IV World Congress Biomechanics

Proceedings CD

Calgary
August 4 - 9, 2002

IV World Congress Biomechanics

Proceedings CD

Calgary

August 4 - 9, 2002

Main Menu

The organizers of the IV World Congress of Biomechanics gratefully acknowledge the support of these institutions

Main Menu

IV World Congress Biomechanics

Table of Contents

To Use this Index: Scroll down or use the bookmarks in the left-hand frame to move to a new location in this index. Click on a **blue paper title** to view that paper. To return to this index after viewing a paper, click the PREVIOUS MENU bookmark in the left frame.

Invited

Cardiovascular Biomechanics

Cardiovascular

Podium

The Engineering of Vascular Substitutes
Nerem, Robert M

Feature of Arterial Blood Flow Associated with the Biological Functions
Tanishita, Kazuo

Application of Models To Understand the Integration of Coronary Vascular Control Mechanisms
Spaan, Jos AE

Effect of Viscous Fluid Stresses on Cells and Bio-Artificial Capsules
Barthès-Biesel, Dominique

Infrastructure for the Iups Physiome Project
Hunter, Peter

Mechanisms Of Mechanotransduction In Cell Processes And Microvilli
Weinbaum, Sheldon

General Biomechanics

General

Podium

Skiing with Carved Skis: Challenges on Performance and Safety
Müller, Erich; Schwameder, Hermann; Schiefermüller, Christian

Has Computer Simulation of Locomotion Delivered All Its Promise in the Past 20 Years?
Vaughan, Christopher L

Biomechanics in Oceanography
Pedley, T J

Injuries in Sport: Reduction Through a Biomechanical Intervention
Elliott, Bruce

Tendon Excursion and Gliding Mechanism
An, K-N; Zhao, C F; Zobitz, M E; Amadio, P C

Critical Issues in the Behavior of Human Skeletal Muscle During Ssc Activities
Komi, Paavo V

Muscle & Musculoskeletal

Muscle

Podium

New Approaches To Integrating Muscle Function And Design From Molecular Biophysics To Whole-Animal
Rome, Lawrence

How Do Biological Motors Work?
Katayama, Eisaku; Uyeda, TQP; Iwane, AH; Ikebe, Mitsuo; Yanagida, Toshio

Orthopeadics

Orthopeadics

Podium

Mechanical Adaptation of Bone Mass and Architecture: Towards a Unified Theory
Huiskes, Rik; Ruimerman, Ronald

Structure Properties of Bone: the Influence of Mechanical and Biologic Stimuli
Goldstein, Steven A

The Small Proteoflycan in Tendon
Vogel, Kathryn G
Biomechanics of Very Soft Tissues
Bilston, Lynne
Cartilage Nanomechanics, Mechanotransduction, And Tissue Engineering
Grodzinsky, Alan; Ortiz, Christine; Seog, Joonil; Dean, Delphine; Ng, Laurel; Jin, Moonsoo; Kisiday, John; Frank, Eliot

Tissue Engineering

Cellular/Molecular

Podium

The Convergence of Cardiovascular Genomics and Endothelial Biomechanics
Davies, Peter F; Helmke, Brian P; Depaola, Natacha; Shi, Congzhu; Rosen, Amy B; Polacek, Denise
Molecular Basis of Cellular Responses To Mechanical Forces
Chien, Shu
Mechanical Stimuli and Endothelial Cell Mechanics
Sato, Masaaki
What Can We Learn From Looking At Biological Processes, One Molecule At A Time
Chu, Steven
Cells, Gels And The Engines Of Life: A Fresh Approach To Biological Motion
Pollack, Gerald

Tissue

Podium

Exploring Structure/Function Relationships in Articular Cartilage Using Novel Experimental Approaches
Broom, Neil
Cartilage Mechanics, Diagnostics And Repair
Buschmann, Michael

Award

Podium

Muscle Force Not Work Defines Muscle Contributions To Forward Progression
Neptune, R R; Kautz, SA; Zajac, FE
Mechanical and Metabolic Requirements of Lateral Stabilization in Human Walking
Donelan, J Maxwell; Shipman, David W; Kuo, AD
Is Sensory Control of the Locomotor System Crucial Or Not?
Yakovenko, Sergiy; Prochazka, Arthur
Residual Stress and Strain in the Lamellar Unit of the Aorta: Experiment and Analysis
Matsumoto, Takeo; Goto, Taisuke; Sato, Masaaki
Effects of Stretching and Shortening on Isometric Forces on the Descending Limb of the Force-Length Relationship in Cat Soleus Muscle
Schachar, Rachel; Herzog, Walter; Leonard, Tim
Muscle Synergies Controlling Ground Reaction Forces During Balance
Ting, Lena H; Macpherson, Jane
Force Depression Following Muscle Shortening of Electrically Stimulated and Voluntarily Activated Human Adductor Pollicis
Lee, Hae-Dong; Herzog, Walter; Won, Young-Doo
Thermal Finite Element Analysis of Osteocyte Kill Zones Achieved with a Cryo-Insult Probe
Reed, Karen L; Brown, Thomas D; Conzemius, Michael G
Smelling With Hairy Little Noses: The Physical Design Of Olfactory Antennae
Koehl, Mimi AR
Experimental Validation of a Computational Model of the Patellofemoral Joint
Elias, John J; Wilson, David R; Adamson, Robert; MacIntyre, Norma J; Cosgarea, Andrew J

Anterior-Cruciate Ligament Forces in the Intact Knee During Normal Gait
Shelburne, Kevin B; Pandy, Marcus; Anderson, Frank; Torry, Mike

The Loading Response Phase of the Gait Cycle is Important To Knee Osteoarthritis
Astephen, JL; Deluzio, KJ; Wyss, UP

Computational Modeling of Flow and Mass Transport in a Microfabricated Array Bioreactor for Perfused 3-D Liver Culture
Kaazempur-Mofrad, MR; Sivaraman, A; Upadhyaya, A; Domansky, K; Powers, MJ; Kamm, RD; Griffith, LG

A Computational Model of Postoperative Knee Kinematics
Chen, Elvis C; Ellis, Randy R; Rudan, John; Bryant, J Tim

Modulation of Anabolic and Catabolic Mechanical Signals in Bone: From Mechanics to Genetics
Judex, Stefan

Symposium

Cardiovascular Biomechanics

Cardiovascular/Respiratory

Podium

Finite Reynolds Number Flows in Three-Dimensional Collapsible Tubes
Hazel, Andrew L; Heil, Matthias

Bioengineering of An Experimental Bioartificial Heart Muscle.
Brackhan, Joseph; Banes, Albert; Cascio, Wayne E

Dynamic Particle/Liquid-Lining Interactions in Peripheral Lung Airways
Weekley, SJ; Rosenzweig, J; King, JR; Waters, SL; Jensen, Oliver

Time-Domain Representation of Ventricular-Arterial Coupling as a Windkessel and Wave System
Tyberg, John; Wang, Jiun-Jr; Shrive, Nigel G; Parker, Kim H

A Novel Age-Related Index of Cardiovascular Function
Niki, Kiyomi; Sugawara, Motoaki; Dehua, Chang; Okada, Takashi; Harada, Akimitsu

Wave Intensity in the Carotid Artery is a New Index of Left Ventricular Systolic and Early Diastolic Performance
Ohte, Nobuyuki; Narita, Hitomi; Niki, Kiyomi; Okada, Takashi; Harada, Akimitsu; Sugawara, Motoaki; Kimura, Genjiro

Non-Invasive Measurement of Wave Intensity - Reproducibility and Effect of Gtn
Jones, Christopher J H; Nicolaides, Eleftherios; Boden, Lucy; Fraser, Alan; Frenneaux, Michael

Shear Stress-Induced Atp Release and Calcium Signaling in Endothelial Cells
Ando, Joji; Yamamoto, Kimiko; Kamiya, Akira

Identification of Genes Regulated by Mechanical Forces Using Microarray Technology in Human Endothelial Cells
McIntire, Larry V; Butcher, ED

The Role of Integrin in Mechanotransduction in Endothelial Cells
Shyy, John Y-J

Stressing Integrins Alters Gene Expression
Wang, Ning

The Free Volume Theory of Mechanochemical Transduction
Frangos, John

Changes of Caveolin-1 in Human Endothelial Cells Exposed To Shear Stress
Sun, Ruijuan; Wang, Xiong; Dong, Xi; Muller, Sylvaine; Stoltz, Jean-Francois

Laminar Shear Stress Induces Vasodilator-Stimulated Phosphoprotein Change in Cultured Human Endothelial Cells
Wei, Lei; Ouyang, JingPing; Muller, Sylvaine; Stoltz, Jean-François; Wang, Xiong

Prediction of Three-Dimensional Orientation of Stress Fibers in Cultured Endothelial Cells Under Cyclic Deformation
Yamada, Hiroshi; Takemasa, Tohru; Yamaguchi, Takami

Studies on the Single Binding Force of LFA-1 and ICAM-1
Zhuang, Fengyuan; Zhao, Hong; Dong, Xi; Li, Xiufeng

Flow Regulation of Gap Junctional Communication and the Functional Compartmentalization of Vascular Endothelium
Depaola, Natacha; Florez, Lucio; Essien, Eno; Polacek, Denise; Kim, Sanghee

Fluid-Structure Interaction And Collagen Remodeling In The Aortic Heart Valve
Baaijens, FPT; Boerboom, Ralf; Bouten, VC Carlijn; Driessen, Niels; Gawlitta, Debbie; Hart, Jurgen de; Peters, Gerrit; Huyghe, Jacques

Developing A Composite, Tissue-Engineered Aortic Valve
Vesely, Ivan; Shi, Yaling; Ramamurthi, Anand

Fabrication And Characterization Of Fibrin-Based Tissue-Equivalent Valves
Neidert, Michael; Oegema, Theodore; Tranquillo, Robert

The Role Of Dynamnic Stresses During Incubation In Increasing Tehv Tissue Strength
Sacks, Michael S; Gulesarian, Kristine; Martin, David; Mayer, John

Biomechanics & Hydrodynamics Of Decellularised Porcine Aortic Heart Valves
Korossis, Sotiris; Booth, Cath; Wilcox, Helen; Watterson, Kevin; Kearney, John; Ingham, Eileen; Fisher, John

Fluid Shear Stress Affects Vascular Smooth Muscle Cell Function
Tarbell, John M; Tada, Shigeru; Garanich, Jeff; Ainslie, Kristy; Civelek, Mete

Poster

Inspiratory Flow in Bronchial Airway Models: Bifurcation Plane Rotation
Caro, CG; Schroter, Robert; Watkins, N; Sherwin, SJ; Sauret, Veronique

Increasing Number of Interconnected Elements in Tensegrity Models Induces a Structural Softening Consistent with Cortical Cytoskeleton Function
Wendling, Sylvie; Cañadas, Patrick; Laurent, Valérie M; Planus, Emmanuelle; Fodil, Redouane; Chabrand, Patrick; Isabey, Daniel

Assessment of Structural Viscoelasticity of Cytoskeleton by Tensegrity Model
Cañadas, Patrick; Laurent, Valérie M; Fodil, Redouane; Planus, Emmanuelle; Wendling, Sylvie; Isabey, Daniel

Effect of Ventilation on Instilled Liquid Transport in the Pulmonary Airways of Rats
Anderson, Joseph C; Dawson, Christopher A; Molthen, Robert C; Haworth, Steven T; Glucksberg, Matthew R; Grotberg, James B

Limitation of Expriatory Flow in Liquid Ventilation
Bull, Joseph L; Reikert, Craig A; Komori, E; Tredici, S; Grotberg, JB; Hirschl, RB

Anatomically Based Models of Blood Flow in the Human Pulmonary Microcirculation
Burrowes, Kelly; Tawhai, Merryn; Hunter, Peter

A Multi-Segmental Model of the Coupling of Inspiratory Flow with the Compliant Nose Structure Assessed in Vivo.
Fodil, Redouane; Brugel, Lydia; Isabey, Daniel; Harf, Alain; Louis, Bruno

Steady Flow and Particle Deposition in Non-Planar Airway Bifurcation Model
Fujioka, Hideki; Schroter, Robert C

Effect of Tissue Viscoelasticity and Lung Surfactant on Eustachian Tube Mechanics
Ghadiali, Samir N; Swarts, J Douglas; Federspiel, William J

The Influence of Cell Topography on Epithelial Cell Stresses During Airway Reopening
Jacob, Anne Marie; Gaver, D P

Use of Computational Fluid Dynamics To Study Inhaled Gas and Particle Trasport in the Nasal Passages
Kimbell, Julia S; Segal, Rebecca A; Asgharian, Bahman

Predicting the Mixing of Ultra-Fine Particles in a Model Lung Acinus
Leeming, Angus; Schroter, Robert C

Pulmonary Epithelial Cell-Matrix Signalling Via Alpha-6/Beta-4 Integrin
Margulies, Susan; Hawk, Michele; Weaver, Valerie

Finite Element Geometric Models of the Human Lung and Diaphragm
Mithraratne, Premakumar; Carden, Geoff; Tawhai, Merryn; Hunter, Peter

Computational Analysis of Inspiratory Heat and Water Vapor Fluxes in the Human Nose
Naftali, Sara; Rosenfeld, Moshe; Wolf, Michael; Elad, David

An Asymptotic Model of Unsteady Airway Reopening
Naire, S; Horsburgh, MK; Jensen, Oliver

General Biomechanics

Biomechanics, Biotechnology and Bioengineering

Podium

Muscle & Musculoskeletal

Musculoskeletal Biomechanics and Movement

Podium

Orthopeadics

Orthopeadics

Podium

Growth Factor Loaded Calcium Phosphate Cement for Bone Regeneration
Blom, EJ; Burger, EH; Waas, MAJ van; Klein-Nulend, J

An Approach for Improving the Performance of Polymeric Macroporous Scaffolds For in Vitro and in Vivo Bone Tissue Engineering Applications
Rzeszutek, K; Baksh, D; Guan, L; Karp, JM; Sarraf, F; Davies, JE

The Use of Robots in Biomechanics - Future Directions
Woo, Savio L-Y; Debski, Richard E; Li, Zong-Ming

Dynamic, In-Vivo Function of Healthy, Acl-Deficient and Acl-Reconstructed Knees: New Insights Using High Frame-Rate Stereo-Radiography
Banks, Scott A

Biomechanics of Knee Replacement - From in Vitro To in Vivo
Zavatsky, AB; Price, AJ; Gill, HS; Oppold, PT; Ward, T; Murray, DW; O'Connor, JJ

Ankle and Subtalar Kinematics of the Ankle Joint with Intact, Injured, and Reconstructed Lateral Ligaments
Rosenbaum, D; Becker, HP; Schmidt, R; Wilke, A; Cordier, E; Neller, S; Claes, L; Bertsch, C; Eils,

He Effect of Damage To the Ligamentous Support of the Arch on the Function of the Posterior Tibialis Tendon.
Imhauser, Carl; Abidi, Nicholas A; Frankel, David Z; Siegler, Sorin

Finite Element Modeling of Total Ankle Replacements for Constraint and Stress Analysis
Mciff, Terence E; Horton, Greg A; Saltzman, Charles; Brown, Thomas D

Mechanical Stability of Ankle Braces Under Passive and Dynamic Loading Conditions
Eils, Eric; Rosenbaum, Dieter; Demming, Christina; Kollmeier, Guido; Thorwesten, Lothar; Völker,

A Finite Element Model of the Foot and Ankle: Validation of Quiet Stance
Ledoux, William R; Camacho, Daniel L A; Ching, Randal P; Sangeorzan, Bruce J

Molecular Mechanisms For Development Of Tendinitis
Wang, James H-C; Yang, Guoguang; Stone, David; Woo, Savio L-Y; Li, Zhaozhu

Computational Simulation Of Treatments Used For Patellofemoral Pain And Instabiity
Elias, John J; Cosgarea, Andrew J

Orthotics Alter Lower Extremity Joint Coupling: a Dynamical Systems Approach
Ferber, R; Davis, I McClay; Williams III, DS Williams

A 3D Finite Element Model of An Implanted Scapula Using Cadaveric Data for Evaluation
Maurel, Nathalie; Diop, Amadou; Irujo, Mercedes; Grimberg, Jean

Free Communication

Other

Poster

Effects of Diabetes on the Strength of the Plantar Skin-Fat Interface
Chen, Yan; Davis, Brian L; Valdevit, Antonio

Tools for Computer-Aided Surgery: Displacement and Velocity Workspaces of the Human Knee
Fuller, John; Murphy, Michael C; Brown, Gregory A

Design of Air Seat Cushion Orthosis for Plegia
Hong, Jung Hwa; Kim, Gyoo Suk; Kim, Jong Kwon; Mun, Mu Seong; Ryu, Jei; Lee, In Huk; Lee, Jong Keun

Method To Measure Sustainable Loads in Sutured Urethral Tissue
Baker, William; Okumu, Kris; Drews, Michael; Martin, R Bruce

Regulation of Motor Unit Recruitment in the Cardiac Muscle
Levy, Carmit; Landesberg, Amir

Simulation of Ultrasonic Waves' Effects on Cervic Cancerous Tissues
Ghalichi, Farzan; Behnia, Sohrab; Ghasemi, Mehdi; Rad, Ehsan Sadigh

Flow Due To a Peristaltic Wave in a Tube
Tadjfar, Mehran; Himeno, Ryutaro

Sonomicrometric Measurements of Eye Displacements
Hurst, William J; Cormier, Joseph M; Duma, Stefan M

On Not Tipping a Stepladder Sideways
Yang, Bing-Shiang; Ashton-Miller, James

Quantitative Evaluation of Microvascular Structure and Comparizon of Regional Microvascularity and Po2 Distribution in Rat Cerebral Cortex
Masamoto, Kazuto; Negishi, Tomoko; Kurachi, Takayoshi; Takizawa, Naosada; Kobayashi, Hirosuke; Tanishita, Kazuo

Foot Function After the Short Term Use of Customs Foot Orthoses
Payne, Craig

Development of a Novel Type of Oesophageal Stent Based on Deployable Tubular Structures
Kuribayashi, Kaori; Jordan, Stephen; You, Zhong

Biotechnology

Biomaterials

Poster

Rapid Manufacturing of Bone Nails with Improved Mechanical Properties
Hoffmann, Jürgen; Fink, Ulrich; Friedrich, Klaus

Sr-Ha Bioactive Bone Cement Characterization and Animal Trials
Lu, WW; Wong, CT; Lu, DS; Cheung, KMC; Luk, KDK; Chan, WK; Leong, JCY

Ecm(Extracllular Matrix) Scaffolds for Tissue Engineering: Biocompatibility and Biodegradability
Grimes, Marguerita; McGloughlin, Tim; Pembroke, Tony

Mechanical Properties and Permeability of Polyelectrolyte Microcapsules (PEMC)
Bäumler, Hans; Mitlöhner, R; Hin, M; Artmann, G; Georgieva, R; Moya, S; Kiesewetter, H

Bonding Strength of Plasma Sprayed Ha Coating on Ti6al4v Alloy Substrate: the Effect of Residual Stress
Yang, Yung-Chin; Chang, Edward

Design and Assembly of a Sterile Nanoscale Orthopedic Biomaterial
Longsworth, John; Eppell, Steven

A Stochastic Model of Fatigue Damage Development in Bone Cement
Evans, Sam L

Residual Stresses Analysis At the Interface Between Hydroxyapatite Coating and Titanium Substrate
Cofino, B; Fogarassy, P; Millet, P; Taiar, R; Lodini, A

Measurement of Residual Stress Due To Volumetric Shrinkage in Bone Cement
Roques, A; New, A; Taylor, A; Baker, D; Browne, M

Biomedical Imaging/Microscopy

Poster

A Fast Circle Finding Technique for Digital Rsa
Thistlethwaite, P; Ronsky, Janet; Gill, HS

Measurement of the Encephalon Physical Parameter with MRI Saturation Transfer Method
Obata, Hideaki; Tokuda, Masataka; Inaba, Tadashi; Matsushima, Shigeru; Kinosada, Yasutomi

In Vivo Motion of the Scaphotrapezio-Trapezoidal (Stt) Joint
Crisco, Joseph J; Kang, Lana; Sonenblum, Sharon; Akelman, E

Analysis of in Vivo Carpal Bone and Ligament Kinematics Using Ct and Mr Data
Upal, Anwar; Pichora, David; Small, Carolyn

The Development of Confocal Arthroscopy for the Assessment of Cartilage Disorders
Kirk, Thomas B; Smolinski, Daniel; Delaney, Peter; Wu, Jian; Miller, Karol; Wood, David; Zheng, Ming Hao

Dynamic Ca2+ Response in Vascular Endothelial Cells Subjected To Various Flows
Chen, Baoguo; Xu, Lisa X; Frankel, Steven H; Haberstroh, Karen M; Plesniak, Michael W; Webster, Thomas J; Wereley, Steve

A Method for Anatomical - Functional Studies of Articular Joints
Martelli, Sandra

On the Use of 3D MRI Velocity Measurements for Computational Flow Simulations
Glor, Fadi P; Westenberg, Josephus J M; Vierendeels, Jan; Danilouchkine, Michael; Verdonck,

Accuracy of Patellofemoral Joint Contact Area Predictions Using Mr Imaging
Moss, Rebecca; Ronsky, Janet

Three-Dimensional Acoustic Microscopy of the Intervertebral Disc: Visualisation of Lamellae, Collagen Bundles and Lesions.
Johnson, Scott; Halliwell, M; Jones, M; McNally, D

Global Optimization for Recovering the Position and Orientation of Free-Form Objects in Medical Imaging Registration Using a New Smoothing Approach
Mahfouz, Mohamed; Hoff, William; Underwood, Robert; Komistek, Richard D; Dennis, Douglas

Three Dimensionnal Reconstruction of the Knee From Biplanar X-Rays
Laporte, S; Skalli, W; Guise, JA de; Mitton, D

Registration of 3D Bone Geometry with Cine-Phase Contrast MRI Data for the Determination of in Vivo Joint Kinematics
Barrance, Peter J; Williams, Glenn; Buchanan, Thomas S

BioMEMS

Poster

Origins of Bipedalism: Evolutionary Morphology Through Finite Element Analysis
Eckhardt, Robert B; Galik, Karol; Senut, Brigitte; Pickford, Martin; Gommery, D; Treil, J

Optical Motion Control of Euglena for Bio-Mems
Itoh, Akitoshi; Toyoda, Yoji

A Color-Coded Video-Based System for Posture and Foot Assessment
Anbarian, Mehrdad; Allard, Paul; Perrault, Ronald; Hinse, Sébastien; Sadeghi, Heydar; Farahpour,

Non-Invasiveassessment of Left Ventricle Function with a Computational Fluid Dynamic Model
Iwase, Hidehito; Liu, Hao; Fujimoto, Shinichi; Himeno, Ryutaro; Hayasaka, Tomoaki

Disintegration and Deformation of Cells and Microcapsules Using Shock Waves and Gas Bubbles for Developing DDS
Tamagawa, Masaaki; Yamanoi, Ichiro

Biosensors

Poster

Development of a Trifilar Pendulum for Measuring Moment of Inertia
Bryant, J Tim; Stevenson, Joan; Zdero, Rad; Hadcock, Lindsay

Hematocrit Determination in Blood Line of Dialysed Patients by Ultrasound
Jaffrin, Michel Y; Fenech, Marianne; Kanj, Bachar; Maasrani, Mahmoud

Changes in Plantar Force, Area and Pressure Within a Single Session Using An In-Shoe Measurement System
Hanke, Timothy A; Tiberio, David

Evaluation of Alternative Material for the Prevention of Pressure Sores
Mootanah, Rajshree; Ranawat, Vijai; Dowell, John

Image Guided Surgery/Virtual Distance Medicine

Poster

An Efficient and Robust ICP Technique for Surface Registration
Cutti, Andrea Giovanni; Cappello, Angelo; Leardini, Alberto

Cardiovascular Biomechanics

Arterial Wall Mechanics

Poster

An in Vivo Experiment-Based Growth Model for Intimal Hyperplasia in Rat Vein Graft
Tang, Dalin; Yang, Chun; Liu, Shu Q

Embolism Bubble Adhesion Force in Excised Perfused Microvessels
Eckmann, David M; Suzuki, Akira

Nanomechanical and Biochemical Properties of Diseased Artery Tissue
Ebenstein, Donna; Chapman, Joan; Li, Cheng; Coughlin, Dezba; Rapp, Joseph; Saloner, David; Pruitt, Lisa

Altered Nana-Order, Micro-Mechanical Property of Pulmonary Artery Smooth Muscle in Primary Pulmonary Hypertension

Shimizu, Juichiro; Nakamura, Kazufumi; Kataoka, Noriyuki; Hashimoto, Katsushi; Hashimoto, Ken; Ohta, Keiko; Fujio, Jerry; Matsubara, Hiromi; Araki, Junichi; Ogasawara, Yasuo; Tsujioka, Katsuhiko; Ohe, Tohru; Kajiya,

Biaxial Tensile Properties of Aortic Aneurysm Tissues Under Equibiaxial Stress

Fukui, Tomohiro; Matsumoto, Takeo; Tanaka, Toshihiro; Ohashi, Toshiro

Biomechanics of Plaque Rupture in Atherosclerosis Coronary Arteries

Brunette, Jean; Mongrain, Rosaire; Tardif, Jean-Claude

Wall Shear Stress With Initiation Of Aneurysm Around Anterior Communicating Artery In Steady Flow Communicating Artery In Steady Flow

Yamaguchi, Ryuhei; Kudo, Susumu; Nakazawa, Nobuhiko; Ujiie, Hiroshi

Flow-Induced Morphological Change of Endothelial Cell and Shear Stress Distribution on the Surface of the Cell

Fukushima, Shuichiro; Fujioka, Hideki; Tanishita, Kazuo

Dynamic Stress Analysis of the Arterial Wall with Finite Element Modeling

Majd, Shervin Ghasemi; Shadpour, Mohammad Tafazzoli; Avolio, Albert

Effects of Sustained Pressure and Strain on Vascular Smooth Muscle Cell Function

Dela Cruz, Sheila Dela; Ginnan, Roman; Singer, Harold A; Bizios, Rena

A Mathematical Model of Arterial Regeneration Over Bioresorbable Grafts

Rachev, Alexander; Kirilova, Miglena

Measuring Effects of Drugs on Arterial Mechanical Properties

van Andel, Carolien J; Sierevogel, Marion J; Pasterkamp, Gerard; Pistecky, Peter V; Borst, Cornelius

Correlation of Mechanical Factors with Intimal Hyperplasia in the Miller's Cuff and Its Application To Optimization of Anastomotic Design

Li, Xue-Mei; Rittgers, Stanley E

Effects of Circumferential Residual Stress on the Circumferential Stress Distribution of the Arterial Wall by Finite Element Modeling

Pour, Nooshin Haghighi; Tafazzoli, Mohammad; Shadpour, Mohammad Tafazzoli; Avolio, Albert

Computational Modelling of Blood Flow and Atery Wall Interaction

Grossman, Debbie; Bailey, Chris; Pericleous, Koulis; Slone, Avril K

Determination of Elastin and Collagen Content in Porcine Aorta

Gundiah, Namrata; Dao, Kim; King, Karen; Pruitt, Lisa

Effect of Shear Stress on the Activation of the Peroxisome Proliferator-Activated Receptors (Ppars)

Formentin, Kitty; Zeng, LingFang; Morgan, Andre P; Shyy, John Y-J

An Investigation of the Effect of Calcium on the Mechanical Function and Structure of Aortic Microfibrils in the Lobster Homarus Americanus

Bussiere, Chantal T; DeMont, M Edwin; Wright, Glenda

Mechanical Aspects of Plaque Redistribution During Angioplasty: Possible Consequences on Vulnerability

Ranga, Adrian; Mongrain, Rosaire; Brunette, Jean; Tardif, Jean

The Contribution of Elastin and Collagen To Residual Strain in Porcine Aorta

Wang, Jingli; Gundiah, Namrata; Pruitt, Lisa

Artificial Heart/Valves

Poster

Incidence of Valve Prosthesis Incline on Left Ventricle Flow Dynamics

Mouret, Frederic; Garitey, Vincent; Derivaux, Frederic; Rieu, Regis

Effects of Oscillation on Elevating Shear Stresses

Sakhaeimanesh, Ali A

Influence of Flow Rate and Axial Position on Shear Stresses

Sakhaeimanesh, Ali A

Stress Analysis on Mechanical Heart Valve Leaflet Using Blood Flow Analysis Through the Valve

Rajaai, S M

Cardiac Mechanics

Poster

Cardiovascular/Respiratory

Podium

Hemodynamics

Podium

Poster

Model Blood Consisting of Dense Suspension of Natural Polymeric Gel Particles
Ohba, K; Ando, T; Yoza, I; Onoue, A; Uragami, T; Miyata, T

Non-Newtonian Effect in the Arterial Blood Flow
Wojnarowski, Józef; Mirota, Kryspin

Cross-Flows Associated with Shear Stress Gradients on the Flow-Endothelium Interaction
Wang, Wen; Lu, Yiling; Lu, Xiyun; Parker, Kim H; Zhuang, Lixian

Measurement of Erythrocytes Deformability with Counter-Rotating Parallel Disk System
Hashimoto, Shigehiro; Oku, Hiroshi; Omori, Masayoshi; Matsumoto, Yuki; Sakaue, Koichi; Ikegami, Kazuhiro

Motion of Rgpiba-Ams Near the Vwf Surface
Tsuji, Tetsuya; Tabata, Takashi; Takeoka, ; Takeoka, ; Ikeda, Yasuo; Tanishita, Kazuo

Is Permanent Arterial Filtration Possible? in Vivo Assesment of a Filtration Device for Embolic Stroke Prevention
Grad, Ygael; Nishri, Boaz; Tanne, David; Einav, Shmuel; Lieber, Bruch B; Yodfat, Ofer

Experimental Analysis of Flow Through Tilting Disk Valve
Raz, Sagi; Avrahami, I; Zaretsky, Uri; Rosenfeld, Moshe; Einav, Shmuel

Numerical Simulation of Sickle Cell Blood Flow in the Transverse Arteriole-Capillary Network
Carlson, Brian; Berger, Stanley A

Influence of Multiple Stenoses on Diagnosis of Peripheral Disease
Bertolotti, Christine; Qin, Zhao; Durand, Louis-Gilles; Soulez, Gilles; Cloutier, Guy

The Effect of Ligand Density on Tether Formation Between Endothelium and Monocytes
Truskey, George A; Levin, Dora J

Respiratory Mechanics

Poster

Self-Excited Oscillations in a Fluid-Beam Collapsible Channel
Cai, Zong Xi; Luo, Xiao Yu

Experimental Study on Air Flow in a Two-Dimensional Channel with An Obstruction Oscillating At 10 Hz To 100 Hz
Matsuzaki, Yuji; Watanabe, Masateru; Aomatsu, Tatsuya; Ikeda, Tadashige

New Method of Three-Dimensional Imaging of Small Airways in Rats with X-Ray Micro-Ct
Sera, Toshihiro; Fujioka, Hideki; Yokota, Hideo; Makinouchi, Akitake; Himeno, Ryutaro

Flow Distribution in a Right Angle Branch During Oscillatory Flow
Tanaka, Gaku; Sakai, Eiji; Hishida, Makoto

Augmented Longitudinal Diffusion in Oscillatory Flow Along a Lateral Grooved Tube Imitated of Trachea with Uneven Inner Surface by Cartilage
Shimizu, Akihiro; Miyahara, Kosuke; Shimizu, Masashi; Ryumae, Saburo

General Biomechanics

Animal

Podium

Shock Absorbing Potential of the Ungulate Digital Cushion
Robilliard, Justine; Burn, JF

The Change in the Rotation Rate of a Bacterium Motor Causes the Difference Between Forward and Backward Swimming Speeds of Vibrio Alginolyticus
Goto, Tomonobu; Ichiba, Makoto; Nakata, Koso; Takano, Yasunari; Magariyama, Yukio

Optimization of Motion of a Mechanical Pectoral Fin
Kato, Naomi; Liu, Hao; Morikawa, Hirohisa

Influence of a Rider To the Back of a Horse in Different Gaits
Frühwirth, B; Peham, C; Scheidl, M

Passive Elastic Properties of Biceps; Contribution To Locomotor Economy in the Horse (Equus Callabus)
Watson, JC.; McGuigan, MP; Wilson, AM

Poster

Kinematics of 90 Degree Running Turns in Wild Mice
Walter, Rebecca

The Effect of Gait Transition on Duty Factor in the Horse (Equus Caballus)
Witte, TH; Lichtwark, GA; Wilson, AM

A Comparison of Joint Mechanics Between Anterior Cruciate Ligament Intact and Deficient Stifles: a New Model of Anterior Cruciate Ligament Disruption
Lopez, Mandi J; Kunz, David; Vanderby Jr., Ray; Heisey, Dennis; Bogdanske, John; Markel, Mark D

Experimental Assessment of Hydrodynamics of a Mechanical Pectoral Fin
Kato, Naomi; Liu, Hao; Morikawa, Hirohisa

Material Properties of Porcine Parietal Cortex
Coats, Brittany; Margulies, Susan S

Bioheat/Cryopreservation

Poster

Effect of Cell Density on Viability of Artificial Tissue After Cryopreservation
Ujihira, Masanobu; Sukegawa, Yumi; Nogawa, Satoshi; Nagoshi, Takako; Mabuchi, Kiyoshi

Heat Characteristic of Non Electrical Incubator..
Ahmadian, MT; Bahramian, F

Air Flow and Temperature Distribution in a Neonatal Incubator
Yun, Sang-Ho; Kwon, Chi-Ho; Kim, Young-Ho

Continuum Mechanics

Poster

Wolff's Law
Qinguo, Gang; Zhuxin, Hua; Guitong, Yang

Dental

Podium

Acousto-Opto-Electromagnetic Properties of Human Dentin Collagen
Tabib-Azar, M; Katz, JL; Spencer, P; Wagh, A; Namura, T; Scott, A; Wang, Y

Finite Element Analysis of a Mandibular Premolar Subjected To Orthodontic Loading: Effects of Periodontal Ligament Thickness and Nonlinear Material P
Toms, Stephanie R; Lemons, Jack E; Eberhardt, Alan W

Fe-Simulation of Bone Modeling Around a Dental Implant in Two-Stage-Healing as Compared To Early Loading
Rong, Qiguo; Lenz, Juergen; Schweizerhof, Karl; Schindler, Hans J; Riediger, Dieter

Experimental Determination of the Center of Resistance of Human Incisors in Comparison with Finite Element Simulations
Dorow, Christina; Krstin, Natasa; Sander, Franz Guenter

Scanning Acoustic Microscope Measurements of Anisotropy of Dentine and Enamel
Sakamoto, Makoto; Kobayashi, Koichi; Sakai, Jun; Maruyama, Yasuo; Itoh, Hidemi

Poster

Sensitivity Analysis on Disc Behavior in Temporomandibular Joint
Tanaka, Masao; Tanaka, Eiji; Todoh, Masahiro; Asai, Daisuke; Kuroda, Yukiko

The Effect of Trabecular Bone Microstructure on Stress Distribution of a Dental Implant
Kim, Han Sung; Lee, Sangup; Cho, Nam-Hyo; Shim, June-Sung; Ko, Jaiyoung

Periodontal Ligament Biomechanics of Intrusive and Extrusive Orthodontic Loading
Toms, Stephanie R; Lemons, Jack E; Eberhardt, Alan W

Tests of Numerical Models of Craniomandibular Mechanics
Iwasaki, Laura; Nickel, Jeffrey; Petsche, Paul; McCall, WD; Marx, David

Plowing Forces and Stress Distribution on the Temporomandibular Joint Disc Surface
Nickel, Jeffrey; Rothe, Laura; Iwasaki, Laura; Beatty, Mark

Evaluation of Slots for Destructive Cerec Restored Premolar by Finite Element Method
Lin, Chun-Li; Chang, Yen-Hsiang

Ergonomics

Poster

Finite Element Modeling

Podium

Poster

Predictions of Infant Brain Injures in Minor Falls and Inflicted Events
Prange, Michael T; Margulies, Susan S

Biomechanical Modeling of Indentation Testing and Application in Plantar Pressure Prediction of Diabetic Foot
Zou, Dequan; Mueller, Michael J; Smith, Kirk; Hastings, Mary; Klaesner, Joseph W

Material Properties of the Human Calcaneal Fat Pad: Validation Experiments
Miller-Young, Janice; Duncan, Neil A

Tissue Stress and Modulus Changes Following Vertebroplasty
Kosmopoulos, Victor; Keller, Tony S; Liebschner, Michael AK

Finite Element Analysis of Median Nerve Insult in the Carpal Tunnel
Petrie, Christopher P; Brown, Thomas D; Steyers, Curtis M

Development of 3D Finite Element Model of Human Foot and Ankle
Zhang, Ming; Cheung, Jason; Fan, Yubo; Leung, Aaron KL

Efficient Finite Element Customisation of a Generic Femur Using the Host Mesh Technique
Fernandez, JW; Blyth, P; Anderson, IA; Hunter, PJ

Validation of Finite Element Model for Prosthetic Socket Design
Goh, James CH; Baidya, Krishna; Lee, Peter VS

Finite Element Study of Trochanteric Gamma Nail for Subtrochanteric Fracture
Sitthiseripratip, Kriskrai; Mahaisavariya, Banchong; Suwanprateeb, Jintamai; Oris, Philip; Bohez, Erik

Influence of Angular Stability of An Internal Spinal Fixator on Implant Loads
Zander, Thomas; Rohlmann, Antonius; Bergmann, G

Oriented Mitosis-Driven Epithelium Reshaping: a Finite Element Study
Brodland, G Wayne; Veldhuis, Jim H

Finite Element Analysis of the Newly Designed Foot Prosthesis for Patients with Partial Foot Amputation
Wu, Yu-Chin; Chen, Weng-Pin; Tang, Fuk-Tan

Influence of a Follower Load on the Mechanical Behavior of the Lumbar Spine
Rohlmann, Antonius; Zander, Thomas; Bergmann, G

Three-Dimensional Fiber-Reinforced Finite Element Model of the Human Anterior Cruciate Ligament
Ali, Ashraf F; Frank, Cy; Shrive, Nigel

Modelling the Solidification of Aqueous Solutions: a Coupled-Field Finite Element Approach
Wan, Richard; Liu, Zhihong; Muldrew, Ken

Growth Mechanics and Adaptation

Poster

Mathematically Modeling Growth and Remodeling of Soft Tissues and Mechanocytes
Humphrey, JD

Mechanical Properties of Cartilage Specimen in Rats -
Kersting, Uwe G; Niehoff, Anja; Morlock, Michael M; Michna, Horst; Brueggemann, Gert-Peter

Measurement of Embryonic Heart Material Properties During Cardiac Looping
Zamir, Evan A; Taber, Larry

Effects of Mechanical Stimuli on the Relaxation Behavior of the Growth Plate Related To Morphological and Biochemical Adaptation in the Rat Model
Niehoff, Anja; Kersting, Uwe G; Zaucke[3], Frank; Morlock, Michael; Sellenschloh, Kay; Brueggemann, Gert-Peter

Impact

Podium

A Novel Algorithm for Estimating Head Impact Magnitude and Location.
Crisco, Joseph J; Greenwald, Richard M; Chu, Jeffrey

Force Characteristics From Drop Landings
Bauer, Jeremy J; Hayes, Wilson C; Snow, Christine M

Acceleration Transients and Transtibial Prosthetic Pylon Attenuation During Gait
Berge, Jocelyn S; Klute, Glenn K; Czerniecki, Joseph M

Control Objectives Change Between Phases of Jumping and Landing Tasks
Costa, KE; McNitt-Gray, J L

Traumatic Brain Injury in An Acceleration-Deceleration Scenario
Chu, Yung-Hua; Bottlang, M

A Method for Assessing the Overall Impact Performance of Helmets Used in Crowd Management Interventions
Dionne, Jean-Philippe; Maach, Ismail El; Makris, Aris

Muscle Activity in the Lower Extremity Damps the Soft-Tissue Vibrations
Wakeling, James; Rozitis, Antra I; Nigg, Benno M

Finite Element Models of Abdominal Organs for Use in Trauma Research
Snedeker, Jess; Rogelj, Joeri; Farshad, Mehdi; Schmidlin, Franz; Niederer, Peter

Impact Attenuation of Landing Activities in Barefoot and Shod
Zhang, Songning; Yu, Yeonjoo

The Cervical Muscle Response During "Whiplash Simulated Motion" with Respect To Gender
Hasselquist, Leif; Goel, Vijay; Wilder, David; Spratt, Kevin; Pope, Malcolm

Poster

The Development of a Keyboard Force Platform
Becker, Theodore; Johnson, Peter W; Dennerlein, Jack Tigh

Transient Foot Ground Reaction Forces and Prosthetic Pylon Attenuation During Gait
Klute, Glenn K; Berge, Jocelyn S; Czerniecki, Joseph M

Comparison of Simulated Projectile and Baton Blow Impacts on Shin Guards Used in Crowd Management Intervention
Dionne, Jean-Philippe; Maach, Ismail El; Semeniuk, Kevin; Makris, Aris

Time-Dependent Properties of the Porcine Kidney Capsular Membrane
Snedeker, Jess; Voide, Romain; Farshad, Mehdi; Schmidlin, Franz; Niederer, Peter

The Propagation of An Impact Force Along the Upper Extremity
Degoede, Kurt M; Ashton-Miller, James; Alexander, Neil B

High-Speed and Continuous Pressure Measurements: a Comparison of Active Pressure Sensors and Pressure Film
Cormier, Joseph M; Stitzel, Joel; Hurst, William J; Duma, Stefan M

Investigation of Skin Abrasion Injuries From High Rate Shear Loading
Cormier, Joseph M; Hurst, William J; Stitzel, Joel; Duma, Stefan M

Assessment of Cushioning Materials: What's the Appropriate Measure?
Tiberio, David; Hanke, Timothy A

Hand Impact Force Reduction in Forward Falls in Young Males: a Prosprctive, Controlled, 3-Month Intervention Trial
Lo, J; McCabe, GN; Okuizumi, H; Ashton-Miller, James

Effects of Midsole Density and Landing Height on Impact Attenuation in Landing
Zhang, Songning; Clowers, Kurt; Kohstall, Charles

The Epidemiology and Biomechanics of Bicycle Handlebar Impact Injuries in Children
McFaull, Steven R

Dynamic, Biomechanical Characteristics of Human Ankle Ligaments
Hopcroft, R; Oakley, C; Suman, S; Manning, P; Lowne, R; Wallace, W A

Molecular and Cellular Biomechanics

Podium

Force Dependence of the P-Selectin/PSGL-1 Bond Dissociation
Marshall, Bryan; McEver, Rodger P; Zhu, Cheng

Dynamic Behavior of Actin Filaments in Cultured Endothelial Cells During Exposure To Shear Stress
Ohashi, Toshiro; Tsuyuki, Kei; Yamamoto, Tsugumasa; Sato, Masaaki

Kinetic Measurements of Surface-Bound P-Selectin/Ligand Interactions
Huang, Jun; Chen, Juan; Zhu, Cheng; Long, Mian

Spreading and Peeling Dymanics in a Model of Cell Adhesion
Hodges, SR; Jensen, Oliver

Experimental Analysis of Lymphatic Cells Motion Under Topographical Control
Mello, A Prina; Volkov, Y; Prendergast, PJ

Interaction of Adhesion Molecules and Lymphocyte Adhesion To Endothelial Cells
Zhao, Hong; Stoltz, Jean François; Zhuang, Feng yuan; Wang, Xiong

Finite Element Modeling and Analysis of Single Cell Micromanipulation Using Magnetic Beads
Karcher, H; Kaazempur-Mofrad, MR; Kamm, RD

Mechanics of Plasma Membrane Vesicles
Kosawada, Tadashi; Schmid-Schönbein, Geert W

Mechanisms for Cell Activation in the Cardiovascular System
Schmid-Schönbein, Geert W; Kistler, Erik; Mitsuoka, Hiroshi; Hugli, Tony

Influence of Glucocorticoid Pretreatment on De-Repression of Gene Expression in Meniscal Explants After Removal From Biomechanical Loading
Natsu-Ume, Takashi; Kydd, Alison; Tsao, Helen; Frank, Cyril B; Shrive, Nigel; Hart, DA

Cyclic Stretch Increases Gene Transfer and Expression in Alveolar Epithelial Cells
Dean, David A; Taylor, Winna; Gokay, Kerimi E; Capaccio, Chris; Glucksberg, Matthew R

Time-Dependent Effect of Interleukin-8 Gene Expression in Endothelial Cells Exposed on Fluid Shear Stress
Wensheng, Zhang; Huaiqing, Chen; Youqin, Chen; Yuan, Yang; Xiaoheng, Liu

Effects of Shear Stress and Lysophosphatidylcholine on Adhesion Modecules Expression of Endothelial Cells
Youqin, Chen; Huaiqing, Chen; Wensheng, Zhang; Xiaoheng, Liu

Functional Changes in Kidney Cells in Response To Sustained Hydrostatic Pressure
Martin, Julie S; Yokota, Hiroki; Haberstroh, Karen M

Soluble Proteins Released by Endothelial Cells in Response To Fluid Flow Affect Smooth Muscle Cells
McCann, Jennifer; Webster, Thomas J; Frankel, Steven H; Plesniak, Michael W; Xu, Lisa X; Wereley, Steven T; Haberstroh, Karen M

Plant

Poster

Overturning Resistance of Rigid Tap Roots
Mickovski, S B; Ennos, A Roland

Simulation

Podium

Influence of Segment Rigidities on Ground Reaction Forces During Landing
Boros, Rhonda L; Challis, John H

Artificial Neural Oscillators as Controllers for Locomotion Simulations and Robotic Exoskeletons
Ferris, Daniel P; Viant, Tiffany L; Campbell, Ryan J

Swing Phase Reduction in Above-Knee Amputee Running
Bohn, Christiane; Shan, Gongbing; Korff, Thomas; Schaper, Hagen; Nicol, Klaus

Modeling of Flow in Cerebral Sidewall Aneurysms: Effect of Aneurysm Size
Mulay, Amol; Hoi, Yiemeng; Bendok, Bernard R; Hoffmann, Kenneth R; Rudin, Stephen

Marker-Based Reconstruction of the Kinematics of a Chain of Segments; a New Method That Incorporates Joint Kinematic Constraints
Klous, Miriam; van Soest, AJ Knoek

Simulating Detailed Kinematics of the Spine - Extrapolation of Function From the 3D Form of Structures Derived From the Visible Human Ct Database
Buford, William L; Andersen, Clark E

Deformation of Bioartificial Capsules in Plane Hyperbolic Flow
Lac, Etienne; Pelekasis, Nikos; Barthès-Biesel, Dominique; Tsamopoulos, John

Effect of Constriction Geometry on Transit of Deformed Neutrophils in Capillaries
Shirai, Atsushi; Fujita, Ryo; Hayase, Toshiyuki

Cooperative Force Analysis of Eleven Muscles During Abduction of the Shoulder
Oizumi, Naomi; Tadano, Shigeru; Narita, Youichi; Iwasaki, Norimasa; Suenaga, Naoki; Minami, Akio

Poster

A Three-Dimensional Mathematical Dynamic Simulation of the Knee Extension Exercise: Effects of Anterior Cruciate Ligament Injury
Caruntu, Dumitru I; Hefzy, Mohamed Samir

Evaluating Possible Techniques for Delaying the Wrist Release: a Computer Simulation Approach
Mackenzie, Sasho; Sprigings, Eric

Theoretical Modeling

Podium

Can Inertial Forces Alone Cause Limb Folding During Protraction?
Preedy, Danielle F; Burn, JF

Antagonistic Muscle Activity in Three-Dimensional Models of the Muscloskeletal System
Jinha, Azim; Ait Haddou, Rachid; Herzog, Walter

An Approximate Analytical Solution for the Planar Spring Mass Model of Locomotion
Bullimore, S R; Usmar, S G; Burn, JF

Hydrodynamics of a Flapping Fin with Interaction of a Body
Liu, Hao; Kato, Naomi; Morikawa, Hirohisa

A Stability Control Model for Human Thorax and Pelvis Movements During Walking
Wu, Q; Swain, R

Comparison of Bilateral and Unilateral Induced Acceleration Analyses of Gait Kinetics
Riley, Patrick O; Kerrigan, D Casey

In Vivo Forces and Motions From Fluoroscopy and Mathematical Modeling
Komistek, Richard D; Kane, Thomas R; Mahfouz, Mohamed; Dennis, Douglas; Haas, Brian D

A Black Box Approach To Modeling the Equine Back as a Flexible Beam
Schobesberger, H; Peham, C

Modeling Locomotion in Crustacean Larvae
Ford, Matthew D; DeMont, M Edwin

Collision Losses During Brachiation: Why Gibbons Have Long Arms
Usherwood, James; Bertram, John

Poster

Pressure Distribution Measurement for Design of Waist Belts in Personal Load Carriage Design
Hadcock, Lindsay; Stevenson, JM; Bryant, J Tim

Can Inverse Dynamics Be Computed with a Rigid Body Model
Böhm, H; Ruder, H

Material Classification of Biaxial Soft Tissue Response
Gloeckner, D Claire; Chancellor, Michael B; Sacks, Michael S

Influences on Eye Location and Posture of Drivers
Fehren, Marion; Thunnissen, Jan; Nicol, Klaus

Biomechanics of Perivascular Flow in Syringomyelia
Bilston, Lynne; Fletcher, David F

Relaxation Function and a Generalized Solution for a Nonlinear Rheological Model of Biological Soft Tissues
Corr, David; Vanderby Jr., Ray; Best, Thomas

A Comparison of ACL Forces During Soft and Stiff Drop-Landings
Pflum, Mary A; Shelburne, Kevin B; Torry, Michael R; Decker, Michael J; Pandy, Marcus G

Mechanical Behaviour of Baseballs During Compressive Loading To Bat-Ball Impact Level
Nichols, Rochelle; Miller, Karol; Elliott, Bruce

Modeling and Visualization of the Mechanical Behaviour of Skeletal Muscle using a Continuum Approach
Lemos, Robson; Epstein, Marcelo; Herzog, Walter; Wyvill, Brian

Modeling of Biomechanics of Tactile Sensation on Fingertips
Wu, John; Dong, Ren G; Schopper, Aaron W; Smutz, W Paul

Self-Sustaining Oscillatory Electromechanical Activity in the Gut
Miftakhov, Roustem; Vannier, Michael

Effective Contact Conditions Between Cementless Coated Hip Implant and Bone
Orlik, Julia; Zhurov, Alexei; Middleton, John

Muscle & Musculoskeletal

Clinical Rehabilitation

Podium

Effects of Varus Wedged Shoe Versus Insole on Knee Joint Loading Characteristcs
Rosenbaum, Dieter; Rödl, Robert; Entrup, Michael; Klein, Dieter

The Resistance of a Knee Joint in Children with Spasticity
Lebiedowska, MK; Fisk, JR

Relation Between Knee Range of Motion Measured Passively and During Gait in Anterior Cruciate Ligament Deficient and Reconstructed Individuals
Grant, John; Zernicke, Ronald F; Mohtadi, Nicholas GH

Identifying Dynamic Instability During Obstructed Gait Following Traumatic Brain Injury
Chou, Li-Shan; Walker, Ann E; Kaufman, Kenton R; Brey, Robert H; Basford, Jeffery R

Improving the Balance Skill of Stroke Patients by Virtual Reality Treadmill Exercise
Chern, Jen-Suh; Yang, Saiwei

Temporal Pattern Recogntion Techniques Can Detect EMG Differences Between Moderate Knee Osteoarthritis Patients and Healthy Controls During Walking
Hubley-Kozey, CL; Deluzio, KJ; Kozey, JW; McNutt, J; Chu, JJ; Caldwell, GE; Stanish, WD

Gait Analysis by Patient Who Have An ACL Deficient Knee
Knoll, Zsolt; Kiss, Rita; Kocsis, László

Head Turns Induce Altered Loading During Standing in Stroke Patients
Lamontagne, Anouk; Paquet, Nicole; Fung, Joyce

Upper Extremity Impairment in Wheelchair Propulsion
Finley, Margaret A; Keyser, Randall E; Stanley, Rhonda; Rodgers, Mary M

Differences in Propulsion Kinetics Between Wheelchair Dependent and Non-Wheelchair Dependent Users
Richter, W Mark; Axelson, Peter W; Cooper, Rory A

Segmental Power During Propulsion in Wheelchair Users with Greater Evidence of Shoulder Injury Overtime
Koontz, Alicia M; Boninger, Michael L; Cooper, Rory A; Towers, Jeffrey D; Ma, Lin

Neuromuscular Function in Anterior Cruciate Ligament Deficient and Uninjured People
Williams, Glenn; Barrance, Peter J; Snyder-Mackler, Lynn; Axe, Michael J; Buchanan, Thomas S

Poster

Are Estimates of Quadriceps Strength Valid? Implications for Clinical Decision Making
Manal, Kurt; Williams, Glenn; Barrance, Peter J; Buchanan, Thomas S

Kinematic Comparison Of Treadmill Gait With Body Weight Suspension Between Unimpaired Subjects And Subjects With Parkinson's Disease
Threlkeld, A Joseph; Cooper, Lance D; Sprenkle, Pamela M; Bertoni, John

Assessment of Sincerity of Effort During Isometric Strength Testing
Challis, John H; Sommer III, HJ

Active Movements of the Shoulder Girdle in Healthy Subjects: a Validity Study
Nadeau, Sylvie; Kovacs, Stéphanie; Gravel, Denis; Moffet, Hélène; Piotte, France; Gagnon, Denis; Hébert, Luc J

Accuracy and Reliability of Q Angle Measurement Methods
Cooper, Ian C; Agnew, Michael J; Mahar, Shannon M; Livingston, Lori

Maximum Antero-Posterior Excursion of the Center of Pressure During Sit To Stand and Standing Sway Movements
Burgess, Robyn M; Challis, John H

Postural Estimates From Digital Images: Inter- and Intra-Tester Reliability
Woo, Timothy K; Pearsall, David J

Biomechanical Directions for the Post-Surgical Recovery of the Acl
Santos, Dario; Fabrica, Gabriel

Evaluation of Tibiofemoral Compressive and Shear Loads in the Medial and Lateral Knee Compartments During Isometric Knee Exercises
Yanagawa, Takashi; Torry, Michael R; Shelburne, Kevin B; Steadman, JR; Sterett, William I

Effects of Target Distance and Size on Reaching Kinematics in Individuals with Hemiparesis
McCrea, Patrick H; Eng, Janice J

Effect of Physical Therapy and Afferent Stimulating Insoles on Motor Abilities in Parkinson Patients
Kimmeskamp, S; Hennig, Ewald M; Milani, TL

Joint Biomechanics

Poster

Locomotion

Podium

Automated Markerless Analysis of Human Walking and Running by Computer Vision
Yam, ChewYean; Nixon, Mark S; Carter, John

Effect of Skin Motion Artefacts on Knee Joint Kinematics
Stagni, Rita; Fantozzi, Silvia; Cappello, Angelo; Brigliadori, Francesco; Leardini, Alberto

A Dual Mass Spring - Dashpot Model of the Exchange of Forces Between the Backpack, Hips and Shoulders During Walking
Lafiandra, Michael; Harman, Everett; Frykman, Peter; Pandorf, Clay

Contributions To Forward Propulsion in Human Gait
Buczek, Frank L; Sanders, James; Concha, M Cecilia; Cooney, Kevin M

Dynamic Stabilization of Rapid Hexapodal Locomotion
Jindrich, Devin L

A Simultaneous Analysis of Multiple Waveform and Constant Gait Measures: Application To Knee Osteoarthritis
Astephen, JL; Deluzio, KJ; Wyss, UP

Metabolic Cost of Generating Horizontal Forces During Walking
Gottschall, Jinger; Kram, Rodger

Effect of Reduced Range of Motion on the Accuracy of the Functional Method of Hip Joint Center Location
Piazza, Stephen J; Okita, Nori; Erdemir, Ahmet; Cavanagh, Peter R

Knee Joint Kinematics and Kinetics in Patients with Moderate Osteoarthritis
Deluzio, KJ; Landry, CSN; Chu, JJ; Hubley-Kozey, CL; Kozey, JW; Caldwell, GE; Stanish, WD

A General Weighted Least Squares Method for Inverse Dynamic Analysis
Su, Anne; van den Bogert, AJ (Ton)

The Effects of Step Uncertainty on Impacts and Contact Kinematics While Running on a Treadmill
Thomas, Joshua; Derrick, Timothy R

Optimized Joint Centres and Axes of Rotation Improve Repeatability of Gait Data
Besier, Thor F; Sturnieks, Daina; Alderson, Jacque; Lloyd, David

Determination of Peak Limb Force From Duty Factor
Knill, K; Witte, TH; Wilson, AM

Poster

Dynamic Gearing At the Limb Joints of Jumping Dogs
Gregersen, Colin; Carrier, David R

The Geometry of Galloping
Butcher, Michael T; Bertram, John; Usherwood, James

Whole Body Biomechanics of Responses To Slips
Cham, Rakié; Moyer, Brian; Redfern, Mark S

Metabolic Cost of Lateral Leg Swing in Human Walking
Shipman, David; Donelan, J Maxwell; Kram, Rodger; Kuo, AD

Visuo-Locomotor Control During Anticipatory Locomotor Adjustments
Vallis, Lori; McFadyen, Bradford J; Gérin-Lajoie, Martin

Socket Comfort and Perceived Functional Ability in Unilateral Transtibial Amputee Patients Using Plaster-Cast and Cad/Cam Manufactured Sockets
Alvarez, Maria; Ronsky, Janet; Aggarwala, R; Harder, J; Zernicke, RF

Effects of Custom Orthotics on Lower Extremity Kinematics, Kinetics and Muscle Activity
Mündermann, Anne; Nigg, Benno M; Humble, R Neil

Adaptations in Lower Extremity Joint Kinetics To Inertial Asymmetries During Walking
Martin, Philip E; Smith, Jeremy; Royer, Todd D

Compensatory Impulse Generation by Individuals with a Unilateral Below-Knee Amputation During Gait Initiation
Tokuno, Craig D; Sanderson, David J; Inglis, J Timothy

Joint Kinematics of Postural Sway Response To Sinusoidal Galvanic Vestibular Stimulation
Latt, L; Redfern, Mark S

Gait Adaptations To Transverse Slopes
Nicolaou, M; Pearsal, D

The Effect of Bracing on Patellofemoral Joint Stress During Free and Fast Walking
Chen, Yu-Jen; Ward, Samuel R; Chan, Li-der; Terk, Michael S; Powers, Christopher M

Muscle Coordination of Movement

Poster

Muscle

Podium

Poster

Soft Tissue Biomechanics

Poster

Sport

Poster

Orthopeadics

Bone

Poster

Cartilage

Poster

Ankle Articular Cartilage Thickness is Accurately Measured with Multi-Detector Computed Tomography (Mdct)
Rudert, Melvin J; Alliman, Kyle; Lundberg, Hannah; El-Khoury, George; Brown, Thomas D; Saltzman, Charles

Are the Articular Contact Stresses in the Knee Joint During Deep Flexion Critical?
Thambyah, Ashvin; Goh, James CH; De, Shamal Das

Matrix Biosynthesis Due To Exogenous Stimuli Differs for Cartilage and Fibrocartilage
Imler, SM; Hunter, CJ; Vanderploeg, EJ; Levenston, ME

A Novel Approach To Measurement of Hoop Strain in the Human Meniscus
Richards, Cristy; Gatt Jr., Charles J; Langrana, Noshir

Prediction of Optimized Diameter of Osteochondral Plugs in Cartilage Repaire
Wu, John; Herzog, Walter; Hasler, Evelyne M

In Vivo Rabbit Patellafemoral Joint Loading Via Surface Stimulation
Craig, Sean; Herzog, Walter

Microindentation Methods for Evaluating Elastic and Viscous Properties of Soft Tissues
Simha, Narendra K; Ravi, Namani; Lewis, Jack L

A Transversely Isotropic and Transversely Homogeneous Model of Cartilage Including Chondrocytes and a Statistical Distribution of Collagen Fibres
Federico, Salvatore; Herzog, Walter; Wu, John; Rosa, Guido La

Effect of Rhein on Intracellular IL-Beta-1 Production and Beta-1 Integrins Expression in Stimulated Chondrocytes
Gigant-Huselstein, C; Dumas, D; Muller, S; Bensoussan, D; Stolz, JF

Tribological Characterisation of Surface Layer of Bovine Articular Cartilage.
Grant, CA; Twigg, PC.; Thompson, J; Jin, ZM

Tribological Evaluation of Therapeutic Lubricants for the Knee
Bell, CJ; Fisher, J; Ingham, E; Forsey, R; Thompson, JI; Stone, MH

Time-Dependent Stress-Strain Analysis of Unconfined Compressed Articular Cartilage Using Confocal Laser Scanning Microscopy
Ihara, Maki; Murakami, Teruo; Sawae, Yoshinori

The Relation of the Compressive Modulus of Articular Cartilage with Its Deformation Response To Cyclic Loading
Barker, Michael K; Seedhom, Bahaa B

Effect of Glycoproteins on Friction Coefficient of Natural and Artificial Joint Surfaces
Kitano, Toshio; Kadoya, Yoshinori; Inui, Kentarou; Yamano, Yoshiki

Effects of Sound Velocity Variation on Cartilage Ultrasound Indentation Measurements
Laasanen, MS; Töyräs, J; Saarakkala, S; Rieppo, J; Korhonen, RK; Jurvelin, JS

Investigations on the Biomechanics of a Osteochondral Implant by Fe Analysis
Turquier, Frederic; Dan, Diane; Smith, Mark; Kamoulakos, Argiris; Downes, Sandra

Joint Replacement

Poster

Use of Local Bodily Landmarks in Acetabular Cup Positioning
Miller, Mark C; He, Jufang; Anderson, Donald D; Sotereanos, Nicholas G

Effect of Polyethylene Thickness on Stresses of An Ankle Joint Implant
Galik, Karol; Miller, Mark C; Smolinski, Patrick J

Bone Resorption in Shoulder Surface Replacement Arthroplasty
Hansen, Ulrich; Hopkins, Andrew

Investigaton of Stresses and Micromotion Between the Liner and the Acetabular Cup in Total Hip Replacement Implants
Romero, Francisco; Amirouche, FML; Gonzalez, Mark; Lewis, Paul; Render, Todd; Ochoa, Jorge

Running on Artificial Hip Joints - is It Wise?
Bowsher, John G; Nevelos, Jim; Pickard, Jenny; Shelton, Julia C

Structural Testing for Symmetry of the Hips by Vibration Technique
Kwong, Kevin; Huang, Xiaolin; Cheng, Jack

Ligament and Tendons

Poster

Immediate Effect of Thermal Modification on the Cadaveric Knee Capsule
Zheng, Nigel; Davis, Brent; Jablonski, Michael; Cain, Lyle; Dugas, Jeff; Andrews, James

Pilot Study of Intracellular Signaling in Post-Operative Tendons
Lai, Jeng-Yu; Gumidyala, Krishna; Houwink, Aletta P; Zhao, Chunfeng; Amadio, P C; An, K-N

Ligament Strength Does Not Decrease with Subfailure Stretches
Crisco, Joseph J; Panjabi, Manohar M

Development of a High Payload Testing System To Study Joint Kinematics and Forces
Debski, Richard E; Darcy, Shon; Gil, Jorge E; Fisk, Jesse; Woo, Savio L-Y

Development and Validation of An Approach To Record and Reproduce Kinematics
Zeminski, Jennifer; Gabriel, Mary T; Thomas, Maribeth; Debski, Richard E; Fu, Freddie H; Woo, Savio L-Y

Kinematics of the Glenohumeral Joint During the Anterior and Posterior Drawer Test
Moore, Susan M; Musahl, Volker; McMahon, Patrick J; Debski, Richard E

Effect of Joint Compression on the Biomechanics of the Intact Acromioclavicular Joint
Costic, Ryan S; Jari, Rajesh; Rodosky, Mark W; Debski, Richard E

Orthopeadics

Podium

The Tensile Properties of the Healing Goat Mcl After a Combined Mcl/Acl Injury
Abramowitch, Steven D; Yagi, Masayoshi; Tsuda, Eiichi; Woo, Savio L-Y

Evaluation of Patella Tendon as a Graft Material for Anterior Cruciate Ligament Reconstruction in An Ovine Model
Barnsdale, Christopher A; Azuma, Hirotaka; Fukushima, Shigenobu; Thornton, Gail; Frank, Cyril B; Shrive, Nigel G

Defining Patellar Tracking Problems Based on 3D, Non-Invasive, in Vivo Measures of Skeletal Kinematics
Sheehan, Frances; Rebmann, Andrea

Muscle Fatigue and Spinal Instability: An Electromyographic Study
Silfies, Sheri P; Karduna, Andrew R

The Effect of Bone Quality on Intra-Medullary Fixation of the Proximal Humerus Using a Retro-Grade Nail
Manning, P; Rajesh, M B; Neumann, L; Parry, M; Wallace, W A

A Biomechanical Analysis of Internal Fixation of Transverse Acetabular Fractures
Demarco, Alyssa L; Bachus, Kent N; Horwitz, Daniel S

The Impact of Anterior Cervical Fusion Upon Cervical Spine Range of Motion and Overall Neck Flexibility
Thinnes, John; Sigler, Sorin; Hilibrand, Alan S; Daffner, Scott; Vaccaro, Alexander R; Alberts, Todd J

Trap May Contribute To Altered Mechanical Properties in Ligament After Chemical Sympathectomy
Dwyer, Kelley W; Provenzano, Paolo P; Muir, Peter; Vanderby Jr., Ray

Investigation of Structure-Property Relationships in Human Femoral Trabecular Bone
Hsu, Steven; Ebenstein, Donna; Issever, Ahi; Pruitt, Lisa; Majumdar, Sharmila

Increasing Age Slows Recovery of Function Following Achilles Tendon Injury in the Rat
Vogelpohl, Lori; Anderson, Donald D; Hale, Joseph E; Stangier, Stefanie D; Guanche, Carlos A

The Effect of Plate Design, Endplate Preparation and Bone Mineral Density on Immediate Stabilization in An Anterior Cervical Plate Fixation Model
Dvorak, Marcel; Pitzen, Tobias; Zhu, Qingan; Gordon, Jeff; Fisher, Charles; Oxland, Thomas

The Effect of a Novel Cage Design on Stabilization in the Lumbar Spine
Johnson, Michael; Zhu, Qingan; Sennett, Andy; Dvorak, Marcel; Fisher, Charles; Oxland, Thomas

Investigation of Cementless Cup Micromotion and Stability After Total Hip Arthroplasty
Aram, Luke; Lehman, Andy; Lewis, Paul; Render, Todd; Ochoa, Jorge; Amirouche, FML; Gonzalez,

Dynamic Testing of Rat Achilles Tendons
Stangier, Stefanie D; Hale, Joseph E; Anderson, Donald D

Subject-Specific Finite Element Modeling of the Human Medial Collateral Ligament
Gardiner, John; Weiss, Jeffrey

Effect of a Compressive Follower Load and a Tensile Force on Intradiscal Pressure and Intersegmental Rotation of the Lumbar Spine
Wilke, Hans-Joachim; Rohlmann, Antonius; Neller, Sylvia; Bergmann, G; Claes, Lutz

Comparison of Fixed and Rotating Bearing Knee Replacements In-Vivo Using a 3Dmotion Analysys Technique: Preliminary Results
Holt, C A; Jones, L; O'Callaghan, P; Roy, S; Wilson, C

Mechano-Acoustic Characterization of Normal, Degenerated and Repaired Cartilage
Töyräs, J; Laasanen, MS; Saarakkala, S; Hirvonen, J; Kiviranta, I; Lappalainen, R; Jurvelin, JS

Anterior Interbody Fusion with Transfacet Screws: a Biomechanical Study
Evans, Sam L; Holt, C A; Jones, L; Dillon, D; Ahuja, S; Davies, P

The Assessment of Cervical Spine Kinematics Using Interventional Mri
Emohare, Osa; McGregor, Alison; Wragg, Paul; Gedroyc, Wladyslaw

The Healing of ACL and Mcl Injuries is Initially Similar But Diverges with Time
Lo, IKY; Marchuk, LL; Leatherbarrow, KE; Sutherland, C; Barclay, Leona; Hart, DA; Frank, CB

In-Situ Chondrocyte Deformation in Early Stage Osteoarthritic (Oa) Articular Cartilage
Clark, Andrea; Herzog, Walter; Matyas, John; Barclay, Leona; Leonard, Tim

The Combined Effects of Disuse and Gonadectomy on Bone Mechanics in Male and Female Rats
Yingling, Vanessa; Brown, Marybeth; Taylor, Jennifer; Kohrt, Wendy; Silva, Matthew; Fisher, Jonathan S; Hasser, Eileen M

Segmental Mobility of the Lumbar Spine During a Prone Press-Up Maneuver in Symptomatic and Asymptomatic Subjects: Assessment Using Dynamic Mri
Kulig, Kornelia; Powers, Christopher; Landel, Robert; Chen, Hung Wen; Fredricson, Michael; Guillet, Marc; Butts, Kim

Biomechanical Analysis of Fixation of Split-Depression Fractures of the Tibia Plateau
Blyth, Mark J; Deo, SD; Frei, Hanspeter; O'Brian, Peter; Blachut, Piotr A; Oxland, Thomas R

Compressive Biomechanics of Fracture and Neurologic Integrity in the Pediatric Spine
Nuckley, David; Hertsted, Suzanne; Tainter, Christopher; Ching, Randal

Shear Stress Stimulates Oxidant Production in Human Cartilage Explants
Martin, James; Heiner, Anneliese

Strain Rate Sensitivity of Ligaments Diminishes At Traumatic Loading Rates
Crisco, Joseph J; Moore, Douglas C; McGovern, Robert D

Predictions of Residual Stresses in Bone Cement for Joint Arthroplasty
Li, Chaodi; Wang, Ying; Schmid, Steven; Mason, James

Mechanism of Intra-Articular Calcaneal Fractures: the Effects of Achilles Tendon Loading
D'Andrea, Susan E; Perusek, Gail P; Praveen, S Solomon; Kuznicki, Jennifer JE; Davis, Brian L

Experimental Evaluation of a Model of Contact Pressure Distribution in the Hip Joint
Armand, Mehran; Merkle, Andrew; Sukal, Theresa; Kleinberger, Michael

Is Damage Development Different in Bones with a Shorter Fatigue Life
George, Winson; Vashishth, Deepak

Spine

Poster

Structural Competence of Osteopenic Thoracolumbar Vertebrae Following Anterior-Wedge Fracture
Alkalay, Ron; Stechow, Dietrich von

Biomechanics of Single-Level Cervical Fusion Techniques: Comparison of Graft-Plate Fusion with An Interbody Cage Device
Diangelo, Denis J; Thomas, Amanda M; Foley, Kevin T

Effect of Osteoporosis in a Disc - Degenerated Lumbar Spine
Varadarajan, Ravikumar; Amirouche, FML; Wagner, Franklin C; Guppy, DrKern

Prolonged Compression of Intervertebral Discs Activates MMP-2
Hsieh, Adam H; Lotz, Jeffrey

Spinal Canal Occlusion in Flexion-Compression : the Effect of Injury Mechanism in An Upper Thoracic Spine Experimental Model
Oxland, Thomas; Zhu, Qingan; Ching, Randy; Lane, Chris; Fisher, Charles; Dvorak, Marcel

Neck Muscle Strains in Whiplash Injury
Vasavada, Anita N; Brault, John; Siegmund, Gunter P

Tissue Engineering

Cardiovascular/Blood

Poster

Effect of Co-Cultured Vascular Smooth Muscle Cells on Pdgf-B Mrna Expression of Endothelial Cells Under Shear Stress
Jiang, Zonglai; Li, Yuquan; Zhang, Yan; Wang, Dong

Biomechanics & Hydrodynamics of Decellularised Porcine Aortic Heart Valves
Korossis, Sotiris; Booth, Cath; Wilcox, Helen; Watterson, Kevin; Kearney, John; Ingham, Eileen; Fisher, John

Liver/Pancreas

Poster

Bile Canaliculi Reformed by Rat Small Hepatocytes, and Its Dynamic Movement
Sudo, Ryo; Kohara, Hiroshi; Mitaka, Toshihiro; Ikeda, Mariko; Tanishita, Kazuo

Skin/Musculoskeletal

Poster

Viscoelastic Characterization of Collagen Gel Constructs
Krishnan, Laxminarayanan; Weiss, Jeffrey; Wessman, Michael D; Hoying, James B; Das, Rosalina

Apoptosis in Ligament After a Sub-Failure Stretch
Provenzano, Paolo P; Muir, Peter; Hao, Zhengling; Vanderby Jr., Ray

Nutrient Diffusion and Flow-Induced Nutrient Transport in 3-D Cell-Scaffold Composites
Botchwey, Edward; Laurencin, Cato T; Levine, Elliot M; Pollack, Solomon R

Chondrocytes and Fibrochondrocytes Respond Differently To Oscillatory Tension
Vanderploeg, EJ; Collier, KR; Imler, SM; Levenston, ME

The Effect of a Cyclic Compressive Strain on the Differentiation of Osteoblast-Like Cell (Mc3t3-E1) in 3-Dimensional Scaffolds
Choi, K; Kim, JK; Park, YS; Bae, EH; Chun, KJ; Lee, TS

Lipoatrophia Semicircularis: a Biomechanical Approach
Goossens, Richard HM; Snijders, Chris J

Novel Alginate-Chitosan Hybrid Fibers as a Scaffold for Tendon Or Ligament Tissue Engineering
Funakoshi, Tadanao; Majima, Tokifumi; Iwasaki, Norimasa; Harada, Kazuo; Nonaka, Sachiko

Chitosan-Based Hyaluronan Hybrid Polymer for Scaffold in Ligament Tissue Engineering
Majima, Tokifumi; Funakosshi, Tadanao; Iwasaki, Norimasa; Harada, Kazuo; Nonaka, Sachiko

Cyclic Strain and Fluid Flow Induce Different Responses in Human Bone Cells
Mullender, M; Haj, AJ El; Yang, Y; Magnay, J; Duin, MA van; Klein-Nulend, J

Effects of Matrix Properties on Intracellular Signaling
Lai, Jeng-Yu; Basford, Jeffery R; Pittelkow, Mark R; Zobitz, Mark E

Fingertip Pulp Mechanics During Voluntary Tapping
Jindrich, Devin L; Becker, Theodore; Dennerlein, Jack Tigh

IV World Congress Biomechanics

Author Index

To Use this Index: Scroll down or use the bookmarks in the left-hand frame to move to a new location in this index. Click on a **blue paper title** to view that paper. To return to this index after viewing a paper, click the PREVIOUS MENU bookmark in the left frame.

A

Alexander, Neil B	Abilities of Young and Old Adults To Adjust Medio-Lateral Step Location During a Forward Fall
Alexander, Neil B	Maximum Toe Flexor Muscle Strength in Healthy Young and Older Adults
Alexander, Neil B	The Propagation of An Impact Force Along the Upper Extremity
Alexander, R McNeill	Work Or Force Minimization as a Criterion for the Evolution of Locomotion
Ali, Ashraf F	Three-Dimensional Fiber-Reinforced Finite Element Model of the Human Anterior Cruciate Ligament
Aliberti, Nicholas J	Biomechanical Evidence for Proprioceptive Function of Lumbar Facet Joint Capsule
Alini, M	Effects of Mechanical Compression on Anabolic and Catabolic Gene Expression in a Rat Tail Model
Alini, M	Occlusion of Vertebral Endplate Openings: a Mechanism for Intervertebral Disc Degeneration?
Alipour, Fariborz	Optimization of Passive Tissue Model Parameters of Intrinsic Laryngeal Adductory Muscles
Alkalay, Ron	Structural Competence of Osteopenic Thoracolumbar Vertebrae Following Anterior-Wedge Fracture
Allain, Jérôme	Protocol for in Vivo Optoelectronic Kinematics Analysis of Shoulder
Allard, Paul	A Color-Coded Video-Based System for Posture and Foot Assessment
Allard, Paul	Reliability of Trunk 3D Kinematics in Clinical Evaluation
Allen, David	An Investigation of the Burst Fracture Mechanism Using a Combined Experimental and Finite Element Approach
Allen, Robert	Lumbar Spine Motion Analysis Via Automatic Segmentation
Alliman, Kyle	Ankle Articular Cartilage Thickness is Accurately Measured with Multi-Detector Computed Tomography (Mdct)
Alperin, Noam	Numerical Simulation of Cerebrospinal Fluid Motion Within a Healthy and Diseased Spinal Canal
Altendorfer, Richard	Self-Stability Mechanisms for Sensor-Cheap Legged Locomotion
Altube, L Altube	Biomechanics of Erythrocyte Agglutination. Determination of Adhesive Specific Energy
Alvarez, Maria	Socket Comfort and Perceived Functional Ability in Unilateral Transtibial Amputee Patients Using Plaster-Cast and Cad/Cam Manufactured Sockets
Amadio, Alberto C	Inter-Group Comparison of EMG Responses of Thigh and Leg Muscles During Gait in Treadmill
Amadio, P C	Digit Resistance Within Short Term After Fdp Tendon Repair in Canine in Vivo
Amadio, P C	Gliding Resistance Versus Work of Flexion -- Two Methods To Assess Flexor Tendon Repair
Amadio, P C	Pilot Study of Intracellular Signaling in Post-Operative Tendons
Amadio, P C	Tendon Excursion and Gliding Mechanism
Amell, Tyler	Force and Muscular Activity During Handwheel Actuation
Amell, Tyler	Strength and EMG of Cervical Muscles in Directional Maximal Voluntary Contraction
Amendola, Annuziato	Preferential Direction of Subtalar Joint Laxity with Interosseous Talocalcaneal Ligament Sectioning
Amimoto, Naoya	Wave-Form Analysis of Electrocardiograph with Spectrum for Screening Test
Aminian, Afshin	Biomechanical Stability Between Two Types of Periacetabular Osteotomies for Surgical Correction of Developmental Deformities of the Hip
Aminian, K	Gait Features Assessment in Hip Osteoarthritis and Total Hip Replaced Patients Based on An Ambulatory System (Physilog)
Amirouche, FML	Effect of Osteoporosis in a Disc - Degenerated Lumbar Spine
Amirouche, FML	Investigation of Cementless Cup Micromotion and Stability After Total Hip Arthroplasty

Amirouche, FML	Investigaton of Stresses and Micromotion Between the Liner and the Acetabular Cup in Total Hip Replacement Implants
Amis, Andrew	Investigations of Some Posterior Ligamentous Structures of the Knee
Amos, Mike	Effect of Shoe Mass on Soccer Kicking Velocity
An, Howard	Biomechanical Effects of Intermediate Screws in Short and Long Anterior Cervical Fusion Constructs
An, K-N	Digit Resistance Within Short Term After Fdp Tendon Repair in Canine in Vivo
An, K-N	Gliding Resistance Versus Work of Flexion -- Two Methods To Assess Flexor Tendon Repair
An, K-N	Modeling of Manual Wheelchair Propulsion Using Optimization
An, K-N	Pilot Study of Intracellular Signaling in Post-Operative Tendons
An, K-N	Quantitative Evaluation of Maximal Working Space and Kinematics of Thumb
An, K-N	Relationship Between Joint Moment Arms and Muscle Function
An, K-N	Stress Analysis of the Rotator Cuff: Model Development and Validation
An, K-N	Stress Transfer To Coronary Vasa Vasorum After Stenting: a Finite Element Model
An, K-N	Tendon Excursion and Gliding Mechanism
An, K-N	The Biomechanics of the Shoulder During Wheelchair Propulsion Up Ramps
Anbarian, Mehrdad	A Color-Coded Video-Based System for Posture and Foot Assessment
Andersen, Clark E	Simulating Detailed Kinematics of the Spine - Extrapolation of Function From the 3D Form of Structures Derived From the Visible Human Ct Database
Andersen, Jesper	Resistance Training Results in An Increased H-Reflex Excitability During Maximal Muscle Contraction But Not At Rest
Andersen, Tina S	High-Frequency Pressure Fluctuations Measured in Heart Valve Patients
Anderson, Donald D	Dynamic Testing of Rat Achilles Tendons
Anderson, Donald D	Increasing Age Slows Recovery of Function Following Achilles Tendon Injury in the Rat
Anderson, Donald D	Use of Local Bodily Landmarks in Acetabular Cup Positioning
Anderson, Frank	Anterior-Cruciate Ligament Forces in the Intact Knee During Normal Gait
Anderson, Frank	Factors That Contribute To Peak Knee Flexion in Normal Swing: Implications for Stiff-Knee Gait
Anderson, Frank	Generating Dynamic Simulations of Movement Using Computed Muscle Control
Anderson, Frank	Induced Positions: Intuitive Quantities for Characterizing Muscle Function
Anderson, Frank	Ligament Forces in the Anterior Cruciate Deficient Knee During Gait
Anderson, Frank	Reaction Forces Induced by Muscles in the Presence of Compliant Contact
Anderson, IA	Efficient Finite Element Customisation of a Generic Femur Using the Host Mesh Technique
Anderson, IA	Geometric Modelling of Skeletal Muscle Using Hermite Elements.
Anderson, Joseph C	Effect of Ventilation on Instilled Liquid Transport in the Pulmonary Airways of Rats
Anderson, Suzanne E	Occlusion of Vertebral Endplate Openings: a Mechanism for Intervertebral Disc Degeneration?
Andersson, Gunnar BJ	Biomechanical Effects of Intermediate Screws in Short and Long Anterior Cervical Fusion Constructs
Andersson, Gunnar BJ	Do Lower Spine Twisting Moments At the Completion of Lift Training Reduce the Likelihood of Back Injury?
Anderst, William J	A Unique Method To Determine Dynamic in Vivo Articular Surface Interaction
Ando, Joji	Shear Stress-Induced Atp Release and Calcium Signaling in Endothelial Cells
Ando, T	Model Blood Consisting of Dense Suspension of Natural Polymeric Gel Particles
Andrews, Brian J	Rocking the Rigid Trunk Can Produce Foot Clearance in MLKAFO Gait
Andrews, DM	Evaluation of a Magnetic Tracking Device for Estimating Cumulative Low Back Compression

Andrews, James	Immediate Effect of Thermal Modification on the Cadaveric Knee Capsule
Andriacchi, Thomas	Knee Rotation in Deep Flexion and Total Knee Replacement Design
Angeli, Thomas	Adjustment of Individual Stimulation Patterns for Fes Cycling
Angeli, Thomas	Cycling by Means of FES: Simulation and Practical Application
Angulo-Kinzler, Rosa M	Effects of Botulinum Toxin a and Muscle Strengthening on Gait
Anseth, Kristi	Crosslinking Density Influences Chondrocyte Morphology and Metabolism in Mechanically Loaded Peg Hydrogels
Antoniou, John	Evidence for Differences in Matrix Turnover in the Developing and Degenerating Human Lumbar Intervertebral Disc
Aoki, Yoshimitsu	Bone-Mulch-Screw/Washer-Loch Fixation of Doubled Flexor Tendon Graft in Anterior Cruciate Ligament Reconstruction
Aomatsu, Tatsuya	Experimental Study on Air Flow in a Two-Dimensional Channel with An Obstruction Oscillating At 10 Hz To 100 Hz
Araki, Junichi	Altered Nana-Order, Micro-Mechanical Property of Pulmonary Artery Smooth Muscle in Primary Pulmonary Hypertension
Araki, Junichi	Logistic Time Constant of Isovolumic Relaxation Pressure-Time Curve in the Left Ventricle
Aram, Luke	Investigation of Cementless Cup Micromotion and Stability After Total Hip Arthroplasty
Arampatzis, Adamantios	Dynamic Variables and Running Injuries
Arampatzis, Adamantios	Kinematics and Kinetics in Pole Vaulting: Energy Storage and Return
Arbeille, Philippe	Venous Return in Lower Limb During Muscular Contraction
Arbogast, Kristy B	Biomechanical Characteristics of Facial Fracture in Children
Archambault, Joanne	Cellular Responses Regulating Signaling and Gene Expression in Tendon Cells
Ariff, Ben	Combining Mri and CFD for Carotid Blood Flow Analysis: a Reproducibility Study
Armand, Mehran	Experimental Evaluation of a Model of Contact Pressure Distribution in the Hip Joint
Arms, Steve	The Testing and Validation of a Fast Response Inclinometer
Armstrong, Neil	The Location of the Elbow Joint Centre of Rotation in Children During Active Flexion-Extension.
Arndt, Anton(Toni)	Natural Frequencies of Femur Bone and Bonepin
Arnoczky, SP	Tensile Load Modulates Inhibition of MMP-1 Expression in Tendons
Arnold, Allison S	Reaction Forces Induced by Muscles in the Presence of Compliant Contact
Aro, Hannu	Molecular Biology of Biomaterial Incorporation with Bone
Aro, Hannu	Precision Measurements of Rsa Method Using a Phantom Model of Hip Prosthesis
Artmann, G	Mechanical Properties and Permeability of Polyelectrolyte Microcapsules (PEMC)
Arts, Theo	Active Myofiber Stress Distribution in Patient Specific Models of Cardiac Mechanics
Arts, Theo	Modeling Electrical and Mechanical Activation Times in the Normal Heart
Arulanandam, Bernard P	Effects of Cyclic Pressure on Select Bone Cell Functions Pertinent To Bone Hoeostasis
Aryal, Ashish	Dynamics of Wound Healing in Airway Epithelial Cells: Gfp-Actin Remodeling
Asai, Daisuke	Sensitivity Analysis on Disc Behavior in Temporomandibular Joint
Asakawa, Deanna Schmidt	Velocity of the Rectus Femoris Muscle After Tendon Transfer Surgery
Asano, Takahisa	Spatial Flow Pattern Difference Between Blood- and Crystalloid-Perfused Myocardium
Asari, Yasushi	Morphology of Endothelial Cells Under Flow Alteration in Vivo
Asgharian, Bahman	Use of Computational Fluid Dynamics To Study Inhaled Gas and Particle Trasport in the Nasal Passages
Ashton-Miller, James	A Loss of Balance is a Loss of Control: the 3-Sigma Hypothesis
Ashton-Miller, James	Abilities of Young and Old Adults To Adjust Medio-Lateral Step Location During a Forward Fall

Ashton-Miller, James	Biomechanical Differences of Fall Arrest Using the Upper Extremity Due To Aging
Ashton-Miller, James	Comparison of Step Variability During Gait on Flat and Irregular Surfaces in Patients with Polyneuropathy.
Ashton-Miller, James	Effects of Age and Gender on Maximum Hip Flexion Power At Low and High Velocities
Ashton-Miller, James	Hand Impact Force Reduction in Forward Falls in Young Males: a Prosprctive, Controlled, 3-Month Intervention Trial
Ashton-Miller, James	Maximum Toe Flexor Muscle Strength in Healthy Young and Older Adults
Ashton-Miller, James	On Low-Cost Strategies for Reducing Fall-Related Injuries in the Elderly
Ashton-Miller, James	On Not Tipping a Stepladder Sideways
Ashton-Miller, James	Pelvic Floor Muscle Strains During Vaginal Brith
Ashton-Miller, James	The Propagation of An Impact Force Along the Upper Extremity
Astephen, JL	A Simultaneous Analysis of Multiple Waveform and Constant Gait Measures: Application To Knee Osteoarthritis
Astephen, JL	The Loading Response Phase of the Gait Cycle is Important To Knee Osteoarthritis
Ateshian, Gerard A	Experimental Verification of the Role of Interstitial Fluid Pressurization in the Frictional Response of Bovine Articular Cartilage
Atherton, John	Mutations of Titin Cause Dilated Cardiomyopathy
Attwells, Renee L	Motion Control Shoes Reduce Midfoot Range of Motion During Running
Aubert, Jean-Thomas	Body Force Distribution in Veins of the Lower Limb During Stationnary Gait
Aubert, Jean-Thomas	Venous Return in Lower Limb During Muscular Contraction
Aubin, CÉ	Biomechanical Modeling of the Scoliotic Spine Reducibility
Aubin, CÉ	Biomechanical Tools To Understand and Predict the Effects of Interventions in Scoliosis
Aubin, CÉ	Muscles and Coordination
Augenstein, Kevin f	Principal Component Analysis of Cardiac Function
Auger, François A	Tissue Engineered Blood Vessels (Tebv) : the Future is Now
Augst, Alexander D	CFD Modeling of the Carotid Artery Using 3D Ultrasound
Augst, Alexander D	Errors Associated with CFD Models Reconstructed From 3D Ultrasound Data
Avela, Janne	Effects of Contraction History on Fascicle Behavior in Shortening Contractions
Avolio, Albert	Dynamic Stress Analysis of the Arterial Wall with Finite Element Modeling
Avolio, Albert	Effects of Circumferential Residual Stress on the Circumferential Stress Distribution of the Arterial Wall by Finite Element Modeling
Avrahami, I	CFD Analysis of Flow Through Mechanical Heart Valves
Avrahami, I	Experimental Analysis of Flow Through Tilting Disk Valve
Avrahami, I	Numerical and Experimental Measurements of the Flow in Pulsatile Ventricle Assist Device
Axe, Michael J	Neuromuscular Function in Anterior Cruciate Ligament Deficient and Uninjured People
Axel, Leon	Three-Dimensional Kinematics of Right Ventricular Systolic Contraction
Axelson, Peter W	Differences in Propulsion Kinetics Between Wheelchair Dependent and Non-Wheelchair Dependent Users
Ayers, David	Can Piece-Wise Linear Interface Models Be Used To Predict the Failure Response of the Cement-Bone Interface?
Ayers, David	Directional Dependence of Early Fatigue Damage in Cemented Total Hip Replacements
Ayers, David	Early Cement Damage Around a Femoral Stem is Focused on the Cement/Bone Interface
Ayers, David	Shrinkage of Vacuum Mixed Cement Causes Interface Gaps and Stress Concentrations in Cement Mantles Surrounding Femoral

B

Bertram, CD	Fluid Velocities Within a Ventricular Assist Device are Highly Sensitive To Pneumatic Drive Conditions
Bertram, John	Collision Losses During Brachiation: Why Gibbons Have Long Arms
Bertram, John	Loss Before Recovery: Some Partial Answers To Old Locomotion Questions
Bertram, John	The Geometry of Galloping
Bertsch, C	Ankle and Subtalar Kinematics of the Ankle Joint with Intact, Injured, and Reconstructed Lateral Ligaments
Besier, Thor F	Knee Loading During Gait and Early Signs of Knee Osteoarthritis in a Meniscectomy Population
Besier, Thor F	Knee Loading in a Meniscectomy Population: a Risk Factor for Osteoarthritis?
Besier, Thor F	Optimized Joint Centres and Axes of Rotation Improve Repeatability of Gait Data
Besson, Arnaud	Simultaneous Strains and Displacements Analysis of Implanted Femurs by in Vitro Study and Finite Element Modelling
Best, Thomas	Anesthetic Effects on Muscle Performance
Best, Thomas	Effects of Joint Angle on Recovery of Torque Following Muscle Stretch Inury
Best, Thomas	Relaxation Function and a Generalized Solution for a Nonlinear Rheological Model of Biological Soft Tissues
Bethune, Allison J	Muscular Response of the Swing Limb and Arms During An Unexpected Slip
Beynnon, Bruce D	Acl Strain During Rehabilitation Exercises, in Vivo
Beynnon, Bruce D	The Biomechanics of the Weightbearing Knee
Beynnon, Bruce D	The Effects of Ligament and Cartilage Properties on the Glenohumeral Joint
Bibby, Susan RS	Nutrition of the Intervertebral Disc; Effects of Pathological Changes
Bicchierini, Mauro	Skin Motion Artefact Characterization From 3D Fluoroscopy and Stereophotogrammetry
Bicknell, C	Characterisation and Simulation of In-Vivo Perhiperal Distal Bypass Grafts
Biden, Ed	Development and Validation of a Joystick Dynamics Model To Predict Operator Input Torque
Biden, Ed	Effect of Joystick Stiffness and Speed on Selected Dynamic Torque Characteristics
Biewener, Andrew A	Contractile Performance of Muscles That Generate Power Vs Minimize Cost/Force
Biewener, Andrew A	In Vivo Muscle Force-Length Behavior During Inclined Hopping in Tammar Wallabies
Biewener, Andrew A	Muscle Work Versus Muscle Force: in Vivo Function of Avian Ankle Extensors
Biewener, Andrew A	Variable Gears in Animal Locomotion: Effects of Speed, Gait and Size
Bigley, Robbie	Estrogen Depletion is Associated with Changes in Osteon Morphology
Bijker, Kirsten E	Prediction of the Metabolic Energy Curve During Running Against Inclines: Implications for Delta Efficiency
Billy, F	Three Dimensional Characterization of Pulsa Tile Flow Beha Vior in the Convergent Region in a Model of Mitral Prolaps. a Particular Velocity Imaging Stud
Bilston, Lynne	Biomechanics of Perivascular Flow in Syringomyelia
Bilston, Lynne	Biomechanics of Very Soft Tissues
Binet, Marc-Herve	Ski Binding Settings and Differences Between Sex
Bird, Nigel	Computational Fluid Dynamics (CFD) Simulation of the Human Biliary System
Bishop, Nicholas	Effect of Interfragmentary Shear and Compressive Stimulation on Bone Healing
Bizios, Rena	Adaptive Responses of Endothelial Cells To Cyclic Pressure
Bizios, Rena	Effects of Cyclic Pressure on Select Bone Cell Functions Pertinent To Bone Hoeostasis
Bizios, Rena	Effects of Sustained Pressure and Strain on Vascular Smooth Muscle Cell Function
Bizot, Pascal	In Vivo Determination of Hip Joint Separtion in Subjects Having Variable Bearing Surfaces
Blachut, Piotr A	Biomechanical Analysis of Fixation of Split-Depression Fractures of the Tibia Plateau

Blankevoort, L	In-Vitro Reports on Anterior Ankle Ligament Damage and Ankle-Joint Laxity: A Review of the Literature
Blankevoort, L	Two Instrumented Tests for Anterior Ankle-Joint Laxity: An Evaluation in the Clinical Setting
Blemker, Silvia	Velocity of the Rectus Femoris Muscle After Tendon Transfer Surgery
Blickhan, Reinhard	Does Leg Retraction Simplify Control in Running?
Blickhan, Reinhard	Fitting Muscle Properties
Blickhan, Reinhard	Leg Design and Jumping in Spiders
Blickhan, Reinhard	Local Feedback Mechanisms for Stable Bouncing
Blickhan, Reinhard	Stable Strategies for Muscle Skeletal Systems
Block, Joel	Asymmetric Dynamic Knee Loading in Advanced Unilateral Hip Osteoarthritis
Blom, EJ	Growth Factor Loaded Calcium Phosphate Cement for Bone Regeneration
Bloomberg, Jacob	Variation in Treadmill Walking Due To Combinations of Visual Scene Motion and Gravity-Assist
Bluestein, Danny	Platelet Activation in Flow Through a Stenosis Model: Comparison Between CFD and Cdpiv Results
Blüthner, Ralph	Biodynamic Data Set for Modelling Car Drivers
Blyakhman, Felix	Contraction of Single Myofibrillar Sarcomeres Occurs in 2.7-Nm Steps and Integer Multiples Thereof
Blyth, Mark J	Biomechanical Analysis of Fixation of Split-Depression Fractures of the Tibia Plateau
Blyth, P	Efficient Finite Element Customisation of a Generic Femur Using the Host Mesh Technique
Blyth, P	Geometric Modelling of Skeletal Muscle Using Hermite Elements.
Bobbert, Maarten F	Stance Limb Contributes To Prevention of Falling After Tripping
Boden, Lucy	Non-Invasive Measurement of Wave Intensity - Reproducibility and Effect of Gtn
Boerboom, Ralf	Fluid-Structure Interaction And Collagen Remodeling In The Aortic Heart Valve
Boesiger, Peter	Numerical Study of Human Aortic Blood Flow: a Comparison Between Healthy and Disturbed Flow Distal To Artificial Heart Valves
Bogdanske, John	A Comparison of Joint Mechanics Between Anterior Cruciate Ligament Intact and Deficient Stifles: a New Model of Anterior Cruciate Ligament Disruption
Boggess, Brian M	Injury Risk Function for the Small Female Wrist
Bohez, Erik LJ	Finite Element Study of Trochanteric Gamma Nail for Subtrochanteric Fracture
Böhm, H	Can Inverse Dynamics Be Computed with a Rigid Body Model
Bohn, Christiane	Swing Phase Reduction in Above-Knee Amputee Running
Bohn, Christiane	The Sensori-Motor Degeneration Revealed by the Center of Pressure Measurement
Bohne, Michael	Differences in Ankle and Knee Joint Stiffness Between Strength-Trained and Aerobic-Trained Athletes When Hopping At a Preferred Frequency
Bohne, Michael	Downhill Hiking with the Use of a Single Hiking Pole Vs. Dual Trekking Poles
Bojsen-Møller, J	Measuring Vastus Lateralis Aponeurosis and Tendon Deformation in Vivo During Maximal Isometric Contraction by Ultrasound
Bond, Quin	Intersegmental Dynamics During Multijoint Arm Reaching: Implications for Control of Limb Movement
Boninger, Michael L	Segmental Power During Propulsion in Wheelchair Users with Greater Evidence of Shoulder Injury Overtime
Booh-Luha, Benjamin	Reliability of Trunk 3D Kinematics in Clinical Evaluation
Boon Ho, Ng	Strain Rate Effect on the Tensile Properties of Flexor Tendon
Boon Ho, Ng	The Effect of Postmortem Freezing Storage on the Tensile Properties of Tendon
Booth, Cath	Biomechanics & Hydrodynamics Of Decellularised Porcine Aortic Heart Valves
Booth, Cath	Biomechanics & Hydrodynamics of Decellularised Porcine Aortic Heart Valves

Borg, F	The Force-Velocity Relation Studied with a Pneumatic Leg-Extension Device
Borg, Thomas K	Analysis of 3-Dimensional Culture of Cardiac Myocytes and Fibroblasts That Simulate Mechanical Conditions in Vivo
Boros, Rhonda L	Influence of Segment Rigidities on Ground Reaction Forces During Landing
Borst, Cornelius	Measuring Effects of Drugs on Arterial Mechanical Properties
Botchwey, Edward	Nutrient Diffusion and Flow-Induced Nutrient Transport in 3-D Cell-Scaffold Composites
Bottlang, M	Comparative Analysis of Joint Compliance by Finite Element Analysis and Electronic Speckle Pattern Interferometry
Bottlang, M	Full-Field Strain Measurement Over Articular Cartilage Cross-Sections with Electronic Speckle Pattern Interferometry
Bottlang, M	Pertrochanteric Fracture Fixation: Effects of Implant Design on Cut-Out Failure Under Dynamic Loading
Bottlang, M	Radiographic Landmark Assessment of the Knee Joint Flexion-Extension Axis
Bottlang, M	Screw and Blade Type Hip Implants Produce Distinct Insertion Forces
Bottlang, M	Swelling of Organotypic Brain Cultures as a Model for Traumatic Brain Injury
Bottlang, M	Traumatic Brain Injury in An Acceleration-Deceleration Scenario
Bourauel, Christoph	Experimental and Numerical Study on the Mechanical Behaviour of the Periodontal Ligament Under Orthodontic Loading
Bourne, M	Effect of Body Posture on Geometry of the Abdominal Aortic Bifurcation
Bouten, VC Carlijn	A Multi-Scale Finite Element Approach To Determine Local Cell and Tissue Deformations
Bouten, VC Carlijn	Fluid-Structure Interaction And Collagen Remodeling In The Aortic Heart Valve
Bovendeerd, Peter	Active Myofiber Stress Distribution in Patient Specific Models of Cardiac Mechanics
Bovendeerd, Peter	Modeling Electrical and Mechanical Activation Times in the Normal Heart
Bowen, Benjamin P	A Role for Molecular Dynamics of Endothelial Cell Lipids in Mechanotransduction
Bowen, Roscoe C	Implications of Hand Trajectories Found in Two Muscular Dystrophy Subjects
Bowman, Kari	Movement Synergy Between the Ankle and Hip Joints During Single Leg Stance
Bowman, Sandy	Effects of Age and Time Period on Joint Kinematics and Kinetics During a Single Step Response
Bowsher, John G	Running on Artificial Hip Joints - is It Wise?
Boyd, Steven K	A Computationally Efficient Algorithm for In-Vivo Bone Failure Prediction on the Trabecular Level: a Combined Experimental and Computational Approach
Boyd, Steven K	Trabecular Tissue Stresses and Strains in Mechanically Induced Anabolic Bone Adaptation: a Finite Element Study
Boyer, Katherine A	Quantification of Soft Tissue Vibration Frequency in Heel-Toe Running
Brackhan, Joseph	Bioengineering of An Experimental Bioartificial Heart Muscle.
Braido, Peter	In Vivo Measurement and Biomechanical Modeling of Thumb Circumduction Range of Motion
Brand, Richard A	Hyperelastic Representation of Hip Joint Capsule: a Finite Element Validation
Brandl, Tanja	Fluid Dynamics and Wall Mechanics in Peripheral Bypass Anastomoses
Braspenning, Sigrid	Contribution of Mono- and Biarticular Muscles To Extending Knee Joint Moments in Runners and Cyclists
Brasseur, James G	Degradation of Drug Tablets and Mixing in the Stomach Using Computer Simulation with the Lattice-Boltzmann Algorithm
Brault, John	Head Restraint Position Affects Occupant Response in Rear-End Collisions
Brault, John	Neck Muscle Strains in Whiplash Injury
Braun, Barry	Influences of Gender and Exercise on ACL Laxity
Braun, Barry	The Association of Estrogen Changes Across the Menstrual Cycle Phases with ACL Laxity in Active Females

Bray, Robert	Angiogenesis and Healing in Rabbit Knee Ligaments
Bressel, Eadric	Bicycle Seat Designs and Their Effect on Pelvic Angle, Trunk Angle, and Comfort in Females During Cycling
Bressel, Eadric	Ground Reaction Forces Transmitted To the Upper Extremity During the Yurchenko Vault and Floor Exercise
Bressel, Eadric	Radiographic Analysis of the Wrist While Gripping a Kayak Paddle
Bressel, Megan E	Bicycle Seat Designs and Their Effect on Pelvic Angle, Trunk Angle, and Comfort in Females During Cycling
Breuls, Roel GM	A Multi-Scale Finite Element Approach To Determine Local Cell and Tissue Deformations
Brey, Robert H	Comparison of Subjective and Objective Measurements of Balance Disorders Following Traumatic Brain Injury
Brey, Robert H	Identifying Dynamic Instability During Obstructed Gait Following Traumatic Brain Injury
Brigliadori, Francesco	Effect of Skin Motion Artefacts on Knee Joint Kinematics
Brizzell, Jason	In Vivo & Noninvasive Load Sharing Among Quadriceps Components in Patellar Malalignment
Brodland, G Wayne	Cell-Cell Interfacial Tension and Cytoplasm Viscosity Can Be Determined Using Parallel-Plate Compression Tests
Brodland, G Wayne	Oriented Mitosis-Driven Epithelium Reshaping: a Finite Element Study
Brodsky, Sergey V	Rescue by Transplantated Endothelial Cells for Ischemic Renal Failure Visualization of Peritubular Capillaries Using Intravital Videomicroscopy
Brogan, D	Stable Forward Dynamic Simulation of Bipedal Gait Using Space-Time Analysis
Brolin, Karin	Influence of Ligamentous Injuries on the Upper Cervical Spinal Kinematics
Brooks, Susan V	Passive Stretches Protect Muscle in Old and Young Mice From Lengthening Contraction-Induced Injury
Broom, Neil	Exploring Structure/Function Relationships in Articular Cartilage Using Novel Experimental Approaches
Brosh, Tamar	Orthodontic Bracket Debonding: in Vivo and in Vitro Debonding Strength and the Related Tooth Damage
Brouwer, Brenda	Postural Control and Strength Among Elderly with and Without a Fear of Falling
Brown, David	Failure Load for Single Screw Versus Single Screw Plus Staple Constructs in the Pediatric Thoracic Spine: Differences Between Plowing and Levering
Brown, Gregory A	Tools for Computer-Aided Surgery: Displacement and Velocity Workspaces of the Human Knee
Brown, Ian E	Biomimetic Approaches To Stable Systems for Functional Electrical Stimulation
Brown, Marybeth	The Combined Effects of Disuse and Gonadectomy on Bone Mechanics in Male and Female Rats
Brown, Stephen	Effects of Expectation During Sudden Undloading of the Hands
Brown, Stephen	Whole-Body Postural Control and Trunk Stability During Sudden Hand Loading
Brown, Thomas D	An Algorithm To Quantify Segmental Lesions in Necrotic Femoral Heads
Brown, Thomas D	Ankle Articular Cartilage Thickness is Accurately Measured with Multi-Detector Computed Tomography (Mdct)
Brown, Thomas D	Finite Element Analysis of Median Nerve Insult in the Carpal Tunnel
Brown, Thomas D	Finite Element Modeling of Total Ankle Replacements for Constraint and Stress Analysis
Brown, Thomas D	Hyperelastic Representation of Hip Joint Capsule: a Finite Element Validation
Brown, Thomas D	Influence of Loading and Local Density on Bone Fracture Toughness Parameters
Brown, Thomas D	Preferential Direction of Subtalar Joint Laxity with Interosseous Talocalcaneal Ligament Sectioning
Brown, Thomas D	Thermal Finite Element Analysis of Osteocyte Kill Zones Achieved with a Cryo-Insult Probe

Browne, M	Assessment of a Novel Femoral Component Removal Technique for Revision Surgery
Browne, M	Characterisation of a Substitute Material To Model Cancellous Bone in In Vitro Implant Migration Studies
Browne, M	Measurement of Residual Stress Due To Volumetric Shrinkage in Bone Cement
Brozoski, Frederick	Comparative Neck Load Measurements In An Instrumented Manikin Exposed To Parachute Drops From A Uh-60 Black Hawk
Bruck, Franz	Dynamic Skiing: Influences of Snow and Ski Properties
Brueggemann, Gert-Peter	Dynamic Variables and Running Injuries
Brueggemann, Gert-Peter	Effects of Mechanical Stimuli on the Relaxation Behavior of the Growth Plate Related To Morphological and Biochemical Adaptation in the Rat Model
Brueggemann, Gert-Peter	Kinematics and Kinetics in Pole Vaulting: Energy Storage and Return
Brueggemann, Gert-Peter	Mechanical Properties of Cartilage Specimen in Rats -
Brueggemann, Gert-Peter	Natural Frequencies of Femur Bone and Bonepin
Brueggemann, Gert-Peter	The Transition From Take-Off To Early Flight Phase in Ski-Jumping
Brugel, Lydia	A Multi-Segmental Model of the Coupling of Inspiratory Flow with the Compliant Nose Structure Assessed in Vivo.
Bruhn, Sven	The Influence of Fatigue on Functional Stability of the Knee Joint
Brumer, Rebecca	Techniques for Safe Landing During An Unexpected Fall: Modulation of Impact Velocity Via the Squat Response
Brunette, DM	Effects of Surface Topography on Cell Behaviour and Tissue Organization.
Brunette, Jean	Biomechanics of Plaque Rupture in Atherosclerosis Coronary Arteries
Brunette, Jean	Mechanical Aspects of Plaque Redistribution During Angioplasty: Possible Consequences on Vulnerability
Brunski, John B	Biomechanical Modeling of Overload At the Bone-Oral Implant Interface
Bryant, J Tim	A Computational Model of Postoperative Knee Kinematics
Bryant, J Tim	Comparison of 3 Measures of Grf; Force Plate, Fscan(r) and Multiple Force Sensors
Bryant, J Tim	Development of a Trifilar Pendulum for Measuring Moment of Inertia
Bryant, J Tim	Pressure Distribution Measurement for Design of Waist Belts in Personal Load Carriage Design
Bryant, J Tim	The Importance of Certain Design Features in a Backpack
Bryant, Stephanie J	Crosslinking Density Influences Chondrocyte Morphology and Metabolism in Mechanically Loaded Peg Hydrogels
Buchanan, Cindy I	Mechanical Function of Leg Muscles in Running Birds
Buchanan, Thomas S	An EMG-Driven Biomechanical Model of the Human Elbow: Fitting a Generic Model To Specific Subjects
Buchanan, Thomas S	Are Estimates of Quadriceps Strength Valid? Implications for Clinical Decision Making
Buchanan, Thomas S	Neuromuscular Function in Anterior Cruciate Ligament Deficient and Uninjured People
Buchanan, Thomas S	Registration of 3D Bone Geometry with Cine-Phase Contrast MRI Data for the Determination of in Vivo Joint Kinematics
Buchanan, Thomas S	Self-Organizing Maps and the Representation of EMG Signals in Terms of Muscular Synergies
Buckley, CP	Integrity of Compression Moulded Uhmwpe Components for Joint Replacement
Buczek, Frank L	Contributions To Forward Propulsion in Human Gait
Buford, William L	Simulating Detailed Kinematics of the Spine - Extrapolation of Function From the 3D Form of Structures Derived From the Visible Human Ct Database
Bull, Anthony	Investigations of Some Posterior Ligamentous Structures of the Knee
Bull, Anthony	The Assessment of Spinal Kinematics During the Application of An A-P Mobilisation

C

Cahuzac, JP	Gait Analysis in Children with Tibial Rotational Abnormalities
Cai, Zong Xi	Self-Excited Oscillations in a Fluid-Beam Collapsible Channel
Cain, Lyle	Immediate Effect of Thermal Modification on the Cadaveric Knee Capsule
Caldwell, GE	Knee Joint Kinematics and Kinetics in Patients with Moderate Osteoarthritis
Caldwell, GE	Temporal Pattern Recogntion Techniques Can Detect EMG Differences Between Moderate Knee Osteoarthritis Patients and Healthy Controls During Walking
Callaghan, JP	Cumulative Loading as An Injury Mechanism: Tissue Considerations
Callaghan, JP	Erector Spinae Flexion Relaxation During Short Duration Slumped Sitting
Callaghan, JP	Evaluation of a Magnetic Tracking Device for Estimating Cumulative Low Back Compression.
Callahan, E	Radiographic Landmark Assessment of the Knee Joint Flexion-Extension Axis
Calzo, R	Comparison of Scaffold Designs for Tissue-Engineered Small-Diameter Graft Applications
Camacho, Daniel L A	A Finite Element Model of the Foot and Ankle: Validation of Quiet Stance
Campbell, Kenneth	Regulated Actin-Myosin Interaction and Sarcomeric Stiffness
Campbell, Rebecca B	Relationship of Animal To Human Methods for in Vivo Tendon Strain Determination in Bipedal Locomotion
Campbell, Ryan J	Artificial Neural Oscillators as Controllers for Locomotion Simulations and Robotic Exoskeletons
Campos, Vasco	An Investigation on the Ventilation of Operating Theatres
Campy, Robert M	Quadriceps Femoris Activation-Force Relationship and Perceived Exertion During Dynamic, Inertial Knee Extension Exercise
Cañadas, Patrick	Assessment of Structural Viscoelasticity of Cytoskeleton by Tensegrity Model
Cañadas, Patrick	Increasing Number of Interconnected Elements in Tensegrity Models Induces a Structural Softening Consistent with Cortical Cytoskeleton Function
Cao, Dongbu	Finite Element Model of the Epidermis-Dermis Interface
Cao, Y	Fatigue and Wear Evaluation of a Novel Artificial Finger Joint
Capaccio, Chris	Cyclic Stretch Increases Gene Transfer and Expression in Alveolar Epithelial Cells
Cappello, Angelo	An Efficient and Robust ICP Technique for Surface Registration
Cappello, Angelo	Effect of Skin Motion Artefacts on Knee Joint Kinematics
Cappello, Angelo	Skin Motion Artefact Characterization From 3D Fluoroscopy and Stereophotogrammetry
Cappello, Joseph R	Biomechanical Efficacy of a Protein Polymer Hyrdrogel for Inter-Vertebral Nucleus Augmentation and Replacement
Cappello, Joseph R	Biomechanical Efficacy of a Protein Polymer Hyrdrogel for Inter-Vertebral Nucleus Augmentation and Replacement
Carden, Geoff	Finite Element Geometric Models of the Human Lung and Diaphragm
Cardoso, Luis	Ultrasound Wave Propagation in Porous Medium. Application To Cancellous Bone
Carlson, Brian	Numerical Simulation of Sickle Cell Blood Flow in the Transverse Arteriole-Capillary Network
Carmody, Chris J	Fluid Structure Interaction of Heart Valves
Caro, CG	Characterisation and Simulation of In-Vivo Perhiperal Distal Bypass Grafts
Caro, CG	Inspiratory Flow in Bronchial Airway Models: Bifurcation Plane Rotation
Carrero, Volker	Robotic Assisted Versus Manual Implantation - a Prospective Study in Primary Total Hip Replacement
Carrier, David R	Dynamic Gearing At the Limb Joints of Jumping Dogs
Carrier, David R	Influence of Increased Rotational Inertia on Human Turning Performance
Carrle, Jeremy	Human Performance-Based Pediatric Wheelchair Prescription
Carter, John	Automated Markerless Analysis of Human Walking and Running by Computer Vision
Cartmell, Sarah	Effect of Perfusion Rate on Cell Seeded 3D Constructs in Vitro

Caruntu, Dumitru I	A Three-Dimensional Mathematical Dynamic Simulation of the Knee Extension Exercise: Effects of Anterior Cruciate Ligament
Cascio, Wayne E	Bioengineering of An Experimental Bioartificial Heart Muscle.
Case, John	Asymmetric Dynamic Knee Loading in Advanced Unilateral Hip Osteoarthritis
Cashman, Peter	The Assessment of Spinal Motion During Rowing
Casolo, Federico	Evaluation of the Relevant Parameters To Predict the Behaviour of Alpine Skis
Castelli, Vincenzo Parenti	Pattern of Articular Contact At the Tibio-Talar Joint in Passive Flexion
Casto, S	A Comparison Between Single-Radius and Multi-Radius Total Knee Arthroplasties for Stand To Sit (An EMG and Kinematic Study)
Catani, Fabio	Skin Motion Artefact Characterization From 3D Fluoroscopy and Stereophotogrammetry
Catani, Fabio	The Role of the Passive Structures in the Mobility and Stability of the Natural and Replaced Human Ankle Joint
Catrysse, Michael	Instrumentation of a Head for the Detection of Loosening by Vibration Analysis
Catrysse, Michael	Monitoring of the Rehabilitation of Patients After Fracture
Catsicas, Stefan	Antero-Posterior Measurements of the Lamellipodium Mechanical Properties in the Migrating Keratocyte
Cattaneo, Paolo M	New Insights Into Orthodontic Load Transfer and Alveolar Bone Remodeling
Cavanagh, Peter R	Are There Threshold Values for Safe Plantar Pressures on Neuropathic Feet?
Cavanagh, Peter R	Effect of Reduced Range of Motion on the Accuracy of the Functional Method of Hip Joint Center Location
Cerati, F	Gait Features Assessment in Hip Osteoarthritis and Total Hip Replaced Patients Based on An Ambulatory System (Physilog)
Cerny, Martin	Fluid Dynamics and Wall Mechanics in Peripheral Bypass Anastomoses
Cerrolaza, Miguel	Biomechanical Testing of An Intramedullary Locked Nailing for Metacarpal Shaft Fractures
Cesinaro, Stefano	A Simple Model To Relate Clinical To Biomechanic Variables in Peripheral Neuropathy
Cha, Sang Hoon	Flow Analysis on the Stented and Non-Stented Lateral Aneurysm Models
Chabran, Ethelle	Venous Return in Lower Limb During Muscular Contraction
Chabrand, Patrick	Increasing Number of Interconnected Elements in Tensegrity Models Induces a Structural Softening Consistent with Cortical Cytoskeleton Function
Chadwick, EKJ	Forward Dynamic Modelling of Shoulder Movements
Chaffin, Don	Biomechanical Differences in Shoulder Loading in Populations During Load-Bearing Tasks
Challis, John H	Assessment of Sincerity of Effort During Isometric Strength Testing
Challis, John H	Influence of Segment Rigidities on Ground Reaction Forces During Landing
Challis, John H	Maximum Antero-Posterior Excursion of the Center of Pressure During Sit To Stand and Standing Sway Movements
Challis, John H	The Contribution of the Arm Swing To Maximum Vertical Jumps
Challis, John H	The Variability of Maximum Vertical Jumps
Chalmers, Gordon R	Soleus H-Reflex Gain in Elderly and Young Adults When Lying, Standing and Balancing
Cham, Rakié	Slip Anticipation Effects on Ground Reaction Forces
Cham, Rakié	Utilizing Biomechanics To Prevent Slips and Falls
Cham, Rakié	Whole Body Biomechanics of Responses To Slips
Chambers, Hank	The Effects of Backpack Loads on Pelvis and Upper Body Kinematics of Adolescent Females During Gait
Chamnongkich, S	A Comparison Between Single-Radius and Multi-Radius Total Knee Arthroplasties for Stand To Sit (An EMG and Kinematic Study)

Chu, Steven	What Can We Learn From Looking At Biological Processes, One Molecule At A Time
Chu, YH	Comparative Analysis of Joint Compliance by Finite Element Analysis and Electronic Speckle Pattern Interferometry
Chu, Yung-Hua	Traumatic Brain Injury in An Acceleration-Deceleration Scenario
Chuang, Chih-Hung	The Finite Element Analysis of Different Fixations for Mandibular Fracture
Chun, Keyoung Jin	Flow Analysis on the Stented and Non-Stented Lateral Aneurysm Models
Chun, KJ	The Effect of a Cyclic Compressive Strain on the Differentiation of Osteoblast-Like Cell (Mc3t3-E1) in 3-Dimensional Scaffolds
Chun, S	Therapeutic Electrical Stimulation with Bions To Rehabilitate Shoulder and Knee Dysfunction
Chung, Ed K	Cervical Spine Facet Capsular Ligament Strain in Midsagittal and Three Dimensional Whiplash-Like Loading
Chung, M	The Effect of Varying Frequencies on the Stimulation of the Aggrecan Promoter of Chondrocytes Embedded in Agarose Gels
Chung, Soon Cheol	A Microstructure Model of Vertebroplasty and Its Mechanical Properties
Chung, Sun G	Aging-Related Changes in Achilles Tendon Reflexes
Chung, Sun G	Biomechanical Changes in Spastic Ankles of Stroke Patients
Chung, Sun G	Intelligent Stretching and Evaluation of Spastic Ankles Using a Portable Device
Cimini Jr., Carlos	Numerical Simulation of the Polymerization of Tooth/Resin Interface for Class V Restorations
Civelek, Mete	Fluid Shear Stress Affects Vascular Smooth Muscle Cell Function
Claes, L	Ankle and Subtalar Kinematics of the Ankle Joint with Intact, Injured, and Reconstructed Lateral Ligaments
Claes, Lutz	Discoligamentous Structures of the Lower Cervical Spine Get Injured in In Vitro Low-Speed Side Collisions
Claes, Lutz	Effect of a Compressive Follower Load and a Tensile Force on Intradiscal Pressure and Intersegmental Rotation of the Lumbar
Claes, Lutz	In Vivo Loads Acting in the Spine and in Spinal Implants
Clark, Andrea	In-Situ Chondrocyte Deformation in Early Stage Osteoarthritic (Oa) Articular Cartilage
Clasey, Jody	A Comparison Between Gait Kinetics in Women with Primary Osteoarthritis and Women with Osteoporosis
Cleary, Richard	Directional Dependence of Early Fatigue Damage in Cemented Total Hip Replacements
Clopeau, T	Drag Coefficient and Reynolds Number in High Butterfly Swimmers
Cloutier, Guy	Influence of Multiple Stenoses on Diagnosis of Peripheral Disease
Clowers, Kurt	Effects of Midsole Density and Landing Height on Impact Attenuation in Landing
Coats, Brittany	Material Properties of Porcine Parietal Cortex
Cochran, Richard P	Regional Differences in Cellular Densities in Human and Ovine Mitral Valves
Cochran, RP	Finite Element Implementation of a Structural Model for Aortic Valve Tissue
Coelho, Alan J	Knee Extensor Torque and Work During Dynamic Contractions Guided by Perceptual Sensations
Coelho, Alan J	Quadriceps Femoris Activation-Force Relationship and Perceived Exertion During Dynamic, Inertial Knee Extension Exercise
Cofino, B	Residual Stresses Analysis At the Interface Between Hydroxyapatite Coating and Titanium Substrate
Coh, Milan	Biodynamic Characteristics of Top Sprinters
Coillard, C	Postural Evaluation of Idiopathic Scoliosis Patients and Adolescent Control Subjects
Coillard, C	Stiffness and Postural Control in Adolescent Control and Idiopathic Scoliosis Patients

Coisne, D	Ee Dimensional Characterization of Pulsa Tile Flow Beha Vior in the Convergent Region in a Model of Mitral Prolaps. a Particular Velocity Imaging Stud
Cole, Neil M	Effects of Age and Gender on Maximum Hip Flexion Power At Low and High Velocities
Cole, Reena	On the Role of Intramural Stress and Strain in the Restenosis of Femoral Artery Bypass Grafts
Colì, L	Flow Studies Connected with Artificial Hemodialysis. Mechanical Investigations and Biomechanical Effects
Collier, KR	Chondrocytes and Fibrochondrocytes Respond Differently To Oscillatory Tension
Collins, David F	H-Reflexes in Human Forearm Muscles are Attenuated During Rhythmic Arm Movement
Collins, James	Effect of Stochastic Electrical Joint Stimulation on Balance Control in Older Adults
Collins, Jim	Age-Related Effects on Momentum Generation and Muscle Activity During Gait-Initiation
Combs, Sarah	Developing Skilled Performance of Spinal Manipulation/Adjusment
Commean, Paul K	Forefoot Structural Predictors of Plantar Pressures During Walking in People with Diabetes and Peripheral Neuropathy
Concha, M Cecilia	Contributions To Forward Propulsion in Human Gait
Conditt, Michael A	A Force-Field Approach To the Adaptive Control and Learning of Arm Movements
Constantinescu, Alina	Implications of a Thick Endothelial Cell Glycocalyx for Microvascular Function in Mice
Contreras, Gabriela	Biomechanical Testing of An Intramedullary Locked Nailing for Metacarpal Shaft Fractures
Conzemius, Michael G	An Algorithm To Quantify Segmental Lesions in Necrotic Femoral Heads
Conzemius, Michael G	Thermal Finite Element Analysis of Osteocyte Kill Zones Achieved with a Cryo-Insult Probe
Cooman, Michel De	Instrumentation of a Head for the Detection of Loosening by Vibration Analysis
Cooney, Kevin M	Contributions To Forward Propulsion in Human Gait
Cooper, Ian C	Accuracy and Reliability of Q Angle Measurement Methods
Cooper, Lance D	Kinematic Comparison Of Treadmill Gait With Body Weight Suspension Between Unimpaired Subjects And Subjects With Parkinson's Disease
Cooper, Rory A	Differences in Propulsion Kinetics Between Wheelchair Dependent and Non-Wheelchair Dependent Users
Cooper, Rory A	Segmental Power During Propulsion in Wheelchair Users with Greater Evidence of Shoulder Injury Overtime
Corazza, Federico	Pattern of Articular Contact At the Tibio-Talar Joint in Passive Flexion
Corazza, Federico	The Role of the Passive Structures in the Mobility and Stability of the Natural and Replaced Human Ankle Joint
Cordier, E	Ankle and Subtalar Kinematics of the Ankle Joint with Intact, Injured, and Reconstructed Lateral Ligaments
Cormier, Joseph M	Computational Modeling and Experimental Validation of Human Eye Interaction with High-Speed Foam Particles
Cormier, Joseph M	High-Speed and Continuous Pressure Measurements: a Comparison of Active Pressure Sensors and Pressure Film
Cormier, Joseph M	Investigation of Skin Abrasion Injuries From High Rate Shear Loading
Cormier, Joseph M	Sonomicrometric Measurements of Eye Displacements
Cornacchia, Tulimar P M	Numerical Simulation of the Polymerization of Tooth/Resin Interface for Class V Restorations
Corr, David	Application of a Nonlinear Model To Describe Ligament Behavior
Corr, David	Effects of Joint Angle on Recovery of Torque Following Muscle Stretch Inury

Corr, David	Relaxation Function and a Generalized Solution for a Nonlinear Rheological Model of Biological Soft Tissues
Corrigan, Catherine Ford	The Influence of Vehicle Roll Rate on Neck Loading During Controlled Vehicle-To-Ground Impacts
Corveleijn, Ruby	Two Instrumented Tests for Anterior Ankle-Joint Laxity: An Evaluation in the Clinical Setting
Corvol, Maite	Cyclic Tensile Stretch Decreases Proteoglycan Production by Anulus Fibrosus Cells Through Production of Nitrite Oxide
Cosgarea, Andrew J	Computational Simulation Of Treatments Used For Patellofemoral Pain And Instabiity
Cosgarea, Andrew J	Experimental Validation of a Computational Model of the Patellofemoral Joint
Costa, KE	Control Objectives Change Between Phases of Jumping and Landing Tasks
Costa, KE	Multijoint Control During Short Duration Movements
Costa, Kevin D	Engineered Tissues as Model Systems for Studying Myocardial Biomechanics
Costic, Ryan S	Effect of Joint Compression on the Biomechanics of the Intact Acromioclavicular Joint
Cotton, John R	Creep Formulation of Strain Accumulation During Tensile Fatigue of Cortical Bone
Cotton, John R	Nonlinear Damage Theory Applied To Two-Step Fatigue Failure Prediction of Bone
Coughlin, Dezba	Nanomechanical and Biochemical Properties of Diseased Artery Tissue
Couillard, Sylvain	Cartilage Deformation of the Feline Patellofemoral Joint Obtained From Laser Scanning
Cowan, Brett	Haemodynamics of the Fontan Connection
Cox, Karen	Molecular and Cellular Analysis of Rotator Cuff Tendinosis in a Rat Overuse Model
Craig, Sean	In Vivo Rabbit Patellafemoral Joint Loading Via Surface Stimulation
Crandall, Jeff	A Numerical Model Predicting Upper Extremity Fractures Due To Airbag Deployment
Crandall, Jeff	Injury Risk Function for the Small Female Wrist
Crandall, Jeff	The Effect of Axonal Injury on the Material Properties of Brain Tissue
Creasy, JL	Therapeutic Electrical Stimulation with Bions To Rehabilitate Shoulder and Knee Dysfunction
Crewther, Blair	A Temporal, Kinematic and Kinetic Analysis of Three Equi-Volume Loading Patterns
Cripton, Peter	Anterior and Posterior Spinal Fixation - An in Vitro Summary
Cripton, Peter	The Influence of Vehicle Roll Rate on Neck Loading During Controlled Vehicle-To-Ground Impacts
Criscione, John	Covariance Amongst Response Terms Will Magnify the Experimental Error That is Inherent in Mechanical Tests on Myocardium
Crisco, Joseph J	A Novel Algorithm for Estimating Head Impact Magnitude and Location.
Crisco, Joseph J	Contact Areas and Ligament Lengths are Abnormal in Patients with Malunited Distal Radius Fracture Despite Normal Radioulnar Kinematics
Crisco, Joseph J	In Vivo Motion of the Scaphotrapezio-Trapezoidal (Stt) Joint
Crisco, Joseph J	Ligament Strength Does Not Decrease with Subfailure Stretches
Crisco, Joseph J	Strain Rate Sensitivity of Ligaments Diminishes At Traumatic Loading Rates
Cristofolini, Luca	A Micromotion-Based Model of Bone-Implant Interface Remodelling
Crivellini, Marcello	Overweight and Obesity in Posture: a Biomechanical Evaluation of Spine Angles
Crocombe, A	Finite Element Simulation of Osseointegrated Trans-Femoral Implant Under Extreme Load Condition
Cronin, John	A Temporal, Kinematic and Kinetic Analysis of Three Equi-Volume Loading Patterns
Croteau, Jeffrey	The Influence of Vehicle Roll Rate on Neck Loading During Controlled Vehicle-To-Ground Impacts
Cruz, Cíntia R	Modification in the Postural Control During Long-Term Standing

D

Dariush, Behzad	A Novel Algorithm for Generating a Forward Dynamics Solution To the Traditional Inverse Dynamics Problem
Darmana, R	Gait Analysis in Children with Tibial Rotational Abnormalities
Darvish, Kurosh K	The Effect of Axonal Injury on the Material Properties of Brain Tissue
Das, Rosalina	Viscoelastic Characterization of Collagen Gel Constructs
David, T	Rheological Properties of the Blood and Local Haemodynamics Modulating Leukocyte Attachment To Selectin-Coated Surfaces
David, Zurakowski	Does Vertebroplasty Alter the Mechanical Response of Osteopenic Vertebrae
Davies, JE	An Approach for Improving the Performance of Polymeric Macroporous Scaffolds For in Vitro and in Vivo Bone Tissue Engineering Applications
Davies, Mark	On the Role of Intramural Stress and Strain in the Restenosis of Femoral Artery Bypass Grafts
Davies, P	A Method for Studying 3D Movement of the Spine in Vitro
Davies, P	Anterior Interbody Fusion with Transfacet Screws: a Biomechanical Study
Davies, Peter F	Shear Stress-Induced Strain Focusing in the Endothelial Cytoskeleton
Davies, Peter F	The Convergence of Cardiovascular Genomics and Endothelial Biomechanics
Davis, Brent	Immediate Effect of Thermal Modification on the Cadaveric Knee Capsule
Davis, Brian L	Effects of Diabetes on the Strength of the Plantar Skin-Fat Interface
Davis, Brian L	Finite Element Model of the Epidermis-Dermis Interface
Davis, Brian L	Mechanism of Intra-Articular Calcaneal Fractures: the Effects of Achilles Tendon Loading
Davis, Brian L	Use of An Instrumented Treadmill in the Evaluation of Amputee Gait
Davis, Champ	Biomechanics of Cervical Spine Surgery: Comparison of Fusion and Nonfusion Instrumentation
Davis, I McClay	A Comparison of Comfort and Rearfoot Control in Custom and Non-Custom Foot Orthoses
Davis, I McClay	Orthotics Alter Lower Extremity Joint Coupling: a Dynamical Systems Approach
Davis, I McClay	Variables Associated with the Incidence of Lower Extremity Stress Fractures
Davis, Jennifer	Dissociation Between Dynamic Stress and Intramuscular Pressure in Isolated Rabbit Tibialis Anterior Muscle
Davis, Jennifer	Intramuscular Pressure is An Indicator of Muscle Force
Davis, Jennifer	The Viscoelastic Behavior of Mouse Extensor Digitorum Longus Single Cells
Davis, N Peter	Axial Stretch of Arteries in Organ Culture
Davis, Stephen	Knee Loading During Gait and Early Signs of Knee Osteoarthritis in a Meniscectomy Population
Davoodi, Rahman	A Biomechanical Model of the Elbow, Forearm and Wrist
Davoodi, Rahman	Biomimetic Approaches To Stable Systems for Functional Electrical Stimulation
Dawson, Christopher A	Effect of Ventilation on Instilled Liquid Transport in the Pulmonary Airways of Rats
de Carvalho Filho, Fabiano	Numerical Simulation of the Polymerization of Tooth/Resin Interface for Class V Restorations
De Clercq, D	Within-Subject Variability of Plantar Pressure Patterns in Barefoot Running
De La Rocja Freitas, Cíntia	Mechanomyographic Signals of the First Dorsal Interosseus Muscle During Isometric Voluntary Contractions
De Smet, Els	Delayed Versus Early Versus Immediate Loading of Oral Implants
de Souza, Jorge Luiz	Postural Alignment with Different Shoes and Barefoot
de Toledo Fleury, Agenor de	Neuromuscular Excitation Patterns of Human Posture Through An Optimal Control Approach
De, S Das	Biomechanics of Transtibial Ptb and Pcast Prosthetic Sockets
De, Shamal Das	Are the Articular Contact Stresses in the Knee Joint During Deep Flexion Critical?

Dean, David A	Cyclic Stretch Increases Gene Transfer and Expression in Alveolar Epithelial Cells
Dean, Delphine	Cartilage Nanomechanics, Mechanotransduction, And Tissue Engineering
Dean, Michael	The Development of a Preliminary Finite Element Model of the 5th Rib
Deban, Stephen M	Influence of Increased Rotational Inertia on Human Turning Performance
Debski, Richard E	Development and Validation of An Approach To Record and Reproduce Kinematics
Debski, Richard E	Development of a High Payload Testing System To Study Joint Kinematics and Forces
Debski, Richard E	Effect of Joint Compression on the Biomechanics of the Intact Acromioclavicular Joint
Debski, Richard E	Kinematics of the Glenohumeral Joint During the Anterior and Posterior Drawer Test
Debski, Richard E	The Use of Robots in Biomechanics - Future Directions
Decker, Michael J	A Comparison of ACL Forces During Soft and Stiff Drop-Landings
Decker, Michael J	Gender Differences in Lower Extremity Shock Absorption During Vertical Drop Landings
Decker, Michael J	Muscle Activation Differences Between the Upper and Lower Subscapularis Muscles During Abduction and Rotation
Decker, Michael J	Quadriceps Weakness Causes An Increase in the Peak Adductor Moment During Gait
DeCock, A	Within-Subject Variability of Plantar Pressure Patterns in Barefoot Running
Defossez, Henri	Quantifying Bone Trabecular Direction From Radiographs
Degoede, Kurt M	The Propagation of An Impact Force Along the Upper Extremity
Dehua, Chang	A Novel Age-Related Index of Cardiovascular Function
Deis, Nathan	Force and Sarcomere Shortening Velocity in Rat Heart
Dejnabadi, H	Gait Features Assessment in Hip Osteoarthritis and Total Hip Replaced Patients Based on An Ambulatory System (Physilog)
Dela Cruz, Sheila Dela	Effects of Sustained Pressure and Strain on Vascular Smooth Muscle Cell Function
DeLancey, John	Pelvic Floor Muscle Strains During Vaginal Brith
Delaney, Peter	Application of Fibre Laser Scanning Confocal Microscopy To Study of the Biomechanics and Microstructure of Articular Cartilage
Delaney, Peter	The Development of Confocal Arthroscopy for the Assessment of Cartilage Disorders
Delassus, Patrick	Comparative Analysis of the Hemodynamics Through Healthy and Diseased Models of the Human Abdominal Aorta
Delbridge, R	Design of a Biofidelic, Instrumented 2.5 Kg Infant Dummy
DeLeo, AT	A Comparison of Comfort and Rearfoot Control in Custom and Non-Custom Foot Orthoses
DeLeo, Joyce A	Role of Local Biomechanics in Temporal Behavioral Responses of Painful Radiculopathy
Delisle, Alain	Handling Missing Marker Coordinates in 3D Analysis
Dellanini, Leah	Bone-Muscle-Limb Morphology and Movement Dynamics/Energetics
Delorme, Sebastien	Kinematic Measurements of Snowboarders' Ankles
Delp, Scott L	Computer Simulation of the Extensor Carpi Ulnaris Transfer To Extensor Carpi Radialis Brevis
Delp, Scott L	Factors That Contribute To Peak Knee Flexion in Normal Swing: Implications for Stiff-Knee Gait
Delp, Scott L	Generating Dynamic Simulations of Movement Using Computed Muscle Control
Delp, Scott L	Induced Positions: Intuitive Quantities for Characterizing Muscle Function
Delp, Scott L	Reaction Forces Induced by Muscles in the Presence of Compliant Contact
Delp, Scott L	Simulation-Based Design of Knee Replacement Surgery
Delp, Scott L	Velocity of the Rectus Femoris Muscle After Tendon Transfer Surgery

Deluzio, KJ	A Simultaneous Analysis of Multiple Waveform and Constant Gait Measures: Application To Knee Osteoarthritis
Deluzio, KJ	An Analytical Description of Kinematic Crosstalk
Deluzio, KJ	Knee Joint Kinematics and Kinetics in Patients with Moderate Osteoarthritis
Deluzio, KJ	Lower Limb Energetics of Normal and Moderate Oa Subjects
Deluzio, KJ	Temporal Pattern Recogntion Techniques Can Detect EMG Differences Between Moderate Knee Osteoarthritis Patients and Healthy Controls During Walking
Deluzio, KJ	The Loading Response Phase of the Gait Cycle is Important To Knee Osteoarthritis
Demarco, Alyssa L	A Biomechanical Analysis of Internal Fixation of Transverse Acetabular Fractures
Demarco, Alyssa L	Head Restraint Position Affects Occupant Response in Rear-End Collisions
Demiralp, C	Contact Areas and Ligament Lengths are Abnormal in Patients with Malunited Distal Radius Fracture Despite Normal Radioulnar Kinematics
Demming, Christina	Mechanical Stability of Ankle Braces Under Passive and Dynamic Loading Conditions
DeMont, M Edwin	An Investigation of the Effect of Calcium on the Mechanical Function and Structure of Aortic Microfibrils in the Lobster Homarus Americanus
DeMont, M Edwin	Modeling Locomotion in Crustacean Larvae
DeMonte, Gianpiero	The Transition From Take-Off To Early Flight Phase in Ski-Jumping
den Berg, Bernard van	Implications of a Thick Endothelial Cell Glycocalyx for Microvascular Function in Mice
Deng, Xiaoyan	Lipid Transport in the Regions of Disturbed Flow:Its Implication in the Development of Arterial Stenoses
Dennerlein, Jack Tigh	Comparison of Clinical Performance and Stabilogram Measures in Patients with Degenerative Lumbar Spinal Stenosis
Dennerlein, Jack Tigh	Fingertip Pulp Mechanics During Voluntary Tapping
Dennerlein, Jack Tigh	Impedance Models of Finger Joints During Typing
Dennerlein, Jack Tigh	The Development of a Keyboard Force Platform
Dennis, Douglas	Global Optimization for Recovering the Position and Orientation of Free-Form Objects in Medical Imaging Registration Using a New Smoothing Approach
Dennis, Douglas	In Vivo Determination of Hip Joint Separtion in Subjects Having Variable Bearing Surfaces
Dennis, Douglas	In Vivo Forces and Motions From Fluoroscopy and Mathematical Modeling
Dennis, Douglas	Muscle Reconstruction and Modeling From Mri-Scan
Dennis, Douglas	Verification of Three-Dimensional Joint Kinematics Determined Using Fluoroscopy: An Error Analysis
Denny, E	A Model of Non-Uniform Lung Parenchyma Distortion
Denoth, Jachen	Inter-Sarcomere Dynamics in Myofibrills and Muscle Fibres - Theoretical Considerations and Simulations
Denoth, Jachen	Visualisation of Inter-Sarcomere Dynamics in Muscle Fibres
Deo, SD	Biomechanical Analysis of Fixation of Split-Depression Fractures of the Tibia Plateau
Depaola, Natacha	Flow Regulation of Gap Junctional Communication and the Functional Compartmentalization of Vascular Endothelium
Depaola, Natacha	The Convergence of Cardiovascular Genomics and Endothelial Biomechanics
Deplano, V	Physiological Flow in a Stented Coronary Bifurcation
Derivaux, Frederic	Incidence of Valve Prosthesis Incline on Left Ventricle Flow Dynamics
Derrick, Timothy R	Lower Back Moment and Postural Parameter Relationships During Asymmetric Lifting
Derrick, Timothy R	The Effects of Step Uncertainty on Impacts and Contact Kinematics While Running on a Treadmill

Desai, Leena	Dynamics of Wound Healing in Airway Epithelial Cells: Gfp-Actin Remodeling
Desjardins, Pierre	Back Muscle Fatigue During Intermittent Prone Back Extension Exercise
Desjardins, Pierre	Handling Missing Marker Coordinates in 3D Analysis
Deutsch, Steven	Understanding the Mechanisms of Mechanical Heart Valve Cavitation
Devereux, Paul	Investigations of Wall Deformation and Hemodynamics
Devine, Elizabeth	Influences of Gender and Exercise on ACL Laxity
Devine, Elizabeth	The Association of Estrogen Changes Across the Menstrual Cycle Phases with ACL Laxity in Active Females
Devita, Paul	Neuromuscular Responses To Knee Osteoarthritis During Stairway Locomotion
Dewen, Jin	Recovery Strategy From Perturbation of the Upper Body During Standing Using Mechanical Energy Analysis
Dewitt, John K	Factors Related To Ball Velocity During An Instep Soccer Kick
Dhaher, Yasin Y	Is Action of Medial Quadriceps Alone Adequate To Stabilize the Knee Against Valgus Loads?
Dhaher, Yasin Y	Reflex Responses To the Medial Knee Ligament Loading: Effect of Hip Angle Change
Dhruv, Neel	Effect of Stochastic Electrical Joint Stimulation on Balance Control in Older Adults
Dial, Kenneth P	Changes in Flight Morphology Influence the Shape of the Avian Power Curve
Diamantopoulos, Panayiotis	Three Dimensional Computer Modelling of the Human Anatomy
Diamond, Scott L	Surfactant Attenuation of Gas Embolism-Induced Thrombin Production
Diangelo, Denis J	Biomechanical Stability of Multi-Level Cervical Spine Instrumentation: Comparison of Constrained Versus Semi-Constrained Anterior Cervical Plates
Diangelo, Denis J	Biomechanics of Cervical Spine Surgery: Comparison of Fusion and Nonfusion Instrumentation
Diangelo, Denis J	Biomechanics of Single-Level Cervical Fusion Techniques: Comparison of Graft-Plate Fusion with An Interbody Cage Device
Diangelo, Denis J	Kinematics of the Cervical Spine: Path of the Instant Axis of Rotation in Flexion and Extension
Dickerson, Clark	Biomechanical Differences in Shoulder Loading in Populations During Load-Bearing Tasks
Dickson, Robert	An Investigation of the Burst Fracture Mechanism Using a Combined Experimental and Finite Element Approach
Dierk, Oliver	Robotic Assisted Versus Manual Implantation - a Prospective Study in Primary Total Hip Replacement
Dierks, TA	Variables Associated with the Incidence of Lower Extremity Stress Fractures
Dietler, Giovanni	Antero-Posterior Measurements of the Lamellipodium Mechanical Properties in the Migrating Keratocyte
Dietz, Volker	Neuronal Co-Ordination of Arm and Leg Movements During Human Locomotion
Diezi, Christian	Ground Reaction Forces on Stairs
Dillon, D	A Method for Studying 3D Movement of the Spine in Vitro
Dillon, D	Anterior Interbody Fusion with Transfacet Screws: a Biomechanical Study
DiMicco, Michael	Response Of The Chondrocyte To Mechanical Stimuli: Physiologic And Injurious Compression
Dines, Monica	Shear-Like Response of Endothelial Cells To Therapeutic Ultrasound
Ding, Z	Effects of Vessel Motion on Right Coronary Artery Hemodynamics
Dingwell, Jonathan B	A Force-Field Approach To the Adaptive Control and Learning of Arm Movements
Dingwell, Jonathan B	Nonlinear Time Series Measures for Quantifying Local Dynamic Stability During Walking
Dingwell, Jonathan B	The Minimum Crackle Hypothesis for Manipulating Mass-Spring Objects Smoothly
Dionne, Jean-Philippe	A Method for Assessing the Overall Impact Performance of Helmets Used in Crowd Management Interventions

Dionne, Jean-Philippe	Comparison of Simulated Projectile and Baton Blow Impacts on Shin Guards Used in Crowd Management Intervention
Dionne, Jean-Philippe	Reduction of Blast Induced Head Acceleration and Concussive Head Injury Potential
Diop, Amadou	A 3D Finite Element Model of An Implanted Scapula Using Cadaveric Data for Evaluation
Diop, Amadou	Protocol for in Vivo Optoelectronic Kinematics Analysis of Shoulder
Diop, Amadou	Simultaneous Strains and Displacements Analysis of Implanted Femurs by in Vitro Study and Finite Element Modelling
Dixon, Paul T	Knee Extensor Torque and Work During Dynamic Contractions Guided by Perceptual Sensations
Dixon, Sharon	Influence of Viscoelastic Heel Inserts on Peak Impact Loading and Peak Ankle Dorsi-Flexion
Dixon, Sharon	The Location of the Elbow Joint Centre of Rotation in Children During Active Flexion-Extension.
Doege, K	The Effect of Varying Frequencies on the Stimulation of the Aggrecan Promoter of Chondrocytes Embedded in Agarose Gels
Dokeh, Jiro	Muscle Work and Force: Energetics of Human Walking
Dokos, Socrates	Shear Properties of Ventricular Myocardium
Dolan, Finbar	3D Finite Element Analysis of An Intravascular Stenting Procedure
Dolenec, Ales	Effect of Fatigue on Leg Kinematic in Running Till Exostion
Domansky, K	Computational Modeling of Flow and Mass Transport in a Microfabricated Array Bioreactor for Perfused 3-D Liver Culture
Dominique, Jean	Ski Binding Settings and Differences Between Sex
Domire, Zachary	The Contribution of the Arm Swing To Maximum Vertical Jumps
Donelan, J Maxwell	Mechanical and Metabolic Requirements of Lateral Stabilization in Human Walking
Donelan, J Maxwell	Metabolic Cost of Lateral Leg Swing in Human Walking
Donelan, J Maxwell	Muscle Work and Force: Energetics of Human Walking
Dong, Ren G	Modeling of Biomechanics of Tactile Sensation on Fingertips
Dong, Ren G	Modeling of Force Response of Fingertips in Keyboard Strikes
Dong, Xi	Changes of Caveolin-1 in Human Endothelial Cells Exposed To Shear Stress
Dong, Xi	Studies on the Single Binding Force of LFA-1 and ICAM-1
Donker, SF	Inter-Limb Coordination in Human Locomotion with Added Mass
Donkerwolcke, Monique	Instrumentation of a Head for the Detection of Loosening by Vibration Analysis
Donkerwolcke, Monique	Monitoring of the Rehabilitation of Patients After Fracture
Doorly, D J	Characterisation and Simulation of In-Vivo Perhiperal Distal Bypass Grafts
Dorow, Christina	Experimental Determination of the Center of Resistance of Human Incisors in Comparison with Finite Element Simulations
Dotti, Mirco	A Micromotion-Based Model of Bone-Implant Interface Remodelling
Dowell, John	Evaluation of Alternative Material for the Prevention of Pressure Sores
Dowling, James	Determination of Inertial Characteristics of the Human Foot Using Dual Energy X-Ray Absorptiometry
Dowling, James	Predicting the Inertial Characteristics of the Human Thigh Using a Geometric Model
Dowling, James	Theoretical Considerations for the Influence of Arm Swing on Vertical Jump Take-Off Velocity
Downes, Sandra	Investigations on the Biomechanics of a Osteochondral Implant by Fe Analysis
Draganich, Louis	The Effects of Early Rollback in Total Knee Replacement on Stair Stepping
Drews, Michael	Method To Measure Sustainable Loads in Sutured Urethral Tissue
Dries, Sebastian	Robotic Assisted Versus Manual Implantation - a Prospective Study in Primary Total Hip Replacement
Driessen, Niels	Fluid-Structure Interaction And Collagen Remodeling In The Aortic Heart Valve

E

Early, Sean	Biomechanical Comparison of the Luque-Galveston and Colorado Ii Methods for Sacropelvic Fixation
Ebara, Sohei	Idiopathic Scoliosis Simulation by Finite Element Analysis with Imbalanced Growth Between Bone and Spinal Ligaments
Ebaugh, David	Effects of Low-Load, High Repetion Motion on Scapular Kinematics
Ebaugh, David	The Pattern of Scapulohumeral Motion - How Stable is It?
Ebbers, Tino	Kinematics of the Heart
Ebenstein, Donna	Investigation of Structure-Property Relationships in Human Femoral Trabecular Bone
Ebenstein, Donna	Nanomechanical and Biochemical Properties of Diseased Artery Tissue
Eberhardt, Alan W	Finite Element Analysis of a Mandibular Premolar Subjected To Orthodontic Loading: Effects of Periodontal Ligament Thickness and Nonlinear Material P
Eberhardt, Alan W	Periodontal Ligament Biomechanics of Intrusive and Extrusive Orthodontic Loading
Ebina, Toshihito	Morphology of Endothelial Cells Under Flow Alteration in Vivo
Eckhardt, Robert B	Origins of Bipedalism: Evolutionary Morphology Through Finite Element Analysis
Eckmann, David M	Embolism Bubble Adhesion Force in Excised Perfused Microvessels
Eckmann, David M	Surfactant Attenuation of Gas Embolism-Induced Thrombin Production
Egan, Edmund A	Biophysical and Biological Research in Lung Surfactant Drug Development
Ehmke, L	Full-Field Strain Measurement Over Articular Cartilage Cross-Sections with Electronic Speckle Pattern Interferometry
Ehmke, L	Screw and Blade Type Hip Implants Produce Distinct Insertion Forces
Eils, Eric	Ankle and Subtalar Kinematics of the Ankle Joint with Intact, Injured, and Reconstructed Lateral Ligaments
Eils, Eric	Mechanical Stability of Ankle Braces Under Passive and Dynamic Loading Conditions
Eils, Eric	The Stabilizing Effect of External Ankle Devices with and Without the Additional Influence of a Shoe
Einav, S	Ecs Adhesion on Silicone Rubber-Rtv 615: a Systematic Study
Einav, S	Numerical and Experimental Measurements of the Flow in Pulsatile Ventricle Assist Device
Einav, Shmuel	Aortic Valve Stenosis - Numerical Study on the Accuracy of Noninvasive Andinvasive Diagnostics
Einav, Shmuel	Arterial Blood Filtration for the Prevention of Ischemic Stroke
Einav, Shmuel	Experimental Analysis of Flow Through Tilting Disk Valve
Einav, Shmuel	Influence of Coronary Vascular Bed Compliance on the Shape of Pressure-Flow Waves
Einav, Shmuel	Is Permanent Arterial Filtration Possible? in Vivo Assesment of a Filtration Device for Embolic Stroke Prevention
Einav, Shmuel	Optimization of a New Blood Filtration Device for Embolic Stroke Prevention
Einav, Shmuel	Platelet Activation in Flow Through a Stenosis Model: Comparison Between CFD and Cdpiv Results
Einav, Shmuel	Shear-Like Response of Endothelial Cells To Therapeutic Ultrasound
Einstein, DR	Finite Element Implementation of a Structural Model for Aortic Valve Tissue
Eklund, J Mikael	Comparison of 3 Measures of Grf; Force Plate, Fscan(r) and Multiple Force Sensors
Ekström, Lars	In Vivo Quantification of Disc Bulging in Different Annular Regions Along a Radial Path
El Haj, Alicia J	Dynamic Cell/Scaffold Interactions:Implications for Bone Tissue Engineering

Elad, David	A Realistic Mechanical Model of the Human Chest Wall
Elad, David	Computational Analysis of Inspiratory Heat and Water Vapor Fluxes in the Human Nose
Elad, David	Intra-Uterine Transport Pattern During Embryo Transfer
Elad, David	Shear-Like Response of Endothelial Cells To Therapeutic Ultrasound
Elad, David	Uterine Biofluid Dynamics
Elder, Geoff	Viscoelastic Stress Relaxation During Acute Passive Stretching and Its Influence on Maximum Voluntary Strength
Elfessi, Abdulaziz	Clinical and Plantar Loading Risk Factors of Subjects with Hallux Valgus
Elias, John J	Computational Simulation Of Treatments Used For Patellofemoral Pain And Instabiity
Elias, John J	Experimental Validation of a Computational Model of the Patellofemoral Joint
El-Khoury, George	Ankle Articular Cartilage Thickness is Accurately Measured with Multi-Detector Computed Tomography (Mdct)
Ellerby, David J	Mechanical Function of Leg Muscles in Running Birds
Ellington, Charles	The Novel Aerodynamics of Insect Flight: Applications To Micro Air Vehicles
Elliott, Bruce	Injuries in Sport: Reduction Through a Biomechanical Intervention
Elliott, Bruce	Mechanical Behaviour of Baseballs During Compressive Loading To Bat-Ball Impact Level
Elliott, Dawn M	Do Constant-Rate Ramp Tests Represent Equilibrium Behaviors in Tendon?
Elliott, Dawn M	Quasi-Linear Viscoelastic Modeling of Tail Tendon Fascicles From Transgenic Mice
Ellis, Henry B	Muscle Activation Differences Between the Upper and Lower Subscapularis Muscles During Abduction and Rotation
Ellis, Jeff	Evaluation of Bileaflet Mechanical Heart Valve Induced Blood Damage During Leakage Flow Using Laser Doppler Velocimetry and Indicators of Platelet Activation
Ellis, Randy R	A Computational Model of Postoperative Knee Kinematics
Ellis, RE	Registration Methods for Computer-Assisted Surgery
Eloot, Sunny	Computational Fluid Dynamics in Hemodialysers
Emohare, Osa	The Assessment of Cervical Spine Kinematics Using Interventional Mri
Endo, Mari	Maximum Toe Flexor Muscle Strength in Healthy Young and Older Adults
Endo, Naoto	Prediction of Torsional Properties of Rat Femur Using Peripheral Quantitative Computed Tomography
Eng, Janice J	Effects of Target Distance and Size on Reaching Kinematics in Individuals with Hemiparesis
Eng, Janice J	Linear Model of Resistance To Passive Stretching in Individuals with Brain Injury: Reliability & Validity
Eng, Janice J	Medial-Lateral Cop Velocity During Standing Relates To Asymmetry and Functional Balance in Individuals with Stroke
Eng, Janice J	Symmetry in Kinetic Variables is Accompanied by Symmetry in Temporal But Not Distance Variables of Gait in Persons with
Ennis, Dan	Studying Electromechanical Behavior in Vivo with MRI Tagging and Epicardial Electrical Mapping
Ennos, A Roland	Overturning Resistance of Rigid Tap Roots
Ensaff, H	Prediction of Scratch Resistance of Metallic Bearing Surface, Articulating Against Uhmwpe, Due To 3rd Body Wear Particles
Ensini, Andrea	Recruitment of Ankle Ligaments Fibres During Passive Flexion
Ensley, Ann E	Analysis of Total Cavopulmonary Connection Fluid Dynamics: Experimental Studies
Entrup, Michael	Effects of Varus Wedged Shoe Versus Insole on Knee Joint Loading Characteristcs
Eppell, Steven	Design and Assembly of a Sterile Nanoscale Orthopedic Biomaterial

F

Farley, Claire T	Spring-Like Force Generation by the Leg in Running
Farrar, Richard	The Effect of Uhmwpe Material and Knee Design on in Vitro Wear of Fixed Bearing and Rotating Platform Mobile Bearing Total Knee Replacements
Farrokhi, Shawn	In Vivo Assessment of the Instantaneous Axes of Rotation of the Lumar Spine in Symptomatic and Asymptomatic Subjects
Farshad, Mehdi	Finite Element Models of Abdominal Organs for Use in Trauma Research
Farshad, Mehdi	Time-Dependent Properties of the Porcine Kidney Capsular Membrane
Fauth, Andrew R	In-Vitro Measurements of Tarsometatarsal Joint Stiffness
Fauth, Andrew R	Plantar Aponeurosis Forces During Simulated Walking
Federico, Salvatore	A Transversely Isotropic and Transversely Homogeneous Model of Cartilage Including Chondrocytes and a Statistical Distribution of Collagen Fibres
Federspiel, William J	Effect of Tissue Viscoelasticity and Lung Surfactant on Eustachian Tube Mechanics
Fehren, Marion	Influences on Eye Location and Posture of Drivers
Fehrmann, Michael	Effect of a Dual Cage on the Mechanical Behaviour of the Lumbar Spine
Fejer, René	Cervical Range of Motion in Asymptomatic Subjects Following Spinal Manipulative Therapy: a Double Blinded Randomised Clinical
Fejer, René	Changes in Range of Motion in the Cervical Spine Following Spinal Manipulation - a Review.
Feldman, AG	Muscles and Coordination
Fenech, Marianne	Hematocrit Determination in Blood Line of Dialysed Patients by Ultrasound
Ferber, R	A Comparison of Comfort and Rearfoot Control in Custom and Non-Custom Foot Orthoses
Ferber, R	Orthotics Alter Lower Extremity Joint Coupling: a Dynamical Systems Approach
Ferber, R	Variables Associated with the Incidence of Lower Extremity Stress Fractures
Ferenczi, Mike	Quantifying Isometric Force-Dependent Energy Release in White Muscle by Comparing Contraction Energetics in Intact and Skinned Fibres
Ferguson, Stephen J	Convective Molecular Transport in the Intervertebral Disc
Fernandez, Julio M	A Unique Sequence of Titin, the Pevk-Domain, is An Entropic Spring That Interacts with Actin
Fernandez, JW	Efficient Finite Element Customisation of a Generic Femur Using the Host Mesh Technique
Fernandez, JW	Geometric Modelling of Skeletal Muscle Using Hermite Elements.
Fernando, Carlos	Biomechanics of the Karate Front Kick
Ferrara, M	A Comparison Between Single-Radius and Multi-Radius Total Knee Arthroplasties for Stand To Sit (An EMG and Kinematic Study)
Ferris, Daniel P	A Comparison of EMG Control Between Distal and Proximal Muscles of the Upper Limb
Ferris, Daniel P	Artificial Neural Oscillators as Controllers for Locomotion Simulations and Robotic Exoskeletons
Fialho, Cíntia Brino	Postural Alignment with Different Shoes and Barefoot
Fink, Ulrich	Development of Orthopedic Implants - a Field of Tension Between Risk Assessment, Pre Clinical and Clinical Testing
Fink, Ulrich	Rapid Manufacturing of Bone Nails with Improved Mechanical Properties
Finley, Margaret A	Glenohumeral Joint Laxity with and Without Rotator Cuff Contraction
Finley, Margaret A	Upper Extremity Impairment in Wheelchair Propulsion
Finley, Margaret A	Wheelchair Propulsion Biomechanics with Upper Extremity Impairment and Fatigue
Finni, Taija	Effects of Contraction History on Fascicle Behavior in Shortening Contractions
Finni, Taija	Jumping Intensity Determines the Behavior of the Fascicle and Tendon Parts of the Vastus Lateralis Muscle
Fioretti, Sandro	Study of Postural Stability by Chaos Theory

Fischer, Alfons	The Acting Wear Mechanisms on Metal-On-Metal Hip Joint Bearings
Fischer, David	Dynamics of Wound Healing in Airway Epithelial Cells: Gfp-Actin Remodeling
Fischer, Paul F	Numerical Simulation of Cerebrospinal Fluid Motion Within a Healthy and Diseased Spinal Canal
Fischer, Paul F	Turbulence Induced Vein-Wall Vibration May Play a Role in Arteriovenous Dialysis Graft Failure
Fischer, Paul	Unstructured Hexahedral Mesh Based on Conduction Temperature Distribution
Fish, Melanie	Estrogen Depletion is Associated with Changes in Osteon Morphology
Fisher, Charles	Are Spinal Facet Loads Influenced by the Fixation Method?
Fisher, Charles	Evaluation of Spinal Implants - Vertebral Bone Density is An Important Factor
Fisher, Charles	Spinal Canal Occlusion in Flexion-Compression : the Effect of Injury Mechanism in An Upper Thoracic Spine Experimental Model
Fisher, Charles	The Effect of a Novel Cage Design on Stabilization in the Lumbar Spine
Fisher, Charles	The Effect of Plate Design, Endplate Preparation and Bone Mineral Density on Immediate Stabilization in An Anterior Cervical Plate Fixation Model
Fisher, J	Experimental and Finite Element Analysis of the Effect of Muscle Forces on Fixation of Cemented Hip Prostheses At Heel Strike
Fisher, J	Fracture of Zirconia on Alumina Hip Prostheses : the Need for Microseparation Testing
Fisher, J	The Kinematics of Hip Joint Simulator Microseparation
Fisher, J	Tribological Evaluation of Therapeutic Lubricants for the Knee
Fisher, J	Wear of Ceramic Matric Composite Hip Prostheses in Simulators Modelling Laxity
Fisher, John	Biomechanics & Hydrodynamics of Decellularised Porcine Aortic Heart Valves
Fisher, John	Biomechanics & Hydrodynamics Of Decellularised Porcine Aortic Heart Valves
Fisher, John	Influence of Swing Phase Microseparation on the Wear of Ceramic on Polyethylene, Ceramic on Ceramic and Metal on Metal Total Hip Replacements
Fisher, John	Long-Term Simulator Wear Study of Surface Engineered Mom Hip Prostheses
Fisher, John	The Effect of Uhmwpe Material and Knee Design on in Vitro Wear of Fixed Bearing and Rotating Platform Mobile Bearing Total Knee Replacements
Fisher, John	Wear of Crosslinked Polyethylene Under Different Tribological Conditions
Fisher, Jonathan S	The Combined Effects of Disuse and Gonadectomy on Bone Mechanics in Male and Female Rats
Fisk, Jesse	Development of a High Payload Testing System To Study Joint Kinematics and Forces
Fisk, JR	The Resistance of a Knee Joint in Children with Spasticity
Flagler, D	Effect of Swelling Pressure on Dynamic Compressive Stiffness of Lumbar Annulus Fibrosis
Flanagan, Sean P	Contribution of the Hip Extensors, Knee Extensors, and Ankle Plantar Flexors Durig Different Squatting Techniques in Older Adults
Flashner, Henryk	Conflict Between Momentum and Balance Control During Landing
Flaud, Patrice	A Non-Invasive Method for the Blood Viscosity Determination
Fleming, Braden	Acl Strain During Rehabilitation Exercises, in Vivo
Fleming, Braden	The Biomechanics of the Weightbearing Knee
Fletcher, David F	Biomechanics of Perivascular Flow in Syringomyelia
Flivik, Gunnar	The Effect of Changing Anteversion on Forces on the Proximal Femur
Florez, Lucio	Flow Regulation of Gap Junctional Communication and the Functional Compartmentalization of Vascular Endothelium
Fodil, Redouane	A Multi-Segmental Model of the Coupling of Inspiratory Flow with the Compliant Nose Structure Assessed in Vivo.
Fodil, Redouane	Assessment of Structural Viscoelasticity of Cytoskeleton by Tensegrity Model

Frankel, Steven H	Dynamic Ca2+ Response in Vascular Endothelial Cells Subjected To Various Flows
Frankel, Steven H	Numerical Modeling of Pulsatile Turbulent Flows in Stenotic Vessels
Frankel, Steven H	Soluble Proteins Released by Endothelial Cells in Response To Fluid Flow Affect Smooth Muscle Cells
Fraser, Alan	Non-Invasive Measurement of Wave Intensity - Reproducibility and Effect of Gtn
Fraser, Scott E	In Vivo Intracardiac Hemodynamics: Does Flow Influence Morphology?
Frayne, Richard	An Investigation of the Burst Fracture Mechanism Using a Combined Experimental and Finite Element Approach
Frayne, Richard	Insights Into In-Vivo Knee Mechanics with Magnetic Resonance Imaging
Frayne, Richard	Quantifying Bone Trabecular Direction From Radiographs
Frazer, Mardy	Using Cumulative Spinal Loading To Assess Jobs, Engineering, and Administrative Controls: a Spinal Perspective
Fredberg, Jeffrey	Microrheology of the Living Cell: are We Built of Glass?
Fredricson, Michael	Segmental Mobility of the Lumbar Spine During a Prone Press-Up Maneuver in Symptomatic and Asymptomatic Subjects: Assessment Using Dynamic Mri
Frei, Hanspeter	A Biomechanical Study Comparingcortical Onlay Allograft Struts and Plates in the Treatment of Periprosthetic Femoral Fractures
Frei, Hanspeter	Biomechanical Analysis of Fixation of Split-Depression Fractures of the Tibia Plateau
French, Andrew S	Sensory Transduction in An Arthropod Mechanoreceptor System
Frenneaux, Michael	Mutations of Titin Cause Dilated Cardiomyopathy
Frenneaux, Michael	Non-Invasive Measurement of Wave Intensity - Reproducibility and Effect of Gtn
Fridén, Jan	Biological and Biomechanical Response of Rat Dorsiflexors To Eccentric Exercise
Fridén, Jan	Clinical and Basic Science Studies of the Deltoid To Triceps Tendon Transfer
Fridén, Jan	Human Upper Extremity Architecture: Implications for Function and Surgical Reconstruction
Fridén, Jan	Increased Desmin in Rat Dorsiflexors After a Single Bout of Eccentric Exercise
Fridén, Jan	Muscle Cellular and Architectural Changes Due To Chronic Spasticity
Friedman, M H	Effects of Vessel Motion on Right Coronary Artery Hemodynamics
Friedman, Morton H	Wall Shear Stress and Albumin Permeability At the Porcine Aortic Trifurcation
Friedrich, Klaus	Rapid Manufacturing of Bone Nails with Improved Mechanical Properties
Frigo, C	Gait Features Assessment in Hip Osteoarthritis and Total Hip Replaced Patients Based on An Ambulatory System (Physilog)
Frigon, Alain	H-Reflexes in Human Forearm Muscles are Attenuated During Rhythmic Arm Movement
Frühwirth, B	Influence of a Rider To the Back of a Horse in Different Gaits
Frykman, Peter	A Dual Mass Spring - Dashpot Model of the Exchange of Forces Between the Backpack, Hips and Shoulders During Walking
Fu, Freddie H	Development and Validation of An Approach To Record and Reproduce Kinematics
Fujihara, Kazutoshi	Biocompatible Osteosynthesis Plates Using Braided Carbon/Peek Composite
Fujiki, Hiroyuki	Microcrack Detection and Mechanical Property Measurement of Bone Using Scanning Acoustic Microscope
Fujimoto, Shinichi	Non-Invasiveassessment of Left Ventricle Function with a Computational Fluid Dynamic Model
Fujio, Jerry	Altered Nana-Order, Micro-Mechanical Property of Pulmonary Artery Smooth Muscle in Primary Pulmonary Hypertension
Fujioka, Hideki	Flow-Induced Morphological Change of Endothelial Cell and Shear Stress Distribution on the Surface of the Cell
Fujioka, Hideki	New Method of Three-Dimensional Imaging of Small Airways in Rats with X-Ray Micro-Ct

Fyfe, D	Foot Roll Over Shapes In Transtibial Amputees: Implications For Prosthetic Alignment
Fyhrie, David P	The Mechanisms and Significance of the Correlation Between Bone Strength and Stiffness

G

Gabel, Udo	A Vertebral Body Replacement for in Vivo Load Measurement
Gabriel, Mary T	Development and Validation of An Approach To Record and Reproduce Kinematics
Gadareh, Kuros	A Biomechanical Study Comparingcortical Onlay Allograft Struts and Plates in the Treatment of Periprosthetic Femoral Fractures
Gagey, Olivier	Protocol for in Vivo Optoelectronic Kinematics Analysis of Shoulder
Gagnon, Denis	Active Movements of the Shoulder Girdle in Healthy Subjects: a Validity Study
Gagnon, Micheline	Learning Processes and Biomechanical Changes While Handling Asymmetrical Loads
Galik, Karol	Effect of Polyethylene Thickness on Stresses of An Ankle Joint Implant
Galik, Karol	Origins of Bipedalism: Evolutionary Morphology Through Finite Element Analysis
Gallant, Troy	Development and Validation of a Joystick Dynamics Model To Predict Operator Input Torque
Gallet, François	Cell-Immersed Microbeads Used as Probes of Cytoskeleton Mechanical Properties
Galli, Manuela	Overweight and Obesity in Posture: a Biomechanical Evaluation of Spine Angles
Galvin, Alison	Wear of Crosslinked Polyethylene Under Different Tribological Conditions.
Gamer, Laura	Molecular and Cellular Analysis of Rotator Cuff Tendinosis in a Rat Overuse Model
Gandevia, SC	Mechanical Coupling of Human Muscles At Very Low Forces
Gao, Fan	Wrenches At the Digit-Object Interface During Prehension
Gao, Yuxin	Effect of Flow Pattern on Vasoactive Mediators Secretion of Cultured Endothelial Cells
Gapeyeva, Helena	Vertical Jumping Performance in 8-12-Year-Old Rhythmic Gymnasts
Garanich, Jeff	Fluid Shear Stress Affects Vascular Smooth Muscle Cell Function
Garbuz, Donald S	A Biomechanical Study Comparingcortical Onlay Allograft Struts and Plates in the Treatment of Periprosthetic Femoral Fractures
Garceau, P	Muscles and Coordination
Garcia, A	Comparison of Scaffold Designs for Tissue-Engineered Small-Diameter Graft Applications
Garcia, Marco A C	Modification in the Postural Control During Long-Term Standing
Garcia, Mariano S	Scaling of Damping: Implications for Stability
Gardiner, John	Subject-Specific Finite Element Modeling of the Human Medial Collateral Ligament
Gardner-Morse, Mack	Spinal Stiffness Increase with Axial Load: Another Stabilizing Consequence of Muscle Activation
Garg, Sunil	Head, Trunk and Pelvis Kinematics During Rapid Head Turning in Standing and Walking
Garitey, Vincent	Hydrodynamics of Mitral Prosthetic Heart Valves: Comparison of Normal Conditions with Atrial Fibrillation Varying the Heart Rate
Garitey, Vincent	Incidence of Valve Prosthesis Incline on Left Ventricle Flow Dynamics
Garland, Phil	Development and Validation of a Joystick Dynamics Model To Predict Operator Input Torque
Garman, Russell	Genetic Variations Influence Bone's Sensitivity To the Loss of Functional Weightbearing
Garry, Joe	Neuromuscular Responses To Knee Osteoarthritis During Stairway Locomotion

Gregor, Robert J	Mechanical Energy Transfer by Two-Joint Leg Muscles During Snatch Lift
Gregor, Robert J	Tai Chi Exercise and the Prevention of Falls in Elderly Transitioning To Frailty
Gregorio, Carol C	Titin Interacts with Murf-1 To Regulate Sarcomeric M-Line and Thick Filament Structure
Greidanus, Nelson V	A Biomechanical Study Comparingcortical Onlay Allograft Struts and Plates in the Treatment of Periprosthetic Femoral Fractures
Grenier, Sylvain G	Coordination of Muscle Activation To Assure Stability of the Lumbar Spine
Grenier, Sylvain G	The Role of Transversus Abdominis in Spine Stability
Griffin, Lanny	Estrogen Depletion is Associated with Changes in Osteon Morphology
Griffith, LG	Computational Modeling of Flow and Mass Transport in a Microfabricated Array Bioreactor for Perfused 3-D Liver Culture
Griffith, T M	Effect of Body Posture on Geometry of the Abdominal Aortic Bifurcation
Grigg, Peter	Measurement of Poisson's Ratio in Rabbit Achilles Tendon
Grigioni, Mauro	Laser Doppler Anemometry in the Evaluation of Mechanical Heart Valves' Hemodynamics
Grill, Franz	Walking with Platform Shoes - Normal Walking Pattern?
Grimberg, Jean	A 3D Finite Element Model of An Implanted Scapula Using Cadaveric Data for Evaluation
Grimberg, Jean	Protocol for in Vivo Optoelectronic Kinematics Analysis of Shoulder
Grimes, Marguerita	Ecm(Extracllular Matrix) Scaffolds for Tissue Engineering: Biocompatibility and Biodegradability
Grimm, C M	Contact Areas and Ligament Lengths are Abnormal in Patients with Malunited Distal Radius Fracture Despite Normal Radioulnar Kinematics
Grimm, Michele J	The High Frequency Material Properties of Brain Tissue as Determined by Ultrasound
Grimm, Michele J	Ultrasonic Assessment of White Matter Properties as a Function of Axonal Orientation
Grodesky, Janene	Variability and Stability Change with Walking Velocity - What is the Relationship Between the Two?
Grodzinsky, Alan	Cartilage Nanomechanics, Mechanotransduction, And Tissue Engineering
Grodzinsky, Alan	Response Of The Chondrocyte To Mechanical Stimuli: Physiologic And Injurious Compression
Grondin, Diane	Determination of the Optimal Forearm Muscles To Monitor with EMG in Ergonomic Studies
Groot, Gert	Prediction of the Metabolic Energy Curve During Running Against Inclines: Implications for Delta Efficiency
Gross, M Melissa	Effect of Expressiveness on the Kinematics of Arm Gestures
Grossman, Debbie	Computational Modelling of Blood Flow and Atery Wall Interaction
Grotberg, James B	Alveolar Transport During Total Liquid Ventilation
Grotberg, James B	Cycle-Induced Flow and Transport in An Alveolus for Partial Liquid Ventilation
Grotberg, James B	Effect of Ventilation on Instilled Liquid Transport in the Pulmonary Airways of Rats
Grotberg, James B	Gravity Effects on Liquid Plug Transport and Distributions in Airway Models
Grotberg, JB	Limitation of Expriatory Flow in Liquid Ventilation
Gruben, Kreg	Pedal Motion Direction and the Control of Foot Force During Pedaling
Grunnet-Nilsson, Niels	Cervical Range of Motion in Asymptomatic Subjects Following Spinal Manipulative Therapy: a Double Blinded Randomised Clinical
Grzybowski, Deborah M	Wall Shear Stress and Albumin Permeability At the Porcine Aortic Trifurcation
Gu, Wy	Effect of Swelling Pressure on Dynamic Compressive Stiffness of Lumbar Annulus Fibrosis
Gu, Wy	Electrical Conductivity of Lumbar Annulus Fibrosis

Guan, L	An Approach for Improving the Performance of Polymeric Macroporous Scaffolds For in Vitro and in Vivo Bone Tissue Engineering Applications
Guanche, Carlos A	Increasing Age Slows Recovery of Function Following Achilles Tendon Injury in the Rat
Guillet, Marc	Segmental Mobility of the Lumbar Spine During a Prone Press-Up Maneuver in Symptomatic and Asymptomatic Subjects: Assessment Using Dynamic Mri
Guimarães, Antônio C S	Mechanomyographic Signals of the First Dorsal Interosseus Muscle During Isometric Voluntary Contractions
Guimarães, Antônio C S	Effective Force and Index of Effectiveness During Cycling
Guise, JA de	A Reproducible Method To Define a Coordinate System for 3D Kinematics Evaluation of the Knee
Guise, JA de	Three Dimensionnal Reconstruction of the Knee From Biplanar X-Rays
Guise, Jacques De	Evaluation of 3D Knee Kinematics with and Without Plantar Orthopaedic Processing
Guitong, Yang	Wolff's Law
Guixing, Qiu	EMG Changes in Paraspinal Muscle of Scoliosis Patients After Spinal Fusion
Guldberg, Robert	Effect of Perfusion Rate on Cell Seeded 3D Constructs in Vitro
Gulesarian, Kristine	The Role Of Dynamnic Stresses During Incubation In Increasing Tehv Tissue Strength
Gumidyala, Krishna	Pilot Study of Intracellular Signaling in Post-Operative Tendons
Gundiah, Namrata	Determination of Elastin and Collagen Content in Porcine Aorta
Gundiah, Namrata	The Contribution of Elastin and Collagen To Residual Strain in Porcine Aorta
Guo, Jiqing	Effects of Sarcomere Length, Ca2+ and Stimulation Rate on Force Generation of Mouse Cardiac Muscle
Guo, LY	Modeling of Manual Wheelchair Propulsion Using Optimization
Guppy, DrKern	Effect of Osteoporosis in a Disc - Degenerated Lumbar Spine
Gupta, Sameer	Directional Dependence of Early Fatigue Damage in Cemented Total Hip Replacements
Gupte, Chinmay	Investigations of Some Posterior Ligamentous Structures of the Knee
Guterl, Kathryn A	Candidate Mechanical Stimuli for Hypertrophy During Early Volume Overload
Guterman, Lee	The Hemodynamic Effects of Parent Vessel Inflow Angle on a Cerebral Sidewall Aneurysm
Gutierrez, Elena M	Center of Mass Displacement During Gait: Normal and Myelomeningocele
Gutierrez, Elena M	Measuring Center of Mass Displacement During Gait: Whole-Body Kinematic Model Vs. Ground Reaction Force Calculation

H

Haan, Arnold de	Bilateral Deficit in Maximum Isometric Force, Neural Drive and Rate of Force Development
Haas, Brian D	In Vivio Determination of Polyethylene Bearing Motion Realtive To the Tibia and the Femur
Haas, Brian D	In Vivo Forces and Motions From Fluoroscopy and Mathematical Modeling
Haber, Idith	Three-Dimensional Kinematics of Right Ventricular Systolic Contraction
Haberstroh, Karen M	Dynamic Ca2+ Response in Vascular Endothelial Cells Subjected To Various Flows
Haberstroh, Karen M	Functional Changes in Kidney Cells in Response To Sustained Hydrostatic Pressure
Haberstroh, Karen M	Soluble Proteins Released by Endothelial Cells in Response To Fluid Flow Affect Smooth Muscle Cells
Haberstroh, Karen	Numerical Modeling of Pulsatile Turbulent Flows in Stenotic Vessels
Hadcock, Lindsay	Development of a Trifilar Pendulum for Measuring Moment of Inertia

Hadcock, Lindsay	Pressure Distribution Measurement for Design of Waist Belts in Personal Load Carriage Design
Haddad, Jeffrey M	Issues in the Interpretation of Continuous Relative Phase
Haenen, W P (Wouter)	Stability of Bipedal Stance; the Contribution of Co-Contraction and Spindle Feedback
Haga, Hisashi	Time-Lapse of Cellular Stiffness Measured with Scanning Probe Microscopy
Hagberg, Mats	Measurement Differences Between Two Wrist Goniometers During Pronation & Supination
Hagemeister, Nicola	A Reproducible Method To Define a Coordinate System for 3D Kinematics Evaluation of the Knee
Hagemeister, Nicola	Evaluation of 3D Knee Kinematics with and Without Plantar Orthopaedic Processing
Haglund-Åkerlind, Yvonne	Center of Mass Displacement During Gait: Normal and Myelomeningocele
Haglund-Åkerlind, Yvonne	Measuring Center of Mass Displacement During Gait: Whole-Body Kinematic Model Vs. Ground Reaction Force Calculation
Hahn, Michael E	A Parameter To Describe Coordination of Hip and Knee Flexion During Obstructed Gait
Hahn, Michael E	Subtle Effect of Walking Speed on Medio-Lateral Center of Mass Motion in Young Adults
Haid, Christian	Correlation Between Radiographic and Clinical Measurement of Sagital Back Shape
Haj, AJ El	Cyclic Strain and Fluid Flow Induce Different Responses in Human Bone Cells
Haklai, R	Ecs Adhesion on Silicone Rubber-Rtv 615: a Systematic Study
Hale, Joseph E	Dynamic Testing of Rat Achilles Tendons
Hale, Joseph E	Increasing Age Slows Recovery of Function Following Achilles Tendon Injury in the Rat
Halford, G	Foot Roll Over Shapes In Transtibial Amputees: Implications For Prosthetic Alignment
Halford, G	Mechanical Energy Loss At The Stump-Socket Interface In Transtibial Prostheses
Hall, Harry	Pertrochanteric Fracture Fixation: Effects of Implant Design on Cut-Out Failure Under Dynamic Loading
Hall, Richard M	Analysis of Wear Performance in Total Hip Replacement
Hall, Richard M	Synergistic Effect of Spatial Resolution and Noise on the Precision and Accuracy of Measurements in Simulated Digital
Hall, RM	Cell Seeded Plasma-Treated Polyester Ligament Under Cyclic Tensile Load-Commissioning of Methodology
Hall, RM	Mathematical Models for the Time-Dependent Characteristics of Spinal Cord Tissue
Halliwell, M	Three-Dimensional Acoustic Microscopy of the Intervertebral Disc: Visualisation of Lamellae, Collagen Bundles and Lesions.
Halliwell, Mike	A New Method for Quantifying Fibre Bundle Orientation Within Intact Intervertebral Discs Using 3-D Scanning Acoustic Microscopy.
Halpern, D	The Effect of Pulsatile Bubble Motion on Surfactant Distribution During Airway Reopening
Hamada, H	Biocompatible Osteosynthesis Plates Using Braided Carbon/Peek Composite
Hamel, Andrew J	In-Vitro Measurements of Tarsometatarsal Joint Stiffness
Hamel, Andrew J	Plantar Aponeurosis Forces During Simulated Walking
Hamill, J	Variables Associated with the Incidence of Lower Extremity Stress Fractures
Hamill, Joseph	Influences of Gender and Exercise on ACL Laxity
Hamill, Joseph	Issues in the Interpretation of Continuous Relative Phase
Hamill, Joseph	Muscle Activation Levels During Running in Varus, Valgus, and Neutral Wedged Shoes

Hardin, E C	Lower Extremity Forces During An Automobile Collision: the Influence of Muscle Properties
Hardy, Warren N	Comparison of Relative Motion Between the Brain and Skull of the Human Cadaver for Rotation in the Coronal and Sagittal Planes
Harf, Alain	A Multi-Segmental Model of the Coupling of Inspiratory Flow with the Compliant Nose Structure Assessed in Vivo.
Haridas, Carlos	Compensatory Corrective Responses Induced by Cutaneous Nerve Stimulation in the Hand and Foot During Walking
Harman, Everett	A Dual Mass Spring - Dashpot Model of the Exchange of Forces Between the Backpack, Hips and Shoulders During Walking
Harrison, Anne L	A Comparison Between Gait Kinetics in Women with Primary Osteoarthritis and Women with Osteoporosis
Hart, DA	An Axisymmetric Biphasic Model of Load Bearing in the Knee Joint
Hart, DA	Influence of Glucocorticoid Pretreatment on De-Repression of Gene Expression in Meniscal Explants After Removal From Biomechanical Loading
Hart, DA	Ligament Autograft Cells Do Not Die by Apoptosis
Hart, DA	The Healing of ACL and Mcl Injuries is Initially Similar But Diverges with Time
Hart, David A	Cyclic Hydrostatic Pressure Increases Both MMP-1 and MMP-3 Mrna Levels, in Mg-63 Osteoblast-Like Cells Under Serum Free Conditions.
Hart, Jurgen de	Fluid-Structure Interaction And Collagen Remodeling In The Aortic Heart Valve
Hart, Michael	Biomechanics of the Karate Front Kick
Hartwig, Erich	Discoligamentous Structures of the Lower Cervical Spine Get Injured in In Vitro Low-Speed Side Collisions
Harwood, Claire L	New Energetics Approaches To Elucidating Mechanisms of Contraction and Relaxation
Hasegawa, Masamitsu	Biomechanical Properties of Acellularized Heart Valves as Bioscaffolds
Hasenkam, J Michael	High-Frequency Pressure Fluctuations Measured in Heart Valve Patients
Hashimoto, Katsushi	Altered Nana-Order, Micro-Mechanical Property of Pulmonary Artery Smooth Muscle in Primary Pulmonary Hypertension
Hashimoto, Ken	Altered Nana-Order, Micro-Mechanical Property of Pulmonary Artery Smooth Muscle in Primary Pulmonary Hypertension
Hashimoto, Ken	Ca2+ Responses and Its Propagation in Cultured Endothelial Cells To Cytosolic Mechanical Stimulation by Laser Tweezers
Hashimoto, Reiji	Rescue by Transplantated Endothelial Cells for Ischemic Renal Failure Visualization of Peritubular Capillaries Using Intravital Videomicroscopy
Hashimoto, Shigehiro	Measurement of Erythrocytes Deformability with Counter-Rotating Parallel Disk System
Hashimoto, Shigehiro	Wave-Form Analysis of Electrocardiograph with Spectrum for Screening Test
Hasler, Evelyne M	Prediction of Optimized Diameter of Osteochondral Plugs in Cartilage Repaire
Hassan, Abdel	Finite Element Analysis of Glenoid Component Version in Total Shoulder Arthroplasty
Hassan, Serhan	Direct Augmentation Restores the Structural Response of Failed Metastatic Defect Vertebrae
Hassan, Serhan	Does Vertebroplasty Alter the Mechanical Response of Osteopenic Vertebrae
Hasselquist, Leif	The Cervical Muscle Response During "Whiplash Simulated Motion" with Respect To Gender
Hasselquist, Leif	Understanding the Relationship of Mass Properties To the Metabolic Cost of Load Carriage: Moment of Inertia
Hasser, Eileen M	The Combined Effects of Disuse and Gonadectomy on Bone Mechanics in Male and Female Rats
Hastings, Mary K	Comparison of Models for the Stress-Strain Relationship of Soft Tissue

Heathfield, T F	Evidence for Differences in Matrix Turnover in the Developing and Degenerating Human Lumbar Intervertebral Disc
Hébert, Luc J	Active Movements of the Shoulder Girdle in Healthy Subjects: a Validity Study
Hefzy, Mohamed Samir	A Three-Dimensional Mathematical Dynamic Simulation of the Knee Extension Exercise: Effects of Anterior Cruciate Ligament
Heiberg, Einar	Kinematics of the Heart
Heiderscheit, Bryan C	Issues in the Interpretation of Continuous Relative Phase
Heiderscheit, Bryan	Ankle Kinematics Using One and Two Segment Foot Models
Heil, Matthias	3D Airway Reopening: the Steady Propagation of An Air Finger Into a Strongly Collapsed Elastic Tube
Heil, Matthias	Finite Reynolds Number Flows in Three-Dimensional Collapsible Tubes
Heil, Matthias	Three-Dimensional Airway Closure: Surface-Tension-Driven Non-Axisymmetric Instabilities Of Liquid-Lined Elastic Tubes
Heine, Richard	An EMG-Driven Biomechanical Model of the Human Elbow: Fitting a Generic Model To Specific Subjects
Heiner, Anneliese	Shear Stress Stimulates Oxidant Production in Human Cartilage Explants
Heini, Paul F	Occlusion of Vertebral Endplate Openings: a Mechanism for Intervertebral Disc Degeneration?
Heinrich, Volkmar	Leukocyte Tethering Under Flow: Model for Interfacial Compression, Viscoelastic Tether Extension, and Cytoskeletal Unbinding
Heinrichs, Bradley E	Head Restraint Position Affects Occupant Response in Rear-End Collisions
Heir, Stig	3D Motion Reconstruction From Uncalibrated 2d Video Sequences - Application To Freestyle ACL Injury Situations
Heise, Gary D	Differences in Ankle and Knee Joint Stiffness Between Strength-Trained and Aerobic-Trained Athletes When Hopping At a Preferred Frequency
Heisey, Dennis	A Comparison of Joint Mechanics Between Anterior Cruciate Ligament Intact and Deficient Stifles: a New Model of Anterior Cruciate Ligament Disruption
Heisey, Dennis	Testing Duration Required To Accurately Predict Ligament Viscoelasticity
Heliams, DB	How Economical is Human Bipedal Locomotion?
Hellmich, Christian	Scale Transition in Bone Elasticity: a Continuum Micromechanics Approach
Helminen, HJ	Collagen Network and Mechanical Properties of Articular Cartilage: Experimental and Numerical Study
Helminen, Taija	Molecular Biology of Biomaterial Incorporation with Bone
Helmke, Brian P	Shear Stress-Induced Strain Focusing in the Endothelial Cytoskeleton
Helmke, Brian P	The Convergence of Cardiovascular Genomics and Endothelial Biomechanics
Hennig, Ewald M	Effect of Physical Therapy and Afferent Stimulating Insoles on Motor Abilities in Parkinson Patients
Hennig, Ewald M	Measurement of Inversion and Eversion Movements of the Foot by Using a Position Transducer
Hennig, Ewald M	Plantar Pressures, Shock and Rearfoot Motion During Running are These Meaningful Quantities for the Prediction of Running Injuries
Hennig, Ewald M	Pressure Patterns Under the Feet of Children, Adults and Overweight Persons - the Influence of Gender -
Hennig, Ewald M	The Use of Skin Pre-Tension To Modify Tibial Bone Acceleration Estimates
Hénon, Sylvie	Cell-Immersed Microbeads Used as Probes of Cytoskeleton Mechanical Properties
Henry, Frank S	Stretch-And-Fold Fractal-Like Aerosol Bolus Spreading in the Rythmically Expanding Alveolated Duct
Herbert, RD	Mechanical Coupling of Human Muscles At Very Low Forces
Herr, Hugh M	Does Leg Retraction Simplify Control in Running?
Herr, Hugh M	Local Feedback Mechanisms for Stable Bouncing
Herr, Hugh M	Running Stability: Limb Rotational Control in Quadrupedal Animals

Herrala, M	The Force-Velocity Relation Studied with a Pneumatic Leg-Extension Device
Herring, Ian P	Computational Modeling and Experimental Validation of Human Eye Interaction with High-Speed Foam Particles
Herrmann, Ariel M	Computer Simulation of the Extensor Carpi Ulnaris Transfer To Extensor Carpi Radialis Brevis
Hertsted, Suzanne	Compressive Biomechanics of Fracture and Neurologic Integrity in the Pediatric Spine
Hertsted, Suzanne	Effect of Strain Rate on Cervical Spine Tensile Mechanics
Hertzberg, Jean	Echo-PIV(r): a Novel Method for the Non-Invasive Measurement of Velocity Vectors Using Ultrasound Imaging
Herzog, Walter	A Transversely Isotropic and Transversely Homogeneous Model of Cartilage Including Chondrocytes and a Statistical Distribution of Collagen Fibres
Herzog, Walter	Acute Bout of Eccentric Exercise in the Rabbit Ta Shows Concomitant Fiber Length Shortening and a Subsequent Shift in the Force-Length Relationship
Herzog, Walter	Antagonistic Muscle Activity in Three-Dimensional Models of the Muscloskeletal System
Herzog, Walter	Biomechanical Modeling of Articular Cartilage: From Macroscale To Microscale
Herzog, Walter	Cartilage Deformation of the Feline Patellofemoral Joint Obtained From Laser Scanning
Herzog, Walter	Changes in H-Reflex Amplitude After Spinal Manipulation in Healthy and Pathological Subjects
Herzog, Walter	Coordination of Cat Gastrocnemius and Soleus During Locomotion Based on Direct Measurement of in Vivo Muscle Forces and
Herzog, Walter	Determining Patterns of Motor Unit Recruitment During Animal Locomotion
Herzog, Walter	Effects of Stretching and Shortening on Isometric Forces on the Descending Limb of the Force-Length Relationship in Cat Soleus
Herzog, Walter	Force Depression Following Muscle Shortening of Electrically Stimulated and Voluntarily Activated Human Adductor Pollicis
Herzog, Walter	Force Enhancement During and Following Eccentric Muscle Contraction
Herzog, Walter	Force Enhancement in Single Skeletal Muscle Fibres on the Ascending Limb of the Muscle Force-Length Relationship
Herzog, Walter	History-Dependence of Force Production in Skeletal Muscle
Herzog, Walter	In Vivo Changes in Muscular Activation Before and After Anterior Cruciate Ligament Transection in the Feline Hindlimb
Herzog, Walter	In Vivo Rabbit Patellafemoral Joint Loading Via Surface Stimulation
Herzog, Walter	In-Situ Chondrocyte Deformation in Early Stage Osteoarthritic (Oa) Articular Cartilage
Herzog, Walter	Modeling and Visualization of the Mechanical Behaviour of Skeletal Muscle using a Continuum Approach
Herzog, Walter	Prediction of Optimized Diameter of Osteochondral Plugs in Cartilage Repaire
Herzog, Walter	The Behavior of Individual Sarcomeres After Stretch in Activated Skeletal Muscle Myofibrils
Herzog, Walter	Variations in the Superimposed Twitch Technique At 100% Mvc
Heschel, Ingo	Geometrically Defined 3-Dimensional Collagen Scaffolds for Tissue Engineering
Heys, Jeffrey J	Aqueous Humor Flow and Passive Iris Deformation
Hijazi, Ibraheem	Investigations of Some Posterior Ligamentous Structures of the Knee
Hilibrand, Alan S	The Impact of Anterior Cervical Fusion Upon Cervical Spine Range of Motion and Overall Neck Flexibility
Hill, NA	A Model for the Development of Intimal Hyperplasia
Hill, NA	Remodelling and Deformation of the Abdominal Aortic Aneurysm

Hille, Ekkehard	Robotic Assisted Versus Manual Implantation - a Prospective Study in Primary Total Hip Replacement
Hillstrom, Howard J	Biomechanical Assessment of the Ankle and Knee During Landing From a Lateral Drop Jump with a Prophylactic Ankle Brace
Himburg, Heather A	Wall Shear Stress and Albumin Permeability At the Porcine Aortic Trifurcation
Himeno, Ryutaro	Flow Due To a Peristaltic Wave in a Tube
Himeno, Ryutaro	Flow in a Realistic Mri-Based Vascular Branch
Himeno, Ryutaro	Multi-Scale Computational Hemodynamics in Cardiovascular System
Himeno, Ryutaro	New Method of Three-Dimensional Imaging of Small Airways in Rats with X-Ray Micro-Ct
Himeno, Ryutaro	Non-Invasiveassessment of Left Ventricle Function with a Computational Fluid Dynamic Model
Himeno, Ryutaro	Separation Patterns in An Arterial Branch Model
Hin, M	Mechanical Properties and Permeability of Polyelectrolyte Microcapsules (PEMC)
Hinder, Mark R	Dynamics Rather Than Equillibrium Point is Controlled in Human Movements
Hingorani, Rittu	Size Effects in Nonlinear Viscoelasticity
Hinrichs, Richard N	Factors Related To Ball Velocity During An Instep Soccer Kick
Hinse, Sébastien	A Color-Coded Video-Based System for Posture and Foot Assessment
Hintermann, Beat	Biomechanical Properties of Total Ankle Arthroplasty and Ankle Arthrodesis
Hinton, DP	Diseased Human Carotid Bifurcations: Histological Correlations To Hemodynamic Factors
Hinz, Barbara	Biodynamic Data Set for Modelling Car Drivers
Hiraizumi, Yutaka	Stiffness Change with Cage Configuration for Anterior Lumber Interbody Fusion
Hirano, Yoichi	Alpine Ski Racing and Optimal Control
Hirasawa, Shin	Comparative Study Between Intra- and Post-Operative Knee Motions After Total Knee Arthroplasty
Hirsch, BE	The Level of Symmetry in the Anthropometric and Mechanical Properties of the Ankle as Determined by a Mechanical/Mri
Hirsch, J	How Networks of Cortical Activity Adapt in Response To Changes In the Type and Quality of Sensory Input During Dynamic Precision Pinch
Hirschl, RB	Limitation of Expriatory Flow in Liquid Ventilation
Hirvonen, J	Mechano-Acoustic Characterization of Normal, Degenerated and Repaired Cartilage
Hishida, Makoto	Flow Distribution in a Right Angle Branch During Oscillatory Flow
Ho, Henry	Fatigue and Wear Evaluation of a Novel Artificial Finger Joint
Ho, Hong-Chang	A Study of Passive Repeatedly Plyometric Method for Training Upper Arm's Strength and Power
Ho, Wei-Hua	A Study of Passive Repeatedly Plyometric Method for Training Upper Arm's Strength and Power
Hodge, W Andrew	Kinematic Observations Across the Spectrum of Total Knee Replacements
Hodges, ANH	The Effects of Stick Construction in the Performance of Ice Hockey Wrist Shot
Hodges, Paul W	Pain and Motor Control of the Spine: Effect and Mechanisms
Hodges, SR	Spreading and Peeling Dymanics in a Model of Cell Adhesion
Hodgson, Antony J	Linear Model of Resistance To Passive Stretching in Individuals with Brain Injury: Reliability & Validity
Hoff, William	Global Optimization for Recovering the Position and Orientation of Free-Form Objects in Medical Imaging Registration Using a New Smoothing Approach
Hoff, William	Verification of Three-Dimensional Joint Kinematics Determined Using Fluoroscopy: An Error Analysis
Hoffman, Allen H	Measurement of Poisson's Ratio in Rabbit Achilles Tendon
Hoffman, Kenneth	The Hemodynamic Effects of Parent Vessel Inflow Angle on a Cerebral Sidewall Aneurysm

Hoffmann, Jürgen	Rapid Manufacturing of Bone Nails with Improved Mechanical Properties
Hoffmann, Kenneth R	Modeling of Flow in Cerebral Sidewall Aneurysms: Effect of Aneurysm Size
Hogan, Harry A	Alcohol and Ovariectomy Effects on Trabecular Bone in Female Rats
Hoi, Yiemeng	Modeling of Flow in Cerebral Sidewall Aneurysms: Effect of Aneurysm Size
Hoi, Yiemeng	The Hemodynamic Effects of Parent Vessel Inflow Angle on a Cerebral Sidewall Aneurysm
Hol, Adrienne T	Motor Adaptations To Changes in Limb Mechanical Properties During Voluntary Gait Modifications
Holden, Simon	Three Dimensional Computer Modelling of the Human Anatomy
Holdsworth, David W	Computed Blood Flow Dynamics in An Anatomically Realistic Cerebral Aneurysm
Hollander, A Peter	Prediction of the Metabolic Energy Curve During Running Against Inclines: Implications for Delta Efficiency
Hollander, A	Evidence for Differences in Matrix Turnover in the Developing and Degenerating Human Lumbar Intervertebral Disc
Hollister, Scott J	Design Method of Porous Scaffold Microstructure Using Computational Simulation for Bone Regeneration
Holm, Allison Kaigle	In Vivo Quantification of Disc Bulging in Different Annular Regions Along a Radial Path
Holm, Sten	In Vivo Quantification of Disc Bulging in Different Annular Regions Along a Radial Path
Holm, Sten	The Sacroiliac Joint, Intervertebral Disc and Muscle Reflexes
Holmes, Jeffrey	Candidate Mechanical Stimuli for Hypertrophy During Early Volume Overload
Holmes, Jeffrey	Engineered Tissues as Model Systems for Studying Myocardial Biomechanics
Holmes, Philip	Self-Stability Mechanisms for Sensor-Cheap Legged Locomotion
Holst, Hans von	Influence of Impact Direction and Duration To the Human Head in Evaluation of Head Injury Criteria: a Numerical Study
Holt, C A	A Method for Studying 3D Movement of the Spine in Vitro
Holt, C A	Anterior Interbody Fusion with Transfacet Screws: a Biomechanical Study
Holt, C A	Comparison of Fixed and Rotating Bearing Knee Replacements In-Vivo Using a 3Dmotion Analysys Technique: Preliminary Results
Holt, Peter	The Assessment of Spinal Motion During Rowing
Homma, Kazuaki	Class Vi Myosin Moves Processively Along Actin Filaments Backwards with Large Steps
Homma, Kazuaki	Myosin V Truncation Mutant with Only One Iq Motif Can Processively Move Along An Actin Filament with 36 Nm Steps
Hondzinski, Jan	Comparing Movements Across Three Visual Conditions in a Step and Reach Task
Hong, Jung Hwa	Design of Air Seat Cushion Orthosis for Plegia
Honl, Matthias	Robotic Assisted Versus Manual Implantation - a Prospective Study in Primary Total Hip Replacement
Hopcroft, R	Dynamic, Biomechanical Characteristics of Human Ankle Ligaments
Hopcroft, R	Failure Analysis of the Lower Limb in Axial Impact Loading
Hopkins, Andrew	Bone Resorption in Shoulder Surface Replacement Arthroplasty
Hopkins, Andrew	Finite Element Analysis of Glenoid Component Version in Total Shoulder Arthroplasty
Hopkins, L	The Hemodynamic Effects of Parent Vessel Inflow Angle on a Cerebral Sidewall Aneurysm
Horak, Fay B	Scaling of Human Postural Control Responses Due To Biomechanical Constraints
Horger, M	The Effects of a Home-Based Forced-Use Intervention on Individuals with Cerebrovascular Accident

Huang, J T	Standing Balance Control Under a Concurrent Attentional Task in Children and Adults
Huang, Jun	Kinetic Measurements of Surface-Bound P-Selectin/Ligand Interactions
Huang, PJ	Gait Analysis After Triple Arthrodesis
Huang, Tsung-Jen	A Biomechanical Analysis of Triangulation of Anterior Vertebral Double-Screw Fixation
Huang, Xiaolin	Structural Testing for Symmetry of the Hips by Vibration Technique
Huang, Xuemei	Forward Dynamic Modeling of Acute Injury: Effective Methods for Optimization, Validation, and Experimentation
Huang, Zheng-Ming	Biocompatible Osteosynthesis Plates Using Braided Carbon/Peek Composite
Hubbard, Mont	Optimal Discus Release Conditions Including Pitching-Moment-Induced Roll
Huber, P	Effect of Head Restraint Properties on Tissue Deformations in the Cervical Spine in Rear-End Motor Vehicle Impacts
Hubley-Kozey, Cheryl	Temporal Activation Pattern Differences Between Those with and Those Without Chronic Low Back Pain
Hubley-Kozey, CL	Knee Joint Kinematics and Kinetics in Patients with Moderate Osteoarthritis
Hubley-Kozey, CL	Lower Limb Energetics of Normal and Moderate Oa Subjects
Hubley-Kozey, CL	Temporal Pattern Recogntion Techniques Can Detect EMG Differences Between Moderate Knee Osteoarthritis Patients and Healthy Controls During Walking
Hughes, AD	Study of Blood Flow in the Human Femoral Artery by CFD
Hughes, Alun D	Assessing the Accuracy of Doppler Velocity Waveforms Using a String Phantom
Hughes, Alun D	Calibration of An Arterial Applanation Tonometer for In-Vivo Pressure Transduction
Hughes, Alun D	CFD Modeling of the Carotid Artery Using 3D Ultrasound
Hughes, Alun D	Combining Mri and CFD for Carotid Blood Flow Analysis: a Reproducibility Study
Hughes, Alun D	Errors Associated with CFD Models Reconstructed From 3D Ultrasound Data
Hughes, S C	Finite Element Simulation of Osseointegrated Trans-Femoral Implant Under Extreme Load Condition
Hugli, Tony	Mechanisms for Cell Activation in the Cardiovascular System
Huiskes, Rik	Mechanical Adaptation of Bone Mass and Architecture: Towards a Unified Theory
Hulejova, Hana	Bone-Friendly Intervertebral Cages
Hulme, P	The Effect of Varying Frequencies on the Stimulation of the Aggrecan Promoter of Chondrocytes Embedded in Agarose Gels
Humble, R Neil	Effects of Custom Molding and Posting of Foot Orthotics on Lower Extremity Kinematics
Humble, R Neil	Effects of Custom Orthotics on Lower Extremity Kinematics, Kinetics and Muscle Activity
Humphrey, JD	Mathematically Modeling Growth and Remodeling of Soft Tissues and Mechanocytes
Hung, Gwo-Feng	Strategy in Reducing Elbow Loading During Fall on An Outstretched Hand
Hunt, Chris M	A Method for Studying 3D Movement of the Spine in Vitro
Hunt, Chris M	Pullout Strength of Pedicle Screws Improves with Palacos Or Cortoss Augmentation
Hunter, Christopher	Oscillatory Compression of Articular Cartilage: Release of Cell Signaling Molecules and the Effect of Conditioned Medium on Chondrocytes in Agarose Ge
Hunter, CJ	Matrix Biosynthesis Due To Exogenous Stimuli Differs for Cartilage and Fibrocartilage
Hunter, Eric J	Optimization of Passive Tissue Model Parameters of Intrinsic Laryngeal Adductory Muscles
Hunter, Peter	A Model of Ventricular Anatomy Based on Structural Measurements From Pig Hearts.
Hunter, Peter	Anatomically Based Models of Blood Flow in the Human Pulmonary Microcirculation

Hunter, Peter Anatomically Based Models of Gas Flow and Gas Exchange in the Human Lung
Hunter, Peter Finite Element Geometric Models of the Human Lung and Diaphragm
Hunter, Peter Infrastructure for the Iups Physiome Project
Hunter, PJ Efficient Finite Element Customisation of a Generic Femur Using the Host Mesh Technique
Hunter, PJ Geometric Modelling of Skeletal Muscle Using Hermite Elements.
Hurst, William J Computational Modeling and Experimental Validation of Human Eye Interaction with High-Speed Foam Particles
Hurst, William J High-Speed and Continuous Pressure Measurements: a Comparison of Active Pressure Sensors and Pressure Film
Hurst, William J Investigation of Skin Abrasion Injuries From High Rate Shear Loading
Hurst, William J Sonomicrometric Measurements of Eye Displacements
Hurvitz, Edward A Effects of Botulinum Toxin a and Muscle Strengthening on Gait
Hurwitz, Debra E Asymmetric Dynamic Knee Loading in Advanced Unilateral Hip Osteoarthritis
Hurwitz, Debra E Peak Hip Joint Moments During Walking and Jogging are Correlated with Proximal Femoral Bone Mineral Density
Hutchinson, John The Locomotor Biomechanics of Large Terrestrial Vertebrates
Huyghe, Jacques Fluid-Structure Interaction And Collagen Remodeling In The Aortic Heart Valve
Hwa-liang, Leo Evaluation of Bileaflet Mechanical Heart Valve Induced Blood Damage During Leakage Flow Using Laser Doppler Velocimetry and Indicators of Platelet Activation
Hwang, I S Standing Balance Control Under a Concurrent Attentional Task in Children and Adults
Hwang, Il-Kyu Effects of Different Padding on the Impact Loading of the Hand During Falling
Hwang, Il-Kyu Effects of the Relative Forearm Velocity on the Impact Force of the Hand During Falling
Hye-Knudsen, Christian T Sudden Loading of the Upper Body Leads To Movement of Both the Lumbar Spine and Pelvis.
Hynd, D Failure Analysis of the Lower Limb in Axial Impact Loading

I

Iatridis, JC Effects of Mechanical Compression on Anabolic and Catabolic Gene Expression in a Rat Tail Model
Ibiwoye, Michael Magnetic Field Visualization in Applications To Pulsed Electromagnetic Field Stimulation of Tissues
Ibiwoye, Michael Pulsed Electromagnetic Field-Dependent Differencesof Collagen Processing in Pre-Osteoblasts
Ibiwoye, Michael Pulsed Electromagnetic Field-Dependent Stimulation of Pre-Osteoblast Proliferation in Vivo
Ichiba, Makoto The Change in the Rotation Rate of a Bacterium Motor Causes the Difference Between Forward and Backward Swimming Speeds of Vibrio Alginolyticus
Ihara, Maki Time-Dependent Stress-Strain Analysis of Unconfined Compressed Articular Cartilage Using Confocal Laser Scanning Microscopy
Ikawa, Eiji Effects of Tendon Sheaths on the Tensile Properties of Mouse Tail Tendon
Ikebe, Mitsuo Class Vi Myosin Moves Processively Along Actin Filaments Backwards with Large Steps
Ikebe, Mitsuo How Do Biological Motors Work?
Ikebe, Mitsuo Myosin V Truncation Mutant with Only One Iq Motif Can Processively Move Along An Actin Filament with 36 Nm Steps
Ikebe, Reiko Class Vi Myosin Moves Processively Along Actin Filaments Backwards with Large Steps

Ikebe, Reiko	Myosin V Truncation Mutant with Only One Iq Motif Can Processively Move Along An Actin Filament with 36 Nm Steps
Ikeda, Mariko	Bile Canaliculi Reformed by Rat Small Hepatocytes, and Its Dynamic Movement
Ikeda, Mariko	Variability and Stability Change with Walking Velocity - What is the Relationship Between the Two?
Ikeda, Tadashige	Experimental Study on Air Flow in a Two-Dimensional Channel with An Obstruction Oscillating At 10 Hz To 100 Hz
Ikeda, Yasuo	Motion of Rgpiba-Ams Near the Vwf Surface
Ikeda, Yasuo	Reconstitution of Gpiba-Mediated Platelet Behavior in Microcirculation
Ikegami, Kazuhiro	Measurement of Erythrocytes Deformability with Counter-Rotating Parallel Disk System
Ikema, Yasunari	Biological and Biomechanical Evaluations on in Vitro Infiltrative Characteristics of Fibroblasts Repopulating in the Necrotized Patellar Tendon
Iken, Mohamed	Effects of Vibration Induced by Inline Skating on Neuromotor Functions
Ilyin, I	Modeling of Extremal Load on Human Knee Joint Ligaments
Imberge, Simone	The Stabilizing Effect of External Ankle Devices with and Without the Additional Influence of a Shoe
Imbiriba, Luís A	Modification in the Postural Control During Long-Term Standing
Imhauser, Carl	He Effect of Damage To the Ligamentous Support of the Arch on the Function of the Posterior Tibialis Tendon.
Imhauser, CW	The Level of Symmetry in the Anthropometric and Mechanical Properties of the Ankle as Determined by a Mechanical/Mri
Imler, SM	Chondrocytes and Fibrochondrocytes Respond Differently To Oscillatory Tension
Imler, SM	Matrix Biosynthesis Due To Exogenous Stimuli Differs for Cartilage and Fibrocartilage
Inaba, Tadashi	Deformation Analysis of Human Left Ventricular Wall Using Mr Tagging Technique
Inaba, Tadashi	Finite Element Analysis of Cardiac Function in Hypertensive Heart Disease
Inaba, Tadashi	Measurement of the Encephalon Physical Parameter with MRI Saturation Transfer Method
Indahl, Aage	The Sacroiliac Joint, Intervertebral Disc and Muscle Reflexes
Ingham, E	Fracture of Zirconia on Alumina Hip Prostheses : the Need for Microseparation Testing
Ingham, E	The Kinematics of Hip Joint Simulator Microseparation
Ingham, E	Tribological Evaluation of Therapeutic Lubricants for the Knee
Ingham, E	Wear of Ceramic Matric Composite Hip Prostheses in Simulators Modelling Laxity
Ingham, Eileen	Biomechanics & Hydrodynamics of Decellularised Porcine Aortic Heart Valves
Ingham, Eileen	Biomechanics & Hydrodynamics Of Decellularised Porcine Aortic Heart Valves
Ingham, Eileen	Influence of Swing Phase Microseparation on the Wear of Ceramic on Polyethylene, Ceramic on Ceramic and Metal on Metal Total Hip Replacements
Ingham, Eileen	Long-Term Simulator Wear Study of Surface Engineered Mom Hip Prostheses
Ingham, Eileen	Wear of Crosslinked Polyethylene Under Different Tribological Conditions.
Inglis, J Timothy	Compensatory Impulse Generation by Individuals with a Unilateral Below-Knee Amputation During Gait Initiation
Inglis, J Timothy	Reflex Responses Graded To Both Perturbation Acceleration and Velocity
Inkster, Lisa	Techniques for Avoiding Hip Impact During Unexpected Sideways Falls
Inkster, Lisa	Techniques for Safe Landing During An Unexpected Fall: Modulation of Impact Velocity Via the Squat Response
Inou, Norio	Individual Stress Analysis of the Human Mandible Under Biting Conditions
Inoue, Haruka	Motion and Contact Analyses of Patello-Femoral Joint After Total Knee Arthroplasty
Inui, Kentarou	Effect of Glycoproteins on Friction Coefficient of Natural and Artificial Joint Surfaces

Ioannou, C	Decreased Proximal Aortic Compliance Causes Systolic Hypertension
Iozzo, Renato V	Quasi-Linear Viscoelastic Modeling of Tail Tendon Fascicles From Transgenic Mice
Ip, WY	Fatigue and Wear Evaluation of a Novel Artificial Finger Joint
Irujo, Mercedes	A 3D Finite Element Model of An Implanted Scapula Using Cadaveric Data for Evaluation
Irving, Malcolm	Quantifying Isometric Force-Dependent Energy Release in White Muscle by Comparing Contraction Energetics in Intact and Skinned Fibres
Isaac, GIsaac	Influence of Interference-Fit on the Initial Stability of Cementless Proximal Femoral Stems
Isabey, Daniel	A Multi-Segmental Model of the Coupling of Inspiratory Flow with the Compliant Nose Structure Assessed in Vivo.
Isabey, Daniel	Assessment of Structural Viscoelasticity of Cytoskeleton by Tensegrity Model
Isabey, Daniel	Cell-Immersed Microbeads Used as Probes of Cytoskeleton Mechanical Properties
Isabey, Daniel	Increasing Number of Interconnected Elements in Tensegrity Models Induces a Structural Softening Consistent with Cortical Cytoskeleton Function
Isaka, Tadao	Mechanical Energy Transfer by Two-Joint Leg Muscles During Snatch Lift
Isasi, AG	Diseased Human Carotid Bifurcations: Histological Correlations To Hemodynamic Factors
Ishibashi, Hiroyuki	Flow Patterns and Preferred Sites of Intimal Thickening in End-To-End and End-To-Side Anastomosed Arteries
Ishiguro, Kenji	Evaluations of Hip Fracture Mechanism and Prevention by Using Dynamic Fe Analyses
Ishiguro, Noriko	Application of Bio-Electrical Impedance Method for Estimating the Ratio of Extensors To Flexors in the Muscle Volume of the Upper
Ishihara, Hirokazu	Intervertebral Disc Metabolism Under Mechanical Load: the Role of Extracellular Physical Factors
Ishikawa, Masaki	Jumping Intensity Determines the Behavior of the Fascicle and Tendon Parts of the Vastus Lateralis Muscle
Isla, N de	Biomechanics of Erythrocyte Agglutination. Determination of Adhesive Specific Energy
Isoletho, Juha	The Transition From Take-Off To Early Flight Phase in Ski-Jumping
Isomichi, Takehiro	Optimal Fixation Sites of the Medial Supporting Structure of the Patellofemoral Joint
Issever, Ahi	Investigation of Structure-Property Relationships in Human Femoral Trabecular Bone
Ito, K	Effects of Mechanical Compression on Anabolic and Catabolic Gene Expression in a Rat Tail Model
Ito, Keita	Convective Molecular Transport in the Intervertebral Disc
Ito, Keita	Effect of Interfragmentary Shear and Compressive Stimulation on Bone Healing
Ito, Keita	Occlusion of Vertebral Endplate Openings: a Mechanism for Intervertebral Disc Degeneration?
Ito, Masamitsu	Behavior of Medial Gastrocnemius Muscle-Tendon Complex During Different Types of Jumping
Ito, Momoyo	Effects of Electro-Acupuncture Stimulation on Systemic and Mesenteric Microvascular Hemodynamics in Anesthetized Rats
Itoh, Akitoshi	Optical Motion Control of Euglena for Bio-Mems
Itoh, Hidemi	Microindentation Analysis of Human Enamel
Itoh, Hidemi	Scanning Acoustic Microscope Measurements of Anisotropy of Dentine and Enamel
Itoh, Ken-ichi	A 2-D Analysis of Temporomandibular Joint Loading Generated During Bilateral Biting At the Molars and Premolars
Ivancic, Paul C	Increased Intra-Abdominal Pressure is Coupled with Trunk Muscle Co-Contraction During Steady State Exertions

J

Jaric, Slobodan	Does Normalization of Muscle Strength for Body Size Depend on the Functional Performance To Be Assessed?
Jawa, Andrew	Do Constant-Rate Ramp Tests Represent Equilibrium Behaviors in Tendon?
Jaworek, Krzysztof	Parametric Identyfication of Lower Limbs During Walking of a Man
Jayaraman, G	Flow Between a Clot Model and a Stenosis
Jeansonne, Jennifer	The Biomechanics of Dart Throwing: Changes During Practice
Jelmini, Sandro	Modeling of Distance in Ski Jumping Using Statistic Models with Random Parameters
Jensen, Bente R	Steadiness in Young and Elderly Before and After a 5-Week Period of Strength Training
Jensen, Kristina	Regional Differences in Cellular Densities in Human and Ovine Mitral Valves
Jensen, Oliver	An Asymptotic Model of Unsteady Airway Reopening
Jensen, Oliver	Dynamic Particle/Liquid-Lining Interactions in Peripheral Lung Airways
Jensen, Oliver	Spreading and Peeling Dymanics in a Model of Cell Adhesion
Jensen, Thomas B	Buffy Coat Concentrate (Agf) with Allograft Improves Implant Fixation
Jiang, Guang-Liang	Dissociation of Pecam-1/Gq with Temporal Gradients in Shear Stress
Jiang, Wentao	Development of a Flow Chamber for Studying Cell Behaviour Under Pulsatile Flow
Jiang, Zonglai	Development of a Flow Chamber for Studying Cell Behaviour Under Pulsatile Flow
Jiang, Zonglai	Effect of Co-Cultured Vascular Smooth Muscle Cells on Pdgf-B Mrna Expression of Endothelial Cells Under Shear Stress
Jiang, Zonglai	Effects of Low Shear Stress on Morphological Remodeling of Organ-Cultured Artery in Vitro
Jiang, Zonglai	Pressure-Induced Expression of Immediate-Early Gene Product C-Jun of the Common Carotid Arteries in Rats
Jichuan, Zhang	Recovery Strategy From Perturbation of the Upper Body During Standing Using Mechanical Energy Analysis
Jim Powell, Jim	Biomechanical Efficacy of a Protein Polymer Hyrdrogel for Inter-Vertebral Nucleus Augmentation and Replacement
Jin, Moonsoo	Cartilage Nanomechanics, Mechanotransduction, And Tissue Engineering
Jin, Moonsoo	Response Of The Chondrocyte To Mechanical Stimuli: Physiologic And Injurious Compression
Jin, ZM	Prediction of Scratch Resistance of Metallic Bearing Surface, Articulating Against Uhmwpe, Due To 3rd Body Wear Particles
Jin, ZM	Tribological Characterisation of Surface Layer of Bovine Articular Cartilage.
Jindrich, Devin L	Dynamic Stabilization of Rapid Hexapodal Locomotion
Jindrich, Devin L	Fingertip Pulp Mechanics During Voluntary Tapping
Jindrich, Devin L	Impedance Models of Finger Joints During Typing
Jinha, Azim	Antagonistic Muscle Activity in Three-Dimensional Models of the Muscloskeletal System
Johansen, Peter	Understanding the Mechanisms of Mechanical Heart Valve Cavitation
Johansson, Hakan	Does Normalization of Muscle Strength for Body Size Depend on the Functional Performance To Be Assessed?
Johnson, Alan	Computational Fluid Dynamics (CFD) Simulation of the Human Biliary System
Johnson, Garth R	Towards the Creation and Validation of a Large Scale Musculoskeletal Upper Limb Model
Johnson, Jeffrey	Forefoot Structural Predictors of Plantar Pressures During Walking in People with Diabetes and Peripheral Neuropathy
Johnson, Matthew E	Measurement of Poisson's Ratio in Rabbit Achilles Tendon
Johnson, Michael	Are Spinal Facet Loads Influenced by the Fixation Method?
Johnson, Michael	The Effect of a Novel Cage Design on Stabilization in the Lumbar Spine

K

Kaufman, Kenton R	Intramuscular Pressure is An Indicator of Muscle Force
Kaufman, Kenton	Comparison of Quantitative Measures of Tremor as Predictors of Surgical Outcome
Kauten, Randy	Monitoring of the Rehabilitation of Patients After Fracture
Kautz, SA	Biomechanical Determinants of Pedaling Energetics: Internal and External Work are Not Independent
Kautz, SA	Muscle Force Not Work Defines Muscle Contributions To Forward Progression
Kautz, SA	Muscle Function During Forward and Backward Walking
Kavcic, Natasa S	Quantifying the Contribution of Individual Muscles To Lumbar Spine Stability
Kawabata, Kazushige	Time-Lapse of Cellular Stiffness Measured with Scanning Probe Microscopy
Kawahara, Norio	Iomechanical Evaluation of Reconstruction Aftre Total Sacrectomy
Kawahara, Norio	Mechanical Evaluation of Spine Reconstruction After Total En Bloc Spondylectomy by Finite Element Analysis
Kawakami, Kensaku	Changes in 3-D Motion and Contact Pressure Distribution After Lateral Ligament Injury of the Ankle Joint
Kawakami, Noriaki	Modeling Skeletal Shape Changes and Growth in Scoliosis
Kawakami, Yasuo	Architecture of Contracing Human Gastrocnemius Muscle: An Aproach From Three-Dimensional Ultrasound Imaging
Kawakami, Yasuo	Behaviours of Muscle-Tendon Complex During Electrical Stimulation with Trains of Linearly Varying Frequency in Humans
Kawakami, Yasuo	Changes in Mechanical Properties of Human Tibialis Anterior Muscle Following Repeated Eccentric Contractions
Kawakami, Yasuo	Effects of Resistance and Stretching Training Programs on the Iscoelastic Properties of Tendon Structures in Vivo
Kawakami, Yasuo	In Vivo Measurement of Muscle Fiber Behavior in the Triceps Surae Muscle During Tensional Summation
Kawakami, Yasuo	In Vivo Muscle Fiber Behavior of the Triceps Surae Muscles
Kawamura, Koichi	Morphology of Endothelial Cells Under Flow Alteration in Vivo
Kawamura, Sadao	Mechanical Energy Transfer by Two-Joint Leg Muscles During Snatch Lift
Kawamura, Shozo	Optimal Fixation Sites of the Medial Supporting Structure of the Patellofemoral Joint
Kawano, Yuji	Design Method of Porous Scaffold Microstructure Using Computational Simulation for Bone Regeneration
Kawasaki, K	Design of a Biofidelic, Instrumented 2.5 Kg Infant Dummy
Kawasaki, Shingo	Deformation Analysis of Human Left Ventricular Wall Using Mr Tagging Technique
Kawchuk, Greg	In Vivo Quantification of Disc Bulging in Different Annular Regions Along a Radial Path
Kaya, Motoshi	Coordination of Cat Gastrocnemius and Soleus During Locomotion Based on Direct Measurement of in Vivo Muscle Forces and
Kearney, John	Biomechanics & Hydrodynamics Of Decellularised Porcine Aortic Heart Valves
Kearney, John	Biomechanics & Hydrodynamics of Decellularised Porcine Aortic Heart Valves
Keenan, Scott M	The Effect of Speed on the Deterministic Origin of Teh Variabilty Present During Human Locomotion
Keenan, Scott M	The Reliability of the Lyapunov Exponent During Treadmill Walking
Kehl, Thomas	Activity Pattern and Joint Motion Profile of Total Knee Patients
Keir, Peter J	Assessment of Crosstalk in Surface EMG of the Forearm
Keir, Peter J	Common Function of Forearm Muscles During Gripping
Keitel, Jürgen	Biodynamic Data Set for Modelling Car Drivers
Keith, Michael W	The Dependence of Wrist Extension Moment on Elbow and Wrist Position After Brachioradialis Tendon Transfer
Keller, Tony S	Posture Dependent Trunk Strength and EMG Activity
Keller, Tony S	Tissue Stress and Modulus Changes Following Vertebroplasty

Kennard, Emma	Synergistic Effect of Spatial Resolution and Noise on the Precision and Accuracy of Measurements in Simulated Digital
Kepple, Thomas M	Examination of Knee Control Via Two Induced Acceleration Models
Kepple, Thomas M	Joint Moment Control of Mechanical Energy Flow During Normal Gait
Ker, Robert F	Tendon Mechanical Properties for Locomotion
Kerckhoffs, Roy	Active Myofiber Stress Distribution in Patient Specific Models of Cardiac Mechanics
Kerckhoffs, Roy	Modeling Electrical and Mechanical Activation Times in the Normal Heart
Kerkhoffs, GMMJ	In-Vitro Reports on Anterior Ankle Ligament Damage and Ankle-Joint Laxity: A Review of the Literature
Kerkhoffs, GMMJ	Two Instrumented Tests for Anterior Ankle-Joint Laxity: An Evaluation in the Clinical Setting
Kern, A	Comparison of Scaffold Designs for Tissue-Engineered Small-Diameter Graft Applications
Kernozek, Thomas W	Clinical and Plantar Loading Risk Factors of Subjects with Hallux Valgus
Kernozek, Thomas W	Model Based Auditory Feedback on the Lifting Technique May Reduce Spinal Moments of Warehouse Workers
Kerrigan, D Casey	Comparison of Bilateral and Unilateral Induced Acceleration Analyses of Gait Kinetics
Kersting, Uwe G	Effects of Mechanical Stimuli on the Relaxation Behavior of the Growth Plate Related To Morphological and Biochemical Adaptation in the Rat Model
Kersting, Uwe G	Mechanical Properties of Cartilage Specimen in Rats -
Kettler, Annette	Discoligamentous Structures of the Lower Cervical Spine Get Injured in In Vitro Low-Speed Side Collisions
Keyser, Randall E	Upper Extremity Impairment in Wheelchair Propulsion
Khalsa, Partap S	Biomechanical Evidence for Proprioceptive Function of Lumbar Facet Joint Capsule
Khanna, Rajesh A	In Vitro Exploration of Synergies Between Fatigue Damage and Proteolysis in Bovine Pericardial Bioprosthetic Materials
Khir, Ashraf W	Calibration of An Arterial Applanation Tonometer for In-Vivo Pressure Transduction
Kido, A	A Leg-Propelled Wheelchair: Biomechanics, Energetics and Modeling
Kiesewetter, H	Mechanical Properties and Permeability of Polyelectrolyte Microcapsules (PEMC)
Kilgore, Kevin L	The Dependence of Wrist Extension Moment on Elbow and Wrist Position After Brachioradialis Tendon Transfer
Kilgus, Douglas	In Vivio Determination of Polyethylene Bearing Motion Realtive To the Tibia and the Femur
Kilner, Philip J	Study of the Intra-Ventricular Blood Flow by CFD and Mri
Kim, C Maria	Medial-Lateral Cop Velocity During Standing Relates To Asymmetry and Functional Balance in Individuals with Stroke
Kim, C Maria	Symmetry in Kinetic Variables is Accompanied by Symmetry in Temporal But Not Distance Variables of Gait in Persons with
Kim, Do Gyoon	Biomechanical Modeling of Overload At the Bone-Oral Implant Interface
Kim, Gyoo Suk	Design of Air Seat Cushion Orthosis for Plegia
Kim, Han Sung	A Microstructure Model of Vertebroplasty and Its Mechanical Properties
Kim, Han Sung	The Effect of Trabecular Bone Microstructure on Stress Distribution of a Dental Implant
Kim, Hyoung-Bum	Echo-PIV(r): a Novel Method for the Non-Invasive Measurement of Velocity Vectors Using Ultrasound Imaging
Kim, Hyung Do	A Microstructure Model of Vertebroplasty and Its Mechanical Properties
Kim, JK	The Effect of a Cyclic Compressive Strain on the Differentiation of Osteoblast-Like Cell (Mc3t3-E1) in 3-Dimensional Scaffolds
Kim, Jong Kwon	Design of Air Seat Cushion Orthosis for Plegia

Kim, Kyu Tae	The Kick in the Deceleration Stage of 100m Track Race
Kim, Kyu-Jung	Biomechanical Differences of Fall Arrest Using the Upper Extremity Due To Aging
Kim, Kyu-Jung	Effects of Different Padding on the Impact Loading of the Hand During Falling
Kim, Kyu-Jung	Effects of the Relative Forearm Velocity on the Impact Force of the Hand During Falling
Kim, Kyunghan	Biomechanical Differences in Shoulder Loading in Populations During Load-Bearing Tasks
Kim, Sang Yong	A Quantitative Assessment of Knee Extensor Spasticity Using Isokinetc Dynamometer
Kim, Sanghee	Flow Regulation of Gap Junctional Communication and the Functional Compartmentalization of Vascular Endothelium
Kim, Seung-Jae	Strain Characteristics of the Foot Arch in Non-Athletes and Athletes During Weight-Bearing, Walking and Running
Kim, Young Eun	Effect of Impact Duration on the Dural-Sac Occlusion
Kim, Young-Ho	Air Flow and Temperature Distribution in a Neonatal Incubator
Kim, Young-Ho	Clinical Application of a Knee-Joint-Controlled Electro-Mechanical KAFO for Polio Patients
Kimbell, Julia S	Effects of Boundary Conditions on Particle Deposition Predictions in Human Nasal Passages
Kimbell, Julia S	Use of Computational Fluid Dynamics To Study Inhaled Gas and Particle Trasport in the Nasal Passages
Kimmel, Eitan	Biofluid Effects of Therapeutic Ultrasound on Biological Tissues
Kimmel, Eitan	Shear-Like Response of Endothelial Cells To Therapeutic Ultrasound
Kimmeskamp, S	Effect of Physical Therapy and Afferent Stimulating Insoles on Motor Abilities in Parkinson Patients
Kimmeskamp, Stefan	Relationship of Perception Vs. the Measurement of Plantar Pressures - a Neurosensory Approach
Kimmeskamp, Stefan	Somatosensory Input in the Control of Human Posture in Patients with Morbus Parkinson
Kimura, Genjiro	Wave Intensity in the Carotid Artery is a New Index of Left Ventricular Systolic and Early Diastolic Performance
King, Albert I	Comparison of Relative Motion Between the Brain and Skull of the Human Cadaver for Rotation in the Coronal and Sagittal Planes
King, Albert I	Numerical Modeling of Human Occupants and Automotive Safety
King, Deborah	Quadruple Jumps in Figure Skating
King, JR	Dynamic Particle/Liquid-Lining Interactions in Peripheral Lung Airways
King, Karen	Determination of Elastin and Collagen Content in Porcine Aorta
King, Michael R	Leukocyte Tethering Under Flow: Model for Interfacial Compression, Viscoelastic Tether Extension, and Cytoskeletal Unbinding
Kingma, Idsart	Co-Activation of Knee Flexors in Isometric Extension Efforts
Kinosada, Yasutomi	Deformation Analysis of Human Left Ventricular Wall Using Mr Tagging Technique
Kinosada, Yasutomi	Measurement of the Encephalon Physical Parameter with MRI Saturation Transfer Method
Kinoshita, Ryo	Starting Friction of Artificial Cartilage Materials in Hyaluronate Solutions
Kinsey, T	A Comparison Between Single-Radius and Multi-Radius Total Knee Arthroplasties for Stand To Sit (An EMG and Kinematic Study)
Kinzl, Lothar	Discoligamentous Structures of the Lower Cervical Spine Get Injured in In Vitro Low-Speed Side Collisions
Kirilova, Miglena	A Mathematical Model of Arterial Regeneration Over Bioresorbable Grafts
Kirk, Brett Thomas	Application of Fibre Laser Scanning Confocal Microscopy To Study of the Biomechanics and Microstructure of Articular Cartilage

Kirk, Thomas B	The Development of Confocal Arthroscopy for the Assessment of Cartilage Disorders
Kirkpatrick, Robert	Regulated Actin-Myosin Interaction and Sarcomeric Stiffness
Kirsch, Robert F	Arm Stiffness and Stability Improved by Fns in C5-C6 Sci
Kirsch, Robert F	Model-Based Development of a Neuroprosthesis for High Cervical Spinal Cord Injury
Kirsch, Robert F	Stiffness of the Human Arm in Three Dimensional Space
Kisiday, John	Cartilage Nanomechanics, Mechanotransduction, And Tissue Engineering
Kiss, Rita	Gait Analysis by Patient Who Have An ACL Deficient Knee
Kistler, Erik	Mechanisms for Cell Activation in the Cardiovascular System
Kitabatake, Akira	CFD Studies of the Intraventricular Diastolic Flow for the Analysis of Color M-Mode Doppler Echocardiogram
Kitamura, Nobuto	Bone-Mulch-Screw/Washer-Loch Fixation of Doubled Flexor Tendon Graft in Anterior Cruciate Ligament Reconstruction
Kitamura, Yoshiaki	The Effect of Overloading on the Patellar Tendon That Underwent Segmental Resection of Its Central One-Third Portion
Kitano, Toshio	Effect of Glycoproteins on Friction Coefficient of Natural and Artificial Joint Surfaces
Kitawaki, Tomoki	Multi-Scale Computational Hemodynamics in Cardiovascular System
Kivekäs, Juha	Effects of Equipment and Performance Characteristics on Ski Jumping Performance
Kivi, Derek	Treadmill Speeds Related To Sprinting Ability
Kiviranta, I	Mechano-Acoustic Characterization of Normal, Degenerated and Repaired Cartilage
Kjær, M	Measuring Vastus Lateralis Aponeurosis and Tendon Deformation in Vivo During Maximal Isometric Contraction by Ultrasound
Klaesner, Joe	Comparison of Models for the Stress-Strain Relationship of Soft Tissue
Klaesner, Joseph W	Biomechanical Modeling of Indentation Testing and Application in Plantar Pressure Prediction of Diabetic Foot
Kleiman, David	A Biomechanical Model of the Elbow, Forearm and Wrist
Klein, Dieter	Effects of Varus Wedged Shoe Versus Insole on Knee Joint Loading Characteristcs
Kleinberger, Michael	Experimental Evaluation of a Model of Contact Pressure Distribution in the Hip Joint
Kleinert, L	Comparison of Scaffold Designs for Tissue-Engineered Small-Diameter Graft Applications
Klein-Nulend, J	Cyclic Strain and Fluid Flow Induce Different Responses in Human Bone Cells
Klein-Nulend, J	Growth Factor Loaded Calcium Phosphate Cement for Bone Regeneration
Kleinschmidt, Th	Flow Evaluation of Stents in Carotid Artery Models
Kleiven, Svein	Influence of Impact Direction and Duration To the Human Head in Evaluation of Head Injury Criteria: a Numerical Study
Klimov, Andrei A	New Energetics Approaches To Elucidating Mechanisms of Contraction and Relaxation
Kloog, Y	Ecs Adhesion on Silicone Rubber-Rtv 615: a Systematic Study
Klous, Miriam	Marker-Based Reconstruction of the Kinematics of a Chain of Segments; a New Method That Incorporates Joint Kinematic
Klute, Glenn K	Acceleration Transients and Transtibial Prosthetic Pylon Attenuation During Gait
Klute, Glenn K	The Material Properties of the Subcalcaneal Tissue in Compression
Klute, Glenn K	Transient Foot Ground Reaction Forces and Prosthetic Pylon Attenuation During Gait
Knauf, Philip	Divalent Ion Induced Adhesion of Neutrophils To ICAM-1 and Vcam-1 Coated Surfaces
Knezevic, Vedran	Engineered Tissues as Model Systems for Studying Myocardial Biomechanics
Knill, K	Determination of Peak Limb Force From Duty Factor
Knoll, Zsolt	Gait Analysis by Patient Who Have An ACL Deficient Knee

Knutzen, Kathleen M	Soleus H-Reflex Gain in Elderly and Young Adults When Lying, Standing and Balancing
Ko, Jaiyoung	The Effect of Trabecular Bone Microstructure on Stress Distribution of a Dental Implant
Ko, Tzu-Hsiang	Effects of a Complete Bypass Graft on the Flowfields in a Host Artery with Different Severity Stenosis
Ko, Tzu-Hsiang	Numerical Study on the Flow Characteristics in a Partially Obstructed Tube with Complete Bypass Graft
Kobayashi, Hirosuke	Quantitative Evaluation of Microvascular Structure and Comparizon of Regional Microvascularity and Po2 Distribution in Rat Cerebral Cortex
Kobayashi, Kochi	Stiffness Change with Cage Configuration for Anterior Lumber Interbody Fusion
Kobayashi, Kochi	Viscoelastic Characterization of Ultra High Molecular Weight Polyethylene
Kobayashi, Koichi	Scanning Acoustic Microscope Measurements of Anisotropy of Dentine and Enamel
Kobayashi, Michiaki	Microcrack Detection and Mechanical Property Measurement of Bone Using Scanning Acoustic Microscope
Kobayashi, Mikio	Morphology of Endothelial Cells Under Flow Alteration in Vivo
Kobayashi, Ryo	Simulation of the Shape Change of a Red Blood Cell At the Entrance of a Capillary
Kobayashi, Shunichi	Flow and Wall Compression in High Grade Asymmetric Arterial Stenosis Models During Pulsatile Flow Experiments
Kobayashi, Toshio	Numerical Simulation of Fluid-Structure Interaction of the Intracranial Artery
Kocsis, László	Gait Analysis by Patient Who Have An ACL Deficient Knee
Koda, Fumikazu	Microindentation Analysis of Human Enamel
Koditschek, Daniel	Self-Stability Mechanisms for Sensor-Cheap Legged Locomotion
Koehl, Mimi AR	Smelling With Hairy Little Noses: The Physical Design Of Olfactory Antennae
Koehler, Danny	Observation of Displacement Steps by Single Myosin Id and Myosin Ii Molecules
Koga, Yoshio	A New Technique for Three-Dimensional Leg Alignment Assessment
Koga, Yoshio	Comparative Study Between Intra- and Post-Operative Knee Motions After Total Knee Arthroplasty
Koga, Yoshio	Motion and Contact Analyses of Patello-Femoral Joint After Total Knee Arthroplasty
Koh, Jason L	In Vivo & Noninvasive Load Sharing Among Quadriceps Components in Patellar Malalignment
Koh, Timothy J	Passive Stretches Protect Muscle in Old and Young Mice From Lengthening Contraction-Induced Injury
Kohara, Hiroshi	Bile Canaliculi Reformed by Rat Small Hepatocytes, and Its Dynamic Movement
Kohl, Peter	Mechanical Effects on Cardiac Myocyte Electrophysiology
Kohno, Syoji	A 2-D Analysis of Temporomandibular Joint Loading Generated During Bilateral Biting At the Molars and Premolars
Kohrt, Wendy	The Combined Effects of Disuse and Gonadectomy on Bone Mechanics in Male and Female Rats
Kohstall, Charles	Effects of Midsole Density and Landing Height on Impact Attenuation in Landing
Koitabashi, Masayuki	A Comparison of Bi-Lateral Deficit in Elite Enduranceand Elite Power Athletes During Drop Jumps
Kokini, Klod	Dependence of Viscoelastic Properties on Collagen Ecm Microstructure
Kokini, Klod	Micro- and Macro-Level 3D Strains Measured in Structurally Varied Collagen Ecms
Kolh, Philippe	Aortic Leak Severity Determines Arterial Elastance And
Koller, Arnold	Correlation Between Radiographic and Clinical Measurement of Sagital Back Shape
Kollmeier, Guido	Mechanical Stability of Ankle Braces Under Passive and Dynamic Loading Conditions
Komatsu, Masayo	Morphology of Endothelial Cells Under Flow Alteration in Vivo
Komi, Paavo V	Critical Issues in the Behavior of Human Skeletal Muscle During Ssc Activities

Komi, Paavo V	Effects of Contraction History on Fascicle Behavior in Shortening Contractions
Komi, Paavo V	Jumping Intensity Determines the Behavior of the Fascicle and Tendon Parts of the Vastus Lateralis Muscle
Komi, Paavo V	Neuromuscular Fatigue During and After Eccentric and Concentric Exercises
Komi, Paavo V	The Transition From Take-Off To Early Flight Phase in Ski-Jumping
Komistek, Richard D	Global Optimization for Recovering the Position and Orientation of Free-Form Objects in Medical Imaging Registration Using a New Smoothing Approach
Komistek, Richard D	In Vivio Determination of Polyethylene Bearing Motion Realtive To the Tibia and the Femur
Komistek, Richard D	In Vivo Determination of Hip Joint Separtion in Subjects Having Variable Bearing Surfaces
Komistek, Richard D	In Vivo Forces and Motions From Fluoroscopy and Mathematical Modeling
Komistek, Richard D	Muscle Reconstruction and Modeling From Mri-Scan
Komistek, Richard D	Verification of Three-Dimensional Joint Kinematics Determined Using Fluoroscopy: An Error Analysis
Komori, E	Limitation of Expriatory Flow in Liquid Ventilation
Komori, Yasunori	Class Vi Myosin Moves Processively Along Actin Filaments Backwards with Large Steps
Kondo, Eiji	Biomechanical Evaluation of a Newly Devised Model for the Elongation-Type Anterior Cruciate Ligament Injury with Partial Laceration and Permanent Elon
Koontz, Alicia M	Segmental Power During Propulsion in Wheelchair Users with Greater Evidence of Shoulder Injury Overtime
Koort, Jyri K	Precision Measurements of Rsa Method Using a Phantom Model of Hip Prosthesis
Korff, Thomas	Swing Phase Reduction in Above-Knee Amputee Running
Korhonen, RK	Collagen Network and Mechanical Properties of Articular Cartilage: Experimental and Numerical Study
Korhonen, RK	Effects of Sound Velocity Variation on Cartilage Ultrasound Indentation Measurements
Korossis, Sotiris	Biomechanics & Hydrodynamics Of Decellularised Porcine Aortic Heart Valves
Korossis, Sotiris	Biomechanics & Hydrodynamics of Decellularised Porcine Aortic Heart Valves
Kosawada, Tadashi	Mechanics of Plasma Membrane Vesicles
Koseki, Michihiko	Individual Stress Analysis of the Human Mandible Under Biting Conditions
Kosmopoulos, Victor	Tissue Stress and Modulus Changes Following Vertebroplasty
Köster, Reinhard W	In Vivo Intracardiac Hemodynamics: Does Flow Influence Morphology?
Kotte, Jiska	Modeling Electrical and Mechanical Activation Times in the Normal Heart
Kour, Anam Kueh	The Proximal Fibers of the Interrosseous Membrane Contributes To Stability in the Radial Dominant Single Bone Forearm
Kourakata, Itaru	Does Orbicularis Oris Make Upper and Lower Lips Compress Each Other?
Kovacs, Stéphanie	Active Movements of the Shoulder Girdle in Healthy Subjects: a Validity Study
Kozerke, Sebastian	Numerical Study of Human Aortic Blood Flow: a Comparison Between Healthy and Disturbed Flow Distal To Artificial Heart Valves
Kozey, JW	Knee Joint Kinematics and Kinetics in Patients with Moderate Osteoarthritis
Kozey, JW	Lower Limb Energetics of Normal and Moderate Oa Subjects
Kozey, JW	Temporal Pattern Recogntion Techniques Can Detect EMG Differences Between Moderate Knee Osteoarthritis Patients and Healthy Controls During Walking
Kram, Rodger	Mechanical Determinants of the Metabolic Cost of Walking: Work, Force and Swing
Kram, Rodger	Metabolic Cost of Generating Horizontal Forces During Walking
Kram, Rodger	Metabolic Cost of Lateral Leg Swing in Human Walking
Kranzl, Andreas	Walking with Platform Shoes - Normal Walking Pattern?
Krasovitski, Boris	Biofluid Effects of Therapeutic Ultrasound on Biological Tissues

Kratzberg, Jarin	Experimental Investigation of the Role of Thrombus on the Pressure-Strain Relationship in Human Abdominal Aortic Aneurysm
Kremser, Christian	Correlation Between Radiographic and Clinical Measurement of Sagital Back Shape
Krieg, James C	Pertrochanteric Fracture Fixation: Effects of Implant Design on Cut-Out Failure Under Dynamic Loading
Krishnan, Laxminarayanan	Viscoelastic Characterization of Collagen Gel Constructs
Krishnan, Ramaswamy	Experimental Verification of the Role of Interstitial Fluid Pressurization in the Frictional Response of Bovine Articular Cartilage
Krosshaug, Tron	3D Motion Reconstruction From Uncalibrated 2d Video Sequences - Application To Freestyle ACL Injury Situations
Krstin, Natasa	Experimental Determination of the Center of Resistance of Human Incisors in Comparison with Finite Element Simulations
Krug, Juergen	Visual Control and Load Effects of Fast Rotational Movements
Ku, David N	Flow and Wall Compression in High Grade Asymmetric Arterial Stenosis Models During Pulsatile Flow Experiments
Kuberka, Melanie	Geometrically Defined 3-Dimensional Collagen Scaffolds for Tissue Engineering
Kubo, Keitaro	Effects of Resistance and Stretching Training Programs on the Iscoelastic Properties of Tendon Structures in Vivo
Kudo, Susumu	Wall Shear Stress With Initiation Of Aneurysm Around Anterior Communicating Artery In Steady Flow Communicating Artery In Steady Flow
Kudoh, Toshiharu	Bone-Mulch-Screw/Washer-Loch Fixation of Doubled Flexor Tendon Graft in Anterior Cruciate Ligament Reconstruction
Kulig, Kornelia	In Vivo Assessment of the Instantaneous Axes of Rotation of the Lumar Spine in Symptomatic and Asymptomatic Subjects
Kulig, Kornelia	Segmental Mobility of the Lumbar Spine During a Prone Press-Up Maneuver in Symptomatic and Asymptomatic Subjects: Assessment Using Dynamic Mri
Kulkarni, S	Assessment of a Novel Femoral Component Removal Technique for Revision Surgery
Kulke, Michael	A Unique Sequence of Titin, the Pevk-Domain, is An Entropic Spring That Interacts with Actin
Kulke, Michael	Passive Elastic Recoil of Titin Adds To the Shortening Speed of Skeletal Muscle Fibers
Kumagai, Kiichiro	Rupture Properties of Thoracic Aortic Aneurysms Using Pressure-Imposed Experiment
Kumar, Shrawan	Force and Muscular Activity During Handwheel Actuation
Kumar, Shrawan	Strength and EMG of Cervical Muscles in Directional Maximal Voluntary Contraction
Kumar, Shrawan	The Role of Torso Muscles in Trunk Twisting
Kums, Tatjana	Vertical Jumping Performance in 8-12-Year-Old Rhythmic Gymnasts
Kunz, David	A Comparison of Joint Mechanics Between Anterior Cruciate Ligament Intact and Deficient Stifles: a New Model of Anterior Cruciate Ligament Disruption
Kunzelman, Karyn S	Regional Differences in Cellular Densities in Human and Ovine Mitral Valves
Kunzelman, KS	Finite Element Implementation of a Structural Model for Aortic Valve Tissue
Kuo, AD	Mechanical and Metabolic Requirements of Lateral Stabilization in Human Walking
Kuo, AD	Metabolic Cost of Lateral Leg Swing in Human Walking
Kuo, AD	Muscle Work and Force: Energetics of Human Walking
Kuo, AD	Passive Dynamic Stability in Human Walking
Kuo, AD	Scaling of Damping: Implications for Stability
Kuo, AD	Scaling of Human Postural Control Responses Due To Biomechanical Constraints
Kuo, Li-Chieh	Quantitative Evaluation of Maximal Working Space and Kinematics of Thumb
Kuo, Mei-Ying	Measurement of Three-Dimensional Kinematics of the Glenohumeral Joint During Manual Wheelchair Propulsion Using Skeletal

L

Leardini, Alberto	An Efficient and Robust ICP Technique for Surface Registration
Leardini, Alberto	Effect of Skin Motion Artefacts on Knee Joint Kinematics
Leardini, Alberto	Pattern of Articular Contact At the Tibio-Talar Joint in Passive Flexion
Leardini, Alberto	Recruitment of Ankle Ligaments Fibres During Passive Flexion
Leardini, Alberto	Skin Motion Artefact Characterization From 3D Fluoroscopy and Stereophotogrammetry
Leardini, Alberto	The Role of the Passive Structures in the Mobility and Stability of the Natural and Replaced Human Ankle Joint
Leatherbarrow, Kate	Ligament Autograft Cells Do Not Die by Apoptosis
Leatherbarrow, KE	The Healing of ACL and Mcl Injuries is Initially Similar But Diverges with Time
Lebiedowska, MK	The Resistance of a Knee Joint in Children with Spasticity
Leblanc, Michele	Angular Momentum of the Non-Throwing Arm in the Javelin Throw
LeBlanc, Steven	Effect of Horizontal Foot Velocity on Impulse in Horizontal Jumping
LeBlanc, Steven	Horizontal-To-Vertical Velocity Tradeoff in Horizontal Jumping
Ledoux, William R	A Finite Element Model of the Foot and Ankle: Validation of Quiet Stance
Ledoux, William R	The Material Properties of the Subcalcaneal Tissue in Compression
Lee, Alex JY	Quantitative Assessment of Balance Ability Among Different Sports Athletes
Lee, CR	Effects of Mechanical Compression on Anabolic and Catabolic Gene Expression in a Rat Tail Model
Lee, DA	Analysis of Strain Fields in Tendon Fascicles Under Tensile Loading
Lee, DA	Structure-Function Relationship in Tendon Fascicles Under Tensile Loading Conditions
Lee, David A	Crosslinking Density Influences Chondrocyte Morphology and Metabolism in Mechanically Loaded Peg Hydrogels
Lee, David A	Dynamic Compression Influences the Synthesis of Nitric Oxide and Pge2 by LL-1B Stimulated Chondrocyte Sub-Populations Cultured in Agarose Constructs
Lee, David V	Influence of Increased Rotational Inertia on Human Turning Performance
Lee, Eun Jung	Engineered Tissues as Model Systems for Studying Myocardial Biomechanics
Lee, Hae-Dong	Force Depression Following Muscle Shortening of Electrically Stimulated and Voluntarily Activated Human Adductor Pollicis
Lee, In Huk	Design of Air Seat Cushion Orthosis for Plegia
Lee, In-Hyeok	Finite Element Human Model for Low Speed Rear Impact Simuation
Lee, J Michael	In Vitro Exploration of Synergies Between Fatigue Damage and Proteolysis in Bovine Pericardial Bioprosthetic Materials
Lee, Jin-Hee	Finite Element Human Model for Low Speed Rear Impact Simuation
Lee, Jong Keun	Design of Air Seat Cushion Orthosis for Plegia
Lee, Kim-Kheng	A Fe Model of the C2-C3 Segment - Gross Responses Under Physiological Loads
Lee, Ming-Yih	Numerical Simulation of Interfacial Stress for Extensive Premolar Cavity Under Different Occlusal Forces
Lee, Ming-Yih	The Finite Element Analysis of Different Fixations for Mandibular Fracture
Lee, Peter VS	Biomechanics of Transtibial Ptb and Pcast Prosthetic Sockets
Lee, Peter VS	Validation of Finite Element Model for Prosthetic Socket Design
Lee, Raymond	The Assessment of Spinal Kinematics During the Application of An A-P Mobilisation
Lee, Richard T	Self-Assembling Peptide Scaffold Promotes Differentiation and Network Formation in Three-Dimensional Culture of Human Microvascular Endothelial Cells
Lee, Robert B	Nutrition of the Intervertebral Disc; Effects of Pathological Changes
Lee, RT	Diseased Human Carotid Bifurcations: Histological Correlations To Hemodynamic Factors
Lee, Sangup	The Effect of Trabecular Bone Microstructure on Stress Distribution of a Dental Implant

Lee, Sang-Wook	Turbulence Induced Vein-Wall Vibration May Play a Role in Arteriovenous Dialysis Graft Failure
Lee, Seung E	Numerical Simulation of Cerebrospinal Fluid Motion Within a Healthy and Diseased Spinal Canal
Lee, Seung E	Unstructured Hexahedral Mesh Based on Conduction Temperature Distribution
Lee, Shiuann-Sheng	Comparative Biomechanical Studies Between Newly Designed Stemless Prosthesis and Conventional Prosthesis
Lee, Shiuann-Sheng	Effects of Different Levels of Transtrochanteric Rotational Osteotomy on the Stress Distributions in the Proximal Femur
Lee, T C	Torsional Fatigue of Cortical Bone
Lee, TS	The Effect of a Cyclic Compressive Strain on the Differentiation of Osteoblast-Like Cell (Mc3t3-E1) in 3-Dimensional Scaffolds
Lee, Vee-Sin	A Fe Model of the C2-C3 Segment - Gross Responses Under Physiological Loads
Leeming, Angus	Predicting the Mixing of Ultra-Fine Particles in a Model Lung Acinus
Lees, Adrian	Electromyographic Analysis of Selected Muscles During a Simulated Soccer Game
Lefebvre, R	Forward Ice Hockey Skating: Comparison of EMG Activation Patterns At Three Velocities
Lefebvre, R	The Effects of Stick Construction in the Performance of Ice Hockey Wrist Shot
Lefebvre, Richard	Effects of Vibration Induced by Inline Skating on Neuromotor Functions
Lefebvre, Richard	Lower Limb Kinematics of Ice Hockey Forward Skating
Legrice, Ian	A Model of Ventricular Anatomy Based on Structural Measurements From Pig Hearts.
Legrice, Ian	Shear Properties of Ventricular Myocardium
Lehman, Andy	Investigation of Cementless Cup Micromotion and Stability After Total Hip Arthroplasty
Lehmann, Fritz-Olaf	Mechanisms of Flight Force Enhancement in Flapping Flight
Leisinger, Bruno	Ground Reaction Forces on Stairs
Lemons, Jack E	Finite Element Analysis of a Mandibular Premolar Subjected To Orthodontic Loading: Effects of Periodontal Ligament Thickness and Nonlinear Material P
Lemons, Jack E	Periodontal Ligament Biomechanics of Intrusive and Extrusive Orthodontic Loading
Lemos, Robson	Modeling and Visualization of the Mechanical Behaviour of Skeletal Muscle using a Continuum Approach
Lenz, Juergen	Fe-Simulation of Bone Modeling Around a Dental Implant in Two-Stage-Healing as Compared To Early Loading
Leonard, Catherine	Angiogenesis and Healing in Rabbit Knee Ligaments
Leonard, Tim	Coordination of Cat Gastrocnemius and Soleus During Locomotion Based on Direct Measurement of in Vivo Muscle Forces and
Leonard, Tim	Effects of Stretching and Shortening on Isometric Forces on the Descending Limb of the Force-Length Relationship in Cat Soleus
Leonard, Tim	In Vivo Changes in Muscular Activation Before and After Anterior Cruciate Ligament Transection in the Feline Hindlimb
Leonard, Tim	In-Situ Chondrocyte Deformation in Early Stage Osteoarthritic (Oa) Articular Cartilage
Leong, JCY	Compressive Strength in Vertebroplasty Under Fatigue Loading
Leong, JCY	EMG Changes in Paraspinal Muscle of Scoliosis Patients After Spinal Fusion
Leong, JCY	Sr-Ha Bioactive Bone Cement Characterization and Animal Trials
Leroux, M	Postural Evaluation of Idiopathic Scoliosis Patients and Adolescent Control Subjects
Leroux, M	Stiffness and Postural Control in Adolescent Control and Idiopathic Scoliosis Patients
Les, Clifford M	The Mechanisms and Significance of the Correlation Between Bone Strength and Stiffness

Leung, Aaron KL	Development of 3D Finite Element Model of Human Foot and Ankle
Leung, Keith	Effects of Different Padding on the Impact Loading of the Hand During Falling
Leuprecht, Armin	Fluid Dynamics and Wall Mechanics in Peripheral Bypass Anastomoses
Leuprecht, Armin	Numerical Study of Human Aortic Blood Flow: a Comparison Between Healthy and Disturbed Flow Distal To Artificial Heart Valves
Leval, Marc de	Computational Fluid Dynamics After Aortic Coarctation Repair
Levenston, Marc E	Oscillatory Compression of Articular Cartilage: Release of Cell Signaling Molecules and the Effect of Conditioned Medium on Chondrocytes in Agarose Ge
Levenston, ME	Chondrocytes and Fibrochondrocytes Respond Differently To Oscillatory Tension
Levenston, ME	Matrix Biosynthesis Due To Exogenous Stimuli Differs for Cartilage and Fibrocartilage
Levin, Dora J	The Effect of Ligand Density on Tether Formation Between Endothelium and Monocytes
Levine, Elliot M	Nutrient Diffusion and Flow-Induced Nutrient Transport in 3-D Cell-Scaffold Composites
Levine, Peter	Intersegmental Dynamics During Multijoint Arm Reaching: Implications for Control of Limb Movement
Levy, Carmit	Regulation of Motor Unit Recruitment in the Cardiac Muscle
Levy, Morris	Rear Wheel Impact Characteristics in Off-Road Cycling
Lewis, Cara	Comparison of Models for the Stress-Strain Relationship of Soft Tissue
Lewis, Jack L	Fracture Toughness of Cartilage by Microindentation
Lewis, Jack L	Microindentation Methods for Evaluating Elastic and Viscous Properties of Soft Tissues
Lewis, Paul	Investigation of Cementless Cup Micromotion and Stability After Total Hip Arthroplasty
Lewis, Paul	Investigaton of Stresses and Micromotion Between the Liner and the Acetabular Cup in Total Hip Replacement Implants
Leyvraz, P-F	Gait Features Assessment in Hip Osteoarthritis and Total Hip Replaced Patients Based on An Ambulatory System (Physilog)
Li, Chaodi	Predictions of Residual Stresses in Bone Cement for Joint Arthroplasty
Li, Cheng	Nanomechanical and Biochemical Properties of Diseased Artery Tissue
Li, Gen-Jia	Measurement of Three-Dimensional Kinematics of the Glenohumeral Joint During Manual Wheelchair Propulsion Using Skeletal
Li, Hongbin	A Unique Sequence of Titin, the Pevk-Domain, is An Entropic Spring That Interacts with Actin
Li, J	Finite Element Simulation of Osseointegrated Trans-Femoral Implant Under Extreme Load Condition
Li, Jimmy	Pulse Effects of Low Intensity Ultrasound Stimulation on Bone Cells Proliferation
Li, Jue	Modelling the Nonlinear Anisotropic Porcine Heart Valves
Li, Li	Different Gait Patterns Can Be Classified by Using Muscular Activity Patterns
Li, Li	Investigating the Differences Between Inertial and Cadence Effects on Neuromuscular Coordination During Cycling
Li, Li	The Biomechanics of Dart Throwing: Changes During Practice
Li, Li	Unique Muscle Activity Patterns Observed During Gait Transitions
Li, Li	Variability and Stability Change with Walking Velocity - What is the Relationship Between the Two?
Li, Song	Differential Modulation of Focal Adhesion Dynamics by Shear Stress and Serum During Endothelial Cell Migration
Li, Xiufeng	Studies on the Single Binding Force of LFA-1 and ICAM-1

Lin, Hsiu-Chen	Stepping Over Obstacles During Locomotion in Anterior Cruciate Ligament Patients
Lin, Hwai-Ting	Muscle Forces Analysis in the Shoulder Mechanism During Wheelchair Propulsion
Lin, James Cheng-An	Pulse Effects of Low Intensity Ultrasound Stimulation on Bone Cells Proliferation
Lin, Po-Chou	Kinematic and Kinetic Analysis of Wheelie Activity
Lin, Ting-Sheng	Biomechanical Eeffects of the Designs on Posterior Resin-Bonded Prostheses
Lin, Wei-Hsiu	Quantitative Assessment of Balance Ability Among Different Sports Athletes
Linder-Ganz, Eran	Biomechanical Interactions of the Pelvis Girdles and Surrounding Soft Tissues: Toward Understanding the Mechanism of Pressure Sore Onset
Linhong, Ji	Recovery Strategy From Perturbation of the Upper Body During Standing Using Mechanical Energy Analysis
Linke, Wolfgang A	A Unique Sequence of Titin, the Pevk-Domain, is An Entropic Spring That Interacts with Actin
Linke, Wolfgang A	Passive Elastic Recoil of Titin Adds To the Shortening Speed of Skeletal Muscle Fibers
Linnamo, Vesa	Neuromuscular Fatigue During and After Eccentric and Concentric Exercises
Lippert, Samuel A	The High Frequency Material Properties of Brain Tissue as Determined by Ultrasound
Lipsitz, Lew	Age-Related Effects on Momentum Generation and Muscle Activity During Gait-Initiation
Lipsitz, Lewis	Dynamics of Cerebral Blood Flow Regulation Using a Lumped Parameter Model
Lipsitz, Lewis	Effect of Stochastic Electrical Joint Stimulation on Balance Control in Older Adults
Litavish, Michael	Comparison of Transient Force Attenuation Between Three Types of Heel Cushions Used in Running Shoes
Liu, Bo	Effects of Low Shear Stress on Morphological Remodeling of Organ-Cultured Artery in Vitro
Liu, Gen-Zhe	Intervertebral Disc Metabolism Under Mechanical Load: the Role of Extracellular Physical Factors
Liu, Hao	Experimental Assessment of Hydrodynamics of a Mechanical Pectoral Fin
Liu, Hao	Hydrodynamics of a Flapping Fin with Interaction of a Body
Liu, Hao	Multi-Scale Computational Hemodynamics in Cardiovascular System
Liu, Hao	Non-Invasiveassessment of Left Ventricle Function with a Computational Fluid Dynamic Model
Liu, Hao	Optimization of Motion of a Mechanical Pectoral Fin
Liu, Heng-Liang	Numerical Simulation of Interfacial Stress for Extensive Premolar Cavity Under Different Occlusal Forces
Liu, Shu Q	An in Vivo Experiment-Based Growth Model for Intimal Hyperplasia in Rat Vein Graft
Liu, W	Biomechanical Stability of Multi-Level Cervical Spine Instrumentation: Comparison of Constrained Versus Semi-Constrained Anterior Cervical Plates
Liu, Wen	Movement Synergy Between the Ankle and Hip Joints During Single Leg Stance
Liu, WH	Effect of Compression on Beta-1 Integrins (CD49d, CD49e) and CD44 Adhesion Molecules Expressed by Articular Condrocytes
Liu, Xiangyi	Anisotropy of Modulus Changes in Trabeuclar Bone Following Shear Overloading
Liu, Y-M	Design of a Biofidelic, Instrumented 2.5 Kg Infant Dummy
Liu, Yong-Ming	The Expression of ICAM-1 Induced by Shear Stress Upregulated Via NFKB Activation
Liu, Yu-Liang	Finite Element Analysis of the Cervico-Trochanteric Stemless Femoral Prosthesis
Liu, Zhihong	Modelling the Solidification of Aqueous Solutions: a Coupled-Field Finite Element Approach
Livengood, Ann L	Biomechanical Assessment of the Ankle and Knee During Landing From a Lateral Drop Jump with a Prophylactic Ankle Brace

Louis, Bruno	A Multi-Segmental Model of the Coupling of Inspiratory Flow with the Compliant Nose Structure Assessed in Vivo.
Lovas, Antal	In Vivo Time-Dependent Tensile Deformability of Human Lumbar Spine Segments, Measured in Traction Bath Therapy in Terms of Aging, Sexes, Weight
Lowne, R	Dynamic, Biomechanical Characteristics of Human Ankle Ligaments
Lowne, R	Failure Analysis of the Lower Limb in Axial Impact Loading
Lownie, Stephen P	Computed Blood Flow Dynamics in An Anatomically Realistic Cerebral Aneurysm
Lu, DS	Sr-Ha Bioactive Bone Cement Characterization and Animal Trials
Lu, Tung-Wu	Measurement of Three-Dimensional Kinematics of the Glenohumeral Joint During Manual Wheelchair Propulsion Using Skeletal
Lu, Tung-Wu	Stepping Over Obstacles During Locomotion in Anterior Cruciate Ligament Patients
Lu, W W	EMG Changes in Paraspinal Muscle of Scoliosis Patients After Spinal Fusion
Lu, William	Fatigue and Wear Evaluation of a Novel Artificial Finger Joint
Lu, WW	Compressive Strength in Vertebroplasty Under Fatigue Loading
Lu, WW	Sr-Ha Bioactive Bone Cement Characterization and Animal Trials
Lu, Xiyun	Cross-Flows Associated with Shear Stress Gradients on the Flow-Endothelium Interaction
Lu, Yiling	Cross-Flows Associated with Shear Stress Gradients on the Flow-Endothelium Interaction
Lucas, Carol	Analysis of Total Cavopulmonary Connection Fluid Dynamics: Experimental Studies
Luchies, Carl	Effects of Age and Time Period on Joint Kinematics and Kinetics During a Single Step Response
Luchies, Carl	The Effects of Age and Feedback on Isometric Knee Force Control Abilities
Luder, Gerhard	Ground Reaction Forces on Stairs
Ludewig, Paula M	The Effect of Forefoot and Arch Posting Orthotic Designs on Hallux-First Metatarsal Kinematics During Gait
Lugner, Peter	Adjustment of Individual Stimulation Patterns for Fes Cycling
Lugner, Peter	Cycling by Means of FES: Simulation and Practical Application
Lugner, Peter	Dynamic Skiing: Influences of Snow and Ski Properties
Luhtanen, Pekka	Effects of Equipment and Performance Characteristics on Ski Jumping Performance
Luk, K D K	EMG Changes in Paraspinal Muscle of Scoliosis Patients After Spinal Fusion
Luk, KDK	Compressive Strength in Vertebroplasty Under Fatigue Loading
Luk, KDK	Sr-Ha Bioactive Bone Cement Characterization and Animal Trials
Lund, Adrian K	Effect of Bumper Design on Whiplash Injury Risk as Measured by Biorid
Lundberg, Hannah	Ankle Articular Cartilage Thickness is Accurately Measured with Multi-Detector Computed Tomography (Mdct)
Luo, Xiao Yu	Computational Fluid Dynamics (CFD) Simulation of the Human Biliary System
Luo, Xiao Yu	Self-Excited Oscillations in a Fluid-Beam Collapsible Channel
Luo, XiaoYu	Modelling the Nonlinear Anisotropic Porcine Heart Valves
Lusardi, Theresa A	Effect of Ethanol on Neuronal Strain Transduction
Lusk, Jason	Center of Pressure Migration During Prolonged Unconstrained Sitting
Luthringer, Kristin	Alcohol and Ovariectomy Effects on Trabecular Bone in Female Rats
Lutz, Gordon J	Biological and Biomechanical Response of Rat Dorsiflexors To Eccentric Exercise
Lutz, Gordon J	Increased Desmin in Rat Dorsiflexors After a Single Bout of Eccentric Exercise
Lyle, Mark	Comparison of Clinical Performance and Stabilogram Measures in Patients with Degenerative Lumbar Spinal Stenosis
Lynch, Heather Anne	Do Constant-Rate Ramp Tests Represent Equilibrium Behaviors in Tendon?
Lyons, Garrett	Micro-Tensile Testing of Individual Trabeculae From Normal, Ageing, and Ovarectomised Rat Bones

M

Mahar, Andrew	Biomechanical Comparison of the Luque-Galveston and Colorado Ii Methods for Sacropelvic Fixation
Mahar, Andrew	Biomechanical Comparison of the Triage Medical Compression Screw To the Synthes Screw for Use in Lower Extremity Fractures and Fusions
Mahar, Andrew	Biomechanical Efficacy of a Protein Polymer Hyrdrogel for Inter-Vertebral Nucleus Augmentation and Replacement
Mahar, Andrew	Biomechanical Stability Between Two Types of Periacetabular Osteotomies for Surgical Correction of Developmental Deformities of the Hip
Mahar, Andrew	Failure Load for Single Screw Versus Single Screw Plus Staple Constructs in the Pediatric Thoracic Spine: Differences Between Plowing and Levering
Mahar, Shannon M	Accuracy and Reliability of Q Angle Measurement Methods
Mahfouz, Mohamed	Global Optimization for Recovering the Position and Orientation of Free-Form Objects in Medical Imaging Registration Using a New Smoothing Approach
Mahfouz, Mohamed	In Vivo Forces and Motions From Fluoroscopy and Mathematical Modeling
Mahfouz, Mohamed	Muscle Reconstruction and Modeling From Mri-Scan
Mahfouz, Mohamed	Verification of Three-Dimensional Joint Kinematics Determined Using Fluoroscopy: An Error Analysis
Mahoney, O M	A Comparison Between Single-Radius and Multi-Radius Total Knee Arthroplasties for Stand To Sit (An EMG and Kinematic Study)
Mainenti, Míriam R M	Modification in the Postural Control During Long-Term Standing
Majd, Shervin Ghasemi	Dynamic Stress Analysis of the Arterial Wall with Finite Element Modeling
Majima, Tokifumi	Chitosan-Based Hyaluronan Hybrid Polymer for Scaffold in Ligament Tissue Engineering
Majima, Tokifumi	Novel Alginate-Chitosan Hybrid Fibers as a Scaffold for Tendon Or Ligament Tissue Engineering
Majumdar, Sharmila	Investigation of Structure-Property Relationships in Human Femoral Trabecular Bone
Makhsous, Mohsen	In Vivo & Noninvasive Load Sharing Among Quadriceps Components in Patellar Malalignment
Makhsous, Mohsen	In Vivo Patellar Tracking in Patellar Malaligned Knees
Makhsous, Mohsen	Modeling of ACL Impingement Using Simm
Maki, Brian E	Importance of Plantar-Surface Mechanoreception in Postural Control
Maki, Koutarou	Individual Stress Analysis of the Human Mandible Under Biting Conditions
Mäkinen, Tatu J	Precision Measurements of Rsa Method Using a Phantom Model of Hip Prosthesis
Makinouch, Akitake	Simulation of Scleral Buckling Operation on An Eyeball by Using Fem Program for Coupling Analysis of Hyperelastic Solid and Static Liquid
Makinouchi, Akitake	Evaluation of Mechanical Stimulus for Trabecular Surface Remodeling Using Digital Image-Based Model
Makinouchi, Akitake	New Method of Three-Dimensional Imaging of Small Airways in Rats with X-Ray Micro-Ct
Makris, Aris	A Method for Assessing the Overall Impact Performance of Helmets Used in Crowd Management Interventions
Makris, Aris	Comparison of Simulated Projectile and Baton Blow Impacts on Shin Guards Used in Crowd Management Intervention
Makris, Aris	Reduction of Blast Induced Head Acceleration and Concussive Head Injury Potential
Mallinson, Gordon	Haemodynamics of the Fontan Connection
Malone, Brian	Ankle Kinematics Using One and Two Segment Foot Models
Maloney, SK	How Economical is Human Bipedal Locomotion?
Manal, Kurt	An EMG-Driven Biomechanical Model of the Human Elbow: Fitting a Generic Model To Specific Subjects
Manal, Kurt	Are Estimates of Quadriceps Strength Valid? Implications for Clinical Decision Making

Mangat, Jasdip	Correlation Between Radiographic and Clinical Measurement of Sagital Back Shape
Manley, Eugene	Testing Duration Required To Accurately Predict Ligament Viscoelasticity
Manley, Eugene	The Effects of Hydration Time on Ligament Viscoelasticity
Mann, Kenneth	Can Piece-Wise Linear Interface Models Be Used To Predict the Failure Response of the Cement-Bone Interface?
Mann, Kenneth	Directional Dependence of Early Fatigue Damage in Cemented Total Hip Replacements
Mann, Kenneth	Early Cement Damage Around a Femoral Stem is Focused on the Cement/Bone Interface
Mann, Kenneth	Shrinkage of Vacuum Mixed Cement Causes Interface Gaps and Stress Concentrations in Cement Mantles Surrounding Femoral
Manning, Keefe B	Understanding the Mechanisms of Mechanical Heart Valve Cavitation
Manning, P	Dynamic, Biomechanical Characteristics of Human Ankle Ligaments
Manning, P	Failure Analysis of the Lower Limb in Axial Impact Loading
Manning, P	The Effect of Bone Quality on Intra-Medullary Fixation of the Proximal Humerus Using a Retro-Grade Nail
Manson, Neil	Rearfoot Motion & Tibial Acceleration in the Running Athlete
Manthei, David	Anesthetic Effects on Muscle Performance
Marai, GE	Contact Areas and Ligament Lengths are Abnormal in Patients with Malunited Distal Radius Fracture Despite Normal Radioulnar Kinematics
Maraj, Brian	Treadmill Speeds Related To Sprinting Ability
Marchuk, Linda	Ligament Autograft Cells Do Not Die by Apoptosis
Marchuk, LL	The Healing of ACL and Mcl Injuries is Initially Similar But Diverges with Time
Margielewicz, Jerzy	The Movement of a Man's Bottom Limb in the Multibond Graphs Representation
Margueratt, Sean D	In Vitro Exploration of Synergies Between Fatigue Damage and Proteolysis in Bovine Pericardial Bioprosthetic Materials
Margulies, Susan S	Material Properties of Porcine Parietal Cortex
Margulies, Susan S	Predictions of Infant Brain Injures in Minor Falls and Inflicted Events
Margulies, Susan	Pulmonary Epithelial Cell-Matrix Signalling Via Alpha-6/Beta-4 Integrin
Marigold, Daniel S	Medial-Lateral Cop Velocity During Standing Relates To Asymmetry and Functional Balance in Individuals with Stroke
Marigold, Daniel S	Muscular Response of the Swing Limb and Arms During An Unexpected Slip
Marinoni, EC	Gait Features Assessment in Hip Osteoarthritis and Total Hip Replaced Patients Based on An Ambulatory System (Physilog)
Markel, Mark D	A Comparison of Joint Mechanics Between Anterior Cruciate Ligament Intact and Deficient Stifles: a New Model of Anterior Cruciate Ligament Disruption
Markopoulou, Ekaterini	A Dynamical Analysis of Parkinsonian Gait
Marks, Michelle	A Non-Invasive Approach for Measuring Sagittal Balance of the Spine
Marks, Michelle	Analysis of Sagittal Balance of the Spine During Various Standing Positions and Gait
Marlow, Darran	Biomechanics of Prone Continuous Passive Motion for Low Back Pain
Marras, W S	Towards the Development of a Cumulative Trauma Metric for Occupationally-Related Musculoskeletal Disorders
Marschel, Peter	Control Mechanisms of the Fluid Shear Response in Circulating Leukocytes
Marsh, J	Radiographic Landmark Assessment of the Knee Joint Flexion-Extension Axis
Marsh, Richard L	Mechanical Function of Leg Muscles in Running Birds
Marsh, Richard	Fitting Muscle Properties
Marshall, Bryan	Force Dependence of the P-Selectin/PSGL-1 Bond Dissociation
Marshall, Bryan	Measuring Spring Constants of the P-Selectin/Psgl-1 Molecular Complexes by Afm
Marshall, I	A Comparative Study of CFD and MRI for Pulsatile Flow in a Carotid Bifurcation Phantom

Matsuda, Takehisa	Engineered Arterial Reconstruction: Integration of Biomechanical, Genetic, and Stem Cell Engineering
Matsumoto, Akihiro	A Gait Orthosis for Paraplegics with a Motor-Driven Knee Joint
Matsumoto, Joseph	Comparison of Quantitative Measures of Tremor as Predictors of Surgical Outcome
Matsumoto, Nobuyuki	Mechanical Energy Transfer by Two-Joint Leg Muscles During Snatch Lift
Matsumoto, Tadami	Evaluation of Shape Accuracy in Ct Based Femur Model for Prosthetic Stem Design
Matsumoto, Takeo	Biaxial Tensile Properties of Aortic Aneurysm Tissues Under Equibiaxial Stress
Matsumoto, Takeo	Residual Stress and Strain in the Lamellar Unit of the Aorta: Experiment and Analysis
Matsumoto, Takeo	Rupture Properties of Thoracic Aortic Aneurysms Using Pressure-Imposed Experiment
Matsumoto, Takeshi	Spatial Flow Pattern Difference Between Blood- and Crystalloid-Perfused Myocardium
Matsumoto, Yuki	Measurement of Erythrocytes Deformability with Counter-Rotating Parallel Disk System
Matsushima, Shigeru	Measurement of the Encephalon Physical Parameter with MRI Saturation Transfer Method
Matsuzaki, Yuji	Experimental Study on Air Flow in a Two-Dimensional Channel with An Obstruction Oscillating At 10 Hz To 100 Hz
Mattila, Kimmo T	Precision Measurements of Rsa Method Using a Phantom Model of Hip Prosthesis
Mattsson, Louise	The Effect of Changing Anteversion on Forces on the Proximal Femur
Matyas, John	In-Situ Chondrocyte Deformation in Early Stage Osteoarthritic (Oa) Articular Cartilage
Matyas, JR	The Effect of Varying Frequencies on the Stimulation of the Aggrecan Promoter of Chondrocytes Embedded in Agarose Gels
Mau, Kenneth	Speed and Cadence Differences Between Cornering and Straight Track Riding in 4km Individual Pursuit
Maurel, Nathalie	A 3D Finite Element Model of An Implanted Scapula Using Cadaveric Data for Evaluation
Maurel, Nathalie	Protocol for in Vivo Optoelectronic Kinematics Analysis of Shoulder
Maurel, Nathalie	Simultaneous Strains and Displacements Analysis of Implanted Femurs by in Vitro Study and Finite Element Modelling
Maurer, Jessica	Locomotion Research Within An Orthopaedics Framework: Successes and Challenges
Maurer, Jessica	Techniques for Avoiding Hip Impact During Unexpected Sideways Falls
Mayer, John	The Role Of Dynamnic Stresses During Incubation In Increasing Tehv Tissue Strength
Mayr, Winfried	Adjustment of Individual Stimulation Patterns for Fes Cycling
McArthur, Tina	Biomechanical Efficacy of a Protein Polymer Hyrdrogel for Inter-Vertebral Nucleus Augmentation and Replacement
McCabe, GN	Hand Impact Force Reduction in Forward Falls in Young Males: a Prosprctive, Controlled, 3-Month Intervention Trial
McCabe, Ron	Anesthetic Effects on Muscle Performance
McCall, WD	Tests of Numerical Models of Craniomandibular Mechanics
McCann, Jennifer	Soluble Proteins Released by Endothelial Cells in Response To Fluid Flow Affect Smooth Muscle Cells
McCarthy, Ian	The Effect of Changing Anteversion on Forces on the Proximal Femur
McCarty, Jeff	Consistency of Putter Trajectory and Golf Putting Accuracy
McClure, Phillip	The Pattern of Scapulohumeral Motion - How Stable is It?
McCorrmick, Kristin	Markov Model Suggests Neuromuscular Aging Affects Short-Range Correlations Present in the Gait Cycle

McCrea, Patrick H	Effects of Target Distance and Size on Reaching Kinematics in Individuals with Hemiparesis
McCrea, Patrick H	Linear Model of Resistance To Passive Stretching in Individuals with Brain Injury: Reliability & Validity
McCrory, Jean	A Comparison Between Gait Kinetics in Women with Primary Osteoarthritis and Women with Osteoporosis
McCulloch, Andrew D	Asynchronous Electrical Activation in a Three-Dimensional Model of Cardiac Electromechanics
McCulloch, Andrew D	Cytoskeletal Defects Alter Myocardial Mechanics Before the Heart Fails
McCulloch, Andrew	Analysis of 3-Dimensional Culture of Cardiac Myocytes and Fibroblasts That Simulate Mechanical Conditions in Vivo
McCulloch, Andrew	Effects of Sarcomere Length, Ca2+ and Stimulation Rate on Force Generation of Mouse Cardiac Muscle
McDermott, Kelly	Molecular and Cellular Analysis of Rotator Cuff Tendinosis in a Rat Overuse Model
McDonald, J	Design of a Biofidelic, Instrumented 2.5 Kg Infant Dummy
McDonough, Daniel	Hydrodynamic Shear and Tethering on E-Selectin Signals Adhesion of Human Neutrophils
McElhaney, James	Biomedical Aspects of Helmet Design
McElhinny, Abigail S	Titin Interacts with Murf-1 To Regulate Sarcomeric M-Line and Thick Filament Structure
McEntire, B Joseph	Comparative Neck Load Measurements In An Instrumented Manikin Exposed To Parachute Drops From A Uh-60 Black Hawk
McEver, Rodger P	Force Dependence of the P-Selectin/PSGL-1 Bond Dissociation
McEver, Rodger	Measuring Spring Constants of the P-Selectin/Psgl-1 Molecular Complexes by Afm
McEwen, Hannah M J.	The Effect of Uhmwpe Material and Knee Design on in Vitro Wear of Fixed Bearing and Rotating Platform Mobile Bearing Total Knee Replacements
McFadden, Alexander	Analysis of 3-Dimensional Culture of Cardiac Myocytes and Fibroblasts That Simulate Mechanical Conditions in Vivo
McFadyen, Bradford J	Visuo-Locomotor Control During Anticipatory Locomotor Adjustments
McFadyen, Bradford J	Walking Around Static and Mobile Upright Obstacles
McFarland, David H	Adapting Body Segment Parameters for Biomechanical Calculations in Children
McFaull, Steven R	The Epidemiology and Biomechanics of Bicycle Handlebar Impact Injuries in Children
McGann, Locksley E	Ice in Tissues
McGill, SM	Torso Positions of Minimum Passive Tissue Strain - Where Do We Sit, Stand and Walk
McGill, Stuart M	Coordination of Muscle Activation To Assure Stability of the Lumbar Spine
McGill, Stuart M	Quantifying the Contribution of Individual Muscles To Lumbar Spine Stability
McGill, Stuart M	The Role of Transversus Abdominis in Spine Stability
McGinnis, Peter M	Twist Angular Momentum During the Pole Vault Take Off
McGloughlin, Tim	Biomaterials as Extracellular (Ecm) Matrices
McGloughlin, Tim	Comparative Analysis of the Hemodynamics Through Healthy and Diseased Models of the Human Abdominal Aorta
McGloughlin, Tim	Ecm(Extracllular Matrix) Scaffolds for Tissue Engineering: Biocompatibility and Biodegradability
McGloughlin, Tim	Investigations of Wall Deformation and Hemodynamics
McGloughlin, Tim	On the Errors Surrounding Hemodynamic Analyses: Comparisons of Various Techniques
McGloughlin, Tim	On the Existence of An Optimum End-To-Side Graft/Artery Junction Geometry To Increase the Patency Rates of Bypass Surgery

McGovern, Robert D	Strain Rate Sensitivity of Ligaments Diminishes At Traumatic Loading Rates
McGowan, Craig	In Vivo Muscle Force-Length Behavior During Inclined Hopping in Tammar Wallabies
McGregor, Alison	The Assessment of Cervical Spine Kinematics Using Interventional Mri
McGregor, Alison	The Assessment of Spinal Kinematics During the Application of An A-P Mobilisation
McGregor, Alison	The Assessment of Spinal Motion During Rowing
McGregor, Alison	The Development of a Preliminary Finite Element Model of the 5th Rib
McGruder, J	The Effects of a Home-Based Forced-Use Intervention on Individuals with Cerebrovascular Accident
McGuigan, MP	Passive Elastic Properties of Biceps; Contribution To Locomotor Economy in the Horse (Equus Callabus)
Mciff, Terence E	Design Factors Affecting the Contact Stress Patterns in a Contempory Mobile Bearing Total Ankle Replacement
Mciff, Terence E	Finite Element Modeling of Total Ankle Replacements for Constraint and Stress Analysis
McIlroy, William E	Importance of Plantar-Surface Mechanoreception in Postural Control
McIntire, Kevin	Movement Synergy Between the Ankle and Hip Joints During Single Leg Stance
McIntire, L	Modulation of Cytochrome P450 (Cyp) 1a1 and 1b1 and Ctgf Expression by Shear Stress
McIntire, Larry V	Identification of Genes Regulated by Mechanical Forces Using Microarray Technology in Human Endothelial Cells
McIntosh, Fiona	Hydrodynamic Shear and Tethering on E-Selectin Signals Adhesion of Human Neutrophils
Mckean, Kelly	Rearfoot Motion & Tibial Acceleration in the Running Athlete
McKee, K	Damped Knee Control for Transfemoral Prostheses in Developing Countries
McLean, Scott G	Forward Dynamic Modeling of Acute Injury: Effective Methods for Optimization, Validation, and Experimentation
McLean, Scott	Determining Neuromuscular Contributions To ACL Injury Risk Via Computer Simulation
McLellan, Lindsay	Different Muscle Activation Patterns During Walking and Response To Common Peroneal Stimulation
McMahon, Patrick J	Kinematics of the Glenohumeral Joint During the Anterior and Posterior Drawer Test
McMorland, Gordon	Changes in H-Reflex Amplitude After Spinal Manipulation in Healthy and Pathological Subjects
McNabb, Mark	Mutations of Titin Cause Dilated Cardiomyopathy
McNabb, Mark	Post-Translation Modification of Titin and Effects on Passive Tension in Cardiac Myocytes.
McNally, D	Three-Dimensional Acoustic Microscopy of the Intervertebral Disc: Visualisation of Lamellae, Collagen Bundles and Lesions.
McNally, Donal	A New Method for Quantifying Fibre Bundle Orientation Within Intact Intervertebral Discs Using 3-D Scanning Acoustic Microscopy.
McNamara, Laoise	Micro-Tensile Testing of Individual Trabeculae From Normal, Ageing, and Ovarectomised Rat Bones
McNeal, Anna	Analysis of 3-Dimensional Culture of Cardiac Myocytes and Fibroblasts That Simulate Mechanical Conditions in Vivo
McNitt-Gray, J L	Control Objectives Change Between Phases of Jumping and Landing Tasks
McNitt-Gray, JL	Conflict Between Momentum and Balance Control During Landing
McNitt-Gray, JL	Multijoint Control During Short Duration Movements
McNutt, J	Temporal Pattern Recogntion Techniques Can Detect EMG Differences Between Moderate Knee Osteoarthritis Patients and Healthy Controls During Walking

McPherson, Moira N	On-Ice Acceleration as a Function of the Wingate Anaerobic Test and a Biomechanical Assessment of Skating Technique in Elite Ice Hockey Players
McPoil, Thomas G	Plantar Pressure Measurements as An Outcome Measure for Interventions Used To Treat Forefoot and Midfoot Pain
McQuade, Kevin	Glenohumeral Joint Laxity with and Without Rotator Cuff Contraction
McVay, Bobby J	Biomechanics of Cervical Spine Surgery: Comparison of Fusion and Nonfusion Instrumentation
McVeigh, Elliot	Studying Electromechanical Behavior in Vivo with MRI Tagging and Epicardial Electrical Mapping
Meaney, David F	Correlates Between Continuum and Microstructural Descriptions of Central Nervous System White Matter
Meaney, David F	Effect of Ethanol on Neuronal Strain Transduction
Mecham, Cherianne	Bicycle Seat Designs and Their Effect on Pelvic Angle, Trunk Angle, and Comfort in Females During Cycling
Mechefske, Dr C	Damped Knee Control for Transfemoral Prostheses in Developing Countries
Meckmongkol, Teerin T	Effect of Expressiveness on the Kinematics of Arm Gestures
Medina, Raul U	A 2-D Analysis of Temporomandibular Joint Loading Generated During Bilateral Biting At the Molars and Premolars
Meehan, Sean	Investigations of Wall Deformation and Hemodynamics
Mehta, Amit	Single Molecule Mechanics and the Myosin Family of Molecular Motors
Meijer, Onno G	Function and Trigger of Changes in Synergy of Lumbar and Thoracic Erector Spinae Muscles.
Meijer, Riske	Effects of Muscle Activation and Seating Posture in Rear End Impact Using a Human Model with a Detailed Neck
Meile, Walter	Basic Problems Associated with Wind Tunnel Measurements and CFD in Sports
Meister, Jean-Jacques	Cell Structure and Function: Plenty of Room for Biomechanics
Melcher, Pia	Biomechanical Analysis of Takeoff To Back Handspring and Backwards Somersault
Mello, A Prina	Experimental Analysis of Lymphatic Cells Motion Under Topographical Control
Melsen, Birte	New Insights Into Orthodontic Load Transfer and Alveolar Bone Remodeling
Menegaldo, Luciano Luporini	Neuromuscular Excitation Patterns of Human Posture Through An Optimal Control Approach
Meng, Chou Siaw	Strain Rate Effect on the Tensile Properties of Flexor Tendon
Meng, Chou Siaw	The Effect of Postmortem Freezing Storage on the Tensile Properties of Tendon
Meng, Hui	The Hemodynamic Effects of Parent Vessel Inflow Angle on a Cerebral Sidewall Aneurysm
Menzel, Gerhard	Biodynamic Data Set for Modelling Car Drivers
Merkle, Andrew	Experimental Evaluation of a Model of Contact Pressure Distribution in the Hip Joint
Merrifield, Robert	Study of the Intra-Ventricular Blood Flow by CFD and Mri
Mertens, Maureen	Molecular and Cellular Analysis of Rotator Cuff Tendinosis in a Rat Overuse Model
Mester, Joachim	Modeling of Slope and Trajectory in Alpine Skiing
Metaxas, Dimitris N	Three-Dimensional Kinematics of Right Ventricular Systolic Contraction
Metzger, Dennis W	Effects of Cyclic Pressure on Select Bone Cell Functions Pertinent To Bone Hoeostasis
Meunier, Alain	Effects of Cyclic Pressure on Select Bone Cell Functions Pertinent To Bone Hoeostasis
Meunier, Alain	Ultrasound Wave Propagation in Porous Medium. Application To Cancellous Bone
Mey, Stefaan De	Study of Left Ventricular Filling: Comparison of Hydraulic and Numerical Modelling
Meyerson, Shari L	Effective Hemodynamic Diameter: a Parameter with Predictive Value for Patency
Meyhöfer, Edgar	Observation of Displacement Steps by Single Myosin Id and Myosin Ii Molecules
Michener, Lori	The Pattern of Scapulohumeral Motion - How Stable is It?

Michna, Horst	Mechanical Properties of Cartilage Specimen in Rats -
Mickovski, S B	Overturning Resistance of Rigid Tap Roots
Middleton, John	A Nonlinear Elastic Transversely Isotropic Constitutive Law for the Pdl: Analytical and Computational Aspects
Middleton, John	Effective Contact Conditions Between Cementless Coated Hip Implant and Bone
Middleton, John	Three-Dimensional Finite Element Analysis of the ACL Under Anterior Tibial Loads
Midura, Ronald J	Pulsed Electromagnetic Field-Dependent Stimulation of Pre-Osteoblast Proliferation in Vivo
Midura, Ronald	Magnetic Field Visualization in Applications To Pulsed Electromagnetic Field Stimulation of Tissues
Midura, Ronald	Pulsed Electromagnetic Field-Dependent Differencesof Collagen Processing in Pre-Osteoblasts
Miesch, Jennifer	Swelling of Organotypic Brain Cultures as a Model for Traumatic Brain Injury
Miftakhov, Roustem	Self-Sustaining Oscillatory Electromechanical Activity in the Gut
Migliavacca, Francesco	Computational Fluid Dynamics After Aortic Coarctation Repair
Mikami, Taisei	CFD Studies of the Intraventricular Diastolic Flow for the Analysis of Color M-Mode Doppler Echocardiogram
Milani, Terese L	Relationship of Perception Vs. the Measurement of Plantar Pressures - a Neurosensory Approach
Milani, Terese L	Somatosensory Input in the Control of Human Posture in Patients with Morbus Parkinson
Milani, TL	Effect of Physical Therapy and Afferent Stimulating Insoles on Motor Abilities in Parkinson Patients
Mileusnic, Milana	Biomimetic Approaches To Stable Systems for Functional Electrical Stimulation
Millar, Karol	Application of Fibre Laser Scanning Confocal Microscopy To Study of the Biomechanics and Microstructure of Articular Cartilage
Miller, Chris	Variation in Treadmill Walking Due To Combinations of Visual Scene Motion and Gravity-Assist
Miller, Doris I	Searching for Optimal Knee Extension Timing in Dives From the Reverse Group
Miller, G Roger	Is Active Force Production of Skeletal Muscles Altered by Collagen Content?
Miller, J	Comparative Analysis of Joint Compliance by Finite Element Analysis and Electronic Speckle Pattern Interferometry
Miller, Karol	Mechanical Behaviour of Baseballs During Compressive Loading To Bat-Ball Impact Level
Miller, Karol	The Development of Confocal Arthroscopy for the Assessment of Cartilage Disorders
Miller, Mark C	Effect of Polyethylene Thickness on Stresses of An Ankle Joint Implant
Miller, Mark C	Torsional Stability of Total Elbow Arthroplasty
Miller, Mark C	Use of Local Bodily Landmarks in Acetabular Cup Positioning
Miller, Mark	Can Piece-Wise Linear Interface Models Be Used To Predict the Failure Response of the Cement-Bone Interface?
Miller, Mark	Directional Dependence of Early Fatigue Damage in Cemented Total Hip Replacements
Miller, Mark	Early Cement Damage Around a Femoral Stem is Focused on the Cement/Bone Interface
Miller, Mark	Shrinkage of Vacuum Mixed Cement Causes Interface Gaps and Stress Concentrations in Cement Mantles Surrounding Femoral
Miller-Young, Janice	Material Properties of the Human Calcaneal Fat Pad: Validation Experiments
Millet, P	Residual Stresses Analysis At the Interface Between Hydroxyapatite Coating and Titanium Substrate
Millett, Peter	Quadriceps Weakness Causes An Increase in the Peak Adductor Moment During Gait

Mizuno, Masashi	Evaluations of Hip Fracture Mechanism and Prevention by Using Dynamic Fe Analyses
Mladenova, Clementina D	Rotations of the Human Knee
Mochizuki, Seiichi	Ca2+ Responses and Its Propagation in Cultured Endothelial Cells To Cytosolic Mechanical Stimulation by Laser Tweezers
Moffet, Hélène	Active Movements of the Shoulder Girdle in Healthy Subjects: a Validity Study
Mogk, Jeremy	Assessment of Crosstalk in Surface EMG of the Forearm
Mogk, Jeremy	Common Function of Forearm Muscles During Gripping
Mohammadi, H	Dynamic Behavior of Sj in Close Phase
Mohtadi, Nicholas GH	Relation Between Knee Range of Motion Measured Passively and During Gait in Anterior Cruciate Ligament Deficient and Reconstructed Individuals
Moisio, Kirsten	Peak Hip Joint Moments During Walking and Jogging are Correlated with Proximal Femoral Bone Mineral Density
Molnár, Peter	In Vivo Time-Dependent Tensile Deformability of Human Lumbar Spine Segments, Measured in Traction Bath Therapy in Terms of Aging, Sexes, Weight
Molthen, Robert C	Effect of Ventilation on Instilled Liquid Transport in the Pulmonary Airways of Rats
Mongrain, Rosaire	Biomechanics of Plaque Rupture in Atherosclerosis Coronary Arteries
Mongrain, Rosaire	Mechanical Aspects of Plaque Redistribution During Angioplasty: Possible Consequences on Vulnerability
Monori, Erika	In Vivo Time-Dependent Tensile Deformability of Human Lumbar Spine Segments, Measured in Traction Bath Therapy in Terms of Aging, Sexes, Weight
Montelpare, William J	On-Ice Acceleration as a Function of the Wingate Anaerobic Test and a Biomechanical Assessment of Skating Technique in Elite Ice Hockey Players
Montgomery, D	Forward Ice Hockey Skating: Comparison of EMG Activation Patterns At Three Velocities
Montgomery, D	The Effects of Stick Construction in the Performance of Ice Hockey Wrist Shot
Montgomery, David	Lower Limb Kinematics of Ice Hockey Forward Skating
Moody, Jill	Neuromuscular Responses To Knee Osteoarthritis During Stairway Locomotion
Mooney, Brian	Pelvic Floor Muscle Strains During Vaginal Brith
Moore Jr., James	Hemodynamic Modeling in Stented Arteries
Moore, DC	Contact Areas and Ligament Lengths are Abnormal in Patients with Malunited Distal Radius Fracture Despite Normal Radioulnar Kinematics
Moore, Douglas C	Strain Rate Sensitivity of Ligaments Diminishes At Traumatic Loading Rates
Moore, Susan M	Kinematics of the Glenohumeral Joint During the Anterior and Posterior Drawer Test
Mootanah, Rajshree	Evaluation of Alternative Material for the Prevention of Pressure Sores
Moraes, Renato	Reprogramming Sit-To-Stand and Sit-To-Walk Movement Sequence Under Different Temporal Constraints
Morag, Erez	Effect of Shoe Mass on Soccer Kicking Velocity
Morales, Abigail	Comparison of Transient Force Attenuation Between Three Types of Heel Cushions Used in Running Shoes
Morales, Nelson	Finite Element Model of the Epidermis-Dermis Interface
Morel, D R	Decreased Proximal Aortic Compliance Causes Systolic Hypertension
Morelli, Sandra	A Novel Equipment for the Assessment of Hand Forces
Morgan, Andre P	Effect of Shear Stress on the Activation of the Peroxisome Proliferator-Activated Receptors (Ppars)
Mori, Daisuke	Computational Fluid Dynamics Simulation of the Blood Flow in the Human Aortic Arch with Its Branches
Mori, Daisuke	Image Based Systematic Modeling of Large Arteries for Clinical Cardiovascular Medicine
Morikawa, Hirohisa	Experimental Assessment of Hydrodynamics of a Mechanical Pectoral Fin

Morikawa, Hirohisa	Flow and Wall Compression in High Grade Asymmetric Arterial Stenosis Models During Pulsatile Flow Experiments
Morikawa, Hirohisa	Hydrodynamics of a Flapping Fin with Interaction of a Body
Morikawa, Hirohisa	Optimization of Motion of a Mechanical Pectoral Fin
Morimont, Philippe	Aortic Leak Severity Determines Arterial Elastance And
Morin, Evelyn L	Comparison of 3 Measures of Grf; Force Plate, Fscan(r) and Multiple Force Sensors
Morin, Evelyn L	The Importance of Certain Design Features in a Backpack
Morin, Frédéric	Effects of Vibration Induced by Inline Skating on Neuromotor Functions
Morino, Taku	Blood Flow Structure Contributing To the Rupture of Cerebral Aneurysm
Morishima, H	Design of a Biofidelic, Instrumented 2.5 Kg Infant Dummy
Moritz, Chet T	Neuromuscular Adjustments for Hopping on a Heavily Damped Surface
Morley, Jeffery	Backpack Loads Carried by School Children
Morlock, Michael M	Activity Pattern and Joint Motion Profile of Total Knee Patients
Morlock, Michael M	Mechanical Properties of Cartilage Specimen in Rats -
Morlock, Michael M	The Influence of Resting Periods on Friction in the Artificial Hip Joint
Morlock, Michael	Biomechanical Testing of An Intramedullary Locked Nailing for Metacarpal Shaft Fractures
Morlock, Michael	Effects of Mechanical Stimuli on the Relaxation Behavior of the Growth Plate Related To Morphological and Biochemical Adaptation in the Rat Model
Morlock, Michael	Robotic Assisted Versus Manual Implantation - a Prospective Study in Primary Total Hip Replacement
Morris, Liam	Comparative Analysis of the Hemodynamics Through Healthy and Diseased Models of the Human Abdominal Aorta
Morrow, Duane	Comparison of Quantitative Measures of Tremor as Predictors of Surgical Outcome
Morrow, Duane	Intramuscular Pressure is An Indicator of Muscle Force
Moseley, G	Pain and Motor Control of the Spine: Effect and Mechanisms
Moseley, Lorimer	Function and Trigger of Changes in Synergy of Lumbar and Thoracic Erector Spinae Muscles.
Moses, Emily	Probabilistic Modeling of Rosette Formation on Selectin/Ligand Interactions
Moshref, Y	Movement Behaviour in Chronic Neck Pain Patients
Moss, Rebecca	Accuracy of Patellofemoral Joint Contact Area Predictions Using Mr Imaging
Moss, Rebecca	Insights Into In-Vivo Knee Mechanics with Magnetic Resonance Imaging
Mössner, Martin	Snow Friction and Drag in Alpine Downhill Racing
Mouchon, W Paul	Computer Simulation of Vibrational Diagnosis of Tha Lossening
Mouchon, W Paul	Numerical Modal Analysis of Cemented Femur Component of Total Hip Replacement
Moulart, Francoise	Monitoring of the Rehabilitation of Patients After Fracture
Mountney, J	Assessment of a Novel Femoral Component Removal Technique for Revision Surgery
Mouret, Frederic	Hydrodynamics of Mitral Prosthetic Heart Valves: Comparison of Normal Conditions with Atrial Fibrillation Varying the Heart Rate
Mouret, Frederic	Incidence of Valve Prosthesis Incline on Left Ventricle Flow Dynamics
Mouzin, Olivier	Buffy Coat Concentrate (Agf) with Allograft Improves Implant Fixation
Mowlem, M C	Assessment of a Novel Femoral Component Removal Technique for Revision Surgery
Moya, S	Mechanical Properties and Permeability of Polyelectrolyte Microcapsules (PEMC)
Moyer, Brian	Slip Anticipation Effects on Ground Reaction Forces
Moyer, Brian	Whole Body Biomechanics of Responses To Slips
Moyle, Keri	Haemodynamics of the Fontan Connection

N

Nichols, Rochelle	Mechanical Behaviour of Baseballs During Compressive Loading To Bat-Ball Impact Level
Nickel, Jeffrey	Plowing Forces and Stress Distribution on the Temporomandibular Joint Disc Surface
Nickel, Jeffrey	Tests of Numerical Models of Craniomandibular Mechanics
Nicol, Klaus	Influences on Eye Location and Posture of Drivers
Nicol, Klaus	Swing Phase Reduction in Above-Knee Amputee Running
Nicolaides, Eleftherios	Non-Invasive Measurement of Wave Intensity - Reproducibility and Effect of Gtn
Nicolaou, M	Gait Adaptations To Transverse Slopes
Nicosia, M	Finite Element Implementation of a Structural Model for Aortic Valve Tissue
Niebur, Glen L	Anisotropy of Modulus Changes in Trabeuclar Bone Following Shear Overloading
Niebur, Glen L	Application of Virtual Experiments To the Study of Trabecular Bone Mechanics
Niederer, P	A Biphasic Constitutive Law for Passive Cardiac Tissue
Niederer, Peter F	Theoretical Model Studies of Fluid-Solid Interactions in the Cervical Spine During Low-Speed Posterior Shoulder Impacts
Niederer, Peter	Finite Element Models of Abdominal Organs for Use in Trauma Research
Niederer, Peter	Time-Dependent Properties of the Porcine Kidney Capsular Membrane
Niehoff, Anja	Effects of Mechanical Stimuli on the Relaxation Behavior of the Growth Plate Related To Morphological and Biochemical Adaptation in the Rat Model
Niehoff, Anja	Mechanical Properties of Cartilage Specimen in Rats -
Nielsen, Jens	Effect of Different Pedal Rates on Endurance and Physiological Responces
Niemi, James	Effect of Stochastic Electrical Joint Stimulation on Balance Control in Older Adults
Nigg, Benno M	Biomechanical Properties of Total Ankle Arthroplasty and Ankle Arthrodesis
Nigg, Benno M	Effects of Custom Molding and Posting of Foot Orthotics on Lower Extremity Kinematics
Nigg, Benno M	Effects of Custom Orthotics on Lower Extremity Kinematics, Kinetics and Muscle Activity
Nigg, Benno M	Muscle Activity in the Lower Extremity Damps the Soft-Tissue Vibrations
Nigg, Benno M	Quantification of Soft Tissue Vibration Frequency in Heel-Toe Running
Nigg, Benno	Foot Sensation as a Predictor for Response To Footwear Interventions
Nightingale, Roger W	Cervical Spine Facet Capsular Ligament Strain in Midsagittal and Three Dimensional Whiplash-Like Loading
Niki, Kiyomi	A Novel Age-Related Index of Cardiovascular Function
Niki, Kiyomi	Wave Intensity in the Carotid Artery is a New Index of Left Ventricular Systolic and Early Diastolic Performance
Niklason, Laura	Mechanical Forces and Engineered Vessels
Nilsson, Niels	Changes in Range of Motion in the Cervical Spine Following Spinal Manipulation - a Review.
Nimgade, Ashok	Comparison of Clinical Performance and Stabilogram Measures in Patients with Degenerative Lumbar Spinal Stenosis
Nishikawa, So	Class Vi Myosin Moves Processively Along Actin Filaments Backwards with Large Steps
Nishino, Katsutoshi	Comparative Study Between Intra- and Post-Operative Knee Motions After Total Knee Arthroplasty
Nishino, Katsutoshi	Motion and Contact Analyses of Patello-Femoral Joint After Total Knee Arthroplasty
Nishino, Mitsuru	Evaluation of Shape Accuracy in Ct Based Femur Model for Prosthetic Stem Design
Nishino, Takashi	Experimental Study of An Artificial Knee Joint with PVA-Hydrogel Cartilage
Nishiya, Takako	Reconstitution of Gpiba-Mediated Platelet Behavior in Microcirculation
Nishri, Boaz	Arterial Blood Filtration for the Prevention of Ischemic Stroke

Nishri, Boaz	Is Permanent Arterial Filtration Possible? in Vivo Assesment of a Filtration Device for Embolic Stroke Prevention
Nishri, Boaz	Optimization of a New Blood Filtration Device for Embolic Stroke Prevention
Niwa, Koichi	The Effect of a Shear Flow on the Uptake of Ldl by An Ec-Smc Bilayer in Culture
Nixon, Mark S	Automated Markerless Analysis of Human Walking and Running by Computer Vision
Nixon, Mark S	Lumbar Spine Motion Analysis Via Automatic Segmentation
Nobile, F	Numerical Simulation of the Cardiovascular System : a Multiscale Approach
Nogawa, Satoshi	Effect of Cell Density on Viability of Artificial Tissue After Cryopreservation
Noiri, Eisei	Rescue by Transplantated Endothelial Cells for Ischemic Renal Failure Visualization of Peritubular Capillaries Using Intravital Videomicroscopy
Noland, Stacia	Movement Synergy Between the Ankle and Hip Joints During Single Leg Stance
Nolte, Lutz P	Surgical Navigation
Nolte, Lutz-Peter	Convective Molecular Transport in the Intervertebral Disc
Nomura, Kiyoe	Blood Flow Structure Contributing To the Rupture of Cerebral Aneurysm
Nonaka, Sachiko	Chitosan-Based Hyaluronan Hybrid Polymer for Scaffold in Ligament Tissue Engineering
Nonaka, Sachiko	Novel Alginate-Chitosan Hybrid Fibers as a Scaffold for Tendon Or Ligament Tissue Engineering
Norley, Chris J	Computed Blood Flow Dynamics in An Anatomically Realistic Cerebral Aneurysm
Normandin, Sarah C	Age Differences in Ability To Absorb Impact Energy in the Upper Extremities During Falls
Normandin, Sarah C	Effect of Age on Ability To Brake a Fall with the Outstretched Hands
Northcut, Eric J	In Vivo Determination of Hip Joint Separtion in Subjects Having Variable Bearing Surfaces
Norton, Karen	Understanding the Relationship of Mass Properties To the Metabolic Cost of Load Carriage: Moment of Inertia
Nosaka, Kazunori	Changes in Mechanical Properties of Human Tibialis Anterior Muscle Following Repeated Eccentric Contractions
Notter, Robert H	Biophysical and Biological Research in Lung Surfactant Drug Development
Novotny, John E	The Effects of Ligament and Cartilage Properties on the Glenohumeral Joint
Nuckley, David	Compressive Biomechanics of Fracture and Neurologic Integrity in the Pediatric Spine
Nuckley, David	Effect of Strain Rate on Cervical Spine Tensile Mechanics
Nugent, Allen	Fluid Velocities Within a Ventricular Assist Device are Highly Sensitive To Pneumatic Drive Conditions
Numoto, Hideki	Localization Detection of Transverse Holes in Intramedullary Nail Inserted Into Femur Using Focused Ultrasound
Nuño, Natalia	Determination of the Parameters for the Finite Element Model of a Debonded Stem-Cement Interface Pertinent To Hip Implants
Nurse, Matthew	Foot Sensation as a Predictor for Response To Footwear Interventions
Nydegger, Thomas	"Flexible" Stabilization of the Spine - is This the Future?
Nygaard, Hans	High-Frequency Pressure Fluctuations Measured in Heart Valve Patients
Nygaard, Hans	Understanding the Mechanisms of Mechanical Heart Valve Cavitation

O

O'Brien, J	Biological Aspects of Disc Degeneration
O'Connor, JJ	Biomechanics of Knee Replacement - From in Vitro To in Vivo
O'Connor, JJ	Integrity of Compression Moulded Uhmwpe Components for Joint Replacement

Oakland, RJ	Mathematical Models for the Time-Dependent Characteristics of Spinal Cord Tissue
Oakley, C	Dynamic, Biomechanical Characteristics of Human Ankle Ligaments
Obata, Hideaki	Deformation Analysis of Human Left Ventricular Wall Using Mr Tagging Technique
Obata, Hideaki	Measurement of the Encephalon Physical Parameter with MRI Saturation Transfer Method
O'Brian, Peter	Biomechanical Analysis of Fixation of Split-Depression Fractures of the Tibia Plateau
O'Brien, Aoife B	Wave Intensity in the Pulmonary Circulation
O'Brien, Aoife	Time-Domain Representation of Ventricular-Arterial Coupling
O'Brien, Thomas	Comparative Analysis of the Hemodynamics Through Healthy and Diseased Models of the Human Abdominal Aorta
O'Brien, Thomas	On the Errors Surrounding Hemodynamic Analyses: Comparisons of Various Techniques
Obusek, John	Understanding the Relationship of Mass Properties To the Metabolic Cost of Load Carriage: Moment of Inertia
O'Callaghan, P	Comparison of Fixed and Rotating Bearing Knee Replacements In-Vivo Using a 3Dmotion Analysys Technique: Preliminary Results
Occleshaw, Chris	Haemodynamics of the Fontan Connection
Ochoa, Jorge	Investigation of Cementless Cup Micromotion and Stability After Total Hip Arthroplasty
Ochoa, Jorge	Investigaton of Stresses and Micromotion Between the Liner and the Acetabular Cup in Total Hip Replacement Implants
O'Connor, John	Simulation of Physiological Muscle Loading in Finite Element Modelling of the Intact Femur
O'Connor, John	The Role of the Passive Structures in the Mobility and Stability of the Natural and Replaced Human Ankle Joint
O'Connor, Kristian	Muscle Activation Levels During Running in Varus, Valgus, and Neutral Wedged Shoes
Oda, Juhachi	Evaluation of Shape Accuracy in Ct Based Femur Model for Prosthetic Stem Design
Oda, Juhachi	Mechanical Evaluation of Spine Reconstruction After Total En Bloc Spondylectomy by Finite Element Analysis
Oda, Jyuhati	Iomechanical Evaluation of Reconstruction Aftre Total Sacrectomy
Oda, T	Changes in Mechanical Properties of Human Tibialis Anterior Muscle Following Repeated Eccentric Contractions
Oda, T	In Vivo Muscle Fiber Behavior of the Triceps Surae Muscles
Oda, Toshiaki	Architecture of Contracing Human Gastrocnemius Muscle: An Aproach From Three-Dimensional Ultrasound Imaging
Oda, Toshiaki	In Vivo Measurement of Muscle Fiber Behavior in the Triceps Surae Muscle During Tensional Summation
Oddou, Christian	Ultrasound Wave Propagation in Porous Medium. Application To Cancellous Bone
Odhner, D	The Level of Symmetry in the Anthropometric and Mechanical Properties of the Ankle as Determined by a Mechanical/Mri
Oegema, Theodore	Fabrication And Characterization Of Fibrin-Based Tissue-Equivalent Valves
Offman, SL	Lower Limb Energetics of Normal and Moderate Oa Subjects
Ogasawara, Yasuo	Altered Nana-Order, Micro-Mechanical Property of Pulmonary Artery Smooth Muscle in Primary Pulmonary Hypertension
Ogasawara, Yasuo	Ca2+ Responses and Its Propagation in Cultured Endothelial Cells To Cytosolic Mechanical Stimulation by Laser Tweezers
Ogasawara, Yasuo	Spatial Flow Pattern Difference Between Blood- and Crystalloid-Perfused Myocardium
Ogawa, Masanobu	Effect of Ankle Joint Constraint by Afo on Maintenance of Standing Posture

Ogden, Lorna	Unique Muscle Activity Patterns Observed During Gait Transitions
Ohashi, Toshiro	Biaxial Tensile Properties of Aortic Aneurysm Tissues Under Equibiaxial Stress
Ohashi, Toshiro	Dynamic Behavior of Actin Filaments in Cultured Endothelial Cells During Exposure To Shear Stress
Ohashi, Toshiro	Rupture Properties of Thoracic Aortic Aneurysms Using Pressure-Imposed Experiment
Ohba, K	Model Blood Consisting of Dense Suspension of Natural Polymeric Gel Particles
Ohe, Tohru	Altered Nana-Order, Micro-Mechanical Property of Pulmonary Artery Smooth Muscle in Primary Pulmonary Hypertension
Ohshima, Hiroshi	Intervertebral Disc Metabolism Under Mechanical Load: the Role of Extracellular Physical Factors
Ohshima, Norio	Biomechanical Analysis of the Design of Endovascular Stents: Influence of Coil-Pitch on Intraluminal Flow Behavior
Ohshima, Norio	Biomechanical Aspects of Tumor Microcirculation: with Special Emphasis on Leukocyte-Endothelium Interactions
Ohshima, Norio	Effects of Electro-Acupuncture Stimulation on Systemic and Mesenteric Microvascular Hemodynamics in Anesthetized Rats
Ohta, Keiko	Altered Nana-Order, Micro-Mechanical Property of Pulmonary Artery Smooth Muscle in Primary Pulmonary Hypertension
Ohta, Yuji	A Gait Orthosis for Paraplegics with a Motor-Driven Knee Joint
Ohte, Nobuyuki	Wave Intensity in the Carotid Artery is a New Index of Left Ventricular Systolic and Early Diastolic Performance
Oi, Nelson	Biomechanical Effects of Intermediate Screws in Short and Long Anterior Cervical Fusion Constructs
Oizumi, Naomi	Cooperative Force Analysis of Eleven Muscles During Abduction of the Shoulder
Oka, Richard	Biomechanical Comparison of the Luque-Galveston and Colorado Ii Methods for Sacropelvic Fixation
Oka, Richard	Biomechanical Comparison of the Triage Medical Compression Screw To the Synthes Screw for Use in Lower Extremity Fractures and Fusions
Oka, Richard	Biomechanical Efficacy of a Protein Polymer Hyrdrogel for Inter-Vertebral Nucleus Augmentation and Replacement
Oka, Richard	Failure Load for Single Screw Versus Single Screw Plus Staple Constructs in the Pediatric Thoracic Spine: Differences Between Plowing and Levering
Okada, Takashi	A Novel Age-Related Index of Cardiovascular Function
Okada, Takashi	Wave Intensity in the Carotid Artery is a New Index of Left Ventricular Systolic and Early Diastolic Performance
O'Kelly, Kevin	Micro-Tensile Testing of Individual Trabeculae From Normal, Ageing, and Ovarectomised Rat Bones
Okereke, E	The Level of Symmetry in the Anthropometric and Mechanical Properties of the Ankle as Determined by a Mechanical/Mri
Okita, Nori	Effect of Reduced Range of Motion on the Accuracy of the Functional Method of Hip Joint Center Location
Oku, Hiroshi	Measurement of Erythrocytes Deformability with Counter-Rotating Parallel Disk System
Oku, Hiroshi	Wave-Form Analysis of Electrocardiograph with Spectrum for Screening Test
Okuizumi, H	Hand Impact Force Reduction in Forward Falls in Young Males: a Prosprctive, Controlled, 3-Month Intervention Trial
Okumu, Kris	Method To Measure Sustainable Loads in Sutured Urethral Tissue
Olabisi, Ronke	Anesthetic Effects on Muscle Performance
Olabisi, Ronke	Effects of Joint Angle on Recovery of Torque Following Muscle Stretch Inury
Oliver, Michele	Development and Validation of a Joystick Dynamics Model To Predict Operator Input Torque

Oliver, Michele	Effect of Joystick Stiffness and Speed on Selected Dynamic Torque Characteristics
Olney, Christine M	Biomechanical Stability of Multi-Level Cervical Spine Instrumentation: Comparison of Constrained Versus Semi-Constrained Anterior Cervical Plates
Olney, Sandra J	Locomotor Research: Present State and Future Directions for Rehabilitation
Olney, Sandra J	Peak Power Changes Respoonsible for Gait Speed Increases in Persons with Stroke Following a Training Program
Olufsen, Mette	Dynamics of Cerebral Blood Flow Regulation Using a Lumped Parameter Model
Omens, Jeffrey	Cytoskeletal Defects Alter Myocardial Mechanics Before the Heart Fails
Omine, Akira	Comparison of Failure Properties of Scar Tissues in Skin, Patellar Tendon , and Medial Collateral Ligament in the Same Rabbits
Omori, Go	Changes in 3-D Motion and Contact Pressure Distribution After Lateral Ligament Injury of the Ankle Joint
Omori, Go	Comparative Study Between Intra- and Post-Operative Knee Motions After Total Knee Arthroplasty
Omori, Go	Motion and Contact Analyses of Patello-Femoral Joint After Total Knee Arthroplasty
Omori, Masayoshi	Measurement of Erythrocytes Deformability with Counter-Rotating Parallel Disk System
Onda, Naoyuki	Motion and Contact Analyses of Patello-Femoral Joint After Total Knee Arthroplasty
Ong, S	Comparison of Scaffold Designs for Tissue-Engineered Small-Diameter Graft Applications
Ono, Koshiro	Minor Neck Injury Mechanism in Low Speed Rear Impact Based on Human Cervical Vertebra Motions
Onoue, A	Model Blood Consisting of Dense Suspension of Natural Polymeric Gel Particles
Ooi, Renn Chan	Computational Fluid Dynamics (CFD) Simulation of the Human Biliary System
Ooi, Yasuhiro	Simultaneous Measurement of Red Cell Velocity and Pressure in Microvessels Revealed Advancement in Phase of Flow Pulse Relative To the Pressure Pulse by P/4
Ookawa, Keiko	Biomechanical Analysis of the Design of Endovascular Stents: Influence of Coil-Pitch on Intraluminal Flow Behavior
Oomens, Cees WJ	A Multi-Scale Finite Element Approach To Determine Local Cell and Tissue Deformations
Oomori, Seiichi	Microcrack Detection and Mechanical Property Measurement of Bone Using Scanning Acoustic Microscope
Oosterwyck, Hans Van	Simulation of Overload-Induced Marginal Bone Resorption Using Anatomical Finite Element Models
Oppold, PT	Biomechanics of Knee Replacement - From in Vitro To in Vivo
O'Reilly, P	Torsional Fatigue of Cortical Bone
Orendurff, Michael	Hamstring Length During Gait Does Not Change After Surgical Hamstring Lengthening
Orendurff, Michael	Surgical Hamstring Lengthening Increases Concentric Muscle Velocity During Gait
Oris, Philip	Finite Element Study of Trochanteric Gamma Nail for Subtrochanteric Fracture
Orlik, Julia	Effective Contact Conditions Between Cementless Coated Hip Implant and Bone
Orr, D	Mechanical Energy Loss At The Stump-Socket Interface In Transtibial Prostheses
Ortiz, Christine	Cartilage Nanomechanics, Mechanotransduction, And Tissue Engineering
Oshima, Marie	Numerical Simulation and Database System for Hemodynamic Study of Cerebral Arteries
Oshima, Marie	Numerical Simulation of Fluid-Structure Interaction of the Intracranial Artery
Oshinski, John	Blood Flow Simulations From Phase Contrast MRI Data for the Measurement of Large Gradient Arterial Wall Shear Stresses
Oskouei, MAE	Variations in the Superimposed Twitch Technique At 100% Mvc

Ouyang, JingPing	Laminar Shear Stress Induces Vasodilator-Stimulated Phosphoprotein Change in Cultured Human Endothelial Cells
Ouyang, JingPing	The Expression of ICAM-1 Induced by Shear Stress Upregulated Via NFKB Activation
Owings, Tammy M	Head Movement Does Not Characterize the Failure of Recovery From An Induced Trip
Owings, Tammy M	Physical Performance Factors and Falls by Older Adults: What is the Weakest Link?
Owings, Tammy M	Reaction Times During a Simulated Baseball-Fielding Task are Influenced by Baseball Velocity, Level of Attention, and Age
Oxland, Thomas R	A Biomechanical Study Comparingcortical Onlay Allograft Struts and Plates in the Treatment of Periprosthetic Femoral Fractures
Oxland, Thomas R	Biomechanical Analysis of Fixation of Split-Depression Fractures of the Tibia Plateau
Oxland, Thomas R	Evaluation of Spinal Implants - Vertebral Bone Density is An Important Factor
Oxland, Thomas R	The Effect of Analysis Method and Calibration Cage Geometry on the Spatial Variation of Rsa Reconstruction Accuracy
Oxland, Thomas	Are Spinal Facet Loads Influenced by the Fixation Method?
Oxland, Thomas	Spinal Canal Occlusion in Flexion-Compression : the Effect of Injury Mechanism in An Upper Thoracic Spine Experimental Model
Oxland, Thomas	The Effect of a Novel Cage Design on Stabilization in the Lumbar Spine
Oxland, Thomas	The Effect of Plate Design, Endplate Preparation and Bone Mineral Density on Immediate Stabilization in An Anterior Cervical Plate Fixation Model
Ozeki, Shigenobu	Evaluations of Hip Fracture Mechanism and Prevention by Using Dynamic Fe Analyses

P

Pääsuke, Mati	Vertical Jumping Performance in 8-12-Year-Old Rhythmic Gymnasts
Padget, Marty	Biomechanical Comparison of the Triage Medical Compression Screw To the Synthes Screw for Use in Lower Extremity Fractures and Fusions
Page, Stephen	Intersegmental Dynamics During Multijoint Arm Reaching: Implications for Control of Limb Movement
Pai, Clive Yi-Chung	Adaptation To Slipping and Fall Prevention
Pai, Yi-Chung	Diminished Stepping Responses Lead To Falls in Both Young and Older Adults
Paillard, Philipps	Digit Resistance Within Short Term After Fdp Tendon Repair in Canine in Vivo
Pain, Matthew	A Comparison of Bi-Lateral Deficit in Elite Enduranceand Elite Power Athletes During Drop Jumps
Pal, Anupam	Degradation of Drug Tablets and Mixing in the Stomach Using Computer Simulation with the Lattice-Boltzmann Algorithm
Palissery, Vinu	Characterisation of a Substitute Material To Model Cancellous Bone in In Vitro Implant Migration Studies
Pallotti, G	Flow Studies Connected with Artificial Hemodialysis. Mechanical Investigations and Biomechanical Effects
Pancanti, Alberto	A Comparision Among Different Tasks Performed by Different Subjects on the Primary Stability of Cementless Stems
Pancanti, Alberto	A Micromotion-Based Model of Bone-Implant Interface Remodelling
Pandorf, Clay	A Dual Mass Spring - Dashpot Model of the Exchange of Forces Between the Backpack, Hips and Shoulders During Walking
Pandy, Marcus G	A Comparison of ACL Forces During Soft and Stiff Drop-Landings
Pandy, Marcus G	Factors That Contribute To Peak Knee Flexion in Normal Swing: Implications for Stiff-Knee Gait

Pandy, Marcus G	Hamstrings Action Alone Cannot Limit Anterior Tibial Translation in Acl-Deficient Gait
Pandy, Marcus G	Induced Positions: Intuitive Quantities for Characterizing Muscle Function
Pandy, Marcus G	Ligament Forces in the Anterior Cruciate Deficient Knee During Gait
Pandy, Marcus	Anterior-Cruciate Ligament Forces in the Intact Knee During Normal Gait
Pandy, Marcus	Effect of Hamstrings Muscle Action on the Stability of the Acl-Deficient Knee
Panjabi, Manohar M	Biomechanical Testing To Quantify Adjacent-Level Effects
Panjabi, Manohar M	Ligament Strength Does Not Decrease with Subfailure Stretches
Panjabi, Manohar M	Models for Whiplash Injury
Panjabi, Manohar M	Spinal Stabilizing System: Consequences of a Subfailure Injury
Papadopoulos, Jim	The Muscular Component of Pedaling Force is Not Well Defined
Papaharilaou, Y	Characterisation and Simulation of In-Vivo Perhiperal Distal Bypass Grafts
Papathanasopoulou, P	A Comparative Study of CFD and MRI for Pulsatile Flow in a Carotid Bifurcation Phantom
Paquet, Nicole	Head Turns Induce Altered Loading During Standing in Stroke Patients
Paquet, Nicole	Head, Trunk and Pelvis Kinematics During Rapid Head Turning in Standing and Walking
Paquette, Caroline	Head, Trunk and Pelvis Kinematics During Rapid Head Turning in Standing and Walking
Parent, Gerald	A Reproducible Method To Define a Coordinate System for 3D Kinematics Evaluation of the Knee
ParentiCastelli, Vincenzo	The Role of the Passive Structures in the Mobility and Stability of the Natural and Replaced Human Ankle Joint
Park, Hee-Dong	A Quantitative Assessment of Knee Extensor Spasticity Using Isokinetc Dynamometer
Park, Sukyung	Scaling of Human Postural Control Responses Due To Biomechanical Constraints
Park, Youngbae	Are Spinal Facet Loads Influenced by the Fixation Method?
Park, YS	The Effect of a Cyclic Compressive Strain on the Differentiation of Osteoblast-Like Cell (Mc3t3-E1) in 3-Dimensional Scaffolds
Parker, Kim H	Calibration of An Arterial Applanation Tonometer for In-Vivo Pressure Transduction
Parker, Kim H	Cross-Flows Associated with Shear Stress Gradients on the Flow-Endothelium Interaction
Parker, Kim H	Time-Domain Representation of Ventricular-Arterial Coupling as a Windkessel and Wave System
Parker, Kim H	Time-Domain Representation of Ventricular-Arterial Coupling
Parker, Kim H	Wave Intensity in the Pulmonary Circulation
Parry, M	The Effect of Bone Quality on Intra-Medullary Fixation of the Proximal Humerus Using a Retro-Grade Nail
Parvataneni, Krishnaji	Peak Power Changes Respoonsible for Gait Speed Increases in Persons with Stroke Following a Training Program
Paskoff, G	Influence of Helmet Mass Properties on Head/Neck Forces During High-Speed Ejection
Pasterkamp, Gerard	Measuring Effects of Drugs on Arterial Mechanical Properties
Pataky, Todd	Tangential Force Sharing Among Fingers During Static Grasping
Patla, Aftab E	Importance of Plantar-Surface Mechanoreception in Postural Control
Patla, Aftab E	Muscular Response of the Swing Limb and Arms During An Unexpected Slip
Patla, Aftab E	Reprogramming Sit-To-Stand and Sit-To-Walk Movement Sequence Under Different Temporal Constraints
Patla, Aftab	Visual Control of Locomotion During Movable-Obstacle Avoidance

Patritti, Ben L	Absolute Heel Sensitivity is Not Related To the Discrimination of Initial Impact Loads Typical of Heel-Toe Running
Patterson, Eann A	Fluid Structure Interaction of Heart Valves
Patterson, Kyle	Biomechanical Analysis of the Effects of a Power Clean Program
Patterson, Ryan C	Alveolar Transport During Total Liquid Ventilation
Patterson, Thomas E	Magnetic Field Visualization in Applications To Pulsed Electromagnetic Field Stimulation of Tissues
Patterson, Thomas E	Pulsed Electromagnetic Field-Dependent Differencesof Collagen Processing in Pre-Osteoblasts
Patterson, Thomas E	Pulsed Electromagnetic Field-Dependent Stimulation of Pre-Osteoblast Proliferation in Vivo
Patton, James	A Force-Field Approach To the Adaptive Control and Learning of Arm Movements
Patwari, Parth	Response Of The Chondrocyte To Mechanical Stimuli: Physiologic And Injurious Compression
Pauk, Jolanta	Parametric Identyfication of Lower Limbs During Walking of a Man
Paul, John	Tensile Properties of the in Vivo Human Gastrocnemius Tendon: Relevance To Function and Locomotion
Paulsen, Peter K	High-Frequency Pressure Fluctuations Measured in Heart Valve Patients
Paulson, D Kent	Comparison of Failure Properties of Scar Tissues in Skin, Patellar Tendon , and Medial Collateral Ligament in the Same Rabbits
Pavan, E	Gait Features Assessment in Hip Osteoarthritis and Total Hip Replaced Patients Based on An Ambulatory System (Physilog)
Pavol, Michael J	Adaptation To Slipping and Fall Prevention
Pavol, Michael J	Diminished Stepping Responses Lead To Falls in Both Young and Older Adults
Pavol, Michael J	Head Movement Does Not Characterize the Failure of Recovery From An Induced Trip
Pavol, Michael J	Physical Performance Factors and Falls by Older Adults: What is the Weakest Link?
Payan, E	Effect of Compression on Beta-1 Integrins (CD49d, CD49e) and CD44 Adhesion Molecules Expressed by Articular Condrocytes
Payne, Craig	Foot Function After the Short Term Use of Custom Made Foot Orthoses
Payne, Craig	Foot Function After the Short Term Use of Customs Foot Orthoses
Pearcy, Mark	Effect of Lesions on the Three-Dimensional Mechanics of the Intervertebral Disc
Pearsal, D	Gait Adaptations To Transverse Slopes
Pearsall, D	Forward Ice Hockey Skating: Comparison of EMG Activation Patterns At Three Velocities
Pearsall, D	The Effects of Stick Construction in the Performance of Ice Hockey Wrist Shot
Pearsall, David J	Postural Estimates From Digital Images: Inter- and Intra-Tester Reliability
Pearsall, David J	The Use of Skin Pre-Tension To Modify Tibial Bone Acceleration Estimates
Pearsall, David	Lower Limb Kinematics of Ice Hockey Forward Skating
Pearsall, David	Measurement of Inversion and Eversion Movements of the Foot by Using a Position Transducer
Peattie, Anne M	Scaling of Damping: Implications for Stability
Pedersen, Douglas R	Bone Morphology Changes in Ddh Hips
Pedersen, Douglas R	Hyperelastic Representation of Hip Joint Capsule: a Finite Element Validation
Pedley, T J	Biomechanics in Oceanography
Peham, C	A Black Box Approach To Modeling the Equine Back as a Flexible Beam
Peham, C	Influence of a Rider To the Back of a Horse in Different Gaits
Peiró, J	Characterisation and Simulation of In-Vivo Perhiperal Distal Bypass Grafts
Pelekasis, Nikos	Deformation of Bioartificial Capsules in Plane Hyperbolic Flow

Pelletier, Michel	Evaluation of 3D Knee Kinematics with and Without Plantar Orthopaedic Processing
Pelot, Ronald P	The Importance of Certain Design Features in a Backpack
Pembroke, Tony	Ecm(Extracllular Matrix) Scaffolds for Tissue Engineering: Biocompatibility and Biodegradability
Peng, Jianbo	Automated Subject-Specific Scaling of Skeletons To Motion-Captured Markers
Pereira, Barry P	The Proximal Fibers of the Interrosseous Membrane Contributes To Stability in the Radial Dominant Single Bone Forearm
Perell, Karen L	Motor Learning Protocol of a Hip Walking Strategy in Individuals with Diabetic Peripheral Neuropathy
Pericleous, Koulis	Computational Modelling of Blood Flow and Atery Wall Interaction
Perié, D	Biomechanical Tools To Understand and Predict the Effects of Interventions in Scoliosis
Périé, Delphine	A Preliminary Evaluation of a Limb-Segment Model for Lifting Tasks
Perktold, Karl	Fluid Dynamics and Wall Mechanics in Peripheral Bypass Anastomoses
Perktold, Karl	Numerical Study of Human Aortic Blood Flow: a Comparison Between Healthy and Disturbed Flow Distal To Artificial Heart Valves
Perrault, Ronald	A Color-Coded Video-Based System for Posture and Foot Assessment
Perraultl, R	Ee Dimensional Characterization of Pulsa Tile Flow Beha Vior in the Convergent Region in a Model of Mitral Prolaps. a Particular Velocity Imaging Stud
Perreault, Eric J	Arm Stiffness and Stability Improved by Fns in C5-C6 Sci
Perreault, Eric J	Experimental Quantification of Muscle Contributions To Whole Limb Stiffness and Stability
Perry, JE	Use of An Instrumented Treadmill in the Evaluation of Amputee Gait
Perry, Stephen D	Importance of Plantar-Surface Mechanoreception in Postural Control
Perusek, Gail P	Mechanism of Intra-Articular Calcaneal Fractures: the Effects of Achilles Tendon Loading
Pesakova, Vlasta	Bone-Friendly Intervertebral Cages
Peters, Brian T	Issues in the Interpretation of Continuous Relative Phase
Peters, David	Biological and Biomechanical Response of Rat Dorsiflexors To Eccentric Exercise
Peters, David	Increased Desmin in Rat Dorsiflexors After a Single Bout of Eccentric Exercise
Peters, Gerrit	Fluid-Structure Interaction And Collagen Remodeling In The Aortic Heart Valve
Petersen, Jennifer	Passive Stretches Protect Muscle in Old and Young Mice From Lengthening Contraction-Induced Injury
Petersen, Kari Skovmand	Cervical Range of Motion in Asymptomatic Subjects Following Spinal Manipulative Therapy: a Double Blinded Randomised Clinical
Peterson, D	Force Enhancement in Single Skeletal Muscle Fibres on the Ascending Limb of the Muscle Force-Length Relationship
Peterson, Sean	High Resolution Micro-Particle Image Velocimetry Measurement of Flows Relevant To Stenotic Vessels
Petit, Y	Biomechanical Tools To Understand and Predict the Effects of Interventions in Scoliosis
Petit, Yvan	Biomechanical Modeling of the Scoliotic Spine Reducibility
Petrie, Christopher P	Finite Element Analysis of Median Nerve Insult in the Carpal Tunnel
Petsche, Paul	Tests of Numerical Models of Craniomandibular Mechanics
Pettazzoni, P	Flow Studies Connected with Artificial Hemodialysis. Mechanical Investigations and Biomechanical Effects
Pfeifer, K	Movement Behaviour in Chronic Neck Pain Patients
Pflum, Mary A	A Comparison of ACL Forces During Soft and Stiff Drop-Landings
Pflum, Mary A	Quadriceps Weakness Causes An Increase in the Peak Adductor Moment During Gait

Pho, Robert W H	The Proximal Fibers of the Interrosseous Membrane Contributes To Stability in the Radial Dominant Single Bone Forearm
Piazza, Stephen J	Effect of Reduced Range of Motion on the Accuracy of the Functional Method of Hip Joint Center Location
Piazza, Stephen J	Effects of Femoral Component Rotational Placement Error in a Dynamic Musculoskeletal Simulation of Total Knee Replacement Motion
Piazza, Stephen J	Plantar Aponeurosis Forces During Simulated Walking
Piazza, Stephen J	Simulation-Based Design of Knee Replacement Surgery
Pichora, David	Analysis of in Vivo Carpal Bone and Ligament Kinematics Using Ct and Mr Data
Pichora, David	Three-Dimensional Motion Tracking of the Forearm Using Surface Markers
Pickar, Joel G	Paraspinal Muscle Spindles Responses To Biomechanical Changes in the Spine
Pickard, Jenny	Running on Artificial Hip Joints - is It Wise?
Pickford, Martin	Origins of Bipedalism: Evolutionary Morphology Through Finite Element Analysis
Pidcoe, Peter	Changes in Ground Reaction Force and Joint Excursions During a Fatiguing Landing Activity
Pierre, Mark C	Stiffness of the Human Arm in Three Dimensional Space
Pijnappels, Mirjam	Stance Limb Contributes To Prevention of Falling After Tripping
Pilgram, Thomas K	Forefoot Structural Predictors of Plantar Pressures During Walking in People with Diabetes and Peripheral Neuropathy
Pilkey, Walter D	Optimal Protection of Humans From Impact
Pincivero, Danny M	Knee Extensor Torque and Work During Dynamic Contractions Guided by Perceptual Sensations
Pincivero, Danny M	Quadriceps Femoris Activation-Force Relationship and Perceived Exertion During Dynamic, Inertial Knee Extension Exercise
Piotrowski, Gary	The Effects of Early Rollback in Total Knee Replacement on Stair Stepping
Piotte, France	Active Movements of the Shoulder Girdle in Healthy Subjects: a Validity Study
Piscitelle, Louis	Understanding the Relationship of Mass Properties To the Metabolic Cost of Load Carriage: Moment of Inertia
Pistecky, Peter V	Measuring Effects of Drugs on Arterial Mechanical Properties
Pittaccio, Simone	Computational Fluid Dynamics After Aortic Coarctation Repair
Pittelkow, Mark R	Effects of Matrix Properties on Intracellular Signaling
Pitzen, Tobias	The Effect of Plate Design, Endplate Preparation and Bone Mineral Density on Immediate Stabilization in An Anterior Cervical Plate Fixation Model
Pizza, Francis X	Passive Stretches Protect Muscle in Old and Young Mice From Lengthening Contraction-Induced Injury
Pizzo, Alaina M	Dependence of Viscoelastic Properties on Collagen Ecm Microstructure
Plamondon, A	Back Muscle Fatigue During Intermittent Prone Back Extension Exercise
Plamondon, André	Handling Missing Marker Coordinates in 3D Analysis
Planus, Emmanuelle	Assessment of Structural Viscoelasticity of Cytoskeleton by Tensegrity Model
Planus, Emmanuelle	Cell-Immersed Microbeads Used as Probes of Cytoskeleton Mechanical Properties
Planus, Emmanuelle	Increasing Number of Interconnected Elements in Tensegrity Models Induces a Structural Softening Consistent with Cortical Cytoskeleton Function
Plesniak, Michael W	Dynamic Ca2+ Response in Vascular Endothelial Cells Subjected To Various Flows
Plesniak, Michael W	High Resolution Micro-Particle Image Velocimetry Measurement of Flows Relevant To Stenotic Vessels
Plesniak, Michael W	Soluble Proteins Released by Endothelial Cells in Response To Fluid Flow Affect Smooth Muscle Cells
Plesniak, Mike W	Numerical Modeling of Pulsatile Turbulent Flows in Stenotic Vessels
Podsiadlo, Pawel	Knee Loading During Gait and Early Signs of Knee Osteoarthritis in a Meniscectomy Population

Poiraudeau, Serge	Cyclic Tensile Stretch Decreases Proteoglycan Production by Anulus Fibrosus Cells Through Production of Nitrite Oxide
Polacek, Denise C	The Convergence of Cardiovascular Genomics and Endothelial Biomechanics
Polacek, Denise	Flow Regulation of Gap Junctional Communication and the Functional Compartmentalization of Vascular Endothelium
Polgár, K	Simulation of Physiological Muscle Loading in Finite Element Modelling of the Intact Femur
Pollack, Gerald	Cells, Gels And The Engines Of Life: A Fresh Approach To Biological Motion
Pollack, Gerald	Contraction of Single Myofibrillar Sarcomeres Occurs in 2.7-Nm Steps and Integer Multiples Thereof
Pollack, Gerald	The Behavior of Individual Sarcomeres After Stretch in Activated Skeletal Muscle Myofibrils
Pollack, Solomon R	Nutrient Diffusion and Flow-Induced Nutrient Transport in 3-D Cell-Scaffold Composites
Pollard, Christine	Influences of Gender and Exercise on ACL Laxity
Pollard, Christine	The Association of Estrogen Changes Across the Menstrual Cycle Phases with ACL Laxity in Active Females
Poncet, Philippe	Estimation of Spinal Deformity in Scoliosis From Geometric Torsion
Poncet, Philippe	Grouping of Scoliosis Patients by Spinal Curve Severity From Torso Surface Data
Poole, AR	Evidence for Differences in Matrix Turnover in the Developing and Degenerating Human Lumbar Intervertebral Disc
Pope, Malcolm	The Cervical Muscle Response During "Whiplash Simulated Motion" with Respect To Gender
Popovic, Dejan	Control of Electrical Therapy Systems for Reaching and Grasping After Stroke
Popovic, Mirjana	Control of Electrical Therapy Systems for Reaching and Grasping After Stroke
Porter, Blaise	Effect of Perfusion Rate on Cell Seeded 3D Constructs in Vitro
Post, Andrew	Shock Absorbing Cross-Country Ski Pole for Dryland Skiing
Potoczny, S	Lower Extremity Support During Toddler Gait
Pottenger, Lawrence	The Effects of Early Rollback in Total Knee Replacement on Stair Stepping
Potthast, Wolfgang	Dynamic Variables and Running Injuries
Potthast, Wolfgang	Natural Frequencies of Femur Bone and Bonepin
Potthast, Wolfgang	The Transition From Take-Off To Early Flight Phase in Ski-Jumping
Potvin, Jim	Determination of the Optimal Forearm Muscles To Monitor with EMG in Ergonomic Studies
Potvin, Jim	Effects of Expectation During Sudden Undloading of the Hands
Potvin, Jim	Muscle Demands and Torque Reactions Associated with Air and Electric Hand Tools
Potvin, Jim	Whole-Body Postural Control and Trunk Stability During Sudden Hand Loading
Potvin, JR	Evaluation of a Magnetic Tracking Device for Estimating Cumulative Low Back Compression.
Pour, Nooshin Haghighi	Effects of Circumferential Residual Stress on the Circumferential Stress Distribution of the Arterial Wall by Finite Element Modeling
Power, Erik D	Computational Modeling and Experimental Validation of Human Eye Interaction with High-Speed Foam Particles
Powers, Christopher M	Biomechanical Analysis of Side-Step Cutting: are Females At Greater Risk for ACL Injury?
Powers, Christopher M	The Effect of Bracing on Patellar Alignment and Patellofemoral Joint Contact Area in Persons with Patellofemoral Pain
Powers, Christopher M	The Effect of Bracing on Patellofemoral Joint Stress During Free and Fast Walking
Powers, Christopher	In Vivo Assessment of the Instantaneous Axes of Rotation of the Lumar Spine in Symptomatic and Asymptomatic Subjects

Powers, Christopher	Segmental Mobility of the Lumbar Spine During a Prone Press-Up Maneuver in Symptomatic and Asymptomatic Subjects: Assessment Using Dynamic Mri
Powers, MJ	Computational Modeling of Flow and Mass Transport in a Microfabricated Array Bioreactor for Perfused 3-D Liver Culture
Prabhu, Ajit	Biomechanical Modeling of Overload At the Bone-Oral Implant Interface
Prange, Michael T	Predictions of Infant Brain Injures in Minor Falls and Inflicted Events
Prätorius, Beate	Somatosensory Input in the Control of Human Posture in Patients with Morbus Parkinson
Praveen, S Solomon	Mechanism of Intra-Articular Calcaneal Fractures: the Effects of Achilles Tendon Loading
Preedy, Danielle F	Can Inertial Forces Alone Cause Limb Folding During Protraction?
Prendergast, Patrick J	3D Finite Element Analysis of An Intravascular Stenting Procedure
Prendergast, Patrick J	Analysis of Acromial Fixation of Gleniod Components Using a 3D Finite Element Model of the Scapula with Comparison To Results Using Photoelasticity
Prendergast, Patrick J	Micro-Tensile Testing of Individual Trabeculae From Normal, Ageing, and Ovarectomised Rat Bones
Prendergast, Patrick	Biomechanical Simulation of Fracture Healing
Prendergast, PJ	Experimental Analysis of Lymphatic Cells Motion Under Topographical Control
Prentice, Stephen D	Motor Adaptations To Changes in Limb Mechanical Properties During Voluntary Gait Modifications
Prentice, Stephen D	Obstacle Avoidance Strategies are Altered Following Total Knee Athroplasty
Preuss, Richard	The Correction of Inertial Ground Reaction Forces Due To a Moving Base of Support
Price, AJ	Biomechanics of Knee Replacement - From in Vitro To in Vivo
Price, Thomas	Muscle Activation Levels During Running in Varus, Valgus, and Neutral Wedged Shoes
Priester, Belinda	Walking with Platform Shoes - Normal Walking Pattern?
Prilutsky, Boris I	Mechanical Energy Transfer Between Adjacent Joints by Two-Joint Muscles
Prilutsky, Boris I	Mechanical Energy Transfer by Two-Joint Leg Muscles During Snatch Lift
Prince, F	Postural Evaluation of Idiopathic Scoliosis Patients and Adolescent Control Subjects
Prince, F	Stiffness and Postural Control in Adolescent Control and Idiopathic Scoliosis Patients
Prince, François	Assessment of Postural Response To An Internal Perturbation
Prince, François	Center of Mass Estimation Based on Zatsiorsky-Seluyanov and Dempster Data
Prince, François	Errors Introduced by the Ground Reaction Forces Approach on Joint Moment Calculation During Gait
Prince, François	Zatsiorsky-Seluyanov's Segment Inertia Parameters for Posture Analysis
Prinzen, Frits	Modeling Electrical and Mechanical Activation Times in the Normal Heart
Prochazka, A	Functional Intraspinal Microstimulation for Restoring Limb Movements After Spinal Cord Injury
Prochazka, Arthur	Is Sensory Control of the Locomotor System Crucial Or Not?
Prosi, Martin	Fluid Dynamics and Wall Mechanics in Peripheral Bypass Anastomoses
Provatidis, Christopher G	On the Relationship Between Bone-Remodeling Rate and Orthodontic Strains Within the Periodontal Ligament
Provenzano, Paolo P	Apoptosis in Ligament After a Sub-Failure Stretch
Provenzano, Paolo P	Application of a Nonlinear Model To Describe Ligament Behavior
Provenzano, Paolo P	Size Effects in Nonlinear Viscoelasticity
Provenzano, Paolo P	Testing Duration Required To Accurately Predict Ligament Viscoelasticity
Provenzano, Paolo P	The Effects of Hydration Time on Ligament Viscoelasticity
Provenzano, Paolo P	Trap May Contribute To Altered Mechanical Properties in Ligament After Chemical Sympathectomy

Pruitt, Lisa	Determination of Elastin and Collagen Content in Porcine Aorta
Pruitt, Lisa	Investigation of Structure-Property Relationships in Human Femoral Trabecular Bone
Pruitt, Lisa	Nanomechanical and Biochemical Properties of Diseased Artery Tissue
Pruitt, Lisa	The Contribution of Elastin and Collagen To Residual Strain in Porcine Aorta
Puers, Robert	Instrumentation of a Head for the Detection of Loosening by Vibration Analysis
Puers, Robert	Monitoring of the Rehabilitation of Patients After Fracture
Puleo, David A	Potential for Combined and Sequential Delivery of Growth Factors To Control Responses At the Cell-Biomaterial Interface
Purbach, B	Experimental and Finite Element Analysis of the Effect of Muscle Forces on Fixation of Cemented Hip Prostheses At Heel Strike
Purbach, Bodo	Quantifying Bone Trabecular Direction From Radiographs
Purcell, Tom	Single Molecule Mechanics and the Myosin Family of Molecular Motors
Purslow, Peter P	Extracellular Matrix Within Muscle and Muscle Cell - Ecm Interactions in Relation To Mechanical Function
Purves, Neil A	On-Ice Acceleration as a Function of the Wingate Anaerobic Test and a Biomechanical Assessment of Skating Technique in Elite Ice Hockey Players
Pustovrh, Janez	An Expert System for Talent Identification and Successful Performance in Ski Jumping

Q

Qi, Gang	Computer Simulation of Vibrational Diagnosis of Tha Lossening
Qi, Gang	Numerical Modal Analysis of Cemented Femur Component of Total Hip Replacement
Qin, Yi-Xian	Trabecular Tissue Stresses and Strains in Mechanically Induced Anabolic Bone Adaptation: a Finite Element Study
Qin, Zhao	Influence of Multiple Stenoses on Diagnosis of Peripheral Disease
Qinguo, Gang	Wolff's Law
Quarteroni, A	Numerical Simulation of the Cardiovascular System : a Multiscale Approach
Quick, David W	Regional Differences in Cellular Densities in Human and Ovine Mitral Valves
Quick, Nancy E	Lower Back Moment and Postural Parameter Relationships During Asymmetric Lifting
Qureshi, Adnan I	The Hemodynamic Effects of Parent Vessel Inflow Angle on a Cerebral Sidewall Aneurysm

R

Rabatin, Ann	Comparison of Quantitative Measures of Tremor as Predictors of Surgical Outcome
Rabatin, Ann	Comparison of Subjective and Objective Measurements of Balance Disorders Following Traumatic Brain Injury
Rabin, Yoed	Thermo-Mechanical Stress as a Limiting Factor of Large Scale Cryopreservation
Race, Amos	Can Piece-Wise Linear Interface Models Be Used To Predict the Failure Response of the Cement-Bone Interface?
Race, Amos	Directional Dependence of Early Fatigue Damage in Cemented Total Hip Replacements
Race, Amos	Early Cement Damage Around a Femoral Stem is Focused on the Cement/Bone Interface
Race, Amos	Investigations of Some Posterior Ligamentous Structures of the Knee

Rassier, Dilson E	History-Dependence of Force Production in Skeletal Muscle
Rassier, Dilson E	The Behavior of Individual Sarcomeres After Stretch in Activated Skeletal Muscle Myofibrils
Ratcliffe, A	Comparison of Scaffold Designs for Tissue-Engineered Small-Diameter Graft Applications
Ratnovsky, Anat	A Realistic Mechanical Model of the Human Chest Wall
Rau, Guenter	Geometrically Defined 3-Dimensional Collagen Scaffolds for Tissue Engineering
Ravi, Namani	Microindentation Methods for Evaluating Elastic and Viscous Properties of Soft Tissues
Rayz, Vitaliy L	Flow in the Stenotic Carotid Bifurcation
Raz, Dalit	Shear-Like Response of Endothelial Cells To Therapeutic Ultrasound
Raz, Sagi	Experimental Analysis of Flow Through Tilting Disk Valve
Raz, Sagi	Platelet Activation in Flow Through a Stenosis Model: Comparison Between CFD and Cdpiv Results
Razaq, Saj	Nutrition of the Intervertebral Disc; Effects of Pathological Changes
Rebmann, Andrea	Defining Patellar Tracking Problems Based on 3D, Non-Invasive, in Vivo Measures of Skeletal Kinematics
Redfern, Mark S	Joint Kinematics of Postural Sway Response To Sinusoidal Galvanic Vestibular Stimulation
Redfern, Mark S	Slip Anticipation Effects on Ground Reaction Forces
Redfern, Mark S	Utilizing Biomechanics To Prevent Slips and Falls
Redfern, Mark S	Whole Body Biomechanics of Responses To Slips
Redfern, Mark	Asymmetries in the Dynamic Structure of the Center-Of-Pressure Time Series
Redhead, JD	Use of An Instrumented Treadmill in the Evaluation of Amputee Gait
Reed, Karen L	An Algorithm To Quantify Segmental Lesions in Necrotic Femoral Heads
Reed, Karen L	Thermal Finite Element Analysis of Osteocyte Kill Zones Achieved with a Cryo-Insult Probe
Rees, J S	The Development of Abfraction Lesions in Teeth
Reid, J	Full-Field Strain Measurement Over Articular Cartilage Cross-Sections with Electronic Speckle Pattern Interferometry
Reid, Susan A	Comparison of 3 Measures of Grf; Force Plate, Fscan(r) and Multiple Force Sensors
Reid, Susan A	The Importance of Certain Design Features in a Backpack
Reikerås, Olav	The Sacroiliac Joint, Intervertebral Disc and Muscle Reflexes
Reikert, Craig A	Limitation of Expriatory Flow in Liquid Ventilation
Reilly, Thomas	Electromyographic Analysis of Selected Muscles During a Simulated Soccer Game
Reinhall, P	Finite Element Implementation of a Structural Model for Aortic Valve Tissue
Reisenberger, Ewald	Basic Problems Associated with Wind Tunnel Measurements and CFD in Sports
Reiss, Caroline	Contribution of the Hip Extensors, Knee Extensors, and Ankle Plantar Flexors Durig Different Squatting Techniques in Older Adults
Rencheng, Wang	Recovery Strategy From Perturbation of the Upper Body During Standing Using Mechanical Energy Analysis
Render, Todd	Investigation of Cementless Cup Micromotion and Stability After Total Hip Arthroplasty
Render, Todd	Investigaton of Stresses and Micromotion Between the Liner and the Acetabular Cup in Total Hip Replacement Implants
Renstrom, Per	The Biomechanics of the Weightbearing Knee
Rentzsch, Reemt	Robotic Assisted Versus Manual Implantation - a Prospective Study in Primary Total Hip Replacement
Requejo, Philip	Conflict Between Momentum and Balance Control During Landing
Requejo, PS	Multijoint Control During Short Duration Movements

Revel, Michel	Cyclic Tensile Stretch Decreases Proteoglycan Production by Anulus Fibrosus Cells Through Production of Nitrite Oxide
Reznick, Nitzan	Shear-Like Response of Endothelial Cells To Therapeutic Ultrasound
Rhee, Kyehan	Flow Analysis on the Stented and Non-Stented Lateral Aneurysm Models
Rhijn, Maarten van	Effect of Interfragmentary Shear and Compressive Stimulation on Bone Healing
Rho, Jae-Young	Time Dependent Deformation During Nanoindentation Test
Riano, Felix	Torsional Stability of Total Elbow Arthroplasty
Ribreau, Christian	Body Force Distribution in Veins of the Lower Limb During Stationnary Gait
Ribreau, Christian	Venous Return in Lower Limb During Muscular Contraction
Ricard, Mark D	Shoulder Biomechanics in Volleyball Spiking: Implications for Injuries
Rice, Sarah	Single Molecule Mechanics and the Myosin Family of Molecular Motors
Richards, Carol C	Walking Around Static and Mobile Upright Obstacles
Richards, Cristy	A Novel Approach To Measurement of Hoop Strain in the Human Meniscus
Richards, Darrin R	Investigation of Golf Club Inertial Properties Via Biomechanical Modeling
Richards, Jason	Variation in Treadmill Walking Due To Combinations of Visual Scene Motion and Gravity-Assist
Richards, KR	Use of An Instrumented Treadmill in the Evaluation of Amputee Gait
Richards, Lorie G	The Effects of Age and Feedback on Isometric Knee Force Control Abilities
Richardson, James K	Comparison of Step Variability During Gait on Flat and Irregular Surfaces in Patients with Polyneuropathy.
Richardson, John D	Three Dimensional Computer Modelling of the Human Anatomy
Richmond, FJR	Therapeutic Electrical Stimulation with Bions To Rehabilitate Shoulder and Knee Dysfunction
Richter, W Mark	Differences in Propulsion Kinetics Between Wheelchair Dependent and Non-Wheelchair Dependent Users
Rickards, Jeremy	Effect of Joystick Stiffness and Speed on Selected Dynamic Torque Characteristics
Riediger, Dieter	Fe-Simulation of Bone Modeling Around a Dental Implant in Two-Stage-Healing as Compared To Early Loading
Rief, Matthias	Single Molecule Mechanics and the Myosin Family of Molecular Motors
Rieppo, J	Effects of Sound Velocity Variation on Cartilage Ultrasound Indentation Measurements
Rietdyk, Shirley	Anticipatory Behaviour During Recovery From Unexpected Perturbations: Younger Verses Older Adults
Rietdyk, Shirley	Consistency of Putter Trajectory and Golf Putting Accuracy
Rieu, Regis	Hydrodynamics of Mitral Prosthetic Heart Valves: Comparison of Normal Conditions with Atrial Fibrillation Varying the Heart Rate
Rieu, Regis	Incidence of Valve Prosthesis Incline on Left Ventricle Flow Dynamics
Riley, Patrick O	Comparison of Bilateral and Unilateral Induced Acceleration Analyses of Gait Kinetics
Ringleb, SI	The Level of Symmetry in the Anthropometric and Mechanical Properties of the Ankle as Determined by a Mechanical/Mri
Rittgers, Stanley E	Correlation of Mechanical Factors with Intimal Hyperplasia in the Miller's Cuff and Its Application To Optimization of Anastomotic
Rivard, CH	Postural Evaluation of Idiopathic Scoliosis Patients and Adolescent Control Subjects
Rivard, CH	Stiffness and Postural Control in Adolescent Control and Idiopathic Scoliosis Patients
Roach, N	The Level of Symmetry in the Anthropometric and Mechanical Properties of the Ankle as Determined by a Mechanical/Mri
Robert, PH	Gait Features Assessment in Hip Osteoarthritis and Total Hip Replaced Patients Based on An Ambulatory System (Physilog)

Roberts, A	Failure Analysis of the Lower Limb in Axial Impact Loading
Roberts, Sally	Biological Aspects of Disc Degeneration
Roberts, Sally	The Structure and Functions of Elastic Fibres in Bovine Intervertebral Disc
Roberts, Thomas J	Mechanical Power Production for Acceleration: the Challenges of Being a Biped
Robertson, Catherine M	Cervical Spine Kinematics Following Sequential Sectioning: Novel Implications for Extension Type Injuries
Robertson, D Gordon E	Biomechanics of the Karate Front Kick
Robertson, D Gordon E	Shock Absorbing Cross-Country Ski Pole for Dryland Skiing
Robertson, DGE	Lower Extremity Support During Toddler Gait
Robertson, Douglas	Forefoot Structural Predictors of Plantar Pressures During Walking in People with Diabetes and Peripheral Neuropathy
Robilliard, Justine	Shock Absorbing Potential of the Ungulate Digital Cushion
Robinovitch, Stephen N	Age Differences in Ability To Absorb Impact Energy in the Upper Extremities During Falls
Robinovitch, Stephen N	Effect of Age on Ability To Brake a Fall with the Outstretched Hands
Robinovitch, Stephen N	Techniques for Avoiding Hip Impact During Unexpected Sideways Falls
Robinovitch, Stephen	Techniques for Safe Landing During An Unexpected Fall: Modulation of Impact Velocity Via the Squat Response
Robinson, J Paul	Dependence of Viscoelastic Properties on Collagen Ecm Microstructure
Robinson, J Paul	Micro- and Macro-Level 3D Strains Measured in Structurally Varied Collagen Ecms
Robinson, James	Investigations of Some Posterior Ligamentous Structures of the Knee
Robinson, Paul S	Quasi-Linear Viscoelastic Modeling of Tail Tendon Fascicles From Transgenic Mice
Robinson, Robert A	An Algorithm To Quantify Segmental Lesions in Necrotic Femoral Heads
Robinson, Shawn	Backpack Loads Carried by School Children
Rock, Ron	Single Molecule Mechanics and the Myosin Family of Molecular Motors
Rodgers, Mary M	Upper Extremity Impairment in Wheelchair Propulsion
Rodgers, Mary M	Wheelchair Propulsion Biomechanics with Upper Extremity Impairment and Fatigue
Rödl, Robert	Effects of Varus Wedged Shoe Versus Insole on Knee Joint Loading Characteristcs
Rodosky, Mark W	Effect of Joint Compression on the Biomechanics of the Intact Acromioclavicular Joint
Roeder, Blayne A	Dependence of Viscoelastic Properties on Collagen Ecm Microstructure
Roeder, Blayne A	Micro- and Macro-Level 3D Strains Measured in Structurally Varied Collagen Ecms
Roeleveld, Karin	Fatigue and Muscle Coordination in Subjects with Patellofemoral Pain Syndrome
Rogelj, Joeri	Finite Element Models of Abdominal Organs for Use in Trauma Research
Rogers, Bob	Development and Validation of a Joystick Dynamics Model To Predict Operator Input Torque
Rogers, Bob	Effect of Joystick Stiffness and Speed on Selected Dynamic Torque Characteristics
Rogers, Carolyn M	Biomechanics of Prone Continuous Passive Motion for Low Back Pain
Rogers, Carolyn M	Developing Skilled Performance of Spinal Manipulation/Adjusment
Rogers, Carolyn M	Obtaining Predictable Lumbopelvic Loads During Spinal Manipulation
Rogers, Mark	Aging-Related Changes in Achilles Tendon Reflexes
Rohlmann, A	Hip Contact Forces - Some Important Observations
Rohlmann, A	Loads on An Internal Spinal Fixator During Sitting
Rohlmann, Antonius	A Vertebral Body Replacement for in Vivo Load Measurement
Rohlmann, Antonius	Effect of a Compressive Follower Load and a Tensile Force on Intradiscal Pressure and Intersegmental Rotation of the Lumbar
Rohlmann, Antonius	Effect of a Dual Cage on the Mechanical Behaviour of the Lumbar Spine
Rohlmann, Antonius	Effect of a Laminectomy on the Mechanical Behavior of the Lumbar Spine
Rohlmann, Antonius	Effect of Bone Graft Position on Loading of Pedicle Screws

Rohlmann, Antonius	In Vivo Loads Acting in the Spine and in Spinal Implants
Rohlmann, Antonius	Influence of a Follower Load on the Mechanical Behavior of the Lumbar Spine
Rohlmann, Antonius	Influence of Angular Stability of An Internal Spinal Fixator on Implant Loads
Rolschau, Frederik	Cervical Range of Motion in Asymptomatic Subjects Following Spinal Manipulative Therapy: a Double Blinded Randomised Clinical
Romano, C	Therapeutic Electrical Stimulation with Bions To Rehabilitate Shoulder and Knee Dysfunction
Romano, D	Therapeutic Electrical Stimulation with Bions To Rehabilitate Shoulder and Knee Dysfunction
Rome, Lawrence	New Approaches To Integrating Muscle Function And Design From Molecular Biophysics To Whole-Animal
Rome, Lawrence	New Energetics Approaches To Elucidating Mechanisms of Contraction and Relaxation
Romero, Francisco	Investigaton of Stresses and Micromotion Between the Liner and the Acetabular Cup in Total Hip Replacement Implants
Rong, Qiguo	Fe-Simulation of Bone Modeling Around a Dental Implant in Two-Stage-Healing as Compared To Early Loading
Ronsky, Janet	A Fast Circle Finding Technique for Digital Rsa
Ronsky, Janet	Accuracy of Patellofemoral Joint Contact Area Predictions Using Mr Imaging
Ronsky, Janet	Effect of Hamstrings Inclusion on Calculation of Joint Contact Force and Stress
Ronsky, Janet	Estimation of Spinal Deformity in Scoliosis From Geometric Torsion
Ronsky, Janet	Grouping of Scoliosis Patients by Spinal Curve Severity From Torso Surface Data
Ronsky, Janet	Insights Into In-Vivo Knee Mechanics with Magnetic Resonance Imaging
Ronsky, Janet	Joint Surface Kinematics During Walking in An in Vivo Model of Osteoarthritis
Ronsky, Janet	Locomotion Research Within An Orthopaedics Framework: Successes and Challenges
Ronsky, Janet	Sensitivity of a Hill Based Muscle Model To Perturbations in Model Parameters
Ronsky, Janet	Socket Comfort and Perceived Functional Ability in Unilateral Transtibial Amputee Patients Using Plaster-Cast and Cad/Cam Manufactured Sockets
Rooij, Lex	A Numerical Model Predicting Upper Extremity Fractures Due To Airbag Deployment
Roper, Janice	Motor Learning Protocol of a Hip Walking Strategy in Individuals with Diabetic Peripheral Neuropathy
Roques, A	Measurement of Residual Stress Due To Volumetric Shrinkage in Bone Cement
Roren, Lasse	Calibration of Kinematic Models for Motion Capture
Rosa, Guido La	A Transversely Isotropic and Transversely Homogeneous Model of Cartilage Including Chondrocytes and a Statistical Distribution of Collagen Fibres
Rosen, Amy B	Shear Stress-Induced Strain Focusing in the Endothelial Cytoskeleton
Rosen, Amy B	The Convergence of Cardiovascular Genomics and Endothelial Biomechanics
Rosen, Vicki	Molecular and Cellular Analysis of Rotator Cuff Tendinosis in a Rat Overuse Model
Rosenbaum, D	Ankle and Subtalar Kinematics of the Ankle Joint with Intact, Injured, and Reconstructed Lateral Ligaments
Rosenbaum, Dieter	Effects of Varus Wedged Shoe Versus Insole on Knee Joint Loading Characteristcs
Rosenbaum, Dieter	Mechanical Stability of Ankle Braces Under Passive and Dynamic Loading Conditions
Rosenbaum, Dieter	The Stabilizing Effect of External Ankle Devices with and Without the Additional Influence of a Shoe
Rosenfeld, M	Numerical and Experimental Measurements of the Flow in Pulsatile Ventricle Assist Device
Rosenfeld, Moshe	Aortic Valve Stenosis - Numerical Study on the Accuracy of Noninvasive Andinvasive Diagnostics

Rosenfeld, Moshe	CFD Analysis of Flow Through Mechanical Heart Valves
Rosenfeld, Moshe	Computational Analysis of Inspiratory Heat and Water Vapor Fluxes in the Human Nose
Rosenfeld, Moshe	Experimental Analysis of Flow Through Tilting Disk Valve
Rosenzweig, J	Dynamic Particle/Liquid-Lining Interactions in Peripheral Lung Airways
Rosol, Michael S	Stress Transfer To Coronary Vasa Vasorum After Stenting: a Finite Element Model
Roth, Christoph	Pertrochanteric Fracture Fixation: Effects of Implant Design on Cut-Out Failure Under Dynamic Loading
Roth, Elliot J	Intelligent Stretching and Evaluation of Spastic Ankles Using a Portable Device
Roth, Ralf	Modeling of Slope and Trajectory in Alpine Skiing
Rothe, Laura	Plowing Forces and Stress Distribution on the Temporomandibular Joint Disc Surface
Rouard, AH	Drag Coefficient and Reynolds Number in High Butterfly Swimmers
Rouhana, Stephen W	Biomechanics in the Design and Development of An Abdomen for Crash Test Dummies
Roy, Amy L	Posture Dependent Trunk Strength and EMG Activity
Roy, Jean-Pierre	Influence of Metatarsophalangeal Joint Bending and Shoe Sole Length on Jump Height Performance
Roy, S	Comparison of Fixed and Rotating Bearing Knee Replacements In-Vivo Using a 3Dmotion Analysys Technique: Preliminary Results
Royer, Todd D	Adaptations in Lower Extremity Joint Kinetics To Inertial Asymmetries During Walking
Royer, Todd D	Identifying the Temporal Limits of Volitional Gait Asymmetry
Royston, Thomas J	Turbulence Induced Vein-Wall Vibration May Play a Role in Arteriovenous Dialysis Graft Failure
Rozitis, Antra I	Muscle Activity in the Lower Extremity Damps the Soft-Tissue Vibrations
Rozumalski, Adam	A Kinematically Constrained Method for Determining Subject Specific Joint Parameters
Rubenson, J	How Economical is Human Bipedal Locomotion?
Rubin, Clinton	Genetic Variations Influence Bone's Sensitivity To the Loss of Functional Weightbearing
Rubin, Clinton	Trabecular Tissue Stresses and Strains in Mechanically Induced Anabolic Bone Adaptation: a Finite Element Study
Rudan, John	A Computational Model of Postoperative Knee Kinematics
Ruder, H	Can Inverse Dynamics Be Computed with a Rigid Body Model
Rudert, James	Torsional Stability of Total Elbow Arthroplasty
Rudert, Melvin J	Ankle Articular Cartilage Thickness is Accurately Measured with Multi-Detector Computed Tomography (Mdct)
Rudert, Melvin J	Preferential Direction of Subtalar Joint Laxity with Interosseous Talocalcaneal Ligament Sectioning
Rudin, Stephen	Modeling of Flow in Cerebral Sidewall Aneurysms: Effect of Aneurysm Size
Rudin, Stephen	The Hemodynamic Effects of Parent Vessel Inflow Angle on a Cerebral Sidewall Aneurysm
Ruff, Christine	Observation of Displacement Steps by Single Myosin Id and Myosin Ii Molecules
Ruhleder, M	Muscular Activity and Strength Testing of Trunk and Hip Extensors: a Reproducibility Study
Ruimerman, Ronald	Mechanical Adaptation of Bone Mass and Architecture: Towards a Unified Theory
Ruina, Andy	Deriving Rowing Coordination Patterns and Boat Rigging From Optimization of a Simple Model
Ruina, Andy	Loss Before Recovery: Some Partial Answers To Old Locomotion Questions

S

Sakai, Yoshitada	Pulsed Electromagnetic Field-Dependent Differencesof Collagen Processing in Pre-Osteoblasts
Sakai, Yoshitada	Pulsed Electromagnetic Field-Dependent Stimulation of Pre-Osteoblast Proliferation in Vivo
Sakamoto, Jiro	Evaluation of Shape Accuracy in Ct Based Femur Model for Prosthetic Stem Design
Sakamoto, Jiro	Iomechanical Evaluation of Reconstruction Aftre Total Sacrectomy
Sakamoto, Jiro	Mechanical Evaluation of Spine Reconstruction After Total En Bloc Spondylectomy by Finite Element Analysis
Sakamoto, Kazuyoshi	Relationship Between Frequency Components of Physiological Tremor and Elastic Load
Sakamoto, Makoto	A New Technique for Three-Dimensional Leg Alignment Assessment
Sakamoto, Makoto	Changes in 3-D Motion and Contact Pressure Distribution After Lateral Ligament Injury of the Ankle Joint
Sakamoto, Makoto	Microindentation Analysis of Human Enamel
Sakamoto, Makoto	Prediction of Torsional Properties of Rat Femur Using Peripheral Quantitative Computed Tomography
Sakamoto, Makoto	Scanning Acoustic Microscope Measurements of Anisotropy of Dentine and Enamel
Sakamoto, Makoto	Viscoelastic Characterization of Ultra High Molecular Weight Polyethylene
Sakaue, Koichi	Measurement of Erythrocytes Deformability with Counter-Rotating Parallel Disk System
Sakhaeimanesh, Ali A	Dynamic Characteristics of the Jellyfish and St. Vincent Artificial Heart Valves
Sakhaeimanesh, Ali A	Effects of Oscillation on Elevating Shear Stresses
Sakhaeimanesh, Ali A	Influence of Flow Rate and Axial Position on Shear Stresses
Sakurai, A	Flow Evaluation of Stents in Carotid Artery Models
Salehi, Abraham	The Effect of Tibial Tray Surface Roughness and Insert Micromotion on Backside Wear
Salem, George	Contribution of the Hip Extensors, Knee Extensors, and Ankle Plantar Flexors Durig Different Squatting Techniques in Older Adults
Salem, George	Relations Between Bone Adaptation and Loading Forces Associated with a Novel Osteoporosis Intervention Program
Salfetnikov, Yuliya	Quadriceps Femoris Activation-Force Relationship and Perceived Exertion During Dynamic, Inertial Knee Extension Exercise
Salmeron, F	Gait Analysis in Children with Tibial Rotational Abnormalities
Salminen, Heli	Molecular Biology of Biomaterial Incorporation with Bone
Salo, Paul	Angiogenesis and Healing in Rabbit Knee Ligaments
Saloner, David	Nanomechanical and Biochemical Properties of Diseased Artery Tissue
Saltzman, Charles	Ankle Articular Cartilage Thickness is Accurately Measured with Multi-Detector Computed Tomography (Mdct)
Saltzman, Charles	Finite Element Modeling of Total Ankle Replacements for Constraint and Stress Analysis
Saltzman, Charles	Preferential Direction of Subtalar Joint Laxity with Interosseous Talocalcaneal Ligament Sectioning
Samarasekera, Dinesh	Evaluation of Spinal Implants - Vertebral Bone Density is An Important Factor
Sambanis, Athanassios	Mechanical Properties of Elastin-Hybrid Tissue Engineered Vascular Constructs
Sampson, H Wayne	Alcohol and Ovariectomy Effects on Trabecular Bone in Female Rats
Sander, Franz Guenter	Experimental Determination of the Center of Resistance of Human Incisors in Comparison with Finite Element Simulations
Sandercock, Thomas G	Experimental Quantification of Muscle Contributions To Whole Limb Stiffness and Stability
Sanders, James	Contributions To Forward Propulsion in Human Gait

Sawaki, Yutaka	Deformation Analysis of Human Left Ventricular Wall Using Mr Tagging Technique
Sawaki, Yutaka	Finite Element Analysis of Cardiac Function in Hypertensive Heart Disease
Scandella, M	Gait Analysis in Children with Tibial Rotational Abnormalities
Scannell, JP	Torso Positions of Minimum Passive Tissue Strain - Where Do We Sit, Stand and Walk
Scattolini, Alessio	Study of Postural Stability by Chaos Theory
Schachar, Rachel	Effects of Stretching and Shortening on Isometric Forces on the Descending Limb of the Force-Length Relationship in Cat Soleus
Schade, Falk	Kinematics and Kinetics in Pole Vaulting: Energy Storage and Return
Schaeffer, Tilman	Antero-Posterior Measurements of the Lamellipodium Mechanical Properties in the Migrating Keratocyte
Schaper, Hagen	Swing Phase Reduction in Above-Knee Amputee Running
Scheidl, M	Influence of a Rider To the Back of a Horse in Different Gaits
Scheidt, Robert A	A Force-Field Approach To the Adaptive Control and Learning of Arm Movements
Scheuffelen, Christoph	The Influence of Fatigue on Functional Stability of the Knee Joint
Schibye, Bente	Exhaustive Back Extension Tests Leads To Gradual Increase in Intra-Abdominal Pressure.
Schie, Carine van	Absolute Heel Sensitivity is Not Related To the Discrimination of Initial Impact Loads Typical of Heel-Toe Running
Schiefermüller, Christian	Skiing with Carved Skis: Challenges on Performance and Safety
Schiffman, Jeff	Effects of Age and Time Period on Joint Kinematics and Kinetics During a Single Step Response
Schiffman, Jeff	The Effects of Age and Feedback on Isometric Knee Force Control Abilities
Schiffman, Jeffrey	Understanding the Relationship of Mass Properties To the Metabolic Cost of Load Carriage: Moment of Inertia
Schima, Heinrich	Aortic Valve Stenosis - Numerical Study on the Accuracy of Noninvasive Andinvasive Diagnostics
Schima, Heinrich	Fluid Dynamics and Wall Mechanics in Peripheral Bypass Anastomoses
Schindelwig, Kurt	Release Setting for An Electronic Alpine Ski Binding
Schindler, Hans J	Fe-Simulation of Bone Modeling Around a Dental Implant in Two-Stage-Healing as Compared To Early Loading
Schmid, P	A Biphasic Constitutive Law for Passive Cardiac Tissue
Schmid, Steven	Predictions of Residual Stresses in Bone Cement for Joint Arthroplasty
Schmid, Th	Flow Evaluation of Stents in Carotid Artery Models
Schmidlin, Franz	Finite Element Models of Abdominal Organs for Use in Trauma Research
Schmidlin, Franz	Time-Dependent Properties of the Porcine Kidney Capsular Membrane
Schmid-Schönbein, Geert W	Control Mechanisms of the Fluid Shear Response in Circulating Leukocytes
Schmid-Schönbein, Geert W	Mechanics of Plasma Membrane Vesicles
Schmid-Schönbein, Geert W	Mechanisms for Cell Activation in the Cardiovascular System
Schmidt, R	Ankle and Subtalar Kinematics of the Ankle Joint with Intact, Injured, and Reconstructed Lateral Ligaments
Schmiedmayer, Heinz-Bodo	Dynamic Skiing: Influences of Snow and Ski Properties
Schmitt, Kai-Uwe	Theoretical Model Studies of Fluid-Solid Interactions in the Cervical Spine During Low-Speed Posterior Shoulder Impacts
Schmölzer, Bernhard	Basic Problems Associated with Wind Tunnel Measurements and CFD in Sports
Schmölzer, Bernhard	Computer Simulated Ski Jumping: the Tightrope Walk To High Performance
Schmölzer, Bernhard	The Influence of Body Mass on the Flight Path in Ski Jumping
Schmölzer, Bernhard	The New Jumping Hill in Innsbruck: Designed by Means of Flight Path Simulations.
Schneider, C	Neural and Biomechanical Organization of Anticipatory Postural Adjustements in Fast Synchronized Stepping and Arm Rising

Schneider, Erich	Activity Pattern and Joint Motion Profile of Total Knee Patients
Schneider, Erich	Effect of Interfragmentary Shear and Compressive Stimulation on Bone Healing
Schneider, Erich	The Influence of Resting Periods on Friction in the Artificial Hip Joint
Schobesberger, H	A Black Box Approach To Modeling the Equine Back as a Flexible Beam
Schoephoerster, Richard T	Rationale for Biomechanical Mimicry in the Design of Artificial Heart Valves
Scholtes, Laura	Predicting the Inertial Characteristics of the Human Thigh Using a Geometric Model
Schopper, Aaron W	Modeling of Biomechanics of Tactile Sensation on Fingertips
Schopper, Aaron W	Modeling of Force Response of Fingertips in Keyboard Strikes
Schretter, Herwig	Dynamic Skiing: Influences of Snow and Ski Properties
Schretter, Herwig	Release Setting for An Electronic Alpine Ski Binding
Schroter, R C	A Model of Non-Uniform Lung Parenchyma Distortion
Schroter, Robert C	Predicting the Mixing of Ultra-Fine Particles in a Model Lung Acinus
Schroter, Robert C	Steady Flow and Particle Deposition in Non-Planar Airway Bifurcation Model
Schroter, Robert	Inspiratory Flow in Bronchial Airway Models: Bifurcation Plane Rotation
Schultheiß, Markus	Discoligamentous Structures of the Lower Cervical Spine Get Injured in In Vitro Low-Speed Side Collisions
Schürch, Samuel	Structural and Functional Aspects of Alveolar and Airway Surfactant
Schuylenbergh, Koenrad	Monitoring of the Rehabilitation of Patients After Fracture
Schwameder, Hermann	Biomechanical Research Methodology in Skijumping: Overview and Perspectives
Schwameder, Hermann	Skiing with Carved Skis: Challenges on Performance and Safety
Schwartz, Lewis	Effective Hemodynamic Diameter: a Parameter with Predictive Value for Patency
Schwartz, Michael	A Kinematically Constrained Method for Determining Subject Specific Joint Parameters
Schweizerhof, Karl	Fe-Simulation of Bone Modeling Around a Dental Implant in Two-Stage-Healing as Compared To Early Loading
Schwieger, Karsten	Robotic Assisted Versus Manual Implantation - a Prospective Study in Primary Total Hip Replacement
Scott, A	Acousto-Opto-Electromagnetic Properties of Human Dentin Collagen
Scott, Melissa M	Individuals with ACL Reconstruction Display Altered Coordination Strategies While Walking and Running
Scovil, Carol Y	Sensitivity of a Hill Based Muscle Model To Perturbations in Model Parameters
Scovil, Carol	Locomotion Research Within An Orthopaedics Framework: Successes and Challenges
Screen, HRC	Analysis of Strain Fields in Tendon Fascicles Under Tensile Loading
Screen, HRC	Structure-Function Relationship in Tendon Fascicles Under Tensile Loading Conditions
Sedel, Laurent	In Vivo Determination of Hip Joint Separtion in Subjects Having Variable Bearing Surfaces
Sedlacek, Radek	Bone-Friendly Intervertebral Cages
Seedhom, Bahaa B	Instantaneous Compressive Modulus of Articular Cartilage in the Joints of the Lower Limb
Seedhom, Bahaa B	The Relation of the Compressive Modulus of Articular Cartilage with Its Deformation Response To Cyclic Loading
Seeley, Matt	Ground Reaction Forces Transmitted To the Upper Extremity During the Yurchenko Vault and Floor Exercise
Segal, Rebecca A	Effects of Boundary Conditions on Particle Deposition Predictions in Human Nasal Passages
Segal, Rebecca A	Use of Computational Fluid Dynamics To Study Inhaled Gas and Particle Trasport in the Nasal Passages
Segers, Patrick	Aortic Leak Severity Determines Arterial Elastance And

Shan, Gongbing	The Sensori-Motor Degeneration Revealed by the Center of Pressure Measurement
Shandas, Robin	Echo-PIV(r): a Novel Method for the Non-Invasive Measurement of Velocity Vectors Using Ultrasound Imaging
Shankaran, Harish	The Nature of Mechanical Forces Regulating Shear-Induced Platelet Activation
Shapiro, Robert	Lower Back Moment and Postural Parameter Relationships During Asymmetric Lifting
Sharkey, Neil A	In-Vitro Measurements of Tarsometatarsal Joint Stiffness
Sharkey, Neil A	Plantar Aponeurosis Forces During Simulated Walking
Sharma, Shiva	Analysis of Total Cavopulmonary Connection Fluid Dynamics: Experimental Studies
Sheehan, Frances T	Towards Understanding in Vivo Knee Joint Musculotendon and Skeletal Dynamics
Sheehan, Frances	Defining Patellar Tracking Problems Based on 3D, Non-Invasive, in Vivo Measures of Skeletal Kinematics
Shelburne, Kevin B	A Comparison of ACL Forces During Soft and Stiff Drop-Landings
Shelburne, Kevin B	Anterior-Cruciate Ligament Forces in the Intact Knee During Normal Gait
Shelburne, Kevin B	Effect of Hamstrings Muscle Action on the Stability of the Acl-Deficient Knee
Shelburne, Kevin B	Evaluation of Tibiofemoral Compressive and Shear Loads in the Medial and Lateral Knee Compartments During Isometric Knee Exercises
Shelburne, Kevin B	Hamstrings Action Alone Cannot Limit Anterior Tibial Translation in Acl-Deficient Gait
Shelburne, Kevin B	Ligament Forces in the Anterior Cruciate Deficient Knee During Gait
Shelburne, Kevin B	Tibiofemoral Kinematics and Contact Patterns are Altered Due To Weakness of the Semitendinosus and Gracilis Muscles
Shelton, JC	Analysis of Strain Fields in Tendon Fascicles Under Tensile Loading
Shelton, JC	Structure-Function Relationship in Tendon Fascicles Under Tensile Loading Conditions
Shelton, Julia C	Running on Artificial Hip Joints - is It Wise?
Shepherd, Duncan E T	Instantaneous Compressive Modulus of Articular Cartilage in the Joints of the Lower Limb
Sherwin, S J	Characterisation and Simulation of In-Vivo Perhiperal Distal Bypass Grafts
Sherwin, SJ	Inspiratory Flow in Bronchial Airway Models: Bifurcation Plane Rotation
Sheth, PN	Stable Forward Dynamic Simulation of Bipedal Gait Using Space-Time Analysis
Sheu, Tony Wh	Computational Hemodynamics and Its Application To Surgeries for Two Congenital Heart Diseases
Shi, Congzhu	The Convergence of Cardiovascular Genomics and Endothelial Biomechanics
Shi, Yaling	Developing A Composite, Tissue-Engineered Aortic Valve
Shi, Yung-Chin	Strategy in Reducing Elbow Loading During Fall on An Outstretched Hand
Shiang, Tzyy-Yuang	A Study of Passive Repeatedly Plyometric Method for Training Upper Arm's Strength and Power
Shigeoka, Cassie	Spring-Like Force Generation by the Leg in Running
Shih, Cheng-Wei	Effect of Orthopaedic Shoes with Orthoses For
Shih, Chun-Hsiung	Finite Element Analysis of the Cervico-Trochanteric Stemless Femoral Prosthesis
Shih, Chun-Shiung	Comparative Biomechanical Studies Between Newly Designed Stemless Prosthesis and Conventional Prosthesis
Shih, William	Single Molecule Mechanics and the Myosin Family of Molecular Motors
Shim, June-Sung	The Effect of Trabecular Bone Microstructure on Stress Distribution of a Dental Implant
Shimizu, Akihiro	Augmented Longitudinal Diffusion In Oscillatory Flow Along A Lateral Grooved Tube Imitated Of Trachea With Uneven Inner Surface By Cartilage
Shimizu, Akihiro	Augmented Longitudinal Diffusion in Oscillatory Flow Along a Lateral Grooved Tube Imitated of Trachea with Uneven Inner Surface by Cartilage

Skilbeck, CA	Rheological Properties of the Blood and Local Haemodynamics Modulating Leukocyte Attachment To Selectin-Coated Surfaces
Skof, Branko	Effect of Fatigue on Leg Kinematic in Running Till Exostion
Skogsbergh, Dennis	Biomechanics of Prone Continuous Passive Motion for Low Back Pain
Skotte, Jorgen	Sudden Loading of the Upper Body Leads To Movement of Both the Lumbar Spine and Pelvis.
Slavin, Mary	Age-Related Effects on Momentum Generation and Muscle Activity During Gait-Initiation
Slone, Avril K	Computational Modelling of Blood Flow and Atery Wall Interaction
Slota, Gregory	Trunk Stability and Muscle Activity: Changes in Perturbation Energy and Preloads
Smaill, Bruce	A Model of Ventricular Anatomy Based on Structural Measurements From Pig Hearts.
Smaill, Bruce	Shear Properties of Ventricular Myocardium
Small, Carolyn	Analysis of in Vivo Carpal Bone and Ligament Kinematics Using Ct and Mr Data
Small, Carolyn	Three-Dimensional Motion Tracking of the Forearm Using Surface Markers
Smeesters, Cécile	Abilities of Young and Old Adults To Adjust Medio-Lateral Step Location During a Forward Fall
Smeesters, Cécile	Effects of Age and Gender on Maximum Hip Flexion Power At Low and High Velocities
Smeesters, Cécile	To Fall Or Not To Fall: the Threshold of Balance Recovery From a Fall
Smeulders, Mark JC	Two Instrumented Tests for Anterior Ankle-Joint Laxity: An Evaluation in the Clinical Setting
Smith, Adam	In Vivio Determination of Polyethylene Bearing Motion Realtive To the Tibia and the Femur
Smith, David	Modeling the Behaviour of Ligaments: a Technical Note
Smith, Erin	Designing Synthetic Polymers with Cell-Adhesive Properties: N-Isopropylacrylamide Polymers Containing Rgd-Peptides for
Smith, Gerald	Rear Wheel Impact Characteristics in Off-Road Cycling
Smith, Jeremy	Adaptations in Lower Extremity Joint Kinetics To Inertial Asymmetries During Walking
Smith, Jeremy	Relationship Between Linear Wrist Velocity and Impulse During Fastball Pitching in Collegiate Pitchers
Smith, Kim	Neuromuscular Responses To Knee Osteoarthritis During Stairway Locomotion
Smith, Kirk	Biomechanical Modeling of Indentation Testing and Application in Plantar Pressure Prediction of Diabetic Foot
Smith, Kirk	Forefoot Structural Predictors of Plantar Pressures During Walking in People with Diabetes and Peripheral Neuropathy
Smith, Mark	Investigations on the Biomechanics of a Osteochondral Implant by Fe Analysis
Smith, Michael L	Adaptive Responses of Endothelial Cells To Cyclic Pressure
Smith, RichardM	Motion Control Shoes Reduce Midfoot Range of Motion During Running
Smith, RKW	The Influence of Ageing and Exercise on Tendon Matrix - Hypotheses for the Initiation and Prevention of Strain-Induced
Smits, Karel	Modeling Electrical and Mechanical Activation Times in the Normal Heart
Smolinski, Daniel	Application of Fibre Laser Scanning Confocal Microscopy To Study of the Biomechanics and Microstructure of Articular Cartilage
Smolinski, Daniel	The Development of Confocal Arthroscopy for the Assessment of Cartilage Disorders
Smolinski, Patrick J	Effect of Polyethylene Thickness on Stresses of An Ankle Joint Implant
Smutz, W Paul	Modeling of Biomechanics of Tactile Sensation on Fingertips
Smutz, W Paul	Modeling of Force Response of Fingertips in Keyboard Strikes

Smyth, Paul	Calibration of Kinematic Models for Motion Capture
Snedeker, Jess	Finite Element Models of Abdominal Organs for Use in Trauma Research
Snedeker, Jess	Time-Dependent Properties of the Porcine Kidney Capsular Membrane
Snijders, Chris J	Lipoatrophia Semicircularis: a Biomechanical Approach
Snow, Christine M	Force Characteristics From Drop Landings
Snyder-Mackler, Lynn	Neuromuscular Function in Anterior Cruciate Ligament Deficient and Uninjured People
Snyder-Mackler, Lynn	Trainging-Induced Changes in Knee Stabilization Strategies After ACL Rupture
Soares, Denise Paschoal	Effective Force and Index of Effectiveness During Cycling
Søballe, Kjeld	Buffy Coat Concentrate (Agf) with Allograft Improves Implant Fixation
Socha, Teresa	On-Ice Acceleration as a Function of the Wingate Anaerobic Test and a Biomechanical Assessment of Skating Technique in Elite Ice Hockey Players
Sochor, Miroslav	Bone-Friendly Intervertebral Cages
Solan, Amy	Mechanical Forces and Engineered Vessels
Solomonow, M	Models of Neuromuscular Disorders in the Spine
Solomonow, M	Neuromuscular Implications of Lumbar Viscoelastic Tissues
Sommer III, HJ	Assessment of Sincerity of Effort During Isometric Strength Testing
Sommers, E	Radiographic Landmark Assessment of the Knee Joint Flexion-Extension Axis
Sommers, Mark B	Pertrochanteric Fracture Fixation: Effects of Implant Design on Cut-Out Failure Under Dynamic Loading
Sommers, Mark B	Swelling of Organotypic Brain Cultures as a Model for Traumatic Brain Injury
Sommers, MB	Screw and Blade Type Hip Implants Produce Distinct Insertion Forces
Sondergaard, Lars	Computational Fluid Dynamics After Aortic Coarctation Repair
Sonenblum, Sharon	In Vivo Motion of the Scaphotrapezio-Trapezoidal (Stt) Joint
Song, Jinlin	Development of a Flow Chamber for Studying Cell Behaviour Under Pulsatile Flow
Sorbetti, Jovina M	Cyclic Hydrostatic Pressure Increases Both MMP-1 and MMP-3 Mrna Levels, in Mg-63 Osteoblast-Like Cells Under Serum Free Conditions.
Sorrentino, Ruth Morey	Mechanical and Performance Aspects of a New Speed Skate Design
Soslowsky, Louis J	Molecular and Cellular Analysis of Rotator Cuff Tendinosis in a Rat Overuse Model
Soslowsky, Louis J	Quasi-Linear Viscoelastic Modeling of Tail Tendon Fascicles From Transgenic Mice
Sotereanos, Nicholas G	Use of Local Bodily Landmarks in Acetabular Cup Positioning
Sotoudeh, M	Comparison of Scaffold Designs for Tissue-Engineered Small-Diameter Graft Applications
Soulez, Gilles	Influence of Multiple Stenoses on Diagnosis of Peripheral Disease
Spaan, Jos AE	Application of Models To Understand the Integration of Coronary Vascular Control Mechanisms
Spaan, Jos	Implications of a Thick Endothelial Cell Glycocalyx for Microvascular Function in Mice
Spencer, P	Acousto-Opto-Electromagnetic Properties of Human Dentin Collagen
Spendiff, MK	A Model for the Development of Intimal Hyperplasia
Spiliotis, AD	Assessment of Techniques Used in Calculating Cell-Material Interactions
Spillmann, Christopher	Divalent Ion Induced Adhesion of Neutrophils To ICAM-1 and Vcam-1 Coated Surfaces
Spratt, Kevin	The Cervical Muscle Response During "Whiplash Simulated Motion" with Respect To Gender
Sprecher, Christoph	The Acting Wear Mechanisms on Metal-On-Metal Hip Joint Bearings
Sprenkle, Pamela M	Kinematic Comparison Of Treadmill Gait With Body Weight Suspension Between Unimpaired Subjects And Subjects With Parkinson's Disease

Steadman, JR	Tibiofemoral Kinematics and Contact Patterns are Altered Due To Weakness of the Semitendinosus and Gracilis Muscles
Stechow, Dietrich von	Direct Augmentation Restores the Structural Response of Failed Metastatic Defect Vertebrae
Stechow, Dietrich von	Does Vertebroplasty Alter the Mechanical Response of Osteopenic Vertebrae
Stechow, Dietrich von	Structural Competence of Osteopenic Thoracolumbar Vertebrae Following Anterior-Wedge Fracture
Stefanyshyn, Darren J	Influence of Metatarsophalangeal Joint Bending and Shoe Sole Length on Jump Height Performance
Stefanyshyn, Darren	Biomechanical Properties of Total Ankle Arthroplasty and Ankle Arthrodesis
Stefanyshyn, Darren	Mechanical and Performance Aspects of a New Speed Skate Design
Steffen, T	Evidence for Differences in Matrix Turnover in the Developing and Degenerating Human Lumbar Intervertebral Disc
Steffen, Thomas	Investigation of the Permeability of Osteoporotic Bone for Cement Augmentation Procedures
Stefoni, S	Flow Studies Connected with Artificial Hemodialysis. Mechanical Investigations and Biomechanical Effects
Stein, RB	A Leg-Propelled Wheelchair: Biomechanics, Energetics and Modeling
Steinman, David A	Computed Blood Flow Dynamics in An Anatomically Realistic Cerebral Aneurysm
Steinman, David A	Template-Based Finite Element Mesh Generation From Medical Images
Sterett, WI	Tibiofemoral Kinematics and Contact Patterns are Altered Due To Weakness of the Semitendinosus and Gracilis Muscles
Sterett, William I	Evaluation of Tibiofemoral Compressive and Shear Loads in the Medial and Lateral Knee Compartments During Isometric Knee Exercises
Sterett, William I	Gender Differences in Lower Extremity Shock Absorption During Vertical Drop Landings
Stergiopulos, N	Decreased Proximal Aortic Compliance Causes Systolic Hypertension
Stergiopulos, Nikolaos	Longitudinal Extension of Muscular Conduit Arteries Affects Distensibility
Stergiopulos, Nikos	Aortic Leak Severity Determines Arterial Elastance And
Stergiou, Nicholas	A Dynamical Analysis of Parkinsonian Gait
Stergiou, Nicholas	Individuals with ACL Reconstruction Display Altered Coordination Strategies While Walking and Running
Stergiou, Nicholas	Individuals with ACL Reconstruction Display Altered Long-Range Fractal Gait Patterns
Stergiou, Nicholas	Markov Model Suggests Neuromuscular Aging Affects Short-Range Correlations Present in the Gait Cycle
Stergiou, Nicholas	The Effect of Speed on the Deterministic Origin of Teh Variabilty Present During Human Locomotion
Stergiou, Nicholas	The Reliability of the Lyapunov Exponent During Treadmill Walking
Stergiou, Nicholas	Variability of the Lower Extremity Segmental Couplings Indicates That Elderly Gait is Less Stable During Stance
Stergiou, Pro	Biomechanical Properties of Total Ankle Arthroplasty and Ankle Arthrodesis
Sterriker, Steven	Clinical and Plantar Loading Risk Factors of Subjects with Hallux Valgus
Sterzing, Thorsten	Measurement of Inversion and Eversion Movements of the Foot by Using a Position Transducer
Sterzing, Thorsten	The Use of Skin Pre-Tension To Modify Tibial Bone Acceleration Estimates
Stevens, Carey	A Model of Ventricular Anatomy Based on Structural Measurements From Pig Hearts.
Stevenson, JM	Pressure Distribution Measurement for Design of Waist Belts in Personal Load Carriage Design
Stevenson, Joan	Comparison of 3 Measures of Grf; Force Plate, Fscan(r) and Multiple Force Sensors

Stevenson, Joan	Development of a Trifilar Pendulum for Measuring Moment of Inertia
Stevenson, Joan	The Importance of Certain Design Features in a Backpack
Stewart, Kristofer	Hyperelastic Representation of Hip Joint Capsule: a Finite Element Validation
Stewart, T	Experimental and Finite Element Analysis of the Effect of Muscle Forces on Fixation of Cemented Hip Prostheses At Heel Strike
Stewart, T	Fracture of Zirconia on Alumina Hip Prostheses : the Need for Microseparation Testing
Stewart, T	The Kinematics of Hip Joint Simulator Microseparation
Stewart, T	Wear of Ceramic Matric Composite Hip Prostheses in Simulators Modelling Laxity
Stewart, Todd D	Influence of Swing Phase Microseparation on the Wear of Ceramic on Polyethylene, Ceramic on Ceramic and Metal on Metal Total Hip Replacements
Steyers, Curtis M	Finite Element Analysis of Median Nerve Insult in the Carpal Tunnel
Stiles, Victoria	Influence of Viscoelastic Heel Inserts on Peak Impact Loading and Peak Ankle Dorsi-Flexion
Stitzel, Joel	Computational Modeling and Experimental Validation of Human Eye Interaction with High-Speed Foam Particles
Stitzel, Joel	High-Speed and Continuous Pressure Measurements: a Comparison of Active Pressure Sensors and Pressure Film
Stitzel, Joel	Investigation of Skin Abrasion Injuries From High Rate Shear Loading
Stoffell, Karl	Knee Loading During Gait and Early Signs of Knee Osteoarthritis in a Meniscectomy Population
Stokes, Ian	Spinal Stiffness Increase with Axial Load: Another Stabilizing Consequence of Muscle Activation
Stoltz, J F	Biomechanics of Erythrocyte Agglutination. Determination of Adhesive Specific Energy
Stoltz, Jean François	Interaction of Adhesion Molecules and Lymphocyte Adhesion To Endothelial Cells
Stoltz, Jean-Francois	Changes of Caveolin-1 in Human Endothelial Cells Exposed To Shear Stress
Stoltz, Jean-François	Laminar Shear Stress Induces Vasodilator-Stimulated Phosphoprotein Change in Cultured Human Endothelial Cells
Stolz, JF	Effect of Compression on Beta-1 Integrins (CD49d, CD49e) and CD44 Adhesion Molecules Expressed by Articular Condrocytes
Stolz, JF	Effect of Rhein on Intracellular IL-Beta-1 Production and Beta-1 Integrins Expression in Stimulated Chondrocytes
Stone, David	Molecular Mechanisms For Development Of Tendinitis
Stone, James	The Effect of Axonal Injury on the Material Properties of Brain Tissue
Stone, Martin H	Influence of Swing Phase Microseparation on the Wear of Ceramic on Polyethylene, Ceramic on Ceramic and Metal on Metal Total Hip Replacements
Stone, Martin H	Long-Term Simulator Wear Study of Surface Engineered Mom Hip Prostheses
Stone, Martin H	The Effect of Uhmwpe Material and Knee Design on in Vitro Wear of Fixed Bearing and Rotating Platform Mobile Bearing Total Knee Replacements
Stone, Martin	Wear of Crosslinked Polyethylene Under Different Tribological Conditions.
Stone, MH	Tribological Evaluation of Therapeutic Lubricants for the Knee
St-Onge, Nancy	A Reproducible Method To Define a Coordinate System for 3D Kinematics Evaluation of the Knee
Stotz, Paula J	Age Differences in Ability To Absorb Impact Energy in the Upper Extremities During Falls
Stotz, Paula J	Effect of Age on Ability To Brake a Fall with the Outstretched Hands
Streepey, Jefferson	Effects of Botulinum Toxin a and Muscle Strengthening on Gait
Streicher, R M	Fracture of Zirconia on Alumina Hip Prostheses : the Need for Microseparation Testing
Streicher, R M	The Kinematics of Hip Joint Simulator Microseparation

T

Tadjfar, Mehran	Separation Patterns in An Arterial Branch Model
Tafazzoli, Mohammad	Effects of Circumferential Residual Stress on the Circumferential Stress Distribution of the Arterial Wall by Finite Element Modeling
Täger, Georg	The Acting Wear Mechanisms on Metal-On-Metal Hip Joint Bearings
Tai, Ching-Lung	A Biomechanical Analysis of Triangulation of Anterior Vertebral Double-Screw Fixation
Tai, Ching-Lung	Comparative Biomechanical Studies Between Newly Designed Stemless Prosthesis and Conventional Prosthesis
Tai, Ching-Lung	Finite Element Analysis of the Cervico-Trochanteric Stemless Femoral Prosthesis
Taiar, R	Residual Stresses Analysis At the Interface Between Hydroxyapatite Coating and Titanium Substrate
Taïar, R	Drag Coefficient and Reynolds Number in High Butterfly Swimmers
Taiebi, MR	Computational Approach for Modeling Blood Flow Through a Pneumatic Driven Vad
Tainter, Christopher	Compressive Biomechanics of Fracture and Neurologic Integrity in the Pediatric Spine
Takagi, Kentaro	Effects of Electro-Acupuncture Stimulation on Systemic and Mesenteric Microvascular Hemodynamics in Anesthetized Rats
Takagi, Kiyoshi	Numerical Simulation and Database System for Hemodynamic Study of Cerebral Arteries
Takagi, Kiyoshi	Numerical Simulation of Fluid-Structure Interaction of the Intracranial Artery
Takahashi, Kazufumi	The Kick in the Deceleration Stage of 100m Track Race
Takano, Eisuke	Prediction of Torsional Properties of Rat Femur Using Peripheral Quantitative Computed Tomography
Takano, Yasunari	The Change in the Rotation Rate of a Bacterium Motor Causes the Difference Between Forward and Backward Swimming Speeds of Vibrio Alginolyticus
Takano, Youhei	Motion and Contact Analyses of Patello-Femoral Joint After Total Knee Arthroplasty
Takanokura, Masato	Relationship Between Frequency Components of Physiological Tremor and Elastic Load
Takashi, Toyoda	Cell Seeded Plasma-Treated Polyester Ligament Under Cyclic Tensile Load-Commissioning of Methodology
Takeishi, Hiroyuku	Stiffness Change with Cage Configuration for Anterior Lumber Interbody Fusion
Takekawa, M	Effects of Surface Topography on Cell Behaviour and Tissue Organization.
Takemasa, Tohru	Prediction of Three-Dimensional Orientation of Stress Fibers in Cultured Endothelial Cells Under Cyclic Deformation
Takemori, Toshikazu	A Regression Model for Predicting Perceived Load
Takemoto, Mami	Spatial Flow Pattern Difference Between Blood- and Crystalloid-Perfused Myocardium
Takeoka,	Motion of Rgpiba-Ams Near the Vwf Surface
Takeshita, Daisuke	Testing the Applicability of Reference Body Segmental Parameter Data To Individual Subjects: An Inverse Dynamics and Numerical Optimization Approach
Takeuchi, Kenzen	Modeling Skeletal Shape Changes and Growth in Scoliosis
Takizawa, Naosada	Quantitative Evaluation of Microvascular Structure and Comparizon of Regional Microvascularity and Po2 Distribution in Rat Cerebral Cortex
Talati, A	How Networks of Cortical Activity Adapt in Response To Changes In the Type and Quality of Sensory Input During Dynamic Precision Pinch
Tamagawa, Masaaki	Disintegration and Deformation of Cells and Microcapsules Using Shock Waves and Gas Bubbles for Developing DDS
Tami, Ivan	Effect of Interfragmentary Shear and Compressive Stimulation on Bone Healing
Tan, Juay-Seng	Evaluation of Spinal Implants - Vertebral Bone Density is An Important Factor
Tan, Kheng Hooi	Finite Element (Fe) Analysis on the Performance Range of Total Knee Replacement- a Preliminary Study

Tanabe, Yuji	A New Technique for Three-Dimensional Leg Alignment Assessment
Tanabe, Yuji	Viscoelastic Characterization of Ultra High Molecular Weight Polyethylene
Tanaka, Eiichi	Evaluations of Hip Fracture Mechanism and Prevention by Using Dynamic Fe Analyses
Tanaka, Eiji	Sensitivity Analysis on Disc Behavior in Temporomandibular Joint
Tanaka, Gaku	Flow Distribution in a Right Angle Branch During Oscillatory Flow
Tanaka, Hiroto	Myosin V Truncation Mutant with Only One Iq Motif Can Processively Move Along An Actin Filament with 36 Nm Steps
Tanaka, Junzo	Effects of Cyclic Strain on Ox-Ldl Uptake Into Macrophages
Tanaka, Masao	Effect of Ankle Joint Constraint by Afo on Maintenance of Standing Posture
Tanaka, Masao	Idiopathic Scoliosis Simulation by Finite Element Analysis with Imbalanced Growth Between Bone and Spinal Ligaments
Tanaka, Masao	Influence of Spasticity on Hemiplegic Ankle Joint Moment
Tanaka, Masao	Sensitivity Analysis on Disc Behavior in Temporomandibular Joint
Tanaka, Tatsuro	Digit Resistance Within Short Term After Fdp Tendon Repair in Canine in Vivo
Tanaka, Tatsuro	Gliding Resistance Versus Work of Flexion -- Two Methods To Assess Flexor Tendon Repair
Tanaka, Toshihiro	Biaxial Tensile Properties of Aortic Aneurysm Tissues Under Equibiaxial Stress
Tang, Dalin	An in Vivo Experiment-Based Growth Model for Intimal Hyperplasia in Rat Vein Graft
Tang, Dalin	Flow and Wall Compression in High Grade Asymmetric Arterial Stenosis Models During Pulsatile Flow Experiments
Tang, Dalin	Stress/Strain Analysis of Arteries with Stenotic Plaques and Lipid Cores
Tang, Fuk-Tan	Finite Element Analysis of the Newly Designed Foot Prosthesis for Patients with Partial Foot Amputation
Tang, Wen-Tzu	Strength Profile and Swing Pattern in Male and Female Elite Golfers
Tanishita, Kazuo	Bile Canaliculi Reformed by Rat Small Hepatocytes, and Its Dynamic Movement
Tanishita, Kazuo	Blood Flow Structure Contributing To the Rupture of Cerebral Aneurysm
Tanishita, Kazuo	Feature of Arterial Blood Flow Associated with the Biological Functions
Tanishita, Kazuo	Flow-Induced Morphological Change of Endothelial Cell and Shear Stress Distribution on the Surface of the Cell
Tanishita, Kazuo	Motion of Rgpiba-Ams Near the Vwf Surface
Tanishita, Kazuo	Quantitative Evaluation of Microvascular Structure and Comparizon of Regional Microvascularity and Po2 Distribution in Rat Cerebral Cortex
Tanne, David	Arterial Blood Filtration for the Prevention of Ischemic Stroke
Tanne, David	Is Permanent Arterial Filtration Possible? in Vivo Assesment of a Filtration Device for Embolic Stroke Prevention
Tanne, David	Optimization of a New Blood Filtration Device for Embolic Stroke Prevention
Tao, Zulai	Effect of Flow Pattern on Vasoactive Mediators Secretion of Cultured Endothelial Cells
Tapper, Janet	Joint Surface Kinematics During Walking in An in Vivo Model of Osteoarthritis
Tarbell, John M	Fluid Shear Stress Affects Vascular Smooth Muscle Cell Function
Tarbell, John M	Understanding the Mechanisms of Mechanical Heart Valve Cavitation
Tardif, Jean	Mechanical Aspects of Plaque Redistribution During Angioplasty: Possible Consequences on Vulnerability
Tardif, Jean-Claude	Biomechanics of Plaque Rupture in Atherosclerosis Coronary Arteries
Tarragô Candotti, Cláudia	Effective Force and Index of Effectiveness During Cycling
Tasevski, Vitomir	Cyclic Hydrostatic Pressure Increases Both MMP-1 and MMP-3 Mrna Levels, in Mg-63 Osteoblast-Like Cells Under Serum Free Conditions.
Tashman, Scott	A Unique Method To Determine Dynamic in Vivo Articular Surface Interaction

Tashman, Scott	Comparison of Relative Motion Between the Brain and Skull of the Human Cadaver for Rotation in the Coronal and Sagittal Planes
Tate, Angela J	A Preliminary Evaluation of a Limb-Segment Model for Lifting Tasks
Tate, Paul	Calibration of Kinematic Models for Motion Capture
Tateshima, Satoshi	Blood Flow Structure Contributing To the Rupture of Cerebral Aneurysm
Taulbee, Dale B	The Hemodynamic Effects of Parent Vessel Inflow Angle on a Cerebral Sidewall Aneurysm
Tavoularis, Stavros	Kinematic Measurements of Snowboarders' Ankles
Tawhai, Merryn	Anatomically Based Models of Blood Flow in the Human Pulmonary Microcirculation
Tawhai, Merryn	Anatomically Based Models of Gas Flow and Gas Exchange in the Human Lung
Tawhai, Merryn	Finite Element Geometric Models of the Human Lung and Diaphragm
Taylor, A	Measurement of Residual Stress Due To Volumetric Shrinkage in Bone Cement
Taylor, Charles A	Simulation Based Medical Planning for Cardiovascular Surgery: Recent Developments
Taylor, D	Torsional Fatigue of Cortical Bone
Taylor, Jennifer	The Combined Effects of Disuse and Gonadectomy on Bone Mechanics in Male and Female Rats
Taylor, M	Influence of Interference-Fit on the Initial Stability of Cementless Proximal Femoral Stems
Taylor, Mark	Characterisation of a Substitute Material To Model Cancellous Bone in In Vitro Implant Migration Studies
Taylor, Mark	Creep Formulation of Strain Accumulation During Tensile Fatigue of Cortical Bone
Taylor, Mark	Finite Element (Fe) Analysis on the Performance Range of Total Knee Replacement- a Preliminary Study
Taylor, Mark	Nonlinear Damage Theory Applied To Two-Step Fatigue Failure Prediction of Bone
Taylor, Mark	Three-Dimensional Finite Element Analysis of the ACL Under Anterior Tibial Loads
Taylor, Paul	Different Muscle Activation Patterns During Walking and Response To Common Peroneal Stimulation
Taylor, Russell H	Coupling Information To Action in the 21'st Century
Taylor, Winna	Cyclic Stretch Increases Gene Transfer and Expression in Alveolar Epithelial Cells
Teboul, Frédéric	Ultrasound Wave Propagation in Porous Medium. Application To Cancellous Bone
Tegdan, Trine	Fatigue and Muscle Coordination in Subjects with Patellofemoral Pain Syndrome
Teixeira, Jose CF	An Investigation on the Ventilation of Operating Theatres
Teixeira, Senhorinha FCF	An Investigation on the Ventilation of Operating Theatres
Telley, I	Inter-Sarcomere Dynamics in Myofibrills and Muscle Fibres - Theoretical Considerations and Simulations
Telley, I	Visualisation of Inter-Sarcomere Dynamics in Muscle Fibres
Telonio, A	Gait Features Assessment in Hip Osteoarthritis and Total Hip Replaced Patients Based on An Ambulatory System (Physilog)
Tencer, AF	Effect of Head Restraint Properties on Tissue Deformations in the Cervical Spine in Rear-End Motor Vehicle Impacts
Teo, Ee-Chon	A Fe Model of the C2-C3 Segment - Gross Responses Under Physiological Loads
Teoh, Swee-Hin	Scaffolds in Cardiovascular Tissue Engineering - Ultra Thin Layer by Layer
ter Keurs, Henk EDJ	Effects of Sarcomere Length, Ca2+ and Stimulation Rate on Force Generation of Mouse Cardiac Muscle
ter Keurs, Henk EDJ	Force and Sarcomere Shortening Velocity in Rat Heart
ter Keurs, Henk EDJ	The Force-Sarcomere Length-[Ca2+]I Relationship in Rat Heart
Terajima, Kazuhiro	A New Technique for Three-Dimensional Leg Alignment Assessment
Terajima, Kazuhiro	Comparative Study Between Intra- and Post-Operative Knee Motions After Total Knee Arthroplasty

Terashima, Shojiro	Changes in 3-D Motion and Contact Pressure Distribution After Lateral Ligament Injury of the Ankle Joint
Terashima, Shojiro	The Effect of Removing Blood and Bone Oil on the Mechanical Strength of Cement-Bone Interaface
Terk, Michael S	The Effect of Bracing on Patellar Alignment and Patellofemoral Joint Contact Area in Persons with Patellofemoral Pain
Terk, Michael S	The Effect of Bracing on Patellofemoral Joint Stress During Free and Fast Walking
Termoz, Nicolas	Assessment of Postural Response To An Internal Perturbation
Thaller, Sigrid	Influence of Gravitation on the Squad Jump: a Computer Simulation
Thambyah, Ashvin	Are the Articular Contact Stresses in the Knee Joint During Deep Flexion Critical?
Thayer, Robert	On-Ice Acceleration as a Function of the Wingate Anaerobic Test and a Biomechanical Assessment of Skating Technique in Elite Ice Hockey Players
Thelen, Darryl G	Abilities of Young and Old Adults To Adjust Medio-Lateral Step Location During a Forward Fall
Thelen, Darryl G	Effects of Age and Time Period on Joint Kinematics and Kinetics During a Single Step Response
Thelen, Darryl G	Generating Dynamic Simulations of Movement Using Computed Muscle Control
Thierfelder, Ludwig	Mutations of Titin Cause Dilated Cardiomyopathy
Thies, Sibylle	Comparison of Step Variability During Gait on Flat and Irregular Surfaces in Patients with Polyneuropathy.
Thinnes, John	The Impact of Anterior Cervical Fusion Upon Cervical Spine Range of Motion and Overall Neck Flexibility
Thistlethwaite, P	A Fast Circle Finding Technique for Digital Rsa
Thom, SA	Study of Blood Flow in the Human Femoral Artery by CFD
Thom, Simon A McG	Assessing the Accuracy of Doppler Velocity Waveforms Using a String Phantom
Thom, Simon A McG	Calibration of An Arterial Applanation Tonometer for In-Vivo Pressure Transduction
Thom, Simon AMcG	CFD Modeling of the Carotid Artery Using 3D Ultrasound
Thom, Simon AMcG	Combining Mri and CFD for Carotid Blood Flow Analysis: a Reproducibility Study
Thom, Simon AMcG	Errors Associated with CFD Models Reconstructed From 3D Ultrasound Data
Thomas, Amanda M	Biomechanics of Single-Level Cervical Fusion Techniques: Comparison of Graft-Plate Fusion with An Interbody Cage Device
Thomas, Joshua	The Effects of Step Uncertainty on Impacts and Contact Kinematics While Running on a Treadmill
Thomas, Maribeth	Development and Validation of An Approach To Record and Reproduce Kinematics
Thompson, Carrie	Movement Synergy Between the Ankle and Hip Joints During Single Leg Stance
Thompson, Cynthia	Effects of Vibration Induced by Inline Skating on Neuromotor Functions
Thompson, J	Tribological Characterisation of Surface Layer of Bovine Articular Cartilage.
Thompson, Jl	Tribological Evaluation of Therapeutic Lubricants for the Knee
Thompson, Mark	The Effect of Changing Anteversion on Forces on the Proximal Femur
Thompson, Rosemary	Effect of Lesions on the Three-Dimensional Mechanics of the Intervertebral Disc
Thornton, Gail	Comparison of Failure Properties of Scar Tissues in Skin, Patellar Tendon , and Medial Collateral Ligament in the Same Rabbits
Thornton, Gail	Evaluation of Patella Tendon as a Graft Material for Anterior Cruciate Ligament Reconstruction in An Ovine Model
Thornton, Gail	Joint Surface Kinematics During Walking in An in Vivo Model of Osteoarthritis
Thorwesten, Lothar	Mechanical Stability of Ankle Braces Under Passive and Dynamic Loading Conditions
Thorwesten, Lothar	The Stabilizing Effect of External Ankle Devices with and Without the Additional Influence of a Shoe
Thrasher, T Adam	Rocking the Rigid Trunk Can Produce Foot Clearance in MLKAFO Gait

Threlkeld, A Joseph	Kinematic Comparison Of Treadmill Gait With Body Weight Suspension Between Unimpaired Subjects And Subjects With Parkinson's Disease
Thunnissen, Jan	Influences on Eye Location and Posture of Drivers
Tian, T	Tensile Load Modulates Inhibition of MMP-1 Expression in Tendons
Tiberio, David	Ankle Kinematics Using One and Two Segment Foot Models
Tiberio, David	Assessment of Cushioning Materials: What's the Appropriate Measure?
Tiberio, David	Changes in Plantar Force, Area and Pressure Within a Single Session Using An In-Shoe Measurement System
Tichy, Petr	Bone-Friendly Intervertebral Cages
Tikunov, Boris	New Energetics Approaches To Elucidating Mechanisms of Contraction and Relaxation
Ting, Lena H	Muscle Synergies Controlling Ground Reaction Forces During Balance
Tingley, Jill	Viscoelastic Stress Relaxation During Acute Passive Stretching and Its Influence on Maximum Voluntary Strength
Tipper, J L	Fracture of Zirconia on Alumina Hip Prostheses : the Need for Microseparation Testing
Tipper, J L	The Kinematics of Hip Joint Simulator Microseparation
Tipper, J L	Wear of Ceramic Matric Composite Hip Prostheses in Simulators Modelling Laxity
Tipper, Joanne	Long-Term Simulator Wear Study of Surface Engineered Mom Hip Prostheses
Tipper, Joanne	Wear of Crosslinked Polyethylene Under Different Tribological Conditions.
Titze, Ingo R	Optimization of Passive Tissue Model Parameters of Intrinsic Laryngeal Adductory Muscles
Tochev, Dimitar	Simulation of Normal Walking Using 3D Modeling
Tochigi, Yuki	Preferential Direction of Subtalar Joint Laxity with Interosseous Talocalcaneal Ligament Sectioning
Todd, Dwight T	The Effect of Tibial Tray Surface Roughness and Insert Micromotion on Backside Wear
Todoh, Masahiro	Effect of Ankle Joint Constraint by Afo on Maintenance of Standing Posture
Todoh, Masahiro	Idiopathic Scoliosis Simulation by Finite Element Analysis with Imbalanced Growth Between Bone and Spinal Ligaments
Todoh, Masahiro	Influence of Spasticity on Hemiplegic Ankle Joint Moment
Todoh, Masahiro	Sensitivity Analysis on Disc Behavior in Temporomandibular Joint
Todorov, Emo	Biomimetic Approaches To Stable Systems for Functional Electrical Stimulation
Tohyama, Harukazu	Biological and Biomechanical Evaluations on in Vitro Infiltrative Characteristics of Fibroblasts Repopulating in the Necrotized Patellar Tendon
Tohyama, Harukazu	Biomechanical Evaluation of a Newly Devised Model for the Elongation-Type Anterior Cruciate Ligament Injury with Partial Laceration and Permanent Elon
Tohyama, Harukazu	Bone-Mulch-Screw/Washer-Loch Fixation of Doubled Flexor Tendon Graft in Anterior Cruciate Ligament Reconstruction
Tohyama, Harukazu	The Effect of Growth Factors on Mechanical Properties of the in Situ Frozen-Thawed Ligament and Gene Expression of Collagen in Extrinsic Fibroblasts
Tohyama, Harukazu	The Effect of Overloading on the Patellar Tendon That Underwent Segmental Resection of Its Central One-Third Portion
Tokish, John	Muscle Activation Differences Between the Upper and Lower Subscapularis Muscles During Abduction and Rotation
Tokuda, Masataka	Deformation Analysis of Human Left Ventricular Wall Using Mr Tagging Technique
Tokuda, Masataka	Finite Element Analysis of Cardiac Function in Hypertensive Heart Disease
Tokuda, Masataka	Measurement of the Encephalon Physical Parameter with MRI Saturation Transfer Method
Tokuno, Craig D	Compensatory Impulse Generation by Individuals with a Unilateral Below-Knee Amputation During Gait Initiation

Tokuno, Craig D	Electromyography of Knee-Joint Muscles in Unilateral Below-Knee Amputees During Walking and Running
Tokushige, Y	Design of a Biofidelic, Instrumented 2.5 Kg Infant Dummy
Tomita, Katsuro	Iomechanical Evaluation of Reconstruction Aftre Total Sacrectomy
Tomita, Katsuro	Mechanical Evaluation of Spine Reconstruction After Total En Bloc Spondylectomy by Finite Element Analysis
Tomita, Yoshihiro	Design Method of Porous Scaffold Microstructure Using Computational Simulation for Bone Regeneration
Tomita, Yoshihiro	Directional Dependency of Sensing Characteristics To Mechanical Stimulus in Osteoblastic Cell
Tomita, Yoshihiro	Evaluation of Mechanical Stimulus for Trabecular Surface Remodeling Using Digital Image-Based Model
Tomlin, G	The Effects of a Home-Based Forced-Use Intervention on Individuals with Cerebrovascular Accident
Toms, Stephanie R	Finite Element Analysis of a Mandibular Premolar Subjected To Orthodontic Loading: Effects of Periodontal Ligament Thickness and Nonlinear Material P
Toms, Stephanie R	Periodontal Ligament Biomechanics of Intrusive and Extrusive Orthodontic Loading
Toni, Aldo	A Comparision Among Different Tasks Performed by Different Subjects on the Primary Stability of Cementless Stems
Toni, Aldo	A Micromotion-Based Model of Bone-Implant Interface Remodelling
Torburn, Leslie	Techniques for Safe Landing During An Unexpected Fall: Modulation of Impact Velocity Via the Squat Response
Tørholm, S	Optimization of Ankle Joint Angle as Function of Trunk Angle in Cycling
Torii, Ryo	Numerical Simulation of Fluid-Structure Interaction of the Intracranial Artery
Torry, Michael R	A Comparison of ACL Forces During Soft and Stiff Drop-Landings
Torry, Michael R	Differences in Kinematics Between Professional and Youth Baseball Pitchers
Torry, Michael R	Evaluation of Tibiofemoral Compressive and Shear Loads in the Medial and Lateral Knee Compartments During Isometric Knee Exercises
Torry, Michael R	Gender Differences in Lower Extremity Shock Absorption During Vertical Drop Landings
Torry, Michael R	Humeral Torque in Youth Baseball Pitchers: Implications for Development of Humeral Retrotorsion
Torry, Michael R	Ligament Forces in the Anterior Cruciate Deficient Knee During Gait
Torry, Michael R	Muscle Activation Differences Between the Upper and Lower Subscapularis Muscles During Abduction and Rotation
Torry, Michael R	Quadriceps Weakness Causes An Increase in the Peak Adductor Moment During Gait
Torry, Michael R	Tibiofemoral Kinematics and Contact Patterns are Altered Due To Weakness of the Semitendinosus and Gracilis Muscles
Torry, Mike	Anterior-Cruciate Ligament Forces in the Intact Knee During Normal Gait
Toshev, Yuli	Model of Active Ankle-Foot Orthosis with Sensors Control
Toshev, Yuli	Simulation of Normal Walking Using 3D Modeling
Toshiaki,	Changes in Mechanical Properties of Human Tibialis Anterior Muscle Following Repeated Eccentric Contractions
Toth, Ladislav	Bone-Friendly Intervertebral Cages
Towers, Jeffrey D	Segmental Power During Propulsion in Wheelchair Users with Greater Evidence of Shoulder Injury Overtime
Townsend, Chris	The Testing and Validation of a Fast Response Inclinometer
Toy, Karen J	Adaptive Responses of Endothelial Cells To Cyclic Pressure
Toyoda, Yoji	Optical Motion Control of Euglena for Bio-Mems

Töyräs, J	Collagen Network and Mechanical Properties of Articular Cartilage: Experimental and Numerical Study
Töyräs, J	Effects of Sound Velocity Variation on Cartilage Ultrasound Indentation Measurements
Töyräs, J	Mechano-Acoustic Characterization of Normal, Degenerated and Repaired Cartilage
Tranquillo, Robert	Fabrication And Characterization Of Fibrin-Based Tissue-Equivalent Valves
Travis, Brandon	Evaluation of Bileaflet Mechanical Heart Valve Induced Blood Damage During Leakage Flow Using Laser Doppler Velocimetry and Indicators of Platelet Activation
Tredici, S	Limitation of Expiratory Flow in Liquid Ventilation
Treil, J	Origins of Bipedalism: Evolutionary Morphology Through Finite Element Analysis
Tremblay, Mathieu	Evaluation of 3D Knee Kinematics with and Without Plantar Orthopaedic Processing
Trevisan, C	Gait Features Assessment in Hip Osteoarthritis and Total Hip Replaced Patients Based on An Ambulatory System (Physilog)
Triano, John J	Biomechanics of Prone Continuous Passive Motion for Low Back Pain
Triano, John J	Developing Skilled Performance of Spinal Manipulation/Adjusment
Triano, John J	Neck Loads During Spinal Manipulation
Triano, John J	Obtaining Predictable Lumbopelvic Loads During Spinal Manipulation
Tricht, Ilse Van	Computational Fluid Dynamics in Hemodialysers
Trimble, K	Back Muscle Fatigue During Intermittent Prone Back Extension Exercise
Trubel, Wolfgang	Fluid Dynamics and Wall Mechanics in Peripheral Bypass Anastomoses
Truskey, George A	The Effect of Ligand Density on Tether Formation Between Endothelium and Monocytes
Tsai, Chien-Lu	Biomechanical Analysis of the Upper Extremity Between Badminton Smash and Tennis Serve
Tsai, S F	Computational Hemodynamics and Its Application To Surgeries for Two Congenital Heart Diseases
Tsamopoulos, John	Deformation of Bioartificial Capsules in Plane Hyperbolic Flow
Tsao, Helen	Influence of Glucocorticoid Pretreatment on De-Repression of Gene Expression in Meniscal Explants After Removal From Biomechanical Loading
Tsapikouni, Theodora	Longitudinal Extension of Muscular Conduit Arteries Affects Distensibility
Tsoumanis, Anastasios D	Reflex Responses To the Medial Knee Ligament Loading: Effect of Hip Angle Change
Tsubota, Ken-Ichi	Evaluation of Mechanical Stimulus for Trabecular Surface Remodeling Using Digital Image-Based Model
Tsuda, Akira	Stretch-And-Fold Fractal-Like Aerosol Bolus Spreading in the Rythmically Expanding Alveolated Duct
Tsuda, Eiichi	The Tensile Properties of the Healing Goat Mcl After a Combined Mcl/Acl Injury
Tsuji, Tetsuya	Motion of Rgpiba-Ams Near the Vwf Surface
Tsujioka, Katsuhiko	Altered Nana-Order, Micro-Mechanical Property of Pulmonary Artery Smooth Muscle in Primary Pulmonary Hypertension
Tsunoda, Daisuke	Flow and Wall Compression in High Grade Asymmetric Arterial Stenosis Models During Pulsatile Flow Experiments
Tsurumaki, Takashi	Motion and Contact Analyses of Patello-Femoral Joint After Total Knee Arthroplasty
Tsutsumi, Masakazu	Finite Element Analysis of Cardiac Function in Hypertensive Heart Disease
Tsuyuki, Kei	Dynamic Behavior of Actin Filaments in Cultured Endothelial Cells During Exposure To Shear Stress
Tsuzaki, Mari	Cellular Responses Regulating Signaling and Gene Expression in Tendon Cells
Tubman, LA	A Leg-Propelled Wheelchair: Biomechanics, Energetics and Modeling
Turcotte, R	Forward Ice Hockey Skating: Comparison of EMG Activation Patterns At Three Velocities

U

V

van Dijk, C Niek	Two Instrumented Tests for Anterior Ankle-Joint Laxity: An Evaluation in the Clinical Setting
Van Dijk, CN	In-Vitro Reports on Anterior Ankle Ligament Damage and Ankle-Joint Laxity: A Review of the Literature
van Emmerik, Richard E A	Issues in the Interpretation of Continuous Relative Phase
Van Hoof, Jack	A Numerical Model Predicting Upper Extremity Fractures Due To Airbag Deployment
Van Hoof, Jack	Effects of Muscle Activation and Seating Posture in Rear End Impact Using a Human Model with a Detailed Neck
Van Horne, Scott Van	Mechanical and Performance Aspects of a New Speed Skate Design
Van Poll, D	In-Vitro Reports on Anterior Ankle Ligament Damage and Ankle-Joint Laxity: A Review of the Literature
van Rey, Elton M	Intelligent Stretching and Evaluation of Spastic Ankles Using a Portable Device
Van Rey, Elton	Aging-Related Changes in Achilles Tendon Reflexes
Van Rey, Elton	Biomechanical Changes in Spastic Ankles of Stroke Patients
Van Rietbergen, Bert	Prospects of Micro- Finite Element Analyses of Bone for Clinical Application
van Soest, AJ Knoek	Marker-Based Reconstruction of the Kinematics of a Chain of Segments; a New Method That Incorporates Joint Kinematic
van Soest, AJ Knoek	Maximal Cycling Power Can Be Slightly Increased by Constraining Leg Kinematics
van Soest, AJ Knoek	Stability of Bipedal Stance; the Contribution of Co-Contraction and Spindle Feedback
van Zwieten, KJ van	Modeling of Extremal Load on Human Knee Joint Ligaments
Vandenbosch, Ryan	Estrogen Depletion is Associated with Changes in Osteon Morphology
Vander Sloten, Jos Vander	Delayed Versus Early Versus Immediate Loading of Oral Implants
Vander Sloten, Jos Vander	Simulation of Overload-Induced Marginal Bone Resorption Using Anatomical Finite Element Models
Vanderby Jr., Ray	A Comparison of Joint Mechanics Between Anterior Cruciate Ligament Intact and Deficient Stifles: a New Model of Anterior Cruciate Ligament Disruption
Vanderby Jr., Ray	Apoptosis in Ligament After a Sub-Failure Stretch
Vanderby Jr., Ray	Application of a Nonlinear Model To Describe Ligament Behavior
Vanderby Jr., Ray	Relaxation Function and a Generalized Solution for a Nonlinear Rheological Model of Biological Soft Tissues
Vanderby Jr., Ray	Size Effects in Nonlinear Viscoelasticity
Vanderby Jr., Ray	Testing Duration Required To Accurately Predict Ligament Viscoelasticity
Vanderby Jr., Ray	The Effects of Hydration Time on Ligament Viscoelasticity
Vanderby Jr., Ray	Trap May Contribute To Altered Mechanical Properties in Ligament After Chemical Sympathectomy
Vanderploeg, EJ	Chondrocytes and Fibrochondrocytes Respond Differently To Oscillatory Tension
Vanderploeg, EJ	Matrix Biosynthesis Due To Exogenous Stimuli Differs for Cartilage and Fibrocartilage
Vannier, Michael	Self-Sustaining Oscillatory Electromechanical Activity in the Gut
Varadarajan, Ravikumar	Effect of Osteoporosis in a Disc - Degenerated Lumbar Spine
Vardimon, Alexander D	Orthodontic Bracket Debonding: in Vivo and in Vitro Debonding Strength and the Related Tooth Damage
Varghese, Sonu S	Numerical Modeling of Pulsatile Turbulent Flows in Stenotic Vessels
Vasavada, Anita N	Neck Muscle Strains in Whiplash Injury
Vashishth, Deepak	Is Damage Development Different in Bones with a Shorter Fatigue Life
Vashishth, Deepak	The Mechanisms and Significance of the Correlation Between Bone Strength and Stiffness
Vaughan, Christopher L	Has Computer Simulation of Locomotion Delivered All Its Promise in the Past 20 Years?

Vaughan, Christopher L	Relationship of Animal To Human Methods for in Vivo Tendon Strain Determination in Bipedal Locomotion
Vaverka, Frantisek	Take-Off Optimization Patterns in Ski Jumping: General Versus Individual Models
Vaz, Marco Aurélio	Functional Adaptation of the Dorsiflexor Torque-Velocity Relation
Vaz, Marco Aurélio	Mechanomyographic Signals of the First Dorsal Interosseus Muscle During Isometric Voluntary Contractions
Vega, A	Electrical Conductivity of Lumbar Annulus Fibrosis
Veldhuis, Jim H	Cell-Cell Interfacial Tension and Cytoplasm Viscosity Can Be Determined Using Parallel-Plate Compression Tests
Veldhuis, Jim H	Oriented Mitosis-Driven Epithelium Reshaping: a Finite Element Study
Venkadesan, M	How Networks of Cortical Activity Adapt in Response To Changes In the Type and Quality of Sensory Input During Dynamic Precision Pinch
Verdonck, Pascal	Aortic Leak Severity Determines Arterial Elastance And
Verdonck, Pascal	Combining Mri and CFD for Carotid Blood Flow Analysis: a Reproducibility Study
Verdonck, Pascal	Computational Fluid Dynamics in Hemodialysers
Verdonck, Pascal	On the Use of 3D MRI Velocity Measurements for Computational Flow Simulations
Verdonck, Pascal	Study of Left Ventricular Filling: Comparison of Hydraulic and Numerical Modelling
Verschueren, S M P	Inter-Limb Coordination in Human Locomotion with Added Mass
Verstraete, Mary C	Backpack Loads Carried by School Children
Vesely, Ivan	Developing A Composite, Tissue-Engineered Aortic Valve
Vesely, Ivan	Tensile Vs. Compressive Glycosaminoglycan Profiles in Normal and Myxomatous Mitral Valves
Vezina, M Johanne	Temporal Activation Pattern Differences Between Those with and Those Without Chronic Low Back Pain
Viant, Tiffany L	Artificial Neural Oscillators as Controllers for Locomotion Simulations and Robotic Exoskeletons
Viceconti, M	Simulation of Physiological Muscle Loading in Finite Element Modelling of the Intact Femur
Viceconti, Marco	A Comparision Among Different Tasks Performed by Different Subjects on the Primary Stability of Cementless Stems
Viceconti, Marco	A Micromotion-Based Model of Bone-Implant Interface Remodelling
Vierendeels, Jan	On the Use of 3D MRI Velocity Measurements for Computational Flow Simulations
Vierendeels, Jan	Study of Left Ventricular Filling: Comparison of Hydraulic and Numerical Modelling
Vink, Hans	Exclusion of Neutral and Polyanionic Plasma Tracers by the Capillary Glycocalyx in Equilibrium and Deformed Configurations Predicts Mechano-Electrochemical Properties in Vivo
Vink, Hans	Implications of a Thick Endothelial Cell Glycocalyx for Microvascular Function in Mice
Vinuela, Fernando	Blood Flow Structure Contributing To the Rupture of Cerebral Aneurysm
Virmavirta, M	The Transition From Take-Off To Early Flight Phase in Ski-Jumping
Visentin, Peter	The Internal-Load Characteristics During Violin Performance
Vito, Raymond P	Stress/Strain Analysis of Arteries with Stenotic Plaques and Lipid Cores
Vito, Raymond	Axial Stretch of Arteries in Organ Culture
Vogel, Kathryn G	The Small Proteoflycan in Tendon
Vogelpohl, Lori	Increasing Age Slows Recovery of Function Following Achilles Tendon Injury in the Rat
Vogt, L	Movement Behaviour in Chronic Neck Pain Patients
Vogt, L	Muscular Activity and Strength Testing of Trunk and Hip Extensors: a Reproducibility Study
Voide, Romain	Time-Dependent Properties of the Porcine Kidney Capsular Membrane

W

Wereley, Steven T	Soluble Proteins Released by Endothelial Cells in Response To Fluid Flow Affect Smooth Muscle Cells
Wessman, Michael D	Viscoelastic Characterization of Collagen Gel Constructs
West, A Nico	Dynamics of Wound Healing in Airway Epithelial Cells: Gfp-Actin Remodeling
West, Jacob	Cervical Range of Motion in Asymptomatic Subjects Following Spinal Manipulative Therapy: a Double Blinded Randomised Clinical
West, Tim	Quantifying Isometric Force-Dependent Energy Release in White Muscle by Comparing Contraction Energetics in Intact and Skinned Fibres
Westenberg, Josephus J M	On the Use of 3D MRI Velocity Measurements for Computational Flow Simulations
Westerhof, Nico	Aortic Leak Severity Determines Arterial Elastance And
Westwood, SM	Rheological Properties of the Blood and Local Haemodynamics Modulating Leukocyte Attachment To Selectin-Coated Surfaces
Wheeler, John	Paraspinal Muscle Spindles Responses To Biomechanical Changes in the Spine
White, Charles	Dissociation of Pecam-1/Gq with Temporal Gradients in Shear Stress
White, D	Foot Roll Over Shapes In Transtibial Amputees: Implications For Prosthetic Alignment
White, Joseph P	Three-Dimensional Airway Closure: Surface-Tension-Driven Non-Axisymmetric Instabilities Of Liquid-Lined Elastic Tubes
White, Klane	Cervical Spine Kinematics Following Sequential Sectioning: Novel Implications for Extension Type Injuries
Whitledge, Jon	Biomechanical Efficacy of a Protein Polymer Hyrdrogel for Inter-Vertebral Nucleus Augmentation and Replacement
Wigström, Lars	Kinematics of the Heart
Wilcox, Helen	Biomechanics & Hydrodynamics of Decellularised Porcine Aortic Heart Valves
Wilcox, Helen	Biomechanics & Hydrodynamics Of Decellularised Porcine Aortic Heart Valves
Wilcox, RK	Mathematical Models for the Time-Dependent Characteristics of Spinal Cord Tissue
Wilcox, Ruth K	Synergistic Effect of Spatial Resolution and Noise on the Precision and Accuracy of Measurements in Simulated Digital
Wilcox, Ruth	An Investigation of the Burst Fracture Mechanism Using a Combined Experimental and Finite Element Approach
Wilde, Brandie	The Selection of Parameters and Pre-Test States in Identifying the Age Effect Through the Center of Pressure (Cop) Measurement
Wilde, Tom De	Simulation of Overload-Induced Marginal Bone Resorption Using Anatomical Finite Element Models
Wilder, David	The Cervical Muscle Response During "Whiplash Simulated Motion" with Respect To Gender
Wiley, Kasey	Anticipatory Behaviour During Recovery From Unexpected Perturbations: Younger Verses Older Adults
Wiliams, Sophie	Long-Term Simulator Wear Study of Surface Engineered Mom Hip Prostheses
Wilke, A	Ankle and Subtalar Kinematics of the Ankle Joint with Intact, Injured, and Reconstructed Lateral Ligaments
Wilke, Hans-Joachim	Discoligamentous Structures of the Lower Cervical Spine Get Injured in In Vitro Low-Speed Side Collisions
Wilke, Hans-Joachim	Effect of a Compressive Follower Load and a Tensile Force on Intradiscal Pressure and Intersegmental Rotation of the Lumbar
Wilke, Hans-Joachim	In Vivo Loads Acting in the Spine and in Spinal Implants
Wilken, J	The Influence of Normal Hormonal Fluctuations in Women on the Biomechanics of Stepping and Cutting
Wilkerson, Jerry	Relationship Between Linear Wrist Velocity and Impulse During Fastball Pitching in Collegiate Pitchers
Willems, Mark ET	Is Active Force Production of Skeletal Muscles Altered by Collagen Content?
Willems, T	Within-Subject Variability of Plantar Pressure Patterns in Barefoot Running

X

Y

Yingling, Vanessa	The Combined Effects of Disuse and Gonadectomy on Bone Mechanics in Male and Female Rats
Yiou, E	Neural and Biomechanical Organization of Anticipatory Postural Adjustements in Fast Synchronized Stepping and Arm Rising
Yoder, Evangeline	Does Simulated Dorsal Kyphosis Alter Lower Limb Kinematic, Kinetic, and EMG Patterns During Gait?
Yoder, Evangeline	Movement Characteristics in Children with Lesch-Nyhan Syndrome (Lns)
Yodfat, Ofer	Arterial Blood Filtration for the Prevention of Ischemic Stroke
Yodfat, Ofer	Is Permanent Arterial Filtration Possible? in Vivo Assesment of a Filtration Device for Embolic Stroke Prevention
Yodfat, Ofer	Optimization of a New Blood Filtration Device for Embolic Stroke Prevention
Yoganathan, Ajit P	Analysis of Total Cavopulmonary Connection Fluid Dynamics: Experimental Studies
Yoganathan, Ajit	Evaluation of Bileaflet Mechanical Heart Valve Induced Blood Damage During Leakage Flow Using Laser Doppler Velocimetry and Indicators of Platelet Activation
Yokota, Hideo	New Method of Three-Dimensional Imaging of Small Airways in Rats with X-Ray Micro-Ct
Yokota, Hiroki	Functional Changes in Kidney Cells in Response To Sustained Hydrostatic Pressure
Yoo, Soo Jin	A Quantitative Assessment of Knee Extensor Spasticity Using Isokinetc Dynamometer
Yoon, Sukhoon	The Variability of Maximum Vertical Jumps
Yoshida, Akira	Iomechanical Evaluation of Reconstruction Aftre Total Sacrectomy
Yoshida, Momoko	A Gait Orthosis for Paraplegics with a Motor-Driven Knee Joint
Yoshitake, Yasuhide	Behaviours of Muscle-Tendon Complex During Electrical Stimulation with Trains of Linearly Varying Frequency in Humans
You, Joshua (Sung)	Does Simulated Dorsal Kyphosis Alter Lower Limb Kinematic, Kinetic, and EMG Patterns During Gait?
You, Joshua (Sung)	Movement Characteristics in Children with Lesch-Nyhan Syndrome (Lns)
You, Zhong	Development of a Novel Type of Oesophageal Stent Based on Deployable Tubular Structures
Young, Alistair A	Principal Component Analysis of Cardiac Function
Young, Alistair	Shear Properties of Ventricular Myocardium
Young, Iain S	New Energetics Approaches To Elucidating Mechanisms of Contraction and Relaxation
Young, Mark RJ	Determination of Inertial Characteristics of the Human Foot Using Dual Energy X-Ray Absorptiometry
Young, Philippe G	Head Impacts: Analytical, Numerical and Experimental Models
Younis, HF	Diseased Human Carotid Bifurcations: Histological Correlations To Hemodynamic Factors
Youqin, Chen	Effects of Hydrogen Peroxide on Endothelial Cells Adhesion Molecules Expression
Youqin, Chen	Effects of Shear Stress and Lysophosphatidylcholine on Adhesion Modecules Expression of Endothelial Cells
Youqin, Chen	Time-Dependent Effect of Interleukin-8 Gene Expression in Endothelial Cells Exposed on Fluid Shear Stress
Yoza, I	Model Blood Consisting of Dense Suspension of Natural Polymeric Gel Particles
Yu, J	The Structure and Functions of Elastic Fibres in Bovine Intervertebral Disc
Yu, Li-niu	Modular Generation and Application of 3D Denture Finite Element Model
Yu, Yeonjoo	Impact Attenuation of Landing Activities in Barefoot and Shod
Yuan, Phillip	Biological and Biomechanical Response of Rat Dorsiflexors To Eccentric Exercise
Yuan, Yang	Time-Dependent Effect of Interleukin-8 Gene Expression in Endothelial Cells Exposed on Fluid Shear Stress
Yun, Sang-Ho	Air Flow and Temperature Distribution in a Neonatal Incubator

Z

Zabjek, K F	Postural Evaluation of Idiopathic Scoliosis Patients and Adolescent Control Subjects
Zabjek, K F	Stiffness and Postural Control in Adolescent Control and Idiopathic Scoliosis Patients
Zabjek, Karl F	Errors Introduced by the Ground Reaction Forces Approach on Joint Moment Calculation During Gait
Zaffagnini, S	Computer Investigation of Cruciate Ligaments Orientation During the Passive
Zahid, A	Evidence for Differences in Matrix Turnover in the Developing and Degenerating Human Lumbar Intervertebral Disc
Zajac, FE	Muscle Force Not Work Defines Muscle Contributions To Forward Progression
Zajac, FE	Muscle Function During Forward and Backward Walking
Zambanini, Andrew	Assessing the Accuracy of Doppler Velocity Waveforms Using a String Phantom
Zambanini, Andrew	Calibration of An Arterial Applanation Tonometer for In-Vivo Pressure Transduction
Zambanini, Andrew	Study of Blood Flow in the Human Femoral Artery by CFD
Zamir, Evan A	Measurement of Embryonic Heart Material Properties During Cardiac Looping
Zamparo, P	The "Evolution" of Bicycle Design and Its Effects on the Efficiency and Economy of Cycling
Zander, Thomas	Effect of a Dual Cage on the Mechanical Behaviour of the Lumbar Spine
Zander, Thomas	Effect of a Laminectomy on the Mechanical Behavior of the Lumbar Spine
Zander, Thomas	Effect of Bone Graft Position on Loading of Pedicle Screws
Zander, Thomas	Influence of a Follower Load on the Mechanical Behavior of the Lumbar Spine
Zander, Thomas	Influence of Angular Stability of An Internal Spinal Fixator on Implant Loads
Zaretsky, U	Numerical and Experimental Measurements of the Flow in Pulsatile Ventricle Assist Device
Zaretsky, Uri	A Realistic Mechanical Model of the Human Chest Wall
Zaretsky, Uri	Experimental Analysis of Flow Through Tilting Disk Valve
Zarins, Christopher K	Morphology of Endothelial Cells Under Flow Alteration in Vivo
Zaro, Milton Antônio	Mechanomyographic Signals of the First Dorsal Interosseus Muscle During Isometric Voluntary Contractions
Zatsiorsky, Vladimir M	Mechanical Energy Transfer Between Adjacent Joints by Two-Joint Muscles
Zatsiorsky, Vladimir M	Wrenches At the Digit-Object Interface During Prehension
Zatsiorsky, Vladimir	Tangential Force Sharing Among Fingers During Static Grasping
Zaucke[3], Frank	Effects of Mechanical Stimuli on the Relaxation Behavior of the Growth Plate Related To Morphological and Biochemical Adaptation in the Rat Model
Zavatsky, AB	Biomechanics of Knee Replacement - From in Vitro To in Vivo
Zborowski, Maciej	Magnetic Field Visualization in Applications To Pulsed Electromagnetic Field Stimulation of Tissues
Zborowski, Maciej	Pulsed Electromagnetic Field-Dependent Differencesof Collagen Processing in Pre-Osteoblasts
Zborowski, Maciej	Pulsed Electromagnetic Field-Dependent Stimulation of Pre-Osteoblast Proliferation in Vivo
Zdero, Rad	Development of a Trifilar Pendulum for Measuring Moment of Inertia
Zebas, Carole J	The Effects of Age and Feedback on Isometric Knee Force Control Abilities
Zee, M de	Optimization of Ankle Joint Angle as Function of Trunk Angle in Cycling
Zehr, E Paul	Are Rhythmic Arm Movements Controlled by a Central Oscillator?
Zehr, E Paul	Compensatory Corrective Responses Induced by Cutaneous Nerve Stimulation in the Hand and Foot During Walking
Zehr, E Paul	H-Reflexes in Human Forearm Muscles are Attenuated During Rhythmic Arm Movement

Zehr, E Paul	Neural Control of Eccentric Contractions
Zeminski, Jennifer	Development and Validation of An Approach To Record and Reproduce Kinematics
Zeng, D	Effects of Vessel Motion on Right Coronary Artery Hemodynamics
Zeng, LingFang	Effect of Shear Stress on the Activation of the Peroxisome Proliferator-Activated Receptors (Ppars)
Zentner, Jelena	Leg Design and Jumping in Spiders
Zernicke, RF	Socket Comfort and Perceived Functional Ability in Unilateral Transtibial Amputee Patients Using Plaster-Cast and Cad/Cam Manufactured Sockets
Zernicke, Ron	Locomotion Research Within An Orthopaedics Framework: Successes and Challenges
Zernicke, Ronald F	Grouping of Scoliosis Patients by Spinal Curve Severity From Torso Surface Data
Zernicke, Ronald F	Relation Between Knee Range of Motion Measured Passively and During Gait in Anterior Cruciate Ligament Deficient and Reconstructed Individuals
Zervas, V	Characterisation and Simulation of In-Vivo Perhiperal Distal Bypass Grafts
Zhang, Baiming	Speed and Cadence Differences Between Cornering and Straight Track Riding in 4km Individual Pursuit
Zhang, Fu-qiang	Modular Generation and Application of 3D Denture Finite Element Model
Zhang, Li-Qun	Aging-Related Changes in Achilles Tendon Reflexes
Zhang, Li-Qun	Biomechanical Changes in Spastic Ankles of Stroke Patients
Zhang, Li-Qun	In Vivo & Noninvasive Load Sharing Among Quadriceps Components in Patellar Malalignment
Zhang, Li-Qun	In Vivo Patellar Tracking in Patellar Malaligned Knees
Zhang, Li-Qun	Intelligent Stretching and Evaluation of Spastic Ankles Using a Portable Device
Zhang, Li-Qun	Mathematical Modeling of ACL Impingement Against the Intercondylar Notch Wall
Zhang, Li-Qun	Modeling of ACL Impingement Using Simm
Zhang, M	Compressive Strength in Vertebroplasty Under Fatigue Loading
Zhang, Mei L	Force and Sarcomere Shortening Velocity in Rat Heart
Zhang, Ming	Development of 3D Finite Element Model of Human Foot and Ankle
Zhang, Ming	Development of a Flow Chamber for Studying Cell Behaviour Under Pulsatile Flow
Zhang, Songning	Effects of Midsole Density and Landing Height on Impact Attenuation in Landing
Zhang, Songning	Impact Attenuation of Landing Activities in Barefoot and Shod
Zhang, Xudong	In Vivo Measurement and Biomechanical Modeling of Thumb Circumduction Range of Motion
Zhang, Yan	Effect of Co-Cultured Vascular Smooth Muscle Cells on Pdgf-B Mrna Expression of Endothelial Cells Under Shear Stress
Zhang, Yan	Effects of Low Shear Stress on Morphological Remodeling of Organ-Cultured Artery in Vitro
Zhang, Yan	Pressure-Induced Expression of Immediate-Early Gene Product C-Jun of the Common Carotid Arteries in Rats
Zhang, Ying M	The Force-Sarcomere Length-[Ca2+]I Relationship in Rat Heart
Zhao, C F	Tendon Excursion and Gliding Mechanism
Zhao, Chunfeng	Digit Resistance Within Short Term After Fdp Tendon Repair in Canine in Vivo
Zhao, Chunfeng	Gliding Resistance Versus Work of Flexion -- Two Methods To Assess Flexor Tendon Repair
Zhao, Chunfeng	Pilot Study of Intracellular Signaling in Post-Operative Tendons
Zhao, Hong	Interaction of Adhesion Molecules and Lymphocyte Adhesion To Endothelial Cells
Zhao, Hong	Studies on the Single Binding Force of LFA-1 and ICAM-1
Zhao, KD	Modeling of Manual Wheelchair Propulsion Using Optimization
Zhao, SZ	A Comparative Study of CFD and MRI for Pulsatile Flow in a Carotid Bifurcation Phantom

BILATERAL DEFICIT IN MAXIMUM ISOMETRIC FORCE, NEURAL DRIVE AND RATE OF FORCE DEVELOPMENT.

Jaap H. van Dieën; Arnold de Haan

Institute for Fundamental and Clinical Human Movement Sciences, Faculty of Human Movement Sciences, 'Vrije Universiteit', Amsterdam, The Netherlands

INTRODUCTION

It has been reported that activity of the motor cortex in one hemisphere reduces the excitability of homologous parts of the opposite hemisphere (Oda and Moritani, 1996). This has been suggested to result in a bilateral deficit in neural drive and force production (e.g.Secher, et al., 1988). However, the existence of such a bilateral deficit has been subject of debate (Herbert and Gandevia, 1996). Three experiments were performed to test the existence of a bilateral deficit in finger flexor and knee extensors muscles.

METHODS

Ten healthy young subjects performed maximum isometric finger flexions bilaterally and unilaterally. In all trials force output and agonist electromyographical activity (EMG) were recorded.

The same protocol was used to test for a bilateral deficit in the knee extensor muscles in 12 subjects. EMG was recorded from the vastus lateralis (VL) and rectus femoris (RF) muscles. In addition, superimposed tetanic stimulation (300 Hz, 80 ms) was used to assess neural drive of the knee extensors. The extra force produced during the tetanic stimulation superimposed on the maximum voluntary effort was divided by the force during a control tetanus prior to the voluntary contraction. The ratio of the superimposed tetanus force and the control tetanus force was used as an estimate of voluntary activation.

In the third experiment, the same 12 subjects performed unilateral and bilateral knee extensions with the instruction to generate force as fast as possible. The peak rate of force development was determined.

RESULTS

In bilateral finger flexions, force output was 22% less than in unilateral exertions ($p = 0.001$). Agonist EMG amplitudes were reduced by similar amounts as force output ($p = 0.015$).

In bilateral knee extension, force output, VL and RF EMG amplitudes were also significantly lower, as compared to unilateral extension by 5%, 8%, and 15% respectively. The voluntary activation as assessed by superimposed stimulation was 4% lower in bilateral contractions ($p = 0.003$).

When subjects were instructed to build up force as fast as possible, the peak rate of force development was 13% lower in the bilateral contraction ($p = 0.002$) as compared to the unilateral contraction.

DISCUSSION

The present study consistently showed a bilateral deficit, albeit with large differences in magnitude between muscle groups and subjects. The deficit values found are within the wide range reported in the literature. It was considered important to show the presence of a deficit in a small muscle group (finger flexors), since Herbert and Gandevia (1996) have argued that the deficit is mainly found in large muscles as a consequence of the difficulties subjects would experience in maintaining their posture during bilateral contractions of large muscle groups. Furthermore, the study confirmed both by EMG data and superimposed stimulation that the bilateral deficit could be attributed to a reduced neural drive.

The deficit in the rate of force rise was on average larger than the deficit in force. This probably reflects the fact that rapidly building up force requires higher activation, than producing the maximum isometric force (de Haan, 1998). This was supported by our EMG data, which showed higher values during force development.

The reductions in voluntary muscle activation, and the consequent reductions in force and rate of force rise in bilateral contractions are of a sufficient magnitude, to substantially affect performance. Since specific training may obviate the bilateral deficit (Howard and Enoka, 1991), this -limiting factor for performance should be taken into account in training for bilateral exertions.

REFERENCES

de Haan, A., (1998) *Exp. Physiol.*, **83** 77-84.
Herbert, R.D., Gandevia, S.C. (1996) *J Appl. Physiol.*, **80** 1351-1356.
Howard, J.D., Enoka, R.M. (1991) *J. Appl. Physiol.*, **70** 306-316.
Oda, S., Moritani, T. (1996) *Eur. J. Appl. Physiol.*, **74** 8-12.
Secher, N.H., *et al.*, (1988) *Acta Physiol. Scand.,* **134** 333-339.

SELF-ORGANIZING MAPS AND THE REPRESENTATION OF EMG SIGNALS IN TERMS OF MUSCULAR SYNERGIES

Jason J. Kutch and Thomas S. Buchanan[1]

Center for Biomedical Engineering Research, University of Delaware, Newark, Delaware USA
[1]buchanan@udel.edu

INTRODUCTION

In order to correctly activate the muscles of a neurologically impaired individual who has lost muscular control, it is necessary to understand what information the CNS normally uses to plan and control movement. We have previously shown that the CNS may control cyclic flexion/extension of the elbow by using the joint moment and a measure of total muscular activity (Kutch & Buchanan, 2001). This previous paper used the linear method of principal components analysis (PCA) to represent the EMG from eight elbow muscles in terms of only two parameters. In this present paper, we would like to generalize our results to consider muscular synergies that are nonlinear.

METHODS

EMG data from eight elbow muscles were collected from three subjects during cyclic flexion/extension using fine-wire EMG electrodes. EMG data were rectified, filtered, and normalized to maximum effort. The elbow joint moment was simultaneously recorded.

A self-organizing map (SOM) is a type of neural network for pattern classification. A description and the SOM algorithm may be found in Haykin (1999). Suppose that we have a cloud of data in an *n*-dimensional space and we would like to represent that data in a two-dimensional space with minimum information loss. Whereas the PCA algorithm can at best fit a hyperplane to the data, a two-dimensional SOM will represent the data with a optimal nonlinear hypersurface.

Each trial consisted of isometric flexion followed by immediate isometric extension at various flexion angles. 10×10 SOM grids were trained on individual trials using only EMG (no moment data).

RESULTS AND DISCUSSION

It has been previously reported that EMG data from multiple muscles can be adequately represented with fewer parameters than an EMG signal from each muscle (Weijs, 1999). For our tasks consisting only of elbow flexion and extension, the EMG from the eight elbow muscles studied could be adequately represented in two dimensions. After a SOM has been trained on the EMG data, the two parameters necessary to define the EMG data are the horizontal and vertical position on the SOM grid. Let z_1 denote the horizontal position and z_2 denote the vertical position. We used these two parameters alone to reconstruct the EMG signal for all eight muscles. Figure 1 shows the results from a sample trial.

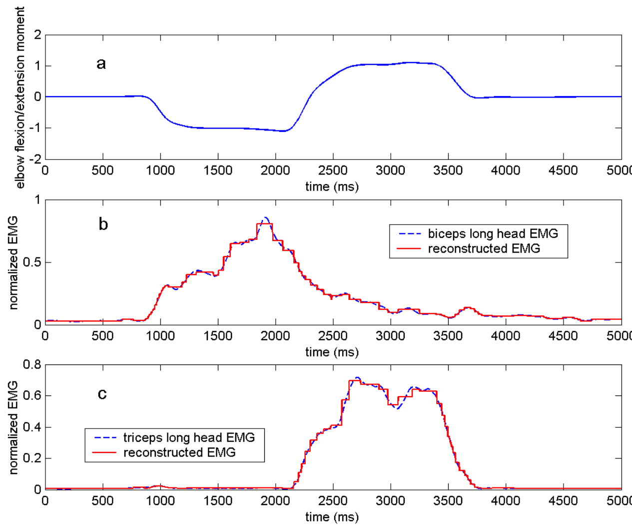

FIGURE 1: *a) The elbow flexion/extension moment in arbitrary units. b) The original and reconstructed biceps long head EMG from this trial. c) The original and reconstructed for the triceps long head EMG.*

We found that even by using a relatively low resolution SOM, better than 96% of the EMG data from the eight muscles controlling this task could be found on a two-dimensional nonlinear surface.

SUMMARY

Eight-dimensional EMG data from the human elbow during flexion and extension can be represented by only two parameters, z_1 and z_2, which specify a position on a two-dimensional SOM. These results suggest that the CNS need only know two parameters to control the activation of the eight muscles involved in this task.

REFERENCES

Haykin, S. (1999). *Neural Networks*, Prentice Hall.

Kutch, J.J., Buchanan, T.S. (2001). *Neuroscience Letters*, **311**, 97-100.

Weijs, W.A. et al. (1999). *Exp. Brain Res.*, **127**, 233-243.

ACKNOWLEDGEMENTS

Supported by NIH grants AR40408 & AR46386.

BIOMECHANICAL MODELING OF INDENTATION TESTING AND APPLICATION IN PLANTAR PRESSURE PREDICTION OF DIABETIC FOOT

Dequan Zou[1], Michael J. Mueller[1], Kirk Smith[2], Mary Hastings[1] and Joseph W. Klaesner[1]

[1]Program in Physical Therapy, Washington University School of Medicine, St. Louis, MO, USA, Email: zoud@msnotes.wustl.edu
[2]Mallinckrodt Institute of Radiology, Washington University School of Medicine, St. Louis, MO, USA

INTRODUCTION

Accurate modeling of soft tissue behavior on the plantar surface of the foot is essential for the prevention and treatment of many foot disorders, such as foot ulcerations in the patients with diabetes. In the present study, a mathematical model of soft tissue mechanical properties was used to model indentation testing on the plantar surface of the foot. The modeling of in vivo indentation testing provides the mechanical properties needed in the finite element analysis (FEA) of the foot.

METHODS

The indentor device combines a load cell, a three-dimensional (3-D) measurement device and a cylindrical stylus with a diameter of 7.9 mm (Klaesner, et al., 2001). The force, displacement measurement from indentor device and timing are collected at 40Hz on a notebook computer via analog-to-digital converter (ADC) and communication ports. The structure and geometry of the bones and soft tissues were measured using three-dimensional spiral x-ray computed tomography (SXCT) imaging method. A two-term Mooney-Rivlin model was used to describe the in vivo biomechanical characteristics of the plantar soft tissue. The strain energy (W) is expressed as a function of principal stretches (λ):

$$W = C_1(\lambda_1^2 + \lambda_2^2 + \lambda_3^2 - 3) + C_2\left(\frac{1}{\lambda_1^2} + \frac{1}{\lambda_2^2} + \frac{1}{\lambda_3^2} - 3\right)$$

For the indentation test, the uniaxial stress per unit undeformed area (p) is given as:

$$p = 2\left(\lambda^2 - \frac{1}{\lambda}\right)\left(C_1 + \frac{C_2}{\lambda}\right)$$

The stress-strain data from the indentation testing on the plantar soft tissue of foot was used to solve for the constants (C_1 and C_2) in the Mooney-Rivlin model. The above material model was used in the FEA to predict the pressure and deformation on the plantar surface of the foot. Three diabetic patients with a history of ulcers on the plantar surface of the foot and three control subjects that were matched for age, gender and body mass index (BMI) (Table 1) were modeled. The geometry data points defining the skin surface and bony contours were extracted from the SXCT images and used to create the models in the ALGOR FEA software (Algor Inc., Pittsburgh, PA). A nonlinear analysis was performed to model the in vivo behavior of the tissue and the contact interaction between the foot and the floor. Peak plantar pressures were collected using the F-Scan system (Software v.4.21, Tekscan, Boston, MA). Tissue and bone structure data from the SXCT measurement provided boundary conditions for the FEA modeling.

Table 1: Age, gender and BMI for subjects

Subject #	Group	Age	Gender	BMI
15	DP	40	M	25.3
30	Control	43	M	24.8
17	DP	80	F	36.6
27	Control	66	F	35.5
36	DP	58	M	38.9
35	Control	44	M	32.3

RESULTS AND DISCUSSION

The stress-strain relation from the indentation measurement was applied in nonlinear 2-dimensional FEA modeling to predict the contact pressure on the plantar surface of foot. Table 2 shows the calculated peak contact pressure and measured peak contact pressure under the second metatarsal head. Good agreements have been observed between the predicted and measured pressure distribution on the plantar surface of the foot.

Table 2: Calculated and measured peak pressure

Subject #	Pressure (kPa) (measured)	Pressure (kPa) (FEA)	Error (%)
15	200.0	218.9	9.5
30	227.0	221.0	2.6
17	303.4	299.4	1.2
27	229.5	251.7	9.7
36	193.1	185.6	3.9
35	206.9	199.3	3.7

SUMMARY

The plantar surface contact pressure prediction results show that the in vivo biomechanical characteristics of the soft tissue from the indentation test may be applied to the FEA modeling of the plantar soft tissue of foot with reasonable accuracy (max. error <10% and avg. error = 5.1%).

REFERENCES

Klaesner, J.W. et al (2001). *IEEE Transactions on Neural Systems and Rehabilitation Engineering*, 9(2): 232-240.

ACKNOWLEDGEMENTS

Funding from NCMRR, NIH under Grant RO1 HD 36895.

MATHEMATICALLY MODELING GROWTH AND REMODELING OF SOFT TISSUES AND MECHANOCYTES

J.D. Humphrey
Department of Biomedical Engineering, Texas A&M University, College Station TX

INTRODUCTION

Diverse research over the past two decades has revealed the ubiquitous role of mechanical factors in controlling structure and function in many types of cells, which are collectively referred to as mechanocytes. Although specific mechanisms of mechanotransduction remain known, it is clear that changes in mechanical stimuli change cell orientation and cytoskeletal structure, cell spreading, migration, contraction, differentiation, proliferation, hypertrophy, and apoptosis, as well as cellular production of many molecules, including surface receptors, adhesion molecules, cytokines, growth factors, proteinases, and vasoactive molecules. Hence, mechanosensitve changes in cellular activity regulate the extracellular matrix, and thus tissue-level responses such as development, tissue maintenance, wound healing, and pathogenesis.

Many different approaches have been suggested for quantifying tissue and cell level mechanics, including growth and remodeling (see Taber, 1995; Cowin and Humphrey, 2000; Zhu et al, 2000; Humphrey, 2002). Herein, it is suggested that a new continuum approach may apply to both cytoskeletal (CSK) and extracellular (ECM) growth and remodeling (G&R) and offer some advantages over other methods.

MATHEMATICAL FRAMEWORK

Connective tissues and cytoskeleton consist of a multitude of important constituents, including primary structural elements such as type I collagen, muscle and elastin or intermediate filaments, actin and microtubules as well as supporting water, proteoglycans, and accessory proteins such as actinin. Because the interactions between solid constituents have yet to be quantified, it may be sufficient under many circumstances to model the ECM or CSK as a solid-fluid mixture wherein the solid is further modeled as a constrained mixture of the structurally dominant solid constituents. For simplicity here, however, let us consider cases where solid-fluid interactions are secondary. Following Humphrey and Rajagopal (2002), let the total (mixture) Cauchy stress $\mathbf{t}$ be

$$\mathbf{t} = -p\mathbf{I} + \phi^f 2\mu\mathbf{D}$$
$$+\frac{1}{\rho}\sum\frac{1}{\det\mathbf{F}_\kappa^j}\int_{-\infty}^{t} m_\alpha^j S^j(\tau)\mathbf{f}_\kappa^j(\mathbf{F}_\kappa)\det\mathbf{F}_\kappa^j d\tau$$

where p enforces incompressible behavior, ϕ^j denotes mass fractions for each constituent j, $\mathbf{D}$ and $\mathbf{F}$ are the stretching and deformation gradient tensors, respectively, $\kappa \equiv \kappa_n$ denotes the natural configuration, which may evolve with G&R, and f^j is the stress response for each j. Finally, m_α is a mass production rate (to be determined via full mixture equations for mass balance) and S^j is a survival function that defines the life-span of each constituent that is produced over time. Finally, note that superscripts f denote fluid, u a constituent that does not turnover rapidly (e.g., elastin, intermediate filaments), and j=1,2 represents constituents that do turnover, such as collagen and muscle or microtubules or actin for the ECM and CSK. Full details are in Humphrey and Rajagopal. The take-home message is that by using a rule-of-mixtures relation for the stress in the solid constituents, we can account for time varying natural configurations and material symmetry while avoiding complex issues with regard to partial tractions on the boundaries (i.e., standard linear momentum applies). Fundamental to implementing this approach, however, are kinetic equations for the mass production and survival as well as how the natural configurations change for each constituent – each nontrivial to find. One role of theory, however, is to identify quantities that must be measured.

CONCLUSIONS

Despite an extensive literature, and copious *observations* of diverse cell responses to a wide variety of applied loads (e.g., via atomic force microscopy, cell poking, magnetic bead cytometry, micropipet aspiration, cell stretching, imposed fluid-induced shear stresses), there is clearly a need for new theoretical frameworks to motivate the design of stringent *experiments* to test competing hypotheses and theories.

REFERENECES

Cowin SC, JD Humphrey (2000) *Special Issue on Soft Tissue Mechanics*. J Elast 61: 1-246.
Humphrey JD (2002) *Cardiovascular Solid Mechanics: Cells, Tissues, and Organs*. Springer-Verlag, NY.
Humphrey JD, KR Rajagopal (2002) A constrained mixture model for growth and remodeling of soft tissue. *Math Model Meth Appl Sci* (in press).
Taber LA (1995) Biomechanics of growth, remodeling, and morphogenesis. *Appl Mech Rev* 48:487-545.
Zhu C, G Bao, N Wang (2000) Cell mechanics: Mechanical response, cell adhesion, and molecular deformation. *Annu Rev Biomed Eng* 2: 189-226.

ACKNOWLEDGEMENTS

This work was supported, in part, by grants from the NSF (BES-0084644) and the NIH (HL-64372).

A STUDY OF PASSIVE REPEATEDLY PLYOMETRIC METHOD FOR TRAINING UPPER ARM'S STRENGTH AND POWER

Wei-Hua Ho[1], Hong-Chang Ho[2], Tzyy-Yuang Shiang[2], Chuan-Show Chen[3]
[1]Tzu-Chi University, Hualien, Taiwan, afa@mail.tcu.edu.tw
[2]National College of Physical Education and Sport, Taoyuang, Taiwan
[3]National Taiwan College of Physical Education, Taichung, Taiwan

INTRODUCTION

Strength and power are important factors in sport competition, and various training methods have been proved to be helpful for athletes (Poprawski, B. 1987). But sport scientists and coaches are still looking for the most efficient method of training strength and power. In order to train muscle power, the function of reflex stretch and phenomenon of stretch-shortening-cycle in neuromuscular system (Komi, P.V. 1984). Furthermore, we were used to design Passive Repeated Plyometric training machine. The purpose of this study was to compare the strength and power trained by traditional weight training and Passive Repeatedly Plyometric (PRP) training method.

METHODS

There were 12 health male subjects divided into 2 groups randomly. The mean age, height and body mass of subjects were 20(±2.2)years, 173.2(±4.7)cm and 71.2(±5.3)kg, respectively. The experimental group was trained by the Passive Repeated Plyometric training machine. The control group used the traditional isotonic weight training method. The training period was 6 weeks, and the training effects were compared by testing bench press and shot-put throwing pre-training and post-training. Average values were considerd significantly different at $P<0.05$.

RESULTS AND DISCUSSION

The pre-training and post-training maximum muscle strength were 85.00(±7.07) kg and 102.50(±12.14) kg for experimental group. The pre-training and post-training muscle power (shot-put throwing) were 4.85(±0.62) m and 5.51(±0.71) m for experimental group. The training effect on maximum strength muscle improved the percentage of experimental group and control group were 20.39(±7.19)% and 15.71(±7.95)%. The training effect on muscle power improved the percentage of were 13.59 (±4.79)% and 6.12 (±6.34)% for experimental group and control group. The statistical results were analyzed by repeated measurement t-test and summarized as followed. The maximum muscle strength were significantly improved after 6 weeks training for both experimental group and control group. But only the experimental group improved the muscle power significantly. By comparing the training effect between experimental and control groups, the muscle power training effect of experimental group is significantly better than control group.

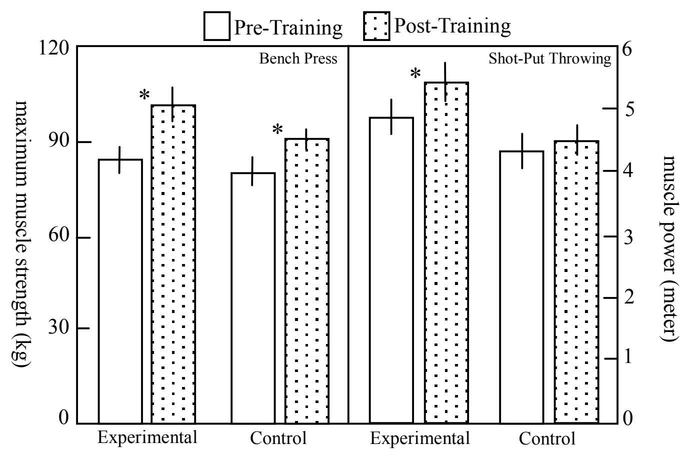

Figure: To compare with the strength and power by traditional (control group) and PRP (experiment group) training method during 6 weeks.

SUMMARY

The results suggested that a good training method should be used to enhance the training effect. PRP training method is not only a good approach to train muscle strength, but also a great method to train muscle power. Further attention should be focus on the EMG analysis to thoroughly understand the mechanism of this training method, and compare with other training approaches.

REFERENCE

Komi, P.V. (1984). Physiological and biomechanical correlates of muscle function: Effects of muscle structure and stretch-shortening cycle on force and speed. *Exercise and Sport Science Reviews*. 12, 81-121.

Poprawski, B. (1987). Aspects of strength, power and speed in shot put training. *National Strength and Conditioning Association Journal*, 9, 39-41.

ACCURACY AND RELIABILITY OF Q ANGLE MEASUREMENT METHODS

Ian C. Cooper[1], Michael J. Agnew[1], Shannon M. Mahar[2], and Lori A. Livingston[1,2]
[1]Dept. of Kinesiology and Physical Education, Wilfrid Laurier University, Waterloo, Ontario, Canada
[2]School of Health and Human Performance, Dalhousie University, Halifax, Nova Scotia, Canada, Lori.Livingston@Dal.ca

INTRODUCTION

The reliability and accuracy of measurement methods must be known if they are to be used in clinical decision-making (Batterham et al., 2000; Brosseau et al., 2001; George et al., 2000). Manual goniometric methods yield reliable (e.g., Byl et al., 2000; Lathinghouse et al., 2000) but not necessarily accurate (France et al., 2001) estimates of the frontal plane Q angle. The purpose of this investigation was to assess the accuracy and reliability of two video-based techniques to identify an improved Q angle measurement method that is both cost- and time-effective.

METHODS

A calibration jig was constructed by attaching a full circle goniometer with 1^{o} increments to two rigid bars. Markers (flat circular adhesive or spherical reflective, 1.25 cm diameter) were affixed to the jig to represent the bony landmarks of the Q angle (Figure 1). One investigator captured video images of ten Q angles of known magnitude for each type of marker. Two other investigators (Testers 1, 2) measured the Q angles by (1) applying a universal goniometer to single-frame hard copy video printouts of the adhesive markers on the jig, and (2) using a PEAK Motus© software/computer system.

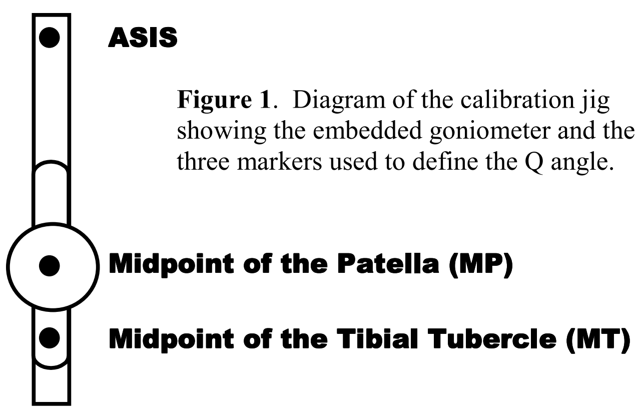

Figure 1. Diagram of the calibration jig showing the embedded goniometer and the three markers used to define the Q angle.

The two types of markers were then affixed by Testers 1 and 2, during separate sessions, to the right ASIS, MP, and MT of 27 young adults. Images were captured on videotape and Q angles were determined using the methods previously described. Before leaving the lab, Q angles for each individual were also measured using manual goniometric techniques.

Two-way ANOVA procedures determined where significant differences, if any, in measured Q angles existed between testers and methods, while intraclass correlation coefficients (ICC[2,1]) were used to assess the accuracy and intertester reliability of the video-based measurement methods.

RESULTS AND DISCUSSION

The ICC[2,1] values (Table 1) indicate that the measurement accuracy of the video goniometry and PEAK Motus© measurement methods is excellent, while intertester reliabilities range from good (0.68) to excellent (>0.75) (Fleiss, 1986).

Table 1: ICC[2,1] for measurement accuracy and intertester reliability.

	Manual Goniometry	Video Goniometry	PEAK Motus©
<u>Accuracy</u>			
Tester 1 vs Jig		0.96	0.79
Tester 2 vs Jig		0.92	0.92
<u>Reliability</u> (Tester 1 vs 2)			
Jig		0.98	0.88
Young adults	0.81	0.79	0.68

Depending upon the method of measurement utilized, mean Q angle values derived from the young adult sample ranged from $9.0^{o} \pm 8.7$ to $12.6^{o} \pm 7.2$ for Tester 1 to $11.7^{o} \pm 8.4$ to $13.0^{o} \pm 6.9$ for Tester 2. In both instances, video goniometry yielded the lowest values while manual goniometry yielded the highest values. For both testers, the mean values obtained via the video goniometric and PEAK Motus© methods varied by about 1^{o}. Statistically significant differences in values between testers or methods, or interaction effects, were not observed.

SUMMARY

The video goniometry method of Q angle measurement is both accurate and reliable. Although more expensive than manual goniometry, it provides a time- and cost-effective method of measurement with known accuracy and reliability characteristics that rival more sophisticated computer-based measurement systems.

REFERENCES

Batterham, A., George, K. (2000). *Phys Ther Sport*, **1**, 54-61.
Brosseau, L., et al. (2001). *Arch Phys Med Rehabil*, **82**, 396-402.
Byl, T., et al. (2000). *J Sports Rehabil*, **9**, 26-34.
Fleiss, J. (1986). *Reliability of Measurement.* Wiley & Sons.
France, L., Nester, C. (2001). *Clin Biomech*, **16**, 710-713.
George, K., et al. (2000). *Phys Ther Sport*, **1**, 19-27.
Lathinghouse, L., Trimble, M. (2000). *J Orthop Sports Phys Ther*, **30**, 211-216.

IS ACTIVE FORCE PRODUCTION OF SKELETAL MUSCLES ALTERED BY COLLAGEN CONTENT?

Mark E.T. Willems, G. Roger Miller and William T. Stauber
Department of Physiology & Pharmacology, West Virginia University,
Morgantown, WV, USA, mwillems@hsc.wvu.edu

INTRODUCTION

Connective tissue of contracting skeletal muscle-tendon complex is involved in lateral (Huijing et al, 1998) and longitudinal force transmission (Patel and Lieber, 1997). Collagen content of skeletal muscles can be altered by exercise training and aging (Kovanen et al, 1987). In this study, we used a rat model of repeated muscle strains that does not lead to increases in muscle mass (Wong and Booth, 1990) to examine the effect of altered collagen content on active muscle force.

METHODS

Female Sprague Dawley rats (4-5 mo) were exposed to repeated stretch-shorten contractions (5x10 repetitions, 5 d/wk for 6 wk) by manually applied ankle rotations between about 140° and 40° with subcutaneous electrical stimulation (70 Hz, 20-40 V, 0.2 ms pulse duration). Functional testing was performed with tibial nerve stimulation (supramaximal voltage, 0.2 ms pulse duration) with frequencies between 5 and 120 Hz. Force of the plantar flexor muscles was recorded as a reaction force under the sole of the foot with knee and ankle held at 90° (Cutlip et al, 1997). For plantar flexor muscles and Achilles tendon, we examined collagen content (hydroxyproline) and collagen cross-links (pyridinoline) using high performance liquid chromatography. Data were analyzed with Student's t test (two-tailed, $P < 0.05$) and presented as mean ± sem.

RESULTS AND DISCUSSION

Weights of plantar flexor muscles remained unaltered [repeated muscle strains: 2114 ± 36 mg (n = 15); control: 2182 ± 28 mg (n = 17)]. Significant increases in collagen content were found in gastrocnemius medialis (30.9%) ($P = 0.019$, n = 7), plantaris (32.3%) ($P = 0.006$, n = 7), soleus (27.6%) ($P = 0.039$, n = 7), and Achilles tendon (3.3%) ($P = 0.014$, n = 7). No changes were observed for collagen cross-links. Six weeks of muscle strains increased the isometric force only at high stimulation frequencies [at 80 Hz by 21% (n = 10, $P = 0.046$), at 100 Hz by 23% (n = 10, $P = 0.030$) and at 120 Hz by 22% (n = 10), $P = 0.032$)] (Fig. 1). An increase in isometric force in the absence of a change in muscle mass could be due to the following factors: 1) an increased number of cross-bridges (i.e. greater forces) per cross-sectional area or 2) a shift in fiber type from low force generating slow-twitch muscle fibers to high force generating fast-twitch muscle fibers. Any of these factors would have resulted in force increases at all stimulation frequencies which was not the case. Increased maximal isometric force resulting from an increase in collagen content of individual plantar flexor muscles and Achilles tendon has not been reported. The mechanism of altered active force production by increased collagen content only at high stimulation frequencies remains undetermined.

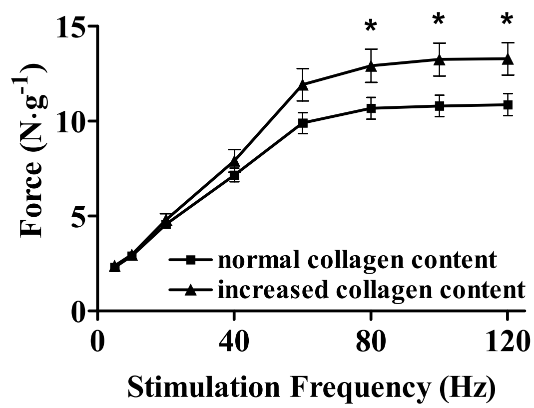

Figure 1: Force-frequency relationship of rat plantar flexor muscle-tendon complex with normal and increased collagen content.

SUMMARY

Repeated muscle strains for a period of 6 weeks which increased the collagen content of skeletal muscles and Achilles tendon of rats was associated with an increase in isometric force production only at high stimulation frequencies.

REFERENCES

Cutlip, R.G., et al (1997). *Med. Biol. Eng. Comput.* **35,** 540-543.
Huijing, P.A., et al (1998). *J. Exp. Biol.,* **201**, 683-691.
Kovanen, V. et al (1987). *Cell Tissue Res*., **248,** 247-255.
Patel, T.J., Lieber R. L. (1997). *Exerc. Sport Sci. Rev*. **25**: 321-363.
Wong, T.S., Booth, F.W. (1990). *J. Appl. Physiol.* **69**, 1709-1717.

ACKNOWLEDGEMENTS

This work was supported by Cooperative Agreement Number R01 OH002918 from Centers for Disease Control and Prevention, USA.

COMPENSATORY IMPULSE GENERATION BY INDVIDUALS WITH A UNILATERAL BELOW-KNEE AMPUTATION DURING GAIT INITIATION

Craig D. Tokuno[1], David J. Sanderson[2], J. Timothy Inglis[3]
UBC Biomechanics Laboratory, University of British Columbia, Vancouver, British Columbia, Canada
[1]tokuno@interchange.ubc.ca; [2]david.sanderson@ubc.ca; [3]tinglis@interchange.ubc.ca

INTRODUCTION

Gait initiation, the transition from quiet stance to steady state gait, requires the unequal generation of forward propulsion from the two lower limbs. The initial stepping, or *lead*, limb generates a peak force of 7% of body weight (BW), while the non-stepping, or *trail*, limb, produces two slightly greater bursts, first in the magnitude of 14% BW, followed by another of 22% BW (Nissan and Whittle, 1990).

For individuals with a unilateral below-knee amputation (BKA), this asymmetrical requirement can be a concern as there are known propulsion deficiencies with the prosthetic limb (Sanderson and Martin, 1997). Because the magnitude of this effect will differ depending upon the role of each limb, it was hypothesized that individuals with a unilateral BK amputation would require distinct movement compensations depending upon the choice of leading limb.

METHODS

Eleven individuals (8 males, 3 females; mean age=44±14) with a unilateral BKA, and 11 age and gender matched controls (8 males, 3 females; mean age=45±12) were recruited for this study. Subjects began each trial by standing with each foot on a separate force platform (Bertec model 4060). After the presentation of a visual stimulus, they were required to initiate gait at their preferred step length. The choice of stepping limb was randomly established by the visual cue. Fourteen trials were completed by each subject, with half of the trials starting with the right leg, the other half leading with the left.

Horizontal impulse values were calculated from the leading and trailing limbs. The starting frame was the start of sway (>4 mm shift from the baseline center of pressure), and the ending frame was the initial toe-off for each particular limb. The two impulses (e.g. impulse from a left lead plus that from a right trail) were then summed to determine the total impulse applied for each trial.

RESULTS AND DISCUSSION

It was found that amputees were concerned with the duration of force application, as they took a significantly longer time to reach the initial toe-off phase ($p<0.001$) (Figure 1A and 1B). The magnitude of peak force was not modulated by the intact limb, as it did not show a significant increase compared to the control conditions. The prosthetic limb did however apply a significantly smaller amount of peak force due to the loss of ankle musculature ($p<0.007$) (Figure 1A and 1B).

To make up for the smaller impulse generated by the prosthetic limb, it was found that regardless of whether it was used as the leading or trailing leg, the intact limb had compensated by significantly increasing its magnitude of impulse generation ($p<0.003$) (Figure 1C). The extent of this compensation was sufficient such that the summed (intact + prosthetic) impulse became comparable to the control conditions.

SUMMARY

Individuals with a unilateral BKA compensated for the limitations of the prosthetic limb by increasing the amount of impulse applied by the intact leg. This was accomplished by altering the duration of force application, without changing the peak force. This strategy was used during gait initiation as the task did require immediate movement. Whether this same strategy is used during perturbations that require immediate stepping deserves further investigation.

REFERENCES

Sanderson, DJ and Martin, PE (1997). *Gait and Posture*, **6**, 126-136.
Nissan and Whittle (1990). Journal of Biomedical Engineering, **12**, 165-171.

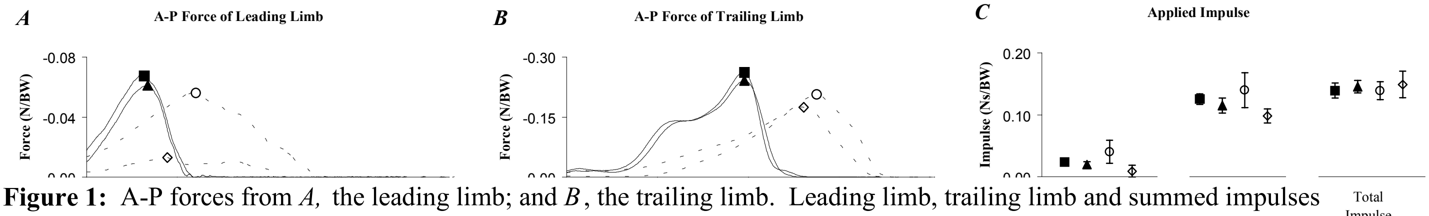

Figure 1: A-P forces from *A,* the leading limb; and *B*, the trailing limb. Leading limb, trailing limb and summed impulses are shown in *C*. (! Left Leg; 4 Right Leg; ∗ Intact Leg; (Prosthetic Leg)

COMPUTATIONAL APPROACH FOR MODELING BLOOD FLOW THROUGH A PNEUMATIC DRIVEN VAD

A. Vakili[1], M. T. Ahmadian[2] and M. Taiebi R.[3]

School of Mechanical Engineering (Biomechanical Engineering Division), Sharif University of Industries.
[1]School of Mechanical Engineering (Biomechanical Engineering Division), TAV1353@YAHOO.COM
[2]Professor of Mechanical Engineering Dept., Sharif University of Industries.
[3]Professor of Aerospace Engineering Dept., Sharif University of Industries.

INTRODUCTION

Study of Blood flow in the vicinity of moving boundaries is widely applicable to various problems in biofluid dynamic. In the present investigation a two-dimensional numerical model of a pneumatic driven VAD is generated, introducing a computational approach for modeling the interaction between moving diaphragm and fluid flow.

NUMERICAL MODELING

The proposed VAD design was made available by the T. Giken Co. In the present study heart valves effect is ignored. The diaphragm thickness is considered infinitesimal and its surface is assumed smooth, uniform and differentiable. Large displacement of the diaphragm results in arising non-linear terms in the equation of motion. The diaphragm is assumed homogen and hyperelastic. Consequently, Hamilton's principle is introduced as governing equation of motion and FEM is used for solving the resulting set of equations.

Blood flow is considered Newtonian, turbulence appearance is ignored and air is considered incompressible. Set of unsteady Navier-Stokes equations governs the behavior of fluid flow, which is solved employing consistent penalty method. Two-dimensional fluid dynamic in a stenosed channel is numerically investigated during physiological pulsation to validate the generated code.

In order to model the interaction between diaphragm and fluid flow at each physical time step, the pressure of the fluid elements, located in the vicinity of the diaphragm, is applied to the diaphragm to determine the diaphragm movement at the subsequent physical time step. The movement of the diaphragm is also imposed to the computational fluid domain as moving boundary condition to compute the behavior of the blood and air flow fields (figure 1).

RESULTS

Performance characteristics of the numerical model of VAD are carried out, which show satisfactory agreement with the obtained results from similar experimental studies and improve the reliability of the computational model (Figure 2). Numerical experiences show that the blood flow regime is usually laminar due to its pulsating nature. Furthermore, during systole phase the shear rate of blood flow is high enough to make the blood behave as a Newtonian fluid whereas during diastole phase some regions with low shear rates are observed in which the blood flow is non-Newtonian.

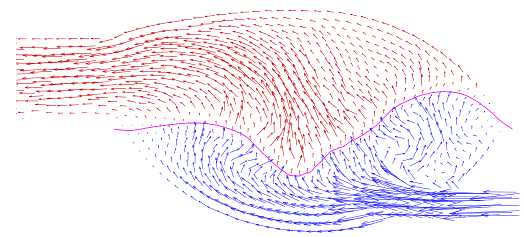

Figure 1: Numerical modeling of interaction between fluid flow and diaphragm movement.

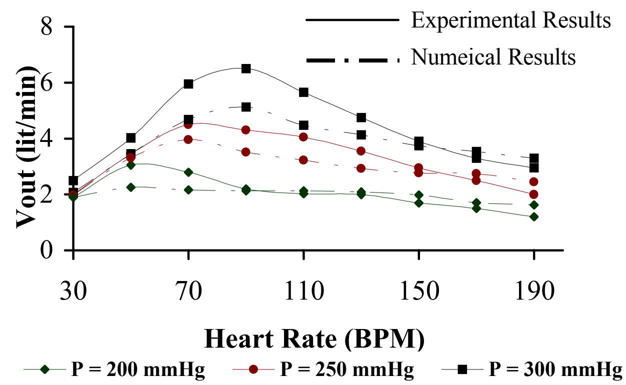

Figure 2: Functional characteristics of numerical model of VAD in comparison with experimental investigation results.

SUMMARY

In this investigation, the interaction of a pulsating blood flow and a moving boundary is well defined and validated, which can be widely applicable to many problems in hemodynamics, such as modeling the blood flow through the arteries, natural heart and any VAD or TAH containing moving boundaries. Furthermore, the computational model of VAD can be easily extended to a 3-D model for more exact results.

REFERENCES

Jin, W., Clark, C. (1994). *J. Biomechanics*, **27**, 697-707.
Kleiber, M. (1989). *Incremental Finite Element Modeling in Non-Linear Solid Mechanics.* ELLIS HORWOOD LIMITED.
Liu, H., Yamaguchi, T. (2001). *ASME J. Biomech. Eng.*, **123**, 88-96.
Oshiro, M. S. et al (1995). *Artificial Organs*, **19**, 274-279.
Vasku, J., Urbanek, P. (1995). *Artificial Organs*, **19**, 535-543.

RELATIONS BETWEEN BONE ADAPTATION AND LOADING FORCES ASSOCIATED WITH A NOVEL OSTEOPOROSIS INTERVENTION PROGRAM

Man-Ying Wang and George J. Salem
Musculoskeletal Biomechanics Research Laboratory, University of Southern California,
Department of Biokinesiology & Physical Therapy, Los Angeles, CA, USA
Email: mwang@usc.edu Web: www.usc.edu/go/mbrl

INTRODUCTION

Bone responds to mechanical loadings that are dynamic, of a high magnitude, of a high loading rate, and exhibit an unusual strain distribution in nature (Chilibeck, 1995). To investigate the relations between external loading characteristics and bone adaptation in humans, we developed an upper extremity dynamic impact-loading model (Wang, 2001). The model is an attempt to provide a practical and accessible osteoporosis prevention program, Dynamic Impact Loading Exercise (DILE), while allowing investigators to characterize potential osteogenic loading stimuli. This paper reports the relations between upper extremity reaction forces and bone adaptations after performing DILE for 6 months.

METHODS

Twenty-four healthy adults (mean age = 29 ± 6 yrs) performed DILE 36 cycles a day, 3 days a week, for a total of 24 weeks. The exercised arm was allocated randomly to either the dominant side or the non-dominant side. In addition, subjects were randomly assigned into either damped loading or non-damped loading treatment arms in order to examine the effects of different loading histories on forearm bone mass. In the damped loading group, subjects performed the DILE on the wall covered with a foam pad. Bone mineral density (BMD), bone mineral content (BMC) and bone cross-sectional area (CSA) at the distal third radius (DR), ultra-distal radius (UD), the area between DR and UD (MID), and total distal 1/3 of radius (Total) were measured on each subject using dual-energy X-ray absorptiometry (DEXA, Hologic QDR1500, Waltham, MA, USA) at the baseline and after 6 months. Subjects were also required to perform 3 loading trials to obtain reaction forces associated with the exercise at the baseline and after 6 months. Reaction forces perpendicular to the wall, including peak loads, peak loading rates, and loading impulse (area under the load/time curve; AUC), were collected by a wall mounted force platform (AMTI, Watertown, MA). Data processing software including Vicon Reporter (Oxford Metrics, Oxford, UK) and Peak Fit (SPSS Inc., Chicago, IL, USA) were used to analyze the reaction forces. Two-tailed Pearson's correlation analyses were employed to investigate the relations between the changes in radial bone mass after 6-month intervention and reaction forces including peak loads, peak loading rates, and AUC.

RESULTS AND DISCUSSION

Table 1 shows the loading forces associated with DILE in the damped and non-damped conditions. Peak loads ($p = 0.28$) and peak loading rates ($p = 0.40$) did not significantly differ between groups because of the large variation among subjects. Statistically significant correlations were not observed between the loading parameters and bone measurements in the *damped* loading group except for a modest correlation between changes in UDBMC and peak loads ($r = .65$, $p < .05$). In the *non-damped* loading group, peak loads during DILE were positively correlated to BMD changes at DR ($r = .73$, $p < .05$), MID ($r = .75$, $p < .05$), and Total ($r = .82$, $p < .01$); and negatively correlated to Total CSA ($r = -.68$, $p < .05$). Moreover, there were positive correlations between the energy absorbed by the radius (AUC) and DRBMC ($r = .65$, $p < .05$), MIDBMD ($r = .76$, $p < .05$), and Total BMD ($r = .75$, $p < .05$), but a negative relation between AUC and UDBMC ($r = -.80$, $p < .01$). No correlations between peak loading *rates* and bone changes were found. These results suggest that the relations between the loading forces and bone changes differed between the two distinct loading programs. In general, bone mass changes in the non-damped loading group were correlated to the peak loads and AUC; whereas, bone mass changes in the damped loading group were independent of loading magnitude. Nevertheless, because the relations varied among the different bone measurement sites, further examination is required to determine the longer-term effects of DILE on bone mass changes and to define the threshold for DILE induced osteogenesis.

SUMMARY

Investigations examining the relations between mechanical loading events and bone adaptation have traditionally used animal models. The upper extremity DILE model was developed to help bridge the gap between the animal and human studies. We found that loading forces associated with the DILE were highly correlated with the bone changes in the non-damped condition. Further analysis is required to identify the optimal mechanical loading factors for osteogenesis.

REFERENCES

Chilibeck, P.D. et al. (1995). *Sports Med,* **19**, 103-122.
Wang, M-Y. et al (2001). *Proceedings of ASB'25,* 211.

Table 1: Reaction forces during the loading phase of DILE in the damped loading and non-damped loading groups (mean ± SD)

	Peak Loads (%BW)	Peak Loading Rates (N/sec)	AUC (N*sec)
Damped loading group	38.2 ± 9.4	4631.7 ± 4236.6	113.7 ± 25.9
Non-damped loading group	50.9 ± 31.0	9146.2 ± 15730.2	119.4 ± 34.4

BIOMECHANICAL DIRECTIONS FOR THE POST-SURGICAL RECOVERY OF THE ACL

Dario Santos and Gabriel Fabrica
Facultad de Ciencias, Universidad de la República, Montevideo, Uruguay. biomec@fcien.edu.uy

INTRODUCTION

The anterior cruciate ligament (ACL) is one of the features of the knee that is most frequently injured (Insall, 1995). One element to take into account during the post-surgical recovery is the tone of the quadriceps muscle. The action of this muscular group is risky for the ACL, as one component of the muscular force tends to move the tibia forwards in regard to the femur, yielding stress on the ACL (Kapandji, 1987). The aim of this paper is to develop a tool that permits to control stress on the ACL during the isometric exercises of the quadriceps for any knee angle.

METHODS

The sample was composed by eight male individuals, which ages ranged from 18 to 35 years. Height, body mass and leg length was recorded for each individual. Strictly profiled X-ray were taken at different knee angles. On each X ray picture, an axis system and the line of action of the patellar ligament were drawn, to determine the lever arm of the quadriceps (Fq). Such moment is given by T = Fq (d_2 sen ϕ), where ϕ is the angle of action of the patellar ligament.

To determine the stress of the ACL, a system in static condition was considered, composed by leg, foot and added mass. A free body diagram was drawn (Figure 1), considering two external forces, Fq and weight (W). The masses of the segments were determined after regression equations (Zatsiorsky, 1998). Through inverted dynamics, it was determined the place on the leg where a mass should be added to achieve a preset stress on the ACL. Data obtained were processed using Matlab 5.3 and ANCOVA analysis was performed.

RESULTS AND DISCUSSION

Stress on the ACL was controlled by equalising the moment arm of the weight of the system (d_l) with the moment arm of the weight of the system, Fq (R/Senϕ).
Significant differences were found in the value of ϕ at different knee angles in individuals of similar anthropometric features. Those differences are associated to the form and position of the patella in regard to the femoral condyles.

Therefore, it is concluded that ϕ is a fundamental variable to choose the place and modulus of the added mass during the quadriceps isometric exercises to control stress on the ACL.

Free body diagram

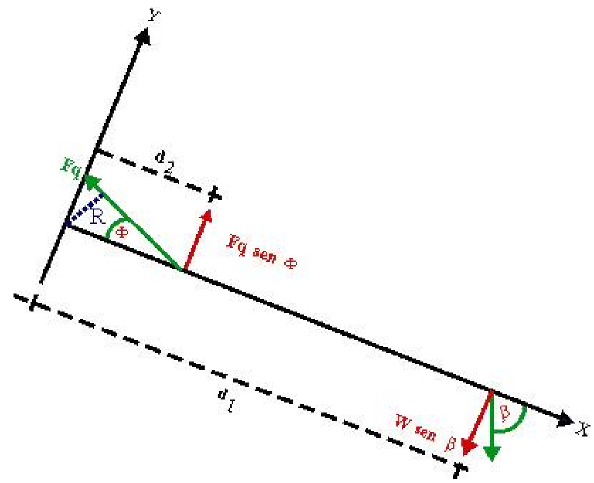

Figure 1

SUMMARY

In this paper, a biomechanical model is proposed, that optimises the rehabilitation of the knee´s anterior cruciate ligament. (ACL). By using a simple model, an equation was obtained, that allows to establish the point where a determined mass has to be put to make the ACL to withstand a pre-set stress at any angle. This constitutes a fundamental tool during the recovery, as the model includes anthropometric features of the patient as well as physical elements.The considered system includes leg, foot and an added mass. Two external forces, the one exerted by the cuadriceps (Fq) and the weight (W). The analysis was carried out in two dimensions. The origin of the axis system was set on a point on the articular surfaces of the inner femoral condyle, in such a way that the model´s X axis corresponds with the geometrical axis of the tibia at any angle of knee flexion. To calculate the mass of the body segments regression equations were used. The variables were obtained through direct measurements on strictly profiled X-ray photographs. The obtained data was used for calcutations from the ecuations derived from the model. The conclusions drawn give new and more accurate criteria for the first recovery stages.

REFERENCES

Insall, J.M. et al (1995). *Surgery of the Knee*. Churchill Livingstone. Edinburgh, 12: 292-329.
Kapandji, I. A. (1987). *The physiology of the joints*. **Vol. 2**. Churchill Livingstone. London.
Zatsiorsky, V. M. (1998). *Kinematics of human motion*.

ON THE ROLE OF INTRAMURAL STRESS AND STRAIN IN THE RESTENOSIS OF FEMORAL ARTERY BYPASS GRAFTS

Reena Cole[1], Mark Davies[1] and Pierce Grace[2]
[1]Stokes Research Institute, Mechanical and Aeronautical Engineering Department,
University of Limerick, Limerick, Ireland; reena.cole@ul.ie
[2]Vascular Surgery Department, Mid Western Regional Hospital, Limerick, Ireland

INTRODUCTION

The cause of stenoses in bypass grafts is as yet unknown, but smooth muscle proliferation and intimal thickening appear to play a major role in the failure of vascular reconstructions. In synthetic grafts significant intimal thickening develops at the anastomosis or just beyond in the distal vessels and usually appears within 2 years of reconstruction [Echave *et al.*(1979), LoGerfo *et al.* (1983)]. The seriousness of this problem is reflected in the very poor patency rates reported for infrapopliteal reconstructions using synthetic grafts: 14% vs. 67% for autologous vein at 5 years (Whittmore, 1995).

Most research into the mechanism of intimal thickening comes from animal and cell culture studies and various biological factors – such as vasoactive, pro-thrombotic and growth factors from platelets – have been identified as important in promoting endothelial cell growth and smooth muscle proliferation [Jawien and Clowes (1991), Malek and Izumo (1995)]. Perktold and Resch (1990) and Friedman (1993) state that atherosclerosis appears to show predilection for more complex regions of the vasculature such as branch regions, which leads to the conclusion that when an artificial branch or bifurcation is introduced, by the addition of a graft bypass, that there will also be a tendency for restenosis. Factors which have been cited as possible reasons for restenosis include: surgical injury, anastomotic angle, material mismatch, wall shear stresses, suture line stresses, and more recently intramural stresses.

There has been much investigation into the effects of fluid dynamics on restenosis, most specifically the effect of wall shear stress. However there are conflicting theories in the literature as to whether it is high [Fry (1968), Caro *et al.* (1969)] or low [Ku *et al.* (1985), LoGerfo *et al.* (1981)] wall shear stress that is to blame. A more recent hypothesis (Nazemi *et al*., 1990), suggests that low wall shear stress contributes to the onset of atherosclerotic plaque formation, with high wall shear stress encouraging plaque growth. Due to the contradictory nature of the wall shear stress theories, other possible factors are being investigated, with one area of interest being the role of mechanical stress and strain in atherogenesis.

Thubrikar and Robicsek (1995, 1997) among others [Thubrikar *et al.* (1990), Perktold and Rappitsch (1995), Salzar *et al.* (1995) and Moore *et al.* (2001)] contend that it is blood pressure induced arterial wall stress that is the principal factor in the localisation of the atherosclerosis in naturally occurring bifurcations in the arterial system. Indeed Roberts (1975) reported that a reduction in mean blood pressure leads to a reduction in mortality.

RESULTS AND DISCUSSION

Initial *in vitro* experiments were made using a model femoral artery and bypass graft, inflated to match a peak systolic pressure of 150mmHg. Images were taken, using a CCD camera, and this allowed strain to be measured.

Using thick shell theory the circumferential stress (σ_H) and longitudinal stress (σ_L) were calculated to be 4.90×10^4 and 1.45×10^4 Nm^{-2} respectively. These values are of a magnitude 10,000 greater than the mean wall shear stress in an adult male, found to be 1.3 ± 0.3 Nm^{-2} by Samijo *et al.* (1997).

These results show that the intramural stress and strain are also an important factor in the restenosis of femoral artery bypass grafts. Further work will involve the measurement of intramural strain *in vivo* using video extensometry and duplex ultrasound.

REFERENCES

Caro, C.G, *et al.*, (1969), *Nature*, **223**:1159
Echave V, *et al.*, (1979), *Surgery* **86**:791
Friedman, M.H., (1993) " *ASME J. of Biomech. Eng.*, **115**, 595-600.
Fry, D.L., (1968) Circ. *Res*., **22**:165
Jawien A, Clowes AW, (1991) In: Bernhard VM, Towne JB (eds). *Complications in Vascular Surgery*, Quality Medical Publishing Inc, 55-64.
Ku, K.N., *et al.*, (1985) *Arteriosclerosis*, **5**:293-302
LoGerfo, F *et al.*, (1981) *Arteriosclerosis*, **1**:235-241
LoGerfo F., *et al.*, (1983) *Ann. Surg.* **197**:479.
Malek, A. and S. Izumo, (1995) *J. Biomech*., **28**:12:1515-1528
Moore, M. M., *et al.*, (2001) *J. of Biomech.,* **34**:3:289-297
Nazemi, M., *et al.*, (1990) *J. Biomech*., **23**:1031-1037
Perktold, K.; and G. Rappitsch, (1995) *J. Biomech.,* **28**:7:845-856
Perktold, K., And M. Resch, (1990) *J. Biomed. Eng*., **12**:111-123
Roberts, W C., (1975) *Am J Med*, **59**:523-532
Salzar, R. S., *et al.*, (1995) *J. Biomech*, **28**:11:1333-1340,
Samijo, S K; *et al.* (1997) *Ultrasound in Medicine & Biology*, **23**:4:583-590
Thubrikar M. J., and F. Robicsek, (1995) *Annals of Thoracic Surgery*, **59**:6:1594-1603
Thubrikar, M. J., and F. Robicsek, (1997) *Atherosclerosis*, **134**:1-2:95
Thubrikar, M J; *et al.*, (1990) *J. Biomech*., **23**:1: 15-26
Whittmore AD, (1995) In: Rutherford RB (ed.) *Vascular Surgery* (4th ed.), WB Saunders Company, 795-814

LONG-TERM SIMULATOR WEAR STUDY OF SURFACE ENGINEERED MOM HIP PROSTHESES

John Fisher[1], Xiao Q Hu[1], Sophie Wiliams[1], Joanne L Tipper[1], Eileen Ingham[1], Martin H Stone[1],
Peter Hatto[2], Graham Berry[3], Cath Hardaker[4] and Graham Isaac[4]

[1]School of Mechanical Engineering, University of Leeds, Leeds LS2 9JT, UK, j.fisher@leeds.ac.uk;
[2]IonBond Ltd; [3]Firth Rixson Superalloys; [4]DePuy International

INTRODUCTION

Polyethylene wear debris-induced osteolysis has led to the re-emergence of clinical interest in metal-on-metal (MOM) hip prostheses. Despite the low wear rates of MOM prostheses, the release and toxicity of metal wear particles and metal ions from corrosion and wear remains a concern. In this study, thick (8-12 μm) surface coatings were investigated with the aim of improving the wear resistance and producing fewer and less toxic wear particles in MOM hip prostheses.

METHODS AND MATERIALS

Twenty eight millimetre diameter MOM hip prostheses were coated (IonBond Ltd., UK) in this study. Four different articulations of heads and inserts, which included CrN v. CrN, CrCN v. CrCN, CrN v. TiN (fully coated) and CrN v. high carbon (HC) CoCrMo (half coated), were tested for 5 million cycles in 25% (v/v) new born bovine serum using a physiological anatomical hip joint simulator (Barbour *et al.* 1999, Firkins *et al*. 2001) and compared to a clinically used MOM bearing couple. Three to five pairs of each bearing couple were studied. Heads and inserts were polished after coating to a surface finish R_a < 0.03 μm. The average volume loss and wear rate was determined gravimetrically from both components for each type of prosthesis.

Metal ion levels in the serum lubricants after the first 0.33 million cycles of the wear test were analysed by atomic absorption spectrometry (AAS, Varian Inc., Surrey, UK). Prior to measurement, the samples were centrifuged at 2000 g for 1 hour to remove the wear debris, and the clear supernatant was used for analysis. Ion levels were determined by the mean of three measurements.

Wear particles were characterised from the serum collected during hip simulator testing at 0.33, 1 and 2 million cycles by transmission electron microscopy (TEM) as described by Tipper *et al*. (1999). The cytotoxicity of CoCrMo, CrN, CrCN and TiN wear debris produced in a simple geometry model in water was assessed by co-culture with U937 macrophages and L929 fibroblast cells. The effect of the wear debris on cell viability was measured. Data was analysed using one way analysis of variance (ANOVA) and the minimum significant difference between means determined using the T-method.

RESULTS AND DISCUSSION

For the MOM couple (Fig. 1), a high bedding-in wear rate was observed in the first million cycles. The coated combinations, however, experienced no bedding-in period and the wear rates remained constantly low throughout five million cycles. After 5 million cycles testing, the wear of the

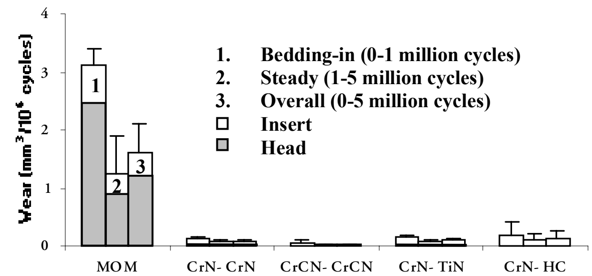

Figure 1: Wear rates from different stages over 5 million cycles.

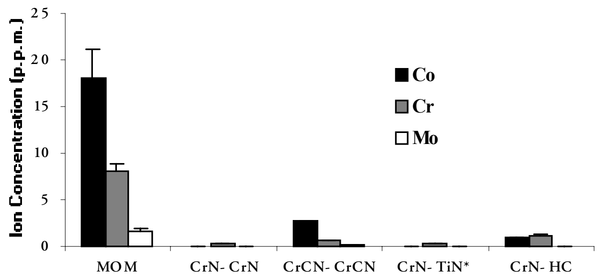

Figure 2: Metal ion levels in the serum lubricants from different prosthesis combinations. *titanium < 1 p.p.m.

three fully coated combinations (CrN v. CrN, CrCN v. CrCN and CrN v. TiN) were at least 38-fold lower compared to the MOM prostheses. The wear of the half coated combination, CrN v. HC, was also at least 13-fold lower. The differences between the wear rates of the surface engineered bearings and MOM prostheses were highly significant (one-way ANOVA and Tukey test, *P<0.01*). The wear particles produced by all combinations were generally less than 30 nm in size, similar in size to the wear debris from MOM prostheses. The metal ion concentrations in the serum lubricants from the three surface engineered systems were at least 6-fold lower than the MOM controls (Fig 2). The cell-culture studies showed that the wear particles from the fully coated surface engineered bearings were at least 10-fold less toxic than the wear particles produced by MOM bearings. These initial findings support the further development and clinical application of surface engineered MOM bearings.

REFERENCES

Barbour, P.S.M. et al (1999). *Proc. Instn. Mech. Engrs., Part H,* **213**, 455-467.
Firkins, P.J. et al (2001). *Proc. Instn. Mech. Engrs., Part H,* **215**, 119-121.
TIPPER, J.L. et al (1999). *J. Mater. Sci.: Mater. Med.*, **10**, 353-362.

ACKNOWLEDGEMENTS

This work was supported by the EPSRC and the DTI.

EFFECT OF BONE GRAFT POSITION ON LOADING OF PEDICLE SCREWS

Antonius Rohlmann, Thomas Zander, Georg Bergmann

Biomechanics Laboratory, University Hospital Benjamin Franklin, Free University of Berlin, Germany, rohlmann@biomechanik.de

INTRODUCTION

After stabilizing a lumbar spine with an internal spinal fixation device pedicle-screw breakage is a common complication. Rohlmann et al [1994] modified the internal spinal fixator after Dick and measured the loads on the implant during many activities. In one of the patients with the telemeterized internal spinal fixation device a pedicle screw broke three months after implantation. The aim of this study was to analyze analytically this unexpected case of pedicle screw breakage.

MATERIAL AND METHODS

Situation that led to a broken pedicle screw

Telemeterized internal spinal fixation devices were implanted in a patient with degenerative instability and a narrow spinal canal in order to measure the fixator loads during daily activities. To realign the lumbar curvature because of wedge-shaped disc space, the motion segments L3-L5 were distracted about 5 mm on the right side. Anterior interbody fusion using bone grafts from the iliac crest was performed three weeks later. The second operation was performed by a minimally invasive microsurgical approach. It involved removing the intervertebral discs L3/4 and L4/5, slightly milling their adjacent vertebral end-plates and inserting the precisely fitted grafts in a ventral position. On removal of the implants three months later, a fatigue fracture was found in the upper right pedicle screw. Unexpectedly, the crack started on the caudal side of the cross-sectional area and progressed cranially [Rohlmann et al. 1998].

Finite element model

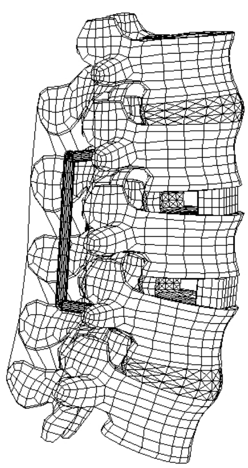

Figure 1: Outer mesh of the finite element model of the lumbar spine with internal fixators and two bone grafts in ventral position.

A three-dimensional, nonlinear finite element model of the human lumbar spine with internal fixators and bone grafts was created to simulate the above described situation (Fig. 1). The element mesh of the vertebrae is based on the model used by Smit [1996]. The nucleus pulposus was simulated by an incompressible fluid-filled cavity and the annulus fibrosus by volume elements with superimposed spring elements representing the fibers. The facet joints could only transmit compressive forces. The capsule of the facet joints and the six ligaments of the lumbar spine were included. The material properties of all tissues were taken from the literature. The internal spinal fixators were simulated by beam elements and the bone grafts by volume elements. Both, ventral and dorsal graft positions were successively simulated. The lower end-plate of the L5 vertebra was fixed and the model was loaded with the body weight and muscle forces representing standing. The finite element model is described in detail elsewhere [Zander et al. 2001].

RESULTS

Figure 2 shows the bending moment in the upper right pedicle screw for standing. When in the finite element model the bone graft position was moved from ventral to dorsal, maximum bending moment within the screw thread (between 17 mm and 52 mm in Fig. 2) changed the sign. Due to the stress concentration factor and a smaller diameter in the threaded compared to the cylinder-shaped part, the highest stresses are in the threaded part of the Schanz' screw close to the non-threaded part.

Figure 2: Bending moment in the upper right pedicle screw

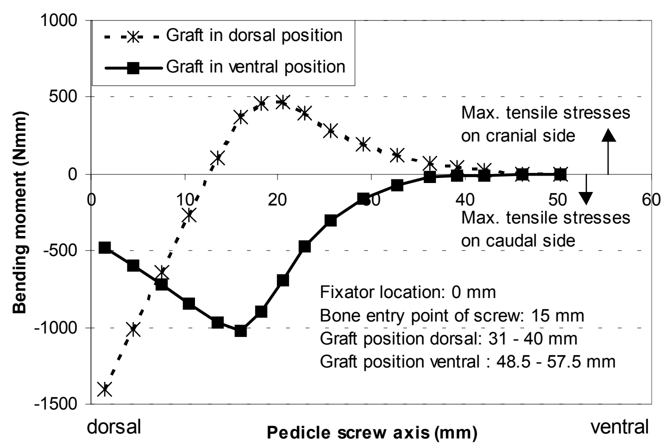

DISCUSSION

In the finite element model the highest stresses in the screw were calculated exactly where the screw broke *in vivo*. The model also predicted the highest stresses in the threaded part on the caudal side of the cross-sectional area when the graft is in a ventral position. This means, the upper right pedicle screw was loaded as during three point bending [Rohlmann et al. 1998]. A graft placed in the center of the end-plate minimizes the stresses in the pedicle screw and thus the risk of breakage.

REFERENCES

Rohlmann, A. et al (1994) *J.Biomech.*, **27**, 961-967
Rohlmann, A. et al (1998) *J.Biomech.*, **31**, 763-767
Smit, T. (1996) *The Mechanical Significance of the Trabecular Bone Architecture in a Human Vertebra*. Shaker
Zander, T. et al (2001) *Clin. Biomech.*, **16**, S73-S80

ON THE EXISTENCE OF AN OPTIMUM END-TO-SIDE GRAFT/ARTERY JUNCTION GEOMETRY TO INCREASE THE PATENCY RATES OF BYPASS SURGERY

Michael Walsh[1], Tim McGloughlin[1] and Pierce Grace[2]

[1] Biomedical Engineering Research Centre, M&AE Dept., University of Limerick, Ireland (tim.mcgloughlin@ul.ie)
[2] Regional Hospital, Dooradoyle, Limerick, Ireland

INTRODUCTION

Hemodynamic flow patterns in distal end-to-side anastomoses are widely implicated in the initiation of the disease formation process, Giddens et al., 1993. The flow patterns created by these graft/artery junctions exert abnormal wall shear stress (WSS) distributions on the endothelial cells (EC) on the bed of the junction, Xiao et al., 1997. The role of WSS in intimal thickening has been the subject of much debate with high WSS, low WSS, WSS gradient, and oscillating WSS theories all being proposed as aetiological factors for anastomotic intimal thickening. All of these theories can be supported by experimental findings and it is possible that each theory has a role to play in the restenosis process. Several surgical techniques exist, including the Taylor Patch and Miller cuff techniques, that use vein cuffs or patches to alter the junction geometry, attempting to improve patency rates of bypass procedures. The flow patterns associated with these surgical approaches can be represented by the angle between the impinging flow and the junction bed, i.e. the Taylor patch creates a lower impinging flow-junction bed angle than the Miller cuff.

MATERIALS AND METHODS

Two idealised geometies, models 1 & 2, were developed to produce different impinging flow–junction bed angles, having angles of 45º and 22.5º respectively. Numerical simulations, using Fluent, a commercially available computational fluid dynamics package, used a non-Newtonian fluid model and time-dependent in-flow boundary conditions. Rigid walls and zero flow in the proximal outflow segment were assumed. The results are presented as distributions of the local gradient in WSS on the junction bed, as described below in equation 1.

$$\tau_g = \left[\frac{d\tau_z}{dz} \Big/ \frac{\tau_{z_a}}{r_a} \right] \qquad \text{Eq 1}$$

where τ_g = normalised spatial WSS gradient, τ_z = WSS, τ_{za} = average WSS on the bed centreline in the host artery and r_a = average radius of the model.

RESULTS AND DISCUSSION

The normalised WSSG distribution for model 1 can be seen as the navy line in figure 1. The profile of this distribution is significant in that in a healthy idealised artery, the local spatial WSSG is zero. Therefore the deviation from zero of the normalised WSSG distribution in figure 1 represents the areas in the junction bed where the EC experience abnormal WSSGs which could be the initiating factors for the disease formation processes. The red line in figure 2 represents the normalised WSSG distribution for the reduced graft/artery angle of model 2. It can be seen that reducing the graft/artery angle reduces the peak values of the normalised WSSG distribution and a consequence of this is the increasing of the bed area over which the abnormal WSSG are experienced.

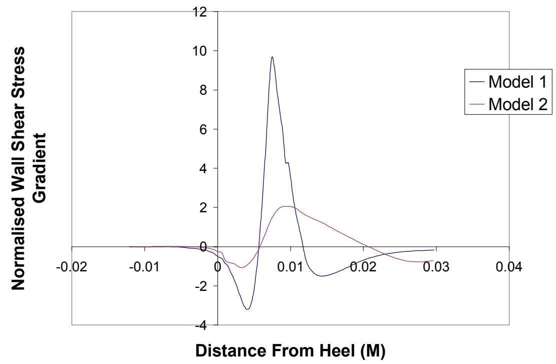

Figure 1 - Normalised WSSG distributions

As a result optimising the graft/artery junction geometry reduces to the simple choice of reducing the peak values in the normalised WSSG distribution or reducing the area over which the normalised WSSG distribution has a non-zero value. Thus, the graft/artery junction can be designed resulting in "optimised" geometries which have characteristics of either a Taylor Patch or Miller Cuff anastomosis. Reported patency rates for the Taylor Patch and Miller cuff techniques include 35% at 3 years, Eagleton et al., 1999, and 38% at 3 years, Kreienberg et al., 2000, respectively. This suggests that the results for each of these techniques are similar to those for conventional bypass grafts, 43% at 3 years, Fichelle et al., 1995. Since both surgical techniques have moderate patency rates it is concluded that an optimum end-to side graft/artery junction geometry, which would significantly increase the patency rates of peripheral bypass surgery, may not exist.

REFERENCES

Giddens, D. P. et al., 1993, "The role of fluid mechanics in localisation and detection of atherosclerosis", *J. of Biomechanical Engineering*, V. 115, pp 588-594.
Xiao, Y. et al., 1997, "Effect of flow recirculation upon endothelial cell height and shape", *BioEngineering Conference, BED* V. 35, pp 537-538.
Eagleton, M.J. et al., 1999, "Femoral-infrapopliteal bypass with prosthetic grafts", *Surgery*, Vol. 26, No. 4, pp 759-764.
Kreienberg, P.B. et al., 2000, "Adjunctive techniques to improve patency of distal prosthetic bypass grafts: Polytetra-fluoroethylene with remote arteriovenous fistulae versus vein cuffs", *J. of Vascular Surgery*, Vol. 31, No. 4, pp 696-701
Fichelle, J.M. et al., 1995, "Infrapopliteal polytetra-fluoroethylene and composite bypass: factors influencing patency", *Annals of Vascular Surgery*, Vol. 9, No. 2, pp 187-196

INCIDENCE OF VALVE PROSTHESIS INCLINE ON LEFT VENTRICULAR FLOW DYNAMICS.

Frederic Mouret, Vincent Garitey, Frederic Derivaux, and Regis Rieu
Laboratory of cardiovascular biomechanics, UMR IRPHE CNRS 6594
Ecole Supérieure de Mécanique de Marseille, Marseilles, France
mouret@esm2.imt-mrs.fr - www.biomeca.org

INTRODUCTION

Diastolic normal flow in the ventricle is characterised by a large vortex that occupies almost the whole cavity. This vortex turns anticlockwise, from the posterior wall along the apex to the interventricular septum and can be clinically observed with color Doppler in apical four-chamber view. When implanting heart valve prosthesis, studies have shown that there is a favourable orientation of the valve with respect to the natural valve leaflets; but no study has paid attention on the incline of the heart valve with regard to the mitral annulus plane. Indeed, clinical observations have put into light an inversion of the rotating sense of the vortex when the prosthesis is veered towards the septum.

METHODS

Using a Dual Activation Simulator of the left heart, flow past heart valve prosthesis in mitral position was studied with Particle Image Velocimetry. A Medtronic-Hall valve was used to reproduce a similar diastolic flow structure than past a natural valve and a Carpentier-Edwards bioprosthesis was successively implanted in "apex directed" position (CEAD) and in "septum directed" position (CESD).

RESULTS AND DISCUSSION

For the CESD, in early diastole, a central jet induces two contrarotatives vortices whose cores move with jet propagation. During deceleration, the jet weakens and is deviated by the apical vortex. The aortic vortex, little fed, is absorbed. In systole, still stronger than the aortic eddy, the apical eddy goes up along the posterior wall then along mitral valve towards the aortic valve. For the CEAD, in early diastole, an important jet follows the posterior wall and a vortex develops in the whole ventricle. During diastasis, due to the absence of flow from the mitral valve, the main vortex develops; an apical contrarotative eddy develops also but stays weak. In systole, the ejection is mainly along the septal wall, the core of the eddy moves below the mitral valve.
The flow past Medtronic-Hall and CEAD present both an anticlockwise vortex and a favourite ejection in systole along the septum through the left ventricular outflow tract. The flow past the CESD presents a clockwise pattern and ejection is principally along mitral valve, opposite to the septum.
When comparing the two inclines, it can be noticed that the flows through the ventricle are different. We can observe a changing in rotating direction when changing the incline of the valve. In the septum inclined case, the interaction of the flow from the mitral valve and the vortex in diastole can create a resistance to ventricle filling. During systole, the ejection is completely asymmetric and could create hemolysis locally.

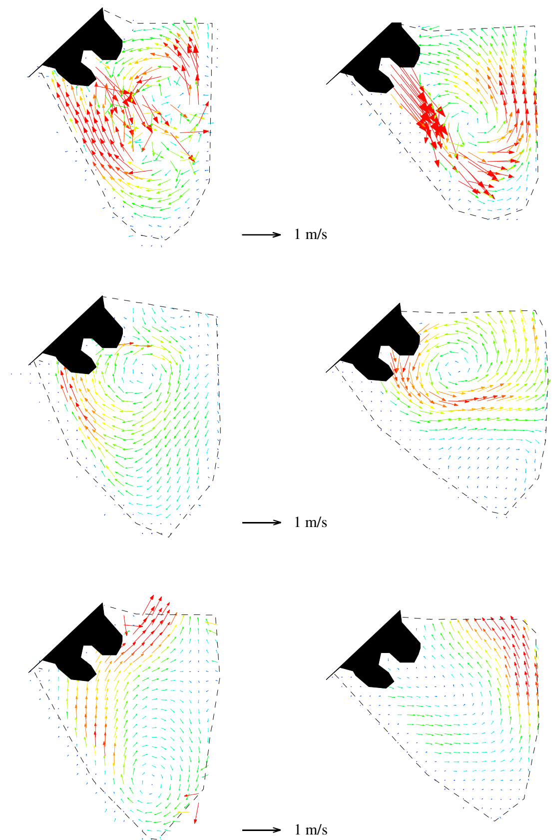

Figure 1: Flow (velocity magnitude) in the ventricle downstream mitral CESD (left) and CEAD (right) in early diastole (top), during diastasis (middle) and in systole (bottom)

CONCLUSION

This study highlights the influence of the valve incline in relation with mitral annulus on the flow in the ventricle. This incline induces an inversion of the rotating motion, a risk of increased valvular resistance during ventricular filling and a risk of hemolysis and endothelial damage. What are the consequences on ventricular function, at short and long term? This inversion could affect left ventricular function recovery. From this study we recommend whenever it's possible that surgeons implant preferably the prosthesis "apex directed"

ACKNOWLEDGEMENTS

The authors would like to thank Dr. JG. Dumesnil and Dr. P. Pibarot from Quebec Heart Institute, Ste Foy, Quebec, Canada.

HYDRODYNAMICS OF MITRAL PROSTHETIC HEART VALVES: COMPARISON OF NORMAL CONDITIONS WITH ATRIAL FIBRILLATION VARYING THE HEART RATE

Frederic Mouret, Vincent Garitey and Regis Rieu
Laboratory of cardiovascular biomechanics, UMR IRPHE CNRS 6594 Ecole Sup. de Mécanique de Marseille, Marseilles, France
mouret@esm2.imt-mrs.fr - www.biomeca.org

INTRODUCTION

Artificial valve substitutes are used to replace incompetent natural heart valves. Due to the inertia of mobile elements and to the functional float of mechanical parts, heart valve prostheses regurgitate. The regurgitant volume is defined as the volume of fluid which flows backwards through a valve during the cardiac cycle. It is represented by the sum of the closing volume (linked to the closing dynamics of the valve) and the leakage volume. Trials are often run in simulated conditions encountered in a healthy young man. However, heart valve implantation is often associated with other pathologies, such as atrial fibrillation. Our aim is to draw close to actual operating conditions of valve prosthesis in vivo, through in vitro trials and to assess the hydrodynamic behavior of artificial valves in normal and pathological conditions.

METHODS

Trials have been achieved on a Dual activation simulator. This test bench has been fully described in Mouret (2000). Both atrial and ventricular contractions are controlled independently allowing the reproduction of physiological signals through a left heart model. Four valves have been tested. The prosthesis is implanted in mitral position. The orientation is similar to usual clinical implantation in vivo. The fluid used to mimic blood has a viscosity analog to blood. The heart rate is set at 50, 70, 90 and 110 bpm successively, mean cardiac output is 5 L/min. These conditions are repeated in normal conditions (E wave magnitude is twice the A wave) and in atrial fibrillation (no A wave, regular heart rhythm).

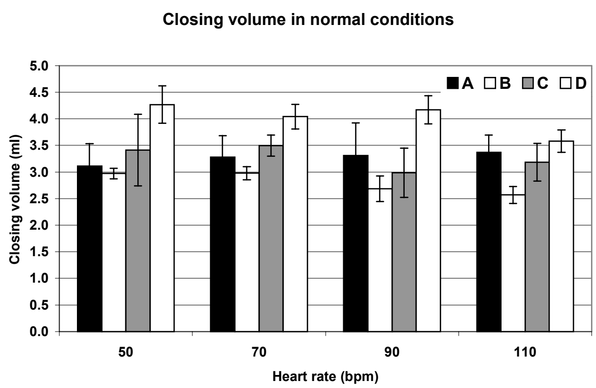

Figure 1: Mean closing volume for all type of valves in normal conditions when varying the heart rate

RESULTS AND DISCUSSION

The different valves have been voluntarily named A, B, C and D to respect the confidentiality in this abstract.

In normal conditions (figure 1), it can be said that the valve B has a significant lower closing volume than the other valves, valves A and C can be considered as similar. In atrial fibrillation (figure 2), valve D has the lower closing volume whatever is the heart rate. Once more valves A and C have a behavior hard to separate the one from the other.
The behavior of valve D in atrial fibrillation could be explained by a greater lift force of the mobile element(s) which induces a position very close to the closed position at the end of diastole.

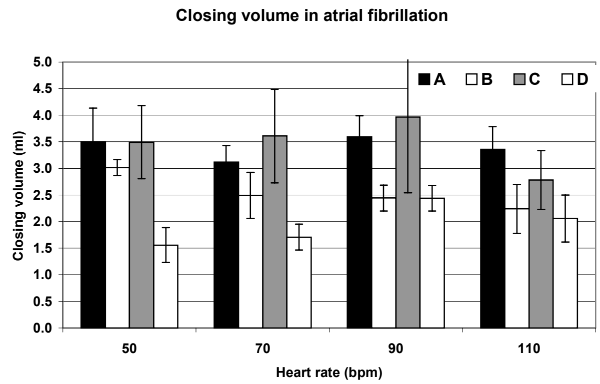

Figure 2: Mean closing volume for all type of valves in atrial fibrillation when varying the heart rate

CONCLUSION

As described by Dellsperger (1983), the closing volume does not vary a lot when changing the heart rate. Nevertheless, a small decrease is observed in some valves at rapid heart rate, probably due to timing in vortex shedding behind leaflets. From these tests, valve B appears to be the best compromise for all flow conditions. It has to be kept in mind that they only concern the regurgitant characteristics of the valves. No conclusion has to be extrapolated to other hydrodynamics parameters. These tests offer important data when considering trials for certification and reinforces the need to test heart valve prostheses in real simulated conditions.

REFERENCES

Mouret et al (2000). *Med Biol Eng Comput*, **38**, 558-561.
Dellsperger et al (1983). *Am J Cardiol* **51**:321-328

ACKNOWLEDGEMENTS

The authors would like to thanks Sulzer Carbomedics (USA), Sree Chitra Tirunal Institute (India) and Medical Carbon Research Institute (USA) for kindly supplying heart valve prostheses.

CO-ACTIVATION OF KNEE FLEXORS IN ISOMETRIC EXTENSION EFFORTS

Idsart Kingma and Jaap H. van Dieën

Institute for Fundamental and Clinical Human Movement Sciences, Faculty of Human Movement Science
Vrije Universiteit, Amsterdam, Netherlands

INTRODUCTION

Co-activation of knee flexors is known to occur in dynamic as well as static knee extension tasks. Simulation studies suggest that hamstrings activation would, except near full extension, aid in reducing forward tibial shear forces (Imran and O'Connor, 1998) thereby reducing the strain on the anterior cruciate ligament (ACL). If an active protection mechanism through hamstrings co-activation would normally be present, hamstrings activation should depend on shear force challenges to the joint. The aim of this study was to test the effect of changes in joint angle, load level and external shear forces on knee flexor co-activation in extension efforts.

METHODS

Ten healthy subjects performed isometric knee extension efforts at 10 knee joint angles (ranging from 5 to 50 degrees of flexion). For each joint angle, external moments of 20, 50 and 80 Nm were applied using a load that was applied perpendicular to the long axis of the shank. All three moments were applied at three distances from the knee joint axis (95, 212 and 307 mm), resulting in three levels of external backward shear force for each moment. The subjects were required to hold the knee joint at each target angle during 5 seconds. An opto-electronic movement registration system (Optotrak) was used to provide a target angle and real-time feedback of the knee joint angle to the subjects. Surface EMG was measured on the Rectus Femoris (RF), Vastus Medialis (VM), Vastus Lateralis (VL), Biceps Femoris (BF), Semitendinosus (ST), Gastrocnemius Lateralis (GL) and Gastrocnemius Medialis (GM) muscles. Rectified EMG signals were averaged over 3 seconds, and a measure of co-activation (EMG/mom) was obtained by dividing EMG by the actual knee extension moment (the externally applied moment plus the moment due to shank mass). For all muscles, ANOVA's were applied with subject, joint angle, external load level and load position as independent variables.

RESULTS

With increasing knee flexion, a strong and non-linear decrease was found for the EMG and EMG/mom (figure 1) of all muscles except GM. EMG of all muscles increased with applied moment ($p<0.001$), suggesting an increase of co-activation with load level. However, this increase was less than proportional, since EMG/mom decreased for all flexor and extensor muscles with increasing load level ($p<0.001$; figure 1 left). The load position affected only the medial knee flexors (ST and GM) and the RF (all $p<0.01$). EMG/mom decreased in the GM (27%) and the ST (12 %) but increased in the RF (9%) at the load position closest to the joint.

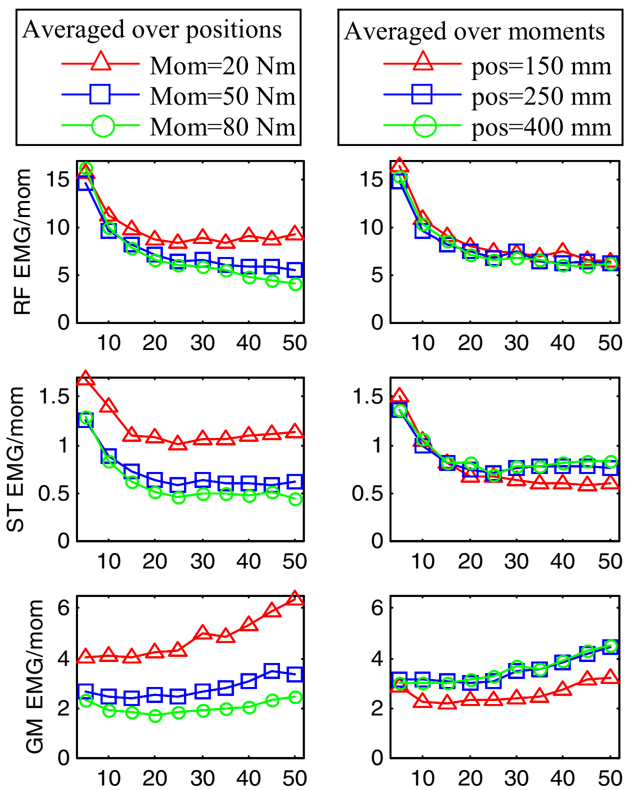

Figure 1: EMG divided by moment against knee angle, for 3 selected muscles, averaged over 10 subjects and over 3 load positions (left) or 3 moment levels (right).

DISCUSSION

The load position closest to the joint causes the largest (externally applied) backward shear force, acting to reduce quadriceps-induced forward tibial shear (Pandy and Shelburne, 1997), and thereby reducing the need for co-contraction. The reduction of medial flexor EMG that we found with loads close to the joint indeed suggests a reduced protective co-activation response.The increase in co-activation near full extension suggests a response to a reduced effectiveness of knee flexors in counteracting shear forces. A reduced level of co-contraction (indicated by EMG/mom) with higher moment levels may be related to the cost of co-contraction (requiring also additional extensor activation).

REFERENCES

Imran, A., O'Connor, J. J. (1998) *Clin. Biomech.* **13,** 153-162.
Pandy, M.G., Shelburne, K. B. (1997) *J Biomech.* **30,** 1015-24.

ELECTROMYOGRAPHY OF KNEE-JOINT MUSCLES IN UNILATERAL BELOW-KNEE AMPUTEES DURING WALKING AND RUNNING

David J. Sanderson and Craig D. Tokuno

School of Human Kinetics, University of British Columbia, Vancouver, BC, Canada
david.sanderson@ubc.ca, tokuno@interchange.ubc.ca

INTRODUCTION

In previous work, Sanderson and Martin (1996;1997) argued that while persons with a below-knee amputation walk symmetrically they do so with dramatically different joint moment patterns at the knee and hip joints. They reported a significant reduction in the prosthetic leg knee-extensor moment for both walking and running, for a group of persons with a unilateral below-knee amputation. It is reasonable to suggest, therefore, that if the joint-moment patterns were different on the prosthetic leg there should be some variation in the activation of the knee-joint musculature. For example, the reported reduced knee extensor moment could have arisen because of increased activation in hamstrings to provide more stability or, conversely a down regulation of vastus lateralis to reduce knee-joint loading. The objective of this project was to provide an analysis of the knee-joint muscular activity during walking and running for a group of unilateral below-knee amputees and an age-matched control group as a means to examine the relationship between the knee-joint moment and muscle activation. It was hypothesized that the activity of vastus lateralis would be reduced in order tomaintain knee-joint stability.

METHODS

Data were acquired as the participants passed over a flush-mounted force platform in the centre of a measurement area of approximately 4 meters in length as part of a 20-meter runway. As the participants passed through the area the six-camera video recording system recorded their movements continuously. Simultaneously, the force platform recorded the loading patterns as the participant passed over the device and the electromyographic system recorded the activity of the vastus lateralis and semitendinosus muscles. Data were collected for three trials at each of two walking speeds (1.2 m/s & 1.6 m/s) and two running speeds (2.7 m/s & 3.5 m/s). A successful trial was one where there was no obvious targeting of the force platform and the average speed remained within ± 3% of the target speed. The sequence for each leg was presented randomly to the participants. Data were recorded from the left and right legs of the non-amputee group and from both the intact and the prosthetic leg of the amputee group providing three limbs for comparison. The EMG data were amplitude normalized to the maximum peak at the slow walk speed and a score of relative activity was computed as:

$$\Delta EMG = \int_{\text{heelstrike}}^{\text{50\%stance}} EMGdt_{VL} - \int_{\text{heelstrike}}^{\text{50\%stance}} EMGdt_{HAMS}$$

RESULTS AND DISCUSSION

Kinematic and kinetic data recorded from these groups were consistent with earlier publications (e.g. Sanderson and Martin, 1996; 1997) showing that the persons with a unilateral below-knee amputation walked with kinematic symmetry but did so with altered hip and knee joint moments. For example, in early stance the knee extensor moment was reduced by 50% compared to the intact and control limbs.

The EMG data, summarized in the table below showed that the ΔEMG values for the prosthetic leg were reduced compared to the other leg conditions for both walking and running conditions. It was concluded that across conditions the activity of the vastus muscle was being down regulated in the prosthetic leg.

Non Amputee	**Slow Walk**	**Fast Walk**	**Slow Run**	**Fast Run**
Vastus lateralis	7024	9849	16890	18791
Semitendinosus	4067	4672	5190	6406
•EMG	2957	5178	11700	12385
Intact				
Vastus lateralis	5758	10512	14297	19983
Semitendinosus	5029	6322	7504	9954
•EMG	729	4190	6792	10029
Prosthetic				
Vastus lateralis	5244	6180	9410	10048
Semitendinosus	5424	6742	6323	6394
•EMG	-179	-562	3087	3654

Table 1. Mean Integrated EMG for the initial 50% of stance.

SUMMARY

This reduced knee-extensor moment arose because of the shift in the degree of activation of the vastus lateralis. These data support the original hypothesis that there is some re-organisation. The goal for the individual appears to be one to provide increased stability to the knee joint during the initial portion of stance, the period when the weight of the body is being taken up by the legs, by reducing the contribution of vastus lateralis and reducing the knee-joint extensor moment.

REFERENCES

Sanderson and Martin (1996). Archives Phys. Med. Rehab. 77, 1279-1285.
Sanderson and Martin (1997). Gait and Posture, 6, 126-136.

INVESTIGATION OF THE DIFFERENCES BETWEEN INERTIAL AND CADENCE EFFECTS ON NEUROMUSCULAR COORDINATION DURING CYCLING

Brian Baum and Li Li
Motor Behavior Laboratory, Louisiana State University, Baton Rouge, LA, USA, LLI3@LSU.EDU

INTRODUCTION

Muscular activity and coordination may be influenced by movement speed and the inertial properties of the limbs. Observed changes in pedal forces, joint moments, and muscular activities have been attributed to inertia, especially at greater pedaling speeds during cycling (i.e. Kautz & Hull, 1983; Li, 1999; Neptune & Herzog, 1999). In these investigations, movement speed and inertia were coupled. Therefore, the purpose of this study was to investigate the effects of cadence and inertial influences on lower extremity neuromuscular coordination during cycling.

METHODS

Sixteen male subjects [mean (SD) age: 23 (5) years, height: 1.8 (0.2) m, mass: 85 (10) kg] cycled at different cadences and with different loads attached to the distal ends of their thighs. Electromyographic (EMG) data were collected from seven muscles of the left lower extremity (see Figure 1). Subjects cycled at 250 W across three pedaling cadences (60, 80, and 100 rpm) and five loads (0, 0.5, 1.0, 1.5, and 2.0 kg) in a random order. Onset, offset, duration, peak magnitude, and peak timing values from the EMG linear envelopes were calculated. Cross-correlation coefficients and phase differences were determined as in Li & Caldwell (1999). Repeated measures ANOVA were used to test statistical significance. Statistical significance of all tests was set at $\alpha = 0.05$.

RESULTS AND DISCUSSION

Neuromuscular coordination and muscular activity patterns displayed differential reactions to cadence and load, as in the muscular responses (exemplar data shown in Figure 1). Timing and magnitudes changed with both greater loads and cadences, but more profound pattern and coordination changes were observed with cadence changes. Results from the cross-correlation technique suggested that coordination changes occurred between mono- and bi-articular antagonists due to cadence but not due to load manipulation. Because of this discrepancy, and that the cross-correlation technique is magnitude insensitive, it is proposed that inertial influences may be more relevant to event magnitudes rather than timing.

SUMMARY

This study aimed to distinguish between inertial and cadence effects on neuromuscular coordination during cycling. Subjects cycled at different cadences and with loads attached to the distal ends of their thighs, and EMG data were collected and analyzed. The results led to the conclusion that movement speed effects have a greater influence on the lower extremity muscles during cycling but the inertial effects were apparent.

REFERENCES

Kautz, S.A., Hull, ML. (1993). *J. Biomech.*, **26**, 155-65.
Li, L. (1999). *Doctoral Dissertation*. University of Massachusetts, Amherst.
Li, L., Caldwell, G.E. (1999). *J. Electromyogr. Kinesiol.*, **9**, 385-9.
Neptune, R.R., Herzog, W. (1999). *J. Biomech.*, **32**, 1021-6.

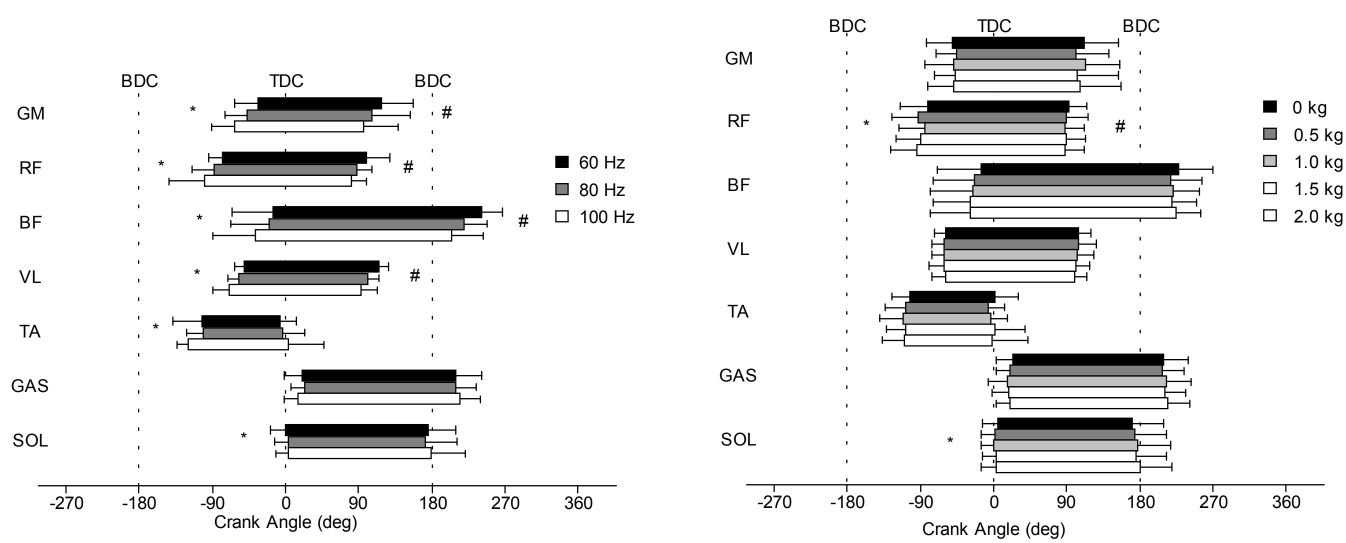

Figure 1. Mean onset, offset, and duration of EMG linear envelopes of gluteus maximus (GM), rectus femoris (RF), biceps femoris (BF), vastus lateralis (VL), tibialis anterior (TA), gastrocnemeus (GAS), and soleus (SOL) across (a) cadence and (b) load conditions. Error bars represent one standard deviation of the mean onset and offset. * and # indicate a significant difference ($p < 0.05$) between cadence or load conditions for onset and offset, respectively.

BIOMECHANICS OF PERIVASCULAR FLOW IN SYRINGOMYELIA

Lynne Bilston[1] and David F. Fletcher[2]

[1] Prince of Wales Medical Research Institute
Barker St, Randwick, NSW 2031, Australia, l.bilston@unsw.edu.au
[2]Department of Chemical Engineering,
University of Sydney, NSW 2006, Australia.

INTRODUCTION

Syringomyelia is a neurological condition in which syringes (fluid-filled cysts) form in the spinal cord. If these syringes are large, they can cause neurological deficits. To date, the exact biomechanical mechanism by which cerebrospinal fluid (CSF) from the subarachnoid space enters the spinal cord to form a syrinx is unknown. One hypothesis suggests that the fluid is pushed into the central canal of the spinal cord from the fourth ventricle in patients with chiari malformations. Alternatively, Stoodley et al (1999) have shown that CSF enters a syrinx through the perivascular spaces in an animal model of syringomyelia, and that this flow is abolished in the absence of arterial pulsations. The aim of this study was to develop a computational fluid dynamic model of flow in the spinal perivascular spaces in order to determine whether arterial pulsations could cause perivascular fluid flow.

METHODS

A 250 μm long segment of a "typical" spinal artery was modelled, with a diameter of 100 microns. The perivascular space was modelled as a 25μm thick annulus surrounding the artery (Thron, 1988). The outer boundary of the perivascular space has been assumed not to deform. The exact amount of arterial wall deformation in the spinal cord is unknown, however in other tissues, small arteries expand by 5-10% during systole Hoeks et al, 1999). Arterial expansion was modelled as a periodic travelling sinusoidal wave of wall deformation in the outer wall of the artery, at 10% of the artery radius (5μm), with a frequency of 1 Hz. Cerebrospinal fluid was modelled as a Newtonian fluid with viscosity of 1.0×10^{-3} Pa.s (Bloomfield et al, 1998).

The flow field was solved using CFX4 (CFX, 2000). This code solves the Navier-Stokes equations using an implicit finite volume method, using a collocated mesh that can be deformed in time to model transient effects. No slip boundary conditions were applied at all walls with the inlet and outlet set as mass flow boundaries. A simulation was run until a quasi-steady-state was reached in which the flux and velocities in the middle of the flow domain had reached a quasi-steady-state.

RESULTS AND DISCUSSION

The simulations showed that the pulsations drive fluid flow in the perivascular space along the same direction that the pulsations travel. Net flow rate was 2.7×10^{-7} kg/s. Figure 1 shows the fluid velocity distribution in the perivascular space at equilibrium. There is a net pressure drop generated of 560Pa as a result of the wall motion.

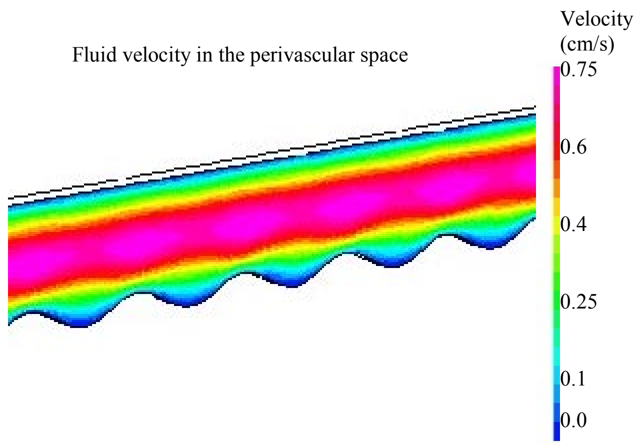

Figure 1: Fluid velocity in the perivascular space model.

SUMMARY

This model demonstrates that fluid can be caused to flow along perivascular spaces as a result of arterial pulsations. This flow may play a role in the development of syringomyelia when there is a disturbance to the outflow or absorption of CSF from within the spinal cord.

REFERENCES

Bloomfield, I. G., et al. (1998). *Ped. Neurosurg.* **28**, 246-251.
Stoodley, M. et al. (1999). *Neurosurgery* **44**, 1065-75.
CFX (2000). *CFX4 User manual*, AEA Technology.
Hoeks, A. P., et al. (1999). *Proc. IMechE. H - J. Eng Med.* **213**, 195-202.
Thron, A.K. (1988) *Vascular anatomy of the spinal cord*, Springer-Verlag.

ACKNOWLEDGEMENTS

The authors would like to thank Dr M Stoodley and Dr A. Brodbelt for their assistance in this work

THE EFFECT OF TRABECULAR BONE MICROSTRUCTURE ON STRESS DISTRIBUTION OF A DENTAL IMPLANT

Han Sung Kim[1], Sangup Lee[1], Nam-Hyo Cho[1], June-Sung Shim[2], Jaiyoung Ko[3]

[1]Institute for Advanced Engineering, Yongin, Kyonggi-Do, Korea, hanskim@iae.re.kr
[2]Dept. of Prosthodontics, College of Dentistry, Yonsei University, Seoul, Korea
[3]Solco Biomedical, Pyongtaek, Kyonggi-Do, Korea

INTRODUCTION

Many previous studies assumed that the mandibular trabecular bones are homogeneous. Moon *et al.* (1997) introduced homogenization method for stress analysis in a dental implant system. They regarded trabecular bone as a structure of unit cell. However, they have the limited accuracy and applicability due to the high degree of material heterogeneity in the trabecular bone structure of mandible. In the present study, a microstructure model for stress analysis in a dental implant system is suggested and the results of the present model and previous models are compared using finite element analysis.

METHODS

A mandibular specimen with a premolar was obtained from a cadaver. The microstructure of the specimen was scanned with micro-CT and captured by BIONIX (CANTiBio Co.). A Micro-FE model in Fig. 1(b) was reconstructed from micro-CT images at mid-sagittal plane of the tooth. Fig. 1 shows the modeling process of this study. A vertical (100N) and horizontal (100N) load was applied to the top surface of the implant system and stress distribution was calculated along the implant surface (Figs. 1,2). For the comparison purpose, the fixed boundary condition in Fig. 1 is applied to the bottom of the mandible. To compare the results of models generated by the previous methods with those of the microstructure model, a homogeneous model of Fig. 1(c) and a D1 bone model with only cortical bone in Fig. 1(d) were also generated and analyzed using commercial finite element software (MSC NASTRAN). In the microstructure model and the D1 bone model, the same material properties (a Young's modulus of 12Gpa, a Poisson's ratio of 0.3) were assigned to elements of cortical bone and trabecular bone. However, in the homogeneous model, a Young's modulus of 345Mpa was used in those of the trabecular bone.

RESULTS AND DISCUSSION

The stress curve across the implant surface is given in Fig.2. The highest tension stresses for all models were on 'A' (Figs. 1,2). The second greatest stresses were on 'C' in both homogeneous model and D1 model, but in microstructure model, they were between 'A' and 'B'. This result indicates that the microstructure of trabecular bone in a mandible needs to be considered in FEA studies to produce reasonable results and thus implant system with high success rate. Since this study is a preliminary investigation, more in-depth studies on the implant system with mandibular trabecular bone need to be followed.

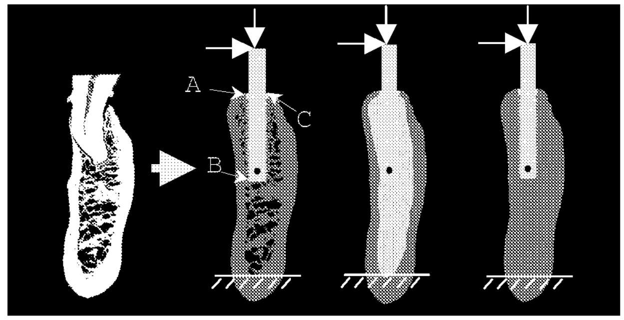

(a) (b) (c) (d)

Figure 1: Modeling process: (a) Micro-CT reconstruction, (b) Microstructure model, (c) Homogeneous model, (d) D1 bone model.

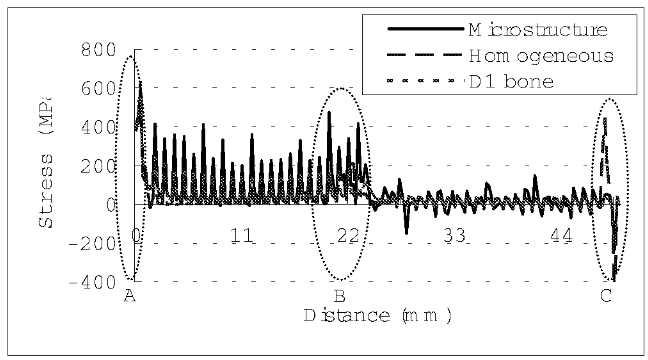

Figure 2: Stress curve along the implant surface.

SUMMARY

Because of the complex geometry in the mandibular trabecular bone, many previous researchers assumed that the mandibular trabecular bones are homogeneous and isotropic. Therefore, the accuracy of the previous models is limited. In this study, a micro-FE model of implant system with mandibular trabecular bone is generated and analyzed. The stress curve along a dental implant surface is compared with that of the previous models. This study shows that microstructure model needs to be considered in FEA studies to produce reasonable results and thus implant system with high success rate.

REFERENCES

Moon, H.J. et al (1997). *J. Med. Eng. Technol.*, **21**, 233-240.

ACKNOWLEDGEMENTS

This study was supported by a grant of the Korea Health 21 R&D Project, Ministry of Heath & Welfare, Republic of Korea. (01-PJ1-PG4-01PT03-0023)

DYNAMICS RATHER THAN EQUILIBRIUM POINT IS CONTROLLED IN HUMAN MOVEMENTS

Mark R. Hinder and Theodore E. Milner*
School of Kinesiology, Simon Fraser University, Burnaby, B.C., V5A 1S6, Canada
* Corresponding author tmilner@sfu.ca tel: 604 291 3398, fax: 604 291 3040

INTRODUCTION

The equilibrium point hypothesis (EPH) was conceived as means whereby the central nervous system could control limb movements by a relatively simple shift in equilibrium position without the need to explicitly compensate for task dynamics. Many recent studies have questioned this view with results that point to the formation of an internal model of the task dynamics (Shadmehr & Mussa-Ivaldi, 1994; Thoroughman & Shadmehr, 2000), while proponents of the EPH still argue for its virtues (Feldman et al, 1998). In this study, we have tested one of the fundamental predictions of the EPH, namely, equifinality.

METHODS

Subjects learned to perform goal-directed wrist flexion movements without visual feedback. A torque motor provided assistance in proportion to the instantaneous velocity, which resulted in underdamped oscillation of the wrist about the final position. Subjects were instructed to produce a single movement and not to react voluntarily to any changes in the assisting torque.

The assisting torque was unexpectedly reduced on random trials by 0%, 25%, 50%, 75% or 100%. These perturbed trials comprised 10% of the total number. Kinematic data and surface EMG of all major wrist muscles was recorded.

Error in the final position was quantified by calculating the difference in final position between perturbed trials and trials immediately preceding the perturbed trials.

Cumulative EMG was analysed to investigate whether motor commands remained invariant between the perturbed trials and preceding trials. Changes in stretch reflex gain and threshold were estimated for flexor muscles by comparing the level of EMG activity during the half cycles of the oscillations corresponding to flexor stretch.

RESULTS AND DISCUSSION

Subjects stopped short of the target on the trials where the magnitude of the assistance was randomly decreased, compared to the preceding control trials (F=14.782, p=0.003), i.e., equifinality was not achieved. This is contrary to the EPH, which predicts that final position should not be affected by external loads that depend purely on velocity. However, such effects are entirely consistent with predictions based on the formation of an internal model of the task dynamics.

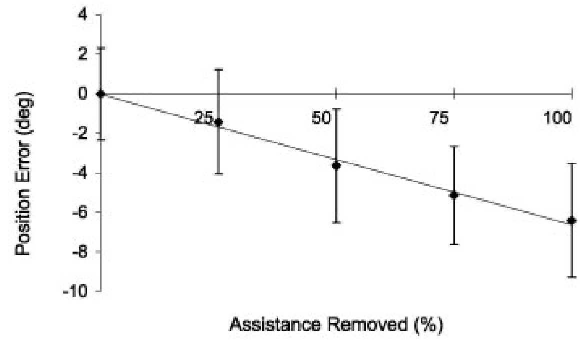

Figure 1 Linear fit of the error in the final position

Cumulative EMG revealed that the motor command remained invariant across all conditions, suggesting that an internal model was formed during learning that was robust to random changes in the assisting torque level.

Analysis of flexor EMG during the oscillations about the target revealed that the level of assisting load did not affect the stretch reflex gain and threshold. Therefore, according to the EPH, the error in final position could not be explained by a reduction in stretch reflex contribution to the motor command, strengthening the case for the formation of an internal model.

SUMMARY

We have shown that one of the fundamental predictions of the EPH, equifinality, does not hold. We conclude that learning leads to the formation of an internal model of the load torque dynamics by the central nervous system which is used for feedforward control of motor commands to muscles.

REFERENCES

Shadmehr, R. & Mussa-Ivaldi, F.A. Adaptive representation of dynamics during learning of a motor task. *J. Neurosci*., **14**, 3208-3224 (1994).

Thoroughman, K.A. & Shadmehr, R. Learning of action through adaptive combination of motor primitives. *Nature*, **407**, 742-747 (2000).

Feldman, A.G., Ostry, D.J., Levin, M.F., Gribble, P.L. & Mitnitski, A.B. Recent tests of the equilibrium-point hypothesis (lambda model). *Motor Control*, **2**, 189-205 (1998).

A VERTEBRAL BODY REPLACEMENT FOR *IN VIVO* LOAD MEASUREMENT

Antonius Rohlmann, Udo Gabel, Friedmar Graichen, Georg Bergmann

Biomechanics Laboratory, University Hospital Benjamin Franklin, Free University of Berlin, Germany, rohlmann@biomechanik.de

INTRODUCTION

In cases involving considerable burst fractures of a vertebral body, post-traumatic kyphosis or tumors of a vertebral body an implant for replacement of a vertebral body is often indicated for restoring normal load-bearing in the anterior spine. Several different implants for this purpose are clinically used. After positioning, the anterior implant is mostly distracted *in situ* by a thread or an expansion mechanism. This provides best contact with adjacent end-plates and three-dimensional stability, thus minimizing the possibility of correction loss or secondary dislocation. If desired, bone cement or bone grafts can be added to the implants. After insertion of a vertebral body replacement the implant takes over the load normally transferred by the anterior column of the spine. The anterior implants are mostly supplemented by a stabilizing implant, e.g. an internal spinal fixation device. The load is then shared at least by the anterior and the posterior implants.

The aim of this paper is to introduce a telemeterized implant for the replacement of a vertebral body which allows the measurement of three force and three moment components.

IMPLANT DESIGN

Synex (STRATEC Medical, Oberdorf, Switzerland) is an implant for vertebral body replacement that meets the above mentioned requirements. It consists of an inner and an outer part both made out of titanium, and a supporting ring. Synex is hollow, smaller than the anterior defect when initially fitted in an undistracted state, and can be distracted *in situ* to the desired height with a special distractor after precise placement in the spinal lesion [Knop et al, 2000]. A self-blocking ratchet mechanism prevents a telescopic shortening of the vertebral body replacement under load.

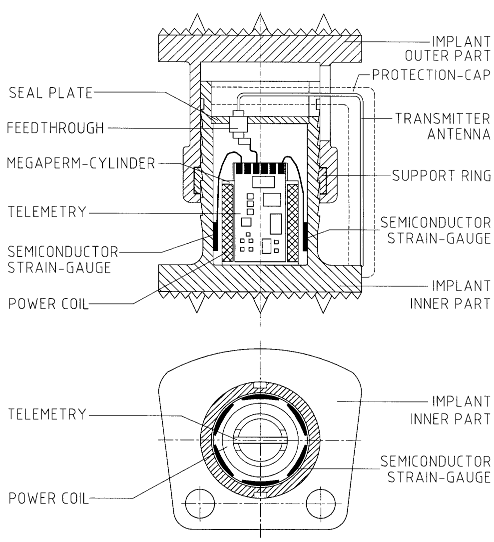

Figure 1: Schematic sketch of the instrumented vertebral-body-replacement implant

DESIGN OF THE TELEMETERIZED IMPLANT

For the instrumentation the original implant was modified. The lateral window of the inner part of the implant was omitted. This necessitated a new anti-twist mechanism. We chose the tongue and groove principle. On the outer side of the cylinder two grooves 0.85 mm deep and 1 mm wide were milled.

To allow the measurement of six load components, six semiconductor strain gauges are glued around the circumference of the inner wall at a distance up to 5 mm from the end-plate (Fig. 1). Two each are glued at +30°, 0°, and –30° to the long axis of the inner part. The telemetry circuit is the same as used for the internal fixator [Graichen et al, 1996]. The telemetric unit was place in a cylinder made out of a material of high permeability (Megaperm 40L, VAC). The secondary coil for the inductive power supply used this cylinder as a core. Megaperm increases the inductivity of the coil reeled on the cylinder, and it shields the circuit against the magnetic field needed to supply the telemetry.

The cylinder-shaped hollow part is hermetically closed by a 1 mm thick titanium seal plate using electron beam welding. In the seal plate an electrical feedthrough used in pacemakers is laser beam welded. The inner side of the niobium wire is connected to the electric circuit of the telemetry unit and the outer side to a niobium wire (diameter 0.5 mm) which serves as a transmitter antenna. A polyethylene cap which is mechanically fixed to the implant protects the wire-antenna against deformation.

In order to adjust to the different heights of the vertebral bodies, two different lengths of the outer part of the implant were manufactured. One combination covers a range from 38 mm to 48mm, the other from 45.5 mm to 58 mm. Two tongues 5 mm long and 1 mm wide are fixed at opposite sides in order to prevent relative turning between inner and outer part.

Prior to implantation, the modified implants are mechanically tested, and calibrated by applying defined forces and moments.

The external telemetry system is the same as for the internal fixators [Graichen et al, 1996; Rohlmann et al, 1994]. For the measurements an induction coil will be placed around the body at the level of the implant. A small loop antenna with an integrated amplifier will be placed on the patient's back near the implant to receive the pulse-interval-modulated signals of the 8-channel telemetry. The patient will be videotaped and the load-dependent signals will be stored on the same videotape. From the signals the forces and moments will be calculated in a PC and the loading curves will be shown online on a monitor.

REFERENCES

Graichen, F. et al (1996) *Med. En.g Phys.*, **18**, 167-174
Knop, C. et al (2000). *Eur.Spine J*, **9**, 472-485
Rohlmann, A. et al (1994) *J.Biomech.*, **27**, 961-967

FATIGUE AND MUSCLE COORDINATION IN SUBJECTS WITH PATELLOFEMORAL PAIN SYNDROME

Gertjan Ettema [1], Trine Tegdan[2] and Karin Roeleveld [1]

[1]Human Movement Science Section, Sport Sciences Programme, NTNU, Trondheim, Norway. email: gertjan.ettema@svt.ntnu.no
[2] Faculty of Health Education and Social Work, Sør-Trøndelag University College, Trondheim, Norway

INTRODUCTION

The patellofemoral pain syndrome (PFPS) is a common knee problem, especially in adolescents and physically active young adults. Abnormal muscle activation of compartments of the Quadriceps Femoris (QF) in PFPS (Callaghan et al., 2001) may disturb the dynamics of the patellofemoral joint, thereby leading to PFPS. In this study intermuscular coordination aspects of the QF under demanding conditions, in this case fatigue, were examined.

METHODS

Twelve subjects with PFPS (3 males, 9 females) and 14 pain free control subjects (4 males, 10 females) volunteered. The groups did not differ for age, height or weight. The average duration of PFPS, as diagnosed by an orthopedic surgeon, was 19,9 (±13,3) months. The subjects were asked to stand on one leg in a semi-squatted position (120 degrees knee flexion) for as long as possible. Position maintenance was checked using digital kinematic recordings (ProReflex). Bipolar surface EMG (sample rate 2000Hz, bandpass-filtered at 10-500Hz) was recorded of oblique vastus medialis (VM_O), vastus lateralis (VL) and rectus femoris (RF). Mean power frequency (MPF) and amplitude (A) were calculated for the start period of the exercise and at exhaustion. The change of MPF (ΔF) and normalised A (ΔA%) during the exercise were used to compare groups.

RESULTS AND DISCUSSION

PFPS subjects demonstrated a shorter time (90.1 ± 48.5s) to exhaustion than the controls (215.7 ± 111.7s) (t-test: $p<0.001$). ΔF and ΔA% results are summarized in Table 1. Both groups, although reporting full exhaustion showed no significant changes in A or MPF. However, a two-factor ANOVA for repeated measures (taking account for individual differences) revealed significant effects of muscle on ΔF. Within a single group, the same effect was found for the controls but not for the PFPS group. A striking finding was that the ΔF values tended to correlate high between muscles in the patient group, but not in the control (Fig. 1). Also a larger proportion of patients than controls showed significant correlations (r considered significant at $p<0.01$) for MPF between muscles during the entire exercise (20 measurement points taken during performance) (group difference by Chi Squared test, p=0.011). These group differences were not found for amplitude.

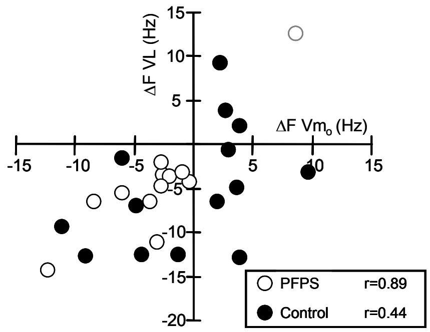

Figure 1: ΔF values VL against VM_o. PFPS correlation is significant ($p<0.001$), when excluding gray data point (as outlier) r reduces to 0.73 (p=0.01).

These results indicate that, regarding the EMG frequency spectrum, PFPS subjects show a more monotone change during fatigue among three QF muscle compared to controls. The physiological basis for the current findings are unclear. However, change in frequency content is a good indicator for fatigue (e.g. Gerdle et al, 2000). Thus, it is suggested that PFPS patients demonstrate a lesser ability to independently adjust certain muscle activation aspects in different muscles (or compartments), which may lead to or may be the result of PFPS. We speculate that PFPS patients show a reduced number of degrees of freedom in QF coordination, and therefore fatigue their QF in a more monotone manner.

REFERENCES

Callaghan, M.J. et al. (2001) *Manual Therapy,* **6**, 27-33.
Gerdle, B. et al. (2000) *J Electromyogr Kinesiol*, **10**, 225-232.

Table 1: Changes in MPF and A during the static exercise.

	VM_o		VL		RF	
	PFPS	Control	PFPS	Control	PFPS	Control
ΔF (Hz)	-3.3 ± 5.3	-0.5 ± 6.5	-4.9 ± 6.8	-5.4 ± 7.7	-2.1 ± 6.9	-6.0 ± 10.23
ΔA%	17.3 ± 68.9	-15.6 ± 30.8	24.1 ± 67.0	-4.4 ± 30.7	20.8 ± 70.4	17.8 ± 51.9

EVALUATION OF A MATHEMATICAL MODEL OF MUSCLE ENERGETICS

Han Houdijk

Institute for Fundamental and Clinical Human Movement Sciences, Faculty of Human Movement Sciences, Vrije Universiteit Amsterdam, The Netherlands. H_Houdijk @ fbw.vu.nl

INTRODUCTION

To simulate submaximal cyclic movements, a model is required that captures both muscle mechanics and energetics. Models that capture muscle mechanics have been described and validated abundantly in the literature. Models that capture muscle energetics are, however, rather scarce and the existing models have not yet been validated adequately. In this study, a model of muscle energetics was evaluated using experimental data of muscle energetics that were obtained from literature.

METHODS

Muscle mechanics were modeled using a Hill-type muscle model as described by Van Soest and Bobbert (1993). Muscle energetics were modeled using a model previously described by Hatze and Buys (1977). This model calculates energy cost as the sum of heat and work produced by a Hill type muscle. Heat production is divided in three components: the cross bridge independent 'activation heat' (a function of stimulation frequency), the cross bridge dependent 'maintenance heat' (a function of active state and contractile element (CE) length), and the 'shortening heat' (a function of CE shortening velocity).

The muscle model was used to simulate a muscle fiber experiment that was performed by Barclay et al. (1993). In this experiment, fiber bundles of mouse slow-twitch m. soleus (SOL) and fast-twitch m. extensor digitorum (EDL) performed iso-velocity contractions at different velocities. Heat and work were measured.

The muscle specific parameters for the mechanical submodel were derived from the experimental data of Barclay et al. (1993). The parameters for the energetics submodel were taken from Hatze and Buys (1977), who had derived these from various animal species under various experimental conditions.

The rate of energy cost (heat + work) and muscle efficiency (work / (heat + work)) were compared between experiment and simulation.

RESULTS

Close agreement existed between the isometric heat production in the experiment and simulation for both SOL and EDL. The rate of energy cost of isometric contraction for SOL was 26.8 vs. 23.8 mW/g for the experiment and simulation respectively. For EDL this amounted to 134.2 vs. 144.0 mW/g.

In accordance with the experimental results, the rate of energy cost for the dynamic contractions of SOL increased almost five-fold between zero and maximal shortening velocity. The model predicted a three-fold increase in energy cost for EDL. This was twice as high as the increase seen in the experimental data. However, the overestimation of the energy cost in the simulation was the result of both an overestimation of the work rate and shortening heat rate. This might be the result of an inaccuracy in the Hill constants provided by Barclay et al. (1993).

The model quite well predicted the relation between shortening velocity and muscle efficiency for both SOL and EDL (fig. 1). Muscle efficiency was overestimated a little for both muscles, but as in the experiment, maximal efficiency was equal between muscles,and the fast-twitch EDL was more efficient at higher relative contraction velocities than SOL.

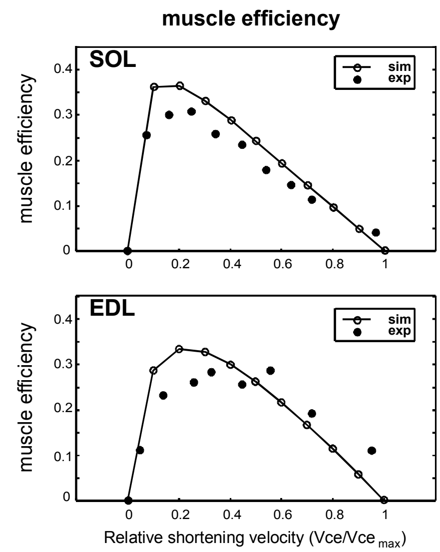

Figure 1: muscle efficiency versus relative CE shortening velocity for SOL and EDL in the **exp**eriment and **sim**ulation.

CONCLUSION

It can be concluded that the model for muscle energetics and its parameters, used in this study, can adequately reproduce muscle efficiency of mammalian muscles during discrete iso-velocity contractions. Our next step in the validation of this model will be to test it for more natural, cyclic stretch-shortening contractions.

REFERENCES

Barclay, C. J. et al. (1993). *Journal of Physiology* **472**, 61-80.

Hatze, H. and Buys, J.D. (1977). *Biological Cybernetics* **27**, 9-20.

Soest, A.J.v. and Bobbert, M.F. (1993). *Biological Cybernetics* **69**, 195-204.

DEFORMATION OF A BIOARTIFICIAL CAPSULE IN PLANE HYPERBOLIC FLOW

Etienne Lac [1], Nikos Pelekasis [2], Dominique Barthès-Biesel [1], John Tsamopoulos [3]
[1] CNRS - UMR 6600, Université de Compiègne, France (etienne.lac@utc.fr)
[2] Department of Mechanical and Industrial Engineering, University of Thessaly, Greece.
[3] Department of Chemical Engineering, University of Patras, Greece.

INTRODUCTION

Cells and vesicles are commonly modelled as capsules, e.g. droplets enclosed in a thin membrane. Capsules are also met in numerous biomedical or pharmaceutical applications. We present a numerical model of the motion and deformation of an initially spherical (radius a) liquid filled capsule freely suspended in a linear shear flow. Both internal and external fluids are Newtonian, have the same dynamic viscosity μ, and obey the Stokes equations, since the particle Reynolds number is very small. The membrane is infinitely thin and hyperelastic with surface shear modulus G_s. We focus on the influence of the membrane rheology on the capsule motion.

METHODS

In an unbounded flow field of velocity $\boldsymbol{v}^\infty$, the velocity $\boldsymbol{v}(\boldsymbol{x})$ of a point on the membrane M, is given by the integral equation (Pozrikidis, 1992):

$$v_i(\boldsymbol{x}) = v_i^\infty(\boldsymbol{x}) - \frac{1}{8\pi\mu}\int_M J_{ij}(\boldsymbol{x},\boldsymbol{y})\,\Delta f_j(\boldsymbol{y})\,dS(\boldsymbol{y}) \ ,$$

where $\Delta\boldsymbol{f}$ represents the viscous stress jump across the interface and the kernel $\boldsymbol{J}$ is a free-space Green's function. For an infinitely thin membrane, $\Delta\boldsymbol{f}$ is equal to load exerted on the elastic interface and is thus related to the elastic tensions tensor $\boldsymbol{T}$ through the membrane equilibrium equation :

$$\nabla_S . \boldsymbol{T} + \Delta\boldsymbol{f} = \boldsymbol{0} \ .$$

The constitutive law of the membrane material relates the tensions to the deformations of the surface. We confront a neo-Hookean law (NH), commonly used for elastomers, and the Skalak et al. (1973) law (SK) where the shear modulus G_s and the area dilatation modulus $(1+2C)G_s$ are of the same order. The undisturbed velocity field $\boldsymbol{v}^\infty$ corresponds to a plane hyperbolic flow of intensity $\dot\gamma$, with components:

$$v_1^\infty = \dot\gamma\, x_1 \qquad v_2^\infty = -\dot\gamma\, x_2 \qquad v_3^\infty = 0$$

An important parameter is the capillary number $\varepsilon = \mu\, a\,\dot\gamma\, / G_s$ that measures the ratio of viscous to elastic forces.

The interface is described with general Lagrangian co-ordinates by means of bi-cubic B-splines, so that very large deformations can be reached with good accuracy. Once their velocity is calculated, the membrane material points $\boldsymbol{x}$ are convected by means of the differential equation $\dot{\boldsymbol{x}} = \boldsymbol{v}(\boldsymbol{x})$.

RESULTS

The hyperbolic flow is created experimentally in the centre of a cell with four contra-rotating cylinders. This device was used by Chang & Olbricht (1993) to measure the deformation of capsules with a nylon membrane. The steady deformation in the extension plane (x_1,x_2) is measured by the Taylor parameter $D_{12} = (L_1-L_2)/(L_1+L_2)$, where L_1 and L_2 denote the particle lengths along axes 1 and 2. As shown on Figure 1, up to a deformation of 10%, the membrane law has no influence and the numerical results match the asymptotic predictions of Barthes-Biesel & Rallison (1981). For larger deformations, the SK law with C=1 captures the strain hardening behaviour of the nylon capsules. The SK law with C=10 is too strain-hardening. Figure 2 shows a comparison between the model (SK, C=1) and experimental profiles.

For large deformations, corresponding to values of ε that depend on the membrane rheology, the membrane tends to buckle and the model fails. The bending rigidity of the membrane should then be taken into account.

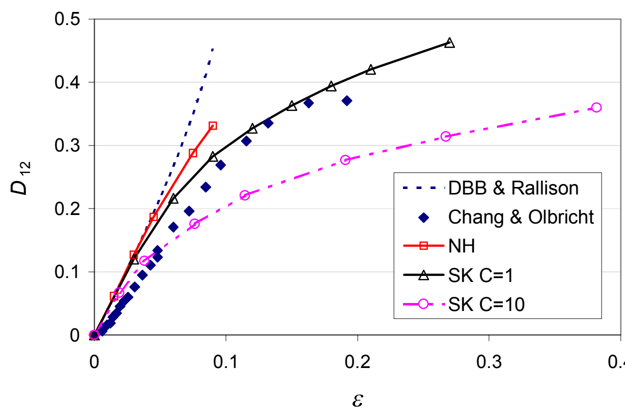

Figure 1 : Deformation vs. capillary number ε for a capsule placed in a hyperbolic flow.

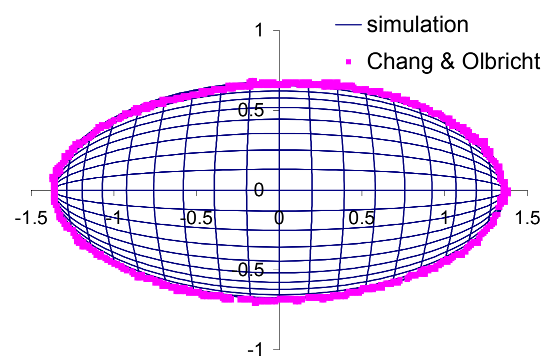

Figure 2 : Comparison between numerical (SK, C=1) and experimental capsule profiles in hyperbolic flow (ε = 0.132).

REFERENCES

Barthès-Biesel D., Rallison J.M. (1981) *J. Fluid Mech.* **113**, 251.
Chang K.S., Olbricht W.L. (1993), *J. Fluid Mech.* **250**, 587.
Pozrikidis C. (1992), *Cambridge University Press*.
Skalak R. et al. (1973), *Biophys. J.* **13**, 245.

MUSCLE ACTIVITY IN THE LOWER EXTREMITY DAMPS THE SOFT-TISSUE VIBRATIONS WHICH OCCUR IN RESPONSE TO IMPACT FORCES

James M. Wakeling, Antra I. Rozitis and Benno M. Nigg

Human Performance Laboratory, University of Calgary, Calgary, Alberta, Canada

INTRODUCTION

Impact shocks are delivered to the body during heel-strike in walking and running. It has been proposed that muscle activity in the lower extremity is tuned in order to minimize the soft-tissue vibrations that would occur after such impacts (Nigg, 1997). Evidence shows that muscle activity is altered in response to heel-strike impacts with different frequency contents (Wakeling et al. 2001), however there is currently no direct evidence linking the frequency of the impact force, the muscle activity and the vibration properties of the soft-tissues. The purpose of this study was to test the hypothesis that there are increases in the damping and natural frequency of the soft-tissues when the frequency of an impact force matched the natural frequency of that tissue.

METHODS

Soft-tissue vibrations were measured using skin mounted accelerometers, and muscle activity using surface EMG sampling at 2400 Hz whilst 20 subjects stood on a vibrating platform. Measurements were made from the soft-tissue groups of the quadriceps, hamstrings, tibialis anterior and triceps surae. Bursts of continuous vibration and bursts of isolated impacts were delivered in a 8×5 randomized, repeated block manner. Input frequencies were varied between 10 and 65 Hz. The power dissipated by soft-tissue, and intensity of muscle activity were determined for each trial. The resonance spectra for the soft-tissues were determined whilst subjects stood on the platform with white-noise displacements.

RESULTS AND DISCUSSION

Tuning responses were categorized when there was a test frequency which resulted in elevated muscle activity or power dissipation. Responses occurred for both the continuous vibration trials and the pulsed impact trials for all four soft-tissues tested, and occurred when the test frequency matched the natural frequency of the soft-tissue (Fig. 1).

The results supported the hypothesis that there are increases in muscle activity and vibration damping when the frequency content of the impacts match the natural frequencies of the soft-tissue. However, there was no evidence to support the hypothesis that if the impact frequency matched the natural frequency of the tissue that there would be an increase in the natural frequency.

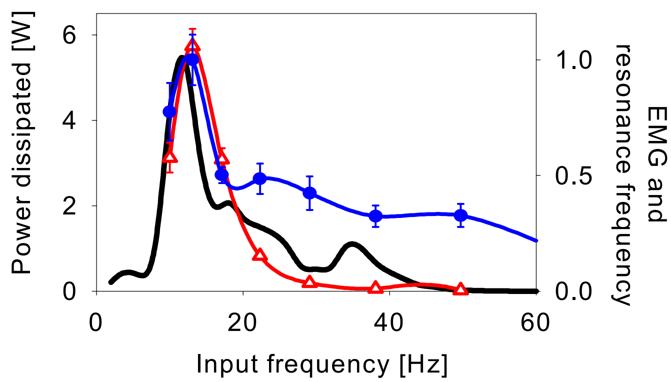

Figure 1. EMG intensity (blue circles), power dissipation (red triangles) and resonance spectra (black line) for the triceps surae whilst subjects were exposed to bursts of continuous vibration. Data (mean ± SEM) are shown for all cases where a response occurred (*N*=18).

The frequency of the impact forces can be modified by the material hardness of a shoe (eg. Frederick et al. 1984; Lafortune et al. 1996). These results thus indicate a mechanism by which the muscle activities in the lower extremity can be altered by changing the material properties of a shoe.

SUMMARY

Muscle activity is used in the soft-tissues to damp the vibrations from impact forces when the frequency of the impact matches the natural frequency of the tissue.

REFERENCES

Frederick E.C. et al (1984). In: *Sport Shoes and Playing Surfaces*. Human Kinetic Publishers, pp190-198.
Lafortune M.A. et al (1996). *J. Biomech.* **29**, 1523-1529.
Nigg B.M. (1997). *Current Opinion in Orthopedics* **8,** 43-47.
Wakeling, J.M. et al (2001). *Eur. J. Appl. Physiol*. **86**, 40-47.

ACKNOWLEDGEMENTS

Drs. Joachim Mester and Clemens Treier, for their support and help in Germany.

DETERMINING PATTERNS OF MOTOR UNIT RECRUITMENT DURING ANIMAL LOCOMOTION

James M. Wakeling[1], Walter Herzog[1] and Doug Syme[2]

[1]Human Performance Laboratory, University of Calgary, Calgary, Alberta, Canada
[2]Department of Biological Sciences, University of Calgary, Calgary, Alberta, Canada

INTRODUCTION

Fast and slow muscle fibres have different electrical properties and conductances. It should be expected that the motor unit action potentials which travel along the fast and slow muscle fibres produce different myoelectric signals, and therefore these may be used to distinguish their activity. The mean EMG frequency is greater for persons with a higher proportion of fast muscle (Sadoyama et al. 1988), and for stimulated contractions with a greater proportion of fast- motor units (Solomonow et al. 1990). However, the myoelectric frequency spectra from distinct fast and slow muscle has not yet been determined. The purpose of this study was to test the hypothesis that fast muscle fibres have higher myoelectric frequency bands than slow muscle fibres.

METHODS

Fine wire EMG was recorded from the medial gastrocnemius of six rats *in situ*, whilst the muscle was stimulated through a tripolar electrode on its nerve. A combination of blocking and innervating stimuli generated isometric contractions with either just slow motor units or a combination of fast- and slow (Solomonow et al. 1990). EMG was also recorded from the white and red myotomal muscle of 16 rainbow trout *Oncorynchus mykiss*, and the medial gastrocnemius and soleus muscles from four cats during *in vivo* locomotion. The intensity of the myoelectric signals was resolved into its components in time-frequency space using wavelet techniques (von Tscharner, 2000). Myoelectric intensity spectra were determined for rat muscle during slow and fast+slow fibre contractions, during various locomotor activities including slow swimming and fast-starts in the fish, and slow walking and rapid paw-shakes in the cat.

RESULTS AND DISCUSSION

EMG intensity spectra were determined when just the slow motor units were activated, and when both fast- and slow-motor units were active in the rat gastrocnemius. Subtraction of these spectra yields the spectra for just the fast- motor units. The fast- and slow- motor units resulted in high and low frequency bands, respectively (Fig. 1).

The fast and slow muscle fibres are anatomically separated in fish, allowing direct recording from these muscle types. The fast and slow fibres generated high and low frequency bands in their intensity spectra in a similar manner to the rat (Fig. 1).

In mammals the fast- and slow-muscle fibres can be mixed within each muscle, making it difficult to determine when each fibre type is active *in vivo*. The cat paw-shake is a predominantly fast-fibre activity (Smith et al. 1980) whereas a larger proportion of slow fibres are active during slow walking. Subtracting the EMG intensity spectra for the paw-shake (fast fibres, blue dashed line, Fig. 1) from that for slow-walking thus results in an estimate of the intensity spectra for the slow fibres in the gastrocnemius (Fig. 1). The estimated intensity spectra for the slow motor units from the medial gastrocnemius was similar to that measured for the soleus muscle which contains predominantly slow fibres (Fig. 1).

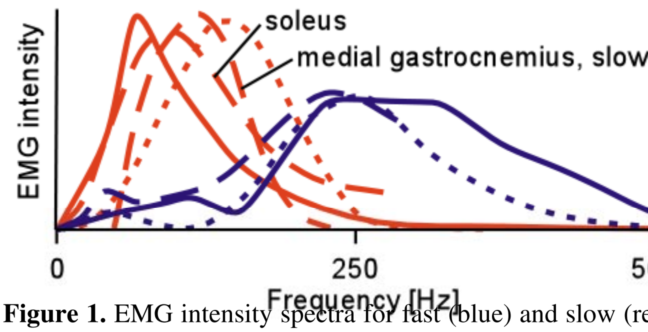

Figure 1. EMG intensity spectra for fast (blue) and slow (red) motor units from the myotomal muscle of the rainbow trout (solid lines), medial gastrocnemius and soleus muscles of the cat (dashed lines), and medial gastrocnemius muscle of the rat (dotted lines).

SUMMARY

The myoelectric frequency spectra from fast- and slow muscle fibres can be characterized by high and low frequency bands, respectively. These bands can be distinguished even during *in vivo* activities. Therefore, these methods may be used to determine the pattern of motor unit recruitment during locomotion.

REFERENCES

Sadoyama, T. et al. (1988). *Eur. J. Appl. Physiol*. **57**, 767-771.
Smith, J.L. et al (1980). *J. Neurophysiol*. **43**, 612-620.
Solomonow, M. et al (1990). *J. Appl. Physiol*. **68**, 1177-1185.
Von Tscharner, V. (2000). *J. Electromyog. Kinesiol*. **10**, 433-445.

BIOMECHANICAL EFFECTS OF INTERMEDIATE SCREWS IN SHORT AND LONG ANTERIOR CERVICAL FUSION CONSTRUCTS

Raghu N. Natarajan, Nelson Oi, Luck Curylo, Gunnar B.J. Andersson and Howard An
Department of Orthopedic Surgery
Rush-Presbyterian-St.Luke's Medical Center, Chicago, Illinois. E-mail : rnataraj@rush.edu

INTRODUCTION

Anterior cervical plating has been accepted as an effective adjunctive procedure to anterior cervical discectomy and fusion (ACDF), particularly in multi-level cases to improve the fusion rate and to provide proper cervical alignment. ACDF with plating can be performed with screws at each end vertebral bodies or segmentally at each end and intermediate vertebral bodies. The purpose of this study is to compare motion and stresses between ACDF constructs with intermediate screws (IS) or without intermediate screws (NIS) in both two and three fused motion segments using a validated finite-element-model (FEM).

METHODS

A three dimensional non-linear finite element model of an intact C3-T1 cervical spine segment was developed using CT scans of 38 year old female normal subject. From this intact model, four different models were developed to include various constructs of anterior plating with interbody fusion models. Anterior plating was 18 mm wide and varied in length depending on the length of the fusion modeled. The screw was of 4.35 mm in diameter. The graft was placed in between appropriate vertebrae so that it occupied about 65% to 75% of the adjacent endplate areas. To simulate the laxity between the screw and the plate, elastic modulus of the plate was assumed as one thousands of the elastic modulus of CoCr. The screw was assumed to be rigidly connected to the bone. The rotation of all the vertebra in the sagittal plane, von Mises stress in the cancellous bone near the screw and the movement of screw with respect to the surrounding bone were extracted from the finite element model results.

RESULTS

As expected, in both 3 level and 4 level platings, intermediate screws (IS) provided lesser total motion as compared to terminal screws (NIS) under flexion/extension moment load (Table 1). Also, 4 level plating produced less total motion as compared to 3 level plating and was more prominent under extension than in flexion. Intermediate screws provided greater rigidity for both short and long plating constructs under flexion and extension.

The von Mises stress in the bone near the screws was higher in the long construct for both IS and NIS cases: 3.0 MPa under flexion and 4.5 MPa under extension. In the shorter construct, maximum stress occurred at the superior vertebra at 1.9 MPa both under flexion and extension. The long construct induced localized (posterior edge of the screw) tensile strain (anterior-posterior direction) in the superior vertebra under flexion moment in both IS and NIS cases while the tensile strain was distributed over 50% of the cross-section in the inferior vertebra under extension moment in NIS case. Flexion produced localized maximum tensile strain of 0.4% (same for both IS and NIS cases) while extension moment produced a distributed tensile strain of 0.3% in NIS and localized strain of 0.2% in IS case. In the shorter construct as well, a similar behavior was observed. Flexion produced a localized strain of 0.3% in both IS and NIS cases while extension induced a distributed strain of 0.2% in the inferior vertebra. Compressive stress in the graft was of higher magnitude in NIS for both short and long plating as compared to IS constructs. Flexion produced maximum graft stress of 4.0 MPa while the graft stress was much higher under extension (13.0 MPa).

CONCLUSION

The most rigid ACDF construct is predicted in the shorter construct with intermediate screws, and the intermediate screws were effective in reducing motion in flexion and extension. The intermediate screws also enhance the construct stability in the long construct greater in flexion than in extension. The results of tensile strain distributed over the cross-section (rather than localized) in the inferior vertebra with terminal screw construct show that chances of screw pullout are greatest in the long constructs. The presence of higher von Mises stresses of the bone around the screw at the inferior vertebrae of the long constructs further enhances the chance of screw pull-out. Graft collapse may be possible in both long and short constructs without intermediate screws, especially under extension moment load. These FEM predictions favor the use of intermediate screws in ACDF and plating cases but should be further validated with experimental studies.

	Total Motion		Motion at Fusion Level	
	3 Level Plating	4 Level Plating	3 Level Plating	4 Level Plating
NIS	9.2 (23.9)	6.9 (15.5)	1.6 (3.9)	3.8 (9.2)
IS	8.7 (23.0)	6.0 (13.7)	1.0 (3.2)	1.8 (7.3)

Table 1: Effect of intermediate screws in both short and long fusion constructs under flexion and extension (values given in bracket) moment loads. The values are given as a ratio : motion due to the external moment for a specific fusion construct / motion in an intact motion segment under same external moment.

DIFFERENT GAIT PATTERNS CAN BE CLASSIFIED BY USING MUSCULAR ACTIVITY PATTERNS

Li Li, Ph.D.

Department of Kinesiology, Louisiana State University, Baton Rouge, Louisiana, USA,LLI3@LSU.EDU

INTRODUCTION

Classification of human locomotion often based on the unique characteristics presented in the kinematic patterns of different modes of locomotion. For example, double or single stance phase are the differences between walking and running. Based on central pattern generator (CPG) theory, Golubisky et al. (1999) suggested four primary gait patterns for bipedal locomotion based on their control mechanisms. There are two different ways to control each leg and the two legs can be in synch or out-of-phase. The theory predicts two primary gaits when the legs are out-of-phase, i.e., walk and run. Theory also predicts two different primary gaits when the legs are in phase, two different hops, i.e., slow and fast hops. The control in each leg should be similar comparing slow hop and running and the control in each leg should be similar comparing fast hop and walking. The purpose of this study was to examine the abovementioned theory using muscular activity patterns during the four proposed gait patterns. Muscular activity patterns were represented by the linear envelops of surface electromyography (EMG).

METHODS

Eight college students recruited as participants of the study. Informed consent forms were signed after the experiment protocol discussed in detail. There were four testing conditions in the experiment: walking at 1.55 m/s and running at 3.1 m/s on a Kistler Gateway treadmill; as well as slow and fast hopping on an AMTI force platform. Vertical ground reaction forces were collected to identify gait cycles. One gait cycle was defined as the time between the initiations of two consecutive ground contacts. EMG data were collected from gluteus maximus (GM), rectus femoris (RF), biceps femoris (BF), vastus lateralis (VL), tibialis anterior (TA), gastrocnemius (GS), and soleus (SL) of both legs. EMG and ground reaction forces were collected in a synchronized fashion at 960 Hz.

Raw EMG data were processed (bias removal, full wave rectification, low pass digital filter – zero lag fourth order ButterWorth with cut off frequency of 6 Hz) to produce their linear envelops. The patterns of the EMG profiles were evaluated by using their temporal parameters (onset, offset, and duration). ANOVA with repeated measures were employed for the statistics analysis.

RESULTS AND DISCUSSION

The frequency of the fast hops was at approximately 5 Hz where the frequency of the slow hops was close to 1 Hz. The EMG patterns of walking and running were comparable with literature (Figure 1). Within each leg, greater amounts of cocontraction were observed in slow hoping, where less cocontraction observed with fast hopping. These observations were more pronounced when focused on the patterns of TA in comparison to GS and SL (see exemplar data in Figure 1). There are four different patterns of locomotion can be defined according to the different muscular activity patterns of lower extremity: 1). alternating muscle activity with limbs out-of-phase: walk; 2). cocontraction muscle activity with limbs out-of-phase: run; 3). alternating muscle activity with in-phase limbs: fast hop; and 4). cocontraction muscle activity with in–phase limb motion: slow hop. These observations agree with the predictions of Golubisky et al., (1999).

REFERENCES

Golubisky, M. et al (1999). *Nature*, **401**, 693-696

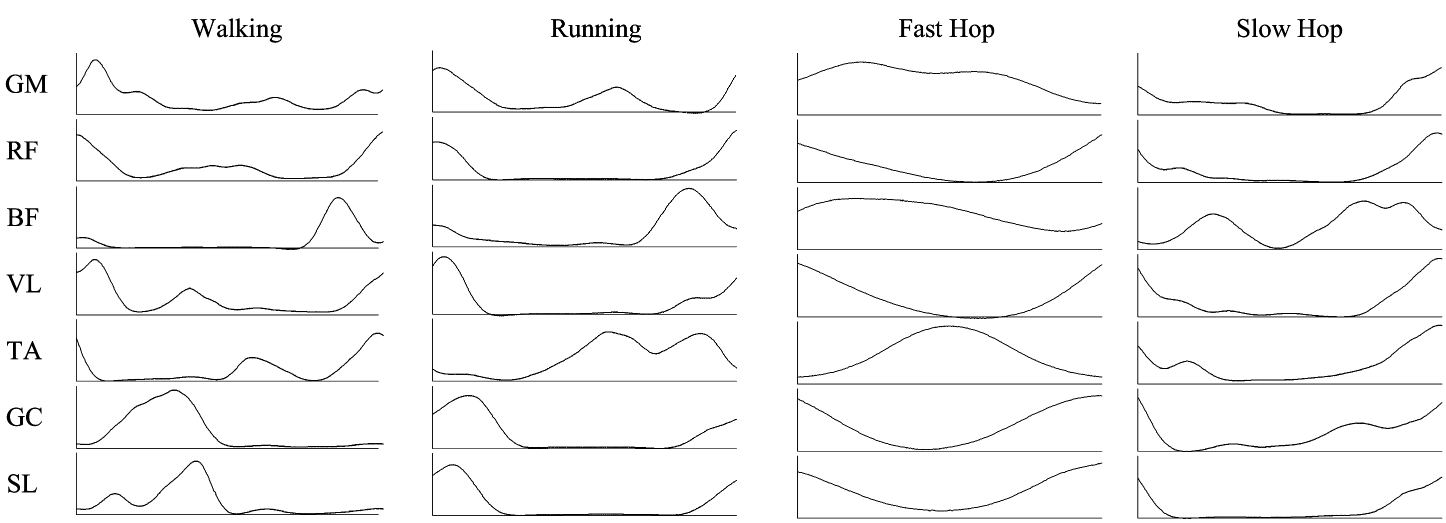

Figure 1. Exemplar data of EMG activity of seven different lower extremity muscles during four different types of locomotion: walking at 1.55 m/s, running at 3.1 m/s, fast and slow hopping. Linear envelops of EMG are graphed for one stride - between two consecutive foot-ground contacts of the same foot. See text for details.

BIOMECHANICAL COMPARISON OF THE LUQUE-GALVESTON AND COLORADO II METHODS FOR SACROPELVIC FIXATION

Andrew Mahar[1], Richard Oka[1], Sean Early[2], Peter Newton[1]

[1] Department of Orthopedics, Children's Hospital, San Diego, CA
[2] Department of Orthopedics, Children's Hospital, Los Angeles, CA

INTRODUCTION

The Luque rod system with Galveston pelvic fixation has become standard for treating childhood and adolescent neuromuscular scoliosis. The Galveston method provides reasonable lumbar-pelvic fixation with a relatively simple method of insertion. Clinical reviews of sagittal plane stability in neuromuscular patients with Galveston fixation performed at our institution have led to concerns regarding the technique's ability to maintain proper lumbar lordosis. Other instrumentation constructs may improve lumbosacral alignment while also preventing recurrence of pelvic obliquity. A biomechanical study evaluated lumbosacral stability of two sacropelvic fixation methods: the standard Luque-Galveston method and the Colorado II sacropelvic fixation method using the Chopin plate-screw block. Construct rigidity was also compared between two proximal fixation methods; one utilizing proximal pedicle screws and the other with proximal sublaminar wires.

METHODS

Eight fresh frozen human cadavers were dissected from L1 to the sacrum. The anterior and posterior longitudinal ligaments and the discs were left intact. The interspinous ligaments and ligmentum flavum were removed to allow passage of 18 gauge sub-laminar wires at L2, L3, L4, and L5. At L1, bilateral 6.5 mm poly-axial pedicle screws were placed. All segmental instrumentation was secured to two 5.5 mm rods contoured for appropriate lumbar lordosis. The proximal pedicle screws were tested in both locked and unlocked conditions. The unlocked condition simulated L1 sub-laminar fixation.

The end of the sacrum was potted in two-part epoxy resin and rigidly bolted to the load cell. The proximal spine was also potted in epoxy resin and attached, with screws, to either a cantilever apparatus for applying bending moments or an axially aligned fixture for torque testing. Intact specimens were tested in an MTS 858 servohydraulic machine, followed by sequential testing of the Galveston and Colorado systems. Proximal fixation was randomized across tests. Torsional testing involved axial rotation performed at 1° per second with torque limits of $\pm$ 2 Nm. Angular displacement and torque data were collected at 20 Hz over 20 cycles. The upper mount of the spine was changed to a cantilever bending apparatus for the flexion/extension bending test. The cantilever allowed application of bending moments of 5 Nm in flexion and extension. Flexion and extension tests were performed for 20 cycles while collecting displacement and force data at 20Hz. Load tests were randomized between spines and constructs. Stiffness was calculated from the linear portion of the load-displacement curve for each test. Data for construct stiffness were analyzed using a two-way analysis of variance ($p<0.05$) with the dependent variables being type of sacropelvic fixation and use of rigid L1 pedicle screws. Tukey *post-hoc* testing was done when significant differences were found to perform multiple comparisons as indicated.

RESULTS AND DISCUSSION

For flexion/extension and torsion testing, significant differences were found when comparing locked conditions to unlocked conditions (Tables 1 and 2). When examining only those constructs that were locked or unlocked (eg. C-U and G-U), there were no statistical differences.

Table 1: Flexion-extension stiffness

	C-U	C-L	G-U	G-L
Mean	0.933	1.384	0.878	1.453
C-U		**0.025**	0.983	**0.008**
C-L	**0.025**		**0.010**	0.967
G-U	0.983	**0.010**		**0.003**
G-L	**0.008**	0.967	**0.003**	
		interaction term =		0.563

Table 2: Torsion stiffness

	C-U	C-L	G-U	G-L
Mean	1.150	2.034	1.445	2.482
C-U		**0.001**	0.466	**0.000**
C-L	**0.001**		**0.030**	0.135
G-U	0.466	**0.030**		**0.000**
G-L	**0.000**	0.135	**0.000**	
		interaction term =		0.588

SUMMARY

The Colorado II and Luque-Galveston methods of sacropelvic fixation demonstrated similar construct stiffness under flexion-extension and torsional loads. Since locking superior instrumentation (pedicle screws) increased the stiffness of the system, rigid fixation at L1 may increase the chances of lumbopelvic fusion. Greater understanding of failure mode differences between systems from retrospective clinical review will influence subsequent biomechanical studies and alterations to the system design.

ACKNOWLEDGEMENTS

Financial support was provided Medtronic Sofamor Danek.

BIOMECHANICAL STABILITY BETWEEN TWO TYPES OF PERIACETABULAR OSTEOTOMIES FOR SURGICAL CORRECTION OF DEVELOPMENTAL DEFORMITIES OF THE HIP

Andrew Mahar[1], Wally Yassir[2], Afshin Aminian[3], Dennis Wenger[1], Peter Newton[1]

[1] Department of Orthopedics, Children's Hospital, San Diego, CA
[2] Department of Orthopedics, Tufts University Hospital, Boston, MA
[3] The Orthopedic Center, Cedar Knolls, NJ

INTRODUCTION

Periacetabular osteotomies are performed for improvement of femoral head coverage in a variety of clinical scenarios. These differ in surgical technique, amount of coverage attainable, and biomechanical strength. The modified triple inominate osteotomy (Tonnis) frees the acetabular fragment from its attachments to the pelvic floor ligaments allowing increased mobility of the osteotomized fragment. The Ganz procedure allows rotation of the acetabular fragment via bone resection and preserves a portion of the posterior ischial column. It is theorized that this allows minimal intraoperative fixation and early postoperative weight bearing. This osteotomy violates the triradiate cartilage, however, and cannot be performed in skeletally immature individuals, making the triple inominate osteotomy a necessary surgical alternative. The purpose of this study was to compare fragment stability following each type of osteotomy.

METHODS

Eight fresh-frozen male cadavers (mean age 39 years ± 4.3 years) were dissected to expose the regions from L1 to the mid-shaft of each femur keeping an intact hip joint capsule and sacrospinous and sacrotuberous ligaments. Each specimen underwent both types of osteotomies, with random assignment to either the right or left side. The acetabular fragments were fixed with AO 4.5 mm cortical screws in three different screw constructs (Figure 1). In addition, the Tonnis osteotomies were fixed with wire across the pubic osteotomy.

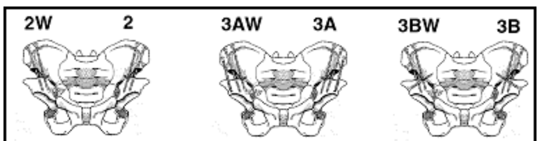

Each specimen was fixed with 2 and 3 screws constructs and then subjected to physiologic loading. The Tonnis osteotomies were also fixed with a pubic wire.

A triad of 4 mm retro-reflective markers was placed on each sacrum at the center sacral line to establish a pelvic coordinate system. Additional marker triads were placed on each acetabular osteotomy fragment and femur. The x, y, and z axes corresponded to the anterior-posterior, medial-lateral, and superior-inferior directions, respectively. The local coordinate system for each fragment was matched to the pelvic coordinate system, establishing a baseline orientation for each fragment relative to the pelvic coordinate system. Each specimen was placed into the testing rig with femurs pointing cephalad and iliac wings pointing caudad. The rig base held each specimen in 8 degrees of anterior pelvic tilt. Loads were applied directly to the superior iliac wings with an MTS 858 machine. Each specimen was cyclically loaded in axial compression from 0 to 450 Newtons for 10 cycles for each screw construct. The loading profile was that of full weight bearing for a 50kg 12-year-old boy, approximating partial weight bearing in an adult. Each specimen underwent loading with the 2, 2W, 3A, 3AW, 3B, and 3BW screw constructs. The order of fixations was randomized to prevent bias from increased osteotomy fragment motion in the later trials. Motion data were sampled at 20Hz for the duration of 10 trials for each screw construct for each cadaver. The maximum and minimum displacements and angular rotations were collected from the final four loading cycles and then averaged. Four 2 (Ganz vs. Tonnis) X 6 (2, 2W, 3A, 3AW, 3B, 3BW) ANOVA's using SPSS statistical analysis software were performed to compare mean displacements and angular rotations among osteotomy type and screw constructs. Post hoc analyses included one independent samples t-test to examine a trend within a particular screw construct and one ANOVA to examine a trend across screw constructs within the Tonnis osteotomy. The Bonferroni corrected significance level was set at $p = 0.008$.

RESULTS

No statistically significant difference in displacement could be found between the Ganz and Tonnis osteotomies ($p = 0.37$). Very little displacement was encountered during loading for all screw constructs, with a range of 0.6 to 1.3 mm on average. Post hoc analysis of the 2W trial (2 screws in Ganz osteotomy vs. 2 screws in Tonnis with pubic wire) approached statistical significance, with the Tonnis osteotomy showing less displacement in this construct ($p = 0.05$). For 3 screw constructs, the addition of a pubic wire adds little to the stability. There were no significant differences in angular motion for any comparison.

CONCLUSION

Small amounts of displacement and angular rotation were noted when comparing the two osteotomies across fixation methods. For partial weight bearing in adult and full weight bearing in pediatric populations, it appears that while 2 antegrade screws provide adequate clinical stability, greater fixation is achieved with 3 screws.

ACKNOWLEDGEMENTS

Thanks are given to Tracey Gaynor, MA, for her expert assistance with the statistical analysis. Funding was provided by a grant from the NOSFF.

MUSCLE SYNERGIES CONTROLLING GROUND REACTION FORCES DURING BALANCE

Lena H. Ting and Jane M. Macpherson

Neurological Sciences Institute, Oregon Health & Science University, Beaverton, OR, 97006 USA
Email: tingl@ohsu.edu

INTRODUCTION

A limited set of functional muscle groupings for controlling ground reaction forces components during balance have been proposed in the standing cat (Jacobs and Macpherson 1996). These groupings are based on correlation analysis of muscle activity and force magnitude and direction associated with automatic postural responses. The current study uses a muscle synergy extraction scheme to determine whether muscle activation patterns observed experimentally can indeed be characterized by additive combinations of a small set of muscle synergies.

METHODS

Cats standing quietly were subjected to translations of the support surface in 16 evenly spaced directions in the horizontal plane (5 cm at 15 cm/s). EMG activity in hindlimb muscles and 3D ground reaction forces at each limb were collected (see Macpherson 1988a, 1988b). Automatic postural responses are typically elicited 60 ms after perturbation onset. Mean EMG levels 60-135 ms after pertubation onset were averaged in each cat for use in the synergy analysis. Corresponding ground reaction forces were taken at 120-195 ms after perturbation onset.

An additive muscle synergy extraction scheme similar to one developed by Tresch, et al. (1999) was used to analyze the 16 different patterns of EMG activity observed across all perturbation directions. Each muscle synergy is a vector with elements constrained to be between 0 and 1. Each element represents the level of activity of one muscle in the synergy. For a given synergy set, a least-squares fit was used to determine the best reconstruction of the experimental data using the muscle synergies and non-negative weighting functions. A gradient search algorithm was used to find muscle synergies that provided the best fit to the experimental data. Random initial synergy values, and different numbers of synergies were used in several searches.

RESULTS AND DISCUSSION

Three muscle synergies were necessary to consistently reproduce >95% of the EMG activity. Synergies were highly repeatable regardless of initial conditions. The first two synergies could be characterized as extensor or flexor muscle groups (Fig. 1A,B). The third (Fig. 1C) was similar to a primarily biarticular group responsible for horizontal plane forces proposed by Jacobs and Macpherson (1996). However, note that muscles are not limited to a single synergy, and muscles do not group simply by anatomical classification.

The synergy weighting functions indicate the level at which each synergy is activated in response to a particular perturbation direction. They tend to vary with the stabilizing forces produced by the limb (Fig. 1).

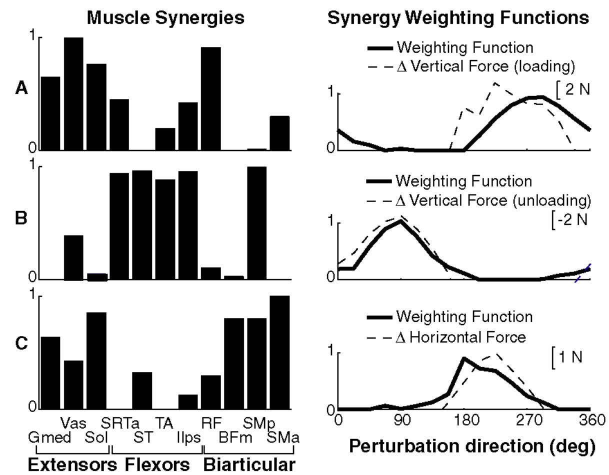

Figure 1: Muscle synergies and weighting functions that reconstruct 98% of experimental data. Synergy A varies with increased loading of the leg, B with unloading, and C with increased horizontal ground reaction force.

SUMMARY

While only EMG information is used in the muscle synergy extraction, the synergy weighting functions that indicate when the synergy is activated bear remarkable resemblance to the Cartesian components of the ground reaction forces produced by the leg. This demonstrates that complex muscle activation patterns observed during automatic postural responses can be reproduced by additive linear combinations of just three muscle synergies. The nervous system may use these synergies to simplify the control of force production in the leg.

REFERENCES

Jacobs, R. and Macpherson, J.M. (1996) *J. Neurophysiol.* **76**: 2402-11
Macpherson, J.M. (1988a) *J. Neurophysiol.* **60**: 204-17
Macpherson, J.M. (1988b) *J. Neurophysiol.* **60**: 218-31
Tresh, M.C, Saltiel, P. and Bizzi, E. (1999) *Nat Neuroscience* **2**:162-7.

ACKNOWLEDGEMENTS

NIH NS29025. LHT is an O'Donnell Foundation Fellow of the Life Sciences Research Foundation.

TEMPLATE-BASED FINITE ELEMENT MESH GENERATION FROM MEDICAL IMAGES

Leila Baghdadi[1,2], Hanif M. Ladak[1,2,3], David A. Steinman[1,2,*]

[1]Imaging Research Laboratories, The John P. Robarts Research Institute, London, Canada, www.irus.rri.ca
[2]Department of Medical Biophysics, University of Western Ontario, London, Canada
[3]Department of Electrical and Computer Engineering, University of Western Ontario, London, Canada
[*]Corresponding author: steinman@irus.rri.ca, www.irus.rri.ca/~steinman

INTRODUCTION

Fluid mechanical factors have been linked to both the initiation and progression of atherosclerotic plaques; however, the exact mechanisms are not clearly understood. Currently, our laboratory is undertaking a study in which we are attempting to correlate plaque progression at the carotid bifurcation with computed fluid mechanical indices. Using black blood magnetic resonance (MR) imaging, arterial geometry and plaque distributions are measured annually in human subjects over a number of years. From each annual MR scan, finite-element meshes of the lumen geometry are generated and patterns of fluid mechanical indices are derived from computational fluid dynamic (CFD) simulations. Creating such finite element meshes requires substantial user effort, and the resulting models can exhibit variability caused by subjective modeling decisions made by the operator. In this abstract we propose a technique to minimize this by using the manually generated "baseline" finite element meshes as a template to be automatically deformed to match "follow-up" MR image data.

METHODS

The initial tetrahedral finite element mesh (e.g., Figure 1a) is first generated from the "baseline" serial MR images using the procedure previously described by Steinman et al. (2002). Briefly, a 2-D discrete dynamic contour (DDC) is used to semi-automatically extract the lumen boundary from each serial MR image. These lumen contours are then used as masks to create a binary 3-D image dataset, within which a 3-D DDC (Ladak et al., 2000) is inflated to provide the 3-D lumen boundary for subsequent octree-based generation of the tetrahedral finite element volume mesh. The deformation procedure begins by manually orienting the initial mesh within the "follow-up" MR image data. An image-based force field is calculated from the 3-D image (Ladak et al., 2000), and then used to drive the vertices of the "baseline" FE mesh to the "follow-up" lumen boundary. To keep the model smooth in the presence of noise and to maintain the quality of the finite elements for subsequent CFD simulation, at each iteration Laplacian smoothing is applied to the deformed surface triangulation and then, with the surface triangles fixed, to the volume tetrahedral elements.

RESULTS AND DISCUSSION

To test this algorithm a "follow up" dataset was created by manually deforming the lumen boundaries of the "baseline" binary 3-D image data to simulate the growth of small plaques (maximum height of 3 and 6 pixels normal to the original wall) at the internal carotid artery just distal to the bifurcation. As illustrated in Figure 1b, automated deformation and smoothing of the mesh was able to capture even a 6-pixel change in the lumen geometry. Element quality, as measured via the radii-ratio metric (Pebay et al., 2001), was found to be comparable to that of the "baseline" mesh.

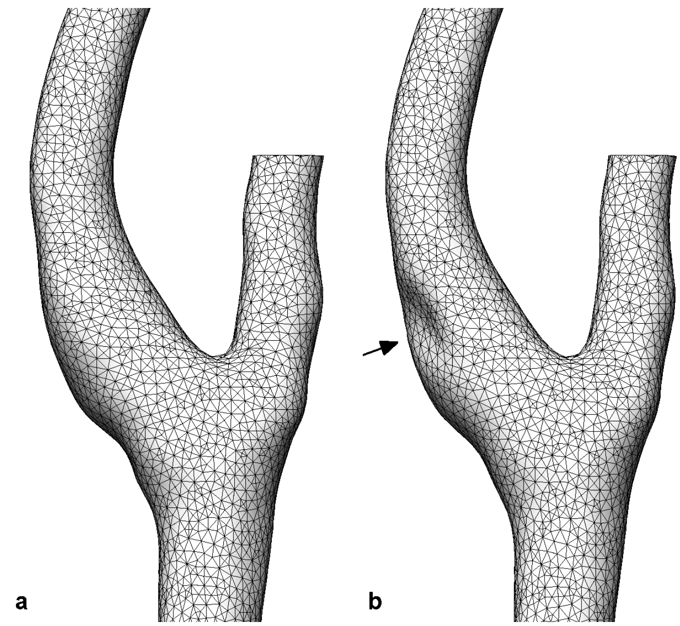

Figure 1: (a) "Baseline" finite element surface mesh; (b) Deformed and smoothed mesh after introduction of the 6 pixel high mild plaque (indicated by arrow).

SUMMARY

Our tests demonstrate that the proposed method can deform the "baseline" finite element mesh to match the corresponding "follow-up" image while maintaining mesh quality. Future work will focus on optimizing the algorithm, via selection of appropriate Gaussian kernel and iteration parameters, to allow for the capture of larger and more complex deformations.

REFERENCES

Ladak H. M. et al. (2000). *J. Biomech. Eng.*, **122**, 96-99.
Pebay, P. P. and Baker, T. J. (2001). *Proc. 10th International Meshing Roundtable*, 327-340.
Steinman D. A. et al. (2002). *Magn. Reson. Med.*, **47**, 149-159.

MODELING OF BIOMECHANICS OF TACTILE SENSATION ON FINGERTIPS

John Z. Wu [1], Ren G. Dong, Aaron W. Schopper, and W. Paul Smutz
National Institute for Occupational Safety and Health, Morgantown, WV, USA. [1] E-mail: jwu@cdc.gov

INTRODUCTION

Tactile perception threshold measurement has been widely used to diagnose the severity of peripheral neuropathy, for example, hand-arm vibration syndrome. The study of biomechanics of the fingertips is vital to enhance an understanding of mechanism of tactile sensation and sensory thresholds. The reported fingertip models (e.g., Phillip and Johnson, 1981; Srinivasan and Dandekar, 1996) do not incorporate the nonlinear and time-dependent effects associated with the anatomical substructures and tissue material properties. The purpose of the present research was to develop a finite element model to simulate the mechanics of tactile sensation of a fingertip.

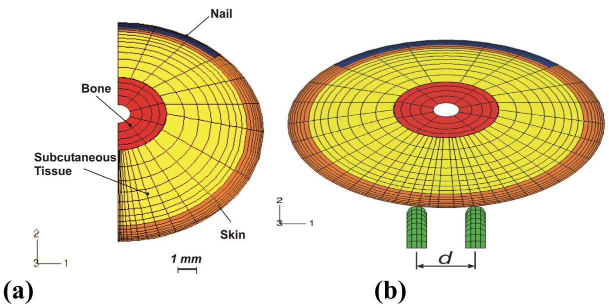

Figure 1: Finite Element Model. **(a):** Multi-layered fingertip model. **(b):** Two-point discrimination (2PT) test

METHODS

The biomechanics of tactile sensation of a fingertip were analyzed using a multi-layered two-dimensional finite element model, as shown in Fig.1a. The fingertip was assumed to be composed of a skin layer, subcutaneous tissue, bone, and nail. The fingertip dimensions were assumed to be representative of index finger of a male subject. The skin tissue, including epidermis and dermis, was assumed to be hyperelastic and linearly viscoelastic. The subcutaneous tissue was assumed to be a biphasic material composed of a fluid phase and a hyperelastic solid phase. The nail and the bone were considered as linearly elastic. Numerical tests were performed to study the mechanics of tactile sensation of the fingertip in two-point (2PT) discrimination tests (Fig.1b). The fingertip was fixed on the center of nail surface, while two indentors (each with a circular contact surface and thickness of 1 mm) were used to deform the skin surface of the fingertip by 1 mm within a ramping period of 1 s. Four numerical tests with different spacing between the indentors (d = 1.5, 2.0, 3.0, and 4.0 mm) were performed. The analyses were performed to compute the displacement, stress, and strain fields within the soft tissue at the state of maximum depression. The mechanical states (stress/strain) of the tissue at a depth of 0.75 mm from the undeformed skin surface, where the Merkel cell receptors are located, were analyzed in the study.

RESULTS AND DISCUSSION

The simulation results reveal that differences in horizontal and vertical strains (E11 and E22, respectively) and strain energy density (SED) developed in the skin at the contact points and at the geometric center of the fingertip vary only slightly with a decrease in the indentor spacing from 4.0 to 3.0 mm (Fig. 2). These differences, however, decrease considerably with a further decrease in the indentor spacing from 3.0 to 2.0 mm. The corresponding differences in the vertical displacement (U2) and shear strain (E12), however, decreased almost linearly with a decrease in the indentor spacing from 4.0 to 1.5 mm.

Figure 2: Normalized variations of horizontal (*E11*), vertical (*E22*) and shear strains (*E12*), vertical displacement (*U2*), and strain energy density (*SED*) as a function of 2PT spacing. The

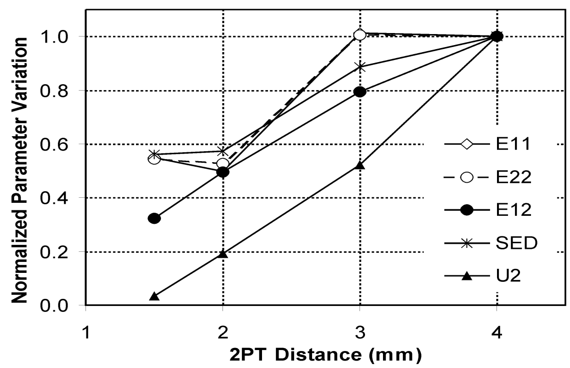

normalized variations were evaluated by [f (contact point of indentor)-f (geometry center)]/ f (contact point of indentor).

SUMMARY

The present analysis suggest that, assuming mechanoreceptors in the dermis sense the stimuli associated with normal strains (E11 and E22) and train energy density (SED) rather than those associated with shear train (E12), the threshold of 2PT discrimination test for the fingertip may lie between 2.0 and 3.0 mm. This analysis is consistent with the experimental observations by Perez et al. (2000) who reported an average 2PT discrimination distance of 2.1 mm in tactile sensation threshold tests of the index finger.

REFERENCES

Perez, C., Holzmann, C. and Jaeschke, H. (2000). *Med Biol Eng Comput,* 38(1), 74-79.
Phillips, J. and Johnson, K. (1981). *J Neurophysiol,* 46(6), 1204-1225.
Srinivasan, M. and Dandekar, K. (1996). *J Biomech Eng,* 118(1), 48-55.

GLIDING RESISTANCE VERSUS WORK OF FLEXION—TWO METHODS TO ASSESS FLEXOR TENDON REPAIR

Tatsuro Tanaka, Peter C. Amadio, Chunfeng Zhao, Mark E. Zobitz, Kai-Nan An
Biomechanics Laboratory, Department of Orthopedics, Mayo Clinic/Mayo Foundation
200 First Street SW, Rochester, MN 55905, e-mail: pamadio@mayo.edu

INTRODUCTION

Two methods for measuring the ability of the flexor tendon to glide following repair are commonly cited in the literature: gliding resistance [1] and work of flexion (WOF) [2]. While the gliding resistance measures the friction force at the tendon-pulley interface, the work of flexion characterizes whole finger function during flexion. The purpose of this study was to compare work of flexion and gliding resistance, in assessing the mechanical outcome of flexor tendon repair.

METHODS

48 mongrel dogs were used. One randomly selected second or fifth flexor digitorum profundus (FDP) tendon was exposed in the paw between the proximal and distal pulleys. A complete laceration was created 5 mm from the distal edge of the proximal pulley on the FDP tendon with the digit in full extension. The tendon was repaired with a modified Kessler technique using 4-0 Supramid loop suture and an epitenon running suture using 6-0 Nylon. Postoperatively, the operated paw was immobilized in a cast. Dogs were sacrificed of 1, 3, 5 or 7 days after surgery.

WOF Measurement: The testing device was composed of a testing frame, an actuator, linear potentiometer, and two load transducers. The distal end of the FDP tendon was exposed and attached to a small load transducer (F_d) which was fixed to the distal phalanx. A K-wire was inserted through the metacarpophalangeal joint with this joint extended to support the specimen in the testing frame. A 0.49 N weight was attached to the proximal end of the extensor tendon. The proximal end of the FDP tendon was connected to a second transducer (F_p), an actuator and a linear potentiometer. The actuator pulled the FDP tendon proximally (2mm/s) to flex the finger against the weight until the full flexion position was reached. Proximal (F_p) and distal (F_d) forces were recorded and plotted against the tendon excursion. Total work of flexion (TWOF) is the area under the F_p curve. The area between the F_p and F_d curves represents the energy expended due to the tendon pulley interaction and is termed internal work of flexion (IWOF).

Gliding Resistance: The same specimens were used to assess the gliding characteristics of repaired tendon after measuring TWOF and IWOF. The proximal pulley, the parietal membrane at the proximal pulley, the visceral membrane of the FDP tendon, the FDS tendon and its insertion were preserved. The vincula of the FDP tendon were cut. A K-wire was inserted through the proximal phalanx to support the specimen in the testing jig. Load transducer, F_2, was attached between the mechanical actuator and proximal FDP tendon. The distal transducer, F_1, was connected to a 4.9N weight. The tendon was pulled proximally by the actuator against the weight at a rate of 2mm/s. The differences between F_1 and F_2 were averaged to represent the gliding resistance (GR).

RESULTS

Average values of work and gliding resistance at each time point are shown in Figure 1. GR was not different significantly at any time point. On the other hand TWOF and IWOF decreased within 5 days after surgery, but there were significant increases at 7 days. Relationships between TWOF and IWOF versus GR for all specimens are shown in Figure 2 and for each sacrifice day in Table 1. Overall, IWOF showed a strong correlation to gliding resistance (r=0.76), while there was little correlation between TWOF and gliding resistance.

Figure 1: Work and Resistance

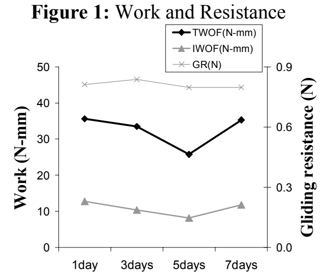

Figure 2: Correlations Between WOF and Gliding Resistance

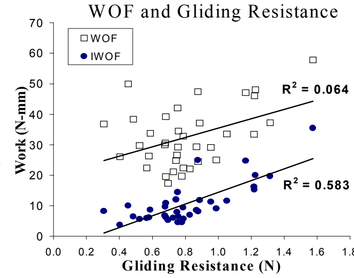

Table 1: Correlation coefficients

Sacrifice Day	GR vs. TWOF	GR vs. IWOF
1 day	r=0.53	r=0.80
3 days	r=0.52	r=0.86
5 days	r=0.45	r=0.92
7 days	r=-0.03	r=0.65

DISCUSSION

Since measurement of TWOF includes external resistance such as joint stiffness, soft tissue resistance, mass of digits, resistance of antagonist muscles and internal resistance, a weak correlation with gliding resistance is not surprising. Meanwhile, IWOF includes variables such as bulk friction, GR, and incremental resistance resulting from adhesions, a strong correlation between gliding resistance and IWOF suggests that the measurement of gliding resistance could be used easily for the assessment of IWOF. Namely, if the correlation between GR and IWOF is strong, it suggests that little adhesion formation may occur. The reduced correlation between GR and IWOF at 7 days post-operative suggests that variations perhaps due to minor adhesion formation may occur at 7 days.

REFERENCES

1. Uchiyama S, et al (1995). JOR **13**: 83-89.
2. Aoki M, et al. J Hand Surg **20B**: 310-313.

ACKNOWLEDGEMENTS

This study was supported by grants from NIAMS(AR44391).

MAXIMUM NET TANGENTIAL FORCE AND MUSCULAR ACTIVITY DURING INDUSTRIAL HANDWHEEL ACTUATION

Tyler Amell[1], Shrawan Kumar[1], Yogesh Narayan[1], and Ambikaipakan Senthilselvan[2]

[1]Ergonomics Research Laboratory, University of Alberta, Edmonton, Alberta, Canada, T6G 2G4
[2]Department of Public Health Sciences, University of Alberta, Edmonton, Alberta, Canada

INTRODUCTION

Large handwheels are used in numerous industries as control devices employed to regulate process and production. Industries such as the petroleum, chemical, waste treatment and power generation commonly use these devices. The task of industrial handwheel actuation requires the exertion of large tangential forces about the control device. These forces are typically generated manually, and have been associated with increased risk of musculoskeletal injury in operators (Amell and Kumar, 2001). The purpose of this study was to determine the maximum two-handed net tangential handwheel force and electromyographic activity of the primary muscles contributing to the task during actuation at various heights, pitch angles, contours of foot support and distances of foot support.

METHODS

Participants were required to exert upon a custom-built handwheel fixed to a force measuring device. All exertions were counter-clockwise in direction. The maximal static two-handed net tangential forces as well as electromyographic (EMG) activity of 20 healthy male participants were recorded with respect to 24 experimental conditions. Four independent variables were examined: 2 handwheel pitch angles (90^{o} and 0^{o} to the horizontal); 2 contours of foot support (flat and convex); 2 distances of foot support (19 cm and 58 cm); and 3 handwheel heights (35, 93 and 168 cm from the grade). Flexor carpis radialis, biceps brachii, anterior deltoid and erector spinae muscle activity at the L4 vertebral level was recorded bilaterally using surface electrodes.

RESULTS AND DISCUSSION

Figure 1 illustrates the mean maximum tangential force for each experimental condition while the mean maximum EMG for each muscle sorted by distance of foot support is depicted in figure 2. Mean maximum tangential forces ranged from 585 N to 760 N. Less force was generated at the 19 cm distance of foot support compared to the 58 cm distance ($p = 0.007$). No statistically significant ($p > 0.05$) main effects were obtained for the pitch angle, contour of foot support or the handwheel height. EMG analysis revealed the flexor carpis radialis and the erector spine to be very active in this task. The mean maximum normalized activity in these muscles was 330% and 230% respectively. The results reveal that handwheel design has an effect upon both maximal tangential force and muscular activity.

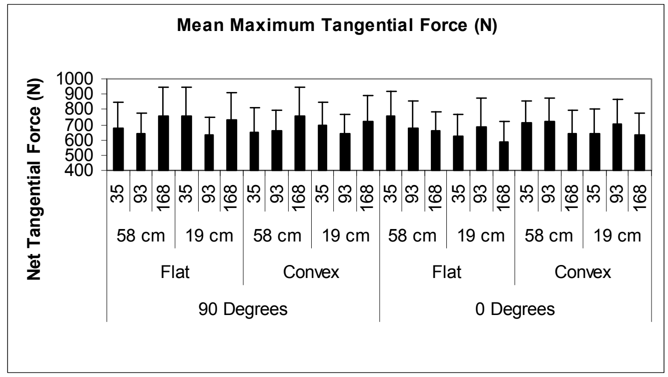

Figure 1: Mean maximum net tangential force sorted by experimental condition for 20 healthy male participants.

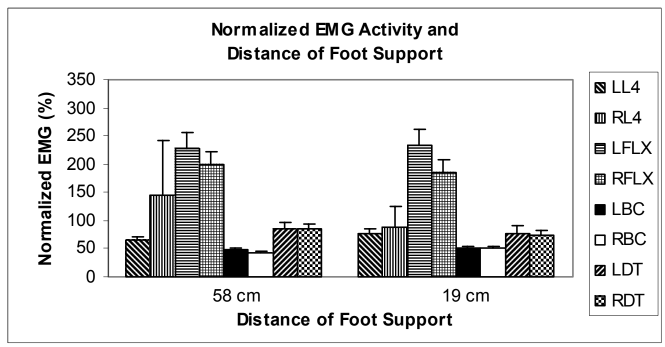

Figure 2: Normalized EMG activity for each muscle studied sorted by distance of foot support for 20 healthy male participants.

SUMMARY

The design of these control devices must consider the strength capabilities as well as the anthropometrics of the operator in order to optimize safety in industrial handwheel operation.

REFERENCES

Amell, T.K., Kumar, S. (2001). Industrial handwheel actuation and the human operator. A review. *International Journal of Industrial Ergonomics*, **28,** 291-302.

ACKNOWLEDGEMENTS

The authors kindly acknowledge the support of the Medical Research Council of Canada (MRC), the Alberta Heritage Foundation for Medical Research (AHFMR), and Syncrude Canada Ltd.

BICYCLE SEAT DESIGNS AND THEIR EFFECT ON PELVIC ANGLE, TRUNK ANGLE, AND COMFORT IN FEMALES DURING CYCLING

Eadric Bressel[1], Cherianne Mecham[1], and Megan E. Bressel[2]
[1]Biomechanics Laboratory, Utah State University, Logan, UT, USA, ebressel@coe.usu.edu
[2]Mountain West Physical Therapy, Logan, UT, USA

INTRODUCTION

As a cyclist leans forward onto the handlebars of a bicycle, undesirable pressure is often applied to the anterior perineum. The pressure applied to the perineum may prevent the pelvis and trunk from moving into an anterior tilt position, which increases the load placed on the seat and lumbar region of the spine (de Vey Mestdagh, 1998; Salai et al., 1999). Newly designed bicycle seats constructed with either no or minimal filling at the anterior-medial region may improve perineal comfort and allow the pelvis and trunk to move into a greater anterior tilt position, however, these latter theories have not been tested. The purpose of this study was to examine if bicycle seats with anterior-medial cutouts influence pelvic angle, trunk angle, and comfort in females during cycling.

METHODS

Ten experienced (M_{age} = 27.14 ± 5.15 yrs) and 10 novice (M_{age} = 21.00 ± 1.41 yrs) female cyclists volunteered as subjects. Subjects pedaled a stationary bicycle with their hands on the tops and drops of the handlebars under three different saddle conditions illustrated in Figure 1.

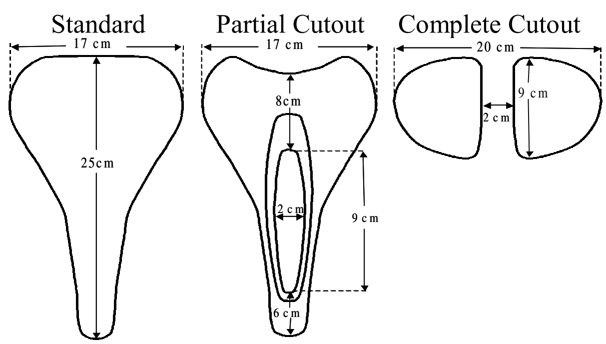

Figure 1: A top view of the three saddle designs and their physical dimensions.

Subjects pedaled for 7 min at each saddle condition while pelvic angle was measured using an inclinometer technique based on the procedures of Walker et al. (1985). Trunk angle was quantified from two-dimensional coordinate data taken from the digitization of reflective markers using a motion analysis system. Kinematic data were calculated with respect to an absolute horizontal reference such that greater angles indicated an anterior tilt of the pelvis and trunk. Comfort level was assessed by having participants subjectively rank the saddles from most to least comfortable. Mean differences were assessed using a repeated-measures analysis of variance with experience level as a between subjects factor. Probability of Type I error was set at .05.

RESULTS AND DISCUSSION

Mean pelvic angles for the partial and complete cutout saddles were 16% and 25% greater respectively, than values for the standard saddle condition in the top handlebar position (Table 1). In the drop handlebar position, pelvic angle data exhibited a similar trend.

Table 1: Mean (± SD) angle data for all subjects on tops

Variable	Pelvic Angle (deg)	Trunk Angle (deg)
Standard	14.18 (7.23)	140.25 (5.30)
Partial Cutout	16.48 (6.44)[a]	139.74 (3.68)
Complete Cutout	17.68 (6.93)[a]	141.62 (3.64)

[a] $p < .05$. Significantly greater than standard saddle condition

Trunk angle data were not different between saddle conditions (Table 1). Fifty percent of the subjects ranked the partial cutout saddle as the most comfortable and 25% ranked the standard saddle as the most comfortable. Angle and comfort data were not different between experienced and novice subjects ($p > .05$).

Our findings indicating a greater anterior pelvic tilt may be appealing because of the potential for reduced stress on the lumbar spine during cycling (Salai et al., 1999), however, a complete anterior cutout design may not be practical during real cycling conditions that rely on the anterior region of the saddle for stability and steering (de Vey Mestdagh, 1998). The partial cutout design may be a good compromise as it maintains stabilizing features of the standard saddle, increases anterior pelvic tilt, and may improve comfort. Comfort and pelvic angle data of this study supports this latter contention.

SUMMARY

These data indicate that complete and partial cutout saddle designs may enhance an anterior pelvic tilt under select cycling conditions and that partial cutout designs may be more comfortable than a standard or complete cutout saddle.

REFERENCES

de Vey Mestdagh, K. (1998). *Appl Ergon*, **29**, 325-334.
Salai, M. et al. (1999). *Br J Sports Med*, **33**, 398-400.
Walker, M.L. et al. (1985). *Phys Ther*, **67**, 512-516.

ACKNOWLEDGMENTS

This study was supported by grants from the Women and Gender Research Institution and the College of Education Pilot Data Grant at Utah State University.

THE CORRECTION OF INERTIAL GROUND REACTION FORCES DUE TO A MOVING BASE OF SUPPORT

Richard Preuss and Joyce Fung

Jewish Rehabilitation Hospital Research Centre, McGill University, Montreal, Québec, Canada, (joyce.fung@mcgill.ca)

INTRODUCTION

The study of postural reactions triggered by surface perturbations often involves the analysis of ground reaction forces (GRF) from a force plate (FP) mounted on a moveable surface. One limitation, however, is that the recorded signal will contain force and moment-of-force components resulting from the inertia of the FP (Force Plate Inertial Components - FPIC). The purpose of this work was to validate a method for calculating the FPIC from the kinematics of the moving platform, so that the FPIC can be subtracted from the recorded signal.

METHODS

Three reflective markers were firmly mounted on the surface of a six-degree-of-freedom motion base (MB) (Fung and Johnstone, 1998). The empty MB (no subject) was subjected to eight different perturbations in the pitch (x) and roll (y) planes, at 45º angles to one another (about the yaw (z) axis). The perturbation stimulus consisted of a ramp signal with a duration of 400ms and a magnitude of 10º. A 6-camera Vicon 512 motion analysis system was used to record the kinematic data (sampling frequency 120Hz) for the MB, while forces were collected from an AMTI (OR6-7) force plate (sampling frequency 1080Hz, digitally re-sampled at 120Hz) firmly mounted on an aluminum plate within the MB. A 2s long trial was collected for each MB perturbation.

The frequency content of the force plate data from the eight perturbation trials was analyzed using a power spectral density function (PSDF), in order to determine an appropriate cutoff frequency for filtering. The filtered signal (filtered using a 4th-order, zero-phase-lag, digital Butterworth filter, cutoff frequency 10Hz) was taken to represent the actual FPIC for each trial.

The kinematic data from the MB perturbations was analyzed using an Euler rotation-matrix algorithm in order to determine the orientation, velocity and acceleration of the MB, as well as the orientation of the gravity vector relative to the MB, for each trial. Using the inertial properties of the force plate, an estimate of the FPIC was calculated from the kinematic data. The calculated FPIC were low-pass filtered (as above) with a cutoff frequency of 6Hz. This filtered, calculated FPIC was then subtracted from the raw force plate data, and the resulting signal was low pass filtered with a cutoff frequency of 10Hz. This result was taken to represent the residual FPIC.

The residual and actual FPIC were then integrated over time as a means to compare the magnitude of the two signals.

RESULTS AND DISCUSSION

The integrated residual FPIC was found to be smaller than the integrated actual FPIC in all components of force and moment (that contained an actual signal), for all MB perturbations. The mean decrease in the integrated signal was 85.5% for Fx, 86.0% for Fy, 45.1% for Fz, 76.9% for Mx, and 74.0% for My (no yaw (Mz) component was present). An example of the actual and residual FPIC is given in figure 1.

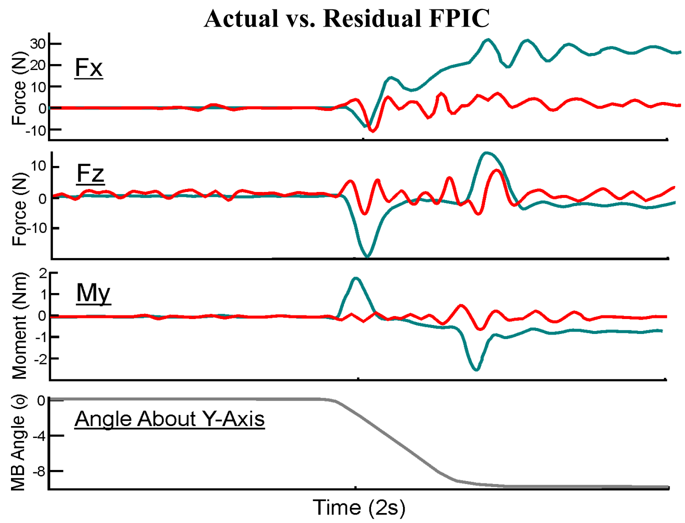

Figure 1: Actual (blue line) and residual (red line) FPIC for a 10º rotation, ramp duration 400ms, about the negative y-axis

Based on these results, when data are collected from a force plate mounted on a moving platform, it is possible to greatly reduce the component of a force plate signal that results from the inertial characteristics of the force plate through analysis of the platform kinematics. The residual FPIC resulting from this technique is due mainly to high frequency noise in the kinematic and force plate data, as well as some noise introduced by the subtraction process itself.

SUMMARY

When a force plate is mounted on a moving platform, a component of the recorded data will result from the inertial characteristics of the force plate (FPIC). An estimate of the FPIC can be calculated from the kinematics of the platform and the inertial characteristics of the force plate, and subtracted from the recorded force plate data, in order to correct the GRF of the subject balancing on the surface.

REFERENCES

Fung,J., Johnstone,E..(1998) *Soc. Neurosci. Abstr.* **24**, 1158

RADIOGRAPHIC ANALYSIS OF THE WRIST WHILE GRIPPING A KAYAK PADDLE

Brad J. Larson[1] and Eadric Bressel[2]
[1]Alpine Orthopaedic Specialists, Logan, UT, USA
[2]Biomechanics Laboratory, Utah State University, Logan, UT, USA, ebressel@coe.usu.edu

INTRODUCTION

It has recently been reported that 61% of the injuries occurring during whitewater kayaking influence the upper extremity and that 21% of the injuries were tendonitis related (Fiore & Houston, 2001). Werner et al. (1997) have argued that the shape of a hand tool, such as a kayak paddle, is directly related to the stress on the upper extremity. For example, repeated physical exertion with the wrist deviated from neutral may cause cumulative trauma that leads to tendonitis (Kroemer, 1992). While the kayaks themselves have undergone many new innovations to improve their performance and comfort, the general shape of the kayak paddle shaft has remained relatively unchanged. It was hypothesized that the wrist exhibits a high degree of radial deviation during kayaking. As this hypothesis has not been previously tested it was the purpose of this study to analyze wrist radial deviation while gripping a kayak paddle.

METHODS

Twenty novice kayakers who were physically active males between the ages of 18-24 years volunteered for this investigation. Wrist deviations were quantified from radiographic images taken in the frontal plane as subjects held a straight shaft kayak paddle (3 cm diameter) according to the illustration shown in Figure 1.

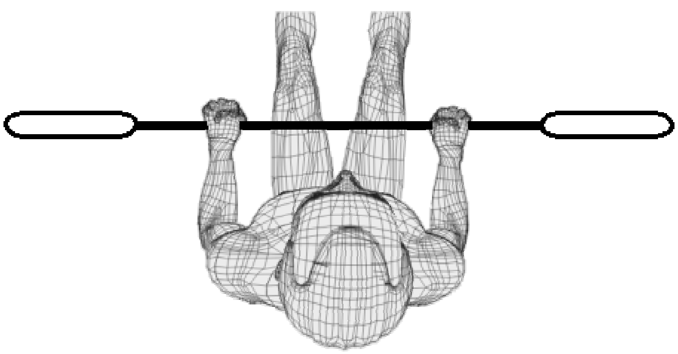

Figure 1: An illustration of the upper extremity position held by subjects while radiographic images were taken of the wrist.

Hands were in pronation, elbows were flexed to 90 deg, and the shoulders were in the anatomical position. This upper extremity position was chosen to reflect a paddle position associated with peak propulsive forces of the pulling arm (Mann & Kearney, 1980). The angle formed between the longitudinal axis of the radius and third metacarpal of the left wrist represented wrist deviation in this study (Figure 2). Descriptive statistics were then applied to angular data.

RESULTS AND DISCUSSION

The results indicated that subjects exhibited a mean radial deviation of 12.45 (± 1.85) deg when gripping a kayak paddle according to Figure 1. Representative data for one subject is shown in Figure 2.

Figure 2: A radiographic image of the left wrist. Lines represent the longitudinal axes used to calculate wrist deviation in the frontal view.

This study was limited to a two-dimensional static analysis under a controlled laboratory condition yet, provides important new information on the potential radial wrist deviations that may occur during kayaking. The mean deviation reported in this study (i.e., 12.45°) approximates population norms for peak ranges reported by Kroemer et al. (1997; 14-22°). Since extreme wrist deviations compromise muscle strength and increase the risk for cumulative trauma (Kroemer, 1992), an ergonomically correct kayak paddle shaft that encourages a neutral wrist position may be warranted.

SUMMARY

The results of this study indicate that kayakers may exhibit approximately 12.45 deg of radial deviation during paddling. Excessive radial deviation may contribute to tendonitis reported in kayakers.

REFERENCES

Fiore, D.C., Houston, J.D. (2001). *Br J Sports Med*, **35**, 235-241.
Kroemer, K.H.E. (1992). *Am Ind Hyg Assoc J***, 53**, 596-604.
Kroemer, K.H.E. et al. (1997). *Engineering Physiology: Bases of Human Factors/Ergonomics*. Van Nostrand Reinhold.
Mann, V.R., Kearney, J. T. (1980). Med Sci Sports Exerc, **12**, 183-188
Werner, R.T.J. et al. (1997). *Clin Biomech*, **12**, 44-51.

STRENGTH AND EMG OF CERVICAL MUSCLES IN DIRECTIONAL MAXIMAL VOLUNTARY CONTRACTIONS

Shrawan Kumar, Yogesh Narayan and Tyler Amell

Ergonomics Research Laboratory, University of Alberta
Edmonton, AB T6G 2G4 Canada

INTRODUCTION

Cervical pain and dysfunction due to whiplash-associated disorders has become a significant health and economic burden to our society (Spitzer, et al. 1995). One of the primary reasons disputes relates to loss of function of affected patients. However, there are no data published in the literature to which the functional capacities of those affected can be compared. Therefore, a study was designed to measure the force generated by superficial cervical muscles (sternocleidomastoids, upper trapezius and splenius capitis) and their pattern of EMG in isometric contraction in sagittal, coronal and intermediate planes.

METHODS

Forty normal young adults (21 male and 19 female) were tested on a specially designed and fabricated cervical strength tester (CST). A load cell (I-250) was inserted below the pivot point at right angles to the arm which would be rotated when pushed by the head due to cervical muscle contraction. The load cell signals were input into the force monitor. Silver, silver chloride surface electrodes of 1 cm diameter were placed with an inter-electrode distance of 2 cm on upper trapezius, sternocleidomastoids and splenius capitis bilaterally. The electrodes were connected to a fully isolated low noise and low non-linearity amplifier system by short cables and tip plugs. The amplification system was run off an internal charged battery and had a CMRR of 130 dB. The strength was measured in N and EMG was measured in µV. The subjects exerted for a 5 s period in a maximal contraction against the upholstered headpiece in 8 direction. After each test the subjects were allowed a minimum of 2-minute rest before starting the next randomized condition. Smoothed EMG tracks were normalized. Torque and EMG were correlated and regression analyses were done to determine predictability of torque from EMG.

RESULTS AND DISCUSSION

The force and EMG (Figure 1) were significantly different between the directions of effort ($p<0.01$). There was a modest correlation between EMG and force ($r = 0.15$ to 0.76; $p<0.01$). EMG output was approximately 66% higher in flexion than in extension while force output was 30% less in flexion than extension. All regressions were significant

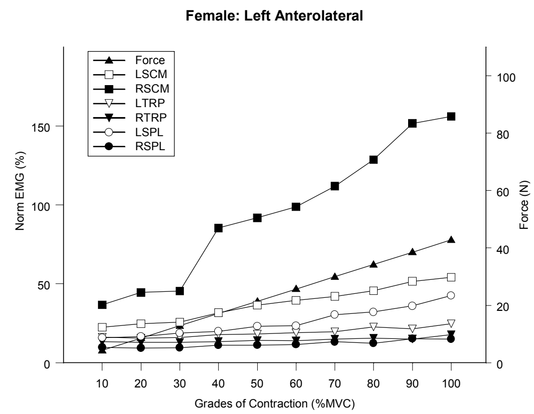

Figure 1: Calibrated force and EMG output of all investigated muscle in left anterolateral flexion at 10% force levels in female sample.

($p<0.01$). The intermediate positions (anterolateral and posterolateral) revealed ratios of force to EMG that were intermediate in relation to force/EMG ratios of pure flexion and extension. The cervical muscle strength and EMG were found directionally dependent. This direction dependence supports the contention that the mode and site of injury to cervical region in automobile accidents may be dependent on direction.

SUMMARY

The cervical muscle strength was found to be highest in extension and lowest in flexion. The strength progressively declined as one moved from posterior to anterior direction. The EMG output in flexion was significantly higher in flexion (66%) than in extension whereas the force was 30% less. The direction dependence of the strength and EMG of the cervical muscles indicate directional dependence of mode and site of injury to cervical region in motor vehicle accidents.

REFERENCES

Spitzer, et al. (1995). Spine 20, 105-475.

ACKNOWLEDGEMENTS

Financial assistance of University of Alberta through SAS program is gratefully acknowledged.

LIPID TRANSPORT IN THE REGIONS OF DISTURBED FLOW: ITS IMPLICATION IN THE DEVELOPMENT OF ARTERIAL STENOSES

Xiaoyan Deng

The State Key Laboratory of Structural Analysis for Industrial Equipment, Department of Engineering Mechanics, Dalian University of Technology, Dalian, China, dengxy@dlut.edu.cn

INTRODUCTION

The early event leading to the genesis of atherosclerosis is the accumulation of cholesterol and other lipids within the intima. These lipid deposits are believed to be derived primarily from plasma lipoproteins particularly low-density lipoproteins (LDL). Because the endothelium of the artery displays low permeability to plasma proteins, the filtration flow across the artery wall may cause a *concentration polarization* of lipids, a well-known mass transport phenomenon, at the blood/wall interface, with an increased lipid concentration from the bulk value towards the interface. Our hypothesis is that the concentration of atherogenic lipids at the luminal surface may vary according to its location in the circulation, even if the bulk concentration remains constant. In areas of disturbed blood flow (flow separation and recirculation) with a low wall shear rate, the luminal surface lipid concentration may be elevated, leading to a greater lipid infiltration and the onset of atherosclerosis in these areas (Deng et al., 1995). The present numerical study is to test this hypothesis.

METHODS

The geometric domain consisted of an axisymmetric tube with a local constriction that served as an arterial stenosis**.** Numerical simulations were carried out assuming a flow rate of 275 ml/min that is the flow rate for the human common carotid artery. The Reynolds number was 250 at this flow rate and the filtration rate was set at 4.0×10^{-6} cm/sec. The Schmidt number used in the computations was between 1.6×10^5 and 6.6×10^5, corresponding to a lipid diffusion coefficient in the range of 2.0×10^{-7} to 5.0×10^{-8} cm^2/sec. The Navier-Stockes equations, in the form of stream-function and vorticity, and a convective-diffusive mass transfer equation were solved numerically using the second upwind finite-difference method. A non-uniform grid was used to minimize the number of nodes while maintaining a sufficient degree of accuracy in the solution.

RESULTS

The numerical results showed that the maximum value of the luminal surface LDL concentration occurred immediately distal to the summit of each stenosis. In the stenosis with a 30% cross-sectional area reduction, the C_w/C_0 distribution curves were rather smooth, compared to those in the more severe stenoses (Fig. 1). Considering that no flow separation occurred distal to the 30% stenosis at Re=250, the sharp peaks recorded by other curves for more severe stenoses were mainly attributed to the flow separation distal to the stenosis. These peaks were in fact located at the exact location corresponding to the flow separation points where the wall shear rate was zero. It was noted that the peak value first increased when the stenosis severity increased from 30 to 40%, then decreased when the severity increased further. The results also showed that the larger the Schmidt number (i.e., the larger the lipids), the higher the peak value of the luminal surface lipid concentration.

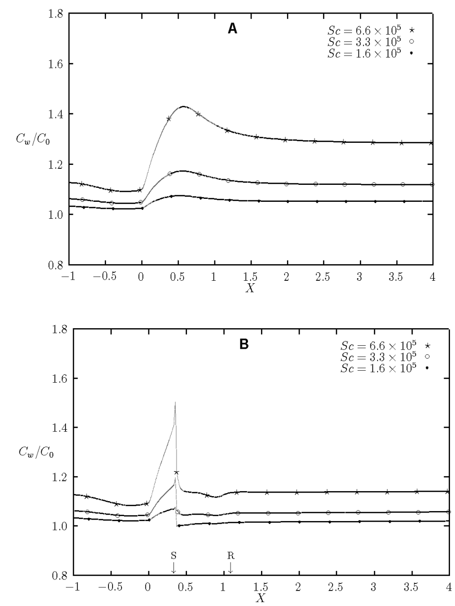

Figure 1: Plots of C_w/C_0 as a function of the distance from the constriction of the stenosis for three different Schmidt numbers. The letters S and R indicate the locations of the flow separation point and the reatachment point, respectively. (A) 30% stenosis (no flow separation). (B) 40% stenosis.

CONCLUSION

In the present of a filtration flow across the arterial wall, lipids accumulated at the arterial wall with the highest concentration occurring at the flow separation point. The results obtained suggest that the fluid layer with highly concentrated lipids in the area of flow separation point may be responsible for the formation and development of the arterial stenosis.

.

REFERENCES

Deng, X.Y. et al. (1995). *Journal of Vascular Surgery*, **21**, 135-145.

RECOVERY STRATEGY FROM PERTURBATION OF THE UPPER BODY DURING STANDING USING MECHANICAL ENERGY ANALYSIS

Wu Ming, Ji Linhong, Jin Dewen, Wang Rencheng and Zhang Jichuan

Dept. of Precision Instrument and Mechanology,Tsinghua University, Beijing 100084,China.
Rehabilitation Engineering Research Center, wum@post.pim.tsinghua.edu.cn

INTRODUCTION

Human body employs multi-joints to recovery from perturbation during standing (Runge, 1999, Tony, 1998). However, little is known about the relationship between balance mode and the intensity of disturbance. Besides, the contribution of each joint, especially the metatarsophalangeal (MP) joint, to balance recovery still needs to be evaluated quantitatively.

METHODS

A 4-degree-of-freedom dynamic model of standing human body, which includes the MP joints, was derived using Kane method. Experiments were performed on 4 healthy adult volunteers, who gave informed consent. Mechanical energy generation and absorption at each joint during the recovery process, was analyzed to identify the balance recovery strategies.

RESULTS AND DISSCUSSION

The results show distinct multi-joints coordination in the recovery process. All joints contribute to balance recovery. However, MP joints and hip joints dominate the contributions to balance recovery from the perturbation of upper body during standing. The ankle and knee joints have less contribution. Balance recovery mode changes with the intensity of disturbance and it is observed that each joint's contribution changes with different balance mode. However, MP joints and hip joints still do dominate contributions to the overall disturbance form upper body. Besides, it is shown that there is a close relationship between the rotation momentum of body relative to MP joint and stability after perturbation of upper body. The stability of human body after perturbation of upper body deteriorates with the increase of the magnitude of rotation momentum of the body.

REFERENCES

C. F. Runge, C.L. Shupert, F.B. Horak, et al. Ankle and hip postural strategies defined by joint torques. Gait and Posture, 1999, 10: 161-170.

Tony Szturm, Bjorg Fallang. Effects of varying acceleration of platform translation and toes-up totations on the pattern and magnitude of balance reactions in humans [J]. Journal of Vestibular Research, 1998, 8(5): 381-397.

ACKNOWLEDGEMENTS

This study was supported by a grant from the NSF of China (No: 30170242), and in part, the "Biped Robot Project" of Tsinghua University.

Table1. Relationship between energy contribution (mean, SD) and balance mode

	No step		One-step		Multi-step	
	momentum 0.13 (0.06)		momentum 0.33 (0.10)		momentum 0.47 (0.25)	
	Generation (%)	Absorption (%)	Generation (%)	Absorption (%)	Generation (%)	Absorption (%)
MP	45.66(14.49)	40.65(15.04)	62.05(10.46)	43.58(27.61)	66.30(5.95)	24.47(32.95)
Ankle	16.15(4.88)	13.32(9.06)	10.56(9.06)	16.18(11.54)	12.09(12.19)	4.90(3.14)
Knee	6.61(3.60)	5.47(2.69)	9.82(6.73)	4.39(3.19)	8.21(4.46)	6.08(5.31)
Hip	31.59(15.68)	40.56(19.62)	17.58(10.60)	35.85(38.59)	13.40(12.41)	64.55(41.16)

INFLUENCE OF SWING PHASE MICROSEPARATION ON THE WEAR OF CERAMIC ON POLYETHYLENE, CERAMIC ON CERAMIC AND METAL ON METAL TOTAL HIP REPLACEMENTS.

Sophie Williams[1], Todd D Stewart[1], Eileen Ingham[2], Martin H Stone[3] and John Fisher[1].

Medical and Biological Engineering.
[1]School of Mechanical Engineering, University of Leeds, Leeds, LS2 9JT. UK (email: mensw@leeds.ac.uk)
[2]Division of Microbiology, University of Leeds, Leeds, LS2 9JT. UK [3]Leeds General Infirmary, Leeds, LS1 3EX. UK

INTRODUCTION

Microseparation of the femoral head and acetabular component can occur following total hip replacement surgery (Dennis *et al*. 2001). Previous studies (Nevelos *et al*., 1999) have shown stripe wear on explanted alumina ceramic on ceramic (COC) bearings. However, COC bearings tested in a standard hip simulator had very low wear rates (0.1mm^3 per million cycles) and no stripe was observed. When swing phase microseparation was introduced into the normal gait cycle, results were more clinically relevant; the wear volume increased (1.7 mm^3 per million cycles) and stripe wear on the femoral head was observed (Stewart *et al.* 2001).

This study aimed to assess and compare the effect of swing phase microseparation on COC, meal on metal (MOM) and ceramic on polyethylene (COP) total hip replacements. Wear rates produced by standard and microseparation conditions were compared.

METHODS

A physiological hip simulator was used to test 28mm femoral heads and acetabular cups. Five pairs of each material combination were tested under each condition. Ceramic components were Biolox Forte HIPed alumina and metal components were cobalt chrome alloy. Components were mounted anatomically, heads underwent flexion/extension -15° to +30° and the acetabular component internal/external rotation ±10°. Loading was applied vertically to approximate *in vivo* conditions. Testing was conducted at 1 Hertz for 5 million cycles in 25% new-born calf serum. Measurements were taken every million cycles. Wear of ceramic and metal components was determined gravimetrically, wear of polyethylene cups was measured geometrically.

Microseparation was achieved by inferior displacement of the head (about 0.8mm) during swing phase which caused the head to contact the inferior rim of the acetabular component. On heel strike, the displaced head contacted the superior rim of the cup; this caused a stress concentration on the head and attributed to the formation of a wear stripe. The head then relocated into the normal articulating position.

RESULTS AND DISCUSSION

Wear rates for different bearing combinations under standard and microseparation conditions are shown in Figure 1.

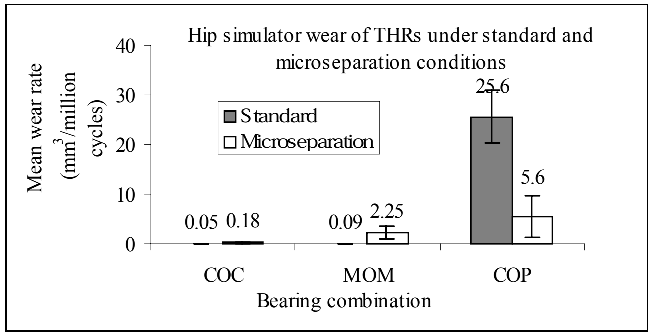

Figure 1: Wear rates (mean ± 95% CL)

Hard bearings (COC and MOM) had lower wear in comparison to COP couples. Hard bearings demonstrated increased wear under swing phase microseparation compared to standard conditions. Some insert rim damage and head stripe wear was observed on all components. Stripe wear on metal heads has not been observed *in vivo*, it is postulated that this is masked by a self polishing mechanism.

COP bearings showed about four times less wear under swing phase microseparation, compared to standard conditions. Evidence suggests that this was due to the entrapment of the lubricant during microseparation resulting in a reduction in wear via a squeeze film mechanism. Microseparation led to the head contacting the superior rim at heel strike causing creep deformation and permanent rim damage. The ceramic head showed no increase in roughness against polyethylene.

CONCLUSION

Swing phase microseparation increased wear of hard on hard bearings (COC and MOM); however, wear remained less in comparison to COP couples. Swing phase microseparation reduced polyethylene wear; indicating that small, controlled amounts of microseparation could be advantageous in these prostheses.

REFERNCES

Dennis D *et al.* (2001) *J Biomechanics* **34** 623-629.
Nevelos J *et al.* (1999) *Biomaterials* **20** 1833-1840.
Stewart T *et al.* (2001) *J Materials Science* **12** 1053-1056.

ACKNOWLEDGMENTS

This work was supported by Action Research, UK Department of Health and the EPSRC.

SHOULDER BIOMECHANICS IN VOLLEYBALL SPIKING: IMPLICATIONS FOR INJURIES

Gary A. Christopher[1] and Mark D. Ricard[2]

[1]Doctoral Student, Oregon State University, Corvallis, OR, garyalan@byu.net
[2]Director, Human Performance Research Center, Brigham Young University, Provo, UT

INTRODUCTION

The potential for overuse injuries in volleyball has been linked to impact magnitude, impact frequency, rate of loading, and number of years of competition.

The purpose of this study was to determine the reaction forces and torques at the shoulder during the volleyball spike and to investigate the relationship between shoulder biomechanics and the potential for injury.

METHODS

Shoulder biomechanics of 11 collegiate volleyball players (6 female, 5 male) were determined using 120 Hz video analysis. Subjects performed at least 10 maximum effort spiking trials toward a region 6 to 9 meters from the center of a regulation height volleyball net.

Retroreflective markers were affixed to the subjects at anatomical landmarks and to the ball. A motion analysis system (Motion Analysis Corporation, Santa Rosa, CA) was used to collect digital images of the volleyball spike. Cameras were positioned to allow image capture from all sides and EVa 6.0.3 software (Motion Analysis Corporation) was used to capture and digitize the spiking trials.

Two trials from each subject were digitized; a DLT algorithm was incorporated to determine the 3D coordinates of the markers. Raw positional data were exported to a custom program for analysis.

RESULTS AND DISCUSSION

Mean maximum ball velocity compared favorably to similarly skilled athletes (Chung, 1988; Chung et al., 1990). A strong positive correlation was found between maximum ball velocity and maximum shoulder compressive force ($r = 0.872$, $p < 0.001$).

While the impact magnitudes (~46-94% BW) and loading rates (~5-15 BW/s) reported herein are relatively small when compared to activities such as running or jumping, the ability of the shoulder to handle impact loading is limited. The dynamic stability of the shoulder complex is generally sufficient for most activities, but any situation that compromises the health of the shoulder musculature can increase the potential for overuse injuries (Norkin and Levangie, 1992).

Cumulative fatigue in the rotator cuff muscles, associated with repetitive overhead motions and/or technique errors, may impair their ability to stabilize the humerus, resulting in superior translation and entrapment of soft tissues, leading to or exacerbating tendinitis and/or impingement. Accumulated microtrauma to the rotator cuff muscles and soft tissues of the shoulder may result in increased symptoms and may limit participation (Briner & Kacmar, 1997; Schaefle, 1993; Watkins, 1994).

SUMMARY

The magnitude and rate of impact loading during volleyball spiking constitute considerable potential for shoulder overuse injuries among volleyball hitters. They are especially prone to biceps tendinitis and impingement syndrome (Briner & Kacmar, 1997; Schaefle, 1993; Watkins, 1994).

REFERENCES

Briner, W. W. J., & Kacmar, L. (1997*). Common injuries in volleyball. Mechanisms of injury, prevention and rehabilitation*. Sports Medicine, **24**(1), 65-71.
Chung, C.S. (1988). *Three-dimensional analysis of the shoulder and elbow joints during the volleyball spike.* Unpublished Doctoral Dissertation, University of Indiana, Bloomington.
Chung, C.S. et al. (1990). *Three-dimensional analysis of the striking arm during the volleyball spike*. Korean Journal of Sport Science, **2**, 124-151.
Norkin, C. C., & Levangie, P. K. (1992). *Joint Structure and Function: A Comprehensive Analysis* (2nd ed.). Philadelphia: F.A. Davis.
Schafle, M. D. (1993). *Common injuries in volleyball: Treatment, prevention and rehabilitation*. Sports Medicine, **16**(2), 126-129.
Watkins, J. (1994). Injuries in volleyball. In P.A.F.H. Renström (Ed.), *Clinical Practice of Sports Injury Prevention and Care* (pp. 360-374). Oxford: Blackwell Scientific.

Table 1: Selected Kinematic & Kinetic Quantities

(mean ± SE)	Units	Male	Female
Maximum Shoulder Internal Rotation Torque	Nm	48.7±4.5	28.3±4.1
	ms[a]	-30.0±4.0	-44.4±3.6
Maximum Shoulder Joint Reaction Force (Compressive)	% BW	89.5±4.8	50.6±4.4
	ms[a]	23.3±2.7	28.4±2.5
	BW/s	14.2±1.0	6.0±1.0
Maximum Shoulder Adduction Torque	Nm	114.7±15.4	63.1±14.0
	ms[a]	34.2±7.1	45.1±6.5
Maximum Ball Velocity (mean ±SD)	m/s	31.2±1.1	19.0±1.0

a. milliseconds before (-) or after (+) start of ball impact.

CLASSIFICATION OF TRABECULAR SURFACES FOR USE IN TISSUE-LEVEL BONE ADAPTATION MODELS

Michal Be'ery and Amit Gefen
Department of Biomedical Engineering, Faculty of Engineering, Tel Aviv University, Tel Aviv 69978, Israel, gefen@eng.tau.ac.il

INTRODUCTION

Trabecular bone is a complex structure composed of interconnected mineralized struts and plates (Odgaard, 2001). It is generally accepted that both its micro-architecture and tissue material properties are dependent upon the applied mechanical stress stimuli. Significant changes in the stress stimuli will affect trabecular morphology, by mechanisms of apposition or resorption of minerals at the trabecular surfaces. In recent years, computational models have been developed to predict alterations in trabecular density and respective elastic properties in response to changes in the stress stimuli (Gefen, 2001). Several two-dimensional models of trabecular lattices could also predict the "tissue-level" changes in surface geometry of individual struts (Mullender et al., 1998; Huiskes et al., 2001). In order to expand the potential of these simulations, parametric representation of trabecular surfaces is needed. In this study, mathematical formulation of typical trabecular surfaces and volumes was developed for their geometric classification, based on optical microscopy.

METHODS

6 specimens were transversally cut from the epiphyseal parts of 5 ovine femurs, using electrically-powered saw, after drying the bones in 85°C for 4.5 hours. The samples were kept at -18°C and defrosted to room temperature before measurements. Geometrical dimensions including base thickness (t_{max}), minimal thickness (t_{min}) and length (L) where recorded for 201 randomly selected trabecular profiles (Fig.1), using optical microscopy (Axiolab A, ZEISS) at a spatial resolution of 0.8 μm. For the purpose of parametric representation, it was assumed that trabecular profiles are symmetric around the x and y axes, and thereby, they could be fitted to the expression

$$y = \pm\left\{\cos\left(\frac{2x}{L}\cos^{-1}\left(\frac{1}{2}\left(2 + t_{\min} - t_{\max}\right)\right)\right) - \left(1 + t_{\min}/2\right)\right\} \qquad (1)$$

Eq. (1) was shown to represent well the trabecular profiles: cross-correlations of real versus fitted geometry yielded average correlation coefficients of 0.87 for the shape overlapping, and 0.97-0.99 and 0.99 for the symmetries around the x and y axes, respectively (n=40). Accordingly, statistical analyses were used to parameterize this relation in order to apply it for classification of human trabeculae.

RESULTS AND DISCUSSION

Linear correlation was found between base and minimal thickness values (R^2=0.71), and thus, the base thickness could be expressed as $t_{max}=\alpha t_{min}+\beta$, with the constants α=1.3736 and β=40.932 μm (Fig. 1). Eq.(1) then becomes

$$y = \pm\left\{\cos\left[\frac{2x}{L}\cos^{-1}\left(1 - \frac{\beta}{2} + \frac{(1-\alpha)(2t-\beta)}{2(1+\alpha)}\right)\right] - \left[1 + \frac{(2t-\beta)}{2(1+\alpha)}\right]\right\} \qquad (2)$$

where t averages t_{min} and t_{max}. The volumes of individual trabeculae with known averaged thickness can be approximated by integrating Eq.(2) to find the solid of revolution about the x axis.

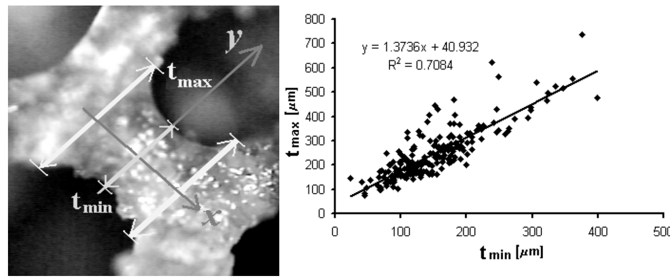

Figure 1: Micrograph of a trabecula (left) and base thickness versus minimal thickness for 201 trabeculae (right).

The histogram of thickness distribution (Fig.2) shows that the thickness of trabeculae may range between 30 and 286% the average thickness. Substitution of characteristic human trabecular dimensions of 1000 and 283 μm in Eq.(2), for the averaged length and thickness, respectively, enabled classification of typical trabecular surfaces (Fig.3). This classification is useful for development of computational simulations of adaptive changes in trabecular morphology.

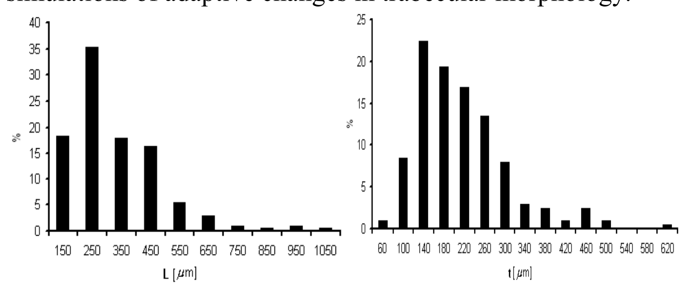

Figure 2: Histograms of lengths (left) and averaged thickness (right) measured for 201 trabeculae.

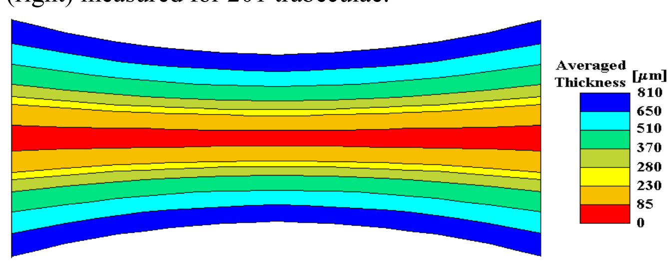

Figure 3: Classification of trabecular surface profiles (for trabeculae of 1000 micron in length).

REFERENCES

Gefen A. (2001). *Proc. 23rd Int. Conf. of IEEE EMBS*, p. 116.
Huiskes R. et al. (2001). *Nature*, **405**, 704-706.
Mullender M. et al. (1998). *Bone*, **22**, 125-131.
Odgaard A. (2001). In: *Bone Mechanics Handbook,* CRC Press.

AN ELECTROMYOGRAPHIC ASSESSMENT OF THE ANTI-G STRAINING MANEUVER

Hsiang-Ho Chen[1], Yi-Chang Wu[2], Ming-Da Kuo[1], Te-Sheng Wen[3]

[1]Inst. of Industrial Engineering & Management, I-Shou University, Kaohsiung, Taiwan, hchen@isu.edu.tw
[2]Inst. Of Aerospace Medicine, National Defense Medical College, Taipei, Taiwan
[3] Aviation Physiology Research Laboratory, Armed Forces Kang-Shan Hospital, Kaohsiung, Taiwan

INTRODUCTION

Combat jet pilots exposed frequently to rapid-onset high-sustained +Gz force are at the risk of G-induced loss of consciousness (G-LOC)(Burton, 1988). The anti-G straining maneuver (AGSM) offers an effective protection against G-LOC and has been the standard high-G tolerance training throughout the world. The AGSM involves a forced exhalation against a partially or completely closed glottis with straining of limb and abdominal muscles during high-sustained +Gz exposures (Comens et al, 1987). By tensing different muscle groups and increasing the intrathoracic pressure, AGSM can significantly increase one's arterial blood pressure to maintain sufficient cerebral blood flow, thereby avoiding G-LOC (McCloskey, 1992). ROC Air Force teaches AGSM to all its fighter pilots as part of their high-G tolerance training. The aim of the present study is to examine the electromyographic (EMG) characteristics of AGSM in order to establish an objective assessment for its training effectiveness.

METHODS

A telemetry EMG (Biotel 99, Glonner Electronic, Steinkirchen, Germany) connected with a data acquisition system (InstruNet, GWI Co., Somerville, MA) was used to obtain the surface electromyography from the subjects. Twenty male subjects who were in good health with no history of any disease were divided into two study groups. Group 1 composed of 8 senior aviation physiological training officers who were already familiar with the techniques of AGSM and had been exposed to high G environments before the study. Group 2 consisted of 12 flight cadets who were undergoing the high-G tolerance training in the Air Force Academy and learned how to perform the AGSM for the first time. For each subject, an Integrated EMG (IEMG) monitored seven groups of respiratory muscles during the performance of AGSM for 30 seconds. The duration of a breathing cycle, the firing rate, the firing sequence, and peak strength of each muscle group were analyzed using a programmable software developed with Matlab 6.0 (MATH Works Inc., Natick, MA).

RESULTS AND DISCUSSION

Data analysis indicate that the mean period of a breathing cycle by the trainers (2.20 ± 0.36 seconds) was significantly longer ($p < 0.001$) than the trainees' (1.86 ± 0.37 seconds). The mean firing rate for the cheek muscle between these two groups were also significantly different (Table 1; $p = 0.001$). In addition, significant differences were found between the two groups in the mean peak strength of the latissimus dorsi muscle ($p = 0.001$), the rectus abdominis muscle ($p = 0.003$), and the sternocleidomastoid muscle ($p = 0.01$). However, the firing sequence was not significantly different between the two groups. We compared the pooled IEMG data for differences between the seven muscle groups and found only the pectoralis major muscle ($p = 0.03$) to be significantly different.

SUMMARY

Our study applied the analytic capability of EMG to examine the physiological differences of AGSM performed by the experienced and the inexperienced. The results indicate that the trainers were able to hold each of their AGSM respiration cycles significantly longer than the trainees could. Furthermore, the peak strengths of the latissimus dorsi muscle, the rectus abdominis muscle, and the sternocleidomastoid muscle reflect the depth of inspiration movement. Most importantly, EMG data among the respiratory muscles studied revealed that the behavior of cheek muscle could be an excellent indicator for the effectiveness and efficiency of the anti-G straining maneuver.

REFERENCES

Burton R.R. (1988). *Aviat Space Enviro. Med,* **59**, 2-5.
Comens, P. et al (1987). *Aviat Space Environ Med*, **58**, 205-210.
McCloskey, K.A. (1992). *Human Factors*, **34**, 409-428.

ACKNOWLEDGEMENTS

This study was funded by a grant from National Science Council, R.O.C. (NSC90-2218-E-214-008)

Table 1: Firing rate of respiratory muscles during L-1 AGSM.

	CM	RA	LD	DP	IC	PM	SCM
Group A	108 ± 35*	69 ± 33	80 ± 42	75 ± 47	73 ± 45	72 ± 50	53 ± 38
Group B	73 ± 28*	65 ± 34	67 ± 28	69 ± 22	65 ± 28	60 ± 19	64 ± 38

CM: cheek muscle, RA: m. rectus abdominal, LD: m. latissimus dorsi, DP: diaphragm, IC: m. intercostals, PM: m. pectoralis major, SCM: m. sternocleidomastoid;
Unit: % of Maximal Voluntary Contraction / Second; * significantly different ($p < 0.05$)

THE EFFECT OF POSTMORTEM FREEZING STORAGE ON THE TENSILE PROPERTIES OF TENDON

Ng Boon Ho[1], Chou Siaw Meng
School of Mechanical and Production Engineering, Nanyang Technological University, Singapore
[1]E-mail: pa10264950@ntu.edu.sg

INTRODUCTION

Postmortem storage has been employed in biomechanical evaluation of living tissues simply because it is not feasible to perform tests on live animal or immediately after sacrifice. It is also often not possible to obtain fresh human specimens instead of fresh frozen cadaveric specimens. Further, cadaveric tendons and ligaments have been used as allografts for transplantation in recent years. Proper storage of allografts is necessary to preserve the biomechanical properties and biological viability for successful transplantation.

Of the many storage methods currently adopted, freezing is most popular for soft tissues preservation as it provides ease of storage and can be carried out at relatively low costs. Researchers have investigated the response of soft tissues to freezing storage but results have been inconclusive. The aim of this study is therefore to elucidate the influence of postmortem freezing storage on the tensile properties of tendons.

MATERIALS AND METHODS

Two hundred and seventy-five chicken FDP tendons were used in this study. Five pieces of tendon specimens were tested within 4 hours after death and the results obtained were recorded as fresh control. Other specimens were divided into 54 groups and stored at 0°C, -20°C or -40°C (8 groups each) within 6 hours after death. A 5565 Instron Universal Testing Machine was employed for the tensile tests and the cross-head speed was set at 60mm/min. Tendons were tested every 5 days for 3 months. Samples were tested in quintuplicate. Mean values of UTS, Strain at Maximum Stress, Elastic Modulus and Energy at Maximum Stress were compared to fresh control at 99% confidence level using the Student's T method.

RESULTS AND DISCUSSION

Upon thawing, tendons which were stored at 0°C became soft and produced unpleasant smell after 5 days. However, no statistically significant changes was found in the cross-sectional area following freezing storage and no variations in the gross shape of the stress-strain curve was recorded for all durations. The tensile properties of digital flexor tendon were not affected during freezing storage at 0°C, -20°C or -40°C for up to 90 days. Generally, there existed no significant deviations from fresh control in the values of UTS, Strain at Maximum Stress, Elastic Modulus and Energy at Maximum Stress. Statistics comparison between groups of same duration showed no discernable differences in tensile properties after storage at 0°C, -20°C and -40°C.

The tensile properties of digital flexor tendon were not affected during freezing storage at 0°C, -20°C or -40°C for duration up to 90 days. These findings were consistent with similar works on ligaments by Viidik and Lewin (1966) and Woo et al. (1986). However, our findings were contradictory with other reported data (Matthews and Ellis, 1968; Dorlot et al., 1980; Turner et al., 1988). Presumably, the differences could be attributed to the employment of different freeze-thaw processes. The comparison between frozen specimens and fresh control in this study has proven that tensile properties of tendon remained unchanged in unprogrammed freezing and rapid thawing processes. The comparison also illustrated that saline solution does not alter the tensile properties of tendon which is contrary to the findings of Viidik and Lewin (1966).

Since results showed no significant changes in tensile properties through out the storage duration, it suggests that tendons can be preserved by freezing for many months, even years, without compensating its tensile properties. However, the duration limit of freezing storage should be determined empirically.

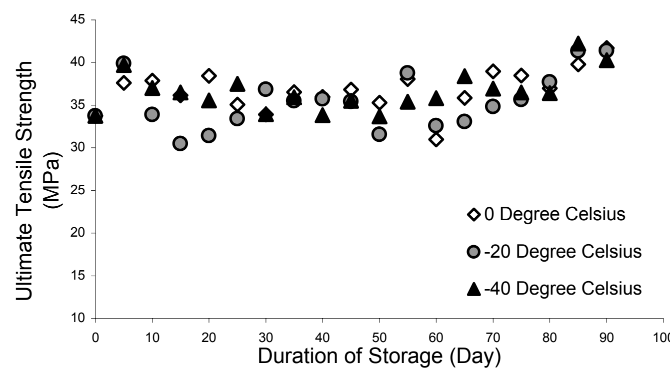

Figure 1: Correlation of tendon strength with the duration of freezing storage.

SUMMARY

Based on the results obtained in this study, we conclude that freezing storage up to 90 days does not alter the tensile properties of digital flexor tendon.

REFERENCES

Viidik, A., Lewin, T. (1966). *Acta orthopaedica scandivica*, **37**, 141-155.
Woo, S. L. et al. (1986). *J. Biomechanics*, **19**, 399-404.
Matthews, L. S., Ellis, D. (1968). *J. Biomechanics*, **1**, 65-71.
Dorlot, J. M. et al. (1980). *J. Biomech. Engng.*, **102**, 190-193.
Turner, W. D. *et al*. (1988). *Clinc. Orthop.*, **230**, 251-256.

STRAIN RATE EFFECT ON THE TENSILE PROPERTIES OF FLEXOR TENDON

Ng Boon Ho[1], Chou Siaw Meng
School of Mechanical and Production Engineering, Nanyang Technological University, Singapore
[1]E-mail: pa10264950@ntu.edu.sg

INTRODUCTION

Tendon, ligament, bone and other biological tissues are known to be viscoelastic material. The change in failure properties of soft tissues at different strain rates is of particular interest in analyzing mechanisms of injury. Bhatia et al. (1992) estimated the extension rates at 60 to 70 mm/min close to tendon speed during gentle active mobilization while Crowninshield and Pope (1976) reported that the traumatic loading of the knee joint in man might occur at strain rates ranging from 50 to 150000 %/s. However, the actual physiologic strain rates during soft tissue injury still remain unknown. Many studies have been conducted to investigate the effect of strain rate on the structural properties of ligament-bone complex but contradicting results were obtained. Further, relatively few studies have evaluated the effect of strain rate on the mechanical properties of tendon. Flexor tendon works under dynamic loading, thus the dependence of tensile properties on strain rate should be determined.

MATERIALS AND METHODS

Seventy-five chicken FDP tendons were used in this study. Tendons were wrapped by saline-soaked gauze and stored at -40°C within 6 hours after death for 16–20 days before testing. A 5565 Instron Universal Testing Machine was employed for the tensile tests. Tendons were tested at 15 different strain rates, namely 0.05, 0.1, 0.25, 0.5, 0.75, 1, 2.5, 5, 7.5, 10, 25, 50, 75, 100 and 150%/s, and samples were tested at each strain rate in quintuplicate. Mean values of UTS, Strain at Maximum Stress, Elastic Modulus and Energy at Maximum Stress were compared at 99% confidence level using the Student's T method.

RESULTS AND DISCUSSION

Results showed that strain rate has little effect on the shape of stress-strain curve. The toe regions were not affected by strain rates but stiffness increased with increasing strain rate. The hypothesis advocated by Piolett et al. (1999) that the strain rate effect mainly acted in the toe region with minimal influence on the linear part of the stress-strain curves was not justified in this study.

Generally, UTS slightly increased as strain rate increased with the lowest mean value observed at the lowest strain rate, 0.05 %/s. The values of Strain at Maximum Stress of all groups did not differ significantly from that at 0.05 %/s except at 1 %/s strain rate. In addition, the increase of strain rate resulted in higher Elastic Modulii and the differences were statistically significant against 0.05 %/s except for lower strain rates of 0.1, 0.25, 0.5 and 1 %/s. In terms of Energy at Maximum Stress, there existed no statistically significant deviations following the increase of strain rate. These findings were consistent with the work of Danto and Woo (1993).

The reason for the strain rate sensitivity of tendon is unknown. A rate sensitive interfibrillar matrix of ground substance is suggested to help maintain the structural integrity of tendon at high strain rate. It is anticipated that lower strain rates permit shearing or gliding between collagen fibres. The shearing eliminates stress sharing among the collagen fibres and this results in uneven stress distribution. As such, only part of the collagen fibres contributes to resisting the applied load. On the other hand at higher strain rates, the rate sensitive interfibrillar matrix of ground substance helps distribute stress among the collagen fibres by limiting interfibrillar shearing. With stress sharing, more collagen fibres are involved in resisting the applied load, thus resulting in stiffer tendon.

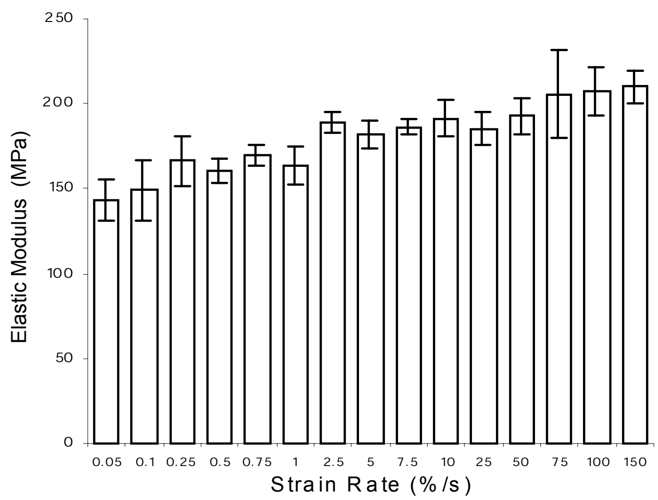

Figure 1: Correlation of tendon stiffness with strain rate.

SUMMARY

Based on the results obtained, we conclude that strain rate affects the tensile properties of tendon significantly. Within the range 0.05 to 150 %/s, the stiffness of tendons increased with the increase of strain rate, with no change in UTS and Strain at Maximum Stress. However, the change in tendon tensile properties was not significant with small change of strain rate.

REFERENCES

Bhatia, D. et al. (1992). *J. Hand Surg.*, **17B**, 550-552.
Crowninshield, D., Pope, H. (1976). *J. Trauma*, **16**, 99-105.
Pioletti, D. P. et al. (1999). *Med. Eng. Phys.*, **21(2)**, 95-100.
Danto, M. I., Woo, S. L. (1993) *J. Orthop.Res.*, **11**, 58-67.

STRAIN CHARACTERISTICS OF THE FOOT ARCH IN NON-ATHLETES AND ATHLETES DURING WEIGHT-BEARING, WALKING AND RUNNING

Seung-Jae Kim
Department of Leisure & Air Sports, Hanseo University, Seosan, Chungnam, Korea
Assistant Professor, sjkim@hanseo.ac.kr

INTRODUCTION

The medial longitudinal foot arch is a unique structure in humans and is reported to have elastic strain energy second only to the Achilles tendon during locomotion (Ker et al., 1987). In vitro and in vivo studies on the foot arch have been performed to identify static and dynamic characteristics (Kogler et al., 1995; Cashmere et al., 1999). However, the actual strain of the foot arch during static and dynamic loading is not well known. This in vivo study tries to answer the following questions: "What strain characteristics does the foot arch have in static and dynamic situations?" and "Is there any training effects of the foot arch?" Therefore, the purpose of this study was to investigate strain characteristics in the foot arch of non-athletes and athletes during weight-bearing, walking and running.

METHODS

Twenty-three male subjects were divided into two groups, 13 non-athletes (NAT) and 10 athletes (AT), in order to investigate training effects of the foot arch. The age of the NAT group which had never been trained as specific athletes was 24.2±2.2 yrs and the age of the AT group which had been trained for 6.8±1.0 yrs as rugby athletes was 21.4±1.6 yrs. Four anatomical landmarks of the longitudinal foot arch, the medial malleolus, bottom of the midline of the posterior calcaneous (CL), navicular tuberocity (NV) and head of the first metatarsal (MT) were marked using black water paint. The arch height was defined as the distance between NV and the ground and the arch length as the distance between CL and MT. The arch height and the arch length were measured with a right-angled square in non weight-bearing and weight-bearing conditions and with a Photosonic 16 mm high speed camera filming at 60 frames/s during walking (1.5 m/s±5%) and running (4 m/s±5%). Strain in weight-bearing, walking and running was calculated as a change in the arch height and the arch length divided by their height and length in the non weight-bearing condition, respectively. The maximum vertical loads during walking (961±151 N) and running (1934±234 N) were measured using a Bertec force-plate. The differences of the NAT and NT groups and the three loading conditions were tested with repeated measures of general linear model in SPSS under .05 level of significance. Post-hoc comparisons were performed with Duncan's test.

RESULTS AND DISCUSSION

Maximum arch height strain among weight-bearing, walking and running showed significant differences in NAT and AT except for the relation between weight-bearing and walking (Figure 1a). Especially, the relation showed a contradictory result that regardless of increasing the loading condition from weight-bearing to walking, maximum arch height strain was negatively decreased in AT. This point needs further research to explain. Maximum arch length strain among weight-bearing, walking and running showed significant differences (Figure 1b). Maximum strain of both the arch height and the arch length between NAT and AT did not show any significant differences according to the three loading conditions.

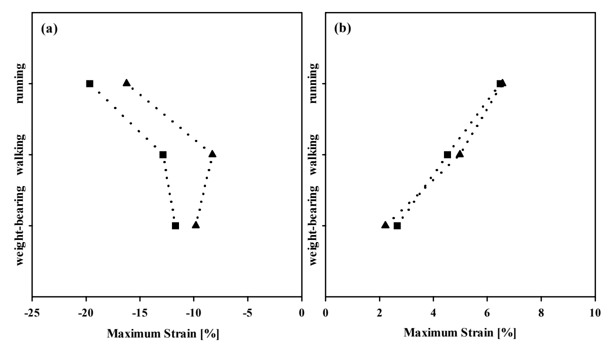

Figure 1: (a) Maximum arch height strain and (b) maximum arch length strain in NAT (■) and AT (▲) during weight-bearing (715±91 N), walking (961±151 N) and running (1934±234 N).

SUMMARY

Maximum arch height strain was negatively increased related to increased loading conditions, except in one AT condition. However, maximum arch length strain was positively increased according to the increased loading conditions. The author cannot find any statistical evidence to support that there will a training effect in strain characteristics of the foot arch, however, a question about a training effect of it is proposed from an exceptional phenomenon of the arch height in AT during walking.

REFERENCES

Cashmere, T. et al (1999). *Foot & Ankle*, **20**, 112-118.
Ker, R.F. et al (1987). *Nature*, **325**, 147-149.
Kogler, G.F. et al (1995). *Clinical Biomechanics*, **10**, 245-252.

KINETIC MEASUREMENTS OF SURFACE-BOUND P-SELECTIN/LIGAND INTERACTIONS

Jun Huang[1], Juan Chen[1], Cheng Zhu[2], and Mian Long[1*]

[1]National Microgravity Laboratory/CAS, Institute of Mechanics, Chinese Academy of Sciences, Beijing 100080, *E-mail: mlong@imech.ac.cn, and [2]George W. Woodruff School of Mechanical Engineering and Wallace H. Coulter Department of Biomedical Engineering, Georgia Institute of Technology, Atlanta, GA 30332, USA.

INTRODUCTION

Receptor/ligand interactions are basic issues to cell adhesion, which are important to many physiological and pathological processes such as inflammatory reaction, tumor metastasis, etc. Selectin/carbohydrate ligand binding have been found to mediate the rolling of leukocytes on endothelial monolayer, the first step of inflammatory cascade, due to the fast kinetic rates. Kinetic rate and binding affinity constants are essential determinants of cell adhesion. Using a well-developed small system probabilistic model and a micropipet aspiration assay, we previously measured the E-selectin/ligand binding on apposed surfaces (two-dimensional (2D) interaction), and compared the 2D kinetics of E-selectin binding to carbohydrate ligands expressed on a human promyelocytic leukemia cell line (HL-60) or a human colon adenocarcinoma cell line (Colo-205). Here we further measured the kinetics of P-selectin/ligand interaction, and compared to that of E-selectin/ligand binding.

MATERIALS AND METHODS

Micropipet aspiration assay has been described previously. Briefly, anti-P-selectin monoclonal antibodies (mAbs) 1478 and S12 were coated on the surfaces of human RBCs using $CrCl_3$ protocol, which are used to capture P-selectin constructs with Lec/EFG (P-Lec/EGF) and with whole extracellular domains (sPs), respectively. Capture mAbs-coated RBCs were then incubated with respective P-selectin constructs before binding to cultured HL-60 cells expressing carbohydrate ligands. Binding probability, P_a, on contact duration, t, of selectin/ligand interaction at the contact area, A_c, was measured experimentally using the micropipet technique, and the kinetic rates and binding affinity were predicted using the small system probabilistic model,

$$P_a = 1 - \exp\{-A_c m_r m_l K_a^0[1-\exp(-k_r^0 t)]\} \qquad (1)$$

where K_a^0 and k_r^0 are zero-force binding affinity and reverse rate, respectively, and m_r and m_l the site densities of selectin and ligands respectively.

RESULTS

Control and blocking experiments were designed to address the binding specificity for P-Lec/EGF and sPs, respectively, binding to the ligands on HL-60 cells. Adhesions were abolished when the P-selectin capture mAb 1478 or S12 was replaced by an isotype-matched irrelevant mIgG1 or when the P-selectin construct was substituted by the E-selectin construct. Adhesions were completely blocked by the anti-P-selectin and anti-PSGL-1 blocking mAbs (PL1). Inclusion of EDTA (5 mM) in the medium also abrogated adhesions (data not shown). These experiments showed that the binding was specifically mediated by P-selectin/ligand interaction.

A typical curve for dependence of binding probability on contact duration was shown in Fig. 1. Using Eq. 1, the zero-force binding affinity and reverse rate of P-selectin/ligand binding can be estimated from the measured data. These numbers were used to compare with E- and P-selectin dissociating from HL-60 cells, as well as with the data from a flow chamber assay.

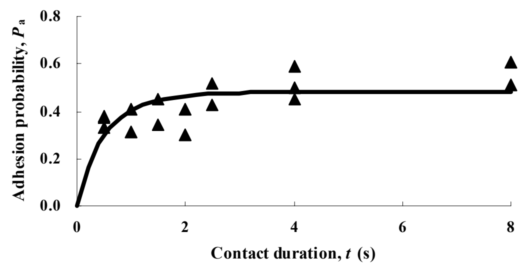

Figure 1. Comparison between measured (H) and predicted (*curve*) adhesion probability, P_a, on contact duration, t, for sPs binding to ligands on HL-60 cells. The theoretical prediction is based on Eq. 1. Each cell pair was used to repeat 100 cycles to estimate the P_a for that cell pair ($N = 17$).

ACKNOWLEDGEMETNS

We thank Rodger P. McEver for generous gifts of the P-selectin constructs and the relative mAbs. Supported by NSFC grants 10042001 and 10072071, a CAS grant KJCX2-L02 and a TRAPOYT Award (ML) as well as by NIH grant AI44902 (CZ).

REFERENCES

Chesla, S.E., Selvaraj, P., Zhu, C. (1998). *Biophys. J.* **75**, 1553-1572.

Long, M., Goldsmith, H.L., Tees, D.F.J., et al. (1998). *Biophys. J.* **76**, 1112-1128.

Long M., Zhao H., Huang K.S., et al. (2001). *Ann. Biomed. Engi.* **29**, 935-946.

McEver, R.P., Moore, K.L., Cummings, R.D. (1995). *J. Biol. Chem.* **270**, 11025-11028.

Zhu C, Long M., Bongrand P. (2002). *Ann. Biomed. Engi.* **30**, Accepted.

PROBABILISTIC MODELING OF ROSETTE FORMATION ON SELECTIN/LIGAND INTERACTIONS

Juan Chen[1], Emily Moses[2], Cheng Zhu[2], and Mian Long[1*]

[1]National Microgravity Laboratory/CAS, Institute of Mechanics, Chinese Academy of Sciences, Beijing 100080, *E-mail: mlong@imech.ac.cn, and [2]George W. Woodruff School of Mechanical Engineering and Wallace H. Coulter Department of Biomedical Engineering, Georgia Institute of Technology, Atlanta, GA 30332, USA.

INTRODUCTION

Rosetting, a simple assay for specific cell-cell adhesion, has been routinely used by immunologists to examine the functionality of the interacting receptors and ligands and to discriminate subclasses of leukocytes. It has not been regarded, however, as a quantitative method, since the measured rosette fraction has not been quantitatively related to the underlying molecular properties. Previously, we have developed a small system probabilistic model and a micropipet aspiration assay to measure and compare the kinetics of E- and P-selectin/ligand binding on apposed surfaces. Here, we use the same concept to model the rosetting experiment and estimate the binding affinity of selectin/ligand interaction from rosette size distribution.

MATERIALS AND METHODS

Rosetting requires two types of cells, typically one of larger size but smaller number and the other of smaller size but larger number. The system used here consisted of a human promyelocytic leukemia (HL-60) cells expressing carbohydrate ligands rosetting with human RBC coated (via $CrCl_3$ coupling) with anti-selectin monoclonal antibodies (mAbs) capturing selectin constructs. Cells were washed, mixed at a ratio of 100 RBC per HL-60 cell, centrifuged at 500 rpm for 5 min, and incubated on ice for 1~2 hr. The cell pellet was gently resuspended, and the rosette size distribution was determined visually under a light microscope. Upon the probabilistic model, rosette size distribution, p_n, the fraction of n RBCs per HL-60 cell, followed the Poisson distribution:

$$p_n = \langle n \rangle^n \exp(-\langle n \rangle)/n! \quad (1)$$

Here, the mean rosette size, $\langle n \rangle$, the average number of RBCs per HL-60 cell, followed quantitatively the formulation (as long as $\langle n \rangle$ is small),

$$\langle n \rangle = A_c m_r m_l K_a N \quad (2)$$

where A_c is the contact area, m_r and m_l the site densities of receptor and ligand respectively, K_a the binding affinity, and N the maximum number of RBC that are geometrically possible to simultaneously contact with a HL-60 cell ($N \approx 12$).

RESULTS

A typical experiment is shown in Fig 1. Excellent agreement was found between theory (*solid curve*) and experiment (*solid bars*) for HL-60 cells rosetting with P-selectin-coupled RBCs. The Poisson simplifying approximation was justified, as the mean rosette sizes were small ($\langle n \rangle = 0.25$) compared to the maximum rosette sizes, N. Using an anti-P-selectin blocking antibody, G1, the rosette size distribution shifted left (*open bars*), which also fitted extremely well with theory (*dotted curve*).

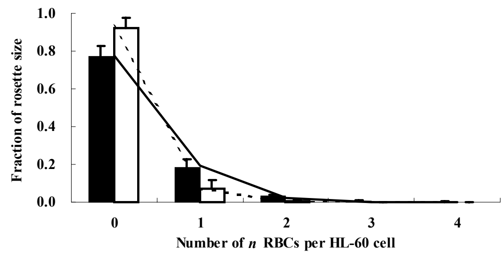

Figure 1. Comparison between measured (*bars*) and predicted (*curves*) rosette size distribution of HL-60 cells with RBCs. The prediction is based on Eq. 1. Bars are the standard deviation.

Cellular binding affinity, $A_c m_r m_l K_a$, was obtained using, Eqs. 1 and 2, to be 0.021 μm^2 for P-selectin/ligand interactions. The value obtained using the present rosetting experiment is consistent with those determined from a micropipet aspiration assay using same molecular and cellular system (data not shown), since the contact area A_c between a HL-60 cell and a RBC in a rosette was in general several folds smaller than that in the micropipet experiment. This supports the validity of these techniques as well as the theoretical models for them, and indicates the reliability of the measured binding affinities.

ACKNOWLEDGEMETNS

We thank Rodger P. McEver for generous gifts of the P-selectin constructs and the relative mAbs. Supported by NSFC grants 10042001 and 10072071, a CAS grant KJCX2-L02 and a TRAPOYT Award (ML) as well as by NIH grant AI44902 (CZ).

REFERENCES

Chesla, S.E., Selvaraj, P., Zhu, C. (1998). *Biophys. J.* **75**, 1553-1572.

Long, M., Zhu, C. (1997). In *1997 Advances in Bioengineering*, **36**, 75-76.

Long M., Zhao H., Huang K.S., et al. (2001). *Ann. Biomed. Engi.* **29**, 935-946.

Salvaraj, P., Plunkett, M.L., Dustin, M. et al. (1987). *Nature*, **326**, 400-403.

SEPARATION PATTERNS IN AN ARTERIAL BRANCH MODEL

Mehran Tadjfar and Ryutaro Himeno

Advanced Computing Center
Institute of Physical and Chemical Research (RIKEN)
2-1, Hirosawa, Wako-Shi, Saitama, JAPAN

INTRODUCTION

In vascular flow study, the flow into arterial branches is of great importance. The tendency for plaque to form around and near the regions of vessel bifurcation is a well-known fact. The role that local hemodynamic factors play in the plaque formation and its local distribution is also accepted. The exact mechanisms of how the hemodynamic factors influence plaque formation and its further development are still subject to debate. See Caro (1994), and Ku (1997). However, it is hypothesized that low wall shear stress regions and regions of high particle residence time are locations of high risk for vascular diseases. Here, we use CFD methods to study the flow separation into a branch model (Fig. 1).

METHODS

The unsteady, three-dimensional, incompressible Navier-Stokes equations are solved using a fast, parallel, and time-accurate finite volume solver (See Tadjfar 2001). The solver is capable of dealing with moving boundaries and moving grids. It is designed to handle complex, three-dimensional vascular systems. The computational domain is divided into multiple block subdomains. At each cross section the plane is divided into twelve sub-zones to allow flexibility for handling complex geometries and, if needed, appropriate parallel data partitioning. A second-order in time and third-order upwind finite volume method for solving time-accurate incompressible flows based on pseudo-compressibility and dual time-stepping technique is used.

RESULTS AND DISCUSSION

The steady flow separation patterns into a 45°-branched tube are studied (Fig 2). The major factors influencing this flow are; The area ratio, defined as the ratio of total cross sectional area of the daughter tubes to the cross sectional area of the mother tube, and the Reynolds number of the incoming flow. At the area ratio of sufficiently higher than one, the flow will separate in the daughter tubes. The magnitude of the area ratio necessary to initiate flow separation is dependent on the value of the incoming flow Reynolds number.

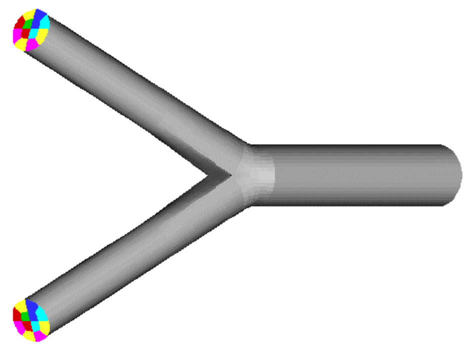

Figure 1: Grid model of the 45°-branched tube.

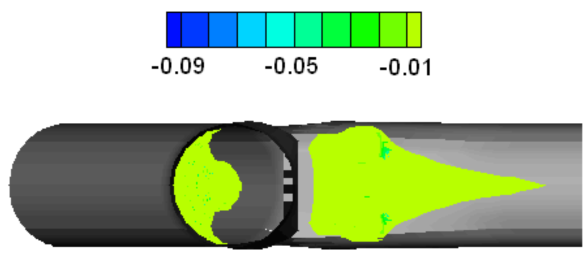

Figure 2: Streamwise velocity contours (backflow part), looking down into the left daughter tube. (Re = 1000 and AR = 2.0).

REFERENCES

Caro, C.G., (1994), *Recent Progress in Cardiovascular Mechanics. Harwood Academi Publishers, pp.197 –213.*

Ku, D. N., (1997), *Ann. Rev. of Fluid Mech. 29, 399-434.*

Tadjfar, M., Himeno, R. (2001), *FED-24967, Proceedings of ASME conference: IMECE-2001, New York, New York.*

Tadjfar, M. and Himeno, R. (2002), *Journal of Biorheology, to appear.*

EFFECT OF CELL DENSITY ON VIABILITY OF ARTIFICIAL TISSUE AFTER CRYOPRESERVATION

Masanobu Ujihira[1], Yumi Sukegawa[2], Satoshi Nogawa[1], Takako Nagoshi[1] and Kiyoshi Mabuchi[3]

[1] School of Allied Health Sciences, Kitasato University, Sagamihara, Kanagawa 228-8555, Japan, uj@kitasato-u.ac.jp
[2] Shirahigebashi Hospital, Sumida-ku, Tokyo 131-0032, Japan
[3] Graduate School of Medical Sciences, Kitasato University, Sagamihara, Kanagawa 228-8555, Japan

INTRODUCTION

Generally, post-thaw viability of cells in cell suspension is higher than that in biological tissue in cryopreservation. Successful cryopreservation with biological tissue is limited due to the complexity of the structure (e.g., Karlsson and Toner 1996), for example, sample size, variety of cells, and cell density. One factor responsible for the difference in the viability between cell suspension and biological tissue is cell density. However, the effect of cell density on post-thaw viability remains unclear.

In this study, we clarified this effect by first preparing artificial tissue that imitated biological tissue, for various cell densities, and then freezing the tissue at various cooling rates. We then observed the structure of artificial tissue stained with hematoxylin and eosin (HE) by optical microscope.

MATERIALS AND METHODS

Human dermal fibroblasts (normal cells obtained from the Kitasato University Hospital) were three-dimensionally cultured for 2 days (5% CO_2, 37°C) in a collagen matrix (Koken Cellgen CS-100, ϕ20×1mm) to imitate biological tissue (artificial tissue). Different cell densities for the artificial tissue were used, from 10^5 to 10^7 cells/cm^3. Five artificial tissues were prepared at each cell density for each experiment; one of them was used for the control (no freezing and thawing) or the observation.

Four artificial tissues were first stacked in a test chamber consisted of a cylindrical test chamber made of polystyrene foam (ϕ24×4mm), then frozen with cooling rates of 0.3 to 50°C/min in a solution of Dulbecco's Modified Eagle Medium (Gibco BRL), 20% Fetal Bovine Serum (Tissue Culture Biologicals), and 10% dimethylsulfoxide, then kept frozen at –196°C for 2 hours, and finally thawed. The collagen matrix was dissolved using collagenase. Post-thaw viability of fibroblasts was evaluated by using a trypan blue exclusion assay. Viable cells were counted by using an erythrocytometer and optical microscope [(Relative Viability) = {(The number of viable cells) / (The total number of cells in the control)} / (The mean viability of the control) × 100 (%)].

The artificial tissue was embedded with paraffin, and sliced by using the microtome. A sliced sample was adhered to the preparation after the HE stain, the structure of the fibroblast in the collagen sponge in each cell density was observed under an optical microscope (Olympus EX50).

RESULTS

The post-thaw viability was high when the cell density was low (10^5 cells/cm^3) and decreased with increasing cell density [Fig. 1, error bars show standard deviation (SD) for n=8]. The post-thaw viability in 10^5 cells/cm^3 was highest at a cooling rate of 3°C/min. The cooling rate indicating highest viability decreased with increasing cell density (1°C/min in 10^7 cells/cm^3). The mean viability in the control tissue was 83.2 ± 9.6% (mean ± SD for n=20). Though cellular contact was not observed with 10^5 cells/cm^3, it was observed with 10^6 and 10^7 cells/cm^3.

DISCUSSION

Two factors are responsible for those results. The first factor is interaction between cells (Acker *et al.* 1999, cell-to-cell contact). From the observation results, cells contacted at cell densities above 10^5 cells/cm^3. Cell-to-cell contact would induce intracellular freezing. Therefore the post-thaw viability decreased with increasing cell density for higher cooling rates (>3°C/min). The second factor is obstruction to dehydration during extracellular freezing. When the cell density was high, fibroblasts in the artificial tissue may have overlapped due to the decrease in the amount of extracellular unfrozen solution during extracellular freezing. The cooling rate indicating highest viability decreased with increasing cell density. In addition, these factors may induce mechanical stress, and may destroy cell or cell membrane for slower cooling rates (<3°C/min). Therefore the post-thaw viability seems to decrease with increasing cell density.

SUMMARY

When the cell density is high, cell-to-cell contact can induce intracellular freezing, and dehydration may be obstructed during extracellular freezing. Therefore, the post-thaw viability and the cooling rate indicating highest viability decreases with increasing cell density.

REFERENCES

Acker, J.P., Larese, A., Yang, H., Petrenko, A., McGann, L.E., 1999, "Intracellular Ice Formation Is Affected by Cell Interactions," *Cryobiology* Vol. 38, pp. 363-371.
Karlsson, J.O.M., Toner, M., 1996, "Long Term Storage of Tissues by Cryopreservation: Critical Issues," *Biomaterials*, Vol. 17, pp. 243-256.

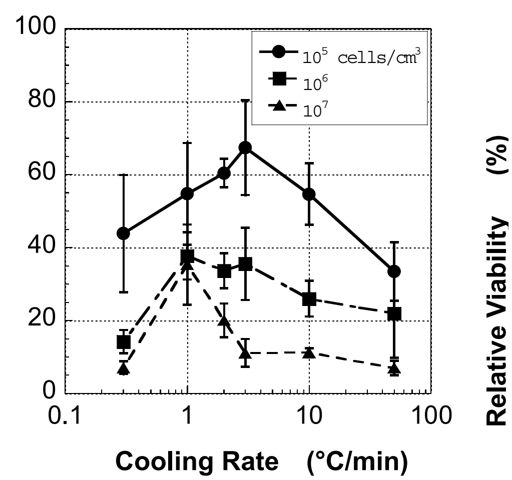

Figure 1 Relationship between relative viability and cooling rate.

EFFECT OF FLOW PATTERN ON VASOACTIVE MEDIATORS SECRETION OF CULTURED ENDOTHELIAL CELLS

Zulai Tao, Jiang Hu, Jia Hu and Yuxin Gao

National Microgravity Lab/CAS, Institute of Mechanics, Chinese Academy of Sciences, Beijing 100080,China,hujohn@sina.com

INTRODUCTION

The recent finding that atherosclerotic lesions occur mainly at specific sites around arterial branches and bifurcations indicates that local flow patterns are involved in atherogenesis. Since the synthetic and secretory functions of vascular endothelial cells are influenced by wall shear stress, it is interesting to study how the secretory patterns of these vasoactive mediators are changed in different flow patterns.

METHODS

Bovine aortic endothelial cells (BAEC) were isolated and cultured. Cells between passages 5 and 11 were used for experiments.

Three kinds of parallel-plate flow chamber were constructed, including rectangle chamber, bifurcation chamber and sudden-expansion chamber. The chamber was connected to a closed-loop flow system and the perfusion medium was driven by syringe pump. The flow field was simulated using the software Fluent. Cells were grown on the glass cover plate and subjected to fluid flow. The release of PGI_2 and ET-1 was determined by assaying perfusion medium samples by radioimmunoassay.

RESULTS AND DISCUSSION

The release of PGI_2 was induced by wall shear stress and was magnitude-dependent for rectangle flow chamber. For bifurcation and sudden-expansion chamber, the release of PGI_2 was lower compared to rectangle chamber at the Re number 37.2(see figure 1). The release of ET-1 was more complex, with low shear stress inducing the secretion and high shear stress inhibiting the secretion. For different flow chamber at the Re number 37.2, the release of ET-1 in bifurcation and expansion chamber was also lower than rectangle chamber (see figure2). In conclusion, the secretory pattern of PGI_2 and ET-1 was different under different flow pattern.

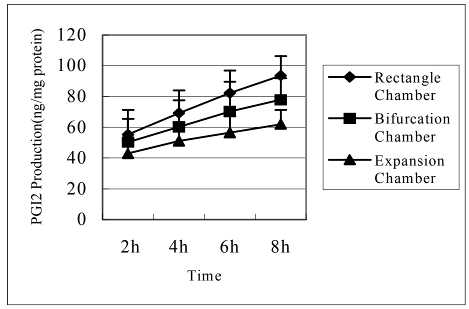

Figure 1: Cumulative PGI_2 release in different flow chambers at Re number 37.2.

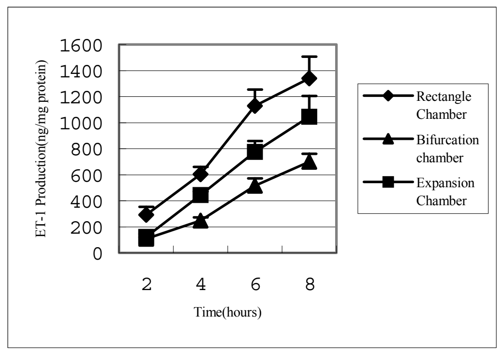

Figure 2: Cumulative ET-1 release in different flow chambers at Re number 37.2.

SUMMARY

Three kinds of flow chamber were constructed and flow patterns were simulated. BAEC monolayers were subjected to these different flow conditions and the release of vasoactive mediators was determined. It was showed the secretion of PGI_2 and ET-1 was affected by flow patterns.

REFERENCES

Nerem, R.M. et al (1998). *Am J Med Sci*,**316**,169-175.
Noris M. et al (1995). *Circ Res*,**76**,536-543.

RELATIONSHIP BETWEEN FREQUENCY COMPONENTS OF PHYSIOLOGICAL TREMOR AND ELASTIC LOAD

Masato Takanokura[1] and Kazuyoshi Sakamoto[2]
[1]Department of Industrial Engineering and Management, Kanagawa University, Yokohama, Japan, takanokura@ie.kanagawa-u.ac.jp
[2]Department of Systems Engineering, The University of Electro-Communications, Tokyo, Japan

INTRODUCTION

Physiological tremor (hereafter referred to as tremor) is an involuntary and continuous oscillation of a limb segment of the healthy human. When no external load is applied to the limb segment, the tremor is composed of two frequency components. It has been proposed that the two frequency components of the tremor are produced by two nervous systems, i.e., the stretch reflex system via the spinal cord and the supraspinal system. The frequency component caused by the stretch reflex system depends on the resonant frequency of the mechanical system of the limb segment. Therefore, some researchers observed that the frequency and the amplitude of the frequency components of the tremor changed with the kind of the limb segment or with the mass of the weight load (e.g., Takanokura and Sakamoto, 2001). The elastic load is an important factor that determines the resonant frequency of the mechanical system. The aim of this study is to investigate the relationship between the frequency components of the tremor in the finger and the elastic load.

METHODS

Subjects were ten healthy males aged 22 to 28. During the experiment, a right index finger of the subject was maintained in a stretched position. The other fingers, the hand, and the forearm were put on a board. The elastic load was applied to the index finger by a tension spring. The subject was asked to pull the tension spring by the index finger and to maintain the finger in a stretched position. When the index finger became horizontal, the tension spring was extended to 5mm from the natural length. Twelve kinds of the tension spring were used. The elastic coefficient ranged from 0.05-0.78N/mm. The tremor was measured by an acceleration sensor (9G111BW, NEC Sanei, Japan). The sensor was placed on the tip of the index finger. The measured signal was fed into a charge amplifier, and then it was stored on a personal computer at a sampling frequency of 200Hz. To quantify the frequency component of the tremor, the power spectrum was calculated by using the autoregressive (AR) model, and the frequency at the peak of the spectrum (i.e., peak frequency) was evaluated.

RESULTS AND DISCUSSION

Figure 1 shows the peak frequency of the tremor spectrum. Under the condition without the elastic load (i.e., 0N/mm), the tremor was composed of two frequency components at around 10Hz and 23Hz. The component at 10Hz did not change with the elastic load. When the elastic load was applied to the finger, the component at 23Hz was split into two components. One of the components did not change with the elastic load, and its frequency was about 23Hz. The other component was shifted to the higher frequency domain. Takanokura and Sakamoto (2001) proposed that the load-dependent component of the tremor was produced by the stretch reflex system, and its frequency depended on the resonant frequency of the mechanical system. Since the resonant frequency increases with the elastic coefficient of the spring, the load-dependent component is shifted to the higher frequency domain. It is considered that the load-independent components at 10Hz and 23Hz are produced by the supraspinal system because these components do not depend on the elastic load. This hypothesis agrees with the suggestion of McAuley et al. (1997) who also observe the three frequency components at 10Hz, 20Hz, and 40Hz under the existence of the elastic load. They suggested that all the components were produced by the supraspinal system. In this study, the load-independent components at 10Hz and 23Hz are also caused by the supraspinal system. However, the load-dependent component is produced by the stretch reflex system because this component depends on the resonant frequency of the mechanical system.

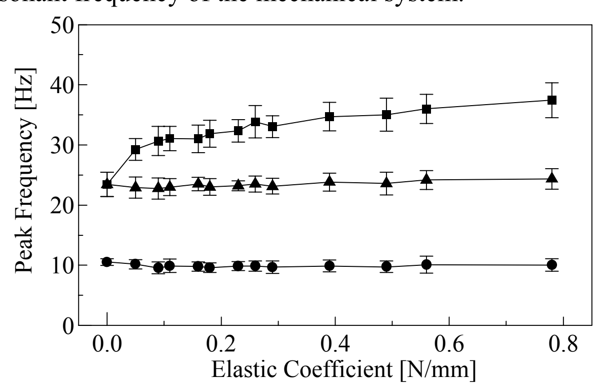

Figure 1: Dependence of peak frequency of tremor spectrum on elastic coefficient of spring.

SUMMARY

The relationship between the frequency components of the tremor and the elastic load is investigated. When the elastic load is applied to the finger, the tremor is composed of three frequency components. The load-independent components at 10Hz and 23Hz are caused by the supraspinal system. The load-dependent component is produced by the stretch reflex system, and its frequency depends on the resonant frequency of the mechanical system.

REFERENCES

McAuley J.H. et al. (1997). *Exp. Brain Res.*, **114**, 525-541
Takanokura M., Sakamoto K. (2001). *Eur. J. Appl. Physiol.*, **85**, 214-225

INFLUENCE OF PLASTIC STRAIN ON THE FATIGUE WEAR OF UHMWPE IN KNEE PROSTHESES

Changhee Cho[1], Teruo Murakami[1], Yoshinori Sawae[1], Nobuo Sakai[1],
Hiromasa Miura[2], Tsutomu Kawano[2] and Yukihide Iwamoto[2]

[1]Department of Intelligent Machinery and Systems, Faculty of Engineering, Kyushu University
6-10-1 Hakozaki, Higashi-ku, Fukuoka 812-8581, Japan, choch@mech.kyushu-u.ac.jp
[2]Department of Orthopaedic Surgery, Faculty of Medicine, Kyushu University
3-1-1 Maidashi, Higashi-ku, Fukuoka 812-8582, Japan

INTRODUCTION

The wear phenomenon of ultra-high molecular weight polyethylene (UHMWPE) in the knee and hip prostheses is one of the major restriction factors on the longevity of these implants. In the retrieved knee prostheses with anatomical design in particular, the most predominant types of wear on UHMWPE tibial components are pitting and delamination. These fatigue wear of UHMWPE are believed to result from the repeated plastic deformation due to high contact stresses. In this study, elasto-plastic contact analyses of the UHMWPE tibial components were performed using FEM to investigate the plastic deformation behavior in the UHMWPE tibial components.

MATERIALS AND METHODS

Two types of analyses were performed in this study. First, static and kinematic contact analyses of simplified knee prosthesis models that consisted of a hemispherical rigid surface with a radius of 30 mm and UHMWPE plates with various thicknesses were performed to investigate the factors that influence the plastic deformation behavior and the fatigue wear mechanism of UHMWPE. Second, in order to investigate the pattern of the generation and progression of the fatigue wear in the UHMWPE tibial component, contact analyses of the UHMWPE tibial components based on geometrical measurement for two retrieved knee prostheses were performed. Figure 1 shows an example of retrieved knee prosthesis (Press-Fit Condylar type, left side, 74 months *in vivo*) in this second type analysis. Nondestructive cross-section observation on the retrieved UHMWPE tibial components was also performed using a micro focus X-ray CT apparatus.
In this study, UHMWPE was assumed to be an elasto-plastic material and simple tensile tests of UHMWPE were carried out in a temperature-controlled container to establish a finite element material model of UHMWPE.

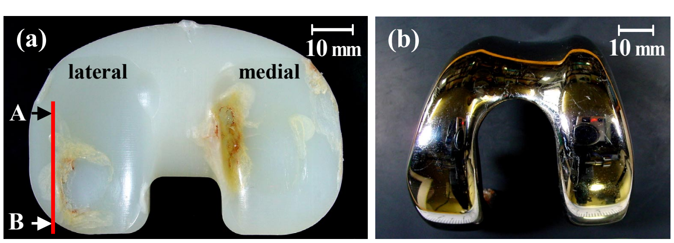

Figure 1: Components of a retrieved PFC type knee prosthesis, (a) UHMWPE tibial component, (b) femoral component.

RESULTS AND DISCUSSION

In the static and kinematic contact analyses of simplified knee prosthesis models, it was found that the magnitudes of the maximum von Mises stress and maximum plastic strain below the surface increase non-linearly with decreasing thickness of the UHMWPE tibial component. It was also found that the lower slip ratios, which mean higher range of rolling motion cause higher plastic strain both on and below the surface than higher slip ratio. These results suggest that thickness of UHMWPE and slip ratio in the knee prosthesis have a significant effect on its fatigue wear mechanism (Cho, C.H. et al, 2001).
In the contact analyses of the UHMWPE tibial components based on geometrical measurement for retrieved knee prostheses, it was found that the maximum plastic strain occurred at approximately 1 mm below the surface (Figure 2). This depth nearly corresponds to the location of subsurface cracks found in the retrieved UHMWPE tibial components (Figure 3). This result suggests that the maximum plastic strain below the surface is closely related to the subsurface crack initiation and delamination in the UHMWPE tibial components.

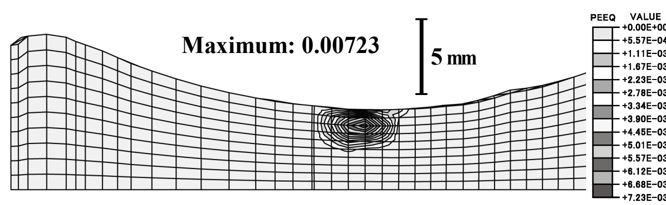

Figure 2: Contour plot of plastic strain in the lateral side of the PFC type UHMWPE tibial component.

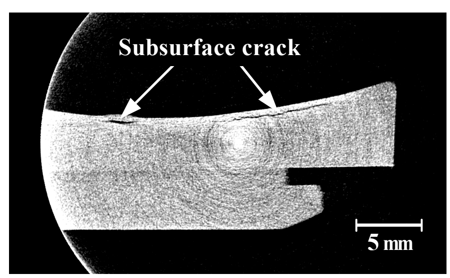

Figure 3: X-ray CT image of the UHMWPE tibial component including subsurface cracks (at line A-B in Figure 1).

REFERENCE

Cho, C.H. et al (2001). *Proceedings of the International Tribology Conference Nagasaki, 2000*, **2**, 1503-1508.

SPEED AND CADENCE DIFFERENCES BETWEEN CORNERING AND STRAIGHT TRACK RIDING IN 4KM INDIVIDUAL PURSUIT

Baiming Zhang, Danny P. K. Chu and Kenneth Mau
Sports Science Department, Hong Kong Sports Institute, Hong Kong, China
Zhangbm@hksdb.org.hk

INTRODUCTION

In track racing, there are two types of track lengths, 250m and 333m. Many coaches and athletes thought that the 4km pursuit track cyclists would maintain a steady velocity to in each round. However, the findings showed that there was a fluctuation of speed during cornering and straight track riding. This fluctuation was produced by the cyclist involuntary. The objective of this study was to determine the differences of speed and cadence of 4km pursuit cyclist between cornering and straight track riding.

METHODS

Totally six elite level track cyclists were employed. There were six trials of 4km pursuit training for each cyclist. The power output, cadence and speed were recorded during the training. A video camera (50Hz) was synchronized with the Schroberer Rad Mebtechnik (SRM) System. The function of video was to provide visual reference for the selection of the cornering and straight track riding data (except starting lap).

RESULTS AND DISCUSSION

Table 1 shows the average speed, cadence and their variations during cornering and straight track riding. The average speed and cadence in straight track riding from 250m and 333m tracks were significantly smaller than in cornering ($p < 0.001$). Moreover, the variation of speed and cadence was significantly increased ($p < 0.001$) with the curvature of the track (i.e. from 333m to 250m). The change in speed and cadence in 250m track was double the 333m track. The reason may due to the increase of centripetal force when riding on a small curvature track. So, the ground reaction force on bike increased. The frictional force between the surface and rear tire would be increased. The frictional force on the rear tire could increase the speed of bike.

The pursuit cyclist could make use of this phenomena - " acceleration in cornering and speed maintenance in straight track". The use of external force for acceleration would have a better result.

SUMMARY

The speed and cadence of 4km track cyclists depended on the whether the cyclist was cornering or straight track riding. The speed during cornering was faster. The speed variation was inversely related with the radius of curvature of track. The radius of curvature in 250m track is smaller than 333m so the speed in 250m track was double the 333m track.

REFERENCES

Broker, J.P., Kyle, C.R. and Burke, E.R.（1999）. Med. Sci. Sports and Exercise, 1677-1685.

Bassett, D.R., Kyle, C.R., Passfield, L., Broker, J.P. and Burke, E.R. (1999）. Med. Sci. Sports and Exercise, 1665-1676.

Table 1：The average speed and cadence variations in straight road and bent curves.

Track	Straight track riding		Cornering		Speed change		Cadence change	
	Speed (km/h)	Cadence (rev/min)	Speed (km/h)	Cadence (rev/min)	S-C	C-S	S-C	C-S
250m	48.38	112.42	49.88	115.73	1.49	-1.62	3.29	-3.58
	±1.03	±2.40	±1.07	±2.51	±0.43	±0.62	±1.02	±1.51
333m	50.15	113.73	50.83	115.18	0.63	-0.80	1.34	-1.71
	±1.09	±2.48	±1.05	±2.35	±0.36	±0.45	±0.81	±1.02

Remark: S-C - from straight to corner ; C-S from corner to straight.

FE-SIMULATION OF BONE MODELING AROUND A DENTAL IMPLANT IN TWO-STAGE-HEALING AS COMPARED TO EARLY LOADING

Qiguo Rong[1], Juergen Lenz[2], Karl Schweizerhof[1], Hans J. Schindler[2] and Dieter Riediger[3]

[1]Institut fuer Mechanik, Universitaet Karlsruhe, Karlsruhe, Germany
[2]Institut fuer Wissenschaftliches Rechnen und Mathematische Modellbildung, Universitaet Karlsruhe, Karlsruhe, Germany
[3]Klinikum fuer Zahn-, Mund-, Kiefer- und plastische Gesichtschirurgie, RWTH Aachen, Aachen, Germany

INTRODUCTION

In dental implantology the classical procedure consists of 1) a healing phase of several months during which the implant is not loaded directly, i.e. the repair zone between the (submerged) implant and bone, containing demineralized bone substance and coagulum, experiences only stresses caused by deformations of the mandible under functional loads, and 2) a subsequent loading phase after the connection of the implant with a suprastructure (two-stage healing). Recently, also a one-stage (early loading) procedure which omits the primary healing phase, has come into use.

This contribution presents a Finite Element (FE) model for the ossification process of the repair zone for the two-stage as well as for the early loading procedure.

METHODS

The geometrical FE model consists of a realistic mandible with a cylindrical titanium implant (diameter: 4 mm) at the site of a premolar (insertion depth: 16 mm). The mandible is loaded by a realistic force distribution of the chewing muscles such that an average periodic chewing force of 100 N is transferred at the premolar site. In the different cross sections of the mandible realistic distributions of cortical and spongy bone are chosen. The thickness of the repair zone around the implant amounts to 500 µm, and a perfect bond between its material and the implant is assumed. The following Young's moduli are used: E_T = 110 GPa for titanium, E_C = 18 GPa for cortical and E_S = 2 GPa for spongy bone, and E_0 = 500 MPa as initial value for the material in the repair zone.

Ossification characterized by an incremental increase ΔE_C and ΔE_S of Young's modulus of elements in the cortical and spongy section of the repair zone, is only allowed if the "stimulus", here chosen as the equivalent stress σ_{eqv}, falls into a so-called "stimulus window" determined by a lower and an upper bound. Too small stimuli ("underloading") and too high stimuli ("overloading") lead to bone resorption, i.e. a small reduction of the actual values of Young's modulus. Furthermore, bone apposition has to follow revascularisation, i.e through "bridging" from the intact bone surface in the direction towards the implant: An increase of Young's modulus is only allowed in an element if it is connected over at least one node via a "bridge" with elements of the intact bone's surface, and if these bridging elements have experienced at least one increase of their Young's modulus under preceding stimuli.

RESULTS AND DISCUSSION

The degree of ossification after the n[th] loading step is defined as $\kappa_{C,S}(n) = \{\sum E_i(n) V_i\} / (E_{C,S} V_{C,S})$ in the cortical (C) and in the spongy (S) section of the repair zone. Here $E_i(n)$ denotes the Young's modulus of the i^{th} element after the n^{th} loading step, V_i its volume, E_C and E_S the target values of the Young's moduli as given above, V_C and V_S the total volume of the repair zone in the cortical and spongy section, respectively.

Parameter studies show that for proper choices $\sigma_{eqv,l}$ and $\sigma_{eqv,u}$ of the lower and upper bound of the stimulus window, all healing processes lead asymptotically to a non-perfect state of ossification (κ_C and/or κ_S < 100 %). The lower bound of the stimulus window determines dominantly the attainable degree of ossification of spongy bone, the upper bound that one of cortical bone. The special choice $\sigma_{eqv,l}$ = 0.3 MPa and $\sigma_{eqv,u}$ = 5 MPa leads to ossification processes as illustrated in Fig. 1. In the two-stage procedure rather high degrees of ossification, κ_C and κ_S, are reached at the end of the first interval (submerged implant), but in the subsequent loading phase κ_C decreases drastically, whereas κ_S experiences a further increase. In contrast to this, in the one-stage procedure κ_C and κ_S grow monotonically to similar asymptotic values.

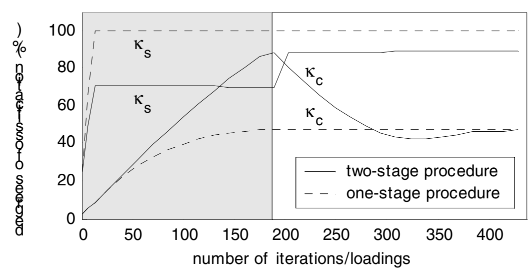

Figure 1: Two-stage and one-stage ossification process.

SUMMARY

The model can simulate certain clinically observed facts: The decrease of κ_C in the second interval of the two-stage procedure clearly corresponds to the well-known crestal bone loss around the neck of the implant and must be attributed to overloading according to this model. The clinically reported success of one-stage implantation is sustained by the computed values κ_C and κ_S. In this case, however, the relative displacements between implant and bone are distinctly higher than in the two-stage procedure.

OPTICAL MOTION CONTOROL OF EUGLENA FOR BIO-MEMS

Akitoshi Itoh[1] and Yoji Toyoda[2]
[1] Department of Mechanical Engineering, Tokyo Denki University, Tokyo, Japan, aitoh@cck.dendai.ac.jp
[2]Graduate School Student, Tokyo Denki University

INTRODUCTION

If the motion of microorganisms can be controlled, we can apply it as living micro machines. In fact, many micro-organisms have the properties of "taxis". The authors have investigated to control the motion of protozoa by applying the galvano-taxis. The results showed that we could control the motion of paramecium and some ciliates by changing the electrical field. The authors also succeeded to rotate the micro impeller by using controlled paramecium. However, this method could not be applicable for mastigophora or sarcodina. Therefore, this study investigates the motion control of protozoa by applying phototaxis. The experimental protozoa are typical photo-responsive mastigophora, *"Euglena gracilis"*. The body length of euglena is about 40-50μm.

BASIC REACTION PROPERTIES OF EUGLENA

Phototaxis of euglena can be classified to two categories, positive phototaxis and negative phototaxis. These phototaxis are occurred by the positive/negative photophobic response, which is the response if the brightness of environment is changed (step-up/step-down). In that case, euglena turns its swimming course about $2/3\pi$ rad. If the optical intensity is gradually changed, euglena swims to/against the light source. This orientation phototaxis is occurred by the stastical accumulation of photophobic response.

After the basic property experiment, it was clarified that the application of the photophobic response is more suitable than that of orientation phototaxis for the individual control of euglena. The response rate of the negative photophobic response is higher than the positive photophobic response.

Therefore, the application of negative photophobic response is suitable to control behavior by changing the optical field.

THE EXAMINATION OF THE CONTROL METHOD

The authors decided the control method as follows. (1)Every area of the experimental pool is illuminated by the strong light. (2)The dark spot is made to capture euglena within it. (3)The motion of the euglena is controlled by moving the dark spot.

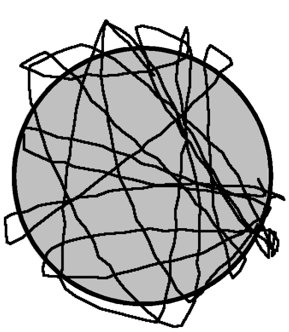

Fig.1 A trace of a euglena in a dark spot

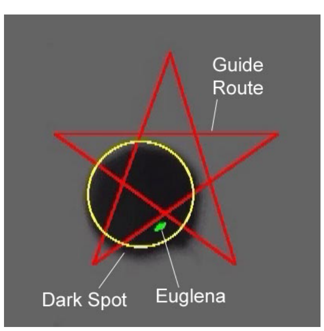

Fig.2 A sequential motion control experiment

The preliminary experiment showed that euglena could be captured in the dark spot by using this control method.

Therefore, the effect of the diameter of the dark spot on the captured time of euglena and on the generation ratio of photophobic response at the bright/dark boundary was investigated. The swimming route of a euglena in 40 seconds when the euglena was captured in the dark spot of ϕ0.4mm was illustrated in Fig.1. Euglena certainly showed photophobic response in the bright/dark boundary. The turning angle of the swimming direction, however, was not fixed in $2/3\pi$ rad, but euglena turned in the various angles.

In some cases, when a euglena turns in the bright/dark boundary, the euglena does not return to the dark field, but escapes to the bright field. Therefore, the returning ratio to the dark field is 80% in the largest. The larger the diameter is, the more the average capturing time and the returning ratio to the dark field increases. Hence, we have to build the control system on the assumption that sometimes euglena escapes from dark spot.

MOTION CONTROL EXPERIMENT

Based on the above results, an experimental system was constructed by using a personal computer and a XY moving table. In this system, a dark spot can be moved by moving the mask on XY table. In this system, the image of the microscope is captured to the personal computer, and the position of the dark spot and that of euglena can be automatically detected.

First, an experiment was done in a condition that a dark spot was sequentially moved without detecting the position of the euglena. To investigate the suitable moving time of the dark spot, the capturing time of a euglena was measured in the condition that the dark spot was moved constantly with reciprocating motion. The results showed that the moving distance of 0.01 - 0.03 mm/s is suitable for the sequential control of euglena. Therefore, a sequential motion control experiment was done. Sometimes euglena is completely followed to the dark spot. However, the capturing of euglena in the dark spot is not stable. Fig.2 is an image processed flame shot of an experimental video.

Therefore, a visual feedback program was made. In this program, the computer always detected the position of the euglena, and if the euglena is escaped from the dark spot, dark spot was moved to the position of the euglena to capture again.

REFERENCES

Itoh, A. (2000). *IEEE/ASME Transactions on Mechatronics,* **5**, 2, 181-188

COMPUTATIONAL FLUID DYNAMICS (CFD) SIMULATION OF THE HUMAN CYSTIC DUCT

Renn Chan Ooi[1] , Xiao Yu Luo[1], S Boon Chin[1], Alan Johnson[2] and Nigel Bird[2]
University of Sheffield, Sheffield, United Kingdom
[1]Department of Mechanical Engineering, r.c.ooi@sheffield.ac.uk
[2]Department of Surgical & Anaesthetic Sciences

INTRODUCTION

Statistical observations by Deenitchin et al (1998) suggested that complex cystic duct geometry is frequent among cholelithiasis patients. Reduction in gallbladder (GB) motility involves its inefficient emptying. Jazrawi et al (1995) showed that gallstone patients had lower GB turnover rate (GB evacuation fraction). Nakayama and van der Linden (1975) observed stratification of the bile in GB and are often regarded as a precursor to gallstone formation. These studies suggest that fluid mechanics of the biliary system may be an important factor in GB diseases. This paper describes the results of CFD simulations in studying the influence of the cystic duct geometry on its resistance and its relation to the GB turnover rate.

METHODOLOGY

Initially, cystic duct was idealised by a 2D channel with staggered baffles to capture the important flow features. A series of such models with varying geometrical and flow parameters was used to study their contribution towards the cystic duct resistance. Then more realistic geometries were employed from patients' 2D X-ray images. Patient A had gallstone and Patient B had a healthy GB. Qualitatively, the former cystic duct was longer with more folds (spirals) than that of the latter. The results were compared with those from idealised models to assess the usefulness of the latter. The numerical simulations were performed using the finite volume based CFD software, Fluent5.

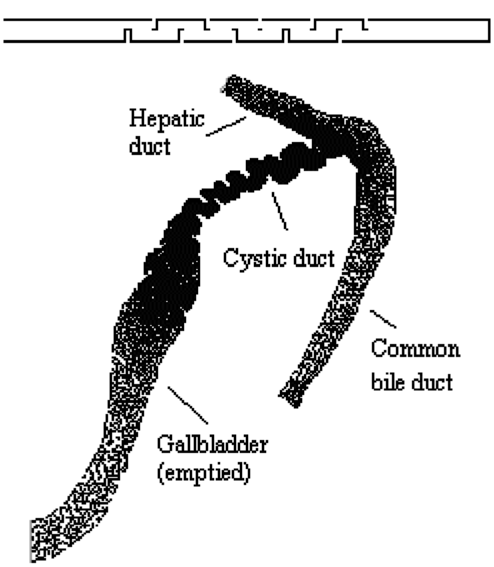

Figure 1: (Top) a typical idealised geometry of the cystic duct and (bottom) computational grid of Patient A’s biliary system.

RESULTS AND DISCUSSION

Boundary conditions were obtained from physiological flow rate measurements. Laminar, steady state flow of Newtonian bile was assumed. The cystic duct resistance, R_n, is defined as:

$$R_n = \Delta P / Q$$

where ΔP = pressure drop across duct, Q = flow rate,
The relative resistance R_d:

$$R_d = R_{n=i} / R_{n=0}$$

where $R_{n=i}$ is the resistance of duct with *i*-number of baffles.

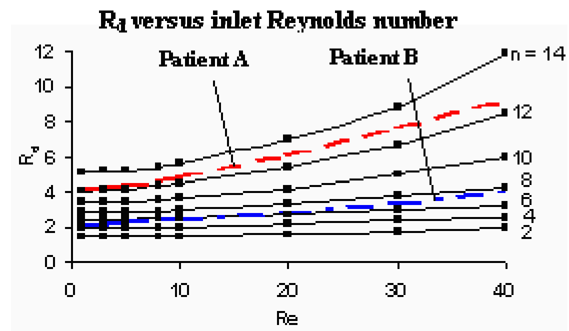

Figure 2: R_d vs Re for various number of baffles (n)

CFD results show that R_d increases with Reynolds number (Re), increasing number of baffles and decreasing baffle spacing. R_d of the two models from patients falls well in the range of the idealised models. Patient A showed higher resistance than patient B, suggesting that its more complex geometry hinders bile flow to and from GB. This may result in reduced GB turnover rate, possibly contributing to gallstone formation. Further simulations on more patients and the GB motility would be required to establish the role of fluid mechanics in GB diseases.

SUMMARY

Numerical simulation of the human cystic duct shows that the flow resistance increases with complexity of the duct geometry. This finding provides promising evidence that fluid mechanics of the biliary system may be a contributing factor to gallbladder diseases. Further work should include *in vivo* and *in vitro* study of the GB motility and the biliary system.

REFERENCES

Deenitchin, G. P. et al (1998). *HPB Surgery*, **11**, 33-37.
Jazrawi, R. P. et al (1995) *Gastroenterology*, **109**, 582-591.
Nakayama, F. and van der Linden, W. (1975). *Surg Gynecol Obstet*, 1975, **141**, 587-90.

THE DEVELOPMENT OF A PRELIMINARY FINITE ELEMENT MODEL OF THE FIFTH RIB.

Michael Dean[1], Anthony Bull[2], Alison McGregor[1]

[1] Department of Musculoskeletal Surgery, Faculty of Medicine, Imperial College of Science, Technology & Medicine, Charing Cross Hospital, London, U.K.
[2] Department of Bioengineering, Imperial College of Science, Technology & Medicine, Exhibition Road, London, U.K.
Email contact: a.mcgregor@ic.ac.uk

INTRODUCTION

Stress fractures of the forth to ninth rib account for between 5% and 14% of injuries amongst competitive rowers, particularly at an elite level (Wajswelner et al 2000). Little is known regarding the aetiology of these fractures but they are thought to be associated with the nature of the sport and its training regimes (Christiansen & Kanstrup 1997). This is further compounded by an inadequate understanding of thoracic biomechanics particularly in terms of force transmission between the upper limb and thorax and how this is influenced by spinal mobility. Previous studies of this problem have only been of an analytical nature (Satou & Konisi 1991). In an attempt to understand these injuries a series of anatomical and mechanical studies were undertaken with the main aim of the study being to develop a finite element (FE) model of the rib.

METHODS

Three cadaveric dissection were undertaken to record the musculoligamentous attachment points and fibre orientation of the left and right fifth ribs in relation to the wider thorax, providing a data set of six ribs. Two additional geometrical data sets were obtained from cadaveric rib CT scans. The three dimensional geometry of the rib was then measured using a custom made box gantry to record the position of predetermined points along the rib. A finite element model was created using the ProEngineer preprocessor. Loading and boundary conditions were applied based on the anatomical details and analysed using ANSYS.

RESULTS

There was considerable inter and intra individual variation in the musculoligamentous attachments to the fifth ribs. There was a similar large variation in the geometry of the ribs for example a 3mm difference in rib length was noted between the left and right sides. However, the application of simple loading conditions analogous to the force transmission through the thorax, to the upper limb during the drive of the rowing stroke showed a force concentration at the anatomical mid auxillary line that is a common stress fracture site in rowers.

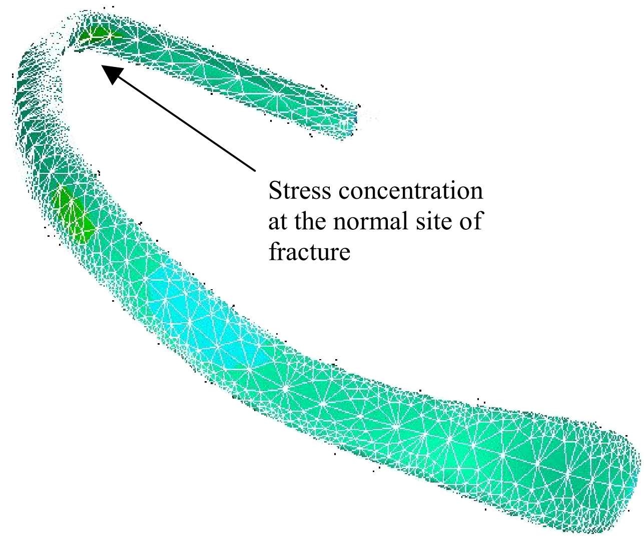

Figure 1~ Finite Element model of the fifth rib with stress concentration at the mid auxillary line.

DISCUSSION

A preliminary FEA model of the rib has been constructed, and the application of different loading conditions to this model has suggested that it may be of value in understanding the mechanical failure of this structure. This is of value due to the immense difficulty of accurately imaging or studying the thorax using conventional imaging or biomechanical methods. Using the experience gained from this study we hope to apply conventional imaging and biomechanical techniques in novel ways to create further FE rib models with interfaces to the rest of the thorax and spine. This will be of use, not only in elucidating the pathogenesis of rib stress fractures in rowers, but also from a wider biomechanical standpoint in particular respiratory and impact biomechanics.

REFERENCES

Wajswelner H, et al (2000). Physical Therapy in Sport **1**:75-84.
Christiansen E., Kanstrup I.L., (1997). Scandinavian Journal of Medicine and Sports **7**:49-52
Satou S., Konisi N, (1991). Journal of the Japanese Orthopaedic Association **65**(9): 708-19.

TIME-DEPENDENT MATERIAL PROPERTIES OF THE PORCINE KIDNEY CAPSULAR MEMBRANE

Jess G. Snedeker[1], Romain Voide[1], Mehdi Farshad[2], Franz Schmidlin[3], Peter Niederer[1]

[1] ETH Zurich, Switzerland, www.biomed.ee.ethz.ch
[2] EMPA Dubendorf, Switzerland
[3] University Hospital, Geneva, Switzerland

INTRODUCTION

A thin capsular membrane helps protect the human kidney during blunt abdominal trauma. Identifying material properties and developing appropriate constitutive models is essential to examining the role of this membrane during impact. While some static mechanical properties of the capsular membrane have been established in the literature (Herbert et al. 1971, and Farshad et al. 1998), presently available renal capsule material test data do not account for the dependency of the stress state on strain rate.

METHODS

Since adult human kidneys are not sufficiently available for material testing, adult pig kidneys were selected as a human analog due to the anatomic and geometric similarity to the human organ. All material tests were performed within 36 hours of animal euthanization. Samples were delicately excised from each kidney using a sheet metal template to yield symmetric samples that could be used for method validation. Tissue samples were kept moist within a physiologic saline solution. The samples were then placed in the clamps of a uniaxial testing machine (Zwick GmbH.).

In order to validate the sample preparation protocol, quasi-static tensile test results were compared between axi-symmetric samples taken from the same kidney. The elastic modulii and ultimate breaking stresses of paired samples were compared to verify test repeatability. Preliminary tests were also performed to examine rate dependent properties The tissues were tested at stretch rates of 0.5%, 5%, and 50%L/s.

RESULTS

The pig kidney capsule exhibits highly variable material behavior both within a single kidney and between different kidneys. Despite this, the experimental protocol yielded similar results for paired samples (figure 1).

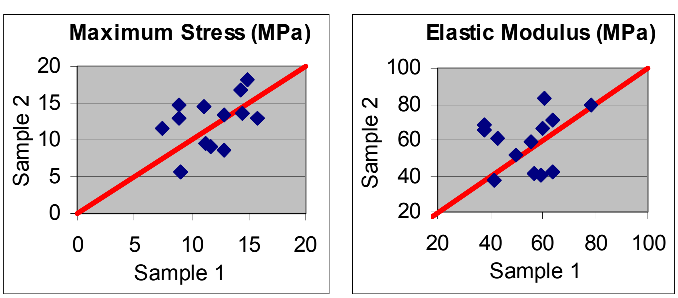

Figure 1. Results of paired samples from the same kidney.

As expected, the capsular membrane behaved viscoelasticly, becoming stiffer with increasing deformation rates (figure 2).

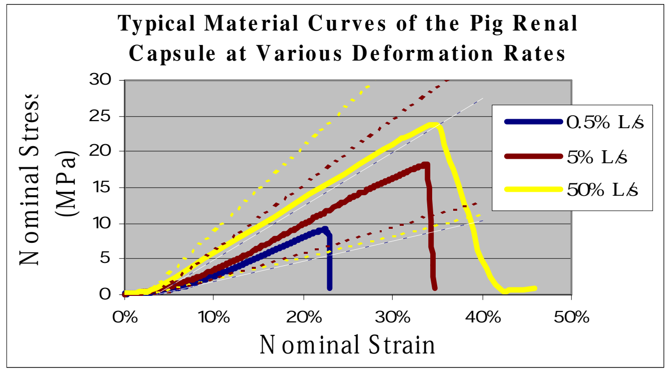

Figure 2. The pig renal capsule becomes stiffer as strain rate increases. Dashed lines indicate standard deviations.

Breaking stress and the corresponding breaking strain were also observed to depend on the rate deformation. Various rate dependent properties are listed in Table 1.

Table 1. Time dependent properties of the pig kidney capsule.

Strain Rate	# Samples	E (MPa)	Max. Stress (MPa)	Max. Strain (%)
0.5 % L/s	17	55 ± 14	11.6 ± 2.7	24.8 ± 5.2
5 % L/s	7	65 ± 29	14.8 ± 4.7	26.9±14.3
50 % L/s	8	73 ± 43	22.6 ± 9.6	29.7 ± 5.1

SUMMARY

Dynamic testing of the porcine renal capsule reveals a heavy material property dependence on deformation rate. To accurately model the kidney under traumatic loads, considerations for the viscoelastic capsule must be made. Future work is to include the development of a viscoelastic finite element trauma model of the renal capsule that is based upon the results of the present study.

REFERENCES

Farshad, M. et al (1998). *J Biomechanics*, **32**, 417-425
Herbert, L.A., et al (1976). *J. Applied Physiology*, **40**, 164-170

ACKNOWLEDGEMENTS

This work was funded by Swiss National Science Foundation grant # 3100-057158.

SIMULATION OF PHYSIOLOGICAL MUSCLE LOADING IN FINITE ELEMENT MODELLING OF THE INTACT FEMUR

K. Polgár[1], H.S. Gill[1], M. Viceconti[2], D.W. Murray[1], J.J. O'Connor[1]
[1]Oxford Orthopaedic Engineering Centre, Nuffield Department of Orthopaedic Surgery, University of Oxford, Oxford, UK
Correspondence to: krisztina.polgar@eng.ox.ac.uk
[2]Laboratorio di Tecnologia Medica, Istituti Ortopedici Rizzoli, Bologna, Italy

INTRODUCTION

Modelling studies are currently used to achieve better understanding of the mechanical environment of the natural and replaced hip joint. It is generally accepted that neglecting certain muscle actions will significantly alter the stress and strain distributions predicted by the finite element model within the bone. However, it is not clear whether each muscle force has to be modelled as distributed over the entire muscle attachment area, or it is acceptable to concentrate the force resultant into a given point, i.e. the attachment area centroid. Modelling the whole muscle insertion requires additional anatomical knowledge and may significantly complicate the model. However, the large size of certain insertion areas may violate the validity conditions of the St. Venant's Principle. Thus, the simplification may significantly alter the calculated stress and strain distribution within the bone tissue.

METHODS

A novel finite element model of the human femur was developed based on the CAD geometric description of the "Muscle Standardised Femur" (Viceconti et al., 2001). During the FE mesh generation procedure, each muscle attachment area was meshed separately on the femoral bone surface. The solid mesh was generated after the complete surface mesh had been defined. Two load cases, representing an instant at 10 % during gait cycle were analysed. The applied force data set was based on the muscle model by Brand et al. (Brand et al., 1986, 1994). In load case 1 (LC1), the effect of all muscle forces attached to the femur were taken into account and applied as concentrated forces at the muscle attachment area centroids. Load case 2 (LC2) represented the physiological load configuration where all muscle force actions were assumed to be uniformly distributed over the areas of their insertions. The displacement boundary conditions were applied to restrict rigid body motion, six degrees of freedom were constrained at the knee.

RESULTS AND DISCUSSION

Calculated displacement of the femoral head was not influenced by the mode of load application. For LC1 the femoral head moved an overall 2.3 mm medially (1.9 mm), posteriorly (1.2 mm) and distally (0.5 mm) relative to the knee. For LC2, the overall displacement differed only slightly, the head moved 2.4 mm in the same direction.

Peak tensile and compressive principal strains in the femoral diaphysis region exceeded 8800 $\mu\varepsilon$ and -9,600 $\mu\varepsilon$ for LC1. The peak principal strain values occurred in the femoral shaft region in the vicinity of the concentrated load application nodes. For LC2, the largest tensile and compressive principal strains were below 680 $\mu\varepsilon$ and -930 $\mu\varepsilon$. When data from those elements containing concentrated muscle force application nodes were excluded, peak tensile and compressive principal strains for LC1 exceeded 1500 $\mu\varepsilon$ and –1900 $\mu\varepsilon$, respectively. Although this is a substantial decrease, the difference between the peak values for simplified and the physiological load cases still exceeded 100 %.

On the internal bone surface no high peak strains were observed for LC1. Principal strains were compared in the internal surface nodes in the region of the concentrated load application. As an example, close to the vastus medialis attachment, compressive and tensile principal strains were still 25% (50 $\mu\varepsilon$) and 40% (30 $\mu\varepsilon$) higher respectively than those for LC2 at a distance of 20 mm (approximately 2.5 times the cortical thickness).

Non-zero normal stress residuals were observed on the internal bone surface around the load application regions. At the gluteus maximus attachment area, peak values of normal stress residuals three times larger for LC1 than for LC2.

CONCLUSION

The results of the current study suggest that when modelling the musculo-skeletal system with FE analysis, St. Venant's Principle should be applied with caution. When the aim of the study is to determine the physiological strain distribution inside the intact bone, realistic representation of the muscle loads transferred to the human femur during activities should be considered. Future work is required to investigate the effects of simplified loading on femurs after joint replacement.

REFERENCES

Viceconti, M., et al. (2001). The Muscle Standardised Femur. Submitted to the *J Biomechanics*

Brand, R.A. et al. (1994). Comparison of hip force calculations and measurements in the same patient. *J. Arthroplasty* **9**, 45-51.

Brand, R.A. et al. (1986). The sensitivity of muscle force predictions to changes in physiological cross-sectional area. *J. Biomechanics* **19**, 589-596.

SELF-SUSTAINING OSCILLATORY ELECTROMECHANICAL ACTIVITY IN THE GUT

Roustem Miftakhov and Michael Vannier

Department of Radiology, University of Iowa, 200 Hawkins Drive, Iowa City, IA 52241, USA; email: roustem-miftakhov@uiowa.edu

INTRODUCTION

Electromechanical conjugation, a fundamental neuromuscular phenomenon in the gut, is responsible for the major motor functions, mixing, grinding, and propulsion of the intraluminal content. It has been speculated that the electrical processes in muscle (slow waves, spiking activity) result from regulatory pacemaker input provided by interstitial cells of Cajal and/or intrinsic nerves. Electrophysiological recordings from the smooth muscle demonstrate self-oscillatory behavior of the syncytium due to randomly occurring and spatially distributed sites of electrical discharges. This implicates the role of intrinsic mechanisms in the regulatory electromechanical activity.

The aims of this study are: i) to model the gut as a biologically active cylindrical tube, and ii) to study numerically the dynamics of the electromechanical wave processes within it.

MODEL DESCRIPTION

The following assumptions are made in the formulation of a model: i) a segment of the gut is formed of the two smooth muscle layers, the longitudinal and circular layers; ii) the longitudinal layer possesses properties of electromechanical anisotropy, while the circular layer demonstrates isotropic characteristics; iii) spatially distributed, weakly connected oscillators define the electromyogenic properties of the syncytium; iv) strong connections among oscillators are provided by the propagating wave of excitation along the syncytium; v) the dynamics of oscillatory activity depends on ion channel function: L - and T - type Ca^{2+}, Ca^{2+} - K^+, Na^+, voltage dependent K^+ and Cl^- channels; vi) the mechanical activity is due to a cascade of intracellular reactions of myosin contractile proteins.

The problem leads mathematically to a combined system of partial and non-linear ordinary differential equations. Boundary and initial conditions assume that both ends of the shell are rigidly fixed and the excitatory signals are applied at the left boundary. Hybrid finite difference and finite element methods of second order accuracy, with respect to spatial and time variables, are used to solve the problem.

RESULTS AND DISCUSSION

The 100 mV 1 s discharge of a pacemaker located on the left boundary produces a wave, 68 – 70 mV, which propagates along the surface of the syncytium towards the right boundary at a constant velocity 0.5 cm /s. The anisotropic electrical properties of longitudinal layer make the front the wave an ellipse, while in the circular layer it forms a ring. Following the activation of contractile proteins, active forces of contraction change the shape of the gut.

The stimulation of the gut by a series of impulses (amplitude 100 mV, duration 1 s, and frequency 0.33 Hz) creates the two spiral waves propagating towards the distal end (fig. 1a, b). After their collision and reflection from the right boundary a strong spike of amplitude 90 mV is produced. It propagates backwards, reaches the middle of the segment and produces a circular wave (fig. 1c). After the wave covers the entire surface of the gut another set of spiral waves is generated. The process is repeated as above (fig. 1d). The pattern of electrical activity causes retrograde propagation of the mechanical wave of contraction-relaxation. The system converts to normal electromechanical activity after application of a sodium channel blocker compound.

SUMMARY

A new numerically discovered phenomenon of self-sustained electromechanical activity in the smooth muscle syncytium could explain normal and pathological motor patterns produced by the organ and observed *in vivo* and *in vitro*. The basis of the theoretical results needs to be established and verified experimentally. It would have enormous implication for our understanding of motor disorders of the gut.

Electrical Activity in the Gut

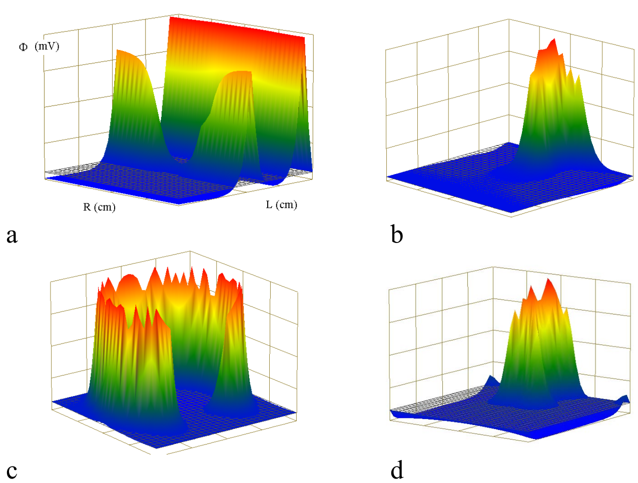

Figure 1: Dynamics of the generation of sustaining self-oscillatory activity in the smooth muscle syncytium of the gut.

GROUPING OF SCOLIOSIS PATIENTS BY SPINAL CURVE SEVERITY FROM TORSO SURFACE DATA

Jacob L. Jaremko[1], Philippe Poncet[1], Janet Ronsky[1], James A. Harder[1], Jean Dansereau[2], Hubert Labelle[2], Ronald F. Zernicke[1]

[1]McCaig Centre for Joint Injury & Arthritis Research, University of Calgary, Calgary, AB
[2]LIS-3D Laboratoire, Ecole Polytechnique & Ste. Justine Hospital, Montreal, PQ

INTRODUCTION

Because spinal curvature in scoliosis often progresses sufficiently to require treatment by bracing or surgery, scoliosis patients are currently monitored by full-spinal X-rays on which the Cobb angle of lateral spinal curvature is measured [1]. If it was possible to detect scoliosis curvature reliably from torso surface shape alone, the harm associated with radiation from these X-rays [2] could be avoided. The relation between surface and spinal deformity, however, is complex and difficult to characterize by linear methods [3-5]. An artificial neural network (ANN) performs nonlinear multivariate regression analysis using several layers of nodes and links analogous to biological neurons. An ANN "learns" generalizable relations between input and output data through repeated presentation of data sets. Here, we trained an ANN to estimate the Cobb angle of scoliosis deformity from asymmetry of the 360° torso surface shape and other non-radiologic data. Since brace treatment in scoliosis would almost certainly begin before the Cobb angle reached 30° and surgery would generally be performed when a curve reached 50° [1], we computed the accuracy with which the ANN categorized patients into three groups based on curve severity (0-30°, 30-50°, >50°).

METHODS

Patients: We had 48 consecutive, consenting scoliosis clinic patients aged 8-18 (38 female) who had never had spinal surgery. The neural network was trained using 89 scans of these patients collected in four semi-annual sessions, and tested using 26 scans of those patients who attended a fifth session. Cobb angles varied from 10-71°.

Imaging: A 3-D torso surface model of each patient was generated from surface coordinates acquired by four laser cameras, and a postero-anterior X-ray was taken as the patient stood in the same position [6].

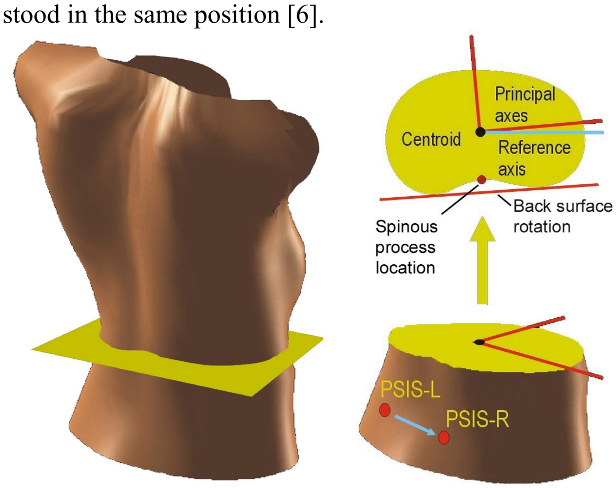

Figure 1: Key indicators of torso surface cross-sectional deformity used in neural-network estimation of scoliosis severity.

Indices: Indices were recorded for each visit of each patient. Genetic algorithm optimization gave a neural network that estimated the Cobb angle from 17 input indices including clinical parameters such as height and body mass index, the maxima and range of surface asymmetry measures such as back surface rotation, cross-sectional eccentricity, spinous process line and cross-section centroid lateral deviation, and asymmetry between left and right halves of cross-sections (Figure 1).

RESULTS

The ANN categorized 83/89 training-set records (93%) and 24/26 test-set records (92%) into the correct group based on curve severity (Cobb angle 0-30°, 30-50°, >50°; Table 1).

DISCUSSION

Neural network analysis of torso surface asymmetry correctly classified >90% of patient-records (whether or not those records had been used for network training) into one of three groups representing those likely to be treated by observation (0-30°), bracing (30-50°) or surgery (50°+). This accuracy encourages further work to detect scoliosis progression in individual patients without repeated X-rays.

REFERENCES

1. Reamy B.V., Slakey J.B. (2001). *Am Fam Physician,* **64**, 111-116. 2. Levy, A.R. et al. (1996) *Spine,* **21**, 1540-1548. 3. Pope, M.H., et al. (1984). *CRC Crit Rev Biomed Eng,* **11,** 157-188. 4. Goldberg, C.J. et al. (2001). *Spine* **26**, 55-63. 5. Stokes, I.A., Moreland, M.S. (1989), *Spine*, **14**, 73-78. 6. Poncet, P. et al. (2000). *Comp Meth Biomech Biomed Eng,* **4**, 59-75.

Curve severity group	Training Set correct	Training Set total	Test Set correct	Test Set total
Mild (Cobb angle 0-30°)	41	43	15	16
Moderate (Cobb angle 31-50°)	30	34	6	7
Severe (Cobb angle 51° +)	12	12	3	3
Total	83	89	24	26
Accuracy score	93.3%		92.3%	

Table 1: Accuracy of neural network categorization of scoliosis patients into treatment groups using torso surface asymmetry data in 115 patients.

FINITE ELEMENT MODELS OF ABDOMINAL ORGANS FOR USE IN TRAUMA RESEARCH

Jess G. Snedeker[1], Joeri Rogelj[1], Mehdi Farshad[2], Franz Schmidlin[3], Peter Niederer[1]

[1] ETH Zurich, Switzerland, www.biomed.ee.ethz.ch
[2] EMPA Dubendorf, Switzerland
[3] University Hospital, Geneva, Switzerland

INTRODUCTION

The abdomen is the largest cavity of the human body and ranks third with regard to injured body regions. Blunt abdominal trauma leads mainly to injuries of the kidney, the liver and the spleen, all of which may result in morbidity or mortality in the injured person. Trauma research has historically focused on other regions of the body (e.g. head, thorax). Therefore the mechanisms of renal trauma are largely unknown. To this end, a high-resolution finite element model of the kidney has been constructed, as well as models of several neighboring organs, specifically the liver and spleen.

METHODS

An image segmentation and organ reconstruction software package was employed to transform 2D Visible Human Female Project (National Library of Medicine) dataset images into 3D polygonal representations. NURBS surfaces were then mapped to the polygonal organ surfaces, and were finally used within commercial meshing software to create robust 3D finite element meshes of the kidney, liver, and spleen.

A combined linear viscoelastic and Ogden hyperelastic material model was developed for the kidney using a least squares fit to experimental test data of pig organs in dynamic compression (Melvin et al. 1974). Since the current project focuses specifically on traumatic effects in the kidney, a more simple Hookean material was used for the spleen and the liver.

RESULTS

Specific information pertaining to the finite element models is listed in Table 1.

Table 1. Abdominal organ FE model specifications.

Organ	Element Type	# of Elements	Material Model (Units MPa)
Kidney	20 Node Hex	165,000	Ogden/Viscoelastic
Liver	4 Node Tet.	14,800	E=2.0, υ=0.4
Spleen	4 Node. Tet.	1,400	E=2.0, υ=0.4

The material model derived for the kidney was an incompressible, isotropic, third order Ogden hyperelastic material (μ_1= 0.15, α_1 = 0.3, μ_2= 0.53, α_2= 0.4, μ_3= -0.01, α3= -9.5) combined with a viscoelastic relaxation function that was implemented via a single term Prony series with constants g_1=0.93 and τ_1=2.5e-4.

Each model was tested for mathematical robustness within a simulation of quasi-static, parallel-plate compression that modelled the experiment used for identifying the material properties of the actual organs. The resultant von Mises stress distributions for all three organs are illustrated in Figure 1.

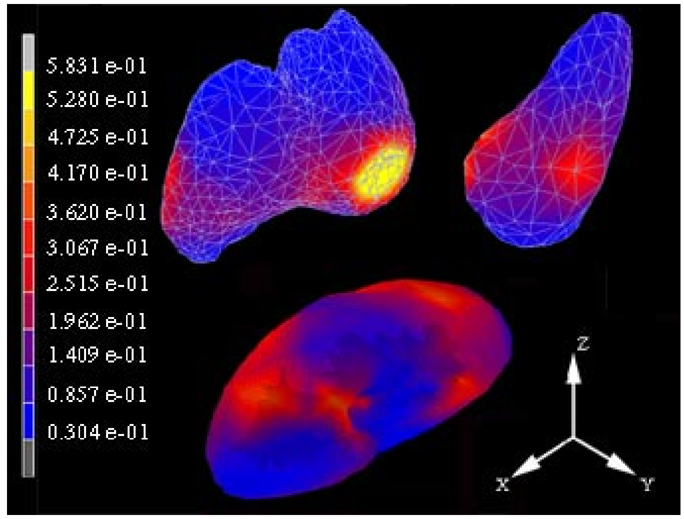

Figure 1. Von Mises stress distributions (clockwise from bottom) for the VHF kidney, liver, and spleen in parallel plate compression, at a nominal strain of 25%. The kidney is compressed along the z-axis, the liver and spleen along the y-axis. The organs are not similarly scaled. Stresses are MPa.

SUMMARY

Working finite element models of the VHF kidney, liver, and spleen have been created. Future models will include other soft organs and tissues, particularly the stomach, pancreas, abdominal fat, and fascia. A completed abdominal model can then be subjected to typical loading patterns derived from accidental impact situations, and exploited to analyze injury mechanisms, evaluate tolerance criteria, and eventually advance injury protection strategies.

REFERENCES

National Library of Medicine (www.nlm.nih.gov)
Melvin, J. et al. (1974). *Proc. 17th STAPP Conf.,* 115-126

ACKNOWLEDGEMENTS

This work was funded by Swiss National Science Foundation grant # 3100-057158.

POSTURAL CONTROL AND STRENGTH AMONG ELDERLY WITH AND WITHOUT A FEAR OF FALLING

Brenda Brouwer, Kristin Musselman and Elsie Culham
School of Rehabilitation Therapy, Queen's University, Kingston, Ontario, Canada, brouwerb@post.queensu.ca

INTRODUCATION

Almost 60% of community dwelling elderly have a fear of falling; well over the 30% of seniors who will experience a fall in a given year (Maki et al 1991). Fear of falling (FF) is of concern as it undermines self-confidence and contributes to self-imposed inactivity or restriction of activities, which may lead to deconditioning. This study explored whether those fearful of falling exhibit deficits in balance ability or physical function compared to non-fearful seniors and whether performance differed based on a 12 month fall history.

METHODS

Seniors recruited from the community were screened to ensure they had no medical conditions affecting balance. They self identified as either restricting their activities due to a concern about falling (FF group) or not (control). The Activities-specific Balance Confidence Scale (ABC) was used to measure FF in terms of subjects' confidence in performing specific daily activities (0 = no confidence; 100 = total confidence). Subjects with a FF were subdivided into those who had and had not fallen in the past 12 months. Participants provided consent and procedures were ethics approved.

Three tests of physical performance were completed in random order: 1) subjects shifted their weight on a force platform by moving about their ankles keeping knees and hips straight. The limits of stability (LOS) were the maximum displacements (cm) of the center of pressure (COP) in anterior, posterior, left and right directions relative to a resting COP position. 2) Isokinetic (60o/sec) flexor and extensor torques were measured about the ankle, knee and hip joints during 5 reciprocal, maximal, concentric contractions. Peak torque (gravity corrected) was normalized to body weight. 3) Natural cadence gait speed was calculated from the time to traverse the central 10 meters of a 15-meter walkway.

RESULTS AND DISCUSSION

Groups matched in age and gender make-up (Table 1). As expected, the FF group had lower ABC scores than controls ($p<0.001$). There were no differences attributable to fall history ($p>0.05$).

Table 1: Subject demographics (mean ± 1 SD)

	Age (yrs)	Male:Female	ABC score
Control (n=25)	76.3 ± 5.2	9:16	90.5 ± 7.9
FF (n=25)	76.4 ± 5.1	9:16	67.5 ± 15.3
No falls (n=13)	74.7 ± 5.3	2:11	70.9 ± 11.0
Falls (n=12)	78.2 ± 4.5	7:5	64.3 ± 18.3

Subjects with a FF were less willing to shift their COP, particularly in anterior and combined anterior-posterior (AP) directions ($p<0.05$; Figure 1). In those who had fallen in the past, LOS were less, but not significantly so. Those with a FF also walked more slowly than controls ($p<0.02$).

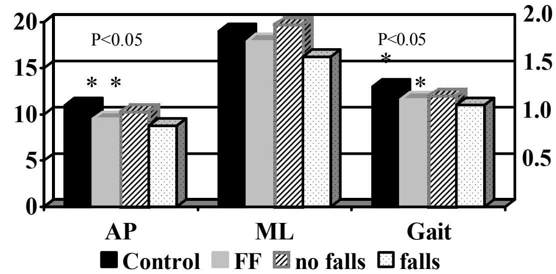

Figure 1: Mean maximal COP displacement (cm) in anterior - posterior (AP) and mediolateral (ML) directions. Gait speed is in m/sec (right axis)

The control group was stronger than the FF group for all muscle groups ($p<0.01$). Differences were most pronounced at the proximal joints (Figure 2).

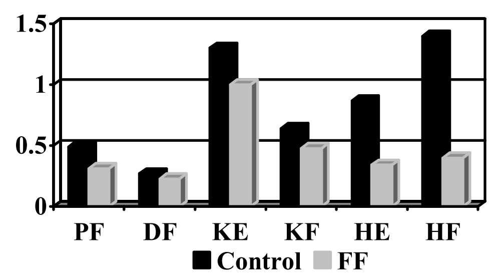

Figure 2: Peak torque (Nm/KgBW) for control and fear of falling (FF) groups. (Subgroups are not shown, as there were no differences based on fall history). PF=plantarflexors; DF=dorsi-flexors; KE=knee extensors; KF=knee flexors; HE=hip extensors; HF=hip flexors.

SUMMARY

Seniors with a self-identified FF had reduced balance confidence accompanied by declines in LOS, walking speed and lower limb strength compared to controls. Deficits appeared more prominent in those who had a prior fall, but not significantly so. The findings indicate limited balance ability and function in the presence of a fear of falling.

REFERENCES

Maki, B.E. et al. (1991). *J. Gerontol* ; 46(4): M123-131.

ACKNOWLEDGEMENTS

This project was funded by the Drummond Foundation.

SOLEUS H-REFLEX GAIN IN ELDERLY AND YOUNG ADULTS WHEN LYING, STANDING AND BALANCING

Gordon R. Chalmers[1] and Kathleen M. Knutzen

Dept. of Physical Education, Health and Recreation, Western Washington University, Bellingham WA, USA. [1]chalmers@cc.wwu.edu

INTRODUCTION

In young adults, the soleus Hoffmann (H-) reflex decreases in size, or gain, when changing from lying to standing (Koceja et al, 1995; Koceja et al, 1993). A decrease in H-reflex size is associated with tasks having greater postural instability (Angulo-Kinzler et al, 1998). In contrast, elderly adults upon standing, on average, show either no change, or an increase in the maximum soleus H-reflex in a reflex recruitment curve (Koceja et al, 1995; Angulo-Kinzler et al, 1998). The goal of this study was to determine in elderly adults if the lack of ability to decrease soleus H-reflex gain when standing is also observed if the elderly adults are challenged with a standing task of greater postural instability.

METHODS

Subjects, 12 young (22 ± 1.4 years, mean ± SD) and 16 elderly (71 ± 4.3 years), were tested in three positions: lying supine, standing with feet spaced at a natural distance apart (wide standing), and standing with the left foot placed directly in front of and touching the right foot (narrow standing). In each position, 12 target right soleus contraction levels were randomly presented, and the subject was provided with feedback on their right soleus EMG. For each contraction level, the subject performed a bilateral isometric ankle plantar flexion contraction and when the feedback EMG level matched the target level a stimulus was delivered to the posterior tibial nerve (voltage producing a M-wave amplitude 25% of the maximum M-wave). For each stimulus, the peak-to-peak amplitude of the M-wave and the H-reflex wave, and the rectified and smoothed background EMG over 0.1 seconds prior to the stimuli were determined. Soleus H-reflex gain was defined as the H-reflex wave amplitude at a given level of motoneuron excitability, the latter reflected by background EMG (Simonsen et al, 1995; Matre et al, 1999) (Fig 1).

Figure 1: EMG data and soleus H-reflex gain calculation for each posture tested, from a young subject. The Y-axis provides the peak-to-peak amplitude of the H-reflex wave and the M-wave. The X-axis provides the background EMG level over 0.1 seconds prior to the delivery of a stimulus. Tests performed in a lying posture (box symbols and solid regression line), stable wide standing posture (circle symbols and large dash regression line), and unstable narrow standing posture (triangle symbols and small dash regression line) are shown. Large filled symbols and regression lines are for H-reflex wave amplitude data, small empty symbols are for corresponding M-wave amplitude data. Note that M-wave amplitude of the stimuli did not vary with body position. The vertical solid line marks the background EMG level used when comparing H-reflex amplitude across the three postures. For this subject, the H-reflex amplitude for the wide standing and the narrow standing postures were a 10% and 32% decrease from the H-reflex amplitude in the lying position.

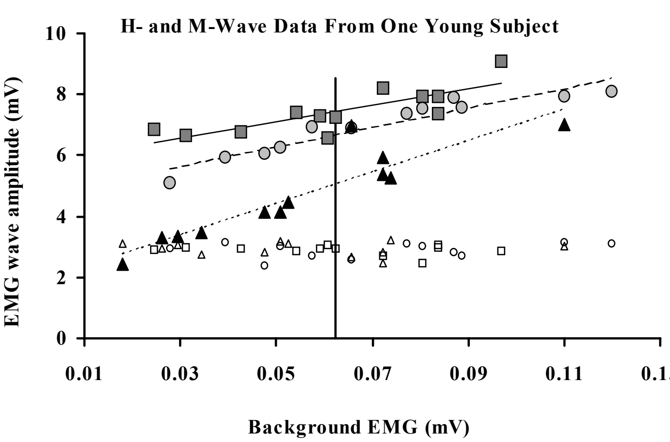

RESULTS

Compared to a lying position, the mean soleus H-reflex gain was significantly lower in the wide standing position for the young subjects (-19 ± 14%, $p < .0125$), but not the elderly (-8 ± 38%), and was significantly lower in the unstable narrow standing posture for both the young (-30 ± 19%, $p < .0125$) and elderly subjects (–28 ± 25%, $p < .0125$).

DISCUSSION

For the range of postural tasks examined, soleus H-reflex gain modulation in the elderly adults had a higher threshold for initiation, but responded dramatically, and similarly to that observed in young adults, when the task difficulty was sufficient.

REFERENCES

Koceja, D.M. et al. (1995). *Electroencephalogr Clin Neurophysiol*, **97**, 387-393.
Koceja, D.M. et al. (1993). *Brain Res,* **629**, 155-158.
Simonsen, E.B. et al. (1995). *Acta Physiol Scand*, **153**, 21-32.
Angulo-Kinzler, R.M. et al. (1998). *J Gerontol A Biol Sci Med Sci*, **53**, M120-M125.
Matre, D.A. et al. (1999). *Clin Neurophysiol*, **110**, 2033-2043.

EXPERIMENTAL DETERMINATION OF THE CENTER OF RESISTANCE OF HUMAN INCISORS IN COMPARISON WITH FINITE ELEMENT SIMULATIONS

Christina Dorow [1] , Natasa Krstin [1] , Franz Guenter Sander [2]

Department of orthodontics, University dental clinic of Ulm, Ulm, Germany

[1] Scientific research assistants, christina.dorow@medizin.uni-ulm.de

[2] Head of department

INTRODUCTION

During an orthodontic treatment, systems of forces and moments are applied to the tooth crown which lead to an initial tooth deflection being mainly controlled by the material properties of the periodontal ligament (PDL). The PDL is a soft biological tissue that attaches the tooth root to the alveolar bone and has an important influence on tooth mobility.

In an orthodontic therapy usually a bodily tooth movement is desired. For that reason the orthodontic force systems have to be designed in a way that no tilting or tipping of the tooth root occurs. The center of resistance (CRE) of a tooth is defined as the point where a force has to be applied to achieve a pure translation of the tooth. Its location is dependent on the shape of the root as well as on the material properties of the embedding of the tooth, i.e. the PDL. Knowledge of the position of the CRE is therefore very important for planning an orthodontic therapy.

METHODS

For the experimental determination of the CRE of human incisors a novel experimental setup has been developed. Tooth deflection was measured by two fiber optic displacement sensors pointing at different locations on the labial surface of the incisor crown. The sensors were fixed to the maxilla using a bite plate. A constant moment was applied to the tooth crown via a motor drive, a stainless steel wire and a bracket that was attached to the tooth crown between the two fiber ends (the experimental setup is shown in figure 1). From the signal of the sensors a two dimensional deflection of the incisor could be calculated and the CRE could be determined.

Realistic and individual three-dimensional geometry models of the measured teeth were generated using computer tomography (CT) data. A novel algorithm has been developed to generate a Finite Element mesh of a tooth unit including PDL and alveolar bone. In a Finite Element simulation the reaction of the tooth to external moments was calculated and the location of the CRE was determined and compared to the experimental results.

RESULTS AND DISCUSSION

When a "square wave" moment was applied to the bracket tooth deflection showed creep and recovery which are typical properties of viscoelastic materials. Using the displacement measured by both sensors and the longitudinal axis of the tooth, the CRE of the incisor could be calculated. From CT data of the measured teeth geometry models were generated (see figure 2) in order to calculate their centers of resistance using the Finite Element Method. The material properties of the PDL were varied and their influence on the location of the CRE was examined.

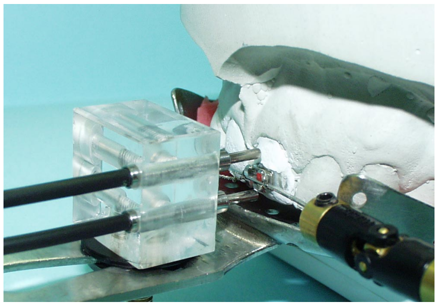

Figure 1: Experimental setup showing the two fiber optic displacement sensors, the motor drive, the wire segment and the orthodontic bracket.

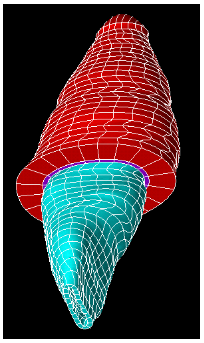

Figure 2: Finite Element Model of a tooth unit including maxillary incisor (blue), PDL (violet) and alveolar bone (red).

SUMMARY

Using viscoelastic material properties for the PDL, the Finite Element simulation was able to represent the measured creep behavior of the incisor. Assuming linear elastic material properties, an elastic modulus of the PDL could be determined by comparing the calculated location of the CRE with the experimental result.

REFERENCES

Dorow, C., Krstin, N., Sander, F.G. (2001). *Proceedings of Computer Methods in Biomechanics and Biomedical Engineering*, to be published

Schneider, J., Geiger, M., Sander, F.G. (2001). *Biomed. Tech.,* **46,** 207-213

OPTIMIZATION OF PASSIVE TISSUE MODEL PARAMETERS OF INTRINSIC LARYNGEAL ADDUCTORY MUSCLES

Eric J. Hunter, Ingo R. Titze, and Fariborz Alipour
National Center for Voice and Speech and Department of Speech Pathology and Audiology,
University of Iowa, Iowa City, Iowa, eric-hunter@uiowa.edu

INTRODUCTION

This research addresses an automated curve fitting strategy to obtain the passive properties of laryngeal muscles in terms of muscle model parameters. The passive properties are important in global shaping and displacement of the larynx, as well as in the control of pitch in speech.

METHODS

Using previously measured stress-strain data from five fresh excised canine laryngeal muscles strained sinusoidally (Figure 1), one-dimensional first-order Kelvin model parameters (Titze, 1996) were obtained through optimization. Optimization was performed using the Nelder and Mead Simplex method when stress-strain patterns predicted by the model were compared to measured cyclic stress-strain patterns. Average parameters were obtained for each muscle type.

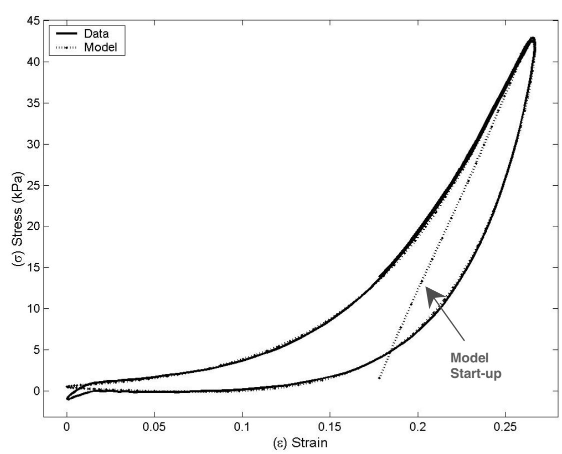

Figure 1: A typical optimized model fit of the muscle data (Specimen 5, LCA). The original muscle data are represented by the solid line.

RESULTS AND DISCUSSION

Optimized parameter values from the single curves were averaged for the five samples of a laryngeal muscle type. After the model overestimated the predicted average stress when using these average values, an average curve representing the five single curves was made for each muscle type and parameter values were optimized for this average curve (Table 1). Fitting the average curve resulted in parameters that best fit the passive characteristics. It was noted that a ratio of the parallel and series time constants was nearly constant regardless of the optimization method.

Table 1. Optimized model parameters for four laryngeal muscles.

Parameters	IA	LCA	PCAo	PCAv
σ_0 (Pa)	1370	784	1560	791
σ_2 (Pa)	6502	270	3690	31.7
ε_1	-0.5	-0.5	-0.5	-0.5
ε_2	-0.000181	-0.0131	0.0223	-0.179
B	6.077	15.5	10.9	15.9
t_p (sec)	0.0904	0.0953	0.084	0.115
t_s (sec)	0.0506	0.0524	0.0484	0.0612
t_p/t_s	1.79	1.84	1.75	1.89

SUMMARY

The automated curve-fitting strategy was able to quantify the stress-strain data with parameters of a muscle model. With the parameters, the model could closely match the measured stress-strain curves. The passive properties could then be used in biomechanical speech models of vocal fold posturing and pitch control. The parallel and series time constants seem to be related to each and may not be independent as the model supposes. The muscle model could be simplified if the time constants are dependent.

REFERENCES

Titze, I. R. 1996. In: P.J. Davis and N.H. Fletcher (Eds.), *Vocal Fold Physiology: Controlling Complexity and Chaos*. Singular Publishing, San Diego, 47-62.

ACKNOWLEGEMENTS

This work was supported by the National Institutes of Health (RO1 DC04347). The authors would like to thank Dr. Niro Tayama and Doug Montequin for their work in muscle data collecting.

DIRECTIONAL DEPENDENCE OF EARLY FATIGUE DAMAGE IN CEMENTED TOTAL HIP REPLACEMENTS

Kenneth Mann, Sameer Gupta, Amos Race, Mark Miller, Richard Cleary[1], David Ayers

Musculoskeletal Science Research Center, Upstate Medical University, Syracuse, New York, USA
[1]Operations Research, Cornell University, Ithaca, New York, USA
mannk@mail.upstate.edu

INTRODUCTION

Determining where fatigue damage or micro-cracks develop in the cement mantle may provide clues into the beginning stages of cement fracture. In the present study we investigate the fatigue damage in a cemented femoral stem model using cadaveric femurs subjected to stair climbing loads. We *hypothesized* that the crack distribution would depend on the circumferential position around the cement mantle. That is, there would be a *directional dependence*. We further hypothesized that the crack distribution would be different for the proximal and distal regions of the cement mantle.

METHODS

Six Charnley Cobra flanged femoral components (DePuy, Inc.) were cemented into fresh-frozen human cadavera using modern cementing techniques. Each construct was loaded using a previously described stair climbing apparatus [Race, 2001] for a total of 300,000 cycles. After loading, each specimen was sectioned in 10mm intervals from the level of the implant collar to the distal tip of the stem. Specimens were grouped as either proximal (sections at 10-50 mm) or distal (sections at 80-110 mm). Crack lengths and angular position of the cracks relative to the center of the stem section were documented for all transverse sections.

The resultant data were analyzed using *circular statistics* [2] where a cyclical scale of 0-360 deg was used. For each cemented implant, a resultant vector with length r_j and angle θ_j was calculated using:

$$r_j = \sqrt{X_j^2 + Y_j^2} \quad and \quad \theta_j = \tan^{-1}\left(Y_j \big/ X_j \right) \quad for \;\; j = 1,6 \quad (six\ cemented\ implants)$$

$$where: \quad X_j = \sum_{i=1}^{n_j} l_i \cos\theta_i \big/ n_j \qquad Y_j = \sum_{i=1}^{n_j} l_i \sin\theta_i \big/ n_j \quad and \quad n_j = total\ \#\ cracks$$

Crack length (l_i) and crack angle (θ_i) were measured for each crack (Fig 1). The measure r represents the dispersion of cracks around the cement mantle; the higher the r, the less uniform the distribution. The θ_j is the mean angle or preferred direction of the crack distribution. Nonparametric statistical analysis was used on these parameters to determine if: (1) the cracks had a non-uniform distribution around the mantle; and (2) the distribution was different for proximal and distal regions of the mantle.

RESULTS AND DISCUSSION

There were a total of 2388 cement cracks in the six cemented femurs (1831 proximal and 557 distal) with an average length of 0.49mm. The frequency of cracks distributed around the cement mantle was not uniform (Fig 1) suggesting a regional variation of cracks with angular position. There was one outlier in this group; this specimen had an inferior cement mantle with substantial stem-cement voids and was excluded from the statistical tests.

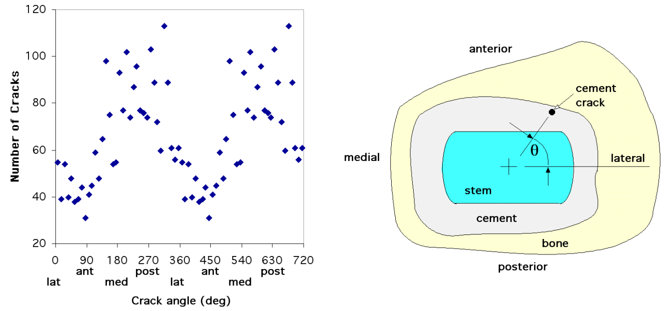

Figure 1: Distribution of cracks (left) and definition of crack angle (right).

The mean angle for all cracks was 249 deg. (Table 1) (posterior-medial direction) and the population of cracks was not uniformly distributed around the mantle ($p < 0.01$). The orientation of the mean angle was also significantly different ($p < 0.02$) for the proximal and distal regions of the cement mantle. In the proximal region, cracks were most often located along the posterior-medial aspect of the mantle. Distally, cracks were most often located along the anterior aspect of the mantle.

Table 1: Ranges and mean of crack distribution of vector strength (r) and orientation (Θ).

	r range of 6 bones	Θ range of 6 bones (deg.)	r (average)	Θ (average) (deg.)
Proximal	0.07-0.28	162.7-296.6	0.14	251.0
Distal	0.04 - 0.16	69.3 - 169.4	0.07	112.3
Total	0.03 - 0.21	158.4 - 326.6	0.09	248.6

DISCUSSION

After fatigue loading, cracks in the cement mantle were not uniformly distributed around the perimeter, nor were the distribution of cracks the same for proximal and distal regions of the constructs. Using circular statistics, we found that both of our initial hypotheses were true. Further work is needed to relate the crack distribution and morphology of the mantle, particularly in the vicinity of trabecular bone that is interdigitated with cement.

REFERENCES

Race, A., Miller, M.A., Ayers, D.C., et al. *Trans Orthop Res Soc*, 2001.

ACKNOWLEDGEMENTS

Support by NIH AR42017 is gratefully acknowledged.

CAN PIECE-WISE LINEAR INTERFACE MODELS BE USED TO PREDICT THE FAILURE RESPONSE OF THE CEMENT-BONE INTERFACE?

Kenneth Mann, Leatha Damron, Amos Race, Mark Miller, and David Ayers

Musculoskeletal Science Research Center, Upstate Medical University, Syracuse, New York, USA
mannk@mail.upstate.edu

INTRODUCTION

Failure of the cement-bone interface is one of the primary mechanisms for clinical loosening of cemented total joint replacements. The etiology of this failure process is poorly understood and predictive models have been insufficient in terms of capturing the mechanics of the failure process. The main goal of this work was to determine if a series of model-specific finite element models (that incorporated a non-linear fracture mechanics approach) could reproduce the failure response of experimentally loaded cement-bone constructs. A secondary aim was to determine how specific changes in the cement-bone interface models, due to lack of specificity of interface parameters, affected the global structural response of the finite element models.

METHODS

A series of eight experimental and corresponding 3-D finite element models were created from human proximal femora. The experimental specimens were CT scanned to document the QCT density of the endosteal trabecular bone, cemented with PMMA using contemporary surgical techniques, followed by sectioning to create the test specimens. Specimens were tested under displacement controlled loading using a custom test fixture (Fig 1A). The corresponding load versus global displacement was measured to represent the structural response to complete failure. Ultimate strength, energy to complete failure, and post-yield softening response were calculated.

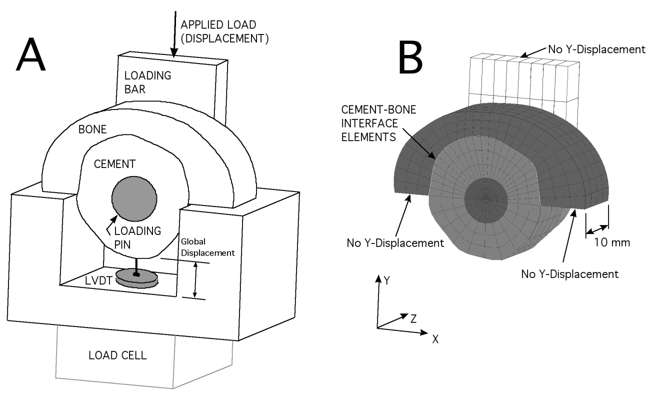

Figure 1: Experimental (**A**) and finite element (**B**) cement-bone specimens.

Finite element models were created for each of the specimens using macrophotographs of the specimens (Fig 1B). Piece-wise linear interface elements were placed at the extent of cement penetration into the bone. The constitutive models were based on a non-linear fracture mechanics formulation that is an extension of the Dugdale-Barenblatt [Kanninen, 1985] approach to predicting fracture. In the normal direction, the interface supports tensile loads up to a peak tensile stress followed by a softening region until the interface no longer supports any load. A similar model was applied in the shear direction, expect the shear model is anti-symmetric. Interface parameter values were assigned to the interface elements based on the amount of bone (CT density) that was interdigitated with the cement (q-int) [Mann, 1997]. Thus the finite element models and interface parameters were based on geometry, material, and interface properties that were assigned using parameters that did not require *a priori* physical loading of the experimental specimens.

RESULTS AND DISCUSSION

There was a strong correlation (r^2=0.8) between experimentally measured and finite element predicted ultimate loads (Fig 2). The average error in predicting ultimate load was 23.9%. In comparison to the ultimate load predictions, correlation and errors for total energy to failure (r^2 = 0.24, avg. error = 38.2%) and displacement at 50% of the ultimate load (r^2 = 0.27, avg. error = 52.2%) were poor. The results indicate that the non-linear constitutive laws could be useful in predicting the initiation and progression of interface failure of cemented bone-implant systems. However, improvements in the estimation of post-yield interface properties from the quantity of bone interdigitated with cement are needed to enhance predictions of the overall failure response.

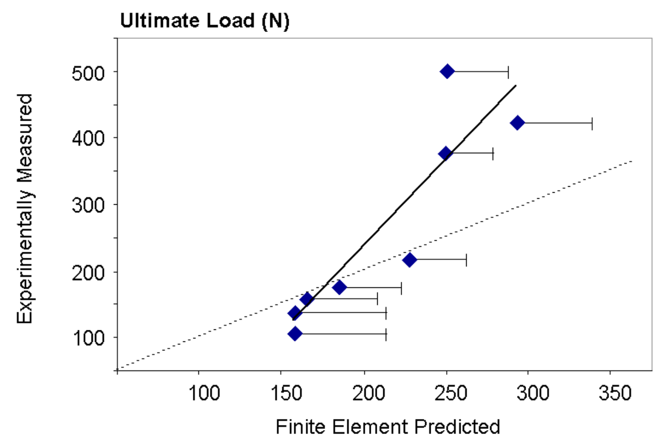

Figure 2: Comparison between measured and predicted ultimate loads. Error bars indicate results using interface constitutive models based on +99% confidence interval values of the q-int data.

REFERENCES

Kanninen, M.F., Popelar, C.H. (1985). *Advanced Fracture Mechanics*, Oxford University Press
Mann, K.A., Werner, F.W., Ayers, D.C., et al. *J Biomechanics* 30(4), 339-346.

ACKNOWLEDGEMENTS

Support from NIH AR42017 is gratefully acknowledged.

EFFECTS OF CYCLIC PRESSURE ON SELECT BONE CELL FUNCTIONS PERTINENT TO BONE HOMEOSTASIS

Jiro Nagatomi[1], Bernard P. Arulanandam[2], Dennis W. Metzger[1,2], Alain Meunier[3], Rena Bizios[1]

1 Department of Biomedical Engineering Rensselaer Polytechnic Institute Troy, NY, USA (Bizios@rpi.edu)
2 Center of Immunology and Microbial Disease Albany Medical College Albany, NY, USA
3 UPRES-A CNRS 7052 Universite D. Diderot - Paris VII Paris, France

INTRODUCTION

Clinical observations (Leblanc *et al.*, 1990; Courteix *et al.*, 1998) have provided evidence that mechanical loading on the skeleton affects bone homeostasis. To date, however, the mechanism(s) that link mechanical stimuli and bone homeostasis, especially at the cellular- and molecular-levels, are yet to be elucidated.

It has been reported in the literature that, when the human skeleton is under loading, the fluid pressure within bone (intraosseous pressure) at such sites as the vertebrae and femoral heads increases proportionally to the applied load (Downey *et al.*, 1988). It is, therefore, possible that the functions of bone cells, which are subjected to changes in intraosseous pressure, are affected under skeletal loading. In an attempt to model this complex mechanical environment of bone *in vivo*, the present *in vitro* study exposed bone cells, namely, osteoblasts and osteoclasts, to controlled regimes of cyclic pressure and examined select cell functions pertinent to bone homeostasis.

METHODS

Rat osteoblasts were isolated, cultured and characterized as described elsewhere (Nagatomi *et al.*, 2001). Bone marrow cells (used as a source of osteoclast progenitor cells) were harvested and cultured using a method adapted from the literature (Hata *et al.*, 1992).

A custom-made, cyclic pressure system (Nagatomi *et al.*, 2001) was used in the present study to expose osteoblasts and bone marrow cells to cyclic pressure. Osteoblasts (in DMEM containing 10% FBS, 50 μg/mL L-ascorbate and 10 mM β-glycerophosphate) on etched glass coverslips and bone marrow cells (in DMEM containing 10% FBS and 10 nM 1,25-$(OH)_2$ vitamin D_3) on devitalized bovine bone slices were exposed to cyclic pressure (10 – 40 kPa at 1.0 Hz frequency) for 1 hour daily for up to 19 consecutive days. Controls were similar cell preparations maintained under standard (no pressure) cell culture conditions for the duration of the experiments.

At the end of the prescribed time periods, mRNA expression for type-I collagen, alkaline phosphatase and osteocalcin by osteoblasts was determined using RT-PCR techniques. Concentrations of collagen and calcium in the extracellular matrix of osteoblasts were determined using commercially available kits. Bone resorption activity by osteoclasts was quantified by measuring the total planar surface area of resorption pits on the surfaces of bone slices.

RESULTS AND DISCUSSION

The results of the present study demonstrated that cyclic pressure stimulated functions of osteoblasts pertinent to new bone formation. Specifically, the results of RT-PCR revealed that mRNA expression for type-I collagen (the main constituent of the organic phase of bone) and alkaline phosphatase (an enzyme important for mineralization of the extracellular matrix) under control conditions declined over the 19-day time period, but was enhanced when osteoblasts were exposed to cyclic pressure (10 – 40 kPa at 1.0 Hz) for 1 hour daily for up to 19 consecutive days. In addition, compared to controls, deposition of collagen into the extracellular matrix of osteoblasts and concentration of calcium (one of the main constituents of the inorganic phase of bone) in this matrix both significantly ($p < 0.05$) increased following exposure to the same regime of cyclic pressure for 19 days.

Furthermore, exposure of bone marrow-derived osteoclasts to cyclic pressure (for 1 hour daily for 7 consecutive days) resulted in significant ($p < 0.05$) decrease in bone resorption. Since the numbers of osteoclastic cells were similar in controls and in cultures exposed to cyclic pressure, it was concluded that the decreased bone resorption observed in the present study was due to reduced osteoclast activity under the mechanical stimulus (and not due to reduced number of cells).

SUMMARY

In summary, the cyclic pressure tested in the present *in vitro* study affects important functions of both osteoblasts and osteoclasts, the cells that affect bone homeostasis. These results, therefore, not only make contributions to bone cell physiology, but also provide cellular/molecular level insights into the relationship(s) between mechanical loading and bone homeostasis.

REFERENCES

Courteix, D., *et al.* (1998). *Osteoporosis Int.* **8**, 152-158.

Downey, D. J., *et al.* (1988). *J. Bone and Joint Surg. [Am]* **70**, 871-877.

Hata, K., *et al.* (1992). *Bone* **13**, 139-146.

Leblanc, A. D., *et al.* (1990). *J. Bone and Miner Res* **5**, 843-850.

Nagatomi, J., *et al.* (2001). *Tissue Eng* **7**, 717-728.

DAMPED KNEE CONTROL FOR TRANSFEMORAL PROSTHESES IN DEVELOPING COUNTRIES

K. McKee and Dr. C Mechefske
Department of Mechanical and Materials Engineering
The University of Western Ontario, London, Ontario, Canada
kmckee@julian.uwo.ca

INTRODUCTION

A rising concern among many international rehabilitation organizations operating in developing countries is to produce a reliable yet inexpensive knee joint for transfemoral prostheses. After an investigation of the transfemoral prosthetics used in both western countries and developing countries was conducted, a novel design concept for a knee joint was devised. A low-cost mechanism involving a dual elastomer system was formulated to replicate the motion of a hydraulic knee control damping cylinder made by Cadence Technologies in Ohio. The hydraulic controller is an industry standard, costing approximately US$1500, and the motion it provides served as the benchmark for this project. The elastomer system devised costs approximately US$18. Comparisons between viscous damping and hysteretic (material) damping were made by considering analytical representations, computational solutions, and experimental analysis. Upon completion of the damping investigation, prototype knee joints were developed, fabricated, and affixed to the ICRC (Red Cross) transfemoral prosthesis.

METHODS

The elastomer system is intended to be maintained in a limited workshop by people with limited technical skills. It must be distributed in remote areas, attached by personnel in a rural clinic, withstand a harsh climate, require little maintenance, and stand up to regular rigorous use. Figure 1 illustrates the dual elastomer concept that was initially designed to be attached posterior to the knee axis of a transfemoral prosthesis.

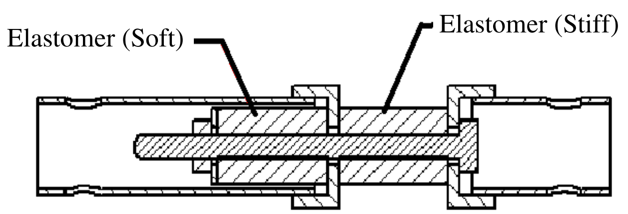

Figure 1: The two-elastomer cylinder design concept

The analytical representation used spring and dashpot models to arrive at a general comparison between the viscous damping of the hydraulic knee controller and the hysteretic damping of elastomer. A second order differential equation was produced and solved to determine the position at any time in the gait cycle. Hysteretic damping for an elastomer was represented by a spring and dashpot in parallel, and characterized by the hysteresis loop on a stress versus strain plot (Kelly, 1993). The computational solution calculated the geometry, material properties, and loss modulus of the elastomer product necessary to replicate the hydraulic knee control cylinder. The experimental analysis involved comparing the spring and damping coefficients for the Catech cylinder and the elastomer prototype by cycling the damping cylinders in an Instron materials testing machine.

RESULTS AND DISCUSSION

Two different prototype knee joints were developed, fabricated, and affixed to the ICRC (Red Cross) transfemoral prosthesis. After design review meetings with two international aid organizations, a third prototype was developed that uses the stainless steel pylon of the ICRC prosthesis as a central shaft for a sliding mechanism.

The elastomer system is much lower in cost and easier to maintain than the hydraulic knee controller. The experimental results showed that the spring return provided by the elastomer meets the amount of spring return in the Cadence system. It was also found that significant damping does exist, however, the current prototype does not provide the target amount of damping as in the hydraulic controller. It is reasonable to accept a lower amount of damping than the target since the design has constraints on cost and size of the elastomer components.

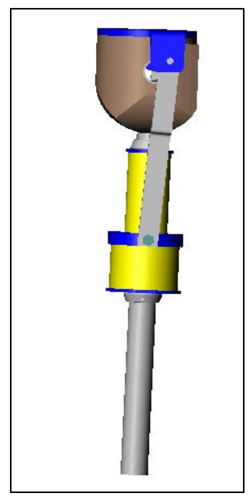

Figure 2: Prototype

SUMMARY

A novel design solution has been formulated for the knee joint of transfemoral prostheses in developing countries. The goal of this study was to include analytical, computational, and experimental comparisons between viscous damping and hysteretic damping. In the future it is hoped that the prototype knee joint will be successful during reliability testing and field trials in a developing country.

REFERENCES

Kelly, S.G. (1993). *Fundamentals of Mechanical Vibrations*. New York: McGraw-Hill.

PARAMETERIC IDENTIFICATION OF LOWER LIMBS DURING WALKING OF A MAN

Jolanta Pauk and Krzysztof Jaworek

Technical University, Automatics & Diagnostics Chair, 15 –351 Bialystok, Poland
jpauk@cksr.ac.bialystok.pl

INTRODUCTION

Identification of different process during human movement depends on data's likelihood and their biomechanical analysis and interpretation. There is a model, which describes relations between velocity of movement, personal data (weight, high and age) and period of time in this paper. The aim of this paper is present coefficients, which allow classify objects to two groups: normal and pathologics.

METHODS

The identification is realised by using of regression's function. We have analysed ankle, knee and hip powers from two groups of adults: 15 normal and 30 hemiplegics. Kinematics and kinetics data were obtained from Centro di Bioingegneria (S.A.F.L.O) in Milan (Italy). Below is the method of identification.

$$\underline{Y}_n = \underline{U}_n \cdot \underline{a}, \qquad \underline{a} = \left(\underline{\underline{U}}^T \cdot \underline{U}\right)^{-1} \cdot \left(\underline{\underline{U}}^T \cdot \underline{Y}\right),$$

$$Y_n = \begin{bmatrix} Y_3 \\ Y_4 \\ Y_5 \\ \vdots \\ Y_{153} \end{bmatrix} \quad \underline{U} = \begin{bmatrix} Y_2 & Y_1 & Y_0 \\ Y_3 & Y_2 & Y_1 \\ Y_4 & Y_3 & Y_2 \\ \vdots & \vdots & \vdots \\ Y_{153} & Y_{152} & Y_{151} \end{bmatrix}$$

where:
n- sample size, $\underline{Y_n}$ – model's output, __ - exploring coefficients, $\underline{U_n}$-model's input.

RESULTS AND DISCUSSION

The results human movement identification is reported below. They are average values over all subjects in each group.

Table 1: Identification's coefficients (mean $\pm SD$)

	I coefficient	II coefficient	III coefficient
Normal	-2.765 $\pm$ 0.203	3.248 $\pm$ 0.512	-1.975 $\pm$ 0.515
Hemiple-gics	-1.905 $\pm$ 0.435	0.956 $\pm$ 0.949	0.342 $\pm$ 0.0.3

Figure 1: Analyse of normal human movement.

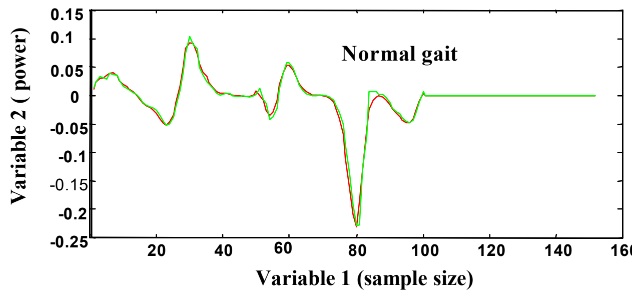

The graphs show human movement (red line – real data, green line – data from model)

Figure 2: Analyse of hemiplegics human movement.

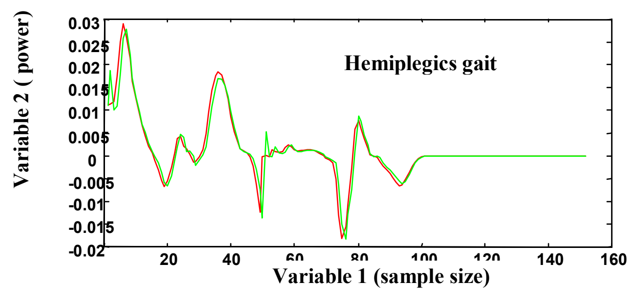

SUMMARY

This method of identification represents human movement in very accurately way during walking a man in sagittal plane. It could be used in bioengineering as assessment of walking recovery.

REFERENCES

Manerowski J., (1999). I*dentification of flying objects model.*
Jaworek K., Pauk J., et al. (2001). *Power correlation between joints during walking of a man.* Gait and Posture, **14**, iss.2, 138.
Jaworek K., Frigo, et al. (2001). *Muscle synergy during locomotion*. Acta of Bioengineering and Biomechanics, **3**, Suppl.1, 113-120.

ACKNOWLEDGEMENTS
Acknowledgements are optional.

QUANTIFYING BONE TRABECULAR DIRECTION FROM RADIOGRAPHS

Henri Dèfossez [1], Peter Walker [1], Mike Wroblewski [2], Bodo Purbach [2], Richard Hall [1].

[1] School of Mechanical Engineering, University of Leeds, Leeds, LS2 9JT, UK, menhjpd@leeds.ac.uk.
[2] Wrightington Hospital NHS Trust, Hall Lane, Appley Bridge, Wigan WN6 9EP, UK.

INTRODUCTION

Increasing evidence supports the necessity to assess bone trabecular structure in addition to mineral density to explain more fully its mechanical properties (Hagiwara, 2000). Radiographs are still routine tools for the examination of initial bone quality. Image-processing techniques developed to describe the trabecular structure from x-ray have regained popularity. This study assessed the precision and accuracy of the matrix, spatial frequency and fractal techniques for the detection of the trabecular direction from a set of test images.

METHODS

A femoral image obtained from a pelvic radiograph digitised at 512 dpi and representative of 1 cm^2 inspired the creation of test images controlling the trabecular thickness (10 pixels), separation (10 pixels) and orientation (60^0). A Laplacian noise was then added at varying intensities (Table 1), as described by Pitas (1993). A software was developed using IDL to implement five image-processing techniques including (a) the Co-occurrence Matrix and the (b) Range Length Matrix analyses presented by Dubus et al (1998), (c) the Spatial Frequency analysis employed by Hagiwara et al (2000) which was modified by pre-processing the image with a Hanning windowing to avoid artefacts in the power spectrum P employed as log[1+P] in order to monitor the high frequencies which otherwise rapidly decrease, (d) the Minkowsky Fractal analysis defined by Jiang et al (1999), and (e) an in house derivation of method (d) only using the processed area intensity. Precision and accuracy were computed at each noise level using 25 images with random noise patterns.

RESULTS

All methods inferred the trabecular direction in the non-noisy image with extreme accuracy and precision (table 1). All methods with the exception of (b) performed well up to a noise of 500 ((a,c) accuracy>99%, SD<3^0, (d,e) >82%, <4^0). Method (b) even failed at the smallest noise level, whilst (a) was correct to a higher noise of 1000. Finally method (e) performed nearly as well as (d), but required less computation.

DISCUSSION

Although method (a) presented the best results, it relied on having a prior knowledge of the trabecular thickness and separation for defining an optimal dimension for the matrix, whereas method (c) presented the second to best results and did not require any trabecular prerequisite. This made (c) the most efficient method. Method (b) relied on the number of pixels of same intensity being in succession. Also even a small noise reduced the long-range values representative of the trabeculae, leading to the observed failure. Finally all methods inferred a mean direction at 90^0 in the noisiest image; as expected since the trabeculae had completely disappeared.

SUMMARY

The Spatial Frequency analysis (c) was the most robust method to infer the textural direction in images including an ideal singular trabecular direction, up to a Laplacian noise of 500. Such high levels of noise are not expected in clinical x-rays; hence these methodologies allow the potential to infer the trabecular direction in clinical studies. This however relies on monitoring the trabeculae that follow a single direction.

REFERENCES

Hagiwara H et al, (2000) *Trans 46th Meet. Orth. Res. Soc* 738.
Pitas I (1993). *Image processing algorithms.* Prentice Hall 45.
Dubus J et al. (1998), *Techniques de l'Ingénieur* ***R630***.
Jiang C et al (1999), *Med. Phys*.,**26**:872-879.

Table 1: Mean and Standard Deviation (SD) of the methods to infer the trabecular direction in a test image at different noise levels.

Perfect and noisy images (Laplacian white noise level given for different Laplacian coefficients).

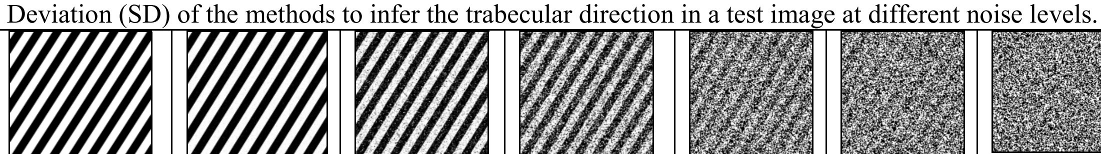

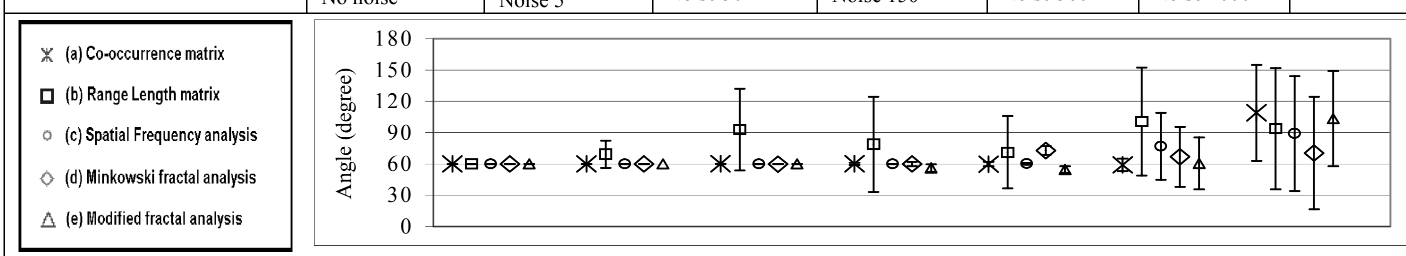

BIOMECHANICAL COMPARISON OF THE TRIAGE MEDICAL COMPRESSION SCREW TO THE SYNTHES SCREW FOR USE IN LOWER EXTREMITY FRACTURES AND FUSIONS

Richard Oka[1], Marty Padget[2], Andrew Mahar[1]
[1] Department of Orthopedics, Children's Hospital, San Diego, CA
[2] Triage Medical Incorporated, Irvine, CA

INTRODUCTION

Orthopedic surgeries involving the foot and ankle have relatively high complication and failure rates. This is related to the magnitude of cyclic load transmitted and applied through this complex joint. First metatarsal fusions, supplementary talar arthrodeses and fixation of medial/lateral malleolar fractures require significant device stability. The compressive ability of fixation screws may lead to earlier callus formation, earlier healing, and thus an earlier return to weight bearing. Devices that increase compressive force across a joint/fracture and that demonstrate greater stability, then, would be considered clinically superior. It was the goal of this study to compare a new type of compression anchor screw to a clinical standard in tests of compression, pullout and three-point bending.

METHODS

Commercially available polyurethane foam (Pacific Research Laboratories, Vashon Island, WA) in 7-lb./ft^3 and 12-lb./ft^3 density molds was selected to simulate cancellous bone. A cortical shell was not included in any of the tests. Based on the type of testing, foam was allocated to different test strategies. Both screw types -- Triage 3.5 x 40-50 mm. & Synthes 3.5 x 50 mm. -- (Figure 1) were inserted into the same foam for each test.

Figure 1: Examples of Triage HCA screw (right) and standard Synthes screw (left).

All screws were inserted manually using the appropriate surgical tools. New screws were used for every test.

For pullout strength in 7-lb./ft^3 and 12-lb./ft^3 foam, an MTS 858 machine applied a displacement at 0.5mm/sec. Maximum tensile force was recorded.

For compression force testing, a miniaturized load cell was inserted between the screw and the 7-lb./ft^3 foam. Maximum compressive force was recorded.

For three-point bending stiffness testing, an MTS 858 machine applied displacement at 2mm/min orthogonal to the screw axis and halfway through the unthreaded shaft until failure (permanent deformation occurred after 1 mm deflection). Bending stiffness was calculated using the linear portion of the curve – using data points from 0N to 250N of applied load.

For each type of testing, data was recorded for 20 tests, (10 per Triage and Synthes screws) averages were calculated within groups, and then compared using a one-way ANOVA ($p<0.05$).

RESULTS AND DISCUSSION

Results for all tests are shown in Table 1. The Triage screw withstood greater pullout force than the Synthes screw (26% more in 7-pound foam, 18% more in 12-lb foam). The Triage screw also demonstrated 82% more compressive force and 23% more bending stiffness than the Synthes screw. In all cases, the statistical differences in performance were highly significant, with *p*-values below 0.001.

	Triage		**Synthes**	
Pullout (N)	**3.5 x 40-50 mm**		**3.5 x 50 mm**	
7-pound foam	98.42	(4.1)	76.85	(8.1)
12-pound foam	214.20	(8.7)	181.92	(7.3)
Compression (N)				
7-pound foam	95.1	(6.5)	52.37	(4.6)
Three-Point Bending Stiffness (N/mm)	965.44	(104.7)	783.46	(30.7)

Table 1: Test data for both groups.

CONCLUSION

Many of the values for both screw types far exceed requirements for a protected environment. However, with greater values for pullout, compression and bending stiffness; the Triage compression screw appears capable of promoting faster recovery to weight-bearing and thus appears to be a better alternative than the current clinical standard.

ACKNOWLEDGEMENTS

Triage Medical Inc provided devices and financial support.

TESTING THE APPLICABILITY OF REFERENCE BODY SEGMENTAL PARAMETER DATA TO INDIVIDUAL SUBJECTS: AN INVERSE DYNAMICS AND NUMERICAL OPTIMIZATION APPROACH

Akinori Nagano, Masae Miyatani, Daisuke Takeshita, and Senshi Fukashiro
University of Tokyo, Tokyo, Japan, cc07725@mail.ecc.u-tokyo.ac.jp

INTRODUCTION

The most basic formula used in inverse dynamics is

$$\vec{F} = m \cdot \ddot{\vec{r}} \quad \text{(Eq. 1)}$$

This formula is typically used to calculate segment inertial forces from acceleration data in inverse dynamics. The basic assumption underlying this procedure is that the values of segment mass, m in (Eq. 1), are readily available (Winter, 1990). Typically body segmental parameter values are estimated by referring to preceding anthropometric studies such as de Leva (1996). However, as there are differences in these parameter values among different individuals, it is not guaranteed that these data reported in preceding studies are always applicable to all individuals.

METHODS

Four movements were performed by a healthy male subject (27 years old, 174 cm, 80 kg): squat jump, counter movement jump, a single squat from standing still, and continuous squats. Two-dimensional kinematic data were recorded at 200 Hz from the right side of the body (MEMRECAM C^2S, NAC, Japan). Anatomical landmarks were digitized automatically, to identify trunk, upper legs, lower legs, and feet segments. Ground reaction force vector (GRF) data were collected using a force platform (9281B, Kistler, Switzerland) at 1000 Hz. Arms were kept on the waist throughout data collection.

Body segmental parameter values reported by de Leva (1996) (mass of segments (m) and position of mass center of segments (p_m)) were used as initial guess for these parameters. Acceleration vectors of segments were determined from video data, which were multiplied by the mass of segments to calculate inertial forces. Finally all the inertial forces (i = 1 through N (# of segments) in Figure 1) and body weight were summed together to obtain the values of ground reaction force calculated through inverse dynamics (GRF_{inv}). GRF_{inv} values were compared with the GRF data measured using a force plate (GRF_{FP}). RMS difference ($GRF_{\Delta RMS}$) between GRF_{inv} and GRF_{FP} were used as the objective function of the numerical optimization process, which modified the values of body segmental parameters to minimize $GRF_{\Delta RMS}$ (Figure 1).

RESULTS AND DISCUSSION

Values of body segmental parameters were modified only slightly through numerical optimization. Therefore, for this subject, the difference of body segmental parameter values from the reference data (de Leva, 1996) was small, suggesting the applicability of those reference data to this subject. This procedure seems to be a useful way to test the applicability of reference body segmental parameter data reported in preceding studies to individual subjects.

REFERENCES

de Leva, P. (1996). *J. Biomechanics*, **29**, 1223-1230.

Winter, D.A. (1990). *Biomechanics and Motor Control of Human Movement*. John Wiley & Sons, New York.

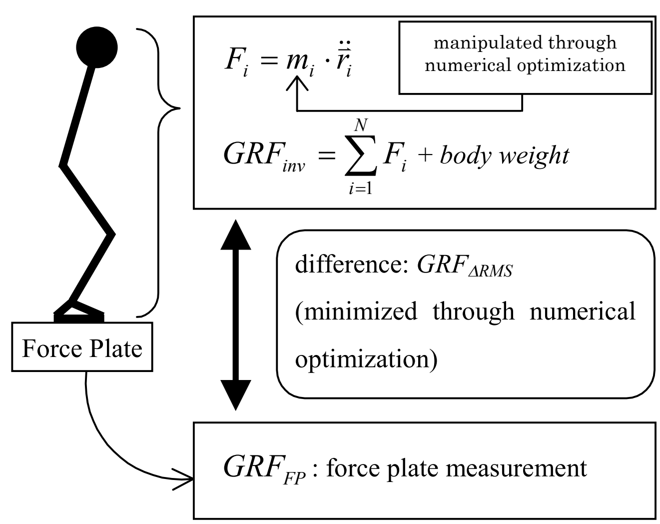

Figure 1: Two ways of obtaining ground reaction force values. GRF_{inv}: inverse dynamics. GRF_{FP}: force plate measurement.

RELIABILITY OF TRUNK 3D KINEMATICS IN CLINICAL EVALUATION

Heydar Sadeghi[1,2,3], Benjamin Booh-Luha[1], Paul Allard[1] , Hubert Labelle[1,2]

[1]Research Centre, Sainte-Justine Hospital, Montreal, PQ, Canada, heidar.sadeghi@umontreal.ca
[2]Department of Medicine, Orthopaedic Surgery, University of Montreal, Montreal, PQ, Canada
[4]Department of Kinesiology, Tarbiat Moallem University, Ministry of Sciences, Research and Technology, Tehran, IRAN

INTRODUCTION

Determining the number of trials that need to be collected to analyse trunk movement is a primary concern in clinical evaluation because non-able-bodied subjects are limited in the number of body motions they can perform without undue pain or exhaustion. To our knowledge, no study has been carried out to determine the minimum number of trials that need to be assessed for 3D main trunk motions as well as the simultaneous motion occurring in other planes, known as coupling motion, using a video-based system.

This study was undertaken to obtain the minimum number of trials required for biomechanical analyses of 3D trunk principal and coupling maximum range of motion (ROM) movements.

METHODS

The ten young able-bodied male subjects who participated in this study had an average age of 27±2 years, height of 1.76±0.2 m and weight of 78±12 kg.

Three different trunk segments were defined as follows: whole trunk (from first vertebra to pelvis; T1-Pelvis), thoracic segment (T1-L1) and lumbar segment (from first lumbar to pelvis; L1-Pelvis). Reflective markers were placed over the spinous processes of T1 and T12 and on the pelvis as shown in Figure 1. The T1 and pelvis markers defined the trunk segment while the T1-T12 and T12-pelvis markers were used for the thoracic and lumbar segments respectively. A high resolution motion analysis video-based system was used to collect the 3D maximum ROM of three different defined trunk sections for five main motions, namely, flexion, right and left bending, and right and left rotations.

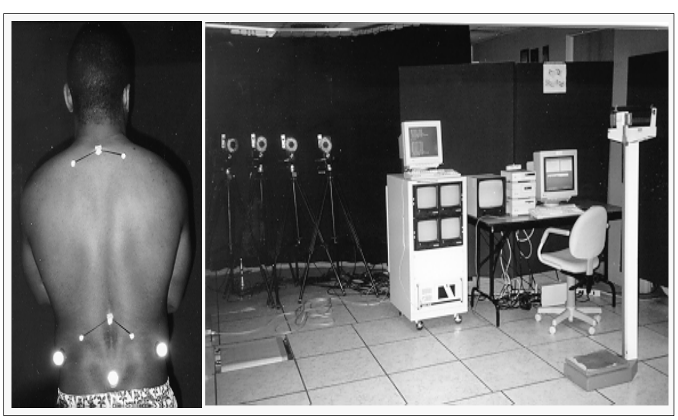

Figure 1: Position of the four cameras and the subject in the calibration space.

Intra-class correlation (ICC)[1] was applied to assess the reliability and to obtain the minimum number of trials required to assess trunk main and coupling motions for the three trunk segments. The ICC values vary from zero to one and like Pearson correlation coefficients, an ICC value close to 1 indicates excellent reliability while a zero value indicates a lack of reliability. The number of trials for the ICC was estimated at 5 in order to have a power of 0.80. For each ICC, the 95% confidence interval (CI) was within ± two standard deviations.

RESULTS and DISCUSSION

Our data are in general agreement with previously published data for back flexion[2,3], right and left lumbar bending[4], right and left lumbar rotation[5] and for coupling movements[6].

The ICCs were in general over 0.80 in different data sets, though some variations existed between trunk segments. Using a cut-off of 0.90 as an indicator, one trial needs to be collected to provide high reliability at the trunk segment, and four trials at the thoracic and lumbar segments. The ICC obtained for parameters at the trunk segment have larger values than the thoracic and lumbar segments, and the thoracic segment has larger ICC values than the corresponding ICCs calculated for the lumbar segment. One explanation may be a variation due to muscle activity in these segments. For coupling motion, variations within and between subjects' performance resulted in lower reliability. Nonetheless, a reliability of 0.74 was observed for the trunk segment with at least four trials.

SUMMARY

As a minimum a single trial is required to have a reliability of 0.84 using a video-based system for five trunk motions measured at three trunk segments. Higher reliability is achievable by collecting five trials. Nonetheless, this finding should be verified in non-able-bodied subjects. For coupling motions, at least four trials are needed for trunk segments, while for the thoracic and lumbar segments more than five trials should be assessed.

REFERENCES

1. Shrout, P.E., Fleiss, J.L. (1979). Psychol Bull, 86: 420-8.
2. Ekstrand, J., Wiktorsson, M., Oberg, B., Gillquist, J. (1982). Arch Phys Med & Rehabil, 63:171-5.
3. Nelson, J.M., Walmsley, R.P., Stevenson, J.M. (1995). Spine, 29: 199-204.
6. Steffen, T., Rubbin, R.K., Baranki, H.G,, Antoniou, J., Marchesi, J., Aebim. (1997). Spine, 22 (2):156-66.
4. Poussa, M., Mellin, G. (1989). Spine, 14:217-9.
5. Pearcy, M.J., Hindle, R.J. (1989). Clin Biomech, 4:73-9.

QUANTITATIVE ASSESSMENT OF BALANCE ABILITY AMONG DIFFERENT SPORTS ATHLETES

Alex J. Y. Lee[1] and Wei-Hsiu Lin[2]

[1]General Education Center, Yu-Da Institute of Business Technology, Taiwan, R.O.C.
Fax: 886-2-37-620525 **Email**: jylee@ms1.ydu.edu.tw
[2]Department of P.E., Tzh-Chi College of Technology, Taiwan, R.O.C.

INTRODUCTION

Balance has been defined as the ability to maintain the center of gravity (COG) over the base of support. It is not only for athletes to perform excellent performance, but also on injury prevention. Previous studies most focus on the difference between injured and uninjured athletes, or determine the effects of specific injury on balance control, or the influence of different training on balance control. In order to determined the long-term specific training effects on balance control. Our study compared the difference between selected sports athletes in 1) static standing steadiness, 2) unstable standing steadiness and 3) unstable dynamic standing steadiness on balance control ability.

METHODS

Three different sports athletes were recruited as subjects: the archer group(21.6±1.3, N=10); the gymnast group(21.6±1.3, N=10) and the control group(nonathletes, 21.6±1.3, N=10). We used Kistler force platform with Bioware 2.0, KAT-2000 with Katwin by BREG, Balance Trainer by TAKEI and the tension meter FB50K by IMADA to measure all subject's static and unstable balance performance. One-way ANOVA was used to examine the statistical differences among each group. Statistical significance was set at α=0.05.

RESULTS

Table 1 is the descriptive characteristic of each group. Table 2 is the Pearson's correlation analysis between each variable. The one-way ANOVA analysis showed that (1) the static standing steadiness of archer were significantly better than the control group, (2) the unstable static balance ability of gymnast group was significantly better than the control group, but the archer group better than control group only in KAT-2000 test, (3) the unstable dynamic balance ability of gymnast group was significantly better than the control group.

SUMMARY

We observed that distinct specific athletes have different balance ability. It was reflected from the different balance test protocol. As a athlete, coach or related researcher must realized the difference were come from individual difference or the training effect of specific exercise participation. According to the results of this study, we suggested that long-term regular specific sport training could significantly alter human body's balance ability. Further research could focuses on the mechanisms of such effects and the alternation. In order to improve the athlete's overall ability, some non-specialized training program must be considered.

REFERENCES

Lord, S. R., Ward, J. A. & Williams, P. (1996). Exercise effect on dynamic stability in older women: A randomized controlled trial., Arch. Phys. Med. Rehabil., 77, 232-236.

Panzer, V. P., Bandinelli, S. & Hallet, M. (1995). Biomechanical assessment of quiet standing and changes associated with aging., Arch. Phys. Med. Rehabil., 76, 151-157.

Table 1. Summary of the descriptive characteristic of each group

	Archer	Gymnast	Control
One-legged static stance with eyes closed(s)	77.3±43.6	32.9±28.7	32.6±31.9
Sum of the distance traveled by COP (cm)	0.28±0.1	0.37±0.1	0.4±0.1
Balance Trainer (20s)	4.3±1.1	3.1±1.4	5.9±1.8
KAT-2000 static balance index	201.2±116.0	138.4±47.9	547.2±237.6
KAT-2000 dynamic balance index	837.2±239.1	708.9±118.9	1049.9±162.9

Table 2. Pearson's correlation analysis between each variable.

	1	2	3	4	5
1. One-legged static stance with eyes closed	——				
2. Sum of the distance traveled by COP	-.34*	——			
3. Balance Trainer	-.17	.21	——		
4. KAT-2000 static balance index	-.09	.51*	.29	——	
5. KAT-2000 dynamic balance index	.00	.28	.39*	.42*	——

DIGIT RESISTANCE WITHIN SHORT TERM AFTER FDP TENDON REPAIR IN CANINE IN VIVO

Chunfeng Zhao, Peter C. Amadio, Philipps Paillard, Tatsuro Tanaka, Mark E. Zobitz, Kai-Nan An
Biomechanics Laboratory, Depertment of Orthopedics, Mayo Clinic/Mayo Foundation
200 First Street SW, Rochester, MN 55905

INTRODUCTION

Postoperative mobilization after flexor tendon repair is effective for reducing adhesion formation. However, safe performance of postoperative therapy can be disrupted by gap formation and tendon rupture. The balance between repaired tendon strength and digit resistance is important to understand. In the short term after surgery, the rough surface and bulk of the repair, soft tissue edema, increased joint stiffness, and later onset adhesion formation increases the work of finger flexion. The purpose of the current study is to investigate digit resistance after short-term flexor tendon repair using an *in vivo* canine model.

METHODS

48 mongrel dogs were used for this study. The second and fifth flexor digitorum profundus (FDP) tendons were exposed through a mid-lateral incision in the paw between the proximal and distal annular pulleys. One FDP tendon was transected at the level of 5 mm proximal to the distal edge of the proximal pulley in digit extension position, and repaired using a modified Kessler technique using 4/0 loop Supramid suture (S. Jackson, Inc. Alexandris, VA) reinforced with a epitenon circumferential running suture. The other digit was closed after tendon exposure without laceration and served as a sham group. The paw and forearm were dressed and immobilized with casting tape to maintain 45^{o} wrist flexion and neutral position after surgery. Dogs were sacrificed at 1, 3, 5, and 7 days (n=12 each). The repaired and sham operated digits and contralateral control digit were harvested by transecting at the mid-level of metacarpal bone.

The testing device consists of a testing frame, actuator, linear potentiometer, and two load transducers (Figure 1). The frame holds the digit to be tested by placing a K-wire through the metacarpal bone. The distal FDP is detached and connected to a small load transducer (BG-1000G, Kulite Semiconductor Products, Inc, Leonia, NJ) that is fixed to distal phalanx. A weight (0.5N) is attached to the extensor tendon. The proximal FDP is connected to a second load transducer which is then connected to the actuator and linear potentiometer. The FDP tendon is pulled proximally (2mm/s) causing digit flexion. Excursion and proximal (F_p) and distal (F_d) forces are recorded. Motion of metal markers embedded in the proximal, middle, and distal phalanx were collected with fluoroscopy during testing and digitized to determine joint angular motions.

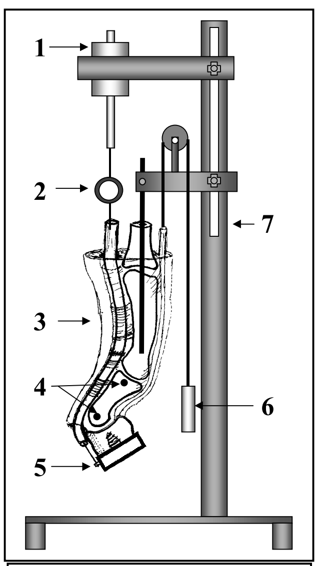

Figure 1: 1) actuator and potentiometer; 2) F_p; 3) specimen; 4) bone markers; 5) F_d; 6) weight; 7) frame

RESULTS

F_p represents the force required to flex the digit with the area under this curve representing total work of flexion (WOF). F_d represents the force transferred to the distal bone to move the digit. The area between F_p and F_d is internal work expended due to resistance between tendon and sheath (IWOF). An end range of motion was chosen for all digits as 40 degrees of flexion.

WOF was not different in control and sham groups at any time point. After repair, WOF was lowest at 5 days ($p<0.05$), while there was no difference among 1, 3, or 7 days. WOF for the repair group was higher than the control group at 1, 3, and 7 days, and higher than the sham group at 1 and 7 days ($p<0.05$). There was no significant difference among control, sham, or repair group at 5 days ($p>0.05$). IWOF in the repair group was higher than the control and sham groups at all time points ($p<0.05$). Within the repair group, IWOF at 5 days was lower than 7 days ($p<0.05$).

DISCUSSION

Resistance to digit motion includes both tendon gliding resistance (internal) and digit joint motion resistance (external). In the normal state, these two resistances are small due to the smooth gliding surfaces and lubricant effects within the tendon sheath and at the joints. After tendon repair, the total WOF increases due to suture technique, soft tissue edema, and effects of wound healing. In the control group, IWOF comprised 17% of the total WOF while after repair IWOF increased to 36% of WOF. The IWOF did not change within 5 days after surgery, although at 7 days there was a significant increase, we believe due to formation of minor adhesions. During rehabilitation the therapists provide forces to overcome external resistance making the internal resistance an important factor influencing tendon gliding. For the dog model used in this study the results suggest that a passive motion therapy should begin no later than day 5 postoperatively.

ACKNOWLEDGEMENTS

Funding provided by NIH (NIAMS) grant AR44391.

Table 1: WOF and IWOF (N-mm) (mean)

Group		1-day	3-day	5-day	7-day
Control	WOF	14.8	13.6	13.8	15.2
	IWOF	3.0	2.1	2.1	2.7
Sham	WOF	15.2	19.4	14.2	17.8
	IWOF	3.0	3.1	2.3	4.2
Repair	WOF	26.0	24.3	16.9	27.0
	IWOF	9.2	9.2	5.6	10.2

LEARNING PROCESSES AND BIOMECHANICAL CHANGES WHILE HANDLING ASYMMETRICAL LOADS

Micheline Gagnon

Département de kinésiologie, Université de Montréal, Montréal, Québec, Canada, micheline.gagnon@umontreal.ca

INTRODUCTION

Low back pain has been a long-standing health problem in manual workers. Experts adopt very different strategies when compared to novices (Authier et al., 1996) and these strategies appear biomechanically safer (Gagnon et al., 2000). As non-directive and free practice did not improve handling strategies in novice workers (Gagnon et al., 2002), it was then hypothesised that a training program focusing on specific experts' strategies would lead to significant biomechanical changes for back loadings and mechanical work in novices.

METHODS

Ten novice workers (men age: 24 yr) were trained in manual handling. The subject viewed a video contrasting experts and novices for handling elements including load manoeuvres (box tilts plus hands placement), feet orientation and trunk asymmetry; the video was commented for mechanical principles. Then the subject practised freely, loading and unloading boxes in a wide range of conditions, and was invited to experiment his own strategies. The experiment itself included the displacement of 3 symmetrical 15-kg boxes from a low 22-cm shelf to another 22-cm shelf at 90º to the subject's left. This sequence was repeated 25 times; a similar session was repeated 3 weeks later. As it was also of interest to investigate the performance of handling asymmetrical boxes, three more sequences were included with 2 asymmetrical 15-kg boxes (height: 30 cm; antero-posterior: 33 cm; width: 42 cm) with the c.g. 30 % forward and 86 % upwards: a pre-test before the training session (trial 1), a post-test following the 25 trials with the symmetrical boxes (trial 2) in the first session and a post-test in session 2, i.e., following the 25 trials with symmetrical boxes (trial 3). The subject was free to choose his lifting techniques. This paper is limited to the analysis of asymmetrical boxes (only one box for each trial per subject).

The 3D kinematic and kinetic data were obtained using 5 video cameras and a large 2.4 x 2.4 m^2 force plate. The net back (L5/S1) loadings included the net 3D moments with axes corresponding to trunk/pelvis orientation. The subject was analysed at take-off (when the box just left the shelf) and deposit (last moment before box contact on the other shelf); the box itself was analysed during transfer (between take-off and deposit) for its trajectory and mechanical work. Analyses of variance with repeated measures on learning were used to determine if the three trials differed significantly; probability values were Greenhouse-Geisser corrected ($P< 0.05$).

RESULTS AND DISCUSSION

Significant differences were only found between the pre-test trial (T1)and the post training trials (Table 1). For T2 and T3, mechanical work done on the load was reduced (about 60 J), due to its reduced path during transfer (46 and 69 cm) and reduced knee flexion at take-off and deposit (about 40º). At take-off, net L5/S1 extensor moments decreased for T2 and T3 (about 25 Nm) and, although not statistically significant, torsion moments then tended to increase; this was attributed to decreased frontal distances but increased lateral distances between the load and L5/S1 for these trials and also to an increase orientation of the feet towards the deposit as shown by the larger angle of feet relative to the take-off shelf (about 30º). Trunk posture was symmetrical and not affected by learning (data not shown). These results are explained by some ergonomic changes, especially the increased use of box tilts (on edges and/or corners) at take-off and deposit which allowed the load to be higher and nearer the subject.

SUMMARY

Contrasting experts/novices' strategies for specific handling elements such as box tilts, feet orientation and trunk posture is an efficient means to train novice workers. They improved very quickly for mechanical work and trunk efforts; however, their change of strategies may not have been optimal, in some cases, as suggested by the slight increase of torsion moments. Formation programs should be based on the observation of workers rather than theoretical concepts alone. These results may guide the specialists involved in formation programs.

REFERENCES

Authier, M. et al. (1996). *Int. J. of Indusr.l Erg.*, **17**, 419-429.
Gagnon, M. et al. (2000). *Clinical Biomechanics*, **15**, 478-488.
Gagnon, M. et al. (2002). *Int. J. of Industr. Erg., **29***, 73-83.

Table 1. Changes for pre-test and post-training trials (N=10)

Variables	Pre-test	Post-training	
	T1	T2	T3
Work on load(J)	129(57)	73*(49)	67*(38)
Path of load(m)	2.13(.52)	1.67*(.50)	1.44*(.44)
Take-off:			
Knee flexion (º)	65(44)	25*(13)	24*(18)
Back total moment(Nm)	210(38)	197(40)	188*(35)
Back extension moment(Nm)	209(38)	187*(46)	178*(45)
Back torsion moment (Nm)	9(6)	34(24)	33(35)
Load front. dist. (m)	0.57(.09)	047*(.09)	0.48*(.09)
Load lat. dist.(m)	0.05(.04)	0.10*(.08)	0.13*(.09)
Feet/shelf pos.[a](º)	16(15)	39*(31)	52*(21)

[a]0º:Feet pointed towards take-off shelf * diff. from T1

EFFECTS OF SUSTAINED PRESSURE AND STRAIN ON VASCULAR SMOOTH MUSCLE CELL FUNCTION

Sheila Dela Cruz[1], Roman Ginnan[2], Harold A. Singer[2], Rena Bizios[1]
[1]Rensselaer Polytechnic Institute, Biomedical Engineering, Troy, NY, delacs@rpi.edu
[2]Albany Medical College, Center for Cardiovascular Sciences, Albany, NY

INTRODUCTION

Various vascular pathologies involve proliferation of smooth muscle cells, but the underlying mechanisms are not fully understood. *In vivo*, the blood vessel wall tissue (including constituent cells) is exposed to various mechanical stimuli such as pressure, strain, and fluid shear stress. Changes in pressure or strain levels due to elevated blood pressure may affect vascular smooth muscle cell functions (Osol 1995). Although the effects of select mechanical stimuli on vascular tissue and cells have been studied individually (Wilson 1993), to date, the effects of combined mechanical stimuli (*i.e.*, models that address the complexity of the pathophysiological milieu) have not been explored yet. The present *in vitro* study used custom made laboratory setups to expose cells to either sustained hydrostatic pressure or combined pressure and strain stimuli and investigated their effects on select vascular smooth muscle cell functions.

METHODS

Rat aortic smooth muscle cells isolated and characterized using established techniques (Geisterfer 1988) were cultured in media composed of 44% Dulbecco's Modified Eagle Medium and 44% Ham's F-12 medium supplemented with 10% fetal bovine serum, 1% antibiotic/antimycotic, and 1% L-glutamine under standard cell culture conditions (that is, a sterile, humidified, 37°C, 95% air / 5% CO_2 environment).

Cell proliferation was examined under the following experimental conditions. For pressure experiments, these cells were seeded on sterile, fibronectin-coated (3 $\mu g/cm^2$) glass coverslips. For simultaneously applied pressure and strain experiments, smooth muscle cells were seeded on sterile, fibronectin-coated (3 $\mu g/cm^2$) biomedical grade silicone sheets. After 24 hours of culture on these two different substrates, these cells were exposed to either sustained hydrostatic pressure (10 cm H_2O or 30 cm H_2O) or combined pressure and strain (10 cm H_2O and 4% strain or 30 cm H_2O and 10% strain), respectively, for up to 7 consecutive days. Control samples were cells seeded on respective, similarly prepared substrates and similar cell-culture conditions, but maintained under 0.3 cm H_20 hydrostatic pressure. All experiments were carried out in a sterile, humidified, 37°C, 95% air / 5% CO_2 environment. At the end of the prescribed time periods, smooth muscle cells were trypsinized and counted using a hemocytometer.

Extracellular-related kinase (ERK) 1 and 2 activity was examined by sodium dodecyl sulfate-polyacrylamide gel electrophoresis (SDS PAGE) and western blot analysis. ERK 1 and ERK 2 activity in controls was compared with that observed in cells exposed to sustained pressure for 10 minutes, 1 hour, 2 hours and 3 hours.

RESULTS

Vascular smooth muscle cell proliferation was similar in controls and in preparations exposed to sustained pressure of either 10 cm H_2O or 30 cm H_2O for 1 and 3 consecutive days. In contrast, after 5 and 7 days, cells that were exposed to either 10 cm H_20 or 30 cm H_2O hydrostatic pressure exhibited significantly ($p < 0.05$) increased cell proliferation compared to controls. For all time points tested, smooth muscle cell proliferation under 10 and 30 cm H_2O sustained pressure was similar.

Compared to respective controls (no mechanical stimuli), simultaneous exposure to sustained pressure of either 10 cm H_2O or 30 cm H_2O and up to 10% strain for 7 days resulted in significant increases ($p < 0.05$ and $p < 0.01$, respectively) in cell proliferation.

SUMMARY

The data of the present study provide evidence that vascular smooth muscle cells responded to sustained hydrostatic pressure in a time-dependent manner (up to 7 days) that was responsive to pressure but independent of the magnitude (that is, either 10 or 30 cm H_2O) of the applied stimulus. Simultaneous exposure of vascular smooth muscle cells to pressure and strain also resulted in increased cell proliferation. These findings may provide cellular-level explanations for the smooth muscle cell proliferation observed in certain pathological syndromes that involve changes in the mechanical milieu of the vasculature.

REFERENCES

Geisterfer, A. A., Peach, M. J., Owens, G. K. (1988). *Circ. Res.*, **62**, 749-756.

Osol, G. (1995). *J. Vasc. Res*, **32**, 275-292.

Wilson, E., *et al*. (1993). *J. Cell Biol*., **123**, 741-747.

EXHAUSTIVE BACK EXTENSION TESTS LEADS TO GRADUAL INCREASE IN INTRA-ABDOMINAL PRESSURE.

Morten Essendrop, Bente Schibye

National Institute of Occupational Health, Denmark
Department of Physiology
me@ami.dk

INTRODUCTION

During back extension when back muscles are isometric contracted at a constant force level until exhaustion the EMG amplitude of the lumbar back muscles remains constant (Bunkens, 1996) or even decreases (Klausen et al., 1978). Even though there is an increase in amplitude for the thoracic part of the back muscles, it is difficult to explain the indications of decreased force output from the lumbar back muscles when the external torque is constant. IAP has been hypothesized to have an influence on the distribution of forces in the lumbar region during back extension (Daggfeldt, 1997). The aim was to study whether IAP increases as the low back muscles fatigue during exhaustive back extension.

METHODS

Ten subjects performed a modified Sorensen test (Jorgensen 1986). Instead of lying completely horizontal, only the trunk was horizontal while the legs were supported on a bench inclined 10° below horizontal (fig. 1). The test was stopped when the subjects could no longer keep the trunk horizontal. Surface EMG was measured bilateral from the lumbar part of m. erector spinae at the level of L3 bilateral, and unilateral from m. internal and external oblique. Sampling rate was 1000 Hz. IAP was measured intra-gastrically with a pressure transducer, inserted through the nose. The measured parameters were compared at five time point: at the start of the test, after 25, 50, 75 % of the endurance time, and at the end of the test. One-Way Repeated Measures Analysis of Variance was used for the comparison.

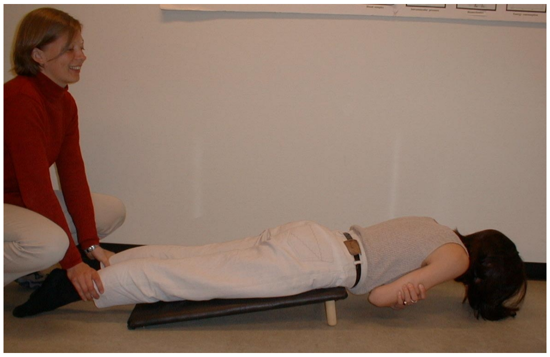

Figure 1. Modified Sorensen test.

RESULTS AND DISCUSSION

The mean endurance time was 270±155 sec. IAP increased significantly through out the test ($P<0.001$) (fig.2). Also the amplitude of the EMG from the abdominal muscles increased ($p<0.002$). For the lumbar part of the m. erector spinae muscles the amplitude of the EMG tended to decrease ($p=0.016$ right side, $p=0.075$ left side) and the EMG median power frequency decreased ($p<0.001$)(fig.2), indicating a decrease in force output from the lumbar part of m.erector spinae. The effect of an increase in IAP and/or increased activity in the abdominal wall could be 1) an increase in stiffness and stability of the spine (Cholewicki et al., 1999; Radebold et al., 2000) 2) a production of an extension torque of the trunk, that if not out-ruled by a flexion torque from abdominal muscle activity, might unload the lumbar spine (Daggfeldt, 1997).

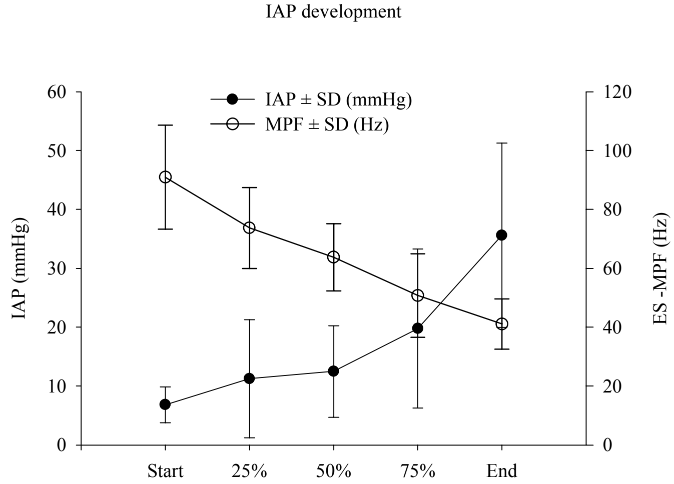

Figure 2. Development in intra-abdominal pressure (left y-axis) and in median power frequency of m. erector spinae (right y-axis), from the start of the endurance test until the end.

SUMMARY

Trunk extension until exhaustion increases IAP and abdominal muscles activity, as the low back muscles become fatigued.

REFERENCE

Bunkens, H. (1996). Thesis. Katholieke Universiteit Leuven
Cholewicki, J. et al (1999). J. Biomechanics, **32**, 13-17.
Daggfeldt, K., Thorstensson, A. (1997) J. Biomechanics, **30**, 1149-1155.
Jorgensen, K., Nicolaisen, T. (1986). Eur. J. Appl. Physiol., **55**, 639-644
Klausen, K. et al (1978). Biomechanics VII A. Baltimore, Universel Park Press, 174-180.
Radebold, A. et al (2000). Spine **25**, 947-954.

JOINT MOMENT CONTROL OF MECHANICAL ENERGY FLOW DURING NORMAL GAIT

Karen Lohmann Siegel, Thomas M. Kepple, and Steven J. Stanhope

National Institutes of Health, Physical Disabilities Branch, Bethesda, MD, USA, karen_siegel@nih.gov

INTRODUCTION

Joint power represents the net effect of a joint moment on the mechanical energy of the whole body, not any one particular body segment. Segmental power techniques (Robertson and Winter, 1980) can account for passive transfer of energy to adjacent segments, but the joint moment responsible for the energy transfer cannot directly be identified. The purpose of the present study was to apply a new technique that can quantify the flow of mechanical energy throughout the body produced by a single joint moment in order to examine the function of the lower extremity during normal gait.

METHODS

While 5 healthy adult subjects walked barefoot at a self-selected speed, ground reaction forces and the movement of reflective targets on the feet, shanks, thighs, and pelvis (HAT) were sampled at 60 Hz using a 2-force platform, 6-camera motion capture system. After applying a low pass filter (6 Hz), segmental velocities and joint moments and powers were calculated from the sampled data. Using a method previously described by Kepple et al (1997), each joint moment or gravity was entered individually into a 7-segment biomechanical model of the subject. Model output included the reaction forces produced at all joints. These output joint reaction forces and the measured gait data were used to calculate segmental power associated with each of the net muscular moments or gravity using the equations described by Robertson and Winter (1980) and Siegel et al (1996). Mechanical energy transfer was calculated from the area under the segmental power curves during selected intervals of stance phase.

RESULTS AND DISCUSSION

Net joint moments were responsible for transferring greater amounts of energy between segments than expected based on the net joint powers. Pairs of moments worked together to balance energy flows through the lower extremity and HAT segments; knee moments vs. gravity in early stance (Fig 1), ankle vs. hip moments in early and middle stance (Fig 2), and knee vs. hip moments in late stance (Fig 3). Each joint moment had a similar effect on the energy level of all segments within the lower extremity, and an opposite effect on the energy level of the HAT. The only exception to this pattern was during the push off phase of gait when the ankle moment was responsible for simultaneously adding energy to all lower extremity segments as well as the HAT (Fig 3).

SUMMARY

Joint power is unable to account for energy transfers due to gravity and underestimates both the type and the amount of work done by the net joint moments on individual segments. Results of this more comprehensive segmental power analysis demonstrated a high level of intralimb coordination showing how muscles with contradictory effects are recruited simultaneously to provide precise control of mechanical energy flow within the body during normal walking.

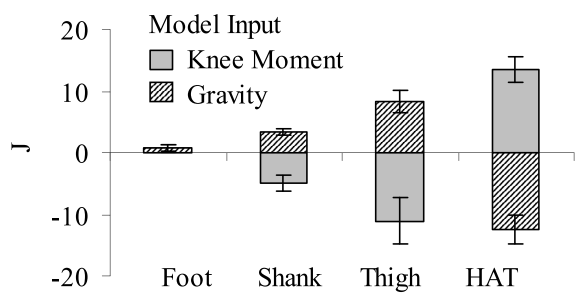

Figure 1: Effects of the knee moment and gravity on mechanical energy transfer into (+) or out of (-) the foot, shank, thigh, and HAT during 0-50% of stance phase.

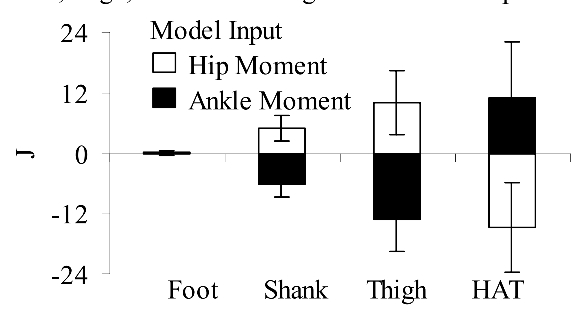

Figure 2: Effects of the hip and ankle moments on mechanical energy transfer into (+) or out of (-) the foot, shank, thigh, and HAT during 10-80% of stance phase.

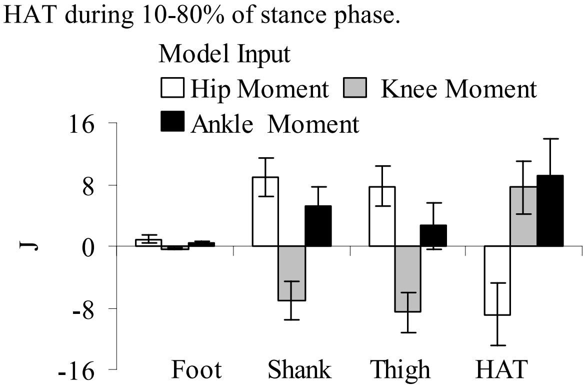

Figure 3: Effects of the hip, knee, and ankle moments on mechanical energy transfer into (+) or out of (-) the foot, shank, thigh, and HAT during 80-100% of stance phase.

REFERENCES

Kepple, TM et al (1997). *Gait & Posture,* **6**, 1-8.
Robertson, DGE, Winter, DA (1980). *J Biomech,* **13**, 845-854.
Siegel, KL et al (1996). *J Biomech*, **29**, 823-827.

REAR WHEEL IMPACT CHARACTERISTICS IN OFF-ROAD CYCLING

Morris Levy[1] and Gerald A. Smith[2]
[1]Biomechanics Laboratory, University of Minnesota Duluth, USA
[2]Oregon State University, USA

INTRODUCTION

There has been significant innovation in bicycle design associated with the rapid development of mountain biking. Making the appropriate choice in suspension fork is often based on subjective statements, with little mechanical testing results available. Recent studies by Orendurff et al. (1996), Pritlove et al. (1998) and Levy et al. (2000) have used similar methods to quantify fork performance while riding over an obstacle. In a study related to this report, Levy et al. measured front wheel antero-posterior impulse as a primary indicator of fork performance. This project was carried out as a follow-up study in which rear wheel peak force and impulse were compared for five fork-frame suspension conditions.

METHODS

Suspension conditions were described by a combination of a particular front suspension fork with either a rigid or suspended frame. The suspended frame (Specialized model FSR) was composed of a dual dampening system (air-spring) located under the seat post, connecting the horizontal bar of the frame to the back wheel. Additional hinges located close to the back wheel axis and above the pedal axis completed the suspension setup. A standard rigid fork/rigid frame system (R-R) was compared with two front suspension forks: air-oil (A-R), and linkage (L-R) design. In addition, the suspended frame was used with the air-oil and linkage design forks (designated A-S and L-S, respectively).

One subject performed repeated trials with each suspension condition. He was instructed to ride passively over the bump slightly elevated out of the saddle. Thirty trials per condition were performed at speeds ranging between 5 and 8 m/s. Each suspension condition was tested across a bump of 6-cm height secured on top of a Kistler force plate. The reaction forces were recorded at 1000 Hz for a period of 0.5 seconds. The data were smoothed using a second-order Butterworth filter with a cutoff frequency of 180 Hz. Braking impulse was calculated by numerically integrating the force-time curve.

RESULTS

Separate ANCOVAs (using speed as a covariate) revealed significant differences both in force and impulse ($p<0.001$). Post-hoc comparisons of force showed significant differences between all conditions except the A-R/A-S and L-R/L-S conditions. All rear wheel braking impulse comparisons were significantly different from each other except the A-S/L-S comparison. In addition, most pairwise comparisons of the total braking impulse showed significant differences. Only the A-R/L-R comparison was not significant.

DISCUSSION

The rigid condition of fork and frame yielded significantly lower peak anterior-posterior forces and impulse than all other suspension conditions when the back wheel contacted the bump. These results are in contrast to front wheel impacts for which rigid forks produce significantly greater force and impulse than suspension forks (Levy et al., 2000). This suggests there is some interaction between front and rear wheel impacts which distributes the total impulse differently perhaps due to a shift of the rider's body positioning. Combining results from our previous study, total braking impulse summed across front and rear wheel impacts were significantly less with suspension components than with rigid fork/frame. While the suspended conditions yielded higher rear wheel braking impulse than the rigid fork condition, the total braking impulse was still significantly smaller with the suspension forks and frames.

SUMMARY

This project compared rear wheel antero-posterior forces and impulses when riding over an obstacle in off-road cycling. The Rigid fork-Rigid frame rear wheel forces and impulses were smaller than all other conditions, while the total impulse (front and rear wheel impacts) was significantly smaller for the various suspension conditions. Total impulse is distributed differently with different suspension conditions, possibly due to a shift of the rider's body positioning.

REFERENCES

Levy, M., & Smith, G.A. (2000). *The Engineering of Sport: Research, Development and Innovation*. Blackwell Science Ltd., 255-264.
Orendurff, M.S., & Smith, G.A. (1996). *Med. Sci. Sports Exerc.*, **28**, S184.
Pritlove, J. et al. (1998). *Proceedings NACOB '98*, 457-458.

ACKNOWLEDGEMENTS

The authors thank Rock Shox, AMP Research and Cyclotopia for their help.

Table 1: Descriptive statistics for various suspension conditions (Mean ± SD)

	A-R	A-S	L-R	L-S	R-R
Peak A-P Force (N)	704.3 ± 54.1	704.9 ± 58.9	669.9 ± 46.0	680.1 ± 65.3	619.8 ± 44.9
Braking Impulse (Ns)	12.8 ± 1.3	11.0 ± 0.5	12.3 ± 1.0	11.0 ± 0.6	10.5 ± 2.4
Total Braking Impulse (Ns)	23.1 ± 1.8	21.0 ± 0.8	23.5 ± 1.5	22.0 ± 1.2	26.3 ± 3.2

MEASUREMENT OF POISSON'S RATIO IN RABBIT ACHILLES TENDON

Allen H. Hoffman[1], Matthew E. Johnson[1] and Peter Grigg[2]

[1]Mechanical Engineering Department, Worcester Polytechnic Institute, Worcester, MA 01609, ahoffman@wpi.edu
[2]Department of Physiology, University of Massachusetts Medical School, Worcester, MA 01655

INTRODUCTION
Poisson's ratio of tendons and ligaments is determined by the transverse deformation under quasi-static uniaxial tension. A negative Poisson's ratio indicates that the transverse dimension increases under axial loading. Many tendons and ligaments are neither circular nor rectangular (Woo et al, 1990; Wren et al, 2000) and this adds to the complexity of determining Poisson's ratio. Tendon properties also depend upon tissue hydration (Haut and Haut, 1997). The purpose of this study was to investigate Poisson's ratio in fresh rabbit Achilles tendons bathed in an osmotically neutral solution.

METHODS
Achilles tendons were harvested from 1-2 kg immature New Zealand white rabbits. The lower legs were amputated at the knee. Each gross Achilles tendon was removed in a closed dissecting chamber maintained at 100% humidity and subdivided into 3 individual tendons that were immediately stored under mineral oil. Individual tendons that were tapered, were discarded. Tendons were mounted axially in a testing apparatus by gripping suture knots tied at the ends of the tendon and were maintained under mineral oil throughout the experiment. Loads and axial displacements were measured using a load cell and an LVDT. The apparatus allowed the tendon to be rotated about its long axis while loaded. The width of the tendon cross section was measured optically using a silhouetting technique. In each experiment an initial state was established, without preconditioning, by applying a small preload (~0.07 MPa) and allowing the tendon to equilibrate for 10 minutes. Then the length was recorded and width measurements were made in 6 transverse planes at equally spaced 30^{o} orientations. At each orientation, the 6 width measurements were averaged. Next, a stress of approximately 0.35 MPa was applied for 30 minutes and another set of width measurements was taken. The primary time constant associated with creep at this stress was about 5 minutes.

RESULTS
Nine tendons from 4 rabbits were tested. The tendon cross sections were well approximated by an ellipse. Fig. 1 is an MRI image of a tendon cross section, from another study, at a stress of approximately 0.07 MPa and provides further evidence of the elliptical shape. Relative to the initial state, the average additional applied stress of 0.36 +/- 0.08 MPa resulted in a strain of 6.9 +/- 3.0 % and an axial modulus of 5.9 +/- 2.4 MPa (n=9). Tendon volume was calculated as the product of length times cross-sectional area. All 9 tendons showed an increase in volume. The average volume increase under load was 7.6%. Since the tendons were elliptical, Poisson's ratio could only be directly measured with respect to the principal axes of the ellipse (Table 1). Negative Poisson's ratios were observed in 8 of 9 tendons. In 7 tendons a negative Poisson's ratio along one axis was accompanied by a positive Poisson's ratio along the orthogonal axis. The Poisson's ratios measured with respect to the principal axes of the ellipse were different, indicating that rabbit Achilles tendons exhibits orthotropic behavior under uniaxial tension.

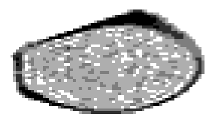

Figure 1. Tendon cross section.

Specimen	Major axis	Minor axis
1	-0.03	-0.43
2	-0.52	0.70
3	-0.28	0.62
4	0.02	-0.39
5	-0.14	0.37
6	-0.82	0.94
7	0.26	0.21
8	0.87	-2.05
9	0.07	-1.46

Table 1. Poisson's Ratio in Mineral Oil

SUMMARY
This study demonstrates that measurements of Poisson's ratio in tendons and ligaments must carefully account for the shape of the tissue cross section. Negative Poisson's ratios were routinely observed. Although tendons and ligaments are often assumed to be isotropic and incompressible, our results show that the validity of these assumptions may be limited. Since the level of hydration affects tendon properties, these results only apply to neutral osmotic solutions.

REFERENCES
Woo, S.L. et al (1990). *J. Biomechanical Engineering*, **112**, 426-431.
Wren, T.A.L. et al (2000). *Trans ORS*, **46**:188.
Haut, T.L., Haut, R.C. (1997). *J. Biomechanics*, **30**, 79-81.

ACKNOWLEDGEMENT
This work was supported by NIH Grant No. NS10783.

EARLY CEMENT DAMAGE AROUND A FEMORAL STEM IS FOCUSED ON THE CEMENT/BONE INTERFACE

Amos Race, Mark Miller, David Ayers and Kenneth Mann

Musculoskeletal Science Research Center, Upstate Medical University, Syracuse, New York, USA
racea@mail.upstate.edu

INTRODUCTION

There is very little information available regarding mechanical aspects of cemented implant loosening and the initiation and development of cement damage. Previous studies have come to a variety of conclusions about the development of cement damage and the relative importance of voids, the stem/cement interface and the cement/bone interface. It is likely that the cement damage process is dependent on the type of stem, the type of cement, the pattern of loading and the boundary conditions of the system. No previous study has quantified cement damage in a cadaveric model. The present study examined the standard Charnley "Cobra" stem with Simplex-P cement under "stair-climbing" loads in a human cadaveric model. Measures of cement damage were derived from the length of cracks in serial transverse sections. Cracks were quantified in order to answer the following two research questions: Does cement damage correlate with applied load? Are cracks preferentially associated with the stem/cement interface, the cement/bone interface or voids?

METHODS

Charnley flanged 45 stems with a satin finish (Ra=0.75μm) were used. Cadaveric femora were selected which were of an appropriate size for the implants (mean age 73yrs, range 59-82). Femora were broached using standard techniques under the supervision of an experienced surgeon. The prostheses were cemented using Simplex-P with contemporary techniques: "bottle brush" lavage, distal plug, vacuum mix, retrograde fill and pressurization. The final position of each prosthesis was controlled by a custom jig. Two non-loaded controls (age 49yrs and 86yrs) were prepared in an identical manner. An MTS axial load frame was used with a custom fixture which produced forces on the femoral head and abductor muscle insertion site which were representative of the peak loads and long axis torques that are experienced by a stem during stem stair-climbing. Loads were applied sinusoidally at 2Hz for 300kcycles at room temperature. Specimens were wrapped in moist gauze to prevent dehydration. All specimens were transversely sectioned at 10mm intervals, from the collar to the distal stem tip. The sections were then stained with a fluorescent dye penetrant and examined using an epi-fluorescence stereo-microscope. In order to confirm that the sectioning and staining process did not introduce artifacts, blocks of surplus cement were sectioned, stained and imaged. Images were recorded using a digital camera and imported into ImagePro for analysis; cracks were identified visually and the auto-trace feature of ImagePro was used to trace them and record their lengths. Crack length data were written to a spreadsheet along with sets of four binary flags indicating the involvement of each crack with stem, void, bone and broached area of cement.

RESULTS AND DISCUSSION

Epi-fluorescence microscopic examination revealed cracks in all of the transverse stem/cement/femur sections. The isolated cement samples which were subjected to the sectioning and staining procedure showed no micro-cracking. In the six cyclically loaded specimens a total of 2419 cracks were recorded, mean crack length was 0.38mm (SD 0.34, range 0.05 to 4.00); total crack length per specimen averaged 152mm (SD 46, range 74 to 205), made up of an average of 403 micro-cracks (SD 120, range 190 to 562). In the two non-loaded control specimens there were 449 micro-cracks with a mean length of 0.24mm (SD 0.15, range 0.05 to 1.00); total crack length per specimen averaged 54mm (47 & 61), made up of an average of 225 micro-cracks (216 & 233).

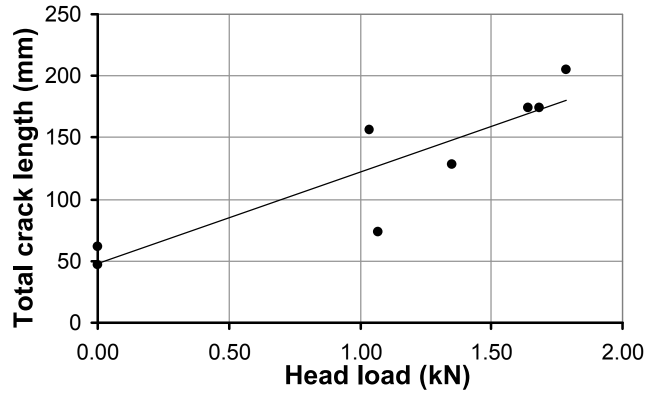

Figure 1: Graph of total crack length versus load applied to the femoral head during fatigue testing.

Total crack length was significantly correlated with femoral head load (R^2=0.799, p=0.0028, Fig 1). There was substantially and significantly more damage at the cement/bone interface than at the stem/cement interface ($p<0.05$). Only a small fraction of micro-cracks involved voids, significantly less than the large fraction involving the cement/bone interface ($p<0.001$).

This study provides an early snapshot of the cement damage process. We found that small micro-cracks are present in cement before loading is applied and that the total number and length of micro-cracks increased with the magnitude of cyclic loading. This suggests that the cement curing process itself may contribute to the initiation of cement failure and that methods of preventing these early micro-cracks may improve the clinical outcome of cemented constructs. The majority of the micro-cracks were associated with the cement-bone interface. Whether these initial micro-cracks coalesce into discreet fracture surfaces that affect the structural integrity of the cemented construct remains to be seen. The role of cement cracks that emanate from bone in the loosening process is a poorly understood phenomenon as most research efforts have focused on the fracture process from voids or from the stem-cement interface. There most certainly would be an interaction between local cement micro-cracks and the remodeling response of adjacent bone due to changes in loading and possibly due to crack generated debris.

ACKNOWLEDGEMENTS

Support from NIH AR42017 and NIH AR47927 is gratefully acknowledged.

THE MOVEMENT OF A MAN'S BOTTOM LIMB IN THE MULTIBOND GRAPHS REPRESENTATION

Józef Wojnarowski, Jerzy Margielewicz

Department of Mechanics, Robots and Machines
Silesian Technical University, Gliwice, Poland; wojnarowski@rmt7.mt.polsl.gliwice.pl

INTRODUCTION

As a result of the process of evolution, the man accepted the perpendicular attitude, producing suitable motorial mechanisms, protecting the maintenance of these attitudes. The structure of connections of bottom limbs, from the point of view of equilibrium and of movement treading, can be fashioned as a system of turned pendulums. It can be proved, that for the maintenance of equilibrium the man uses, specified stability mechanisms, and in the movement treating, the stabilisation of a man is assured by hesitations being characteristic for oscillations. Both, the perpedicular attitude and the characteristic attitude for a man being in movement, are disturbed by a system of external and internal forces. The first of them are consequence of the realization of conscious assignments of movement of a man, the second result from the external environment.

METHODS

A kinematic and dynamic analysis of a model of a man's bottom limb when using the bond graph method, is presented. The conclusion and the main idea of this work is the presentation of a dynamic model of a man's bottom limb. This model makes it possib1e to examine kinematic and dynamic characteristics resulting from extorsions to muscles. The man's bottom limb is modelled as an open variable kinematic chain of a configuration varying in time. Differential equations describing such an attitude in a specified unit of time, are strongly non-linear ones. Contrary to manipulators and industrial robots, values exorting the movement are a result of muscles. A non-classic approach of modelling the dynamics of a man's bottom limb, is presented. The method of bond graphs [2] proposed by H. Paintera in 1961, was originally formulated to analyse steady and unsteady electrical systems. This method has been enlarged to be used for mechanical systems by D.Karnopp and R.Rosenberg [1]. For the procedure of modelling, the method of bond graphs presents the most concise way to describe joined elements or reactions between them for a specified system. The method of bond graphs is considered as a topological method, as it describes the structure sequence of a system, as during modelling, as also during the analysis. For modelling the kinematics, special attention was paid to determine the velocity and acceleration of specified points of the limb. Based on the kinematic scheme of a man's bottom limb (Fig. 1a) multibond graphs are designed (Fig. 1b), in which zero – numerated nodes represent adding of angular and linear velocities, whereas one- numerated nodes represent velocities of specified ponds of the bottom limb.

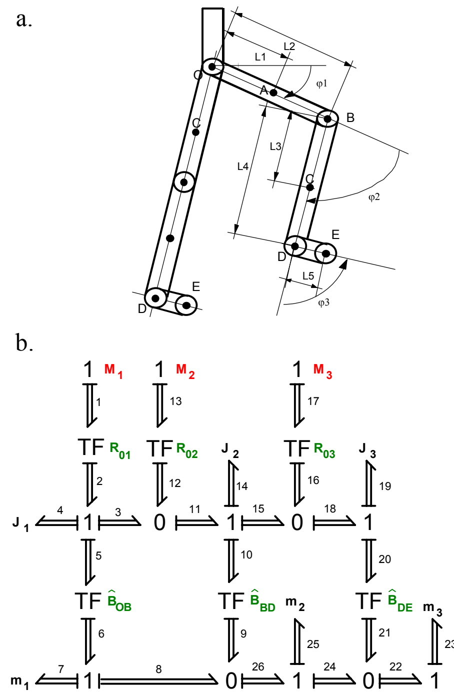

Figure 1: A bottom limb: a) Kinematic scheme, b) Multibond graphs

The method of multibond graphs (Fig. 1b), as a structure af zero - numerated nodes nad one- numerated nodes as also of transformers, represents a set of equations, which can be directly described in an open way, or when using a computer program - to carry out respective computations.

SUMMARY

The described method of modelling the walking process, when using the multibond graphs for a kinematic and dynamic analysis, allows it for simulation tests to neglect the stage of generation of differential equations of the movement. This method allows also to modify, in a simple way, the structure of multibond graphs, in adding additional movement elements of the bottom limb.

REFERENCES

1. Karnopp D.; Rosenberg R.C.: *Analysis and Simulations of Multiport Systems. The Bond Graph Approuch to Physical System Dynamic*. The M.I.T. Press. Cambridge Massachusetts and London 1968.
2. Wojnarowski J.: *Application of graphs and structural numbers in modelling vibrations mechanical systems* [in Polish], PWN Wrocław – Warszawa 1981

MODELING OF FORCE RESPONSE OF FINGERTIPS IN KEYBOARD STRIKES

John Z. Wu [1], Ren G. Dong, Aaron W. Schopper, and W. Paul Smutz
National Institute for Occupational Safety and Health, Morgantown, WV, USA. [1] E-mail: jwu@cdc.gov

INTRODUCTION

An extended exposure to repeated loading on the fingertip has been associated with many vascular, sensorineural, and musculoskeletal disorders in the fingers, such as carpal tunnel syndrome (Beck-Foehn, 1992) and hand-arm vibration syndrome (Bovenzi et al., 1988). A better understanding of the pathomechanics of these sensorineural and vascular diseases in fingers requires a formulation of a biomechanical model of the fingertips and analyses to predict the mechanical responses of the soft tissues to dynamic loading. In the present study, a model based on finite element techniques has been developed to simulate the mechanical responses of the fingertips to dynamic loading.

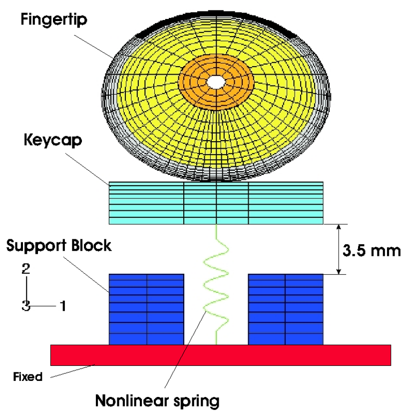

Figure 1: Model of the response of a fingertip to keystroke.

METHODS

The mechanical responses of the fingertip were analyzed using a multi-layered two-dimensional finite element model (Fig. 1). The fingertip was assumed to be composed of a skin layer (representing epidermis and dermis), subcutaneous tissue, bone, and nail. The dimensions of the fingertip were assumed to be representative of the index finger of a male subject. The skin tissue, including epidermis and dermis, was assumed to be hyperelastic and linearly viscoelastic. The subcutaneous tissue was assumed to be a biphasic material composed of a fluid phase and a hyperelastic solid phase. The nail and the bone were considered as linearly elastic. The numerical experiment (Fig. 1) was designed to simulate the experiments reported by Rempel et al. (1994). The keyboard was composed of a hard plastic keycap, a rigid support block, and a nonlinear spring. The contact between the fingertip and the keycap was assumed to be frictionless. A gap of 3.5 mm was considered between the support block and keycap at the undeformed state. The force-displacement relation of the nonlinear spring was determined on the basis of the experimental data of Apple Extended II keyboard with Alps KCM QSIII switches (Rempel et al., 1994). The numerical tests were performed in a quasi-static manner, assuming negligible inertia effects of the mass of the model.

RESULTS AND DISCUSSION

Fig. 2 shows the comparison of the numerical simulation with the experimental data reported by Rempel et al. (1994). The time history of the force response during a keystroke typically demonstrates three phases (Fig.2a): I - keyswitch depression, II - impact of the fingertip on the keycap, and III – compression and release of the fingertip pulp. During the first phase, the finger depresses the nonlinear spring (representing the switch activation), and the deformation of the fingertip is small. A relative large impact force occurs during the second phase, which is associated with the deceleration of the participating masses, i.e. the masses of fingers and arm. Since the effects of the inertia were neglected in the proposed model, the impact force was not predicted in our simulations. The second peak force in the time history is associated, mainly, with the compression of the fingertip pulp, and occurs over a greater time duration than the first force peak. The effects of inertia are negligible during the third phase. The predicted force responses of the fingertip during keystroke phases I and III agree well with the experimental data (Fig. 2).

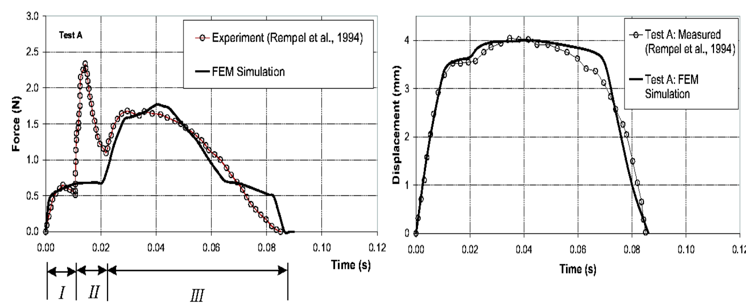

(a) **(b)**

Figure 2: Comparisons of the time-histories of the force response and the displacement excitation of the fingerpad during keystroke obtained in the simulations with those experimental data reported by Rempel et al. (1994). **(a)** Force response of the fingerpad. **(b)** Displacement excitation curves of the arterial bone within the fingertip.

SUMMARY

The proposed model is capable of predicting the time-dependent behavior of the fingertip under dynamic loading, for example, time-dependent force response, energy dissipation, and time-dependent stress/strain distributions within soft tissue of the fingertip. The limitation of the proposed model is that the effects of finger and hand inertia, which participate in the impact interactions between the fingertip and the contacting plate or keyboard, are neglected.

REFERENCES

Bovenzi, M. et al. (1988) *Int Arch Occup Environ Health*, 61, 25-34.
Beck-Foehn, M. (1992) *Nervenarzt*, 63, 467-472.
Rempel, D. et al. (1994) *J Biomech*. 27, 1101-1104.

ORIENTED MITOSIS-DRIVEN EPITHELIUM RESHAPING: A FINITE ELEMENT STUDY

G. Wayne Brodland[1] and Jim H. Veldhuis[2]

Department of Civil Engineering, University of Waterloo, 200 University Avenue West, Waterloo, Ontario, Canada N2L 3G1
[1]Professor, brodland@uwaterloo.ca
[2]Research Associate

INTRODUCTION

During cell division, the orientation of the mitotic plane is typically determined by the long axis of the mother cell. In certain cases, however, the mitotic planes tend to occur at a fixed angle with respect to a global reference frame (Hertzler and Clark). The latter pattern is called oriented mitosis, and it has been hypothesized as driving certain kinds of in-plane reshaping in epithelia.

THE FINITE ELEMENT MODEL

To test this hypothesis, a cell-level, finite element-based model was developed (Chen and Brodland, 2000). In that formulation, the internal volume of each n-sided cell is represented using n, triangular finite elements. These elements are assigned a viscosity μ, a value that is assumed to embody the effective viscosity of the cytoplasm with its embedded filamentous networks and organelles. To model the interfacial tensions that arise along each cell edge, rod-like elements are used. These tensions embody the actions of microfilaments, microtubules, the cell membrane and cell-cell adhesions (Chen and Brodland, 2000). To study mitosis, the original formulation was enhanced so that cells could be divided according to one of several user-specified patterns.

RESULTS

Figure 1A shows the initial configuration of a square patch of 50 cells that was used for the simulations reported here. When the cleavage plane was determined by the long axis of the mother cell, the patch remains square and if the daughter cells are programmed to grow following division, the patch grows isotropically. When all cleavage planes are horizontal and daughter cells do not grow, the patch narrows and elongates (Fig. 1B). When oriented mitosis and growth occur together, the patch changes shape and its area increases (Fig. 1C).

DISCUSSION AND CONCLUSIONS

When oriented mitosis occurs and the number of cells has doubled, geometric considerations predict a maximum patch aspect ratio of 2:1. The simulations show that oriented mitosis actually produces this amount of reshaping. The simulations also show that the degree of reshaping is independent of the rate of daughter cell growth. Thus, oriented mitosis is found to be not only effective, but highly efficient, in reshaping epithelia. Since the simulations show the degree of reshaping that can be attributable to oriented mitosis, they provide a benchmark against which experimental studies and hypotheses about epithelium reshaping can be compared.

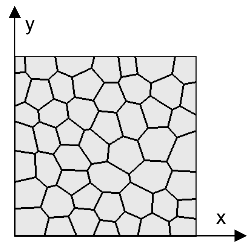

A. Initial Configuration

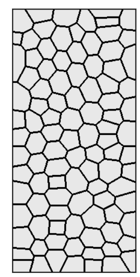

B. Oriented Mitosis but no Growth
(All cleavage planes were parallel to the x-axis)

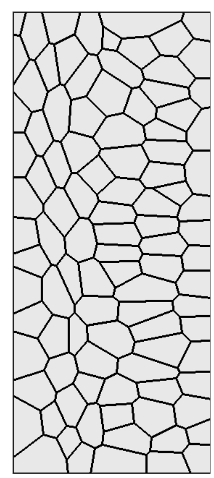

C. Oriented Mitosis and Growth.

Figure 1: Simulation Results

REFERENCES

Chen, H.H., and Brodland, G.W. (2000). Cell-level finite element studies of viscous cells in planar aggregates, *ASME Journal of Biomechanical Engineering*, **122**, 394-401.

Hertzler, P.L., and Clark, W.H. (1992). Cleavage and gastrulation in the shrimp *Sicyonia Ingentis*: Invagination is accompanied by oriented cell division, *Development,* **116**, 127-140.

CELL-CELL INTERFACIAL TENSION AND CYTOPLASM VISCOSITY CAN BE DETERMINED USING PARALLEL-PLATE COMPRESSION TESTS

Jim H. Veldhuis[1] and G. Wayne Brodland[2]

Department of Civil Engineering, University of Waterloo, 200 University Avenue West, Waterloo, Ontario, Canada N2L 3G1
[1]Research Associate
[2]Professor, brodland@uwaterloo.ca

INTRODUCTION

One of the standard ways to determine the surface tension of embryonic tissues (Foty and Steinberg, 1995) is to compress a mass of tissue between a pair of parallel plates (Fig. 1). Cell-level computer simulations of the test cycle led to a more complete understanding of the mechanics of the test.

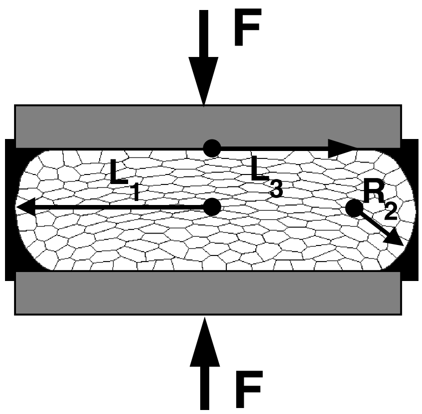

Figure 1: The Parallel-Plate Compression Test

THE FINITE ELEMENT MODEL

These tests were based on a cell-level finite element-based model (Chen and Brodland, 2000). In that formulation, the internal volume of each n-sided cell is represented using n triangular finite elements. These elements are assigned a viscosity μ, a value that is assumed to embody the effective viscosity of the cytoplasm with its embedded filamentous networks and organelles. To model the interfacial tensions that arise along each cell edge, rod-like elements are used. These tensions embody the actions of microfilaments, microtubules, the cell membrane and cell-cell adhesions (Chen and Brodland, 2000).

RESULTS AND DISCUSSION

The cells shown in Fig. 1 were actually produced by taking an approximately circular mass of cells and compressing them between parallel plates. When the plates are brought to rest, the reactive force due to deformation of the viscous cytoplasm suddenly stops, and the load drops from the value shown as B_1 in Fig. 2 to that shown as B_2. As the plates are held at a fixed spacing, the cells anneal. That is, the interfacial tension γ_{CC} that acts along the boundaries between individual cells causes all elongated cells to shorten and increase in width until their aspect ratios approach one. Formulas that relate cell shape to stress, like those developed by Brodland et al. (2000), can be used to calculate the strength of this interfacial tension from the change in load between B_2 and C. Finally, the surface tension γ_{CM} of the cells can be determined from the load at C using the methods of Foty and Steinberg (1995).

Families of simulations of this type confirm that the load-deflection curve produced in parallel-plate compression tests is produced by three properties of the cells: the effective viscosity of the material in the cells, the strength of the cell-cell interfacial tensions, and the strength of the surface tension at the boundary between the cells and the surrounding medium. They also show that these contributions correspond to the values labelled, respectively, as F_{cyto}, F_{CC} and F_{CM} in Fig. 2.

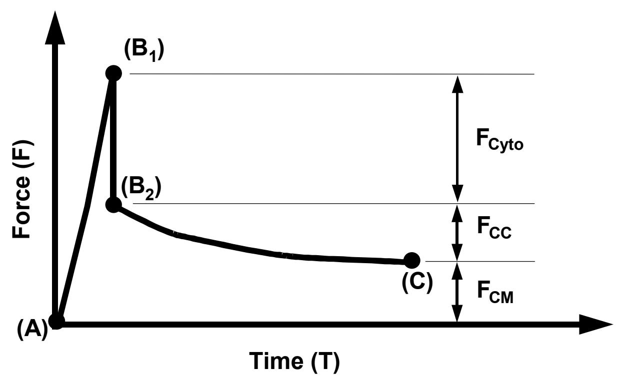

Figure 2: Contributions to the Load-Time Curve Attributable to the Mechanical Properties μ, γ_{CC} and γ_{CM}

REFERENCES

Brodland, G. W., Veldhuis, J. H. and Chen, D. (2000). How cell shape affects the stresses in a cell sheet, *2000 Advances in Bioengineering* (BED Vol 48), Conway, T. A., ed., ASME New York, 79-80.

Chen, H. H. and Brodland, G. W. (2000). Cell-level finite element studies of viscous cells in planar aggregates, *ASME Journal of Biomechanical Engineering*, **122**, 394-401.

Foty, R. A. and Steinberg, M. S. (1995). Liquid properties of living cell aggregates, in: *Interplay of genetic and physical processes in the development of biological form*, Beysens, D., Forgacs, G. and Gaill, F., eds., World Scientific, Pub. Co. Pte. Lt., 63-73.

HUMERAL TORQUE IN YOUTH BASEBALL PITCHERS: IMPLICATIONS FOR DEVELOPMENT OF HUMERAL RETROTORSION

Michelle B. Sabick[1], Michael R. Torry[1], and Richard J. Hawkins[2]

[1]Steadman♦Hawkins Sports Medicine Foundation and [2]Clinic, Vail, CO, USA, Michelle.Sabick@shsmf.org

INTRODUCTION

The effect of repetitive throwing on developing athletes is not well understood, in part because there is little data describing the biomechanics of youth pitchers, and in part due to unique aspects of the developing skeleton such as joint laxity, underdeveloped musculature, and open epiphyseal plates. Increased humeral retrotorsion, the angle between the axis of the femoral head and the axis of the elbow joint, has been noted in the throwing arms of pitchers, but its cause has not been determined. If this adaptation is due to throwing as some suggest (Pieper, 1998), it likely results from a torque about the long axis of the humerus. The large joint forces generated during the pitching motion have been previously documented, but the relationship between pitching biomechanics and torque on the humerus has not been studied. The aim of the current study is to evaluate the proposed mechanism of development of humeral retrotorsion in light of biomechanical data.

METHODS

Fourteen youth baseball pitchers were filmed at 120 Hz using two high-speed video cameras. The locations of 21 body landmarks were digitized and their three-dimensional locations were calculated using the DLT method (Abdel-Aziz & Karara, 1971). Joint kinetics at the shoulder and elbow were computed using inverse dynamics (Fleisig et al., 1996; Werner et al., 1993). The net humeral forces and torques were defined as the difference between force and torque values at the proximal and distal ends of the humerus. Kinetic data was normalized in time to facilitate comparisons among players.

RESULTS AND DISCUSSION

A description of the subject population is provided in Table 1. The largest net force acting on the humerus was an axial force causing tension. This force was largest in magnitude, -378 ± 81 N, just after ball release. The largest net torque about the humerus was a torque about the long axis of the humerus that reached a "maximum" value of -35.3 ± 6.6 Nm (Figure 1). The negative value of this torque signifies that it tended to rotate the distal end of the humerus externally relative to the proximal end. This humeral axial torque peaked during the late cocking phase of the pitch. After ball release, the humeral torque was negligible for the remainder of the motion.

During the cocking phase of the pitch, there is an internal rotation torque at the shoulder while the forearm and hand are externally rotating, resulting in a torque about the shaft of the humerus. This torque is consistent with the development of increased humeral retroversion, in which the distal humerus displays increased external rotation relative to the proximal humerus. The peak humeral torque developed in these subjects was 66-78% of the torque required to fracture the adult humerus (Schopfer et al., 1994; Lin et al., 1998). The magnitude of torque required to deform the youth humerus is unknown. However, the cartilage of the epiphysis is known to have poor resistance to torsion, and is not as strong as bone (Bright et al., 1974).

Table 1. Description of the subject population.

	Age (yr)	Height (m)	Mass (kg)	Ball V (m/s)
Mean	13	1.54	43.8	21.6
S.D.	--	0.08	8.6	1.8
Range	--	1.42 - 1.69	33.7 - 66.4	17.9 - 23.7

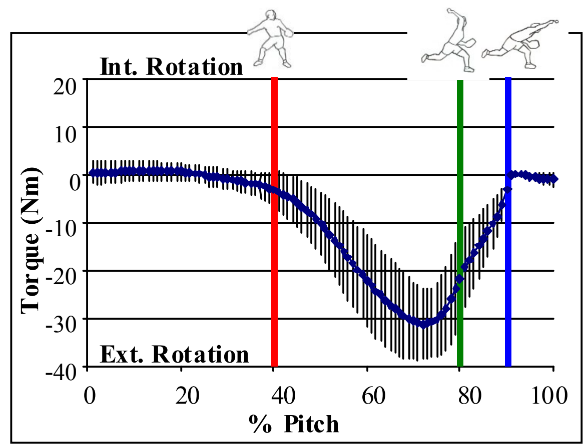

Figure 1. Humeral torque throughout the pitching motion.

SUMMARY

The direction of the axial torque acting on the humerus during the late cocking phase of the throwing motion is consistent with the development of increased humeral retrotorsion. The magnitude of this torque is the same order of magnitude as the torque required to break the adult humerus. Given that epiphyseal cartilage is weaker than bone in torsion, this torque may be sufficient to cause adaptive changes in the proximal humeral epiphysis resulting in increased humeral retrotorsion noted in throwers, supporting the assertions of Pieper (1998).

REFERENCES

Abdel-Aziz, Y., Karara, H. (1971). *Proc of Am Soc Photogram Symposium on Close Range Photogram*, 1-19.
Bright R. W. et al (1974). *J Bone Jt Surg*, **56A**, 688-703.
Fleisig, G. S. et al (1996). *Sports Med*, **21**(6), 421-37.
Lin, J. et al (1998). *Clin Orthop,* **351**, 203-13.
Pieper, H. G. (1998). *Am J Sports Med*, **26**(2), 247-53.
Schopfer A. et al (1994). *J Orthop Trauma*, **8**(5), 414-21.
Werner, S. L. et al (1993). *J Orthop Sports Phys Ther*, **17**(6), 274-8.

GAIT ANALYSIS BY PATIENT WHO HAVE AN ACL DEFICIENT KNEE

Zsolt Knoll MD.[1], Rita Kiss PhD.[2], László Kocsis PhD.[3]

[1] Senior surgeon, Fund MEDICaMENTOR, Budapest, Hungary knoll@elender.hu
[2] Senior researcher, Hungarian Academy of Sciences, Research Group of Structures, Budapest, Hungary
[3] Assoc. Professor, Biomechanics Laboratory Budapest University of Technology and Economist, Budapest, Hungary

INTRODUCTION

At present, not too much is known about the function of the knee during the activities of daily living in patients who have a deficient anterior cruciate ligament (ACL) (Andriacchi 2000, 1993, 1997) The goal of our study was a better understanding of the changes in function of the knee that occur while patients who have a deficient ACL in one knee walk.

MATERIALS AND METHODS

Twenty patients who had unilateral, isolated deficiency of ACL diagnosed arthroscopy or MRI data. The study population consisted of twelve men and eight women. The mean age was 34.70±3.1 years; the mean height 1.74±0.12 meters and the mean weight 78.1±20.2 kilograms. Each patient was examined clinically with IKDC test. The measuring of the human motion was investigated by zebris CMS-HS ultrasound-based motion measurement system during treadmill-walking. The triplets are attached to the sacrum, right and left thigh, and right and left calf. The anatomical models consider each limb segment to be a rigid body, linked to each other by a joint. The triplets are attached to the segments and virtually linked by a pointer to the anatomical points in such a way, that the registered movement of each triplet enables the calculation of the position of the selected anatomical points, and thereby representing the movement.

RESULTS AND DISCUSSION

Firstly basic gait parameters (step-length, step-width, gait-cycle time), were calculated from coordinates of anatomical points (Whittle, 1998). The flexion-extension motion is characterized by the knee's angle-time function. The newly defined ACL-movement is a displacement between two ACL characterized points namely a displacement between tibial tubercle and femoral lat. epicondyle. The calculated parameters are summarized in Table 1.

Table 1: The gait parameters of healthy and ACL deficient limb

Knee	ACL deficient	Healthy
Step-length [mm]	349 – 670	405 – 700
Step-width [mm]	8 – 80	4 – 71
Maximum of the knee angle [degree]	41.1 - 76.4	45.9 – 81.7
Minimum of the knee angle [degree]	0.5 – 18.8	1.7 – 27.4
ACL movement [mm]	7.50 – 41.9	5.7 – 31.1

The step-length of the affected limb was smaller (12-45%) than healthy. The length of the stance phase of the deficient limb was longer (8-27%) than healthy. The flexion-extension motion plot of knees with ACL deficiency (angle of the knee) showed a flattering of the support phase and a reduction of the peak knee flexion (5-34%) and extension (2-20%) (Figure 1). The ACL-movement of affected knee was significant greater (3-293%) than normal.

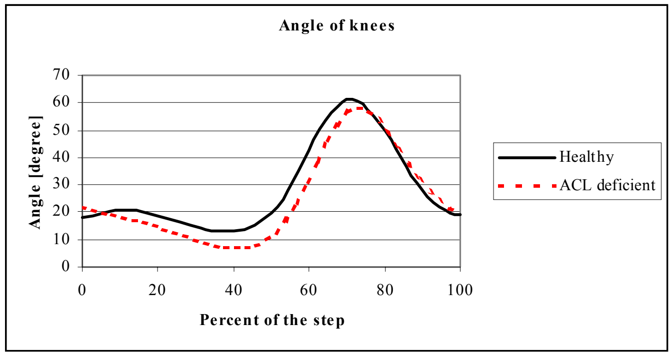

Figure 1: The flexion-extension motion plot of the healthy and the ACL deficient knee

SUMMARY

The findings in this study indicate that when the ACL is deficient the movement of the knee may be performed in an abnormal manner. The special developed gait-analysis can be useful for evaluating patients who have an ACL injury because it detects subtle changes in the movement of the knee.

REFERENCES

Andriacchi, T.P., Alexander, E. J. (2000). *J. of Biomechanics*, **33**, 1217-1224.
Andriacch,i T.P., Birac, D.(1993). *Clin.l Orthop. Rel. Res.*, **288**, 40-47.
Andriacchi T.P, et al (1997). *Sportorthopadie – Sporttraumatologie*, **13**, 153-160.
Whittle, M.W. (1998) *Gait analysis. An introduction.* Butterworth, Heinemann.

ACKNOWLEDGEMENTS

The research is sponsored by Hungarian Academy of Sciences, by Széchenyi István Stipendium (Rita Kiss), by MEDICaMENTOR Fund (Zsolt Knoll) and the Hungarian Research Fund.

OPTIMIZATION OF ANKLE JOINT ANGLE AS FUNCTION OF TRUNK ANGLE IN CYCLING

M. de Zee[1], S. Tørholm[1], M. Damsgaard[1], H.H.C.M. Savelberg[2], and J. Rasmussen[1]

[1]Institute of Mechanical Engineering, Aalborg University, Aalborg, Denmark
The AnyBody Group: http://anybody.auc.dk
[2]Department of Human Movement Sciences, Faculty of Health Science, Maastricht University, Maastricht, The Netherlands

INTRODUCTION

Savelberg *et al.* (2001) showed experimentally that manipulating the trunk angle, or rather manipulating the muscles spanning the hip joint, affects both the kinematics and the recruitment of the leg muscles during cycling. Their subjects showed more plantar flexion during the upstroke with the upper body leaning backward compared to other trunk positions (upright, forward). The change of muscle recruitment was not only restricted to the muscles spanning the hip joint, but affected the muscles in the lower leg as well. This implies that the human body is able to optimize the intermuscular coordination for different bicycle and/or body configurations.

The aim of this project is to simulate the experiment of Savelberg et al. using the general body modeling system AnyBody based on inverse dynamics, which is capable of analysis and optimization of complicated 3-dimensional musculo-skeletal models. It has been shown that AnyBody is able to optimize movement for partially unknown motions like the ankle angle during cycling (Rasmussen *et al.*, 2001). In this study we shall optimize the ankle angle for different trunk angles in cycling using two different objective functions. The simulation results will be compared with Savelberg *et al.* (2001).

METHODS

AnyBody's model of the lower extremities comprises all the significant muscles crossing the ankle, knee and hip, totaling 64 muscles in the two legs. Muscle data are compiled from (Delp, 1995). The muscles are Hill type with force/length and force/velocity dependency according to an adaptation of (Zajac, 1989).

The cycling computer simulations were done at a cadence of 70 rpm and an average mechanical output of 200 W. The ankle angle was optimized for three body configurations: 1) trunk angle 50° (forward), 2) trunk angle 90° (upright), and 3) trunk angle 105° (backward), see also figure 1.

For each optimization we used two different object functions:

1. Minimize the sum of rms muscle stresses over the cycle
2. Minimize metabolic energy consumption

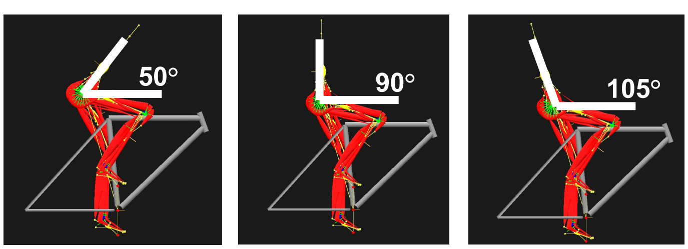

Figure 1: The three body configurations for which the ankle angle was optimized.

RESULTS

Figure 2 shows the optimized ankle angle curves for the three different body configurations optimized with the different objective functions.

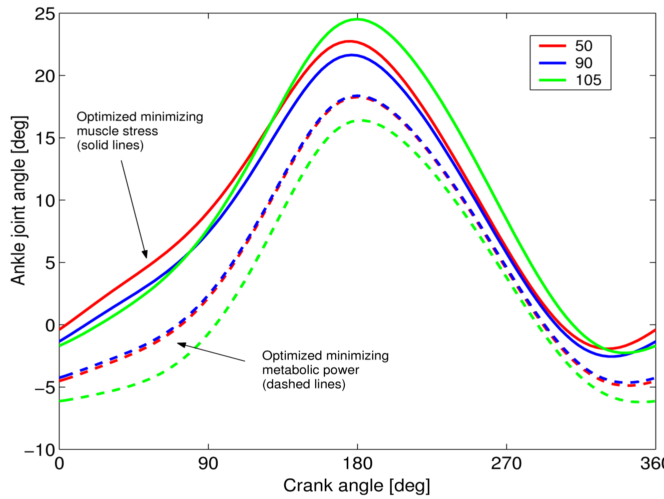

Figure 2: Ankle joint angle as function of trunk angle. Solid lines: optimized by minimizing muscle stress. Dashed lines: optimized by minimizing metabolic power.

DISCUSSION

The results shows that the objective function of minimizing muscle stress shows the same tendency as the experimental results of Savelberg *et al.* with regards to the backward position. The absolute differences, though, are smaller than in the experiments. The optimization results imply that during cycling minimizing metabolic power is not the most important criterion for the human body during cycling, which is in line with other literature (Chen *et al.*, 1999). We believe that minimizing muscle stress is a better objective function for cycling, but more verification is still necessary.

REFERENCES

Chen,B., Jones,N.L., and Killian,K.J. (1999) *J.Physiol.* **518,** 933-940.
Delp,S.L. (1995) (http://isb.ri.ccf.org/data/delp/Muscle_parameter.txt)
Rasmussen,J., Damsgaard,M., and Christensen,S.T. (2001) ISB XVIIIth Congress, Zürich, Switzerland (Abstract)
Savelberg,H.H.C.M., van de Port,I.G.L., and Willems,P.J.B. (2001) ISB XVIIIth Congress, Zürich, Switzerland (Abstract)
Zajac,F.E. (1989) *Crit.Rev.Biomed.Eng.* **17,** 359-411.

ACKNOWLEDGEMENTS

This work was supported by the Danish ResearchAgency, and by the Danish National Research Foundation.

THE EFFECT OF UHMWPE MATERIAL AND KNEE DESIGN ON *IN VITRO* WEAR OF FIXED BEARING AND ROTATING PLATFORM MOBILE BEARING TOTAL KNEE REPLACEMENTS

Hannah M J McEwen[1], Richard Farrar[2], Martin H Stone[3] and John Fisher[1]

[1] Medical and Biological Engineering, University of Leeds, Leeds LS2 9JT, U.K. email: j.fisher@leeds.ac.uk
[2] DePuy International, a Johnson and Johnson company, Leeds, U.K.
[3] Leeds General Infirmary, Leeds, U.K.

INTRODUCTION

Reduction of ultra high molecular weight polyethylene (UHMWPE) surface wear in total knee replacement (TKR) bearings may delay the onset of osteolysis and subsequent loosening of components. The rotating platform (RP) mobile bearing TKR design decouples bearing motions by allowing linear rotation at the tray-insert counterface, hence reducing the multidirectional motion at the femoral-insert articulation. The aim of this study was to compare the effects of TKR design and bearing material on UHMWPE wear using a physiological knee simulator.

MATERIALS AND METHODS

Twelve (n = 12) LCS RP mobile bearing TKR (DePuy) were investigated. Six RP inserts were machined from GUR1050 UHMWPE and were sterilised using gas plasma methods (1050 GP), as used commercially. The remaining six inserts were machined from GUR1020 UHMWPE and were packaged in foil pouches prior to sterilisation by 4.0 MRad γ-irradiation in a vacuum (1020 GVF). These were compared with six (n = 6) PFC Sigma (DePuy) fixed bearing TKR with curved 1020 GVF UHMWPE commercially used inserts. Testing was completed on a six-station force/displacement controlled knee simulator using the inputs specified in Table 1 (frequency = 1Hz). The test lubricant was 25% (v/v) newborn calf serum with 0.1% (m/v) sodium azide solution in sterile water. Components were tested in the simulator for five million cycles. Volumetric wear was calculated from the mass loss of the inserts, adjusted using unloaded soak controls, and using densities of 0.932 and 0.934 mg/mm^3 for the 1050 GP and 1020 GVF bearings, respectively. The wear rate for each test was defined as the slope of the linear regression line of cumulative wear versus number of cycles completed.

Table 1: Kinematic inputs for knee simulator studies.

	FE	AF	AP	TR
PFC Σ	0 – 58 °	max 2600 N	0 – 10 mm	± 5°
LCS RP	0 – 58 °	max 2600 N	-262 – 110 N	± 5°

FE = flexion-extension (ISO14243 1999); **AF** = axial force (ISO14243 1999); **AP** = anterior-posterior translation with displacement control (Lafortune *et al* 1992) for PFC and force control (ISO14243 1999) for LCS; **TR** = tibial rotation (Lafortune *et al* 1992)

RESULTS AND DISCUSSION

The PFC Sigma fixed bearing knees exhibited a significant (p < 0.01) threefold higher wear rate in comparison to the LCS RP mobile bearing knees while no significant difference (p = 0.20) in wear rate was observed between the two RP mobile bearing materials (Fig. 1).

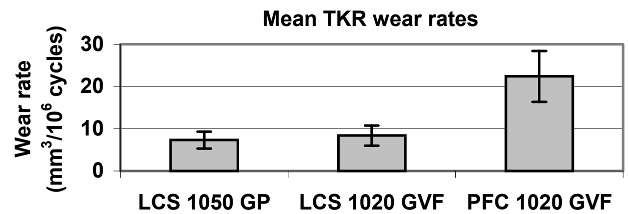

Figure 1: Mean wear rates with 95% confidence limits.

The RP mobile bearing design decouples knee motions between the femoral-insert and the tray-insert articulating surfaces. Most of the rotation occurs at the tray-insert interface, which is a simple unidirectional rotation motion that is known to produce low wear (Marrs *et al* 1999, Wang *et al* 1996). Consequently, the femoral-insert articulation experiences very low rotation so the motion at this articulation is also generally unidirectional and similarly has a low wear rate. The unique design of the rotating platform mobile bearing knee translates complex input motions into more unidirectional motions, thus benefiting from a reduced wear rate due to decreased cross shear on the molecularly oriented UHMWPE in comparison to the more multidirectional PFC Σ fixed bearing knees. Crosslinked polyethylenes exhibit improved wear rates when subjected to multidirectional motion (Wang *et al* 1996) but this advantage is not realised when the motion is more unidirectional (Marrs *et al* 1999). There was no significant advantage observed when the moderately crosslinked 1020 GVF bearing material was utilised for the RP bearings in comparison to the non-crosslinked 1050 GP.

CONCLUSIONS

Under high rotation kinematics, the use of RP mobile bearing knees significantly reduced the volumetric wear rate of UHMWPE in comparison to fixed bearing components. The use of crosslinked UHMWPE bearing materials had no significant effect on LCS RP wear. Thus, TKR design is an important factor in the reduction of UHMWPE wear.

REFERENCES

ISO14243 (1999)
Lafortune M.A. *et al* (1992) J. Biomech., **25**, 347-357.
Marrs H. *et al* (1999) J.Mats.Sci.Mats.Med., **10**, 333-342.
Wang A. *et al* (1996) Proc.Instn.Mech.Engrs. **210H**, 141-155.

COMBINATIONS OF CYCLE LENGTH AND RATE ARE CHOSEN TO MINIMIZE THE MUSCLE POWER REQUIRED IN HUMAN RUNNING

Toshimasa Yanai[1] and James G. Hay[2]
[1]School of Physical Education, University of Otago, Dunedin, New Zealand, tyanai@pooka.otago.ac.nz
[2]Department of Sport and Exercise Science, University of Auckland, Auckland, New Zealand

INTRODUCTION

Experimental data on many forms of human cyclic locomotion suggest that the graphical forms of the relationships of cycle length (CL) vs speed (S) and cycle rate (CR) vs S are common across all forms of such locomotion, except those in which one of the two factors (CL or CR) is held constant throughout the range of Ss studied (Figure 1). There are many practically-feasible combinations of CL and CR that a subject might choose to use when locomoting at a given speed. It appears, however, that a subject consistently select that combination that is consistent with the characteristic curves shown in Figure 1. The obvious question that follows from this observation is "What is the criterion they use in making their selection from the many available combinations of CL and CR for each S?"

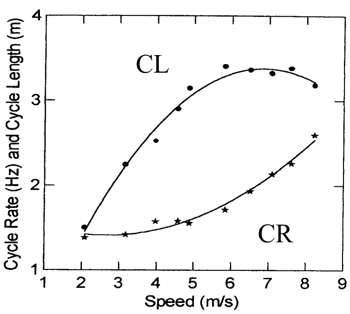

Figure 1: Typical CR vs S and CL vs S relationships for longitudinal (within-subjects analysis of human running.

The purpose of this study was to test the hypothesis that, in human running at a given speed, subjects select the combination of cycle length and cycle rate that minimizes the peak power generated by the muscles.

METHODS

A two-dimensional model of a runner consisting of a trunk and two legs was defined. A force actuator controlled the length, and a torque actuator controlled the amplitude and frequency of the backward and forward swing, of each leg. The sum of the peak powers generated by the actuators was determined for a range of CRs (1-4 Hz) at each of a series of Ss (2-10 m/s). The combination of CL and CR requiring the least sum of the peak powers at each S was taken to be the ideal combination. Two constraints were imposed: the maximum amplitude of the forward and backward swing of the legs (± 50°), and the minimum ground contact time needed to maintain steady state running (0.12 s).

RESULTS AND DISCUSSION

The CR and CL vs S relations derived on the basis of the strategy that minimizes the peak power generated by the actuators (Figure 2) generally showed a similar pattern to those exemplified in Figure 1. CL was the primary factor accounting for increases in S in the low-speed range and CR was the primary factor in the high-speed range. The results thus supported the hypothesis of the study. The natural process of selecting CR-CL combinations for human running might, therefore, be said to have similar characteristics to the process of solving a constrained optimization problem.

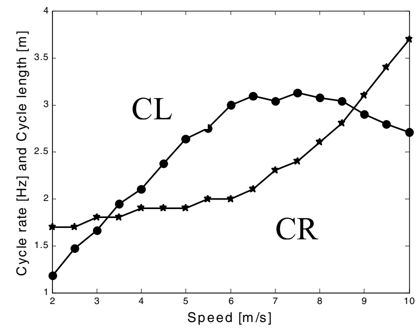

Figure 2: CL and CR vs S relationships that minimized the peak power required

The constraints played important roles in determining CR and CL vs S relationships. The anatomical constraint stopped CL from increasing beyond approximately 3.2 m (Figure 3). With a near-constant CL in the high-speed range (from 6.5 to 10 m/s), CR increased in a near-linear fashion throughout the range. When the temporal constraint was imposed in addition to the anatomical constraint, CL started to decrease at S approximately 7.5 m/s. With CL decreasing, CR increased rapidly at the high-speed end (from 7.5 to 10 m/s).

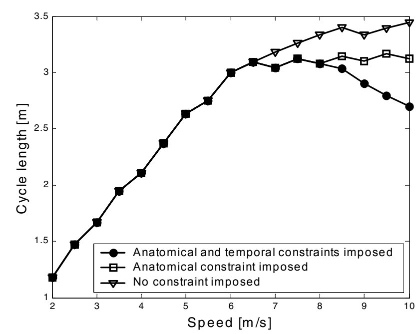

Figure 3: Effects of the constraints

SUMMARY

The results of this study demonstrated that CR-CL combinations that minimized the peak power generated by the actuators matched well the CR-CL combinations naturally selected by human subjects. The results also showed that the anatomical constraint prevented the CL from increasing beyond a certain limit; and the temporal constraint forced the CL to decrease, and the CR to increase substantially, at high speeds. The results suggest that a runner may be able to improve the performance through some form of physical training that makes the anatomical constraint less restrictive. Future studies to examine the practicality of this suggestion and the effectiveness of such a training approach are indicated.

AUTOMATED MARKERLESS ANALYSIS OF HUMAN WALKING AND RUNNING BY COMPUTER VISION

ChewYean Yam, Mark S. Nixon, John N. Carter
Image, Speech and Intelligent System, Electronics and Computer Science, University of Southampton.

INTRODUCTION

Very often, analysis of gait kinematics exploits invasive data acquisition techniques, e.g. attaching a goniometer and accelerometer, using a multiple exposure camera technique [Murray67] with reflective, and markers [O'Malley93] on the subject's body. These can be expensive, laborious and inconvenient. More importantly they encumber the natural manner of walking and running. Human walking and running is a highly sophisticated system involving multiple factors interacting simultaneously. Naturally, it is difficult to model human locomotion realistically. A considerable amount of work (in biomechanics) seeks to model human walking [Mochan80], running [McGeer90] or both [Alexander92] aiming to understand or explain the mechanism underlying these move-ments, but not for realistic modelling or imitation.

We have developed an automated non-contact and markerless analysis system using computer vision techniques. A structural motion model derived from forced coupled oscillators, which can describe the spatio-temporal characteristics of human running and walking gaits [Yam02], serves as the basis of an evidence gathering technique used to extract leg motion. Naturally, concern over marker movement is now replaced by concern of the features extracted. In this respect, evidence gathering approaches have known optimal performance, especially in respect of noise and occlusion.

METHOD

The fronto-parallel views of 20 healthy subjects (5 females and 15 males, age:22-45, weight:45-100kg, height:156-192cm) walking (2.8-5.5km/h) and running (6.5-13.9km/h) normally on a treadmill at their preferred speeds are filmed with a digital camera. The video clips are digitised into image files. Edge maps are obtained via the Sobel edge detector. Temporal template matching that considers the whole sequence of edge maps is applied to extract the motion of a whole gait cycle. The structural motion model serves as the basis of this evidence gathering technique. The length of the thigh and lower leg, their absolute rotation angles and the hip's motion can be extracted and computed simultaneously. These measurements can then be used for further analysis. The process is automatic following pre-selection of some control parameters.

RESULTS AND DISCUSSIONS

Fig. 1 shows the extracted rotation angles of a subject's thigh (when walking) and lower leg (when running) superimposed on manually labelled data. The gross motions are captured well and appear very close to the manual labelled data which could however be erroneous. **Fig. 2a** shows an image with the extracted motion superimposed. This technique extracts the front of the legs and we shall later determine its relationship to the conventional labelling on the bone structure. Due to temporal (1/2 period) and spatial (sequence of oscillation) symmetry, this technique can extract both legs, and hence handle self-occlusion. Here, only the thigh and lower leg rotation are considered, with potential extension to ankle rotation.

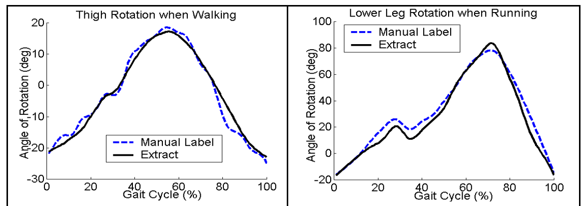

(a) (b)

Fig. 1: Automatically extracted absolute angles of (a) thigh when walking and (b) lower leg when running.

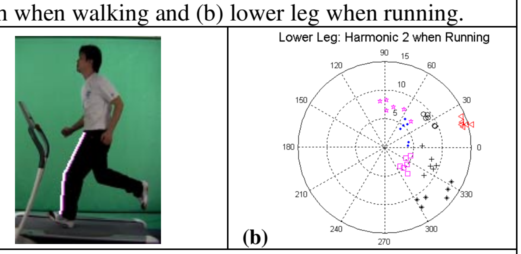

(a) (b)

Fig. 2: (a) Automatically extracted leg motion; (b) phasor plot of lower leg rotation when running; different symbols represent different subjects.

Fig. 2b shows the 2nd harmonic Fourier description for lower leg motion. It suggests individuality, in that people's movement clusters in different places. Experimentation shows that running actually has more variability than walking. The capability to extract individual characteristics in gait patterns suggests that it is indeed appropriate for future investigation in analysis of gait biomechanics. This non-contact, markerless and automated feature extraction process is invariant to gait mode (walking or running) and speed, so is feasible for analysis, especially with a large subject population.

REFERENCES

Alexander, R. M. (1992). *Phil. Trans. R. Soc. Lond.* B. **338**, 189-198. McGeer, T. (1990). *Proc. R. Soc. Lond.* B. **204**, 107-134. Mochan, S. et al (1980). *Math. BioSc.* **52**, 241-260. Murray, M.P. (1967). *American J. of Phy. Med*. **46**, 290-332. O'Malley, M. et al (1993). *Med. & Biol. Eng. & Comp.*, **31**, 392-398. Yam, C.Y. et al (2002), *ACCV*, accepted.

THE KINEMATICS OF HIP JOINT SIMULATOR MICROSEPARATION

T Stewart[1], S Williams[1], J L Tipper[2], R M Streicher[3], E Ingham[2], J Fisher[1]
[1]Mechanical Engineering, The University of Leeds, Leeds LS2 9JT, UK, T.D.Stewart@Leeds.ac.uk
[2]Division of Microbiology, The University of Leeds, Leeds LS29JT UK
[3] Stryker SA, Scientific and Clinical Affairs, Florastr. 13, CH-8800 Thalwil, Switzerland.

INTRODUCTION

It has been recently discovered that hip joint separation occurs during normal gait (1). Reproducing this motion in hip simulators results in contact of the femoral head with the rim of the acetabular insert at heel-strike. For ceramic prostheses this results in localised intragranular fracture of the femoral head in the form of a stripe of wear and localised intragranular fracture of the insert rim at the point of impact. The result produces similar wear mechanisms, wear volumes, and wear debris to those found in retrieved ceramic components and their surrounding tissues and is now the most clinically relevant means of testing ceramic bearings (2,3). The purpose of this study was to compare the biomechanics and wear of two methods of microseparation simulation on one hip design.

MATERIALS AND METHODS

28mm Biolox Forte Alumina components were used.

Method 1-Leeds MKII Hip Simulator. A small lateral to medial load was applied to the acetabular insert with a spring, which, during the swing phase when the joint load was reduced, produced medial (~400 μm) and superior translation of the insert as it tracked around the head (Position 1 to 2). Upon reapplication of the joint load at heelstrike this resulted in contact between the head and the superior rim of the insert (Position 2) before joint relocation (Position 1). Severity was altered by adjusting the swing phase axial load which, when reduced made it easier for the spring to overcome friction and to produce superior translation between the head and insert. The increased momentum and impact energy modelled greater laxity and a more severe microseparation condition.

Method 2-Prosim Hip Simulator. An inferior load was applied to the femoral head using an actuator, which, during the swing phase when the joint load was reduced, produced a separation of (~700 μm) between the components. Upon separation this resulted in contact of the head with the inferior rim of the insert producing lateral displacement of the head as it tracked around the insert rim (Position 1 to C). Upon re-application of the joint load at Heel-Strike this resulted in superior translation of the head which then collided with the superior rim of the insert (Position 2) before relocation (Position 1).

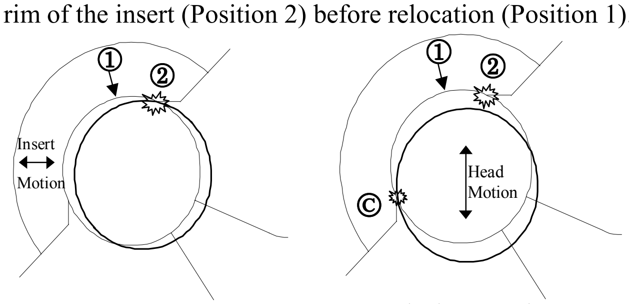

Method 1- Leeds MKII Method 2 – Prosim

Figure 1. Centre of contact.

RESULTS

Wear results from the two methods are shown in Figure 2.

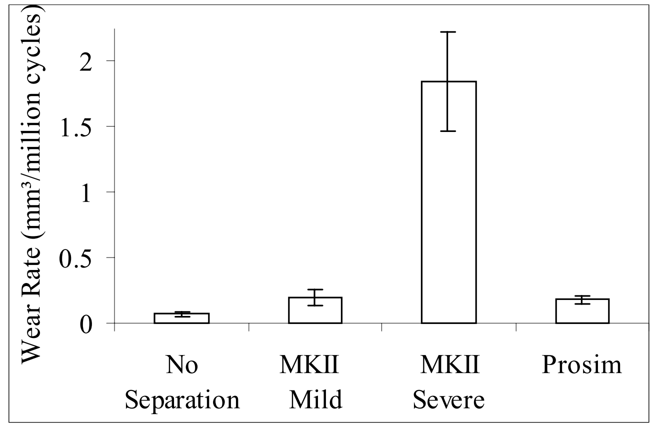

Figure 2. Long Term Wear of AL-AL Under Microseparation.

DISCUSSION

The two methods of microseparation investigated have anatomical positioning of the components with the insert mounted superior to the head, however, they have different mechanics, wear patterns, and wear volumes. In Method I, medial translation of the insert produced a superior wear scar on the head and insert in the form of a stripe. The loading vector in this method was vertically downwards through the insert, essentially perpendicular to the contact. Impact was, therefore, very direct and included the momentum of the insert and its holder. A deeper and more pronounced stripe of wear resulted. In Method 2, inferior translation of the head produced little effect at the inferior rim of the insert, however, superior translation of the head at heelstrike produced a wear scar at the superior rim of the insert. The loading vector in this method was along the axis of the femoral head and tangential to the contact at heelstrike (30° Flexion). Impact was a glancing blow with very little effect of momentum. A long, thin, less pronounced stripe of wear resulted.

In-vivo wear results from the current generation of prostheses are limited, however, wear volumes ~0.5 mm³/million cycles have been reported suggesting that both methods are capeable of producing repeatable clinically relevant wear results (3).

REFERENCES

1. A V Lombardi et al, J. Arthroplasty, 15, 702-709, 2000.
2. J E Nevelos et al, J. Arthroplasty, 15, 793-795, 2000.
3. T Stewart et al, JMS Mat. In Med., 12, 1053-1056, 2001.

ACKNOWLEDGEMENTS

The research was funded by Stryker Howmedica Osteonics, the Arthritis Research Campaign and Action Research

FRACTURE OF ZIRCONIA ON ALUMINA HIP PROSTHESES : THE NEED FOR MICROSEPARATION TESTING

T Stewart[1], J L Tipper[2], R M Streicher[3], E Ingham[2], J Fisher[1]
[1]Mechanical Engineering, The University of Leeds, Leeds LS2 9JT, UK, T.D.Stewart@Leeds.ac.uk
[2]Division of Microbiology, The University of Leeds, Leeds LS29JT UK
[3] Stryker SA, Scientific and Clinical Affairs, Florastr. 13, CH-8800 Thalwil, Switzerland.

INTRODUCTION

Extremely low wear (<0.1 mm³/million cycles) has been reported for Zirconia femoral Heads articulating against Alumina Inserts for hip prostheses under normal laboratory hip simulation conditions and this bearing combination has been introduced into clinical use (1,2). However, improved testing conditions which model mild and severe swing phase joint separation are now available. This has shown for Alumina bearings to produce more clinically relevant wear results (3,4). The purpose of this study was, therefore, to evaluate the wear performance of Zirconia heads against Alumina inserts using microseparation simulation techniques.

MATERIALS AND METHODS

Two commercially available materials were tested: Zirconia (“ZR”, ISO 13356) and 3rd Generation Hot Isostatic Pressed (HIPed) Alumina (“AL”, ISO 6474). A six station anatomical hip simulator was used with 25% bovine serum lubricant. The procedure of microseparation involved applying a small lateral to medial load to the acetabular insert with a spring, which, during the swing phase when the joint load was reduced, produced a medial (400 μm) and superior translation of the insert relative to the head. On heelstrike, with re-application of the joint load, this resulted in impact between the head and the superior rim of the insert before joint relocation. Conditions were altered by adjusting the swing phase load in the simulator from 400 N for mild conditions, to 50 N for severe conditions. The reduced load made it easier for the medial separation force to overcome friction and to produce superior translation between the head and insert, thus producing more momentum and impact energy. The variable swing phase load represented varying degrees of joint laxity.

RESULTS

The simulator produced a regular pattern of micro-separation over the 5 million cycle test duration. Under mild microseparation a very faint stripe of wear was formed on two of the three Zirconia heads, which increased the surface roughness R*a* from < 0.005 μm to ~0.08 μm. The third femoral head was visibly undamaged. Stripes on the two Zirconia femoral heads under mild conditions were ~ 0.75 mm wide and ~10 μm deep. Under severe microseparation prolonged squeaking was observed from the bearings. A large stripe of wear was formed on all three of the Zirconia heads, which increased the surface roughness R*a* from < 0.005 μm to between 0.09 and 2.1 μm. After 2 million cycles one acetabular insert and one femoral head fractured along the worn stripe and rim areas. Stripes on the Zirconia femoral heads under severe conditions were ~ 5 mm wide and up to 250 μm deep (components are shown in Figure 1).

X-ray Diffraction of the femoral heads after severe microseparation revealed up to 35% phase transformation of the Zirconia from tetragonal to monoclinic had occurred within the worn stripe area.

Figure 1. Fractured Alumina Insert (Middle) and Zirconia Head (right) after severe microseparation.

DISCUSSION

Under mild microseparation simulation conditions the wear of Zirconia heads against HIPed Alumina inserts was very low (0.05 mm³/million cycles) suggesting potentially superior performance in-vivo to Alumina against Alumina. However, under severe microseparation conditions gross femoral head and insert rim wear were observed on the components after 1 million cycles producing a wear rate of 10.6 mm³/million cycles. The high wear additionally produced fracture of one acetabular insert across the worn rim area, and fracture of one Zirconia femoral head across the stripe wear area. The results suggest that Zirconia may have a threshold stress level, which if exceeded may result in catastrophic wear. Zirconia femoral heads against Alumina acetabular inserts are not recommended for clinical use.

REFERENCES

1. F Villermaux *et al*, Trans. Soc. Biomat, 135, 1999.
2. C. Kaddick *et al*, 4th CeramTec Symposium, 96-101, 1999
3. J E Nevelos et al, J. Arthroplasty, 15, 793-795, 2000.
4. T Stewart et al, JMS Mat. In Med., 12, 1053-1056, 2001.

ACKNOWLEDGEMENTS

The research was funded by Stryker Howmedica Osteonics and the Arthritis Research Campaign.

WEAR OF CERAMIC MATRIC COMPOSITE HIP PROSTHESES IN SIMULATORS MODELLING LAXITY

T Stewart[1], J L Tipper[2], R M Streicher[3], E Ingham[2], J Fisher[1]
[1]Mechanical Engineering, The University of Leeds, Leeds LS2 9JT, UK, T.D.Stewart@Leeds.ac.uk
[2]Division of Microbiology, The University of Leeds, Leeds LS29JT UK
[3] Stryker SA, Scientific and Clinical Affairs, Florastr. 13, CH-8800 Thalwil, Switzerland.

INTRODUCTION

Next generation ceramic matrix composites are now available for hip prostheses as alternative to Alumina (AL). These new Zirconia Toughened Alumina (ZTA) materials are reported to offer improved toughness without a significant reduction in hardness, making them more flexible for designers (1). There is, however, no published experimental data on the wear of ZTA-ZTA and ZTA-AL under microseparation conditions that have been shown for AL-AL to provide clinically relevant wear rates, wear mechanisms and wear debris (2,3). The purpose of this study was to evaluate the long-term wear performance of ZTA-ZTA and ZTA-AL in a hip joint simulator incorporating severe swing phase microseparation.

MATERIALS AND METHODS

Two commercially available materials were tested: Zirconia Toughened Alumina (ZTA- Biolox Delta) and 3rd Generation Hot Isostatic Pressed (HIPed) Alumina (AL-Biolox Forte). A six station anatomical hip simulator was used with 25% bovine serum lubricant and three components of each type. The procedure of microseparation involved applying a small lateral to medial load to the acetabular insert with a spring, which, during the swing phase when the joint load was reduced, produced a medial (400 μm) and superior translation of the insert relative to the head. On heelstrike, with re-application of the joint load, this resulted in impact between the head and the superior rim of the insert before joint relocation. A swing phase load of 50 N was used to model a severe level of joint laxity.

RESULTS

The simulator produced a regular pattern of micro-separation for the 5 million cycle test duration. During the initial 1 million cycles a stripe of wear was formed on all of the heads of both ZTA–AL and ZTA-ZTA bearing combinations, which increased the surface roughness R*a* from < 0.005 μm to ~ 0.1 μm. Wear volumes are summarised in Figure 1 along with previous wear results of AL-AL where bedding-in and steady-state wear rates of 4.0 and 1.84 mm^3/million cycles were reported under the same severe testing conditions (3). The wear of ZTA-AL was significantly less than the wear of AL-AL with a bedding-in wear rate of 0.99 mm^3/million cycles during the initial 1 million cycles followed by a reduced steady-state wear rate of 0.51 mm^3/million cycles. The wear of ZTA-ZTA was significantly less than the wear of AL-AL and also less than the wear of ZTA-AL with a bedding-in wear rate of 0.32 mm^3/million cycles during the initial 1 million cycles followed by a steady-state wear rate of 0.12 mm^3/million cycles.

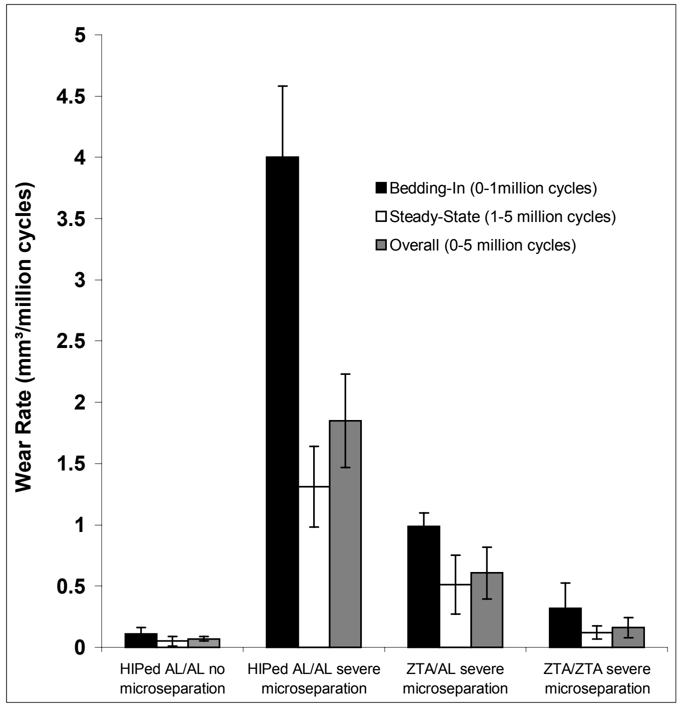

Figure 1. Average Wear Rates ± SE, n=3

DISCUSSION

Long term *in-vitro* microseparation of ZTA heads against ZTA inserts and ZTA heads against Alumina inserts produced overall average wear rates 3 and 12 times lower than previously observed with Alumina ceramic bearings under the same severe conditions representative of high joint laxity. The results suggest that ZTA heads articultaing against ZTA inserts and ZTA heads articulating against AL inserts may have better resistance to microseparation wear compared to AL on AL. The overall production of less wear debris from the new alumina matrix composite material, combined with its reported improved toughness makes it a potentially more flexible alternative to the more traditional Alumina for hip prostheses.

REFERENCES

1. Rack et al, 4th Int. CeramTec Symp. eds L Sedel and G Willmann ,141-145, 1999.
2. J E Nevelos et al, J. Arthroplasty, 15, 793-795, 2000.
3. T Stewart et al, JMS Mat. In Med., 12, 1053-1056, 2001.

ACKNOWLEDGEMENTS

The research was funded by Stryker Howmedica Osteonics and the Arthritis Research Campaign.

EFFECT OF A DUAL CAGE ON THE MECHANICAL BEHAVIOR OF THE LUMBAR SPINE

Antonius Rohlmann, Thomas Zander, Michael Fehrmann, Georg Bergmann

Biomechanics Laboratory, University Hospital Benjamin Franklin, Free University of Berlin, Berlin, Germany

INTRODUCTION

Degenerative changes in the lumbar spine sometimes require an intercorporal fusion. The respective disc has to be removed partly and replaced by a bone graft or an implant. The main task of a disc replacement is to keep the two adjacent vertebral bodies at a defined distance in order to avoid the postdiskectomy syndrome. The implants are primarily spacers and, because of their design, they are called cages. They are often implanted in pairs together with cancellous bone. The concerned spinal level is often additionally stabilized by a posterior or anterior implant.

The aim of this study was the analytical investigation of changes in intersegmental rotation and in stress distribution due to insertion of a dual threaded cage and additional stabilization using an internal spinal fixation device.

METHODS

A three-dimensional nonlinear finite element model of the whole lumbar spine was created [Smit, 1996; Zander et al, 2001]. Each annulus fibrosus consisted of volume elements and superimposed spring elements; the latter represents the fibers of the annulus. The nucleus pulposus was simulated by means of an incompressible fluid-filled cavity. The facet joints were modeled to transmit only compression forces. All seven ligaments were included in the finite element model. According to their function, they were modeled as tension-only spring elements with nonlinear elastic behavior.

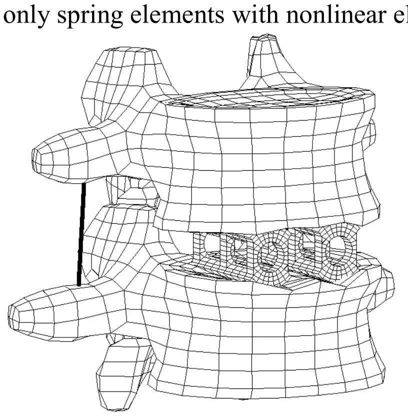

Figure 1: Element mesh of a dual cage (Proximity Lumbar Interbody Fusion System), adjacent vertebrae and internal fixator

After verification of the finite element model of the intact lumbar spine with experimental data the disc L2/3 was partly removed. In the intervertebral space a model of a paired cage (Proximity Lumbar Interbody Fusion System of Sulzer Medica) was inserted in anterior-posterior direction (Figure 1). This threaded cage has a central longitudinal hole and four flattened sides and is made out of titanium. A monosegmental internal spinal fixation device bridging the cage was added to the finite element model using beam elements.

The model was successively loaded with pure moments of 7.5 Nm in the three anatomical main planes and optionally with a preload on the cage. The preload was simulated by reducing the distance between the pedicle screws at the longitudinal rod of the fixator by 0.5 mm. A follower load [Patwardhan et al, 1999; Rohlmann et al, 2001] of 250 N simulated the stabilizing effect of the local muscles acting directly on the lumbar spine. This compressive load has a path tangentially to the spinal curvature and a stabilizing effect against buckling. The finite element program ABAQUS was used.

RESULTS

A monosegmental internal fixation device reduced the overall deformation of the lumbar spine model by about 20% during flexion and lateral bending. The additional implementation of a dual cage had then only a minor effect. For the loading case extension, the sum of intersegmental rotation was also reduced by a fixator but it increased again after insertion of a dual cage. The implants had only a minor influence on the sum of intersegmental rotation for the loading case torsion. They also had only a small effect on the adjacent segments.

In the vertebral endplates, which were in contact with the cage, stress distribution was strongly affected by the cage. A preload on the cage had a drastic influence on the maximum stresses in the interface between cage and vertebral body.

DISCUSSION

When a dual cage is implanted together with an internal spinal fixation device, intersegmental rotation is markedly reduced in the corresponding segment for the loading cases flexion and lateral bending and slightly reduced for the loading cases extension and axial rotation.

The contact area between cage and vertebral body is smaller than between disc and vertebral body. Additionally, a cage is stiffer than a disc. These are the main reasons for the noticeable increase of stresses after insertion of a dual cage. A preload, applied by shortening of the fixators, causes a small intersegmental rotation at that level. This in turn reduces the contact area between cage and vertebral body. Together with the increased load due to the preload these are the reasons for the much higher peak stresses compared to the case without a preload. During implantation of a cage the preload should be chosen advisedly to prevent subsidence of the cage into the vertebral body. For the same reason, vertebral endplate should not be weakened more than absolutely necessary.

REFERENCES

Patwardhan, AG. et al (1999) *Spine*, **24**, 1003-1009

Rohlmann, A. et al (2001) *Spine*, **26**, E557-E561

Smit, T. (1996) *The Mechanical Significance of the Trabecular Bone Architecture in a Human Vertebra*. Shaker

Zander, T. et al (2001) *Clin. Biomech*., **16**, S73-S80

EFFECT OF A LAMINECTOMY ON THE MECHANICAL BEHAVIOR OF THE LUMBAR SPINE

Thomas Zander, Antonius Rohlmann, Georg Bergmann

Biomechanics Laboratory, University Hospital Benjamin Franklin, Free University of Berlin, Berlin, Germany

INTRODUCTION

Severe spinal stenosis is often treated by dorsal decompression. Dependant on the degree of stenosis mono- or bilateral hemifacetectomy, hemi- or bilateral laminectomy or even laminectomy on two levels is indicated. The operative resection of a facet capsule and of posterior bony parts of a vertebra reduces the spinal stability which may lead to an increase of deformation and loads at that level. The amount of instability produced by these procedures is still a matter of debate.

The aim of the present finite element study was to determine the influence of different degrees of resection of posterior elements on the mechanical behavior of the lumbar spine.

METHODS

A three-dimensional, nonlinear finite element model of the human osseoligamentous spine segment L2 to the superior part of S1 was created (Figure 1).

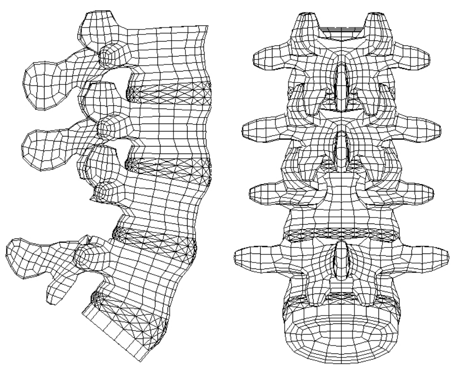

Figure 1: Outer mesh of the finite element model of the spine segment with laminectomy

The element mesh of the vertebrae is based on the model used by Smit [1996]. The nucleus pulposus was simulated by an incompressible fluid-filled cavity and the annulus fibrosus by volume elements with superimposed spring elements representing the fibers. The facet joints could only transmit compressive forces. The capsule of the facet joints and the six ligaments of the lumbar spine were included. The mainly nonlinear material properties of all tissues were taken from the literature. The model was successively loaded in flexion/extension, right/left lateral bending, and right/left axial rotation with pure moments up to 7.5 Nm. Different situations were studied, including left hemifacetectomy, bilateral hemifacetectomy, left hemilaminectomy, laminectomy, and two level laminectomy. This was done by successive resection of posterior parts of the vertebrae at the affected level. The finite element model is described in detail elsewhere [Zander et al. 2001]. The finite element program ABAQUS was used. The intact computer model was validated by reference to experimental data from *in vitro* measurements [Rohlmann et al. 2001; Zander et al. 2001].

RESULTS

Calculated intersegmental rotation angles at the level L4/L5 lay in nearly all cases within the ranges measured by Quint et al (1998) for the corresponding situation. The highest values were found for flexion. A laminectomy had only a negligible effect on intersegmental rotation for extension and lateral bending. Intersegmental rotation increased markedly after laminectomy for flexion while for axial rotation it increased already after a hemifacetectomy. In the latter case further resection of posterior elements had only a minor influence on the intersegmental rotation angle. Extending the laminectomy to the segment L5/S1 had only a negligible effect on intersegmental rotation angles for all loading cases studied. A degenerated disc, however, reduced intersegmental rotation, especially for flexion.

A laminectomy had only a negligible effect on the maximum von Mises stresses in the annuli for the loading cases extension and lateral bending. It increased stresses for flexion while stresses rose already after a hemifacetectomy for axial rotation.

The degree of resection of dorsal osseous and ligamentous elements had only a minor effect on intradiscal pressure for the loading cases flexion, extension, and lateral bending. Merely for axial rotation intradiscal pressure increased markedly after hemifacetectomy. Intradiscal pressure in the adjacent discs was not affected by a laminectomy.

DISCUSSION

The influences of different degrees of resection of posterior vertebral parts on the mechanical behavior of the lumbosacral spine was studied using the finite element method.

A good agreement between our numerical results and the experimental data measured by Quint et al. (1998) could be ascertained. During axial rotation, a hemifacetectomy had already an influence on the mechanical behavior of the lumbosacral spine. The resection of further parts had only a minor effect during this loading case. During lateral bending and extension, the parameters studied were only slightly affected by the different degrees of resection. During flexion, the mechanical behavior of the lumbar spine was only slightly influenced by resections up to a hemilaminectomy.

REFERENCES

Quint, U. et al. (1998) *Z Orthop* , **136**, 350-357

Rohlmann, A. et al (2001) *Spine*, **26**, E557-E561

Smit, T. (1996) *The Mechanical Significance of the Trabecular Bone Architecture in a Human Vertebra*. Shaker

Zander, T. et al (2001) *Clin. Biomech.*, **16**, S73-S80

MECHANO-ACOUSTIC CHARACTERIZATION OF NORMAL, DEGENERATED AND REPAIRED CARTILAGE

J Töyräs[1], MS Laasanen[2,3], S Saarakkala[3], J Hirvonen[3], I Kiviranta[4], R Lappalainen[1] and JS Jurvelin[1,3]

[1]Department of Applied Physics, University of Kuopio, Kuopio, Finland, e-mail: Juha.Toyras@uku.fi
[2]Department of Anatomy, University of Kuopio, Kuopio, Finland
[3]Department of Clinical Physiology and Nuclear Medicine, Kuopio University Hospital, Kuopio, Finland
[4]Department of Surgery, Division of Orthopaedics and Traumatology, Jyväskylä Central Hospital, Jyväskylä, Finland

INTRODUCTION

Softening of articular cartilage (AC) and degradation of superficial collagens are signs of incipient osteoarthrosis (OA). We have developed a handheld ultrasound indentation instrument enabling assessment of cartilage mechanical and acoustic properties (Laasanen 2002). In this study, capability of the instrument to distinguish between normal and degenerated AC was studied. In addition, we evaluated feasibility of high frequency ultrasound imaging to quantify tissue repair after autologous chondrocyte transplantation (ACT) and to detect spontaneous, enzymatic or mechanical cartilage damage.

MATERIALS AND METHODS

The ultrasound indentation instrument (Fig. 1) consists of a contact ultrasound transducer installed to the tip of an Artscan 200 instrument. Dermascan-C 20 MHz ultrasound instrument was used for B-mode ultrasonic imaging. Bovine patellar AC were visually classified to four different grades: 0-intact (n=11), 1-slightly discoloured (n=5), 2-superficial defect (n=6), 3-deep defect (n=8). Osteochondral samples (n=30, dia.=19 mm) were drilled from the classified sites. Dynamic moduli of the samples were measured with the novel instrument by manually inducing several instantaneous compressions (prestress 215 kPa, strain 4%). Thickness and deformation was determined from ultrasound signal using the time of flight principle with predetermined sound velocity (1627 m/s). Dynamic modulus was calculated by assuming instantaneous incompressibility of cartilage (Hayes 1972). High-resolution material testing device was used for reference measurements (Töyräs 1999) with a stress-relaxation protocol (10% prestrain, 10% step, 2 mm/s) in unconfined compression. Ultrasound reflection coefficient was determined as a ratio of the maximum amplitude recorded from saline-cartilage interface and amplitude recorded from a perfect reflector. To evaluate capability of ultrasound for detecting superficial cartilage damage, 12 extra samples were prepared. The samples (n=6, dia.=6 mm) were gently damaged by sliding a sample against a 120 grit abrasive (pressure 56 kPa, total sliding distance 20 mm) or (n=6, dia.=16 mm) digesting with collagenase (Töyräs 1999). Cartilage healing after ACT was studied in pigs (n=8). Full thickness cartilage lesion (dia.=6 mm) was created on the femoral groove and subsequently repaired using ACT (Brittberg 1999). In control animal, lesion was created but left unrepaired. After follow up of three months the tissue repair was analysed with ultrasonic and microscopic techniques.

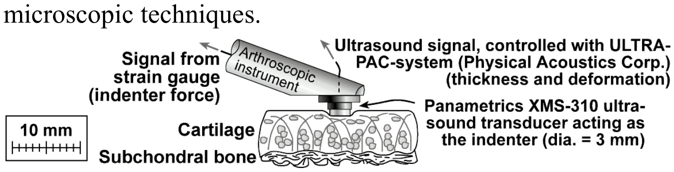

Figure 1. Ultrasound indentation measurement geometry.

RESULTS AND DISCUSSION

Linear correlation between ultrasound indentation modulus and reference dynamic modulus was R=0.993 (p<0.0001, n=30) (Fig. 2A). The instrument distinguished different degenerative grades (Fig. 2B). Large SD of intact cartilage dynamic modulus revealed insensitivity of visual grading of cartilage quality. Ultrasound imaging illustrated sensitively spontaneous, enzymatic or mechanical degradation (Fig. 3) and provided high resolution images on cartilage repair in ACT repaired porcine joints (Fig. 4).

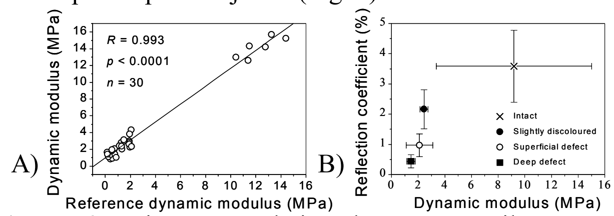

Figure 2: Linear correlation between cartilage modulus (ultrasound indentation) and the reference modulus (A). Mean values (± SD) of modulus and ultrasound reflection coefficient in intact or degenerated cartilage (B).

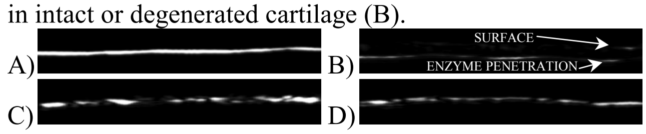

Figure 3: Ultrasound images of articular surface in normal (A), collagenase degraded (B), mechanically degraded (C) and spontaneously degenerated cartilage (grade 1) (D).

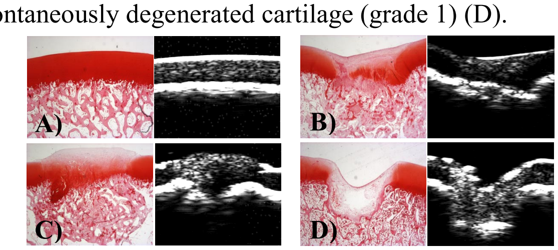

Figure 4: Ultrasound and light microscopic (safranin O-stain) images of intact (A), repaired (B and C) and unrepaired (D) porcine joints.

SUMMARY

The ultrasound indentation instrument was capable of quantifying absolute cartilage stiffness and diagnosing progression of tissue degeneration. Ultrasound imaging detected spontaneous, enzymatic or mechanical degradation sensitively and provided high resolution images on cartilage and subchondral bone in ACT repaired porcine joints.

REFERENCES

Brittberg, M. et al. (1999), *Clin Orthop*, S147-55.
Laasanen, M.S. et al. (2002), *Trans Orthop Res Soc*, **27**.
Hayes, W.C. et al. (1972), *J Biomech*, **5**, 541-51.
Töyräs, J. et al. (1999), *Phys Med Biol*, **44**, 2723-33.

EFFECTS OF SOUND VELOCITY VARIATION ON CARTILAGE ULTRASOUND INDENTATION MEASUREMENTS

MS Laasanen[2,3], J Töyräs[1], S Saarakkala[3], J Rieppo[2], RK Korhonen[1,2] and JS Jurvelin[1,3]

[1]Department of Applied Physics, University of Kuopio, Kuopio, Finland, e-mail: Jukka.Jurvelin@uku.fi
[2]Department of Anatomy, University of Kuopio, Kuopio, Finland
[3]Department of Clinical Physiology and Nuclear Medicine, Kuopio University Hospital, Kuopio, Finland

INTRODUCTION

Earlier studies report sound velocities (*c*) of 1600-1800 m/s for articular cartilage (Myers 1995; Töyräs 1999). Some discrepancy exist, while velocities up to 2428 m/s were reported for human ankle cartilage (Yao 1999). In this study, we measure *c* in normal, enzymatically degraded and osteoarthrotic (OA) bovine cartilage and evaluate relationships between *c* and cartilage composition or mechanical properties. Further, effect of variation of *c* on determination of cartilage thickness (*h*) and dynamic modulus (*E*) with an ultrasound indentation instrument (Laasanen 2002) was analyzed.

MATERIALS AND METHODS

Three sample groups were harvested. Group 1: Cartilage disks (*n*=30, dia.=4 mm) were obtained from femoral medial condyle (*n*=6, FMC), lateral patellofemoral groove (*n*=6, LPG), medial tibial facet (*n*=6, MTF), patella (*n*=6, PAT) and talus (*n*=6) of intact bovine joints. Group 2: 30 bovine patellar cartilage samples (11 visually normal and 19 having visible degenerative changes, dia.=4 mm) were prepared. Group 3: Patellar cartilage disks (bovine, *n*=18, dia.=4 mm) were harvested and digested with trypsin (*n*=6, inducing severe proteoglycan (PG) depletion), chondroitinase ABC (*n*=6, slight and specific PG depletion) and collagenase (*n*=6, specific collagen degradation) (Laasanen 2002). Cartilage *c* (groups 1-3) and *E* (groups 2 and 3) were measured with a high-resolution mechano-acoustic material testing instrument under unconfined compression (Fig. 1A). PG concentration was determined using the digital densitometry (Panula 1998). Finally, the effect of recorded variation in *c* (group 1) on the error in *h* and *E*, as determined with ultrasound indentation instrument (Fig 1B), was simulated by modelling cartilage to be instantaneously incompressible and isotropic (Hayes 1972). Sound velocity of 1630 m/s (bovine knee mean) and 1721 m/s (talus mean) were used in the simulations.

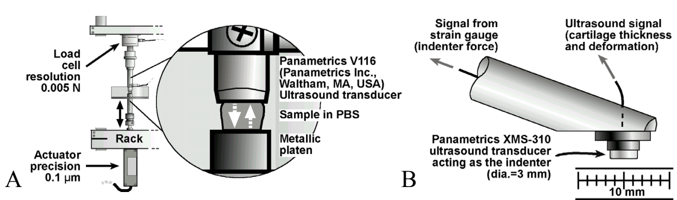

Figure 1: Mechano-acoustic material testing instrument used for determination of cartilage dynamic modulus and sound velocity (A). Tip of the ultrasound indentation instrument (B).

RESULTS AND DISCUSSION

Sound velocity correlated positively with PG concentration and with *E* (Fig. 2). It showed, however, only a minimal topographical variation in bovine cartilage (Table 1). Realistic variation of *c* induced minimal errors (<3%) on *h* and *E,* as determined with the ultrasound indentation technique (Table 1). Degradation of collagens or PGs induced only minor decrease in *c*, while *E* decreased significantly (Table 2).

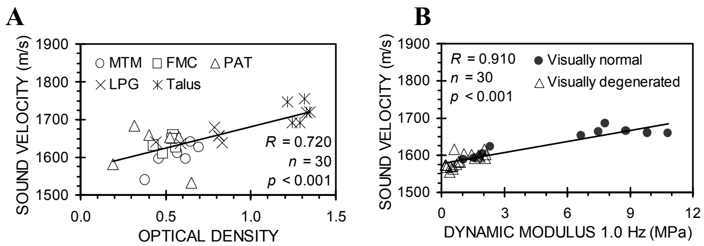

Figure 2: *c* correlated positively with PG content (optical density of safranin-O stained sections) in visually normal cartilage (A) and with *E* in normal/degenerated cartilage (B).

Table 1: *c* and *h* of bovine knee and talus cartilage. Simulated errors of *h* and *E* in ultrasound indentation (mean ± SD) when assuming a constant sound velocity (joint mean *c*).

	MTF	FMC	PAT	LPG	Talus
c [m/s]	1602 ± 35	1638 ± 18	1627 ± 58	1652 ± 16	1721 ± 26
h [µm]	1346 ± 276	1310 ± 380	1543 ± 186	1398 ± 137	435 ± 53
h error [%]	1.97 ± 2.00	0.95 ± 0.66	2.88 ± 1.90	1.33 ± 0.98	1.14 ± 0.85
E error [%]	0.22 ± 0.15	0.27 ± 0.30	0.28 ± 0.31	0.24 ± 0.25	0.85 ± 0.64

Table 2: *c* and *E* (mean ± SD) before and after degradation.

	Trypsin	Chond. ABC	Collagenase
c before [m/s]	1618 ± 22	1605 ± 10	1606 ± 31
c after [m/s]	1596 ± 13*	1605 ± 18	1580 ± 23
E before [MPa]	5.37 ± 4.02	3.11 ± 0.61	3.66 ± 1.85
E after [MPa]	3.30 ± 2.82*	2.40 ± 0.62*	2.26 ± 2.30

*p<0.05 Wilcoxon's signed-ranks test.

SUMMARY

Although *c* was found to correlate with cartilage composition and modulus it was nearly constant in tested cartilage. Enzymatic degradation of tissue PGs and collagen decreased *c* only minimally (mean -1.0%). We could not verify the high *c*, reported earlier for human cartilage (Yao 1999). Current results propose that a constant (joint mean) *c* may be utilised to obtain a clinically acceptable accuracy for *h* and deformation during ultrasound indentation measurement. This enables a reliable ultrasound indentation measurement for determination of cartilage modulus *in situ* and possibly *in vivo*.

REFERENCES

Hayes, W.C. et al (1972), *J Biomech*, **5**, 541-51.
Laasanen, M.S. et al (2002), *Trans Orthop Res Soc*, **27**.
Myers, S.L. et al. (1995), *J Rheumatol*, **22**, 109-16.
Panula, H.E. et al. (1998), *Ann Rheum Dis*, **57**, 237-45.
Töyräs, J. et al. (1999), *Phys Med Biol*, **44**, 2723-33.
Yao, J.Q. et al. (1999), *Rheumatology (Oxford)*, **38**, 1269-71.

THE ASSESSMENT OF CERVICAL SPINE KINEMATICS USING INTERVENTIONAL MRI

Osa Emohare[1], Alison McGregor[1], Paul Wragg[2], Wladyslaw Gedroyc[2]

[1] Department of Musculoskeletal Surgery, Faculty of Medicine, Imperial College of Science, Technology & Medicine, Charing Cross Hospital, London
[2] Interventional MRI Unit, St Mary's Hospital, London
Email contact: a.mcgregor@ic.ac.uk

INTRODUCTION

To date the living mechanics of the spine, particularly the neck, are not well understood. This is in part due to inadequate methods with which the movements of the neck can be assessed. The ability to record and measure intersegmental motion is paramount if we are to understand conditions such as whiplash injury, and instability. Radiographic assessment has formed the basis for this research, particularly lateral x-ray views of cervical flexion and extension and more recently the use of videofluoroscopy images. Both of these methods have been fraught with problems including ionizing radiation exposure, magnification errors and image quality. The ionising nature of the radiation particularly limits serial studies of neck function and studies of large populations. The evolution of open or interventional magnetic resonance (IMR) scanners allow dynamic imaging of patients in the scanner in weight loaded positions. Therefore, the aim of this study was to investigate the use of IMR imaging to assess intersegmental motion of the cervical spine.

METHODS

20 normal subjects (10 females, 10 males, mean age 25.4 ± 3.7 years) were recruited into this study. Subjects with a history of neck pain that required intervention, current neck pain or problems within the past 6 months were excluded from participation in the study. Subjects were scanned using a General Electric Signa SPI0 Interventional MRI scanner. This is an open MRI scanner consisting of 2 connected but opposing ring "doughnuts" magnets. The gap between these magnets is 56cm generating a uniform field of 0.5Tesla. The patients were scanned in sitting with their neck in neutral and in flexed and extended positions. Sagittal images of the spine were obtained in each position. From these sagittal images, measurements of intersegmental motion were made using the methodology described by Dupuis *et al.,* 1985, the repeatability of such measures from MRI has been previously reported (McGregor *et al.,* 2001).

RESULTS

It was possible to get clear images of the cervical spine in neutral, flexed and extended positions from which measures of motion could be obtained. The table below illustrates the mean ± standard deviations of A-P angular rotations and associated horizontal translation occurring at each level during flexion and extension. Greatest angular motion was noted to occur between C4-C7, which is in agreement with previous studies whilst greater translation occurred in the upper cervical region.

DISCUSSION

These preliminary findings suggest that interventional MRI has the potential to assess cervical spine kinematics and the findings appear to be in agreement with previously published data. This combined with the non-invasive nature of this imaging medium suggest that long term follow-up studies of cervical instability and fusion patients are possible in the future.

REFERENCES

Dupuis, P.R. et al (1985). Spine, **10**(3),262-276.
McGregor, A.H et al (2001). Clin Orth **392**,341-348.

	Flexion		**Extension**		**Total A-P Arc**	
	Rotation (degrees)	**Translation (mm)**	**Rotation (degrees)**	**Translation (mm)**	**Rotation (degrees)**	**Translation (mm)**
C2/3	13.6±3.5	0.5±1.0	1.6±1.4	-0.8±1.2	15.2±3.3	2.3±1.1
C3/4	14.8±3.7	0.9±0.9	2.7±1.7	-1.3±1.1	17.4±4.0	2.6±1.3
C4/5	14.9±3.7	1.0±0.7	3.7±2.7	-1.0±1.1	18.5±4.8	2.2±1.2
C5/6	14.4±3.3	0.9±0.6	3.8±2.8	-0.1±1.1	18.2±3.6	1.7±0.9
C6/7	13.7±4.0	0.8±0.5	3.4±3.0	-0.3±0.8	17.1±4.0	1.4±0.6
C7/T1	12.5±2.5	1.0±0.9	1.4±2.3	0.2±0.8	13.9±2.9	1.4±1.0

WRENCHES AT THE DIGIT-OBJECT INTERFACE DURING PREHENSION

Fan Gao, Vladimir M. Zatsiorsky[1], Mark L. Latash
Department of Kinesiology, The Pennsylvania State University, PA 16802, USA
[1] vxz1@psu.edu

INTRODUCTION

To construct multifunctional hand prostheses and robotic hands, engineers should be aware of the wrenches (forces and moments) acting on individual digits during manipulative tasks. This knowledge is also essential for understanding object manipulation. The available data on digit-object interactions are limited.

METHODS

Subjects (n=8) stabilized a handle with an attachment that allowed for change of external torque from –1.5 Nm to 1.5 Nm, Figure 1. Wrenches (forces and moments) exerted by the digit tips on the object were recorded.

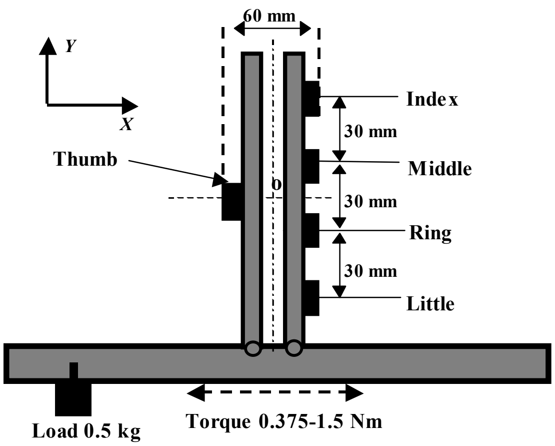

Figure 1. Schematic drawing of the handle.

RESULTS

In all tasks, the index finger did not contribute, or contributed very little, to load holding: its force was directed either downward or horizontally, Figures 2 and 3. With the exception of the large (>–0.375 Nm) supination efforts, the middle, ring and little fingers produced forces in the same direction. The force vectors were almost parallel. The points of force application were systematically displaced with the torque, with the exception of the little finger. Across all torque conditions, the shear forces of the four fingers combined (IMRL force) and the shear force of the thumb increased or decreased in opposite directions while the normal forces of the thumb and IMRL changed in sync from 19.2 N at a zero torque to 46.3 N at a torque 1.5 Nm. During the large supination torques the IMRL shear force was directed downward and the thumb supported the entire weight of the apparatus. The relationships between the shear and normal force of the thumb and IMRL had a V-like shape. The total moment of the normal finger forces accounted for approximately 2/3 of the torque exerted on the object.

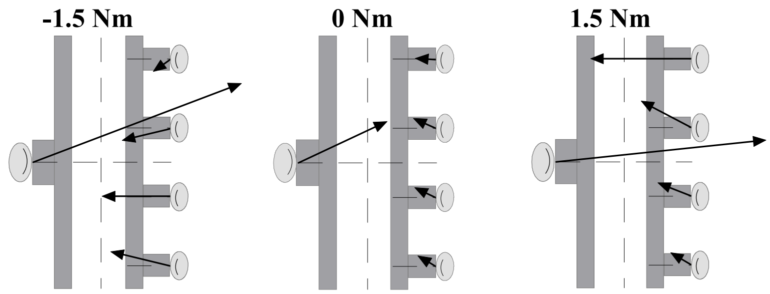

Figure 2. Force vectors at the digit tips, group average.

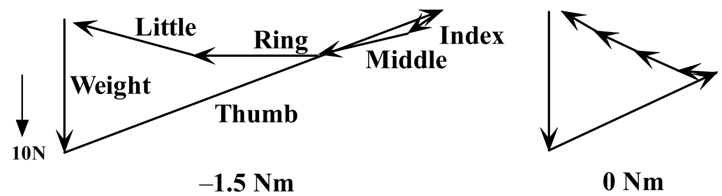

Figure 3. Force polygons. The vertical downward arrows represent gravitational forces, other arrows represent the forces of the thumb, index, middle, ring and little fingers, respectively, in a counterclockwise sequence.

DISCUSSION

As compared with other dexterous tasks, the task explored in this study looks rudimentary. The subjects were asked to hold a handle while resisting an external torque and load. The task is similar to those used in robotic manipulation: a gripper grasps an object and rotates it. Relatively simple control strategies are used to perform these tasks in robotics applications: all the fingers receive a similar command for grasping and the resistance is provided by apparent stiffness of the digits – when the fingers deflect from a nominal position they exert larger forces (Mason, Salisbury 1985; Doersam, Fischer 1998). The finger force direction is not specifically controlled and depends on the peripheral interactions between the fingertips and the object. The human interaction with a hand-held object seems more complex.

REFERENCES

Doersam, T., Fischer, T., 1998. Aspects of controlling a multifinger gripper. *Engineering Application of Artificial Intelligence* **11**(1), 87-96.

Mason, M.T., Salisbury, J.K. 1985. *Robot Hands and the Mechanics of Manipulation*. Cambridge, MS: The MIT Press.

IMMEDIATE EFFECT OF THERMAL MODIFICATION ON CADAVERIC KNEE CAPSULE

Nigel Zheng, Ph.D., Brent Davis, M.D., Michael Jablonski, M.D., Lyle Cain, M.D., Jeff Dugas, M.D., James Andrews, M.D.

American Sports Medicine Institute
1313 13th Street South, Birmingham, Alabama 35205, USA, nigelz@asmi.org

INTRODUCTION

Patellofemoral pain syndrome is one of the most widely diagnosed disorders involving the knee and includes a number of conditions resulting in pain of the anterior portion of the knee (Fulkerson, J.P. et al 1985, Goldberg, B.1997). Imbalanced and over-stretched joint capsule and surrounding tissue of the patellar may cause the patella to be translated to one side or the other, onto the edges of the intercondylar notch, as the knee flexes and extends. Thermal modification has been used to alter mechanical properties of soft tissues in order to regain their lost functions (Wall, M.S. et al 1999). The objectives of this study were to test biomechanically the thermal shrinkage of the knee capsule and its effects on the patella tracking in the intercondylar notch by comparing the lateral translation of the patella. The lateral translation and stiffness of the knee capsule were compared among healthy subjects, cadaver knees pre and post thermal shrinkage, and cadaver knee post open surgery.

METHODS AND MATERIALS

Knee capsule thermal modification was performed on cadaver specimens using Mitek VAPR. The tissue shrinkage was applied to the medial portion of the capsule. Lateral translation of the patella was measured with lateral force applied to the patella before and after the process. Open medial reefing of the medial capsular structures was conducted at last during open surgery. Nine fresh frozen cadaver specimens were used for the study. The test was repeated after open surgery. To establish the baseline for the lateral stiffness of the knee capsule, nine healthy subjects were tested on both legs after they filled out consent forms.

Lateral translation of the patella was recorded using a LVDT translation sensor (Macro Sensors, Pennsauken, NJ). The lateral force applied to the patella was recorded using a Flexiforce force sensor (Tekscan, South Boston, MA). A custom made adaptor was used to hold the sensor and apply force. Both force and translation sensors were connected to a computer via a data acquisition board (Data Translation, Boston, MA). Data were collected and stored for further analysis. A custom made frame was used to hold specimens during test. Subjects were lying on an exam table during test.

Each test was repeated three times. Subjects were instructed to relax during tests. The peak force applied, the peak translation and the stiffness were analyzed. Repeated measure analysis of variance (ANOVA) was used to compare the differences.

RESULTS

No significant differences were found between genders and between left and right knees for healthy subjects. There were no significant differences of the peak force, peak displacement and stiffness between healthy subjects and the cadaver knees. No significant differences of the cadaver knees were found between pre and post thermal shrinkage. Cadaver knees after open surgery showed significant higher stiffness than healthy subject, cadaver knee pre thermal shrinkage and post thermal shrinkages ($p<0.001$). No significant differences of the force applied were found among cadaver pre, post thermal shrinkage and open surgery. Cadaver knees post open surgery showed significant less displacement than healthy subjects, cadaver pre thermal shrinkage and post thermal shrinkage. No significant differences of the displacement were found among healthy subjects, cadaver knees pre and post-thermal shrinkage. Table 1 shows the forces, displacements and stiffness.

Table 1 Forces (F), displacements (D) and stiffnesses (S) for healthy (H) subjects and cadaver (C) knees pre thermal shrinkage (TS), post thermal shrinkage and post open surgery (OS).

GROUP	F (N)	D (mm)	S (N/mm)
H Subjects	17.57 ± 4.79	10.67 ± 3.72	1.91 ± 0.92
C pre TS	23.22 ± 4.50	10.55 ± 1.92	2.27 ± 0.54
C post TS	22.90 ± 3.23	10.87 ± 1.88	2.15 ± 0.43
C post OS	25.26 ± 3.90	5.73 ± 1.86	5.10 ± 2.53

SUMMARY

The application of thermal energy to the medial capsular structures of human cadaver knees caused no statistical or clinically appreciable differences in lateral patellar displacement or medial structure stiffness compared to pre-treatment values. Open medial reefing of the medial capsular structures caused a 46% decrease in lateral patellar displacement compared to pre-treatment values and a 222% increase in medial structure stiffness compared to pre-treatment values. Further clinical study is needed to investigate the long-term effect of thermal modification.

REFERENCES

Fulkerson, J.P. et al (1985). Clin Orthop 196-205.
Goldberg, B. (1997). Pediatr.Ann 26, 32-35.
Wall, M.S. et al (1999) J Shoulder.Elbow.Surg 8, 339-344.

PREDICTION OF SCRATCH RESISTANCE OF MEATLLIC BEARING SURFACE, ARTICULATING AGAINST UHMWPE, DUE TO 3RD BODY WEAR PARTICLES

M. Mirghany, H. Ensaff, Z.M. Jin

Department of Mechanical and Medical Engineering, University of Bradford, Bradford, BD7 1DP, UK.

INTRODUCTION

Within a hip prostheses, the metallic surface of Stainless Steel (SS) articulating against ultra high molecular weight polyethylene (UHMWPE) experiences scratches. These are related to the presence of entrapped particles such as UHMWPE, SS, bone and bone cement. The main type of debris that causes scratches on the metallic surface has not been clearly identified. Most clinical studies (Que and Topoleski, 2000) suggested that metal and bone debris are capable of plastically deforming the metal surface and causing scratches. However, materials as soft as UHMWPE were also claimed to be capable of causing SS to deform plastically under certain contact condition (Davidson et al. 1994).

The purpose of this study was to use the finite element (FE) method to investigate the resistance of plastic deformation of the articulating surfaces due to entrapped debris in SS-on-UHMWPE combinations, in particular to examine the metallic bearing surface as a first indication of the likelihood of producing scratches.

MATERIALS AND METHOD

A simple 2D axi-symmetric FE model was constructed to simulate an entrapped wear particle between two bearing surfaces. Both spherical and diamond-shaped wear particles were considered. The length of the bearing surfaces was chosen to be at least 4 times that of the radius of particle. The load was applied to the bearing surfaces through a contact pressure, determined from a particular hip implant. Therefore, for a spherical particle with a radius of 10 µm and maximum contact pressure of 15 MPa, the load applied to the FE model would be 0.042 N. The contact problem thus formulated was solved using ABAQUS 5.8. All the materials considered were treated as elastic-perfect-plastic with properties given in Table1. Potential failure (plastic deformation) of the metallic surface was assessed by comparing the von Mises stress prediction with the yield stress.

RESULTS AND DISCUSSION

Figure 1 shows the prediction of von Mises stress against the load applied for both the bearing surfaces and a spherical bone particle with a 10 µm radius. The corresponding deformation of the wear particle and the bearing surfaces is also shown under a load of 0.003 N (1.06 MPa). It is clear that even under these small loads, all the materials considered are deformed plastically, clearly indicating the potential scratch damage on the SS surface due to the bone wear particle. This was also found to be true for the metallic wear particle, under even smaller loads and sharp-edged cement particles. However, no plastic deformation of the metallic bearing surface was found for spherical cement particles.

CONCLUSION

Both SS and bone particles have been predicted to cause plastic deformation of the SS bearing surface when articulating against UHMWPE. This supports the presence of scratches observed from clinical studies previously reported.

REFERENCES

Que L, Topoleski LDT (2000), *Journal of Biomedical Materials Research*, **3**, 322-330.

Davidson, J. A., Poggie, R. A. and Mishra, A. K. (1994), *Bio-Medical Materials and Engineering,* **4,** 213-229.

ABAQUS 5.8 (1997) *ABAQUS/Standard,* Hibbitt, Karlsson & Sorensen, Inc., USA.

Further enquiries should be addressed to Dr. ZM Jin
Email: Z.M.Jin@Bradford.ac.uk

ACKNOWLEDGEMENTS This work is funded by the EPSRC-UK.

Table1: The mechanical properties of the materials

Material	Young's Modulus (GPa)	Poisson's ratio	Yield stress (MPa)
SS	210	0.3	200
UHMWPE	1.1	0.4	11.23
Bone	17	0.3	125
Bone cement	2.4	0.33	73

Figure1: Prediction of maximum von Mises stress against load for an entrapped spherical bone particle between stainless steel and UHMWPE bearing surfaces.

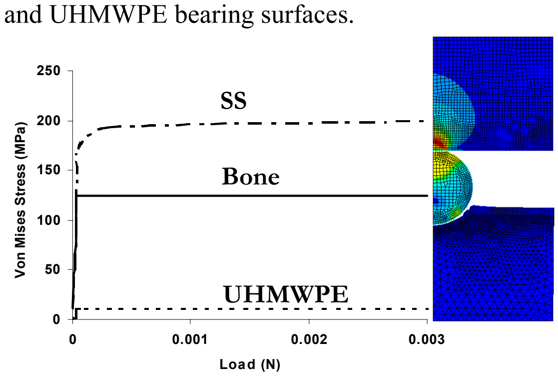

CYCLIC TENSILE STRETCH DECREASES PROTEOGLYCAN PRODUCTION BY ANULUS FIBROSUS CELLS THROUGH PRODUCTION OF NITRITE OXIDE

Francois Rannou[1,2,3], Maite Corvol[1], Michel Revel[2], John Y.-J. Shyy[3] and Serge Poiraudeau[1,2]
INSERM U530, UFR Biomedicale des Saints-Peres, Paris, France, 75006.
Reseau Federatif de Recherche sur le Handicap IFR 25, France.
Division of Biomedical Sciences, University of California, Riverside, CA, USA, 92521-0121.
Email address: francois.rannou@ucr.edu

INTRODUCTION

Degeneration of the intervertebral disc (IVD) is a major factor associated with low back pain and is a prerequisite to disc herniation. Although mechanical forces are important modulators in remodeling IVD tissue, the underlying molecular mechanism remains to be investigated.

The aim of this work was to study at molecular level the effects of cyclic tensile stretch (CTS) on proteoglycan (PG) production by anulus fibrosus (AF) cells.

METHODS

AF cells of rabbit IVD were cultured at high density on flexible-bottomed culture plates. CTS was applied with use of a pressure-operated instrument to deform the plates (Flexercell Strain Unit).

The ^{35}S-labeled PGs newly synthesized and secreted from AF cells were measured under basal conditions and after CTS application. The cell content of aggrecan and biglycan messenger RNA (mRNA) was determined by Northern blotting. The elution profile on Sepharose 2B columns revealed PG aggregability after $^{35}SO_4$ incorporation. Nitrite oxide (NO) production was evaluated by use of Griess reaction.

RESULTS AND DISCUSSION

The amount of ^{35}S-labeled newly synthesized PGs that accumulated in the cellular pool or were secreted in the culture medium did not change when CTS was applied with 1% elongation at 1 Hertz frequency.

In contrast, with 5% elongation at 1 Hertz frequency, the level of newly synthesized PGs in the cellular pool and in the culture medium was significantly reduced after 8 hours of stimulation (30% and 21% respectively) and further reduced at 24 hours (43% and 41% respectively). Introducing the protein synthesis inhibitor cycloheximide had no effect on this result. Neither aggrecan and biglycan expression nor PG physical properties were modified. The level of NO production significantly increased by 3.5 times after 8 hours of 5% elongation. Introducing the nitric oxide synthases inhibitor N^G-methyl-L-arginine (L-NMA) eliminated the effects of CTS on NO and PG production.

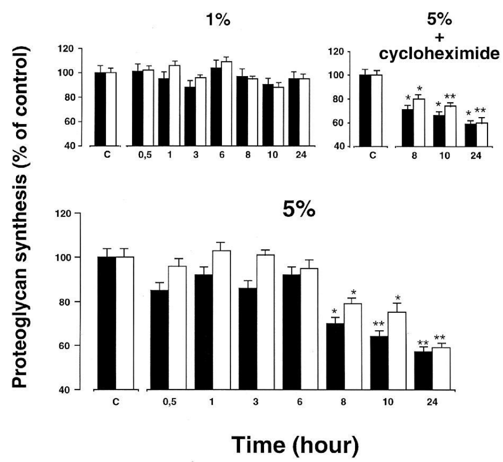

Figure 1: Effect of CTS (1% and 5% elongation at 1 Hertz frequency) on level of production of ^{35}S-labeled newly synthesized (black columns) and secreted (white columns) PGs by stretched AF cells as compared with unstretched cells (C).

SUMMARY

Under our culture conditions, CTS regulates PG production by AF cells in a dose dependant manner through a post-translational event depending on NO production. These results suggest that CTS can participate in the regulation of the IVD matrix by decreasing PG production through NO regulation. This result could be of interest in developing local therapeutic strategies aimed at inhibiting IVD degeneration.

ACKNOWLEDGEMENTS

This study is supported in part by : Societe Francaise de Rhumatologie (SFR), Fondation de l'Avenir, Institut National de la Sante Et de la Recherche Medicale (INSERM), Ministere des Affaires Etrangeres (programme Lavoisier), Fondation Bettencourt Schueller, and a UCR Biomedical Sciences general set up found.

DIFFERENCES IN KINEMATICS BETWEEN PROFESSIONAL AND YOUTH BASEBALL PITCHERS

Michelle B. Sabick[1], Michael R. Torry[1], and Richard J. Hawkins[2]
[1]Steadman♦Hawkins Sports Medicine Foundation, and [2]Steadman♦Hawkins Clinic, Vail, CO, USA, Michelle.Sabick@shsmf.org

INTRODUCTION

While there is little data describing the biomechanics of youth baseball pitchers, understanding the mechanics of this group is important for several reasons: (1) the population of youth pitchers is much larger than that of elite athletes, (2) injuries due to overuse and poor throwing mechanics are common in youth pitchers, and (3) the pitching mechanics of less skilled pitchers may lead to different stresses on the upper extremity than occur in professional pitchers. Unique aspects of the developing skeleton make it susceptible to a spectrum of injuries not commonly seen in adult athletes. Although these injuries are most likely due to the musculoskeletal changes occurring during growth, they may also be, at least in part, due to pitching technique. The aims of the current study were to compare youth pitching biomechanics with that of elite adult pitchers and to identify important differences that might explain common injuries seen in the youth pitcher population.

METHODS

Twenty-five professional and 14 youth baseball pitchers were filmed at 120 Hz using two high-speed video cameras. The locations of 21 body landmarks were digitized and their three-dimensional locations were calculated using the DLT method (Abdel-Aziz & Karara, 1971). Three-dimensional position data was filtered using a fourth order Butterworth filter with a cutoff frequency of 13 Hz. From the marker coordinates, the kinematics of the pitching elbow and shoulder were calculated using a standard technique (Fleisig et al., 1996; Werner et al., 1993). Kinematic data was normalized in time to facilitate comparisons and so group mean values could be calculated.

RESULTS AND DISCUSSION

Descriptive statistics for the two groups are provided in Table 1. There are three important findings from our kinematic data. First, the peak shoulder internal rotation and elbow extension angular velocities of the youth pitchers were greater than those of the professional pitchers. Second, the youth pitchers used less shoulder external rotation than the professional pitchers. Peak shoulder external rotation in youth pitchers was 166 ± 9°, compared with 182 ± 13° in professionals ($p<0.001$). The most striking difference between the groups was in their trunk motion. The peak rotational velocities of both the upper trunk and pelvis were greater in youth baseball pitchers than in professional pitchers. Peak upper trunk rotational velocity was 2102 ± 324°/s in youth pitchers and 1193 ± 176°/s in professional pitchers ($p<0.001$, Figure 1).

Table 1. Mean (S.D.) values describing the subject groups.

	Age (yr)	Height (m)	Mass (kg)	Ball V (m/s)
Pro	26.8 (2.9)	1.88 (0.05)	88.7 (9.2)	38.8 (2.0)
Youth	13 (0)	1.54 (0.08)	43.8 (8.6)	21.6 (1.8)

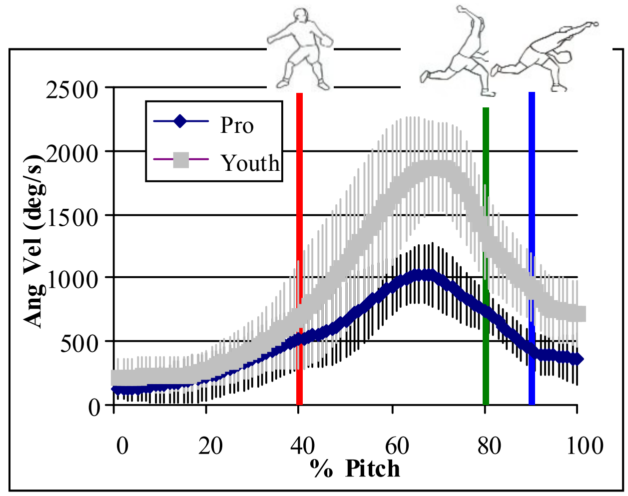

Figure 1. Upper trunk angular velocity of the two groups.

In contrast to the published literature (Fleisig et al., 1999), we found several significant kinematic differences between youth and professional pitchers. Our data support the observation that youth baseball pitchers control their trunk motion in a less efficient way than elite pitchers (Ireland & Hutchinson, 1995). Peak pelvis rotation velocity occurred near the time of stride foot contact in the professionals, while it occurred much later in the youth pitchers. Proper timing of pelvis and upper trunk rotation are necessary to effectively transfer energy from the trunk to the throwing arm (Fleisig et al., 1996). Therefore, increased trunk rotational velocity may be a compensation for improper timing of segment rotations or insufficient muscle strength (Ireland & Hutchinson, 1995) in youth pitchers. Improper energy transfer from the trunk to the upper extremity may lead to the increased shoulder internal rotation and elbow extension velocities in youth pitchers compared to the professionals. Our data also indicates that trunk rotation is related to the peak shoulder distraction force during the pitch.

SUMMARY

Significant kinematic differences were found between youth and professional pitchers. The greatest differences were in trunk rotation, likely to make up for a lack of upper body strength or proper timing in youth pitchers. Improper trunk control may have implications for shoulder injuries in youth pitchers, such as proximal humeral epiphysitis.

REFERENCES

Abdel-Aziz, Y., Karara, H. (1971). *Proc of Am Soc Photogram Symposium on Close Range Photogram*, 1-19.
Fleisig, G.S. et al (1996). *Sports Med*, **21**(6), 421-37.
Fleisig, G. S. et al (1999). *J Biomech*, **32**(2), 1371-5.
Ireland, M. L., Hutchinson, M. R. (1995). *Clin Sports Med*, **14**(3), 533-569.
Werner, S.L. et al (1993). *J Ortho Sport Phys Ther*, **17**, 274-8.

MECHANICAL AND PERFORMANCE ASPECTS OF A NEW SPEED SKATE DESIGN

Scott Van Horne, Darren Stefanyshyn, Ruth Morey Sorrentino

Human Performance Laboratory, University of Calgary, Calgary, AB, Canada

INTRODUCTION

Speed skating has seen many innovations in the last five years. The most note worthy is the induction of the klapskate. The klapskate permits the shoe to rotate on a hinge relative to the blade. Therefore, allowing plantar flexion with the blade remaining flat, gliding on the ice (Houdijk, 2001).

Raps Co. has recently developed a new skate, coined the "3D", where the klap mechanism is mounted at an offset angle, meant to create a more natural push movement. The klap mechanism is rotated 10 degrees about an axis through the transverse plane, and rotated 14 degrees about an axis through the frontal plane. Therefore, as the Raps klap opens the foot is either more everted throughout the rotation or the blade is more vertical, than with the regular klap.

The 3D was speculated to affect biomechanics in the frontal and transverse plane. More specifically it was speculated that the 3D mechanism would cause a decreased horizontal impulse during the end of the push phase, when the klap is opening, resulting in a less effective push and a slower overall speed. Also, it was speculated that the 3D would cause a greater maximum frontal plane ankle moment, and a greater ankle eversion.

The purpose of this study was to analyze kinetics and kinematics of the lower leg and foot throughout a speed skating push, and to test the above speculations.

METHODS

Eight experienced speed skaters participated in the study. All eight performed a test speed skating push with their own boot and klap mechanism compared to the Raps boot with 3D mechanism (exp1). Subjects performed 6 trials with each condition, kinematic and kinetic data were collected in the lab while, on a modified slideboard apparatus. Five subjects performed on-ice, pre-test and post-test, 100m and 400m, time trials for three conditions: (1)their own boot and mechanism, (2)their own boot and 3D mechanism, (3)their own boot and regular Raps mechanism (exp2). The 3rd condition was included to control for different types of metal used in the mechanism and blade. A two week training period on the 3D mechanism was implemented between the pre and post-test. All performance tests were done on a 400m oval track. Exp 1 was analyzed with a paired t-test (α = .05). Exp 2 was analyzed with an ANOVA (α = .05).

RESULTS AND DISCUSSION

In exp1, when subjects wore there own boot and mechanism opposed to the Raps boot and 3D mechanism they had a 2.1% higher horizontal impulse (integral of the force-time curve). No significant differences were found in the maximum frontal plane moment at the ankle joint or in the minimum angle scribed by the ankle joint about the frontal axis (ankle eversion), indicating that the mechanics at the ankle were unaffected by the 3D mechanism.

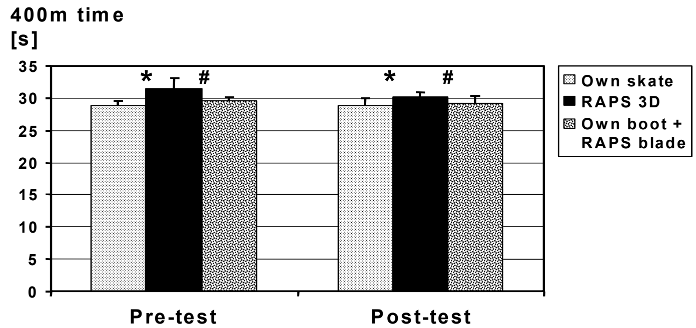

Figure 1: Time to complete a maximal effort 400m lap. Data presented are averages and standard deviations for five subjects. * indicates a significant differences between conditions 1 and 2. # indicates a significant difference between conditions 2 and 3.

In exp 2 a significant difference was found during the pre-test and post-test between condition 2 and conditions 1 and 3, during the 400m time trial. Pre-test results had subjects with the 3D taking an average of 2.7 seconds longer. Post-test results had subjects with the 3D taking an average of 1.2 seconds longer. The 100m time trial showed no significant differences. The above results indicate some sort of detriment of the 3D occurring potentially during the turns, and during constant velocity skating. If during the turn, the horizontal force is decreased the resulting velocity will be decreased or the radius of the skating path will be increased, both resulting in a slower overall lap time. Also, if a smaller horizontal impulse is generated during the straight there will be less acceleration of the center of mass perpendicular to the direction of the pushing blade, and a decreased forward velocity.

REFERENCES

Houdijk, H. (2001). The Klapskate; Shifting Gears in Speed Skating. Ph.D. Thesis. Amsterdam: Vrije Universiteit.

Table 1: Mean values and standard deviations for different push-off mechanics with 3D and regular klap. Significance indicated by *

Variable	Vertical Impulse (Ns)	Horizontal impulse (Ns)	Frontal Ankle Moment (Nm)	Frontal Ankle Angle (º)
3D klap	351.65 (28.60)	176.65 (25.92) *	89.65 (24.10)	84. 87 (6.63)
Regular klap	358.80 (35.24)	180.33 (25.77) *	86.92 (20.50)	83.22 (5.13)

INFLUENCE OF A FOLLOWER LOAD ON THE MECHANICAL BEHAVIOR OF THE LUMBAR SPINE

Antonius Rohlmann, Thomas Zander, Georg Bergmann

Biomechanics Laboratory, University Hospital Benjamin Franklin, Free University of Berlin, Berlin, Germany

INTRODUCTION

The spine is stabilized mainly by muscle forces, and little is known about these forces. Several groups have recommended pure moments in the three anatomical planes without an axial preload. The great advantage of pure moments is that all levels bear the same constant load. The reason for no preload is that even low preloads lead to buckling of multisegmental specimens and thus to uncontrolled motion. Patwardhan et al. [1999], by introducing a follower load, were the first to present a feasible technique for the experimental application of a physiological spine load. A follower load is a compressive load applied along a follower load path that approximates the tangent to the curve of the spine, thus subjecting the whole specimen to nearly pure compression. It has a similar effect as the short local muscles. The aim of this study was to show analytically the influence of a follower load on the mechanical behavior of the lumbar spine.

METHODS

A three-dimensional, nonlinear finite element model of the human osseoligamentous lumbar spine was created (Fig. 1).

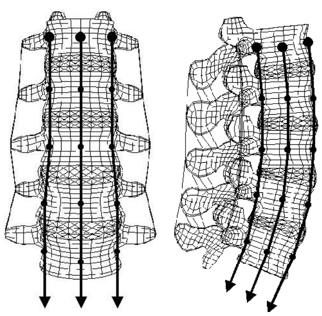

Figure 1: Outer mesh of the finite element model of the lumbar spine with follower load.

The element mesh of the vertebrae is based on the model used by Smit [1996]. The nucleus pulposus was simulated by an incompressible fluid-filled cavity and the annulus fibrosus by volume elements with superimposed spring elements representing the fibers. The facet joints could only transmit compressive forces. The capsule of the facet joints and the six ligaments of the lumbar spine were included. The mainly nonlinear material properties of all tissues were taken from the literature. First, the model was successively loaded in flexion/extension, right/left lateral bending, and right/left axial rotation with moments up to 10 Nm. In a second step the model was loaded by an additional follower load [Patwardhan et al, 1999; Rohlmann et al, 2001] of 250 N to simulate the stabilizing effect of the local muscles acting directly on the lumbar spine. The load was generated by four forces acting on the circumference of each vertebral body, their lines of action leading to the corresponding points of circumference of the adjacent vertebral bodies (Fig. 1). The finite element model is described in detail elsewhere [Zander et al. 2001]. The finite element program ABAQUS was used. The computer model was validated by reference to experimental data from *in vitro* measurements [Rohlmann et al. 2001; Zander et al. 2001].

RESULTS

Flexion/extension

A follower load had only a minor influence on intersegmental rotation but it increased intradiscal pressure strongly to physiological values. Intradiscal pressure was higher for extension than for flexion.

Lateral bending

For lateral bending too, a follower load had only a negligible effect on intersegmental rotation. Without a follower load, intradiscal pressure increased with increasing bending moment, up to a moment of about 2 to 3 Nm. For higher bending moments intradiscal pressure decreased. When a follower load was also applied, intradiscal pressure decreased with increasing moment. For all bending moments intradiscal pressure was significantly higher when a follower load was applied.

Axial rotation

Again, a follower load had only a minor influence on intersegmental rotation. Intradiscal pressure increased slightly with the applied torsional moment. A follower load shifted the pressure curves to physiological values.

DISCUSSION

The effect of a follower load on intradiscal pressure and intersegmental rotation of the lumbar spine was determined using the finite element method. Good agreement was achieved with experimental data [Rohlmann et al, 2001]. Both methods showed that a follower load has only a minor effect on intersegmental rotation.

In this study, a follower load of only 250 N was applied but even when it was increased to 1000 N the computer model remained stable. A follower load should not simulate the body weight but the short local muscle forces which stabilizes the spinal segments and which depend on several factors. The body weight has to be stabilized by the global muscles.

A follower load increases the intradiscal pressure to physiological values, stabilizes the spine so that additional single forces representing a muscle can be applied, and in contrast to a preload, has only a minor influence on lumbar lordosis.

REFERENCES

Patwardhan, AG. et al (1999) *Spine*, **24**, 1003-1009

Rohlmann, A. et al (2001) *Spine*, **26**, E557-E561

Smit, T. (1996) *The Mechanical Significance of the Trabecular Bone Architecture in a Human Vertebra*. Shaker

Zander, T. et al (2001) *Clin. Biomech.*, **16**, S73-S80

EFFECTS OF HYDROGEN PEROXIDE ON ENDOTHELIAL CELLS ADHSION MOLECULES EXPRESSION

Chen Huaiqing[1] Chen Youqin[1] Zhang Wensheng[1] Liu Xiaoheng[1] Xiong Wang[2]
[1]Institute of Biomedical Engineering, West China Medical Center, Sichuan University, Chengdu 610041, chq@wcums.edu.cn
[2]LEMTA-UMR-CNRS 7563, Vandoeuvre, France

INTRODUCTION

Ischemia is a central pathomechanism in many acute and chronic diseases. Both persistent ischemia and subsequent organ reperfusion are frequently associated with leukocyte infiltrates, and this inflammatory response play a major role in causing ischemia associtaed organ dysfunction and damage(Yamazaki et al,1993). Leukocyte infiltration requires a chain of reactions between endothelial cells (EC) and leukocyte that initially retards intravascular leukocyte flow and finally leads to leukocyte transmigration through the endothelial monolayer. These events are mediated by sequential interaction of different endothelial adhesion molecules with cell surface receptors on leukocytes. A crucial step between the initial contact and final transmigration of leukocytes is their tight adhesion to EC, which is mainly mediated by the endothelial transmembrane receptors intercellular adhesion molecule-1 (ICAM-1) and vascular adhesion molecule-1 (VCAM-1). One of the cytotoxic products of neutrophil, promotes the adhesion of neutrophil to EC(Ichikawa et al,1997). The objectives of the present study were to investigate the effects of H_2O_2 on adhesion molecules expression in cultured human umbilical endothelial cells (HUVEC).

METHODS

Endothelial cells were isolated from human umbilical cord veins by collagenase treatment as described by Jaffe and modified. The Endothelial cells between 2 and 4 passage were treated with H_2O_2 at different concentrations. Surface expressions of ICAM-1, VCAM-1 and E-selectin were labeled by incubating the cells with fluorescence monoclonal antibodies of anti- ICAM-1, VCAM-1 and E-selectin in dark. Data acquisition and analysis were performed using an flow cytometry.

RESULTS AND DISSCUSSION

The results showed that: 1) after treated with 250 μmol/L H_2O_2, ICAM-1 expression increased(Fig.1). VCAM-1 expression was maximally induced 2h after stimulation, and then gradually descended. It was also observed that 3h after simulation, the E-selectin expression began to be up-regulated significantly, and peak induction was obtained 5h after H_2O_2 stimulation. 2) Concerning the treatment of HUVECs with different concentrations of H_2O_2, ICAM-1 and VCAM-1 were maximally induced by 250 μmol/L H_2O_2. E-selectin peak induction was obtained by 350 μmol/L H_2O_2(Fig.2).

These results have extended previous observation which showed that adhesion molecules expression on endothelium was a critical factor in the H_2O_2-induced neutrophil adhesion to the endothelium. This study may contribute to the comprehension of the adhesion and transmigration of leukocytes in ischemia-reperfusion injuries (Willam et al, 1999).

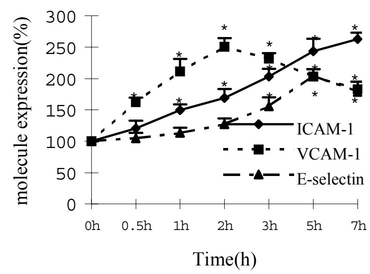

Fig.1 Time course of adhesion expression induced by H_2O_2

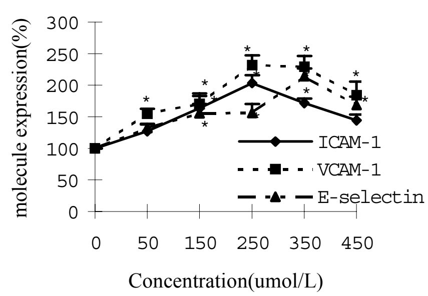

Fig.2 The effects of different concentrations of H_2O_2 on expression of adhesion molecules

SUMMARY

Cytotoxic product, H_2O_2, of neutrophils contributed to ischemia reperfusion injury can increase the expression of adhesion molecules in ECs. Therefore, H_2O_2 may promote the inflammation process.

REFERENCES

Yamazaki T, et al.(1993). Am J Pathol.1993, **143:** 410-417
Ichikawa H, et al (1997). *Circ Res,* **81:**911-931
Willam C, et al (1999). *Am. J. Physiol.,***276** : H2044-H2052

ACKNOWLEDGEMENTS

We thank the National Natural Science Foundation of China (No.39830110), and the China Medical Board of New York (CMB).

TIME-DEPENDENT EFFECTS OF INTERLEUKIN-8 GENE EXPRESSION IN ENDOTHELIAL CELLS EXPOSED ON FLUID SHEAR STRESS

Zhang Wensheng[1] Chen Huaiqing[1] Chen Youqin[1] Yang Yuan[2] Liu Xiaoheng[1]

[1]Institute of Biomedical Engineering, West China Medical Center, Sichuan University, Chengdu 610041, chq@wcums.edu.cn
[2]Research Unit of Medical Genetics, West China Hospital, Sichuan University, Chengdu 610041

INTRODUCTION

Vascular endothelial cells not only are the natural barrier, which separates flowing blood from the wall of vascular vessels, but also mediate a variety of physiological and pathological processes. Fluid shear stress plays an important role in vascular biology. In vivo, endothelial cells are continuously exposed to mechanical shear stress generated by the flowing blood. Previous studies have identified that the exposure of vascular endothelial cells to fluid mechanical forces can modulate the expression of many genes involved in vascular physiology and pathophysiology (Papadaki, 1997). In order to investigate that IL-8 mRNA expression of endothelial cells is not only regulated by chemical factors, but also by mechanical stresses, we employed quantitative reversal transcription-polymerase chain reaction (qRT-PCR) to assay the expression of IL-8 mRNA and its time course in human umbilical vein endothelial cells (HUVECs).

METHODS

Endothelial cells were isolated from human umbilical cord veins by collagenase treatment as described by Jaffe and modified. The cells were grown in M199 medium and the cells used were mainly prior to passage 3 or 4. Cell culture was maintained in a humidified 5% CO_2/95% air incubator at 37°C. A flow system was established according to the design previously described (Chen HQ, 2001). The same cultured medium was used to shear HUVECs. Shear stresses of 2.2, 4.2, and 6.1 dyne/cm^2 under laminal flow were generated by a peristaltic pump. Cells from static controls or from shear experiments were washed twice with PBS, and total cellular RNA was isolated by TRIzol reagent according to manufacturer`s manual. Quantitative RT-PCR assay involves LightCycler™ technology. Experimental protocol were performed by instruction manual of LightCycler-RNA Amplification Kit SYBR Green I.

RESULTS AND DISSCUSSION

Quantitative RT-PCR analysis revealed that IL-8 mRNA did not express in HUVECs untreated with fluid shear stress. IL-8 mRNA expression increased (7.7×10^6, 7.0×10^6, and 5.1×10^6 copies, respectively) when HUVECs exposed to the three shear stress for 1h, and it reached the summit (increased ~3.3, 2.1, and 2.9-fold, respectively) when HUVECs exposed to shear stress for 2h. Then IL-8 expression gradually decreased to 73%, 87%, and 89% respectively against 2h shear stress treatment at 3h of stimulation by shear stress and remained at a constant level (2.3×10^6~2.2×10^5 copies) throughout the time course of the study. The increase of IL-8 mRNA expression by shear stress was time-dependent(Fig.1). IL-8 gene expression in response to shear stress was very similar to NF-κB in response to shear stress. The induction of IL-8 gene expression by fluid shear stress is probably due to the activation of NF-κB. Shear stress can activated AP-1 and NF-κB latent in the cytoplasm through mechanical signal transduction pathways (Lan, 1994). It is reasonable to conclude that translocated AP-1 and NF-κB may activates IL-8 transcription (Roebuck KA, 1999). These considerations suggest that IL-8 expression induced by shear stress in HUVECs may play an important role in the genesis and development of both inflammation and arterio-atherosclerosis.

SUMMARY

This in vitro study demonstrates the expression of IL-8 gene can be regulated by shear stress. Shear stress induces the HUVECs to express IL-8 mRNA in a time-dependent fashion.

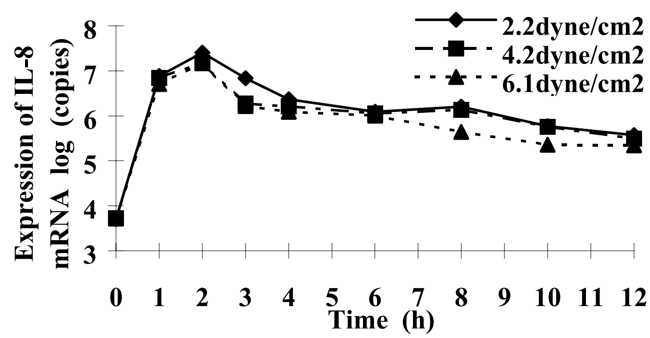

Fig. 1 Time-dependent relation of the expression of IL-8 mRNA in HUVECs exposed to shear stress

REFERENCES

Chen HQ, et al (2001). *J Biomed Eng*, **18**, 64-67. (in Chinese)
Lan Q, et al (1994). *Biochem Biophys Res Commu.*, **201**, 950.
Papadaki M and Eskin SG (1997). *Biotechnol Prog.*, **13**, 209.
Roebuck KA (1999). *J Interf Cytok Res*, **19**, 429-438.

ACKNOWLEDGEMENTS

We thank the National Natural Science Foundation of China (No.39830110), and the China Medical Board of New York (CMB).

EFFECTS OF SHEAR STRESS AND LYSOPHOSPHATIDYLCHOLINE ON ADHESION MOLECULES EXPRESSION OF ENDOTHELIAL CELLS

Chen Youqin Chen Huaiqing Zhang Wensheng Liu Xiaoheng

[1]Institute of Biomedical Engineering, West China Medical Center, Sichuan University, Chengdu 610041, chq@wcums.edu.cn

INTRODUCTION

Numerous studies suggest that normal function of the endothelium is critical in limiting the development of atheroclerosis. Impairment of these endothelial cells-mediated processes has been postulated to play a central role in the pathogenesis of atherosclersis.Extensive monocyte recruitment is an early phenomenon associated with the development of atherosclerotic lesion(Ross, 1999). Although the molecular mechanisms are not completely understood, monocyte recruitment into these early lesions may involve changes in endothelial adhesion for monocyte, in which adhesion molecules expressed by endothelial cell play an active role. In vivo, the function of endothelial cells is not only affected by the chemical factors, but also by the mechanical factors. The purpose of this article was to investigate the induction of adhesion molecules expression by synergistic effects of Lysophosphatidylcholine (Lyso-PC) and shear stress in cultured human umbilical vein endothelial cells (HUVEC).

METHODS

Endothelial cells were isolated from human umbilical cord veins by collagenase treatment as described by Jaffe and modified. A flow system was established according to a described design (Chen et al, 2001). The Endothelial cells between 2 and 4 passage were seeded on a 25mm×75mm slide to confluence, which can provides 1.5-2.0×10^5 cells for the following protocol. The slide of endothelial cell monolayers subjected to shear stress (2.2 or 4.2 dyne/cm^2) or treated with 30 μg/ml Lyso-PC for 5hr, and were either exposed simultaneously to Lyso-PC and shear stress for 5hr, or two stimuli were applied sequentially. The medium was maintained at a constant pH by gassing with 5% CO_2 and 95% air, and the temperature was maintained at 37°C. By immersing the flow system in a water bath. Laminar shear stress was generated by a peristaltic pump. Surface expression of ICAM-1, VCAM-1 and E-selectin was studied by incubating the cells with fluorescence labeling monoclonal antibodies of anti- ICAM-1, VCAM-1 and E-selectin in dark. Data acquisition and analysis was performed using an flow cytometry.

RESULTS AND DISSCUSSION

Comparing with the control group, shear stress or Lyso-PC can alone up-regulate the expression of ICAM-1 and VCAM-1, but can not increase the expression of E-selectin. When the shear stress and Lyso-PC are applied simultaneously on HUVECs, the expression of ICAM-1 and VCAM-1 are increased more significantly than that in the control group, but are not higher than that in the only Lyso-PC group. Activating the cells with Lyso-PC prior to shear stress, or with shear stress prior to Lyso-PC incubation, result in a significantly higher expression of ICAM-1, VCAM-1 and E-selectin, especially at low shear stress (2.2 dyne/cm^2). We suggest that shear stress or Lyso-PC up-regulated ICAM-1 expression, which accounts for the increase of neutrophil adhesion to endothelial cells in the inflammatory response (Sampath, 1995). The increase of VCAM-1 expression can be correlated to the increase of monocyte adhesion in the low shear stress regions of arteries, and may play an important role in monocyte recruitment into the atherosclerotic lesions(Mohan, 1999). However, a sequential action of the shear stress or Lyso-PC induced an even greater expression of ICAM-1 and VCAM-1, thus it can be seen that the response of shear stress in combination with endothelial activation may increase the ability of these cells to recruit leukocytes under settings of inflammatory and atherosclerosis even under an otherwise unfavorable mechanical environment.

SUMMARY

A sequential action of the shear stress and Lyso-PC induces high expression of ICAM-1 and VCAM-1. Thus it could be understood that the flow shear stress in combination with endothelial activation by chemical factors may increase the ability of endothelial cells to recruit leukocytes even under the mechanical environment unfavorable for cell adherence.

REFERENCES

Ross R.(1999). *N Engl J Med*, **340,** 115-126

Chen HQ, et al (2001). *J Biomed Eng*, **18**, 64-67. (in Chinese)

Sampath R, et al (1995). Ann Biomed Eng. 23, 247-256.

Mohan S (1999). Am. *J Physiol..*, **276**, C1110-1106.

ACKNOWLEDGEMENTS

We thank the National Natural Science Foundation of China (No.39830110), and the China Medical Board of New York (CMB).

THE ASSESSMENT OF SPINAL MOTION DURING ROWING

Peter Holt[1], Peter Cashman[2], Anthony Bull[2], Alison McGregor[1]

[1] Department of Musculoskeletal Surgery, Faculty of Medicine, Imperial College of Science, Technology & Medicine, Charing Cross Hospital, London
[2] Department of Bioengineering, Imperial College of Science, Technology & Medicine, Exhibition Road, London
Email contact: a.mcgregor@ic.ac.uk

INTRODUCTION
Low back pain is a common problem amongst competitive rowers at all levels. It is not clear why this occurs. Currently little is known regarding the kinematics of the spine during rowing and its relationship to rowing technique and to the loads generated during rowing. The present study sought to address this and to examine the effects of fatigue and stretching on these movements.

METHODS
A method was developed for measuring rowing technique on a Concept IIC rowing ergometer by combining the use of an electromagnetic motion capture system, The Flock of Birds (Ascension Technology, USA) to record the motion of the spine and pelvis (Bull & McGregor 2000) and a load cell (Oarsum, Australia) to record the force produced at the ergometer handle. The outputs from these two systems were synchronised and continuously recorded using custom software. Thirteen elite national and international oarsmen (mean age 22.4, S.D. 0.1 years) were recruited into this study. Using the experimental system, rowing stroke profiles were quantified in terms of lumbopelvic kinematics and stroke force profiles during a one hour training rowing piece, with recordings being taken at the start of the session and at quarterly intervals during the hour session. Seven of the athletes returned the following week and repeated the experimental protocol with the addition of a brief rehydration and stretching break of 3 minutes 30 minutes into the rowing piece, to establish whether this would have any impact on the stroke profiles.

RESULTS
The figure alongside depicts a typical force curve output starting at the catch position together with a measure of the lumbar spine motion during the stroke with quantification of lumbar spine motion relative to the stroke force profile
Using this data, the rowing stroke was divided into key stages, and the curve gradients, angles of curvature and force magnitudes were obtained. These variables were calculated for each of the 4 sample periods over the one hour test and were compared using analysis of variance. This revealed marked changes and increases in the amount of spinal motion ($p<0.001$) during the hour rowing piece (-0.7º±1.4 at the start of the training piece and –2.3º±2.3 at the end). This led to a later percentage value for maximum spinal extension as the back had to move through a greater range to achieve the same finish position (36.3º±4.3 to 38.0º±8.5). This suggests that in trying to maintain a consistent stroke force profile athletes were utilising greater ranges of spinal motion as they fatigued. The inclusion of a break in the middle of the training program appeared to reduce some of these changes.

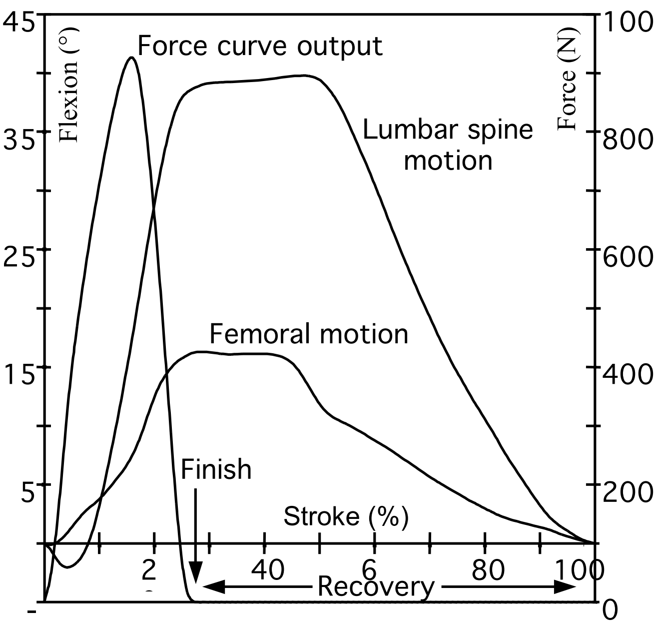

DISCUSSION
The findings of this study provide a clearer understanding of the mechanics of rowing. Subtle but definite changes in the kinematics were noted as a result of fatigue and these changes may be associated with potential injury mechanisms. The effect of including the brief break during training suggests that such changes in technique are reversible, but further detailed work is required in this area.

REFERENCES
Bull, A.M.J. & McGregor, A.H. (2000). Clin Biomech **15**(10),772-776

THE CERVICAL MUSCLE RESPONSE DURING "WHIPLASH SIMULATED MOTION" WITH RESPECT TO GENDER

Leif Hasselquist[1], Vijay Goel[2], David Wilder[3], Kevin Spratt[3], Malcolm Pope[4],
[1]U.S. Army Natick Soldier Center, Natick, MA, USA; E-mail: leif.hasselquist @Natick.army.mil
[2]Department of Bioengineering, The University of Toledo, Toledo, OH, USA
[3]Department of Biomedical Engineering, The University of Iowa, Iowa City, IA, USA
[4]Liberty Safework Centre, University of Aberdeen, Aberdeen, UK

INTRODUCTION

The cervical muscle's involvement in whiplash has just recently been addressed (Brault, 1998; Magnusson, 1998, 1999). Epidemiological results show women have higher rates of whiplash than men (Spitzer, 1995). We hypothesized that the cervical muscle responses influence the biomechanics of whiplash and would be different between genders.

METHODS

The 24 subjects (12M, 12F) were seated on a car seat mounted on a sled propelled by a spring and latch release mechanism and was accelerated less than .5 g. The sled mass was normalized by gender. There were 6 randomized unexpected trials (4 release, 2 w/o release). Auditory and visual cues were masked. Bilateral surface EMG recorded sternocleidomastoid (Scm), paraspinals (Para), and trapezius (Trap) using bipolar pre-amplified electrodes acquired at 1000 Hz. Normalized EMG were analyzed using Wavelet Analysis. The Motion Monitor (Innovative Sports Training, Inc.) and a 6^o of freedom magnetic sensor tracking system (Ascension Tech.) collected 3-D kinematics and were synchronized to EMG. Sensors were attached to sled, head, T1, T12, and sacrum. An accelerometer on the sled insured reproducibility of acceleration.

RESULTS AND DISCUSION

Significant anthropometric differences between genders were identified (Table 1). Results show a significant interaction of gender to muscle with respect to duration of muscle contractions (p = .00018) and reaction times with respect to head and torso motion for all directions (x ant. -post, y med.-lat., z sup. -inf.) (p < .0001) (Fig.1-2). The coplanar and coupled motions of the head and cervical spine in reference to the torso is due to the anatomical structure of the cervical vertebrae and floppy nature of the head. Females showed an increase in torso angular acceleration, angular velocity, and greater kyphotic torso and cervical lordosis positions. The frequency of head and neck movement was ~2-3Hz and is representative of the range for whiplash research (~2-8 Hz). Synchronization of EMG with kinematics indicates eccentric muscle responses which when coupled with the frequency and smaller muscle mass may increase female's risk of injury.

Table1: Mean Subject Age and Selected Anthropometry (SD)

	Female (N=12)	Male (N=12)	*P (*p<0.05)*
Age (yrs)	24.67 (5.71)	30.33 (8.42)	0.0668
Mass (kg)	65.64 (8.51)	80.72 (16.77)	.011*
Height (cm)	169.58 (5.68)	175.33 (5.88)	0.0234*
HeadCir^3/ NeckCir^2	170.18 (19.76)	140.82 (14.56)	0.004*
Cer. Flex. (^{o})	72.8 (2.2)	66.5 (5.2)	0.0008*

Figure 1: Male Muscle Response: x= ant. -post. y= med.-lat., and z =sup.-inf.; 1=ScmR, 2=ScmL, 3=ParaR, 4=ParaL, 5=TrapR, and 6=TrapL

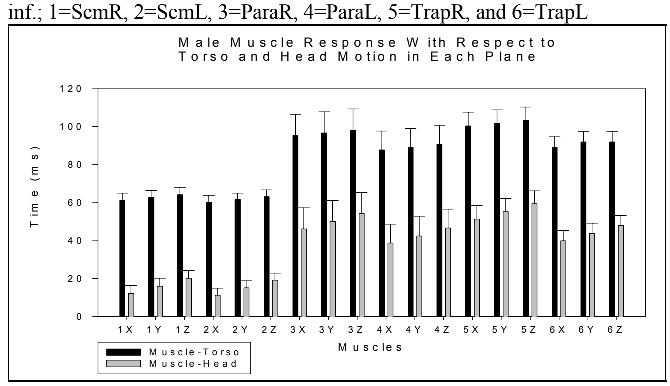

Figure 2: Female Muscle Response: x=ant. -post., y= med.-lat., and z =sup.-inf.; 1=ScmR, 2=ScmL, 3=ParaR, 4=ParaL, 5=TrapR, and 6=TrapL

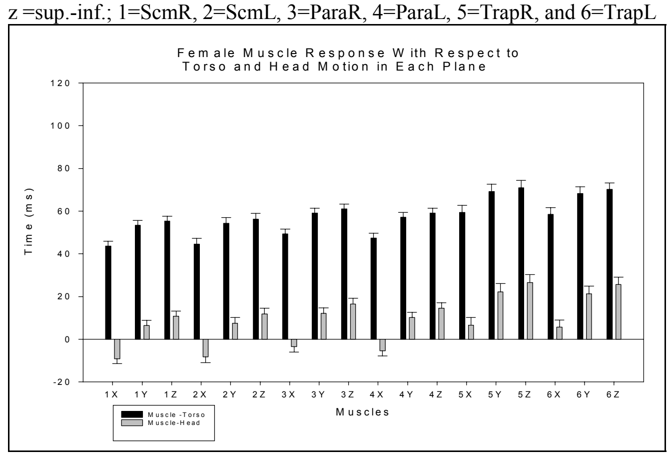

SUMMARY:

The cervical muscle's response to perturbations is rapid enough to effect biomechanical responses. In frequency ranges of 2-8 Hz the amplitude of the head acceleration is augmented, and oscillation about a center of rotation low in the body may induce large angular movements due to the linear component of acceleration delivered to the cervical vertebrae. Female muscle onset times are related to the timing and frequency of the movement of the torso and head. These factors plus angular accelerations, increased kyphosis, and eccentric contraction may increase female cervical injuries (Ono, 1997).

REFERENCES:

Brault, J. et al (1998) *Arch Phys Med Rehabil*, **79**, 72-80
Magnusson, M. et al (1998) *Proc 43rd ORS Conf,* ORS
Magnusson, M. et al (1999) *Eur. Spine J,* **8**, 118-125
Ono, K. et al (1997) *Proc 41st Stapp Car Crash Conf*, SAE
Spitzer, W. et al (1995) *Spine,* **20**, 9S-73S

THE PROXIMAL-DISTAL SEQUENCE IN OVERARM THROWING AND THE EFFECT OF BALL WEIGHT

Roland van den Tillaar and Gertjan Ettema

Department of Sport Science, Norwegian University of Science and Technology, Trondheim, Norway
rolandv@svt.ntnu.no

INTRODUCTION

In overarm throwing, the temporal proximal-distal sequence (TPDS) of the different segments of the upper body is theoretically of major importance for the generation of high speed (e.g. Herring & Chapman, 1992). However, experimental data are inconclusive on this issue: whereas Jöris et. al. (1985) found supporting evidence, other studies have found that in overarm throwing this sequence does not occur between the shoulder and elbow segments (Hosikawa and Toyoshima, 1976). In the present study, this issue was further investigated under various loading conditions (i.e. ball weight). It was hypothesized that heavier ball weight may create relatively higher reaction forces that could affect movements in the slender distal and more bulky proximal segments differently.

METHODS

Seven Norwegian experienced male handball players performed maximum speed throws, using 7 different balls that only differed in weight (0.2-0.8 kg.), Each ball was used 5 times, in random order. The throwing target was a 0.5 by 0.5m square at approximately shoulder height (1.65m) at a 4m distance. Displacement of ball and segments (wrist, elbow, shoulder and hip) was recorded using a ProReflex motion capture system (five infrared cameras, 240Hz.) Linear velocity (v) and acceleration of ball and velocity of segments was calculated using a 5-point differentiating filter on the absolute 3D displacement. The force applied to the ball was calculated as the product of its acceleration and mass. The moment of ball release was identified as the time where a sudden and dramatic separation of wrist and ball occurred. Angular velocity (ω) of elbow, wrist and shoulder were also analysed.

RESULTS AND DISCUSSION

Ball weight had a negative effect on ball velocity (r=-0.91 or higher). This relationship with ball weight was also apparent for maximum linear velocity of the wrist and elbow, as well as the maximum elbow extension velocity and internal rotation of the shoulder. The maximum force applied to the ball increase with ball weight (r=-0.64).
The maximum linear velocity of the shoulder occurred later in time than that of the elbow (t-test, $p<0.001$) (figure 1). Furthermore, the maximal angular velocity of the wrist occurred earlier than that of the elbow ($p<0.001$), which is confirming finding by Hong et. al. (2001). The maximal internal rotation velocity of the shoulder did not occur before ball release (figure 1), which was also found by Matsuo et al. (2001).
No effect of ball weight on relative timing of the aforementioned kinematic events were found. The sequential order of segment movements remained unaltered when changing ball weight.
An explanation for the early maximum elbow velocity could be that the elbow extension causes an enhanced reactive force on the elbow segment, reducing its speed: in figure 1 this is indicated by the coincidence of onset of elbow extension and maximum elbow segment linear velocity. The shoulder segment is not necessarily influenced by this in the same manner.

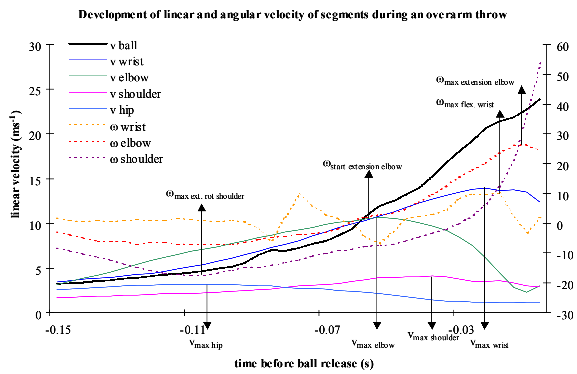

Figure 1: Example of linear and angular velocity.

Also the early occurring maximum wrist flexion velocity is not according to TPDS. The reason of this may be because of the biarticular characteristic of the majority of the wrist flexors that have a significant elbow flexion action as well (Ettema, et al., 1998). Elbow extension may therefore initiate early flexion of the wrist.

SUMMARY

Ball weight does not have a substantial effect on coordinative timing aspects in overarm throwing by experienced handball players. The timing is not in accordance with the generally accepted proximal-distal joint sequence. It is therefore concluded that, within the boundaries of the experiment (i.e. throwing a relatively light object) the proximal-distal sequence in overarm throwing does not hold. Furthermore, this movement sequence seems the result of a built-in coordination strategy rather than of external reaction forces (generated by the ball mass).

REFERENCES

Ettema, G. et al. (1998) *Human Mov. Sci.*, **17**, 201-220.
Herring R.M., Chapman A.E. (1992) *J. Biomech.*, **25**, 1173-1184.
Hong, D. et al. (2001) J. *Electromyography Kinesiology*, **11**, 95-112.
Hoshikawa, T., Toyoshima, S. (1976) *Biomechanics V-B.* University Park Press, 109-117.
Jöris, H. et al. (1985) *J. Biomech.*, **18**, 409-414.
Matsuo, T. et al. (2001) *J. Appl. Biomech.*, **17**, 1-13.

EFFECT OF DIFFERENT PEDAL RATES ON ENDURANCE AND PHYSIOLOGICAL RESPONCES DURING CYCLING AT HIGH SUB-MAXIMAL EXTERNAL POWER

Jens Steen Nielsen[1], Ernst Albin Hansen[1], and Gisela Sjøgaard[2]
Email: js.nielsen@sportmed.sdu.dk
[1]Institute of Sports Science and Clinical Biomechanics, University of Southern Denmark, Odense
[2]National Institute of Occupational Health, Copenhagen, Denmark

INTRODUCTION

Freely chosen pedal rate (FCPR) increases with increased external power (Hansen et al. 2002). Interestingly, at low sub-maximal external power the FCPR is considerable higher than the pedal rate at which oxygen uptake is the lowest, i.e. the most efficient pedal rate. However, as the external power increases the FCPR and the most efficient pedal rate seem to merge. Accordingly, it was recently shown that FCPR and the most efficient pedal rate were similar during cycling at external power corresponding to 80% of the maximal oxygen uptake (VO_{2max}) (Brisswalter et al. 2000). Efficiency is an important factor affecting endurance during cycling at sub-maximal external power. It was therefore hypothesized that cycling at high sub-maximal external power with FCPR would result in a prolonged endurance compared with higher as well as lower pedal rates. The purpose of the present study was to examine this hypothesis.

METHODS

Twenty males (26.3±3.5 years, 178±5 cm, and 73.3±7.5 kg) volunteered. A progressive test was performed on a Monark cycle ergometer (Monark AB, Varberg, Sweden) with a pedal rate of 80 rpm for determination of VO_{2max} and external power corresponding to 90% of VO_{2max} (W90%). Another test was performed on a racing bicycle placed a motorized treadmill (Woodway GmbH, Weil am Rhein, Germany) for 5 min at W90%. This test was performed to determine the FCPR. The set-up allowed the subjects to freely choose a pedal rate in the range of the pedal rates typically used during road cycling. The subjects were allowed 3 min to experiment with the gear ratio before selecting their FCPR. During the final 2 min the FCPR was maintained while external power, heart rate (HR), and pulmonary gas exchange were measured. Subsequently, 3 endurance tests were performed on a Monark cycle ergometer at the FCPR (determined on the treadmill), FCPR-25%, and FCPR+25%, in randomized order. The tests were performed at the same weekday and hour of the day. Endurance was determined as the time from start to the point of time where the subjects were unable to maintain the target pedal rate minus 10%. Douglass bags were collected between the 3. and the 5. min for measurement of oxygen uptake (VO_2), pulmonary gas exchange and respiration exchange ratio (RER). At the 5. min also blood lactate concentration (using an YSI Model 1500 Sport, YSI Incorporated, Yellow Springs, USA), heart rate (HR), and rating of perceived exertion (RPE) were measured. In all tests the external power and HR were measured with a SRM crank dynamometer (Schoberer Rad Messtechnich, Jülich, Germany).

RESULTS AND DISCUSSION

The progressive test resulted in VO_{2max} of 4.418±0.61 l/min, maximal HR of 190±10 beats/min, blood lactate concentration of 12.2±2.0 mM, and RER of 1.20±0.05. Further, W90% was determined to be 325±47 W while FCPR at W90% was 78±11 (59-96) rpm. During treadmill cycling with FCPR the VO_2, RER, and V_E were 4.115±0.57 l/min, 1.11±0.07, and 127.5±24,3 l/min, respectively. During the endurance tests pedal rates were 58±88, 78±11, and 96±13 rpm at $FCPR_{-25\%}$, FCPR, and $FCPR_{+25\%}$, respectively. There was no difference between external power in endurance tests performed with the three different pedal rates. Endurance time at $FCPR_{-25\%}$ and FCPR were 19% and 25% longer compared to $FCPR_{+25\%}$ (Tab. 1).

	$FCPR_{-25\%}$	FCPR	$FCPR_{+25\%}$
Endurance (sec)	547±1701	589±239	441±188[a]
VO_2 (l/min)	4.016±0.55	4.091±0.57 [b]	4.298±0.54[a]
V_E (l/min)	116±25	121±27	134±31[a]
Lactate (mM)	7.4±2.0	8.1±2.1	10.1±2.5[a]
HR (beats/min)	175±8	176±11	181±7[a]
RPE	17.0±1.4	16.7±1.2	17.2±1.8

Tab. 1 Results from the endurance tests. [a]=significantly different from $FCPR_{-25\%}$ and FCPR. [b]=significantly different from $FCPR_{-25\%}$ and $FCPR_{+25\%}$.

SUMMARY

We showed that endurance time during cycling at high sub-maximal external power was 19-25% longer at FCPR and $FCPR_{-25\%}$ compared with $FCPR_{+25\%}$. The shorter endurance time at $FCPR_{+25\%}$ compared with FCPR could be explained by the higher energy expenditure at this pedal rate as identified by higher values of HR, VO_2, blood lactate concentration, and V_E. Interestingly, VO_2 was lower at $FCPR_{-25\%}$ compared with FCPR and endurance time could therefore be expected to be longer at $FCPR_{-25\%}$ compared with FCPR. However, decreasing the pedal rate results in higher mean and peak pedal forces that might cause a higher peripheral strain feedback during pedaling and thereby limit the time to exhaustion i.e. the endurance.

REFERENCES

Brisswalter, J. et al (2000). *Int J Sports Med*, **21**, 60-64.
Hansen, E.A. et al (2002). *J Biomech*, **35**, 277-285.

NEUROMOTOR ACCOMMODATION TO MULTIPLE TRANSFEMORAL PROSTHESIS ALIGNMENTS

Mark D. Geil, Ph.D. (mark.geil@hps.gatech.edu)
Georgia Institute of Technology, Atlanta, Georgia

INTRODUCTION

The alignment of a lower-limb prosthesis involves the spatial orientation of the components with respect to one another. Prosthetists usually conduct dynamic alignment based on observation of gait and a few simple measures. It is unclear what outcomes of gait the practitioner considers most desirable, and while a set of gross gait deviations is avoided, the goals of dynamic alignment are generally prosthetist-specific. This investigation sought to quantify gait outcomes when multiple practitioners "optimally" aligned the same prosthesis for the same subject. The investigators hypothesized large variability in self-selected walking speed, ground reaction force, and joint kinematics.

METHODS

The study measured the kinematics and kinetics of the gait of a single subject walking with a prosthesis aligned by five different prosthetic practitioners. The subject was a 36 year old active male unilateral left transfemoral amputee 10 years post-trauma. The prosthesis included an ischial containment socket, Mauch knee, and Otto Bock 1C40 foot. Informed consent was obtained.

Although all were actively practicing, practitioners ranged widely in certification and years of experience. The subject in the study was a certified prosthetist, and was included among the five practitioners. For each analysis, the prosthesis was disassembled distal to the socket. Each practitioner assembled and aligned the components based on whatever measurement and gait observation he or she deemed necessary. The subject was then allowed time to become accustomed to the alignment and an instrumented gait analysis was conducted.

After a static trial quantified weight-bearing alignment, kinematics were measured at 60 Hz and kinetics at 300 Hz while the subject walked at a comfortable, self-selected speed. Wherever possible, markers remained on the prosthetic components upon disassembly; care was taken to return any removed markers to the same location for each analysis.

RESULTS

Instrumented gait analysis revealed quantifiable static frontal and sagittal plane differences in the alignments conducted by different practitioners. Despite the differences in the alignments of the practitioners, mean self-selected velocity of gait showed only small differences between practitioners' alignments, with a range of 0.116 m/s (Table 1). Ground reaction forces were also similar, with a three-hump pattern specific to amputee gait (Hubbard and McElroy, 1994).

Given the differences in static alignment, differences in intersegmental angles during gait were surprisingly small, suggesting that the alignment of the different practitioners produced a consistent gait pattern. Angles for the prosthetic knee were most consistent, while the contralateral knee (Fig. 1) showed only slight differences in the alignment of P5 in late swing/early stance phase. Ankle angles in the varying alignments were also very similar. Alignment changes to the ankle angle are apparent in differences in the swing phase portion of the prosthetic ankle angle curves, as the ankle is non-weight bearing and is not affected by remote joints.

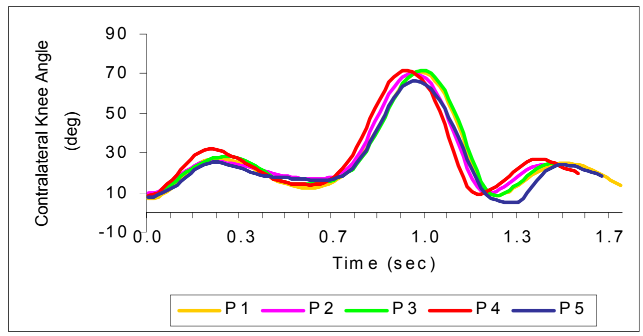

Figure 1: Representative intersegmental contralateral knee angle vs. time for each practitioner's alignment.

DISCUSSION

Several researchers have spoken of the goal of "optimum alignment." The data in the present study illustrate the difficulty of defining this optimum. Practitioners in the study appeared to use differing alignment strategies, including bilateral static joint angle symmetry vs. zero pelvic obliquity. Nonetheless, kinematics were very similar, disproving the hypothesis. This result suggests the potential for alignment deviation as a tool to assess an amputee's neuromotor control strategies for optimizing gait. Furthermore, until optimum alignment can be more clearly defined, automated or computerized alignment may not be necessary.

REFERENCES

Hubbard, W.A., McElroy, G.K. (1994). *Prosth Orth Int*, **18**, 142-149.

Table 1: Mean velocity of gait and peak bilateral ground reaction force averaged for 5 trials for each practitioner's alignment.

Alignment		P1	P2	P3	P4	P5
Mean Velocity, m/s, (std. dev.)		1.17 (0.08)	1.21 (0.04)	1.20 (0.04)	1.29 (0.03)	1.24 (0.05)
Peak Vertical GRF (N)	prosthesis side	956.23	964.83	976.57	1000.63	1020.18
	contralateral side	1012.70	1054.70	1031.75	1091.32	1098.65

THE INFLUENCE OF FATIGUE ON FUNCTIONAL STABILITY OF THE KNEE JOINT

Sven Bruhn / Walter Rapp / Christoph Scheuffelen / Albert Gollhofer
Institute for Sport and Sport Science, University of Freiburg, Sven.Bruhn@sport.uni-freiburg.de

INTRODUCTION

Stability of the knee joint in functional situations relates on active stabilisation by muscle contraction. Neuronal activation and mechanical output of muscle contraction are depending among others on the history of fatigue and recovery of the related muscles. Thus it can be assumed, that functional joint stability is influenced by muscle fatigue (Rozzi et al., 1999). The purpose of the study was to measure the influence of muscle fatigue on functional stability of the knee joint.

METHODS

15 mail students underwent a fatiguing incremental step test. Work load was enhanced 20W every minute until exhaustion starting from zero. Power output, heart rate and EMGs of knee stabilizing muscles were recorded during testing. The EMGs were integrated over the medium ten seconds of each loading minute and mean power frequency of this time period was calculated with the raw EMGs.

Pre and post fatigue, functional stability of the knee joint was measured while the leg was axially loaded using a dynamic stimulus. 19 single stimuli were applied. Each single stimulus was averaged over the 15 subjects. Anterior tibial displacement as well as the compensating reflexes of knee joint muscles measured with a new instrumentation.

RESULTS AND DISCUSSION

During the incremental test, iEMGs continuously enhanced indicating increasing demands on muscle power output. Mean power frequency of the raw EMGs increased first, indicating higher frequencies of motor units discharge and additional recruitment of motor units with fast twitch muscle fibres as a reaction on higher demands on muscle power output. During the last increments, the mean power frequency of m. vastus medialis decreased indicating the exhaustion of the first fast twitch muscle fibres (fig. 1).

Mean power frequency was reduced during the stability test both before and after the destabilizing stimulus was induced. After the fatiguing incremental test, it took nearly twice as much activity (iEMG) for the subjects to stand upright, than before. On the other hand, the reflex activity was reduced in relation to the activity during upright stance after fatigue (fig. 2) (Wojtys et al., 1996).

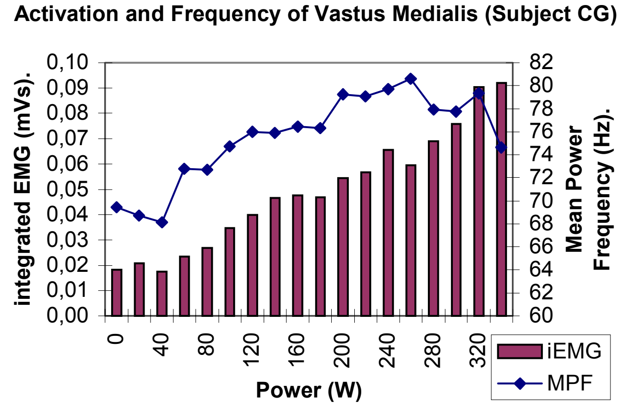

Figure 1: Amount and frequency of neuromuscular activation of m. vastus medialis of subject CG during the fatiguing test.

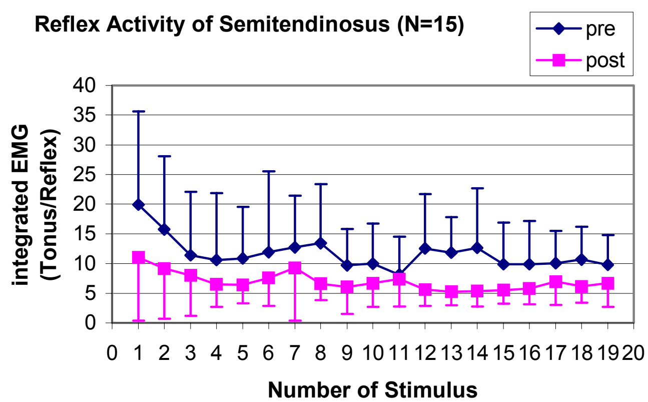

Figure 2: Reflex activation (iEMG) in relation to muscle tone pre- and post-fatigue 120ms after the stimulus was induced.

SUMMARY

Functional stability of the knee joint after fatigue has to rely on passive stabilizers rather, than on active stabilisation by voluntary or reflex activity of the knee joint muscles. As the mechanical output of the active component of the functional stability seems to be reduced in case of fatigue and because the strength of the passive stabilisers is limited, fatigue can significantly enhance the risk of injury.

REFERENCES

Rozzi, SL.; Lephart, SM.; Gear, WS.; Fu, FH. (1999). *Am J Sports Med* **Vol. 27, No. 3,** 312-9
Wojtys E M; Wylie B B; Huston L J. (1996). *Am J Sports Med* **5,** 615-621

THE EFFECTS OF STICK CONSTRUCTION IN THE PERFORMANCE OF ICE HOCKEY WRIST SHOT

T-C Wu[1], D. Pearsall[1,2], A.N.H. Hodges[1], R. Turcotte[1], R. Lefebvre[3], D. Montgomery[1], H. Bateni[2]

[1]Department of Kinesiology & Physical Education, [2]Physical & Occupational Therapy, McGill University, Montréal, Québec, Canada
[3]Bauer-Nike Hockey Inc., St. Jerome, QC, Canada

INTRODUCTION

In the game of ice hockey, a stick is one of the most vital piece equipment because it is used for shooting, passing, and stick handling in playing the game (Pearsall et al, 1999). A wrist shot is swung forward in snapping or pushing action to propel the puck upwards of 20 m/s, and this movement may be broken into four or five phases: draw back (optional), (a) blade positioning, loading, (b) pushing and (c) follow through, Figure 1. Several factors are thought to influence the outcome of the shot such as skill level, body strength, stick material type and ice surface condition. The purpose of this study was to investigate the performance of the wrist shot as affected by different stick types.

METHODS

Ten interuniversity or college level male subjects volunteered to participate in a shooting test of this study. Each subject used his own gloves and skates and performed the shooting task which consisted of three wrist shots with three different constructions of stick shaft: a medium (M), a stiff (S) and a carbon composite (C) on a force platform (AMTI). Subjects had a thirty second rest interval and a two-minute pause between stick types. The order of subjects and the types of stick were randomized. Each stick had nine reflective markers placed every 0.10 m. A hockey net was placed 8 m away and a sports radar gun (SR 3000) was placed behind the net to record the puck velocity. In addition, a high speed camera (Redlake, 480 frames/second) recorded the movement and deflection of the stick as seen in the sagittal plane. All the data were analyzed by APAS, Biobench, Statistica and Excel software programs.

RESULTS AND DISCUSSION

With regards to various stick models in the wrist shot, several variables were analyzed including velocity, vertical force, stick bending (θ) and attacking angles (β), and shaft deflection (δ). In the wrist shot, no significant difference was observed in all the variables, Table 1. The results may suggest that the stick characteristics were quite similar among all three different stick types. However, a high positive correlation of r = 0.6 ~ 0.7 was observed between shot velocity and vertical force, stick bending and shaft deflection. This indicated the important relationship between stick mechanical construction and shot performance.

Figure 1. The phases of the wrist shot include the (a) blade positioning; loading; (b) pushing and (c) follow through.

Table 1. Stick mechanical measures for stick types

	C	SD	M	SD	S	SD
V (m/s)	14.7	4.5	14.7	4.4	14.1	4.3
F_v (N)	44.5	26.0	43.6	28.9	44.8	36.5
θ (deg)	10.4	5.6	12.4	6.1	9.4	4.8
β (deg)	50.6	31.6	50.5	32.2	58.9	29.8
δ (m)	0.03	0.02	0.04	0.02	0.03	0.01

SUMMARY

These research results showed similar findings as Pearsall et al, 1999 & 2001 on the slap shot performance. They both suggest different stick stiffness properties did not significantly nor substantially affect puck velocity. Some questions still remain unanswered from this study. For example, in this experiment the criteria for the performance was based on peak velocity of the shot; however, other performance criteria such as accuracy of puck shot placement as well as passing, receiving, and stick handling should be examined with respect to stick design. Therefore, more in depth studies are needed to address the importance of the stick mechanical construction.

REFERENCES

Pearsall, D.J. et al (1999). *Sports Engineering.* **2**, 3-11.
Pearsall, D.J. et al (2001). *Proceedings of ISBS'01*, 74-77.

ACKNOWLEDGEMENTS

The authors would like to acknowledge research grant support from National Science and Engineering Research Council (NSERC) of Canada and Bauer-Nike Hockey Inc.

FUNCTION AND TRIGGER OF CHANGES IN SYNERGY OF LUMBAR AND THORACIC ERECTOR SPINAE MUSCLES.

Jaap H. van Dieën[1]; Claudine Lamoth[1]; Onno G. Meijer[1]; Wiebe de Vries[1]; Lorimer Moseley[2]

[1]Institute for Fundamental and Clinical Human Movement Sciences, Faculty of Human Movement Sciences, 'Vrije Universiteit', Amsterdam, The Netherlands; 2 Prince of Wales Medical Research Institute, University of New South Wales, Sydney, Australia

INTRODUCTION

In a recent study, trunk muscle synergies were found to be different in low back pain (LBP) patients compared to controls (Dieën et al., submitted). Across a range of tasks, the activation of the lumbar erector spinae muscle (ES) relative to the thoracic ES was higher in the patients. Furthermore, it was shown by model simulation that this altered synergy would enhance trunk stability. In the present paper, we will present data from two experiments to further explore the functionality and specificity of this behavior. The first experiment gave support to the adaptive nature of the behavior, by showing that it was displayed in healthy subjects in response to a challenge of trunk stability. The second experiment addressed the trigger of this behaviour in LBP. Pain and fear of pain were experimentally induced to study their effects on the ES synergy. It was found that especially fear of pain is a potent trigger of the mode of behaviour found in LBP patients.

METHODS

In the first experiment 9 subjects performed symmetric and asymmetric lifts of 15 kg containers, with a stable or unstable content (ice or water). After lifting, the load was held at hip height. EMGs of lumbar and thoracic erector spinae muscles were recorded. The dependent variable was the ratio of mean lumbar over mean thoracic rectified and averaged EMG amplitude averaged over 1s of the holding phase.

In the second experiment 9 subjects walked on a treadmill at velocities of 2.2, 3.8, 4.6 and 5.4 km/hr. EMGs were recorded as in experiment 1. The experimental conditions were walking, walking after injection of isotonic saline in the lumbar back muscles (no pain), walking after injection of hypertonic saline (severe pain), and walking while expecting electric skin stimulation in the low back area above tolerance (fear of pain). The latter stimulus was not actually applied. The dependent variable was the ratio of mean lumbar over mean thoracic EMG amplitude averaged over strides.

Repeated measures 2-way ANOVAs were used to test for effects of the independent variables on the ratio of lumbar over thoracic EMG amplitudes after logarithmic transformation. In case of sphericity violations, Wilk's λ was used as the test statistic.

RESULTS AND DISCUSSION

The ratio of lumbar over thoracic ES activity was higher when holding the unstable load, as compared to holding the stable load ($F = 6.4$, $p = 0.036$; Figure 1). Symmetry of the lift had no effect. This finding supports the adaptive nature of the relative increase of lumbar ES activity.

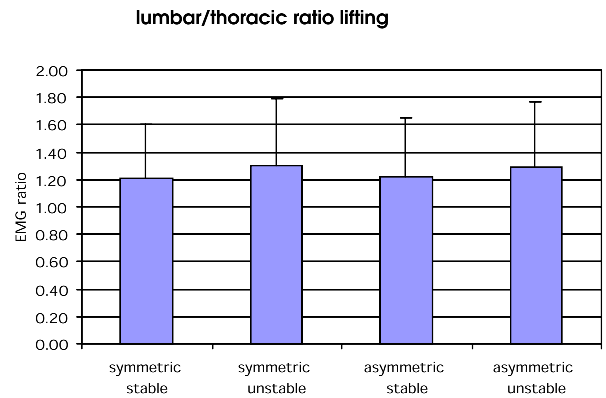

Figure 1: Mean lumbar over thoracic EMG ratio in holding stable and unstable loads. Bars indicate one SD.

In experiment 2, the ratio of lumbar over thoracic ES EMG was significantly affected by the stimulus condition ($\lambda = 0.157$, $p = 0.008$; Figure 2). This was mainly due to a difference between the skin stimulation condition and all other conditions. There was no significant velocity effect. The finding that the skin stimulation condition triggered the change in synergy suggests that it is an aspecific response to fear.

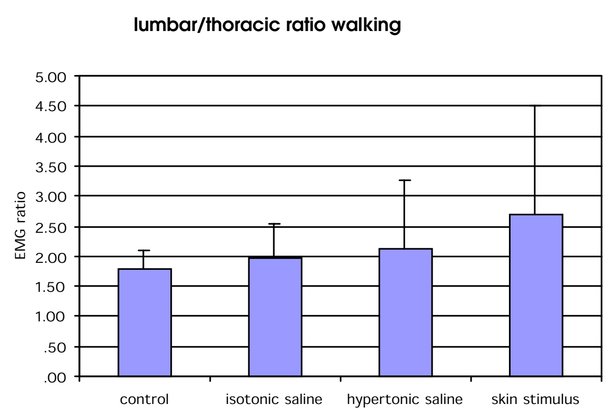

Figure 2: Mean lumbar over thoracic EMG ratio in walking under various stimulus conditions. Bars indicate one SD.

Although the adaptive nature of the relative increase in lumbar ES activity was supported, this behavior was shown to be an aspecific response that could be indced by fear of pain alone.

REFERENCES

Dieën, JHvan, Cholewicki J, Radebold A. (submitted.)

ACUTE BOUT OF ECCENTRIC EXERCISE IN THE RABBIT TA SHOWS CONCOMITANT FIBER LENGTH SHORTENING AND A SUBSEQUENT SHIFT IN THE FORCE-LENGTH RELATIONSHIP

Tim Butterfield[1], Walter Herzog
Faculty of Kinesiology, University of Calgary, Calgary, AB, Canada
[1]timb@kin.ucalgary.ca

INTRODUCTION

It is well accepted that eccentric exercise can cause severe muscle injury and soreness. However, there is anecdotal evidence that eccentric training (conditioning) of muscle dramatically reduces the incidence and severity of muscle injury and might completely abolish muscle soreness following a given protocol of eccentric exercise. One theory for such a repeated bout effect involves an increase in serial sarcomere number. This adaptation may be due to overstretch and damage of activated sarcomeres on the descending limb of the force-length relationship, resulting in an increase serial sarcomere number and a shift in the force length relation to the right (Morgan, 1990). Koh and Herzog (1998) found a small but significant 3% increase in sarcomere number when rabbit TA was subjected to chronic eccentric exercise, but through a relatively short range of motion (70^o-105^o). Quantification of muscle fiber lengths compared to whole muscle lengths in the cat medial gastrocnemius during eccentric contraction has been studied by Griffiths (1991) and indicates that fibers may actually shorten during eccentric contraction. The aim of this study was to investigate the fiber length changes during isometric and eccentric exercise in the rabbit TA and the effects of an acute bout of eccentric exercise on the force-length relationship.

METHODS

1 New Zealand White Rabbit was anesthetized and placed supine in a sling, after a nerve cuff electrode was placed on the left sciatic nerve, an E shaped force transducer was placed on the distal tendon of the left TA, and sonomicrometry crystals were inserted into the proximal and distal regions of a superficial fascicle in the left TA to measure fiber lengths throughout the experiment. The left foot was strapped into a foot-plate attached to a stepping motor specifically designed for the rabbit. An external torque cell attached between the foot-plate and motor allowed the recording of torque at the ankle joint. Supramaximal stimulation was determined after connecting the nerve cuff electrode to the stimulator (1.6 V, frequency 150 Hz). Range of motion around the ankle joint was determined to be 55^o to 155^o. Peak isometric forces at 21 different angles were measured by stimulating the peroneal nerve at every 5^o of ankle joint plantar flexion starting at 55^o. Three single twitches were given immediately before and after a 2 second isometric contraction with a two minute rest between bouts. Immediately following, an eccentric exercise protocol was utilized consisting of 5 sets of 10 eccentric contractions with a two minute rest between sets. Supramaximal stimulation (1.6 V, frequency 150 Hz, pulse duration 0.1ms, train duration 550ms) was applied to the sciatic nerve at the onset of plantar flexion through a range of motion of 40^o at the ankle joint (65^o to 105^o) at 72.3^o sec^{-1} with 180^o considered full plantar flexion. Immediately following the eccentric protocol, the isometric protocol was repeated without allowing time for recovery between stimulations. The rabbit was euthanized with an overdose of pentobarbital, and both hindlimbs were fixed in 10% neutral phosphate buffered formalin solution at 155^o ankle joint angle.

RESULTS

Single twitch forces resulted in potentiation effects in joint torque, which diminished over time and at longer muscle lengths. A shift to the right of the force-length relationship was seen in the peak isometric force of the TA after the eccentric protocol, however no shift was seen for joint torque measurements. During isometric contractions, at every angle, fiber lengths decreased. During the eccentric exercise protocol average fiber lengths also decreased, with the decrease in fiber length being greatest at the onset of contraction but elongated as plantar flexion increased, but fiber length never returned back to the starting length. The net fiber length, therefore, remained shorter than the starting length throughout the entire set of repetitions. These results will be systematically explored in a set of greater than six animals.

REFERENCES

Griffiths, RI. (1991). Shortening of Muscle Fibres During Stretch of the Active Cat Medial Gastrocnemius Muscle: The Role of Tendon Compliance, *Journal of Physiology*, **436**, 219-236.

Koh T.J., Herzog W. (1998). Eccentric Training Does Not Increase Sarcomere Number in Rabbit Dorsiflexor Muscles, *Journal of Biomechanics*, **31**, 499-501.

Morgan D.L. (1990). New Insights Into the Behavior of Muscle During Active Lengthening, *Biophysical Journal*, **57**, 209-221.

ACKNOWLEDGEMENTS

The authors would like to thank Tim Leonard for his technical advice and expertise.

AN APPROXIMATE ANALYTICAL SOLUTION FOR THE PLANAR SPRING MASS MODEL OF LOCOMOTION

S. R. Bullimore[1], S. G. Usmar, and J. F. Burn

Department of Anatomy, University of Bristol, Southwell Street, Bristol, BS2 8EJ
[1]Corresponding author: sharon.bullimore@bris.ac.uk

INTRODUCTION

The spring mass model (Blickhan, 1989; McMahon and Cheng, 1990) has been one of the most influential models of locomotion in recent years. The animal is represented by a point mass, supported on a massless, linear, perfectly elastic spring. This simple model predicts the mechanics of locomotion in running, hopping and trotting animals remarkably well (Blickhan and Full, 1993; Farley *et al.*, 1993). Two forms of the model have been described. In the *one-dimensional* model, the spring bounces vertically, modelling hopping in place. In the *planar* model, the spring rotates through the vertical, modelling forward hopping or running. The equations of motion for the one-dimensional model can be solved analytically, so that algebraic relationships between the input and output parameters can be derived. However, this powerful approach cannot be applied to the planar model because its equations of motion are non-linear and have to be solved numerically. The aim of the present study was to derive an approximate analytical solution for the planar spring mass model and to validate it by comparison with a numerical solution and with experimental data.

METHODS

An approximate analytical solution to the planar model was obtained by making a simplifying assumption and employing standard techniques for solving second order differential equations. A numerical solution was obtained using a fourth order Runge-Kutta algorithm (step size: 0.0001 s). These two solutions were evaluated for various input parameter values and initial conditions. For each combination of values, the contact time and minimum spring length predicted by each method were compared.

In addition, kinetic and kinematic data were collected from 3 running humans, 3 trotting horses and 3 trotting dogs. The kinematic data were used to determine input parameter values and initial conditions for the model. The peak forces and stance times predicted by the analytical solution were compared to the experimental data and the percentage error in each prediction was calculated.

RESULTS AND DISCUSSION

The predictions for contact time and spring length obtained from the analytical solution were very similar to the predictions of the numerical solution (figure 1). This suggests that the analytical solution is a good approximation to the true solution of the planar spring mass model.

The analytical solution also predicted stance time and peak vertical ground reaction force in humans, horses and dogs to within 10 % of measured values. This suggests that it is a good predictor of ground reaction forces in humans and quadrupedal mammals.

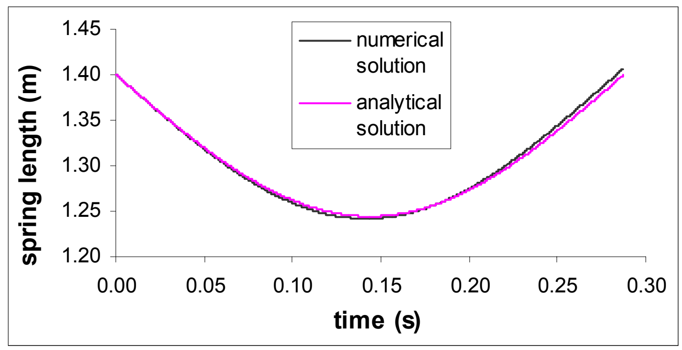

Figure 1: Comparison of a numerical solution and an approximate analytical solution to the planar spring mass model, showing the close correspondence between the two.

SUMMARY

An approximate analytical solution was obtained for the planar spring mass model of locomotion. The predictions of the solution were similar to those of a numerical solution and to ground reaction force data obtained from three different species. The derivation of an approximate analytical solution to the planar spring mass model will allow the implications of this important model to be explored in greater depth than has previously been possible.

REFERENCES

Blickhan, R. (1989). *J Biomech*, **22**, 1217-1227.
Blickhan, R., Full, R. J. (1993). *J Comp Physiol A*, **173**, 509-517.
Farley, C. T. et al (1993). *J Exp Biol*, **185**, 71-86.
McMahon, T. A., Cheng, G. C. (1990). *J Biomech*, **23**, 65-78.

TIBIOFEMORAL CONTACT POINTS RELATIVE TO FLEXION ANGLE MEASURED WITH MRI

Dan K. Ramsey [1] Per Wretenberg [1,2], and Gunnar Németh [1,2].
[1] Department of Surgical Sciences, Section for Orthopaedics, Karolinska Institute, Stockholm, Sweden dan.ramsey@kbh.ki.se
[2] Department of Orthopaedic Surgery, Karolinska Hospital, Stockholm, Sweden

INTRODUCTION

Magnetic resonance images (MRI) is a non-invasive method to accurately record knee structures of living subjects with precise 3D coordinates. Iwaki et al. (2000) and Hill et al. (2000) used MRI to measure tibiofemoral contact points but only in the sagittal plane.

METHODS

MR-images (1.5 tesla (T) Sigma System) were taken from the right knee of sixteen subjects with no history of knee dysfunction. A customized adjustable orthosis positioned the knee at 0°, 30° and 60° flexion. The leg was strapped to minimize movement and prevent external rotation at the hip. Angles were verified from the sagittal MR images. Co-ordinates for the contact areas were obtained from MRI and the centroid calculated. Position of the contact point was referenced to the most lateral and distal patellar tendon insertion site, the anatomical reference point (Figure 1).

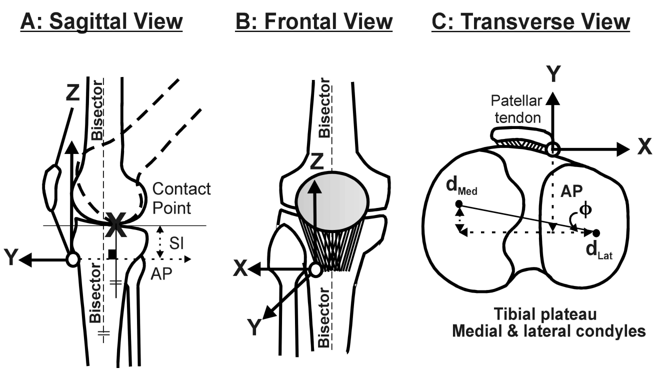

Figure 1: Position of the contact point with respect to the anatomical reference frame for each plane.

Co-ordinates were expressed relative to the inherent MRI reference frame. When the knee was flexed, the co-ordinates were transformed mathematically and aligned with the anatomical reference frame (Figure 2). Movement was reported as changes of the contact point's position relative to the fixed anatomical coordinate system for each angle.

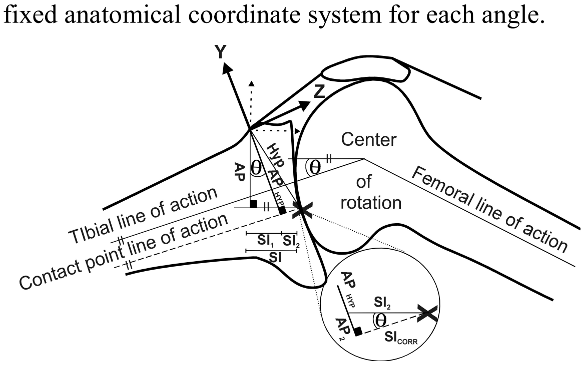

Figure 2: Method to correct contact position.

RESULTS AND DISCUSSION

Figure 3 illustrates the relative position of the tibial contact points with respect to the anatomical reference point for 0º, 30º and 60º.

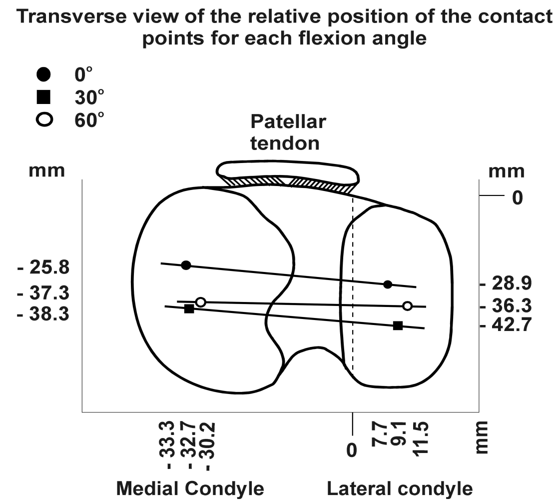

Figure 3: Mean tibiofemoral contact positions for each plane at 0°, 30°, and 60°.

Overall, contact points on the lateral tibial condyle were positioned further posteriorly. Displacements posteriorly were slightly greater than medially. Comparing movements, contact motion progressed posteriorly 12.5 mm vs. 13.8 mm, inferiorly 6.2 mm vs. 9.7 mm and laterally 0.6 mm vs. 1.4 mm for the medial and lateral condyles respectively. The predominant posterior displacement suggests femoral rolling. With increased flexion to 60°, the contact points moved anteriorly 1.0 mm vs. 6.4 mm, superiorly 2.4 mm vs. 4.7 mm and continued laterally 2.5 mm vs. 2.4 mm for the medial and lateral condyles respectively. Only the lateral contact point displaced anteriorly, indicative that motion along medial femoral condyle was almost pure sliding. Iwaki et al. (2000) and Hill et al. (2000) suggest the posterior and inferior deflections may result from a combination of factors. When flexing to 30°, the contact point is drawn down along the sloping tibial plateau. Due to the differing radii of the anterior and posterior femoral condyles, the bony contact point is transferred posteriorly because the femur "rocks" from the anterior onto the posterior articular surface

REFERENCES

Iwaki, H., et al. (2000). Tibiofemoral movement 1: The shapes and relative movements of the femur and tibia in the unloaded cadaver knee. *J Bone Joint Surg Br* **82**, 1189-95.

Hill, P.F., et al. (2000). Tibiofemoral movement 2: The loaded and unloaded living knee studied by MRI. *J Bone Joint Surg Br*, **82,** 1196-98.

FINITE ELEMENT (FE) ANALYSIS ON THE PERFORMANCE RANGE OF TOTAL KNEE REPLACEMENT (TKR) – A PRELIMINARY STUDY

Kheng Hooi Tan, Andrew New and Mark Taylor

Bioengineering Sciences Research Group, School of Engineering Sciences, University of Southampton, Southampton, United Kingdom. Email: rtan@ses.soton.ac.uk

INTRODUCTION

Replaced knees are likely to undergo a wide range of loading and kinematics in different patients as shown in several video-fluoroscopy studies (Stiehl et al., 1999; Banks et al., 1993). However, at present, TKR performance especially in terms of kinematics and wear of the polyethylene component, are only evaluated under a limited range of kinematic conditions, as a standard gait cycle (Walker et al., 1997, Walker et al., 2000). Thereforce, there is a need to exam the TKR over a wide range of patient to assess the 'performance envelop' of replaced knees. Such kinematics studies can then be used to study the effects on polyethylene stresses and wear as a result of variable loading conditions. The aim of this study was to predict the performance range of TKR in terms of kinematics and surface contact pressure as a result of a range of applied forces.

METHOD

A previously developed three-dimensional explicit FE model (Godest et al., 2002) of a PFC Sigma total knee was used. The femoral component was modeled as rigid body using four noded shell elements. The polyethylene was modeled using hexahedral elements with an elastic-plastic material model. The femoral component was allowed to translate in the proximal-distal direction, to rotate about its transverse (flexion-extension) and frontal (varus-valgus) axes. The tibial component was allowed to translate in the anterior-posterior, medial-lateral directions and to rotate about its longitudinal axis. An inferiorly directed axial force tending to compress the insert (F_c) was applied at the center of gravity of the femoral component and an anterior-posterior force (F_{ap}) applied to the tibial component. Torque was applied to the joint via two nodes that were tied externally at the medial and lateral side of the tibial component. Medial and lateral springs were used to represent the soft-tissue structures of the knee. The standard loading states were defined according to the experimental protocal used in the Stanmore knee simulator (Walker et al., 1997). The affects of loading parameters were simulated by multiplying the standard loading states by factors of 1.3 and 0.7 to serve as upper and lower bounds respectively. These values were chosen as they give forces appropriate of the range likely patient masses. There were 3 variables (A-P force, I-E torque and axial force), each with an upper and a lower bound; hence there was a total of eight analyses.

RESULTS AND DISCUSSIONS

The performance range of the knee model is shown in Figure 1. The results were compared with the control model. The plots for A-P displacement are not shown because they showed a consistent pattern for all the gait analyses as reported by Godest et al. The maximum A-P displacement output was when the model was subjected to high A-P force, low axial force and low torque. The minimum A-P displacement output was when the model was subjected to low A-P force and high axial force. High axial force thus appeared to give more stability to the model. The difference between the maximum and minimum peak A-P displacement was 2 mm. For the I-E rotation, the model subjected to high torque, high A-P force and low axial force exhibited the highest rotational angle changes. While low torque, low A-P force and low axial force cause the lowest rotational angle. The difference between the highest and the lowest rotational angle was approximately 4.4 degree. The highest contact pressure occurred in the model subjected to low axial force. The reason for this was that the relative component motions were higher as a result of the high A-P force, causing a smaller contact area. The lowest contact pressures were generated in the model subjected to low torque, A-P force and axial load.

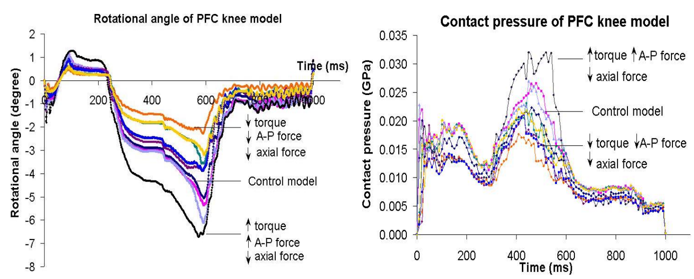

Figure1: Performance range of PFC knee model. High bound (↑), low bound (↓).

CONCLUSION

Variations of approximately 2 mm in A-P displacement and 4 degrees in I-E rotation were observed. A performance envelop was obtained for each of the kinematic funtions. In general, the trends in the A-P displacements and I-E rotations are similar, regardless of variations in the applied loads whereby only the magnitudes changed. This study highlights the importance of examining the performance envelop. However, systematic variations in the applied loading conditions are not sufficient to explain the wide variations in kinematics observed *in vivo*.

REFERENCES

Banks, S. C., Hodge, W. A. (1993). *Proceedings of ORS*, 428.
Godest, A.C. et al (2002). *J. Biomechanics*, **35**, 267 - 275.
Stiehl, J. B. et al (1999). *Cli. Orth. Rel. Res.*, **364**, 139 – 148.
Walker, P. S. et al (1997). *J. Biomechanics*, **30**, 83 – 89.
Walker, P. S. et al (2000). *Cli. Orth. Rel. Res.*, **372**, 290 – 301.

ACKNOWLEDGEMENTS

The author would like to acknowledge DePuy International, Leeds, U.K., for their financial support.

VARIABILITY OF THE LOWER EXTREMITY SEGMENTAL COUPLINGS INDICATES THAT ELDERLY GAIT IS LESS STABLE DURING STANCE

Max J. Kurz, Nicholas Stergiou and Cory M. Millhollin
HPER Biomechanics Laboratory, University of Nebraska at Omaha
Email: mkurz@mail.unomaha.edu Web: www.unocoe.unomaha.edu/hper.htm

INTRODUCTION

Previous investigations have suggested that the elderly have an unstable gait pattern (Winter et al., 1990). However, the definition of stability in elderly gait is not well understood. The variability of segmental couplings can be used to determine the stability of a movement pattern (Diedrich and Warren, 1995). A low amount of variability in the segmental couplings indicates a stable movement pattern; while high amount of variability in the segment couplings indicates an unstable movement pattern (Diedrich and Warren, 1995). Evaluation of the variability present in the lower extremity segmental couplings can provide scientific evidence of the stability present in the elderly gait pattern. Therefore, the purpose of this investigation was to evaluate the variability present in the lower extremity segmental couplings for the elderly gait. We hypothesized that the elderly would have greater variability in the lower extremity segmental couplings during the stance phase due to an unstable gait pattern.

METHODS

Ten young (Age = 25.1 $\pm$ 5.3 yrs.), and ten elderly women (Age = 74.6 $\pm$ 2.55 yrs.) participated in this investigation. Sagittal kinematics (60 Hz) were collected while walking at a self-selected pace on a treadmill. Dynamical Systems Theory (DST) tools were used to evaluate the variability present in the lower extremity segmental couplings. Phase portraits were constructed from the angular positions and velocities of the lower extremity segments. Relative phase (RP) curves were utilized to define the lower extremity segmental couplings during the stance phase. RP curves were calculated by subtracting the phase angles of the distal and proximal segments for the following relationships: foot-shank, and shank-thigh. Mean ensemble RP curves were calculated for all RP segmental relationships. Mean variability in the RP relationships was calculated by averaging the absolute values of the standard deviations for all points of the mean ensemble RP curve. Statistical differences between the two groups (Elderly vs. Young) were noted with independent t-test ($p < .05$).

Table 1. Mean (SD) RP variability for both groups. All values are in degrees.

	Foot-Shank	Shank-Thigh
Elderly	6.6 (1.8)*	9.9 (2.4)*
Young	4.8 (.9)	6.3 (1.4)

* significantly different between groups at .01 alpha level

RESULTS AND DISCUSSION

Our hypothesis that the elderly would have greater variability in the lower extremity segmental couplings during stance was supported by this investigation (Table 1). The elderly had greater variability in both lower extremity segmental relationships. An increase in variability of the couplings is associated with decreased stability (Diedrich and Warren, 1995). Based on this investigation, it was evident that elderly gait is less stable during the stance phase (Figure 1). Differences in variability of the segmental couplings were most pronounced during the early and late portions of the stance phase (Figure 1). A decreased amount of stability during these portions of the stance phase may be due to the loose-packed position of the joints where there is greater dependence on the surrounding joint musculature.

SUMMARY

The elderly lower extremity displays a more variable segmental coupling pattern. The increased variability indicated that the elderly have a less stable gait pattern during the stance phase. Examination of the interactive behavior of the segments offers new insights on the stability of elderly gait patterns that may not be evident otherwise.

REFERENCES

Diedrich and Warren (1995). *J. Experimental Psychology,* **21(1)**:183-202.
Winter et al. (1990). *Physical Therapy,* **70(6)**:340-347.

A.
B.

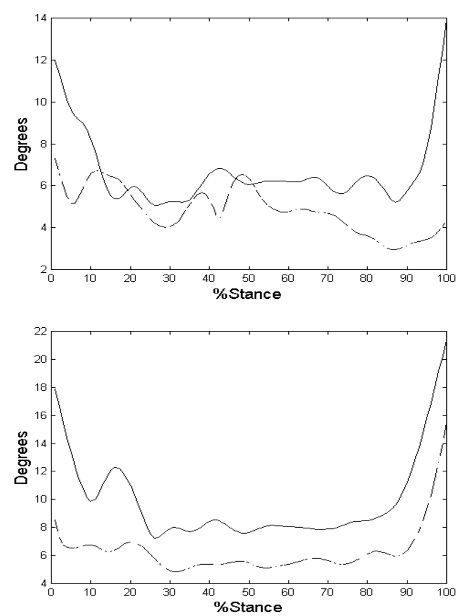

Figure 1. Mean ensemble RP variability curves during the stance phase where A is the foot-shank and B is the shank-thigh. The young is the dashed line, and the elderly is the bold line.

NUMERICAL MODELING OF PULSATILE TURBULENT FLOWS IN STENOTIC VESSELS

Sonu S. Varghese[1], Steven H. Frankel[1], Karen Haberstroh[2], Mike W. Plesniak[1], Thomas J. Webster[2], Steve T. Wereley[1], and Lisa X. Xu[1, 2]

[1]School of Mechanical Engineering and [2]Department of Biomedical Engineering
Purdue University West Lafayette, Indiana, 47907, USA
frankel@ecn.purdue.edu

INTRODUCTION

Blood flow under pathological conditions, such as atherosclerosis, involves narrowing of the artery lumen, referred to as a stenosis, which together with flow pulsatility can result in periodic generation of turbulence despite relatively low Reynolds numbers for such flows (typical Reynolds number range is 1 to 4000 depending upon the size of the vessel (Ku 1997, Berger et al., 2000)). This turbulent flow can affect flow resistance and mixing rates, and can ultimately impact platelet coagulation rates. Vessel compliance can also affect flow stability and turbulence generation. Due to difficulties in making *in vivo* measurements of local velocity profiles and shear stress under pulsatile flow, computational fluid dynamics (CFD) has begun to play a major role in improving our understanding of biofluid flows in general and blood flow in arteries in particular. Recent CFD work has focused on pulsatile stenotic flows accounting for fluid-structure interaction, non-Newtonian effects, and irregular geometry. However, the effects of transitional or turbulent flow have not been addressed to a similar degree.

METHODS

Pulsatile turbulent flow in stenotic vessels has been numerically modeled using the Reynolds-Averaged-Navier-Stokes equation approach. The commercially available CFD code, FLUENT, has been used for these studies. Four different laboratory experiments and geometries were modeled. The first two involved pulsatile turbulent flow in a round tube and a plane channel, while the second two involved pulsatile flow through two different axisymmetric stenoses. Two different two-equation turbulence models (standard and RNG) were employed to study their influence on the results.

RESULTS AND DISCUSSION

It was found that the tube and channel flow results were in reasonable agreement with previously measured experimental data and previous numerical simulations regardless of the turbulence model used. For the stenotic flows, the experiment by Ohja et al. (1981) and by Ahmed and Giddens (1984) were modeled. The results showed that the RNG turbulence model was in much better agreement with the data than the standard two-equation turbulence model with regard to predicting the centerline velocity distribution (see Fig. 1), the vortex shedding process, and the spatial distribution of the turbulent kinetic energy distal to the stenosis. For the stenotic flows, wall shear stress peaked in the region of the stenosis and minimum values were observed in regions distal to the stenosis where flow separation occurred.

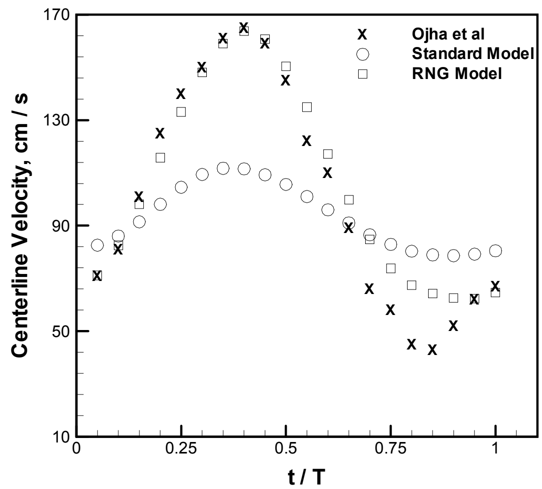

Figure 1. Centerline velocity vs. time for Ohja et al. showing better agreement using RNG model.

REFERENCES

Ahmed, S. A., Giddens, D. P., (1984), *J. Biomechanics*, **17**, 695-705.
Berger, S. A., Jou. L-D, (2000), *Ann. Rev. Fluid Mech.*, **32**, 347-382.
Ku, D., (1997) *Ann. Rev. Fluid Mech.*, **29**, 399-434.
Ohja, et al., (1981), *J. Fluid Mech.*, **13**, 173-197.

ACKNOWLEDGEMENTS

We are grateful to the B.F.S. Schaeffer Award and the Showalter Trust Award for funding for this work.

INDIVIDUALS WITH ACL RECONSTRUCTION DISPLAY ALTERED COORDINATION STRATEGIES WHILE WALKING AND RUNNING

Max J. Kurz, Nicholas Stergiou, and Melissa M. Scott
HPER Biomechanics Laboratory, University of Nebraska at Omaha
Email: mkurz@mail.unomaha.edu Web: www.unocoe.unomaha.edu/hper.htm

INTRODUCTION

Although it has been suggested that segmental coordination is necessary for a stable gait pattern (Hamill et al., 1999; Stergiou et al., 2001), few studies have attempted to determine if ACL reconstruction affects lower extremity coordination during the stance phase. Potentially, evaluation of the lower extremity coordination during the stance phase may provide information about the health and dynamic stability of the reconstructed leg. The purpose of this investigation was to evaluate the segmental coordination of ACL reconstructed individuals while walking and running. We hypothesized that individuals with ACL reconstruction would have different segmental coordination strategies during the stance phase while walking and running.

METHODS

Ten fully rehabilitated subjects (3.4 yrs on average after the surgeries were performed) who had undergone ACL reconstruction using an autogenous patellar tendon graft, and ten healthy controls participated in this investigation. Sagittal kinematics (60 Hz) were collected while the subjects walked and ran on a treadmill. The stance phase was evaluated for fifteen consecutive footfalls for each subject. Phase portraits were constructed from the angular positions and velocities of the lower extremity segments. Relative Phase (RP) curves were utilized to define coordinative strategies during the stance phase. RP curves were calculated by subtracting the phase angles of the distal from proximal segment for the following relationships: foot-shank and shank-thigh. Mean ensemble RP curves were calculated for both segmental relationships. From the mean ensemble curves the Mean Absolute Relative Phasing (MARP) was evaluated. MARP were calculated by averaging the absolute values for all points of the mean ensemble RP curve. Statistical differences between the two groups (ACL reconstructed vs. control) were noted with an independent t-test ($p < 0.05$).

RESULTS AND DISCUSSION

Our hypothesis that individuals with ACL reconstruction would have different coordination strategies during the stance phase while walking and running was supported. During walking, differences between the groups were noted for both the foot-shank and the shank-thigh (Figure 1). During running, differences between the groups were noted only between the foot-shank (Figure 1). No differences were found for the shank-thigh relationship during running. This lack of difference may be due to the increased inertial contributions of the segments during running. An alternative explanation is that coordinative changes in the other joints, such as the ankle and possibly the hip, helped to maintain stability at the knee.

SUMMARY

Individuals with an ACL reconstruction display different coordination strategies during the stance phase while walking and running. These control strategies may be related to the surgical reconstruction of the joint. Analysis of the coordination patterns during the gait cycle offers a noninvasive way to assess ACL surgical interventions.

REFERENCES

Hamill et al. (1999). *Clinical Biomechanics*, **14**:297-308.
Stergiou et al. (2001). *Clinical Biomechanics,* **16**:213-221.

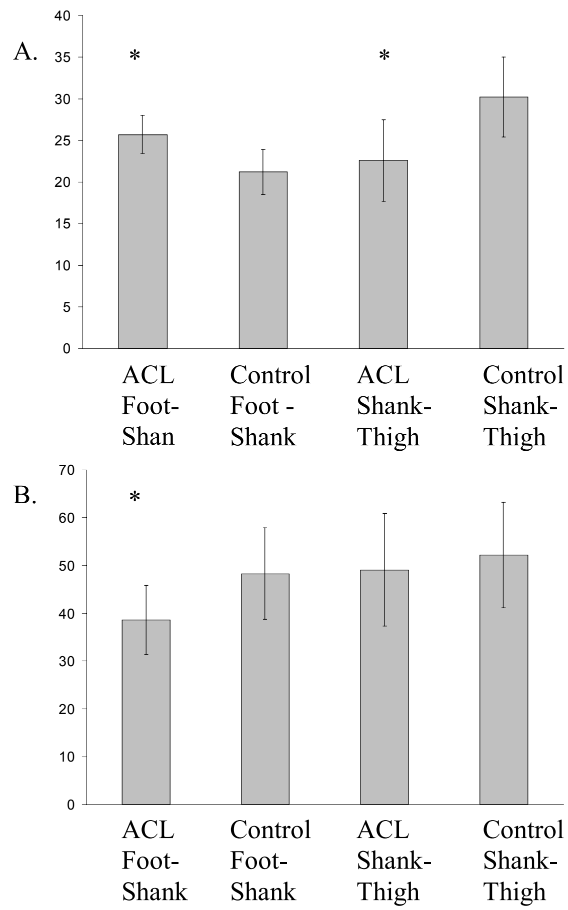

Figure 1. Mean RP and standard deviation values for the respective segmental relationships investigated where A is walking and B is running. Values are presented in degrees. (*significantly different from control group at $p<0.05$)

INDIVIDUALS WITH ACL RECONSTRUCTION DISPLAY ALTERED LONG-RANGE FRACTAL GAIT PATTERNS

Max J. Kurz and Nicholas Stergiou
HPER Biomechanics Laboratory, University of Nebraska at Omaha
Email: mkurz@mail.unomaha.edu Web: www.unocoe.unomaha.edu/hper.htm

INTRODUCTION

Previous investigations have indicated that gait patterns are fractal (Hausdorff et al., 1995). A fractal gait pattern suggests that subtle variations in the gait pattern are not "noise". Instead, these variations are due to long-range power-law correlations from preceding footfalls (Hausdorff et al., 1995). Breakdown of the fractal-scaling pattern has been found to be dependent on the health and dynamic stability of the neuromuscular system (Hausdorff et al., 1995). Currently, there are several clinical measures of static knee stability (i.e., KT 1000), but there are no such measures for dynamic stability of the ACL reconstructed joint. We speculated that a lower fractal-scaling value would be related to a decreased dynamic stability and health of the reconstructed joint. To test our hypothesis, we evaluated the effects of ACL reconstruction on fractal-scaling for walking and running gait patterns.

METHODS

Ten fully rehabilitated subjects (3.4 yrs on average after the surgeries were performed) who had undergone ACL reconstruction using an autogenous patellar tendon graft, and ten healthy controls participated in this investigation. Sagittal kinematics (60 Hz) were collected while the subjects walked and ran on a treadmill for 40 seconds. The unfiltered time series for the ankle and knee joint angles were used to classify the fractal nature of the gait pattern. Log-log power spectral density (PSD) plots were constructed from the kinematics. The slopes of the plots can characterize the presence of long-range fractal correlations in the gait patterns (Hausdorff et al., 1995). A slope of zero indicates random noise in the time series. Slopes greater than zero indicate more self-similar or fractal gait pattern. Statistical differences between the two groups were examined with an independent t-test ($p< .05$).

RESULTS AND DISCUSSION

Although there were no significant ($p>.05$) differences between the two groups for both conditions, the ACL reconstructed subjects had lower slope values for both knee and the ankle joints while walking and running (Table 1). A lower slope value suggested a more variable gait pattern that is less dependent on previous fluctuations in the gait pattern (Figure 1). Previously, it has been suggested that lower slope values are due to neuromuscular deficiencies and, a lower slope value can be an indicator of decreased stability of the gait pattern (Hausdorff et al., 1995). It is possible that these trends seen in the reconstructed ACL subjects may be due to such neuromuscular deficiencies and a lack of stability in the reconstructed joint (Buzzi et al., 2001).

Table 1. Mean (SD) slopes of the log-log PSD plots.

	Walk		Run	
	Ankle	Knee	Ankle	Knee
ACL	.65 (.1)	1.8 (.4)	.72 (.2)	1.5 (.4)
Control	.72 (.2)	2.0 (.4)	.83 (.3)	1.6 (.6)

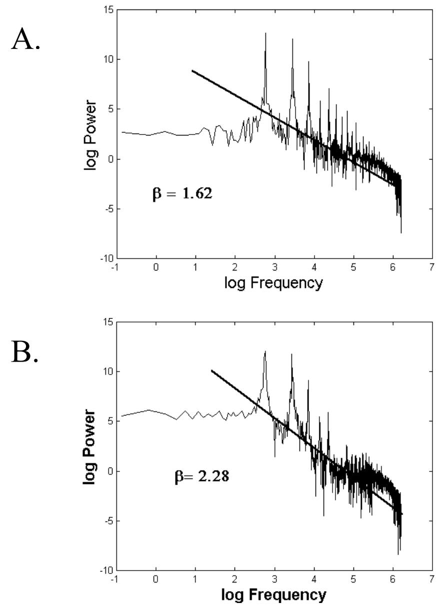

Figure 1. Exemplar knee joint log-log PSD plots during walking where A is an ACL reconstructed knee and B is a control knee.

SUMMARY

Individuals with ACL reconstruction display a more random fractal-scaling gait pattern. A more random pattern suggests that the joint has less neuromuscular control and stability. Analysis of the fractal properties of gait patterns offers a noninvasive way to assess the dynamic stability and health of the joint.

REFERENCES

Hausdorff et al.(1995). *J. Applied Physiology*, **78**:349-358.
Buzzi et al. (2001). *Proceedings of ASB '2001*, San Diego, p. 295.

BIOMECHANICAL EFFICACY OF A PROTEIN POLYMER HYDROGEL FOR INTER-VERTEBRAL NUCLEUS AUGUMENTATION AND REPLACEMENT

Andrew Mahar[1], Richard Oka[1], Jon Whitledge[2], Joseph R. Cappello[2], Jim Powell[2], Tina McArthur[2], Joseph Cappello[2]

[1] Department of Orthopedics, Children's Hospital, San Diego, CA
[2] Protein Polymer Technologies, Inc., San Diego, CA

INTRODUCTION

Degenerative intervertebral discs are a common clinical occurrences in the lumbar spine. This pathology may present with low back pain and/or pain in the lower extremities and the worst cases require surgical treatment. The removal of the nucleus pulposus (nucleotomy) is often performed through a posterior-lateral approach without any replacement of the material. While this surgery may be successful, the optimal situation would be to remove the painful disc and replace the material with something that maintains disc height and provides axial support. Previously, collagen repair devices have been theorized but with little reported biomechanical data. Therefore, new materials based on injectable protein polymer hydrogels (IPPH) have been developed. This study compared axial strain during mechanical loading of human cadaveric vertebral segments with those augmented by two IPPH disc nucleus augmentation materials.

METHODS

Ten adult, human lumbar spines were first radiographed to eliminate pathological specimens. Motion segments were then harvested between T12 through S1. Using the radiographs, measurements of native disc height were calculated. All further displacements during testing were attributed to disc mechanics. The posterior elements were removed leaving an intact PLL and posterior annulus. Individual specimens were tested using force control in a MTS 858 machine ("native"). The testing involved cyclic loading between 35kg and 75kg at 1Hz for 20 cycles. Further testing involved a sequential 30-minute static load at 5kg, a static load of 75kg for 60 minutes and a final 30-minute static load at 5kg (Figure 1).

Figure 1: Displacement due to axial load

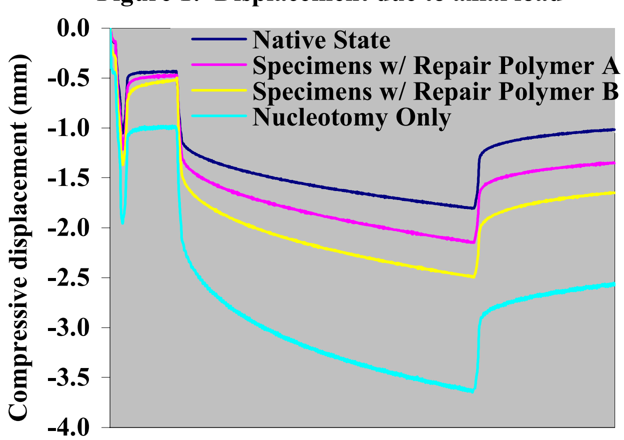

Displacement and force data were sampled at 5Hz for the duration of the test. This paradigm allowed for evaluation of both creep and recovery tests. Following "native" specimen testing, the nucleus was removed via an anterior annulotomy and replaced with a randomly selected IPPH (polymer A or B) using a custom injection device. Identical testing was then repeated. A single control specimen was tested post-nucleotomy without augmentation. Maximal strain was calculated at the end of the creep test and statistical significance was tested with a one-way ANOVA ($p<0.05$).

RESULTS AND DISCUSSION

An average of 4.2cc of disc nucleus material was removed from each specimen. The IPPH materials did not extrude during any part of the tests. The strains experienced in the repair groups were greater than the strains for the native state. However, these differences were not statistically significant (Table 1). There were also no significant differences between the two types of protein hydrogels.

Table 1: Strain data for native and repaired discs.	Native Strain	Injected Strain
Repair Polymer A		
Mean (n=5)	**0.136**	**0.188**
Standard Deviation	0.023	0.045
Repair Polymer B		
Mean (n=5)	**0.148**	**0.219**
Standard Deviation	0.046	0.064
Overall Mean(n = 10)	**0.141**	**0.204**
S.D.	0.033	0.055
Nucleotomy Only	0.122	0.346

CONCLUSION

Composition B displayed slightly greater maximum deflection than did composition A, and both were slightly greater than native discs. The mean final recovery for both repair groups was within 0.75 mm of native. The mean spontaneous recovered height was within 1.2mm. These preliminary data indicate that IPPH hydrogels may demonstrate adequate mechanical properties as disc augmentation devices.

ACKNOWLEDGEMENTS

Financial support was provided by SpineWave Incorporated.

MARKOV MODEL SUGGESTS NEUROMUSCULAR AGING AFFECTS SHORT-RANGE CORRELATIONS PRESENT IN THE GAIT CYCLE

Max J. Kurz, Nicholas Stergiou and Kristin McCorrmick
HPER Biomechanics Laboratory, University of Nebraska at Omaha
Email: mkurz@mail.unomaha.edu Web: www.unocoe.unomaha.edu/hper.htm

INTRODUCTION

Step-to-step variability during gait appears to be correlated with the preceding footfalls (Hausdorff et al., 1995). It has also been suggested that this variability is related with the health of the neuromuscular system (Hausdorff et al., 1995). To further understand the effect of aging on the step-to-step variability, we utilized a Markov Model. The Markov Model suggests that the fluctuations in the behavior of the joints are dependent on short-range correlations in the gait cycle (Lay, 2000). Therefore, the behavior of the joints for the next footfall is dependent on the behavior exhibited in the preceding footfalls. The Markov Model suggests that fluctuations in the movement behavior of the joints exponentially decay to a steady state gait pattern (Lay, 2000). In this investigation, we speculated that the Markov Model would identify that neuromuscular aging affects the short-range correlations present in the gait cycle. Modifications in the short-range correlations would in turn result in a different steady state gait pattern.

METHODS

Markov models were developed from the gait patterns of ten young (Age = 25.1 $\pm$ 5.3 yrs.) and ten elderly women (Age = 74.6 $\pm$ 2.55 yrs.). Sagittal kinematics (60 Hz) were collected while walking on a treadmill. Joint angles were calculated for the ankle, knee and hip. Forward selection regression equations were used to predict the behavior of the lower extremity joints. Such that the ankle joint was regressed on the knee and hip, the knee joint was regressed on the ankle and hip, and the hip joint was regressed on the ankle and knee. The change in the coefficient of determination, as predictors were added to the model, and the remaining unexplained variance ($1-R^2$) of the regression equation were used to develop probability vectors. The probability vectors described the interactive behavior of the respective lower extremity joints. Short-range correlation matrices (M) presented below, were developed from the probability vectors of each of the respective joints. Each column of the matrix represented a probability vector for the ankle (column 1), knee (column 2) and hip (column 3).

$$M_{Elderly} = \begin{pmatrix} .56 & .82 & .41 \\ .03 & .04 & .10 \\ .41 & .14 & .49 \end{pmatrix} \qquad M_{Young} = \begin{pmatrix} .8 & .05 & .04 \\ .02 & .19 & .76 \\ .18 & .76 & .20 \end{pmatrix}$$

Utilizing the short-range correlation matrices (M), Markov Models were solved for a sequence of footfalls until a steady state gait pattern was achieved:

$$\mathbf{X}_{k+1} = M\,\mathbf{X}_k \qquad \text{for } k = 0, 1, 2, \ldots$$

A steady state was achieved when $\mathbf{X}_k$ converged to a specific value and there were minimal fluctuations from one k to the next.

RESULTS AND DISCUSSION

The results of our investigation suggest that short-range correlations in the gait pattern are affected by age (Table 1). The steady state gait pattern for the elderly suggested that 52% of the gait pattern was dependent on the behavior of the ankle. Thus our model concurs with previous studies that have suggested the elderly have altered gait patterns due to the behavior of the ankle (Judge et al., 1996). Additionally, the steady state gait pattern for the young suggested that the gait pattern was not dependent on the behavior of the ankle (Table 1). Rather the young steady state gait pattern was dependent on the equal contributions of the hip and knee (Table 1). Based on our model, it was apparent that fluctuations in the gait cycle determined the selected steady state gait pattern. Short-range correlations are similar to neuromuscular "memory" of the preceding footfalls. Our model suggests that neuromuscular memory is dependent on age. Changes in neuromuscular memory may be responsible for the altered kinematics in the elderly. The degeneration of the neuromuscular system, that is associated with aging, appears responsible for the loss of neuromuscular memory.

SUMMARY

Short-range correlations are affected by neuromuscular age. Our model suggested that short-range correlations resulted in a steady state gait pattern that was dependent on the behavior of the ankle in the elderly.

REFERENCES

Hausdorff et al.(1995). *J. Applied Physiology*, **78**:349-358.
Judge et al. (1996). *J. Gerontology*, **51A**:303-312.
Lay (2000). *Linear Algebra and it Applications*. Addison-Wesley:New York.

Table 1. Components of the steady state gait pattern for the elderly and young

	Ankle	Knee	Hip
Elderly	.52	.06	.42
Young	.06	.47	.47

SCALE TRANSITION IN BONE ELASTICITY: A CONTINUUM MICROMECHANICS APPROACH

Christian Hellmich[1] and Franz-Josef Ulm[2]

Department of Civil and Environmental Engineering, Massachusetts Institute of Technology, Cambridge, Massachuestts, USA
[1]Postdoctoral Fellow; on leave from: Vienna University of Technology (TU Wien), Vienna, Austria
[2]Associate Professor

INTRODUCTION

The hierarchical organization of bone and its mechanical implications has attracted researchers for hundreds of years. Continuously improved experimental techniques have revealed features of astonishing complexity, rendering the mechanical understanding (even of the elastic behavior) of this material class challenging.

METHODS

In this contribution we approach the problem within the framework of continuum micromechanics, where a material phase is defined not by the pure presence of matter components, but by their mechanical activation through strains. For bone, we propose a two step homogenization procedure: Within a representative volume element of 100 to 200 nm, hydroxyapatite (HA) crystals build up a crystal foam (polycrystal) where the inter-crystalline space is filled with water and organic matter (homogenization step I). Part of the (organic) collagen molecules are linked to the crystal foam (Ca-bridges), reinforcing the polycrystal in the form of cylindrical inclusions at the ultrastructural scale of mineralized tissues, i.e. 5 to 10 microns (homogenization step II). Within the same homogenization step, we account for the microporous space (Haversian channels, inter-trabecular space) by means of cylindrical pore inclusions, which, interestingly, are suitable for both trabecular and cortical bone.

RESULTS AND DISCUSSION

The proposed micromechanical model allows for fairly precise prediction of ultrastructural and macroscopic elasticity properties of all different kinds of bone. The model is based on three (constant) intrinsic stiffness values for HA, collagen, and water, which are tissue-independent. The input of the model are the tissue-specific volume fractions of HA, collagen, and of the micro-porous space, which are accessible via various imaging techniques or chemical experiments. This is illustrated by evaluation of a large data base (more than 1000 stiffness values).

Continuum micromechanics allows for the development of a general macroscopic bone material law without the use of any regression parameters. Notably, the three basic tissue-independent stiffness constants are directly determined from (tissue-independent) experiments. We expect a high clinical relevance of such a material law for bone failure risk assessment by means of structural analyses (e.g. in the framework of Finite Element analyses).

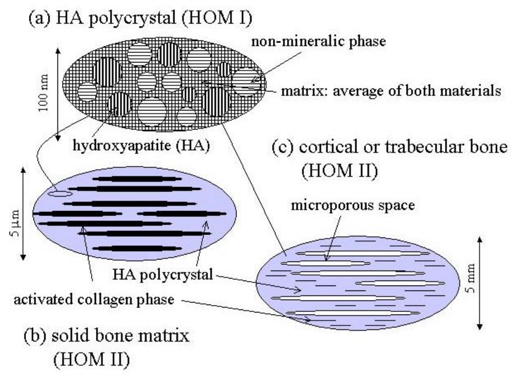

Figure 1: Two step homogenization procedure to perform scale transition from (a) the nanolevel to (b) the ultrastructure (solid bone matrix), or to (c) the microstructure (macroscopic bone material)

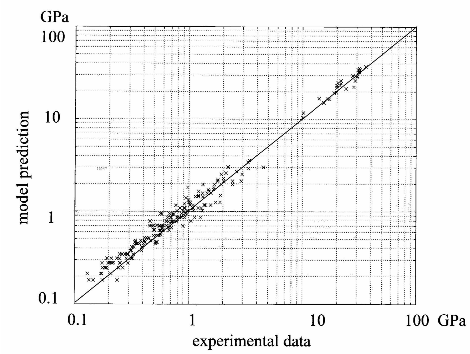

Figure 2: Comparison between experimental stiffness values and micromechanical model answers at levels (b) and (c)

REFERENCES

Lees, S., (2001). *Elastic properties and measurement techniques of hard tissue*, Chapter 7 of Levy, Bass, and Stern (2001), *Handbook of Elastic Properties of Solids, Liquids, and Gases, Vol III,* Academia Press.

Zaoui, A., (1997). *Structural morphology and constitutive behavior of microheterogeneous materials*, pages 291-347 of Suquet, P. (1997), *Continuum Micromechanics,* Springer, Wien – New York.

KINETICS OF CONTINUOUS HOPPING TO VOLUNTARY EXHAUSTION

Darren J. Dutto

Biomechanics Laboratory, California State Polytechnic University, Pomona, Pomona, CA, USA
e-mail: ddutto@csupomona.edu

INTRODUCTION

Stretch-shortening cycle exercise performed to fatigue has been shown to impair the ability to produce force (Golhofer, 1987). Force production during ground contact is governed by the stiffness of the leg system (Blickhan, 1989). The purpose of this study was to show that during fatigue, hoppers have altered stiffness of the leg while maintaining a specific hopping frequency, and leg kinematics would reflect the change in stiffness.

METHODS

Eighteen, physically active college age students participated. Each subject performed a hopping bout to voluntary exhaustion. Hopping was performed to an electronic metronome at a rate of 2 hz on a force platform. Force data were sampled at 1200 Hz for 5 seconds at the beginning and end of the exercise bout. Sagittal plane kinematics of the right leg were recorded with a Motion Analysis Corp. system at a rate of 120 hz.

Actual hopping rate, peak vertical ground reaction force, contact time, and vertical impulse were determined from the force data. Displacement of the center of mass was calculated by double-integration of the acceleration-time data. Stiffness was estimated as the ratio of peak vertical force and center of mass displacement. Ankle and knee angles and angular velocities during the ground contact phase of the hop were determined. Differences in measured variables were assessed with a univariate ANOVA ($\alpha = 0.05$).

RESULTS AND DISCUSSION

Results from twelve subjects were included, as the remaining six subjects had greater than 3% deviation in hopping rate from beginning to end. The remaining 12 subjects maintained a fairly consistent hopping rate for the duration of the test (Table 1), which on average was 7 min.

Table 1: Summary data and statistical results (mean ± s.d.)

	Beginning	End	*p*
Rate (hz)	2.02 ± 0.01	2.03 ± 0.04	0.369
Stiffness (kN/m)	22.1 ± 7.5	17.7 ± 6.0	0.101
CM Disp. (m)	0.13 ± 0.01	0.14 ± 0.01	0.104
Peak Force (BW)	4.1 ± 0.5	3.4 ± 0.4	0.002
Contact Time (s)	0.25 ± 0.03	0.30 ± 0.03	0.002
Impulse (bw/s)	0.25 ± 0.03	0.19 ± 0.04	0.001

Subjects had a decrease in peak impact force and increased foot contact time with fatigue. The vertical impulse decreased by 20% (Table 1) despite increased foot contact time, resulting in decreased hopping height. The average displacement of the center of mass during foot contact remained constant.

Force-displacement curves show that subjects tended to decrease stiffness of the leg system during ground contact. An example of the force-displacement curves for one subject is shown in Figure 1. A non-significant decrease in stiffness with fatigue was observed (Table 1). Differences in ground reaction force and contact time were associated with reduced stiffness.

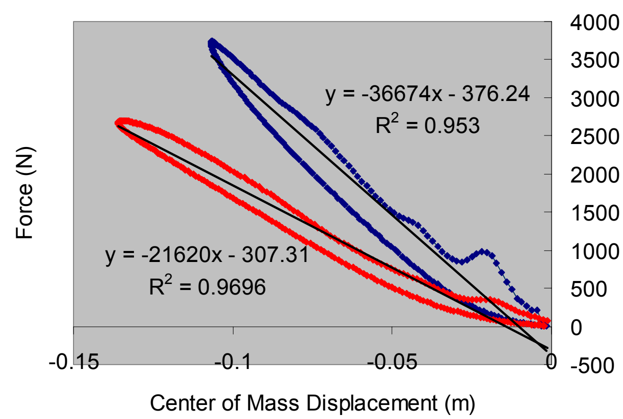

Figure 1: Force-displacement curves for one subject. The blue (higher) curve was obtained from the beginning and the red (lower) curve at the end of the test bout. Each curve represents an ensemble average of 10 hops.

Ankle range of motion was observed to decrease by 6º (*p*=0.01) on average and knee range of motion to increase slightly, indicating that perhaps the knee and ankle are changing roles in producing vertical propulsion.

SUMMARY

Fatigued hoppers are able to maintain a set hopping rate despite a reduction in the stiffness of the leg. It appears that stiffness is adjusted to maintain rate, resulting in decreased impulse, peak force, and increased contact time when fatigued.

REFERENCES

Blickhan, R. (1989). *J. Biomech.* **22**, 1217-1227.
Golhofer, A., et al. (1987). *Int. J. Sports Med.* **8**,71-81.

ACKNOWLEDGMENTS

Thanks to Carlo Reyes and Chris Jablonski for assistance with data collection and reduction.

EFFECTIVE FORCE AND INDEX OF EFFECTIVENESS DURING CYCLING

Cláudia Tarragô Candotti [1,2]; Denise Paschoal Soares [1]; Carlos Dreyer Neto [1]; Jefferson Fagundes Loss [1] and Antônio Carlos Stringhini Guimarães [1]

[1] Exercise Research Laboratory, Federal University of Rio Grande do Sul, RS, Brazil, shujeffe@ufrgs.br
[2] Health Science Center, University of Vale do Rio dos Sinos, RS, Brazil

INTRODUCTION

Cycling and triathlon are growing as competitive sports in Brazil. More athletes are getting involved in these activities and that has demanded a more scientific approach from coaches. The understanding of the complex bicycle-cyclist has, for quite some time, attracted the interest of scientists. The application of force on the pedal is an attractive subject of study given the implications that it has on the effectiveness of the effort that is exerted by the athletes. The aim of this study was to implement a methodology proposed by Lafortune et al. (1983) and used by Ericson et al. (1988) to calculate the effective force exerted on the pedal (EF) and an index of effectiveness (IE). The system will be used for scientific purposes as well as a source of feedback for coaches and athletes.

METHODS

Subjects: One cyclist, one triathlete (both professionals) and one non-athlete.
Instrumentation: Two systems were used: (1) a home-made 2D strain-gauge instrumented pedal to determine the normal and tangential forces and (2) a 2D video system (Peak Performance) to measure the pedal and crank-angles.
Protocol: The subjects performed two bouts of 3 minutes each, using two different gear ratios (53x13; 53x17), at their preferred cadence. The subjects used their own bicycles which were mounted on a stand-roll.
Data Analysis: The MATLAB software was used to calculate mean values of the resultant force (RF), EF and IE (ratio between the EF and RF) for ten revolutions of each trial, using force information from the instrumented pedal and geometry data from the video (Figure 1).

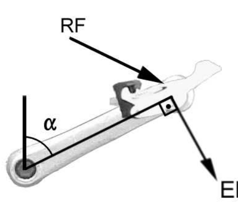

Figure 1: Crank angle (α), Resultant Force (RF) and Effective Force (EF).

RESULTS AND DISCUSSION

Figure 2 shows the mean of the 10 cycles for the IE, expressed as a function of the crank angle (0 degrees = crank vertical and upward). Pronounced differences between subjects are noticed in all quadrants for gear ratio 53x12 (Figure 2a) and in the first, third and fourth quadrants for gear ratio 53x17 (Figure 2b). Negative results indicate that subject is imposing himself extra load to the opposite lower limb.

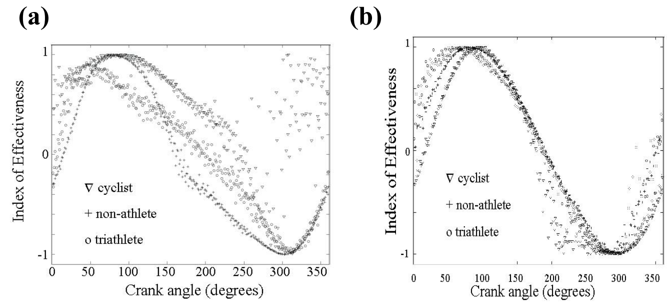

Figure 2: IE during cycling: (a) 53x12 and (b) 53x17.

Table 1 shows the mean IE calculated for ten revolutions. The cyclist achieved the best mean IE for the 53x12 gear ratio followed by the triathlete and non-athlete. Interestingly, however, the non-athlete obtained the second best IE for the gear ratio 53x17. These results can be used to monitor the cycling technique of these subjects as well as to discuss technical aspects of pedaling with coaches and athletes.

Table 1: IE mean in each gear ratio for full 360 degrees angular displacement.

Subjects	**53x12**	**53x17**
Triathlete	0,04	-0,03
Cyclist	0,49	0,23
Non-athlete	-0,14	0,09

SUMMARY

A methodology based on pedal force measurements and geometry of the pedal and crank was implemented to calculate the effective force applied on the pedal and an index of effectiveness during pedaling. The goal was to provide scientific support to cycling athletes and coaches.

REFERENCES

Ericson, MO & Nisell,R. Efficiency of pedal forces during ergometer cycling. *Int. J. Sports Med*., 9: 118-122, 1988.
Lafortune, MA & Cavanagh, PR. Effectiveness and efficiency during bicycle riding, in Matsui, H., K. Kobayashi (eds): *Biomechanics VIII-B*. Champaign, IL, Human Kinetics Publishers: 928-936, 1983.

ACKNOWLEDGEMENTS

CNPq, PIBIC/UFRGS e SNE/MET, Brazil.

MEASUREMENT OF EMBRYONIC HEART MATERIAL PROPERTIES DURING CARDIAC LOOPING

Evan A Zamir and Larry A Taber*

Department of Biomedical Engineering
Washington University, St. Louis, MO
*lat@biomed.wustl.edu

INTRODUCTION

Cardiac looping is a fundamental developmental process that is the first morphogenetic sign of lateral (left-right) asymmetry in the vertebrate embryo. The biophysical mechanism that drives the early linear heart tube to bend and rotate dextrally (rightward) into a c-shaped loop is still unknown, although several genetic and epigenetic factors have been implicated (Harvey, 1998). There have been some theoretical mechanical models of looping (Taber et al., 1995). What has been lacking in models of looping are appropriate material properties for the tissue. Our lab has developed a poking device, which not only gives force-displacement data, but also allows us to analyze the shape of indentation and input that information into a finite element (FE) model to determine material properties. A simulated annealing (SA) algorithm is used to optimize the agreement between the experimental and model results.

EXPERIMENTAL PROCEDURES

The heart poker is a piezoelectric driven cantilever beam assembly with a flexible glass beam attached to a rigid support. When the tip of the beam contacts the heart the beam deflects while the tissue underneath deforms. The force of indentation is proportional to the amount of beam deflection. We measure the displacement of the tip by monitoring a small ink spot that is placed on the tip. The entire experiment is captured on video, which allows us to gather additional information about the two-dimensional shape or contour of the edge of the heart during poking. Preliminary stiffness measurements of the HH stage 12 heart reveal that the inner curvature (IC) is stiffer than the outer curvature (OC). The mean stiffness of the OC was 0.149mdyn/μ, compared to 0.373mdyn/μ for the IC.

MODEL AND OPTIMIZATION

To determine the constitutive law or material properties for the heart an appropriate model and optimization method is needed. There are several experimental and computational limitations that influence our choices, but many of these may be overcome in the future. To begin with we are gathering visual information about the indentation from one perspective, so we assume the tissue is isotropic in the model. Ideally, we would poke the heart in one direction, and then rotate the heart and poke in an orthogonal orientation. Because the optimization may take hundreds, if not thousands, of iterations, it is ideal to have as simple a model as possible. In our case we created an axisymmetric FE model with contact boundary conditions in ABAQUS (see **Fig. 1**). This model takes on the order of seconds to run, as opposed to a full 3D model, which would take tens of minutes. At least, for the isotropic case, we have verified that the results from our axisymmetric model are nearly the same as those for a full 3D curved tube model. We are using a SA algorithm (Corana et al., 1987) with a least-squares cost function to minimize simultaneously the force and displacement data during indentation. There are two main advantages in using this method, besides the simplicity of the algorithm. The first advantage is that we can search a very large parameter or state space with many possible minima. We have no *a priori* way of knowing what an initial guess for the model parameters should be, so that a traditional non-linear least-squares approach, such as Levenberg-Marquardt, may easily get stuck in local minima that are not the global optimum. The second advantage is that the SA algorithm, in general, does not require the calculation of derivatives, which usually involves finite-differencing in models that do not have analytical solutions, such as ours.

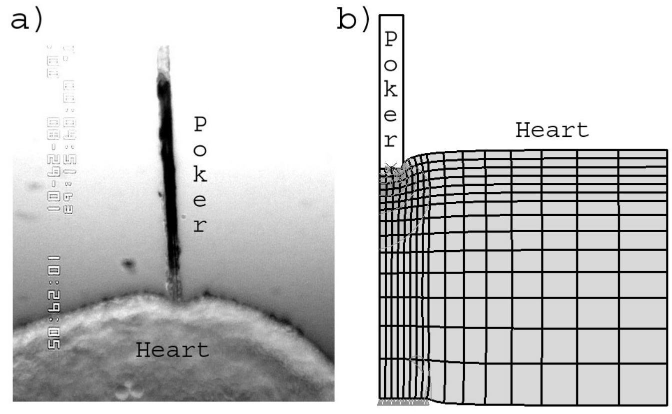

indentation.

REFERENCES

Taber, L.A. et al (1995). *Dev Dyn*, **203**, 42-50.
Corana, A. et al (1987). *ACM Trans on Math Soft*, **13**, 262-280.
Harvey, R.P. (1998). *Semin Cell Dev Biol*, **9**, 101-108

REFLEX RESPONSES GRADED TO BOTH PERTURBATION ACCELERATION AND VELOCITY

Gunter P. Siegmund[1,2], David J. Sanderson[1], J. Timothy Inglis[1]

[1]School of Human Kinetics, University of British Columbia, Vancouver, BC, Canada
[2]MacInnis Engineering Associates, Richmond, BC, Canada, gunters@maceng.com

INTRODUCTION

Reflex responses to postural perturbations have been shown to vary with platform acceleration, velocity and displacement (Diener et al., 1988; Maki and Ostrovski, 1993). The relative influence of these platform kinematic descriptors on the reflex response has not, however, been evaluated. In the current study, the gradation in reflex response of the neck muscles and kinematic response of the head and torso were studied in seated subjects using different combinations of platform acceleration and velocity. It was hypothesized that the timing and amplitude of both the reflex neck muscle response and the induced head and torso kinematics would vary with both stimulus properties.

METHODS

Following IRB approval, thirty subjects (15F, 15M) underwent 47 forward horizontal perturbations while seated in a car seat mounted on a linear motor. Seven different perturbations were constructed from one of three peak accelerations (low L_a=7.8, medium M_a=14.7, high H_a=21.7 m/s²) to reach one of three constant velocities (L_v=0.25, M_v=0.50, H_v=0.75 m/s). The L_aH_v and H_aL_v combinations were not used. Each subject first underwent 11 M_aM_v perturbations to achieve a stabilized response and was then exposed to a randomized series of 36 perturbations: 12 M_aM_v perturbations, and 4 of each of the remaining 6 perturbations. Onset and root-mean squared (RMS) amplitude of the sternocleidomastoid (SCM) and cervical paraspinal muscles were measured using surface electromyography (EMG). Torso and head acceleration onset were determined from accelerometers, whereas peak mastoid acceleration, neck retraction (horizontal displacement of the mastoid relative to the manubrium) and head extension angle were computed from data acquired with an Optotrak system. One-way repeated-measures analyses of variance, Scheffé post-hoc tests and a significance level of 0.05 were used to assess response differences between the seven perturbations. Linear regressions were then used to quantify the relative influence of platform acceleration and velocity on responses.

RESULTS AND DISCUSSION

The onset and amplitude of the neck muscle responses and the head and torso kinematic responses varied between the different perturbations. Muscle activation occurred earlier at higher platform accelerations and lower velocities (Table 1a) and followed a pattern similar to the duration of the platform acceleration (Table 1b). In contrast, onset of torso and head accelerations occurred earlier at higher platform accelerations, but did not vary with platform velocity (Table 1c,d). SCM EMG amplitude and peak kinematic amplitudes increased with both higher platform acceleration and velocity (Table 1e-h), although the relative influence of platform acceleration and velocity was not the same for all response variables. For instance, early kinematic peaks (e.g., vertical mastoid acceleration; Table 1f) correlated more strongly with platform acceleration (r^2=0.80) than velocity (r^2=0.47), whereas late kinematic peaks (e.g., peak retraction; Table 1g) correlated more strongly with platform velocity (r^2=0.95) than acceleration (r^2=0.42).

a) SCM onset (ms)

Acceleration	L_v	M_v	H_v
H_a		68 (6)	71 (6)
M_a	68 (4)	71 (5)	74 (6)
L_a	72 (4)	74 (6)	

b) Acceleration duration (ms)

Acceleration	L_v	M_v	H_v
H_a		43	60
M_a	33	60	85
L_a	60	110	

c) Torso acceleration onset (ms)

Acceleration	L_v	M_v	H_v
H_a		17.6 (2.2)	17.7 (1.9)
M_a	19.7 (2.2)	19.5 (1.8)	19.7 (2.0)
L_a	21.5 (2.3)	21.9 (1.9)	

d) Head acceleration onset (ms)

Acceleration	L_v	M_v	H_v
H_a		26.2 (4)	26.8 (4.3)
M_a	29.5 (4.0)	29.3 (4.3)	29.8 (4.4)
L_a	32.2 (4.9)	32.2 (4.4)	

e) SCM EMG amplitude

Acceleration	L_v	M_v	H_v
H_a		1.03 (0.19)	1.40 (0.46)
M_a	0.54 (0.23)	1	1.13 (0.34)
L_a	0.48 (0.20)	0.57 (0.22)	

f) Vertical mastoid acceleration

Acceleration	L_v	M_v	H_v
H_a		1.39 (0.26)	1.63 (0.26)
M_a	0.68 (0.13)	1	1.12 (0.25)
L_a	0.43 (0.07)	0.54 (0.14)	

g) Retraction

Acceleration	L_v	M_v	H_v
H_a		1.03 (0.03)	1.44 (0.08)
M_a	0.55 (0.06)	1	1.42 (0.08)
L_a	0.52 (0.06)	0.95 (0.10)	

h) Head extension angle

Acceleration	L_v	M_v	H_v
H_a		1.08 (0.07)	1.64 (0.14)
M_a	0.54 (0.07)	1	1.60 (0.16)
L_a	0.51 (0.07)	0.96 (0.15)	

Velocity

Table 1: Mean (SD) of selected variables as a function of platform acceleration (L_a, M_a, H_a) and velocity (L_v, M_v, H_v). Increasing line weights correspond to homogeneous groups of significantly earlier times or greater amplitudes. Amplitude variables normalized to the M_aM_v perturbation.

SUMMARY

Our hypothesis that the timing and amplitude of the muscle and kinematic responses would vary with both platform acceleration and velocity was accepted. Moreover, the combined influence of platform acceleration and velocity on the amplitude of the SCM muscle response indicated sensory encoding of both stimulus properties, and underscored the importance of controlling the detailed platform kinematics when studying responses to postural perturbations.

REFERENCES

Diener, H.C. et al. (1988). *J. Neurophysiol.*, **59**, 1888-1905.
Maki, B.E., Ostrovski, G. (1993). *Gait & Posture*, **1**, 93-104.

ACKNOWLEDGEMENTS

Physical Medicine Research Foundation, Natural Sciences and Engineering Research Council of Canada, Science Council of British Columbia.

A COMPARISON OF JOINT MECHANICS BETWEEN ANTERIOR CRUCIATE LIGAMENT INTACT AND DEFICIENT STIFLES: A NEW CANINE MODEL OF ANTERIOR CRUCIATE LIGAMENT DISRUPTION

Mandi J. Lopez[1,3], David Kunz[2], Ray Vanderby, Jr.[2], Dennis Heisey[2], John Bogdanske[1], and Mark D. Markel[1]

[1]Comparative Orthopaedic Research Laboratory and the [2]Department of Biomedical Engineering
University of Wisconsin-Madison, Madison, WI. [3]lopezm@svm.vetmed.wisc.edu

INTRODUCTION

The canine model of osteoarthritis (OA) following anterior cruciate ligament (ACL) transection is one of the best characterized and most commonly used.(Marshall, 1996) It has been suggested that joint capsular thickening in ACL deficient canine knees may stabilize the joint over time.(Hulse, 1983) We have developed a model by which the canine ACL is intentionally overtreated with monopolar radiofrequency energy (MRFE) using an arthroscopic approach. The ACL then undergoes progressive deterioration until complete disruption at a predictable time point after treatment. We also undertook this project to evaluate the contribution of joint capsule (JC) after progressive canine ACL deterioration and rupture.

METHODS

Ten skeletally mature female crossbreed dogs, weighing 24 - 37 kg each were used in this study. MRFE (70°C, 25W) was applied to the ACL of one randomly selected knee arthroscopically with a 2 mm diameter electrode (TAC-C probe, Oratec Interventions, Inc.) and an Oratec MRFE generator (Electrothermal System ORA-50^{tm}). The contralateral knee was sham operated. Treated ACL's ruptured approximately 54 days after surgery (Mean 54 days, SEM 1.2). The animals were sacrificed 16 weeks (n=5) or 26 weeks (n=5) after rupture of the MRFE treated ACL, and the hind limbs were stored at –70°C until biomechanical testing. Anterior-posterior (AP) translation was evaluated with load cycles of +/- 40N. Following AP translation tests, medial-lateral (ML) rotation tests were performed with 2 test cycles of 4 Nm. AP laxity and ML rotation were evaluated at 30°, 60°, and 90° of flexion. All testing was first done with intact JC and then with JC removed.

A factorial model with all interactions was used to compare time, capsule status, ligament status, and angle. Because all treatments except time were within-animal treatments, a split plot model for incomplete data was used. Significance was set at $P < 0.05$.

RESULTS AND DISCUSSION

AP translation: A preliminary ANOVA showed a significant interaction to include JC by ACL (P = .02) and a trend for ACL by time (P = .07) (Fig. 1).

ML rotation: Significant interactions included the presence of JC (P =.0001), and angle by ACL (P = .0012) (Fig. 2).

Overtreatment of the canine ACL with MRFE using an arthroscopic approach is a highly predictable and reproducible model of OA that avoids variables introduced by surgery to transect the ACL. This study showed a significant stabilizing influence of JC against AP translation in ACL deficient knees, though this effect did not change significantly in the time period between sample collections. The ACL was also a significant stabilizing influence against ML rotation.

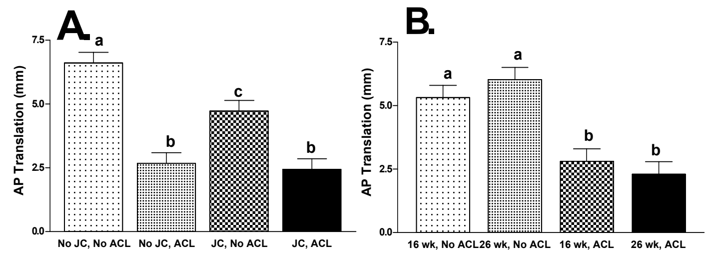

Fig. 1 AP translation (mean ± SEM) of canine knees with and without ACL or JC (A); and with and without ACL's 16 and 26 weeks post-rupture (B). Columns with different letters are significantly different from one another (P < .05).

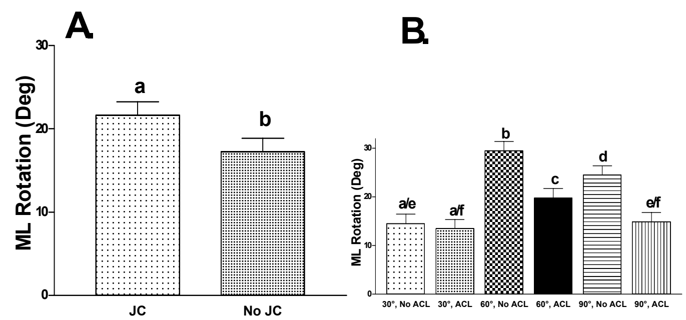

Fig. 2 ML rotation (mean ± SEM) of canine knees with and without JC (A) and at different flexion angles with and without ACL's (B). Columns with different letters are significantly different from one another (P < .05).

SUMMARY

This study describes a model in which ACL's predictably rupture approximately 8 weeks after arthroscopic surgery. This model avoids significant surgical variables. Based on the results of this study, the JC is a significant stabilizing influence in the canine ACL deficient knee. Further, the best angle to test motion in ACL deficient canine knees appears to be 60° of flexion.

REFERENCES

Marshall K. et al (1996) J. Rheumatol. 23, 338-342.
Hulse D.A. et al (1983) Vet. Surg. 12,109-112.

EFFECTS OF DIFFERENT PADDING ON THE IMPACT LOADING OF THE HAND DURING FALLING

Il-Kyu Hwang, Keith Leung, and Kyu-Jung Kim, Ph.D.

Department of Mechanical Engineering, University of Wisconsin-Milwaukee, Milwaukee, WI, USA, kimk2@uwm.edu

INTRODUCTION

Efficacy of wrist guards in preventing forearm injuries has been a subject of debate (Giacobetti 1997). It has been reported (Kim 2001) that the current wrist guards have less effectiveness in reducing the peak impact force with a high frequency mode. Accordingly, other padding materials should be sought for effective absorption of the impact energy during falling. Several materials such as rubber, Sorbothane, etc., have been commonly used in biomechanics/ ergonomics fields for vibration isolation and injury prevention. The purpose of this study was to measure the impact loading of the hand with various padding materials under simulated impact conditions and to analyze their biomechanical effects.

METHODS

A total of fifteen young male and female adults participated in this experiment. The subject with eyes closed was asked to put the forearm at 30˚ from the horizontal and to maintain the initial tension of 50 N into the load control cable (Fig. 1). Then the cable was released at random and the hand hit a commercial force plate (Type 4060, Bertec, Columbus, OH) covered with a 1-in thick wooden plate. The subject repeated each of the trials three times with different padding conditions such as a bare hand (BH), a Sorbothane glove (SO), a commercial wrist guard (WR), and an air-pocket on the palm (AP). A miniature accelerometer (EGA-F, Entran Devices, Fairfield, NJ) was attached on the dorsum of the hand. The impact force and acceleration of the hand were collected at a sampling rate of 10 kHz. From the impact force profile, the maximum impact force (F_{max}), its occurrence time (T_{max}) after touchdown, and loading rate ($G_{zi} = F_{max} / T_{max}$) were estimated. A logarithmic decrement technique was used to obtain the damped natural frequency (ω_d) and damping ratio (ζ). The impact velocity (v_i) at touchdown was estimated by integrating the acceleration profile. Paired t-tests were used for statistical comparison (p=0.05).

RESULTS AND DISCUSSION

The impact parameters under each padding condition were summarized in Table 1. The estimated impact velocities and effective masses for each condition were approximately the same, demonstrating the consistency of the impact trials under the given initial cable tension and arm angle. The impact response from the AP was significantly different from the other padding conditions, while the rest of them made no significant difference with each other. Compared with the BH condition, the AP condition had similar damping ratio but much lower damped natural frequency (61 Hz vs. 95 Hz). This indicated that the AP introduced a 60% decrease in effective stiffness and 40% decrease in effective damping constant. The impact force profile for the AP condition became flatter with a smaller peak impact force and longer peak time, resulting significantly slower loading rate. This is a highly desirable feature for impact attenuation and subsequent pain on the hand.

SUMMARY

Upon impact testing of the hand with various padding materials the air pocket (AP) demonstrated highly desirable characteristics as a padding material for impact absorption during falling.

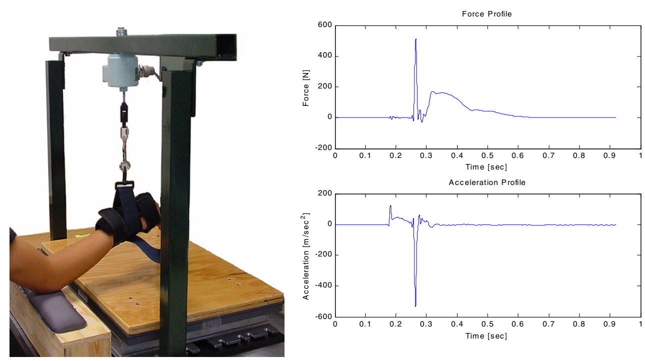

Figure 1. Isolated force measurement system for the impact testing of the forearm (left) and corresponding measured impact force and acceleration of the hand (right).

Table 1. Impact parameters under various padding conditions. (S.D. in parentheses)

	F_{max} (BW)	T_{max} (msec)	G_{zi} (BW/sec)	v_i (m/sec)	ω_d (rad/sec)	ζ
Bare Hand (BH)	0.69 (0.16)	12 (4)	67.9 (32.6)	2.0 (0.5)	594.3 (166.2)	0.20 (0.05)
Sorbothane (SO)	0.75 (0.16)	11 (3)	74.0 (25.2)	2.1 (0.4)	542.0 (75.9)	0.25 (0.06)
Wrist Guard (WG)	0.72 (0.14)	11 (2)	70.5 (18.4)	2.1 (0.4)	493.0 (106.8)	0.24 (0.04)
Air Pocket (AP)	0.48 (0.08)	19 (10)	29.1 (5.8)	2.0 (0.3)	379.9 (182.0)	0.19 (0.09)

REFERENCES

Chiu, J., Robinovitch, S. N. (1998). *J. Biomech*, **31,**1169-1176
Giacobetti, F.B. et al (1997). *Am. J. Sports Med* **25**, 223-225.
Kim, K. J., et al. (2001). *ASME BED*-Vol. **50**, 271-272

EFFECTS OF THE RELATIVE FOREARM VELOCITY ON THE IMPACT FORCE OF THE HAND DURING FALLING

Jong-Hoon Nam, Il-Kyu Hwang, and Kyu-Jung Kim, Ph.D.

Department of Mechanical Engineering, University of Wisconsin-Milwaukee, Milwaukee, WI, USA, kimk2@uwm.edu

INTRODUCTION

Falling during various sports activities often results in serious forearm injury. The impact force on the hand is a major cause of such injuries. It has been reported that the impact force has characteristic bimodal shape, having distinct high and low frequency modes. To characterize the nature of the two modes of impact, a few biomechanical models were used to predict the impact response of the forearm (Kim 1997, Chiu 1998). However, little is known on the effect of the faller's activity before landing on the impact force of the hand, especially the upper extremity movement.

METHODS

Our previous experimental data from simulated cable-released falls (Kim 2001) were used for comparison. The impact force profiles were decomposed into the high and low frequency (or passive impact and active braking) force components using spectral techniques. The body was modeled as a linear 2-DOF mass-spring-damper system with two Voigt models in series. The resultant damping matrix was decomposed into proportional damping. The two effective masses m_1 (trunk, head, and legs) and m_2 (arm complex) were assigned to be proportional to the mass moments of inertia of the body and the arm complex. The sum of the two weight forces was set equal to the magnitude of the measured steady state force. The mass moments of inertia were obtained from the anthropometric data. A logarithmic decrement technique for the passive impact force component was used to estimate the damping (ζ_2) and damped natural frequency (ω_2) of the arm complex. The active braking force component was used to estimate the damped natural frequency of the body (ω_1). The damping ratio of the body, ζ_1 was varied between 0.5 and 0.7 to have a best least square fit to the impact force profile. The impact velocity of the whole body was estimated using the law of energy conservation. The ratio of the initial velocities between the arm complex and the body (VR $= v_{arm}/v_{body}$) was varied to find the effect of the arm movement on the impact force transmitted to the hand. The weight and height of the subject were 60.7 kg and 1.72 m, respectively.

RESULTS AND DISCUSSION

The damped natural frequencies for the two impact modes were found to be ω_1=8 *rad/s*, ω_2=100 *rad/s* and the damping ratio of the arm complex was ζ_2=0.22. To avoid the highly non-linear beginning portion of the impact force, a time delay was introduced (40 *msec*). The simulation results with various ζ_1 and VR were summarized in Table 1. Best fitting was obtained with ζ_1 =0.6 and VR=1.2 (Fig 1). The VR substantially affected the peak impact and peak braking forces. An increased VR from 1.0 to 1.5 would significantly increase the peak impact force from 382 *N* to 560 *N*, while the peak braking force would be also increased from 420 *N* to 460 *N*. In other words, harder landing would increase both the peak impact and peak braking forces simultaneously. This was also confirmed in our earlier experimental data (Kim 1997) that under time critical situations a subject tended to have harder landing with faster upper extremity movement before landing, resulting in higher peak impact and braking forces after touchdown.

SUMMARY

This simulation study confirmed that the faller's activity before touchdown would affect the subsequent impact absorption of the body.

Table 1 Results of various simulations. F_{max1} and F_{max2} are the peak impact and peak braking forces after touchdown, respectively.

ζ_1	0.5	0.6			0.7
v_{arm} / v_{body}	1.2	1.0	1.2	1.5	1.2
$F_{max\,1}(N)$	439	382	445	560	453
$F_{max\,2}(N)$	455	420	437	460	428

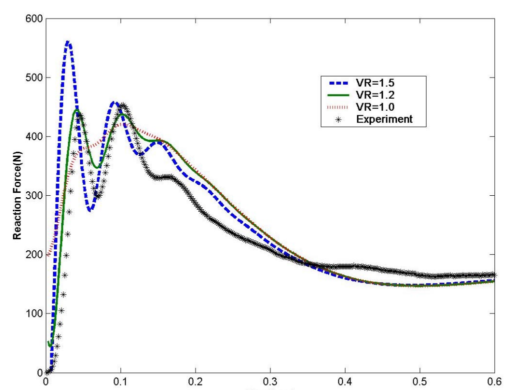

Figure 1 Effect of VR on the impact force of the hand.

REFERENCES

Kim, K. J. et el (1997). *ASME BED* **37**, 328-329
Kim, K. J. et el (2001). *ASME BED* **50**, 271-272
Chiu, J., Robinovitch, S. N. (1998). *J. Biomech*, **31,**1169-1176
Hsiao, E. T., Robinovitch, S. N. (1998). *J. Biomech*, **31,**1-9

FLOW IN THE STENOTIC CAROTID BIFURCATION

Stanley A. Berger and Vitaliy L. Rayz
Department of Mechanical Engineering, University of California, Berkeley, CA 94720, saberger@me.berkeley.edu

INTRODUCTION

We have concentrated our studies on the blood flow in the carotid artery bifurcation, a site especially prone to the development of atherosclerotic plaques. Plaque development is strongly influenced by rapid changes of shear stress at the artery wall. Under certain conditions the plaque may rupture, leading possibly to stroke. Fully three-dimensional, unsteady numerical simulations have been carried out for realistic geometries.

METHODS

A three-dimensional model of a severely stenotic carotid bifurcation has been created using MR images of an atherosclerotic plaque. An unstructured grid was then generated on the domain to be used for the numerical solution of the incompressible Navier-Stokes equations. To obtain an optimum grid three models with different grid densities were created and analyzed. Newtonian behavior has been assumed in most of our studies, but we do also consider the possible effects of non-Newtonian behavior. The walls of the artery are assumed to be rigid. The CFD Research Corporation finite-volume package CFD-ACE(U) was used for discretization and solution of the equations. The equations are numerically integrated over each of the computational cells, the resulting integrated equations then solved by an iterative, implicit pressure correction algorithm (SIMPLEC). The boundary conditions are zero velocity at the walls, uniform velocity at the inlet, and fixed pressure at both outlets. For steady flow simulations the initial values for velocity and pressure were set equal to zero. A steady-state solution was used as the initial condition for the unsteady simulations. Steady and transient simulations were made to assess non-Newtonian effects in the flow.

RESULTS AND DISCUSSION

Numerical solutions of the governing equations have been obtained for each of the grid density models for steady Newtonian flow at different Reynolds numbers. The quality of the grids was evaluated by comparing the velocity fields obtained for each grid. A model with 60,781 tetra cells was found to be adequate for the current analysis, and subsequent simulations were done for this grid only. This grid as well as a cross-section plane showing the stream-wise velocity distribution are shown in Figure 1. A large recirculation region can be observed in the carotid sinus upstream of the stenosis. A high velocity jet develops in the narrowest stenotic part of the internal carotid artery. Another large recirculation zone is formed downstream of the stenosis. The unsteady flow simulations show a rapidly growing high-speed jet formed at the stenosis in the systolic part of the pulse. A large recirculation zone can be observed downstream of the plaque. During diastole the jet diminishes and the flow is more stagnant. In the non-Newtonian flow simulations the jet is less pronounced but the recirculation area downstream of the plaque is increased.

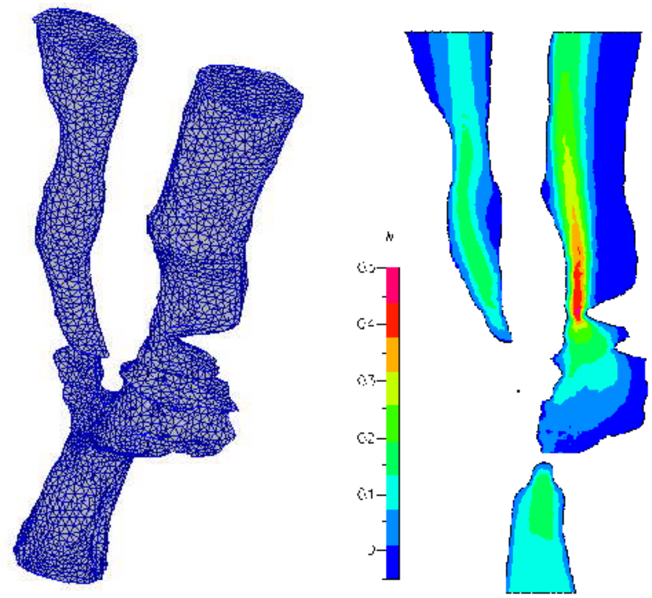

Figure 1. Unstructured 3D grid and stream-wise velocity distribution for steady flow at Reynolds number of 200.

SUMMARY

A three-dimensional model of the carotid artery bifurcation has been created and steady and unsteady Navier-Stokes equations were solved numerically. The results show qualitative agreement with the previous work done for a two-dimensional model as well as with the flow visualization results obtained by co-investigators.

REFERENCES

Berger, S.A. and Jou, L-D. (2000). *Annual Review of Fluid Mechanics*, **32**, 347-382.

Stroud J.S. et al (2002). "Numerical analysis of flow through a severely stenotic carotid artery bifurcation," *Journal of Biomechanical Engineering* (ASME), (in press, to appear in Feb. 2002).

Stroud, J.S. (2000). *Numerical Simulation of Blood Flow in the Stenotic Artery Bifurcation.* Ph.D. Thesis, University of California, Berkeley.

ACKNOWLEDGEMENTS

The authors wish to acknowledge the support of NIH Grant HL 61823.

BIOMECHANICS OF PRONE CONTINUOUS PASSIVE MOTION FOR LOW BACK PAIN

John J. Triano, DC, PhD[1,2,3], Carolyn M. Rogers, MS[1], Darran Marlow, DC[1], and Dennis Skogsbergh, DC[1]

1. Texas Back Institute, Plano, TX, 6300 W. Parker Rd, Plano, TX 75093; jtriano@texasback.com
2. Joint Biomedical Engineering Program, University of Texas at Arlington & Southwestern Medical Center, Dallas, TX.
3. Texas Chiropractic College, Pasadena, TX.

INTRODUCTION

This project was designed to quantify the biomechanics of continuous passive motion (CPM) applied in a prone recumbent posture during treatment for patients with lower back pain. CPM has been available for management of postoperative joint rehabilitation for decades. Only in the past few years has it been applied to low back complaints. Reinecke et al (1994) demonstrated comfort preference with a cycling lumbar support cushion, changing the seated lumbar lordosis. Van Deursen and colleagues (2000) have introduced axial rotation using small alternating motions (0.08 Hz) of a motorized seat pan. Patients reported reduction of back pain. If effective in reducing pain for seated sufferers, CPM may be useful directly in therapy to reduce symptoms and encourage cartilage repair in patients with disc or facet disease. A first step to investigate clinical utility is the determination of mechanism of action and is the intent of this study.

METHODS

The study was conducted in two parts: first, to measure spinal kinematics during CPM and second, to measure the loads transmitted through the spine during CPM. Five volunteer subjects (age 37 ± 9.3 years) completed informed consent and participated in the study. A motorized treatment table (Leader Health Technologies, Inc. Port Orchard, WA) able to provide CPM to the lower body was modified to incorporate an AMTI force plate capable of measuring reaction loads for 6 degrees of freedom (DOF). Subjects laid in prone recumbence on the table with the lumbopelvic junction positioned above the pivot axis of the table to maximize the flexion motion at that level. CPM was induced (10 deg) at the midrange velocity (0.24 Hz) for table settings that were capable of ranging from 0.05 Hz to 0.5 Hz. Load transformation equations were used in conjunction with distance estimates (± 1 cm) from the force plate center to the L5/S1 disc to quantify the loads transmitted through the lumbopelvic junction. Load estimates were expressed as a proportion of body mass index and body weight for pooling of data across subjects. Fidelity of the table-force plate system in reporting accurate reaction loads was independently confirmed (Rogers 2001). Intersegmental motions of the lumbar spine were obtained separately by interposing the table in the imaging window of a fluoroscopic C-arm. Subjects were repositioned in prone recumbence and flexion of the torso was invoked to end-range table motion. An inclinometer recorded the maximum table motion and digitized fluoroscopic images were used to estimate the maximum intersegmental displacements at the L3/4, L4/5 and L5/S1 disc levels.

RESULTS

Inclinometer measure of maximum table motion was 35 degrees for all subjects. Vertebral angular displacement averaged 16.7 (± 2.6) degrees for maximum table motion of 35 degrees. The ratio of table to available vertebral motion is approximately 0.48. Loads transmitted through the lumbopelvic junction at 10 degrees of flexion angle showed smooth, sinusoidal form with primary components consisting of axial compression / traction (up to 9.4 ± 0.09 % BW), anteroposterior shear (up to 1.16 ± 0.004 % BW) and flexion moments (up to 0.76 ± 0.005 % BMI).

DISCUSSION

Vertebral motions induced during prone, recumbent CPM can be controlled as a function of the table motion settings in flexion. The loads that are induced by movement of the lower body against a fixed upper body are small compared to body weight and body mass index. Van Deursen et al observed loads and motions far smaller that were effective in reducing severity of suffering. Clinical testing of prone CPM, as a means to manage painful episodes and enhance tissue repair during rehabilitation of low back pain patients, seems warranted.

SUMMARY

Prone CPM invokes intervertebral displacements and loads that are proportional to body mass and of sufficient amplitude to be hypothesize that they may be clinically meaningful.

REFERENCES

Reinecke S.M., et al (1994). *J Spinal Disord,* **7,** 29-35.
Rogers C.M. (2001). *Response Characteristics and Fidelity Analysis of a Spinal Manipulation Treatment Table with an Imbedded Force Plate.* UT Southwestern Medical Center at Dallas and UT at Arlington.
Deursen D.L, et al. (2000). *J of Biomech,* **33,** 695-700.

DEVELOPING SKILLED PERFORMANCE OF SPINAL MANIPULATION/ADJUSTMENT

John J. Triano, DC, PhD[1,2,3] , Carolyn M. Rogers, MS[1], Sarah Combs, DC, MS[3],
David Potts, DC[3], Kenneth Sorrels, DC[3], Marion McGregor, DC, MSc[3]

1. Texas Back Institute, Plano, TX, 6300 W. Parker Rd, Plano, TX 75093; jtriano@texasback.com
2. Joint Biomedical Engineering Program, University of Texas at Arlington & Southwestern Medical Center, Dallas, TX.
[3]Texas Chiropractic College, Pasadena, TX.

INTRODUCTION

Spinal manipulation / adjustment is inherently mechanical, applying loads to the spine and inducing motions (Triano 2001, Triano and Schultz 1997). An important factor for selecting a doctor is their qualifications (Abbott 1988). A profession's authority relies on the demonstration of skill and effectiveness (Kaiser Family Foundation 2000). Common wisdom holds that successful care is influenced by the skill of the treating doctor; in this case, mechanical skill.

Cohen et al (1995) demonstrated that physicians trained but unpracticed in procedures were no different than novice manipulators in performance. Curtis et al (2000) trained primary care physicians in manipulative methods over 18 hours across three sessions. They state, "By design, the physicians were not experts...." If skilled performance is related to outcome, can methods of training be harnessed to improve it, optimize results and minimize complications? As yet, there is no objective means to assess skill, therefore, the contribution of skill to outcome remains undefined. This project tested the strategy of rehearsal and quantitative feedback as a means of enhancing mechanical skill development using a standard reference performance criterion (Triano et al 2002).

METHODS

An instrumented treatment table (Leader 900 Z with AMTI) recorded manipulation loads acting on an imbedded force plate. Inverse dynamics estimated the loads transmitted at the L5 disc (Triano 2001, Triano and Schultz 1997, Cohen et al 1995). Performance of HVLA by two groups of students was compared over one-trimester. All students were trained in select procedures in the standard curriculum (SC). Students were randomly assigned to one of two groups. In the first group, 19 subjects followed the (SC) training. The second group consisted of 20 subjects who used the hand held Dynadjust instrument (DI), providing automated feedback, adding a daily rehearsal (home practice using 10 repetitions each). Student performance of test procedures was measured at the beginning (T1), middle (T2) and end of the trimester. Difference scores were calculated between test intervals T1, T2, and T3 and tested statistically by Student's-t and Fisher's exact tests. Primary outcomes included changes in preload, peak amplitude, slope and direction of load application.

RESULTS AND DISCUSSION

Lumbar - Peak amplitudes demonstrated significant differences by group. Preload improved 10.5% for SC and 52.5% for DI group ($p=0.0009$). The SC amplitude increased for transverse force ($p = 0.0439$). The DI group significantly changed for sagittal force ($p = 0.0229$) and lateral bending moment ($p = 0.0182$). The rate of loading decreased 79.3 N/Sec (±435.6 N/Sec) for the SC while the DI showed a 742 N/Sec (±345.2) increase ($p = 0.0000$). The flexion rate decreased (50.2±120.4 Nm/Sec) in the SC but over three times as much (173.2 ±32.4 Nm/Sec) for the DI ($p=0.0074$). Lateral bending slowed 135.4 Nm/Sec (±286.9 Nm/Sec) in the SC but increased (210.2 ±29.11 Nm/Sec) in the DI ($p=0.0000$).

Cervical and Thoracic - Similar results were observed in the cervical and thoracic procedures. Amplitudes were significantly different based on training ($0.00458 < p < 0.0773$). Rates and durations likewise differed ($0.0024 < p < 0.0745$).

A skilled task requires the ability to produce specific action on demand (Higgins 1991). Advanced skill can moderate actions to accommodate complex problem solving. Home rehearsal with automated feedback creates larger differences in performance than standard curriculum training, more rapidly increasing the level of skill.

SUMMARY

Independent quantitative measures were used to assess results of training in the performance of mechanical procedures. Students using the Dynadjust instrument demonstrated significantly greater change in performance of select HVLA procedures for cervical, thoracic and lumbar regions. Future work is likely to result in optimizing training and permit even greater improvement.

REFERENCES

Abbott A. (1988). *The System of Professions an Essay on the Division of Expert Labor.* The University of Chicago Press
Cohen E et al. (1995). *J Manipulative Physiol Ther,* **18**, 347-52.
Curtis P et al. (2000). *Spine,* **22**, 2954-9.
Higgins, S. (1991). *Physical Therapy,* **71**, 121-139.
Kaiser Family Foundation/Agency for Healthcare Research and Quality National Survey on Americans as Health Care Consumers: An Update on the Role of Quality Information, Dec. 2000 (conducted 7/31-10/13, 2000)
Triano J.J., Schultz A.B. (1997). *Spine,* **22,** 1955-64.
Triano J.J. (2001). *The Spine,* **1,** 121-30.
Triano J.J. et al. (2002). Defining a Reference Standard for Performance Characteristics in Spinal Manipulation, *JMPT* (In submission)

OBTAINING PREDICTABLE LUMBOPELVIC LOADS DURING SPINAL MANIPULATION

John J. Triano, DC, PhD[1,2] and Carolyn M. Rogers, MS[1,2]

1. Texas Back Institute, Plano, TX, 6300 W. Parker Rd, Plano, TX 75093; jtriano@texasback.com
2. Joint Biomedical Engineering Program, University of Texas at Arlington & Southwestern Medical Center, Dallas, TX.

INTRODUCTION

Spinal manipulation has become more widely used for the management of spine-related pain over the past two decades. With the aging of America, more elder patients with degenerative disease, osteoporosis and prior spinal surgery (Triano et al 1997) are receiving treatment than ever before. Little epidemiological data is available with respect to potential risks of these procedures as a function of patient co-morbidity. However, common clinical practice provides for modifications to manipulative procedures to accommodate structural changes associated with disease and surgery. This project was devised to systematically explore modifications to manipulation procedures in order to understand how to systematically control loads acting on the spine. Earlier work (Triano and Schultz 1997, Triano 1998, Triano 2000) suggests that patient postures and experienced manipulator effort can alter the loads that the spine undergoes. Quantitative knowledge of these parameters may be helpful in preventing complications from this treatment in patients that are older or have complex spinal conditions.

METHODS

This study was conducted in three parts. First, loads acting on the lumbopelvic region during typical high velocity, low amplitude (HVLA) procedures were measured using a specially instrumented treatment table described previously (Triano and Schultz 1997, Triano 1998). A standard treatment table (Leader Health Technologies, Inc. Port Orchard, WA) was modified to incorporate an AMTI force plate capable of measuring reaction loads for 6 DOF. Load transformation equations were used in conjunction with distance estimates (± 1 cm) from the force plate center to the L5/S1 disc to quantify the loads transmitted through the lumbopelvic junction. Fidelity of the table-force plate system in reporting accurate reaction loads was independently confirmed. The typical procedure used for this study was defined by averaging the measured loads from 22 procedures performed on 11 volunteer subjects by 6 physicians with experience ranging from 1.5 to 24 years. Using a load-transformation computer modeling technique, the effects of systematic variation in patient posture were estimated. Second, relative intersegmental postures associated with lumbopelvic flexion and lateral bending were quantitatively defined. Five subject volunteers (age 37 ± 9.3 years) completed informed consent and participated in the study. Intersegmental motions of the lumbar spine were obtained separately by positioning the lumbopelvic region according to feasible treatment extremes in flexion, extension and lateral bending while in a fluoroscopic C-arm. Displacements at the L3/4, L4/5 and L5/S1 disc levels were determined from digitized fluoroscopic images. Systematic intersegmental displacements from the measures were introduced to the computer model in the third step of the study, using small angle increments until the total range of displacements was achieved. Results were associated with specific postural variations.

RESULTS AND DISCUSSION

The matrix of 3 dimensional rotations derived from fluoroscopic measures included flexion ($0 < \alpha < 9.2$), axial rotation ($0 < \beta < 55$) and lateral bending ($-10.2 < \delta < 17.2$) defined in terms of reference to the initial anatomical position. Postural variation resulted in sequential transition in the amplitudes of force and moment components acting on the lumbopelvic spine that range from 25% to 261%. In the case of shear force acting across the spine from left to right (frontal plane), the direction of loading was able to be modified without changing the input manipulation load.

Quantitative knowledge of this type is useful in understanding the applications and limitations of manipulative procedures. Long a procedure based on empirical observation alone, this type of data can now be used in further computer modeling to explore how these procedures might effect patients with complex or post-surgical changes. Such models limit the risk to patients while maximizing information that can help develop realistic and safer treatment protocols.

SUMMARY

Systematic modification of patient posture theoretically may be used to control the amplitude of select components of manipulation loads acting on the spine. Capacity of operators performing these procedures to intentionally achieve specific loads systematically may now be assessed.

REFERENCES

Triano J.J. et al (1997). *J Rehabil Res & Develop,* **34,** 394-403.
Triano J.J., Schultz A.B. (1997). *Spine,* **22,** 1955-64.
Triano J.J. (1998). *Biomechanical analysis of motions and loads during spinal manipulation.* University of Michigan
Triano J.J. (2001). *The Spine*, **1,** 121-30

FLOW AND WALL COMPRESSION IN HIGH GRADE ASYMMETRIC ARTERIAL STENOSIS MODELS DURING PULSATILE FLOW EXPERIMENTS

Shunichi Kobayashi[1], Takeshi Horie[1], Daisuke Tsunoda[1], Hirohisa Morikawa[1], Dalin Tang[2], David N. Ku[3]
[1] Faculty of Textile Science and Technology, Shinshu University, Ueda, Nagano 386-8567, Japan, shukoba@giptc.shinshu-u.ac.jp
[2] Mathematical Sciences Department, Worcester Polytechnic Institute, Worcester, MA 01609, USA
[3] School of Mechanical Engineering, Georgia Institute of Technology, Atlanta, GA 30332-0405, USA

INTRODUCTION

High grade stenoses can limit blood flow and produce conditions in which the artery may collapse. This resultant compression may be important in the development of atherosclerotic plaque fracture and subsequent thrombosis or distal embolization. We used an asymmetric experimental model that closely approximates the arterial disease situation where the entire stenosis is compliant. This study was to examine flow rate, pressure, stenosis severity and eccentricity characteristics inducing collapse under pulsatile flow.

METHOD

The diseased carotid artery was modeled using an elastic hydrogel shaped in the form of a stenosis. Figure 1 illustrates the asymmetric stenosis shape of the hydrogel model. Nominal stenosis severity (percent stenosis) St and eccentricity Ec of the stenosis model are given by,

$$St = (D - Ds)/D \times 100\ [\%], \quad Ec = e/((D-Ds)/2) \times 100\ [\%],$$

where D and Ds are diameter at straight portion and throat of stenosis, respectively. e is the distance between the center of straight portion and the center of the throat.

Pulsatile flow was perfused through the hydrogel stenosis model. The computer controlled gear pump which works as alternative current component, was connected to upstream tube. The upstream pressures was set as 100+/-30mmHg and downstream pressure was changed. Sagittal section image of stenosis was made a video signal by the B-mode of a Duplex ultrasound scanning.

RESULTS AND DISCUSSION

The stenosis model caused a phase difference of flow rate and pressure between upstream and downstream. The phase difference in the stenosis model is accounted by the compliance of the straight portion (tube) of the stenosis model and the resistance of stenosis.

Ultrasound images of sagittal section of stenosis model (70% St, 100% Ec) are shown in Figure 2. For the average downstream pressure (P_{2ave}) of 0mmHg, the full collapse during the whole cycle occurs. Table 1 shows the P_{2ave} when the first outbreak of collapse is occurred. P_{2ave} increases with an increase in eccentricity and a decrease in stenosis severity. This is accounted by the geometrical stiffness against collapse. Thinner part of the post stenosis tends to collapse. The phase of the first outbreak of collpase was generally around the end of systole (higher flow rate at post stenosis).

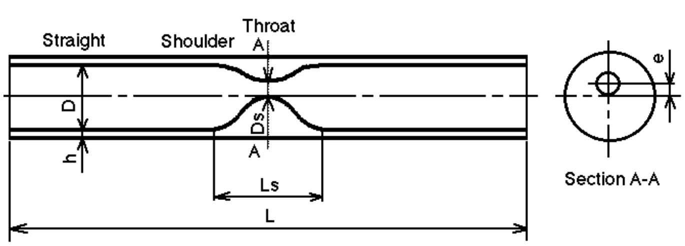

Figure 1: Schematic representation of the stenosis models. L=110 mm, Ls=16mm, D=8mm, h=1mm.

SUMMARY

The results indicate that a combination of percent stenosis and eccentricity would be a more accurate indicator for wall compression. The wall compression, in turn, may contribute to plaque rupture.

ACKNOWLEDGEMENT

This research was supported in part by US NSF grant DMS-0072873.

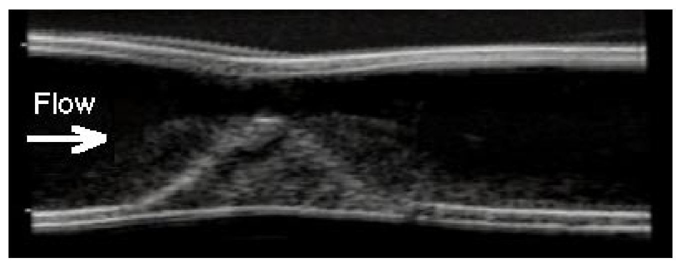

(1) P_{2ave}=70mmHg, Phase: 24 degrees.

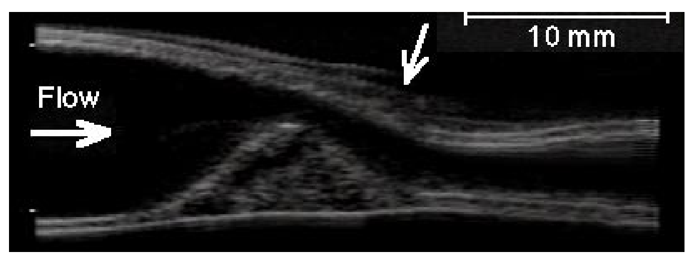

(2) P_{2ave}=0mmHg, Phase: 24 degrees

Figure 2: Ultrasound images of sagittal section of stenosis model (70% Stenosis severity (% stenosis), 100% eccentricity). The arrow points the collapse

Table 1: Average downstream pressure (P_{2ave}) when the first outbreak of collapse is occurred

St [%] \ Ec [%]	0	50	100
70	5	7	12
75	1	7	8
80	0	4	4

[mmHg]

FLOW DUE TO A PERISTALTIC WAVE IN A TUBE

Mehran Tadjfar and Ryutaro Himeno

Advanced Computing Center
Institute of Physical and Chemical Research (RIKEN)
2-1, Hirosawa, Wako-Shi, Saitama, JAPAN

INTRODUCTION

In the human body the most common method of transporting fluid is through peristaltic pumping. Peristalsis occurs in the transport of urine from kidneys to bladder in the ureter, transport of food bolus through the oesophagus, gastro-intestinal tracts, and the ejection of semen from male reproductive organ amongst many. The vast lymphatic system all over the body is using peristalsis to circulate lymph through the blood stream. The lymph vessels have one way valves and smooth muscle medial layer, which contract periodically to perform the peristaltic pumping. Here, we use CFD methods to study the peristaltic flow in a tube initiated by a single wave motion (Fig. 1).

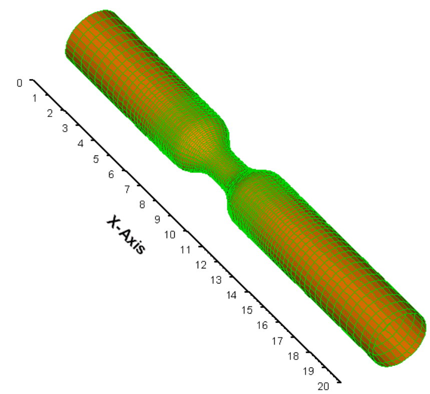

Figure 1: Grid model of the peristaltic wave in a tube.

METHODS

The unsteady, three-dimensional, incompressible Navier-Stokes equations are solved using a fast, parallel, and time-accurate finite volume solver (See Tadjfar 2002). The solver is capable of dealing with moving boundaries and moving grids. It is designed to handle complex, three-dimensional vascular systems. The computational domain is divided into multiple block subdomains. At each cross section the plane is divided into twelve sub-zones to allow flexibility for handling complex geometries and, if needed, appropriate parallel data partitioning. A second-order in time and third-order upwind finite volume method for solving time-accurate incompressible flows based on pseudo-compressibility and dual time-stepping technique is used.

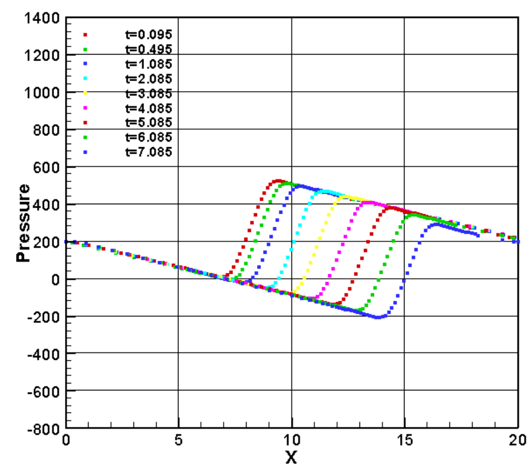

Figure 2: The pressure distribution along the centerline of the tube at different times.

RESULTS AND DISCUSSION

Considering an initial sinusoidal activation signal for the muscle wall results in a "tear-drop" wall shape coming out of the interaction (See Carew and Pedley). This shape is the result of some fluid being pushed into the tube (by some relevant mechanism involved in that particular case). After the initial dilation of the tube there is a region of constant maximum stretched diameter caused by some time lag before the surrounding muscle tissues contract the lumen back to its original diameter. This passive filling and active contraction with some associated time lag causes the formation of the "tear-drop" shape on the tube wall. It is the numerical solution of the unsteady 3-D Navier-Stokes equations for the "tear-drop" shaped wall waves that is the subject of this study. After an initial transient period a pressure gradient is created that carries the fluid downstream along the tube (Fig 2).

REFERENCES

Carew, E.O., and Pedley, T.J., (1997), *ASME J. Biomech. Eng., Vol. 119, pp.66-76.*

Tadjfar, M. and Himeno, R. (2002), *Journal of Biorheology, to appear.*

COMPARISON OF TRANSIENT FORCE ATTENUATION BETWEEN THREE TYPES OF HEEL CUSHIONS USED IN RUNNING SHOES

Arnel Aguinaldo, Michael Litavish, and Abigail Morales
Motion Analysis Laboratory, Children's Hospital, San Diego, CA
Correspondence: aaguinaldo@chsd.org, Online: www.sandiegogaitlab.com

INTRODUCTION

As the foot strikes the ground, the momentum from the moving limb rapidly changes, resulting in a transient force transmitted up the skeleton. The repetitive transmission of this force has been suggested to be a contributing factor in the development of joint degradation (Radin, et al., 1972). Although the foot has internal structures that help attenuate this impact shock, footwear with rearfoot cushioning soles have been proven to provide effective impact attenuation (Hennig, et al., 1993). Impact forces are dependent on the mechanical properties of the interface between the ground and the foot, as well as on the activity in which the moving limb is involved. Since various footwear manufacturers use different materials to provide impact attenuation, it is unknown whether shoes with different heel cushions provide the same level of attenuation during walking and running. Therefore, the purpose of this investigation was to evaluate the effects of three types of footwear with different heel midsole cushions on transient forces, measured through the initial vertical ground reaction force following footstrike.

METHODS

Eight male and two female subjects participated in the study after signing informed consent forms approved by the hospital's Institutional Review Board. Each subject walked and ran a 12-meter runway while eight high-speed cameras (Motion Analysis Corporation, Santa Rosa, CA) collected coordinate data from a cluster based marker set used to define the pelvis, thigh, and shank segments. Three force platforms (AMTI, Watertown, MA) with a natural frequency of 450 Hz were used to collect ground reaction forces (GRF) at a sampling rate of 1000 Hz. A heelstrike transient (impact) force was identified, as defined by Whittle (1999), by a quick spike in force superimposed in the upslope of the initial GRF peak occurring in the first 30 ms after footstrike during walking (Figure 1), approximately 15% of the gait cycle. Additionally, plantar-dorsi flexion was measured to verify ankle position at footstrike. Walking and running sessions were conducted with each of the following shoes: Shoe 1 (polyurethane), Shoe 2 (mechanical cushion), and Shoe 3 (EVA material). Transient forces from each shod session were compared to each other and to the barefoot condition using a 4-level repeated measures ANOVA.

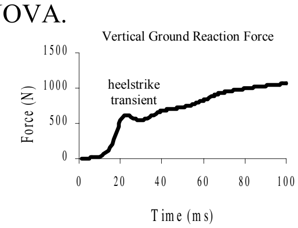

Figure 1: Heelstrike transient force (impact peak)

RESULTS AND DISCUSSION

Figure 2a shows the walking heelstrike transients for each condition. There were significant differences found between Shoe 1 and Shoe 2, as well as between Shoe 2 and barefoot conditions. No differences in plantar-dorsiflexion were found for walking. However, there was an increase in plantarflexion (-3° ± 1°) at footstrike during barefoot running. Thus, initial GRF peaks of barefoot running were removed from the statistical analysis, which resulted in a significant difference found in impact peaks between Shoes 1 and 2 (Figure 2b).

Footwear provides an additional layer of protection against impact forces. However, the differences in shoe construction complicate the analysis of how impact attenuation occurs with footwear (Clarke, et al., 1983). Shoe 2 utilizes a midsole system of four columns that are each a two-level dynamic cushion (Iso-Dynamics, Cleveland, OH) designed with a loading response similar to that of a linear hydraulic shock absorber. In this study, Shoe 2 exhibited the lowest heelstrike transient during walking. Conversely, Shoes 1 and 3, which are manufactured with polyurethane and ethylene vinyl acetate (EVA) midsoles, respectively, attenuated walking heelstrike transient less effectively than Shoe 2. Although impact forces during barefoot running were not analyzed, due to the apparent midfoot strike at initial contact, the initial GRF peaks during running showed that Shoe 2 dissipated the vertical impact force more effectively than Shoe 1.

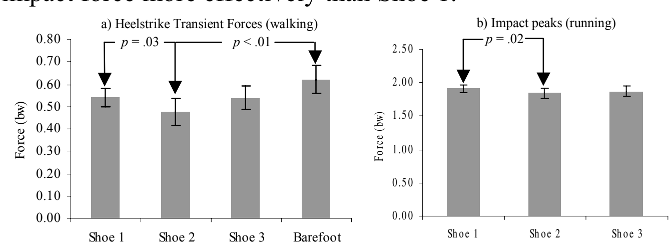

Figure 2: Impact forces during a) walking and b) running

SUMMARY

Impact forces were measured with three shoe types during walking and running. The mechanical cushioned shoe exhibited the lowest transient forces. It was found that impact forces varied with shoe type and, therefore, should be carefully evaluated when selecting shoes for injury prevention.

REFERENCES

Clarke, T.E., et al. (1983). *Intl J Sports Med*, **4**(4), 247-251.
Hennig, E.M. et al. (1993). *J App Biomech*, **9**(4), 306-314.
Radin, E.L. et al. (1972). *Lancet*, **4**, 519-522.
Whittle, M.W. (1999). *Gait & Posture*, **10**, 264-275

FLOW ANALYSIS ON THE STENTED AND NON-STENTED LATERAL ANEURYSM MODELS

Kyehan Rhee[1], Moon Hee Han[2], Sang Hoon Cha[3] and Keyoung Jin Chun[4]

[1] Department of Mechanical Engineering, Myongji University, Yongin, Korea, khanrhee@mju.ac.kr
[2] Department of Radiology, Seoul Natonal University Hospital, Seoul, Korea
[3] Department of Radiology, Choongbuk National University Hospital, Chungju, Korea
[4] Korea Institution of Industrial Technology, Chonan, Korea

INTRODUCTION

Endovascular technique using a tubular shaped stent has been developed and successfully used in treating wide neck aneurysms. A self-expandable stent is introduced via a small catheter and placed at the aneurysm neck. A stent can promote thrombosis formation inside the aneurysm sac by stagnating intraaneurysmal flow, and provide biocompatible passage of the parent artery by neointimal formation on the stent wall. Thrombus formation and neointima growth may be affected by the flow characteristics inside the aneurysm. We want to clarify velocity and wall shear stress changes by stenting under physiological flow for the lateral aneurysm models, and explore the effects of stent porosity and aneurysm geometry on the flow fields inside the aneurysm sac.

METHODS

Transparent models with different lateral aneurysm shapes are manufactured using a glass model as a male mold. A male wax model made from the glass model is enclosed in an acryl box, and transparent silicone resin (Sylgard 184, Dow-Corning) is poured. After silicone resin is cured, wax is melted out and an acryl box is removed. Both models have parent artery diameter (D) of 5 mm and neck width of 14 mm, and the lateral aneurysm model 1 (L1) has dome height (the distance between neck and fundus) of 4.8 mm while the lateral aneurysm mode 2 (L2) has dome height of 6 mm. The stents used in this study have porosity of 0.86 (stent 1) and 0.79 (stent 2) respectively, and length of 20 mm. The aneurysm model is inserted into a mock circulation loop, which can generate physiological flow waveform. We use a flow visualization method incorporating photochromic dye in order to observe the flow fields and measure the wall shear rates. We visualize flow motion at five different axial locations along the aneurysm wall – maximally dilated location (pt.3), 0.3D (pt.2) and 0.6D(pt.1) proximal location, 0.3D(pt.4) and 0.6D(pt.5) distal location. Wall shear rates are measured at each location for five different phases of a flow cycle (T: period) – early acceleration (t/T=0.05), mid acceleration (t/T=0.13), peak (t/T=0.21), early deceleration (t/T=0.26) and late deceleration (t/T=0.35).

RESULTS AND DISCUSSION

Intraaneurysmal flow activity was significantly reduced in the aneurysm models with a stent. The magnitude and pulsatility of shear rate were also decreased significantly in the stented aneurysm models. The shape of the aneurysm sac and the stent porosity did not affect the intraaneurysmal flow patterns and wall shear rate distribution significantly. The magnitudes of wall shear rates were less than 100 sec^{-1} along the aneurysm wall during a flow cycle in the stented lateral aneurysm models (Figure1). Since intraaneurysmal fluid motion, the magnitude and pulsatility of wall shear rate were significantly reduced in the stented models, insertion of a stent may provide more thrombogenic hemodynamic environment inside the aneurysm. Further study will be performed to elucidate the hemodynamic effects on the thrombus formation and neointima development on the stent wall.

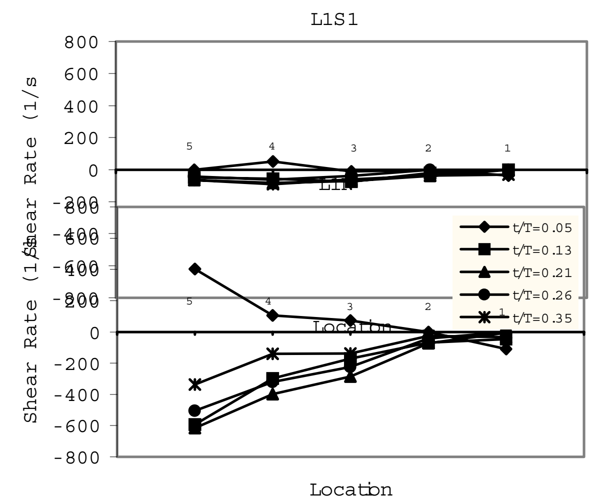

Figure 1: Wall shear rates along the aneurysm wall for five different phases in the lateral aneurysm model without a stent (L1N) and with a stent 1(L1S1).

REFERNCES

Lieber, B.B. et al (1997). *Annals of Biomed Eng* , **25**, 460-469.
Marks, M.P. et al (1994). *Radiology*, **191**, 441-446.
Rhee, K., Tarbell, J.M. (1994). *J. Biomechanics*, **27**, 329-338.
Wakhloo, A.K. et al (1994). *Am J Neuroradiol*, **15**, 493-502.

ACKNOWLEDGEMENTS

This work was supported by grant No. 2000-2-20500-008-2 from the Basic Research Program of the Korea Science & Engineering Foundation.

A TEMPORAL, KINEMATIC AND KINETIC ANALYSIS OF THREE EQUI-VOLUME LOADING PATTERNS

John Cronin and Blair Crewther
Sport Performance Research Centre - Auckland University of Technology. john.cronin@aut.ac.nz

INTRODUCTION

Loads greater than 60-70% 1RM are thought fundamental to the development of maximal strength and an important stimulus for muscle hypertrophy [4 5]. In strength trained athletes even greater loading intensities (80-100% 1RM) are thought critical for the development of maximal strength [3]. However, a number of studies have found light load (10-30% 1RM) explosive training to be equally effective in enhancing a variety of performance measures (including strength and increases in CSA) as compared to heavier weight training (75-85% 1RM) [1 2 6]. In light of the inconsistencies of research in this area, this study investigated whether three training loads (30%, 60% and 90% 1RM) equated by volume, differed in terms of their temporal, kinematic and kinetic characteristics.

METHODS

Twelve (7 males and 5 females) experienced weight trainers (mean age and weight were 30.2 ± 10.6 years and 75.8 ± 13.0 kg respectively) were assessed on an instrumented isoinertial supine squat machine. Testing was conducted over two sessions. In the first session the one repetition maximum (1RM) of each subject was established. The second session involved subjects performing a set at 30%, 60% and 90% of their 1RM. Each set was equated by volume (% 1RM x reps) to ensure that total mass lifted between conditions was identical. The instructions to the subjects for all repetitions were to move the load as "explosively" as possible. The sequence in which each subject performed the three sets was randomised to negate order and fatigue effects.

RESULTS AND DISCUSSION

Significantly ($p < 0.05$) greater total time under tension during the eccentric (41-53%) and concentric phases (27-31%) was observed for the 30% 1RM condition as compared to the other two conditions. Similarly the lighter loading intensity resulted in significantly greater total eccentric (9-19%) and concentric (14-24%) force output as compared to the other two conditions. If time under tension and high forces are the critical stimuli to strength development then the greater total force and greater total duration under tension of the 30% 1RM condition would seem superior. However, if force x time under tension (impulse) is the critical stimulus for producing strength and hypertrophic change, the concentric impulse associated with the 90% 1RM condition would appear superior (29-42%). It has also been suggested that total work done is important for muscle hypertrophy [6]. Greater total work (9-24%) was associated with the 30% 1RM condition.

SUMMARY

Research studying the temporal, kinematic and kinetic characteristics of a set rather than a single repetition provides better insight into the changes and adaptations that may occur with the repeated application of a training stimulus. Such research is more likely to contribute to our understanding of how various training programmes optimize strength and power development.

REFERENCES

1. Dahl, H.A., R. Aaserud, R., Jensen, J. (1992). *Med. Sci. Sports Exerc.* 24, S55.
2. Harris, G., et al (2000). *J. Strength Cond. Res.* 14, 14-20.
3. Komi, P., Hakkinen, K. (1988) In:The olympic book of sports medicine. Oxford: Blackwell Scientific Publications.
4. MacDougall, J.D. (1992) In: *Strength and power in sport*, Oxford: Blackwell Scientific Publications.
5. McDonagh, M.J.N., Davies, C.T.M. *Eur. J. Appl. Physiol.* 52, 139-155, 1984.
6. Moss, B. et al (1997). *Eur. J. Appl. Physiol.* 75, 193-199.

Table 1: Temporal and kinetic characteristics during eccentric and concentric contractions at 30%, 60% and 90% 1RM.

Variables	30% 1RM Mean (SD)	60% 1RM Mean (SD)	90% 1RM Mean (SD)	F value (p)
Total Duration of Eccentric Contraction (s)	2.673 (0.350) $^{\alpha}$	1.591 (0.266) $^{\delta}$	1.285 (0.249)	80.2 (0.000)
Total Duration of Concentric Contraction (s)	2.530 (0.263) $^{\alpha}$	1.764 (0.153) $^{\delta}$	1.869 (0.233)	56.8 (0.000)
Total Eccentric Mean Force (N)	4829 (1323) $^{\alpha}$	4409 (1139) $^{\delta}$	3925 (1001)	62.1 (0.000)
Total Concentric Mean Force (N)	5084 (1370) $^{\alpha}$	4399 (1112) $^{\delta}$	3876 (984)	86.4 (0.000)
Total Eccentric Impulse ($N \cdot sec^{-1}$)	2116 (567)	2319 (695)	2535 (936)	3.13 (0.063)
Total Concentric Impulse ($N \cdot sec^{-1}$)	2111 (536) $^{\alpha}$	2591 (724) $^{\delta}$	3632 (1093)	58.4 (0.000)
Total Eccentric Work (J)	1433 (414) $^{\alpha}$	1311 (372) $^{\delta}$	1168 (328)	66.2 (0.000)
Total Concentric Work (J)	1510 (437) $^{\alpha}$	1309 (371) $^{\delta}$	1153 (321)	86.9 (0.000)

Key: $^{\alpha}$ - 30% 1RM significantly different to 60% & 90% 1RM. $^{\delta}$ - 60% 1RM significantly different to 90% 1RM.

A GAIT ORTHOSIS FOR PARAPLEGICS WITH A MOTOR-DRIVEN KNEE JOINT

Yuji OHTA[1], Momoko YOSHIDA[1], Yoichiro SHINOYA[2], Akihiro MATSUMOTO[2],
Noritaka KAWASHIMA[3], Kimitaka NAKAZAWA[3], and Hideo YANO[3]

[1] Ochanomizu University, Tokyo, Japan, yuji@cc.ocha.ac.jp, [2] Toyo University, Kawagoe, Japan,
[3] National Rehabilitation Center for the Disabled, Tokorozawa, Japan

INTRODUCTION

Various kinds of orthopedic devices have been developed to assist walks and stances in paraplegic patients up to now. Furthermore, the devices have been combined with functional electric stimulation techniques to reduce the effort needed and to walk farther. In this study we developed a new gait orthosis featuring the rotating knee joint mechanism powered by a linear actuator, and tested it with a spinal cord injury patient.

MATERIALS AND METHODS

Figure 1 shows the schematic diagram and the photograph of the device we developed. A linear motion actuator was mounted at the back of the knee joint of an Advanced Reciprocating Gait Orthosis (ARGO). The actuator consists of a low-inertia DC motor (3557, Faulhaber, Switzerland) and a ball screw (Kuroda Precision Industries Ltd., Japan). The stroke length of the linear actuation and the maximum knee rotational angle were set at 15 cm and 70 degree, respectively. As shown, the mechanism mounted is compact and its weight is 0.8 kg. We used Ni-H rechargeable batteries featuring both lightweight and large capacity (HR-3US, 1600 mAh, Sanyo Co., Japan). From the viewpoint of safety, we adopted an infrared switch to control knee action in case that a user might be caught by a cable and fall down. The switch is placed on an arm crutch handle and pushed by a user itself along with every step. Furthermore, the knee joint of ARGO stays locked throughout extension phase. It is unlocked by the actuator through flexion phase and is locked again at heel strike. We measured the gait of a patient (male, 23 yrs, T12) with this device on, by using the vicon system (Oxford Metrics Co., UK) at the sampling rate of 60Hz.

RESULTS AND DISCUSSION

Figure 2 shows the self-paced gait of the patient with and without the device. As shown, the walking pattern with the device was found to be close to healthy subject's one. The walking speed with the device was about 0.4 m/s, which could be faster by trainings. The knee joint rotated about 40 degree at maximum flexion. The patient expressed that the effort required for walking was drastically reduced due to the device. The fully-charged battery could last for about one hour walk without exchange. The relationship between the foot-floor clearance of the device and the mechanism must be studied through further experiments.

SUMMARY

We developed a new gait orthotic device for paraplegics. The feature is the motor-driven knee joint mechanism which makes patient's gait close to healthy one. Through preliminary experiments with a patient, we found that the walking speed was about 0.4 m/sec, and we make sure that the effort for walking was reduced by rotating the knee joint during swing phase.

REFERENCES

Marsolais, E. B. et al (2000). *J. Spinal Cord Med.*, **23**, 100-108.
Greene, P. J. and Granat, M. H. (2000). *Clin. Biomech.*, **15**, 536-540.

ACKNOWLEDGEMENTS

This study was supported by Tateishi Science and Technology Foundation.

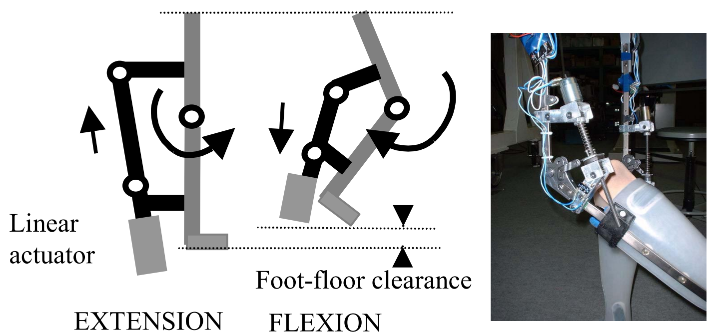

Figure 1 Mechanism of the motor-driven knee joint and its photograph at flexion.

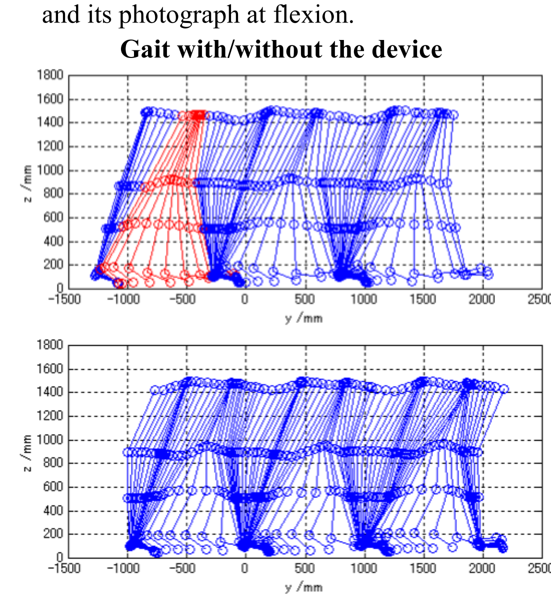

Figure 2 Measurement of the gait (right leg) with (*lower*) and without (*upper*) the device.

GEOMETRIC MODELLING OF SKELETAL MUSCLE USING HERMITE ELEMENTS

Fernandez, J.W.* Blyth, P. Anderson, I.A. and Hunter, P.J.

Bioengineering Institute, University of Auckland, New Zealand
*jw.fernandez@auckland.ac.nz

INTRODUCTION

This abstract explores the convenience and computational efficiency of cubic Hermite volume elements for use in anatomically accurate finite element models of skeletal muscles. Other three-dimensional studies of skeletal muscle have used linear based elements [Gentaro et al, 2000]. By comparison, Hermite elements use high order interpolation and describe high geometric gradients with low element numbers. This provides a basis for incorporating a fibre distribution also interpolated using cubic Hermite shape functions. Further, the derivative continuity at nodes provides benefits when considering contact mechanics.

METHODS

Using the finite element analysis software CMISS (developed by the Bioengineering Institute, University of Auckland) 9 muscles associated with knee joint function were modelled. The procedure involved the following steps: A bi-linear surface mesh was developed for a specific muscle from axial slices of the visible human data set [Ackerman, 1998]; constant spacing allowed for a consistent mesh (Fig. 1a). Data points were orthogonally projected onto the mesh surface and defined as material coordinates. Using a least-squares fitting algorithm [Bradley et al, 1997] the difference between the original data and orthogonal projections was minimised. This was achieved through an optimisation routine which varied the nodal derivative parameters (Fig. 1b). Following this, volume elements were generated by linearly extruding to a central node, defined as the geometric mean of an axial slice (Fig. 1c).

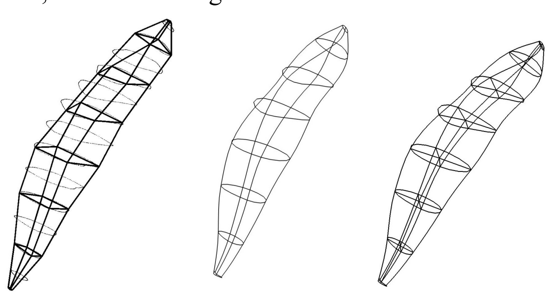

a) **b)** **c)**

Figure 1: a) Linear mesh with data points for rectus femoris muscle; **b)** Fitted surface; **c)** Volume elements created by extruding to central nodes;

RESULTS

The results in Table 1 were obtained using a 180 MHz O2 computer (SGI, CA, USA). Element numbers were chosen to give a root mean square (RMS) difference of less than 2mm (with an average of 1.33 mm over 9 muscles). Fitting time averaged 48.4 seconds over 9 fits.

Muscle	**nodes**	**elements**	**data points**	RMS **(mm)**	**time (sec)**
Rectus femoris	32	28	1607	0.84	47.00
Vastus lateralis	60	54	2404	1.96	86.00
Vastus medialis	63	56	1779	1.94	90.00
Tensor fascia latae	42	36	442	0.95	34.00
Gracilis	32	28	820	1.85	27.00
Biceps long head	48	42	1534	1.50	54.00
Biceps short head	28	24	846	1.15	31.00
Semimembranosus	20	16	1482	1.27	39.00
Semitendinosus	28	24	879	0.51	28.00
Average	39	34	1310	1.33	48.4
s.d.	14.2	13.1	575.4	0.5	22.7

Table 1: Results for 9 muscles

DISCUSSION

Hermite basis functions dramatically reduce element numbers needed to describe complex geometry (an average of 34 elements for the 9 muscles modelled). A further benefit is the ability to define curvature within a mesh volume, improving description of muscles with high internal geometric gradients, such as the vastus group which wrap around the femur. Additionally our design accommodates muscle bifurcation such as that seen in the gastrocnemius. Currently, the contact between muscles in the human knee is being investigated. The Hermite elements allow for a smooth contact surface and reduce the contact search time with lower element numbers.

SUMMARY

Cubic Hermite elements are suitable for the finite element modelling of limb muscles. They provide realistic visualisation for such applications as virtual surgery. Model customisation using patient specific-data obtained from MRI and CT is also being explored, with the intent of producing a diagnostic and therapeutic tool.

REFERENCES

Ackerman, M.J. (1998). *Proceedings of the IEEE*, **86**(3): 504-511.
Bradley et al. (1997). *Annals of Biomedical Engineering*, **25**, 96-111.
Gentaro et al. (2001). *Proceedings Computer Animation 2001*, Seoul, Sth Korea, Nov 7-8.

EFFICIENT FINITE ELEMENT CUSTOMISATION OF A GENERIC FEMUR USING THE HOST MESH TECHNIQUE

Fernandez, J.W.* Blyth, P. Thrupp, S.F. Anderson, I.A. and Hunter, P.J.

Bioengineering Institute, University of Auckland, New Zealand
*jw.fernandez@auckland.ac.nz

INTRODUCTION

Patient-specific models are of interest in modelling and surgical planning. Previously published techniques for model customisation have required long processing times [Viceconte et al, 1998]. He we present a new highly efficient procedure using 24 key landmark points to customise a generic femur to patient data, capturing important features of patient geometry. In addition, the high order elements employed allow for a continuous surface curvature and may prove a useful aid in visualisation. By comparison, other models typically use linear elements [Couteau et al, 2000].

METHODS

Using the finite element analysis software CMISS (developed by the Bioengineering Institute, University of Auckland) a tri-cubic Hermite host mesh was defined to enclose the generic femur, and subdivided into three regions giving separate control of the head, shaft and condyles (Fig. 1). The generic mesh was described by 416 bi-cubic Hermite elements. Twenty-four key landmark data points were chosen along with the corresponding projection points on the data set in question. The landmark points and femur mesh nodes were defined as fixed material coordinates within the host mesh and inherently transformed as the host mesh was deformed. The host mesh was constrained to deform in certain directions. Using a least-squares algorithm the difference between the landmark and projection data was minimised [Bradley et al, 1997]. The fitting procedure varied nodal coordinates and derivatives to achieve the host configuration with the minimum overall root mean square (RMS).

To validate this method, a sample of 5 femur datasets were used (4 scans of cadaveric femurs and the visual human dataset [Ackerman, 1998]), each containing on average 2400 points with varying geometrical features. The 4 femurs were suspended over a laboratory bench and data was collected using a hand-held laser scanner (FastSCAN™, Applied Research Associates, ChCh, NZ).

RESULTS

Using a 180 MHz O2 computer, (SGI,CA,USA) the fitting process took less than 100 seconds. The algorithm yielded an average RMS of 3.09mm with a standard deviation of 0.15mm. Operator time for positioning the projection points was less than 5 minutes.

DISCUSSION

The efficiency of this technique allows for the rapid generation of patient and sub-population specific models in the design and testing of prostheses, and in surgical planning. Particular attention has been paid to ensuring the accuracy of parameters such as neck-shaft angle, femoral head size, and neck length, key features of interest to orthopaedic surgeons and important for stress analysis. Further, the key landmark points used are easily identified on saggital and coronal MRI images. Other methods such as that described by [Couteau et al, 2000] use segmentation of CT scans to obtain data and hence require long pre-processing times. [Viceconte et al, 1998] analysed this and other methods and report times in the order of 250-520 minutes and operator times of 380-690 minutes. In contrast, by manually selecting 24 points our processing time is significantly reduced.

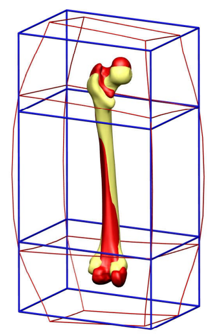

Figure 1: The yellow (light) generic bone is transformed to the red (dark) customised bone.

SUMMARY

This abstract presents a novel means for customisation of human bone geometry with generation of patient specific models on a PC from minimal MRI or CT scans in under 10 minutes. This accurate surface geometry can be used to generate volume meshes automatically. It has widespread applications from stress analysis to surgical simulation and planning, and may be adapted to other organs such as skeletal muscle.

REFERENCES

Ackerman, M.J. (1998). *Proceedings of the IEEE*, **86**(3): 504-511.
Bradley et al. (1997). *Annals of Biomedical Engineering*, **25**, 96-111.
Couteau et al. (2000). *Journal of Biomechanics*, **33**, 1005-1009.
Viceconti et al. (1998). *Medical Engineering & Physics*, **20**, 1-10.

EXPERIMENTAL ASSESSMENT OF HYDRODYNAMICS OF A MECHANICAL PECTORAL FIN

Naomi Kato[1], Hao Liu[2] and Hirohisa Morikawa[3]

[1]Tokai University, School of Marine Science and Technology, Department of Marine Design and Engineering,nkato@scc.u-tokai.ac.jp
[2]The Institute of Physical and Chemical Research(RIKEN), Division of Computer and Information, hliu@postman.riken.go.jp
[3]Shinshu University, Faculty of Textile Science and Technology, Department of Functional Machinery and Mechanics
hmorikw@giptc.shinshu-u.ac.jp

INTRODUCTION

Many marine animals thrive in near shore, high-energy environments where rapidly changing flow velocities created by surges, currents, and breaking waves present extreme challenges to precision maneuvering and hovering performance. Many near-shore fishes employ one or more pairs of oscillating fins to increase both stability and maneuverability. It is reasonable to believe that these highly maneuverable fishes serve as excellent biological templates for the design of man-made vehicles with extreme maneuvering and stealth capabilities.

Kinematic studies indicate that pectoral fin movements are variable among species and across a range of swimming speeds with complex fin ray patterns. Lindsey (1978) referred to propulsion by oscillation of pectoral fins as “Labriform swimming mode” after Labridae. Labriform swimming consists of *drag-based* labriform swimming mode at low swimming speeds and *lift-based* labriform swimming mode at higher swimming speeds. The former is characterized by the rowing action of pectoral fins forming a high angle to the horizontal axis of fish body. The latter is characterized by the flapping action of pectoral fins forming a small angle to the horizontal.

This paper experimentally discusses the hydrodynamic characteristics of a flapping, rowing and feathering fin system in terms of drag-based labriform swimming mode and lift-based labriform swimming mode.

MECHANICAL PECTORAL FIN

To experimentally and numerically assess the hydrodynamic characteristics of flapping, rowing and feathering fin system in a precise manner, a compact Three-Motor-Driven Mechanical Pectoral Fin (3MDMPF) (Kato et. al., 2002) device with high speed capability and precise movement was manufactured(see Fig.1). The device is equipped with a force sensor measuring normal force acting on the rigid fin and a torque sensor measuring torque around a fin shaft. Potentiometers for measuring angles of rowing motion, flapping motion and feathering motion are installed inside the device.

The rowing angle, the feathering angle, and the flapping angle were varied sinusoidally.

An open water test of the mechanical pectoral fin was carried out in a water-circulating tank, with measurement section of 2.2 m long, 1.4 m wide and 0.9 m deep. The hydrodynamic characteristics were investigated in terms of the following items.

(1) Phase difference between the rowing motion and the feathering motion, $\Delta\phi_{FE}$, without the flapping motion for drag-based labriform swimming mode,
(2) Phase difference between the rowing motion and the flapping motion, $\Delta\phi_{FL}$, with $\Delta\phi_{FE}$ of $90°$ for drag-based labriform swimming mode,
(3) Phase difference between the feathering motion and the flapping motion with $\Delta\phi_{FE}$ of $0°$ for lift-based labriform swimming mode,
(4) Non-dimensional frequency, K, which is defined as

$$K = c \cdot \omega_{fin} / U \qquad (1)$$

(c: chord of fin, ▪ :angular frequency, U: uniform speed)
(5) Frequency change in still water and
(6) Non-sinusoidal feathering motion without uniform flow.

SUMMARY

Experimental tests by a compact mechanical pectoral fin device making a flapping motion , rowing motion and feathering motion in a precise manner revealed that the effect of the flapping motion on the propulsive force coefficient and the propulsive efficiency of the drag-based labriform swimming mode is remarkable not only in uniform flow, but also in still water.

The propulsive efficiency of lift-based labriform swimming mode reaches 40% at the maximum, that is larger than in the case of drag-based swimming mode.

Non-sinusoidal feathering motion of the drag-based labriform swimming mode in still water can generate propulsive force in the X direction with small hydrodynamic forces in the Y and Z directions.

REFERENCES

Lindsey,C.C (1978):Form, Function and Locomotory Habits in Fish, In “Fish Physiology VII Locomotion”, edited by W.S.Hoar and D.J.Randall, Academic Press, pp.239-313
Kato,N.,Liu,H.,Morikawa,H.(2002). *Proceedings of 12th Int. Offshore and Polar Engineering Conf.* (submitted)

ACKNOWLEDGEMENTS

This research is funded by Office of Naval Research (Grant No. N00014-01-1-0501) as the project title “US-Japan Cooperative Research on Biology-Inspired Precision Maneuvering of Underwater Vehicles”.

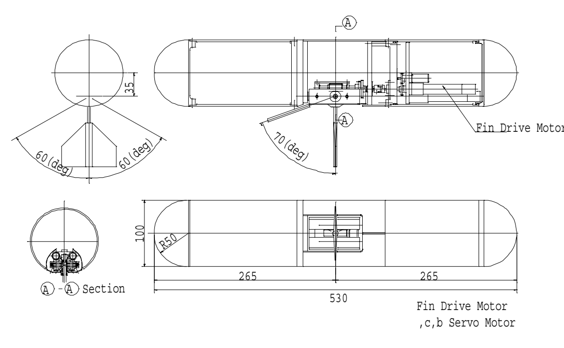

Figure 1 A cylindrical body with a 3mdmpf

A MICROSTRUCTURE MODEL OF VERTEBROPLASTY AND ITS MECHANICAL PROPERTIES

Gye Rae Tack[1], Han Sung Kim[2], Hyung Do Kim[1], Soon Cheol Chung[1]

[1]Dept. of Biomedical Eng., Konkuk University, Chungju, Chungbuk, Korea, grtack@kku.ac.kr
[2]Institute for Advanced Engineering, Yongin, Kyonggi-Do, Korea

INTRODUCTION

Osteoporosis is defined as a systemic skeletal disease caused by low bone mass and microstructure deterioration of trabecular bone. Li *et al*. (1995) has shown that a drug therapy (PTH: Parathyroid hormone) increases the bone mass and thus bone strength. Vertebroplasty is a surgical procedure for the treatment of osteoporotic vertebrae. This procedure includes puncturing vertebrae and filling with Polymethylmethacrylate (PMMA). In the present study, several (intact, aged, hormone treated and bone cement treated) 2D models for the treatment of osteoporotic vertebrae are analyzed and the relative effects of drug therapy and bone cement treatment are compared using finite element analysis.

METHODS

Five 2D finite element models of the same relative density (0.134) were generated for intact vertebral trabecular bones using Voronoi diagram method suggested by Silva and Gibson (1997). For direct comparison with results of Silva and Gibson, these models were allowed to have the same trabecular tissue properties as those used in their models. Displacement boundary conditions were applied to simulate a uniaxial compression test for the longitudinal direction. Five models for aged bones with the relative density of 0.114 were also generated and analyzed for each model using commercial finite element software (ANSYS 5.7; ANSYS, Inc.).

In order to compare the results of hormone-treated model given by Silva and Gibson with those of bone cement-treated model, five models for each case were analyzed. In this study, hormone-treated models have the same relative density (0.134) as that used in models of Silva and Gibson. In bone cement-treated models, to show the effect of bone cement treatment, the same relative density (0.114) as that of the intact bone model was used and bone cement was modeled by shell element.

RESULTS AND DISCUSSION

The results of the present analysis for hormone-treated models show an excellent agreement with those given by Silva and Gibson. Modulus and strength of hormone-treated models were approximately 30% of those of intact models and they were about 60% of those of the bone cement-treated models (Figures 1, 2). From these results, it is found that the bone cement treatment is likely to decrease the incidence of vertebral fractures, compared with the drug therapy. Since this study is a preliminary investigation, more in-depth studies on the 3D models of human vertebral trabecular bone need to be followed.

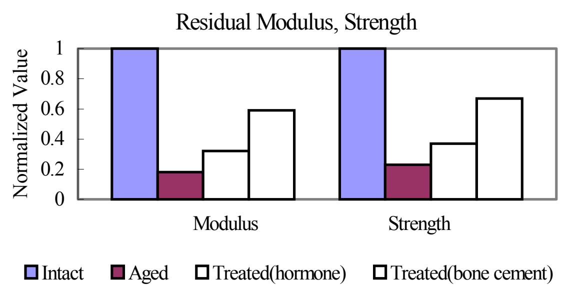

Figure 1: Effective Young's modulus and strength of each models.

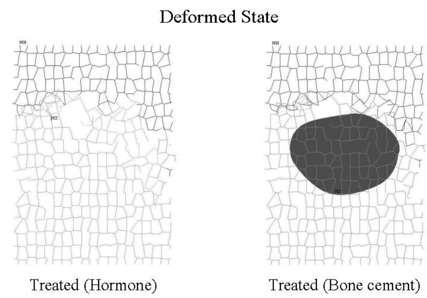

Figure 2: Deformed state of treated models.

SUMMARY

It is reported that the mechanical properties of vertebral trabecular bone depend on the density and the mass of bones. Silva and Gibson studied the treatment of age-related bone loss using drug therapy. However, the relative effect of drug therapy and bone cement for osteoporosis treatment is not reported yet. In this study, several 2D models of human vertebral trabecular bone are analyzed by finite element method. The mechanical behaviors of the vertebral trabecular bone treated by the drug therapy and the bone cement are compared. This study shows that bone cement treatment is more effective strategy than drug therapy to prevent the degradation of bone strength.

REFERENCES

Gibson, L.J., Ashby, M.F. (1997). *Cellular Solids: Structure & Properties*. Cambridge University Press
Li, M. et al (1995). *Bone*, **16**, 629-635.
Silva, M.J., Gibson, L.J. (1997). *Bone*, **21**, 191-199.

ACKNOWLEDGEMENTS

This study was supported by a grant (HMP-98-G-1-010) of the HAN (Highly Advanced National) Project, Ministry of Heath & Welfare, R. O. K.

OPTIMIZATION OF MOTION OF A MECHANICAL PECTORAL FIN

Naomi Kato[1], Hao Liu[2] and Hirohisa Morikawa[3]
[1]Tokai University, School of Marine Science and Technology, Department of Marine Design and Engineering, nkato@scc.u-tokai.ac.jp
[2]The Institute of Physical and Chemical Research(RIKEN), Division of Computer and Information, hliu@postman.riken.go.jp
[3]Shinshu University, Faculty of Textile Science and Technology, Department of Functional Machinery and Mechanics, hmorikw@giptc.shinshu-u.ac.jp

INTRODUCTION

Kinematic studies indicate that pectoral fin movements are variable among species and across a range of swimming speeds with complex fin ray patterns. Lindsey (1978) referred to propulsion by oscillation of pectoral fins as "Labriform swimming mode" after Labridae. Labriform swimming consists of *drag-based* labriform swimming mode at low swimming speeds and *lift-based* labriform swimming mode at higher swimming speeds. The former is characterized by the rowing action of pectoral fins forming a high angle to the horizontal axis of fish body. The latter is characterized by the flapping action of pectoral fins forming a small angle to the horizontal.

To experimentally and numerically assess the hydrodynamic characteristics of flapping, rowing and feathering pectoral fin system in a precise manner, a compact Three-Motor-Driven Mechanical Pectoral Fin (3MDMPF) (Kato et. al., 2002) device with high speed capability and precise movement was manufactured. The device is equipped with a force sensor measuring normal force acting on the rigid fin and a torque sensor measuring torque around a fin shaft. Potentiometers for measuring angles of rowing motion, flapping motion and feathering motion are installed inside the device.

The most important task using 3MDMPF is to establish an optimal match between the fin geometry and the motion in terms of optimal control force generation. The optimal parameters of the fin motion to generate the maximum control force in a particular direction were obtained experimentally by combining the experimental device and Hooke-Jeeves non-linear optimization method.

In this work, the optimal parameters of the fin motions were obtained so as to generate the maximum control force in X, Y, Z directions in terms of effects of uniform flow and motion pattern. Namely, motion parameters were optimized in a uniform flow or in still water, and in drag-based labriform swimming mode or in lift-based labriform swimming mode.

EXPERIMENTAL SETUP

The rowing angle ϕR, the feathering angle ϕFE, and the flapping angle ϕFL, were varied sinusoidally using the following definitions.

$$\phi_R = \phi_{R0} - \phi_{RA} \cdot \cos(\omega_{fin} \cdot t)$$

$$\phi_{FE} = \phi_{FE0} - \phi_{FEA} \cdot \cos(\omega_{fin} \cdot t + \Delta\phi_{FE})$$

$$\phi_{FL} = -\phi_{FLA} \cdot \cos(\omega_{fin} \cdot t + \Delta\phi_{FL}) \quad (1)$$

Experimental device is composed of the cylindrical body with the 3MDMPF, a computer for data generation and analysis with AD and DA boards and a computer where the optimization program runs and the second data processing for hydrodynamic coefficients.

The uniform velocity and the frequency were taken as 0.2 m/s and 1.25 Hz, respectively. Two kinds of initial conditions corresponding to the drag-based labriform swimming mode and the lift-based labriform swimming mode were given.

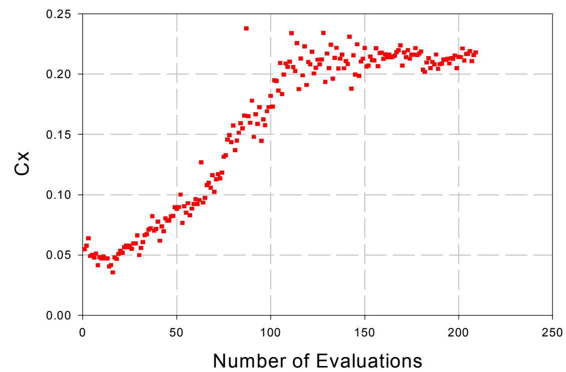

Figure 1: Variation of propulsive force coefficients during procedure of optimization for drag-based swimming mode in still water

SUMMARY

We have revealed through the optimization of motion of a mechanical pectoral fin that the lift-based labriform swimming mode rather than the drag-based labriform swimming mode is suitable for generation of propulsive force in uniform flow, while the drag-based labriform swimming mode rather than the lift-based labriform swimming mode is suitable for generation of propulsive force in still water.

REFERENCES

Lindsey,C.C (1978):Form, Function and Locomotory Habits in Fish, In "Fish Physiology VII Locomotion", edited by W.S.Hoar and D.J.Randall, Academic Press, pp.239-313

Kato,N.,Liu,H.,Morikawa,H.(2002). *Proceedings of 12th Int. Offshore and Polar Engineering Conf.* (submitted)

ACKNOWLEDGEMENTS

This research is funded by Office of Naval Research (Grant No. N00014-01-1-0501) as the project title "US-Japan Cooperative Research on Biology-Inspired Precision Maneuvering of Underwater Vehicles".

HYDRODYNAMICS OF A FLAPPING FIN WITH INTERACTION OF A BODY

Hao Liu[1], Naomi Kato[2] and Hirohisa Morikawa[3]

[1]The Institute of Physical and Chemical Research (RIKEN), Division of Computer and Information, hliu@postman.riken.go.jp
[2]Tokai University, School of Marine Science and Technology, Dept. of Marine Design and Engineering, nkato@scc.u-tokai.ac.jp
[3]Shinshu University, Faculty of Textile Science and Technology, Dept of Functional Machinery & Mechanics. hmorikw@giptc.shinshu-u.ac.jp

INTRODUCTION

Biological fluid dynamics associated with interaction between an oscillating wing or fin and a body is very common in animal swimming and flying. Many fishes thrive in extreme environments as fast currents and present excellent maneuvering performance by means of pectoral fins. Birds and insects beat their wings rapidly for hovering, and darting flight, in performing high stability and maneuverability. These locomotion mechanisms can be transferred from fluid dynamic viewpoint to the basic problem of the interactions among the wing or fin, the body and the surrounding flow. Interaction between an oscillating body and the flow about it has been the main subjects in studying biological fluid phenomena (Liu et al., 1998) but very few studies can be found, that deal with the hydrodynamics of a flapping wing or fin with consideration of the interaction of a body it attaches onto.

METHODS

We developed a computational fluid dynamic (CFD) simulator for biological fluid dynamics about realistic swimming and flying animals, which has been recently upgraded to be able to deal with a multi-body object. The simulator specified for the current problem is based on a solver for unsteady, incompressible Navier-Stokes equations developed by Liu et al., 1998, in which a geometric model and a kinematic model are incorporated. Upon the establishment and modification of the CFD simulator the following issues are taken into account: 1) build-up of a CFD simulator with special focus on modeling of unsteady hydrodynamics of a single flapping fin; 2) build-up of a CFD simulator with special focus on modeling of unsteady hydrodynamics of a body and a flapping fin.

In this paper we first discuss the verification and validation of our method by comparison with the measured hydrodynamic forces of a mechanical flapping pectoral fin with a cylinder body in Fig. 2(Kato et al., 2002) and furthermore address the hydrodynamics in terms of interaction between the fin and the body.

RESULTS AND DISCCUSSIONS

Computed results of a body-fin model undergoing rowing and feathering motions in uniform flow at a Reynolds number of 1.597×10^4 and the reduced frequency of 3.0 was illustrated in Fig. 1-2. Time variation of coefficients of hydrodynamic forces Cx, Cy was plotted in Fig. 1. With influence of the inflow, timing of the occurrence of the maximum thrust, zero thrust and minimum thrust changes slightly compared with those of the fin in stillwater. Flow pattern around the fin are shown in terms of velocity vectors, instantaneous streamlines, and pressure contours at instant when the Cx is max. Unlike the leading- and trailing edge vortex pattern about the fin in still water, the inflow obviously changes the vortex structure around the fin largely, leading to a long wake behind the fin. The interaction between the body and the fin likely extends significant influence on the feature of the wake structure and hence the force generation.

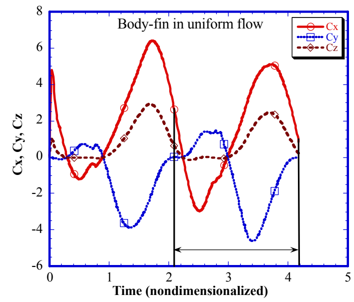

Fig. 1 Hydrodynamic forces

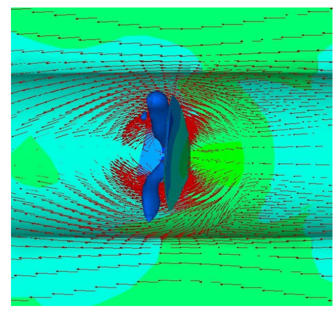

Fig. 2 Flow pattern

SUMMARY

An integrated CFD simulator has been established and validated for computational modeling of biological fluid dynamics associated with realistic multi-body model. An extended study on hydrodynamics of a flapping fin with interaction of a body shows that the hydrodynamic performance of the flapping fin can be affected significantly by the existence of the body.

REFERENCES

Liu, H. and Kawachi, K. (1998): A numerical study of insect flight", *Journal of Computational Physics*, **146**(1), 124-156.
Kato,N.,Liu,H.,Morikawa,H.(2002). *Proceedings of 12th Int. Offshore and Polar Engineering Conf.* (submitted)

ACKNOWLEDGEMENTS

This research is funded by Office of Naval Research (Grant No. N00014-01-1-0501) as the project titled "US-Japan Cooperative Research on Biology-Inspired Precision Maneuvering of Underwater Vehicles".

STRESS/STRAIN ANALYSIS OF ARTERIES WITH STENOTIC PLAQUES AND LIPID CORES

Dalin Tang[1], Chun Yang[2], Jie Zheng[3] and Raymond P. Vito[4]
[1]Mathematical Sciences Department, Worcester Polytechnic Institute, Worcester MA USA 01609, dtang@wpi.edu
[2]Mathematics Department, Beijing Normal University, Beijing, China
[3]Mallinkcrodt Institute of Radiology, Washington University School of Medicine, St. Louis, MO USA
[4]School of Mechanical Engineering, Georgia Institute of Technology, Atlanta, GA USA

INTRODUCTION. There has been increasing evidence that stenotic plaque may rupture under physiological conditions and cause fatal subsequential atherosclerotic diseases such as myocardial infarction, cerebral stroke, etc. In our prior studies, computational models with fluid-structure interactions were introduced to quantify pressure and stenosis severity conditions under which critical flow conditions (negative pressure, low and oscillating shear stress, high shear stress at the throat, flow separation) and artery compression which may be directly related to stenosis plaque rupture (Tang et al., 2001). It was found that wall stress/strain distributions are of very local nature and extremely sensitive to plaque structure and mechanical property changes. It is well known that stenotic plaques have complex structures and their mechanical properties vary widely (Beattie et al. 1998). In this paper, finite element models are introduced to perform stress/strain analysis of stenotic arteries where stenosis plaque structure and mechanical properties are added into our consideration.

METHOD. MRI images of human carotid artery plaque were supplied by Dr. Zheng from Washington University School of Medicine. Those images were digitized and smoothed before they were used in the numerical simulation. Mechanical properties of the artery wall, fibrous plaque, calcification and lipid were taken from Beattie (1998), Huang (2001) and our prior studies. Idealized 2-D and 3-D geometries of the stenotic arteries with fibrous plaque and lipid pools were used to find correlations between artery maximum stress/strain and structure of the plaque and imposed pressure conditions.

A finite element software package ADINA (ADINA R & D, Inc., Watertown, MA, USA) is used to solve the models for structure only and stress/strain analysis with fluid-structure interactions. The package has been extensively tested and verified with hundreds of engineering applications. Mooney-Rivlin material is used for the solid material while incompressible Navier-Stokes equations are used for the fluid. Parameter evaluations were performed for several typical cases and results are given below.

RESULTS AND DISCUSSION.
2-D MRI image-based structure analysis. Two cases are considered, one with smaller lipid pool which is further away from the lumen, other with larger lipid pool with a sharp angle close to the lumen area. The latter is more prone to rupture. Different internal pressures are imposed in the lumen. Stress/strain distributions are obtained for the arteries with and without lipid pools to find out the magnitude and location of maximum stresses. Then idealized geometries are used to perform parameter evaluation with incremental changes in pressure load and position of lipid pool.

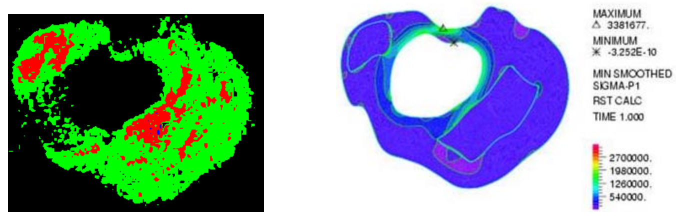

Fig. 1. MRI image of human carotid artery with fibrous cap, calcification and lipid pool (left) and contour plot of wall stress showing location and magnitude of maximum stress

3-D simulation for stenotic arteries with lipid pool. Arteries with streamlined asymmetric stenosis are used to simulate blood flow and artery stress/strain distributions under physiological conditions. Lipid pool of varying sizes and shapes are enclosed in the stenosis plaque to evaluate its effect on wall stress and flow behaviors. 3-D images will also be reconstructed from 2-D MRI images and used in the simulation.

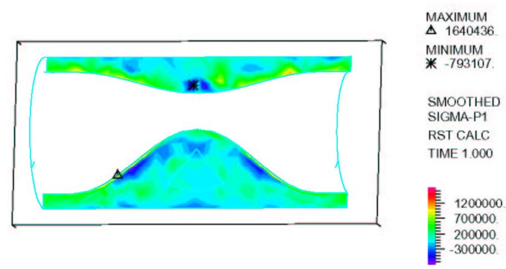

Fig. 2. Stress distribution for a 3-d asymmetric stenosis with an irregular lipid pool in the stenosis plaque. Unit: dyn/cm^2 .

CONCLUSION. Stress/strain distribution is very sensitive to plaque structure and mechanical property variations. Maximum stress increases rapidly as the sharp angle of the lipid pool gets closer to lumen. 3-D simulations provide more realistic predictions which may be helpful to identify stenoses which are more prone to plaque cap rupture. However, reconstruction of 3-D domain from 2-D MRI images and solution of those 3-D realistic models are very challenging.

ACKNOWLEDGMENT This research was supported in part by NSF grant DMS-0072873. Helpful discussions and advices from Drs. Roger Kamm, Richard T. Lee, and Hayden Huang are happily acknowledged.

REFERENCES
Beattie D. et al (1998), *J. Biomech. Engng*., **120**, 602-607.
Huang H. et al (2001), *Circulation*, **103**, 1051-1056.
Tang, D. et al(2001), *J. Biomech. Engng.*, **123**, 548-557.

MULTI-SCALE COMPUTATIONAL HEMODYNAMICS IN CARDIOVASCULAR SYSTEM

Hao Liu[1], Wei Shyy[2], Tomoki Kitawaki[3], and Ryutaro Himeno[1]
[1]The Institute of Physical and Chemical Research (RIKEN), Computer and Information Division, Wako, Saitama, Japan
hliu@postman.riken.go.jp, himeno@postman.riken.go.jp
[2]University of Florida, Department of Aerospace Engineering, Mechanics & Engineering Science, Gainesville, USA
Wei-shyy@ufl.edu
[3]OMRON Institute of Life Science Co. Ltd., Japan
tomoki-kitawaki/OLS@ns2.omron.co.jp

INTRODUCTION

Multi-scale computation in hemodynamics can help enhance our understanding of circulation at different levels. It can also help contribute to the computation-aided predictive medicine. The motivation for developing this approach is a pragmatic one: the scale disparity associated with hemodynamics is too vast to be simultaneously handled with adequate resolution, without modeling, by any existing and foreseeable computational tools. For example, 3D modeling of an isolated artery, even with a faithfully reconstructed anatomic model based on medical-images, requires information supplied from the rest of the blood circulation system in order to define physiological realistic inflow and/or outflow conditions. However, direct simulations of the full circulation system ranging from the large blood vessel to capillaries are not possible with today's computational capabilities. In order to simplify the task, lower dimensional approaches, such as 0D and 1D modeling can provide the information such as flow-pressure relationship, thus offering required boundary conditions for detailed simulations of a particular portion of the circulation system. A combined 0D/1D and 3D modeling can establish an efficient, multi-scale computational model in cardiovascular hemodynamics. In this paper we highlight our recent efforts in developing such a multi-scale computational model along with results of blood flows in human aortic arch with bifurcations.

METHODS

The PAtient-Specific Simulator (PASS) for hemodynamics that we developed (Liu, et al., 2001) has formed a foundation for the simulation-based diagnosis and surgery. PASS is an integrated system, involving an image-based morphological model, a realistic physiological model, and a multi-block, computational mechanical model. The morphological modeling system can reconstruct an anatomic model for vessels and/or organs based on medical images of MRA, US, and CT X-ray, and generate meshes for computation. The physiological modeling is measurement-based, in which blood velocity and pressure are measured by techniques such as MRA and Doppler US. It offers boundary conditions needed by the detailed simulation through a quasi-static hydraulic model.

In this study we have incorporated a recently developed 1D computational model for cardiovascular system into the PASS model. The model can handle unsteady viscous flow as well as generalized arterial viscoelastic dynamics (Kitawaki et al., 2001). It has been validated with measurements of pressure waves in a silicone rubber tube, which indicates that our model can predict the wave propagation and reflection more reasonable than several conventional 1D methods. We are aiming at establishing an interactive, multi-scale model in which, not only the global 1D model can provide boundary conditions for the local 3D model in terms of flow rate Q and pressure P, but also that the 3D model with realistic geometry can be used to improve the 1D model in terms of feedback of the detailed flow information such as pressure drop.

RESULTS AND DISCCUSSIONS

We select a prototypic cardiovascular model of human aorta arch involving bifurcations. The velocity-based boundary conditions at inlet and outlets are based on the 1D model in terms of flow rate and pressure. An extensive study is carried out to investigate how the ratio of flow rates among the outlets affects the flows in the aorta model as shown in Fig. 1, in which

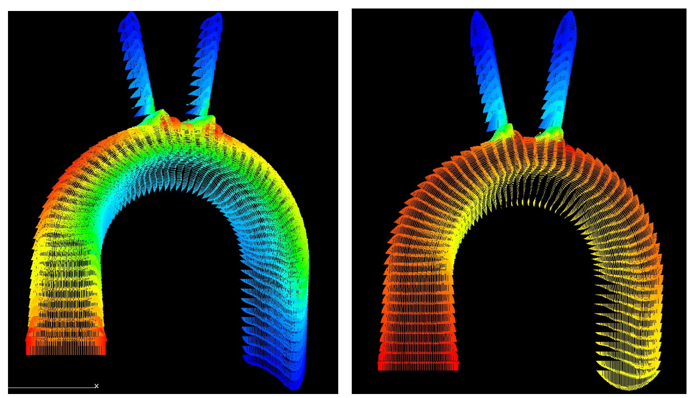

a) Free velocity conditions b) Flow rate-based conditions
Figure 1: Comparison of flows in an aortic arch model under two BC conditions

the color denotes the pressure decreasing from red to blue. Given a flow rate ratio between the descending aorta and the bifurcations of 7/3, the computed flow in both the aorta and in the LSA (Left Subclavian Artery) and BTA (Brachiocephalic trunk Artery) show apparent difference compared with the case (a) where the velocities at three outlets are set free. The pressure is fixed to be zero at the outlet of descending artery and is set free at both outlets of LSA and BTA.

REFERENCES

Liu,H.et al.(2001): *Proceedings of symposium on computational hemodynamics. USNCCM VI, 540*
Kitawaki,T. et al.(2001): *JSME International Journal, Special issue on Biomechanics. (submitted)*

ACKNOWLEDGEMENTS

This research is supported by the national project of Computational Biomechanics in RIKEN, Japan.

COMRESSIVE STRENGTH IN VERTEBROPLASTY UNDER FATIGUE LOADING AN EXPERIMENTAL AND A FINITE ELEMENT MODELLING ANANLYSIS

WW Lu[1], KT Yeung[1], KMC Cheung[1], C.T. Wong[1], M Zhang[2], KDK Luk[1], JCY Leong[1]

[1] Department of Orthopaedic Surgery, Queen Mary Hospital, The University of Hong Kong; Hong Kong
[2] Jockey Club Rehabilitation Engineering Centre, The Hong Kong Polytechnic University; Hong Kong

INTRODUCTION

Using minimally invasive techniques to inject bone cement for treating fractured or osteoporotic vertebral body(VB) has significant clinical potential. However, the effect of bone cement volume on the stiffness of VB cannot be evaluated in a more quantitative way and is still under investigation. Also, present studies show concern on the effect of one-off compression on VB. This approach, however, has neglected the clinical reality, which VB of patient bear body-weigh loading day to day consecutively. In this study, experimental testing and finite element model (FEM) of VB was constructed to investigate the effect of volume of bone cement used under fatigue loading.

MATERIALS AND METHODS

Mechanical properties of VB and bone cement were collected for modeling of FEM. ISO5833 guided the testing procedure for finding the properties of bone cement. Specimens of L1 to L5 VB of over 65-year-old cadaveric female were extracted. Soft tissue and posterior elements were removed. The VB were scanned by DEXA for confirmation of VB osteoporotic properties. The VB specimens were then divided into two groups, one without cement injected and one with bone cement injected, using cement delivery system – Parallax.

The first group of VB specimens (without bone cement injected) was scanned with 1.25mm CT scanning. The CT numbers in Hounsfield units (HU) were converted to bone mineral density (BMD) in g/cm^3. The elastic moduli of trabecular centrum were calculated by BMD value[1].

Compression load was applied on VB by MTS machine. It was loaded at 0.5% strain/s and loaded to 1.78% which exceeded yield point of the VB, unloaded, and then reloaded to 10% strain to obtain the real damaged VB. The CT data was imported into a finite-element modeling software, ANSYS, for developing a FEM model of the VB. The elastic constants of yield elements with reduced properties were replaced[2] as:

$$\%\Delta \text{Elastic constant} = \frac{227 \times \text{strain}\%}{\text{strain}\% + 6.18}$$

The model was reloaded and the damaged FEM VB was simulated. Structural stiffness was calculated by the steepest slope of load-deflection curve over displacement range, appeared in the loading (S_1) and reloading (S_2) cycle.

Virtual implant of bone cement Different volume of bone cement 2ml, 4ml, 6ml and 8ml was injected into the second group of VB specimens respectively and then CT scanned. With reference to the pattern under CT, bone cement was virtually implanted into the damaged VB FEM model with different volume. The stiffness of VB with different volume of bone cement implanted was found. The value of stiffness was compared with that of damaged and intact VB without bone cement implanted. VB with bone cement implanted was then performed compressive fatigue loading of about 20,000 cycles, and the data was input in FEM model as fatigue loading condition. FEM model was further validated by comparing the FEM model of a damaged VB with the experimental results.

RESULTS & DISCUSSION

Table I shows the result of compression test on bone cement. (Composite ratio: Resin 4g (Si-HA 3.9g, Fumed Silica 0.1g, BPO 0.011g), Filler blend 6g) It was used for finding mechanical properties for FEM modeling.

It was found that the stiffness of all VB specimen with bone cement injected exceeds stiffness without bone cement in damaged VB. After injection, stiffness of the spine recovered to 112% of the intact condition ($p<0.01$). Average failure strength of the spine after injection and 20,000 loading cycles was 5056 N. The stiffness was increased proportional to the increased the bone cement volume ($r=0.84$).

Fatigue loading test is a better way for studying stress behavior as it is close to clinical reality. Performing fatigue loading cycle in FEM model could be used to simulate the VB under long term clinical follow up.

Table I: Compression testing result of bone cement

	F (N)	σ (MPa)	ΔL (mm)	υ
1	3214	118	3.6	0.30
2	2951	108	3.6	0.24
3	3455	126	3.6	0.22
4	3124	115	3.0	0.28
5	3377	125	3.6	0.27
6	2325	86	3.2	0.25

(F-fracture force; σ-compressive strength; ΔL-compressive displacement; υ-poisson ratio)

REFERENCES

[1]Keaveny *et al. J of Orthopaedic Research* 1997;17:346-53
[2]Kopperdahl *et al. J of Orthopaedic Research*;1998 18(5):685-91

ACKNOWLEDGEMENTS:

Financial support from the Hong Kong Research Grant Council (RGC) 7249/99M.

Sr-HA BIOACTIVE BONE CEMENT CHARACTERIZATION AND ANIMAL TRIALS

W.W. Lu[1, 2], C.T. Wong[1], D.S. Lu[1], K.M.C. Cheung[1], K.D.K. Luk[1] and W.K. Chan[2], J.C.Y. Leong[1]

[1]Department of Orthopaedic Surgery, Faculty of Medicine, The University of Hong Kong; Hong Kong;
[2]Department of Chemistry, Faculty of Science, The University of Hong Kong; Hong Kong

INTRODUCTION

It has been reported that using minimally invasive bone cement injection for treating vertebral body fracture or stabilizing osteoporosis has been used clinically in recent years. Conventional poly(methyl methacrylate) (PMMA) bone cement has been used in orthopaedic surgery for over 40 years. However, it does not encourage bone ingrowth, has a high exothermity, and monomer toxicity. New bioactive bone cement was designed to overcome the disadvantage of PMMA. The purposes of this study were to further character the new injectable bioactive bone cement designed specifically for spinal surgery and to conduct animal trials.

MATERIALS AND METHODS

The bioactive bone cement contains a filler blend and a resin blend. The filler blend contains Strontium-containing hydroxyapatite (Sr-HA), fumed silica and benzoyl peroxide (BPO). The resin blend contains bisphenol A diglycidylether dimethacrylate (Bis-GMA), poly(ethylene glycol) methacrylate (PEGMA) and *N,N*-dimethyl-*p*-toluidine. The materials used were less toxic when compared with methyl methacrylate (MMA), which was the major component in conventional PMMA bone cement.

Strontium-containing hydroxyapatite was synthesized by the wet method and was characterized by Fourier Transform Infrared (FTIR) spectroscopy, X-ray diffraction (XRD) spectroscopy and Electron-dispersive X-ray (EDX) analysis. Strontium can act as a radiopaque.
The ratio of mixture in the resin blend was adjusted so that the mechanical properties suited the usage on surgery. The ratio of the filler and resin blend was adjusted and the setting time and temperature were monitored during the mixing of bone cement.

New Zealand white rabbits (n=10) were used for animal test. Bone cement was injected into the hole in ilium at rabbits. X-ray film was taken periodically post-operation to observe the bone cement in the ilium. The rabbits were sacrificed 3 months post-operation. Another four rabbits were performed as a control with conventional PMMA bone cement. The bone and bone cement interface was observed by Scanning Electron Microscopy (SEM) and Electron-dispersive X-ray (EDX) analysis. Histology of the bone with bone cement section stain with giemsa and eosin was performed.

RESULTS AND DISCUSSION

Strontium-containing hydroxyapatite (Sr-HA) was synthesized successfully. The spectra of Sr-HA from Fourier Transform Infrared (FTIR) spectroscopy and X-ray diffraction (XRD) spectroscopy have the pattern as hydroxyapatite. From Electron-dispersive X-ray (EDX) analysis, strontium, calcium and phosphorus were found which were elements in Sr-HA(**Fig. 1**).

Setting time and temperature is a key issue for orthopaedic surgery using bone cement. The setting time of the bone cement can be adjusted from 8 to 16 minutes. The maximum temperature was between 45 and 60 °C.
The bone cement can be seen on X-ray film. The bone cement was not absorbed. By Scanning Electron Microscopy (SEM) and Electron-dispersive X-ray (EDX) analysis, the bone and bone cement interface can be observed clearly. The bone cement is bioactive which bond to the bone without soft tissue separation. The EDX pattern of bone cement was similar to that of bone except peaks of strontium and silica were found in the cement. Histology of the bone with bone cement section stain with giemsa and eosin was examined and the bone in growth on the bone cement interface was observed.

SUMMARY

A bioactive bone cement which has many advantages over conventional PMMA bone cement was studied. The bone cement was injectable, with less toxic monomers, have lower setting temperature and reasonable setting time and mechanical strength suitable for orthopaedic surgery.

REFERENCES

WW Lu, KMC Cheung, YW Li et al. ***Spine***, 2001:26:24,2684.
Y.W. Li, J.C.Y. Leong, W.W. Lu et al. ***J. Biomed. Mater. Res***. 2001: **52**, 164-170.

ACKNOWLEDGEMENTS:

Financial support from the University of Hong Kong CRCG.

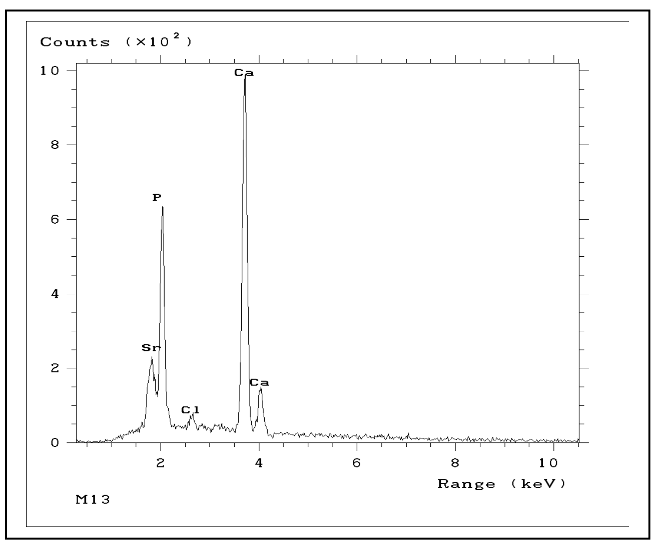

Fig. 1 EDX of Sr-HA Bioactive Bone Cement

PULSE EFFECTS OF LOW INTENSITY ULTRASOUND STIMULATION ON BONE CELLS PROLIFERATION

Walter Hong-Shong Chang[1], Jui-Sheng Sun[2], James Cheng-An Lin[1] and Jimmy Li[1]

[1]Department of Biomedical Engineering, Chung Yuan Christian University, Chung-Li, Taiwan, ROC. whchang@cycu.edu.tw
[2]Department of Orthopedic Surgery, National Taiwan University Hospital, Taipei, Taiwan, ROC

INTRODUCTION

Ultrasound wave is a longitudinal sound wave that causes high-frequency compression and expansion of the medium which can lead to pressure variations. The stimulatory effect of ultrasound on the fracture healing has been well established during the last decade [1]; but the mechanism is still pending. Many physical parameters of the ultrasound may be involved in different biological effects. The aim of our investigation is to study the possible mechanism of the pulse effects of ultrasound stimulation on the bone cells proliferation.

METHODS

Osteoblast-like cells were isolated from sequential enzymatic digestion of neonatal rat calvaria. After 6 days culture, confluent osteoblast cells were detached from the petri dish, counted and subdivided into 3-cm wells. All dishes were then underwent ultrasound stimulation at a well-maintained temperature (37±1^{o}C) as described below (Fig.1).

The osteoblasts were stimulated at the intensity of 150 mW/cm^2 (temporal average intensity) with different pulse waveform (continuous wave (CW), 1:1, 1:4, 1:9) for 15 min. The frequency of ultrasound stimulation is 1 MHz and the pulse-repeated frequency at 100Hz. The rate of cell proliferation was monitored by measuring the rate of BrdU incorporation into osteoblasts by immunofluorescence staining.

RESULTS AND DISCUSSION

The results showed that the adding of pulsed ultrasound stimulation can enhance the osteoblast-like cells proliferation. The osteoblasts cell counts increased significantly after treatment of pulsed ultrasound stimulation. The PGE2 concentrations in culture medium also increased significantly. But the treatment of continuous wave of ultrasound did not affect both the osteoblasts cells counts and the PGE2 secretion.

The results suggested that pulsed wave played an important role during the ultrasound stimulation. Cells were excised (or stimulated ???) during cycles of pulse on-off and the proliferation were also activated at the same time. Indeed, it is exactly this interaction that we believe contributes to the osteogenic potential of pulse strain.

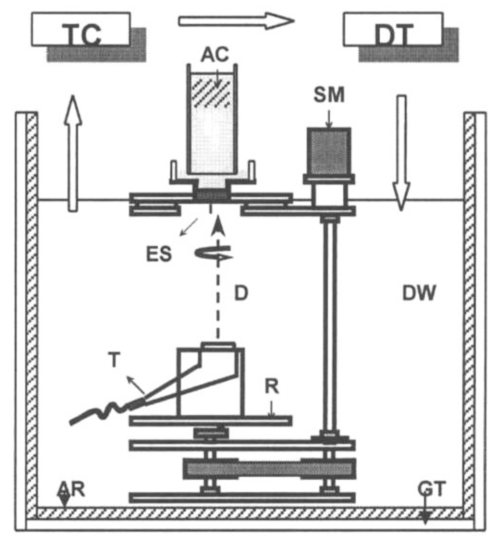

Figure 1: Schematic diagram of the experimental arrangement for the ultrasound stimulation. AC = Absorption Chamber; AR = Absorption Rubber; D = Distance from transducer to cell flask, 240mm; DT = Degas Tank; DW = Distilled Walter; ES = Exposure Sample; GT = Glass Tank; R = x-y Roter; SM = Stepping Motor; T = Transducer; TC = Temperature Controller.

SUMMARY

In this study, we established the pulse effects of ultrasound stimulation on the bone cells proliferation. The results showed that pulsed ultrasound stimulation got significantly responses to bone cells proliferation than continuous ultrasound stimulation does.

REFERENCES

1. Kristiansen TK. Ryaby JP. McCabe J. Frey JJ. Roe LR. (1997) *Journal of Bone & Joint Surgery - American Volume.* 79(7): 961-73.

ACKNOWLEDGEMENTS

This project was supported in part by NHRI-EX91-8925EL and NSC90-2213-E002-130. We thank their financial support.

COMPUTATIONAL FLUID DYNAMICS SIMULATION OF THE RIGHT CORONARY ARTERY MOVING WITH THE CARDIAC WALL

Hiroyuki Hayashi and Takami Yamaguchi

Dept. Mechatronics and Precision Engineering, Tohoku University, Aoba 01, Sendai 980-8579,
hayashi@pfsl.mech.tohoku.ac.jp, takami@pfsl.mech.tohoku.ac.jp

INTRODUCTION

The beating motion of the heart wall, to which the major coronary arteries are fixed, is interesting, due to its possible mechanical influence on the flow inside the artery, and hence its effect on atherogenesis. In this study, we conducted a computational fluid dynamics (CFD) simulation using a simplified model of the right coronary artery, which deforms with heart contractions. The results are discussed with respect to the local hemodynamics characteristics, particularly the streamline pattern and the wall shear stress distribution.

METHODS

The CFD model of the right coronary artery consisted of a coiled pipe with an ordinary helix as a centerline, surrounding a cylinder that simulated the heart. The diameter and height of the cylinder changed over time at a given rate. The volume reduction in one beat of the cylinder was 75%; *i.e.*, the ejection fraction (EF) was 0.75.

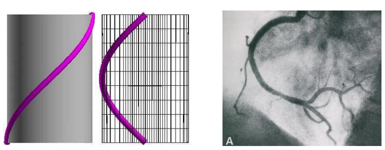

Figure 1: CFD model and angiogram of the right coronary artery.

The coupling of the wall and fluid motions was based on a previously reported method, in which the wall motion is assumed quasi-steady compared to the development of the flow. Three different modes of changes in the shape of the CFD model were examined to investigate the effect of the time dependent curvature and tosion of the right coronary artery on the flow. The unsteady inflow velocity perpendicular to the inlet cross section was defined by a cosine function of phase 180° different from the time evolution of the change in volume (Figure 2). The Reynolds number was 300, defined by the maximum inflow velocity and the diameter of the inlet cross section. One cardiac cycle was assumed to last for one second, *i.e.*, the heart rate was assumed to be 60 beats/min.

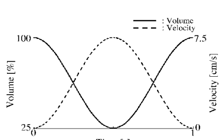

Figure 2: The time evolution of the change in volume (solid line) and inflow velocity (dots).

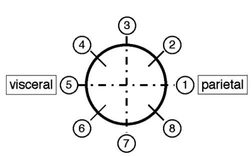

Figure 3: Observation posts of the WSS data along the circumference of the cross section midpoint.

RESULTS AND CONCLUSIONS

Representative results are given by the streamline patterns and corresponding WSS distribution at a cross section in the middle of the right coronary artery model at a phase between the early systole and the late diastole, shown in Figure 4. The observation post numbers of the WSS distribution in Figure 4 correspond to the numbers shown in Figure 3.

Many interesting features of the fluid dynamics are evident in Figure 4. Characteristic changes in the streamline and WSS distribution appeared when the flow was decelerated. Useful information about the specific mechanisms for the formation, growth, and breakdown of coronary plaque can be obtained from an analysis of the results under various physiological conditions.

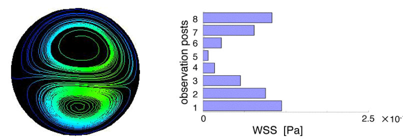

(a) volume change of the heart with a constant diameter to height ratio.

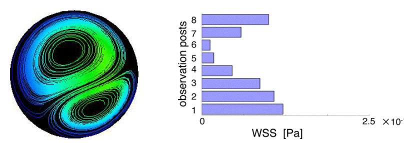

(b) volume change of the heart with only the height changed.

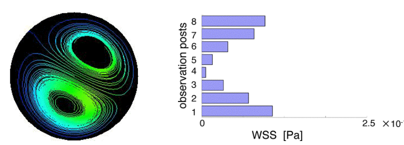

(c) volume change of the heart with only the diameter changed.

Figure 4: Streamline patterns and corresponding cross-sectional distribution of the WSS.

REFERENCES

T. W. Taylor, H. Okino and T. Yamaguchi. (1994), *Three-dimensional analysis of left ventricular ejection using computational fluid mechanics*, Journal of Biomechanical Engineering, Vol.116(1) pp.127-130

T. W. Taylor, H. Suga, Y. Goto, H. Okino and T. Yamaguchi. (1996), *The effects of cardiac infarction on realistic three-dimensional left ventricular blood ejection*, Journal of Biomechanical Engineering, vol.118(1) 106-110

H Hayashi and T. Yamaguchi. (2002), *A simple Computational Model of the Right Coronary Artery on the Beating Heart Effects of the Temporal Change of Curvature and Torsion on the Blood Flow* , Biorheology, submitted.

THE EFFECT OF MEDIAL TRANSLATION ON TIBIAL LOAD AND STRESS DISTRIBUTIONS IN TOTAL KNEE PROSTHESES

Jiann-Jong Liau[1], Cheng-Kung Cheng[1,*] and Chun-Hsiung Huang[1,2]

[1]Orthopaedic Biomechanics Laboratory, National Yang Ming University, Taipei, Taiwan. ckcheng@ortho.ym.edu.tw
[2]Department of Orthopaedic Surgery, Mackay Memorial Hospital, Taipei, Taiwan

INTRODUCTION

Alignment is an important consideration in many clinical situations, such as fracture reduction, deformity correction and total knee arthroplasty. Significant changes in the axial alignment of the femur and tibia may alter the loading and stress distributions in the knee joint[1]. The purpose of this study was to investigate the effect of medial translation on tibial load and stress distributions in two different designs of total knee prostheses.

METHODS

Three-dimensional finite element models of the tibiofemoral joint of knee prostheses for two different designs were constructed. The sagittal radii of the femoral and tibial components were identical in those two knee prostheses. In the frontal plane, the high conformity flat-on-flat design (HFF model) has the same curvatures in femoral and tibial components with a radius of 120 mm. The high conformity curve-on-curve design (HCC model) has a smaller curvature in femoral and tibial components with a radius of 70 and 72 mm respectively. The medial translation (0.25, 0.5 and 1.0 mm) of the femoral component relative to the tibial component were simulated. A compression load of 3000 N was applied to the tibiofemoral joint at 0¢Xof flexion. The contact forces on the medial and lateral tibial components and the maximum von-Mises stress calculate from finite element analysis was used to investigate the effect of medial translation on the tibial load and stress distributions.

RESULTS AND DISCUSSION

The contact force on the medial and lateral parts of tibial component was showed in Figure 1. The difference of contact force between medial and lateral parts increased when the distance of medial translation of femoral component relative to the tibial component increased. The maximum difference of contact force on medial and lateral parts of tibial component relative to total contact force was 89% and 11% in the HFF and HCC models respectively. The HFF design showed a severe asymmetrical load distribution when medial translation of femoral component occurred. The maximum von-Mises stress of the tibial component was showed in Figure 2. In comparing with the neutral position, the greatest increase of von-Mises stress was 92.5% in HFF model. Again, the greater the displacement of the femoral component moved medially, the greater increase in maximum von-Mises stress.

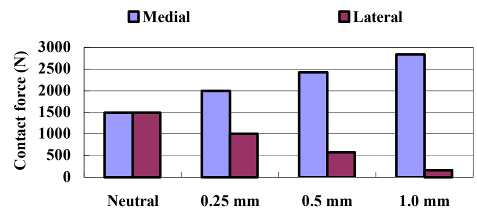

(a)

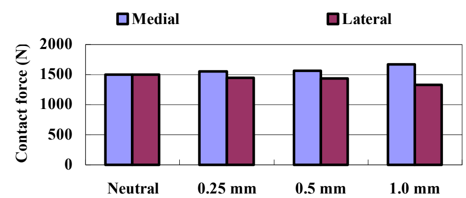

(b)

Figure 1: The load distributions on tibial component in (a) Flat-on-Flat design and (b) Curve-on-Curve design when femoral component was translated medially.

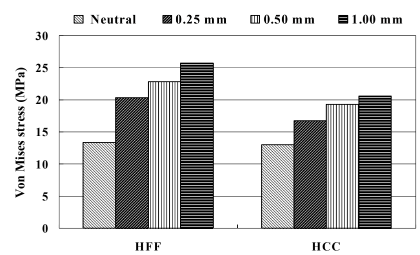

Figure 2: The maximum von-Mises stress in the tibial component of those two knee designs under maltranslation conditions.

SUMMARY

The high conformity flat-on-flat design showed a severer asymmetrical load distribution and greater increase of von-Mises stress than the high conformity curve-on-curve design when the medial translation of femoral component occurred. Therefore the flat-on-flat design of knee prosthesis would increase the risk of polyethylene wear under maltranslation conditions.

REFERENCES

1. Chao EYS, et al. (1994). Orthop Clin North Am, 25: 379-86.

EFFECT OF LESIONS ON THE THREE-DIMENSIONAL MECHANICS OF THE INTERVERTEBRAL DISC

Rosemary Thompson, Mark Pearcy and Timothy Barker

Centre for Rehabilitation Science and Engineering, Queensland University of Technology, Brisbane, Australia
rosemary.thompson@ao-asif.ch

INTRODUCTION

Progressive degenerative changes of the intervertebral disc are related to increased age and will thus affect a large proportion of the population. Macroscopically, degeneration in the intervertebral disc can be characterised by concentric tears, radial tears and rim lesions (Thompson et al, 2000). Initiation of degeneration is poorly understood. However, once initiated degeneration affects the mechanics of the intervertebral joint (Nachemson et al., 1979) and this may lead to further degeneration. Hence, it is important to understand how individual intervertebral disc lesions affect the mechanics of the spinal joint during physiological motion and how this may lead to further degeneration.

METHODS

A robotic materials testing facility was used to perform the mechanical tests on sheep spinal motion segments. The robot was a Kawasaki PH260 (Kawasaki, Japan, 1989) and it was controlled by a digital signal processing card (20 MHz PMAC PC, Delta Tau, USA). Three-dimensional force data acquisition was achieved using a JR3 50M31 force transducer (JR3, California, USA). This system offers a solution to the restrictions of a traditional engineering testing facility as it is capable of motion with six degrees of freedom and is able to dynamically test specimens through the full range of motion.

Sheep intervertebral joints were used as they provide a good biomechanical model for the human lumbar spine (Wilke et al, 1997). The L1-L2 and L3-L4 levels in the sheep spine were used to represent the corresponding motion segment in humans. As humans do not have a sixth vertebra, the L5-L6 level was used to represent the L4-L5 level in the human.

Physiologically accurate motions of flexion/extension, lateral bending and axial rotation were performed on pre-conditioned, isolated disc motion segments. These tests created the data for future reference. The following three sets of tests were performed after the creation of an intervertebral disc lesion. The three lesions created were radial tears, rim lesions and concentric tears. Radial tears were created by inserting a thin bladed knife vertically into the left postero-lateral portion of the disc. Concentric tears were placed in the anterior of the disc and created according to Fazzalari et al, 2001. Rim lesions were produced by inserting a blade horizontally into the anterior anulus on the right side. The order of insertion depended on the specimen's level, and each tear was the initial tear created for at least one of the levels. After the creation of each lesion, all three motions were performed and compared to the original, undamaged test.

RESULTS AND DISCUSSION

The mechanical factors examined from this study were the size of the neutral zone, maximum moment resisted by the intervertebral disc during each motion and the hysteresis of the response. Radial tears and concentric tears had no effect on any of the studied mechanical factors. A right, anterior rim lesion increased the neutral zone by approximately 1.5 degrees and reduced the maximum moment resisted by the intervertebral disc by approximately 20% during extension in L1/L2 specimens. Rim lesions were also found to reduce the maximum moment resisted by the intervertebral disc in lateral bending and axial rotation for all levels by approximately 15% and 25% respectively. Rim lesions did not affect the hysteresis of intervertebral disc motion.

These results suggest that the presence of a rim lesion in the intervertebral disc reduces the capability of the intervertebral disc to control motion and other spinal elements would be required to compensate. This could lead to overloading of the spinal ligaments, muscles and zygapophysial joints, which may result in damage to these structures. This could commence a cycle of degenerative changes to the spinal elements that is instigated by the mechanical response of the intervertebral joint to loading.

SUMMARY

The mechanical effects of intervertebral disc lesions were examined by experimentally introducing lesions into sheep intervertebral discs and comparing the mechanical response of the injured joint to the joint's response prior to the creation of the lesions. Rim lesions were found to reduce the intervertebral disc's mechanical integrity during all motions.

REFERENCES

Fazzalari, N. et al (2001). *Spine* **26**(23): 2575-2581.
Nachemson, A. et al (1979). *Spine* **4**(1): 1-8.
Thompson, R. et al (2000). *Spine* **25**(23): 3026-3035.
Wilke, H. et al (1997). *Spine* **22**(20): 2365-2374.

COMPUTATIONAL MECHANICAL ANALYSIS OF THE PLATELETS ADHESION USING A COMBINED STOKESIAN DYNAMICS METHOD AND DISCRETE ELEMENT METHOD

Kouichirou YANO[1], Takami YAMAGUCHI[2]
1) Department of Mechanical and System Engineering, Nagoya Institute of Technology, Nagoya, Japan,
kouichiro@pfsl.mech.tohoku.ac.jp
2) Deprtment of Mechatronics and Precision Engineering, Graduate School of Engineering, Tohoku University, Sendai, Japan,

INTRODUCTION

Platelets play an important role in blood coagulation, particularly in the formation of primary thrombi. The aggregation of platelets, which initiates primary thrombi formation, is thought to be mediated by the von Willebrand factor (vWF). The vWF is a long-chain macromolecule that exists in a soluble form in the blood flow and an insoluble form in the vessel wall. The vWF plays a more important role in pathological thrombosis formation than in the normal hemostatic process, due to its ability to sense and react to hemodynamic stress.

In this study, we analyzed the mechanical interactions between platelets, the vessel wall, and the vWF, using both a Stokesian dynamics method (SDM) and a discrete element method (DEM) that can treat solid elements in a flow without assuming continuity.

METHOD

A two-dimensional (2D) mechanical model of a blood vessel, platelets, and the vWF was constructed. The mechanical interactions between individual platelets, and the interactions between the platelets and vessel walls that were mediated by the vWF, were modeled as shown in Fig. 1. Here, the vWF was assumed to act at a relatively remote distance from the direct collision of components, and a vWF molecule was assumed to produce only a tensile force at a certain distance from the other elements (platelets or the wall). Furthermore, it was assumed that only repulsive forces were generated in the direct interactions.

(a) Between platelets (b) Between a plateletand a wall

Fig.1 Mechanical models of interaction mediated by the vWF

A 2D Couette flow model was used in the present study, and the influence of other blood constituents, including red blood cells, was neglected. The fluid force acting on the particles was calculated using the SDM.

RESULTS AND DISCUSSION

The variable strength of the chemical binding between the platelets and vWF's was simulated by changing the number of receptors (Nre) on the vWF. The destruction process of the primary thrombus under the influence of the blood flow was then modeled.

Fig. 2(a) shows the results for Nre = 0. Since the only force acting between the platelets and the vessel wall in this model is the repulsive force, the simulated platelets separate from the aggregation individually. Fig. 2(b) shows the results for Nre = 5. When there are both repulsive forces due to direct collisions and tensile forces due to the vWF between platelets or between platelets and the vessel wall, the modeled platelets moved together to form an aggregation in the blood flow. Fig. 2(c) shows the results for Nre = 10. Larger platelet aggregations are observed, since the number of receptors is twice as large as the former case, resulting in a much larger binding force. The time evolution of the number of aggregations is shown in Fig. 3. The number of receptors, and hence the total binding force between the platelets and the vWF, significantly affects the destruction process of the primary thrombus.

Two simulation methods were used in the present study: the DEM to describe the direct collision mechanism between solid elements, and the SDM to describe fluid-solid interactions. This combination has the potential to simulate the discontinuous movement of blood constituents such as platelets.

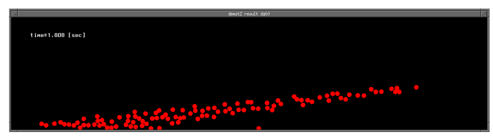

(a) Nre=0

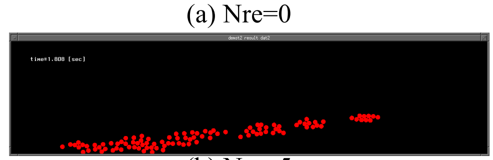

(b) Nre=5

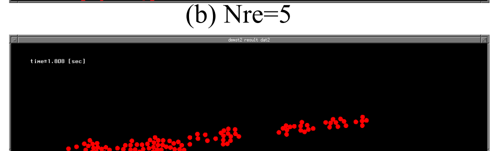

(c) Nre=10

Fig.2 Simulated results of a thrombolytic process under influence of the blood flow

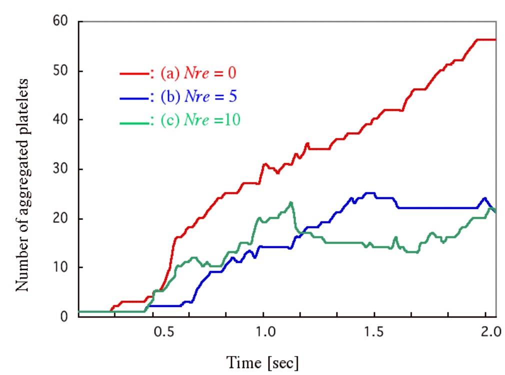

Fig.3 Time cause of the number of aggregated platelets

BIOMECHANICAL EVALUATION OF A NEWLY DEVISED MODEL FOR THE ELONGATION-TYPE ANTERIOR CRUCIATE LIGAMENT INJURY WITH PARTIAL LACERATION AND PERMANENT ELONGATION OF FIBERS

Eiji Kondo[1], Harukazu Tohyama[1], Masanori Yamanaka[1], Akio Minami[2], Kazunori Yasuda[1]
[1]Department of Medical Bioengineering & Sports Medicine and [2]Department of Orthopaedic Surgery,
Hokkaido University School of Medicine, Sapporo, Japan. yasukaz@med.hokudai.ac.jp

INTRODUCTION

The elongation-type anterior cruciate ligament (ACL) injury, in which the ligament is permanently elongated with partial laceration and permanent elongation of collagen fibers, frequently occurs in athletes. For this type of ACL injury, we have had no therapeutic methods except for the reconstruction of the whole ACL to repair the injured site in the substance. To develop new therapeutic methods involving gene therapy for this type of ACL injury, it is necessary to establish a model of this injury. Previous studies have reported a few models for the partial laceration-type ACL injury (O'Donoghue et al., Wiig et al., Hefti et al.). In these models, however, collagen fibers that are not lacerated in the substance remains thoroughly intact. Therefore, it is necessary to develop a more suitable model for this specific ACL injury. We have developed a new ACL injury model with partial laceration and permanent elongation of collagen fibers. The purpose of this study is to biomechanically evaluate this ACL injury model using rabbits.

MATERIALS AND METHODS

A total of 27 skeletally mature female rabbits were used for this study. In each animal, after the anteromedial and posterolateral half of the right ACL were transected with a scalpel at the proximal and the distal one-third levels, respectively, the ACL was stretched by applying an anterior drawer force of 10N to the tibia at 90° of knee flexion (Fig 1). No immobilization was applied after surgery. Nine rabbits were sacrificed at 0, 6, and 12 weeks after surgery, respectively. Seven out of the 9 rabbits were used for biomechanical evaluation, and the remaining 2 were used for histological observation. The left knees were used to obtain normal control data. In biomechanical evaluation, the anterior-posterior (A-P) translation of the knee was measured using a tensile tester with a 5-DOF fixture under ± 10N A-P loads at 30, 60, and 90° of knee flexion. Then, the cross-sectional area (CSA) of the ACL was measured with a video dimension analyzer. The structural properties of the femur-ACL-tibia complex (FATC) were determined in tensile testing at a cross-head speed of 20 mm/min. In each study, statistical analyses were made using the ANOVA with the post-hoc Fisher PSLD test for multiple comparisons.

RESULTS

(1) At 0 weeks (immediately after surgery), the ACL length of the injured knee was significantly elongated to 110 % of its original length, and the A-P translation was significantly greater than the normal knee (Table 1). At 6 and 12 weeks, the ACL length of the injured knee remained significantly greater than the normal value. There were no significant differences among the 0-, 6-, and 12-week periods. The CSA did not significantly change over time. (2) The A-P translation of the injured knee also remained significantly greater than the normal value at 6 and 12 weeks. (3) Concerning failure modes, each specimen was torn at the mid-substance of the ACL. The maximum load and the stiffness of the injured FATC were significantly lower than the normal control values at 0, 6, and 12 weeks. (4) Histologically, alignment of collagen fibers in the mid-substance of the injured ACL appeared to be irregular with significant cellular proliferation at 6 and 12 weeks.

DISCUSSION

This study demonstrated that this newly devised procedure significantly increased the ACL length and the A-P translation of the knee, and that it drastically decreased the structural properties of the FATC to 28% of the normal value at 0 weeks and 48% at 12 weeks. This fact showed how the quantitative procedure can create serious injury in the ACL substance with partial laceration and permanent elongation of collagen fibers. We believe that the model we have developed is useful to study new therapeutic methods, such as gene therapy, cell therapy, and so on, for the elongation-type ACL injury.

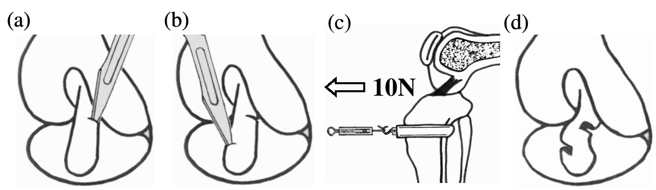

Figure 1: The elongation-type ACL injury model.

REFERENCES

O'Donoghue DH et al(1966). *J Bone Joint Surg* **48A**,503-519.
Wiig ME et al (1990). *J Orthop Res* **8**, 425-434.
Hefti FL et al (1991). *J Bone Joint Surg* **73A**, 373-383.

Table 1: Results of mechanical test after partial laceration and permanent elongation of the ACL

	Tissue dimension		*A-P translation (mm)*			*Structural properties of the FATC*	
	ACL length (mm)	Cross-sectional area (mm2)	30°	60°	90°	Maximum load (N)	Stiffness (N/mm)
Control	10.5 ± 0.8	6.4 ± 0.7	2.0 ± 0.5	1.6 ± 0.3	1.0 ± 0.3	361.8 ± 51.8	136.4 ± 23.6
0 weeks	11.5 ± 0.8*	6.1 ± 0.9	2.6 ± 0.4*	2.4 ± 0.5*	1.6 ± 0.3*	102.5 ± 28.5*	43.1 ± 12.0*
6 weeks	11.5 ± 0.9*	5.8 ± 0.8	3.0 ± 0.6*	2.4 ± 0.3*	1.7 ± 0.4*	146.4 ± 50.9*	65.2 ± 13.1*
12 weeks	11.5 ± 0.7*	5.8 ± 1.3	3.2 ± 0.5*	2.8 ± 0.7*	2.1 ± 0.5*	174.9 ± 60.8*	73.9 ± 25.7*

* $p<0.05$ (vs Control), Mean±SD, n=7 for each

SPREADING AND PEELING DYMANICS IN A MODEL OF CELL ADHESION

S.R. Hodges[1] and O.E. Jensen[2]

[1]Department of Applied Mathematics and Theoretical Physics, University of Cambridge, Sliver Street, Cambridge CB3 9EW, UK; Email: srh34@damtp.cam.ac.uk
[2]Centre for Mathematical Medicine, School of Mathematical Sciences, University of Nottingham, University Park, Nottingham NG7 2RD, UK; Email: O.E.Jensen@nottingham.ac.uk

INTRODUCTION

The adhesion of blood-borne cells to activated endothelium is of fundamental importance in the body's response to injury or inflammation. In order to understand better the competition between viscous forces, elastic cell membrane forces and adhesive forces associated with specific receptor-ligand bonds, we consider a theoretical model system in which a two-dimensional cell, modeled as an extensible membrane under tension containing fluid of constant volume, adheres to a plane surface. We treat three situations: *sedimentation*, where an initially circular cell settles onto the wall under the action of adhesive forces (and during which the membrane at the base of the cell spreads dynamically over the wall); *aspiration*, where the cell is removed from the wall under the action of an external force, applied to the top of the cell and acting normal to the wall (and during which the base of the cell peels off the wall); and *rolling*, where the cell tank-treads over the wall in the presence of a shear flow, spreading at the leading edge of the cell's base and peeling at the rear.

METHODS

We model binding kinetics following Dembo *et al.* (1988), using a continuum description of bond mechanics and treating individual molecular bonds as Hookean springs with rates of bond formation and breakage dependent on bond extension. If binding kinetics occurs rapidly compared to flow timescales, the binding forces are equivalent to a contact potential that is long-range attractive and short-range repulsive. The flow in the thin gap between the cell and the wall is described using lubrication theory; viscous stresses in the cell's interior are neglected. The membrane tension is assumed large enough compared to adhesive forces that, in equilibrium, the cell binds to the wall over a region that is long compared to the bond length, but short compared to the cell radius R; on lengthscales comparable to R, the cell in this case appears to meet the wall with a small but well-defined equilibrium contact angle θ_0. The presence of microvilli or glycocalyx is neglected. Numerical simulations of a nonlinear evolution equation for the gap thickness are used to describe sedimentation and aspiration. The simulations are used to motivate and justify calculations based on thin-film asymptotics that relate the effective dynamic contact angle θ to the speed V at which the membrane spreads over, or peels off, the adhesive wall. A force balance on a rolling cell, in which the imposed viscous shear force balances components of the membrane tension acting in different directions at each effective contact line, is used to obtain a relation between the rolling speed V and the imposed shear rate. Full details appear in Hodges and Jensen (2002).

RESULTS

During sedimentation, the cell moves down onto the wall and the contact region at the base of the cell spreads sideways. Fluid just outside this region is trapped between the membrane and wall, creating a locally high fluid pressure that causes viscous bending of the membrane, reducing the effective dynamic contact angle $\theta(V)$ beneath θ_0. During aspiration, viscous effects create a low fluid pressure where the membrane peels from the wall, causing bending of the membrane in the opposite sense, elevating $\theta(V)$ above θ_0. During rolling, the relation between the speed of a tank-treading cell and shear rate is found to be independent of viscosity at low rolling speeds and when binding kinetics is rapid, but viscosity-dependent at higher speeds and when binding is slower.

DISCUSSION AND SUMMARY

The model presented here aims to highlight the potential importance of thin-film hydrodynamics and membrane deformation in controlling spreading and peeling rates of a cell adhering to a plane substrate. In the situation when viscous dissipation in the suspending fluid provides the dominant resistance to spreading and peeling, a cell is predicted to tank-tread at a speed dependent on shear rate but not shear stress. The model may therefore provide an explanation for experimental reports of such behavior seen with rolling neutrophils but not with rigid beads (Smith *et al.* 2001). Substantial model refinements are required before reliable comparison can be made with *in vivo* systems, however.

REFERENCES

Dembo, M. *et al.* (1988). *Proc. R. Soc. Lond. B* **234**, 55-83.
Hodges, S.R. and Jensen, O.E. (2002) *J. Fluid Mech. (to appear)*.
Smith, M.L. *et al.* (2001). *FASEB J.* **15** A393.

ACKNOWLEDGEMENTS

SRH was supported by an EPSRC Studentship

EFFECTS OF VARUS WEDGED SHOE VERSUS INSOLE ON KNEE JOINT LOADING CHARACTERISTCS

Dieter Rosenbaum, Robert Rödl, Michael Entrup, Dieter Klein

Movement Analysis Lab, Orthopaedic Department, University Clinics Münster, Münster, Germany, diro@uni-muenster.de

INTRODUCTION

In patients suffering from varus gonarthrosis a treatment goal is to relieve pain by unloading the degenerative medial compartment of the knee joint. This may be endeavored with either surgical (high tibial osteotomy) or conservative treatment (braces or shoe modifications). Varus wedged shoes or insoles have been shown to provide a medial thrust of the force vector thereby reducing the adductor moment in the knee (Crenshaw 2000; Ogata 1997; Sasaki 1987; Yasuda 1987). However, the two methods have not been compared yet regarding their effectiveness in reducing the loading of the knee joint. Therefore, the present study investigated the effect of wedged insoles versus wedged shoes with respect to knee joint kinematics and kinetics in a healthy population.

METHODS

Twenty-nine subjects (14 ♂, 15 ♀, age 40.7±15.8 years, body mass 72.9±13.2 kg, height 172±8 cm) participated in the study and walked with customized shoes (Puma Inc., model “Street Cat”) in four different conditions: neutral shoes, shoes with a varus wedged sole, shoes with a valgus wedged sole and shoes with a valgus wedged insole.

Motion data was recorded during walking at self-selected, controlled speed on a 12 m walkway with a 6-camera system (Motion Analysis Inc.) and two force plates (AMTI). Temporal-spatial parameters as well as kinematic and kinetic parameters related to the knee and ankle joint were analyzed for each subject and averaged across multiple trials for each condition (Orthotrak).

RESULTS

The results indicate that the shoe modifications lead to significant changes in knee moments (Fig. 1). The medial wedge increased the knee joint loading. The lateral wedge as well as the insole led to the expected decrease of the varus moment with the insole being less effective. However, the changes in the knee joint have to be transferred through the ankle joint complex that is subjected to higher loading (Fig. 2).

DISCUSSION

The results demonstrate the biomechanical effectiveness of conservative treatment of gonarthrosis with shoe modifications even though the clinical impact remains to be investigated in patients. The reduced varus moment will lead to an unloading of the medial compartment in varus gonarthrosis that is expected to reduced the patient’s pain situation. However, it has also been demonstrated that these effects have to be passed on though the distal joints which might lead to stress in these regions that has to be tolerated.

REFERENCES

- Crenshaw SJ, Pollo FE, Calton EF (2000) *Clin Orthop* **375**, 185-92.
- Ogata K, Yasunaga M, Nomiyama H (1997) *Int Orthop* **21**, 308-12.
- Sasaki T, Yasuda K (1987) *Clinical Orthopaedics.* **221**, 181-87.
- Yasuda K, Sasaki T (1987) *Clinical Orthopaedics.* **215**, 162-72.

ACKNOWLEDGEMENTS

Thanks are due to „PUMA AG Rudolf Dassler Sport“, Herzogenaurach für providing the shoes and „Orthopädieschuhtechnik Krursel“, Münster for the shoe modifications and insoles.

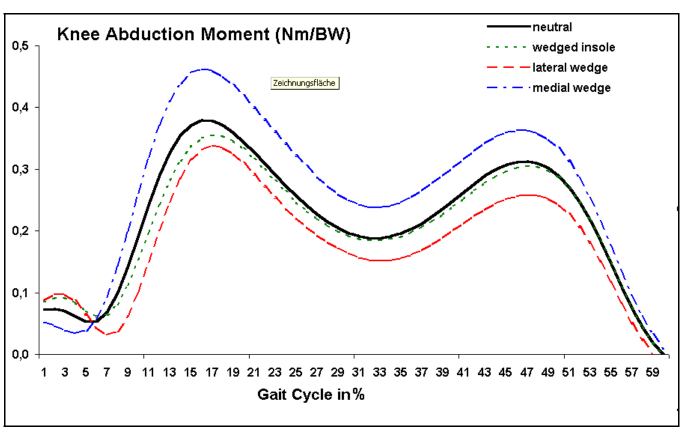

Fig. 1: Increased knee abduction moment with medial wedge and decreased moment with lateral wedge or insole.

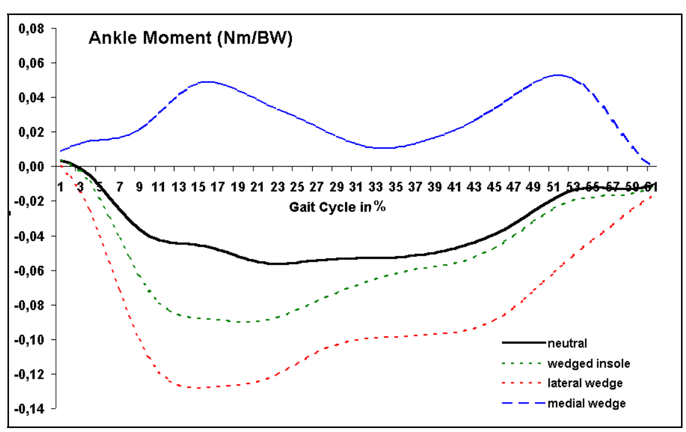

Fig. 2: Ankle eversion moment with medial wedge and inversion moment with lateral wedge or insole.

A COMPARISION AMONG DIFFERENT TASKS PERFORMED BY DIFFERENT SUBJECTS ON THE PRIMARY STABILITY OF CEMENTLESS STEMS

Alberto Pancanti, Marco Viceconti and Aldo Toni

Laboratorio di Tecnologia Medica, Istituti Ortopedici Rizzoli, Bologna, Italy - http://www.ior.it/tecno/

INTRODUCTION

The failure of cementless total hip replacements is mostly caused by aseptic loosening (Malchau, et al, 2000). Many authors consider the bone-implant relative micromotion early after surgery (primary stability) as the main biomechanical cause of aseptic loosening in cementless implants ((Soballe, et al, 1992). Animal and retrieval studies associate the failure of the osseointegration process to primary micro-movements above 100-200 μm (Soballe, et al, 1992). Assuming constant all the other factors, the final outcome of the osseointegration process clearly depends on the forces induced in the operated joint during the early stages after surgery.

All studies on the rehabilitation program stress the importance of the gradual allowance of weight bearing and the use of orthopaedic support (Bilotta, et al, 1992). However, the joint forces are not only function of the allowed weight bearing, but also of the type of task the patient is performing, as well as of the strategy adopted to perform it. An in vitro orthopaedic biomechanics study confirmed that the magnitude of micromotion at the entire contact surface depends also on the magnitude and the direction of the external forces and thus on the tasks subjects are performing (Saponara Teutonico, et al, 2001).

Aim of the present study is to evaluate the influence of the type of task, as performed by various subjects, on the primary stability of a cementless stem.

METHODS

The study was based on the finite element model of a human femur implanted with a cementless anatomical stem, modelling frictional contact at the bone implant interface. The model was fully validated in a previous work against primary stability experimental measurements (Viceconti, et al, 2000). Cancellous and cortical bone were both considered homogeneous materials. The first was assumed isotropic, with a Young's modulus of 1000 MPa; the second was assumed transversally isotropic with a longitudinal and transversal Young's modulus of 16300 MPa and 6600 MPa, respectively. The cementless stem, made of titanium alloy, was modelled with a modulus of 105000 MPa.

Only the hip joint force, acting on the head of the prosthesis, was considered in the load cases representing different activities. In a previous study, it was found that neglecting the muscle forces altered the predicted peak micromotion of only 1% (Pancanti, et al, 2001). Data on four patients performing nine different tasks were available from the telemetry measurements collected by Bergmann and co-workers (Bergmann, et al, 2001). Hip contact forces and the subject-specific anteversion angles were used. A fifth dataset was obtained by averaging the results of all patients. All force values were expressed as percentage of body weight. The predicted peak micro-movements were used to describe the primary stability and to compare each task performed by each patient.

RESULTS AND DISCUSSION

The critical tasks were found out to be patient-specific (table 1). The largest peak micro-movement was predicted for patient #1, patient #2 and for average patient during stair climbing. However for patient #3 and patient #4, the worst tasks were fast walking and double-single-double stance cycle respectively.

Table 1: Peak bone–implant relative micromotion predicted under the action of the joint loads.

	Patient-1	Patient-2	Patient-3	Patient-4	Average	Range
downstair	-	66	80	97	77	31
fastwalk	-	62	**89**	81	72	27
kneebend	-	34	69	51	54	34
norwalk	95	60	71	77	69	35
sitdown	75	49	65	58	54	26
slowwalk	-	74	67	77	68	9
st212	-	62	74	**113**	67	51
standup	80	66	58	63	68	22
upstair	**123**	**77**	81	101	**80**	46
Range	48	43	31	62	26	

The variability predicted between tasks was found comparable to that between subjects. Double-single-double stance cycle induced a variability among patients of 51 μm, while the largest variability among tasks was 62 μm for patient #4.

Considering that the study is based on a generic anatomy, the inter-subject differences can be explained only with the different patients' movement strategies.

SUMMARY

In this work, we tried to compare different tasks performed by different patients on the primary stability of cementless stems by the use of a finite element model, previously validated. Data here reported suggest that no task can be identified as the most critical. In addiction the differences between subjects performing the same task resulted as much relevant as the differences between tasks performed by the same patient.

REFERENCES

Malchau, H., et al., (2000), *Proceeding of AAOS 2000*, 1-16.
Soballe, K., et al., (1992). *Acta Orthop Scand,* **63**, 128-40.
Bilotta, T. W., et al., (1992). *Chir Organi Mov,* **77**, 447-9.
Saponara Teutonico, A., et al., (2001), *Proceeding of ORS '01*,
Viceconti, M., et al., (2000). *J Biomech,* **33**, 1611-8.
Pancanti, A., et al., (2001). *J Biomech, submitted.*
Bergmann, G., et al., (2001). *J Biomech,* **34**, 859-871.

A MICROMOTION-BASED MODEL OF BONE-IMPLANT INTERFACE REMODELLING

Marco Viceconti, Mirco Dotti, Alberto Pancanti, Luca Cristofolini and Aldo Toni

Laboratorio di Tecnologia Medica, Istituti Ortopedici Rizzoli, Bologna, Italy - http://www.ior.it/tecno/

INTRODUCTION

Total hip replacements fail mostly because of aseptic loosening (Malchau, et al, 2000). In controlled experiments the bone-implant relative micromotion appears to influence interfacial bone resorption more than any other biomechanical factor (Soballe, et al, 1992). The osseointegration process observed in stable implants is impaired by interface micro-movements above 30-50 μm, and even reverted to fibrous tissue differentiation if the amplitude is higher than 100-150 μm (Soballe, et al, 1993). The bonding between bone and implant can be broken if the interface shear stress exceed the strength limit, typically of 5-6 MPa (Soballe, et al, 1992).

The present study is aimed to model this process with a single computational model, and to use it to predict the secondary stability of an implant depending on the initial interface conditions obtained during surgery.

METHODS

The study was based on the finite element model of a human femur implanted with a cementless anatomical stem. The model, accounting for the large-sliding frictional contact occurring at the interface, had been previously validated against *in vitro* measurements of primary stability (Viceconti, et al, 2000). The material properties were derived from the literature and the load case was designed to simulate the instant of peak hip force during stair climbing (Bergmann, et al, 2001).

The adaptive algorithm was implemented as a macro-program with the Ansys programming environment (APDL). A first finite element analysis computed the bone-implant relative micromotion at each interface element, initially assumed in *standard* condition (i.e. frictional contact). The finite element analysis was repeated until the process converged to a stable configuration, adjusting in each iteration the status of each contact element on the basis of the following rules: i) elements exhibiting a micromotion higher than 100 μm were modified to simulate the presence of an interstitial gap of 0.7 mm (*loosened* condition); ii) elements with a micromotion below the 30 μm were modified to simulate a fully bonded interface (*integrated* condition); iii) bonded elements with a shear stress higher than 5 MPa were configured back to the standard condition. The proposed adaptation model is fully identified with only three parameters: two threshold micromotion and the shear strength. Four complete adaptation simulations were performed, varying the initial configuration of the model. The first, considered the reference model, was run assuming that initially the entire implant surface was in standard condition. A second simulation was run assuming that initially the entire bone-implant surface was in loosed condition. Two intermediate initial configurations were also considered, assuming that only the two regions with the highest contact pressure in the reference model (proximal-anteromedial and distal postero-lateral regions) had an initial gap. In the first simulation the gap was simulated only in the proximal region, where in the second simulation it was assumed to be present at both locations. The peak total elastic micromotion induced by the stair-climbing load in the initial model was taken as an indicator of the so-called *primary stability*. The same value, as predicted by the final converged model, was assumed to represent *secondary stability*.

RESULTS AND DISCUSSION

All simulations reached an oscillatory convergence, in which the model switched between two stable configurations. The results of both configurations are reported.

The primary stability of the reference model was 115 μm. With this initial configuration the adaptation simulation converged to a final configuration in which 80-81% of the interface area was integrated, and 18-19% in standard condition. The secondary stability of this final model was 23-29 μm. The gap in the proximal region increased the peak micromotion to 242 μm. However, the simulation produced very similar results, with 80-81% of interface in integrated condition and 19-20% in standard condition. The secondary stability was 21-24 μm. The results remained almost unchanged also when the initial configuration considered an interface gap also in the distal region. Only when the initial condition simulated a generalised interface gap, the primary peak micromotion increased to 1475 μm, which prevented any osseointegration.

From these preliminary results the model seems to provide meaningful results. Although a validation study is currently in progress, the very simple nature of the model relies on a few assumptions proposed by other authors on the basis of experimental observations, ensuring that the predicted configuration are at least plausible. Once validated and included into a MonteCarlo simulation to provide a statistical perspective to the predictions, the proposed algorithm may become a very useful instrument in orthopaedics biomechanics.

REFERENCES

Malchau, H., et al., (2000), *Proceeding of the AAOS '00*, 1-16.
Soballe, K., et al., (1992). *J Orthop Res,* **10**, 285-299.
Soballe, K., et al., (1993). *J Bone Joint Surg Br,* **75**, 270-8.
Soballe, K., et al., (1992). *Acta Orthop Scand,* **63**, 128-40.
Viceconti, M., et al., (2000). *J Biomech,* **33**, 1611-1618.
Bergmann, G., et al., (2001). *J Biomech,* **34**, 859-871.

PREDICTION OF TORSIONAL PROPERTIES OF RAT FEMUR USING PERIPHERAL QUANTITATIVE COMPUTED TOMOGRAPHY

Makoto Sakamoto[1], Satoru Uchihashi[2], Kenji Sato[3], Jun Sakai[1, 3], Eisuke Takano[3], Naoto Endo[4] and Toshiaki Hara[2]

[1]Biomechanics Laboratory, Department of Health Sciences, Niigata University School of Medicine, Niigata, Japan, sakamoto@clg.niigata-u.ac.jp
[2]Department of Mechanical Engineering, Niigata University, Niigata, Japan
[3]Department of Mechanical Engineering, Niigata College of Technology, Niigata, Japan
[4]Department of Orthopaedic Surgery, Niigata University School of Medicine, Niigata, Japan

INTRODUCTION

Assessment of bone material quality by means of peripheral quantitative computed tomography (pQCT) offers a wide perspective for bone research employing non-invasive procedures. The method of pQCT is able to determine volumetric bone mineral density, cross-sectional bone area, moment of inertia of area, and polar moment of inertia of area. Ferretti et al. (1996) described the mechanical validation of a pQCT-derived index of rat femur using a three-bending test. Jämsä et al. (1998) compared pQCT and a three-point bending test in evaluating the mechanical strength of mouse cortical bones. Hasegawa et al. (2001) investigated the association of grip strength and muscle cross-section with pQCT-derived torsional indexes at two human radial sites. Lind et al. (2001) evaluated the relationships between the torsional properties of rat humerus and geometrical parameters obtained by pQCT. They showed that significant correlation existed between area-related variables, stiffness, and torsion at failure. However, these relationships were not strong enough. The objective of this study was to predict torsional properties of rat femur utilizing pQCT.

MATERIALS AND METHODS

We used forty-eight Sprague-Dawley rat femora at ages of 10, 13, 16 and 24 weeks. The femora were stored at -10°C until pQCT and torsional test. The cross-section of each femur was scanned at mid-diaphysis using pQCT (XCT-960, Stratec, Pforzheim, Germany) in air. CT scans had a slice thickness of 2.5 mm and a voxel size E (0.148 mm). The value of Strain/Stress Index for polar (SSI_p) was calculated using volumetric bone mineral density and geometric parameters of cortical bone as follows:

$$SSI_p = \int_n (r_i^2 \rho_i / \rho_0) da / r_{\max} \qquad (1)$$

where r_i is the each distance of voxel to the center of gravity, $r_{\max}$ is the maximum distance of a voxel to the center of gravity, a is the area of a voxel, ρ_i is the each measured volumetric cortical density and ρ_0 is the normal physiological bone mineral density (1200mg/cm^3). A biaxial testing machine (858 MiniBionix, MTS, Minnesota, USA) was used to apply the torsion for the mechanical test. Whole bone specimens were tested to failure in torsion at a rate of 0.2°/sec with no axial load during the test. The torsional stiffness and strength (maximum torque) were obtained from the torque-rotation angle curve.

RESULTS AND DISCUSSION

The torsional stiffness and strength increased with increasing the age of rat. Nevertheless, the maximum rotation angle decreased with increasing the age of rat. Experimentally measured torsional stiffness correlated strongly (r=0.95) with SSI_p. The correlation between torsional strength and SSI_p was also strong, r=0.91 (Figure 1). In this study, we assessed the validity of using the pQCT-derived index SSI_p as a good predictor of whole bone torsional stiffness and strength over a range of 10 to 24 weeks old of rat bone size. Jämsä et al. (1998) estimated different pQCT variables and their relation to bending strength of mouse femur and tibia, the pQCT-derived index and cross-sectional cortical area were the best predictors of breaking force and stiffness. Their findings were well in accordance with the present study.

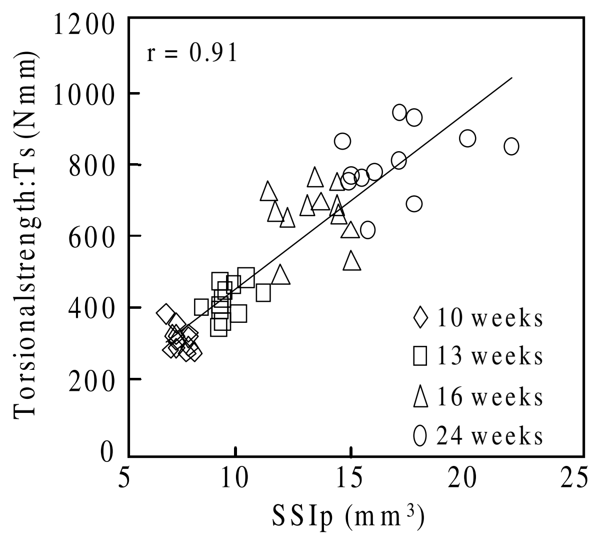

Figure 1: The relationship between torsional strength and SSI_p.

REFERENCES

Ferretti, J. L. et al. (1996). *Bone*, **18**, 97-102.
Hasegawa, Y. et al. (2001). *J. Biomech.*, **34**, 497-503.
Jämsä, T. et al. (1998). *Bone*, **23**, 155-161.
Lind, P. M. et al. (2001). *Bone*, **29**, 265-270.

SCANNING ACOUSTIC MICROSCOPE MEASUREMENTS OF ANISOTROPY OF DENTINE AND ENAMEL

Makoto Sakamoto[1], Koichi Kobayashi[1], Jun Sakai[2], Yasuo Maruyama[3] and Hidemi Itoh[3]

[1]Biomechanics Laboratory, Department of Health Sciences, Niigata University School of Medicine, Niigata, Japan, sakamoto@clg.niigata-u.ac.jp
[2]Department of Mechanical Engineering, Niigata College of Technology, Niigata, Japan
[3]Tohoku University Graduate School of Dentistry, Sendai, Japan

INTRODUCTION

Knowledge of the mechanical properties of teeth and the tissues from which they are formed is important to aid understanding of their mechanical behavior under physiological loading conditions. Studies on the elastic modulus of dentine are numerous and the values obtained extend over quite a wide range (Stanford et al., 1958; Lehman, 1967; Watts et al., 1987; Rees and Jacobsen, 1994). Nevertheless, studies on enamel are lacking due to the difficulty in preparing and testing extremely small specimens. The purpose of this study was to measure the elastic anisotropy of human and bovine dentine and enamel using a scanning acoustic microscope (SAM).

MATERIALS AND METHODS

216 human dentine and enamel specimens were obtained from 36 molar permanent teeth. 143 bovine specimens were obtained 15 molar teeth. Both human and bovine teeth were sliced into small rectangular specimens with a microcutter and polished with a buffing machine under constant water irrigation. The perpendicular direction of the specimen was aligned with the tooth axis and specimen cross-section was approximately 1×1 mm. A 50 MHz ultrasonic transducer and lens of SAM were used to transmit and receive acoustic waves in pulse echo mode. The delay time between acoustic waves reflected from the bottom of the specimen was measured using a digital oscilloscope. The acoustic velocity is equal to twice the thickness of the specimen divided by the delay time. The elastic wave propagation theory predicts relations between the elastic modulus, E, density ρ, and acoustic velocity, c, of the following form:

$$E = (1+\nu)(1-2\nu)\rho c^2 /(1-\nu) \tag{1}$$

where ν is the Poisson's ratio. We measured the elastic moduli of longitudinal and transverse directions of dentine and enamel.

RESULTS AND DISCUSSION

There was no significant difference between the longitudinal and transverse elastic moduli for human dentine (Fig. 1). However, the longitudinal modulus was higher than transverse modulus for human enamel. The ratio of elastic anisotropy of human enamel was about 1.1. For bovine enamel, the longitudinal elastic modulus was also higher than transverse modulus and the ratio of elastic anisotropy was about 1.2 (Fig. 2). The enamel is composed of prisms, which are built up in an orderly fashion. These prisms run roughly parallel to the tooth's surface. Although the enamel prisms across a section of tooth do actually appear as curved lines, particularly around the cuspal region, this effect would be very complicated to anisotropy. The SAM technique is capable of further development and if it could be used in conjunction with localized determinations of the density and composition it would be a powerful tool for elucidating the relationship between structure and elastic properties.

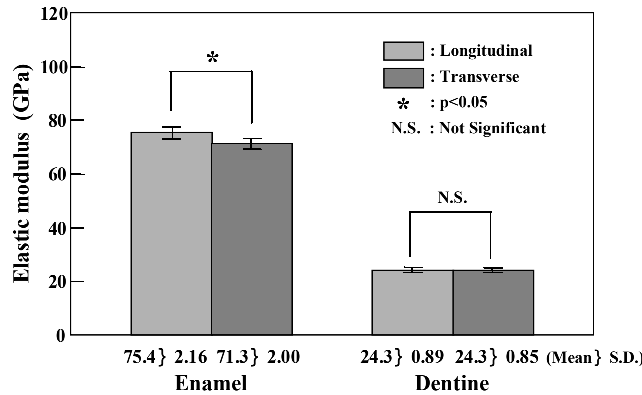

Figure 1: Longitudinal and transverse elastic moduli of human teeth.

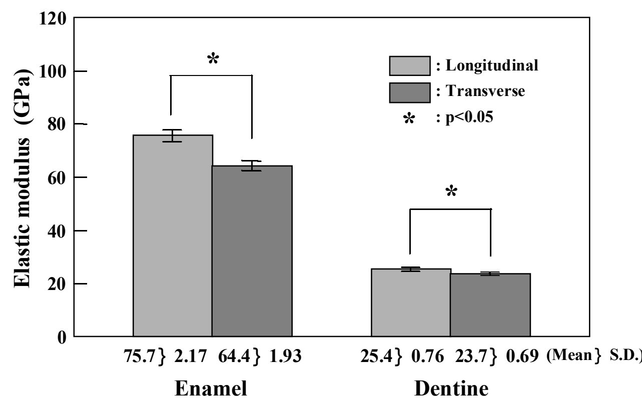

Figure 2: Longitudinal and transverse elastic moduli of bovine teeth.

REFERENCES

Lehman, M. L. et al. (1967). *J. Dent. Res.*, **46**, 197-201.
Rees, J. S., Jacobsen, P. H. (1993). *Clin. Mater.*, **14**, 35-39.
Stanford, J. W. et al. (1958). *J. Amer. Dent. Asso.*, **57**, 487-495.
Watts, D. C. et al. (1987). *J. Dent. Res.*, **66**, 29-32.

WEAR OF CROSSLINKED POLYETHYLENE UNDER DIFFERENT TRIBOLOGICAL CONDITIONS

Alison Galvin, Joanne Tipper, Martin Stone, Eileen Ingham and John Fisher
Medical and Biological Engineering, University of Leeds, Leeds, LS2 9JT, UK. j.fisher@leeds.ac.uk

INTRODUCTION

Crosslinking has been extensively introduced to reduce the wear of ultra high molecular weight polyethylene (UHMWPE) in artificial joints. McKellop *et al.* (1999) reported that UHMWPE crosslinked with 5MRad of radiation produced an 83% reduction in wear in hip joint simulator studies compared to non-crosslinked material. Muratoglu *et al.* (2000) showed an 85% reduction in wear with 10MRad material. These simulators applied different kinematic conditions, but both used high concentrations (90-100%) of serum in the lubricant. Other studies have shown smaller reductions in wear with crosslinking (Endo *et al.* 2000). Although there is a general consensus that crosslinked UHMWPE reduces wear, there is considerable variation in the percentage reduction achieved in different studies. The aim of this study was to compare the effects of changes in serum concentration, kinematics and counterface condition on the wear of UHMWPE for three different levels of crosslinking.

METHODS

Wear pins were machined from UHMWPE GUR 1050. Crosslinking was achieved using gamma irradiation at 0, 5 and 10MRad. The counterface was stainless steel. Tests were run in a six station multidirectional pin on plate rig. Initial tests used 95% (v/v) and 25% (v/v) serum as lubricants. Three different counterface conditions were then tested at ±60° rotation, smooth Ra~0.007µm, medium scratches Rp~0.8µm, and high scratches Rp~1.8µm with 25% (v/v) serum. The final test used similar counterfaces with ±20° rotation. Wear was determined gravimetrically and wear factors were calculated.

RESULTS

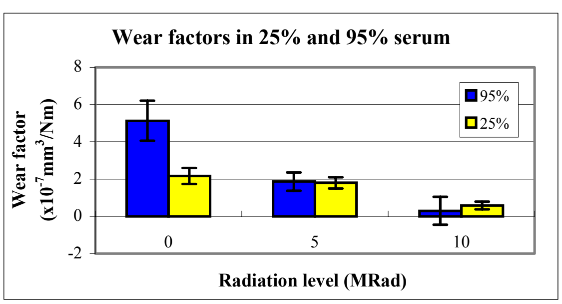

Figure 1: Wear factors in 95% and 25% serum lubricant.

The wear rates in the different serum concentrations at ±60° rotation on smooth counterfaces are shown in Figure 1. With both concentrations of serum there was a reduction in wear as crosslinking levels increased. The mean wear factors for the different counterfaces at ±60° are presented in Figure 2. The wear rate increased with increasing scratch height for each material. The mean wear factors for the different counterfaces at ±20° rotation are shown in Figure 3. They showed a similar pattern to the ±60° rotation results.

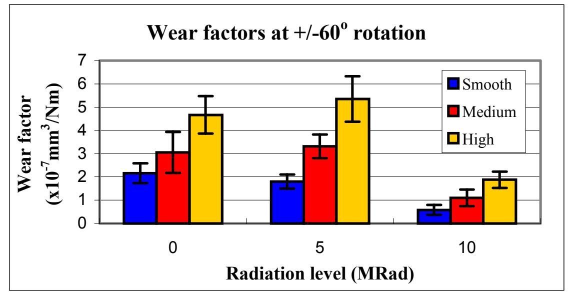

Figure 2: Wear factors at ±60° rotation.

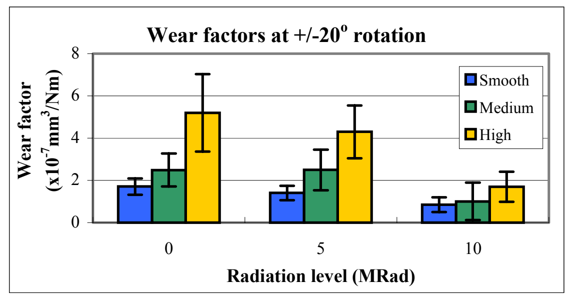

Figure 3: Wear factors at ±20° rotation.

DISCUSSION

The largest reduction in wear rate produced by crosslinking was observed with the high concentrations of bovine serum. At lower serum concentrations (25% (v/v)) as defined by the ISO standard, the reduction in wear produced by crosslinking was lower. The results from different counterface conditions at ±60° rotation showed that the smooth counterface gave the greatest percentage reduction in wear factor between non and highly crosslinked material. Damage to the counterface increased the wear rates for all the materials with both kinematic conditions. Altering the kinematics to a lower angle of rotation, which introduced less cross shear frictional energy, has implications if using crosslinked polyethylene in the hip and knee, as the different kinematics seen in each joint give different levels of cross shear frictional energy. In conclusion the reduction in wear produced by crosslinking was critically dependent on protein concentration, kinematic conditions and counterface roughness.

REFERENCES

McKellop *et al*. (1999) *Trans. Soc. Biomats.* 323.
Muratoglu, *et al.* (2000) *6th World Biomats. Cong. Trans*. 865.
Endo, *et al.* (2000) *6th World Biomats. Cong. Trans.* 872.

PRECISION MEASUREMENTS OF RSA METHOD USING A PHANTOM MODEL OF HIP PROSTHESIS

Tatu J. Mäkinen[1], Jyri K. Koort[1], Kimmo T. Mattila[2] and Hannu T. Aro[1]

University of Turku, Turku, Finland, hannu.aro@utu.fi
[1] Department of Surgery, [2] Department of Diagnostic Radiology

INTRODUCTION

RSA (Radiostereometric Analysis) has become one of the recommended techniques for premarket clinical evaluation of new joint implants designs (Kärrholm et al. 1997). The method allows high precision measurements of three-dimensional movements from radiographs (Önsten et al. 2001). However, the method is technically very demanding. A meticulous assessment of possible error sources is mandatory during standardization of the method in each research unit.

METHODS

A phantom model was constructed (Fig. 1). A threaded cup was securely fixed to a plastic pelvis. The femoral component was inserted to the medullary canal of a plastic femur. Care was taken to ensure that there was no movement between bony and prosthetic components. Tantalum markers (n=8 for the femoral and n=13 for the acetabular side) were inserted to the components with glue. A uniplanar type of RSA setup with two portable radiographic units was used. Two series were performed. First, 10 double examinations were performed so that the tubes were not repositioned and position of the phantom model was not changed (Series 1). This correlates to the optimum situation, the best precision obtained with the applied setting. Next, 10 double examinations were performed so that the tubes were repositioned and position of the phantom model was changed between double examinations (Series 2).

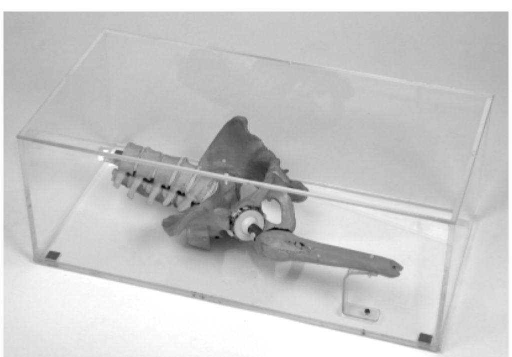

Figure 1: Phantom model

This correlates to the clinical situation where patient is examined at different time points. Digital X-ray films were scanned with a high-resolution scanner (UMAX PowerLook 2100 XL, Taiwan) and analysed with UmRSA 4.1 (RSA BioMedical Innovations AB, Umeå, Sweden) software. The calculated displacements of the femoral and acetabular components between double examinations were used to determine the limits of significant migration in the x, y and z axes defined as the 99% confidence limit (CL). Mann-Whitney test was used to analyze the statistical significance of the differences observed between the two series.

RESULTS AND DISCUSSION

In Series 1, the minimal significant (99% CL) translations and rotations varied between 18-103 µm and 0.03-0.33 degrees, respectively (Table I). For translations, the precision was highest along the longitudinal axis (y-axis) and lowest along the sagittal axis (z-axis). In Series 2, repositioning of the X-ray tubes and the phantom between double examinations resulted in statistically significant differences when compared with the values of Series 1 in four out of 12 calculations. Of the four significant differences, three were found in evaluation of the acetabular component, reflecting the limited space for scattering of the acetabular component markers.

SUMMARY

When using RSA-method, standardization and calibration procedures should be performed with phantom models in order to avoid unnecessary radiation exposure of the patients. The present model gives the means to establish and to follow the intra-laboratory precision of the RSA method. The model is easily applicable in any research unit and allows the comparison of the precision values in different laboratories of multicenter trials.

REFERENCES

Kärrholm J. et al. (1997). *Clin Orthop*, **344**, 94-110.
Önsten I. et al. (2001). *J Orthop Res*, **19**, 1162-1167.

Table I: Minimal significant translations and rotations for femoral and acetabular components based on double examinations

	Translation of the femoral component (µm)			Translation of the acetabular component (µm)			Rotation of the femoral component (degree)			Rotation of the acetabular component (degree)		
	x axis	y axis	z axis	x axis	y axis	z axis	x axis	y axis	z axis	x axis	y axis	z axis
Series 1	22	18	61	41	27	103	0.08	0.33	0.03	0.09	0.11	0.06
Series 2	51	41	95	79	56	212	0.13	0.31	0.10	0.25	0.07	0.07
p-value	NS	NS	NS	NS	0.029	NS	0.015	NS	NS	0.011	0.019	NS

OPTIMAL PEDAL RATE FOR MAXIMAL POWER PRODUCTION IN CYCLING IS NOT RELATED TO FREELY CHOSEN PEDAL RATE AT SUB-MAXIMAL EXTERNAL POWER

Ernst Albin Hansen[1] and Gisela Sjøgaard[2]
[1]Institute of Sports Science and Clinical Biomechanics, University of Southern Denmark, e.hansen@winsloew.sdu.dk
[2]National Institute of Occupational Health, Copenhagen, Denmark

INTRODUCTION

Cyclists seek to maximize performance during competition, and efficiency is an important factor affecting performance at sub-maximal external power. Efficiency is affected by pedal rate and therefore it is pertinent to reveal factors affecting freely chosen pedal rate (FCPR) during cycling. Recently, we showed that e.g. crank inertial load affects FCPR. Thus, for a group of subjects FCPR was higher at high compared with low crank inertial load (Hansen et al. 2002). Hautier et al. (1996) showed that the proportion of fast twitch fibers in m. vastus lateralis, expressed in terms of cross sectional area, was related to optimal pedal rate for maximal power production. The purpose of the present study was to determine the optimal pedal rate for maximal power production (OPMP) for each subject in a group that was characterized by a large variation in fiber type composition in m. vastus lateralis. Further, to test the hypothesis of a relationship between OPMP and FCPR during cycling at sub-maximal external power.

METHODS

Twenty healthy males of age 26.3±3.5 years, height 178±5 cm, and body mass 73.3±7.5 kg volunteered. The subjects had a needle biopsy taken from the middle section of m. vastus lateralis. Sodium dodecyl sulfate polyacrylamide gel electrophoresis (SDS-PAGE) was used in a MHC analysis performed on each muscle sample. MHC isoform (I, IIa, and IIx) content was determined. Cycling sessions were performed in a custom-built set-up with a racing bicycle placed on a motorized treadmill. Optimal pedal rate for maximal power production (OPMP) was determined in a session consisting of 12 isokinetic maximal cycling bouts at preset pedal rates of 30-140 rpm in steps of 10 rpm (randomized). Treadmill speed and gear ratio were matched to attain the target pedal rates. Peak crank power was calculated from crank arm velocity, determined from the pedal rate, and the peak crank torque. Freely chosen pedal rate (FCPR) was measured in another session consisting of cycling at external power corresponding to 40 and 70% of the maximal oxygen uptake (VO_{2max}), at 80 rpm. These external powers had previously been determined in a progressive test to exhaustion. $p<0.05$ was considered statistically significant.

RESULTS AND DISCUSSION

A large range in fiber type composition was documented, the data being presented as mean ±1SD (range): 64±16 (21-97)% MHC I, 33±14 (4-65)% MHC IIa, and 3±5 (0-15)% MHC IIx. FCPR was 74±11 (56-88) rpm and 80±11 (61-102) rpm at external power corresponding to 40 and 70% VO_{2max} (at 80 rpm), respectively ($p<0.05$). Maximum peak crank power was 1412±229 (990-1924) W and occurred at the optimal pedal rate of 122±18 (91-153) rpm. There was a high correlation between % MHC I and OPMP: OPMP (rpm) = -0.87 MHC I (%) +176.15, r=-0.81, $p<0.05$ (Fig. 1). There was a low correlation (r=-0.47) between % MHC I and maximum peak crank power but no correlation when maximum crank peak power was expressed per kg body weight, thigh weight, or muscle extensor weight. Further, there was no significant correlation between OPMP and FCPR.

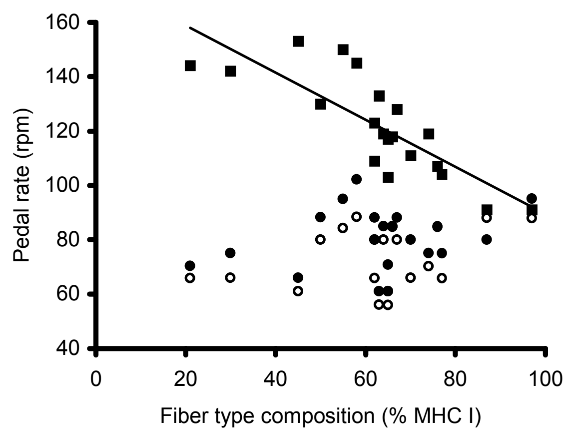

Fig. 1: Pedal rate as a function of % MHC I. n=20. ■ represent optimal pedal rate for maximal power production (OPMP). ○ and ● represent freely chosen pedal rate (FCPR) at external power corresponding to 40 and 70% VO_{2max} (at 80 rpm), respectively.

SUMMARY

We showed a high correlation between fiber type composition and optimal pedal rate for maximal power production. Thus, subjects with a high % MHC I demonstrated a low optimal pedal rate compared to subjects with a low % MHC I. This confirmed data from Hautier et al. (1996). The optimal pedal rate for maximal power production was no key factor when individuals freely chose a pedal rate during cycling at sub-maximal external power. Subjects with high % MHC I freely chose a pedal rate close to the optimal pedal rate for maximal power production. Subjects with low % MHC I tended to choose lower pedal rates, favoring high gross efficiency.

REFERENCES

Hansen, E.A. et al (2002). *J Biomech*, **35**, 277-285.
Hautier, C.A. et al (1996). *Eur J Appl Physiol*, **74**, 114-118.

SELF-EXCITED OSCILLATIONS IN A FLUID-BEAM COLLAPSIBLE CHANNEL

Zong Xi CAI & Xiao Yu LUO
Department of Mechanical Engineering, University of Sheffield, S1 3JD, UK
X.Y.Luo@shef.ac.uk

INTRODUCTION

Flow in collapsible tubes is studied extensively in the recent few decades not only due to its relevancies in physiological applications, but also due to its interesting dynamic phenomena. Self-excited oscillations are frequently discovered in a Starling resistor set up of such a system in laboratories. Some of these oscillations have been reproduced by a two dimensional fluid-membrane model (Luo & Pedley, 1996), which may in principle, be realized a laboratory. The fluid-membrane model, however, suffers from several *ad hoc* approximations: the wall stiffness was ignored, and elastic wall was assumed to move either in the vertical or the normal directions. Although these assumptions may be acceptable for the steady flow simulations, their influences on the unsteady flows, especially on the self-excited oscillations, need to be carefully evaluated.

This paper studies the unsteady flow in a collapsible channel using a new, improved fluid-beam model, where a plane strained elastic beam with large deflection is used. Thus the solid mechanics of the wall is taken care of properly, and the above *ad hoc* assumptions are not longer required.

METHOD

A finite element code for unsteady flow is developed to solve the coupled nonlinear fluid-structure interactive equations simultaneously, and an adaptive mesh with rotating spines is used to enable a movable boundary. Small perturbations are applied on the steady solutions of the system and the time evolution of the unsteady solutions are subsequently computed. In addition, the code is modified to solve the corresponding eigen-value equations so that the linear stability of the system can be also investigated.

RESULTS AND DISCUSSION

The results of the new model are computed and compared with the fluid-membrane models. There are several interesting discoveries. First, the self-excited oscillations in the new model are qualitatively similar to those from the previous fluid-membrane model if the wall stiffness is very small. This implies that the fluid-membrane model is a good approximation for a very thin wall material (which is usually too thin for biological materials, however). Secondly, the critical value of the tension no longer exists in the new model if the wall stiffness is big enough. In addition, small amplitude oscillations are found which seem to exist exclusively in the new model with the wall stiffness included. The occurrences of these small amplitude oscillations are closely predicted by the neutral stability curve obtained from the linear stability analysis of the system. These oscillations then change into the large amplitude irregular non-linear ones via the period doublings as the tension/wall stiffness is further decreased from the neutral stability points. One finding of interest is that unlike the small amplitude oscillations, these large amplitude non-linear oscillations tend not to oscillate around their corresponding steady solution when perturbed, but they oscillate around a different operation point, see figure below.

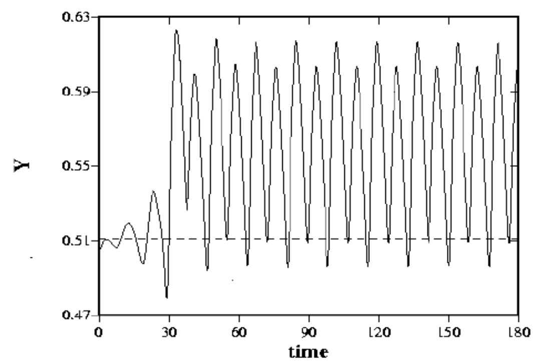

Figure: The oscillation of the centre point of the beam,Y, is shifted away from its steady solution. Re=300.

SUMMARY

Unsteady flow in a fluid-beam interactive model is simulated by using a finite element code. Both small and large amplitudes self-excited oscillations are discovered. The small amplitude oscillations agree very well with the neutral stability curve obtained from the linear stability analysis. The large amplitude oscillations are of non-linear nature and often present highly irregular and chaotic-like waveforms. Results are also compared with those of the previous fluid-membrane model, and their differences are discussed.

REFERENCE

Luo XY & Pedley, TJ, 1996, A numerical simulation of unsteady flow in a 2-D collapsible channel, *J. Fluid Mech.* 314, 191-225.

ACKNOWLEDGEMENT

This work is supported by the EPSRC, Grant No. GR/M07243. Special thanks are due to Professor T. J. Pedley for helpful discussions.

OVERTURNING RESISTANCE OF RIGID TAP ROOTS

S B Mickovski and A Roland Ennos
Shool of Biological Sciences, University of Manchester, 3.614. Stopford Bldg., Oxford Rd., Manchester M13 9PT, UK
Contact: slobodan.mickovski@stud.man.ac.uk

INTRODUCTION

The vast majority of self-supporting plants are likely to be pushed sideways by a herbivore or even more likely by the wind and either topple or lean permanently – a phenomenon known as 'lodging'. To neutralise lateral loads these plants are expected to have strong roots with at least one rigid element that will resist with its bending resistance, while the surrounding soil resists with its compressive resistance. Engineers have formulated the theory of laterally loaded piles that can be used to explain the behaviour of tap root systems.

This study combined engineering theory with practical biology by modelling different sizes of simple rigid tap roots, embedding them at different depths in different soil media, and pulling them over, recording the overturning moment along the way.

MATERIALS AND METHODS

Spruce and balsa dowels (∅=4.2, 6.3, 8.5 and 12.7mm, all of them 33cm long) were used as model tap roots. Ten replicas of each diameter were embedded in two different soil media (river sand and compost – agricultural soil) at three different depths (3, 5 and 7cm). The models were laterally pulled over at a constant rate using INSTRON testing machine. The force *vs.* displacement was plotted and the type of the soil failure was recorded. Aspect ratios (the ratio between the diameter of the tap root and embedment depth) were calculated presuming that the amount of material required to resist overturning force is minimised when the bending strength of the tap root equals the resistance to rotation.

RESULTS

Log-log regression (Figure 1) showed that the overturning resistance of the model tap roots increased with the third and second power of the embedment depth, in sand (r^2=0.99) and in agricultural soil (r^2=0.86) respectively. They showed that the model diameter was also a significant factor in resisting overturning, but only in agricultural soils, where overturning resistance was more or less proportional to diameter.

Log [depth] vs. Log [M] graph for models in both media

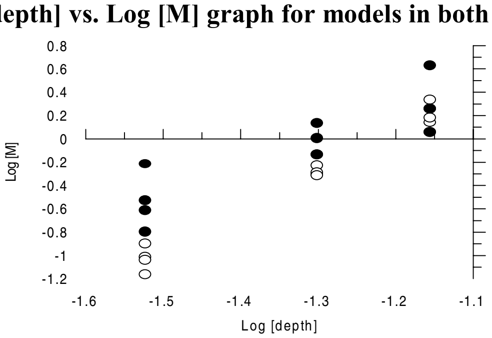

Figure 1. Log [depth] *vs.* log [overturning moment] graph for models in sand (○) and in agricultural soil (●)

In sandy soil there was little consistent increase of overturning moment with model diameter. In fact, smaller diameter roots were actually more firmly anchored at low depths in sand. The optimal aspect ratio for the models in sandy soils ranged from 15.5 to 15.7, and for the models in agricultural soil from 14.1 to 14.6. Models that showed the largest resistance, were in all cases those with an aspect ratio of 7 to 9.

DISCUSSION

Results are comparable to the ones predicted in earlier works based on the engineering theory of laterally loaded piles. Sandy soil failed in shear locally around the tap root and it rotated around a point on or very close to the root tip. The resistance to overturning in this case comes from the shear strength of the soil around the tap root and does not change with diameter.

In agricultural soil, the tap root rotated around a point between the soil surface and the root tip and the passive earth pressure below that point acted together with the soil shear strength in resisting overturning.

This kind of root system is unstable and likely to fail under small loads above the ultimate ones, and the strength of the tap root itself is likely to further limit the overturning resistance of tap root dominated systems. The stability of such root systems is naturally improved by reinforcing the base of the tap root (larger cross-sectional area where the stresses are highest) often accompanied by formation of the 'I' beam shaped cross sectional area, or developing a hollow shape strengthened around the outside of the root.

Embedment depth to root diameter ratio turned out to be more important in cohesionless soils where the lack of cohesion could be partially replaced by the larger surface areas on which the soil will shear during overturning. Adaptations might include splitting the large rigid root into a group of thinner deeply embedded tap roots with a larger surface area, positioning the tap root under a certain angle from the vertical as in some desert shrubs, or simple proliferation of thick lateral roots.

REFERENCES

Broms, B.B. (1964*) Jour. of Soil Mech. and Found. Div. Proc. of ASCE*, **SM3**, 123-156
Broms, B.B. (1964) *ibid.,* **90**, 27-63
Crook, M.J. and Ennos, A.R. (1993). *Jour. Of Exp. Botany*, **44**, 1219-1224
Ennos, A.R. (1993). *Functional Ecology*, **6**, 71-78
Ennos, A.R. (2000). *Adv. in Botanical Res*., **33**, 123-128
Goodman, A.M. et al (2001). *Annals of Botany*, **87**, 397-404.
Mattheck, C. (1993). *Design in der Natur. Der Baum als Lehrmeister*. Rombach-Verlag, Freiburg

COMPUTATIONAL FLUID DYNAMICS SIMULATION OF THE BLOOD FLOW IN THE HUMAN AORTIC ARCH WITH ITS BRANCHES

Daisuke Mori[1] Tomoaki Hayasaka[2] and Takami Yamaguchi[1]
[1]Department of Mechatronics and Precision Engineering, Tohoku University, Sendai, Japan
daisuke@pfsl.mech.tohoku.ac.jp
[2]The Institute of Physical and Chemical Research (RIKEN), Wako-shi, Japan

INTRODUCTION

We have been studying the flow in the human aortic arch from a hemodynamics perspective with respect to vascular diseases using a computational fluid dynamics (CFD) method (Mori and Yamaguchi, 2001). Initially, we examined the complicated geometry of the arch, focusing on the three-dimensional (3-D) non-planar distortion in its configuration, while not fully considering the major branches at the top of the arch. In this study, we construct an aortic arch model for CFD simulations that incorporates both non-planarity and the major branches, using a set of magnetic resonance (MR) images, and discuss their combined effects on blood flow.

METHODS

The branching structure of the aortic arch can be simplified as a major pipe, i.e., the aortic arch, with three major branches connected to it. Using the differential geometry modeling method (Mori and Yamaguchi, 2001), the aortic trunk and the three branches were each constructed individually based on their centerlines using 3-D reconstructed MR images. There were regions in each model in which the corresponding computational grids overlapped, so we combined the models to form a single computational domain of the arch with its branches. To model each vessel geometrically, we used the interactive clinical interface for MR images developed by Hayasaka et al. (2001). Fig. 1 shows an MR image, and the CFD model constructed from it. In order to use the overset grid, the velocity vectors and pressure for each grid in the overlapping regions must be interpolated and transferred from one region to the other at every computational step. The transferred data were always regarded as part of the boundary conditions in the recipient region. The CFD computations used a commercial program, SCRYU version 1.4 (Software Cradle, Osaka, Japan).

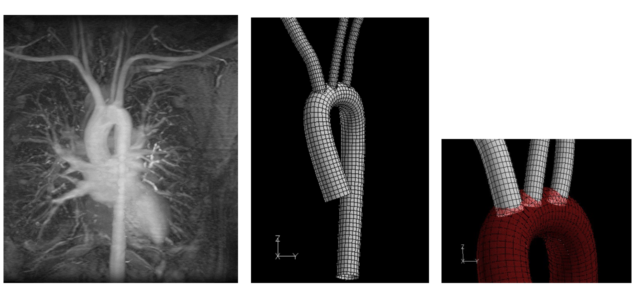

(a) (b) (c)

Figure 1: A CFD model of the aorta constructed by curve fitting the centerline to a cubic spline function. (a) 3-D reconstructed MR image. (b) CFD models of the aorta. (c) Overlapping region.

RESULTS AND CONCLUSION

Figures 2 and 3 show the secondary flow at a given cross section, and the wall shear stress (WSS) distribution under a steady uniform inflow condition with a Reynolds number (Re) of 1600, respectively. As shown in Figs. 2a-c, the flow along the arch consisted of a large right-handed rotational flow in the descending part of the arch, and a large left-handed rotational flow at the end of the arch. These characteristics of the global flow are similar to the results obtained using our arch model without branches (Mori and Yamaguchi, 2001). On the other hand, the secondary flow in the branches differed in each branch and showed unique structures, probably due to the asymmetric 3-D structure of the arch. This study demonstrated that the combined method of differential geometrical modeling based on the vascular centerline, with overset meshing for the branches, is a powerful means of conducting a CFD analysis of the blood flow in the aortic arch.

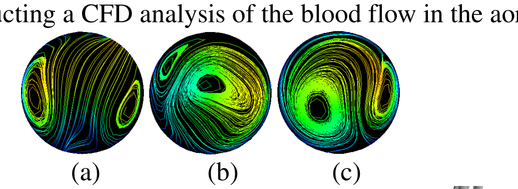

(d) (e) (f)

Figure 2: The streamline patterns in cross sections of the model of the aortic arch and its three major branches (steady uniform inflow, Re = 1600).

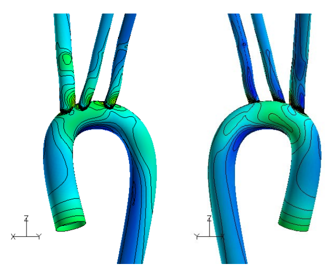

(a) Left lateral (b) Right lateral

Figure 3: The wall shear stress distribution viewed from different directions (steady uniform inflow, Re = 1600).

REFERENCE

Mori, D., Yamaguchi, T. (2001). *Proceedings of International Workshop on MIAR 2001*, 111-116
Hayasaka, T. et al (2001). *Proceedings of the 2001 Bioengineering Conference, BED-50*, 563-564.

FINITE ELEMENT SIMULATION OF OSSEOINTEGRATED TRANS-FEMORAL IMPLANT UNDER EXTREME LOAD CONDITION

W. Xu, J. Li, A Crocombe and S. C. Hughes
Centre for Biomedical Engineering, School of Engineering,
University of Surrey, Guildford, Surrey, GU2 5XH UK, W.Xu@Surrey.ac.uk

INTRODUCTION

The traditional limb prosthesis is interconnected with residual limb via a "socket". The load put upon the prosthesis limb transfers through soft tissue to the human skeleton. As the result of wearing socket type of prostheses, muscles and skin is likely to be traumatized. The osseointegrated titanium implants have achieved impressive clinical results in the dental and maxillofacial treatment for over 20 years [1]. A similar technique has been recently extended to orthopedic applications for attaching prosthetic limb to the residual stump of the amputee. This technique inserts a titanium implant into the long axis of the principal bone of the stump. The distal end of the implant connected to an abutment that penetrates through the skin to provide direct prosthesis limb attachment. This method could overcome the disadvantages of socket type limb attachment. The preliminary clinical trials, conducted principally in Sweden within the Branemark Osseointegration Centre, Gothenburg and consequently Queen Mary's hospital in London, has shown encouraging result.

However, due to the malfunction of the prosthetic limb and accidentally loss balance of the prosthetic limb wearer, significant overload could be put on to the abutment, implant and bone. At the Queen Mary's hospital five cases have developed a plastic deformation of the abutment. None of these cases leaded to a failure of osseointegrated connection between the implant and bone. This indicates that the bone-implant osseointegrative interface may somehow withstand higher stress impact. To investigate the interfacial stress under an overload condition, the finite element methods were used.

METHOD

To simulate the stress situation at the bone-implant interface, 3 dimensional bone and implant FE models were created. The bone model was created direct form CT scans of the trans-femoral amputee. A computer program was developed to carry out 3D reconstruction of the solid model of the femur and implant in the format of Ansys parametric language. The detail of the 3D reconstruction of the solid model of the femoral and implant is discussed in a separate paper of authors[2].

Since the load put up on the abutment is cause by a collision while the amputee fall over, the actual load is unknown. To work out the collision load, the deformation simulation of a simple nonlinear FE abutment model was carried out. The result of the simulation in terms of direct reaction force put up on the abutment was used as input for the further study of bone-implant interfacial stress under collision loading.

RESULTS AND DISCUSSION

To investigate the effect of the collision load on bone-implant interfacial stress, Von Mises stress and the equivalent strain were used to represent FE modelling results. In order to compare the stress situation between normal load and collision load condition, two models were evaluated and showed a general pattern with the maximum stress located near to distal femur and the stress near the end part of implant taking a relatively low value with more uniform distribution.

The result shows that the interfacial stress under a normal load situation is much smaller that the collision condition. The stress level under a collision load condition reaches the fracture load of the human bones, although these only takes place in few isolated places. This indicates that the osseointegrated interface is able to repair an overload injury through the bone remodelling or other mechanisms.

SUMMARY

The following conclusions were drawn from this study. As it is expected that the stress under the collision load condition is much higher than the normal load condition. The stress level at the collision condition reaches fracture stress of the human bone, although there are only few small areas at the bone-implant interface reaches this level. Since the full recoveries were observed in all overload cases, it indicated that the osseointegrated interface possess self-repairing capability. Further clinical investigation needs to be carried out for clarification.

REFERENCE

[1] P. I. Branemark et al, "Osseointegration in Skeletal Reconstruction and Joint Replacement" (1994)

[2] J Li et al , The 3D Reconstruction of Femur Attached with a Distal Osseointegrated Implant, 5th Inter Symp. on Biomechs and Biomed Eng., 1 - 3 Nov. 2001, Rome, Italy.

ACKNOWLEDGEMENT

The authors would like to thank finacial support from EPSRC to the first author.

PRESSURE-INDUCED EXPRESSION OF IMMEDIATE-EARLY GENE PRODUCT C-JUN OF THE COMMON CAROTID ARTERIES IN RATS

Zonglai Jiang, Zhiqiang Yan, Yan Zhang, Xiangqun Yang
Institute of Biomedical Engineering, Changhai Hospital, Shanghai 200433, China

INTRODUCTION

Mechanical stress have been thought to play a role in vascular remodeling but the mechanism remains to be determined. The proliferation and neointimal formation of vascular smooth muscle cells are the critical events in the arterial remodeling, in which immediate-early response gene product c-Jun, a transcription factor, may play a important role. In order to understand the mechanism of mechanical stress affecting the remodeling, pressure- induced expression of c-Jun in the common carotid arteries was studied in rats.

METHODS

The common carotid arteries were perfused with both high pressure (160mmHg) and normal pressure (80mmHg) for 0.5, 1, 3 and 6 hours in SD rats *in vivo*. Expression of immediate-early response gene product c-Jun in the arteries was examined by immunohistochemistry and computer image processing methods.

RESULTS AND DISCUSSION

The results revealed that c-Jun was weakly expressed at 1h, then increased at 3 h and 6 h after the arteries exposing to normal pressure. While positive immonohistochemical product of c-Jun was existed at 0.5h after the onset of high pressure , then increased markedly up to 6h in the arteries. There was significant difference between two groups (Fig.1). It was shown that expression of c-Jun of the arteries could be induced by the pressure, which was also in response to the pressure sensitively. The immediate-early response gene product c-Jun may play an important role in mechanical stress-mediated arterial remodeling.

Fig.1 The relative area of the positive product of c-Jun
* P < 0.01 *vs* normal pressure

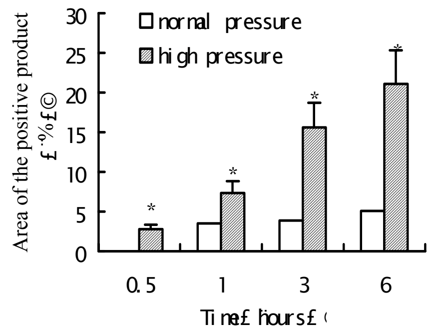

SUMMARY

To investigate the mechanism of mechanical regulation of arterial remodeling, the pressure-induced expression of c-Jun in the common carotid arteries was studied in rats. The results are shown that expression of c-Jun of the arteries can be induced by pressure, which may play an important role in mechanical stress-mediated arterial remodeling.

REFERENCES

Suggs WD, Olson SC, Mardnani D. (1999). Suegery, 126 (2):443-449
Morawitez H, Ma YH, Vives F, et al. (1999). *Circ Res*, 84 (6):678-687
Gan L, Doroudi R, Hagg U, et al.(2000). *FEBS Lett*, 477(1-2): 89-94

ACKNOWLEDGEMENTS

This project was supported by the National Nature Science Foundation of China (No.10132020).

EFFECTIVE CONTACT CONDITIONS BETWEEN CEMENTLESS COATED HIP IMPLANT AND BONE

Julia Orlik[1], Alexei Zhurov[2] and John Middleton[2]
[1]Fraunhofer Institut Techno- und Wirtschaftsmathematik, Kaiserslautern, Germany
[2]Biomechanics Research Unit, University of Wales College of Medicine, Cardiff, UK, zhurovai@cardiff.ac.uk

INTRODUCTION

Treatment for hip osteoarthritis focuses on decreasing pain and improving joint movement. When conservative methods of treatment fail, it is necessary to replace the affected joint with an artificial joint prosthesis. Nowadays there are two types of hip prosthesis: cemented and cementless. The cementless coated hip prosthesis represents approximately 35% of the European market and is regarded as being particularly promising. The surface of the coating is made rough and porous with the idea that the bone, which is in direct contact with the coating, grows into the microvalleys and pores to provide enhanced stability and rapid osseointegration.

We consider mature femoral cortical bone that is in contact with a hip implant having a rough coating. The bone is assumed to be separated from the implant by a thin layer of microscopic peaks and valleys formed on the surface of the coating. The size of the peaks and valleys is very small compared with the macrosize of the implant stem and bone, which makes the direct application of the FEM for the calculation of the bone–stem contact problem prohibitively costly. A way out is to replace the rough layer with physical microcontact boundary conditions by a surface with some effective macrocontact boundary conditions. The macrocontact conditions can then be used in FEM models, allowing one to avoid extremely costly computations in regions with different size scales.

The aim of the research is to investigate the dependence of the bone–implant contact conditions on the microgeometry and mechanical properties of the coating. To achieve this aim, unlike Hansson & Norton (1999), who use semi-empirical approximate relations, we develop an asymptotic homogenisation procedure based on theoretical results of Yosifian (1999) and extend the approach of Jäger et al (1997, 1998) and Belyaev et al (1998) to elastic contact problems.

ASSUMPTIONS

We assume that the contact areas are known, thus confining ourselves to linear problems. From the mechanical point of view, the contact zones are known only if the micropeaks (punches) either have plane summits and equal heights (e.g., are parallelepipeds or cylinders) or have arbitrary geometry but all free space is filled by bone (i.e., the bone is in ideal contact with the implant).

We make the following assumptions: (i) the problem is linearly elastic; (ii) the microcontact surfaces are known, and consequently, the problem is linear; (iii) either there is no friction or Coulomb's friction law is adopted, and hence, the shear stresses at the contact boundary are either zero or proportional to the normal stress; (iv) the bone and implant materials are homogeneous; and (v) there is a small parameter, ε, the ratio of the characteristic dimension of the interface irregularities to the characteristic length of the bone–implant interaction zone, which allows application of an asymptotic homogenisation procedure. In our theoretical models, we treat the implant and coating as being rigid, since their Young's modulus is much greater than that of the bone.

STATEMENT OF PROBLEM, HOMOGENISATION PROCEDURE AND BASIC RESULTS

We consider two contacting domains with interface having a pattern represented by periodically arranged identical peaks with plane or spherical summits. It is assumed that the domains are bounded and periodic boundary (contact) conditions are imposed. We write out the equilibrium equations and constitutive elastic relations with contact and boundary conditions, and then rewrite the problem in a weak (variational) formulation.

Further, we apply a two-scale asymptotic homogenisation procedure, employing some results of Yosifian (1999), to obtain a homogenised variational equation and write out the corresponding homogenised problem in the strong formulation. This problem involves the averaged contact conditions, which replace the microcontact layer.

At the next stage, we solve the homogenised problem, calculate the macrodisplacements and stresses in the bone domain with the averaged boundary conditions obtained. Then, extending techniques of Jäger et al (1998) to elasticity, we find an approximation to the microstresses in the boundary layer by a formal asymptotic expansion, and finally insert this approximation into a microstrength condition to predict the occurrence of fracture in the bone under the applied loading.

The main theoretical result obtained is a general expression of the effective normal contact stiffness for arbitrary microgeometry of the interface; formulas for some special geometries are also presented.

In computations, we use the finite element software package ANSYS. Various designs are considered using the effective normal contact stiffness obtained above. The results are compared with the cases of smooth interface. Fracture regions are predicted for various loadings.

Acknowledgment
We wish to acknowledge support from the European Commission, project CRAF-1999-70359, to undertake this research.

REFERENCES

Hansson, S., Norton, M. (1999). *J. Biomech.*, **32**, 829–836.

Yosifian, G.A. (1999). *Some Unilateral Boundary Value Problems for Elastic Bodies with Rugged Boundaries*, Preprint 99-18 (SFB 359), Heidelberg.

Jäger, W. et al (1998). *Trans. Moscow Math. Soc.*, **59**, 135–157.

Jäger, W. et al (1997). *Applicable Analysis*, **65**, 205–223.

Belyaev, A.G. et al (1998). *Sib. Math. J.*, **39** (4), 621–644.

EFFECT OF CO-CULTURED VASCUAR SMOOTH MUSCLE CELLS ON PDGF-B mRNA EXPRESSION OF ENDOTHELIAL CELLS UNDER SHEAR STRESS

Zonglai Jiang, Yuquan Li, Yan Zhang, Dong Wang

Institute of Biomedical Engineering, Changhai Hospital, Shanghai 200433, China

INTRODUCTION

The effect of vascular smooth muscle cells (VSMCs) on the PDGF-B mRNA expression of co-cultured endothelial cells (ECs) under shear stress had been studied to provide some experimental data for preventing the development of restenosis resulted from VSMCs proliferation in the vascular graft.

METHODS

A new co-culture model of ECs-VSMCs, which mimicked the interior architecture of native vessel and also imitated the interaction patterns between ECs and VSMCs and a flow chamber system for the co-culture model were established, in which 0 ~ 40dyn/cm^2 steady laminar flow shear stress can be obtained. The level of PDGF-B mRNA of ECs cultured alone (SCss) and co-cultured with VSMCs (CCss) exposed to shear stress were investigated by the methods of *in situ* hybridization and image analysis. Both controls of ECs cultured alone (SC) and co-cultured with VSMCs (CC) were maintained under static conditions.

RESULTS AND DISCUSSION

In static condition, the content of PDGF-B mRNA expression of co-cultured ECs was lowered in comparison with ECs alone-cultured. Under shear stress, PDGF-B mRNA expression of co-cultured ECs was increased in transient manner at 1hr after the onset of shear stress and then returned to the level lower than the static level of co-cultured Ecs at 6 hr after being exposed to shear stress. The transient increasing time of PDGF-B mRNA expression of co-cultured ECs reached a maximum earlier than that of ECs cultured alone. Under shear stress, PDGF-B mRNA expression of ECs co-cultured with VSMCs is lowered, which may be favor of inhibiting VSMCs proliferation.

Fig. 6 Gray value of PDGF-B mRNA ISH in ECs

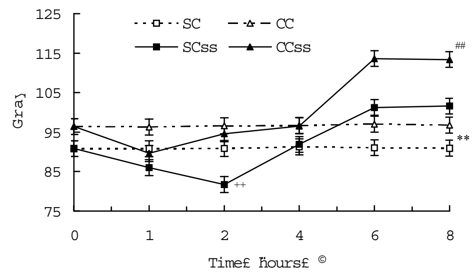

**(SC vs CC, p<0.01) ; ## (CCss vs CC, p<0.01); ++ (SCss vs CCss, p<0.01)

SUMMARY

To understand the effect of VSMCs on PDGF-B mRNA expression of co-cultured ECs under shear stress, the level of PDGF-B mRNA of ECs cultured alone and co-cultured with VSMCs exposed to shear stress were studied by the methods of *in situ* hybridization and image analysis. The results shown that PDGF-B mRNA expression of ECs co-cultured with VSMCs is lowered under shear stress, which may be favor of inhibiting VSMCs proliferation.

REFERENCES

Liu SQ. (1999). *Crit Rev Biomed Eng*, 27(1&2):75-148
Mondy JS, Lindner V, Miyashiro JK, et al. (1997). *Circ Res,* 81(3): 320-327
Cong XZ, Jiang ZL, Li YQ, et al. (2001). *J Med Biomech*, 16(1):1-5

ACKNOWLEDGEMENTS

This project was supported by the National Nature Science Foundation of China (No.10132020, 30070179).

EFFECTS OF LOW SHEAR STRESS ON MORPHOLOGICAL REMODELING OF ORGAN-CULTURED ARTERY IN VITRO

Bo Liu, Zonglai Jiang, Yan Zhang, Xiangqun Yang

Institute of Biomedical Engineering, Changhai Hospital, Shanghai 200433, China

INTRODUCTION

Changes of blood flow can effect the morphometry of vessel. Shear stress may influent proliferation of vascular cells, but it is difficult to control the stress quantitively of in an intact vessel, however, the mechanism of mechanical regulation of vascular remodeling remains to be understood. To explore the biological influence of shear stress on intact artery, we established an organ-culture system of artery under stress *in vitro* and the relationship between stress and vascular remodeling was studied.

METHODS

The common carotid arteries of pigs were cultured under 20 (S20), 5 (S5) and 0 (S0) dyn/cm^2 of shear stress in the system for 1, 4 and 7 days, the pressure 100mmHg was maintained during the culture . Uncultured artery was used as control group (C). Morphometry of arteries, such as inner diametr, wall area and wall thickness, were studied with computer image processing methods. The α-actin of vascular smooth muscle cells (VSMCs) was stained by immunohistochemical methods and cells of vascular wall were also observed by transmission electron microscope.

RESULTS AND DISCUSSION

The results showed that arterial remodeling occurred obviously under low shear stress, expressed as decreasing of inner diameter and wall area and increasing of wall thickness and ratio of wall thickness to inner diameter (Fig. 1). Some VSMCs changed from contractile phenotype to synthetic phenotype under low shear stress. The relative area of α-actin decreased. The nucleus became twisted , bigger and rounder, it's array complicated, and nucleoli could be obviously observed in VSMCs. It was shown that the vascular remodeling reduced by low shear stress is different from that of the alteration of pressure in the morphological changes, which suggested that they have different mechanism. Phenotype switch of VSMCs is the base of vascular remodeling under low shear stress.

SUMMARY

To explore the biological influence of low shear stress on intact artery, the common carotid arteries were cultured under low shear stress in the organ-culture system of artery under stress *in vitro*. Changes in the arteries were studied with morphological, immunohistochemical, electron microscopical and computer image processing methods. Morphological remodeling of them occurred obviously under low shear stress, and it is different from that of the alteration of pressure in the morphological changes, which suggested that they have different mechanism.

Fig. 1 Morphometry of arteries under low shear stress

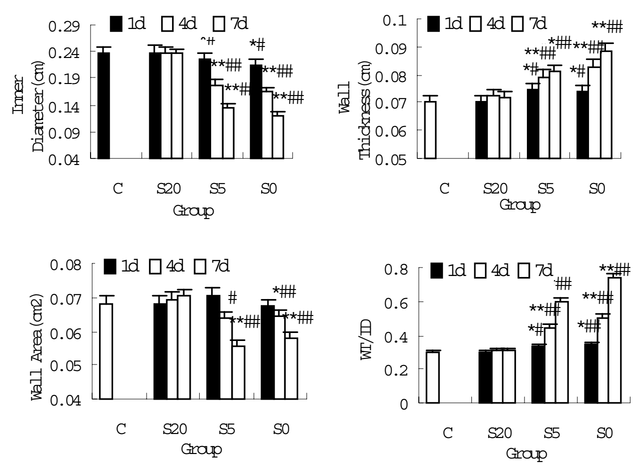

* $p < 0.05$,** $p < 0.01$ *VS* C; # $p < 0.05$, ## $p < 0.01$ *VS* S20

REFERENCES

Zarins CK, Zatina MA, Giddens DP, et al. (1987). *J Vasc Surg,* 5：413~420

Gooch KJ, Dangler CA, Frangos JA. (1997). *J Cell Physiol,* 171：252~258

Konstantin G, Birukov, Stephanie Lehoux, et al. (1997). *Circ Res*, 81：895-903

ACKNOWLEDGEMENTS

This project was supported by the National Nature Science Foundation of China (No.10132020, 10072075).

CHANGES IN GROUND REACTION FORCE AND JOINT EXCURSIONS DURING A FATIGUING LANDING ACTIVITY

Michael Madigan[1] and Peter Pidcoe[2]

[1]Department of Engineering Science & Mechanics,Virginia Tech, Blacksburg, VA, mlm@vt.edu
[2]Department of Physical Therapy,Virginia Commonwealth University, Richmond, VA

INTRODUCTION

Past landing studies have investigated the effect of several performance factors on lower extremity loads in an effort to characterize their roles in injury development. Neuromuscular fatigue may also play a role in injury development, but its effect on lower extremity loads has received limited attention in the literature. The purpose of this investigation was to quantify changes in the vertical component of the ground reaction force (GRFv) and joint excursions during a fatiguing landing activity.

METHODS

The fatiguing landing activity was developed with two goals in mind. First, the resulting muscle fatigue pattern should be "functionally realistic" in that it may include multiple muscle groups. This is in contrast to studies that have fatigued a single muscle group. Second, the protocol should allow changes in landing biomechanics to be monitored continuously as fatigue progresses from a pre-fatigued state to exhaustion. This is in contrast to studies that have reported only pre- and post-fatigue data.

Twelve male subjects who were physically active and had no recent history of lower extremity injury volunteered to participate. Subjects were asked to perform a fatiguing landing activity until exhaustion. The landing activity involved an alternating sequence of 2 single-leg landings (25 cm height), and 3 single-leg squats. The landings were the biomechanical event of interest, and the squats were integrated into the activity to facilitate neuromuscular fatigue. Single-leg landings were used to avoid potential asymmetries in bilateral landings. Ground reaction force and lower extremity kinematics were sampled during the landings. A repeated measures ANOVA with posthoc Dunnett's test was used to determine the significance of changes from initial values for each variable of interest.

RESULTS AND DISCUSSION

As subjects fatigued, the GRFv maximum decreased an average of 12.2% ($p<.01$), the temporal location of the GRFv maximum was not found to vary significantly, the GRFv impulse (calculated from impact to 200 msec after impact) decreased an average of 5.9% ($p<.01$), and the GRFv maximum loading rate increased an average of 4.5%, but was not statistically significant ($p>.05$). Sagittal plane joint excursions increased upon landing as subjects fatigued. Hip flexion increased an average of 2.9° ($p>.05$), knee flexion increased an average of 5.4° ($p<.05$), and ankle dorsi flexion increased an average of 3.8° ($p<.01$). These changes were found to occur in a curvilinear manner as subjects fatigued with the degree of nonlinearity varying between the variables.

These findings suggest a decreased ability of subjects to decelerate upon landing when fatigued. The decrease in GRFv impulse indicates that less of the downward deceleration occurred during the first 200 msec after impact, and (presumably) more deceleration occurred after this time interval. This is supported by the increase in joint excursions upon landing. The nonlinear rate of change of these variables as fatigue progressed indicates that the decreased ability to decelerate the body did not occur in a linear manner.

The fatigue pattern in the lower extremity was induced by a closed kinetic chain activity (squatting) in an attempt to elicit a fatigue pattern that may be more functional compared to a single fatigued muscle group. A limitation of this study was that the resulting fatigue pattern was poorly defined.

SUMMARY

A closed kinetic chain activity was used to progressively fatigue subjects during a landing activity, and the resulting changes in GRFv and joint excursions were quantified. Results suggested a decreased ability of subjects to decelerate upon landing when fatigued. A nonlinear rate of change of GRFv variables and joint excursions indicated that this decreased ability did not progress in a linear manner.

ACKNOWLEDGEMENTS

The authors would like to thank the International Society of Biomechanics for financial support of this work. We would also like to thank AdidasAmerica for sponsoring this study by providing footwear to all participants.

FLOW STUDIES CONNECTED WITH ARTIFICIAL HAEMODIALYSIS. MECHANICAL INVESTIGATIONS AND BIOMECHANICAL EFFECTS

D. Liepsch[1], G. Pallotti[2], P.Pettazzoni[2], L.Colì[2], S.Stefoni[2]

[1]Institut für Biotechnik. e.V., University of Applied Sciences Munich, Germany and
[2]Faculty of Medicine and Surgery,University of Bologna,Italy
Pallotti@df.unibo.it

INTRODUCTION

Arterial venous shunts are commonly used for dialysis treatment of diabetes patients. The procedures are well established. However, many of these shunts create problems and have to be reexamined. The problems that arise include inflammation at the shunt site which must be treated with antibiotics, and stenosis, both within the shunt and downstream in the arteries. In the worst case, the shunt must be replaced for treatment to continue. This, however, can only be repeated once before the shunt site is no longer viable. This increases discomfort, inconvenience and possible danger to the dialysis patient.

METHODS

Several typical shunts were studied to determine whether flow disturbances within the shunt can give rise to these complications. Many studies have already demonstrated the importance of the hemodynamic factors in the pathogenesis of vascular disease. These factors include the pulsatility of flow, the elasticity of the vessel, the non-Newtonian flow behavior of blood, and, very importantly for shunts, the vessel geometry. In model studies, intimal changes have been observed in bends and bifurcations, regions of vessel construction and vessel stenosis. In these regions, the flood flow changes abruptly and this contribute to arterial disease.

RESULTS AND DISCUSSION

We prepared several one-to-one, true-to-scale elastic silicon rubber models of different arterieovenous shunts. The shunt models were based on angiographic studies of dialysis patients at the University of Bologna. These models have a similar compliance to that of the human blood vessel. The flow was visualized in these models using a photoelasticity apparatus and a birefringent blood-like fluid. This method is suitable to analyze the spatial configuration of flow profiles, to differentiate laminar flow from disturbed flow, and to visualize flow separation, vortex formation and secondary flow.

It could be seen that arteriovenous shunts create disturbances that are not found under physiologically normal flow conditions. The X-formed AV shunt was shown to be very unsatisfactory, creating significant flow disturbances. High velocity fluctuations were found within the shunt. These could lead, for example, to aneurysm formation. A less objectionable configuration would be an end-to-end AV shunt. This formation, however, creates other complications. For example, the hand does not get enough blood and parts of the hand lose feeling. The recommended shunt would be an end-to-side anastomoses. In this case, attention should be given to the placement geometry, so that additional flow disturbances are minimized. Several models as well as patient angiographic studies will be discussed.

SUMMARY

This haemodynamic investigation concerns the problems connected with the application to artificial kidney of the patient. The hemolysis-mechanical effects that arise include inflammation at the shunt site which must be treated with antibiotics, and stenosis, both within the shunt and downstream in the arteries. Several tipical shunt were studied to determine whether flow disturbance within the shunt can give rise to these complication

REFERENCES

Kute, S.M., Vorp, D. A. (2001). The effect of proximal artery flow on the hemodynamics at the distal anastomosis of a vascular bypass graft: computational study. *J. of Biomedical Engng.* **123** , 277-283.

Stehbens, W.E., Liepsch, D.W., Poll, A.., Erhardt, W. (1955). Recording of unexpectedly high frequency vibrations of blood vessel walls in experimental arteriovenous fistulae of rabbits using a laser vibrometer. *Biorheology* ,**32**, 631-641.

Sloop, G. D., Fallon, B., Zieske A.W.,(2002). Atherosclerotic plaque-like lesions in synthetic arteriovenous grafts: implications for atherogenesis. *Atherosclerosis,* **160***,* 133-139.

Xue-Mei, Li, S. Rittgers (2001). Hemodynamic factors at the distal end-to-side anastomosis of a bypass graft with different POS: DOS flow ratios. *J. of Biomedical Engng.* **123**, 270-276.

ERECTOR SPINAE FLEXION RELAXATION DURING SHORT DURATION SLUMPED SITTING

Nadine M. Dunk and Jack P. Callaghan

Department of Human Biology and Nutritional Sciences, University of Guelph, Guelph, Ontario, Canada
E-mail: jcallagh@uoguelph.ca

INTRODUCTION

The link between back pain and seated work has been attributed to the required flexed curvature of the lumbar spine (Wilder and Pope, 1996). The ligaments and muscles are the two most frequently proposed sources of low back pain. Given the association of back pain with seated spine postures we were driven to examine whether the flexion relaxation phenomenon occurred in seated postures which could load the passive structures, a potential source of pain. Flexion relaxation (FR) refers to a sudden onset of myoelectric silence in the erector spinae (ES) muscles of the back during standing full forward flexion (Floyd and Silver, 1955). While many studies have documented FR in standing postures, there have been few studies that have examined this phenomenon in seated spine postures.

METHODS

Surface EMG recordings were collected from the right and left thoracic (at the level of T9) and lumbar erector spinae (at the level of L3) on 22 subjects (11 male, 11 female). Lumbar flexion/extension angle was measured using a 3-Space ISOTRAK. Five trials each of standing full forward flexion and seated forward flexion (rounding of the lumbar spine to a "slouched" seated posture) were collected. The flexion-extension cycle was comprised of three different phases (Figure 1).

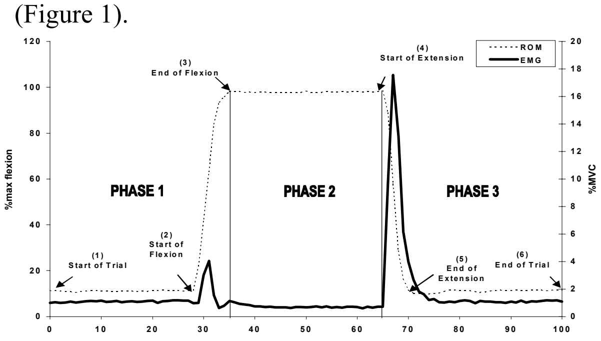

Figure 1: Lumbar flexion and EMG for one channel illustrating the three phases of the flexion-extension cycle.

Both the EMG and 3-Space signals were 6-point ensemble averaged based on events identified from the 3-Space data (Figure 1). FR was defined in standing flexion if the EMG values during the FR phase were within 1%MVC of the levels during upright standing and in seated flexion when the EMG values during the FR phase were at least 1%MVC less than the levels during upright sitting.

RESULTS

Approximately 80% of all subjects exhibited FR in all muscles during standing flexion. Twenty-one out of the twenty-two subjects tested exhibited FR in their thoracic erector spinae in sitting (Figure 2). However, the lumbar erector spinae muscle group remained at relatively constant activation levels regardless of seated posture. The lumbar spine was flexed on average to approximately 36% of maximum standing flexion during upright sitting and 52% of maximum flexion in the slumped posture. FR occurred during seated flexion at an average angle of 46.6% of maximum flexion. The average angle at which FR occurred in standing flexion was 84.1%.

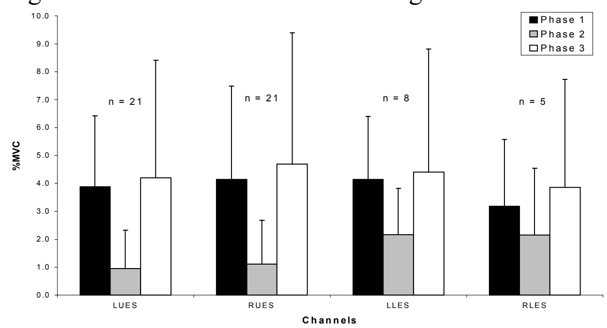

Figure 2: Sitting EMG levels for subjects classified as exhibiting flexion relaxation

DISCUSSION

The most common theory about why FR occurs in standing flexion involves the passive tissues being stretched to a point where they can support the moment imposed on the low back (Kippers and Parker, 1984; Toussaint et al, 1995). FR occurs in seated flexion at a lumbar flexion angle that is much less than standing FR. This would appear to support the mechanical idea that FR is a response to the passive tissues being able to support the imposed moment, which would be less in seated flexion and thus the passive tissues would be capable of supporting the moment at a smaller lumbar angle. Since the myoelectric activity of the lumbar erector spinae did not increase and the thoracic activity decreased, it is likely that the passive tissues of the vertebral column were loaded to support the moment at L4/L5. Ligaments contain a large number of free nerve endings, which act as pain receptors and therefore could be a potential source of low back pain during seated work.

REFERENCES

Floyd WF, Silver PHS. (1955). *J Physiol*, **129**, 184-203.
Kippers V, Parker AW. (1984). *Spine*, **9**, 740-745
Toussaint HM et al (1995). *J Biomech*, **28**, 199-210
Wilder DG, Pope MH. (1996). *Clin Biomech,* **11**, 61-73.

LOCALIZATION DETECTION OF TRANSVERSE HOLES IN INTRAMEDULLARY NAIL INSERTED INTO FEMUR USING FOCUSED ULTRASOUND

Yoshihisa Minakuchi[1], Hideki Numoto[2] and et al.
Faculty of Engineering, Yamanashi University, 4-3-11 Takeda, Kofu-shi, Yamanashi, Japan
[1]Professor, minakuti@ccn.Yamanashi.ac.jp
[2]Orthopaedic Surgery of Isawa Kyoto Hospital, Japan

INTRODUCTION

It is not easy to insert a locking screw into the distal transverse hole for fixing the intramedullary nail and the broken human bone [1]. Generally, the X-ray image is used to detect the transverse holes [2]. But the X-ray exposure has very crucial problem for doctors and patients. In this paper, the central position of the transverse holes in the nail inserted into the pig femur was detected by the linear scanning using a focused ultrasound. Moreover, the interlocking accuracy of locking screw was investigated.

EXPERIMENTS

The pig femur specimen inserted with the nail was made. The nail is a brass bar with the diameter of 12mm and two holes of 5mm. Figure 1 shows the measurement apparatus for detecting a nail hole by a focused ultrasound. The specimen was immersed in the water at 36℃ and the focused probe (Frequency:1MHz, Focal distance:70mm, Transducer diameter:13mm) was set on the water surface of 40mm apart from the intramedullary nail in conjunction with a target device (ACE Med.). The focused probe was moved linearly every 0.1mm toward the y-direction using a handle. The wave velocity through water was set at 1500m/s. The ultrasound was propagated toward the specimen, and then the probe position and the echo height were measured by the echo reflected from the nail surface. After determining the center of the nail hole, the locking screw was inserted into the pig femur specimen along a guide sheath.

RESULTS AND DISCUSSION

Figure 2 shows an example of the echo waveform reflected from the specimen. The marks of ①, ② and ③ indicate the echoes from the outside of femur, the inside of femur and the nail surface, respectively. It was found that the echo from the nail surface was able to catch by the ultrasound. Figure 3 shows the relations between echo heights and measuring positions obtained by the echo ③ in Fig.2. The central position of the transverse nail hole was located at the largest echo height in Fig.3. The reason is that the distance between the focused probe and the top face of nail is the shortest propagation path of the sound wave, and the echo reflected from the top face of nail has the largest power. Moreover, the locking screw could insert into the transverse nail hole with a high accuracy.

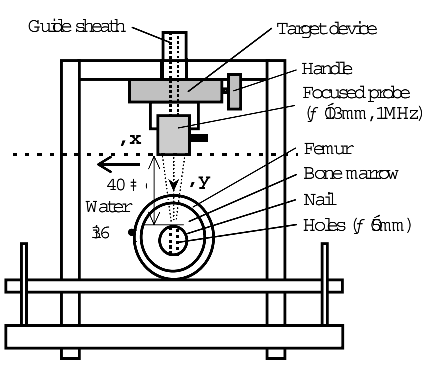

Figure 1: Measurement apparatus for detecting a nail hole by focused ultrasound.

SUMMARY

(1) The central position of a transverse hole in the intramedullary nail inserted into the pig femur specimen can detect by the largest echo height position reflected from the nail surface.
(2) The locking screw can insert into the hole center with a high accuracy using focused probe.

REFERENCES

[1] Minakuchi, Y., et al., J. Japan Soc. Welfare Eng., **1**, pp.39-43 (1999).
[2] Barry, T. P, Clin. Orthop., **182**, pp.160-164 (1984).

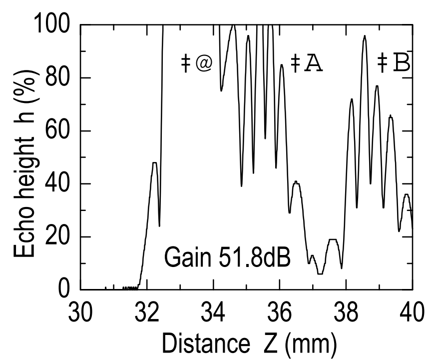

Figure 2: Echo waveform from outside of femur ①, inside of femur ② and nail surface ③.

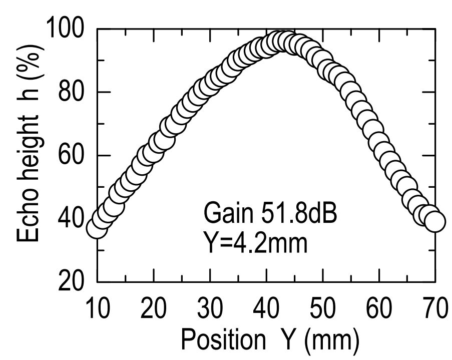

Figure 3: Echo heights to measuring positions.

IMPLICATIONS OF HAND TRAJECTORIES FOUND IN TWO MUSCULAR DYSTROPHY SUBJECTS

Roscoe C. Bowen[1], Rami Seliktar[1], Tariq Rahman[2], MichaelAlexander[3]
Drexel University Philadelphia PA 19104
[1]School of Biomedical Engineering
AI duPont Hospital for Children, Wilmington DE, 19803
[2]Pediatric Engineering Research Lab
[3]Rehabilitation Medicine

INTRODUCTION

Muscular dystrophy (MD) is a progressive disease affecting muscle function. In the upper limb, the proximal muscle groups are affected first, and the disease progresses toward the distal muscles. This results in individual having insufficient power to lift their arm against the force of gravity while still having a reasonable grasping capability.
The present study inquires: if movement in a planar workspace is still possible how does the disease affect hand trajectory when performing tasks in that workspace. Several researchers (Abend et al., 82; Flash and Hogan., 85; Soechting and Flanders, 91; Marasso, 81) have shown that in able-bodied subjects, point-to-point hand movements produce essentially straight-line hand paths and uni-modal velocity profile along the path. This is true for almost all point pairs and has been a strong argument for movement planning in terms of hand motion versus joint angles (Marasso, 81).

METHODS

Two male subjects were tested, one with Duchenne's type MD age 14 and the other with Becker's type MD age 19. Subjects were seated at a test table and were asked to reach for several targets, moving to each target and returning to the start position before moving on to the next target until all targets were acquired. Targets were fixed at 30, 60, 90, and 120 degrees attitudes (see Fig 1), at a distance of the length of a fully extended arm. An air bearing was used to "float" the arm so as to minimize friction. Motion of the arm was monitored with MacReflex kinematic data acquisition system.

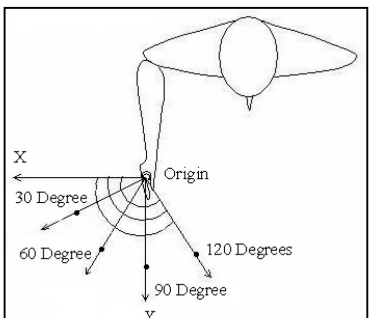

Figure 1: From the starting position shown the subject reached for targets placed at each attitude 1/2 the distance of the subjects arm length

RESULTS AND DISCUSSION

Both subjects produced essentially straight hand paths, to and from the target and unimodal velocities as illustrated in Figure 2. Subjects tended to use large trunk rotations and tilt to assist them in projecting their hand throughout the workspace. It appears that transfer of momentum from the trunk to the arm may be a key component for compensating for muscular weakness in the arms.

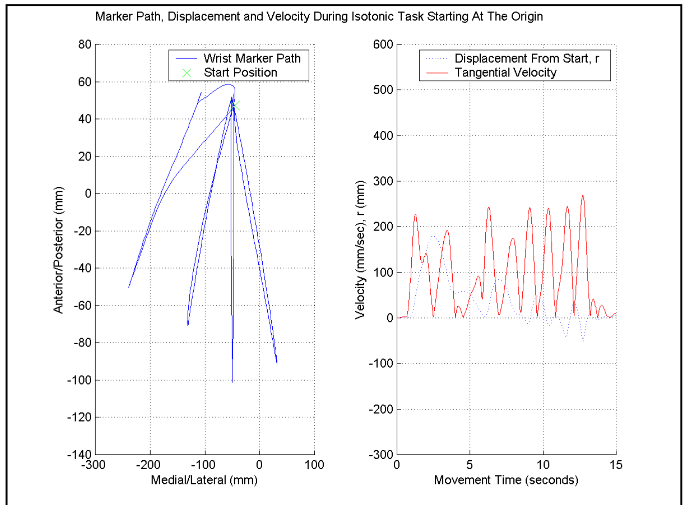

Figure 2: Trajectory Kinematic profile for subject with Duchenne's type MD.

SUMMARY

Mechanisms of compensation are employed to enable the MD subjects tested to move their arms throughout a planar workspace. To the extent that conclusions can be derived from the two subjects tested, mechanisms of compensation were chosen in such a manner that maintains the hand trajectory characteristics similar to those reported in healthy individuals. The fact that the hand path and velocities are similar to healthy subjects supports the contention by Marasso (81) that planning for movement occurs in the hand-space.

REFERENCES

Abend, et al., (1982). *Brain,* 105: 331-348.
Flash, T., and Hogan, N. (1985). *J. Neurosc.,* 5:1688-1703.
Soechting, J. and Flanders M. (1991). *Exercise and Sport Science Reviews,* 19: 389-418.
Marasso, P., (1981). *Exp Brain Res.,* 42: 223-227.

ACKNOWLEDGEMENTS

This project was supported in part by the Drexel-Jefferson seed grant program, Drexel project #991057. We would also like to acknowledge the in-kind support of the AI duPont Hospital for children, by allowing the use of their facilities.

THE PROPAGATION OF AN IMPACT FORCE ALONG THE UPPER EXTREMITY

Kurt M. DeGoede[1,4], James A. Ashton-Miller[1,2] and Neil B. Alexander[2,3]

University of Michigan, Ann Arbor, Michigan 48109
[1]Biomechanics Research Laboratory, Department of Mechanical Engineering, http://me.engin.umich.edu/brl/
[2]Institute of Gerontology, [3]Geriatrics Section, Department of Internal Medicine
[4]Present Address: Elizabethtown College, Elizabethtown, PA, degoedek@etown.edu

INTRODUCTION

A fall onto an outstretched arm is often the cause of wrist, elbow and/or shoulder injuries (Loder and Mathew 1988), perhaps due to the initial large high-frequency component of reaction force between the arm and the ground, rather than the later and smaller lower-frequency component. Lumped-parameter model simulations of a fall onto an outstretched arm have predicted attenuation and delay of the peak impact force applied at the hand by the time it reaches the shoulder (Chiu and Robinovitch 1998). We tested the hypotheses that **(a)** the deflection of the shoulder occurred significantly after the early peak hand reaction force and **(b)** the rate of force transmission through the limb is a function of initial elbow angle at impact.

METHODS

A total of 40 subjects (20 young (mean [SD] age 25 [3] years; 20 older subjects: 70 [3] years, with equal gender representation) participated in the study. Subjects were seated in a rigid, high-backed, steel-framed chair with a 4 cm wide spine support designed to securely support the torso in the mid-sagittal plane, while permitting free motion of the scapulae. A ceiling-mounted, instrumented, padded, ballistic pendulum (3.5 Kg) impacted both stationary hands at 1.8 m/s at a location in front of the shoulder with elbow angles of 130, 150, 170 degrees (DeGoede et al. 2002). Three trials were conducted for each elbow angle. Kinematic data from markers located on the arm, forearm and torso were obtained at 300 Hz using an Optotrak® 3020 system, and from the bimanual pendulum force transducers at 1,800 Hz. We assumed that deflection of a kinematic marker is proportional to the force acting at that location. The mean (SD) latencies were found when the hand force and kinematic marker displacements (a) initially exceeded preset baseline rate thresholds ('start'), and then (b) first returned below threshold ('end') were found, along with the timing of the peak force applied to the hand. A repeated measure analysis of variance (rm-ANOVA) was used to test the hypotheses after calculating average latency times for each subject. Two-sided, post-hoc paired t-tests were performed to examine the relationships between initial elbow angle and deflection initiation times.

RESULTS AND DISCUSSION

The peak contact force occurred 7±1 msec after initial contact and the impact impulse lasted a total of 18±3 msec. Upper extremity location systematically affected the impact force propagation latency (rm-ANOVA, $p<0.001$): (a) the elbow started to deflect as the contact force approached its maximum

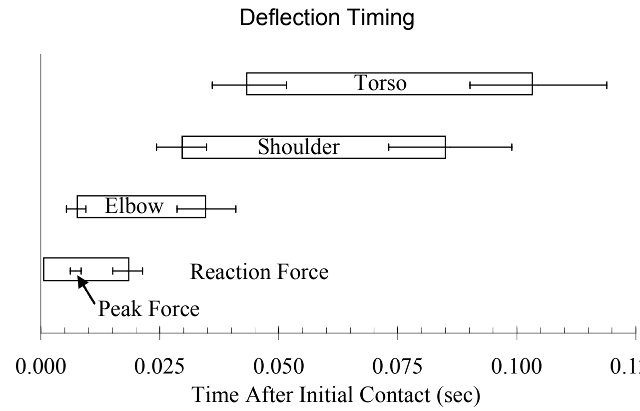

Figure 1: Timing of the mean (SD denoted by error bars) initiation (left end of box) and termination (right end) deflections observed at different points along the arm

(start: 7±2 msec; end: 35±6 msec); (b) the shoulder deflected posteriorly just after the end of the impact force impulse (start: 30±5 msec); (c) the torso first deflected at 44±8 msec (Fig. 1). The initial elbow angle also affected the latencies (within-subject, rm-ANOVA $p<0.001$). In the more extended arm configuration: (a) time-to-peak force and initiation of elbow rotation each increased by approximately 4 msec ($p<0.001$); and (b) posterior deflections at the shoulder, torso and chair occurred earlier (8, 21, and 16 msec, respectively; $p<0.001$). Short- (~40 ms) and long-loop reflexes (>80 ms) latencies are precluded from protecting wrist or elbow tissues in a fall, because significant additional delays (~100 msec) are required to increase muscle tension.

SUMMARY

The shoulder did not deflect until well after the impact force at the hand had returned to baseline levels. This validates lumped mass models suggesting that the initial impact force spike is principally due to arm inertial effects. Thus in a fall to the ground the peak force applied to a wrist should be independent of the contralateral wrist impact time.

REFERENCES

Chiu, J., Robinovitch, S.N. (1998). *J. Biomech.* **31**: 1169-76.
DeGoede, K.M. et al (2002). *J. Biomech. Eng.* In Press.
Loder, R.T., Mathew, H.E. (1988). *Am Fam Physician* **37**: 327-338.

ACKNOWLEDGEMENTS

PHS grant P01 AG10542 and P30 AG 08808

THE STABILIZING EFFECT OF EXTERNAL ANKLE DEVICES WITH AND WITHOUT THE ADDITIONAL INFLUENCE OF A SHOE

Eric Eils, Simone Imberge, Lothar Thorwesten, Klaus Völker, Dieter Rosenbaum
Movement Analysis Lab, Orthopaedic Department, University Clinics Münster, Münster, Germany, eils@uni-muenster.de

INTRODUCTION

External ankle stabilizing devices (braces, tape) are commonly used for treatment, rehabilitation and prophylactic purposes in sports. There is evidence that the use of these devices reduce ankle sprains in high risk sporting activities like soccer or basketball (1). However, this is only valid for sports where an external device is used in combination with a shoe. Ankle sprains are also among the most common injuries in sports like dancing or gymnastics were no shoe are used (2, 3), and it remains unclear if the stabilizing effects of the brace/shoe complex is transferable to a situation without shoe. Therefore, the aim of the present investigation was to quantify the stabilizing effects of three external ankle devices tested with and without shoe to make recommendations for sports where shoes are not worn.

METHODS

25 healthy subjects participated in the study (26±3 yrs, 178±7 cm, 71±10 kg). A mechanical fixture was developed to measure the mobility of the ankle joint complex in three planes with a standardized torque. Subjects lay supine with one leg fixed in the apparatus, the foot placed on a foot plate and the tibia fixed at two points. Rotation axes for plantar/dorsiflexion, inversion/eversion and internal/external rotation were aligned with the intermalleolar axis, the long axis of the foot on the level of the subtalar joint and the longitudinal axis of the tibia, respectively. To determine the individual torque, the leg was fixed without braces and rotated in each direction to the limits of comfort. The maximum torque for each direction was then used for all conditions and the rotational displacement were measured.

Three stabilizing devices (Semi-rigid-Aircast, Soft-Dynastab, Tape) were applied to the subject's leg by the same investigator. Condition with and without shoe were carried out by using two pairs of shoes where one was cut at the lateral and medial part to remove additional stability of the upper material. The order of the eight testing conditions was randomized. Three trials for each direction were measured and the individual means were calculated. Restriction of motion in relation to the no brace/no shoe condition was calculated for each direction. For statistical analysis a two way repeated measures ANOVA (shoe, external device) with the α-level set to 5% was used.

RESULTS

In the no brace/no shoe condition the following ranges of motion were determined: 42°±11° inversion, 31°±13° eversion, 47°±8° plantar flexion, 35°±6° dorsiflexion, and 35°±11° internal rotation, and 39°±8° external rotation. The corresponding mean torques were 6.2 Nm±3.2 inversion, 7.1 Nm±3.1 eversion, 9.7 Nm±4.7 plantar flexion, 17.6 Nm±6.0 dorsiflexion, 6.7 Nm±2.8 internal rotation, and 6.1 Nm±3.0 external rotation. The ANOVA revealed that both main effects (shoe, external device) were significant ($p<0.01$) for all directions of motion and a significant interaction between shoe and external devices was found ($p<0.01$) except for total rotation. Range of motion between shoe and no-shoe increased for all conditions and in all directions (Fig. 1). Tape and Aircast provided highest stability in all directions in combination with the shoe, but without shoe Tape and Dynastab showed best restriction of motion for most directions. Significant loss of stabilization between shoe and no-shoe ($p<0.001$) was only found for the Aircast for inversion, eversion, plantar flexion and total rotation.

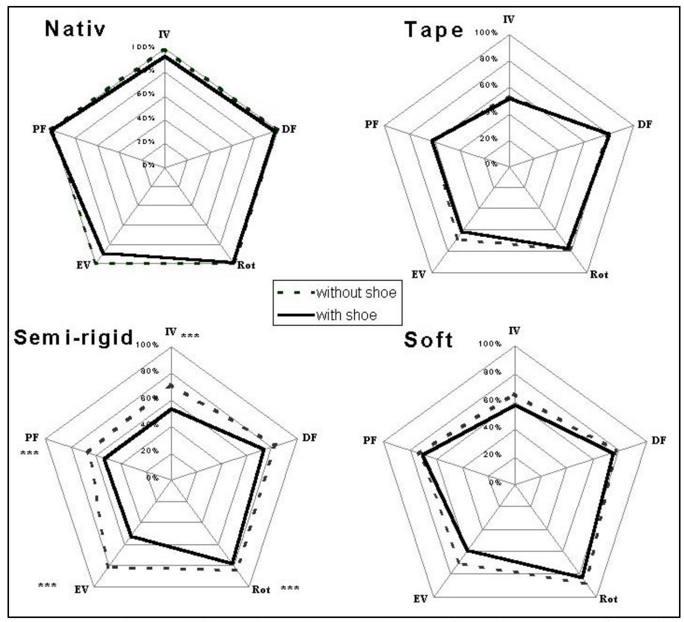

Fig. 1. Passive stability of each condition in five directions of motion (IV=inversion, EV=eversion, PF=plantar flexion, DF=dorsiflexion, Rot=total rotation) with and without shoe. The values are normalized to the no brace/no shoe condition (=100%).The size of the area in the spider web becomes smaller with a more pronounced stabilizing effect. ***=p<0.001.

DISCUSSION

Although changes between shoe and no-shoe were minimal for Tape it may not be recommended for use in sports because it is well described that the stabilizing effect is lost after 20 minutes of exercise (4). The stirrup-design brace obtained a high degree of stability from the shoe and without shoe it showed less stability for most directions than the lace-on brace. Therefore, lace-on braces may be recommended to provide stability for sports like dancing or gymnastics.

REFERENCES

1. Quinn K. et al. (2000), *Cochrane Database Syst Rev*.
2. Hamilton WG. (1988) *Clin Sports Med* 1988; 7(1).
3. Lindner KJ/ Caine DJ.(1990) *Can J Sport Sci*; 15(4).
4. Verhagen E.A. et al. (2001). *Sports Medicine* 2001; 31(9).

A COMPARATIVE STUDY OF CFD AND MRI FOR PULSATILE FLOW IN A CAROTID BIFURCATION PHANTOM

S.Z. Zhao[1], X.Y. Xu[1], P. Papathanasopoulou[2], I. Marshall[2]
[1]Department of Chem. Eng. and Chem. Tech., Imperial College, UK, s.zhao@ic.ac.uk
[2] Department of Medical and Radiological Sciences, Edinburgh University, Edinburgh, UK

INTRODUCTION

Local hemodynamics is considered to play an important role in the initiation and development of atherosclerosis (Ku et al., 1985). Flow quantification techniques such as magnetic resonance imaging are commonly used to study arterial hemodynamics. An alternative and complementary approach uses numerical simulations. A combined MR imaging and computational fluid dynamics (CFD) modelling study was carried out for pulsatile flow in a carotid bifurcation phantom. The aim of the study was to quantify differences in velocity and wall shear stress obtained from the two approaches. The geometry and inlet velocity images from MR scans were used as boundary conditions for CFD calculations of the complete flow field in the model, and CFD results were compared with the MR measurements. Wall shear stress (WSS) derived from direct MR velocity measurements was also compared with the CFD predictions.

METHODS

Scanning was carried out on a 1.5-T GE Signa scanner (GE Medical, Milwaukee) equipped with Echospeed gradients. An anthropomorphically realistic healthy human carotid bifurcation model was employed in the experiment. Velocity measurements were made using a retrospectively gated three-dimensional phase contrast gradient-echo sequence that generated velocity-encoded images for each component at 18 frames. Its parameters were TR/TE=25/7 ms, pixel size 0.5 mm and slice thickness 1mm.

Structured computational mesh for the carotid phantom was generated from the high-resolution MRI images after segmentation and smoothing (Long et al., 1998). A commercial package CFX4 was used to solve the Navier-Stokes equations governing the time-dependent flow. For the inlet boundary condition, the MR measurements at the entrance were mapped onto the computational grid at inlet. Time-varying flow ratio between two branches calculated from MR velocity images was used for outflow boundary conditions. Finally, the WSS vectors were calculated from direct MR measurements by a home developed software package (Köhler et al., 1999).

RESULTS AND DISCUSSION

Figure 1 shows MRI and CFD results in the mid-sinus. General features are the occurrence of highly skewed flow with slow velocities at the outer wall and high velocities at the flow divider wall in the bifurcation plane (R-L plane), as well as well-defined M-shaped profiles along the anterior-posterior axis (in A-P aspect). The agreement between MRI and CFD acquired velocities is generally good, given some uncertainties for low velocities due to 5% measurement error. WSSs predicted from CFD were compared with those derived from MRI alone at peak and minimum flow phases. Reasonably good agreement was also achieved especially at the phase of minimum flow.

(a)

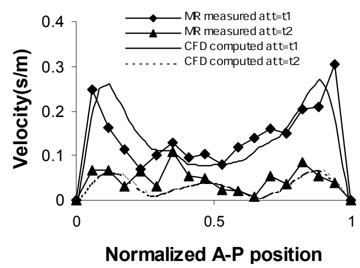

(b)

(outer wall) (flow divider)

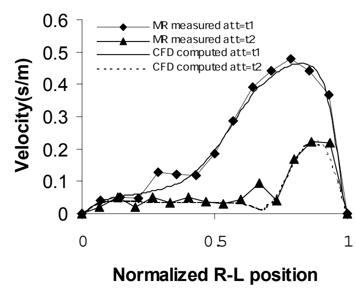

Figure1 Velocity profiles in the carotid sinus at peak (t1) and late systole (t2) (a) R-L (b) A-P

SUMMARY

Comparisons of computed and MRI measured velocity profiles in a carotid phantom under transient flow condition have shown good agreement for both well-behaved flow and disturbed flow, with difference in peak velocity less than 8%. We are currently comparing the MR derived WSS vectors with CFD predictions.

ACKNOWLEDGEMENT|S

This work is supported by EPSRC. The authors would like to thank Dr. Quan Long for developing the package of reconstructing geometry model and processing velocity images, and Dr. Uwe Köhler for WSS software.

REFERENCES

Ku, D.N., Giddens. D.P., Zarins, C.K., Glagov, S.(1985) Arteriosclerosis, 5,293
Long, Q., Xu, X.Y., Collins, M.W., Bourne, M., Griffith, T.M.(1998) Compu Methods Programs Biomed, 56, 249
Köhler, U. et al. (1999)Proc. ESMRMB, 157

TORSIONAL FATIGUE OF CORTICAL BONE

P.O'Reilly[1], D. Taylor[1], T.C.Lee[1,2]
[1]Department of Mechanical and Manufacturing Engineering, Trinity College, Dublin 2, Ireland. [2]Department of Anatomy, Royal College of Surgeons in Ireland, Dublin 2, Ireland.

INTRODUCTION

Fatigue tests on bone are usually conducted in tension and/or compression. Very little work has been carried out to date on torsional fatigue of bones or machined bone specimens. Torsinal loading is of interest because it occurs in vivo and because bone being anisotropic, may be relatively poor at resisting longitudinal shear stresses. In this study the objectives were to construct a rig to deliver pure torsional loading; to compare fatigue test data in torsion and compression and to study the development of damage (cracking) in torsion.

METHODS

The rig was designed to convert the linear displacement of the actuator on an Instron servohydraulic testing machine into a rotational displacement of the bone; the load cell of the Instron was used to sense the load being applied to the bone. Ten chicken metatarsal bones were tested; the bones were gripped by having their ends encased in modelling plaster. The rig was also used to test bovine cortical bone samples of circular cross section (5mm gauge diameter). Sixteen samples were tested. Tests were carried out in load control at 3Hz with a stress ratio of 0.1;. Failure was defined in terms of a fixed increase in amplitude, since catastrophic failure often did not occur, especially in the bovine specimens (see below). A Finite Element model was created to enable us to find the maximum stress in the bone during testing; this was validated using strain gauges. Fluoro-chelating dyes were used before and during testing to label damage (cracks) for later examination using optical and scanning-electron microscopy.

RESULTS AND DISCUSSION

Fig. 1 shows the stress range versus cycles to failure for the bovine samples and also for specimens taken from the same source which were tested in axial compression [3]. A similar plot exists comparing the torsional fatigue results for torsional fatigue on chicken metatarsal bones with previous data from compressive fatigue on chicken tibiae.The bovine bone was found to be plexiform structure [1] which greatly influenced the crack propagation. And this is evidenced in histology and electron microscopy photographs. Cracks in the chicken and bovine bone tended to grow to lengths of a several millimetres in a stable manner without causing catastrophic failure. Large amounts of creep[2] or plastic ratcheting were observed on the plots of position displacement for the bovine and chicken bone tests.

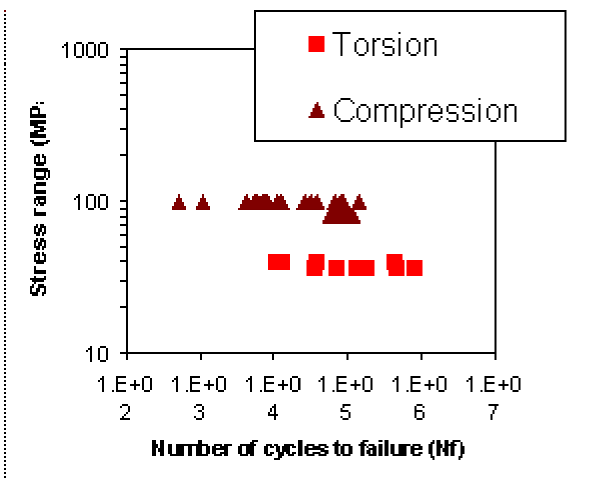

Figure 1: Fatigue test data for bovine compact bone specimens, tested in torsion and axial compression. The stress axis shows the maximum principal stress applied.

SUMMARY

Results showed that bone is much weaker when tested in cyclic torsion than in axial compression. Previous work has shown that bone is only slightly weaker in axial tension than it is in compression; here we found a difference of more than a factor of two in terms of the maximum principal stress. In the case of the whole chicken bones there may also be differences due to the fact that we are comparing two different bones (metatarsal and tibia) as well as two modes of loading. However this is not the case for the bovine bone, where we used the same source of material and the same type of specimen for both torsion and compression.

REFERENCES

1] Martin, R.B., Burr, D.B. and Sharkey, N.A. (1998) Skeletal Tissue Mechanics New York: Sprenger-Verlag.
[2] Lakes, R., Saha, S. (1979) Cement Line Motion in Bone. Science 204 501-503.
[3] Taylor D, O'Brien F, Prina-Mello A, Ryan C, O'Reilly P and Lee TC. (1999). J.Biomechanics 32:1199-1203.

STUDY OF BLOOD FLOW IN THE HUMAN FEMORAL ARTERY BY CFD

S.Z.Zhao[1], A.Zambanini[2], Q.Long[1], A.D.Hughes[2], S. A.Thom[2] and X.Y.Xu[1]

[1]Department of Chem. Eng. and Chem. Tech., Imperial College, UK, s.zhao@ic.ac.uk
[2]Clinical Pharmacology, National Heart and Lung Institute, Imperial College, UK

INTRODUCTION

The presence of atherosclerotic plaques has been shown to be associated with particular geometric features of arteries. This is believed to be mediated through local hemodynamic factors such as wall shear stress. Atherosclerotic disease of the superficial femoral artery (SFA) is common and is a major cause of peripheral vascular disease. The SFA is a curved and tortuous artery. We have previously reported that significant gender and anatomical site differences exist for SFA tortuosity and curvature. The present study was designed to examine the effects of femoral artery geometry on wall shear stress distributions with emphasis on clarifying the site-specific nature and gender difference for the incidence of arterial disease.

METHODS

The SFA was imaged by MRI in 18 normal subjects. Velocity and wall shear stress distribution in anatomically realistic models of human SFA were computed using the finite volume method. In order to investigate the effect of geometry alone, all simulations were carried out under the same flow conditions. To understand the influence of overall geometry on wall shear distributions, the lowest wall shear stress (LWSS) at each transverse grid plane was determined for the whole vessel segment. Two wall shear stress measures were then derived from the LWSS for each vessel: the time averaged LWSS and the minimum LWSS occurring in a cardiac cycle. To investigate regional differences of wall shear stress measurements in upper, mid and lower segments of SFA were compared.

RESULTS AND DISCUSSION

In all arteries features, such as highly spiral flow and spiral wall shear stress distribution when the artery enters the adductor canal (as shown in Figure 1), were seen. Particularly noteworthy was the complex secondary flow pattern which may include structures such as a single vortex, a double vortex and C-shaped vortex surrounded by two relatively thin layers developed within a single vessel. The region of artery in the adductor canal was exposed to the lowest shear stress in both men and women. This corresponds well with the strong predilection for atheroma formation at this site in at risk individuals. There was also significant difference in average LWSS and minimum LWSS between males and females(average LWSS: 1.84±0.33(male), 2.44±0.34(female), $p<0.01$; minimum LWSS: 1.02±0.42(male), 1.79±0.26(female),$p<0.001$) due to differences in vessel tortuosity. This study suggests that high vessel curvature and tortuosity result in localized sites of low average and minimum LWSS. Shear stress in SFA is also lower in men than women. These observations may explain differences in the distribution of atheroma in SFA and the increased burden of peripheral vascular disease in men.

(a)

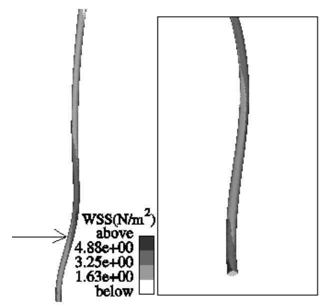

(b)

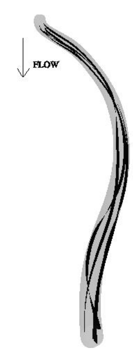

Figure 1 (a) Spiral wall shear stress distribution and (b) spiral flow pattern in the femoral artery.

ACKNOWLEDGEMENTS

This work was supported by the British Heart Foundation.

MODEL OF ACTIVE ANKLE-FOOT ORTHOSIS WITH SENSORS CONTROL

Slavyana Milusheva[1], Mihaela Kalaidjieva[1], Nikolay Zlatov[2], Yuli Toshev[1]
[1]Institute of Mechanics and Biomechanics, Bulgarian Academy of Sciences, Bulgaria, ytoshev@imbm.bas.bg
[2]Manufacturing Engineering Centre, University of Cardiff, United Kingdom

INTRODUCTION

Ankle-foot orthoses are used mainly in case of disability of neurological origin (cerebral palsy, stroke, spinal cord injury) or musculoskeletal origin (trauma, ageing). Due to the motor control disorder the observed result is usually abnormal ankle-foot position and forefoot or flatfoot initial ground contact during gait.

METHODS

The principles of active control could be illustrated using Fig.1. Using relatively hard orthosis footpad the system "foot-orthosis" could be determined as pseudo-rigid system. In this case active ankle-foot flexion (dorsiflexion) and extension could be realised using external drive force (electrical, pneumatic or hydraulic).

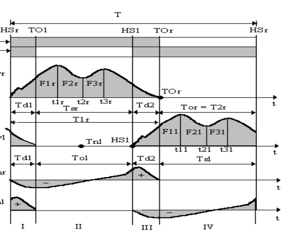

Figure 1: The vertical (index v) and the horizontal (index h) ground reactions of the right (index r) and left (index l) lower limbs during walking. F1r, F2r, F3r, F1l, F2l, F3l – extreme force values; t1r, t2r, t3r, t1l, t2l, t3l – time parameters of the extreme force values; T1r, T1l - stance phases; T2r, T2l - swing phases; Td1, Td2 - double supports; Tr, Tl - step phases (stance + swing).

If we suppose that the left limb is abnormal, the control signals to realise suitable ankle flexion/extension must be: (a) In the moment T_{nl} (in the interval t_{1r} - t_{3r}) during the stance phase of the normal (right) limb, the first control signal must provoke ankle flexion of the abnormal (left) limb; (b) In the moment HSl (heel strike left) the second control signal must provoke ankle extension of the same left limb (abnormal); (c) In the moment TOr (toe off right) the third control signal must provoke drive switch-off in order to assure the stance phase of the abnormal (left) limb.

The sensors situation is as following: (a) The first sensor is situated under the front foot part of the normal limb (the right) and using adequate software generates control signal in the moment T_{nl} (ankle flexion of the abnormal limb); (b) The second sensor is situated under the rear orthosis part (left limb) and generates control signal in the moment HSl (ankle extension of the abnormal limb); (c) The third sensor - situated under the toe of the normal limb (the right) generates control signal in the moment TOr (drive switch-off in order to assure the stance phase of the abnormal limb).

Two additional warning/training sensors (WTS) could be mounted on the orthosis to control the transversal (right/left) dynamic equilibrium.

RESULTS AND DISCUSSION

A scheme of our active ankle-foot orthosis (electrical drive) with branched metal splint is shown on Fig. 2. Both branches (positions 4 and 5) have supporting function. On the end of the rear branch (under the heel) is mounted a sensor (position 6) to generate a control signal in the moment of HSl.

Figure 2: Active orthosis model: 1- buckle; 2 – metal splint; 3 – motor; 4 – rear branched metal splint; 5 – fore branched metal splint; 6 – sensor under the heel; 7 - polypropylene crust for the shank; 8 – belt; 9 – polypropylene crust for the foot.

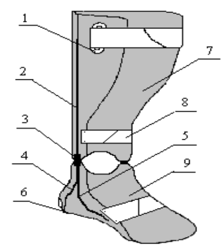

Using CAD/CAM technology (SolidWorks) different models of the system "ankle-foot-orthosis" are developed (Fig.3). Three types of drives could be used – electrical, hydraulic and pneumatic. The final evaluation should be verify during the clinical experiments.

Figure 3: CAD/CAM model of active ankle-foot orthosis

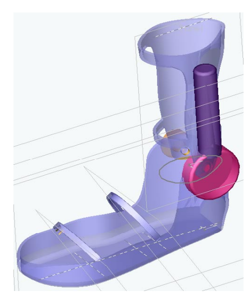

SUMMARY

New approach for design of active orthoses is presented. One model is proposed and generated using CAD/CAM system.

REFERENCES

Toshev, Y.et al (2001*). Proceedings of the 13th ISB Congress, Zurich*, 318.

EFFECTS OF MECHANICAL STIMULI ON THE RELAXATION BEHAVIOR OF THE GROWTH PLATE RELATED TO MORPHOLOGICAL AND BIOCHEMICAL ADAPTATION IN THE RAT MODEL

Anja Niehoff[1], Uwe Kersting[2], Frank Zaucke[3], Michael Morlock[4], Kay Sellenschloh[4], G.-P.Brüggemann[1]
[1]Institute for Biomechanics, German Sport University of Cologne, Cologne, Germany, Niehoff@hrz.dshs-koeln.de
[2]Institute for Individualsport, German Sport University of Cologne, Cologne, Germany
[3]Institute for Biochemistry II, Medical Faculty, University of Cologne, Cologne, Germany
[4]Biomechanical Section, Technical University of Hamburg-Harburg, Hamburg, Germany

INTRODUCTION

The adaptation of the growth plate in response to physical loading was investigated in previous studies with clinical intention of bone lengthening. About the effect of physical loading through exercise on the growth plate exists only limited information. There are occasional studies which had shown morphological adaptation (Nyska et al., 1995, Swissa-Sivan et al., 1989). Alterations of the mechanical properties and the relation between mechanical, morphological and biochemical components of the plate were not analysed.
The purpose of this study was to investigate the effects of physical loading on the laod-relaxation behavior of the distal femoral growth plate in relation of morphological and biochemical alterations in a rat model.

METHODS

Ninety 3 weeks old female Sprague-Dawley rats were randomly assigned to a high trained exercise (n = 30), a low trained exercise (n = 30) and a non-active control group (n = 30). The exercise groups were trained in a running wheel with voluntary exercise. Food and water was available ad libitum and the rats housed on a 12 h/12 h light/dark cycle.
10 animals of each group were sacrified after four weeks, the next ten after eight weeks and the last ten after 12 weeks. The rats were decapitated and the femurs were obtained. The bones of the left hindlimb were frozen at –80 °C until mechanical testing on a material test machine (Zwick Z2.5/TN 1S). The femur was placed horizontally so that the distal growth plate was loaded in shear direction. The load was applied by a c-formed stamp adapted individually to the form of the plate from lateral to medial to the whole epiphysis using a 100 N load cell. The specimens were preloaded with 0.5 N and three cycles of a load-relaxation series began. For each cycle a shear load of 6 N was first applied, followed by a relaxation at that strain for 500 s. Then load was reduced to 0.5 N for 500 s. After the three cycles there was a total relaxation for 15 min. Then the three load-relaxation cycles were repeated. We analysed the relaxation behavior after 3 s, 10 s, 60 s and 500 s from each cycle of the two tests series.
The distal epiphysis of the right femur was fixed in Bouin solution, decalcified in EDTA for four weeks and blocked in paraffin. After suitable enzymatic pretreatment immunohisto-chemical staining with antibodies directed against type I (Sigma, Germany), type II (Calbiochem, Germany), type X (Girkontaite et al., 1996), matrilin-3 (Klatt et al., 2000) and osteonectin (kindly provided by Dr. R. Timpl, Matinsried, Germany) was performed and detected with the AEC method.

RESULTS AND DISCUSSION

The load-relaxation test of the growth plate showed a typical curve for viscoelastic materials (Fig. 1). The plate of the high and low trained groups relaxed in average faster after all analysed periods of time and after 4, 8 and 12 weeks of exercise, whereas the low trained groups differed only slightly from the control groups. Alterations were detected in morphology and expression of matrix proteins.

Load-relaxation curve

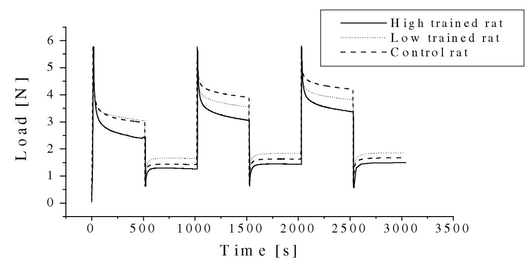

Figure 1: Load-relaxation curve from the growth plate of a high trained, low trained and control rat.

We conclude, that physical loading influences the relaxation behavior of the distal femoral growth plate of rats. The plates of the exercise groups are more permeable. The effects seem to depend on the dose of exercise.

SUMMARY

We investigated the effect of dose running exercise on the relaxation behavior, morphological and biochemical components of the distal femoral growth plate in a rat model.
Adaptations are found in all analysed properties.

REFERENCES

Girkontaite, I. et al. (1996). *Matrix Biol*, **15**, 231-238.
Klatt, A.R. et al. (2000*). J Biol Chem*, **275**, 3999-4006.
Nyska, M. et al. (1995). *Int J Exp Pathol*, **76**, 241- 245.
Swissa-Sivan, A. et al. (1989). *Bone Miner*, **7**, 91-105.

ACKNOWLEDGEMENTS

We thank Prof. Dr. M. Paulsson, Institute for Biochemistry II, Medical Faculty, University of Cologne and Prof. Dr. H. Michna, Institute for Tumor Research and Morphology, German Sport University of Cologne for their support.

THE EXPRESSION OF ICAM-1 INDUCED BY SHEAR STRESS UPREGULATED VIA NFκB ACTIVATION

Yong-Ming Liu[1], Sylvaine Muller[2], Baohua WANG[1], Jing-Wei Yang[1], Hai-Lu Yang[1], Jing-Ping Ouyang[1]
[1]Department of Pathophysiology, Medical College of Wuhan University, Wuhan, China, hybs@public.wh.hb.cn
[2]Mécanique et Ingénierie Cellulaire et Tissulaire, UMR 7563, UHP-CNRS-INPL-CHU, Nancy, France

INTRODUCTION

Shear stress can influence the structure, function and metabolism of VECs.

Intercellular adhesion molecule-1 (ICAM-1) is an important adhesive molecules inter cell adhesion. The expression and distribution of ICAM-1 can be changed by shear stress. It has demonstrated that ICAM-1 is associated with rearrangement cytoskeleton F-actin. However, the exact mechanisms of signal transduction are not clear.

The nuclear transcription factor NFκB is the p50-p65 heterodimers existing in plasma. It is report that NFκB can be activated by shear stress, and then enters into the nucleus to bind the SSRE promoter region specifically.

The objective of this study is to test the hypothesis that shear stress leads to the upregulation of ICAM-1 via the activation of NFκB.

METHODS

Human umbilical veins endothelial cells (HUVECs) were cultured on the cover slides coated with 0.1% gelatin. The cells were divided into different groups randomly. Except the static control, the cells were exposed to 3 shear stresses (2 Pa, 1 Pa, 0.2 Pa) for 4h, 37℃. The tyrosine kinase inhibitor Herbimycin A (875 nM, 1h) and the Cytochalasin D (5μM, 1h) which could depolymerize the F-actin of cytoskeleton were used before shear stress.

The changes of expression of ICAM-1 and NFκB were measured by immuno-histochemistry. Reverse Transcription-Polymerase Chain Reaction (RT-PCR) was used to detect the mRNA of ICAM-1.

RESULTS AND DISCUSSION

The expression of ICAM-1 mRNA induced by shear stress (2 Pa) is higher than static ($p<0.01$). It is reduced after using the Herbimycin A ($p<0.05$) and Cytochalasin D ($p<0.01$) compared with shear stress.

As the same, the expression of NFκB is the most significant by 2 Pa shear stress ($p<0.01$). After using the Herbimycin A and Cytochalasin D, NFκB expression decrease induced by shear stress.

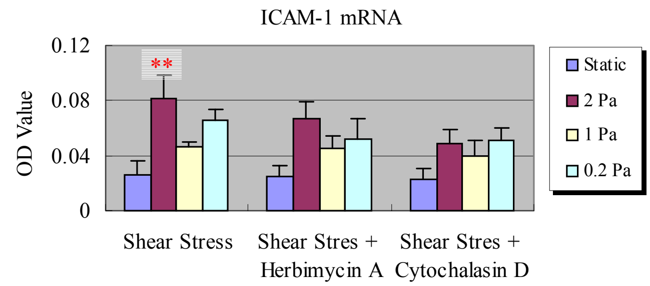

Figure 1: The expression of ICAM-1 mRNA induced by different shear stress (** $p<0.01$, *vs* static).

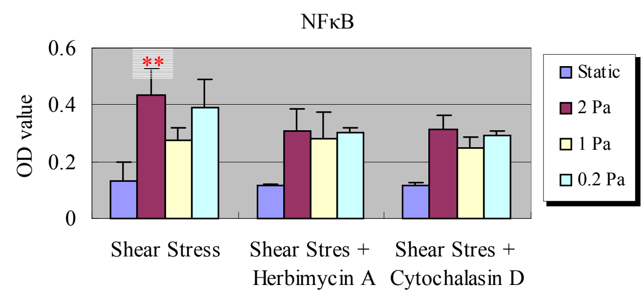

Figure 2: The expression of NFκB by different shear stress.

SUMMARY

Higher Shear stress can increase the expression of ICAM-1 and mRNA. The results suggest that the shear stress, mechanical signal, can be transmitted from the membrane to plasma by tyrosine kinase, and then transduce into nucleus as biochemical signals by cytoskeleton, upregulate the expression of ICAM-1 in molecular level via the activation of transcription factor NFκB.

REFERENCES

Tsuboi H, et al (1995). *Biochem Biophys Res Commun*, **206**, 988-96.
Malek AM, et al (1999). *J Mol Cell Cardiol*, **30**, 693-5.
Aplin AE, et al (1999). *Curr Opin Cell Biol,* **11**,737-44.
Imberti B, et al (2000). *Microvasc Res,* **60**, 182-8.

ACKNOWLEDGEMENTS

This work was partly supported by Association Franco-Chinoise pour la Recherche Scientifique & Technique (AFCRST，Grant N° PRA B00-09), FRANCE.

PEAK HIP JOINT MOMENTS DURING WALKING AND JOGGING ARE CORRELATED WITH PROXIMAL FEMORAL BONE MINERAL DENSITY

Kirsten Moisio[1], Dale R. Sumner[1, 2], and Debra E. Hurwitz[1, 2]
[1]Department of Anatomy, Rush Medical Center, Chicago IL 60612
[2]Department of Orthopedic Surgery, Rush Medical Center, Chicago IL 60612, dhurwitz@rush.edu

INTRODUCTION

The relationship between mechanical loading and its effect on bone mass is well accepted (Wolff 1892). Many studies have investigated the effects of mechanical stimuli on bone mass and architecture. While it is clear that mechanical loading strongly influences bone mass and architecture it is unclear what relationship exists between bone mineral density (BMD) and joint loads as assessed during gait analysis. Since walking is one of the most frequently performed activities, and one of the most commonly prescribed types of exercise for building bone mass, its contribution to load history and bone mass needs to be identified. Given that the dynamic loads during jogging are greater than those during walking, the loads during jogging may be even more influential on bone mass. The purpose of this study was to test the hypothesis that peak hip joint moments during gait and jogging were correlated with proximal femoral BMD in a group of normal subjects.

METHODS

A group of 31 normal subjects (18 females, 13 males) with an age range of 30-49 yrs. underwent gait analysis using methods described previously (Andriacchi et al., 1997) and dual energy x-ray absorptiometry (DXA). Gait data were collected using an optoelectronic system (CFTC) and a multicomponent force plate (Bertec). The BMD of the proximal femora was determined by DXA (Lunar DPX-L). Univariate Pearson correlations were calculated to determine the individual effects of external joint moments, height and weight on BMD. A stepwise multiple regression model was used to determine how much of the BMD variability could be explained by height, weight, or joint moments during walking and jogging.

RESULTS AND DISCUSSION

During walking the internal and external rotation, and abduction moments had the strongest correlations with BMD (Table 1). For jogging, the adduction, flexion, and external rotation moments had the strongest correlations with BMD (Table 2).

The multiple regression analyses from the walking data indicated that higher correlations were found for the neck and greater trochanter when two moments entered the model. For instance, 40% of the variability in the greater trochanter BMD on the right side was explained by the combination of the external rotation (21%) and internal rotation (19%) moments. For the jogging data, the addition of other variables did not increase the correlations.

SUMMARY

Peak hip joint moments from walking and jogging were correlated with proximal femoral BMD. This suggests that joint loading during gait reflects the loading history, which presumably plays an important role in determining adult BMD.

Walking	Neck		Greater trochanter		Ward's triangle	
	R	L	R	L	R	L
Flexion	.27	.27	.33	.20	.23	.30
Extension	.26	.13	30	.29	.12	.06
Abduction	.20	.33	**.41***	**.36***	.16	**.39***
Adduction	.33	.35	.32	.35	.23	.24
Internal rotation	**.48****	**.43***	**.41***	**.52****	**.37***	.27
External rotation	.29	**.40***	**.48****	.33	.30	.34
Height	.30	**.38***	.26	.27	.22	.25
Weight	**.37***	.28	**.39***	**.40***	.31	.26

Table 1 Walking-Univariate correlations (r values) for joint moments (Nm), height (m), weight (kg), and BMD (g/cm^2) for right and left sides.*= significant at the 0.05 level, **= significant at the 0.01 level, R=right side, L=left side.

Jogging	Neck		Greater trochanter		Ward's triangle	
	R	L	R	L	R	L
Flexion	**.37***	**.46****	**.57***	**.48****	.28	.28
Extension	.10	.06	.16	.10	.02	-.21
Abduction	.08	.14	.09	.10	.13	.093
Adduction	**.44***	**.53****	**.42***	**.56****	.31	**.40***
Internal rotation	.08	.01	.02	-.11	.07	-.07
External rotation	**.38***	**.56****	**.41***	**.51****	.23	**.45***

Table 2 Jogging-Univariate correlations (r values) for joint moments (Nm) and BMD (g/cm^2) for right and left sides.* = significant at the 0.05 level,**= significant at the 0.01 level, R=right side, L=left side.

REFERENCES

Wolff (1892). *The Law of Bone Remodeling.* Springer, Berlin
Andriacchi, T.P. et al. (1997) *Musculoskeletal dynamic locomotion and clinical applications.* New York, Raven Press

ACKNOWLEDGEMENTS

NIH grant #AR46225; Promotion of Doctoral Studies Scholarship, American Physical Therapy Association

NEUROMUSCULAR EXCITATION PATTERNS OF HUMAN POSTURE THROUGH AN OPTIMAL CONTROL APPROACH

Luciano Luporini Menegaldo[1,2], Agenor de Toledo Fleury[1,2], Hans Ingo Weber[3]

[1] Control Systems Group, São Paulo State Institute for Technological Research - IPT
P.O. Box 0141, CEP 01064-970, São Paulo-SP, Brazil, e-mail: lmeneg@ipt.br
[2] University of São Paulo, Polytechnic School, Department of Mechanical Engineering
[3] Pontifical Catholic University of Rio de Janeiro, Department of Mechanical Engineering

INTRODUCTION

The present work deals with the numerical synthesis of open-loop neuromuscular activations patterns in human postural tasks, using a new biomechanical model and optimal control algorithms. Through the optimal control approach, neuromuscular activations can be estimated as the body performs a movement prescribed by initial and terminal kinematic conditions, at the same time that an objective function is minimized. In this case, the motor task does not have to be physically performed and measured, therefore, the biomechanical system can be virtually modified, by an orthopedic surgery for example, and the functional results evaluated accordingly. As the biomechanical posture model is a highly non-linear, multi-degree-of-freedom and unstable system, several analytical and numerical related problems should be found and addressed in other motor tasks associated to orthopedic surgery simulations.

METHODS

The multi-body model analyzed is a three-link inverted pendulum representing the human body segments of the shank, thigh and HAT (head, arms and trunk), as shown in Menegaldo (2001). This model is driven by 10 muscular actuators, expressed by nondimensional, 2nd order, non-linear equations of activation and contraction dynamics. Musculo-tendon geometry was parameterized through leasts-squares regression equations using data from a musculoskeletal modeling software (Musculographics Inc., 1997). The optimal control algorithms were developed and implemented based on the Polak's Consistent Approximation Theory framework by Schwartz (Polak, 1997; Schwartz and Polak, 1996). This method is based on a Runge-Kutta discretization of system dynamics, and over the same mesh, control vectors are represented in a spline-coefficient functional subspace. This leads to a very precise control representation. For testing of the algorithms behaviour, the postural task has been the same for all simulations, with the knee initially flexed by an angle $\pi/6$ and trunk kept upright and all muscle forces initially zero. Endpoint constraints have been imposed null to every angle and angular velocity at the final time, except for tolerances.

RESULTS AND DISCUSSION

Simulation results for kinematics and muscle excitation (control), activation and force are shown for two fixed simulation final times. Physiologically feasible patterns of muscle activations have been obtained.

Due to the dynamical characteristics of the problem, several numerical difficulties have arisen, and the numerical experiments performed suggest the need of careful estimation of the initial control guess, a gradual charge of constraints and an appropriate choice of the optimization tolerances.

SUMMARY

This work shows a biomechanical model of human posture, comprising 10 equivalent musculotendon actuators and three links (shank, thigh and HAT - Head, Arms and Trunk), and the use of optimal control techniques to generate open-loop raising-up movements from a squatting position. The optimal control algorithms are based on the Consistent Approximations Theory (Schwartz and Polak, 1996), where the continuous non-linear dynamics is represented in a discrete space by means of a Runge-Kutta integration and the control signals in a spline-coefficient functional space. The adopted numerical methodology guarantees a fine precision on the control representation, using a control mesh as fine as the integration mesh. Due to the highly non-linear and unstable nature of posture dynamics, specific strategies must be used to achieve numerical algorithm convergence. Results for muscular excitations and angular displacements are shown for two simulation final times, and excitation patterns obtained through numerical simulations are discussed.

REFERENCES

Menegaldo, L.L. (2001), *Biomechanical modeling and optimal control of human posture using algorithms based on consistent approximations theory* (in portuguese). Ph.D. thesis. Polytechnic School, University of São Paulo.

MusculoGraphics Inc. (1997), *SIMM Software for Interactive Musculoskeletal Modeling, Version 1.2.5, User Manual*.

Polak, E. (1997), *Optimization: Algorithms, and Consistent Approximations*, Springer-Verlag.

Schwartz, A.L., Polak, E. (1996). *SIAMM Journal of Control and Optimization* **34**, 1235-1296.

ACKNOWLEDGEMENTS

The authors are gratefully acknowledged to Fundação de Amparo à Pesquisa do Estado de São Paulo (FAPESP) for funding this research project and to Conselho Nacional de Desenvolvimento Científico e Tecnológico (CNPq), for the scholarships.

GAIT ANALYSIS IN CHILDREN WITH TIBIAL ROTATIONAL ABNORMALITIES

R. Darmana(1), F. Salmeron(2), M. Scandella(2), E. Martinez(1), JP Cahuzac(2)

(1) INSERM, Laboratoire de Biomécanique, Hôpital Purpan, Toulouse, France (robert.darmana@toulouse.inserm.fr).
(2) Hôpital des Enfants, Département d'Orthopédie, Toulouse, France.

INTRODUCTION

Rotational abnormalities of lower limbs are the most fréquent causes of examinations in paediatric orthopaedics. The goal of this study is to find the modifications of gait kinematic and dynamic parameters du to the presence of these abnormalities and to research what could be their consequences on joint behavior in adult life.

MATERIAL AND METHOD

Children have been classified in three groups, without sex differentiation :

	RG	ITT	ETT
N	12	12	12
Age (years) (sd)	8.3 (2.9)	10.1 (2.1)	10.5 (2.7)
Tibial torsion (°) (sd)	20 (4.1)	8.1 (4.17)	42.7 (10.6)

Table 1: RG=reference group, ITT=insufficiency external tibial torsion group (in-toeing gait), ETT=exagereted external tibial torsion group (out-toeing gait).

Measurements performed were :

- ground reaction forces Fz and Fy (force-plate INCA 44, Captels, Montpellier, France) on a 16 meters long walkway, 3 records were performed for each foot;
- lower limbs motion: hip flexion/extension and adduction/abduction, knee flexion/extension, ankle dorsal flexion and plantar flexion, foot rotation (ELITE opto-electronic system, BTS, Milan, Italy) on the same walkway, 10 records were performed for each leg.

RESULTS

For the vertical component force Fz a significant difference was found only for ITT group, in Fz1 (heel strike) and Fz2 (midstance) components, Fz1 was 15% greater than reference group and Fz2 was reduced of 18%.

Lower limbs motion capture has shown that hip extension and adduction were significantly reduced ($p<0.05$) for the two groups of respectively 20 and 30%. Knee flexion was never modified. For ITT group, since hell strike and during all the stance phase, foot position was internal; during the swing phase an internal movement appear in opposite to the reference group for which the rotation at this time is 30° external sens. For ETT group the amplitude of this rotation was 11° in more. For ankle flexion, a significant 25% reduction was found for the maximum of plantar flexion in propulsive phase for the two groups ITT and ETT.

DISCUSSION

A very little number of biomechanical works have been found about lower limbs rotationnal abnormalities. Somme experimental studies on cadavers like these of Grijalvo and Laville (1) have shown an increasing of stress in the one side patello-femoral contact du to the torsional effect in knee given by rotational abnormality. In 1995, Liu (2) measured a decreasing of the three components of ground reaction force in children with in-toeing walking. We found in opposite, in comparison with reference group, a vertical reception force (Fz1) more important, a Fz2 component less important and no statistical difference for Fz3. In our study, Fy2 was greater than reference group. To our knowledge, not any kinematic studies exist about gait with rotational abnormalities of children. In the clinical field, Turner (3) et Yagi (4) in 1994, in a radiological study in adults, have shown that a relation exists between tibial torsion and knee pathologies. So, the increasing of fore-aft propulsion force (Fy2) and the internal or external position of foot which creates a torque around tibial axis can be on a mechanical point of vue the cause of stress increasing in patello-femoral contact and so can be the origin of knee pathologies.

CONCLUSION

External and internal tibial torsion modifie gait kinematic and dynamic parameters. The results of this study are in agreement with experimental works and it seems that these results prove the biomechanical origin of articular cartilage damage.

REFERENCES

(1) Grijalvo PH, Laville JM, Cahuzac JP, Bonnevialle P, Lebarbier P, Pasquié M. Les syndromes rotuliens chez l'enfant. Acta Orthopedica Belgica, Tome 49, fasc. 4, 1983.
(2) Liu XC, Fabry G, Van Audekercke R, Molenaers G, Govaerts S. The ground reaction forces in the gait of intoeing children. J Pediatr Orthop 1995, Part B, 4,1, 80-85.
(3) Turner MS. The association between tibial torsion and knee joint pathology. Clin Orthop 1994, 302, 47-51.
(4) Yagi T. Tibial torsion in patients with medial-type osteoarthrotic knees. Clin Orthop 1994, 302, 52-56.

POSTURAL ALIGNMENT WITH DIFFERENT SHOES AND BAREFOOT

Cíntia Brino Fialho[1], Paulo Cabral[2], and Jorge Luiz de Souza[3]

Exercise Research Laboratory (LAPEX), Federal University of Rio Grande do Sul (UFRGS), Porto Alegre, RS, Brazil
[1] Mastership student of Physical Education at UFRGS, cbfialho@portoweb.com.br
[2] Journalist and videomaker of LAPEX's Multimedia Center
[3] Ph.D. in Physical Education at UFRGS

INTRODUCTION

There is a disparity among scientific results concerning the corporal segments' position in the maintenance of standing position when wearing shoes. Opila et al. (1988) and Lee et al. (2001) found changes in the knee and in the ankle of the evaluated subjects either standing and walking. On the other hand, Franklin et al. (1995) did not find changes in the knee joint with the increase of the heel height. In pursuit of additional information that may contribute with the researchers of this area, this research investigates the changes in the position of the head, shoulder, hips, knee, and ankle corporal segments in the sagittal plane in barefoot individuals, in individuals wearing high-heeled shoes, and in the ones wearing running shoes.

METHODS

Six female individuals were evaluated, with mean age, height, and weight of 23,17 years old (±6,83), 160,17 cm (±5,83), and 54,02 kg (±2,98), respectively.

Adhesive markers measuring 1 cm of diameter were fixed on five anatomical points (external auditory meatus, acromioclavicular joint, center of femur's greater trochanter, femoral epicondyle, and lateral malleolus). A sixth marker was fixed in the leg, 5 cm above lateral malleolus. In this point, a reference vertical straight line was drawn. All the five points were evaluated in relation to that vertical straight line in the three conditions proposed in this study: 1) barefoot; 2) wearing running shoes (with a 2,5 cm-height sole); and 3) wearing high-heeled shoes (8 cm). From that straight line, it were established three levels forward and three levels backward (each level is 1,8 cm in height) that would permit to verify the position of the anatomical points (postural alignment) in the sagittal plane.

The subjects' posture was filmed (Sony DSR PD 150 digital camera) during 15 seconds, with a sampling rate of 30Hz in each condition. The first 5 seconds of images were eliminated, and it was analyzed one image per second, during the next 10 seconds.

RESULTS AND DISCUSSION

The results of the statistical tests (Chi^2 and Fisher) showed that the localization of the anatomical points of external auditory meatus (head), acromioclavicular joint (shoulder), and femur's greater trochanter (hips) stay in levels closer to the reference straight line in the high- heeled condition when compared to the barefoot situation ($p<0,05$). In the femoral epicondyle's (knee) position, there were significant statistical variances in different levels in the three conditions of the study ($p<0,05$). Similar results were found in previous studies (Opila et al., 1988; Lee et al., 2001; Franklin et al., 1995).

CONCLUSION

There are changes in the position of anatomical points (postural alignment) in standing position, wearing high-heeled shoes, comparatively to the barefoot condition.

There are variances of the femoral epicondyle's position (knee), which has placed itself in different levels, varying in the barefoot, running shoes, and high-heeled shoes conditions.

REFERENCES

Franklin, M.E. et al. (1995). Effect of positive heel inclination on postures. *JOSPT*, **21** (2), 94-99.
Lee, Chang-min et al. (2001). Biomechanical effects of wearing high-heeled shoes. Elsevier, *International Journal of Industrial Ergonomics,* **28**, 321-326.
OPILA, K. A. et al. (1988). Postural alignment in barefoot and high-heeled stance. *Spine,* **13** (5), 542-547.

ACKNOWLEDGEMENTS

We thank professors Milton Zaro and Marcelo Cardoso, respectively, for the help in the data collection and in the statistical treatment of this study.

THE RESISTANCE OF A KNEE JOINT IN CHILDREN WITH SPASTICITY

M.K. Lebiedowska and J.R. Fisk
Southern Illinois University, School of Medicine, Springfield, Illinois, USA, mlebiedowska@siumed.edu

INTRODUCTION

Spasticity coexists with many neurological disorders, including cerebral palsy. The resistance of a joint in spasticity may be increased as a result of velocity (Lance,1980) or position (Powers et al 1988) dependent on stretch reflexes and/or contractures. The resistance of a limb is evaluated with subjective clinical scales (Ashworth, Tardie). The application of complex torque devices to quantify spasticity in clinical settings is limited. The hand-held force transducer was used to identify the passive stiffness (Stein et al 1996) and rigidity (Prochazka et al. 1997) in patients. The aim of this study was to determine whether or not the resistance of a knee joint can be measured with the hand-held force transducer and electrogoniometer in children with spasticity.

METHODS

We evaluated 20 able-bodied children and 18 children with spasticity related to cerebral palsy. A shank of a child was extended and then flexed. The pulling torque was measured with a hand-held force transducer as a function of the knee angle which was measured with an electrogoniometer (Biometrics, Ltd.). The knee motion, force, and EMG activity of knee muscles were collected at three velocities. Analog signals were digitized at 333 Hz (Axoscope, Axon Instruments, Inc.). The velocity and acceleration were determined by differentiating the motion signal (MATLAB, MathWorks Inc.). The Torque-Angle (Tq-α) functions describing the resistance of a joint were determined for each velocity. The torque due to the pathological changes Tq_a was calculated as a result of the of the subtraction of mass (m, r), inertia (I), and viscoelastic properties of a joint (K, B) from the overall torque (Fig.1):

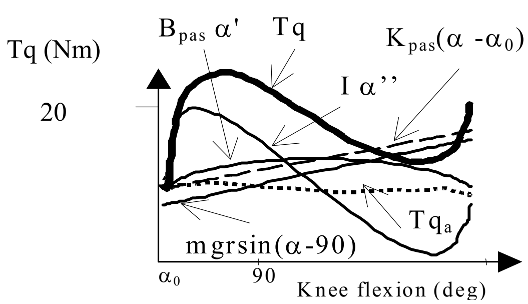

Figure 1 The components of the torque used to move the limb segment with velocity (α') and acceleration (α'').

$$Tq_a = Tq - (I \alpha'' + B \alpha' + mgr \sin (\alpha-1.58) + K (\alpha-\alpha_0))$$

Mass, inertia and passive viscoelastic properties were estimated from the anthropometric measures (Winter,1990, Lebiedowska and Fisk, 1999). The slope of a Tq–α function at the initial position K_0, the work done to overcome the torque Tq_a and the activation of knee muscles were calculated and the regression equations between velocity of pull were established (Statistica, StatSoft Ltd.).

RESULTS ANS DISCUSSION

During knee flexion and extension, the slope K_0 of the Tq-α function was slightly higher in patients, but the increase related to velocity α' was similar in able-bodied children (K_0=0.127+0.23α', r=0.8, flexion) and in patients (K_0=0.08+0.24 α', r=0.58, flexion). The work W_a done by the examiner to overcome the changes induced by spasticity increased much more rapidly in patients (W_a=0.012+0.0091α', r=0.48, flexion) than in able-bodied children (W_a=0.0026+0.0058 α', r=0.37, flexion). The activation A of rectus femoris (A=2.56+1.49 α', r= 0.42, flexion) and hamstring (A=2.8 +1.27 α', r= 0.23, flexion) muscles increased with the velocity of motion in patients, but not in able-bodies children. A similar increase of slope K_0 and a more rapid increase of work W_a in patients than in able-bodied children suggest that W_a better discriminates patients. The different patterns of muscle activation were identified in our patients. The differentiation between the neural (muscle activation) and mechanical (contractures) origin of the increased resistance was possible in the individual patients. The study showed that the velocity-dependent resistance of a knee joint can be measured with the aid of a hand-held transducer and an electrogoniometer in a pediatric population. The combination of mechanical and EMG parameters should be used to discriminate patients v. able-bodied subjects and to determine the origin of changes.

SUMMARY

The resistance of a knee joint was measured in 20 healthy children and in 18 children with cerebral palsy. It was concluded that the velocity dependence of stretch reflexes can be measured with the aid of a simple hand-held force transducer and an electrogoniometer attached to a joint. The method helps to differentiate between neural and mechanical origin of changes and different types of muscle activation in patients.

REFERENCES

Lance J.W. (1980) Spasticity: disordered motor control. Chicago: Yearbook Medical, 485-494.
Lebiedowska Mand Fisk J.(1999) *Clin Biomech*, **14**: 653-660.
Powers R.K. et al. (1988) Neurol , **23**:115-124
Prochazka A., et al (1997) *Mov. Disord* , **12**, 24-32.
Stein, R.B. et al (1996) *IEEE Transactions on Rahabilitation Egineering,***4**,201:211.
Winter D.A.(1990) *Biomechanics and Motor Control of Human Movement*. Wiley, Interscience, New York.

EXPERIMENTAL ANALYSIS OF LYMPHATIC CELLS MOTION UNDER TOPOGRAPHICAL CONTROL

A. Prina Mello[1], Y. Volkov[2], P.J. Prendergast[1]
[1]Bioengineering Group, Department of Mechanical Engineering, Trinity College, Dublin 2, Ireland, www.biomechanics.ie
[2]Department of Clinical Medicine, Trinity College Dublin, St. James's Hospital, Ireland

INTRODUCTION

The migration of malignant cells starts with the invasion of blood and lymphatic vessels, which then move, through the vessel walls, into the adjacent tissue. This process that is carried out by lymphatic cells is highly unpredictable. They frequently continue moving indefinitely until death, or else they regress (Trinkaus, 1984).

It may be proposed that an understanding of the motility of these cells is a key step in further analysis of metastasis formation. Interestingly the shape of the cells seems to be important. Their rigidity or deformability, which is related to their cytoskeleton, is a significant factor in determining the capability of motion.

To control metastasis spreading, quantitative information on the *in vivo* migration process must be acquired. Therefore, it is necessary to recreate, *in vitro,* the complex nature of the migration process through the vessel walls carried out by malignant and normal cells.

METHODS

Cell type and culture

Two human lymphatic cells were involved in this study: normal *Peripheral Blood T Lymphatic* cell (PBTL) and a malignant cell, *T lymphoma HUT 78* (HUT). Briefly, PBTLs were pre-activated with PMA (phorbol-myristate-acetate) (Sigma, ST. Louis, MO, USA). HUT cells line 78 (ATCC, Manassas, VA, USA) were used non-treated or pre-activated by PMA in the same concentration for sixty minutes, as described in by Volkov *et al*. (1998).

HUT 78 or activated PBTL (10-20x10^3/well) were added on top of a plane bioglass coated with monoclonal antibodies (mAb) to α-chain of LFA-1. This mAb was able to to induce cytoskeletal rearrangement in T cells (*polarization*). Cell motility experiments were performed using a bioglass plane or micropatterned (Prina Mello *et al*., 2001).

RESULTS AND DISCUSSION

Migration of T cell on unconstrained ECM-coated surface

Migration of single-cell was measured, quantitatively, by using a "persistent random walk" method (Othmer, *et al*., (1988)). A series of tests was carried out to measure the cell-centroid variation on a population of activated cells.

The cells were investigated on unconstrained surface for a hour. Means and standard errors for the motile fraction cells are summarised in Table 1.

TABLE 1. Average results of HUT 78 and PBTL on treated plane surface, under LFA-1 and PMA-LFA-1.(Polarisation = 20 minutes).

Cell type	Receptor	Cells tracked	Single Cell Cell velocity (μm/minute)	Cells % Cell Motile
PBTL	PMA,LFA-1	20 (n_f=13)	5.667 ± 2.243	74.9 ± 10.3
HUT 78	LFA-1	20 (n_f=13)	3.763 ± 1.331	60.4 ± 7.9

Migration of T cell on constrained ECM-coated surface

Quantitative cell migration measurements were carried out to compare HUTs and PBTLs when under unidirectional constraint. Cells were activated inside the channel in order to confine their migration. Results are shown in Table 2.

TABLE 2. HUT 78 and PBTL on micropatterned surface.

Cell type	Receptor	Cell tracked	Single Cell Cell velocity (μm/minute)	Cells % Cell Motile
PBTL	PMA,LFA-1	15 (n_f=10)	1.603 ± 0.702	65.2 ± 15.3
HUT 78	LFA-1	15 (n_f=10)	0.560 ± 0.260	72.4 ± 21.3

Experimental distributions of cell speed were following a normal distribution curve, see Fig. 1.

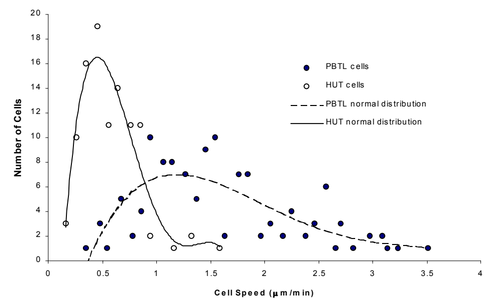

FIGURE 1. Cell speed distributions on micropatterned substrate. HUTs speed distribution (continuous line), and PBTLs (dashed). HUTs speed mean X=0.457 μm/min; PBTL mean X=1.266 μm/min.

SUMMARY

A quantitative *in vitro* analysis for cell migration was carried out to observe, and interpret, the *in vivo* response of some T lymphatic cell types to inflammatory process. The difference in migration between PBTLs and the HUTs is evident from the results shown. These results highlight a slower dynamic response of the HUTs in comparison to the PBTLs on both the two surfaces. Under constrained ECM, the PBTLs had a shorter persistence time compared to the HUTs due to their smaller size. PBTLs changed their direction more frequently then HUTs, when following the channel. Therefore, it seems that surface topography can discriminate the migration of these two cells, this may prove useful in identifying normal from malignant T cells.

REFERENCES

Trinkaus, J.P., (1984). *Cells into organs.* Prentice-Hall, N.J., USA.
Volkov, Y. *et al*., (1998). *J. Immunology*, **161**, 6487-6495.
Prina Mello, A. *et al*., (2001). *Proc. 5th Int. Conference in Cellular Engineering*, **ST_1-7**, Aachen, Germany.
Othmer, H.G. *et al*., (1988). *J. Math. Biol*., **26,** 263-298.

ACKNOWLEDGEMENTS

This work was supported from HEA under the Programme for Research in Third Level Institutions PRTLI programme.

ON THE USE OF 3D MRI VELOCITY MEASUREMENTS FOR COMPUTATIONAL FLOW SIMULATIONS

Fadi P. Glor[1], Josephus J. M. Westenberg[2], Jan A. Vierendeels[3], Michael Danilouchkine[2], Pascal Verdonck[1]
[1] Cardiovascular Mechanics and Biofluid Dynamics Department, Ghent University, Gent, Belgium, fadi@navier.rug.ac.be
[2] Department of Radiology (Division of Image Processing), Leiden University Medical Center, Leiden, The Netherlands
[3] Department of Flow, Heat and Combustion Mechanics (Fluid Mechanics Laboratory), Ghent University, Gent, Belgium

INTRODUCTION

Magnetic Resonance Imaging (MRI) allows for geometry as well as velocity measurements. This aspect is highly interesting since it provides hemodynamic data (such as wall shear stress) that are of big importance related to the prediction and diagnosis of atherosclerosis.

A drawback for MRI hemodynamic diagnosis is the long acquisition time required and the cost of an MRI session. The coupling of MRI acquisition with computational fluid dynamics (CFD) allows to calculate the velocity profiles when MRI data is not present due to lack of scan time. The combined technique allows the number of scans to be reduced to a set of geometrical scans and a limited number of additional velocity scans, equal to the number of in- and outflow sections contained in the model.

This study aimed to quantify the reliability of MRI velocity scans, and to prescribe the best way of implementing the measured velocity data in the CFD tool.

METHODS

Figure 1a shows the set-up used in this study. It consists of a MRI version of a UHDC Flow Pump Shelley (Numatics 225-3728 24VDC 6.0 Watts, Shelley Limited, London Ontario, Canada), a rigid u-tube manufactured out of agar gel (for good MRI-contrast; internal diameter 8 mm, bend radius 25 mm) and an ultrasonic flow probe for flow rate measurements (HT207 Transonic Flowmeters; Transonic, Ithaca, New York, USA). Steady (Re=220, 267 and 882) and unsteady (Dean Number = 66.1, 77.1 and 191, Womersley Number = 11) flows were set. An extra inflow tube was introduced for full development of the flow profile.

Calculations with uniform or parabolic inlet flow profiles were compared to calculations with profiles obtained from 3D MRI velocity measurements.

RESULTS AND DISCUSSION

Figure 1 (b-d) shows the secondary flow for simulations with different inflow boundary conditions in the second steady case. Figure 2 (e) shows the measured secondary flow. All simulations compare very well to the measured one, which implies reliability of the MRI measurements (maximal errors around 10% for axial velocities). The simulations using MRI measurements seem to compare better to the MRI measurements. The explanation for this observation can be

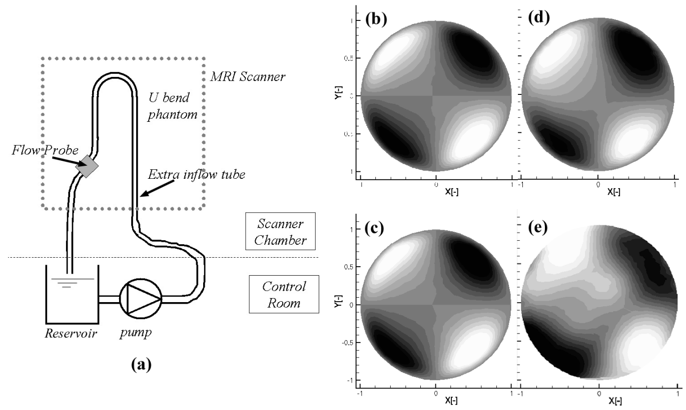

Figure 1: a. Set-up; **b-d** vertical velocity profiles in the tube at 120 degrees through the bend, using as inflow boundary conditions: **b.** Uniform inflow; **c.** Parabolic inlet; **d.** MR measurements as inlet BC; **e.** Velocity profile at 120 degrees as measured by MR. WHITE=3mm/s, BLACK=-3mm/s.

found in the fact that the computational model uses the accurate geometry specifications provided. Furthermore we must take into account that the phantom is included in a flow circuit applying a theoretically specified flow. In reality, the geometry and (more probably) the flow profile is imperfect, changing the flow in a way detectable by MRI. This means that setting a disturbed flow as boundary condition (measured by MRI), will result in a different flow profile, which is closer to the real profile. This observation denotes clearly the advantage of using scaled MRI velocity data as inflow boundary condition.

If the velocity measurements are not corrected for PVE, the unfiltered errors will compromise the convergence of the simulation. If no scaling is applied to the MRI measured velocities, the flow rate will be incorrect. This seriously influences the hemodynamic parameters.

SUMMARY

When corrected for the partial volume effect and scaled to match the flow rate, the use of MRI velocity measurements as boundary condition is preferred above uniform, parabolic or fully developed flow profiles based on the flow rate.

ACKNOWLEDGEMENTS

This work is funded by Ghent University (BOF grant 01112500) and the Dutch Heart foundation. PAM-FLOW and PAMGEN3D, software used for mesh generation and flow calculations, are trademarks from ESI software.

FOREFOOT STRUCTURAL PREDICTORS OF PLANTAR PRESSURES DURING WALKING IN PEOPLE WITH DIABETES AND PERIPHERAL NEUROPATHY

Michael J. Mueller[1], Mary Hastings[1], Paul K. Commean[2], Kirk Smith[2], Thomas K Pilgram[2], Douglas Robertson[3], and Jeffrey Johnson[4]
[1]Program in Physical Therapy, Washington University School of Medicine, St. Louis, MO, USA, muellermi@msnotes.wustl.edu
[2]Electronic Radiology Laboratory, Mallinckrodt Institute of Radiology, [4]Department of Orthopaedic Surgery, Washington University School of Medicine, St. Louis, MO, USA, [3]Radiology Department, University of Pittsburgh Health Systems, Pittsburgh, PA

INTRODUCTION

Structural and functional factors have been shown to predict approximately 50% of the variance of peak plantar pressures (PPP) at the hallux and first metatarsal head during walking in asymptomatic subjects (Morag and Cavanagh, 1999). High PPP during walking in people with diabetes (DM) and peripheral neuropathy can cause skin breakdown. The objective of this study was to determine the ability of selected measures of foot structure and function to predict regional PPP at the great toe and the five metatarsal heads during walking in people with diabetes mellitus (DM) and peripheral neuropathy.

METHODS

Twenty people with DM and peripheral neuropathy (mean age 55 $\pm$ 9 years, 6 female, 14 male, BMI = 33 $\pm$ 8, duration of DM = 21 $\pm$ 11 years) were tested. Measures of foot structure were taken from 3-dimensional images constructed from spiral x-ray computed tomography (SXCT) with established accuracy and included metatarsal phalangeal angle (hammer toe), soft tissue thickness under each metatarsal head, hallux valgus, forefoot arthropathy, Morton's Index, and calcaneal angle (Smith, et al., 2001). Soft tissue stiffness under the metatarsal head was measured with an indentor device. Ankle dorsiflexion range of motion (DFROM) was measured with a goniometer. Toe out angle was measured during walking using ink and the moleskin method. PPP data were recorded during barefoot walking and during SXCT data acquisition using the F-Scan system (Software v.421, Tekscan, Boston, MA). PPP recorded during walking were registered with metatarsal head location using data from SXCT. Hierarchical multiple regression analysis was used to predict regional peak plantar pressures at the great toe and metatarsal heads from selected structural and walking variables.

RESULTS AND DISCUSSION

Hammer toe deformity was the single most important variable, accounting for 19-45% of the PPP variance at 5 of the 6 forefoot locations. Combinations of structural and walking variables accounted for 47-71% of the variance. Table 1 contains the significant predictors of PPP at each of the 6 locations on the foot in their order of entry into the hierarchical multiple regression equation.

Table 1: Significant Predictors of Regional PPP

Region	Predictor	r	R^2*	p*
Great Toe	Hammer Toe (1)	-.67	.45	.001
	Subject Weight	.21	**.56**	.001
Met Head 1	Hallux Valgus	.45	.21	.045
	Morton's Index	.63	.41	.011
	Subject Weight	.29	**.47**	.014
Met Head 2	Hammer toe (2)	.59	.35	.006
	Soft tissue thick	-.50	.53	.002
	Toe out angle	-.15	.67	<.001
	Subject Weight	.35	**.71**	.001
Met Head 3	Hammer toe (3)	.62	.38	.004
	Soft tissue thick	-.26	.47	.005
	Calcaneal Angle	.33	.52	.007
	Soft tissue stiff	.82	**.57**	.010
Met Head 4	Hammer Toe (4)	.44	.19	.050
	Calcaneal Angle	.57	.39	.015
	DF ROM	.52	.47	.018
	Toe out angle	-.07	**.53**	.019
Met Head 5	Hammer Toe (5)	.64	.41	.002
	Morton's Index	.38	.50	.003
	Toe out angle	-.14	**.55**	.004

*overall model, Met=Metatarsal,

SUMMARY

Of the variables studied, hammer toe deformity was the most important single variable to predict forefoot PPP in people with DM and peripheral neuropathy. These results, coupled with clinical studies linking hammer toe deformity to plantar ulcers, highlight the importance of this foot deformity for its contribution to PPP and forefoot skin breakdown. In addition to hammertoe deformity, soft tissue thickness and soft tissue stiffness under the metatarsal heads were important for predicting PPP during walking. These variables should be included in computational models to predict plantar stresses to the forefoot and to devise interventions (i.e., orthotic devices or surgery) to minimize the stress.

REFERENCES

Morag E. and Cavanagh P.R. (1999). *J. of Biomechanics*, **32**, 359-370.
Smith, K.E. et al (2001). *Arch Phys Med & Rehabil*, **82**, 925-929.

ACKNOWLEDGEMENTS

Funded by NCMRR, NIH, RO1 HD36895

RELATION BETWEEN KNEE RANGE OF MOTION MEASURED PASSIVELY AND DURING GAIT IN ANTERIOR CRUCIATE LIGAMENT DEFICIENT AND RECONSTRUCTED INDIVIDUALS

John A. Grant[1], Ronald F. Zernicke[2] and Nicholas G.H. Mohtadi[1]
[1]Sport Medicine Centre and [2]Human Performance Lab
Faculty of Kinesiology, University of Calgary, Calgary, Alberta, Canada, grantja@ucalgary.ca

INTRODUCTION

Gait adaptations are well documented in both anterior cruciate ligament deficient (ACLD) and ACL reconstructed (ACLR) patients and have been related to quadriceps avoidance (Berchuck et al, 1990) or hamstrings facilitation (Beard et al., 1996). While functional gait assessment of a patient's rehabilitation progress may be ideal, it is not generally used in a standard clinical rehabilitation setting. It would, therefore, be important to know if measures that can quickly and reliably be performed in the clinic are associated with functional performance. The purpose of this study was to determine the level of association between clinical goniometric measures of knee range of motion (ROM) and ROM during gait in ACLD and ACLR patients.

METHODS

Thirty-two consecutive patients (17 males and 15 females) booked for ACL reconstruction with a bone-patellar tendon-bone graft at a university sport medicine clinic were invited to enroll. Patients (16-59 yr) were undergoing their first ACL reconstruction. Eighteen right knees and 14 left knees were reconstructed. Worker's Compensation patients and elite athletes were excluded.

Patients underwent assessments 1 wk before and 12 wk after surgery. All patients followed a standardized rehabilitation program in the first 3 post-operative months. ROM exercises started on post-operative day 1 and patients were discharged from hospital the day of surgery with instructions for weight bearing as tolerated.

Patients were first measured for passive knee extension ROM while resting in a prone position with the knee and leg hanging pendant from the end of the exam table. Knee flexion was measured with the patient in supine position. A strap was placed around the ankle, and the patient was instructed to pull the foot towards the gluteal region as far as was comfortable. The included angle between the thigh and the leg was measured with a standard plastic goniometer (each arm was 31.5cm).

Joint markers were affixed to the greater trochanter, lateral femoral condyle, and lateral malleolus of each lower extremity. Sagittal plane video data were collected with a Sony® digital video camera at 30 Hz. The shutter speed was set to 1.3 ms. Patients walked barefoot to eliminate the variation due to shoe wear. Patients practiced walking through the field of view three times before three trials per limb were recorded. Patients walked at a self-selected pace.

Digital video data were digitized using HU-M-AN® software. ROM data were smoothed using a Butterworth filter (cut-off frequency of 5Hz). Maximal flexion and extension values for each trial were extracted. The average flexion and extension values for the three trials were used for analysis.

Range of motion data were analyzed using Stata 6.0 (Stata Corp., College Station, Texas). Pearson Product Moment Correlations were calculated to determine the strength of the association between passive knee ROM and knee ROM during gait. Correlations were calculated separately for the surgical limb, the non-surgical limb and for the difference between the non-surgical and surgical limbs (NS-S). Correlations were determined for both ACLD and ACLR conditions.

RESULTS

Table 1: Correlation (r) between passive and gait ROM

Comparison	r	n
Pre-Op Extension, Surgical Limb	0.17	32
Pre-Op Extension, Non-Surgical Limb	-0.25	32
Pre-Op Flexion, Surgical Limb	0.32	30*
Pre-Op Flexion, Non-Surgical Limb	0.06	28*
Pre-Op Extension Difference (NS-S)	0.08	32
Pre-Op Flexion Difference (NS-S)	0.35	30*
12 Week Extension, Surgical Limb	0.13	32
12 Week Extension, Non-Surgical Limb	0.37	32
12 Week Flexion, Surgical Limb	0.40	29*
12 Week Flexion, Non-Surgical Limb	0.28	29*
12 Week Extension Difference (NS-S)	0.16	32
12 Week Flexion Difference (NS-S)	0.15	30*

* Missing flexion data; "n" indicates number per group

DISCUSSION

The results of this preliminary study showed that there was little-to-moderate association between maximal knee flexion/extension and that demonstrated during gait in ACLD and ACLR patients. Previous studies showed that ACL-compromised individuals tended to flex more than controls throughout the stance phase of gait (Beard et al., 1996; DeVita et al., 1997). That may have been due to neuromuscular adaptations that reduced anterior tibial translation near full extension rather than actual limitations in knee ROM and those adaptations may have, in part, explained the lack of association shown in the present study.

REFERENCES

Beard, D.J. et al. (1996). *Gait & Posture*, **4**, 83-88.
Berchuck, M. et al. (1990). *JBJS*, **72A**, 871-877.
DeVita, P. et al. (1997). *Med. Sci. Sports Exerc.*, **29**, 853-859.

Supported in part by the Alberta Heritage Foundation for Medical Research, the Calgary Health Region, the Calgary Orthopaedic Research & Education Fund and the Olympic Oval Fund. Industrial Support was provided by AirCast Inc. and Fitter International Inc.

THE EFFECT OF SPEED ON THE DETERMINISTIC ORIGIN OF THE VARIABILITY PRESENT DURING HUMAN OF LOCOMOTION

Scott M. Keenan[1] and Nicholas Stergiou[1]
[1]HPER Biomechanics Lab, University of Nebraska at Omaha, Omaha, NE, USA
Email: nstergiou@mail.unomaha.edu Web: www.unocoe.unomaha.edu/hper.htm

INTRODUCTION

Slower speeds have shown to lead to increased variability during walking (Winter, 1983). That was also found to be true with neuropathic patients (Dingwell et al., 2000). However, Dynamical Systems Theory (DST) predicts that the least amount of variability (a highly stable state) will be present at a self-selected pace. When the system is perturbed, then variability increases. Based on DST, variability in locomotion can then be modeled as a parabola. This model has also been supported by energy expenditure data. Dingwell et al., (2000), using a surrogate data technique, have shown that variability in human locomotion is not the result of noise in the system, but it has deterministic origin. The purpose of this study was to expand on the above Dingwell et al work and examine the effect of speed on the deterministic origin of locomotion. We hypothesized that changes in speed may eventually introduce sufficient noise in the system that can mask the deterministic origin of the variability present during human locomotion.

PROCEDURES

Twenty subjects (range: 19-35 yr) attended 5 test sessions on 5 different days. On the first day, the subjects walked on a treadmill to establish a comfortable self-selected pace. This pace was used as the baseline speed for subsequent testing. Following this procedure, the subjects were required to walk for 5 minutes at 5 different speeds: baseline, 10% and 20% faster, and 10% and 20% slower. The same procedure was used for running. A quartz shear piezoelectric accelerometer (PCB Piezotronics) was attached to subjects' distal anteromedial aspect of the right tibia with a tight elastic wrap. The time series from the accelerometer data sampled (180 Hz) were surrogated using a phase randomization technique (Theiler et al. 1992). Phase randomized surrogates of the time series were generated by computing Fourier transforms (FFT) of the original data, randomizing the phase spectra, and computing inverse FFTs. Surrogation removes the deterministic structure from the original data sets, generating a random equivalent with the same mean, variance, and power spectra as the originals. Subsequently, Lyapunov Exponent (LyE) values were calculated from both the original and the surrogate counterparts and statistically compared. If significant differences are found between the two data sets, then the original is not a randomly derived data set. The LyE for both sets were calculated using the Chaos Data Analyzer software (Sprott & Rowlands, 1992). Mean group values were calculated for LyE for both the original and surrogate data sets and for each running and walking speed. The means were grouped and analyzed statistically using t-tests ($p < 0.01$).

RESULTS AND DISCUSSION

The average baseline speeds were 1.35 $m{\bullet}s^{-1}$ and 2.45 $m{\bullet}s^{-1}$ for walking and running, respectively. Significant differences in LyE between the original and surrogate data sets were found for all speeds and for both walking and running (Table 1). This result confirmed that the original data sets were not randomly derived and had deterministic origin and refuted our hypothesis. As it has been indicated (Pool, 1989), such deterministic behavior may allow the nervous system to adapt to changing conditions, while generating effective movement patterns.

SUMMARY

The time series collected from a tibia located accelerometer were analyzed with nonlinear tools and specifically with a surrogation technique. Our results confirmed that variability in human locomotion has a deterministic origin and changes in speed can not alter such a conclusion. The fluctuations that exist between each stride should not be considered noise but adaptations from stride to stride.

REFERENCES

Dingwell, J.B. et al. (2000). *J. Biomech.*, 33, 1269-1277.
Pool, R. (1989). *Science*, **243**, 604-607.
Sprott, J., Rowlands, G. (1992). *Chaos Data Analyzer*. American Institute of Physics.
Theiler, J. et al. (1992), Physica D, 58:77-94
Winter, D.A. (1983). J. of Motor Behavior. 15, 302-330

Table 1: LyE values evaluated for both modes of locomotion (group means). S= surrogate data

	20%Slower	10%Slower	Self-Selected	10%Faster	20%Faster
WALK - LyE	0.164	0.158	0.161	0.167	0.156
WALK – SLyE	0.391	0.401	0.404	0.404	0.412
RUN – LyE	0.155	0.161	0.172	0.165	0.159
RUN – SLyE	0.439	0.431	0.432	0.438	0.423

THE RELIABILITY OF THE LYAPUNOV EXPONENT DURING TREADMILL WALKING

Scott M. Keenan[1] and Nicholas Stergiou[1],
[1]HPER Biomechanics Laboratory, University of Nebraska at Omaha, Omaha, NE, USA
Email: nstergiou@mail.unomaha.edu Web: www.unocoe.unomaha.edu/hper.htm

INTRODUCTION

Continuous human locomotion has been showed to vary from one stride to the next. The examination of variability has been traditionally conducted using standard deviations across multiple strides. However, such an approach implies that locomotion is a sequence of independent strides. Nonlinear tools, such as the Lyapunov Exponent (LyE), have been shown to provide a more detailed analysis and can possibly reveal information about underlying control mechanisms (Dingwell et al., 2000; Stergiou et al., 2000). The Lyapunov Exponent (LyE) allows biomechanists (Dingwell et al., 2000; Stergiou et al., 2000) to examine variations during locomotion that have been called noise in the past. The LyE is defined as a measure of the rate at which nearby trajectories in phase space diverge (Sprott & Rowlands, 1992). However, no studies have been conducted to evaluate the reliability or stability of LyE. Specifically, the number of continuous footfalls that are required to achieve a stable value for LyE remains unknown. The purpose of this study was to investigate this problem during treadmill walking.

PROCEDURES

Twenty subjects (range: 19-35 yrs) with no known pathologies were asked to walk on a treadmill at a self-selected pace. A quartz shear piezoelectric accelerometer (PCB Piezotronics) was securely attached to subjects' distal anteromedial aspect of the right tibia with a tight elastic wrap. The time series from the accelerometer data sampled (180 Hz) were analyzed using the Chaos Data Analyzer software (Sprott & Rowlands, 1992). The footfalls were analyzed starting with the initial five. Then, five footfalls were added to each subsequent analysis, until all 80 footfalls were included. The LyE was calculated for each one of the analyses groups. All LyE calculations were performed using five embedded dimensions. The embedded dimension, a description of the number of dimensions needed to unfold the structure of a given dynamical system, was calculated from a Global False Nearest Neighbors (GFNN) analysis (Abarbanel, 1996). Mean LyE group values for the grouped footfalls were analyzed statistically using repeated measures ANOVA ($p<0.05$) with a Tukey test as post-hoc.

RESULTS AND DISCUSSION

The ANOVA results showed significant differences between the LyE values. This indicated the LyE values changed from the initial five footfalls when more footfalls were added to the analysis. The post hoc analysis revealed that at the initial five and ten footfalls, the LyE was significantly smaller in comparison with all the other conditions. There were significant differences between the initial fifteen footfalls and the fifty through eighty footfalls. The initial twenty and thirty footfalls were also significantly different from the seventy and seventy-five. It can be observed (Table 1), that as the number of footfalls and data points increase, the values became statistically similar. It can then be concluded that the differences observed from five through fifteen footfalls may be due to the lack of data points. The data points analyzed for the initial five were 1,000, while the total number for all eighty was 16,000.

SUMMARY

The time series collected from a tibia located accelerometer were used to calculate the LyE. The LyE is a measure of the stability of a dynamical system and its dependence on initial conditions. Our results confirmed that after thirty footfalls the LyE is a statistically stable nonlinear tool. This finding can help narrow the number of data points and footfalls needed for an accurate assessment of the LyE during treadmill walking.

REFERENCES

Abarbanel, H.D.I. (1996). *Analysis of Observed Chaotic Data*, Springer-Verlag.
Dingwell, J.B. et al. (2000). *J. Biomech.*, 33, 1269-1277.
Sprott, J., Rowlands, G. (1992). *Chaos Data Analyzer*. American Institute of Physics.
Stergiou, N. et al. (2000). *Proceedings of the ASB'00*, 75-76.

ACKNOWLEDGMENTS

Supported by the University Committee on Research of the University of Nebraska at Omaha.

Table 1: Group means of footfalls (FF). Statistical differences between number of footfalls are shown in superscripts

	5 FF$^{15-80}$	**10 FF$^{25-80}$**	**15 FF$^{50-80}$**	**20 FF$^{70-75}$**	**25 FF**	**30 FF$^{70-75}$**	**35 FF**	**40 FF**
WALK - LyE	0.131	0.144	0.155	0.158	0.160	0.157	0.161	0.163
	45 FF	**50 FF**	**55 FF**	**60 FF**	**65 FF**	**70 FF**	**75 FF**	**80 FF**
WALK - LyE	0.166	0.170	0.170	0.170	0.171	0.172	0.174	0.170

THE SENSORI-MOTOR DEGENERATION REVEALED BY THE CENTER OF PRESSURE MEASUREMENT

Gongbing Shan[1], Christiane Bohn[2] and Ge Wu[3]
[1]Department of Kinesiology, University of Lethbridge, AB. Canada; [2]Institute for Movement Science, University of Muenster, MS, Germany; [3]Department of Physical Therapy, University of Vermont, VT, USA

INTRODUCTION

The frequency of falls and fall-related injuries increases with age. An early identification of potential fallers will help to reduce the frequency of falls. Unfortunately our current methods of prediction, which are based on the analyses of data collected across different biomechanical tests, are consequently contradictory and impractical (Daubney et al. 1999; Maki, 1993), because the measurement techniques used are too complicated and diverse (Hill et al. 1999). Hence, a simple, highly reliable method of prediction is desired by practitioners. The purpose of this study was to develop a practical and quantitative way for diagnosing the age-related degeneration of human sensori-motor function in order to predict the potential fallers. Contrary to the current methods, this research utilized the Artificial Neural Network (ANN) to predict the degeneration of sensori-motor function related to age while keeping the measurement simple. Only the Center of Pressure (COP) was utilized in this study.

METHOD

The method is based on the following facts. Because COP is related to one's involuntary control in quiet stance, it should reflect the CNS integration of sensory inputs from the visual, vestibular and somatosensory systems Therefore, parameters derived from COP captures, i.e. excursion length, maximum displacement, mean and maximum velocity as well as acceleration of COP, can represent the human sensori-motor ability. The redundancy and non-linearity of sensori-motor systems relates these parameters to one another. This relationship looks much like a web. If one point (one parameter) on the web is changed, the others will be changed also. One suitable tool for capturing the "web-relationship" is the ANN modeling. Recent studies (Koike et al, 1995) have showed that the ANN model could predict the behavior of a biological system successfully. Furthermore, body weight (BW) and body height (BH) would also influence the net-like interaction of the human sensori-motor system and should be considered in the building of the ANN model. Based on the above matters, an ANN model of 3 layers was established (Figure 1). For capturing the relationship between COP and age-related sensor-motor function, the ANN model had 26 inputs (P_1 to P_i, i=26) in the input layer; 60 non-linear neurons in the hidden layer; and 2 linear neurons in the output layer. The 26 inputs were: BW & BH, length, max excursion, mean and max velocity as well as acceleration of the COP in the anterior-posterior and medial-lateral direction with eyes open or closed (BW & BH + 6 parameters × 2 COP excursions in 2 directions × 2 visual conditions = 26 inputs). The two targets were age and fall-history (0 – non faller or 1 – faller). After ANN training, the first layer weights (W_{ij}) and second layer weights (W_{jk}) were fixed, so that one could use the model and a new measurement to predict the age (output y_1) of the new subject and fall possibility (output y_2). The predicted age would indicate the declining rate of one's sensor-motor function, e.g. if a predicted age is 65 years for a 60 year old subject, it would mean that the declination of the sensori-motor system of this subject is faster than those individuals whose data are applied to train the ANN model.

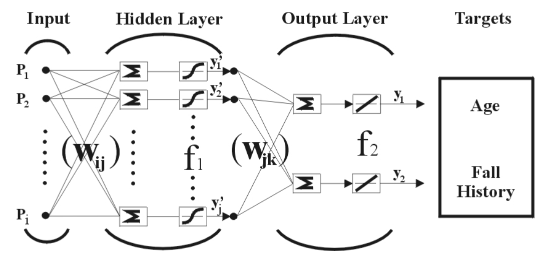

Figure 1: Design of the ANN model.

Two female groups of subjects were tested in this study: a young group (<22 yrs of age, N=6) and an aged group (>55 yrs of age, N=4). During the test, each subject was asked to stand quietly for 10 s, with either eyes open or closed. The COPs under the feet were measured by an AMTI force plate. Two more female subjects (21 and 68 years old) were also involved in the test and their data were applied for testing the accuracy of the prediction of the ANN model.

RESULTS AND DISCUSSION

Because there were no fallers in the subjects, the ANN was only trained by the data of non-fallers. Hence, the prediction of the model at present state is limited on diagnosing the degeneration of sensori-motor function related to age. The prediction results for the two subjects are: 23 for a 21-years old student and 64 for a 68 years old senior.

The long-term aim of this study is to develop a quantitative method for diagnosing the degeneration of sensori-motor function in order to predict potential fallers. The philosophy is to simplify the present measurements, at the same time to increase the reliability of the prediction. This philosophy would let the outcomes be practitioner-friendly. The primary result reveals that this philosophy has huge potential to reach its final goal. It is clear that the accuracy of the prediction of ANN model depends on the amount of data for ANN training. The more subject data collected, the higher the accuracy. Therefore, a large number subject tests (age from 18 - 65+) and new ANN models are going to be done.

SUMMARY

This study revealed that one could utilize a simple measurement (COP) and ANN model to predict sensori-motor degeneration related to age.

REFERENCES

Daubney M.E. et al. (1999). Phys Ther, Dec, 79:12, 1177-85
Hill K. et. al (1999). Aust N Z J Pub. Health, Feb, 23:1, 41-8
Koike Y., Kawato M. (1995).Biol Cybern, 73:291-300
Maki BE (1993). Med Biol Eng Comput, 31:4, 355-62

THE INTERNAL-LOAD CHARACTERISTICS DURING VIOLIN PERFORMANCE

Peter Visentin[1] and Gongbing Shan[2]
[1]Department of Music, [2]Department of Kinesiology, University of Lethbridge, Lethbridge, Alberta, Canada

INTRODUCTION

Overuse syndrome is a common injury among musicians. It is defined as excessive use of body parts so that the accumulation of small micro-trauma exceeds human physiological limits (Dawson et. al., 1990). Studies on professional musicians, as well as college and high-school-aged music students show that 43% - 66% (Zara, 1992; Brown, 1997) of musicians need to stop performing for extended periods because of overuse syndrome. Regrettably, there is currently little quantitative research in this area, inhibiting the development of effective industry practices that focus on improving economic training and learning. Consequently, this study initiates an examination of internal loads occurring during violin performance, with the aim of supplying the characteristics of the load, and providing a foundation that could lead to the design of practices that reduce incidences of overuse syndrome in musicians.

METHOD

In this study, only shoulder loads were examined, as shoulder injuries account for up to 25% of all injuries and are the most prevalent type of injury among professional violinists (Fry, 1988). The method applied uses EMG and kinematic measurements as well as inverse dynamic modeling. Two channels of EMG (DelSys) were used to capture deltoid muscle activity. A nine-camera VICON v8i system was used to capture upper body movement and synchronize EMG and kinematic data. The captured 3D kinematic data was then applied onto a ten-segment model for inverse dynamic analysis in order to determine the joint moments and forces loading the shoulders. The resultant calculated loads together with EMG measurements were utilized to reveal shoulder load characteristics. The ten segments in the violin model were head, trunk, both upper arms, lower arms and hands as well as bow and violin.

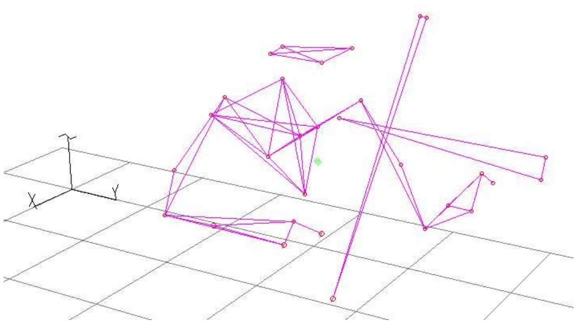

Fig. 1: A 3D reconstruction of violin performance.

Six professionals (two university professors and four Calgary Philharmonic Orchestra violinists) participated in the study. They age from 38 to 46, with no currently known injuries. Both legato (smooth) and spiccato (bounced) bowing techniques were evaluated for six continuous minutes each. For each technique, subjects performed a common skill (a two octave G-major scale) at three separate speeds (two minutes each): low (legato-50, Spiccato-144 bows/min.), medium (legato-100, Spiccato-432 bows/min.), and high speed (legato-200, Spiccato-576 bows/min.). Multiple EMG and kinematic samples were gathered at each speed, so that internal loads and EMG data could be examined throughout the full cycle of the skill.

RESULTS AND DISCUSSION

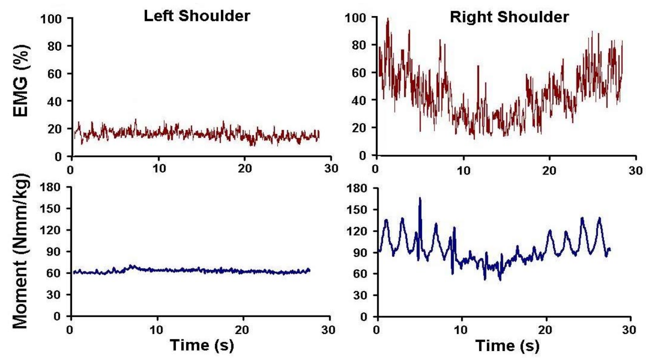

Fig. 2: Normalized EMG envelopes and calculated shoulder joint moments of a trial. Measurements began on the G-string (lateral), cycling to the E-string (medial) and back.

EMG and inverse dynamic analysis both reveal that: a) the left shoulder has a relatively constant load (static) regardless of the string used or the bowing technique or speed b) the load on the right shoulder (dynamic) varies in a larger range and is highest on the G-string and the lowest on the E-string (Fig.2), with the lowest level comparable to left shoulder loads; c) legato technique results in higher right shoulder loads than spiccato; and d) higher performance speeds result in lower internal loads and EMG readings, indicating slow-speed bowing to be more physiologically challenging than fast bowing. Interestingly, despite the significant left and right shoulder differences revealed by this study, shoulder injury rates are comparable (Fry, 1988), suggesting that lower intensity static loads (left side) may lead to micro-trauma more easily than dynamic loads (right side).

SUMMARY

The results of this study suggest that overuse syndrome in violinists is exacerbated by: a) slow-speed bowing techniques and excessive G-string use (right shoulder), and b) constant lower-level static loads (left shoulder).

REFERENCES

Brown A.N. (1997). *Med Probl Perform Art*, 5:117-119
Dawson D.M. et. al (1990). *Entrapment Neuropathies*, 358
Fry H.J.H. (1988).*Int J Music Educ*, 11:3-16
Zara C. (1992). *Med Probl Perform Art*, 7:48-51

ACKNOWLEDGEMENTS

Research was supported by Alberta Learning Research Excellence Envelope & the Calgary Philharmonic Orchestra

THE SELECTION OF PARAMETERS AND PRE-TEST STATES IN IDENTIFYING THE AGE EFFECT THROUGH THE CENTER OF PRESSURE (COP) MEASUREMENT

Brandie Wilde and Gongbing Shan
Department of Kinesiology, University of Lethbridge, Lethbridge, Alberta, Canada

INTRODUCTION

Much research has been done to study the neural control abilities in aging individuals utilizing COP measurement (Daubney 1999). Multiple parameters derived from the COP test, such as peak-to-peak (P-P) value, curve length (CL), velocity and acceleration of COP excursion, were proposed to identify the age-effect on the sensori-motor system (Suomi 1994, Fitzgerald 1994). Unfortunately, the analyses based on these parameters are often contradictory (Daubney et al. 1999)**.** On the other hand, not until now have the pre-test states been taken into account. A pre-test state refers to the activity just before the test. A study done by Carroll (1992) showed that the first 20-second timely excursion in a center of pressure (COP) measurement varied greatly from the measurements following the first 20 seconds, which suggests there would be a transfer phase between the pre- and test-state. Un-standardized COP tests could be the reason for the conflicting situations in the previous studies. Our intent is to research the influence of the states of the body prior to measurement as well as all possible parameters derived from a COP test in order to determine the most effective way for applying the COP test in analyzing the age-effect on human sensori-motor system.

METHOD

This study explored the influences of three pre-test states, sitting, standing and walking, on COP excursion; as well as eleven parameters to see which one(s) can sufficiently identify the age-effect. The parameters were divided into two groups – absolute and relative parameters. The seven absolute parameters consist of p-p values in anterior-posterior (a-p) and medial-lateral (m-l) direction, CL, mean and max velocity as well as acceleration of the COP excursion. The four relative parameters were normalized p-p values (normalized by foot length) and the swing angles of centre of mass (COM) in a-p and m-l directions, which are defined by ½ p-p values divided by subject COM height. The COM heights were obtained through a regression equation (Shan, 1999), which utilize body weight and height as independent parameters. A random sample of 17 seniors (60-92yrs), and 21 students (20-25 yrs.) were obtained. Measurements of their foot length, shoulder width, height (m) and weight (kg) were taken and utilized to normalize as well as standardize (shoulder width = stand width) the COP tests. By the use of Kistler force platform, a 40 second quiet stance was used for the series of COP measurements. Each measurement was assessed in the first 20 seconds, second 20 seconds and total (40 s) by using the 11 parameters. The three pre-test states were applied as follows: the first following a two-minute period of sitting; the second being after at least a minute's worth of standing; and the third subsequent to a walk, at normal walking pace, for 200 m. Each of these trials was done three times for a total of nine measurements. A vision condition was also added to these trials. The subjects were asked to follow the same procedure as outlined, however while standing on the platform their eyes were closed. The added 9 trials (eyes closed) resulted in a total of 18 measurements per subject. Finally, ANOVA was utilized to determine the significances among pre-test states, and parameters in the identifying the age-effect.

RESULTS AND DISCUSSION

It was found that the aged individuals had in average a higher p-p value in both directions in the absolute and relative evaluations. Their COM swing angle (relative parameter) was also greater in both directions. However, the students showed higher max and average excursion speed and acceleration to the aged as well as a larger curve length. The results above suggest that the involuntary control of young adults is more dynamic (faster, however in a smaller range) than the aged. It was also noted that there was a more drastic change between the first and second 20 s in the younger subjects as opposed to the elderly. The calm-down effect (the decline of p-p value) is significant ($p<0.05$) in the young group, while hard to notice in the aged group, which suggests there is a transfer phase (control pattern change) between pre-test and test states for the young group. The transfer phase could be the reason for contradictory results in the previous studies. The ANOVA results reveal that 56 out of 66 parameters (3 pre-test states × 2 vision conditions × 11 parameters) are significantly different between young and aged in the second 20 s interval, while there are only 40 for both the first 20 s and total. Another indication of the ANOVA results is that the best pre-state possible for the identification of the age-effect is walking. This has a more obvious transfer phase and is almost 100% different between the two groups of subjects. A different avenue to reaching a unique identification is to use relative parameters. The ANOVA results showed that 24 out of 24 parameters are significantly different ($p<0.05$), while only 32 out of 42 absolute parameters are significant.

SUMMARY

Thus, to determine the age-effect on a subject's balance, a walking pre-state with a measurement after 20 s standing would be recommended. The relative parameters would also be the most effective.

REFERENCES

Carroll, J.P. et al. (1992) *J. of Biomechanics,* 26, 409-416
Daubney, M.E. et al. (1999). *Phy. Therapy,* 79, 1177-1185
Fitzgerald J.E.(1994) *Acta Oto-Laryngologica*, 114(2):115-9
Shan, G.B. (1999) Münster:Lit, ISBN 3-8258-4274-6
Suomi R, et al. (1994) Arch. Phy. Med. & Rehab., 75:205-9

ACKNOWLEDGEMENTS

This research was supported by the UofL Research Fund.

AXIAL STRETCH OF ARTERIES IN ORGAN CULTURE

N. Peter Davis, Hai-Chao Han, and Raymond Vito
George W. Woodruff School of Mechanical Engineering
Georgia Institute of Technology
raymond.vito@me.gatech.edu

INTRODUCTION

In vivo, arteries remodel in response to their mechanical environment. Many studies have shown that artery wall thickness increases when pressure increases and that artery diameter increases as blood flow increases. If axial stretch also leads to remodeling of the arterial wall, this may provide a way to engineer new arterial tissue for use in coronary bypass and other applications where arterial grafts would be beneficial. Lengthening existing arteries that have proven performance as bypass conduits could facilitate completely arterial revascularization.

Organ culture was chosen as the means to investigate the lengthening of arteries by mechanical stretch. Much greater control of mechanical environment is possible with organ culture compared to *in vivo* studies, and the native architecture of the tissue itself is maintained.

METHODS

Carotid arteries (4.8 ± 0.3 mm outer diameter) were harvested from 100-150 kg farm pigs and mounted in a perfusion organ culture system that was modified from a previous design (Han and Ku, 2001) for the application of axial stretch. Culture medium was DMEM plus 10% newborn calf serum. Arteries were perfused at pulsatile physiologic pressure and flow conditions (100 ± 20 mm Hg with average wall shear stress of 15 dyn/cm^2). Axial stretch was applied to arteries during culture using linear motors controlled by a PC running custom C-code. Control arteries were maintained at the physiologic stretch ratio of 1.5 while stretched arteries were cultured with a constant axial stress of 250 kPa. Culture period was 7 days.

Proliferation was detected by BrdU incorporation during the last 24 hr of culture and subsequent antibody detection in 5-μm histologic sections. Vasomotor response was tested on whole arteries the last day of culture while arteries were still mounted in the perfusion circuit. Differences between means were considered significant at $p < 0.05$.

RESULTS AND DISCUSSION

Though stretched arteries reached an average stretch ratio of 2.13 ± 0.07 during culture, neither stretched nor control arteries showed any permanent increase in no-load length. Tissue volume was found to decrease in both groups, but stretched arteries showed a significantly lower volume loss of 15% compared with the 27% loss in controls.

Figure 1 shows that more proliferating cells were located in the intimal and adventitial layers than in the media. Stretched arteries had significantly higher proliferation in the intima than controls. Overall, stretched arteries showed slightly higher proliferation than controls, but the difference was not significant. Total medial smooth muscle population did not change significantly over the 7 days of culture for either group, indicating that stretch under these conditions produced no cumulative proliferative changes in that layer. Though axial stretch at 250 kPa for 7 days did not appear to be a growth stimulus for the medial smooth muscle population, the intimal layer responded significantly to stretch at 250 kPa for 7 days. Both groups of arteries showed strong contraction to norepinephrine and relaxation to sodium nitroprusside at the end of culture. No morphological differences were observed between H&E sections from either group.

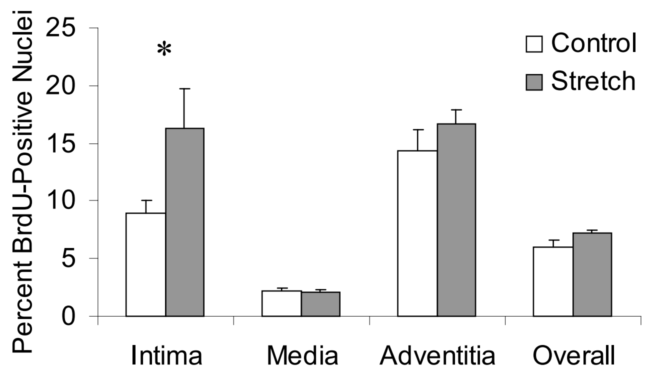

Figure 1. Proliferation within the three arterial wall layers. * $p<0.05$.

SUMMARY

Arterial integrity and morphology were unaffected by stretch, and vasomotor response was good in both stretched and control arteries. Even though the arteries did not show significant growth under these conditions, they endured considerably larger stretch than the *in vivo* condition without evident damage. Therefore, these arteries are quite resilient under axial stretch, and lengthening might be accomplished by optimizing the stretch protocol.

REFERENCES

Han, H-C, Ku, DN. (2001). *Ann Biomed Eng,* **29**, 467-475.

ACKNOWLEDGMENTS

Support for this work was provided by the ERC program of the National Science Foundation under Award Number EEC-9731643 and by a Beginning Grant-in-Aid Award from the American Heart Association. Porcine arteries were generously donated by Holifield Farms of Conyers, GA.

FORCE DEPRESSION FOLLOWNG MUSCLE SHORTENING OF ELECTRICALLY STIMULATED AND VOLUNTARILY ACTIVATED HUMAN ADDUCTOR POLLICIS

Hae-Dong Lee[1] Walter Herzog[1] and Young-Doo Won[2]

[1] Human Performance Laboratory, Faculty of Kinesiology, University of Calgary, Calgary, Alberta, Canada
Email: lee@kin.ucalgary.ca & walter@kin.ucalgary.ca Web address: http://www.kin.ucalgary.ca/
[2] College of Physical Education, Chosun University, Kwang-Ju, Korea. Email: ydwon@hanmail.net

INTRODUCTION

Force depression following active muscle shortening has been demonstrated, using artificial electrical stimulation, for in-vitro and in-situ animal muscle/fibre preparations (Abbott & Aubert 1952; Edman et. al. 1993; Herzog & Leonard 1997; Maréchal & Plaghki 1979) and for in-vivo human muscles (Cook & McDonagh 1996; de Ruiter et. al. 1998). Recently, it was demonstrated that force depression also exists for human voluntary knee extensions (Lee et. al. 1999). However, force depression did not depend on the shortening magnitude and speed (Lee et. al. 2000), in contrast to what has been consistently observed for electrically stimulated preparations. Therefore, in order to fully describe force depression in human skeletal muscles and to investigate the influence of neuromuscular control in voluntary contractions, it is necessary to make direct comparisons of force depression between electrically stimulated and voluntarily activated muscles.

The purpose of this study was to investigate force depression for in-vivo human adductor pollicis during voluntarily activated and electrically stimulated contractions.

METHODS

Subjects (n = 6) performed isometric contractions following active muscle shortening with the thumb adductor muscle using voluntary and electrical stimulation. The shortening conditions were systematically varied [i.e., magnitudes (10, 20 and 30° at a constant speed of 20°/s) and speeds (20, 60 and 300 °/s over a constant magnitude of 30°)]. Each test contraction was repeated three times in a random order, and isometric reference contractions were performed before and after the three test contractions. All isometric contractions were performed at a fully adducted thumb position. Muscle force and joint angle were continuously recorded using a custom-designed dynamometer (Lee et. al. 2001), and muscle activation was monitored with electromyography and the interpolated twitch force (ITF) (Merton 1954). Using ANOVA with repeated measures and Bonferroni post hoc comparisons, force depression (FD), defined as the difference in the steady-state isometric force following shortening and the isometric reference force, the root mean square (RMS) values of EMG, and the ratios of ITF to the resting twitch force (RTF) were compared among the test conditions (α=0.05). All results are presented as means ± 1 S.E.M.

RESULTS AND DISCUSSION

Mean force depression across all tests was 21±4% and 15±3% for the voluntary and the electrically stimulated contractions, respectively. Force depression was directly related to the magnitude of shortening and was inversely related to the speed of shortening (Fig.1&2). These result agrees with observations for electrically stimulated preparations (de Ruiter et. al. 1998), but not with those observed for human voluntary knee extensions (Lee et. al. 2000). Muscle activation of the adductor pollicis was similar across contractions for all voluntary tests, whereas for human knee extensors, activation was not constant across isometric reference and shortening test trials (Lee et. al. 2000). We propose therefore, that force depression during voluntary and electrically stimulated contractions is similar, as long as activation in the voluntary contractions remains constant. Furthermore, we speculate that for small hand muscles, activation may be kept constant and maximal for different contractions, whereas for the big muscles of the limbs, this may not be necessarily correct.

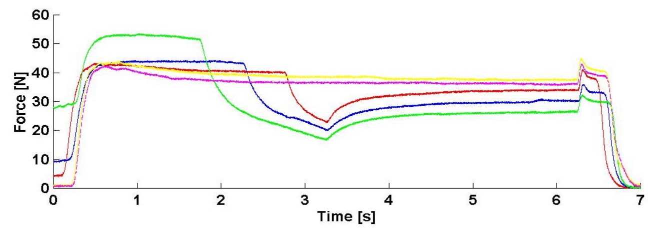

Figure 1. Force-time histories of purely isometric and isometric contractions following shortening with varying magnitudes (10, 20 and 30° at a constant speed of 20°/s).

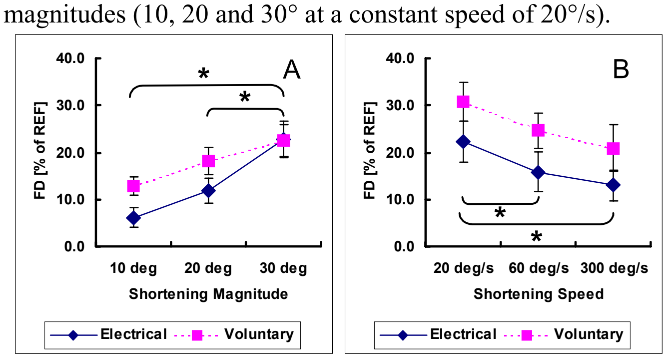

Figure 2. Force depression following muscle shortening of varying magnitudes (A) and speeds (B) (for collapsed means across each shortening condition: *, $p < 0.05$)

REFERNCES

Abbott & Aubert (1952) *J. Physiol.* **117**, 77-86.
Cook & McDonagh (1996) *J. Appl. Physiol.* **81**, 384-392.
De Ruiter, et. al. (1998) *J. Physiol.* **507**, 583-591.
Edman, et. al. (1993) *J. Physiol.* **466**, 535-552.
Herzog & Leonard (1997) *J. Biomech.* **30**, 865-872.
Lee, et. al. (2001) *Proceedings of the ISB* 21-21.
Lee, et. al. (1999) *J. Appl. Physiol.* **87**, 1651-1655.
Lee, et. al. (2000) *J. Biomech.* **33**, 917-923.
Maréchal & Plaghki (1979) *J. Gen. Physiol.* **73**, 453-467.
Merton (1954) *J. Physiol.* **123**, 553-564.

A COMPARISON BETWEEN GAIT KINETICS IN WOMEN WITH PRIMARY OSTEOARTHRITIS AND THOSE WITH OSTEOPOROSIS

Jean L. McCrory, Anne L. Harrison, and Jody L. Clasey
Biodynamics Laboratory and Body Composition Core Laboratory, University of Kentucky, Lexington, KY, USA
mccrory@uky.edu

INTRODUCTION

Osteoporosis (OP) and osteoarthritis (OA) are recognized as major age-related health problems that disproportionately affect women. Of women over age 65, an estimated 33% will sustain an osteoporotic hip fracture and approximately 86% will show evidence of lower extremity OA (Wardlaw, 1998).

Interestingly, many of the predictors for OP and OA are inversely related, which has led to the theory that these diseases are mutually exclusive of one another (Dequecker et al., 1996). By definition, individuals with OP have low bone density. Individuals with OA have been shown to have elevated bone mineral density (BMD) (Stewart and Black, 2000). Hurwitz et al. (1998) related BMD to biomechanics by reporting that people with hip OA had greater femoral bone density and greater hip adduction moments than a control group did. This is in accordance with Wolff's law, which states that bone density is proportional to the amount of force to which the bone is exposed (Woo et al., 1981).

The purpose of this investigation was to determine if the gait kinetics differ between women with OP and women with OA. It was hypothesized that women with knee OA will have greater ground reaction forces and joint moments than the women in the OP group.

METHODS

Thirty-one post-menopausal women aged 50 to 85 received a standing bilateral A-P knee x-ray and a DXA scan of their femoral neck. Women with knee OA rated 2 or 3 on the Kellgren-Lawrence scale were placed in the OA group (n=10, 68.3±7.4yrs, 1.62±0.06m, 79.4±12.8kg). Women with proximal femoral BMD two SD below normal were placed into the OP group (n = 7, 74.4±7.9yrs, 1.64±0.06m, 61.2±10.0kg).

On a subsequent visit, a gait analysis was performed on each subject using a 6-camera Motion Analysis Inc. system (60 Hz, Santa Rosa, CA) interfaced with a Kistler force plate (600 Hz, Winterthur, Switz.). Retroreflective markers were placed on the foot, shank, thigh, and pelvis to determine 3D movement patterns. After subjects had become accustomed to walking on the 20m laboratory runway in the marker set, 5 good trials of the most affected leg (OA group) or a random leg (OP group) were collected. A trial was termed "good" if the subject struck the force plate with the designated foot with no visible alteration in gait mechanics. An ANOVA was performed on the passive and active peaks for the following measurements: ground reaction force, hip and knee compression forces, and hip and knee adduction moments.

RESULTS AND DISCUSSION

With the kinetic variables normalized to the subjects' BW, no variables were significantly different between groups. However, it is more physiologically relevant to compare the non-BW normalized values (in N) between groups because Wolff's law deals with actual magnitude of force exposure. The OA group had greater values ($p<.05$) for the passive and active peaks in ground reaction forces, hip and knee compressive forces, and hip adduction moment (Table 1).

Table 1: Significant kinetic variables

Variable	OA	OP
Psv GRF Pk (N)	847.2±178.1	660.1±115.1
Act GRF Pk (N)	841.6±114.1	688.9±103.1
Psv Hip Comp Fc (N)	712.9±132.2	549.4±96.7
Act Hip Comp Fc (N)	689.4±87.4	561.3±96.7
Psv Knee Comp Fc (N)	810.1±170.6	621.5±111.9
Act Knee Comp Fc (N)	738.2±97.2	621.4±95.4
Psv Hip Add Mom (Nm)	724.1±275.7	542.2±153.6
Act Hip Add Mom (Nm)	632.7±212.1	460.6±161.4

The average femoral neck BMD of the OA group was 109.2±12.1% of aged matched normal while the OP group averaged 89.2±9.7% of normal. Like the women with hip OA studied by Hurwitz et al. (1998), the women in the knee OA group in the current study had large hip adduction moments increased femoral neck BMD. Whalen et al. (1988), in the "daily load hypothesis" theory, stated that BMD is directly related to the GRF magnitude. Future work will involve testing a healthy control group to determine if the values of this group fall between those of the diseased populations of this study.

SUMMARY

Body weight is related to the differences in the gait kinetics between the OA and OP groups. Because the OA group was significantly heavier than the OP group, the magnitude of lower extremity force exposure was significantly larger in the OA group. This supports the theory that these two diseases are on opposite ends of the same continuum.

REFERENCES

Dequecker, J., et al. (1996). *Br. J Rheum*. **35**: 813-829..
Hurwitz, D.E. et al. (1998). *J. Biom*. **31**: 919-925.
Stewart, A. and Black, A.J. (2000). *Cur. Opin Rheum*. **12**: 464-467.
Whalen et al. (1988). *J. Biom*. **21**: 825-837.
Wardlaw, G.J. (1988). *Am. Dietc Assn*. **88**: 17-25.
Woo et al., (1981) *J Bn Jt Surg*. **63-A**, 780-786.

MODELING OF DISTANCE IN SKI JUMPING USING STATISTIC MODELS WITH RANDOM PARAMETERS

Sandro Jelmini , Reposoir 23, 1007 Lausanne, Switzerland; sandro@balelec.ch
Mathematics Department, Swiss Institute of Technology, Lausanne, Switzerland

INTRODUCTION

Ski jumping, as an outdoor sport is dependent on weather conditions and it is now important for promoters to be able to make the right choice concerning, among others, the inrun given to the jumpers. Statistics offers a solution to make more "objective" choices, using data about the jumpers, the hills and the weather, thus making use of all the information we have about the *history* of the jumpers and the hills. One possibility is to model the lengths of the jumps in ski jumping with a statistical theory called *Bayes Theory*. A simplified approach to the *Bayes Theory* would be the following: the jumpers represent a population for which the distribution (with parameters) is known (approximately at least) or supposed to be known. Each jumper is one individual of this population with his own parameters.

METHODS

Before applying the *Bayes Theory,* some "classical" graphical analyses were made in order to sort the jumpers and the hills and to understand various correlation. The data we used are the World Cup results of seasons 1997/1998 and 1998/1999. All data was sorted into 3 categories: data on the jumpers (6), data on the jumping hills (3) and data on each jump of the competition (2 x 16). Different classical methods were first used to analyze the data. **Histograms and boxplots** give a global view of each jumper and hill distribution. This shows which jumpers are most regular and which have the best mean length. A similar evaluation can be made for hills, showing which hill allows the longest jumps in mean and which are the most difficult to jump. The **Principle Components Analysis** method gives us a graphical idea of different (sub-) classes or sectors in which we could put jumpers on one side and hills on the other. As we create the diagram for all jumpers and all hills at once, the various "clouds" or classes appearing correspond to jumpers that have similar results on similar hills. The table of correlation linked to the PCA gives the correlation between the hills.

The first step to find a **model** using the information we have is to make a simple **linear regression**. Two models were found to estimate the length of a jump with the help of different methods as the stepwise and the ANOVA. The first model taking a particular jumper and the second taking different characteristics of a person. Both models allow us to compare the model with the reality (something that has happened) or to predict the result of a jumper or a person with given characteristics. Comparing the first model with the data we used, the mean difference between the model and the reality for a given jump is less than 2%, i.e. 2.5m on a 125m jump. The more data we have, the more exact this estimation should be, also as a "prediction". The second model gives the estimate length of a jump for a person with given characteristics (height, weight, birth year, year of beginning,…).

The Bayes theory can be use in different levels: standard, empirical or hierarchical. The first and most easy result is to suppose that the length x of a jump for each jumper i, written x_i , has a Normal distribution with mean μ_i and variance σ^2; σ^2 is known but μ_i has itself a Normal distribution with mean υ and variance τ^2, both known (the results based on the whole population on K120 hills give: υ = 111.47 meters & τ^2 = 120.55;). We have: $x_i \sim N(\mu_i, \sigma^2)$ and $\mu_i \sim N(\nu,\tau^2)$ which is the *a priori law* on parameter μ_i.

The posterior distribution of μ_i knowing x is given in S. Jelmini (2000). Taking $\vec{x} \sim N(\vec{\mu},\Sigma)$ and $\vec{\mu} \sim N(\vec{\nu},\Lambda)$ with any Σ and any Λ, we find the posterior distribution for a more general case. Suppose now that each jumper "has his own variance". We suppose that the different persons are independent to each other and that two jumps of a same person are independent and identically distributed. If J is the number of jumps on the particular hill h (h=1,…,H with H the number of hills), the *a posteriori law* for jumper i is then:

$$\begin{pmatrix}\mu_{ih}\\ \vdots \\ \mu_{ih}\end{pmatrix} \Big| X \sim N_J\left(\mu_{\pi ih}, V_{\pi ih}\right) \text{ with}$$

$$\mu_{\pi ih} = \left(\frac{1}{\tau^2} \mathrm{I}_J + \Sigma_{ih}^{-1}\right)^{-1} \left(\frac{1}{\tau^2} \mathrm{I}_J \begin{pmatrix}\nu\\ \vdots \\ \nu\end{pmatrix} + \Sigma_{ih}^{-1} \begin{pmatrix}x_{ih1}\\ \vdots \\ x_{ihJ}\end{pmatrix}\right) \;\&$$

$$V_{\pi ih} = \left(\frac{1}{\tau^2} \mathrm{I}_J + \Sigma_{ih}^{-1}\right)^{-1}$$

RESULTS

Models and parameters have been found for, among others, different linear regressions and a Bayes model with the same number of jumps for each person (taking only the competitions on K120 hills into consideration). As has been said, the data analyzed for this work came from results of seasons 1997/1998 and 1998/1999. The best results - or at least the most complete results - would obtain through stepwise updates of the database after each jump of each competition. This would provide an "instant" situation of the parameters for each jumper and each competition. It would then be possible during a competition to predict how long the next jumpers would normally jump if they were performing in their "mean" level.

This could be a very interesting model for the FIS (International Ski Federation) to be able to choose a good inrun length, based on all the different parameters (hill, temperature, weather, jumpers, etc.).

REFERENCES

- S. Jelmini (2000), *Modèles statistiques à paramètres aléatoires: modélisation des longueurs en saut à skis et théorie du risque,* Mathematics Department (Prof. S. Morgenthaler), Swiss Institute of Technology, Lausanne, Switzerland.
- Ch. Robert (1992), *L'analyse statistique bayesienne*, Ed. Economica, Paris.

TESTS OF NUMERICAL MODELS OF CRANIOMANDIBULAR MECHANICS

Laura Iwasaki[1] , Jeffrey Nickel[1], Paul Petsche[2], W.D. McCall[3], David Marx[4]
[1]University of Nebraska Medical Center, College of Dentistry, Lincoln, NE, liwasaki@unmc.edu
[2]Private Practice, Colorado Springs, CO
[3]State University of New York, Buffalo, NY, [4]University of Nebraska, Lincoln, NE

INTRODUCTION

In humans, muscle recruitment during static biting and chewing varies depending on bite force (BF) direction. Directional information is provided by periodontal ligament mechanoreceptors. Given that BF directions can vary during biting, it is unknown whether there is an overlying neuromuscular objective which governs the mix of forces produced by the masticatory muscles. The mix of muscle forces determines the magnitudes and directions of temporomandibular joint (TMJ) loads, and thus, is clinically important. The aim of this project was to test hypotheses that could account for the muscle outputs during static BFs that produce moments on molar and incisor teeth. Models of minimization of joint loads (MJL) and muscle effort (MME) were tested. Seven living subjects provided subject-specific data that included: i) effective TMJ eminence morphology and ii) muscle activities, which were used to test the models.

METHODS

Effective Eminence Morphology: The effective eminence morphology of the TMJ represents the sagittal plane projection of the trajectory of the TMJ stress-field as the mandibular condyle translates downward and forward from a molar biting position to an incisor biting position. The shape of the effective eminence was measured using a videographic technique. The shape of the trajectory was digitized and described as a third order polynomial. A numerical model was used to predict the shape of the effective eminence based on MJL and the individual's three-dimensional (3-D) craniomandibular (CM) geometry. A linear regression analysis was used to test the model predictions by comparison with *in vivo* data from the same subject.

Muscle forces during biting: Indwelling and surface EMG were used to measure muscle activity as a surrogate for muscle force. Data were collected from the right and left masseter, temporalis, medial pterygoid, lateral pterygoid, and digastric muscles during biting on the first molar and central incisor teeth. BF position on a given tooth was varied across the occlusal table to produce a systematic variation of + and – moments about the center of resistance of the teeth. The biting tasks were simulated in the models. Predicted data using the subject specific 3-D CM geometry were based on i) MJL or ii) MME. The data were compared using a statistical analysis consisting of both general linear and mixed methods in order to determine if MJL or MME model predictions fit the actual data better. A random coefficient method is effective in determining which subjects have the actual muscle outputs predicted better by the MME model and which by the MJL model. Therefore, the accuracy of the statistical analysis was based on prediction of muscle outputs, rather than using measures of variance.

RESULTS AND DISCUSSION

A range of eminence shapes was measured. Slope differences varied by as much as 3 to 1 between the subjects. Linear regression analysis resulted in an R^2 of 0.94. **T** tests indicated no significant difference between predicted and measured effective eminence morphologies. The results showed that in most subjects the MME model predictions fit the actual muscle outputs better than the MJL muscle predictions did ($p < 0.001$, Table 1). However, for molar biting in one subject, the MJL model predicted the measured data. In another subject, both the MJL and MME model results fit the measured muscle activities. A similar pattern of results was found for incisor biting.

SUMMARY

Muscle recruitment during isometric biting appears to be consistent with the objectives of MME but, depending on the individual, location of biting, and direction of BF, single individuals matched predictions of MJL.

Table 1: Multiple Regression Analysis of Predicted and Measured Muscle Outputs During Biting

Molar Biting	**Degrees of Freedom**	**F- Value**	**P- value**
MME Model (after fitting MJL Model)	1	50.64	<0.0001
MME Model and Subject	6	5.02	<0.0001
Incisor Biting	**Degrees of Freedom**	**F- Value**	**P- value**
MME Model (after fitting MJL Model)	1	16.8	< 0.0001
MME Model and Muscle Output	4	3.66	0.0064

IDENTIFYING DYNAMIC INSTABILITY DURING OBSTRUCTED GAIT FOLLOWING TRAUMATIC BRAIN INJURY

Li-Shan Chou [1], Ann E. Walker [2], Kenton R. Kaufman [2], Robert H. Brey [3] and Jeffery R. Basford [4]
[1] Department of Exercise and Movement Science, University of Oregon, Eugene, OR
[2] Department of Orthopedic Surgery, [3] Department of Otorhinolaryngology and [4] Department of Physical Medicine and Rehabilitation
Mayo Foundation, Rochester, MN
E-mail: chou@oregon.uoregon.edu

INTRODUCTION

Sensation of imbalance has been troublesome for as many as 30% of patients following a traumatic brain injury (TBI) despite an often unremarkable neurological and physical exam (Alves et al., 1986; Cicerone and Kalmar, 1995). Given that additional injuries may occur due to consequences of unsteadiness or imbalance during locomotion, it is important to reveal the influence of TBI on an individual's ability of balance control during balance-challenged activities, such as walking and stepping over obstacles. This information may enhance the development of TBI rehabilitation and education programs and lead to increased safety and faster integration into the community. Therefore, the purpose of this study was to develop a quantitative measurement system to identify dynamic instability during gait of individuals with TBI.

METHODS

Ten subjects (6 men and 4 women, ranging in age from 19 to 62 years, and at least 3 months post injury) with documented TBI and complaints of "imbalance" or "unsteadiness" while walking and ten age, gender, and stature-matched healthy individuals were recruited for this study. Subjects were instructed to walk along a 10m walkway at a comfortable self-selected speed while barefoot. Whole body kinematic data were collected from each subject using a six-camera ExpertVision™ system during unobstructed level walking and when stepping over an obstacle of height corresponding to 2.5%, 5%, 10%, or 15% of the subject's height. The order of obstacle height was randomly selected. A 13-link biomechanical model of the body was used to compute the kinematics of the whole body's COM (Chou et al., 2001). A two-way ANOVA with repeated measures of obstacle height was used to test for group differences and obstacle height effect on the temporal-distance parameters, range of motion of the COM and its peak velocities in three orthogonal directions during the crossing stride.

RESULTS AND DISCUSSION

Post-TBI subjects adopted a gait pattern with a significantly slower walking speed ($p=0.02$) and shorter stride length ($p=0.018$) than controls during all obstacle conditions. The walking speed was found to decrease linearly ($p<0.001$) as obstacle height increased. Significantly smaller/slower COM movement in the A-P direction ($p\leq 0.012$) was also observed in post-TBI subjects than controls. The A-P COM range of motion and peak forward velocity decreased linearly ($p<0.001$) as obstacle height increased.

Although neither significant group nor obstacle height effects were detected for the step width, significantly greater/faster COM movement in the M-L direction ($p\leq 0.007$) was found in post-TBI subjects than controls during all obstacle conditions (Figure). The M-L COM range of motion and peak velocity were also found to increase linearly ($p<0.001$) with obstacle height.

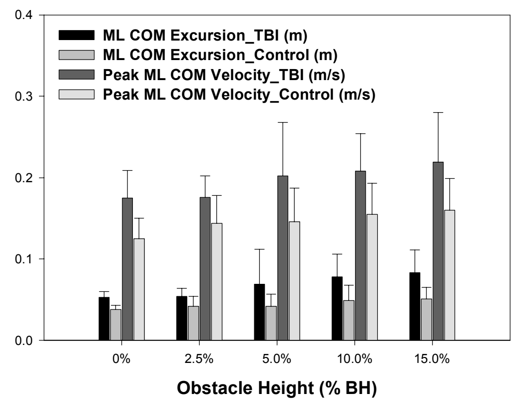

Stepping over a higher obstacle was found to impose a greater perturbation on the M-L COM motion in the TBI subjects than normal individuals. Also, magnitudes of the M-L COM excursion and peak velocity of the TBI subjects are similar to those reported for the balance-impaired elderly adults (Hahn et al., 2001), which indicate poor balance control in the frontal plane. Our data also imply that the feasible range of COM movement during which balance can be successfully maintained in the sagittal plane has been reduced in the TBI subjects relative to their controls.

SUMMARY

Examining the COM motion provides an objective measurement to better document complaints of instability not observable on clinical examination for individuals who suffered a TBI. Subjects with a TBI may be under a greater risk of sideways instability/falling during obstacle crossing.

REFERENCES

Alves, W.M. et al. (1986) *J. Head Trauma Rehab* 1: 1-12.
Cicerone, K.D., Kalmar, K. (1995) *J. Head Trauma Rehab* 10: 1-17.
Chou et al. (2001) *Gait & Posture* 13: 17-26.
Hahn et al. (2001) *Proceedings of the ASB*, pp. 241-242.

ACKNOWLEDGEMENTS

This study was supported by the Mayo Foundation.

PLOWING FORCES AND STRESS DISTRIBUTION ON THE TEMPOROMANDIBULAR JOINT DISC SURFACE

Jeffrey Nickel, Laura Rothe, Laura Iwasaki , Mark Beatty
University of Nebraska Medical Center, College of Dentistry, Lincoln,NE, jnickel@unmc.edu

INTRODUCTION

The development of degenerative joint disease of the temporomandibular joint (TMJ) is related to the degeneration of the fibrocartilaginous disc. It is thought that shear and tractional force-induced stresses on the disc surfaces may account for early disc degeneration. The clinical evidence that the lateral portion of the disc is the location where failure occurs most often suggests that there is an asymmetric distribution of these stresses. Considering tractional forces, movement over the surface of the disc is likely to produce both frictional forces and plowing forces due to deformation of the cartilage. Although it is known that surface friction on the TMJ disc is very low ($\mu_S < 0.005$[1]), the magnitude of plowing forces has not been reported. It is possible that plowing forces are very much greater and, therefore, a more important factor in developing stresses on the disc surface. With respect to asymmetric distribution of compressive stresses, no data are as yet reported on the temporospatial distribution of compressive stresses under the TMJ disc during stress field translation over the disc surface. This project tested the hypotheses that 1) plowing forces are significantly greater than frictional forces on the surface of the TMJ disc, and 2) asymmetric distribution of compressive and shear stress occurs under the TMJ disc during stress-field translation.

METHODS

Fifty-six porcine TMJ discs were used in a laboratory apparatus to measure plowing forces on the surface of the disc, and pressure distribution under the disc during movement of an acrylic indenter over the top surface of the disc. Each disc remained hydrated in warm saline until it was statically loaded with 11 N for either 10 s or 1 min., after which the acrylic indenter was moved over the surface of the disc at peak velocities of 117 ± 2.6 mm/s. This velocity is consistent with peak velocities measured *in vivo* in humans. The position and velocity of the movement were controlled by a computer-driven force generator. The indenter was instrumented to measure plowing forces during movement. Beneath the discs, a linear array of 9 pressure-sensitive transducers measured changes in compressive stress in real time. Measurement accuracy was ±5 Pa. Data measuring the position of the indenter, pressure data, and plowing forces were recorded digitally at a sampling frequency of 300 Hz per channel. Each experiment was performed twice per disc, with 2 hours intervening between experiments to allow for disc rehydration.

To test the hypothesis that plowing forces are significantly greater than frictional forces, data analysis involved identifying peak plowing forces, and calculating a coefficient of plowing ($\mu_{plowing} = Force_{plowing} / Force_{normal}$) for comparison to published data of the surface friction on the TMJ disc. Asymmetry in stress distribution under the TMJ disc was determined from pressure data under the leading and following edges of the stress field with respect to indenter position over the TMJ lateral and medial portions. Shear stresses and normalized pressure gradients were calculated and compared to disc position. A general model of shear stress magnitude was calculated from the distribution of peak compressive stress under the disc[2].

RESULTS AND DISCUSSION

Measured $\mu_{plowing}$ were, on average, two orders of magnitude greater than published data of the static coefficient of friction (μ_{static}[1], $p < 0.001$). Duration of loading affected plowing. Static loading for 60 s increased plowing forces by 23% compared to 10 s of loading. Peak compressive stresses under the disc were in excess of 80 Pa. The first pass of the indentor caused leading edge compressive stress gradients to be nearly twice that of the following gradients ($p < 0.001$). After the third pass, no significant differences in gradients were found. For all cycles, average shear stresses were 2.2 times greater for the lateral half compared to the medial half of the disc ($p < 0.01$, range 0.6 – 6.3).

SUMMARY

Plowing forces are the most significant source of tractional forces on the TMJ disc surface. Peak plowing forces occur just after the start of movement. The viscoelastic character of the disc is the reason for the temporal changes seen in the plowing forces, and compressive stresses after the indentor made multiple passes over the disc. The asymmetric distribution of greater shear stresses are consistent with clinical findings of common sites of degenerative joint disease.

REFERENCES

[1]Nickel, J.C. and McLachlan, K.R. (1994). *In vitro measurement of the frictional properties of the tempormandibular joint disc.* Arch oral Biol 39: 323-331.
[2]Armstrong, C.G. (1986). *An analysis of the stresses in a thin layer of articular cartilage in a synovial joint.* Eng Med 15: 55-61.

ACKNOWLEDGEMENTS

Supported by a UNMC College of Dentistry Student Research Fellowship.

DOWNHILL HIKING WITH THE USE OF A SINGLE HIKING POLE VS. DUAL TREKKING POLES

Julianne Abendroth-Smith [1], Ed.D. and Michael Bohne [2]
[1] Willamette University, Salem OR; jabendro@willamette.edu
[2] University of Northern Colorado, Greeley CO USA

INTRODUCTION

Single hiking poles have long been used by hikers, but the use of two trekking poles has recently gained popularity. The purpose of this project was to examine possible benefits of hiking downhill at different gradients while using different poling combinations. Peak GRFs and braking forces (BFs) were examined for conditions of pole use (no poles, one pole, or two poles), gradient (15 and 25 degrees) and gender.

METHODS

Thirteen healthy, well-conditioned adults with recent hiking experience volunteered (7 men, 6 women). All signed informed consents. Procedures included hiking up and down a wooden ramp, with instructions to "hike with purpose". The single hiking pole was used with the dominant hand while the opposite leg struck the force plate. After practice, ten successful trials per condition (counterbalanced) were collected and analyzed. Force data was collected using a Bertec force plate (1000 Hz), mounted flush with the ramp. Video (60 hz) was obtained for later analysis. Means (SD) were calculated for each condition. All force data was normalized to body mass (N/kg). Peak GRFs and BFs (N/kg) were examined for differences between gradient, pole use and gender, using a 3-way repeated measures ANOVA.

RESULTS AND DISCUSSION

Statistically significant differences ($p<.05$) were noted for changes in GRFs between the two gradients ($F=31.8$, df=1 $p<.01$). Though not statistically significant, trends were noted for interactions between grade, poles, and gender (Figure 1).

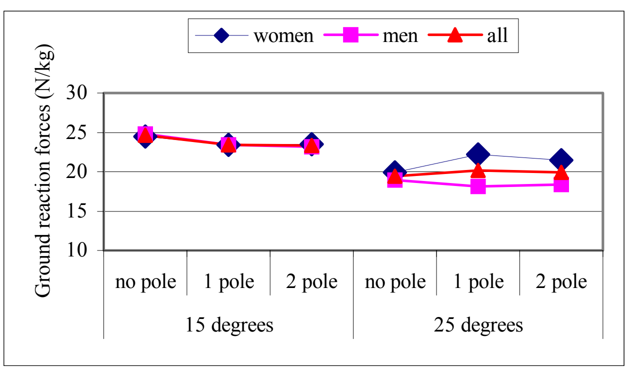

Figure 1. Peak GRFs for men and women at two gradients.

Specifically, GRFs overall were greater than in previously reported studies (Abendroth-Smith & Bohne, 2001; Knight & Caldwell, 2000; Schwameder et al., 1999; Willson et al., 2001). In addition, the normalized forces were less at the steeper gradient for all conditions of pole use. Braking forces were noted to be less than in previous studies (Figure 2). It is unclear whether these experienced hikers exhibited greater velocities or hiked with greater determination, as if they were hiking a mountain trail.

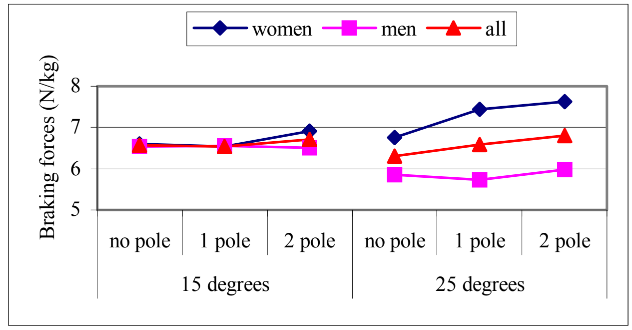

Figure 2. Peak braking forces at 15 and 25 degree gradients.

A trend was noted for decreasing GRFs at the lower gradient with the addition of one and two poles, although individual variation was great. Similar to previous reported work (Abendroth-Smith & Bohne, 2001), the women demonstrated higher forces with pole use than without, at least for the steeper gradient, with the forces at their greatest for the single pole use. Men, overall, demonstrated the lowest forces with the single pole use at the steeper gradient. No conditions were statistically significant for the braking forces. Women demonstrated greater braking forces at both grades with the dual pole use, while men maintained a similar braking pattern irrespective of pole condition.

SUMMARY

Individual variation in GRF and BF was high in single vs. dual pole use among the participants. Overall, men preferred the single hiking pole, and women, the dual poles, especially at the steeper gradient. Strategies behind pole use as a possible benefit, appear to vary as well. While some participants were able to reduce forces with the use of one or two poles, others demonstrated an increase in forces. The mechanisms behind the strategies are currently unknown, but examining muscle use in conjunction with force output may provide some answers. Lastly, symmetry needs to be examined, especially with the single pole use, to see if any benefits are applicable to both sides of the body.

REFERENCES

Abendroth-Smith, J., & Bohne, M. (2001). *Proceedings, 25th ASB Meeting*. San Diego. pp. 443-444.

Knight, C., & Caldwell, G. (2000). *Med Sci Sport Exer.* **32**(12). 2093-2101.

Schwameder, H., et al. (1999). Abstracts, XVIIth ISB Congress. Calgary. pp. 257.

Willson, J., et al. (2001). *Med Sci Sport Exer.* **33**(1). 142-147.

QUADRICEPS WEAKNESS CAUSES AN INCREASE IN THE PEAK ADDUCTOR MOMENT DURING GAIT

[1]Mary A. Pflum, [1]Michael R. Torry, [2]Peter Millett, [1]Michael J. Decker, [1]J.R. Steadman
[1]Steadman♦Hawkins Sports Medicine Foundation, Vail, CO, mike.torry@shsmf.org
[2]Department of Orthopedics, Harvard University School of Medicine, Boston, MA

INTRODUCTION

Many knee pathologies are associated with quadriceps muscular inhibition and weakness, and knee osteoarthritis (OA) has been shown to be a long term outcome of such neuromuscular deficiencies (Brandt et al., 1999; Slemenda C., et al., 1997). As reviewed by Suter and Herzog (2000), there is considerable support for the role of muscular inhibition and weakness as a factor in the initiation and progression of knee OA. The difficulty in directly assessing the role muscle weakness may have on knee joint function and its relationship to in vivo knee load stems from the inability of researchers to utilize a repeated measures study design where muscular weakness can be induced and removed (safely) and the effects of muscular weakness evaluated in an otherwise healthy population. Torry et al. (2000) has shown that experimentally induced intra-articular knee joint effusion can reduce quadriceps activation during gait. The purpose of this study was to determine whether muscular weakness of the quadriceps of the human knee joint can increase the magnitude of the adductor moment during the stance phase of the gait cycle.

METHODS

A modified Helen Hayes marker set (Kadaba et al., 1990) and a 120 Hz five camera Motion Analysis system were used to record the 3D kinematic and kinetic gait profiles of 7 healthy subjects (22.4±3.2 yrs; 1.84±0.5 meters, 85.9.8±13.0 kg) prior to and after infusion of 20-cm^3 of 0.9% saline into the intra-articular knee joint capsule. Quadriceps weakness due to the infusion was confirmed by testing isometric strength via a knee extension exercise (knee position = 30 degrees) utilizing a Cybex dynamometer. After isometric knee extensor torque was recorded, the subject immediately performed the post-effusion analysis, walking at similar speeds for both pre- and post-effusion conditions. Three trials of pre- and post-effusion gait data were collected, filtered (5 Hz), and processed to yield select GRF variables, knee kinematics and the adductor moment using previously described methodology (Sharma et al., 1998). Differences between test conditions were compared with a one-way repeated measures ANOVA (alpha = 0.10).

RESULTS AND DISCUSSION

The 20-cm^3 infusion caused a mean decrease in isometric knee extensor peak torque of 10.4 ± 4.1%. After quadriceps weakness was confirmed, the subjects walked with a more flexed knee ($p<0.01$) and reduced stance time ($p=0.02$). The peak magnitude of the vertical GRF increased ($p=0.02$), but the loading rate of this force did not change ($p=0.50$). The peak adductor moment (Figure 1) increased ($p=0.01$). However, the impulse of adductor moment and the time to the peak adductor moment did not change between conditions ($p=0.50$ and $p=0.23$, respectively).

These results suggest that 20-cm^3 of effusion can cause a 5-15% reduction in isometric peak torque output of the quadriceps muscles. An apparent effect of this quadriceps weakness was a significant increase in the peak adductor moment during gait. Since this moment has been reported to be indicative of medial joint loading (Sharma et al, 1998), muscular weakness of the quadriceps may dispose individuals to higher loads and degenerative changes. These results may also help explain why conservative treatments such as quadriceps strength training may improve functional capacity and reduce pain in osteoarthritic individuals.

SUMMARY

Because the individuals in this study were healthy, the results cannot be attributed to any rival or adaptive factors (injury or surgery) to produce these outcomes. Thus, based on these preliminary results, quadriceps weakness can be considered an independent risk factor for increased adductor during gait. From these data, we speculate that muscular weakness may be a significant risk factor in the initiation and progression of knee joint OA.

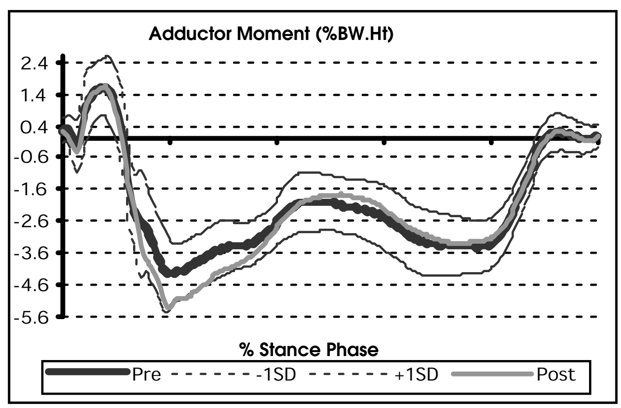

Figure 1: Time series plot of knee adductor moment pre and post-effusion. Negative values = adductor while positive values = abductor moments; Black = pre-effusion, gray = post-effusion conditions.

REFERENCES

Brandt K.D. et al., (1999) *J Rheumatol*., **26**:2431-2437.
Slemenda C., et al. (1997) *Ann. Intern. Med*., **127**:97-104.
Suter E., Herzog W., (2000) *Exerc. Sp. Sci. Rev.*, **28**:15-18.
Torry M.R. et al., (2000) *Clin. Biomech.,* **15**:147-159.
Kadaba M.P., et al., (1990) *J. Orthop. Res*., **8**:383-392.
Sharma L., et al. (1998) *Arth. & Rheum*., **41**:1233-1240.

LIGAMENT AUTOGRAFT CELLS DO NOT DIE BY APOPTOSIS

Kate Leatherbarrow, Ian Lo, Linda Marchuk, David Hart and Cyril Frank
McCaig Centre For Joint Injury and Arthritis Research, Calgary, Alberta, Canada
cfrank@ucalgary.ca

INTRODUCTION

Following reconstruction, tendon grafts undergo a modification process involving cell death, revascularization and repopulation of the graft with cells of extrinsic origin, and remodeling (Amiel and Kuiper 1990). Because cells are responsible for maintenance and production of the extracellular matrix, cell death may be in part responsible for grafts being replaced by scar-like tissue, resulting in inferior mechanical properties (Spindler et al. 1996). The purpose of this study was to characterize changes in cellularity of and early ligament autograft and determine if any cells undergo apoptosis.

METHODS

Thirteen New Zealand White rabbits were used. The rabbit MCL autograft was used in this study because it represents an idealized ligament reconstruction, being fresh, extraarticular and anatomical (Sabiston et al. 1990). In the right leg of each experimental animal, the femur-MCL-tibia graft was surgically removed, rinsed in saline, and orthotopically reinserted in the harvest site (Sabiston et al. 1990). Two animals each were sacrificed at time points 4,7,10,14 and 21 days post operatively, as well as 3 normal controls. 6μm paraffin sections were analyzed for *in situ* DNA fragmentation, indicating apoptosis, using the TUNEL assay (Gavrieli et al. 1992) (ApopTag kit, Intergen Co., NY). Nuclei were counterstained with DAPI (Vectashield, Vector Laboratories, CA) and slides were viewed by fluorescence microscopy. Positive controls showed 100% positive staining.

RESULTS AND DISCUSSION

Few apopotic cells were observed in the normal MCL (Fig. 1A,B). In the 4 day graft, cellularity was similar to the normal ligament with few apoptotic cells (Fig. 1C,D). After 7 days, large acellular areas were observed (Fig. 1E,F), and after 10 days, new cells began to infiltrate the graft. By 21 days, the grafts were repopulated with round cells and were becoming revascularized (Fig. 1G). Apoptosis was observed these repopulating cells as well as in the infiltrating blood vessels (Fig. 1H).

These results suggest that although a dramatic loss of cellularity took place in these grafts, this was apparently not due to apoptotic mechanisms. However, new cells infiltrating the MCL did demonstrate apoptosis. Determining which subset of the infiltrating cells die by apoptosis and which survive to form the mature graft may lead to a better understanding of the mechanical deficiencies of the remodeled graft (Sabiston 1990), and therapies to improve the quality of ligament reconstructions.

Figure 1: TUNEL assay for apoptosis

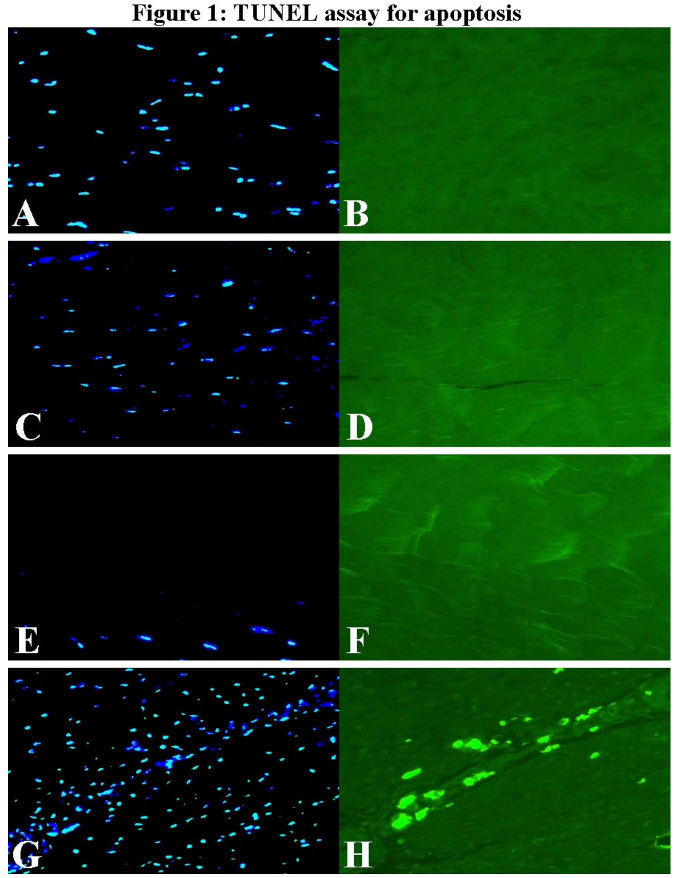

Figure 1: Normal MCL (A,B) and MCL autografts at 4 (C,D), 7 (E,F) and 21 days (G,H) post-surgery. A,C,E,G are DAPI nuclear counterstained and B,D,F,H are corresponding FITC labeled images for apoptotic cells (Magnification = 100x).

SUMMARY

This study confirms that the early loss of cellularity in fresh rabbit MCL autografts is not due to apoptosis, but that cells repopulating the graft during healing do exhibit apoptotic activity. We speculate that this will be true of other dense connective tissue grafts as well. Further understanding of the biologic processes following graft reconstruction may lead to novel therapeutic interventions, improving the mechanical integrity of all mature grafts.

REFERENCES

Amiel, D., Kuiper, S., (1990). In: *Knee Ligaments: Structure, Function, Injury, and Repair*. Raven Press.
Gavrieli, Y. et al. (1992). *J. Cell Biol.*, **119**, 493-501
Sabiston, P. (1990). *J. Orthop. Res.*, **8**, 35-45
Spindler, K.P. et al. (1996). *J. Orthop. Res.*, **14**, 384-9.

CYCLIC HYDROSTATIC PRESSURE INCREASES BOTH MMP-1 AND MMP-3 mRNA LEVELS, IN MG-63 OSTEOBLAST-LIKE CELLS UNDER SERUM FREE CONDITIONS.

Vitomir Tasevski, Jovina M. Sorbetti, Nigel G. Shrive and David A. Hart.
McCaig Centre for Joint Injury and Arthritis Research, Faculty of Medicine,
University of Calgary, Alberta, Canada. vtasevsk@ucalgary.ca

INTRODUCTION

The skeleton is exposed to mechanical forces of varying types and degrees. Individual cells respond to these biomechanical stimuli in different ways. The MG-63 osteosarcoma cell line is a commonly used model of human osteoblasts, producing both osteocalcin and bone specific alkaline phosphatase (Lajeunesse, D. et al). The effect of cyclic hydrostatic pressure (HP) on DNA, RNA and specific mRNA levels for both Matrix Metalloproteinase-1 and 3 (MMP-1, MMP-3) was investigated to determine whether HP alters overall osteoblast metabolism and viability, or whether it affects the expression of specific genes involved in bone remodeling.

METHODS

Cells were routinely maintained in DMEM F-12, containing 10% Fetal Calf Serum (FCS). Cells were seeded into NUNC 6-well plates at 2 X 10^5 cells per well, grown for 2 days in complete media, intensively washed, and maintained in serum free medium, for 20 hours. They were then transferred to a purpose built pressure chamber and subjected, at 37^{o}C, to 30 cycles of cyclic HP for one minute (0-0.8 MPa) followed by 14 minutes at atmospheric pressure (total time = 4 hours). Control cells were maintained in either serum free or complete growth medium, at 37^{o}C, for 24 hours. DNA was solubilised with DNAzol and quantified using absorbance measurement (260 nm). RNA was extracted using Trizol and a QIAGEN RNeasy kit, quantified using SYBRgreen fluorscence measurement and reverse transcribed (QIAGEN Omniscript). Polymerase chain reaction (PCR) was performed on 30 ng of cDNA, with primers directed against human Glyceraldehyde-3-phosphate dehydrogenase GAPDH, MMP-1 and MMP-3. PCR product separated on 2% agarose gels and visualised with ethidium bromide. RFLP Scanalytics software was used to calculate intergrated density values for the genes in question. An unpaired t-test with unequal variances was used in the statistical evaluation.

RESULTS AND DISCUSSION

When MG-63 cells were deprived of FCS for a period of 24 hours the quantity of both DNA and RNA measured was significantly reduced ($p < 0.001$) compared to those cells maintained in complete growth media. There was, however, no significant change in DNA/RNA ratio. When MG-63 cells were subjected to cyclic HP for the last 4 hours of a 24 hour serum free incubation, the quantity of both DNA and RNA as well as DNA/RNA ratio was unchanged compared to serum free control cells (Table 1).

Condition.	DNAµg/well	RNAµg/well	DNA/RNA Ratio
10% FCS	28.5 ± 9.12	11.3 ± 0.60	2.46
Serum free	14.6 ± 2.36	4.85 ± 1.32	3.01
Serum free (HP)	17.1 ± 2.26	5.29 ± 2.36	3.23

Table 1. Quantity of DNA (µg), RNA (µg), and DNA/RNA ratio. Data expressed as Mean ± 2 SD per well (n=3).

Detected mRNA for GAPDH, MMP-1 and MMP-3 in complete growth media was designated to be 100%. Serum free conditions (24 hours), resulted in a significant decrease ($p < 0.001$) of mRNA for MMP-1 and MMP-3. Cyclic HP for the last four hours of the 24 hour serum free incubation, significantly increased ($p < 0.001$) mRNA for both MMP-1 and MMP-3, with no change seen for GAPDH (Figure 1). The percentage increase was similar for MMP-1 and MMP-3. No change in the expression of transcription factors Cbfa1, c-fos or c-jun was detected under these conditions (data not shown). Whether specific sites within the promotor regions encoding MMP-1 and MMP-3 are sensitive to HP, requires further investigation.

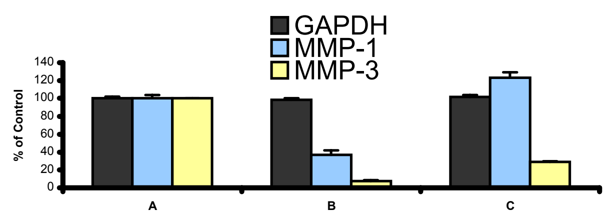

Figure 1. mRNA (Mean ± SEM) for GAPDH, MMP-1 and MMP-3 in **(A)** 10% FCS medium, **(B)** Serum free medium and **(C)** Serum free medium under hydrostatic pressure (n=6).

SUMMARY

The data indicate that specific mRNA expression of MMP-1 and MMP-3, in MG-63 cells, is increased following exposure to intermittent HP. DNA and RNA as well as mRNA levels for GAPDH, however, remained constant. These results are consistent with the proposal that *in vivo* mechanical loading can profoundly effect osteoblast gene expression and bone remodeling.

REFERENCES

Lajeunesse, D. et al (1990). J.Bone Miner. Res., **5** , 915-922.

BONE-MULCH-SCREW/WASHER-LOCH FIXATION OF DOUBLED FLEXOR TENDON GRAFT IN ANTERIOR CRUCIATE LIGAMENT RECONSTRUCTION - BIOMECANICAL EVALUATION ON THE EFFECT OF INITIAL GRAFT TENSION USING CYCLIC ELONGATION -

Toshiharu Kudoh[2] , Harukazu Tohyama[1] , Nobuto Kitamura[1] , Yoshimitsu Aoki [2] , Akio Minami [2] , Kazunori Yasuda [1]
[1]Department of Medical Bioengineering & Sports Medicine and [2] Department of Orthopaedic Surgery,
Hokkaido University School of Medicine, Sapporo, Japan, tohyama@med.hokudai.ac.jp

INTRODUCTION

The doubled hamstring tendon (HT) graft has been widely used in anterior cruciate ligament (ACL) reconstruction. Several investigators, however, have reported that this graft fixed with sutures has some disadvantages compared to the BTB graft. One of them is that the stiffness of the femur-graft-tibia (FGT) complex with the HT is lower (Yamanaka et al.). To increase the stiffness of the FGT complex with the HT, a new fixation procedure with the Bone-Mulch-Screw/WasherLoc (BMSW) system has recently been developed, and the biomechanical properties immediately after surgery was evaluated by To et al. However, biomechanical behaviors of the FGT complex reconstructed using this system during and after cyclic loading have not been clarified. In order to understand these biomechanical behaviors, Numazaki et al. showed the importance of initial graft tension as a mechanical condition. The purpose of this study is to carify the effect of initial graft tension on biomechanical behaviors of the FGT complex reconstructed with the doubled flexor tendon (FT) graft and the BMSW system, during and after cyclic elongation.

METHODS

Based on our previous study (Yamanaka et al.), a porcine ACL reconstruction model was used in this study. In this model, a pair of digital FT was trimmed so that their cross-sectional area became 7 and 14 mm^2, respectively. Twenty-one porcine knees were used. In each knee, ACL reconstruction was performed with the doubled FT graft, which was fixed using the BMSW system (Arthrotek, Naples, FL). Then, the FGT specimens were randomly divided into 3 groups (n=7 in each group). For the 3 groups, a tensile load of 20 N, 80 N, and 140 N, respectively, was applied to the graft for 2 minutes as an initial graft tension. Then, cyclic elongation of 2 mm was applied 5000 times to the FGT complex at 0.2 Hz. Finally, each FGT specimen underwent the tensile failure test at a crosshead speed of 50 mm/min. Statistical comparisons were made using a one-way ANOVA and Fischer PLSD tests.

RESULTS

(1) The peak load values at the first cycle were significantly different among the 3 groups (Fig. 1). The peak load rapidly decreased during the first 1000 cycles in each group. At the 5000th cycle, we found a significant difference in the peak load between the 20-N and 80-N groups, while there were no significant differences between the 80-N and 140-N groups. (2) After cyclic elongation, the initial stiffness (the slope in the toe-region of the load-displacement curve) of the FGT complex in the 20-N group was significantly lower than that in the 80-N and 140-N groups, while there were no significant differences between the latter two groups (Fig. 2). The magnitude of the initial graft tension did not significantly affect the linear stiffness or the ultimate failure load of the FGT complex (Fig. 2).

DISCUSSION

The present study demonstrated, first, that the cyclic elongation significantly affect biomechanical behaviors of the FGT complex reconstructed using the HT and the BMSW system under each initial tension. Secondly, an increase of initial graft tension from 20 N to 80 N significantly increased the peak load at the 5000th cycle and the initial stiffness of the FGT complex after cyclic elongation. However, an increase of initial tension from 80 N to 140 N did not significantly affect any mechanical parameters after cyclic elongation. Therefore, the increase of initial tension beyond 80 N has no biomechanical benefits for ACL reconstruction using this system.

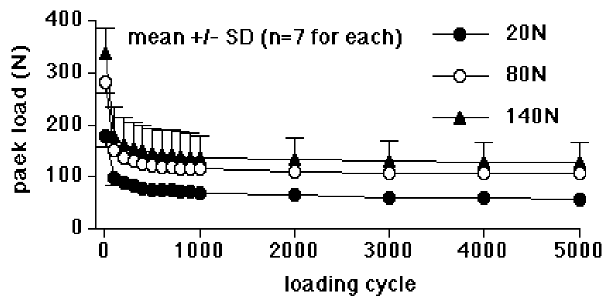

Figure 1 The peak load of the graft during cyclic loading.

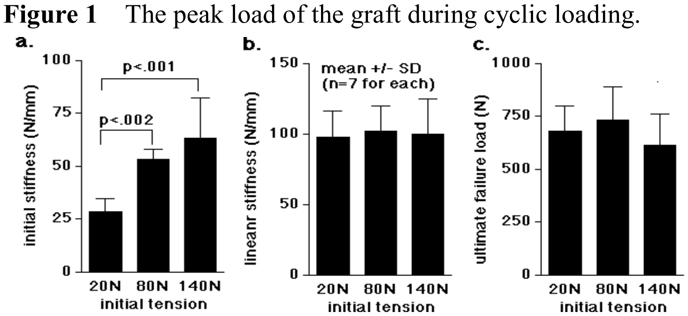

Figure 2 The initial stiffness (a), the linear stiffness (b), and the ultimate failure load (c) of the FGT complex.

REFERENCES

Yamanaka M., et al (1999). Am. J. Sports Med., **27,** 772-777.
To, J.T., et al (1999). Arthroscopy, **15,** 379-387.
Numazaki , H. et al (in press). Am. J. Sports Med.

ACKNOWLEDGEMENTS

The Bone-Mulch-Screw/WasherLoc system was provided by Arthrotek.

BIOLOGICAL AND BIOMECHANICAL EVALUATIONS ON *IN VITRO* INFILTRATIVE CHARACTERISTICS OF FIBROBLASTS REPOPULATING IN THE NECROTIZED PATELLAR TENDON

Yasunari Ikema[1, 3], Harukazu Tohyama[1], Hideki Nakamura[2], Fuminori Kanaya[3], Kazunori Yasuda[1]
[1]Department of Medical Bioengineering & Sports Medicine and [2]Center Research Institute, Hokkaido University School of Medicine, Sapporo, Japan, tohyama@med.hokudai.ac.jp
[3]Depatment of Orthopaedics Surgery, Ryukyu University School of Medicine, Okinawa, Japan.

INTRODUCTION

It is necessary to clarify functional characteristics of various fibroblasts in order to make progression in tissue engineering for the tendon and ligament tissues. Recent studies have shown that fibroblasts repopulating in the skin wound are phenotypically distinct from normal dermal fibroblasts (Schaffer et al.). Few studies, however, have been conducted to clarify the difference in functional characteristics between the fibroblasts repopulating in the necrotized tendon, which are commonly observed in the tendon autograft, and the fibroblasts that exist in the normal tendon. The purposes of this *in vitro* study were: 1) to compare infiltrative characteristics of the repopulating fibroblast (RF) and the normal fibroblast (NF) derived from the patellar tendon (PT), and 2) to compare the effects of the fibroblast infiltration on mechanical properties of the PT matrix between the RFs and the NFs.

METHODS

A total of 36 skeletally mature rabbits were used in this study. Isolation of fibroblasts: In 18 animals, the right PT was frozen *in situ* with liquid nitrogen to kill intrinsic fibroblasts of the tendon (Ohno et al). Subsequently, only the RFs repopulated in the right PT, and only the NFs existed in the left PT in each animal at 6 weeks. Each tendon was harvested and incubated in DMEM with 10% FBS for 2 weeks. Thus, the RFs and the NFs were separately obtained from these explants. Cells at the first passage were used for all experiments. In vitro infiltration into the matrix: The cultured RFs and NFs were seeded into collagen gel so that the concentration became $5x10^6$ cells/ml. The bilateral PTs were harvested from the remaining 18 rabbits, and underwent the *in vitro* freeze-thaw treatment using liquid nitrogen. Thus, we prepared a total of 36 acellular PTs. Then, each PT was sharply divided into 3 thin PT matrix specimens (1x2x15mm) along with the long axis. The 3 specimens were implanted into the 3 types of collagen gel clot, in which the RFs, NFs, and no cells (Control) were seeded, respectively. Evaluation: Twelve (36 specimens) out of the 36 PTs were evaluated at 1, 3, and 6 weeks after implantation, respectively. At each period, 6 (18 specimens) out of the 12 PTs were analyzed using a confocal laser microscope (CLM), and we counted the total number of cells scattering in a unit volume (750 x 500 x 25 μm). The remaining 6 PTs (18 specimens) were used for tensile testing to determine the mechanical properties. The strain was measured with a video dimension analyzer.

RESULTS

(1) Infiltration of the RFs was limited only in the superficial portion of the specimen at 6 weeks, while the NFs infiltrated into the deep portion at the same period (Fig. 1). Cells were not observed in the control specimens. The total number of the NFs significantly increased over time, but that of the RFs did not significantly change (Fig. 2-a). The total number of the RFs was significantly less than that of the NFs at each period. (2) Tensile testing showed that there were no significant differences in the elastic modulus among the specimens involving the RFs, those involving the NFs, and those involving no cells (Fig. 2-b).

DISCUSSION

This study demonstrated that the *in vitro* infiltrative ability of the RF into the tendon matrix is significantly lower than that of the NF. However, infiltration of the RFs and the NFs did not significantly affect the elastic modulus of the tendon matrix. Our previous *in vivo* study showed that the RFs infiltrated into the deep portion of the *in situ* frozen-thawed PT at 6 weeks, and that the infiltration significantly deteriorated the mechanical properties of the tendon matrix (Tohyama et al). These drastic differences between the *in vitro* and *in vivo* studies imply that some unknown factors that exist only in the *in vivo* condition may affect infiltrative characteristics and functions of the RF.

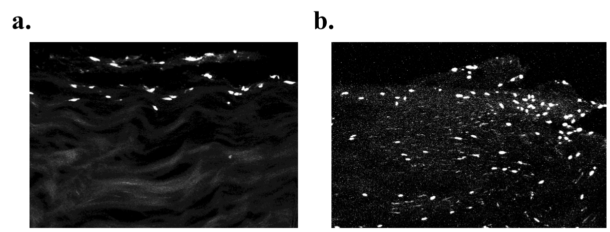

Figure 1: Three-dimensional distribution of RFs (a) and NFs (b) observed using a CLM with Propidium Iodide at 6 weeks.

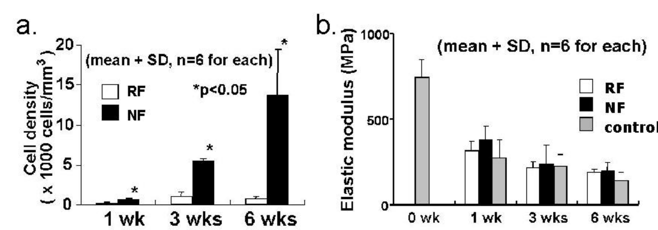

Figure 2: Quantitative analysis of cell infiltration (a) and the elastic modulus of the PT matrix with cell infiltration (b).

REFERENCES

Schaffer, R. et al (1999). Int. J. Biochem. Cell Biol., **29,** 231-239.
Ohno, K. et al (1993). J. Orthop. Res., **11,** 592-602.
Tohyama, H. et al (2000). J. Biomech. Eng., **122,** 594-599.

THE EFFECT OF OVERLOADING ON THE PATELLAR TENDON THAT UNDERWENT SEGMENTAL RESECTION OF ITS CENTRAL ONE-THIRD PORTION - BIOMECHANICAL EVALUATION OF THE REGENERATED TISSUE AND THE RESIDUAL TENDON -

Harukazu Tohyama[1] , Kazunori Yasuda[1] , Yoshiaki Kitamura[2], Ei Yamamoto[3], Kozaburo Hayashi[2]
[1]Department of Medical Bioengineering & Sports Medicine, Hokkaido University School of Medicine, Sapporo, Japan,
[2] Biomechanics Laboratory, Graduate School of Engineering Science, Osaka University, Toyonaka, Japan, and
[3]Department of Mechanical Engineering, School of Biology-Oriented Science and Technology, Kinki University, Wakayama, Japan
tohyama@med.hokudai.ac.jp

INTRODUCTION

The central one-third portion of the patellar tendon (PT) is resected to obtain a substitute for ligament reconstruction. Many studies have shown that the space made by the resection is filled with a regenerated fibrous tissue. However, much remains unknown on biomechanics of the PT that underwent the segmental resection. In previous biomechanical studies on this issue, the regenerated tissue and the residual tendon were not distinguished. Our recent study using a rabbit model, however, has clarified that the mechanical properties of the residual tendon significantly deteriorate at 6 weeks, and that the properties of the regenerated tissue remarkably improve over time, reaching the properties similar to the residual tendon (Tohyama et al. 2001). Then, we should ask what effects mechanical environments give to the regenerated tissue and the residual tendon. The purpose of this study is to clarify the effect of overloading applied to the PT that underwent the segmental resection of its central one-third portion on the mechanical properties of the regenerative tissue and the residual tendon.

METHODS

A total of 32 skeletally mature female rabbits (3.0±1.0 kg) were used. In each animal, we surgically made a full-thick defect at the central portion of the right PT (3-mm wide and 15-mm long). In the left PT, we performed the *sham* operation. After this treatment, the animals were divided into two groups (n=16, each), and they were allowed unrestricted activities in their cage. At 3 weeks after the first operation, the medial portion of the right PT was additionally resected in Group 1 in order to overload the remaining tendon portion and the regenerated tissue. In Group 2, the sham surgery was performed at the 3-week period. Again, they were allowed unrestricted activities in their cage. At 6 and 12 weeks after the first operation, 8 rabbits were sacrificed for mechanical testing. Before sacrifice, the blood-flow in the regenerated tissue was measured with a laser Doppler flowmeter. In each rabbit, we longitudinally divided the patella-tendon-tibia complex (PTTC) specimen into 2 portions, the regenerated tissue and the residual (lateral) tendon. For each PTTC specimen, a tensile test was performed with a tensile tester. Strain was measured using a video dimension analyzer.

RESULTS

In Group 1, the blood flow was 225±34% and 213±47% of the sham-operated tendon at 6 and 12 weeks, respectively, while it was 194±106% and 140±47%, respectively, in Group 2. The ANOVA showed that blood flow was significantly greater in Group 1 than in Group 2 (p=0.039), while there were no significant differences between the periods. Concerning the tensile strength and the modulus of the residual tendon, these parameters of Group 1 were significantly lower than those of Group 2 (Fig. 1). Regarding these parameters of the regenerative tissue, there were no significant differences between Groups 1 and 2 (Fig. 2).

DISCUSSION

This study demonstrated, first, that overloading significantly deteriorated the mechanical properties of the residual tendon. This result is supported by our previous study on the effect of overloading on the PT (Yamamoto et al. 1999). Secondly, the present study showed that overloading did not significantly affect the mechanical properties of the regenerated tissue. The results suggest that the responses to overloading are significantly different between the regenerated tissue and the residual tendon. The difference may be caused by functional differences of fibroblasts that exist in the regenerated tissue and the residual tendon. As to clinical relevance, excessive overloads should be avoided in the early phase after harvesting the central one-third portion of the PT for ligament reconstruction.

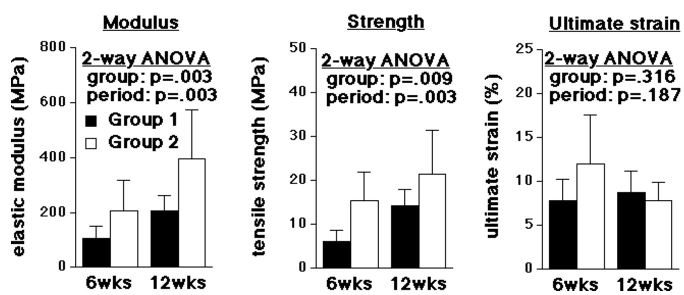

Figure 1 Mechanical properties of the residual tendon

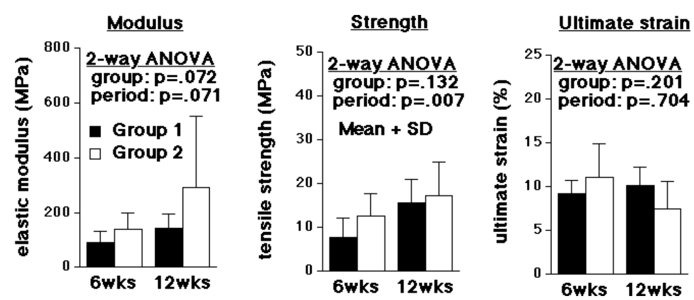

Figure 2 Mechanical properties of the regenerated tissue.

REFERENCES

Tohyama, H., et al (2001), Trans 4^{th} Combined ORS, 76.
Yamamoto, N., et al (1999), J. Biomech. Eng., **121**, 323-329.

BIOMECHANICAL ANALYSIS OF THE EFFECTS OF A POWER CLEAN PROGRAM ON THE FIRST STEP OF THE SPRINT START

Kyle Patterson, Estelle Abdala, Mitell Sison and Alan Hreljac
Biomechanics Laboratory, California State University, Sacramento, California
Communicating Author: kyle_patterson@hotmail.com

INTRODUCTION

The purpose of this study was to examine the effects of a power clean training program on biomechanical aspects of a sprint start out of the starting blocks for novice sprinters. If the effects of the power clean training program are significant, then coaches at the high school and college level could consider using a systematic power clean training program as a part of their strength and conditioning programs.

METHODS

The subjects used in this study were 10 active healthy novice male sprinters ages 20-25 (M=22.7 +/- 1.9 y). The participants were split into an experimental group and a control group, each with five subjects. Three days prior to and following the experimental treatment (six week power clean training program), kinematic and kinetic data were collected on all subjects performing the sprint start in the Biomechanics Lab at CSU Sacramento.

RESULTS AND DISCUSSION

Findings suggest that the power clean training program increases the vertical and propulsion ground reaction forces. In addition, the velocity of plantar flexion was increased. According to Young et al. (1995) increase in velocity and increase in GRF lead to a decrease in the propulsion phase of sprinting. This decrease in propulsion phase is needed to increase speed. Thus, the power clean training program could increase speed.

Figure 1: Maximal vertical force for both groups from pretest to posttest. The * represents significance increase from pretest to posttest.

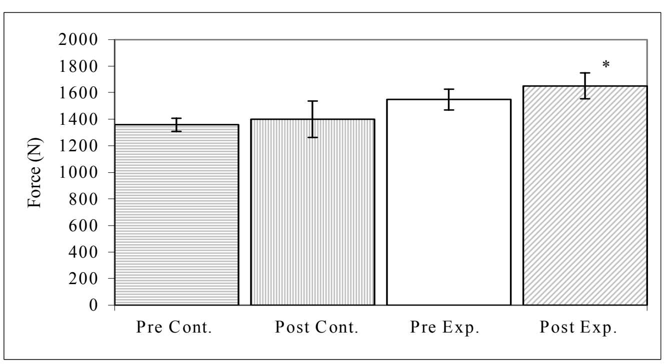

The experimental group showed a significant increase between pretest (683 +/- 47 N) and posttest (716 +/- 60 N) for the maximal propulsion force. Experimental group showed a significant increase between pretest (1548 +/- 78 N pretest vs. 1651 +/- 97 N posttest) and posttest maximal vertical force (Figure 1) while there were no differences between the pre- and posttests of the control group. This showed a relationship between GRF and leg strength. Young et al. (1995) established a positive relationship between leg strength and sprinting speed. Therefore, it can be suggested that the power clean training program would have a positive effect on sprinting speed.

SUMMARY

The power clean training program attributed to the increased ground reaction forces of the experimental group as demonstrated by the increase in the vertical force, which can be due to the development of the knee extensors and the plantar flexors.

More power generated by the legs would lead to an increase in ground reaction forces. Statements by Harman (1994) support Weyand et al. (2000) and this study by supporting the development of strength of sprinters and thereby increasing the ground reaction forces as found in this study. Takano (1992) stated that power cleans are important to the development of speed, which may be why the experimental group subjects significantly increased their plantar flexion velocity. Thus, a power clean training program could lead to an increase in speed.

Young et al. (1995) found that more leg strength is essential for increased GRF, which could lead to an increase in speed. This study demonstrates that a power clean training program could lead to increases in ground reaction forces during a sprint start. It is assumed that the training program increased the strength of the experimental group, but is not known because EMG and isokinetic testing were not performed.

REFERENCES

Harman, E. (1994). *National Strength and Conditioning Association Journal*, **16(2),** 59-65.
Takano, B. (1992). *National Strength and Conditioning Association Journal*, **14(1),** 68-71.
Weyand, P.G, et al. (2000). *Journal of Applied Physiology*, **89**, 1991-1999.
Young, W., McLean, B., & Ardagna, J. (1995). *Journal of Sports Medicine and Physical Fitness*, **35**, 13-19.

NUMERICAL STUDY ON THE FLOW CHARACTERISTICS IN A PARTIALLY OBSTRUCTED TUBE WITH THE COMPLETE BYPASS GRAFT

Tzu-Hsiang Ko
Department of Mechanical Engineering, Lunghwa University of Science and Technology, Taiwan, R.O.C
Associate Professor, thko@mail.lhu.edu.tw

INTRODUCTION

The coronary bypass surgery is usually operated on the patients with severe or moderate stenosis in their coronary arteries. The bypass graft is implanted on the obstructed host artery and induces blood to flow bypass the obstruction. In order to resolve the flow characteristics in the graft and host arteries, many investigators performed studies on the flow phenomena from the hemodynamic view points. In the earlier researches, the end-to-side anastomsis flow model was most frequently employed (Hofer et al., 1996; Ethier et al., 1998). In such a model, the host artery was assumed to be 100%-area severity stenosis, and the "end " was to simulate the completely obstructed wall while the "side" was to simulate the subsection of the bypass graft. Uniform or paraboloid velocity distributions were specified at the side inlet and only the flow fields in the subsections of the bypass and the host artery were analyzed. However, the bypass graft is usually with curvature. The flow entering the bypass graft will be influenced by the curvature and become complex flow patterns accompanied with secondary flow. Neither the uniform nor the paraboloid velocity distribution assumed at the bypass inlet is precisely correct. On the other hand, when the coronary bypass surgery is operated , the stenosis may not be exactly 100%-area severity in the host artery. Blood may still be possible to pass through the contracted region of the host artery as well as flow through the bypass graft. To implement more realistic situations, further investigations on the anastomotic flow with the complete bypass graft and the partially obstructed host artery should be worthwhile. The present paper investigates the flow characteristics in a model composed of the complete bypass graft and a 90%-area obstructed host tube.

METHODS

The geometry of the model is shown as Fig. 1. The flow is assumed as three dimensional, incompressible, laminar and steady. The continuity equation and the Naviar-Stokes equation are solved numerically by SIMPLEC scheme. The grid layout is also shown in Fig.1. Uniform velocity distributions are assumed at the inlet and the fully developed condition is assumed at the outlet.

RESULTS AND DISCUSSION

Fig. 2 shows the flow fields on the symmetric plane and three selected slices of the model. Some fluids flow through the contracted area with very high speed. The velocity can be as high as twice of inlet velocity. The calculated results show that only about 14% inlet mass flows through the contracted area of the host tube, and 86% inlet mass flows through the bypass graft. Four low velocity regions can be found on the flow fields. They distribute on the lower front region of the contracted area, the upper and lower regions downstream of the contracted area, and the entrance of the bypass graft. The recirculations which appear in the four low velocity regions are closely relevant to the blood flow rate. In the entrance region of the bypass, the larger velocity occurs at outer side of the bypass, and as the flow develops toward the downstream, the larger velocity flow transfers toward the inner side of the bypass. This result clearly comes of the curvature effect. The velocity fields shown on the slices A, B and C indicated the development of the secondary flow structures. These flow characteristics prove the assumptions of the uniform or paraboloid flow distribution at the bypass inlet which were made in the end-to-side model are not precisely correct

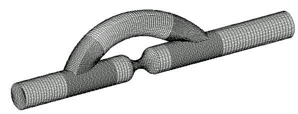

Fig. 1 The geometry and grid layout of the model

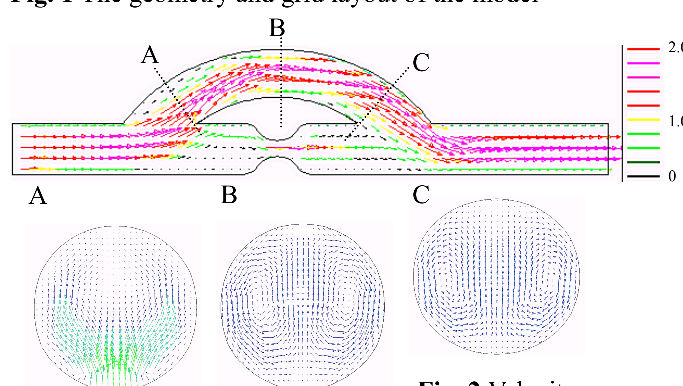

Fig. 2 Velocity distributions (Normalized by inlet velocity)

SUMMARY

The flow characteristics of the complete bypass graft and the partially obstructed host tube are investigated. The flow fields consists of one recirculation zone in the bypass graft and three recirculation zones in the host tube. The secondary flow structure appears in the bypass graft because of the curvature effect. This makes the velocity distribution in the bypass is neither uniform nor paraboloid which is usually assumed in the end-to-side model. The present study provides more realistic information of the flow fields.

REFERENCES

Hofer, M. et al. (1996). *J. Biomechanics*, **29**, 1297-1308
Ethier, C. R. et al. (1998). *J. Biomechanics*, **31**, 609-617

FLOW-INDUCED MORPHOLOGICAL CHANGE OF ENDOTHELIAL CELL AND SHEAR STRESS DISTRIBUTION ON THE SURFACE OF THE CELL

Shuichiro Fukushima[1], Hideki Fujioka[2], and Kazuo Tanishita[1]
[1]Institute of Biomedical Engineering, Keio University, Yokohama, Japan, fuku@tani.sd.keio.ac.jp
[2]Biomedical Engineering Department, University of Michigan, MI, USA

INTRODUCTION

Endothelial cells elongate and align due to flow exposure (Levesque and Nerem, 1985). Considering microscopic flow characteristics at individual cell level, which are defined by the cell surface geometry, the morphological change of the cells seems to be adaptive response (Barbee et al., 1995; Fukushima et al., 2001; Satcher et al., 1992; Yamaguchi et al., 2000). To address the mechanisms for the adaptive response, it is necessary to examine how the mechanical environment changes by the adaptation process. Therefore, we measured cell surface geometry during flow exposure, and determined shear stress distribution on the surface.

METHODS

Cultured bovine aortic endothelial cells were subjected to steady flow by using parallel-plate flow chamber. The flow induced macroscopic shear stress of 1.5 Pa on the cell surface when the surface was assumed to be flat. During the flow exposure, the same group of cells was tracked, and the surface geometry of the cells was measured by using confocal laser scanning microscopy (Fukushima et al., 2001).

Flow field near the measured cell surface was simulated by computational fluid dynamics (CFD). To simulate the conditions in the parallel-plate flow chamber, constant nominal shear rate was applied at inflow plane of computational domain so as to maintain a 1.5 Pa wall shear stress at bottom plane.

RESULTS AND DISCUSSION

At the beginning of the flow exposure, the shape of the cells in the confluent condition was polygonal without alignment. After 24 h, cell motility was changed, and the number of elongated cells was increased. The direction of migration was not necessarily the same as that of the macroscopic flow, but is always influenced by the surrounding cells. After 30 h, the number of cells aligned with the direction of the macroscopic flow. Mean height for the 13 cells (Fig. 1) was decreased after 30 h (24 h: 3.2±1.4 µm, 30 h: 3.2±1.5 µm, 36 h: 2.9±1.3 µm).

With such morphological change, mean shear stress for the 13 cells was decreased with time course (24 h: 1.91±0.57 Pa, 30 h: 1.81±0.59 Pa, 36 h: 1.78±0.61 Pa). However, there were some cells on which mean shear stress for each cell was increased, and morphological change of each cell was not always adaptive. The results show the importance of interaction with surrounding cells for the adaptive response as cell layer.

REFERENCES

Barbee, K.A. et al. (1995). *Am. J. Physiol.*, **268**, H1765-1772.
Fukushima, S. et al. (2001). *JSME Int. J. C*, **44**, 972-981.
Levesque, M.J., Nerem, R.M. (1985). *J. Biomech. Eng.*, **107**, 341-347.
Satcher, R.L. et al. (1992). *J. Biomech. Eng.*, **114**, 309-316.
Yamaguchi, T. et al. (2000). *J. Biomech.*, **33**, 115-126.

Figure 1: Wall shear stress distribution on cell surface. Solid line is contour of cell surface (interval: 1 µm). The label is given to the same cell. Arrow indicates macroscopic flow direction.

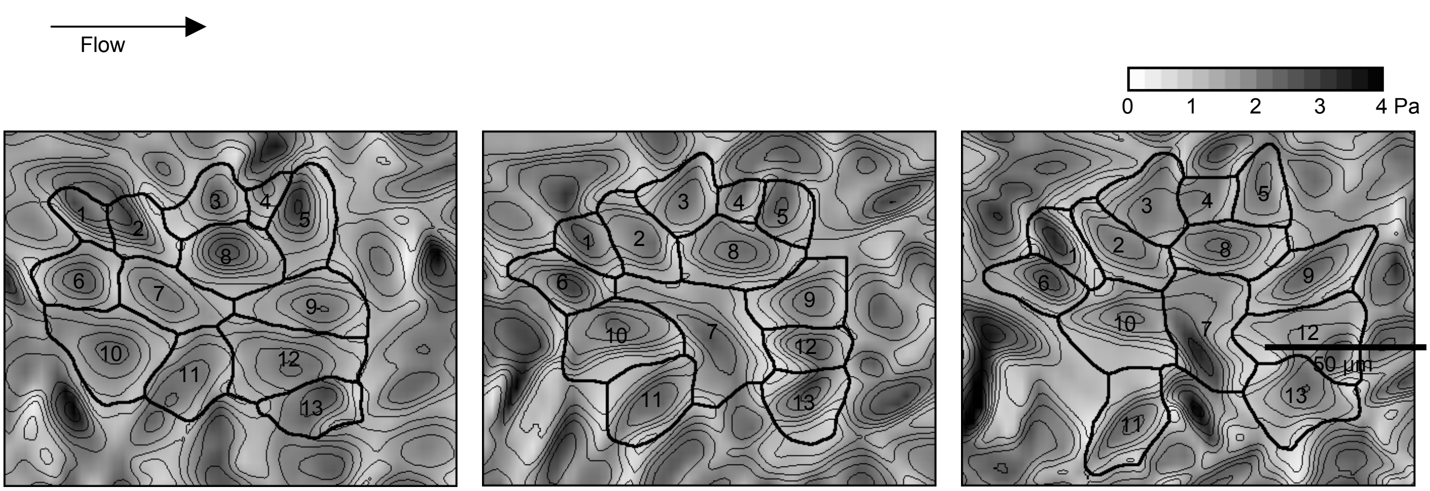

(a) 24 h (b) 30 h (c) 36 h

GAIT ANALYSIS AFTER TRIPLE ARTHRODESIS

WL. Wu[1] , YM. Cheng[2], PJ. Huang[2]
[1]Department of Physical Therapy, Foo-Yin Institute of Technology, Taiwan, sc100@mail.fy.edu.tw
[2]Department of Orthopedic Surgery, Kaohsiung Medical University, Taiwan

INTRODUCTION

Triple arthrodesis is a procedure that fuses the subtalar joint, talonavicular joint, calcaneocuboid joint. At the follow-up examination, Beischer et. al. have found the abnormal moment and power generation at the ankle and decreased angular range of motion in ankle and ipsilateral knee joints are associated with triple arthrodesis. It seems that triple arthrodesis may influence biomechanic mechanics of lower limbs. For more precisely evaluate the potential biomechanic mechanics, the goal of this proposal is to utilize gait analysis combined with foot pressure analysis to study movement disorders after triple arthrodesis.

METHODS

In total, 10 triple arthrodesis surgery cases were recruited for the experiment. The HIRES ExpertVision motion analysis system (Motion Analysis Corporation), an AMTI force platform (Advanced Medical Technology, Inc., Newton, MA) and Pedar foot pressure system (Novel gmbh, Germany) were used in this study. Twenty-one simplified point (Helen Hays) marker set for full body gait analysis was used in OrthoTrak analysis. Joint kinematics and kinetics were computed. In addition, foot contact patterns were recorded using insole pressure system. The database of age-matched normal subjects built in OrthoTrak package was obtained for comparison. Repeated measures analysis of variance was used to compare the differences in the kinematic and kinetic parameters. Differences were considered significant when the P value was less than 0.05.

RESULTS AND DISCUSSION

A clinically apparent valgus alignment of the heel was found in all patients. In temporal/spatial parameters, significant difference between normal subjects and surgical patients were identified. A significantly longer (12%) support time, an increased (11%) step length and a reduced walking velocity (21%) were observed on the patients' feet ($P < 0.05$). We found there are significant differences between patient group and control group in the ankle dorsi/plantarflexion. On the other hand, there were not significant differences between sound side and affected side in surgical group The range of motion of the surgical group was significant less than the normal group in ankle dorsi/plantarflexion ($p<0.05$). On average, it was reduced by 9^o (50%) compared with the normal group. From the result of passive range of motion examination, we supposed that loss of bilateral ankle range of motion in sagittal plane was not a consequence of a mechanical block to this motion. The passive range of motion was significant larger than the active range of motion in ankle dorsi/plantarflexion. The motions of the ankle joint in coronal plane (Pro/supination) are shown in Figure 1. It was observed that there are high variations in affected side of the foot, it may present the non-homogeneity in triple arthrodesis gait patterns. It meant that there are more than one pattern existed in the pathological pro/supination movements. During the latter two thirds of the stance phase of gait, the subtalar joint normally inverts (supinated). This locks the transverse tarsal joint and creates a rigid forefoot. For the "Supinated group" patients with triple arthrodesis, motion of the ankle joint in the coronal plane indicated an increase in inversion (supination) before toe-off, progressing to a relatively neutral or slightly everted position shortly before heel strike. Contrarily, motion of the ankle joint in the coronal plane for "Pronated group" patients increased in varus (pronation) direction through whole gait cycle. At toe-off phase, the subtalar joint normally reaches peak invertion. These motions create an effective lever arm through which the tricepts surae can exert its action. It explained why the abnormal posture of the arthrodesed foot diminished peak of gastrocnemius-soleus power generation. Our studies also have confirmed that the group of hindfoot supination often results in symptomatic force concentrations beneath the medial metatarsals, whereas hindfoot pronation produces increased lateral metatarsal weightbearing. It is because that the forefoot rotates relative to the hindfoot for maintaining universal metatarsal contact with the floor.

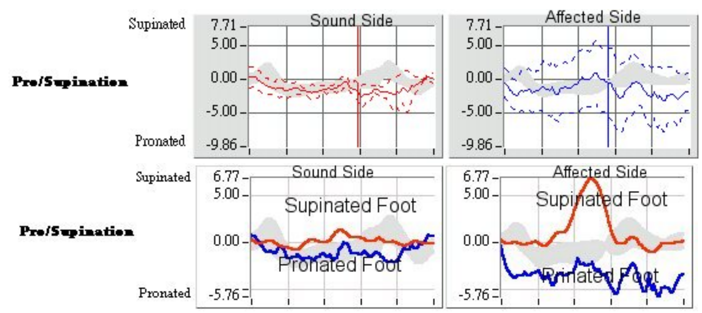

Figure 1: The angular motions of ankle joint in coronal plane. Upper layer: There are high variations in affected side; Lower layer: There are two patterns existed in the pathological pro/supination movements.

SUMMARY

Our results offer objective and quantifiable information to monitor the surgical effect through comparison of analytic and objective parameters.

REFERENCES

Beischer AD. et al (1999) *Foot & Ankle International*, **20(9)**, 545-53.

VALIDATION OF FINITE ELEMENT MODEL FOR PROSTHETIC SOCKET DESIGN

James CH Goh [1,2], Krishna P Baidya 1, Peter VS Lee [1,2,3]
[1] Department of Orthopaedic Surgery, National University of Singapore
[2] Division of Bioengineering, National University of Singapore
[3] Defense Medical Research Institute, Singapore

INTRODUCTION
CAD/CAM in prosthetics only offers controlled socket reproduction technique based on conventional method. Finite element (FE) method, when introduced to a CAD/CAM system, can provide quantitative feedback prior to socket manufacturing. The objective of this paper is to develop a FE model from geometry data acquired from a commercial CAD system, to optimise the modelling time and to validate the modelling technique using a test object.

METHOD
Cylindrical shaped test object was fabricated from viscous RTV silicon. The test object has a co-axial, cylindrical stainless steel mandrel. The test object and mandrel were scanned separately at 1mm layer thickness. An integration program (i-Link), developed in-house, reads CAD model data and parameter files containing load, boundary conditions and material properties in batch mode (Figure 1). It then automatically refines the CAD geometry, maps the parameter data on to the refined geometry and generates FE codes for optimized meshing in ANSYS.

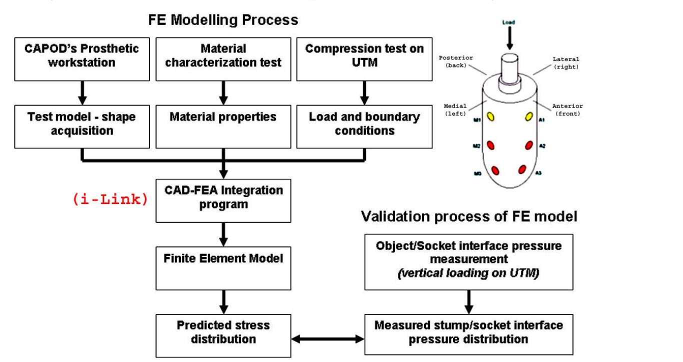

Figure 1: Schematic of the FE modeling and validation process

Effect of different volume layer thickness to describe the geometry was also checked.

The FE model consists of 8-noded hexahedral elements, with 13600 nodes and 10900 elements utilized for the model based on a 5mm volume layer thickness. The Silicon test object material properties was described as M-R hyper-elastic with C_{01} = -2.013e-3 and C_{10} = 2.782e-3Mpa. Standard properties (E=210GPa, ν=0.31) were used for the stainless steel mandrel. Vertical loading of 700N was introduced via the proximal section area of the mandrel. Fixed nodal boundary condition at the test object's surface was assumed.

The physical test object was mounted in the UTM machine (Instron-8874) and loaded vertically. Twelve specially constructed strain gauge type transducers distributed uniformly along the socket length in the 4-quadrant captured the pressure. Data were captured at peak load of 700N. Measured pressure values were compared with the FE predictions from models with different volume layer thickness.

RESULTS AND DISCUSSION
Table 1 shows that interface pressure patterns predicted by the FE model of the test object under vertical loading were similar to the measured patterns.

		Measured (kPa)	Predicted (kPa)	% difference
Anterior	proximal	45.95	45.89	-0.13
	middle	77.82	78.12	0.39
	distal	103.68	108.23	4.39
Posterior	proximal	44.21	45.97	3.98
	middle	80.79	79.56	-1.52
	distal	119.29	114.76	-3.80
Medial	proximal	46.17	43.12	-6.61
	middle	91.76	80.32	-12.47
	distal	104.14	110.45	6.06
Lateral	proximal	53.24	48.92	-8.11
	middle	79.71	80.74	1.29
	distal	114.54	112.82	-1.50

Table 1: Comparison of FE predicted and measured pressure (based on 5mm layer thickness model)

Figure 2 shows the comparison of prediction between models developed with two different volume layer thicknesses.

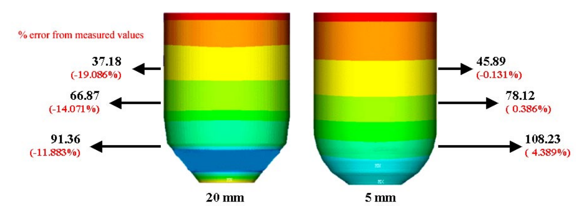

Figure 2: comparison of predicted values for different volume layer thickness (corresponding to front view)

A comparison between the different layer thickness models revealed that predictive ability improved with finer volume layer. However, the computational time increased significantly (Table 2), which may be a cause of concern when coupled with CASD system.

		Comparison with experimentally measured values				
		Over estimation		Under estimation		
Volume layer thickness	Computation time (min)	no. of sites	Max. (%)	no. of sites	Max. (%)	RMS of % difference
4mm	23	6	6.32	6	8.28	4.805
5mm	17	5	6.06	7	12.47	5.458
10mm	14	2	1.03	10	17.75	8.377
15mm	10	-	-	12	23.05	11.467
20mm	9	-	-	12	29.77	19.228

Table 2: Effect of layer thickness on predictive ability

A finite element model was successfully developed from direct CAD data using an integration program. The model was able to predict interface pressure with reasonable accuracy (<10% error). Hence, efficacy of the FE model generation technique from CAD data was demonstrated and can be further integrated with prosthetic CASD system.

BIOMECHANICS OF TRANSTIBIAL PTB AND PCAST PROSTHETIC SOCKETS

James CH Goh, Peter VS Lee, SY Chong, S Das De
Department of Orthopaedic Surgery, National University of Singapore, SINGAPORE

INTRODUCTION

Difficulties are faced by many prosthetists in consistently producing satisfactory socket fit. Some major causes arise from inadequate training and experience of the prosthetist in the patellar-tendon-bearing (PTB) socket technique. In 1965, Murdoch[1] introduced a pressure-casting concept where fluid was used to apply uniform pressure around the stump, which produced the Dundee socket. However, an indentation to the patella tendon was implemented. In 1968, Gardner[2] introduced a pneumatic pressure sleeve that wrapped the entire stump during cast taking. Kristinsson[3] used the same pressure casting concept by using air as a medium in the Icelandic Roll On Silicone Socket (ICEROSS) system. Rectifications were done by adding padding over the bony areas of the stump during the casting process in a non-weight bearing fashion i.e. not standing. The theory supporting these various attempts in pressure casting techniques is known as Pascal's principle of fluid dynamics. This concept of using hydrostatic pressure still raises many questions in the prosthetic field today. Using similar pressure casting technique, a pressure cast (PCast) system was developed. This system produces a socket without any rectifications. In this study, a comparison between the PCast and PTB sockets was done using stump/socket interface pressure.

METHODOLOGY

Five unilateral transtibial amputees volunteered for this study. Figure 1 shows the PCast setup. The PCast system requires the patient to place his stump in a pressure chamber. He was requested to stand in this normal standing position without any aid. Pressure was applied to the stump. A positive mould was then generated without any rectifications and the final socket fabricated using traditional lamination methods. PCast and PTB test sockets with 16 measurement sites each was made for each subject. The sites were basically openings made in the socket to allow pressure transducers to be mounted such that contact can be made with the stump. The pressure transducer assembly which includes a load cell manufactured by Entran International, USA was similar to that described in Lee et al[4]. The pressure transducers were connected to the VICON 370 3D motion analysis system in conjunction with 2 Kistler force platforms. Pressure and gait data were acquired simultaneously when the subjects were standing and walking at each subject's self-selected speed.

Figure 1: Subject with stump in PCAST tank.

RESULTS AND DISCUSSION

In general, pressure magnitudes were lower in the PCast socket than the PTB socket. Furthermore, the PCast socket exhibited less pressure concentration i.e high pressure at specific areas. This is expected, as the PCast socket had no rectifications done while the PTB socket made use of certain pressure tolerant
areas for weight bearing. From the pressure profiles, two main observations were made. The first group had higher pressure concentration at the distal end in the PCast socket or higher pressure concentration at the proximal brim in the PTB socket. The second group had similar pressure profile in both sockets especially at toe-off (refer to Figure 2).

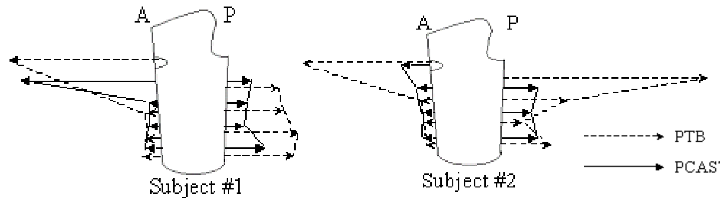

Figure 2: Anterior-posterior pressure profile of subject #1 exhibiting similar pressure profile (left) and subject #2 exhibiting high pressure profile at the proximal brim in the PTB socket (right) at toe-off.

The first group exhibited similar results to a study done by Convery et al[5] on one subject who exhibited a 'ring' of high pressure near the patellar tendon 'bar'. However, in the second group, the hypothesis to 'let nature determine the most realistic and achievable pressure distribution' may hold true; though reasons on why it does not occur in all subjects need more research. But one big advantage in this PCast technique is removing all manual dexterity and inter-prosthetist variances. While the PCast and PTB sockets belong to two different schools of thought, it is still difficult, at this time to conclude which is the best socket as there are constant dynamic forces at work in a socket during gait. There are still questions on the mechanical stability and internal dynamics of the limb, enclosed and acting in such an environment[3]. The best socket will be the one that suits a patient's activity level, stump condition and rehabilitation needs.

REFERENCES

1. Murdoch G (1965). The Dundee socket for below knee amputation. Prosthetic International, 3(4/5), 15-21.
2. Gardner H (1968). A pneumatic system for below-knee casting. Prosthetic International, 3 (4/5), 12-14
3. Kristinsson O (1992). Pressurised casting instruments. 7th World Congress ISPO, Chicago, 43.
4. Lee VSP, Spence WD, Solomonidis SE (1997). Stump/socket interface pressure as an aid to socket design in prostheses for trans-femoral amputees – a preliminary study. Engineering in Medicine. Vol 211, 167-180.
5. Convery P, Buis AWP (1999). Socket/stump interface dynamic pressure distributions recorded during the prosthetic stance phase of gait of a trans-tibial amputee wearing a hydrocast socket. Prosthetic and Orthotics International, 23, 107-112.

CHANGES IN 3-D MOTION AND CONTACT PRESSURE DISTRIBUTION AFTER LATERAL LIGAMENT INJURY OF THE ANKLE JOINT

Kensaku Kawakami[1], Go Omori[2], Shojiro Terashima[3], Makoto Sakamoto[4], Toshiaki Hara[5]
[1]Graduate School of Science and Technology, Niigata University, 8050 Ikarashi 2, Niigata, 950-2181, Japan, far.k2@bh.wakwak.com
[2]Depertment of Orthopaedic Surgery, School of Medicine, Niigata University
[3]Depertment of Mechanical and Control Engineering, Niigata Institute of Technology
[4]Depertment of Health Sciences, School of Medicine, Niigata University
[5]Depertment of Mechanical Engineering, Niigata University

INTRODUCTION

Ankle sprains are one of the most common sports injuries. In particular, lateral ligament injuries such as those of anterior talofibular ligament (ATF) and calcaneofibular ligament (CF) cause ankle instability and may lead to cartilage damage. Several biomechanical studies have described the kinematics (Cass, et al., 1984; Siegler, et al., 1996) and contact pressure distribution (Driscoll, et al., 1994; Christensen, et al., 1994) of the talocrural joint. Nevertheless, few studies have evaluated both kinematics and contact pressure under dynamic conditions. The purpose of this study was to evaluate changes in 3-D dynamic motion and contact pressure distribution in the ankle joint before and after an ATF and CF cut. We also assess the efficacy of the Aircast (Airstrap Ankle Brace, Summit, NJ/USA) on correcting ankle instability.

MATERIAL AND METHODS

Five fresh frozen musculoskeletally intact cadavaric ankles were examined. Each ankle including all of the associated soft tissue was mounted on a specially designed frame that preserved five degrees of freedom motion. The direct linear transformation (DLT) technique was used to measure the 3-D motion of the talocrural joint, and an electric conductive rubber sensor was inserted into the talocrural joint space to determine the contact pressure distribution. The ankle joint was tested from 15 degrees of dorsiflexion to 15 degrees of plantarflexion under application of an axial tibial force 100 N. Four different experimental conditions were examined in succession for each ankle: 1) intact, 2) ATF cut (ATF (-)), 3) CF cut (Both (-)), and 4) with Aircast (Air). A paired t-test was used for statistical analysis and $p<0.05$ was defined as the level of significance.

RESULTS

The intact talus pronated with dorsiflexion. After an ATF cut, a significant increase in supination was observed for each flexion angle in comparison with the intact ankle. Supination significantly increased after a combined ATF/CF cut in comparison with after an ATF cut alone. The angle of talus pronation with the Aircast was close to that of the intact ankle, and no significant differences were observed in motional properties under the two conditions (Fig.1). For all other motion parameters including abduction-adduction, anterior-posterior translation, and medial-lateral translation, no significant changes were observed under the four experimental conditions.

The area of contact on the talus for intact ankle moved anteriorly and laterally with increasing dorsiflexion. A similar trend in contact area movement was observed after an ATF cut. However, an area of high pressure was observed in the medial aspect of the articular surface. A similar tendency was demonstrated after a combined ATF/CF cut. However, no significant changes were found in the contact characteristics following the Aircast.

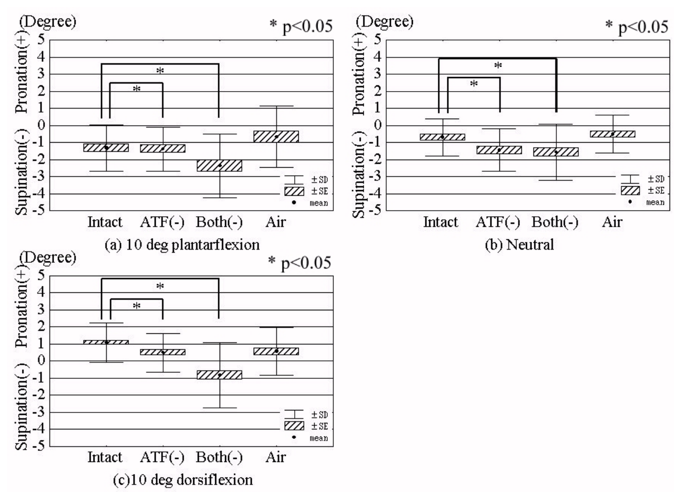

Figure 1: Pronation-spination angle at: (a)10 degrees plantarflexion, (b)Neutral position, (c)10 degrees dorsiflexion.

DISCUSSION AND CONCLUSIONS

The present results showed an increase in supination after a lateral ligament cut and medial shift in the high contact pressure area on the articular surface. These findings demonstrate the mechanics of talus cartilage injury after ankle sprain. Abnormal increases in supination angle after a lateral ligament cut were recovered by the Aircast, which suggests its clinical utility.

REFERENCES

Cass,J.R., et al. (1984). *Foot Ankle*, **5**, 142-149
Siegler,S., et al. (1996). *J. Biomech.*, **29**, 943-947
Driscoll,H.L., et al. (1994). *JAPMA*, **84**, 491-498
Christensen,J.C., et al. (1994). *JAPMA*, **84**, 537-547

FINITE ELEMENT STUDY OF TROCHANTERIC GAMMA NAIL FOR SUBTROCHANTERIC FRACTURE

Kriskrai Sitthiseripratip*[1], Banchong Mahaisavariya[2], Jintamai Suwanprateeb[3], Philip Oris[4], Erik L. J. Bohez[1], Jos Vander Sloten[4], Hans Van Oosterwyck[4]

[1]Industrial Systems Engineering, Asian Institute of Technology, Pathumtani, Thailand, msc997247@ait.ac.th

[2]Faculty of Medicine, Siriraj Hospital, Mahidol University, Bangkok, Thailand.

[3]National Metal and Materials Technology Center, Bangkok, Thailand.

[4]Biomechanics and Engineering Design, Katholieke Universiteit Leuven, Leuven, Belgium

INTRODUCTION

A trochanteric gamma nail (TGN) is widely used for trochanteric and subtrochanteric fracture fixation. The fracture in the subtrochanteric region shows higher biomechanical stresses than the fracture occurring in the trochanteric region, which may result in a higher failure rate of the implant. This study aimed to investigate the mechanical performance of a TGN fixation of subtrochanteric fracture by a finite element method. Five different locations of the transverse subtrochanteric fracture were determined, starting from the lesser trochanter and more distally with an interval of 10 mm. For each of these fracture locations, the stress distributions in the TGN were evaluated. Analyses were also performed for different conditions of fracture, i.e. stable and unstable types of fracture.

METHOD

A three-dimensional FEM of the proximal femur was created from the average geometry derived from CT-scans of 108 Thai cadaveric femora. Four-noded tetrahedral elements were used to build up the mesh of the proximal femur and the TGN. Linear elastic isotropic material properties were assigned to all materials involved in the model. Different material properties were attributed to different femoral regions and stainless steel was assigned to the material properties of the TGN. The performance of the TGN in the unstable condition is evaluated by assigning a low E-modulus value to the fracture zone. The femoral model was fully fixed at the distal end (no displacement). The one-legged stance load configuration was used in this study. The load condition consisted of a joint reaction force applied to the femoral head and an abductor muscle force applied to the greater trochanter.

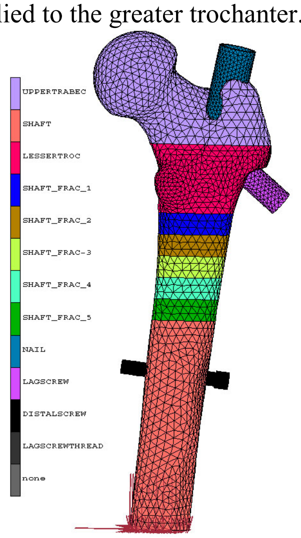

Fig. 1 FE model of subtrochanteric fractures and TGN

RESULTS AND DISCUSSION

The results showed that the average Von Mises stress at the distal locking screw hole in the nail has a trend to increase with the fracture location occurring closer to the distal locking screw hole in both stable and unstable fracture conditions, while the stress magnitude in the lag screw hole does not significantly change in the stable fracture condition but it has a trend to decrease in the unstable condition. This is due to the improper functioning of the lag screw when the fracture occurs more distally and closer to the distal locking screw hole.

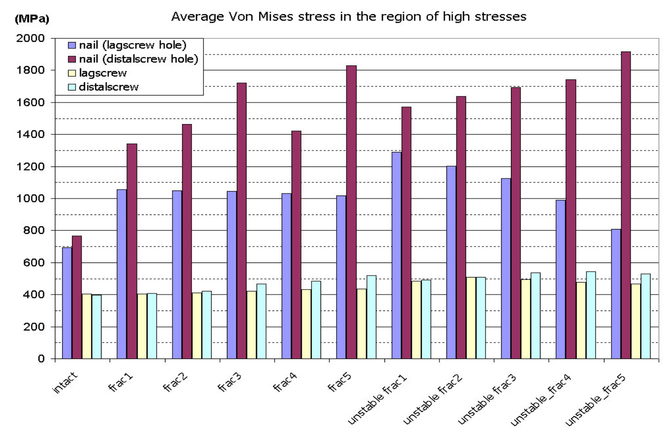

Fig. 2 Average Von mises stress in the TGN

SUMMARY

From the results, it can be concluded that

1. The distal locking screw hole is the critical region in the TGN for the fixation of a low subtrochanteric fracture as the stress at the distal locking screw hole under one-legged stance exceeds the UTS of stainless steel (1.100 MPa), therefore leading to a possible failure of the nail.
2. The stress magnitude in the TGN for the fixation of an unstable subtrochanteric fracture is usually higher than for a stable subtrochanteric fracture.
3. The following modifications at the distal part of the nail can be suggested: changing into a solid nail or reducing the size of the distal locking screw hole and the distal locking screw.

REFERENCES

Sitthiseripratip K. et al. (2001). Proceedings 18^{th} of the International Society of Biomechanics 2001.

ACKNOWLEDGEMENTS

The authors would like to acknowledge the National Metal and Materials Technology Center (MTEC), Thailand and the ASIMED Project K.U. Leuven-AIT, Flemish Inter-university Council (VLIR), Belgium for their financial support and facilities.

BEHAVIOR OF MEDIAL GASTROCNEMIUS MUSCLE-TENDON COMPLEX DURING DIFFERENT TYPES OF JUMPING

Masahiro Suzuki[1], Ken Nemoto[1], Sadao Kurokawa[2], Masamitsu Ito[1]
[1]Nippon Sport Science University, Tokyo, Japan itom@nittai.ac.jp
[2] Joshibi University of Art and Design, Tokyo, Japan

INTRODUCTION

The purpose of this research was to determine the role of tendionus structures during jumps with counter-movement by observing the behavior of the muscle-tendon complex (MTC) using real-time B-mode ultrasonography.

METHODS

Six healthy males participated in the present study as subjects. They performed following four different vertical jumps:

1) counter movement jump from the standing position (CMJ),
2) squat jump starting at the lowest position in CMJ, (SJcmj)
3) drop jump from the height of 20cm (DJ),
4) squat jump starting at the lowest position in DJ (SJdj).

Kinematic, kinetic, electromyographic and ultrasonographic data were collected during the movements.

The movements were filmed at 250Hz with a high speed digital video camera. Ground reaction force was recorded using a force platform. From these data, joint moment and power around the ankle (M_a and P_a, respectively) were computed through a link segment model.

Longitudinal ultrasonic images of the medial gastrocnemius (MG) were scanned using a B-mode ultrasound device with a 7.5MHz probe (Figure 1). These images were scanned at 60Hz and stored in a built-in cinememory of the device for 400ms before the take-off, while they were recorded on videotapes at 30Hz for 600ms from 1s to 400ms before the take-off. Fascicle lengths (L_f) and pennation angles (α) were measured using NIH-image software.

MTC length (L_{MTC}) of MG was estimated from knee and ankle joint angles (θ_k and θ_a, respectively) using the equation proposed by Grieve et al.(1978). Tendinous structure's length (L_t), moment arm length (r), MG tendon force (F_t^{MG}), MG muscle force (F_m^{MG}) were calculated as follows;

$L_t = L_{MTC} - (L_f * \cos\alpha)$

$r = \Delta L_{MTC} / \Delta\theta_a$

$F_t^{MG} = k^{MG} * (M_a / r)$

$F_m^{MG} = F_t^{MG} / \cos\alpha$

, where k^{MG} represents the ratio of physiological cross sectional area of MG among plantar flexors.

RESULTS and DISCUSSION

Vertical jump heights of CMJ (0.44±0.05m) and DJ (0.40±0.05m) were significantly higher than those of SJcmj (0.40±0.05m) and SJdj (0.31±0.04m), respectively.

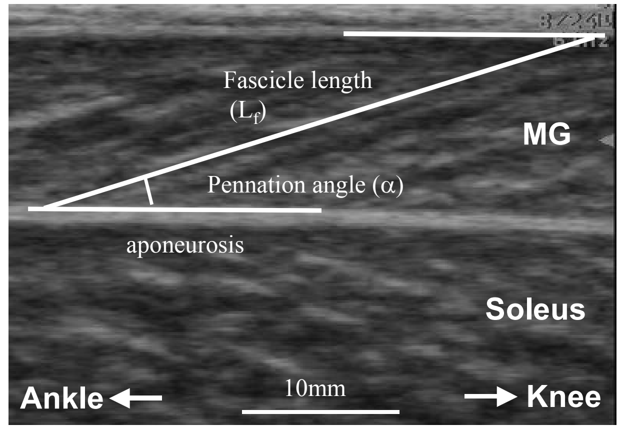

Figure 1 Ultrasonic image of MG.

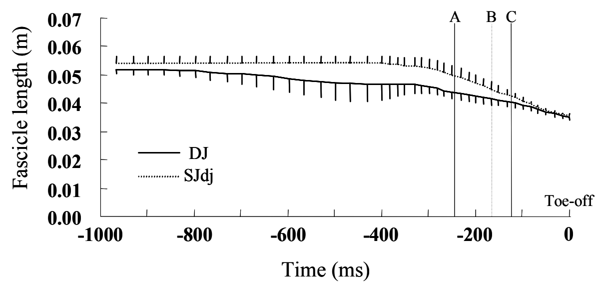

Figure 2 Changes in L_f during DJ and SJdj. **A**: Landing during DJ; **B**:onset of the ankle angle change increase during SJdj; **C**: onset of the ankle angle increase during DJ.

Behaviors of MTC, fascicle and tendon structure during CMJ were similar to those of SJcmj. There was no significant difference in peak joint power. In DJ, MTC and tendon structures were rapidly stretched immediately after landing, while such a phenomena was not observed in the other jumps. During MTC lengthening in DJ, fascicles were actually shortening at relatively slow velocities (Figure 2). Although elastic energy stored was greater in CMJ and DJ compared with their counterparts, released energy during tendon shortening was greater in SJcmj and SJdj. It could be concluded that jumps with counter movements were advantageous, partly because fascicles could use their higher force regions of force-velocity relationship by virtue of tendon elastic properties during jumps with counter movements.

REFERENCES

Greive D.W. et al. (1978). Biomechanics IV-A, 405-412.
Kurokawa S. et al. (2001). J. Appl. Physiol. **90**, 1349-1358.

STIFFNESS CHANGE WITH CAGE CONFIGURATION FOR ANTERIOR LUMBER INTERBODY FUSION

Kochi Kobayashi[1,2], Hiroyuki Takeishi[1], Yoshisada Sato[3], Toshiyuki Shirahata[4] and Yutaka Hiraizumi[4]

[1]Faculty of Engineering, Chiba Institute of Technology, Narashino, Japan, k_kobay@msi.biglobe.ne.jp
[2]Biomechanics Laboratory, Department of Health Sciences, Niigata University School of Medicine, Niigata, Japan
[3]Mon-naka Orthopedic Clinic
[4]Department of Orthopedic Surgery, Showa University

INTRODUCTION

Anterior lumber interbody fusion (ALIF) cages have been accepted as suitable spinal fusion devices for laparoscopic surgery. Since two-ALIF cage insertion is the most common surgical procedure, many studies have been reported on the stabilizing potential of two-cage insertion, indicating that the stability of instrumented specimen was at least the same as that of intact specimen (Kanayama et al., 2000; Tsantrizos et al., 2000). However, little research has been done on effects of the number and direction of inserts on the stability (Tencer et al., 1995). The objective of this study is to examine the change in stiffness with the number and direction of ALIF cages toward reducing operation time and minimizing invasion for ALIF surgery.

MATERIALS AND METHODS

Fourteen fresh porcine functional spinal units of L4-5 and L5-6 levels were retrieved and stored at -20°C in plastic bags until testing. They were dissected of muscle and fat tissues, leaving the intervertebral discs and the osteoligamentous structures intact. After drilling a pilot hole into the disc manually, a threaded interbody fusion cage (Hollow Modular Anchorage, AESCLAP, Germany) was inserted. The cage configurations tested were as follows: (1) a single cage placed centrally and anteriorly, (2) a single cage placed laterally, (3) two cages placed anteriorly, and (4) a single cage placed anterolaterally. Each vertebral body of implanted specimen was fixed in a stainless pot with dental plaster. The bottom pot was secured to the lower base of an Instron-type material testing machine. The top pot was connected to a specially designed loading device, which consisted of pulleys, wires and rod joints and transferred an upward motion of the position-controlling platform of the testing machine to flexion, extension, lateral bending and axial rotation. Maximum torque applied with an axial compression of 70N was 2.5Nm for flexion, extension and lateral bending while 4Nm for axial rotation. Angular motions were detected using a video dimensional analyzing system.

RESULTS

Figure 1 shows the stiffness achieved by the four different cage configurations and the intact stiffness. In flexion, a single cage constructed laterally or anterolaterally and two cages placed anteriorly had significantly higher stiffness than intact, and the single-cage construct was stiffer in anterolateral than in anterior. In the other loading modes, no significant differences were observed in stiffness between instrumented and intact specimens and among the four configurations of construction.

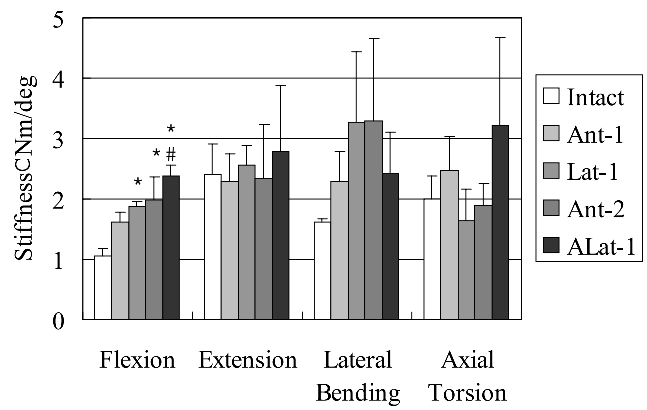

Figure 1: Mean values and standard errors of stiffness for intact and implanted specimens (* $p<0.05$ vs intact; # $p<0.05$ vs Ant-1).

DISCUSSION AND CONCLUSIONS

Significant increase in stiffness observed only for flexion implies that the placement of ALIF cage enhanced anterior support for flexion. On the other hand, since the facet joints played a dominant role in the kinematics of the spine for the other loading modes, the effect of cage insertion was negligible when compared with flexion. There was no significant difference between the anterior two-cage and the anterolateral single-cage constructs. Therefore, although this study addresses only the initial stiffness afforded by different ALIF cage configurations, it is concluded that the anterolateral single-cage construct should be further investigated for clinical implementation.

REFERENCES

Kanayama, M. et al (2000). *J. Neurosurg* (*Spine 2*), **93**, 259-265
Tencer, A.F. et al (1995). *Spine*, **20**, 2408-2414
Tsantrizos, A. et al (2000). *Eur. Spine J.*, **9**, 14-22

EFFECT OF CONSTRICTION GEOMETRY ON TRANSIT OF DEFORMED NEUTROPHILS IN CAPILLARIES

Atsushi Shirai[1], Ryo Fujita[2] and Toshiyuki Hayase[3]
Institute of Fluid Science, Tohoku University, Sendai, Japan
[1]Research Associate, Tohoku University, shirai@ifs.tohoku.ac.jp
[2]Graduate Student, Tohoku University
[3]Professor, Tohoku University

INTRODUCTION

On the average, neutrophils are significantly less deformable than erythrocytes and, once they are deformed, they require considerable time to recoil to their initial spherical shape. For this reason, initial cell shape influences the transit time of neutrophils through constrictions in narrow capillaries. In this research, the flow of a neutrophil in a capillary with two constrictions was investigated numerically, in terms of the transit time of the cell through the second constriction after it had been deformed by passing through the first one.

MODELING AND NUMERICAL PROCEDURE

In this research, numerical analysis was performed in an axisymmetric cylindrical coordinate system to obtain the flow of a neutrophil through two constrictions in a cylindrical capillary. The neutrophil was initially a sphere with a radius of 4 μm and was modeled as a Maxwell interior bounded by a thin isotropic elastic membrane. Shear modulus and viscosity of the interior were 186 Pa and 31 Pa·s, respectively. The membrane was pre-stressed and the cortical tension was 3.1×10^{-5} N/m. Since the thickness of the membrane was set at 1 nm and Young's modulus was 10^{-4} Pa, the tension could be treated as an interfacial surface tension between the cell interior and the surrounding plasma. The Poisson ratio of the interior was set at 0.4999.

The capillary segment was a straight cylinder, 5100 μm in length and 6 μm in radius, with two constrictions. The shape of each constriction was an arc, the ratio of the length to the height being 8:1. The throat radius, R_{min1} and R_{min2}, of each constriction was chosen from 2.50, 2.75 and 3.00 μm, respectively. The center of the first constriction was set 100 μm downstream of the upper end of the segment and that of the second one was set at the distance L_c downstream of the center of the first constriction. To mimic the endothelial layer of the constrictions, an imaginary vessel wall was set in each constriction 0.1 μm apart from the actual wall. Plasma flowed through this wall, but the cell was deformed along the surface.

Plasma is an incompressible Newtonian fluid with a viscosity of 1.2×10^{-3} Pa·s and a density of 1.03×10^{3} kg/m^3. No-slip conditions were assumed at the vessel wall and the cell surface. Pressure of 0 Pa was prescribed for the upstream boundary of the capillary segment, with a pressure drop, ΔP, of 40 Pa along the segment. Adhesion of the neutrophil to the endothelium was not considered here.

RESULTS AND DISCUSSION

Figure 1 shows the time required by the deformed neutrophil to pass through the second constriction. Broken lines are the transit times of spherical cells. In this figure, the transit times approach these lines as the distance L_c between the two constrictions increases, since the cell gradually recoils to its initial spherical shape during on its way to the second constriction after it has passed the first one. The effect of the throat radius R_{min1} of the first constriction on the transit time is large for the small throat radius R_{min2} of the second constriction and for L_c.

In a previous study (Huang et al. 2001), transit time of neutrophils passing through the pulmonary capillary network was investigated. The transit of each neutrophil was modeled based on blunt-ended micropipette experiments on spherical neutrophils there. Our last research study (Shirai et al. 2001) showed that the inlet geometry of the pipette affects the transit time and denoted that actual transit can be shorter than that obtained by the micropipette model. In addition to that result, the present result suggests that the transit time of neutrophils passing through the pulmonary network may be much shorter due to the non-spherical shape of the cell entering the second constriction.

SUMMARY

Transit time of a neutrophil through the second constriction after it had been deformed by passing through the first one was investigated numerically. It was clarified that the maximum radius of the deformed cell greatly affects the transit time.

REFERENCES

Huang, Y. et al (2001). *J. Appl. Physiol.*, **90**, 545-564.
Shirai, A. et al (2001). *Proc. 1st Int. Symp. Adv. Fluid Info.*, 125-130.

ACKNOWLEDGEMENTS

The numerical simulation was carried out by the use of the super-computer, ORIGIN 2000, at the Institute of Fluid Science, Tohoku University.

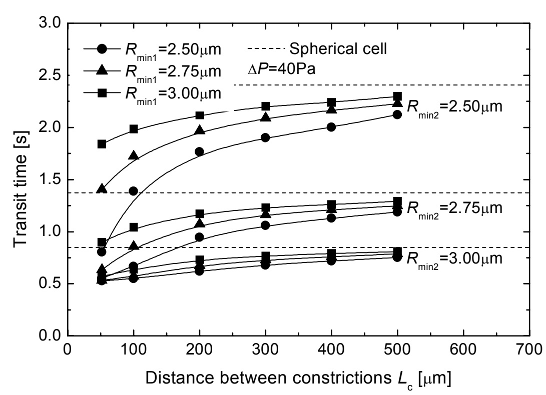

Figure 1: Effect of distance L_c between constrictions on transit time of a neutrophil passing through the second constriction.

DEVELOPMENT OF A MOBILE HOME CARE MONITORING SYSTEM USING THE COMPUTER NETWORK

[1]Akie Ukai and [2]Takami Yamaguchi
[1]Dept. Mech. Eng., Nagoya Institute of Technology, Gokiso-cho,Showa-ku,Nagoya, Japan, akie@pfsl.mech.tohoku.ac.jp
[2]Department of Mechatronics and Precision Engineering, Graduate School of Engineering, Tohoku University

INTRODUCTION

Recently, an increasing number of attempts to adapt multimedia communication to medical care have been reported. It is our belief that while high technology may be necessary for medical practice, spiritual support is more important in medical care. Therefore, we proposed the concept of a Hyper Hospital to offer patients a means of effective human communication during medical care. The original Hyper Hospital was a novel medical system constructed on a computer and multi-media based network, in which the major human-machine-human interface was a virtual reality dedicated to the patients. In the present study, we describe a home-care-type telemedicine network, a recent development in the Hyper Hospital project, based on various modern mobile telecommunication technologies.

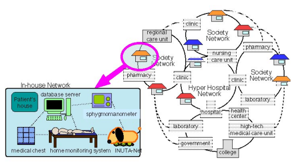

Fig.1: Hyper Hospital Network

The Hyper Hospital network is composed of numerous networked units, such as local health care authorities, regional nursing care units, high-tech medical centers, etc., as shown in Fig. 1. Each unit in the network contains its own networks. The network within the home is designed as a combined inter-network with special tasks or functions. These include the collection of information regarding the patient's physiological condition and behavior, and control of a variety of support facilities in the house. Every functional unit in the network is equipped with a server function that allows information to be broadcast over the network using HTTP protocols. The network system has a unified user interface, based on a WWW interface.

INUTA-NET: ONE FUNCTIONAL UNIT

A functional unit is a general term that we use to describe equipment that is connected to an in-house local area network (LAN); each functional unit acts as a server and provides various types of medical and technical support. Face-to-face communication is the best way to obtain information from patients and make them feel at ease. One of the functional units developed to implement this is an electronic pet called the "INUTA-net" (INU means "dog" in Japanese). The INUTA-net is a semi-automatic robot that looks like a toy dog, and is equipped with monitoring and communication interfaces (Fig. 2). It provides remote interactive facilities to monitor a patient, and is controlled by a combination of distant caretakers and family or friends through the network. The design principle of this system is that patients can be monitored closely without introducing nervous or mental stress. The patients may even enjoy themselves, playing with the 'pet' or talking with people remotely, such as doctors, family members, or friends, by using the INUTA-net communication facility.

Fig.2: INUTA-net

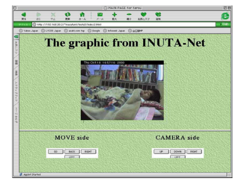

Fig.3 : Web page

A sample web page is shown in Fig. 3. To ensure privacy, all users must provide their usernames and passwords when accessing this page. The picture at the center of the display is a monitor screen from the CCD camera on the INUTA-net. The INUTA-net and the CCD camera can be controlled by clicking on the buttons shown below the screen: the left button moves the INUTA-net, and the right button operates the camera. The INUTA-net has 3 computers, a control PC, a network-managing PC, and a computer built into the camera. All of the computers have server ability, and each constitutes an internal network, using a TCP/IP connection. In this way, the load of each PC can be reduced, and functions can be substituted or added easily. In this study, three additional functions were developed and implemented. First, an emergency alert system was added to allow the patient to report his or her own unusual situation by sending a report in a mail appended to the CCD camera picture. Second, a user identification system was implemented to allow a patient to identify anyone accessing the system. Third, an LCD monitor was included, located in front of the INUTA-net shown in Fig. 2, to display the access log for the system, which provides information such as the frequency and duration of users' access to the Web page. Two logs are displayed: one for the username, and the other for the access time.

CONCLUSIONS

The INUTA-net functional unit was successfully controlled over the Internet through a WWW interface. It is therefore possible to build a home-care telemedical system for the mental and spiritual support of users that allows maximum freedom, and a flexible network construction that can grow and be modified according to the patient's needs.

ACKNOWLEDGMENTS

Part of this work was supported by Health Sciences Research Grants for Comprehensive Research on Aging and Health, from the Ministry of Health and Welfare, Japan, 1999-2001 (Chief Researcher: K. Nakajima, National Institute of Longevity Sciences), 13C-3 (Chief Researcher T. Tamura), and a grant from the Suzuken Memorial Foundation.

BASIC PROBLEMS ASSOCIATED WITH WIND TUNNEL MEASUREMENTS AND CFD IN SPORTS

Ewald Reisenberger[1, 3], Walter Meile[1], Bernhard Schmölzer[2] and Wolfram Müller[2]

[1] Institute of Fluid Mechanics and Heat Transfer, Graz University of Technology, Austria
[2] Institute of Medical Physics and Biophysics, Karl-Franzens University Graz, Austria
[3] Communicating author, erei@fluidmech.tu-graz.ac.at

INTRODUCTION

Performance in many sports is determined not only by the motor abilities of the athlete, but to a large extend by aerodynamic features of the athlete's body and his equipment (Schmölzer, Müller 2002; Hanna 1996). The aerodynamic problems to be solved with human bodies in the air flow are a challenging task: Both approaches, wind tunnel measurements and computational fluid dynamics (CFD), have to be applied carefully when results with high accuracy are to be obtained. In order to point out the basic problems, we study the aerodynamic characteristics of a simple flat plate by means of wind tunnel measurements and CFD. The same approach can be applied to objects with complex geometries, including human bodies. The accuracy of the lift and drag coefficients obtained with the relevant objects of a particular sport determines the prediction accuracy of flight path calculations.

METHODS

Wind tunnel measurements have been performed in a Göttingen type tunnel of Graz University of Technology. This tunnel has a cross section area of 2x1.5 m^2 and allows wind speed up to 40 m/s. For CFD calculations FLUENT, a CFD-program with finite volume approach has been used. The influence of inaccuracies in lift and drag measurements on the flight path prediction in ski jumping is reported here exemplarily, using a computer model approach that has been described recently (Müller et al 1995, 1996; Schmölzer, Müller 2002).

RESULTS AND DISCUSSION

The classical results of Flachsbart (1932) for drag and lift coefficients of a flat plate (length 1m, aspect ratio 5:1) are taken as reference and are compared with present results (Figure 1). The velocity distribution around the flat plate calculated with CFD is shown in Figure 2. For example, the increase of lift values by 1% throughout the flight phase for the simulation of a ski jump at the new jumping hill in Innsbruck resulted in a jump length increase by 2.5 m. Deviations of lift and drag value measurements depend on wind tunnel blockage effects and interferences between model and mounting devices. These effects determine the accuracy of wind tunnel measurements. Mathematically, the flow field is described by the Reynolds Averaged Navier-Stokes equations (RANS) which exhibit major inherent difficulties. The CFD approach leads to approximated solutions for velocity, pressure and density distributions. The prediction accuracy depends on various factors of influence, e.g. the boundary conditions and especially the applied turbulence model.

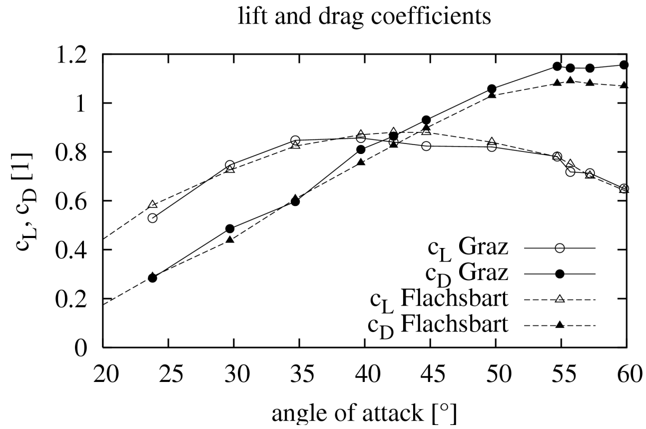

Figure 1: Lift (c_L) and drag (c_D) coefficients versus angle of attack - experimental results for the 5:1 flat plate.

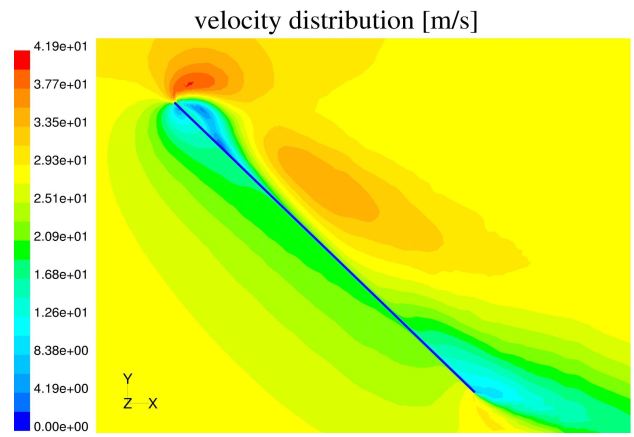

Figure 2: CFD simulation: 5:1 flat plate at 44.7° angle of attack. Free stream velocity U_0 = 30 m/s; c_D = 0.94 ; c_L = 0.94

REFERENCES

Müller, W. et al (1995). *Nature* **375**, 455.
Müller, W. et al (1996). *J. Biomech.* **29/8**, 1061-1068.
Hanna, R.K. (1996). *The Engineering of Sport*. Balkema.
Schmölzer, B., Müller, W. (2002). *J. Biomech.*, accepted.
Flachsbart, O. (1932). *Ergebnisse der Aerodynamischen Versuchsanstalt zu Göttingen* **4**, 96 - 100.

ACKNOWLEDGEMENTS

We gratefully acknowledge the financial support from the Austrian Research Funds (FWF) under grant Nr. P14388-TEC and the cooperation with the IOC and FIS.

EFFECTS OF CYCLIC STRAIN ON OX-LDL UPTAKE INTO MACROPHAGES

Hiroshi Miyazaki[1], Junzo Tanaka[1], Shinya Nakagawa[2], and Kozaburo Hayashi[1]
[1]Biomechanics Laboratory, Div. of Mechanical Science, Dept. of Systems and Human Science,
Grad. School of Engineering Science, Osaka University, Toyonaka, Osaka, Japan, oboe@me.es.osaka-u.ac.jp (H.M.)
[2]Nestle Japan Co., Shimada, Shizuoka, Japan

INTRODUCTION

Macrophages (Mϕ) play an important role in the initiation and development of atherosclerosis. Mϕ differentiated from monocytes in the intima take up such modified LDL as oxidized LDL (ox-LDL) and, then, turn into foam cells. These Mϕ are always subjected to cyclic strain induced by pulsatile blood pressure. Because cyclic strain affects the morphology and the phagocytosis for latex particles of Mϕ (Miyazaki and Hayashi, 2001), it should also have an influence on the formation of foam cells. In the present study, Mϕ attached to silicone rubber sheet were cultured under the cyclic strains of 5 and 10 % amplitudes, and the effects of strain on ox-LDL uptake were studied.

MATERIALS AND METHODS

Peritoneal Mϕ were obtained from 6-week old female C57BL/6J mice 4 days after the intraperitoneal injection of 3% thioglycollate. They were washed with Ca^{2+}- and Mg^{2+}-free Hanks' balanced salt solution (HBSS) and, then, were suspended in RPMI-1640 medium supplemented with 10% FCS and antibiotics.

Silicone rubber sheets were placed in a tissue culture dish after making their surface hydrophilic by the treatment with sulfuric acid, and the above-mentioned cell suspension was poured into the dish. After 2 hour preincubation at 37˚C, the sheets were rinsed with HBSS to remove non-attached cells. The Mϕ were cultured for 24 and 48 hours under 5 % cyclic strain (S(5)-24h and S(5)-48h groups, respectively), or 10 % strain (S(10)-24h and S(10)-48h groups, respectively) at 1 Hz frequency, or under no strain (NS-24h and NS-48h groups, respectively) at 37˚C. Then, the Mϕ of S and NS groups were cultured in a medium containing ox-LDL for another 2 hours under the same strain and no strain conditions, respectively. Control data were obtained from the cells which were cultured with ox-LDL for 2 hours immediately after the above-mentioned preincubation (C group). A negative control group cultured for 2 hours without ox-LDL was also prepared (NC group).

After culture, the cells adhered to each sheet were stained with Oil-Red O. The numbers of the attached cells and stained cells, and the area occupied by lipids were determined in three different areas using an optical microscope and an image analyzer.

RESULTS AND DISCUSSION

The number of attached cells per 1 mm^2 was smaller in S group than in NS and C groups. Cyclic strain decreased the number of attached cells, and this change was significant at 48 hours. This result suggests that some Mϕ were detached from the sheets by strain. However, there were no significant differences in the numbers of stained cells among all the groups except for NC group; the number of stained cells was much smaller in NC group than in the other groups. The percentage of stained cells was significantly larger in S group than in NS and C groups. There were no significant differences in the percentage between S(5) and S(10) groups. The area occupied by lipids was larger in S group than in NS and C groups, although the differences were not significant. No significant differences were observed between S(5) and S(10) groups. These results indicate that cyclic strains of 5 and 10 % amplitude have almost the same effects on ox-LDL uptake into Mϕ, and suggest that the effects of cyclic strain is saturated at or less than 5 % amplitude.

SUMMARY

Effects of the magnitude of cyclic strain on ox-LDL uptake into murine peritoneal Mϕ were assessed after they were cultured under the cyclic strain conditions of 5 and 10 % amplitudes at 1 Hz frequency for 24 and 48 hours. Cyclic strain enhanced ox-LDL uptake into Mϕ regardless of strain magnitude. However, there were no significant differences in the percentage of lipid accumulating cells and in the area occupied by lipids between 5 and 10 % strain groups.

REFERENCES

Miyazaki, H., Hayashi, K. (2001). *Bio-Med. Mater. Eng.*, **11**, 301-309.

ACKNOWLEDGEMENTS

This work was financially supported in part by the Grant-in Aids for Scientific Research (A)(2) (nos. 09358020 and 12308047) from the Ministry of Education, Culture, Sports, Science and Technology, Japan.

A QUANTITATIVE ASSESSMENT OF KNEE EXTENSOR SPASTICITY USING ISOKINETIC DYNAMOMETER

Duk Hyun Sung, MD. PhD., Sang Yong Kim, MD., Hee-Dong Park, MD., Soo Jin Yoo, MPE.
Department of Physical Medicine and Rehabilitation, Sungkyunkwan University School of Medicine,
Samsung Medical Center, Seoul, Korea. dhsung@smc.samsung.co.kr

INTRODUCTION

Mechanical pendulum test has been used to quantify spasticity. But velocity dependent increase in tonic stretch reflex, which is a critical characteristic of spasticity, cannot be evaluated with the pendulum test. The purpose of this investigation was to determine the biomechanical parameter to quantify the degree of spasticity that would be useful in the clinical setting.

METHODS

Knee extensor muscles of 60 limbs of 47 patients, which were spastic by clinical modified Ashworth scale (MAS), were studied. The muscle was stretched by a isokinetic dynamometer (Cybex 6000®, Cybex Inc. USA) 5 times with the each velocity of 60°/sec, 120°/sec, 180°/sec, 240°/sec in the range of 0~90° of knee and generated eccentric torque during stretch was measured. Each subjects was asked to relax as much as possible during test period. Four parameters (torque onset angle(TOA), peak torque angle(PTA), peak torque(PT), peak torque area(PTA)) were measured at each stretch velocity (fig 1). Then, linear regression analysis was performed in relationship between each parameter and stretch velocity to find the slope of the linear regression curve. This slope, which reflects the sensitivity to the rate of stretch, was compared with clinical modified Ashworth scale using a Spearman's correlation coefficient.

RESULTS

The slope of TOA and PTA had negative value so that they showed the decreasing trend of their value as stretch velocity increased. On the other hand the slope of PT and PTA had positive value that meant that the slope increased as stretch velocity increased.

The slope of PT and PTA were positively and significantly correlated with clinical MAS score (p<0.05). However the slope of the TOA and PTA showed poor correlation with clinical MAS (table 1).

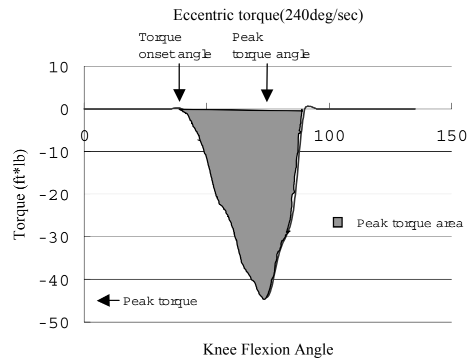

Figure 1. Definition of torque onset angle(TOA), peak torque angle(PTA), peak torque(PT), peak torque area(PTA)

SUMMARY

As clinical degree of spasticity increases, eccentric resistive torque generated by knee extensor increases. The slope of peak torque and peak torque area in linear regression curve between each parameter and stretch velocity can be useful parameters in quantify spasticty of knee extensor.

REFERENCES

Lamontagne A, et al.(1997). Impaired viscoelastic behaviour of spastic plantar flexors during passive stretch at different velocities. *Clinical Biomechanics*, **12,** 508-515

Table 1. Correlation with clinical Modified Ashworth Scale

Parameter	Correlation coefficient(r)(mean)	Determination coefficient(R^2)(mean)
TOA	0.056	0.003
PTA	-0.022	0.000
PT	0.564*	0.318
PTA	0.516*	0.266

* Significant at p<0.05, two-tailed test

GAIT ANALYSIS AND ENERGY CONSUMPTION OF NEW DESIGN PROSTHESIS WITH BELOW KNEE AMPUTEES: A PILOT STUDY

Gwo-Feng Huang ,You-Li Chou ,Fong-Chin Su, and Pei-His Chou

Institute of Biomedical Engineering of National Cheng Kung University ,Tainan, Taiwan
Division of Orthopedic Surgery, Kaohsiung Medical University, Kaohsiung ,Taiwan

INTRODUCTION

This study use new is to design a prosthesis equipped with an air cooling system so that the sweat due to high temperature and humidity inside the socket can be reduced. There is a fan with 5cm diameter at the below part of socket which is controlled by a humidity sensitive circuit. The fan switch (power FET2SK2134) will operate and draw out the humid air inside the socket when the humidity inside the socket is beyond 80% relative humidity (RH). The maximal velocity is 0.45m/sec and measured in experiment. The humid air will come out through the holes on the pylon. The fan turned off when the humidity drop to a comfort level again. The purpose of this study is to find out the characteristic of new prosthesis design for clinical physicians and prosthetists reference. Scientifically measure was used the dynamic gait characteristics of the amputee by using motion analysis and to measure the energy consumption for the below-knee amputee when wearing the solid ankle cushion heel (SACH), single axis and multiple axis prosthetic feet.

METHODS

Twenty male unilateral, including 15 right and five left, transtibial amputees were selected as subjects for this study. The 20 subjects tested were divided into two groups, a vascular group and a traumatic group. Using a six-camera motion analysis system, the subjects walked at a self-selected comfortable walking speed for three trials. Energy consumption was detected while walking by metabolic measurement cart. Subjects walked on the treadmill few times for trial and warm up. When subjects' HR reached 60% of the maximum HR (220-Age), measurements of energy consumption parameters were started to record for a minimum of 2 min. Subjects walked on the treadmill at speeds of 1,1.5 and 2 miles per h on slopes of grades 0 , 4 and 8 with the three kinds of prosthetic feet. Subjective results are additionally determined via questionnaire after testing.

RESULTS AND DISCUSSION

The results of motion analysis showed statistically significant differences at $P < 0.05$ between the vascular and traumatic groups in the linear measurements of velocity, cadence, stride length and single limb stance.

Hip, knee and ankle joint motion of three new socket type prostheses were also analyzed via motion analysis and significant differences ($p<0.05$) were found in the sound side and prosthetic side. Motion analysis system and two forceplates are used to analyze the ground reaction force when heel strike and toe off. There are significant difference between sound side and prosthetic side at heel strike but not at toe-off with three types of prosthetic (Fig.1). Comparing the HR, respiratory rate (RR) and energy consumption rate, traumatic group is more efficient than vascular group (Table 1). According to the result of questionnaire, multiple axis feet are the most comfortable type and single axis feet are the next. SACH type is the worst ones in comparison with the two types mentioned above.

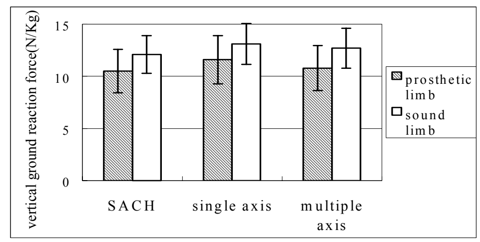

Fig. 1: The average vertical ground reaction forces that occur shortly after contact (n=20) The prosthetic limb is compared to the sound limb to evaluate symmetry for each prosthetic foot.

Table 1: Energy consumption parameters collected during 2 minutes of walking averaged across all feet tested.

Energy parameters	Traumatic	Vascular	Control	p-value
HR	110.2 ± 8.26	127.3 ± 10.23	108.6 ± 6.35	0.001*
O2 pulse	0.16 ± 0.03	0.12 ± 0.02	0.17 ± 0.02	0.001*
RR	22.3 ± 1.75	27.56 ± 2.28	21.18 ± 2.56	0.001*
Energy rate	12.3 ± 2.18	17.17 ± 1.86	10.38 ± 2.23	0.005*
RER	0.82 ± 0.07	0.92 ± 0.08	0.81 ± 0.05	0.017*

SUMMARY

Using the quantitative measures of motion analysis, some significant differences were found in kinetics and kinematics of the new design prosthesis with various feet tested. These data provide information about the dynamic performance of the various feet, which can be helpful in prescribing the optimal prosthetic foot for individual amputees.

REFERENCES

Huang,G.F.,Chou,Y.L. (2000). Gait and Posture, **12,**162-168.
Huang,G.F.,Chou,Y.L.(2001)**.**Biomedical Engineering Applications,Basis&Communications,**13**,99-107.

ACKNOWLEDGEMENTS

This research was supported by the DOH88-HR-817, NHRI-GT-EX89E817P, NHRI-EX90-8817EP

CFD STUDIES OF THE INTRAVENTRICULAR DIASTOLIC FLOW FOR THE ANALYSIS OF COLOR M-MODE DOPPLER ECHOCARDIOGRAMS

Masanori Nakamura[1], Shigeo Wada[1], Taisei Mikami[2], Akira Kitabatake[3], Takeshi Karino[1]
Hokkaido University, Sapporo, Japan, nakamura@bfd.es.hokudai.ac.jp
[1]Research Institute for Electronic Science, [2]College of Medical Technology, [3]Graduate School of Medicine

INTRODUCTION

A color M-mode Doppler echocardiogram (CMD) is a spatiotemporal map of flow velocity along one axis and has been applied to clinical evaluation of the left ventricular (LV) diastolic function. We carried out a CFD study of intraventricular flow during early diastole to analyze a relationship between the intraventricular flow and the LV diastolic function, and to clarify how this relationship is reflected on a CMD.

METHOD

The geometry of the luminal surface of the LV at its maximum expansion is determined so that it approximates the general anatomy of a human LV. For simplicity, it is assumed that the geometry is symmetric with respect to the bisector plane of the mitral and aortic orifices, and that the crosssection of the LV obtained by cutting it with a plane radiated out from the line of intersection of the planes containing the two valve orifices is ellipsoid.

The ventricular wall is moved under two assumptions; 1) the movement of the ventricular wall is not affected by the intraventricular blood flow, and 2) a point on the wall moves in the direction of a line connecting the point and the centroid of the crosssection of the LV obtained by the same manner as described above. A spatial distribution of the moving velocity of the wall is fixed throughout the simulation, and it is set that the moving velocity of the wall takes the maximum at the apex and decreases as going away from the apex to the mitral and aortic orifices.

Computer simulations of intraventricular flow during early diastole are carried out for the cases of the LVs with a normal diastolic function and a poor diastolic function by giving large and small volume changes to the LV, respectively. As an initial condition, blood in the LV is assumed to be at a standstill. After advancing a time step and giving a volume change to the LV model, a further expanded model is constructed. The Navier-Stokes and continuity equations are solved by the use of ANSYS-FLOTRAN ver.5.6 (distributed by Cybernet Systems Co. Ltd., Tokyo). As boundary conditions, zero pressure is given to the LV entrance, and a moving velocity of the wall is applied to the ventricular wall based on a non-slip condition. This process is repeated until the time reaches the end of early diastole (t = 0.24 sec).

RESULTS AND DISCUSSIONS

Regardless of the diastolic function of the LV, there is the formation of an annular vortex that surrounds the inflow via the mitral orifice and constricts it. Figure 1 shows instantaneous streamlines of the intraventricular flow at a late stage of early diastole (t = 0.20 sec). A comparison of the size and position of the vortex between Fig. 1 (a) and (b) shows that the vortex in the LV with a normal diastolic function is larger and its center is closer to the apex.

A spatiotemporal map of the inflow velocity expressed in the same manner as CMD obtained from the CFD results for each case is shown in Fig. 2 (a) and (b). A blue region indicates the region where the velocity of fluid elements is larger than 70% of the spatiotemporal maximum velocity in the early diastolic phase, called aliasing area. It is clearly seen that the aliasing area for the LV with a normal diastolic function is sharply elongated compared to that for the other case.

The annular vortex forming in the LV narrows and constricts the passage of inflow and helps the fluid elements in the inflow maintain their velocities even when coming in the cavity of the LV. With the development of the vortex, the constricted point of the inflow moves towards the ventricular apex, causing a shift of the high-velocity portion of the inflow towards the apex. This appears as elongation of the aliasing area in CMD. These results suggest that a clinical diagnosis of the LV diastolic function with CMD is based on evaluation of the development of the intraventricular vortex during early diastole.

ACKNOWLEDGEMENTS

This work was supported by the Research Grant for Cardiovascular Diseases (12C-12) from the Ministry of Health and Welfare of Japan and by the Ministry of Education, Science, Sports and Culture, Grant-in-Aid for Scientific Research (B), No. 13480284, 2001.

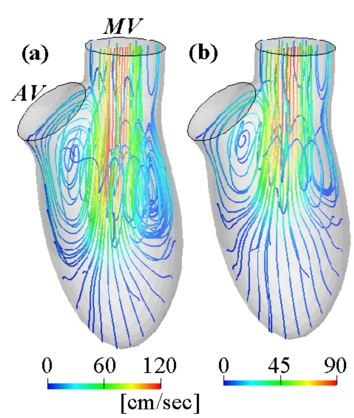

Figure 1: Streamlines in the LV with a normal diastolic function (a) and the LV with a poor diastolic function (b). *MV*: mitral orifice, *AV*: aortic orifice.

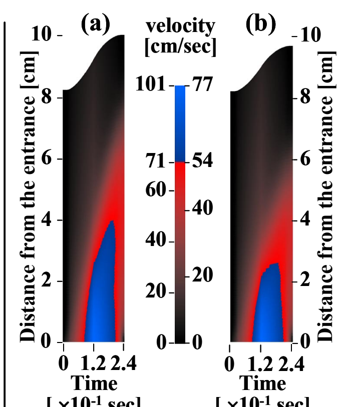

Figure 2: CMDs obtained with CFD for the LV with a normal diastolic function (a) and the LV with a poor diastolic function (b).

DYNAMIC STRESS ANALYSIS OF THE ARTERIAL WALL WITH FINITE ELEMENT MODELING

Shervin Ghasemi Majd[1],Mohammad Tafazzoli Shadpour[1] , Albert avolio[2]

[1]Department of Biomedical Engineering, Amir Kabir University of Technology (Tehran Polytechnic), Tehran Iran ,tafazoli@cic.aku.ac.ir
[2]School of Biomedical Engineering, The University of New South Wales, Sydney , Australia

INTRODUCTION

Cardiovascular diseases are among leading causes of death. Increase of mechanical tensile stress in the arterial wall leads to an altered arterial function, and structural degeneration. This investigation aimed to determine distribution of arterial wall tensile stress due to a harmonic internal pressure.

METHODS

Finite element modeling was used to evaluate Von Mises stress distribution in a typical model of cross section of human aorta with differing mechanical parameters and arterial wall structures. The applied pressure was sinusoidal in the range of 80-120 mm Hg with the frequency of 60 bpm to simulate physiological pulse for a healthy human being. The model included a 10 degree section of the aortic wall with appropriate boundary conditions to allow the modeling of the entire arterial wall cross section with radial expansion. The model consisted of 2440 elements, 7550 nodes with 8 node quadratic 2D elements and plane strain conditions.

RESULTS AND CONCLUSION

Results showed a general decrease in maximum Von Mises stress on the luminal side compared to the static analysis. This decrease was 23%, for the arterial pulse of 60 bpm , and Young's modulus of elasticity (E) of 300 KPa . The stress profile showed a maximum value (S_{max}) on the luminal side and a minimum value on the adventitia side . An increase in E resulted in an increase of S_{max} value with a non-linear trend (Figure 1).

With the introduction of viscoelastic modulus to the model, a further decrease in the amplititude of the resultant stress wave was observed . Figure 2 shows a typical profile of maximum and minimum values of the Von Mises stress caused by the sinusoidal pressure . A ratio of C/E (the ratio of viscoelastic modulus to elastic modulus) equivalent to 12.5% resulted in a phase lag of *5.4* degrees between applied pressure and deformation , and for the value of 31 .4 % this was elevated to 14.4 degrees.

It can be concluded that in the stress analysis of the arterial wall , the effects of dynamic pressure and material properties should be considered . It is recommended that a fatigue analysis based on the stress results of application of dynamic pressure may contribute to a better understanding of arterial dysfunctioning with age and hypertension .

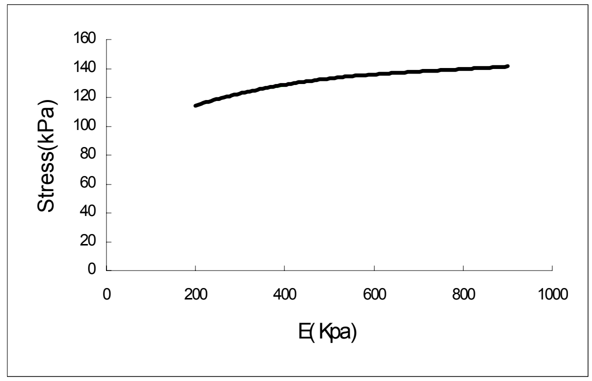

Figure l: Effects of Young's modulus of elasticity of arterial wall on maximum Von Mises stress with a harmonic blood pressure.

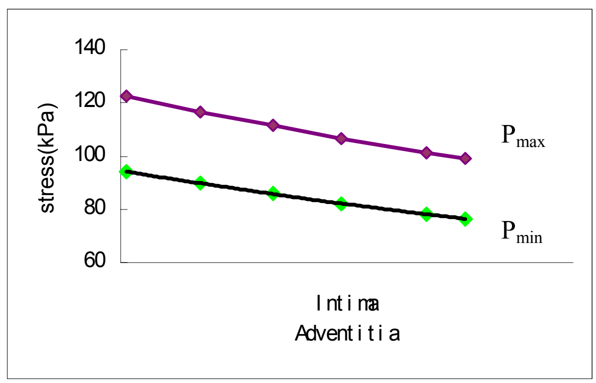

Figure 2: Von Mises stress profiles across arterial wall caused by maximum and minimum values of pressure wave.

REFERENCES

Avolio A., Jones D., Tafazzoli-Shadpour M., Quantification of alterations in structure and function of elastin in the arterial media, Hypertension. 1998. 32;170-175.

Tafazzoli-Shadpour M. , Analysis of mechanical stress in arteries with change in wall structure properties PhD Thesis, UNSW, 1999

Takashi I. ,In Vivo Viscoelastic behavior in the human aorta, Cir Res.1990. 66:1413-1419

THE EFFECT OF A CYCLIC COMPRESSIVE STRAIN ON THE DIFFERENTIATION OF OSTEOBLAST-LIKE CELL (MC3T3-E1) IN 3-DIMENSIONAL SCAFFOLDS.

K.Choi[1], J.K. Kim[1], Y.S. Park[1], E.H. Bae[1], K.J. Chun[2], T.S. Lee[3]
[1]Biomedical Research Center, Korea Institute of Science and Technology, Seoul, Korea choi@kist.re.kr
[2]Korea Institute of Industrial Technology, Seoul, Korea
[3]Mechanical Design Laboratory, Sogang University, Seoul, Korea

INTRODUCTION

Tissue engineering technologies has widely been applied to develop artificial bone tissues for the treatments of bone fractures and other skeletal diseases. Among the parameters which affect in vitro bone regeneration, mechanical stimuli have been considered to be a key factor. In this study, we examined the effect of an applied cyclic compressive strain on the growth and differentiation of mouse osteoblast-like cells (MC3T3-E1) cultured in 3-dimensional chitosan scaffolds.

METHODS

MC3T3-E1 cells, a mouse osteoblast-like cell line, were grown in α-minimal essential medium containing 10% fetal bovine serum (FBS), 100μg /ml penicillin-streptomycin. Cells were maintained in a humidified incubator at 37°C with 5% CO_2, 95% air and were subcultured every 3 days. For mechanical stimuli studies, these cells were seeded to 3- dimensional chitosan scaffolds (Regen Biotech. Inc., Seoul, Korea).at 1×10^6 cells/scaffold.

A cyclic compressive strain was applied to the specimens using a specially-designed testing apparatus which also allows the cells to be simultaneously visualized using an inverted microscope. The cyclic compressive strain (2.5%) was applied over a period of 17 days with 150 cycles per day at a frequency of 0.5Hz. Image processing methods are utilized for taking image at indicated times and detecting a level of cell deformation. The amount of protein and alkaline phosphatase activity were evaluated for the degree of differentiation and proliferation at the indicated times (day 4, 7, 10, 14, 17).

Total protein was estimated for finding the level of cell proliferation using Bredford method and alkaline phosphatase was estimated for knowing the time of cell differentiation using a commercially available kit (Sigma, USA).

RESULTS AND DISCUSSION

The total amount of protein produced in the control group was higher than the mechanically stimulated group. This was due to cell death for the nodule formation of the mechanical stimuli group which resulted from cell differentiation. During the MC3T3-E1 cell differentiation, alkaline phosphatase was used as a mark of osteoblast differentiation. The alkaline phosphatase activity increased slightly in the control group, however, no statistically significant maximum point was observed. In the mechanical stimuli group, it increased significantly and reached its peak level on day 7, statistically significant maximum point (P<0.05), which represents the beginning of cell differentiation. Nodule formation have also been observed through the microscope since day 7. Conclusively, it could be noted that the effects of the differentiation in the mechanically stimulated group was significant.

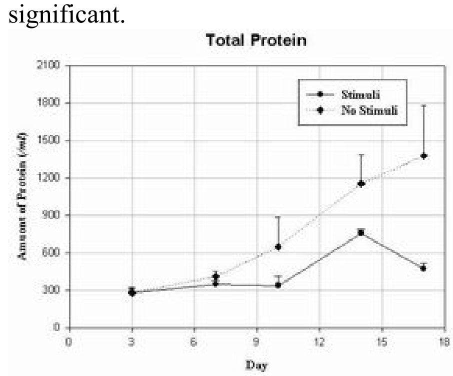

Figure 1. The amount of total protein produced by cells.

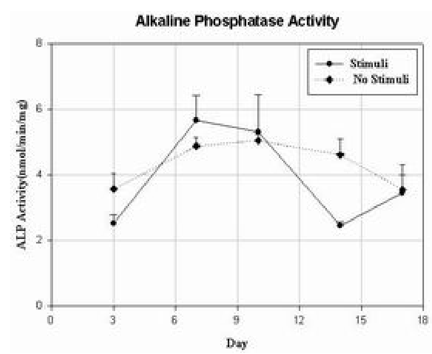

Figure 2. The alkaline phosphatase activity of cells.

SUMMARY

In this study, an osteoblast-like cell line was cultured in 3-dimensional chitosan scaffolds and a cyclic compressive strain was applied to this scaffold. The effects of the mechanical stimuli were significant in the cell proliferation and differentiation process as well as calcification process.

REFERENCES

J.Y. Choi et al.(1996). *J. of Cellular Biochem*. 61, 609-618
Lidan You et al.(2001). *J. of biomechanics* 34,1375-1386

LIPOATROPHIA SEMICIRCULARIS: A BIOMECHANICAL APPRAOCH

Richard H.M. Goossens[1] and Chris J. Snijders[2]
[1]Delft University of Technology, Faculty of Design, Construction and Production
Landbergstraat 15, 2628 CE Delft, The Netherlands, r.h.m.goossens@io.tudelft.nl
[2]Erasmus University Rotterdam, Medical Faculty, Department Biomedical Engineering and Technology
POBox 1738, 3000 DR Rotterdam, The Netherlands

INTRODUCTION

Lipoatrophia Semicircularis (LS) is a highly characteristic dermatosis, which represents as semiannular depressions from loss of subcutaneous fat, symmetrically distributed on the anterolateral aspects of both thighs, and occurs predominantly in young women(De Groot 1994).

In literature different causes are postulated. Bloch and Runne (Bloch and Runne 1978) state that semicircular lipoatrophy represents an ischemic atrophy of the fatty tissue, manifested by repeated microtraumata (corners of wash- basins, dressing tables or desks). De Groot (De Groot 1994) suggests that pressure from a chair on the posterior aspect of the thighs, possibly in combination with direct pressure from a desk on the anterior aspect, caused the condition in these patients. More recently Hermans et al. (Hermans, Hautekiet et al. 1999) found remarkable posture differences between the LS group and the group without LS were found: less use of the lumbar support of the chair, static sitting postures and a too high seat surface of the office chair were characteristics of the subjects with LS. These observations were confirmed by higher pressure measurements for the subjects with LS.
The common aspect of all studies is that some relation is made with the mechanical load of the thighs and LS.

Aim of the present study is to gain insight into the factors that play a role in the mechanical load of the anterolateral thighs in relation with different ways of body support by different office chairs.

METHODS

A simple biomechanical model shows that the load on the seat that is mainly concentrated at the ischial tuberosities is effects in an extra load of the anterolateral thighs (figure 1).

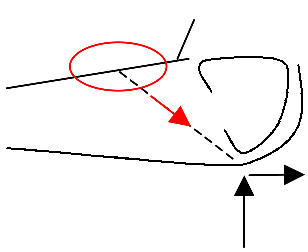

Figure 1. Pressure and shear on the buttocks effects in tension on a small area on the upper leg (elipse).

The hypothesis is that this extra tension in the proximal part of the upper thigh will result in deformation of the tissue and as a result of that a reduction of the blood flow.
The blood flow was measured as skin oxygen(tension with the Transcutaneous Oxygen/Carbon Dioxide Monitoring System on three places of the upper leg (figure 2) of 10 healthy young women (between 20 and 30 years of age). The drop in skin oxygen tension compared to standing was recorded in three sitting situations; high shear force, low shear force and sitting without the use of the backrest but with a too high seat surface.

RESULTS AND DISCUSSION

In figure 2 it can be seen that the drop in skin blood flow is highest when high shear forces act on the buttocks, as is predicted by the model.

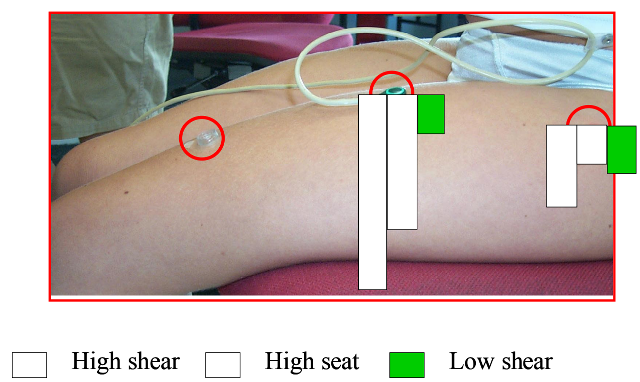

Figure 2. Three load situations on the thigh and the effect on skin blood flow.

The above finding might indicate that shear force on the tuberosities plays an important role in the cause of LS.
In a follow-up test 28 LS patients were given a 'low shear' office chair. After 13 weeks LS was diminished in 17 of the cases (60%).

REFERENCES

Bloch, P. H. and U. Runne (1978). "[Lipoatrophia semicircularis in the male. Coincidence of arterial variations and micro-traumas as a possible disease cause]." *Hautarzt* 29(5): 270-2.
De Groot, A. C. (1994). "Is lipoatrophia semicircularis induced by pressure?" *Br J Dermatol* 131(6): 887-90.
Hermans, V., M. Hautekiet, et al. (1999). "Lipoatrophia semicircularis and the relation with office work." *Appl Ergon* 30(4): 319-24.

TRANSIENT DYNAMIC BEHAVIOR OF OCCLUDER IN MECHANICAL AORTIC BILEAFLET CARDIAC VALVE (SJ) IN CLOSE PHASE USING FINITE STRIPS METHOD

M.T.Ahmadian[1], H.Mohammadi[2] (hadi_mohammadi@hotmail.com)

[1.] Associate Professor, Mechanical Engineering Department, Sharif University of Technology, TEHRAN,IRAN, [2.] MS Mechanics

INTRODUCTION Transient dynamic analysis of occluder in aortic bileaflet cardiac valve in close phase is considered. The fluid analysis (Blood) is based on the control volume with moving boundaries in the vicinity of the occluders. Governing equations including continuity and momentum equation in unsteady state are used for calculations of backflow and its velocity. Exerting external forces contain gravity and pressure effect and its dynamic balancing on occluder about pivot axis gives angle, velocity of occluder tip and impact forces between occluder and its housing in a function of time in close phase. Results indicate that the maximum impact force between occluder and its housing is in the range of 75-140 N that takes 35-45 milliseconds (ms). Governing equations are equation of motion for the occluder including momentum as the occluder rotate about its hinge pivot. The model used in this analysis is assumed to have 38 mm leaflet valve diameter such as a St.Jude bileaflet valve.

METHODS For simulation of the aortic space and proper approximation in solution, the following assumptions is mained. For simplification of analysis and computing, it was assumed that the flow is unidirectional in the axis direction. Due to complexity of the projected area between the circular occluder and circular orifice area at various positions of the occluder during closing the orifice on the occluder, cross sections were also assumed to be rectangular in the initial study. It was also assumed that the flow is laminar and velocity is uniform at every cross section in the control volume as well as the inlet. Thus, the effect of viscous diffusion in the short period of valve closure was neglected. The backflow is separated into flows through minor and major flow orifice at the entrance section. The analysis simulates the valve dynamics in the aortic position and it was assumed that the pressure of the fluid will be the same as that of the ventricle with the occluder in the fully open position at the initiation of valve closing. It was also assumed that the pressure of ventricular chamber is uniform. On the other hand, the fluid through section passes through converging channel between the occluder and the wall. Hence, velocities and pressures vary continuously through the converging channel. Because the control volume has moving boundaries and their shape varies according to time, unsteady conditions and the unsteady Bernoulli's equation" should be considered for the analysis. The steps of the calculations is shown in figure 1.

RESULTS The governing equation of motion for the occluder was solved by forth order Runge Kutta method. The average aortic pressure at closing varied between 10.7-16.0 kpa (80-120 mmHg) and was assumed constant during closing. For the final condition for step II fig.1, the occluder was assumed to have reached the resting position when the occluder angle of the successive time increment is less than "0.5" degree after impact. It takes about 10-18 ms before occluder comes to rest in the fully closed position after impacting against the housing. The maximum velocity at the occluder tip is in the range of 7-8 m/s. Gao and Hwang have reported that the maximum velocity of the occluder tip of bileaflet valve 4.5 to 4.8 m/s (Dia.=24mm)[1].

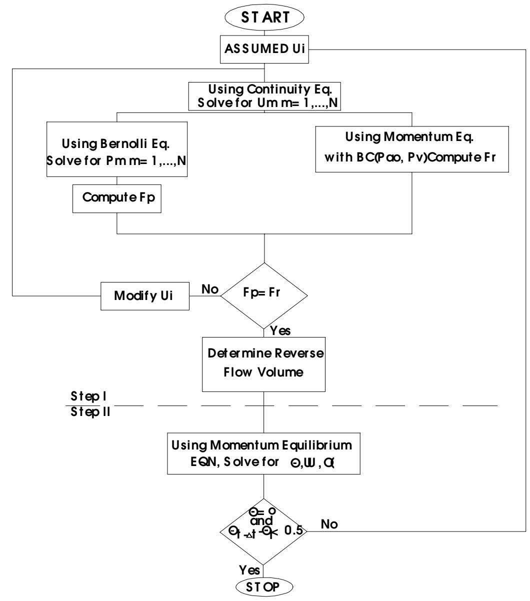

Fig 1- Flow Chart of the Computational Scheme

The backflow exhibit oscillation similar to that of the occluder, but the net backflow volume is about 5.5 cc. Sabban and Stein have measured the closing backflow to be about 3 cc(Dia.=24mm)[2].

SUMMARY With the application of continuity and momentum equation, the closing backflow is calculated in the range of 1.5 to 5.5 cc with various initial opening angles in aortic section. As the initial opening angle decrease, the backflow volume decreases. The maximum backflow velocities are in the range of 3-5 m/s. The position of the occluder as a function of time and the tip velocity were calculated by the solving the governing equations of motion with the fluid pressure and equivalent gravitational force as external forces. It was also possible to calculate the relative velocity of the fluid against the occluder tip. The calculation values of the tip velocity and backflow volume are in the agreement with the previous experimental analysis. Hence, the theoretical method employed in this study, appear to be suitable. How ever, several assumptions to this study must be pointed out.

REFERENCE [1]Gao G.X., Xu C.C., "Laser Assessment of Leaflet Closing Motion in the Prostheses Heart Valve", J. of Biomechanical Engineering, 1990, Vol. 12, pp. 477-481

[2] Sabban H.N., Stein P.D., "Comparative Study of the Amount of Backflow Produced by Fourth Type Aortic Valve Prostheses", J. of Biomechanical Engineering, 1984, Vol. 106, pp. 66-71. Cardiac Valve Prostheses", J. of Biomedical Engineering, 1991, Vol. 24, pp. 333-341.

MEASUREMENT OF HEAT CHARACTERISTICS OF A NEW INCUBATOR WITH A CHEMICAL ENERGY SOURCE USING INVERSE PROBLEM SOLUTION AND FINITE ELEMENT METHOD.

M.T.Ahmadian[1], , F.Bahramian[2]
[1]Associate Professor, Mechanical Engineering Department, Sharif University of Technology, Tehran, Iran
[2]MS Mechanics, E-Mail:f_bahramian@hotmail.com

INTRODUCTION

Generally, babies are kept adequately warm at home and hospitals, some times it is necessary to transfer the baby, in this case, it is important to keep the baby warm during transportation. Most developing countries are unable to afford the high costs of commercial incubators, and sufficient personnel to supervise their use and maintenance are not available. A new transport incubator was designed, which produces heat via an exothermic crystallization reaction initiated by a metal disc in a plastic container. A new incubator was made with blue Styrofoam with K= 0.025 W/mk. The number of chemical bags was considered as a mechanism for control of the inside temperature of the incubator.

METHOD

In order to develop a thermodynamic model of this device, the first law of thermodynamic is used in a control volume of enclosure.

$$(1)\ (mc_p)_{air}\dot{T} = \sum UA(T_r - T) + \dot{q}_b + \dot{q}_s + (mc_p)_{in}(T_r - T)$$

$(mc_p)_{air}$: heat capacity of the air, $(mc_p)_{in}$: heat capacity rate of the incoming fresh air or oxygen, T : inside temperature, T_r : ambient temperature, $\dot{q}_s$: heat transfer from the sodium acetate, $\dot{q}_b$: rate of heat loss from baby, $\sum UA$: total heat transfer coefficient of incubator walls, $\dot{q}_s$ & $\sum UA$: unknown

Due to the complex geometry and the heat transfer mechanism in the enclosure the value of $\sum UA$ can not be calculated accurately by means of the conventional formula or numerical methods. Therefore, $\sum UA$ is obtained experimentally. The non-linear regression method known as parameter estimation is used to obtain the unknown parameters by using numerical and experimental method.

In experimental part of this method, the inside temperature of enclosure is measured using thermocouples and a Pico TC-08 data logger.

Initially this method is used to find the time dependent behavior of $\dot{q}_s$. The rate of heat released by the chemical, $\dot{q}_s$, is partly due to the heat generation from crystallization process, and partly due to the heat capacity of the chemical. As the rate of heat transfer of the chemical is time dependent, thus the conventional calorimeter method is not appropriate. Therefore, the parameter estimation method is used to find the time dependent behavior of $\dot{q}_s$. In order to obtain $\dot{q}_s$, an insulated flask is used and the thermodynamic model of the air in the flask is solved by above method.

$$mc_p \frac{dT}{dt} = UA(T_r - T) + \dot{q}_s$$

mc_p : heat capacity of the air, T : inside temperature of the flask, T_r : ambient temperature, UA : total heat transfer coefficient from the aie inside the flask to the environment. When $\dot{q}_s$ is determined Eq.(1) is solved by parameter estimation method.

RESULTS AND DISCUSSION

As the results show, the amount of heat generation of sodium acetate is:

$$(2)\ \dot{q}_s = 2.27 + 5*10^4 t - 10^{-7} t^2 + 6.7*10^{-12} t^3$$

The average amount of UA was calculated based on different number of bags in the canopy, shown in Table 1.

Table1-UA for Canopy

No. of Bags	3	4	7
UA(W/k)	1.94±0.30	3.±0.30	5.24±0.66

Considering the value of UA in the table it is clear that UA is increasing with the increasing the number of chemical bag. However other factors such as ambient temperature and the location of the bags do not significantly influence the value of UA. Finally, this model was numerically verified by MSC/NASTRAN Software.

SUMMARY

In this research a thermal model was developed for a new non-electric infant transport incubator. The source of heat comprises a super saturated solution of sodium acetate. In the thermal modeling of the incubator the amount of heat generation is considered. Condition of the chamber in relation to the baby and chemical heat source was studied. The total heat transfer coefficient UA for different ambient temperature was calculated. The proper number of chemical bags with respect to ambient temperature and the conditions of the chamber are estimated in this paper.

REFERENCES

F.P. Incorpera, D.P.Dewitt, "Introduction to heat transfer" 2nd Ed.,John Wiley & Sons,1996.

J.V. Beck, K.J. Arnold, "Parameter Estimation in Engineering & Science", John Wiley & Sons,1997.

LONGITUDINAL EXTENSION OF MUSCULAR CONDUIT ARTERIES AFFECTS DISTENSIBILITY

Martin A. Zulliger, Naomi T. M. R. Kwak, Theodora Tsapikouni, Nikolaos Stergiopulos
Laboratory of Hemodynamics and Cardiovascular Technology, Swiss Federal Institute of Technology, Lausanne (EPFL), Switzerland
martin.zulliger@epfl.ch

INTRODUCTION

With progressing age large arteries diminish their longitudinal stretch (λ_z). This may eventually result in tortuosity. Further, increased age is also associated with loss of vessel distensibility or compliance, frequently also associated with hypertension. We show data from muscular porcine carotids measured *ex vivo* that suggest a possible biomechanical link between the decrease of λ_z and the loss of distensibility.

METHODS

Muscular segments of porcine carotid arteries (n=8) were harvested at the local slaughterhouse and transported in PBS (with Ca^{++} and Mg^{++}) on ice to our laboratory. Immediately upon arrival, the adventitia was carefully removed and approximately 3 cm long segments were mounted on a longitudinally extensible support in a PBS bath with Ca^{++}, Mg^{++}, and Glucose (11.1 mM) held at 37°C. Then, the arteries were pressurized to a physiological pressure of 100 mmHg.

Using a high-precision ultra-sound tracking device (NIUS, Omega Electronics, Switzerland) pressure-diameter (p-d) and pressure-wall thickness (p-h) curves were measured in three different vascular smooth muscle (VSM) states. In the order we proceeded in, these VSM states were normal VSM tone, totally contracted VSM (KCl, 90 mM), and totally relaxed VSM (sodium nitroprusside (SN), 100 µM). In each state the measurement was performed for both λ_z=1.4 and λ_z=1.8 (randomized order) after 5 preconditioning inflation-deflation loops (0-150 mmHg) and allowing time for adequate equilibration and drug exposure.

To form mean curves and to perform Student paired t-tests where appropriate, the Langewouters function (Langewouters, 1984) was fitted to raw data to calculate p-d and p-h values at pressure intervals of 10 mmHg. From these the vessels distensibility D was obtained applying:

$$D = \frac{1}{d^2}\frac{\partial}{\partial p}d^2 \qquad (1)$$

Similarly, from the fitted functions, the Hudetz incremental elastic modulus (Hudetz, 1979) was calculated at 0.05 intervals of circumferential stretch (λ_θ):

$$H_{\Theta\Theta} = \frac{1}{2}\left(\frac{r_o \cdot r_i^2}{\left(\left.\frac{\partial r_o}{\partial p^*}\right|_{p^*=p}\right)} + p \cdot r_o^2\right) \cdot \frac{1}{r_o^2 - r_i^2} \qquad (2)$$

where $r_i = d/2$ and $r_o = (d+h)/2$ are the inner and outer radii of the artery's wall.

RESULTS

Distensibility was found to differ significantly ($p<0.05$) over the entire physiological range (50-150 mmHg) in its normal tone (Figure 1) and totally passive VSM states. In the totally contracted VSM state distensibility remained uninfluenced by the longitudinal stretch.

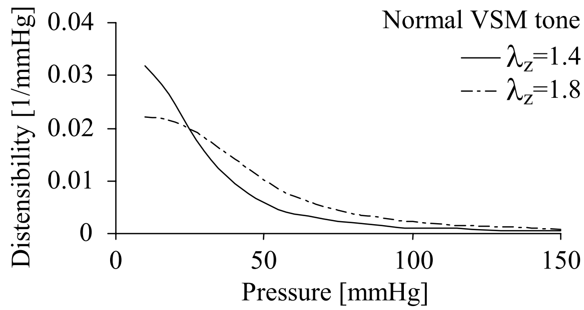

Figure 1: Distensibility of porcine carotid arteries (n=8) at different longitudinal stretch under normal VSM tone. Above 50 mmHg less elongated arteries are significantly stiffer ($p<0.02$).

The Hudetz elastic modulus was found to be virtually identical for the totally contracted and totally relaxed VSM state. Normal tone VSM modulus were slightly elevated, though not significantly, at λ_z=1.8.

DISCUSSION

The apparent passive and active material properties (Hudetz elastic modulus) of the carotid artery remain unaffected by changes in λ_z even though VSM tone might change. Nevertheless, the functional property (distensibility) of the artery is significantly changed, even in its passivated state. Both small λ_z and low distensibility appear with progressing age as well as changes in material composition and properties. The data presented above suggests, that a change in longitudinal stretch in itself is sufficient to change arterial distensibility.

REFERENCES

Langewouters, G. J., et al. (1984), J Biomech 17(6): 425-35.
Hudetz, A. G. (1979), J Biomech 12(9): 651-5.

ACKNOWLEDGEMENTS

This work is supported by the Swiss National Science Foundation (0021-055665.98).

BIOMECHANICAL EVALUATION OF RECONSTRUCTION AFTER TOTAL SACRECTOMY

Hideki Murakami[1], Katsuro Tomita[1], Norio Kawahara[1], Akira Yoshida[1] , Jiro Sakamoto[2] and Jyuhati Oda[2]

[1]Department of Orthopaedic Surgery, Kanazawa University, Kanazawa, Japan
[2]Department of Human and Mechanical Systems Engineering, Kanazawa University, Kanazawa, Japan

INTRODUCTION

Among sacral tumors, aggressive benign bone tumors such as chordoma, giant cell tumor and chondrosarcoma are the most common. If a malignant tumor or an aggressive benign tumor is excised with an intralesional margin, the likelihood of local recurrence apparently increases and this can lead to fatal disease. Therefore, en bloc sacrectomy with enough tumor free margin is indicated even though the continuity between the pelvis and spine are sacrificed. Radical excision of a sacral tumor involving the 1st sacral vertebra necessitates a total sacrectomy, to be followed by reconstruction of the continuity between the spine and the pelvis. However, the sufficient reconstruction procedure has not been established yet. Some authors have previously described such a reconstruction. One of the methods is a modified Galveston reconstruction (MGR) using the Galveston method. However, there has been no mechanical analysis of these reconstructions. In this study, finite element analysis was carried out to evaluate reconstruction models after total sacrectomy.

METHODS

We have mechanically evaluated two reconstruction methods: modified Galveston reconstruction (MGR) and novel reconstruction (NR) developed by us. In the first method which is commonly used reconstruction, after insertion of pedicle screws into the 3rd, 4th and 5th lumbar vertebrae and two bilateral iliac screws into two iliac bones, these screws are connected by two spinal rods. The second model consists of both posterior and anterior instrumentations. Posterior instrumentation consists of pedicle screws inserted into the 3rd, 4th, and 5th lumbar vertebrae, iliac screws inserted into posterior iliac crest and two rods, which connect them. Anterior instrumentation consists of two screws inserted into inferior endplate of the 5th lumbar vertebra, a sacral rod connected with both sides of the pelvis through these screws and a sleeve augmentation of the pelvis. The three-dimensional MGR and NR models were reconstructed to clarify the stress concentration on the bones and instruments using finite element analysis. A finite element model of the reconstruction model was made based on computed tomographic images taken of a healthy adult male. Material properties were assumed according to the literature. The boundary conditions considered were for 960 N weight applied vertically to upper surface of the 3rd lumbar vertebra and the bottom of the pelvis being fixed. Half region was used in the analysis because of the symmetry.

RESULTS AND DISCUSSION

Generally, a risk of breakage or loosening at the points in which undue stress concentrated is higher. In MGR model, maximum Mises stress (14 MPa) at the bones was observed at a region of the lateral cortical bone around the inferior iliac screw. This stress is less than the yield stress of cortical bone (83 MPa). However, concerning the instruments, high stress (1042 MPa) was observed at a region of the spinal rod between the L5 pedicle screw and the iliac screw. This stress is higher than the yield stress of the titanium alloy (860 MPa). If the patient were to stand or sit immediately after the reconstruction, there is the risk of fracture of the instruments because of high stress in the spinal rods. A large load was transmitted from the lumbar vertebrae to the pelvis via the posterior rods only and excessive stress was concentrated at the spinal rod. Breakage of the spinal rod at this juncture has been found clinically. So in order to avoid stress concentration in MGR, it is necessary to add anterior support. In NR model, stress concentration was observed at the region of the connection between the sacral rod and the screws. The maximum stress was 400 MPa, which is lower than the yield stress of the titanium alloy. In the bones, stress concentration was observed at the region of the insertion of the sacral rod in the pelvis. The maximum stress was 77 MPa, which is just lower than the yield stress of the cortical bone. Excessive stress concentration was not detected in NR model. A 48-year-old female underwent NR for a giant cell tumor of sacrum. At the 20-month follow-up, she was healthy, with no recurrence or metastasis. The spine and the pelvis were stabilized well and no failure of spinal instrumentation was noted.

SUMMARY

In MGR, there is a strong possibility that the rod might fail. Patients should avoid weight-bearing until the grafted bone is fused. In NR, no particular stress concentration was detected. We concluded that the NR has a low risk of instrument failure and loosening after a total sacrectomy.

Figure 1: MGR

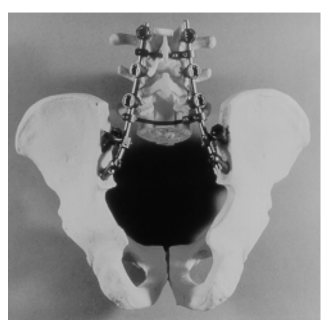

Figure 2: NR

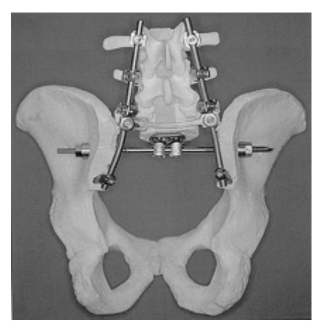

THE NEW JUMPING HILL IN INNSBRUCK: DESIGNED BY MEANS OF FLIGHT PATH SIMULATIONS

Wolfram Müller and Bernhard Schmölzer
Institute of Medical Physics and Biophysics, Karl-Franzens University Graz, Austria
Communicating author, wolfram.mueller@uni-graz.at

INTRODUCTION

A modelling concept that considers the relationship of the aerodynamic lift and drag forces ($F_l = \frac{\rho}{2} \cdot w^2 \cdot L$; $F_d = \frac{\rho}{2} \cdot w^2 \cdot D$) on the flighing position by means of tabulated input functions for $F_l = F_l(t)$ and $F_d = F_d(t)$ has been described in detail before (Müller et al 1995, Müller et 1996, Schmölzer and Müller 2002). The model is based on the non-linear and coupled equations of motion that are valid for any object in air (with a given air density ρ). The gravitational force and the forces due to the airstream (w = u – v, w being the resulting airstream vector, u wind velocity, v velocity of motion of the object) determine the flight path with a given set of initial conditions and parameters. The application of this computer model to the design of jumping hills (Müller 1997) and a detailed analysis of the accuracy of this modelling approach have been described before (Schmölzer and Müller 2002).

METHODS

Here, we focus on the analysis of the landing impact which depends on one hand on the flight velocity and the flight path angle at landing and on the other hand on the geometric properties of the landing hill: At landing, the athlete has to compensate the momentum perpendicular to the landing slope. In order to "translate" the language of physics into terms that can easily be understood, we compare this momentum with the one that corresponds to a jump onto a horizontal plane from a height h_l (*equivalent landing height* h_l). There are several possibilities to obtain an increased jump length in the simulation. We can vary the approach velocity υ_0 , or the velocity perpendicular to the ramp at take-off υ_{p0} , apply a wind blowing up the hill, use a shallow ramp angle, shift the L = L(t) or the D = D(t) function, or reduce the mass m. All these simulation protocols would result in similar characteristics in relationship to of h_l on the obtained jump length l. Here, different jump lengths have been obtained by increasing the approach velocity υ_0 in the simulation protocol.

RESULTS AND DISCUSSION

We have suggested a jumping hill profile for Innsbruck that deviates remarkably from all other previous profiles: In Innsbruck (I in Figure 1, K = 120m) the equivalent landing height h_l increases continuously with increasing jump length l and does not show a kink from which the equivalent landing height would increase rapidly as do all other profiles that have been built before. Figure 1 also shows examples of other profile characteristics: The new jumping hill in Innsbruck I_120 shows several advantages when compared to conventional profiles: 1. No abrupt increase of the landing impact beyond a certain jump length (increased safety and fairness). 2. Decreased sensitively to wind (increased fairness). 3. Decreased sensitively to the approach velocity (makes it easier to run a competition).

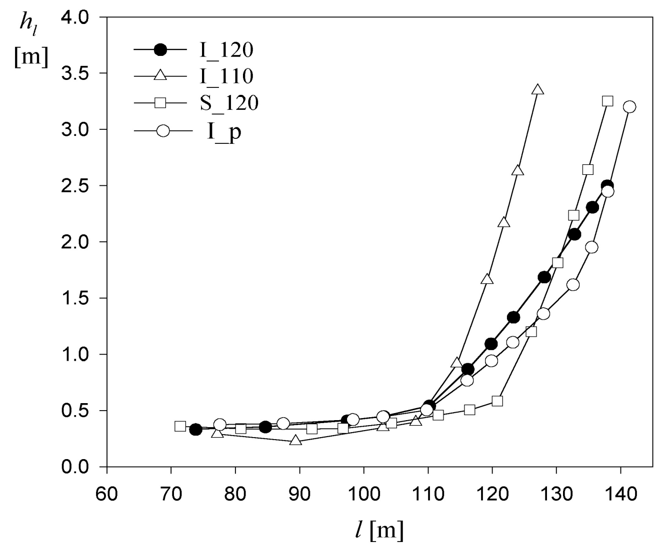

Figure 1: Dependency of h_l on the jump length l
I_120: new profile Innsbruck; I_110: old profile Innsbruck; S_120 Sapporo; I_p planed without computer simulation, has not been built in Innsbruck because of the dangerously rapid increase of h_l from l = 134m on.

SUMMARY

The computer simulation of ski jumping enables the design of "custom-made" jumping hill profiles. The characteristics of a jumping hill can be determined and optimised in all details in advance. This scientifically based approach can save large amounts of money when compared to trial and error approaches that might need to be corrected afterwards.

REFERENCES

Müller, W. et al. (1995). *Nature*, **375**. 455.
Müller, W. et al. (1996) *J. Biomech*, **8**. 1061-68.
Müller, W. (1997). In: *Science and Skiing*, 36-48.
Schmölzer, B., Müller, W. (2002) *J. Biomech*, (accepted).

ACKNOWLEDGEMENTS

Supported by: Austrian Science Fund FWF (P14388TEC), IOC, FIS, Land Steiermark

EVALUATION OF SLOTS FOR DESTRUCTIVE CEREC RESTORED PREMOLAR BY FINITE ELEMENT METHOD

Chun-Li Lin[1] and Yen-Hsiang Chang[2]
[1]Department of Mechanical Engineering, Chang Gung University, Tao-Yuan, Taiwan, cllin@mail.cgu.edu.tw
[2]Operative Dentistry, Chang Gung Memorial Hospital, Tao-Yuan, Taiwan.

INTRODUCTION

A large field of destructive premolar, such as a remaining tooth fractures after extensive MOD restoration is a common and complicated clinical biomechanical problem. Generally traditional restorative methods (direct and indirect) are employed exhaustively to repair the destructive tooth. In recent years, CAD/CAM technology has added the new option of producing chairside ceramic restorations for repairing a large decimated tooth. However, the long-term success of a ceramic restoration relates to the mechanical integrity arising from the restorative engineering design (Chen et al., 1999; Lin et al., 2001). The aim of this study was therefore to determine the biomechanical aspects of various CEREC restorative tooth designs using linear and nonlinear finite element (FE) analyses.

METHODS

An intact maxillary second premolar was selected. The CEREC system was used to restore the extensive destruction induced by previous MOD restoration failures in which the lingual cusp was lost. The restored tooth was embedded and sliced serially to expose the tooth-resin sections. An in-house program was employed to detect the boundaries for different materials from each sectioned scanning image. Four FE restored tooth models (Fig. 1-a and Table 1) were constructed using a commercial package (ANSYS) through contour stacking, Boolean operations and mesh generation procedures. Bonded (linear) and contact (nonlinear) interfacial fixations were modeled to simulate the adaptations between the tooth structure and restorative material. Interfacial (normal and shear) stresses were then calculated using self developed program for four restored teeth with two occlusal forces (12 simulated models in total) to evaluate the biomechanical interactions.

RESULTS AND DISCUSSION

The extensive ceramic restoration fabricated using the CEREC system without any reinforced design usually has doubtful structural stability and adhesion-bonded strength for long-term use. A reinforced design, such as a slot considered for increasing the tooth/ceramic interface, is an attempt to improve the clinical performance. However, the simulated results indicated that the stress values (Table 1) at the buccal wall increased with slot designs for both a bonded and debonding interface when a single occlusal force acted on the tooth. This was because the lateral micro-motion of the restorative ceramic was constrained by the slot and induced the lingual bevel surface to receive higher compression under the bending moment effect (Fig. 1-b). In contrast, the interfacial stresses decreased with slot designs when the tooth received uniform occlusal pressure. These results implied that different occlusal forces affect the interfacial stress distribution and might be a more important factor than preparation design. Therefore slot-reinforcement effects seem to be doubtful in a tooth that subjected to a lateral load.

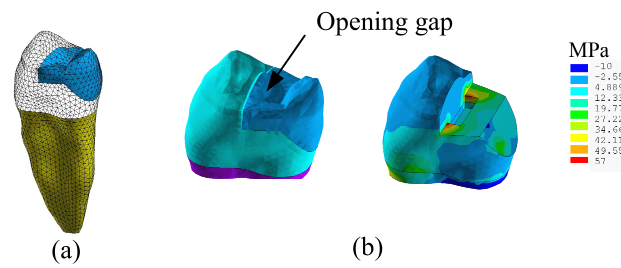

Figure 1: (a) One of the restored FE models, (b) Displacement and max. principle stress patterns for a 1mm slot design with debonding condition.

SUMMARY

Based on the limited data, we conclude that the extensive destruction in a premolar can be restored directly through normal CEREC procedures without other reinforcement designs. Utilizing occlusal adjustments to reduce the lateral bending moment does redistribute the tooth/ceramic interfacial stresses. Further *in-vitro* and *in-vivo* studies are needed to validate the conclusions of this study.

REFERENCES

Chen, H.Y. et al (1999). *J. Prosthet Dent*, **82**, 468-475.
Lin, C.L. et al (2001). *J. Oral Rehabil*, **28**, 576-585.

Table 1: Peak interfacial and maximum principle stresses at buccal wall for four restored teeth.

Restored types	Interfacial stresses (single force with bonded condition) (MPa)		Interfacial stresses (uniform occlusal pressure with bonded condition) (MPa)		Max. principle stress (single force with contact condition) (MPa)
	Tension	Shear	Tension	Shear	
Without slot	9.07	12.25	16.1	13.27	35.711
With central slot (1mm depth)	9.53	14.32	14.98	11.74	56.168
With central slot (2mm depth)	10.00	14.38	14.83	11.59	67.81
With lingual slot (1mm depth)	9.56	14.60	14.71	13.27	33.97

COOPERATIVE FORCE ANALYSIS OF ELEVEN MUSCLES DURING ABDUCTION OF THE SHOULDER

Naomi Oizumi[1], Shigeru Tadano[2], Youichi Narita[2], Norimasa Iwasaki[1], Naoki Suenaga[1], and Akio Minami[1]
[1]Orthopaedic Surgery, Graduate School of Medicine, Hokkaido University, Sapporo, Japan noizumi@med.hokudai.ac.jp
[2] Devision of Mechanical Science, Graduate School of Engineering , Hokkaido University, Sapporo, Japan

INTRODUCTION

It is difficult to directly examine the muscle force in living subjects. Many muscles are acting cooperatively in a human shoulder, therefore, computed simulation may be useful in analyzing the muscle force. In this study, a method of numerical analysis of muscle force during shoulder abduction was described.

METHODS

Three-dimensional muscloskeletal model was created from normal volunteer's CT data of the shoulder. Muscle vector was modeled by a straight-line vector from the insertion to the origin of each muscle. Analyzed muscles were F1; anterior fiber of deltoid, F2; middle fiber of deltoid, F3; posterior fiber of deltoid, F4; supraspinatus, F5; infraspinatus, F6; subscapularis, F7; teres minor, F8; teres major, F9; long head of biceps, F10; short head of biceps, F11; triceps. Figure 1 shows the three-dimensional model for analysis. Muscle force was calculated from equilibrium equations of force and moment using sequential quadratic programming (SQP) method as optimization. Objective function was determined as the total sum of the square of the muscle force divided by the physiological cross sectional area. For the muscles originated from wide area (F1-6), the optimization method was also used in selecting the proper point of the origin for each abduction angle. Static analyses were performed for every 5° of abduction of the glenohumeral joint in a scapular plane.
The analyzing results were compared with the data of electromyography (EMG), which was obtained from the same volunteer.

RESULTS AND DISCUSSION

Results of the muscle force analysis were shown in Figure 2. Middle fiber of deltoid (F2) demonstrated remarkably large force. Supraspinatus (F4), anterior fiber of deltoid (F1), and infraspinaus (F5) followed it. Posterior fiber of deltoid (F3), subscapularis (F6), and teres minor (F7) were acting at late phase of abduction. These results qualitatively corresponded with the integrated EMG activity.
The current model for numerical analysis using optimization was useful in predicting muscle forces cooperatively acting for the shoulder movement.

SUMMARY

Numerical analysis of muscle force during shoulder abduction using optimization method was demonstrated in this study. Three-dimensional muscloskeletal model was build from normal volunteer's CT data. SQP method was applied to calculate muscle forces from equilibrium equations of force and moment. The results of analysis qualitatively corresponded with the integrated EMG activity.

REFERENCES

Meek, S.G., Wood, J.E., et al. (1990). *Multiple Muscle Systems.* Springer-Verlag Press.
Crowninshield, R.D., Brand R.A. (1981). *J. Biomech.*, **11**,793-801.
Karlsson, D., Peterson, B. (1992). *J. Biomech.,* **25**,189-199.

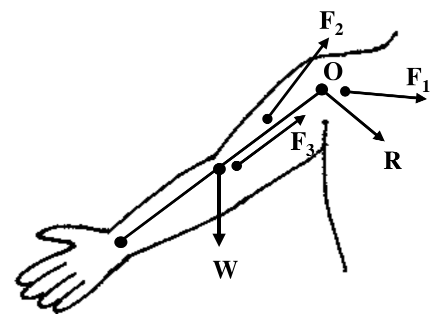

Figure 1: Three-dimensional model of upper limb (O; center of rotation, F; muscle force (i=1~11), R; reaction force over the joint, W; self weight of the upper limb)

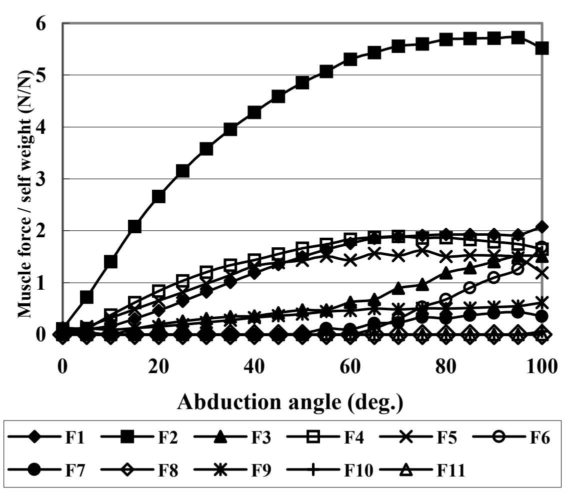

Figure 2: The results of the muscle force analysis

STRUCTURE-FUNCTION RELATIONSHIP IN TENDON FASCICLES UNDER TENSILE LOADING CONDITIONS

Screen, HRC[1]; Lee, DA[1,2]; Bader, DL[1,2]; Shelton, JC[1,2]
[1] IRC in Biomedical Materials, Queen Mary University of London, London, UK,   H.R.C.Crane@qmul.ac.uk
[2] Medical Engineering Division, Department of Engineering, Queen Mary University of London, London, UK

INTRODUCTION

The collagen within a tendon fibres are interspersed with tenocytes, arranged in rows following the crimp. Under strain, these fibres straighten and align to the direction of loading, creating local strain fields within the tendon matrix (Screen et al, 2002). When subjected to mechanical stimuli, tenocytes initiate matrix remodelling through various mechanotransduction pathways (Banes et al, 1999). In this study we have investigated the relationship between applied strain and local strain fields in tendon, in order to develop an understanding of tendon strain mechanics.

METHODS

Collagen fascicles were teased from the tails of male Wistar rats within 2 hours of death, and kept moist in a paper towel soaked with PBS. Fascicles were then subjected to one of two test procedures, as described below.

Macroscopic examination: Thirty fascicles were subjected to quasi-static tensile testing to failure using a mechanical test machine (Elastomer, MTS). Fascicles were kept moist by continual spraying with PBS, and strained to failure at a rate of 1mm.min^{-1}. Tests were recorded using a CCD camera.

Microscopic examination: The cell nuclei of twenty-five fascicles were stained with the vital fluorescent stain acridine orange (5µl.ml^{-1} of DMEM), for 1 hour at room temperature. Each specimen was gripped in a novel mechanical test rig, mounted on the stage of a confocal microscope, which enabled visualisation of cells. Tenocytes from a region approximately equidistant from each grip, were imaged, and the nuclei motion used as a measure of strain, as previously described (Screen et al, 2002). Relative displacements between cell nuclei along the same fibre, and between fibres were recorded as intra-group strains and inter-group displacements respectively. Fascicles were strained in 1% increments to a strain of 8-10%, when cells could no longer be visualised.

RESULTS AND DISCUSSION

Stress-strain curves for individual fascicles were repeatable, and similar in form to those characteristic of bulk tendons. Figure 1a shows curves for five individual fascicles. The estimated modulus for a single fascicle was also recorded in figure 1b. The mean maximum modulus of fascicles was found to be 197 MPa ± 37.5, occurring at approximately 8% applied strain. Fascicles failed at a mean strain of 14.3% ± 1.88. Crimp straightening could be detected by macro and micro examination, and was normally distributed, occurring at an average strain of 1%. Nuclei aligned to the collagen fibres under strain (figure 2), and the fascicle was observed to narrow, often to 50% its original width.

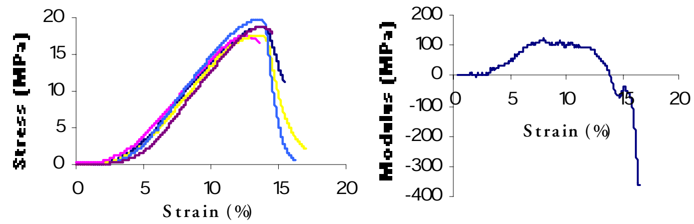

Figure 1a. Stress-strain curves for five typical rat-tail fascicles strained at 1mm.min^{-1} to failure **b.** Modulus curve for a single, representative fascicle

Once nuclei had aligned to the collagen fibres, there was little further increase in intra-group strains with increasing applied strain. By contrast, inter-group displacements continued to increase steadily. This suggests that fascicles stretch by a mechanism involving sliding between adjacent fibres. Video footage of fascicle failure displayed macro sliding between fibres, visible at an average strain of 13%. Sliding appears to provide a continual elongation mechanism for the fascicle, leading to eventual failure.

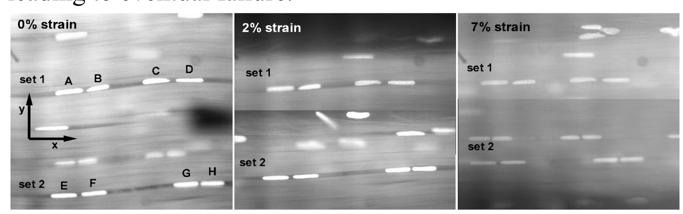

Figure 2. Relative motion of rat-tail tendon nuclei at 0, 2 and 7% applied strain

SUMMARY

Applied strain was not transmitted wholly to the cell nuclei, as tenocytes only experienced tensile strains of up to 2%. Sliding appears to provide a mechanism enabling further fascicle elongation, hence mechanotransduction pathways may in fact be stimulated by smaller strains than previously suggested (Zeichen, 2000). Cell alignment, or the shear stresses associated with fibre sliding may stimulate mechanotransduction pathways. Equally tightening of the matrix may apply compressive strains to cells, or fibre motion may strain the cell processes and initiate mechanotransduction.

ACKNOWLEDGEMENTS
This work was funded by the Engineering and Physical Sciences Research Council (EPSRC).

REFERENCES

Banes, AJ et al (1999). *Osteoarthritis Cartilage* **7** (141-153)
Screen, HRC et al (2002). *Trans Orthop. Res. Soc.***47** (604)
Zeichen et al (2000). Am. J. Sport. Med. **28** (888-892)

ANALYSIS OF STRAIN FIELDS IN TENDON FASCICLES UNDER TENSILE LOADING

Screen, HRC[1]; Lee, DA[1,2]; Bader, DL[1,2]; Shelton, JC[1,2]

[1] IRC in Biomedical Materials, Queen Mary University of London, London, UK, H.R.C.Crane@qmul.ac.uk
[2] Medical Engineering Division, Department of Engineering, Queen Mary University of London, London, UK

INTRODUCTION

Tendon is composed predominantly of type I collagen fibres, possessing a natural periodic crimp. These fibres are interspersed with cells, termed tenocytes, which are aligned in rows, following the crimp (Kastelic et al, 1978). Under tensile elongation, the fibres straighten, exposing tenocytes to a range of mechanical stimuli. The mechnical environment will induce matrix remodelling by the tenocytes (Banes et al, 1999).
In order to examine the associated mechanotransduction pathways, it is important to determine local tissue strains in tendon, and establish the mechanisms for tendon elongation.

MATERIALS AND METHODS

Fascicles were teased from the tails of male Wister rats, aged between 4 and 6 months, within two hours of death. They were then placed in the vital stain acridine orange (5μl.ml^{-1} in PBS), for 1hr at room temperature, to stain the cell nuclei. Samples were gripped in a novel test rig, mounted on the stage of an inverted confocal microscope, which enabled visualisation of the cell nuclei during mechanical testing (Screen et al, 2002).
Samples were strained in 1% increments, at a rate of 10mm.min^{-1}. The specimens were held at each strain level, whilst nuclei were imaged. A z-series of horizontal images, taken at 15 μm intervals, was recorded through the thickness of the tendon. Samples were strained to maximum values of up to 5% strain, and then returned to zero in 1% increments.
The centre coordinate of each nucleus was located in three-dimensional space, and plotted graphically using Matlab. The horizontal z coordinate of each nucleus was taken as the plane in which the nucleus was brightest. Sections through the sample were superimposed, in order to measure intra-group strains between nuclei in two-dimensions, as previously described (Screen et al, 2002).

RESULTS AND DISCUSSION

Three groups of nuclei in different focal planes within the body of the each sample fascicle were chosen for analysis. The application of strain resulted in fibre rotation, and alignment to the direction of strain, as well as fibre translation within the fascicle matrix, as shown in figure 1. Bulk fascicle rotation also occurred under tensile strain, suggesting that fascicular structure is helical in nature. Intra-group strains were recorded during the straightening of the crimped collagen fibres, after which point, little further increase in local strains was measured, as seen in figure 2. Upon removal of applied strain, fibre crimping was restored, returning the local strains intra-group to zero.

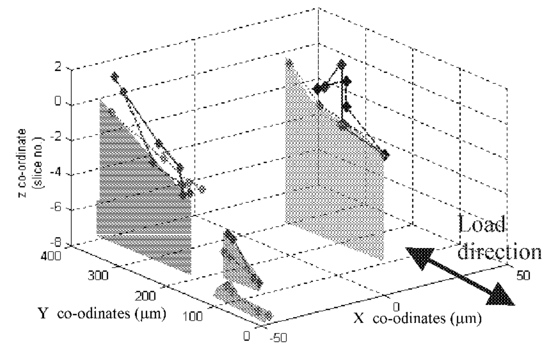

Figure 1. 3 D plot, depicting nuclei coordintes with applied strain at 0% (dashed lines) and 1% (solid lines)

As strain was removed, collagen fibres were also seen to return to their initial location within the fascicle matrix. In addition, the fascicle returned to its original helical structure. No permanent damage to the fascicle was visible in any samples.

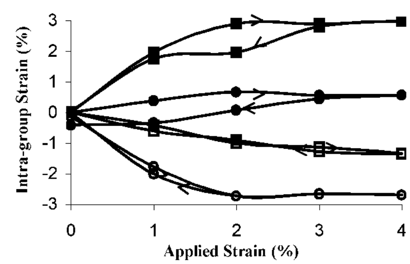

Figure 2. Intra-group strains in relation to applied strain in four cell groups of a representative fascicle.

SUMMARY

Tensile strain is transmitted through tendons via a straightening mechanism, followed by reorientation and sliding of the crimped collagen fibres. Local strain fields within the fascicle were significantly less than the applied strains, suggesting applied strain is not transmitted wholly at the level of the nucleus. Fibre reorientation under strain may induce other potential mechanotransduction pathways, involving fibre shearing and/or compression.

ACKNOWLEDGEMENT
This work was funded by the Engineering and Physical Sciences Research Council (EPSRC).

REFERENCES
Banes, AJ et al (1999). *Osteoarthritis Cartilage* 7, 141-153
Kastelic, J et al (1978) Connective Tissue Research, 6 (11-23)
Screen, HRC et al (2002). *Biorheology (in press)*

THE EFFECT OF REMOVING BLOOD AND BONE OIL ON THE MECHANICAL STRENGTH OF CEMENT-BONE INTERAFACE

Shojiro Terashima[1] and Takahiro Seki[2]
[1] Dept. of Mechanical & Control Eng., Niigata Institute of Technology, Niigata, JAPAN, george@mce.niit.ac.jp
[2] e–medical Orthopaedic Clinic, Niigata, JAPAN

INTRODUCTION

We hypothesized that removal of blood and bone oil improves the mechanical strength of the cement-bone interface. In this study, using cancellous bone, we compared the mechanical shear strength of cement-bone interface with and without blood and bone oil.

METHODS

Six pairs of ox tibiae were used. Each proximal tibia was osteotomized 20mm below the medial plateau, and vertical holes (7.5 mm diameter) were drilled in the tibiae. Each cut surface was washed using palsatile lavage to clean out bone debris.

Two cases of experiment were carried out to investigate each influence of blood and bone oil. To examine the influence of remaining blood, one side of the 3 pairs of tibiae was soaked in a fresh human blood to simulate bleeding from the bone (*BLOOD+*), and the other side was left as it is (*BLOOD-*). Likewise, to learn the effect of removing bone oil, one side of the 3 pairs tibiae was cleaned using 1 percent aqueous surfactant used as food additive (*OIL-*), and the other side saline solution (*OIL+*).

Doughy cement (Simplex P) was injected into each hole using a caliber syringe under pressure. Then, 3 cross sections of 10 mm thickness were sliced off from the proximal tibiae, and each cylindrical cement buried in the bone plates was pushed-out by Instron Mechanical Test Machine. The maximum load at failure was converted to an interface shear stress (ISS). 103 and 117 pieces of cylindrical cement were pushed to test the effect of blood removal, as the groups of *BLOOD+* and *BLOOD-*, respectively. Likewise, 139 and 121 pieces of cement were used to test the effect of oil removal using surfactant, as *OIL-* and *OIL+*.

RESULTS AND DISCUSSION

The ISS (means ± 1 S.D.) of the result of with and without blood or bone oil are shown in the Figure 1. The ISS of *BLOOD+* and *BLOOD-* were 2.3(1.1) MPa and 2.7(1.3) MPa, respectively, so the ISS of *BLOOD-* shows an increase of 18 percent as compared with *BLOOD+*. The ISS of *OIL+* was 2.6(1.5) MPa, and *OIL-* was 3.8(1.9), so the ISS of *OIL-* shows an increase of 46 percent as compared with *OIL+*. Statistically significant differences were found in the ISS between *BLOOD+* and *BLOOD-* ($p<0.01$, Student's t-test), and *OIL+* and *OIL-* ($p<0.0001$, Welch's t-test). Removal of blood and bone oil obviously improved the ISS.

Removal of blood and bone oil remarkably increased the mechanical strength probably through the improvement of microlock between cement and bone by the removal of the interposing material. Some papers described that cleaning out blood and bone debris on the bone surface gives satisfactory strength. However, other authors suggest that bone oil membrane decreases the mechanical strength, more than other factors. One of the reasons for it will be that bone oil on the surface will not be removed completely, even by applying the palsatile lavage system using only saline solution.

Figure 1: Comparison of Interface Shear Stress (Mean ±

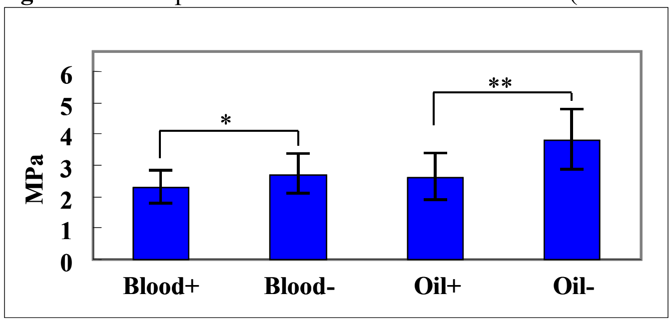

1S.D.). *p<0.01, **p<0.0001 by t-test.

SUMMARY

We evaluated the effect of removing blood or bone oil on the mechanical strength of the cement-bone interface using ox cancellous bone. The results suggest that removal of blood or bone oil within the cancellous bone is essential to improve the strength of the bone-cement interface.

REFERENCES

Mann K. A., et al., (1998). 44th *Orthopaedic Research Society*, pp.764
Martin H. Stone, et al., (1989). *Journal Bone and Joint Surgery*, vol71-B, No. 2, pp217-221
G. C. Bannister, et al., (1988). *Engineering in Medicine*, pp131-133
William R. Krause, et al., (1982). *Clinical Orthopaedic Related research*, No. 163, pp290-299
Jeff P. Davies, et al., (1987) *J Biomed Mater Res*, vol.21, pp. 719-730
R. S. M. Ling, et al., (1991). *Techniques in Orthopaedics*, vol. 6, ISSUE 3, pp.34-39, 1991

COMPUTATIONAL FLUID DYNAMICS AFTER AORTIC COARCTATION REPAIR

Simone Pittaccio[1], Francesco Migliavacca[2], Gabriele Dubini[2], Lars Sondergaard[1], Yun Xu[3], Marc de Leval[1]
[1] University College London at Great Ormond Street Hospital, London, UK
[2]Laboratory of Biological Structure Mechanics, Politecnico di Milano, Milan, Italy
[3]Department of Chemical Engineering and Chemical Technology, Imperial College, London, UK

INTRODUCTION

Coarctation of the aorta is a congenital narrowing of the upper descending aorta, generally adjacent to the site of attachment of the ductus arteriosus, which is sufficiently severe that there is a pressure gradient across the area. It accounts for about 6.5% of congenital heart disease. It can be treated using surgery or interventional cardiac catheterisation, although the surgical approach is far more common. The statistical significance of coarctation on the whole of congenital heart diseases makes it important to try and find a way of assessing the outcomes of its treatment quantitatively. The purpose of this study is to evaluate the local fluid dynamics of repaired coarctations using computational methods based on data collected from single cases.

METHODS

Two patients (age 13 and 21, respectively) were selected among those who underwent a successful surgical treatment for aortic coarctation at Great Ormond Street Hospital, London, UK. The patients were scanned with a Siemens Magnetom Vision MR Scanner (1.5 T). The geometrical data were acquired through a fi3d sequence with gadolinium injection (TR=5.0ms, TE=2.0ms, slice thickness 1.5mm, FoV=188×300, flip angle 25°). Velocity mapping was performed with a cine phase contrast fl2d sequence using the same scanner (max velocity 250cm/s, TR=324.7ms, TE=5.0ms, slice thickness 6.0mm, FoV 300×300, flip angle 30°, 24 images in a cardiac cycle).

Image segmentation was performed using Mimics (Materialise N.V., Leuven, Belgium), while geometrical modelling was made by means of Rhinoceros (Robert McNeel & Associates, Seattle, USA). CFD mesh, consisting of tetrahedral elements, was generated with GAMBIT (Fluent Inc, Lebanon, USA). Pulsatile flow simulations were carried out under Newtonian fluid and laminar flow assumptions using finite element method based CFD solver FIDAP (Fluent Inc, Lebanon, USA). Upstream velocity data obtained from MR velocity mapping were imposed as inlet boundary conditions through a FORTRAN subroutine.

RESULTS AND DISCUSSION

The geometries obtained are realistic. Results of the CFD simulations show that, apart from the influence that a suture line may have on wall properties, blood flow is reverted to a qualitatively and quantitatively normal pattern when an end-to-end anastomosis coarctation repair is considered successful according to surgical and clinical evaluation.

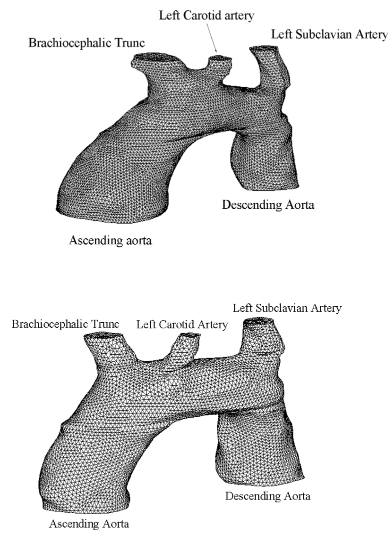

Figure 1: Aortic arch models reconstructed from MR.

REFERENCES

Long, Q. et al (1998). *Comput Methods Programs Biomed.,* **56**(3), 249-59
Wood N. B. et al (2001). *J Magn Reson Imaging.*, **13**, 699-713
Long Q. et al (1997). *Proceedings of Medical Image Understanding & Analysis,* Oxford*,* 117-120

INVESTIGATIONS OF WALL DEFORMATION AND HEMODYNAMICS AT DISTAL FEMORAL BY-PASS ANASTOMOSES

Paul Devereux, Tim McGloughlin and Sean Meehan

Department of Mechanical and Aeronautical Engineering, University of Limerick,
Co. Limerick, Republic of Ireland.
paul.devereux@ul.ie

INTRODUCTION

A major problem with small calibre vascular by-pass grafts is their relatively low patency rates of between 3-5 years (Verhelst et al., 1997). Thrombus formation and the formation of intimal hyperplasia (IH) at both the bed and suture line of the anastomosis are key events in the failure of such grafts. The presence of IH at the suture line is believed to be caused by the compliance mismatch between the host artery and the synthetic graft, with IH formation along the bed of the junction caused by the impinging blood flow (Ballyk et al., 1998). Numerical simulations using both FE and CFD techniques were carried out to assess the effect that arterial wall deformation has on wall shear stress gradients and distributions, along with flow patterns through the anastomosis.

METHODS

Finite element analysis of an idealised 45° femoral anastomosis, using MSC Marc Mentat 2000 software, was carried out to assess the extent of deformation occurring at the junction.

This deformed geometry was then exported to Gambit 2.0 and a grid independent mesh for use in the CFD analysis was created. Once this mesh was generated it was exported to Fluent 6.0 where a steady flow analysis of fluid flow through the deformed geometry was completed. The fluid modelled by Fluent 6.0 incorporated the non-Newtonian behaviour of blood by using the Carreau model of viscosity.

The un-deformed model of the anastomosis was also subjected to a CFD analysis, using the same velocity boundary conditions and fluid properties as for the deformed case.

RESULTS AND DISCUSSION

Upon completion of the finite element analysis, it was evident that relatively large deformations occur along the suture line, the heel, toe and bed. The geometry of the anastomosis is forced to distort in an attempt to accommodate the deformation occurring along the suture line. The heel and toe are forced down towards the bed, with the bed of the junction rising (Figure 1). These deformations are not accounted for when a rigid wall CFD analysis is carried out and it is for this reason that this deformed geometry was recreated in Gambit 2.0 and subjected to a steady flow CFD analysis. A steady flow analysis with identical inlet and outlet boundary conditions was completed with the non-deformed geometry.

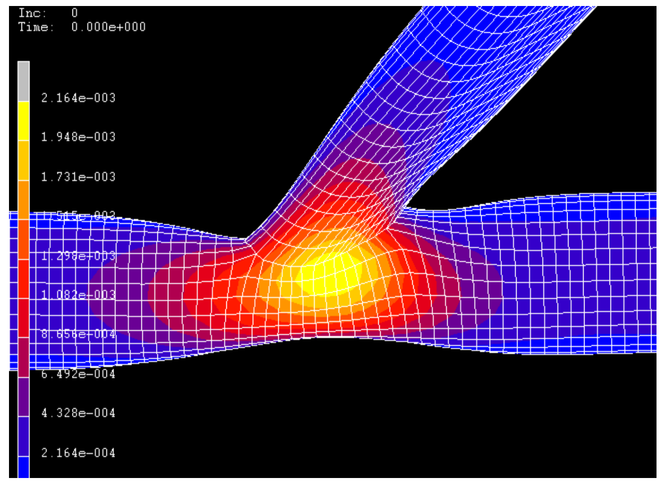

Figure 1: Deformation of femoral anastomosis

It was evident that the flow patterns through the deformed geometry, along with wall shear stress gradients and distributions were significantly different to the results obtained from the non-deformed geometry.

SUMMARY

Investigations of junction hemodynamics have traditionally assumed the arterial wall as being rigid. It is clear from this study that, for more compliant arteries, large deformations may occur which has a significant effect on the junction hemodynamics. Along with the variation in flow patterns through the deformed geometry in comparison to the non-deformed geometry, variations in wall shear stresses gradients and distributions along the bed of the artery have implications concerning the formation of intimal hyperplasia at this location.

REFERENCES

Ballyk, P.D. et al (1997). *Journal of Biomechanics,* **31**, 229-237.

Verhelst, R. B. et al (1997). *Annals of Vascular Surgery,* **11**(5), 505-509.

MECHANICAL EVALUATION OF SPINE RECONSTRUCTION AFTER TOTAL EN BLOC SPONDYLECTOMY BY FINITE ELEMENT ANALYSIS

Jiro Sakamoto[1] , Atsushi Kakuuchi[1], Tomoyuki Akamaru[2], Norio Kawahara[2], Juhachi Oda[1] and Katsuro Tomita[2]
Kanazawa University, Kanazawa, Ishikawa, Japan
[1] Department of Human and Mechanical Systems Engineering, sakamoto@t.kanazawa-u.ac.jp
[2]Department of Orthopaedic Surgery

INTRODUCTION

Total en bloc spondylectomy is the most efficient surgical treatment to prevent recurrence of malignant vertebral tumors (Tomita et al., 1997). In this surgery, a tumorous vertebra is totally removed and replaced by a titanium mesh cage filled morselized bone graft, and spinal instrumentation is carried out by using pedicle screw system. It is considered that bone fusion and remodeling of the grafting depend on mechanical stress condition. Although initial stability and rigidity of the reconstructed structure have been evaluated experimentally (i.e. Oda et al, 1999), mechanical stress condition has not been sufficiently investigated. In this study, finite-element analysis of the reconstructed structure was carried out and stress condition was discussed.

METHODS

In our previous study (Sakamoto et al, 2001), mechanical loading test of the reconstructed structure was performed using human cadveric spine (T10-L4) of 90 years old male with no spinal diseases. T12 was replaced by the titanium mesh cage. Finite-element model of the reconstructed structure was made based on CT images taken from the experimental specimen. Finite-element analysis corresponding to the loading test was carried out, and effectiveness of the FE model was ensured.
Tow types of spinal reconstruction are available in clinical use. One is the multilevel posterior instrumentation (MPI), and another is the short circumferential instrumentation (SCI). MPI has posterior devices at T10-L2 using pedicle screws and spinal rods. SCI has anterior and posterior instruments between T11 and L1 in left side. Mechanical stress occurred in the instruments and the vertebrae were evaluated by finite-element analysis for both the reconstructions. Advantages and disadvantages of the reconstruction were discussed comparing the results. FE model of the MPI is shown in Fig.1. Boundary condition was assumed as natural standing situation.

RESULTS AND DISCUSSION

Stress of the spinal rod was larger in MPI than in SCI. On the other hand, load occurred in the titanium mesh cage was smaller in MPI than in SCI. Fig.2 shows energy stress distribution in upper surface of L1, which connects with the titanium mesh cage. Energy stress of MPI is larger, and stress distribution of SCI is not symmetry. Stress condition in the interface between vertebra and the mesh cage is important for considering bone fusion. SCI can reduce stress in the posterior instruments, but it is not advantageous in the viewpoint of promotion of bone fusion.

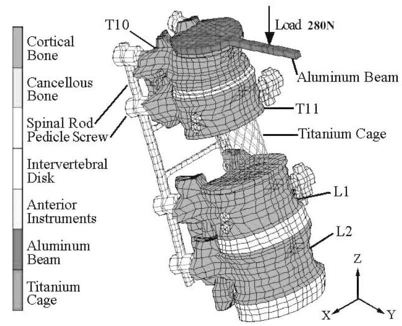

Figure 1: Finite-element model of the spine reconstructed structure in the case of MPI.

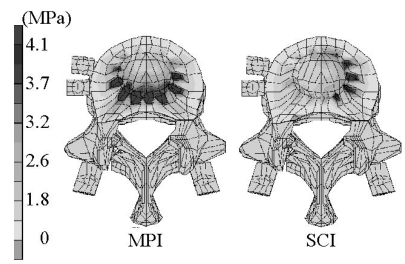

Figure 2: Energy stress distributions on upper surface of L1 in comparison between MPI and SCI.

SUMMARY

Mechanical evaluation of the spine reconstructed structure after the total en bloc spondylectomy was carried out by using finite-element analysis. Finite-element models were fabricated for the two typical reconstruction methods, which were MPI and SCI. In the stress analyses, it was observed that SCI was favorable to reduce stress of posterior instruments and MPI was advantageous to promote bone fusion between bone graft and vertebra.

REFERENCES

Tomita, K., Kawahara, N., et al. (1997), *Spine*, 22(3), 324-333.
Oda, I., et al. (1999), *Spine*, 24(16), 1634-1638.
Sakamoto, J., Oda, J., et al. (2001), *Proc.2001 Bioengineering Conf. ASME*. 50, 825-82

DEFORMATION ANALYSIS OF HUMAN LEFT VENTRICULAR WALL USING MR TAGGING TECHNIQUE

Tadashi Inaba[1], Masataka Tokuda[1], Yutaka Sawaki[1], Hideaki Obata[1], Shingo Kawasaki[2] and Yasutomi Kinosada[3]
[1]Department of Mechanical Engineering, Mie University, Tsu 514-8507, Japan, inaba@mach.mie-u.ac.jp
[2]Matsushita Memorial Hospital, Moriguchi 570-8540, Japan
[3]Department of Medical Informatics, Gifu University, Gifu 500-8705, Japan

INTRODUCTION

To evaluate the cardiac contractility from a mechanical point of view by analyzing the deformation of the myocardial wall is useful for a quantitative evaluation of the extent of heart disease. In this research work, the deformation of the left ventricular wall in normal humans and patients with a hypertrophy of the myocardial wall is analyzed by using a magnetic resonance tagging technique, and a difference in the cardiac contractility of each heart disease is discussed.

METHODS

Ten normal human volunteers, eight patients with a hypertrophic cardiomyopathy (HCM), and seven patients with a hypertensive heart disease (HHD) were imaged with a 1.5 T superconducting magnet (Signa, GEMS, USA). Multiphase tagged images were obtained in a cardiac short-axis view at an equatorial location of the left ventricle. The deformation of the left ventricular wall was analyzed by tracking intersections of tagged stripes throughout systole. The components of the Green's strain tensor within a triangular region defined by three adjoining intersections were calculated, and the calculated strain tensor in each triangular region was translated to polar coordinates where the origin is a center of the left ventricular cavity.

RESULTS AND DISCUSSION

Figure 1 shows the strain components at end systole in the normal humans. From this figure, it is recognized that the radial strains and the circumferential strains in all regions indicate positive and negative values, respectively. It is also observed that dispersions among ten subjects in the circumferential strains are considerably small. From theses results, so far as the deformation of the myocardial wall at a short-axis section in normal humans is discussed, it is considered that the myocardial wall dominantly contracts in a circumferential direction, and that there is no significant difference among subjects about an amount of contraction of the myocardium. Figure 2 shows typical examples of distribution of the circumferential strains at end systole in the normal humans (a and b), the patients with a HCM (c and d), and the patients with a HHD (e and f). As seen in these figures, the circumferential strain in a local region in the patients with a HCM, especially the septal wall in figure 2c and the anterior wall in figure 2d, decreases compared with those in the normal humans, while the circumferential strains in the patients with a HHD are similar to those in the normal humans. From these results, it is considered that HCM is a heart disease accompanied with a reduction of an amount of contraction of the myocardium in a local region, and that the cardiac contractility in HCM and that in HHD are different, although both of them are heart diseases accompanied with a hypertrophy of the myocardial wall.

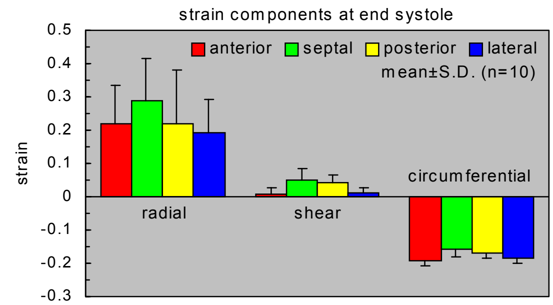

Figure 1: Strain components at end systole in normal humans.

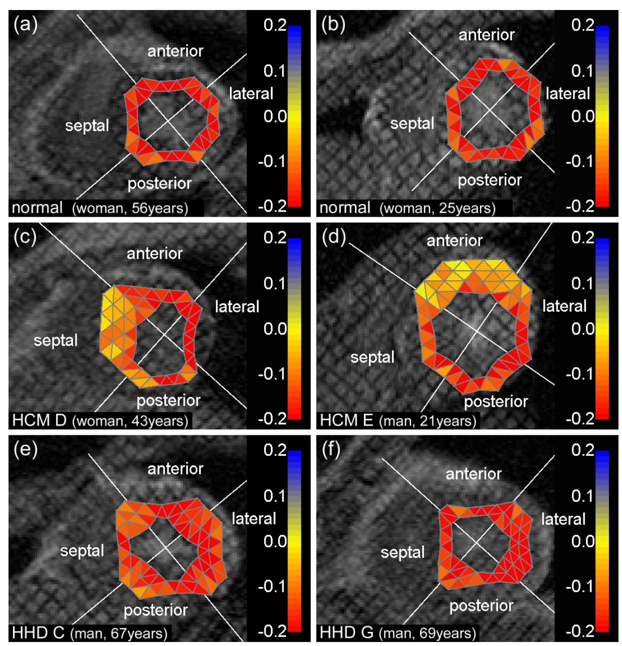

Figure 2: Typical examples of distribution of circumferential strains at end systole.

REFERENCES

Axel, L., Dougherty, L. (1989). *Radiology*, **171**, 841-845
Inaba, T., et al (1997). *JSME Int. J.*, Ser. C, **40**-4, 637-642

MEASURING VASTUS LATERALIS APONEUROSIS & TENDON DEFORMATION *IN VIVO* DURING MAXIMAL ISOMETRIC CONTRACTION BY ULTRASOUND

J. Bojsen-Møller, P. Hansen, P. Aagaard, M. Kjær and S.P. Magnusson. Sports Medicine Research Unit/Team Danmark, Bispebjerg Hospital, Copenhagen, Denmark. E-mail: jbm01@bbh.hosp.dk

INTRODUCTION

Recent development in high definition ultrasonography (US) permits observation of intramuscular connective tissue (CT) displacement during isometric contraction, *in vivo*. Displacement may be regarded as a function of CT deformation, that enables assessment of material properties such as stiffness or compliance. The method has been extensively used in recent years (Magnusson et al. 2001, Kubo et al. 2000), however there is limited information available regarding the reproducibility of the method. Furthermore, the analysis of displacement has been performed manually by digitizing video images frame by frame, which is a labor intensive method associated with potential error due to investigator bias. The purpose of the present study was to evaluate reproducibility of the method, and further to introduce an automated tracking tool.

METHODS

Eight male subjects participated in the study. Using a very rigid test frame, the subjects were positioned in a sitting position with a 90° flexion of the hip and knee joints. The subjects performed two (trial 1&2) isometric knee extensions (10s. ramp, 5min. apart). Knee extensor force and real time US video images of VL aponeurosis displacement were on-line sampled. MVC and VL aponeurosis maximal displacement (MD) was determined, the latter using a newly developed frame by frame automated US video tracking software based on pyramidal implementation of the Lukas Kanade tracking feature (Bouguet, J.Y. 2001). One video sequence from each subject was analysed repeatedly (>6 times) by two experienced observers, and MD was determined as the largest obtainable displacement value. To assess the accuracy of the tracking algorithm software a separate experiment was performed, in which an injection needle (∅ 0.5 mm) embedded in sonography gel was moved parallel to the US transducer while a video sequence was recorded. Subsequently individual frames were digitized and the displacement manually measured with respect to the calibration markers (10 mm apart) of the ultrasound image. The tracking software was then applied to the video sequence, and the results were compared to the corresponding digitised values. The values of displacement obtained from the two methods diverged less than 0.2 mm, indicating an acceptable degree of accuracy of the tracking algorithm.

RESULTS & DISCUSSION

Data are presented as mean±SD: MVC: trial1; 3025±706 N, trial2; 3016±671 N, MD: trial1; 11.4±2.6 mm, trial2; 11.2±2.5 mm, MVC and MD yielded no difference between trials: r^2=0.97, 0.92, CV=2.87%, 4.64%, respectively. Inter- and intraobserver US-deformation reliability were r^2=0.95 & 0.99, CV=3.12% & 1.24% and mean differences=0.2 mm & 0.1 mm, respectively. In conclusion, isometric quadriceps MVC force and corresponding VL displacement can be measured in a reproducible (intra-day) manner, and the automated tracking tool may be considered accurate. The present methodology can be used to assess CT material properties, and further to evaluate the response to physical training, which have not previously been thoroughly examined despite the potential influence on sports performance.

REFERENCES

Bouguet, J. Y. Pyramidal implementation of the Lucas Kanade feature tracker. Description of the Algorithm. http://sourceforge.net/projects/opencvlibrary . 1-12-2001. Ref Type: Electronic Citation

Kubo, K., H. Kanehisa, Y. Kawakami, and T. Fukunaga. Elasticity of tendon structures of the lower limbs in sprinters. Acta Physiol Scand. 168: 327-335, 2000.

Magnusson, S. P., P. Aagaard, S. Rosager, P. Dyhre-Pouelsen, and M. Kjaer. Load-displacement properties of the human triceps surae aponeurosis in vivo. J Physiol 531: 277-288, 2001.

IMPROVING THE BALANCE SKILL OF STOKE PATIENTS BY VIRTUAL REALITY TREADMILL EXERCISE

Jen-Suh Chern[1,2], Saiwei Yang[1], Wei-Shun Huang[1] Lu-Lu Yan[3], Fu-Kang Liu[3]
[1]Institute of Biomedical Engineering, National Yang Ming University, Taipei, Taiwan, swyang@bme.ym.edu.tw
[2]Department of Occupational Therapy, Chang Gung University, Tao-Yuan Taiwan
[3]Cheng-Hsin Rehabilitation Medical Center, Taipei, Taiwan

INTRODUCTION

Restoration of functional ambulation is one of the major goals in the rehabilitation for nonambulatory hemiparetic patients. Recent studies found that functional therapeutic task, such as treadmill training could effectively restore walking ability and improve gait pattern. However, there were still 40% of those who restored walking ability in hospital failed to regain walking ability when returned to community. To improve the effect of treadmill training, virtual reality (VR) technology was added to the traditional treadmill-training program to construct a more interactive and diverse balance-training program. The hypothesis is that the additional visual biofeedback from VR scenery could further increase the training effect and balance skill.

MATERIAL AND METHODS

A VR based treadmill system as shown in Figure 1, a VR scenery was synchronized by a speed/position sensor and progressed according to the treadmill speed that was tailored by the therapist in corresponding to each patient's balance control capacity. A 20 minutes program with eight right and left turns was constructed by 3D web Master VR software. A suspension system was mounted for safety.

14 hemiparetic patients were recruited from local medical center and randomly divided to training or control group. The training group underwent treadmill training with interactive VR program and the control group participated in the traditional treadmill training only. All subjects were exposed to 3 weeks training (20 mins a session, three sessions a week). Both groups were tested by the following three tasks pre- and after training as the evaluation parameters of balance skills: stand still for 5 seconds (for quiet stance stability), sit-to-stand, and level walking in the most comfortable speed (for dynamic balancing skill). The loci of COP of the first two tasks were recorded using a pressure mat (RS-scan, Belgium). The change of foot pressure during sit-to-stand and walking was recorded by F-scan (TekScan, USA). Mann-Whitney U test was used to test the difference in training effect between groups.

RESULTS AND DISCUSSSION

Both groups failed to show significant improvement in quiet stance stability. However, the experimental group did showed significantly more symmetric posture in the process of sit-to-stand transfer, which means that more weight was loaded over affected lower extremity for the experimental group (Figure 2). In addition, the stance phase of the sound leg deceased from 90% of the gait cycle to 60%, which is more comparable to the normal pattern.

SUMMARY

The static balance ability failed to show the training effect might be due to the ceiling effect. More challenging test may be required to detect the balance change for subjects with higher balance skill in this study. However, the visual flow stimulation and more physical practice of weight shifting might results in the significant improvement of the body sway and balance ability in training group as shown by the performance of sit-to-stand transfer. In summary, the virtual reality technology can make the treadmill training more divers, more challenging, and more attractive to the participant, which were believed to facilitate learning effect.

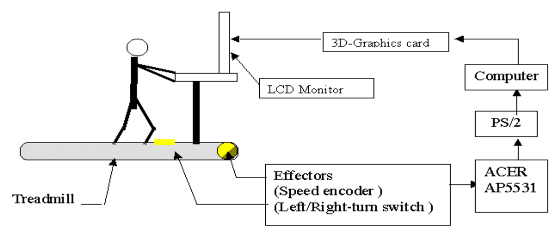

Figure 1: VR Based treadmill system

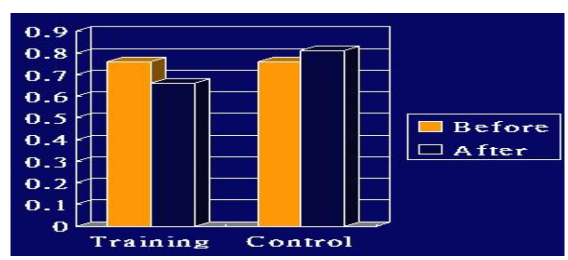

Figure 2: The symmetric index during sit-to-stand

REFERENCES

Hess, S. et al. (1995). *Stroke*, **26**, 976-981.
Shumway-Cook, A.S., Woollacott, M.H. (2001). *Motor Control: Theory and Practical Applications*.

ACKNOWLEDGEMENT

This study was supported by NSC, Taiwan (90-2614-B010-002-M47)

ECM (EXTRACELLULAR MATRIX) SCAFFOLDS FOR TISSUE ENGINEERING APPLICATIONS: BIOCOMPATIBLITY AND BIODEGRADABILITY

Marguerita Grimes [1], Dr. Tim McGloughlin[1], and Dr. Tony Pembroke[2]

[1]Biomedical Engineering Research center, Dept. of Mechanical and Aeronautical Engineering, University of Limerick, Ireland
[2]Dept. of Chemical and Environmental Science, University of Limerick, Limerick Ireland

INTRODUCTION

Replacement of damaged tissue/organs remains a significant problem. Standard therapies such as transplantation are limited by donor shortages and alternatives such as drug therapies, and surgical reconstruction frequently fail in long term applications (Kim et al., 1999). Scientists have come to believe that tissue engineering may provide a viable solution. The most commonly used approach is the utilization of an exogenous 3-D ECM scaffold to bring the appropriate cell types into contact in a suitable environment (Ratcliffe 2000). This work investigated the biocompatibility and biodegradability of 3 such ECM scaffold materials of biological origin- ECM1, ECM 2 and ECM 3 using L929 mouse fibroblasts for *"in vitro"* studies.

METHODS

Biocompatibility was assessed using the Direct Contact and Indirect Contact assay in accordance with ISO 10993-5: "Tests for Cytotoxicity -In Vitro Methods". Total cellular protein concentration was assessed using the BCA assay (Bicinchoninic acid assay) and the metabolic activity was assessed by the MTT assay. Cell viability was investigated using the Giesma staining procedure.

The effect of hydrolytic degradation on ECM1was investigated by a timed degradation study with ECM 1 being incubated in PBS (phosphate buffered saline) pH 7.4 at 37^{0}C. ECM 1was removed at timed intervals dried and weighed. The sample extract were assessed via the BCA assay to determine if protein is being released during degradation. We also assessed the thermal stability if ECM 1 using Thermogravimetric analysis (TGA).

RESULTS AND DISCUSSION

It was found that the presence both directly and indirectly (elutant extract) of ECM 1, ECM 2, and ECM 3 caused an increase in the production of cellular protein assessed via the BCA assay and also in an increase in cell metabolic activity assessed via the MTT assay. Figure 1 compares the % protein conc vs. % metabolic activity for cells in direct contact with the various ECM materials and control materials (PE -ve and PVC +ve). This suggests that ECM 1-3 have bioactive properties causing a positive effect on cell behaviour. Giesma staining proved that cells were viable and appeared capable of supporting cell adhesion and proliferation which are desirable parameters for a tissue engineering scaffold.

It was found that ECM1 degraded hydrolytically over time. Following a 3 month period the mass of ECM1 had decreased approximately 35%. We also observed that samples subjected to a repeat sterilization process degraded at a faster rate-following 3 month period mass had decreased approx. 60%. TGA analysis was significant as it was found that ECM 1 in its dry form contained 12% water. This has significant implications for storage and shelf life of ECM 1 as it has also been shown to be affected by hydrolysis.

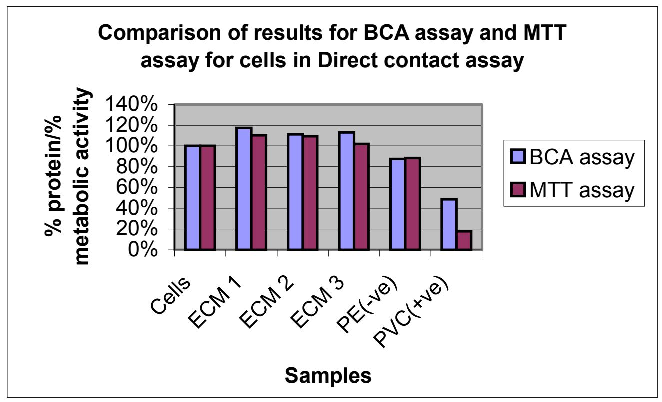

Figure 1: Shows the comparison of results for BCA assay and MTT assay in Direct Contact assay.

SUMMARY

ECM 1, ECM2, and ECM 3 appear to be bioactive materials capable of supporting cell adhesion and proliferation. ECM1 is degraded by hydrolytic degradation and repeated sterilization results in an increased rate of degradation. ECM1 (dry) contains 12% water which has significant implications for storage and shelf life of the materials.

REFERENCES

Kim, B.S., Mooney, D.J., Development of biocompatible synthetic extracellular matrices for tissue engineering. TIBTECH 1999, 16:224-229.

Ratcliffe, A., Tissue engineering of vascular grafts. Matrix Biology 2000, 19:353-357.

LONG-TIME MEASUREMENT OF IN VIVO BONE STRAINS WITH A NEWLY DESIGNED TELEMETRIC SYSTEM

Ei Yamamoto

Department of Mechanical Engineering, School of Biology-Oriented Science and Technology,
Kinki University, Naga, Wakayama, Japan, ei@fmec.waka.kindai.ac.jp

INTRODUCTION

It is well accepted that mechanical strain plays an important role in regulating bone formation and resorption. Therefore, in vivo bone strain measurements have been described by many investigators. However, knowledge of the pattern of the in vivo strain is limited to relatively short-time measurements. Although the short-time measurements determine the peak strain during vigorous activities, a detailed profile of the frequency and duration of the in vivo strains remains unclear.

The purpose of the present study is to determine the long-time pattern of in vivo bone strains. For this purpose, we have newly designed a telemetric system for the determination of the in vivo strains, and applied it to the long-time measurement of the strain pattern induced in the rabbit femur.

METHODS

A telemetric system which we have newly designed eliminates the need for long trailing wires from animals. Therefore, the system can be applied to in vivo strain measurements for free-moving animals. A sender unit (Fig. 1) is composed of a Wheatstone bridge circuit, an amplifier circuit, and a radio transmitter equipped with a VF converter. After the frequency signal, which corresponds to the bone strain, is transmitted to a receiver, the corresponding output voltage signal is recorded.

A single element waterproofing strain gauge was bonded to the anterior part of midshaft of a rabbit femur. The lead wires of the gauge were connected to the telemetric system which was attached to the animal body. Three hours after implanting the gauge, the output voltage from the telemetric system was continuously recorded for 6 hours. After the data collection, the femur with the strain gauge was harvested from the rabbit. The calibration curve, which is described by the relation between the bone strain and the output voltage from the telemetric system, was obtained from a cantilever loading test. The in vivo strains induced in the femur were calculated with this calibration curve.

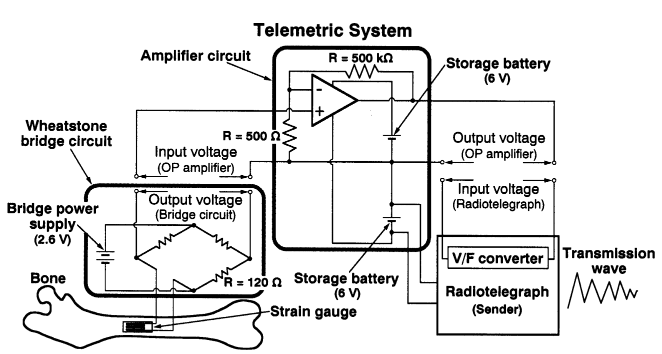

Figure 1: Telemetric system (sender).

RESULTS AND DISCUSSION

Figure 2 shows the in vivo strain pattern continuously measured for 6 hours. Although the in vivo strains were over a wide range, the femur was subjected to compressive strains much more frequently than tensile ones. The pattern of the in vivo strains measured with the telemetric system corresponded to the observation of activities in the animal. This result indicates that the system which we have designed has the potential for accurate determination of in vivo bone loading conditions. The peak compressive strains obtained from the present study were approximately -2500 $\mu\varepsilon$. These values were similar to those measured by nontelemetric strain gauge technique in the past studies. For example, Rubin and Lanyon (1982) reported that peak compressive strains are generally conceded to be about -2000 to -3000 $\mu\varepsilon$ in most animals.

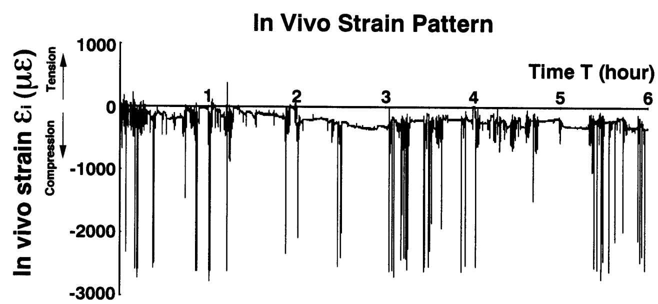

Figure 2: In vivo strain pattern measured for 6 hours.

SUMMARY

We have newly designed a telemetric system for the long-time measurements of in vivo bone strains. Using this system, we could continuously measure the pattern of the in vivo strains during the normal activities, such as eating, resting, and walking.

REFERENCES

Rubin, C. T., and Lanyon, L. E. (1982). *J. Exp. Biol.*, **101**, 187-211.

ACKNOWLEDGEMENTS

This study was financially supported in part by the Grant-in-Aid for encouragement of Young Scientists (E. Yamamoto, no. 11750087) from the Ministry of Education, Science and Culture, Japan, and by the Kinki University Special-Grant-in-Aid Research Project.

THE KICK IN THE DECELERATION STAGE OF 100M TRACK RACE

Kazufumi Takahashi[1], Kyu Tae Kim[2] and Sachio Usui[3]
Graduate School of Hiroshima University, Higashi-Hiroshima, Hiroshima, Japan
[1]Department of Health and Sports science, kazu6754@hiroshima-u.ac.jp
[2]Department of health science
[3]Faculty of Integrated Arts and Science

INTRODUCTION

The deceleration stage of 100m sprint, it was known that both contact and flight times are longer than in the constant speed stage. Contact time was divided into eccentric (negative) and concentric (positive) work phase according to the vertical movements of the center of gravity (CG). In the eccentric phase, the foot-contact played the braking role; the CG vertically dropped and decelerated slightly. The effect of kick motion in the deceleration stage of 100m track race was researched.

However there were no research dealing relationships between kick and CG, especially about kick motion of ankle at concentric phase.

Thus the purpose of this study was to clarify the availability of kick motion of ankle and to suggest the better kick in the deceleration stage during 100m sprinting.

METHODS

Subjects were 14 highly trained college male sprinters. Two digital video cameras were set up in the main stand at a frequency of 60 frames per second (SONY LCH-VX2000), and the running form in 80-85m interval was recorded in the 100m track race. DLT method was used to analyze angle of ankle joint at contact phase and displacement of CG.

The Pearson's product-moment correlations between variables were calculated. Statistical significance was set at the $p<0.05$ level.

RESULTS AND DISCUSSION

The relationship between vertical displacement of CG and displacement of ankle angle at concentric phase were indicated in Fig.1. And the relationship between horizontal displacement of CG at flight phase and displacement of ankle at concentric phase was showing Fig.2. Both coefficients of correlations (Fig1, 2) were significant ($p<0.01$).

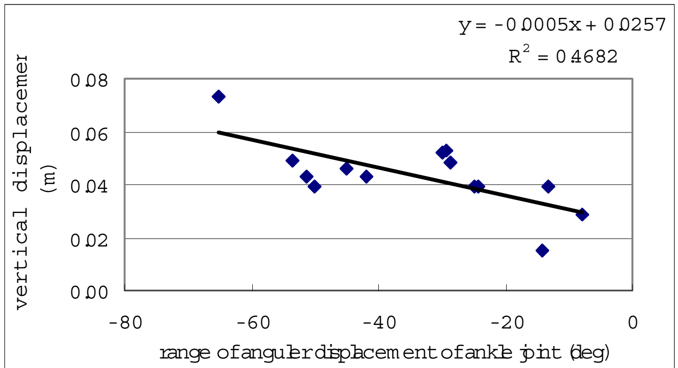

Fig1 Relationship between vertical displacement of CG and displacement of ankle angle at concentric phase

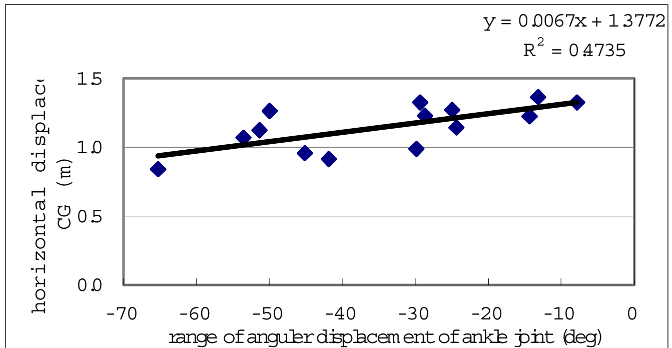

Fig2 Relationship between horizontal displacement of CG at flight phase and displacement of ankle at concentric phase

SUMMARY

Kick motion of ankle at concentric phase has little advantage to run faster. Because of the displacement of CG was significantly increase vertically and less gained horizontally.

REFERENCE

Ito A, et al. (2000). *Japanese Journal of Biomechanics in Sports & Exercise*, **4 (2)**, 159-163.

Mero, A. et al (1992). *Sports Medicine*, **13 (6)**, 376-392.

Moravec, P. et al (1988). *New Studies in Athletics*, **3**, 61-96.

TRIBOLOGICAL CHARACTERISATION OF SURFACE LAYER OF BOVINE ARTICULAR CARTILAGE.

Grant C.A*, Twigg P.C., Thompson, J.[1] and Jin Z.M.

Department of Mechanical and Medical Engineering, University of Bradford, West Yorkshire, BD7 1DP, U.K.
[1]DePuy International Ltd., St Anthony's Road, Leeds, LS11 8DT, UK
* Corresponding e-mail address: c.a.grant1@bradford.ac.uk

INTRODUCTION

The surface layer of articular cartilage plays an important role in its tribological function for synovial joints. Kobayashi *et al* (1996) have found a surface "amorphous layer" using a cryo-scanning electron microscope. These authors further suggested that this amorphous layer mainly consisted of proteoglycan molecules. This is different from the superficial layer of articular cartilage, which mainly consists of a collagen-fibril network and chondrocytes. Similar observations were made by Sasada (1999), Ikeuchi & Oka (1999) and Sawae & Murakami (1999). However, these authors refer to this layer as a "gel layer", in which the condroitin or keratin sulphates composing the leaves of the proteoglycan subunit are hydrated. The purpose of this study is to further characterise and compare the tribological properties of the surface layer of healthy and degraded articular cartilage.

MATERIALS AND METHOD

A commercially available D3100 Nanoscope IIIa AFM (Digital Instruments, Santa Barbara) and Hysitron nanoindenter is used to image the surface topography of bovine articular cartilage and to determine the force-distance relationship. AFM investigations on dry or desiccated samples give topographic and nanoindentation results that are unrepresentative of the living tissue. Therefore, in order to eliminate the adhesion and surface tension forces that affect scanning probe testing of the hydrated tissue, a fluid cell is to be incorporated into this experimentation. Phosphate buffer solution (PBS) is used as the hydration media within the fluid cell. Fluid tapping mode is employed for imaging the surface, from which surface roughness data is accumulated. Spherical diamond indenters with different tip radii are utilized for nanoindentation of the surface to examine the variation of biphasic properties of the cartilage sample with and without a gel layer. Chemical and mechanical degradation of the sample is used to replicate degenerated and diseased cartilage specimens.

Mathematical models are developed to predict the force-distance relationship, based on both fluid and solid mechanics. The fluid mechanics approach uses lubrication theory, while the solid mechanics approach is based on the biphasic theory for articular cartilage.

RESULTS AND DISCUSSION

Results from the AFM tapping mode scanning are discussed in the context of asperity amplitude and frequency across the surface using bearing curve analysis. Comparison of results from the nanoindentation of healthy and degraded cartilage reveals how the gel layer affects the properties of the cartilage. These results are discussed in the context of current lubrication theory.

REFERENCES

Ikeuchi, K. and Oka, M. (1999). The joint lubrication with water in articular cartilage. *Proc. of 26th Annual Meeting of the Japanese Society for Clinical Biomechanics and Related Research*, Kyoto, 43.

Kobayashi, S. *et al* (1996). Cryoscanning electron microscopy of loaded articular cartilage with special reference to the surface amorphous layer. *J Anat*., 188 (Pt 2), 311-22.

Sasada, T. (1999). Lubrication of human joints – nature of joint friction and "surface gel hydration lubrication". *Proc. of 26th Annual Meeting of the Japanese Society for Clinical Biomechanics and Related Research*, Kyoto, 40.

Sawae, Y. & Murakami, T. (1999). Surface layer of articular cartilage observed by atomic force microscopy in liquid – morphology and role in joint lubrication. *Proc. of 26th Annual Meeting of the Japanese Society for Clinical Biomechanics and Related Research*, Kyoto, 46.

ACKNOWLEDGEMENTS

The authors would like to acknowledge the Engineering and Physical Sciences Research Council (EPSRC) and DePuy International Ltd., Leeds for financial support.

DOES NORMALIZATION OF MUSCLE STRENGTH FOR BODY SIZE DEPEND ON THE FUNCTIONAL PERFORMANCE TO BE ASSESSED?

Slobodan Jaric, Ulrika Aasa, Margareta Barnekow-Bergkvist, Hakan Johansson
Centre for Musculo-Skeletal Research, National Institute for Working Life, Umea, Sweden

INTRODUCTION

Although the relationship between muscle strength and body size has attracted a considerable attention of researchers, the normalization of muscle strength for body size has been arbitrarily applied through the professional literature. A specific problem appears when the tested muscle strength is assumed to serve for assessment of the functional movement performance in various sports, ergonomic, therapeutic and other movement related literature. In particular, since performance of various functional tests may also be related with body size, the optimal normalization of muscle strength for body size may differ when different functional movement abilities are assessed. The present study investigates this problem on two important groups of functional performance/ability tests: the tasks based on overcoming gravitational and inertial resistance of subject's own body, and the tasks of exerting force against external objects.

METHODS

Healthy, male and physically active university students (N=21, aged 20-28 years) were tested on vertical jump, standing football kick, seated medicine ball throw and standing maximal isometric lift. A standard isokinetic apparatus was also used in order to test the isokinetic MVC (60°/s) of muscle groups active in the tested functional tasks. The MVC was thereafter related with the recorded performance of four functional tests as either non-normalized or normalized (per kg of body mass) strength.

RESULTS AND DISCUSSION

Subjects' body mass was 80.4 ± 9.8 kg, while their height was 182 ± 8 cm. The tested strength (averaged across the subjects) revealed the following results: 77 ± 15 Nm in shoulder flexors, 67 ± 12 Nm in elbow extensors, 192 ± 39 Nm in hip flexors, 209 ± 52 Nm in hip extensors, and 231 ± 45 Nm in knee extensors. The averaged across the subjects results obtained in the functional performance tests were as follows: the height of the vertical jump was 38 ± 6 cm, the peak foot velocity in the standing football kick was 14.7 ± 1.7 m/s, the peak hand velocity in the seated medicine ball throw was 4.3 ± 0.5 m/s, while the force recorded in the standing maximal isometric lift was 1440 ± 220 N.

Table 1 depicts the main result of the study: the relationship between the functional movement performance and strength of the active muscle groups. The tested performance that required exerting muscle force against one's own body (i.e., vertical jump and standing football kick) demonstrated stronger association with normalized than with the non-normalized strength in all five tested relationships ($p < 0.05$; Wilcoxon matched pairs test). The tested performance based on exerting muscle force against external objects (i.e., seated medicine ball throw and standing maximal isometric lift) demonstrated the opposite result ($p < 0.05$).

The obtained results could be interpreted from the prospective of the role of body size in both muscle strength and functional performance tests. It is well known that muscle strength increases with body size. Since the velocity of rapid body movements is likely to be body size independent, the muscle strength applied in order to predict the movement performance should also be size independent (i.e., normalized). However, since the functional performance of acting by force against external object is well known to increase with body size just like muscle strength, normalization of muscle for body size is redundant (or, alternatively, both muscle strength and functional performance should be normalized).

SUMMARY

The results obtained generally suggest that the requirement for normalization of muscle strength for body size may depend of the type of functional movement performance to be assessed. Therefore, further research is needed in order to provide comprehensive and reliable classification of functional performance tests from the prospective of the role of body size.

ACKNOWLEDGEMENTS

The study was supported in part by grants from The Swedish Sport Research Council and The Swedish Council for Work Life Research.

Table 1: Correlation coefficients observed between the functional performance tests and strength of active muscle groups

movement performance vs. muscle strength	vertical jump		standing football kick			seated medicine ball throw			standing isometric lift	
	hip E	knee E	hip F	hip E	knee E	shoulder F	elbow E	hip F	hip E	knee E
non-normalized strength	r=0.26	r=0.27	r=0.13	r=0.57*	r=0.36	r=0.43*	r=0.57*	r=0.41	r=0.59*	r=0.30
normalized strength	r=0.28	r=0.43*	r=0.29	r=0.63*	r=0.54*	r=0.25	r=0.37	r=0.27	r=0.27	r=0.01

* $p < 0.05$ (N=21); E = extensors; F = flexors

AN INVESTIGATION OF THE BURST FRACTURE MECHANISM USING A COMBINED EXPERIMENTAL AND FINITE ELEMENT APPROACH

Ruth Wilcox[1], David Allen[2], David Barton[1], Richard Hall[1/2], David Limb[2], Robert Dickson[2]
[1]School of Mechanical Engineering, University of Leeds, Leeds, UK. Email: menrkw@leeds.ac.uk
[2]Musculo-skeletal Services, St. James's Hospital, Leeds, UK

INTRODUCTION

Following a burst fracture, decompressive surgery is often recommended on the basis of imaging alone. However there is doubt as to whether the fragment position seen on post-injury CT scans represents the true extent of the occlusion produced during the fracture process (Limb et al., 1995). Several experimental studies have modelled the burst fracture in the laboratory, but few authors have studied the detailed dynamics of the event due to the high impact speed. Further, only limited data can be obtained from such models since invasive measurements would affect the fracture mechanism. The aim of this study was to combine experimental data with a finite element model to provide greater understanding of the underlying mechanics of the fracture event.

METHODS

A drop-mass method described previously (e.g. Tran et al., 1995) was used to create burst fractures in bovine spinal segments at different impact energies. During the event, the specimens were filmed by high-speed video along the canal and externally. After fracturing, each specimen was dissected and a detailed examination of the damage recorded. A finite element model, based on CT images of one of the specimens was also created and processed using LS Dyna (Livermore Software, CA). The model comprised an entire motion segment including posterior elements and the posterior longitudinal ligament (PLL). Validation of the model was carried out by comparison of component displacements with the video images. The combined evidence of the finite element and experimental models was used to build an understanding of the fracture mechanism.

RESULTS

The high-speed video footage showed the external damage to the specimen during impact. At high impact energies, the transverse processes were seen to rotate posteriorly and some cracking of the posterior of the vertebral body was observed.
Dissection of 38 specimens showed damage corresponding to the burst fracture pattern described by Denis (1983). At the lowest impact energy (20J) no or minimal cracking of the vertebra was recorded. At medium impact energies, a Denis type C fracture was observed, with a wedge of bone and endplate cartilage. At impact energies above 100J, type A fractures were increasingly found, with the fragment including bone from both endplates. There was a positive correlation between the impact energy and mass of the fragment ($r = 0.708$, $p<0.001$). The posterior longitudinal ligament was always intact.

The dynamic finite element model showed that as the specimen compressed, the articular processes were forced apart. This caused the transverse processes to rotate, as was observed on the video footage. The movement of the articular processes led to a tensile force being transmitted through the pedicles, and produced localised regions of high tensile strain in the posterior of the vertebral body (Figure 1). Fracture was initiated at these sites approximately 2 ms after impact. Further analysis of the fragment projection into the spinal canal showed it being reflected back by action of the PLL.

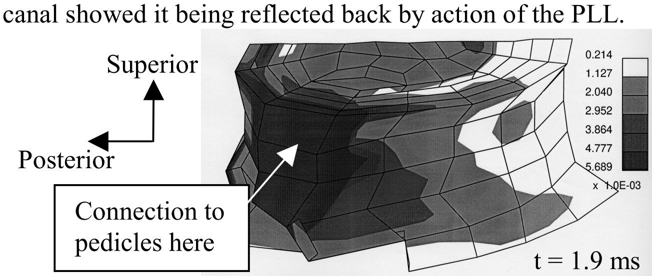

Figure 1: Maximum principal strain in half the vertebral body

DISCUSSION

Several authors have suggested that the increased pressure in the cancellous bone causes high hoop stresses in the cortex that lead to tensile failure. Although this does occur, it does not explain why the fracture initiates at the particular positions on the cortex. The finite element and experimental models show that the motions of the articular processes cause fracture by generating high tensile strains in the region of the pedicles.
The combined experimental and computation approach to investigating the burst fracture has yielded a greater understanding of the dynamics of the fracture mechanism. The results provide further evidence of how the bone fragment may be produced and projected into the spinal canal. The specimen dissections show that the fragment is often attached to the endplate and the posterior longitudinal ligament remains intact, causing the projected fragment to be recoiled back towards the vertebral body, as was also shown in the finite element model. The findings confirm previous experimental work (Wilcox et al., 2001) and demonstrate that the greatest canal occlusion occurs before the fragment is recoiled and will not be represented by post injury imaging of the patient.

REFERENCES

Denis, F. (1983). *Spine,* **8,** 817-831.
Limb D., Shaw, D.L., Dickson, R.A. (1995). *J. Bone Jnt. Surg.*, **77**, 774-777.
Tran, N.T., Watson, N.A., Tencer A.F. et al. (1995). *Spine*, **20**, 1984-1988.
Wilcox, R., Boerger, T., Barton, D. et al. (2001). *Transactions of the ORS,* p. 0279.

A NOVEL EQUIPMENT FOR THE ASSESSMENT OF HAND FORCES

Sandra Morelli, Daniele Giansanti, Gianni Maccioni, Claudia Giacomozzi, Velio Macellari
Biomedical Engineering Laboratory, Istituto Superiore di Sanità, Rome, Italy
Corresponding author: C. Giacomozzi, claudia.giacomozzi@iss.it

INTRODUCTION

A good level of hand muscular activity and ability to manage objects is mandatory for maintaining an adequate quality of life. In terms of forces exerted through the tendons of deep flexors which mainly act on the distal inter-phalangeal joints, most studies only assess the action of the 4 fingers (Li et al., 1998; Li et al., 2001). Thumb was instead rarely included in the studies (Kilbreath et al., 1994; Kilbreath et al., 1995; Li et al., 1998). A special equipment has been purposely designed and constructed at the authors' laboratory to assess the force each finger exerts under isometric conditions. A dedicated software with a visual bio-feedback allows the patient to follow pre-established force profiles according to well defined trajectories. Validation and calibration tests proved the system to be accurate and reliable. It allows to analyse the effects of different strategies of central neural system in managing thumb activation, the reciprocal influence of fingers of one or both hands, the effects of mechanical constraints. The visual feedback, then, renders it particularly attractive in rehabilitation.

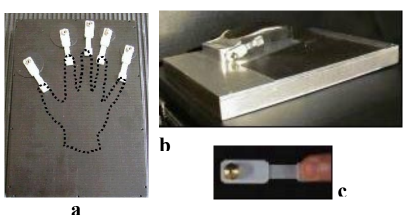

Fig. 1. Devices – a) top view of right FK; b) lateral view of right MS; c) detail of the key.

METHODS

Two devices have been realised for each hand: a flat keyboard (FK) with five keys to measure the force each finger exerts against the corresponding instrumented key; a mouse-like support (MS) equipped with one key only, to measure the force the thumb exerts while grasping a mouse-like metallic handle. Each key consists of a quasi-rectangular aluminum bar (63.5mm long, $169mm^2$ of contact surface), instrumented with a full estensimetric bridge which measures its flexion when the finger presses against it. The devices and a detail of the key are shown in Fig. 1. The key on the MS is 90° rotated around the longitudinal axis of the finger. When the hand is fixed aside the mouse, the same key allows the measurement of the force exerted by little finger adductor. During measurement, both devices are inserted in a flat support which maintains hand, wrist and forearm in a fixed position and guarantees for a stable contact between fingers and keys. A dedicated software provides: tools for data acquisition and processing; on-line visual feedback; force profiles programmable as for amplitude, shape and duration. A few experiments have been conducted on 4 healthy volunteer to test the system *"on-the-field"*. Each subject was asked to perform different tasks of isometrically pressing against the devices, three times each in random sequence. Maximum force was identified for each task of interest.

RESULTS AND DISCUSSION

Repeatability was tested for each key at 10, 20, 30, 40 and 50N, 10 random measurements for each step, thus taking into account for eventual repositioning errors. The worst response in terms of mean of deviations was around 3% of the measured value (input force 10N). For forces greater than 20N the response always spread less than 1% (range 0.2-1.0). Responses were strictly linear; angular coefficients ranged from 0.744 to 1.233, and R^2 values ranged from 0.998 to 1.000.

As an example of the system outputs, different strategies of hand force delivering are reported in Fig. 2. Fig. 2a shows the different percentual contribution of the thumb and the remaining 4 fingers to the total maximum voluntary contraction (MVC) expressed on the FK. Fig. 2b reports three cases in which the influence of the contralateral hand while grasping the mouse results in three dramatically different effects (reduction (a), invariance (b), increase (c)).

The system is self-contained, easily transportable and easy to use. We believe it's a promising tool both for diagnosis and therapy, for fields like biomechanics, clinics, forensic medicine and occupational medicine.

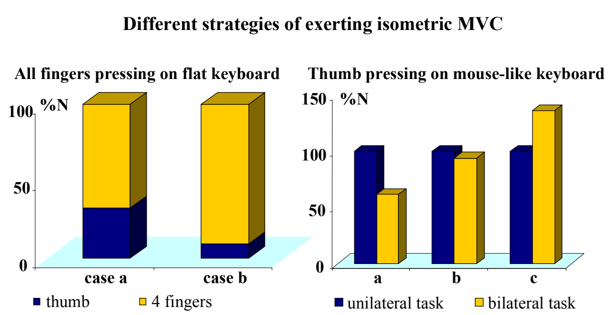

Fig. 2. – On the left: the thumb contribution to the total force exerted on the FK is significantly smaller in case b. On the right: the thumb grasping-pressing force during a bilateral task is reduced (a), unchanged (b) and increased (c), with respect to the unilateral task.

REFERENCES

Kilbreath SL, Gandevia SC (1994) *J Physiol.*,479(3),487-97.
Kilbreath, S.L. et al (1995). *Neurosci Lett.,* 201(3), 203-6.
Li, Z.M. et al (1998). *Exp Brain Res.*, 122(1), 71-8.
Li, Z.M. et al (2001). *Exp Brain Res.*,140(1), 86-94.

A SIMPLE MODEL TO RELATE CLINICAL TO BIOMECHANIC VARIABLES IN PERIPHERAL NEUROPATHY

Claudia Giacomozzi[1], Stefano Cesinaro[1], Velio Macellari[1], Luigi Uccioli[2], Emanuela D'Ambrogi[2]
[1]Biomed. Eng. Lab., Istituto Superiore di Sanità, Rome, Italy; [2]Dept. Internal Medicine, University of Rome, Italy
Corresponding author: C. Giacomozzi, claudia.giacomozzi@iss.it

INTRODUCTION

Peripheral neuropathy is a frequent and serious complication of diabetes. From a biomechanic point of view, it results in significant alterations of gait, widely investigated in terms of foot-floor interaction (Uccioli et al, 2001). From a deeper analysis, however, changes are also found at the level of the ankle articular complex, as for limited joint mobility and reduced muscular strength (Mueller et al, 1995).

The challenge of this study was to associate the alterations of biomechanic parameters measured at the ankle complex to concurrent alterations of physical and clinical parameters of diabetic patients, with or without neuropathy.

METHODS

22 healthy volunteers (9 females, 13 males) have been included in the study as a control group, matched for age and physical characteristics with the diabetic patients. The pathologic group was formed by 60 diabetics, 26 females and 34 males, whose VPT (vibratory perception threshold) was measured according to the existing guidelines (Young et al, 1997) and included in the study as the only clinical independent variable of the model.

Joint mobility and muscular functionality of both patients and volunteers were accurately assessed by means of a dedicated device, designed and constructed at the authors' lab (Giacomozzi et al, 2000). The device allows the measurement of angular excursions of the ankle complex in the three anatomical planes, and of torques expressed around the three corresponding axes when exerting maximal voluntary isometric contractions of the leg muscles. Peak values have been identified for each parameter and for each patient. For control group, a set of statistical regressive models have been considered whose independent variables were sex, age, height, body weight and body mass index (BMI). The best-fitting model was then applied to the pathologic group, too, with the inclusion of clinical variable VPT among the independent factors of the model.

Table 1: Mean values and standard deviations of independent variables of patients and controls which have been included in the regressive model

	Cases	Age (yrs)	Height (cm)	Weight (kg)	BMI (kg/m^2)	VPT (V)
Controls	22	50.41 (±14.6)	168.55 (±8.8)	71.00 (±11.3)	24.86 (±2.6)	-
Diabetics	60	53.97 (±12.8)	168.20 (±9.7)	76.42 (±15.6)	26.97 (±4.8)	13.00 (±8.3)

RESULTS AND DISCUSSION

Mean values and standard deviations of the independent variables are reported in Table 1 for patients and controls. Student's t-test confirmed that there were no statistically significant differences between the two groups for age, height and weight (p=0.05 for BMI).

The statistical model which best fitted the biomechanic parameters of the ankle complex functionality was the Piecewise linear regression model with computer-fixed breakpoint. It is a sort of multiple linear regression whose angular coefficient changes from a fixed point on. For any of the angular excursion or torque in any of the three anatomical plane, the model succeeded in explaining more than 90% of variance for controls. The same model, with the same independent variables plus VPT, explained up to 80% of variance in presence of neuropathy.

As an example, Fig. 1 shows the results of the application of the piecewise model to estimate the torque generated by a maximal plantar flexion (sagittal plane), starting from a neutral position (90° between foot and leg). Fig. 1a plots the observed versus the estimated values for controls; fig. 1b plots the same values for diabetic patients; fig. 1c compares the good fitting of the appropriate model for patients, and the bad fitting obtained by applying to patients the coefficients corresponding to the same parameters for controls. This last comparison is important to highlight two main findings: i) relationships among physical and biomechanic characteristics change with respect to a normal condition when diabetic peripheral neuropathy takes place, even if in a early stage; ii) suitable clinical variables must be necessarily included in the model to take into account at least for part of the observed biomechanic alterations.

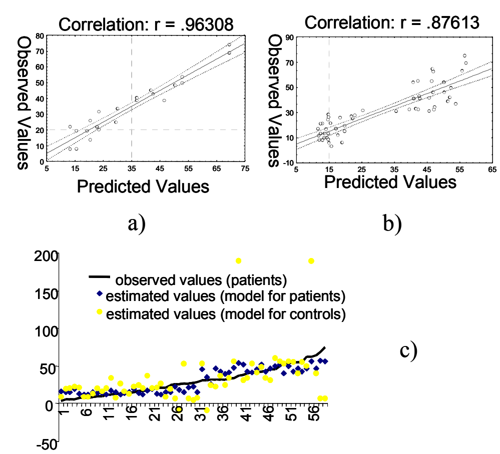

Piecewise linear model to estimate dorsal flexion torque

Figure 1: a) observed vs predicted values for controls; b) observed vs predicted values for patients; c) bad fitting, of model found for controls, to patients observed values.

REFERENCES

Uccioli L. et al (2001) Clin Biomech 16(5), 446-54.
Mueller M.J. et al (1995) Phys Therapy 75(8), 684–693.
Young M.J. et al (1997) Diabetes Care.
Giacomozzi C. et al (2000) Proc of Int Ankle Symposium Ulm, Germany 2000, 57-65.

ECS ADHESION ON SILICONE RUBBER–RTV 615: A SYSTEMATIC STUDY

J.-P. E. Martinez[1], R. Haklai[2], S. Einav[1], Y. Kloog[2], Y. Lanir[3]
[1]Department of Biomedical Engineering, Faculty of Engineering, Tel Aviv University, Tel Aviv 69978, Israel, jpelisha@eng.tau.ac.il
[2]Department of Neurobiochemistry, Faculty of Biological Sciences, Tel Aviv University, Tel Aviv 69978, Israel
[3]Department of Biomedical Engineering, The Institute of Technology -Technion, Haifa, Israel

INTRODUCTION

Silicone rubber RTV 615 is a suitable material for the building of artery models since it is compliant, highly transparent and easy to process. However, surface modification is necessary to reduce its hydrophobicity to enhance adsorption of adhesive proteins and cellular adhesion (Ratner et al.1996). Different methods are described in the literature for the treatment of various silicone rubbers, but they were found to be ineffective on RTV 615 or non applicable to tube's lumen. Therefore, a systematic study of ECs adhesion on silicone rubber RTV 615 has been done.

METHODS

The investigated parameters included: surface treatment (acid vs base), time (0', 10', 30', 60'), amination, topography (fine vs rough) and protein contact (collagen, fibronectin, gelatin, serum). Surfaces have been characterized for their roughness, surface energy (Wilhelmy slide method - LaPorte, 1997) and molecular structure (TOF-SIMS) after surface treatment and prior to protein contact. Bovine aortic ECs (BAECs) were seeded. Micrographs (phase contrast microscopy and fluorescence microscopy for Hoechst staining) were quantitatively imaged and analyzed.

RESULTS

The optimal time treatment to reduce surface hydrophobicity was 30', base inducing a change of 10º in the contact angle. Acid and base, respectively, increased the number of adherent and spread cells by 10 and 100 fold. Gelatin has been found to promote the best cellular adhesion after acid treatment and fibronectin after base treatment. After 45 hours culture, ECs reach local confluence aside to empty area so called "capillary forms" on surfaces treated by base followed by fibronectin contact (fig.1, a & b), whereas acid treatment followed by amination and fibronectin contact induced a uniform cell distribution on the surface but without confluence and very few cell-cell contacts (fig.1, c). Full cell confluence was obtained by acid treatment followed by amination and collagen contact (fig.1, d).

CONCLUSIONS

The results show the feasibility to culture ECs on RTV 615, using surface modification methods that are applicable to tube's lumen. They provide formulae to reach cell confluence or, alternatively, uniform cell distribution with no cell-cell contacts.

BAECs Adhesion on RTV

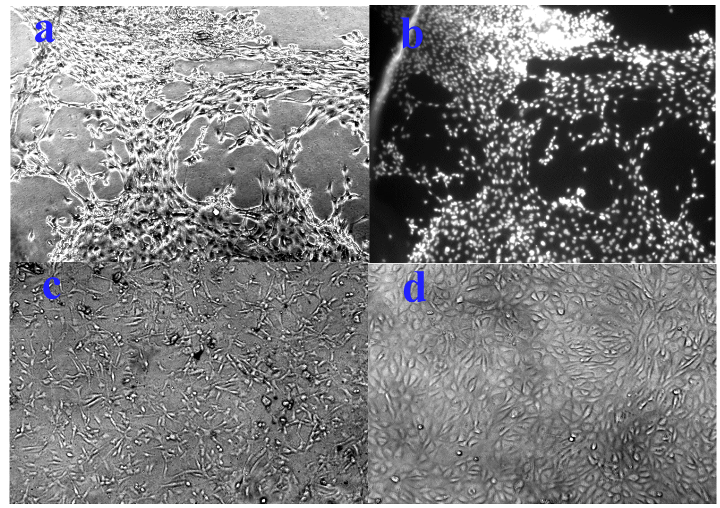

Fig. 1: BAECs adhesion on RTV: a) base treatment and fibronectin - "capillary forms" and local confluence; b) as in a, stained cell nuclei; c) acid treatment, amination and fibronectin - uniform, sparse cell distribution; d) acid treatment, amination and collagen - full confluence.

REFERENCES

LaPorte, R.J. (1997) *Hydrophilic Polymer Coatings for Medical Devices*. Technomic Publishing, Lancaster

Ratner, B.D., Hoffman, A.S., Schoen, F.J., Lemons, J.E. (1996) *Biomaterials Science - An Introduction to Materials in Medicine*. Academic Press, San Diego.

THE EFFECT OF HORIZONTAL FOOT VELOCITY ON IMPULSE IN HORIZONTAL JUMPING

Steven LeBlanc
School of Health and Human Performance, Dalhousie University, Halifax, Nova Scotia, Canada
Steve.LeBlanc@dal.ca

INTRODUCTION

It has often been stated by researchers and coaches that athletes should use an active landing, or "pawing" action, when performing the horizontal jumps in track and field athletics; namely the long jump and triple jump. This technique is seen as a means of reducing braking impulses, thus reducing losses in the horizontal velocity of the total-body centre of mass during the support phase of the takeoff. To date, this concept has received relatively little attention in the research on jumping (LeBlanc, 1997). The purpose of the present study was to examine the pre-contact horizontal foot velocities relative to the total-body centre of mass (i.e., the level of activeness) and the horizontal and vertical impulses encountered during the support phase during short-approach horizontal jump takeoffs. It was hypothesized that greater levels of activeness would lead to reduced braking impulses while leaving the propulsive and vertical impulses unaffected.

METHODS

Kinematic data was collected using standard two-dimensional video analysis techniques (NTSC 60 Hz), and kinetic data was collected from a force platform (300 Hz). Five experienced, non-elite jumpers performed five trials each of two-, three- and four-step approach long jump-style takeoffs. This resulted in a total of 75 trials to be analysed. The subjects represented a heterogeneous sample of jumpers from all four jumping disciplines (one male LJ, one female LJ/TJ, one male HJ, one female LJ/TJ/HJ, one male PV) in hopes of more clearly identifying trends in the data as compared to previous research (Koh & Hay, 1990a,b).

The statistical analysis examined the relationships between the level of activeness (**rVf**) and five dependent measures: horizontal braking impulse (**FTb**), horizontal propulsive impulse (**FTp**), change in horizontal velocity of the total-body centre of mass (**dVh**), net vertical impulse (**FTv**), and theoretical flight distance (**D**). A regression model (see Equation 1) was used to examine the relationships between activeness and the dependent variables. As well as rVf, the model incorporated a subject variable, mass, and the horizontal and vertical touchdown velocities of the total-body CM (**tdVh**, **tdVv**) as predictors. It was deemed to be evidence of a significant relationship if the regression analysis resulted in a model with a large F-value, a large R^2 value, a significant p-value for **rVf**, and a β coefficient for **rVf** whose sign agreed with the hypothesized relationship.

$$\mathbf{Y} = \beta_0 + \beta_1\mathbf{subj} + \beta_2\mathbf{rVf} + \beta_3\mathbf{mass} + \beta_4\mathbf{tdVh} + \beta_5\mathbf{tdVv}$$

Equation 1: Multiple regression model.

RESULTS AND DISCUSSION

The subjects used active landings (-2.61±1.11 m/s) in 73 of 75 short approach jumps. The ground contact resulted in a net loss of horizontal velocity of the CM (-1.14±0.30 m/s) and a net gain in vertical velocity of the CM (2.92±0.42 m/s) in all 75 trials. The mean impulses during contact were: **FTb** = -85.11±23.07 Ns; **FTp** = 3.14±1.00 Ns; **FTv** = 343.30±61.54 Ns. Theoretical flight distances were calculated to be 2.01±0.36 m. Based upon the results of the regression analysis, it was determined that **rVf** was significantly related to **FTb** (F=28.69, R^2=65.2%, p=0.002, β_2=-6.68), **dVh** (F=16.97, R^2=51.9%, p=0.025, β_2=-0.07), and **FTv** (F=94.42, R^2=86.3%, p=0.000, β_2=13.1). No significant relationship was found between **rVf** and either **FTp** or **D**.

SUMMARY

It was found that: 1) greater activeness reduced the braking impulse; 2) level of activeness was not related to propulsive impulse; 3) greater activeness reduced the loss in horizontal velocity; 4) greater activeness reduced the net vertical impulse; and 5) level of activeness was not related to theoretical flight distance. From this analysis, it was evident that the use of the active landing technique affects more than just the braking impulse. Further research is necessary to clarify the effectiveness of the active landing technique to improve horizontal jump performance.

REFERENCES

Koh, T.J. & Hay, J.G. (1990a). Landing leg motion and performance in the horizontal jumps I: the long jump. *Int'l J of Sports Biomech*, **6**, 343-360.
Koh, T.J. & Hay, J.G. (1990b). Landing leg motion and performance in the horizontal jumps II: the triple jump. *Int'l J of Sports Biomech*, **6**, 361-373.
LeBlanc, J.S. (1997). The use of active landings in the horizontal jumps. *Biomechanics in Sports XV*, 125-131.

ON THE ERRORS SURROUNDING HEMODYNAMIC ANALYSES: COMPARISONS OF VARIOUS INVESTIGATIVE TECHNIQUES

Thomas O Brien, Michael Walsh, Tim McGloughlin
Biomedical Engineering Research Centre, Dept. Mech. & Aero. Eng., University of Limerick, Limerick, Ireland

INTRODUCTION

Hemodynamic factors have been widely implicated in the development of atherosclerosis. Abnormal wall shear stress (WSS) gradients and distributions along with regions of flow separation are thought to be the principle disease influencing factors in the vascular system (Giddens, 2001). There is a range of experimental and numerical techniques available to researchers to investigate the blood velocity profiles and wall shear stresses at various disease prone sites. Principle among these are; the numerical methods based on the finite element (FE) and finite volume (FV) methods, which are both accurate and efficient, and the experimental *in vitro* technique, laser Doppler anemometry (LDA), with its high spatial and temporal resolution. The purpose of this study was to perform a detailed comparison on the aforementioned techniques with a view to establishing how differences between the results may be reduced and which of the two numerical methods gave closer correlation to experimentally derived results.

MATERIALS AND METHODS

The geometry of interest that was chosen for this study was that of a 6mm idealised graft-artery bypass junction. This geometry was selected as it causes such phenomena as flow separation, recirculation and stagnation. An idealised 45° graft-artery junction was machined and polished into a plexiglas block for 1-D LDA studies. The model was investigated using two different transient inlet velocity boundary conditions, namely a femoral resting pulse and a carotid resting pulse. A non-Newtonian fluid was used. Velocity profiles were determined at various axial and radial positions through the junction.

The numerical studies were carried out on models according to the conditions described above. A 6mm idealised 45° graft-artery junction was generated and meshed in Gambit 1.3 (Fluent, Europe) using approximately 100,000 brick elements. This was then exported as a structured mesh for solution in Fluent 4.5 (Fluent, Europe) and as an unstructured mesh in FIDAP 8.6 (Fluent, Europe). The velocity boundary conditions and fluid properties were as for the experimental analysis. Simulations were performed on a 1GHz, 512Mb RAM, Dell Dimension 4100.

RESULTS

Results were obtained at the mean decelerating velocity for both pulses as this was found to have particularly severe WSS gradients and distributions. Results were compared by plotting the 2D velocity profiles through the junction (figure 1) and establishing the percentage differences between them, using the LDA profiles as a benchmark.

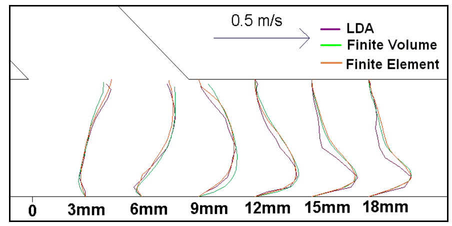

Figure 1: Velocity profiles through junction for resting pulse.

In addition, WSS acting along the bed of the artery were compared for the three methods. The WSS for the LDA investigations were determined by curve-fitting the experimental data (figure 2).

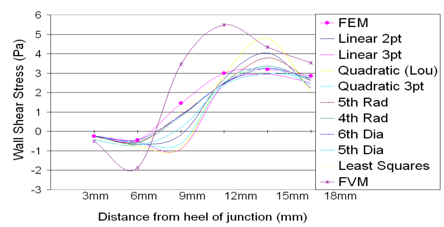

Figure 2: WSS acting along bed of artery for resting pulse.

DISCUSSION

There are significant differences between the three investigative techniques. Comparisons of the two pulse results showed that the LDA method may be pulse point dependant. In addition, the FE velocity profiles gave better agreement to the LDA than did the FV profiles. The FV method gave higher WSS results than the FE method though was approximately 60% more efficient.

REFERENCE

Giddens, D.P *et al*. (2001) “Pulsatile Flow in an End-to-Side Vascular Graft Model: Comparison of Computations With Experimental Data”. *Journal of Biomechanical Engineering*, Volume **123**, Issue 1, pp. 80-87.

COMPARATIVE ANALYSIS OF THE HEMODYNAMICS THROUGH HEALTHY AND DISEASED MODELS OF THE HUMAN ABDOMINAL AORTA

Liam Morris[1], Thomas O Brien[1], Tim McGloughlin[1], Don Giddens[2], Patrick Delassus[3]
[1]Biomedical Engineering Research Centre, Dept. Mech. & Aero. Eng., University of Limerick, Limerick, Ireland
[2] Georgia Tech/Emory, Department of Biomedical Engineering, Atlanta, Georgia, USA
[3]Galway/ Mayo Institute of Technology, Galway, Ireland

INTRODUCTION

Abdominal Aortic Aneurysms (AAAs) are a major cause of death in Western societies. While the factors that effect their development and growth are not fully understood, there are a number of surgical techniques available that seek to prevent rupture of the aneurysm and the subsequent haemorrhaging by attaching a prosthetic graft within the aneurysm (Uflacker *et al.*, 1998). The objective of this study was to quantify the normal conditions that exist within a healthy human abdominal aorta. These results were then compared to corresponding results from an abdominal aortic aneurysm and also for flow through a prosthetic graft that followed the curvature of the diseased aneurysm.

MATERIALS AND METHODS

2D Time of Flight Angiography (TOF) was carried out on a healthy human volunteer using a 1.5T Philips Magnetic Resonance (MR) Imager with a view to determining the geometrical data and velocity boundary conditions for the descending abdominal aorta. Computerised Tomography (CT) was carried out on an abdominal aortic aneurysm using a Siemens CT scanner with a view to determining its geometry. The geometrical models were assembled using Mimics 6.3 (Materialise) and exported as IGES files for meshing in Gambit 1.3. (Fluent, Europe). The prosthetic graft model was generated in ProEngineer 2000i^2 (Parametric Technologies) according to the dimensions of a commercially available graft (Perouse Laboratoires, France) and its centerline curvature was matched to that of the AAA. Upon determining grid independence, the models were investigated using the numerical solvers FIDAP 8.6 (Fluent, Europe) and FLUENT 6.0 (Fluent, Europe). The pulsatile velocity boundary conditions as determined from MR were applied at the inlets of the models observing continuity between models. Blood was assumed to be a Newtonian fluid with $\mu = 0.0035$Pa-s and $\rho = 1050$Kg/m^3 (Nichols & O' Rourke, 1998).

RESULTS

The principle results of interest were the magnitudes and gradients of the Wall Shear Stresses (Nerem, 1992) and the velocity profiles acting in each of the models (figure 1). The effects of the geometrical curvature in the diseased aorta were investigated. In addition, the axial forces acting on the prosthetic graft were quantified and compared to normal aortic conditions. It was found that the peak WSS acting in the healthy aorta was approximately 3Pa as opposed to the prosthetic graft where the WSS was found to be approximately 15Pa in places. WSS gradients were found to be much larger in the diseased and prosthetic models than the healthy one. The aneurysm was found to be particularly tortuous having a major effect on the blood velocity profiles.

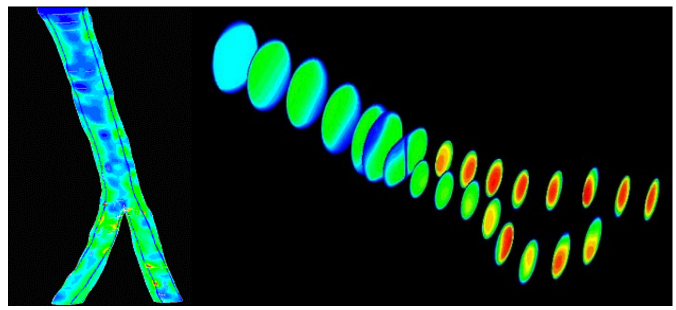

Figure 1: WSS for the normal aorta and velocity profiles for the prosthetic graft.

CONCLUSION

There are particularly significant differences between the wall shear stress gradients and distributions in the models described above. The tortuous nature of the aneurysm has major implications for the blood flowing through the aorta and also any surgically implanted grafts.

REFERENCES

Uflacker, R. *et al.,* (1998). Abdominal Aortic Aneurysm Treatment*, Journal of Vascular and Interventional Radiology*, **9**: 51-60.

Nichols, W. & O' Rourke, M. F. *McDonalds Blood Flow in Arteries*, Edward Arnold. 4th Ed, 1998.

Nerem, R., (1992). Vascular fluid mechanics, the arterial wall and atherosclerosis, *Journal of Biomechanical Engineering*, **114**: 274-281.

ACKNOWLEDGEMENTS

The authors wish to thank the radiology departments at Emory University Hospital, Atlanta, and the Regional Hospital Limerick. This work was funded by Enterprise Ireland.

OSTEOLYSIS OF THE FEMORAL SHAFT AFTER IMPLANTATION OF A CEMENTED HIP PROSTHESIS – BIOMECHANICAL ASPECTS

Holger Grabski, Barbara Behnke, Götz von Foerster and Alexander Katzer
ENDO-Klinik, Holstenstraße 2, D-22767 Hamburg (Germany)

INTRODUCTION

Osteolysis of the femoral shaft is a rare late complication after implantation of a cemented hip prosthesis. The etiology of this secondary phenomenon, which eventually results in loosening of the prosthesis stem, is unknown.

METHODS

To investigate the frequency and possible causes of femoral osteolysis, we analysed the radiographs of 495 patients with the diagnosis "early prosthesis loosening" treated at the ENDO-Klinik Hamburg between 1990 and 2000. 53 of these patients had areas of lysis in the femoral shaft. Of these, one female patient had lysis in both femurs. In 52 the lysis had occurred after primary implantation, and in one after an aseptic exchange operation. Therefore osteolysis of the femoral shaft occurred in 12.9% of "early loosenings", or 0.2% of primary total hip replacements in this 10-year period (n = 24.764). For standardized biomechanical in vitro-analysis concerning the cyclic load behaviour of prosthesis stems of different thicknesses in connection with the different cementing fixation techniques the VICON-System was used.

RESULTS AND DISCUSSION

The mean age of the patients was 51.5 years, which is markedly lower than the mean age of coxarthritis patients. The proportion of male patients was greater than the female. The period of implantation was on average 7.7 years, which is significantly shorter than the general average. There was no predominance of the right or left side, and no correlation to concomitant diseases.

During the exchange operations, arrosion of the femoral cortex, without interruption of the continuity of the bone, and toxic-granulomatous synovitis were observed. Histologically, this was a fibro-histiocyte reaction with foreign body giant cells and zirconium dioxide / polyethylene inclusion and areas of circumscribed necrosis. Florid or purulent foci were not observed. Detailed evaluation reveals that the following factors must be discussed as possible causes of focal osteolysis of the femoral shaft after implantation of a cemented hip prosthesis:

1) Thickness of prosthesis stems
2) Torsional stability and design of the prosthesis stem
3) Cementing technique
4) Lateral offset
5) The time of intraoperative reduction
6) Age and gender of patients

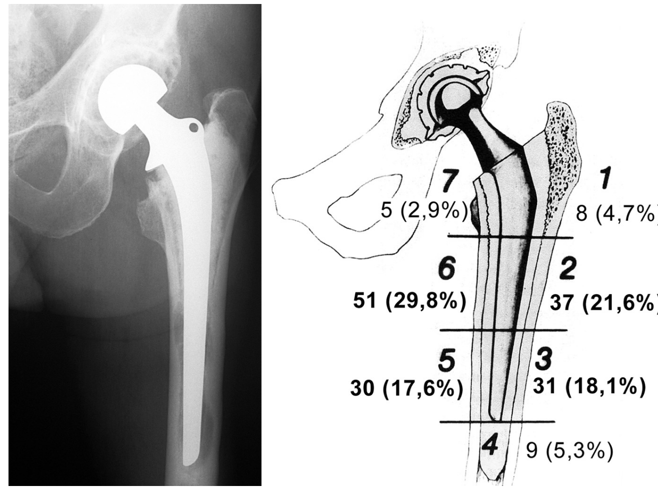

Figure 1: Distribution of femoral shaft osteolysis according to GRUEN's classification

SUMMARY

Regarding the in vivo-findings and in vitro-results, our biomechanical data confirm the recommendation of using maximum thickness in stem prosthesis design in combination with vacuum cementing technique in order to minimize complication rate in total hip arthroplasty by means of isolated femoral shaft osteolysis especially in high demanding and younger patients.

REFERENCES

Gruen T.A., McNeice G.M., Amstutz H.C. (1979):
Modes of failure of cemented stem-type femoral components. A radiographic analysis of loosening.
Clin. Orthop., **141**, 17-27

Katzer A., Behnke B., von Foerster G. (2001):
Osteolysis of the femoral shaft after implantation of a cemented hip prosthesis
Journal of Biomechanics, **34**, 68

TRIBOLOGICAL EVALUATION OF THERAPEUTIC LUBRICANTS FOR THE KNEE

Bell CJ[1], Fisher J[1], Ingham E[2], Forsey R[1], Thompson JI[3], Stone MH[4]
[1]School of Mechanical Engineering, University of Leeds, C.Bell@leeds.ac.uk; [2]Department of Microbiology, University of Leeds; [3]DePuy International (a Johnson & Johnson Company), Leeds; [4]Department of Orthopaedic Surgery, Leeds General Infirmary, UK.

INTRODUCTION

Intra-articular injection of hyaluronic acid (HA), is an increasingly popular treatment for pain relief in knee osteoarthritis (OA). Clinical studies (Huskisson & Donnelly, 1999) have reported the benefits of such treatments, but the mechanism of action is poorly understood. The aim of this study was to develop a series of *in vitro* OA models, which could be used to investigate the potential benefits of intra-articular injections of HA. These results were validated against data from *in vitro* tests on human OA cartilage.

MATERIALS AND METHODS

Start-up frictional properties were investigated as these are dependant on boundary lubrication mechanisms (Forster & Fisher, 1996). Bovine cartilage is readily available and known to give repeatable measurement of friction coefficient (Forster & Fisher, 1996). Bovine femurs from healthy, skeletally mature animals were retrieved within 12 hours of commercial slaughter. Cartilage plates (approx. 30mm x 15mm) and plugs (9mm diameter) were cut from the distal femur. Samples were stored in Ringers solution and frozen (-20°C). Prior to testing, specimens were defrosted at 40°C and treated with Folch Reagent to remove any residual lipids. For all tests the pin was loaded onto the plate for ten minutes prior to measurement. Frictional force was measured with a piezo-electric transducer and data captured on an oscilloscope for analysis. A 25N load was applied, and the sliding velocity of the plate was 4mm/s (fig 1). This model has been used to test lubricants in a boundary lubrication regime (Forster & Fisher, 1996).

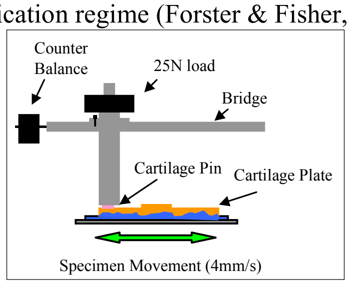

Figure 1: Schematic of Test Rig

Three *in vitro* OA models were developed to determine the severity of disease state at which the lubricants are most effective. The 'healthy' model used cartilage as retrieved. The 'intermediate' damage model was developed to represent mild OA. This involved coring a 3mm diameter plug from the plate followed by biochemical degradation with papain (30 mins at 1500units/ml). The third model was a 'highly damaged' model used to represent advanced OA. This used coarse sandpaper to remove greater than 50% of the cartilage thickness. Human samples were retrieved from patients undergoing total knee replacement for OA. Samples were frozen in Ringers (-80°C) until tested. Human samples were graded using the ICRS System (International Cartilage Repair Society). Ringers was the control lubricant as this has previously been shown to produce friction levels comparable to synovial fluid (Forster & Fisher, 1996). Three HA-based preparations were evaluated: a low molecular weight HA (MW = 700,000); a high MW HA (MW = 3,000,000); and a cross-linked HA (MW = 6,000,000). Results were analysed using one-way ANOVA with individual differences determined using the T-method. All data plotted as averages ± 95% confidence intervals.

RESULTS

Results for all bovine models showed an increase in friction for each successive damage level, which replicates the human OA results. Results for the 'healthy' bovine model correlated well with those from human samples of ICRS grades 0-1. The use of HA produced a significant ($p<0.05$) reduction in friction compared to Ringers, for both 'healthy' bovine and low grade human OA cartilage (fig 2). Both 'intermediate' and 'highly damaged' models showed a reduction in friction coefficient for the high MW HA compared to Ringers, but this difference was not statistically significant. High grade human OA cartilage however did show a significant reduction in friction coefficient for the high MW HA.

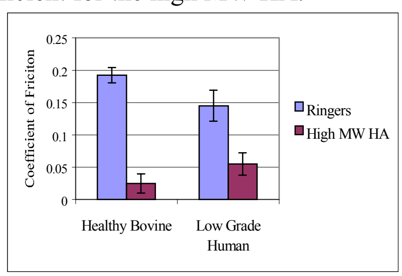

Figure 2: Comparison of friction coefficient for 'healthy' bovine and human cartilage in Ringers and high MW HA

DISCUSSION

This study shows that boundary lubrication by HA is important for healthy and diseased cartilage. Results from the 'healthy' bovine model showed good correlation with low grade OA cartilage, for all lubricants tested. The inability to demonstrate this in our bovine 'damage' models could be due to a variation in the damage states produced. The results produced by these simple *in vitro* bovine 'damage' models did not replicate the effect of HA on human OA cartilage.

REFERENCES

Huskisson & Donnelly (1999). *Rheumatology*. **38**:602-607
Forster & Fisher (1996). *Proc Instn Mech Engrs*, **210**:109-119

INFLUENCE OF GRAVITATION ON THE SQUAD JUMP: A COMPUTER SIMULATION

Sigrid Thaller and Martin Sust
Institute of Sports Sciences, Karl-Franzens-University Graz, Austria
sigrid.thaller@uni-graz.at

INTRODUCTION

How high can an astronaut jump on the moon? In vertical jumping the force F accerlerating the center of mass can be measured via the ground reaction force. This force F consists of the forces produced by the muscles, including arm movements, in the positive direction (up) and the weight of the subject in the negative direction (down). A change in the gravitational field obviously leads to a change of weight, but the inertia of mass remains the same. In addition, the changed velocity of the movement leads to altered muscle forces due to Hill's relation between force and contraction velocity. With the help of a simple mathematical model the influence of the gravitation on the vertical jump is simulated.

METHODS

The squad jump is described by a Hill-type model of an extensor based on Sust (Ballreich , Baumann 1996.). This model consists of three parts, describing the force produced in the muscle (Hill), the innervation of the muscle, and the relation between the force in the muscle and the force acting outside due to the geometry of the joint. These parts together with Newton's law lead to a nonlinear second order differential equation which is solved numerically using MATLAB©. There is only a small number of parameters used: one parameter for the innervation, three for Hill's force-velocity relation, 5 for describing the geometry of the joint, and furthermore, the mass, the gravitation, the initial position and the initial velocity for the equation of motion. Several simulations were performed using different values of parameters for the biomechanical and physiological properties of the subjects

RESULTS AND DISCUSSION

In a first series of simulations we decreased the gravitational constant while we increased the mass such that the weight, i.e. the product of gravitation times mass, was kept constant. All other parameters of the subject were left unchanged. As a result the height of the jump increased with decreasing gravitational constant, while the velocity at take off, i.e. the velocity of the center of mass at the time when the subject looses ground contact, decreased. Figure 1 shows the velocity at take off, the jump height (measured from the ground), and the total energy produced by the muscle, as a function of the gravitation for one subject. The shape of these curves depends on the individual properties of the subject. In order to examine the interindividual differences between the subjects and their influence on the height of the squad jump we performed a simulation of jumps on earth (gravitation $g = 9.81\ m/s^2$) and on the moon ($g = 1.65\ m/s^2$). We were able to find values of parameters in such a way that on earth subject A jumped higher than subject B, whereas on the moon, subject B was better in jumping (Table 2). Subject A is assumed to have a slower innervation and a lower maximal possible contraction velocity of the muscle. Thus on earth, where the time until take off is longer and therefore the velocity of the movement is slower than on the moon, these individual properties of subject A are less limiting than on the moon.

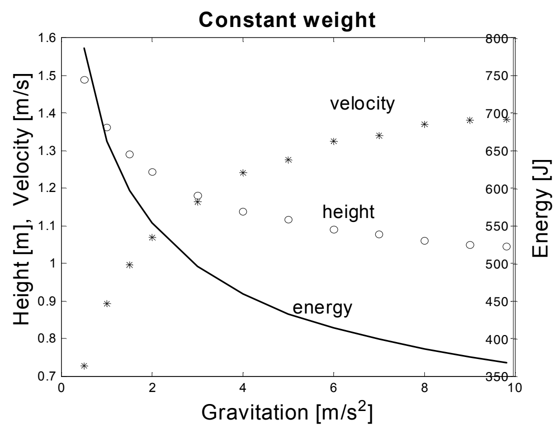

Figure 1: Height, velocity at take off, and energy of the squad jump, as a function of gravitation. The weight of the subject is held constant by adding additional mass.

Table 1: Comparison of height (measured from the ground) of a squad jump on earth and on the moon, performed by two subjects with different individual muscle properties.

	height [m] subject A	height [m] subject B
earth	1.11	1.08
moon	2.36	2.46

SUMMARY

The influence of the gravitation on the resulting height of a vertical jump depends crucially on the individual physiological and biomechanical properties of the subject. In different gravitational environments different properties are limiting factors for the movement.

REFERENCES

Ballreich, R., Baumann, W. (1996). *Grundlagen der Biomechanik des Sports*. Ferdinand Enke Verlag Stuttgart.

SYNERGISTIC EFFECT OF SPATIAL RESOLUTION AND NOISE ON THE PRECISION AND ACCURACY OF MEASUREMENTS IN SIMULATED DIGITAL RADIOGRAPHS

Ruth K Wilcox[1], Emma Kennard[1], Richard M Hall[1,2]
[1]School of Mechanical Engineering, University of Leeds, Leeds, UK, [2]Musculoskeletal Services, CSB, St James's University Hospital, Leeds, UK. r.m.hall@leeds.ac.uk

INTRODUCTION

The accurate and precise measurement of wear in the clinical environment is necessary for effective patient management. Further, such improvements would increase the power associated with clinical trials in which level of wear was an outcome measure. Recently several groups have devised automated techniques based on digital image processing (Shaver et al 1997, Martell and Berdia 1997) that have shown improved precision when compared to manual methods in the laboratory environment. However, artefacts within the experimental protocols used to simulate wear add additional sources of error. The aim of this study was to investigate the effect of noise and spatial resolution on the accuracy and precision of penetration measurements from simulated radiographs of cemented Charnley prostheses.

METHOD

Ten images were generated using a graphical programming language (IDL, Research Systems Inc., USA). The images depicted a perfect circle and arc to represent the femoral head and wire marker respectively, with the same dimensions as a standard Charnley THR, but differing in head position relative to the socket. Each ideal image was then used to generate 15 more images corrupted by reductions in spatial resolution followed by different levels of white Laplacian noise. The reduction of spatial filtering was chosen to encompass the range of modulation transfer functions exhibited by hospital radiography systems. All 160 images were analysed by a single operator using custom-designed software that had been developed previously in-house employing an algorithm similar to that given by Shaver et al (1997)

RESULTS

The error in penetration depth and direction were calculated for each analysis. The bias and precision for each level of noise were represented by the mean and root mean square error (RMS) respectively and are shown in Figures 1a and 1b for the penetration depth measurements. The errors were found not to be dependent on the magnitude or direction of the wear, except at extremely low levels of penetration depth (<0.1 mm). Here large variations in the penetration angle were apparent and these values were not included in the overall analysis. No discernable pattern was observed in the relationship between the mean error and the level of corruption (Figure 1a). The RMS errors were found to increase with increasing noise and, to a lesser extent, with increasing levels of filtering (Figure 1b). Similar results were observed for the penetration direction measurements.

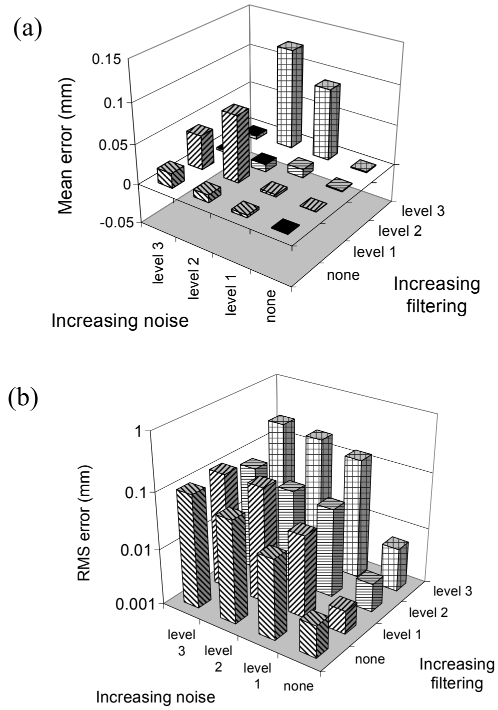

Figure 1: (a) Mean error and (b) RMS error in penetration depth for different levels of image corruption.

DISCUSSION

The use of simulated radiographs are useful in characterizing the effects of different image processing techniques and noise in a more controlled manner whilst decoupling the effects of the laboratory simulated wear. The precision was found to be strongly dependent on the level of noise whilst the effects of spatial resolution had less of an effect. When combined, effects of changes in spatial resolution and noise appear not to be linear. The results indicate that these new assessment techniques are highly dependent on the level of image corruption that can occur within these images. The reduction in the level of precision in the most severely affected images is probably clinically significant in that the RMS value obtained here is of the order of the penetration likely to occur in the first two years of a Charnley type hip.

REFERENCES

Martell, J., Berdia, S. (1997) *J. Bone Joint Surg.* **79A** 1635-1641
Shaver S.M., Brown, T.D., Hillis, S.L. et al (1997). *J. Bone Joint Surg.* **79A** 693-700
The authors acknowledge ARC for their support of this project (Grant number H0581).

GROUND REACTION FORCES ON STAIRS

Alex Stacoff, PhD[1], Christian Diezi[1], Gerhard Luder[1], Edgar Stüssi, PhD[1], Bruno Leisinger[1], Inès A. Kramers – de Quervain, MD,[1,2]

[1]Laboratory for Biomechanics, ETH Zürich, Schlieren, Switzerland; stacoff@biomech.mat.ethz.ch
[2]Bircher Klinik Susenberg, Zürich, Switzerland

INTRODCUTION

Normative data of the vertical ground reaction force (GRF) of stair ascent and descent is rare in the related literature. Most previous investigators (Andriacchi et al. 1982; McFayden, 1988; Savvidis et al. 1999) tested on 2-4 steps only, a test which is not representative to daily housing situations. The goals of the study were: (i) to identify typical patterns of vertical GRF in ascending and descending stairs, (ii) to test the reliability of parameterization of selected points on the vertical GRF curve, and (iii) to test left-right symmetry during stair ascent and descent.

METHODS

Nineteen healthy test subjects (between 27 and 83 years) were tested when walking on level ground, and during ascent and descent on stairs with 20 deg. (flat), 31 deg. (standard) and 41 deg. (steep stair) of inclination; thus a total of 7 test conditions. Each test subject repeated all test conditions 10-12 times. Parameterization of two consecutive steps of the vertical GRF curves was performed with a computer routine adapted from Aebersold (1980; Fig. 1) and checked for reliable detection. To test gait symmetry, the symmetry index described by Herzog et al. (1989) was used.

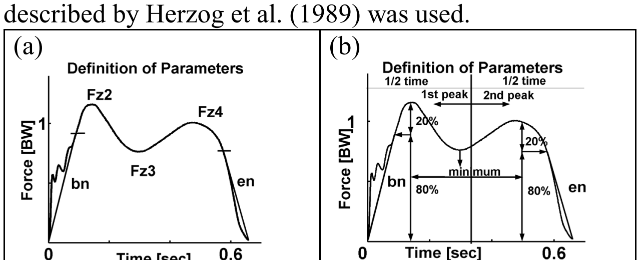

Figure 1: (a) Detection and (b) definition of selected parameters of the vertical GRF measured during level walking (after Aebersold, 1980).

RESULTS AND DISCUSSION

To (i): Generally, during ascent and descent a two-peak wave form of the vertical GRF was detected. In contrast to level gait the second peak (Fz4) was generally higher in stair ascent during push-off (Fig. 2a) and the first (Fz2) in stair descent (Fig. 2d) during touchdown. However, in stair ascent, curves with similar peaks (Fig. 2b) and in stair descent, curves with only one peak (Fig. 2e), as well as complex forms (Fig. 2c, 2f) were also found.

To (ii): GRF parameters defined for level gait (Fig. 1) were reliably detected for each individual in 100%. In stair

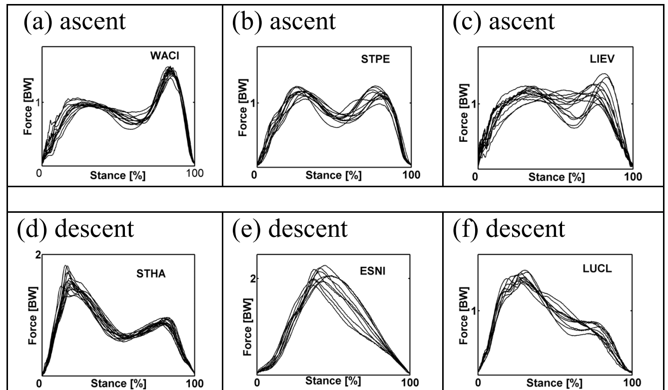

Figure 2: GRF curves: (a) Fz4 larger than Fz2, (b) same magnitude of Fz2 and Fz4, (c) complex form, (d) Fz2 larger than Fz4, (e) one peak and (f) complex form.

ascent the correct detection for all parameters was between 87.4% and 100%, in stair descent between 59.7% and 100% on average. Consequently, trials with incorrect detection were omitted from the data pool. To (iii): The remaining data showed significant left-right asymmetries over all parameters, subjects and test conditions in 31.2% (ANOVA $p<5\%$); the differences being unsystematic, however. When applying the symmetry index, asymmetries were found between 2.9% and 40.2% on average. Parameters bn and en showed larger asymmetries (between 6.8% and 40.2%) than Fz2 and Fz4 (between 3.1% and 18.0%), reflecting the difficulty of an exact definition of certain parameters of GRF on stairs.

SUMMARY

Vertical GRF curves of stair ascent and descent were detected with two peaks, but other wave forms (one peak, complex forms) were also present. In addition the GRF proved to be less reproducible compared to level walking; thus, the parameterization of the GRF was found to be less reliable. The results showed that significant left-right asymmetries occurred in about 30% of the test parameters, the index revealing asymmetry between 3% and 40%. Therefore, asymmetries of around 5% reported for patients may not necessarily be pathological.

REFERNCES

Aebersold P. Dissertation, Univ. Bern, 1980; Andriacchi TP et al. JBJS, 62A, 1982; Herzog et al. MSSE, 21, 1989; McFayden et al., J of Biomech. 21, 1988; Savvidis et al., Biomed. Technik, 44, 1999.

ACKNOWLEDGEMENTS

Swiss National Foundation (Grant No: 3200-055651.98).
SULZER Medica, Orthopedics Ltd. ESK Switzerland.

VISUALISATION OF INTER-SARCOMERE DYNAMICS IN MUSCLE FIBRES

I Telley[1], KW Ranatunga[2], J Denoth[1]
[1]Laboratory for Biomechanics, Department of Materials, ETH Zürich, Wagistrasse 4, 8952 Schlieren, Switzerland
[2]Department of Physiology, School of Medical Sciences, University of Bristol, Bristol BS8 1TD, UK
Correspondence to denoth@biomech.mat.ethz.ch

INTRODUCTION

We recently developed a mechanical model (Denoth et al, 2002) that can explain phenomena like extra tension, sarcomere popping and homogenisation. The model assumes that random or systematic differences exist in force generation in single sarcomeres and shows that they can lead to non-uniform behaviour, especially if some sarcomeres are working on the descending limb of the force-length curve. Experiments using sarcomere visualisation in single mammalian muscle fibres have given evidence of non-uniform sarcomere behaviour after stretching in active but not in relaxed muscle fibres.

METHODS

Single skinned fibres (~1mm long) from rabbit psoas muscle were set up for visual data acquisition by attaching them on two small stainless steel hooks. One hook was connected to a force transducer (AE 801, AME), the other to a liver arm and a micromanipulator that allowed manual stretching and releasing of the fibre (accuracy of length change was 1µm). The fibre was relaxed and Ca-activated adopting standard procedures (see Coupland et al., 2001, for details on the solutions). Image data acquisition was performed with an inverted microscope (Olympus), a CCD camera with a VCR, a PC video grabber and image processing software (SCION).

RESULTS AND DISCUSSION

We showed in several earlier simulations that only a slight diversity in maximal isometric force in some or every sarcomere leads to non-uniform behaviour such as sarcomere popping (Denoth et al. 2002), phenomena that were predicted by Morgan (Morgan et al. 1990). While stretching after activation, some sarcomere operate on the plateau and were only slightly stretched, other weaker sarcomeres were shifted into the titin scaffold where they can possibly remain stable after releasing the fibre to its original length (Fig. 1).

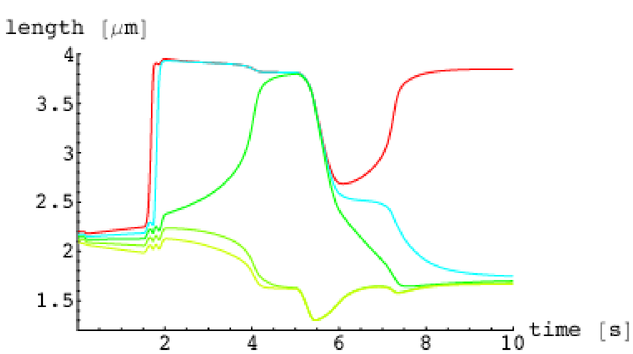

Figure 1: Sarcomere length simulation during stretch-release (40% of resting length) for an activated 5-sarcomere myofibril. Stretch, 1.5 – 2 s; release, 5 – 6 s.

The stretch-release experiment on fibres showed similar effects to the simulations. While in relaxed state the observed region showed a homogeneous striation pattern and a sharp peak in image fourier analysis, in active state some sarcomeres remained longer after stretching the fibre (see Fig. 2). Stretches were about 40% of the fibre length as used in the simulation.

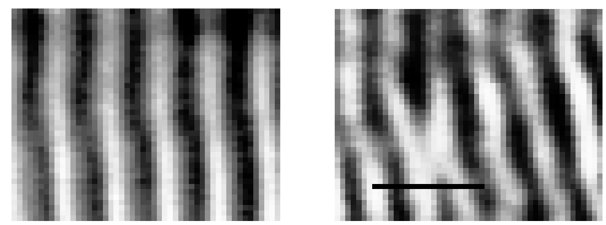

Figure 2: Visual images of a fibre in relaxed (left) and active state (right) after stretching, scale bar is 5µm.

The muscle fibre force recording showed transient behaviour unlike the model. The discrepancy may be partly due to the fact that the simulations were only for single myofibrils and did not take account of a network of parallel structures with inter-connections as is the case for a muscle fibre.

SUMMARY

These preliminary experiments show that after large stretches the sarcomere uniformity is disturbed and new stable arrangements are possible where some sarcomeres are much longer than others. Our plan for the future is to investigate the behaviour of single myofibrils at large stretches and also to adapt the mechanical model for non-steady situations.

REFERENCES

Coupland, M., Puchert, E., Ranatunga, K.W. (2001) *Temperature dependence of active tension in mammalian muscle fibres*, J Physiol, **536.3**, 879 – 891

Denoth, J., Stüssi, E., Csucs, G., Danuser, G. (2002) *Single muscle fiber contraction is dictated by inter-sarcomere dynamics*, J Theor Biol. In Press.

Morgan, D.L. (1990) *New insights into the behavior of muscle during active lengthening*, Biophys J, **57**: 209 – 221

INTER-SARCOMERE DYNAMICS IN MYOFIBRILLS AND MUSCLE FIBRES – THEORETICAL CONSIDERATIONS AND SIMULATIONS

J Denoth, I Telley, G Danuser
Laboratory for Biomechanics, Department of Materials, ETH Zürich, Wagistrasse 4, 8952 Schlieren, Switzerland
Correspondence to denoth@biomech.mat.ethz.ch

INTRODUCTION

We have developed a generic framework for analysing inter-sarcomere dynamics (Denoth et al, 2002). The complexity of a ‘real’ muscle fibre is addressed through rigorous coupling of the sarcomere and myofibril models in a system of differential equations. Our objective is to find an accurate description of (a) a myofibril as a linear motor composed of in series coupled sarcomeres and (b) a fibre as a linear motor composed of parallel coupled myofibrils. Emphasis of this work is put on systematic treatment of sarcomeres and not on the molecular modelling of the active and passive elements in them. With the current method we have found mathematical explanations for mechanisms such as sarcomere popping, homogenisation, extra tension, permanently changed tension or creep phenomena.

METHODS

Properties of the system of differential equations (DE) were examined based on a down-stripped model, which permits the derivation of analytical solutions. The system of differential equations for the complete model was solved by numerical methods, where in contrast to other work in the literature, we confine ourselves to relatively short myofibrils up to 30 sarcomeres. In both cases the inter-sarcomere dynamics in length- and force-controlled experiments were analysed.

RESULTS AND DISCUSSION

<u>(a) Myofibril:</u> In force-controlled experiments the inter-sarcomere dynamics is determined independently for each sarcomere. On the ascending limb and the plateau of the force-length relation of the active element, the sarcomere length resists a perturbation; the mechanical state is stable and is characterized by a relaxation time τ ($\tau \approx$ 1-5 s). On the descending limb of the force-length relation of the active element, the sarcomere length will not resist perturbations if the slope of the total force-length function (contractile and passive elements) is negative; the mechanical state is unstable, the relaxation time τ is about 1-5 s.

Length-controlled experiments are governed by a coupling of sarcomeres. The behaviour is much more complex and we have shown that experimentally observed phenomena such as popping or creeping can be explained with the dynamic coupling of the DEs associated with each sarcomere. In mathematical terms the response of such a system can be described by N independent modes, where one mode is a linear combination of the N sarcomeres involved. Similar to simple sarcomeres, the modes are characterized by a stability parameter and the relaxation time, however here unstable modes can affect multiple sarcomeres.

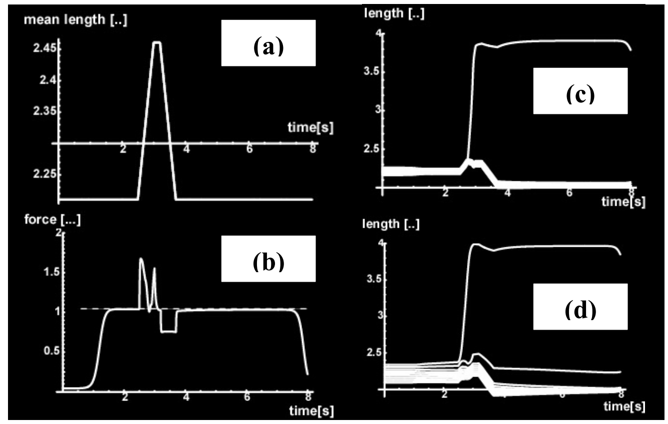

***Figure 1**: Stretch-release experiment of a two-myofibril system. External length control displayed as a length-time curve of the mean sarcomere length (a). Force development in the fibre (b). Length-time curve of the sarcomeres of myofibril 1 (c) and the sarcomeres of myofibril 2 (d). Note: Stable modes in myofibril 1 may not prevent the popping of a sarcomere in myofibril 2.*

<u>(b) A single fibre:</u> Adjacent myofibrils are mechanically connected through the Z-line scaffold. The cross links are expected to stabilize the system; a local instability will be attenuated by ‘stable’ sarcomeres in neighbouring parallel myofibrils. However, the simulations show that unstable sarcomeres (or modes) in a myofibril may not be stabilized by sarcomeres on the plateau (or stable modes) of the immediate neighbouring myofibril (Figure1).

SUMMARY

A rather simplistic mechanical description of the contractile and passive elements in the sarcomere is sufficient to predict observations from single fibre experiments that are seemingly contradictory. It turns out that the large variability of possible fibre responses is the result from a convolution of multiple rules, each of them defining a certain characteristics of the single sarcomere. With this work we provide a comprehensive model platform for consistent interpretation of single fibre experiments.

REFERENCES

Denoth, J. et al. *Single muscle fiber contraction is dictated by inter-sarcomere dynamics,* J. theor. Biol. (2002). In Press.

LOWER BACK MOMENT AND POSTURAL PARAMETER RELATIONSHIPS DURING ASYMMETRIC LIFTING

Jason C. Gillette[1], Timothy R. Derrick[2], Nancy E. Quick[3], and Robert Shapiro[3]
[1]Center for Biomedical Engineering, University of Kentucky, Lexington, Kentucky, USA, jcgill2@uky.edu
[2]Health and Human Performance Department, Iowa State University, Ames, Iowa, USA
[3]Department of Kinesiology and Health Promotion, University of Kentucky, Lexington, USA

INTRODUCTION

Increased risks of injury during asymmetric as compared to symmetric lifting have been predicted by both biomechanical and epidemiological studies [Chaffin, 1999]. The selection of appropriate ergonomic indicators to quantify the effect of asymmetric lifting on lower back loading remains an area of active research. The goals of this study were: a) to determine the effects of asymmetry and object mass on L5/S1 joint moments and b) to examine relationships between L5/S1 joint moments and other postural parameters during lifting.

METHODS

Six subjects (mass 74 ± 12 kg, three males, three females) with no history of back pain volunteered for this study. The subjects lifted a milk crate loaded either with a self-selected, moderate amount of mass (12 ± 2 kg) or half this amount. These subjects lifted the crate free-style from floor level in front of their feet to waist level at 0°, 30°, 60°, or 90° of asymmetry to the right as mapped out on the floor for guidance. In total, three repetitions of two object masses at four asymmetry levels were performed, resulting in 24 lifting trials for each subject. The subjects stood on force platforms (Bertec Corp.) sampled at 960 Hz and wore reflective markers that were tracked by a six-camera video system (Motion Analysis Corp.) at 60 Hz. Centers of pressure (COP) and joint angles were calculated. A three-dimensional model of the human body was utilized to estimate joint moments at the L5/S1 intervertebral disc [Kingma, 1996]. Multivariate ANOVA (SAS Institute, Inc.) was performed to test the dependence of the L5/S1 joint moments on object weight and lifting asymmetry (significance at $p < 0.05$).

RESULTS

Maximum L5/S1 extension moments were significantly greater when lifting the heavier load as compared to the lighter load. Maximum L5/S1 lateral bending moments were greater for 60° and 90° asymmetry than for 0° when lifting the heavier load. In addition, maximum L5/S1 twisting moments were significantly greater for 90° asymmetry with the lighter load and for 60° and 90° asymmetry with the heavier load. Correlation coefficients between the anterior/posterior (A/P) COP and the L5/S1 extension moments averaged above 0.7 (Fig. 1), and correlations between the L5/S1 flexion angle and the L5/S1 extension moments averaged over 0.8 for all lifting conditions. Correlation coefficients between the L5/S1 twisting angle and the L5/S1 twisting moments averaged below –0.5 for 90° with the lighter load and for 60° and 90° with the heavier load.

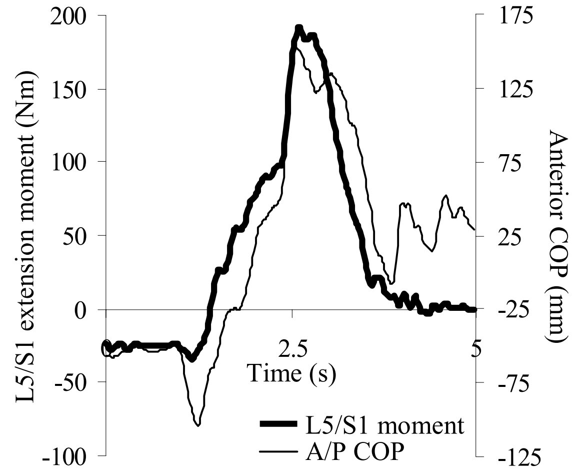

Figure 1: A representative example showing the relationship between A/P COP and L5/S1 extension moments.

DISCUSSION

Maximum L5/S1 extension moments increased when lifting the heavier load, but were not significantly affected by the degree of lifting asymmetry. Along those lines, studies have found spinal compression forces that have even decreased with lifting asymmetry [van Dieen, 1999]. However, when lifting the heavier load, maximum L5/S1 lateral bending moments significantly increased from 30° to 60° asymmetry. This may suggest that lateral bending effects are of most concern after passing a certain threshold of asymmetry, which becomes more pronounced with increased lifting loads.

The estimation of L5/S1 joint moments requires an elaborate experimental setup that may not be possible to implement in the field. For example, COP could be determined using foot-based pressure sensors, and L5/S1 angle measurements could be measured by a Lumbar Motion Monitor [Marras, 1998]. Both A/P COP and L5/S1 flexion angles were correlated with L5/S1 extension moments and may serve as practical ergonomic measures. For L5/S1 twisting moments, the L5/S1 twisting angle appears promising for the more extreme asymmetry conditions that are of particular concern.

REFERENCES

Chaffin, D.B., Andersson, G.B.J., Martin, B.J. (1999). *Occupational Biomechanics*. John Wiley & Sons.
Kingma, I., et al. (1996). *Hum. Mov. Sci.*, **15**, 833-860.
Marras, W.S., Davis, K.G. (1998). *Ergonomics*, **41**, 817-834.
van Dieen, J.H., Kingma, I. (1999). *J. Biomech.*, **32**, 681-687.

COULD MOBILE BEARING KNEE PROSTHESIS REDUCE STRESS CONCENTRATION UNDER SURGICAL MALALIGNMENT?

Chang-Hung Huang[1], Jiann-Jong Liau[1], Cheng-Kung Cheng[1], Chun-Hsiung Huang [1, 2]
[1]Institute of Biomedical Engineering, National Yang-Ming University, Taipei, Taiwan, ckcheng@ortho.ym.edu.tw
[2]Department of Orthopaedic Surgery, Mackay Memorial Hospital, Taipei, Taiwan

INTRODUCTION

Fixed bearing total knee prosthesis (TKP) has been proved to be clinically successful. However, lossening and wear were still the long-term failure in fixed bearing knee prostheses. Mobile bearing TKP is designed to resolve these problems (Buechel F.F. and Pappas M.J.). The polyethylene bearing of mobile TKP can move relatively on the interface between bearing and tibial baseplate, which can decrease constraint force. In addition, the tibiofemoral joint is high conformity in contacting surfaces, so that it could reduce the contact pressure to prevent polyethylene wear. The malalignment of knee prosthesis was hypothesized to accelerate the polyethylene wear. The study was to investigate the difference in contact pressure between fixed and mobile bearing TKP under malalignment condition.

METHODS

At first, we modified the locking mechanism of fixed bearing (U-knee, ROC) to mobile bearing, the polyethylene insert can rotate on the tibial baseplate. These curvatures (moderate conformity) in the tibiofemoral contact surface of the mobile bearing was kept the same as fixed bearing. Malalignment of total knee replacement was simulated and the contact pressure in the tibiofemoral joint was measured by using Fuji prescale film and digital image analysis. The simulated malalignments include the mediolateral translation (0.5 and 1 mm), anteroposterior translation (2 and 4 mm) of the tibial component relative to the normal position. Further, Femoral component was positioned internal/external rotation (1, 3, 5 and 10 degrees) relative to tibial component. The compressive load was 3000 N to simulate the maximum contact force during human gait cycle.

RESULTS AND DISCUSSION

The maximum contact pressure of fixed bearing design was significantly higher than the mobile design when the tibial component was translated anteriorly 4 millimeter (Fig. 1). The maximum contact pressure of fixed bearing design was also significantly higher than the mobile bearing design when the tibial component was translated medially or laterally. In malrotation test, only at the internal or external 10 degrees, the maximum contact pressure of the fixed bearing design was significantly higher than the mobile bearing design. The maximum increase of contact pressure in anterioposterior maltranslation were 7.63 and 7.62 percent relative to the neutral contact situation in fixed and mobile bearing designs respectively. In mediolateral maltranslation, there were 23.3 percent in fixed bearing design and 22 percent in mobile bearing design. However, in the internal/external malrotation, the increase of maximum contact pressure in fixed bearing design was 27.1％ which was much higher than mobile bearing design (22.4％). The maximum contact pressure in the fixed bearing design was always higher than the mobile bearing design under malalignment situations. Mobile bearing knee prosthesis could reduce stress concentration because polyethylene insert can internal/external rotate on the metal tibial tray while simulated surgical malalignments occurred. There were some limitations in this study such as: the nonhomogeneous of Fuji pressure film and inaccuracy dimensions of the fixture would influence the measured result of maximum contact pressure.

SUMMARY

The mobile bearing design has smaller maximum contact pressure than the fixed bearing design when the malalignment of tibiofemoral joint of knee prosthesis was simulated. Even though, the design is moderate conformity in tibiofemoral contact surface. The mobile bearing has an advantage to accommodate the surgical malalignment than fixed bearing design. To provide better wear resistance in mobile bearing design, the high conforming design in the tibiofemoral contact surface can be considered.

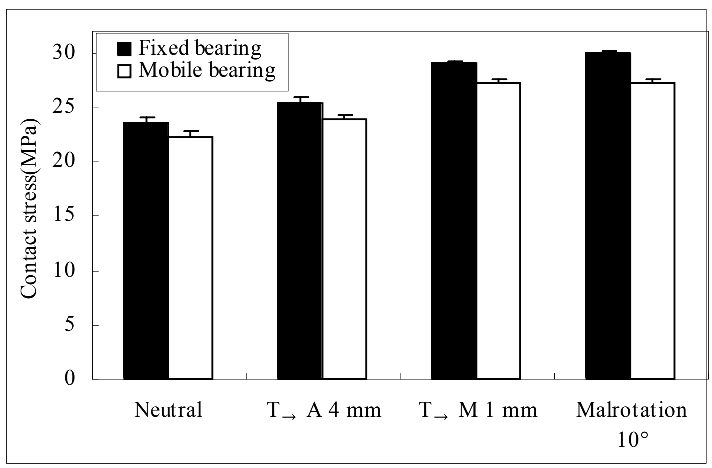

Figure 1: Contact pressure of fixed and mobile bearing under different surgical malalignments.
T→A 4 mm: Tibial component was translated anteriorly 4 mm.
T→M 1 mm: Tibial component was translated medially 1 mm.
Malrotation 10°: Femoral component was malrotated 10 degree.

REFERENCES

Buechel F.F., Pappas M.J., (1986). *Arch Orthop Trauma Surg*, **105**, 197-204.

MUSCLE FORCES ANALYSIS IN THE SHOULDER MECHANISM DURING WHEELCHAIR PROPULSION

Hwai-Ting Lin[1], Hong-Wen Wu[2], and Fong-Chin Su[1]
[1]Institute of Biomedical Engineering, National Cheng Kung University, Tainan, Taiwan, fcsu@mail.ncku.edu.tw
[2]School of physical therapy, China Medical College, Taichung, Taiwan

INTRODUCTION

Epidemiological studies have shown that there is a high prevalence of shoulder injuries in wheelchair users. The high incidence of upper extremity musculoskletal problems may be due to the low efficiency of wheelchair propulsion. To lessen the injury probability and to enhance the efficiency of wheelchair propulsion, biomechanical analysis of the contribution of arm- and shoulder muscles to the joint moments during wheelchair propulsion is essential. The purpose of this study was to determine the muscle contraction forces around the shoulder during wheelchair propulsion based on the measured segment motion and the estimated limb mass/inertia property of the wheelchair user.

METHODS

Eleven muscles were included in the shoulder model, while the motion of the entire body was considered in the dynamic analysis of the system. The wheelchair propulsion of a normal subject at level ground with the self-select speed was captured using an Expert Vision™ motion analysis system (Motion Analysis Corporation, U.S.A.) at a 60Hz sampling rate. Using the inverse dynamic problem solution and Newtonian analysis, the joint resultant forces and moments at shoulder were quantified. The indeterminate problem was solved using an optimization technique by minimizing the sum of the squares of muscle stresses. Additional inequality constraints on muscle force and stress output were considered, thus making the present formulation a "mini-max" problem. Sequential quadratic programming and a steepest decent algorithm were used to search for the unique solution. The wheelchair propulsion EMG data reported in the literature were used to qualitatively assess the validity of the theoretically predicted muscle forces and stresses.

RESULTS

We divided the wheelchair propulsion cycle into propulsion and recovery phase for results presentation. Anterior deltoid increased the muscle contraction force at the beginning of the propulsion phase and reached the maximum force 462N at the middle of propulsion phase then decreased to zero at the end of propulsion phase. Pectoralis major also had minor significant contraction force during the propulsion force, whereas the other muscles were relatively quiescent. During the recovery phase, all muscles had smaller contraction forces than in propulsion phase. Posterior deltoid and pectoralis major had larger contraction forces among all muscles (Fig. 1).

DISCUSSION

Direct measurement of muscular forces is invasive and currently impractical. A proper biomechanical model is helpful in understanding the state of muscle contraction in response to both internal and external loading on the skeletal system. Previous electromyography (EMG) data for the wheelchair propulsion (Chow et al., 2001) showed that the anterior deltoid experiences peak activity in the propulsion phase, and the pectoralis major and posterior deltoid had significant muscle activity in the recovery phase which corroborates with our results. Nevertheless, the triceps brachii had high muscle activity in the propulsion phase in the EMG data that didn't show in our results. That may caused from the EMG data reflected the muscle activity that could not represent real muscle contraction force. The physiological cross-sectional area (PCSA) of the muscle also affected the muscle contraction force. The present study provided the first attempt to quantitate individual muscle contraction during wheelchair propulsion. This model and the analysis technique will aid in elucidating the underlying pathomechanics leading to various overuse syndromes involving the shoulder.

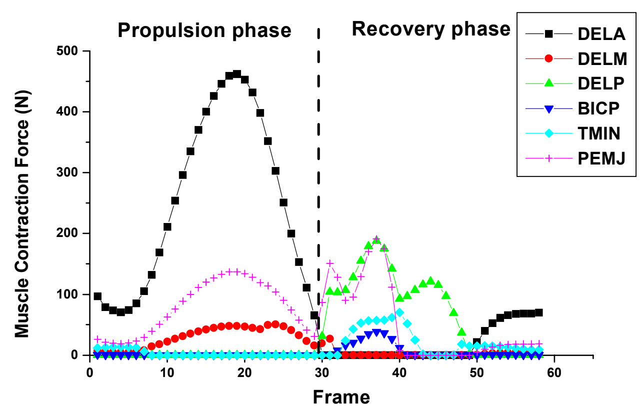

Fig. 1 The muscle contraction force during wheelchair propulsion (DELA: anterior deltoid; DELM: middle deltoid; DELP: posterior deltoid; BICP: biceps long head; TMIN: teres minor; PEMJ: pectoralis major).

REFERENCES

Van der HELM, F.C.T., Veeger H.E.J. (1996). J. Biomechanics, 29, 39-52.
Chow J.W. et al (2001). Medicine & Science in Sports & Exercise, 33, 476-484.

ACKNOWLEDGMENT

Support from the National Health Research Institutes grant NHRI-EX90-9019EL, TAIWAN, ROC.

CORRELATION BETWEEN RADIOGRAPHIC AND CLINICAL MEASUREMENT OF SAGITAL BACK SHAPE.

Christian Haid[1] Jasdip Mangat[1] Christian Kremser[2] Arnold Koller[3]
[1]Univ.-Klinik f. Orthopaedie, Biomechanik, Schoepfstr. 41, A-6020 Innsbruck, christian.haid@uibk.ac.at
[2]Dept. of Radiology, Innsbruck
[3]Institut fuer Sport und Kreislaufmedizin, Innsbruck

INTRODUCTION

The measurement and assessment of the shape of the human back is an important area of research. Spinal Mouse© and Zebris© system are now becoming more widely used for the specific purpose of back shape and mobility measurements. In both cases, by tracing the superficial shape of the subjects back, intelligent algorithms, within the systems software, computes information concerning the relative position of the vertebral bodies, of the underlying bony spinal column. To make qualitative judgments about spinal posture by observing surface curvature, is based on the assumption, that the surface curvature consistently reflects the underlying curvature of the vertebral column (Refshauge 1994). This study was therefore designed to test the validity of both systems, by comparing measurements with those of a gold standard, - an Orthopaedic surgeons analysis of Magnetic resonance images. Additionally, with reference to the gold standard measurements, the correlation between back and spinal shape was also investigated.

METHODS

15 male subjects age 19 – 37 were examined in 3 different postures, by 3 different methods – Zebris, Spinal Mouse, and Magnetic Resonance Image analysis. The measurements were conducted with the subject in the lying flat posture (Straight), a posture whose requirement to make the lumber spine more lordotic (Lordotic), and a posture being used to examine the back/spine curvature, when the lumber spine is made more kyphotic (Kyphotic). Clinical measurements from the magnetic resonance images, of the surface of the back and the spinal shape, conducted by an experienced orthopaedic surgeon, were also made. From the results, a comparison between the three measurement systems could then be made, as well as the possibility of evaluating the relationship between back shape and spinal curvature. It was essential, to ensure the subject was positioned in exact postures within all measurements. A specially built horizontally aligned bed, to enable exact repetition of postural stance, was therefore designed and constructed for measurements purposes. The results from Zebris and Spine Mouse system was immediately available in the form of a medical report. However, the MRI radiographs required further examination from an spinal orthopaedic surgeon. The orthopaedic surgeon measured all the required clinical parameters for each subject. The parameters taken from the images were the Cobb angle according to the lumbar and thoracic surface as the gold standard, and the Cobb angle of the bony spine.

RESULTS AND DISCUSSION

Results obtained from each system during patient examinations, are displayed on a clear and easy to understand report sheet. The absolute values of Thoracic kyphosis, and Lumber lordosis, of both surface and spinal curvatures, from clinical analysis of MRI's obtained, are shown in table (1). Differences in the absolute angles, determined by both Zebris and Spinal Mouse systems, in comparison to the respective gold standard measurements, are small for the Thoracic spine (<2.5°), but higher for the Lumbar spine.

SUMMARY

It is evident from the large standard deviation seen in all measurements obtained, that spine/back shape changes, as a consequence of postural alterations, varies from person to person. Many factors may influence this variation, such as body mass index and poor postural stance. It is clearly evident, that the correlation between surface and spine is an individually determined variable. All surface measurement devices can give acceptable results in the thoracic region of the spine.

REFERENCES

Refshauge, K.M., et al (1994). *Spine*, 19, 19, 2180-2185.

Table 1: Mean Difference between absolute values of MRI Surface (gold standard) and Spinal Curvatures.

Posture	Lumber Spine		Thoracic Spine	
	mean	S D	mean	S D
Straight	-12.5°	+/- 8.3°	- 3.5°	+/-6.3°
Lordotic	-15.5°	+/- 7.6°	- 0.1°	+/-4.1°
Kyphotic	-12°	+/- 11°	6.1°	+/-7.9°

VARIABILITY AND STABILITY CHANGE WITH WALKING VELOCITY--WHAT IS THE RELATIONSHIP BETWEEN THE TWO?

Janene Grodesky, M.Ed., Li Li, Ph.D., and Jan Hondzinski, Ph.D.
Department of Kinesiology, Louisiana State University, Baton Rouge, Louisiana, USA, LLI3@LSU.EDU

INTRODUCTION

Researchers have attempted to determine locomotion system stability using variability, such as the standard deviation (SD) of step duration, as an indicator. Furthermore, the increase in variability was related to the decrease in system stability (Brisswalter & Mottet, 1996; Newell & Corcos, 1993; Hamill, et al., 1999). Although variability and stability have been defined in different theoretical frames, the relationship between the two remains unclear. In addition, there is no empirically effective definition of stability. Thus, the purpose of this study was to design a method, based on the Dynamical Systems Theory, to measure stability, identify trends in variability and stability, and examine the relationship between these variables across walking speeds.

METHODS

Five participants of 20.2 ± 0.7 years of age, 63 ± 11 kg, and 1.67 ± 0.08 m were recruited. The participants signed informed consent forms after the testing protocol was discussed in detail. Reflective markers were placed on the anatomical landmarks of the hip, knee, ankle, and 5th metatarsal-phalange joint of the right leg. Lower extremity kinematics was collected at a sampling rate of 100 Hz using a Qualisys System (Glastonbury, CT, USA). Five trials of 5 minutes were performed at each of 6 different speeds (0.67, 0.80, 0.94, 1.07, 1.21, & 1.34 m/s) randomized within and across subjects. During each trial, a mechanically triggered visual perturbation was introduced when the participants attained a stable stride pattern, which was targeted to be synchronous with heel contact of the right foot. Variability of locomotion was measured by calculating the SD of the knee joint angle ensemble curve across five strides during stable treadmill walking. Stability was calculated as the duration required for participants to resume their normal walking pattern after the gait was affected by the perturbation. A two factor (gait mode and speed) repeated measures ANOVA was used for statistical analysis. Pearson correlation coefficient was calculated to determine the relationship between variability and stability across the various walking speeds.

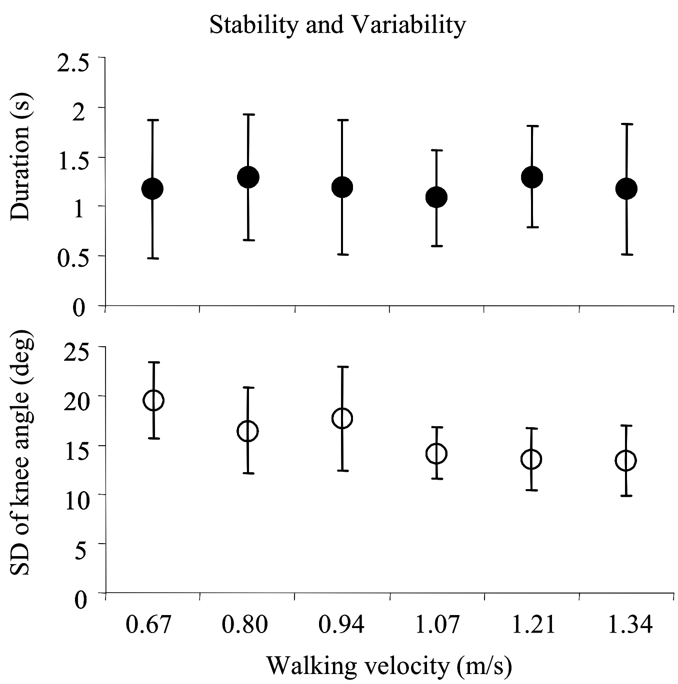

Figure 1. The trend of stability and variability changes with walking velocity. Stability was measured as the duration that it takes for the system to recover from a perturbed gait. Variability was measured as the sum of the standard deviation (SD) of the knee joint angle ensemble curve for five non-perturbed cycles.

RESULTS AND DISCUSSION

The perturbations were introduced with a mean absolute latency of .059 s (6% of the gait cycle) after heel contact. The reliability of the variability and stability measurements were reported as reliable in a previous study with an Intraclass Correlation Coefficient (ICC) of 0.80 and 0.83, respectively (unpublished data). The results indicated that stability was insensitive to change in walking speed ($p > 0.9$), while variability decreased as walking speed increased ($p > 0.05$, Figure 1). In addition, no significant correlation between variability and stability was observed ($p > .05$). These data indicate that variability is not a dependable indicator of locomotion stability. Thus, although we cannot conclude that variability and stability measures are separate entities, we suggest that measurement other than variability should be used to describe locomotion system stability.

SUMMARY

The present study showed that trends in variability and stability were different across walking speeds. Also, there was no significant correlation observed between variability and stability. Based on these results we suggest that variability should not be used as an indicator of stability, and stability should be measured directly, independent of variability, when studying locomotion.

REFERENCES

Brisswalter, J., Mottet, D. (1996). *Canadian Journal of Applied Physiology*, **21**, 471-480.
Hamill, J. et al. (1999). *Clinical Biomechanics,* **14**, 297 – 308.
Newell, K.M & Corcos, D.M. (1993). *Variability and Motor Control*. Champaign: Human Kinetics.

ACKNOWLEDGEMENT

This project is supported by Louisiana Board of Regents Grant (2000-5)-7.

BIOMECHANICAL INTERACTIONS OF THE PELVIS GIRDLES AND SURROUNDING SOFT TISSUES: TOWARD UNDERSTANDING THE MECHANISM OF PRESSURE SORE ONSET

Eran Linder-Ganz and Amit Gefen
Department of Biomedical Engineering, Faculty of Engineering, Tel Aviv University, Tel Aviv 69978, Israel, gefen@eng.tau.ac.il

INTRODUCTION

Pressure sores, caused by extensive and prolonged loading of tissues, are reported to appear in every 10th hospitalized adult, and are considered one of the most severe complications in geriatric and paralyzed patients. Many studies explored the interfacial mechanical stresses between the recumbent or sitting body and the supporting surfaces (Brosh and Arcan, 2000). However, recent simple biomechanical models of the pelvis indicated that elevated stresses, which could potentially lead to ulceration, are found internally, under the bony prominences of the pelvis (Bosboom et al., 2001). The goal of the present study was, therefore, to develop a realistic, anatomically accurate three-dimensional (3D) model of the pelvis region, in order to apply it for analysis of the mechanical conditions leading to onset of pressure sores.

METHODS

The 3D anatomy of a 5mm-thick cross-section taken around the sacrum was reconstructed from the Visible Human (male) digital database. The bones, cartilage, muscles, colon, ileum, major blood vessels, fascia and skin were segmented and their contours transferred to a solid modeling software package (SolidWorks 2001), for building the solid volumes which described the slice shown in Fig.1. The 3D slice geometry was then transferred to a finite element solver (NASTRAN 2001) for its structural analysis under body loading in the recumbent posture. This far, tissues were assumed to be homogenous, isotropic and elastic materials, with their properties adapted from previous reports (Gefen et al., 2000). Predictions of internal stress distribution were validated experimentally by comparing simulated to measured contact pressures, which were acquired by means of polyester pressure sensitive films (Sensor Products). Simulations of representative stress states in vulnerable populations (elderly and diabetics) were developed by increasing the stiffness of the skin and fascia to 6 times their normal values, in order to mimic the results of aging or disease (Gefen et al., 2001).

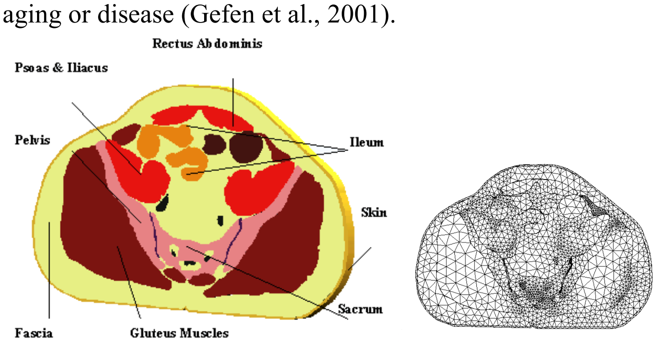

Figure 1: Structural model of the pelvis and surrounding tissues (left) and its finite element mesh (right).

RESULTS AND DISCUSSION

The distribution of von Mises stresses (Fig. 2) demonstrated sites of intensified loading in the muscular and soft connective tissues underlying the bony prominences of the pelvis. The maximal internal stresses at these sites (~350 KPa) exceeded the interfacial compression by two orders of magnitude.

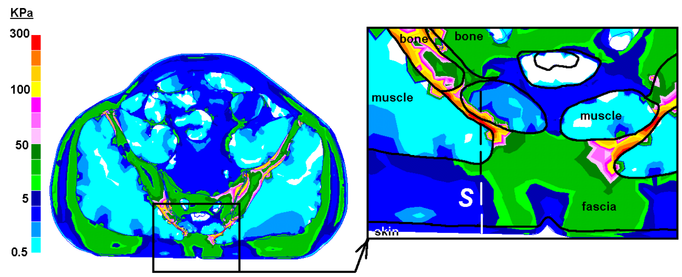

Figure 2: The distribution of von Mises stresses (with a region of interest magnified under the bony prominences of the pelvis) during recumbency. A linear path *S* is defined for characterizing the rise in stress in the soft tissues across it, towards the bone surface.

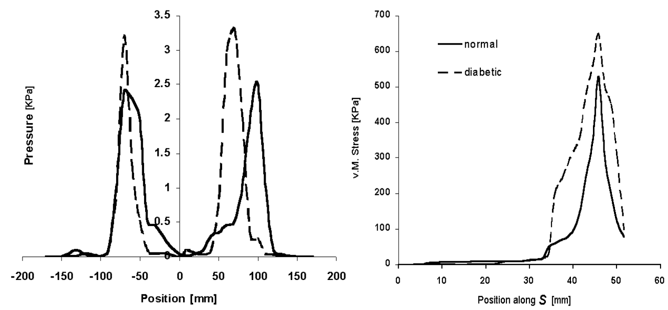

Figure 3: The distributions of pressure under the model's contact area with the supporting surface (left) and of internal von Mises stresses (right) along the path *S* (as marked on Fig. 2) for different stiffness properties of the fascia and skin simulating normal and diabetic tissues.

Distributions of contact pressures under the model's contact area with the surface (Fig. 3) are in agreement with our experimental results. In simulations of the altered distribution of internal and interfacial stresses with the progression of diabetes, where soft connective tissues are stiffened (Gefen et al., 2001), it was shown that maximal stresses may rise by 33% at the surface and by 22% internally, around the sacrum. This indicates the vulnerability of diabetic patients to onset of pressure sores, and the model has the potential of being an aid in design of seats and beds for this and other populations.

REFERENCES

Bosboom et al. (2001). *ASME Bioeng. Conf.*, **50**,853-4.
Brosh, T. Arcan, M. (2000). *Clin. Biomech.* **15**, 217-9.
Gefen, A. et al. (2000). *J. Biomech. Eng.*, **122**, 630-9.
Gefen, A. et al. (2001). *Clin. Biomech.*, **16**, 921-5.

VISUAL CONTROL OF LOCOMOTION DURING MOVABLE -OBSTACLE AVOIDANCE

Luiz Santos and Aftab Patla
Gait & Posture Lab, University of Waterloo, Waterloo, Ontario, Canada

INTRODUCTION

Perceiving changes in the environment is very important to implement avoidance strategies during locomotion. Usually avoidance strategies can be planned in advance using visual feedforward information (Patla, et.al., 1991). When there is a sudden change in the environment, however, it is necessary to make on-line adjustments in gait pattern in accordance with the direction and magnitude of the environmental change. This study investigates how visual information about a moving obstacle is used to implement on-line changes in adaptive patterns.

METHODS

Kinematic and kinetic data of seven participants (22-25 yr) was collected using 25 active markers. Participants were asked to walk and step over an obstacle (14 cm high) placed 100 cm in front of a force platform. They were told that the obstacle could move forward or stay static. For half of the trials (n=40) the obstacle remained static (V0) and in the other half the obstacle moved forward at one of two velocities (V1= 25, and V2= 60 cm/s). All trials were randomized. The obstacle motion was triggered at the toe off of the lead limb by the force platform. Velocities of toe, heel and Center of Mass (COM) were analyzed at three different points in time: Pos0 (when the foot reached the initial position of the obstacle), Pos1 (when the foot was on the top of the obstacle), and heel contact (HC). Toe Clearance (TC) was measured at Pos0 and at Pos1 (Figure 1a).

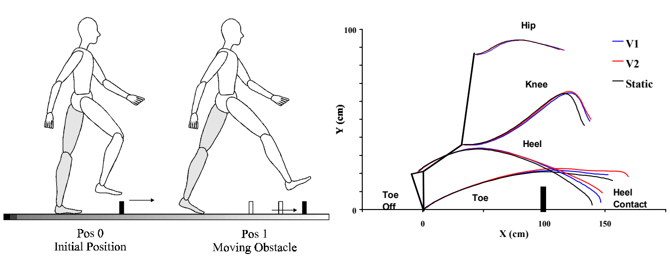

(a) (b)

Figure 1: (a) Experimental set up; (b) Sample limb profiles.

RESULTS AND DISCUSSION

All subjects were able to step over the obstacle in both static and moving conditions. The sagittal trajectory (XY) of the toe and the heel (Figure 1b) were affected by the obstacle conditions. Vertical displacement of the toe and heel were scaled to obstacle velocity. Displacement was higher for the fastest velocity (V2). Measures of TC, step length (SL), COM, and toe velocity (vertical and horizontal) were significantly affected by obstacle velocity. TC at Pos0 was significantly affected by the velocity conditions ($F_{(2,12)}$ =5.31, p=0.022). Both velocity conditions (V1 and V2) were different from the static condition (V0). The time from toe-off to Pos0 was approximately 250 ms and was not significantly different among the velocities ($F_{(2,12)}$=1.78, p=0.20). This result suggests that there is a common response for the initial toe elevation. Although the magnitude of toe elevation was the same for both velocity conditions, the vertical velocity of the toe was significant scaled to all obstacle velocities ($F_{(2,12)}$ =29.14, p=0.0001 - Figure 2a), which suggests on-line acquisition of direction specific visual information.

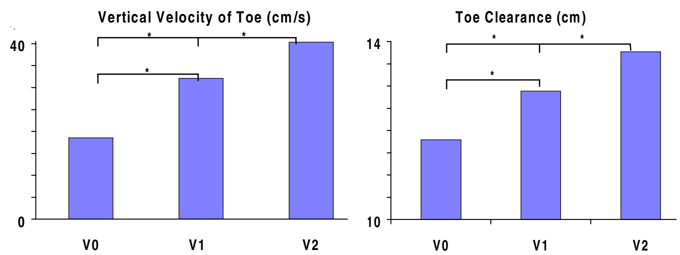

(a) (b)

Figure 2: Significant measures

The values and the time of TC calculated at Pos1 were significant different and were scaled to the obstacle velocity (value: $F_{(2.12)}$=13.84, p=0.0008; time: $F_{(2.12)}$=78.97, p=0.0001, Figure 2a,b). The same result was found for the vertical velocity of COM ($F_{(2.12)}$= 70.56, $p < 0.0001$; V0: -3.56 cm/s; V1: -5.84; V2: -9.54). The horizontal velocity of the toe was only affected by the fast velocity condition (V2), and only at Pos0 ($F_{(2.12)}$= 5.11, p=0.0247) and at HC ($F_{(2.12)}$= 5.68, p=0.0184). The anterio-posterior velocity of the COM was only significantly different at HC ($F_{(2.12)}$=18.79, p=0.0002). Both anterio-posterior velocity of COM and SL were scaled to the obstacle conditions (VelCOM – V0:155.8 cm/s, V1: 166.3 cm/s; V2: 180.2 cm/s ; SL – V0: 157.0 cm, V1: 164,6 cm, V2: 172.5 cm).

SUMMARY

The findings suggest that direction and magnitude specific visual information about the moving obstacle were used to control on-line adaptive locomotor patterns.

ACKNOWLEDGEMENTS

The authors appreciate the assistance of Milad Ishac and the financial support of CAPES, UnB – Brazil, and NSERC - Canada.

REFERENCES

Patla, A.E.; Prentice, S.D. Robinson, C. & Neufeld, J. (1991). *J. Exp. Psych.Human Perc. Perform.*, 17, **3**, 603-634.

INJURY RISK FUNCTION FOR THE SMALL FEMALE WRIST

Stefan M. Duma[1], Brian M. Boggess[2], Jeff R. Crandall[2], Conor B. MacMahon[2]
[1]Virginia Tech, Impact Biomechanics Laboratory, Blacksburg, VA Duma@vt.edu
[2]University of Virginia, Automobile Safety Laboratory, Charlottesville, VA

INTRODUCTION

In addition to falls on the outstretched hand, the interaction between a deploying side airbag and the upper extremity has been shown in to result in wrist injuries as the hand becomes entrapped in the handgrip (Duma, 2001). The purpose of this paper is to develop a continuous injury risk function that can be used to predict wrist injuries at any force level from falls or from impact in an automobile crash environment.

METHODS

A total of 17 (n=17) axial impact experiments were performed on the wrists of small female cadavers. Small female cadaver upper extremities were used to develop the wrist tolerance as a conservative estimate of the most vulnerable section of the population. The test configuration was designed to impact the palm and force the wrist into compression. The energy source used to apply the axial loads was a pneumatic impactor. The applied axial pulse from the impactor was configured to match the force onset rate, impulse, and peak force in order to simulate a dynamic load profile. The upper extremities were disarticulated at the mid-shaft humerus and supported by two cables that held the elbow in 90° of flexion. The forearms were kept intact in order to preserve the load distribution through the interosseous ligament. Instrumentation included an impactor load cell (Model 1968, Robert A. Denton Inc., Rochester Hills, MI) to measure applied axial load, accelerometers (Model 7264a, Endevco Inc., San Juan Capistrano, CA) on the impactor mount for mass compensation, and magnetohydrodynamic angular rate sensors (Model ARS-04E, ATA Sensors Inc., Albuquerque, NM) on the hand and forearm to measure wrist flexion during the event. All tests were recorded with high speed color video at 1000 fps. The bone mineral density of each specimen was determined by using the Osteogram® technique (CompuMed Inc., Los Angeles, CA), and injury analysis was performed using radiographs and detailed necropsy. .

RESULTS AND DISCUSSION

Post-test necropsy revealed that 9 of the 17 tests resulted in wrist injuries (Table 1). The injury patterns were consistent to those observed from cases studies of fall data and cadaver tests with side airbags and included fractures of the scaphoid, lunate, distal radius, and distal ulna. The peak impactor force ranged from 344 N to 3616 N and the initial wrist extension angle ranged from 55° to 62°. Analysis of the high speed video showed that the hand remained in contact with the handgrip and did not separate until the end of the impact loading event. Logistic regression analysis showed that the injury outcome was independent of specimen age ($p = 0.99$), mass ($p = 0.31$), stature ($p = 0.69$), and bone mineral density ($p = 0.49$). The lack of dependence on subject anthropometric parameters was attributed to the narrow sample size in this group of experiments, which consisted only of small female specimens.

Table 1: Specimen mass, test data, and resulting injuries.

TEST	Subject Body Mass (kg)	Peak Force (N)	Force Onset Rate (N/ms)	Momentum Transfer (Ns)	Observed Injuries
1	41	1199	174	12.6	None
2	41	2001	738	17.0	Distal Radius fx Ulna Styloid fx
3	66	1794	352	14.1	None
4	66	2007	508	21.5	Scaphoid fx Distal Radius fx Ulna Styloid fx
5	63	1412	182	14.4	None
6	55	890	140	9.2	None
7	65	1657	435	16.1	Distal Radius fx Ulna Styloid fx
8	91	2708	893	26.8	Scaphoid fx
9	71	2212	242	21.8	None
10	52	3358	430	28.9	Scaphoid fx
11	67	2385	758	28.4	Distal Radius fx
12	55	2653	395	24.0	Distal Radius fx Scaphoid fx
13	65	418	38	5.1	None
14	91	4336	1006	33.2	Distal Radius fx
15	71	4698	1460	36.3	Distal Radius fx Ulna Styloid fx Lunate fx
16	52	2584	571	16.2	None
17	67	1242	269	13.5	None

Using the injury outcome as the binary variable, a logistic regression analysis was performed. The peak impact forces were mass scaled to the 5th percentile female (Eppinger, 1984) to provide an injury risk function suitable for the 5th percentile female test dummy. The analysis produced an injury risk function that predicts a 50% risk of injury at a wrist load of 1700 N ($p = 0.0037$) where 'x' is the applied axial wrist load:

$$\text{Probability of Wrist Injury } (x) = \frac{1}{1+e^{(4.40-0.00259\cdot x)}}$$
For the 5th Percentile Female

Based on the similarities in impact load profile and observed injury patterns between these tests and fall experiments (Chiu, 1998) and side airbag tests (Duma, 2001), it is suggested that the injury risk function will accurately predict the risk of wrist injuries in the both environments.

REFERENCES

Chiu, J., Robinovitch, SN., (1998) Prediction of upper extremity impact forces during falls on the outstretched hand, *J Biomech*, 31(12):1169-76.

Duma, S.M., Boggess, B.M., Crandall, J.R., H, S.R., (2001) Upper extremity interaction with a side airbag: the effect of a door handgrip. 17th ESV Conference, Netherlands.

Eppinger, R.H., Marcus, J.H., Morgan, R.M., (1984) Development of dummy and injury index for NHTSA's thoracic side impact protection research program, SAE Paper No. 840885.

A STABILITY CONTROL MODEL FOR HUMAN THORAX AND PELVIS MOVEMENTS DURING WALKING

Q. Wu[1] and R. Swain[2]
Department of Mechanical and Industrial Engineering, University of Manitoba, Winnipeg, Manitoba, Canada R3T 5V6
[1]Associate Professor, cwu@cc.umanitoba.ca, [2]Graduate Student

INTRODUCTION

The essence of human walking is to move the upper body from one place to another with reliable stability. Furthermore, the vertical and lateral pelvic motion plays a crucial role in the stabilization of the upper body and, they are two of the six major determinants of gait. Thus, the study of upper body stability with complex pelvic motion is important (Wu *et al.,* 1998), but has not been studied properly. The challenge is that though the controller can be designed to keep the stability, it often can not produce the responses similar to those from natural systems.

In this work, we develop a mathematical model of human thorax and pelvis moving in the frontal plane during walking. The upper body is modeled as a two-link inverted pendulums. The base point moves freely in the same plane. A continuous controller is designed based on Lyapunov's stability theory to guarantee the system stability. The system response and the control torques are further compared with those based on gait measurement, and we found they match reasonably well.

METHODOLOGY

Figure 1. Two-link Model of the thorax and pelvis

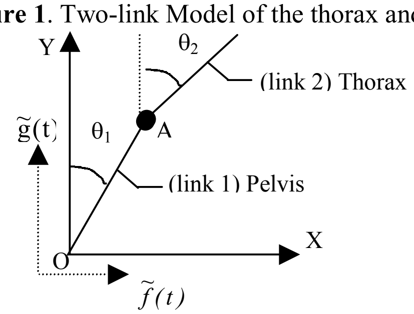

The two-link model is shown in Figure 1. The motion of the base point is described by $\tilde{f}(t)$ and $\tilde{g}(t)$ in the inertial *OXY* system. The general dynamic equations are shown as follows:

$$M\ddot{\Theta} + C(\Theta,\dot{\Theta})\dot{\Theta} + G(\Theta) + \tilde{F}(\Theta)\ddot{\tilde{f}}(t) + \tilde{G}\ddot{\tilde{g}}(t) = R \qquad (1)$$

where $\tilde{F}(\Theta)\ddot{\tilde{f}}(t)$ *and* $\tilde{G}(\Theta)\ddot{\tilde{g}}(t)$ are vectors related to the effects of base motion. M is the inertia matrix. R is the vector of control torques applied on each link. The controller is designed to stabilize the system at the upright position as:

$$R_1 = -k_1\theta_1 - k_{1d}\dot{\theta}_1 - (m_1a_1 + m_2l_1)\left|\ddot{\tilde{f}}(t)\right| sgn(\dot{\theta}_1) - (m_1a_1 + m_2l_1)\left|\ddot{\tilde{g}}(t)\right|\left|\theta_1\right| sgn(\dot{\theta}_1) \qquad (2a)$$

$$R_2 = -k_2\theta_2 - k_{2d}\dot{\theta}_2 - m_2a_2\left|\ddot{\tilde{f}}(t)\right| sgn(\dot{\theta}_2) - m_2a_2\left|\ddot{\tilde{g}}(t)\right|\left|\theta_2\right| sgn(\dot{\theta}_2) \qquad (2b)$$

where g is the gravitational acceleration, m_i, and l_i ($i=1,2$) are the mass and length of each link. a_1 is the distance from the base point O to the center of mass of link 1, and a_2 is the distance from point A to the center of mass of link 2 (see Figure 1). $sgn(\dot{\theta}_i)$ ($i=1,2$) denotes a sigma function.

A Lyapunov function is constructed as follows to prove that the system is stable about the upright position.

$$V = \frac{1}{2}(\dot{\vec{\Theta}}^T \mathrm{M}\dot{\vec{\Theta}}) + (m_1a_1 + m_2l_1)g(\cos\theta_1 - 1) + m_2a_2g(\cos\theta_2 - 1) + \frac{1}{2}k_1\theta_1^2 + \frac{1}{2}k_2\theta_2^2 \qquad (3)$$

where $\vec{\Theta} = \{\theta_1, \theta_2\}^T$. $k_2 > m_2a_2g$ and $k_1 > (m_1a_1 + m_2l_1)g$. M is the inertial matrix shown in equation (1).

RESULTS AND DISCUSSIONS

To substantiate the capacity of our model towards describing the dynamics of the human thorax and pelvis during walking, the simulations were compared with those from gait measurements. For the sake of brevity, only the pelvic angle and torque are shown in Figure 2, and they match reasonably well.

In this paper, we have demonstrated the development of a dynamic model for human thorax and pelvis during walking with the following important features: (1) the system stability is guaranteed, (2) the effects of translational pelvic motion are included, and (3) the motion and the torques similar to those of humans can still be produced. This model can serve as a framework for further development of more realistic models of human locomotion systems

REFERENCE

Wu, Q., Sepehri, N., Thornton-Trump, A. B., Alexander, M. (1998). *Computer Methods in Biomechanics and Biomechanical Engineering*, **1**, 247-259.

Figure 2. Comparison between the pelvic angles and torque: (—) from the model and (----) from the gait

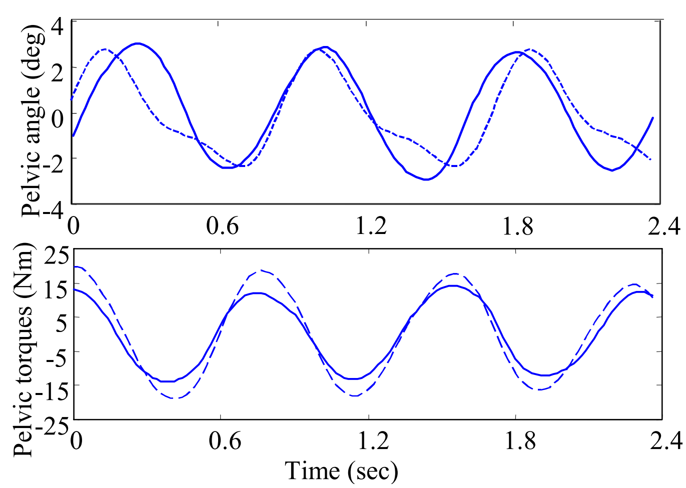

STUDY OF THE INTRA-VENTRICULAR BLOOD FLOW BY CFD AND MRI

Quan Long[1], Robert Merrifield[2], Philip J Kilner[3], X Yun Xu[1] and Guang-Zhong Yang[2]
[1] Dept. of Chem. Eng. & Chem. Tech., Imperial College, London, UK q.long@ic.ac.uk
[2] Dept. of Computing, Imperial College, London, UK.
[3] Cardiovascular MR Unit, Royal Brompton Hospital, Imperial College, London, UK

INTRODUCTION

Detailed investigation of flow patterns in the Left Ventricle (LV) could improve our understanding of heart function and dysfunction. In the present study, the time-dependant structure of the LV was recorded by cine magnetic resonance imaging (MRI) in multiple planes, allowing the reconstruction of a 4D model of the LV cavity. With this information, quantitative intra-ventricular flow patterns were predicted by CFD simulations.

METHODS

Imaging was performed using a Siemens Sonata 1.5T MR system. A multi-slice cine True-FISP imaging sequence was used to acquire 7 short axis slices at 14 phases providing complete spatial and temporal coverage of the LV. All images were acquired within a single 20 second breath-hold so as to minimize registration errors caused by respiratory movement. Segmentation and reconstruction of the LV structure was performed using proprietary software. This allowed the capture of detailed spatial and temporal properties of the endocardial border from reformatted images representing short axis, long axis and M-Mode acquisitions. The LV structure was modelled as the union of a pair of deformed cylinders delineating the inflow and outflow tracts.

Structured numerical volume mesh was generated for the LV cavity at each of 14 phases in a cardiac cycle. B-splines were used to interpolate between measured time points to produce a total of 50 meshes in a cycle. The meshes have the same structure for each model. A finite volume based CFD solver (CFX4) was employed to perform flow simulation from the beginning of systole. During systole, a constant pressure was specified at the outflow plane and no flow was allowed through the inflow plane. During diastole, the outflow plane was closed while the inflow plane was opened with a constant pressure specified. The opening area of the inflow plane was allowed to vary with time. The simulation was carried out for five complete cycles to achieve a periodic solution (where the velocity variation between the last two cycles was less than 3% at test points in the LV model).

RESULTS AND CONCLUSION

CFD simulations were carried out on 3 asymptomatic subjects. For each case, velocity vectors and pressure distributions in the LV models were predicted. Examples of the model geometry, numerical mesh (Figure 1) and velocity vectors in a long axis plane (Figure 2) are shown.

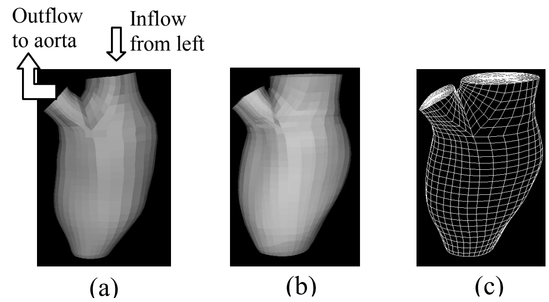

Figure 1. Geometry of the ventricle at (a) mid-systole, (b) mid-diastole and (c) structure numerical mesh.

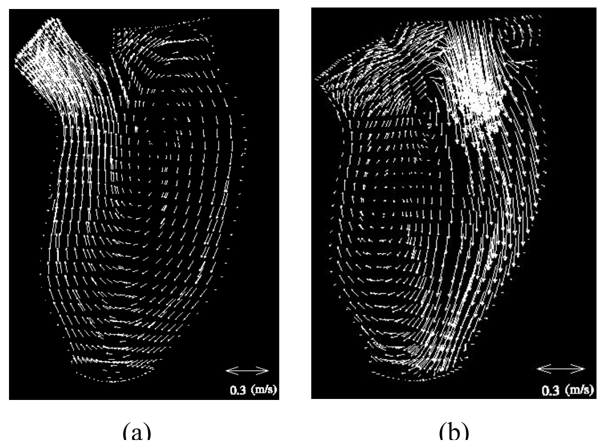

Figure 2. Velocity vectors in a left ventricular long axis plane at (a) mid-systole and (b) mid-diastole. Vorticity is seen in both cases.

A general feature of intra-ventricular flow as predicted by these methods was large-scale vorticity in the cavity for much of the cardiac cycle. For a given wall geometry, the computed shape, size, location, duration and even directionality of vortices were found to be highly dependent on the size, location and orientation of the inlet orifice representing the mitral valve. Effects of different inlet orifices, and hence inlet boundary conditions, on flow patterns in the models will be presented at the conference.

ACKNOWLEDGEMENT

This study is sponsored by the British Heart Foundation (FS/2001002)

HEMATOCRIT DETERMINATION IN BLOOD LINE OF DIALYSED PATIENTS BY ULTRASOUND

Michel Y. Jaffrin, Marianne Fenech, Bachar. Kanj and Mahmoud Maasrani
UMR 6600, Biomechanics and Biomedical Engineering
Technological University of Compiegne, BP 20529, 60205 Compiegne, France

INTRODUCTION

Blood volume monitoring during dialysis is important since hypotension, which occurs in about 30% of patients is thought to be related to hypovolemia caused by fluid removal. An ultrasonic technique for blood volume monitoring, proposed by Schneditz and coworkers [1], consists in measuring the sound speed in blood which depends upon blood density and therefore on hematocrit and protein concentration. They proposed an empirical linear relationship between blood water concentration (BWC) and hematocrit.

The purpose of this work is to propose a more accurate method which takes into account patient plasma protein concentration and its variation.

THEORETICAL BACKGROUND

By definition, the BWC is given by

$$BWC = \frac{100 M_w}{M_w + M_p + M_{hg}} \qquad (1)$$

where M_w is the water mass per liter of blood, M_p the mass of plasma proteins and lipids and M_{hg} the red cell mass including cell membrane, Since a liter of pure water weighs 993 g at 37°C, the water mass in g/l of plasma at a protein concentration Cp in g/l is

$$M_{wpl} = 1012 - 0.913\, C_p \qquad (2)$$

Since 1 liter of red cells contains 735 g/l of water, we can express the water mass per liter of blood as

$$M_w = (1012 - 0.913\, C_p)(1 - H/100) + 7.35\, H \qquad (3)$$

Assuming that the plasma lipids represent 8.2% of the protein concentration (the average percentage) the plasma lipids and proteins mass per liter of blood is given by

$$M_p = 1.082\, C_p\, (1 - H/100) \qquad (4)$$

Finally, since the hemoglobin mass is 340 g/l and the cell membrane 21 g/l we write .

$$M_{hg} = (340 + 21)\, H/100 = 3.61\, H \qquad (5)$$

Combining eqs 1 to 5 we obtain for BWC

$$BWC = \frac{100[1012 - 0.913 C_p (1 - H/100) - 2.77 H]}{1012 + 0.169 C_p (1 - H/100) + 0.84 H} \qquad (6)$$

Assuming proteins and red cells conservation during dialysis, we write

$$C_p(100 - H)/H = C_{p0}(100 - H_0)/H_0 \qquad (7)$$

MATERIAL AND METHODS.

Tests were carried out under medical supervision on six patients of the Compiegne Dialysis Center, for a total of 11 runs. The generator used was a Fresenius 4008 H equipped with a blood volume monitor (BVM). Blood samples where sent to a commercial laboratory for measuring hematocrit by a Coulter counter coupled with a spectro-photometer. These measurements were used as controls.

RESULTS AND DISCUSSION

Individual correlations between hematocrits measured by the lab and BWC measured by the BVM are displayed in Fig.1 for each patient. The general correlation obtained by pooling all data for the 11 runs is found to be

$$H_L = 298.9 - 3.1755\, BWC \quad (R^2 = 0.7335) \qquad (8)$$

The standard deviation was 1.78% and the mean deviation was –0.02%.

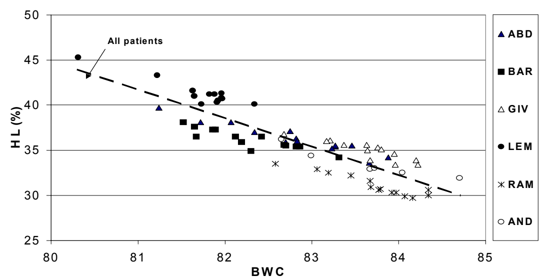

Figure 1:Correlation between control hematocrits and BWC in the 11 runs.

Proposed method

The new method consists in calculating in each patient the variation of H and C_p from BWC and the initial protein concentration estimated from the last available blood test. Eqs 6 and 7 are solved for H and C_p respectively as

$$H = \frac{1012(100 - BWC) - C_p(0.169 BWC + 91.3)}{277 - 0.913 C_p + (0.84 - 0.00169 C_p) BWC} \qquad (9)$$

$$C_p = \frac{C_{p0} H (100 - H_0}{H_0 (100 - H)}) \qquad (10)$$

For calculating the hematocrit during each dialysis run from BWC supplied by the BVM we have eliminated C_p in Eq. (9) using Eq.(10). The result is a quadratic equation for H of the form

$$aH^2 - bH + c = 0 \qquad (11)$$

where the coefficients a,b,c are functions of C_{p0} and BWC. This equation is solved analytically. The agreement between control hematocrits and those calculated from Eq.(9) for the 11 runs using measured protein concentration is very good. The standard deviation has been reduced to 1.08% (from 1.78%with Eq. 8) with a mean deviation of -0.24%. This precision is equivalent to that of the spectrophotometric method used as control.

REFERENCE

1. Schneditz D, Pogglitsch H, Horina J, Binswanger U. *Kid Inter 1990; 38: 803-806.*

ACKNOWLEDMENTS

The support of Fresenius Medical Care is acknowledged.

THERMAL FINITE ELEMENT ANALYSIS OF OSTEOCYTE KILL ZONES ACHIEVED WITH ACRYO-INSULT PROBE

Karen L. Reed[1] (Email: karen-reed@uiowa.edu), Thomas D. Brown[2,1], Michael G. Conzemius[3]
[1]Departments of Biomedical Engineering and [2]Orthopaedic Surgery, University of Iowa, Iowa City, IA
[3]Veterinary Teaching Hospital, Iowa State University, Ames, IA

INTRODUCTION Osteonecrosis remains a major unsolved problem in orthopaedic hip surgery, responsible for about 10% of the primary cases and 20% of the societal cost of total hip arthroplasty (Mont, 1995). To help in devising head-preserving surgeries, we have recently developed a method of creating segmental lesions by using a cryogenic probe (Reed, 2001) in the emu, a large biped which progresses to femoral head collapse (Conzemius, 2000).

In order to parametrically modulate the shape and size of the kill zone (ice ball) produced *in vivo* with the cryogenic probe, a thermal finite element model has been developed, and validated using bench-top surgical simulations. The model has been implemented to guide the intraoperative protocol to determine freezing time to achieve a specified kill-zone.

METHODS A closed-circulation cryo-insult probe, (Figure 1) previously described (Reed, 2001), consists of an outer and inner tube (15 gage and 21 gage 316 stainless steel thin-walled tubing). The outer tube is wrapped in 37 gage high-resistance heating wire, and coated with Teflon for protection. The tip of the probe is thermally isolated from the heated shaft by a small piece of Ultem (polyetherimide). Type T thermocouples are located at the tip and just above the Ultem insulator, so that shaft temperature can be controlled intraoperatively.

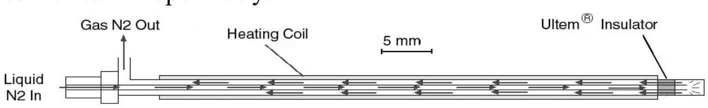

Figure 1: Schematic of the closed-circulation cryogenic probe

An axisymmetric thermal finite element model of this probe was developed, using Patran 9.0 for pre-processing (HKS, Pawtucket, RI), and ABAQUS 6.2 for analysis (MSC, Los Angeles, CA). The probe is surrounded by an "infinite" field of a 1% agarose-water gel (whose thermal conductivity matches that of cancellous bone) (Biyikli, 1986). Tip and shaft temperature boundary conditions consisted of curves taken directly from experimental data. Additionally, a far-field boundary condition of room temperature (or emu body temperature, for *in vivo* simulations) was imposed. Model validation consisted of comparing simulated temperature-time curves with those achieved experimentally.

There were three differences between the validation and *in vivo* models: *in vivo* simulations (1) consisted of multiple freeze-thaw cycles, (2) started at emu body temperature (instead of room temperature), and (3) included the warming effects of blood flow in the femoral head.

To simulate blood flow, all substrate (bone tissue bed) elements had a volumetric heat source,

$$q_p = \eta(T_S)*\rho_p*C_{Pp}*\beta*[T_C-T_S]$$

where: q_p = power (W/cm^3); $\eta(T_S)=1$ if Ts>273 K, 0 if Ts<273 K; ρ_p=blood density (g/cm^3); Cp_p=blood spec. heat (J/g*K); β=blood perfusion rate (g/g*s); T_C=element temperature (K); and T_S=body temperature (K).

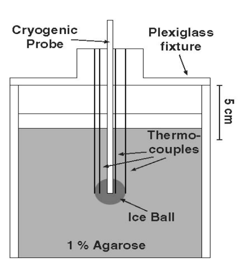

Figure 2: Experimental probe testing setup

The experimental probe testing setup (Figure 2) consisted of 5 type T thermocouples, embedded in the agarose gel at locations ranging from 0 mm to 12 mm from the cryogenic probe. Liquid nitrogen was circulated through the probe using a Cryogun (Brymill Cryogenic Systems, Ellington, CT). Data were collected using LabVIEW (National Instruments, Austin, TX).

Operator control of cryo-insult was via valve attenuation of liquid N_2 flow to the probe, rather than by probe temperature set point. Therefore, time-variant probe temperatures (recorded experimentally) were used to drive the simulation.

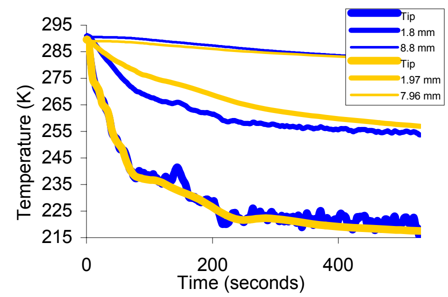

Figure 3: Comparison of experimental (dark) and FE (light) temperature histories during a 9-minute freeze

RESULTS Experimental and validation simulations showed close correspondence in temperature-time curves at various radii (figure 3), and similar ice-ball expansion rates. Validation trials were conducted for nine-minute cryo-insults (a time similar to that previously used, empirically, for emu surgeries).

In vivo freeze-thaw cycles showed a decrease in freeze-front expansion, and an increase in thaw rates, due to femoral head blood perfusion. Additionally, as expected, there was a slight increase in ice-ball radius during subsequent freezes, due to a lower "initial" temperature of the surrounding tissue (Figure 4).

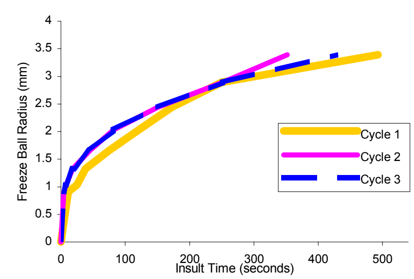

Figure 4: Computed *in vivo* ice ball radii for three consecutive nine-minute freeze-thaw cycles

DISCUSSION
This validated FE model has proven invaluable as a means to predictably modulate lesion sizes for our *in vivo* emu surgeries.

SUMMARY A finite element model describing the temperature fields surrounding a cryogenic probe has been developed and validated. This model has been used to estimate the temperature history of bony tissue during local surgical freezing, for the purpose of creating osteonecrotic lesions.

AKNOWLEDGEMENTS NSF Graduate Research Fellowship and NIH Grant #46601

REFERENCES Biyikli et al. (1986) *J Biomed. Mater. Res.***20(9)**, Conzemius et al. (2000) *ORS Proceedings* p. 206, Mont and Hungerford (1995) *JBJS* **77A**, Reed and Brown (2001) *ASB Proceedings* p.8

KNEE EXTENSOR TORQUE AND WORK DURING DYNAMIC CONTRACTIONS GUIDED BY PERCEPTUAL SENSATIONS

Paul T. Dixon[1], Alan J. Coelho[2], and Danny M. Pincivero[3]

[1]Department of Bioengineering, The University of Toledo, pdixon@eng.utoledo.edu
[2]Department of Physical Education, Health and Recreation, Eastern Washington University, acoelho@ewu.edu
[3]Department of Kinesiology, The University of Toledo, danny.pincivero@utoledo.edu

INTRODUCTION

The ability to accurately replicate graded levels of knee extensor torque based on subjective feelings of perceived exertion has been shown to be over-estimated during isometric contractions (Pincivero et al, 2000) and lifting tasks (Kumar et al, 1994). The purpose of this study was to examine knee extensor peak torque (PT) and work (W) production during isokinetic contractions guided by perceptual sensations.

METHODS

Fifteen males and 15 females were evaluated for maximum knee extensor strength, via isokinetic testing at 1.05 rad•s^{-1}. Immediately following 5 maximal-effort contractions, subjects were instructed to "think about the feelings in their quadriceps during the contraction, and to assign a rating of 10 to those feelings". Following 2 min of rest, subjects were asked to sit quietly and to "think about the feelings in their quadriceps and to assign a rating of 0 to those feelings".

Subjects performed 3 voluntary knee extensions, separately, at the following perceptual intensities: 1, 2, 3, 4, 5, 6, 7, 8, and 9, in a random order. For each contraction, subjects were instructed to "contract their muscles to a level that feels like a (assigned number)". During each contraction, subjects were instructed to view a 10-point scale while the investigator pointed to the selected number. During all testing, subjects were blinded to the absolute torque values they were generating. Peak torque, and knee extensor W were determined over the middle 1.22 rad of extension for each contraction. The second 2 contractions were averaged and normalized to the 3 highest values of the maximal efforts.

RESULTS AND DISCUSSION

The results demonstrated a significant increase in normalized knee extensor peak torque ($F_{8,224}$=118.87, $p<0.05$) and work ($F_{8,224}$=132.31, $p<0.05$) across perceived exertion levels 1 to 9 (Figure 1). No significant gender, or gender by perceived exertion interactions for any of the isokinetic variables were noted. Subjects were found to under-estimate their effort at perceived exertion levels 1-2 for PT, and 1-3 for W. In this regard the normalized torque was over-produced (i.e., comparison with expected values of 10% at perceived exertion level 1, 20% at perceived exertion level 2, etc.). Peak torque was found to be statistically similar to the expected values at perceived exertion levels 3-6, and perceived exertion levels 4-6 for W. At higher perceived exertion levels (7-9), over-estimation was observed as normalized PT and W was under-produced from the expected values.

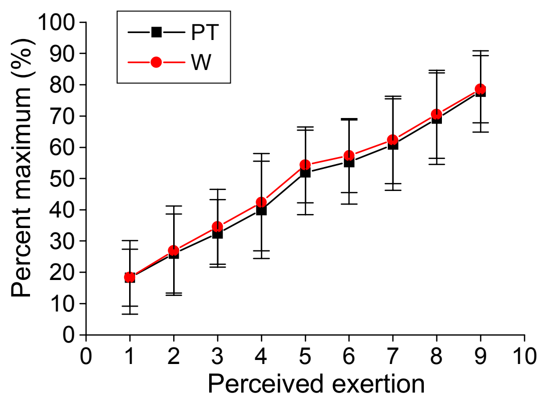

Figure 1: Normalized knee extensor PT and W across perceived exertion levels 1 to 9.

SUMMARY

The major findings indicate that the ability to accurately replicate PT and W during dynamic knee extension efforts appears to be attenuated at relatively low and high levels of perceived exertion. In concurrence with Kumar and Simmonds (1994), torque replication appeared to be accurate during moderate-level contractions.

REFERENCES

Kumar, S., Simmonds, M. (1994). The accuracy of magnitude production of submaximal precision and power grips and gross motor efforts. *Ergon*. **37**: 1345-1353.
Pincivero, D.M., et al. (2000). Quadriceps femoris activation and accuracy across the perceptual range. *Arch Physiol Biochem*. Proceedings of the XIth Congress of the Canadian Society of Biomechanics. **108** (1-2): 160.

ACKNOWLEDGEMENTS

This study was supported by an Eastern Washington University Faculty Research Grant (2001-02) awarded to A.J.C.

A MULTI-SCALE FINITE ELEMENT APPROACH TO DETERMINE LOCAL CELL AND TISSUE DEFORMATIONS

Roel G.M. Breuls, Bram G. Sengers, Cees W.J. Oomens, Carlijn V.C. Bouten, Frank P.T. Baaijens

Eindhoven University of Technology, Department of Biomedical Engineering
P.O.Box 513, 5600 MB Eindhoven, The Netherlands
Ph. (+31) (0)40-2473027, Fax. (+31) (0)40-2447355
R.G.M.Breuls@tue.nl

INTRODUCTION

Mechanical stimuli play an important role in cellular processes such as growth, adaptation and cellular breakdown. Knowledge of local cells strains can aid in our understanding of these processes. However, defining local cell strains within a tissue is difficult. First, local cell strains are a complex function of tissue strain due to the local microstructural architecture. In turn, tissue strains are influenced by the presence of cells. Moreover, cell and matrix properties vary in time due to remodeling. To incorporate these phenomena, we adopted a finite strain multi-scale finite element approach (Breuls et. al., 2002). This approach is used to the study role of the local microstructure's physical and geometrical heterogeneity on resulting cell and tissue strains.

METHODS

In the multi-scale FE approach, the macroscopic tissue is represented by a macroscopic FE model (Figure 1). To each macroscopic integration point, a micro FE model is assigned, representing the underlying local microstructure.

Multi-scale Finite Element Approach

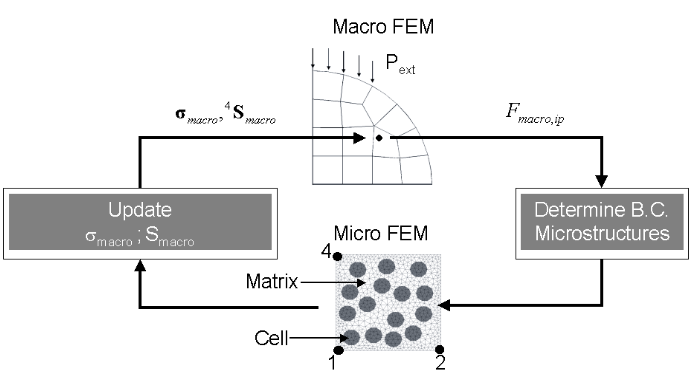

Figure 1: Flow chart of the Multi-scale FE approach.

The macroscopic finite strain FE model supplies boundary conditions for the finite strain microstructural models. These detailed microstructural FE models predict local cell loads. In turn, the microstructural FE models supply the macroscopic stresses and effective stiffnesses using a computational homogenization procedure. Thus, macroscopic behavior is completely determined on the basis of the underlying microstructure – irrespective of its complexity. To deal with the relative large computational times, the approach has been implemented on a parallel computing system (Beowulf Cluster).

To investigate the effect of microstructural architecture on individual cell loads, we simulated the compression of an engineered muscle tissue construct.

RESULTS

In Fig. 2, the results of the simulations show that:

1) Average cell loads highly depend on local architecture.
2) Individual cell loads vary a factor 5 due to heterogeneity.
3) Cell strains exceed macroscopic tissue strains with an order of magnitude.
4) Strain distributions within a cell are heterogeneous.

Multi-scale Simulation

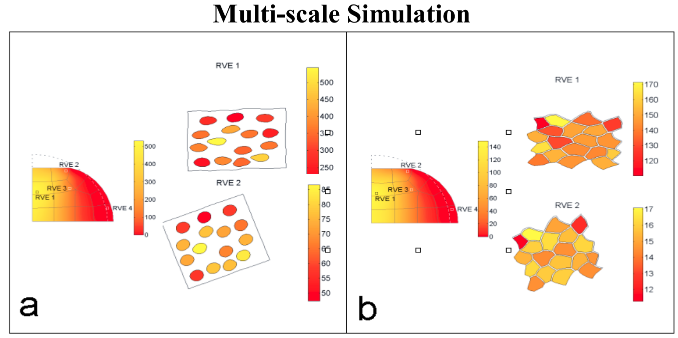

Figure 2: Results of multi-scale simulations with two different microstructural meshes.

SUMMARY

A multi-scale finite element approach, has been adopted to define local cell loads in an engineered tissue construct. The model incorporates a detailed analysis of an arbitrary complex microstructure and contemplates the influences of microstructural properties on the effective macroscopic tissue properties. Simulations indicate that the local microstructural architecture has a profound impact on cell and tissue strains. The multi-scale approach provides a framework to study these cell and tissue strains.

REFERENCES

R.G.M.Breuls et al., (2002), Journal of Biomech. Eng., In press.

PREFERENTIAL DIRECTION OF SUBTALAR JOINT LAXITY WITH INTEROSSEOUS TALOCALCANEAL LIGAMENT SECTIONING

Yuki Tochigi[1], Charles L. Saltzman[1], Annuziato Amendola[1], Melvin J. Rudert[1], Thomas E. Baer[1] and Thomas D. Brown[1, 2]
Department of Orthopaedic Surgery[1] and Biomedical Engineering[2], University of Iowa
IowaCity, Iowa, USA <tochigiy@mail.medicine.uiowa.edu>

INTRODUCTION

Injury of the interosseous talocalcaneal ligament (ITCL) has been recognized as the most important cause of subtalar instability; however diagnosis of this injury remains difficult due to the lack of an accepted clinical test. We conducted a cadaveric experimental study to identify the appropriate direction for a clinical drawer examination for ITCL injuries. In this investigation, we found the neutral zone laxity of the subtalar joint under applied multi-directional transverse forces, and determined a dominant direction of subtalar joint laxity involved with ITCL sectioning.

METHODS

Four fresh frozen cadaveric specimens were placed in a custom-loading fixture for multi-directional laxity tests. The fixture allowed six tests at 30 degree increments in the transverse plane (**Figure 1**). The anterior direction was defined as 0 degrees, the lateral as 90 degrees, the posterior as 180 degrees, and the medial as 270 degrees. The fixture was mounted in a material-testing machine (MTS-810) that supplies and controls the force. Seven cycles of loading to +/- 60N, using a ramp function with a loading frequency of 0.1Hz, were applied in each test. After four preconditioning cycles, the next three cycles of the load-displacement response were collected. After completing six loading directions in the intact condition, the specimen underwent ITCL sectioning, and the tests were repeated.

RESULTS AND DISCUSSION

The load-displacement relationship was characterized by a sigmoid curve (**Figure 2**). A flat region, where stiffness was near 0, was observed on and about the 0 force. To describe this portion of the load-displacement response, the displacement between +/- 10N of load was defined as the neutral zone laxity. A neutral zone laxity was measured for both positive-to-negative and negative-to-positive drawer forces. The neutral zone laxity portion of the load-displacement curve was characterized by large displacement values that were produced by the application of small magnitude of force. Increases of the neutral zone accompanying sectioning the ITCL serve as an objective basis for indexing laxity.

The largest increase in laxity occurred in the 300°-120° direction with sectioning of the ITCL (**Table 1**). On average, a 38.3 +/-18.9 % increase was observed in the 300°-120° direction, in contrast, the mean increase among the 0°-180°, 30°-210° and the 60°-240° directions was only 13.7 +/- 14.6 %. Based on these data we believe that clinical assessment of ITCL integrity should be done along an axis roughly defined from the posterior aspect of the lateral malleolus to the anterior aspect of the medial malleolus.

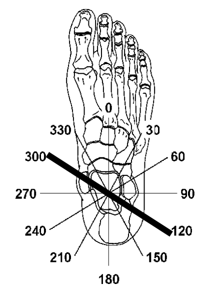

Figure 1 Testing directions of the multi-directional laxity test. The bold line shows the dominant direction of subtalar laxity increasing with ITCL sectioning.

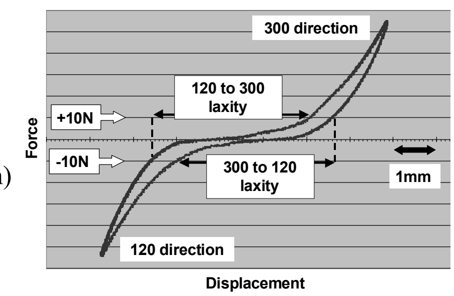

Figure 2 Typical load-displacement relationship (Intact condition, 300°-120° direction)

SUMMARY

Multi-directional transverse laxity tests were studied for the subtalar joint, to identify the appropriate direction for a clinical examination for ITCL injuries. The result suggests that an axis roughly defined from the posterior aspect of the lateral malleolus to the anterior aspect of the medial malleolus is the dominant direction of subtalar laxity increase with ITCL sectioning.

REFERENCES

Toyama, H., et al. (1995). *J Orthop Res*. **13**: 609-614

Table 1 Increase of subtalar laxity with ITCL sectioning (mean +/- SD)

Direction	300°-120°	330°-150°	0°-180°	30°-210°	60°-240°	90°-270°
Intact (mm)	3.4 +/- 0.4	4.1 +/- 0.5	3.4 +/- 0.6	2.7 +/- 0.6	2.7 +/- 0.6	3.2 +/- 0.4
ITCL sectioning (mm)	4.6 +/- 0.1	4.9 +/- 0.6	4.0 +/- 0.3	2.9 +/- 0.6	2.9 +/- 0.6	4.0 +/- 0.5
Laxity Increase (%)	38.3 +/- 18.9	22.5 +/- 8.2	19.6 +/- 11.5	7.5 +/- 7.5	14.1 +/- 19.4	23.2 +/- 19.5

THE LOCATION OF THE ELBOW JOINT CENTRE OF ROTATION IN CHILDREN DURING ACTIVE FLEXION-EXTENSION.

Louise Wood[1], Neil Armstrong[1], Vivienne Barrett[2], Sharon Dixon[1]
[1]School of Sport and Health Sciences, University of Exeter, Exeter, United Kingdom. Louise.e.wood@exeter.ac.uk.
[2]The Somerset MRI centre, Somerset, United Kingdom

INTRODUCTION
The centre of rotation (COR) of a joint undergoing a specified action has been used to detect movement abnormalities, to estimate musculotendinous moment arms and to predict the loading of a joint and its associated soft tissue structures. The elbow COR has been observed to remain fixed throughout flexion-extension in adults, (For example, Chao and Morrey, 1978). These studies examined the COR in cadavers and therefore it is uncertain whether this COR can be applied to active joint movements. It is also not known whether this COR location can be applied to children, since bone development during and post-puberty may influence the elbow articulation and its consequent movement, (Jaramillo and Waters, 1997). Therefore, the purpose of this study was to derive co-ordinates for the elbow joint COR during active flexion-extension in children, in order to examine whether the COR location remained fixed or moved, and agreed with the adult literature.

METHODS
Thirty one children volunteered to participate in the study. The subject characteristics are presented in Table 1. All children were pre-pubertal according to Tanner's indices of pubic hair.

Table 1. Subject characteristics. Values are means (standard deviations).

	N	Age (y)	Mass (kg)	Stature (m)	Arm length (cm)	Forearm length (cm)
Boys	15	9.7(0.3)	34.11(10.73)	1.39(0.08)	28.9(1.7)	21.1(1.5)
Girls	16	9.5(0.3)	32.39(5.47)	1.37(0.04)	28.3(1.3)	20.3(0.8)
Total	31	9.6(0.3)	33.22(8.34)	1.38(0.06)	28.6(1.5)	20.7(1.2)

To estimate the elbow joint COR throughout the flexion-extension range of motion, the elbow was fixed in 5 positions of elbow flexion (90°, 70°, 50°, 30° and 10°) within the integral body core of a Magnetic Resonance Imager (Philips 0.5 Tesla Powertrak 1000 system). At each angle sagittal plane T1 spin echo images were taken (slice thickness 4mm, slice gap 0.4mm), during isometric elbow flexion. The method described by Reuleaux (1875) cited by Maganaris et al (1998) was used to estimate the COR location. Therefore 4 CORs were derived for the 5 elbow angles scanned. This analysis was performed 6 times for each subject. To compare the COR location throughout the range of motion and between individuals, co-ordinates were derived for each COR by placing axes relative to the long axis of the humerus and also the trochlea, (Figure 1).

To examine whether the COR remained fixed or moved throughout flexion-extension, separate repeated measures ANOVA tests were performed using each subject's mean x, and y co-ordinates for each COR, respectively. An alpha level of 0.05 was accepted as significant. Since boys and girls were grouped together in the previous ANOVA analyses, non-parametric Mann-Whitney U tests were also used to examine if there were significant sex differences in any of the COR co-ordinates.

RESULTS AND DISCUSSION
There were no significant differences in either the x or y co-ordinates for any of the CORs for the group as whole (boys and girls combined), or between boys and girls. Therefore the mean COR x co-ordinate, and y co-ordinate were determined from the 4 COR locations. This provided a fixed COR position for the children for elbow flexion-extension (Figure 1).

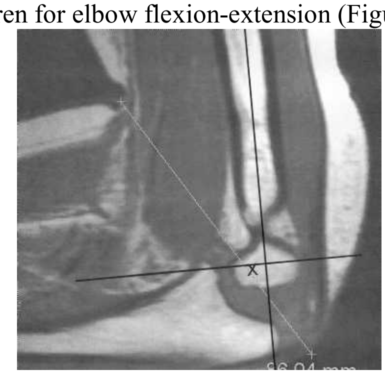

Figure 1. Axes and fixed COR position (x) for active elbow flexion in 9/10 year old children. Scale: 1mm=0.52mm.

The co-ordinate derived for the 9/10 year old boys and girls during isometric elbow flexion positioned the COR approximately on the centre of the trochlea. This is in agreement with the COR positions identified for adult cadavers. In this study, the fixed position of the COR was defined by the co-ordinate (-3.75mm, -1.45mm) relative to the internal axes (Figure 1). This COR co-ordinate can be used for subsequent estimates of muscle-tendon moment arms according to the geometric technique (Pandy, 1999).

REFERENCES
Jaramillo, D., Waters, P.M. (1997). In *Magnetic Resonance Imaging. Clinics of North America. The elbow.* **5**. Editor, Rosenberg, Z.S. WB Saunders Company.
Maganaris, C.N. et al (1998). *Journal of Physiology*, **510**, 977-985.
Pandy, M.G. (1999). *Exercise and Sport Sciences Reviews*, **27**, 79-118.
Chao, E.Y., Morrey, B.F. (1978). *Journal of Biomechanics*, **11**, 57-73.

IN VIVO ASSESSMENT OF THE INSTANTANEOUS AXES OF ROTATION OF THE LUMBAR SPINE IN SYMPTOMATIC AND ASYMPTOMATIC SUBJECTS

Shawn Farrokhi (farrokhi@usc.edu), Kornelia Kulig, Judy Burnfield, Christopher Powers
Department of Biokinesiology and Physical Therapy, University of Southern California, Los Angeles, California, USA

INTRODUCTION

The location of the instantaneous axis of rotation (IAR) is within the boundaries of a joint in non-pathologic conditions. Pathology, however, may alter joint kinematics, including the location of the IAR. The purpose of this study was to describe the sagittal plane location of the IAR for individuals with and without low back pain. It was hypothesized that a greater number of the IARs would be located outside of the functional spinal unit (FSU) in symptomatic compared to asymptomatic individuals.

METHODS

Eight individuals (four pain-free, four symptomatic; 22-43 y.o.) consented to participate in this study. Symptomatic subjects reported non-specific low back pain that increased with extension. Dynamic imaging of the lumbar spine was performed using a vertically open MR system (0.5 Tesla, Signa SP, General Electric Medical Systems, Milwaukee, WI, USA). Subjects were positioned prone with the lumbar spine centered within the magnet. A surface coil was secured to the anterior and posterior lower torso using cloth tape. Using their arms, each subject was instructed to arch their back as far as they were able to without causing additional pain (Figure 1).

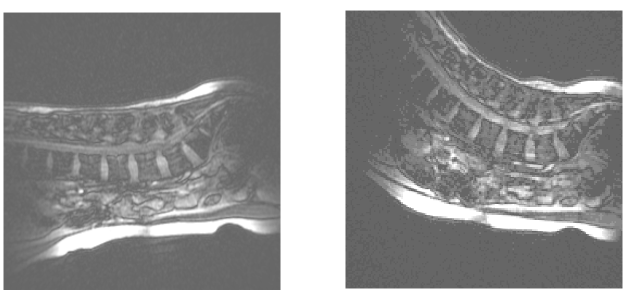

Figure1. Sagittal view of the resting (left) and final extended (right) position of the lumbar spine for a prone press-up.

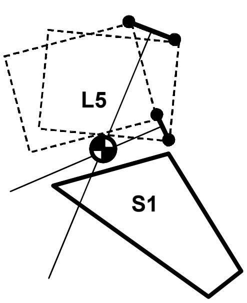

Figure 2. The Reuleaux Method (● = IAR for L5-

MR images of the resting and final extended positions for each individual were used to calculate the IAR for each FSU using the Reuleaux method (Broc 1997; Haher, 1991; Pearcy, 1988). Due to the clarity of the posterior borders of the vertebrae, the posterior superior and posterior inferior landmarks of the superior and inferior vertebral bodies were chosen to calculate the IAR (Figure 2). Only FSUs L3-L4, L4-L5, L5-S1 were analyzed, as these units are more frequently symptomatic.

RESULTS AND DISCUSSION

Overall, asymptomatic subjects presented with less variability in the location of the IAR for each FSU and, with the exception of one subject, all of the IARs were within the anterior elements of the FSU (Figure 3). The locations of the IAR for symptomatic subjects were more dispersed, and in many cases, were located outside of the anterior elements compared to the asymptomatic subjects. The results of a Chi–square test comparing whether the IAR was located inside or outside the FSU approached significance ($\chi^2 = 3.23$, p= 0.07), however, additional subjects are required to clarify these findings. A literature review suggests that these data present the only in vivo evidence of altered IAR location for symptomatic compared to asymptomatic individuals while performing an active movement.

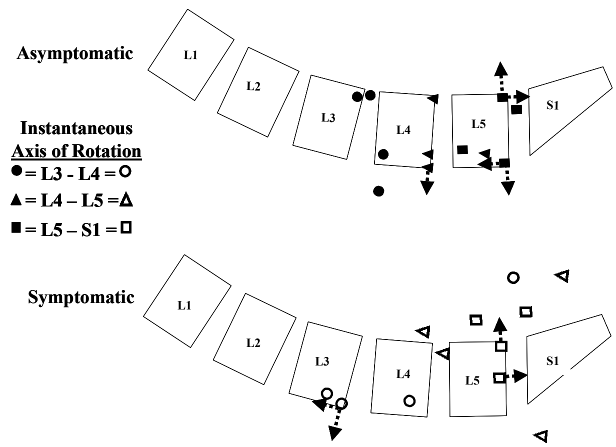

Figure 3. Location of the IAR for L3-L4, L4-L5, L5-S1 for asymptomatic (top) and symptomatic (bottom) subjects. Arrows indicate the direction of linear motion when rotation was not observed.

SUMMARY

These data provide insight into the effects of pathology on lumbar spine mechanics. Changes in the IAR associated with pathology likely alter the length of the moment arms for the lumbar spine musculature and therefore the relative demand imposed upon the musculo-skeletal system.

REFERENCES

Broc, G.G., et al. (1997) *Spine*. **15,** 605-612.
Haher T.R., et al. (1991) *Spine*. **16,** S312-S318.
Pearcy M.J., Bogduk N. (1988) *Spine*. **13,** 1033-104.

DRAG COEFFICIENT AND REYNOLDS NUMBER IN HIGH BUTTERFLY SWIMMERS

R. Taïar[1], T. Clopeau[2]. A .H. Rouard[3]

[1] Redha TAÏAR : * Laboratoire d'Analyse des Contraintes Mécaniques (L.A.C.M.)
UFRSTAPS. Bât 6 - Moulin de la Housse *51687 Reims cedex 2*
Tel : (33) 06-63-28-60-04 ; Fax : (33) 03-26-91-38-06 ; e-mail : redha.taiar@univ-reims.fr
[2] MAPLY, CNRS UMR 5585, UFR Mathématiques. Université Claude Bernard Lyon 1, Bât. 101, 43, Bd. Du 11 Novembre 1918. 69622 Villeurbanne, France
[3] Département STAPS de CHAMBERY Université de Savoie BP 1104 - 73011 CHAMBERY Cedex

INTRODUCTION

The drag opposed by a fluid to a moving body is proportional to the drag coefficient, the frontal surface area and the square of the relative velocity between body and fluid (Vogel, 1994). The aim of our study is to determine the relationships between drag coefficient (DC) and the Reynolds number Re for a high level athletic swimmer .

MATERIAL AND METHODS

Within the Kinematic method (Taïar et al., 1999), we defined three most propulsive positions .They were: the end of the external sweep (beginning of the cycle), the end of the internal sweep (middle of the cycle), and the end of the thrust (end of the cycle). These three positions were reproduced using a real size mannequins articulated in real velocity conditions. The mannequins has been fixed on his gravity center, represented by his hip, by the mean of a steel stem. The force measurement is therefore concentrated in this point. The mannequins has been carried during 50 meters at velocity from 1.4 to 2.1 $m.s^{-1}$, covering the velocity scale from regional to international levels. The tangential contact force measured during the experimentation represents the drag in the moving swimmer's direction.

RESULTS AND DISCUSSION

In our model, for a given swimmer and for the corresponding Re values (fig.1), the DC is more important at the end of the internal sweep (middle of the cycle) that in the beginning of cycle (end of the external sweep) and in the last position of thrust (end of the cycle). In middle of cycle, the superior members are in a vertical plan, perpendicular to the swimmer's displacement, giving a bigger drag coefficient due to an increase of the frontal surface area. We used the theory of turbulence to find the DC as a function of Log Re (see Schlichting et al. 2000) and a very good agreement between the theory and our experimental observations is found. The drag is smallest in the least propulsion positions of the swimming cycle (beginning and end of cycle). In these 2 positions, the superior and lower members are globally at the alignment of the trunk. The swimmer searches a streamline position profiled with a body. The model corresponding to the fastest swim is the best streamline for the swimming. The best swimmer is characterised by the least resistance along the cycle , compared to the other swimmers. We can say that the drag coefficient depends on the movement adopted by the swimmer. This drag coefficient is principally reduced by the frontal surface area. For the best swimmer the lower members are less bent, his superior members are more lengthened in the beginning of cycle and his head is less raised at end of cycle.

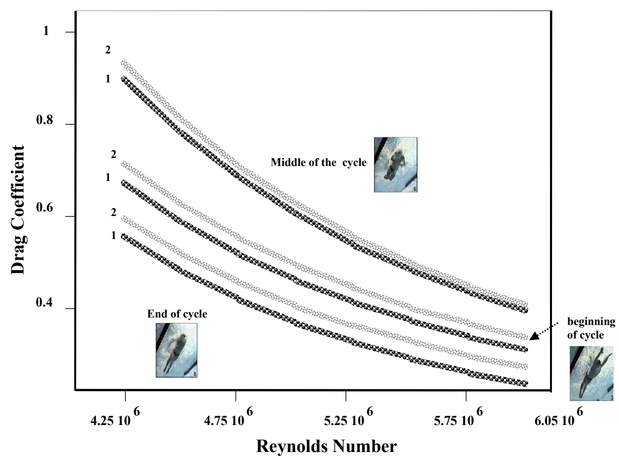

Figure 1: Relation between the drag coefficient and the Reynolds number

ACKNOWLEDGEMENT

We thank Professor Andro Mikelic (a good swimmer) for his advises in applications of the theory of turbulence.

REFERENCES

Taîar R, Sagnes P, Henry C, Dufour AB and Rouard AH. (1999).Hydrodynamics optimization in butterfly swimming : position, drag coefficient and performance. Journal of Biomechanics 32 : 803-810.

H. Schlichting, K. Gersten, Boundary-Layer Theory, 8th Revised and Enlarged Edition, Springer-Verlag, Berlin, 2000

Vogel, S. (1994) Life in Moving Fluids. 2nd Edn. Princeton University Press, Princeton, 467 p.

HIGH-SPEED AND CONTINUOUS PRESSURE MEASUREMENTS: A COMPARISON OF ACTIVE PRESSURE SENSORS AND PRESSURE FILM

Joseph M. Cormier, Joel D. Stitzel, William J. Hurst, and Stefan M. Duma
Virginia Tech, Impact Biomechanics Laboratory, Blacksburg, VA. Duma@vt.edu

INTRODUCTION

Obtaining pressure measurements during a high-speed event is a common task. The use of Fuji film may be suitable for low-speed applications, or where the normal pressure remains fairly constant. However, the practicality of Fuji film diminishes in cases where a shear force is present or in cases where a continuous pressure reading is needed. Reed *et al.* (1992) used Fuji film to quantify the normal pressure exerted onto an object in the path of a deploying airbag. Depending on the orientation of the airbag relative to the Fuji film a shear force will exist and may introduce inaccuracies. In this case an active sensor may be more advantageous. Harris *et al.* (1999) compared the area of contact measured by Fuji film to the K-scan sensor. The results showed that the Fuji film measured an area 11-36% lower than the area measured by the K-scan sensors. Both the K-scan and the FlexiForce sensors use the same resistive ink technology; however, the K-scan is limited to a sampling frequency of 127 Hz, which makes it inadequate for recording pressures during a high speed event (Tekscan, South Boston, MA). The purpose of these experiments is to compare the use of Fuji film and FlexiForce sensors to record normal pressures during a high-speed event.

METHODOLOGY

To compare the utility of FlexiForce sensors and Fuji film, a high speed shear test apparatus capable of applying normal pressure was manufactured. The test set-up allowed for an initial pressure to be applied to a stationary, rectangular polycarbonate plate. A pneumatic cannon was used to impact the plate with a projectile, accelerating it to speeds ranging from 86 m/s to 105 m/s. Two types of Fuji film were used: medium, with a range of 10-50MPa and low with a range of 2.5-10MPa (Fuji Photo Film CO., Tokyo, Japan). The Fuji film sheets were placed on top of four FlexiForce sensors which were rigidly mounted to the test stand. This arrangement was held in constant contact with the polycarbonate plate by the initial preload applied to the stand as it traveled under the sensors. A protective sheath was used to limit the shear force exerted onto the Fuji film and sensors. A pressure pulse was created through the use of a raised segment along the short axis of the polycarbonate plate. The pressure exerted onto the FlexiForce sensors was recorded at 28,400 Hz during the event. High speed color video was recorded at 7100 frames per second to track the motion of the polycarbonate block.

RESULTS

A total of 18 tests were conducted, and the peak velocity during the tests was 96.7 m/s with a mean of 78.6 m/s. The peak pressure recorded by the FlexiForce was 4 MPa with a mean of 1.2 MPa. The pressure vs. time graph is shown in Figure 1. The corresponding Fuji film used for the same test is shown in Figure 2. The Fuji film sheets used during the tests were digitized and their resulting pressure was determined using the color scale provided by the manufacturer. The Fuji film sheets shown in Figure 2 were exposed to the same event. The medium film shows a pressure of approximately 25 MPa, whereas the low film shows a pressure of 10 MPa. There were 9 instances in which the medium scale Fuji film indicated a pressure reading. In none of the tests did the FlexiForce measure a pressure higher than 10 MPa, which is the minimum range of the medium Fuji film.

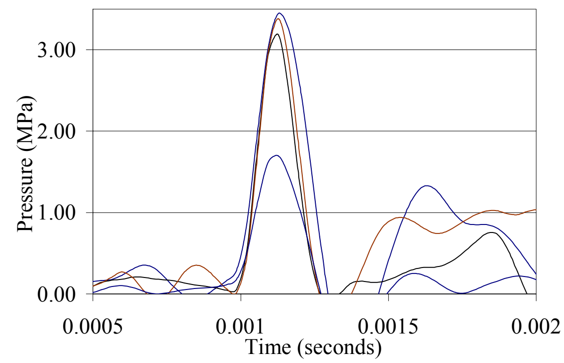

Figure 1: Pressure measured by FlexiForce sensors

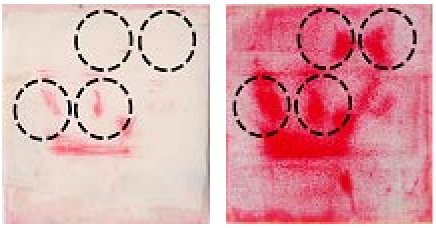

Figure 2: Medium (left) and Low (right) Fuji film results, dotted lines show position of FlexiForce sensors

CONCLUSIONS

The differences in the pressure measurement between the Fuji film and the FlexiForce may be due to shear effects during the event. The FlexiForce sensors are less sensitive to shear forces and therefore would measure a lower pressure than the Fuji film, which is affected by shear. Another source of error arises when considering the deformability of the Fuji film itself. If the film sheets are forced to bend around any type of contour, or if an edge exists, the film becomes more sensitive in that area. In summary, the FlexiForce's ability to sample at extremely high frequency and produce continuous signals make it an ideal sensor for pressure measurements.

REFERENCES

Harris, ML, Morberg, P,Bruce WJM,Walsh, WR, 1999: An Improved Method for measuring tibiofemoral contact areas in total knee arthroplasty: a comparison of K-scan sensor and Fuji film, *J. Biomech* **32** 951-8.

Reed, M, Schneider L,Burney R, 1992: Investigation of airbag induced skin abrasion: Proceedings of the 36th Stapp Car Crash Conference, Society of Automotive Engineers, Warrendale, PA,.

DECREASED PROXIMAL AORTIC COMPLIANCE CAUSES SYSTOLIC HYPERTENSION

N. Stergiopulos,. C. Ioannou, I. Startchik[1], A. Kalangos[1], M. J. Licker[1], D. R. Morel[1]
Laboratory of Hemodynamics, Swiss Federal Institute of Technology (EPFL), Lausanne, Switzerland.,
[1]University Hospital of Geneva, Geneva, Switzerland

INTRODUCTION

Total arterial compliance, principally determined by the elastic properties of the aorta and large arteries, together with peripheral resistance, are the two major arterial parameters that contribute to heart load. . Decreased compliance results in an increased pulse wave velocity so that the backward reflected wave contributes to elevation of systolic pressure [1,2]. Acute experiments in intact animals have shown that a decrease in aortic compliance, without a change in peripheral resistance, results in an increased pulse pressure due to elevation of systolic pressure and a reduction in diastolic pressure [3]. Studies on isolated hearts have shown that decreased arterial compliance has little effect on systolic pressure but does affect diastolic pressure. Using a new experimental animal model we aimed to show that systolic hypertension could result from a decrease in arterial compliance without a change in vascular resistance.

METHODS

Fourteen minipigs were divided into two equal groups, a sham operated group and a banding group. All animals had a pressure transducer and a flow probe implanted in the ascending aorta. In the banding group, a Teflon prosthesis was wrapped around the aortic arc. Data were recorded immediately after instrumentation, after banding (only in the banding group), at 2 days postoperatively and at 2 months postoperatively.

RESULTS AND DISCUSSION

After banding, aortic compliance decreased by 52±13% (±SEM) ($p<0.01$) while systolic pressure increased by 37±8% ($p<0.05$) and pulse pressure by (87±31%, $p<0.01$). Diastolic pressure, mean blood pressure, cardiac output and systemic vascular resistance did not change significantly. Aortic characteristic impedance increased 2.5 times, suggesting a 6-fold decrease in proximal aortic compliance due to the banding. The amplitudes of the forward and reflected pressure waves increased by 96±41% and 174±46%, respectively, while the time delay between the two decreased by 36±7%.

Figure 1 shows typical recordings of aortic pressure and flow performed in the same animal, before and after banding as well as on the 2nd post-operative day after banding. Immediately following banding, peak and mean flow were somewhat reduced, recovering to slightly higher values in the post-operative (2-day) period. Immediately following banding, systolic aortic pressure, however, was significantly increased and even increased further in the post-operative period. Following banding, the pressure wave shape was characterized by a late systolic increase, which is attributed to the early arrival of the reflected wave.

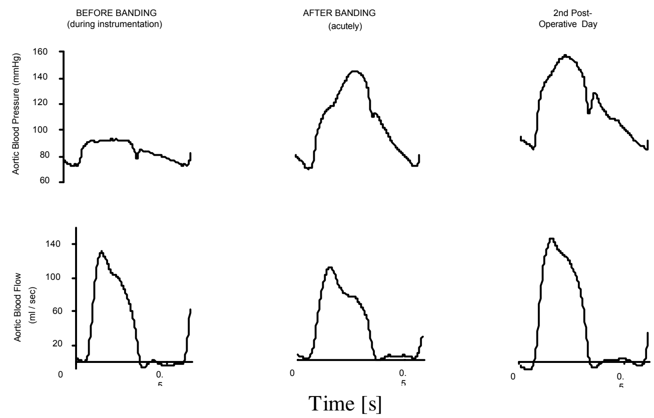

Figure 1: Example of ascending aortic pressure and flow curves taken before and immediately after banding during the day of instrumentation as well as on the 2nd postoperative day. A significant increase in the systolic pressure and rise in pressure is observed after banding, which is maintained post-operatively. Flow is not significantly altered after banding.

SUMMARY

We conclude that decreased proximal aortic compliance results in an increase in systolic pressure, without a change in diastolic pressure or cardiac output, due to an increase in the amplitudes of the forward and reflected waves as well as from an earlier return of the reflected wave. Our model therefore mimics normal ageing, where arterial compliance is decreased and systolic pressure is increased, without changes in peripheral resistance, cardiac output, or diastolic pressure.

ACKNOWLEDGEMENTS

This study is supported by the Swiss National Science Foundation (grant number: 32-59171.99).

A MATHEMATICAL MODEL OF ARTERIAL REGENERATION OVER BIORESORBABLE GRAFTS

Alexander Rachev and Miglena Kirilova
Institute of Mechanics, Acad. G. Bonchev Str., bl 4, 1113 Sofia, Bulgaria
rachev@bgcict.acad.bg

INTRODUCTION

There exists an increasing interest in use of bioresorbable material for fabricating vascular prostheses. The graft dissolves over post-implant time forming a scaffold for tissue ingrowth that leads to development of a neo-vascular conduit. Experimental studies have shown that during resorption process the graft decreases in thickness whereas the newly developed arterial tissue progressively thickens. Geometrical changes are accompanied by softening of the graft material while at the same time the arterial tissue becomes more organized and its elastic modulus increases. The interrelation between the resorption process and factors driving the arterial regeneration are poorly understood. This study aims to test some hypothetical mechanisms of neo-artery formation by comparing the theoretical predictions of a mathematical model with experimental data available in the literature.

METHODS

The artery/graft complex is considered as a two-layered thick-walled tube made of elastic incompressible materials (Fig.1). Under physiological pressure the vessel undergoes finite deformations. The modulus of the graft material is assumed to decay monotonically over post-implant time.

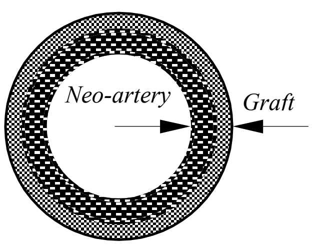

Figure 1: Schematic representation of the artery/graft complex

It was postulated that the rate of change in wall thickness of the neo-artery is driven by the deviation of the current mean circumferential stress from certain “equilibrium” values. Increase of arterial thickness is concomitant with corresponding decrease in thickness of the resorbable graft. The rate of change of arterial modulus depends on the abnormal pulsatile stretch of the arterial wall estimated through the deviation of the current arterial compliance from its baseline value.

Formation of a regenerated artery is described by a system of two non-autonomous first order differential equations for the evolution of the neo-artery dimensions and changes in the mechanical properties of the wall material. The system is coupled to the equation of equilibrium under constant transmural pressure and equations describing changes in the geometry and mechanical properties of the resorbable prosthesis.

RESULTS AND DISCUSSION

Using data available in the literature the model parameters were specified and the governing equations were numerically solved. The theoretical predictions of the model for time variation of the neo-arterial wall thickness (Fig.2), and time course of the arterial elastic properties (not shown) are in qualitative agreement with the experimental data reported by Greisler H. et al, (1987) for regeneration of rabbit aorta over PGA graft.

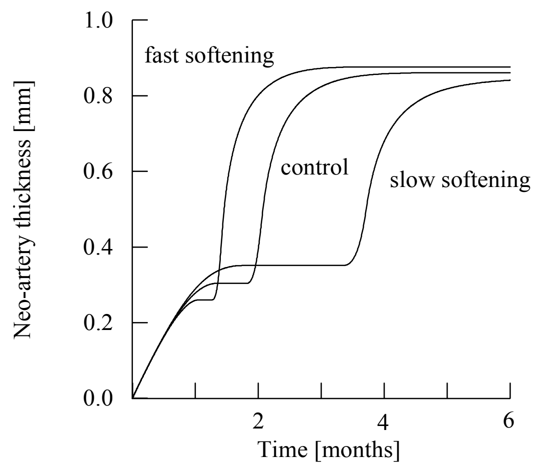

Figure 2: Time variation of neo-arterial thickness for different rate of softening of the graft material.

It was shown that a rapid resorption of graft material leads to overloading of the neo-artery tissue before it is sufficiently organized to bear load. This might lead to bursting or aneurismal dilatation, as had been experimentally observed (Greisler H. et al, 1987).

SUMMARY

The results obtained supported the hypothesis that arterial regeneration over a bioresorbable graft is an adaptive process that is influenced and modulated by mechanical factors. If the mean circumferential stress and pulsatile stretch are accepted as major determinants of the vessel wall regeneration, the process is self-limiting and leads to formation of a vessel with dimensions and mechanical properties close to those of a normal artery.

REFERENCES

Greisler H. et al (1987). *Arch. Surg.*, **122**, 715-721.

INVESTIGATION OF SKIN ABRASION INJURIES FROM HIGH RATE SHEAR LOADING

Joseph M. Cormier, William J. Hurst, Joel D. Stitzel, and Stefan M. Duma
Virginia Tech, Impact Biomechanics Laboratory, Blacksburg, VA. Email: Duma@vt.edu

INTRODUCTION

Although airbags have been shown to reduce the incidence of life threatening injuries, they have increased the risk of minor injuries such as skin injuries. A study of the National Automobile Sampling System (NASS) found that 66% of front seat occupants exposed to an airbag deployment incur a skin injury, and 47% of these injuries are attributed directly to the airbag itself (Jernigan 2001). It is suggested that there are two general injury mechanisms for airbag induced skin injuries: normal pressure from perpendicular contact of the airbag with the face and thoracic areas, and shear loading as the airbag expands and interacts with the upper extremities. Reed *et al.* (1992) performed studies on human volunteers to elucidate the potential for skin abrasion caused by airbag deployment. Reed concluded that normal loading alone induced enough pressure to cause skin abrasions. The work done by Reed seems applicable only to the perpendicular type loading, and would not accurately predict skin injuries from shear loading. Moreover, a study of airbag induced skin injuries found that the upper extremity is the most often injured body region at 42% of all airbag induced skin injuries (Jernigan, 2001). Given the large incidence of upper extremity airbag induced skin injuries, the shear loading injury mechanism that is likely responsible for these injuries, and the location of the airbag seams in this region. The purpose of the current study is to develop a technique for evaluating skin abrasions caused by shear loading at high velocities.

METHODOLOGY

Airbag fabric with four different seams was obtained and prepared for testing by cutting it into a rectangular shape and mounting to a polycarbonate plate. The mounting was such that the fabric was held in tension along all four directions. Porcine skin was chosen for the current study due to its similarities with human skin. Before the skin was removed from the animal, tension lines were drawn on the skin to facilitate the recreation of the *in vivo* tension of the porcine skin. The test apparatus allowed for the application of an initial normal load to be applied to the skin. A step velocity was applied to the fabric mount by an aluminum projectile released from a pneumatic impactor. Previous research done by Reed (1992) found that airbag velocities above 85 m/s (190 mph) resulted in skin abrasions for normal loading. Based on this criterion, the target fabric velocity for the current study was established at 89 m/s (200 mph). The fabric seam was situated such that it moved over the surface of the skin as the fabric mount was struck by the projectile and was pushed out from under the skin. The tissue stage was prepared with Fuji film sheets, both low and medium sensitivities and Flexi-Force pressure sensors (Tekscan, South Boston, USA). A total of four sensors were used, each with a sensing diameter of 9.5 mm. Data acquisition was configured to record the pressure exerted on the skin by the airbag seam and sampled at a frequency of 28400 Hz. High-speed digital color video was used to capture the motion of the fabric mount and video was recorded at 7100 frames per second. This frame rate allowed sufficient resolution of the fabric block in motion to facilitate velocity calculations and track the event. Visual examination of the skin was facilitated using ultraviolet black light and orange filters. Based on visually determining which section received the highest degree of abrasion, three sections of skin were removed for histology.

RESULTS AND DISCUSSION

The histology analysis showed that all tests resulted in abrasions with the exception of the control tests (Table 1). The abrasion score indicates depth: 1-2 epidermis, 2-3 transition, 3-4 dermis. In no instance did the abrasion remove the full thickness of the dermis. The abrasions varied from a slight removal of the epidermis, to a partial removal of the dermis (Figure 1). The analysis of the results obtained from these tests shows that it is possible to measure the effects of seam design alone without external effects of airbag inflator design.

Test	Seam Type	Peak Pressure (MPa)	Peak Velocity mph (m/s)	Abrasion Score
1	Control	1.50	210 (93.9)	0.00
2	Control	1.46	215 (96.1)	0.00
3	1	1.88	234 (104.6)	2.16
4	1	1.83	216 (96.6)	2.21
5	2	1.86	197 (88.1)	2.79
6	2	1.89	201 (89.9)	2.81
7	3	1.82	195 (87.2)	3.48
8	3	1.49	202 (90.3)	3.31
9	4	1.61	197 (88.1)	1.65
10	4	1.52	205 (91.6)	1.71

Table 1: Summary of Abrasion Test Results

Figure 1: Digitized histology section showing total removal of epidermis and partial removal of dermis.

REFERENCES

Jernigan, G. :Investigation of injury patterns in automobile collisions. Masters Thesis, Virginia Tech, Blacksburg VA, 2002.

Reed, M., Schneider L.,Burney R.: Investigation of airbag induced skin abrasion. Proceedings of the 36th Stapp Car Crash Conference, Society of Automotive Engineers, Warrendale, PA, 1992.

AN ALGORITHM TO QUANTIFY SEGMENTAL LESIONS IN NECROTIC FEMORAL HEADS

Karen L. Reed[1], Robert A. Robinson[2], Michael G. Conzemius[4], Thomas D. Brown[3,1]
[1]Departments of Biomedical Engineering, [2]Pathology, and [3]Orthopaedic Surgery
University of Iowa, Iowa City, IA
[4]Veterinary Teaching Hospital, Iowa State University, Ames, IA
Email: karen-reed@uiowa.edu

INTRODUCTION Approximately 25,000 new cases of femoral head osteonecrosis (ON) present each year in the U.S. To help clarify the pathology, we have recently developed a cryo-insult technique for creating segmental lesions (Reed, 2001) in the emu, a large biped in which osteonecrosis progresses to femoral head collapse (Conzemius, 2000). Osteonecrosis is characterized by the presence of dead osteocytes in histological sections of the affected bone. Quantification of lesion morphology is important in assessing our ability to create reproducible segmental lesions. An automated osteocyte identification and quantification algorithm is here reported to aid in this process.

METHODS Viable osteocytes can readily be identified in haematoxylin and eosin-stained slides by their nuclei, which appear as dark purple spots within a bright local field. Dead osteocytes present as empty lacunae – a small light-colored hole with no nucleus present – in the trabeculae (Figure 1).

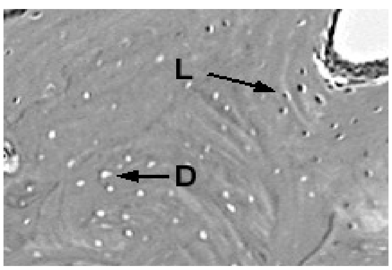

Figure 1 Stained bone showing live (L) and dead (D) osteocyte locations

An automatic detection algorithm to quantify the location of both live and dead osteocytes was written to take advantage of these morphological features. The algorithm, written in PV-Wave (VNI, Houston, TX), reads in eight-bit grayscale images and scans them for features signaturing osteocytes or empty lacunae (Figure 2). The flagged regions are then tested for aspect ratio, size, and contrast relative to the average background color. If a region is identified as an osteocyte or an empty lacuna, its centroid is found and its status is determined by the presence/absence of a dark spot. The algorithm's output is a list of osteocyte-center locations (pairs of x and y coordinates), and a binary value that indicates the osteocyte's status (1=alive, 0=dead)

The algorithm also provides the user with visual feedback, in the form of light and dark circles around the locations identified as live and dead respectively (Figure 3). Thus, the user can verify that the algorithm has correctly identified all points, and he/she can interactively correct any errors.

PERFORMANCE AND VALIDATION Four representative sections of a femoral head slice were chosen for validation purposes. A pathologist (R.A.R.) manually identified all of the live and dead osteocytes in each section, and their locations and status were recorded. The algorithm then performed the same operation, and the pairs of lists were compared for all four sections. The results, summarized in Table 1, show very good agreement between total detected percentage of viable osteocytes in each section.

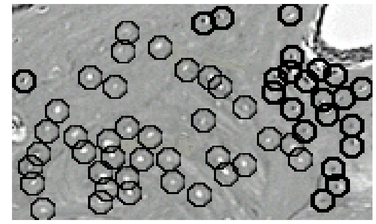

Figure 3 Stained bone with osteocytes and empty lacunae circled

Section #	% alive (H)	% alive (A)	Rel. Discrepency
1	31.41	28.26	0.100
2	96.36	93.08	0.034
3	51.60	50.56	0.020
4	50.51	51.90	-0.027

Table 1 Summary of validation results, human reader (H), vs. algorithm (A)

DISCUSSION Until now, assessing the shape and size of segmental osteonecrotic lesions has been entirely qualitative. However, for the purposes of further developing the emu as a model for osteonecrosis, quantification of lesions now emerges as an important tool in assessing the extent of tissue damage.

As a protection against errors in image analysis, the algorithm relies on a knowledgeable human to verify the completed reads, and make corrections if needed to each file scanned. This strategy of keeping a human in the loop, while allowing the algorithm to perform the bulk of the tedious work, allows necrotic lesions to be (relatively) quickly and accurately mapped.

Fully automated histology analysis tools have been developed for "high volume" production settings, such as identifying abnormal pap smears. To our knowledge, however, such assessments have not previously been coupled with spatial registration of normal/abnormal regions, or to quantify the degree of abnormality.

SUMMARY As development of the emu animal model for osteonecrosis progresses, it has become important to quantify necrotic lesion shape, size, and location. Therefore, an algorithm to identify live and dead osteocytes was developed for the purpose of quantifying these morphological characteristics.

ACKNOWLEDGEMENTS NSF Graduate Research Fellowship, NIH grant #AR46601

REFERENCES Conzemius et al. (2000) *ORS Proceedings* p. 206
Reed and Brown (2001) *ASB Proceedings*, p.8

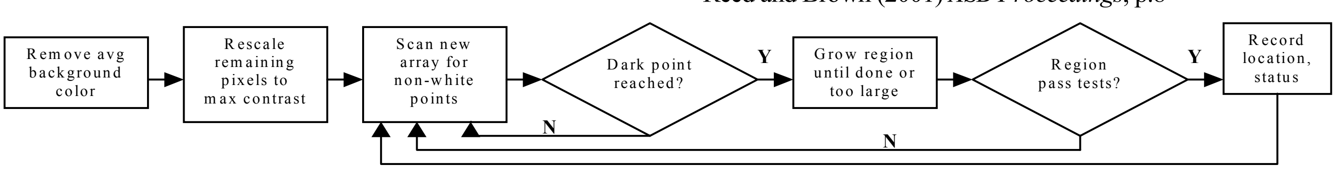

Figure 2: Flowchart describing the basic algorithm design

FINITE REYNOLDS NUMBER FLOWS IN THREE-DIMENSIONAL COLLAPSIBLE TUBES

Andrew L. Hazel[1] and Matthias Heil[2]
Department of Mathematics, University of Manchester, UK
[1]ahazel@maths.man.ac.uk [2]M.Heil@maths.man.ac.uk

INTRODUCTION

Many biological transport systems consist of elastic tubes conveying viscous fluid: e.g., the cardiovascular, respiratory and renal systems. If the transmural (internal minus external) pressure within such tubes falls below a critical value, the tube buckles and a strong fluid-structure interaction can occur. The interaction is responsible for phenomena such as flow limitation during forced expiration and the development of self-excited oscillations that cause wheezing in the airways and the Korotkoff sounds heard during sphygmomanometry.

MODEL DESCRIPTION

Following the earlier work of Heil (1997), we consider the flow of an incompressible, Newtonian fluid of viscosity μ, density ρ and average speed U through an elastic tube of undeformed diameter D, length L and bending modulus, K. The 3D Navier-Stokes equations, used to describe the fluid flow, are coupled to the equations of geometrically non-linear shell theory, which determine the tube's deformation. The coupled system of equations is solved numerically by a finite element method.

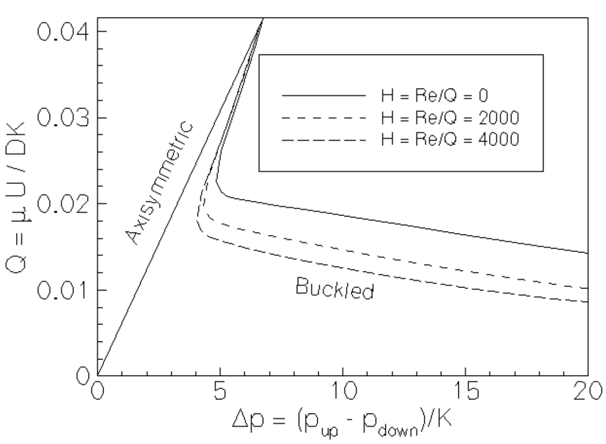

Figure 1: Non-dimensional flow rate, Q, as a function of the pressure drop, Δp, along an elastic tube (L/D=5) for a constant upstream transmural pressure. Results are shown for three different values of the parameter H, where H=0 corresponds to Stokes flow.

Two dimensionless parameters govern the system: (i) $\mathrm{Re} = \rho UD/\mu$, the Reynolds number, representing the ratio of inertial to viscous forces and (ii) $Q = \mu U/DK$, a dimensionless flow rate, that represents the ratio of viscous to elastic forces. A third dimensionless parameter $H = \mathrm{Re}/Q$ depends only upon the material properties of the system and is constant in any experiment involving a given tube and a given fluid.

RESULTS

Results will be presented illustrating the effects of fluid inertia upon the macroscopic behaviour of the system. For example, Figure 1 shows the relationship between the flow rate and the pressure drop along the tube when the upstream transmural pressure is held constant. At finite Reynolds numbers, the Bernoulli effect causes the tube to collapse more strongly than when Re = 0, resulting in a lower flow rate at any given pressure drop.

We shall also describe the three-dimensional flow fields and contrast them to those predicted by previous two-dimensional models (e.g. Rast 1994). In 3D, flow separation is open and tends to give rise to structures such as horseshoe vortices, see Figure 2.

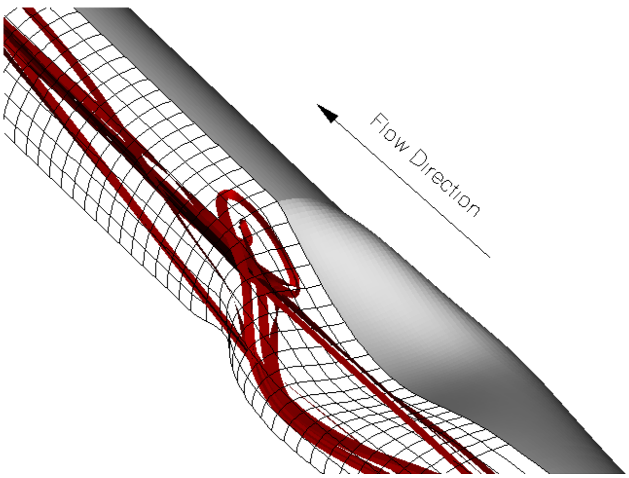

Figure 2: Steady flow through an elastic tube at Re = 255.

REFERENCES

Heil, M. (1997) Stokes flow in collapsible tubes: computation and experiment. *J. Fluid Mech*. **353**, 285-312.

Rast, M. P. (1994) Simultaneous solution of the Navier-Stokes and elastic membrane equations by a finite-element method. *Int. J. Num. Meth. Fluids.* **19**, 1115-1135.

BIOMECHANICAL DIFFERENCES IN SHOULDER LOADING IN POPULATIONS DURING LOAD-BEARING TASKS

Clark Dickerson[1], Kyunghan Kim, Diane Adamo, Bernard Martin, and Don Chaffin
HUMOSIM Laboratory, Center for Ergonomics, University of Michigan, Ann Arbor, Michigan, USA
[1]Corresponding Author: cdickers@umich.edu

INTRODUCTION

The role of the shoulder in load-bearing tasks for non-injured populations has been studied extensively (Chaffin et al, 1999). This contrasts to limited examinations of load handling by special populations. However, wheelchair users are highly susceptible to shoulder injuries (Koontz, 1998). This suggests that higher biomechanical tissue loading in the shoulder may occur during task performance by physically limited persons.

METHODS

Three groups of 10 volunteers participated: control (CG), spinal cord injured (SCI), and chronic low back pain sufferers (LBP). Motion capture data was recorded for seated load delivery tasks (25% of extended arm static shoulder strength). Targets were at 3 azimuths (0° [Target #3-10], 45°[#12-20], 90°[#22-30]), 4 heights and 2 horizontal distances. Target numbers increase with height then distance (i.e. 3-5 @ 0° near; 7-10 @ 0° far). Surface electromyography recordings were taken from the upper trapezius (UT), anterior deltoid (AD), infraspinatus (IF), and pectoralis major (PM), and normalized with respect to maximum voluntary contractions (NsEMG). Resultant external dynamic shoulder moments were calculated using a previously described model (Dickerson et al, 2001), and were normalized by subject body weight (NEDSM).

RESULTS AND DISCUSSION

NEDSM values increased both with increased reach distance and increased target height across all three groups (Figure 1). Both target location and subject group had a significant effect in determining NEDSM values (ANOVA, $p < 0.01$). LBP subjects had significantly higher NEDSM levels than both SCI and CG groups, as identified by Tukey post hoc analysis ($p < 0.01$ for both), though there was no statistical difference between SCI and CG NEDSM values ($p = 0.34$). This may relate to discomfort associated with torso twisting and bending for LBP. Minimizing torso movement may transfer loading to the shoulder via the outstretched loaded arm.

Figure 2 shows a comparison for the anterior deltoid NsEMGs. Pronounced trends existed for NsEMG values with respect to target location and group (ANOVA, $p < 0.01$). For all muscles, LBP NsEMG values were higher than CG ($p < 0.01$). SCI NsEMG values were higher than CG for the AD and PM ($p < 0.01$). This indicates that the groups have different muscle activation patterns.

SUMMARY

This study identified significant differences in biomechanical loading of the shoulder for loaded tasks performed by different populations. It also affirms the necessity for studying injured populations, as they may be at increased risk of injury due to higher tissue loading and muscle use. Interpreting underlying causes of this loading may aid in universal interface design.

REFERENCES

Chaffin et al (1999) *Occupational Biomechanics* (*3rd*). Wiley.
Dickerson C., et al (2001). *ASB Proceedings '01*, 235-236.
Koontz, A et al (1998). *RESNA Proceedings '98*

ACKNOWLEDGEMENTS

The Automotive Research Center and the HUMOSIM consortium partners contributed to this research.

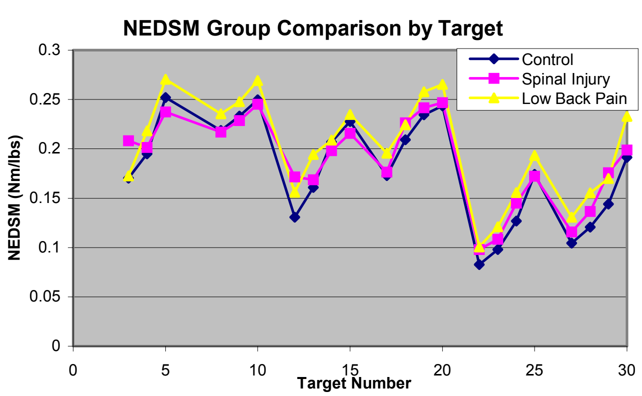

Figure 1: NEDSM Group Comparison. LBP NEDSM is significantly higher than CG and SCI NEDSM, possibly due to LBP mechanisms to minimize moments on the lower back.

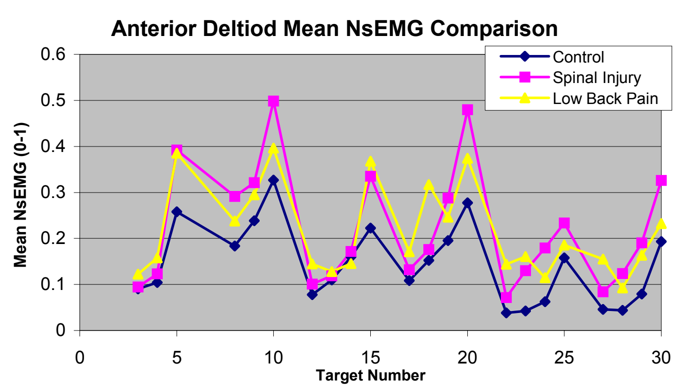

Figure 2: NsEMG for AD. The SCI had the highest NsEMG values for AD and PM, while the LBP had the highest values for UT and IF, suggesting different motion strategies.

INFLUENCE OF ANGULAR STABILITY OF AN INTERNAL SPINAL FIXATOR ON IMPLANT LOADS

Thomas Zander, Antonius Rohlmann, Georg Bergmann
Biomechanics Laboratory, University Hospital Benjamin Franklin, Free University of Berlin, Germany, rohlmann@biomechanik.de

INTRODUCTION

Several different internal spinal fixation devices are available. Most of them have an angular fixed connection between pedicle screws and the longitudinal rod. Some of the implants act like tension-banding implants thus requiring a stable anterior spinal column and a connection between pedicle screws and longitudinal rod which allows angular motion. Angular movable implants can adapt to different situations, for example graft resorption, thus allowing the bone to take over a great part of the spinal load, which reduces the risk of implant breakage. It is still a matter of debate whether an internal fixator should be flexible or rigid.
The aim of this study was to determine analytically implant loads for both, angular fixed implants and implants which allow angular motion between screws and rod.

MATERIAL AND METHODS

A three-dimensional, nonlinear finite element model of the human lumbar spine was created. The element mesh of the vertebrae is based on the model used by Smit [1996]. The nucleus pulposus was simulated by an incompressible fluid-filled cavity and the annulus fibrosus by volume elements with superimposed spring elements representing the fibers. The facet joints could only transmit compressive forces. The capsule of the facet joints and the six ligaments of the lumbar spine were included in the computer model. The mainly nonlinear material properties of all tissues were taken from the literature. The lower end-plate of the L5 vertebra was fixed and the model was successively loaded with pure moments of 7.5 Nm acting in the three anatomical main planes. The finite element model is described in detail elsewhere [Zander et al. 2001]. The finite element program ABAQUS was used. After studying the intact lumbar spine, paired bisegmental internal spinal fixators bridging the L3 vertebra were inserted without a preload. Different angular connections between pedicle screws and longitudinal rod were simulated. Most of the upper bridged disc was replaced by a bone graft (Figure 1).

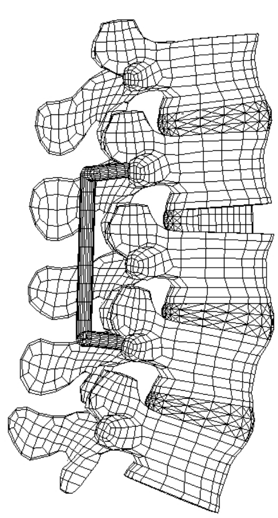

Figure 1: Outer mesh of the finite element model of the lumbar spine with internal fixators and a bone graft.

RESULTS

An internal fixator considerably reduces the angular motion in the bridged region for flexion and lateral bending (Table 1). For extension, angular motion was higher after insertion of an angular unstable fixator and a bone graft than for the intact spine. The finite element model predicts higher angular motion for implants with an angular movable fixator than for angular fixed ones. This is most pronounced for the loading cases extension and axial rotation.

	Intact spine	Angular fixed	Angular movable
Flexion	8.8°	0.8°	0.9°
Extension	6.5°	5.0°	8.2°
Lateral bending	9.8°	1.6°	2.0°
Axial rotation	6.0°	3.4°	6.5°

Table 1: Angular motion between L2 and L4 vertebrae

Angular stability of the fixator has a marked influence on axial forces on the implant for extension and axial rotation, but a minor one for flexion and lateral bending (Table 2).

	Angular fixed	Angular movable
Flexion	92	85
Extension	-69	-129
Lateral bending	149	140
Axial rotation	3	-20

Table 2: Maximum axial forces (N) on the internal fixators

The resultant bending / torsional moments in the fixators were mostly much higher for the angular fixed than for the angular movable implant (Table 3).

	Angular fixed	Angular movable
Flexion	0.37	0.31
Extension	1.00	0.40
Lateral bending	1.02	0.58
Axial rotation	1.39	0.09

Table 3: Maximum resultant bending / torsional moments (Nm) in the implants

DISCUSSION

An angular movable connection between pedicle screws and longitudinal rod reduces the bending moments on the implants and increases the intersegmental motion in the bridged region. It requires, however, a stable anterior spinal column which has then to transfer the loads. For the implant studied the pedicle screws and the longitudinal rod are not in the same plane. This is the reason why small bending moments were calculated in the longitudinal rod for the angular movable implant.

REFERENCES

Smit, T. (1996) *The Mechanical Significance of the Trabecular Bone Architecture in a Human Vertebra*. Shaker
Zander, T. et al (2001) *Clin. Biomech.*, **16**, S73-S80

SIMULATION OF NORMAL WALKING USING 3D MODELING

Dimitar Uzunov[1], Dimitar Tochev[1], Nikolay Zlatov[2], Yuli Toshev[1]
[1]Institute of Mechanics and Biomechanics, Bulgarian Academy of Sciences, Canada
[2]Manufacturing Engineering Center, University of Cardiff, United Kingdom

INTRODUCTION

The human locomotion involves a three-dimensional motion of a multiple linkage system, which demands coordinated control by the central nervous system. The main focus of the present study is simulation of normal walking using 3D modeling. A group of twenty normal male subjects between 18-25 years was studied.

METHODS

Four original force-plates TA-4 (Fig. 1) are used to obtain force and temporal data during walking. The platforms have a minimum resonant frequency of nearly 200 Hz and allow continuos records both of the vertical and the horizontal components of the ground reactions (for every leg) during three gait cycles). Two groups of gait parameters are analysed (Fig. 2). The parameters are defined separately for the right (index *r*) and the left (index *l*) leg. A total of six (*F1r, F2r, F3r, F1l, F2l, F3l*) force parameters and fourteen temporal parameters are defined in our previous work (Angelova et al., 1998). Six of the temporal variables express the chronological incidences of occurrence of the defined force parameters (*t1r, t2r, t3r*, *t1l, t2l, t3l*). The rest eight parameters are the step periods (T≈*Tr*≈*Tl*), the periods of stance phase (*T1r, T1l*), the periods of swing phase (*T2r, T2l*) and the periods of double support (*Td1, Td2*).

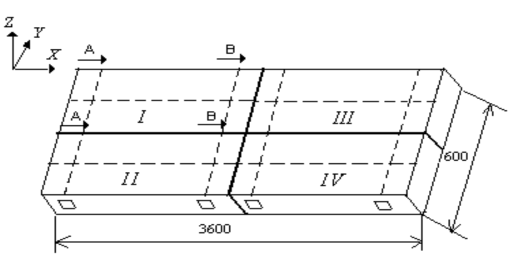

Figure 1. Four force-plates TA-4 (I, II, III, IV) for measuring the vertical and the horizontal components of the ground reactions during walking.

HUMAN BODY MODEL

A symmetrical model of the human body with 14 segments is used. Following the model we have to calculate the lengths of 8 segments, to determine their mass, as well as the location of segment mass center on its longitudinal axis. We will also need to determine the main central inertial moments of each segment. We propose an algorithm that enables to determine all necessary geometrical and mass-inertial parameters, using only L [cm] and M [kg].

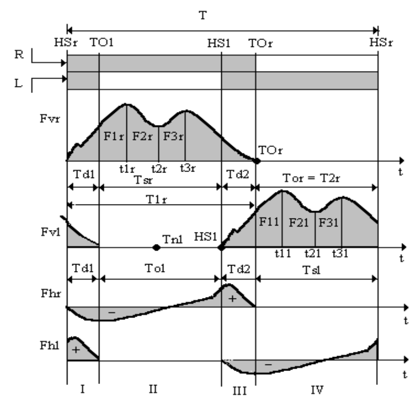

Figure 2: The vertical (index *v*) and the horizontal (index *h)* ground reactions of the right (index *r*) and left (index *l*) lower limbs during walking.

RESULTS AND DISCUSSION

One of the most convenient temporal criteria is: $k = (T1r/Td2)/(T1l/Td1)$, due to its sensibility to the walking asymmetry. The 3D simulation (Fig. 3) is based on our experimental results including the criterion *k* and the following whole body parameters: volume=0.076 m^3; surface area = 2.119 m^2; density=1000 kg/m^3; mass=75.954 kg. The principal moments of inertia in the center of gravity during the double support are: I_x=1.700 $kg.m^2$; I_y=11,334 $kg.m^2$; I_z=12,230 $kg.m^2$

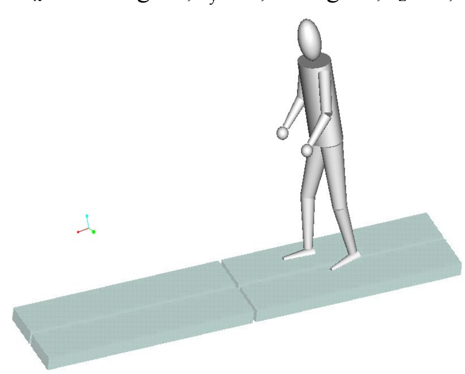

Figure 3: Walking simulation using CAD 3D generation

SUMMARY

Using experimental data 3D walking simulation is realized.

REFERENCES

Angelova, L. et al. (1998) *J. Theoretical and Applied Mechanics*, **18**, 16-21.

MEASURING EFFECTS OF DRUGS ON ARTERIAL MECHANICAL PROPERTIES

Carolien J. van Andel[1,2], Marion J. Sierevogel[2], Gerard Pasterkamp[2], Peter V. Pistecky[1] and Cornelius Borst[2]
[1]Man-Machine Systems, Delft University of Technology, Delft, The Netherlands, c.j.vanandel@wbmt.tudelft.nl
[2]Experimental Cardiology, University Medical Center Utrecht, The Netherlands

INTRODUCTION

Many problems in cardiology and cardiovascular research are associated with vascular mechanics. Endothelial cells and smooth muscle cells sense their mechanical environment and respond with metabolic changes (Liu et al, 2000) Restenosis after percutaneous coronary interventions can be a result of these cellular changes (Orford et al, 2000). Drugs that might play a role in the prevention of restenosis are being studied on a cellular level by many researchers. However, the use of drugs might have an effect on the mechanical properties of the vessel wall as a whole. In this study, we used a relatively easy and quick method to determine changes in the circumferential and axial stress-strain relations of isolated coronary arteries. We studied the effects of two drugs, a matrix metalloproteinase (MMP) inhibitor and a collagen synthesis inhibitor on the circumferential and axial mechanical properties of the arterial wall.

METHODS

Animal models. 1) Atherosclerotic Yucatan minipigs, approximately 2 years of age with an average weight of 40 kg were used. Pigs had been fed an atherogenic diet for 9-10 months. Pigs were treated with the MMP-inhibitor BB-2983 for 42 days (n=2) or served as controls (n=2). A proximal and distal part of each right coronary artery was measured within 24 hours after termination. 2) Non-atherosclerotic Yucatan minipigs, approximately 2 years of age and an average weight of 30 kg. Pigs were treated with a collagen synthesis inhibitor for 42 days (n=4) or served as control (n=2). One segment of each right coronary artery was measured within 6 hours after termination.

Measurements of mechanical properties. Axial and circumferential mechanical properties were measured by subjecting arterial segments to inflation and axial tension in vitro. The segments were cannulated and connected to a tensile testing machine in order to regulate lengthening of the segment and to measure axial force. The segments were inflated with and bathed in Tyrode solution at a constant temperature of 37 ^{0}C. The external diameter of the artery during inflation was measured with a dual beam laser-micrometer. The measurements were repeated while the vessels were held at different levels of constant axial pre-stretch λz. Assuming arterial wall incompressibility, the Green-Lagrange strains ($E\theta$, Ez) and second Piola-Kirchhoff stresses ($S\theta$, Sz) in the circumferential (θ) and axial (z) direction can be calculated for the middle surface of the vessel wall.

RESULTS AND DISCUSSION

In the atherosclerotic pigs, the right coronary arteries of the MMP inhibitor group showed a significant reduction in axial stress when increasing the axial pre-stretch ($p=0.02$ at $\lambda z=1.4$), compared with the control group (fig.1). In the non-atherosclerotic pigs, the collagen synthesis inhibitor group showed a large increase in axial stress at increasing axial pre-stretch ($p=0.06$ at $\lambda z=1.5$), which was not found in the control group. In both pig models, no differences in circumferential stress were observed among groups.

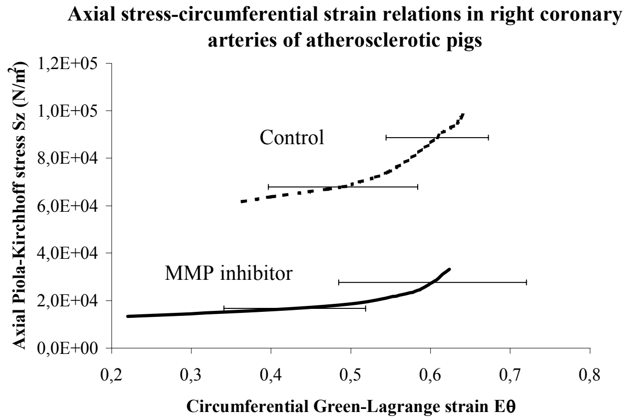

Figure 1: Axial stress versus circumferential strain relation of right coronary arteries of atherosclerotic pigs at $\lambda z=1.4$. The continues line indicates the MMP inhibitor group and the interrupted line the control group, horizontal lines indicate standard deviations.

Clearly, these drugs have an effect on the mechanical behavior of the vessel wall, which can be assessed with a relatively small amount of measurements. Dobrin et al (1984) showed that in canine and human vessels, tensile strength and wall integrity depends on intact collagen. Any disruption of this collagen fiber network causes structural and mechanical alteration of the artery. Axial stiffening due to axial stretch and internal pressure was largely absent in the MMP inhibitor group, which might point to a possible effect of the MMP inhibitor on the mainly axially oriented collagen fibers in the adventitia. The increase in axial stiffening of the vessel wall by the collagen synthesis inhibitor was surprising since this inhibitor is thought to reduce collagen content in the arterial wall. Further research is necessary, but these mechanical experiments could support the testing of long term effects of drugs.

REFERENCES

Liu, S.Q. et al (2000). *J Biomech Eng*, **122**,31-38.
Orford, J.L. et al (2000). *Am J Cardiol*, **86**, 6H-11H
Dobrin, P.B. et al (1984). *Arch Surg*, **119**, 405-409

ACKNOWLEDGEMENTS

C.J. van Andel was supported by the Technology Foundation STW (grant UGN 66.4183) in the Netherlands. M.J. Sierevogel was supported by the Sorbo Foundation.

UNIQUE MUSCLE ACTIVITY PATTERS OBSERVED DURING GAIT TRANSITIONS

Lorna Ogden and Li Li
Department of Kinesiology, Louisiana State University, Baton Rouge, Louisiana, USA, lli3@lsu.edu

INTRODUCTION

Often the approach to investigating gait related variables, including muscular function, at transition speeds entailed conducting tests at speeds held constant from one test to the next (Prilutsky & Gregor, 2001). Estimated transition speeds would be included within these tests; few did the protocols call for testing while transition was in progress. In a study on the response of vertical ground reaction force (VGRF) to gait transitions, Li and Hamill (in press) reported that VGRF exhibited transition specific patterns several steps before gait transitions. In order to produce these transition specific VGRF patterns, muscles might act accordingly with transition specific coordination. This study investigated muscular activity during continuously changing speeds, which may better resemble the transition process, in order to further detail and quantify neuromuscular changes during gait transitions.

METHODS

Twelve healthy adults, 18-41 years of age, were recruited as participants. Informed consent was obtained. Experiment was conducted on a treadmill with embedded force platforms (Kistler, Amherst, NY, USA). Gait transitions were induced by the speed of the treadmill changing with constant acceleration. Walking was identified by double stance phases where running was identified by double flight phases. Reflective markers were placed on the anatomical landmarks of hip, knee, ankle, heel, and 5th metatarsal joint. Bipolar surface electrodes were positioned on the subjects' skin over the muscular bellies of the gluteus maximus (GM), rectus femoris (RF), vastus lateralis (VL), biceps femoris (BF), tibialis anterior (TA), gastrocnemius (GAS), and soleus (SOL). Electromyographic (EMG) data were collected at 960 Hz. Five transition trials were conducted for both progression modes: walk-to-run (WR) and run-to-walk (RW), and five interval trials were collected for both walk and run at constant speeds. The mean of recorded transition speeds (MTS) was calculated from the preceding transition trials.

The experimental protocol includes four conditions: WR and RW transitions, as well as walking and running at different but matched constant speeds. Five trials were included in each condition. For the transition conditions, each trial refers to one step. Five steps proceed the gait transitions were analyzed. The mean speed of each of these steps (trials) was different since they led to gait transitions with a constant acceleration. There were five different constant speed trials for both walking (WC) and running (RC), the speeds were MTS - 0.6, MTS - 0.3, MTS, MTS + 0.3, and MTS + 0.6 mph. EMG data of one step from each trial was selected for further analysis. Peak magnitude and duration of EMG activities were examined across trials and conditions. Two factor (condition and trial) repeated measures ANOVA was employed for statistical analysis ($\alpha = .05$).

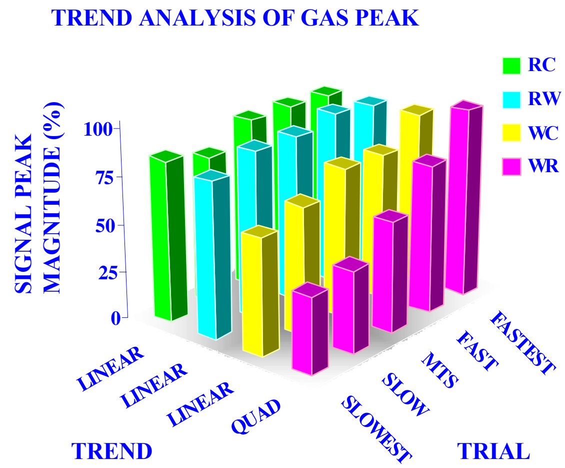

Figure 1: Condition/trial interaction graph for the relative peak magnitude of the GAS. Peak magnitude increased with speed in a linear fashion for all conditions but one condition. Peak magnitude increased quadratically with speed in the WR condition.

RESULTS AND DISCUSSION

A significant condition/trial interaction (see Figure 1 for example) for burst peak magnitude was observed for GM, RF, VL, TA, GAS, and SOL. EMG activity intensity in some of the muscles changed with the locomotion speed in a quadratic fashion (for example, GM and RF in WR). However these quadratic changes with locomotion speed were only observed in transition related trials but not in interval trials even though the range of speed was comparable. Significant condition/trial interactions for muscle burst duration were also observed. Similar as to the EMG activity intensity, quadratic response to speed change was also observed with EMG activity duration. Again, these quadratic trends were only observed in transition related trials (GAS in RW) but not in locomotion at constant velocity. These results indicate that preparation for gait transition occurs before observed kinematic changes and triggers of gait transitions should be studied accordingly.

SUMMARY

Transitional specific muscular activity was observed in the study. Neuromuscular changes occur steps before the observed gait transition. These results suggest that gait transition related studies should be conducted with changing speed rather than constant velocity in the same range.

REFERENCES

Li, L., Hamill, J. (in press). *Research Quarterly for Exercise and Sport*.

Prilusky, B., Gregor, R. (2001). *J. Biomechanics,* **204**, 2277-2287.

THREE-DIMENSIONAL MOTION TRACKING OF THE FOREARM USING SURFACE MARKERS

Eding Mvilongo[1,2], Carolyn F. Small[1,2], David Pichora[2]
[1]Queen's University, Kingston, Ontario, Canada, mvilongo@me.queensu.ca
[2]Human Mobility Research Centre, Kingston General Hospital, Kingston, Ontario, Canada

INTRODUCTION

Rheumatoid arthritis is a systemic inflammatory disease. When affecting the wrist joint, it generates pathological changes causing a decrease in the range and consistency of motion and leading to joint instability and loss of hand function (Taleisnik, 1989). Restoration of strength and motion by means of a complete wrist replacement, known as arthroplasty, is a preferred treatment option for severe cases of rheumatoid arthritis (Swanson, 1973; Swanson, 1981). In order to set objective criteria for evaluating motion with wrist implants, normal motion, or kinematics, of the wrist joint therefore needs to be defined. Studies of upper limb 3D kinematics including forearm pronation-supination have been done *in vivo* statically, but not yet dynamically using skin markers. The goal of this project is twofold. First, we want to validate a testing protocol that would enable us to characterize, from skin markers, dynamic forearm pronation-supination both *in vitro* and *in vivo*. Secondly, we want to establish if skin motion patterns can be used to describe bone motion during *in vivo* pronation-supination for an asymptomatic subject.

METHODS

A mechanized model of a human forearm (Sawbones, Pacific Research Laboratories, Inc.) was initially used with a custom-built apparatus to validate motion analysis software developed in-house for pronation-supination kinematics. Upon validation, we used a cadaver arm for standard optoelectronic motion tracking (OPTOTRAK, Northern Digital Inc.) of the wrist and the forearm during dynamically induced flexion-extension, radioulnar deviation and pronation-supination. Surface markers were placed on the forearm and at the elbow (Figure 1). Position data was collected during 3 different testing cycles. Three sets of CT scans (GE Light Speed Plus) with our specimen in different semi-static positions were also done for later work involving the computation of a skin motion artefact correction algorithm.

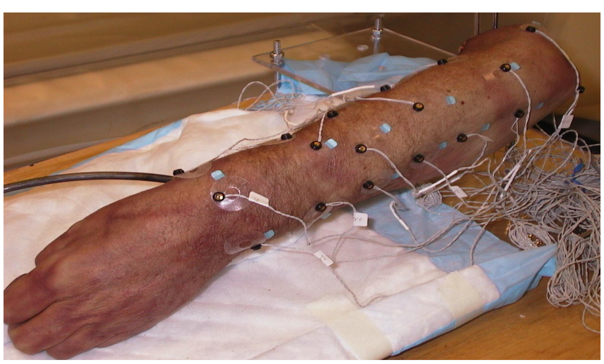

Figure 1: Surface markers on the upper limb specimen

RESULTS AND DISCUSSION

We were successful setting up a testing apparatus and protocol for dynamic pronation-supination motion. We used the collected position data in our in-house motion analysis software to measure the Euler angles and the Screw Displacement Axis parameters resulting from motions of the hand, the radius and the ulna. Table 1 displays sample results of kinematic data collected following a validation experiment.

Table 1: Sample results for Euler angles; flexion-extension (θ), radioulnar deviation (ϕ) and pronation-supination (ψ)

Trial number	Wrist position	Euler angles (degrees)		
		ϕ	θ	ψ
1	45° flexion	-9.09	-46.05	4.74
2	neutral	1.37	8.29	13.47
3	45° extension	-4.32	47.10	4.12

We are now looking at the skin motion artefact created following the utilization of surface markers during optoelectronic data acquisition by relating position data of anatomical landmarks to that of the markers. We are estimating the motion relative to the ulna during testing by using skin motion data from CT images of the upper limb in the different semi-static positions. We are also in the process of verifying if a valid correction algorithm can be developed so that skin motion artefact could be expressed in terms of a transformation matrix applied to the underlying bones, relating the surface markers to the bony landmarks.

SUMMARY

Normal kinematics of the forearm need to be defined so as to quantitatively determine the extent of altered motion due to the presence of rheumatoid arthritis and to set objective criteria for evaluating motion with forearm implants. This project aims to validate a testing protocol that would enable us to describe the three-dimensional kinematics of forearm pronation-supination from skin markers, and establish if skin motion patterns can ultimately be used to accurately describe bone motion during *in vivo* pronation-supination for an asymptomatic subject.

REFERENCES

Swanson,A.B. (1973). Orthopedic Clinics of North America **4,** 383-394.
Swanson,A.B. (1981). *Surgical Clinics of North America* **61,** 369-382.
Taleisnik,J. (1989). *Hand Clin.* **5,** 257-278

TEMPORAL PATTERN RECOGNTION TECHNIQUES CAN DETECT EMG DIFFERENCES BETWEEN MODERATE KNEE OSTEOARTHRITIS PATIENTS AND HEALTHY CONTROLS DURING WALKING

C.L. Hubley-Kozey [1], K.J. Deluzio [2], J.W. Kozey [3], J.McNutt [1], J.J. Chu[4], G.E.Caldwell[4], W.D. Stanish [5]
[1] Schools of Physiotherapy, clk@is.dal.ca, [2] Biomedical Engineering, and [3] Health and Human Performance, Dalhousie University, Canada, [4] Dept. of Exercise Science, University of Massachusetts, USA, [5] Faculty of Medicine, Dalhousie University, Canada.

INTRODUCTION
Early detection of mild to moderate knee osteoarthritis (OA) may assist in the development of effective therapeutic strategies to slow down or possibly reverse disease progression. There is strong evidence that mechanical factors play a role in the pathogenesis of OA. Since the muscles surrounding the knee joint produce forces for movement, stability and impact attenuation, identifying muscle activation patterns unique to OA may assist in developing particular therapies that focus on altering neuromuscular control strategies. The purpose of this study was to quantitatively compare temporal electromyographic (EMG) profiles of the knee muscles during walking between those who have been diagnosed with moderate OA and those with healthy knees (CON). In an attempt to stress the system normal and a fast walking speed conditions were compared. Although motion and force data were collected simultaneously with the EMG data, this paper will focus on the EMG results.

METHODS
EMG data were collected from CON and patients with moderate OA (scored 1 or 2 on the Kellgren and Lawrence scale). Subjects gave informed consent (approved by Ethics Committee), completed the SF-36 health survey and the OA subjects completed the WOMAC. After skin preparation, Ag/Ag Cl surface electrodes were attached in standard locations over the vastus lateralis (VL), vastus medialis (VM), rectus femoris (RF), lateral hamstring (LH), medial hamstring (MH), medial (MG) and lateral gastrocnemius (LG) muscles of the affected limb for the OA group, and a randomly selected limb for the CON. EMG signals were amplified (BP 10 - 1000 Hz, CMRR 115dB, input impedance ~ 10 Gohm) using an AMT-8 EMG system (Bortec Inc., Calgary, Al) and were digitized at 1000 Hz using the analogue data capture feature of the Qualysis™ motion analysis system. Each subject performed, in random order, five trials of their normal selected speed (C1), and a fast walk (C2) (150% of the normal speed). Following the test trials, subjects performed six standardized maximal voluntary isometric contractions (MVIC) for each muscle site. Raw EMG signals were full-wave rectified, low pass filtered at 6 Hz, and for the test trials were amplitude normalized to %MVIC and time normalized (% gait cycle) from heel strike to heel strike on the measured limb. The Karhunen-Loève Expansion was applied to the data set of all time-normalized profiles. The weighting coefficients for each muscle derived for each principal component pattern (PC_i) were the main dependent measures in the mixed model ANOVAs. For each muscle, trial effects were tested followed by group and speed main effects and interactions ($\alpha = 0.05$) using Minitab statistical software package (11Xtra).

RESULTS
The mean age for the CON was 44 ±9 and 57.8 ± 14 years for the OA. The WOMAC score ranged from 89-113. No differences were found between groups for walking speed. Ninety eight percent of the variance in the profiles for the seven muscles was contained in 10 PCs. There were no significant trial effects ($p>0.05$) for any muscle or speed, indicating consistency in the temporal patterns. Significant group by speed interactions ($P<0.05$) were found for all three quadriceps sites and for the two hamstring muscles. Post hoc analysis revealed that the statistical differences occurred in the higher speed, C2, trials rather than the slower, C1, trials. The quantitative EMG similarities for C1 and differences for C2 identified by the statistical analysis for VL is evident in the ensemble average profiles in Figure 1.

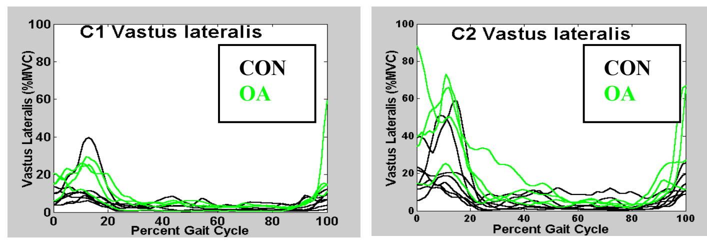

Figure 1 %MVIC versus % gait cycle for VL.

DISCUSSION AND CONCLUSION
The EMG waveform data revealed differences in muscle activation patterns between the two groups primarily at the faster walking speed condition. The differences in the PCs for VL captured the double peak and the high amplitude at heel strike in the temporal waveform for the OA group for C2. For the MH and LH, the significant PC corresponded to the high amplitude of activity at heel contact and a burst of activity during late stance for the OA group in particular for C2. The disproportionately higher amplitude of knee flexor coactivity at heel strike may reflect a guarded response to pain, whereas the burst during the weight transfer phase may reflect a stabilizing response as the knee moment changes from a flexor moment to an extensor moment. These data support that at normal walking speeds the temporal activation patterns were similar between groups. However, differences were exaggerated when the system was stressed at higher speed. The higher activity from both knee flexors and knee extensors and the differences in patterns need to be further explored, in particular given the trend for lower external flexor moments for the OA group at the fast walking speed. These data support that the neuromuscular control patterns are different for those with moderate OA compared to healthy knees.

ACKNOWLEDGEMENT
Thanks to A. Horne, S. Landry and S. Offmann for assistance with data collection and analysis.

CFD MODELING OF CAROTID BIFURCATION BLOOD FLOW USING 3D ULTRASOUND

Alexander D. Augst[1], Dean C. Barrat[2], Alun D. Hughes[2], Simon A.McG. Thom[2], X. Yun Xu[1]
Departments of [1]Chemical Engineering, [2]Clinical Pharmacology, Imperial College, London, UK, **a.augst@ic.ac.uk**

INTRODUCTION

Computational Fluid Dynamics (CFD) flow simulation techniques have the potential to enhance our understanding of how haemodynamic factors are involved in atherosclerotic plaque formation. In order to model blood flow and predict wall shear stress for individual patients using CFD, an accurate description of vascular geometry is necessary. 3D X-ray angiography and magnetic resonance angiography (MRA) have been used for gathering this information in vivo, but recently 3D ultrasound imaging has emerged as an alternative. We describe the application of a novel 3D ultrasound imaging system to extract vessel geometry for CFD studies of the human carotid artery bifurcation.

METHODS

3D ultrasound scans of human carotid artery bifurcations were carried out on 8 subjects. The 3D ultrasound system used in this study is based on a standard 2D ultrasound scanner (HDI 5000, ATL-Philips Ltd, Bothell, MA, USA), and an electromagnetic position and orientation measuring (EPOM) device (Ascension Technology Inc, Vermont, USA) (Barratt 2001a and b). During the scan, the transducer probe is swept slowly over the subject's neck and images are acquired on the peak of each ECG R-wave. Two separate data sets were recorded on detection of a trigger pulse: a set of 2D images from the scanner and the orientation and position of the ultrasound probe from the EPOM device. The digital images were stored on the scanner and later downloaded onto a PC to be analyzed off-line. The EPOM data was used to accurately determine the location of each acquired ultrasound image within a 3D volume. Blood velocity information was also acquired in the proximal common and external carotid artery (CCA and ECA, respectively) using pulsed Doppler ultrasound. Time-dependent center-stream velocities were used as input data for the CFD simulations. The acquired transverse images were then segmented using purpose-built software, which allowed points on the vessel wall to be manually defined. A smooth cubic spline or ellipse was fitted to these points, as appropriate. Thus, a series of cross-sectional contours were produced that define the geometry of the vessel. In order to reduce spatial reconstruction artefacts in the reconstructed vessel, a cubic smoothing spline was fitted to the centroids of the contours. Each contour was then realigned so that it's centroid coincided with the fitted centerline curve. The vessel surface was reconstructed by fitting smoothing splines to successive contour points.
The surface splines were used by a commercial CAD/CAE package (ICEM-DDN) to produce the input file for the grid generator (ICEM-Hexa). Using the CAD tool, the internal carotid artery (ICA) was extended linearly in order to move the outflow boundary far enough away from the carotid bulb. This was deemed necessary as relevant flow features were expected to occur in this region which might have been affected by a nearby boundary. The semi-automatic Hexa tool allows the generation of a fully structured hexagonal cell grid for the designated solver CFX-4.4.
Flow simulations were carried out under pulsatile flow conditions using a non-Newtonian fluid. Fully developed flow was assumed at inlet while time-varying outflow divisions between ICA and ECA were determined from Doppler data. The oscillatory shear index (OSI) and time averaged wall shear stress magnitude (TAWSS) were calculated.

RESULTS AND DISCUSSION

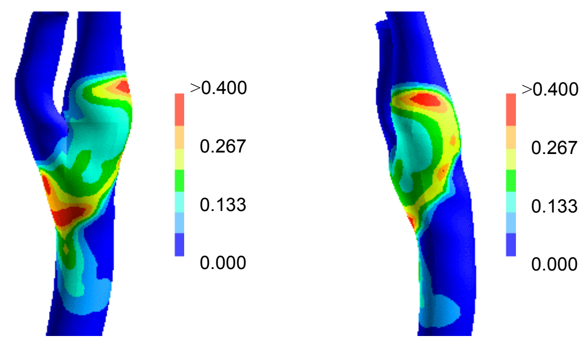

Figure 1: OSI shown for sample bifurcation.

It can be seen in Fig.1 that particularly high values of OSI occur in the carotid bulb and at the bifurcation region proximal to the ECA where the CCA starts to increase in diameter. Analogous patterns were observed on all subjects.

SUMMARY

It has been demonstrated that 3D ultrasound is a viable alternative to other established vascular imaging techniques for generating accurate 3D geometric input data for CFD simulations. Future work will include evaluation and improvement of the methods described in this paper using phantom and in vivo studies.

REFERENCES

Barratt, D.C., Davies, A.H. et al.(2001a). *Ultrasound Med. Biol.*,**27**,957-968
Barratt, D.C., Davies, A.H. et al.(2001b*). Ultrasound Med. Biol.*,**27**,1421-1425

INFLUENCE OF INTERFERENCE-FIT ON THE INITIAL STABILITY OF CEMENTLESS PROXIMAL FEMORAL STEMS

A.S.Wong[1], A.New[1], G.Isaac[2] and M. Taylor[1]

[1]Bioengineering Sciences Group, University of Southampton, Southampton, SO17 1BJ, United Kingdom, asw@soton.ac.uk
[2]DePuy International, St. Anthony's Road, Leeds, LS11 8DT, United Kingdom

INTRODUCTION

Cementless press-fit stems have become a common design concept in present hip joint replacement. Cementless stems are pressed into a canal that is slightly smaller than the femoral stem to create an interference-fit to provide greater initial stability and bone contact. A number of finite element (FE) studies have modelled cementless hip stems, but they have neglected to model the interference-fit. The influence of interference on the initial stability, bone strain and contact area has yet to be quantified. This preliminary study will address these issues.

METHOD

A FE model was constructed based on computer-tomography (CT) scans of a male human femur and implanted with a proximally porous coated IPS stems (DePuy). This stem was designed to be implanted into an under-reamed cavity to produce an interference-fit of up to 0.375mm. The elastic modulus of the bone was assumed to have a relationship with apparent density in the form $E = 2875\ \rho^3$ [Carter and Hayes, 1977]. The elastic modulus of the titanium stem was 116 GPa.

Initially, two models were analysed, with (model EI) and without (model E) a modest inteference of 0.1mm, and assuming elastic material properties for bone. On observing significant bone strains, the analyses were repeated assuming elastic-perfectly plastic bone properties with a yield strain of 1.5% (models EP and EPI). For all models, a coefficient of friction of 0.6 was assumed at the bone-implant interface and loads were applied as suggested by Bergmann [Hip 98 cd]. The micromotions and bone strains are reported at the bone-stem interface at six cross-sections from the proximal (L1) to distal (L6) portion of the porous-coated area.

RESULTS AND DISCUSSION

The minimum principal strain at the bone interface was significantly higher in the interference-fit models (Fig. 1). The elastic-plastic model showed significant plastic deformation, which suggests greater bone damage. However, the addition of plasticity to the models did not influence the micromotion values (Table 1.).

Axial micromotions were smaller in the models with interference-fit due to residual stresses at the interface. The micromotion values are large in comparison to similar studies. The inclusion of an interference-fit reduced the peak micromotions by only 10-30 µm.

Contact areas in the interference-fit models were significantly higher as compared to the no interference-fit models. When loaded, greater contact with the stem was maintained due to elastic recovery of the interference-fit.

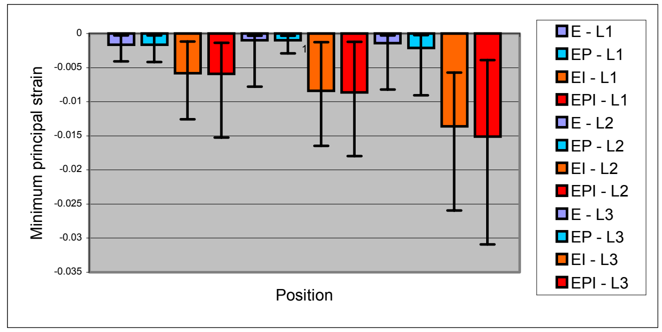

Figure 1. Mean minimum principal strain of L1, L3 and L6. Error bars showed the minimum and maximum minimum principal strain values at the cross-sections.

Model	Maximum axial micromotion, µm					
	1	2	3	4	5	6
E	183.1	228.0	198.8	189.1	163.7	194.7
EP	183.2	228.1	198.9	189.4	164.1	194.8
EI	150.2	205.8	167.2	171.3	150.6	177.4
EPI	148.4	205.7	166.8	169.4	148.6	177.6

Table 1. Maximum axial micromotions

SUMMARY

The predicted micromotions were high in this study, particularly around the anterior and posterior regions of the stem. The application of multiple load cycles may reduce the magnitude of the micromotions, by allowing the stem to 'bed in' [Kuiper and Huiskes, 1996], particularly for the elastic-plastic models. The results suggested that the inclusion of an interference-fit only marginally improved the stability of the stem, although the contact area was increased. The strain distribution was dominated by the interference-fit and this lead to significant bone damage (in some areas up to 1.5% minimum principal plastic strain). This may result in adverse bone resorption, in the early post-operative period. This raises the question, is there an optimum degree of interference, which minimises the degree of bone damage, but provides adequate initial stability and bone contact? Further work is required to study this in greater details.

REFERENCES

Carter, D.R., Hayes, W.C. (1977). J. Bone and Joint Surgery, **59A**, 954-962.
[Hip 98] Bergmann et al. (2001) J. Biomechanics, **34**, 859-871 and Heller et al. (2001) J. Biomechanics, **34**, 883-893
Kuiper, J.H., Huiskes, R. (1996). J. Orthopaedic Research, **14**, 36-43

INTRA-UTERINE TRANSPORT PATTERN DURING EMBRYO TRANSFER

Sarit Yaniv [1], Osnat Eytan [2], Ariel J. Jaffa [2] and David Elad[1]
[1]Department of Biomedical Engineering Faculty of Engineering, Tel-Aviv University, Tel-Aviv 69978, Israel, elad@eng.tau.ac.il
[2]Ultrasound Unit, Lis Maternity Hospital, Tel-Aviv Sourasky Medical Center, Tel-Aviv 64239, Israel

INTRODUCTION

Embryo transfer (ET) is the last stage of extra-corporal fertilization better known as in vitro fertilization (IVF). The ET procedure is performed 1-2 days after fertilization with a thin catheter, which is filled with 2-3 embryos in a fluid medium. The catheter is inserted into the uterus with its tip near the fundus at the top of the uterus (Schoolcraft et al., 2001). While fertilization in the laboratory occurs with relatively high success rates (>90%), the overall success of take home baby is still very low (<25%). Once the embryo enters the uterus, the ultimate goal is implantation at a fundal area to ensure a successful pregnancy. It has been demonstrated that intrauterine fluid motions, which are induced by myometrial contractions, may transport the embryo towards its implantation site (Eytan & Elad, 1999). In the present study, we analyzed the transport characteristics of ET by utilizing a model of a fluid-filled thin catheter inserted within a two dimensional (2D) channel with oscillating walls.

METHOD

The transport phenomena during the procedure of ET are simulated by a thin fluid-filled catheter inserted within a 2D channel which represents the intrauterine cavity (Fig. 1). Uterine peristalsis is simulated by a sinusoidal wall motility on both sides of the channel. The fluid that contains the embryos is injected into the channel via the catheter in either a constant or time varying speed. The initiation of the injection is synchronized with the position of the channel wall at the cross-section that coincides with the catheter tip. The time-dependent nonlinear governing equations for laminar flow of an incompressible fluid with constant viscosity are solved in a discrete form by FIDAP. Mesh points are clustered around the catheter and along the walls, where large gradients of velocity were expected. A total of 64,500 quadrilateral elements are used for the present simulation. The transport patterns of embryos during embryo transfer are analyzed for various parameters of the catheter and the channel.

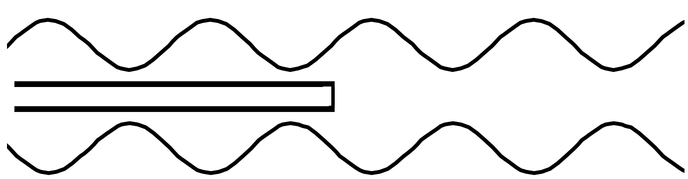

Figure 1: Schematic description of ET in the sagittal cross-section of the uterus.

RESULTS

Simulations of intrauterine fluid flow pattern during the process of ET show that the higher the injection speed, the smaller the dependence of axial propagation on the peristaltic motion. As the injection stops, the trajectories of massless particles that represent potential embryos are determined entirely by the peristalsis and the channel characteristics. When the magnitude of injection velocity is of the same order as that of wall motility, the axial displacement of the particles is significantly affected by the synchronization of the onset of fluid injection with the wall motility. At higher injection velocities the trajectories of these particles are independent of the onset timing of the injection.

DISCUSSION

The presence of the catheter in the uterine cavity changes the normal intrauterine fluid flow. The speed of injection of the embryos from the catheter controls their dispersion within the uterine cavity. At high injection speeds the embryos are transferred forward and may reach the fundus (end of the channel) within one time period. When the magnitude of the injection speed is of the same order as that of the peristaltic wave speed, the embryos trajectories are mostly dominated by the peristaltic motion of the uterine walls, which may resemble to the natural process. This study may explain some of the biomechanical aspects involved in techniques of ET that may be responsible for the low rate of implantation after successful procedures of fertilization in the laboratory.

REFERENCES

Eytan O. and Elad D. (1999). *Bull Math Biol*, **61**, 221-238.
Schoolcraft W.B. *et al*. (2001), *Fertil Steril*, **76**, 863-870.

STUDY OF POSTURAL STABILITY BY CHAOS THEORY

Sandro Fioretti (fioretti@bioma.ee.unian.it) and Alessio Scattolini
Dipartimento di Elettronica ed Automatica – University of Ancona – Ancona - Italy

INTRODUCTION

In the present research, the problem of characterizing postural stability is approached from the perspective of nonlinear dynamics and chaos theory (Yamada, 1995). "Chaotic" is a term assigned to a deterministic non-linear process which is strongly sensitive to the initial conditions and system's parameters. Particularly, the dominant (largest) Lyapunov exponent λ_1 quantifies the exponential divergence of initially close state-space trajectories and gives an estimate of the amount of chaos in a system (Wolf et al, 1985). The goal of this study was to verify if the dominant Lyapunov exponent relative to the center of foot pressure (CoP) time series is able to characterize the degree of postural stability when different bases of support and different vision conditions are considered.

METHODS

Five normal, healthy adult volunteers (25±3 years) participated in this study. We collected CoP data for 120 s using an extensimetric platform (Bertec) at a sample frequency of 100 Hz; the subjects stood barefoot, looking straight ahead at a fixed point in a quiet room with their arms relaxed at the sides. The CoP data were filtered by a 4^{th} order Butterworth low-pass filter (cut-off frequency 5 Hz). For each subject we performed six different acquisitions, one for each experimental condition: (1) eyes-open, feet together (*FT*), (2) eyes-closed, feet together, (3) eyes-open, feet 30º (*F30º*), (4) eyes-closed, feet 30º, (5) eyes-open, right foot forward 10 cm ($F_{dx}A$), (6) eyes-closed, right foot forward 10 cm. Starting from a single-dimensional measurement vector (y_i), i=1,N_s, $\mathbf{x}_i$-trajectory points in an m-dimensional embedding phase-space can be defined according to the time-delay method (Takens, 1981):

$$\mathbf{x}_i \equiv (y_i, y_{i+\tau}, \ldots, y_{i+(m-1)\tau}) \qquad i=1,\ N_s-(m-1)\tau$$

where y_i are CoP (AP or ML) data, τ is the time delay, m is the embedding dimension. Parameters τ and m have been calculated by mutual information (Fraser et al., 1986) and false-nearest-neighbors method (Kennel et al., 1992) respectively. The computation of the dominant Lyapunov exponent was performed using the algorithm proposed by Wolf et al.(1985).

RESULTS AND DISCUSSION

The optimal values for τ and m resulted 30 and 3 respectively. Table 1 shows the largest Lyapunov exponents computed for the mediolateral component (ML) of the subjects. A similar behavior was obtained for the anteroposterior component (AP) too. Repeatability has been verified on one subject (Subject-5) that performed the experimental protocol three times in three different days.

Table 1: Largest Lyapunov exponent (λ_1) for the ML component of the CoP. Subject-5 was tested three times in three different days to verify repeatability.

ML	*Eyes-open*			*Eyes-closed*		
m = 3, τ =30	*FU*	*F30º*	$F_{dx}A$	*FU*	*F30º*	$F_{dx}A$
Subject-1	0.299	0.161	0.194	0.354	0.168	0.267
Subject-2	0.292	0.168	0.289	0.317	0.225	0.306
Subject-3	0.125	0.098	0.124	0.175	0.138	0.152
Subject-4	0.138	0.114	0.247	0.274	0.168	0.318
Subject-5.1	0.243	0.169	0.208	0.331	0.221	0.314
Subject-5.2	0.212	0.183	0.196	0.298	0.241	0.269
Subject-5.3	0.229	0.174	0.189	0.281	0.197	0.225

The eyes-closed condition and the precariousness in the base of support resulted in an increment of the largest Lyapunov exponent λ_1. Being λ_1 proportional to the instability of a process, results shown in Table 1 confirm that this parameter can be assumed as an index of postural instability. Besides, the experimental condition characterized by the lower λ_1 value was relative to the eyes-open and *F30º* task, that is the most stable posture.

SUMMARY

Because of the nonlinearity of the posture system, the CoP oscillation during quite standing is a good candidate to measure the chaotic movement of stance. Since the largest Lyapunov exponent λ_1 resulted positive, the postural system can be assumed to be chaotic. With respect to other parameters of the chaos theory (like f.i. the Lyapunov spectrum) the computation of the dominant exponent is a robust procedure resulting in a parameter that is repeatable and strictly connected to the stability of the system. With respect to classical posturographic parameters the dominant exponent together with other quantifiers of chaos theory can be more directly connected to the posture control mechanisms.

REFERENCES

Yamada, N., (1995). *Human Mov. Science*, **14**, 711-726.
Wolf, A. et al., (1985). *Physica D*, **16**, 285-317.
Takens, F, (1981). *Detecting Strange Attractors in Turbulence.* Springer, Berlin, **898**, 366-381.
Fraser, A.M. and Swinney, H.L., (1986), *Phys. Rev. A*, **33**, 1134-1140.
Kennel, M.B. et al (1992*), Phys. Rev .A*, **45**, 3403-3411

ML	*Eyes-open*			*Eyes-closed*		
m = 3, τ =30	*PU*	*P30º*	$P_{dx}A$	*PU*	*P30º*	$P_{dx}A$

TEMPORAL ACTIVATION PATTERN DIFFERENCES BETWEEN THOSE WITH AND THOSE WITHOUT CHRONIC LOW BACK PAIN

Cheryl Hubley-Kozey [1] and M. Johanne Vezina [2]
[1] School of Physiotherapy, Dalhousie University, NS clk@is.dal.ca [2] Physiotherapy Department CFSU(0) HCC Ottawa ON

INTRODUCTION
Trunk stabilization through appropriate neuromuscular responses to external perturbations (McGill, 1999) and the association between decreased trunk stability and mechanical low back pain (LBP) (Cholewicki and McGill, 1996) has provided the impetus to improve therapeutic LBP exercises. Concepts such as synergistic and antagonist coactivation are deemed important neuromuscular control strategies for stabilization (Granata and Wilson, 2001). Since the electromyographic (EMG) signal is a time-varying waveform of muscle activity, quantifying the temporal activation patterns in response to a sequence of perturbations should improve our understanding of muscle coactivation. This study compared (between those with LBP and those without) EMG waveforms recorded while subjects performed a task that challenged the neuromuscular system to respond to a sequence of perturbations while maintaining a neutral spine. Karhunen-Loève (KL) Expansion reduced the waveforms and two hypotheses were tested: all muscle sites were activated with the same temporal pattern and the temporal patterns were the same between the two groups.

METHODS
Twenty-four men without LBP (CON) and 14 men with chronic LBP (> 7 weeks) gave informed consent (approved by Ethics Committee). LBP subjects filled out Roland-Morris, Oswestry and six-point pain scales. Meditrace Ag/Ag Cl surface (Graphics Control, Ca) electrodes were attached in standard locations over 7 muscle sites: right lower (LRA) and right upper rectus abdominus (URA); right (REO) and left external oblique (LEO); right erector spinae ES; right (RMT) and left multifidus (LMT). EMG signals were amplified (BP 10 - 1000 Hz, CMRR 115dB, input impedance ~ 10 Gohm) using an AMT-8 EMG system (Bortec Inc., Calgary, Ab). Subjects repeated 5 trials of an exercise performed in supine which incorporated an abdominal hollowing maneuver, followed by leg-lifting and lowering tasks, while maintaining a neutral spine position (Vezina and Hubley-Kozey, 2000). The EMG signals were digitized at 1000 Hz using a Tecmar Lab Master A to D board (12-bit resolution, Scientific Solutions Inc., Oh) and a General Basic Software Program on an IBM PC. EMG signals were full-wave rectified, low pass filtered at 6 Hz, amplitude normalized to the average amplitude (%AVG) over the exercise and time normalized to 100% from start to end of the exercise (%Time). The KL Expansion was applied to the data set of all time-normalized profiles (X=101*1330) and the weighting coefficients (WC_i) derived for each principal component pattern (PC_i) were the main dependent measures. Trial effects were tested, then two-factor (muscle and group) mixed ANOVA models tested interactions and main effects for each WC_i separately (α = 0.05) using Minitab statistical software package (11Xtra). Post hoc analyses were performed on significant results.

RESULTS
The mean age for the CON was 32 ± 8 and for the LBP was 39 ± 5 years. The mean Roland, Oswestry, pain scale scores and number of years with LBP were 4.3 ± 4, 19.4 ± 14, 1.6 ± .6 and 7.7 ± 4.8, respectively. Ninety-six percent of the variance in the waveforms was contained in 3 PCs. There were no significant trial effects ($p>0.05$). There was significant ($p<0.05$) group and muscle main effects for WC_1 and group by muscle interactions for both WC_2 and WC_3. The RMT was the only muscle site that produced significant differences between the two groups for WC_2, whereas significant differences for all muscles except ES and LMT were found for WC_3. There were no significant differences among muscle sites for the CON for either WC_2 or WC_3, whereas numerous differences were found among muscles for the LBP. The statistical differences captured the qualitative differences illustrated in the group ensemble average profiles for each muscle illustrated below.

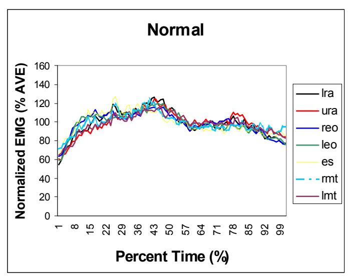

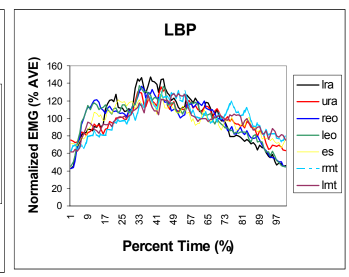

DISCUSSION AND CONCLUSION
Moderately disabled LBP subjects used different temporal activation patterns than CON subjects. The LBP subjects had greater variation in amplitude over time. As well, the differences among muscles for the LBP subjects demonstrated a lack of synergistic and antagonistic coactivation, whereas the CON group recruited all seven muscles in a coordinated manner as illustrated in the ensemble average profiles. These data provide a quantitative basis for developing a diagnostic classifier of neuromuscular control impairments associated with LBP, and in future could help direct therapeutic interventions in particular those aimed at muscle reeducation.

REFERENCES
Cholewicki J, McGill SM. Clin Biomech (1996). 11,1-15.
McGill SM. J Can Chirop Assoc (1999). 43, 71-86.
Granata KP, Wilson SE. Clin Biomech (2001).16, 650-659.
Vezina MJ, Hubley-Kozey CL. Arch Phys Med Rehab (2000). 81, 1370-1379.

ERRORS ASSOCIATED WITH CFD MODELS RECONSTRUCTED FROM 3D ULTRASOUND DATA

Alexander D. Augst[1], Dean C. Barrat[2], Alun D. Hughes[2], Simon A.McG. Thom[2], X. Yun Xu[1]
Departments of [1]Chemical Engineering, [2]Clinical Pharmacology, Imperial College, London, UK, a.augst@ic.ac.uk

INTRODUCTION

Computational fluid dynamics (CFD) is widely being used to gain insight into the complex flow patterns in human arteries. This can be done using idealized or realistic vascular geometries. For the latter an appropriate imaging technique is required to generate an accurate representation of the blood vessel. 3D X-ray angiography and magnetic resonance angiography (MRA) have been used for gathering this information in vivo, but recently 3D ultrasound (3DUS) imaging has emerged as an alternative. This study assessed the reproducibility of this procedure from image acquisition, to reconstruction to CFD simulation. A carotid artery bifurcation phantom was used for this purpose.

METHODS

An anthropomorphic carotid artery phantom (R.G. Shelly Ltd, Ontario, Canada) (Smith 1996) constructed from a set of silicon tubing in a tuning fork shape embedded in agar solution was scanned three times using 3D ultrasound. The lumen of the phantom was filled with a glycerol solution with a similar acoustic velocity to blood.
The 3D ultrasound system used was based on a standard 2D ultrasound scanner, and an electromagnetic position and orientation measurement (EPOM) device (Barratt 2001a and b). During the scan, the transducer probe was swept slowly over the open surface of the phantom. Two separate data sets were recorded: a 2D image from the scanner and the orientation and position of the ultrasound probe from the EPOM device. These sets were acquired on detection of a trigger pulse at a fixed time interval of 800ms. Digital images were then stored on the scanner and later downloaded to a PC to be analyzed off-line.
The acquired images were segmented using purpose-built software. The software was used to manually define points on the vessel wall to which a smooth cubic spline or ellipse was fitted, as appropriate. Thus, a series of cross-sectional contours was produced which define the geometry of the vessel. In order to reduce spatial artifacts in the reconstructed vessel, a cubic smoothing spline was fitted to the centroids of the contours. Each contour was then realigned so that its centroid coincided with the fitted centerline curve. The vessel surface was reconstructed by fitting smoothing splines to successive contour points (Barratt 2002). The surface splines were used by a commercial CAD/CAE package (ICEM-DDN) to produce the input file for the grid generator (ICEM Hexa). The semiautomatic Hexa tool allows the generation of a fully structured, multi-block hexagonal cell grid for the designated solver CFX-4.4.

Four CFD models were generated for the carotid bifurcation phantom studied, one from the corresponding CAD data describing its true geometry, and one based on each of the three 3D ultrasound scans.
Flow simulations were carried out for all four models under pulsatile flow conditions using a non-Newtonian, blood-mimicking fluid model. A 60:40 outflow ratio between the internal and external vessels was used which was determined from the ratio of the exit diameters of these vessels. Time-integrated parameters such as the oscillatory shear index (OSI) and time averaged wall shear stress magnitude (TAWSS) were calculated as well as instantaneous values of wall shear stress (WSS) magnitude and corresponding WSS vectors.

RESULTS AND DISCUSSION

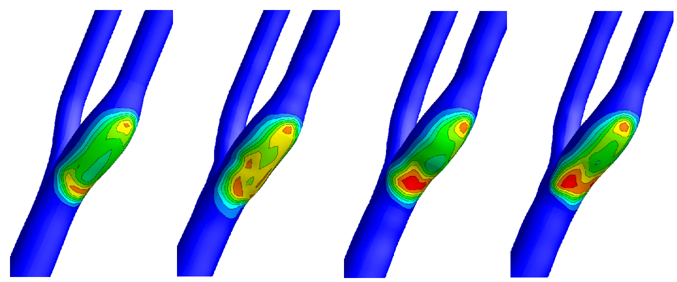

Figure 1: OSI for CAD, Scan 1, Scan 2, Scan 3.

There was good agreement between the localization of areas of high OSI in the CAD generated set (left) and the three scans. This was also true for other wall shear stress indices. This may be attributed to the high geometric accuracy of 3D ultrasound reconstructions (Barratt 2002).
RMS errors for OSI calculated along a contour at location 1.75mm proximal to the apex of the bifurcation were found to be 0.0623, 0.0262 and 0.0314 (the full range of OSI values was 0 to 0.43 (CAD)).

SUMMARY

3D ultrasound has proved to be a highly accurate imaging method. It allows the reconstruction of blood vessels suitable for highly significant CFD-modeling.

REFERENCES

Smith, R., Rutt B.(1996). *Acad Radiol*.,**3**,898-911
Barratt, D.C., Davies, A.H. et al.(2001a). *Ultrasound Med. Biol.*,**27**,957-968
Barratt, D.C., Davies, A.H. et al.(2001b). *Ultrasound Med. Biol.*,**27**,1421-1425
Barratt, D.C. (2002), Ph.D. Thesis, London University

GAIT FEATURES ASSESSMENT IN HIP OSTEOARTHRITIS AND TOTAL HIP REPLACED PATIENTS BASED ON AN AMBULATORY SYSTEM (PHYSILOG)

B. Najafi[1] , K. Aminian[1], H. Dejnabadi[1], C. Frigo[2], E. Pavan[2], A. Telonio[2], C. Trevisan[3], F. Cerati[3], E.C. Marinoni[3] , P.-F. Leyvraz[4] and Ph. Robert[1]

[1]Swiss Federal Institute of Technology (EPFL), Institute for Biomedical Engineering , Lausanne, Switzerland, bijan.najafi@epfl.ch

[2]Centro di Bioingegneria, Fnd. Don Gnocchi ONLUS-IRCCS, Politecnico di Milano, Milano, Italy

[3]Department of Orthopaedic Surgery, University of Milano Bicocca, San Gerardo Hospital, Monza, Italy.

[4]Hôpital Orthopédique de la Suisse Romande, Lausanne, Switzerland

INTRODUCTION

Osteoarthritis is the most frequent joint pathology throughout the world. Obtaining objective, dynamic and quantified data allowing the evaluation of patients' progress before and after hip arthroplasty is crucial. Gait analysis can be used for evaluating improvement in such patients, since walking is the principal human physical activity. Comprehensive gait analysis usually includes kinematics, kinetics, and electromyography. A complex instrumentation is thus required that only can be installed in a dedicated laboratory. These techniques are valuable to support clinical decisions and to evaluate the results. However, in several instances, a simplified analysis, concentrated on few selected gait parameters, can be valuable as well. Recently, we have proposed a new ambulatory system for gait analysis (Physilog) and validated its performances for normal and abnormal walking (Aminian et al., 2002). The aim of this study is to show the efficacy of Physilog system for clinical gait analysis in orthopaedics.

METHODS

Lower limbs movement during walking was measured using four miniature gyroscopes attached on each shank and thigh. Each sensor measured the angular rotation rate parallel to the mediolateral axis. The signals were digitized (12 bit) at a sampling rate of 200 Hz by a very light portable data logger (Physilog, BioAGM, CH), and stored for off-line elaboration. Spatial-temporal parameters of gait were determined according to a kinematic model. Measurements were taken from 7 patients with hip coxarthrosis (60±9 yrs old), 6 patients with total hip prosthesis (69±4 yrs old) and 8 aged-matched healthy subjects as controls (63±4 yrs old). In addition, the quality of life score (SF36) was used to evaluate pain and function in patients and control subjects Each subject was asked to perform 10 walking trials at his/her habitual pace.

RESULTS AND DISCUSSION

A total of 106, 80 and 83 gait cycles were obtained from patient with hip coxarthrosis, patients with total hip prosthesis and control subjects, respectively. Lower performances were obtained for patient with coxarthrosis compared to patient with hip prosthesis and control subjects. In particular, the range of shank, thigh and knee rotation in sagittal plane were significantly lower for coxarthrosis patients compared to other subjects. As it can be seen in Figure 1, the range of shank rotation in coxarthrosis patients was significantly different than control group ($p<0.001$). However SF36 score can not clearly discriminate between these two groups. Among the temporal parameters, the difference between initial and terminal double support showed a significant change between control and coxarthrosis patients ($p<0.01$), as well as between control and hip prosthesis patients ($p<0.05$). Moreover, stride velocity and stride length were significantly lower for coxarthrosis patients than other subjects ($p<0.05$).

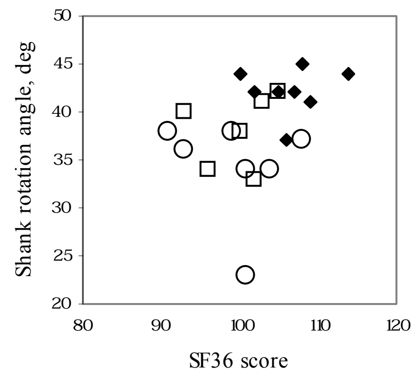

Figure 1: Range of shank rotation angle for coxarthrosis (o), hip prosthesis (□) and control (♦) subjects compared to SF36 score.

The proposed method reveals a promising monitoring tool for functional evaluation of gait improvement. It allows measuring temporal and spatial parameters of gait (stance, swing, single and double support, stride velocity, stride length, range of knee, shank and thigh rotation) during a long period of walking and supplying in this way the stride-to-stride variability. Because of its portability and its low weight, this new device interferes minimally with the usual activity of the subjects. Therefore, contrary to other devices that require laboratory setting, Physilog allows to monitor the subjects in their usual environment and provides information that is probably as close as possible to the "real-world''.

REFERENCE

Aminian K., Najafi B et al (2002), Spatio-temporal Parameters of Gait Measured by an Ambulatory System Using Miniature Gyroscopes. *J. Biomech.*,'in press'

COMPARISON OF BILATERAL AND UNILATERAL INDUCED ACCELERATION ANALYSES OF GAIT KINETICS

Patrick O. Riley[1] and D. Casey Kerrigan[2]
[1]Department of PM&R, Harvard Medical School, Boston, MA, USA
[2]Department of PM&R, U. of Virginia, Charlottesville, VA, USA

INTRODUCTION

Induced acceleration analysis is an extremely useful tool for understanding coupled dynamics of posture control and gait. Meglan (1991) stated that a whole body model was required for an induced acceleration analysis. Kepple (1997) employed such a model to analyze propulsion and support functions during single support. We have performed induced acceleration analyses using a single limb model (Riley 1999, 2001a, 2001b). In doing so, we presumed that a single limb model is complete if all external forces are taken into account. While this assumption is common in analysis of dynamic systems, it is appropriate to test its validity. We do this by comparing the stance limb hip, knee, and ankle moment contributions to propulsion and support derived from bilateral models to the results of our unilateral analysis. We hypothesize that the analysis is sensitive to constraint formulation. We further hypothesize that with appropriate use of constraints, unilateral and bilateral models will provide similar.

METHODS

Ten subjects (5 female) from our database of healthy young control subjects were selected for analysis. The average subject age, height and mass were 26.6±3.9 years, 1.7±0.1 m, and 65.0±12.9 kg, respectively. Kinematic data were sampled at 120 Hz. Force plate data were sampled at 1080 Hz. Subject specific seven segment bilateral models (right and left thigh, leg and foot segments and a pelvis/upper-body segment) were developed. Two versions of the models were developed, one with pelvic motion constrained and the second with the pelvic motion unconstrained during the model kinematic assembly process and inverse dynamic analyses. For both origin constraint formulations, two different foot constraints were imposed during the induced acceleration analyses. First, the foot position was constrained at the center of pressure during stance. Second, the foot rotation was also constrained. Thus, four different bilateral models (two forms of origin constraint and two forms of foot constraint) were evaluated. The trunk was assumed to be rotationally stabilized in space. The contributions of each limb's ankle, knee, and hip moments to propulsion and support were compared to the corresponding contributions defined by the unilateral model.

RESULTS

The models with the origin unconstrained yielded relatively poor agreement between kinematic accelerations and the summed induced accelerations. Of the two origin-constrained models, the model with both foot position and rotation constrained in foot-flat yielded better acceleration correlations than the model with only the foot position constrained. For the foot position constrained model the Pearson correlation coefficient was 0.63 for the foot position and rotation constrained model r=0.79. Qualitatively, acceleration agreement was excellent during single support, and marginal in double-support

The stance limb joint moment contributions to anterior/posterior and vertical origin accelerations of the constrained bilateral and unilateral models are comparable (Figure 1). For example, all models indicate that the hip moment contribution to anterior/posterior acceleration of the model origin is positive in early-stance and in late-swing, and negative in late-stance. Similarly, there is agreement on a strong positive late stance ankle moment contribution to origin anterior/posterior. The magnitudes of the contributions are, however, very sensitive to model formulation.

DISCUSSION

As hypothesized, the analysis was sensitive to model formulation. While the question of how complete a complete model needs to be, remains unanswered. Constraints can, it appears, be used effectively to represent unmodeled segments and forces. However, quantitative results are very sensitive to model formulation. The fundamental principle of induced acceleration analyses is that each degree of freedom influences every other degree of freedom. In seeking to validate a model for quantitative application of induced acceleration analyses, it will be best to begin with a model that represents as many of the body's degrees of freedom as possible (Riley 1990, Meglan 1991, Krebs 1992, Hutchinson 1994).

REFERENCES

Hutchinson et al. 1994 IEEE Trans Rehab Eng; 2: 49-56.
Kepple et al. 1997 Gait & Posture, 6: 1-8.
Krebs et al. 1992 Physical Therapy; 72: 505-14.
Meglan. 1991 Thesis, Ohio State University.
Riley et al. 2001a Journal of Biomechanics; 34: 197-202.
Riley, Kerrigan. 2001b Clinical Biomechanics; 16: 681-7.
Riley, Kerrigan. 1999 IEEE Trans Rehab Eng; 7: 420-6.
Riley et al. 1990 Journal of Biomechanics; 23: 503-6.

ACKNOWLEDGMENTS

This work was supported by the Selby Collin Davis Foundation and by the Milton Fund, HMS. Additional support was provided by NIH-K24-HD01351.

Figure 1. Bilateral and Unilateral Model contributions to A/P acceleration.

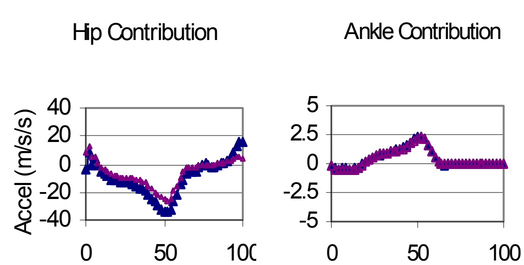

SONOMICROMETRIC MEASUREMENTS OF EYE DISPLACEMENTS

William J. Hurst, Joseph M. Cormier and Stefan M. Duma
Impact Biomechanics Laboratory, Virginia Tech, Blacksburg, VA Duma@vt.edu

INTRODUCTION

Every year there are over 2.4 million reported cases of eye injuries in the United States, and of these injuries, 30,000 result in permanent vision loss in at least one eye (Luder, 2000). While many researchers have attempted to investigate the fundamental injury mechanisms of eye trauma, there is a void of research that accurately quantifies the amount of stress and strain experienced by the eye during an impact event. Many different approaches have been attempted to measure the response of the eye to impact loading, including high-speed photography, scanning laser tomography, and ultrasound biomicroscopy; however, these methods do not accurately measure the response of the eye to deformation in both time and three-dimensional space.

Sonomicrometry allows for real-time three-dimensional measurements to be obtained. This technique allows for sampling frequencies of over 6.5 kHz with a 0.015mm resolution. Also, the piezoelectric transducer crystals used may be as small as 0.7mm in diameter. Sonomicrometric transducers have been used in various other types of medical biological studies including: length measurements of operating skeltal muscles, tendons, cardiac muscle, and respiratory tissues (Kamel, 2001). The purpose of this study is to determine the if sonomicrometry may be used to measure the dimensions of the eye.

METHODS

For this study two transducer configurations were tested: an equitorial configuration and a cornea to optic nerve configuration. In both configurations peizoeletric transducers were placed on diametrically opposite ends of the globe (Figure 1). Two compression plates were used to compress the eye along the axis being measured. Attached to these plates was a linear voltage differential transformer (Mitutoyo, Japan), which measures the distance between the plates, and two sonomicrometer transducer crystals (Sonometrics, London, Ontario, Canada), which measure the axial length of the eye.

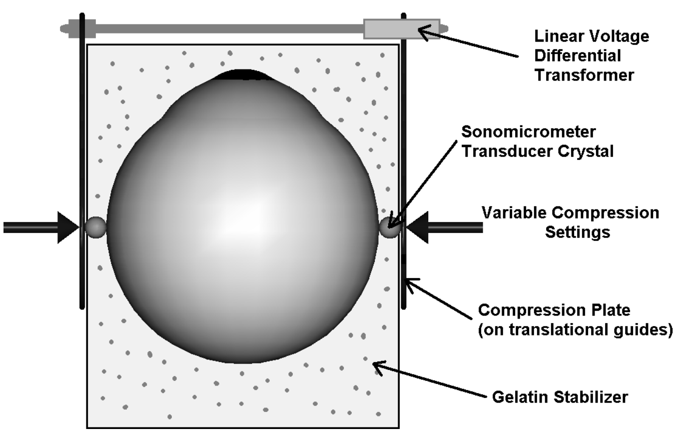

Figure 1: Test setup for equatorial configuration.

The eye was compressed to different levels ranging from 0% to 36% of the original axial length. At each level, measurements were recorded from both sources.

RESULTS AND DISCUSSION

Comparing the data shows that there are small errors (maximum error of 0.82%) that occur with the use of sonomicrometry in this experiment (Table 1). Although these errors exist, they are very small and do not significantly effect the precision of the measurements. The results do not indicate any significant increase in error based on the configuration. This study was conducted using simplified configurations that may be used to measure distortions of the eye. Future research will be done to evaluate the ability to perform three-dimensional measurements.

Table 1: Summary of error data obtained from comparing the linear voltage differential transformer data and the sonomicrometry data. The maximum error values are indicated in bold type.

	Sonomicrometry Measurement (mm)	Compression Ratio (%)	Error	
			(mm)	(%)
Equatorial Configuration	22.88	0	0.04	0.19
	21.88	4	0.10	0.45
	20.88	9	**0.14**	0.65
	19.88	13	0.11	0.58
	19.00	17	0.07	0.35
	17.88	22	0.08	0.47
	16.88	26	0.12	**0.70**
	15.75	31	0.07	0.41
	14.75	36	0.03	0.17
Cornea to Optic Nerve Configuration	22.75	0	0.03	0.13
	21.75	4	0.02	0.07
	20.75	9	0.07	0.34
	19.75	13	0.04	0.18
	18.75	18	0.08	0.42
	17.75	22	0.04	0.22
	16.63	27	0.10	0.63
	15.50	32	0.10	0.61
	14.63	36	**0.12**	**0.82**

REFERENCES

Kamel, K.S., Mazer, C.D. (2001). *Critical Care Medicine*, **29**, 344-350

Luder, G.T. (2000). *J. Opthalmology*, **107,** 1472-1475

ACKOWLEDGEMENTS

Tissues supplied by Old Dominion Eye Foundation, Roanoke, VA

IS ACTION OF MEDIAL QUADRICEPS ALONE ADEQUATE TO STABILIZE THE KNEE AGAINST VALGUS LOADS?

Yasin Y. Dhaher[1] and Leonard E. Kahn[2]
[1,2] Sensory Motor Performance Program, Rehabilitation Institute of Chicago, Chicago, IL, USA, y-dhaher@northwestern.edu
[1] Dept. of Phys. Med. & Rehabilitation, Northwestern University Medical School, Chicago, IL, USA
[2] Dept. of Biomedical Engineering, Northwestern University, Evanston, IL, USA

INTRODUCTION
Upon examination of knee joint geometry, the medial moment arms of the vastus medialis obliquus (VMO) and longus (VML) in the coronal plane create an expectation for both muscles to generate adduction moments in the joint. Such actions in the coronal plane have implications in medio-lateral joint stability. However, this simple assumption has never been tested analytically or experimentally. We sought to determine the torque resulting from activating each of these muscles independently.

METHODS
A mathematical model of the patello-femoral joint was introduced using a basis-function method to accurately represent the contact surfaces as C^2 continuous functions. In the model, which was derived from theVisible Human right knee joint (Visible Productions, Ft. Collins, CO), the quadriceps were represented as five separate forces (figure 1) (Dhaher et. al, 2000 and Dhaher & Kahn, 2001). As the model solves patellar equilibrium for a given tibio-femoral joint orientation and relative quadriceps forces, we examined the resulting joint torques when VMO and VML were independently activated with no force contribution from the other vasti (Thiranagama, 1990).

Corroboration of the computational results was achieved *in vivo* by stimulating the same muscles. Four subjects participated and had their shanks fixed to a beam at the end of a 6-axis load cell. The VMO and VML were selectively stimulated using intramuscular electrodes and the resulting joint torques were recorded.

Figure 1: Graphical representation of the contact surfaces, coordinate systems, and muscle and tendon forces in the model.

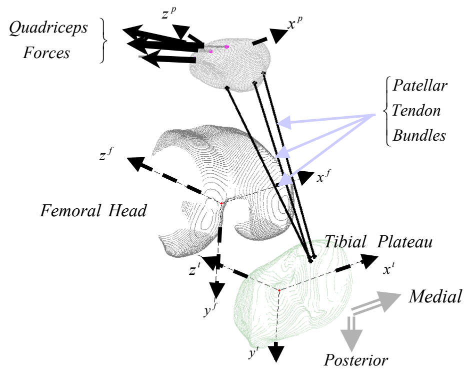

RESULTS AND DISCUSSION
Contrary to what was expected, independent activation of the VML and VMO in the model produced abduction moments at the knee. The abduction moment ranged increased from approximately 15% to 40% of the extension moment with increasing knee flexion angle (figure 2). Similar results were obtained *in vivo*, as shown in the figure.

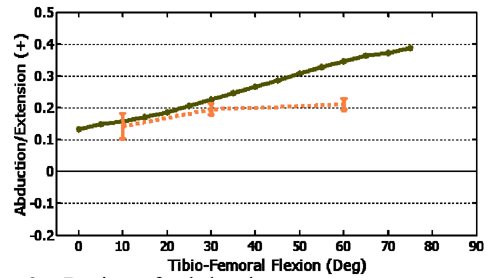

Figure 2: Ratio of abduction torque to extension torque created by the VMO in the model (solid) and *in vivo* (dashed) at multiple flexion angles

SUMMARY
The effect of the individual medial quadriceps muscles on tibiofemoral joint torques was examined in a novel 3-D computational model. Our model results were validated by *in vivo* stimulation of the same muscles. In both model and experimental data, the medial extensors produced torque to abduct the shank (~20% of flexion torque), which is contrary to what should happen according to simple examination of the joint. It is likely that this counterintuitive result arose from the complex interaction between the patellar and femoral contact surfaces. Although significant, the selective role of the medial extensors in generating the appropriate stabilizing torque in secondary directions is questionable. Our data suggest that in the presence of an abduction torque applied to the knee, the individual medial quadriceps cannot produce the necessary adduction torque to stabilize the knee. Co-activation of all muscles (medial and lateral) with medial muscles exhibiting larger responses is an alternative strategy that may be mechanically more favorable (Dhaher et al, 2002).

REFERENCES
Dhaher, Y.Y. et. al (2000). *J. Biomechanics*, **33**, 901-909
Dhaher, Y.Y., Kahn, L.E. (2001). *J. Biomech. Eng.*, in review
Dhaher, Y.Y. et. al (2002). *J. Biomchanics*, in review
Thiranagama, R. (1990). *J. Anatomy*, **170**, 193-198

ULTRASOUND WAVE PROPAGATION IN POROUS MEDIUM. APPLICATION TO CANCELLOUS BONE.

Luis Cardoso[1], Frédéric Teboul[2], Christian Oddou[1], and Alain Meunier[2]
CNRS ESA 7052, Biomécanique et Biomatériaux Ostéo – Articulaires,
[1]LMP Paris 12, 61 av. du Général de Gaulle, 94010 Créteil, [2]LRO Paris 7, 10 av. de Verdun, 75010 Paris.

INTRODUCTION

Bone pathologies such as osteoporosis lead to drastic changes in the architecture, mineral content and mechanical properties of cancellous bone. Non invasive characterisation of such tissues can be performed using ultrasonic methods. Indeed, the acoustic waves properties are affected by the spatial orientation, complexity and polyphasic nature of this material. Biot's theory of propagation of elastic waves in a fluid saturated porous solid (Biot 1956), has been used in order to evaluate the ultrasound propagation in bovine cancellous bone (Williams 1992). In such media, acoustic waves were shown to propagate following two modes with different velocities (Hosokawa and Otani 1997-98). This parametric study, leading to the variation of the two waves velocities as function of both porosity and orientation of the structure, is shown to be in fair agreement with experimental in vitro tests associated with attenuation measurements.

MATERIALS AND METHODS

14 bovine and 60 human trabecular bone samples were tested in vitro, using an immersed transmission method with a pulsed excitation. The parallel-faced cubic samples of about 1cm^3 volume, were machined from different cancellous specimens of bovine or human femoral heads and from femoral and tibial human condyles. Broadband ultrasound transducers at central frequency of 2,25MHz (6mm OD) were used. Wave velocities were measured using a conventional transmission technique.

EXPERIMENTAL RESULTS

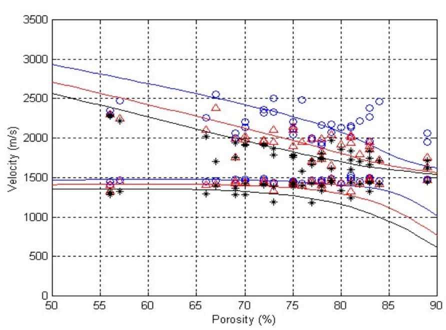

Figure 1.

The two predicted longitudinal propagation modes were observed in both human and bovine cancellous bone. Due to the limited size of the available samples, both waves generally superimposed and were separated in the frequency domain using digital filtering. Figure 1 shows the measured fast and slow waves in three orthogonal directions obtained when testing 38 human femoral head specimens as a function of bone porosity. It is clear that for a single homogenous specimen (with a unique porosity) the measures of acoustic velocities are orientation dependant. Therefore, the elastic properties of cancellous bone cannot be accurately predicted with the sole value of the local porosity. For this reason, a theoretical model based on Biot's Theory was developed and applied to these data. This model takes into account a Structural Parameter (SP) based on trabecular orientations. From the model, this parameter was computed for each specimen and each measured direction. Figure 2 shows the fast and slow wave velocities measured on bovine specimens as a function of both porosity and Structural Parameter. The figure clearly show that each direction corresponds to a well defined value of SP that is independent from the specimen's porosity. Solid lines presented in figure 1 corresponds to the same theoretical model, using an averaged SP value for each direction.

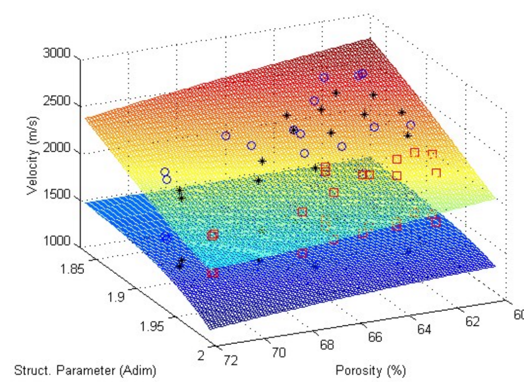

Figure 2.

DISCUSSION AND CONCLUSION

In such in vitro tests, the two longitudinal propagation modes predicted by the model were clearly observed and quantified in both human and bovine cancellous bone. The measured slow wave velocities were always of the same order of magnitude as the sound velocity in the aqueous fluid phase alone. On the contrary the measured fast wave velocities demonstrated a high range of variation depending upon both the degree of porosity and the orientation of the trabecular structure with respect to the ultrasound beam direction.

Either in the experimental measurements or in the theoretical data for highly porous samples, the slow wave attenuation could be lower than the attenuation of the fast wave. This finding may be a cause of concern when considering in-vivo measurements of very osteoporotic specimens for which the only measurable velocity could be related to the propagation of the slow wave mode, thus characterising more the fluid phase than the solid one.

REFERENCES

Biot, M. A. J. Acoust Soc Am 28:166-178 & 179-191;1956.
Williams, J. L. J Acoust Soc Am 91:1106-1112;1992.
Hosokawa, Otani. J Acoust Soc Am 101:558-562; 1997.
Hosokawa, Otani. J Acoust Soc Am 103:2718-2722; 1998.

BACKPACK LOADS CARRIED BY SCHOOL CHILDREN

Jeffery Morley, Mary C. Verstraete and Shawn Robinson
Department of Biomedical Engineering, The University of Akron, Akron, OH 44325-0302
mary@biomed.uakron.edu

INTRODUCTION

The popularity of backpacks among school age children in the United States has increased significantly over the past few decades. Public media (USA Today 2000, US News & World Report 1999, Business Week 1999), in addition to several scholarly sources (Negrini, et al. 1999, Grimmer, et al. 1999, Hong and Brueggemann 2000, Pascoe, et al. 1997, Wang, et al. 2001), have recently highlighted the possible risks to children carrying heavy loads in their backpacks to and from school. The adolescent spine differs from the adult spine in that it represents structures in variable stages of growth. Chronic conditions may predispose children to further problems later in life. The purpose of this study was to determine the average load carried by children aged 12-13 during a typical school day.

METHODS

Six junior high/middle schools in the greater Akron area were contacted to assist in evaluating the loads carried in backpacks to and from school. Letters were sent home to parents requesting their permission to weigh their child, their child's backpack and to allow their child to answer a few questions about their age, potential back and shoulder pain, and participation in sports. Once permission was received, the investigators made an appointment with the principal of the school to visit the school on an unannounced day to measure these variables.

A physicians scale, accurate to 0.5 lb, was brought to the school to ensure that all weights were consistently measured. The investigators set up the scale in a private setting designated by each school to avoid the effects of peer pressure and other potential psychological factors. Each student was then brought to this location with their backpack loaded with a "typical" amount of books and materials that they would normally carry to and from school. The child was weighed and their height was measured without their backpack and then the pack was weighed separately. The child was then asked several questions: 1) their age, 2) their gender, 3) whether they experience any pain in their back or shoulders (if they answered "yes", they were asked to discuss the frequency and type), 4) if they participated regularly in type of sports or exercise. All data were recorded anonymously.

RESULTS AND DISCUSSION

Of the six schools that agreed to participate, 111 students were included in the study. Of these students, 69 were female (mean weight 52.5 kg and mean height 157.0 cm) and 42 were male (mean weight 53.8 kg and mean height 160.1 cm). Table 1 presents the results of comparing the weight of the student and the weight of their backpack. Table 2 lists the results of the questions regarding existing pain in the shoulders or back.

Table 1: Percent of Body Weight Carried in Backpacks

	0%-10%	10%-20%	20%-30%	30%-40%
Girls	11	42	15	1
Boys	12	21	10	1
Total	23	63	25	2

Table 2: Pain Reported by the Subjects

	Pain	Neck Pain	Shoulder Pain	Back Pain	Other
Girls	43	2	34	17	2
Boys	21	1	14	12	1
Total	64	3	48	29	3

Of the 111 children studied, 21% of them carried between 0 and 10% of their bodyweight, 57% carried between 10 and 20%, and 23% carried between 20 and 30%. A total of 58% of these students also reported some type of existing pain in their neck, shoulders or back. These numbers indicate that a potential connection exists between the amount of load carried in the backpack and the occurrence of pain in these students.

SUMMARY

The results of this study show that school children, age 12-13, are carrying between 0 to 40% of their body weight in their backpacks to and from school on an average day. Most of the students also indicated that they typically wore their backpacks using only one of the two shoulder straps, thus distributing this weight in an asymmetric manner to primarily one shoulder. The results of this study will be used to provide input to an ongoing research project investigating the actual forces and moments incurred on the lower back due to this applied load.

REFERENCES

Grimmer, K.A., et al. (1999). *Spine*, **24**(21), 2262-2267.
Hong, Y., Brueggemann, G.P. (2000). *Gait and Posture*, **11**, 254-259.
Negrini,S., et al. (1999). *The Lancet*, **354**, 74.
Pascoe, D.D., et al. (1997). *Ergonomics*, **40**(6), 631-641.
Wang, Y., et al. (2001). *Ergonomics*, **44**(9), 858-869.
Business Week, (Aug. 16, 1999), (3642), 115.
USA Today (Nov 2000), **129**(2666), 6.
US News & World Report, (Oct 11, 1999), **127**(14), 17.

PATTERN OF ARTICULAR CONTACT AT THE TIBIO-TALAR JOINT IN PASSIVE FLEXION

Federico Corazza[1,3], Rita Stagni[2,3], Alberto Leardini[3], Vincenzo Parenti Castelli[1]
[1] DIEM - Università degli Studi di Bologna, Italy, federico.corazza@ior.it
[2] DEIS – Università degli Studi di Bologna, Italy
[3] Movement Analysis Laboratory, Istituti Ortopedici Rizzoli, Bologna, Italy

INTRODUCTION

The knowledge of the articular contact patterns at the human tibio-talar joint (Ti-Ta) is fundamental for the understanding of the joint kinematics and mechanics and to enhance biomechanics-based clinical treatments. Most of the contact area estimates from the literature are limited by the invasive measuring techniques. Studies have also rarely reported areas on the tibial mortise, and no studies have been performed in unloaded conditions. Motion analysis has successfully been used to assess these areas without any interference with the frictionless articulation (Kura et al., 1998). Clinical treatments, such as arthrodesys, arthroplasty and ligament reconstruction, would benefit from the results of this work. In the present study, the pattern of contact of the Ti-Ta joint during passive flexion is reported using a novel technique based on Roentgen Stereophotogrammetric Analysis (RSA) and a 3D digitiser.

METHODS

Passive flexion tests (Leardini et al., 1999) were performed on three anatomical preparations from amputation. RSA was used to reconstruct the position of four tantalum balls embedded in the tibia and in the talus, at several different positions of unconstrained passive flexion. This provided a discrete representation of the ankle joint neutral path (Leardini et al., 1999). After RSA, each specimen was dissected, and a large number of points was digitised on the trochlea tali (TTa) and on the tibial mortise (TiM). Digitisation also of the tantalum balls allowed the reconstruction of these points in a common reference coordinate system, at each of the different flexion positions. The articulating surfaces were then modelled by thin plate splines, delimited by standard B-splines interpolating the border points. The distance between the modelled points of the TTa and TiM was mapped on the two articular surfaces, for each reconstructed joint position. A distance threshold was set to detect the closest areas for each specimen. The position of the contact area centroid was calculated with respect to the three principal axes of inertia of each modelled surface.

RESULTS AND DISCUSSION

The contact area moved anteriorly on both articular surfaces with dorsiflexion (Do). Taken x as the posterior-anterior principal inertia axis, and y as the medio-lateral (see Fig. 1), the contact area was located in the most posterior part of the surfaces at maximum plantarflexion (Pl) (mean TiM x: -60%). For increasing angles of Do, the contact area moved to the lateral zone in all the specimens, and reached its most anterior position at maximum Do (mean TiM x: +29%). These findings are partially supported by the literature (Kura et al., 1998; Driscoll et al., 1994), although obtained in different conditions. The area was clearly found to be smallest at 50% Do (mean TiM CA: 3%), largest at 50% Pl (mean TiM CA: 13%) (see Tab. 1), whereas more variable results have been reported previously (Kura et al., 1998).

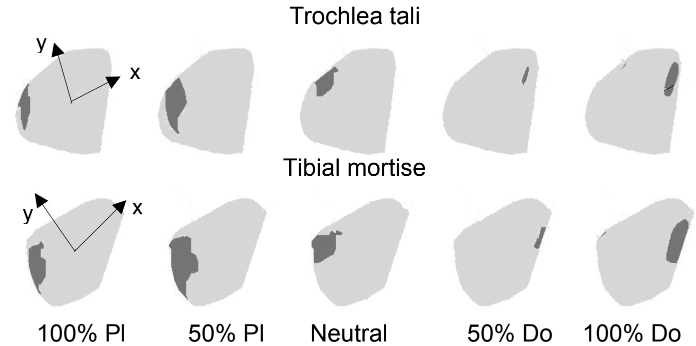

Figure 1: Contact areas on the articular surfaces, both seen from above, for five flexion positions in one typical specimen.

	Do+/Pl- (%)	*Specimen A*			*Specimen B*			*Specimen C*		
		CA%	*x%*	*y%*	*CA%*	*x%*	*y%*	*CA%*	*x%*	*y%*
TTa	-100	4.4	-78.6	34.8	12.8	-62.1	28.6	9.1	-62.9	47.3
	-50	9.0	-64.4	36.0	9.4	-49.2	45.3	9.0	-53.5	54.5
	Ne	4.2	-40.7	66.5	6.9	-42.7	50.4	5.0	-22.9	75.3
	50	0.8	65.1	22.7	5.4	-27.7	53.8	1.5	44.5	79.6
	100	5.0	70.5	13.4	4.6	-22.0	54.7	4.9	65.8	35.1
TiM	-100	8.3	-70.9	39.2	19.0	-40.3	37.4	11.4	-68.7	19.5
	-50	15.4	-63.3	39.2	14.5	-29.3	46.5	9.4	-68.1	25.7
	0	8.5	-47.3	67.1	8.6	-27.5	53.0	4.4	-49.5	50.6
	50	1.7	61.0	-40.3	5.9	-25.9	55.8	1.4	37.1	72.4
	100	8.7	50.5	-33.8	5.9	-27.0	56.5	5.6	62.6	22.6

Table 1: Normalized values of contact area (CA) and contact centroid in the principal axis coordinates (x,y).

SUMMARY

These findings provide a useful characterization of the contact pattern at the Ti-Ta articulation. A well defined pattern of anterior motion of the contact area on the tibial mortise supports the hypothesis that the ankle behaves as a mechanism in passive flexion.

REFERENCES

Driscoll, H.L., et al. (1994). *J.Am.Pod.Med. Ass.*, **84**, 491-498.
Kura, H., et al. (1998). *Clin. Biomech.*, **13,** 365-370.
Leardini, A., et al., (1999). *J. Biomech.*, **32**, 111-118.

CROSSLINKING DENSITY INFLUENCES CHONDROCYTE MORPHOLOGY AND METABOLISM IN MECHANICALLY LOADED PEG HYDROGELS

Stephanie J. Bryant[1], Kristi S. Anseth[1,2], Tina T. Chowdhury[3], David A. Lee[3], and Dan L. Bader[3]
[1]Department of Chemical Engineering, and the [2]Howard Hughes Medical Institute, University of Colorado, Boulder, CO 80309, USA
[3]IRC in Biomedical Materials and Medical Engineering Division, Department of Engineering, Queen Mary, University of London, Mile End Road, London E1 4NS, United Kingdom, d.l.bader@qmw.ac.uk

INTRODUCTION

From a tissue engineering perspective, photopolymerizable hydrogels based on poly(ethylene glycol) are attractive for their ability to be gelled *in situ* with controlled architecture and desired macroscopic properties. However, in designing an *in situ* forming cell-scaffold, it is important to understand the impact of mechanical loading on cells within the scaffolds. During normal activity, articular cartilage is subject to mechanical loading, which causes cell deformation and alters biosynthesis within the tissue. Therefore, this study tests the hypothesis that changes in hydrogel properties, in the form of the crosslinking density, can influence the morphology and the metabolism of seeded chondrocytes in response to loading.

MATERIALS AND METHODS

Construct Preparation. Bovine articular chondrocytes were isolated from the metacarpalphalangeal joints of 18-month old steers via a sequential enzyme digestion with pronase (700 U/ml, Sigma) and collagenase (300 U/ml, Sigma). Poly(ethylene glycol) dimethacrylate (PEGDM, MW=3000) was synthesized [Sawhney,1993] and the PEGDM macromer was dissolved at concentrations from 10-20% (w/w) in PBS or water. Cytocompatible photoinitiating conditions 0.05% (w/w) and 0.012% (w/w) (I2959, Ciba Geigy), for 10 and 20% PEGDM gels, respectively, were employed [Bryant,2000]. The isolated chondrocytes were suspended in the macromer/initiator solution to a final concentration of $50x10^6$ cells/ml and polymerized using 365 nm light at an intensity of ~2 mW/cm^2 for 10 minutes.

Cell Morphology . A confocal laser scanning microscope was used to visualize and measure cells embedded in PEG hydrogels following previously described techniques [Knight,1996]. Briefly, chondrocytes in cell-hydrogel constructs of rectangular shape (4x4x3 mm^3) were stained with 5μM Calcein-AM (Molecular Probes), a viable fluorescent probe. Using a fabricated test rig [Knight,1996], the cell-hydrogel constructs were compressed from 0% to 20% strain and 50 cells/construct (4 constructs) were visualized at 0 and 20% gel strain. A horizontal image through the center of the cell was obtained, and the cell diameters were measured parallel (X) and perpendicular (Y) to the axis of compression. The deformation index (DI) is defined as X/Y.

Cell Metabolism Cell-hydrogel constructs of cylindrical shape (4 mm diameter, 5 mm height) were incubated in culture for 24 hours. The constructs were placed in a specially designed cell-straining apparatus [Lee,1997] and subjected to compressive strains from 0% to 15% in a sinusoidal waveform at a frequency of 1 Hz for 48 hours. The constructs were removed and digested in a papain solution (5μl/ml papain (Sigma, P3125), 10 mM l-cysteine-HCl, 100 mM phosphate, and 10mM EDTA at pH 6.3) for 15 hours at 60°C, and the glycosaminoglycan content [Farndale,1982] and total DNA content [Rao,1992] were measured. Statistical analysis was performed using a Student's t-test with a confidence level of 0.05 unless otherwise specified.

RESULTS AND DISCUSSION

By varying the PEGDM macromer concentration, a range of crosslinking densities (ρ_x) is obtained to yield gels with the same chemistry but different network structures. PEGDM gels were prepared from solutions containing 10 and 20% PEGDM macromer, which produced gels of different ρ_x values. In addition, ρ_x influences many of the macroscopic gel properties. For example, an increase in ρ_x results in a decrease in water content, but an increase in gel mechanics.

The DI of chondrocytes was measured in the unstrained and strained states of the two seeded PEG gels (Table 1). At 0% gel strain, the mean DI for both systems was approximately unity, suggesting rounded morphology characteristic of differentiated chondrocytes. When the gels were subjected to 20% strain, the DI decreased in both systems, but interestingly, the cells embedded in the more tightly crosslinked gel deformed more ($p<0.001$) than the cells within the more loosely crosslinked gel. These data suggest that the overall macroscopic differences, which exist between the gel systems, may lead to variations in the local strain adjacent to the cells.

Table 1. DI for chondrocytes seeded in PEG hydrogels with two crosslinking densities after a 24 hour culture period (mean±SD (N=200)).

	10% PEGDM	20% PEGDM
$DI_{0\% \text{ gel strain}}$	0.99 ± 0.08	0.99 ± 0.08
$DI_{20\% \text{ gel strain}}$	0.80 ± 0.10	0.72 ± 0.11

Table 2. GAG content (μg GAG / μg DNA) for constructs subjected to a 15% dynamic strain at 1 Hz (mean±SE (N=24)).

	10% PEGDM	20% PEGDM
Unloaded	3.6 ± 0.2	1.7 ± 0.09
Loaded	3.4 ± 0.1	1.5 ± 0.06

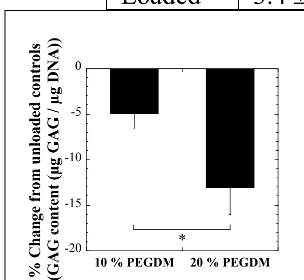

Figure 1. The percentage change from unstrained controls for GAG content in PEG gels (mean ± SE (N=24)) *p<0.05

When the cell-scaffolds were dynamically loaded for a 48 hour period during 72 hours of culture, the GAG content was statistically lower in the more highly crosslinked system in both the unloaded and loaded state. In addition, GAG production was inhibited in both systems by the application of strain, but the percentage change from unloaded to loaded was statistically greater in the more crosslinked gel. Therefore, during the first three days of culture when limited matrix has been produced, crosslinking density appears to play an important role in the mechanotransduction pathways in chondrocytes photo-encapsulated in PEG hydrogels.

ACKNOWLEDGMENTS

The authors would like to thank NIH for their support through a research grant (R01 DE12998), and NSF and GAANN fellowships to SJB. Support is also provided by the EPSRC, UK.

REFERENCES

Bryant, S. et al. (2000). *J Biomater Sci Polym Ed*,**11**,439-57.
Farndale, R.W. et al. (1982). *Connect Tissue Res*,**9**,247-8.
Knight, M. et al. (1996). *Cell Eng*,**1**,97-102.
Lee, D., et al. (1997). *J Ortho Res*,**15**,181-8.
Rao, J. et al. (1992). *Anal Biochem*,**207**,186-92.
Sawhney, A.S. et al. (1993). *Macromolecules*,**26**,581-7.

MUSCULAR RESPONSE OF THE SWING LIMB AND ARMS DURING AN UNEXPECTED SLIP

Daniel S. Marigold[1], Allison J. Bethune[2], and Aftab E. Patla[2]

[1]Rehabilitation Research Lab, Graduate Program in Neuroscience, University of British Columbia, Vancouver, British Columbia, Canada, dsmarigo@interchange.ubc.ca
[2]Gait and Posture Lab, Department of Kinesiology, University of Waterloo, Waterloo, Ontario, Canada

INTRODUCTION

Falls among the elderly are a major source of death and morbidity (Hsiao & Robinovitch, 1998). Slipping is a common cause of these falls (Pai & Iqbal, 1999). Reactive recovery responses are crucial in maintaining dynamic stability following unexpected destabilizing events such as a slip and accordingly, it is important to understand the nature of these responses. The role of the swing limb (i.e. the unperturbed limb) in the recovery response to an unexpected slip is not well known. The importance of this limb is reflected in the recent finding that the critical time for regaining stability following the onset of slip is during the first double support phase of the gait cycle (You et al., 2001).

The purpose of this study was to investigate the role of the swing limb in the reactive recovery response following an unexpected slip. The muscular activity of this recovery response is described here.

METHODS

Ten (6 female and 4 male) healthy, young adults from the University of Waterloo participated in this experiment. A slip was induced when participants stepped directly on a set of steel rollers with their right foot. The rollers (static & dynamic coefficient of friction equal to 0.04 & 0.03, respectively) were mounted on a force plate, sat flush in the middle of a 6.5 m long, 3.8 cm elevated wooden walkway and were visible at all times. Each participant travelled along the walkway a total of 20 trials. In each trial, participants were not aware of the rollers' surface (locked/no slip or unlocked/slip). At a random trial after the initial 10, 6 consecutive slips were induced.

Bipolar surface electromyography (EMG) electrodes were used to record the muscle activity of the unperturbed limb (i.e. the swing limb that did not make contact with the rollers) including rectus femoris (RF), biceps femoris (BF), tibialis anterior (TA), and the medial head of gastrocnemius (MG). In addition, bilateral gluteus medius (RGM and LGM), erector spinae (RES and LES), and deltoid (RD and LD) muscles were recorded. All raw EMG analog signals were sampled at 1200 Hz for 6 seconds. For analysis, the raw EMG signals were full-wave rectified and low-pass filtered at 10 Hz with a custom program. Each muscle response profile for a slip trial was determined by subtracting the ensemble average profile of the control trials from the slip trial. The control trials used were the unperturbed trials prior to the first slip. A one-way (Muscle) repeated measures ANOVA on muscle onset latency was performed for the first slip trial. Post hoc analysis consisted of Tukey's HSD test with significance set at $p<0.05$.

RESULTS AND DISCUSSION

The ten muscles showed a significant difference in onset latency (Figure 1) in response to the first slip trial ($F_{9,79} = 5.103$, $p < 0.001$). Post-hoc analysis revealed that MG was significantly delayed compared to all muscles except LGM and RGM. Furthermore, RGM was significantly delayed compared to all muscles except MG and LGM. The remainder of the muscles were activated in the range of 140 – 162 ms following the onset of the first slip trial (see Figure 1).

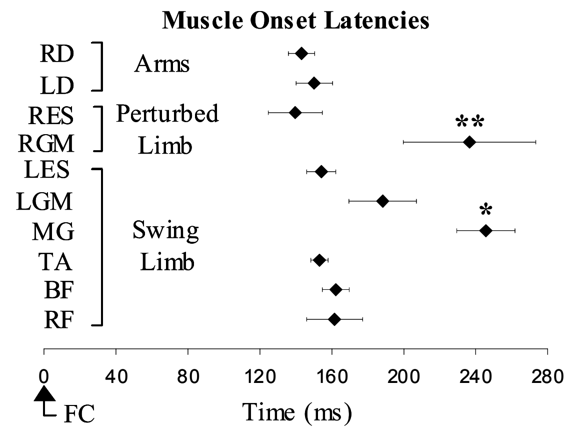

Figure 1: Muscle onset latencies in response to an unexpected slip during locomotion. FC = foot contact on rollers. Significant at $p<0.05$ compared to all muscles except LGM & RGM (*) and to all muscles except MG & LGM (**).

The muscle onset latencies for the swing limb were slower than previously found in responding to an unexpected slip during locomotion (Tang et al., 1998). However, it is evident that interlimb coordination is crucial in maintaining dynamic stability following an unexpected slip (Marigold & Patla, 2002; Tang et al., 1998). The pattern of muscle activity observed serve specific functions: the musculature is activated rapidly to allow the limb to quickly land and provide stability. This was demonstrated by 70% of the participants as they briefly terminated swing before continuing the limbs' trajectory. Furthermore, the fact that the arm muscles responded quickly suggests they are vital in recovering balance as supported by recent data (Marigold & Patla, 2002). The arms serve to control body center of mass by shifting it more anteriorly after it is forced backwards by the slip.

ACKNOWLEDGEMENTS

This study was supported by a grant from NSERC, Canada.

REFERENCES

Hsiao, E.T., Robinovitch, S.N. (1998). *J Biomech*, **31**, 1-9.
Marigold, D.S., Patla, A.E. (2002). *J Neurophysiol*, in review.
Pai, Y-C., Iqbal, K. (1999). *J Biomech*, **32**, 779-786.
Tang, P-T. et al. (1998). *Exp Brain Res*, **119**, 141-152.
You, J-Y. et al. (2001). *Clin Biomech*, **16**, 167-173.

CHANGES IN PLANTAR FORCE, AREA AND PRESSURE WITHIN A SINGLE SESSION USING AN IN-SHOE MEASUREMENT SYSTEM

Timothy A. Hanke and David Tiberio
Department of Physical Therapy and Department of Kinesiology - Human Performance Laboratory
University of Connecticut, Storrs, CT, USA, timothy.hanke@uconn.edu

INTRODUCTION

Evaluating a variety of in-shoe pressure-relief materials with the F-Scan System (Tekscan Inc., Boston, MA, USA) revealed decreased peak plantar forces over subsequent trials during a single experimental session. This could not be explained by subject performance as all subjects used different sensors and were paced at their preferred walking speed on a treadmill. To further understand the consistency of in-shoe sensors and their plantar force measurements during walking (cf., Rose et al, 1992), we describe changes in force, area and contact pressure using a set of in-shoe sensors for one experimental session.

METHODS

One healthy 49 y/o male performed treadmill walking at a self-selected speed (2.8 miles/hr.). F-Scan sensors were equilibrated using an air bladder system and calibrated using the F-Scan software (v.4.21). Eleven trials were collected: s1 with sensors (baseline); m2-9 walking with sensors and a PORON® material (Rogers Corp., Rogers, CT, USA) replaced each trial with a new set of the same material to avoid temperature or wear-related changes; s10 with sensors only; and s11 with sensors after re-calibration. Data was collected for 15s at 100Hz after 30-45s of walking.

RESULTS AND DISCUSSION

Figure 1: Plantar force and area decrease with time.

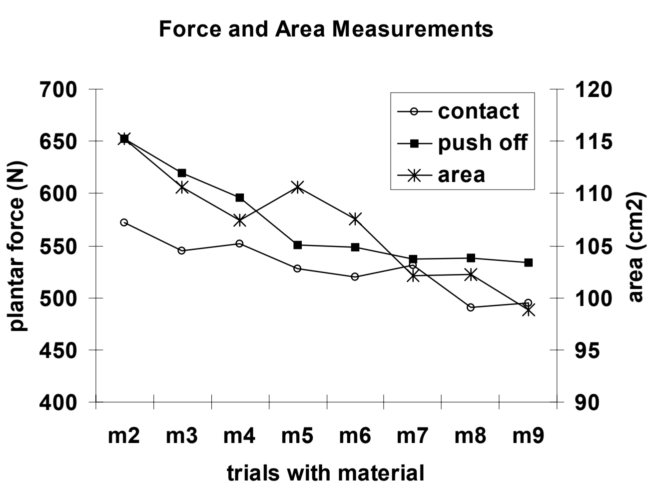

There was a significant decrease in the peak of the average total plantar force (contact + push off) (repeated measures ANOVA, $F(7,63) = 52.78$, $p<.001$) as well as sensor reporting area ($F(7,63) = 9.06$, $p<.001$) across m trials (Figure 1). There was a trial effect for the peak of the average total contact pressure for m trials ($F(7,63) = 2.29$, $p=.038$). However, post hoc analysis revealed only the m2m8 comparison to be significant ($p=.005$). Comparisons m2m7 and m2m9 were not different ($p>.07$). See Figure 2.

Figure 2: Total contact pressure across trials.

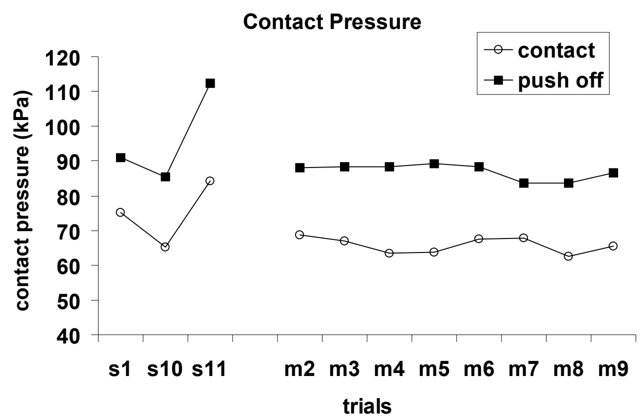

Force and area measurements decreased with subsequent trials within a single session. The decrease in force and area resulted in the total contact pressure remaining relatively stable across trials. Additional calibration at the end of the session significantly altered total contact pressure (compare s10-s11).

SUMMARY

Although additional observations would strengthen the results, plantar pressure may be a more prudent variable over force when studying in-shoe materials across trials within a single session. Additional calibrations may not aid in comparing early and late trials. Finally, an "extended calibration" procedure (F-Scan manual) may require validation in studies examining effects of <u>different</u> in-shoe materials across trials.

REFERENCES

Rose, N.E. et al (1992). *Foot Ankle*, **13(5)**, 263-70.

ACKNOWLEDGEMENTS

Supported by a grant from Rogers Corp., Rogers, CT, USA.

PERICARDIUM-MEDIATED EQUALIZATION OF LEFT AND RIGHT VENTRICULAR OUTPUTS

Carol A. Gibbons Kroeker[1], Nigel G. Shrive[2], and John V. Tyberg[1]
Departments of Physiology & Biophysics[1] and Civil Engineering[2],
University of Calgary, 3330 Hospital Dr. NW, Calgary, Alberta, T2N 4N1; kcagibbo@ucalgary

INTRODUCTION

Although it is generally accepted that the pericardium plays an important role in equalizing left ventricular (LV) and right ventricular (RV) outputs, the mechanism has never been clearly demonstrated. The pericardium may mediate this equalization because of its stress-strain relationship, which is very distensible at low strains, but much stiffer at higher strain levels. Hence, at low strains (and low pericardial pressures), the size of the heart can increase relatively easily within the pericardium and there is little to no interaction between the ventricles. At higher strains, however, where the pericardium is stiff, the size of the heart will change very little with any further increase in load. Hence, any increase in the area of one ventricle must be accompanied by a decrease in the area of the other. The aim of this study was to show that the pericardium is important in equalizing LV and RV outputs on a beat-to-beat basis. We produced large, sudden changes in atrial volume and assessed the effects in terms of pericardial and ventricular pressures, dimensions, and outputs.

METHODS

Experiments were performed on 8 open-chest anaesthetized dogs. Aortic, left and right ventricular, atrial, and pericardial pressures were recorded, as well as LV and RV dimensions. Aortic and pulmonary flows also measured, from which LV and RV outputs or stroke volumes (SV) were calculated. To effect changes in atrial volumes, a reservoir was designed which allows rapid (~300 ms, during systole) infusion or withdrawal of 20-25 mL blood into or out of either the left or right atrium (LA or RA). Haemodynamic parameters were recorded for several beats before and for several beats after an infusion or withdrawal. LVEDP was decreased by a vena caval occlusion, or increased by volume loading. Inflations and deflations were repeated several times at various LVEDP's. This protocol was then repeated with the pericardium removed.

RESULTS AND DISCUSSION

With LA or RA infusions, there was a rise in ipsilateral transmural pressure, diameter and output (SV). With the pericardium present, there was also a compensatory decrease in transmural pressure, diameter, and SV on the contralateral ventricle. Further, the sum of the ipsilateral increase and contralateral decrease in outputs closely matched the initial infused volume (see Figure 1A). With LA or RA withdrawal, the opposite changes were observed, with the overall sum again closely corresponding to the initial withdrawal. In all cases, the response was quick (75-85% of complete response in the first beat post- infusion or withdrawal), with LV and RV SV's returning to control values within 3-4 beats. With the pericardium removed, there was again an increase in the ipsilateral ventricular output with LA or RA infusions. However, there was no compensatory decrease in SV seen in the contralateral ventricle. Similar results were observed with LA or RA withdrawals. With the pericardium removed, the sum of the excess and deficit SV's did not match the infused or withdrawn volume (see Fig. 1B). These results show that the pericardium is essential for rapid biventricular equalization of the LV and RV outputs.

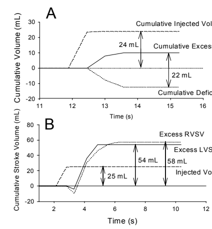

Figure 1: LA infusions with and without the pericardium.

To assess the accuracy of the biventricular compensatory response, with and without the pericardium, the sum of the cumulative changes in LVSV and RVSV are plotted as a fraction of the infused or withdrawn volume and shown against pericardial pressure (Figure 2). With the pericardium intact, the ratio was very close to one, indicating excellent equalization of LV and RV outputs and compensation for the initial infusion or withdrawal. Once the pericardium was removed (pericardial pressure equal to zero), however, LV and RV outputs were not equalized and, within the observation interval, compensation was not achieved. When the EDP's and pericardial pressures were lowered, there appeared to be a reduced ability to equalize the LV and RV outputs. At these low pressures, the data approached that seen with the pericardium removed. That is, the sum of the excess and deficit stroke volumes did not equate so well with the infused or withdrawn volumes.

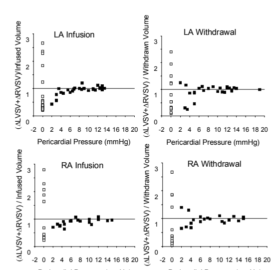

Figure 2: The effect of pericardial pressure on the accuracy of the biventricular compensatory response ((ΔLVSV+ΔRVSV) /infused or withdrawn volume). Filled squares, pericardium closed; open squares, pericardium open.

SUMMARY

This study clearly demonstrates that the pericardium is necessary to effect precise and rapid equalization of LV and RV outputs. When the pericardium was intact and its pressure at least 5 mm Hg, a sudden increase in atrial volume caused an ipsilateral increase in ventricular output and a compensatory contralateral decrease. Likewise, a decrease in atrial volume caused an ipsilateral decrease in SV and a contralateral increase. In all cases, the sum of the excess and deficit stroke volumes closely matched the infused or withdrawn volume. This interaction was lost when the pericardium was removed. With low pericardial pressures, the interaction diminished. We have demonstrated strong beat-to-beat equalization of ventricular outputs mediated by the pericardium. These results may be important in exercise when lung throughput is greater, and with orthostatic hypotension.

TORSO POSITIONS OF MINIMUM PASSIVE TISSUE STRAIN –WHERE DO WE SIT, STAND AND WALK?

Scannell, J.P. [1] and McGill S.M.
Faculty of Applied Health Sciences, University of Waterloo, Ontario, N2L 3G1.
[1] Communiucating Author: jscannell@sympatico.ca

INTRODUCTION

The purpose of this study was to quantify the lumbar spine position of minimal strain and to investigate the posture related differences in the lumbar passive tissue strain levels endured during sitting, standing and walking trials.

Passive tissue strain is a recognized cause of mechanical low back pain (MLBP) (Kumar 2001). Yet to date the position of least lumbar passive tissue strain (elastic equilibrium) has not been quantified and it is not known if, without training, we assume the position of elastic equilibrium in ADL. Elastic equilibrium was identified following which the lumbar passive tissue strain in ADL was calculated by comparing the lumbar position in ADL to the position of elastic equilibrium.

METHODS

Eighteen female participants (6 hypolordotic, 6 hyperlordotic and 6 controls) were recruited from a pre-screened group of 150 undergraduate university students (without a history of LBP). Lumbar elastic equilibrium, the resting position of the lumbar spine in the absence of muscle activation, was identified after bending moments were applied by an assistant to the lumbar torso while the participant lay on a frictionless jig and simultaneous angular displacements of the T12 relative to S1 were recorded. Angular displacements of the lumbar spine were recorded during sitting, standing and walking trails and compared to the position of elastic equilibrium to identify the level of passive tissue strain. One-way ANOVA was used to perform statistical analysis.

RESULTS AND DISCUSSION

A 'zone' (neutral zone), rather than a specific lumbar position, of low tissue strain was found. The size and location of the neutral zone was not significantly different ($p > 0.5$) between different postural groups.

Regardless of their natural lumbar posture all participants sat in lumbar elastic flexion and walked with lumbar spine positions within their neutral zone. Both the hypolordotic group and the control group also stood within their neutral zones but the hyperlordotic group stood in elastic extension. Lumbar spine positions assumed during walking were consistently within the neutral zone indicating the absence of passive tissue strain during walking (Figure 1)

Positions either flexed (as found during sitting) or extended (as the hyperlordotic group were during standing) of the neutral zone imply that some passive tissue is beyond elastic strain and the tissue safety margin is reduced. The passive tissue strain was found to be specific to the hypolordotic and hyperlordotic classification.

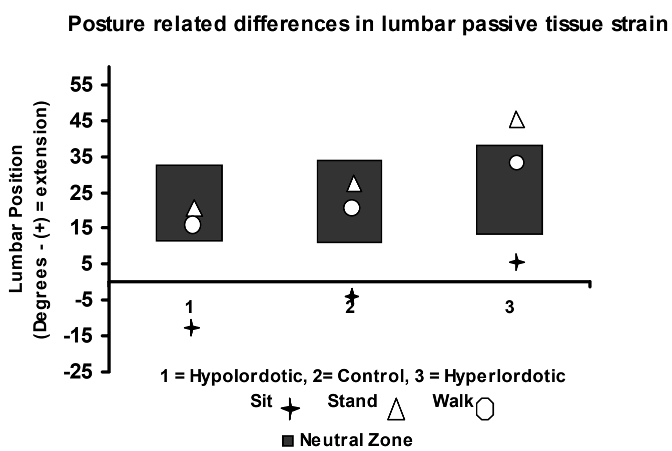

Figure 1: The neutral zone of each group, indicated by the black bars, is the zone of lumbar positions of least passive tissue strain. The average group lumbar spine position (50% level of the APDF) during the sitting, standing and walking trails in the pre-training test are shown relative to the group NZ. Positions outside the neutral zone are indicative of passive tissue strain and are indicative of a greater risk of tissue failure. The hypolordotic group sat significantly further from (more flexed of) their NZ than the hyperlordotic group.

SUMMARY

A 'zone' of lumbar spine positions where the passive tissue strain is low was found. Depending on an individual's natural lumbar posture, sitting and standing impose greater passive tissue strains than walking.

REFERENCES

Kumar, S. (2001). *Ergonomics,* **44**, 17-47

LOWER EXTREMITY SUPPORT DURING TODDLER GAIT

S. Potoczny[1], D.G.E. Robertson[1] and H. Sveistrup[1, 2]

Motor Control Laboratory, University of Ottawa, Ottawa, Ontario, Canada
[1]School of Human Kinetics, [2]School of Rehabilitation Sciences

INTRODUCTION

A net support moment of the lower limb, M_s, is defined as the sum of the moments at the hip, knee and ankle during the stance phase of walking. For adults, the net support moment during stance prevents collapse and brings about push-off (Winter 1980, 1991). It has been proposed (Breniere & Bril, 1988) that children within their first few months of independent walking actually "walk while falling", whereas adults "fall while walking." For children this implies that the vertical acceleration of the centre of gravity remains negative through single support and becomes positive only during double support. The purpose of this study was to characterize the M_s patterns of toddlers in their first year of independent walking and to determine if the proposed "walk while falling" is reflected by a negative M_s.

METHODS

Four toddlers aged 12, 16, 21 & 22 months with 2, 3, 7 & 12 months of independent walking, respectively, participated in this study. Surface markers were placed on the ASIS, sacrum, greater trochanter, lateral condyle, tibial tuberosity, lateral malleolus, heel and fifth metatarsal head. Toddlers walked independently at their own speeds across two AMTI force plates. A minimum of nine trials were analyzed for each toddler. Kinematic data were collected using three VHS cameras and processed using the Ariel Performance Analysis System. Force and kinematic data were analyzed and combined using Biomech software (Robertson, 2002) to calculate net joint and support moments. All moments were normalized to body weight.

RESULTS AND DISCUSSION

Support and lower limb moment curves during the stance phase for all trials from one toddler along with corresponding data (mean +/- st. dev.) from adults are plotted in Figure 1 (extensor moments being positive). This toddler's M_ss are much smaller and lack the double hump profile of adults. In 6 of 11 trials, the M_s were negative during the first 20% of stance of toddler gait corresponding to the period of weight transfer. In adults, the M_s at contact was always positive. The negative support moments lend credence to the suggestion that toddlers do not anticipate foot contact and are less stable on the lower limb at contact. The toddlers were able to provide an extensor M_s for the rest of stance bringing about push-off. Toddler ankle and hip joint moments followed similar patterns as those recorded for adult gait. Knee joint moments were negligible suggesting that toddlers may lock their knee creating a rigid segment. Regulation of stance phase seems to occur at the ankle and hip joints.

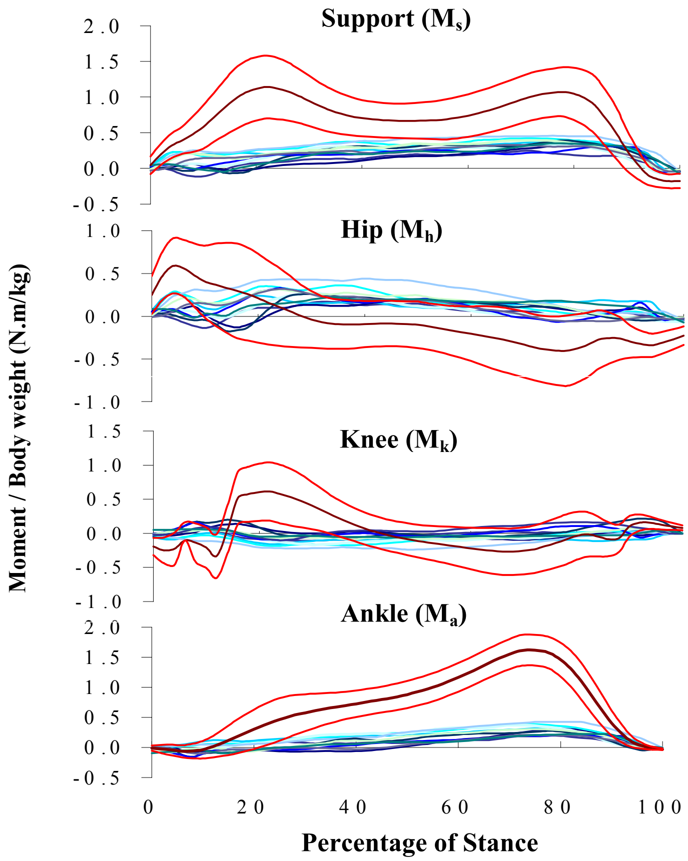

Figure1: Support and joint moments of force for a 2-month walker and averaged adult data (the latter from Winter, 1991).

SUMMARY

Early walking is characterized by a negative support moment of the lower limb during the first 20% of stance as the toddler attempts to position the body to create the support necessary to prevent a fall. Toddlers are less stable throughout stance and are therefore more susceptible to falls due to their reduced support moments.

REFERENCES

Breniere, Y., Bril B. (1988). *Sciences de la Vie*, **11**, 617-622.
Robertson, D.G.E. (2002). http://www.health.uottawa.ca/biomech/csb/software/biomech.htm.
Winter, D.A. (1980). *J. Biomechanics*, **13**, 923-927.
Winter, D.A. (1991). *The biomechanics and motor control of human gait.* University of Waterloo Press.

ACKNOWLEDGEMENTS

Partly funded by an NSERC, operating grant. SP holds an OGS scholarship. HS is a Career Scientist with MHLTC, Ont.

IN VIVIO DETERMINATION OF POLYETHYLENE BEARING MOTION REALTIVE TO THE TIBIA AND THE FEMUR

Richard D. Komistek[1], Brian D. Haas[1], Douglas Kilgus[2], Adam Smith[2], Scott A. Walker[1]
[1]Rocky Mountain Musculoskeletal Research Laboratory, Denver, Colorado, rkomistek@rmmrl.org
[2]Wake Forest Baptist Medical Center, Winston-Salem, North Carolina

INTRODUCTION

Previously, in vivo kinematic studies have determined that axial rotation patterns are quite variable between implant type and specific subjects. Previously, kinematic studies have determined that subjects having a mobile bearing TKA experience axial rotation, but it was unknown as to whether the bearing was rotating. (Stiehl, 1997) Therefore, the objective of this present study was to analyze the in vivo kinematics for subjects having a mobile bearing prosthesis to determine if the polyethylene rotates relative to the femoral and/or the tibial components.

METHODS

Femorotibial contact positions for ten subjects having a mobile bearing TKA, implanted by a single surgeon, were analyzed using video fluoroscopy. Each subject, while under fluoroscopic surveillance, performed a weight-bearing deep knee bend to maximum flexion. Video images were downloaded to a workstation computer and analyzed at varying degrees of knee flexion. Each polyethylene component had four metallic beads, inserted at known positions. Using a 3D model-fitting process, the femoral, tibial and polyethylene insert components were overlaid onto the fluoroscopic images. Initially, the polyethylene insert was made transparent, allowing visualization of the four metal beads. Then, the polyethylene insert was made viewable and analyzed relative to the metal femoral and tibial components.

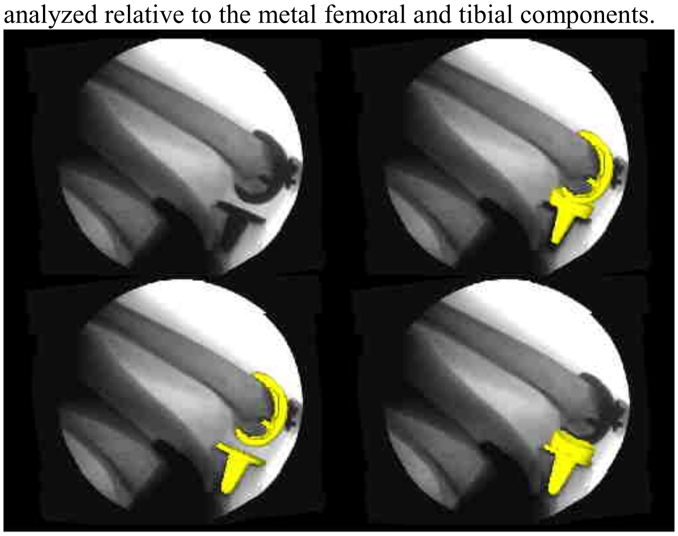

Figure 1. Example of overlay progression used in this process. First the femoral component and polyethylene were fit to the image. Second, the tibia relative to the existing femoral component was fit. Finally, the polyethylene was inserted with respect to the tibia.

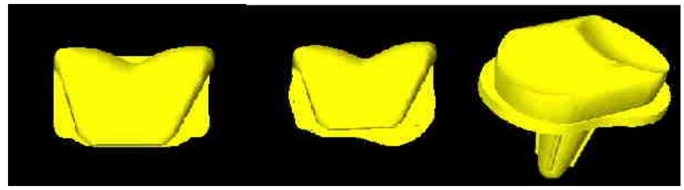

Figure 2. Axial rotation of the femur on the polyethylene was negligible in most subjects. However, the poly rotation on the tibial tray proved that the bearing rotates throughout increasing flexion.

RESULTS AND DISCUSSION

All of the subjects experienced polyethylene bearing rotation relative to the metal tibial base and minimal rotation relative to the metal femoral component. On average, relative to the tibial base, the subjects experienced 4.7^o (2.1 to 7.9^o) of polyethylene bearing rotation. The subjects experienced a similar amount of femoral component rotation, relative to the tibial base. On average, the subjects experienced 4.0^o (-0.7 to 10.0^o) of rotation of the femoral component relative to the tibial base. Therefore, on average, subjects experienced only 0.7^o of rotation for the femoral component relative to the polyethylene bearing. Also, on average, from full extension to 90^o of knee flexion the subjects experienced –2.9 mm of posterior femoral rollback of their lateral condyle and –0.4 mm of their medial condyle.

SUMMARY

This is the first study to determine the in vivo rotation of the polyethylene bearing for subjects having a mobile bearing TKA. The results from this study determined that the polyethylene bearing was rotating relative to the metal tibial component, but little motion of the femoral component relative to the polyethylene bearing was discovered relative to the metal. Therefore, as the femoral component axially rotated the polyethylene bearing was rotating a similar amount in the same direction. Since bearing rotation occurs under in vivo conditions, subjects' knees implanted with a mobile bearing prosthesis may be subjected to lower amounts of contact stress.

REFERENCES

Stiehl, J. B., Dennis, D. A., Komistek, R. D., et al (1997), *In vivo kinematic analysis of a mobile bearing total knee prosthesis*. Clin Orthop, **345**:60-66.

IN VIVO FORCES AND MOTIONS FROM FLUOROSCOPY AND MATHEMATICAL MODELING

Richard D. Komistek[1], Thomas R. Kane[2], Mohamed Mahfouz[1], Douglas A. Dennis[1], Brian D. Haas[1]
[1]Rocky Mountain Musculoskeletal Research Laboratory, Denver, Colorado: rkmositek@rmmrl.org
[2]Stanford University, Stanford CA

INTRODUCTION

Understanding the forces across the human lower extremity joints are of considerable interest to the clinician and implant manufacturers. In the past, telemetric hip implants have been used to determine the forces across the hip joint, but the forces at the knee joint have yet to be validated. Recently, video fluoroscopy has been utilized to accurately determine the in vivo kinematics of human joints during various activities. The objective of this study was to predict muscle and joint forces from a mathematical model utilizing fluoroscopy as the input motion data.(Komistek, 1998)

METHODS

Utilizing Kane's Dynamics, a mathematical model of the human lower extremity was developed. Using Autolev©, a symbolic manipulator soft-ware package, 18 equations of motion were explicitly derived using $F_r + F_r^* = 0$, r=18. Eighteen auxilliary generalized speeds were modeled in the velocity and angular velocity equations and were then constrained after the system kinematic equations were derived. While under fluoroscopic surveillance, one subject was asked to perform gait and deep knee bends at various speeds. The kinematic data, derived using fluoroscopy, was then used as input to a mathematical model and the predicted knee joint, quadriceps muscles and patellar ligament forces were plotted with respect to time, percent gait cycle and knee flexion angle.

RESULTS AND DISCUSSION

While walking at a normal speed, femorotibial force just after heel-strike was 1.9 times body weight (x BW) and 2.2 x BW just before toe-off (Figure 1). The patellofemoral force ranged from 0.3 to 0.5 x BW. The force in the quadriceps and patellar ligament ranged from 0.9 to 1.2 x BW, in the opposite direction of each other. The A/P forces in the knee were 0.1 and 0.4 (0.3 to 0.5) x BW at the femorotibial and patellofemoral joints, respectively. During a deep knee bend, the femorotibial force ranged from 0.5 to 1.8 x BW and the patellofemoral force increased from 0.1 x BW at full extension to 3.2 x BW at 90o of knee flexion (Figure 2). During a deep knee bend, the quadriceps force (0.1 to 2.3 x BW) was greater than the patellar ligament force (0.1 to 1.4 x BW). The model was very sensitive to the angle between the patellar ligament and the tibia. Varying this angle increased the femorotibial force during gait to 3.5 x BW.

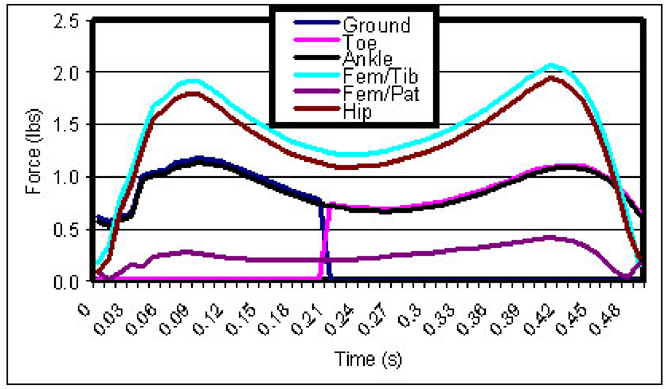

Figure 1. Interaction forces during stance-phase of gait.

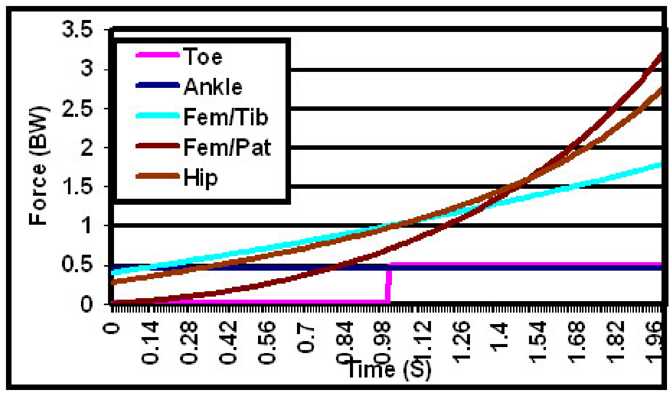

Figure 2. Interaction forces during a deep knee bend.

SUMMARY

Although we have not been able to validate the derived knee forces using a subject having a telemetric knee, the predicted hip forces using the model were very similar. Therefore, it can be assume that the knee forces should also be accurate, or our modeled system would have predicted inaccurate hip forces. In the future, we hope to validate the model using a subject having a telemetric knee. The results from this study have revealed that patellar motion does influence the forces throughout the lower extremity. Simultaneous kinematic (fluoroscopy) and kinetic (mathematical model) data for subjects having a total knee replacement will provide valuable information for implant testing and future development.

REFERENCES

Komistek, R.D., Stiehl J.B., Paxson, R.D., et al (1998). Mathematical model *of the lower extremity joint reaction forces using Kane's method of dynamics: A technical note.* J Biomechanics, **31**:185-189.

OBSTACLE AVOIDANCE STRATEGIES ARE ALTERED FOLLOWING TOTAL KNEE ARTHROPLASTY

Jeannette M. Byrne and Stephen D. Prentice
Gait and Posture Laboratory, University of Waterloo, Waterloo, Ontario, Canada
jmbyrne@ahsmail.uwaterloo.ca

INTRODUCTION

As locomotion involves coordinated movement of all lower limb joints, the effects of total knee arthroplasty (TKA) on function can be fully understood only by investigating bilateral lower limb function. Such research, by defining the bilateral motor changes resulting from TKA, will assist in the design of treatment programs for use with this population and also provide a deeper understanding of plasticity in the neuromuscular system. The primary purpose of the current study will, therefore, be to determine how TKA alters not only surgical knee function, but also how kinetic patterns in the remaining lower limb joints are affected. To accomplish this goal an obstacle avoidance task will be examined.

METHODS

Six individuals, an average of 20 months post right TKA (2 male, 4 females, mean age 73 years) and a group of 6 healthy participants (3 males, 3 females, mean age 76.6 years) were studied. Participants performed a total of 48 walking trials, divided equally among 3 conditions – unobstructed walking and clearing a 6cm and 18cm obstacle. Sixteen trials were performed at each height (8 right limb lead; 8 left limb lead). An Optotrak motion analysis system was used to collect kinematic data from both the right and left limbs. Bilateral ankle, knee and hip moments and powers were calculated using an inverse dynamics analysis. These results were used to determine rotational ankle, knee and hip work and translational hip work. Statistical analysis consisted of two separate two-way repeated measures ANOVAs to determine if surgical and non-surgical limb function differed from that of healthy, control limbs ($\alpha = 0.01$).

RESULTS AND DISCUSSION

Qualitatively, most patients exhibited decreased surgical knee flexion moments during early swing (Fig 1a). Deficits in surgical knee flexor work were also observed (obstacle x limb interaction P=0.009; Fig 1a). Post-hoc analysis of this interaction demonstrated differences between surgical and healthy limbs were significant at both heights ($\alpha < 0.01$). As knee flexor work during elevation (toe off to toe over obstacle) primarily flexes the knee (MacFadyen & Winter 1991), this decrease in knee work would account for deficits in active surgical knee flexion previously reported in these same individuals (Byrne 2001). Knee flexor work during early swing also passively flexes the hip and ankle via intersegmental dynamics (Patla & Prentice 1995). Deficits in surgical knee work would, therefore, result in members of the TKA group having less passive hip flexion and potentially less overall surgical hip flexion. As such a decrease in hip flexion would have deleterious effects on toe clearance, members of the TKA group increased surgical hip work (18cm height) (Fig 1a). This increase approached significance (p =0.0328) and occurred in conjunction with greater surgical hip flexor

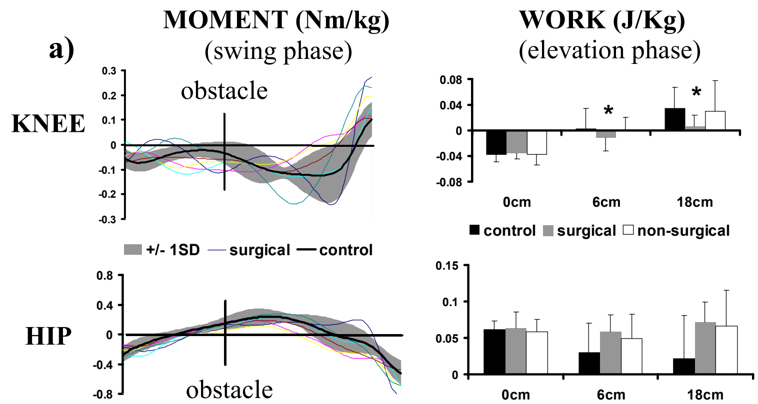

Figure 1: a) knee, hip moment and work (18cm obstacle)
b) translational hip work
(* significant difference between surgical and control limbs)

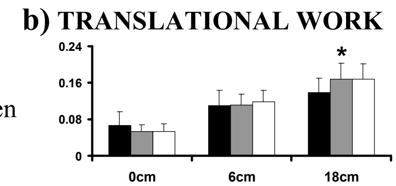

moments (Fig 1a). Although not significant, it is felt the increase in hip work was sufficient to ensure hip flexion was maintained. Surgical limb translation hip work increased at both obstacle heights (P = 0.0024;Fig 1b). Post-hoc analysis revealed this increase was significant only at the 18cm height. This increase can be understood by examining lower limb kinematics during swing. While members of the TKA group exhibited normal hip and ankle flexion, surgical knee flexion decreased, resulting in an overall decrease in surgical limb flexion (Byrne 2001). Despite this decrease, toe clearance was maintained. As translational hip work represents the stance limb's contribution to toe elevation, increases in translational hip work during surgical limb lead provided additional swing hip elevation, thereby, enabling members of the TKA group to maintain toe clearance despite decreased surgical knee flexion.

SUMMARY

The results demonstrate that while surgical knee function is clearly deficient following TKA, kinetic changes also occur at the surgical hip. These changes help compensate for surgical knee deficits, enabling these individuals to successfully negotiate obstacles.

REFERENCES

McFadyen B & Winter DA (1991). *Neurosci Res Commun,* **9**,37-41.
Byrne (2001) Unpublished Master's thesis. *U. Waterloo.*
Patla AE & Prentice SD (1995) *Exp Brain Res,* **106**,499-504.

AKNOWLEDGEMENTS

The authors wish to acknowledge the financial support of MRC and CIHR and the assistance of M. Ishac.

IN VIVO DETERMINATION OF HIP JOINT SEPARTION IN SUBJECTS HAVING VARIABLE BEARING SURFACES

Richard D. Komistek[1], Douglas A. Dennis[1], Laurent Sedel[2], Curt D. Hammill[1], Eric J Northcut[1], Pascal Bizot[2]
[1]Rocky Mountain Musculoskeletal Research Laboratory, Denver, Colorado, rkomistek@rmmrl.org
[2]Laribroisiere Hopital, Paris France

INTRODUCTION

Previous in vivo kinematic analyses of the hip joint have determined that femoral head separation from the medial aspect of the acetabular component occurs in metal-on-polyethylene THA (Dennis, 2001). The present study analyzes subjects having either an alumina-on-alumina (AOA), alumina-on-polyethylene (AOP), metal-on-metal (MOM) or metal-on-polyethylene (MOP) THA during gait and an abduction/adduction leg lift to determine if the incidence of hip joint separation (femoral head sliding on the acetabular cup insert) varies based on articular surface material.

METHODS

Forty subjects were analyzed in vivo using video fluoroscopy. Ten subjects had a AOA THA, ten an AOP THA, ten a MOM THA, and ten had a MOP THA. All THA subjects were implanted by two surgeons and were judged clinically successful (Harris hip scores >90.0). Each subject performed normal gait on a treadmill and an abduction/adduction leg lift maneuver while under fluoroscopic surveillance. The two-dimensional (2D) fluoroscopic videos were converted into 3D using a computer automated model-fitting technique. Each implant was analyzed at varying flexion angles to assess the incidence of hip joint separation.

RESULTS AND DISCUSSION

During gait and the abduction/adduction leg lift, no separation was observed in subjects having an AOA THA or in subjects having a MOM THA (Figure 1). Similar to our previous studies pertaining to subjects having a THA with a polyethylene acetabular insert, all ten subjects having a MOP THA and 6/10 subjects having an AOP THA experienced hip joint separation. The maximum amount of separation was 7.4 mm for a subject having an AOP THA and 3.1 mm for a subject having a MOP THA. The maximum amount of separation occurred during mid-stance to toe-off (Figure 2).

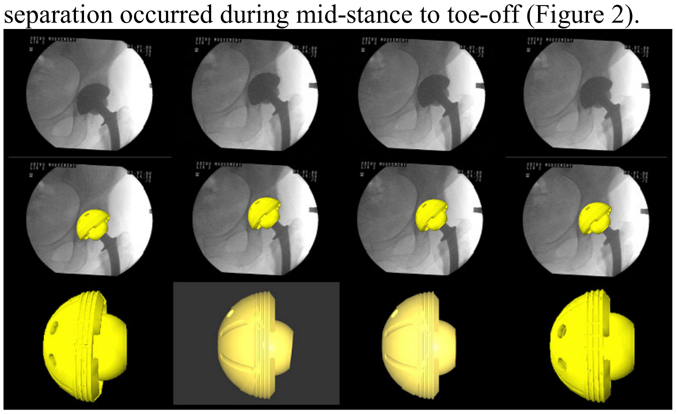

Figure 1. Fluoroscopy images of final fit overlay and component positioning of a subject having an alumina-on-alumina THA. Images are shown during gait activity at heel-strike, 33%, 66% and toe-off.

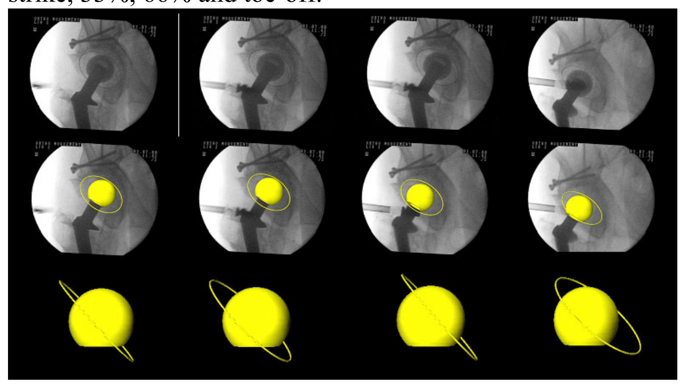

Figure 2. Fluoroscopy images of final fit overlay and component positioning of a subject having an alumina-on-polyethylene THA. Images are shown during gait activity at heel-strike, 33%, 66% and toe-off.

SUMMARY

This study shows femoral head separation from the medial aspect of the acetabular component can occur in the presence of a polyethylene liner. The femoral head often remains in contact with the liner, hinging superolaterally. Previous studies have only reported hip separation (femoral head sliding) to occur during non-weightbearing conditions. The presence of hip separation during stance-phase of gait may suggest that the inertia of the contra-lateral leg induces the acetabular cup to separate away from the femoral from mid-stance to toe-off. Potential detrimental effects resulting from hip joint separation include premature polyethylene wear, component loosening (secondary to impulse loading conditions) and hip instability. Wear may be enhanced due to creation of multidirectional wear vectors or excessive loads due to eccentric femoral head pivoting. The absence of separation observed in AOA and MOM THA designs may be related to increased wettability of these materials and tighter radial tolerances resulting in a cohesive lubrication film. This data may be of value in hip simulation studies to better duplicate wear patterns observed in retrieval analyses and assist in the understanding of the lubrication regime and wear rates in AOA and MOM designs, allowing for the synthesis of prosthetic components that minimize wear and optimize kinematics.

REFERENCES

Dennis, D.A., Komistek, R.D., Northcut, E.J., et al, (2001). *In vivo determination of hip joint separation and the forces generated due to impast loading conditions*. J Biomehanics, **34**: 623-629.

NORMALIZATION OF SURFACE EMG SIGNALS - COMPARISON AMONG EFFORT, JOINT POSITION AND PROCESSING METHOD

Nigel Zheng, Ph.D., Brian Ragan, Paul Marvar, Glenn Fleisig, Ph.D., Steve Barrentine, M.S.
American Sports Medicine Institute
1313 13th Street South, Birmingham, Alabama 35205, USA, nigelz@asmi.org

INTRODUCTION

EMG signals have been used for diagnosis of disease, evaluation of different exercises, and estimation of muscle forces (Zheng, N et al, 1997). EMG results are affected by numerous factors during data detection and processing (De Luca, C. 1997), however these factors are often ignored and/or not reported when normalizing EMG. The objective of this study was to evaluate the effects of contraction effort, joint angle, and data processing method during isometric contraction of the quadriceps muscles.

METHODS AND MATERIALS

Ten healthy subjects (5 male, 5 female) with no history of knee injury volunteered as subjects. The dominant leg was tested with the subject seated. Three pairs of surface electrodes (Medicotest Marketing, Inc. Ballwin, MO) were placed on the muscle belly of the vastus medialis (VM), vastus lateralis (VL), and rectus femoris (RF). A load cell (Omega Engineering) was installed to directly measure force applied by the dominant leg near the ankle. The force signal was collected at 1000 Hz. Synchronized EMG signals from the three muscles were recorded at 1000 Hz with a Myosystem 2000 (Noraxon USA, Inc., Scottsdale, AZ). Signals were converted from analog to digital data and stored with an ADS system (Motion Analysis Corp., Santa Rosa, CA). Tests were conducted at 30, 60 and 90 degrees of knee flexion with maximum, 75% and 50% effort voluntary isometric contraction for 3 seconds. Each test was repeated three times. Subjects were allowed to take a 2-minute break between tests.

Data were passed through a high-pass 4th order butter filter and rectified. Four different processing methods were then used: integration (INT), low-pass filter with cut-off frequency of 25 Hz (LPS), root-mean-square (RMS) and average rectified value (ARV). For each processing method, the mean value of the middle second was calculated and averaged for the three tests each subject performed for each condition. The coefficient of variability (COV) among the three tests was also calculated. Repeated measures analysis of variance (ANOVA) was used to identify significant ($p<0.05$) differences in mean EMG and COV among effort, knee angle, and data process for each muscle (SPSS Inc, Chicago, USA).

RESULTS AND DISCUSSION

EMG data is commonly scaled by the EMG magnitude of maximum voluntary isometric contraction (MVIC). While this is a common approach, Lawrence and De Luca (1983) suggested that the variability of EMG during maximum effort was high to make it a poor choice for normalization. As expected, the current study showed that mean value of EMG and force both were highest with maximum effort and lowest with 50% effort. However their COV were not significantly different among effort levels. Thus, the choice of effort for normalization trials would affect the magnitude but not the consistency of scaled data.

The mean values of EMG for the VM and VL muscles varied significantly with knee flexion angle, and were highest with 90^{o} knee flexion and lowest with 30^{o}. COV varied with knee angle, and were lowest at 60°. For the RF muscle, mean values and COV for different knee angles showed no significant differences. Thus, the choice of isometric position should be considered and reported when isometric data are used for normalization, as the magnitude and consistency of scaled data may be affected.

EMG results varied significantly among the different data processing methods. Mean values were greatest with the INT method and least with the ARV method. COV was the least with INT and no differences among others. Each of these methods has virtue and has been used in EMG analysis. The current study does not suggest that one method is superior, but that the choice of method can affect the results and should therefore be reported.

SUMMARY

Normalization is often used in EMG data analysis. MVIC has the highest magnitude and the choice of using MVIC is no better or worse than 75% or 50% effort level. The choice of joint position and processing method should also be considered and reported. Different joint angles should be considered for different muscles to obtain MVIC or other level VIC. Because of variability, multiple trials are always a good idea. The choice of result parameter (e.g., global peak of 3 seconds, peak of the middle second and average of the middle second) also affects results. The choice of effort, position, and processing method is important not only for the quality of an individual study, but also for comparison of various studies and clinical application of EMG testing.

REFERENCES

De Luca, C (1997). J. Appl. Biomechanics, 13, 135-163.
Lawrence, J.H. and De Luca, C. J. Appl. Physiol. 54:1653-9
Zheng, N. et al (1997) J. Biomechanics, 31, 963-967

ON NOT TIPPING A STEPLADDER SIDEWAYS

Bing-Shiang Yang and James A. Ashton-Miller
Biomechanics Research Laboratory, Department of Mechanical Engineering
University of Michigan, Ann Arbor, MI, U.S.A. bsyang@umich.edu

INTRODUCTION

Falls from ladders are the second most frequent cause of injury involving falls from elevation. A fall caused by tipping a stepladder over sideways is the most common cause of stepladder accidents (and the second most common cause involving ladder accidents) (Björnstig et al., 1992). Faergemann et al. (2001) suggested that overreaching laterally is the most common cause of falls from stepladders. In the elderly, standing on a raised surface is considered as one of the three most-challenging activities of daily living (Powell et al. 1995). The purpose of this study, therefore, was to use a biomechanical model, validated by experiment, to analyze in the frontal plane, the factors determining the stability of an individual during the lateral weight shift associated with climbing or descending a stepladder. We examined the effect of (a) altering the height of stance step, H, as a percentage of body height (BH), (b) altering the bipedal foot separation distance, and (c) the velocity with which the individual shifts his/her weight laterally from bipedal to unipedal stance.

METHODS

A stepladder was modeled as a rigid, planar, inverted "U" structure of variable height with 10% body mass (representing step height, expressed as a % of body height) and of fixed width resting on flat ground. We modeled a human shifting from double support to single support at the middle of the step as an inverted pendulum. The torque acting at its pivot joint represented the moment applied about the midpoint of the step by the stance foot-step reaction force. Its magnitude was constrained by the value of the product of body weight times foot width, and by the average ankle inversion/eversion strengths for young males (Ottaviani, 1995). The length and mass of the inverted pendulum corresponded to the average young male (Winter, 1990). Simulation inputs at contralateral foot lift-off included initial inclination angle of the pendulum center of mass (COM) from the vertical, initial COM angular velocity. A fourth-order Runge-Kutta method was used to solve the equations of motion in this MATLAB® simulation and a 'Bang-Bang' control strategy to control the joint torque. The controller objective was to bring COM over the stance foot width, or base of support (BOS), with zero residual COM velocity. When the total torque applied to the stepladder exceeded the torque required to lift one leg of the stepladder, then the ladder was deemed 'unstable'. The feasible phase plane operating region was then found. To validate model predictions, five healthy young males were each asked to transfer weight in 7 trials from bipedal stance onto one foot at the middle of a step located at 0 and 22% of body height (BH). Kinematic measures on pelvic, torso and leg motions were obtained at 100 Hz using an Optotrak 3020 system, while foot reaction forces were measured at 100 Hz using two AMTI force plates under the stepladder legs and an F-Scan pressure distribution system under the stance foot.

RESULTS AND DISCUSSION

The stability region was found to be strongly dependent on height of step on which the subject stood, the initial COM displacement related to BOS given by the initial foot separation distance, and velocity of the weight shift (Fig. 1). The stable region was 80% smaller when the human stood on a step at 22% of body height than when the human stood on the ground. Moreover, the higher the step was, the narrower the feasible range of COM velocities was. These model predictions were supported by the experimental data. This simplified model generally identified the feasible region of stepladder stability under lateral weight shift conditions. EMG analyses of gluteus medius activity supported the 'bang-bang" control strategy assumption.

Region of Stability

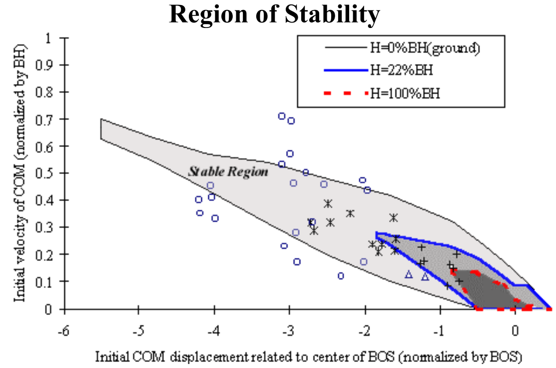

Figure 1: Model-predicted region of stability (lines). Experimental data points are also shown (*: successful (no ladder tilt) recovery trials for H=0%BH; ○: failed (ladder tilt) recovery trials for H=0%BH; +: successful recovery trials for H=22%BH; Δ: failed recovery trials for H=22%BH).

SUMMARY

The model provided a reasonable prediction of the circumstances under which a human can cause a stepladder leg to inadvertently lose ground contact. The higher the step, the narrower the bipedal base of support should be, and the slower the COM should be moved.

REFERENCES

Björnstig, U., Johnsson, J. (1992). *J. Safety Res*, **23**, 9.
Faergemann, C., Larsen, L. B. (2001). *J. Safety Res*, **32**, 333.
Ottaviani, R. A. et al., (1995). *Am J Sport Med*, **13**, 418.
Powell, L. E. et al. (1995). *J. Gerontol Med Sci*, **50**, M28.
Winter, D. A., (1990). *Biomechanics and Motor Control of Human Movement*. Wiley.

VERIFICATION OF THREE-DIMENSIONAL JOINT KINEMATICS DETERMINED USING FLUOROSCOPY: AN ERROR ANALYSIS

Mohamed Mahfouz[1,2], William Hoff[2], Richard Komistek[1], Douglas Dennis[1]
[1]Rocky Mountain Musculoskeletal Research Laboratory, Denver, Colorado, mmahfouz@rmmrl.org
[2]Colorado School of Mines, Golden Colorado

INTRODUCTION

A method was developed to analyze the accuracy of a 3D-to-2D image registration system that has been used successfully in joint kinematics studies (Dennis, 1996; Mahfouz, 2002). This system, determines the relative pose of femoral and tibial knee implant components from single plane X-ray fluoroscopy images. The accuracy analysis method used cadaver images very similar to "in vivo" clinical X-ray fluoroscopy images, and a completely independent method for determining the ground truth poses based on the use of an optical sensor. The objective of the study was to conduct an unbiased characterization of the accuracy of the 3-D to 2-D registration method.

METHODS

The sensor used in this study was an Optotrak 3020 system (Northern Digital Inc., Waterloo, Canada), which is a position-tracking device that tracks infrared LED's by using three fixed linear array CCD cameras. Shallow registration holes (5/64") were drilled into the femoral and tibial components of a posterior cruciate retaining knee implant. The holes were distributed throughout the components in a non-collinear arrangement. These holes were used to establish a reference frame for each implant component using the optical sensor. The implants were laser scanned and a polygonal surface model was created for the femoral, the tibial component.

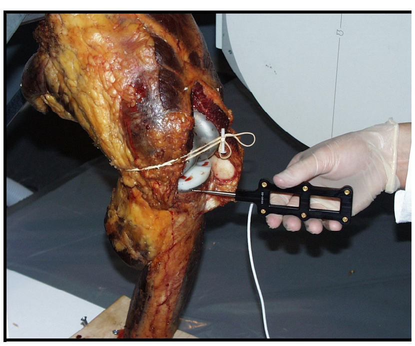

Figure 1 The Optotrak probe was used to determine the location of the registration points.

The locations of the registration holes on the surface models were found by manually placing virtual beads (balls) of the same size as the probe tip in the holes located on the surface of the generated models. The coordinates of the beads were recorded in the implant model coordinate reference frame. The 3D-to-2D registration system operated fully autonomously, after initial model placement by the operator. The optimization process in the 3D-to2D-image registration system was allowed to converge, and the pose results were recorded without any adjustment or intervention.

Table 1 Differences of poses derived from our method and those derived from Optotrak sensor (Sagittal plane).

	Mean	SD
X trans (mm)	-0.338	0.323
Y trans (mm)	0.130	0.472
Z trans (mm)	-0.494	1.640
X rotation (deg)	-0.125	0.550
Y rotation (deg)	-0.351	0.592
Z rotation (deg)	-0.006	0.971

Table 2 Estimated standard deviation of errors due to our process only in the Sagittal plane.

	SD
X trans (mm)	0.001
Y trans (mm)	0.429
Z trans (mm)	1.622
X rotation (deg)	0.427
Y rotation (deg)	0.501
Z rotation (deg)	0.727

A surgeon implanted both components into a fresh cadaver. The Optotrak probe was used to measure the (x, y, and z) coordinates of the registration holes in the femoral and tibial components while simultaneously video recording the X-ray fluoroscopy (Figure 1).

RESULTS AND DISCUSSION

With the exception of the Z (out of plane) translation, the mean difference in translation was less than 0.34 mm in all directions, and the standard deviation of translation errors was less than 0.50 mm in all directions. Error is higher for translation along the Z axis (the direction perpendicular to the image plane) because the registration method is much less sensitive to displacements in that direction. The mean difference in rotation was less than 0.50 degrees about any axis, and the standard deviation of rotation is less than 0.70 degrees about any axis (Table 1 and 2).

SUMMARY

The accuracy analysis method in this study is unique in that it used data very similar to "in vivo" clinical X-ray fluoroscopy images, unlike other work that uses clean laboratory images or synthetic data. Also, a completely independent method for determining the ground truth was developed, unlike some previous work that uses ground truth derived from X-ray data. This gives a true characterization of the accuracy of our 3-D to 2-D registration method. This approach could be used for determining ground truth for testing other registration methods.

REFERENCES

Dennis, D.A., Komistek, R.D., Hoff, W.A., et al (1996). *In vivo knee kinematics derived using an inverse perspective technique*, Clin Orthop. **331**:107-117.

Mahfouz, M., Hoff, W.A., Komistek, R.D., et al, (submitted 2002). *A robust method for registration of three-dimensional knee implant models to two-dimensional fluoroscopy images.* IEEE Transactions.

ASSESSMENT OF CUSHIONING MATERIALS: WHAT'S THE APPROPRIATE MEASURE?

David Tiberio and Timothy A. Hanke
Department of Physical Therapy & Human Performance Laboratory, University of Connecticut, Storrs, CT, USA
david.tiberio@uconn.edu

INTRODUCTION

Assessment of cushioning insoles / materials is often performed using plantar pressure measurements. Regardless of which measurement system is used, investigators must decide what dependent variable / measure provides the most appropriate insight into the cushioning properties of different materials. Mechanical testing of impact g-force does not take into account the interaction between the material and the human neuro-musculo-skeletal system.

METHODS

Twelve subjects hopped repetitively on one leg for 5 seconds on a force platform (AMTI, Watertown, MA, USA) with a F-Scan sensor (Tekscan, South Boston, MA, USA) in their sport shoe. The force plate data was sampled at 200Hz and the F-Scan data at 100 Hz. There was a 3 minutes rest between material conditions. The sequence of the tested materials was the same, but the starting order was changed for each subject. Each 5 - second trial resulted in 10-12 hopping cycles.

The peak vertical force (FZ) for each hop was averaged to produce a mean for each material for each subject. The peak value for the total contact pressure (TCP) from the F-Scan was averaged in the same manner. Five "box pressures" (BP) were determined using the F-Scan software for the hallux and 4 metatarsal head regions. The box with the highest pressure values was selected for each subject.

Inspection of the data revealed intra-subject variability across materials. There were substantial differences in FZ for the different materials, possibly due to the subjective comfort assessment of each participant. In order to minimize this effect, the FZ was divided by the subject's body weight to produce a body weight unit (BWU) for each material. This BWU was then used to evaluate both the TCP and the BP data.

RESULTS AND DISCUSSION

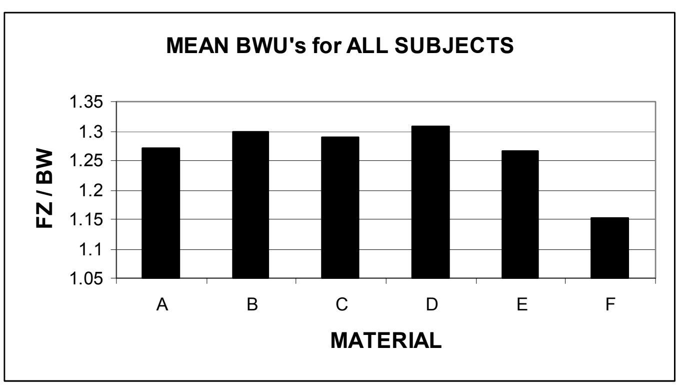

Figure 1. FZ for different materials normalized by BW.

Since the subjects were landing on the force plate with different BWU values, the TCP was normalized (Figure 2). This substantially changes the relative cushioning efficacy of the materials.

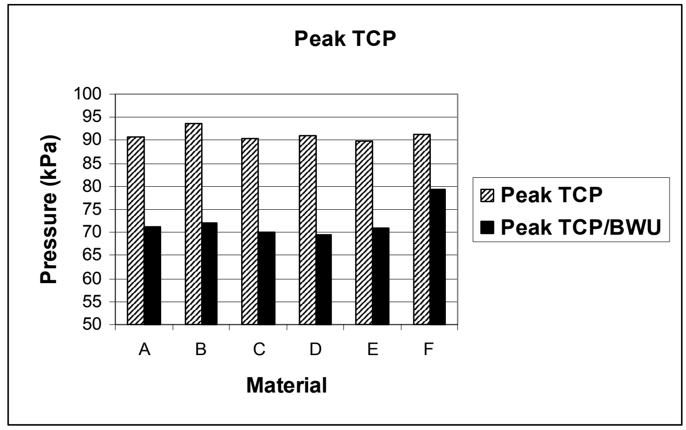

Figure 2. Effect of normalizing TCP by BWU on the relative rankings of cushioning effectiveness.

Figure 3 shows a comparison of the TCP and the BP for the different materials. The relative rankings of materials from lowest to highest pressure are different for the BP compared to TCP. Material E had the highest BP / BWU, but the third lowest TCP / BWU.

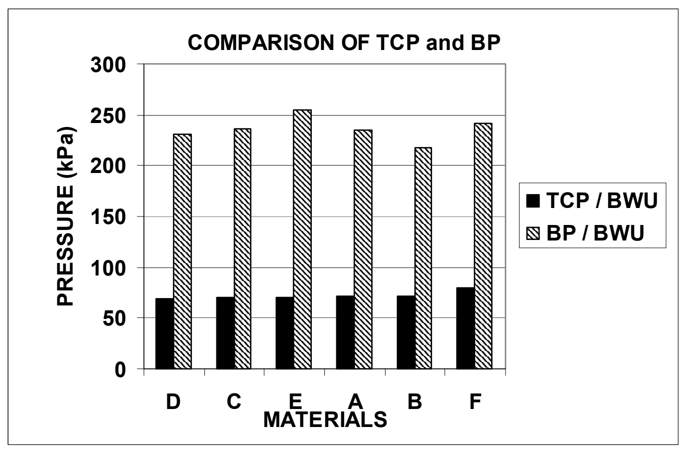

Figure 3. Materials ranked in order of TCP, compared to BP.

Even when normalized by BWU, the materials differed in effectiveness. This would suggest that, for hopping, materials do not have the same cushioning efficacy in high pressure areas of the foot when compared to the total contact pressure.

SUMMARY

We contend that the use of BWU to normalize FZ and pressure measures is important when testing different materials. TCP and BP are different measures of cushioning.

ASSESSING THE ACCURACY OF DOPPLER VELOCITY WAVEFORMS USING A STRING PHANTOM

Andrew Zambanini, Nicholas W. Witt, Dean C. Barratt, Simon A. McG Thom, Alun D. Hughes

Department of Clinical Pharmacology, National Heart & Lung Institute, Imperial College, London, UK
a.zambanini@ic.ac.uk

INTRODUCTION

Non-invasive techniques such as magnetic resonance and Doppler ultrasound imaging are popular methods used to determine flow velocity waveforms in arteries. These data are subsequently used for clinical applications such as wave intensity analysis, computational fluid dynamics modelling and the determination of volumetric flow. Previous work has suggested that peak velocities may be over-estimated using pulsed wave Doppler ultrasound (Hoskins, 1999). Real-time automated peak and mean frequency tracing algorithms have therefore been developed and are less variable than manual measurements (Rickey & Fenster, 1996). The aim of our study was to determine which of these two algorithms is most accurate for determining the flow velocity waveform.

METHODS

A string phantom (Gamex RMI, Middleton, USA) with an O-ring rubber filament was immersed in a tank containing degassed water at a temperature of 36°C (acoustic velocity 1522 m s^{-1}) and used as a moving target. The string was rotated using a stepper motor controlled by an electronic waveform generator programmed with 4 types of waveform; a constant speed of 35cm/s (P1), a single phase positive waveform with a peak velocity of 100cm/s (P2), a two phase positive waveform with peak velocities of 75 cm/s (P3), and a triphasic waveform with both positive and negative velocities with peak velocity of 90 cm/s (P4). The speed of the drive wheel on the string phantom was determined over successive periods of 17ms using a shaft encoder linked via a microcontroller to a PC.

An L12-5 linear-array transducer and HDI5000 ultrasound scanner (ATL, Bothell, USA) were used to acquire signals from the string phantom. This system provided real-time automated peak and mean frequency tracing algorithms and allowed digital data to be transferred to a PC for further analysis. Following simultaneous acquisition of the Doppler and shaft encoder data (5s for P1, 10 waveforms for P2-P4), ensemble averaging was performed to generate velocity waveforms from the shaft encoder (S) together with peak (Pk) and mean (M) Doppler for each string phantom program. Pk and M were compared with S by determining the root mean square (RMS) errors.

RESULTS

Pk overestimated the true velocity (S) in all cases. Figure 1 illustrates the differences between Pk, M and S for the triphasic waveform P4. The RMS errors are summarized in table 1 and confirm that there was very little difference between M and S for all generated waveforms.

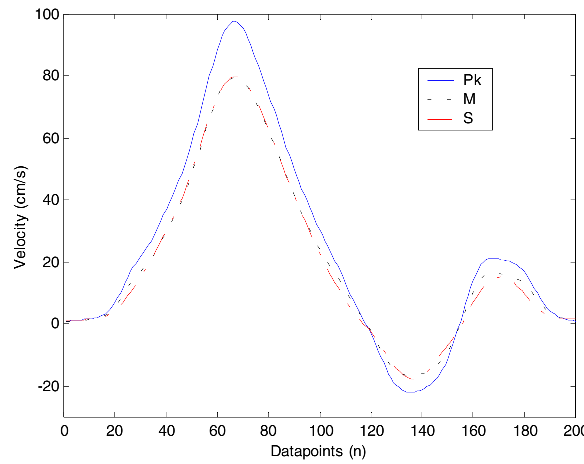

Figure 1: Peak (bold) & Mean (dashed) Doppler waveforms compared with the shaft encoder waveform for P4

SUMMARY

In the Doppler ultrasound system tested, the mean Doppler tracing algorithm was found to be more accurate than the peak for determining the velocity waveform for a string phantom. In order to avoid significant errors in velocity measurements, it is recommended that the accuracy of other ultrasound systems should be assessed using this method.

REFERENCES

Hoskins, P.R. (1999). *Proc Instn Mech Engrs* **213 Part H**, 391-400.

Rickey, D.W. & Fenster, A. (1996). *Ultrasound Med Biol vol* **22**(1)*:*61-73.

ACKNOWLEDGEMENTS

We would like to thank Dr. Keith Humphries for lending us the original string phantom.

Table 1: RMS error in peak and mean Doppler velocity waveforms compared with the shaft encoder waveform

String Program	**P1**	**P2**	**P3**	**P4**
Peak Doppler RMS error (cm/s)	16.9	12.5	7.0	7.6
Mean Doppler RMS error (cm/s)	2.0	1.0	1.7	1.5

HAND IMPACT FORCE REDUCTION IN FORWARD FALLS IN YOUNG MALES: A PROSPECTIVE, CONTROLLED, 3-MONTH INTERVENTION TRIAL

J. Lo, G.N. McCabe, H. Okuizumi, and J.A. Ashton-MillerBiomechanics Research Laboratory,
University of Michigan, Ann Arbor, MI USA. E-mail: joshualo@umich.edu

INTRODUCTION

Fall-related injuries of the upper extremities are common at any age because of the magnitude of the impact force acting on the limb (Myers et al. 1993). Accordingly, a reduction of impact forces is key to reducing fall impact-related injuries. It has recently been shown that after a brief, 10 minute, instructional intervention, healthy subjects can volitionally reduce the impact force on the upper extremity by 27% during standardized forward falls (DeGoede, 2002). Using this paradigm, we explore two hypotheses in young males using forward falls: (1) the reduction in impact forces obtained after the 10 minute instructional intervention during the baseline visit was not due to self-learning; (2) in a prospective, controlled, trial conducted without practice, the impact forces in the intervention group would not differ significantly from the untrained controls at 3 or 12-week follow-up.

METHODS

20 young males, without previous fall trainings, participated in the study (mean±SD: age=25±2 years, body weight=69±8 kgf, and height=173±3 cm). Subjects were leaned forward, restrained by a waist harness until a cable supported them with a tension of 30% body weight. Both shoulders were then lowered to 1 meter from the ground. Upon cable release, the subject was instructed to arrest the fall with both hands, and body segment kinematics were measured at 200 Hz using an Optotrak 3020 system. The impact forces on both hands were collected at 2 kHz using dual AMTI force plates. The subjects were divided randomly into two groups, 10 in the intervention and 10 in the control. At the baseline visit, each subject in the intervention group was asked to perform 5 falls without instruction (termed "natural falls"). The subjects were then given a 10-min intervention consisting of instructions on how to reduce impact by minimizing the hand-ground relative velocity at impact. After intervention, the subjects performed another 5 falls (termed "reduced-impact falls"). They were then asked to perform, without practice or instructions, 5 reduced-impact falls at the 3-week and 12-week follow-up visits. The control group followed a similar experimental protocol to that of the intervention group, except that they received no instructions during the intervention period and merely repeated their natural falls after the 10-min break and at the follow-up visits. A two-way repeated-measures analysis of variance was used to test the hypotheses using $p < 0.05$.

RESULTS AND DISCUSSION

The first hypothesis was supported in that, during the baseline visit, the intervention group volitionally reduced the impact forces by 11.4% ($p=0.0024$) over initial values, whereas the subjects in the control did not decrease their impact forces significantly (0.3%, $p=0.96$, Figure 1). The second hypothesis was supported in that, at 3 and 12 weeks follow-up, the mean impact forces of both groups were not different ($p=0.62$). Interestingly, across all subjects, impact force at 12 weeks follow-up was significantly less than that at baseline($p=0.007$).

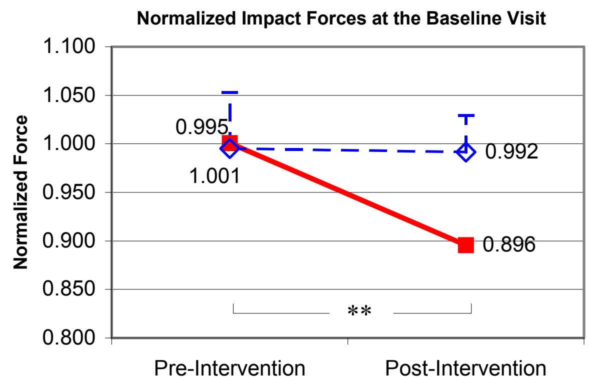

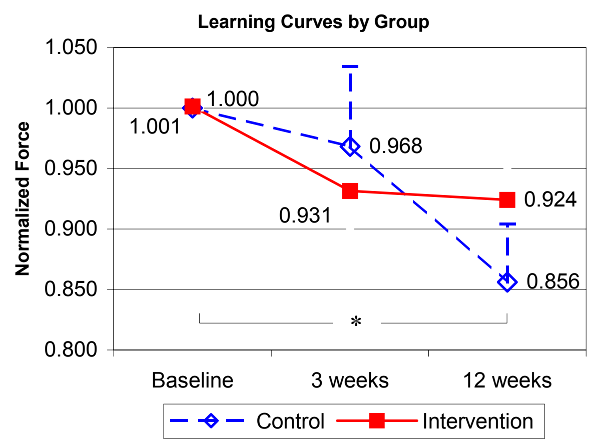

Figure 1: Top: Average impact forces at the baseline visit, by group. Bottom: Learning curves by group. (Bars denote standard error; forces are normalized by the mean of the five first 'natural' falls at baseline).

SUMMARY

Healthy young males can volitionally reduce impact forces after 10-minute instruction, and the control group data show this was not due to self-learning. The challenging nature of this fall-arrest task did induce, without practice, self-learning in the 3 months study period.

REFERENCES

Myers, E. R., et al. (1993). *Calcif. Tissue Int.,* **52**, 199-204
DeGoede, K. M. et al., (2002). *J. Biomech*. (In Press).

ACKNOWLEDGEMENTS

NIH Grants: P60 AG08808 and P01 AG10542.

THE ROLE OF TRANSVERSUS ABDOMINIS IN SPINE STABILITY

Sylvain G. Grenier, Stuart M. McGill
Occupational Biomechanics Laboratory, University of Waterloo, Waterloo, Ontario, Canada
Contact: sggrenie@ahsmail.uwaterloo.ca

INTRODUCTION

There is a perception in clinical circles that recruitment of transversus abdominis (TA) through abdominal hollowing (drawing in the navel) is advantageous because it increases stability without augmenting the compressive load on the spine. The abdominal hollowing recruitment technique was originally conceived to re-train TA recruitment and not to directly improve stability. This was thought to be important because TA has been found to be deficient in those with a previous low back injury (Hodges, 1998). The purpose of this research was to evaluate, through a model, the mechanical contribution of TA to spine stability.

METHODS

Over a period of twenty-five seconds a 10Kg bilateral weight was held in a neutral standing posture: relaxed for five seconds, abdominal hollow for five seconds, relax for five, abdominal brace for five and relax for the final five seconds. Lumbar spine kinematics were recorded in 3D and EMG was recorded from 7 channels bilaterally.

The model used in this experiment has been fully described by Cholewicki and McGill (1996). Some modifications were made to include TA. Ten fascicles were added bilaterally, five originating on the tip of the spinous process where the supraspinous ligament attaches, the others originating from the transverse process of the lumbar vertebrae. The ten fascicles converge on a point 60cm directly lateral of L5. This arrangement was conceived to reproduce the coronal plane action of TA on the lumbar spine while minimizing its moment generation potential.

The abdominal activation levels were artificially adjusted to imitate “ideal” hollowing (HLW) and bracing (BRC) strategies. The extensor activation levels were left untouched. For HLW, transversus abdominis and internal oblique were activated at 20% of maximum voluntary contraction (MVC) while the rectus abdominis and external oblique were activated at 1% MVC. The BRC strategy required all abdominals activated at 20%. Two additional trials were simulated one where rectus abdominis and external oblique were activated at 20% while TA and internal oblique were activated at 1% (NoIO/TA) and another where TA was deactivated (NoTA). The change in compression and stability between bracing and reference trials was expressed as a percentage change.

$$\boldsymbol{\%change = \left(\frac{BRC - REF}{BRC}\right) \times 100}$$

RESULTS AND DISCUSSION

As a means of increasing stability in the lumbar spine HLW is not as effective as BRC. BRC improved stability over HLW by 95.43% with only a 18.98% increase in compression. NoIO/TA decreased stability by 88.5% relative to BRC with a 8.3% decrease in compression (Table 2). Removing only TA from the BRC pattern decreased stability by 55%.

The mechanical effect of TA on stability has not, to our knowledge, been reported in the literature. The force generated by our TA equivalent was on the order of 10 N for a 20% MVC contraction. This compares Tesh et al.'s (1987) reported thoracolumbar fascia tissue tolerance of 335N. They also report that IAP may contribute as much as 40% of the restorative moment in lateral bending. Our own work shows that IAP contributes significant stiffness especially in the neutral posture. However for comparison purposes this can be safely neglected because a hollowing strategy is unlikely to generate greater IAP than bracing. Others have also suggested that general cocontraction balanced against the load is most effective in attaining and maintaining stability (Granata and Orishimo, 2001).

CONCLUSION

General bracing of the abdominal girdle should be advocated where greater spine stability is required. This is not say that abdominal hollowing is not a valid training tool for TA activation. Under conditions of surprise perturbation prompt recruitment of TA countering increased IAP may be critical until the remaining torso muscles can be recruited, once the CNS has determined the nature of the perturbation. It might be useful to compare the maximum load that could be stabilized by TA against the load generated by unexpected perturbations.

Table 1: The percent increase in stability with a minimal increase in compression (CMP) of BRC over every other strategy in the simulation is clear. The muscle compression (MCMP) values reported are the reference values.

% Δ from BRC	Stability	CMP	MCMP
BRC vs. HLW	95.43	18.98	316N
BRC vs. NoIO/TA	88.50	8.36	351N
BRC vs. NoTA	55.47	8.32	354N

REFERENCES

Cholewicki, McGill. (1996). *Clin Biomech*.,**11(1)**, 1-15.
Hodges, Richardson. (1996). *Spine*. **21**, 2640-2650.
Tesh, Shaw-Dunn, Evans. (1987). *Spine*, **12(5)**, 501-508.
Granata, Orishimo. (2001). *J Biomech*. **34**, 117-1123.

MUSCLE RECONSTRUCTION AND MODELING FROM MRI-SCAN

Mohamed Mahfouz[1,2], Richard Komistek[1], Scott Walker[1], Douglas Dennis[1]
[1]Rocky Mountain Musculoskeletal Research Laboratory, Denver, Colorado, mmahfouz@rmmrl.org
[2]Colorado School of Mines, Golden Colorado

INTRODUCTION

Medical imaging techniques such as Magnetic Resonance (MR) can noninvasively capture patient information specifics about the geometric and material properties of bone and muscle. Hence, MRI makes it possible to measure physiological cross-sectional area (PCSA) of leg muscles of healthy human subjects, which are much larger than PCSAs of cadaveric leg muscles that have been used in biomechanical simulation. The objective of this study was to use MRI to construct 3D models of human bone and soft-tissues and to compare the accuracy of the models with CT images.

METHODS

The entire lower limb of a healthy 30-year-old male subject was imaged using a fat-suppressed three-dimensional sequence (SPGR; 1.5T). Multiple overlapping MRI scans were required to complete the entire lower limb. Markers were attached to the subject skin and distributed throughout the leg in a non-collinear arrangement. These markers were used to register (3D–to-3D rigid transformation) the MRI volumetric data segments after the data sets have been geometrically corrected, due to gradient field nonlinearties and magnetic field inhomogeneities (using a specially designed calibration phantom). After correction of MR inhomogeneities, morphological operators were used to finally segment the muscle and bone. Bone segmentation was performed using a method based on deformable contours models (Terzopoulos, 1991; Terzopoulous, 1987). The segmentation methods used were mainly automated. Manual segmentation was performed only when the automated methods failed to separate a muscle, and in this case, the bone at the articular cartilage of the knee joint. More then sixteen muscle were segmented including all the knee flexors and extensors and the major ankle joint muscles.

RESULTS AND DISCUSSION

Muscle and bone segmentation results from MR scanning were successful (Figure 1). Good quality surface model for each muscle was created from the segmented volumes and the entire flexors and extensors muscles of the knee joint were created. The interfaces between the muscles and tendons were created as well (Figure 2). The results for this initial in vivo analysis were encouraging for 3D model development of muscles and bone models. Bone models created were similar in accuracy to the models constructed using CT images.

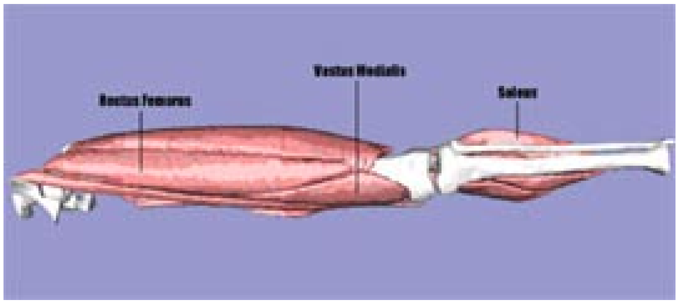

Figure 1. Selected muscles of the lower extremity.

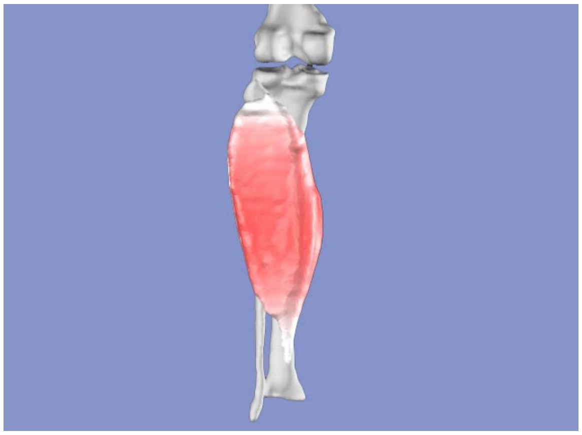

Figure 2. Muscle –Tendon interface Soleus.

SUMMARY
The objective of this study was to develop a 3-dimensional muscle model that is capable of predicting and simulating loads acting on knee, hip or ankle joint. The simulation method will employ modern finite element analysis techniques such as real muscle geometries, appropriate constitutive behavior and muscle interaction. Finite element models will provide appropriate computations required for evaluation of muscle and joint loads of a patient preoperatively.

REFERENCES

Terzopoulos, D., Metaxas, D., (1991) *Dynamic 3D Models with Local and Global Deformations: Deformable Superquadrics.* IEEE Trans. Pattern Analysis and Machine Intelligence, **13**: 703-714
Terzopoulous, D. (1987) *On Matching Deformable Models to Image*". Tech. Rept. 60. Schlumberger Palo Alto Research. Reprinted in Topical Meeting on Machine Vision, Technical Digest Series, (Optical Society of America, Washington, DC) **12**: 160-167.

A UNIQUE METHOD TO DETERMINE DYNAMIC *IN VIVO* ARTICULAR SURFACE INTERACTION

William J. Anderst and Scott Tashman
Motion Analysis Lab, Bone and Joint Center, Henry Ford Hospital, Detroit, MI
Email:anderst@bjc.hfh.edu

INTRODUCTION

This paper describes a unique method to calculate and visualize the proximity of articular bone surfaces during movement. This information may be useful in the study of osteoarthritis, in biomechanical modeling, and in identifying normal and pathological joint mechanics. As an example of this technique, the distances between tibia and femur articulating surfaces during hopping in uninjured and anterior cruciate ligament (ACL) reconstructed knees are presented.

METHODS

Kinematic Data: Under IRB approval and after acquiring informed consent, three 1.6mm tantalum spheres were implanted into both tibias and femurs during ACL reconstructive surgery. Data was acquired during one-legged hopping and treadmill running 6 months after surgery. Kinematic data was collected using a biplane radiographic system capable of tracking implanted radiopaque markers in 3D at a rate of 250 frames/s with a dynamic accuracy of $\pm$ 0.1mm (Tashman, 1995). 3D marker coordinates were determined using previously described techniques (Tashman, 1999).

Computed Tomography Data: Computed tomography (CT) data was collected after marker implantation (1mm slices, 0.5859mm x 0.5859mm resolution). The CT scans were reconstructed into 3D solid figures (Treece, 1999). The locations of the vertices in the solid figure mesh were used to calculate the area and centroid of each triangle in the solid figure.

Implanted tantalum marker locations were identified in the CT scans and combined with vertex information from the bone surface mesh to determine the relationship between implanted markers and bone surface centroids. This information, combined with the tracked radiopaque marker data, made it possible to calculate the minimum distance between bone surfaces on the tibia and femur at each instant. Surface polygons were color-coded according to the minimum distance between bones at each polygon centroid. The color-coded joint surfaces were displayed and animated using the freely available Geomview (www.geomview.org) software package.

RESULTS AND DISCUSSION

Figure 1 shows the color-coded surfaces of the uninjured and ACL reconstructed femur and tibia after landing from a one-legged hop.

Differences are evident between the uninjured and reconstructed joints. The uninjured joint shows an asymmetric distribution in medio-lateral contact patterns on the tibia, indicating the tibia was internally rotated relative to the femur. The reconstructed joint, however, showed a symmetric distribution of contact on the tibia. This difference could indicate that ACL reconstruction did not restore normal internal-external rotation of the tibia relative to the femur for this subject.

This tool for calculating and visualizing bone surface motion *in vivo* during dynamic movements may provide insight into cartilage deformation and damage. Additionally, it can provide information on the dynamic interaction between articular surfaces such as rolling and sliding contact and areas of close contact. It also can identify changes in joint surface motion over time. None of this information can be obtained using conventional 3D motion analysis.

REFERENCES

Tashman, S. (1995). *Proc. Am. Soc. Biomech*., Stanford, CA.
Tashman, S. et al.(1999). *Proc. Orthop. Res. Soc*.,Anaheim, CA.
Treece, G.M. et al. (1999). *Computers and Graphics,* 23 **(4)**.

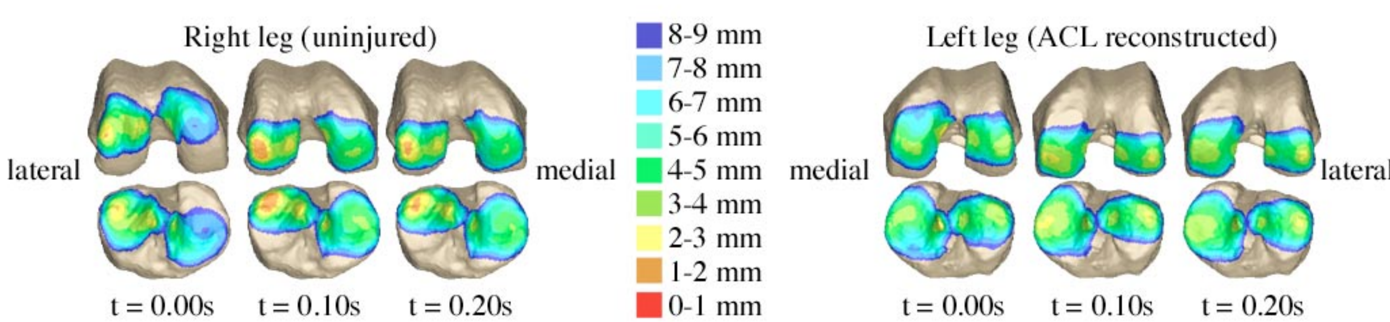

Figure 1: Color mapped distance between femur and tibia for the uninjured and ACL reconstructed knee of one subject. Time instants are post-touchdown for one-legged hopping.

QUADRICEPS FEMORIS ACTIVATION-FORCE RELATIONSHIP AND PERCEIVED EXERTION DURING DYNAMIC, INERTIAL KNEE EXTENSION EXERCISE

Danny M. Pincivero[1], Robert M. Campy[2], Yuliya Salfetnikov[2], and Alan J. Coelho[2]
[1]Human Performance and Fatigue Laboratory, Department of Kinesiology, The University of Toledo, danny.pincivero@utoledo.edu
[2]Department of Physical Education, Health and Recreation, Eastern Washington University

INTRODUCTION

The purpose of this study was to examine the effects of relative inertial load on QF muscle activation and perceived exertion during single-leg, knee extension exercise.

METHODS

Fifteen males and 15 females were evaluated for the maximum amount of weight they could lift once (1-RM) with their right leg during knee extension (Power Systems Inc.). Subjects performed 2 repetitions at loads equivalent to 20-90% (10% increments) of their 1-RM, in a random order. Subjects were instructed to: 1) lift the weight and achieve full knee extension (concentric phase), 2) hold the weight in the knee extended position for approximately 2 s (isometric phase), and 3) lower the weight in slow and controlled manner (eccentric phase).

Immediately following the 1-RM, subjects were instructed to "think about the feelings in their quadriceps during the contraction, and to assign a rating of maximal to those feelings". Following 2 min of rest, subjects were asked to sit quietly and to "think about the feelings in their quadriceps and to assign a rating of 0 to those feelings". Immediately prior to the sub-maximal contractions, subjects were instructed to "think about the feelings in your quadriceps during the contractions, and give a number from the scale about how your quadriceps feel", via a modified Borg (1982) category-ratio scale.

Muscle activation was assessed through surface EMG for the VM, VL, and RF muscles (sampling rate=1000 Hz, bandpass filtered 20-500 Hz). Pre-amplified, bipolar circular electrodes were placed on each muscle with a fixed 2 cm inter-electrode distance. Raw EMG activity was full-wave rectified and integrated over the concentric phase of the exercise, and at each sub-maximal lifting level, was converted to a 1 s average, and normalized to the recorded activity during the 1-RM.

RESULTS AND DISCUSSION

The results demonstrated a significant load effect as VM, VL and RF muscle EMG increased from 20-90% 1-RM ($F_{7,196}$= 156.72, $p<0.05$) (Figure 1). Rectus femoris EMG was found to increase significantly more than the VL from 30-40%, and 50-60% 1-RM. The results revealed a significant intensity main effect ($F_{7,189}$=195.49, $p<0.001$) for the perceived exertion responses. The findings demonstrated that perceived exertion was significantly ($p<0.05$) lower than the specific expected values on the CR-10 scale from 10-60% 1-RM, and was not different from 70-90% 1-RM. The results also revealed that the perceived exertion response was fit to the following power function: $R=9.998 \bullet S^{1.467}$, where R=predicted perceived exertion response, and S=relative lifting load.

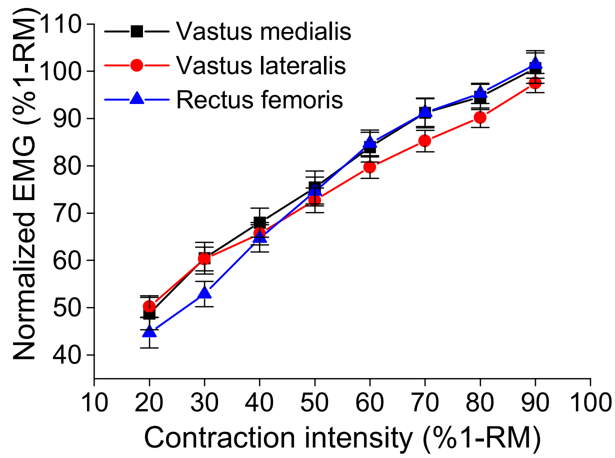

Figure 1: Normalized QF muscle EMG activity during the concentric phase of knee extension from 20-90% 1-RM.

SUMMARY

The major findings indicate that as a function of relative inertial load during dynamic knee extension exercise, RF EMG appears to increase more than the VL at moderate loads. Equivalent activation of the superficial QF muscles, however, appears to predominate throughout the range of lifting loads, while the perceptual sensation (i.e., perceived exertion) is more sensitive at relatively higher lifting intensities.

REFERENCES

Borg, G.A.V. (1982). Psychophysical bases of perceived exertion. *Med Sci Sports Exerc*. **14**:377-81.

ACKNOWLEDGEMENTS

This study was supported by an Eastern Washington University Faculty Research Grant (2000-01) awarded to D.M.P.

STRATEGY IN REDUCING ELBOW LOADING DURING FALL ON AN OUTSTRETCHED HAND

Paul Pei-Hsi Chou[1] , You-Li Chou[2] , Shen-Kai Chen[1] , Yung-Chin Shi[2], Gwo-Feng Hung[2], Tun-Chin Wu[2]
[1]Department of Orthopedic Surgery, Kaohsiung Medical University, Kaohsiung, Taiwan, chou0626@ms3.hinet.net
[2]Institute of Biomedical Engineering, National Cheng-Kung University, Tainan, Taiwan.

INTODUCTION

Approximately 75% of all fractures sustained by children occur in the upper extremities during a fall onto an outstretched hand. The majority of these injuries involve the wrist and forearm, but the elbow alone accounts for approximately 10 percent of all fractures in children. Clinically, there are far more extension type of supra-condylar fractures of the elbow than flexion type. Furthermore, posterolateral instability of the elbow can be reproduced with forearm supination and mild elbow flexion. These evidences stress the importance of elbow flexion in the upper extremity trauma. Therefore, the purpose of this study is to investigate the effect of different initial elbow flexion angles on joint loading during a fall on the outstretched hand.

METHODS

Twenty male subjects volunteered in this study. Their average age was 23.8 years, with an average height of 171.7 cm, and average weight of 62.9 Kg. A hinge elbow brace was used to limit the elbow extension without interfering the elbow flexion. A suspension system was designed to release the subject from 5 cm above the ground. Simulating a fall on the outstretched hand, each subject fell on the force plate with his elbow in four elbow flexion angles: 0°, 20°, 40°, and unlimited degree. A Motion Analysis System (Motion Analysis Inc., Santa Rosa, CA, U.S.A.), two Kistler force plates (Model 9281B, Kistler Instruments AG, Winterthur, Switzerland), and a workstation computer were used to collect data.

RESULTS AND DISCUSSION

The ground reaction force curve was characterized by a high frequency peak F_1 at the moment of impact. The second low frequency peak F_2 occurred soon after F_1 (Fig. 1).

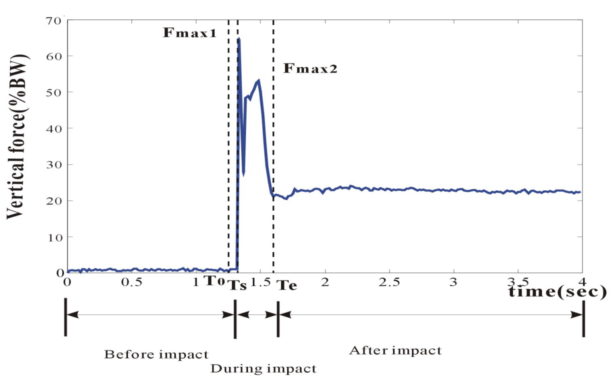

Figure 1: This is a ground reaction force (GRF) curve.
T_0 : release of subject from the suspension system.
Ts : the moment of impact. **Te :** the end of impact.

At the moment of impact, the F_1 was significantly different among various initial elbow flexion angles ($p<0.001$). The impact force F_1 decreased significantly with increased elbow flexion (Fig. 2).

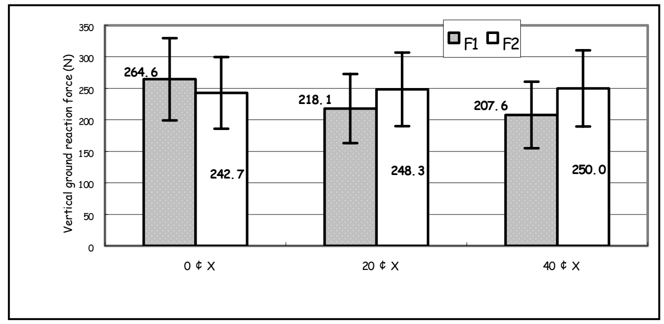

Figure 2: Peak ground reaction force F1, F2 (y-axis), vs. degree of initial elbow flexion angle (x-axis).

In a study by Chiu and Robinovitch, a fall height greater than 60 cm was predicted to be hazardous in producing distal radial fracture of the wrist. However, only the motion of shoulder and wrist were considered in their two-mass model to simulate a fall on the outstretched hand. In addition to the effective dampers and springs of wrist and shoulder, the elbow played a very important role of energy dissipation. Taking the effect of elbow motion into consideration, our three-mass-model was more precise in simulating the motion of upper extremity during a fall.

CONCLUSION

In conclusion, the loading biomechanics of the elbow joint differs with various initial flexion angles. With the increasing elbow flexion at the moment of impact, the impact force (F1) decreases but the elbow extension moment (M1) increases. On the contrary, the impact force (F1) is at maximum when the elbow is fully extended upon impact. Therefore, fall on the outstretched hand with elbow in full extension should be avoided. Additionally, a forward fall with mild elbow flexion maybe a better strategy to reduce impact force and to reduce injury.

REFERENCES

Chou, P.H., Chou, Y.L., Lin, C.J., et al. (2001). *Clin Biomech*, **16**, 888-894.

ACKNOWLEDGEMENTS

This study was supported by the National Science Council in Taiwan (NSC 89-2314-B-037-102-M08).

COMPARISON OF STEP VARIABILITY DURING GAIT ON FLAT AND IRREGULAR SURFACES IN PATIENTS WITH POLYNEUROPATHY

Sibylle Thies, James K. Richardson[1], and James A. Ashton-Miller

Biomechanics Research Laboratory, Department of Biomedical Engineering, and [1]Physical Medicine and Rehabilitation, University of Michigan, Michigan, USA. sthies@umich.edu

INTRODUCTION

Patients with a diffuse polyneuropathy (PN), which is characterized by a distal-to-proximal gradient decrement in lower extremity sensation and strength, have a 20-fold higher risk for falls and 6-fold higher risk for fall-related fractures than matched controls (Richardson, 1992). PN patients report difficulty when walking on uneven surfaces, particularly in low-light conditions. We are not aware of studies of how humans, whether impaired or healthy, adjust their gait on uneven ground. We tested the primary (null) hypothesis that elderly PN patients would not alter their stepping pattern when walking on an uneven surface under low-light as compared to a flat surface under normal light. Similarly, secondary hypotheses were tested that the uneven surface would not affect (a) step time, or (b) average gait speed.

METHODS

Twenty PN patients (64.1 ± 10.3 yrs; 15 males), in a full-body safety harness and identical walking shoes, were asked to walk a 6-m walkway at their comfortable speed under two conditions: on flat linoleum-tiled floor under normal lighting (> 600 lux, 10 trials), and on a standardized uneven surface (1.5 cm-high, multiple randomly-arranged triangular wooden prisms located under industrial carpeting) under low lighting (<90 lux, 10 trials). Kinematic measures of step width and step length were obtained during double support at 100 Hz using optoelectronic markers placed over both ankles (via Optotrak 3020 system), while two pairs of foot switches (heel, metatarsal) indicated dual support times. The standard deviation served as the measure of variability. A marker over the umbilicus was used to determine the average gait speed. Two-sided, paired t-tests (P<0.05) were used to test the hypotheses.

RESULTS AND DISCUSSION

The primary hypothesis was rejected in that the patients demonstrated an increased step width (7.7%, p=0.003) and increased step width variability (16.8%, p<0.001) on the uneven surface. The secondary hypotheses were also rejected in that significantly increased step time variability (42.0%; p<0.001), decreased step length (4.1%, p=0.004) and gait speed (6.5%, p=0.004) were found on the uneven surface. On the uneven surface, 8 patients exhibited a total of 34 steps that crossed the midline (defined as "cross-over" steps, Figure 1). Significantly fewer cross-over steps were observed on the flat surface: 3 patients exhibited a total of 4 cross-over steps. Cross-over steps are dangerous because they increase the risk for a trip via swing foot toe contact with the stance foot heel, particularly when the prior step is shortened. A detailed kinematic analysis of three cross-over steps on the uneven surface revealed that, following an unexpected stance foot perturbation, the torso marker veered laterally for about 0.5 second prior to alteration of the swing leg trajectory. In all three cases the next step was shorter (~3 cm) and wider (~4 cm), than average for the subject. This seemed to be part of the recovery strategy for mediolateral plane balance. This is the first quantification of human stepping patterns on an uneven surface.

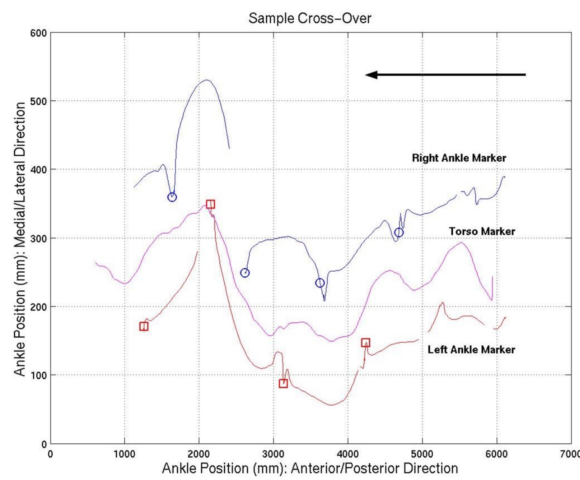

Figure 1: Top-view of sample kinematics of cross-over step (left foot crossing in front of the right while walking in the direction of the arrow on the uneven surface). Squares and circles show position of left and right ankles, respectively, at "foot-flat".

SUMMARY

An uneven surface and low lighting caused PN patients to significantly increase their step width and step time variability, and increase the number of unintended 'cross-over' steps, despite decreased step length and gait speed.

REFERENCES

Richardson, J.K. et al (1992). *JAGS*, 40, 1008-12.

A LOSS OF BALANCE IS A LOSS OF CONTROL: THE 3Σ HYPOTHESIS

Alaa A. Ahmed[1], M.S. and James Ashton-Miller[1,2], PhD.
Biomechanics Research Laboratory
Departments of [1]Biomedical and [2]Mechanical Engineering
University of Michigan, Ann Arbor, MI, U.S.A.[aaahmed@umich.edu]

INTRODUCTION

Happily, not every 'loss of balance' results in a fall, yet every fall is preceded by a 'loss of balance' (LOB). Surprisingly, a precise, physical description of a LOB is lacking. We propose that a LOB is the fundamental requirement for the CNS to initiate a compensatory response aimed at preventing a potential fall and/or subsequent injury. We posit that a 'loss of balance' is a loss of control (LOC) in engineering terms, causing the system to become temporarily unstable about the current operating point. In the event of a perturbation during gait, such as a trip, the controller must compensate for the temporary LOC through a change in control strategy in an attempt to regain stability about a new operating point. As long as this new operating point does not involve a fall, the event is classified as a 'temporary' LOC, else we define it post-hoc as a 'terminal' LOC. Our goal was to identify LOC in a challenging balancing task, and then to examine the reliability of this algorithm in predicting an impending compensatory response. We tested the primary hypothesis that the instant of loss of control (T_{LOC}) can be identified by using a 3Σ threshold criterion on the controller error signal (see below). The secondary hypothesis, that any compensatory response will lag the instant of LOC by at least 100ms, was also tested.

METHODS

Twenty healthy, young adult volunteers (10 females) aged 18-25 years were tested. They were seated in a sturdy, four-legged experimental chair with a rigid back and head rest (Fig.1a). The subjects were asked to use only their dominant leg forefoot to push themselves slowly backwards until they (and the chair) were perfectly balanced for as long as possible over its rear legs, P, with no foot-ground contact. Each subject performed ten trials with their eyes open. A 200 N force transducer under the dominant foot, sampled at 100 Hz, recorded the vertical and horizontal reaction forces (Fig.1b). The position of three LEDs on the head and two on the chair were tracked using an Optotrak 3020 system at 100 Hz. An error signal was formed from the difference between the expected system output due to the given force input and the actual output, chair acceleration. LOC was defined to have occurred once the error signal crossed a threshold level set at three standard deviations (3Σ) above the mean value in a 2-second-wide moving window that trailed the current time instant, t, by 100 msec. The mean and standard deviation of these data were used to calculate the threshold at time t (Fig.1c). Terminal LOC was confirmed by impact of the chair rear frame, F, with the ground after it had rotated 30^{o} within 2 sec. The occurrence of a natural righting response, a large acceleration of the head in flexion (relative to the chair), was defined as a compensatory response, and evidence of LOC perception. Reaction time (RT) was defined as the latency of this response following LOC (Fig.1d).

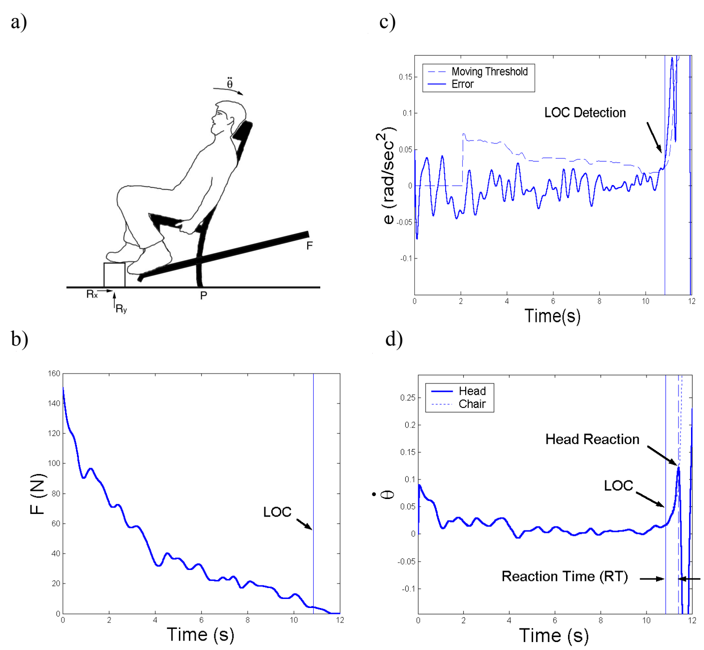

Figure 1: Single subject data (see text)

RESULTS AND DISCUSSION

The 3Σ algorithm successfully identified LOC in 98.0% of 197 trials and was supported by the presence of a compensatory response an average of 451 msec later in 95% of the trials. Short RTs were associated with large angular accelerations at T_{LOC}, and vice versa. No gender effects were observed. The optimal threshold level was found to be 3Σ; lower levels resulted in more false positives, while higher levels resulted in delayed LOC detection times. It is noteworthy that the 3Σ hypothesis does not depend on a vertical angular reference.

SUMMARY

The results support the definition of a loss of balance as being a loss of control. LOC was successfully identified, as was the latency of the following righting response.

ACKNOWLEDGEMENTS

NIH Grants P01 AG 10542 and P60 AG 08808

HIGH RESOLUTION MICRO-PARTICLE IMAGE VELOCIMETRY MEASUREMENTS OF FLOWS RELEVANT TO STENOTIC VESSELS

Sean D.Peterson[1], Michael W.Plesniak[1], Steven T. Wereley[1],
Steven H. Frankel[1], Karen M. Haberstroh[2], Thomas J.Webster[2], and Lisa X. Xu[1, 2]

[1]School of Mechanical Engineering and [2]Department of Biomedical Engineering
Purdue University, West Lafayette, Indiana, 47907, USA
plesniak@ecn.purdue.edu

INTRODUCTION

Blood flow under pathological conditions, such as atherosclerosis, involves a narrowing of the artery lumen, referred to as a stenosis, which together with flow pulsatility can result in periodic generation of turbulence despite relatively low Reynolds numbers. Laminar flow chambers have frequently been used to subject cells to known shear stresses (Frangos, 1988). However, the shear stresses are typically inferred from idealized theory for two-dimensional fully developed laminar flow between infinite parallel plates. We have measured the velocity fields within a typical laminar flow cell to examine how uniform the velocity and shear stress field is across the apparatus and how well it is predicted by theory. Application to turbulent stenotic flows is underway.

METHODS

Velocity fields within the flow chamber were obtained using micro-Particle Image Velocimetry (μ-PIV). The μ-PIV system consists of a pulsed Nd:YAG laser, a fast interline transfer CCD camera, and an epifluorescent microscope which captures two consecutive images of a fluorescent particle seeded flow illuminated by the laser. A 0.00038% concentration of 1 μm diameter seed particles and a 20X microscope lens were used to image a 300x300 μm area within the flow cell. The flow cell was a narrow channel 330 μm deep, 34.2 mm wide, and 74.1 mm long. Water (20C) was pumped through the chamber by a gear pump at a flow rate of 37.3 ml/min. One hundred image pairs were taken at each measurement volume within the chamber and temporally averaged to obtain the velocity.

.

RESULTS AND DISCUSSION

The spanwise velocity profiles at the inlet and in the center of the flow cell chamber are shown in Fig. 1. Each vector within the flow channel is an average of 1280 vectors in the μ-PIV interrogation region. A typical μ-PIV vector field is shown in the upper left part of Fig. 1. This is an average of five instantaneous realizations, from which a single vector is obtained. Additionally, three near-wall μ-PIV images are presented with average velocity profiles overlaid on the two images along the chamber centerline. The overall spanwise profile shows an interesting asymmetry about the streamwise centerline. The fluid near the bottom wall (opposite to the injection port) has a lower velocity than the fluid near the opposing wall. Also, near the injection slot wall, the velocity vectors are angled down towards the wall. This is because the injection slot does not span the entire channel.

These measurements show that even in a carefully designed and constructed flow apparatus, slight dimensional variances result in differences in the flow to which the cells are subjected. This illustrates the importance of measuring the velocity and associated shear stress field directly.

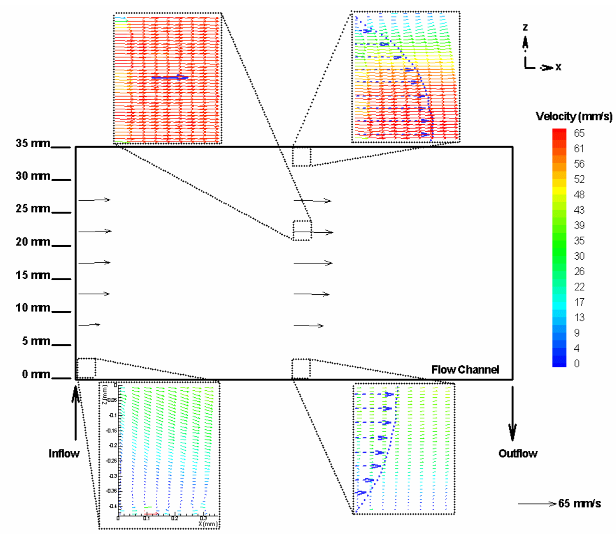

Figure 1. Micro-PIV Measurements in Laminar Flow Cell.

REFERENCES

Frangos, J.A., McIntire, L.V, and Eskin, S.G. (1988) "Shear Stress Induced Stimulation of Mammalian Cell Metabolism," *Biotech. & Bioeng.* **32**, 1053-1060.

ACKNOWLEDGEMENTS

We are grateful to the Showalter Trust for funding for this work and to Prof. Fred Pavalko (Department of Cellular and Integrative Physiology) of Indiana University Purdue University Indianapolis (IUPUI) for providing the flow chamber and for helpful discussions.

IMPACT ATTENUATION OF LANDING ACTIVITIES IN BAREFOOT AND SHOD

Songning Zhang and Yeonjoo Yu
Biomechanics/Sports Medicine Laboratory, The University of Tennessee, Knoxville, Tennessee, USA, szhang@utk.edu

INTRODUCTION

Impact loading is tremendous during the landing phase of sports activities. It can be dissipated through footwear, various connective tissues and skeletal muscles in the body. Effects of footwear on protection of the body from impact loading have been researched extensively in walking and running (Cavanagh et al., 1981; De Wit et al., 2000). However, few studies addressed its effects on impact and shock attenuation during more vigorous sport activities such as landing. Therefore, the purpose of this study was to investigate effects of shod and landing heights on impact force and shock attenuation during landing activities.

METHODS

Ten healthy and physically active male subjects (age: 20.4 ± 2.9 yrs, body mass: 77.0 ± 9.5 kg, 182.9 ± 5.6 cm) volunteered to participate in the study. A video camera (60 Hz, Panasonic) was used to obtain kinematic data of the right sagittal view; a force platform (AMTI) was used to measure ground reaction force (GRF) during the testing trials. Two miniature (1.7 g) accelerometers (A353B17, PCB) were used to measure accelerations (ACC) at the forehead and the distal tibia. Signals from the accelerometers and the force platform were sampled at 1200 Hz. The subjects performed 5 trials of step-off landings in each of eight testing conditions that are combinations of 4 landing heights (30, 45, 60 and 75 cm) and 2 surfaces (barefoot and athletic shoe). The subjects were instructed to land the right foot on the force platform with the left foot on the adjacent floor. The order of the surface conditions was randomized at each height; the landing height was increased from 30 to 75 cm. The raw coordinates of the reflective markers were smoothed using a fourth-order and zero-lag Butterworth digital filter. The cutoff frequency was individually chosen for the each x and y coordinate of the reflective markers using an optimized algorithm. A Shannon algorithm was used to reconstruct the video signal from 60 Hz to 240 Hz (Hamill et al., 1997). A 4 x 2 (height x surface) repeated measures analysis of variance was used to evaluate selected GRF, ACC and kinematic variables ($p < 0.05$).

RESULTS

The GRF results showed that the forefoot peak GRF (F1) in the shod landing was significantly greater than that in the barefoot landing at 45, 60 and 75 cm. The rearfoot peak GRF (F2) in the barefoot landing was significantly greater than that in the shod landing at 30, 45 and 75 cm levels. The impulse integrated from contact to 100 ms only showed a significant difference at 30 cm. Meanwhile the peak head ACC (Hmax) for the barefoot was smaller than that for the shod at two higher heights; the peak tibia ACC (LMax) for the barefoot was significantly greater than that for the shod at all landing heights. The shock attenuation index (Index) was calculated as:

$$Index = (1 - \frac{HMax}{LMax}) \times 100$$

Its result also demonstrated significantly greater values across all heights for the barefoot landing. The kinematic data showed that a greater contact angle for the ankle and a lesser contact angle for the knee joint at two lower heights in the barefoot landing.

Table 1. Mean values of selected GRF and ACC variables

Surface	Height	F1	F2	Impulse	HMax	LMax	Index
Shod	1	13.4	54.3	2.5	2.6	18.3	84.4
	2	21.5	59.3	2.7	3.3	23.8	85.2
	3	29.6	65.4	2.9	3.6	28.5	87.0
	4	36.9	75.9	3.1	4.5	38.2	88.1
Barefoot	1	13.1	65.2	2.3	2.3	30.1	90.6
	2	19.4	76.2	2.6	2.7	37.7	91.7
	3	26.0	81.0	2.8	3.0	47.5	92.1
	4	30.9	91.2	2.9	3.2	63.9	94.0

F1 & F2: N/kg, Impulse: Ns/kg, HMax & LMax: g, Index: %.

DISCUSSION

The results from this study showed significantly attenuated impacts at the forefoot contact in the barefoot landing. This may be due to conscious and active neuromuscular intervention because of increases in the perceived threat to the body. In the shod conditions, the impact experienced by the body was actually greater indicating a reduced conscious effort due to decreases in the perceived threat. The result indicates the importance of the material and construction at the forefoot area of footwear used in landing related sport activities. At the heel contact, greater impact forces were observed in the barefoot landing; the shoe provided additional cushion to the body. Therefore, it also indicates the importance of the midsole material and construction in the reafoot region of sport footwear. In addition, the kinematic results suggest that there may be a neuromuscular adaptation at the two lower heights.

REFERENCES

Cavanagh, P. R., et al. (1981). *Biomechanics VII-b*. Baltimore: University Park Press.
De Wit, B., et al. (2000). *J Biomech,* **33**, 269-278.
Hamill, J., et al. (1997). *J Appl Biomech.,* **13**, 226-238.

ACKNOWLEDGEMENTS

This study was supported by a grant from adidas America, Inc.

HAMSTRING LENGTH DURING GAIT DOES NOT CHANGE AFTER SURGICAL HAMSTRING LENGTHENING

Michael Orendurff
Gait Analysis Lab, Center of Excellence for Limb Loss Prevention and Prosthetic Engineering,
Veterans Hospital, Seattle, Washington, USA. morendurff@hotmail.com.

INTRODUCTION

When individuals walk in crouch and have tight hamstrings, surgical muscle lengthening may be undertaken in an effort to increase knee extension during gait. Several studies have evaluated hamstring length in children with cerebral palsy crouch gait, and suggested that their hamstring musculotendinous units are often of normal length (Delp, et al., 1998; Thompson, et al., 2001). Nevertheless, improvements in knee extension are seen following surgical hamstring lengthenings (Rethlefsen, et al., 1999), suggesting that the treatment is effective in increasing knee extension in gait despite the normal length of these muscles. The goal of this study was to evaluate joint kinematic changes, muscle length and muscle velocity after surgical hamstring intervention.

METHODS

Twenty-three individuals (40 sides) with cerebral palsy who underwent computerized gait analysis and hamstring lengthening surgery were reviewed retrospectively. All individuals underwent medial and lateral hamstring lengthenings; 22 sides also underwent adductor lengthenings, 9 sides had distal femoral derotational osteotomies, 5 sides had iliopsoas lengthenings, 4 sides underwent rectus femoris transfers, 4 sides had triceps surae lengthenings and 2 sides had subtalar fusions at the time of their hamstring surgery. Nine sides had hamstring surgery only. Gait data was collected with a 6-camera Vicon 370 system prior to and about one year following surgery. Three dimensional kinematics and kinetics were calculated in vicon clinical manager. Kinematic measures included maximum knee extension in single limb stance, maximum knee flexion, maximum hip extension in single limb stance, maximum hip flexion. Biceps femoris, rectus femoris, and vastus lateralis muscle lengths were calculated from the kinematic data using the methods of Visser, et al., (1990). Muscle velocity data was calculated using a 3-point finite difference algorithm. Maximum and minimum muscle lengths and velocities were extracted preop and postop. Variables were compared preop to postop using repeated measures ANOVAs. An alpha level of $p < 0.05$ was chosen a priori.

RESULTS

Table 1. Sagittal knee and hip kinematics before and after surgical hamstring lengthening. n = 40 sides (23 individuals). * indicates significance at $p < 0.05$.

	Preop	Postop	*p*-value
Knee			
Maximum Extension	30.1 ± 13.1°	7.6 ± 13.0°	<0.0001*
Maximum Flexion	57.8 ± 10.2°	45.5 ± 12.6°	<0.0001*
Hip			
Maximum Extension	13.7 ± 14.7°	11.2 ± 15.9°	0.1575
Maximum Flexion	49.3 ± 10.1°	54.5 ± 11.7°	0.0033*

Table 2. Muscle lengths (%anatomic neutral length) and velocities (%anatomic neutral length / %gait cycle) before and after surgical hamstring lengthening. n = 40 sides (23 individuals). * indicates significance at $p < 0.05$.

	Preop	Postop	*p*-value
Biceps Femoris			
Maximum Length	15.2 ± 3.6	16.1 ± 4.1	0.0989
Minimum Length	3.1 ± 4.7	2.8 ± 5.4	0.6356
Shortening Velocity	0.58 ± 0.20	0.60 ± 0.17	0.4540
Lengthening Velocity	-0.35 ± 0.13	-0.43 ± 0.10	0.0207*
Rectus Femoris			
Maximum Length	7.9 ± 2.3	6.2 ± 4.2	0.0053*
Minimum Length	2.2 ± 2.4	-2.5 ± 2.4	<0.0001*
Shortening Velocity	0.22 ± 0.13	0.35 ± 0.20	<0.0001*
Lengthening Velocity	-0.34 ± 0.14	-0.46 ± 0.20	<0.0001*
Vastus Lateralis			
Maximum Length	11.1 ± 1.8	8.9 ± 2.2	<0.0001*
Minimum Length	5.9 ± 2.6	1.2 ± 2.9	<0.0001*
Shortening Velocity	0.25 ± 0.11	0.35 ± 0.12	<0.0001*
Lengthening Velocity	-0.32 ± 0.12	-0.42 ± 0.14	<0.0001*

DISCUSSION

Despite surgical lengthening, hamstring length did not significantly change during gait from preop to postop, consistent with Delp, et al., (1998) and Thompson, et al., (2001). However, subjects showed a marked increase in knee extension in single limb stance, supporting the effectiveness of this intervention in improving crouch gait. Hamstring muscle-tendon length is much more dependent upon hip flexion than knee flexion, and hip flexion increased only in late stance, and then by just 5° from preop to postop. It is likely that hamstring tension is much lower postop, and that preop the individuals reached similar lengths with much greater tension. This reduction in tension at the functional length may account for the improvements observed, but in vivo tension measurements during gait were not made in this study. Hamstring shortening velocity did not change, but lengthening velocity did, suggesting that at the new tension level, eccentric contraction of the hamstring in single limb stance did not elicit spasticity as readily as was the case preop. The quadriceps showed improvements in all parameters, indicating that their function may have been improved. The results help to explain why hamstring length may be normal in individuals with crouch gait both preop and postop despite improvements in knee extension following surgical intervention.

REFERENCES

Delp, S.L., et al., (1996) *J Orthop Res,* **14,** 144-151
Thompson, N.S., et al., (2001) *J Pediatr Orthop,* **21**, 383-387
Rethlefsen, S., et al., (1999) *J Pediatr Orthop B,* **8**, 75-79
Visser, J.J., et al., (1990) *Eur J Appl Physiol,* **61**, 453-460

EFFECTS OF MIDSOLE DENSITY AND HEIGHT ON IMPACT ATTENUATION IN LANDING

Songning Zhang, Kurt Clowers and Charles Kohstall

Biomechanics/Sports Medicine Laboratory, The University of Tennessee, Knoxville, Tennessee, USA, szhang@utk.edu

INTRODUCTION

Effects of shoe properties on impact attenuation have been researched extensively with mixed results. Lafortune and Hennig (Lafortune et al., 1992) reported significantly lower initial peak tibia acceleration and acceleration transient rate in the athletic shoes and street shoes compared to the barefoot during walking. Nigg et al. (Nigg et al., 1987) found no significant effects of running shoes with different midsole densities on peak vertical ground reaction forces (GRF) in running. Therefore, the purpose of this study was to examine effects of shoe midsole densities on impact shock attenuation during a landing activity.

METHODS

Nine healthy and intercollegiate male athletes (age: 20.2 ± 1.9 yrs, body mass: 77.4 ± 5.1 kg, 1.82 ± 0.07 m) participated in the study. Instrumentation. A digital video camera (120 Hz, JVC) was used to obtain right sagittal kinematic data; a force platform (AMTI) was used to measure GRF during the testing trials. Two miniature (1.7 g) accelerometers (A353B17, PCB) were used to measure accelerations (ACC) at the forehead and the distal tibia. Signals from the accelerometers and the force platform were sampled at 1200 Hz. An electrogoniometer (Penny and Gile) was placed on the left knee joint to monitor consistency of the maximum knee flexion during landing performance. Subjects wore three pairs of basketball shoes (adidas) that have identical construction and are differed only by the midsole density: soft (Shore C: 40), normal (Shore C: 55), and hard (Shore C: 70) midsole. The subjects performed five step-off landing trials in each of nine test conditions that are a combination of three different shoes and three different pre-determined heights. The three jump heights were determined individually based upon the potential energy (PE) of a subject. A “mid-size” person of 80 kg landing from 0.60 m with a potential energy of 470.9 J was chosen as a 100% PE condition. A 70% and 130% PE were computed accordingly; three heights were then determined based on the body mass of individual subjects. A Shannon algorithm was used to reconstruct the video signal from 60 Hz to 240 Hz. A 3 x 3 (surface x height) repeated measures analysis of variance was performed on selected GRF and ACC variables with the significance level set at $p < 0.05$.

RESULTS

The GRF results showed that the first peak GRF (F1) in the normal and hard midsoles was significantly greater than that in the soft midsole at the low and median PEs (Table 1). The difference of the second peak GRF (F2) was significant between the normal and hard midsoles and between the soft and hard midsoles at the median PE, and between the soft and hard midsoles at the high PE. The accelerometer data indicated that the peak head ACC (HMax) of the normal and hard midsoles were significantly greater than that of the soft midsole at the median and high PEs (Table 1). A greater peak tibia ACC (LMax) for the hard midsole was observed compared to the other midsoles at the median PE. At the high PE, the peak tibia ACC of the hard midsole was also significantly greater than that of the soft midsole. A higher shock attenuation index (as a ratio HMax and LMax) was also observed for the hard midsole at both median and high PEs compared to the soft shoe.

Table 1. Mean values of selected GRF and ACC variables

PE	Midsole	F1	F2	HMax	LMax	Index
Low	Soft	19.4	57.5	3.49	24.6	86.2
	Normal	20.9	58.7	3.5	26.7	87.1
	Hard	21.6	63.9	3.6	30.6	88.1
Med	Soft	29.3	67.1	4.0	34.5	88.5
	Normal	30.6	66.5	3.8	35.4	89.0
	Hard	30.7	81.0	4.4	46.4	90.6
High	Soft	41.2	78.2	4.7	49.2	90.0
	Normal	42.4	81.4	5.0	52.6	90.1
	Hard	42.6	87.6	5.1	59.8	91.2

Unit: F1 & F2 - N/kg, HMax & LMax - g, Index - %.

DISCUSSION

Gross and Nelson (Gross et al., 1988) found no significant differences in peak GRF and ACC values across three different surfaces in barefoot landings. Our results are also different from that of Nigg et al. (Nigg et al., 1987). On the other hand, Lafortune and Hennig (Lafortune, &Hennig, 1992) were able to detect significant effects of more compliant shoe on shock attenuation. The results from this study indicated that the forefoot (F1) and rearfoot (F2) impact forces were attenuated with the softer shoes, but occurred at the different PE levels. The peak head and tibia shock waves were also attenuated to certain extents. The results from this study suggest that shoes with more compliant midsole provide better cushion in the landing activities.

REFERENCES

Gross, T. S., Nelson, R. C. (1988). *Med. Sci. Sports Exerc.,* **20**, 506-514.
Lafortune, M. A., Hennig, E. M. (1992). *Clin. Biomech.,* **23**, 360-363.
Nigg, B. M., et al. (1987). *J. of Biomech.,* **20**, 951-959.

ACKNOWLEDGEMENTS

This study was supported by a grant from adidas America, Inc.

CORRELATION OF MECHANICAL FACTORS WITH INTIMAL HYPERPLASIA IN THE MILLER'S CUFF AND ITS APPLICATION TO OPTIMIZATION OF ANASTOMOTIC DESIGN

Xue-Mei Li[1] and Stanley E. Rittgers[2]
[1]Department of Biomedical Engineering, Duke University, Durham, NC, USA
[2]Department of Biomedical Engineering, The University of Akron, Akron, OH, USA

INTRODUCTION

Mchanical factors are believed to be among the primary causes implicated in stimulating the formation of anastomotic intimal hyperplasia (IH). Although these factors have been analyzed by several groups employing computational simulations [Hofer (1996), Ballyk (1998)], none of these studies were based on a realistic large strain model for wall stress analysis nor did these studies attempt a direct correlation of the amount of IH with mechanical factors. Furthermore, optimizations of anastomotic designs to diminish IH formation have only considered the hemodynamic factors which were present in the physiologically loaded anastomotic geometry. Therefore, the purposes of this study were to: 1) simulate the mechanical environment by using a large strain finite element analysis (FEA) and a pulsatile computational fluid dynamics (CFD) analysis, 2) establish a regression relationship between IH and mechanical factors, 3) to provide an insight to the reduced IH formation in the venous cuffed anastomosis, and, 4) optimize the anastomotic design by altering the mechanical factors present in the regression relationship obtained above.

METHODS

An ePTFE cuffed distal end-to-side anastomosis was constructed for computational analysis in accordance with clinic procedures described by Kissin et al. (2000). A large strain and deformation FEA was used to analyze the wall strain and stress distribution in the anastomosis under the application of physiological loading. The deformed anastomotic geometries were then used as the wall boundaries for pulsatile CFD analysis. The maximal principle wall strain, wall shear stress, and oscillatory shear index (OSI) were calculated. Multiple linear regression analysis was employed in an effort to establish relationships between the amount of IH obtained by Kissin et al. (2000) in a chronic (4 wk.) porcine implant and these mechanical factors. The regression relationship was applied to biomechanical factors in similarly constructed venous cuffed anastomosis in order to explain the reduced amount of IH as also obtained by Kissin et al. (2000). Finally, an optimized design has been performed of a single component ePTFE anastomosis to control the mechanical factors involved in the regression relationship for the purpose of facilitating surgery and reducing IH.

RESULTS AND DISCUSSION

A distinct feature of the FEA derived wall mechanics was that the expansion of the cuffs caused elevated strains and stresses along the artery floor as well as at the heel and toe regions in the anastomosis. The hemodynamics were characterized by a large central vortex in the cuff region during most of the cardiac cycle, which was suppressed by a forward stream motion during the acceleration phase and then divided by a backward stream during the reversing phase. The multiple linear regression equation for IH vs. strain, ε, and oscillatory shear index, OSI, was:

$$\mathrm{IH}(\mu\mathrm{m}) = -1397 + (2765 \times \varepsilon) + (1034 \times \mathrm{OSI}) \quad (R^2=0.999,\ p<0.05) \tag{1}$$

with a standardized regression equation of:

$$\mathrm{IH} = (0.91 \times \varepsilon) + (0.80 \times \mathrm{OSI}) \tag{2}$$

Taking the values for ε and OSI calculated for the venous cuff simulation and substituting them into Eqn. (1) predicted values of IH of 527 μm, 616 μm, and 213 μm at the heel, middle floor, and toe, respectively. Compared to the values of IH obtained by Kissin et al. (2000) at four weeks implantation (13 μm, 10 μm, and 9μm at the heel, middle floor, and toe, respectively), these predicted IH amounts were much greater (>20X) than those actually present. This implies that unaccounted for biological factors may work against the stimulating effect of the mechanical factors. The optimized anastomotic design showed that a laterally constrained, donut shaped, single component ePTFE graft/cuff generated a uniformly reduced wall strain and a partially reduced OSI under physiological loading which, thus, should suppress the IH formation at the heel, toe and middle artery floor.

CONCLUSIONS

A large strain model is necessary to resolve important biomechanical features in the vascular anastomotic analysis. Maximal principle wall strain and OSI account for the formation of intimal hyperplasia directly proportionally and equivalently in an ePTFE cuffed anastomosis. Based on our model, the reduced amount of intimal hyperplasia in the venous cuffed anastomosis is not due to the extensibility of the cuff material nor to a beneficial influence of its unique shape on the hemodynamic environment. A clipped, donut shaped, single component ePTFE anastomosis uniformly reduced the wall strain and partially reduced the OSI compared to the traditional approach.

REFERENCES

Hofer et al. J Biomech, 1996; **29**:1297-1308.
Ballyk et al. J Biomech, 1998; **31**:229-37.
Kissin et al. J Vasc Surg, 2000; **31**, 69-83.

A REPRODUCIBLE METHOD TO DEFINE A COORDINATE SYSTEM FOR 3D KINEMATICS EVALUATION OF THE KNEE

Maxime Van de Putte [1, 2] maxime.vandeputte@etsmtl.ca, Nicola Hagemeister [1], Gerald Parent [1], Nancy St-Onge [1, 4], J.A. de Guise [1,3]
[1]Laboratoire de recherche en imagerie et orthopédie (LIO), CHUM Hôpital Notre-Dame, Montréal (Québec), [2]Université de Montréal, Montréal (Québec), [3]École de Technologie Supérieure, Montréal (Québec), [4]Institut de réadaptation de Montréal, Montréal (Québec)

INTRODUCTION

When 3D kinematics are recorded, parameters are generally represented in a local coordinate system for a clinically sound interpretation of the data (calibration). The difficulty in defining a correct joint coordinate system in the knee, without the use of medical imaging (Rx) resides in the precise positioning, in space, of anatomical landmarks (i.e.: The femoral condyles, antero-superior iliac spine and the postero-superior iliac spine). Techniques described in the literature generate errors of a significant nature. Our research group (LIO) has developed a technique based on a functional approach already proposed by Cappozzo (1984) and using less anatomical landmarks. The proposed technique includes a postural approach to define the neutral position of the knee (0° of flexion and extension). The hypothesis is that errors incurred by the definition of the anatomical landmarks would be diminished through a more functional approach.

METHODS

In this experiment, reproducibility of both techniques (LIO and Cappozo 1984) was evaluated in 5 subjects by three observers. The 3D kinematics of the subjects were recorded while they were walking on an instrumented treadmill after 5 minutes of habituation. Mean kinematic parameters (knee flexion/extension, abduction/adduction, tibial rotation, antero-posterior, medio-lateral and vertical translations) were calculated from 30 gait cycles using the two different calibrating methods (5 calibrations per technique per observer for the same sample of gait).

Evaluation of mean error for each observer and for all observers were then carried out to evaluate the results obtained for each calibrating technique. Repeatability was assessed through intra class correlation coefficient (ICC) (Kadaba 1989). A Student t test was then used to determine if the discrepancies discovered between the two calibrating techniques were of a significant nature.

RESULTS AND DISCUSSION

On the 5 subjects that have been recorded to date, our calibration technique has given results that suggest an equal or higher reproducibility of the calibrating technique, compared to the one proposed by Cappozzo (table1). The Student t test analysis as shown that errors yielded by our calibrating technique were smaller than those produced by Cappozzo's technique in abduction/adduction and tibial rotation for the intra-observer study. The inter-observer study has shown that our calibrating technique generated errors that were statistically smaller from Cappozzo's in all parameters except for flexion/extension (fig.1). The proof of a higher reproducibility of our technique could diminish the possibility of error due to the difficulty to locate the anatomical landmarks.

	Flex/Ext	*Abd/Add**	*Tibial rot**	*A-P Trans*
LIO	0.996	0.851	0.925	0.645
	0.002	0.145	0.079	0.128
Cappozzo	0.997	0.474	0.356	0.467
	0.003	0.235	0.149	0.344

Table 1: ICC and standard deviation for both calibrating techniques, results obtained by observer #1 on 5 subjects (* p<0.05).

Mean Error, LIO vs Cappozzo

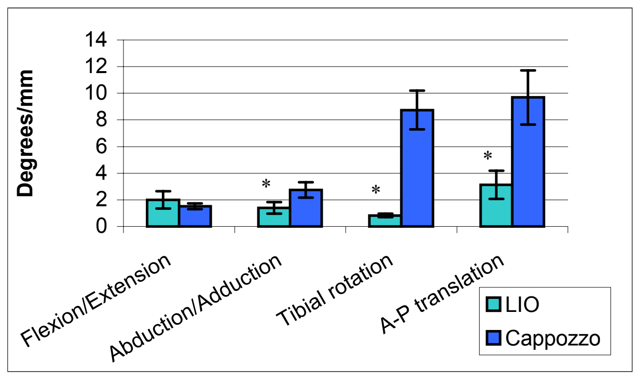

Figure 1: Mean error in both calibrating techniques, inter-observer study (* p<0.05)

SUMMARY:

The goal of this study is to develop a new technique for the precise positioning of the local coordinate systems necessary for the 3D knee kinematic analysis. Our technique, which is based on a functional approach for the determination of local coordinate systems, has yielded results that are more reproducible than those obtained using Cappozzo's method.

REFERENCES

Cappozzo, A., (1984). Gait analysis methodology. *Human Movement Science,* **3**, 27-50.
Kadaba, H.K. et al. (1989) Repeatability of Kinematic, Kinetic, and Electromyographic Data in normal Adult Gait. *J. Orthop. Res.*, **7**, No.6.

FRACTURE TOUGHNESS OF CARTILAGE BY MICROINDENTATION

Jack L. Lewis[1] and Narendra K. Simha[2]
[1]Department of Orthopaedic Surgery, University of Minnesota, USA
[2]Department of Mechanical Engineering, University of Miami, USA

INTRODUCTION

Cartilage strength is important as a measure of cartilage function; reduction of strength reflects degradation of the matrix. Although important, there are few methods for measuring cartilage strength. Tensile tests are the most common method, but they do not reflect the failure mode of cartilage and it is difficult to fabricate the small specimens needed for these tests. An alternative method for strength measurement is microindentation, in which an indenting tip penetrates the surface. Small tissue volumes can be tested without the need to prepare regularly shaped small specimens. However, traditional nanoindentation methods[1] used with metals and other hard materials do not work with soft time dependent materials. Methods are proposed for overcoming these limitations and deducing a fracture toughness value for cartilage from microindentation tests.

METHODS

Cartilage from bovine patella was indented using a NanoindenterXP (MTS, Inc.). Bone/cartilage specimens approximately 10 x 10 x 4 mm were adhered to a holder and bathed with PBS. Indents were made with a conical indenter with diamond tip of included angle of 67^0. After finding the surface, the tissue was loaded at a rate of 4 mN/sec to a maximum load. To assess penetration, in test Group 1 indents with maximum loads of 75, 100, 150, 200, 300, and 400 mN were performed. After testing the cartilage was bathed in India Ink and examined in a dissecting microscope. In each of Groups 2 and 3, 3 indents each of maximum load of 300 mN and 400 mN were performed. In group 4, 3 indents of 300 mN and 3 indents of 400 mN were performed and the specimen prepared for histology and depths of the indents measured from the slides.

Depth of penetration was predicted by assuming that the rate of work done, the power, increases rapidly whenever penetration occurs. After an initial penetration, as determined from the power rate, all displacement that occurs during elevated power rate was considered penetration displacement. These were summed to give the total penetration. The penetration, or fracture work, done was the sum of work done during the penetrating displacements. Fracture toughness was defined as the work during penetration divided by one-half the penetrated surface area of the conical tip.

RESULTS AND DISCUSSION

Comparing the power and India Ink stain images suggests that rapid change in the power is a reliable indicator of penetration. The predicted depth of penetration was not different from the depth measured by histology ($p>.5$). The predicted fracture toughness for the 300 mN indents was identical with the predicted fracture toughness for the 400 mN indents, for both Groups 2 and 3. The pooled results for Group 2 is different from the results for Group 3, probably reflecting variation over the patella surface[2]. The fracture toughness of Groups 2 and 3 are compared with the fracture toughness for bovine cartilage measured by Adams et al[3] using a modified single edged notch test. There was no difference between the Adams results and the present results (Figure 1).

SUMMARY

A value of fracture toughness of cartilage can be

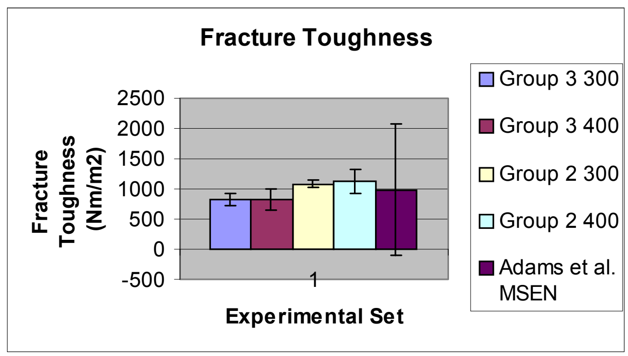

measured by microindentation. The predicted penetration depth agrees well with direct measurement by histology. The predicted fracture toughness agrees well with values measured by a macroscopic test. The microindentation method is promising as a new tool for measuring failure properties of cartilage and other soft tissues.

REFERENCES

1. Oliver, W.C. and Pharr, G.M., J. Mat. Res. 7:1564 1583, 1992. 2.Chin-Purcell, M. and Lewis, J.L., J. Biomech. Engr., 118:545-556, 1996. 3. Adams,D.J. et al., Trans. Ortho. Res. Soc., 1999, p.653.

ACKNOWLEDGEMENTS

Materials Research Science and Engineering Center, University of Minnesota, NSF DMR-9809364.

EFFECT OF SHOE MASS ON SOCCER KICKING VELOCITY

Mike Amos and Erez Morag
Nike Sports Research Laboratory, Nike, Beaverton, Oregon, USA
michael.amos@nike.com

INTRODUCTION

Foot speed is an important trait of skilled soccer players. It assists them in maneuvering the ball past opposing defenders and enables them to make first contact with the ball in a 50/50 challenge. It is generally recognized that changes in shoe characteristics which improve foot speed are advantageous.

Increases in shoe mass have been shown to require increased energy expenditure. In steady-state running Frederick (1983) predicts an increase of 1% VO_2 for every 100 grams of additional shoe mass. During an activity such as soccer where rapid changes in speed and direction occur which require large foot accelerations this energy cost may be even higher.

The purpose of this study was to evaluate the influence of shoe mass on soccer kicking velocity.

METHODS

Fourteen skilled male soccer players performed 3 maximal effort kicks in each of 5 shoe mass conditions; 215, 344, 381, 431, and 482 g. The dominant foot and a 2-step approach were used in each kick. The ball was kicked straight forward. Ball pressure was 12 PSI.

High speed video (1000 Hz) recorded the motion of markers placed on the lateral fibula, the lateral malleolus, and the 5th metatarsal head. Foot velocity was calculated from these markers and the ball was treated as a marker to measure ball velocity.

EMG (1000 Hz) was collected and used to measure activation in 5 muscles in the kicking leg (tibialis anterior, lateral/medial quadriceps, and lateral/medial hamstrings). The signals were bandpass filtered (10-350 Hz), rectified, and low-pass filtered (20 Hz) to create linear envelope curves and expressed as a percentage of maximal voluntary contractions for each muscle. Mean activation levels were calculated for i) 50 ms before ball contact (BC), ii) during BC, and iii) 100 ms after BC.

RESULTS AND DISCUSSION

Shoe mass had a significant effect on peak foot velocity ($p=0.002$); as shoe mass increased foot velocity decreased.

There was no significant difference in the resulting ball velocity between shoe conditions ($p=0.510$). Striking the ball with added shoe mass seems to have compensated for the reduced foot impact velocity to create an equivalent ball velocity.

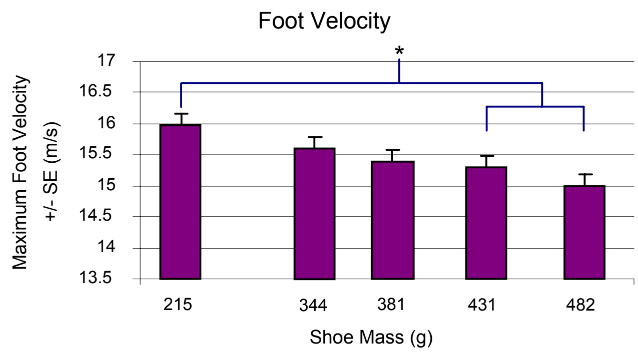

Figure 1: Peak foot velocities during maximal effort kicks. Note the reduction in velocity with increased shoe mass.

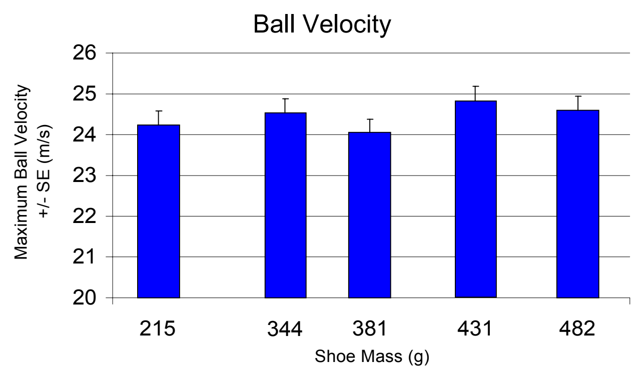

Figure 2: Peak ball velocities resulting from maximal effort kicks. Ball velocity is unchanged by varying shoe mass.

No differences were detected in EMG activity between shoe conditions for any of the muscles or time intervals monitored ($p=0.534-0.992$). It may be that any existing differences in muscle activation between shoe conditions were masked by the natural variability in kicking technique.

SUMMARY

Increases in foot velocity were observed during kicking in lighter shoes. This was accomplished without detectable change in muscle activation level or resulting ball velocity. Therefore, potential advantages from increased foot speed and agility can be attained with lighter shoes while maintaining ball kicking velocity.

REFERENCES

Frederick, E.C. (1983). *Biomechanics IX-B,* 295-300, Human Kinetics Publishers.

NEUROMUSCULAR RESPONSES TO KNEE OSTEOARTHRITIS DURING STAIRWAY LOCOMOTION

Paul DeVita, Jill Moody, Stacey Beam, Jovita Jolla, Kim Smith, Chris Mizelle, Joe Garry, and Tibor Hortobagyi
Biomechanics Laboratory, East Carolina University, Greenville, NC, USA

INTRODUCTION

While pain due to knee osteoarthritis (OA) limits movement capabilities (Hurwitz et al 2000), secondary muscle deficits including less quadriceps activation and strength (Hurley et al 1993) also affect movement. Knee OA subjects had reduced knee extensor torques in level walking and in stair ascent compared to healthy controls (Fisher et al 1997, Kaufman et al. 2001). Although other populations with reduced knee muscle function (i.e. ACL injured and healthy older adults) have shown increases in either hip and/or ankle muscle function (DeVita et al, 1998, 2000), compensatory functional increases have not been reported in knee OA patients. We hypothesized that knee OA is associated with a neuromuscular reorganization during gait such that reductions in knee extensor function will be compensated by increases in other lower limb muscles. The purpose of this study was to identify the effects of knee OA on lower extremity joint torques and powers during stairway locomotion.

METHODS

Eleven knee OA and 12 healthy subjects (mean ages: 57 & 49 yr) were tested in stair ascent and descent on a 4-step stairway instrumented with a force plate. Presence of OA was verified by a physician and with X-rays. Steps were 20 cm high and 27 cm deep. Floor reactions and sagittal plane kinematics were obtained during ascent and descent and combined with inverse dynamics to calculate hip, knee, and ankle joint torques and powers. Support torque and total power curves were calculated as the sum of the individual joint torques and powers. Extensor angular impulse and work at each joint were derived from these data and compared between groups with t-tests, $p<0.05$.

RESULTS AND DISCUSSION

While support torque and total power were not different between groups, OA increased the hip extensor angular impulse 250% to offset the 25% reduced knee extensor angular impulse compared to healthy subjects in ascent. These torques produced 220% more work at the hip and 19% less work at knee in the OA group. Peak hip torques were similar between groups but the phase of extensor torque lasted longer in OA. Ankle torque and power were nearly identical between groups in ascent. Descent torques and powers had fewer differences than ascent. Healthy subjects had 8% more plantarflexor impulse that did 36% more work compared to OA subjects in stair descent.

Our knee torque results were similar to those of Kaufman et al for ascent but not descent. They reported ~77% higher peak knee torque in healthy vs. OA and we had a ~75% difference (see figure). Kaufman et al also had higher knee torque in descent vs. ascent while we had the opposite result. Since subject and stairway characteristics and subject kinematics (not reported here) were similar between studies, we cannot explain these differences at this time.

We concluded that knee OA caused a reorganization of the neuromuscular control strategy in stair ascent such that ascent was performed with greater effort from the hip extensors and less effort from the knee extensors. We found less support for our hypothesis in descent since only the ankle muscles performed differently between groups.

REFERENCES

DeVita, P. et al. (1998). *Med. Sci Sports Exer*. **30**, 1481-1488.
DeVita, P. et al. (2000). J. Appl. Physiol., **88**, 1804-1811.
Fisher, N.M. et al. (1997). *Disability & Rehab.*, **19**, 47-55.
Hurley, M.V. et al. (1993). *Brit. J. Rheumatol*. **32**, 127-131.
Hurwitz, D.E. et al. (2000). *J. Orthop. Res.*, **18**, 572-579.
Kaufmann, K.R. et al. (2001). *J. Biomech*. **34**, 907-915.

Figure 1. Mean joint torque curves. * in areas with OA different than healthy. OA - solid lines, Healthy - dashed lines.

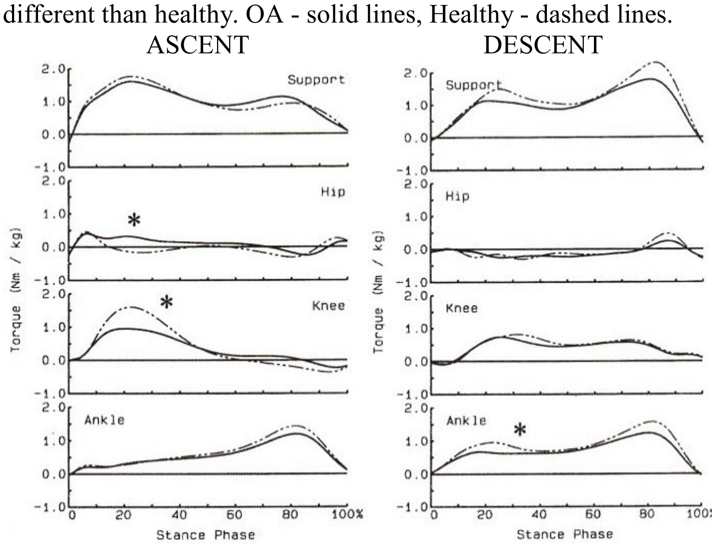

Table 1. Mean (sd) angular impulse (Nms/kg) and work (J/kg) values. * OA vs. Healthy, $p<0.05$

Angular Impulse:	Support	Hip	Knee	Ankle	Work:	Total	Hip	Knee	Ankle
Ascent: OA	0.78 (0.25)	0.20 (0.15) *	0.24 (0.08) *	0.45 (0.08)		1.25 (0.25)	0.22 (0.19) *	0.60 (0.17) *	0.58 (0.14)
Healthy	0.70 (0.14)	0.08 (0.05)	0.32 (0.10)	0.45 (0.08)		1.29 (0.12)	0.10 (0.06)	0.74 (0.20)	0.62 (0.16)
Descent: OA	0.69 (0.20)	-0.12 (0.09)	0.25 (0.10)	0.49 (0.15) *		-1.00 (0.14)	-0.10 (0.05)	-0.49 (0.18)	-0.30 (0.08)*
Healthy	0.75 (0.14)	-0.11 (0.07)	0.27 (0.12)	0.53 (0.10)		-1.12 (0.18)	-0.08 (0.02)	-0.55 (0.28)	-0.41 (0.07)

A COLOR-CODED VIDEO-BASED SYSTEM FOR POSTURE AND FOOT ASSESSMENT

Mehrdad Anbarian[1,2], Paul Allard[1], Ronald Perrault[3], Sébastien Hinse[1,3], Heydar Sadeghi[1] and Nader Farahpour[2]
[1]University of Montreal, Canada; [2]Bu-Ali Sina University, Hamadan, Iran; [3]Cryos Technology Inc. Joliette, Canada
Tel: +1 514 343-5601 Email: paul.allard@umontreal.ca

INTRODUCTION

The diagnostic of foot ailments is still based on qualitative assessment often neglecting compensatory actions observed in the lower limbs and pelvis (Morag and Cavanagh, 1999). There is a need for systems that can quickly and clinically provide quantitative clinical information on foot ailments while considering other body posture parameters. This paper reports on the use of a color-coded video-based system for foot disorders assessment. Before this system can be used for the diagnostic of foot ailments, the number of trials required for an evaluation needs to be established and the intra-tester reliability determined.

METHODS

Seven females and three males young healthy adults (21.1 + 1.8 years old age) participated in this study. A color-coded video-based system was developed to assess the postural attitude of the whole body, body segments such as the trunk, lower limbs or parts like the foot. This system consists of a black and white digital camera connected to a film grabber operating in a PC environment. The subject stands inside an open ended, three-sided black structure facing the camera. Normally, the subject uncovers the body parts to be analyzed. Fluorescent lights ensure a uniformly lit body surface and appropriate contrast of the exposed flesh.

Fourteen camera images consisting of the anterior and posterior views of the lower limbs, the anterior view of the knee, the posterior view of the pelvis and the anterior, posterior, medial and lateral views of the feet as well as posterior views of the feet in flexion in weight-bearing position were taken of each subject. These 14 digital pictures formed a single set data from which 43 parameters were measured (3-5 angles on each image) and calculated for two, three and four trials.The intra-class correlation coefficient (ICC) was used to estimate the number of trials. This was followed by ANOVAs ($p<0.05$) to determine of significant difference between all the calculated ICCs. Intra-tester reliability was tested with three evaluators using data collected from data previously collected on one of the 10 subjects.

RESULTS

The average ICC values for all 43 parameters measured from 14 camera images and calculated for two, three and four trials was 0.84. There was not significant difference between the sets of trials. Data from both feet were combined and reported according to the images taken. For example, the lateral foot image includes all the parameters taken on this view for both feet. Average ICC values for the lower limbs and pelvis were 0.90±0.09. The foot parameters had ICC values ranging from 0.74 to 0.95 with an average of 0.82±0.10. The medial, postero-anterior and foot views had mean ICCs of 0.80 and above. The antero-posterior view ICC was close to 0.80 at 0.79 while the lateral foot parameters had the lowest mean ICC at 0.68±0.24. The average intra-tester reliability was 0.86 with 35 postural parameters having ICC value 0.7. Eight parameters had a mean ICC of 0.51.

DISCUSSION

This system was evaluated because of the good quality of the numerical photographs and its ability to apply a color code to the images. From the numerical pictures, the patient's morphology was immediately recognizable thus making a qualitative comparison with previous images easy.

Our mean ICC value (0.84) did not increase significantly with additional trials. Overall, the measured parameters had an excellent reliability, which do not warrant additional trials so that a single set of images can be used for clinical evaluations. The mean of intra-tester reliability was excellent except for 8 angles that displayed poorer reliability. Their reliability can be improved by defining more precisely how these angles should be measured.

CONCLUSION

These results support the idea that a color-coded video-based system can be reliably used for assessing patients with foot ailments.

SUMMARY

There is a need for a system that can quickly and clinically provide a relevant body posture evaluation as well as information on foot ailments. This paper reports on the use of a color-coded video-based system for assessing foot disorders. More specifically the number of trials required for a clinical evaluation and the intra-tester reliability were determined. The average ICC values for 43 angles measurements taken from 14 camera images and calculated for two, three and four trials was 0.84. The intra-tester reliability was good to excellent on 35 of the 43 measured postural parameters. These results support the idea that a color-coded video-base measurement system can be reliably used for assessing patient with foot ailments.

REFERENCES

Morag, E. and Cavanagh, P.R. (1999). Structural and functional predictors of regional peak pressures under the foot during walking. J. of Biomech. 32, 359-370

BIOMECHANICS & HYDRODYNAMICS OF DECELLULARISED PORCINE AORTIC HEART VALVES

Sotiris Korossis[1], Cath Booth[2], Helen Wilcox[2], Kevin Watterson[3], John Kearney[4], Eileen Ingham[2], John Fisher[1]
[1] School of Mechanical Engineering, University of Leeds, Leeds, UK menskoro@leeds.ac.uk, [2] Division of Microbiology, University of Leeds, Leeds, UK, [3] Leeds General Infirmary, Leeds, UK, [4] Yorkshire Regional Tissue Bank, Pinderfields Hospital, Wakefield, UK

INTRODUCTION

There is no adequate heart valve substitute for long term implantation for the majority of patients (Korossis 2000). For elderly patients bioprosthetic tissue valves with a life expectancy of 10-15 years provide a satisfactory solution. The heart valve substitute of choice for patients with a greater life expectancy is the mechanical heart valve. However, these valves require long-term anticoagulation therapy. For young adults and children there is a need to deliver a heart valve that will develop with the patient. Homograft valves have been used in this patient group, but they do not retain viability following transplantation. Tissue engineered heart valves coupled with recellularisation have the potential to grow with the patient. An approach is to use natural tissue matrices, either of xenograft or allograft nature. The major challenge in this approach is to develop effective decellularisation techniques to remove foreign cellular elements while retaining the biomechanical integrity of the valvular matrix. This study investigated the effect of sodium-dedocyl-sulfate (SDS), as a decellularisation treatment, on the biomechanical integrity and hydrodynamics of porcine aortic heart valves.

METHODS

Left coronary leaflets were dissected from fresh porcine aortic valves within 4 hours of slaughter. The leaflets were divided into 6 groups and treated according to the protocols listed in Table 1. Haematoxylin and eosin histological staining was performed to all the groups to assess the degree of decellularisation. Circumferential and radial specimens were cut from each of the 6 leaflet groups and tested under uniaxial tensile loading to failure. Whole porcine aortic roots were also treated with 0.1% (w/v) SDS in hypotonic buffer and their functionality was assessed by pressurising them to physiological pressures (120 mmHg) and by subjecting them to simulated pulsatile flow.

Table 1: Leaflet treatments used in the biomechanical study.

Fresh (control)
Isotonic buffer (control)
Hypotonic buffer (control)
Isotonic buffer + 0.03%(w/v) SDS (control)
Hypotonic buffer + 0.03%(w/v) SDS
Hypotonic buffer + 0.1%(w/v) SDS

RESULTS AND DISCUSSION

Isotonic buffer or isotonic buffer with SDS did not alter the biomechanical properties. However, they were not effective decellularisation treatments. Treatment with 0.03% and 0.1% (w/v) SDS in hypotonic buffer produced complete accellularity while retaining the network of elastin, collagen and glycosaminoglycans (Booth 2002). These protocols produced modest changes in the biomechanics of the leaflets by reducing their elastin and collagen phase slopes, as well as by increasing their transition and failure strains. However, the treatments did not affect the strength of the leaflets (Korossis 2002). Whole porcine aortic roots treated with 0.1% (w/v) SDS in hypotonic buffer and pressurized to 120mmHg presented complete leaflet competence, whereas, when they were subjected to pulsatile flow showed reduced transvalvular pressure gradients (Figure 1) and similar regurgitation volumes compared to fresh, untreated roots. Regarding leaflet kinematics, the treated roots exhibited similar levels of leaflet free edge bending strains compared to the fresh control, as well as physiological opening and closing actions (Figure 2).

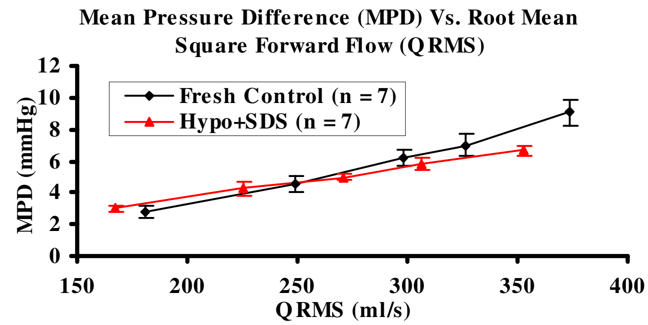

Figure 1: Pressure difference vs. root mean square forward flow for fresh and SDS-treated aortic roots (mean ± 95% C.I.).

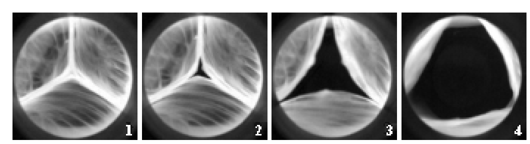

Figure 2: Leaflet kinematics of SDS-treated aortic valve.

SUMMARY

The decellularisation protocol used in this study, incorporating SDS in hypotonic buffer, produced complete accellularity of porcine aortic leaflets, causing modest changes in their extensibility. The absence of dead cells as foci for calcification, the retention of the elastin, collagen and glycosaminoglycans, as well as the promising leaflet kinematics and the retention of the leaflet matrix compliance and strength, form a promising platform for further studies. Further work will investigate whether the treated leaflets have adequate durability and will consider *in vitro* recellularisation and penetration of the cells in the leaflet matrix.

REFERENCES

Korossis, S.A. et al (2000). *Bio-Med Mat Eng*, **10**, 83-124.
Booth, C. et al (2002). *J Heart Valve Dis* (In press)
Korossis, S.A. et al (2002). *J Heart Valve Dis* (In press)

ON THE CORRELATION BETWEEN NEGATIVE NEAR-WALL SHEAR STRESS IN HUMAN AORTA AND VARIOUS STAGES OF CHF

M. Gharib[1] and M. Beizaie[2]

[1]Aeronautics and Bioengineering, California Institute of Technology, Pasadena, CA 91125, USA, mory@caltech.edu
[2]Orqis™ Medical, 20914 Bake Parkway, Suite 112, Lake Forest, CA 92630, USA, masoud@orqis.com

INTRODUCTION

The critical effect of NYHA Class III and IV CHF is the reduced blood flow in descending aorta that results from mild to severe reduction in cardiac output, which usually accompanies low EF. In these patients the heart tries to compensate by beating faster, but reduced blood flow combined with increased heart rate can lead to a retrograde flow adjacent to the wall and thereby a negative shear stress along the vessel walls during each cardiac cycle. Our studies show that near-wall negative shear stress can result from the existence of either an entire-retrograde flow at normal heart rates or a Womersley type phase delayed near-wall retrograde flow at high HR and low EF conditions. Previous studies suggest a number of possible harmful responses of the blood-vessel endothelial linings to the reversal of shear stress along the vessel walls. In this study, we try to map the correlation between the level of retrograde flow in descending aorta and the severity of CHF.

METHODS

A compliant aortic loop with appropriate pressure and flow instrumentation, was used. A Harvard pulsatile blood pump (HP) generated the aortic flow and the descending aorta model was totally immersed in water. In the first set of experiments, we used two liters each of three mixtures of distilled water and glycerin with a kinematic viscosity of 1, 2, and 4 cS, respectively. In the second, we used two liters of property filtered, anti-coagulated diluted bovine blood with an effective kinematic viscosity of 4 cS. The flow field was mapped using a GE-Vingmed System 5 platform with a 10 MHz probe. The resulting images were analyzed with Caltech's Digital Ultrasound Speckle Image Velocimetry (DUSIV) technique.

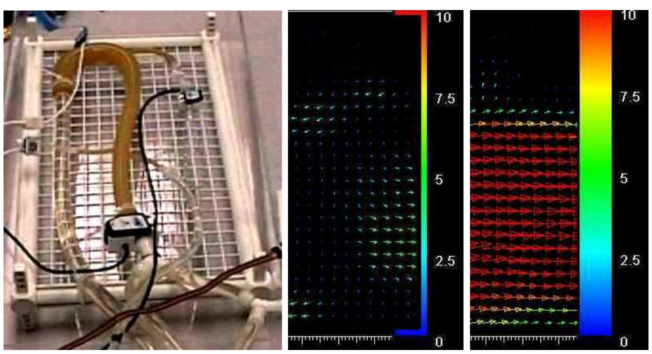

Figure 1: Orqis™ Medical's compliant descending aortic model (left) and typical DUSIV results from bovine-blood experiments, showing near-wall retrograde flow during diastole (center) and its absence during systole (right); mean flow was always positive at about 2.25 lpm, 110 bpm, giving Re = 470, Wo = 21.5.

RESULTS AND DISCUSSION

We have shown that near-wall retrograde flow does indeed happen under certain conditions of aortic flow rate and frequency. We have charted these conditions via an empirical relationship between Reynolds and Womersley numbers. Also, we have demonstrated a strong correlation between the level of retrograde flow and the transition from Class II to III in CHF patients.

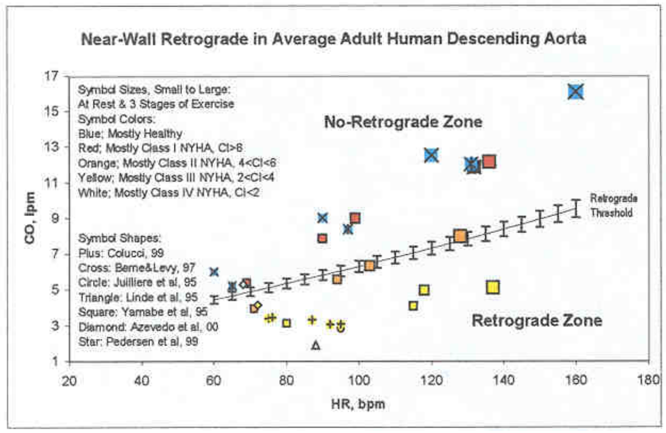

Figure 2: Variation of near-wall retrograde threshold as a function of cardiac output and heart rate, compared to clinical data from previous investigators.

We also have shown that the retrograde conditions can be reduced or eliminated by increasing the aortic flow

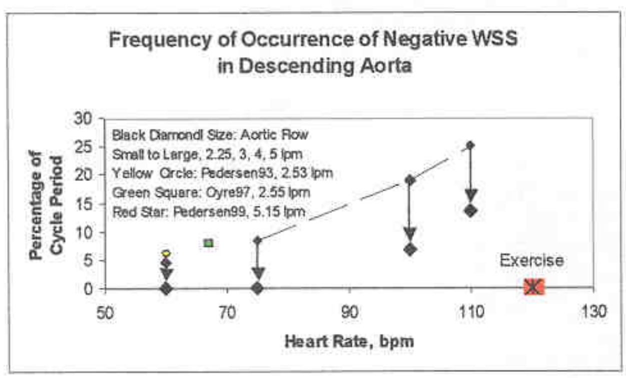

Figure 3: Frequency of occurrence of near-wall retrograde as a function of heart rate.

REFERENCES

Gharib M., Beizaie M. (2002). On the correlation between negative near-wall shear stress in human aorta and various stages of CHF. Submitted to *Circulation Research*.

VELOCITY OF THE RECTUS FEMORIS MUSCLE AFTER TENDON TRANSFER SURGERY

Deanna Schmidt Asakawa[1,3,4], Silvia Blemker[1], Garry Gold[2,3], and Scott Delp[1]
Depts. of [1]Mechanical Engineering and [2]Radiology, Stanford University, Stanford, California
[3]Diagnostic Radiology Center, VA Health Care System, Palo Alto, California [4]djasakawa@stanford.edu

INTRODUCTION

Rectus femoris transfer surgery is performed to improve knee flexion in persons with cerebral palsy who walk with a stiff-knee gait (Perry, 1987). In this surgery, the rectus femoris muscle is detached from the patella and reattached to a tendon that inserts posterior to the knee in an attempt to convert the muscle from a knee extensor to a knee flexor. However, outcomes of the surgery are variable. The purpose of this study was to gain insight into the action of the rectus femoris muscle after tendon transfer surgery using dynamic magnetic resonance imaging. Cine phase contrast magnetic resonance imaging (cine-PC MRI) accurately captures the anatomy and the velocity of tissues during joint motion (Drace and Pelc, 1994; Sheehan *et al*., 1998). Based on the direction of the muscle tissue velocity, one can identify a muscle's action (e.g., as the knee extends, the knee extensors move superiorly and the knee flexors move inferiorly). We used cine-PC MRI to test the hypothesis that the transferred rectus femoris muscle acts as a knee flexor and therefore moves inferiorly with knee extension.

METHODS

We acquired axial plane cine-PC MR images in the proximal thigh of 5 control subjects (5 limbs) and 6 subjects (10 limbs) with cerebral palsy who had undergone rectus femoris transfer surgery. Each subject was positioned supine in the 1.5T GE scanner with the lower limb between dual radiofrequency coils. Subjects were imaged as the investigator moved their knee passively through 100 repeated cycles of knee extension/flexion at a rate of 35 cycles/min. Images were acquired with a 17ms TR, 36x27cm FOV, 256x128 matrix, and 20 cm/s encoding velocity with 24 time frames representing a motion cycle. On the velocity images we prescribed 0.25-cm square regions in the rectus femoris (RF), vastus intermedius (VI), and semitendinosus (ST) and the average superior-inferior velocity within these regions was computed for each time frame using MATLAB.

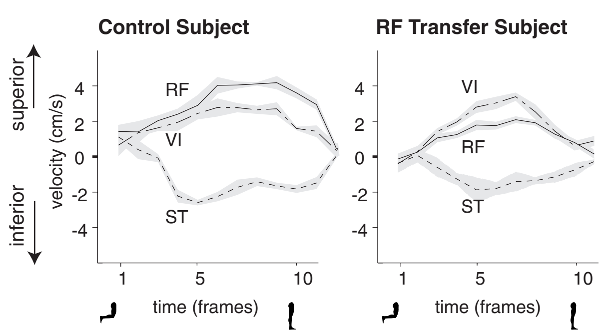

Figure 1. Average (lines) and standard deviation (shaded regions) of superior-inferior muscle velocities measured from cine-PC MR images acquired during knee extension.

RESULTS

In the control subjects, the RF and VI, knee extensors, had velocities in the superior direction and the ST, a knee flexor, had velocity in the inferior direction during knee extension (Fig. 1). In the RF transfer subjects, the RF also had velocities in the superior direction during knee extension despite its insertion posterior to the knee. The RF/VI velocity ratios (Table 1) demonstrate that the control subjects had maximum RF velocities greater than the maximum VI velocities; in contrast, the RF transfer subjects had RF velocities less than VI velocities. These results indicate that RF transfer surgery does not convert the RF to a knee flexor, but the surgery does diminish the muscle's capacity for knee extension.

Table 1. Maximum Muscle Tissue Velocities[1] in cm/s

Limb	RF Velocity	VI Velocity	RF/VI Ratio
1	1.4	1.6	0.9
2	1.5	2.5	0.6
3	1.1	1.6	0.7
4	2.0	3.3	0.6
5	0.1	3.0	0.0
6	1.1	2.7	0.4
7	1.9	2.5	0.8
8	2.9	4.4	0.7
9	1.6	3.0	0.5
10	2.3	2.5	0.9
Controls	3.8 ± 0.2	2.1 ± 0.8	1.9 ± 0.3

[1]Positive values indicate velocity in the superior direction

DISCUSSION

The rectus femoris muscle did not move in the direction of the knee flexors in any of the 10 limbs that had undergone a rectus femoris transfer. This result is surprising considering that its path is surgically altered to insert into a knee flexor muscle or tendon. One possible explanation is that scar tissue may form after surgery, constraining the motion of the muscle and diminishing the force transmitted to its distal tendon. Our results indicate that the mechanism for improved knee flexion in some subjects following rectus femoris transfer is unlikely to be a knee flexion moment generated by the rectus femoris.

REFERENCES

Drace, J. and Pelc, N. (1994). *Radiology*, **193**(2), 423-429.
Perry, J. (1987). *Dev Med Child Neurol*, **29**, 153-8.
Sheehan, F. et al. (1998). *J Biomech*. **31**, 21-26.

ACKNOWLEDGEMENTS

A. Bagley and G. Rab at Shriners Hospitals for Children, Northern California. Funded by NIH Grant HD38962 and T32 GM63495, the Whitaker Foundation, and the AAUW.

STIFFNESS OF THE HUMAN ARM IN THREE DIMENSIONAL SPACE

Mark C. Pierre and Robert F. Kirsch
Biomedical Eng. Dept., Case Western Reserve University, 10900 Euclid Ave, Cleveland, OH 44106
E-mail:mcp6@po.cwru.edu

INTRODUCTION

The goal of this work was to measure the dynamic characteristics of the arm, including its endpoint mass, viscosity, and stiffness. These dynamic characteristics depend on inherent musculo-skeletal properties, skeletal geometry and neuromuscular interactions. Previous studies of posture and movement focusing on single muscles, single joints, or movements in the horizontal plane may not have revealed critical features of natural neural control. In this study, we have added the capability to measure the endpoint stiffness of the arm in three dimensions while the subject isometrically exerts forces in three-dimensional space.

METHODS

The dynamic stiffness of the human arm is the relationship between a displacement imposed at the endpoint of the arm and the forces that result from that displacement. The endpoint stiffness was estimated using data obtained during stochastic displacement perturbations applied to the hand by a robotic manipulator (Acosta, et al. 2000). The subject's trunk and wrist were constrained so that only the arm was free to move. The dynamic input-output relations between the three displacements and three forces were determined using a frequency domain non-parametric system identification technique (Bendat & Piersol, 1986, Perreault et al 1999). This technique identifies a set of nine transfer functions that assume linearity for small displacements about a particular posture.

RESULTS AND DISCUSSION

It has been shown that second order models using inertial (I), viscous (B), and stiffness (K) parameters can be used to accurately represent endpoint transfer functions (Perreault et al 1999). The inertial, viscous, and stiffness properties are dependent on the direction of the input. We characterized these directional properties by representing the endpoint stiffness as an ellipsoid, created by plotting the force responses to a unit displacement applied to the identified stiffness values. This is the extension of a previous two-dimensional method used to plot ellipses (Mussa-Ivadi, et al. 1985)

Figure 1 shows an ellipsoid as the central figure surrounded by three two-dimensional projections that aid in visualizing the three dimensional content of the ellipsoid. This figure is shaded to highlight the varying stiffness. Areas with the highest stiffness are shaded lightly and areas of low stiffness are dark. Relative to the figure, the subject would be oriented with their shoulders parallel to the X-axis facing the positive Y-direction. The endpoint of the hand would be located in the center of the ellipsoid at location (0, 0,0).

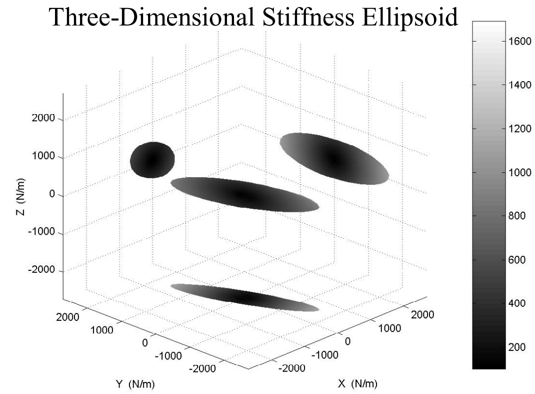

Figure 1. The three-dimensional stiffness ellipsoid is the center most object. The three surrounding ellipses are projections of the ellipsoid onto each plane. Shading correlates to the stiffness magnitude; lighter being stiffer.

SUMMARY

This abstract outlines a non-parametric method for characterizing thee-dimensional arm dynamics in response to stochastic perturbations. The method assumes no prior knowledge about the system dynamics except linearity in the presence of small displacements. In addition, this technique differs from previous techniques because it includes all three dimensions, a much more meaningful evaluation for arm postures. Thus, this test can be used to more fully determine system structure under natural three-dimensional conditions.

Preliminary results show that this method is suitable for characterizing changes in three-dimensional endpoint stiffness. In addition, the graphical ellipsoid is an important tool to help visualize the complex dynamic properties of the arm. Future work will concentrate on testing the dynamic properties of the arm in functional positions. Ultimately, this technique will be used to quantify stiffness changes due to functional neuromuscular stimulation of paralyzed muscles in individuals with spinal cord injury.

REFERENCES

Mussa-Ivaldi, F., Hogan, N, Bizzi, E. (1985). *J. Neuroscience*, **5**, 2732-2743.
Bendat, J.S., Piersol, A.G., (1986) *Random Data*: *Analysis and Measurement Procedures*. New York: Wiley.
Perreault, E.J., Kirsch, R.F., Acosta, A.M. (1999). Biol Cybern, **80**, 327-337.
Acosta, A.M., Kirsch, R.F., Perreault, E.J. (*2000).* J. Neuroscience Methods, **102**,177-86.

ACKNOWLEDGEMENTS

Supported by NIH HD32653 (RFK) NIH 2T32GM07535-24 (MCP) and NSF 9972747.

BIOLOGICAL AND BIOMECHANICAL RESPONSE OF RAT DORSIFLEXORS TO ECCENTRIC EXERCISE

David Peters, Ilona Barash, Michael Burdi, Phillip Yuan, Jan Fridén, Gordon J. Lutz and Richard L. Lieber
rlieber@ucsd.edu; Departments of Orthopaedics and Bioengineering
University of California, San Diego School of Medicine, La Jolla, CA 92037

INTRODUCTION

Eccentric contraction (EC) of skeletal muscle can result in tissue injury and decreased force output (Proske and Morgan, 2001). Reported structural changes after EC include Z-disk streaming (Fridén *et al.* 1981), extreme sarcomere length changes (Talbot and Morgan, 1996), loss the intermediate filament protein desmin (Lieber *et al.* 1996), inclusion of plasma fibronectin (Fridén *et al.* 1991), and expression of embryonic myosin heavy chain (Lieber *et al.* 1994). However, the relative timing of these events is not known. Such information would permit development of a mechanistic hypothesis that explains muscle response and remodeling after EC, especially in a rat model, where a plethora of antibodies and gene sequences are available.

METHODS

The experimental subjects for this study were young, male Sprague-Dawley Rats with an average size of 433.9 ±4.2g (mean±SEM, n =30). All procedures were approved by the University of California and V.A. Medical Center Committees on the Use of Animal Subjects in Research. To induce eccentric contractions, rat dorsiflexors were activated at 100 Hz by placing a nerve cuff around the peroneal nerve while actively plantarflexing the foot using a dual-mode servo motor (Cambridge Tech, Model 6650) similar to that previously reported for the rabbit model (Lieber *et al.* 1994). Angle ankle was rotated 38° over 400 ms corresponding to a fiber length change of about 10% and a sarcomere length change from 2.48±0.069 µm to 2.87±0.048 µm in the extensor digitorum longus (EDL) muscle. Thirty ECs, at two minute intervals, were imposed upon the muscle and then joint torque and tissue were analyzed 6, 12, 24, 48, 72 and 168 hours later. Muscle tissue was snap frozen and sectioned for immunohistochemical staining with monoclonal antibodies against desmin (an intermediate filament protein; DER-11, Novocastra), fibronectin (signaling increased membrane permeability; EDA, Sigma), embryonic myosin heavy chain (MHC, expression signaling regeneration; 1.652, Novocastra) and vimentin (an intermediate filament protein expressed in infiltrating macrophages; VIM-V9, Novocastra). The number of fibers showing a positive immunostain were directly counted by light microscopy at 25X magnification.

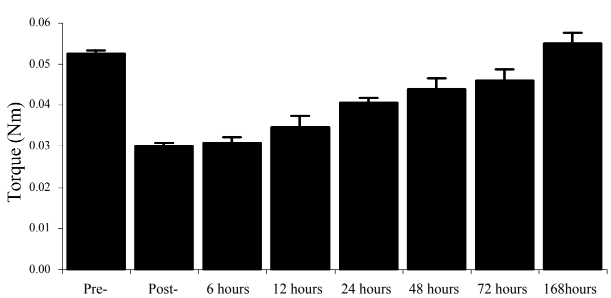

Figure 1: Dorsiflexion torque prior to (Pre-) and at various times after 30 eccentric contractions separated by 2 minutes.

RESULTS

Initial dorsiflexion torque was .053±.00095 Nm, decreased to .030±.00082 Nm immediately after the eccentric exercise bout and recovered monotonically to control levels after 168 hours (0.055±0.00026 Nm; Fig. 1). In contrast, cellular events were staggered in time and resolved over varying time courses (Fig. 2). For example, the most rapid structural change was loss of immunostaining for the intermediate filament protein, desmin (Fig. 2, solid bars), which was maximal at 12 hours and resolved within 72 hours. Changes in vimentin and fibronectin paralleled one another, peaking 24 hours after EC and being nearly resolved after 7 days (Fig. 2, open bars and hatched bars respectively). Finally, expression of the MHC protein became significant 48 hours after exercise and was still increasing 7 days later (Fig. 2, stippled bar).

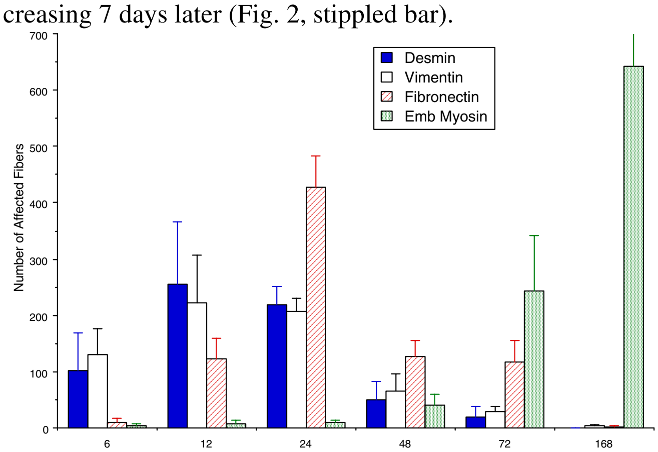

Figure 2: Number of fibers showing change from control for the protein shown at various times (hours) after the EC bout.

DISCUSSION

These data reveal an injury/repair process whereby loss of desmin immunostaining signifies the first stage of the process. Such loss may be due to depolymerization of the intermediate filament system, loss of the desmin antibody's epitope or even selective proteolysis. In any case, this change is followed by a transient increase in cellular permeability as indicated by fibronectin labeling and infiltration of macrophages as indicated by vimentin staining. Finally, the embryonic MHC is upregulated, which may lead to the observed functional recovery. The relationship among these events as well as their necessity (if any) to muscle hypertrophy remain unclear.

REFERENCES

Fridén *et al*. (1981) *Experientia* **37**: 506-507.
Lieber *et al*. (1994) *J. Appl. Physiol***. 77**: 1926-1934.
Lieber *et al*. (1996) *J. Appl. Physiol.* **80**: 278-284.
Proske and Morgan. (2001) *J. Physiol. (Lond.)* **537**: 333-345.
Talbot and Morgan. (1996) *J. Mus. Res. Cell Mot.* **17**: 261.

ACKNOWLEDGMENTS

Support from NIH AR40050, the V.A. Rehab R&D Service and the Swedish Medical Research Council.

ASYMMETRIC DYNAMIC KNEE LOADING IN ADVANCED UNILATERAL HIP OSTEOARTHRITIS

Najia Shakoor[1], Debra E. Hurwitz[1,2], Rohita Shah[2], Susan Shott[3], Joel A. Block[1], John P. Case[1,4]
[1]Section of Rheumatology, Rush Medical College
Departments of [2]Orthopedic Surgery and [3]Obstetrics and Gynecology, Rush Medical College
[4]Division of Rheumatology, Cook County Hospital, jcase@rush.edu
Chicago, Illinois, USA

INTRODUCTION

Dynamic joint loading has been shown to be an important factor in the pathogenesis of lower extremity osteoarthritis (OA). For instance, the peak external knee *adduction moment* during gait has been correlated with radiographic OA severity (Sharma et al., 1998) and may be predictive of subsequent radiographic progression (Wada et al., 2000; Hong et al., 2001). It is likely that abnormal loading of one lower extremity joint due to pain, disease or deformity will result in altered loading in the other joints (either on the same or contralateral side of the body).

We recently investigated the sequence of lower extremity total joint replacements in OA patients and showed that the evolution of endstage lower extremity OA is *not random.* Patients who have an initial unilateral total *hip* replacement (THR) for OA require a subsequent *contralateral* total knee replacement (TKR) significantly more frequently than they do an *ipsilateral* TKR (Shakoor et al., 2001). The objective of the present study was to relate the evolution of endstage OA to dynamic joint loading. The hypothesis tested was that patients with unilateral endstage *hip* OA have higher dynamic knee loads at the *contralateral knee* relative to *the ipsilateral knee.*

METHODS

The knee joint loads during gait on the ipsilateral and contralateral sides of 49 preoperative THR patients with unilateral hip OA were compared. All patients had gait analysis using an optoelectronic camera system and a multi-component force plate (Andriacchi et al., 1997). Walking trials at a speed of approximately 1 m/s were chosen for analysis. Three dimensional moments were calculated using inverse dynamics. The peak medial compartment force at the knee was also estimated using the gait data in conjunction with a statically determinate model (Schipplein and Andriacchi, 1991).

The Friedman test was used to identify differences in the peak external knee adduction moment and peak medial compartment load at the knee ipsilateral and contralateral to the preoperative hip.

RESULTS

Dynamic loading in these patients with endstage hip OA differed between the extremities. The peak knee adduction moment and the peak medial compartment load were both *significantly higher* at the *knee contralateral* to the preoperative hip relative to the knee ipsilateral to the preoperative hip (see Table 1).

Table 1: Adduction Moment and Medial Compartment Load

	Adduction Moment (%BW*Ht)	**Medial Compartment Load (BW)**
Contralateral Knee	1.7 (±1.0)*	1.9 (±0.6)**
Ipsilateral Knee	1.3 (±0.9)	1.1 (±0.5)

*p=0.003 **p<0.001

DISCUSSION

Previous studies have also suggested the clinical importance of asymmetric loading in the evolution of lower extremity OA. An investigation of traumatic amputees found a significantly higher incidence of radiographic knee OA at the non-amputated limb when compared to age-matched healthy controls (Melzer et al., 2001). Biomechanical evaluations of such amputees revealed higher load-bearing on the knee of the non-amputated limb (Eberhart et al, 1954). The results from the current study extend the concept of asymmetric knee loading and OA evolution to a non-amputee population.

These are the first data to reveal a relative loading differential between the knees of preoperative THR patients, which may explain the asymmetric development of endstage knee OA (TKR requirement) in these subjects. Further investigation is necessary to discern how early in the course of hip OA differential loading develops, and its relationship to alterations in neuromuscular limb control.

REFERENCES

Sharma, L. et al (1998). *Arthritis Rheum*, **41**, 1233-40.
Wada, M. et al (2000). *Osteoarthritis Cartilage*, **8**, S8.
Hong, R. et al (2001). *Arthritis Rheum*, **44**, 2950.
Shakoor, N. et al (2001). *Arthritis Rheum*, **44** (suppl), S380.
Andriacchi, T.P. et al (1997). *Basic Orthopaedic Biomechanics.* Ravens Press, Ltd., 2nd ed., 37-69.
Schipplein, O.D. and Andriacchi, T.P. (1991). *JOR*, **9**, 113-19.
Melzer, I. et al. (2001). *J Rheum*, **28**, 169-72.
Eberhart, H.D. et al. (1954). The locomotor mechanism of the amputee. In Klopstet P.L. and Wilson P.D., Eds., *Human Limbs and their Substitutes.* McGraw Hill.

MICRO- AND MACRO-LEVEL 3D STRAINS MEASURED IN MICROSTRUCTURALLY VARIED COLLAGEN ECMS

Blayne A. Roeder[1], Klod Kokini[1,2], Jennifer E. Sturgis[3], J. Paul Robinson[2,3], Sherry L. Voytik-Harbin[2,3]
[1] School of Mechanical Engineering
[2] Department of Biomedical Engineering
[3] Department of Basic Medical Sciences
Purdue University, West Lafayette, Indiana, USA

INTRODUCTION

In vivo, cells reside in a three-dimensional (3D) framework known as the extracellular matrix (ECM). The structure and composition of the ECM conveys to cells biochemical as well as biomechanical information critical to maintenance of tissue form and function. Mechanical loads applied to tissues have been shown to affect many fundamental cellular processes; however, little is known regarding how loads are transmitted through the ECM to cells and how those load ultimately affect cellular function. A model ECM consisting of a 3D matrix of type I collagen fibrils was used to further understand how mechanical loads are transmitted from a macro (tissue) level to the a micro (cellular) level. Specifically, collagen ECMs with different microstructures were loaded in tension and both 3D macro- and micro-level strains were measured and compared.

METHODS

Collagen ECMs were manufactured by neutralizing an acid solution of collagen type I (Sigma Chemical Co.) to desired concentration and pH. Collagen content and polymerization pH were varied to create micro-structurally varied collagen ECMs (Roeder et al., 2002). The neutralized solution was polymerized in a "dog-bone" shape by incubating the ECM at 37°C in a humidified environment for at least 18 hours before testing. Combined confocal-mechanical experiments (Voytik-Harbin et al., 2002) acquired 3D images of collagen ECM microstructure and images of the ECM cross-section (width & thickness), as specimens were incrementally loaded in tension (1.0 mm/min). 3D images tracked a specific location (an approximately 150×150×35 μm volume) inside the collagen ECM. Digital volume correlation was then used to measure 3D tensorial strains in microstructure of the collagen ECM (Roeder et al., 2001). Macro-level strains were derived from cross-sectional area images (ε_{22} & ε_{33}) and applied strains (ε_{11}). Shear strains were not measured at the macro-level.

RESULTS AND DISCUSSION

Previously, alterations in microstructural properties such as fibril length, diameter and density were found to substantially change macroscopic material properties such as modulus and failure strength of collagen ECMs (Roeder et al., 2002). Here, micro-level strains were determined and correlated with macro-level strains in mechanically loaded collagen ECMs with varied microstructure. For example, the means of six independent components of the lagrangian strain tensor measured in the microstructure of a 1.0 mg/ml, pH 7.4 collagen ECM are compared to macro-level strains, as tensile loads (1-direction) were applied to the specimen (Figure 1). Error bars indicate the standard deviation of the strains measured in the image volumes. In the loading direction, macro-level strains applied to the sample increased linearly, while the micro-level strains initially paralleled this behavior but leveled off at higher loads. Similarly, transverse strains (ε_{22} & ε_{33}) decreased substantially as loads were applied, but the micro-level strains were lower in magnitude than the macro-level strains at higher loads. Understanding how the micromechanical behavior of collagen ECMs is related to their macroscopic behavior will help elucidate how the ECM microstructure acts to functionally transmit loads from the tissue (macro) level to cellular (micro) level. Such relevant information regarding micromechanical loads at the cellular level will prove invaluable in the design of future tissue engineered devices.

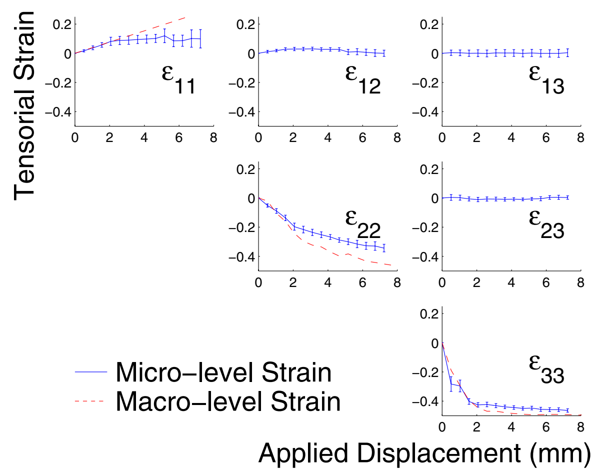

Figure 1: 3D strains measured at the micro- and macro-level in a 1.0 mg/ml collagen ECMs as the specimen was stretched in the 1-direction.

REFERENCES

Roeder, B.A. et al. (2001). *Annals of Biomedical Engineering*, **29**(S1), S148.
Roeder, B.A. et al. (2002). *In Press, Journal of Biomechanical Engineering* **124**.
Voytik-Harbin, S.L. et al. (2002). *Submitted, Microscopy and Microanalysis.*

ACKNOWLEDGEMENTS

This research was funded in part by NSF Integrative Graduate Education and Research Training (IGERT) Program in Therapeutic and Diagnostic Devices Grant DGE-99-72770, and Purdue University Vice President Academic Reinvestment Initiative entitled "Comprehensive Cell Biology Imaging and Analysis Facility". Blayne A. Roeder is an NSF/IGERT fellow.

BIOMECHANICS OF CERVICAL SPINE SURGERY: COMPARISON OF FUSION AND NONFUSION INSTRUMENTATION

Denis J. DiAngelo[1], Kevin T. Foley[2], Champ Davis[1], and Bobby J. McVay[1]
[1]School of Biomedical Engineering, The University of Tennessee Health Science Center, Memphis, TN, ddiangelo@utmem.edu
[2]Department of Neurosurgery, The University of Tennessee Health Science Center, Memphis, TN

INTRODUCTION

Anterior cervical discectomy or anterior cervical decompression is an acceptable surgical method for the treatment of cervical spondylosis or other spinal disc diseases. The gold standard for surgical treatment is fusion and can include spinal instrumentation. However, clinical studies have shown that motion at spinal segments adjacent to a fused region increases over time and may cause adjacent segment disease. Multiple factors have been implicated, including number of levels fused, health condition, post-operative alignment, and rigid fixation. An alternative approach to fusion surgery of the cervical spine is to restore motion to the diseased joint using an artificial cervical joint (ACJ). The objective was to compare the biomechanical stability of two single-level cervical procedures: graft fusion with anterior cervical plate (GAP) versus an artificial cervical joint (ACJ).

METHODS

Five human cadaveric cervical spines (C2-T1) were procured and screened with AP and lateral radiographs to exclude those with disease. Three different spine conditions were analyzed: i) harvested (H), ii) implanted ACJ , and iii) instrumented GAP. The ACJ spine consisted of a single level discectomy with subsequent disc replacement using the "Bristol" disc. An Orion™ anterior cervical plate (Medtronic-Sofamor Danek, Memphis, TN) was used for the graft-plated constructs. The specimens were nondestructively tested in flexion/extension, lateral bending, and axial rotation. Measurements included overall spine motion, individual vertebral motions, and applied load and moment. Global (C2-T1) rotational stiffness was calculated and normalized to the harvested condition to control intrinsic differences in the specimens. The relative rotations at the superior (S), operated (O) (C5-C6), and inferior (I) motion segment units (MSU) were normalized with the respect to the overall rotation of those three (S+O+I) MSUs. Paired t-tests ($p<0.05$) were used to statistically analyze the normalized motion and stiffness data.

RESULTS

There was no significant difference ($p<0.05$) in the stiffness values between the H and ACJ spines for all modes of testing. There were significant differences between GAP and both the H and ACJ conditions. The normalized rotations at the operated and adjacent segments for flexion/extension and lateral bending are shown in Figure 1. Similar results occurred in axial rotation. There was no significant difference in the normalized motion between the H and ACJ conditions at all three levels and loading modes. There was a significant difference between the GAP and ACJ spine conditions at all three levels for all three loading modes.

MSU Rotations

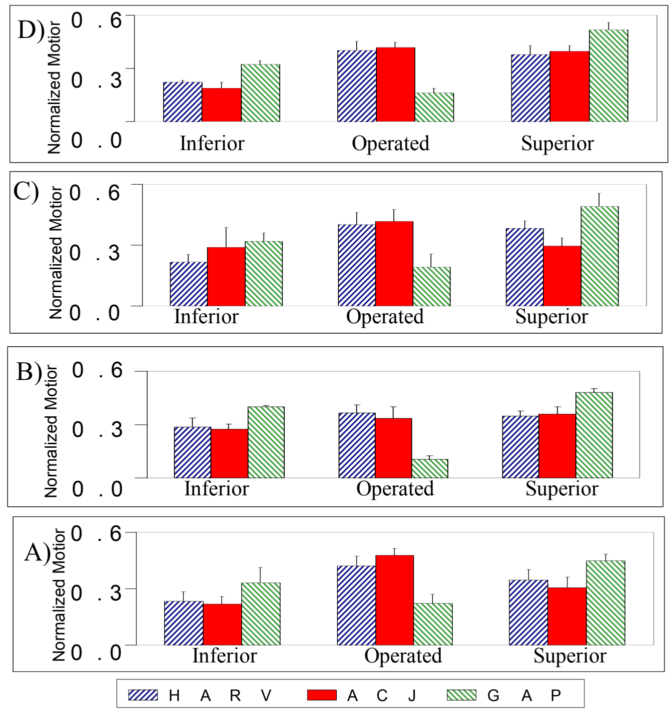

Figure 1: Relative MSU Rotations. A) Flexion, B) Extension, C) Right Lateral Bending, and D) Left Lateral Bending. (Mean + one standard deviation.)

DISCUSSION

Clinical studies have reported increased loading at adjacent segments following fusion surgery. Lost motion at the fusion site may increase adjacent segment motion, that overtime, may lead to degenerative wear of the adjacent discs. In this study, the GAP did significantly alter the motion and at the operated and adjacent MSUs compare to the H and ACJ spine conditions. Additional surgery may be required. The ACJ did not significantly alter motion at the superior, implanted, or inferior MSUs relative to the harvested spine condition, nor did it change the stiffness. There are two differing viewpoints on adjacent segment disease: i) the disease is part of the natural aging process and ii) the MSUs adjacent to a fused level experience a significant increase in motion that enhances the disease. We found that the single-level plated procedure caused a significant increase in motion at the adjacent segments, which clinically may contribute to the advancement of adjacent segment disease. Use of the artificial cervical joint did not alter the adjacent segment motion patterns and is less likely to promote adjacent segment disease.

ACKNOWLEDGMENTS

Medtronic Sofamor Danek, Memphis, TN.

KINEMATICS OF THE CERVICAL SPINE: PATH OF THE INSTANT AXIS OF ROTATION IN FLEXION AND EXTENSION

Denis J. DiAngelo[1], Keith A. Vossel[1], and Kevin T. Foley[2]
[1]School of Biomedical Engineering, The University of Tennessee Health Science Center, Memphis, TN, ddiangelo@utmem.edu
[2]Department of Neurosurgery, The University of Tennessee Health Science Center, Memphis, TN

INTRODUCTION

Two-dimensional motion of a joint can be described by the Instant Axis of Rotation (IAR). Calculation of the IAR depends on the experimental set-up, anatomical structure, mathematical reduction technique, and accuracy of the measurement equipment. For the cervical spine, no accurate calculations of the IAR path exist; typical vertebral measurements only include the rotational components. The objective of the study was to determine the IAR of the cervical spine for flexion-extension loads *in vitro*.

METHODS

Six human cadaveric cervical spines (C2-T1) were procured and mounted in a programmable testing system. A previously developed *in vitro* testing protocol that replicated physiologic flexion and extension motion (DiAngelo et al., 1997) was used (see Figure 1). Measurement of the vertebral motions were made using a custom-built optical joint measurement system (JMS) that had an improved resolution (10 microns). The motion data were then used to calculate the IAR coordinates of each motion segment unit (MSU). Several statistical tests were performed to analyze the IAR data, including comparison between the experimental IAR and a theoretical IAR zone (anterior half of subjacent body). Using the JMS, the theoretical error in calculating the coordinates of the IAR was less than 1 mm. However, using a conventional system (100 to 500 micron resolution), the IAR error increased 7 to 10 mm.

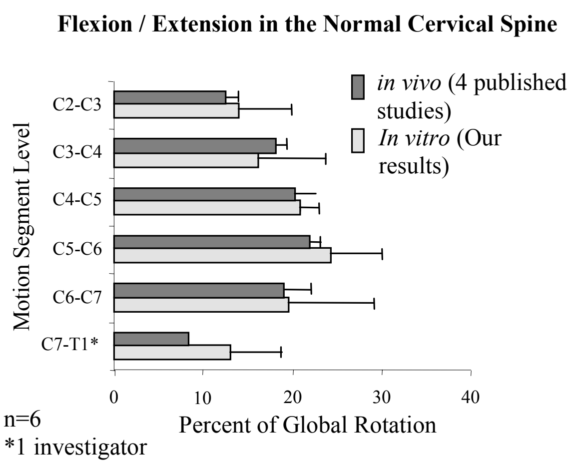

Figure 1: Relative MSU Rotation of the Harvested Spine. Mean + one standard deviation of the combined flexion/extension rotations for the *in vitro* harvested spine compared to published *in vivo* data. (Ameco et al, 1991; Dvorak et al, 1998; Lind et al, 1998; White and Panjabi, 1990)

RESULTS AND DISCUSSION

The average location of the IAR positions of the harvested cervical spine on an upright representative spine model is shown in figure 2 for flexion and extension loading. The shift in the position of the IAR between extension and flexion was significant (paired t-test, $n=6$, $p<0.05$). The standard deviations of the IAR positions (comparing between different spines) averaged ± 9 mm along the anterior/posterior axis of the spine and ± 8 mm in the dorsal/ventral direction. A two-way ANOVA test was also performed to determine the fraction of local IAR points that laid in the theoretical zone (i.e., anterior half of subjacent body). In extension, 10% of the IAR points were within the predefined zone. During flexion, 14% of the IAR points laid within the theoretical IAR zone. The combined flexion/extension motion of an individual, intact cervical MSU varies between 5° and 15°. To calculate their IAR path, smaller angular measurements (2°) were needed. Using the improved JMS, the IAR of the cervical spine was found to lay in the subjacent body near the facet joints during extension and moved towards the center of the subjacent vertebral body during flexion. This change was significant.

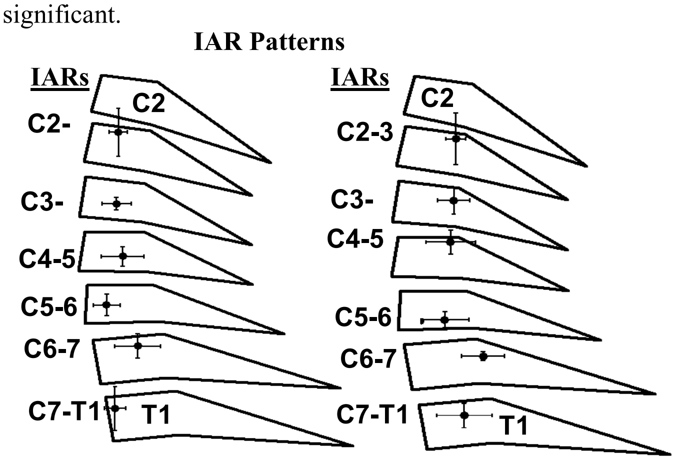

A) Flexion B) Extension

Figure 2: Individual MSU IAR positions. A) Flexion and B) Extension. (Mean plus one standard deviation.)

ACKNOWLEDGMENTS

The Whitaker Foundation.

REFERENCES

Amevo B, et al (1991) *Clin Biomech*, 6:31-37.
DiAngelo D, et al (1997) *1997 Adv. Bioeng*, pp 211 - 212.
Dvorak J, et al (1998) *Spine*; 13:748.
Lind B, et al (1988) *Spine*: 162-167.
White A., Panjabi M. (1990) Clinical Biomechanics of the Spine, JB Lippincott Co., Philadelphia.

BIOMECHANICAL STABILITY OF MULTI-LEVEL CERVICAL SPINE INSTRUMENTATION: COMPARISON OF CONSTRAINED VERSUS SEMI-CONSTRAINED ANTERIOR CERVICAL PLATES

Denis J. DiAngelo[1], Kevin T. Foley[2], W. Liu[1], and Christine M. Olney[1]
[1]School of Biomedical Engineering, The University of Tennessee Health Science Center, Memphis, TN, ddiangelo@utmem.edu
[2]Department of Neurosurgery, The University of Tennessee Health Science Center, Memphis, TN

INTRODUCTION

Recent clinical experience has shown that anterior cervical plating does not prevent construct failure in multi-level cervical corpectomy (Vaccaro et al, 1998). We have also shown that anterior cervical plating reverses the load transfer through multi-level strut-grafts and may promote pistoning of these grafts (DiAngelo et al, 2000). The design of the anterior cervical plate (ACP) may contribute to this phenomenon. The purpose of this study was to compare the graft loading mechanics of two different anterior cervical plating systems; one with a constrained screw-plate interface versus another with a semi-constrained, translational screw-plate interface.

METHODS

Ten cadaveric cervical spines (C2-T1) were harvested and mounted in a programmable tester and loaded in flexion and extension. Five spine conditions were evaluated: harvested (H), (C4-C6) corpectomy (C), strut-graft alone (GA), strut-graft with constrained anterior cervical plate (CACP), and strut-graft with translational anterior cervical plate (TACP). The Orion™ cervical plating system was used for the CACP conditions and the Premier™ plating system was used for the TACP condition (Medtronic – Sofamor Danek, Memphis, TN). Five spines were tested with each plating system. Following harvested and corpectomy testing, the spine was decompressed and a force sensing strut-graft (FSSG) was inserted into the corpectomized region and lengthened to achieve a 20N pre-load. Graft loads were measured prior to and after plate application. A previously developed *in vitro* testing protocol was adopted, i.e., target moment at T1 of 3Nm with limit checks of 40° total spine rotation, 5Nm maximum bending moment, 75N actuator load, or 200N maximum graft load (DiAngelo et al, 2000). Measurements included vertebral motion, applied load and moment, and load transferred through the FSSG. Global (C2-T1) rotational stiffness was calculated and normalized to the harvested condition to control intrinsic differences in the specimens. Output from the FSSG and mean relative rotations were compared at nondestructive end limits of flexion and extension. A one-way ANOVA ($p<0.05$) was used to determine the statistical differences between the strut-graft pre-load and end-load of the CACP and TACP conditions in flexion and extension, and the normalized motion data of the graft-alone, TACP, and CACP conditions.

RESULTS AND DISCUSSION

Application of either anterior cervical plate increased the global (C2-T1) stiffness and decreased the local (C3-C7) motion. Values of the FSSG pre-loads, end-load, and change in load are shown in Table 1. Flexion of the SG spine loaded the FSSG; extension unloaded the FSSG. With both plates, these load transfer patterns were reversed. The CACP construct produced significantly higher graft loads in extension than the TACP construct ($p<0.001$) and GA spine ($p<0.001$), which may promote graft pistoning and lead to construct failure. Importantly, there was no significant difference in graft loads in extension between TACP and GA constructs. In flexion, there were no significant differences in graft loads amongst the three constructs. The CACP construct produced significantly higher pre-load than the TACP (in both extension ($p<0.001$) and flexion ($p=0.003$)) and the GA constructs (in both extension ($p<0.006$) and flexion ($p<0.005$)). However, there were no significant differences in pre-load between TACP and GA constructs in both extension and flexion. There were significant differences between the change in pre-load and end-load values for the CACP and TACP spines, in both extension ($p<0.001$) and flexion ($p=0.025$). However, no significant differences occurred between the TACP and GA constructs in both extension and flexion. Values of the normalized local (C3-C7) motion are shown in Table 2. During flexion, there were no significant differences between the GA, CACP, or TACP conditions. During extension, there were significant differences between the CACP versus GA ($p<0.001$) and CACP versus TACP ($p<0.03$). In summary, the semi-constrained, translational plate did not produce significant changes in strut-graft loads, which would be considered biomechanically advantageous in this setting.

Table 1: FSSG Loads in Extension and Flexion

Measurement Condition		FSSG Load (N) GA	TACP	CACP
Preload	Flexion	23(3)	21(11)	59(21)
	Extension	18(3)	7(5)	40(13)
Max Load at 8°	Flexion	33(9)	15(16)	15(19)
	Extension	15(3)	24(6)	140(48)
Change in Preload	Flexion	10(7)	10(11)	44(27)
	Extension	2(2)	16(7)	101(39)

Table 2: (C3-C7) Motion Normalized to Harvested

Measurement Condition	Normalized Motion Relative to H: GA	TACP	CACP
Flexion	0.84(0.23)	0.68(0.25)	0.47(0.37)
Extension	1.0(0.14)	0.67(0.34)	0.27(0.18)

ACKNOWLEDGMENTS

The Whitaker Foundation and Medtronic-Sofamor Danek.

REFERENCES

DiAngelo D et al (2000) *Spine*, 25(7): pp. 783-795.
Vaccaro A, et al (1998) *J Spinal Disorders*, pp. 410-5.

CONTRIBUTION OF THE HIP EXTENSORS, KNEE EXTENSORS, AND ANKLE PLANTAR FLEXORS DURING DIFFERENT SQUATTING TECHNIQUES IN OLDER ADULTS

Sean P. Flanagan, George J. Salem, Man-Ying Wang, Serena Sanker, and Caroline Reiss
Musculoskeletal Biomechanics Research Laboratory, Department of Biokinesiology and Physical Therapy, sflanaga@usc.edu
University of Southern California, Los Angeles, California, USA

INTRODUCTION

Different lower extremity exercises can be used to improve, retain, or restore functional independence in older adults. Two such exercises are the squat (SQ) and the box squat (BS), an activity where one squats down onto a stable surface before rising. We hypothesized that these activities would invoke different lower extremity demands and that they could be used to preferentially target specific muscle groups in elders. Thus, the purpose of this investigation was to characterize the contributions of the hip extensors, knee extensors, and ankle plantar flexors during two functional squatting activities in older adults

METHODS

Twenty healthy, older adults (ages 70-85) performed SQ to a self-selected depth and BS onto a stool at a standardized height of 43.8 cm. Each subject completed three trials of each exercise, and both exercises were performed during the same session. Joint kinetics were obtained using inverse dynamics techniques. The angular impulse of each joint was obtained by integrating the hip, knee, and ankle moment curves over an entire repetition. A support impulse was calculated as the sum of the three joint impulses. The contribution of the lower extremity extensor muscle groups was determined by diving the individual joint impulses by the support impulse. Results were averaged across the three trials. Comparisons between SQ and BS were made with paired t-tests.

RESULTS AND DISCUSSION

SQ generated a 51.2% greater knee extensor impulse ($p < 0.01$), a 157.9% greater plantar flexor impulse ($p < 0.01$), and a 31.3% greater total support impulse ($p < 0.01$) than BS (Table 1). Conversely, BS generated a 8.1% greater hip extensor impulse than SQ ($P = 0.50$). Results are expressed as a percentage of the total support impulse in Figure 1.

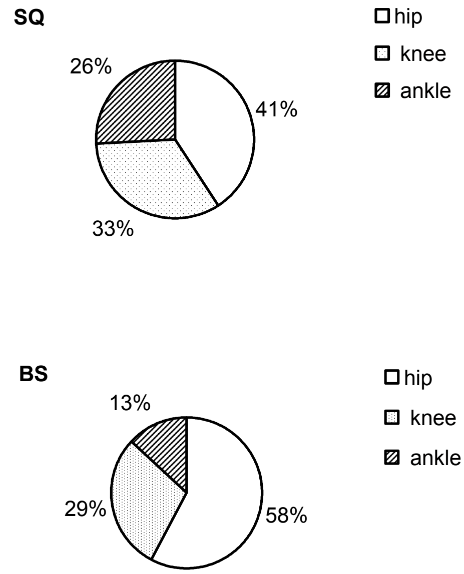

Figure 1. Relative contributions of the hip extensor, knee extensor, and ankle plantar flexor impulses.

Findings suggest that SQ and BS activities require different lower-extremity motor programs that may preferentially target different muscle groups in older adults. SQ generates greater knee extensor and ankle plantar flexor impulses; thus, this activity may be preferred by clinicians prescribing exercise for elders with knee and ankle weakness. Conversely, BS generates a greater hip extensor impulse and a greater hip contribution to the total support impulse. This exercise may be most beneficial for elders with hip weakness. In older adults without identified lower extremity weakness, the SQ appears to be the preferred exercise because it generates the greatest total support impulse.

SUMMARY

This study demonstrates statistically significant differences in the generated joint impulses associated with SQ and BS activities in older adults. Future investigations should characterize the muscle recruitment patterns, joint powers, joint work, and relative participant preference associated with these activities.

ACKNOWLEDGEMENTS

This research was supported by NIA AG19320-01

Table 1. Angular Impulse (Nmm*s/kg) during SQ and BS

Exercise	Hip Impulse	Hip Percent	Knee Impulse	Knee Percent	Ankle Impulse	Ankle Percent	Support Impulse
Normal Squat	1929 ± 889	41 ± 11%	1582 ± 760	33 ± 11%	1126 ± 539	26 ± 10%	4738 ± 1485
Box Squat	2085 ± 919	58 ± 11%	1046 ± 846	29 ± 14%	476 ± 204	13 ± 7%	3608 ± 1472

A FINITE ELEMENT MODEL OF THE C2-C3 SEGMENT – GROSS RESPONSES UNDER PHYSIOLOGICAL LOADS

Vee-Sin Lee[1], Ee-Chon Teo[2*], Kim-Kheng Lee[2], Kok-Yong Seng[1], Hong-Wan Ng[2] and Lih-Duen Neo[1]
[1]Defence Medical Research Institute, Defence Science & Technology Agency, Singapore
[2]School of Mechanical & Production Engineering, Nanyang Technological University, Singapore
[*]Corresponding author E-mail: mecteo@ntu.edu.sg

INTRODUCTION

The human cervical spine can be sub-divided into four units, each with a unique morphology that determines its kinematics and its contribution to the functions of the complete cervical spine. While literature delineating the biomechanical characteristics of the atlas, axis and the typical cervical spine abound, there remain a dearth of studies with regards to the biomechanics of the C2-C3 junction, from which the typical cervical spine commences. The present study of developing and exercising a finite element (FE) model of the C2-C3 segment was undertaken to partially fill the gap in the literature by quantifying its gross behavior under various physiological loads.

MATERIALS AND METHODS

A 3-dimensional FE model of the C2-C3 segment based on a 68-year old male cadaveric spine was developed. The model was developed based on previously reported digitizing techniques, modeling methodology and material models. The C2-C3 segment was subjected to bending moments in the anatomic sagittal, frontal and transverse planes. Five incremental loads of 300 Nmm each were applied uniformly across the superior articular surfaces of C2, while the inferior vertebral body of C3 was rigidly constrained in all directions. The rotational components of relative motion between the C2 and C3 segments under increment moment to maximal moments of 1500 Nmm were computed.

RESULTS AND DISCUSSION

The FE model of the C2-C3 segment (Fig.1) comprised 4580 "8-noded" solid elements for the definition of the bony structures and the intervertebral disc, and 181 tension cable elements represented the spinal ligaments. Surface-to-surface contact elements were used to simulate the joints between the C2 inferior and C3 superior articulating surfaces.

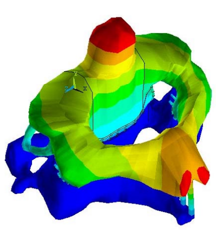

Figure 1: The FE model of C2-C3

The gross biomechanical response of the C2-C3 segment displayed varying non-linear and stiffening characteristics under different loads (Fig 2).

Under applied moments in the sagittal plane, the C2-C3 model exhibited greater stiffness in the extension direction at high loads (>400 Nmm), but at low loads (0 – 400 Nmm), the spinal segment was stiffer under flexion. The variation in stiffness was insignificant for flexion, but the increase in stiffness was discernable between 200 – 400 Nmm in the extension direction.

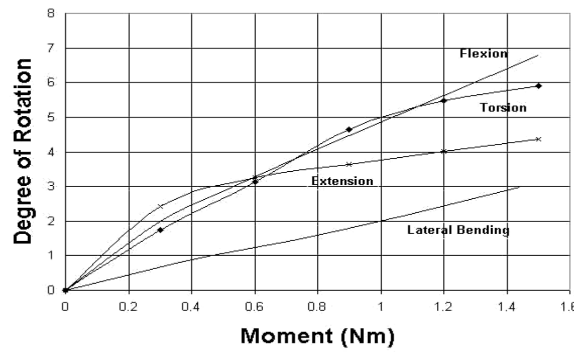

Figure 2: C2-C3 Responses under various loads.

Under axially applied incremental torsion loads, the model exhibited gradual stiffening. Coupled motion – in the form of lateral bending in the frontal plane – was observed. In lateral bending exertions, the model predicted a maximum angular motion of 3^{o} at 1400 Nmm, and no variation in stiffness was noted throughout the loading history. The model also predicted coupled motion in the transverse plane.

The simulation of the 45^{0}-inclined facet joints via moving contact elements greatly influenced the kinematics of the C2-C3 segment, while the spinal ligaments and the intervertebral disc controlled the range of motion in all the body planes considered in the present study.

SUMMARY

A 3D FE model of the C2-C3 spinal segment was developed and reported for the first time based on previously published methodology and materials for the lower cervical spine. As such, appreciable levels of confidence in the aforementioned results are expected. The non-linear response and range of motion of the C2-C3 segment were observed to be the concerted efforts of all spinal components and the orientation of articular facets. The model has the potential to supplement various *in vitro* and *in vivo* studies to further the understanding of human cervical spine biomechanics under different load-displacement vectors.

REFERENCES

Bogduk, N., Mercer, S. (2000) *Clin. Biomechanics*, **15**, 633-648.
Teo, E.C., Ng, H.W. (2001) *J. Biomechanics*, **34**, 13-21.
Teo, E.C., Ng, H.W. (2001) *Med. Eng. Phys,* **23**, 155-164.
Ng, H.W., Teo, E.C. (2001) *J. Spinal Disord,* **14**, 201-210.

SUBTLE EFFECT OF WALKING SPEED ON MEDIO-LATERAL CENTER OF MASS MOTION IN YOUNG ADULTS

Michael E. Hahn and Li-Shan Chou
Department of Exercise and Movement Science, University of Oregon, Eugene, OR, USA
E-mail:chou@oregon.uoregon.edu

INTRODUCTION

Adequate dynamic stability during gait may be demonstrated by a controlled COM displacement or a well-modulated COM velocity profile. A greater and faster COM motion in the frontal plane, with a slower walking speed, was demonstrated in older adults and individuals with balance disorders (Kaya et al., 1998; Chou et al., 2000). It is not clear how much if any of this increased COM motion is due to a slower walking speed alone. Recent studies showed peak M-L velocity of the COM to be invariant in healthy children (~9 yrs) walking at three different speeds (Cherng, 2001; Hughes et al., 2001). However no data have been reported for the effect of walking speed on COM motion in adult population. The purpose of this study was to quantify the effect of walking speed on COM motion in young adults. It was hypothesized that frontal plane COM motion is not affected by the walking speed.

METHODS

Sixteen young adult subjects (eight per gender; mean age, 24.6 yrs) without neurological or musculoskeletal impairment were asked to walk barefoot, over level ground, in three conditions of chosen speed. The first condition was their preferred gait, and then a noticeably faster condition followed by a noticeably slower condition. Trajectory data were collected using a six-camera HiRes™ system (Motion Analysis Corp., Santa Rosa, CA). Position of the whole-body COM was then calculated using a 13-segment link model, and linear velocities were calculated using the GCVSPL algorithm. A two-way ANOVA with repeated measures of walking speed was used to test for significant effects of gender and/or walking speed on COM displacements and peak velocities.

RESULTS AND DISCUSSION

There were no significant gender effects for any of the variables tested. Significant effects of walking speed were found for all variables tested (Table 1). The M-L COM displacement decreased as walking speed increased, however the peak M-L velocity was significantly less for both the fast and slow walking speeds when compared with the normal pace. Although these differences were significant, they are relatively small (~1cm in displacement and ~1cm/s in peak velocity), which reflects a robust and precise control of COM motion in the frontal plane of healthy young adults. Furthermore, these walking speed-induced differences are much less than those differences reported between healthy young and elderly (Chou et al., 2000) or between healthy elderly and patients with vestibular dysfunction (Kaya et al., 1998) during level walking.

SUMMARY

Findings of this study demonstrated that, in young adults, walking with a faster/slower speed causes a subtle but significant change in the frontal plane COM motion. This information provides more insight into the use of COM motion as an objective measurement of dynamic stability. It remains to be seen what effects walking speed may have on COM motion in elderly adults.

REFERENCES

Cherng, R-J. et al. (2001) *Proceedings of the 18th ISB Congress*, 26.
Chou, L-S. et al. (2000) *Proceedings of the 24th ASB Meeting, pp. 93-94.*
Hughes, et al. (2001) *Proceedings of the 25th ASB Meeting, pp. 299-300.*
Kaya, B.K. et al. (1998) *J. Gerontol* **53A**: M126-134.

ACKNOWLEDGEMENTS

This work was supported by the Oregon Medical Research Foundation.

Table 1. Gait velocity and COM parameters (Mean ± SD)

	Slow	Normal	Fast	p-value
Gait Velocity (m/s)	1.032 ± 0.117	1.287 ± 0.092	1.653 ± 0.184	$p < 0.001$
COM Displacement (m)				
Anterior-Posterior	1.217 ± 0.057	1.333 ± 0.059	1.490 ± 0.092	$p < 0.001$
Medio-Lateral	0.040 ± 0.007	0.037 ± 0.005	0.032 ± 0.006	$p < 0.001$
Vertical	0.031 ± 0.005	0.035 ± 0.005	0.038 ± 0.005	$p < 0.001$
Peak COM Velocity (m/s)				
Anterior-Posterior	1.159 ± 0.134	1.437 ± 0.110	1.831 ± 0.202	$p < 0.001$
Medio-Lateral	0.137 ± 0.015	0.149 ± 0.021	0.125 ± 0.031	$p = 0.004$
Upward	0.148 ± 0.025	0.188 ± 0.026	0.245 ± 0.039	$p < 0.001$
Downward	0.149 ± 0.032	0.199 ± 0.038	0.245 ± 0.028	$p < 0.001$

A PARAMETER TO DESCRIBE COORDINATION OF HIP AND KNEE FLEXION DURING OBSTRUCTED GAIT

Michael E. Hahn and Li-Shan Chou
Department of Exercise and Movement Science, University of Oregon, Eugene, Oregon
E-mail:chou@oregon.uoregon.edu

INTRODUCTION

During obstacle crossing, healthy adults increase toe-ground/obstacle clearance from an average of 3 cm during level walking to approximately 10-15 cm over an obstacle (Chen et al., 1991; Patla et al., 1996; Chou et al., 1997) to minimize the risk of tripping. The hip, knee and ankle joints of the swing limb are modulated for phase and amplitude of flexion to ensure appropriate elevation of the swing foot over the obstacle (Patla et al., 1996). Due to a different proximity of the swing foot at the time of toe-off with the location of the obstacle, strategies with emphasis on different joints are adopted to elevate the swing foot to clear the obstacle (McFayden and Winter, 1991; Patla et al., 1996; Chou et al., 1997). The purposes of this study was to define a parameter that could describe different coordination strategies of hip and knee flexion of the leading and trailing limbs during obstacle crossing and to examine its relationship with the obstacle height in healthy young adults.

METHODS

Six healthy young adults (mean age, 24.8 years) were recruited for this study. Whole body kinematic data were collected using a six-camera HiRes™ system (Motion Analysis Corp., Santa Rosa, CA) during unobstructed walking and when stepping over an obstacle of height corresponding to 2.5%, 5%, 10%, or 15% of the subject's body height (BH). All trials were conducted at a comfortable self-selected walking speed while barefoot. The order of obstacle height was randomly selected. Flexion angles of the hip and knee joints were plotted one against the other, from toe-off to heel-strike for each limb. A coordination slope was then calculated to represent the overall trend of joint coordination for each limb (Fig. 1). Graphical midpoints were calculated between toe-off (LTO, TTO) and heel-strike (LHS, THS). For each limb, the slope of the line between the midpoint and the apex of the coordination curve represented the overall hip/knee coordination during the obstacle-crossing stride. A one-way ANOVA with repeated measures for obstacle height was used for each limb to test the effect of obstacle height on coordination of the hip and knee.

RESULTS AND DISCUSSION

During unobstructed walking, the coordination slope between knee and hip flexion had an average value of 0.181, which implies a favor of flexing knee joint to the swing foot with the floor. This can be explained from the aspect of energy efficiency. During obstacle crossing, the coordination slope of the leading limb demonstrated a value from 0.447 ± 0.09 for the lowest obstacle to a value of 0.602 ± 0.06 over the highest obstacle. A significant effect of obstacle height on the joint coordination slope of the leading limb was identified

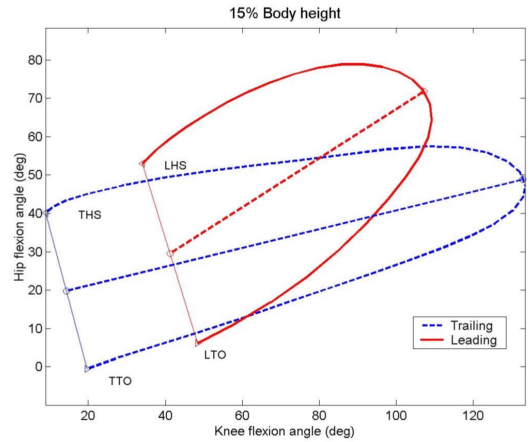

Figure 1. Representative joint coordination plot of the 15% BH obstacle condition, defining the slope of each limb.

($p=0.001$). These greater values of the coordination slope reflect that a relatively greater contribution from the hip flexion, as compared to the knee flexion, is required to safely step over a higher obstacle. The coordination slope of the trailing limb increased slightly from that of unobstructed walking to an average value of 0.247 ± 0.06 across all obstacle heights. This indicated that the joint coordination strategy of the trailing limb remains unchanged regardless of obstacle height, with foot elevation being achieved primarily through knee flexion

SUMMARY

The joint coordination slope provides us information on the overall strategy adopted by the swing limb when walking on different terrains. Inability to coordinate motion of hip and knee joints may result in obstacle contact, increasing the risk of tripping and falls. Results of this study could potentially serve as a baseline for comparing the functional strategies adopted by patients with joint pathology, muscular strength deficits or post-surgical complications.

REFERENCES

Chen, H-C et al. (1991) *J Gerontol* **46**: M196-203.
Chou, L.-S. et al. (1997) *J Biomech* **30**: 331-337.
McFayden, B. F. and Winter, D.A. (1991) *Neurosci Res Commun* **9**: 37-44.
Patla, A.E. et al. (1996) *J Mot Behav* **28**: 35-47.

ACKNOWLEDGEMENTS

This study was supported by the Oregon Medical Research Foundation.

BIOMECHANICAL PROPERTIES OF TOTAL ANKLE ARTHROPLASTY AND ANKLE ARTHRODESIS

Victor Valderrabano[1], Beat Hintermann[1], Benno M. Nigg[2], Darren Stefanyshyn[2], Pro Stergiou[2]

[1] Clinic of Orthopaedic Surgery, University of Basle, Kantonsspital, 4031 Basel, Switzerland; v.valderrabano@bluewin.ch
[2] Human Performance Laboratory, Kinesiology, University of Calgary, Calgary, Alberta, Canada

INTRODUCTION

Ankle arthrodesis and total ankle arthroplasty are the surgical treatment possibilities for severe ankle arthritis. The ankle arthrodesis is a well-established and accepted method, but has a few biomechanical and clinical disadvantages: Gait abnormality, degeneration of adjacent joints, pseudoarthrosis, stress fractures. The new total ankle replacement (TAR) generation shows encouraging clinical results and represent nowadays a valuable alternative to the ankle fusion. Although biomechanical comparison studies could provide important data for determination of the future development in this field, they are still extremely rare. The purpose of this in vitro study was therefore to determine the biomechanical characteristics of the ankle before and after ankle arthrodesis and after implantation of three currently used total ankle prostheses. The ankle range of motion (ROM), ankle movement transfer and the talar coupled movement were investigated.

METHODS

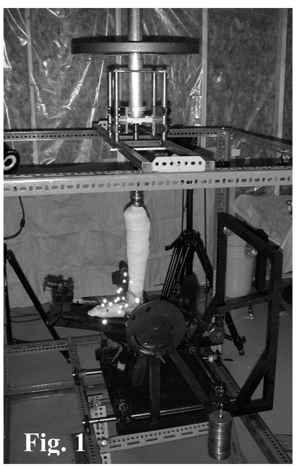
Fig. 1

A 6 degrees-of-freedom device (Fig. 1) with an axial load of 200 N, and a camera high speed video system (Motion Analysis Corporation, Santa Rosa, CA, USA) were used. Data collection was performed on 6 fresh frozen cadaveric leg specimens after insertion of reflective hindfoot bone markers and performance of the different ankle surgeries. All five conditions (normal ankle, ankle fusion, AGILITY [AGILITY™ Total Ankle System, DePuy Inc., USA], S.T.A.R. [Scandinavian Total Ankle Replacement, Waldemar Link, Hamburg, Germany], HINTEGRA [HINTEGRA®, Newdeal SA, Vienne, France]) were performed in each case on the same foot. Three-dimensional bone marker positions were calculated using a direct linear transformation (DLT) procedure (EVA software, version 6.0). The 3-D co-ordinates of the markers were transferred into other software for analysis (Kintrak, version 6.0, The University of Calgary, Calgary, AB, Canada). Relative joint angles and translations were calculated as rotations or shift between the bones of interest for a specific movement. The input movements were performed dynamically and statically (100N). Significant condition effects were detected using ANOVA and paired student t-tests.

RESULTS

ROM: Compared to the normal condition, the ROM for dorsi-plantarflexion had the highest change for the ankle arthrodesis. The total ROM for eversion/inversion was slightly decreased by the fused ankle, not changed by the three-component prostheses (HINTEGRA, S.T.A.R.) and increased by the two-component prosthesis (AGILITY). The ROM for internal and external tibial rotation was not altered by the AGILITY and HINTEGRA ankle, but it was significantly reduced by the ankle arthrodesis. S.T.A.R. showed a significant shift of the total ROM towards internal tibial rotation.

Movement Transfer: While dorsi-/plantarflexion of the foot, ankle joint fusion increased the movement transfer to tibial rotation by a 2.4 factor and to eversion-inversion by a 18.5 factor; whereas, this movement transfer did not change for all prosthesis conditions. The movement transfer between foot eversion and tibial rotation was found to decrease for all ankle prostheses.

Talar movement: In the normal ankle, dorsi-plantarflexion movement was coupled with rotation of the talus about its longitudinal axis and medio-lateral talar shift. While the three-component prostheses (HINTEGRA, S.T.A.R.) did not show no changes to the normal condition, AGILITY was significantly decreased and therefore constrained in both coupled movements.

DISCUSSION AND SUMMARY

Physiological range of motion and intact coupled movements of the ankle are very important for natural human foot function. A pathological ROM or movement transfer result in abnormal gait kinematics and high rate of second degeneration and injuries. The ankle fusion alters the normal biomechanics with a decrease of ROM and an increase of movement transfer leading to an overstress of neighboring joints. The total ankle prostheses changed the kinematics parameters of the ankle joint complex less than the ankle arthrodesis. The three-component total ankle prostheses were shown to replicate the normal ankle joint closer as the two-component design. In the surgical treatment of severe ankle arthritis an anatomical shaped, three-component total ankle replacement can be seen as the biomechanical "gold-standard".

REFERENCES

Kofoed,H. and Stürup,J. (1994): Comparison of ankle arthroplasty and arthrodesis. A prospective series with long-term follow-up. *Foot*, **4**:6-9

Hintermann,B., Nigg,B.M., Sommer,C., and Cole,G.K. (1994): The transfer movement between tibia and calcaneus. *Clin. Biomech.*, **9**:349-355

Michelson,J.D., Schmidt G.R., Mizel M.S.(2000): Kinematics of a total arthroplasty of the ankle: comparison to normal ankle motion. *Foot and Ankle Int.*, **21**:278-284

FINITE ELEMENT MODEL OF THE EPIDERMIS-DERMIS INTERFACE

Nelson Morales[1,2], Dongbu Cao[2], Yan Chen[2], Brian L. Davis[2]
[1]NASA Glenn Research Center
[2]Department of Biomedical Engineering - Cleveland Clinic Foundation

INTRODUCTION

Usually, when the skin is represented using finite element models, the interface between the epidermis and dermis is shown as a flat line. In reality, this interface is not flat, but rather consists of so-called “rete ridges“ (Figure 1). Neglecting the ridges can yield to incorrect results because of the large difference in stiffness between the two layers (one order of magnitude). These irregularities could prevent relative slipping between layers when the skin is subjected to shear loads. Thus the purpose of the current study was to obtain a quantitative effect of different epidermal-dermal (E-D) configurations and compare these with the flat configuration.

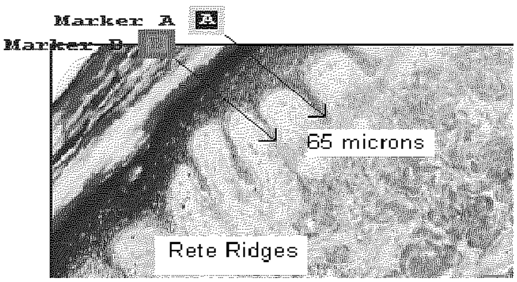

Figure 1: Epidermis-dermis beneath first metatarsal head

METHODS:

A 3D finite element model of a small section of the skin was created to compare the effects of the ridges and their frequency. Four different configurations were investigated: one flat and three others with sinusoidal ridges at the epidermal-dermal interface. The model was initially created in a 2D plane (x-y plane) and later extruded in the z-direction. The overall size of each model was 3mm x 1mm x 0.2 mm. Each model had approximately 140,000 elements and 155,000 nodes. The model was preprocessed in PATRAN© and analyzed using the commercial finite element model code, ABAQUS©. All the models were analyzed separately.

The ridge sizes were compared to real sample data obtained from the skin of the soles of cadaver feet. Ridge spacing was measured using ResView 3.0. The ridge spacing obtained was 65 µm. This is similar to the width used in the finite element model, 56 µm (high frequency). The other two configurations, mid-frequency (100 µm), and low frequency (252 µm), are variations that may simulate other skin regions or skin conditions. The material properties given to the model were linear elastic. The elasticity moduli used were20 MPa for the dermis, and 200 MPa for the epidermis. Vertical and shear loads were applied in the x-z plane. The loads consisted of a compressive load of 200 kPa (to simulate the body weight on the foot) and a shear stress of 20 kPa (to simulate the friction forces when walking). Constraint boundary conditions were applied on the top nodes to prevent free body motion.

RESULTS

All the configurations were compared on the basis of their Von Mises stress. The table below shows a summary the Von Mises (VM) stresses for all the configurations. These stress values occur at the interface region and represent local peak values. Also, since VM stress does not indicate whether the stresses are compressive or tensile, principal stresses were examined. It was found that the values given below are associated to compressive (negative values) stresses at the interface. The overall peak stress of the model was very similar in all the configurations (550 kPa), but it occurred at the constrained region, away from the epidermis-dermis interface. Also, the models stress distribution in the regions away from the epidermis-dermis interface was very similar in all the configurations.

Table 1: VM Stress at E-D interface for all configurations

Configuration	VM Stress Range in Dermis (kPa)	VM Stress Range in Epidermis (kPa)
Flat	246-283	250-273
Low frequency	400-480	75-90
Mid frequency	400-520	64-75
High frequency	380-504	55-73

DISCUSSION

As shown above, representing the epidermis-dermis interface as a flat interface can yield inaccurate results. These results neglect the peak stresses at the interface. Including rete ridges in the model reveals that the interface stress are approximately twice as much as a model without the ridges. Although models like these can be computer intensive, submodeling can be used to obtain results of a larger region, such as the entire foot, relatively faster without using excessive computing resources. Also, it can be noticed that the models with the three different ridges yielded very similar results.

REFERENCES

Thompson, D.L. (1997). *Finite Element Modeling of the Diabetic Foot*. Unpublished Master’s Dissertation, Ohio State University.

ACKNOWLEDGEMENT

Support for this project was provided by the Juvenile Diabetes Research Foundation.

AN AXISYMMETRIC BIPHASIC MODEL OF LOAD BEARING IN THE KNEE JOINT

Samer Adeeb[1], Dave Hart[2], Cy Frank[3], and Nigel Shrive[4]
McCaig Centre for Joint Injury and Arthritis Research, University of Calgary, Calgary, Alberta, Canada
[1]B.Sc. Civil Engineering, smadeeb@ucalgary.ca
[2]Professor and Head, Dept. of Microbiology & Infectious Diseases
[3]McCaig Professor of Joint Injury and Arthritis Research
[4]Killam Research Chair

INTRODUCTION

The objective of this study is to examine the load distribution in the knee joint between the articular cartilage and the meniscus and the role of the interstitial fluid in stress distribution in the tissues.

METHODS

An axisymmetric finite element model of the knee joint was developed, based on geometric approximations obtained from the literature for the menisci and the articular cartilage. The solid phase of the meniscus was modeled with anisotropic material properties, being much stiffer circumferentially than radially. The joint was studied under an axial load of approximately double the average human body weight (1400 N) applied in 0.34 seconds using a commercial FEM package (ABAQUS 6.1). The initial gap between the articular cartilage surfaces was varied from 0mm to 1mm in 0.25mm steps. The meniscus and the articular cartilage were modeled as saturated biphasic materials consisting of solid and interstitial fluid. Stress states in the meniscus were compared with the locations of the different meniscal cell phenotypes identified earlier[(Hellio Le Graverand, 2001)].

RESULTS AND DISCUSSION

Load deflection curves obtained from our model for different initial gaps between the cartilage layers are similar to the experimental results obtained from porcine and human knee joints[(Shrive, 1974)].The vertical loads between the femur and the tibia are mainly carried by the intersitial fluid. The presence of the meniscus decreases the magnitude of the pore water pressure and the stresses in the articular cartilage compared to the meniscus deficient knee. The meniscus carries 50-75% of the load depending upon the initial gap between the articular cartilage surfaces.
The state of stress in the meniscus varies tremendously from inner to outer radius. At the inner periphery, there are high hydrostatic fluid pressures and low circumferential tension, whereas the opposite occurs at the outer periphery (**Fig. 1, 2**). Interestingly, these different stress states correspond with the varying cell phenotype detected in the rabbit meniscus[(1)]. Chondrocytic cells are observed towards the inner periphery, with increasing cellular networks and processes to the outer edge where the cells are fibrocytic and aligned predominantly circumferentially.

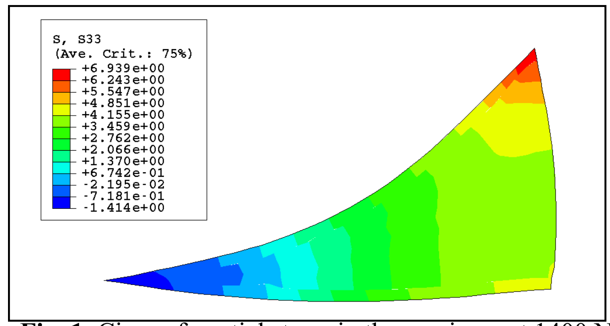

Fig. 1. Circumferential stress in the meniscus at 1400 N.

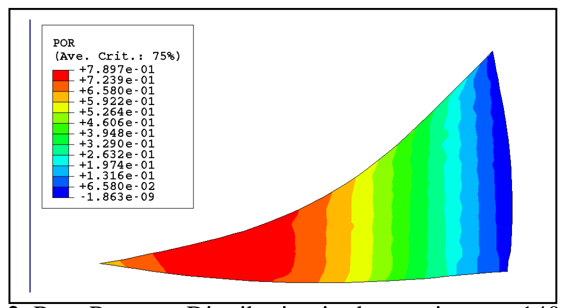

Fig. 2. Pore Pressure Distribution in the meniscus at 1400 N.

SUMMARY

Modeling soft tissues as a biphasic mixture of a solid and a fluid phase demonstrates the behavior of those tissues under compression as a nearly incompressible material with very low shear properties. The results obtained also show how the morphology of the meniscus is well adapted for transmitting load across the knee.

REFERENCES

Hellio Le Graverand, M.P. et al. (2001). *Journal of Anatomy* 198(5), 525-536.
Shrive, N.G. (1974). *D.Phil. Thesis. University of Oxford.*

ACKNOWLEDGEMENTS

We gratefully acknowledge the support of CAN for this work.

MODELING THE BEHAVIOUR OF LIGAMENTS: A TECHNICAL NOTE

Samer Adeeb[1], Nigel Shrive[2], Cy Frank[3] and David Smith[4]
McCaig Centre for Joint Injury and Arthritis Research, University of Calgary, Calgary, Alberta, Canada
[1]B.Sc. Civil Engineering. smadeeb@ucalgary.ca
[2]Killam Research Chair
[3] McCaig Professor of Joint Injury and Arthritis Research
[4]Associate Professor, Engineering and Built Environment, the University of Newcastle, Australia

INTRODUCTION

Ligaments are composed of solid matrix and fluid phases. When ligaments are stretched, an increase in volume would be expected to lead to a negative pore pressure inside the tissue. This pressure would, in turn, cause an inward flux of fluid. However, experiments have shown that when the ligaments are stretched, there is an outward flux of fluid(Hannafin, 1994) suggesting a decrease in volume. We have investigated this unique behaviourand have found three mechanisms which may contribute to the expected observations: the slackness of the bibres before stretching can lead to a decrease in volume upon straightening; a poisson's ratio higher than 0.5 from the axial to the lateral direction (as recorded in the literature(Hewitt, 2001)) due to the very high level of anisotropy of the tissue; and a constant osmotic pressure that causes the swelling of the tissue before loading(Thornton, 2001), together with a certain level of anisotropy These mechanisms may not be the only ones to cause the observed fluid exudation on tensile loading.

METHODS

Each mechanism was studied separately. For the case of fibre slackness, a simple mathematical model was used with a parabolic curve for the outer fibres (a barrel shaped ligament). The value of the volume change after straightening of the fibres was calculated and shown to be lower than the initial volume (**Fig. 1**). For the case of high poisson's ratio in anisotropy, a finite element model of a ligament was constructed and analysed through poro-elastic theory. The ligament was taken to be 12 mm long and 2 mm in diameter. Axisymmetric elements were used. A high level of anisotropy was implemented with three values for the ratio of lateral strain to longitudinal strain taken 0.3, 0.5 and 0.7. The same finite element model was used with a smaller poisson's ratio (0.3). To assess osmotic swelling a constant positive pore pressure was imposed on the surface simulating an osmotic pressure which caused the tissue to swell with time. The ligament was then stretched for different levels of anisotropy measured by the values of E_2/E_1 (Longitudinal stiffness/horizontal stiffness) and G/E_1 (in plane shear stiffness/horizontal stiffness). The ligament was considered to exude fluid when –at one point during the stretching process– all the values of the fluid pressure inside the ligament were higher or equal to the imposed osmotic pressure.

RESULTS AND DISCUSSION

Results of the simple mathematical model show that for curved fibres, very small strains are required to straighten the fibres. However, these strains cause a tremendous decrease in volume, depending upon the slackness of the fibres. For the finite element model with different poisson's ratio, results show that for a poisson's ratio higher than 0.5, the ligament tends to exude fluid. Finally, the osmotic pressure that tends to swell the ligaments is another cause for the phenomenon of fluid exuding from ligaments. Results show that the value of the imposed osmotic pressure that would cause fluid exudation depends on the anisotropy of the material. For high stiffness in the longitudinal direction and low shear stiffness, the value of the osmotic pressure required to exude fluid is less than that required for a ligament with less longitudinal stiffness and higher shear stiffness.

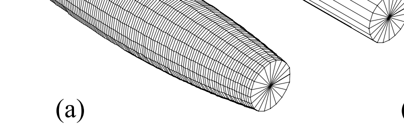

(a) (b)

Fig. 1. (a) The assumed barrel shape of the ligament before stretching. (b) Ligament shape after stretching.

SUMMARY

Ligaments tend to exude fluid upon stretching. This phenomenon was investigated and was related to one or more of three mechanisms: Slackness of fibres; high poisson's ratio; and the osmotic pressure that causes ligament swelling.

REFERENCES

Hewitt, J.et al (2001). *J. Orthopaedic Research*, **19**, 359-364.
Hannafin, J.A., Arnoczky S.P. (1994). *J. Orthopaedic Research,* **12(3)**, 350-356.
Thornton, G.M. et al (2001). *J. Orthopaedic Research,* **19(5)**, 845-851

THE "MINIMUM CRACKLE" HYPOTHESIS FOR MANIPULATING MASS-SPRING OBJECTS SMOOTHLY

Jonathan B. Dingwell[1], Christopher D. Mah[2], and Ferdinando Mussa-Ivaldi[2]
[1]Department of Kinesiology and Health Education, The University of Texas, Austin, TX
[2]Sensory Motor Performance Program, The Rehabilitation Institute of Chicago, Chicago, IL
Email: jdingwell@mail.utexas.edu Web: http://www.utexas.edu/education/kinesiology/motorbe/dingwell.html

INTRODUCTION

Humans make "smooth" movements during point-to-point reaching tasks, adopting optimal "minimum jerk" trajectories (Flash & Hogan, 1985), defining in effect the lowest order polynomial (5^{th}) to satisfy the boundary conditions (BC) imposed by the task. Tasks where the end-point of a non-rigid object is controlled impose additional BC on reaching, requiring new optimal solutions. Indeed, humans adopt very different kinematics when manipulating mass-spring objects (Dingwell et al., 2002). This study determined if these kinematics are also optimally smooth in the same sense as minimum jerk.

METHODS

The task studied was reaching to a target with a mass-on-a-spring attached to the hand. The object's dynamics were:

$$M_O\ddot{r}_O = -K_O\left(r_O - r_H\right) \qquad (1)$$

where M_O=object mass, K_O=object stiffness, r_O=object displacement, and r_H=hand displacement. Both the hand and object were to be stationary (i.e. $\dot{r}_O = \ddot{r}_O = \dot{r}_H = \ddot{r}_H = 0$) at the beginning ($t = 0$) and end ($t = T$) of the movement. Minimum jerk trajectories cannot satisfy all of these BC. Therefore, we propose a cost function for this task that minimizes the mean squared "crackle" (5^{th} derivative of displacement) along r_O:

$$C\left[r_O(t)\right] = \frac{1}{2}\int_0^T \left\{d^5/dt^5\left[r_O(t)\right]\right\}^2 dt = \frac{1}{2}\int_0^T \left[\overset{\cdot\cdot\cdot\cdot\cdot}{r}_O\right]^2 \qquad (2)$$

Solving the Euler-Poisson equation (Flash & Hogan, 1985) subject to this cost function gives a general 9^{th} order polynomial solution for $r_O(t)$. Applying the appropriate BC gives:

$$r_O(t) = L\left[70\left(\frac{t}{T}\right)^9 - 315\left(\frac{t}{T}\right)^8 + 540\left(\frac{t}{T}\right)^7 - 420\left(\frac{t}{T}\right)^6 + 126\left(\frac{t}{T}\right)^5\right] \qquad (3)$$

Hand trajectories are obtained by substituting (3) into (1) and solving for $r_H(t)$. Contrary to minimum jerk predictions, the minimum crackle hypothesis predicts that faster movements or movements made with objects of lower resonant frequency (f) will require bi-phasic hand movements (Fig. 1B).

To test these predictions, 12 young healthy subjects (6M+6F; age = 28.7±3.0 yrs) made targeted reaching movements with their dominant arm using a robot (Fig. 1A) that imposed forces simulating various mass-spring objects. Subjects were given 1-2 days (2-4 hours) to become skilled at the task, but were not told *how* to solve the task. Subjects were then tested under a variety of task conditions to compare their movements with those predicted by the minimum crackle model.

RESULTS

All subjects exhibited uni-phasic or bi-phasic hand movements under task conditions where the minimum crackle hypothesis predicted that they should (e.g. Fig. 2). Furthermore, all subjects switched from uni-phasic to bi-phasic hand movements (and back again) when the task conditions changed accordingly. Subjects exhibited behavior generally consistent with all predictions made by the minimum crackle model.

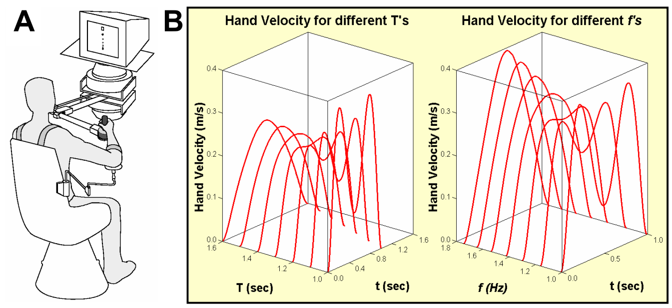

Figure 1: *A*: 2-DOF robot used to simulate mass-spring objects. *B*: Predicted hand velocity profiles for (left) different total movement times (T) and (right) different object resonant frequencies (f).

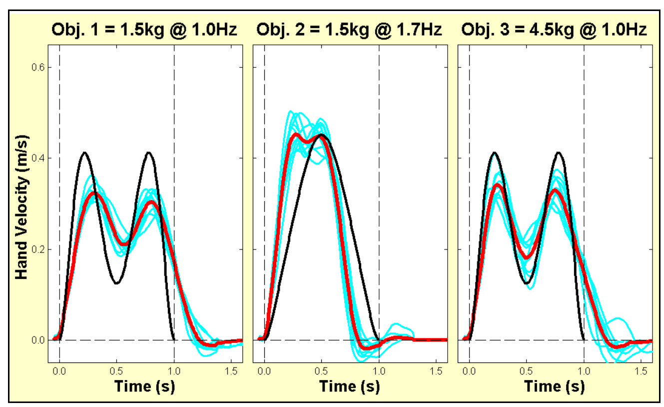

Figure 2: Predicted ("ideal") and actual hand velocity profiles for a typical subject reaching with 3 different mass-spring objects.

DISCUSSION AND SUMMARY

These results demonstrate that the ability of humans to generate smooth movements extends beyond simple reaching, to manipulation tasks involving non-rigid objects that impose additional degrees-of-freedom on the system being controlled (i.e. the arm). This does *not* necessarily mean that the brain is explicitly computing "crackle", but it does provide further evidence that "smoothness" in this sense is a general principle that guides movement planning and control.

ACKNOWLEDGEMENTS

Partial funding was provided by NIH grants F32-HD08620-01 & T32-HD07418 and by NSF grant NSF-BES-9900684.

REFERENCES

Flash T, Hogan N (1985) ***J. Neurosci.***, 5 (7): 1688-1703.
Dingwell JB et al., (2002) ***J. Neurophysiol.***, In Press.

ECHO-PIV®: A NOVEL METHOD FOR THE NON-INVASIVE MEASUREMENT OF VELOCITY VECTORS USING ULTRASOUND IMAGING

Hyoung-Bum Kim[1], Jean Hertzberg[1], and Robin Shandas[1,2]
[1]Dept. of Mechanical Engineering, University of Colorado, Boulder, Boulder, CO, USA
2 Cardiovascular Flow Research Laboratory, The Children's Hospital / University of Colorado Health Sciences Center, Denver, CO USA shandas.robin@tchden.org

INTRODUCTION

The inherent angle-limitation of current ultrasound Doppler imaging techniques precludes the ability to quantify parameters such as fluid stress, vorticity, or complex velocity profiles. Such information should allow clinicians to develop a more comprehensive picture of cardiovascular hemodynamics non-invasively. We have recently developed a novel method to measure multiple-components of velocity using high frame rate (>100 fps) echocardiography coupled with contrast imaging. This method, Echo-PIV®, is an *in vivo* equivalent of laser-based particle image velocimetry methods used *in vitro* for flow quantitation.

METHODS

The utility of Echo-PIV® to quantify various flow conditions was tested in a series of *in vitro* flow phantoms ranging from simple steady and pulsatile flows (0.5 – 3 L/min) through a tube, to complex pulsatile flow (30 – 80 cc/beat; 50 –80 bpm) through a bileaflet mechanical heart valve. High frame rate echocardiography (>100 fps) and contrast imaging (Optison®) was used to image the flow patterns from both short and long axis views. Each image frame was digitally stored without compression and transferred to an off-line analysis system. A two-dimensional spatial cross-correlation algorithm was used to extract mean spatial shift of contrast particles within smaller sub-windows (16X16 pixels; 32X32 pixels) of the image frame. The local 2D velocity vector was then obtained by dividing the spatial shift vector by the time difference between consecutive frames.

RESULTS AND DISCUSSION

Figures 1 and 2 show velocity vector plots from the steady-flow tube studies (1) and the bileaflet mechanical valve (2). Figure 1 shows that Echo-PIV can measure velocity profiles across an arterial or venous cross-section; this information can be used to compute wall and fluid shear stresses. Figure 2 shows the two side jet flows issuing obliquely from the valve as well as the central jet.

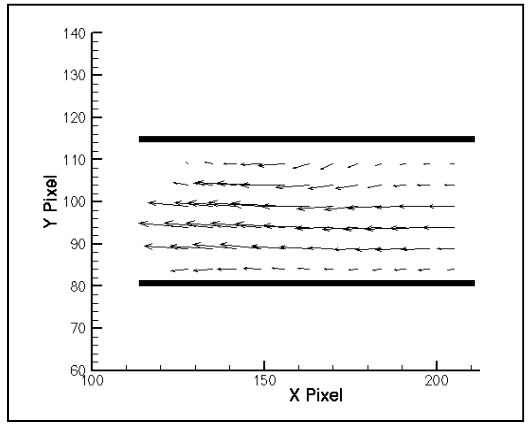

Figure 1: Velocity vectors for steady flow through an arterial model as measured by Echo-PIV®.

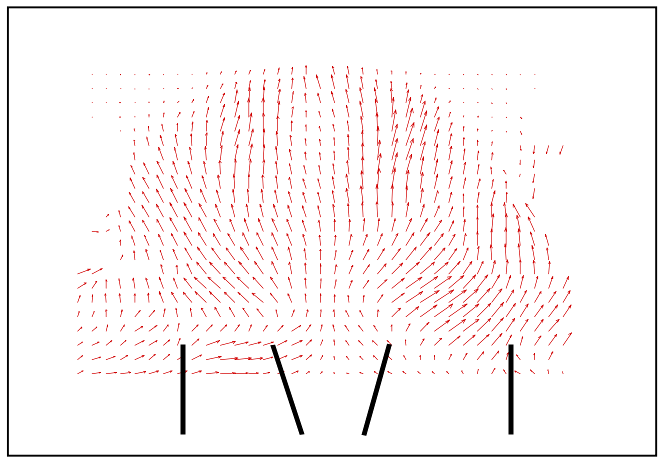

Figure 2: Velocity vectors immediately distal to a bileaflet mechanical heart valve (S,C,S: side, central, side orifices).

SUMMARY

Echo PIV® appears to be a promising method for the non-invasive measurement of multiple velocity vectors *in vivo* without angle limitations, and should raise the accuracy of hemodynamic information that can be obtained using echocardiography.

ACKNOWLEDGEMENTS

This project was supported in part through grants from the American Heart Association and the National Institutes of Health (HL-67393-01).

DERIVING ROWING COORDINATION PATTERNS AND BOAT RIGGING FROM OPTIMIZATION OF A SIMPLE MODEL

David Cabrera and Andy Ruina
Human Power and Robotics Laboratory, Theoretical and Applied Mechanics, Cornell University, Ithaca, NY, USA
http://www.tam.cornell.edu/~ruina/hplab/index.html

INTRODUCTION

Trusting that the rowing stroke has been nearly optimized by the evolution of the sport, we attempt to explain current competitive rowing techniques by optimizing the performance of a simple model. The model is thus verified by its ability to predict various kinematic and force data found in actual rowing.

Once such realism has been achieved, the model can be used to check the advantages of various possible design changes for racing boats. It is hoped, for example, that the ideas could help test changes in rigging on a person-by-person basis, for upwind or downwind races, making use of work by the coxswain, etc.

More generally, however, finding which optimization criteria make for the best matches with used-technique validates the overall modeling strategies for better understanding of other human and animal activities.

METHODS

We develop a mathematical model of the mechanics of the rowing stroke that is quasi-one-dimensional. Momentum balance only in the fore-aft direction is considered. Mass is distributed in two places, the boat and the rower's gut. The controlled degrees of freedom are leg length, back angle, and arm length as functions of time. The arc-like motion of the oar blade and handle is considered when calculating the fore-aft mechanics. That is, we allow the oar to sweep through large angles instead of assuming small angular motion as is done in some other simple models. The oar is flexible and the oar blade has wing-like lift and drag properties in the water. Hand raising is assumed to be timed so that there is zero-splash and hand lowering is timed just when the bending of the oar is relieved. We use computer optimization of the coordination (leg length, back angle, and arm length as functions of time) to maximize the boat speed (or minimize race time) with given rower performance limitations. In the simplest model the rower's average rate of metabolic cost is bounded and metabolic cost is proportional to the joint work of the leg, back, and arm actuators (counting negative work as slightly costly). In this optimization we can also leave free to optimize the oar length and oarlock position (fore-aft and outboard).

We parameterize the control functions of the body part motions in time using periodic cubic splines. The splines consist of knots which are evenly spaced in time and, thus, the body displacements at the knot times are the parameters over which we optimize. The knot values, as well as a few rigging parameters, determine, through the simulation, both the metabolic cost and the boat speed. In addition to the metabolic work limitation, we place upper and lower bounds on the amount the various body parts can displace. Matlab®'s nonlinearly constrained optimization routine, 'fmincon', is used to determine the optimal coordination strategy as well as the optimal boat rigging parameters. The model and optimization criteria are evaluated in terms of how well they predict present rigging practice and present popular rowing technique as determined by available kinematic and force data.

RESULTS AND DISCUSSION

We have been able to "derive" both rowing technique and common rigging as well as might be hoped with a simple model. Due to the flatness of the objective function, once constrained, near the optimum, we see very little change in the average boat speed when searching in this neighborhood of the parameter space. Therefore, we find multiple coordination strategies which produce similar average boat speeds at a given metabolic cost. However all of these strategies have some common features, the most conspicuous of which is the near absence of negative-work by all of the body parts.

SUMMARY

Our quasi 1D model, with 2D oar mechanics, with an energy based model of human performance, is surprising predictive of some aspects of rowing coordination. That is, even without putting any bounds on the strengths of any muscles, or indeed any information about the muscles at all, much of rowing can be explained. Overall this predictive ability adds some credence to the view that energetics has an important role in explaining human and animal coordination patterns.

REFERENCES

Williams, K.R., Cavanagh, P.R. (1983). *J. Biomechanics*, **16**, **2**, 115-128.

ACKNOWLEDGEMENTS

This work has been partially funded by a NSF biomechanics grant on the mechanics of locomotion.

THE FINITE ELEMENT ANALYSIS OF DIFFERENT FIXATIONS FOR MANDIBULAR FRACTURE

Chih-Hung Chuang[1], Ming-Yih Lee[1,] Lun-Jou Lo[2] and Chun-Li Lin[1]
[1]Department of Mechanical Engineering, Chang Gung University, Tao-Yuan Taiwan, d9022003@stmail2.cgu.edu.tw
[2]Craniofacial Surgery, Chang Gung Memorial Hospital, Tao-Yuan, Taiwan

INTRODUCTION

Plates and screws fixation system is commonly used to fix the bone segments for craniofacial trauma fracture and malformation orthopedics. The long-term success of surgery is influenced by biomechanical aspects, such as stress concentration and bone remodeling that related to the insecure fixation philosophies. However, quantification guideline cannot identify by clinical experiences and experimental approaches. Therefore, computer analysis is needed to use as a complemental tool to understand the mechanical interactions between fixation system and surrounding bone.

METHODS

Medical image software (MIMICS 6.3) was employed to process coronal CT data of a healthy male mandible. A 3D FE model included cortical and cancellous bone was constructed in FEA package (ANSYS 5.6) through self-developed program that transformed CT data to ANSYS. Reducing Young's modulus procedure was used to simulate for mandibular fracture volume and four types of fixation philosophies were then designed to model different fixation system. The mandibular condyle and coronoid process was constrained as the boundary conditions. Vertical occlusive forces were applied as the loading conditions at premolar and molar symmetrizing to the symphysis. The peak von Mesis stresses and the displacements for all designs were calculated to investigate the mechanical responses.

RESULTS AND DISCUSSION

The peak stress and displacement of fixation type A were lower than B, C and D (Table 1). However, considered about the anatomy and parasumphysis location of mandible that fixation type D might be the better chose among four designs. This was because the higher bending moment acted on the B and C fixation that might cause the excessive stress concentration and displacement. These biomechanical interactions could lead the bone surrounding screws damage and malocclusion during healing. After bone healing, the stresses distribution and displacements of the bone surrounding screws was observed no significantly.

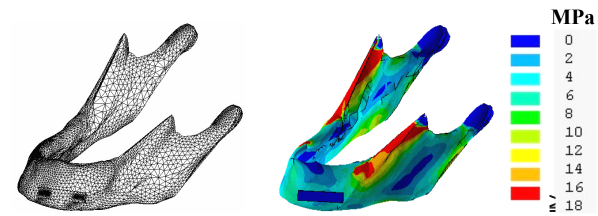

(a) **(b)**

Figure 1: **(a)** The mandible FE model; **(b)** The von Mesis stress patterns for D fixation type.

SUMMARY

Based on the limited data, the results indicated that fixation philosophies might influence the stress redistribution near the screws and surrounding bone.

REFERENCES

Huang et al (2001). *J. Oral Maxillofac Surg*, **59,** 1199-1210
Schuller-Gozburg et al (1999). *J. Biomechanics*, **32,** 511-520

ACKNOWLEDGEMENT

We acknowledge the technical assistance of Mr. Ming-Shin Huang, Chang Gung Memorial Hospital, Tao-Yuan, Taiwan

Table1: The peak von Mesis stresses and the displacements for four fixation types.

Fixation Types Plate and screw (PS) ; Cortical bone (CB)			Fracture case		Healed case	
			Max. von Mesis stress (MPa)	Displacement (10^{-6}mm)	Max. von Mesis stress (MPa)	Displacement (10^{-6}mm)
A	2 plates with 8 screws	PS	626.66	1.04	62.88	0.633
		CB	145.03	1.02	5.00	0.719
B	1 plate with 4 screws	PS	1376	1.26	41.56	0.590
		CB	490	1.20	4.90	0.686
C	1 plate with 2 screws (wide)	PS	3428	2.99	34.47	0.590
		CB	645.20	30.0	6.69	0.686
D	1 plate with 2 screws (close)	PS	1143	1.03	17.52	0.379
		CB	393.19	0.894	4.80	0.475

TANGENTIAL FORCE SHARING AMONG FINGERS DURING STATIC GRASPING

Todd Pataky[1], Vladimir Zatsiorsky, and Mark Latash
Department of Kinesiology, The Pennsylvania State University, University Park, Pennsylvania, USA
[1] tcp120@psu.edu

INTRODUCTION

Multi-finger grasping is statically indeterminate; the number of unknown finger forces exceeds the number of equilibrium equations. As such, normal force sharing has received substantial attention in the literature (e.g. Santello and Soechting, 2000). Far fewer studies exist in the literature regarding tangential finger forces (e.g. Flanagan et al., 1999). Tangential force sharing for "natural" prismatic grasping (4 fingers opposing the thumb) has not been addressed. The purpose of this study was to examine the tangential (load sustaining) force sharing at the fingertips as a function of both load magnitude and load direction.

METHODS

Eight subjects (age: 28.1 ± 5.9 years) were required to grasp a handle "as lightly as possible, while keeping the handle stationary". The handle was free to rotate about a central axis (Figure 1) to tightly prescribe a zero net moment. Three loads (250, 750, 1250 g) were applied to the handle in both the downward and upward vertical directions. Upward loading was achieved with a leveled steelyard mechanism (Figure 1). Fingertip forces were registered with multi-axis force transducers (ATI, North Carolina, USA).

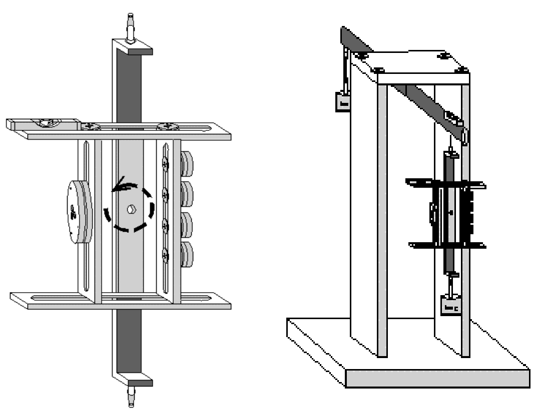

Figure 1: Rotating handle to prevent moment production (left); steelyard mechanism to achieve upward loading (right).

RESULTS AND DISCUSSION

Load sharing (% of the total tangential force) was evidently not constant (Figure 2). The mean sharing pattern changed more notably with load direction than with load magnitude. Notably, the thumb decreased its tangential force by about 15% of the total load when required to resist the applied load by pushing in a downward direction. The index finger conversely increased its tangential force by about 15% of the total load. The standard deviations associated with these percentages were less than 4% for the majority of conditions. Note that subjects were free to choose any tangential force sharing pattern desired provided that the sum of these forces was equal in magnitude and opposite in direction to the load. It may be expected that individual subjects select distinct sharing patterns because of the large number of possible patterns, but this was not observed. Another trend that was observed was the fact that the thumb did not produce 50% of the total tangential force. This indicates that the tangential forces contributed to a supination moment (for downward loading) and a pronation moment (for upward loading) despite constant hand posture.

SUMMARY

1) This is the first study to examine tangential force sharing, and patterns of this sharing have been presented.
2) The tangential force sharing pattern was more markedly affected by load direction than by load magnitude.
3) The subjects selected quite similar tangential force sharing patterns despite the high degree of redundancy in the task.

The current line of work will be important for understanding object manipulation, where the gravitational field can change with respect to the hand.

REFERENCES

Flanagan, J.R. et al. (1999). *Neurophysiology*, **81**, 1706-1717.
Santello, M., Soechting, J.F. (2000). *Experimental Brain Research*, **133**, 457-467.

Figure 2: Mean tangential force sharing among the fingers across different loads. Positive load indicates upward load. The exploded black pie slice corresponds to the thumb, and clockwise from the thumb: index, middle, ring, little.

EVALUATION OF SPINAL IMPLANTS - VERTEBRAL BONE DENSITY IS AN IMPORTANT FACTOR

Juay-Seng Tan, Brian K. Kwon, Dinesh Samarasekera, Marcel F. Dvorak, Charles G. Fisher and Thomas R. Oxland
toxland@interchange.ubc.ca
Department of Orthopaedics, University of British Columbia, Vancouver, British Columbia, Canada

INTRODUCTION

The current ASTM standard for spinal implant constructs uses synthetic elements as vertebral surrogates and therefore does not address bone-implant interface issues. Presumably, this interface is important since it is a frequent site of clinical failure. Variation in implant designs could result in different degrees of trabecular bone failure at the interface and by testing implants in synthetic materials, this important factor is not evaluated. Therefore, devices tested using ASTM test standards may give clinicians and regulatory bodies a false sense of security with respect to implant performance due to their limited scope. The purpose of this study was to contrast the mechanical behaviour of pedicle screws in cadaveric vertebrae versus synthetic surrogates.

METHODS

Short-term physiologic axial compression and bending moment were cyclically applied to pedicle screws inserted in lumbar vertebrae and UHMWPE. The maximum applied load consisted of a 300N vertical force and a moment arm of 35mm resulting in a 10.5Nm bending moment (Figure 1). These loads were based on *in vivo* measurements (Rohlmann 1997). Loads were applied to a hinged PE block superiorly and the inferior vertebrae and PE were rigidly clamped. An optoelectronic system (Optotrak 3020, Northern Digital Inc., Waterloo, Canada) was used to detect motion of the screw with respect to the bone and PE in each test. Motion of the inferior pedicle screws with respect to vertebrae and PE at the end of 100 cycles were compared. Eight lower lumbar vertebrae (L3, L4, L5) were tested and one PE was tested 8 times. One side of each vertebra was overdrilled so as to compare between motion of pedicle screws in normal insertion and loosened pedicle screws. The vertebrae were from a previous indentation test and the pedicles were all intact. Lateral DEXA bone mineral density of these specimens ranged from 0.30 to 1.04 g/cm^2 with a mean of 0.70 g/cm^2. An unpaired t-test was used to determine if there was any difference between the translation and rotation ranges between screws in UHMWPE and screws in bone inserted in the normal fashion. A paired t-test was used to compare between pedicle screws in normal and in overdrilled holes.

RESULTS AND DISCUSSION

Motions of pedicle screws in PE were significantly smaller than in vertebrae (Figure 2). There was a trend that specimens with higher bone mineral densities had lower translation and rotation ranges. The kinematics of the screw was affected by bone mineral density. Screws inserted in high-density bone were pivoting about a point between screw head and screw tip, whereas screws inserted in low-density bone underwent a translation and a rotation under each cycle of load. It was clear that bone mineral density affects the kinematics of the screw and the bending points on it.

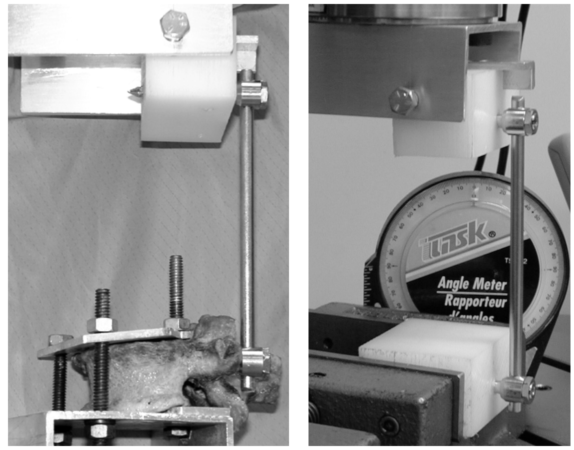

Figure 1: Test setup used to compare motion of pedicle screw in bone and in UHMWPE.

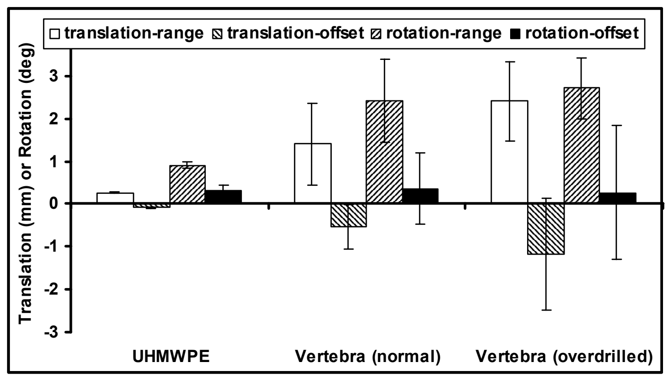

Figure 2: Motion of pedicle screw in UHMWPE was significantly lower than motion in vertebrae ($p < 0.005$). There was no significant difference for screw motion in the vertebrae between normal insertion and after overdrilling.

CONCLUSION

The kinematics of pedicle screws in bone and in PE are different in terms of the range of motion, pivoting and bending points of the screws and in terms of the effects of bone mineral density. The kinematics of the screws in bone is more relevant to clinical modes of failure. The fixation at the bone-implant interface can be quantified during short-term cyclic testing when an appropriate model is used, as demonstrated in this study.

REFERENCES

Rohlmann, A., Bergmann, G., Graichen, F. (1997), *J. Biomechanics*, **30**, 41-47.

ACKNOWLEDGEMENTS

The financial supports of the Canadian Institute for Health Research and Synthes Spine are gratefully acknowledged.

EFFECTS OF AGE AND TIME PERIOD ON JOINT KINEMATICS AND KINETICS DURING A SINGLE STEP RESPONSE

Carl W. Luchies[1], Yongsoek Won[1], Jeff M. Schiffman[2], Darryl G. Thelen[3], Sandy Bowman[4]
[1]Department of Mechanical Engineering, University of Kansas, Lawrence, E-mail: luchies@ku.edu
[2]U.S. Army Natick Soldier Center, Natick, MA.
[3]Engineering Program, Hope College, Holland, MI.
[4]Physical Therapy Department, Watkins Health Center, University of Kansas, Lawrence.

INTRODUCTION

Aging increases the frequency of injurious falls in the elderly (Tinetti, 1989). Taking a step is a strategy often used to arrest an impending fall when balance disturbances are encountered during activities of daily living. The generation of rapid, coordinated muscle actions about lower extremity joints is believed to be an important biomechanical component underlying successful stepping responses. The purpose of this study was to investigate the effect of age and time period (double stance, single stance, and landing) on the kinematics and kinetics at the ankle, knee, and hip joints used to execute a single step in response to a posterior waist pull.

METHODS

The performance of using a single step for balance recovery in response to a posterior waist pull was measured in 11 young adult (mean age 23.7, *SD* = 4.1 yrs) and 11 old adult (mean age 69.6 yrs, *SD* = 5.2 yrs) healthy female participants. Each participant gave her informed written consent as approved by the institution's review board on human experimentation. The posterior waist pulls were produced using an electronically released weight and cable system (Luchies, 1999). Foot-support surface reactions (AMTI) and body segment kinematics (Optotrak, NDI) were measured and analyzed using an inverse dynamics model (Vaughn, 1999) to determine the ankle, knee, and hip joint kinematics and power time histories during three time periods: double stance, single stance, and landing (Figure 1). Step foot liftoff and landing times, step length, height, and average speed were also determined. A two-way MANOVA was conducted on the dependent variables. Significant main effect findings ($p < 0.05$) were followed up with an ANOVA on each variable. Type I error was controlled for by using the Bonferroni Method.

RESULTS AND DISCUSSION

The old adults, compared to young adults, had earlier liftoff times ($p < .05$), earlier landing times ($p < .01$), shorter step lengths ($p < .001$), shorter in step height ($p < .005$), and slower average step speeds ($p < .001$). The old adults, compared to young adults, had significantly smaller flexion/extension joint excursion angles at the step leg ankle ($p < .005$), knee ($p < .05$), and hip ($p < .001$).

The landing period, compared to the double stance period, resulted in significantly larger flexion/extension joint excursion angles at the step leg ankle ($p < .05$), knee ($p < .001$), and hip ($p < .001$); larger power generation for the step leg knee ($p < .001$); and larger power absorption for the step leg ankle ($p < .001$) and hip ($p < .001$).

The landing period, compared to the single stance period, resulted in significantly larger joint excursion angles at the step leg ankle ($p < .001$); larger power generation in the step leg ankle ($p < .001$), knee ($p < .05$), and hip ($p < .001$); and larger power absorption in the step leg ankle ($p < .001$), knee ($p < .005$), and hip ($p < .05$).

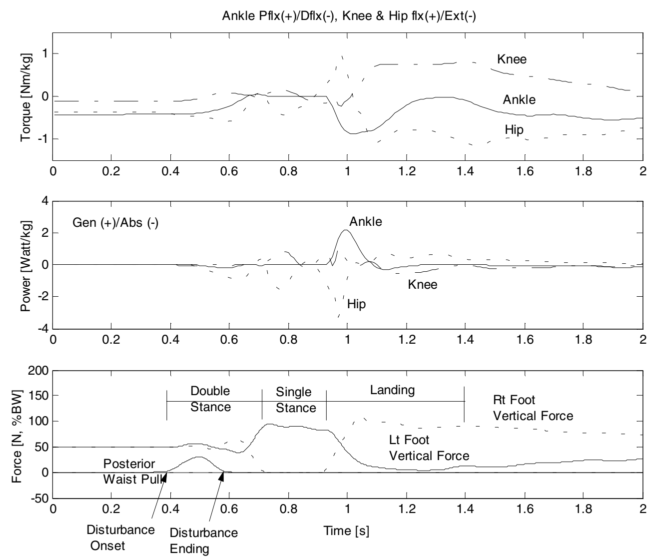

Figure 1: Foot forces, step leg joint powers and torques.

SUMMARY

Significant age and time period effects were found in the kinematics and kinetics in the step leg for a single step taken in response to a posterior waist pull. Older adults, compared to younger adults, stepped earlier and with a smaller step, resulting in smaller joint excursion angles. Despite the differences in kinematics, the underlying joint powers were similar between the two groups. Step landing resulted in larger joint powers than step initiation or swing. Thus, the landing period may represent the most challenging period of the stepping response in terms of joint kinetics, especially for those with limited capacity to generate muscle power quickly.

REFERENCES

Luchies, C.W. et al. (1999). *J Gerontol Med Sci,* 54A:M140-44.

Tinetti, M.E. et al. (1989). *N Eng J Med,* 320**:**1055-1059.

Vaughn, C.L. et al. (1999). *Dynamics of Human Gait* (CD-ROM), 2nd Ed, Kiboho Publisher.

ACKNOWLEDGEMENTS

This study received financial support from the American Federation for Aging Research and NIH (R15 AG13759-01). We gratefully acknowledge the assistance of Antonis Stylianou, Greg King, and Dr. Teresa Cathers.

ESTIMATION OF SPINAL DEFORMITY IN SCOLIOSIS FROM GEOMETRIC TORSION

Philippe Poncet[1], Jacob L. Jaremko[1], Janet Ronsky[2], James Harder[3], Jean Dansereau[4], Hubert Labelle[5], Ronald F. Zernicke[1,2]

[1]Dept. of Surgery, University of Calgary, 3330 Hospital Drive NW, Calgary, Alberta, Canada T2N 4N1, poncet@ucalgary.ca, [2]Dept. of Mechanical and Manufacturing Eng., University of Calgary, [3]Alberta Children's Hospital, Calgary, [4]Ecole Polytechnique of Montreal and [5]Ste-Justine Hospital, Montreal, Canada

INTRODUCTION

The shape of a curved line that passes through thoracic and lumbar vertebrae is often used to study spinal deformity with measurements in "auxiliary" planes that are not truly three-dimensional (3-D). Here we propose a new index, the geometric torsion (3-D intrinsic property of a curve), which could uniquely describe the spinal deformity. In this study we assessed whether geometric torsion could be effectively used to predict spinal deformity with the aid of multiple linear regression.

MATERIALS AND METHODS

Anatomical landmarks (6 points per vertebra) were obtained from multi-view radiographic reconstruction and used to generate 3-D model of the spine and rib cage of 28 patients. Fourier series best fitted to the vertebral centroids approximated the spinal shape. For each patient, spinal deformity indices were computed. Torsion was calculated (Frenet formulas) and 20 derived parameters were recorded. Torsion inputs were used in a multiple linear regression model for prediction of key spinal indices.

RESULTS AND DISCUSSION

The primary clinical Cobb angle (mainly thoracic) was predicted well, with r=0.89 using all 20 inputs of torsion or r=0.83 (Figure 1) using just two (maximal value and range of torsion in curve).

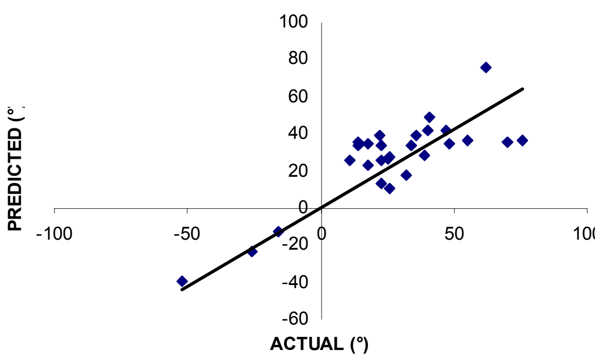

Figure 1: Actual vs. predicted Cobb angle. Data points are plotted for the 28 primary curves with the regression best-fit line (y=0.8456x).

Torsion was also well related (Figure 2) to the orientation of plane of maximal deformity (r=0.87). Torsion was less accurate but still significant in predicting maximal vertebral axial rotation (r=0.77).

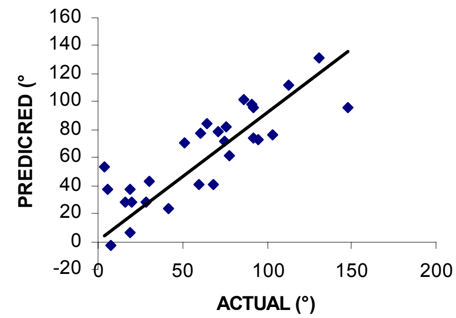

Figure 2: Actual vs. predicted orientation of plane of maximal deformity. Data points are plotted for the 28 primary curves with the regression best-fit line (y=0.9208x).

SUMMARY

This preliminary study showed promising results for the use of geometric torsion as an alternative 3-D index of spinal deformity. As expected, the orientation of the plane of maximal curvature, a quasi 3-D measure based on the overall lateral and sagittal curvature of the spine, correlated closely to the geometric torsion. The use of various input variables tended to improve predictive accuracy, though usually only slightly. Careful selection and combination of input indices, therefore, is essential to provide appropriate information and further improve the linear regression model predictive capacity.

Future work will focus on more patients and subgroups, and use of an artificial neural network, a high-order non-linear system, to improve correlations and study the reliability of geometric torsion as an accurate marker of scoliosis progression.

ACKNOWLEDGEMENTS

Funding: Arthritis Society of Canada, Fraternal Order of Eagle's, Hospital for Sick Children Foundation.

FINITE ELEMENT ANALYSIS OF THE NEWLY DESIGNED FOOT PROSTHESIS FOR PATIENTS WITH PARTIAL FOOT AMPUTATION

Yu-Chin Wu[1], Weng-Pin Chen[1] and Fuk-Tan Tang[2]

[1]Department of Biomedical Engineering, Chung Yuan Christian University, Chungli, Taiwan, wpchen@cycu.edu.tw
[2]Department of Rehabilitation, Chang Gung Memorial Hospital, Kweishan,Taiwan

INTRODUCTION

The aim of this research was to explore the biomechanics of two types of partial foot amputation: hallux amputation (HA), and transmetatarsal amputation (TMA) before and after the intervention of the newly designed total contact foot prostheses. The prosthesis was designed based on a total contact insole with filler at the amputation site. The plantar stress distributions before and after the intervention of foot prostheses were quantified using finite element analyses.

METHODS

Three different foot models (normal, HA and TMA) were created in the SolidWorks2000 CAD software and finite element models were created in the Patran2000 FEA software. The prostheses were modeled as total contact insole with filler and the thickness were ranging from 2 to 5mm. Young's moduli and Poisson's ratios for the bone, cartilage and soft tissue were adopted from literature. The prosthesis was made of Microcelpoff and Softsponge. The loading condition for the analysis was assumed that the foot be pushed by a rigid plane vertically from plantar side in 20mm/sec and continued for 1 sec (Fig. 1). Loading was divided into 20 increments.

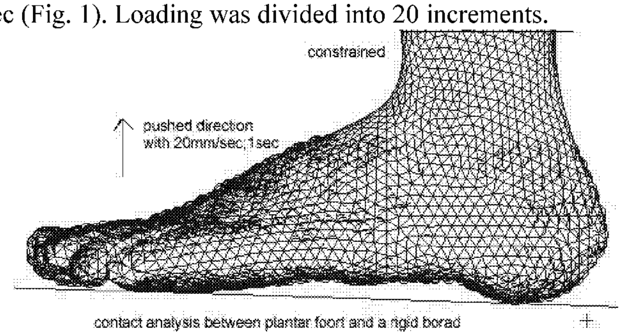

Figure 1: The boundary conditions used for analysis.

The maximum stress and strain values were calculated when the reaction force at the constrained tibial surface was equal to 600N simulating single leg stance condition. Plantar foot is divided into 5 different regions as M1 to M5 (Fig. 2), for comparison before and after footwear intervention.

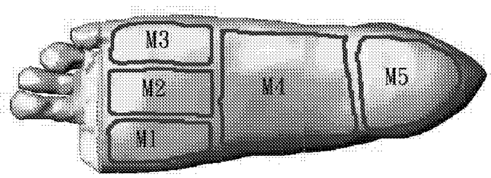

Figure 2: Five plantar regions: M1 to M5.

RESULTS AND DISCUSSION

Results showed that total contact prostheses could contribute over 60% of the plantar pressure reduction (Fig. 3), excluding M4 area of TMA foot. Peak plantar pressure was found to be higher in amputation feet than normal ones. Excluding M5 (plantar calcaneus) area, total contact prosthesis can reduce the peak pressure value to under 100kPa. This proves the effect of plantar pressure reduction by the special geometry and material combination of the total contact prostheses. Maximum von Mises strain also decreased 10% after wearing total contact footwear for normal foot, but increased for amputation feet. This may be resulted from the different load transfer path due to skeletal structure changes.

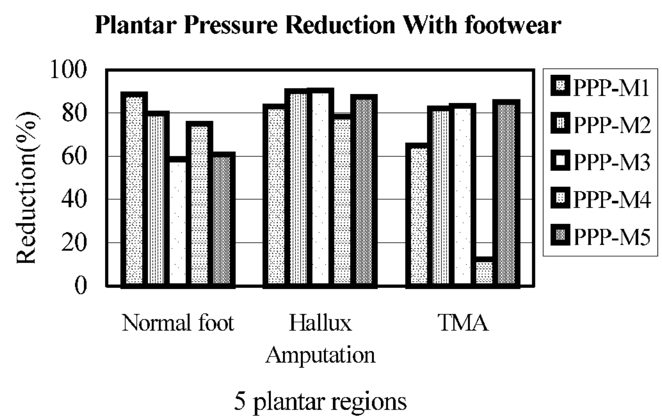

Figure 3: Peak Plantar Pressure(PPP) reduction in 5 plantar regions (M1 to M5) after wearing total contact prosthesis.

SUMMARY

This study can be a reference on the plantar pressure and skeletal stress distributions in foot amputation and prosthetic design. It is possible to evaluate different material and geometry combinations to design a more optimal prosthesis for patients with partial foot amputation.

ACKNOWLEDGEMENTS

This research was supported by the National Science Council, ROC. (grant no.:NSC 89-2614-E-033-001)

FINITE ELEMENT ANALYSIS OF THE CERVICO-TROCHANTERIC STEMLESS FEMORAL PROSTHESIS

Weng-Pin Chen[1], Yu-Liang Liu[1], Chun-Hsiung Shih[2] and Ching-Lung Tai[1,2]

[1]Department of Biomedical Engineering, Chung Yuan Christian University, Chungli,Taiwan, wpchen@cycu.edu.tw
[2]Department of Orthopaedic Surgery, Chang Guang Memorial Hospital, Kweishan, Taiwan

INTRODUCTION

Stemless-type prostheses, such as, surface replacement have been used during the early developing stage of hip arthroplasty. However, the high stresses occurred at the femoral head and the acetabulum jeopardized its development. A new stemless prosthesis was designed for solving the stress-shielding effect and the osteolysis caused by the wear debris often seen in stem-type prostheses. The objective of this study is to investigate the biomechanical performance of the newly designed Cervico-Trochanteric (C-T) stemless prosthesis by comparing the stress distributions with the traditional stem-type PCA (porous-coated anatomic) prosthesis using three-dimensional finite element models.

METHODS

Four finite element models were created for the intact femur, C-T implanted (with two fixation screws) femur, C-T implanted (with three fixation screws) femur, and PCA implanted femur. The geometry of the femur was based on a standardized composite femur. The finite element models for the C-T prosthesis, two screws, three screws and PCA prosthesis were created and shown in Fig. 1. The element type used was 10-node (2nd order) tetrahedral element. Material properties for each different material (cortical bone, cancellous bone, titanium alloy, Co-Cr alloy) were considered to be linear, elastic. Loading condition of single-legged stance was considered.

RESULTS AND DISCUSSION

The von Mises stress distributions on the medial side of the femur for the four models are shown in Fig. 2. and Fig. 3. The results can be summarized as:

1. Von Mises stress in the proximal, medial femur for the C-T implanted model was higher than that of the intact model and the PCA-implanted model.
2. Stress-shielding effects were significantly eliminated for the C-T-implanted models (with 2 or 3 fixation screws) as compared with PCA-implanted model.
3. No significant difference in von Mises stress distribution for the C-T-implanted model with 2 or 3 fixation screws.
4. There is no significant stress concentration around the fixation screws.

CONCLUSIONS

Based on the results, we found that the C-T implanted femur has more physiological stress distribution on the proximal femur than that of PCA prosthesis. C-T prosthesis can prevent the osteolysis caused by the wear debris. It can provide immediate stabilization of the implant and the preservation of endosteal vascularity.

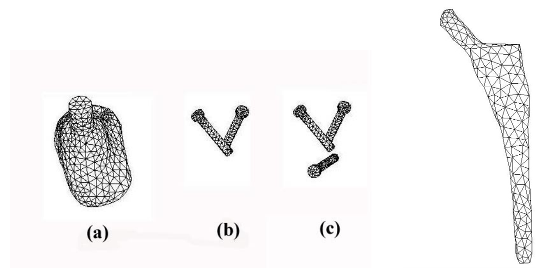

Figure1: Finite element mmodels of (a) C-T prosthesis, (b) 2 screws, (c) 3 screws, and (d) PCA prosthesis.

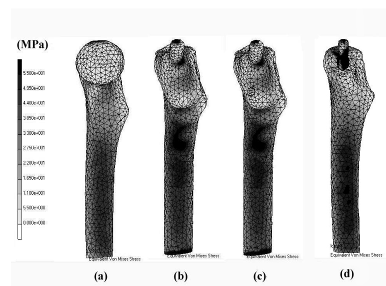

Figure 2:Von Mises stress distributions on the medial side of femur for (a) intact, (b) C-T (2 screws), (c) C-T (3 screws), and PCA implanted models. (unit: MPa)

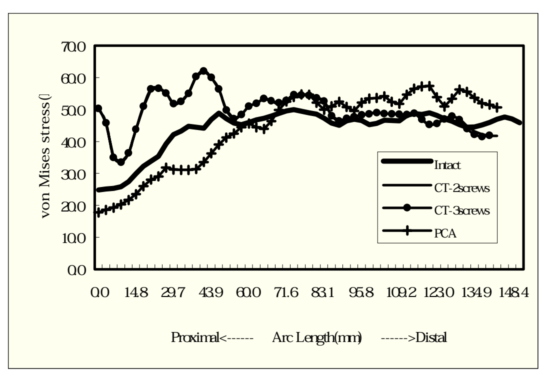

Figure 3: Von Mises stress distributions on the medial side of the femur for four different models. (unit: MPa)

ACKNOWLEDGEMENTS

This research was supported by the National Science Council, ROC. (grant no.: NSC-90-2320-B-033-001-M08)

MUSCLE ACTIVATION AND THREE-DIMENSIONAL KINEMATICS OF UPPER EXTREMITY IN TENNIS VOLLEY

Lin-Hwa Wang[1], Kuo-Cheng Lo[3], Chia-Ching Wu[2] and Fong-Chin Su[2]

[1]Department of Physical Education & [2]Institute of Biomedical Engineering, National Cheng Kung University, Tainan, TAIWAN
[3]Physical Education Section, Kun Shan University of Technology, Tainan, TAIWAN

INTRODUCTION

Volley is one of important techniques in tennis competition. There are two distinctly different volley types: the punch volley and the drop volley. Understanding of three-dimensional (3D) kinematics and muscle activities in upper limb in four phases of volley, introductory backswing, forward acceleration, impact and follow through, would provide the basic guidelines of the tennis training and the tennis evaluation. The purpose of this study was to investigate the kinematics and EMG signals of the trunk and upper extremity during punch volley and drop volley.

METHODS

12 male tennis players with right hand dominant were recruited in this study. A full 3D kinematic model of trunk and upper extremity was developed for studying tennis volley. 21 markers were placed on selected anatomic landmarks unilaterally to define the coordinate system of the trunk, pelvis, upper arm, forearm and hand. The HiRES motion system with six cameras (Motion analysis Corp., Santa Rosa, CA, USA) was used to collect the position of the reflective markers at sampling rate of 240 Hz. Ten trials were sampled for each subject. Euler angles were used to describe the 3D joint movements of trunk and upper extremity with respect to their neutral posture.

Muscle activities were determined using a surface EMG system (Motion Lab Systems, Inc., USA). 8 surface electrodes were attached to the flexor carpi radialis (FCR), extensor carpi radilis (ECR), brachioradialis (BRR), biceps and triceps brachii (BIB & TRB), antero-middle and postero- middle deltoids (AMD & PMD), and pectoralis major (PCM) muscles of the dominant arm. The maximum effort 5-sec isometric contraction was performed for each muscle/muscle group before the experimental trials to obtain maximum EMG level of the selected muscles for normalization.

RESULTS AND DISCUSSION

Each joint movements of upper extremity of dominant arm and trunk during the forehand volley were showed in Fig. 1. In punch volley, more trunk and shoulder movements were used to generate more kinetic energy and with less movement in wrist joint to stabilize and cause more reflection the kinetic energy of ball. However, the drop volley had more movements in wrist joint to absorb the kinetic energy and control the reflection angle and position of ball. The same results pattern were showed in backhand volley between punch and drop types.

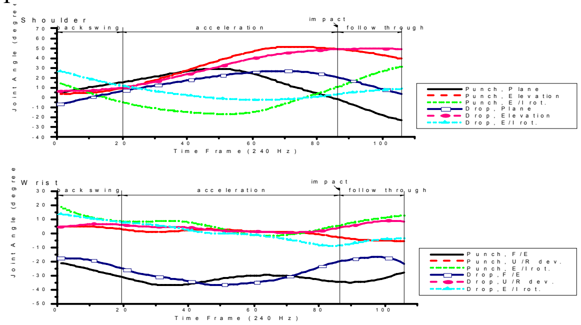

Fig. 1: Joint movements of shoulder and wrist joints in forehand punch and drop volley.

Punch volley required more muscle activation than drop (Fig. 2), especially for backhand punch trials. All muscles showed strong activity during the acceleration phase except the biceps. For forehand volley, the FCR, BBR and PCM were the dominant muscle that compare to the ECR, TRB, AMD and PMD muscles in backhand volley.

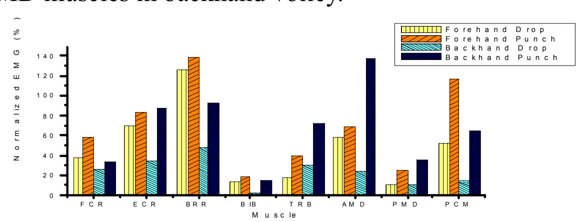

Fig. 2: Normalized maximum EMG levels

Understanding of the 3D joints movements and muscle activities of upper extremity during the different types of tennis volley will allow the tennis player and coach to improve the performance of tennis technique.

REFERENCES

Chow, J.W. et al (1999). Medicine & Science in Sports & Exercise, **31(6)**, 846-854.

Van Gheluwe, B., Hebbelinck, M. (1986). International Journal of Sports Biomechanics, **2**, 88-99.

ACKNOWLEDGMENT

Support from the National Science Council grants NSC89-2314-B-006-134-M08, TAIWAN, ROC

EFFECTS OF DIFFERENT LEVELS OF TRANSTROCHANTERIC ROTATIONAL OSTEOTOMY ON THE STRESS DISTRIBUTIONS IN THE PROXIMAL FEMUR

Jean-Bue Chen[1,2], Weng-Pin Chen[2], Shiuann-Sheng Lee[3]

[1]Department of Orthopaedic Surgery, Tao-Yuan General Hospital, Department of Health, Chungli, Taiwan
[2]Department of Biomedical Engineering, Chung Yuan Christian University, Chungli, Taiwan, wpchen@cycu.edu.tw
[3]Department of Orthopaedic Surgery, Chang Gung Memorial Hospital, Kweishan, Taiwan

INTRODUCTION

Transtrochanteric rotational osteotomy (TRO) is an alternative solution besides total hip arthroplasty (THA) for relatively younger avascular necrosis (AVN) patients. The concept of the TRO is to move the weight-bearing necrotic area to a non-weight-bearing region by rotational osteotomy. The objective of this study is to investigate the effects of four different trastrochanteric rotational osteotomy levels on the stress distributions of bone and fixation devices using finite element analysis. Dynamic hip screw (DHS) fixation system was used .We hoped that through this research a guideline for the osteotomy level for the TRO can be established.

MATERIALS AND METHODS

CT image data of a standardized composite femur was used to create a 3-D finite element intact femur model. Based on the intact model, four models simulating four different levels of osteotomy line together with the implanted DHS fixation system were created and shown in Fig. 1. The four models were defined as DHS-1 (normal transtrochanteric line), DHS-2 (0.5cm distal), DHS-3 (1cm distal) and DHS-4 (1.5 cm distal). The total numbers of elements used for the four models were: 28430 (DHS-1), 28555 (DHS-2), 29139 (DHS-3), and 30666 (DHS-4). A vertical loading of 2000N was applied on the femoral head and finite element analyses were performed using a FEA software (MARC2000).

RESULTS

The von-Mises stress distributions of the four different TRO models are shown in Fig. 1. The peak von Mises stresses on each component of the DHS devices (screws, plates and lag screw) for the four different models are shown in Fig. 2. The stresses increased on the osteotomy interface and the fixation devices as the osteotomy line moves distally. There was a significant stress rise when the osteotomy line moves from DHS-2 to DHS-3 as seen from Fig. 2. The stiffness value for the femur-implant complexes were found by calculating the 2000N loading divided by the longitudinal displacement at the loading point. each model was calculated respectively (Intact: 3086 N/mm, DHS-1: 2989 N/mm, DHS-2: 2753 N/mm, DHS-3: 2113 N/mm, and DHS-4: 1165 N/mm).

DISCUSSION AND CINCLUSION

Results concluded that the osteotomy line should be carefully designed and limited to no more than 0.5 cm distal to the intertrochanteric line because high stress concentration and loss of lateral cortical buttress will possibly lead to early mechanical failure. The DHS-1 model has a stiffness value (2989 N/mm) closer to that of the intact femur (3086 N/mm) than other models. Therefore, DHS-1 is suggested from the stability consideration.

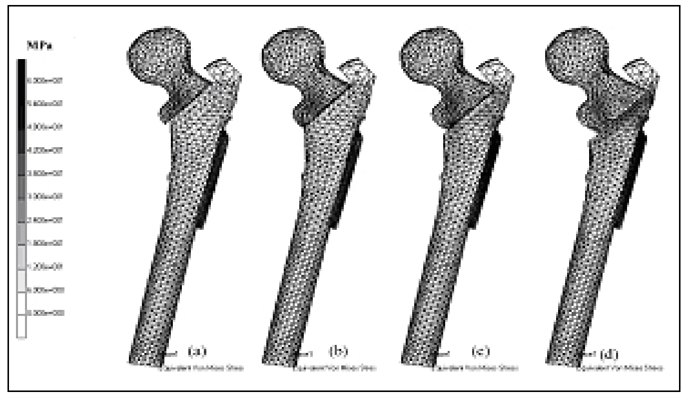

Figure 1: The von-Mises stress distributions of four TRO models at different osteotomy levels. (a) DHS-1 (b) DHS-2 (c) DHS-3 (d) DHS-4 (unit: MPa)

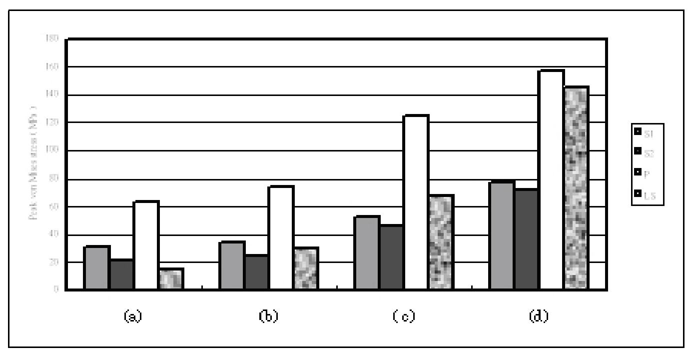

Figure 2: The peak von Mises stresses for each part of DHS fixation devices (screw 1, screw 2, plate and lag screw). (a) DHS-1, (b) DHS-2, (c) DHS-3, (d) DHS-4.

ACKNOWLEDGEMENTS

This research was supported by the National Science Council, ROC. (grant no.: NSC-90-2320-B-033-001-M08)

AIR FLOW AND TEMPERATURE DISTRIBUTION IN A NEONATAL INCUBATOR

Sang-Ho Yun, Chi-Ho Kwon, Young-Ho Kim
Department of Biomedical Engineering, Research of Medical Engineering,
Research Institute for Medical Instrumentation & Rehabilitation Engineering,
Technology Innovation Center for Medical Instruments, Yonsei University
yhkim@dragon.yonsei.ac.kr

INTRODUCTION

Careful considerations of temperature, airflow, and humidity should be made for an effective control of neonatal incubator. The temperature differences inside an incubator lead to neonate heat loss, hypothermia and apnea, which are closely related to air flow and air velocity(Libert et al, 1997). Many studies have been performed to visualize major airflow patterns in many different fields other than inside a commercial incubator(Yamaguchi et al, 1996). However, the turbulent airflow characteristics in the incubator were not considered in their studies. In the study, flow visualizations, hot-wire velocity measurements and computational fluid dynamics were performed to determine the airflow characteristics inside a neonatal incubator.

METHODS

The incubator chamber had a long inlet at the right side of the neonate and an exit of similar size and shape at the left side of the neonate so that the major airflow in the incubator chamber would be of a transverse directional nature. An anatomically correct neonate model is designed using a three-dimensional laser scanner system and a rapid prototyping machine.

The flow visualization system consisted of a flood light, a digital video camera, a slit light system and a smoke generator. Hot wire measurements along the contour of neonate 0.2cm distant from the neonate's body, were employed to measure local airflow velocities and fluctuations.

A three-dimensional steady-state convective heat transfer in the incubator with a neonate model was computed using a pressure-based finite-volume software, CFD-ACE (CFD Research Corporation, U.S.A.).

RESULTS AND DISCUSSION

Motion pictures of smoke particles have demonstrated that flow in the incubator was turbulent, unsteady and three-dimensional. Flow was separated at the wall near the inlet, which resulted from the interaction between the air stream and vortex layers springing from the corners of the incubator(Figure 1(a)). Disturbances from the corners of the incubator chamber and the sharp angle of entry of the incubator might affect the airflow instability. Computational fluid dynamics provided more detailed information on the airflow fields in the incubator. As shown in Figure 1(b), airflow from the inlet formed a large-rotating vortex near the middle of the incubator chamber and partly moved towards the exit, similar to airflow visualization results.

(a) Flow visualization (b) CFD

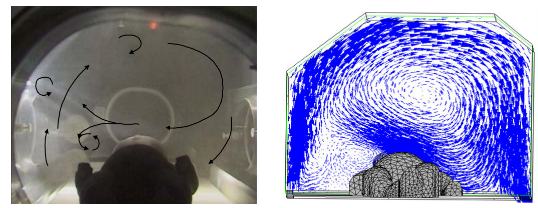

Figure 1: Flow pattern on the neonate's transverse plane.

Skin temperature distributions of the neonate were observed uniform temperatures of about 34°C on the neonate's anterior aspect. Convective heat transfer increased where air velocity was large. Temperatures at the right armpit and the crotch were 36.1°C, and the temperature at the left surface of the neck was 35.3°C. Temperatures at the medial aspects of both thighs were high, where weak stationary vortices were found. Results from computational fluid mechanics showed that a warmer temperature was maintained on the neonate's right aspect, especially near the neck, the armpit and the crotch, where air was relatively stationary. Heat losses were larger at the forehead region, but smaller in the extremities, which was similar to a previous study (Sarman et al, 1992).

SUMMARY

Flow fields from flow visualizations, hot-wire measurements, and computational fluid dynamics inside a neonatal incubator were very similar both qualitatively and quantitatively. The small eddies produced between the neonate and the mattress might interfere with convective and evaporative heat transfers from the neonate. Therefore, it is important to eliminate eddies around the neonate for future designs of neonatal incubators.

REFERENCES

Libert, J. P. et al (1997). *Crit. Rev. Biomed. Eng.*, **25**, 287-370.
Yamaguchi, T. et al (1996). *Frontiers Med. Biol. Eng.*, **7**, 129-141.
Sarman, I. et al (1992). *Am. J. Perinatol.*, **9**, 239-246.

ACKNOWLEDGEMENTS

This work was partially supported by RRC program of MOST and KOSEF

INFLUENCES OF GENDER AND EXERCISE ON ACL LAXITY

Christine Pollard, Elizabeth Devine, Barry Braun, Joseph Hamill
Biomechanics Laboratory, University of Massachusetts, Amherst, Massachusetts, USA

INTRODUCTION

Numerous investigators have reported a higher incidence of anterior cruciate ligament (ACL) injury in women than in men (Arendt et al., 1995). Multiple factors have been associated with this disproportionate incidence of injury. It has been suggested that females may be at greater risk of injury due to greater ACL laxity. Investigators have also suggested an increase in ACL laxity following exercise (Steiner et al., 1986). In addition to these changes in laxity associated with exercise, changes in ACL laxity across the menstrual cycle phases have also been reported (Heitz et al., 1999). The purpose of this study was to determine if there were differences in the effect of exercise on ACL laxity between males and females. In addition, the influence of exercise on ACL laxity across the menstrual cycle phases was investigated.

METHODS

Subjects consisted of six females (age: $\bar{x}$ =26 years, mass: $\bar{x}$ =64 kg) with a history of a normal menstrual cycle lasting 28-32 days and six males (age: $\bar{x}$ =24 years, mass: $\bar{x}$ =82 kg). All subjects had intact knee ligaments bilaterally and exercised on average at least five times a week for thirty minutes. Female subjects were assigned to start data collection at either the onset of menses or the onset of ovulation depending on which event came first after signing the informed consent to participate. Ovulation was determined by a positive test on an ovulation kit. Serial estrogen levels of the female subjects were measured via radioimmunoassay procedures.

Knee laxity was measured with a KT-1000 knee arthrometer at 20 degrees of knee flexion with a displacement force of 89N. Displacement was recorded to the nearest 0.5mm. Estrogen levels and ACL laxity were measured for the female subjects at specific times to represent the three menstrual cycle phases. These times were at onset menses (menstrual phase), days 10 and 12 post onset menses (follicular phase), and days 7 and 9 post ovulation (luteal phase). ACL laxity of the male subjects was measured on three different days with 10-12 days between each measurement.

For each data collection session, ACL laxity was measured just prior to an exercise protocol and immediately following the exercise protocol. The exercise protocol consisted of fifteen minutes of treadmill running at a self-selected pace, two minutes of weaving, two minutes of cutting and twenty-five jump downs from a twelve-inch surface.

A repeated measures ANOVA (gender x laxity x subjects) was used to test for significant differences in the change in knee laxity values between females and males and across the different menstrual cycle phases ($p \leq 0.05$).

RESULTS AND DISCUSSION

There were no significant differences in the effect of exercise on ACL laxity between males and females (Figure 1). In addition, the effect of exercise did not differ across the menstrual cycle phases (Figure 2). However, there were significant differences in ACL laxity between genders both pre-exercise and post-exercise.

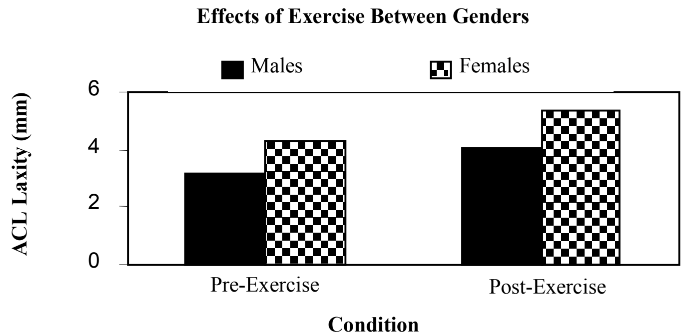

Figure 1: Influences of Gender and Exercise on ACL Laxity.

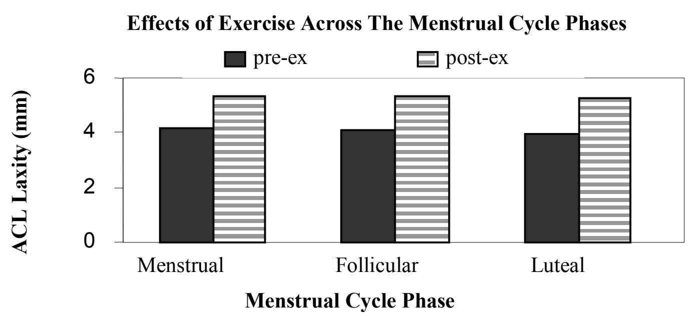

Figure 2: Influences of Exercise on ACL Laxity Across the Menstrual Cycle Phases.

SUMMARY

These results suggest that ACL laxity is increased in both genders following an exercise protocol. This increase in laxity due to exercise does not appear to differ in females across the menstrual cycle phases. However, females demonstrate greater ACL laxity than do males both pre and post exercise.

REFERENCES

Arendt, E., Dick, R. (1995). *Am J Sports Med.* **23**(6), 694-701.
Heitz, N.A. et al. (1999). *J Athl Train.* **34**(2), 144-149.
Steiner, M.E. et al. (1986). *Am J Sports Med.* **14**(1), 24-29.

VISCOELASTIC STRESS RELAXATION DURING ACUTE PASSIVE STRETCHING AND ITS INFLUENCE ON MAXIMUM VOLUNTARY STRENGTH

Derek Weir, Geoff Elder, and Jill Tingley
School of Health & human performance, dalhousie university, halifax, nova scotia, canada, HTTP://WWW.DAL.CA/HAHP

INTRODUCTION

Increased muscular compliance following a bout of acute passive stretching (APS) could potentially modify the length-tension characteristics of the stretched muscle, thereby altering its maximal force-generating capacity at any given joint angle. Two recent studies investigated the effects of 30 (Fowles, Sale, & MacDougall, 2000) and 60 min (Avela, Kyrolainen, & Komi, 1999) of APS on the isometric maximum voluntary contraction (MVC) of the plantar flexors and decreases of 28 and 24%, respectively were reported. Whether less extensive stretching regimes would have similar detrimental effects on MVC however, remains in question. In addition, the exact nature of any such MVC decrement has not yet been clearly established. The purpose of this study was to investigate viscoelastic stress relaxation in the human plantar flexors *in vivo* during APS, to establish whether this response would reduce maximal strength, and if so, to determine the mechanisms responsible for the decrease.

METHODS

Fifteen female subjects underwent a series of five plantar flexor stretches, where the ankle was passively extended to within 2° of their maximum dorsiflexion (D) range of motion and held for 120 s. MVC, with twitch interpolation, and the electromyographic (EMG) and torque output of the mechanically induced stretch reflex (SR) were assessed before (Pre) and immediately following (Post-test$_1$) APS at 20° D, along with the electrically induced maximal Hoffmann reflex (H_{max}) and maximal mass compound action potential (M_{max}). MVC, SR, and M_{max} measures were then assessed again (Post-test$_2$) at an increased angle (26 ± 1° D), to test if the length-tension relationship had been altered. EMG was recorded from the soleus (SOL), medial gastrocnemius (MG), and tibialis anterior (TA) using bipolar surface electrodes.

RESULTS

During APS there was a significant decrease in passive torque with time (120 s) and stretch (1-5) but the decrease was less as more stretches were performed (Figure 1). Following APS, there was a 7% reduction in MVC torque ($P < 0.05$) and a 13% reduction in SR torque ($P < 0.05$). SR EMG recorded from SOL and MG was also reduced by 27% ($P < 0.05$) and 22% ($P < 0.05$), respectively. The ratio of H_{max} to M_{max} EMG did not differ significantly at Post-test$_1$, nor did the H_{max} and M_{max} torque responses. At Post-test$_2$, MVC and SR EMG (SOL and MG) recovered to pre-stretch values, while the SR and M_{max} torques increased to 19 and 13% above Pre, respectively ($P < 0.05$). There were no significant changes in motor unit activation between any of the tests.

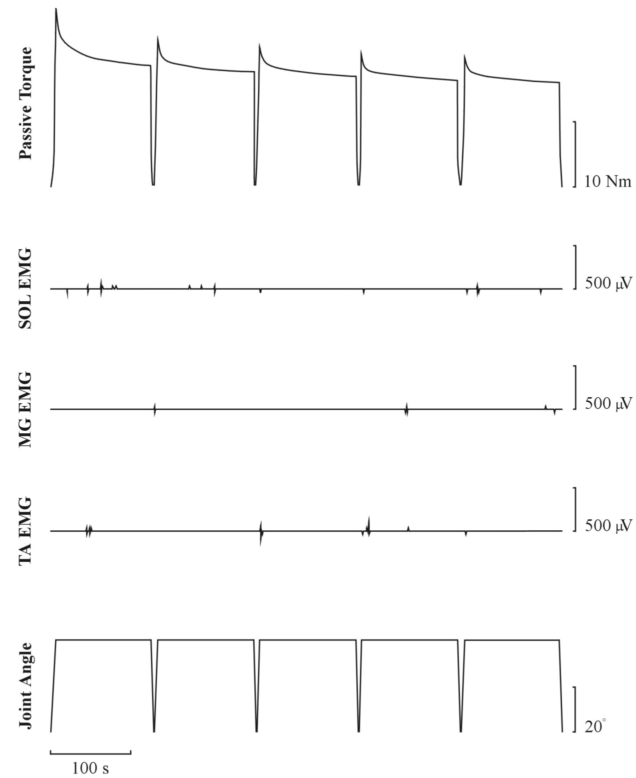

Figure 1: Data recording of APS for one subject. *Top*: passive torque record. *Middle*: raw EMG recorded from SOL, MG, and TA. *Bottom*: ankle angle displacement. The torque record indicates stress relaxation in the absence of any significant EMG activity.

DISCUSSION

The results of this study provide new evidence to suggest that decreases in maximal strength following shorter bouts of APS are the result of mechanical changes in the stretched muscle, rather than reduced neural drive. The decrease in MVC was associated with a marked decrease in passive torque at any given joint angle and the fact that MVC was restored with the application of additional stretch indicates that the decrease was most likely caused by an alteration in the length-tension properties of the plantar flexors. Although APS reduced SR excitability in a resting state, it is not believed that changes in afferent drive and/or motoneuron excitability influenced these findings, as the decrease and subsequent increase in MVC was not associated with any change in motor unit activation.

REFERENCES

Avela, J., Kyrolainen. H., & Komi, P.V. (1999). *J. Appl. Physiol.*, **86**, 1283-1291.

Fowles, J.R., Sale, D.G., & MacDougall, J.D. (2000). *J. Appl. Physiol.*, **89**, 1179-1188.

FLUID VELOCITIES WITHIN A VENTRICULAR ASSIST DEVICE ARE HIGHLY SENSITIVE TO PNEUMATIC DRIVE CONDITIONS

Allen Nugent and Chris Bertram

Graduate School of Biomedical Engineering, University of New South Wales, Sydney, Australia , (www.gsbme.unsw.edu.au)

INTRODUCTION

Both bulk flow performance and valve-generated water hammer are strongly affected by the drive conditions of a pulsatile ventricular assist device (VAD) (Umezu et al. 1989). Indeed, these considerations influence the design of VADs as well as the control algorithms of their actuators. However, little attention has been paid to small-scale effects of drive conditions, such as the influence on the time-varying fluid velocity at particular locations within the VAD.

The Spiral Vortex (SV) VAD was designed to minimise undesirable fluid-mechanical phenomena and haemolysis. With a tangential inflow tract and an axial outflow tract, flow stasis and prolonged residence are eliminated. Previous investigations of the device have revealed highly organised flow patterns and good washout of peripheral surfaces (Umezu et al. 1991).

METHODS

From 3-inch cast acrylic sheet, a model of the SV VAD was fabricated with flat, polished, orthogonal exterior walls. This was connected to a mock circulation consisting of a Windkessel model of the aorta and a blood bag for the left atrium. A blood-analogue fluid formulated from NaI and glycerol gave dynamic similarity with blood while matching the refractive index of the acrylic to better than 4 decimal places, essential for making LDA measurements within the complex shape of the VAD interior.

At each of nearly 700 nodes in a 5mm-spaced Cartesian measuring grid, 2-component LDA data were taken until 10,000 samples were accumulated or 5 minutes had elapsed. Between 25 and 360 cycles (model heart beats) were required, and these were overlaid in the correct phase prior to statistical analysis of the ensembles.

Velocity components parallel to the projection of the inflow tract onto the equatorial plane (U) and parallel to the outflow tract (W) were measured. The pneumatic drive pressure (DP), mock aortic and left atrial pressure, and aortic flow-rate were sampled simultaneously.

Model heart rate was 68 min^{-1} and systolic fraction was 35 %. Drive pressure and vacuum were adjusted for physiological systemic parameters within the mock circulation.

During the investigation, it was discovered that the vacuum setting on the pneumatic driver was marginally excessive, resulting in what appeared as a small downward spike on the DP waveform immediately prior to systole. Close inspection of this feature, which arises from stretching of the diaphragm, suggested that the magnitude and duration of excess negative DP might be sufficient to affect flow velocities within the VAD, and the reality of this effect was examined by comparison of data from certain locations with new data obtained after reducing the vacuum.

RESULTS AND DISCUSSION

Waveforms of the W-component of velocity at sites within the outlet tract were found to be most affected by excess vacuum, displaying a sigmoid perturbation, with a peak-to-peak amplitude of 0.6 to 0.9 m/s, coinciding with the unwanted feature on the DP waveform. U-component waveforms at these sites were less affected. Velocities within the inflow tract were apparently unaffected, as were those nearer the diaphragm.

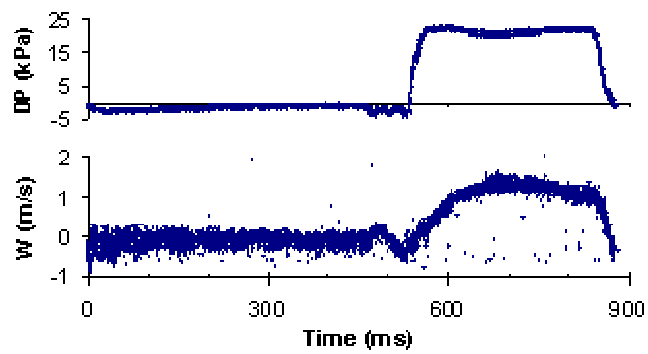

Figure 1: Drive pressure and outflow tract W-velocity in the presence of excess drive vacuum.

It is likely that velocities at sites near the diaphragm are indeed perturbed, but that the amplitude is small relative to the data scatter. The cross-sectional area in the neck of the outflow tract of the SV VAD is only 6 % of that at the equatorial plane (diaphragm-housing junction), so that a small perturbation distributed over the latter region is effectively magnified by the convergent geometry.

The required adjustment of vacuum that restored normal drive conditions was barely palpable, and too small to observe on the vacuum gauge. This observation highlights the sensitivity of pneumatic VADs to drive conditions, while the findings above reinforce the importance of optimising drive conditions.

SUMMARY

Deleterious flow behaviour within a blood pump may result from very fine misadjustments of pneumatic drive conditions.

REFERENCES

Umezu, M. et al. (1989). *Jpn. J. Artif. Organs*, **18**, 719–722.

Umezu, M. et al. (1991). *Proc. Artificial Heart* **3**, 107–116.

THE ASSOCIATION OF ESTROGEN CHANGES ACROSS THE MENSTRUAL CYCLE PHASES WITH ACL LAXITY IN ACTIVE FEMALES

Christine Pollard, Elizabeth Devine, Barry Braun, Joseph Hamill
Biomechanics Laboratory, University of Massachusetts, Amherst, Massachusetts, USA

INTRODUCTION

Women have been reported to experience four to eight times the number of anterior cruciate ligament injuries (ACL) as men (Arendt et al., 1995). Researchers have investigated a variety of factors that may affect this disproportionate incidence rate. Recent work has focused on potential hormonal influences on injury due to the difference in estrogen levels between genders. More specifically, investigators have focused on the influences of high estrogen levels during specific times of the menstrual cycle. These authors have suggested that changes in circulating estrogen levels across the menstrual cycle phases may contribute to this higher incidence of injury. This potential factor has stemmed from recent *in vitro* work that has reported that physiologic levels of estrogen may significantly reduce ACL fibroblast proliferation and rate of collagen synthesis (Liu et al., 1997). This reduction may be associated with changes in ligament laxity.

Within the normal menstruating female, serum estrogen typically fluctuates from low levels during the menstrual phase to high levels during the follicular phase and then decreases to moderately high levels during the luteal phase. The purpose of this study was to determine if there were changes in ACL laxity associated with estrogen changes across the menstrual cycle phases in active females.

METHODS

Subjects consisted of six females (age: $\bar{x}$ =26 years, mass: $\bar{x}$ =64 kg) with a history of a normal menstrual cycle lasting 28-32 days and intact knee ligaments bilaterally. All subjects exercised on average at least five times a week for thirty minutes. Subjects were assigned to start data collection at either onset menses or at onset ovulation depending on which event came first after signing the informed consent to participate. Ovulation was determined by a positive test on an ovulation kit.

Knee laxity was measured with a KT-1000 knee arthrometer at 20 degrees of knee flexion with a displacement force of 89N. Displacement was recorded to the nearest 0.5mm. Serum estrogen levels and ACL laxity were measured at specific times to represent the three phases of the menstrual cycle. These times were at onset menses (menstrual phase), days 10 and 12 post onset menses (follicular phase), and days 7 and 9 post ovulation (luteal phase). Serial estrogen levels were measured via radioimmunoassay procedures.

A repeated measures analysis of variance (laxity x phase x subjects) was used to test for the presence or absence of significant differences in knee laxity values across the different menstrual cycle phases ($p \leq 0.05$).

RESULTS AND DISCUSSION

There were no significant differences in ACL laxity between the menstrual cycle phases (Figure 1). However, there was a significant increase in estrogen between the menstrual and the follicular phase (Figure 2). The estrogen level in the luteal phase was similar to both the menstrual and follicular phase levels. These findings suggest that ACL laxity in females is not associated with changes in circulating estrogen levels.

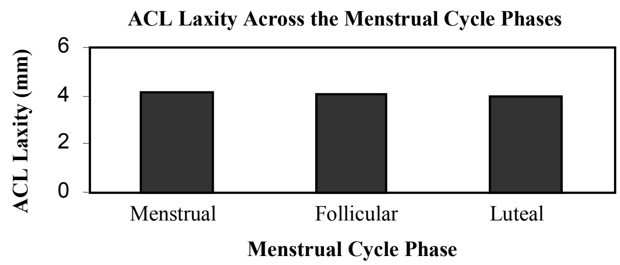

Figure 1: ACL laxity across the menstrual cycle phases.

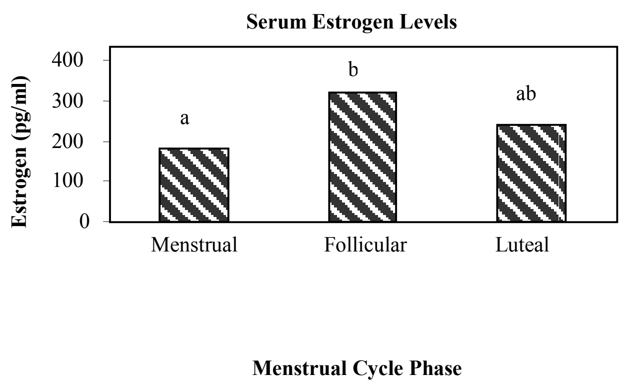

Figure 2: Estrogen levels across the menstrual cycle phases (phases with like letters are not significantly different).

SUMMARY

Although *in vitro* investigations have suggested that the ACL may be at greater risk of injury when exposed to higher levels of circulating estrogen, there does not appear to be a clinically significant association between ACL laxity and changes in serum estrogen across the menstrual cycle phases. However, it is important to consider that this study focused on knee laxity and did not address lower extremity dynamics. Future studies are necessary to begin to investigate the effects of circulating hormones on lower extremity dynamics.

REFERENCES

Arendt, E., Dick, R. (1995) *Am J Sports Med.* **23**(6), 694-701.
Liu, S.H. et al. (1997) *Am J Sports Med.* **25**(5), 704-709.

A DYNAMICAL ANALYSIS OF PARKINSONIAN GAIT

Ugo H. Buzzi[1], Nicholas Stergiou[2], and Ekaterini Markopoulou[3]
[1]Motor Development Laboratory, University of Michigan, Ann Arbor, Michigan, USA
[2]Biomechanics Laboratory, University of Nebraska at Omaha, Omaha, Nebraska, USA
[3]Department of Neurology, University of Nebraska Medical Center, Omaha, Nebraska, USA

INTRODUCTION

Parkinson's disease is a debilitating neurological condition that affects over 1 million people in the US. Previous work has found significant differences in the kinematic walking patterns and increases in variability in parkinsonian gait (Murray, 1978). However, these changes in the variability of parkinsonian gait and their underlying nature have received little attention. The purpose of this study was to examine the underlying organizational dynamics of parkinsonian gait.

METHODS

Six subjects suffering from idiopathic Parkinson's disease (age=66.0±7.7 yrs) and six healthy controls (age=63.5±7.0 yrs) participated in the study. Parkinson's subjects undergoing dopamine therapy were asked to refrain from taking their medication the morning of data collection. Kinematic data from 30 continuous footfalls (avg=2378 data points/trial) were collected using two cameras (60Hz) while the subjects walked on a treadmill at their self-selected pace. Sagittal 3D angles of the right hip, knee, and ankle were calculated. Lyapunov exponents (LyE) and correlation dimensions (COD) of the angles were calculated for both groups and were analyzed using the Chaos Data Analyzer (Sprott & Rowlands, 1992). LyE is a measure of the stability of a dynamical system and its dependence on initial conditions. COD describes the geometric dimension of a dynamical system in state space. All calculations were performed using 5 embedded dimensions. The embedded dimension is the number of dimensions needed to unfold the structure of a given dynamical system. It was calculated using a Global False Nearest Neighbor analysis (Abarbanel, 1996). All data were also surrogated using a phase randomization technique (Theiler et al., 1992). Surrogation removes the deterministic structure from the original data set, generating a random equivalent. LyE of the surrogate data set (S-LyE) is then calculated. If significant differences are found between the LyE and S-LyE, then the original is not a randomly derived data set. Lastly, the approximate entropy (ApEn), a measure of the regularity of a data series was computed for all data sets (Pincus, 1991). Small ApEn values (≅ 0) indicate less complexity (greater periodicity) in the data, while higher values (≅ 2) indicate greater complexity (increased randomness). Mean group values for ApEn, LyE, S-LyE and COD of both groups were analyzed using t-tests ($p<0.05$).

RESULTS AND DISCUSSION

All LyE values for both groups were significantly different from their surrogate counterparts indicating that variability in all time series may be deterministic in nature. Knee and ankle COD values were significantly higher for the Parkinson's group. No significant differences were found between groups for the hip COD, or for the LyE and ApEn for any of the joints. However, all values for the Parkinson's group at all joints were higher suggesting a more random (noisier) behavior in comparison with the control group. Increased noise in the Parkinson's group may be attributed to changing constraints as a consequence of pathophysiological changes in the brain. Previously reported changes in gait kinematics in the Parkinson's patients may result from adjustments by the neuromuscular system to compensate for the increased noise.

SUMMARY

Variability in parkinsonian and healthy gait was found to be deterministic in nature suggesting that the inherent variability generated by the neuromuscular system may still be intact in this pathological group. If the basal ganglia is the neuro-source of this disorder (Conley & Kirchner, 1999), then it can be speculated that the mechanisms that are responsible for the deterministic nature of variability in gait are not housed there. The higher values reported in all variables for the parkinsonian gait, indicated that changing constraints associated with the disease may lead to increased behavioral noise during gait.

REFERENCES

Abarbanel HDI, (1996). *Analysis of Observed Chaotic Data*, Springer-Verlag
Conley SC, Kirchner JT. (1999). *Postgrad Med*, **106**, 39-52.
Knutsson E. (1972). *Brain*, **95**, 475-486.
Murray MP. (1978). *Am J of Phys Med*, **57**, 278-294.
Pincus SM. (1991). *Proc. National Acad. Sci. '91*, 2297-2301
Sprott J, Rowlands G. (1992). *Chaos Data Analyzer*. American Institute of Physics.
Theiler et al (1992). *Physica D*, **58**, 77-94.

Table 1:Group means of LyE, COD, ApEn, and S-LyE.

	LyE			COD			ApEn			S-LyE		
	Hip	Knee	Ankle	Hip	Knee	Ankle	Hip	Knee	Ankle	Hip	Knee	Ankle
Parkinson's	0.0723 ±0.018	0.1572 ±0.031	0.1790 ±0.025	2.0775 ±0.117	3.5495* ±0.337	3.8973* ±0.162	0.2773 ±0.012	0.3919 ±0.101	0.3903 ±0.040	0.1792† ±0.039	0.2742† ±0.030	0.3030† ±0.029
Control	0.0708 ±0.027	0.1295 ±0.033	0.1513 ±0.049	2.0152 ±0.057	3.1633 ±0.251	3.5153 ±0.309	0.2737 ±0.026	0.3571 ±0.065	0.3874 ±0.109	0.2108† ±0.031	0.2773† ±0.035	0.3208† ±0.017

*sig. diff. from control; †·sig. diff. from original ; $p<0.05$

BILE CANALICULI REFORMED BY RAT SMALL HEPATOCYTES, AND ITS DYNAMIC MOVEMENT

Ryo Sudo[1,2], Hiroshi Kohara[1], Toshihiro Mitaka[2], Mariko Ikeda[1], Kazuo Tanishita[1]
[1]Department of System Design Engineering, Keio University, Yokohama, Kanagawa, Japan, sudo@tani.sd.keio.ac.jp
[2]Department of Pathology, Cancer Research Institute, Sapporo Medical University, Sapporo, Hokkaido, Japan

INTRODUCTION

Small hepatocytes, which are known to be hepatic progenitor cells, can be isolated from an adult rat liver (Mitaka et al., 1999). They can rapidly proliferate with maintaining hepatic functions such as albumin secretion, and formed a monolayer colony consisting of 20 to 30 cells within 10 days. About 10 days after plating, many colonies were surrounded by hepatic nonparenchymal cells such as liver epithelial cells and stellate cells, and, several days later, rising/piled-up cells appeared in the colonies. In such colonies, translucent belts are formed between the piled-up cells under phase-contrast microscopy. As time in culture, they developed into anastomosing network, which seem to be bile canaliculi (BC). We investigated whether this BC-like structure has ability to be functionally active and how it works as a pump to transport components.

METHODS

Hepatic cells, including small hepatocytes, were isolated from an adult rat liver and cultured. Double fluorescent immunocytochemistry for BC proteins (MRP2: multidrug-resistance-associated protein 2, 5NT: 5'-Nucleotidase, ectoATPase) and actin was carried out. Phase-contrast images of BC formed in a colony were digitally recorded at the 20-second intervals for 2 hours. To observe flux within BC, CellTracker™, which is fluorescent dye and secreted into BC, was microinjected into one of the piled-up cells in a colony. Then, time-lapse fluorescence images were recorded at the 5-second intervals for 5 minutes. We also assessed the effects of calcium ionophore A23187 and Endothelin-1 on BC contractions to investigate the mechanism of contractile motion. Before and after the dose of these reagents, time-lapse images were recorded at the 20-second intervals for 3 hours.

RESULTS AND DISCUSSION

Immunostaining of BC proteins showed that BC proteins were distributed in the intercellular space that coincided with the translucent belts formed in the piled-up cells. In addition, actin was intensively positive around BC-like structures corresponding to the expression of BC proteins.

Figure 1A shows phase-contrast images of the piled-up colony in which anastomosing BC network developed well. The calculated light intensity of each segment in figure 1A is graphically shown in figure 1B. Contraction and dilatation of reformed BC occurred in the experimental period (Fig. 1C-E). This contractile motion may have a relation to the intracellular Ca^{2+} level, because the treatments of A23187 and Endothlin-1 resulted in the enhancement of BC contraction. We also found that reformed BC contract synchronously through the adjacent cells.

Microinjected CellTracker™ was metabolized and fluorescein was secreted into BC. Soon after the injection, bright fluorescence was observed in the cytoplasm and a line of fluorescence extended in the direction of the tip of the colony. A few minutes later, the tracer was clearly detected in 4 cells distant from the injected cell.

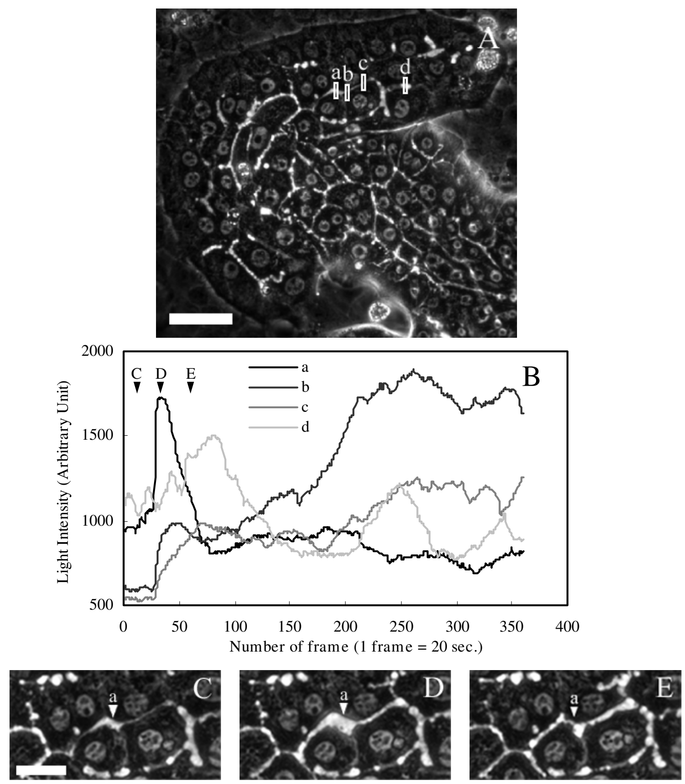

Figure 1: Phase-contrast images and graphical representation of BC contraction. Scale bars, 50 µm (A) and 20 µm (C).

SUMMARY

This is the first experiment that demonstrates tubular structures of BC *in vitro* have a motility to transport the components. The results in this study suggest that reformed BC by rat small hepatocytes may be functionally active and have a contractile activity in a synchronized manner.

REFFERENCES

Mitaka, T. et al (1999). *Hepatology*, **29**, 111-125.

COMPUTATIONAL FLUID DYNAMICS MODEL ANALYSIS OF THE BLOOD FLOW IN THE CIRCLE OF WILLIS

Makoto HARAZAWA, Takami YAMAGUCHI
Department of Mechatronics and Precision Engineering, Graduate School of Engineering,
Tohoku University, Sendai, Japan., harazawa@pfsl.mech.tohoku.ac.jp

INTRODUCTION

Blood is supplied to the brain via four arteries: two internal carotid arteries and two vertebral arteries. To increase the reliability of the supply of blood to the brain, these arteries are interconnected at the base of the brain, where they form a closed arterial circle, called the circle of Willis. However, their anastomoses vary considerably. If some of the anastomoses are very small, or absent, the safety of the blood supply is jeopardized. This is particularly important in diseases such as cerebral thrombosis when the blood flow is obstructed unilaterally. In such cases, redistribution of the blood supply is thought to be strongly affected by the geometric configuration of the anastomoses. Cerebral aneurysms, which may induce serious cerebrovascular disease, preferentially occur at the circle of Willis, and the complex blood flow pattern is suspected of influencing the development of aneurysms. Again, this is dependent on the complex geometry of the circle. Therefore, we conducted a computational fluid dynamics (CFD) simulation of the blood flow in the circle of Willis, focusing on the relationship between the geometric configuration and the redistribution of blood flow under changing inlet flow conditions.

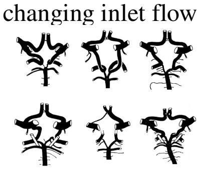

Fig. 1: Typical variations of the circle of Willis.(Adachi, 1928)

METHODS

The circle of Willis consists of multiple inlet and outlet vessels. They have a complex 3D geometry, with a very wide variety of atypism (Adachi, 1928). We built a generic 2-dimensional model of the circle of Willis (Fig. 2).

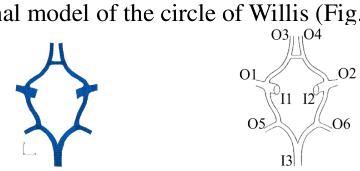

(a) CFD model (b) schematic model (Adachi, 1928)

Fig. 2: CFD model and the circle of Willis.

The CFD computation used SCRYU ver. 1.9 (Software Cradle, Osaka, Japan). The governing equations were the Navier-Stokes equations for an incompressible Newtonian fluid with the properties of water. The boundary conditions at every inlet consisted of a steady uniform inflow velocity perpendicular to the cross section. The Reynolds numbers of inflow velocity are listed in Table 1. At the outlet, the boundary conditions were zero pressure and zero velocity gradient. No-slip walls were assumed.

Table 1: The Reynolds number of inflow velocity.

TYPE	1-1	1-2	1-3	1-4	1-5	2-1	2-2	2-3	2-4	2-5	3-1	3-2	3-3	3-4	3-5
Inlet 1	500	375	250	125	0	500	375	250	125	0	500	375	250	125	0
Inlet 2	500	500	500	500	500	500	500	500	500	500	500	500	500	500	500
Inlet 3	500	500	500	500	500	250	250	250	250	250	0	0	0	0	0

RESULTS

Representative results are shown in Figs. 3 and 4. Fig. 3 shows the velocity vectors, and Fig. 4 shows the pressure distribution. Fig. 5 shows the change in flow at other outlets that resulted from changing the inflow conditions at inlet 1. At outlet 1, which is close to inlet 1, the change in the flow was proportional to the change in the inlet flow at inlet 1. At outlets 3 and 5, on the contralateral side, relatively little change in the flow was observed. In contrast, there was little change in the flow of outlet 1, on the contralateral side. The outflow from outlet 1, which is directly connected to inlet 1, was significantly affected. However this effect was diminished by bypass flows from inlet 3. Therefore, the outflow from outlets 4 and 6 was spared relatively.

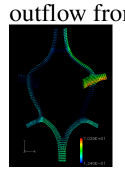

Fig. 3: Velocity vector.

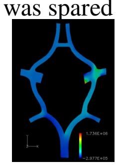

Fig. 4: Pressure distribution.

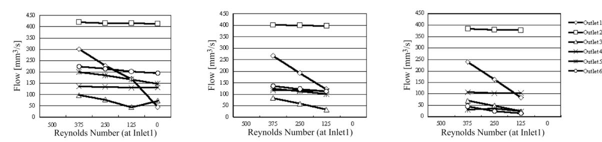

(a) I3; Re=500. (b) I3; Re=250. (c) I3; Re=0.

Fig. 5: Flows by changing inflow conditions.

CONCLUDING REMARKS

This study found that geometrical factors, such as mode of connection and proximity of inlets and outlets, significantly affected the redistribution of the blood flow when unilateral alterations of the flow occurred in the circle of Willis. This was not shown in previous studies using one-dimensional simulations equivalent to an electric circuit analogy (Hillen et al., 1988; Lodi and Ursino, 1999). This clearly shows the need for true fluid dynamical studies using a more realistic three-dimensional model based on real data obtained from both healthy and diseased subjects.

REFERENCES

B ADACHI. (1928). *Das Arteriensystem der Japaner, Band1*. 116-134. Maruzen, Japan.
B Hillen, BA Drinkenburg, HW Hoogstraten, L Post. (1988). *Analysis of flow and vascular resistance in a model of the circle of Willis, J Biomech*, **21**(10), 807-14.
CA Lodi, M. Ursino. (1999). *Hemodynamic effect of cerebral vasospasm in humans: a modeling study., Ann Biomed Eng*, **27**(2), 257-73

EXPERIMENTAL STUDY ON AIR FLOW IN A TWO-DIMENSIONAL CHANNEL WITH AN OBSTRUCTION OSCILLATING AT 10 HZ TO 100 HZ

Yuji Matsuzaki, Masateru Watanabe, Tatsuya Aomatsu and Tadashige Ikeda
Department of Aerospace Engineering, Nagoya University, Chikusa, Nagoya, Japan
matsuzaki@nuae.nagoya-u.ac.jp

INTRODUCTION

In a human body, flows of blood, air and body fluids in flexible vessels such as blood vessels, air ways, etc., produce many kinds of static and dynamic phenomena, which are mostly very complex from mechanical view points. To understand physiological and pathological aspects of such phenomena, it is essential to observe them in vivo as well as perform both related experiments on artificial conditions and analytical studies. In the case of the flexible tubes the dynamic behaviors of the flow and the tube are very complicated due to an interaction between flow pressure and tube deformation (Matsuzaki & Matsumoto, 1989; Matsuzaki, et al., 1994). To produce phonetic sounds, a pair of vocal chords oscillate over 200 to 1,000 Hz with very small amplitudes (Ikeda & Matsuzaki, 2001). One of difficult issues is to evaluate the fluid pressure distribution on the oscillating wall experimentally and analytically (Matsuzaki & Fung, 1976; Matsuzaki & Ikeda, 1998; Ikeda & Matsuzaki, 1999). In this paper we present experimental results on flow pressures in a two-dimensional flow channel with an obstruction oscillating at low to high frequencies up to 100 Hz in order to provide quantitative information on the flows passing through the oscillating narrow passage.

METHOD

The flow channel is shown in Fig. 1 and a magnified view of the test section is given in Fig. 2. The air was sucked from the atmosphere to a vacuum. The flow was obstructed by a trapezoidal block modeling a vocal chord. Static pressures were measured at the center of the narrowed passage, and its 10mm upstream and downstream, that is, p(0), p(-10) and p(10), respectively. The level surface of the trapezoid was periodically moved in a vertical direction with amplitude of 0.05mm at given frequency and clearance to the wall. The pressure was measured for several sets of Reynolds and Strouhal numbers, changing the flow rate, the frequency of the level surface and the initial clearance.

RESULTS AND DISCUSSION

In a frequency range less than 10 Hz the flow behaved quasistatically. The narrower the obstructed passage became, the smaller the static pressure p(0) was. Above 30 Hz, the moving effect of the block surface was clearer with increasing frequency. For instance, the pressure amplitudes of p(0) and p(10) became smaller, but the amplitude of p(-10) larger. At 70 Hz, the phase relationship between the passage clearance and the static pressure changed clearly in an opposite way to that of 10 Hz. At 100 Hz, the amplitude of p(0) showed two peaks.

SUMMARY

The static pressure was measured around the oscillating obstruction at low frequencies to 100 Hz. The high frequency oscillation of the obstruction in the air flow channel has strong influences on the static pressures and their phase difference.

REFERENCES

Ikeda, T., Matsuzaki, Y. (1999). *J. Biomech. Eng.*, **121**, 153-159.
Ikeda, T., Matsuzaki, Y. (2001). *J. Biomech. Eng.*, **123**, 571-579.
Matsuzaki, Y., Fung, Y.C. (1976). *J. Applied Mech.*, **98**, 227-231.
Matsuzaki, Y., Matsumoto, T. (1989). *J. Biomech. Eng.*, **111**, 180-184.
Matsuzaki, Y., et al. (1994) *J. Biomech. Eng.*, **116**, 469-476.
Matsuzaki, Y., et al. (1998). *J. Biomech. Eng.*, **120**, 594-601.

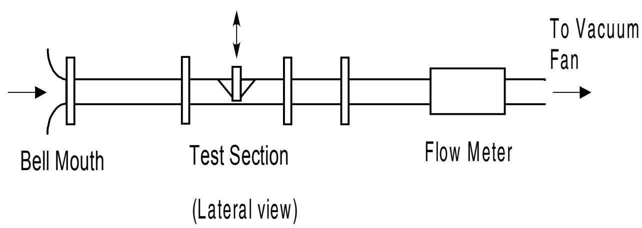

Figure 1: Flow channel with an oscillating obstruction in a test section.

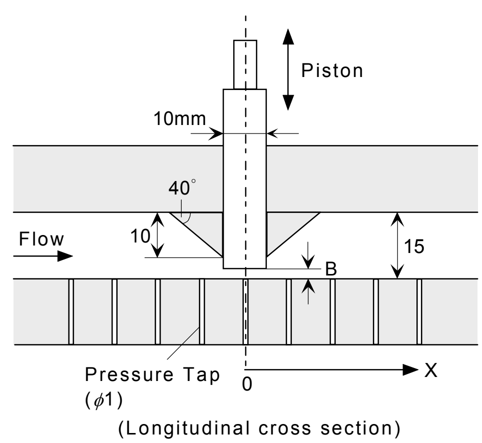

Figure 2: Test section with an oscillating obstruction driven by a piston (pressures were measured at x=-10, 0 and 10 mm).

BIOMECHANICS OF THE KARATE FRONT KICK

D. Gordon E. Robertson, François Beaulieu, Carlos Fernando and Michael Hart
Biomechanics Laboratory, School of Human Kinetics, University of Ottawa, Ottawa, Ontario, Canada

INTRODUCTION

The front kick (*mae geri*) in karate is one of the strongest and most easily mastered kicks. This project examined the powers produced by the lower extremity joints of the kicking leg of two elite (fourth dan) martial artists performing both closed and open stance front kicks. The purpose was to determine the contributions and sequencing of the ankle, knee and hip moments.

METHODS

The subjects (one a specialist in Tae-kwon-do, the other in Karate) kicked against a padded board held by an assistant while filmed by a VHS camera. The subjects performed several trials each using both an open stance (kicking leg back) and closed stance (legs beside each other). The video was digitized with the Ariel Performance Analysis System and analyzed with the Biomech Motion Analysis System (Robertson, 2002). Inverse dynamics were used to compute the net moments and their associated powers for the ankle, knee and hip joints.

RESULTS AND DISCUSSION

The powers produced by the ankle moment of force were too small to warrant analysis. Figure 1 shows the angular velocities, moments of force and their powers for the knee and ankle of a typical trial. Notice that the moments of force of the hip and knee reverse direction at precisely the same instant just prior to contact with the board (right arrow). This was common to all trials and both subjects.

The powers produced by the closed stance kicks, as expected, always produced larger moments and powers than the closed stance kicks. Obviously, the added range of motion enabled the subjects to generate greater impulses and foot velocities.

The sequencing of the moments were consistent across all trials and both subjects. The motion began with almost simultaneous flexing of the hip and knee joints. The hip flexors were responsible for flexing both joints as shown by the burst of positive work done by the hip flexors while the knee moment of force was relatively inactive.

After the hip reached its maximum velocity, the hip moment of force became extensor (presumably due to eccentric contraction of the gluteals) causing the hip to slow its flexion and begin knee extension. Not surprisingly, based on similar research on the mechanics of sprinting (Lemaire & Robertson, 1989) the knee extensor moments did not contribute to increasing knee extension. Instead, the knee moment was flexor producing negative (eccentric) work to presumably protect the knee from hyperextension at the end of the kick.

SUMMARY

Peak powers were greater for the open stance than the closed stance. The hip extensors and flexors were the prime movers of both the hip and knee actions. The knee moments were primarily used to reduce knee flexion and extension during the kick.

REFERENCES

Lemaire, E.D., Robertson, D.G.E. (1989) Track & Field J, 35, 13-17.

Robertson, D.G.E., Mosher, R.E. (1985) *Biomechanics IX-B*, 533-538

Robertson, D.G.E. (2002) http://www.health.uottawa.ca/-biomech/csb/software

Figure 1: Typical angular velocities (top), moments of force (middle) and moment powers (bottom) of the knee and hip moments during an open stance karate front kick. Left arrow indicates lifting of kicking leg; right arrow is contact.

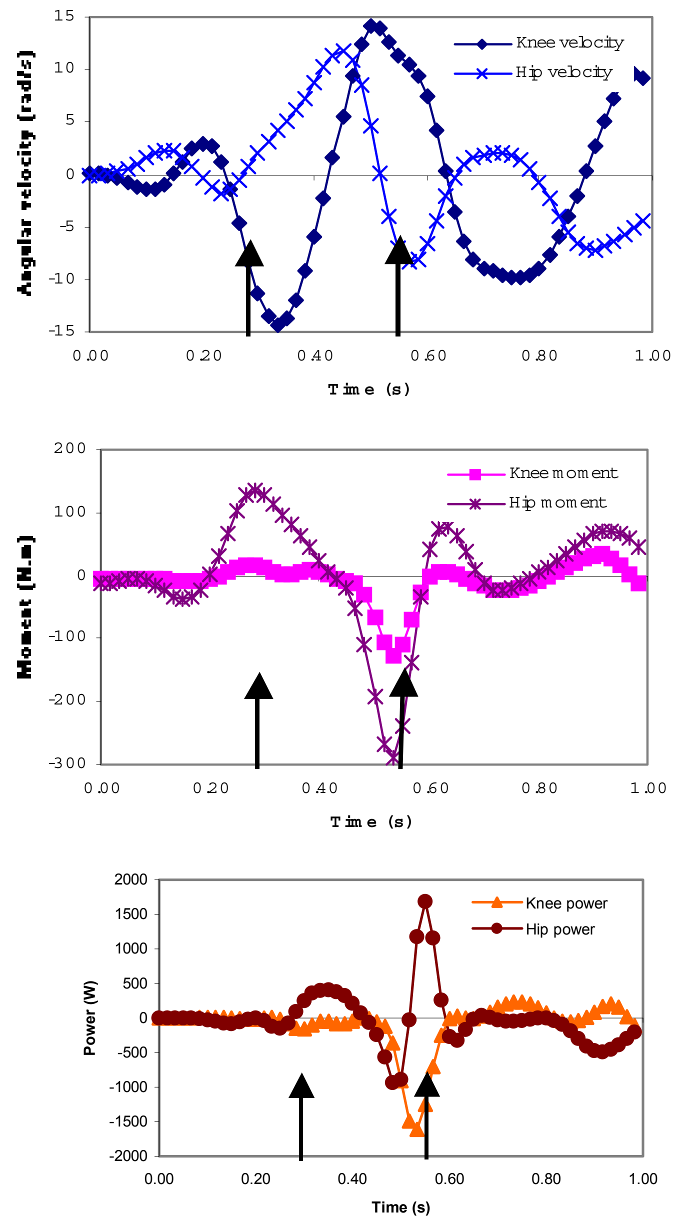

CLINICAL APPLICATION OF A KNEE-JOINT-CONTROLLED ELECTRO-MECHANICAL KAFO FOR POLIO PATIENTS

Sung-Jae Kang and Young-Ho Kim

Department of Biomedical Engineering, Institute of Medical Engineering,
Research Institute for Medical Instrumentation & Rehabilitation Engineering,
Technology Innovation Center for Medical Instruments, Yonsei University
yhkim@dragon.yonsei.ac.kr

INTRODUCTION

The ideal knee joint of KAFO (Knee-Ankle-Foot Orthosis) should provide the stability in stance and the foot clearance in swing. To achieve these two important functions, many researches have been performed on the control of the knee joint in KAFO (Long and Ross, 1972; Yang, 1975; Suga et al, 1998; Lehmann, and Stonebridge, 1978). However, clinical evaluations on patients with those KAFOs have not been successful yet. In the present study, an electro-mechanical KAFO to satisfy both the stability in stance and the knee flexion in swing was developed and evaluated in eight polio patients with the motion analysis.

METHODS

A knee joint control algorithm suitable for eight polio patients who are lack of stability in pre-swing was developed and various control systems and circuits were also designed. Knee flexion angles and knee flexion moments were measured on those polio patients with the developed KAFO using electrogoniometers and the three-dimensional motion analysis system. Temporal gait parameters in the controlled-knee gait with the developed KAFO were also compared with the locked-knee gait as well as the normal gait

RESULTS AND DISCUSSION

The designed foot switch system successfully determined the gait cycle of eight polio patients to control the knee joint of KAFO, resulting in the passive knee flexion or foot clearance during swing phase. From the three-dimensional gait analysis for polio patients, it was found that the controlled-knee gait with the developed electro-mechanical KAFO showed the knee flexion of 40°～45° at an appropriate time during swing phase and maximum knee flexion moment of 6.07N·m. In addition, the developed electro-mechanical KAFO revealed the possibility to correct toe drag and circumduction in an involved limb that are frequently found in polio patients.

Vertical movements of COG in controlled-knee gait (gait with the developed electro-mechanical KAFO) were significantly smaller than those in locked-knee gait (gait with the locked knee joint), and correspondingly controlled-knee gait reduced approximately 40% less energy consumption during horizontal walking.

More efficient gait patterns could be obtained, when various rehabilitation training and therapeutic programs as well as the developed electro-mechanical KAFO were applied for polio patients

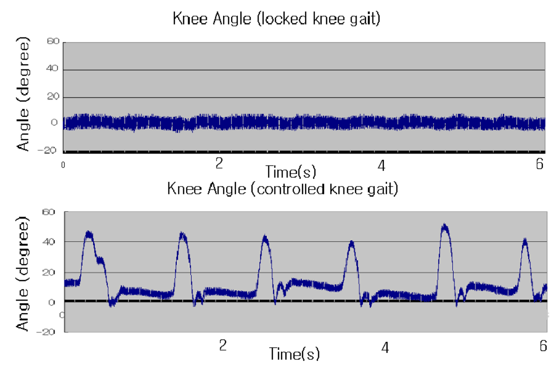

Figure 1: Knee flexion angles in the locked-knee gait and the controlled-knee gait

SUMMARY

In this study, an electro-mechanical KAFO whch an improved clutch control algorithm was developed and clinically evaluated on eight polio patients. From three-dimensional gait analysis, the maximum knee flexion angle in controlled-knee gait was 40°～45°. The temporal parameters and knee flexion pattern for controlled-knee gait showed a good agreement with those in the normal gait. The developed KAFO system with the automatic knee joint control could be a useful tool for polio patients.

REFERENCES

Long, I., Ross, C. (1972), CPRD, *National Academy of Sciences, 1972*
Yang, P. Y. (1975) , Ph.D. dissertation, *The Ohio State Univ., 1975*
Suga, T. et al (1998), *P & O International*, **22**, pp. 230-239.
Lehmann, J. F. and Stonebridge, J. B. (1978.). *Arch Phys Med Rehabil*, **59** : 430-437.

ACKNOWLEDGEMENTS

This work was partly supported by RRC program of MOST and KOSEF.

SHOCK ABSORBING CROSS-COUNTRY SKI POLE FOR DRYLAND SKIING

Andrew Post and D. Gordon E. Robertson
Biomechanics Laboratory, School of Human Kinetics, University of Ottawa, Ottawa, Ontario, Canada

INTRODUCTION

Some research has gone into the forces that are produced during the pole plant phase of cross-country roller skiing (Street & Frederick, 1995; Komi, 1988; Millet at al., 1998a,b,c). Due to the hard surface (usually asphalt) into which the roller skiers plant their poles there are much higher forces travelling through the pole than with ordinary snow skiing. These high ground reaction forces have been identified as a possible cause of injuries to the wrists, elbows and shoulders of roller skiers.

To date few studies have tried to resolve this problem by inserting a shock absorbing mechanism into the ski pole. In the present experiment pole forces were examined before and after a shock absorbing mechanism (a spring) was inserted into a normal Nordic ski pole. The spring was inserted into the shaft of a carbon fibre cross-country ski pole between the handle and the shaft.

METHODS

To simulate the load created by the arm, a 1.13 kg mass was attached to the handle above the spring. The ski pole was dropped from a support that was set up over a force platform (Kistler). The pole was dropped five times for each of the four pole/height conditions: 20 and 40 cm with and without the modification. The pole was suspended by a fish line and the drop height was measured by an anthropometer to ensure repeatable impulses. The force platform was covered with a steel plate to protect it from the carbide tips of the ski pole. The resonant frequency of the force platform was measured to be approximately 780 Hz.

RESULTS AND DISCUSSION

The peak vertical forces for the 20 cm trials were 458+/-66 N and 404+/-45 N for the standard versus modified poles, respectively. The peak vertical forces for the 40 cm trials were 766+/-49 N and 615+/-64 N for the standard versus modified poles, respectively. Thus, the spring reduced the peak vertical force by 11.8% for the 20 cm drop height and 19.8% for the 40 cm drop height. Figure 1 shows vertical force histories for the normal and modified poles for the 40 cm drop. Notice that the spring dissipates the impact forces by spreading the forces over a longer duration and creating negative vertical forces.

The reduced peak forces are comparable to those reported by Wells (1988) for cross-country skiers on snow. Presumably, the spring has reduced the peak forces low enough to prevent stress related injuries.

SUMMARY

In summary, the trials to test the modified ski pole successfully simulated a standard pole plant on a harder than snow surface. The results showed that the forces were reduced by the shock absorbing system that was installed on the ski pole. While the modified pole was successful in a laboratory environment it is essential to estimate its durability and its functionality in a field setting for its use by the general public and athletes.

REFERENCES

Komi P.V. (1988) Amer Ski Coach Vol **11**(5).

Kannus P., Niittymaki S., Jarvinen M. (1988) Scand J of Sports Sci **10**, 17-21.

Millet G.Y., Hoffman M.D., Candau R.B., Clifford P.S. (1998a,b) Med & Sci Sports & Exer **30**, 1637-1633, 1645-1653.

Millet G.Y., Hoffman M.D., Candau R.B., Buckwalter, J.B., Clifford P.S. (1998c) Med & Sci Sports & Exer **30**, 755-762.

Street M.G. & Frederick E.C. (1995) J Appl Biomechanics, **11**, 245-256.

Wells R. (1988) Proc. 5th Conference of Can Soc for Biomechanics. 166.

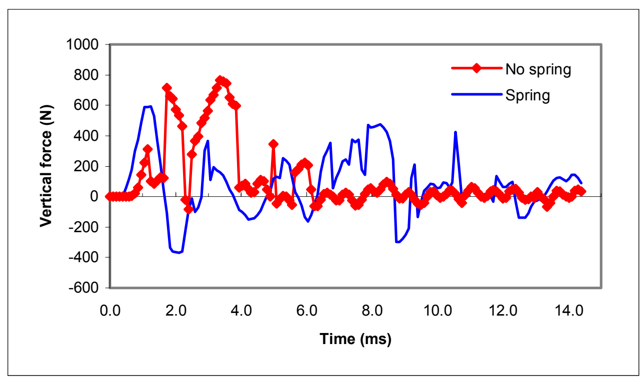

Figure 1: Vertical forces for the 40 cm drop height for modified (spring) and normal (No spring) ski poles.

EFFECTS OF A COMPLETE BYPASS GRAFT ON THE FLOWFIELDS IN A HOST ARTERY WITH DIFFERENT SEVERITY OF STENOSIS

Tzu-Hsiang Ko
Department of Mechanical Engineering, Lunghwa University of Science and Technology, Taiwan, R.O.C
Associate Professor, thko@mail.lhu.edu.tw

INTRODUCTION

When moderate or severe stenosis occurs in the coronary arteries, the coronary bypass surgery will be operated. The effects of the bypass graft on the flowfields are closely relevant to the severity degree of stenosis. In the earlier studies, the end-to-side anastomsis flow model which assumed 100%-area severity stenosis was most frequently used (Hofer et al., 1996; Ethier et al., 1998). The flowfields obtained from the model could be very different from the realistic cases with only partially obstructed host arteries. To implement the flow characteristics in the host artery with different severity degree of stenosis, the present paper focuses on the anastomisis flows in tubes with different degree obstructions, and investigates the bypass effects on the flowfields.

METHODS

The geometry of the model is shown as Fig. 1. The flow is assumed as three dimensional, incompressible, laminar and steady. The continuity equation and the Naviar-Stokes equation are solved numerically by SIMPLEC scheme. The grid layout is also shown in Fig.1. Uniform velocity distributions are assumed at the inlet and the fully developed condition is assumed at the outlet.

RESULTS AND DISCUSSION

Three different obstructed degrees, including 70%, 80% and 90%-area obstructed cases were studied in the present paper. Figs. 2(a), (b) and (c) showed the flowfields on the symmetric plane for the three cases respectively. The highest velocity appeared at the contracted area in all three cases. The highest velocity in 90%-area obstructed cases was about twice of the inlet velocity, and in the 70%-area obstructed case, the highest velocity was only about 1.75 times of the inlet velocity. The difference might induce different shear stresses at the contracted region. Four low velocity zones appear in three cases similarly. They distributed at the entrance of the bypass, the lower zone upstream of the contracted region and the upper and lower zones downstream of the contracted region. When three different cases were compared, the low velocity zone at the bypass entrance was widest in the 70%-area obstructed case, and the low velocity zones occurring at the other three regions were widest in the 90%-area obstructed case. There were recirculations on the low velocity regions, and were prone to accumulate the damaged particles and substances. Fig. 3 compared the mass fractions entering the bypass. The mass fractions entering the bypass in the three cases were about 60%, 73% and 86% respectively. Though the mass fraction directly flowing through the contracted region was the smallest in the 90%-area obstructed case, the velocity was highest in three cases as mentioned previously. The high velocity fluid entering the downstream of the contracted area would induce high shear stresses which were believed to be an important factor relevant to the success of the bypass graft surgeon.

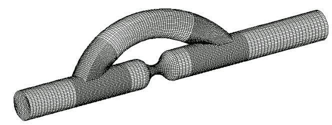

Fig. 1 The geometry and grid layout of the model

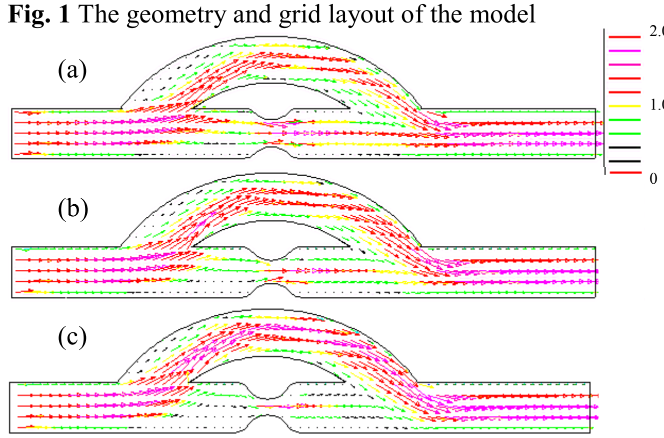

Fig.2 Velocity distributions for (a)70% (b)80% and (c) 90%-area obstructed cases (normalized by inlet velocity)

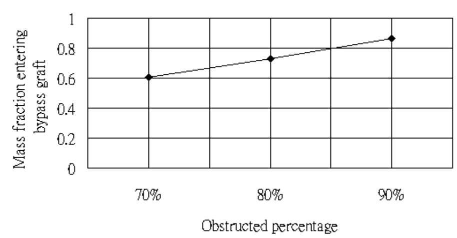

Fig. 3 Mass fraction entering the bypass graft for different obstructed cases

SUMMARY

The flow characteristics in a 70%, 80% and 90%-area obstructed host tube with a complete bypass graft were investigated. The flowfields in three cases showed very different features. The results were also different from those in the earlier studies which used the end-to-side model. The present study provided more realistic simulations as for preliminary design information.

REFERENCES

Hofer, Michael (1996). *J. Biomechanics*, **29**, 1297-1308
Ethier, C. R. et al. (1998). *J. Biomechanics*, **31**, 609-617

MEASUREMENT DIFFERENCES BETWEEN TWO WRIST GONIOMETERS DURING PRONATION & SUPINATION

Peter W. Johnson [1], Per Jonsson [2] and Mats Hagberg [2]

[1] Department of Environmental Health, University of Washington, Seattle, WA, petej@u.washington.edu
[2] Section of Occupational Medicine, Göteborg University, Göteborg, Sweden

INTRODUCTION

Pronation and supination has been shown to affect the measurement accuracy of wrist goniometers. The purpose of this study was to determine whether there were differences in measurement accuracy between two different goniometers, over a wide range of pronation and supination (P/S).

METHODS

Eight subjects moved their wrist between -40° and 40° of flexion/extension (F/E) and -10° and 20° of radial/ulnar (R/U) deviation in four different P/S positions: 90° pronation (90 P); 45° pronation (45 P); 0° neutral (0 N) and 45° supination (45 S). Crosstalk and offset errors were compared between the goniometer systems and across the various P/S positions.
Two electrogoniometers were tested: System A consisted of a biaxial, single transducer goniometer (Biometrics; model XM-65; Gwent, UK), System B consisted of a biaxial, two-transducer goniometer integrated into a fingerless glove. (WristSystem, Greenleaf Medical, Palo Alto, California, USA). The sensing elements in System B were the exact same design as System A's and manufactured by the same company (Biometrics; Gwent, UK).

A tiltable, adjustable-height table (Part 50642, Förbandsmaterial AB, Partille, Sweden) combined with a calibration fixture (Greenleaf Medical; Palo Alto, CA) was used to repeatedly position each subject's forearm and wrist in known pronation/supination, flexion/extension and radial/ulnar angles. The goniometers were calibrated in 90° of pronation.

RESULTS AND DISCUSSION

As shown in Figure 1, offset errors in F/E were encountered during P/S and both systems experienced similar F/E offset errors. R/U offset errors were also encountered with both systems during P/S; however, the trends in R/U offset errors between systems were roughly equal but opposite in direction. As shown in Figure 2, System A was prone to more R/U crosstalk than System B and the amount of R/U crosstalk with System A was dependent on the P/S position. F/E crosstalk was present with both goniometer systems and dependent on P/S. Movement from 90 P to 45 S caused a synchronous twist/rotation in both the F/E and R/U signal with System A, whereas with System B, there was virtually no twist/rotation with the F/E movements and a small amount of P/S twisting/rotation with the R/U movements.

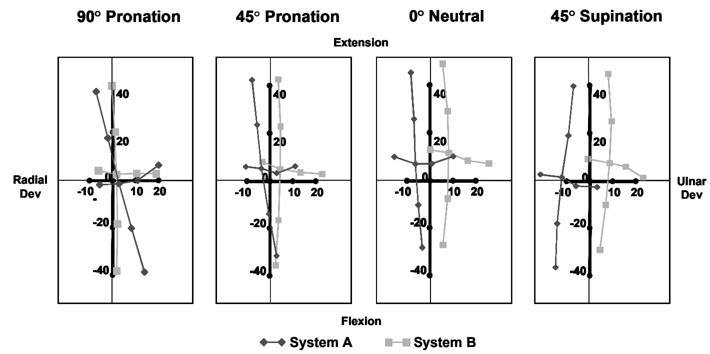

Figure 1: The effects of pronation and supination on measurement accuracy [n=8]. The bold black identity lines indicate the actual movements.

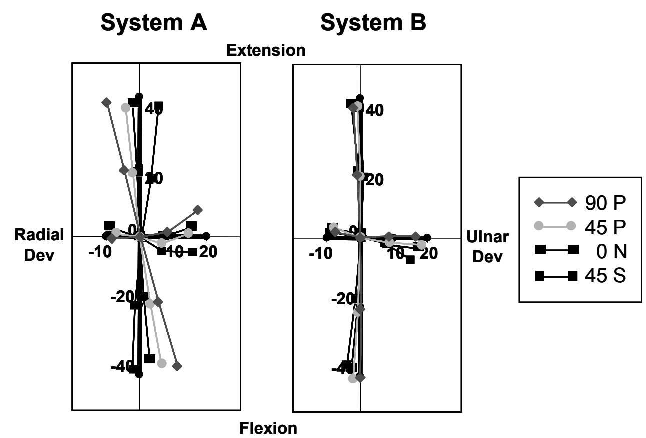

Figure 2: The effects of pronation and supination on F/E and R/U crosstalk grouped by goniometer system [n=8]. Offset errors in the various P/S positions from Figure 1 have been adjusted so the origins of each P/S position are aligned.

SUMMARY

Goniometer crosstalk is an important source of measurement error and results from a twisting of the goniometer transducer. System B demonstrates that design changes can reduce transducer twist and the resultant crosstalk. The calibration position will affect wrist angle measurements and the magnitude and direction of measurement errors. To minimize offset errors, goniometers should be calibrated/zeroed in the most common P/S position or in the mid-range of anticipated P/S positions. When possible, goniometers should not be calibrated in one P/S position and used another P/S position, otherwise offset error will result.

HEAD TURNS INDUCE ALTERED LOADING DURING STANDING IN STROKE PATIENTS

Anouk Lamontagne, Nicole Paquet and Joyce Fung

Jewish Rehabilitation Hospital Research Center & McGill University, Montreal, Canada.
(Anouk.Lamontagne@mcgill.ca)

INTRODUCTION

Stroke patients have difficulties maintaining balance while walking with voluntary head turns (Kairy et al. 2000). How postural adaptations to fast head turns in stroke patients differ from those of healthy individuals, however, is unclear. Our objective was to compare postural adaptations to horizontal head turns during standing between stroke patients and healthy subjects by examining the loading forces (GRF), body center of mass (CoM) and center of pressure (CoP).

METHODS

Eight patients (aged 56-79 yrs) with a hemiparesis (right=4, left=4) secondary to a first ischemic stroke and 4 healthy controls (aged 54-76 yrs) were evaluated during standing with their feet apart at shoulder width. An illuminated arrow panel located in front of the subjects indicated the direction for voluntary head turns. Head turn directions were randomly delivered in the right and left directions (3-6 trials per direction), interspersed with catch trials (6-12 trials) with no head turn. Subjects were instructed to turn the head as fast and as quickly as possible in the direction indicated by the arrow and to keep the head turned for 3s. A Vicon[tm] 3-D motion analysis system with six infrared cameras was used to record body segment displacements at 120 Hz. Body CoM was calculated based on kinematics using a 9-segment model. Two AMTI (OR6-7) force plates, embedded in the floor, were used to record GRF under each foot and the net displacement of the body CoP was calculated. Changes in GRF with respect to baseline values were calculated using integrals over sequential time windows (see Figure). In addition, maximum displacement of the body CoM and CoP, as well as the mean absolute difference between CoP and CoM, were analyzed.

RESULTS

Patients performed amplitudes of head turn similar to controls, but at slower velocities. Mean peak head turn velocities were 335 (±124) deg/s for the controls and 237 (±63) deg/s for the patients. In the controls (Figure), GRF were characterized by an unloading-loading pattern of the limb ipsilateral to the direction of the head turn. In the patients (Figure), head turns ipsilateral to the paretic side caused the same unloading-loading pattern of the paretic limb, but this was immediately followed by an unloading of the paretic limb. During contralateral head turns, a systematic unloading of the paretic limb was observed. Note that very little if no changes in GRF took place before the onset of head turns in both groups. CoM and CoP in patients and controls were shifted toward the side of the head rotation. The shifts in body CoM were small and similar between groups and directions of head turn (range: 3.5 - 4.1 mm). CoP displacements, however, were larger in the patients (ipsilateral=11.6mm, contralateral=11.9mm) than in the controls (8.0 mm), resulting in a larger CoP-CoM difference. These shifts in CoM and CoP represented more than 3 times the peak-to-peak displacements observed in trials with no head turns for the controls. In the patients, peak-to-peak displacements of CoM and CoP were similar between trials with and without head turns.

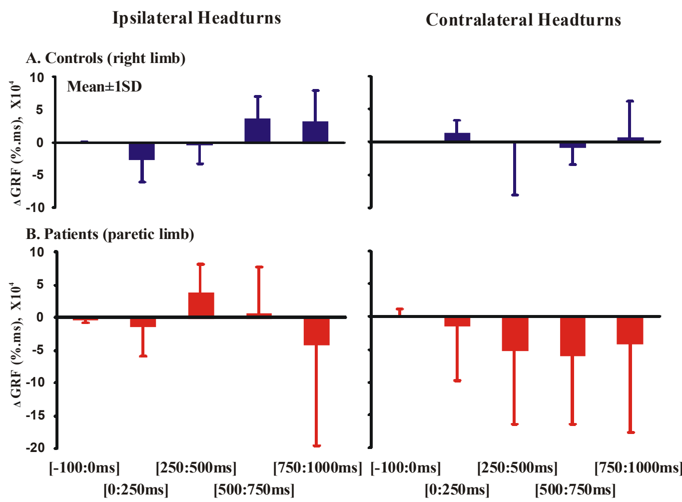

Changes in vertical ground reaction forces (GRF) during horizontal headturns

DISCUSSION AND CONCLUSIONS

GRF patterns indicate that stroke patients minimize loading of the paretic limb during horizontal head turns, in contrast with healthy subjects who show a typical unloading-loading pattern of the limb ipsilateral to the direction of the head turn. The inability to load the paretic limb likely explains the lack of increase in CoM and CoP excursions during trials with head turns as compared to trials without head turns. The larger CoP-CoM differences and the slower head turn velocities in patients suggest the maintenance of a larger safety margin due to postural instability (Corriveau et al. 2000).

REFERENCES

Kairy D., Paquet N., Fung J. (2000). *Physiotherapy Canada,*52,S98

Corriveau H. et al. (2000). *Diabetes Care*,23,1187-1191.

EFFECTS OF AGE AND GENDER ON MAXIMUM HIP FLEXION POWER AT LOW AND HIGH VELOCITIES

Cécile Smeesters[1,3], Neil M. Cole[2] and James A. Ashton-Miller[1]
[1]Biomechanics Research Laboratory, University of Michigan, Ann Arbor, MI, USA
[2]Bio Logic Engineering Inc., Dexter, MI, USA
[3]Communicating author cecile.smeesters@gme.usherb.ca

INTRODUCTION

The ability to complete a compensatory step in time to arrest an on-going forward fall can require the hip flexor muscles to maximize power (Schultz et al., 1997). Mean step velocity of older males in single-step recovery from their maximum forward lean is approximately 350º/sec (Wojcik et al., 1999). However, age and gender effects on maximum hip flexion strengths have only been reported for isokinetic velocities up to 210º/sec (Cahalan et al., 1989). The literature contains reports showing significant gravitational and inertial measurement artefacts as well as narrowing isokinetic windows at higher isokinetic velocities. We used a custom dynamometer that made corrections for these effects. Our null hypothesis was that neither age nor gender would significantly affect the maximum hip flexion power (torque x angular velocity) developed in healthy adults.

METHODS

The custom dynamometer had a stiff, low rotational inertia lever arm providing a smooth, adjustable, passive resistance throughout the range of motion (ROM); visual feedback of results; and dedicated angular position and torque sensors. From the measurements obtained, velocity, acceleration, rate of torque and power were calculated, and corrections for the leg lever inertia and gravity were made. The subject's upper body was secured so that the dominant leg hip joint was aligned with the center of rotation of the lever arm. The tested leg was secured to the lever arm at the ankle with the tested knee near full extension. Twenty-four young (18-26yrs) and 24 older (65-84yrs) healthy adults, with equal numbers of males and females, were tested at five randomly ordered resistance levels spanning the range of achievable velocities for each subject. Except for the maximum resistance level or zero velocity isometric test where the angle was maintained at 0º, the ROM was from 0º to 90º. The subjects were instructed to swing their leg "as fast and as hard as possible" until it was decelerated by a soft stop. Maximum instantaneous hip flexion power, velocity and torque over the ROM were measured (Figure 1). Linear curves were fitted to each subject's maximum torque over the ROM versus maximum velocity over the ROM data. Quadratic curves were fitted to each subject's maximum power over the ROM versus maximum velocity over the ROM data. Age and gender effects on maximum achievable hip flexion kinetic power, torque and velocity were assessed with repeated measures analyses of variance (rm-ANOVA).

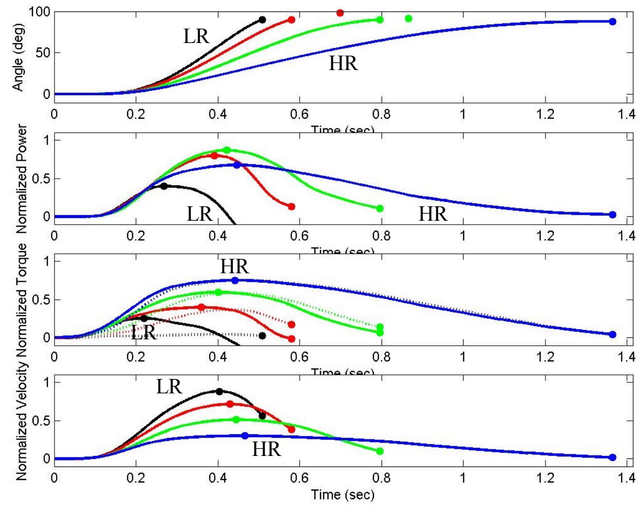

Figure 1: Average (N=48) normalized angle, velocity, torque and power versus time from low (LR) to high resistances (HR).

RESULTS AND DISCUSSION

Age and gender significantly affect the maximum achievable kinetic power, torque and velocity (all $p<0.005$). Maximum achievable hip flexion power decreased 21% and 16% with increasing age for males and females, respectively, due to a decrease in both maximum torque and velocity (Table 1). The maximum achievable kinetic velocities ranged from 244º/sec to 508º/sec. The substantial age-related reduction in older adult hip flexor muscle power may underlie the diminished ability, especially in older women, to take a sufficiently rapid step to arrest a forward fall (Wojcik et al., 1999).

Table 1: Percentage Decrease With Age of Torque (T), Power (P) and Velocity (V) at the Maximum (Max) Points

	TMax	PMax			Vmax		
	T	T	V	P	T	V	P
Female	25%	31%	21%	49%	44%	21%	50%
Male	17%	20%	16%	37%	30%	14%	39%

REFERENCES

Schultz, A.B. et al. (1997). *Muscle Nerve*, **Suppl. 5**, 60-64.
Wojcik, L.A. et al. (1999). *J. Gerontol.*, **54A**, M44-50.
Cahalan, T.D. et al. (1989). *Clin. Orthop.*, **246**, 136-145.

ACKNOWLEDGEMENTS

PHS grants R42 AG13587, PO1 AG10542 and P60 AG08808.

NEW METHOD OF THREE-DIMENSIONAL IMAGING OF SMALL AIRWAYS IN RATS WITH X-RAY MICRO-CT

Toshihiro SERA [1], Hideki FUJIOKA [2], Hideo YOKOTA [3], Akitake MAKINOUCHI [4], Ryutaro HIMENO [3], Robert C. SCHROTER [5] and Kazuo TANISHITA [6]

[1] Center for Life Science and Technology, Keio University, Yokohama, Japan, sera@tani.sd.keio.ac.jp
[2] Biomedical Engineering Department, University of Michigan, Michigan, U.S.A.
[3] Advanced Computing Center, The Institute of Physical and Chemical Research (RIKEN), Wako, Japan
[4] Integrated V-CAD System Research Program, The Institute of Physical and Chemical Research (RIKEN), Wako, Japan
[5] Department for Bioengineering, Imperial College of Science, Technology and Medicine, London, U.K.
[6] Department of System Design Engineering, Keio University, Yokohama, Japan

INTORODUCTION

Small airways consist of tapered, curved, branching tubes with various length and diameter, and their geometry influence mechanical dynamics in airways (airflow structure, surfactant transport and particle deposition). In the previous studies, the cast models and the fixed preparations were available to analyze large airway geometry [1-3]. However, the airway geometry, especially small airways, may be changed in the stage of preparations and it varies during respiration. In this study, we propose the new technique to visualize the small airways at high resolution without requiring fixed preparation.

METHODS

We visualized small airways of the excised rat lungs without fixed preparation. The radiopaque solution was induced into blood and stained to lung tissue without airways by the permeability. In our technique, lung tissue without air, for example pulmonary arteries and airway wall, exhibits a higher intensity than airway lumens.

Animal Preparation

After male Wister rats (300 ± 30 g) were anesthetized with pentobarmital sodium (50 mg/kg ip), they were exsanguinated and cardiac arrest was induced by 0.2 g/ml KCl solution. The water mixed this a radiopaque media, Sodium diatrizoate (Sigma Chemical, St Louis, MO) in the quantity 0.8 g/ml, was induced into an inferior vena cava. After the solution was stained to lung tissue for 1 h, the lungs were removed.

Imaging

The small airways were visualized by a microfocal X-ray CT system (MCT-CB100MF, Hitachi Medical Corp., Japan, Tokyo). This system consisted of microfocal cone-beam X-ray source (spotsize: 7 μm), X-Y-Z-Θ rotation stage, an image intensifier and 12 bit CCD camera. The Resolution was 480 × 480 pixel and 1 voxel size was 13 μm. In one rotation, the number of slice images was obtained 200 images.

The excised rat lung induced by the radiopaque solution was placed into a Plexiglas cylinder in. It was mounted on the rotation stage, and it took 2.5 min to rotate around 360°.

RESULTS AND DISCUSSION

Fig. 1 shows the example continuous micro-CT images (slice pitch: 52 μm). The radiopaque solution was stained to lung tissue, and so airway lumens had a lower intensity. Using our technique the continuous and complex branching airways were visualized in detail physiologically.

The edge lines of target airways could be identified using a threshold method. Fig. 2 shows the three dimensional structure, which was reconstructed from the continuous edge lines.

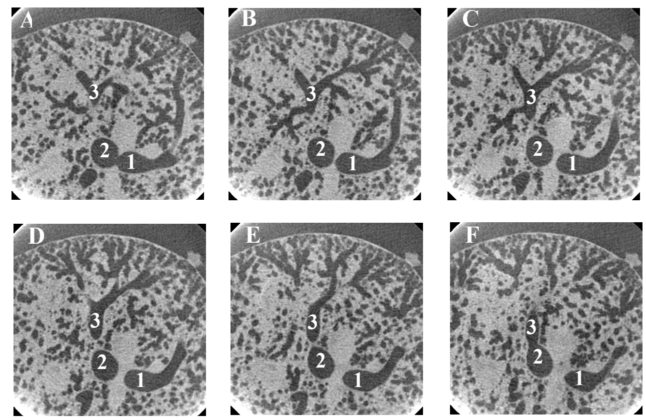

Fig. 1: The continuous images of micro-CT (Scale bar = 500 μm). From image (A) to image (F), airway (1) and airway (2) were branching, otherwise airway (2) and airway (3) were merging.

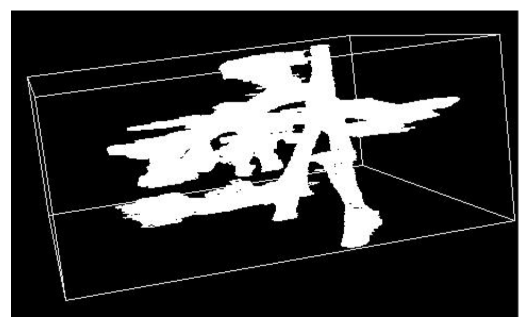

Fig. 2: Three dimensional reconstruction image form the continuous edge lines (width: 6.24 mm and height: 2.59 mm).

SUMMARY

We stained the radiopaque solution to lung tissue by the permeability and visualized by a microfocal CT system, and so we visualized small airways physiologically in detail. Using this new visualization technique, the geometry of small airways, diameter and length as well as branching angle and curvature, can be analyzed in detail when lung volume is variable.

REFFERNCES

1 Weibel, E. R. (1963). *Morphometry of the Human lung*. New York: Academic
2 Horsfield, K. et al (1971). *J. Appl. Physiol.* **31**, 207-217.
3 Hammersley, J. R., and Olson, D. E. (1992). *J. Appl. Physiol.* **72**, 2402-241.

FLOW IN A REALISTIC MRI-BASED VASCULAR BRANCH

Mehran Tadjfar and Ryutaro Himeno
Advanced Computing Center
Institute of Physical and Chemical Research (RIKEN)
2-1, Hirosawa, Wako-Shi, Saitama, JAPAN

INTRODUCTION

Many researchers use CFD to study the mechanics of blood flow in the human vascular system. The emphasis is shifting from averaged, idealized geometric models into realistic patient-specific models taken from MRI images or other advanced imaging techniques (Taylor et al. 1998). In order to use the results of CFD for clinical diagnoses or surgical planning, one needs to have fairly accurate representation of the given patient's vascular system or at least in the region of interest. This involves fairly smooth geometrical model of the region and an accurate description of the inlet and outlet flow conditions. Here, we use CFD methods to study the flow based on an accurate grid representation of a realistic MRI-based arterial branch (Fig. 1).

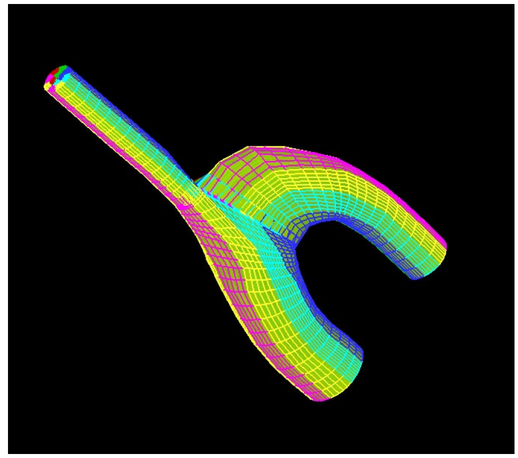

Figure 1: Grid model of the MRI-based branch.

METHODS

The unsteady, three-dimensional, incompressible Navier-Stokes equations are solved using a fast, parallel, and time-accurate finite volume solver (See Tadjfar 2002). The solver is capable of dealing with moving boundaries and moving grids. It is designed to handle complex, three-dimensional vascular systems. The computational domain is divided into multiple block subdomains. At each cross section the plane is divided into twelve sub-zones to allow flexibility for handling complex geometries and, if needed, appropriate parallel data partitioning. A second-order in time and third-order upwind finite volume method for solving time-accurate incompressible flows based on pseudo-compressibility and dual time-stepping technique is used.

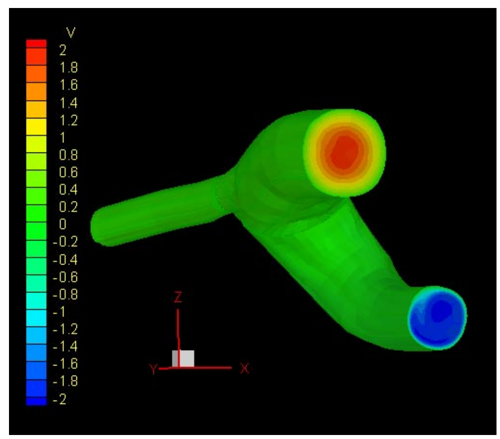

Figure 2: Axial velocity distribution into (top) and out of (bottom) the main vessel.

RESULTS AND DISCUSSION

We have developed tools to convert arterial branches from MRI-images to solid surface geometries. A structured grid is generated from these solid surfaces for the use in the flow simulation. We can obtain all the flow properties for both steady and unsteady flow simulations (see Fig. 2). From the simulation data, we can obtain the shear and normal stresses on the arterial walls. The intention is to use the results of these simulations based on the MRI-images obtained from a patient base for the study of arterial diseases.

REFERENCES

Taylor, C. A., Hughes, T. J. R., and Zarins, C. K., (1998), *Comp. Meth. Appl. Mech. Eng., Vol. 158, pp. 155-196.*

Tadjfar, M. and Himeno, R. (2002), *Journal of Biorheology, to appear.*

QUANTITATIVE EVALUATION OF MICROVASCULAR STRUCTURE AND COMPARIZON OF REGIONAL MICROVASCULARITY AND PO2 DISTRIBUTION IN RAT CEREBRAL CORTEX

Kazuto Masamoto[1], Tomoko Negishi[1], Takayoshi Kurachi[2], Naosada Takizawa[3], Hirosuke Kobayashi[4], and Kazuo Tanishita[2]
[1]School of Fundamental Science and Technology, Graduate School of Keio University, Yokohama, 223-8522, Japan, kaz@tani.sd.keio.ac.jp, [2]Department of System Design Engineering, Keio University, Yokohama, Japan,
[3]Center of Information Science, Kitasato University, Sagamihara, Japan,
and [4]Department of Medicine, Kitasato University School of Medicine, Sagamihara, Japan

INTRODUCTION

Cerebral oxygen demand is very large and normal brain function depends on continuous oxygen delivery. One of the most important parameters in the oxygen delivery process is a microvascular structure where the oxygen is mainly supplied through to tissue. Regional differences in the microvascular networks and density are generally known (Duvernoy, H.M.). However, the quantitative differences in the microvascular structure are not clear, and whether the regional varieties of the microvascularity respond a subsistent oxygen demand in tissue is subsequently unclear. To clarify the quantitative differences in the microvascularity in the local cerebral regions, we developed a quantitative evaluation of the microvascular structures by means of a resin injection method with fluorescent dye. In addition, to confirm whether the microvascular structure is influenced by the oxygen demand, we investigated the relationships between the regional microvascularity and Po2 distribution in both the different function areas and their laminar regions in rat somatosensory cortex.

MATERIALS AND METHODS

The experiments were performed on male Wistar rats (290-320 g) anesthetized with sodium pentobarbital (50 mg/kg bw, i.p). To visualize the microvascular structure in the brain, prepolymerized methacrylate resin mixed with fluorescent dye (Lumogen® F Red 300, BASF) was perfused through the left ventricle. After the fixation of the blood vessels, the whole brain was removed and then its coronal sections were developed (Fig. 1A). The microvascular structure, within the functional areas in the primary somatosensory cortex (S1HL: hindlimb region, S1FL: forelimb region, and S1Tr: trunk region) based on the brain map (Paxinos and Watson), was observed by a laser scanning confocal microscope (Oz, NORAN). Analysis of the vascularity was performed by the isolating regions of interesting (ROI) in each functional area (Fig. 1B). To produce the binary ROI of the selected regions, a threshold of discrimination was applied. Then, to estimate the number density of the blood vessels in the ROI, we calculated the number density of the black pixels skeletonized from the casting molds of the vessels in the ROI (Fig. 1C).

Po2 distribution in the functional areas was measured by micro-coaxial oxygen electrodes (Lübbers Type) penetrating vertically from the brain surface by 20-µm step intervals.

RESULTS AND DISCUSSION

The high vascular density region was found in the middle cortical layers (III-V) in all functional areas we observed (Fig. 2). This agrees with the human cortical microvascularization (Torre, F. R. 1998) and this suggests that the large vascularity reflects the high oxygen demand, because the highest cerebral glucose utilization was found in the layer IV (Wress, A. 1990) where the neural inputs from thalamus directly connect.

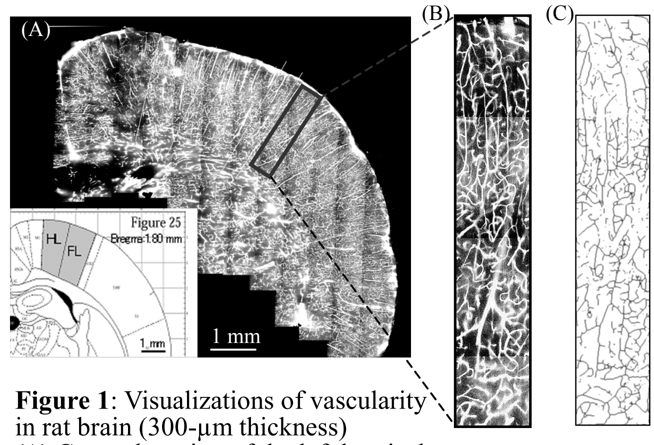

Figure 1: Visualizations of vascularity in rat brain (300-µm thickness)
(A) Coronal section of the left hemisphere
(B) Selected region of interesting (ROI) in a functional area.
(C) Skeletonized section of the binary ROI (from Fig. 1(B))

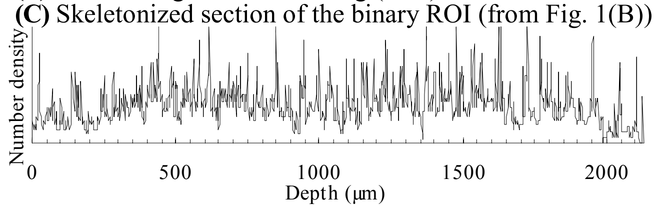

Figure 2: Number density of black pixels (vascularity) in ROI

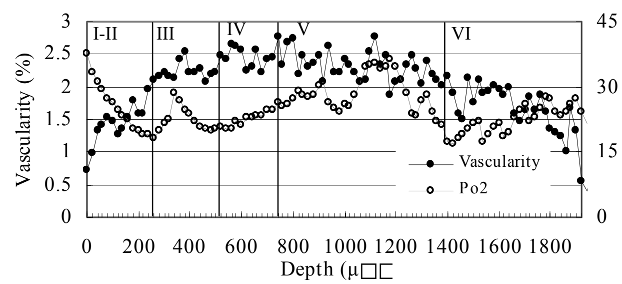

Figure 3: Comparison of the vascularity and Po2 distribution in the area S1HL (Layer I-VI)

Some inconsistent points between the vascularity and Po2 distribution was found in the superficial layers (I-II). Such as the vascularity increased from the surface, in contrast, the Po2 decreased (Fig.3). This implies that disproportion of the oxygen supply to the oxygen demand may exist in the cerebral superficial regions.

REFERENCES

Duvernoy, H.M. (1999). *The Human Brain –Surface, Three-Dimensional Sectional Anatomy with MRI, and Blood Supply.* SpringerWienNewYork, 431-473

Paxinos, G. and Watson, C. (1998). *The Rat Brain.* Academic Press

Torre, F.R. et al (1998). *The Anatomical Record*, **251**, 87-96

Wress, A. et al (1990). *Anat Embryol*, **181**, 603-614

EVALUATION OF SHAPE ACCURACY IN CT BASED FEMUR MODEL FOR PROSTHETIC STEM DESIGN

Jiro Sakamoto[1] , Tanzo Sugimori[2], Ayumi Kaneuji[2], Mitsuru Nishino[2], Juhachi Oda[1] and Tadami Matsumoto[2]
[1] Dept. Human and Mechanical Systems Engineering, Kanazawa University,
Kanazawa, Ishikawa, Japan, sakamoto@t.kanazawa-u.ac.jp
[2]Department of Orthopaedic Surgery, Kanazawa Medical University, Kanazawa, Japan

INTRODUCTION

Three-dimensional CAD model of hip joint is required for development of total hip prosthesis and stress analysis by finite-element method. The authors have been classified proximal femur canal shape of Japanese osteoarthrosis (OA) patients by using 3D models based on CT images to develop total prosthetic stem fitting specially for Japanese OA (Hasegawa, et al., 2000). Although shape accuracy of the 3D model is very important to develop the total hip stem, it has not ensured sufficiently. In this study, a 3D femur model constructed from CT images was compared with corresponded real femur, and accuracy of the model was evaluated.

MATERIALS AND METHODS

A femur of 50 years-old female with OA was subjected to evaluate accuracy of the 3D model. The right leg was resected because of a malignant tumor. CT images of the femur were obtained before the resection. The CT images were inputted into image processing software (MedVision, Evergreen Technologies Inc.), and cortical outlines and canal lines were extracted in each section. These lines were transferred to CAD software (Unigraphics, Unigraphics Solution Inc.), and then 3D model was constructed by interpolation based on the lines. On the other hand, the resected femur was embedded in resin mold, and parallel sliced specimens were prepared. Photographs of the cross sections were taken from the specimens as same as CT scan. The 3D model based on the real femur was constructed in same way to make the 3D model based on CT images. These models are comparable each other by overlapping operation of CAD. Overlapping image of the real and CT based model is shown in Fig. 1. Bone axis, lesser trochanter and center of femoral head are matched up each other in the overlapping.

RESULTS AND DISCUSSION

The outlines and canal lines of the real and CT based model in frontal plane are shown is Fig.2. Gap between each canal line of the real and CT based model was measured in some horizontal plane. In the figure, ”level” denotes distance from the lesser trochanter level. The gap value means shape error of the CT based model related to the real femur. The canal lines corresponded well each other in distal part below the level of +15mm. Maximum gap is 1.5mm at the medial side of lesser trochanter level. If the CT based model is used to design the prosthetic stem shape, we have to pay attention that error of the model can be over 1mm.

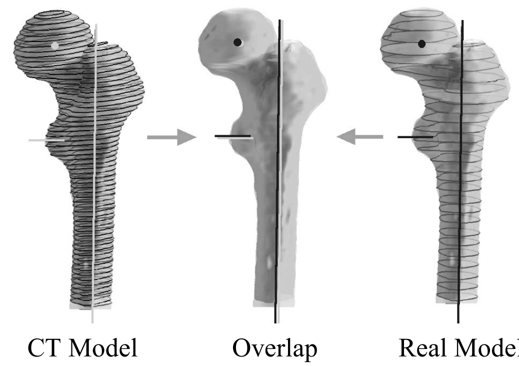

Figure 1: 3D overlapping image of the real and CT based model of proximal femur.

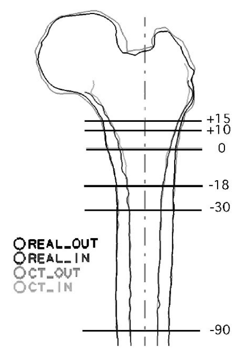

Level	Medial	Lateral
+15	0.30	0.48
+10	0.34	0.45
0	1.51	0.34
-18	0.27	0.56
-30	0.46	0.19
-90	0.38	0.08
Average	0.54	0.35

(mm)

Figure 2: Gap of the canal line between the real and CT based model in frontal plane.

SUMMARY

Shape accuracy of 3D femur model created by CT images was evaluated in comparison with precise model based on cross section images of the real femur. Proximal canal surfaces of the two models were compared each other by overlapping in CAD software. Over 1mm error was observed in the CT based model. We have to consider such error range when the CT based model is used to design of prosthetic stem fit to proximal femur canal.

REFERENCES

Hasegawa, Y., Sakamoto, J., et al. (2000). *Proceedings of 10th Int. Conf. Biomed. Engineering*, 169-170.

FLOW BETWEEN A CLOT MODEL AND A STENOSIS

A. Sarkar[1] and G. Jayaraman
Center for Atmospheric Sciences, Indian Institute of Technology Delhi,
Hauz Khas, New Delhi – 110016, INDIA.
[1]Present Address : Bioengineering, University of Washington, Seattle. USA. anamika@bioeng.washington.edu

INTRODUCTION

A pathological condition is encountered when some blood constituents deposited on the artery wall get detached from the wall, join the blood stream again and form a clot which can lead to complete blockage of the blood vessels. Doffin and Chagneau (1981) set up an experiment and showed that the velocity profiles, of the steady component of the flow, experience considerable changes in the unsteady flow field by the steady streaming, especially for low values of the frequency parameter. We analyse the model proposed by them, to study the effect of the height of the clot model and frequency parameter on the physiological parameters of the flow.

MATHEMATICAL MODEL

We model the artery as a rigid tube with radius R_o. Fig.1 shows the schematic diagram of the stenosed artery in the presence of a clot model in the cylindrical coordinate system (R,θ,Z). The flow is axi-symmetric and oscillatory in nature. It is assumed that the development of the stenosis is axisymmetric over the length of the artery. It is also assumed that the clot model is axisymmetric.

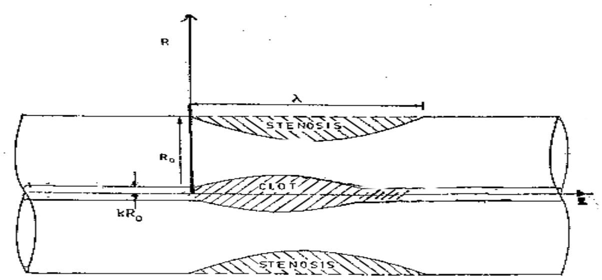

Fig. 1 The schematic diagram of the stenosed artery with a clot model inside.

The equations of motion in non dimensional form become,

$$\frac{\partial u}{\partial r} + \frac{u}{r} + \frac{\partial w}{\partial z} = 0$$

$$\alpha^2 \frac{\partial w}{\partial \tau} + R_{en}\delta\left(u\frac{\partial w}{\partial r} + w\frac{\partial w}{\partial z}\right) = -R_{en}\frac{\partial p}{\partial z} + \left(\frac{\partial^2 w}{\partial r^2} + \frac{1}{r}\frac{\partial w}{\partial r}\right) + \delta^2\frac{\partial^2 w}{\partial z^2}$$

$$\delta^2\alpha^2 \frac{\partial u}{\partial \tau} + R_{en}\delta^3\left(u\frac{\partial u}{\partial r} + w\frac{\partial u}{\partial z}\right) = -R_{en}\frac{\partial p}{\partial r} + \delta^2\left(\frac{\partial^2 u}{\partial r^2} + \frac{1}{r}\frac{\partial w}{\partial r} - \frac{u}{r^2}\right) + \delta^4\frac{\partial^2 u}{\partial z^2}$$

where R_{en} is the Reynolds Number, u and w are the velocities in the radial and axial directions respectively, p denotes the pressure, $\alpha = R_o\sqrt{(\omega/\nu)}$ is the Womersley number (ω = angular velocity and ν = kinematic viscosity) and δ is the geometric parameter. The no slip boundary conditions give $w = u = 0$ at $r = r_s(z)$ and $r_c(z)$, where $r_s(z)$ and $r_c(z)$ describe the non dimensional stenotic wall and geometry of the clot model. Also, we assume constant volume flux say, $Q = \cos(\tau)$ at every instant along the tube. Using lubrication theory, we develop a series solution in powers of δ for frequency parameter, α, either small or very large. Asymptotic analysis is done to study the flow field separated into three regions (i) region near the clot model (ii) core region and (iii) region near the stenotic wall.

RESULTS AND DISCUSSIONS

The solutions are obtained for two different geometries of stenosis. *Geometry 1*: $r_s(z) = 1-\delta_1 e^{-\pi 2(z-0.5)2}$, which is a Gaussian curve with peak (δ_1) at z = 0.5 and *Geometry 2*: A fitted curve based on data after coronary angioplasty PTCA (Back and Denton (1992)) The clot model is described by the function $r_c(z) = k+\delta_2\, e^{-\pi 2(z-zd-0.5)2}$ where δ_2 is the maximum height attained by the clot at z = zd+0.5, k is the radius of the inner tube which keeps the clot model in position and zd represents the axial displacement of the clot. The table shows the comparison of induced mean pressure gradient at the end of the stenosis, p_s, and maximum absolute value of shear stress, T_s, for different values of δ_2 for *Geometry* 1 and 2 ($\alpha = 5$, zd = 0).

Table : Comparison of mean pressure gradient, p_s and maximum absolute value of shear stress, T_s

	p_s			T_s		
Geometry	*1*		*2*	*1*		*2*
δ_2=0.2	δ_1=0	δ_1=0.16		δ_1=0	δ_1=0.16	
0.05	-0.29	-0.087	1.12	0.067	0.094	0.201
0.1	-0.51	-0.329	0.76	0.106	0.195	0.329
0.15	-0.70	-0.528	0.48	0.393	0.396	0.456
0.2	-0.85	-0.696	0.25	0.474	0.842	0.874

The streamline patterns show distinct boundary layer characteristics at both the stenotic wall and the wall of the clot when the frequency parameter is small. Results are sensitive to not only the geometries of the stenotic wall but also to the position of the clot model.

REFERENCES

1. Doffin ,J. and Chagneau, F., *J.Biomech.*, **14**, No:3,143-148,1981.
2. Back,L.H. and Denton, T.A., *Adv. Bioeng.*,**22**,337-340,1992.

MICROINDENTATION ANALYSIS OF HUMAN ENAMEL

Jun Sakai[1, 3], Makoto Sakamoto[2], Fumikazu Koda[3], Yasuo Maruyama[4], Hidemi Itoh[4], Toshiaki Hara[5]
[1]Graduate School of Science and Technology, Niigata University, Japan, jsakai@po.niigata-ct.ac.jp
[2]Depertment of Health Sciences, Niigata University School of Medicine
[3]Depertment of Mechanical Engineering, Niigata College of Technology
[4] Tohoku University Graduate School of Dentistry
[5]Depertment of Mechanical Engineering, Niigata University

INTRODUCTION

The mechanical properties of hard tooth tissues are considerable interest in the field of dental research. The hardness of dentine and enamel has been studied by a number of researchers who have used spherical (Renson and Braden, 1971), Knoop (Meredith et al., 1996) and Vickers (Ryge et al., 1961; Curry and Brear, 1990) indenters. Evans and Wilshaw (1976) have used a microindentation test to obtain the fracture toughness of ceramic materials. Hassan et al. (1981) utilized a similar technique to determine the fracture toughness of human enamel. However, this technique was difficult to detect cracks developed by the wedge-shaped corners of the Vickers' indenter. In this study, we investigated the fracture toughness and hardness of human enamel utilizing a microindentation method with a laser scanning microscopy.

MATERIALS AND METHODS

Forty-eight enamel specimens were obtained from sixteen human molars. Enamel specimens were transversely sliced into thin layers 1.0 mm thick from upper, middle and lower positions of teeth. The perpendicular direction of specimen was aligned with the tooth axis. Each specimen was polished with a buffing machine. After being polished, specimens were stored in saline. The specimens were tested on a Vickers microhardness tester (MVK-H1, Akashi, Japan), equipped with a diamond pyramid indenter, using 1.96, 2.94 and 4.9 N applied loads for 30 seconds. The surface of specimen was covered with a wet tissue between indentation. The indentation diagonal and crack size were measured with a laser scanning microscopy (OLS1100, Olympus, Japan). Vickers microhardness, H_V, is defined applied load divided by the surface area of the indentation. The fracture toughness, K_{IC}, is defined as (Lewis et al., 1981):

$$K_{IC} = \frac{1.4}{\pi^{3/2}\tan\phi} \cdot \frac{P}{c^{3/2}} \quad (1)$$

where c is length of crack developed by the wedge-shaped corners of indentation, P is applied load and ϕ is half-angle of Vickers indenter at 74 degrees.

RESULTS AND DISCUSSION

Mean values for Vickers hardness and fracture toughness of enamel with confidence intervals at the 95% level were calculated for different positions and applied loads, and are presented graphically in Figs. 1 and 2. No significant differences were observed for hardness. The fracture toughness at the middle position was higher than that at the upper position. The value of fracture toughness was found within the range of 0.8 to 1.1 $MN/m^{3/2}$. The advantages of the microindentation method lies in its ability to provide fracture toughness measurement not only on small specimens, but in localized areas as well. Further studies can be performed using this method to determine the anisotropic and inhomogeneous effects on the fracture toughness of enamel.

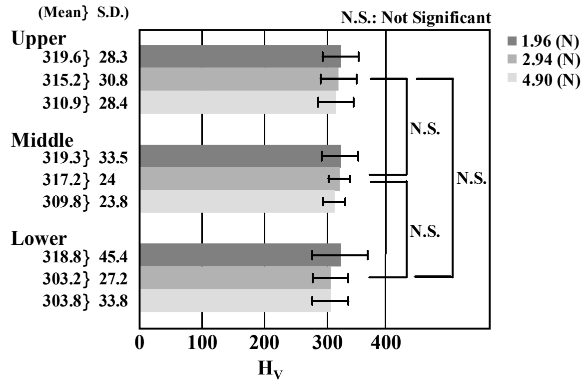

Figure 1: Vickers hardness of human enamel.

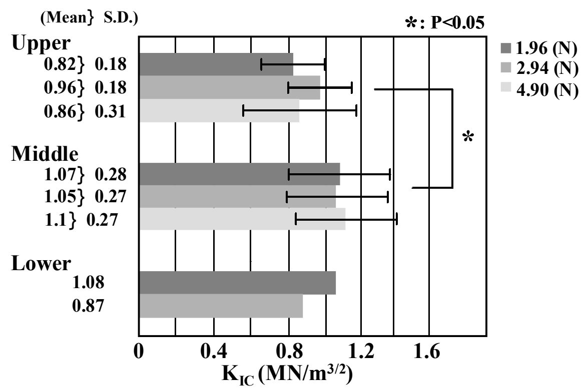

Figure 2: Fracture toughness of human enamel.

REFERENCES

Curry, J. D., Brear, K. (1990). *J. Mater. Sci. Mater. Med.*, **1**, 14-20.
Evans, A. G., Wilshaw, T. R. (1976). *Acta Metallurgica*, **24**, 939-956.
Hassan, R. et al. (1981). *J. Dent. Res.*, **60**, 820-827.
Lewis, M. H. et al. (1981). *J. Mater. Sci.*, **16**, 3437-3446.
Meredith, N. et al. (1996). *Arch. Oral Biol.*, **41**, 539-545.
Renson, C. E., Braden, M. (1971). *Arch. Oral Biol.*, **16**, 563-572.
Ryge, G. et al. (1961). *J. Dent. Res.*, **40**, 1116-1126.

STRESS DISTRIBUTION ON A LEUKOCYTE FLOWING THROUGH A NON-UNIFORM MICROVESSEL WITH AN ENDOTHELIAL SURFACE LAYER

Masako Sugihara-Seki
Faculty of Engineering, Kansai University, Suita, Osaka, Japan, sekim@kansai-u.ac.jp

INTRODUCTION

It is well known that cells in the circulation respond to stresses exerted by the blood flow in various circumstances. Recently, an important response of circulating leukocytes to fluid stresses has been reported in physiological and inflammatory states (Moazzam et al 1997; Fukuda et al 2000). In the present study, we numerically examine the fluid stresses acting on the surface of a freely floating leukocyte, in the presence of an irregularity of the vessel lumen and an endothelial surface layer (ESL). Interior surfaces of blood vessels are lined with a layer of bound or adsorbed macromolecules, named as ESL, whose physiological implications are discussed (Vink, Duling 1996; Secomb et al 1998; Pries et al 2000; Feng, Weinbaum 2000). Here, the effect of the ESL on the stresses acting on a flowing leukocyte is examined.

METHODS

We consider the motion of a leukocyte freely floating in a non-uniform microvessel with or without an ESL. For simplicity, the leukocyte is modeled as a rigid sphere, and the ESL is approximated as a porous medium with a constant Darcy permeability K_0 and a constant thickness w. The particle is suspended in an incompressible Newtonian fluid (viscosity μ) flowing through a circular cylinder whose wall has a protrusion with a sinusoidal shape into the lumen with height h, as shown in Fig. 1. In the present analysis, penetration of the particle into the ESL is not treated.

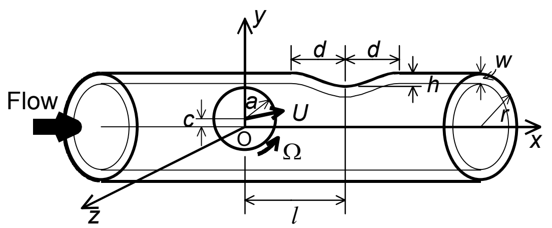

Figure 1: Configuration.

Assuming that the inertia of the fluid and the particle can be neglected, the resultant force and moment on the particle vanish at each instant, and the motion of the fluid obeys: $\nabla \cdot \boldsymbol{u} = 0$ and $-\nabla p + \mu\, \nabla^2 \boldsymbol{u} - K\boldsymbol{u} = 0$, where p and $\boldsymbol{u}$ denote the pressure and the velocity vector of the fluid, respectively, and $K = K_0$ in the ESL and $K = 0$ otherwise. These equations are solved numerically by a finite element method, under the non-slip boundary condition at the surfaces of the particle and the vessel wall.

RESULTS AND DISCUSSION

Straight uniform vessel (*h* = 0): The thickness of the ESL is estimated to range from 0.5 μm to more than 1 μm (Pries et al 2000). Estimates of K_0 showed at least $\approx 10^8\,\mathrm{dyn \cdot s / cm^4}$ for microvessels (Secomb et al 1998), indicating that flow penetrates only a short distance (approximately 0.1 μm) into the ESL. This implies smaller effective cross-sectional area of the microvessel compared to that with no ESL, so that the presence of the ESL enlarges the flow velocity (and the shear rate) at constant flow rates. Thus, a suspended particle experiences higher stresses on its surface when the ESL is present. This tendency is enhanced as the gap distance between the particle surface and the edge of the ESL is decreased.

Non-uniform vessel: Figure 2 shows examples of the computed flow velocity, the pressure contours and the distribution of the shear stress on the particle surface, in the presence of both ESL and protrusion of the vessel wall. This corresponds to the case of a leukocyte with 8μm diameter flowing through a 16μm microvessel with a protrusion of 1.6μm height and an ESL of 1μm thickness with $K_0 = 1.56 \times 10^8\ \mathrm{dyn \cdot s / cm^4}$. Compared to the cases when one or both of the ESL and the protrusion are absent, much larger variations of the shear stress and the pressure are observed on the particle surface near the gap region. When the mean flow velocity across the vessel cross-section $U_m = 1\mathrm{mm/s}$ and $\mu = 0.01\mathrm{dyn \cdot s/cm^2}$, the variation of the pressure over the particle surface is approximately 106 dyn/cm^2 and that of the shear stress is approximately 63 dyn/cm^2, in the case shown in Fig. 2. Due to the rotation of the particle, its surface always experiences these variations as it translates.

REFERENCES

Feng, J., Weinbaum, S. (2000). *J. Fluid Mech.* **422**, 281-317.
Fukuda, S. et al (2000). *Circ. Res.* **86**, e13-e18.
Moazzam, F. et al (1997). *Proc. Natl. Acad. Sci.* **94**, 5338-5434.
Pries, A.R. et al (2000). *Pflugers Arch – Eur. J. Physiol.* **440**, 653-666.
Secomb, T.W. et al (1998). *Am. J. Physiol.* **274**, H1016-1022.
Vink, H., Duling, B.R. (1996). *Circ. Res.* **79**, 571-589.

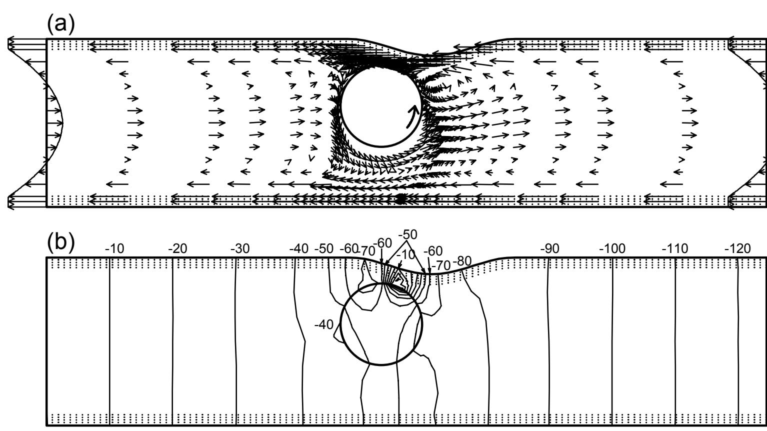

Figure 2: Velocity vectors at z=0 relative to the translational velocity of the particle in the x-direction (a), pressure contours at z=0 (numbers represent the values of $p/(\mu U_m / r)$) (b), and the distribution of the shear stress on the particle surface (c), at $a/r = 0.5$, $c/r = 0.2$, $h/r = 0.2$, $d/r = 1$, $l/r = 0.6$, $w/r = 0.125$, and $K_0 r^2/\mu = 10^4$.

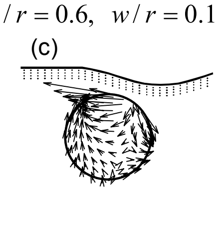

TIME-DEPENDENT STRESS-STRAIN ANALYSIS OF UNCONFINED COMPRESSED ARTICULAR CARTILAGE USING COMFOCAL LASER SCANNING MICROSCOPY

Maki Ihara [1] Teruo Murakami[2] and Yoshinori Sawae[2]
[1]Dept. of Intelligent Machinery and Systems, Graduate School of Engineering, Kyushu University, Fukuoka, Japan, maki@tribo1.mech.kyushu-u.ac.jp
[2]Dept. of Intelligent Machinery and Systems, Faculty of Engineering, Kyushu University, Fukuoka, Japan

INTRODUCTION

Articular cartilage has viscoelastic property based on high water content, and the flow behavior of water concerns the deformation of articular cartilage under compression state. In addition, its depth-dependent complicated structure causes complex stress-strain field. In this study, we investigated the structural response of time-dependent stress-strain behavior under unconfined, axial and static compression.

METHODS

Full depth rectangular blocks of articular cartilage including subchondral bone were prepared from the medial femoral condyle in knee joints of 4 -5 months porcines, and hemi-cylindrical test specimens which has a radius of 3 mm were cut from them. None of the joints exhibited any visible signs of degeneration.

For fluorescent microscopy, cells within articular cartilage are stained with the viable fluorescent probe, 5- Chloromethyl fluorescein diacetate. The direct observation of depth-dependent deformation of articular cartilage became possible by taking fluorescent stained chondrocytes as marker.

Test specimens were compressed at ramp period of 1.0 s to strains of up to 15% using a specially designed test rig whose indenter was controlled by a micrometer head. And the indentation alumina plate was impermeable. It was mounted on the stage of confocal laser scanning microscope which was used to visualize the cells within the articular cartilage. Test specimens were kept hydrated in a bath of PBS.

We took the time-dependent successive images during 120 s immediately after compression. After that, the scanning was executed at 300 s, 900 s, 1200 s.

RESULTS AND DISCUSSION

We observed time-dependent strain of articular cartilage by monitoring stained chondrocytes within articular cartilage. We confirmed viscoelastic stress relaxation under compression. Results indicated that the zone-specific changes of articular cartilage under compression predicted that the strain of the upper part in the middle layer immediately after compression may be larger than equilibrium and mechanical environment around chondrocytes in this layer changed largely than equilibrium. These processes are important to elucidate the deformation mechanism of articular cartilage in the osteoarthritis.

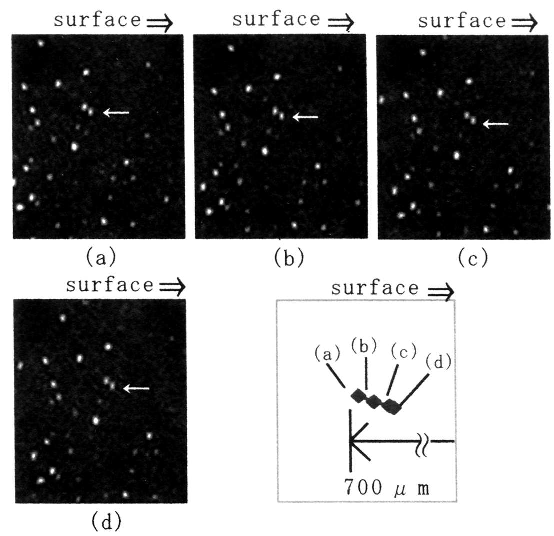

Figure 1: Time-dependent displacement of chondrocyte in cartilage at (a)5s, (b)30s, (c)120s, (d)300s after unconfined compression

SUMMARY

Articular cartilage has viscoelastic property and it is impossible to explain its mechanical environments easily. We made the special test rig to compress articular cartilage up to constant strain, and using the confocal laser scanning microscopy we could make it possible to monitor time-dependent and depth-dependent strain of articular cartilage.

REFERENCE

Robert,M.,Michael,K.,et al(1996). *Annals of Biomedical Engineering*,**24**,500-512,

STANDING BALANCE CONTROL UNDER A CONCURRENT ATTENTIONAL TASK IN CHILDREN AND ADULTS

R. J. Cherng[1*], J. T. Huang[1], I. S. Hwang[1], F. C. Su[2]
[1]Department of Physical Therapy, [2]Institute of Biomedical Engineering National Cheng Kung University, Tainan, Taiwan, R.O.C.
*Email: rjc47@mail.ncku.edu.tw

INTRODUCTION

Many studies in aging have demonstrated the mechanisms for regulating balance in standing and walking interact with high level cognitive systems and may share similar attention resources (Teasdale 1993, Shumway-Cook et al. 1997). Research on children also shows that attention is related to learning and fine motor control. Whether attention affects the children's postural and balance control is less investigated. The purpose of this study was to investigate the effect of a concurrent attentional task on the standing balance performance in children and young adults.

METHODS

Ten children (age, 9.4 ± 3.5 range 5-13 years; height, 141.2 ± 20 range 116-158.5 cm; mass, 34.8 ± 11.8 range 20.5-48.5 kg) and ten young adults (age, 20.8 ± 0.7 range 20-22 years; height, 165.7 ± 5.1 range 157-171 cm; mass, 56.7 ± 7.3 range 50.5-74 kg) participated in this study. The effect of a concurrent attentional task (tone detection) on standing balance was investigated under four sensory conditions: (1) eyes open, fixed foot support, (2) eyes close, fixed foot support, (3) eyes open, compliant foot support, and (4) eyes close, compliant foot support. The fixed foot support was the metal force plate surface and the compliant foot support was a medium-density foam (40.5-cm x 40.5-cm x 7.5-cm section) placed on top of the force plate. The tone-detection task involved playing an auditory signal (a 250 Hz pure tone) to the right or left of the subjects every two seconds. The subjects were required to press a left or a right button as soon as they heard the tone. The task varied at two levels of difficulty: easy (stimulus and response were spatially compatible, e.g., left tone left button) and hard (where stimulus and response were spatially incompatible, e.g., left tone right button). A force platform (Kistler 9284) was used to collect the ground reaction force at a sampling rate of 500 Hz for 20 s. The sway area of center of pressure was calculated and used to represent the subject's standing balance.

RESULTS AND DISCUSSION

Figure presents the subjects' standing balance under three attentional conditions (no concurrent task, low-demand task and high-demand task) and four sensory conditions. Results showed that children generally presented greater COP sway area than adults did ($F_{1, 18}$ =30.01, $p < .0001$). The effect of attentional task was also significant. Subjects showed smaller COP sway area with concurrent attentional task than without concurrent attentional task ($F_{2, 36}$=19.05, $p < .0001$). The effect of the attentional task was not different in children than in adults (($F_{2, 36}$ =1.65, n.s.).

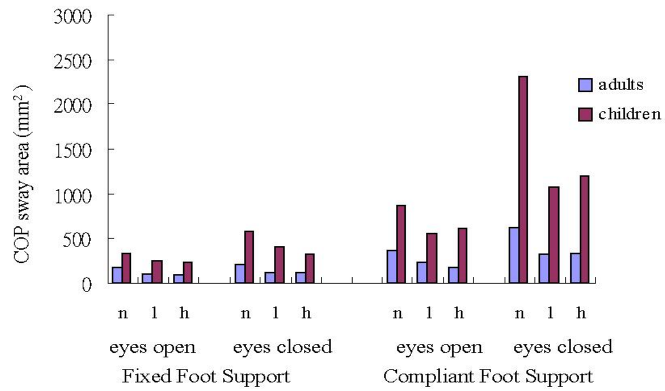

The results showed that the concurrent attentional task did not negatively affect the balance performance. Rather it improved the standing stability of both children and young adults. The effect was not different in low demand and high demand attention tasks. Although these results are not the same as those reported in the literature with elderly subjects, they are not different from the results of Vuillerme et al (2000). Vuillerme et al. showed that postural stability was better while concurrently performing a reaction time task than while maintaining balance alone condition. The discrepancy between our results and those studies based on the elderly subjects may be explained as follows. Aging caused deterioration of the peripheral system. As a result, a task (such as standing) which normally is taken to be easy and automatic by children and young adults will require attention in the elderly. This renders the elderly especially vulnerable under a divided-attention situation. By contrast, children and young adults apparently cope with the situation with a different strategy. In our study, it appeared that the effect of the concurrent attentional task was an increase of the subjects' alertness and their body stiffness, thereby an increase in their standing stability.

REFERENCES

Teasdale, N. et al (1993). *Exp Aging Res*, **19**, 1-13.
Shumway-Cook, A. et al (1997). *J. Gerontol A Biol Sci Med Sci*, **52A**, M232-240.
Vuillerme N. et al (2000). *Neuroscience Letters*, **291**, 77-80.

ACKNOWLEDGEMENTS

This study was partially supported by NSC 90-2314-B006-129 and Summer Student Fellowship of Medial College, NCKU.

NON-INVASIVE ASSESSMENT OF LEFT VENTRICLE FUNCTION WITH A COMPUTATIONAL FLUID DYNAMIC MODEL

Hidehito Iwase[1], Hao Liu[1], Shinichi Fujimoto[2], Ryutaro Himeno[1], and Tomoaki Hayasaka[1]

[1]Division of Computer and Information, The Institute of Physical and Chemical Research (RIKEN)
2-1, Hirosawa, Wako-shi, Saitama
[2]Nara Medical University, 840, Shijochou, Kashiwara-shi, Nara

INTRODUCTION

We have been developing a computational fluid dynamic modeling of left ventricle hemodynamics for a purpose of clinical application. In our previous model, velocity boundary conditions at aorta- and mitral valve in left ventricle were defined using measured physiological data with pulse Doppler method. With consideration of non-invasive assessment of left ventricle function, a multi-scale modeling of combined lumped model and detailed 3D model can be of great significance. In this study, we aim at coupling of the previous 3D model with a recently developed lumped model for cardiovascular system, in which the influence of left atrium and aorta are accounted for in terms of resistance, compliance, and inductance[(1)] (Fig. 1).

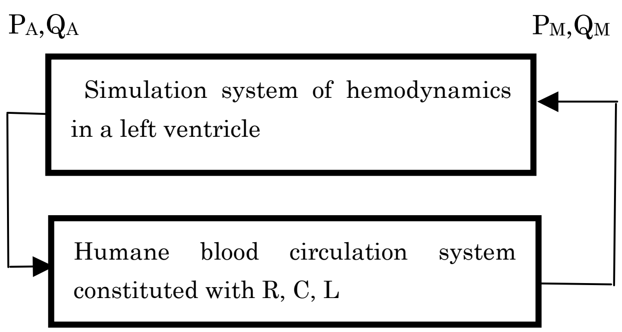

Figure 1: A multi-scale computational model for left ventricle hemodynamics.

METHODS

In the two-chamber-view modeling[(2)] method that we developed for numerical analysis of blood flow in a left ventricle, we reconstruct the anatomic model of a human left ventricle by applying two-chamber-view modeling to two phase echocardiogram images. In the unsteady solutions to the 3D incompressible Navier-Stokes equations, fluid is assumed to be homogeneous and Newtonian. The governing equations are discretized and solved in a manner of finite volume method. A 0D model for circulation system is expressed by a lumped constraint model, which is constituted with resists, compliances, and inductances. A combined computational system of the 0D and 3D models is hereby established for simulation of hemodynamics in left ventricle. The 0D model is used to provide boundary conditions for the detailed 3D model at inlet, the mitral valve and outlet, the aortic valve, in terms of pressure and flow flux. Therefore, the lumped model can provide time-varying flow boundary conditions at the mitral valve.

RESULTS AND DISCUSSIONS

Fig. 2a-d illustrates the morphological modeling of a left ventricle computer model based on ultrasonic images recorded in two mutual perpendicular cross sections, and shows flow pattern at early diastole when the mitral valve opens. Note that an asymmetric vortex ring is detected. Right after the closure of the mitral valves the vortex flow inside the left ventricle are observed and a rapid rise in pressure is also detected, which eventually results in a steep pressure gradient when approaching to the systole before the aortic valve opens.

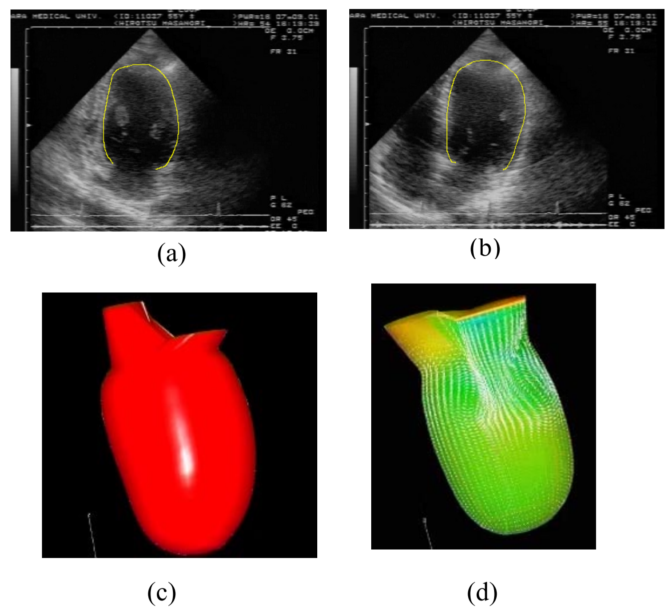

Figure 2: Morphological and CFD modeling of left ventricle

REFERENCES

(1) E.B. Shim, R. D. Kamm and K. S. Chang, *Proceedings of 2001 Bioengineering Conference ASME.*
(2) H. Iwase, H. Liu, R. Himeno, and S. Fujimoto,, *Proceedings of ASME MECE, 2001.*

ACCURACY OF PATELLOFEMORAL JOINT CONTACT AREA PREDICTIONS USING MR IMAGING

Rebecca Moss and Janet Ronsky
Department of Mechanical and Manufacturing Engineering and Human Performance Laboratory, University of Calgary, Calgary, Alberta, Canada. jlronsky@ucalgary.ca

INTRODUCTION

Abnormal joint contact mechanics are commonly speculated to be an initiating factor in cartilage degeneration. Magnetic resonance imaging (MRI) provides a non-invasive technique for evaluating cartilage contact. However, specific evaluation of the sources and magnitudes of error are limited. This study evaluates the error sources in surface reconstructions and predicted joint contact area in a loaded patellofemoral (PF) joint obtained with MRI.

METHODS

A fast spin echo pulse sequence (T2 weighting, 90° flip angle, TR = 5400 ms, TE = 80 ms, bandwidth = 15.63 kHz, 1 NEX, 140 mm FOV, 512x512 readout matrix, echo train length = 9) and an anterior neck coil were used to image five fresh porcine knees. The joint was loaded in a custom loading apparatus prior to imaging. The Non-Maxima Suppression (Devernay, 1995) semi-automated technique of edge detection was used to identify articular cartilage profiles. The Thin Plate Spline technique (Boyd et al., 1999) was used for surface reconstruction and data smoothing. PF joint contact region was determined by measuring the distance along surface normals projected from regular intervals on one (base) articular surface to its intersection with the opposing (target) surface. All points where this distance was less than a threshold value were defined to be in contact. In the absence of a gold standard, a comparative measure with staining and multi-station digital photogrammetry (MDPG) (Ronsky et al., 1999) was used to evaluate the accuracy and repeatability of the joint surface and contact modeling procedures based on MRI (Figure 1). Sensitivity of the contact area to: image digitization repeatability, surface smoothing, resampling interval, base surface and proximity threshold was analyzed.

RESULTS AND DISCUSSION

The perimeter of the contact pattern obtained from MR images is accurate within approximately 2.5 mm, as measured radially from the centroid of the stained contact area. The uncertainty in the calculated contact area is approximately 16%. Intra-user variability (based on 3 repeat trials) resulted in contact area differences of 1% or less, while inter-user digitization errors increased the differences in contact area to as much as 10%. Introduction of surface smoothing did not result in a consistent increase or decrease in contact area across the five specimens. The difference in contact area between the smoothed and original surfaces ranged from –6.1% to 6.0%. For all specimens the difference in calculated contact area resulting from changes in the smoothing factor (ranging from 0.25 to 1.45) was less than the difference between any of the smoothed surfaces and the original surface. A 0.32 mm grid size, applied to all specimen images, provided the optimal trade off between accuracy and computational time. Selection of base surface resulted in mean differences in contact area ranging from 0.2%-2.7%. The patella was the most appropriate base surface based on contact area calculations on analytical surfaces. A contact proximity threshold of 0.2 mm was determined as optimal, based on comparison with the staining technique.

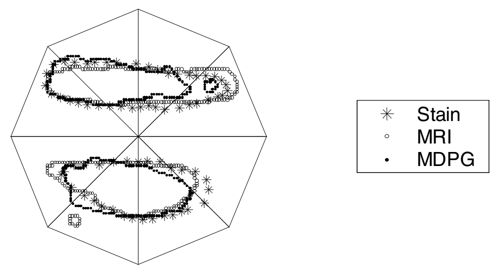

Figure 1: Comparison of contact area perimeter from staining, MRI and MDPG techniques for porcine specimen #5, using a proximity threshold of 0.2 mm. Solid lines indicate regions used for inter-technique comparisons.

SUMMARY

These study findings illuminate factors that influence the accuracy of joint contact predictions based on MR imaging in fresh joints. The largest sources of error were MR image quality, repeatability of edge detection and the sensitivity of the contact area to proximity threshold. Image digitization error is minimized with a single user, even with semi-automated edge detection algorithms. Some smoothing of the surface data is required due to MR image noise and distribution of digitized surface points. This technique is suitable for an assessment of contact area trends associated with joint motion or major injury, where changes in contact area of greater than roughly 20% are anticipated.

REFERENCES

Boyd S.K. et al. (1999). J. of Biomech. Eng., **121**, 525-532.
Devernay F. (1995). Institut National de Recherche en Informatique et en Automatique, **2724**, 1-20.
Ronsky J.L., et al. (1999). J. of Biomech. Eng., **121**, 196-205.

ACKNOWLEDGEMENTS
Financial: NSERC, AHFMR
Technical: Western Canada MRI, R. Frayne

MECHANICAL ENERGY TRANSFER BY TWO-JOINT LEG MUSCLES DURING SNATCH LIFT

Tadao Isaka[1], Boris I. Prilutsky[2], Robert J. Gregor[2], Nobuyuki Matsumoto[1] and Sadao Kawamura[1]
[1]Human Robotics Laboratory, Ritsumeikan University, Shiga, JAPAN, isaka@se.ritsumei.ac.jp
[2]Center for Human Movement Studies, Georgia Institute of Technology, Atlanta, GA, USA

INTRODUCTION

Weight lifting and especially the snatch lift is one of the most power-demanding sport events. The lifters are required to generate a great deal of muscular power and to effectively transfer this power to the barbell. Therefore, the analysis of mechanical power and energy generation and transfer in weight lifting is important for the understanding and improving the athletic performance. It has been suggested that the performance in explosive movements can be improved due to the energy transfer by two-joint muscles between adjacent joints (Bobbert, van Ingen Schenau, 1988). The purpose of this study was to analyze the mechanical energy transfer by two-joint muscles during the 'pull phase' of the snatch lift.

METHODS

Experiment: Five healthy male subjects participated in this study. One subject was a competitive weightlifter (skilled) and the other ones were American football players who had some experience in the snatch lift (unskilled). Each subject performed two to three snatch lifts of each of the three barbell weights: 50, 70 and 80% of their best current result. A high-speed video system was employed to record subject and barbell's displacement data during the snatch lift. At the same time, two force platforms were recording the ground reaction forces under each foot. Surface EMG during the snatch was sampled from the following muscles: gastrocnemius, vastus medialis, rectus femoris, semitendinosus, biceps femoris, gluteus maximus, erector spinae and rectus abdominals. The EMG signals were low-pass filtered, normalized to the peak EMG in the 80%-snatch lift, and then used to estimate muscle forces. Only the pull phase of the snatch (from the barbell lift-off to the feet lift-off) was analyzed.

Estimation of energy transfer by two-joint muscles: First, muscle forces during the snatch were calculated as a function of the activation and muscle velocity using a muscle model. Parameters of the model were optimized by minimizing the difference between the calculated joint moments and the joint moments found using inverse dynamics. Trials where no reasonable agreement between predicted and experimentally obtained total joint powers occurred were not considered. Power of individual muscles, power produced by individual muscle moments at the joints, and joint power were calculated. The amount and direction of energy transfer by two-joint muscles were determined as described earlier (Prilutsky, Zatsiorsky, 1994, Prilutsky et al, 1996).

RESULTS AND DISCUSSION

During the pull phase of the snatch lift, peaks of joint power (up to 1200 W) occurred in the second part of the pull in all subjects. During this period of the maximum power production, the direction of energy transfer by two-joint muscles in unskilled subjects was from the knee to the hip (by the hamstring, HA) and from the knee to the ankle (by the gastrocnemius). This energy transfer and the EMG results indicate the primary contribution of the one-joint knee extensors in power generation in unskilled subjects. During the same period, the skilled subject demonstrated in addition a substantial energy transfer from the hip to the knee by the rectus femoris (RF; 22% of work done at the knee; Fig. 1). This energy transfer was the consequence of the high activation of the RF in late pull. A simultaneous energy transfer from the knee to the hip by the HA and from the hip to the knee by the RF was suggested to assist extensions in both the knee and hip joints (Lombard, 1903). A further analysis is needed to fully understand the significance of the found energy transfer mechanisms for the snatch performance.

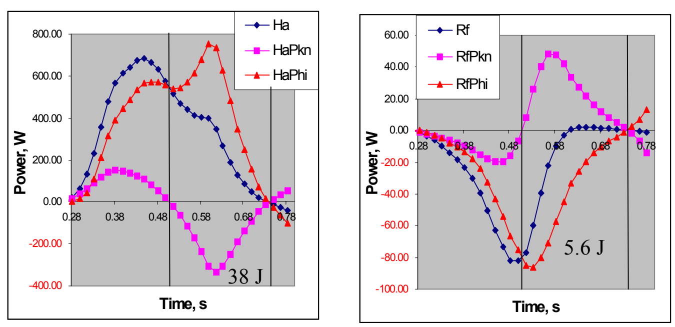

Figure 1: Power of HA and RF and power produced by moments of these muscles at the knee and hip (characters 'kn' and 'hi', respectively). Skilled subject; 83%-snatch. The two vertical lines indicate approximately the last third of the pull phase. During this period, the HA transported from the knee to the hip 38 J (26% of work at the hip); the RF transported from the hip to the knee 5.6 J (22% of work at the knee).

REFERENCES

Bobbert, M.F., van Ingen Schenau, G.J. (1988) *J.Biomech.*, **21**, 249-262
Lombard, W.P. (1903) *Am. Phys. Educ. Rev.*, **8**, 141-145.
Prilutsky, B.I., Zatsiorsky, V.M.(1994) *J. Biomech.*, **27**,25-34.
Prilutsky, B.I. et al (1996) *J. Biomech.*, **29**, 391-403.

DOES ORBICULARIS ORIS MAKE UPPER AND LOWER LIPS COMPRESS EACH OTHER?

Itaru Kourakata[1] , Tomokane Kurosawa[2], and Toshiaki Hara[2]
[1]Graduate School of Niigata University, Niigata, Japan, itaru@tmbio7.eng.niigata-u.ac.jp
[2]Department of Engineering, Niigata University, Niigata, Japan

INTRODUCTION

Because of the complexities of its anatomical layout and physiology, functional correlation between lip-closing force or movement and each individual perioral muscle is not cleared. Although some "mouth robots" have been recently presented, which generates lip configuration like human speaking typical vowels, another adopting two rubber tubes imitating upper and lower lips plays brass instruments, and so forth, it is hard to say they are well modeled on the basis of musculo-skeltal aspects. Thus in this paper authors present the experimental results comparing bilabial closing force, puckering force, and contact pressure distribution on teeth buccal surface between human and artificial lip developed.

MATEIRIAL AND METHODS

Modeling: To create the shape of dental arch and oral cavity easily acrylic pipe with 64 mm in outer diameter was used. The material was once cut and bonded with approximately 120 degree of crossing angle. For soft tissue surrounding dental arch very soft two silicon rubber sheets with a few millimeter thickness was processed and attached on to the pipe by straps. Three wires were liken to muscles considering levator anguli oris (LAO), depressor anguli oris (DAO), and buccinator (BUCC). One wire as LAO ran from its starting point of one side to modilus node fixed on rubber surface, piercing through lower lip, and led to another side. Modeling DAO was similar to LAO but upside down. BUCCs were connected to modilus nodes in both sides respectively. These three wires were pulled anteriorly by independent three pneumatic cylinders.

Measurements: A new force transducer for measuring bilabial closing force and its distribution on lip aperture was prepared, which had five measuring arms on which strain gages were attached and the thickness of one arm was only 2.6 mm, so that the closing force could be measured in natural and neutral form of lip. Contact pressure sensor using electric conductive rubber was also thin enough less than 1 mm and it was inserted between silicon rubber and pipe. Tensions of wires were changed from 0 to 36N in stepwise, however, strengths of LAO and DAO were set in same value. Lip configurations and bilabial forces obtained are shown in fig. 1. The same items by five young adult subjects were also measured. In this case subjects were ordered to close lip, pucker, pull POM meter adjusting to designated %MVC with observing output values from transducers. Simultaneously SEMG of orbicularis oris superior and inferior (OOS, OOI), LAO, DAO, and mentalis were recorded. Measured SEMG signals were analyzed to reveal strength of correlation between their amplitudes and mechanical parameter obtained by transducers. Besides zero-lag correlation coefficients between two of four signals, which were all rectified and low-pass filtered.

RESULTS AND DISCUSSION

EMG analysis showed statistically strong coordination of LAO and DAO than any other muscle combinations and linearities of these two muscles' activities to almost all mechanical parameters (two-way ANOVA with Fisher's LSD test). Further more it is very interesting that lip model without orbicularis oris that shortens lip itself demonstrated to produce bilabial closing forces. Distribution pattern of bilabial forces in the model was similar to the human subjects; however, its magnitude at the center was so much less than at distal region. Thus modeling the function of orbicularis oris will be the key to replicate human lip movement and mechanics.

REFERENCES

Gilbert, J., Ponthus, S. (1998). J. Acoust. Soc. Am., **104**, 1627-1632

Kourakata, I. et al. (2001). JSME Int. J. Ser. C, **44**, 1142-1151.

Wohlert, A. B. (1996). J. Speech Hear. Res., **39**, 761-770.

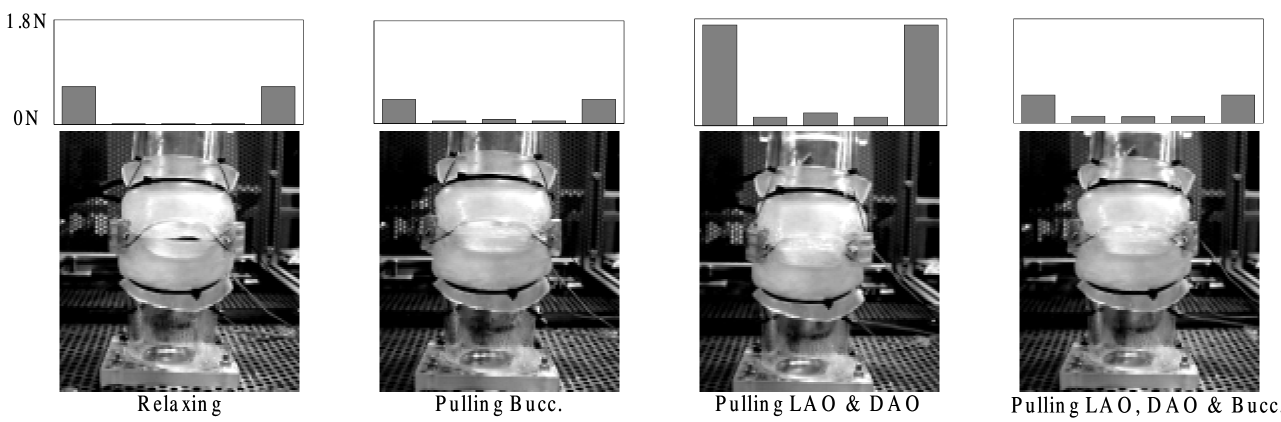

Fig. 1 Lip configuration and distribution of bilabial closing forces at some conditions of muscle tensions.

EFFECTS OF CIRCUMFERENTIAL RESIDUAL STRESS ON THE CIRCUMFERENTIAL STRESS DISTRIBUTION OF THE ARTERIAL WALL BY FINITE ELEMENT MODELING

Nooshin Haghighi Pour[1], Mohammad Tafazzoli (tafazoli@cic.aku.ac.ir), Shadpour[1], Albert Avolio[2]
[1]Department of Biomedical Engineering, AmirKabir University of Technology (Tehran Polytechnic), Tehran, Iran,
[2]School of Biomedical Engineering, The University of New South Wales, Sydney, Australia.

INTRODUCTION
Stress distribution of the arterial wall is an important factor in biomechanics of arteries. It has been suggested that excessive stress leads to arterial degeneration and lesion formation. Mechanical stress in arterial wall consists of two components, the first one is caused by external load (blood pressure) and the second is residual stress. If a ring of an artery is cut in radial direction it opens. The degree of opening is determined by the opening angle (Figure 1) which is a determinant of circumferential residual stress. This investigation aimed to study effects of circumferential residual stress on the total circumferential stress distribution with the differing mechanical parameters.

METHODS
Finite element modeling was used to evaluate circumferential residual stress in a typical model of cross section of human aorta. The modeling was performed through introduction of different opening angles to models. Then an internal pressure equivalent to a typical mean arterial pressure (100 mm Hg) was applied and stress results were obtained. The residual stress values were compared to the stress caused by blood pressure. The models consisted of lamellar structures with lamellar and interlamellar layers with different values of Young's modulus of elasticities of two types of layers ($E_1$and E_2). The appropriate boundary conditions were introduced to the model to allow radial expansion. The average number of elements were 3000 (depending on the θ value), with 8 node quadratic 2D element and plane strain conditions.

RESULTS AND COCLUSION
Circumferential residual stress along arterial thickness consists of two components. A compressive component with a maximum value on intima side and a tensile component with a maximum value on adventitia side. When an artery is exposed to blood pressure a tensile stress profile will be resulted with a maximum value on the luminal side and a minimum value on the adventitia side. Then the effect of compressive residual stress on luminal side is to compensate part of maximum tensile stress, and therefore decreases severity of tension on endothelial lining.

Results show that residual stress values are influenced by structural and mechanical parameters. An increase in θ results in an increase in residual stress values (Figure 2). The maximum compressive residual stress compensates 17.3% of maximum tensile stress for θ=50°, and 32.6% for θ=90°. The stiffening of arterial wall resulted in an increase of residual stress. Results showed that for all models the circumferential residual stress profile is nonlinear and the neutral location (zero stress) is dependent on mechanical parameters, but approximately is close to the middle of wall thickness on luminal side.

It was concluded that arterial circumferential residual stress plays an important role in stress analysis of arterial wall. The amount of residual stress is a function of mechanical and structural parameters. Depending on the situation, the circumferential residual stress can compensate part of maximum tensile stress on endothelial lining. The evaluation of arterial residual stress is recommended for different arteries, ages, and geometrical locations, such as bifurcations and curvatures. Also it can be applied in pathological situations such as presence of atherosclerotic

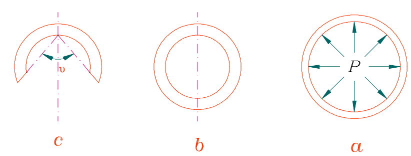

Figure1: A schematic view of cross section of arterial wall, a: pressurized, b: without pressure and with residual stress, and c: without residual stress showing an opening angle.

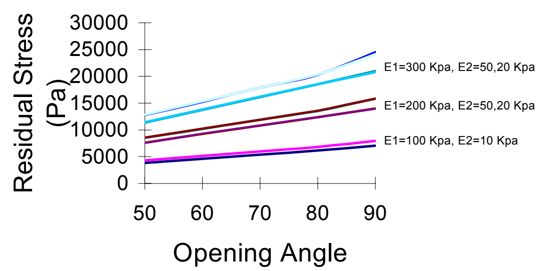

Figure 2: The increase of circumferential residual stress with the increase of θ for different E_2 and E_1 values.

REFERENCES
Tafazzoli-Shadpour M., Analysis of Mechanical Stress in Arteries With Change in Wall Structure Properties. PhD thesis, UNSW, 1999.

Delfino A, Stergiopulos N, Moore J.E, Jr and Meister J.J, Residual Strain Effects on the Stress Field in a Thick Wall Finite Element Model of the Human Carotid Bifurcation. Journal of Biomechanics 30,8,777-786,1997.

THE EFFECT OF CHANGING ANTEVERSION ON FORCES ON THE PROXIMAL FEMUR

Mark Thompson[1], Ian McCarthy[1], Gunnar Flivik[1], Louise Mattsson[2], Leif Ryd[3], Lars Lidgren[1]
1. Department of Orthopaedics, Lund University Hospital, Lund, Sweden
2. Scandinavian Orthopaedic Laboratory, Lund University Hospital, Lund, Sweden
3. Department of Orthopaedics, Linköping University Hospital, Linköping, Sweden
corresponding author: mark.thompson@ort.lu.se

INTRODUCTION

Recent investigation of the one-year post-op. migration of the femoral component of Total Hip Replacement (THR) using Radio Stereometric Analysis (RSA) demonstrated increased migration into retroversion at one year with lower post-op. anteversion as measured by CT scan (Hermann, 2000). Early migration of the femoral stem into retroversion is reported to be predictive of early failure (Alfaro-Adrian *et al.* 1999).

Heller *et al.* (2001) reported an increase of up to 28% in Hip Joint Reaction (HJR) force by increasing anteversion up to 30° in patient-based musculo-skeletal models. They did not report the effect upon the moment about the prosthesis long axis, which is important for the stability of the implant.

This study investigated the effects of changing anteversion on the moment acting around a femoral prosthesis stem.

METHODS AND MODELS

A Vicon gait analysis system with five cameras was used to capture the gait kinematics of a subject with anteversion of 18°. These data were then used as input for a standard scaled musculoskeletal model with an implied anteversion of 18°. Data collection and modelling were based upon Davis *et al.* (1991) and muscle force distribution on Crowninshield (1978).

Changes in the anteversion of the model were simulated by two methods. The first accommodated the change by a rotation of the entire lower limb distal to the femoral neck, as in Heller *et al.* The second method maintained the attitude of the lower limb while changing the rotation of the femoral neck. The anteversion angles were chosen to vary from –5° to +30.

A simplified sensitivity study was performed, calculating the HJR moment about the prosthesis stem and muscle moments about the hip joint with changing anteversion. Force data for maximum stem torsion during stair climbing, muscle attachments and femoral neck orientation were obtained from HIP98 (Bergmann, 2001). An anteversion of 18° was used.

RESULTS AND DISCUSSION

The HJR moment about the stem was -1.5 %BWm, tending to decrease anteversion. This decreased to -2.2 %BWm at -5° anteversion and increased to -1.0 %BWm at +30°. The largest transverse plane muscle moments about the joint centre were due to the abductors (-1.1 % BWm), vastus lateralis (-1.1 % BWm) and vastus medialis (-0.6 % BWm). The moments with the largest changes using method 1 are reported in Table 1.

Table 1: Transverse muscle moment changes with anteversion of -5° and +30°. itb is iliotibial band, tfl is tensor fasciae latae.

	abductor	proximal itb	proximal tfl
-5°	+76%	-35%	+14%
+30°	-41%	+15%	-10%

Method 2 predicts slightly larger changes, opposite in sign to those predicted by method 1.

The increased rotational migration of a prosthesis may be explained simplistically by the change in moment arm of the HJR. However the changes in muscle moments show that the anteversion will have a large effect upon the system of forces acting on the proximal femur. Further, this effect depends upon how the change in angle is accommodated, a question which has yet to be addressed.

Of necessity the effect of changing anteversion from an average or "normal" value was investigated. Representing the clinical situation of correction of abnormal anteversion would be complicated by the variation of other morphological parameters related to the anteversion.

SUMMARY

Reducing the anteversion angle increases the magnitude of the peak moment of the HJR, tending to decrease anteversion, about a femoral stem. Assumptions about the accommodation of the change of angle determine the muscle moment changes.

REFERENCES

Alfaro-Adrian, J. *et al.* (1999). *Int. Orthop.,* **23**, 140-144.
Bergmann, G. (2001). *HIP98.* Free University, Berlin.
Crowninshield, R.D. (1978). *J. Biomech. Eng.* **100**, 88-92.
Davis, R.B. *et al.* (1991). *Hum. Mov. Sci.,* **10**, 575-587.
Heller, M.O. *et al.* (2001). *Clin. Biomech.,* **16**, 644-649.
Herman, K.L. (2000). PhD Thesis. Radiology Dept., Rigshospitalet, Copenhagen University.

ACKNOWLEDGEMENTS

This research was supported by a Marie Curie Fellowship (to MT) of the European Community programme Improving Human Research Potential under contract number HPMF-CT-2000-01033. Disclaimer: the European Commission is not responsible for any views or results expressed. Support from the Medical Faculty, Lund University and the Swedish Medical Research Council (Project 9509) is gratefully acknowledged.

OPTIMAL FIXATION SITES OF THE MEDIAL SUPPORTING STRUCTURE OF THE PATELLOFEMORAL JOINT

Mitsumasa Matsuda[1], Takuzo Iwatsubo[1], Shozo Kawamura[1], Takehiro Isomichi[1]
Shinichi Yoshiya[2], Kiyonori Mizuno[2], Masahiro Kurosaka[2] and Hirotsugu Muratsu[3]

Kobe University, Kobe, Japan
[1]Dept. Mechanical Engineering, matsuda@mech.kobe-u.ac.jp
[2]Dept. Orthopedic Surgery
[3]Orthopedic Surgery, Kakogawa Hospital

INTRODUCTION

The medial supporting structure of the patellofemoral joint (MSS) is ligament complex that restrains lateral patellar displacement. Injury to the MSS ligament complex has been described as the result of a blow to the lateral aspect of the knee in flexion or extension motion. When MSS ligament complex deficiency is present with patellofemoral instability, reconstruction of MSS is required. Graft insertion site is one of the important factors that affect the results of reconstruction of MSS ligament complex. Theoretical reconstructive procedure to restore the function of the MSS ligament complex has not been established. The purpose of this study was to locate and describe the possible ligament insertion sites for surgical reconstruction of MSS ligament complex that satisfied normal motion of intact cadaver knee.

METHODS

The three dimensional geometry of the articular surface of the femur, tibia and patella were constructed from successive cross sectional plane CT images in normal knee from fresh cadaver. The three dimensional position and angular orientation of the knee during active knee flexion and extension were recorded with magnetic position sensor (3SPACEFASTRAK, Polhemus, U.S.A.). The motions of patella were recorded and compared while knee was flexed and extended under conditions of MSS ligament complex retained and MSS ligament complex dissected, respectively.

RESULTS AND DISCUSSION

From these data, MSS ligament complex restrained lateral patellar displacement near full extension position, but had little effect for knee flexion (Fig.1). Computer search technique was adopted to determine the length of graft route that traced through articular surface. The distance between femoral and patellar ligament insertion sites were calculated as a function of the knee flexion angle. All the ligament insertion sites, where the graft became tight near full extension and non-tensioned during knee flexion of the intact knee motion, were determined.
The optimum graft insertion sites were determined. The distance of graft route was calculated from clinically popular medial apex on the patella to any location on the femur. The proximal to the medial femoral condyle was obtained for the femoral graft insertion site (Fig. 2). This site nearly coincided with the femoral attachment site of medial patellofemoral ligament (MPFL), which worked as primary stabilizer against lateral patellar displacement.

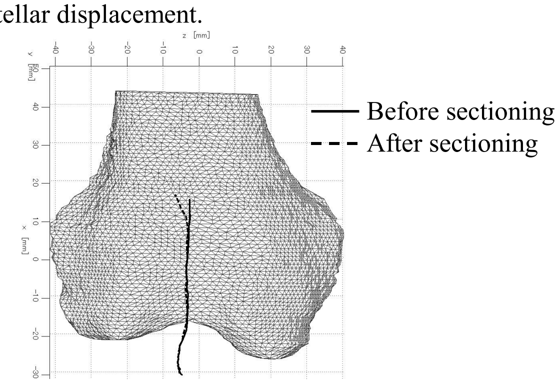

Fig.1 Patellar motion in simulated active knee extension before and after sectioning the medial supporting structure

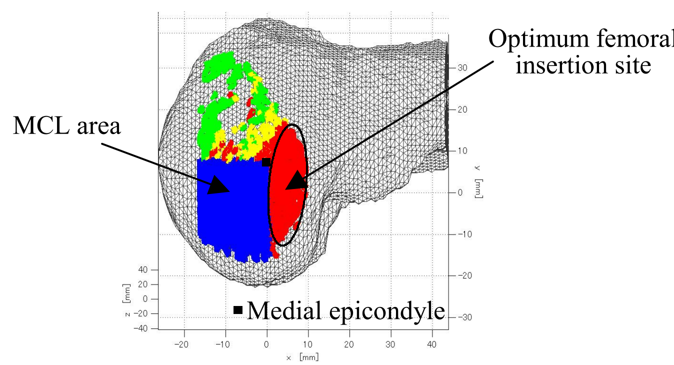

Fig.2 Femoral insertion site

SUMMARY

Optimum femoral ligament insertion site of the graft was found to be located proximaly to the medial femoral condyle and the optimum patellar ligament insertion site was located at the central medial surface of patella.

REFERENCES

Colan, T. et al (1993). J Bone Joint Surg 75A : 682-693.
Hautmaa, P.V. et al (1998) Clin Orthop 349 : 174-182.
Avikainenn, V.J. et al (1993). Clin Orthop 297 : 12-16.

COMPARISON OF MUSCLE SYNERGIES BETWEEN GENDERS USING AN INNOVATED PERTURBATION SYSTEM

Chen-Yu Lo[1,2], Saiwei Yang[1], Jia-Rong Yang,[1]
[1]Institute of Biomedical Engineering, National Yang Ming University, Taipei, Taiwan, swyang@bme.ym.edu.tw
[2]School of Physical Therapy, China Medical College, Taichung, Taiwan

INTRODUCTION

Postural perturbations are often used to investigate human balance and postural control. The Clinical Test for Sensory Interaction in Balance is one of the method which has been proposed for clinically assessment of the influence of sensory interaction on postural stability in the stance .The purpose of this study was to develop a new dynamic balance assessment system with multi-direction perturbations and to study the muscle synergy difference between genders and dynamic balance mechanism after sudden perturbation.

METHODS

A new designed perturbation-balance system consisted of three modulus, center of gravity (COG) measuring system, motor driven system, and pneumatic inflation system. The COG measurement system consisted of 60cm x 60cm square platform with a load cell at each corner and having it's bottom freely attached to a ball and socket base. The motion of the platform was controlled by a motor driven system with two main linkages driven by two servomotors. The platform could be rotated in anterior-posterior (AP), medial-lateral (ML), and circumgyration (CC).
Six-female and six-male healthy young subjects with average ages of 23.8 old were participated. Each subject performed anterior-posterior (AP), medial-lateral (ML), and counter-clockwise (CC) perturbations at the frequency of 0.3Hz and 0.6Hz with eyes closed and opened. Each trail had two perturbed amplitudes 5 and 10 degrees. The total experiment consisted of 22 trails. Ten channels EMG (MA300, Motion Lab. Inc, USA) were attached on the major flexor and extensor of lower extremities. The loci of center of foot pressures were recorded by insole type pressure sensors (Fscan, Tekscan, USA). Maximum displacement in X-Y directions, loci of COG, and balance score, plantar pressure, and muscle synergies corresponding to the perturbation orientation were analysed.

RESULTS AND DISCUSSSION

The results showed that the balance score of female subjects was significantly higher than male subjects, 17 out of 22 trails had significantly differences (Fig. 1). The rest items were also comparable but there was no difference between male and female at 0.6Hz, ML, 5/10 degrees. The perturbation phase and foot pressure change showed that subjects had a better motor synergy at 0.3Hz for non-precaution perturbations, but at 0.6Hz had the better synergy once got used to the perturbation sequence. The EMG data revealed that the erector spinae was acting at all perturbation tests. In the anterior perturbation, gastrocnemius and biceps femoris of both legs were acting (Fig 2), while in the posterior perturbation, tibialis anterior and rectus femoris of both legs were firing. At the counter clockwise rotation, right gastrocnemius, left gastrocnemius, right tibialis anterior, left tibialis anterior were acting in order. Besides, the EMG signals of lower extremity and foot pressure were significantly related to the motions of AP/0.6Hz / 5 degrees, ML/0.6Hz /5 degrees and CC/0.3Hz/5 degrees.

SUMMERY

Female in general shows better synergy ability than male
The lower extremity muscles were alternative firing in sequence according to the direction of perturbations.

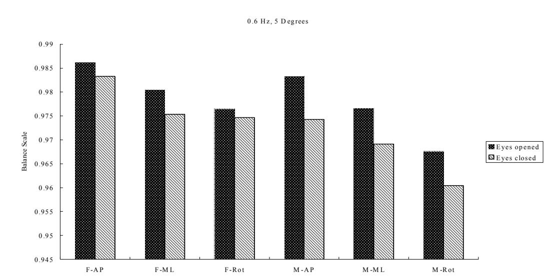

Table 1: The balance scores of female and male in different types of perturbations

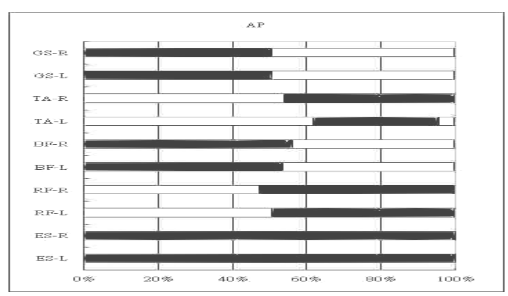

Figure 1: The muscle synergies in different orientation

REFERENCES

Maki, B.E. (1986). *Med Bilo. Eng. &Comp*, **24**, 561-568.
Shumway-Cook, A., Woollacott, M.H. (1995). *Motor Control: Theory and Practical Applications*.Wiliams & Wikins

ACKONOLOGEMENT

This study was supported by NSC, Taiwan (89-2614-B010-004-M47)

KINEMATIC AND KINETIC ANALYSIS OF WHEELIE ACTIVITY

Po-Chou Lin[1], Jyh-Jong Chang[1,2], Chien-Chih Chen[1,2], Fong-Chin Su[1]
[1]Institute of Biomedical Engineering, National Cheng Kung University, Tainan, TAIWAN
[2]School of Rehabilitation Medicine, Kaohsiung Medical University, Kaohsiung, TAIWAN

INTRODUCTION

A wheelie is executed when the user pops the front casters off the ground and balances on the rear wheels, and it is useful in many situations, just as climbing a curb, turning in confined spaces, or negotiating uneven terrain. To maintain the balance, the position of the center of mass (COM) must be within the base of support (BOS). In the case of wheelie performing, the performer keeps the COM in the small BOS with integrating hand and trunk strategies. McInnes et al. reported that vision played an important role in the maintenance of a stationary wheelie. Kirby et al. found the new wheelie aid provided stability and wheelie-like function with maneuverability. Bonaparte et al. suggested wheelie performers appear to use a proactive balance strategy in maintaining a stationary wheelie. However, how the hand push and pull and trunk movements play their roles in maintaining the stability of wheelie performing is not clear. Therefore, the purpose of this study was to investigate the hand push force and center of pressure of the user-wheelchair system in wheelie activity

METHODS

Ten normal subjects (age 20.6±1.5 years, weight 64.7±6.3kg, height 171.3±5.2cm) participated this study. They had learned this skill for about one month before test. A six-camera Expert Vision™ video-tracking system (Motion Analysis Corp, CA, USA) was used to collect the three-dimensional trajectory data of the markers placed on the wheelchair. A standard type manual wheelchair with an instrumented wheel consists of a six-component load cell was used to collect the forces and moments applied on the hand-rim by users. Two force plates were used to collect the ground reaction forces of the wheelchair. Subjects were requested to keep both wheels of the wheelchair on two force plates, respectively, during tests. Every subject was asked to perform 5 trials from level to wheelie up for 10 seconds.

RESULTS AND DISCUSSION

When performing wheelie, subjects had to strike backward slightly for preparing to push forward. The first forward striking was used to pop the front casts off ground, so this pushing would result in the maximum tangent force (Ft), axial moment (Ma), and pitch (tilt) angle (Ap). The maximum Ap was occurred after the maximum Ft and Ma. Then, the second back ward striking was applied to pull the trunk back for balance. Forward tilting moment caused by back ward striking was used to react the backward tilting moment caused by body weight and first backward tilting moment to prevent back falling. Therefore, second backward striking played an important role in performing wheelie. In the stable balance, the magnitudes of Ft and Ma on the pushrim were small. Instead, the trunk movement was used for balance control. The Ap was 23.7±0.6 degrees, and it was greater than previous study,13.6 ± 2.3 degrees, by Bonaparte (2001). The difference of wheelchair COM and sitting position would affect Ap. The maximum forward displacement of center of pressure during wheelie activity was only 5.4±6.3cm in order to keep the wheelchair on the force plate. In stable state, the displacement of center of pressure was very small. The total normal force (Fn) of force plates was decreased during first backward pushing because body forward tilting made a forward moment of wheel axle. After that, the Fn was increased during first forward pushing and reached to the maximum value when attaining to the maximum Fn and Ma.

Table 1. Push force of the hand and pitch angle in wheelie activity

	Ft (N)	Ma (N-m)	Ap (deg)
1st Backward^{Max}	72.2±9.7	35.9±6.1	
1st Forward^{Max}	125.4±7.5	71.7±4.2	29.2±1.8
2nd Backward^{Max}	63.4±7.5	36.7±4.8	23.6±0.9
Balance	3.0±9.0	0.01±5.2	23.7±0.6

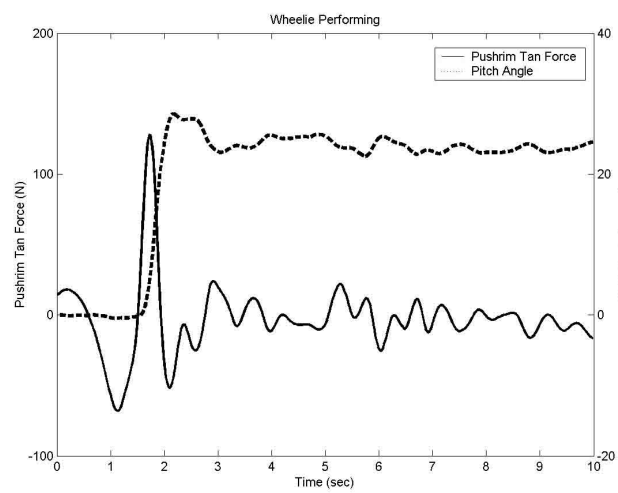

Figure 1. Tangential pushrim force and pitch angle of the wheelchair in performing wheelie.

CONCLUSION

Subjects needed a backward pulling to easily perform wheelie. The body backward tilting reacted with the first forward pushing which brings the maximum pitch angle. In stable state, the Ft and Ma were small because of good trunk control. Results of this study would help the wheelchair user in learning the wheelie skill.

REFERENCES

Bonaparte JP et al. (2001). Arch Phys Med Rehabil, **82**, 475-9
Kirby RL, et al. (2001). Arch Phys Med Rehabil, **82**, 380-90.
McInnes et al. (2000). Arch Phys Med Rehabil, **81**, 1081-4.

ACKNOWLEDGMENT

Support from the National Health Research Institutes grant NHRI-EX90-9019EL, TAIWAN, ROC.

EVALUATIONS OF HIP FRACTURE MECHANISM AND PREVENTION BY USING DYNAMIC FE ANALYSES

Eiichi Tanaka[1], Sota Yamamoto[1], Shigenobu Ozeki[1], Kenji Ishiguro[1], Atsushi Harada[2], Masashi Mizuno[2]
[1]Department of Mechano-Informatics & Systems, Nagoya University, Furo-cho, Chikusa-ku, Nagoya, Japan
tanaka@mech.nagoya-u.ac.jp
[2]Chubu National Hospital, Gengo, Morioka-cho, Obu, Japan

INTRODUCTION

Hip fracture is frequently observed among the elderly. It is mainly caused by fall and impairs the ability of the patient to stand and walk. Because of the increase in the population of elderly age, this fracture is one of the most serious clinical problems in the field of orthopedics.

Hence we evaluate the effects of dynamic loading and shock absorption by padding on hip fracture using finite element analyses. Firstly, we evaluated the stress distribution in femur neck during fall. Then we discussed the effects of soft tissue of thigh and material properties of hip protector on the prevention of hip fracture.

METHODS

A finite element model of thigh for dynamic analysis with body segments was constructed by modifying our previous model. The morphology of the femur model was determined based on the data from cadaveric femur of 8 Japanese elderly females. The mechanical properties of femur were identified on the basis of bone density referring to Snyder and Schneider, Peacock et al. and Lotz et al. Hip pads of a hard and a soft type were also modeled. Falls on concrete ground were simulated. The impact velocity was taken from van den Kroonenberg et al. The Analyses were performed by LS-DYNA Version 950 (Livermore Software Technology).

RESULTS AND DISCUSSION

Simulation results showed that stress concentrations were observed in the basicervical region in every case. An example of

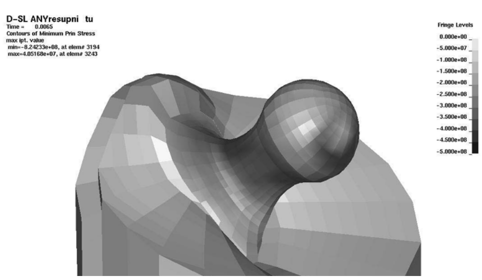

Figure 1: Minimum principal stress distribution in femur neck (on concrete ground with a hard hip pad)

the minimum principal stress distribution in the femur neck is shown in Fig. 1. Against concrete ground, the fracture risk in this region was reduced by soft tissue and hip pad but there was no difference between the protection effects of two materials of hip pad as shown in Fig. 2.

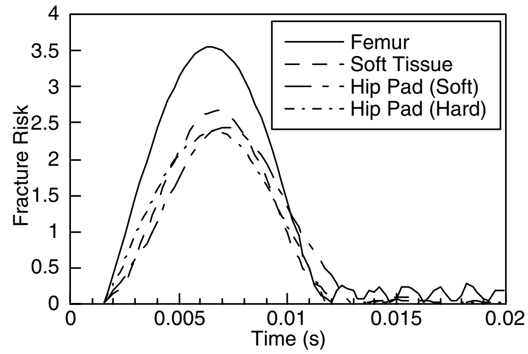

Figure 2: Time variations of minimum principal stress in basicervical region of femur neck (against concrete ground)

SUMMARY

The effects of soft tissue and hip pads on the prevention of hip fracture were evaluated by using dynamic finite element analyses. The results showed that the fracture risk in the basicervical region was reduced by soft tissue and hip pad but there was no difference between the protection effects of two materials of hip pad. The optimal design and material of hip pad for fracture prevention will be discussed in detail in the next step.

REFERENCES

Tanaka, E., et al. (2001). *Proceedings of IMMM2001*, 275-282.
Snyder, S. M., Schneider, E. (1991). *J. Orthopaedic Res.*, **9**, pp. 422-431.
Peacock, M. et al. (1998). *Osteoporosis Int.*, **8**, 231-239.
Lotz, J. C. et al. (1991). *J. Biomech. Engin.*, **113**, 353-360.
Van den Kroonenberg, A. J. et al. (1996). *J. Biomechanics*, **29**, 807-811.

ACKNOWLEDGEMENTS

This study is supported by a Grant-in-Aid for Scientific Research (B) from JSPS (No. 13450044) and Health Sciences Research Grants (Comprehensive Research on Aging and Health, No. H11-Choju-016) from MOHLW/Japan.

PREDICTORS TO DISCRIMINATE REACH MOVEMENT IN CEREBRAL PALSY

Jyh-Jong Chang[1,3], Tong-I Wu[1], Jer-Hao Chang[1,2], and Fong-Chin Su[1]
[1]Institute of Biomedical Engineering, [2]Department of Occupational Therapy,
National Cheng Kung University, Tainan, Taiwan
[3]School of Rehabilitation Medicine, Kaohsiung Medical University, Kaohsiung, Taiwan

INTRODUCTION

Reach and grasp movements involve basic and important motor control in the independence of daily living activities. Learning skills and control of electronic aids to daily living are also affected by the control ability in reach movement for children with cerebral palsy (CP). However, few kinematic studies were involved in reach movement for children with CP. This study used a kinematic model to assess the quantity and quality of reach movement in children with CP compared with normal control, and to establish a predictive model for the discrimination of reach movement.

METHODS

Twenty-eight subjects, 14 normal children (Mean Age (SD) = 11.41(2.57)) and 14 children with CP (Mean Age (SD) = 9.88(2.75)), were assigned to control and experimental groups. Each subject was positioned in a restrictive seat and in front of a height-adjustable table to normalize his/her relative posture and asked to reach a button (1.6 cm in diameter, located at a sternal level and arm-length away from the subject) with his/her dominant hand in a self-natural pace method. Retroreflective spherical markers were placed on the fingertip, wrist joint, lateral epicondyle of the elbow, and acromion process. The trajectories of the reaching movements were collected using a 6-camera motion analysis system. The movement duration (MD), time to maximum velocity (TMV), time to maximum acceleration (TMA), and normalized jerk score (NJS) were computed for comparison. Descriptive statistics, GLM multivariate procedure and discriminative analysis were utilized to examine the data.

RESULTS AND DISCUSSION

The results show children with CP group had prolonged MD, delayed TMV and TMA, and higher NJS in the index tip movement than the control group (Table 1). In the velocity profiles, children with CP showed increased rate during the acceleration phase and demonstrated multiple drops (oscillations) during the deceleration phase when compared with the normal control (Figure 1). Feedback control is important for children with CP in reach movement. Discriminative analysis revealed NJS and TMA could discriminate the reach movement between normal children and children with CP with 89.3 % total correction rate (Table 2). Two diplegias and one left hemiplegia with nearly normal dominant hand function were misclassified to the normal group and all the normal controls were correctly classified. These results showed NJS and TMA were sensitive to changes in reach movement and useful in the assessment of control in reach movement.

SUMMARY

This study suggests that NJS and TMA are good predictors to discriminate reach movement between normal and children with CP. These predictors are also useful indexes to present the treatment effect and quality of control in reach movement.

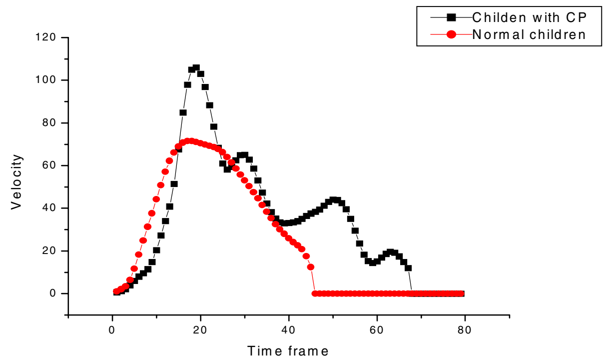

Fig. 1. Typical reach movement velocity profiles between normal and CP children.

Table 1. Group differences between CP and control on temporal-distance variable

Para-meters	Mean (SD) Normal	CP	F-value	Effect Size
MD	0.69(0.14)	0.97(0.35)	11.13	0.31
TMA	0.10(0.03)	0.21(0.10)	14.96	0.37
TMV	0.27(0.05)	0.36(0.12)	4.86	0.16
NJS	40.25(17.1)	170.31(133.5)	21.80	0.47

Table 2. Summary table for model including NJS and TMA (N=28)

	Diagnosis	Predicted Group Membership Normal	CP	Total
N	Normal	14	0	14
	CP	3	11	14
%	Normal	100.0	0.0	100.0
	CP	21.4	78.6	100.0

89.3% of original grouped cases corrected classified.

ACKNOWLEDGMENT

Support from the National Science Council grant NSC 90-2213-E-006-029, TAIWAN, ROC.

REFERENCES

Alberts, J.L., et al (2000). Disruptions in the reach-to-grasp actions of Parkinson's patients. Exp Brain Res, **134**, 353-62.
Smeets, J.B., Brenner E. (1999). Grip formation as an emergent property. Response To commentaries on "A new view on grasping". Motor Control, **3**, 316-25.

COMPUTATIONAL HEMODYNAMICS AND ITS APPLICATION TO SURGERIES FOR TWO CONGENITAL HEART DISEASES

Tony W. H. Sheu[1] and S. F. Tsai[1]
[1]Scientific Computing and Cardiovascular Simulation Laboratory, National Taiwan University
73, Chou-Shan Rd., Taipei, Taiwan 106, R. O. C., sheu@sccs.na.ntu.edu.tw

INTRODUCTION

Numerical investigation into the total cavopulmonary connection (TCPC) blood flow and arterial switch operations (ASO) were conducted by solving the three-dimensional Navier-Stokes equations. We consider the total cavopulmonary connection (TCPC) operation, which is specifically used to treat hearts with essentially a single ventricular chamber. The operation ends with construction of a right atria lateral tunnel that connects the IVC to the transected end of the SVC, which is anastomosed to the right and main pulmonary arteries. Transposition of the great arteries (TGA) is a congenital heart disease. The abnormality is that the aorta arises from the right ventricle and the pulmonary artery from the left ventricle. A septal defect, another congenital abnormality of heart development in the fetus, permits abnormal blood circulation from the left (high pressure) side of the heart to the right (low pressure) side. This may result in excessive blood flow through the lungs and can cause pulmonary hypertension and heart failure.

METHOD

The blood under investigation is a Newtonian fluid, which is treated as being homogeneous and incompressible. Based on the above assumptions, the working equations for non-pulsatile flow simulation of the vascular system, Ω, are made dimensionless as follows:

$$\frac{\partial u_i}{\partial x_i} = 0 \,, \tag{1}$$

$$\frac{\partial}{\partial x_m}(u_m\, u_i) = -\frac{\partial p}{\partial x_i} + \frac{1}{\mathrm{Re}}\frac{\partial^2 u_i}{\partial x_m\, \partial x_m} \,. \tag{2}$$

RESULTS AND DISCUSSION

Throughout this TCPC study, we presented for three cases with different offset values. The offset is defined as the distance between the centers of two caval anastomoses. In view of the importance of wall shear stress, we show its distribution on the entire vessel wall. It is seen that the wall shear stresses are smaller in magnitude on the outer wall of the bifurcated pulmonary arteries. This zone is clinically very risky since it is susceptible to atherosclerotic lesions.

To provide theoretical evidence that the SRGA (Spiral relationship of the normally related Great Arteries) arterial switch operation outperforms that of the Lecompte procedure, we evaluate the pressure on the vessel surface and compute the wall shear stress from the computed velocities. It is found that SRGA surgery has lower pressure and higher shear stresses, compared with those obtained from the Lecompte operation. Evidence is also provided in verifying that the SRGA manoeuvre is less susceptible to stenosis. We also show that SRGA is the operation of choice for the ASO from the point of view of energy. Assessment of two anatomies is done by computing the total energy loss coefficient and the hydraulic dissipated power index.

SUMMARY

In this study, the three-dimensional Navier-Stokes equations for incompressible blood flow have been solved in order to numerically assess two ASO and TCPC surgeries. From the hemodynamic point of view, the ASO surgery with the spiral manoeuvre outperforms the Lecompte operation based either on the shear stress distribution or the pressure distribution. Our three-dimensional calculations reveal that regions with low shear stresses are located at the nondivider walls of bifurcation. Particle tracers reveal that the blood flow is featured by spiraling motion. Through this study, we could depict a clear flow structure. The complexity of the flow field results from the axial velocity shifting towards the inner walls and the rapidly developing secondary flow. To accurately indicate where blood flow separates and then reattaches, we have applied the theoretically rigorous topology theory to find critical lines based on the computed limiting streamlines.

REFERENCES

Dubini, G. et al (1996), A numerical fluid mechanical study of repaired congenital heart defects application to the total cavopulmonary connection, *J. Biomechanics*, **29**, 111-121.
De Leval et al (1988), Total cavopulmonary connection: a logical alternative to atriopulmonary connection for complex Fontan operation, *J. Thorac. Cardiovasc Surg.*, **96**, 682-695.
Chiu, I. S. et al (2000), Modified arterial switch operation by spiral reconstruction of the great arteries in transposition, *Ann. Thorac. Surg.*, **69**, 1887-1892.

AORTIC LEAK SEVERITY DETERMINES ARTERIAL ELASTANCE AND HEART-ARTERIAL COUPLING IN AORTIC REGURGITATION

Patrick Segers[1], Philippe Morimont[2], Philippe Kolh[2], Nikos Stergiopulos[3], Nico Westerhof[4] and Pascal Verdonck[1]
[1]Hydraulics Laboratory, Institute Biomedical Technology, Ghent University, Belgium; [2]Hémoliège, Centre Hospitalier Universitaire, University of Liège, Belgium; [3]Biomedical Engineering Laboratory, EPFL, Lausanne, Switzerland; [4]Laboratory for Physiology, ICaR-VU, Vrije Universiteit Amsterdam, The Netherlands

INTRODUCTION

Effective arterial elastance (E_a; mmHg/ml), introduced as a measure of the arterial load on the heart, is approximated by the ratio of left ventricular end-systolic pressure and stroke volume, and combines steady and pulsatile load components. E_a can be combined with E_{max} (mmHg/ml; the slope of the left ventricular end-systolic pressure-volume relation) to form the heart-arterial coupling parameter E_a/E_{max}. The E_a/E_{max} parameter is extensively used in studies considering mechanico-energetic aspects of heart-arterial coupling. In aortic valve regurgitation (AR), the normal heart-arterial interaction is disturbed by the leaking aortic valve with the severity of the aortic leak being an important modulator of cardiovascular hemodynamics. Although E_a and E_{max} can still be calculated from measured pressure-volume (P-V) loops, the pattern of these P-V loops is in part determined by the aortic regurgitation itself, and aortic leak severity should therefore interfere with the E_a/E_{max} concept. The aim of this study is to assess (i) how E_a relates to arterial properties and leak severity, and (ii) the validity of E_a/E_{max} as a heart-arterial coupling parameter in AR.

METHODS, RESULTS AND DISCUSSION

The study is based on human data obtained from a study on vascular adaptation in chronic AR (Devlin et al., 1999) . These data allowed us to assess the parameters of a computer model of heart-arterial interaction (Segers et al., 2000). In particular, total peripheral resistance (R; in mmHg/(ml/s)) and aortic leak severity - expressed as leak resistance ($R_{L,ao}$; in mmHg/(ml/s)) - were quantified for different patient subgroups (Table 1)

Table 1: Computer model parameters assessed for 3 patient groups (Devlin et al., 1999)

	group I	group IIa	group IIb
E_{max}	2.15	0.62	0.47
E_a	1.24	0.66	0.90
R	1.90	0.60	0.85
$R_{L,ao}$	0.35	0.05	0.20

A parameter study demonstrated that $R_{L,ao}$ was the main determinant of E_a (Figure 1). With all other parameters constant, valve repair would increase E_a to 2.81, 1.08 and 1.54 mmHg/ml in groups I, IIa and IIb, respectively.

It has been shown theoretically that for a given preload and inotropic state of the left ventricle (LV), stroke work (SW) is determined by E_a/E_{max} and maximal when E_a/E_{max} = 1. This relation was derived under the assumption that SW can be approximated by the product of stroke volume and end-systolic pressure which, obviously, is an assumption violated in AR. We found no straightforward relation between E_a/E_{max} and SW, not even after normalization of the data, and SW is not maximal for E_a/E_{max} = 1.

For a given E_a/E_{max}, LV pump efficiency (estimated as the ratio of SW and LV systolic pressure-volume area) was lower than the theoretical predicted value, except for the simulations with intact aortic valve.

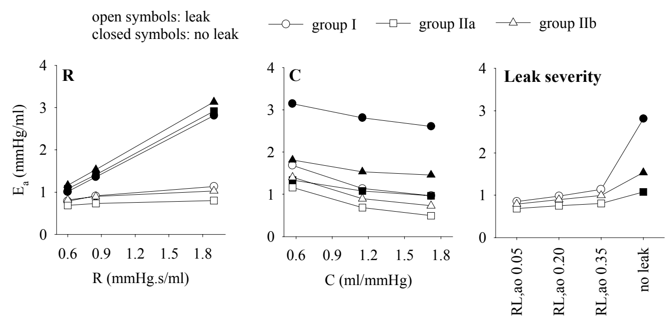

Figure 1: Contribution of total peripheral resistance (R), total arterial compliance (C) and leak severity to arterial elastance in conditions of AR, and for identical cardiac and arterial conditions, but with an intact aortic valve (closed symbols).

SUMMARY

In summary, we have shown that in AR, effective arterial elastance (E_a) is determined not only by arterial mechanical properties, but mainly by the severity of the aortic leak. In these conditions, it seems more appropriate to characterize the arterial system by specific system properties (total peripheral resistance, arterial compliance, valve leakage) rather than by a global parameter such as E_a. Furthermore, in AR, the assumptions leading to the conceptual heart-arterial coupling framework linking E_a/E_{max} to mechanico-energetic parameters, are violated. As such, the use of E_a/E_{max} as a coupling parameter in general or as a mechanico-energetic regulatory parameter in particular, is questionable in these conditions.

REFERENCES

Devlin, W.H. et al. (1999). *Circulation*, **99**:1027-1033
Segers, P et al. (2000). *Hypertension,* **36**:760-765.

ACKNOWLEDGEMENTS

P. Segers is funded by a post-doctoral grant of the Fund for Scientific Research - Flanders, Belgium (FWO-Vlaanderen).

INDIVIDUAL STRESS ANALYSIS OF THE HUMAN MANDIBLE UNDER BITING CONDITIONS

Norio INOU[1], Michihiko KOSEKI[1] and Koutarou MAKI[2]

[1] Graduate School of Science and Engineering, Tokyo Institute of Technology, Tokyo, Japan, inou@mech.titech.ac.jp
[2] Department of Orthodontics, Showa University, Tokyo, Japan

INTRODUCTION

The purpose of this study is to examine biomechanical characteristics of the human mandible in occlusion. The mandibular body has a complicated shape and receives various masticatory forces under biting conditions. To obtain the exact mandibular model, an automated modeling method based on CT images was developed. Stress analyses were performed under bilateral and unilateral bitings. This research proposes a synthesized method to evaluate mechanical rationality of the bone using these computational results.

METHODS

The modeling method is composed of four processes. The first provides a voxel space of a bone from the CT images. The second distributes nodal points in the space. The third generates tetrahedral elements with the nodal points by use of Delaunay triangulation. The fourth finishes accurately the model by removing excessive elements.

For stress analysis in the biting condition, we consider four kinds of masticatory muscles. The masticatory forces were assumed to be proportional to sectional area of muscles. The muscular directions were determined from the reconstructed 3D image of the mandible.

The boundary conditions were set as follows. Condyles can turn in any direction like a pivot. One side of condyle can also move along the X-axis. The moments around the X-axis produced by reaction forces and muscular forces should adjust the balance as following equations.

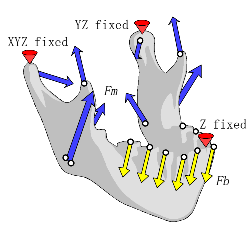

$$\Sigma\, Rm_i \times Fm_i + \Sigma\, Rb_i \times Fb_i = 0$$

$$\Sigma\, Fm_i + \Sigma\, Fb_i + \Sigma\, Fr_i = 0$$

Figure 1: Boundary conditions

RESULTS AND DISCUSSION

Stress analyses were performed under bilateral and unilateral biting conditions. Reaction forces at the teeth in the bilateral biting conditions were measured by a pressure sheet. Reaction forces under the unilateral biting conditions were given to half side of the dental arch so that the total value of the reaction forces is nearly equal. Stress analyses were performed by CAEFEM (Concurrent Analysis Co.).

The analytical results were synthesized by choosing the highest value among the stresses for each nodal point. The obtained stressed map covers the wide area of the mandible. This suggests the mechanical rationality of mandible.

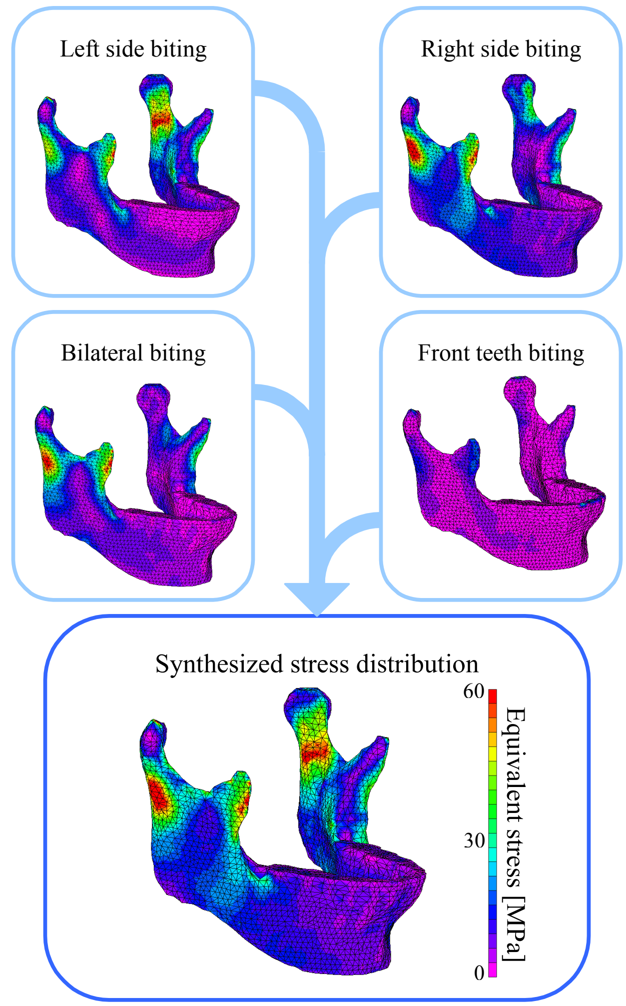

Figure 2: Calculated Stress distributions under several biting conditions and stressed map synthesized with these results

CONCLUSION

An individual simulation method of the human mandible based on X-ray CT data was proposed. An evaluation method to synthesize analytical results under multi-loading conditions was also proposed. The computational results showed that the mandible could be explained from biomechanical viewpoints. The proposed method will be applicable to other bones.

Ca^{2+} RESPONSES AND ITS PROPAGATION IN CULTURED ENDOTHELIAL CELLS TO CYTOSOLIC MECHANICAL STIMULATION BY LASER TWEEZERS

Noriyuki Kataoka[1,3], Ken Hashimoto, Seiichi Mochizuki, Yasuo Ogasawara[1],
Katsuhiko Tsujioka[2] and Fumihiko Kajiya[1,3]

[1] Department of Medical Engineering and [2] Department of Physiology, Kawasaki Medical School, Okayama, Japan, [3] Department of Cardiovascular Physiology, Okayama University Graduate School of Medicine and Dentistry, Okayama, Japan,
kataoka@me.kawasaki-m.ac.jp

INTRODUCTION

We have hypothesized that the cytoplasmic micro-mechanical strain and its associated cytoskeletal structures are playing major roles in mechano-sensing mechanism of endothelial cells. To test this hypothesis, the cytosolic Ca^{2+} responses of endothelial cells to the mechanical stimulus by laser tweezers without direct contact, were investigated.

METHODS

Bovine aortic endothelial cells (ECs) were cultured on a glass bottom cell culture dish until confluent. ECs were loaded with Fura red (40μM) and Fluo-4 (20μM) for 30min. The laser beam (1064nm, SIGMA KOKI, Japan) was focused on the nucleus of a single EC. The nucleus was moved slightly without any contact, and the fluorescent images were taken every 1 sec with a real time confocal laser microscope (CSU-10;YOKOGAWA, Japan). The stored images on a computer (PowerMac G4, Apple Computer, USA) were decomposed in the RGB format and the changes of the cytosolic Ca^{2+} of ECs were estimated with the ratio images of the Fluo-4 image (Green) to the Fura red images (Red) (Budel S. et al. 2001).

RESULTS AND DISCUSSION

After the laser beam focus was moved, the cytosolic Ca^{2+} gradually increased in the EC (Fig.1(A)). In contrast, in EC which were irradiated by the laser beam without any movement of the laser beam focus, the cytosolic Ca^{2+} did not increase (Fig.1(B)). The Ca^{2+} wave was propagated from the stimulated EC to the surrounding ECs non-uniformly (Fig.2). The Ca^{2+} wave propagation time between ECs in the visual field was within 10-20 sec, indicating cell-to-cell electrical coupling. Thus, the micro-strain induced by the micro-movement of the nucleus can be a trigger of the cytosolic Ca^{2+} increase and bring about the Ca^{2+} wave propagation.

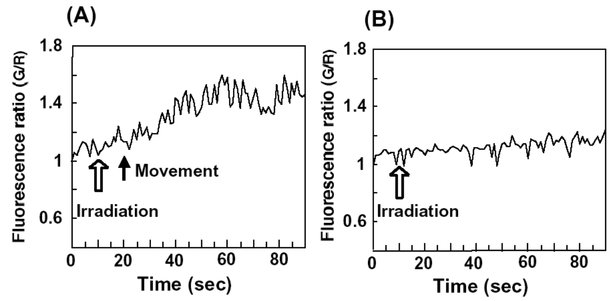

Figure 1: Typical traces of the change of the cytosolic Ca^{2+} in EC stimulated by a laser tweezers. (A) with the laser beam movement and (b) without the laser beam movement.

SUMMARY

When the nucleus of one EC was slightly moved by laser tweezers, the cytosolic Ca^{2+} increased immediately in the same EC and the Ca^{2+} wave was propagated from the stimulated EC to the surrounding ECs non-uniformly. The micro-strain induced by the micro-movement of the nucleus can be a trigger of the cytosolic Ca^{2+} increase and the Ca^{2+} wave propagate probably by an electrical communication.

REFERENCES

Budel S. et al. (1998). *Am. J. Phyiol.,* **281**, H1156-62.

ACKNOWLEDGEMENTS

The authors would like to thank Prof. Jean-Louis Benny at University of Geneva and Prof. Jean-Jacques Meister at Swiss Federal Institute of Technology for helpful discussion with them.

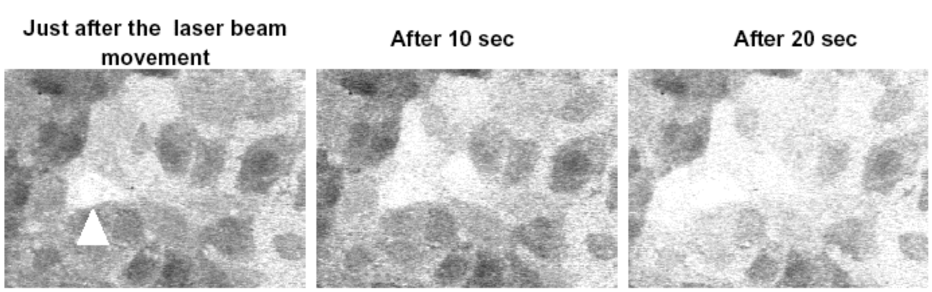

Figure 2: Cytosolic Ca^{2+} wave propagation from the stimulated endothelial cell by a laser tweezers.

COMPARATIVE STUDY BETWEEN INTRA- AND POST-OPERATIVE KNEE MOTIONS AFTER TOTAL KNEE ARTHROPLASTY

Katsutoshi Nishino[1], Yoshio Koga[1], Kazuhiro Terajima[2], Go Omori[3], Shin Hirasawa[4] and Toyohiko Hayashi[4]
[1]Department of Orthopaedic Surgery, Niigata Kobari Hospital, Niigata, Japan, nishi@jkl.bc.niigata-u.ac.jp
[2]Department of Physical Therapy, Niigata University of Health and Welfare, Niigata, Japan
[3]Department of Orthopaedic Surgery, Faculty of Medicine, Niigata University, Niigata, Japan
[4]Department of Biocybernetics, Faculty of Engineering, Niigata University, Niigata, Japan

INTRODUCTION

We have developed a real-time monitoring system of the femorotibial joint motion during total knee arthroplasty (TKA)[1]. Nine knee motions in eight patients have been measured intraoperatively. The motion data was evaluated as movement of contact point between the femorotibial articular surfaces (Figure 1). Consequently, two different types were observed with respect to anteroposterior translation of the contact point: (a) roll-back pattern and (b) paradoxical pattern relative to the tibial surface during knee flexion[1)]. In order to validate the significance of these patterns, post-operative knee motion was measured, and then intra- and post-operative knee motions were compared.

MATERIALS AND METHODS

Post-operative knee motion was measured using a six degree-of-freedom electro goniometer set on the lateral side of thigh and shank[2)]. Radiographic marker was mounted on each end of the goniometer. By bi-planar radiography, three-dimensional position of the marker was detected. Three-dimensional position of the TKA component on the radiographic image was estimated by using the matching technique[3)] between the projective image of the component and its three-dimensional computer model. From these position data, positional relationship between the marker and the component was estimated. By combining the positional relation data with the motion data obtained from the goniometer, the motion of the femoral component relative to the tibial one was obtained. The motion data was expressed the movement of the contact point. Seven knees in six patients after TKA, who measured the motion intraoperatively (movement pattern (a) in five knees and pattern (b) in two knees), were studied at six months after TKA. As total knee system, three different types were used: (1) Genesis I cruciate retaining (CR) type; (2) Genesis II CR type and (3) Genesis II posterior stabilized (PS) type (Smith & Nephew, Richards, USA). Knee motion was measured with and without body-weight bearings. In order to evaluate the laxity of the knee, the hyperextension angle was evaluated from the sagittal radiographic image.

RESULTS AND DISCUSSION

Average hyperextension angle was 2.6 degrees in pattern (a) and 6.1 degrees in pattern (b). At maximum extension angle, the contact point in pattern (b) was located posteriorly by comparison with one in pattern (a). Difference between the post-operative knee motion in pattern (a) and one in pattern (b) was observed with regard to amount of anteroposeterior translation of the contact point with and without body-weight bearings. Difference between the knee motion in CR type and one in PS type wasn't detected. These seemed to be related to difference of the joint tightness. Therefore, the intraoperative knee-motion monitoring system was verified to be potentially acceptable to predict the post-operative knee motion.

REFERENCES

1) Hayashi, T., Nishino, K., et al. (1998). *44th Annual Meeting Orthopaedic Research Society*, 704.
2) Terajima, K., Terashima, S., et al. (1994). *Clinical Biomechanics and Related Research*, 383-391.
3) Fukuoka, Y., Hoshino, A., et al. (1999). *IEEE Transactions on Rehabilitation Engineering*, **7**(2), 228-233.

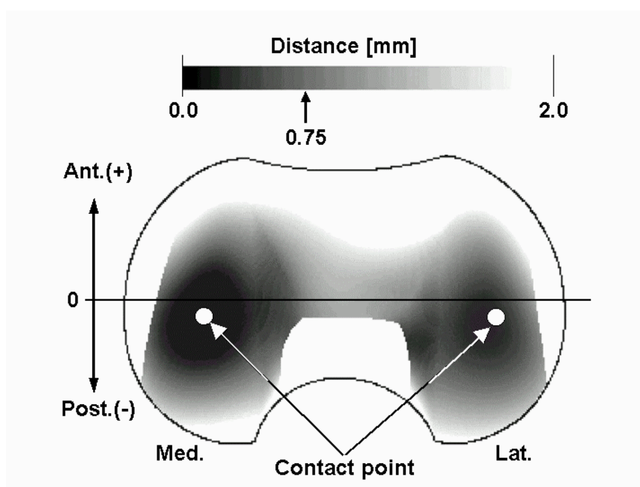

Figure 1: Visualization of the distance between TKA components and the contact points on the tibial surface.

THE EFFECT OF A SHEAR FLOW ON THE UPTAKE OF LDL BY AN EC-SMC BILALER IN CULTURE

Takeshi Karino[1], Tatsunori Kado and Koichi Niwa
Research Institute for Electronic Science, Hokkaido University, Sapporo, Japan
karino@bfd.es.hokudai.ac.jp

INTRODUCTION

It is suspected that wall shear stress plays an important role in the pathogenesis and localization of atherosclerosis in the human arterial system. Thus the effects of a shear flow on the transport of low density lipoprotein (LDL), known to be an atherogenic substance, from flowing blood to an arterial wall has been studied by many investigators by using a monolayer of cultured vascular endothelial cells, and measuring the effects of wall shear stress on the uptake of LDL and its analogues by the endothelial cell (EC). However, it is questionable whether a monolayer of ECs can be used as a model of an arterial wall where ECs are forming only the inner surface of a thick wall consisting of the internal elastic lamina and layers of smooth muscle cells (SMC), fibroblasts, and various matrix fibers. Therefore we prepared EC-SMC bilayers which we considered a model closer to an arterial wall by seeding ECs directly over the SMCs and co-culturing them, and tested whether the EC-SMC bilayers behave in the same manner as monolayers of ECs in the uptake of LDL and microspheres.

MATERIALS AND METHODS

Bovine aortic SMCs were seeded on the inner surface of a 35-mm diameter Falcon culture dish at a cell density of 5×10^4 cells/cm^2 and cultured for 5 days in an Iscove's modified Dulbecco's medium (IMDM: Sigma Chemicals) containing fetal calf serum at 20% by volume, 100 U/ml penicillin, 100 μg/ml streptomycin, and 50 μg/ml ascorbic acid in a 95% air and 5% CO_2 humidified atmosphere at 37°C. Then bovine aortic ECs were seeded directly over the SMCs at a cell density of 5×10^4 cells/cm^2 and they were co-cultured for 5 days until the ECs became confluent and completely cover the SMCs, forming an EC-SMC bilayer.

The effects of a shear flow on the uptake of macromolecules were studied using three different substances, that is, DiI-LDL (Biomed. Tec., Stoughton, MA) as a model of LDL, DiI-Ac-LDL (Biomed. Tec.) as a model of oxidized LDL, and fluorescent polystyrene latex microsphere (FluoSheres: Molecular Probes, Eugene, OR) whose diameter was approximately the same as that of LDL (20 nm).

The effects of a shear flow on the uptake of these substances were tested as follows. A 35-mm diameter culture dish in which an EC-SMC bilayer was prepared was filled with 2 ml of IMDM containing fetal calf serum at 20% and either DiI-LDL (4.0 μg/ml) or microspheres (1.35×10^{14} particles/ ml) or DiI-Ac-LDL (4.0 μg/ml). The culture dish was then set to a 32-mm diameter rotating-disk shearing apparatus keeping a distance of 0.5 mm between the EC- SMC bilayer and the disk, and exposed the ECs to a mean wall shear stress of 0 and 10 dynes/cm^2 for 2 hours at 37°C in a cell culture incubator in a 95% air and 5% CO_2 humidified atmosphere.

After finishing the flow experiment, the EC-SMC bilayer was rinsed with a phosphate buffer solution (PBS) and then removed from the dish by using 2 ml of PBS containing a surfactant (0.2% Triton-X100). The ECs and SMCs dispersed in the PBS were lysed by the addition of collagenase (Sigma Chemicals, St. Louis, MO) at a final concentration of 0.1% and incubating the solution for 15 minutes at 37°C. The amount of the LDL, microsphere, and Ac-LDL taken up by the EC-SMC bilayer was assessed by measuring the fluorescence intensity of the solution using a spectrofluorometer (FP-750, Jasco, Japan) and converting it to the concentration of the substance. The results were compared with those obtained with a monolayer of ECs prepared from the same stock of cells as those used to prepare the EC-SMC bilayer.

RESULTS AND DISCUSSION

The uptake of LDL and microspheres by an EC-SMC bilayer was much greater than that by a monolayer of ECs. A shear flow which imposed a mean wall shear stress of 10 dynes/cm^2 to the ECs augmented the uptake of both LDL and microspheres by a monolayer of ECs but not by an EC-SMC bilayer. The uptake of Ac-LDL was almost the same by both a monolayer of ECs and an EC-SMC bilayer, indicating that it was taken up only by ECs forming the luminal surface of the EC-SMC bilayer. However, as shown in Figure 1, in both the cases, the uptake of Ac-LDL was significantly reduced by the imposition of a shear flow, suggesting that the mechanism of the uptake of Ac-LDL by ECs is very different from that of LDL.

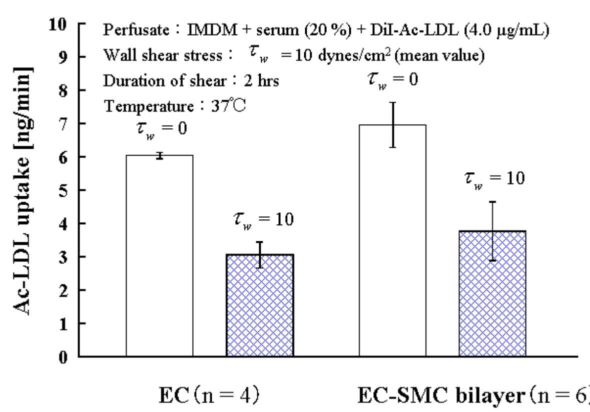

Figure 1: Effects of a shear flow on the uptake of Ac-LDL.

MECHANICAL PROPERTIES AND PERMEABILTY OF POLYELECTROLYTE MICROCAPSULES (PEMC)

Hans Bäumler[1], R. Mitlöhner[1], M. Hin[1], G. Artmann[2], R. Georgieva[1], S. Moya[3], H. Kiesewetter[1]
[1]Institute of Transfusion Medicine, Humboldt University of Berlin, D-10098 Berlin, Germany
[2]Dept. of Applied Biophysics, TFH Aachen, D-52428 Jülich, Germany
[3] Max Planck Institute of Colloids and Interfaces, D-14424 Potsdam-Golm, Germany

INTRODUCTION

Microcapsules in the 100nm to 10µm size range are of both scientific and technological interest, since they have potential applications as nano- and micro-containers. Liposomes represent a well-known example of spherical closed thin films, which in addition to their numerous applications as model biological membranes, have already been employed as drug delivery systems in pharmaceutics and cosmetics [Lasic 1993]. Their limited stability and low permeability for polar molecules, however, imposes serious limitations for general use. Microcapsules fabricated from polyelectrolytes offer advantages in that they are permeable to small polar molecules and are extremely stable against chemical and physical influences [Caruso et al. 1998, Klitzing and Möhwald 1995, Bäumler et al. 2000]. Both types of closed films are, however, limited by their spherical shape, which precludes producing capsules with anisotropic properties. Biological cells possess a wide variety of shapes and sizes, and thus using them as templates allows producing capsules with a wide range of morphologies [Neu et al. 2001].

METHODS

Polyelectrolyte microcapsules (PEMC) were prepared on decomposable/dissolvable biological templates like red blood cells. The PEMC were prepared by consecutive multiple adsorption of the polyanion poly(styrene sulfonate) [PSS], dextransulfate and human serum albumin and the polycation poly(allylamine hydrochloride) [PAH] as well as chitosan/chitosansulfate onto glutardialdehyde treated red blood cells as template, which was decomposed after completing the coating by a hypochlorate solution.

Deformability properties of PEMC were studied by means of micropipette technique and confocal laser scanning imaging. The morphological and permeability properties of the PEMC were characterised by atomic force microscopy, confocal laser scanning microscopy, transmission electron microscopy, and electrophoretic mobility.

RESULTS AND DISCUSSION

The diameter of the PEMC increased in dependence on the composition of the polyelectrolyte shell by up to 2/3 of the original size. Due to the elastic behaviour of the shell the PEMC recovers to the original shape and size.

The wall thickness as well as the bending modulus (BM) of the PEMC was depended on the number of layers and the used polyelectrolytes. The thickness was in the range between 7 and 28 nm and the BM was between $3.5\cdot10^{-15}$ and $1.8\cdot10^{-14}$, 4 to 5 magnitudes larger than the BE of red blood cells [Evans 1973]. If lipids were added to the polyelectrolyte layers the capsules cannot be visibly deformed by micropipette suction up to 10^4 N/m^2.

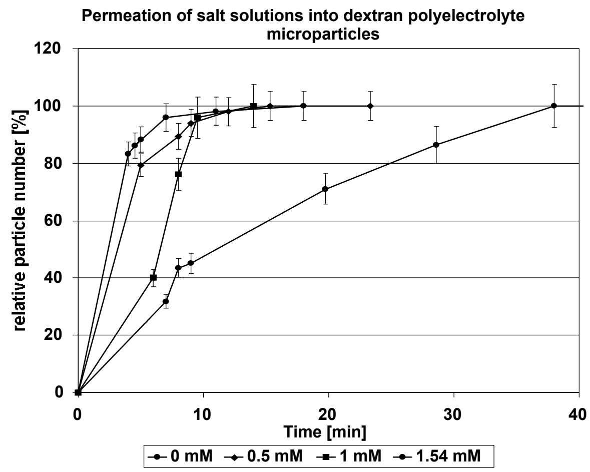

The PEMC are permeable for salt ions and charged macromolecules. The permeability depends on the salt concentration, the used polyelectrolytes and the number of layers.

SUMMARY

PEMC are a new type of microparticles, permeable to small polar molecules and are extremely stable against chemical and physical influences. They show elastic behaviour and the bending modulus depends on the number of polyelectrolyte layer as well as on the kind of polyelectrolyte. The permeability of the PEMC can be varied in the M_w range of a few Dalton up to some kDa.

ACKNOWLEDGEMENT

This work was supported by grant 01K0-31P2813 of the Federal Ministry of Research and Technology of Germany.

REFERENCES

Bäumler et al. 2000, J. Microencapsulation, 17:651-655
Caruso et al. 1998, J.Phys. Chemistry B, 102:2011-2016
Evans, E. 1983, Biophys J. 43:27-30
Klitzing and Möhwald 1995, Langmuir, 11:3554-4559
Lasic 1993, Liposomes: From Physics to Applications, Amstdam, Elsevier
Neu et al. 2001, J. Microencapsulation, 18:385-395

FINITE ELEMENT ANALYSIS OF CARDIAC FUNCTION IN HYPERTENSIVE HEART DISEASE

Masakazu Tsutsumi, Akiyoshi Shiomi, Tadashi Inaba, Yutaka Sawaki and Masataka Tokuda
Department of Mechanical Engineering, Mie University, Tsu 514-8507, Japan, tsutsumi@bio.mach.mie-u.ac.jp

INTRODUCTION

In order to estimate quantitatively the mechanical functions of the left ventricle, the authors have constructed a fundamental numerical simulation system based on a finite element ventricle model connected with both an electric stimulus transmission model and a blood circulation system model. In this research work, the biomechanical cardiac functions supposed the heart with hypertensive heart disease (HHD) are analyzed by using the proposed numerical simulation system.

MATHEMATICAL MODEL OF LEFT VENTRICLE AND FINITE ELEMENT SIMULATION

The mathematical models of the left ventricle are composed of the mechanical model of the myocardial fiber, the electric stimulus transmission model and the blood circulation system model. As the circulation system model, a simplified electric circuit analogy model (see figure 1) is employed in the present numerical simulation. The installation of the fiber orientation into the finite element model is realized by transforming the standard element in the local coordinate system to the real element in the global coordinate system. The 3-dimensional geometry of the left ventricle is here assumed to be a prorate spheroid for simplicity. The isoparametric parallelepiped finite elements (198 elements in total) are arranged along the ventricular wall. The mechanical properties of the myocardial fiber and the other various material constants are not determined for a specific individual, but chosen on the basis of studies up to the present as well as the experience and knowledge of medical doctors.

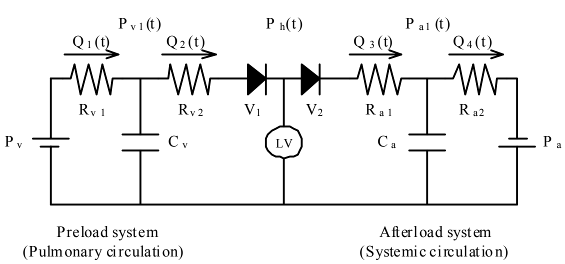

Figure 1: Schematic representation of blood circulation system model.

RESULTS AND DISCUSSIONS

In the present study, the analysis of the cardiac functions supposed the heart with HHD was performed with the following process.

(1) By decreasing the aortic compliance (Ca in afterload system shown in figure 1), the cardiac functions in the elevated blood pressure conditions were estimated.

(2) In the elevated blood pressure condition, by increasing the initial (end diastole) wall thickness, the cardiac functions in the hypertensive hypertrophic conditions were estimated.

Figure 2 show time courses of circumferential strain during systole and stroke volumes in a cardiac cycle for several Ca values. From figure 2, it is recognized that both of the circumferential strain and the stroke volume decrease together with a decrease of the Ca value, that is, an increase of the blood pressure. Figure 3 show time courses of circumferential strain and stroke volumes for several wall thicknesses. From figure 3, it is confirmed that both of them increase together with an increase of the wall thickness. From these simulated results, it is considered that the an amount of contraction of the myocardium decreases when the heart becomes the elevated blood pressure condition. It is also considered that the hypertrophy of the myocardial wall in HHD is one of acclimatization developments to compensate a reduction of the stroke volume.

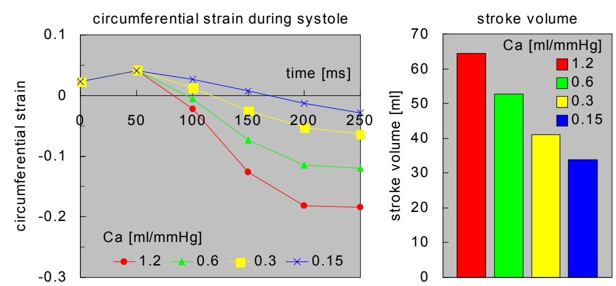

Figure 2: Cardiac functions for several Ca values.

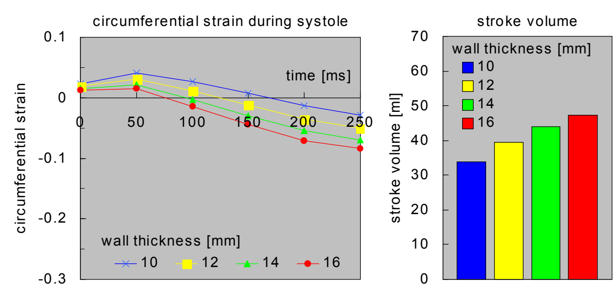

Figure 3: Cardiac functions for several wall thicknesses.

REFERENCES

Sawaki, Y., et al (2000). *Clinical Application of Computational Mechanics to the cardiovascular System*, Ed. Yamaguchi, T., Springer-Verlag Tokyo, 49-58

BIODYNAMIC DATA SET FOR MODELLING CAR DRIVERS

Barbara Hinz, Helmut Seidel, Gerhard Menzel, Jürgen Keitel, Ralph Blüthner
Federal Institut for Occupational Safety and Health, Berlin, Hinz.Barbara@baua.bund.de

INTRODUCTION

The examination of the transmission of vibration to drivers and their reduction is an essential task for occupational biomechanics.

The ISO 5982 (2001) describes the biodynamic data of seated individuals subjected to z-axis whole-body vibration. A human model is derived. The range of the data in this ISO is determined from the results in 18 publications. The defined values considered special conditions (posture, exposure, hard seat without backrest) for drivers of off-road, heavy road and industrial vehicles. However this ISO mention the lack of a data base for the condition car driving. A new item of the International Standard Organization (ISO) will tackle that problem and this paper provides a relevant data set.

METHODS

23 voluntary male subjects (body masses (BM) 58.2 kg – 106 kg; body heights (BH) 160 cm – 186.9 cm) and 22 female voluntary subjects (BM between 51.5 kg and 84.1 kg; BH 154 – 175 cm) were selected. Anthropometric parameters were determined in the standing and sitting posture. The test subjects sat in an relaxed, leaned and subjectively comfortable posture, the hand on the legs on three different car seats and on one lab seat with a rigid seat pan and with the backrest of a car seat. They were exposed to three vertical exposures: E1 – broad-band random vibration with a frequency weighted (ISO 2631, 1997) r.m.s. value (awz) of 0.3 ms^{-2}; E2 – car typical signal for driving of a main road, awz = 0.7 ms^{-2}; E3 – car typical signal for driving of a main road, awz=1.4 ms^{-2}. The accelerations (a) were measured at the seat basis in z-direction (z) (B200, HBM), at the seat- and backrest-cushion in z- and x-directions (Type 4322 mounted in a rubber disc, B&K). The resulting force at the interface between the test subject and the seat was measured using three force cells (KWH 100, Messelektronik) for the rigid seat. Markers on relevant body points were acquired (Motion Analysis System, Qualysis) to quantify the posture. The transfer functions (nondimensional ratio of the response at the cushions to the forced vibration at the basis) to the backrest were determined for all seats, to the seat cushion for the car seats only. The impedance and the apparent mass were calculated for the rigid seat (ISO 5982, 2001 , 3.1 and 3.2).

RESULTS AND DISCUSSION

Rigid seat: The mean values (MV) of the peaks of the moduli of the impedance and apparent mass were lower during E3 and occurred for men and women at the lower frequency. For the men higher values of moduli were registered. The mean apparent mass for car seat conditions exhibited lower values range below 4 Hz than in ISO 5982 (Fig.1). The peaks of the mean absolute values of the transfer functions from the seat basis to

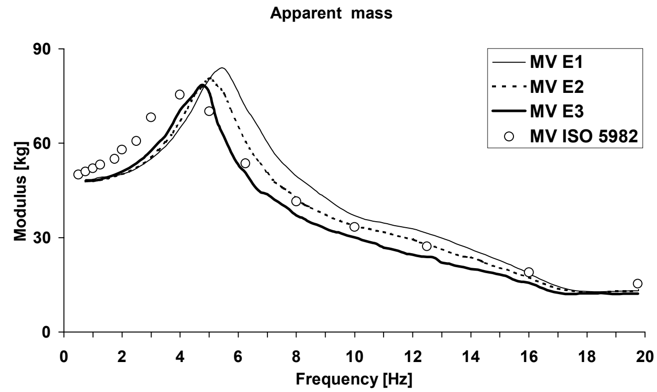

Figure 1: MV (N=55) of the modulus of the apparent mass

the acceleration in x-direction at the backrest shows higher values at the lower frequencies for E3. The mean absolute values were higher for men up to 6.5 to 8 Hz with the lower frequency at E3. In the upper frequency range the women showed higher mean absolute values.
Car seats: Two transfer functions were calculated: az at the seat basis to az at the seat cushion (STF) and to the ax at the backrest cushion (BTF). A dependence of the mean absolute values of STF and BTF from the intensity was found, slightly modified by the used seat, in a similar way as for the hard seat. This dependence is more distinctly for STF than for BTF. The mean absolute values of STF and BTF were higher for men up to 6 Hz, above that frequency the values of women were higher. The individual STF and BTF show a great variability.

SUMMARY

Based on the presented results an amendment of the ISO 5982 for car seats should consider the following aspects: the transmission to the backrest, the transmission properties of soft seats, the intensity dependence of the transmissions, the gender as an essential factor for the transmission, and the range of the interindividual variability. Further experimental research work is needed in order to find a represent range of biodynamic values for car seats.

REFERENCES

ISO 5982 (2001). Mechanical vibration and shock – Range of idealized values to characterize seated-body biodynamic response under vertical vibration. International Organization for Standardization, Geneva.
ISO 2631/1 (1997). Evaluation of human exposure to whole-body vibration – Part 1: General requirements. International Organization for Standardization, Geneva.

EFFECTS OF ELECTRO-ACUPUNCTURE STIMULATION ON SYSTEMIC AND MESENTERIC MICROVASCULAR HEMODYNAMICS IN ANESTHETIZED RATS

Kentaro Takagi, Shinjiro Yamaguchi, Momoyo Ito and Norio Ohshima [1]
Department of Biomedical Engineering, Institute of Basic Medical Sciences, University of Tsukuba,
Tsukuba Science City, Ibaraki, Japan. [1] ohshima@md.tsukuba.ac.jp

INTRODUCTION

Electro-acupuncture therapy has recently been recognized as a complementary treatment for various diseases and symptoms. Electro-acupuncture stimulation (EAS) is known to evoke various reflex responses by activating afferent nerve fibers. A number of reports have indicated that EAS affect autonomic functions via somato-autonomic reflex. However, little has been known about the effects of EAS on the hemodynamics in the target organ particularly from the viewpoints of the microcirculation (Yamaguchi *et al*., 2001). We therefore intended to assess the effects of the EAS on microvascular and systemic hemodynamics by using an intravital microscope-television system.

MATERIALS AND METHODS

Experiments were performed using adult male Wistar rats (250-300 g) anesthetized with urethane (1.1 g/kg). Respiration was maintained using a ventilator. Blood pressure and heart rate (HR) were continuously recorded throughout the experiments. Rectal temperature was monitored and maintained at 37-38℃ using a temperature control system. An intravital microscope-television system was used throughout the experiments. The mesentery was exteriorized on a stage designed for intravital microscopy. During each experiment, an arteriole was continuously visualized by a CCD camera, and recorded by a video cassette recorder. Inner diameter of the arteriole was measured on a replayed standstill TV frame by use of an image processor. The red blood cell (RBC) velocity was measured by the dual-sensor method developed by the authors (Sato and Ohshima, 1988). Two acupuncture needles inserted through the skin up to the underlying muscles of the hindpaw. EAS was performed by passing current between these two needles for 30 s at differed current intensities using an electrical stimulator.

In the first series of experiments, to investigate stimulus intensity-response relationships, in term of systemic hemodynamics and microvascular RBC velocity, were examined. EAS was applied to a hindpaw at current intensities of 1.0-10.0 mA.

In the second series of experiments, to identify the peripheral neural pathway of hemodynamic reflex response evoked by EAS, pharmacological studies using several vasoactive substances, such as local anesthesia (lidocaine), α-adrenergic receptor antagonist (phentolamine), β-adrenergic receptor antagonist (propranolol), and cholinergic receptor antagonist (atropine), were administrated. Systemic and microcirculatiory hemodynamic changes accompanying administration of these drugs were analysed. EAS was applied at current intensities of 5.0 mA.

RESULT AND DISCUSSION

The EAS of intensity over 3.0 mA applied to the hindpaw evoked intensity-dependent increase response in mean arterial pressure (MAP), HR, and arteriolar RBC velocity. Thus, it indicated a quantitative relation exsisted between current intensity of EAS and these hemodynamic changes. In some cases of the experiments, localized vasoconstriction of the arteriole was induced by EAS. These results suggested that effect of EAS on the mesenteric microhemodynamics was mainly attributable to increase of the systemic blood pressure, but partly due to vasoconstrictive effect.

The EAS-induced increase responses in MAP, HR, and arterioler RBC velocity were abolished after somatic afferent blockade by subcutaneous injection of local anesthesia to the stimulated site. Such increase responses in MAP and RBC velocity were also abolished by the intravenous injection of α-adrenergic receptor antagonist, while these responses were not abolished by the intravenous injection of β-adrenergic receptor antagonist or cholinergic receptor antagonist. While, increase response in HR was abolished by the administration of β-adrenergic receptor antagonist. These results suggested that these responses were induced by somato-sympathetic reflex mediated via α-adrenergic receptors in the vascular smooth muscles.

SUMMARY

In the present study, effects of EAS on systemic and mesenteric microvascular hemodynamics were directly observed. EAS evoked the intensity-dependent response of stimulus in systemic and microvascular hemodynamics. It was cralified that the increase response in RBC velocity in the mesenteric arteriole by EAS depends mainly on arterial pressure but partly is affected by localized vasoconstriction of the arteriole as well. Pharmacological experiments using several vasoactive substances indicated that the pressor response by EAS was induced by somato-sympathetic reflex mediated via somatosensory nerve and α-adrenergic receptors in the vascular smooth muscles.

REFERENCES

Sato, M. and Ohshima, N. (1988) *Biorheology*, **25**, 279-288.
Yamaguchi, S. *et al*. (2001) *Autonomic Neuroscience*, **88**, 160-166.

ACKNOWLEDGEMENTS

Partly supported by a Grant for "Research for the Future" Program (JSPS-RFTF 96I00202) from the Japan Society for the Promotion of Science (JSPS), and Research Grants from Japanese Ministry of Education, Science and Culture, and a Grant from the Tsukuba Advanced Research Alliance (TARA) Center of the University of Tsukuba.

FOOT FUNCTION AFTER THE SHORT TERM USE OF CUSTOM MADE FOOT ORTHOSES

Craig Payne
School of Human Biosciences, La Trobe University, Melbourne, Australia
c.payne@latrobe.edu.au

INTRODUCTION

Foot orthoses (FOs) are widely used in clinical practice for what is assumed to be biomechanical dysfunction. Many studies have previously investigated the immediate kinematic effects of FOs, but little is known about the longer term effects of FOs on foot function. The aim of this project was to determine foot function when custom FOs were first used and then again at 4 weeks.

METHODS

Consecutive patients needing rigid custom FOs at a podiatry teaching clinic were recruited for this project. Custom made FOs were made over a negative plaster cast of the foot in its defined neutral position. When orthoses were first issued, foot function was determined using the Pedar in-shoe pressure measuring system. Subjects were measured walking for approximately 10 steps in canvas shoes with and without their FOs. This was repeated again at approximately 4 weeks after the subjects had been using the FOs. Using the NovelWin software, 6 steps of each trial were averaged. Masks were created over the hallux, first metatarsal head, lateral forefoot, arch and heel areas to calculate mean pressure and the pressure tine integral in each masked area. Contact time for the averaged steps to check if velocity was consistent between trials.

RESULTS AND DISCUSSION

36 subjects were recruited (10 were lost to follow-up). The left foot of 26 subjects was used for the analysis. Mean time between baseline and follow up was 29.5 (±10.3) days. Repeated measures ANOVA showed that the velocity within subjects of each trial were consistent enough for further analysis ($p=0.31$). The results of the pressure variables are reported in Tables 1 & 2. Post hoc analysis showed, as expected, differences between the use of FOs and no FOs both at baseline and at follow up. However, no differences were found between foot function at baseline and at follow up without the use of FOs. Similarly, no differences were found in foot function at baseline and follow up with the use of FOs, indicating that no adaptation or changes occur to foot function in the parameters we measured over a 4 week period of using FOs.

SUMMARY

This study has shown that there are no adaptive changes in foot function in the short term in the parameters used. This does not rule out the possibility of longer term changes.

Table 1: Mean pressure

	No orthoses at baseline	Orthoses at baseline	No orthoses at follow up	Orthoses at follow up	ANOVA
Hallux	12.9 (±4.6)	13.7 (±4.6)	12.6 (±5.0)	13.5 (±5.1)	p=0.38
First MPJ	9.5 (±1.7)	9.2 (±2.4)	9.8 (±1.6)	9.3 (±2.1)	p=0.37
Lateral forefoot	13.1 (±1.9)	10.8 (±1.8)	13.5 (±2.1)	10.9 (±2.0)	p=0.000[a]
Arch	2.7 (±0.95)	4.2 (±1.2)	2.6 (±0.8)	4.0 (±1.3)	p=0.000[b]
Heel	11.9 (±2.0)	10.2 (±1.8)	12.3 (±1.7)	10.8 (±2.0)	p=0.000[c]

Table 2: Pressure time integral

	No orthoses at baseline	Orthoses at baseline	No orthoses at follow up	Orthoses at follow up	Repeated measures
Hallux	57.1 (±19.8)	64.6 (±19.4)	53.6 (±23.3)	65.5 (±24.8)	p=0.005[a]
First MPJ	64.4 (±15.1)	51.3 (±14.9)	64.1 (±14.7)	48.9 (±13.7)	p=0.000[b]
Lateral forefoot	87.8 (±19.8)	68.9 (±16.3)	87.7 (±19.3)	67.8 (±17.1)	p=0.000[c]
Arch	26.0 (±10.6)	39.7 (±10.6)	24.2 (±9.1)	36.7 (±10.8)	p=0.000[d]
Heel	63.1 (±10.7)	50.2 (±10.9)	60.6 (±11.0)	52.7 (±14.7)	p=0.000[e]

BIOMECHANICAL ANALYSIS OF THE DESIGN OF ENDOVASCULAR STENTS: INFLUENCE OF COIL-PITCH ON INTRALUMINAL FLOW BEHAVIOR

Eiki Akagawa[1,2], Keiko Ookawa[3] and Norio Ohshima[3]
[1]Graduate School of Comprehensive Human Sciences, University of Tsukuba, Tsukuba Science City, Ibaraki, Japan
[2]New Energy and Industrial Technology Development Organization (NEDO) Fellow
[3]Department of Biomedical Engineering, Institute of Basic Medical Sciences, University of Tsukuba, ohshima@md.tsukuba.ac.jp

INTRODUCTION

Neointimal hyperplasia is considered partly responsible for the restenosis after treatment with indwelling interventional endovascular stents. From the biomechanical viewpoints, it is expected that if the design of endovascular stents is optimally modified as to control blood flow velocity close to the vessel wall, such stents could prevent development of neointimal hyperplasia. The objective of the present study is, therefore, to examine whether adjusting coil-pitch of the coil stents is able to regulate blood flow condition near the vascular wall.

MATERIALS AND METHODS

To analyze the changes of detailed flow pattern caused by the indwelling endovascular stents, the flow was visualized in an *in vitro* mock perfusion circuit. A single-coil endovascular stent (SUS316L; wire diameter = 0.5 mm, coil diameter = 4 mm; coil-pitch = 2.5, 5, or 10 mm) was placed at the center of a glass tube (4 mm i.d., 6 mm o.d.), and a physiological saline containing a diluted suspension of rat erythrocytes chosen as tracer particles (adjusted at a value of hematocrit of 0.1%, viscosity of 1.0 mPa) was perfused at a flow rate of 30-90 mL/min.

The behavior of the erythrocytes within the glass tube was video-recorded at 250 frames/s under a microscope, and was subjected to off-line image analysis. Video images obtained by observing focused planes parallel to the longitudinal axial section in the glass tube were scanned at an interval depth of 0.4 mm, and the velocity were measured by tracing trajectories of erythrocytes from the frame-by-frame analysis.

RESULTS AND DISCUSSION

A complex and three-dimensional spiral flow pattern due to the secondary flows was observed in the vicinity of the stent. Figure 1 shows the flow velocity profiles in the glass tube indwelt with coil stent. The reduction of the velocity near the vessel wall was linearly correlated with the decrease in coil-pitch significantly ($p < 0.01$), particularly at the higher flow rates (correlation coefficient with the volumetric flow rate of 60 mL/min, $r = 0.56$; with the volumetric flow rate of 90 mL/min, $r = 0.55$).

The conventional endovascular stents have been considered to work by resisting mechanically to inwardly protruding vascular wall. Whereas, the present study pointed out a possibility of a new design concept of suppressing neointimal hyperplasia by adjusting intraluminal blood flow.

It now has been widely accepted that region of the low shear stress (< 0.4 N/m^2) exposed to the vascular wall was localized at atherosclerosis-prone site. Based on the results of the present study concerning the relationships between the flow velocity near the wall and the coil-pitch of the indwelling stent, we can estimate the wall shear stress of any given stented vessels. In the case of human abdominal aorta indwelt with coil stents, therefore, the coil-pitch should be over 6 mm in length in order to exceed the lowest level of shear stress of 0.4 N/m^2.

SUMMARY

To analyze blood flow behavior, we constructed an *in vitro* perfusion system. The flow velocity near the vessel wall was affected by the coil-pitch of the indwelling endovascular stents, which fact suggests a possibility to improve the stent design.

ACKNOWLEDGEMENTS

This study was partly supported by a Grant for "Research for the Future Program" (JSPS-RFTF 96I00202) from the Japan Society for the Promotion of Science (JSPS), and a Grant-in-Aid from Japanese Ministry of Education, Culture, Sports, Science and Technology.

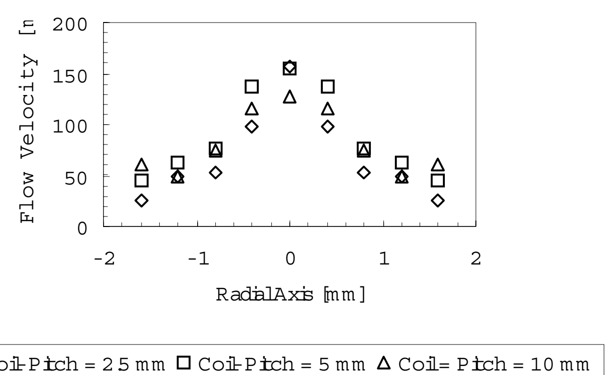

Figure 1: Flow velocity profiles within the glass tube.

COMPUTER INVESTIGATION OF CRUCIATE LIGAMENTS ORIENTATION DURING THE PASSIVE RANGE OF MOTION OF NORMAL KNEES

S. Zaffagnini, S. Martelli, F. Acquaroli
Rizzoli Orthopaedic Institutes, Biomechanics Lab., Bologna, Italy
Contact author: s.martelli@biomec.ior.it

INTRODUCTION

Cruciate ligaments of the knee have been extensively studied for anatomical and surgical reasons. Several authors have reported data on ligaments elongations, stress and strain, but no quantitative data are reported in the literature regarding the orientation of anterior cruciate ligament (ACL) and posterior cruciate ligament (PCL) fibers during passive range of motion (1,2,3,6). The goal of this study is to start filling this gap of information for normal knees.

METHODS

In this study we examined, qualitatively and quantitatively, 8 normal cadaver knees. The passive range of motion of each defrosted and intact joint was recorded using the 6-degrees-of-freedom electrogoniometer FARO Arm (Faro Technologies, Lake Mary, USA). Then the joint was exposed to digitize the articular surfaces of tibia and femur, ACL and PCL insertion boundaries, couples of 9 fibers insertions on ACL and PCL. Computer elaboration of the recorded data enabled the reconstruction of the joint and ligaments relative position during the passive range of motion. This method has been previously used for anatomical or kinematic studies (Martelli 2000) and is currently under patent process (E.P. 00128769.7 , Dec 30, 2000).

The 3D orientation of single ligaments' fibers was measured reporting the angle between the line joining each fiber insertions with following three planes :

- a plane fitting the tibial plateaux, computed using a least square algorithm, named "tibial plateaux plane" (I);
- a plane fitting the femoral ACL insertion area, computed using a least square algorithm, named "femoral notch plane" (II);
- a plane perpendicular to the tibial plateaux directed in the medio-lateral direction, named "third plane" (III).

Figure 1 reports the planes used for ACL orientation in knee 2.

The ACL 9 fibers were split into antero-medial and postero-lateral ones, in order to evaluate bundles orientation. The PCL 9 fibers were classified as postero-lateral and antero-medial. Then we computed the average orientation of the two bundles in all knees.

RESULTS AND CONCLUSIONS

The inclination of ACL with respect to the tibial plateaux decreases with flexion from 56° to 33°. Orientation of ACL with respect to the femoral notch increases with flexion from 4° to 58°. The ACL orientation in a medio-lateral direction changes from 24° to 52°. The postero-lateral and the antero-medial bundle have different angular variations, mainly with respect to the tibial plateaux and medio-lateral direction.

The inclination of PCL with respect to the tibial plateaux decreases with flexion from 43° to 28°. Orientation of PCL with respect to the femoral notch ranges from 36° to 51°. The PCL orientation in a medio-lateral direction decreases with flexion changes from 45° to 25°. The postero-lateral and the antero-medial bundle have different angular variations, mainly with respect to the medio-lateral direction.

This quantitative and qualitative information not only increases the anatomical knowledge of the ACL and PCL, but could also be important in developing or improving the surgical strategy for their reconstruction.

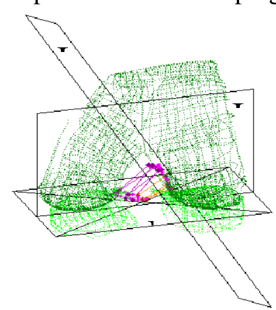

Figure 1: Reference planes used for computing ACL fibers orientation.

REFERENCES

Amis R, Amis A (1994), *J. Biomechanics* ; 27 :13-24
Daniel D., Akeson W., O'Connor J, (1990), Raven Press
Fuss F, (1989*) Am J of Anatomy*; 184:165-176
Martelli S, Pinskerova V. *J Bone Joint Surg* (in press).
Martelli S, Zaffagnini S, et al. (2000) *Computer Methods & Programs in Biomedicine*; 62 77-86.
Mommersteeg T, Koolos et al., (1995), *J Anat* ; 187:461-471.

EXPERIMENTAL STUDY OF AN ARTIFICIAL KNEE JOINT WITH PVA-HYDROGEL CARTILAGE

Aneta Nicoleta Suciu[1], Takuzo Iwatsubo[1], Mitsumasa Matsuda[1] and Takashi Nishino[2]
Kobe University, Kobe, Japan
[1]Department of Mechanical Engineering, 981d846n@yku.kobe-u.ac.jp
[2]Department of Chemical Science and Engineering

INTRODUCTION

Wear is one of the main reasons of failure of the artificial knee joint (AKJ) fixation into the host bone, due to the biological reaction against wear debris. In the modified design of the AKJ, proposed by Iwatsubo et al. (2001), a poro-elastic hydrated layer covers the tibial plateau and micro-pockets are machined on the surface of the femoral head (Fig. 1). Taking as reference the case of a smooth femur, theoretically was found that the friction coefficient reduces in the presence of the micro-pockets. In order to check this result, first (present work) we intend to perform wear tests for a smooth femur. Further on we plan to compare the wear data, obtained with and without micro-pockets on the femoral component.

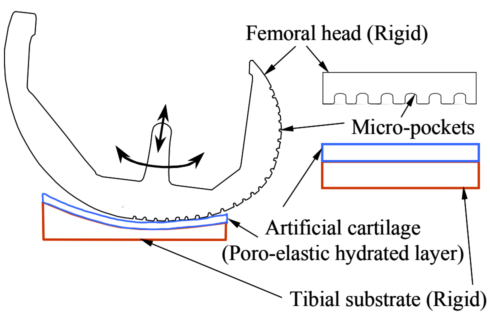

Figure 1: Modified design of the AKJ

MATERIALS AND METHODS

Femoral head is considered as a circular plate of 25 mm diameter (surface roughness, R_a = 0.02 μm), made in stainless steel. The artificial cartilage material is polyvinyl alcohol hydrogel (PVAH), prepared using the cyclic freezing/thawing method (Stammen et al. 2001). The PVAH layer has a water content w = 77% and a thickness t = 2, 3, 4 mm. In the creeping test (Fig. 2.a), due to the water exudation, the residual

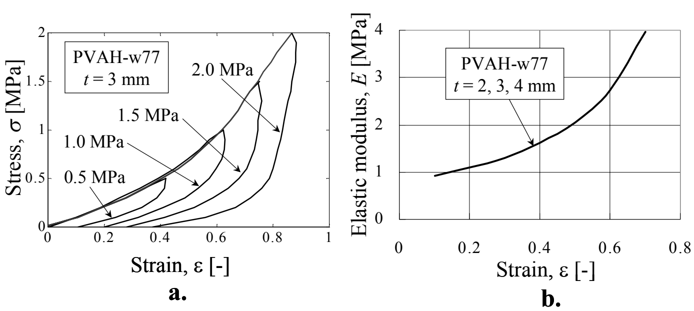

Figure 2: Mechanical characteristics of PVAH-w77

strain was ε = 0.27 for σ_{max} = 1.5 MPa (F = 735 N), but the PVAH layer recovered after rehydration. The elastic modulus increases with the strain increasing (Fig. 2.b) but does not depend on layer's thickness. Fig. 3 illustrates the wear test rig. AC servomotor drives the ball-screw. The ball-nut translates together with the slider of the LM guide and the water tank, following the ISO-14243 anterior-posterior displacement pattern. The PVAH is bonded on the tibial substrate and immersed in the water tank. The loading screw produces a force, which is applied on the femoral head via lamella spring. It is possible to measure the displacement, load and wear volume (e.g., by using a spectrophotometer we measure the absorbance of the solution in which wear debris were dissolved). Tests on a smooth femoral head against PVAH reveals a wear factor on order of 10^{-4} $mm^3/(Nm)$ and a friction coefficient about 0.1-0.2.

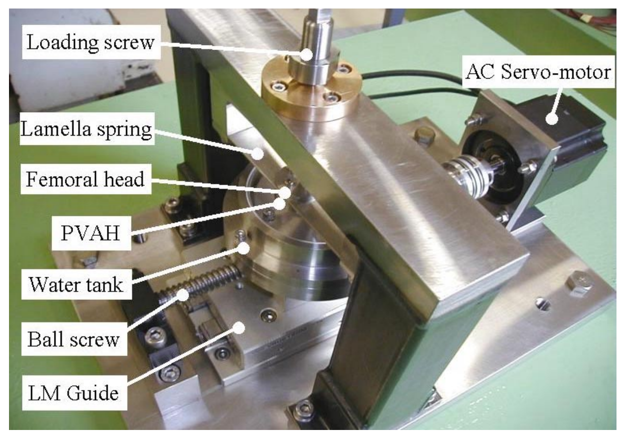

Figure 3: Photo of the wear test rig

SUMMARY

The prepared PVAH can operate up to 1.5 MPa pressure. The elastic modulus increases with the strain and does not depend on layer's thickness. The wear and friction measurements for a smooth femur against PVAH represent the reference data for the further studies of a femoral head with micro-pockets.

REFERENCES

Iwatsubo, T., et al. (2001). *2001 Bioengineering Conference*, ASME, BED **50,** 447-448.
Stammen, J.A., et al. (2001). *Biomaterials*, **22**, 799-806.

NOVEL ALGINATE-CHITOSAN HYBRID FIBERS AS A SCAFFOLD FOR TENDON OR LIGAMENT TISSUE ENGINEERING

Tadanao Funakoshi[1], Tokifumi Majima[1], Norimasa Iwasaki[1], Kazuo Harada[2], Sachiko Nonaka[2], Yoshihiko Maekawa[2], Akio Minami[1] and Shin-Ichiro Nishimura[3]
[1]Dept. of Orthopaedic Surgery, Hokkaido University Graduate school of Medicine, Sapporo, Japan, t-funa@med.hokudai.ac.jp
[2]Chemical Biology Institute, Inc., Sapporo, Japan
[3]Laboratory of Bio-Macromolecular Chemistry, Hokkaido University Graduate School of Science, Sapporo, Japan

INTRODUCTION

Several materials (non-absorbable prostheses, collagen, synthetic biodegradable polymers, natural biodegradable materials) have been used for scaffolds in tendon or ligament tissue engineering. The scaffold should provide adequate sites for attachment and growth of enough cells to survive and function in vivo.

Recently, it has been reported that alginate and chitosan, natural biodegradable materials, have been good potential for biocompatible and biodegradable scaffold. Chitosan has various biological functions such as wound healing, antibacterial activity. Moreover, chitosan and alginate are easily prepared and a natural biopolymer available in plenty. On the other hand, the strength of these materials has been required to be improved. We developed new hybrid fibers consisted from Alginate and Chitosan. The aim of this study was to evaluate feasibility of novel Alginate-Chitosan Hybrid fibers as potential biomaterials.

METHODS

<u>Biomechanical Study.</u> Tensile tests for five samples of each material, Polyglactin 910 (Vicryl®), Alginate, Alginate-0.05%Chitosan Hybrid fibers (Cos-Y 0.05), Alginate-0.1%Chitosan fibers (Cos-Y 0.1), were performed at a cross-head speed of 20 mm/min. The cross-sectional area was determined with the non-contact method using microscope and video dimension analyzer.

<u>Cell Attachment.</u> Fibroblasts were isolated from the patellar tendon of Japanese White rabbit under sterile conditions. Cells were maintained in culture using standard procedures and used at passage 2. The concentration of fibroblasts suspension was 1.4×10^7 cells/ml. Cell adhesion study was performed as follows, (Nishimura 1985. Int. J. Biol. Macromol,7, 100-104). Briefly, the fibrous samples were cut into 7mm length, and packed in small Teflon tubes (30mm length, 7.0 mm inner diameter). Then, fibroblasts suspension (0.1mL) was loaded on the column for 15minutes, and then washed out with phosphate-buffered saline (1mL) after loading. The number of fibroblasts retained on the fiber was estimated by the microscopic observation of washing solution. Results were analyzed using One-way Factorial ANOVA and Fisher's PLSD test. Difference was considered significant for $p<0.05$.

RESULTS AND DISCUSSION

<u>Biomechanical Study.</u> Tensile strength in hybrid polymers was significantly lower than that in the alginate polymers. The guluronic acid chains of alginate ionically bind each other via the calcium ions. That may be replaced by chitosan in the Alginate-Chitosan Hybrid fiber. This may explain the mechanical inferiority in hybrid polymers.

<u>Cell Attachment</u> The number of washed out fibroblasts in Vicryl were significantly higher than that in the other polymers. The adhesivities in Cos-Y 0.05 and Cos-Y 0.1 were better than that in Vicryl and Alginate. On the other hand, the total amount of adhered fibroblasts was not affected by the increase in degree of content of chitosan. Zielinski (1994 Biomaterials,15, 1049-1056) reported a cationic hydrogel such as chitosan provides a matrix necessary to maintain anchorage-dependent cell attachment and spreading. Our results were consistent with those reports.

In conclusion, novel Alginate-Chitosan Hybrid fiber showed great potential as desirable biomaterials for tendon or ligament tissue engineering.

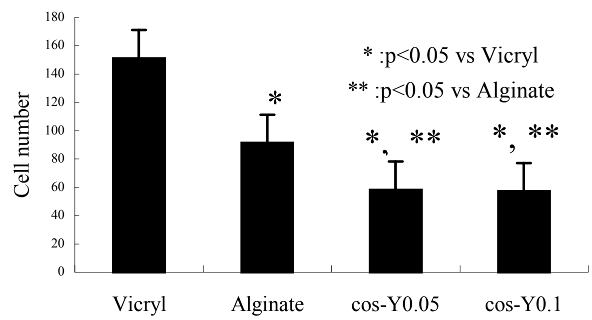

Figure 1: Number of unattached cells in each material

ACKNOWLEDGEMENTS

Supported by Northern Advancement Center for Science & Technology in Hokkaido

Table 1: Material properties of scaffolds

Material Properties	Vicryl	Alginate	Cos-Y0.05	Cos-Y0.1
Tensile strength (Mpa)	886.2 ± 7.7	274.1 ± 7.6	223.1 ± 3.6	235.2 ± 4.6
Strain at Failure (%)	28.1 ± 0.6	9.0 ± 1.0	10.6 ± 0.5	12.3 ± 0.44

CHITOSAN-BASED HYALURONAN HYBRID POLYMER FOR SCAFFOLD IN LIGAMENT TISSUE ENGINEERING

Tokifumi Majima[1], Tadanao Funakosshi[1], Norimasa Iwasaki[1], Kazuo Harada[2], Sachiko Nonaka[2], Yoshihiko Maekawa[2], Akio Minami[1] and Shin-Ichiro Nishimura[3]
[1]Dept. of Orthopaedic Surgery, Hokkaido University school of Medicine, Sapporo, Japan, tkmajima@med.hokudai.ac.jp
[2]Chemical Biology Institute, Inc., Sapporo, Japan
[3]Laboratory of Bio-Macromolecular Chemistry, Hokkaido University Graduate School of Science, Sapporo, Japan

INTRODUCTION

Severe ligament and tendon injuries are frequently treated with autograft transplantation. However, biological grafts are not ideal replacements. The use of autografts will necessarily results in donor site morbidity. Furthermore, the grafts initially undergo necrosis after the implantation. This is the main reason why the biological grafts often do not provide adequate mechanical strength until a long term remodeling process is done.

Resorbable scaffolds seeded with cells are potential alternatives to biological grafts. Currently, most of these constructs for tissue engineering have been based on collagen scaffolds. On the other hand, the major limitation is that collagen scaffolds are allogenic. Also, collagen scaffolds suffer from batch-to-batch variability, making consistent reproduction of these constructs difficult. To solve this problem, we developed new hybrid materials consisted from chitosan and hyaluronan (HA). It was reported that chitosan could promote the healing of skin wound. Moreover, chitosan is not immunogenic. HA has been shown to improve healing of a variety of tissues by means of trophic effects through binding, delivery of growth factors, cell adhesion, and anti-inflammatory effects. The purpose of this study is to investigate material properties and fibroblasts adhesion behavior of chitosan-based HA hybrid polymer.

METHODS

Polymer fibers of Polyglactin 910 (vicryl®, Ethicon Co, NJ) were used as a control material. Chitosan polymer fibers and chitosan-based HA hybrid polymers (Chitosan/0.05HA: Chitosan:HA = 8%:0.05%, Chitosan/0.1HA: Chitosan:HA = 8%:0.1%) were originally developed in our laboratory.

<u>Measurement of Material Properties</u>

Tensile tests for five samples of each material were performed at a cross-head speed of 20 mm/min. The cross sectional area was determined with the non-contact method using microscope and video dimension analyzer.

<u>Cell Adhesion Study</u>

Fibroblasts were isolated from the patellar tendon of a Japanese white rabbit under sterile conditions. Cells were isolated and maintained in culture using standard procedures and used at second passage. The fibroblasts suspension was concentrated to 1.4×10^7 cells/ml using a hemocytemeter. Cell adhesion study was performed according to our previous study (1985, Int. J. Biol. Macromol, 7, 100-104). Briefly, the fibrous samples were cut into 7 mm pieces and packed in Teflon tube (30 mm length, 7 mm inner diameter) and then 0.1 ml of fibroblasts suspension was loaded on the column. The cells were allowed to adhere in a humidified incubator for 1 hour. Each column was gently rinsed with 1 ml of phosphate-buffered saline and the number of unattached cells was quantified by the microscopic observation of rinsed solution. Five parallel samples were used for each polymer fibers. Statistical comparison was performed using one-way ANOVA and Fisher's PLSD test. Difference was considered significant for $p < 0.05$.

RESULTS AND DISCUSSION

Mechanically, new materials were significantly weaker than control polyglactin fibers. On the other hand, strain at failure in new polymers showed significantly stiffer than control fibers. This strain characteristic of new polymers may be beneficial for ligament scaffold. HA significantly increased chitosan polymer strength (Table 1). This may be attributable to water binding affinity of HA during manufacturing process of air-drying. The current study showed that the adhesivity of fibroblasts was significantly higher in the new polymer materials. Moreover, HA significantly increased cell adhesion to the polymers (Fig. 1).

SUMMARY

Material properties and cell adhesivity were investigated in newly developed chitosan polymer fibers and chitosan-based HA hybrid polymers. Chitosan-based HA hybrid polymers showed great potential as a desirable biomaterials for use in a tissue scaffold. Further in vivo study should be conducted.

Table 1: Material properties of scaffolds

Material	Tensile Strength (MPa)	Strain at Failure (%)
Vicryl®	886.2 +/- 7.7	28.1 +/- 0.6
Chitosan	128.1 +/- 4.9*	4.3 +/- 0.4*
Chitosan/0.05HA	152.6 +/- 5.4*,**	6.1 +/- 0.7*
Chitosan/0.1HA	217.6 +/- 8.5*,**	3.2 +/- 0.3*

*: P<0.05 vs. vicryl, **: p<0.05 vs. Chitosan, Mean +/- SE

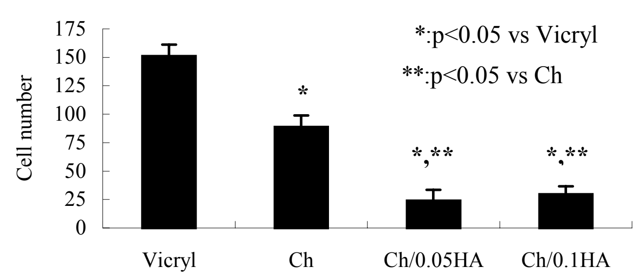

Figure. 1: Number of unattached cells in each material

ACKNOWLEDGEMENTS

Supported by Northern Advancement Center for Science & Technology in Hokkaido

SHEAR-LIKE RESPONSE OF ENDOTHELIAL CELLS TO THERAPEUTIC ULTRASOUND

Eitan Kimmel[1,2], Monica Dines[1], Dalit Raz[2], David Elad[2], Shmuel Einav[2] and Nitzan Reznick[3]
[1]Faculty of Agricultural Engineering, Technion IIT, Haifa 32000, Israel. agreita@tx.technion.ac.il
[2]Department of Biomedical Engineering, Tel-Aviv University, Tel-Aviv 69978, Israel
[3]Faculty of Medicine, Technion IIT, Haifa 32000, Israel

INTRODUCTION

Our long-term goal is to utilize therapeutic ultrasound (TUS) as a stimulus for angiogenesis and vascular regeneration. Stimulation of new capillary growth under ischemic conditions is crucial in preventing large damage following major events such as acute infarction, and kidney or liver dysfunction. It has been demonstrated that TUS induces cell proliferation and migration, collagen synthesis, stimulation of growth factors, production of cytokines, regeneration of skeletal myofibrils, migration of smooth muscle cells and angiogenesis. The physical interaction of TUS with tissues is complex and intensity (and frequency) dependent. Cavitational erosion of surfaces due to bubble collapse and high velocity jet formation as well as thermal effects are associated with the high range of intensities of TUS. The relevant mechanisms for the lower range of TUS intensities, which are used in this investigation, are associated with bubble pulsation and micro streaming, and transverse (shear) waves.

Regarding TUS and angiogenesis, this study concerns TUS and its effect on blood vessels in general and on the endothelium in particular. We hypothesize that low intensity TUS induces localized shear stresses on the endothelial cell (EC) layer. This is based on evidence for TUS-induced intercellular spaces between the first two outermost cell layers of fish epidermis (Frenkel et al. 1999), and on the physical similarities, in relation to ultrasound, between the epithelium and endothelium at the tissue/liquid interfaces.

It is known that biomechanical forces act on endothelial cells to modulate their structure and function. For instance, shear stresses induced by the flowing blood, influence permeability to macromolecules and accumulation of lipoproteins. They affect angiogenesis and lately were found (unpublished) to regulate the level of expressed receptors such as VEGFR-1 and VEGFR-2 (Vascular Endothelial Growth Factor Receptors) and angiopoietin receptors (e.g. Tie-1 and Tie-2). VEGFR-2 (Flk-1) receptor is known to enhance the proliferation of endothelial cells, mediate chemotaxis (migration), and increase the vascular permeability. VEGFR-1 (Flt-1) is connected with communication between the endothelial cells. Tie-2 involves in expansion of the endothelium, matrix association and pericyte recruitment and Tie-1 involves in capillary development and endothelial cell integrity. Both Tie-1 and Tie-2 play a role in the late phase of angiogenic capillary growth and in survival of the endothelium.

The following study is about sonication of endothelial cells *in vitro.* It describes the changes of viability, the variations in level of angiogenic molecules and the morphological changes in the EC after exposure to TUS.

METHODS

TUS was applied to confluent Bovine Aortic Endothelial Cells (BAEC), kept in DMEM low glucose 10% calf serum under 5% CO_2/95% air in a humidified incubator at 37^{O}C. The medium contained also 2mM L-Glutamin, 1 μg/ml Gentamycin, 20 μg/ml Streptomycin, and 20U/ml Penicillin. The EC were exposed to TUS (frequency 1.5MHz, intensity 1W/cm^2, continuous mode) for time durations that vary from 5 to 30 minutes. Western blot analysis and immunoblotting were used to test the expression of VEGF receptors Flk-1 and Flt-1, and angiopoietin receptors Tie-1 and Tie-2. Viability was tested using XTT kit, Hocht and direct counting.

RESULTS AND DISCUSSION

The expression of Flk-1 was increased significantly after 30 minutes of exposure to ultrasound. At the same time no change was observed in Tie-2 levels. Preliminary data indicates that TUS induces changes in Tie-1 and Flt-1. These regulations of the angiogenic factors correspond with the results of shear stress stimulation of EC obtained in a cone-and-plate apparatus (unpublished). Hours after treatment we observe that in comparison to control sonicated EC have fewer and smaller extensions, and their boundaries appear more round and monotonous. This might be the result of disconnected adhesion sites and may serve as indirect indication of TUS-induced shear stresses. Also, treated BAECs show no preferred orientation as expected from the random nature of bubble's micro streaming and the localized shear stresses, which are generated by bubble pulsations near a surface. No sign of cavitational erosion is found in this study as indicated by the fact that EC viability is not at all reduced by the TUS.

We conclude that low intensity TUS influence angiogenic mechanism in BAEC *in-vitro* and might have an effect on the functioning of the cardiovascular endothelium *in-vivo*. The regulating effect of TUS on angiogenic factors in BAEC point to the possibility that shear stresses are involved.

REFERENCES

Frenkel, V. et al. (1999). *Ultras. Med. Biol*. **26**, 473-480.

ACKNOWLEDGEMENT

This work is supported by the Israeli Ministry of Science.

A REGRESSION MODEL FOR PREDICTING PERCEIVED LOAD

Masaru Hotehama[1], Jeff Janert[2], and Toshikazu Takemori[1]
[1]R&D Department, Osaka Gas Co., Ltd
[2]Visiting Researcher R&D Department, Osaka Gas Co., Ltd

INTRODUCTION

The purpose of this research is to develop a regression model between torque and perceived load, which will be integrated with commercial software called "Digital Human" or "Computer Mannequin".
The paper describes a best-fit regression model and its comparison with other types of regression models.

METHODS

Ten subjects performed biceps MVC on a biceps isolation bench (isolation MVC) and again while seated and without any back support (non-isolation MVC). The subjects then curled a bucket of unknown weight but between 1kg and 10kg for 15 trials and reported what percentage of their biceps MVC the weight represented each time. Afterwards to validate the algorithm derived from the previous 15 trials; the same ten subjects then moved the unknown weight from the floor to a 10 centimeter platform again while seated and without back support (living scene).

RESULTS AND DICUSSION

Table1 shows regression models (linear and nonlinear) and the population R^2 values for the torque normalized with the Max torques on non-isolation MVC movement and isolation MVC movement, and average of prediction error on living scene. The best fit function for the isolation MVC is (Perceived Load)%=43.593*(Normalized reported torque percent of Max Torque)+80.886. The algorithm validation error between the isolation normalized algorithm and the real application data is 11.91%. The average error of each subject's perceived load between 1st time and 2nd time is 9.23%, and standard deviation is 9.28. So prediction error is small enough to predict a perceived load on bicep.

Figure1 shows the living scene data normalized by isolation MVC and nonlinear regression line. The variation in data is seen between 0.5 and 1. But almost all data is close to nonlinear regression line.

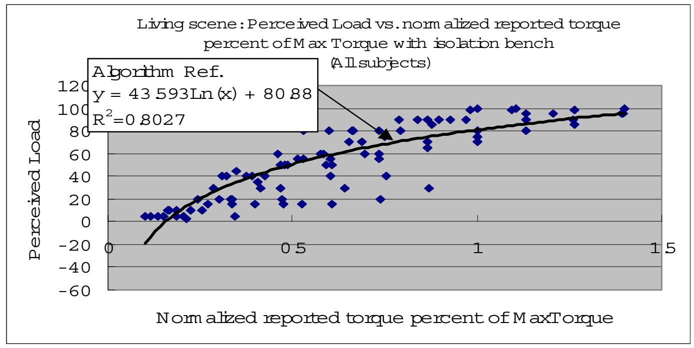

Figure 1: Living scene "real-life" validation of biceps isolation bench MVC normalized data and nonlinear regression line for all 10 subjects.

SUMMARY

We developed a regression model for predicting perceived load based on biceps maximum voluntary contraction. The best fit function for the isolation MVC is (Perceived Load)%=43.593*(Normalized reported torque percent of Max Torque)+80.886. The algorithm validation error between the isolation normalized algorithm and the real application data is 11.91%. The error is small enough to predict a human sensation on bicep.

If we develop other parts model and integrate these functions to computer mannequin, we will be able to predict a personal perceived load by measuring max torque.

REFERENCES

White(1998). *Measuring Pain*, Acupuncture in Medicine November **16** No.2
Marras, Solonomow, Westgaard, Ankrum(2000). *Interpreting EMG Results*. Proceedings of the IEA 2000/HFES 2000 Congress

ACKNOWLEDGEMENTS

This study is supported by the Ministry of Economy, Trade and Industry and the New Energy and Industrial Technology Development Organization (NEDO), as a part of the project of "Behavior-Based Human Environment Creation Technology"

Table 1: comparison regression function, R^2 value and average of prediction error on non-isolation MVC and isolation MVC

	regression model	R^2 value	prediction error average (%)
normalized by non-isolation MVC	y = 98.489x + 5.6714	0.7688	13.98
	y = 42.292Ln(x) + 91.2	0.7967	12.10
normalized by isolation MVC	y = 80.331x + 3.1265	0.7870	13.08
	y = 43.593Ln(x) + 80.8	0.8027	11.91

BIOCOMPATIBLE OSTEOSYNTHESIS PLATES USING BRAIDED CARBON/PEEK COMPOSITE

K Fujihara[1], Zheng-Ming Huang[1], S.Ramakrishna[1], K.Satkunanantham [2] and H.Hamada[3]
[1] Division of Bioengineering
[2] Department of Orthopaedic Surgery
The National University of Singapore, 9 Engineering Drive 1, Singapore 117576
[3] Division of Advanced Fibro Science
Kyoto Institute of Technology, Matsugasaki, Sakyo-ku, Kyoto 606-8585, Japan

INTRODUCTION

It is well known that rigid metal plates induce bone atrophy during the healing of fractured bone. This phenomenon is widely recognized as stress shielding and the problem is the large stiffness mismatch between metal plates and human cortical bone. Hence primary objective of this research project is to design and develop a less rigid and biocompatible braided carbon fiber fabric reinforced PEEK composite osteosynthesis plate for the treatment of long bone fractures.

FABRICATION METHODS OF BIOCOMPATIBLE OSTEOSYNTHESIS PLATES USING BRAIDING TECHNIQUES

In this study, braiding techniques were adopted to fabricate composite bone plates. Firstly, a new type of commingled yarn, called micro-braiding yarn (***Figure 1 [a]***) was made. This yarn was made by inserting three reinforcing carbon fiber yarns (diameter = $7\mu m$, 1000 filaments) into a tubular braid of 10 matrix PEEK fiber yarns (230 dTEX, 30 filaments). The feature of this yarn is such that the reinforcing and matrix fibers were mixed uniformly, which results in good impregnation of PEEK matrix into carbon fibers. More over, PEEK fibers wrap carbon fibers effectively and reduce the possibility of release of broken fibers. The micro-braiding yarn was used to make the flat braided fabrics with braiding angle θ (***Figure 1* [b]**). The braided carbon/PEEK composite osteosynthesis plate (***Figure 1* [c]**) was fabricated using optimized compression molding conditions, an average pressure of 5.6MPa and temperature of 400C^{o} for 60 minutes.

RESULTS AND DISCUSSION

As shown in ***Fig.2***, bending moment and stiffness of the composite bone plates decreased with increasing braiding angle and the specimens showed 7.07 ~ 8.14 [Nm] maximum moment and 0.316 ~ 0.359 [Nm/deg.] stiffness with varied braided angles. These values correspond to 38.2 ~ 44.0% of the maximum moment and 26.6 ~ 30.2% of the stiffness of stainless-steel bone plate values. These mechanical properties can be varied with different size of the micro-braiding yarn or braiding structure of composite. That means braided composite osteosynthesis plates offer the desirable and suitable mechanical design for each patient regardless of sex and age. It is considered that braided composite plates are holding promise of a better bone fixation as compared with conventional metal plates.

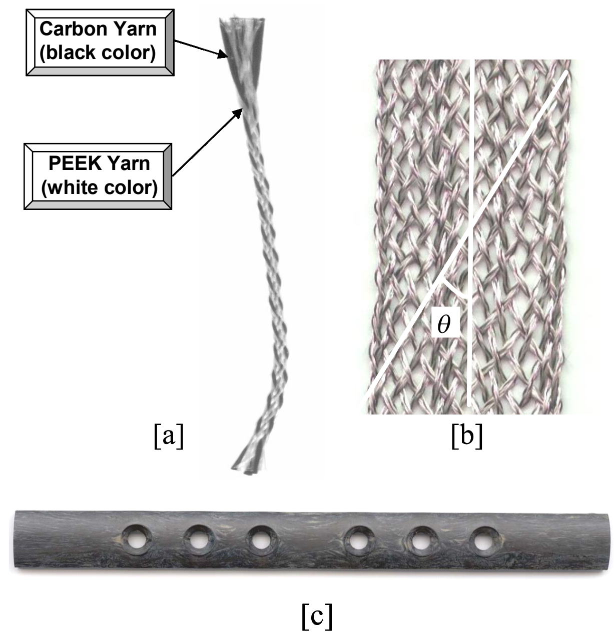

Figure 1: Photographs of [a] a micro-braiding yarn comprising carbon and PEEK fibers, [b] flat braided fabric, and [c] composite plate.

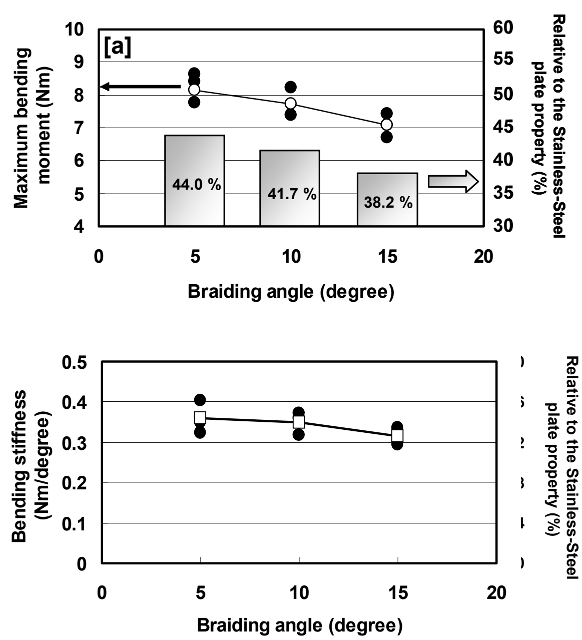

Figure 2: [a] Maximum bending moment and [b] bending stiffness with different braiding angles on braided carbon/PEEK composite bone plates.

COMPARATIVE BIOMECHANICAL STUDIES BETWEEN NEWLY DESIGNED STEMLESS PROSTHESIS AND CONVENTIONAL PROSTHESIS

Ching-Lung Tai[1], Chun-Shiung Shih[1,2], Shiuann-Sheng Lee[1] and Weng-Pin Chen[3]
[1]Department of Orthopaedic Surgery, Chang Gung Memorial Hospital, Kweishan, Taiwan, ortholab@adm.cgmh.org.tw
[2]Department of Orthopedic Surgery, Chung Shan Hospital, Taipei, Taiwan
[3]Department of Biomedical Engineering, Chung-Yuan Christian University, Chungli, Taiwan

INTRODUCTION

Total hip arthroplasty (THA) has proven to be a successful surgical technique in the past thirty years due to the improvement of prosthetic design, biomaterials and surgical technique. However, the complication of local bone loss still remains an unsolved problem during the long-term application. No femoral prostheses were free of such complications. Stress-shielding effect was thought to be the main factor that result in local bone loss after prosthesis implantation. In order to eliminate the stress shielding effect that traditional prosthetic femora encounters in long-term application, we developed a new designed stemless prosthesis (Cervico-Stemless prosthesis, C-S prosthesis), Figure 1. An integral and systematic biomechanical experiment was conducted by using this C-S prosthesis, and the results were compared with that of traditional femoral prosthesis.

METHODS

We measured the surface strains of proximal femora *in-vitro* on conditions of one-leg stance using synthetic femora and MTS testing machine under 1,000 Newtons loading. The surface strains of implanted femora are compared between C-S and traditional PCA prosthesis after insertion of C-S prosthesis in cases of (A) Two screws fixation; (B) Three screws fixation and (C) Cement fixation. The experimental set-up was shown in Figure 2.

RESULTS AND DISCUSSION

The percentage of surface strains as compared to intact femora for C-S and traditional prosthetic femora was shown in Figure 3. The results was summarized as follows:

1. The stress shielding phenomena of C-S prosthetic femora were significantly eliminated in all insertion conditions as compared to the PCA case.
2. As for C-S prosthetic femora, there exists similar stress distribution between each insertion condition. No significant difference of surface strains was found.

SUMMARY

Based on the results of this current study, we concluded that the newly designed C-S prosthesis possess the following superiority:

1. More physiological stress distribution on the proximal femur;
2. Prevention of endosteal femoral osteolysis;
3. Immediate stabilization of the implant;
4. Preservation of endosteal vascularity; and
5. Capacity for later femoral revision.

Figure 1: The newly designed C-S prosthesis.

Figure 2: The strain measurement of C-S prosthetic femora.

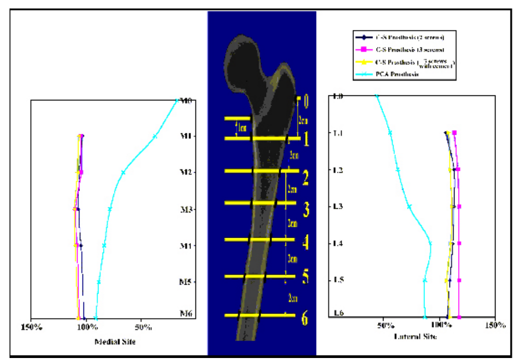

Figure 3: The percentage of surface strains as compared to intact femora for C-S and traditional PCA prosthetic femora.

REFERENCES

Collis D.K. et al, (1991)*J. Bone Joint Surg[Am],***73A**, 593-597
Joshi A.B. et al, (1993) *J. Bone Joint Surg[Br],* **75**, 616-623.
Shih C.H. et al, (1997) *Clin. Biomech,* **12**, No. 7: 482-490.

ACKNOWLEDGMENTS

We acknowledge the financial support of the National Science Council, ROC. (NSC89-2314-B- 182A-191)

SIMULATION OF THE SHAPE CHANGE OF A RED BLOOD CELL AT THE ENTRANCE OF A CAPILLARY

Shigeo Wada and Ryo Kobayashi
Research Institute for Electronic Science, Hokkaido University, Sapporo, Japan
wada@bfd.es.hokudai.ac.jp

INTRODUCTION

It is well known that a red blood cell (RBC) has an ability to pass through a capillary with a diameter smaller than that of the cell by changing its shape flexibly. The flexibility of an RBC arises from the mechanical properties of the cell membrane consisting of a lipid bilayer and an underlying skeletal network (Mohandas and Evans, 1994). However, it also depends on the shape of an RBC taking a shell structure. Therefore, in order to understand the flexibility of an RBC, it is necessary to describe the behavior of an RBC which deforms 3-dimensionally into various shapes based on the properties of the membrane. In this study, we simulated the shape change of an RBC passing through a capillary using our elastic network-model of an RBC (Wada et al., 2000).

METHODS

The whole membrane of an RBC was divided into small triangular elements (4484 elements with 2244 nodes). Each edge of the element was expressed by a linear spring with an elastic resistance, k_s. An element was connected with the neighboring elements by a plate spring having an elastic resistance, k_b, which resisted to the change of the contact angle between them. It was assumed that the element also resisted to the change in both the area of each element and the total surface area of the membrane, and it had an expansion moduli for the local area change, k_a, and for the global area change, k_A. Furthermore, the resistance to the change in volume of an RBC was expressed by a bulk modulus of the cell, k_V.

When an external force is applied to an RBC to cause a shape change, elastic energies are generated as the results of stretching of the linear spring, bending of the plate spring, area expansion of the element and the membrane, and volume change of the cell. Here, these elastic energies were mathematically expressed as a function of position vector at each node of the elements. Based on the energy principle, the shape of an RBC was determined by finding nodal positions that minimized the sum of the elastic energies. Since the derivative of the total energy with respect to the position vector at a node provides an internal force acting on the nodal point, this was accomplished by solving the equation of motion of mass points assigned to the nodes which were moved by the internal force and an external force applied.

The values of elastic resistances were chosen to be $k_s = 1.5\times10^{-2}$ dyn/cm and $k_b = 1.0\times10^{-6}$ dyn, which were equivalent respectively to a shear modulus and a bending stiffness of an RBC membrane shown in literatures (Mohandas and Evans, 1994; Hansen, 1996). The expansion modulus for local area change, k_a, was determined to be 0.5 dyn/cm based on experimental data obtained by an aspiration test (Mohandas and Evans, 1994). The expansion modulus, k_A, and bulk modulus, k_V, were set to be 5.0 dyn/cm and 1.0×10^{-6} dyn/cm^2, respectively, so that the calculations could be carried out successfully keeping the surface area of the membrane and the volume of the RBC almost constant.

RESULTS AND DISCUSSION

It was assumed that the shape of an RBC in a natural state (stress free state) was a biconcave disc with a diameter of 8.30 μm, a minimum thickness of 1.01 μm, a maximum thickness of 2.18 μm, a surface area of 138 μm^2, and a volume of 122 μm^3. Simulation was carried out from a state where the RBC was approaching the entrance of a capillary with a diameter of 6 μm by aligning its axis with the axis of the capillary.

Figure 1 shows the shape change of an RBC as the cell was drawn in the capillary by a suction pressure of 50 dyn/cm^2. The total elastic energy generated in the RBC increased until the cell was completely drawn in the capillary. The internal force acting on the membrane which increased with increasing the elastic energy resisted to the shape change of the RBC. However, in going deeper in the capillary, the shape of the RBC gradually changed in such a manner that it decreased the total elastic energy and pass through the capillary easily.

REFERENCES

Hansen, J. C. et al. (1996). *Biophys. J.*, **70**, 146-166.
Mohandas, N., Evans, E. (1994). *Annu. Rev. Biophys. Biomol. Struct.* **23**, 787-818.
Wada, S. et al. (2000). *Proc. 10th Intern. Conf. on Biomed. Eng.*, 435-436.

ACKNOWLEDGEMENTS

This work was supported by the Grant-in-Aid for Scientific Research (B), No. 13480284, by the Ministry of Education, Science, Sports and Culture of Japan.

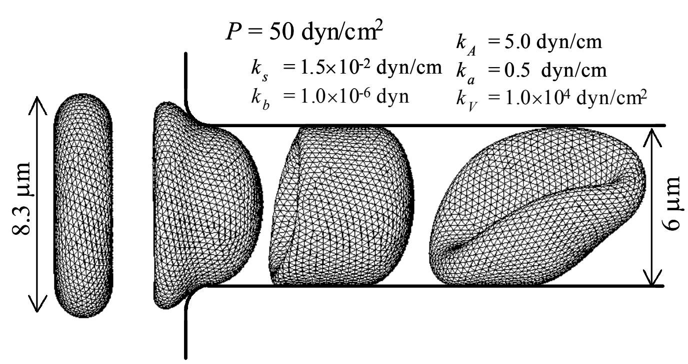

Figure 1: Shape change of an RBC at the entrance of a capillary.

ADJUSTMENT OF INDIVIDUAL STIMULATION PATTERNS FOR FES CYCLING

Margit Gföhler[1], Thomas Angeli[1], Peter Lugner[2] and Winfried Mayr[3]

[1]Department of Machine Elements, Vienna University of Technology, Vienna, Austria, email: margit.gfoehler@tuwien.ac.at
[2]Department of Mechanics, Vienna University of Technology, Vienna, Austria
[3]Department of Biomedical Technics and Physics, University of Vienna , Vienna, Austria

INTRODUCTION

By Functional Electrical Stimulation (FES) of leg muscles paraplegics can coordinate the movement pattern of pedaling. As paralyzed muscles are mostly weakened and only a limited number of effective leg muscles can be reached by surface electrodes it is important to convert the generated muscle forces into drive power with high efficiency. Therefore, before the test person starts cycling on a mobile tricycle, tests are performed on a test bed (Gföhler et al., 2001) for determination of the optimal individual stimulation pattern.

METHODS

The paraplegic test person is seated on a specially adapted wheelchair, the relative position of crank and chair and also the angle of the backrest can be adjusted (Fig. 1). A four bar linkage allows the pedal to rotate on an optimized noncircular pedal path (Angeli et al., 1999). A specially developed measuring crank allows measurements of the three orthogonal forces applied to the crank. The knee angle is measured by a goniometer. For the pedaling experiments the gear motor can either fix the crank at a given angular position (static measurements) or drive the crank with a given angular velocity (dynamic measurements).

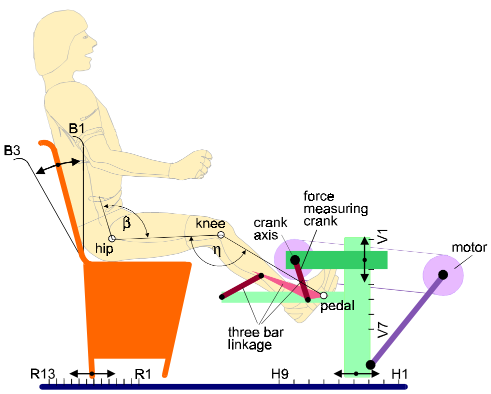

Figure 1: Scheme of the test bed.

The geometry of the rider-cycle system (vertical and horizontal distance between hip joint and crank axis, backrest inclination) and the influence of the stimulation parameters (threshold / max. stimulation voltage, stimulation frequency) are tested by variation of the different parameters. The generated crank loads and drive torque are measured, and optimal stimulation intervals are determined for each stimulated muscle individually. Afterwards dynamic measurements at a given crank angular velocity with all muscles stimulated together show which power output can be achieved during one full rotation of the crank.

RESULTS AND DISCUSSION

Figure 2 shows the results of dynamic measurements with stimulation of the hamstrings.

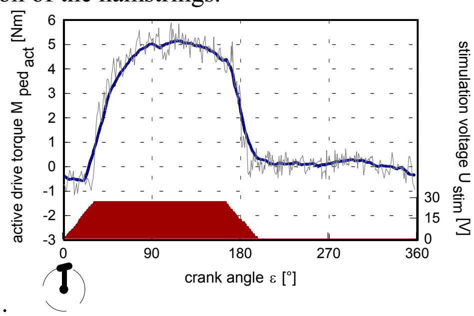

Figure 2: Measurements with stimulation of the hamstrings at crank angular velocity 25 rpm in the individually optimized stimulation interval: stimulation voltage and resulting active drive torque (due to active muscle forces) applied to the crank during one full rotation

SUMMARY

As paralyzed muscles are mostly weakened and only a limited number of effective leg muscles can be reached by surface electrodes it is important for FES cycling to convert the generated muscle forces into drive power with high efficiency. This study describes how to optimize the stimulation patterns for FES cycling with static and dynamic tests on a test bed for an individual paraplegic test person.

REFERENCES

Gföhler M. et al. (2001). *IEEE Trans. Neural. Syst & Rehab. Eng.*, **9**, 169-180.
Angeli T. et al. (1999). *Med. & Biol. Eng. & Comp.*, **37**, Supp. 2, 326-327.

ACKNOWLEDGEMENTS

This work was supported by the Austrian Science Foundation FWF and Otto Bock Austria.

A BIPHASIC CONSTITUTIVE LAW FOR PASSIVE CARDIAC TISSUE

D.-E. Bakman, Y. Loosli, P. Schmid, P. Niederer
Institute of Biomedical Engineering, University and ETH Zurich, Zurich, Switzerland
bakman@biomed.ee.ethz.ch

INTRODUCTION

Myocardial tissue consists of a variety of different components, among them, muscle fibres, collagen, coronary vessels, blood and interstitial fluid. The pronounced anisotropy of the tissue is characterized by the architecture of the highly crosslinked muscle fibres (Schmid 1997). Passive myocardial tissue has furthermore non-linear viscoelastic constitutive characteristics (Fung 1981). The intravascular fluid flow, in turn, is influenced by the contraction (systole) and relaxation (diastole) processes, such that an effective compressibility may be simulated by an unbalanced fluid exchange.

In order to simulate the redistribution of coronary blood in the ventricular wall during the deformation (passive filling phase), a biphasic formulation (fluid + solid) has been developed for the myocardium to be applied during the diastolic phase.

CONSTITUTIVE EQUATIONS

In this study the myocardial tissue is considered as a mixture of an incompressible inviscid fluid phase (representing the coronary blood) and a nearly incompressible anisotropic solid phase. Each phase is homogeneous and no material exchange occurs between the two constituents.

The stress tensor of the fluid ($\boldsymbol{\sigma}^{\mathbf{f}}$) is calculated by the relation

$$\boldsymbol{\sigma}^{\mathbf{f}} = -p\frac{\phi^f \rho_T^f}{\rho}\mathbf{I} \tag{1}$$

whereas the stress on the solid phase ($\boldsymbol{\sigma}^{\mathbf{s}}$) is given by

$$\boldsymbol{\sigma}^{\mathbf{s}} = -p\frac{\phi^s \rho_T^s}{\rho}\mathbf{I} + \boldsymbol{\sigma}^{\mathbf{E}} \tag{2}$$

Thereby, ρ_T^α is the true density, $\rho_T^\alpha(\underline{x},t) = \dfrac{dm^\alpha(\underline{x},t)}{dV^\alpha(\underline{x},t)}$, and ϕ^α is the local volume fraction of the αth constituent:

$$\phi^\alpha(\underline{x},t) = \frac{dV^\alpha(\underline{x},t)}{dV(\underline{x},t)}, \quad \alpha = s: \text{solid}, \quad \alpha = f: \text{fluid} \tag{3}$$

ρ is the density of the mixture, $\rho = \rho^s + \rho^f$ (4)

$$\text{with } \rho^\alpha(\underline{x},t) = \frac{dm^\alpha(\underline{x},t)}{dV(\underline{x},t)} \tag{5}$$

$\boldsymbol{\sigma}^{\mathbf{E}}$ is the solid stress which in general is derived from the strain energy function, W. Huyghe (1991) proposed a formulation for this function for use in a passive heart model:

$$\boldsymbol{\sigma}^{\mathbf{E}}(\boldsymbol{\varepsilon},t) = \frac{\partial\left(C(J-1)^2\right)}{2\cdot\partial\boldsymbol{\varepsilon}} + \int_0^t G(t-\tau)\cdot\frac{\partial\boldsymbol{\sigma}^{\mathbf{el}}(\boldsymbol{\varepsilon}(\tau))}{\partial\tau}\cdot d\tau \tag{6}$$

Here, C is the bulk modulus, J the Jacobian, $\boldsymbol{\sigma}^{\mathbf{el}}$ the anisotropic elastic response of the material and G(t) the scalar reduced relaxation function

$$G(t) = \left[1 + \int_0^\infty \Psi(s)\cdot e^{-\frac{t}{s}}ds\right]\cdot\left[1 + \int_0^\infty \Psi(s)\cdot ds\right]^{-1} \tag{7}$$

with $\Psi(s) = \dfrac{d}{s} + \Psi^0$ if $s_1 \le s \le s_2$ and $\Psi(s) = 0$ elsewhere.

$\boldsymbol{\sigma}^{\mathbf{el}}$ is given by: $\sigma_{ij}^{el} = \dfrac{1}{2}\left(\dfrac{\partial W^{el}}{\partial\varepsilon_{ij}} + \dfrac{\partial W^{el}}{\partial\varepsilon_{ji}}\right)$ (8)

$$W^{el} = c^n\{\sum_{i=1}^{3}(\exp(a^{cf}\varepsilon_{ii}) - a^{cf}\varepsilon_{ii}) + \sum_{i\neq j}\sum_{j\neq i}(\frac{1}{2}(\exp(a^b\varepsilon_{ii})$$
$$- a^b\varepsilon_{ii})(\exp(a^b\varepsilon_{jj}) - a^b\varepsilon_{jj})) - 6\} + c^s\{\exp(\frac{a^s}{2}\sum_{i\neq j}\sum_{j\neq i}\varepsilon_{ij}\varepsilon_{ij}) - 1\}$$

The fluid flux into the biphasic medium is defined as

$$\underline{J} = \phi^f(\underline{v}^f - \underline{v}^s) \tag{9}$$

where $\underline{v}^f$ and $\underline{v}^s$ are the fluid and solid velocities, respectively.

The constitutive equation for the momentum supply $\underline{\pi}$, representing the internal force between the two phases, reads

$$\underline{\pi} = \frac{\mathbf{K}}{\phi^f}\underline{J} - \frac{p}{\rho}\underline{u}(\underline{v}^s\cdot\underline{\nabla}\rho^s + \underline{v}^f\cdot\underline{\nabla}\rho^f) \text{ with } u_i = \frac{1}{3(v_i^f - v_i^s)} \tag{10}$$

where $\mathbf{K}$ a positive definite diagonal tensor whose terms describe the diffusive resistance coefficients.

DISCUSSION

The equations ((1), (2), (6) and (10)) describe the constitutive behavior of the myocardial tissue. The effective compressibility of the heart, due to the intravascular fluid flow, as well as its anisotropic structure and its non-linear viscoelastic behaviour are also considered. In this formulation the time dependence of the blood flux was not taken into account, however, a pulsatile coronary blood flow can be implemented. The biphasic formulation (equations (1), (2) and (10)) presented here is not limited to the myocardium and can also describe the mechanical behaviour of other soft tissues.

REFERENCES

Fung, Y. C. (1981). *Biomechanics: Mechanical Properties of Living Tissues*. Springer-Verlag.
Huyghe, J. M. et al (1991). *Journal of Biomechanics*, **24**, 841-849.
Schmid, P. et al (1997). *Technology and Health Care*, **5**, 29-43.

CELL SEEDED PLASMA-TREATED POLYESTER LIGAMENT UNDER CYCLIC TENSILE LOAD- COMMISSIONING OF METHODOLOGY

Mostafa Raïf[1], Toyoda Takashi[1] and Bahaa Seedhom[2]
Division of Bioengineering, Rheumatology and Rehabilitation Research Unit, Leeds Medical School, Leeds, UK
1 Postdoctoral Research Fellow, 2 Reader and Director of Research

INTRODUCTION

Plasma treatment of polyester ligament structures has been shown to render the material hydrophilic and increase cell adhesion to it (Rowland et al (2000)). In this work we describe methodology, apparatus and report early results of an investigation into the cell proliferation and morphological changes of cells when seeded on a plasma-treated polyester ligament scaffold, which is then subjected to cyclic tensile strains.

METHODS

Cell culture: Primary cultures of Synovial fibroblasts were prepared from Metatarsophalangeal bovine joints by enzymatic digestion with collagenase.
Mechanical load application: A special apparatus was designed which allowed the application of a cyclic tensile load, of varying amplitude at a frequency of 1 Hz, on the cell seeded ligament scaffolds while being gripped and placed in culture medium within an incubator at 37°C. The design allowed visual monitoring of the cell seeded ligament scaffold with light microscopy, during prolonged tests

Cytotoxicity test: The cytotoxicity of scaffold grips was investigated using synovial fibroblasts in cell monolayer culture. The scaffold grips were partially immersed and partially projecting out of the culture dish. The grips materials tested were 303 and 316 stainless steel, Titanium (Ti) and Delrin.

Cell proliferation: The ligament scaffolds were seeded with synovial fibroblasts. After four days in culture, the scaffolds were incubated in a serum free medium for 24 hours. Subsequently, a cyclic tensile load of amplitude of 150N (producing 5% cyclic tensile strain) was applied for a period of 6 hours. The cell-seeded scaffolds were then incubated for a further 24 hours. Effect of cyclic strain on cell proliferation was assessed using Blue Trypan. The controls (unloaded cell seeded scaffolds, both **within** and **without** the grips) were carried out under the same conditions.

Optical microscopy analysis
The loaded and unloaded cell seeded scaffolds (one of the two control groups) were fixed with 3.7% formaldehyde for 5 minutes. They were then washed with PBS and stained with Toluidine Blue O for 5 minutes.

RESULTS AND DISCUSSION

Efficacy of the apparatus: A mechanical test was carried out to examine the capacity of the grips to hold the implant whilst applying cyclic tensile load. The test demonstrated that these grips could successfully hold the implant in place after the application of a tensile load of 150N amplitude, at a frequency of 1 Hz throughout 300,000 load cycles.

Toxicity: contrast optical microscopy and the cell cytotoxicity studies showed that the 316 stainless steel was the most biocompatible of the alloys tested when partially immersed in the culture medium and partially projecting out of the culture dish.

Cell proliferation: The application of cyclic strain for 6 hours was associated with an increase in the number of cells of some 8% observed in the loaded ligament scaffolds, above those observed in seeded but unloaded scaffolds.

Morphological changes: In the *unloaded control* group the cells are randomly oriented, Figure 1-a, and although cellular morphology varied from one cell to another, a fibroblastic shape is the most typical. In the *loaded scaffolds* most of the cells are oriented in the direction of the load (scaffold filaments), Figure 1-b, and most of the cells acquired a spindle-shape typical of ligament fibroblasts, Figure 1-c.

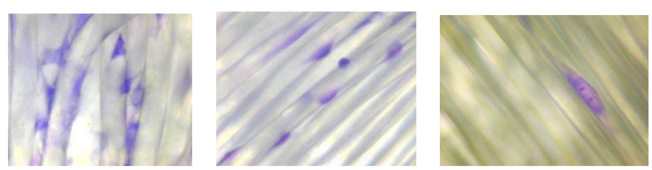

(a) (b) (c)

Figure 1: Morphology of bovine synovial cells seeded on plasma-treated polyester ligament scaffold, (a): Controls, (b): Cells on loaded scaffold, (c): higher magnification of b.

CONCLUSION

We have developed a viable methodology for seeding fibroblasts onto plasma treated polyester ligament scaffolds and subjecting these, for prescribed periods, to cyclic loads at a physiological frequency in order to investigate and monitor cell proliferation; morphology and metabolism.

REFERENCE

ROWLAND, R.J.R., ET AL (2000) Proceedings 9th International Conference on Polymers in Medicine & Surgery. Danube University, Krems, Austria,

MATHEMATICAL MODELS FOR THE TIME-DEPENDENT CHARACTERISTICS OF SPINAL CORD TISSUE

Oakland, R J[1]; Wilcox, R K[1]; Hall, R M[1]; Barton, D C[1]
[1]School of Mechanical Engineering, University of Leeds, Leeds, LS2 9JT, UK. +44 113 233 2164, Email: menrjo@leeds.ac.uk

INTRODUCTION

It is becoming increasingly important to develop accurate mathematical models of human tissue for use in finite element analysis. For modeling the impingement of bone fragments on the spinal cord during fracture, mechanical properties of the spinal cord are required but only limited data is available. The viscoelastic behaviour over 1 minute has been studied (Bilston, 1996), but no authors have investigated extended relaxation. The aim of this study was to investigate the time-dependent characteristics of spinal cord and fit mathematical models to both loading and stress-relaxation data obtained.

METHODS

Experimental - Samples of intact bovine spinal cord (80mm-120mm) were taken from their dural sheath and placed in a sealed container of preheated isotonic saline solution (37^0C). Individual specimens were then fitted with two clips around the central section to mark the gauge length and the specimen ends were placed into fixation devices loaded with dry ice to hold the sample firm. Care was taken not to stretch the specimen as the fixations were attached to the lower base and upper load cell of a bench top tensile testing machine (Shimadzu, JN). A preload of 0.5N, representing a strain of approximately 3-5% was then applied to each specimen. A videoextensometer (Messphysk ME-46) was used to identify the gauge length and determine the extension caused by the uniaxial load on the specimen. For each test, 15 conditioning cycles were performed before samples were elongated to a maximum nominal strain at a preset strain rate ($0.023s^{-1}$) and held for 15 minutes.

Mathematical Models – A quasilinear model developed by Fung (1993) was used to model the cord behaviour during loading. Using the same elastic response function as Bilston (1996), the following expression for the stress response was obtained:

$$\sigma(t) = AB\varepsilon_0 \sum_i G_i \left[\frac{1}{\frac{1}{\tau_i} + B\varepsilon_0} \left(e^{B\varepsilon_0 t} - \left(e^{\frac{-t}{\tau_i}} \right) \right) \right] \qquad 0 < t < t_1$$

It was also attempted to fit the quasilinear model to the stress-relaxation data but this was deemed unsuccessful due to the extended relaxation period tested.

A Maxwell-Kelvin four-element model was therefore used to model the cord behaviour during relaxation. Substituting the elastic and viscous elements in the relaxation response of a four-element viscoelastic model gives:

$$\sigma(t) = E_1 e^{(t_1 - t)\tau_1} + E_2 e^{(t_1 - t)\tau_2}$$

RESULTS

A total of 10 tests were successfully carried out, and data from each test were fitted to the models using a generalised reduced gradient non-linear optimisation algorithm (Microsoft Excel Solver, Microsoft, WA) to obtain values for each of the parameters. The results of each model are summarised below:

Quasilinear Model

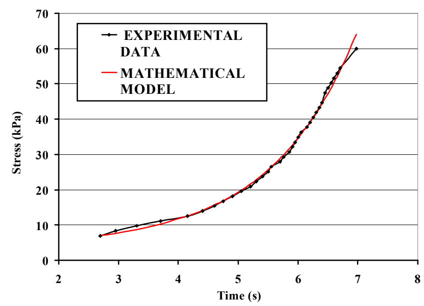

	Mean ± S.D.
τ_1	0.64 ± 0.12
τ_2	0.36 ± 0.07
τ_3	229 ± 0.34
A	-8.91 ± 2.40
B	34.10 ± 2.61
G_1	-1.41 ± 0.21
G_2	-0.53 ± 0.13
G_3	0.49 ± 0.13

Model Parameters

Figure 1: Typical Stress-Time Plot during Loading

4-Element Model

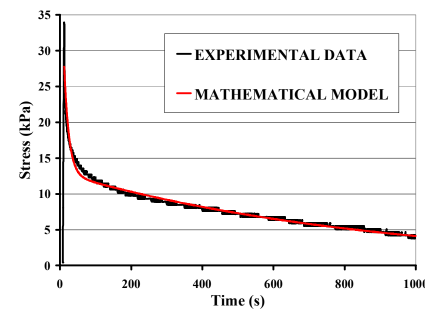

	Mean ± S.D.
E_1 (kPa)	17.42 ± 5.84
E_2 (kPa)	21.65 ± 7.45
τ_1 (sec^{-1})	$6.7E^{-4}$±$1.3E^{-4}$
τ_2 (sec^{-1})	0.08 ± 0.01

Model Parameters

Figure 2: Typical Stress-Time Plot during Relaxation

DISCUSSION

The results of the experimental tests show a non-linear 'J-shaped' stress-strain response during loading and clear viscoelastic properties upon relaxation. The quasilinear model developed to describe the behaviour of the spinal cord was found to describe the material behaviour adequately during loading, but was deemed unsuccessful for modelling the extended relaxation. The 4-element model appeared to fit the relaxation behaviour well. The parameters from both models are therefore useful for finite element simulations of the spinal cord under different loading conditions.

REFERENCES

Bilston, L.E., Thibault, L.E. (1996). *Annals of Bio. Eng.* **24**, 67-74.
Fung, Y.C. (1993). *Biomechanics: Mechanical Properties of Living Tissues.* New York: Spinger-Verlag.

THE RELATION OF THE COMPRESSIVE MODULUS OF ARTICULAR CARTILAGE WITH ITS DEFORMATION RESPONSE TO CYCLIC LOADING

[1]Michael K. Barker, B.Eng., M. Sc., Ph.D. and [2]Bahaa B. Seedhom B.Sc., PhD*

Division of Bioengineering, Rheumatology and Rehabilitation Research Unit, Leeds School of Medicine, University of Leeds, Leeds. UK.

[1] Snow Senior Bioengineer, DePuy International, Leeds, [2] Reader in Bioengineering and Director of Research, b.b.seedhom@leeds.ac.uk

INTRODUCTION

This study was focused on the relationship between the compressive modulus of cartilage and its deformation under cyclic loading conditions – particularly those arising during level walking, which is the most predominant of human activities. Other parameters that influence cartilage deformation under these conditions are the duty cycle parameters including: the frequency of load application, the amplitude of the applied load, the ratio of the loading duration to that of recovery within a loading cycle and the number of loading cycles applied. It is likely that effects of these parameters on cartilage deformation have not been investigated because of the limited variation in them. It is interesting, however, that no study has so far investigated the effect of the large range of modulus (1- 20 MN/m2), on the deformation of cartilage and this may well be because of the expectation that this relation would be a simple inverse one. This study has focused on this aspect because of both the intrinsic viscoelastic nature of cartilage and the influence of flow of the interstitial fluid during the application of cyclic load on cartilage that naturally occurs during locomotion.

METHODS

Twenty-four osteochondral plugs were harvested at eight specific sites from 3 fresh cadaveric knees. The cartilage tested thus had the widest possible range of compressive modulus as that observed across the knee in previous studies. Cartilage specimens were immersed in Hanks balanced salt solution, which was maintained at 37°C, and were subjected to the same cyclic loading regime representative of a typical walking cycle, for over 1 hour using a specialized indentation apparatus (Barker and Seedhom (1997)). The viscous and elastic components of matrix strain and the creep rate were measured throughout the entire experiment. The cartilage 'instantaneous' compressive modulus of each osteochondral plug was determined using methodology developed in our laboratory (Shepherd and Seedhom (1997)).

RESULTS AND DISCUSSION

The values of *'instantaneous compressive modulus* ranged from 1 to 19.5 MN/m^2. *Elastic strain decreased exponentially* with the compressive modulus; specimens with a modulus less than 4 MN/m^2 experienced elastic strains in the range 0.18 and 0.36, whereas stiffer specimens experienced strains between 0.05 and 0.13. *Viscous strain increased linearly* with cartilage compressive modulus and was as low as 0.02 at the lower values of the modulus but increased to 0.22 for a compressive modulus of 18 MN/m^2.

The rate of creep under cyclic load had an inverse linear relationship with the cartilage stiffness. The strain response of soft specimens approached steady state by 200 cycles but that of stiff specimens approached it by 1300 cycles. Subsequent experiment corroborated the view that this difference in the viscous behavior of stiff and soft cartilage is mostly related to the interstitial fluid flow rather than to intrinsic viscoelasticity of the cartilage matrix.

The total strain (sum of elastic and viscous strain components), had a bimodal relationship with the compressive modulus, and had a minimum that corresponded to the midrange value of the modulus (10 MN/m^2). A hypothesis is proposed that cartilage adapts its matrix components so as to minimize the total strain in response to the most prevalent loading regime that it is subjected to.

REFERENCES

Barker, M. K. and Seedhom, B, B., (1997); Articular cartilage deformation under physiological cyclic loading without a tare load apparatus and measurement techniques; Journal of Biomechanics, 30: 377-381.

Shepherd, D. E. T. and Seedhom, B, B. (1997); A technique for measuring the compressive modulus of articular cartilage under physiological loading conditions with preliminary results, Engineering in Medicine, Proceedings Institute of Mechanical Engineers, 211: 155-165.

EVALUATION OF FRICTION AND WEAR PROPERTIES OF PVA HYDROGEL AS ARTIFICIAL CARTILAGE

Kazuhiro Nakashima, Teruo Murakami and Yoshinori Sawae
Department of Intelligent Machinery and Systems, Faculty of Engineering, Kyushu University,
Hakozaki, Fukuoka City, Japan, nakaji@mech.kyushu-u.ac.jp

INTRODUCTION

Although a great number of total joint replacements have been carried out particularly for diseased hip and knee joints, in certain cases, serious tribological problems such as loosening and wear occurred. Therefore authors investigated another rubbing surface as joint replacement, namely, artificial cartilage material by using PVA (polyvinyl alcohol) hydrogel. And in a condition of walking motion at knee joint simulator, PVA hydrogel showed low friction by fluid film lubrication. However, in thin film lubrication like mixed lubrication the wear of PVA hydrogel was increased against the zirconia ceramics.
In this study to investigate the possibility of clinical use of PVA hydrogel, the pair of PVA hydrogel as lower specimen and PVA hydrogel or natural articular cartilage as upper specimen was examined.

METHODS

PVA hydrogel was made by repeated freezing method (degree of saponification:99.4-99.8mol%, EWC: 79%, repeating process: 5 cycles).
Friction and wear properties of PVA hydrogel as artificial cartilage was investigated in a reciprocating tester. In the test a elliptical surface of PVA hydrogel or natural articular cartilage was used as upper specimen and PVA hydrogel plate was used as lower specimen. The sliding speed was 20mm/s, the total sliding distance was 3km, the stroke was 35mm (rectangular wave) and the load was 9.8, 4.9, 2.94 N. The lubricants were saline solution containing protein and hyaluronic acid (HA). The wear was evaluated by the wear grade based on difference of surface structure observed by microscopy or naked eye.
The film thickness was calculated to confirm that mixed lubrication occurred. The equations proposed by D.Dowson et al. was used.

RESULTS AND DISCUSSION

Figure 1 shows surface structure images after reciprocating test (lower specimen: PVA hydrogel, upper specimen: natural articular cartilage, load: 9.8N, lubrication: saline + 0.5wt% HA). In PVA hydrogel as lower specimen the wear was mild. In natural artificial cartilage as upper specimen, however, the severe wear was observed. The addition of proteins, i.e., albumin and globulin could reduce the wear of articular cartilage as shown in figure 2. The boundary film of protein is effective for the natural articular cartilage.

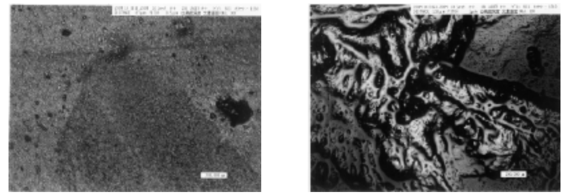

Figure 1: Surface structure images after reciprocating test (lubricant: saline + 0.5wt% HA, left: lower PVA hydrogel, right: upper natural articular cartilage)

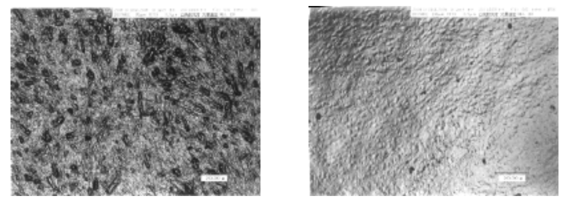

Figure 2: Surface structure images after reciprocating test (lubricant: saline + 0.5wt% HA + 0.7wt% globulin, left: lower PVA hydrogel, right: upper natural articular cartilage)

In the rubbing pair of PVA hydrogel against itself, although the upper PVA specimen showed significant wear, the addition of albumin and globulin could reduce wear. In PVA hydrogel the lubricant containing protein was effective to make boundary layer. Therefore, the artificial cartilage of PVA hydrogel is expected to be clinically applicable in biological environment in low loaded joint replacement.

SUMMARY

To evaluate the tribological behavior of PVA hydrogel, the simplified reciprocating test was conducted for sliding pairs of PVA hydrogel against natural articular cartilage or PVA hydrogel. In both pairs of PVA hydrogel and natural articular cartilage or PVA hydrogel, the lubricant containing protein effectively reduced wear.

REFERENCES

Murakami, T., Sawae, Y., Nakashima, K., Fisher, J., (2000) *Thinning Films and Tribological Interfaces / D.Dowson et al.* 317-327
Dowson, D., Yao, J Q., (1994) *Proc Instn Mech Engrs* **Vol 208** *Part J,* 43-52

ACKNOWLEDGEMENTS

Sodium hyaluronate was supplied by Seikagaku Corporation

INSTANTANEOUS COMPRESSIVE MODULUS OF ARTICULAR CARTILAGE IN THE JOINTS OF THE LOWER LIMB

Duncan E T Shepherd[1] and Bahaa B Seedhom[2]

Division of Bioengineering, Rheumatology and Rehabilitation Research Unit, Leeds Medical School, University of Leeds, Leeds. UK.

[1]Lecturer in Bioengineering (now Department of Bio-Medical Physics & Bio-Engineering, University of Aberdeen), [2]Reader in Bioengineering and Director of Research, b.b.seedhom@leeds.ac.uk

INTRODUCTION

In previous studies, we determined the topographic variation in cartilage compressive modulus on the entire articular surfaces of knee and ankle joints (Swann and Seedhom (1993), Yao and Seedhom (1993), Shepherd and Seedhom (1999). These studies showed that the compressive modulus (whether measured as a 'creep' or 'instantaneous' modulus) was related to the regional variation in the prevalent stresses occurring in these two joints. Thus cartilage was stiff (had a high modulus) where the prevalent stress was high, whereas cartilage subjected to predominantly low stress was soft, (had a low modulus). These data supported the hypothesis that cartilage responds to the predominant mechanical stress and so adapts its mechanical properties. These data provide necessary (but not sufficient) evidence in support of our mechanical conditioning hypothesis of articular cartilage. Because the knee and ankle joints used in the previous studies were from different populations it was not possible to extrapolate from the data obtained so far whether it was viable to propose the hypothesis that properties of cartilage of joints in the lower limb were also related to the prevalent stresses acting in these joints i.e. those arising during locomotion. To test this hypothesis it was necessary to survey the properties of cartilage on the entire articular surfaces of groups of hip, knee and ankle joints where each set is from the ipsilateral side. In this presentation we report some of the findings of this investigation.

METHODS

Eleven sets of fresh human lower limb joints, obtained from the ipsilateral side from eleven cadaveric donors, were used in this study. The 'instantaneous' modulus was determined using a specially developed indentation apparatus (Shepherd and Seedhom, 1997) that allowed application of load on articular surfaces at a physiological rate, and so from the measured indentation and cartilage thickness at a particular site, the modulus was calculated for a specific geometry of contact. Measurements were made at some 50 sites in each hip, 70 sites in each knee and 35 in each ankle. The average modulus for the entire joint surface of each joint and the topographical variations in the modulus within each joint were examined for all eleven sets, and subjected to statistical analysis.

RESULTS AND DISCUSSION

Within each set of joints (hip, knee and ankle) the ankle *always* had a significantly greater mean compressive modulus than the hip and knee ($p<0.001$- $p<0.05$). In seven sets of joints there was no significant difference between the mean compressive moduli of the knee and hip joints. In three sets of joints the compressive modulus of the knee was significantly greater than that of the hip ($p<0.001$-$p<0.01$), while in only one set of joints was the compressive modulus of the hip significantly greater than that of the knee ($p<0.01$). The topographical variations in the cartilage instantaneous compressive modulus over the surfaces of the lower limb joints were matched by differences in the prevalent stresses occurring in different areas of each joint. The results of the present study corroborate previous findings and show that the site specific stresses and corresponding values of the instantaneous cartilage compressive modulus over the surfaces of lower limb joints were correlated ($r = 0.82$ at $p<0.01$), thus adding credence to the conditioning hypothesis of cartilage by prevalent stress.

REFERENCES

Swann, A.C. and Seedhom B.B. (1993). The Stiffness of normal articular cartilage and the predominant acting stress levels, British Journal of Rheumatology, 32: pp 16-25.

Yao, J.Q. and Seedhom, B.B. (1993). Mechanical conditioning of articular cartilage to prevalent stress, British Journal of Rheumatology, 33: pp 16-25.

Shepherd, D.E.T. and Seedhom, B.B. (1997); A technique for measuring the compressive modulus of articular cartilage under physiological loading conditions with preliminary results, Engineering in Medicine, Proceedings Institute of Mechanical Engineers, 211: pp 155-165.

Shepherd, D.E.T. and Seedhom, B.B. (1999). The 'instantaneous' compressive modulus of human articular cartilage in joints of the lower limb, Rheumatology, 38: pp 124-132.

STUDY OF LV FILLING:COMPARISON OF HYDRAULIC AND NUMERICAL MODELING

Stefaan De Mey, Jan Vierendeels and Pascal Verdonck
Institute of Biomedical Techmology, Ghent University, Ghent, Belgium.

INTRODUCTION

The aim of this study is to compare the findings in a hydraulic LV filling model with numerical simulations in a 2D axi-symmetric LV filling model.

METHODS

The left heart model (De Mey et al, 2000) consists of an atrium (LA) connected to a truncated ellipsoidal left ventricle (LV). Hydraulic model experiments of LV filling were done for varying relaxation (τ = 45, 60 and 90 ms), LA pressure (LAP = 3, 10 and 30 mmHg) and compliance (C = 0.45 and 1.35 ml/mmHg). Flow propagation of LV filling (v_p) is calculated from measured color M-Mode (CMD) images. The hydraulic experiment results are fitted to a multiple linear regression model (General Linear Model, GLM) with v_p the dependent variable to test for significant variables. Hydraulic experiment results are compared to numerical simulations derived from a 2D axi-symmetric numerical LV filling model (Vierendeels et al, 2000).

RESULTS AND DISCUSSION

Figure 1 compares CMD images obtained in the hydraulic model experiment and the according numerical model simulations corresponding for varying settings. Overall, a good qualitative agreement is observed. The GLM modeling the hydraulic experiment results has a F-value of 82.9 (adjusted r^2 = 0.82, $p < 0.001$). A significant ($p < 0.001$) influence of τ, C and LAP is found. Overall, a moderate, but significant correlation is found ($r = 0.67$, $p < 0.01$) between numeric and hydraulic experiment results. Numerical model results are however consistently lower.

In the numerical model an ambiguous influence of compliance is noticed. Visual inspection of CMD images shows a curved isovelocity contour that can be approximated in a bilinear way. Close to the base, the front is steeper (higher v_p) than further into the LV (lower v_p). The slower v_p, obtained when using the isovelocity contour that goes deeper in the LV can be explained by a stagnation point of the traveling vortices, occurring in the stiff LV, but not in the compliant LV. As can be verified in figure 1 (A) and 1 (B), this stagnation point moves towards the apex with decreasing τ. Because the closer to the apex a stagnation point is situated, the less influence it has on calculated v_p values, this mechanism possibly explains the merging of v_p values for low τ values in the computer model.

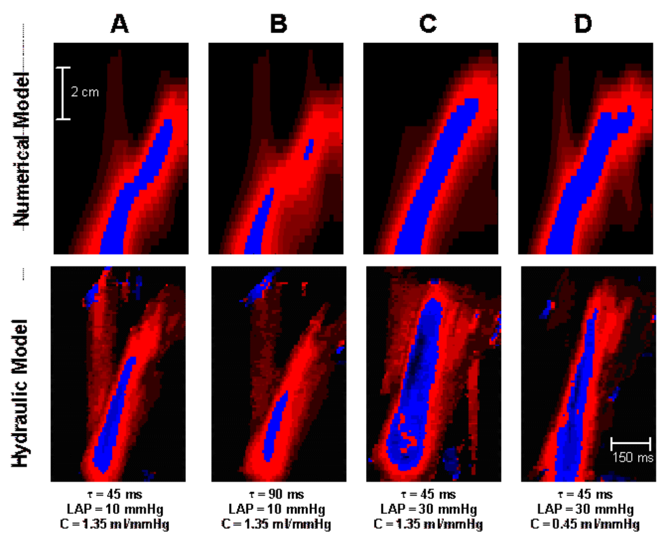

Figure 1: Calculated CMD images using the numerical model (top) and corresponding measured CMD images in the hydraulic model experiments (bottom) for varying time constant of relaxation (τ), LA pressure (LAP) and compliance (C).

SUMMARY

The interaction between v_p and LV diastolic variables is studied in a numerical model and compared to corresponding hydraulic model results. Overall a good agreement is found. v_p increases with increasing LA filling pressure and decreases with increasing τ. A decrease in compliance augments v_p in the region of the LV base but decreases v_p due to stagnation of the vortex at the mid-level of the LV.

REFERENCES

De Mey, S. et al (2000). *Circulation*, **102**, 1775. A new model for the experimental validation of left ventricular filling characteristics (abstract).

Vierendeels, J. et al (2000). *J Biomech Eng*, **122**, 667-674. Computer simulation of intraventricular flow and pressure gradients during diastole.

ACKNOWLEDGEMENTS

SDM was a recipient of a grant from the Institute for the Promotion of Innovation by Science and Technology in Flanders.

A BIOMECHANICAL ANALYSIS OF TRIANGULATION OF ANTERIOR VERTEBRAL DOUBLE-SCREW FIXATION

Ching-Lung Tai[1], Shih-Hao Chen[1], Tsung-Jen Huang[1], Weng-Pin Chen[2] and Robert Wen-Wei Hsu[1]
[1]Department of Orthopaedic Surgery, Chang Gung Memorial Hospital, Kweishan, Taiwan, ortholab@adm.cgmh.org.tw
[2]Department of Biomedical Engineering, Chung-Yuan Christian University, Chungli, Taiwan

INTRODUCTION

Anterior spinal instrumentation of the thoracic and lumbar spine has gained in popularity since Dwyer et al developed the cable system in 1964. However, implant loosening, screw breakage and cut-throughs have been noted clinically when using Dwyer or Zielke's Ventrale Derotations Spondylodese (VDS) instrumentations. To avoid these complications, one may use an anterior vertebral screw to penetrate the second cortex, or even a double-screw instrumentation using two parallel and pentrated screws to provide a stronger fixation. Bi-cortical screw purchase of vertebral body in anterior spinal fixation is well recognized to achieve optimal stabilization of implants. However, the potential hazards of penetration of anterior vertebral cortex screws that might cause neurovascular or organs injuries.

METHODS

Single-screw with bi-cortical purchase and various modes of double-screw fixation in anterior vertebral bodies were done using Trifix vertebral screws (San Andrio, CA, USA, Fig. 1.A) to assess the biomechanical stability of each fixation mode. The pullout forces of two parallel or triangulated anterior double-screw fixation with uni-cortical or bi-cortical purchase, were compared with that of single-screw with bi-cortical purchase. Four porcine spines were used for biomechanical analysis and bone mineral density was measured on each individual specimen before test. Single-screw with bi-cortical purchase and double-screws with 4 different modes of fixation which includes group A: triangulated with one screw penetration; group B: triangulated with no screw penetration; group C: two parallel with two screws penetration; and group D: two parallel with no screw penetration, were sequentially allocated into T11-L6 (totally 31 vertebrae) vertebrae. The experimental set-up were shown in Fig. 1.B and Fig. 2

RESULTS AND DISCUSSION

The results (Figure 3) demonstrate that the magnitudes of pullout force for various double-screw fixation modes are significantly higher as compared to the mode of single-screw bi-cortical purchase ($p<0.05$). However, in pullout tests of double-screw fixation, there is no statistically significance between group B and group C ($p=0.144$).

SUMMARY

In anterior vertebral double-screw fixation, the triangulated with no screw penetration mode can achieve ideal stability as those of two parallel with two screws penetration mode that is commonly advocated clinically. Therefore, the risks of placing anterior vertebral screws with cortical penetration can be avoided.

REFERENCES

Dywer, A.F. et al (1970).*J. Bone Joint Surg,* **52B**, 782-787
Lieberman I.H. et al (1998). *Spine* **23**, 908-910
Ogon M. et al (1996). *Spine* **21**, 2728-2734
Horton W.C. et al (1996). *Spine* **21**, 439-444

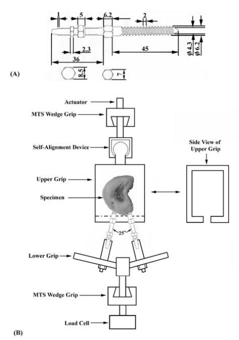

Figure 1: (A) The implanted vertebral screw and (B) Experimental set-up for triangulated implantation.

Figure2: The pullout test of single-screw fixation mode.

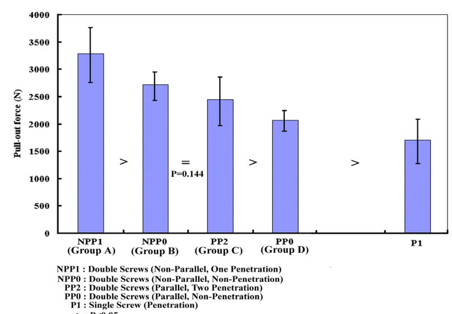

Figure 3: The pullout forces of the single-screw with bi-cortical purchase and double-screw with four modes of fixation.

ACKNOWLEDGEMENTS

We acknowledge the financial support of the National Science Council, ROC. (NSC89-2314-B- 182A-191)

BIODYNAMIC CHARACTERISTICS OF TOP SPRINTERS

Milan Coh, Bojan Jost, Milan Zvan
Faculty of Sport, University of Ljubljana, Slovenia, milan.coh@sp.uni-lj.si

INTRODUCTION

Sprinting velocity is the product of stride rate and stride length. Both parameters are interdependent and individually conditioned with the processes of central regulation of movement, morphologic and physiologic characteristics, motor abilities and energy factors. Sprint, as a motor stereotype of human locomotorics, consists of repetitions of strides. The length of the stride depends mainly on body height or leg length and the force developed by the extensors of the hip, knee and ankle joints in the contact phase. On the other hand, stride rate depends on the functioning of the central nervous system on the cortical and sub-cortical level and is strongly genetically determined. The ratio between both parameters is individually defined and automated. Increasing stride rate results in shorter stride length and vice-versa. Maximal sprinting velocity is actually the result of an optimal relation between the stride length and stride rate of the athlete. The aim of our study was to find which morphologic and kinematic characteristics most differentiate sprinters in the competitive 100m sprint results. The flying 20m test was used to measure the kinematic parameters of maximal velocity and the low start 20m run for the kinematic characteristics of the starting acceleration.

METHODS

Twenty-four sprinters participated in the experiment. They were divided into two groups of twelve subjects according to their competitive 100m sprint time. In the first, better group (Group A), the average age was 23.9 ± 3.88 years, average 100m sprint time 10.52 ± 0.19s, the best athlete's time 10.21s. In the second, worse group (Group B) the average age was 22.7 ± 4.05 years, average 100m result 11.09 ± 0.12s, the best 100m time 10.92s. Measurements of the 100m sprint were performed on a track with a tartan surface. The two 20m tests were performed indoors on a tensiometric carpet (Ergo tester - Bosco) of length 20m and width 0.80m. Each subject performed four runs. Specially written software (Sprint) was used to obtain the following kinematic parameters: stride rate and frequency, contact times and flight times. The flying start and low start 20m times were measured with a system of infrared photocells. The morphologic characteristics of the sprinters were assessed with a battery of seventeen measures, obtained by the procedures proposed in the International Biologic Programme (IBP) and measured by a professionally trained medical team. The SPSS statistical package was used for data analysis.

RESULTS AND DISCUSSION

The results show that elite sprinters do not differ significantly in the morphological parameters in connection with their 100m time. Only the diameter of the knee measure is on the verge of statistical significance. The athletes are equal in body height, leg length, body mass, thigh and calf circumferences. The differences in skin-folds are somewhat more noticeable but not statistically significant. Sprinters in the better group have in general a little less subcutaneous fat in the stomach, thigh and forearm areas. This can be seen also from the proportion of fat , which is 0.4% larger in group B than in group A. The better sprinters group has 1.59% more muscular mass than the group with worse sprinting times. They differ significantly ($p<0.01$) in the starting acceleration ability and in maximal velocity. The contact time of maximal velocity and starting acceleration is that factor which significantly ($p<0.01$) differentiates between better and worse sprinters. The maximal stride rate parameter is on the verge of statistical significance ($p=0.05$). Better sprinters have a 4 cm longer stride than worse ones, but this difference is not statistically significant, nor is the difference between the groups in stride length and rate in the starting acceleration. The results show that the most important generator of differences ($p<0.01$) in sprinting quality among the kinematic parameters is contact time. Luhtanen and Komi (1980) divide the contact phase of the sprinting stride into two parts: braking phase and propulsion phase. The sum of both is total contact time, amounting for elite world-class sprinters to 80 – 85ms. (Mero, Komi & Gregor, 1992). The most important role in economical sprint running goes to the ratio between the braking phase and the propulsion phase, which should be 40:60. The shorter the braking phase, the lesser the reduction in horizontal velocity of the body centre of gravity – BCG . The average contact time of the better group of our sprinters is 89.7ms, the worse group 95.6ms.

REFERENCES

Mero, A.,Komi,.V.,& Gregor,R. (1992). *Biomechanics of Sprint Running*. Sport Medicine, 13(6):376-392

Luhtanen, P.,& Komi, P. (1980). *Force-power-and elasticity-velocity relationship in walking, running and jumping.* European Journal of Applied Physiology, 44(3):279-289.

FLOW DISTRIBUTION IN A RIGHT ANGLE BRANCH DURING OSCILLATORY FLOW

Gaku Tanaka, Eiji Sakai and Makoto Hishida
Department of Electronics and Mechanical Engineering
Chiba University, Chiba, Japan
tanaka@meneth.tm.chiba-u.ac.jp

INTRODUCTION

The presence of unidirectional flow in the avian lung is thought to be effected by aerodynamic valves (Scheid et al., 1972). Previous studies suggest that the aerodynamic valves may be largely attributable to the flow distribution in a airway branch in a steady inspiratory flow (Wang et al., 1988). In this study, the flow distribution in a right angle branch during oscillatory flow was studied to clarify the flow unsteady effects on the aerodynamic valves.

METHODS

Figure 1 shows the experimental apparatus. The working fluid is water and three straight acrylic tubes (primary, main, and side branch, i.d., 22mm; length, 1m) function as the right angle branch. A pulse generator installed at one end of the primary tube generates sinusoidal oscillatory flow. The main and side branches terminate in large reservoirs. Reservoirs connect by connecting duct (i.d. 110mm). The temporal variation of flow rate in each tube was measured by a laser-Doppler velocimeter, and pressure differences by a pressure transducer. Flow patterns at the bifurcation were visualized with a tracer method. The experimental conditions were characterized by the dimensionless tidal volume V_T/a^3 and the frequency parameter $\alpha\ (= a(\omega/\nu)^{0.5})$, and were chosen to match the conditions corresponding to the high frequencies of avian panting.

RESULTS AND DISCUSSION

Based on the flow rate measurements in the main and side branches (Q_m, Q_s), we found the three different flow regimes (Fig. 2). When V_T/a^3 or α^2 is relatively small, Q_m and Q_s are the same at all times during an oscillation (zone 1). When V_T/a^3 and α^2 increase, asymmetrical flow distribution causes the net flow between the main and side branches (zone 2). Zone 3 is the transition regime between zone 1 and 2.

Figure 3 shows typical flow rate waveforms in zone 2 in (a) the main branch and (b) the side branch. Q_m and Q_s are normalized by the amplitude of the flow rate in the primary tube $Q_{p,\,max}$ and time t is normalized by the oscillation period T. t/T = 0–0.5 corresponds to the inspiratory dividing flow and t/T = 0.5–1.0 corresponds to the expiratory merging flow. The temporal variation of Q_m and Q_s agree well with a sine curve, but the mean flow rate ($Q_{m,\,mean}$, $Q_{s,\,mean}$) deviate from zero. Since the flow rate waveform in the primary tube is a purely oscillatory flow, this mean component indicates the net flow from the side branch to the main branch.

The occurrence of the net flow is related to the direction-dependent flow separation at the bifurcation. The magnitude of the net flow was correlated with the mean pressure difference between the main and the side branches. The results also show that the net flow is further enhanced by the constriction installed at the entrance to the bifurcation.

SUMMARY

Oscillatory flow in a right angle branch causes a steady net flow from the side branch to the main branch. The net flow magnitude increases with the increase of the amplitude of flow rate in the primary tube.

REFERENCES

Scheid, P., et al. (1972). *Repir. Physiol.,* **14**, 83-95.
Wang, N., et al. (1988). *Respir. Physiol.,* **73**, 111-124.

ACKNOWLEDGEMENTS

This study was partially supported by a Grant-in-Aid for Encouragement of Young Scientists from the Ministry of Education, Science and Culture, Japan, and by Casio Science Promotion Foundation.

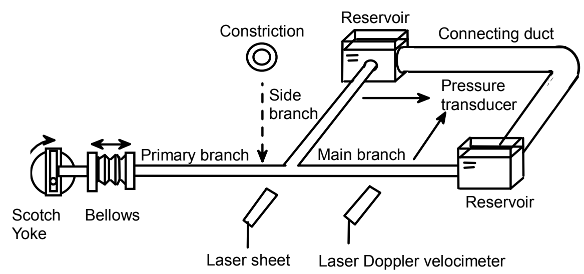

Figure 1: Experimental apparatus

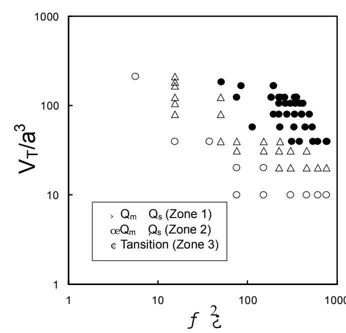

Figure 2: Flow regime diagram

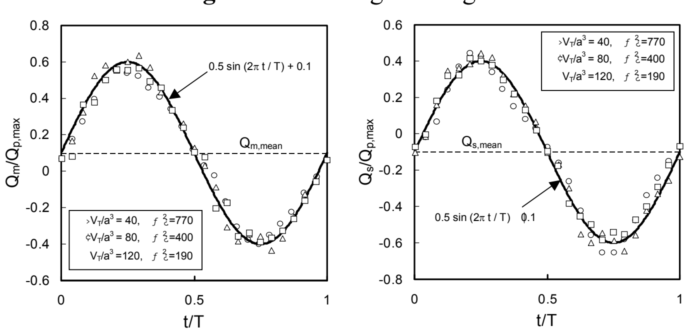

(a) main branch (b) side branch

Figure 3: Typical flow rate waveforms in zone 2

CERVICAL RANGE OF MOTION IN ASYMPTOMATIC SUBJECTS FOLLOWING SPINAL MANIPULATIVE THERAPY: A DOUBLE BLINDED RANDOMISED CLINICAL TRIAL.

René Fejer, Kari Skovmand Petersen, Frederik Gothen Rolschau, Jacob West and Niels Grunnet-Nilsson
Institute of Sports Science and Clinical Biomechanics, University of Southern Denmark, Odense, Denmark, RFejer@Health.sdu.dk

INTRODUCTION

Patients often express increased flexibility following spinal manipulative therapy (SMT) of the cervical spine. Most studies seem to show that SMT increases range of motion (ROM) of the cervical spine (Cassidy 1992, Nansel 1989, Nilsson 1996), and recently a study has demonstrated a significant increase in ROM following SMT on patients with cervicogenic headache (Whittingham 2001). The question remains, though, whether SMT improves cervical ROM in asymptomatic subjects with lower normal ROM.

METHODS

Twenty-three females (age ranging 20-29 years) with lower normal active cervical ROM - but otherwise asymptomatic - volunteered for this study. After one-week baseline the subjects were randomised into two groups. One group received a placebo treatment (using an Activator locked to 'zero amplitude'), and the other group received cervical SMT (toggle recoil for upper cervicals and diversified for lower cervicals). Both groups were treated 6 times over a 3-week period. Each group then had a one-week follow-up period. Recordings on active cervical ROM were made once a week using the CROM device giving a total of 6 recordings for the treated group and 7 recordings for the placebo group (see below). All recordings were calculated as mean-of-three in rotation and lateral flexion. Flexion-extension was not recorded.

All subjects had prior to the randomization been told that the study was a comparison of two different treatment techniques; hence no subject was aware that a placebo treatment was used. Due to ethical considerations the placebo group was offered the same treatment as the other group and additional recordings were made.

RESULTS AND DISCUSSION

The mean active ROM for rotation and lateral flexion are shown in figures 1 and 2. There are no statistical significances in any of the recordings except for the placebo group receiving the additional treatments. This was only true for rotation ($P=0.009$) but not for lateral flexion. However, at that point of time the subjects knew they received true SMT. Therefore, bias cannot be ruled out.

CONCLUSION

Spinal manipulative therapy does not significantly alter the active cervical range of motion on asymptomatic females.

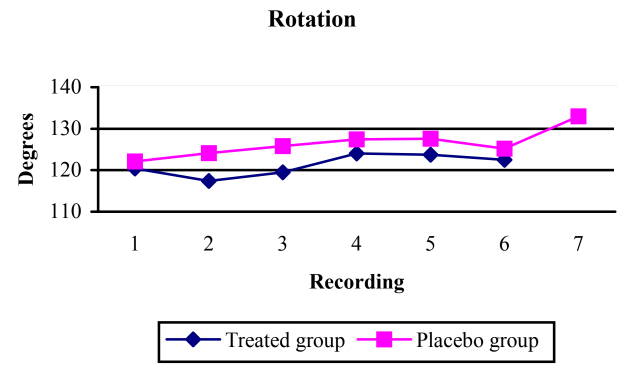

Figure 1: Cervical ROM for rotation.

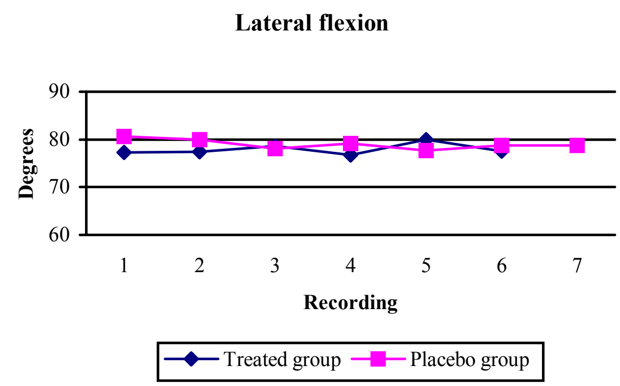

Figure 2: Cervical ROM for lateral flexion.

REFERENCES

Cassidy D., et al (1992). *J. Manipulative Physiol. Ther*. **15**, 570-575

Nansel D.D., et al (1989). *J. Manipulative Physiol Ther*. **12**, 419-427

Nilsson, N. et al (1996). *J. Manipulative Physiol Ther*. **19**, 165-168

Whittingham W., Nilsson N. (2001). *J. Manipulative Physiol. Ther.*

ACKNOWLEDGEMENTS

The authors wish to thank Henrik Lauridsen, DC for treating the volunteers.

TIME-LAPSE OF CELLULAR STIFFNESS MEASURED WITH SCANNING PROBE MICROSCOPY DEPENDING ON CELL MIGRATION

Masafumi Nagayama*, Hisashi Haga and Kazushige Kawabata
Division of Physics, Graduate School of Science, Hokkaido University, Sapporo, Japan
*masafumi@skws.sci.hokudai.ac.jp

INTRODUCTION

Cell migration plays an important role in phenomena raging from healing of wounded tissue to self-organizing of the early embryo. Many kinds of molecular components involved in cell migration have been identified. Recently, various studies of their functions are investigated at a rapid rate. However, it is not still clear how these components work harmoniously as an integrated system. Then, we have focused on the relation between mechanical properties of migrating cells and rearrangement of biomolecular components such as actin filaments and focal adhesions. In this study, to clarify the cooperative mechanism for cell migration, we measured the time dependence of the local stiffness distribution of living fibroblasts with Scanning Probe Microscopy (SPM).

METHODS

The SPM measures topography by scanning a cantilever, which has a tip at its end, over the surface of a sample. This has been used to image a wide variety of biological samples in liquid environment. Furthermore, the SPM has been also applied to measuring such mechanical properties as stiffness since the tip is directly in contact with the sample.

Stiffness imaging was carried out using force modulation mode. This mode has higher temporal and spatial resolution than any other method. In this mode, we can obtain a 128×64 pixels image only for 6 minutes. So, this is quite effective to examine relation between temporal change of stiffness and cell migration. The viscoelasticity of the sample was estimated from a sample strain against an external periodic stress by the method based on the linear viscoelastic theory. The experiments were performed under the physiological condition (34°C HEPES-buffer).

RESULTS AND DISCUSSION

Sequential images of the local stiffness distribution in living fibroblasts (NIH3T3) were captured every 10 minutes using force modulation mode (Fig. 1). The measurements were carried out over 60 minutes, which corresponds to the average time period of the intermittent cell migration. We found the following relations: Once the cells started to move, the stiffness in the nuclear portion was drastically reduced. On the other hand, while the cells were staying at one position, the stiffness distribution was quite stable. Previous immunofluorescence observations with chemical doping strongly suggest that the local elasticity is mainly attributed to actin filaments rather than microtubules. We propose a model that change of tensional force acting along the stress fibers induces the cell migration. To verify this assumption, we examine temporal variations of the local stiffness when actin-myosin interaction is controlled with antagonist or growth factor.

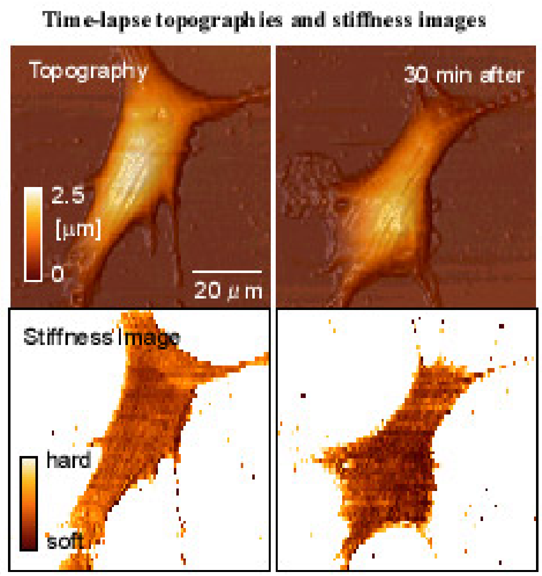

Figure 1: Topography and stiffness image measured with SPM simultaneously. Sequential pair of identical cell is shown.

SUMMARY

We measured the sequential images of the topography and the local stiffness distribution of living fibroblasts by SPM. We discovered a clear correlation between the change of the local stiffness distribution and the intermittent cell migration. To explain this correlation, we propose that the tensional force acting along the stress fibers would change with the cell migration.

REFERENCES

Haga, H., et al. (2000). *Ultramicroscopy*, **82**, 253-258.
Haga, H., et al. (2000). *J. Electron Microsc.*, **49**, 473-481.
Nagayama, M., et al. (2001). *Cell motil. Cytoskel.*, **50**, 173-179

THE INFLUENCE OF BODY MASS ON THE FLIGHT PATH IN SKI JUMPING

Bernhard Schmölzer and Wolfram Müller
Institute of Medical Physics and Biophysics, Karl-Franzens University Graz, Austria
Communicating author, b.schmoelzer@aon.at

INTRODUCTION

A recent anthropometrical study has shown that all ski jumpers are very light. 15 of 92 investigted athletes were in thinness class I according to the WHO classification, the lowest body mass index (BMI) was 16.6 kg m^{-2} , the BMI mean value was 19.6 kg m^{-2} (Müller, 2002). However, within this group of low weight athletes no correlation between body weight and World Cup ranking has been found indicating that some of the athletes go beyond the limits of reason .
The earliest analytical model of ski jumping was made by Straumann (Straumann, 1927). Here, a computer model that is based on the equations of motion and that considers the positional changes of a ski jumper during the flight phase is used for the analysis of the effects associated with low body weight. The effects have to be seen in the context of other factors that affect jump distance (Müller et al., 1995; Müller et al., 1996; Schmölzer, Müller, 2002).

METHODS

The computer model is based on the equations of motion and uses tabulated functions for the lift L=L(t) and drag D=D(t) areas corresponding to the athletes positions during the flight. A reference jump based on sets of wind tunnel measurements with 1:1 models of ski jumpers in current equipment (2001/2002) formed the basis for the computer simulation studies discussed here. For all simulations the new profile of the jumping hill in Innsbruck (K = 120m) has been used. The modelling approach and the wind tunnel measurements have been described in detail recently (Schmölzer, Müller, 2002).

RESULTS AND DISCUSSION

Figure1a shows the decrease of jump length with increasing weight of the athlete with his equipment. The jump length l was 120 m when the mass was set to 65 kg, the approach velocity to v_0 26.0 m s^{-1}, and the take off velocity perpendicular to the ramp v_{p0} to 2.5 m s^{-1} (Virmavirta, 2001). The mass m profoundly influences the jump length l and the velocity of motion along the flight path. The jump length l was only 106.1 m with m = 80 kg and increased to 133.2 m with m = 50 kg. One kg less mass increased the jump length by 0.9m (linear approximation). Additionally, with a lower body mass the landing is eased due to a pronounced reduction of the landing speed. Filled circles in Figure 1b indicate pairs of m and v_0 values required to obtain a given jump length of 120 m. The advantage associated with 1 kg less mass can be compensated by a 0.05 m/s increase in the approach velocity.
Possible changes to the regulations that would make it less attractive to be extremely underweight are being discussed.

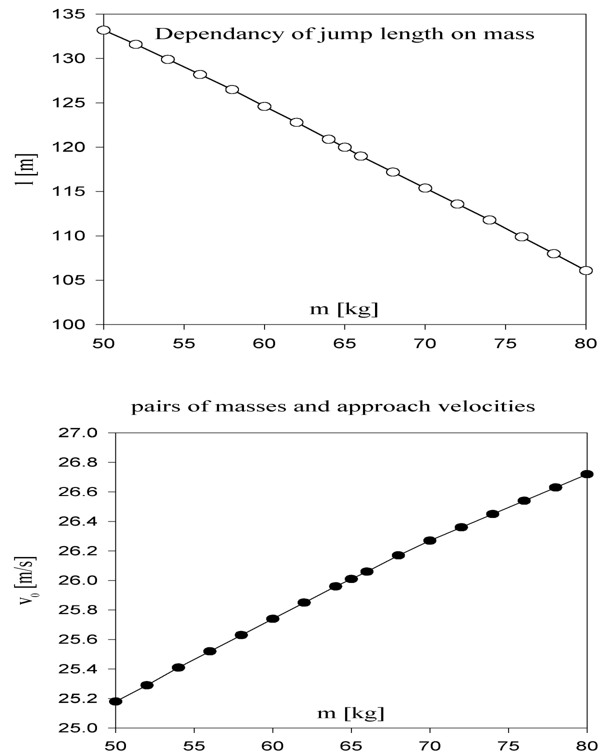

Figure 1: a) Influence of body mass m on the jump lenght l .
b) Pairs of values m and v_0 that result in an unaltered jump length of 120m.

Beside a higher v_0 value also an increased v_{p0} would compensate higher weight. Aerodynamically advantageous equipment components for heavier athletes (e.g. larger skis) could provide a tool to solve the underweight problem in ski jumping.

REFERENCES

Müller, W. (2002). *Proceedings of ACSM 2002* (in press).
Straumann, R. (1927). In: *JB Schweiz. Skiverband*, 34-64.
Müller, W. et al. (1995). *Nature*, **375**. 455.
Müller, W. et al. (1996) *J. Biomech*, **8**. 1061-68.
Schmölzer, B., Müller, W. (2002) *J. Biomech*, (accepted).
Virmavirta, M. et al. (2001) *J. Biomech,* **34**. 465-470.

ACKNOWLEDGEMENTS

Supported by: FWF (P14388TEC), IOC, FIS

AUGMENTED LONGITUDINAL DIFFUSION IN OSCILLATORY FLOW ALONG A LATERAL GROOVED TUBE IMITATED OF TRACHEA WITH UNEVEN INNER SURFACE BY CARTILAGE

Akihiro Shimizu[1], Kosuke Miyahara[2], Masashi Shimizu[2] and Saburo Ryumae[2]
[1] Department of Mechanical Engineering, Tokyo National College of Technology, 1220-2, Kunugida, Hachioji, Tokyo, Japan
ashimizu@io.mei.titech.ac.jp
[2]Graduate School of Information Science and Engineering, Tokyo Institute of Technology, Ookayama, Meguro, Tokyo, Japan

INTRODUCTION

Respiration is attained despite small tidal volume breathing and large dead space in the trachea. Uneven inner surface configuration by cartilage of trachea may influence on the effective diffusivity. Ye had reported augmentation of diffusion by oscillatory flow of water in a lateral grooved tube. Measurements of CO_2 concentration in the oscillatory flow in tubes with several groove widths have been carried out.

METHODS

Inner diameter of the test tube was 18mm, and inner surface configuration was composed by combination of aluminum rings with rectangular cross section as shown in figure 1. Depth of the groove of each configuration was 2mm and Bottom width and top width of it are described in table 1. Total length of the test tube was 3025mm, consisting of the part from the entrance to injecting point of 1260mm and from there to sensing point of 500mm, and further 1265mm to the open end. Oscillatory flow was generated by piston(ƒÓ50) connected with a reciprocating block double slider-crank mechanism driven by AC servomotor. CO_2 gas was injected simultaneously with the lower dead point of the piston. Non-dispersive infrared analyzer measured CO_2 concentration.

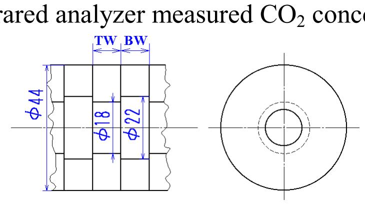

Figure 1: Inner surface configuration along the grooved tube.

RESULTS AND DISCUSSION

Values of $(D_{eff}/D_{mol}-1)/(V^2/a^6)$, where D_{eff} is effective diffusivity, D_{mol} is molecular diffusivity, V is stroke volume and a is the inner radius of the tube, are shown in figure 2. The difference between the effective diffusivity obtained and the theoretical one in the oscillatory flow in a straight tube is increasing with the increase of Womersly number. As for the bottom width of the groove, wide width of groove gives relatively large augmentation on the effective diffusivity.

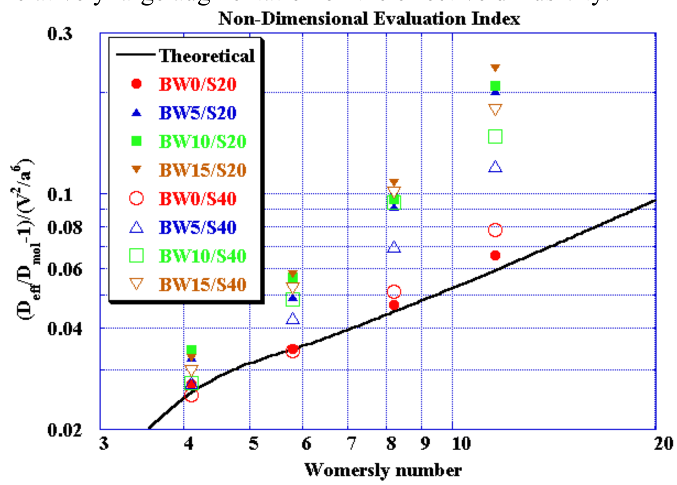

Figure 2: Evaluation index derived from non-dimensional effective diffusivity and non-dimensional stroke volume. Solid curve indicates the theoretical value for laminar flow in a straight tube.

SUMMARY

The effective diffusivity of CO_2 in oscillatory flow along tubes with the lateral grooves has been measured. The difference between the effective diffusivity through the lateral grooved tube and one through the smooth straight tube is increasing with the increase of Womersly number. The effective diffusivity is more augmented by each inner surface configuration with the increase of the width of the groove within the region of the present experimental condition.

REFERENCES

Ye Xiaofeng, Shimizu Masashi, *Augmented longitudinal diffusion in grooved tubes for oscillatory flow*, *Int. J. Heat and Mass Transfer*, **44**(2001), 633.

Watson, E. J., *J. Fluid Mech.* **133**(1983), 233.

Table 1: Piston stroke and dimension of the top and the bottom width of each lateral groove of inner surface [mm]

Item	BW0/S20	BW0/S40	BW5/S20	BW5/S40	BW10/S20	BW10/S40	BW15/S20	BW15/40
Piston stroke	20	40	20	40	20	40	20	40
Top width	10	10	10	10	10	10	10	10
Bottom width	0	0	5	5	10	10	15	15

COMPUTATIONAL FLUID DYNAMICS IN HEMODIALYSERS

Sunny Eloot, Dirk De Wachter, Ilse Van Tricht and Pascal Verdonck
Hydraulics Laboratory, Institute of Biomedical Technology, Ghent University, Belgium
Sunny.Eloot@rug.ac.be http://navier.rug.ac.be/

INTRODUCTION

Hemodialysis is a renal replacement therapy during which blood of a patient is circulated through an extracorporeal hollow fiber or packed membrane sheets module. Blood and dialysis fluid are circulated countercurrently on opposite sides of a porous membrane which permits the passage of waste metabolites and water but restricts the transfer of blood proteins and blood cells from the blood towards the dialysis fluid. In a hollow fiber dialyser, blood flows inside the capillaries while dialysis fluid flows around them.

AIM OF THE STUDY

While other studies [Nordon,1997] only provide information about macroscopic flow patterns in dialysers, product optimisation should be based looking more in detail at transport processes and fluid properties inside the dialyser. Therefore, this study aims to investigate the effect of flow, bloodviscosity and dialyser dimensions on flow in a hollow fiber dialyser using computational fluid dynamics.

METHODS

A three-dimensional finite volume model of the blood-dialysate interface over the complete length of the dialyser is developed (Fluent 5.4). Assuming the fibers spaced in a hexagonal lattice and based on symmetry, one twelfth part of a single fiber can be isolated (Figure 1), characterised by an

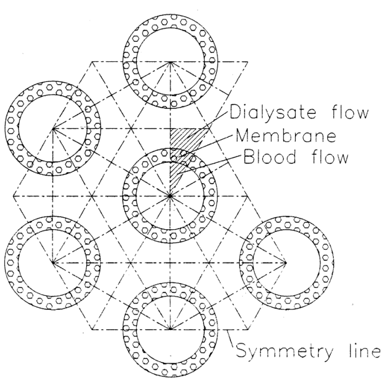

Figure 1 : Hexagonal lattice of the hollow fiber dialyser

axial to radial dimension ratio of 1000.

Different equations govern blood and dialysate flow (Navier-Stokes and continuity) and transmembrane water transport (Darcy). Blood is modelled as a non-Newtonian fluid with a viscosity varying in radial and axial direction because of the influence of the local cell concentration, the small diameter of the capillaries (Fahraeus-Lindqvist effect) and the local shear rate. Based on in vivo measurements, the dialysate flow is assumed to be an incompressible, isothermal laminar Newtonian flow with a constant viscosity. The permeability characteristics of the membrane, produced of modified or regenerated cellulose or synthetic polymers, are obtained from laboratory tests for forward and backfiltration [Eloot,accepted]. The oncotic pressure, which is exerted by the plasma proteins and opposes the hydrostatic transmembrane pressure, is implemented as a function of cell concentration. Moreover, the reduction of the overall permeability caused by the adhesion of a protein layer on the membrane, is implemented as a series of resistances.

RESULTS

Assuming a constant blood and dialysate inlet flow of 250 and 500ml/min respectively, outlet pressures of 10kPa and 5Pa respectively, the pressure distribution renders an overall water filtration flow of 45ml/min as expected theoretically and in vivo, while no backfiltration occurs. As blood flows through the dialyser, the water removal causes hemoconcentration and, as a consequence, the mean viscosity increases with 50%. Figure 2 demonstrates the radial viscosity variation caused by a plug flow of blood cells at the axis and a plasma layer near the membrane wall. The pressure distribution in the blood compartment deviates only slightly from linearity (0.3% at blood in and outlet) due to the water removal.

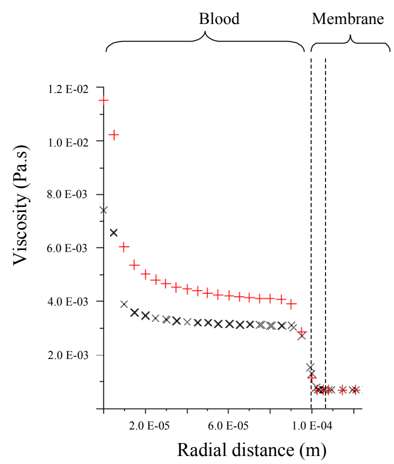

Figure 2 : Radial viscosity distribution at inlet (x) and outlet (+).

CONCLUSION

The presented model allows to investigate in detail the impact of hemodialyser dimensions and transmembrane flow on the blood flow and blood viscosity.

REFERENCES

Nordon, R.E., Schindhelm, K. (1997). *Artif Organs* **21**, 107-115.

Eloot, S. et al. (accepted). *Int J Artif Organs*.

ACKNOWLEDGEMENTS

This research was financially supported by Fresenius Medical Care (Germany).

BIOMECHANICAL EFFECTS OF THE DESIGNS ON POSTERIOR RESIN-BONDED PROSTHESES

Chih-Han Chang[1], Ting-Sheng Lin[1] and Chun-Li Lin[2]
[1]Institute of Biomedical Engineering, National Cheng Kung University, Tainan, TAIWAN
[2] Department and Graduate Institute of Mechanical Engineering, Chang Gung University, Tau-Yuan, TAIWAN

INTRODUCTION

Resin-bonded (RB) prosthesis has become an alternative to replace missing teeth in clinical dentistry in recent years. However, the retention rate of RB prostheses was still unsatisfied especially when it is applied to the posterior region. Many studies have focused on the improvement of adhesion and enhanced the bonding strength between metal and abutment teeth. The investigations of in the biomechanical aspect of RB prostheses, on the other hand, were insufficient due to the difficulties in experimental setup and clinical observation. Unlike conventional fixed partial dentures, the guidelines of posterior RB prostheses, such as retainer thickness, occlusal rest seats and retention grooves were still unclear and needed further investigation. Finite element (FE) analysis provides more complete information than traditional experimental approaches and its reliability has been validated by several researches. The objective of this study is to investigate the biomechanical effects of posterior RB bridges with different design parameters by 3D FE analysis.

METHODS

The replicas of the abutment teeth (a second premolar and second molar) and metal bridgework were fabricated based on the actual teeth. The structure was embedded in an epoxy block. Low speed saw was used to obtain the biopsy of this posterior RB prosthesis serially. An in-house image processing system was employed to track the contour of each slice and transferred into finite element packages (ANSYS 5.6). A mesh model of posterior RB prosthesis was constructed by isotropic 8-node brick elements. Five levels of retainer thickness, reduced gradually from 1.0mm to 0.2mm, were adopted. The designs with and without occlusal rest seats and retention grooves were also investigated. In order to study the effects of the direction of functional cusp in posterior mandible, the loadings were decomposed into vertical and horizontal (buccal direction) forces respectively. The abutment teeth were assumed with only one material (dentin) for simplification. The mechanical properties of metal (Ni-Cr alloy, E=188000MPa, ν =0.28) and abutment teeth (dentin, E=18600MPa, ν =0.31) were referred from other studies. All nodes below cementoenamel junction were fixed in all directions as the boundary condition. Peak tensile stress at the interface between metal and abutment teeth was selected as the judgment index to predict the failure probability quantitatively.

RESULTS AND DISCUSSION

The effect of horizontal force has greater effect than vertical force. Peak tensile stress reduced exponentially as the retainer thickness increased. Occlusal rest seats help to decrease interface stresses slightly when vertical force was applied but this phenomenon did not observe for horizontal loading. The retention groove design has the ability to resist buccal displacement and deformation, but the interfacial tensile stresses tend to concentrate on the edge of distal grooves and raise the probability of interface debonding.

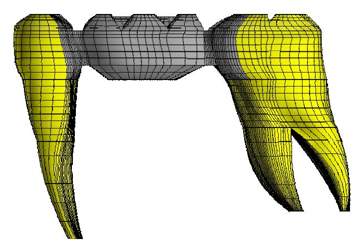

Figure 1: Finite element mesh mode of posterior RB prosthesis

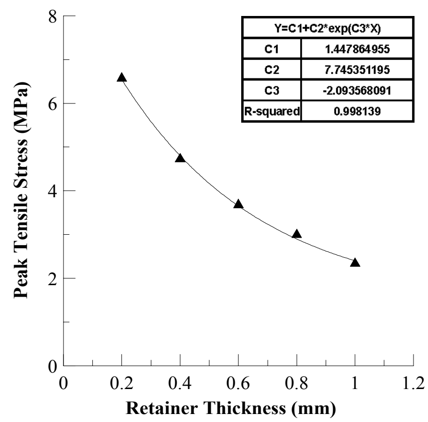

Figure 2: Relation of retainer thickness and peak tensile stress in second molar under horizontal force

General questions, contact: Prof. Chih-Han Chang email: cchang@mail.bme.ncku.edu.tw

SUMMARY

Retainer thickness was the most effective support in the framework designs. The effects of occlusal rest seats and retention grooves were not significant in this study.

REFERENCE

Morris, H.F. (1989). *J. Prosthet Dent*, **61**, 160-169.

CALIBRATION OF AN ARTERIAL APPLANATION TONOMETER FOR IN-VIVO PRESSURE TRANSDUCTION

Andrew Zambanini [1], Ashraf W. Khir [2], Kim H. Parker [2], Simon A. McG Thom [1], Alun D. Hughes [1]
[1] Clinical Pharmacology, National Heart & Lung Institute, St. Mary's Hospital, a.zambanini@ic.ac.uk
[2] Physiological Flow Studies Group, Department of Bioengineering,
Imperial College, London, UK

INTRODUCTION

Non-invasive methods for determining the arterial pressure waveform at peripheral sites have become increasingly popular for use in wave intensity analysis, computational fluid dynamics modelling and pulse wave analysis. Although applanation tonometry has been shown to accurately represent the pressure wave morphology, current methods calibrate the amplitude of the waveform at sites other than the brachial artery using brachial diastolic and mean arterial pressures. We have developed an alternative approach using an in-vitro calibration of the tonometer.

METHODS

A pressure phantom was constructed using 1cm diameter latex tube placed within a similarly sized Dacron graft. An intravascular pressure catheter (8F SVPC-684A, Millar Instruments, Houston, USA) was introduced into the phantom and the system was filled with saline to achieve a static pressure of 50 mmHg. A high fidelity strain gauge tonometer (SPT 301, Millar Instruments, Houston, USA) was placed externally 1cm distal to the catheter and attached to a stand for hands-free measurements. Rapid active filling and passive drainage of the phantom using saline and a syringe achieved variations in pressure. Pressure data from tonometry and invasive catheter measurements were sampled simultaneously at 250Hz. A series of pressure waveforms were generated over three different applied applanation pressures and provided the data needed to develop a calibration algorithm.

Using the same tonometer, pressure waveforms were obtained from the right brachial artery in 30 resting human subjects [10 normals, 10 treated hypertensives and 10 untreated hypertensives, 27 men, mean (±SD) age 52 (±14) years] with simultaneous measurement of the blood pressure in the left arm using a semi-automated sphygmomanometer [mean BP 143/85 mmHg (range 98-221/65-128)]. Following use of the calibration factor and correcting for mean arterial pressure, comparisons were made between pressures determined by tonometry and sphygmomanometry.

RESULTS

There was a linear relationship between the intraluminal catheter and tonometry pressure measurements in the phantom. However, the slope of the linear regression line increased linearly with increased applanation pressure (figure 1).

Figure 1: The relationship between tonometric and catheter pressures in a phantom. The applanation pressures were 12.3 mmHg (Study 1), 119.9 mmHg (Study 2) and 167.8 mmHg (Study3) respectively and the tonometry pressures plotted were corrected for these.

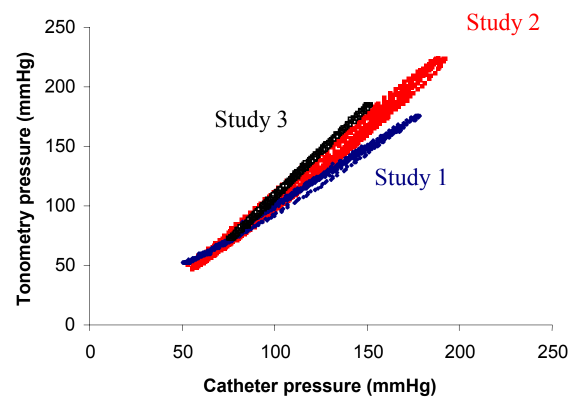

The slopes and intercepts from these linear regression lines were used to develop the correction algorithm for tonometry pressures (P) taking into account applanation pressure (P_a) and measured tonometry pressure (P_t):

$$P=0.04P_aP_t+0.60P_t-0.32P_a+34.2$$

When applied to brachial tonometry waveforms in vivo, there was a significant correlation between the calibrated tonometry and sphygmomanometry pressures (y=0.93x + 6.90, r=0.996, p<0.0001). The mean difference (±SD) in sphygmomanometry and tonometry pressures was 1.4 (±9.9) mmHg.

DISCUSSION

By calibrating a tonometer in-vitro, we have developed a non-invasive method for determining the pressure waveform accurately in the peripheral arteries of man. This method can be applied to other sites such as the carotid artery where direct non-invasive measurement of systolic and diastolic pressure is not feasible.

A 2-D ANALYSIS OF TEMPOROMANDIBULAR JOINT LOADING GENERATED DURING BILETRAL BITING AT THE MOLARS AND PREMOLARS

Makoto Abe[1], Toyohiko Hayashi[2], Yasuo Nakamura[2], Ken-ichi Itoh[3], Raul U. Medina[4], Syoji Kohno[4]
[1]Graduate of School of Science and Technology, Niigata University
[2]Department of Biocybernetics, Faculty of Engineering, Niigata University
2-8050, Ikarashi, Niigata, 950-2181, Japan, makoto@jkl.bc.niigata-u.ac.jp
[3]Department of Information and Electronics Engineering, Niigata Institute of Technology
1719, Fujihashi, Kashiwazaki, 945-1195, Niigata, Japan
[4]Department of Removable Prothodntics, Graduate of School of Medical and Dental Science
2-5274, Gakkochodori, Niigata, Japan

INTRODUCTION

In order to clarify the control mechanism during static bilateral biting, we have been analyzing the controllability of TMJ loading achieved by coordinative activities of the masticatory muscles. In the present study, we estimated TMJ loading in actual biting by applying subject's data of bite force and EMG activity into a static 2-D jaws model, in an attempt to validate to what extent TMJ loading was optimized.

METHODS

A 2-D jaw model consisted of a rigid-body model of the jaws and a rigid-body spring model of TMJ (Itoh, K. and Hayashi, T., 2000). The jaw model incorporated the masticatory muscles such as the masseter (including the internal pterygoid), the temporalis and the lateral pterygoid. The bite force was assumed to be applied at a point of either the molars or premolars.The muscle force was estimated firstly from its cross-section area, normalized EMG data and the intrinsic muscle strength (Prium, G.J., et al, 1980). Then, the estimated muscle forces were corrected in order that the bite force estimated from the muscle forces agreed with the actual bite force measured by means of a pressure sensitive film (Dental Prescale 50HR), under the assumption that the intrinsic muscle-strength of the masseter and temporalis muscles can be corrected proportionally.Three male subjects with a set of bilateral acrylic splints mounted on the lower molars or premolars were asked to generate the maximal voluntary bite force. EMG activity of the superficial masseter muscle, the anterior and posterior portions of the temporalis muscle were recorded bilaterally by means of a bipolar surface electrode with a diameter of 12 mm and the inter-polar distance of 15 mm. Our previous papers reported that the magnitude of TMJ loading can be minimized under the same bite condition merely by adjusting the forces of the masseter and temporalis muscles (Itoh, K., et al, 1997). Then, such minimum TMJ loading was computed in each experiment.

RESULTS AND DISCUSSION

Figure 1 demonstrates a typical result of the estimated TMJ-loading ($\mathbf{f}_j$) and the minimun TMJ loading ($\mathbf{f}_{j,min}$), and corresponding load distribution in the disk under the two biting conditions. In the molar bite, TMJ-loading $\mathbf{f}_j$ was not necessarily minimized, while it was nearly minimized in the premolar bite. Such remarkable results were also observed in all other subjects. In the molar bite, the ratio of the TMJ loading versus the bite force was relatively small (0.47 on average), and the load was concentrated primarily in the intermediate zone of the disk. In the premolar bite, on the contrary, the ratio was relatively large (0.90 on average), and the load was distributed throughout the disk. This suggested that TMJ loading is optimized to some extent even in actual biting in accordance with the bite condition.

SUMMARY

The present study assessed the optimization of TMJ loading in actual biting by applying subject's data of bite force and EMG activity into a static 2-D jaws model. Results were summarized as follows: 1) in the molar bite, TMJ loading was not necessarily minimized, and was focused primarily on the load-bearing portion of the disk; and 2) in the premolar bite, TMJ loading was nearly minimized, and was distributed throughout the disk.

REFERENCE

Itoh, K., et al (1997). *Frontiers Med. Biol. Engng.*, **8**, 123-138.
Itoh, K. and Hayashi, T. (2000). *Frontiers Med. Biol. Engng.*, **10**, 17-31.
Pruim, G.J., et al (1980). *J. Biomech.*, **13**, 755-763.

ACKNOWLEDGEMENTS

We would like to thank Y. Mukawa, Y. Kohno, K. Yamada, and G. Cynthia, Niigata University, for their assistance in the experiments.

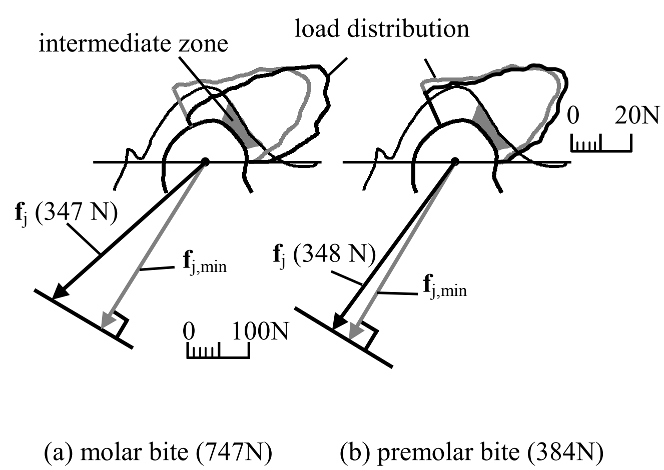

Figure 1: Estimated and minimized TMJ loading vectors and corresponding load distributions for subject 1: (a) molar bite and (b) premolar bite.

HOW ECONOMICAL IS HUMAN BIPEDAL LOCOMOTION?

J. Rubenson[1], D.B. Heliams[2], S.K. Maloney[3], P.C. Withers[4], G.B.M. Martin[5], D.G. Lloyd[1] and P.A. Fournier[1]
Department of: [1]Human Movement and Exercise Science, [3]Physiology, [4]Zoology, [5]Agriculture
University of Western Australia, Crawley, W.A., Australia, (www.hm.uwa.edu.au)
[2] Fauna Technologies, Gosnells W.A., Australia

INTRODUCTION

Since the pioneering work of C.R. Taylor and colleagues (1970) it has generally been acknowledged that humans are uneconomical runners compared to animal species of the same mass. More ambiguous, however, is how humans' energy cost of transport (J/kg/m) compares to similar size species during other shared locomotor tasks where the mechanical basis of movement is different from that of steady-speed level running. To address this issue we chose to compare the energy costs of transport of humans and a more economical bipedal runner of similar mass, the ostrich (Taylor et al, 1982), during level running, incline running and walking. These locomotor tasks were chosen because each depends on a different mechanism for generating the mechanical work of locomotion; during level running much of the mechanical work is supplied via the release of elastic strain energy stored in tendons; during incline running by the muscles themselves; and during walking by a 'pendulum-like' exchange between kinetic and gravitational potential energy of the body's center of mass (Dickinson et al, 2000).

METHODS

Four elite human runners (66.1 ± 5.1 kg; mean ± S.D.) and four ostriches (66.1 ± 6.1 kg; mean ± S.D.) were trained to run and walk on a motorized treadmill over a range of speeds both on the horizontal and on a 5% and 10% incline. The humans' and birds' rates of oxygen consumption were measured at rest and during treadmill locomotion using the same open-flow metabolic system.

RESULTS AND DISCUSSION

The rate of oxygen consumption during level running in humans, and hence energy cost of transport, exceeded that of ostriches by nearly 40% (Fig. 1a). However, during walking and incline running the difference in energy cost of transport disappears (Fig. 1 a,b). This finding supports the earlier view that human walking may not be exceptionally economical (Alexander, 1991). Our data also indicates that the additional vertical work of running up-hill may be relatively inexpensive in humans. Possible mechanisms for these observations are discussed.

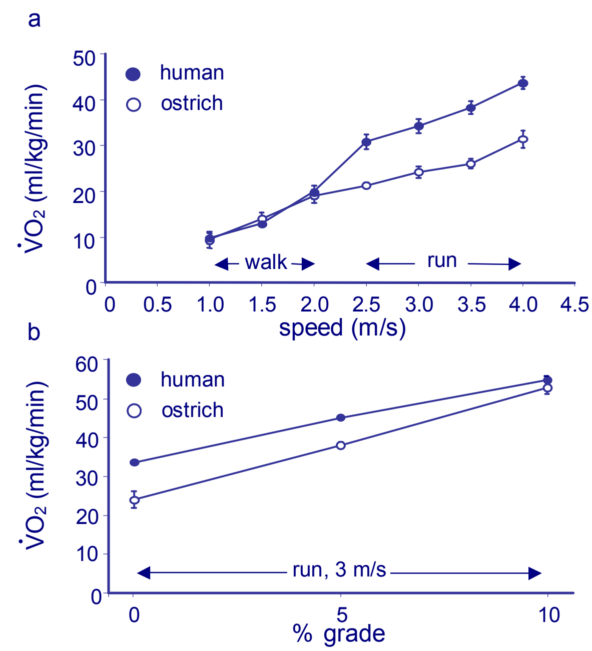

Figure 1: The mass-specific rate of oxygen consumption ($\dot{V}O_2$; means ± S.E.) in humans and ostriches as a function of (**a**) speed and (**b**) incline.

SUMMARY

Despite level running being more expensive for humans than for ostriches this difference disappears when running on steep inclines or during walking. This raises the intriguing question of whether the difference in the cost of transport among animal species of similar mass may be, in general, largest for level running and smallest for walking and incline running, an important consideration given that walking is the preferred mode of locomotion for many terrestrial animal species and that several live in a heterogeneous landscape.

REFERENCES

Alexander, R.M. (1991) in *Biomechanics in Evolution,* Raynor, J.M.V. & Wootton, R.J. ed, Cambridge University Press 225-266.
Dickinson, M.H. et al (2000) *Science*, **288**, 100-106.
Taylor, C.R. et al (1970) *Am. J. Physiol*, **219**, 1104-1107.
Taylor, C.R. et al (1982) *J. Exp. Biol.*, **97**, 1-22.

A METHOD FOR STUDYING 3D MOVEMENT OF THE SPINE IN VITRO

C. M. Hunt[1], C. A. Holt[1], L. Jones[1], S. L. Evans[1], S. Ahuja[2], D. Dillon[2], P. Davies[2] and J. Howes[2]
[1]Division of Materials and Minerals, Cardiff School of Engineering, Cardiff University,
P O Box 925, The Parade, Cardiff, CF24 0YF, UK. HUNTCM@CARDIFF.AC.UK
[2]University Hospital of Wales, The Heath, Cardiff CF14 4XY, Wales, UK

INTRODUCTION

The purpose of this study was to develop a technique for monitoring the effect of spinal instrumentation on the range of motion occurring within the spine. The method was then applied to a pedicle screw system inserted into a lumbar spinal section to determine the behavior of various spinal constructs under loading.

METHODS

The technique was based on a method developed for the study of human gait (Holt et al, 2000), using infrared cameras to view the movement of marker clusters attached to the body segments to be studied. The Soderkvist and Wedin (1993) approach is used to define three interrelated coordinate sets defined within the marker cluster, body segment, and the laboratory measurement volume. The relative motion of one body segment to the other is defined through manipulation of these transformation matrices.

The technique was used to determine the effect of cross-linked pedicle screw systems on the behaviour of calf spine sections loaded in vitro. Five calf lumbar spine sections consisting of the L3-L5 vertebrae had a fracture simulated at the L4 level. They were then loaded with 2Nm moments to cause flexion/extension, left & right lateral bending and left & right axial rotation. Each section was tested with four implant arrangements: unimplanted, pedicle screws & rods only, pedicle screws & rods with one or two cross-links. At each load and implant arrangement the motion of L3 relative to L5 was calculated to determine the range of motion (ROM).

The ROM mean values and standard deviations were checked for significance using paired two tailed T tests (significance level $p=0.05$).

RESULTS AND DISCUSSION

The results showed that pedicle screws and rods, used on their own, have a significant effect on the rotation occurring within the section ($p=0.008$, $p=0.022$, $p=0.02$ for flexion/extension, lateral flexion and rotation respectively). When compared to using screws and rods alone, the only significant improvement found by the introduction of cross-links was a reduction in the amount of axial rotation. In this case the addition of one cross-link showed a significant improvement over just screws & rods ($p=0.017$). Two cross links showed a further significant improvement over one ($p=0.04$). The results for axial rotation are shown in figure 1.

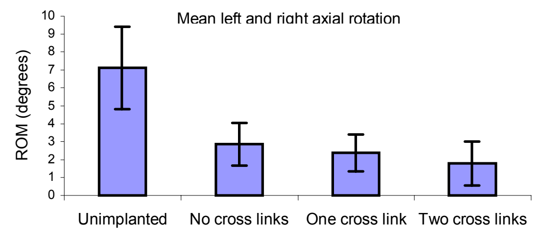

Figure 1: Axial range of motion with various combinations of implant

The technique originally used to analyze knee movement has been successfully applied to the study of the motion of the spine and has confirmed results found in a previous study (Dick et al 1997). The advantage of this approach is that it allows simultaneous determination of the motion of the spine in all six degrees of freedom. This allows an enhanced understanding of the coupled movement of the spine and will be of great benefit in determining the effect of spinal implant systems.

SUMMARY

A new technique has been developed which has advanced the understanding of the effect of instrumentation on the behaviour of the spine in vitro. It has shown that the use of cross-links in pedicle screw implant systems reduces the amount of axial rotation and that using two cross-links has a greater effect than one.

REFERENCES

Holt C.A. et al (2000). *Computer methods in Biomechancis and Biomedical Engineering,* **3**. Gordon and Breach Science Publishers SA
Soederkvist I, Wedin P (1993). *Journal of Biomechanics,* **26**, 1473-1477
Dick J.C. et al (1997). *Spine,* **22**, 370-375

ACKNOWLEDGEMENTS

We would like to thank Stratec Medical for supplying the implants used in this study.

PULLOUT STRENGTH OF PEDICLE SCREWS IMPROVES WITH PALACOS OR CORTOSS AUGMENTATION

*Sam L Evans[1], Sashin Ahuja[2] and Chris M Hunt[1]
[1]Division of Materials and Minerals, School of Engineering, Cardiff University,
P O Box 925, The Parade, Cardiff, CF24 0YF, UK *EvansSL6@cardiff.ac.uk
[2]University Hospital of Wales, The Heath, Cardiff CF14 4XY, Wales, UK

INTRODUCTION

Spinal instrumentation is used extensively in the treatment of the spine. Pedicle screw implants systems use screws driven into the pedicles to provide a mounting point for a structure that runs between two or more vertebrae. It has been found that in some conditions (such as at the ends of long span fixations, or in the presence of osteoporosis) the pedicle screws can lose purchase in the bone and pull out, leading to failure of the treatment.

This work aimed to test whether the pullout strength of pedicle screws could be improved by augmenting their fixation with either low viscosity bone cement or a bioactive bone-substitute.

METHODS

The experiments were carried out using Cortoss (a bone substitute produced by Orthovita) and Palacos LV (a low viscosity cement produced by Schering-Plough). Five-calf lumbar vertebra were used to test each of the materials. Each vertebra had a cement or bone-substitute augmented screw inserted into a randomly selected pedicle, and a non-augmented screw inserted into the other. In this way each augmented pedicle screw had its own paired, non-augmented screw mounted in the same vertebra. Bone cement was used to provide a flat surface for a loading plate attached to the posterior of each pedicle. The shafts of the screws were coated with PTFE tape to prevent the cement adhering to them and affecting the results. Once the vertebrae had been prepared the pedicle screws were pulled out using a tensile testing machine and the load at pullout recorded.

The tests produced paired results for augmented and non-augmented pedicle screws. After testing, means and standard deviations were calculated for the augmenting material and their non-augmented pairs. Paired, two-tailed T-tests with a significance level of $p=0.05$ were then used to compare the augmented results with the paired non-augmented results. Two-tailed unpaired T-tests were also used to compare the two types of augmenting material and also the two control groups.

RESULTS AND DISCUSSION

Both Palacos LV and Cortoss significantly increased the pullout strength ($p=0.0213$ and $p=0.0029$ respectively). Comparison of the Palacos and Cortoss results suggested no significant difference between them ($p=0.79$). There was no significant difference between the spines used ($p=0.41$).

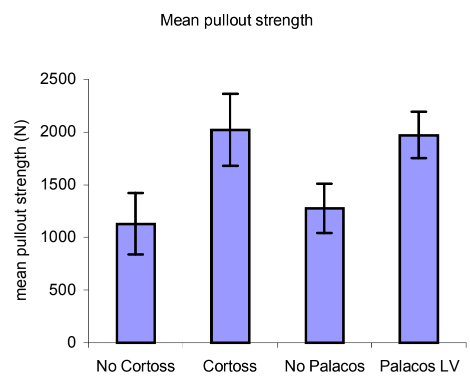

Figure 1: Mean pullout strengths and standard deviations for the paired Cortoss and Palacos LV tests

The results suggest that augmentation with bone cement or bone-substitute can increase the pullout strength of pedicle screws. No significant difference was found between the two augmenting materials. In the long term the bone-substitute may stimulate bone growth, increasing bone density in the vicinity of the pedicle screw and increasing the pullout strength further. This test did show that even without the formation of new bone, the bone-substitute is as effective at increasing pullout strength as the low viscosity cement.

SUMMARY

- Augmentation with Cortoss or Palacos significantly increased pullout strength of pedicle screws.
- There was no significant difference between Cortoss and Palacos.

ACKNOWLEDGEMENTS

We would like to thank Orthovita (Cortoss) for providing funding for this study.

EXPERIMENTAL AND FINITE ELEMENT ANALYSIS OF THE EFFECT OF MUSCLE FORCES ON FIXATION OF CEMENTED HIP PROSTHESES AT HEEL STRIKE

B. Afsharpoya[1], T. Stewart[1], D. C. Barton[1], J. Fisher[1], B Purbach[2], M. Wroblewski[2]
1. School of Mechanical Engineering, The University of Leeds, LS2 9JT, UK, menba@leeds.ac.uk
2. Wrightington Hospital, Appley Bridge, Wigan UK.

INTRODUCTION

The bending, or strain, in a cemented hip prostheses is shielded by the increased stiffness of the implant and cement, and further restricted by actions of the muscle forces acting to stabilise the joint throughout the range of complex physiological motions. Due to anatomical complexity in-vitro studies of cemented hip fixation have either been simplified experimental models in the stance phase of gait with only limited use of muscle forces, or complex finite element models which lack validation [1,2,3]. Consequently a clinically relevant in-vitro model which reproduces the cement mantle fracture seen in-vivo is required. It is postulated that at heel strike where high bending moments exist, incorporating the actions of the Glutei and Vastus muscle groups will cause increased bending strains within the cement mantle and a more physiological model of fixation. The purpose of the study was to develop an experimental and finite element model of femoral stem fixation at heel strike and to determine the effects of muscle forces on the resulting strain produced.

MATERIALS AND METHODS

Depuy C-stem femoral stems were cemented into Sawbone composites femurs by an orthopaedic surgeon. Each femur was rotated into the heel strike position of the gait and fixed distally. Muscle force positions and vectors at heel strike [4,5] were applied by means of springs and pulleys with their forces measured by load cells as shown in Table 1. Eight uni-axial strain gauges were applied to the lateral, medial, anterior and posterior surfaces of the femur. Strain gauge and load cell outputs were monitored by a PC data acquisition system.

Table1**.** Joint and muscle forces

Force	F_x (N)	F_y (N)	F_z (N)
Joint	520	203	-1711
Gluteus maximus	498	-479	630
Gluteus medius	350	-0.53	398
Gluteus minimus	218	-55	325
Vastus medialis	-5	-22	-243
Vastus lateralis	14.7	-20	-294

IDEAS software was used to build a solid model of the Sawbone and hip prosthesis. Isotropic 20-node parabolic elements were used to mesh the solid model. The Young's moduli of stem, cement, epoxy and polyurethane foam were 210, 2.28, 11.5 and 0.41 GPa respectively.

RESULTS

Figure 1 shows predicted and measured surface strains for the implanted femur without muscle forces. Results show good agreement indicating that the FE model is valid. Predicted surface strains with and without muscle forces are shown in Figure 2. Tension was decreased anteriorly (b) and increased laterally (h) while compression increased medially (c,d) and decreased posteriorly (e,f,g) by the addition of muscle forces.

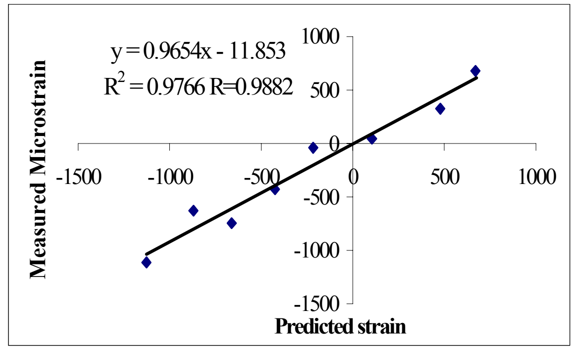

Figure 1: Measured vs. predicted surface strains without muscle forces

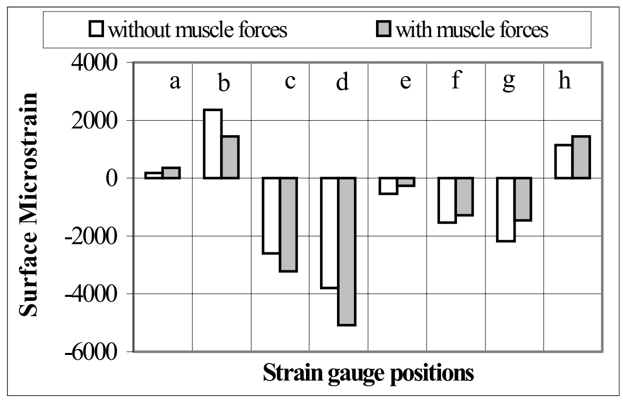

Fig. 2**:** Predicted surface strains with/without muscle forces

DISCUSSION

The experimental and predicted strains within the femur at heel strike were in close agreement both with and without muscle forces. The addition of the glutei and vastus muscles reduced the strain anteriorly and posteriorly, while increasing the strain medially and laterally. The increased medial/lateral bending produced at heel strike increases the stresses at the implant/cement/bone fixation interfaces. With the addition of proximal debonding of the cement mantle, it is predicted that this loading will lead to high torsional stresses and reproduce the cement mantle failure as seen *in vivo.*

REFERENCES

1. Stolk J. et al.(2001). J Biomech., 34, 917-925.
2. Joshi M.G. et al.(2000), J Biomech., 33, 1655-1662.
3. Cheal J.C. et al.(1992), J Orthop. Res, 10, 405-422.
4. Brand R.A. et al.(1982),J Biomech Eng,104,304-310.
5. Dostal W.F. et al (1981), J. Biomech., 14, 803-812.

ACKNOWLEDGEMENTS

The research was funded by the John Monk Trust UK.

THE EFFECTS OF AGE AND FEEDBACK ON ISOMETRIC KNEE EXTENSOR FORCE CONTROL ABILITIES

Jeff M. Schiffman[1], Carl W. Luchies[2], Lorie G. Richards[4], Carole J. Zebas[3]
[1]U.S. Army Natick Soldier Center, Natick, MA. E-mail: Jeffrey.Schiffman@natick.army.mil
[2]Department of Mechanical Engineering, [3]Department of Health, Sport and Exercise Science, University of Kansas, Lawrence.
[4]Department of Occupational Therapy Education, University of Kansas Medical Center, Kansas City, Kansas.

INTRODUCTION

Mixed results exist regarding the effects of age on force variability during a force control task (Enoka, 1999; Graves 2000, Hortobagyi, 2001). While past research used continuous feedback designs, most ADLs require the monitoring of internal feedback for submaximal forces. The purpose of this study was to investigate the effects of age, feedback, and force level on isometric knee extensor force control ability.

METHODS

Twenty young (YA, 25.8 ± 2.7 yrs) and 20 older (OA, 71.8 ± 2.0 yrs) adult healthy male participants maintained a steady force in knee extension (knee joint set at 60 degrees flexion) at two levels of force (20% and 60% MVC) with and without visual bandwidth feedback for 8 seconds. The upper and lower bandwidth limits were defined as ± 6.1 Nm. The on-screen feedback consisted of a green light with "Push more" and a red light with "Push less" above it which illuminated whenever force production fell below or rose above the bandwidth limits. Variables examined were force variability, bias, and time in bandwidth.

Strength was measured using the Cybex 6000 isokinetic dynamometer system (Lumex, Inc.) interfaced with a computer data acquisition system. The voltage output from the dynamometer was sampled at 200 Hz and filtered. A three-way MANOVA (age x force x feedback) was performed on the 3-trial average of the variables. p values less than 0.05 were considered significant. Significant findings were followed up with ANOVAS and pair wise testing.

RESULTS AND DISCUSSION

As force increased, variability increased for both groups, with YA having greater increases in variability (Table 1). Variability was significantly higher for the YA at the 60%, though the actual difference was small (1 Nm), suggesting that the two groups performed quite similarly which would be consistent with past research (Graves, 2000; Tracy, 2000). The main effect of feedback on variability was not significant. The variability from the feedback condition may be more similar to our no feedback condition in contrast to continuous feedback conditions of other studies.

Table 1. Age x force (%MVC) effects on Force Variability

	YA, 20%	OA, 20%	YA, 60%	OA, 60%
Mean	0.863	0.7255	3.1262	2.1003
SD ±	0.357	0.4752	1.2814	1.1397

Increase in age, decrease in force level, and presence of feedback resulted in significantly less bias away from bandwidth midline. Bias was larger with an increase in force for the feedback condition and for the feedback removed condition (Figure 1). At 60% MVC, bias was significantly larger for the feedback removed condition. It has been suggested that OA have a larger safety margin because of age-related impairments in tactile and proprioceptive sensation. Therefore we expected, consistent with the results, that the OA would use more force in our task than the YA. The YA produced just enough force to be within the bandwidth, while the OA produced more force than required, even when feedback was removed. Both OA and YA spent more time within the bandwidth at 20% compared to 60% MVC and with feedback than without (figure 1). Time in bandwidth decreased as force increased with feedback and without. Time in bandwidth decreased in the feedback removed condition at 20% MVC and at 60% MVC.

Figure 1. Feedback x Force Interaction Effect Means and Standard deviations for Time in Bandwidth and Bias

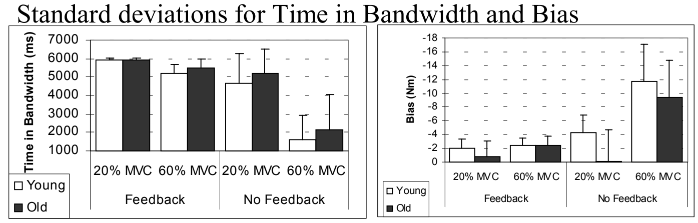

SUMMARY

Both groups were fairly accurate at accomplishing the task, though the higher force was harder to control. The visual feedback improved performance in terms of time spent in bandwidth and safety margin but had little affect on force variability. Older adults performed with a higher safety margin and statistically less variability. Further study is needed to examine the effects of feedback paradigms (intermittent versus continuous feedback) on submaximal force control ability.

REFERENCES

Enoka, R.M. et al (1999). *Progress Brain Res.* **123**:389-395.
Graves, A.E. et al (2000). *J. Neurophys*. **83**:2030-2039.
Hortobágyi, T. et al (2001). *J. Geron:Bio Sci.* **56A**:B38-B47.
Tracy, B.L. et al (2000). *Med Sci Sports Exerc.* **32**: S244.

ACKNOWLEDGEMENTS

We gratefully acknowledge the support from the Center on Aging KUMC and the assistance of Drs. Pamela Duncan, Stephanie Studenski, Patricia Pohl, Joan McDowd, Teresa Cathers, Dennis Wallace as well as Pam Klaesbisch.

MODEL BLOOD CONSISTING OF DENSE SUSPENSION OF NATURAL POLYMERIC GEL PARTICLES

K. Ohba[1], T. Ando[1], I. Yoza[1], A. Onoue[1], T. Uragami[2] and T. Miyata[2]
Kansai University, Suita, Osaka, 564-8680 Japan, ohbak@ipcku.kansai-u.ac.jp
[1]Dept. of Mechanical and Systems Engrg., [2]Dept. of Applied Chemistry

INTRODUCTION

Simulating blood flow in experiments *in vitro* are very important to derive effective and precise results in the studies of the pathogenic mechanism of cardiovascular diseases, such as arteriosclerosis, and the development of artificial organs. However, it was difficult to make a similar flow pattern to the actual blood with a simple fluid, such as glycerol solution, because the actual blood is a non-Newtonian fluid, and obeys the Casson's diagram. These complicated flow properties are mainly caused by the motion of the red blood cells. Therefore, we have developed a tiny particle of natural polymeric gel as a model of human red blood cell (RBC), and have made a high concentration suspension of these particles in water and physiological salt solution as a realistic model of human blood [1].

MATERIALS AND METHODS

The model RBC (MRBC) was made of alginic acid calcium gel, and was of a spherical shape and very soft and elastic. Its average diameter was about 10 μm, which was very similar to human RBC, although its shape was not so-called biconcave. Shear rate $d\gamma/dt$ and shear stress τ of the human blood with 45% hematocrit (volumetric concentration) of the RBC at the temperature of 37°C and the model blood with 45% hematocrit of the MRBC at the temperature of 15°C were measured by using a cone-plate viscometer. The motion of each MRBC in the various range of shear rate was observed using a rheoscope system consisted of an inverted microscope, a cone-plate viscometer, and a high-speed video camera. The elasticity of the MRBC was also visualized and measured using a micromanipulator.

RESULTS AND DISCUSSION

Figure 1 shows the Casson's diagram, i.e. $\sqrt{d\gamma/dt}$ versus $\sqrt{\tau}$ obtained from the present model blood and the human blood. It can be seen from Fig. 1 that the present model blood obeys the Casson's diagram and agrees very well with that of real blood. All the curve of this model blood obey the Casson's diagram regardless of various concentrations and temperatures, although the yield stress and the gradient of the curves for the model blood shows a little dependence on concentration and temperature, which is considered to be partly due to the variation of the viscosity of water with temperature. The coefficients of viscosity calculated from the above curves in the case of four different concentrations and six different temperatures show clear shear thinning, and agree very well with that of the human blood in the case shown in Fig. 1. Furthermore, in the region of low shear rate less than about 100/sec, visualization of the MRBC motion revealed formation of aggregates of the MRBC, which is a very similar phenomenon as real RBC forms a rouleaux when shear rate is lower than about 100/sec. The relationship between the deformation of the spherical MRBC and the force applied on it obeyed the Hertz's contact theory, and the total Young's modulus of the MRBC was 0.075MPa for $\nu = 0.5$ and 0.10MPa for $\nu = 0$, where ν is the Poisson's ratio.

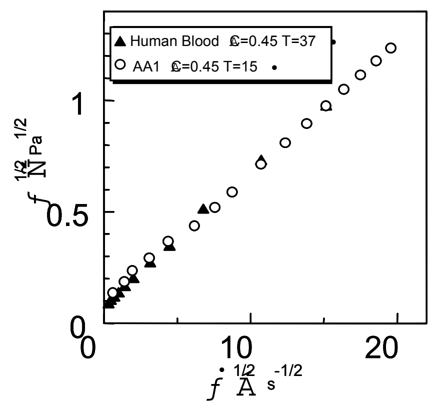

Fig. 1 Casson's diagram of human blood and model

SUMMARY

The above experimental results show that the present model blood has almost same rheological characteristics as actual human blood, and that it can be used as a powerful substitute of actual human blood to make a precise experiments *in vitro* .

REFERENCES

[1] K.Ohba *et al.*, Proc. 11th Symp. on Bio-medical and Physiol. Engrg. (SICE), pp.365-368, 1996 [in Japanese].

SKIN MOTION ARTEFACT CHARACTERIZATION FROM 3D FLUOROSCOPY AND STEREOPHOTOGRAMMETRY

Silvia Fantozzi[1], Rita Stagni[1], Angelo Cappello[1], Mauro Bicchierini[1], Alberto Leardini[2] and Fabio Catani[2]
[1] Dipartimento di Elettronica Informatica e Sistemistica, Università di Bologna, Italy, fantozzi@ior.it
[2] Movement Analysis Laboratory, Istituti Ortopedici Rizzoli, Bologna, Italy

INTRODUCTION

Routine gait analysis is critically limited by skin motion artefact (SMA). The analysis of this artefact on patients with external fixators (Cappozzo et al.,1996) and on volunteers with percutaneous pins (Manal et al, 2002) is limited by the restrictions to skin sliding. Moreover, only a small number of markers has been analysed. The knowledge on the amount and direction of the SMA is therefore limited. It is necessary to better characterize this artefact in order to achieve higher accuracy in gait analysis data. In the present study the SMA was characterized non invasively collecting data from a patient with a total knee replacement by means of stereophotogrammetry and 3D fluoroscopy simultaneously.

METHODS

One patient operated of total knee replacement was analysed during stair climbing (SC) and sit-to-stand/stand-to-sit (STS) activities with fluoroscopy and stereophotogrammetry. Nineteen reflecting markers were uniformly attached laterally on the skin of the thigh, ten on the shank, and one reflecting/radiopaque on the patella for temporal synchronization. Moreover, three reflecting/radiopaque markers were placed in the fluoroscope field of view for spatial registration. The marker trajectories were reconstructed by means of a stereophotogrammetric system with 5 TV cameras (e-Motion, Padova, Italy). The accurate 3D pose of the prosthesis components was reconstructed from each 2D fluoroscopic projection with an iterative procedure using a CAD model based shape matching technique (Banks et al., 1996). The skin marker trajectories on the thigh and shank were reported in the corresponding prosthesis component reference frames. The displacements were calculated with respect to the initial frame.

RESULTS AND DISCUSSION

Markers on the thigh exhibited a much larger movement with respect to markers on the shank, particularly during STS (Figure 1 and 2). In particular, the markers located posteriorly on the thigh were more affected by SMA. In SC the displacement involved in the thigh and in the shank were comparable (Figure 2). The maximum amount of displacement of the markers located posteriorly on the thigh during STS was 40.0, 51.5, and 55.3mm along the antero/posterior, medio/lateral and vertical direction, respectively. In the shank, the maximum displacements were 31.4, 32.4 and 32.4 mm along the antero/posterior, medio/lateral and vertical direction, respectively. These displacements enable a rationale identification of the optimal location of markers depending on the segment and on the motor task under analysis. This technique can be applied to a large number of subjects.

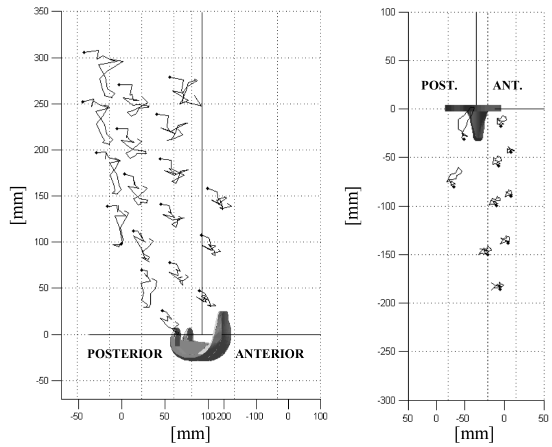

Figure 1: Skin markers trajectories in the femoral (left) and tibial (right) component reference frame during a trial of STS.

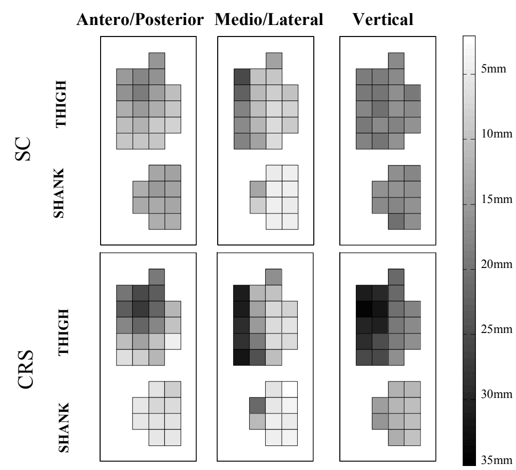

Figure 2: Root mean square value of the three components of the marker displacement vector, during the execution of SC and STS.

SUMMARY

Displacement as large as about 50mm was observed in markers attached on the thigh. The extension of this novel technique to a larger number of subjects will allow to identify the optimal location of markers in order to study with higher accuracy knee kinematics in gait analysis.

REFERENCES

Manal, K., et al. (2000). *Gait & Posture*, **11**, 38-45.
Cappozzo, A., et al. (1996). *Clin. Biomech.* **11**(**2**), 90-100.
Banks, S. A., et al. (1996). *IEEE Trans. Biomed. Eng*, **43**(**6**), 638-648.

CHARACTERISATION OF A SUBSTITUTE MATERIAL TO MODEL CANCELLOUS BONE IN *IN VITRO* IMPLANT MIGRATION STUDIES

Vinu Palissery, Mark Taylor and Martin Browne
Bioengineering Sciences Research Group, School of Engineering Sciences, University of Southampton,
Highfield, Southampton, SO17 1BJ, UK. vinu@soton.ac.uk

INTRODUCTION

Progressive fatigue failure of supporting cancellous bone with inadequate bone remodelling has been suggested as a possible cause of implant migration [Taylor et al., 1997]. There is no preclinical migration test that has accounted this factor. An analogue material with uniform and consistent properties similar to cancellous bone would provide a simplified idealised model for a preliminary *in vitro* analytical and experimental migration studies simulating the worst-case scenario. Wide variation in the properties of cancellous bone will affect the reproducibility of experimental results. Substitute materials to cancellous bone used in *in vitro* studies are normally chosen based on a similar structure and static compressive behaviour to that of cancellous bone [Szivek et al., 1993], and no comparison of fatigue behaviour has been reported. In this study a rigid closed cell polymer foam (HEREX C®70.55) of density 60 kg/m^3 was tested to assess its fatigue behaviour for use as a cancellous bone substitute in migration studies.

EXPERIMENTS AND METHODS

Reduced section cylindrical specimens of foam were tested under static and cyclic loads. Strength and modulus of the material, calculated from five specimens each in tension and compression, were consistent though the material was stronger in tension (strength = 1.45MPa, modulus = 48.9MPa) than in compression (strength = 0.64MPa, modulus = 39.9MPa). Fatigue tests in tension and compression, conducted under load control, were carried out at various stress levels at a frequency of 2Hz. Secant modulus and translation of hysteresis loop along the strain axis (creep) at various cycles were determined for each test. Secant modulus determined from a preconditioning test, prior to each fatigue test, was used to normalise the stress.

RESULTS AND DISCUSSION

Qualitatively, the static behaviour of HEREX C®70.55 was similar to cancellous bone. Strength and modulus, which fall in the lowest range of cancellous bone, were consistent with a standard deviation less than 10%. Under compressive cyclic loading with a non-zero mean stress cancellous bone shows accumulation of strain and modulus degradation with number of cycles [Bowman et al., 1998], where the number of cycles to failure and secondary state creep rate are related to normalised stress by means of power law relationships. There are no tensile fatigue tests reported for cancellous bone. Similar findings were observed for the analogue material. Figure 1 shows creep and modulus reduction of the foam against life fraction in compression fatigue. Numbers of cycles to failure and creep rate were related to normalised stress by a power law relationship in both tension and compression (Figure 2). The degree of creep and modulus reduction was low compared to that of cancellous bone in compression fatigue. Generally there was more creep and modulus reduction in compression than in tension for the analogue material. This is probably because the material was stronger in tension than in compression, which is normally the reverse in the case of bone. This research does not intend to replicate the mechanical behaviour of cancellous bone quantitatively; however the methods may be used to propose a protocol that could be used for the selection of suitable analogue *in vitro* test medium for assessing implant performance under cyclic loading.

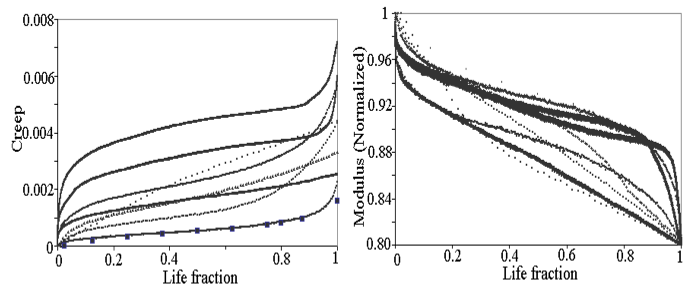

Figure 1: Creep and modulus degradation against life fraction in compression fatigue

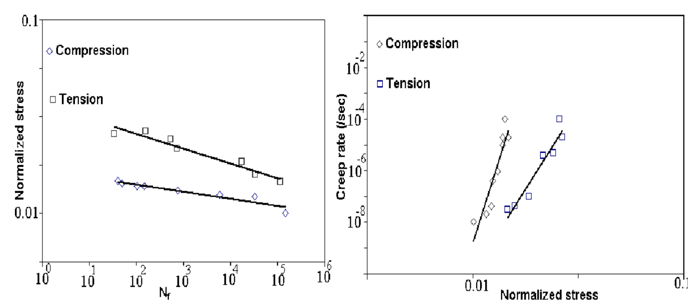

Figure 2: Power law relationship between number of cycles to failure (N_f) and creep rate with normalized stress (Logarithmic plot)

REFERENCES

Taylor, M. and Tanner, K. E. (1997), *JBJS*, **79-B**, 181-182.
Szivek, J. A. et al (1993), *J. App. Biomat.*, **4**, 269-272.
Bowman S. M. et al (1998), *J. Biomech. Engg.*, **120**, 647-654.

ACKNOWLEDGMENTS

The authors would like to thank Cremascoli Fry Ortho Ltd. (UK) for their financial support.

ROTATIONS OF THE HUMAN KNEE

Clementina D. Mladenova

Institute of Mechanics, Bulgarian Academy of Sciences
Acad. G. Bonchev Str., Block 4 , Sofia 1113, Bulgaria
Email: clem@bgcict.acad.bg,

INTRODUCTION

It is necessary to display the kinematic data of the knee in a suitable parameter space, so that the diagnostic test reacts with sensitivity to the respective damage (cf Gillner 1999 and Mannel 1999). In this connection a mathematical description of the knee rotations is presented through an efficient parameterization of the rotation group already used by the author in multibody systems for modeling and control, i.e. using vectors of rotations 'c' which are elements of a Lie group and have clear and simple
composition law.

KNEE GEOMETRY

The knee is the intermediate joint of the lower limb. It is mainly a joint with one degree of freedom which allows the end of the limb to be moved towards or away from its root. The knee has an accessory, i.e. second degree of freedom: rotation of the long axis of the leg, which only occurs when the knee is flexed. The first degree of freedom is related to the transverse axis XX' around which occur movements of flexion and extension in a sagittal plane. This axis *XX'*, lying in a frontal plane, runs through the femoral condyles horizontally.
The second degree of freedom of the joint is related to rotation around the long axis $Y\,Y'$ of the leg with the knee flexed. The axis *ZZ'* (broken line) is running anteroposteriorly and at right angles to the other two axes. This axis does not represent a third degree of freedom but, owing to a measure of 'play' at the joint, side-to-side movements occur. In full extension these movements disappear and if they still persist they must be considered, as a rule, as abnormal.

KNEE ROTATIONS

The present paper breaks the standard frames of considering multibody systems motion and presents a unified treatment of robot dynamics using the ideas from Lie groups and differential geometry (see Mladenova 1990, Mladenova 1991). Since the properties of the parameterization of the rotation group in three dimensional space $SO(3)$ more or less influence over the efficiency of the dynamic model, we use vector - parameters c, which make a Lie group with a clear geometrical sense and a simple composition law, they are linear and symmetrical with respect to all components, and play role of new generalized coordinates, different from the standard joint displacements.
We introduce :
rotation angle - α (around X axis), β (around Y
axis), (around Z axis) and the vectors c_1, c_2 , c_3 which are the vector-parameters describing the rotations around X, Y, Z axes respectively.
The basic rotations are:
- Flexion (rotation around Z axis)
$c_1 = (0, 0, \tan(\gamma/2))$;
- Rotation (rotation around Y axis)
$c_2 = (0, \tan(\beta/2), 0)$;
- Adduction (rotation around X axis)
$c_3 = (\tan(\alpha/2), 0, 0)$;
- Rotation + Flexion = $< c_2 , c_1 >$ - this means the composition law of the group
- Flexion + Rotation = $< c_1 , c_2 >$ - this means the composition law of the group, where the composition (group) law of the vector-parameters is:
$c' = < c_1 , c_2 > = (c_1 + c_2 + c_1 \times c_2)/(1 - c_1\, c_2)$
$c'' = < c_2 , c_1 > = (c_2 + c_1 + c_2 \times c_1)/(1 - c_2\, c_1)$.

SUMMARY

The present approach allows efficient presentations of the basic kinematic and dynamic relations so that the last to be successfully applied in the virtual dynamic simulations, for the control and mechanics of human movement systems, for biomechanical investigations and motor control of human gait.

REFERENCES

Mladenova, C. (1990). *J. Intell. & Robot. Syst.*, No.3, 349-363.
Mladenova, C. (1991). *Rob. & Comp. Integr.*, Vol.8, No.4, 233-242.
Gillner, S. et al (1999). *Proc. Conf. Biomechanics Meets Roboitics, Modelling and Simulation of Motion*, Heidelberg - Germany, November 8-11.
Mannel, H. et al (1999). *Proc. Conf. Biomechanics Meets Robotics, Modelling and Simulation of Motion*, Heidelberg - Germany, November 8-11.

3D FINITE ELEMENT ANALYSIS OF AN INTRAVASCULAR STENTING PROCEDURE USING AN NIROYAL STENT

Caitriona Lally[1], Patrick J. Prendergast[1] and Finbar Dolan[2]
[1]Department of Mechanical Engineering, Trinity College, Dublin 2, Ireland, calally@tcd.ie
[2]Medtronic AVE, Parkmore Industrial Estate, Galway, Ireland

INTRODUCTION

Coronary heart disease may be treated by the deployment of a stent within the stenosed artery, however, in-stent restenosis occurs in 20-50% of stented vessels (Grewe *et al.*, 2000). Tissue prolapse and high stresses within a stented vessel have been hypothesised to increase the probability of in-stent restenosis. This study aims to quantify the stresses induced within an idealised cylindrical vessel, by deploying an NIROYAL stent within the vessel using the Finite Element Method (FEM). We wish to establish if stresses in the vessel wall and tissue prolapse within the stent repeating units could play a role in the initiation of the restenotic process.

The ultimate objectives of this study are to generate a computational model of restenosis using the stress distribution within the vessel wall as a stimulus and subsequently determine the probability of restenosis within various stent designs.

METHODS

The geometry of one repeating unit of a fully expanded 2.5 mm diameter NIROYAL stent was determined using a coordinate measurement technique (Prendergast *et al,* 2002). A full 3D segment of the stent, with a radial thickness of 0.1 mm and an inner diameter of 2.5 mm, was generated based on the geometry of the repeating unit.

To describe the stress-stretch behaviour of the artery wall a reduced 9-parameter Mooney-Rivlin hyperelastic constitutive equation was used. Experimental stress-stretch data, obtained from uniaxial and equibiaxial tensile tests conducted on human femoral arterial tissue, was used to determine the specific hyperelastic constants in the constitutive equation (Prendergast *et al.*, 2002*)*. The coronary artery was modelled with a thickness of 0.5 mm and a diameter of 2 mm.

The analysis was carried out in two load steps. Initially the stent elements were deactivated and the vessel was expanded beyond the stent by applying a luminal pressure of 70 kPa. The stent elements were then activated in the second load step and the luminal pressure removed. Due to the nature of the vessel material, which was modelled as a hyperelastic material and is therefore completely elastic, the vessel attempted to return back to its original configuration upon removal of the pressure. However, contact surfaces defined on the outer surface of the stent and on the inner lumen of the vessel ensured that the vessel was scaffolded open by the stent.

The stent was assumed to be rigid and therefore completely restrained during the analysis, whilst restraining the proximal and distal faces of the vessel simulated longitudinal tethering of the vessel.

RESULTS AND DISCUSSION

Tissue prolapse (i.e. narrowing of the lumen as a result of elastic deformation of the vessel wall) was observed between the struts of the stent to a maximum of 0.1 mm within each stent unit, see Fig. 1 (a).

Von Mises stress magnitudes of up to 460 kPa were observed to be induced in the arterial vessel where the stent struts contacted the lumen of the vessel, see Fig. 1 (b).

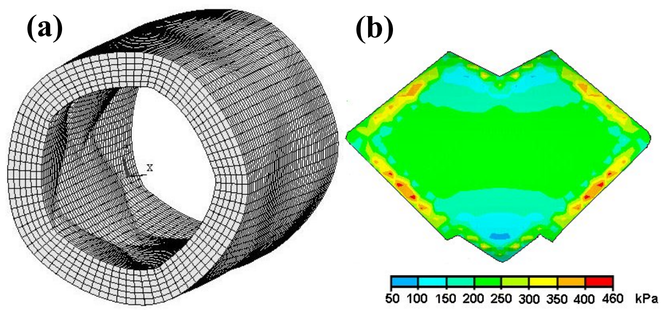

Figure 1 *(a) Deformation of a cylindrical vessel after deployment of an NIROYAL stent, (b) Von Mises stress distribution within the vessel wall for one repeating stent unit*

CONCLUSION

From this study it is clear that the stress distribution, as well as the degree of tissue prolapse, within stented vessels may be determined using FEM. Tissue prolapse observed within the stented vessel contributes to lumen loss and also induces high stresses within the vessel which may act as a stimulus for in-stent restenosis. An analysis to determine the effect that elastic recoil of the stent has on the stress distribution within the vessel, where the stent is allowed to deform elastically, will be carried out in a future study.

REFERENCES

P.H. Grewe *et al.*, (2000). *J Am Coll Cardiol*, **35**: 157-163.
P.J. Prendergast *et al.*, (2002). "Analysis of Prolapse in Cardiovascular Stents: A Constitutive Equation For Vascular Tissue and Finite Element Modelling", (In Submission).

TRAJECTORY ANALYSIS OF CATCHING MOTION BY A HAND USING THREE-DIMENSIONAL POSITION SENSOR

Nobuo Sakai, Teruo Murakami and Yoshinori Sawae

Department of Intelligent Machinery and Systems, Kyushu University, Fukuoka, Japan.
Bionic Design Laboratory, sakai@mech.kyushu-u.ac.jp

INTRODUCTION

The application of robots to the human-care system for elder or disabled people is required, but the direct application of existing industrial robot has difficult problem. Namely human-care robots or machines encounter a minor collision with human body directly. Machines coexisting in human livings must be designed with a lot of consideration about soft and smooth touch to human body. In robotics research field, the structure of human body and human motion has served as an inspiration to propose a design that could be used to build more useful system. A situation that a human touches directly to another person in a hand may be found in a daily life. In such situation, a condition of human mind largely affects the feeling impression of another person. In this study we set up the following scenario to investigate the catching motion within humans: The subjects were asked to support a human body falling backward by placing their hand on the falling person's back either gently or without limits. The purpose of this study is to speculate how to generate and to control a trajectory for robots or machines touching to human directly.

METHODS

When we measure a human voluntary motion, the first question we have to consider is how subjects have consciousness or peculiar effort. We evaluated the dependence of the trajectory and contact force on the subject's consciousness in a catching motion for a falling person. Subjects were sufficiently instructed to have the mind in which subjects catch a falling human softly. To discuss the difference for subject's mind, another situation was arranged so that the subject push back to escape a falling person.

A trajectory of subject's hand was measured by three-dimensional position sensor using an electromagnetic signal. Position sensor was attached on metacarpal bone. A tactile sensor was attached on a back of falling person to estimate contact force. Experimental process is as follows;

(1) Subject stands in a person's back within an area of reaching by subject's hand; (2) Subject puts one's hand to tactile sensor attached on person's back to give a cue for falling backward; (3) Person falls backward with fixing knee and hip joints straight; (4) Subject reaches out a hand to the back of falling person to support him or her in a medium position; (5) Subject pushes the falling person to the starting state; (6) Subject settles a hand in the starting position. Measured position data were translated to a coordinate system having X-axis along a linear motion line and a coordinate origin at starting position of a hand. The data were recorded at 120 Hz and filtered using Savitzky-Gollay method to estimate the velocity directly.

RESULTS AND DISCUSSION

An example of measured trajectory and contact force with the mind for softly touching is shown in Fig.1. Each number in figure corresponds to each action stated above. At a time of action near (4), velocity transition was different from that in Fig.2, in which the data were measured by a subject without the mind for softly touching. In the situation that subject supported a falling human softly in mind, velocity profile was smooth transition at early touching time. As to the touching force profile, estimated maximum force in Fig.1 was the same as in Fig.2. But it is clear that integration of time dependent force transition was evaluated to be larger in soft touching. This result implies that the comfortable contact action required more energy than simple escaping motion evaluated in this experiments.

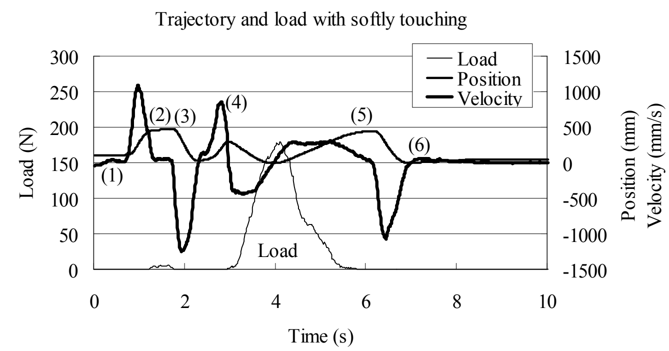

Figure 1: Trajectory and touching load for supporting a human with the mind for softly touching.

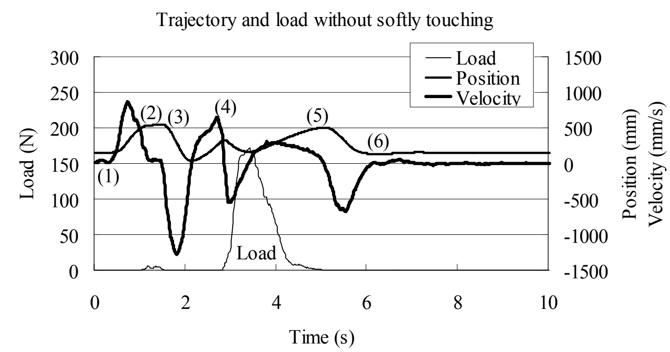

Figure 2: Trajectory and touching load for supporting a human without the mind for softly touching.

SUMMARY

The experimental result indicated that in the supporting motion for a falling person the direct contact action considering a feeling of satisfaction required not only energy evaluation but also special time-depending force transition profile or trajectory profile.

REFERENCE

Zhang, X., Kuo, A.D., Chaffin, D.B.: *Optimization-based differential kinematic modeling exhibits a velocity-control strategy for dynamic posture determination in seated reaching movements. J. Biomechanics*, **31**, 1035-1042.

EFFECT OF LOADING RATE ON THE DURAL-SAC OCCLUSION

Young Eun Kim[1] and Jae Yong Ahn[2]
[1]Dept. of Mechanical Engineering, Dankook University, Seoul, Korea, yekim@dankook.ac.kr
[2]Samsung Cheil Hospital, Dept. of Orthopedic Surgery, Sungkyunkywn University, Seoul, Korea

INTRODUCTION

Spinal stenosis has been defined as a narrowing below the lowest limit of the ranges for normal vertebral canal size. For static loading condition, disc and ligamentum flavum were the main causes for generating stenosis. Among the various types of loading conditions, impact loading, which induces spinal fractures, leases energy rapidly over a short time period. In this case, fractured vertebral bony segment pose a great treat to the spinal cord. In this study therefore improved the previously developed finite element model (Kim et al. 2001) of the spinal motion segment to reflect the response of the dural-sac occlusion by the bony fragment under varying impact durations

METHODS

A finite element model of L3/L4 lumbar spinal motion segment which consist of all ligament, dural-sac and bone fragment was developed. The ligamentum flavum was modeled by four-node shell element in order to be able to analyze the slackening. By performing the modal analysis of the ligamentum flavum, the third mode, which is closed to the slackened shape, was chosen and small amount of initial displacements were assigned to create desired deformed shape. Occlusion of dural-sac was modeled by utilizing the surface contact scheme. The contact between two surfaces assigned slave and master elements was restricted not to penetrate the master side. Figure 1 shows the developed FE model including bony fragment. To simulate the damping phenomena in the motion segment, structural damping was assigned to the disc element. The impact load applied to the top of the L3 vertebral body was assumed to be a triangular impulsive force with variable impact duration. A maximum compressive force of

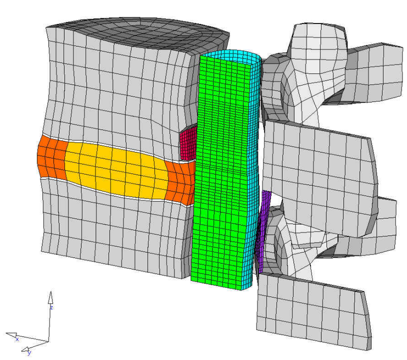

Figure 1: Developed 3-D FE motion segment model including dural-sac and bony fragment

6kN was chosen for this study to simulate the actual situation of initial fracture in the human spine.

RESULTS AND DISCUSSION

High loading rate(short impact duration) produced relatively large dural-sac occlusion compare to low loading rate(large impact duration) as shown in figure 2. In this case, impinged bony fragment resulted dural-sac occlusion. In comparison, at the low loading rate, very small dural-sac occlusion was calculated and main causes of occlusion were disc bulging and slackened ligamentum flavum similar to the static loading case. Experimental study with post injury radiography (Tran et al. 1995) showed bigger spinal canal encroachment at high loading rate than at low loading rate. This encroachment difference was due to the total volume of the generated burst facture. Contrast to previous experimental study, we used only one fragment for this analysis, but similar results were calculated for different loading rates.

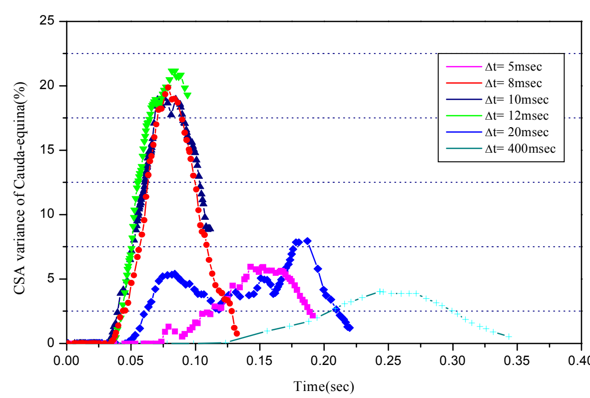

Figure 2: Cross sectional area variation of dural-sac for different impact duration

SUMMARY

Use of the finite element technique to address the role of impact loading rate in producing dural-sac occlusion is presented. Fractured bony fragment at the posterior wall of the cortical shell produced different amount of occlusion according to impact duration(loading rate) changes.

REFERENCES

Kim Y.E. et al(2001). *J of Musculoskeltal Research*, 5(in press)
Tran N.T et al.(1995). *Spine*, 20, 1984-1988

EFFECTS OF TENDON SHEATHS ON THE TENSILE PROPERTIES OF MOUSE TAIL TENDON

Noritaka Yamamoto and Eiji Ikawa
Biomechanics Laboratory, Department of Mechanical Engineering, Faculty of Science and Engineering,
Ritsumeikan University, Kusatsu, Shiga, Japan, noritaka@se.ritsumei.ac.jp

INTRODUCTION

Tendons and ligaments have such hierarchical structures as fascicles, fibers, and fibrils. They were enveloped by sheaths. The basic knowledge of their structure and mechanical properties is essential to the biomechanics of tendons and ligaments.

A rat tail tendon was composed of several fascicles enveloped by a sheath (peritenon, epitenon, or reticular membrane) (Kastelic et al., 1978; Rowe, 1985; Strocchi et al., 1985). In this study, we developed a new method by which tensile tests were performed observing the microstructure of a tendon and its fascicles with a light microscope, and studied the effects of tendon sheaths on the mechanical properties of mouse tail tendon.

METHODS

Male DD-y mice age 4 weeks weighing 18.5±0.5 g (Mean± S.E.) were used. Tendons having the length of 35 mm were resected from mouse tails (Figure 1). They were divided into two portions in the direction of the length. The distal portions were stretched to failure. In the proximal portions, fascicles were resected from a sheath and stretched to failure.

For mechanical testing, a specially designed micro tensile tester was mounted on a microscope stage. Small acrylic blocks were attached to both ends of each specimen with cyanoacrylate adhesives. One of the blocks was fixed to a load cell, and the other one was fixed to the crosshead of a linear actuator. The specimen was immersed in a saline solution and stretched to failure by moving the actuator at the speed of 0.1 mm/sec. The microstructure of the specimen was observed using a differential interference microscope, and the images were recorded on a video recorder.

We confirmed that there were no significant differences in the mechanical properties of fascicles between the proximal and distal portions.

RESULTS AND DISCUSSION

In each specimen, the maximum load of a tendon (distal portion) was larger than the sum of that of its fascicles (proximal portion) (Figure 2). There were statistically significant differences between these mean values. The differences might be attributable to mechanical interaction between fibers as well as between fibers and ground substance induced by binding fascicles with the sheath.

In conclusion, tendon sheaths are a basic microstructural component to determine the tensile properties of mouse tail tendon.

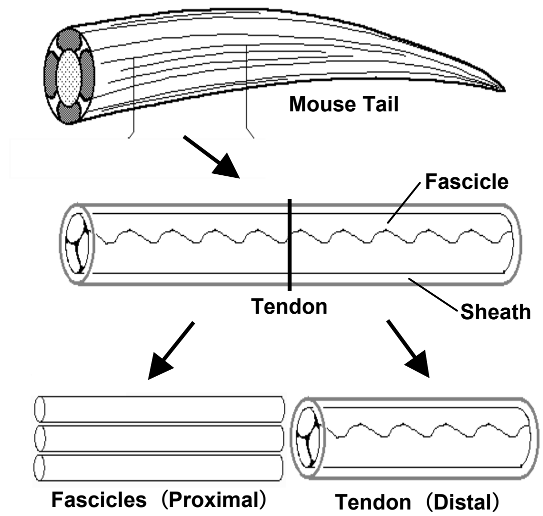

Figure 1: Resection of a tendon and its fascicles from a mouse tail.

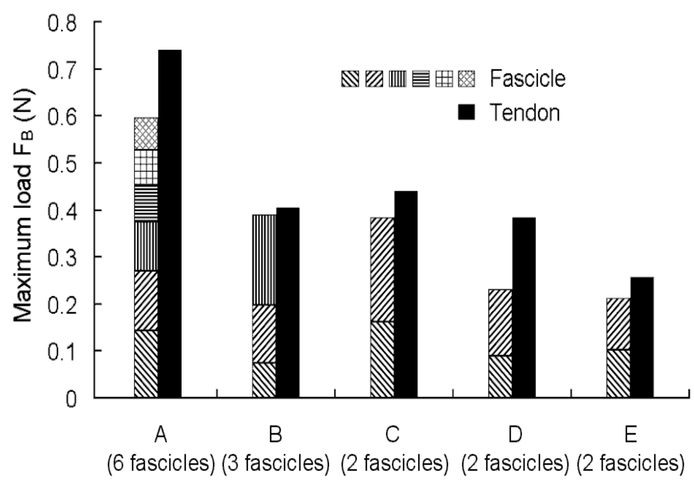

Figure 2: Maximum load of a tendon and its fascicles in each specimen (A ~ E).

REFERENCES

Kastelic, J. et al. (1978). *Connect. Tissue Res.*, **6**, 11-23.
Rowe, R.W.D. (1985). *Connect. Tissue Res.*, **14**, 9-20.
Strocchi, R. et al. (1985). *J. Anat.*, **140**, 57-67.

ANTICIPATORY BEHAVIOUR DURING RECOVERY FROM UNEXPECTED PERTURBATIONS: YOUNGER VERSES OLDER ADULTS

Shirley Rietdyk and Kasey Wiley
Biomechanics Laboratory, Purdue University, West Lafayette, Indiana, USA (srietdyk@sla.purdue.edu)

INTRODUCTION

Research on young adults indicates that during unexpected perturbations, the response was based on an anticipation of the perturbation magnitude (Rietdyk et al., 1999). The purpose of this research was to examine the anticipatory component of the older adult's response to determine the effect of age-related delays and degenerations.

METHODS

To date, three healthy older adults (mean age: 69) have participated in the study. The subjects received unexpected trunk perturbations in different directions and at different sites. The centre of pressure (COP) was determined from the forceplate (AMTI), and the centre of mass (COM) was determined from a 10-segment model (14 IREDs, Optotrak, NDI). Anticipatory behaviour was measured as the phase relationship between the COM and COP (determined from the cross-correlation, Winter et al., 1998). Corrections to the COP were documented by the third time derivative of the COP (Hogan, 1984). Responses were compared to data for 10 younger subjects (mean age: 26; Rietdyk et al., 1999).

RESULTS AND DISCUSSION

For both young and older participants, the COP acts to corral and decelerate the COM (Fig. 1). The average phase lead of the COP for the older adult was almost twice as long (elderly: 198 +/- 51 ms (mean correlation at 198 ms = 0.951); young: 109 +/- 37 ms (mean correlation at 107 ms = 0.976)($p<0.01$)). This increased phase lead can be interpreted two ways: (1) the system takes longer to respond in the elderly or (2) that the nervous system has anticipated the age-related delays and attempts to provide greater time for the response. The first possibility is addressed by comparing the COM acceleration and the difference between the COP and COM displacement (Winter et al., 1998); no differences were found between the young and elderly. Therefore, the nervous system appears to be compensating by providing more time.

The extended phase lead can be problematic if the COM displacement is predicted incorrectly: The subject must detect errors and make corrections in COP displacement (see A in Fig. 1). Multiple corrections are evidenced by the third time derivative (jerk) of the COP (Hogan, 1984): the elderly show peak jerk values which are 25 times greater than the young subjects (elderly: 848.2 m/s^3; young: 33.8 m/s^3)($p<0.01$). If the error is not detected, balance is compromised, as demonstrated in Fig. 1 (bottom panel). At time 0.8 s, the COM is still moving towards the edge of the foot, but the COP turns around, and heads back to correct for any overshoot (B in Fig. 1). The nervous system anticipated that the peak COP

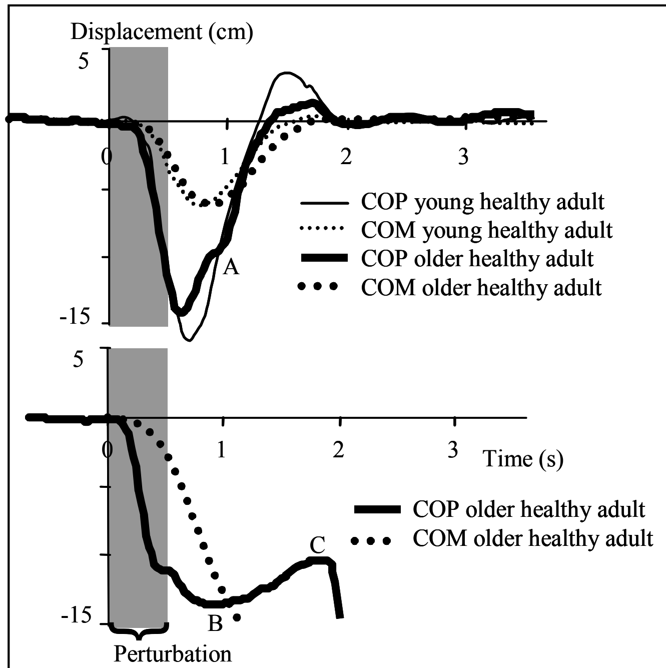

Figure 1: COP-COM relationship: a typical response (top panel) and a stepping response (bottom panel).

displacement was adequate to decelerate and turn around the COM in the immediate future. However, the COM does not decelerate and is heading for the edge of the base of support. It takes another 0.9 s to detect the mistake, decelerate and turn around the COP (C in Fig. 1) in an unsuccessful attempt to corral and decelerate the COM. The participant had to take a step in order to prevent a fall.

SUMMARY

During recovery from an unexpected perturbation the nervous system appears to compensate for age-related delays by anticipating the magnitude of the disruption, and providing a COP-COM phase lead almost two times longer than younger adults. This adaptation appears to put the older adult at increased risk of losing balance because they need to rely more extensively on feedback, and degenerations in the feedback system may compromise their ability to anticipate the excursion or to detect errors.

REFERENCES

Hogan, N. (1984). *J. Neurosci.,* **4**: 2745-54.
Rietdyk, S. et al. (1999). *J.Biomech.,* **32**: 1149-58.
Winter, D.A. et al. (1998). *J. Neurophys.,* **80**: 1211-21.

ACKNOWLEDGEMENTS

Supported by the Purdue Research Foundation.

BONDING STRENGTH OF PLASMA SPRAYED HA COATING ON TI6AL4V ALLOY SUBSTRATE: THE EFFECT OF RESIDUAL STRESS

Yung-Chin Yang[1] and Edward Chang
Department of Materials science and engineering, University of Cheng-Kung, Tainan, Taiwan
[1]fatchin@cubic.mat.ncku.edu.tw

INTRODUCTION

For the durability of the system to succeed in application, the residual stress of plasma-sprayed HA coatings on a titanium substrate for orthopedic use might be very important, but was seldom considered. In this study, we investigated the influence of residual stress in HACs on the bonding strength of plasma-sprayed HA on titanium substrates.

EXPERIMENTAL

Seven HACs were plasma sprayed on Ti-6Al-4V substrates by varying the cooling effect and the coating thickness (Table 1). To evaluate the residual stress of the HACs, the "$\sin^2\psi$" technique of XRD method [1] was used. The Young's modulus value E = 16.2 GPa [2] was instead of the value 110 GPa for residual stress calculation. The bonding strength of HAC/Ti was tested using a standard adhesion test (ASTM C-633).

RESULTS AND DISCUSSION

The thicker 200µm HAC exhibited higher residual stress than that of thinner 50µm HAC coating (Table 1). The Table 1 also showed the residual stresses of the HACs with the various substrate temperatures. The max. temperature of HA5 without cooling during the plasma spraying was above 500 ^{o}C and it revealed the highest residual stress (26 MPa, compressive). This was due to the higher thermal expansion mismatch between coating and substrate during cooling from an elevated temperature to room temperature. In contrast, the max. temperature of the substrates were lower when cooling media were used. For the HA1, the lowest residual stress (18.0 MPa) was obtained due to a lower thermal expansion mismatch.

Fig. 1 shows the variation in bonding strengths of the HACs with the corresponding residual stresses. The HA1 with the lowest residual stress exhibited a higher bonding strength than the others; the HA5 displayed the lowest bonding strength apparently due to its high residual stress. The observation that the specimen with higher residual stress exhibited lower bonding strength can be explained in term of the compressive residual stress in the HAC, which could cause the coating to delaminate from the substrate [3].

CONCLUSION

Compressive residual stress weakened the bonding at the interface of the HA and the Ti-substrate. Then, in turn, the weakened bonding at the interface of the HA and the Ti substrate resulted in a decrease in the bonding strength.

REFERENCES

1. Cullity, B.D. (1980). *Elements of x-ray diffraction*: 2nd Ed. Reading, MA: Addison-Wesley. 447-478.
2. Yang, Y.C. et al (2000). *Biomaterials*, **21**, 1327-1337.
3. Evans, A. G. et al (1983). *Oxidation of Metals,* **20**, 196-216.

Table 1: Residual stresses of the various HACs

	Max. temp. of substrate	Residual stress
50 µm	---	-14.9 MPa
200µm	---	-17.1 MPa
HA1	330~400°C	-18.0 MPa
HA2	350~400°C	-18.8 MPa
HA3	410~430°C	-20.2 MPa
HA4	415~440°C	-22.3 MPa
HA5	480~520°C	-26.6 MPa

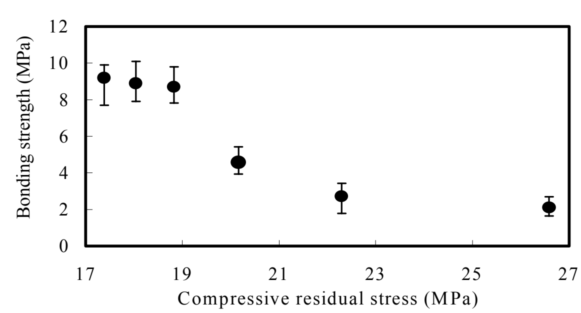

Figure 1: Variation of bonding strength of the HACs with compressive residual stresses.

NUMERICAL AND EXPERIMENTAL MEASUREMENTS OF THE FLOW IN PULSATILE VENTRICLE ASSIST DEVICE

I. Avrahami[1], M. Rosenfeld[1], S. Einav[1], U. Zaretsky[1] and K. Affeld[2]

[1]Departement of Biomedical Engineering, Tel Aviv University, Israel. idita@eng.tau.ac.il
[2]Humboldt University Berlin, Germany.

INTRODUCTION

Some of the most important factors that affect the longevity of the ventricle assist devices (VADs) are their hemodynamic properties. Interaction of blood with the moving components, stagnation regions or high shear stresses may promote thrombosis and hemolysis with detrimental effects on the operation of the VAD. The study of the flow field inside the VAD is, therefore, is of great importance both for optimising existing designs and for developing new ones. In the presented study, the Berlin Left Ventricle Assist Device (LVAD) [1], with the improved energy converter unit, has been investigated both numerically and experimentally.

METHODS

For the investigation of the flow field in the blood chamber of the Berlin LVAD, an experimental Continuous Digital Particle Imagining Velocimetry (CDPIV) was combined with a computational fluid dynamics (CFD) analysis in moving boundaries. These tools complemented each other to result into a comprehensive description of the complex 3D, viscous and time-dependent flow field inside the artificial ventricle.

For the numerical analysis, a commercial finite element package was used to solve the Navier-Stokes equations (FIDAP, Fluent Inc., Evanston).

For the experimental analysis, an optically clear elastic model of the LVAD was placed inside the CDPIV system. The CDPIV system is capable of sampling 15 velocity vector fields per second, based on image-pairs intervals lower than 0.5 millisecond.

RESULTS

Figure 1 shows typical vector plots as obtained from the numerical and experimental analyses.

(a) (b)

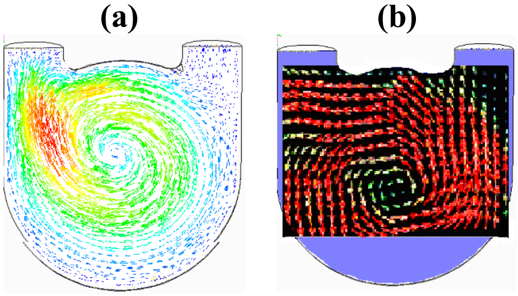

Figure 1: Velocity vector plots at central cross-section at peak diastole as obtained from (a) the numerical analysis and (b) the experimental analysis.

The flow inside the blood chamber was characterized with high velocity jet through the mitral valve in the beginning of diastole, a rotation flow filling the chamber during diastole and a complete washout during systole. No permanent stagnation regions were found in the mid-section of the blood chamber. High shear stresses (in the order of 2000dyne/cm^2) were found for a short duration (0.05 sec) at peak diastole near the walls and during peak systole (up to 1000dyne/cm^2).

Continuous sequences of experimental images, followed by their calculated velocity and vorticity transient fields, are given as animated presentation of the distensible VAD. The experimental results of both groups (German and Israeli) were similar and were used for validating the CFD simulations. The results obtained from the experimental and numerical simulations were also in good agreement with previous works (Rosenfeld et al, 2002).

Once validated, the CFD results provided a detailed 3D and time dependent description of the flow field, allowing the identification of stagnation or high shear stress regions.

SUMMARY

CDPIV method had some limitations in analysing high velocities, wall shear stress and 3D flow field. However, After the validation of the numerical model, the detailed numerical simulation were very useful providing valuable information that was hard or even impossible to obtained experimentally such as shear stresses or 3-D flow.

The simulation of the membranes motion was essential for demonstrating the exact flow behaviour during systole. Modelling the S-shape valves in their fully open phase is recommended to extract the accurate circulation dynamic during diastole.

REFERENCES

[1] Affeld, K., A. Ziemann, and L. Goubergrits. Flow in Artificial Heart Valves and in Cardiac Assist Devices. in Ninth International Conference on Biomedical Engineering. 1997. Singapore.

[2] Rosenfeld, M., Avrahami, I. and Einav, S., "Unsteady Effects on Flow Across Tilting Disk Valves" Journal of Biomechanical Engineering, Feb. 2002

ACKNOWLEDGEMENTS

The research is supported by a grant from G.I.F., the German-Israeli Foundation for scientific Research and Development, and the Drown Faundation.

ANALYSIS OF WEAR PERFORMANCE IN TOTAL HIP REPLACEMENT

Richard M Hall
School of Mechanical Engineering, University of Leeds & Musculoskeletal Services
St James's University Hospital, Leeds, UK, r.m.hall@leeds.ac.uk

INTRODUCTION

One of the most crucial issues facing total hip arthroplasty is socket loosening and its relationship to wear. Whilst considerable research has focused on the acquisition of wear data from radiographs and retrieved samples, little attention has been paid to the most appropriate data analyses. Indeed, two articles (Lewis 2000, Pedersen et al 2000) have incorrectly indicated that a non-normal distribution of the wear data is a barrier to the use of appropriate parametric statistics, in particular, regression or associated methods. Using the bootstrap method this paper explores the errors that may arise in deviations from the regression assumptions for such analyses.

METHOD

Most calculations of the penetration rate are based on ordinary least squares (OLS) regression including studies that evaluate the mean. OLS regression is most efficient if four assumptions are found to be true (Hamilton 1992):

1. The independent variable has fixed values.
2. The errors have a mean equal to zero.
3. The errors have constant variance (homoscedastic).
4. The errors are not correlated with each other.

The standard errors (se) of the coefficients are unbiased if these assumptions hold. The incorporation of a non-normal error assumption is unnecessary for OLS unless the *t* and *F* distributions are used in subsequent analyses. This is, in itself, only true if the central limit theory (CLT) does not apply. Two data sets are used to explore these underlying assumptions, 1) wear data from retrieved metal backed acetabular components and 2) from retrieved Charnley sockets. In both cases the penetration was determined using shadowgraphic techniques and the service life from clinical records. The penetration rate was determined using traditional parameter estimation and the boostrapping technique (Efron et al 1986). Three regression models were used:

1. Simple linear model with no residual weighting.
2. As in 1 with residual weighting equal to $(\text{time})^2$.
3. As in 2 but with the regression constant = 0. Here, the mean penetration rate is identical to that gained from calculating the mean from individual penetration rates.

The bootstrap technique resamples the data with replacement and provides an improved estimate of the se in settings where the traditional method is untrustworthy.

RESULTS

Using model 1 each of the data sets displayed heteroscedastic residuals and as such violated assumption 3. The results gained for data sets 1 are displayed in Table 1. The parameters 'a' and 'b' indicate the constant term and the coefficient, which is the penetration rate, from the regression. The prefix 'se' indicates the standard error gained from standard regression analyses whilst * indicates that derived from the bootstrap distribution. Both data sets 1 and 2 are large (n>30) and it is probable that the central limit theorum (CLT) will apply. Indeed two of the plots (Figure 1), which indicates the variation in the penetration rates, are approximately normal. Estimate b3 using model 3 indicated a mild deviation from normality although the effect may not be serious. Of the two good models, 2 is the most efficient. Similar results were gained for data set 2.

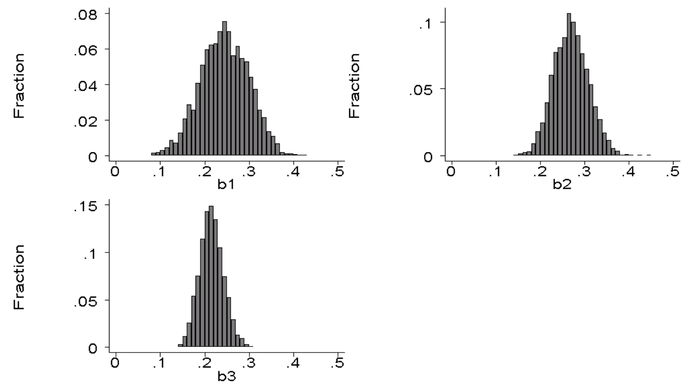

Figure 1: The bootstrap distributions for the penetration rate estimation (b1, b2, b3) using each of the models 1, 2 and 3 respectively (data set 1).

Parameter	Model 1	Model 2	Model 2
a	0.233	-0.131	-
se(a)	0.254	0.075	-
se(a)*	0.207	0.069	-
b	0.166	0.206	0.184
se(b)	0.022	0.018	0.014
se(b)*	0.022	0.015	0.014

Table 1: Results from the bootstrap method (data set 1).

DISCUSSION

The different models produce differing parameter estimations together with their standard errors, with Model 1 being less efficient than Model 2. Evidence here suggests that the penetration rate sampling distribution, determined from the traditional analyses (Model 3), departs from normality which may invalidate results gained from using the *t* or *F* test. It is recommended that penetration data be analysed using model 2 with regression diagnostic routinely undertaken to check the underlying assumptions. The use of inferential statistics may become problematic in situations where the CLT does not hold, that is in small samples less than 30 data points with extreme outliers.

REFERENCES

Pedersen D. et al (2000). Trans. 46th Meeting ORS, pg 577.
1) Lewis G. (2000). JBJS **82A** 281-7.
2) Hamilton L. C. (1992) Regression with Graphics (Duxbury).
3) Efron et al (1986) Statistical Science **1** 54-77.

AORTIC VALVE STENOSIS – NUMERICAL STUDY ON THE ACCURACYOF NONINVASIVE AND INVASIVE DIAGNOSTICS

Yael Danai [1], Shmuel Einav [1], Moshe Rosenfeld [2], Heinrich Schima [3]
Department of [1]Biomedical Engineering and [2]Fluid Mechanics, Faculty of Engineering
Tel Aviv University, Tel Aviv 69978, Israel. danai@eng.tau.ac.il
[3]Department of Cardiology, Vienna General Hospital, University of Vienna, Vienna, Austria

INTRODUCTION

The assessment of aortic valve stenosis is of great clinical significance. In the present study the evaluation of the flow field factors on valve area calculation and the accuracy of Doppler Ultrasound and Cardiac Catheterization in the determination of valve area, is done by studying computer models of the flow in the immediate neighborhood of the valve, varying systematically the flow rate and the valve area. For Doppler measurements the flow rate is evaluated using the PISA (Proximal Isovelocity Surface Area) technique, and the effective valve area is determined using the continuity equation based on the velocity field. For Catheterization technique the Gorlin equation is applied based on the measured volumetric flow rate and the pressure gradient. The numerical results were compared with the in-vitro results of Schima *et. al*. (1999).

METHOD

An axisymmetric numerical model was constructed to simulate the aortic valve flow using a time-depended CFD analysis to predict the flow characteristics during the cardiac cycle through axisymmetric straight channel with diameter of 3.0 cm. Disk type plates (2 mm thickness) with central orifices of 0.5, 1.0 or 1.5 cm^2 were used to model stenosis of various degree of severity. The pulse rate was held constant at 60 bpm, with an ejection time of 0.37 sec. The Navier-Stokes equations were solved using FIDAP (Fluent Inc., Evanston) for incompressible, laminar flow with constant viscosity.
The PISA method uses the velocity field proximal to the orifice to estimate the flow rate (see Fig.). Clinically and experimentally the velocity field is obtained through the use of 2-D CDFM (Color Doppler Flow Mapping) that is capable of extracting only the velocity components aligned with the signal of the transducer beam. It is therefore less accurate in contrast with computational simulations where the velocity components can be obtained at every node. This set of equations and the appropriate boundary and initial conditions determine the velocity and pressure drop in the analyzed domain.

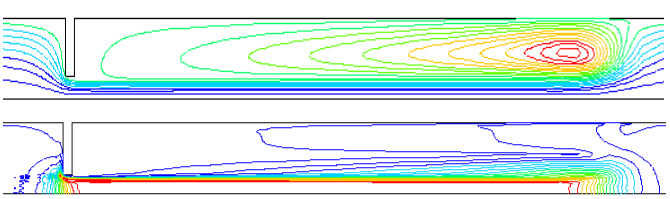

Streamlines (top) and Speed contours (bottom) at peak systole

The flow field was analyzed for several phases of the cardiac cycle, for varied orifice size and for different flow rates. The calculated flow rate was compared to the real flow values as given by the initial conditions of the model, and the calculated valve areas were compared to the in-vitro findings, using both Doppler and Catheterization techniques.

RESULTS AND DISCUSSION

Numerical simulations provide knowledge on the instantaneous velocity and pressure fields throughout the cardiac cycle therefore enables accurate valve area calculations at any chosen time. The PISA approximation of flow rate was found to yield accurate results near the peak flow for small orifice sizes, allowing accurate calculation of the effective orifice area.
The in-vitro measurements uses volumetric flow rate during the entire ejection time, mean pressure drop and mean velocity. The measurements show significant overestimation of the valve area, both by Doppler and by Catheterization techniques, due to incorrect use of continuity and Gorlin equations. Correction factors were set using computer simulations: the Gorlin formula was modified by the addition of ‘discharge coefficient’, the continuity equation was modified by setting a correction factor that compensated on using measured velocities (maximum velocities instead of average velocities), according to the flow profile. The incorporation of these correction factors enables accurate calculations (error<5%) of the valve area.

SUMMARY

Numerical analysis of the aortic valve is very complicated by the large 3-D motion of the highly flexible leaflets in a compliant system of fluid and structure. Using simplifications in the numerical study enabled its solutions and provided an insight on the flow characteristics, and on noninvasive and invasive methods for calculating the effective valve area.
The current work employs Fluid-Structure Interaction (FSI) simulations, which simulated flow through rigid channel with flexible leaflets, using an arbitrary Lagrange-Euler (ALE) formulation. The objective is to analyze the leaflets movement during the cardiac cycle and to characterize the flow field through it.

REFERENCES

Baumgartner *et. al.* (1999) *J Am Coll Cardiol* **33** (6), 1655-61.

DISINTEGRATION AND DEFORMATION OF CELLS AND MICROCAPSULES USING SHOCK WAVES AND GAS BUBBLES FOR DEVELOPING DDS

Masaki Tamagawa[1] and Ichiro Yamanoi[2]
Department of Energy Conversion Science, Graduate School of Energy Science, Kyoto University, Kyoto, Japan
[1]Lecturer, tama@energy.kyoto-u.ac.jp
[2]Graduate Student, yamanoi@tvd.energy.kyoto-u.ac.jp

INTRODUCTION

Recently shock wave phenomena in living tissues are being widely applied in the fields of medical and chemical enigineering, such as extracorpreal shock wave lithtripsy or bioprocess for environmental protection (Genenger,1997). In the bioporcess, a buuble inside the cell is broken by shock waves to rise efficiency of disintegration of cells. In the same mechanism, we propose a Drug Delivery Systems (DDS) using shock waves (Tamagawa, 2001). In this systmes, a microcapsule including a gas bubble is flown in the blood pipe, and finally broken and drug is reached to the affcted part in the body as same as traditional DDS(Fig.1). In these process, the mechanism for deformation and disintegration of cells depend on the parameter of elasticity of cells or microcapusles, diameter of bubbles and position of the bubbles. It is nesessary to investigate these fundamental mechanism for desgin of the capsule in DDS and bioprocess. This paper describes the trial making of microcapsules and observation of deformation of a bubble near the curved elastic wall.

EXPERIMENTAL MODELS AND METHODS

In order to investigate possibilities to make microcapsules in small scale, the prototype capsules in mm scale are produced using alginic acid-sodium (0.3-0.7 %), small gum Arabic, and calcium chloride. By pouring liquid and bubbles into these capsules using injector, the three-layer experimental model (membrane, liquid and bubble) can be made as shown in Fig.2. In the next step, to observe deformation process of a bubble in a cell or microcapsule, the bubble near the curved elastic wall made of Gelatin is observed when plane shock wave works on it in the shock tube apparatus. Here silicone oil is used as the surrounding liquid.

RESULTS AND DISCUSSION

Taking high-speed photograph of bubble deformation using framing tube, time histories of bubble radius are obtained in case of various curvatures of gelatin wall and distance from the wall. Figure 4 shows the maximum radius of a bubble with changing distance from the wall and the curvature. R_0, R_{max}, b_o mean initial radius, maximum radius, initial distance respectively. From the result, it is found that by controlling the curvature of the wall and initial position of a bubble there is a point to have large deformation, which tends to be collapsed easily. This is one of the results to aid design of DDS or bioprocess for cell-integration.

REFERENCES

Genenger B.(1997) Verfahren zum Aufschluss von Gasfoemige Stoffwechse-produkte erzeugenden mikroorganismen, *PATENT Nr-DE-197 15 819*
Tamagawa, M., Akamatsu, T.(2001) *JSME Intl J.* C 44-4, 1031-1040

ACKNOWLEDGEMENTS

A part of this work is being supported by the grant in aids by a Grant-in-Aid for Scientific Research from the ministry of Education, Culture, Sports, Science and Technology, Japan (Scientific Research (B):13450074)

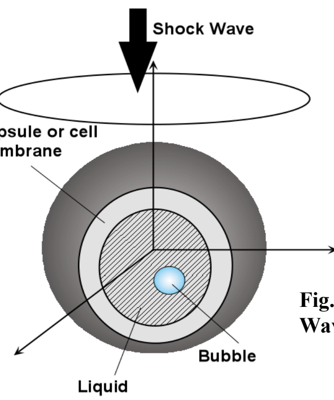

Fig. 1 Concept for Shock Wave-DDS and Bioprocess

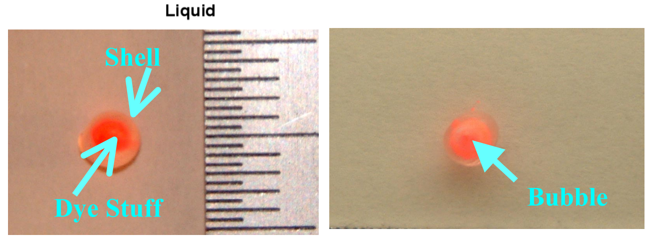

Fig.2 Experimental model for microcapsule

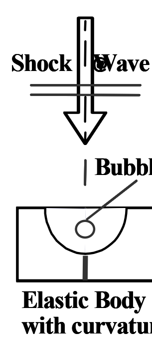

Fig.3 Experimental model for observation of bubble behavior by shock waves

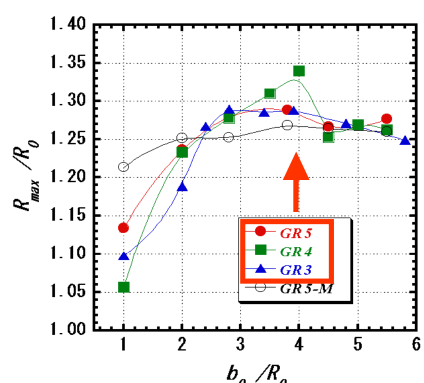

Fig.4 Maximum radius of a bubble with distance from the gelatin wall

INTER-GROUP COMPARISON OF EMG RESPONSES OF THIGH AND LEG MUSCLES DURING GAIT IN TREADMILL

Isabel C.N. Sacco [1,2]; Alberto C. Amadio[2].

[1] Physical Therapy, Speech and Ocupational Therapy dept.- School of Medicine – University of São Paulo, Brazil, icnsacco@usp.br

[2] Laboratory of Biomechanics – School of Physical Education and Sport – University of São Paulo, Brazil.

INTRODUCTION

Biomechanical changes in neuropathic patient's gait have been reported, as well motor strategies created to compensate their somatosensorial deficits (Cavanagh et al. 1992; Abboud et al., 2000, Sacco et al., 2000). The present investigation aims at comparing the EMG activity in the leg and thigh muscles during treadmill locomotion between a neuropathic patients group (DG) and a non-diabetic group (CG).

METHODS

Thirty-six voluntary adults of both sexes from the University Hospital were assigned to 2 groups: DG- with neuropathy confirmed, and a healthy non-diabetic group (CG). We used a Gaitway treadmill (Kistler) and six surface EMG electrodes (Delsys) that were placed on the motor point of the gastrocnemius lateral, tibialis anterior, and vastus lateral of both legs. CG subjects achieved an average walking velocity in a treadmill of 4.6±0.4 km/h and DG subjects, 3.8±0.4 km/h. EMG signals were acquired 3 times at 1000 Hz, aquisition time of 12 s, resulting in 30 supports for each foot. The EMG signal were rectified, filtered, integrated and normalized by the mean value and by support time. Inter-groups comparisons of each electromyographic variable were made through the use of the t test and Mann-Whitney test. The Ethical Committee of the University Hospital approved the protocol.

RESULTS AND DISCUSSION

The EMG pattern of the DG was expressively different from the CG (fig. 1). We observed significantly inter-groups differences in the activation of the right vastus lateral (P=0.032), its first activation peak in CG subjects was at 7.4% of support time and in DG it was at 10.3%. The activation beginning and the peak activation of the right gastrocnemius lateral in the DG subjects were delayed. The right and left tibialis anterior activation was also significantly different between groups (R: P=0.042, L: P=0.022). The first activation peak of right tibialis anterior in CG subjects was at 1.4% of support time and in DG it was at 8.2%. The first activation peak of left tibialis anterior in CG was at 3.0% of the support time and in DG it was at 9.7%. And we also observed lower EMG magnitudes for the vastus lateral in DG subjects.

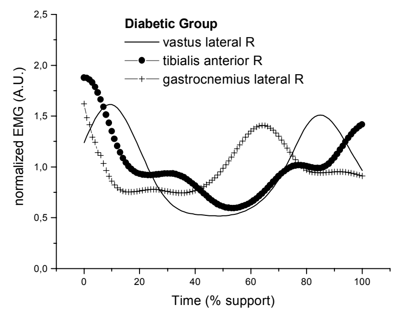

Figure 1: Mean curve of linear envelopes of the right vastus lateral, tibialis anterior and gastrocnemius lateral of DG.

Another important aspect to detach is the lower coefficient of variation of the EMG of both groups. This fact was also observed by Dingwell et al. (2000) and it is discussed that the restrictive treadmill environment impose a locomotor pattern extremely reproductive with lower variability.

REFERENCES

Abboud R.S. et al. (2000). ***Cl. Biomechanics***, **15**, 37-45.

Cavanagh P.R. et al. (1992). ***Diabetic Medicine***, **9**, 469-74.

Dingwell et al. (2000). ***J. Biomechanics***, **33**, 1269-77.

Sacco I.C.N. et al. (2000). ***Cl. Biomechanics***, **15**, 196-202.

ACKNOWLEDGEMENTS

We acknowledge FAPESP/Brazil for the important financial support during all the development of the project #98/09992-4.

MUSCULAR ACTIVITY AND STRENGTH TESTING OF TRUNK AND HIP EXTENSORS: A REPRODUCIBILITY STUDY

Ruhleder M., Segieth C., Vogt L., Banzer W.
Johann Wolfgang Goethe-University, Institute of Sports Sciences, Frankfurt/Main, Germany
Dept. of Sports Medicine, ruhleder@sport.uni-frankfurt.de

INDRODUCTION

Methods have been developed to evaluate the strength of hip surrounding muscles and to examine the effects of rehabilitation measures following implantation of endoprotheses (Shih et al. 1994; Horstmann et al 1995). The purpose of this study was to evaluate the test-retest reproducibility of SEMG activity of selected lumbopelvical muscles and their amount of activity during the “lateralflexion” maneuver, which has been described and already used in clinical practice (Stutz & Schreiber 1999).

METHOD

In a standardized testing procedure 11 healthy subjects (f=4, m=7, age 26.7 ± 3.0 years, range 22-32 years) without a history of hip pain performed three maximal isometric contractions (MVC) in three randomized positions: leg abduction (supine lying), trunk extension (from prone position) and “lateralflexion” (supine lying, body side was randomly selected). During the “lateralflexion” maneuver the subjects were instructed to rotate their pelvis in the frontal plane in order to reduce the distance between the iliac crest and the rib cage. The “lateralflexion” maneuver against an invincibly resistance is thus characterized by the attempt of a left- respectively right-concave curve of the low back in the frontal plane. Maximal isometric strength and bilateral SEMG activity of the gluteus medius and the lumbar erector spinae muscles were recorded with 1000Hz/channel (Biovision®, Wehrheim, Germany). The electrode placement was oriented on international standards (Frericks et al. 1999). MVC was performed over a period of five seconds with a rest of three minutes between trials. All measurements were taken from the neutral position on one day (1h-intervall) within one electrode application. MVC with the highest force peak was determined and the mean SEMG activity was calculated. The average SEMG activity during the “lateralflexion” maneuver was analyzed in relation to the maximum voluntary contraction which was considered as 100% muscle activity. For the verification of normality of sampling distribution the Kolmogorov-Smirnov test was carried out. Students t-test for paired samples were calculated for differences of relative myoelectrical activity during the “lateralflexion” maneuver between test and retest.

RESULTS AND DISCUSSION

Students t-test showed no significant differences for the average SEMG activity between test and retest for both muscles (figure 1). Correlation coefficient ranged from r = 0.78-0.97 ($p < 0.05$). In relation to the MVC the results revealed a higher muscle activity of the gluteus medius muscle than the lumbar erector spinae during “lateralflexion”. It seems that the erector spinae muscle had a more stabilizational function during the “lateralflexion” maneuver (figure 2).

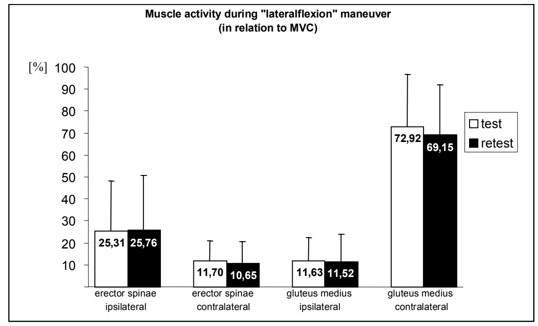

Figure 1: Test retest activity during the “lateralflexion” maneuver in relation to the maximum voluntary contraction (MVC was considered as 100% muscle activity) ($p>0.05$)

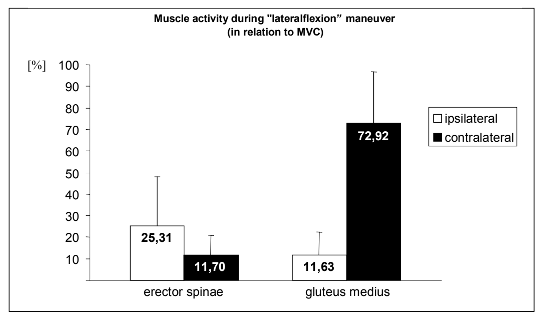

Figure 2: Muscle activity during the “lateralflexion” maneuver in relation to the maximum voluntary contraction (MVC was considered as 100% muscle activity)

SUMMARY

The findings of this study encourage the implementation of the proposed method for strength testing in clinical practice and rehabilitation.

REFERENCES

Freriks B. et al. (1999). *European Recommendations for Surface ElectroMyoGraphy, results of the SENIAM project.* (SENIAM **8**), 15-53

Horstmann T. et al. (1995). *Z Orthop **133**, 562-567*

Shih et al. (1994). *Clin Orthop* **302**, 115-120

Stutz R., Schreiber U. (1999). Entwicklung von standardisierten Messmethoden im Rehabilitationsprozess anhand komplexer funktioneller Zusammenhänge. Beispiel Hüftgelenk. *Kongressband VRF, Euromed Klinik, Fürth*

HANDLING MISSING MARKER COORDINATES IN 3D ANALYSIS

Pierre Desjardins,[1] André Plamondon,[2] Sylvie Nadeau,[1,3] Alain Delisle[2]
[1]Centre de recherche interdisciplinaire en réadaptation du Montréal métropolitain, site Institut de réadaptation de Montréal, Montréal, Québec, Canada
[2]Institut de recherche Robert-Sauvé en santé et en sécurité du travail, Montréal
[3]École de Réadaptation, Faculté de médecine, Université de Montréal

INTRODUCTION

Three-dimensional (3D) task analysis is an important part of biomechanics studies. Kinematics data is obtained by reconstruction of spatial motion of markers on all mobile segments (Veldpauss et al. 1988). Typically, joints between biomechanical segments are used as anatomical points and skin markers are chosen to provide simple relations with those joints. Analysis are frequently contaminated by missing coordinates (Muijtjens et al. 1997) and some trials end up being rejected because of the missing markers (Nussbaum et al. 2000).

The purpose of this paper is to present a simple mathematical formulation that can be used to retrieve the coordinates of markers hidden during a task. A strategy based on the smoothness of the variation of distance between points is devised, which leads to an automated computer procedure for retrieving hidden skin markers or missing joint coordinates (missing 3D points). This approach has the advantage of not being restricted to the frequent rigid-body assumption.

METHODS

The mathematical formulation does not require a specific biomechanical model except that all skin markers on a segment are considered to be attached to the joints of that segment.

Let assume that A, B and C are three points in the laboratory space and that point B is some time missing. Let dL_{ab} be the distance between points A and B. One can compute the distances dL_{ab}, dL_{bc} and dL_{ac} using a frame where all three points are present. Let also the distances dL_{ab} and dL_{bc} vary monotonically with time in such a way that they can always be interpolated over time with quintic splines. There is no restriction on dL_{ac} except that points A and C should be present when computing the coordinates of missing point B.

Point B is on a sphere of radius around point A and, simultaneously, on a sphere of radius around point C. The intersection of the two spheres is a circle which lies in a plane with its normal passing through the coordinates of A and C. Let point E be at the centre of the circle. The distance of the plane and point A is then given by a proportion which is a function only of the length dL_{ab}, dL_{bc} and dL_{ac}, which can be calculated using the Pythagorean theorem.

$$dL_{ae} = \frac{(dL_{ab}^2 + dL_{ac}^2 - dL_{bc}^2)}{2.0(dL_{ac})} \quad (1)$$

Vectors in the laboratory reference frame can also represent points A, B and C. Thus the equation of a plane containing point B is given by:

$$\frac{\vec{C}-\vec{A}}{dL_{ac}} \bullet \vec{P} = \frac{\vec{C}-\vec{A}}{dL_{ac}} \bullet \vec{A} + dL_{ae} \quad (2)$$

where $\vec{P}$ is the vector in the laboratory reference system associated with the coordinates of a point lying in the plane.

To retrieve point B, let assume that there are other points monotonously linked to B. For each pair of monotonously linked points a plane is expressed using equation 2. Note that these points do not need to be on the same segment; for example, for a human elbow two points close to the wrist and two others close to the shoulder can be used. Because the coordinates of point B are common to all planes, the set of plane equations is used to calculate these coordinates borrowing the common solution of linear algebraics with the singular-value decomposition technique.

RESULTS AND DISCUSSION

A mathematical procedure that can retrieve missing coordinates of a point in a 3D volume has been presented. This procedure is easy to implement in an automatic algorithm. It is based simply on the ability to determine the distances of the missing point (e.g. B) from its neighbours (e.g. A and C). This means that the two distances dL_{ab} and dL_{bc} have to be known or interpolated at all times during the trial.

SUMMARY

It was found that a set of four non-coplanar monotonously linked points, always gives the coordinates of a missing point.

REFERENCES

Veldpaus, F. E. et al. J. of Biomechanics 1988;21:45-54.
Muijtjens, A. M. M. et al. J. of biomechanics 1997;30:95-98.
Nussbaum, M. A. et al. Human movement science 2000;19:797-816.

ACKNOWLEDGEMENTS

This study was supported by a grant from NSERC Canada.
Dr. Nadeau is supported by a scholarship from the CIHR.

EFFECT OF INTERFRAGMENTARY SHEAR AND COMPRESSIVE STIMULATION ON BONE HEALING

Nicholas Bishop, Maarten van Rhijn, Ivan Tami, Erich Schneider, Keita Ito
AO Research Institute, Davos, Switzerland, keita.ito@ao-asif.ch

INTRODUCTION

Mechanical deformation of the callus modulates fracture healing, i.e. tissue proliferation and differentiation. Clinically, shear has been associated with delayed- and non-unions. In a rabbit model, transverse shear first led to non-unions (Yamagishi & Yoshimoto, 1955), but then oblique shear stimulated healing (Park *et al*, 1998). Although both studies applied interfragmentary (IF) shear, local deformations and their deviatoric/volumetric components, as implicated in mechanotransduction theories (Pauwels 1980), may not have been similar. In this study, the effect of torsional IF deformation, (pure deviatoric), axial IF deformation (deviatoric and volumetric), and rigid fixation on fracture healing was compared in an *in vivo* ovine model.

METHODS

In 3 groups of 6 Swiss Alpine sheep each, a 2.4 mm mid-diaphyseal tibial transverse gap osteotomy was created and stabilized with a custom unilateral external fixator. The fixator was rigidly locked or accurately applied axial or torsional motion. 120 sinusoidal loading cycles were applied daily with 25% minimum (compressive) principal peak IF strain at 0.5Hz. IF displacements were 0.6 mm axially and 7.2° in torsion with load limits of 360 N and 1670 Nmm, respectively. After 8 weeks, the sheep were sacrificed. Transverse CT scans were made to measure gap density and osteotomy stiffness was measured by 4-point bending in and out of the pin plane. This study was approved by the Animal Experimentation Commission of the Veterinarians Office of the Canton Graubünden.

RESULTS AND DISCUSSION

Circumferential analysis of CT scans around the bone axis indicated that highest density tissue formed caudally, where the soft tissue coverage is greatest (Fig 1). Mean density of gap tissue was highest in the torsional group around the entire bone. The rigid and axial groups had similar mean density of gap except caudal-laterally where the former was denser. Analysis of consecutive radial rings indicated higher gap tissue mean density in torsional vs. axial group for the medullary and intracortical regions, but externally their values converged (Fig. 1). The torsional group produced denser callus than the rigid group in the medullary and external regions but was similar intracortically. Stiffnesses were similar in the torsional and rigid groups, 69±29% and 64±26% (of intact contralateral tibia) respectively, and lower in the axial group (41±25%).

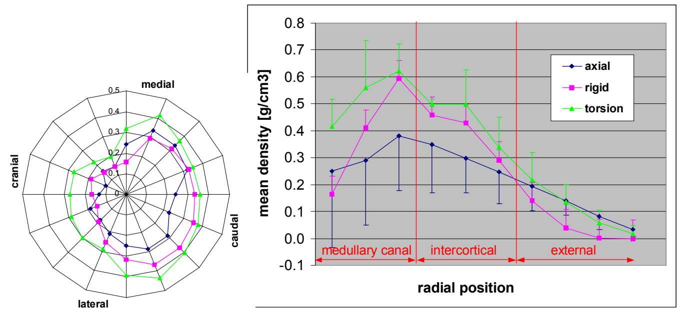

Figure 1: Mean angular (left) and radial (right) tissue density distribution.

In general, healing in the torsion group was most advanced. This is contrary to the view that shear deformation compromises fracture healing. Since there is relatively little volumetric deformation in the torsion group (or related fluid flow), it would appear that volumetric stimuli (including fluid flow) are less stimulatory than the deviatoric deformations. This is in contradiction with recent theories which involve fluid flow (Lacroix and Prendergast 1999).

It would also appear that the axial group has less advanced healing than the rigid group. This is the only group with significant volumetric deformation so this parameter may therefore be responsible for the retarded healing.

SUMMARY

These results indicate that interfragmentary shear is not detrimental to fracture healing. They are consistent with the concept that shear deformation stimulates and compressive hydrostatic pressure retards bone healing (Carter et al 1988). Future histological evaluation may indicate further differences between groups and will be compared with finite element analysis of local mechanical conditions to explore mechanotransduction mechanisms in more detail.

REFERENCES

Yamagishi & Yoshimoto (1955). *J Bone Joint Surg*, **37A**:1035-68.
Park et al (1998). *J Bone Joint Surg*, **80A**:868-77.
Carter et al (1988). *J Orthop Res*, **6**:736-48.
Pauwels (1980). *Biomechanics of the Locomotor Apparatus*, 107-37.
Lacroix & Prendergast (1999). *Proc 23rd Am Soc Biomech*, 276-7.

MOVEMENT BEHAVIOUR IN CHRONIC NECK PAIN PATIENTS

C. Segieth[1], Y. Moshref[1], L. Vogt[1], K. Pfeifer[2] and W. Banzer[1]
Johann Wolfgang Goethe-University, Institute of Sports Sciences, Frankfurt/Main, Germany
[1] Dep.of Sports Medicine, c.segieth@sport.uni-frankfurt.de
[2] Otto-von-Guericke University, Institute of Sports Sciences, Training and Health, Magdeburg, Germany

INTRODUCTION

Although back pain is the most costly musculoskeletal problem affecting industrialized nations (Van Tulder et al.1997), a general lack of knowledge exists concerning the etiology and specific symptoms related to chronic neck pain (CNP).
Some studies already described the importance of cervical motion analysis (Highland et al. 1992) and examined the kinematics in patients with neck pain (Hagen et al. 1997), but it still remains unclear how adaptations to muscle pain accommodates the coordination and interaction of neck and shoulder movements.
The purpose of this study was to investigate how pain modulates the kinematic of the cervical spine in a defined sample of chronic neck pain sufferers compared to healthy control subjects.

METHODS

Sixteen chronic neck pain (CNP) patients (f = 10, m = 6, mean age 55.8±2.8 yr), who had cervical pain on at least half the days in the past 12–18 months, and eighteen age matched controls (f = 10, m = 8, mean age 56.6±3.5 yr) performed ten repetitive maximal cervical movement cycles (flexion /extension, axial rotation, lateral flexion) at a self-determined velocity (patients: 39.9±14.4°/s]; controls: 37.5±15.6°/s).
To collect the kinematic data of the cervical spine a three-dimensional ultrasonic movement analysis system (Zebris CMS 70®, Germany) was used. Maximum oscillation angles (ROM, degrees) of the various movements were calculated for amplitude analysis. To describe the movement variability in the maximum oscillation amplitudes the intra-subject coefficients of variation (CV %) were determined. The computed maximum difference was characterized by the absolute differences between the minimum and maximum oscillation amplitudes of iterated movement cycles (Figure1). Pain intensity was obtained by visual analogue scales (VAS).

Figure 1: Maximum difference of ten repetitive cervical spine movements in the frontal plane for one patient.

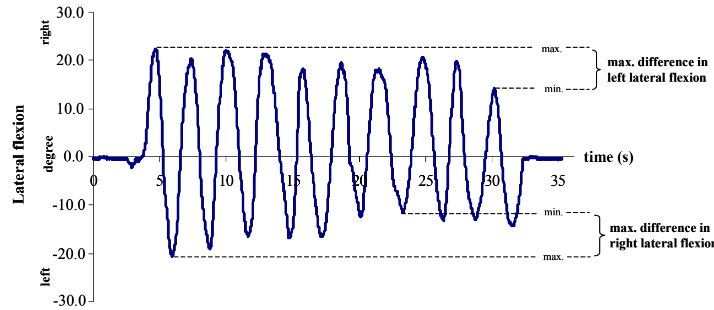

RESULTS AND DISCUSSION

The average pain rating of the CNP patients indicated moderate neck pain intensity (mean 37±8).
The independent t-test revealed a significant decreased range of motion (ROM) in the CNP group for all anatomic planes ($p<0.05$), except for the lateral flexion to the right. The maximum differences and variability parameters showed significantly increased values in the CNP group in all directions ($p<0.001$)(Table 1).

SUMMARY

This study confirmed that CNP patients compared to healthy subjects show a typical restriction in the max. range of motion (ROM) and significant differences in variability parameters (CV, max. difference) calculated for the repeated movement cycles.

REFERENCES

Hagen, K. et al. (1997). *Spine* ,**22**(13), 1501-1507.
Highland, T.R. et al. (1992). *Spine* ,**17**(6), 77-82.
Van Tulder, M.W. et al. (1997). *Spine*, **22**:76-82.

Table 1: ROM (Range of Motion), Max. difference and Coefficient of Variation for the CNP group (n = 16) vs. the controls (n = 18), (Mean±SD),(A: Flexion / Extension; B: Rotation right / left; C: Lateral flexion right / left)

	ROM (degree)		Max. difference (degree)		CV (%)	
	CNP group	controls	CNP group	controls	CNP group	controls
A	40.7±19.9/44.3±18.5	56.3±8.5/67.3±10.2	10.2±5.6/10.7±5.5	3.9±1.8/3.4±1.7	12.1±12.0/11.3±9.5	2.9±1.4/1.9±0.9
B	56.5±18.9/52.6±17.4	68.6±6.6/75.4±7.6	11.6±2.7/9.9±2.8	3.8±2.2/3.4±2.0	7.9±3.8/8.1±7.2	2.1±1.1/1.8±1.0
C	27.9±14.1/25.5±9.6	35.2±6.9/35.0±6.6	9.6±2.1/8.6±2.7	4.9±3.3/4.7±2.6	13.3±4.0/12.0±3.4	5.1±2.6/5.4±3.0

EFFECT OF GLYCOPROTEINS ON FRICTION COEFFICIENT OF NATURAL AND ARTIFICIAL JOINT SURFACES

Toshio Kitano, Yoshinori Kadoya, Kentarou Inui, and Yoshiki Yamano

Department of Orthopaedic Surgery, Osaka City University Graduate School of Medicine
1-4-3 Asahimachi Abenoku OSAKA, 545-8585 JAPAN
tkitano@med.osaka-cu.ac.jp

INTRODUCTION

Failure in lubrication mechanism causes Orthopaedic complications, Osteoarthrosis for natural joint and loosening of artificial joint. When Hydrodynamic lubrication breaks down, boundary lubrication becomes dominant. In this condition, boundary lubricating molecular e.g., Glycoproteins or Phospholipid becomes important. Synovial fluid of natural joint and Periprosthetic fluid after total joint arthroplasty mainly contains Glycoproteins in addition to Hyarulonic acid. It has been hypothesized that constituents and conditions of Glycoproteins affect the lubrication properties in natural and artificial joint. The purpose of this study is to test this hypothesis, comparing the effects of Glycoproteins on friction coefficient between natural and artificial joint

METHODS

Four lubricants were tested in this study: L01; 0.033M Tris buffer + sodium hyaluronate (HA) 3 mg/ml, L02; L01 + bovine albumin (ALB) 12 mg/ml, L03; L01 + bovine Gamma-globulin (GLB) 8 mg/ml, L04; L01 + ALB 12 mg/ml + GLB 8 mg/ml. Each lubricant was tested at 8 different pH values varying from 6.5 to 8.6. CF of cartilage against cartilage and ultra-high molecular weight polyethylene (UHMWPE) against Co-Cr-Mo alloy (CoCrMo) were measured with a mechanical spectrometer using the cylindrical joint surface model.
Normal stress 150kPa was applied to the natural joint surface model and 250kPa was applied to the artificial joint surface model.

RESULTS AND DISCUSSION

Addition of GLB decreased CF of cartilage against cartilage (Ca-Ca) while the addition of ALB did not decrease CF (Fig.1). Addition of ALB or GLB increased CF of UHMWPE against CoCrMo (PE-CoCr) at the low velocity range independent of lubricant viscosity while addition of ALB or GLB decreased CF at the middle and high velocity range in lubricant viscosity dependent manner (Fig.2).

The difference of boundary lubrication properties between artificial and natural joint has been observed. Addition of GLB decreased CF in natural joint model at the entire range of speed under boundary lubrication condition. On the other hand, addition of ALB or GLB increased CF in artificial joint model at the low speed at which boundary lubrication is dominant. Failure of joint lubrication produces many problems in natural synovial joint as well as in the artificial joint. The boundary lubrication plays an important role in joint lubrication after the failure of fluid film lubrication. The results obtained in this study support that surface modification of artificial surface might improve boundary lubrication properties by affecting the adsorption ability of boundary lubricant layer and that the regulation of synovial fluid might improve Osteoarthrosis conditions of natural joint.

REFERENCES

Kitano, T., Ateshian, G.A. (2001). *J. Biomech*, **34**, 1031-1037.

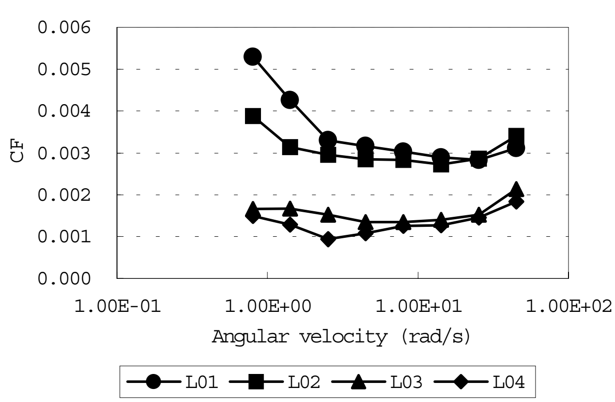

Fig.1 Angular Velocity - CF Curve (Ca-Ca)

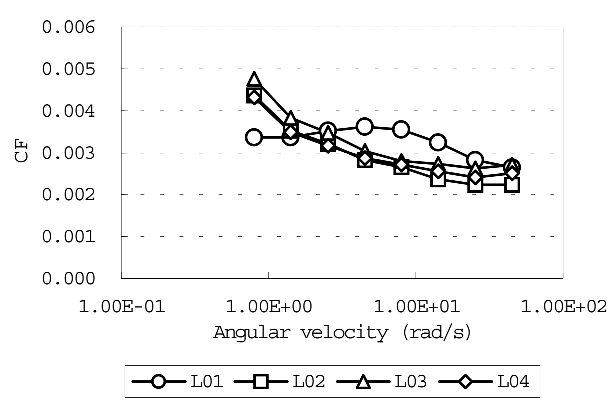

Fig.2 Angular Velocity - CF Curve (PE-CoCr)

INTERACTION OF ADHESION MOLECULES AND LYMPHOCYTE ADHESION TO ENDOTHELIAL CELLS

Hong Zhao[1,2], Jean François Stoltz[1], Feng yuan Zhuang[2], Xiong Wang[1]

[1] LEMTA - UMR-CNRS 7563, Vandoeuvre-lès-Nancy, France, hong.zhao@hemato.u-nancy.fr
[2] Research Institute, China-Japan Friendship Hospital, Beijing 100029, China

INTRODUCTION :

Interactions of lymphocyte function-associated antigen-1 (LFA-1) with intercellular adhesion molecule-1 (ICAM-1) play an important role in a number of cellular events, for example, the leukocyte adhesion and transendothelial migration in inflammation. The aim of this work was to investigate the adhesion mechanism of LFA-1 and ICAM-1 interaction by a newly developed micropipette method (Chesla et al., 1998) and a commonly used flow chamber technique.

METHODS :

A normal human RBC was coated with soluble ICAM-1 by an improved chromium chloride coupling method. This RBC interacted either with a SKW-3 cell (human T cell leukemia) or with a normal human lymphocyte (HLC), both of these two cells expressed LFA-1 on their surface. The two interacting cells were respectively held by a pair of micropipettes with negative pressure and brought into contact using a computer-controlled micromanipulator system. The contact area was kept constant and the contact duration was varied over a range from 1 to 16 seconds. Using the RBC as a force transducer through its deformation for judging the happening of adhesion, an adhesion probability (Pa) was obtained. In parallel, a flow chamber system was also used in this work. Human umbilical vein endothelial cells (HUVEC) were cultured on glass coverslides coated with 1% gelatin and these slides were assembled to a commonly used rectangular flow chamber for shear experiments. A syringe pump generated steady flows corresponding to values of shear stress of 0.17 and 0.7Pa at the surface of endothelial monolayer. A suspension of SKW-3 ($1x10^6$/ml) would be injected into the flow chamber. The number of firmly adhered SKW-3 cells (Nad) was counted with the help of an image acquisition and analysis program (Visilog 5.1).

RESULTS AND DISSCUSSION:

Phytohemagglutinin (PHA) stimulation resulted in a significant increase in the adhesion probability of lymphocytes compared with nonstimulated ones (P<0.001) (Table 1). But Tetramethylpyrazine (TMP) treatment could significantly inhibit such increase. These effects were confirmed by experiments on firm adhesion of SKW-3 on HUVECs under low shear conditions (Figure 1). It was found a significant positive correlation between the Pa and Nad obtained by the two methods.

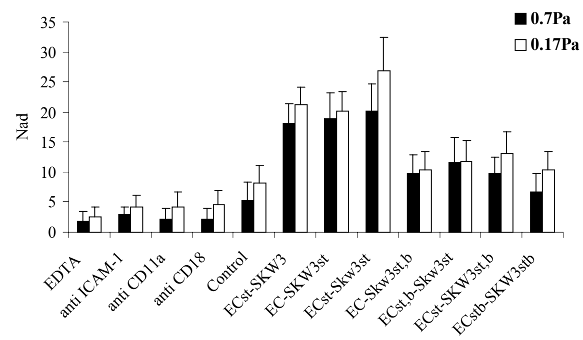

Figure 1 : Number of firmly adhered lymphocytes to endothelial cells in different groups at two shear stresses (0.7 and 0.17 Pa).

SUMMARY:

This study demonstrates that the interaction between ICAM-1 and LFA-1 plays an important role in cell adhesion. The experiments on the changes of cell adhesion induced by TNF-α, PHA or TMP show a good concordance between the results obtained by the two techniques used.

REFERENCES :

Chesla SE, et al. (1998). *Biophys. J,* ***75***, 1553-1572.
Zhao H, et al. (2001). *Clin. Hemorehol. Microcirc.* **23**, 145-151.

ACKNOWLEDGEMENTS:

This work was partly supported by the Association Franco - Chinoise pour la Recherche Scientifique & Technique AFCRST (Grant N° PRA B98-07), and the Region Lorraine (Grant N° 99/469-SJE), *France.*

Table 1 : Adhesion probability (Pa) and number of firmly adhered cells (Nad)

Parameters	Control	PHA	PHA+TMP
Pa (RBC-SKW-3)	58 ± 10	74 ± 12***	36 ± 4 ##
Pa (RBC-HLC)	32 ± 4	42 ± 3*	18 ± 11 ##
Nad (0.7Pa)	5 ± 3	18.9 ± 4***	9.8 ± 3 ##
Nad (0.17Pa)	8.2 ± 3	20.2 ± 3***	10.4 ± 3##

(*p < 0.02, ***p < 0.001 compared with the control group ; ##p < 0.01 compared with the PHA stimulated group).

FORWARD DYNAMIC MODELLING OF SHOULDER MOVEMENTS

E.K.J. Chadwick and F.C.T. van der Helm
web: http://mms.tudelft.nl/ email: e.k.j.chadwick@wbmt.tudelft.nl
Man-Machine Systems, Dept. of Mechanical Engineering, Delft University of Technology, Delft 2628CD, The Netherlands

INTRODUCTION

Biomechanical models can be used in surgical planning to assess the outcome of an operation, and are particularly useful in performing sensitivity analyses. This aspect of computer assisted surgery (CAS) requires sophisticated models that are accessible to clinicians and are sufficiently fast in operation. Inverse-dynamic models suffer from two main problems. The first of these is that the kinematics of the simulation must be known in advance and the second is that the optimisation of muscle forces makes the models slow. Forward-dynamic models assume no prior knowledge of kinematics, but do require a neural input. The aim of this study was to develop a large-scale, forward-dynamic model that is fast in operation and could be used in CAS. The success of the model was assessed by its ability to reproduce measured movements.

METHODS

An inverse-dynamic model including an inverse dynamic muscle model of the upper limb (Happee and van der Helm, 1995) was used to calculate the required neural input for a recorded movement (forward flexion of the humerus - from -15° to +15° in the sagittal plane), sample time 0.012s. A set of optimised muscle forces was calculated based on a quadratic cost function (sum of squared muscle stresses weighted by muscle volume), and these muscle forces were converted into neural inputs by use of a muscle model. This model was a Hill-type muscle model with a contractile element, series and parallel elastic elements and three state variables (length of contractile element, activation and excitation). The model was then rewritten to allow forward-dynamic simulations, and the same neural input used to try to recreate the measured kinematics.

RESULTS AND DISCUSSION

Figure 1 shows the combination of muscle forces used by the model to generate the movement. Acceleration of the humerus into forward flexion is primarily achieved by the supra- and infraspinatus muscles, and deceleration is then produced by deltoideus posterior and triceps. Although this seems to be a reasonable combination of muscle forces, the resulting motion (Fig. 2) deviates considerably from the desired pattern (-15° to +15°). Given the number of steps between the neural input and the kinematic output, and the complexity of the model this result is surprisingly good - a smooth anteflexion of the humerus has been simulated. In a complex multiple DOF system muscle forces must balance each other for each DOF in order to obtain a stable solution. Discretization of neural inputs, linear interpolation and the three-step time-delay in an inverse dynamic muscle model result in modelling noise. Future work will focus on improving the estimates of neural input. Using the forward-dynamic and inverse-dynamic models together and feeding the error in predicted kinematics back into the inverse-dynamic loop, the calculated neural inputs can be optimised.

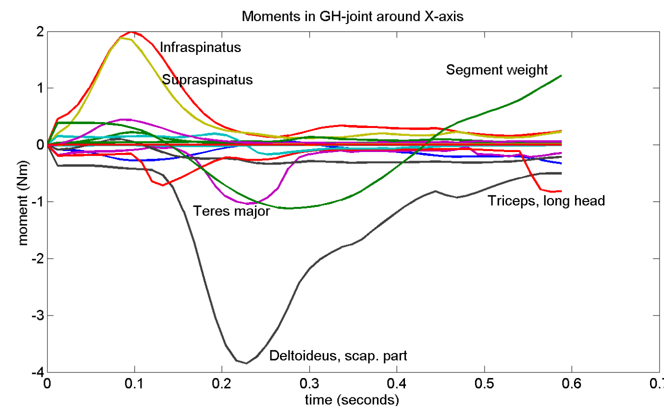

Figure 1 Muscle contributions to the flexion moment during fast forward flexion of the humerus.

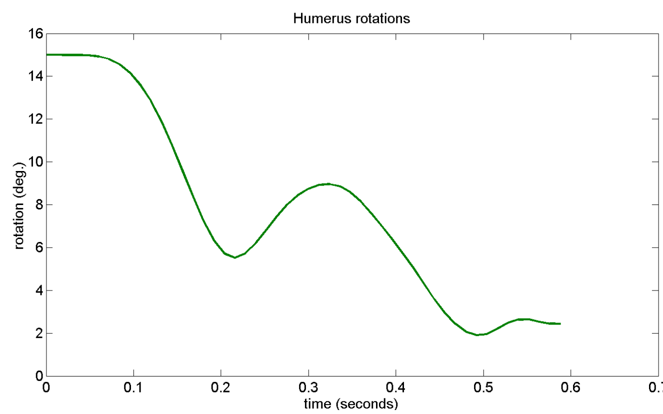

Figure 2 Elevation angle of the humerus during the anteflexion.

REFERENCES

Happee R, Van der Helm FCT (1995). *The control of shoulder muscles during goal directed movements, an inverse dynamic analysis*. J. Biomechanics 28(10), 1179-1191.

DESIGN AND ASSEMBLY OF A STERILE NANOSCALE ORTHOPEDIC BIOMATERIAL

John Longsworth, Steven Eppell
Case Western Reserve University
Department of Biomedical Engineering
jrl22@po.cwru.edu

INTRODUCTION

An ideal biomaterial bone substitute should facilitate bone healing and be resorbed by the body. Although they have been proven to facilitate bone healing, hydroxyapatite ceramics cannot be resorbed in vivo or in vitro due to their highly crystalline structure (Yuasa et al. 2001). It is also questionable whether more current bone cements that better mimic the crystallinity of bone minerals will be completely resorbed by the body (Yuasa et al. 2001). It has been postulated that the size of the crystals may influence their resorbabilty by the body, as shown by the fact that nanocrystallline hydroxyapatite grains are readily degraded by osteoclasts (Webster et al. 2001). This could be due to the fact that the smaller crystals have a larger surface area to volume ratio, resulting in a larger surface area per gram of the crystal being exposed. It has been theorized that the size of the mineralites in bone may be determined by the spacing between the collagen monomer repeats in the collagen fibrils (Hodge 1989). By using collagen fibrils as a scaffold, our lab has succeeded in making a synthetic bone biomaterial composed of collagen fibrils and nanometer-sized apatites that closely resemble the dimensions of bone apatites. The objective of this current project was to create a sterile collagen composite using aseptic technique for further testing in osteoclast cell cultures.

MATERIALS AND METHODS

The protein content of collagen monomer in acid (Vitrogen), was verified by trypsin digestion followed by SDS-PAGE in the manner described by Bruckner and Prockop (1981). Trypsin digests collagen polypeptides that are not in the form of intact monomers, thus it can be used to test that a solution contains triple helical collagen monomers. All composite assembly steps were done in a laminar flow hood. Solutions were sterilized using 0.2-micron bottle top filters. Fibril assembly in vitro was achieved using the simultaneous neutralization warming method (Holmes et al. 1986). After fibril self-assembly, the pH of a mineralization solution, which simulates the ionic concentrations of body fluid, was raised from 7.4 to 8.2 to initiate precipitation of calcium. The fibrils were added to the mineralization solution and allowed to incubate for 24 hours. After mineralization, the fibrils were washed multiple times with ethanol to remove excess solution and macro-sized minerals. Some samples were prepared for SEM imaging by progressive ethanol dehydration. These samples were then coated with palladium and imaged in an environmental SEM in full vacuum mode. Samples were loaded into cell chambers to hold down the collagen and create a well-defined surface. The composites were incubated in α-MEM at 37° C for 14 days.

RESULTS

SDS-PAGE showed that the protein was still intact after trypsin digestion, indicating that the starting solution was composed of triple helical collagen. The results exhibited bands for the $\alpha 1$ and $\alpha 2$ chains (the alpha band), a band for two crosslinked α chains (beta band) and a band for three crosslinked α chains (gamma band), identical to literature from results [4]. As shown by the SEM, fibers were successful assembled sterilely in vitro, and no large crystals were found. After incubating the composites for 14 days no signs of infection were detected.

DISCUSSION

The results of the trypsin digestion show that the collagen we are working with is composed of primarily triple helical monomers, rather than individual polypeptide chains. Analysis by SEM shows that the self-assembly protocol we utilize results in a meshwork of collagen fibrils several microns in length. The resulting material has also shown to be sterile, since incubating the samples for several days does not result in any kind of infection. Further cell based work with this material is now possible.

REFERENCES

T. Yuasa, Y. Miyamoto, K. Ishidawa, M. Takechi, M. Nagayma, K. Suzuki. (2001). *J Biomed Mater Res,* **54**, 344-350.

T.J. Webster, R.W. Siegel, R. Bizios. (2001). *Biomaterials,* **22**, 1327-1333.

A.J. Hodge. (1989). *Connect Tissue Res.,* **21**, 137-147.

P. Bruckner and D.J. Prockop. (1981). **110**, 360-368.

D.F. Holmes, M.J. Capaldi, J.A. Chapman. (1986). *Int. J. Biol. Macromol.,* **8**, 161-166.

NONLINEAR DAMAGE THEORY APPLIED TO TWO-STEP FATIGUE FAILURE PREDICTION OF BONE

John R. Cotton[1], Peter Zioupos[2], Keith Winwood[2], and Mark Taylor[1]
[1]Bioengineering Science Research Group, School of Engineering Sciences, University of Southampton, Highfield, Southampton, SO17 1BJ, UK. Email: jcotton@soton.ac.uk
[2]Department of Materials & Medical Sciences, Cranfield University, Shrivenham, SN6 8LA, UK

INTRODUCTION

Fatigue failure prediction in bone is desirable for orthopedic implant design. Load cycle magnitude varies during normal function. Also, fatigue-induced creep and stiffness loss redistributes stress with time. Thus, to predict failure *in vivo*, a theory accommodating variable stress magnitudes must be generated and validated.

Zioupos and Casinos (1998) tested femoral cortical bone from a 44 year-old male, *in vitro*, in two-step loading fatigue. Predictions based upon linear Palmgren-Miner theory produced a systematic error: high/low stress steps overestimate life and low/high steps underestimate life. A possible improvement on this theory ties damage accumulation to stiffness loss. We have been collecting data on the reduction of Young's modulus during uniform cyclic fatigue (Winwood, et al. 2001). Herein, we use modulus degradation relationships from current work to formulate a nonlinear damage theory and predict the published two-step fatigue test results.

METHODS

Fatigue (0-tension) was performed, as published (Zioupos, et al. 1996), on 10 samples from a 55 year-old male. Damage, defined as the modulus loss ($1-E/E_0$), was taken from the crosshead movement of the testing system. The tangent modulus, E_0, was calculated from a low-stress pretest. Data was fitted to the most appropriate of the three damage laws identified by Zioupos, et al. (1996),

$$D = 1-\left(E/E_0\right) = 1-\left[1-\left(n/N_f\right)^{(1-\alpha)^{-1}}\right]^{(1+\beta)^{-1}} \qquad (1)$$

Parameters ($1-\alpha$) and ($1+\beta$) were determined from an non-linear regression analysis and fitted as functions of normalized stress, σ/E_0. These relationships for α and β, were combined with uniform cyclic S-N data (Zioupos and Casinos, 1998) to predict failure for the published two-step experiments. The nonlinear prediction method is shown graphically in figure 1.

RESULTS

From mechanical tests, damage was seen to accumulate according to equation 1, with parameters α and β fitting

$$\begin{aligned} \mathrm{Log}(1-\alpha) &= -2300\,\sigma/\mathrm{E}_0 + 19. \\ \beta &= -31000\sigma/\mathrm{E}_0 + 205. \end{aligned} \qquad (2)$$

To relate intrinsic differences between individuals, σ/E_0 values in equation 2 were multiplied by a correction factor of 0.80. This was the ratio of σ/E_0 values needed to predict the same cycles to failure between the two individual's S-N curves. No other tuning was used between the two data sets. Model predictions are presented in figure 2.

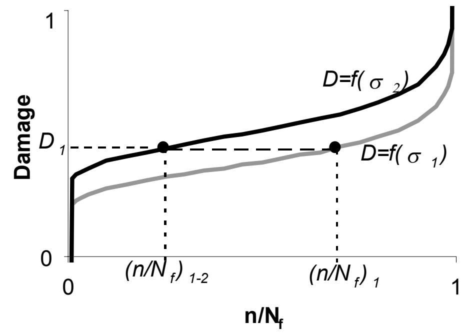

Figure 1: Prediction of failure in two-step loading with a nonlinear damage theory. Damage, D_1, was calculated from the first-step values σ_1 and $(n/N_f)_1$. Then, the equivalent life fraction $(n/N_f)_{1-2}$ was calculated. The second-step life fraction is $(n/N_f)_2 = 1-(n/N_f)_{1-2}$.

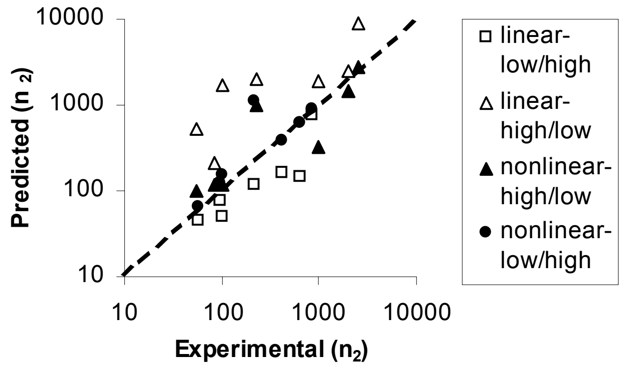

Figure 2: Prediction accuracy for cycles to failure, n_2. Scatter around the dashed line, $y = x$, using the nonlinear theory is less than linear Palmgren-Miner theory (r^2 of 0.71 and 0.39 respectively).

SUMMARY

The nonlinear theory shown here improved prediction of remaining life despite using modulus data from a different individual. The stress-step order dependency (high/low vs. low/high) is not seen in the nonlinear theory, removing the systematic error seen in Palmgren-Miner theory.

REFERENCES

Zioupos, P., Casinos, A.(1998). *J. Biomech.*, **31**, 825-833.
Zioupos, P., et al. (1996). *J. Biomech.*, **29**, 989-1002.
Winwood, K., et al. (2001) *XVIIIth ISB Congress*, P721.

ACKNOWLEDGEMENTS

Funded by EPSRC (UK) grant GR/M59167.

THREE DIMENSIONAL CHARACTERIZATION OF PULSA TILE FLOW BEHAVIOR IN THE CONVERGENT REGION IN A MODEL OF MITRAL PROLAPS. A PARTICULAR VELOCITY IMAGING STUDY.

F. Billy[1], D. Coisne[2], R. Perrault[1]
[1] L.E.A UMRCNRS 6609, Poitiers University, France.
[2] Cardiology Department, Poitiers University Hospital , France.
d.coisne@chu-poitiers.fr

INTRODUCTION

Ultrasound imaging of laminar flow towards the regurgitant orifice has been widely used for valvular regurgitant flow rate assesssment[1]. Nevertheless, the behavior of flow distribution in this zone is not exactly described by ultrasound techniques, even using 3D color Doppler reconstruction, due to technical and fundamental limitations[2-4]. This study was designed to characterize the pulsatile flow behavior in an in vitro model of mitral prolaps using a 3D particular velocity imaging (3DPVI) technique

METHODS

Our experimental heart model is represented by two cylindrical chambers simulating ventricular and atrial cavities separated by a perforated wall between two half cylinders placed symmetrically in opposition as shown on fig l. The cylinder diameter was 40mm. Physiological pressure conditions have been provided by a pump governed by a synthesizer signal generator. The viscosity of the fluid was designed to mimic blood (3.6 cp at 20°).
The velocity measurements were made by PVI method, using silica particles illuminated with a 1 mm laser light plane. Each plane in longitudinal and transversal plane was separated by 5 mm (fig1). We obtain velocity fields every 50 ms all over the cardiac cycle (600 ms). Based on orthogonal 2D vectors, we calculated the 3D velocity field.

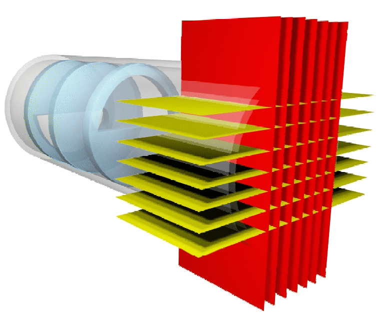

Fig 1: experimental model and PVI reconstruction method

RESULTS

This 3D reconstruction method gave us exact representation of flow dynamics in the convergent region.

Figure 2 show 3D PVI velocity fields upstream the orifice at peak ejection time. In this particular model of mitral regurgitation, we note that 3D isovelocity profiles are complex and the hemispheric assumption usually used in clinical setting for flow rate calculation is not accurate in this configuration.

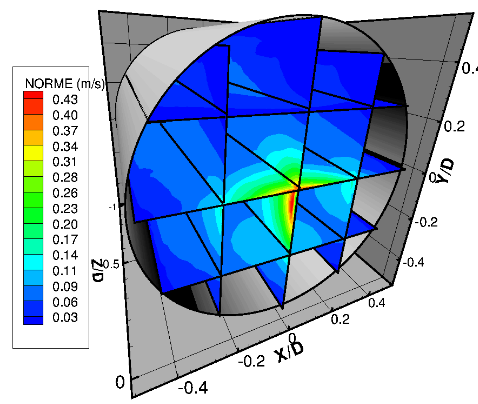

Fig 2: Orthogonal views of velocity field in the convergent region

SUMMARY

This study was designed to characterize the pulsatile flow behavior in an in vitro model of mitral prolaps using a 3D particular velocity imaging (3DPVI) technique. We generate a complex pulsatile flow convergent field using a mitral prolaps regurgitant model. Bi-dimensional velocity vectors were calculated using particular velocity imaging. Flow is lighted by a 1mm thickness laser plan and particular velocity vectors are measured by PVI software. Based on orthogonal 2D vectors, we calculated the 3D velocity field.
Conclusion. Perfect knowledge of the 3D velocity vectors distribution is crucial for developing new tools for flow regurgitant rate quantitation. Our model gives us exact characterization of flow in a complex pulsatile mode of mitral regurgitation.

REFERENCES

1. Enriquez-Sarano, M. et al. *J Am Coll Cardiol* **25**, 703-9 (1995).
2. Shiota, T. et al. *J Am Coll Cardiol* **27**, 1511-8 (1996).
3. Li, X. et al. *J Am Soc Echocardiogr* **12**, 1035-44 (1999).
4. DeGroot, C. et al. *Ultrasound Med Biol* **26**, 989-99. (2000).

A BLACK BOX APPROACH TO MODELING THE EQUINE BACK AS A FLEXIBLE BEAM

Schobesberger H, Peham C
Clinic for Orthopedics in Ungulates, Veterinary University Vienna, Austria
christian.peham@vu-wien.ac.at

INTRODUCTION

Back pain and diseases of the spine constitute significant problems in equine sports and veterinary medicine. Mathematical models have become one of the basic and renowned methods for examining the biomechanical behavior of the back. Han et al. (1995) have formulated such a model for the human spine using kinematic and EMG data. Van den Bogert et al. (1989) have built models of the whole horse with rigid segments, but they are not realistic enough for in-depth analysis. In our study we propose a novel approach to define a biomechanical model of the equine back.

METHODS

We have measured the EMG of the long back muscle of 15 horses without back pain during lateroflexion and extension, while simultaneously recording the motion of the back by a kinematic tracking system. Out of these data sets, we derived a linear transfer function (TF) for two positions on the back (spinous process of thoracical vertebra T16 and T12) relating the EMG to the actual movement of the back (equation (1). $TF(s) = \frac{X(s)}{F_{EMG}(s)}$ (1) with s denoting the complex frequency. We evaluated the transfer function by computing the correlation coefficient (CC) between the output of the TF and the actual kinematic measurement.

Consequently we related the transfer function to the general motion equation in the frequency domain. Equation (2) shows the general motion equation in its canonical form in the time domain and its corresponding description in the frequency domain,

$$f_{EMG}(t) = m \cdot \ddot{x} + D \cdot \dot{x} + K \cdot x \Leftrightarrow$$

$$\Leftrightarrow F_{EMG}(s) = m \cdot s^2 \cdot X(s) + D \cdot s \cdot X(s) + K \cdot X(s) \qquad (2)$$

$$with \;\; F_{EMG}(s) = \frac{X(s)}{TF(s)} \Rightarrow TF = \frac{1}{m \cdot s^2 + D \cdot s + K} \qquad (3)$$

with s denoting the complex frequency, and m as coefficient for inertia, D for damping and K for the spring constant. By comparison of the coefficients we obtained relevant parameter estimates equating the filter polynomial to the general motion equation in the frequency domain (equation 3). The derived parameters were used for the simulation of the back as a flexible beam. The mathematical parts of our work were done using MATLAB™ (Mathworks, Inc.), the flexible beam was simulated in ADAMS™ (Mechanical Dynamics, Inc.).

RESULTS

During lateroflexion to the left, we achieved a pooled correlation coefficient (CC) of 0.711 for position T16 and a pooled CC of 0.701 for position T12. Lateroflexion to the right resulted in a pooled CC of 0.731 for T16 and a pooled CC of 0.695 for T12, and extension in a pooled CC of 0.878 for T16 and a pooled CC of 0.852 for T12. We obtained the coefficients of the polynomial of the transfer function by a least squares fit to the measured frequency response data. In the ensuing step we modeled the equine back as a flexible beam using the advanced simulation software ADAMS™ .

DISCUSSION

We now propose a novel approach to model the equine back. Using EMG and locomotion data from 15 horses, we have derived the transfer function (TF) in the frequency domain for certain positions on the back. The high correlation achieved between calculated and measured data show that a linear black box model can be sufficient to derive a simple mathematical relation (TF) between EMG input and position output. This enabled us to identify necessary material characteristics (m, D, K) to simulate the equine back as a flexible beam, and in preliminary experiments we were able to demonstrate the similarity of the motion of the real and the simulated back. Once this correspondence has been proven statistically valid, we will be able to subject the modeled equine spine to all kinds of load and vibration stress regimes, and explore its dynamical behavior during physiological and pathological scenarios, as well as its contribution to general locomotion at different gaits. This will greatly enhance the insight into the nature of the motion of the equine spine. Furthermore, the model will be of great potential value for clinical practice in providing a new means of diagnosing equine back problems.

SUMMARY

The aim of our work was to establish a biomechanical model of the equine back, based on kinematic and surface electromyo-graphic data of horses without back pain. Our approach in order to do so, consisted of four essential steps: Step 1) to measure the horses kinematically and electromyographically, 2) to identify the mechanical system by computing a linear transfer function relating the EMG to the kinematic data, and determining the validity of the linear transfer function, 3) to relate the transfer function to the general motion equation to acquire relevant parameter estimates, and 4) to model the equine back as simple flexible beam.

REFERENCES

Han JS, et al. (1995) Loads in the spinal structures during lifting: development of a 3D comprehensive biomechanical model. *European Spine Journal* 4, 153-168

Van den Bogert AJ, et al. (1989) Simulation of quadrupedal locomotion using a dynamic rigid body model. *Journal of Biomechanics* 22, 33-41

STRESS TRANSFER TO CORONARY VASA VASORUM AFTER STENTING: A FINITE ELEMENT MODEL

Mark E. Zobitz[1], Michael S. Rosol[3], Mario Goessl[2], Malyar M. Nasser[2], Kai-Nan An[1], Birgit Kantor[3]
[1]Biomechanics Laboratory, Department of Orthopedics, [2]Department of Physiology and Biophysics,
[3]Department of Internal Medicine and Cardiovascular Diseases
Mayo Clinic/Mayo Foundation, 200 First Street SW, Rochester, MN 55905, e-mail: zobitz.mark@mayo.edu

INTRODUCTION

In-stent restenosis is a major health issue in the US. It is characterized by excessive cell proliferation. The underlying mechanisms are not well understood. Vasa vasorum are nutrient vessels in the outer wall of coronary arteries (Kantor, 1999; Kantor, 2000). Damage and manipulation to vasa result in neointimal proliferation and subsequent artery stenosis. We hypothesized that stents damage vasa during balloon inflation and through sustained compression by the individual stent struts. The aim of this study was to develop a finite element analysis (FEA) model of stented coronary arteries to determine stresses induced in the vessel wall in order to predict vasa compression by the stent, which could initiate the restenotic process.

METHODS

A 3D FEA model of the coronary artery wall was developed using ABAQUS (HKS, Inc., Pawtucket, RI) finite element software. The model was created for half of the artery using 8-node brick elements and consisting of 19,000 nodes and 15,500 elements (Fig. 1). The outer diameter was 7.3mm and the final expanded lumen diameter 3.3mm. Vasa were modeled in the wall at a location 70% of the wall thickness. The vessel wall was modeled as isotropic, linear elastic, and incompressible (E=1.0MPa (7501mmHg), ν=0.49). Boundary conditions were applied to the symmetry plane while the outer wall of the vessel was free to expand radially. An internal pressure of 95mmHg was applied to simulate the mean blood pressure. Two sizes of vasa were modeled; 50 and 150 μm diameter. Two degrees of stent diameter expansion were considered (16% and 34%). The expanded 3D stent geometry was simulated from 3D microscopic-CT images (Jorgensen 1998). Stent expansion was simulated by applying radial displacements to the nodes of the vessel wall surface where stent contact would occur. Data were analyzed through a plane in the midsection of the model with a radial path chosen from the lumen through the vasa vasorum to the outer wall. All stresses are reported as Von Mises equivalent stress in mmHg.

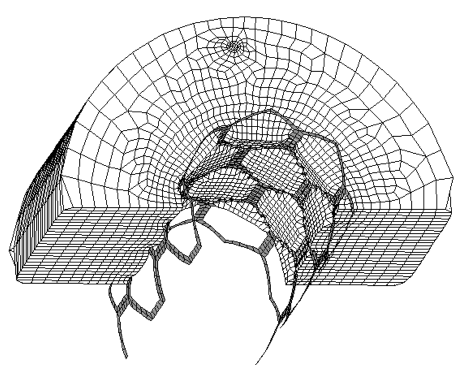

Figure 1: FEA model after 34% stent expansion.

RESULTS

Fig. 2 shows the stress contours through a plane in the midsection of the model. On the luminal stented side, stresses were greater than 1,500mmHg with a maximum of 4,000 and 10,000mmHg for 16% and 34% expansions, respectively. The stress decreased in a non-linear manner with increased distance from the lumen (Fig. 3). In the region where vasa are located, stresses exceeded 500 and 1,000mmHg for the two expansions. In comparison, prior to stenting, stresses in the wall induced by the blood pressure were lower (<30mmHg).

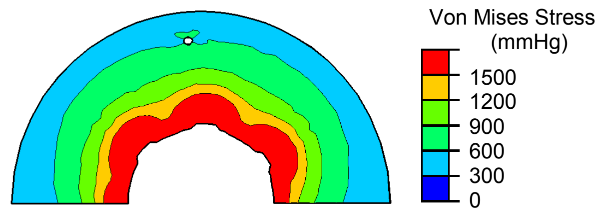

Figure 2: Stress contours following 34% stent expansion.

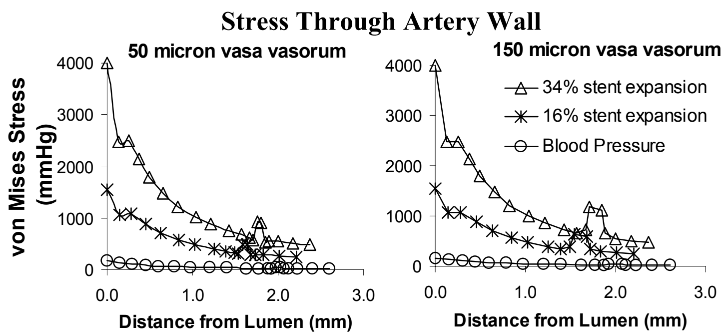

Figure 3: Von Mises stress as a function of distance from lumen before and after stent expansion.

DISCUSSION

This study demonstrates a dramatic increase in stresses within the vessel wall in response to stent implantation including the region where vasa vasorum are located. Therefore, it would be expected that these stresses are sufficient to compress the vasa and impair vessel wall perfusion. The subsequent hypoxia can lead to increased release of growth factors and to cell proliferation and restenosis. This model can be used to predict stresses induced by various stent types and to optimize stent design to minimize impact on vasa vasorum.

REFERENCES

Kantor, B. et al (1999). *Int J Cardiovascular Interv*, **2**, 79-80.
Kantor, B. et al (2000). *Curr Interv Cardiol Rep*, **3**, 204-12.
Jorgensen, S.M. et al (1998). *Am J Physiol*, **275**, H1103-114.

ACKNOWLEDGEMENTS

This study was funded by the Whitaker Foundation (RG-00-0299) and the American Heart Foundation (00-60427Z-02). We gratefully acknowledge Dr. Erik L. Ritman.

SUDDEN LOADING OF THE UPPER BODY LEADS TO MOVEMENT OF BOTH THE LUMBAR SPINE AND PELVIS.

Henrik Naesborg, Christian T. Hye-Knudsen and Jorgen Skotte.
National Institute of Occupational Health, Denmark, Department of Physiology
hen@ami.dk

INTRODUCTION

In laboratory setups studying sudden loading of the upper body pelvic fixation is often used. Both semi-seated (Cholewicki et al 2000) and standing (Stokes et al 2000, Skotte et al 2001) procedures have been used to immobilize the pelvis. A pilot study by Andersen (2001) has indicated that pelvic rotation occurs when the pelvis is tightly fixed by a non-elastic belt. Ignoring pelvic rotation may tend to overestimate lumbar flexion. This could lead to errors in biomechanical modeling. The aim of this study was therefore to describe and quantify the movement of the pelvis and the lumbar spine when healthy subjects are fixed at the pelvis and exposed to a sudden perturbation of the upper body.

METHODS

Ten subjects participated in the study. The experimental set-up is illustrated in Figure 1. The external force on the subject was momentarily increased from 3 N to 60 N through a steel wire attached to the subject via a shoulder harness. A Peak Motus video system (50 Hz) was used to collect the 2D coordinates of reflective markers placed on C7, T2, T4, L1, L3, L5, midpoint between right and left posterior superior iliac spine (PSIS), anterior superior iliac spine (ASIS) and the great trochanter (see fig. 1). The combination of 2 different body postures (erect and 30° of trunk forward inclination) and loads (no load and 15% of body weight (BW) in a box held in the hands) was randomly applied to the subjects. The pelvis was firmly fixed to a wooden plate by a non-elastic belt. Pelvic rotation and lumbar flexion was defined as change in pelvic angle (P_{angle}) and lumbar angle (L_{angle}) respectively according to Figure 1. A two-Way Repeated ANOVA ($p<0.05$) was used to test the effect of body position and load. If interaction was

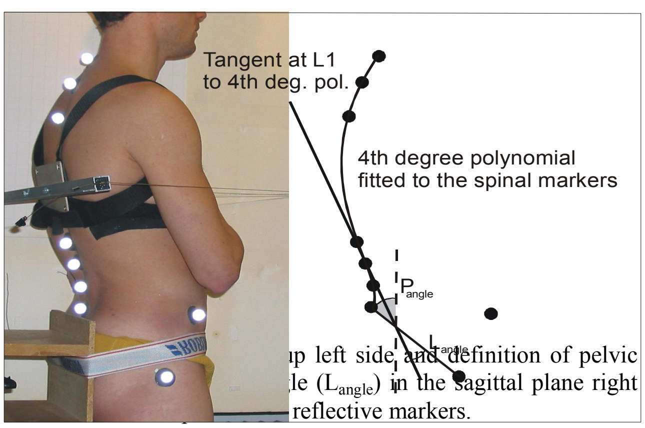

...up left side and definition of pelvic ...le (L_{angle}) in the sagittal plane right ... reflective markers.

found One-Way Repeated ANOVA was used.

RESULTS AND DISCUSSION

Movement caused by the perturbations resulted in less forward pelvic rotation in the inclined position compared to standing erect ($p=0.004$). No difference was seen between the two load conditions ($p=0.085$) (fig.2A). For lumbar flexion interaction was seen between position and load ($p=0.021$). Less flexion of the lumbar spine was observed in the inclined position compared to standing erect despite load level ($p\leq0.005$). Less lumbar flexion was also detected in the erect position with a load ($p=0.031$) while in the inclined position an extra load did not affect the degree of lumbar flexion ($p=0.091$) (fig. 2B). The significant pelvic rotation caused by a sudden perturbation indicates that lumbar flexion is overestimated if not corrected for pelvic rotation. The overestimation seems to be larger in inclined postures were smaller movement of the lumbar spine was distinct. The smaller lumbar flexion and pelvis rotation in the inclined position indicates an increased stiffness in both the lumbar spine and around the hip joint.

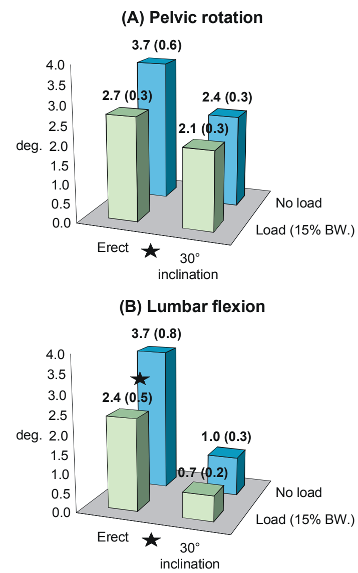

Figure 2. Mean (SE) pelvic rotation (A) and lumbar flexion (B) in degrees.
★indicates significance

SUMMARY

After a sudden perturbation of the upper body both lumbar flexion and pelvic rotation are seen even if the pelvis is firmly fixed. In future experiments the pelvis and spine should to some degree be considered as a combined movable unit even when the pelvis is fixed.

REFERENCE

Andersen, T.B. (2001).*Thesis*. University of Copenhagen.
Cholewicki, J. et al (2000). *J. Biomechanics,* **33**, 1377-1385.
Skotte, J. et al (2001). *Proceedings at the XVIII*th *ISB congress 2001,*145.
Stokes I.A.F. et al (2000). *Spine*, **25**, 1957-1964.

STARTING FRICTION OF ARTIFICIAL CARTILAGE MATERIALS IN HYALURONATE SOLUTIONS

Teruo Murakami, Ryo Kinoshita, Yoshinori Sawae and Kazuhiro Nakashima
Dept. of Intelligent Machinery and Systems, Faculty of Engineering, Kyushu University, Fukuoka, Japan
tmura@mech.kyushu-u.ac.jp

INTRODUCTION

To improve the longevity of artificial joints, the authors have investigated the application of compliant artificial cartilage. In the previous knee joint simulator tests foe walking motion, the improvement of lubrication mode was confirmed in knee prosthesis with PVA (polyvinyl alcohol) hydrogel layer lubricated with hyaluronate solution containing protein. For variuous daily activities, however, the high friction at starting motion after long standing is another problem in compliant rubbing materials. In this study, the influence of lubricants on the starting friction in sliding pair of compliant material of PVA hydrogel and polyurethane as artificial cartilage against hard material.

METHODS

Test apparatus to measure the starting friction was constructed, in which the upper stainless steel cylindrical roller of 30 mm radius is rubbed against the lower flat plate specimen of PVA hydrogel or segmented polyurethane of 2 mm thickness. PVA hydrogel of 79 % water content was prepared by repeated freezing-thawing method. Elastic modukus of PVA hydrogel is 1 MPa and that of polyurethane is 19.9 MPa. After the definite loading time with constant load of 37 N for 5 s, 1 min, 5 min, 15min, 30 min and 60 min, the lower plate and moving support was driven at 4 mm/s by means of lineared motor. The frictional behavior was observed by the signal from strain gauges on leaf spring with upper stationary specimen. Three kinds of 1.0 wt% solutions for sodium hyaluronate (HA) of different molecular weight, i.e., 0.58 x 10^6, 1.00 x 10^6 and 1.98 x 10^6 were used as lubricants. Higher molecular weight corresponds to higher viscosity.

RESULTS AND DISCUSSION

After the lower specimen started to move, the friction increased gradually to the maximum value and then decrease to steady value as coefficient of friction of about 0.04 to 0.05.
The maximum friction value after starting is defined as the starting friction. The starting friction increased with the loading time before starting. PVA hydrogel exhibited siginificantly lower starting friction less than 0.12 even after loading of 60 min as shown in Fig.1. Higher molecular weight of sodium hyaluronate reduced the starting friction. This is caused by viscous effect of hyaluronate solution to maintain the squeeze film formation. For HA of 0.58 x 10^6 and 1.00 x 10^6, the immersion in HA solution for 14 days reduced the friction. Therefore, the lower starting friction less than 0.1 appears to be maintained for PVA hydrogel with high water content. This fact suggests that the PVA has better frictional property as artificial cartilage.
On the contrary, polyurethane with higher stiffness and higher strength showed very high starting friction such as 2.2 after 60 min loading for all HA solutions. This high friction can induce the loosening of the compliant surface layer in usual daily activities after long standing. However, the immersion of the polyurethane specimen in HA solution for 14 days could remarkably reduce the starting friction to about 0.5 as coefficient of friction. HA of 1.00 x 10^6 exhibited the lowest value of 0.3. This fact indicates the possibility of polyurethane as artificial cartilage after surface modification.

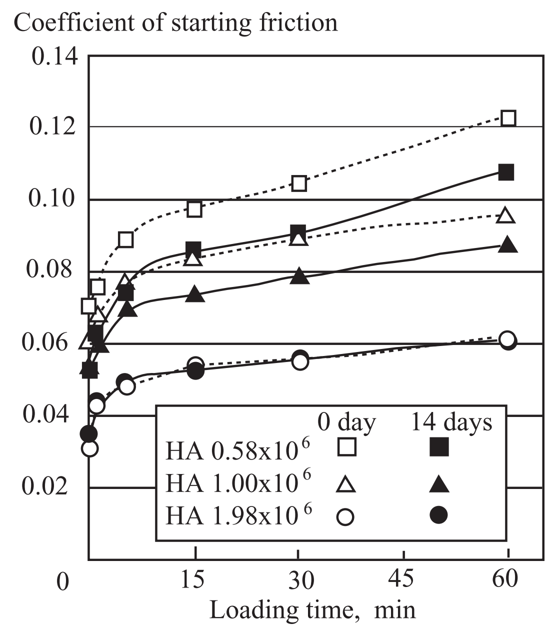

Figure 1: Influence of loading time, molecular weight of sodium hyaluronate and immersion in HA solutions on starting friction for PVA hydrogel againt stainless steel

SUMMARY

The variation of starting friction for PVA hydrogel and polyurethane as artificial cartilage was examined. It was indicated that the higher molecular weight HA solution is effective to reduce friction for PVA and the immersion in medium molecular weight HA solution is effective for polyurethane.

REFERENCES

Murakami T. et al.(1998), *Proc. Instn. Mech. Engrs. Part H, J. Eng. in Medicine,* **Vol. 212**,. 23-35.

THREE-DIMENSIONAL SCANNING ACOUSTIC MICROSCOPY OF THE INTACT INTERVERTEBRAL DISC: VISUALISATION OF LAMELLAE, COLLAGEN BUNDLES AND LESIONS.

S. Johnson [1], M.Halliwell [2], M. Jones[2] and D. McNally [1]

[1]Institute of Biomechanics, School of Mechanical, Materials, Manufacturing Engineering and Management. University of Nottingham, Nottingham. UK

[2]Department of Medical Physics and Bioengineering. United Bristol Healthcare NHS Trust. Bristol. UK.

INTRODUCTION

The intervertebral disc plays a key role in the aetiology of low back pain. A disc consists of a fluid-like nucleus pulposus constrained laterally by the fibrous annulus fibrosus (AF). The AF has a complex structure that comprises concentrically organised lamellae composed of collagen bundles embedded within a proteoglycan matrix and arranged at specific orientations with respect to the spine; the direction of fibre orientation alternates between successive layers. The collagen fibres act to reinforce the disc and are critical to its mechanical function. Lesions cause disruption to the organised structure and are involved in the failure of the disc. Visualisation of disc structure has relied previously upon time consuming and destructive methods, such as histology, that do not enable structures to be observed within intact specimens; this precludes repetitive testing of the same specimen. The present study employs non-destructive scanning acoustic microscopy (SAM) to visualize the normal disc structure and examine the three dimensional morphology of pathological lesions within the AF.

METHODS

Eight porcine lumbar discs and adjacent vertebrae were dissected free from soft tissue and the posterior vertebral elements removed to enable access to the entire disc circumference. Discs were then mounted into a water bath contained within the SAM. The SAM consists of a 50MHz transducer (axial resolution 30µm; penetration depth approx. 2mm), 4-stepper motor driven stages controlled via a PC and a bath for coupling medium. The transducer operates in pulse-echo mode and images are displayed so that the amplitude of echoes reflected from tissue boundaries determines the brightness of the display. The time difference between the propagation of the initial pulse and the echo's return gives a measure of the depth of the reflecting surface.

A 3-D data set consisting of between 256 and 800 slices of a region of interest (ROI), of variable size, was acquired from one of three circumferential locations: the anterior AF, the antero-lateral AF and the postero-lateral AF. Typically, the scanned ROI included the AF and part of the adjacent vertebral body, in two of the discs the ROI was restricted to an area of approximately 2mm^2 to maximize structural detail from the AF. The 3-D data sets are viewed in the three orthogonal planes; X, Y and Z using a multi-planar slice display. A 3-D projection of the data was also generated to enable the complete ROI to be viewed.

RESULTS AND DISCUSSION

A typical 3-D data set viewed in the three orthogonal planes is shown in Figure 1. Viewed in the transverse and sagittal planes (Fig. 1 a, b), the AF is characterised by strong alternate light and dark banding; the former represent the boundary between adjacent lamellae. Lamellae could be followed between their insertions in adjacent vertebral bodies. Collagen bundles are clearly visible in images generated perpendicular to the disc surface, as if looking at the surface of a tangential cut through the AF; bundle orientation alternates between adjacent lamellae (Fig. 1 c). A 3-D projection view of the complete 3-D data set reveals both the lamella structure and the orientation of collagen bundles within each lamella (Figure 1d). Lesions, characterized by an hypoechoic region within the AF, were observed in 2 of the 8 specimens; all were located at the periphery and had a "Discuss" shaped 3-D morphology. The lesions were arranged circumferentially and may represent either small circumferential lesions or areas of delamination.

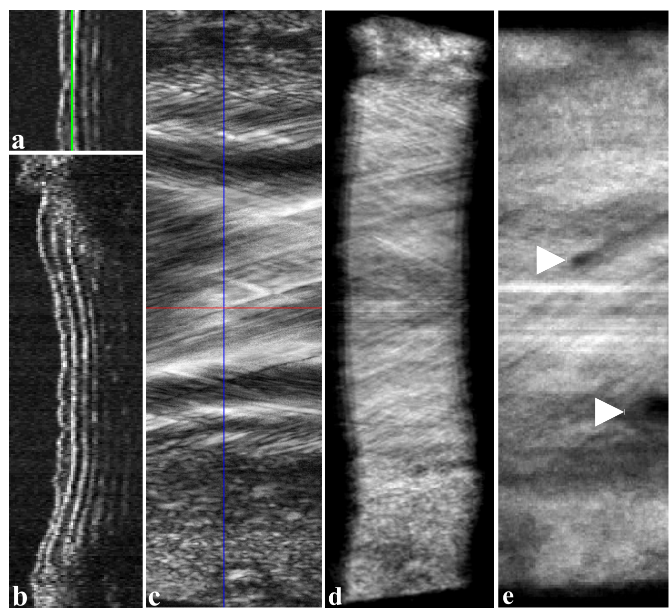

Figure 1: Visualisation of disc structure. (a) transverse, (b) saggital and (c) tangential planes. (d) 3-D projection of data. (e) Projection showing lesions in the AF (closed arrow heads).

SUMMARY

The lamella and collagen bundle structure were readily visible using 3-D SAM. Discrete lesions with a characteristic "Discuss" morphology were observed within the peripheral AF. SAM enables non-destructive imaging of disc structure that may be used to improve understanding of the relationship between disc structure, function and mechanical degeneration.

EFFECT OF BODY POSTURE ON GEOMETRY OF THE ABDOMINAL AORTIC BIFURCATION

P L Cheong[1], M Bourne[2], T M Griffith[2], X Y Xu[1]
[1]Deparment of Chemical Engineering & Chemical Technology, Imperial College, London SW7 2AZ, UK, p.cheong@ic.ac.uk
[2]Department of Diagnostic Radiology, University of Wales College of Medicine, Cardiff CF14 4XN, UK

INTRODUCTION

Haemodynamic factors have been postulated to be responsible for the focal nature of atherosclerosis, and local patterns of blood flow are strongly dependent on vascular geometry. The existence of geometric risk factors for atherosclerosis has thus been proposed, as certain anatomical features might favour a flow environment that is pathogenic (Friedman et al 1983).

The aorto-iliac bifurcation is known to exhibit a high incidence of plaque formation. Attempts have therefore been made to characterise haemodynamic conditions quantitatively in the abdominal aorta and its bifurcation using computational fluid dynamics (Taylor et al 1998, Long et al 1997). However, flow simulations have usually been performed with geometries based on data acquired from subjects lying in the supine position during magnetic resonance (MR) scanning. Different body postures might alter the aortic bifurcation geometry, which could affect the simulated haemodynamics greatly. Moreover, people do not spend their whole lives in the supine position, so if the flow simulations are to represent *in vivo* arterial flows satisfactorily, it becomes necessary to understand how changes in body posture affect geometry and hence flow at the aortic bifurcation. To our knowledge, the effects of body posture on aortic bifurcation geometry have not previously been studied.

METHOD

Two subjects were scanned between the renal bifurcation and the ilio-femoral bifurcation with a 1.5T whole body MR scanner using 2D time-of-flight (TOF) technique. Each subject was scanned supine and prone. Models of the aorto-iliac bifurcation were reconstructed from a series of cross-sectional images using our own image segmentation and geometry reconstruction programme.

RESULTS AND DISCUSSION

Fig. 1 shows the 3D geometry of the bifurcation reconstructed from images acquired in the supine position. For each subject, bifurcation geometries in the two postures were analysed in terms of branching angles, curvatures, shape factors, 3D vessel centre lines and position of bifurcation (high or low). The non-planarity is measured by the average perpendicular distance from the centre lines to the reference plane which is formed by the last points on each vessel centre line in the bifurcation region. In the present study, the bifurcation region covers an area one diameter proximal to and distal from the bifurcation apex. Fig. 2 shows the centre line of the aorto-iliac bifurcation of the same subject acquired in the supine and prone positions with non-planarity values of 0.5155mm and 0.1081mm respectively. These changes in geometry may be important, as they might strongly affect the local haemodynamics.

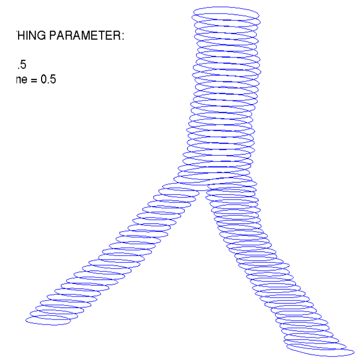

Figure 1: A human aorto-iliac bifurcation reconstructed from MR images acquired in the supine position.

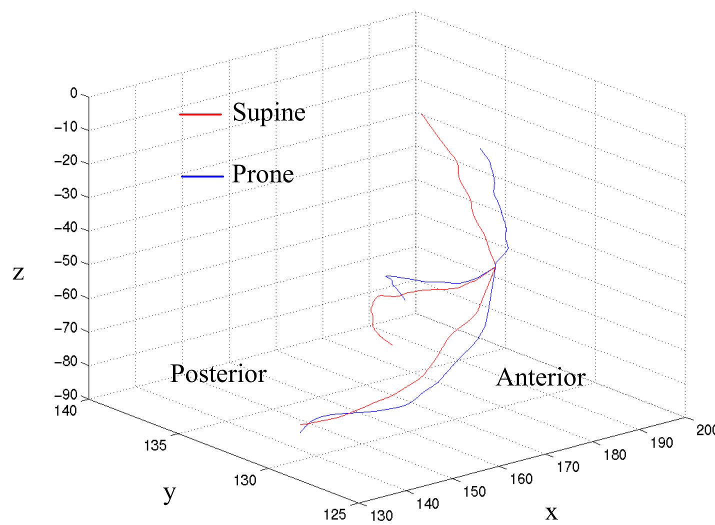

Figure 2: Centre line of a human aorto-iliac bifurcation in two different body postures. x, y, and z are the co-ordinates in mm.

SUMMARY

The importance of this study is that it demonstrates changes in the geometry of the abdominal-aortic bifurcation following alterations in posture. The effects of such alterations in geometry on local haemodynamics remain to be determined.

REFERENCES

Friedman MH et al (1983) *Atherosclerosis*, **46,** 225-231.
Long Q et al (1997). *Internal Med.* **5**, 33-39.
Taylor CA et al (1998). *Annals of Biomed. Eng.,* **26,** 975-987.

ACKNOWLEDGEMENT

This project is sponsored by British Heart Foundation.

OVERWEIGHT AND OBESITY IN POSTURE: A BIOMECHANICAL EVALUATION OF SPINE ANGLES

Federica Sibella[1], Manuela Galli[1], Marcello Crivellini[1]
[1]Bioengineering Department, Politecnico di Milano, Milano, Italy
e-mail: sibella@biomed.polimi.it web site: www.gaitlab.biomed.polimi.it

INTRODUCTION

The loading condition of the spine in obese subjects results certainly excessive and sometimes it can lead to biomechanical modifications and pathological alterations of the musculo-skeletal system. A quantitative assessment of the spine angles in the sagittal plane during quiet standing in normal and overweight subjects provides useful biomechanical information about the effect of an anomalous body weight increasing on the spine.

The main aim of this study was to evaluate biomechanical aspects of the spine loading condition by calculating spine angles overweight and obese patients in comparison to normals.

METHODS

We analyzed a total number of 26 women (mean age 32.5 s.d. 5.91 years) divided into 4 subgroups in relation to BMI value: 1) underweight (6 subjects), mean BMI 19.81, s.d. 0.86 2) normal weight (10 subjects), mean BMI 22.33 s.d. 1.55 3) overweight (5 subjects), 26.21 s.d. 1.09 4) obese (5 subjects), mean BMI 38.94 s.d. 8.99 .

A motion measurement system (ELITE, bts@, IT) provided the 3D coordinates of reflective passive markers and a force platform (AMTI, Newton, MA) provided the ground reaction forces and the trajectory of the Centre of Pressure. In particular, 11 markers were placed over the spinosus processes every two vertebrae from c7 to sacrum. Each subject was asked to stand on the force platform in orthostatic indifferent position with eyes open for three successive acquisition trials. Each trial was 30 secs long. This abstract is focused only on kinematic aspects. The curve that interpolates all the 11 points in the sagittal plane was found using an algorithm based on cubic splines. From this curve two significative angles parameters were extracted: angle of lordosis (θ_L) and angle of kyphosis (θ_C).

RESULTS AND DISCUSSION

A significative correlation between increasing BMI and a variation of the calculated parameters lordotic angle (θ_L) and cifotic angle (θ_C) was found: for increasing values of BMI a decreasing value of the two considered angles was to notice (see Figure 1 and 2). The decrease of the lordotic angle (θ_L), in relation to an increasing value of the BMI is a sign of an iper-lordotic posture in obese women This result confirms the conclusions of some previous studies that used radiographic images as a tool to investigate spine angles in obese subjects. The decrease of the kyphotic angle (θ_C), in relation to an increasing value of the BMI is a sign of an iper-kyphotic posture in obese women. This is probably due to a spine overloading and it seems to be a way to compensate the iper-lordotic posture, in order to maintain a good balance during quiet standing.

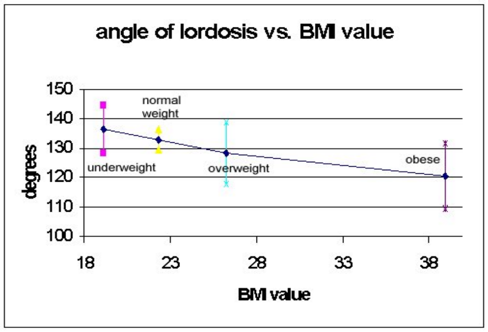

Figure 1: angle of lordosis in relation to BMI value

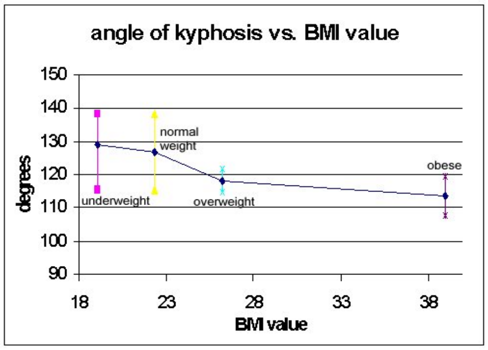

Figure 2: angle of kyphosis in relation to BMI value

SUMMARY

As a conclusion, we can say that these results, obtained with a non-invasive optoelectronic device, confirm previous results, obtained with a more invasive tool (radiographic images). The simple biomechanical model that we used to define spine angles in the sagittal plane, can help to get information about the posture of any kind of subject and maybe try to explain different attitudes from a biomechanical point of view.

REFERENCES

Kapteyn T.S.: "*Data processing of posturographic curves*", Agressologie, (1972)**; 13B:** 29-34;

Murray M.P., Seireg A.A., Sepic S.B.: "*Normal postural stability and steadiness: quantitative assessment*", J. Bone Joint Surg., (1967); **23:** 831-838

NUMERICAL SIMULATION OF INTERFACIAL STRESS FOR EXTENSIVE PREMOLAR CAVITY UNDER DIFFERENT OCCLUSAL FORCES

Heng-Liang Liu[1], Ming-Yih Lee[1], Yen-hsiang Chang[2] and Chun-Li Lin[1]
[1]Department of Mechanical Engineering, Chang Gung University, Tao-Yuan, Taiwan, gerry@ms65.url.com.tw
[2]Operative Dentistry, Chang Gung Memorial Hospital, Tao-Yuan, Taiwan

INTRODUCTION

Traditionally, the extensive cavity restoration has to spent large amount of efforts and time-consuming by direct or indirect method. The CAD/CAM systems are adequate to fabricate all-ceramic restoration for extensive cavity. However, interfacial bonded strength between tooth tissue and restoration material is suspected after restored by CAD/CAM system. The objective of this study was to estimate the interfacial stresses for extensive premolar cavity with various designed restoration shape under different occlusal loading.

METHODS

An intact premolar was designed for extensive cavity shape, depth was from lingual cusp tip to high of contour and width was from fissure line to lingual cusp. Restoration was then performed using CEREC system (Sirona Dental Systems, Bensheim, Germany). The 3D finite element model (Fig. 1(a)) of restored premolar with sound material properties (enamel, dentin, pulp, and ceramic) was generated in ANSYS (Ansys Inc, Houston, USA, 1994) after embedded, sliced, image process, caught material contour procedures. Other four individual cavity finite element models were developed by modify element material properties in the zone of cavity areas. All designed shape of restorations have the same dimensions except width distance from fissure line to lingual wall (D). The various width distances are average divided from 2/3D to 1D. Premolars were individual subject to 200N with 45 degrees incline acted on tooth and restoration, respectively, near the interface between natural tooth and restoration. An in-house program was used to combine with ANSYS to calculate the interfacial stress for five different cavity designs with two occlusal forces.

RESULTS AND DISCUSSION

The interfacial stresses (normal and shear) obtained for each design are listed in Table 1 (Fig. 1(b)). Higher normal stress on buccal and lingual wall inducing by bending moment increased restoration width in the restored premolars under the same occlusal loading condition. In addition, larger normal stress on interfacial bonded areas by occlusal force acting on natural tooth than on restorative material for longer moment arm under the same restoration shape design.

SUMMARY

Under limited data, occlusal contact adjustment might be an essential factor than shape design for extensive cavity in clinic.

REFERENCES

Arola D., Galles L.A., (2000). *J. of Dentistry*, **29**, 63-73.
Fischer H., Dautzenderg G., Marx R., (2000). *Dental Materials*, **17**, 289-295.
Ausiello P., et al (2001). *J. of Biomechanics*, **34**, 1269-1277.

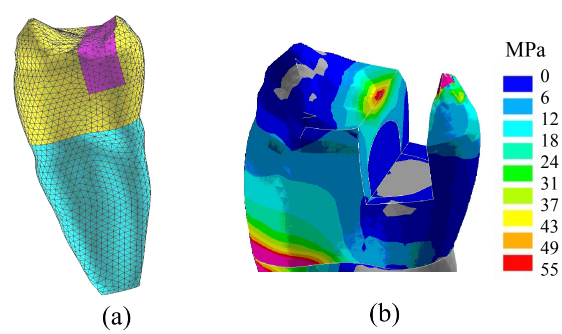

Fig. 1: (a) 3D restored premolar finite element model; (b) Maximum principle stress due to occlusal loading placed on tooth in Design 5

Table 1: The maximum normal stress within each design by two different occlusal loadings (MPa)

Interfacial Area	Contact Location	Design 1 (8/12D)	Design 2 (9/12D)	Design 3 (10/12D)	Design 4 (11/12D)	Design 5 (1D)
Baccal Wall	Natural Tooth	36.94	51.63	52.39	52.93	55.09
	Restoration	46.86	48.29	48.21	49.22	49.99
Lingual Wall	Natural Tooth	33.48	39.02	43.05	43.99	65
	Restoration	7.92	8.00	7.47	7.42	6.64

CYCLIC STRAIN AND FLUID FLOW INDUCE DIFFERENT RESPONSES IN HUMAN BONE CELLS

Mullender, M[1], El Haj, AJ[2], Yang, Y[2], Magnay, J[2], van Duin, MA[1], Klein-Nulend, J[1]
1 Dept. Oral Cell Biology, ACTA-Vrije Universiteit, Amsterdam, The Netherlands, m.mullender@fbw.vu.nl
2 Centre for Science and Technology in Medicine, Dept. Biomedical Eng., Stoke-on-Trent, UK.

INTRODUCTION

When bone is subjected to mechanical loads, osteocytes and osteoblasts have been shown to produce signaling molecules, which mediate bone remodeling (Burger, 1999). It is thought that osteocytes detect these mechanical loads by sensing fluid flow through the lacuno-canalicular network in bone. Osteoblasts, however, are located on the bone surface. They may also be directly stimulated by mechanical strain. The objective of this study was to examine if fluid flow or direct cell strain induces the production of signaling molecules or matrix proteins in bone cells. Therefore, we subjected primary human bone cells to either pulsating fluid flow (PFF) or cyclic strain (CS) *in vitro*. The production of nitric oxide (NO) and prostaglandin E_2 (PGE_2) was measured. Both are early mediators in mechanically induced bone formation. To evaluate the effect on matrix production, the amount of collagen type I was measured.

METHODS

Primary human bone cells were obtained from bone fragments of three patients (1.5; 14; 16 yrs.). The outgrowing bone cells were cultured in α-MEM with 10% FBS. Second-passage primary cultures were treated with pulsating fluid flow (PFF) or cyclic strain (CS). Cells were plated on polylysine coated glass slides and incubated for 24 h in DMEM with 2% FBS. The cells were then loaded for 1 h by PFF (0.6±0.3 Pa, 8.5 Pa/sec, 5 Hz) or CS by four-point bending (~1000 μstrain, 1 Hz). Control cultures were kept accordingly, without loading. All cell cultures were post-incubated until 24 h after loading. The conditioned medium was assayed for NO, measured as nitrite (NO_2^-), using the Griess reagent and for PGE_2 by enzyme-immunoassay. Cells were harvested for measurement of total protein and DNA. The quantity of collagen I was analyzed by Western Blot. Data were analyzed using the general linear model. A $p<0.05$ was considered as significant.

RESULTS

The total amount of DNA did not differ between treatment and control groups. Treatment with PFF caused a significant increase in the production of NO during flow (Figure 1B). PFF stimulated PGE_2 production up to 12-fold after 24h post incubation. CS also stimulated the release of NO significantly (Figure 1A), but not PGE_2 (Figure 1C). PFF inhibited and CS stimulated the production of collagen type I (Figure 2).

DISCUSSION

Fluid flow through the lacuno-canalicular system is believed to be a key mechanism by which osteocytes sense mechanical loads. They are considered to convey this information to cells at the bone surface by signaling molecules. Our results showed that primary human bone cells responded to pulsating fluid flow by an increased release of such molecules. However, the production of the matrix protein collagen I was inhibited by PFF. In contrast, CS stimulated the production of collagen I and did not stimulate PGE_2 release. The release of NO was upregulated by both PFF and CS.

We have shown previously that human bone cells respond to CS by an upregulation of c-fos expression, a transcription regulator of matrix production. Stretch activated channels and integrin mediated pathways are critical for this response but not PGE_2 (Peake, 2000). This might explain the increased collagen production and the lack of PGE_2 response after CS. The results suggest that bone cells can discriminate between strain directly applied through the substrate and strain induced by flow-derived shear stress. Furthermore, activation of these different mechanical pathways may either stimulate or inhibit the production of matrix proteins.

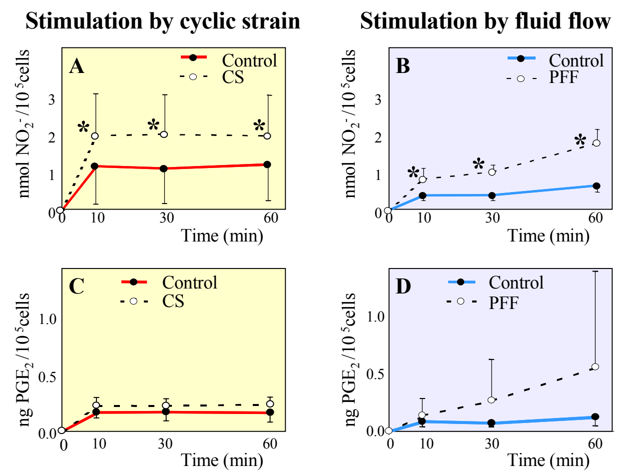

Figure 1: Both CS and PFF stimulated NO release (**A**, **B**). PGE_2 did not increase after CS (**C**). PGE_2 increased after PFF (**D**), but this was significant only after 24 h post incubation.

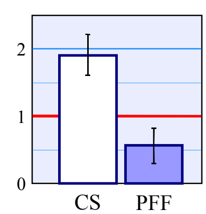

Figure 2: Collagen I expression is given as load over control ratio (no response gives a ratio of 1). CS stimulates collagen I production, whereas PFF inhibits collagen I production.

REFERENCES

Burger E.H., Klein Nulend J., 1999, *FASEB J.* **13** S101-12.
Peake M.A. et al. 2000, *J. Appl. Physiol*. **89**: 2498-2507.

ACKNOWLEDGEMENTS

This work was supported by the European Commission Community Research, project BITES (QLK3-1999-00559)

NON-NEWTONIAN EFFECT IN THE ARTERIAL BLOOD FLOW

Józef Wojnarowski[1] and Kryspin Mirota[2]
[1] Silesian Technical University, Gliwice, Poland
[2] Bielsko-Biala Technical University, Bielsko-Biala, Poland

INTRODUCTION

One of the most important questions of hemodynamics is the question about manner of flow rheology specification. In this present paper, Hagen - Poiseuille's model has been used in analysis of influences of human blood state parameters, such as hemocritic number and level of protein in plasma (more precisely fibrinogen and globulin level) on type of behaviour of velocity field in cross-section of blood vessel.

METHODS

Phenomenon of blood flow in a main vessel can be described by equation system of mass and momentum balances:

$$\frac{1}{r}\frac{\partial}{\partial r} r u_r + \frac{1}{r}\frac{\partial u_\theta}{\partial \theta} + \frac{\partial u_z}{\partial z} = 0, \tag{1}$$

$$\rho\left(\frac{\partial u_z}{\partial t} + u_r\frac{\partial u_z}{\partial r} + \frac{u_\theta}{r}\frac{\partial u_z}{\partial \theta} + u_z\frac{\partial u_z}{\partial z}\right) = -\frac{\partial p}{\partial z} + \left(\frac{1}{r}\frac{\partial}{\partial r} r\tau_{rz} + \frac{1}{r}\frac{\partial \tau_{\theta r}}{\partial \theta} + \frac{\partial \tau_{zz}}{\partial z}\right). \tag{2}$$

In the case of flow through a vessel, a longitudinal dimension of a canal is essentially higher than a cross-section dimension, and therefore an axial component of transport is several times greater than radial and tangent. Therefore these transport components can be dropped.

A phenomenological model equation requires a definition of a stress-strain relationship. In this work Walburn-Schneck empirical model has been applied. By substituting of constitutive equation into (1) and (2), we have after integration

$$u_z = -\frac{1-c_3H}{2-c_3H}\left(2c_1 e^{c_2H + c_4\frac{TPMA}{H^2}}\right)^{\frac{1}{c_3H-1}}\left(\frac{dp}{dz}\right)^{\frac{1}{1-c_3H}} R^{\frac{2-c_3H}{1-c_3H}}\left(1-\left(\frac{r}{R}\right)^{\frac{2-c_3H}{1-c_3H}}\right) \tag{3}$$

formulae of velocity distribution in arterial cross section and

$$\lambda = 2^{4-c_3H}\frac{c_1}{\rho u^{1+c_3H} D^{1-c_3H}} e^{c_2H + c_4\frac{TPMA}{H^2}}\left(\frac{4-3c_3H}{1-c_3H}\right)^{1-c_3H}. \tag{4}$$

hydrodynamics friction coefficient.

RESULTS AND DISCUSSION

Obtained equation (3), (4) describes an arterial flow phenomena by velocity distribution and pressure drop with regards to real blood state parameters. Let's consider, as an example, the distribution of blood velocity in a vessel cross section. Figure 1 presents distribution of velocity in dimensionless, as a function of radial co-ordinate.

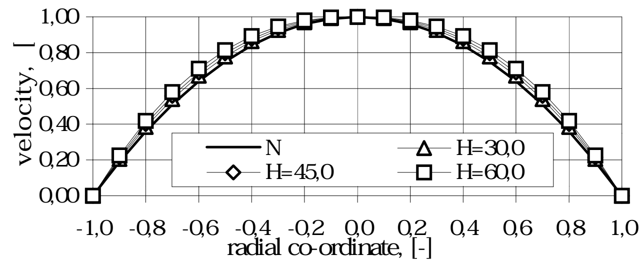

Figure 1: Dimensionless velocity distribution in a vessel cross section for Newtonian (N) and non-Newtonian (hematocrit 30, 45, 60 ml/100ml) fluid

SUMMARY

Performed detailed analysis shows the following regularities connected with hematological and flow parameters:

- strong influence of pseudo-plastic properties; due to decreasing shear velocity;
- decreasing of value of maximal velocity in relation to average velocity, what is confirmed by more flat profile of velocities together with increase of hematocrit number and proteins level measured by *TPMA* indicator;
- essential sensitivity of considered parameters on hematocrit number and simultaneously several times less sensitivity to changes of levels of fibrinogens and globulins.

Non-Newtonian effects and their consequences are more and more important in case when blood composition would be different from proper (regular) one for human body - what indicates that it occurs a particular correlation between pathological states of blood flow system.

REFERENCES

Rodkiewicz Cz. (1983). *Arteries and Arterial Blood Flow*,., Springer Verlag, 1-12

Wojnarowski J., Mirota K. (1999). *Proceedings of Tenth World Congress on the Theory of Machines and Mechanisms*, Vol.5, 1841-1846

Wojnarowski J., Mirota K. (2001). *Acta of Bioengineering and Biomechanics*, 655-662

PEAK POWER CHANGES RESPONSIBLE FOR GAIT SPEED INCREASES IN PERSONS WITH STROKE FOLLOWING A TRAINING PROGRAM

Krishnaji Parvataneni and Sandra Olney
Human Mobility Research Group, Queen's University, Kingston, Canada, K7L 3N6

INTRODUCTION

Gait speed is arguably the single best measure of motor performance, correlating highly with most measures of impairment, disability and health outcome (Bohannon, 1992, Berg et al., 1989). Muscle groups of the lower limb generate and absorb the power required to walk at a safe speed in typical patterns (Winter, 1987). In order of size of the power generators in normal individuals they are: A2, ankle plantarflexors at push-off; H3, hip flexors at pull-off; H1, hip extensors in early stance; K2, knee extensors in early stance. K3 is an important absorber at push-off. Knowledge of the power changes occurring with increased speeds would enable clinicians to target specific muscle groups for retraining. The purpose of this study was to determine the changes in power produced by lower limb muscle groups of persons with stroke who increased their speed of walking after a training program.

METHODS

We examined the peak powers from the hip, knee and ankle of 28 persons (age = 64.2yrs ± 11.7) with chronic stroke (onset time = 4.8yrs ± 7) before and after a training program of 10 weeks, all of whom had an increase in their gait speed. The gait data were collected using a Peak Motus two-dimensional motion analysis system (Peak Performance Technologies Inc., Englewood, Co.), with an AMTI force platform (Advanced Mechanical Technologies Inc., Newton, MA) and subjected to inverse link segment analysis (Winter, 1979). One trial each from the affected and unaffected side with similar speeds were selected for data analysis.

RESULTS AND DISCUSSION

The walking speed after training as measured from the gait analysis trials averaged 0.83m/s (± 0.33), which was significantly faster than the baseline speed, which averaged 0.69m/s (± 0.31). The descriptive statistics and comparisons of peak powers at major points in the gait cycle from the affected and unaffected sides, before and after training are presented in Table 1. The results show an overall increase in average peak power generation at the hip, knee and ankle on the affected as well as the unaffected sides. The largest increase in peak power generation was observed in the ankle plantarflexors (A2) on the affected side (0.74 ± 1.16 W/kg) followed by the ankle plantarflexors (A2) on the unaffected side (0.46 ± 0.98 W/kg). The next largest increases were by the hip extensors (H1) in early stance on the affected side (0.25 ± 0.5 W/kg) and flexors (H3) at pull-off on the unaffected side (0.26 ± 0.32 W/kg).

To show the distribution of increases across subjects, we identified subjects with peak power increases of greater than 0.1W/kg. Of the 28 subjects, 21 subjects showed increases on the affected side in A2, 18 in H3, and 11 in H1. On the unaffected side, 20 subjects showed increases in A2, 19 in H3 and 13 in H1. Increase in peak power absorption by the knee extensors (K3) on the affected side was observed in 25 subjects and in 23 subjects on the unaffected side.

The importance of plantarflexor training on both sides is clear from these results, and one would expect gait training stressing push-off to be beneficial. Similarly, training of affected hip extensors (H1) and encouragement of the "push-from behind" on the affected side should be helpful. Hip flexor training on the unaffected side, and accentuation of pull-off is also indicated. Further research should be directed at assessing the effectiveness of training potentially compensatory muscle groups that were less used: affected side H2, and unaffected side H1.

REFERENCES

Bohannon, R.W. (1992). *Int J Rehabil Res*, **155**, 246-248.
Berg K., Wood-Dauphinee, S. et al (1989). *Physiotherapy Canada*, **41**, 304-311.
Winter, D.A. (1987). *The Biomechanics and Motor Control of Human Gait.* University of Waterloo Press
Winter, D.A. (1979). *Biomechanics of Human Movement.* John Wiley & Sons

Table 1. Mean and Standard Deviations of ankle hip and knee peak powers normalized to body weight (W/kg), from the affected and unaffected sides, before and after treatment.

Power	Affected side		Unaffected side	
	Before	After	Before	After
Plantarflexor generation, A2	1.34 ± 1.15	2.07 ± 1.22	2.43 ± 1.74	2.89 ± 1.91
Hip extensor generation, H1	0.44 ± 0.39	0.69 ± 0.56	0.54 ± 0.41	0.66 ± 0.47
Hip flexor generation, H3	0.57 ± 0.56	0.67 ± 0.40	0.76 ± 0.42	1.02 ± 0.56
Knee extensor generation, K2	0.17 ± 0.21	0.29 ± 0.28	0.22 ± 0.41	0.29 ± 0.3
Knee extensor absorption, K3	-0.63 ± 0.55	-0.88 ± 0.79	-0.99 ± 0.65	-1.43 ± 1.03

RECRUITMENT OF ANKLE LIGAMENTS FIBRES DURING PASSIVE FLEXION

Rita Stagni[1], Alberto Leardini[2], Andrea Ensini[2]
[1] Dipartimento di Elettronica, Informatica e Sistemistica, Università degli Studi di Bologna, Italy, stagni@ior.it
[2] Movement Analysis Laboratory, Istituti Ortopedici Rizzoli, Bologna, Italy

INTRODUCTION

The knowledge of ligament fibre recruitment at the human joints is fundamental for the analysis of mobility, joint motion as controlled by articular surfaces and ligaments, and stability, joint resistance to relative movement of the bones when load is applied. Previous experimental and modelling studies have shown that ankle motion is guided by fibres within the CaFi and TiCa ligaments, which remain approximately isometric through passive flexion (Leardini et al, 1999). The purpose of this study was to identify more precisely the ligament fibres that guide this motion, to distinguish them from those that only limit motion.

METHODS

Three skeleto-ligamentous lower leg preparations including tibia, fibula, talus, calcaneus and intact ligaments were tested. Four spherical 0.8 mm diameter tantalum balls were stuck on the cortex of each of the four bones. Starting from maximum passive plantarflexion, the specimen was stopped in a series of different joint positions, increasing dorsiflexion until a little resistance from the joint was felt. Two roentgen tubes exposed simultaneously both the calibration cage and the specimen in each flexion position. The 3-D co-ordinates of the 16 tantalum balls were then reconstructed in each of the joint positions using standard RSA techniques (Selvik, 1989). The areas of origin and insertion of the main ankle ligaments, the tantalum balls and a series of anatomical landmarks were digitised by means of a 3D digitiser (FARO Technologies, Inc.). Calcaneofibular (CaFi), anterior talofibular (ATaFi), posterior talofibular (PTaFi), tibiocalcaneal (TiCa), deep anterior (DATiTa) and deep posterior (DPTiTa) tibiotalar were examined. The Singular Value Decomposition technique (Challis, 1995) was used to match RSA- and FARO- based ball positions. Eleven representative fibres were mapped in each of the ligaments. The instantaneous length of each fibre of each ligament was calculated in percentage of its maximum, hereinafter called Effective Length Fraction (ELF) of the fibre. ELF Variation (ELFV) from maximal plantarflexion to maximal dorsiflexion was also calculated.

RESULTS AND DISCUSSION

Figure 1 shows that the most anterior fibres of the CaFi ligament and the medio-anterior fascicle of fibres of the TiCa show the smallest variation with respect to their maximal elongation. The ELFV values in Table 1 confirm that the TiCa and CaFi ligaments are the ones, which remain most isometric, with a RMS value of the mean ELFV of 5.2% and 4.1% respectively.

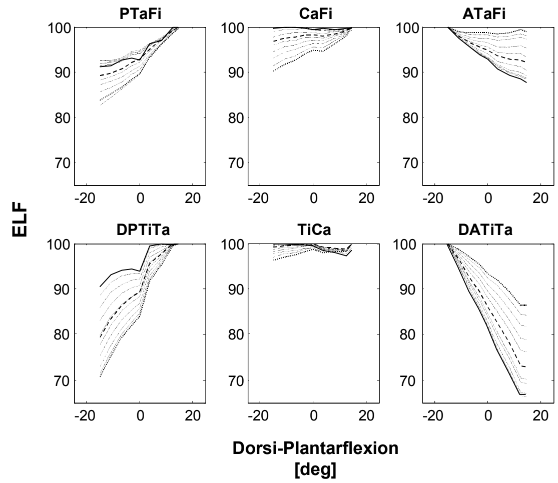

Figure 1: ELF of each fibre of each ligament for a representative specimen. The most anterior (solid bold line), the middle (bold dashed line) and the most posterior (bold dotted line) fibres are depicted.

ELFV	Lateral Side			Medial Side		
	PTaFi	CaFi	AtaFi	DPTiTa	TiCa	DATiTa
Post	11.2	7.4	-0.5	37.8	9.5	-16.0
II	10.2	6.5	-1.5	36.9	8.8	-18.3
III	9.6	5.3	-2.5	35.6	7.3	-20.2
IV	9.0	4.8	-3.8	34.2	5.9	-22.2
V	9.9	3.9	-5.1	32.2	4.5	-24.4
Mid	8.7	3.2	-6.3	30.1	3.3	-26.9
VII	6.7	2.6	-8.0	28.3	2.2	-28.7
VIII	6.2	1.8	-9.7	25.5	1.0	-29.3
IX	5.0	1.1	-11.2	22.4	-0.1	-30.4
X	4.3	0.5	-12.4	19.3	-1.1	-31.3
Ant	5.8	0.3	-13.6	16.5	-2.2	-30.7
RMS	8.2	4.1	8.1	29.8	5.2	25.8

Table 1: Mean value of ELFV over the three specimens for each of the 11 fibres of each of the 6 ligaments.

SUMMARY

Fibres within the CaFi and TiCa ligaments, which remain almost isometric along the passive Do/Pl range, have been identified. These are supposed to control and guide ankle motion in a preferred passive path, whereas all the other ligament fibres limit motion to resist external load. Fibre recruitment analysis in unloaded conditions provides the necessary geometrical basis for future studies of the mechanics of the ankle joint complex.

REFERENCES

Challis, J.H. (1995). *Med Eng Phys*, **17(2)**, 83-90.
Leardini, A., et al. (1999). *J Biomech*, **32(2)**, 111-118.
Selvik, G. (1989). *Acta Orthop Scand Suppl*, **232**, 1-51.

FINITE ELEMENT ANALYSIS OF GLENOID COMPONENT VERSION IN TOTAL SHOULDER ARTHROPLASTY

Andrew Hopkins[1], Ulrich Hansen[1] and Abdel Hassan[2]
[1] Biomechanics Section, Department of Mechanical Engineering, Imperial College, London, UK.
[2] Apley Research Fellow, St.Thomas Hospital, London, UK.

INTRODUCTION

Complications with Total Shoulder Arthroplasty are generally associated with failure of the component replacing the scapular articulation. One of the suggested mechanisms for the implant failure is the destruction of the cement mantle used to bond the prostheses to the bone. Cement degeneration is associated with the development of excessive tensile loads within the mantle.

A major complication of TSA surgical reconstruction is the difficulty associated with maintaining a suitably versed articular surface post-operatively. The version of the glenoid cavity relative to the scapular plane has been reported to vary, on average, by 7º from the central axis for patients suffering from rheumatoid arthritis (Couteau et al. 2001). The placement of the implant is generally evaluated using pre-operative CT scans, however variations such as geometric distortion and realignment of the trabecular structure of the glenoid due to rheumatoid arthritis may suggest to the surgeon an incorrect alignment/version of the component.

It is proposed that this variation of implant version from an anatomically ideal reconstruction might result in the generation of excessive tensile stresses within the cement mantle of the glenoid component. This in turn would cause destruction of this bonding interface and thus loosen the component. It has been suggested that this loosening will over time propagate into the 'rocking-horse' mechanism.

MATERIALS AND METHODS

A 3D Finite Element Analysis was performed upon four different scapulae, two of which represent a patient exhibiting rotator cuff deficiency and two models representing rheumatoid patients. Implant placement and version were discussed and simulated in the models in consultation with an orthopaedic surgeon. The suggested anatomically ideal version was modelled as were several of the probable off-set prosthesis inclinations.

Material properties were assigned to the models using interpolation between greyscale value, apparent density and Young's modulus (Rice et al. 1988, Schaffler & Burr 1988), and these values were modified for the cases of rheumatoid arthritis using simulated material properties (Dalstra et al. 1996). Anisotropy within the trabecular structure of the glenoid (Mansat et al. 1998) has been introduced to the models using a region based method.

A distributed pressure loading is applied to the contact surface upon the glenoid component using the theory of non-conforming surfaces (Johnson 1985). The scapula bone was reduced to the superior lateral quarter as this was the principal area of interest.

Primary consideration is to be taken of the maximum principle stresses developed within the cement mantle. This is used to examine the percentage by volume of cement expected to survive a repetitive loading of 10 million cycles (Murphy et al. 2000).

RESULTS

Analysis of the different cases of version suggest that a variation in the sites of implant anchorage within the trabecular bone plays a significant factor in the distribution of stresses developed within the cement mantle. This effect was seen to be particularly pronounced within the rheumatoid simulations, where degenerated bone stock produced a more significant probability of cement mantle failure due to tensile stress peaks.

CONCLUSIONS

FEA can provide a useful resource of data regarding survivability of prostheses under conditions difficult to simulate within a laboratory experiment. The potential for misalignment or misplacement of an implant during surgery is a very real possibility, which could eventually be eliminated if techniques for optimisation of the anchorage sites for the prostheses are investigated sufficiently pre-operatively.

This study suggests that the interpretation of geometry and material property distribution, pre-operatively and during surgery, is critical to the long-term success of a procedure such as TSA.

REFERENCES

Couteau et al. (2001) J. Shoulder & Elbow Surg., 116-122.
Rice et al. (1988) J. Biomech., 155-168.
Schaffler and Burr (1988) J. Biomech., 13-16.
Dalstra et al. (1996) Proc. 10th Conf. E.S.B., 178.
Mansat et al. (1998) J. Shoulder & Elbow Surg., 109-115.
Johnson (1985) Contact Mechanics, Cambridge Univ. Press.
Murphy (2000) Proc. 12th Conf. E.S.B., 160.

ACKNOWLEDGEMENTS

This work was funded by the Engineering and Physical Sciences Research Council, UK.

ARCHITECTURE OF CONTRACING HUMAN GASTROCNEMIUS MUSCLE: AN APROACH FROM THREE-DIMENSIONAL ULTRASOUND IMAGING

Toshiyuki Kurihara, Yasuo Kawakami, Toshiaki Oda, Kentaro Chino, Tetsuo Fukunaga
Department of Life Sciences (Sports Sciences), University of Tokyo, Komaba, Japan, t-kuri@mti.biglobe.ne.jp

INTRODUCTION

Architectural parameters of skeletal muscles such as fascicle length, pennation angles, muscle thickness and tendon length are often studied. Recent in vivo approaches to the architecture of contracting human muscle have shown that muscle architecture changes by contraction even in isometric actions (Kawakami et al, 2000; Kawakami et al, 1998; Fukunaga et al, 1997). To understand the contraction-induced changes in muscle architecture, however, information on three-dimensional morphology of the whole muscle is necessary. The purpose of this study is to describe architectural changes in human gastrocnemius muscle upon contraction by using the 3D ultrasonography.

METHODS

The subject's right foot was firmly attached to an electric dynamometer. The ankle joint was fixed at 90 deg, and the knee joint was positioned at 0 deg. During the ultrasound data acquisition, the subject was asked to relax (rest condition, as reference), then to maintain isometric contractions at five force levels (20, 40, 60, 80, 100%MVC).

With the use of B-mode ultrasonography, cross-sectional images of muscles and tendinous tissues (tendons and aponeuroses) are visualized in a two-dimensional plane. In the present study, we employed this method to visualize them in a three-dimensional space. For this purpose, an electromagnetic position sensor was attached to the ultrasonic transducer to provide position and orientation information for each image acquired. Then all the serial ultrasonic images (recorded at 30 frames/s) were stored in a computer simultaneously with the positional information, from which fascicles and tendinous tissues were reconstructed three-dimensionally (Fig. 1).

RESULTS AND DISCUSSION

Preliminary results for 2 healthy male subjects showed that the length of muscle belly part of gastrocnemius was monotonically decreased as the force increased, but the length changes of aponeuroses as a function of force levels were nonlinear and different between the deep and superficial parts (Fig. 2). In addition, the reconstructed muscle showed three-dimensional deformation of both aponeuroses upon contraction. It was also shown that the muscle thickness was not constant over the force levels.

Work is in progress to improve the accuracy and validity of the present methodology and measured variables. In the further study, we will investigate the intramuscular variation of fascicle architecture.

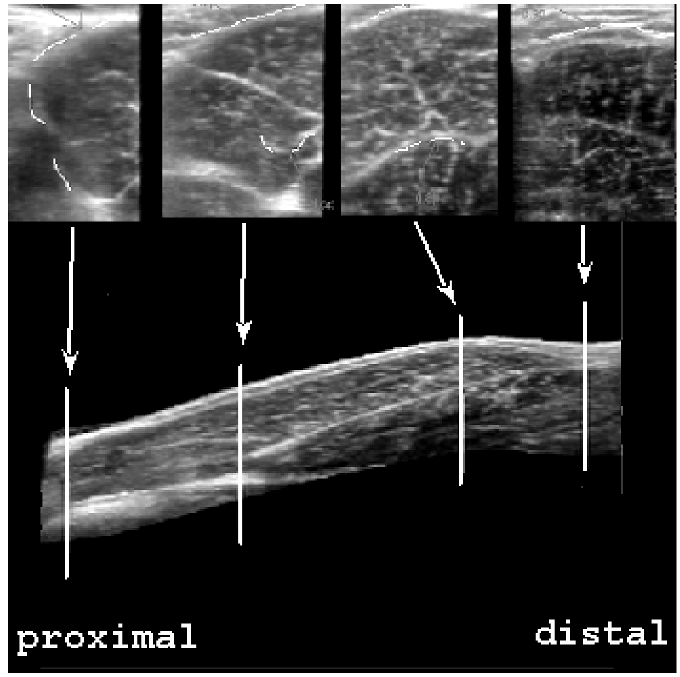

Figure 1. A typical example of ultrasound images of the gastrocnemius muscle at 40%MVC. (top: four examples of cross-sectional images, bottom: reconstructed longitudinal image)

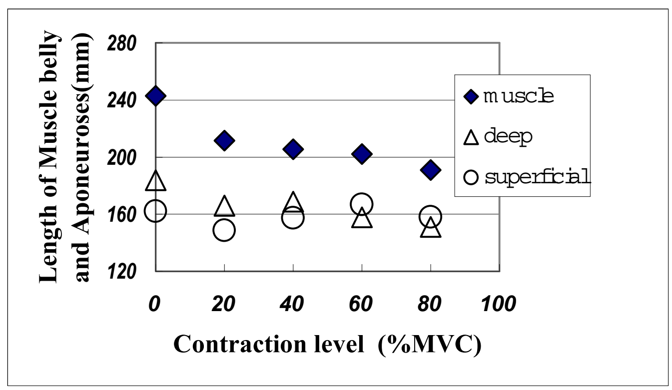

Figure 2. A typical example of the length of the muscle belly part, deep and superficial aponeuroses as a function of contraction levels.

REFERENCES

Fukunaga, T. et al (1997). *J. Appl. Physiol.*, **82**: 354-358
Kawakami,Y. et al (1998). *J. Appl. Physiol.*, **85**: 398-404
Kawakami,Y. et al (2000). *J. Appl. Biomech.*, **16**: 88-98
Lam, E.W. et al (1991). *Arch. oral Biol.*, **36**: 845-853
Scott, S.H. et al (1993). *J. Anat.*, **182**: 249-257

EFFECT OF SKIN MOTION ARTEFACTS ON KNEE JOINT KINEMATICS

Rita Stagni[1], Silvia Fantozzi[1], Angelo Cappello[1], Francesco Brigliadori[1], Alberto Leardini[2]
[1] Dipartimento di Elettronica, Informatica e Sistemistica, Università degli Studi di Bologna, Italy, stagni@ior.it
[2] Movement Analysis Laboratory, Istituti Ortopedici Rizzoli, Bologna, Italy

INTRODUCTION

The reliability of clinical gait analysis is limited by the effect of Skin Motion Artefacts (SMA). Joint angles are calculated from trajectories of markers located on the skin of the subject under analysis. This procedure is based on the erroneous assumption that markers are rigidly connected with the underlying bony segment. How and to which extent SMA affect joint kinematics is a crucial issue. This has been investigated considering subjects wearing external fixators (Cappozzo et al., 1996) or other bone tracking devices (Manal et al., 2000), which limit SMA. The purpose of the present work was to investigate the effect of SMA in absence of skin sliding constraints and to evaluate the best location of skin markers (SM) for the reconstruction of knee kinematics.

MATERIALS AND METHODS

One patient operated of total knee replacement was acquired during stair climbing (SC) and sit-to-stand/stand-to-sit (STS) activities with fluoroscopy and stereophotogrammetry at the same time. Nineteen markers were uniformly attached laterally on the skin of the thigh, ten on the shank (Figure 1).

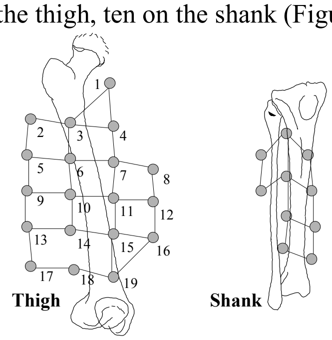

Figure 1: Skin markers distribution on the thigh and shank of the analysed subject.

The accurate 3D kinematics of the prosthesis components was reconstructed from the 2D single fluoroscopic view with an iterative procedure using CAD model based shape matching techniques (Banks et al., 1996). The position of the femoral component was calibrated in one reference position using four different clusters of SMs on the thigh: complete (CM: markers 1-19), proximal (PR: markers 1-8), central (CT: markers 5-12) and distal (DT: markers 9-19) subsets. The tibial component was calibrated in the same reference position with respect to the 10 SMs tibial cluster. The 3D prosthesis components kinematics was then reconstructed from the SM clusters (Challis, 1995).

Knee angles were calculated with Grood and Suntay convention (1983) from the 3D kinematics of prosthesis components obtained from fluoroscopy and SM. The Root Mean Square Value (RMSV) of the difference between knee angles evaluated from SM and fluoroscopy in percentage of their corresponding range for STS and SC, was calculated for CM, PR, CT and DT clusters.

RESULTS AND DISCUSSION

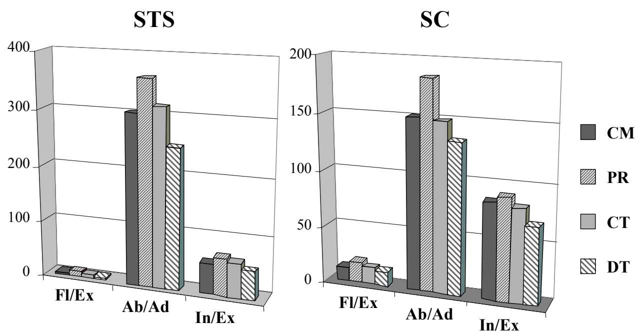

Figure 2: RMSV of the difference between knee angles evaluated from SM and fluoroscopy in percentage of the range for STS and SC, evaluated for CM, PR, CT and DT clusters.

The Fl/Ex angle was the least affected by SMA for both motor tasks with a maximum RMSV of the difference of 15% in SC considering the PR cluster. The Ab/Ad angle was the most affected by SMA: RMSV in the range 250% (DT) – 361% (PR) for STS, 134% (DT) – 185% (PR) for SC. These results suggest a better reconstruction of knee rotations can be obtained with the DT cluster, as observed for the In/Ex angle also, with a RMSV ranging between 50% (DT) and 67% (PR) for STS, and between 69% (DT) and 91% (PR) for SC.

SUMMARY

These experimental observations provide a quantification of SMA effects and a useful indication for the selection of the most appropriate cluster of markers for the reconstruction of knee kinematics during clinical gait analysis. Knee Ab/Ad angle was the most affected by SMA. The cluster positioned in the distal area of the femur performed the best in the recostruction of knee kinematics.

REFERENCES

Banks, S.A., et al. (1996). *IEEE Trans Biomed Eng*, **43(6)**, 638-648.
Cappozzo, A., et al. (1996). *Clin Biomech*, **11(2)**, 90-100.
Challis, J.H., (1995). *Med Eng Phys*, **17(2)**, 83-90.
Grood, E.S., Suntay, W.J. (1983). *J Biomech Eng*, **105(2)**, 136-144.
Manal, K., et al. (2000). *Gait & Posture*, **11**, 38-45.

A NEW METHOD FOR QUANTIFYING FIBRE BUNDLE ORIENTATION WITHIN INTACT INTERVERTEBRAL DISCS USING 3-D SCANNING ACOUSTIC MICROSCOPY.

Scott Johnson[1], Mike Jones[2], Mike Halliwell[2] and Donal McNally[1]
[1]Institute of Biomechanics, School of Mechanical, Materials, Manufacturing Engineering and Management. University of Nottingham, Nottingham. UK
[2]Department of Medical Physics and Bioengineering. United Bristol Healthcare NHS Trust, Bristol. UK.

INTRODUCTION

The collagen fibres of the intervertebral disc, particularly those in the annulus fibrosus (AF), act to reinforce the disc and are critical to its mechanical functioning. The fibres are grouped into bundles within lamellae and are tilted by approximately 60-65º with respect to the spinal axis; the direction of fibre tilt alternates between adjacent lamellae (Marchand and Ahmed, 1990). Changes in the orientation of collagen fibres enables the disc to accommodate structural distortions associated with axial compression, torsion and flexion. Previous methods used to investigate collagen orientation have employed destructive methods that preclude repetitive observations of structural changes within the same disc specimen. A new method of quantifying bundle orientation within intact discs through direct visualization of the collagen structure using scanning acoustic microscopy (SAM) has been developed. The findings of a preliminary study are described in this abstract.

METHODS

Four porcine lumbar discs and adjacent vertebrae were dissected free from soft tissue and the posterior vertebral elements removed. Each specimen was loaded into a manually operated screw-press capable of applying axial compression. The screw-press and disc were mounted into a water bath within the SAM. The SAM consists of a 50 MHz transducer (theoretical axial resolution 30μm), 4-stepper motor driven stages controlled via a PC and a bath for coupling medium. The transducer operates in pulse-echo mode and images are displayed so that the amplitude of echoes reflected from tissue boundaries determines the brightness of the display. The time difference between the propagation of the initial pulse and the echo's return gives a measure of the depth of the reflecting surface.

A 3-D image of the ventral surface of each disc specimen was acquired: i) before compression, ii) after application of first maximal compression and, iii) after application of a second maximal compression. Maximal compression was defined as the maximum amount of reasonable torque the author (SJ) could apply to the screw press without causing damage to the disc. The load applied to the disc was unknown, the aim of this preliminary study was to ascertain whether a change in disc structure and fibre bundle orientation could be detected.

Visualisation of the bundles structure between insertions in the cranial and caudal vertebrae is complicated by the circumferential and axial curvatures of the disc. To enable the orientation of the bundles to be viewed between their insertions, a method was devised to extract the bundle structure from individual lamellae.

The 3-D ultrasound data was viewed using a multi-planar slice display. Markers were manually placed within the substance of the two most superficial lamellae to map the contour of the lamellae. Structural detail between markers was resampled using linear interpolation and displayed as a separate image. Put simply, this method enables individual lamellae to be "peeled" from the 3-D volume and visualized. Analysis of the fibre orientation was performed using the Hough transform.

RESULTS AND DISCUSSION

Changes in the internal structure of the AF with compression were clearly evident in acoustic images (Figure 1a, b). The collagen bundle structure from individual lamellae was successfully extracted from the 3-D volumes and displayed as separate images (Figure 1c). Calculated fibre angles from the fours disc specimens in an uncompressed state varied between 40-50º to the spinal axis; much lower than that reported in previous studies (60-65º; Marchand and Ahmed, 1990). This discrepancy may have arisen if the 3-D volumes have not been corrected to give anatomically accurate dimensions of the disc. After compression, fibres tended to become orientated more horizontally, as predicted by McNally and Arridge, 1995).

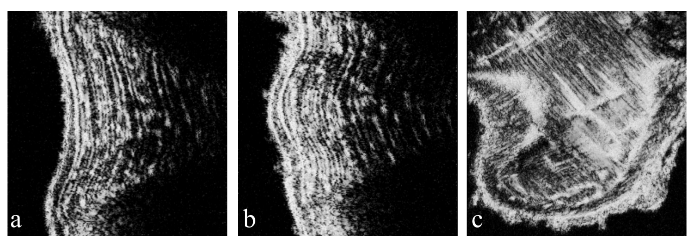

Figure 1: Sagittal views of a disc (a) uncompressed and (b) compressed. (c) Collagen bundle structure from a single lamella "peeled" from the 3-D volume.

SUMMARY

Analysis of fibre orientation was performed using a novel non-destructive technique involving 3-D SAM. Visualisation of collagen bundle structure within individual lamellae and the relative changes in bundle orientation following mechanical loading, can be observed using this technique. Determination of the precise orientation of the bundles with respect to the spinal axis requires further development. This technique provides information regarding the internal structure and mechanics of discs, and may be used to compliment information obtained through *in vitro* mechanical testing.

REFERENCES

Marchand, F., Ahmed, AM. (1990). *Spine,* **15**, 402-410.
McNally, DS., Arridge, RG. (1995). *J.Biomech,* **28**, 53-68.

EXPERIMENTAL VALIDATION OF A COMPUTATIONAL MODEL OF THE PATELLOFEMORAL JOINT

John J. Elias[1], David R. Wilson[2,3], Robert Adamson[2], Norma J. MacIntyre[3] and Andrew J. Cosgarea[1]

[1]Department of Orthopaedic Surgery, Johns Hopkins University, Baltimore, MD, elias@meric.info
[2]Orthopaedic Biomechanics Lab, Beth Israel Deaconess Medical Center and Harvard Medical School, Boston, MA
[3]Department of Mechanical Engineering and Human Mobility Research Centre, Queens University, Kingston, Ontario

INTRODUCTION

A computational model has been created to help orthopaedic surgeons predict how variations in patellofemoral anatomy and loading conditions influence the pressure applied to the cartilage during computationally simulated functional activities. This study was performed to determine how well this model predicts variations in the patellofemoral force and pressure distributions.

METHODS

Two cadaver knees were flexed from extension to near 90° in a rig that simulated a weight-bearing squat. The patellofemoral force distribution was measured continuously with a pressure sensor (Iscan, Tekscan), and movement of the tibia, femur and patella was tracked with a motion analysis system (PCReflex, Qualisys). Anatomical landmarks were digitized and a mapping procedure was used to determine the force and pressure distribution on the patellar surface through the flexion range (Wilson, 2002). Measurements were made for Q-angles of 0°, 5° and 10°.

Geometric models of each knee were constructed from CT images (Analyze, Mayo Foundation). The Q-angle was varied to simulate each experimental test. The tibia was flexed about the femur in 10º intervals. The patella was flexed, and aligned with the femur by aligning the posterior patella with a parallel surface within the trochlea. A static force analysis of the tibia determined the patella tendon force, which was used to quantify the quadriceps force (Huberti, 1984). For these input forces, the patellofemoral pressure distribution was quantified using the discrete element analysis technique (Elias, 2002). Variations in the total patellofemoral force, the ratio of the force applied to the lateral cartilage to the total force, and the position and magnitude of the medial and lateral pressure peaks were compared to the experimental results. The pressure peaks were normalized by the peak lateral pressure at the deepest flexion angle for a Q-angle of 5° to compare the experimental and computational results.

RESULTS AND DISCUSSION

For the 5° Q-angle, the model predicted force increases over the range of motion of 105% and 69% for knees 1 and 2, respectively, while these changes were measured to be 121% for knee 1 and 65% for knee 2. The model predicted the experimental finding that increasing the Q-angle from 0° to 10° increased the relative force on the lateral compartment (averaged over the flexion range) by 8% to 12%.

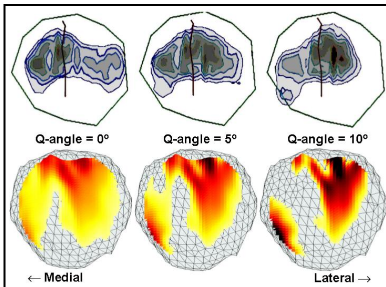

Fig. 1: Measured (top) and predicted (bottom) pressure distribution (flexion = 80°, knee 1).

The model predicted an increase in the peak pressure with flexion, as was found in the experiments. Increasing the Q-angle shifted the area of concentrated contact pressure laterally (Fig. 1) and increased the peak lateral pressure (Fig. 2). Predictions for knee 1 were more accurate than for knee 2.

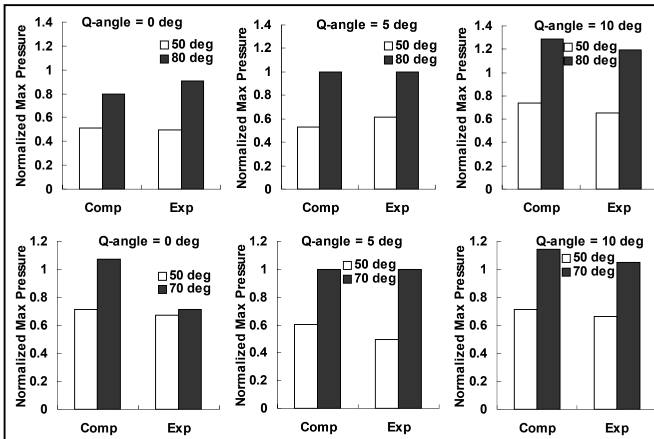

Fig. 2: Variations in the computational (Comp) and experimental (Exp) peak lateral pressure with the flexion angle and Q-angle for knee 1 (top) and knee 2 (bottom).

SUMMARY

The computational model predicted how the patellofemoral force and pressure distributions vary with the flexion angle and Q-angle. This model will allow clinicians to predict how surgical procedures will influence patellofemoral biomechanics for computationally simulated activities.

REFERENCES

Wilson, D.R. et al (2002). *J Biomech*, in press.
Huberti, H.H., et al (1984). *J Orthop Res*, **2**, 49-54.
Elias, J.J., et al (2002). *Transactions of ORS '02*, 896.

ACKNOWLEDGEMENTS

Funding was provided by the Whitaker Foundation, a Bristol-Myer/Squibb/Zimmer Center of Excellence Award, and the Natural Sciences and Engineering Research Council (Canada).

FINITE ELEMENT MODELING AND ANALYSIS OF SINGLE CELL MICROMANIPULATION USING MAGNETIC BEADS

H. Karcher, M.R. Kaazempur-Mofrad and R.D. Kamm
Department of Mechanical Engineering and Division of Bioengineering and Environmental Health
Massachusetts Institute of Technology, Cambridge, MA

INTRODUCTION

The objective of this study is to provide insight in the mechanical reaction of the cell during magnetocytometry experiments (application of a controlled force to a single cell via magnetic microbeads). A computational finite element model is developed to analyze the forcing of one microbead on a cell monolayer and determine the patterns of induced mechanical stress/strain fields. Detailed distribution of displacement and stress fields can then be used to: (i) determine the mechanical properties of the cells, (ii) correlate the localized stress/strain patterns to biological responses of the cell, and finally (iii) offer a simple theoretical model to explain the experimental observations.

MODEL DESCRIPTION

Geometry and Material Properties. The model consists of two parts: the magnetic bead of diameter 4.5µm and the cell monolayer. The cell monolayer is itself composed of (i) a cylinder (20µm high and 60µm wide) accounting for the cytoskeleton and (ii) an infinitely thin plate featuring the membrane and the actin cortex. The model allows for increasing the contact surface between the bead and the membrane. The magnetic bead is modeled as a homogeneous, isotropic elastic (Hook) model with Young' s modulus of E=10,000 Pa and Poisson's ratio of ν=0.30 (McVittie, 2000). The cell membrane and actin cortex are assumed as incompressible homogeneous, isotropic viscoelastic (Maxwell) model with bending stiffness of $D=2.10^{-19}$ N.m and shear viscosity of $\mu=10^{-3}$ dyn.s./cm (Hwang, 1997; Evans, 1983). The cytoskeleton too was modeled as Maxwell model with shear modulus and viscosity of G_C=100 Pa and μ_C = 100 Pa.s. (Yamada, 2000)

Boundary conditions. A zero-displacement is imposed at the bottom surface, i.e. the cell monolayer is fixed to a rigid substrate. No other constraint is imposed on the perimeter of the cell monolayer (free stress). The magnetic forcing on the bead is represented by a 0.5µm displacement imposed in 2s at the center of the bead.

Solution Techniques. A finite element model was developed using a commercially-available software ADINA (Watertown, MA). The mesh consisted of 2016 quadrilateral elements with 31,495 nodes. The thin membrane was modeled with a single layer of nodes and shell elements.

RESULTS AND DISCUSSION

A linear relationship between reaction and displacement at the center of the bead is observed with slope 28pN/µm. It is however possible that a further displacement of the bead gives rise to non-linearity. The stress field appears localized at the vicinity of the bead (cutoff radius of 5-8µm) and dominated by shear stress rather than pressure. The displacement field (see Fig.1) exhibits a pulling/squeezing pattern characteristic of the bead rolling. More interesting is the existence of a zero-displacement zone right below the bead. Work is currently underway to impose a greater displacement to probe the degree of microbead's rolling/translation.

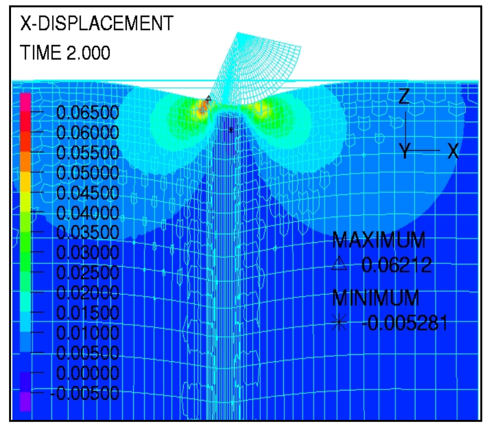

Fig. 1: Displacement field in the x-direction. Cross-sectional view. The displacement is imposed along the x-direction. Only a part of the bead (unfilled light blue line network) is displayed.

SUMMARY

A computational FEM model is developed for the magnetocytometry micromanipulation of the cell. The model provides a robust tool for analysis of detailed strain/stress fields induced in the cell monolayer. Correlation of the computational model and experimental findings promises to shed light on the mechanical properties of the cell and their variation under different mechanical/biological stimulations.

REFERENCES

Evans EA. *Bending elastic modulus of red blood cell membrane derived from buckling instability in micropipet aspiration tests*. Biophysical Journal **43**:27-30, 1983.
Hwang CW and Waugh RE. *Energy of dissociation of lipid bilayer from the membrane skeleton of red blood cells*. Biophysical Journal **72**:2669-2678, 1997.
McVittie A. *Pathways for mechanotransduction in pressurized airway epithelial cells*. S.M. Thesis, Department of Mechanical Engineering, Massachusetts Institute of Technology, 2001.
Yamada S. *et al*. *Mechanics of living cells measured by laser tracking microrheology*. Biophysical Journal **78**:1736-1747, 2000.

THE VARIABILITY OF MAXIMUM VERTICAL JUMPS

Sukhoon Yoon[1] and John H. Challis[2]

[1] Biomechanics/Sports Medicine Lab, The University of Tennessee, Knoxville, Tennessee, USA, syoon1@utk.edu
[2] Biomechanics Laboratory, Department of Kinesiology, The Pennsylvania State University, University Park, Pennsylvania, USA

INTRODUCTION

The kinematics and kinetics of maximum vertical jumps have been the subject matter of a large number of studies. However, little attention has been given the variability of the performance of maximum vertical jumps. The purpose of this study was to examine for a group of subjects the variability of a series of maximum vertical jumps. The study analyzed the kinematics and kinetics of the jumps, and computed intra-subject (within-subject) and inter-subject (between-subjects) variability.

METHODS

Ten healthy male subjects (age: 25.3 ± 3.1 years; height: 177.5 ± 5.8 cm; body mass: 73.4 ± 8.5 kg) each performed ten maximum countermovement vertical jumps. Force plate (Type 4080s, Bertec) and kinematic (Pro-Reflex System) data were collected from the initiation of movement until the instant of take-off. From these data resultant joint moments were computed. For each subject and the group data the coefficients of variation (CV; Winter, 1983) were computed for the joint angles, angular velocities, ground reaction forces, and resultant joint moments.

RESULTS

The mean jump height was 0.33 ± 0.072 m; the mean CV for the subject in jump height was 5.1 ± 2.7%. The intra- and inter-subject joint angle and angular velocity profiles all showed low variability (Table 1), with the trend, seen throughout these results, that the intra-subject variability was lower than the inter-subject variability.

Table 1: The mean (± standard deviation) of the coefficients of variation for the intra-subject and inter-subject joint angle and angular velocity profiles for the vertical jumps.

Joint	Joint Angle		Joint Angular Velocity	
	Intra-Subject	Inter-Subject	Intra-Subject	Inter-Subject
Ankle	2.3 % ± 0.7	6.9 %	13.4 % ± 4.2	20.2 %
Knee	4.1 % ± 1.4	9.7 %	12.6 % ± 3.5	23.2 %
Hip	4.3 % ± 1.0	8.1 %	11.7 % ± 2.3	20.7 %

The horizontal ground reaction force profiles were produced with larger relative variability than the vertical forces (Table 2). The mean peak horizontal ground reaction force was 2.2 ± 0.3 $N.kg^{-1}$, which is much smaller than the mean of the peak vertical ground reaction force for all subjects that was 22.8 ± 2.6 $N \cdot kg^{-1}$, where the ground reaction force data have been normalized with respect to each subject's body mass.

Table 2: The mean (± standard deviation) of the coefficients of variation for the intra-subject and inter-subject ground reaction force profiles for the vertical jumps.

Ground Reaction Force	Intra-Subject	Inter-Subject
Horizontal	40.9 % ± 9.8	84.0 %
Vertical	8.3 % ± 1.9	19.0 %

The resultant joint moment profiles all showed the lowest variability at the knee joint followed by ankle and hip joints (Table 3). This trend was consistent across all subjects, and for the inter-subject data. The variability of the support moment (sum of all extensor moments) was very similar to that of the ankle joint.

Table 3: The mean (± standard deviation) of the coefficients of variation for the intra-subject and inter-subject resultant joint moments for the vertical jumps.

Joint	Intra-Subject	Inter-Subject
Ankle	14.8 % ± 2.3	28.1 %
Knee	12.7 % ± 1.9	25.7 %
Hip	20.6 % ± 4.3	36.9 %
Support	15.0 % ± 2.1	28.8 %

DISCUSSION

Vertical jumping has received considerable attention in experimental and modeling studies. This study addressed the variability of maximum vertical jumps. The data from this study were contrasted to data on the variability of human gait and running (Winter, 1983, 1991). The jumping task had much lower variability, it is hypothesized that this lower variability was due the maximal nature of the task, and/or because jumping has a relatively invariant movement pattern.

This study has investigated the variability of the kinematics and kinetics of maximal vertical jumps. It has demonstrated that for this maximal task, the jumps are produced very consistently both intra- and inter-subject. It would be interesting to see if this trend exists for the other maximal tasks. The study provides guidance for design of studies of jumping, as the low variability of all measures vindicates those studies that select only one trial from a sequence of trials for detailed analysis

REFERENCES

Winter, D.A. (1983). *J. Biomech.,* **16**, 91-97.
Winter, D.A. (1991). *Biomechanics and Motor Control of Human Gait: Normal, Elderly, and Pathological.* Waterloo: University of Waterloo Press.

CALIBRATION OF KINEMATIC MODELS FOR MOTION CAPTURE

Iain W. Charlton, Paul Tate, Paul Smyth and Lasse Roren

Vicon Motion System Ltd, 14 Minns Business Park, West Way, Oxford, UK, OX2 0JB
www.vicon.com

INTRODUCTION

In the past, the measurement of human kinematics through marker based motion capture has relied on relationships between marker triads (technical – anatomical calibration, Williams *et el*., 1996, Murray, 1999). Furthermore, knowledge of the constraints provided by the skeleton has only been utilized recently (global optimisation, Lu and O'Conner, 1999). Such constrained models are sensitive to estimates of the joint centres, segment lengths and marker locations. The use of statistical information in marker position and joint locations is also rarely used to contribute to the overall quality *and confidence measure* in estimated kinematic data.

We present a method for utilising generalised kinematic models of the skeleton and optimising the parameters using confidence measures in both the initial and the improved estimate based on the range of movement measured.

METHODS

A parameterised lower limb skeletal model was used, containing joint locations, joint types, segment lengths and marker locations on the various segments. Data was captured at 120Hz over 4 seconds from a single subject performing a relatively large range of motion with the legs.

Using standard algorithms, the model markers were fitted to measured marker data by minimising the Mahalonobis distance (statistical measure) in the error between model and measured marker co-ordinates for each time frame.

Calibration of the skeletal model was then performed by optimising the locations of markers, joint centres and segment lengths. This was done by minimising the Mahalonobis distance in marker error for a number of time frames simultaneously as a function of the skeleton model parameters. This was augmented by minimising the Mahalonobis distance in the difference between the original and predicted model parameters. A-priori estimates of the covariance in model marker locations and other model parameters were used in the calculation of Mahalonobis distances in both cases. A standard Levenberg – Marquardt algorithm was used to solve these equations.
Following each calibration step, a new kinematic fit was performed and the whole process repeated until a suitable convergence criterion in fit residual was met.

RESULTS AND DISCUSSION

The RMS fit residual for the initial model was 29.3mm, which rapidly reduced to 2mm after 3 iterations of the calibration procedure. Little improvement in the residual took place subsequently (Figure 1). Several discontinuities in the joint angles were also removed by the calibration process.

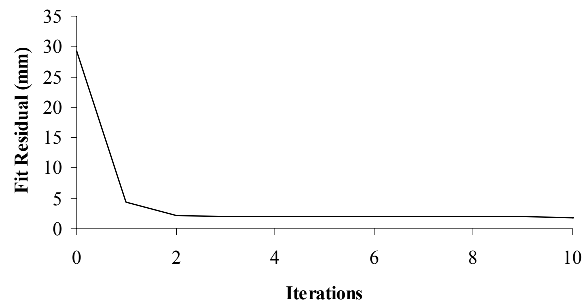

Figure 1: RMS residual in fit during the calibration process.

SUMMARY

A method is presented for optimising generalised skeletal models, which accounts for confidence in the model accuracy. Also, the nature of the kinematic models is divorced from the calibration process, allowing varying complexity and different types of model to be used.

Convergence of the calibration algorithm to an order of magnitude less than the fit residual is rapid. Furthermore, confidence in the optimised model parameters is available retrospectively, allowing quick assessment of the suitability of captured data for the calibration process.

REFERENCES

Lu, T.W and O'Connor, J.J. (1999). *J. Biomech*, **32**, 129-134.
Murray, I.A. (1999) Determining upper limb kinematics and dynamics during everyday tasks. Ph.D. Thesis, Newcaslte University, UK.
Williams, J.R., Leardini, A., & Catani, F. (1996). *Proc. Meeting of the British Orthopaedic Research Society, Oswestry, UK.*

BIOMECHANICAL DIFFERENCES OF FALL ARREST USING THE UPPER EXTREMITY DUE TO AGING

Kyu-Jung Kim, Ph.D.[1], James A. Ashton-Miller, Ph.D.[2]

[1]Department of Mechanical Engineering, University of Wisconsin-Milwaukee, Milwaukee, WI, USA, kimk2@uwm.edu
[2]Department of Mechanical Engineering and Applied Mechanics, University of Michigan, Ann Arbor, MI, USA

INTRODUCTION

Falls impose significant threats to the health of older adults. Especially, fractures of the upper limb account for approximately one third of total osteoporotic fractures. A great majority of the upper limb fractures occur as a result of using the upper extremity to break a forward or backward fall and a subsequent direct impact of the fractured site. Earlier epidemiology and clinical studies failed to incorporate the aspects of the faller's activities during falling. It is unclear whether a specific age group of fallers who experience upper limb fractures has some characteristic body reactions during the fall incidence.

METHODS

Ten old males were volunteered to participate (Mean: age = 66.4 years). Ten healthy young males with matched height and weight were also volunteered as a control group (Mean: age = 24.1 years). A subject wearing a safety harness was standing on a narrow platform. Four different distances between the base of the platform and the wall-mounted force plate were maintained at 40 cm, 60 cm, 80 cm, and 100 cm, respectively. Two different types of falling mode were repeated three times at each distance. With hands down, a subject voluntarily initiated the forward lean at the comfortable speed and broke the fall by putting the hands on the force plates (self-initiated falls). With hands down, a subject was leaning forward at 10 degrees vertically into the lean control cable. The cable was released after a random time delay (0~5 sec) and the subject broke the fall by the same way above (cable-released falls). The 3-dimentional positions of the markers at each joint in the upper extremity were recorded at 300 Hz using an optoelectronic motion analysis system. The impact forces on the hand were simultaneously recorded. To test the effects of fall distance, age, or falling mode on the impact force and joint kinematics parameters, fully-factorial multiple analysis-of-variance (ANOVA) was conducted.

RESULTS AND DISCUSSION

The measured impact force demonstrated a characteristic bimodal pattern with two distinct impact (F_1) and braking (F_2) peaks (Chiu 1998, Kim 2001). The fall impact conditions were moderate compared to the reported fracture loading (Table 1). From the ANOVA, the falling distance showed statistically significant effects on all the impact force and timing parameters ($p<0.05$) except for the peak impact time ($p=0.846$). The age effect was demonstrated in the timing parameters ($p<0.04$). Similar results were obtained from the ANOVA for the joint kinematic parameters. The falling distance affected all the kinematic parameters ($p<0.0005$). The age effect was noted in the wrist and elbow joint angles at touchdown ($p<0.0005$). The old adults (OA) tended to extend their wrists less but extend their elbows more at touchdown than the young adults (YA) or have more outstretched arms

The falling mode (self-initiated vs. cable-released) had another major effects on all the parameters from the ANOVA ($p<0.018$), except again for the peak impact time ($p=0.189$). The OA showed more dramatic differences in their performance between the two different types of falling. Especially, at closer positions (40 or 60 cm), the OA had a 10 to 15 times higher peak impact force ($p<0.05$ from post hoc t-tests) and a 3~4 times shorter peak braking time ($p<0.05$) in cable-released falls. Subsequently, the joint kinematic parameters were significantly different between the two types of falling mode at those positions ($p<0.02$).

SUMMARY

Though having similar physical capabilities of successfully arresting falls, the OA demonstrated more detrimental impact and kinematics conditions under the circumstance with limited available reaction time.

Table 1. Peak impact (F_1) and peak braking forces (F_2), and corresponding occurrence times after touchdown (T_1 and T_2, respectively) for cable-released falls. (Mean±S.D.).

Distance	Group	F_1 [BW]	F_2 [BW]	T_1 [msec]	T_2 [msec]
40 cm	YA	0.25±0.13	0.23±0.07	34±10	153±29
	OA	0.43±0.19*	0.24±0.05	39±13	110±28
60 cm	YA	0.29±0.18	0.29±0.05	36±12	185±66
	OA	0.28±0.14†	0.26±0.04	46±17	170±49
80 cm	YA	0.32±0.19	0.35±0.06	47±24	191±78
	OA	0.20±0.17	0.31±0.04	43±27	204±76
100 cm	YA	0.42±0.28	0.42±0.05	39±17	143±46
	OA	0.31±0.23	0.37±0.04	46±30	168±34

* Statistical age group difference on post hoc t-test ($p<0.05$; $p=0.08$†).

REFERENCES

Kim, K. J. et el (2001). *ASME BED* **50**, 271-272
Chiu, J., Robinovitch, S. N. (1998). *J. Biomech*, **31,**1169-1176

THE FORCE-VELOCITY RELATION STUDIED WITH A PNEUMATIC LEG-EXTENSION DEVICE

F Borg, M Herrala
Jyväskylä University/Chydenius Institute, Kokkola, Finland

INTRODUCTION

The purpose of the present study was to find out whether a simple Hill-modell for the muscle could be useful for understanding the results obtained using an off-the-shelf pneumatic leg extension exercise machine (non-isokinetic).

MATHEMATICAL MODEL

We use one of the simplest versions of the Hill-modell as described e.g. by W Herzog (1995). Accordingly the force-velocity relationship may be written as

(1) $$\frac{v}{v_0} = \frac{1-\frac{F}{F_0}}{1+c\frac{F}{F_0}} \qquad \frac{F}{F_0} = \frac{1-\frac{v}{v_0}}{1+c\frac{v}{v_0}}$$

where F_0 is the isometric maximum force, and v_0 is the maximum contraction velocity. We have only one parameter c, the so called *shape parameter*. Generally, a higher value for c suggests a muscle with a higher proportion of fast twitch fibers. Using the scaled variables $u = v/v_0$ and $f = F/F_0$ the force-velocity relation describes a symmetric curve. From this one sees that the power $P = Fv$ attains its maximum at the midpoint of the curve for which

(2) $$u = f = \frac{\sqrt{1+c}-1}{c}$$

Nigg and v. d. Bogert (1995) quote a typical value around $c = 2.5$ for the shape parameter which corresponds to a maximum power output at velocity $v = 0.35\ v_0$ and force $F = 0.35\ F_0$.

METHODS

A pneumatic resistance machine (HUR Co, www.hur.fi) was used for recording MVC leg extensions employing varying resistance levels (2 to 8 bars). An inclinometer measures the angle of the lever (a measure of the joint angle) and a force transducer measures the torque exerted by the lower leg. Also isometric tests were performed in order to obtain the maximum isometric force. If we map the maximum torque versus maximum angular velocity for the tests we get points that generally lie quite close to a downsloping line as expected from the force-velocity relation. The shape parameter c for each subject was calculated by solving (2) for c by setting $f =$ TQp/TQ0, where TQp is the torque measured at maximum power output and TQ0 is the isometric maximum. Since c is quite sensitive to the variations in the f we get a quite high variation in c between individuals. However, using a data set provided by Raimo Kuhanen (Kultu, Research Institute of Exercise Medicine) comprising 25 subjects, we were able to do some statistics.

RESULTS AND DISCUSSION

Measurements from 25 male (semipro hockey team) were analyzed (right leg). Computing the shape parameter as described above we obtained an average value of 3.04 ± 2.23. The average of the scaled torque (which is the same as scaled force) TQp/TQ0 was 0.35 ± 0.06 which may be compared to the quoted value of 0.35; i.e., $c = 2.5$. The maximum velocity VEL0 measured at the lowest load is naturally an under-estimate of the true maximum velocity. From the average velocity at maximum power, VELp, which was found to be 410 deg/s (7.16 rad/s), we can estimate the average of the maximum velocity v_0 as VELp/0.35 = 1170 deg/s (20.4 rad/s), which is about 0.66 m/s for a quadriceps muscle assuming a moment radius of 3.3 cm. Above we have neglected the muscle length factor. More accurate results could likely be obtained taking this into account, but as a first approximation (1) will do as the joint angle region for maximum power were quite similar for all subjects. An interesting observation is that if we fit a straight line (which works quite well)

(3) $$TQ = a \cdot VEL + b$$

to the measured torques and velocities (a straight line approximation of the force-velocity curve) it is found that the a and b parameters are strongly correlated. This can be easily explained on the basis of (1) if we suppose that (3) is close to a tangent to the curve (1). Indeed, (1) would then predict a relationship

(4) $$a = -\frac{1}{v}b + \frac{F}{v}$$

where v is the velocity and F the force at the tangent point. Indeed, when we calculated the averages of 1/VEL and TQ/VEL for the 3 bar resistance level tests we got 0.00238 s/deg and 0.255 N m s/deg respectively, to be compared with the regression line $a = -0.00238\ b + 0.258$ for the a and b parameters of the test group (correlation coefficient being -.80).

SUMMARY

Our cursory study shows that the simple Hill-modell (1) can help explain some important features of the data obtained with the pneumatic leg extension machine and thus suggests future comparisions with more detailed models.

REFERENCES

Herzog W. (1995). Muscle. *Biomechanics of the Musculo-skeletal System* (eds Nigg B. M., Herzog W.). Wiley. p. 173.

Nigg B. M., van den Bogert A. J. (1995). Simulation. (Ibidem.) p. 561.

EFFECT OF A COMPRESSIVE FOLLOWER LOAD AND A TENSILE FORCE ON INTRADISCAL PRESSURE AND INTERSEGMENTAL ROTATION OF THE LUMBAR SPINE

Hans-Joachim Wilke[1], Antonius Rohlmann[2], Sylvia Neller[1], Georg Bergmann[2], Lutz Claes[1]

[1]Dept. of Orthopaedic Research and Biomechanics, University of Ulm, Ulm, Germany, hans-joachim.wilke@medizin.uni-ulm.de
[2]Biomechanics Laboratory, University Hospital Benjamin Franklin, Free University of Berlin, Germany, rohlmann@biomechanik.de

INTRODUCTION

Various loading conditions are used for investigations on the spine. This makes a comparison of different studies difficult. Pure moments in the three anatomical main planes have the great advantage that all spine levels are exposed to the same constant load.
Patwardhan et al. (1999) introduced a follower load which stabilizes the spine considerably. A follower load is a compressive load applied along a follower load path that approximates the tangent to a curve of the lumbar spine, thus subjecting the whole lumbar spine to nearly pure compression. Loading the spine in tension is difficult to realize in normal life since muscle forces will prevent this. However, passive traction may be possible in the operating theatre under anesthesia. The behavior of a disc under axial tension is not fully understood.
The aim of this study was to determine the influence of a follower load up to 280 N and an axial tensile load up to 240 N on intradiscal pressure and intersegmental motion of the lumbar spine.

MATERIAL AND METHODS

Ten fresh-frozen, human cadaveric lumbar spines were tested. All soft tissue was removed, leaving the capsules, ligaments, and other supporting structures intact. Biomechanical testing was performed in a spine loading apparatus (Wilke et al., 1994). The specimens were stepwise loaded and unloaded with a follower load of up to 280 N with steps of 20 to 30 N and then with an axial tensile force of up to 240 N with steps of 10 to 20 N. This loading procedure was performed twice. During the first loading only translation but no angular motion of the upper vertebra was allowed, while during the second loading unconstraint motion of the upper vertebra was possible.
The compressive follower load was applied to the specimens using a cable and dead weights. The cable was passed through the center above of the cranial L1 vertebral endplate and guided through eyelets fixed laterally on both sides in the middle of the a.p. diameter of each vertebral body. Thus the load path followed the curvature of the lumbar spine in the sagittal plane. Because the cable guides moved with the vertebrae, the load path approximated the tangent to the spinal curve also when the spine was deformed under loading (Rohlmann et al, 2001).
Intradiscal pressure was measured in each disc by flexible pressure transducers. They had a constant diameter of 1.2 mm. Intersegmental motion was measured simultaneously at each level using an ultrasound based 3D motion analysis system. This system was fixed to the frame of the spine tester and to each mobile segment of the specimen.

RESULTS

Intradiscal pressure increased nearly linearly at all levels with increasing follower load. For an axial tensile force up to about 100 N the pressure changes as function of the force were nearly the same as during compression. For higher tensile forces the pressure changes were only small. The different disc levels showed the same tendency, however, the maximum pressure was higher for the upper than the lower levels. Constraining angular motion of the L1 vertebra had only a minor influence on intradiscal pressure.
The deformation of the specimens due to a follower load was relatively small in the case where the L1 vertebra could rotate freely. It occurred mainly in the sagittal plane. For a follower load of 280 N the average total angle in that plane was about 5.5° and for the tensile force of 240 N it was around 4.5°. The lordotic curvature of the specimens decreased for both loading cases. A follower load caused nearly the same angular motion changes at all levels while a tensile force led to higher deformations in the lower than in the upper lumbar spine. The interspecimen differences were high, especially at the levels L3-L4 and L4-L5. When angular motion of the L1 vertebra was constrained, the deformation of the specimens was negligible.

DISCUSSION

The results of this study with a follower load are in agreement with those of previous studies (Rohlmann et al, 2001, Patwardhan et al, 1999). An axial tensile force of up to 100 N led to nearly the same relative intradiscal pressure changes as a reduction of 100 N follower load to the unloaded state. A further increase of the axial tensile force had only a slight effect on intradiscal pressure. For both, follower load and axial tensile load, the deformations of the specimens were similar. The specimens were straightened and their lordotic curvature decreases. In the case of follower load the cable guides on the lateral side of the vertebra were responsible for this straightening. A vertical compressive load without cable guides would have increased the curvature of the specimens.
Constraining angular motion of the L1 vertebra during loading had only a minor effect on intradiscal pressure but a considerable one on the angular deformation of the specimen. These deformations were relatively small and had therefore obviously only a slight effect on intradiscal pressure.

REFERENCES

Patwardhan, AG. et al (1999) *Spine*, **23**, 537-542
Rohlmann, A. et al (2001) *Spine*, **26**, E557-E561
Wilke HJ et al (1994) *Eur. Spine J.*, **3**, 91-97

PASSIVE STRETCHES PROTECT MUSCLE IN OLD AND YOUNG MICE FROM LENGTHENING CONTRACTION-INDUCED INJURY

Timothy J. Koh[1], Jennifer M. Petersen[2], Francis X. Pizza[2], Susan V. Brooks[1]

[1]Institute of Gerontology, University of Michigan, tjkoh@uic.edu
[2]Department of Kinesiology, University of Toledo

INTRODUCTION

Conditioning with lengthening contractions protects skeletal muscles in young and old animals from subsequent lengthening contraction-induced injury, although muscles in old mice appear to adapt more slowly (McBride et al., 1995;Brooks et al., 2001). Lengthening contractions and associated damage are not required for inducing protection in young mice, as stretches of passive muscle and isometric contractions protect muscle from injury in these mice (Koh and Brooks, 2001). We tested the hypothesis that passive stretches and isometric contractions would also protect muscle in old mice from contraction-induced injury.

METHODS

Extensor digitorum longus (EDL) muscles from young (3 month old) and old (24 month old) mice were subjected *in situ* to lengthening contractions either with or without prior conditioning with passive stretches or isometric contractions (n=7-9 each group). Conditioning was performed using 75 repetitions at 0.25 Hz of either passive stretches of 20% strain relative to optimal muscle fiber length (L_f) or 75 isometric contractions at L_f with stimulation at 150Hz. Two weeks after conditioning, 3 sets of 75 lengthening contractions were performed using strain of 20% Lf initiated 100ms after 150Hz stimulation. Three days after lengthening contractions, maximum isometric force was measured *in situ* and muscles excised for histological analysis. Injury was assessed by the deficit in maximum isometric force (Po) compared to that measured before lengthening contractions. Data were analyzed using two-way analysis of variance.

RESULTS AND DISCUSSION

Mouse mass was significantly greater for old versus young mice ($p < 0.05$), whereas EDL muscle mass, initial Po, and specific Po did not differ significantly, and were virtually identical (Table).

Table. Body mass, EDL muscle mass and Po for young and old mice. Means and standard errors shown. *significantly different from young (p<0.05).

	Young	Old
Body mass (g)	26.4 (0.6)	30.3 (0.6)*
EDL mass (mg)	10.3 (0.2)	10.6 (0.2)
Po (mN)	397 (11)	396 (11)
Specific Po (N/cm^2)	23.4 (0.6)	22.8 (0.6)

Unconditioned muscle from both young and old mice showed large force deficits following the lengthening contraction protocol ($p < 0.05$; Figure). There was a significant effect of conditioning on the force deficit ($p < 0.05$) but no significant effect of age. There was also no significant interaction effect. Post-hoc analysis using the Student-Neumann-Keuls test indicated that only conditioning with passive stretch significantly reduced the force deficit. These results demonstrate that conditioning with passive stretch protects skeletal muscle in both young and old animals from subsequent lengthening contraction-induced injury, with no difference in protection between young and old mice.

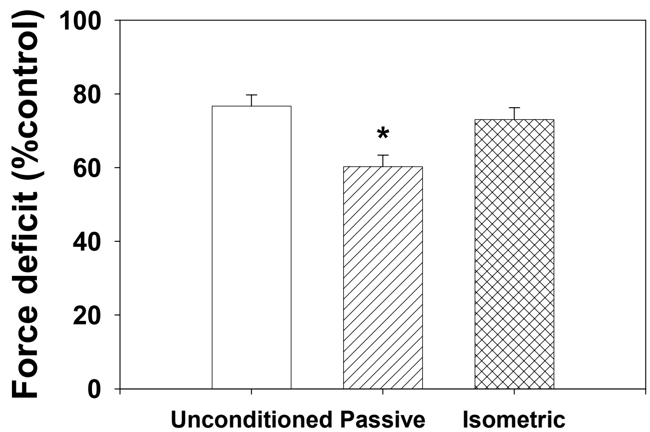

Figure. Force deficits 3 days after 225 lengthening contractions for unconditioned EDL muscles and muscles conditioned with passive stretches or isometric contractions. Data from young and old animals were grouped for this figure. Means and standard errors shown. *significantly different from unconditioned (p<0.05).

SUMMARY

The major finding of this study was that a single bout of passive stretches protected EDL muscles in both young and old animals from subsequent lengthening contraction-induced force deficits. Additional assays of injury including percentage of overtly injured fibers and inflammatory cell involvement are ongoing. The results of this study may have implications for protecting muscle in old individuals from damage.

REFERENCES

Brooks, S.V. et al. (2001). J Gerontol 56, B163-171
Koh, T.J., Brooks, S.V. (2001) Am J Physiol 281, R155-161
McBride, T.A. et al. (1995) Mech Ageing Dev 83, 185-200

ACKNOWLEDGMENTS

This research was supported by NIA AG06157, AG00114.

BLOOD FLOW STRUCTURE CONTRIBUTING TO THE RUPTURE OF CEREBRAL ANEURYSM

Taku Morino[1], Kiyoe Nomura, Takatsugu Yamauchi[2], Kazuo Tanishita[3], Satoshi Tateshima[4], Yuichi Murayama and Fernando Vinuela

[1]Center for Life Science & Technology, Keio University, Yokohama, Japan, taku@2000.jukuin.keio.ac.jp
[2]Core Flow Technologies Inc., Fuchu, Tokyo, Japan
[3]Dept. of System Design Engineering, Keio University, Yokohama, Japan
[4]Dept. of Radiological Sciences, UCLA, Los Angeles, CA, USA

INTRODUCTION

The overall morbidity and mortality for aneurysmal subarachnoid hemorrhage is unacceptably high, even though most cerebral aneurysms do not rupture. The decision to perform preventive treatment for unruptured aneurysms must be based on a prediction of which aneurysms are likely to rupture. However, there are no reliable predictors for rupture now. Ujiie et al. reported that intra-aneurysmal flow was classified into two patterns according to aspect ratio (dome depth/neck width) and one was associated with rupture (1999). We measured detailed flow structure with PIV and LDV in realistic cerebral aneurysm models based on CT images in order to discuss the relationship between rupture and blood flow structure.

METHODS

We built three realistic rigid models of cerebral aneurysm by photoforming method. Model 1 is an unruptured middle cerebral bifurcation aneurysm, model 2 is a ruptured middle cerebral aneurysm, and model 3 is an unruptured basilar tip aneurysm. The flow waveform in the parent arteries was simulated to the physiological pulsatile flow in cerebral arteries. Maximum/mean/minimum Reynold's number was 680/520/410 for model 1 and 2, and 800/430/340 for model 3. Frequency parameter was 6.0 for model 1 and 2, and 5.0 for model 3. We used a laser Doppler velocimeter (LDV) and particle image velocimetry (PIV) for the velocity measurement and estimated wall shear stress.

RESULTS AND DISCUSSION

We found that intra-aneurysmal flow was classified into two patterns according to aspect ratio, which corresponds to Ujiie et al.'s study (1999). One consisted only of single circulating flow in model 1 (Figure 1-a) and 3, the other consisted of circulating flow and recirculating flow in the bleb in model 2 (Figure 1-b). Model 2 is ruptured aneurysm and the flow pattern as in Fig.1-b seems to be associated with rupture.

Figure 2 shows wall shear stress distribution in model 2. The values were extrapolated in order to match with that in human cerebral aneurysms. It had a peak at the bleb ($x^* = 0$). Rupture of cerebral aneurysm occurs preferentially at bleb. Therefore, high wall shear stress might be related to the rupture.

SUMMARY

We measured detailed velocity profiles with PIV and LDV in realistic cerebral aneurysm models based on CT images and also estimated wall shear stress. Physiological pulsatile flow in cerebral arteries was completely simulated in the parent arteries. Intra-aneurysmal flow was classified into two patterns and one seemed associated with aneurysmal rupture. Wall shear stress had a peak at bleb. That implies that cerebral aneurysm ruptures at bleb.

REFERENCES

Ujiie H. et al. (1999). *Neurosurgery45.1, 119-129*

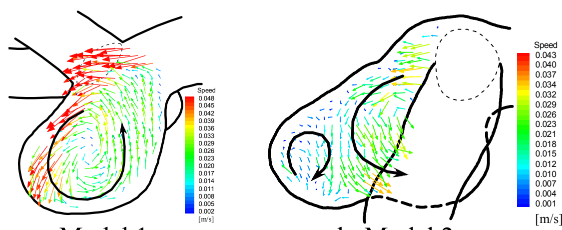

a. Model 1 b. Model 2

Figure 1: Velocity profiles measured with PIV. a, Maximum phase in model 1. b, Minimum phase in model 2.

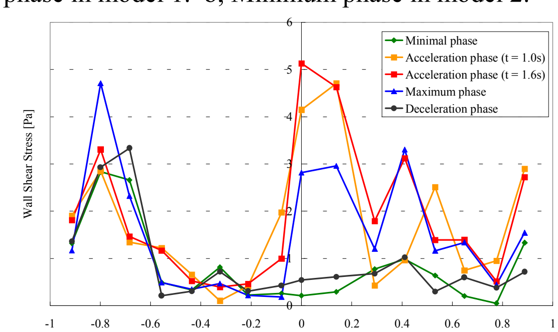

Figure 2: Wall shear stress distribution in model 2. Horizontal axis stands for normalized measurement points. Vertical axis stands for wall shear stress.

ANESTHETIC EFFECTS ON MUSCLE PERFORMANCE

Ronke Olabisi, John Webster, Ron McCabe, David Manthei, Thomas Best

Departments of Biomedical Engineering, Orthopedic Surgery, and Family Medicine
University of Wisconsin, Madison, Wisconsin, USA
Contact: olabisi@surgery.wisc.edu

INTRODUCTION

The effects of two anesthetic protocols on stretch-injured and healthy rabbit skeletal muscle were assessed. The torque-producing capabilities of the tibialis anterior and the extensor digitorum longus muscles were measured at ankle joint angles of 0°, 30°, 60° and 90°. Isometric torque measurements were made at various intervals before and after an eccentric stretch injury to the right leg. One anesthetic protocol utilized an intramuscular injection of ketamine, xylazine and acepromazine; the other anesthetic was inhaled isoflurane. Torque data were obtained under each anesthetic for both healthy and injured legs.

METHODS

The injury system comprises a geared electric motor, a loading frame, a torque sensor, an angular position sensor, a closed loop control system, and disposable electrodes. The nerve stimulator provides a 50 Hz. pulse rate, 0.5-ms pulse width and variable current output.

To stimulate the peroneal nerve, two electrodes were used to direct current through the desired tissues. A small incision distal to the ankle over the dorsum of the foot exposed the TA tendon. The encapsulating fascia was then cut away. Both TA tendons were exposed, the right for the purposes of injury, the left as a sham operation. Once the surgery was complete, the rabbit was situated in the test apparatus such that its right leg was aligned so that the knee joint was at 90º and the foot permitted to follow the physiologic rotation of the ankle joint. An angular displacement of 90 degrees was applied to the ankle joint of an anesthetized rabbit while its hind leg was stabilized, the tibialis anterior tendon shortened, and the peroneal nerve stimulated to consistently produce a stretch injury. All animals were injured at 1.4 cm of tendon pre-shortening and stimulated with 2.8 mA of current. Talocrural joint angles 0, 30, 60 and 90 degrees were obtained in random order for each leg.

All rabbits were tested immediately prior to injury and immediately post injury. They were again tested at 4, 12, 18 and 24 hours post injury, followed by further testing at 3,5, and 7 days. Rabbits 1-5 were anesthetized with 1.5 cc intramuscular injection into the gluteus maximus for a total of 3 ccs of a 3:1:1 ketamine: acepromazine:xylazine; redoses were 1 cc of ketamine as needed. Rabbits 6-10 were anesthetized with 3-5% isoflurane per 1.5-2 L O_2.

RESULTS AND DISCUSSION

In the first set (rabbits 1-5), considerable time was required for the rabbits to recover from the intramuscular anesthetic, and the testing schedule on day 1 proved to be particularly stressful to the animals. Rabbit 4 died under initial injection. Rabbit 1 showed extreme sensitivity after Day 1 and could not be stimulated via surface stimulation. Under direct neural stimulation the muscle would not contract and the animal was sacrificed on Day 3 with an assumed neuropathy. Rabbit 2 showed similar sensitivity on Day 3 and no data were obtained on subsequent days. On Days 5 and 7, Rabbit 2 could tolerate stimulation although very low torque values were obtained. In each rabbit a steady decline in joint torque was observed for both the injured and sham control legs over the first 24hr with recovery in the following 3 days.

The rabbits anesthetized with isoflurane (Group 2; Rabbits 6-10) recovered from the anesthetic much more rapidly, and hence the testing schedule on day 1 was less stressful. The hypersensitivity demonstrated by the first group of animals was absent in the second group. Unlike the first group, Rabbits 6-10 showed no loss of joint torque in the sham control legs. The torque loss induced in the injured leg recovered in a similar fashion to the animals in Group 1.

SUMMARY

Ketamine has been linked to increased muscle acetylcholinesterase activity (Ingals et al, 1996). Veterinary evidence also links it to neuropathies in certain animals. (Schiffman and Lopez). The high doses required in our protocol appeared to have caused cumulative damage that was irreversible. Thus, it appears that at least for multiple time points of testing, inhalational isoflurane is preferable to intramuscular anesthetic regimens when assessing muscle and joint function.

REFERENCES

Ingals, Christopher P. et al (1996), *J. Applied Physiology*, **80**, 332-340.

Schiffman, Beth, and Lopez, Mandi, (2001), Department of Vetinary Medicine, U of Wisconsin, *Personal correspondence.*

MODELING OF EXTREMAL LOAD ON HUMAN KNEE JOINT LIGAMENTS

I. Ilyin[1], V. Sholukha[1], A. Zinkovsky[1], K.J. van Zwieten[2]

[1]St.Petersburg State Technical University, St.Petersburg, Russia
[2]Limburg University Centre, Diepenbeek, Belgium

INTRODUCTION

In the sport medicine, prosthesis and rehabilitation it is necessary to evaluate the dynamical loads on joint tissues during different motions. Usually, experimental simulators are used. However such experiments require a great deal of time and expense. In contrast the virtual simulators allows relatively quickly and accurate adjusting the model and evaluating dynamical load in the joint components during wide range of desirable motions. The goal of this work was to create the most realistic virtual mechanical model of the knee joint and to perform modeling allowed us to calculate a dynamical load on the main ligaments of the knee during so dangerous for Anterior Cruciate Ligament (ACL) motions, as jump landing and downhill skier backward fall.

METHODS

The mechanical simulator of the knee joint was created using ADAMS™ (Mechanical Dynamics, Inc., Ann Arbor, MI, USA) software. The application of the commercially available software allows us to create a universal tool for investigation loads in the knee joint. The knee model includes femur, fibula, tibia, meniscuses and surrounded soft tissues. Lateral and medial meniscuses are placed on the plateau of the tibia. Their movement is limited by corresponding ligaments. Each femoral condyle was modeled by two merged spheres, as described in (O'Connor J. et al., 1990) for the flat case. The anterior spheres are in contact with the patella implementing sphere-plane contact model, but the posterior spheres are in contact with spherical upper surfaces of the meniscuses. The contact forces are based on the Hertz's model of interaction, including stiffness, damping and friction. The lateral and medial meniscuses and condyles have surface of different curvatures. Therefore such model provides the tibio-femoral internal/external rotation in the joint (Ilyin I. et al, 2001).
The model includes cruciate, collateral and meniscus ligaments as well as patellar tendon. Each ligament or tendon was simulated by several nonlinear springs. The dependencies of force on deformation were obtained by spline approximation of real experimental data obtained in (Woo S. L-Y., D.J. Adams, 1990). All groups of muscles also were simulated by springs and dampers.
The simulator was evaluated in well-explored motion - curtsey, and then was applied for modeling of dynamical loads on cruciate ligaments during landing on heel after jump and during downhill skier backward fall.

RESULTS AND DISCUSSION

As the result of this work the virtual three-dimensional model of the human knee joint was developed, that allows exploring extremal loads in the joint.
The adequacy of this model to the real human knee was demonstrated by modeling the good explored motion - curtsey. The dependences of main ligament tension on the angle of knee flexion were obtained.
The model was applied to numerical modeling of dynamical loads in the knee joint during the landing on the heel after jump on the slippery and not slippery surfaces with different visco-elastic properties. This movement leads to anterior-posterior displacement of the thigh relatively to the shank at the moment of landing that results in tension of cruciate ligaments. It was shown that at the landing on the slippery surface, when the leg slips out under the man, the tensile force of ACL doubles tensile force of posterior cruciate ligament. Such landing on the relatively extended leg can lead to ACL rupture for older persons if the jump is 50 cm high. Then the ACL tension exceeds 1000 N.
The dynamical load on ACL during the downhill skier backward fall was analyzed. The following was revealed:

- During the backward fall the shank moves forward relatively to the thigh. The maximum load on ACL corresponds to maximum horizontal acceleration of the shank, which is achieved at the knee flexion angle equal to 90 degrees.
- Decrease of the angle between top of the ski boot and ground decreases the risk of ACL injury up to 20%.
- Increase of quadriceps contraction during the backward fall proportionally decreases the maximum load on ACL.
- Maximum load on ACL proportionally increases with increase of skier's weight.

Thus, there was developed a universal tool to explore different type of injury-dangerous motions of the knee joint.

REFERENCES

O'Connor, J. et al (1990). *Geometry of the knee. In: Knee Ligaments: structure, function, injury, and repair*, edited by D. Daniel, et al., 163-199.
Woo S. L-Y., D.J. Adams (1990). *The tensile properties of human anterior cruciate ligament (ACL) and ACL graft tissues. In: Knee Ligaments: structure, function, injury, and repair*, edited by D. Daniel, et al., 279-289.
Ilyin I., V. Sholukha, A. Zinkovsky (2001). *Computer modeling of knee joint motion. Proceedings of ISCSB*, Milan, 71-74

EFFECTS OF JOINT ANGLE ON RECOVERY OF TORQUE FOLLOWING MUSCLE STRETCH INURY

Ronke Olabisi, David Corr, Thomas Best

Departments of Biomedical Engineering, Orthopedic Surgery, and Family Medicine
University of Wisconsin, Madison, Wisconsin, USA
Contact: olabisi@surgery.wisc.edu

INTRODUCTION

Measurement of joint torque provides important information about recovery following muscle injury in animal models (Warren et al, 1999). The torque-joint angle profiles for normal and stretch-injured muscle were determined in 6 New Zealand White rabbits. Isometric torque-producing capabilities of the tibialis anterior (TA) and extensor digitorum longus (EDL) muscles were measured at talocrural joint angles of 0°, 30°, 60° and 90° (90° corresponds to full plantar flexion). Torque data were obtained under isoflurane anesthesia at several time points post-injury to determine the effects of joint angle and time post-injury on recovery following a controlled muscle stretch injury (Fig 1-3).

METHODS

The injury system consists of a geared electric motor, a loading frame, a torque sensor, an angular position sensor, a closed loop control system, and disposable electrodes. The nerve stimulator provides a 50 Hz. pulse rate, 0.5-ms pulse width and variable current output.

The animals were anesthetized with 3-5% isoflurane/1.5-2 L O_2. A current-driven surface neural stimulation system was designed and fabricated to produce TA muscle tetany. This non-invasive system provides reproducible and consistent stimulation of the TA without co-contraction of the antagonist hamstrings. Prior to muscle stimulation, the TA tendon was pre-shortened 1.4cm with a customized tendon-shortening device. An angular displacement of 90 degrees was then applied to the ankle joint while the peroneal nerve was simultaneously stimulated to produce a stretch injury at the TA myotendinous junction. Pilot testing demonstrated an order effect, thus the angle order (0, 30, 60, 90 deg) was kept the same through experiments on all 6 animals.

All rabbits were tested immediately prior to injury and immediately post injury. They were again tested at 4, 12, 18 and 24 hours post injury, followed by further evaluation at 3,5, and 7 days. Data are plotted as Mean +/- SEM (Figs 1-3).

RESULTS AND DISCUSSION

Torque deficits were most apparent at the intermediate angles (30° and 60°) compared with 0° and 90° (Figs 1 and 2). The magnitude of change in joint torque was largest in the first 24hr after injury (Figs 1 and 2). There was a noticeable torque deficit at all joint angles in the control leg immediately following injury (Fig 3).

Fig 1. Torque vs. Angle over Time post Injury (Injured leg)

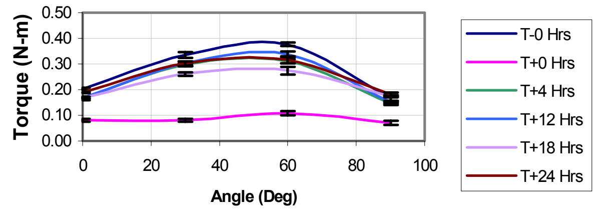

Fig 2. Torque vs. Angle over Time post Injury (Injured Leg)

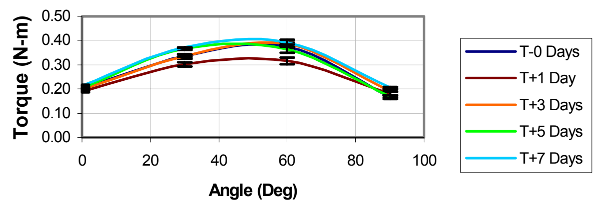

Fig 3. Torque vs. Angle over Time (Control Leg)

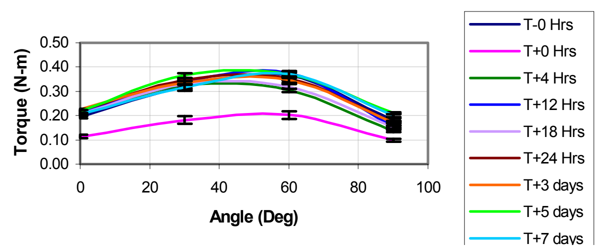

SUMMARY

There appears to be a continual decline in muscle performance in the first 24hr following stretch injury. However, a less severe deficit was also observed in the control leg immediately post injury that may reflect a host defense response, or perhaps an anesthetic effect. Loss in muscle performance following injury also appears to be effected by joint angle. Together, these findings may suggest early intervention to prevent the initial loss of muscle strength following stretch injury.

REFERENCES

Warren GL (1999), *Sports Med* **27**(1), 43-59.

CONTRIBUTION OF MONO- AND BIARTICULAR MUSCLES TO EXTENDING KNEE JOINT MOMENTS IN RUNNERS AND CYCLISTS

Hans H.C.M. Savelberg and Sigrid Braspenning
Department of Human Movement Sciences, Nutrition and Toxicology Research Institute Maastricht, Maastricht University, The Netherlands. hans.savelberg@bw.unimaas.nl

INTRODUCTION

Generally differences in muscle properties, due to training, ageing or genetic predisposition, are studied by measuring maximal joint moments. For several reasons this approach gives limited information. Firstly, differences or adaptation in numbers of sarcomeres in series are neglected. To understand dynamic behaviour this knowledge is essential [Lieber and Fridén, 2000]. Secondly, this approach neglects that generally several muscles contribute to a joint moment. Moreover, control of the direction and magnitude of an external force requires tuning of the recruitment of mono- and biarticular [ant]agonists [Van Ingen Schenau *et al.*, 1992]. Consequently, adaptation of individual muscles to different movements are not uniquely represented by the maximal joint moment. In this study it is hypothesized that in all involved muscles functional differences or adaptations will exist for movements requiring different control of external force, *i.c.* cycling and running. It is expected that these adaptations are not independent. Also maximal joint moment will not be a sufficient measure to monitor this kind of differences.

METHODS

On a dynamometer ten runners [>20km/wk] and ten cyclists [>100km\wk] performed voluntary maximal, isometric knee extensions at twenty different combinations of knee [0 30 60 85 110degrees] and hip joint angles [0 40 70 100degrees]. The active knee joint moment was assessed. A model was used to determine RF length for each hip/knee joint combination [Hawkins and Hull, 1991]. This set up allowed to calculate changed contributions of both biarticular RF and monoarticular vasti to the knee joint moment [Herzog *et al.*, 1991].

RESULTS

No difference in maximal knee joint moment was found. However, the range of joint moments registered for the runners was smaller than for the cyclists, indicating that the runners had a flatter curve. Also the cyclists reached the maximal joint moment at more flexed knee joint angles. The latter was reflected in the knee joint angle at which the vasti contribute maximally: for runners this occurred at 74 degrees for the cyclists at 81 degrees [Figure 1]. Also the increase in joint moment contribution by the vasti in the studied knee joint range was larger for the cyclists than the runners. For the RF no significant differences between both groups were found. It seems that the range of joint angles studied coincided with the ascending part of the force-length curve of the RF for the runners and the top of the curve for the cyclists [Figure 2].

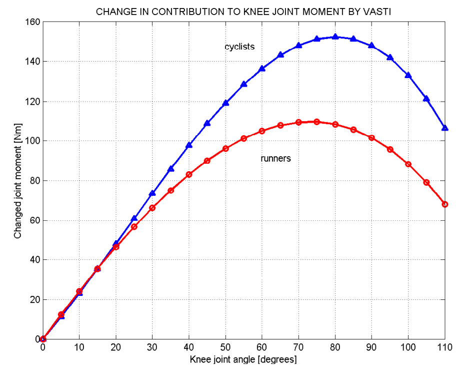

Figure 1: Change in contribution of vasti to knee extending moment as a function of knee joint angles for cyclist [triangles] and runners [circles]

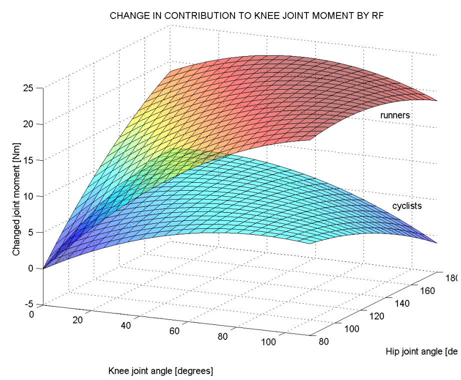

Figure 2: Change in contribution of the RF to knee extending moment as a function of knee and hip joint angles for cyclists [lower surface] and runners [upper surface].

DISCUSSION

This study showed that differences in properties of mono- and biarticular knee joint extensors underlie similar maximal knee joint moment. For runners the optimal length of RF occurs to be larger than for cyclists, this might represent a larger number of sarcomeres in series [Herzog *et al.,* 1991]. The difference in optimal vasti length cannot unequivocally be addressed to the number of sarcomeres, alternatively it can be explained by a shift in maximal force ratios between the three heads of vasti. When knee and hip joint angle patterns for cyclists and runners are compared to the moment-angle diagrams, it occurs that cyclist use their vasti around optimal length, while runners operate on the lower part of the ascending limb. Both groups use their RF around optimal length. These different properties will lead to different ratios between both muscle groups in runners and cyclists. Since tuning between mono- and biarticular muscles affects direction of external force, it can be suggested that these different properties affect the co-ordination.

REFERENCES

Hawkins,D., Hull, M.L. [1991]. *J.Biomech.* **23**: 487-494.
Herzog, W. *et al.* [1991]. *Med.Sci.SportsExer.*, **23**: 1289-1296.
Lieber, R.L., Fridén, J. [2000]. *Muscle Nerve*, **23**: 1647-1666.
Van Ingen Schenau, G.J. *et al.* [1992]. *Neurosci.*, **46**: 197-207.

DISCOLIGAMENTOUS STRUCTURES OF THE LOWER CERVICAL SPINE GET INJURED IN *IN VITRO* LOW-SPEED SIDE COLLISIONS

Hans-Joachim Wilke[1], Annette Kettler[1], Markus Schultheiß[2], Lothar Kinzl[2], Lutz Claes[1], Erich Hartwig[2]

[1]Institute of Orthopaedic Research and Biomechanics, University of Ulm, Helmholtzstr. 14, D-89081 Ulm,
Tel.: ++49 (0)731/50023482, Fax.: ++49 (0)731/50023498, e-mail: : hans-joachim.wilke@medizin.uni-ulm.de
[2]Department of Trauma-, Hand- and Reconstructive Surgery, University of Ulm, Steinhövelstr. 9, D-89075 Ulm

INTRODUCTION

The role of ligamentous structures of the upper cervical spine in whiplash injury is still controversially discussed. Especially the alar ligaments are often deemed to be responsible for long lasting clinical symptoms. These ligaments protect the upper cervical spine against excessive lateral bending and axial rotation movements, which mainly occur in side collisions. The objective of the present in vitro-study therefore was to examine whether the alar ligaments or any other structures of the cervical spine are damaged in side collisions.

METHODS

An acceleration apparatus was designed, which allows acceleration of cadaveric cervical spine specimens in any desired direction. Its basic components are a pneumatic acceleration unit, a sled and a railtrack, which is 9m in length.

On the sled the cervical spine specimens are fixed on a damped pivot table, which is allowed to tilt passively around an axis, which is aligned perpendicular to the direction of the acceleration. This damped pivoting movement accounts for the passive movements of the trunk during collision.

In order to guaranty adequate inertia, a dummy head was designed with a weight of 4.5kg. It can easily be mounted on the occiput of the cadaveric specimens. On the sled, before acceleration, this dummy head is suspended with a suspension cord, which is cut t_0 in order to allow the head to move completely unconstrained and to ensure physiological loading of the specimens.

Six human osteoligamentous cervical spine specimens (occiput to T1) were subjected to incremental 90°-side collision from the right without head contact beginning with 1g, followed by 2g, 3g, 4g, ... until structural failure occurred.

For quantification of functional injuries, the three-dimensional flexibility of each single segment of the specimens was tested in a spine tester before and after each acceleration.

RESULTS

The sled acceleration pulses always had a duration of about 125ms. During the "1g"-collision, the maximum sled acceleration was in median 1.3g, during the "2g"-collision 2.4g and during the "3g"-collision 3.8g whereas the maximum resultant head acceleration was always nearly two-fold higher. Integration of the filtered accelerometer data resulted in a velocity change •v of the sled of 4.3 km/h in the 1g-collision, 8.1 km/h in the 2g-collision and 12.5 km/h in the 3g-collision.

In all six specimens structural failure always occurred in the lower cervical spine and always affected the left facet joint capsules and the intervertebral discs. In four specimens this damage occurred during the 2g-collision, in one during 3g's and in one during 4g's.

The flexibility of the specimens mainly increased in the lower cervical spine in lateral bending and to a minor extend in axial rotation. In flexion and extension almost no destabilizing effect could be observed.

DISCUSSION

Low-speed side-collisions mainly seemed to stress discoligamentous structures of the lower cervical spine. The upper and middle cervical spine including the alar ligaments might have been less stressed since the bending moment arising from the weight of the head increases towards the lower segments.

Since the effect of muscle forces could not have been taken into account, the present in vitro study has to be deemed a "worst case scenario". The measured critical sled acceleration of 2g to 4g until structural failure can therefore not directly be transferred to reality. However, clinically the lower cervical spine also seems to be more often affected by whiplash than the upper and middle cervical spine.

CONCLUSION

In vitro low-speed side collisions caused functional and structural injury to discoligamentous structures of the lower cervical spine but not to the alar ligaments.

ACKNOWLEDGEMENTS

This work was supported by the Deutsche Forschungsgemeinschaft DFG (HA 3276/1-1) and the University Hospital of Ulm, Germany (P.648).

CROSS-FLOWS ASSOCIATED WITH SHEAR STRESS GRADIENTS ON THE FLOW-ENDOTHELIUM INTERACTION

Wen Wang[1], Yiling Lu[1, 2], Xiyun Lu[2], Kim H Parker[3] and Lixian Zhuang[2]

[1]Medical Engineering Division, Department of Engineering, Queen Mary, University of London, London, UK. wen.wang@qmul.ac.uk
[2]Department of Mechanics and Mechanical Engineering, University of Science and Technology of China, Hefei, China
[3]Department of Bioengineering, Imperial College of Science, Technology and Medicine, London SW7 2BY, UK

INTRODUCTION

Vascular endothelial cells respond to fluid shear stress in a variety of ways (e.g. Davies, 1995). The close correlation between the early atherosclerotic lesions and branches of human arterial systems suggests that large gradients of the wall shear stress near arterial branches may play a role in the initiation and development of atherosclerosis. A number of studies have investigated the effects of fluid shear stress gradients on vascular endothelium (e.g. Tardy, *et al.* 1997). This study examines the effects of flows on endothelial cells, focusing on the local flow field near the wall where endothelial cells exist. Emphasis is given to cross-flows associated with shear stress gradients (or fluid accelerations) in the flow direction, and their effects on movement of molecules and biological cells in the fluid to endothelial cells on the boundary wall.

THEORETICAL CONSIDERATIONS

For simplicity, we limit our analysis to two-dimensional flows and use local polar coordinates for any smooth boundaries (shown in Figure 1). Shear stress at any point, e.g. point P, on the wall is

$$\tau_{R\theta} = \mu\left(\frac{1}{R}\frac{\partial V_R}{\partial \theta} + \frac{\partial V_\theta}{\partial R} - \frac{V_\theta}{R}\right)_{Wall}.$$

With no slip boundary conditions, i.e. $V_R \equiv 0, V_\theta \equiv 0$, the wall shear stress gradient in the flow direction

$$G \equiv \frac{\partial \tau_{R\theta}}{R\partial\theta} = \frac{\mu}{R}\left(\frac{\partial^2 V_\theta}{\partial\theta\partial R}\right)_{Wall}.$$

Continuity of fluid gives

$$\frac{\partial V_\theta}{\partial \theta} = -\left(R\frac{\partial V_R}{\partial R} + V_R\right).$$

With no slip conditions, we have

$$\left(\frac{\partial V_R}{\partial R}\right)_{Wall} \equiv 0 \qquad \text{...........(A)}$$

hence, the shear stress gradient

$$G = -\frac{\mu}{R}\left(R\frac{\partial^2 V_R}{\partial R^2}\right)_{Wall}.$$

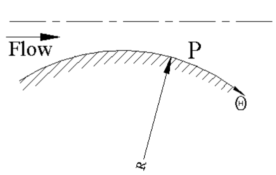

Figure 1. Local polar coordinates for point P on the boundary.

At given θ values, Taylor series of the V_R at point $R+\xi$ are

$$V_R(R+\xi) = V_R(R) + V_R'(R)\xi + \tfrac{1}{2}V_R''(R)\xi^2 + \cdots$$

where $'$ represents the differentiation with respect to the R. Since $V_R = 0$ and $V_R' = 0$ at the wall (from equation A),

$$V_R(R+\xi) = \tfrac{1}{2}V_R''(R)\xi^2 = -\frac{G}{2\mu}\xi^2 \qquad \text{.............(B)}$$

RESULTS AND DISCUSSION

From equation B, we find that near the boundary wall, the cross-flow velocity V_R is proportional to – G. Figure 2 representing a schematic of the cross-flows, indicates that when shear stress gradients are positive (i.e. $G > 0$), there are fluid convections towards the boundary wall, and vice versa.

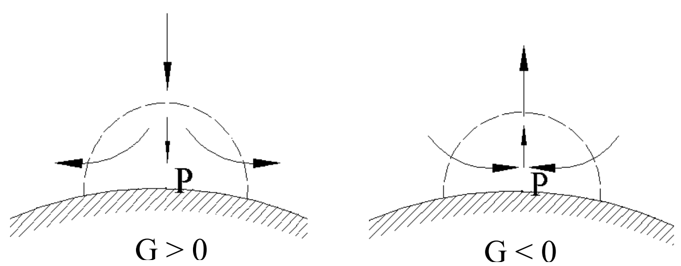

Figure 2. Schematics of cross-flows associated shear stress gradients G.

Depending on the flow geometries and conditions, the cross-flows, V_R may be comparable to or much smaller than the bulk flow, V_θ, but is still present provided there are changes in the wall shear stress (i.e. non-zero shear stress gradients). This is true for any smooth boundary walls, including parallel plate surfaces used in *in vitro* endothelial cell studies. The cross-flow convection, associated with shear stress gradients, affects the movement of molecules and cells in the fluid to endothelial cells at the boundary, as well as the dispersion of particles released by the endothelium into the fluid stream.

SUMMARY

This study addresses a related phenomenon of the effects of shear stress gradients on endothelial cells. We demonstrated that for any smooth boundaries, there are cross-flow fluid convections either towards or away from the boundary associated with local shear stress gradients. These convections influence the movement of biological cells and particles in the fluid to endothelial cells at the boundary, contributing to the interaction between endothelial cells and fluid shear stress gradients.

REFERENCES

Davies, PF (1995). *Physiol Rev* **75**: 519-560.
Tardy, Y, Resnick, N, Nagel, T, Gimbrone, MA and Dewey, CF (1997) *Arterioscler. Thromb. Vasc. Biol.* **17**, 3102-3106.

Supported by the National Science Foundation, China

ON-ICE ACCELERATION AS A FUNCTION OF THE WINGATE ANAEROBIC TEST AND A BIOMECHANICAL ASSESSMENT OF SKATING TECHINIQUE IN ELITE ICE HOCKEY PLAYERS

Neil A. Purves, Moira N. McPherson, William J. Montelpare, Teresa Socha, Robert Thayer

Research Centre, School of Kinesiology, Lakehead University, Thunder Bay, Ontario, Canada
mmcphers@gale.lakeheadu.ca

INTRODUCTION

Success in ice hockey depends on an individual's ability to accelerate from a standing start or from a change in direction. Previous research to determine those factors which provided the greatest contribution to on-ice acceleration has been limited to 2D biomechanical analyses of skating technique, without regard for the influence of physiological measures. The purpose of this study was to predict on-ice acceleration in elite ice hockey players using peak anaerobic power and kinematic variables from a 3D analysis of the biomechanics of skating technique. A sub purpose of this study was to examine the variability of skating technique at the elite level.

METHODS

The study involved the analysis of 37 ice hockey players from the Florida Panthers and Los Angeles Kings participating in a 1999 Prospects Camp. The players completed a 30 second, maximal intensity Wingate anaerobic cycle ergometer test against a resistance of 0.095 kg.kg bodyweight^{-1}. Peak anaerobic power was calculated and recorded as the highest anaerobic power value produced during any of the five second intervals. One week following the Wingate anaerobic test, the players performed two maximal, on-ice accelerations over a distance of 20 meters, while being recorded at 60Hz by two, Panasonic ™ CL-350 digital cameras mounted on Peak Performance ™ pan/tilt heads. The Peak Performance 3D Video Analysis System and a 23 point spatial model were used to extract the raw coordinates for the fastest of the two trials for each player, as measured by a photoelectric timer. The system was then used to smooth the raw data and produce a 3D image. Center of mass and specific kinematic variables were measured at push-off and touchdown for the first five strides. Time, velocity and average acceleration were measured 1.52m, 3.03m, 4.54, and 6.06 from the first push-off. Descriptive statistics for all kinematic data were performed using SPSS™. Exploratory principal components factor analyses (PCA) were performed using SAS™ to a) filter the set of predictor variables by eliminating confounding kinematic variables from further analyses, and b) identify the underlying relationships between groups of kinematic variables which represent important characteristics of ice hockey skating. Performance measures for strides loading in series within variable sets identified by the PCA were transposed into a single composite score using a log-log transformation of the power function. Multiple regression analyses using a backward stepwise approach was used to determine the set of variables that best predict on-ice acceleration. The variability in skating technique was examined using estimates of skewness and kurtosis for the variables identified by the PCA and predictive equation.

RESULTS AND DISCUSSION

The results of the PCA highlighted three latent variables that described key characteristics of skating. The loadings on each latent variable indicated that in order to optimize performance players should attempt to maximize their push-off during the first stride, prepare for propulsion with knees fully flexed at touchdown, and maintain an efficient body position throughout acceleration to maximize propulsion. Regression analysis revealed that the time to skate six meters is best predicted by player eight, stride length, propulsive time, peak anaerobic power, hip and knee angle at push-off on the first stride, hip abduction angle at push-off, and toe-to-centre of mass distance at touchdown on the third stride. The homogeneity of variance in the measures that predicted skating performance indicated that little variability exist in the skating technique used by ice hockey payers at the elite level.

SUMMARY

Exploratory factor analyses were used to filter the set of kinematic data by eliminating confounding kinematic variables and to identify and quantify the relationship between kinematic measures that together described important characteristics of ice hockey technique. The use of the log-log transformation of the power function to transpose raw scores within a variable set into a single composite score captured the progressive nature of the skating stride without masking the unique contribution of each individual stride. The inclusion of peak anaerobic power in the regression model demonstrates the importance of combining physiological and biomechanical measures in an attempt to accurately describe or predict sport performance.

REFERENCES

Allinger, T.L., van den Bogert, A. (1997). Med. Sci. Sports Exerc. 29(2), 279-286.
Van Ingen Schenau, G.L., de Boer, R.W., de Groot, G. (1987). Int. J. Spt. Biomech. 3, 419-431.
Marino, G.W. (1983). Res. Quart. 54(3), 234-238.
Marino, G.W. (1979). Res. Quart. 50(1), 55-59

ACKNOWLEDGEMENTS

The author would like to acknowledge Carlos Zerpa for his technical support.

COMPARISON OF CLINICAL PERFORMANCE AND STABILOGRAM MEASURES IN PATIENTS WITH DEGENERATIVE LUMBAR SPINAL STENOSIS

Maura Iversen[1,2,3], Ashok Nimgade [3,4], Mark Lyle[1] and Jack Dennerlein [4]

[1]Human Performance Laboratory, Department of Physical Therapy, Simmons College
[2] Brigham & Women's Hospital, [3] Harvard Medical School, [4]Harvard School of Public Health, Boston, MA

INTRODUCTION

Over two million US adults endure substantial activity limitation because of chronic low back pain each year (Lavsky-Shulan et al, 1985). Degenerative lumbar spinal stenosis (LSS) is a progressive syndrome characterized clinically by exacerbation of symptoms with lumbar extension and relief with flexion (Katz, 1994). Symptoms of degenerative LSS generally worsen with lumbar extension and improve with flexion. Clinically, these patients demonstrate a higher prevalence of balance disturbances with static and dynamic activities and decreased proprioception.

The Timed Up and Go (TUG) test (Podsiadlo et al, 1991) assesses functional independence and is useful because it describes realistic mobility activities including fall risk situations. The purpose of this study is to describe the relationship between stabilogram (Collins, 1995) measures of postural sway and motor control and performance measures commonly used in clinical settings. It is hypothesized that stabilogram measures and balance performance tests will present a consistent clinical profile in patients with symptomatic degenerative LSS. It is further hypothesized that patients with more severe disease will demonstrate greater dysfunction that patients with milder disease.

METHODS

A descriptive case series was used to compare clinical performance and outcomes measures with stabilogram assessments of balance. Four patients (3 female, 1 male) with clinically confirmed degenerative LSS were recruited from the Spine Center of a large tertiary care institution. Eligibility criteria included: (i) age 55 years and older; (ii) back, buttock and/or leg pain exacerbated by lumbar extension, and (iii) physician's judgment that the patient had clinically significant LSS and low back pain > 6 months. Subjects were excluded if: (i) they reported an increase in pain with lumbar flexion; (ii) had h/o low back surgery, or epidural steroid injection within the last 6 months; (iii) had medical problems that limited their function more than low back pain.

Patients were examined by a physical therapist and completed a demographic questionnaire, the Short Form -36 (Ware et al., 1993), and the Walking Capacity and Symptom Severity form (Stucki et al, 1996), developed specifically for older adults with LSS and related spinal disorders. The Cumulative Index Rating Scale was completed on each patient (Linn et al, 1968). A standard six-degree-of-freedom force plate measured the position of the center-of-pressure (COP) under the feet during 30 seconds of quiet standing with and with eyes closed over 10 trials. Stabilogram-diffusion analysis of the COP trajectories provided steady-state behavior and functional interaction of the neuromuscular mechanisms underlying the maintenance of erect posture (Collins et al, 1995). Patients also completed the Timed-Up and Go Test (Podsiadlo et al, 1991).

RESULTS AND DISCUSSION

The summary parameters from the three components, the physical exam, the health survey, and the force plate COP trajectories are presented in Table 1. These pilot data are all within range of expected values for LSS patients. The absolute stabilogram measures, specifically the larger critical time transition, indicated that LSS patients rely more on open loop control for balance . Correlation with the clinical parameters is not obvious; however, the one subject with a long time up and go parameter had longer critical times in the eyes open stage, suggesting the visual perception influences the person's postural control. Furthermore, the subject with the highest CIRS score had the lowest critical times suggesting this subject may not have impaired balance control.

This study, of course, is limited in the number of patients and it is therefore difficult to draw any major conclusions. However, the data do contain several trends pertaining to visual feedback in the stabilogram data and the clinical test parameters relating to risk of fall.

REFERENCES

Katz JN:. Rheum Dis Clin North Am 1994; 20:471-483 .
Lavsky-Shulan M, J Am Geriatr Soc 1985; 33: 23-28.
Podsiadlo DJ Am Geriatric Soc 1991;39:142-148.
Stucki G, Spine 1996;21(7):796-803.
Ware JE, SF-36 Health Survey Manual and Interpretation Guide. Boston: The Health Institute, 1993.

Table 1: Demographic and Clinical Features of Patients with Lumbar Spinal Stenosis (LSS)

Subject	Age (yrs)	Mean TUG (s)	CIRS Score	QS Closed R critical (s)	QS Open R critical (s)	SF-36 physical	LSS function
1 (001)	66.6	7.75	5	1.06	0.93	64	1.2
2 (011)	72.8	7.31	10	0.91	0.84	25	2.6
3 (020)	76.1	11.28	6	1.06	1.22	15	2.4
4 (033)	61.7	9.0	5	1.06	1.03	60	1.4

COMPARISON OF FIXED AND ROTATING BEARING KNEE REPLACEMENTS *IN –VIVO* USING A THREE-DIMENSIONAL MOTION CAPTURE TECHNIQUE: PRELIMINARY RESULTS

C. A. Holt[1], L. Jones[1], P. O'Callaghan[2], S. Roy[2], C. Wilson[2]
[1]Division of Materials and Minerals, Cardiff School of Engineering, Cardiff University,
P O Box 925, The Parade, Cardiff, CF24 0YF, UK. HOLT@CARDIFF.AC.UK
[2] Department of Physiology, Faculty of Medical and Health Sciences, University of Auckland, Private Bag 92019, Auckland, NZ
[3]University Hospital of Wales, The Heath, Cardiff CF14 4XY, Wales, UK

INTRODUCTION

One of the requirements following total knee arthroplasty, apart from the principle goal of pain reduction, is the return to normal function with stability of the joint during normal daily activity. The purpose of this study was to develop a technique for monitoring the functional effect of fixed and rotating bearing knee replacements *in-vivo*. A method was developed [Holt et al, 2000] to measure clinical knee rotations and is applied to four subject groups, with knee function classified as: normal, pre-operative osteo-arthritic, post-operative fixed and rotating bearing TKR (FTKR and RTKR respectively).

METHODS

A method has been developed [Holt et al, 2000] to calculate knee rotation and translation using marker clusters placed on the thigh and shank. Six degrees of freedom of the knee are calculated using the Joint Co-ordinate System [Grood and Suntay, 1983] with transformation matrices relating marker cluster and bony axes [Soderquist and Wedin, 1993]. Marker clusters rather than single marker placements minimise skin movement artefact and errors associated with standard optical motion analysis techniques [Capello et al, 1997].

The validated method [1] is applied to an on-going clinical trial to study knee function of normal subjects in comparison with pre-operative osteo-arthritic and three to twelve months post-operative TKR allowing a measure of return to normal knee function and a consideration of knee replacement design compatibility with initial functional specification. A major aim of the study is to investigate the external-internal tibial rotation range of motion (EIROM) as an indication of functional outcome and the patient group is thus further defined as having either FTKR or RTKR designs.

RESULTS AND DISCUSSION

Static jig tests and dynamic normal gait validation showed repeatability for rotation and translation measures. Comparison of subject categories introduced into the clinical trial shown in figure 1 indicates mean EIROM for different groups sizes. Preliminary results are given for the majority of FTKR subjects and the study is continuing to increase subject numbers for both FTKR and RTKR. With greatest recovery after 12 months, both knee designs provide a return to normal EIROM with implications regarding TKR design.

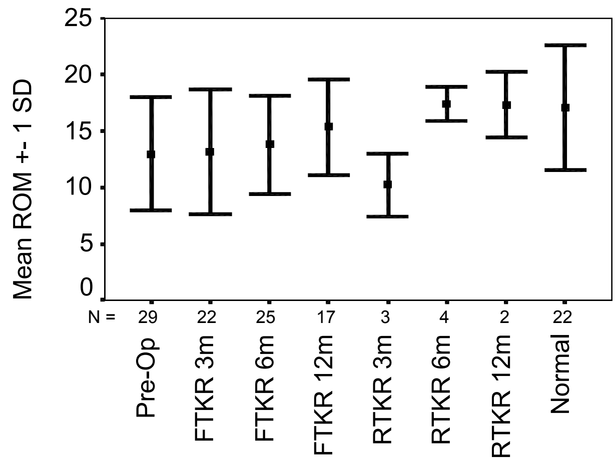

Figure 1: Mean external-internal tibial range of motion for pre-op, FTKR and RTKR post-op and normal subjects (m = months post-op)

SUMMARY

A movement analysis technique using marker clusters is used to study the effect of fixed and rotating bearing knee replacement components on post-operative knee function in vivo. Preliminary results indicate a return to normal function for both sets of patients after a 12-month recovery period.

REFERENCES

Holt C.A. et al (2000). *Computer methods in Biomechancis and Biomedical Engineering,* **3**. Gordon and Breach Science Publishers SA
Grood ES and Suntay WJ, (1983) J. Biomechanical Eng., **105(2)**, 136-144
Soderkvist I, Wedin P (1993). *Journal of Biomechanics,* **26**, 1473-1477
Capello A, Cappozzo A, Della Croce U and Leardini A, (1997) Three-dimensional analysis of human locomotion, Chapter 8, John Wiley and Sons Ltd., ISBN 0 471 96949 3

ACKNOWLEDGEMENTS

We would like to thank DePuy International for their continuing support for this study.

INFLUENCE OF A RIDER TO THE BACK OF A HORSE IN DIFFERENT GAITS

B. Frühwirth[1], C. Peham[1], M. Scheidl[3]
[1]Clinic for Orthopedics, Veterinary University Vienna, Vienna/Austria
[3]FH Wieselburg, Wieselburg/Austria

INTRODUCTION

Back pain and diseases of the spine are known as significant problems in equine sports and veterinary medicine. Information about the strains and stresses that a horse encounters while being ridden might be an important link between symptomatic description and functional diagnosis, and thus might improve prevention, treatment and management of back pain. Up to now, the biomechanics of the equine back under conditions usually present today, especially while being ridden, have not yet been sufficiently investigated.

The aim of this study is to compare the pressure distribution and motion of the horses back with different loads (with and without rider), applied in different gaits.

MATERIALS AND METHODS

We measured 12 horses (age 7-25 years, 410-650 Kg, various breed, different training levels) without clinical signs of back pain (Licka et al. 1998).

All horses were analysed in three different gaits (walk, sitting trot, gallop) with rider, and in walk and trot without rider. For this investigation the regularly used saddles of each horse were taken. The fit of the saddles was checked by a veterinarian and the saddler of the Spanish Riding school of Vienna.

Measurements were carried out from the right side, with a system of six cameras (Motion Analysis Corporation). The pressure distribution under the saddle was recorded with the PLIANCE saddle mat (NOVEL Inc., Munich). At least five recordings of each combination were taken with the two simultaneously triggered measuring systems. From the pressure distribution we calculated the maximum overall force (MOF) in relation to the mass of rider and saddle, and the Centre of Pressure (COP) of the overall force. The range of back motion was determined at T5, L4, and S1.

RESULTS AND DISCUSSION

The MOF and the COP with and without rider is shown in table 1. Our results demonstrate, that force transmission in walk is more stable with rider (less variation of the COP) than without (only saddle). The rider's weight concentrates the load on a smaller area. In trot the situation is reversed. The COP varies more when ridden (table 1). The MOF is about six times higher when ridden in walk, and about seven times in trot. There was no significant difference in lateral motion of the back between ridden and unridden horse.

One of the most important problems in equestrian sports is to fit the saddle properly to a horses back. To achieve a proper fit it is extremely recommendable to know the accurate stress applied by saddle and rider. This investigation potentially enables us to estimate and predict the behaviour of the back under certain load and stress regimes. This again constitutes a fundamental building block for developing a biomechanical model of the equine back, and for designing and refining new saddle types.

REFERENCES:

HARMAN, J.C.: Practical use of a computerised saddle pressure measuring device to determine the effects of saddle pads on the horse's back. Journal of Equine Veterinary Science 14, 606-611, 1994.

JEFFCOTT, L.B., HOLMES, M.A., TOWNSEND, H.G.G.: Validity of saddle pressure measurements using force-sensing array technology – Preliminary studies. The Veterinary Journal, 158, 113-119, 1999.

LICKA, T., PEHAM, C.: An objective method for evaluating the flexibility of the back of standing horses. Equine Veterinary journal, 30 (5), 412-415, 1998.

ACKNOWLEDGEMENTS

This study was supported by the Austrian Science Fund Project P13915.

We would like to thank Mr. Desmond O`Brien for his active participation in the measurements and for checking the fits of the saddles.

Table 1: The maximum overall forces (MOF) [N/kg].

	Mean			SD		
	Walk	Trot	Gallop	Walk	Trot	Gallop
MOF-r	12.13	24.26	27.15	1.17	4.56	4.37
MOF-ur	2.07	3.61	-	1.19	1.59	-
CoPx-r	2.87	4.76	2.99	0.64	3.51	1.72
CoPy-r	3.49	9.98	8.66	1.19	4.92	1.96
CoPx-ur	5.32	4.28	-	2.32	1.10	-
CoPy-ur	4.69	4.63	-	4.52	1.68	-

(r denoting "ridden", ur "unridden"; x, y spatial co-ordinates) .

THE EPIDEMIOLOGY AND BIOMECHANICS OF BICYCLE HANDLEBAR IMPACT INJURIES IN CHILDREN

Steven R. McFaull

Injury Section, Health Surveillance and Epidemiology Division, Centre for Healthy Human Development
Population and Public Health Branch, Health Canada, E-mail: steven_mcfaull@hc-sc.gc.ca

INTRODUCTION

Head and upper extremity injuries are frequent in bicyclists. Abdomino-thoracic injuries, although less common, are potentially serious. The handlebar of the bicycle has been implicated in serious and sometimes fatal injuries to the abdominal organs for over 30 years (Bergqvist et al, 1985). However, details as to the mechanism of such injuries and the mechanics of the impact have only recently been addressed (Winston et al, 1998).

The purpose of the present study is twofold: *i)* to describe the circumstances of abdomino-thoracic bicycle handlebar impact injuries in Canada's principal injury surveillance database (CHIRPP) and *ii)* to develop a simple mechanical model of various handlebar impact scenarios to determine the potential magnitude of the impact forces involved and any variables which may be important in prevention and control efforts.

METHODS

The Canadian Hospitals Injury Reporting and Prevention Program (CHIRPP) is an injury surveillance system supported by Health Canada that has been collecting Information on circumstances of injuries since 1990 in ten pediatric and 5 general hospitals across Canada. The entire database (1,098,334 records as of March 2001) was searched for records involving abdomino-thoracic injury (s) coupled with the handlebars as the direct cause of injury.

Epidemiological information from CHIRPP and other details were used to formulate the mechanical model which estimates the compressive force of the impact based on the pre-crash velocity of the bicycle, the impact angle, the mass of the child and the bicycle and the location of the centre of mass of the bicycle-rider system. The results of the model are compared to data on the compressive tolerances of the liver and spleen (Sturtz, 1995).

RESULTS AND DISCUSSION

A total of 650 cases (76.6% males), or about 1.5% of all bicyclist cases in the database, were identified. Almost half (47.9%) of all cases involved children aged 5-9 years, which proportion is larger than that for all bicyclist cases (38.1%, $p<0.005$). Of the cases with enough detail regarding the mechanism, 39.8% involved a spearing impact (handlebar end) and 30.1% were frontal impacts across the horizontal aspect of the handlebar. The typical profile of handlebar impact injuries involves a child, between the ages of 6 and 11 years, a low velocity, single-party (non-motor vehicle) event, losing control of the bicycle due to a surface irregularity, falling on or progressing into the handlebars and suffering an abdominal injury. The low velocity of such events optimizes the conditions for the child to interact with the bicycle in contrast to a catapult-type scenario, which occurs more often with older riders at higher speeds, often involving motor vehicles. At least one-fifth (19.1%) of the cases involved injuries to internal organs (16.7%) or to abdominal blood vessels or abdomino-thoracic muscle tissue (2.4%). Almost three-quarters of the cases involved only superficial injuries upon presentation, however in the literature (e.g. Spitz, 1999) there is often a diagnostic delay in up to 67%-86% of cases with internal injuries due to blunt trauma. It is possible that some of the injuries diagnosed as superficial in the emergency department were later found to be more serious.

Table 1 details the results of a simulation of the model. Clearly, the angle of impact is an important parameter in the resulting compressive force experienced by the child. The spleen appears particularly vulnerable, and in children the spleen and the liver are more exposed below the ribs compared to adults.

Table 1. The compressive impact force (N) as a function of the impact angle at different subject anthropometries for a spearing mechanism. An impact angle of 0 degrees indicates the handlebar perpendicular to the coronal plane. Subject is a male traveling at a pre-crash velocity of 2.23 m/s. Liver and spleen columns are compressive tolerances (N), Sturtz (1995).

Angle (deg.)	3rd %ile 5 years	50th %ile 10 years	97th %ile 13 years	Liver	Spleen
5	6,981	8,474	14,272	2,649	785
15	2,351	2,854	4,806	2,649	785
25	1,440	1,748	2,943	2,649	785
45	860	1,045	1,759	2,649	785
90	608	739	1,244	2,649	785

SUMMARY

Handlebar impact injuries are rare but potentially very serious and considering the young age of the victims and the vulnerability of the child's abdomen, prevention efforts are important. The simple mechanical model reveals the potential for high impact forces relative to the organ tolerances.

REFERENCES

Bergqvist, D. et al (1985). *Injury*, **16**, 217-20.
Winston, F.K. (1998). *Pediatrics*, **102**, 596-601.
Sturtz, G. (1995). *Biomechanics of impact injury and injury tolerances of the abdomen, lumbar spine and pelvic complex,* Society of Automotive Engineers.
Spitz, D.J. (1999). *Am J. Emerg Med*, **17**, 244.

ADAPTING BODY SEGMENT PARAMETERS FOR BIOMECHANICAL CALCULATIONS IN CHILDREN

Timothy K Woo[1] and David H. McFarland

Scientific Development Department, Biotonix inc., Montreal, Canada
[1]e-mail: woot@biotonix.com web site: www.biotonix.com

INTRODUCTION

Using appropriate body segment parameters for the age, sex and perhaps ethnicity of the intended population is crucial for biomechanical modeling. There is a renewed interest in looking at the development of biomechanical characteristics of children at different life stages. Despite this, the most readily available and widely used data for various body segments parameters comes from the classic studies using elderly adult, Caucasian male cadavers. Clearly, such parameters are not applicable to young children, as the body segment proportions change during development. During adulthood, a person's head and neck represents 8.1% (Dempster 1955) of the total body weight where as a five year old child's head will represent 18.1% (Jensen 1986) of their total body weight.

To find the appropriate body segment data, we began a systematic review of the available literature and data sets to arrive at a consensus of appropriate biomechanical parameters for children. Our particular focus was to use these data sets to adapt the center of gravity calculations and moment of force calculations for children of different developmental ages for the Biotonix BioPrint system. This is a web-based musculo-skeletal assessment and corrective exercise system. The purpose of this paper is to demonstrate the potential problems of inappropriately applying adult to infant/child calculations of center of gravity and moment of force estimations.

PROCEDURE

A single-segment moment of force (Chaffin1984) and a center of gravity estimation (Enoka 1994) were calculated twice, once using adult body segment parameters (Dempster 1955) and once using children's body segment parameters (Jensen 1986). These biomechanical formulas were applied to three female subjects (mean age 13.3) as well to simulated postures of children aged 4 to 15 in quiet standing with a 5° anterior head position. The simulated posture used anthropometric measures collected by Pheasant (1986). The differences in using adult parameters versus children's parameters were plotted in the graphs shown in the results.

RESULTS AND DISCUSION

The following two figures show the differences in using adult versus children's body segment parameters in the center of mass calculation and moment of force calculation of the head and neck. Figure 1 shows the differences in calculated center of mass (mean 11.9 SD 2.4). The difference between children and adult center of gravity decreases as age increases. This trend is normal, as the children age, their body's will become more similar to those of adults. A noticeable decrease in the difference in center of mass is observed beginning at age 10 and 11. This is due to the rapid growth that is associated with puberty.

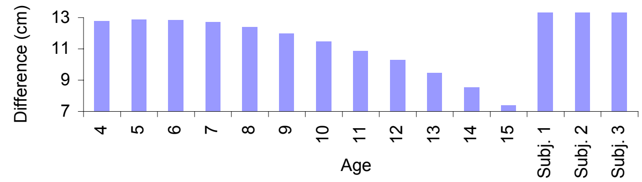

Figure 1. The underestimated vertical difference in calculated center of mass using adult parameters in place of children's

Figure 2 shows the difference in moment of forces of the head and neck. Adult parameters underestimate the moment until the age of 13. At the age of 15 there is a large overestimation of the moment of force. This increase is partially due to the body segment parameters that are used in children. The linear changes in body segment parameters are not appropriate during adolescence when puberty occurs as major growth occurs during this period.

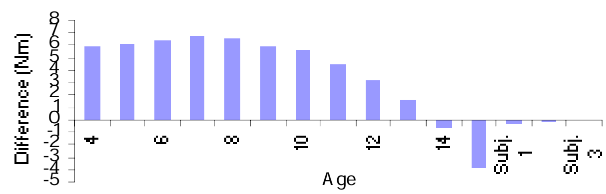

Figure 2. The underestimated difference in moments of force using different adult parameters in place of children's

SUMMARY

The results of this study show the importance of using appropriate body segment parameters in biomechanical modeling. Although the body segments may not be perfect, it is important to utilize the parameters that best suit the population to eliminate as many of the confounding factors as possible.

REFERENCES

Chaffin, D., Anderson G.B.J. (1984). *Occupational biomechanics,* Wiley & Sons

Dempster, W.T. (1955). *Space requirements of the seated operator. WADC Technical Report.* Wright-Paterson Air Force Base

Enoka, R.M. (1994). *Neuromechanical basis of kinesiology.* Human Kinetics

Jensen, R.K. (1986). *Journal of Biomechanics,* **19**, 359-368

Pheasant, S.T. (1986). *Body space: anthropometric ergonomics & design,* Taylor and Francis

NUMERICAL SIMULATION OF FLUID-STRUCTURE INTERACTION OF THE INTRACRANIAL ARTERY

Ryo Torii[1], Marie Oshima[2], Toshio Kobayashi[2] and Kiyoshi Takagi[3]

[1]School of Mechanical Engineering, The University of Tokyo
[2]Institute of Industrial Science, The University of Tokyo
[3]School of Medicine, Teikyo University

INTRODUCTION

Over 90% of subarachnoid hemorrhages are caused by rupture of cerebral aneurysms. Although the risk of rupture is known to be under 1%, aneurysms are usually operated if they are identified. On the other hand, the risk of postoperative sequelae is over 10% (The international study of unruptured intracranial aneurysms investigators, 1998). Thus it is important to predict risk factors of rupture of cerebral aneurysms in order to avoid unnecessary surgeries. Since it is reported that growth and rupture of aneurysms are associated with hemodynamic factors, the authors have been conducted a study to predict growth and rupture of cerebral aneurysms using numerical simulation. In this paper, numerical method for interaction between blood flow and arterial wall is developed. Results are compared with those of numerical simulations with rigid arterial wall. Especially, as WSS (wall shear stress) is an important factor for cerebrovascular disorders (Malek, A. M., et. al., 1999), effects of elastic arterial wall on WSS distribution are investigated.

COMPUTATIONAL METHODS

For fluid calculation with moving domains, ALE (arbitrary Lagrangian-Eulerian) FEM (Finite Element Method) is used to descretize both Navier-Stokes and the continuity equations. For structural calculation, FEM is used to descretize the equilibrium equation with the elastic constitutive law. Fluid and structural equations are iteratively solved by exchanging pressure and displacement at the boundaries.

COMPUTATIONAL MODEL

Three dimensional geometry of the ICA (internal carotid artery) is extracted from CT (Computed Tomographic) angiography (see Figure 1). The arterial wall is assumed to be elastic body with thickness of 0.3 mm. The elastic coefficient and Poisson's ratio are 1.0Mpa and 0.4 respectively. Womersley velocity profile is used for the inflow boundary condition. The outflow boundary conditions are assumed to be traction free, and the wall boundary conditions for fluid are non-slip, respectively. The inflow and outflow boundaries are fixed in structural calculation. The Reynolds number varies from 80 to 430. All calculations were performed on SGI Origin2000.

RESULTS AND DISCUSSIONS

The maximum deformation of elastic arterial wall is small (6.54×10^{-6} [m], about 0.164 % of diameter of ICA). But from comparison of instantaneous WSS distributions between elastic and rigid wall calculations, WSS distributions are different as shown in Figure 2. The difference can be explained by following two effects of interaction between blood flow and arterial wall. Firstly, as indicated by the arrow in Figure 2 (a), the centerline of elastic artery moves in the outward direction of curvature and velocity gradient near inside arterial wall becomes higher than that in case of rigid wall. Thus the location and magnitude of the maximum WSS are changed. The maximum WSS is 297 dyn/cm^2 in elastic wall calculation while that is 160 dyn/cm^2 in rigid wall calculation. Secondly, irregularity of arterial wall is smoothed by fluid force and overall WSS distribution varies. These results indicate that effect of elastic arterial wall on blood flow simulation is considerable.

SUMMARY

Numerical simulations of the internal carotid artery were performed considering elasticity of arterial wall. As a result, it is shown that effect of elastic arterial wall on WSS distribution is significant even though wall deformation is small. Thus it indicates that elasticity of arterial wall is essential in numerical simulation of blood flow.

REFERENCES

The international study of unruptured intracranial aneurysms investigators (1998), *New England J. Med.*,**339**-24, 1725-1733
Malek, A. M., et. al., (1999), *JAMA*, **282**-21, 2035-2042

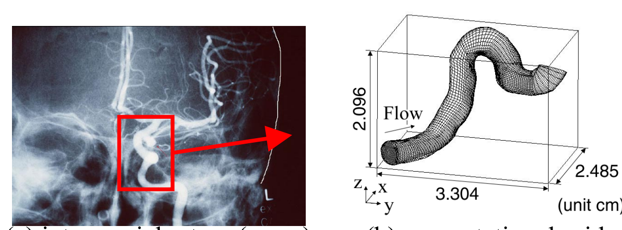

(a) intracranial artery (x-ray) (b) computational grid

Figure 1: computational model

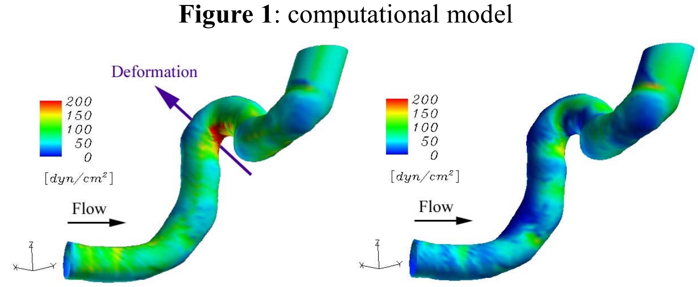

(a) elastic wall (b) rigid wall

Figure 2: instantaneous WSS distribution at the end of systole

ANTERIOR INTERBODY FUSION WITH TRANSFACET SCREWS: A BIOMECHANICAL STUDY

S.L. Evans[1], C. A. Holt[1], L. Jones[1], D. Dillon[2], S. Ahuja[2] and P. Davies[2]

[1]Division of Materials and Minerals, Cardiff School of Engineering, Cardiff University,
P O Box 925, The Parade, Cardiff, CF24 0YF, UK. EAVNS SL6@CARDIFF.AC.UK
[2]University Hospital of Wales, The Heath, Cardiff CF14 4XY, Wales, UK

INTRODUCTION

Transfacet screws are widely used to provide additional stability in anterior spinal surgery. The aim of this study was to determine whether it is better to implant transfacet screws before or after implanting an anterior cage for interbody fusion. A 3D motion analysis technique based on methods previously used for measuring knee movement has been modified to measure relative movements of two vertebral bodies [Hunt et al, 2001], and this technique was used in the present study.

METHODS

L4/L5 calf spines segments were mounted on a base plate using 6.5mm cancellous screws and bone cement. A second smaller plate was attached to the superior surface of the upper vertebral body for attachment of the loading jig. Marker clusters were attached to both upper and lower vertebral bodies using Kirschner wires. Three anatomical landmarks on each vertebral body were identified using a marked pointer to establish the anatomical axis system. 2Nm moments were applied about each anatomical axis and the resulting movements were measured using a Qualisys motion analysis system. Rotations and translations about each anatomical axis were then calculated using the method previously described.

For one group of five specimens transfacet Magerl screws were implanted, followed by a Syncage implant (Stratec), and a in a further five tests the anterior cage was implanted first.

RESULTS AND DISCUSSION

Implanting the cage first produced a significantly smaller range of motion, both in flexion/extension (p=0.02) and in axial rotation (p=0.03). In lateral bending the range of motion was reduced, but the difference was not statistically significant (p=0.38).

When the cage is implanted first, the vertebral bodies are distracted so that the posterior longitudinal ligament (PLL) is taut, and the facet joints are locked. The screws then provide some additional stability. If the screws are implanted first, they tend to prevent tensioning of the PLL so that the range of motion is much greater.

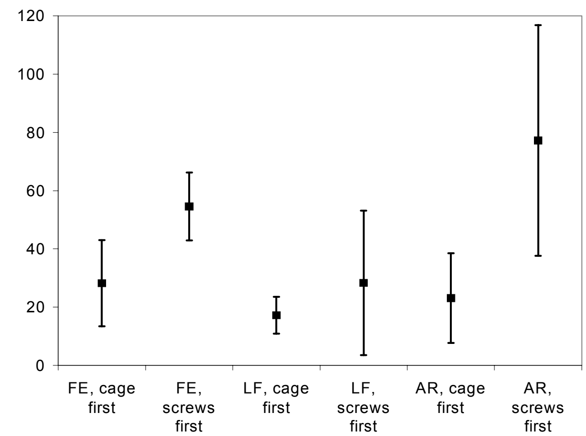

Figure 1: Range of motion in flexion- extension (FE), lateral flexion (LF) and axial rotation (AR) as a percentage of the unimplanted range of motion (±standard deviation).

SUMMARY

Implanting the cage before the transfacet screws resulted in a much more stable construct, which should promote successful fusion. This difference is ascribed to the tensioning effect of inserting the cage on the posterior longitudinal ligament.

REFERENCES

Hunt, C.M., Evans, S.L., Holt, C.A., Jones, L., Ahuja, S., Dillon, D., Davies P. and Howes J. (2001). *5th Symposium on Computer Methods in Biomechanics and Biomedical Engineering. ITALY*

ACKNOWLEDGEMENTS

We would like to thank DePuy International for their continuing support for this study.

LUMBAR SPINE MOTION ANALYSIS VIA AUTOMATIC SEGMENTATION

Yalin Zheng[1], Robert Allen[2] and Mark S. Nixon[1]

yz99r@ecs.soton.ac.uk

[1]Department of Electronics and Computer Science, University of Southampton, Southampton, SO17 1BJ, UK.

[2]Institute of Sound & Vibration Research, University of Southampton, Southampton, SO17 1BJ, UK.

INTRODUCTION

Low back pain is a very common problem and the consequent cost is enormous. In spite of its prevalence, however, it is still difficult to obtain accurate diagnosis. Mechanical disorder is now often regarded as the main cause. Presently, a number of studies are directed at measurement of spine kinematics. Since the lumbar spine is a deep-rooted structure, this has been difficult until digital videofluoroscopic (DVF) imaging was developed [Breen et. al. 1989]. In this paper, DVF is used to acquire the motion sequence of the lumbar spine, to solve the problems with manual location of the vertebrae within the sequence, a spatio-temporal Hough transform (STHT) [Zheng et. al. 2001] has been developed to automatically locate vertebrae in DVF images and results of tests are very promising.

METHODS

During DVF image acquisition, the subject lies on a table which can be moved at a controlled rate. A major advantage of DVF is that it can capture a whole motion sequence with a radiation dose that is lower than a single X-ray plate of the lumbar spine. This reduction, however, incurs deteriorated image quality and causes problems with edge detection. Phase congruency [Kovesi 1999], which detects edges by phase information, is used here for improved edge detection. Phase congruency has significant advantage over most of the gradient-based methods as it can cope with uneven contrast and brightness within the image. Fig. 1 (b) shows convincing results in L5 edge (L*n* is the *nth* vertebra of the lumbar spine).

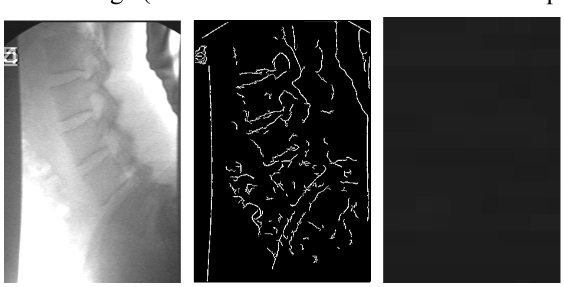

(a) (b) (c)

Figure 1: DVF image, edge map and extraction results.

The Hough transform (HT) is a powerful tool in computer vision for extracting objects in images by evidence gathering in a parameter space [Leavers 1993]. Here an STHT has been developed to locate five lumbar vertebrae in each frame of a selected sequence while the subject moves from a neutral position into flexion, then back through neutral to extension, and finally to neutral position. The new STHT differs from the traditional HT in that it considers not only the parameter space, but also the spatio-temporal information, that is, the relationships between vertebrae within a single frame as well as throughout the whole sequence. However, the huge search space involved leads to increased computational cost. To solve this problem, a genetic algorithm [Goldberg 1998] is employed to find the optimal values of a "fitness function" which is the combination of the two terms discussed above. Aided by the spatio-temporal information, the STHT can provide us with more robust results. Fig. 1 shows a DVF image, its edge map and vertebral extraction results.

RESULTS

The extraction results from the STHT enable us to conduct further kinematic study of the lumbar spine. Fig. 2 shows the motion pattern in the *x* direction of the centers of five lumbar vertebrae moving from full flexion to extension, and reveals a sinusoidal feature. In data acquisition the interface between the moving lower and the static upper sections of the table was at the level of L3. This is to maximise the focus on the whole lumbar spine. It explains why L3 moves less than the other four segments.

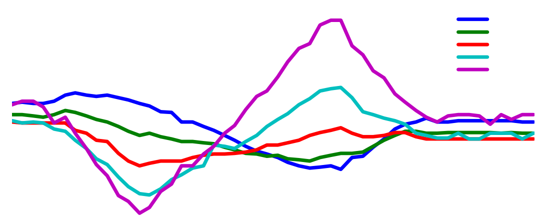

Figure 2: Motion pattern of the lumbar spine.

CONCLUSION

Our method shows potential for automatic extraction of the vertebrae in moving DVF images of the lumbar spine. We are currently applying this to a large database of spine motion from which the kinematics at the segmental level will be produced. Further validation studies using a calibration model are also being undertaken.

REFERENCES

Breen, A. et al (1989). *J. of Med. Eng & Tech*, **13**, 109-113
Kovesi, P. (1999). *Videre: J. of Comp Vision Research*, **1**, 3-26
Leavers, V. (1993) *CVGIP: Image Understanding*, **58**, 250-264
Goldberg, E. (1998) *Genetic Algorithms in Search, Opt. and Mach. Learning*. Addison-Wesley
Zheng, Y et al (2001). *Proceedings of EMBC'01*, Istanbul

NUMERICAL SIMLUATION AND DATABSE SYSTEM FOR HEMODYNAMIC STUDY OF CEREBRAL ARTERIES

Marie Oshima[1], Kiyoshi Takagi[2] and Motoharu Hayakawa[3]

[1]Institute of Industrial Science, University of Tokyo, 4-6-1 Komaba Tokyo 153-8505 Japan, marie@iis.u-tokyo.ac.jp
[2]Teikyo University, School of Medicine, School of Medicine, 2-11-1 Kaga Itabashi-ku Tokyo, Japan
[s]Tujita Health University, School of Medicine, 1-98 Dengakugakubo, Kutsukake-cho, Toyoake-shi, Aichi, Japan

INTRODUCTION

The paper aims to investigate the relationship between cerebrovascular geometry and hemodynamics in order to predict rupture and creation of cerebral aneurysms. The authors have been developing a numerical simulation system, which consists of medical image–based geometric modeling, grid generation, finite element fluid simulation, and scientific visualization (Oshima, 2001). A database system is designed so as to organize and analyze medical imaging, physiological, and numerical data. Using 15 cases of the middle cerebral artery (MCA) calculations from the database system, the multivariate analysis are performed to estimate a maximum wall shear stress. The results are compared and show good agreement with those of numerical analysis. It is found that diameter of the MCA, ratio of diameter of branching to that of the MCA, and bifurcation angle between the MCA and brunching arteries are important geometric factors in determining maximum wall shear stresses.

MEDICAL IMAGE-BASED SIMULATION SYSTEM

Due to over-tessellated polygonal surfaces extracted from CT images, smoothing operation is carried out combining polygon reduction technique (Garland, 1997) and smoothing technique (Taubin, 1995). After construction of geometric model, computational grids are generated for the finite element analysis of incompressible Newtonian blood flow. The inflow boundary conditions are prescribed using velocity data at the entrance of the MCA measured by the transcranial Doppler ultrasound technique. Overall procedure for the numerical system is summarized in Figure 1.

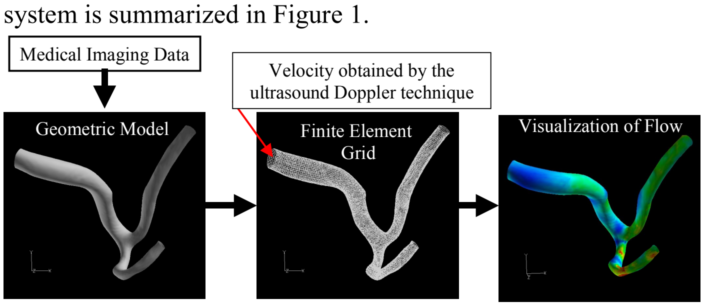

Figure 1: Flowchart of overall Simulation System

MULTIVARIATE ANALYSIS USING DATABASE

The present database system can deal with text data as well as graphic data such as visualization pictures and movies. For the multivariate analysis, 6 parameters are chosen to represent the vascular geometry as follows: 1)diameter of the MCA(D_p), 2)the ratio of the diameter of brunching artery to that of the MCA(D_1/D_p and D_2/D_p), and 3)angle between brunching artery and MCA(α_1,α_2) and between two brunching arteries (α_3).

RESULTS AND DISCUSSION

The multivariate analysis is conducted for 15 cases to examine effects of vascular geometry on the maximum wall shear stress. Comparison of the simulation and the estimation results are described in Figure 2. The analysis shows that the parameters, D_p, D_1/D_p, and $\alpha_1$affect the magnitude of maximum wall shear stress. As a results, the magnitude of maximum wall shear stress decreases associated with increase in D_p, D_1/D_p, and α_1.

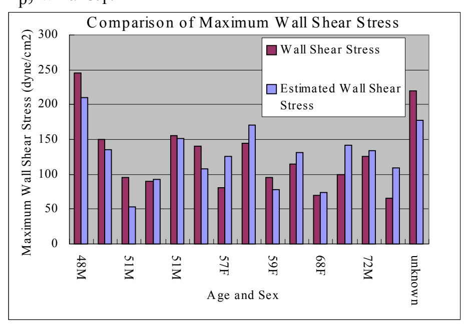

Figure 2 : Maximum wall shear stress of numerical results and estimated values by multivariate analysis.

SUMMARY

The medical image-based simulation and database system is developed to evaluate effects of cerebrovascular geometry on hemodynamics. A total of 15 cases for the MCA are analyzed. The multivariate analysis is conducted to estimate the maximum wall shear stresses using 6 geometric parameters and results in good agreement with the simulation results. It is shown that the wall shear stress are affected by 3 parameters (diameter of MCA, and ratio of diameter and angles of branching to that of the MCA). The magnitude of maxim wall shear stress decreases as those of 3 parameters increases.

REFERENCES

Garland, M., et al (1997). ACM SIGGRAPH 97 Conference Proceedings, 209-216.

Oshima, M. (2001). Compt. Methods Appl. Mech. Engrg., *191*, 661-67.

Taubin, G. (1995). Proceedings of the 22nd annual ACM Conference on Computer Graphics, 351-35

A DUAL MASS SPRING – DASHPOT MODEL OF THE EXHANGE OF FORCES BETWEEN THE BACKPACK, HIPS AND SHOULDERS DURING WALKING

Michael LaFiandra[1], Everett Harman[1], Peter Frykman[1], Clay Pandorf[1]
[1]U.S. Army Research Institute of Environmental Medicine, Natick, MA 01760-5007, USA
E-mail: michael.lafiandra@na.amedd.army.mil

INTRODUCTION

A model describing the exchange of forces between the backpack, hips and shoulders during walking is proposed (Figure 1). The intent of the model is to provide backpack designers with a simple tool that can give them the information needed to design backpacks that better distribute the forces between the hips and shoulders. The model is described by the following equation:

$$F_{BP} = k_{hip}x + c_{hip}\dot{x} + k_{shoulder}x + c_{shoulder}\dot{x}$$

x, and $\dot{x}$ represent vertical instantaneous displacement, and velocity (respectively) of the backpack's center of mass (COM), F_{BP} together with the $mass_{BP}$*gravity are all the external forces acting to accelerate the backpack's COM. k represents the stiffness of the springs at the hips and shoulders, and c represents damping at the hips and shoulders.

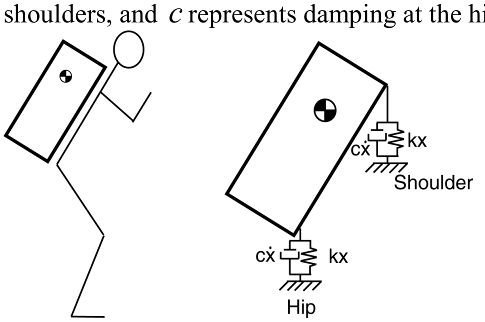

Figure 1 Dual Mass Spring-Dashpot Model of Backpack.

The model is designed to predict the vertical force acting on the hips and shoulders based on the vertical force acting on the backpack COM, the stiffness and damping at the shoulders and the stiffness and damping at the hips. Stiffness and damping for the shoulders and hips are separate terms in the model, consequently there is no assumption that the stiffness or damping at the shoulders is equal to the stiffness or damping at the hips. However, the model does capture the fact that differences in stiffness and damping at the shoulders will affect stiffness and damping at the hips.

METHODS

One male volunteer 22 years old walked on a treadmill at 1.34 m/s with 3 backpack weights 134, 267 and, 401 N (30, 60, and 90 pounds). Hip-belt tension and backpack COM location were constant for all backpack-walking conditions. The backpack had a lightweight polymeric frame with force transducers between the hip-belt and frame. The pack was designed to only make contact with the upper back and shoulders and the hips. Force data was sampled from the force transducers at 1000 Hz. Kinematic data of the motion of the backpack COM were collected at 100 Hz. Thirty seconds of data were collected from the subject, yielding on average approximately 25 strides of data. The instantaneous vertical force acting on the BP COM was calculated from its mass and instantaneous vertical acceleration. Vertical force on the shoulders (and upper back) was calculated as the difference between the vertical force on the BP COM and the vertical force on the hips.

The values of stiffness and damping terms were based on the force acting on the BP COM. Values of stiffness and damping ranging from 0 to 20 were substituted in the model and used to predict the forces acting at the hips and shoulder. The predicted shoulder and hip forces were then compared (using linear regression) to the forces at the shoulders and hips that were calculated from the kinematic and transducers data respectively. The values of stiffness and damping that yielded the highest r^2 were retained for the subsequent analysis. In order to determine the robustness of the values of stiffness and damping terms across backpack mass conditions, the model was used to predict hip and shoulder forces while the subject carried the 60 and 90 pound backpack. In all cases, the strength of the prediction of the model was determined using 2 linear regressions (for hip and shoulder separately), with predicted force as the dependent variable and the force calculated from the transducers or kinematics as the independent variable.

RESULTS

k_{hip} = 2; $k_{shoulder}$ = 2; c_{hip} =4; and $c_{shoulder}$ = 12 yielded the highest r^2 values (0.82 for hip; 0.93 for shoulder) for predicting *both* the hip and shoulder force. It should be noted that other values of stiffness and damping resulted in higher r^2 values for the shoulder, however this resulted in lower r^2 values for the hip. These stiffness and damping values were used to predict hip and shoulder force for the same subject walking with a 60 and a 90-pound backpack. The r^2 values for the 60-pound pack were 0.74 (hip) and 0.81 (shoulder); the r^2 values for the 90-pound pack were 0.86 (hip) and 0.87 (shoulder).

DISCUSSION

The increase in damping at the shoulders may result from the shoulders bearing a much greater proportion of the backpack mass during walking (LaFiandra et al. in press). More research is required to substantiate this hypothesis. The lower r-squared values obtained for the 60-pound backpack suggests it may be necessary to re-tune the model for different backpack masses. We also conducted a between subject test of the model's robustness, the results of which are forthcoming.

REFERENCES

LaFiandra, M. et al. (in press). *Med Sci Sport Exerc*.

PLANTAR APONEUROSIS FORCES DURING SIMULATED WALKING

Ahmet Erdemir[1,2], Andrew J. Hamel[1], Andrew R. Fauth[1,2], Stephen J. Piazza[1,2,3,4] and Neil A. Sharkey[1,2,4]

[1]Center for Locomotion Studies, The Pennsylvania State University, University Park, PA
[2]Department of Kinesiology, The Pennsylvania State University, University Park, PA
[3]Department of Mechanical and Nuclear Engineering, The Pennsylvania State University, University Park, PA
[4]Department of Orthopaedics and Rehabilitation, The Pennsylvania State University, Hershey, PA
e-mail: *steve-piazza@psu.edu* url: *www.celos.psu.edu*

INTRODUCTION

The plantar aponeurosis (PA) originates from the medial tubercle of the calcaneus and inserts on the phalanges through complex network of fibrous tissues. It is known to be a major contributor to arch support via the "windlass mechanism" and has the potential to transfer Achilles tendon forces to the forefoot (Hicks, 1954). Recently, Hamel et al. (2001) investigated the influence of plantar fasciotomy on forefoot loading and Carlson et al. (2000) examined PA strain in relation to toe extension and Achilles force. However, the load transfer mechanism between the Achilles tendon and the forefoot under lifelike conditions remains poorly understood. The objectives of this study were to measure PA force during cadaver simulations of walking and to determine its magnitude relative to Achilles tension.

METHODS

Seven cadaver feet (age: 66 ± 20 y; BM: 57.2 ± 10.0 kg) were tested in a Dynamic Gait Simulator (DGS; Sharkey and Hamel, 1998). The DGS prescribes knee kinematics and applies forces to the tendons of extrinsic foot muscles to reproduce foot motion and the ground reaction forces occurring during the stance phase of walking. The PA was exposed by dissecting a strip of superficial plantar tissue (~ 2 cm) anterior to the calcaneal origin. A fiberoptic cable was passed through the PA perpendicular to its longitudinal axis to measure PA force (Komi et al., 1996). Tendon forces applied by the DGS, ground reaction forces, and raw fiberoptic output from the PA during walking simulations were recorded simultaneously.

Following experimental measurements, the transducer was calibrated *in situ* by applying known forces to the PA using a materials testing device (MTS Sys. Corp.). The specimen was placed in a fixture with the calcaneus and forefoot potted and midfoot structures except the PA dissected. The fixture aligned the longitudinal axis of the PA with the loading axis of the MTS. The calibration loading rate approximated loading rates experienced in the walking simulations, and cable migration was monitored to reduce the potential for error (Erdemir et al., *in press*).

RESULTS AND DISCUSSION

PA tension increased gradually until push-off (Figure 1). Peak forces (0.6-1.5 BW) were found to be lower than the model predictions of Giddings et al. (2000). The fiberoptic technique may be subject to errors due to twisting of the PA, but the PA forces measured were well below published PA failure loads (Kitaoka et al., 1994). A linear fit using data from all specimens revealed PA force to be a function of Achilles tension (PA force = 0.47 x AT force + 0.041 BW, $R^2 = 0.58$).

The PA is loaded substantially during stance phase as a combined result of toe extension and contraction of the extrinsic plantarflexors and was shown to be a vital structure for load transmission during normal gait. Surgeries involving partial or full fasciotomy may alter this load transfer mechanism and disturb dynamic function of the foot.

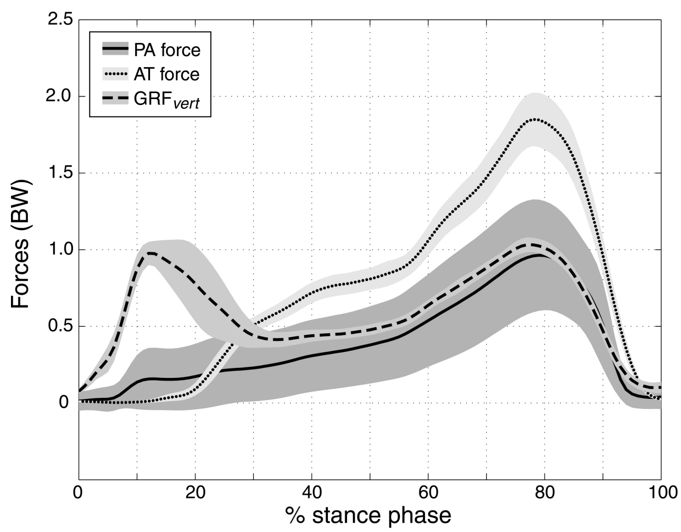

Figure 1. Plantar aponeurosis, Achilles and vertical ground reaction forces, normalized by body weight (mean ± SD).

REFERENCES

Carlson, RE et al (2000) *Foot Ankle*, **21**, 18-25.
Erdemir, A et al (*in press*) *J Biomech*
Giddings, VL et al (2000) *Med Sci Sports Exerc*, **32**, 627-634.
Hamel, AJ et al (2001) *Clin Orthop*, **393**, 326-334.
Hicks, JH (1954) *J Anat*, **88**, 25-31.
Kitaoka, HB et al (1994) *Foot Ankle*, **15**, 557-560.
Komi, PV et al (1996) *Eur J Appl Physiol*, **72**, 278-280.
Sharkey, NA, Hamel, AJ (1998) *Clin Biomech*, **13**, 420-433.

ACKNOWLEDGMENTS

This study was partially supported by International Society of Biomechanics matching dissertation grant.

IN-VITRO MEASURMENTS OF TARSOMETATARSAL JOINT STIFFNESS

Andrew R. Fauth[1], Andrew J. Hamel, and Neil A. Sharkey[1,2]

Center for Locomotion Studies, The Pennsylvania State University, University Park, PA
[1]Department of Kinesiology, The Pennsylvania State University, University Park, PA
[2]Department of Orthopaedics and Rehabilitation, The Pennsylvania State University, Hershey, PA
email: nas9@psu.edu url: www.celos.psu.edu

INTRODUCTION

The tarsometatarsal joints (TMT) of the midfoot are complex articulations involving the three cuneiforms, the cuboid, and the metatarsal bones. Since the medial TMT joints are located along the medial longitudinal arch, the torsional stiffnesses of these joints play important roles in arch deformation, force transfer, and energy storage during gait (Lakin, 2001).

Stokes et al. (1976), used metatarsal geometry, force data, and quasi-static calculations to estimate the axial loads, shear loads, and bending moments routinely imposed on the TMT joints. Recently, Jacob (2001) improved on Stoke's calculations by incorporating more precise metatarsal geometry and forefoot loading criteria. Knowledge of TMT joint stiffness, as defined by torque versus angular displacement curves, could provide a basis from which to judge the accuracy of these computational estimates. Yet, there is little, if any, empirical data concerning the structural properties of the TMT joints. The objective of this *in vitro* study was to determine the torsional stiffness of the 1st TMT joint under physiologic moments.

METHODS

Six cadaver feet were dissected to yield intact midfoot sections composed of the mid-tarsal (navicular, cuboid, and cuneiform) and metatarsal bones. Care was taken to preserve the joint capsule and ligamentous structures at the 1st TMT. The tarsus of each sample was potted in PMMA to a level just proximal to the TMT joint line, and the 1st metatarsal head was fitted with a linkage for distal load application. The preparation was then mounted in an unconstrained testing apparatus, which applied force to the metatarsal head in a direction perpendicular to the long axis of the bone.

Each specimen was cyclically loaded in sequential fashion to pre-determined peak torque levels: 2.5, 5.0, 7.5, and 10 N-m. For each peak torque, ten conditioning cycles were executed, followed by six test cycles. Joint loading was conducted at 0.05 Hz; force and displacement data were sampled at 100 Hz. Data were averaged over the six test cycles and across all specimens, and then curve fit to obtain mean torque-angle curves for each peak torque level.

RESULTS AND DISCUSSION

The 1st TMT joint displayed nonlinear behavior, indicated by the dependence of joint stiffness on flexion angle ($T=K(\theta)*\theta$). A least squares curve fit defined 1st TMT joint stiffness as $K(\theta) = 3.23*10^{-4}\ \theta^3 + 3.85*10^{-4}\ \theta^2 + 1.04*10^{-3}\ \theta + 0.0693$ (Fig.1). The torque versus angular displacement curves displayed a transition point at approximately 4 degrees of dorsiflexion, which corresponded to a joint torque of 0.4 Nm. Below this threshold, joint stiffness was essentially constant at 0.1 Nm/deg. Beyond the 4 degree threshold, joint stiffness changed markedly as a function of dorsiflexion as characterized by the cubic polynomial, $K(\theta)$. For example, at a higher angular displacement of 9 degrees, joint stiffness increased to 0.34 Nm/deg.

Previous quasi-static models of the 1st TMT generalize the contributions of soft tissue by combining different muscle actions into one force vector, and neglecting the contributions of supporting structures such as the plantar fascia, which may lead to an overestimation of joint torque (Jacob 2001). The joints tested in this study dramatically increased in stiffness beyond a threshold displacement of approximately 4 degrees dorsiflexion, which is also the normal limit of motion defined by Wanivenhaus (1989). Taken together, these data suggest that the joint torques experienced at the 1st TMT during normal dynamic conditions may be substantially lower than values predicted by previous computational analyses.

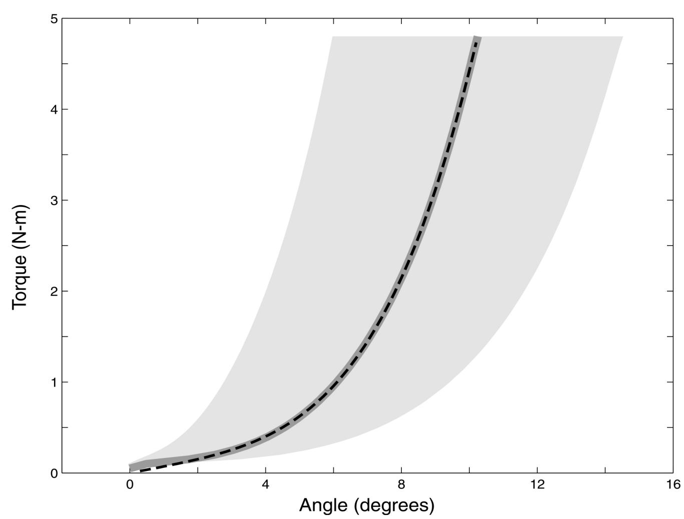

Figure 1. Mean torque-angle curve with standard deviations for 6 first TMT joints. The dashed line, $T= K(\theta)*(\theta)$ represents the non-linear polynomial that defines joint stiffness.

REFERENCES

Lakin R.C. et al. (2001). *Bone Joint Surg*. **83,** 520-528.
Jacob H.A.C. (2001). *Clin Biomech*. **16**, 783-792.
Stokes A.F. et al. (1979). *J. Anat*., **129**, 579-590.
Wanivenhaus A., Pretterklieber M. (1989). *Foot and Ankle* **9**, 154-157.

ACKNOWLEDGEMENT

This work was supported by NIH grant 5 R01 HD37443-02.

WITHIN-SUBJECT VARIABILITY OF PLANTAR PRESSURE PATTERNS IN BAREFOOT RUNNING.

De Cock A. [1], Willems T[2]., Stal S. [1] and De Clercq D. [1]
[1]University of Ghent, Departement of Movement and Sport Sciences, Watersportlaan 2, 9000 Ghent
[2]University of Ghent, Departement of Rehabilitation Sciences and Physiotherapy, De Pintelaan 185 6K3, 9000 Ghent
dirk.declercq@rug.ac.be

INTRODUCTION

Dynamic plantar pressure measurements offer a unique opportunity to asses foot functioning during stance phase in running. However a biomechanical or clinical interpretation has to take within-subject, or between-trial variability into account. Only Cornwall and McPoil (2000) studied within-subject variability for LMFI (Lateral-Medial Force Index) and LMAI (Lateral-Medial Area Index) obtained during 3 trials of barefoot walking. Intraclass Correlation Coefficient (ICC) values were .386 and .374 respectively.
The purpose of this study was first to investigate the between-trial variability for a large number of variables deduced from plantar pressure measurements. Second, difference was studied between left foot and right foot pressure data.

METHOD

Plantar pressure data were collected from 80 healthy undergraduate physical education students without lower extremity abnormalities. A footscan pressure plate (RsScan nv., 2m x 0.4m, 16384 sensors, 480 Hz, dynamic calibration with AMTI) was mounted in the middle of a 16.5m long wooden running track. The subjects were asked to run barefoot at a speed of 3.3m/s (+/- 0.17m/s). Prior to the measurements, all subjects performed habituation trials. Three valid left and three valid right stance phases were measured. After testing one observer placed 8 regions (medial heel, lateral heel, metatarsal heads I to V and hallux) on the footprints for all trials. Temporal data (i.e. time to peak pressure, instants on which the regions make contact and instants on which the regions end footcontact) peak pressure data and relative and absolute impulses were calculated for all 8 regions. Eight medio-lateral ratio's were calculated at four instants of the footcontact, namely initial contact (IC), midstance (Mst) – i.e. contact of one of the metatarsal heads –, foot flat (FF) – i.e. contact of all metatarsal heads – and heel off (HO). Excursion ranges of these ratio's were calculated over three intervals (IC-Mst, Mst-FF and FF-HO) and also medio-lateral displacements of center of pressure. Between-trial variability was investigated by using ICC (SPSS 10.0). Differences between left foot trials and right foot trials was studied by using a paired sample T-test.

RESULTS AND DISCUSSION

The ICC values are summarized for 5 categories of plantar pressure variables in table 1. ICC values for total contact time are .843 for the left foot and .789 for the right foot, and therefore temporal variables are absolute reported.
In general, peak pressure variables and impulses, show rather high ICC values (mostly above 0.7). The temporal variables show very different ICC values with between-trial variability becoming lower during forefoot contact. This is also true for the medio-lateral ratio's. Also the impulses showed high ICC values for the regions in the forefoot, but lower ones for the heel regions. On the other hand, peak pressure variables showed an overall low between-trial variability. Medio-lateral COP displacements showed low ICC values. Two factors may play a role here. First, these variables are calculated on time instants and over time intervals and therefore timing dependent (with rather large variability). Second, in each footprint the observer had to define a foot axis (metatarsal II – middle of the heel) as a reference for COP location. A minor shift of this axis in the three trials may induce between trial variability. Most variables deduced from plantar pressure measurements during barefoot running display good ICC (26% > 0.7) to sattisfactory ICC (68% > 0.5) with mid-forefoot contact period in favour. Higher variability is assumed present due to the transient nature of initial heel contact. In the second part of the study, differences between left foot contacts and right foot contacts were found, especially in the calculated values of the medio-lateral ratio's. Also peak pressure variables showed differences between left and right foot.
In conclusion, for interpreting purposes it is important both (1) to measure a sufficient numner of trials, and (2) to analyse left and right foot trials seperately.

REFERENCE

Cornwall, MW, McPOil, TG (2000). Analysis of the center of pressure gait line and its relationship to rearfoot motion, *emed Scientific Meeting, 2-6 August 2000*

ACKNOWLEDGEMENTS

This study was partly supported by BOF-RUG 01109001.

Table 1: ICC values for between trial variability and the significant differences between left foot and right foot trials

	ICC values for the left trials between	ICC values for the right trials Between	Left-right variability Significant difference
Temporal variables:			
- **time to peak pressure**	.424 and .735	.326 and .670	3 of 8
- **time to first contact**	.607 and .698	.578 and .715	1 of 8
- **time to end contact**	.755 and 827	.427 and .776	1 of 8
Peak pressure variables	.539 and .831	.579 and .865	4 of 8
Medio-lateral COP displacements	.090 and .729	.099 and .594	0 of 7
Impulses			
- **absolute**	.572 and .818	.448 and .839	3 of 8
- **relative**	.585 and .854	.361 and .820	3 of 8
Medio-lateral ratio's	.144 and .769	.187 and .712	24 of 44

REACTION TIMES DURING A SIMULATED BASEBALL-FIELDING TASK ARE INFLUENCED BY BASEBALL VELOCITY, LEVEL OF ATTENTION, AND AGE

Tammy M. Owings[1], Sarah L. Lancianese[1], Elissa Lampe[1], and Mark D. Grabiner[1, 2]

[1] Department of Biomedical Engineering, Cleveland Clinic Foundation, Cleveland, Ohio, USA
[2] School of Kinesiology, University of Illinois at Chicago, Chicago, Illinois, USA
Email: owings@bme.ri.ccf.org

INTRODUCTION

Nearly 90% of catastrophic injuries in youth baseball occur by direct contact of a baseball or a baseball bat to the head, neck, or chest of the youth (Rutherford et al., 1984). The potential for injury is increased if the time required for a batted ball to reach a given field location is less than the reaction time of the player. This project investigates the reaction times of young baseball players performing a simulated fielding task and characterizes how ball velocity and level of attention influence reaction time for various age groups of boys and girls.

METHODS

Fifty boys and 50 girls (ages 8-16 years) who participate in competitive/recreational baseball programs were recruited. Each youth stood in a standard fielding position and were asked to simulate a baseball catch when a baseball was projected towards them. A pitching machine, located 45 feet away and directed toward the youth, was employed to project the baseballs. A safety net, located 10 feet in front of the youth (i.e., between the youth and the pitching machine), was used to protect the youth from the incoming baseball. Forty trials were performed. Trials were randomly blocked by level of baseball velocity: 60 mph and 75 mph. Within each block, trials were randomly divided between two levels of attention: full attention and split attention. Examples of split attention tasks include counting backwards, naming familiar objects, or spelling difficult words. Split attention tasks varied between trials and were gauged to the age of the youth. The data collection included motion capture of the baseball and of three reflective markers placed on the youth's baseball glove. The instant of ball projection was quantified with an accelerometer and synchronized with the motion capture data. Reaction time was calculated as the time from the instant of ball projection until initial motion of the baseball glove. Statistical analysis involved a 2x2 (ball velocity by level of attention) repeated measures ANOVA using age as a covariate and sex as a between-subject factor.

RESULTS AND DISCUSSION

When the ball was projected at 75 mph, reaction times were significantly faster than when the ball was projected at 60 mph ($p<0.01$). Reaction times were significantly faster when the youth were at full attention compared to split attention ($p<0.01$). The older age groups had significantly faster reaction times compared to the younger age groups ($p<0.01$). Reaction times did not differ significantly between boys and girls ($p>0.05$). A significant sex by level of attention interaction was identified ($p<0.01$). All other interactions were not significant (all $p>0.05$).

Surprisingly, the faster ball velocity produced faster reaction times. It is currently unknown if ball velocities greater than 75 mph would elicit faster reaction times. Another unexpected finding was the sex by level of attention interaction. For the full attention trials, boys and girls did not differ in reaction time. For the split attention trials, girls reacted 20 msec slower than during the full attention trials, whereas boys showed no change in reaction time between the full attention and the split attention trials. Although this suggests that girls had a more difficult time performing multiple tasks, the delay in reaction time during the split attention trials was expected.

REFERENCES

Rutherford, G.W. et al. (1984). *Hazard Analysis: Baseball and Softball Related Injuries to Children 5-14 Years of Age.* Washington, DC: US Consumer Product Safety Commission.

ACKNOWLEDGMENTS

Funded by a grant from The National Operating Committee on Standards for Athletic Equipment. The opinions expresses herein are those of the authors and do not necessarily reflect the opinions of the Committee.

Table 1: Reaction times (msec) for youth (n=100) performing a simulated fielding task (mean ± standard deviation).

	Boys				Girls			
	60 mph		75 mph		60 mph		75 mph	
Age	Full	Split	Full	Split	Full	Split	Full	Split
8-9 yrs	223 ± 27	215 ± 42	202 ± 43	207 ± 29	220 ± 40	231 ± 50	200 ± 54	219 ± 60
10-11 yrs	225 ± 29	227 ± 52	194 ± 26	190 ± 30	210 ± 36	239 ± 97	187 ± 29	235 ± 44
12-13 yrs	184 ± 19	209 ± 56	179 ± 27	183 ± 42	184 ± 42	213 ± 55	173 ± 45	216 ± 66
14-15 yrs	194 ± 25	191 ± 28	172 ± 20	164 ± 48	189 ± 42	213 ± 55	176 ± 45	194 ± 66
16 yrs	181 ± 33	183 ± 32	177 ± 23	171 ± 28	189 ± 25	211 ± 44	179 ± 29	187 ± 36

STEADINESS IN YOUNG AND ELDERLY BEFORE AND AFTER A 5-WEEK PERIOD OF STRENGTH TRAINING

Jesper Sandfeld[1], Bente R. Jensen[2]
[1]National Institute of Occupational Health, Denmark (Jes@ami.dk)
[2]Institute of Exercise and Sports Sciences, University of Copenhagen

INTRODUCTION

At present, not only the young but also the elderly part of the work force uses computer and computer mouse to solve the daily tasks at work. These instruments require extensive fine motor control skills, which seem to be reduced with age (Grimby & Saltin, 1983, Enoka et al. 1999, Laursen et al. 2001). Loss of fine motor control skills as e.g. impaired steadiness may affect the ability to perform everyday working tasks. The aim was to study hand-steadiness in young and elderly and to evaluate the effect of training.

METHODS

25 subjects participated in the study. 12 young (27 ± 2.6 yrs. (SD), 6 females, 6 males.) and 13 elderly (67 ± 3.8 yrs. (SD), 6 females, 7 males).

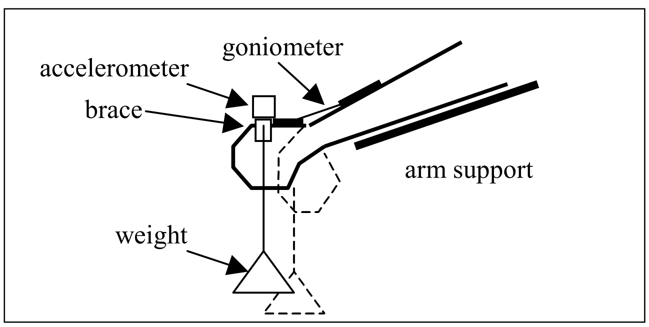

Figure 1. The experimental set-up

The subjects performed wrist extension/flexion tasks. Wrist movements measured with electro-goniometer were displayed on a computer screen. The task for the subjects was to follow a pre-defined trace displayed on a computer screen (duration = 20 s), which required the subject to perform a wrist extension (concentric contraction) from a vertical to a horizontal position for 7 s (constant angular velocity of 12.8°/s), maintain the horizontal wrist position for 6 s (isometric) and finally to lower the hand (eccentric) back to vertical position (7 s).
The task was performed 12 times. Three times with each of 4 loads: 0 (hand weight), 4, 12.5 and 25% of isometric maximum voluntary contraction (MVC). The loads are average loads, calculated on the basis that the moment arm changes during the movement described. Test order was randomised. Hand-steadiness was measured as standard deviation of the acceleration.
Training consisted of 5 weeks of heavy strength training of arm and shoulder muscles. Three sessions each week with 3 sets of 4-8 repetitions for each muscle group were obligatory. Steadiness and wrist extensor muscle strength (isometric and dynamic (isokinetic in Biodex System 3)) were measured before and after the 5 weeks of training.

RESULTS AND DISCUSSION

Before training, steadiness during concentric wrist extension was significantly reduced in the elderly group compared to the young at the loads 0, 4 and 12.5 %MVC ($p \leq 0.05$). Changes in fine motor control during ageing are considered to be due to neurological and morphological changes. After training the isometric MVC in the wrist extensor muscles in the young group increased 12.4% ($p \leq 0.05$), but only a tendency to an increase in dynamic strength was found (10%, $p=0.1$). In the elderly group the isometric MVC increased 12.0% and dynamic strength increased 14.0% ($p \leq 0.05$). A 5-week training period mainly influences neurological factors. Thus, changes in steadiness due to training are assumed primarily to be an effect of changes in the neurogical parameters. After training an improvement in steadiness was found in the young group at the load of 4%MVC ($p \leq 0.05$). For the elderly group steadiness improved for loads corresponding to 0, 4, 12.5%MVC ($p \leq 0.05$) (Fig 2). Steadiness measured during isometric and eccentric contraction mirror to a large extent the results from the concentric contraction, indicating a general improvement of hand-steadiness.

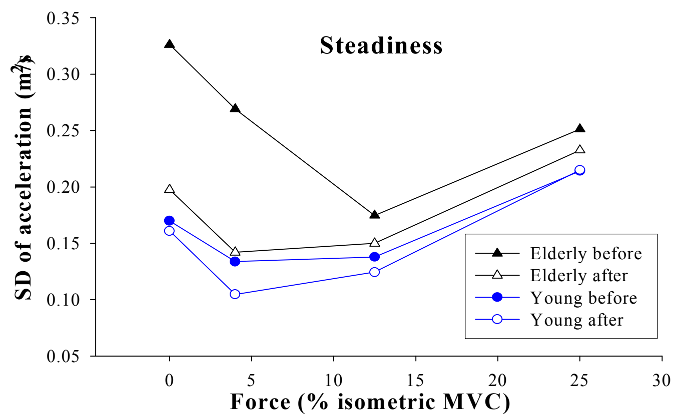

Figure 2: Steadiness during concentric wrist extension before and after heavy strength training.

CONCLUSION

After training the hand-steadiness of the elderly group during concentric wrist extension reached the pre-training levels of the young group. This indicates that changes in steadiness due to age to a large extent are a result of neurological changes, which can be reversed by a short period of strength training.

REFERENCES

Grimby, G., Saltin, B. (1983). *Clinical Physiology,* **3**, 209-218.
Enoka, R.M. et al. (1999) *Prog. in Brain Research., Vol 123, chapter 34.* Elsevier Science
Laursen, B., Jensen, B.R., Ratkevicius, A. (2001). *European Journal of Applied Physiology,* **84**(4), 329-36

UPPER EXTREMITY IMPAIRMENT IN WHEELCHAIR PROPULSION

Margaret A. Finley[1,2,3], Randall E. Keyser[1], Rhonda Stanley[1] and Mary M. Rodgers[1,2]

[1]University of Maryland School of Medicine, Baltimore, MD USA
[2]Baltimore Veterans Administration Medical Health Care System, Baltimore, MD, USA
[3] Communicating Author: mfinley@som.umaryland.edu

INTRODUCTION

Many manual wheelchair users (MWCU) have upper extremity impairment (UEI) due to paralysis or motor control deficits. In spite of their UEI, these individuals are functionally independent. Maximal isometric strength has been reported to have an inverse relationship to physical strain during certain functional tasks. (Dallemeijer, 1996) Additionally, level of spinal lesion was directly related to dynamic propulsion characteristics, however, without specific classification of UEI. (Dallemeijer, 1996,1994) The purpose of this study was to compare biomechanical characteristics of dynamic (MzD) and static (MzS) propulsive moments in functionally independent MWCU with and without UEI. It was hypothesized that 1) MWCU with UEI would demonstrate smaller MzD and MzS compared with those without UEI and 2) relationship exists between UEI and specific functional tasks.

METHODS

Subjects included 38 MWCU (12 with UEI, 26 without UEI, mean age = 38.1±8.4 years, WC use = 11.3±8.4 years). Following informed consent and medical screening, propulsion mechanics were measured during a maximal exercise test to exhaustion (defined as volitional inability to sustain the target velocity of 3km/hr). A wheelchair ergometer instrumented with a PY-6 six-component force/torque transducer (Bertec Corp, Worthington, OH) in the wheel hub was used to measure handrim forces and moments. Orientation of the x-y-z transducer coordinates was tangential (forward+), radial (up+) and medial-lateral (into the wheel+), respectively. MzD was defined as the propulsive moment occurring at the peak power output (POpeak). Handrim data was collected at 360 Hz and averaged over three cycles. For the MzS, subjects placed their hands at top-dead -center of their wheel and gave three maximal forward propulsion efforts with the wheelchair held stationary. Force from this maximal propulsive motion was collected at 30Hz using a uniaxial (200 lb max) force transducer (Transducer Technologies, Temecula, CA) attached to the rear aspect of the wheel. For MzS, peak force from each of the three trials was averaged and mathematically converted to moments based on the radius of the wheel. All subjects performed a 13 item functional test developed to assess level of independence in MWCU. The Wheelchair Users Functional Assessment (WUFA©) includes home and community mobility skills. (Feliciano,1994)

Pearson product moment correlations determined relationships between MzD, MzS and the 13 functional tasks ($r^2 \geq 0.3$). ANOVA was used to determine if differences existed between the groups in MzD, MzS and tasks correlated to these measures ($p \leq 0.05$). ANCOVA determined differences in MzD between groups with POpeak covaried.

RESULTS

Total WUFA scores (UEI = 83.5, without UEI = 84.0) and MzS (UEI = 24.2Nm, without UEI = 31.8 Nm) were not different between the groups. Four tasks (wheelchair propulsion of street crossing, ascending a ramp, and ascending a curb, and rising from the floor to wheelchair) correlated to the propulsive measures and POpeak (Table1). POpeak ($p< 0.01$) and MzD ($p = 0.025$) were significantly lower for the UEI group. However, when POpeak was covaried, MzD was not different between those with UEI and those without UEI.

Table 1: Pearson Product Moment Correlation of Biomechanical Measures vs Functional tasks

	Street crossing	Ramp	Curb	Floor-WC
MzD	0.47	0.54	0.48	0.35
MzS	0.56	0.44	0.44	0.46
POpeak	0.61	0.54	0.69	0.50

DISCUSSION/CONCLUSION

Although static and dynamic measures were lower in the MWCU with UEI, there was no difference in their level of functional independence. Correlations found were similar to findings in previous studies. MWCU with UEI were able to propel at the same proportion of their maximum effort as those without UEI. These findings may provide insight into how MWCU with UEI remain functionally independent.

REFERENCES

Dallmeijer, A. et al (1996) Spinal Cord; 34, 729-735
Dallmeijer, A et al (1994) J Rehab Res Dev; 31(2), 120-128
Feliciano, et al. **(**1998) APTA Sect Res Newsletter 30(3): 10.

ACKNOWLEDGEMENTS

The Veterans Affairs Rehabilitation Research and Development Service (Merit Review Board Project #B2168RA) supported this project.

INVESTIGATIONS ON THE BIOMECHANICS OF AN OSTEOCHONDRAL IMPLANT BY FE ANALYSIS

Frederic Turquier[1], Diane Dan[2], Mark Smith[1], Argiris Kamoulakos[2], Sandra Downes[1]

[1] Smith&Nephew Group Research Centre, York YO10 5DF, England, frederic.turquier@smith-nephew.com
[2] Engineering System International, 94 513 Rungis, France

INTRODUCTION

Articular cartilage repair is one of the key fields in tissue and cell engineering. However, very few studies deal with the mechanical environment required to enhance this process (Smith C. 2001, Wu J. Z. 2001). The goal of this study is to investigate the biomechanics of an osteochondral implant once in place. More specifically, the combined influence on the implant performance of the articular surface alignment mismatch (V1), the implant material properties (V2), and the implant/host integration (V3) has been studied under static loading conditions.

METHODS

The investigations were carried out with a 3D Finite Element model of a "ball in a socket" which represented the human medial knee compartment (femoral condyle on the tibial glenoid). The effect of the meniscus was taken into account by removing 40% of the load. The focal defect was assumed cylindrical (r = 8 mm), limited to the femoral cartilage and located at the vertical of the contact point. The cartilage, subchondral plate and trabecular bone were represented. Geometrical features and material properties, which were assumed isotropic homogeneous and linear elastic, corresponded to average values found in the literature. The implant was composed of two layers : the fabric (3.5 mm thick) and the cover (1 mm thick). It matched the defect in terms of radius. Finally, a standing up equivalent static load (176.58 N) was applied vertically onto the femur (Figure 1).

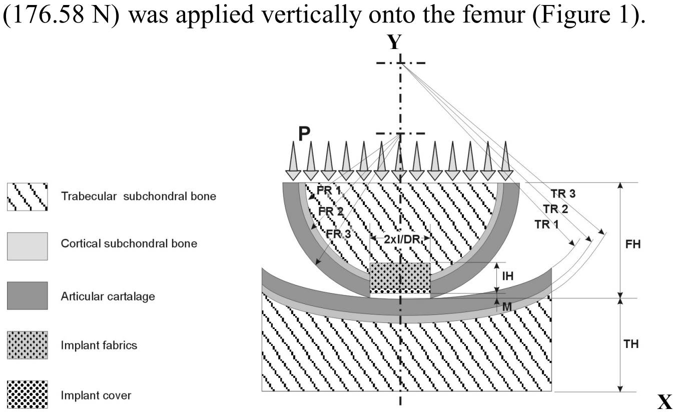

Figure 1 : Section of the system with implant

V1 took the values 0 mm and –0.5 mm. The variations of V2 corresponded to $E_{implant\ fabric}$ of 30% and 75% $E_{cartilage}$ (E defined as the Young Modulus). V3 equalled total (T) and zero (N*) integration at the implant/host radial interface. The combination of these 3 variables resulted in 8 different configurations including the ones used as references : with (D_{ref}) and without (N_{ref}) damage. The numerical simulations were performed with the code PAM SAFE (ESI Group).

RESULTS AND DISCUSSION

The result coherence and consistency were checked, and the model was judged suitable for qualitative purpose.
The model simulated the primary mode of failure related to a chondral focal defect. Indeed, the simulations showed a large deformation of the femoral cartilage at the edge delimited by the focal defect. This resulted in maintaining a large contact area with a moderate increase of the normal/vertical stresses compared to the healthy tissue configuration (N_{ref}). However, the tensile radial strains (X) in the cartilage corner rose up by +425% (Figure 2).

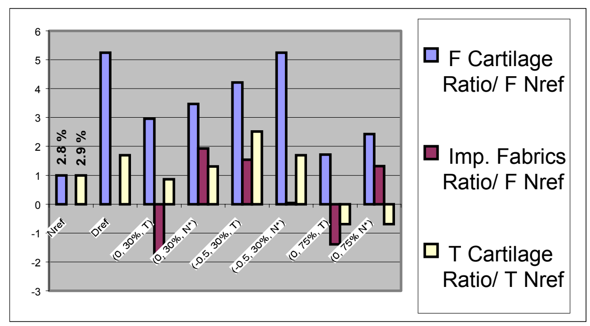

Figure 2 : Radial strains in cartilage and implant fabric

When $E_{implant\ fabric}$ equalled to 30% of $E_{cartilag}$ and V3 took N*, the increase of the tensile radial strains was reduced to +250%. Moreover, maximum radial (X) and normal (Y) strains within the fabric were found to be significantly higher than in the healthy tissue. In addition to the above results, it was found that, with the - 0.5 mm positioning mismatch below the articular surface, the implant behaved as void filler with no mechanical contributions. Finally, the implant material properties appeared to be very influential on the mechanical response.

CONCLUSION

The implant works against the primary failure mode by taking part of the total load, and by limiting directly the radial deformation when it interacts with the wall of the focal defect. With V1 equals to -0.5 mm, almost no load is transferred by the implant and therefore it behaves as a void filler. V2 was found very influential. Indeed, V2 drives the stiffness of the implant and consequently controls the load sharing. Due to the numerous modelling assumptions, the results have to be considered from a qualitative point of view only. Further steps will consist of refining the model and carrying out a sensitivity study.

REFERENCES

Smith C. and al., (2001). *Proceedings of ORS 2001*, 0442
Wu J. Z. and al., (2001). *Proceedings of ORS 2001*, 0429

MICROSTRUCTURAL ASSESSMENT OF TRABECULAR BONE FAILURE BEHAVIOR

Ara Nazarian[1,2], Martin Stauber[2] and Ralph Müller[1,2]

[1]Orthopedic Biomechanics Laboratory, Beth Israel Deaconess Medical Center, Harvard Medical School, Boston, MA, USA
[2]Institute for Biomedical Engineering, Swiss Federal Institute of Technology, Zürich, Switzerland

INTRODUCTION

Osteoporosis occurs most frequently in post-menopausal women and the elderly. It is defined as a systemic skeletal disease characterized by low bone mass and micro-architectural deterioration of bone tissue, with a concomitant increase in bone fragility and fracture risk[1,2]. Until recently the structural analysis of these fractures has been limited to two-dimensional sections. More recently, an image-guided technique, utilizing micro-compression in combination with micro-computed tomography (micro-CT), has been developed, which allows direct three-dimensional visualization and quantification of fracture progression on the microscopic level[3]. The goal of this project was first, to design a new micro-mechanical testing system, composed of the micro-compression device (MCD) and the material testing and data acquisition system (MTDAQ), and second, to validate the testing system to perform step-wise testing of trabecular bone specimens using image-guided failure analysis (IGFA).

METHODS

IGFA is based on time-lapsed compression and imaging of bone specimens. The testing protocol consists of applying sequential compression steps of 0%, 2%, 4%, 8%, 12%, 16% and 20% global nominal strain, while simultaneously measuring nominal stress. The specimen is imaged after each strain step to observe microstructural deformation. The MCD is designed to house the test specimens and act as a transportable link between the mechanical testing and micro-CT imaging. Previously, the MCD was loaded axially via a standard Instron-type mechanical testing system. The axial strain was applied through a pushpin on the MCD cap and locked manually. This combination introduced errors in the form of strain application fluctuation, due to reduced sensitivity of the testing machine at small strains, and the application of unknown manual torque in the strain locking process. In order to alleviate these problems, the MCD is instead interfaced with the MTDAQ. This system is designed to introduce axial strain to the specimen using a custom micro-stepping compression actuator. Also, an onboard LVDT measures the applied strain of the specimen. To establish accuracy and reproducibility of this new device, a total of 61 specimens were cored along the principal trabecular axis and cut into cylinders of ∅ 8 mm x 12 mm for human vertebral specimens (n=31), and ∅ 8 mm x 16 mm for whale vertebral bone (n=20) and ERG aluminum foam (n=10) specimens. The specimens were then divided into two groups with similar mass and densities and one group was tested from 0-20% strain based on conventional continuous mechanical testing, while the other was tested from 0-20% strain using IGFA.

RESULTS

Mechanical properties obtained from the continuous and step-wise methods were not significantly different for aluminum foam, whale and human trabecular bone specimens. Both testing methods yielded very similar stress-strain graphs with almost identical elastic and plastic regions. In aluminum specimens a general trend of buckling was observed within the structure due to imposed strain, where the individual structural elements throughout the entire specimen tended to bend and buckle. However, failure was observed differently in whale and human trabecular bone specimens. In these cases, a transaxial subregion of the specimen would fold dramatically with the associated individual trabeculae experiencing high levels of deformations such as bending and buckling, whereas the remaining regions and elements were kept relatively intact. It was observed that although the mineral phase of the bone failed in a brittle manner, it showed a very ductile post failure behavior indicating that the collagen network is able to keep the trabeculae together over a large range of strains.

DISCUSSION

A novel MTDAQ was successfully designed and validated for step-wise IGFA and time-lapsed micro-CT imaging. One of the limitations of the system was the load frame compliance, which can be partially accounted for if incorporated in the strain measurements of the specimens. Another limitation was the method of displacement measurement, which measures the displacement of the end-effector. In order to measure the specimen's mid-axis strain, a novel strain measurement technique is currently under investigation. In summary, step-wise micro-compression yielded the same mechanical properties as classical continuous tests for porous materials, and IGFA provided insight in the pre and post failure behavior of these structures.

REFERENCES

1. Kanis, JA, (1994). Osteoporosis. Blackwell Science
2. Kleerekoper et al. (1985). Calcif. Tiss. Int, 37, 594-597
3. Müller et al, Technology and Health Care, 6, 433-444

MICROCRACK DETECTION AND MECHANICAL PROPERTY MEASUREMENT OF BONE USING SCANNING ACOUSTIC MICROSCOPE

Hiroyuki Fujiki[1], Michiaki Kobayashi[1], Seiichi Oomori[1] and Yukio Nakatsuchi[2]

[1]Department of Mechanical Engineering, Kitami Institute of Technology, Kitami, Hokkaido, Japan
fujiki-hiroyuki/me@king.cc.kitami-it.ac.jp
[2] Department of Orthopedic Surgery, National Nagano Hospital, Ueda, Nagano, Japan

INTRODUCTION

Microcracks in bone are assumed to increase the risk of bone fractures and to stimulate bone remodeling. Several methods of histochemical staining have been reported to detect the microcracks in fresh and undecalcified sections of bone. However, in order to clarify the process of the insidious micro bone fractures, it may be important to know the biomechanical changes of bone properties surrounding the microdamages. In this paper, the detection of microcracks in bone without staining and the measurement of mechanical properties around the microcracks were attempted using the scanning acoustic microscope (SAM).

MATERIALS AND METHODS

The femurs of old females (65 years old and 86 years old) and of young beagle dog (8 months old) were harvested and trimmed into some parts with a bone saw. The specimen was embedded in Specific20 (Struers), anacrylic resin consolidated in lower temperature, with impregnation by a vacuum pump and the surface of specimen was polished with diamond papers.

H-SAM200 (Hitachi Construction Machinery Co.) was used as the SAM machine and a 200MHz of ultrasound was used in the observation. Four kinds of measurement were performed: acoustic impedance obtained from C-mode imaging, ultrasound velocity from XZ-mode imaging, elastic modulus and density calculated from the intensity of reflected wave by comparison with that of aluminum.

RESULTS AND DISCUSSION

Figure 1 shows the C-mode image sample. As shown in this figure, microcracks were detected easily by SAM though it was difficult to find the cracks by optical microscope with no staining.

Figure 2 shows the distribution of bone density around the microcrack shown in Fig. 1. It was clarified that micro scale distribution of material properties of bone could be measured using SAM and the density and the elastic modulus of bone were decreased around microcracks.

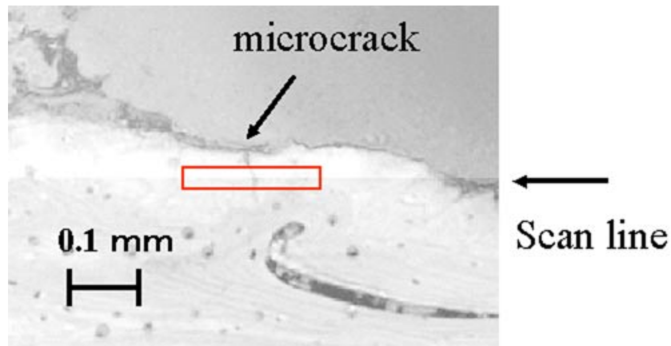

Figure 1: C-mode image at trochanter major of old female. Red rectangular indicates the measured area for mechanical properties.

In the measurement of young beagle dogs, microcracks were also detected and low density material was found at a microcrack. It would be estimated as the callus by its mechanical properties, and this indicates the development of the callus in the repair process of microcrack same as in that of macro scale bone fracture.

CONCLUSION

By SAM measurement, microcracks in bone were detected easily without staining and it was clarified that the mechanical properties around microcracks decrease and the occurrence of callus in repair process of microcrack are predicted. SAM could be utilized for identification of microcracks as well as for evaluation of its microscale biomechanical properties.

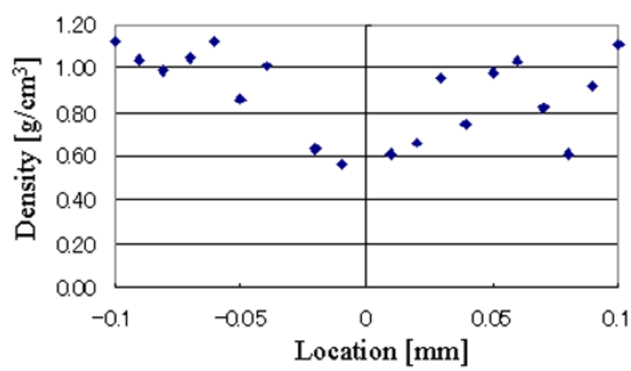

Figure 2: Distribution of density around the microcrack shown in Fig. 1. The density decreases around the crack.

KINEMATICS OF THE HEART

Pernilla Selskog[1], Einar Heiberg[1,2], Tino Ebbers[2], Lars Wigström[1,2] and Matts Karlsson[1]
Linköpings universitet , Linköping, Sweden
[1]Dept. of Biomedical Engineering, [2]Dept. of Medicine and Care

INTRODUCTION

The heart muscle (myocardium) has anisotropic, non-linear and time-dependent mechanical properties and is a complex three-dimensional structure. During the cardiac cycle, the myocardium undergoes large elastic deformations as a consequence of the active muscle contraction along the muscle fibers and their relaxation, respectively. A four-dimensional (4D) description (three spatial dimensions + time) of the mechanical properties of the myocardium may be of interest in the assessment of myocardial function. Time-resolved 3D phase contrast MRI makes it possible to quantify all three-velocity components, which is necessary to accurately describe the velocities in the heart. We present a method for estimation of myocardial kinematics using 3D time-resolved phase contrast MRI.

METHODS AND RESULTS

The 3D cine phase contrast MRI pulse sequence provides velocity vector information in a 3D spatial grid throughout the cardiac cycle (Wigström et al 1996). Unwanted magnetic gradient fields produced according to the Maxwell equations and phase shifts due to Eddy currents in the coils of the MRI scanner are compensated for. Saturation pulses in the S/I direction are used to reduce the signal from the blood. The data set consists of 32 time frames, each containing a 256x256x32 grid with vectors and gray scale data describing the velocities and anatomy, respectively.

Clinically relevant kinematic parameters, such as strain and strain rate, can be calculated from the velocity data. In order to describe the myocardial properties throughout the heart cycle we need to track discrete sites on the myocardium. This can be achieved by defining a parametric finite element mesh for the myocardium. The velocity information may then be used to track the motion of nodes in the mesh. The borders of the myocardium, necessary to define the mesh, can be found by selecting the traces which return to their starting point, as discussed by Ebbers et al (Ebbers 2001) and shown in Figure 1

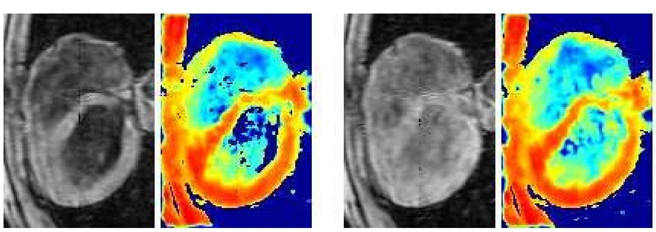

Figure 1: Segmentation using particle trace (magnitude and myocardial probability).Left:Early diastole, Right:Mid-diastole

The deformation of the mesh will describe the deformation of the myocardium and the trajectory data can thereby be used for strain calculations.

Kinematic parameters, such as strain and strain rate, are represented by tensors, which for three dimensions will have nine components. A visualization method enabling interpretation is therefore needed.

Tensors may be visualized as an ellipsoid in each data point. The three axis of the ellipsoid represent the eigenvectors (principal directions) of the tensor and the length of the axis represent the three eigenvalues (principal values), respectively. This visualizes both magnitude and direction of, for example, the deformation rate of the myocardium (Selskog et al 2001).The results of the tensor visualization method are shown in Figure 2, here displaying strain rate in a region of interest on a surface in the left ventricular myocardium (left). The orientation of the ellipsoids represents the main direction of instantaneous deformation at this time in the cardiac cycle (middle and right) The ellipsoids are colored according to the largest eigenvalue (sorted by magnitude) and the surface color represents the sum of the squares of the eigenvalues.

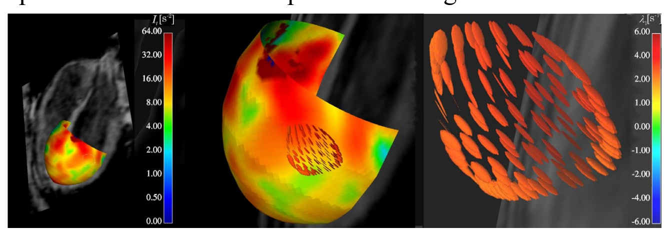

Figure 2: Tensor visualization using ellipsoids.

DISCUSSION

A method is suggested that allows a 4D description of the mechanical properties of the myocardium. The borders of the myocardium are successfully defined in the velocity data, enabling calculation of kinematic parameters, such as strain. The visualization method displays the full tensors, revealing the main direction of deformation or deformation rate. Complete strain and strain rate tensors represent a step towards quantification of myocardial motion and increased understanding of the complex mechanical properties of the heart. Using phase contrast velocity measurements also provides the possibility of adding blood flow information for a more complete description of cardiac dynamics.

REFERENCES

Wigström, L. et al (1996). *Magn Reson Med*;**36**:800-803

Ebbers, T. (2001). *Dissertations No 690*, Linköpings universitet, Linköping, Sweden.

Selskog, P. et al (2001). *Proceedings of the ISMRM*, p1870.

MEASUREMENT OF ERYTHROCYTES DEFORMABILITY WITH COUNTER-ROTATING PARALLEL DISK SYSTEM

Shigehiro Hashimoto[1], Hiroshi Oku[1], Masayoshi Omori[1], Yuki Matsumoto[1], Koichi Sakaue[1], Kazuhiro Ikegami[1], Hajime Otani[2], Hiroji Imamura[2]

[1]Biomedical Systems, Dept. of Electronics, Information and Communication Engineering, Osaka Institute of Technology, Osaka, Japan, hasimoto@elc.oit.ac.jp
[2]Dept. of Thoracic and Cardiovascular Surgery, Kansai Medical University

INTRODUCTION

Erythrocytes deform to pass through capillary in micro-circulation. Deformability of erythrocytes is an important parameter to maintain blood circulation. To measure erythrocytes deformation, several methodology have been designed in the previous studies. Measurement of erythrocytes deformability is available to detect their sublethal damage and to design micro-capsule like artificial erythrocytes. In this study, erythrocytes deformability was quantitatively evaluated with shear stress responsiveness in the counter-rotating parallel disk system.

METHODS

A parallel-disk-type rheoscope system has been designed and manufactured. In the system, Couette-type shear field is induced in the fluid between two counter-rotating disks, which are made of transparent silica glass (5 mm thickness, 80 mm diameter). The distance was maintained 0.1 mm between two disks supported with ball bearings (100 mm diameter). The rotating speed (<0.4 rad/s) was regulated with a stepping motor, which is controlled by a computer. The shear rate (<200 1/s), which is calculated from the velocity deference (<20 mm/s) between two disks and from the dimension between two disks, is constant regardless of the distance from the disk. An erythrocyte can be observed under shear without translational movement , when it is suspended at the stationary plane in the middle part of the shear field. Deformation of erythrocytes was viewed at a distance of 27 mm from the rotational axis through an optical-phase-contrast microscope with an objective lens of 20 magnifications, which has a long focal length of 6.9 mm. The picture was recorded with a charge coupled device camera at a shutter speed of 0.001 s, with a video tape recorder, and with a computer. Human erythrocytes were suspended in a dextran water solution (hematocrit of 0.5%, viscosity between 0.02 Pa s and 0.06 Pa s) and were sheared between two counter rotating disks at 25 degrees C.

Erythrocytes deform from biconcave to ellipsoid in Couette-type of shear field. Erythrocytes deformation was quantified with an elongation index (E), which was calculated from the length of major axis (L) and that of the minor axis (W) by $E=(L-W)/(L+W)$. E becomes zero in a sphere (L=W), and approaches to unity as the deformation advances (L>>W). The elongation index (E) was plotted as a function of shear stress (S), and the fitting exponential curve was calculated by $E=C(1-\exp(-S/R))$, Where C is the critical elongation and R is the shear stress responsiveness.

RESULTS AND DISCUSSION

The dextran concentration in medium does not affect on shear stress responsiveness. Erythrocytes deformation is not governed by shear rate, but by shear stress in these shear condition. Couette-type flow has an advantage to quantify the shear, because uniform shear rate is applied to the whole space. The counter rotating rheoscope is a devise to observe sheared cells, which are suspended at the stationary plane in the middle part of Couette-type flow without contact between cells and surfaces. Increase of stiffness of the disks minimizes secondary flow.

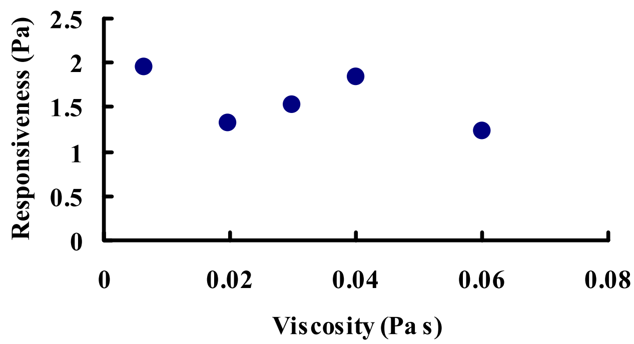

Figure 1: Relation between medium viscosity and shear stress responsiveness.

SUMMARY

The designed experimental system has enough geometrical accuracy to evaluate shear stress responsiveness. The present study shows that erythrocyte deformation is not governed by shear rate, but by shear stress.

REFERENCES

Hashimoto, S., Hikita, S., Sasada, T. (1992). *Trans. 4th World Biomaterials Congress*, 347.
Hashimoto, S., (2000). *Trans. 6th World Biomaterials Congress*, **2**, 929.
Schmit-Schoenbein, H., Wells, R. (1969). *Science*, **165**, 288.
Sutera, S.P., et al. (1983). *Blood Cells*, **9**, 485-495.

ACKNOWLEDGEMENTS

This work was supported in part by a Grant-in-Aid for Scientific Research from the Japanese Ministry of Education, Culture, Sports, Science and Technology.

INFLUENCE OF VISCOELASTIC HEEL INSERTS ON PEAK IMPACT LOADING AND PEAK ANKLE DORSI-FLEXION

Sharon Dixon and Victoria Stiles

School of Sport and Health Sciences, University of Exeter, Exeter, United Kingdom. s.j.dixon@exeter.ac.uk.

INTRODUCTION

Viscoelastic heel inserts have been reported as a successful intervention for the treatment of Achilles tendon pain (MacLellan and Vyvyan, 1981). However, the mechanism by which these inserts reduce Achilles tendon pain is not clear. One suggested explanation is that they reduce peak impact loading as the heel strikes the ground. Although viscoelastic heel inserts have been shown to reduce peak impact deceleration when placed in dress shoes (Light et al. 1980), a study on the effect of full-length inserts in running shoes reported no influence on peak impact loading (Nigg et al., 1988). An alternative suggested mechanism by which heel inserts are a successful treatment is that they result in a raised heel during midstance, causing a reduction in peak ankle dorsi-flexion, and thus a reduction in Achilles tendon strain. The potential of heel inserts to reduce peak ankle dorsi-flexion has previously been demonstrated in a barefoot study in which the heel was raised using high density ethyl-vinyl acetate inserts attached to the rear of the foot (Dixon and Kerwin, 1999). However, the influence of viscoelastic inserts placed in the rear of running shoes is not fully understood. The purpose of the present study was to investigate the influence of viscoelastic heel inserts during running. It was hypothesised that the placement of viscoelastic heel inserts in running shoes would reduce peak impact loading and would also result in a reduction in peak ankle dorsi-flexion.

METHODS

Seven distance runners volunteered to participate in the study. Each runner performed eight shod running trials at 3.83 $m.s^{-1}$ (±5%) under each of three conditions: no insert, insert1 (7.5mm maximum thickness), insert2 (15mm maximum thickness). Both inserts were constructed from the same viscoelastic material and were tapered along a length of 80 mm. For each running trial, force plate data were collected for a right-footed ground contact (AMTI, 600Hz). Sagittal plane kinematic data were collected simultaneously using a Peak optical system (Peak Technologies, 120Hz). Ankle joint angles were determined using markers placed at the knee, ankle and toe, with an increase in angle defined to indicate an increase in ankle joint dorsi-flexion.

Group mean values were calculated for peak magnitude and rate of loading of impact force, time of occurrence of peak impact force and peak ankle dorsi-flexion angle for each of the running conditions. Significant differences between the baseline (shoe only) condition and the insert conditions were tested using an ANOVA with repeated measures ($p<0.05$).

RESULTS AND DISCUSSION

Mean group values and standard deviations for all variables are illustrated in Table 1. Although there appears to be a tendency for impact loading to be reduced by the use of increased viscoelastic material at the heel, none of the observed reductions were significant. Peak ankle dorsi-flexion was found to be reduced with the use of an increased thickness of heel insert, with insert2 causing a significant reduction compared with the no insert condition ($p<0.05$).

Table 1. Peak impact force and time of occurrence, peak rate of loading and peak ankle dorsi-flexion for each of the running conditions. Mean values (standard deviation). (* $p<0.05$).

	no insert	insert1	insert2
Peak impact force (Bodyweights)	2.20 (0.60)	2.04 (0.46)	2.01 (0.46)
Time of Peak impact force (ms)	33.5 (4.2)	34.0 (5.7)	34.4 (5.8)
Peak rate of loading (Bodyweights.s^{-1})	126.3 (41.2)	117.6 (46.0)	113.0 (43.7)
Peak ankle dorsi-flexion (degrees)	95.1 (2.8)	93.9 (1.0)	92.0* (2.5)

The hypothesis that viscoelastic heel inserts reduce peak impact loading when placed in running shoes is not supported by the results of the present study. This agrees with the findings of Nigg et al. (1988) for full-length inserts, and is likely to be the result of running shoes already providing sufficient heel cushioning. The hypothesis that viscoelastic heel inserts reduce peak ankle dorsi-flexion during running is supported in the present study, but only for the thicker of the two inserts. It is therefore suggested that for optimum treatment of Achilles tendon pain an insert of maximum thickness greater than 7.5mm may be preferred to a thinner insert.

SUMMARY

The results of the present study highlight the role of increased heel lift when using a viscoelastic heel insert intervention in running shoes.

REFERENCES

Dixon, S.J. and Kerwin, D.G. (1999). *J. Appl. Biomech.* **15**, 139-151.
Light et al. (1980). *J. Biomech.* **13**, 477-480.
MacLellan, G. and Vyvyan, B. (1981). *Brit. J. Sports Med.* **15**, 117-121.
Nigg, B.M et al. (1988). *Am. J. Sports Med*. **16**, 70-78.

EXPERIMENTAL INVESTIGATION OF THE ROLE OF THROMBUS ON THE PRESSURE-STRAIN RELATIONSHIP IN HUMAN ABDOMINAL AORTIC ANEURYSM

Madhavan L. Raghavan[1], Jarin Kratzberg[1] and Erasmo Simão da Silva[2]
[1]Department of Biomedical Engineering, University of Iowa, Iowa City, IA
[2]Department of Surgery, University of São Paulo School of Medicine, São Paulo, SP, Brazil

INTRODUCTION

An abdominal aortic aneurysm (AAA) – a focal dilation of the human abdominal aorta – typically contains substantial amounts of thrombus lining the inner wall. It has been hypothesized that thrombus may act like a cushion to reduce the pressure-induced stress in the AAA wall, thus lowering its risk of rupture (Wang, 2001). To investigate this hypothesis, we experimentally measured and compared the strain in human AAA with and without thrombus using autopsy specimens.

METHODS

Experimentation: Four AAA specimens were harvested from cadavers during autopsies performed at the Service for Confirmation of Deaths, São Paulo University School of Medicine. The specimens varied in size (4 – 8 cm) and amounts of thrombus. Each specimen was hung from a frame using 3 hooks at marked locations. A ruler was also hung beside the AAA. A tripod-fixed digital camera was placed such that it faces the anterior portion of the AAA at its elevation. A balloon connected to a pressure gauge was inserted from the proximal end. Using the balloon, the AAA was inflated to 0, 80, 100, and 120 mmHg. Simultaneously, the AAA was photographed using the digital camera at each of the four pressures. This procedure was repeated by placing the digital camera at the left, posterior and right views also. Next, the AAA was removed from the frame and all the thrombus inside the AAA was scrapped out intraluminally. The AAA was then hung back in the frame taking care to ensure that it is hung from the same three hooks at exactly the same points. This ensured that the anterior, left, posterior, and right views of the thrombus-free AAA are not different from the earlier position with thrombus. The specimen was once again gradually inflated and photographs similarly taken for all four pressures from all four views.

Data Analysis: The outline of the AAA on the individual images for all the specimens and the ruler were digitized using Scion Image (ver 4, Scion Corp, Frederick, MD). A custom-written Visual Basic algorithm was used to import the digitized outlines into Microsoft excel, convert distances to cm using ruler measurements, calculate the area inside the AAA for all four views at the four pressures, determine the % change in area from 0 through 80, 100, and 120 mmHg for each view and the overall average for all views combined.

RESULTS AND DISCUSSION

Of the four AAA, AAA# 1&2 were large (dia >7cm) and had substantial amounts of thrombus. AAA# 3&4 were relatively small (dia < 5 cm) with moderate amounts of thrombus. The view-averaged % change in area for AAA# 1, 3 & 4 was significantly higher without thrombus than with it. AAA #2, exhibited low % change in area, but it was slightly greater with thrombus than without it. Figure 1 graphically illustrates the results.

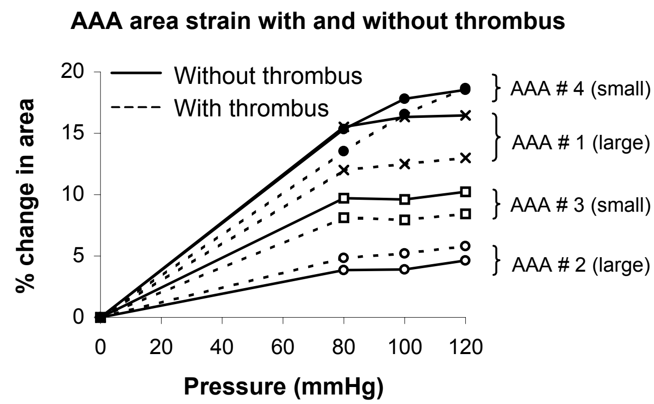

Figure 1: Percent change in area - pressure relationship for the four AAA studied with and without thrombus. The area strain is an average of individual % change in area from the four views.

SUMMARY

We have experimentally investigated the role of thrombus on the AAA wall strain. It appears from the results that thrombus is indeed reducing the strain on the AAA wall, lending support to the hypothesis that thrombus reduces wall stress and therefore rupture risk. AAA #2 alone showed a reverse result, but appeared to exhibit relatively low strain in the pressure range studied. It is unclear whether digitization/experimental error magnified by its low strain may have caused this or if this is indicative of a genuine phenomenon. Study of a larger population coupled with detailed analysis of the type and configuration of thrombus is ongoing to investigate further.

REFERENCES

Wang, D.J., et al (2001). *Proceedings of ASME Bioengineering Conference*, **BED-50**, 685-686

EVALUATION OF MECHANICAL STIMULUS FOR TRABECULAR SURFACE REMODELING USING DIGITAL IMAGE-BASED MODEL

Ken-ichi Tsubota[1], Taiji Adachi[2], Yoshihiro Tomita[2] and Akitake Makinouchi[3]

[1]Division of Computer and Information, Advanced Computing Center, The Institute of Physical and Chemical Research (RIKEN), Wako, Japan, tsubota@postman.riken.go.jp
[2]Division of Mechanical Engineering, Faculty of Engineering, Kobe University, Kobe, Japan
[3]Integrated V-CAD System Research Program, The Institute of Physical and Chemical Research (RIKEN), Wako, Japan

INTRODUCTION

Trabecular bone remodeling is caused by cellular activities on trabecular surface driven by a local mechanical stimulus. To understand and predict trabecular structural changes due to remodeling, it is important to clarify *in vivo* mechanical stimulus at microstructural level. In this study, local stress nonuniformity as a mechanical stimulus for trabecular surface remodeling was evaluated using digital image-based finite element model of rat vertebral body.

METHODS

A digital image-based model for a center part of rat L1 vertebral body was constructed from X-ray micro CT data, as shown in Fig. 1. A bone element was 12.8 μm on each side, and assumed to be a homogeneous and isotropic material with Young's modulus 20 GPa and Poisson's ratio 0.3. As a daily loading condition, compressive displacement was applied to the upper plane of the image-based model to apply the total loads 10 N. Finite element analysis was conducted to calculate local nonuniformity of Mises equivalent stress $\Gamma = \ln(\sigma_c/\sigma_d)$ (Adachi et al., 1997) over the trabecular surface in central hexahedron cancellous region, as indicated by dotted lines in Fig. 1. Here, σ_c denotes the stress at the point $\boldsymbol{x}_c$ on trabecular surface, and σ_d denotes the neighbor stress around the point $\boldsymbol{x}_c$:

$$\sigma_d = \int_S w(l)\sigma_r dS \Big/ \int_S w(l) dS . \qquad (1)$$

In Eq.(1), σ_r denotes the stress at the point $\boldsymbol{x}_r$ on the trabecular surface S, l denotes the distance between the points $\boldsymbol{x}_c$ and $\boldsymbol{x}_r$, and $w(l)$ is a weight function decreasing to the distance l. σ_d was evaluated within a sensing distance $l_L = 200$ μm in this study.

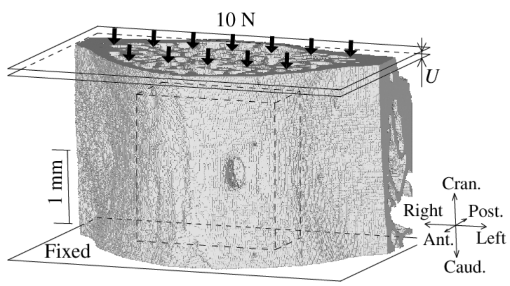

Figure 1: Image-based model of rat vertebral body.

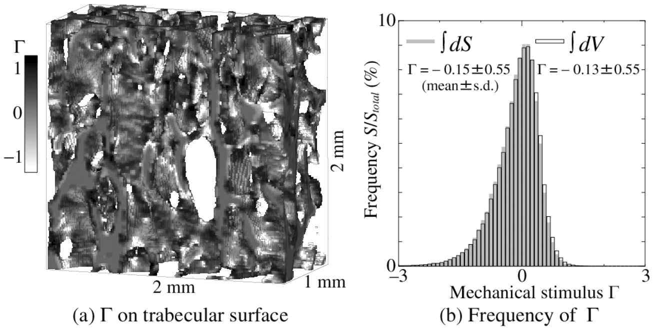

Figure 2: Mechanical stimulus Γ in cancellous region obtained by image-based finite element method.

RESULTS AND DISCUSSION

Mechanical stimulus Γ on trabecular surface was distributed depending on trabecular microstructure, as shown in Fig. 2(a), although the vertebral body was under simple external loading. This result indicates digital image-based finite element method is useful in quantifying mechanical stimulus at trabecular level for three-dimensionally complicated structure in the actual bone. Considering a role of osteocyte as a mechanosensor, mechanical stimulus Γ in the case of integrating over the volume dV in Eq. (1) was also obtained. Frequency of the mechanical stimulus, defined by normalized trabecular surface area S/S_{total} to the mechanical stimulus Γ, showed that mechanical stimulus Γ for volume integration was shifted to formation side ($\Gamma > 0$) compared to that for surface integration, as shown in Fig. 2(b). This result suggests that osteocytes existing in bone matrix would play an important role in maintaining an amount of bone volume.

CONCLUSION

Mechanical stimulus for trabecular surface remodeling was evaluated using digital image-based finite element model of rat vertebral body considering *in vivo* three-dimensionally complicated trabecular structure. The proposed simulation method would be useful in understanding mechanosensory system in trabecular surface remodeling.

REFERENCES

Adachi, T. et al (1997). *JSME Int. J.*, **40**, 782-792.

THE HEALING RESPONSE OF ACL AND MCL INJURIES IS INITIALLY SIMILAR BUT DIVERGES WITH TIME

Lo IKY, Marchuk LL, Leatherbarrow KE, Sutherland C, Barclay L, Hart DA, Frank CB
McCaig Centre For Joint Injury And Arthritis Research, University Of Calgary, Calgary, AB, Canada, email: cfrank@ucalgary.ca

INTRODUCTION

Medial collateral ligaments (MCLs) heal with the formation of scar tissue. In contrast, for reasons which remain unclear, anterior cruciate ligament (ACL) injuries are said to have a poor or absent healing (scarring) response (reviewed in Lo et al, 1999). However, recent studies have suggested that in some cases, particularly in partial ACL injuries, the ACL can exhibit some signs of a healing response although this has not been well characterized (Hefti et al., 1991). The purpose of this study was to evaluate a subset of extracellular matrix molecules during MCL and ACL healing in the ovine model.

METHODS

13 skeletally mature, female suffix-cross sheep were utilized for the study. 4 animals were used as normal control animals. In 9 animals, the right leg was used as the experimental limb and the left leg as an additional contralateral control. The MCL was transected at the joint line and the posterolateral band (PL) of the ACL was then transected and allowed to retract. The anteromedial (AM) band and posterior cruciate ligament were left undisturbed. The animals were allowed to recover with unrestricted activities. The midsubstance of the MCL and PL-ACL scar was harvested at 0, 6 and 12 weeks following injury. Tissue was analyzed by reverse transcriptase polymerase chain reaction (RT-PCR) and immunohistochemistry. RT-PCR was performed as previously described (Boykiw et al., 1998) for biglycan, decorin, type I collagen and type III collagen using sheep-specific primer sets. Results were normalized to the housekeeping gene GAPDH. Indirect immunofluorescence microscopy was performed using 7 µm paraffin sections and antibodies to decorin (P Scott) and biglycan (P. Roughleyy) using standard immunohistochemical techniques. All comparative sections were incubated simultaneously and visualized and photographed on an Axiostop 2 plus fluorescence microscope (Zeiss, Germany) under standardized exposure times. One-way ANOVA with post-hoc t-tests and Bonferroni correction were used to determine differences between groups.

RESULTS

At 6 weeks, changes in mRNA levels were strikingly similar in the MCL and PL-ACL scar tissue. mRNA levels for biglycan, type I collagen and type III collagen were increased in both the PL-ACL and MCL scar tissue of injured legs versus uninjured contralateral or normal controls ($p<0.008$). In addition, decorin mRNA levels were significantly decreased in the MCL ($p=0.01$) and ACL ($p=0.001$) at 6 weeks. At 12 weeks, both MCL and PL-ACL scar tissue continued to demonstrate similar changes with increased mRNA levels for type I and III collagen ($p< 0.001$). In addition, the MCL scar tissue biglycan mRNA levels were increased ($p<0.02$) and decorin mRNA levels were decreased ($p<0.04$). In contrast, in 12 week PL-ACL scar tissue, biglycan mRNA and decorin mRNA levels were not significantly different from controls.

To confirm differences seen at the mRNA level, immunofluorescence microscopy was performed for decorin and biglycan. In the MCL, immunofluorescent staining for decorin was decreased at 6 and 12 weeks while biglycan was increased at 6 and 12 weeks when compared to normal controls. However, in the PL-ACL, immunofluorescent detection of decorin decreased in 6 week scars but appeared to increase at 12 weeks. Immunofluorescent detection of biglycan was increased in both 6 week and 12 week PL-ACL scars when compared to normal but appeared to decrease at 12 weeks when compared to 6 weeks scars.

DISCUSSION

Following injury, many authors have suggested that the ACL does not heal or fails to show any evidence of a healing response. Our results suggest that following partial ACL injury, new tissue can form in the gap containing cells, which undergo similar extracellular matrix molecule changes to those in healing MCLs at 6 weeks. By 12 weeks however, the scarring response appears distinctly different. While the MCL of the sheep continues to demonstrate increased biglycan and decreased decorin levels, the PL-ACL demonstrated decreased biglycan and increased decorin levels when compared to 6 week PL-ACL scars. These proteoglycans have been previously identified as being altered in the rabbit MCL healing model (Boykiw et al., 1998), suggesting some similarities between the healing responses of different species.

Interestingly, increased biglycan levels have been associated with other models of chronic scarring including hypertrophic scar formation in skin or kidney fibrosis (Scott et al., 1996; Yamamoto et al., 1994). Thus, the decreased levels of biglycan when compared to MCL scars or 6 week PL-ACL scars may indicate that the scarring response may be inadequate or prematurely halted in PL-ACLs. In addition, decorin appeared to increase at 12 weeks in the ACL scar. With its known action of inhibiting collagen fibrillogenesis, increasing decorin levels may prevent or inhibit collagen fibril formation and thus scarring (Vogel et al., 1984). Although these changes may be secondary effects, they may also be potential factors in the eventual failure of functional healing of the ACL.

REFERENCES

Lo et al (1999) *Arthroscopy*,**15**,301-6.
Hefti et al (1991) *J. Bone Joint Surg.*,**73**,373-83.
Boykiw et al (1998) *J. Orthop. Res.*,**17**,371-8.
Scott et al (1996) *Clin. Sci.*,**90**,417-25.
Yamamoto et al (1994) *Kidney Int.*,**45**,916-27.
Vogel et al (1984) *Biochem. J.*, **223**, 587-97.

MOTION OF *R*GPIBα-AMS NEAR THE VWF SURFACE

Tetsuya Tsuji[1], Takashi Tabata[1], Shinnji, Takeoka[2], Yasuo Ikeda[3], and Kazuo Tanishita[4]

[1]Center for Life Science and Technology, Keio University, Yokohama, Japan, tetsuyatsuji@2000.jukuin.keio.ac.jp
[2]Department of Polymer Chemistry, Waseda University, Tokyo, Japan
[3]Department of Internal Medicine, Keio University, Tokyo, Japan
[4]Department of System Design Engineering, Keio University, Yokohama, Japan

INTRODUCTION

Platelet transfusion is the only effective therapy for bleeding associated with thrombocytopenia. However, platelet suspension has several serious problems such as the insufficiency or the transmitting of virus. To break these problems, substitutes for platelets have been desired. Even though many substitutes have proposed, any products couldn't be employed in clinical, because there is no methodology for assessing the haemostatic functions of such substitutes. In present study, we assessed the ability of platelet substitute *r*GPIbα-AMS, which interacts with ristocetin induced platelet aggregation, and then, at the first step to evaluate the ability, we observed the adhesive motion under flow condition.

METHODS

We used rectangular channel consisted of two glass plates and upper and lower chambers to fix them. Two glass plates, the thickness of 200 µm, were placed with an interval of 200µm. The interval was applied as the rectangular channel. One glass plate was coated with vWF (100 µg/ml), and the another with BSA (1%). *r*GPIbα-AMS was labeled with fluorescein isothiocyanate (FITC), and excited with argon-ion laser (ILT4590, Ion Laser Technology). Steady flow was introduced by gravity at an upper chamber. Because of transparency, we used red cell ghosts suspension prepared with hypotonic lysis method. The motion of flowing near the wall was obtained by using a High Speed Camera (SPEED CAM+, WeinBerger) with an Image Intensifier (XX1420AA, Delft Electronic Products). The Image was processed with NIH Image (U.S. National Institute of Health) and abstracted the single particle images. Then we identified the same particle and measured the concentration profile and the drift velocity.

RESULTS AND DISCUSSION

The concentration profiles of *r*GPIbα-AMS at high shear rate showed the near-wall excess (NWE). The highest concentration was 5 times as high as that at the center, whereas it was 2.4 times at low shear rate (Figure 1). Many previous works demonstrated the NWE of platelet-sized particles, and NWE was thought to accelerate the interaction between platelets and injured vessel wall. So it seems that *r*GPIbα-AMS has a property to arrest bleeding haemorheologically. *r*GPIbα-AMS adhered to vWF surface, although no interaction observed with BSA surface. In the time-series, *r*GPIbα-AMS flowing near the vWF surface moved more randomly, since several particles adhered the wall (Figure 2). This behavior seems to contribute to the thrombus formation.

REFERENCES

Takeoka, S. et al (2000). *Biomacromolecules*, **1**, 290-295

ACKNOWLEDGEMENTS

We would like to thank Prof. Takeoka. for preparation of *r*GPIbα-AMS. This work was supported by Health Science Reserch Grants, Reserch on Advanced Medical Technology, Ministry of Health, Labour and Welfare, Japan.

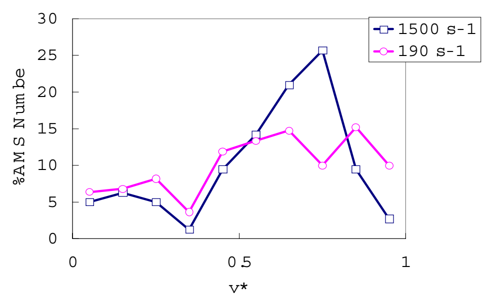

Figure 1: concentration profiles of *r*GPIbα-AMS. y* is the normalized y coordinate, and y*=0 means the center of channel.

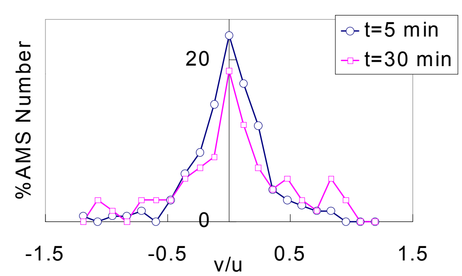

Figure 2: time-series of drift velocity at 190 s^{-1}. v: drift velocity. u: vertical component against v. As v/u increases, the motion becomes more randomlv.

EFFECT OF HAMSTRINGS MUSCLE ACTION ON STABILITY OF THE ACL-DEFICIENT KNEE

Takashi Yanagawa[1], Kevin Shelburne[1], Frank Serpas[2], and Marcus Pandy[2]
[1]Steadman♦Hawkins Sports Medicine Foundation, Vail, Colorado, takashi.yanagawa@shsmf.org
[2]Department of Biomedical Engineering, University of Texas at Austin

INTRODUCTION

Knee-extension exercise is a common component of rehabilitation regimens aimed at maintaining quadriceps muscle strength following injury to the ACL. Unfortunately, this exercise may cause large anterior tibial translations (ATT) when the ACL is absent. Excessive ATT may lead to damage to the meniscus and other passive structures inside the knee. Several studies have shown that hamstrings co-contraction can reduce ATT in the ACL-deficient (ACLD) knee. Hagood et al. (1990) reported hamstring co-activation at all speeds during maximal isokinetic knee extension exercise. Relatively little is known, however, about the *amount* of hamstrings activation needed to keep ATT within normal limits during knee extension exercise. Also, no results are available for the effects of hamstrings muscle action on stability of the ACLD knee during isokinetic knee extension. The purpose of this study was to quantify the effect of hamstrings muscle action on stability of the ACLD knee during isokinetic extension exercise at various speeds. The limit of knee-joint stability was defined as the peak ATT calculated for maximum isometric contractions of the quadriceps in the ACL-intact knee in the absence of hamstrings co-contraction.

METHODS

Modeling and forward-dynamics simulation were used to study the interactions between knee-extension speed, hamstrings co-contraction, and ATT. Isokinetic knee extension was simulated using a sagittal-plane model of the knee and lower leg. The geometry of the model bones was adapted from cadaver data. Tibiofemoral and patellofemoral articulation were each modeled as single-point contact. Eleven elastic elements described the geometric and mechanical properties of the knee ligaments and posterior capsule. The model was actuated by eleven musculotendinous units. The path of each muscle was represented by a straight line, except when it contacted and wrapped around the bones and other muscles (Shelburne and Pandy, 1997). The lower leg was distally constrained by its connection to the massless arm of a simulation isokinetic exercise machine. It was assumed for the duration of each simulated exercise that the quadriceps were fully activated and that the other muscles (including hamstrings) were fully deactivated. However, the passive forces developed by the muscles were taken into account. Details of the simulations are described by Serpas et al. (in press).

RESULTS AND DISCUSSION

ATT was inversely related to extension speed in the ACLD knee. There was also an inverse relationship between ATT and hamstrings co-contraction level at all extension speeds. Some amount of hamstrings activation was needed at all speeds to stabilize the model ACLD knee. Although peak ATT decreased as extension speed increased, the decrease was insufficient to prevent excessive ATT (knee instability), even at the highest extension speeds (360 deg/sec). However, relatively low levels of hamstrings activation were needed to stabilize the ACLD knee at speeds above 300 deg/sec. For example, the hamstrings must be activated at least 35% of maximum for the model ACLD knee to remain stable during isometric extension; in contrast, when the model knee was extended at a rate of 360 deg/sec, only 10% of maximum hamstrings activation was needed (Fig. 1). If a rehabilitation program is to include isokinetic exercise as an adjunct to thigh muscle strengthening, it will be important to ensure that the ACLD patient is capable of co-contracting his/her hamstrings during this exercise; otherwise, excessive ATT over time may cause damage to the menisci and other passive structures, resulting in further degeneration of the joint.

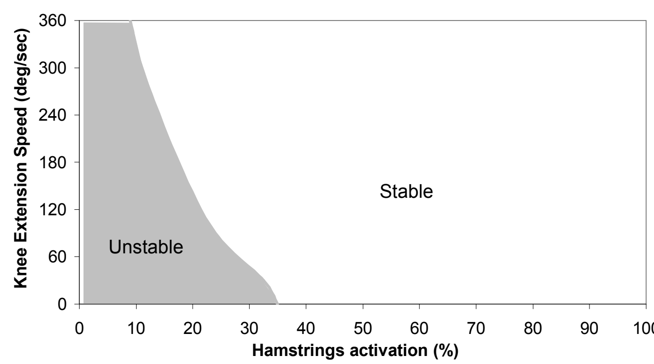

Figure 1: Hamstrings contraction required for knee stability at all isokinetic speeds.

SUMMARY

If ACL-deficient patients can be trained or artificially stimulated to co-contract their hamstrings muscles during isokinetic knee extension, then this exercise is appropriate for maintaining strength of the thigh muscles without compromising anterior stability of the knee. The results of this study also suggest that hamstrings co-contraction is more effective than low-resistance extension exercise as a therapy for conservative treatment of the ACLD knee.

REFERENCES

Hagood, S., et al. (1990). Am J Sports Med **18**(2): 182-7.
Serpas, F., et al. (in press). Compu Meth in Biomech and Biomed Eng.
Shelburne, KB, Pandy, MG (1997). J Biomech **30**(2): 163-76.

MODELING OF MANUAL WHEELCHAIR PROPULSION USING OPTIMIZATION

LY Guo[1&2], KD Zhao[1], FC Su[2], K-N An[1]
[1]Orthopedic Biomechanics Laboratory, Mayo Clinic, Rochester, MN 55905
[2]Institute of Biomedical Engineering, National Cheng Kung University, Tainan, 701 TAIWAN

INTRODUCTION

Collection of biomechanical data is essential for understanding handrim wheelchair propulsion. Biomechanical models can add to our understanding by clarifying how upper extremity segments and muscles interact to execute the motor task. Therefore, we have developed a two-dimensional model of the upper arm, forearm, and wheelchair wheel to study different aspects of the man-machine environment, including the mechanical constraints and effectiveness of force application while propelling a wheelchair. The goal of this study is to develop and validate the model as well as present predictions of handrim kinetics during wheelchair propulsion.

METHODS

A planar model was developed at incremental changes in wheel angle throughout the propulsion cycle. Anthropometric and strength data were collected from subjects as inputs to the model and model predictions of handrim force and progression moment were compared to those collected from the subjects during quasi-static wheelchair propulsion.

Analytic Modeling

The analytical model is comprised of three segments (the upper arm, lower arm and hand, and hand to wheel hub) (Fig. 1). At each hand position, the unknown forces on the handrim (F_h) are obtained by maximizing the progression moment about the wheel axle (M_o),

subject to the following equality and inequality constraints:

$$M_s = P_s \times F_h$$
$$M_e = P_e \times F_h$$
$$M_o = P_r \times F_h$$
$$-M_{se} \le M_s \le M_{sf}$$
$$-M_{ee} \le M_e \le M_{ef}$$

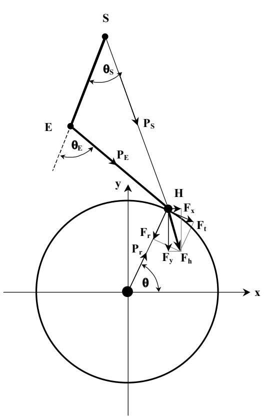

Figure 1: Analytical model of wheelchair propulsion mechanics

where M_s and the M_e are the flexion/extension moments at the shoulder and elbow joints, respectively, due to the force F_h. P_s, P_e, and P_r are the position vectors of the shoulder, elbow, and wheel axle relative to the point of force application on the handrim. M_{se}, M_{sf} and M_{ee}, M_{ef} are the maximum shoulder and elbow joint strengths in extension and flexion.

Experimental Measurement

Five healthy male subjects (30 to 40 years old) participated in this study. Lengths of the upper arm and forearm as well as the shoulder position relative to the wheel axle, were obtained.

Isometric shoulder and elbow flexion and extension strengths throughout the ranges of motion were measured using a KinCom125 AP®, and fitted to second order polynomials as function of joint angle. An instrumented wheelchair developed in our laboratory was used to measure applied handrim forces and moments on the handrim at wheel angles (θ) of 120, 105, 90, 75 and 60 degrees during static wheelchair propulsion.

RESULTS AND DISCUSSION

The model predicted a progression moment that is larger at the initial and terminal propulsion positions (i.e. wheel angles of 120 and 60 degrees respectively) and is smaller in mid-propulsion. The experimental results supported this finding (Table 1). This phenomenon may result from a mechanical disadvantage of the upper arm musculature at mid-propulsion. At mid-propulsion, the reaction force on the hand is nearly perpendicular to the moment arms of the force about the shoulder and elbow. Thus, even small forces result in large moments at the two joints. Differences in force direction are quite small between model and experiment at all propulsion positions. Differences in force magnitude and progression moment between model and experiment were smaller in the initial and mid propulsion hand positions than in the terminal propulsion (Figure 2).

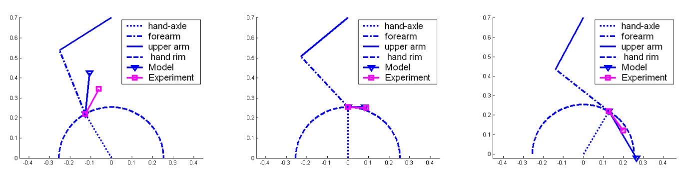

(A) (B) (C)

Figure 2: The difference in force magnitude and force direction between model and experiment at wheel angles of 120°(A) 90° (B) 60° (C)

SUMMARY

A planar model has been successfully developed and validated which could be useful in examining the mechanics of wheelchair propulsion and in wheelchair design and fitting. In the future, the model will be further refined to include muscle dynamics and to be three-dimensional.

ACKNOWLEDGEMENT

This study is supported by grants NIH HD 33806 (USA) and NHRI-EX90-9019EL (Taiwan)

Table 1. Comparisons of the progression moment (N-m) between model and experiment

Wheel Angle	120°	105°	90°	75°	60°
Model	45.4 (8.9)	33.9 (10.0)	31.2 (10.7)	63.8 (18.0)	91.3 (26.3)
Experiment	52.7 (9.8)	42.8 (7.9)	38.6 (3.8)	42.2 (4.3)	44.5 (4.3)

COMPUTATIONAL MODELLING OF BLOOD FLOW AND ARTERY WALL INTERACTION

Debbie Grossman, Chris Bailey, Koulis A. Pericleous and Avril K. Slone

Centre for Numerical Modelling and Process Analysis University of Greenwich, Old Royal Naval College
10 Park Row, Greenwich, LONDON SE10 9LS United Kingdom
E-mail D.Grossman@gre.ac.uk

INTRODUCTION

The study of diseases of the Circulatory System is an increasingly active research area. Since annually this accounts for approximately 40% of all the deaths in the United Kingdom. Traditionally, studies have been carried out on either blood flow phenomena or arterial wall behaviour, with a variety of models being used for both. Newtonian and non-Newtonian models for blood flow see C.A. Taylor *et al,* and shell theory amongst others, for the arterial wall.

Clinical research has shown that there is two-way interaction between the artery wall and blood flow, which must be considered if the arterial wall behaviour is to be modelled accurately. Some attempts are now being made to couple the two distinct models of the two phenomena. However this usually involves the linking of two very different commercial codes e.g. S.Z. Zhao *et al* used CFX and ABAQUS, which provides a number of additional complications. Here we will present details on a research effort that is developing novel, closely integrated solution procedures for both blood flow and artery wall deformation. At this stage of the work 3D results will be demonstrated where the blood is non-Newtonian and the artery wall elastic.

METHODOLOGY

Due to the multiphysics nature of the problem there are three distinct parts to the solution: (1) Blood flow, (2) Artery wall behaviour and (3) Interaction between the two.

(1) BLOOD FLOW

For the blood flow a conventional computational fluid dynamics method is used with a choice of models for bloods non-Newtonian properties namely the Power-law and Casson's Equation.

(2) ARTERY WALL BEHAVIOUR

Here initially the wall was modelled as a single layered elastic wall. This is expanded to 2 layers based on the fact that the intima (inner layer) of the aorta is a single layer of cells so has little impact on the wall behaviour, G.A. Holzapfel *et al*. Various studies have determined that the arterial wall behaviour is non-linear and viscoelastic it is our intention to incorporate these properties into the model in future.

(3) INTERACTION

The approach presented here is based on that presented by A. Slone *et al* who employed a dynamic mesh approach to dynamic fluid structure interaction for an aircraft wing in fluid flow. In the case of transient runs, the finite volume analysis is performed at the end of each fluid time step, the mesh is deformed and the fluid flow is calculated for the next time step using the deformed mesh.

RESULTS

At this stage of the work simple 3D geometric results will be demonstrated where the blood is non-Newtonian and the artery wall a two layered elastic material. In this case the effects of the blood on the artery wall are considered, where the fluid pressure is applied to the artery wall.

It is hoped to include a realistic pressure pulse and corresponding arterial wall movement based on actual data taken in vivo from a dog.

SUMMARY

A single software framework PHYSICA is being used to provide solutions for both the blood flow (using CFD techniques) and the corresponding artery wall deformation (using FV method) with results from each feeding directly back into the next time step. It is our intention to demonstrate the one-way fluid-structure interaction between non-Newtonian blood flow and a compliant linear elastic artery wall within a 3 dimensional model.

REFERENCES

Taylor C.A., Hughes T.J., Zarins C.K, Computer methods in applied mechanics and engineering, (1998) Vol. 158, 155-196.
Zhao S.Z., Xu X.Y., Collins M.W., Proc Inst. Mech Engrs, 1998, Vol. 212 Part H, 241-252.
Holzapfel G.A., Gasser T.C., Ogden R.W. (2000) J. Elasticity, Vol. 61, 1-48.
Slone A, Pericleous k, Bailey C, (2000), AIAA.
Physica Multi-physics modelling code see web site Physica.gre.ac.uk

IN-SITU CHONDROCYTE DEFORMATION IN EARLY STAGE OSTEOARTHRITIC (OA) ARTICULAR CARTILAGE

Andrea Clark[1], Walter Herzog[1], John Matyas[2], Leona Barclay[2] and Tim Leonard[1]
University of Calgary, Calgary, Alberta, Canada
[1] Human Performance Laboratory, Faculty of Kinesiology walter@kin.ucalgary.ca
[2]The McCaig Centre for Joint Injury and Arthritis Research

INTRODUCTION

Chondrocytes and their nuclei deform throughout the depth of articular cartilage in proportion to the magnitude of applied compression (3). Furthermore, deformation alters the biosynthetic activity of normal chondrocytes in vitro (5). Little is known about how compression influences the magnitude and local variation of chondrocyte deformation in situ, and if these parameters change with disease. Our aim was to evaluate variations in chondrocyte deformation throughout intact specimens of early stage OA cartilage subjected to uniform static compression.

METHODS

Six cats were euthanised 16 weeks post-unilateral anterior cruciate ligament transection (ACL-T), a model of OA (4). A cylindrical, metal indentor was used to apply a surface pressure of 9MPa to the centre of the articular cartilage of the experimental femoral groove and patella. After load relaxation, the cartilage was fixed in RHT fixative (1) and full-thickness osteochondral blocks were harvested from identical anatomical sites in experimental and contralateral specimens. Sections stained with toluidine blue were examined under the light microscope.

RESULTS

Morphologically, the contralateral knees were grossly normal with the experimental knees showing typical initial signs of degeneration. Histologically, the experimental patellar cartilage had increased in thickness and showed decreased matrix staining in the superficial layer compared to contralateral and healthy patellae. Furthermore, chondrocytes from the superficial and middle layers of experimental patellae were more rounded (Fig 1a), arranged in clusters, and had an increased volume density. These changes were not observed in the experimental femoral grooves.

Static compression decreased the aspect ratio of chondrocytes throughout the depth of both tissues (Fig 1). Comparison with results obtained from healthy articular cartilage (1) showed that this decrease was similar for OA and healthy femoral cartilage, however differed in the superficial and middle layers of patellar cartilage. The change in aspect ratio of superficial and middle layer patellar chondrocytes being smaller in magnitude in OA compared to healthy tissue (Fig 1a).

DISCUSSION

The results of this study demonstrate architectural and compositional adaptation in patellar articular cartilage 16 weeks post ACL-T. Furthermore, in the indented superficial and middle layers of patellar cartilage, chondrocytes in OA tissue flattened less than chondrocytes in healthy tissue. In contrast these differences were not observed in the femoral groove cartilage.

The contrast in pathology between patellar and femoral groove articular cartilages demonstrated here was also evident (though

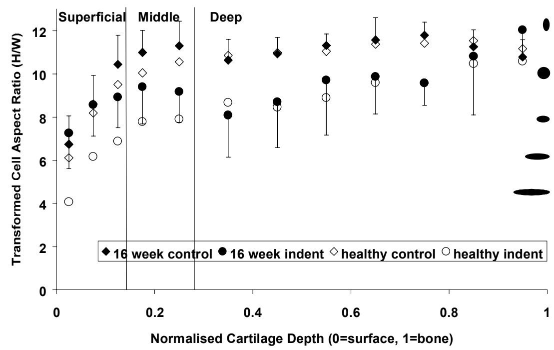

(a)

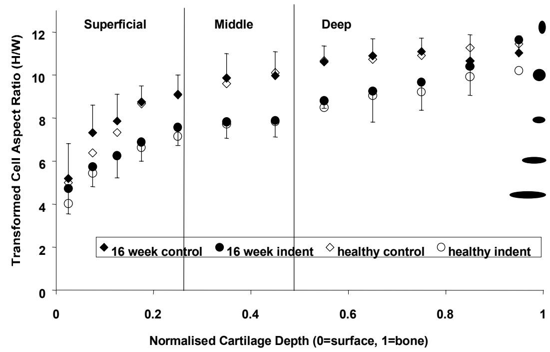

(b)

Figure 1: Graphs of transformed chondrocyte aspect ratio (CAR) (y={3xln[CAR]}+10) as a function of cartilage depth for (a) patellar and (b) femoral groove tissues. Each graph compares healthy (n=4) and OA (n=1) tissue in the unindented control and indented state. Values of CAR have been averaged (±SD) within 5 or 10% bins throughout the cartilage depth so that n>10 cells for each bin. Representative ellipses placed at their corresponding values of transformed aspect ratio are shown pictorially on the right.

different in nature) >57 months post ACL-T in the cat (1). Together, these results demonstrate the site specific nature of cartilage adaptation with the progression of OA, even across articulating cartilage surfaces of the patellofemoral joint. We speculate that this is caused by the differing nature of the load experienced by the surfaces and the variations in the cartilage properties across the joint in healthy tissue. Furthermore, the site specific architectural and compositional adaptation of cartilage with OA influences the deformation, and presumably, the metabolic response of chondrocytes in situ.

REFERENCES

1. Clark, A. et al., 2000. *Trans Orthop Res Soc* **46**,104
2. Clark, A. et al., 2001. *Proc XVIIIth Int Soc Biomech,*162
3. Guilak, F. et al., 1995. *J Biomechanics* **28**,1529
4. Herzog, W. et al., 1993. *OA Cart* **1**,243
5. Wong, M. et al., 1997. *J Orthop Res* **15**,189

ACKNOWLEDGEMENTS

CIHR and The Arthritis Society

QUANTITATIVE EVALUATION OF MAXIMAL WORKING SPACE AND KINEMATICS OF THUMB

Li-Chieh Kuo[1] Fong-Chin Su[1] Haw-Yen Chiu[2] Kai-Nan An[3]

[1]Institute of Biomedical Engineering, National Cheng Kung University, Tainan, TAIWAN, fcsu@mail.ncku.edu.tw
[2]Section of Plastic Surgery, Department of Surgery, National Cheng Kung University, Tainan, TAIWAN
[3]Biomechanics Laboratory, Div. of Orthopedic Research, Mayo Clinic, Rochester, MN, USA

INTRODUCTION

Recently, a method of measuring the actual area of fingertip motion using the motion analysis system was developed (Chiu & Su, 1996). This scientific and objective method complemented the traditional evaluations of assessing an injured finger. However, it was not suitable for measuring the motor function of the thumb. The major movement of the finger is in the flexion/extension plane associated with little rotation and lateral movement. Thus, the area of fingertip motion is concentrated to a two-dimensional plane. However, the motion of the thumb is completely different from that of the other digits with broadly ranging movements in a three-dimensional space. Assessing the volume covered by the moving track of thumb tip in three-dimensional space would be more precise, but more complicated than the current methods for another digits. The maximal working space of the thumb-tip is defined as the maximal motion range of the thumb-tip movement in the 3-D. This working space is formed by the largest range of motion of each joint of the thumb. It also means that it is impossible for the movements of thumb-tip to exceed this maximal working space. The objective of this study was to develop a quantitative evaluation method of measuring maximal working space and to establish a kinematics model of the thumb.

METHODS

Fifteen adults without previous and present injuries of the thumb and three patients were recruited in this experiment. Six normal subjects were involved in the first part of the study to assess the reliability of the measurement of the thumb tip motion by the motion analysis system. Nine normal subjects and three patients were studied to assess the value of maximal working space and kinematics of the thumb. Since the length of the thumb influences the volume of working space, the length of each thumb studied was measured before the motion analysis investigation. The maximal motion space was evaluated by the ExperVision™ motion analysis system (Motion Analysis Corp, CA, USA). Eleven retro-reflective markers, 4 mm in diameter, were placed on the dorsal side of the thumb. The subjects were asked to adopt two extreme motion patterns (A and B) of the thumb to form the maximal working space when filmed by the video camera (Fig. 1). Through registering, reconstructing the markers and transforming the coordinate systems, a computer software system was developed for numerical integration to compute the maximal working volume and the kinematics of the thumb.

RESULTS AND DISCUSSION

The reliability of the repeated measurements of the maximal motion area of the thumb-tip movement was calculated as 0.89. The two motion paths formed by the two designed movements are shown in Fig. 2a. The maximal working space of the thumb-tip motion is shown in Fig. 2b. The linear relationship between the maximal volume and the thumb length was also determined: *Motion area* $(cm^2) = 0.677 \times$ *(finger length)*^{2}. The angular variations of each joint of the thumb were also calculated and are illustrated in Fig. 3.

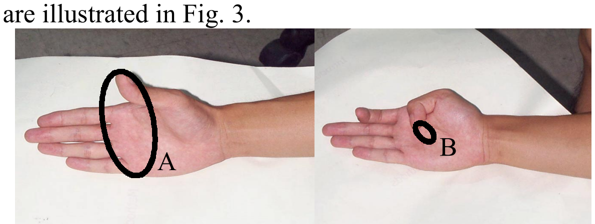

Figure 1: The two designed movements (A and B) of the thumb to form the maximal working space of the thumb-tip motion

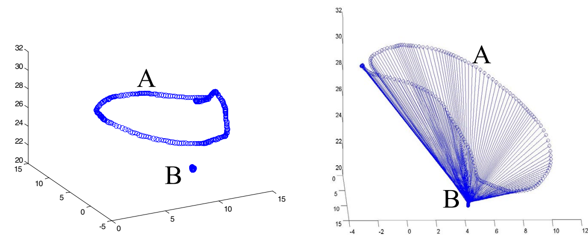

Figure 2: The two motion paths (left) and maximal working space of the thumb-tip motion in the 3D (right)

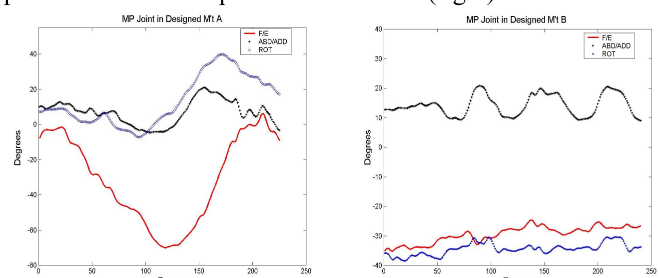

Figure 3: The goniometry through entire movement of MP joint of the thumb of one subject

SUMMARY

A quantitative evaluation method for assessing the motion impairment of the thumb has been developed. In this study, both an evaluation method of the maximal working space of the thumb tip, as well as kinematic model of the thumb, were developed.

REFERENCES

An, K.N., Bejjani, F.J.(1990). *Hand Clinics*, **6**, 393-403.
Chiu, H.Y., Su, F.C. (1996). *J. Hand Surg.*, **21B**, 604-608.
Chiu, H.Y. et al (1998). *J. Hand Surg.*, **23B**, 53-56.
Chiu, H.Y. et al (1998). *J. Hand Surg.*, **23B**, 788-791.

ACKNOWLEDGEMENTS

This work was supported by National Science Council grant NSC89-22218-E-006-066 and NSC89-2314-B-006-082, TAIWAN.

INCREASED DESMIN IN RAT DORSIFLEXORS AFTER A SINGLE BOUT OF ECCENTRIC EXERCISE

Ilona A. Barash[1], David Peters[1], Gordon J. Lutz[1], Jan Fridén[2] and Richard L. Lieber[1]
rlieber@ucsd.edu; Departments of Orthopaedics and Bioengineering
[1]University of California, San Diego School of Medicine, La Jolla, CA 92037
[2]Department of Hand Surgery, Göteborg University, Göteborg, Sweden

INTRODUCTION

Eccentric contraction (EC) causes skeletal muscle injury and decreased force output (Proske and Morgan, 2001). Even a single bout of EC is known to prevent subsequent injury (Morgan and Allen, 1999), but the mechanism of this protection is unknown. One of the earliest changes detected in muscle after EC is a loss of desmin immunohistochemical staining within minutes after the contractions begin (Lieber et al, 1996). This study demonstrates two points: it demonstrates "protection" from EC-induced muscle injury in a rat model and shows that one long term effect of EC is to increase the relative amount of desmin in the muscle.

METHODS

All procedures were approved by the University of California and V.A. Medical Center Committees on the Use of Animal Subjects in Research. Thirty EC's, at two minute intervals, were induced by stimulating the peroneal nerve of male Sprague-Dawley rats at 100Hz while the foot was actively plantarflexed using a dual-mode servo motor (Cambridge Tech, Model 6650), similar to that previously reported for the rabbit model (Lieber et al, 1994). Ankle angle was rotated 38° corresponding to a fiber length change of 12% in the tibialis anterior (TA) muscle. Joint torque and tissue were analyzed 6, 12, 24, 48, 72, and 168 hours after the EC bout. One group of animals (the "protected" group) was exposed to <u>two bouts</u> of ECs separated by 72 hours, with torque measured 48 hours after the second EC bout. Muscles were snap frozen and a 25μm thick cross-section was taken from the central belly of the TA and immediately extracted on ice in SDS-PAGE sample buffer. Western blots were run, in triplicate, from each time point using antibodies to desmin (DER-11, Novocastra; 1:100) and actin (A4700, Sigma; 1:100,000), along with desmin and actin standards on each gel. Data are presented as mean±SEM and were analyzed by one way ANOVA with Fisher's PLSD *post hoc* test when appropriate.

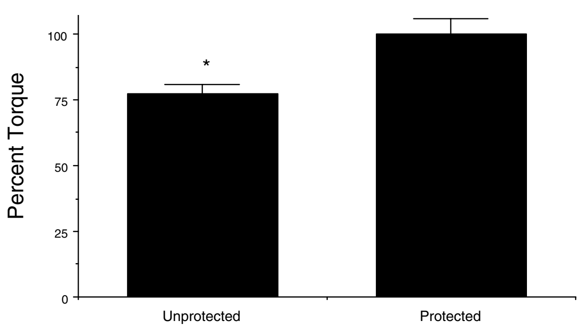

<u>Figure 1:</u> Dorsiflexion torque measured 48 hours after EC, normalized to pre-EC torque. The protected group underwent two bouts of ECs separated by 72 hours. The unprotected group generated 77.3±3.7% of pre-EC torque while the protected group generated 99.8±6.2% of pre-EC torque.

RESULTS

Isometric dorsiflexion torque measured 48 hours after a single bout of EC was only 77% of torque measured prior to EC ($p<0.01$, asterisk Fig. 1). Maximum isometric torque measured 48 hours after the second bout of EC, however, was not decreased, *i.e.*, the muscle was protected from EC-induced injury (Fig. 1). These data demonstrate functional protection of the muscle from injury after a single EC bout. Structurally, we measured a three-fold increase in the ratio of desmin to actin from control levels of 0.00435±0.000661 to 0.0125±0.00125 168 hours after EC ($p<0.0001$, Fig. 2).

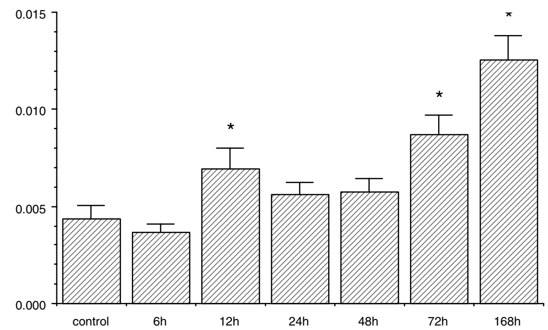

<u>Figure 2:</u> Desmin/actin ratio measured from Western blots at various time points after a single EC bout (asterisks, $p<0.05$).

DISCUSSION

These data reveal that one bout of ECs in this model protect against subsequent injury induced by ECs. Maximum isometric dorsiflexion torque was significantly decreased 48 hours after a bout of 30 ECs compared to original torque values, but this decrease did not occur if the muscles were preconditioned by a bout of eccentric contractions 72 hours earlier. The second result is that the relative amount of desmin in muscle cells increases after a single bout of eccentric contractions. It is unknown whether this desmin is incorporated into the cytoskeleton and whether increased desmin is directly responsible for the protective effect observed. Future studies are required to localize the newly synthesized desmin and to determine its structural role (if any) in muscle cell force transmission (Sam et al. 2000).

REFERENCES

Lieber et al. (1994) *J. Appl. Physiol.* **77:** 1926-1934.
Lieber et al. (1996) *J. Appl. Physiol*. **80:** 278-284.
Morgan and Allen. (1999) *J. Appl. Physiol*. **87:** 2007-2015.
Proske and Morgan. (2001) *J. Physiol. (Lond.)* **537:** 333-345.
Sam et al. (2000) *Am. J. Physiol.* **279:** C1116-C1122.

ACKNOWLEDGMENTS

Supported by NIH grant AR40050, the V.A. Rehab R&D Service and the Swedish Medical Research Council.

EVALUATION OF ALTERNATIVE MATERIAL FOR THE PREVENTION OF PRESSURE SORES

Rajshree Mootanah[1] Vijai Ranawat[2] and John Dowell[3]

[1]Research Fellow, Bioengineering Research Group, Anglia polytechnic University, Chelmsford, Essex, UK, r.mootanah@apu.ac.uk
[2]Vijai Ranawat, Orthopaedic Surgeon, the North Middlesex Hospital, London, UK, vijairanawat@hotmail.com
[3]John Dowell, Orthopaedic Consultant, Broomfield Hospital, Chelmsford, Essex, jkdowell@lineone.net

INTRODUCTION

Pressure sores are potentially serious complications caused by capillary closure due to extended periods of immobilisation. Capillary blood flow pressure ranges between 22 and 32 mm Hg (Landis, 1930) and when externally applied loads create localised pressure above this level, blood flow is likely to be obstructed and circulation is reduced, resulting in pressure sores. Excessive and prolonged pressure excludes blood from the skin and subcutaneous layers and may cause thromboses, ulcer and necrosis. A variety of products are used in hospitals to reduce pressure sores, but most are very costly and harbour bacteria and therefore could transmit infections when re-used.

In hospitals, the incidence of pressure ulcers seems to range from 2.7% (Gerson, 1975) to 29.5% (Clarke and Kadhom, 1988). The yearly UK costs of pressure sore treatments have been estimated to be £755 million (West and Priestley, 1994). The aim of this study is to investigate the potential use of more cost effective disposable products, without compromising on efficacy.

METHODS

Currently marketed (jelly pad) and novel (bubble wrap) pressure relief products were used in this study to compare pressures generated when a subject sat on the different products. The X-sensor pressure mapping system, which consists of a thin mat containing grids of miniature force sensors, was placed between the subject and the pressure relief products, one at a time, to electronically record information on pressure distributions. The pressure relief system was placed on a support surface similar to theatre bed.

Pressure data were recorded every second for 10 seconds while the subject was sitting on each of the pressure relief products. Each test was repeated five times and the average pressure data was computed. Pressure information for each product was compared.

RESULTS AND DISCUSSION

Average and peak pressure values recorded for the different pressure relief products are shown in figure 1. These results show that bubblewrap seems to be a better pressure relief product than jelly pad. Two to four layers of bubblewrap give seem to be the optimum number. It was observed, in general, that when the bubblewraps were placed in opposite directions, the values of peak and average pressures were lower than when they were placed in the same direction.

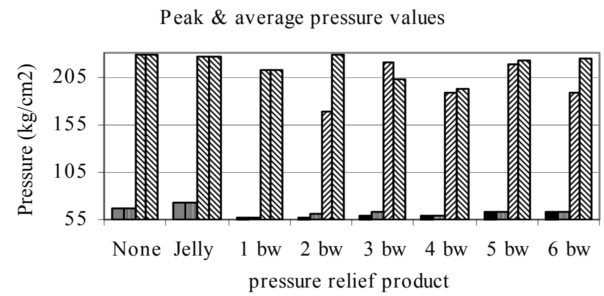

Figure 1: Peak and average pressure values for different pressure relief products; bw stands for bubblewrap

The pressure mapping system only records values of normal pressures and does not give any indication of values of shear forc
es generated. The extent of sideways motion of the bubblewrap indicates low possibility of shear build-up. However, further investigations need to be carried out to evaluate shear forces resulting from the different products.

SUMMARY

Based on the above investigations, we believe that bubblewrap is a better product for the prevention of pressure sores. Bubblewrap results in lower peak and average pressure values than jelly pad. Moreover, bubblewrap is cheap, disposable and is less likely to transmit infections.

REFERENCES

Landis, E. (1930). Heart, 15, 209-228.
Gerson, L.W. (1975). Int J. Nurs. Stud., 12(4):2014
Clarke, M., Kadhom, H.M. (1988). J. Adv. Nurs. 13(3): 36573.
West, P., Preistley, J. (1994). Health Serv. J. 14 April: 20-22.

ACKNOWLEDGEMENTS

The authors wish to thank De Puy Int. Ltd., Prof. D. King, Mr P. Ingle Mr. K. Cheah and APU graduate school.

EFFECTS OF MATRIX PROPERTIES ON INTRACELLULAR SIGNALING

Jeng-Yu Lai[1], Jeffrey R. Basford[2], Mark R. Pittelkow[1], Mark E. Zobitz[3]
Departments of Dermatology[1], Physical Medicine & Rehabilitation[2], and Orthopedics[3], Mayo Clinic, Rochester, MN, USA

INTRODUCTION

Cell responses to external electrical, hormonal, and mechanical stimuli result in signal transduction processes that alter gene expression. Mechanical stimuli, in particular, are known to affect cell differentiation. However, our knowledge is fragmented. While the cytoskeletal system is important in intracellular signal transduction and proteoglycans appear to interact with the cytoskeleton, no studies have correlated matrix properties and intracellular signal transduction. At least part of the signal transduction pathway that mediates responses to mechanical forces is coupled to activation of extracellular signal-regulated kinases (ERK) and c-Jun N-terminal kinase (JNK) which, in turn, regulate downstream transcription factors and nuclear events linked to specific cell responses (Xia *et al,* 1995). This project investigated the changes in the extent of activated ERK as a function of matrix property.

METHODS

Gels of various ratios of polyacrylamide (A) and BIS (B) were produced (Table 1, Pelham *et al,* 1997). The gels were tested with a dynamic mechanical analyzer (TA Instruments, New Castle, DE) to determine the Young's modulus (E) over a frequency range of 1-200 Hz. Numerical modeling was performed using JMP software (SAS Institute, Cary, NC).

Table 1. Gels for Modeling

	1	2	3	4	5	6
Acrylamide (%)	40	40	40	20	10	20
BIS (%)	1.38	0.69	0.34	0.69	0.34	0.34

The gels that were intended to support cell growth contained growth medium, in lieu of water. Normal human epithelial keratinocytes were isolated from neonatal foreskin and were seeded on the gel surfaces at a density of 2×10^5 per plate. Cell cultures were lysed with 100 microliters of MAPK solution (Auclair *et al,* 1999). Extracts were heated at 100° C for 5 min, loaded onto a 12% polyacrylamide gel for PAGE, and transferred to a membrane. The membrane was blotted against activated ERK 1/2 and total ERK.
The images were scanned and measured by the Scion Image software (Scion Corp., Fredrick, MD). Expression of total ERK served as control.

RESULTS AND DISCUSSION

The Young's modulus of the gels were found to be consistent, except gel 1 (Figure 1). The averages at 80 Hz were used for modeling. The model was determined to be $E = -13.57 + 1.72A + 34.73B$, $R^2 = 0.97$.
The expression of activated ERK is shown in Figure 2, Series 1. Since there is no apparent correlation between the Young's modulus and the expression, we suspected that the matrices were much stiffer than physiological state. Therefore, less stiff matrices were produced and the result was shown in Figure 2, Series 2. Unexpectedly, the expression of activated ERK did not completely correlate with the Young's modulus. However, correlation could be observed when the constituents of the gels were compared (Table 2).

Table 2. Ratios of Gels and ERK Expression

A (%)	20	20	20	30	10	10
B (%)	0.69	0.34	0.17	0.34	0.34	0.17
ERK	1.43	1.10	0.47	1.00	0.63	1.06
E*	44.79	32.64	26.73	101.44	15.44	9.53

*Calculated Young's modulus (kPa) based on the model.

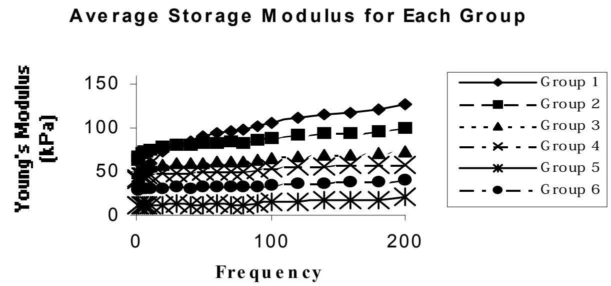

Figure 1. Young's Modulus.

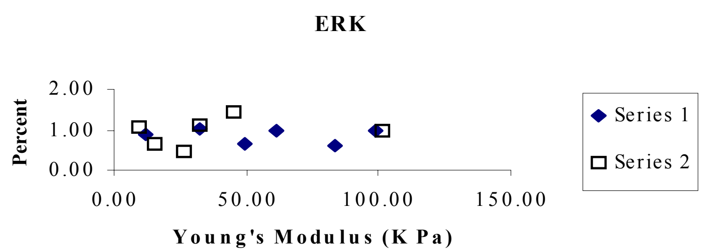

Figure 2. ERK Expressions.

Based on the results, we concluded that the Young's modulus alone is not a good predictor for cellular responses. That is, the mechanical property of a matrix, determined by both stiffness and flexibility, will affect cellular physiology. Additionally, the ratio between acrylamide and BIS can affect the pore size, which could influence cellular physiology. Integrin expression and activity on the cell surface may also play an important role. Knowledge obtained from these studies may lead to new therapeutic modalities for diabetic and other chronic wounds.

REFERENCES

Auclair M *et al.*, *J Clin Endocrinol Metab* 84: 3197-206., 1999
Pelham RJ, Jr. and Wang Y, *PNAS U S A* 94: 13661-5, 1997
Xia Z, Dickens M, Raingeaud J, Davis RJ and Greenberg ME, *Science* 270: 1326-31., 1995

ACKNOWLEDGEMENTS

This project was supported by NIH grant T32 HD 07447.

ERRORS INTRODUCED BY THE GROUND REACTION FORCES APPROACH ON JOINT MOMENT CALCULATION DURING GAIT.

Danik Lafond, Mathieu Charbonneau, Karl F. Zabjek and François Prince

Laboratoire du mouvement, Centre de réadaptation Marie-Enfant, Hôpital Ste-Justine.
Department of Kinesiology, University of Montreal, P.O. Box 6128, Downtown Station Montreal, Quebec, CANADA, H3C 3J7

INTRODUCTION

When attempting to calculate the joint moment, it is generally accepted that the inverse dynamics solution, initially described by Bresler and Frankel (1950), is the most accurate approach. Although the inverse dynamics solution (M_{ID}) has known intrinsic errors, few authors point out that the ground reaction force vector approach (M_{GRF}) may introduce more important bias in the estimation of joint moments. To our knowledge, no extensive comparison of joint moments profile has been done using both the M_{ID} and M_{GRF} approaches. The purpose of this study is to compare the two approaches and to document the potential misinterpretation of gait pattern introduced by the use of the M_{GRF} approach.

METHODS

Three OPTOTRAK® position sensors (Northern Digital, Waterloo, Ontario, Canada) and two force platforms (AMTI, Watertown, MA, USA) were used to collect kinematic and kinetic data simultaneously during each gait trial. Using the same kinematics and force platform data, joint moments in the sagittal plane at the ankle, knee and hip were calculated under M_{ID} and M_{GRF} approaches in eighteen elderly subjects. The M_{GRF} were then determined by the dot product of the ground reaction force amplitude and its orthogonal distance from the axis of rotation at each joint. Trigonometric solutions were used to calculate the lever arm between ground reaction force vector and the joint axis of rotation. To estimate the error on joint moment associated with the use of M_{GRF}, the standard error (S_e) at the ankle, knee and hip joints was calculated. The S_e allows the importance of the error in magnitude associated with the use of the M_{GRF} approach while the inverse dynamic solution served as the "gold standard". To estimate the bias on the temporal sequence of joint moment, the time delay between the corresponding curve's peaks and crossing zero of M_{ID} and M_{GRF} was used. The timing lag was calculated in percentage of stance phase.

RESULTS AND DISCUSSION

A typical joint moment time-series curve for each joint is presented at Figure 1. It is noted that the M_{GRF} and the M_{ID} time-series are quite similar at the ankle joint. Therefore, at the hip, the differences in magnitude become larger and it is clearly seen that hip extensor moment from M_{GRF} calculation is delayed compared with the M_{ID} leading to opposite polarity of joint moment during the late stance phase.

The magnitude of the S_e was 1.6 N·m, 3.4 N·m and 11.4 N·m respectively at the ankle, knee and hip joints. Discrepancies were found to be as high as 40 N·m at the hip. The results also indicate that hip and knee moments estimated by M_{GRF} are delayed when compared to M_{ID}. The M_{GRF} approach increases the hip extensor moment duration up to 39% of stance phase (mean of 8.2%). This result is shown in a proportion of 80% (66/84) of trials and 89% (16/18) of subjects. These temporal errors lead to an opposite polarity of joint moment during the late stance phase. Therefore, a hip extensor moment could be identified instead of a true hip flexor moment. As noted by Wells (1981), the largest error is seen at push-off, where the accelerations of the segments are greatest.

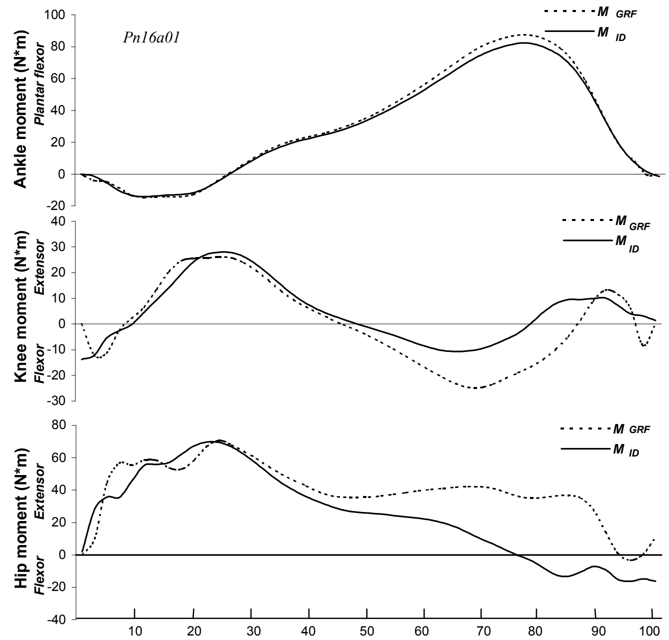

Figure 1. Graphical representation of joint moments obtained by M_{GRF} and M_{ID}.

These biases may lead to wrong conclusions in pathological gait analysis. As a clinical tool, joint moment profile should be as precise as possible to make appropriate decisions and intervention. The results showed magnitude and temporal errors that may lead to wrong identification of muscle activity, particularly around push-off. Therefore, it is concluded that M_{GRF} is not a good estimation of joint moment profile, even in a clinical setting.

REFERENCES

Bresler, B. & Frankel, J.P. (1950). *Trans. ASME.* **72**, 27-36.
Winter, D.A. (1979). *Biomechanics of Human Movement*. John Wiley & Sons.
Winter, D.A. (1986). *Physical Therapy*. **66**, 998-1000.
Wells, R.P. (1981). *Bull Prosth Research*. **18**, 15-19.

PELVIC FLOOR MUSCLE STRAINS DURING VAGINAL BIRTH

Kuo-cheng Lien, Brian Mooney, John O.L. DeLancey[1] and James A. Ashton-Miller

Biomechanics Research Laboratory, Departments of Mechanical Engineering, and [1]Obstetrics and Gynecology,
University of Michigan, Michigan, USA. kclien@umich.edu

INTRODUCTION

One in nine American women suffer from the debilitating conditions of incontinence and pelvic organ prolapse. The greatest risk factor for developing these conditions is the vaginal delivery of a child (Foldsprang, 1992). The pathomechanics of the injury are not well understood, although excess tissue strain may be implicated. There are, however, no estimates of the magnitude or location of the maximal tissue strains during human birth. This is partly due to the three-dimensional anatomic complexity of the pelvic floor structures and their hidden location. The goal of this research was to estimate the magnitude of the average strains in each of the pelvic floor muscles during the second stage of labor.

METHODS

A healthy 34 year-old nulliparous woman gave written informed consent to have her pelvis imaged using a 1.5 T magnetic resonance (MR) scanner. The outlines of each of the pelvic pelvic bones, muscles and organs were traced on 30 consecutive 5-mm axial sections, digitized, and imported into an engineering graphics program (IDEAS™). The serial sections were lofted to yield a 3-D model of the female pelvis and pelvic floor. Using descriptions of origins and insertions in the anatomic literature, the origins and insertions of the levator ani muscles were identified on the pelvis. 24 parallel-fibered muscle bands, 1 - 5mm thick and 5 – 10mm wide, were used to represent the left and right pelvic floor muscles: ilococcygeus, pubococcygeus, puborectal and puboperineus. As a first-order approximation, the 3rd, 50th, and 97th fetal head diameters (at 42 week gestation) were represented by spheres of equivalent diameter. We modeled the incremental descent of the model fetal head relative to the ischial tuberosities, as it passes around the pubic bone following the Curve of Carus. As the descent progressed, the different bands of the pelvic floor muscles were successively engaged by the head and then stretched. The strain in each band was calculated for each stage of descent (Figure 1).

RESULTS AND DISCUSSION

The results for the 50th centile head show that the iliococcygeal muscle bands were engaged by 0.55 cm head descent, the pubococcygeal muscles by 2.5 cm descent, and the puborectal and puboperineus muscles by 4.4 cm descent (Fig.1). The puboperineus muscle was the last muscle to be engaged, yet was strained more than any other muscle band: its maximum strain reached 300%. A single passive stretch exceeding 50% strain in a striated muscle from a non-gravida causes pliometric injury (Brooks et al., 1995). It is therefore a biological wonder that pelvic floor muscle can tolerate much larger apparent strains without injury. Hormonal mechanisms are likely involved. Preliminary findings from our MR study suggest, however, that a significant proportion of nulliparous women were injured during vaginal delivery. Muscle defects, visible on MR scans six months postpartum, appear in the regions of greatest muscle strain predicted by the present simulation (Mooney, et al., 2002).

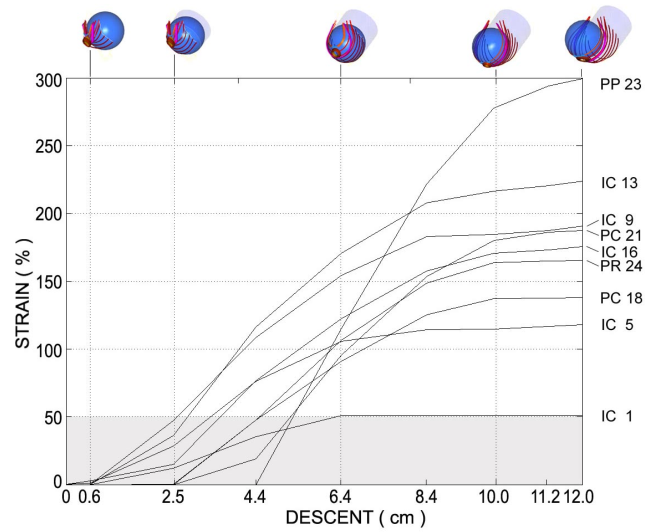

Figure 1: *The relationship between fetal head descent (abscissae, in cm; icons from simulation at top) and the resulting muscle strain (ordinate, in percent) for selected muscles. The labels at right identify the puboperineus (PP), iliococcygeus (IC), pubococcygeus (PC), and puborectal (PR) muscle bands. The largest strains are induced in the puboperineus (PP) muscle, the last muscle to be engaged by the fetal head. Bands within each muscle are numbered by a numerical suffix in a dorsal-to-ventral direction. The shaded area represents usual non-injurious operating region of passive striated muscle in response to a single stretch.*

SUMMARY

These are the first estimates of pelvic floor muscle strains during human birth. The maximum apparent muscle strain, 300%, was found in puboperineus, late in the second stage of labor.

REFERENCES

Brooks, S.V. et al., *J. Physiol.,* **488**, 459.
Mooney B. et al., (2002) *Science*, Submitted.
Foldsprang A. et al. (1992) *J. Epid. Comm Health* **46**, 595.

A NOVEL ALGORITHM FOR ESTIMATING HEAD IMPACT MAGNITUDE AND LOCATION

Joseph J. Crisco[1], Richard M. Greenwald[2], Jeffrey Chu[2]

[1]Dept. of Orthopaedics, Brown Medical School/Rhode Island Hospital and Div. of Engineering, Brown University, Providence, RI
[2]Simbex, Lebanon, NH. E-mail: joseph_crisco@brown.edu

INTRODUCTION

Concussions are a major injury in sports. While head accelerations are the likely injury mechanism, the correlation between head acceleration and concussion injury has not been established. Current systems for measuring head accelerations are costly or not applicable for wide spread use in sports. This paper presents an algorithm for estimating peak head acceleration and impact location using an array of low-cost single-axis accelerometers.

METHODS

Algorithm: It is assumed that the intersection of a horizontal plane with the head is a circular cross-section (HCS), described by a radial coordinate system with the origin at the center, 0° posterior, and 90° to the right. A given number (n) of single-axis accelerometers are located about and normal to the HCS with the axis towards the center. The HCS is assumed to behave as a rigid body accelerated by a single impact in the plane of the HCS. Given these assumptions, it can be shown that the acceleration components normal to the HCS vary as the cosine of the location on the HCS. Thus, from the n peak accelerations and the location of each accelerometer, the algorithm determines the magnitude and location of the impact using a least-squares curve fit of a cosine function with two variables: amplitude and phase shift. The amplitude is then the peak impact acceleration to the HCS and the phase shift is the impact location on the HCS. In application, these values are the linear head acceleration and the hit location.

Numerical Simulation: A parametric study was performed by examining the effect of n, and the effect of random noise on the location and the acceleration magnitudes of each accelerometer. A wide range of parameter sets were studied, but for the results reported here, the specific parameters were set at n = 3, located at 120°, 0° and 120° about the HCS. The standard deviations in the noise were set at 5° degrees and 5% for accelerometer location and peak, respectively. The simulation was repeated 10 times with impacts located at increments of 5° around the HCS.

Experimental Testing: Testing was performed using a twin-wire drop system (ASTM F1446) with a tri-axial accelerometer mounted at the center of gravity (CG) of a standard ISO headform. A specially designed array of single-axis accelerometers (n = 3) was fitted to the headform in the horizontal plane, which defined the HCS. Three drops (2.2 m/s) were performed at each of several locations around the HCS. The algorithm was used to predict the peak impact acceleration and impact location. These values were compared to the CG acceleration of the headform and the known impact locations.

RESULTS AND DISCUSSION

In the numerical simulation, errors were most sensitive to accelerometer location compared to errors in peak acceleration. For the given set of parameters studied here, the maximum standard deviation of the error in the predicted peak acceleration was 9%, and the maximum standard deviation of the hit location error was approximately 6°.

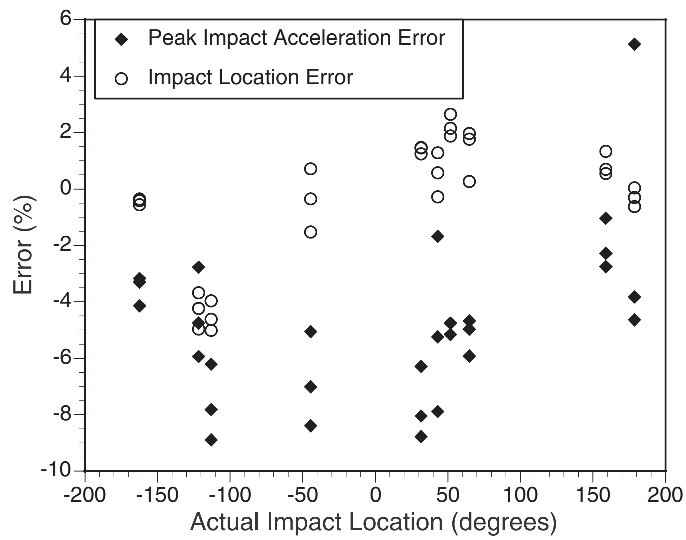

Figure 1: The error in the estimated peak acceleration and location of an impact to a headform from experimental drops.

Experimentally, the estimated peak impact acceleration averaged 5.4% lower than headform CG acceleration with an average 3.2% error in impact location (Figure 1). Limitations of the current algorithm include 2D impacts only on the transverse plane, and estimation of only linear acceleration. Using this algorithm, a system with several low-cost single axis accelerometers placed orthogonal to the surface of the head can provide estimates of head acceleration within 10% of measured accelerations, allowing widespread data collection of head impacts in sport.

SUMMARY

A new algorithm for measuring head acceleration from impacts was developed, studied with numerical simulation, and validated by experimental testing. This algorithm provides a cost-effective approach for studying head impacts and concussion injuries which was heretofore not possible.

ACKNOWLEDGEMENTS

This work was supported in part by NIH 1R43HD40473

STRUCTURAL COMPETENCE OF OSTEOPENIC THORACOLUMBAR VERTEBRAE FOLLOWING ANTERIOR-WEDGE FRACTURE

Ron N Alkalay, Dietrich von Stechow
Orthopedic Biomechanics laboratory, Beth Israel Deaconess Medical Center, Boston, MA.

INTRODUCTION

Age related vertebral compression fractures cause significant physical and psychological impairments. Although data exists on the ability of osteopenic vertebrae to carry compressive loads and the use of imaging methods to predict vertebral fracture, little is known on the effect of low rate fracture on the structural integrity and consequent mechanical load carrying ability of such vertebra under complex loads, both immediately post-fracture and after a recovery period.

METHODS

Nineteen thoracic and lumbar vertebrae from three spines, aged 65-78 years, were radiographed to estimate the body posterior and anterior height and their Bone Mineral Density measured using DXA (Hologic 2000+, Hologic, MA). A custom testing jig was employed to test the vertebrae to failure using a hydraulic test system (1331, Instron, Canton, MA) under combined compression-flexion at a rate of 5mm/min. Failure was defined as 50% reduction in the vertebra anterior height or a reduction of 10% in maximum load. A 6DOF load cell (MC5, AMTI, MA) was employed to measure the resulted forces and moments and displacement to failure measured via the material testing system with the data acquired using LabView (National Instruments, TX) at the rate of 10Hz. The failed vertebrae were allowed to recover for 30 min, the vertebral body heights re-measured and the vertebrae re-tested. Matched pair analysis was used to test for difference in maximal failure load and stiffness, estimated from the linear portion of the load–displacement curves, between the two tests for each of the measured parameters (JMP, SAS, NC).

RESULTS AND DISCUSSION

Vertebral BMD yielded a mean and standard deviation of ($0.5 \pm 0.1 g/cm^2$) for L1 indicating the donor spines to be osteoporotic. The vertebral body failed by a continuous reduction in its anterior height with the vertebral body anterior and posterior heights showing a mean reduction of 19.2% and 7.2%. At the end of the 30 minutes recovery period, the vertebral body regained 5.3% and 2.1% of its height respectively. Compared to the intact vertebrae, the post-recovery vertebrae showed a highly significant reduction in its ability to resist applied compression-flexion loading, Table 1. For example, the ultimate compressive load and flexion moment were reduced by an average of 28% with the compressive stiffness reduced by 40%, Table 1 Clearly, when comparing the estimated stiffness for the in-plane forces and moments the recovered vertebra underwent significantly higher deformations per applied load (Table 1). However, apart from lateral bending, the remaining load responses did not differ significantly (Table 1).

Table 1 Mechanical parameters measured for the intact and the recovered vertebrae

Mechanical parameter	Intact	Fractured*	Significance
Compression force/N	1581 ± 441	1082 ± 313	<.001
C. stiffness/$N.mm^{-1}$	-536 ± 542	-262 ± 186	<.001
Flexion moment/Nm	53 ± 23	34± 11	<0.0001
F. stiffness/$Nm.mm^{-1}$	-11 ± 12	-8 ± 7	<0.001
A-P. Shear force /N	354 ± 185	272 ± 103	<0.0001
A-P. stiffness/$N.mm^{-1}$	-96 ± 97	-74 ± 56	<0.01
Lat.-Bending /Nm	3 ± 7	3 ± 4	<0.05
L-B.stiffness /$Nm.mm^{-1}$	-1 ± 2	-1 ± 1	N.S
Lat. Shear force /N	-15 ± 66	-28 ± 41	<0.01
L-S.stiffness/$N.mm^{-1}$	5 ± 17	5 ± 9	N.S
Torque/Nm	-0.04 ± 0.2	0.03 ± 0.2	N.S
T. stiffness/$Nm.mm^{-1}$	-0.0± 0.2	0.1 ± 0.3	N.S

Mean±S.D, A-P:Anterior-Posterior, Lat:Lateral.*Post-test+ 30min.

This study investigated the effect of flexion-compression fracture on the structural competence of failed and recovered osteopenic thoracolumbar vertebrae. Compared to the intact vertebrae, the failed vertebrae exhibited a significant reduction in structural load carrying ability and increased deformation, particularly in the plane of loading (Table 1). However, the mean reduction in axial compression, flexion and anterior-posterior strength were 23-28% of the intact vertebrae, whilst out of plane response, although showing a high reduction, were highly variable. Furthermore, the fractured vertebrae presented a marked rebound of the vertebral body heights. This data suggests osteopenic vertebrae having recovered for a period of time, to retain a substantial load carrying ability. In assessing the elderly patient without neurological compromise, this residual structural competence ought to be considered in deciding on the appropriate treatment modality.

SUMMARY

The residual structural competence of failed osteopenic thracolumbar vertebrae having undergone recovery, in response to complex loads, was investigated. The recovered vertebrae, although showing decreased competence and higher deformation under the applied loads, did retain a significant portion of their initial competence when compared to the intact vertebrae.

MOTOR ADAPTATIONS TO CHANGES IN LIMB MECHANICAL PROPERTIES DURING VOLUNTARY GAIT MODIFICATIONS

Stephen D. Prentice and Adrienne T. Hol
Gait and Posture Lab, Department of Kinesiology, University of Waterloo, Waterloo, Ontario, Canada
sprentic@healthy.uwaterloo.ca

INTRODUCTION

The ability to safely walk through a cluttered environment involves the formation of precise limb trajectories to eliminate the risk of trips and falls. The central nervous system must have a fine awareness for specific limb dynamics in order to seemlessly superimpose these discrete voluntary movements upon the ongoing locomotor actions. The success of this integration depends greatly on how well the neural and mechanical systems interact. The role of limb dynamics in the formation of locomotor strategies is not fully understood and it is not clear as to how well the locomotor control system can adapt to changes in limb mechanics. The purpose of this study was to examine how the locomotor control system can adapt its movement strategies following a change in the inertia of the leg segment of both lower limbs.

METHODS

Eight participants were instructed to perform two walking tasks: level unobstructed walking and walking over a 30cm obstacle, under three limb weighting conditions (NW: non-weighted, W: weighted, WR: weight removed). A total of 90 trials (15 trials for each walking/weighting condition) were completed in the following order: level walking–NW, obsructed walking–NW, level walking–W, obstructed walking–W, obstructed walking–WR and level walking–WR. During obstructed trials, the obstacle was positioned midway between the left and right foot contacts of a step halfway along the walkway and the starting position was fixed such that the right foot always led over the obstacle. For the block of weighted trials, a custom weight (4.5kg) was attached bi-laterally on the centre of mass of each leg segment.
Kinematic data for the limbs and trunk were obtained using an OPTOTRAK 3D motion measurement system (f_s= 60Hz & low-pass filtered at 6Hz). Linear envelop EMG was recorded (f_s=240 Hz) bilaterally from: rectus femoris, biceps femoris, tibialis anterior and soleus. Kinematic data and force plate data were used to determine joint moments and powers using inverse dynamics. Initial analyses have focused on performance during the obstacle condition.

RESULTS AND DISCUSSION

Kinematic, kinetic and EMG data of the initial trials of the weighted trials over the obstacle were compared to the average profiles of the non-weighted conditions. Overall, the joint kinematics were very similar following the addition of the mass with the largest changes being observed as an increased knee extension during swing (Fig. 1). During early swing, there is a marked decrease in the knee flexor power genearation (Fig. 1) which is predominate in NW obstacle conditions (McFadyen & Winter, 1991; Prentice & Patla,

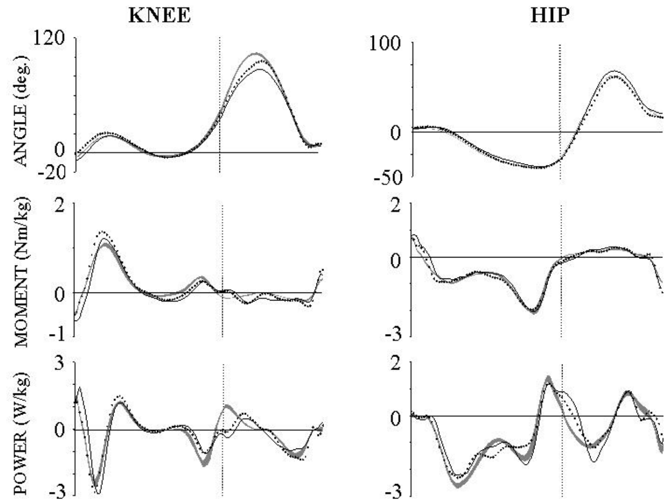

Figure 1: Knee & hip kinematics and kinetics. Profiles are from one subject during the obstacle condition. Grey = mn ± 95%CI of NW(n=15), thick = 1st trial W, dotted = 10th trial W.

1995). This reduced knee action was accompanied by a prolonged hip pull off power. Fluctuations in the moment and power profiles of the hip and knee indicate the poor initial estimation of limb mechanics which becomes more refined in the later exposures to the obstacle to resemble that reported previously under weighted conditions (Reid & Prentice, 2001). These modifications in joint kinetics indicate that even during the initial exposure to the obstacles with added weight, individuals were able to produce an altered yet immature movement strategy.

SUMMARY

Individuals were able to rapidly adapt to the new mechanical limb properties. There was a brief period in which the nervous system explored the nature of the change in limb dynamics to further refine the appropriate response. The resulting strategy was not simply a magnitude adjustment of the actions used in the non-weighted conditions but involved a different muscle activation pattern and thus a different locus of energy generation that was gradually developed during the initial exposures to the obstacle.

REFERENCES

McFadyen BJ & Winter DA (1991). *Neurosci Res Comm* **9**, 37-44
Prentice & Patla (1995) *Exp Brain Res*, **114**, 500-506.
Reid MJ & Prentice SD (2001). *Neurosci Res Comm*,**29**,79-87.

ACKNOWLDEGEMENTS

This work was supported by NSERC and we would like to thank J.Groves, J.Byrne & E.Hasler for their assistance.

PREDICTIONS OF INFANT BRAIN INJURES IN MINOR FALLS AND INFLICTED EVENTS

Michael T. Prange and Susan S. Margulies
Department of Bioengineering, University of Pennsylvania, Philadelphia PA margulies@seas.upenn.edu

INTRODUCTION The majority of serious traumatic brain injury in infants and toddlers is due to child abuse and abused children with brain injury have a worse outcome than those with accidental brain injury (Billmire and Myers 1985, Ewing-Cobbs et al., 1998).The suspicion of abuse often arises when the event history appears not to correspond to the injury in the child. Because the mechanisms of head injuries due to shaking, shaking with impact, and falls are not yet established, the differentiation between accidental and inflicted head injury is problematic. This study develops axonal injury predictions in the infant using a finite element model.

METHODS A 3-D finite element model of a 1 month old infant head, infant material properties, axonal tissue injury thresholds, and typical loading conditions were combined to predict the incidence of axonal injury during abusive and accidental events. The brain geometry was extracted from resonance (MR) images obtained from the radiology database at the Children's Hospital of Philadelphia, with IRB approval. The brain tissue was modeled as a nonlinear, homogenous, isotropic, viscoelastic, incompressible material, with parameters fit to experimental data obtained from mixed gray/white matter brain specimens from newborn piglets (Prange, 2002). Scenarios simulated were limited to inertial loading events with no contact or contact with a widely distributed load to the skull with no anticipated skull fracture. Simulated events included a 1.5m fall onto 10cm thick mattress foam, a shake without impact, an inflicted impact onto the mattress foam. Because these events were assumed to produce little or no significant skull deformation, the loads were approximated as purely inertial, and the skull was represented as a rigid material.

After convergence analysis, simulations were performed (ABAQUS/Explicit, HKS Inc.) using loads we obtained with a custom-designed instrumented infant dummy experiencing these events. Tissue deformations were computed by the finite element model and subsequently transformed to regional axonal injury predictions, using injury thresholds we determined from purely inertial porcine studies. Because of the lack of high-rate data for the infant skull, suture, and bridging vein properties, and little experimental data regarding in vivo motion at the skull/brain boundary, no predictions of subdural hemorrhage or skull fracture can be made and injury predictions in this study were limited to only axonal damage.

RESULTS Detailed comparisons were performed between predicted regional stress/strains and actual injures in these regions for the same controlled movements in the newborn piglet (N=6). The output parameters investigated, peak maximum principal strain (pkE1), peak maximum shear strain (pkSSTRAIN), and peak maximum shear stress (pkSSTRESS), all correlated well with occurrence of axonal injury. Injury threshold values were determined to be 0.336, 0.282, 0.299kPa, for pkE1, pkSSTRAIN, and pkSSTRESS, respectively.

Simulations of the loads measured from 1.5m falls onto mattress foam were mostly translational, and produced peak strain and stress levels below axonal injury thresholds for infants. Shakes and moderate inflicted impact scenarios produced higher strains and stresses than the fall simulation, but less than 1% of the brain volume was expected to experience axonal injury. The severe inflicted impact event was associated with the largest load, and resulted in the largest strain and stress levels and extent of injury, with axonal injury predicted in 11-30% of the brain, depending on the output parameter used in the evaluation. Regions injured were primarily in the subcortical and deep white matter regions.

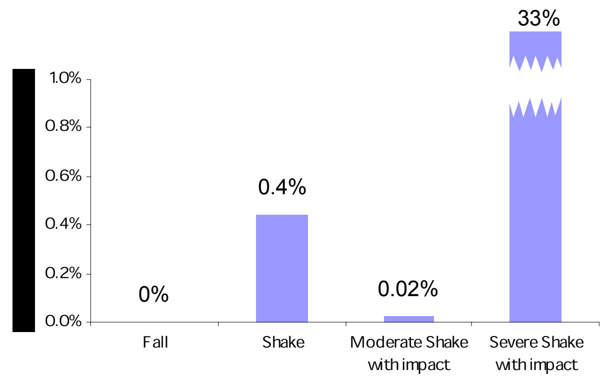

DISCUSSION The rigid skull approximation may underestimate the extent of injury with impact. However, this study supports the theory that shaking alone is not expected to produce significant primary axonal injury in the infant, but that axonal injury may occur with inflicted impacts onto soft materials.

REFERENCES

Billmire M, Myers P. (1985) *Pediatrics,* **75**, 340-342.
Ewing-Cobbs L, et al. (1998) *Pediatrics* **102**, 300-307.
Prange, M.T., Margulies, S.S. (April, 2002) *J. Biomech Eng*., in press.

ACKNOWLEGEMENTS

Support was provided by NIH-NINDS R01/NS39679 and CDC–NCIPC R49/CCR312712.

HYPERELASTIC REPRESENTATION OF HIP JOINT CAPSULE: A FINITE ELEMENT VALIDATION

Kristofer J. Stewart, Douglas R. Pedersen, Richard A. Brand, and Thomas D. Brown
Orthopaedic Biomechanics Lab, 2181 Westlawn Building,
University of Iowa, Iowa City, IA 52242
E-mail: kristofer-stewart@uiowa.edu Web: poppy.obrl.uiowa.edu

INTRODUCTION

Contemporary computational models (Scifert, 1999), which are used extensively to study total hip impingement and dislocation, allow for the practical incorporation of the effects of joint capsule on both motion and the loads transmitted to other parts of the joint. However, these models to date have not included mechanical representation of the hip capsule. Since capsule insufficiency is clinically regarded as predisposing to dislocation, incorporating capsule representation is an important aspect of making these models yet more credible.

METHODS

In a series of ten cadaver specimens, quantitative mechanical properties of the hip capsule were obtained experimentally for the entire intact structure, and subsequently for eight individual sectors of the hip capsule (Stewart, 2001). Material properties (i.e., structural tangent stiffness, failure load, ultimate strength, tangent modulus) were calculated using the load-displacement and geometric data collected for each of the sectors. The load-displacement curves provide the basis for adding hyperelastic representation to an existing finite element (FE) model. Of the various hyperelastic material models available in the ABAQUS 6.2 finite element library, the Yeoh model (a variation of the reduced-polynomial strain energy function) satisfactorily fits the experimental data. Eight sectors, meshed with continuum elements having Yeoh hyperelastic material characteristics, are incorporated into a whole-joint FE model at proper anatomical insertion points.

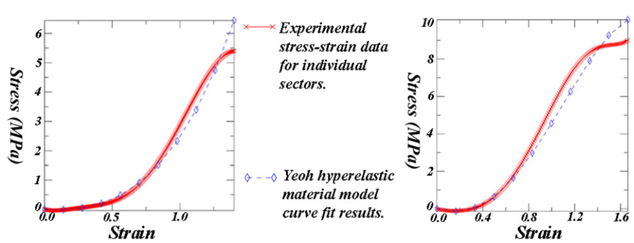

Figure 1: Two samples of Yeoh model fit to physical data.

A size-scalable FE mesh, developed using 1-mm serial section data from the Visual Human database, provdies detailed anatomic zoning of the hemi-pelvis and femur (Fig 2A). This model replicates the whole-capsule cadaveric hip tensile tests by distracting the femur away from the acetabulum in the direction of the femoral neck axis.

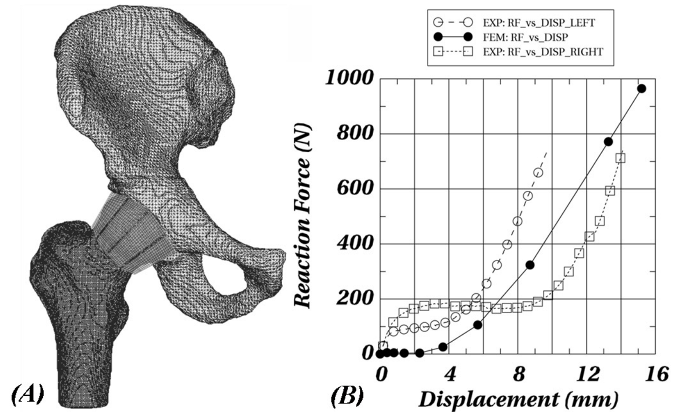

Figure 2: (A) Rigid Bezier surface mesh used for whole-capsule joint distraction validation exercises, (B) and the resulting comparison of experimental and computational load-displacement curves.

RESULTS AND DISCUSSION

Initial validation exercises of the FE model reveal a load-deformation behavior similar to that obtained from the physical experiments (Fig 2B).

This "soft tissue" finite element model can now be used to parametrically investigate and quantify the effects of hip joint capsule on joint kinetics and dislocation mechanics. Specific parametric series of interest include generalized capsulo-ligamentous laxity and stiffness deficit (or absence) of individual capsule structures.

REFERENCES

Stewart, K.J. et al. (2001). *Proceedings of 25th Annual Meeting, American Society of Biomechanics*, LaJolla, CA, 411.

Scifert, C.F. et al. (1999). *Computer Methods in Biomechanics and Biomedical Engineering*, **2**, 139-147.

ACKNOWLEDGEMENTS

This study was supported in part by NIH 46601. We wish to acknowledge the technical contributions of Dr. Nicole Grosland and Dr. Anneliese Heiner.

ARE ESTIMATES OF QUADRICEPS STRENGTH VALID? IMPLICATIONS FOR CLINICAL DECISION MAKING

Kurt Manal, Glenn Williams, Peter Barrance and Thomas S. Buchanan

Center for Biomedical Engineering Research. University of Delaware, Newark, DE. USA. manal@udel.edu

INTRODUCTION

Weakness of the quadriceps muscle group is common following anterior cruciate ligament (ACL) injury and reconstruction (Heimstra et al., 2000). Quadriceps strength is assessed indirectly by measuring the patient's maximum knee extension moment. Patient positioning and concomitant contraction of the hamstrings can reduce the magnitude of the extension moment, and therefore the perceived strength of the quadriceps. It is important to understand how these factors affect the magnitude of the extensor moment, because the results of such testing are used in surgical decision making, rehabilitation progression and "return to sport" (Williams et al., 2001). The purpose of this study was to examine how subject positioning and co-contraction of the hamstrings can reduce the knee extension moment. We hypothesized that these factors can lead to an underestimation in quadriceps strength of approximately the same value used clinically to define quadriceps weakness (i.e., 10%-20%).

METHODS

(1) A biomechanical model of the leg (Delp et al., 1990) was used to estimate how small changes (± 10º) in knee and hip angle from a prescribed testing position alter the moment generating potential of the quadriceps. The extension moment in each position was expressed relative to the moment with the model in 70º & 90º of knee and hip flexion. Muscle activations for the hamstrings and quadriceps were set at 0.0 & 1.0 respectively (i.e., to simulate a case of zero co-contraction).

(2) EMGs from 6 ACL deficient subjects were recorded during isometric, maximal knee extension and flexion with the knee and hip in 70º & 90º of flexion. EMGs for the medial (MH) and lateral hamstrings (LH) were processed as described in Lloyd & Buchanan (1998). Muscle activity for the MH & LH during the knee extension trials was expressed relative to the activity recorded during maximal knee flexion. This was done for the involved and uninvolved legs of each subject.

RESULTS AND DISCUSSION

Percent change in knee extension moment due to varying knee and hip angle ± 10º is displayed in Figure 1. Note that these data were calculated using the biomechanical model of the leg. Joint configurations for which the extensor moment changed by more than ±5% are shaded in red. The extensor moment was underestimated by 11% with the knee and hip extended 10º from the prescribed test position. In contrast, the moment was 8% greater with the knee and hip in +10º of flexion.

The magnitude of the flexor activity during maximal knee extension is displayed in Figure 2. An assumption when making side-to-side strength comparisons is that the antagonistic activity of the hamstrings is the same for both legs. In general, this was not the case for the subjects tested in this study (i.e., the data in Fig. 2 do not fall on the diagonal line). For example, MH activity of the involved leg for subject "*" was 22% of the peak value recorded during maximal flexion, while muscle activity for the MH of the uninvolved leg was only 9%. Also note that muscle activity for the flexors during knee extension was generally greater than 10% of the muscle's peak value during flexion. This is significant because the moment arms for MH & LH are close to their maximum values with the leg in the position tested. Using the EMG data for subject "*" and the biomechanical model of the leg, we estimated that the knee extension moment would be 18% weaker for the involved leg due to the greater hamstrings activity. Moreover, positioning the involved leg in greater knee and hip extension would further undermine the perceived quadriceps strength. The magnitude of this "error" is significant because it lies in the same range used clinically to define quadriceps weakness (i.e., side-to-side differences of 10%-20%). This finding was consistent with our hypothesis.

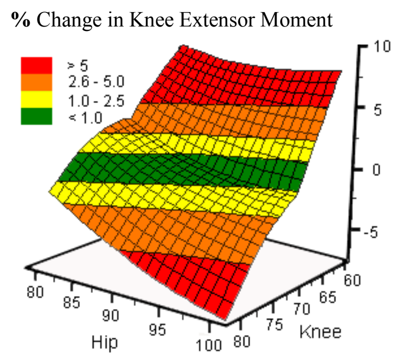

Figure 1. % change as a function of position from test angle. NB: (+) values represent a decrease in the moment.

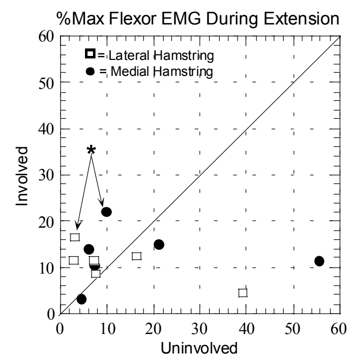

Figure 2. % Max MH & LH muscle activity during knee extension (n=6). "*" = data for same subject.

SUMMARY

Preliminary results for a group of ACL deficient subjects demonstrate that noteworthy activity of the hamstrings is present during quadriceps strength testing. The clinical relevance of this work is that modified testing procedures may be needed to better evaluate quadriceps strength.

REFERENCES

Heimstra,L.A. et al (2000). *Med Sci Sports Exerc*,**32**,1472-79.
Lloyd,D.G.,Buchanan,T.S.(1996).*J Biomech Eng*,**118**,367-76.
Williams,G.N. et al (2001). *J Orthop Sports Ther*, **31**,546-566.
Delp,S.L et al (1990). *IEEE Trans Biomed Eng*,**37**, 757-67.

ACKNOWLEDGMENTS

This work was supported in part by NIH AR46386.

THE TENSILE PROPERTIES OF THE HEALING GOAT MCL AFTER A COMBINED MCL/ACL INJURY

Steven D. Abramowitch, Masayoshi Yagi, Eiichi Tsuda, Savio L-Y. Woo

Musculoskeletal Research Center, Department of Orthopaedic Surgery, University of Pittsburgh
Pittsburgh, PA. 412-648-2000. Fax: 412-648-2001. decenzod@msx.upmc.edu

INTRODUCTION

The optimal animal model for the study of a combined injury to the medial collateral ligament (MCL) and anterior cruciate ligament (ACL) has yet to be established. With the high incidence (<50%) of ACL graft failure and joint deterioration in the rabbit and canine models, an animal model is needed in which long-term ACL reconstructions are successful (Yamaji 1996, Woo 1990). The large knee joint and robust activity level of the goat is attractive for studies of ligament healing (Ng 1995). Thus, the objective of this study was to determine the structural properties of the healing goat femur-MCL-tibia complex (FMTC) and the mechanical properties of the healing goat MCL at 6 weeks after a combined MCL/ACL injury.

METHODS

Eight skeletally mature female Saanen goats (weight 37.3±4.3 kg) were used in this study. The ACL of the right knee was transected and reconstructed with a bone-patellar tendon-bone autograft. Subsequently, a mop-end tear was created in the MCL (Weiss 1991). The contralateral knee served as a sham-operated control. The goats were allowed free cage activity after surgery. At 6 weeks, the animals were euthanized and the hind legs were harvested for biomechanical testing. Specimens (8 healing and 6 sham-operated) were dissected leaving an FMTC. The cross-sectional area of the MCL was measured using a laser micrometer (Lee 1990). Each FMTC was positioned in custom designed clamps and fixed to an Instron™ testing machine (model 4502) in a 37ºC saline bath. The FMTC was loaded to failure at 10 mm/min. Strain was measured by tracking two reflective markers on the midsubstance using a Motion Analysis™ system (VP320). Structural properties of the FMTC (stiffness, ultimate load) and mechanical properties of the MCL substance (tangent modulus between 3%-7% strain) were calculated from the resulting load-elongation and stress-strain curves, respectively (Scheffler 2001). Statistical analysis was performed using an unpaired t-test. Significance was set at $p < 0.05$.

RESULTS AND DISCUSSION

The ACL graft was intact after 6 weeks. Grossly, each healing MCL was darker and less shinny than the MCLs in the sham-operated controls. Further, no joint surface deterioration or osteophyte formation was observed. The cross-sectional area of the healing MCL was 2.7 times larger than that of the sham-operated MCL ($p<0.05$; Table 1). In terms of the structural properties of the FMTC, the stiffness and ultimate load at failure of the healing FMTC was less than 50% and 27% of that for the sham-operated FMTC, respectively ($p<0.05$; Table 1). In terms of the mechanical properties of the MCL substance, the tangent modulus of the healing MCL was less than 13% of that for the sham-operated MCL ($p<0.05$).

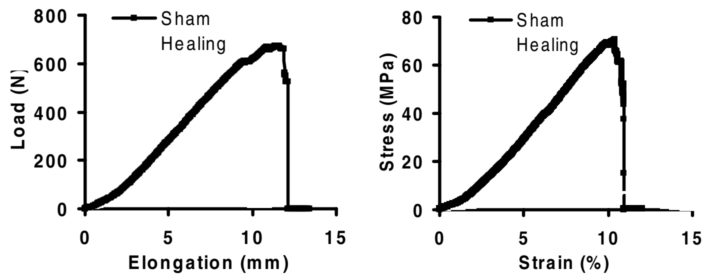

Figure 1: Typical load-elongation and stress-strain curves.

This study determined the tensile properties of the healing goat MCL at 6 weeks after a combined MCL/ACL injury treated with ACL reconstruction. The parameter values of sham-operated controls are similar to those found previously (Scheffler 2001). Further, the parameter values of the healed MCL range from 29% to 52% lower than those reported for an isolated MCL injury using the goat model. This result may be attributed to severity of injury to the knee. Overall, the goat model is suitable for studying the combined MCL/ACL injury as the results are consistent with those observed using other animal models, yet none of the complications were observed.

REFERENCES

Yamaji, T. et al (1996) *JOR*, **14**, 223-7.
Woo, S. L-Y. et al (1990) *JBJS*, **72-A**, 382-92.
Ng, G. Y. et al (1995) *JOR*, **13**, 602-8.
Weiss, J. A. et al (1991) *JOR*, **9**, 516-28.
Lee, T.Q. et al (1988) *JBME*, **110,** 110-4.
Scheffler, S. U. et al (2001) *Ann Biomed Eng*, **29**, 173-80.

ACKNOWLEDGEMENTS

The funding from NIH grant #AR41820 is greatly appreciated.

Table 1: Structural Properties of the FMTC and Mechanical Properties of the MCL (mean ± sd;*p<0.05).

	Stiffness (N/mm)	Ultimate Load (N)	Cross-sectional Area (mm^2)	Tangent Modulus (MPa)
Healing Group (n = 8)	37.4 ± 23.1*	193.2 ± 148.8*	23.3 ± 10.2*	99.3 ± 59.1*
Sham-Operated Control (n = 6)	75.6 ± 23.0	719.7 ± 88.9	8.6 ± 1.7	773.3 ± 254.8

DISSOCIATION BETWEEN DYNAMIC STRESS AND INTRAMUSCULAR PRESSURE IN ISOLATED RABBIT TIBIALIS ANTERIOR MUSCLE

Jennifer Davis[1], Kenton K. Kaufman[2], Richard L. Lieber[1], Email: rlieber@ucsd.edu
[1] University of California and Veterans Administration Medical Centers, San Diego, CA. & [2]Mayo Clinic, Rochester, MN.

INTRODUCTION Reports in the literature suggest that intramuscular pressure (IMP) may serve as a reliable index of muscle force measured. Recently, it was shown that IMP predicts relative active and passive isometric muscle stress in animal models (Davis et al., 2001). However, since movement is dynamic, the purpose of this study was to quantify the relationship between IMP and dynamic muscle stress during both concentric and eccentric contractions.

METHODS The experimental model was the tibialis anterior (TA) of the New Zealand White rabbit (mass=2.5 $\pm$0.5 kg, n = 10). The knee was fixed in a custom jig, TA exposed, and distal tendon attached to a servomotor (Model 300B, Aurora Scientific Inc.). A cuff electrode was placed around the peroneal nerve for muscle activation (Pulsar 6Bp Stimulator FHC Inc.). A 360 µm fiber optic pressure sensor (Luna Innovations Inc.) was inserted in line with the long axis of the fibers. The force-velocity relationship was generated during activation of the muscle at 60 Hz for 650 ms with a 2-minute rest interval between each contraction. Fiber length (L_f) was calculated from muscle length using a 0.67 fiber length-to-muscle length ratio. For concentric and eccentric contractions, muscle length was initially set to L_0+5%L_f or L_0-5%L_f respectively. The experiment ended with 2 contractions that combined both shortening (and lengthening) in opposite order. Tension records were converted to stress using the muscle's calculated physiological cross sectional area (PCSA).

RESULTS AND DISCUSSION The TA muscle force-velocity curve had the classic shape of a rectangular hyperbola, which was characterized by a V_{max} of 5.5L_f/s and a P_0 of 230±18.6kPa (Fig. 1A). This compared favorably with Close's (1972) classic values for mammalian muscle. The shape of the IMP-velocity curve mimicked the shape of the force-velocity curve for concentric contractions but with much higher variability (Fig. 1B). The corresponding points on the IMP-velocity demonstrated a maximum IMP (I_0) of 24±6.3 mmHg and at V_{max} IMP decreased to 5.9±13.3 mmHg. For the eccentric portion of the IMP-velocity curve, a precipitous drop in pressure relative to I_0 was observed (Fig. 1B). Combined contractions demonstrated a profound history effect. The stresses at various points during the protocol were designated as seen in figure 2A. The protocol was repeated, reversing the order contractions. For the combined protocol that began with shortening (Fig. 2B), muscle stresses were significantly different as revealed by one-way ANOVA ($p<0.0006$). Values for IMP at each of these points displayed reproducible but unexpected relative levels. For example, I_{01} was <u>greater</u> than I_0 in spite of the fact that P_{01} was <u>lower</u> than P_0. Further, while P_E was <u>greater</u> than P_{01} due to eccentric contraction, I_E was <u>lower</u> than I_{01} (Fig. 2C). A similar dissociation was observed for the protocol that began with lengthening. In summary the combined protocol demonstrated both a history effect and an order effect between combinations. The reason for these effects is not clear but may relate to transducer movement, tissue fluid flow or muscle volume changes.

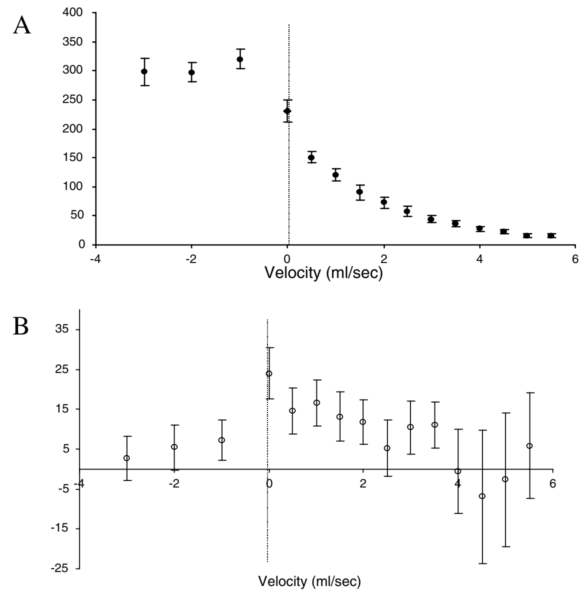

<u>Figure 1:</u> (A) Stress-velocity relationship for all velocities tested, (B) Corresponding IMP velocity relationship (n = 10, Bars =SEM).

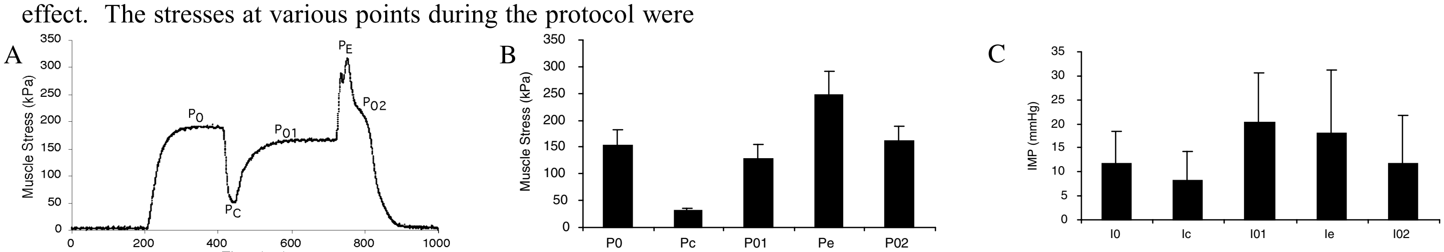

<u>Figure 2</u> (A) Sample of the time course of stress during shortening protocol. (B) Average stress achieved during shortening protocol. (C) Average IMP achieved during the shortening protocol. Abbreviations: P_0, initial isometric stress, P_C, concentric stress, P_{01}, isometric stress at first length change, P_E, eccentric stress, and P_{02}, isometric stress at the starting length. Corresponding IMP was defined as I_0, I_C, I_{01}, I_E, and I_{02}.

REFERENCES:

Close, R.I. (1972) *Physiol. Rev.*, **52**, 129-197.
Davis, J., Kaufman, K.K., Lieber, R.L. (2001) *Proc. Am. Soc. Biomech.***25,**149-150.

USE OF LOCAL BODILY LANDMARKS IN ACETABULAR CUP POSITIONING

Mark C Miller[1,2], Jufang He[2], Donald D Anderson[3], and Nicholas G Sotereanos[2]

[1]Duquesne University, Pittsburgh, PA, millermark@duq.edu
[2]Allegheny General Hospital, Pittsburgh, PA; [3]Minneapolis Sports Medicine Center, Minneapolis, MN

INTRODUCTION

Dislocation after total hip arthroplasty is a common complication frequently caused solely by improper acetabular cup orientation. Current practices for establishing cup orientation vary substantially and systems using computerized imaging and intraoperative display have been developed to provide consistent results (McCollum, DiGioia). However, most facilities do not have access to emerging technologies and the cost is substantially increased because each procedure requires CT or MRI data. The purpose of this study was to investigate a new method for positioning the acetabular cup based on bony acetabular landmarks that are readily identified intraoperatively after reaming.

METHODS

Three landmarks that would be unaffected by osteophyte formation were selected: 1) the most lateral point of the ischial sulcus, which is also the lowest point of the sulcus when felt with a blunt-tipped probe; 2) the saddlepoint at the confluence between the iliopubic eminence and the superior pubic ramus, which is also effectively five millimeters from the acetabular rim along the ridge of the pubic ramus; 3) the most superior point of the acetbulum, which intra-operatively is used to establish the overhang of the acetabular cup: when viewed radiographically, the most superior point is also the most lateral. Note that the points on the sulcus and ramus are inferior to the rim of the acetabulum and establish the level of the cup inside the reamed cavity.

The use of landmarks for component orientation can be judged to be successful if neither dislocations nor other mechanical problems occur in practice. Given that an acceptable post-operative range of motion should essentially recreate pre-operative functionality and not constrain restored activity, post-operative cup orientation may be expected to approximate native acetabular orientation. In clinical practice, however, cup abduction is estimated in pre-operative planning so that the native acetabulum is equal to or is less than the cup abduction. Therefore, the hypotheses of the study were that the landmarks 1) would provide a low dislocation rate clinically and 2) would recreate native cup anteversion but have less abduction.

To establish the clinical validity of the landmark method of cup placement, the technique was used in 329 total hip arthroplasties from 1996 to 2000 and the patients were followed until July 2001, with an average follow-up of 2.5 years. A special device was constructed to quantify *in vitro* acetabular orientation. The device used a sequence of body-based rotations of a gimbal to physically display the amount of rotation on carefully scribed scales accurate to 0.5 degrees. To establish the relationship of the acetabulum itself to the resulting three-dimensional cup orientation, the orientation of the acetabuli in 14 acetabuli in seven pelvises from cadavers was measured. Then, after reaming, cups were placed in the pelvises using the landmark method and the cup orientation was measured again.

RESULTS AND DISCUSSION

In the clinical study, two dislocations occurred after arthroplasty. One occurred at 4 months while the patient was using a recumbent bicycle in physical therapy and the second dislocation occurred in the recovery room. Both cases were reduced with conscious sedation and treated with hip abduction orthotics for 12 weeks. There were no subsequent dislocations, giving a favorable dislocation rate of 0.61%.(DiGioia)

In the laboratory study of seven pelvises, the anteversion of the cups after implantation was similar to the value of the native acetabulum. The post-operative anteversion and abduction were respectively 0.7 degrees more and 7.1 degrees less than the pre-operative measures. (Table 1) Statistical analysis with corrected, paired t-tests showed no significant differences between pre- and post-operative cases.

Proper orientation of the acetabular cup in total hip arthroplasty based on the patient's bony anatomic landmarks can significantly reduce the dislocation rate. The landmark method of cup placement reproduces native anteversion and provides good superior coverage of the femoral head. In conclusion, surgeons can effectively use landmarks to orient acetabular cups without additional equipment.

Table 1: Pre- and Post-operative Orientation

	Mean [°]	S.D.
Preoperative Abduction	44.3	5.7
Postoperative Abduction	37.2	10.
Preoperative Anteversion	31.1	5.5
Postoperative Anteversion	31.8	11.

REFERENCES

1) McCollum, DE et al. (1990), *CORR*, **261**: 159-170.
2) DiGioia, AM et al.(1998), *CORR*, **355**: 8-22.

ACKNOWLEDGEMENTS

The design and fabrication skills of John DesJardins are gratefully acknowledged.

EVALUATION OF PATELLA TENDON AS A GRAFT MATERIAL FOR ANTERIOR CRUCIATE LIGAMENT RECONSTRUCTION IN AN OVINE MODEL

Christopher A. Barnsdale, Hirotaka Azuma, Shigenobu Fukushima, Gail M. Thornton, Cyril B. Frank, Nigel G. Shrive

McCaig Centre for Joint Injury and Arthritis Research,
University of Calgary, 3330 Hospital Dr. NW, Calgary, Alberta, Canada, T2N 4N1
Email: chris-barnsdale@btinternet.com

INTRODUCTION

One option for anterior cruciate ligament (ACL) reconstruction in humans uses an autologous central third of the patella tendon (PT) graft. To be successful, such PT grafts must structurally replace the features of the ACL. The same logic is true for grafts in animal models of ACL injury. Our goal is to create a sheep model of ACL injury and PT replacement, if the PT can, in fact, replace the key functions of the normal ACL. To that end, the ovine ACL and its two component parts (anteromedial (AM) and posterolateral (PL) bands) must be related mechanically and compared with a PT graft to determine both their structural and material behavior. This is the first step in determining potential efficacy of an appropriately sized PT graft to replace part or all of the normal ACL. Our hypothesis was that the PT and ACL bands would have similar material properties.

METHODS

PTs and ACLs from fifteen skeletally mature Suffolk-Cross sheep were tested uniaxially to failure: PT (n=5), ACL-AM (n=5) and ACL-PL (n=5). Bone-PT-bone complexes were mounted uniaxially in an MTS system with the patella mounted at 45° relative to the long axis of the tibia. The PT was sized to a 4mm central portion, aligned with the actuator, and its length and area measured using digital calipers and custom area calipers, respectively. The complex was elongated to failure at 50mm/min measuring load vs. time. Whole bone-ACL-whole bone complexes were mounted at 60° flexion (tibial/femoral long axes) (*Figure 1*) and one ACL bundle was then cut. The ACL was aligned with the actuator and its length and area measured. The ACL was elongated to failure at 50mm/min. Cross-sectional area, failure load and failure stress of PT and ACL were compared using Student's t-tests and power was calculated.

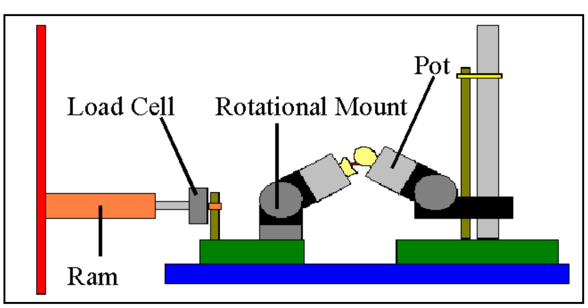

***Figure 1* – MTS Sheep Table for Uniaxial ACL Testing**

RESULTS AND DISCUSSION

The cross-sectional area of the ACL-AM, ACL-PL and PT were similar. In this preliminary study, failure load comparison between the PT and ACL-PL revealed a significant difference. The failure load comparison between the PT and ACL-AM was significant (p=0.03) but had low power (P=0.5). Likewise, comparison of failure stresses of the PT to both the ACL-PL and ACL-AM were significantly different but also had low power (p=0.04 and P=0.5). The failure load and stress of sheep central third PT grafts were statistically significantly less than the ACL-AM and ACL-PL (*Figure 2*). However, due to the preliminary nature of this study, only the comparison between the failure load of the PT and ACL-PL was statistically powerful. Power analysis indicated that the sample size must be doubled (P=0.8). Contrary to our hypothesis, these preliminary results suggest that PT failure stress was less than the ACL-AM and ACL-PL; thus, such grafts would have to be larger than the original ACL to achieve the same structural strength.

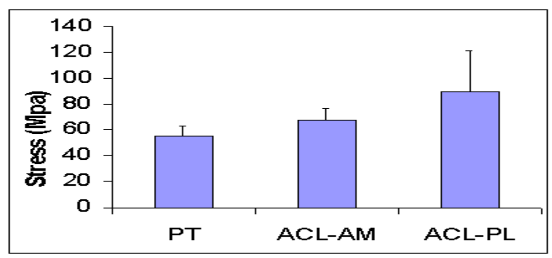

***Figure 2* – Mean Failure Stresses of Sheep Tissues**

SUMMARY

The failure properties of sheep central third PT grafts were compared to both AM and PL bundles of the ACL. The failure load and stress of the PT grafts were significantly less than the ACL-PL and ACL-AM. The sample size of the current study (n=5) must be doubled to confirm that these statistically significant results are also statistically powerful. The data from this preliminary study reveals both structural and material inferiority of the PT, which suggests that the PT may not be an appropriate graft material for the ovine ACL-AM, ACL-PL or whole ACL.

ACKNOWLEDGEMENTS

CIHR, AHFMR, TAS

BIOMECHANICS OF SINGLE-LEVEL CERVICAL FUSION TECHNIQUES: COMPARISON OF GRAFT-PLATE FUSION WITH AN INTERBODY CAGE DEVICE

Denis J. DiAngelo[1], Amanda M. Thomas[1], and Kevin T. Foley[2]
[1]School of Biomedical Engineering, The University of Tennessee Health Science Center, Memphis, TN, ddiangelo@utmem.edu
[2]Department of Neurosurgery, The University of Tennessee Health Science Center, Memphis, TN

INTRODUCTION

Anterior cervical graft fusion alone or supplemented with an anterior cervical plating system may be used to treat the diseased cervical spine. An anterior cervical plate is intended to restore the mechanical integrity of the operated spine and decrease graft complications. An alternative method to single-level graft fusion is to use an interbody device. The objective of this study was to compare the biomechanical stability of a graft-plated construct with an interbody cage device.

METHODS

Six human cadaveric cervical spines (3 male and 3 female, average age 79.3 ±5 years) were biomechanically tested in four conditions: 1) harvested (H), 2) single-level discectomy with graft alone (GR) (Cornerstone SR, Regeneration Technologies, Inc. Alachua, FL), 3) graft with anterior cervical plate (GAP) (Atlantis plating system; Medtronic Sofamor Danek, Memphis, TN), and 4) one centrally located interbody fusion device (CAGE) (BAK/C, Sulzer Spine-Tech, Minneapolis, MN). The spines were mounted in a programmable tester and loaded in flexion and extension, right and left lateral bending, and right and left axial rotation. Measurements included vertebral motions, overall spine rotation, and applied load and moment. Global (C2-T1) rotational stiffness was calculated and normalized to the H condition to control intrinsic differences in the specimens. The relative rotations at the superior (S), operated (O), and inferior (I) motion segment units (MSU) were normalized with respect to the overall rotation of those three (S+O+I) MSUs and compared. A one-way ANOVA ($p<0.05$) was used to statistically analyze the normalized motion and stiffness data.

RESULTS AND DISCUSSION

The moment values of the altered spine conditions normalized to the harvested condition are listed in Table 1. In flexion, lateral bending, and axial rotation, the normalized moments increased; in extension, they decreased. There were no significant differences between the instrumented conditions, although the GAP condition typically had the greatest value. The normalized motion data are given in Table 2. For flexion, extension, and lateral bending, the motion normalized to the harvested condition at the operated level decreased. There were no significant differences in the normalized motion patterns between the graft-plated spines and the spines having an interbody cage. The distribution of the motion at the operated and adjacent segments for flexion and extension loading is shown in Figure 1. For both instrumented conditions, there was a trend in decreased motion at the operated site that was compensated by the adjacent segments.

ACKNOWLEDGMENTS

Medtronic-Sofamor Danek, Memphis, TN.

REFERENCES

DiAngelo D et al, 2000, *Spine*, 25(7): pp 783-795.

Table 1: Normalized Moment Relative to Harvested Condition. (Mean value; Standard deviation in brackets.)

Loading Condition	Normalized Moment		
	GA	CAGE	GAP
20° Flexion	3.8 (1.9)	4.3 (2.6)	5.5 (4.0) *
18° Extension	0.7 (0.6)	0.6 (0.4)	0.9 (0.7)
16° Right Bending	2.6 (1.3) *	2.6 (1.0) *	2.8 (1.0) *
16° Left Bending	2.3 (1.2)	1.9 (0.3)	2.4 (1.2) *
11° Right Rotation	1.7 (1.2)	1.5 (0.8)	3.0 (1.6) *
9° Left Rotation	1.2 (0.3)	1.2 (0.4)	1.5 (1.1)

* Indicates a significant difference ($P<0.05$) exists between the altered spine condition and the harvested condition.

Table 2: Operated-Level Motion Normalized to Harvested Condition. (Mean value; Standard deviation in brackets.)

Loading Condition	Normalized Motion Relative to H		
	GA	CAGE	GAP
20° Flexion	0.8 (0.6)	0.7 (0.7)	0.2 (0.1) *
18° Extension	0.6 (0.5)	0.4 (0.2) *	0.2 (0.1) *
16° RL Bending	0.6 (0.3)	0.6 (0.4)	0.6 (0.5)
16° LL Bending	0.5 (0.3) *	0.5 (0.3) *	0.2 (0.2) *
11° Right Axial	0.5 (0.6)	0.2 (0.2) *	0.5 (0.5)
9° Left Axial	1.2 (1.1)	0.8 (0.4)	0.8 (1.1)

* Indicates a significant difference ($P<0.05$) exists between the altered spine condition and the harvested condition.

Relative MSU Rotations

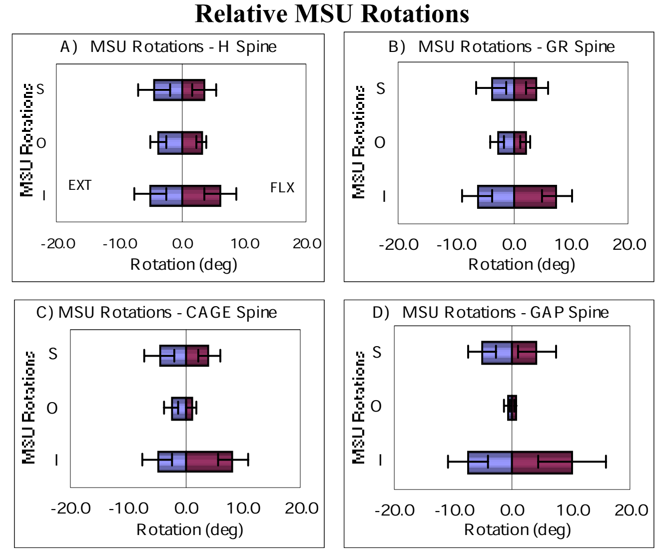

Figure 1: Relative MSU rotations of the operated level for different spine conditions during flexion and extension. A) Harvested, B) Grafted, C) Cage and D) Graft with Plate.

DYNAMICS OF CEREBRAL BLOOD FLOW REGULATION USING A LUMPED PARAMETER MODEL

Mette Olufsen[1], Ali Nadim[2], and Lewis Lipsitz[3]
[1]Department of Mathematics, North Carolina State University, Raleigh, North Carolina
[2]Keck Graduate Institute, Claremont Graduate University, Claremont, California
[3]Hebrew Rehabilitation Center for Aged, Beth Israel Deaconess Medical Center, and Harvard Medical School, Boston, Massachusetts

INTRODUCTION

Cerebral blood flow dynamics is analyzed to study changes in key parameters (systemic and cerebrovascular resistances) during posture change from sitting to standing. The model sheds light on vascular adaptation to hypotensive stress, and can help to determine some of the changes in cerebral autoregulation that occur during hypertension.

METHODS

Existing data for 10 healthy young and 10 hypertensive subjects from Doppler measurements of cerebral blood velocity in the middle cerebral artery (MCA) and Finapres pressure in the finger are analyzed. Measurements show that as the subject stands up pressure falls and the blood flow pulse widens (Lipsitz 2000). The MCA blood flow is modeled using a three-element windkessel model represented by a circuit with two resistors (R_S, R_P) and a capacitor (C_S), (Olufsen 2002). The model input is the finger pressure p_F and the output is the flow q_{MCA} in the MCA. From this circuit we have derived an equation for impedance $(Z = P/Q)$ of the MCA.

$$\frac{P_F}{Q_{MCA}} = \frac{R_P + R_S + i\omega\, C_S R_S R_P}{1 + i\omega\, C_S R_P} \equiv Z_w(\omega)$$

Let Z_m be the impedance obtained from the measurements. Then, the parameters for the model can be determined by fitting the impedance of the model to the impedance of the data. The zero- and large-frequency limits of the model yield relations that only involve the resistances:

$$\lim_{\omega\to\infty} Z_W(\omega) = R_S, \quad \lim_{\omega\to 0} Z_W(\omega) = R_S + R_P$$

The compliance C_S can be computed from analyzing the modulus of the impedance $|Z|$ as a function of frequency. We have estimated the model parameters in two ways; getting a parameter for each of the three intervals (sitting, transition, and standing) and getting parameters on a beat-to-beat basis.

RESULTS AND DISCUSSION

Using the measured pressure as input we were able to compute the flow in the MCA, compare it with the measured flow, and extract the dynamic changes of the model parameters during posture change (see Figure 1). The results show that during posture change, the mean flow and pressure and their ratio (the total resistance) fall (for ~10 s) and then increase (for ~10 s) to a new steady state (in fact the total resistance increases slightly before it falls). The peripheral resistance increases significantly in the beginning before it falls as the total resistance. As expected the heart rate goes up for about 10-15 s, and then it falls to the new steady state. These results can be explained as follows: Immediately after standing the arterial pressure falls because of blood pooling in the legs and splanchnic circulation. The reduction in arterial pressure may unload the baroreceptors in the carotid arteries, aortic arch, and cardiopulmonary circulation, causing reflex cardio-acceleration and systemic vasoconstriction. When cerebral autoregulation becomes engaged approximately 10 s after the initial fall in pressure, cerebrovascular resistance decreases as expected, to restore blood flow back to baseline. The initial increase in cerebrovascular resistance may explain the widening of the cerebral blood flow pulse velocity, observed in the young subjects. In fact, our model confirms this hypothesis. If we modify the cerebrovascular resistance to prevent its increase (as seen in the hypertensive subjects) due to the initial response by the baroreceotors, the blood flow pulse does not widen.

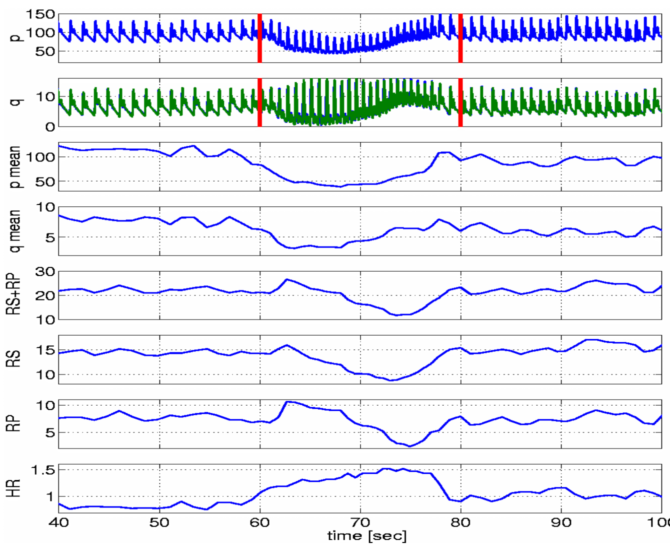

Figure 1: Traces show (top to bottom) pressure [mmHg], flow [cm^3/s], mean pressure, mean flow, total resistance, systemic and cerebrovascular resistance [mmHg s/cm^3] and heart rate [beats/s] as a function of time.

RERENCES

L.A. Lipsitz et al. (2000), *Stroke*, 31:1897-1903.
M.S. Olufsen et al. (2002), *Am J Physiol*, 282:R611-22.

ACKNOWLEDGEMENTS

NSF GIG DMS-9631755, NIA #AG05134, HRCA #AG05134

FORCE DEPENDENCE OF THE P-SELECTIN/PSGL-1 BOND DISSOCIATION

Bryan Marshall[1], Rodger P. McEver[2], and Cheng Zhu[1]

[1]Schools of Mechanical Engineering and Biomedical Engineering, Georgia Institute of Technology, Atlanta, GA 30332, USA, cheng.zhu@me.gatech.edu, [2]Warren Medical Research Institute and Departments of Medicine and Biochemistry and Molecular Biology, University of Oklahoma Health Sciences Center, Oklahoma City, OK 73104, USA.

INTRODUCTION

The interaction between P-selectin and its ligand P-selectin glycoprotein ligand 1 (PSGL-1) mediates leukocyte tethering and rolling on the endothelium of the blood vessel wall. The binding of these two molecules plays a critical role in the inflammatory response. Because it occurs in a mechanically stressful environment, this transient interaction depends not only on the kinetic rates but also their dependence on force.

An atomic force microscope (AFM) was utilized to study the force dependence of the disassociation kinetics of the P-selectin/PSGL-1 bond. Previously we employed two separate methods: 1. a constant force was applied to the bond and the lifetime distribution was recorded as a function of force, 2. the bond was loaded to failure at a constant rate and the rupture force distribution was recorded as a function of loading rate. The kinetic parameters estimated from the two methods were very different. Here we report a new method used to determine the source of the discrepancies.

METHODS

P-selectin was purified from human platelets and reconstituted in a supported lipid bilayer by using the method of vesicle fusion on a coverslip precoated with a polymer. Monomeric soluble (s)PSGL-1 was secreted by CHO cell transfectants and coupled to a Thermomicroscopes cantilever tip using the capture antibody PL2.

Experiments were done by repeatedly moving the PSGL-1 in and out of contact with the P-selectin bilayer. Lifetime experiments consisted of four phases: Approach, Contact, Retraction, and Holding. The force applied to a bond was controlled by the distance the cantilever was retracted from the surface of the P-selectin bilayer, the further the distance, the larger the force. Loading rate experiments consisted of only three phases: Approach, Contact, and Retraction. Bonds were loaded at constant rate until rupture occurred.

RESULTS AND DISCUSSION

In the lifetime method, the mean lifetime was interpreted as the inverse of the off-rate. The mean lifetime of the P-selectin /PSGL-1 bond displayed a biphasic dependence on force, which initially increased with force and then decreased. This indicated the presence of a catch bond with long lifetime at low force, which transitioned into a slip bond at 11 pN.

In the loading rate method, the peak force from the rupture force histogram was plotted against the log of the loading rate. Data so analyzed exhibited two line segments, which was interpreted as the presence of a slip bond with two energy barriers, suggesting fast disassociation with much shorter bond lifetimes than those actually measured in the lifetime assay.

To reconcile the differences between these two methods, a new method was used to simultaneously analyze the two sets of data. Regardless the method used to obtain them, data were analyzed by plotting the cumulative probability of bond disassociation against the time to bond rupture, starting from the instant when the bond is first loaded (Figure 1).

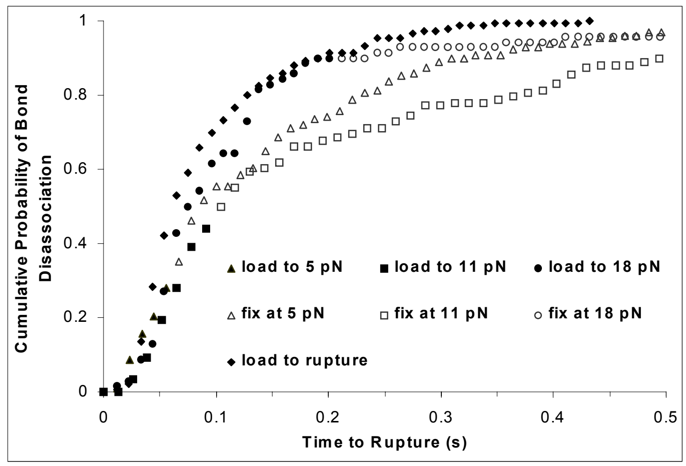

Figure 1: Three sets of data from the lifetime method (loading rate ~ 100 pN/s) are compared with one data set from the loading rate method (loading rate ~ 300 pN/s).

All four data sets display the same behavior while the bond is being loaded. Once a constant force is applied to the bond, the behavior deviates. The constant force appears to stabilize the bond, necessitating a second set of kinetic parameters to model its behavior. It is during this deviation that the catch bond becomes visible. Without probing the bond at a constant force, the loading rate method was unable to detect the catch bond. This suggests that the off-rate of the P-selectin/PSGL-1 bond cannot be described as a function of force but a functional of the force history.

ACKNOWLEDGEMENTS

This work was supported by NIH grants AI44902 and HL65631 and a Whitaker Foundation Graduate Fellowship (BM).

VISCOELASTIC CHARACTERIZATION OF COLLAGEN GEL CONSTRUCTS

Laxminarayanan Krishnan[1], Jeffrey A. Weiss[1], Michael D. Wessman[1], James B. Hoying[2], Rosalina Das[1]
[1]Dept of Bioengineering, University of Utah, 50 S Central Campus Drive, Rm 2480, Salt Lake City, UT 84112. (jeff.weiss@utah.edu)
[2]Biomedical Engineering Program, The University of Arizona, 1230 E. Speedway Blvd, Tucson, AZ 85721

INTRODUCTION

Extracellular matrix (ECM) tissue constructs are simplified systems for in vitro study of conditions such as injury, healing and tumorogenesis. Quantification of changes in material properties of ECM constructs can elucidate fundamental biological processes that occur during wound healing and assist in developing design strategies for functional tissue-engineered constructs. Our interest stems from ongoing studies of angiogenesis in vitro (Hoying et al., 1996), with application to optimization of musculoskeletal soft tissue healing. As a prerequisite to this work, the present objectives were to design and characterize a system for in vitro viscoelastic characterization of collagen gels, and to use the system to characterize the effects of strain rate, equilibrium strain level and test day on material properties of the gels.

MATERIALS AND METHODS

Collagen I gels were polymerized at 37°C in custom chambers between fixed and moveable anchor posts, yielding an aspect ratio of 4:1. Gels were polymerized through holes in the posts, providing a firm anchor for uniaxial tensile testing (Fig 1).

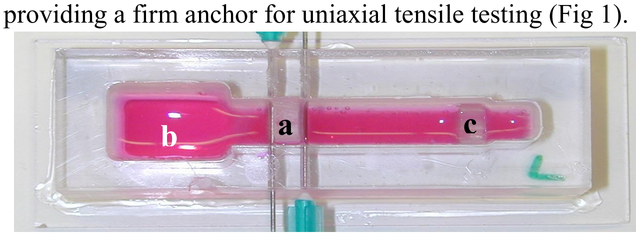

Fig 1: Acrylite chambers with polymerized gel. (a) Actuating post, (b) reservoir, (c) fixed post (c) attached to base of chamber.

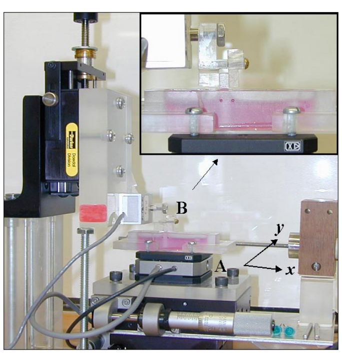

Fig 2: Photograph of test device.
Inset: interface with load cell.

The system used a piezoelectric stage (PiezoJena, Hopedale, MA) to apply sinusoidal strains (Fig 2). The stage (***A***) was driven by signals from a function generator and an LVDT (Schaevitz, Hampton, VA) tracked displacement. Chambers were mounted to the stage and the mobile anchor interfaced (***B***) with a load cell (Transducer Tech, Temecula, CA, acc ±0.00012N). Sinusoidal oscillations (1% mag.) were applied about equilibrium strain levels of 2, 4 and 6%. Linear viscoelasticity theory was used to calculate dynamic stiffness (M, Pascals) and phase shift (ϕ, radians) as a function of equilibrium strain level and frequency:

$$M = \frac{A_\sigma}{A_\varepsilon}; \qquad \phi = \phi_\sigma - \phi_\varepsilon .$$

Here (A_ε,ϕ_ε) and (A_σ,ϕ_σ) are the amplitude and phase of the strain-time and stress-time data, respectively. Two sets of gels (N=11 in each group) were tested on 1st and 7th day of culture.

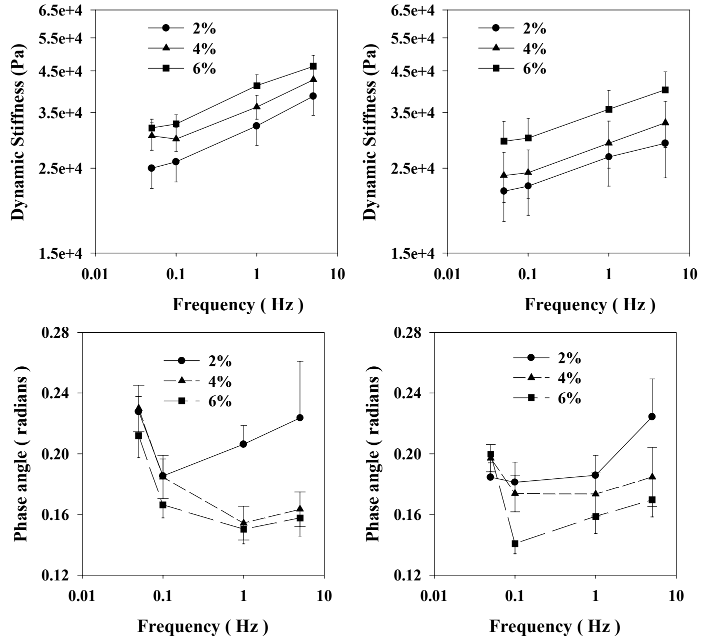

Fig 3: Dynamic stiffness and phase shift at Day 1 (left col) & Day 7 (rt. col).

RESULTS

Dynamic stiffness increased with frequency and strain level ($p<0.001$, Fig 3). For a given strain level there was no significant change in dynamic stiffness (p=0.346,0.155,0.249) and phase shift with day of testing. The phase shift decreased up to 1 Hz and then increased. Equilibrium stresses showed an increase with increasing strain level ($p<0.001$) without significant effect of test day (p=0.832).

DISCUSSION

Stiffening of the gels was not seen – this might be expected by an increase in stabilization of collagen fibers (Hayashi, 1974). A linear increase in dynamic stiffness and decrease in phase angle up to 1 Hz is consistent with studies on cell-populated matrices (Wakatsuki, 2000). The change in phase shift with frequency cannot be explained by quasilinear viscoelastic theory. Over the range of frequency tested, the damping goes down up to 1 Hz and then increases again at higher frequencies, indicating that the most viscous behavior is at low and high frequencies. With this new device and data on native gels material properties, the influence of vessel fragments and growth during angiogenesis can now be examined.

REFERENCES

1. Hayashi,T., Nagai,Y. (1974). *J Biochem*, **75**, 651-54 **2.** Hoying,J.B.et al (1996) *In Vitro Cell Dev Biol Anim*, **32**(7), 409-19 **3.** Wakatsuki,T.et al (2000) *Biophys J*, **79**, 2353-68.

ACKNOWLEDGEMENTS

Supported by Aircast Foundation (#RF699).

ACCURACY OF NON DIFFERENTIAL GPS FOR DETERMINATION OF SPEED OVER GROUND

Witte T.H. Wilson A.M.

Structure and Motion Lab, The Royal Veterinary College, North Mymms, Hatfield, Herts AL9 7TA England

INTRODUCTION

In studies of human and animal locomotion many measures are expressed relative to speed. Speed is easily determined during treadmill exercise but when making measurements during over-ground locomotion average speed is often determined by chronometry over a pre-measured track (Schutz & Herren, 2000). Differential GPS and/or double-frequency receivers have been shown to provide accurate speed measurements, but such units are heavy (4kg) and expensive (Terrier *et al*, 2000). Recent developments in GPS technology for car navigation and incorporation into mobile phones mean that it is now possible to buy an OEM module GPS that weighs as little as 7g with the potential to program as a data logger (Steiner *et al*, 2000). Such a unit has immense potential for logging and subsequent downloading of speed data during field exercise. The accuracy of such systems is unclear with most manufacturers reporting velocity accuracies of 0.1 to 0.2ms^{-1}. Speed is calculated through a combination of position differentiation and measurement of Doppler shift of the carrier wave, meaning that speed accuracy is not just a function of the accuracy and drift in position data. Unfortunately, no detailed information is available about how such calculations are made. This study was designed to evaluate the accuracy of GPS speed measurement under varying conditions.

METHODS

A bicycle speedometer was modified to transmit a pulse once per wheel revolution via a radiotelemetry link. The bicycle was ridden around the 6th lane of a 400m running track at speeds of 10, 15 and 20 kmh^{-1}. The GPS receiver (RoyalTek REB-2100) was fixed to the helmet of the rider and speed over ground, position dilution of precision (PDOP) and satellites used were logged once per second.

A second experiment was undertaken at 15kmh^{-1} with an aluminium shield fixed so as to block satellite reception on one side of the antenna. This meant that the effect of changing the satellites used for the position fix could be examined as the cyclist went round the track

Data were logged in LabView and instantaneous speed calculated from the telemetered pulses. Comparison of actual speed and GPS speed was undertaken and the effect of satellite number, speed, PDOP and whether on a bend or straight examined on a total of 185 samples.

RESULTS AND DISCUSSION

The mean speed measured by the GPS was 0.063ms^{-1} lower than the speed determined from the cycle wheel. The mean random error (i.e. mean unsigned difference between GPS and cycle speed) was 0.16ms^{-1} and 50% of the values were within 0.12ms^{-1}. The error was not a function of speed (0.079ms^{-1} at 10kmh^{-1}, .222ms^{-1} at 15kmh^{-1}, 0.183ms^{-1} at 20kmh^{-1}).

PDOP varied between 2.5 and 50 during the study. PDOP is inversely proportional to the volume of the pyramid formed by lines running from the receiver to 4 satellites observed and has a multiplicative effect on the position error value. No effect on random error was however observed until PDOP reached a value of 9. Number of satellites used (range 3-6) also had no effect on accuracy of speed determination. There was no difference in the mean speed difference or the random error as a function of straight or bend – we had expected an under estimate of velocity because the GPS would "cut" the corner. Changing satellite also appeared to have little or no effect on velocity – no jump was observed in either the positional or speed data.

SUMMARY

GPS can be used to determine speed over ground with 50% of readings within 0.12ms^{-1} of the true value. The accuracy of speed determination was preserved even when the positional data was degraded due to poor satellite number or geometry. Some smoothing of the speed data is evident.

REFERENCES

Schutz, Y., Herren, R. (2000) *Med. Sci. Sports Exerc.* **32(3)** 642-646

Steiner, I., *et al* (2000) *Physiol & Behav.* **71** 589-596

Terrier, P., *et al* (2000) *J. Biomech.* **33,** 1717-1722

ACKNOWLEDGEMENTS

We acknowledge funding from the Horserace Betting Levy Board, London.

DEFINING PATELLAR TRACKING PROBLEMS BASED ON 3D, NON-INVASIVE, IN VIVO MEASURES OF SKELETAL KINEMATICS

Frances Sheehan[1,2,3] and Andrea Rebmann[1,3]
[1]Mechanical Engineering Department, The Catholic University of America, Washington, D.C. USA (sheehan@cua.edu)
[2]Physical Disabilities Branch and [3]Diagnostic Radiology, The National Institutes of Health, Bethesda, MD. USA

INTRODUCTION

Despite the frequency of reported knee pain, especially patellofemoral (PF), there is still a lack of specificity in diagnosing the pathology causing this pain, due primarily to limited clinical and research tools for the direct and non-invasive measurement of *in vivo* musculoskeletal dynamics. This leads to confusion when designing treatment plans and to difficulty in assessing the efficacy of any intervention. Broad categories such chondromalacia, anterior knee pain, or maltracking are often too quickly accepted as a diagnosis without the underlying etiology being researched. With the advent of new imaging technologies allowing the non-invasive study of *in vivo* musculoskeletal kinematics during volitional tasks, we have an opportunity to revisit these broad classifications in order to develop more specific diagnosis that can be correlated with specific impairments. Our previous work has shown both cine phase contrast magnetic resonance imaging (cine-PC MRI) and fast-PC MRI to be accurate and precise in acquiring such 3D measures. With this knowledge, we have begun to study the kinematics of compromised joints, specifically PF maltracking.

METHODS

The study included a total of five unimpaired subjects (29.0±7.9years, 1.7±0.3m, 60.8±11.8kg; 8 knees) who had no history of knee pathology or pain and one subject (28 years, 1.75m, 75kg) clinically defined as having patellofemoral pain syndrome (PPS) with suspected maltracking. For the PPS subject, data were collected on her more severely impaired knee. All subjects were placed in a supine position within a 1.5 GE CX imager and were asked to flex and extend their knee, from full extension to ~40° of flexion, at 35 cycles/minute. Images were taken in the sagittal plane at the approximate centerline of the femur and patella using a fast-PC protocol (2nex, TR=9msec, 2 views/acquisition, imaging time=2:48). The fast-PC protocol was not available during the imaging session with the PPS subject. Therefore, the impaired knee was scanned using a cine-PC protocol (2nex, TR=21 msec, imaging time=5:33). In order to establish anatomically based reference frames, fastcard anatomical images were taken in 3 axial planes during the movement, as well. Using Fourier integration algorithms developed previously (Zhu, et al. 1996), regions on the patella, femur, and tibia were selected (at t=0) and tracked in 3D space throughout the motion cycle. Data were translated into 3D xyz body-fixed orientation angles (flexion, tilt, and twist) describing the patellar and tibial orientation relative to the femur.

RESULTS

The unimpaired data was similar to that previously acquired (Sheehan, Zajac, Drace, 1999). Specifically, the unimpaired subjects showed very little change in patellar tilt angle [RPTA = (max PTA) - (min PTA at or near full extension) = -4.7±3.3°)], as the knee extended (Fig 1). The impaired knee demonstrated a rapid lateral change at the end of the extension cycle (RPTA=-28.2°). Also, this subject noted that the required ~5.5 minutes of movement for the cine-PC exam began to aggravate her knee joint slightly.

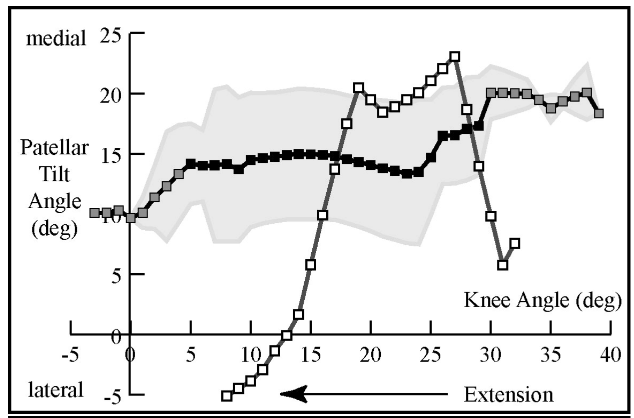

Figure 1: Patellar Tilt Angle (PTA). The filled boxes represent the average unimpaired PTA (±1SD-grey area). Not all subjects had the same knee range of motion, due to variations limb lengths. Thus, the dark gray boxes represent the regions where less than one half of the subjects are represented in the average. Open boxes represent the PTA from the impaired subject.

DISCUSSION

These preliminary results are highly encouraging in terms of our ability to use PC MRI to quantify the underlying kinematics pathologies linked to PF pain. The rapid change in the patellar tilt angle may be indicative of high stresses being placed on the cartilage of the PPS subject when the patella contacts the femur. Enrollment of additional impaired and unimpaired subjects into this study is currently underway so that statistically significant differences between these populations can be identified. Based on our previous precision study and the comments of our impaired subject, we would highly recommend the use of fast-PC over cine-PC MRI in future studies due to its slightly higher precision and shorter imaging times.

REFERENCES

Zhu, et al. (1996). *Magn. Reson. Med.*, **35,** 471-80
Sheehan, Zajac, Drace (1999). *J of Biomech. Eng.*, **121**, 650-656

VARIATION IN TREADMILL WALKING DUE TO COMBINATIONS OF VISUAL SCENE MOTION AND GRAVITY-ASSIST

Chris Miller [1], Ajitkumar Mulavara [2], Jason Richards [1] and Jacob Bloomberg [3]
[1] Neurosciences Laboratory, Wyle Laboratories, Houston, TX, USA
[2] Department of Otorhinolaryngology, Baylor College of Medicine, Houston, TX, USA
[3] Neurosciences Laboratory, NASA Johnson Space Center, Houston, TX, USA
E-mail: chris.miller1@jsc.nasa.gov

INTRODUCTION

Variations in optic flow have been shown to alter postural adjustments during treadmill walking (Warren, et al., 2001; Bardy, et al., 1999). Kram's group has examined the effects of gravity-assist on body kinematics during treadmill walking (Griffin, et al., 1999; Donelan and Kram, 1997; Kram, et al., 1997). However, little is known about the interaction between visual flow cues and body unloading during locomotion. Miller, et al. (2001) have shown that scene motion and gravity-assist together increase the variability of torso orientation during treadmill walking. The purpose of this study was to determine if the combination of visual scene motion and partial gravity-assist (i.e., body unloading) alters gait temporal parameters and foot placement during treadmill locomotion.

METHODS

Five subjects (3 male; 2 female; age 30 ± 4.4 yrs; weight 70.3 ± 8.6 kg; height 170.8 ± 8.3 cm) participated in this study. A pneumatic device, called the "Pogo", provided gravity-assist. Subjects were strapped into the Pogo's harness system, which is designed to allow for six degrees of freedom. While in the Pogo, subjects walked on a motorized treadmill at 4 km/hr (2.5 mi/hr). A virtual office scene was back-projected on a screen placed 1.5 meters in front of the subject. During a 60-second trial, the scene remained stationary for the first 30 seconds (sec), then rotated in either pitch, roll or yaw for the remaining 30 sec. The Pogo was set to three gravity-assist levels: 1/3 body-weight (BW); 2/3 BW; 1 BW (i.e., no assist). Three trials were recorded for each scene rotation and gravity-assist combination (27 total). Kinematic (Motion Analysis Corp, Santa Rosa, CA) and footswitch (Motion Lab Systems, Baton Rouge, LA) data were recorded from 15 sec before the start of scene motion to 15 sec after the start of scene motion (i.e., T_0+15 sec to T_0+45 sec).

Using footswitch data, temporal variables and duty factor were determined. The step direction (the angle of the line segment starting at the foot's xy-position at toe-off to the subsequent heel contact) and stride length were calculated with kinematic data. The variances of the step direction, step length and temporal parameters were computed over all analyzed gait cycles within both the static scene and scene motion periods of each trial. A paired t-test was used to determine significant increases in the variance of the parameters during scene motion as opposed to that during steady state ($p < 0.05$).

RESULTS AND DISCUSSION

Variability of step direction (Figure 1) increased during scene motion (p=0.003), as did the duty factors for both feet (left: p=0.002; right: p=0.006). Stride length did not significantly increase, nor did the gait temporal parameters, except for left-foot step time (p=0.029) and right-foot stance time (p=0.022).

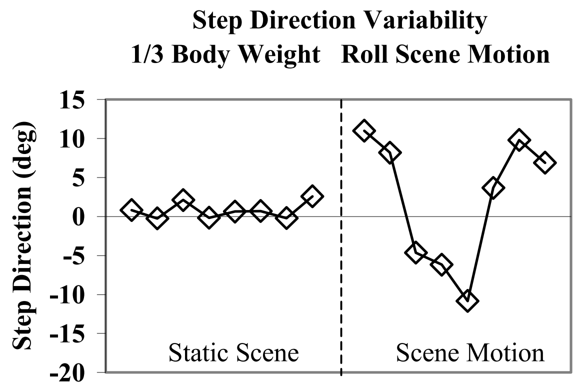

Figure 1: Plot showing step direction in the xy-plane (in degrees) for a representative trial in which the subject experienced 1/3 BW and the visual scene rotated in roll. Each symbol represents one gait cycle.

SUMMARY

The combination of visual scene motion and gravity-assist significantly increased the variability of foot placement and duty factor during treadmill walking. Stride length variability was not affected. Given that the combination of gravity-assist and visual scene motion affect walking kinematics, varying treadmill harness tension and visual scenes within a variable practice program may be implemented as an in-flight training tool or countermeasure to minimize the effects of space flight on balance and coordination.

REFERENCES

Bardy, B., et al. (1999). *Perception & Psychophysics*, **61(7)**, 1356-68.
Donelan, J., Kram, R. (1997). *J. Exp. Biol,* **200**, 3193-201.
Griffin, T., et al. (1999). *J. Appl. Physiol.*, **86(1)**, 383-90.
Miller, C., et al., (2001). *Soc. Neurosci. Abstr,* **27**, 940.4.
Kram, R., et al. (1997). *J. Exp. Biol*, **200**, 821-6.
Warren, W., et al. (2001). *Nat. Neurosci.*, **4(2)**, 213-6.

DIMINISHED STEPPING RESPONSES LEAD TO FALLS IN BOTH YOUNG AND OLDER ADULTS

Michael J. Pavol[1], Eileen F. Runtz[2], and Yi-Chung Pai[1]

[1]Department of Physical Therapy, University of Illinois at Chicago, Chicago, IL
[2]Department of Physical Therapy and Human Movement Sciences, Northwestern University, Chicago, IL
e-mail: mpavol@uic.edu

INTRODUCTION

Falls are a significant source of morbidity and mortality in older adults (Sattin,1992). In order to reduce the incidence of falls by older adults, it is important to determine exactly why these falls occur. In particular, are there age-differences in the responses to a perturbation that place older adults at a higher risk of falling than the young? To date, there has been no direct comparison of the responses leading to actual falls by young and older adults. This study investigated whether age-differences exist in the mechanism of falling versus recovery upon an unexpected and novel slipping perturbation.

METHODS

An unexpected and novel forward slip was induced, using bilateral low-friction platforms, during a sit-to-stand task in 60 young and 41 older ($\geq$65 yrs.) healthy, safety-harnessed adults. After 4 normal sit-to-stand trials, a 24cm slip was induced just after seat-off. Kinematics of 26 markers were recorded (Peak Performance, CO). Outcomes were classified into recoveries, assists, or falls, based on the extent of hip descent and the force on the safety harness. Falls were further classified by whether or not a step was initiated before the "fall." Fisher's exact test identified differences in outcome occurrence. One- or two-way ANOVAs investigated effects of age group and/or slip outcome on selected kinematic variables. Variables were the horizontal position and velocity (Xcom, VXcom) of the body center of mass (COM) relative to the more posterior heel, the vertical height and velocity (Zhip, VZhip) of the bilateral hip midpoint, and step length. Events of interest were slip onset, mid-slip, the start of hip descent, step initiation (init.), and step touchdown (TD). Step timing was determined from recorded ground reaction forces (AMTI, MA).

RESULTS AND DISCUSSION

A greater proportion of older than young adults fell (76% vs. 30%; p<.001). Stepping occurred in all but one recovery, but "no-step" falls comprised 20% and 34% of falls by young and older adults, respectively, with no difference in the proportion of no-step falls between age groups (p=.26). The state of the body at slip onset, the slip duration, and the COM backward velocity at mid-slip all differed between age groups, yet none of these variables differed between recoveries and falls.

Instead, falling was related to the kinematics of hip descent and of the first step (Table 1). Fallers underwent a greater change in Zhip and VZhip between first step initiation and touchdown and placed their stepping foot less posterior to the COM. The hips of older adult fallers, both step and no-step, also began to descend from a lower height. Increased hip descent, indicative of a "collapse" of the support (non-stepping) limb, together with a less posterior stepping foot placement, arguably reflect a diminished stepping response in those who fell. The no-step fallers then represent those individuals in whom the stepping response was diminished to the point of near-absence. It is most likely that these diminished stepping responses reflect a poor selection or scaling by the central nervous system (CNS) of the response to an unexpected and unfamiliar perturbation.

Increased falling in older adults might thus be attributable to more frequent mis-selection or mis-scaling of a recovery response by the CNS. The fact that older fallers began to descend from a lower hip height might also indicate that decreased lower extremity strength contributed to increased falling by older adults. Finally, regardless of slip outcome, older adults placed their stepping foot less posterior to the COM than the young. In fact, older adults were more likely than young to employ a second backward step for recovery (89% vs. 34%; p<.01). These results suggest a multi-factorial source of the decreased ability of older adults to recover and that training of recovery responses might reduce falling.

REFERENCES

Sattin, R.W. (1992). *Ann Rev Pub Health*, **13**, 489-508.

ACKNOWLEDGEMENTS

Funded by NIH R01-AG16727 and the Whitaker Foundation.

Table 1: Kinematic variables related to the falls by young and older adults (mean ± SD) (bh = body height; ft len = foot length)

Variable		Young		Older		
		Recover (n = 31)	Fall:Step (n = 11)	Recover (n = 8)	Fall:Step (n = 18)	Fall:No-Step (n = 10)
Zhip at hip descent	(%bh)	52.1 ± 1.4	51.1 ± 1.8	51.3 ± 1.0	47.9 ± 2.2 ¶	47.9 ± 2.2 ¶
ΔZhip, step init. to TD	(%bh)	-1.2 ± 1.6	-5.8 ± 2.6 §	-0.3 ± 1.7 †	-3.1 ± 1.9 † §	–
ΔVZhip, step init. to TD	(%bh/s)	-17.5 ± 17.6	-31.7 ± 22.8 ‡	-19.5 ± 16.3	-38.4 ± 28.2 ‡	–
Xcom at step TD	(%ft len)	39.0 ± 23.8	6.5 ± 31.5 §	20.7 ± 21.1 *	-15.3 ± 27.8 * §	–

* $p \leq .01$ vs. Young; † $p \leq .001$ vs. Young; ‡ $p \leq .01$ vs. Recover; § $p \leq .001$ vs. Recover; ¶ $p \leq .01$ vs. Older Recover

PRESSURE DISTRIBUTION MEASUREMENT FOR DESIGN OF WAIST BELTS IN PERSONAL LOAD CARRIAGE SYSTEMS

L. Hadcock, J.M. Stevenson, J.T. Bryant
Ergonomics Research Group, Queen's University, Kingston, ON
9ljh2@qlink.queensu.ca

INTRODUCTION

In previous research studies, two types of backpacks have been modeled, a shoulder-based model and a shoulder plus waist belt model. In the shoulder-based model, a strap sensor in the lower shoulder strap allowed the lumbar and shoulder reaction forces to be resolved (MacNeil, 1996). This model was validated with 20 subjects and accurately predicted shoulder (r=0.92, for four of five packs) and lumbar discomfort (r=0.93) (Stevenson, 1995). The second model added a waist belt and other straps such as load lifters and sternum straps. To resolve the forces, a standardized torso was mounted on a force platform with a second load cell at the L3 level to separate shoulder and waist components. This model was considered less successful because of the indeterminacy of friction and an inadequate understanding of the waist belt forces (Rigby, 1999). Therefore, the purpose of this study was to design a standardized method of comparing waist belt features and designs, independent of the rest of the pack, to define and validate the mathematical model of the backpack.

METHODS

A standardized lower torso model with known mathematical properties was constructed. The lower torso was designed to be unisex with the waist circumference matching that of a 50th percentile man. The waist-to-hip ratio was 0.8, an acceptable value for both genders. It was covered with Bocklite, a skin analog, which represented a person with 3% body fat. Tekscan sensors were affixed to the Bocklite surface to record pressures applied by the waist belt. The torso was mounted on a jig that was placed a[...]. The geometric shape of the torso allowed for the measured Tekscan pressures to be converted to vector normals and subsequently resolved and summed as single forces and moments acting on the torso. These calculated values were compared to those measured by a six-degree of freedom load cell beneath the torso model and a load application device. Loads were applied with the calibrated application device and the results of the Tekscan and load cell measurements were compared. A simplified shoulder was attached to a second load cell at L3 above the torso as a method to mount the pack with minimal contact on the upper torso. Different waist belt designs could be easily isolated and compared while being loaded realistically with the specific pack design.

Figure 1. Standardized Torso Model

RESULTS AND DISCUSSION

Resolved force data from the calibrated force plate and a load application device showed good agreement. The Tekscan results were consistently lower than both of the other instruments, by up to 45%. The vector resolution of measured Tekscan forces in the X, Y, and Z directions were proportionally accurate, relative to the direction of the applied force, indicating that the sensel location coordinates and their calculated normal vectors were not the major source of error. Simple summation of the individual sensel measurements provided force measurements greater than the applied forces. This indicated the need for the use of a mathematical model for resolving the forces on a curved surface. A coefficient of friction was measured using an inclined plane with the same properties as the torso model. Results were only marginally more accurate when this coefficient of friction was included in the calculations.

SUMMARY

Preliminary results indicate that the standardized torso model is a useful design tool that can realistically model and compare waist belt forces. The measurement of contact pressures with Tekscan sensors requires better calibration to be considered a valid design tool.

REFERENCES

MacNeil, S.K., (1996), *M.Sc. Thesis*, Queen's University, Kingston, ON (unpublished).
Rigby, A, (1999), *M.Sc. Thesis*, Queen's University, Kingston, ON (unpublished).
Stevenson, J.M., et al (1995) R & D of an Advanced Personal Load Carriage System, DCIEM #W7711-4-7225/01-XSE.

ACKNOWLEDGEMENTS
This research was funded by DCIEM, DND, Toronto, Canada.

EFFECTS OF DIABETES ON THE STRENGTH OF THE PLANTAR SKIN-FAT INTERFACE

Yan Chen, Brian Davis, Antonio Valdevit
Department of Biomedical Engineering, Cleveland Clinic Foundation, Cleveland, USA
cheny@bme.ri.ccf.org

INTRODUCTION

Foot ulceration is one of the most common complications of diabetes mellitus. Research has suggested that the plantar skin–fat interface may be the site for initial ulcer formation since peak first principal stresses at this location dramatically increase with changes in material properties and boundary conditions (Thompson, 1997). The goal of this study was to compare the skin-fat interface strength in diabetic and non-diabetic feet.

METHODS

For 21 diabetic (68±2.4 years) and 17 non-diabetic (74.6±3.8 years) foot specimens, the plantar skin surface was cut into a 9x2 array from the first metatarsal head (row 1) to the anterior heel (row 9) and divided down the medial/lateral axis. Each strip of skin was 1 cm wide and 2 mm deep. The skin was clamped to a load cell and tension was applied at a rate of 1 mm/sec as the skin was peeled off the underlying fat tissue. During testing the foot specimen was held in a supine position in a custom designed jig that was placed on top of a transitional unit that could move in both x and y directions to keep the peeling force vertical to the peeling site. This unit was then mounted on a universal MTS machine. The mean peeling force over the entire removal process was calculated and normalized to the width of the skin strip (i.e. F=N/cm).

RESULTS

The strength of the skin-fat interface was significantly different

	Diabetic group (n=21)		Non-diabetic group(n=17)	
	Medial	Lateral	Medial	Lateral
Row 1	32.2±6.7	38.2±10.6	31.9±13.6	30.8±9.6
Row 2	33.2±9.2	36.1±12.7	29.0±9.4	30.4±7.9
Row 3	30.7±8.7	31.2±11.4	26.0±8.5	25.1±9.3
Row 4	28.1±8.0	28.7±9.1	24.7±8.6	24.4±10.5
Row 5	26.1±7.5	26.4±7.1	22.5±7.7	24.4±10.5
Row 6	28.3±9.5	29.6±7.8	22.7±7.9	24.4±9.5
Row 7	32.7±10.0	31.9±9.0	24.5±8.7	26.5±9.8
Row 8	34.4±9.9	34.2±10.7	29.3±8.9	27.7±10.2
Row 9	46.7±16.5	42.5±15.3	35.9±14.4	34.7±13.9

Table 1. The mean and standard deviation for the mean skin-fat strength (N/cm) at different regions across the plantar surface of the foot.

($p<0.05$) with the diabetic strips requiring greater skin removal force (Table 1). There was no significant difference between medial and lateral strips within both groups. The skin-fat strength decreased with age in the non-diabetic group ($p<0.00$, Fig 1), but this trend did not exist in the diabetic group.

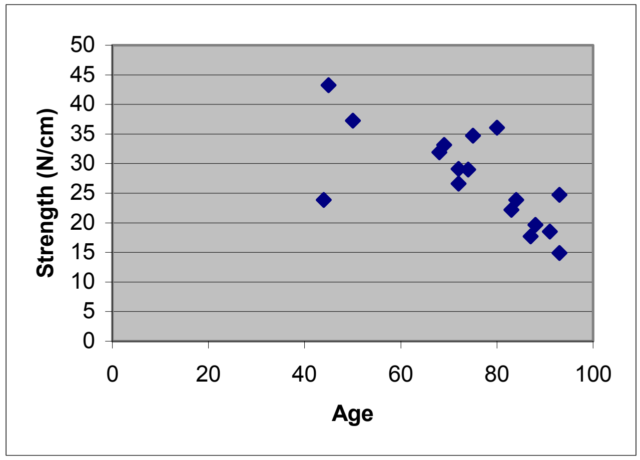

Fig 1. Skin-fat interface strength vs age in the non-diabetic group.

DISCUSSION

This experiment demonstrated that the strength of the skin-fat interface in the diabetic group was higher than in the non-diabetic group. Due to tissue property changes and bone deformity, diabetic patients usually experience elevated vertical stress at the foot-ground interface. The strength of the skin-fat interface might be an adaptive response to this elevated vertical stress. The trend with age in the non-diabetic group might also be explained by this assumption. In general, people become less active with age, which implies less stress under the foot, and thus lower skin-fat interface strength. In the diabetic group, as age increases, the stress concentration might be greater because of changes taking place in the foot due to diabetes, thus the decreasing trend with age did not exist in the diabetic group.

REFERENCES

Thompson, D.L (1997). *Finite Element Modeling of the Diabetic Foot.* Unpublished Master's Dissertation, Ohio State University.

TESTING DURATION REQUIRED TO ACCURATELY PREDICT LIGAMENT VISCOELASTICITY

Eugene Manley[1], Paolo Provenzano[1], Dennis Heisey[2], Roderic Lakes[3] and Ray Vanderby, Jr. [1]

[1]Departments of Biomedical Engineering and Orthopedic Surgery, [2]Department of Surgery, and [3]Departments of Biomedical Engineering and Engineering Physics, University of Wisconsin, Madison, WI, USA, vanderby@surgery.wisc.edu

INTRODUCTION

Extensive viscoelastic testing has been performed on ligaments and tendons, but only (King, et al. 2000) has studied the viscoelastic effects over extended continuous time durations. Our goal is to test ligaments under creep and stress relaxation with the intent of determining how much time needs to be allocated to effectively obtain viscoelastic behavior of ligaments. The goal is to reduce the testing time needed for specimens so that more specimens can be prepared and analyzed in a shorter time frame.

METHODS

Male Sprague-Daley rats (300±50g) were used in all experiments. Specimen harvesting and testing were adopted from the methods of Provenzano, et al. (2001) as was some of the data. The animals were divided into two groups, creep (n=9) or stress relaxation (n=14). The stress relaxation (SR) samples consisted of two phases, eight subjected to 1000s of testing and six subjected to 10,000s of testing. The data from the first three decades (1-1000s) of all samples were pooled together, and then data based on the six long term duration (10,000s) were analyzed separately. All of the samples were subjected to a ramp-up to creep and relaxation.

Data analysis was done on the specimens to determine an adequate time frame for testing ligaments in both creep and relaxation to accurately predict ligament behavior. Both the Standard Regression approach (columns 1-2 in the Tables) and the Random Coefficients (columns 3-6 in the Tables) approach were applied.

RESULTS AND DISCUSSION

Table 1. Creep Standard Regression and Random Coefficients

Time (s)	mean[1]	SD[2]	E[M][3]	SD(I)[4]	SD(E[M])[5]	CV[6]
<10	0.089	0.056	0.088	0.052	0.018	20%
<100	0.091	0.039	0.091	0.039	0.013	14%
<1000	0.079	0.030	0.079	0.030	0.010	13%

Table 1 shows the data for the standard approach of averaging regression coefficients versus the random coefficient approach for creep. Testing for 1000seconds only produces a 1% increase in accuracy of the measurement of ligament behavior as shown by the CV. The extra degree of precision will not affect results to any significant degree.

Table 2. S.R. Standard Regression and Random Coefficients

Time (s)	mean[1]	SD[2]	E[M][3]	SD(I)[4]	SD(E[M])[5]	CV[6]
>10	-0.029	0.019	-0.029	0.019	0.0051	18%
>100	-0.033	0.019	-0.033	0.019	0.0050	15%
>1000	-0.032	0.017	-0.032	0.017	0.0044	14%
>10000	-0.033	0.018	-0.033	0.017	0.0047	14%

Table 2 shows the stress relaxation standard regression rates versus the random coefficients. Testing for 1000 seconds is again shown to only increase the accuracy of the data by 1% from the first two decades. Testing for a fourth decade offers no increase at all in data accuracy.

Random coefficients accounts for the variability in individual samples by separating out the material property (creep and relaxation) from the testing variability. The log linear model of the form: strain=a+b*$\log_e$(time) for creep, and $\log_e$(stress)= a+b*$\log_e$(time) for stress relaxation. It is clearly shown that testing for durations longer than 100seconds does not offer any significant increase in the accuracy of the measurements of creep and relaxation. Though not shown, the data separated for just the four decades showed that there are large variations in linearity through the fourth decade. Due to variability of testing these materials, most information is obtained at the beginning of testing that cannot be used later.

[1]Average of Standard Regression coefficients for each sample
[2]Standard deviation of Standard Regression coefficients
[3]Random Coefficients estimate of material property (creep or relax.)
[4]Estimated std. dev. of individual increments of creep or relaxation
[5]Standard error of the estimated creep or relaxation, E[M]
[6]Percent coefficient of variation: 100*SD(E[M])/E[M]

SUMMARY

Our statistics show you can reliably predict material behavior by doing short duration tests for a large number of samples.

REFERENCES

King, G.J.W. et. al (2000). *J. Orthop Res*,**18**, 678-681.
Provenzano, P. et al (2001). *Ann Biomed Eng*, **29**: 908-914.

ACKNOWLEDGEMENT

Funding by NSF (#CMS-9907977) and G.E.R.S & G.E.M. Fellowships (E.M.)

VERTICAL JUMPING PERFORMANCE IN 8-12-YEAR-OLD RHYTHMIC GYMNASTS

Helena Gapeyeva[1], Tatjana Kums[2], Mati Pääsuke[1], Jaan Ereline[1]

University of Tartu, Tartu, Estonia
[1]Laboratory of Kinesiology and Biomechanics, Institute of Exercise Biology, spbiol@ut.ee
[2]Institute of Sports Pedagogy

INTRODUCTION

The vertical jumps can be used as a model to study explosive force-generating capacity of the lower extremities. A squat jump consists of a concentric muscle action of the leg extensor muscles while counter-movement jump consists of an eccentric-concentric muscle action. It has been shown to have a potentating effect of stretch-shortening cycle to vertical jumping performance in young adult subjects (Bosco et al, 1982), however, the age-related differences of this potentating effect are poorly understood. The aim of the study was to compare the vertical jumping performance in 8-10- and 11-12-year-old female rhythmic gymnasts.

METHODS

The vertical jumping performance in young female rhythmic gymnasts recorded before the competition (I group, n=7, and II group, n=9; Table 1).

Table 1: Anthropometrical characteristics of gymnasts

Characteristics	I group	II group
Age (years)	8.7±0.3	11.7±0.2 ***
Height (cm)	137.0±2.8	149.0±2.3 **
Body mass (kg)	31.0±1.5	37.2±0.1.0 **
BMI ($kg \cdot m^{-2}$)	16.5±0.6	16.8±0.2
Training period (years)	2.4±0.5	3.1±0.7

Gymnasts performed the squatting jumps (SJ), counter-movement jumps (CMJ) and counter-movement jumps with the help of arms (CMJA), and a 30 s hopping test (HT) on a force platform PD-3A (VISTI, Russia) with the dimensions of 0.75x0.75 m and natural frequency of 150 Hz. Three maximal SJ, CMJ and CMJA recorded on-line and the trial with the best height of jump (H) was analysed in each case. The vertical velocity of take-off (Vv), height of jump (H) and peak vertical ground reaction force (VGRF) recorded.

RESULTS AND DISCUSSION

The Vv was significantly higher in CMJA as compared to SJ and CMJ (Table 2) for both groups (p<0.01). Gymnasts of II group had greater Vv in all kinds of jumps in comparison with I group. The older gymnasts had greater values of height of jump in all types of jumps. There were no differences in Vv and H of jump in SJ as compared to CMJ for both groups (p>0.05). The VGRF of SJ was significantly lower (p<0.05) in comparison with CMJ and CMJA for II group, and difference of VGRF was not significant for I group. Younger gymnasts had the lower mean power of jumps (11.8±0.6 and 15.6±1.2 W in I and II group, respectively) and bigger decrease of power during the HT (p<0.05) as compared to II group (42.0±3.9 and 36.2±3.6%, respectively).

Table 2: Vertical jumping performance characteristics of 8-10- (I group) and 11-12-years-old rhythmic gymnasts

Parameters	Type of jump	I group	II group
Vv ($m \cdot c^{-1}$)	SJ	1.81±0.05	2.13±0.06 **
	CMJ	1.80±0.06	2.16±0.06 **
	CMJA	2.18±0.04	2.42±2.17 **
H (cm)	SJ	18.4±1.0	23.3±1.3 *
	CMJ	19.6±1.1	23.9±1.4 *
	CMJA	24.1±0.9	30.0±1.7 *
VGRF (N)	SJ	488.3±50.1	494.4±24.3
	CMJ	511.4±57.6	527.6±42.6
	CMJA	550.1±65.0	594.0±39.2

Significance of difference in characteristics between groups:
* p<0.05; ** p< 0.01; *** p<0.001

SUMMARY

The significant increase in vertical jumping height during puberty is well documented (Häkkinen et al, 1989). Younger gymnasts cannot use positive effect of stretch-shortening cycle to vertical jumping performance in counter-movement jumps (Bobbert et al, 1996). It has been suggested that the expression of muscle strength is dependent on myelination of the motor nerves, which is not completed until sexual maturity (Brooks and Fahey, 1985).

REFERENCES

Bosco, C. et al (1982) *Acta Physiol. Scand.* **114**, 543-550
Häkkinen, K. et al (1989) *J. Sports Med. Phys. Fitn.* **29**, 27-35
Bobbert, M.F. et al (1996) *Med. Sci. Sports Exerc.* **28**, 1402-1412
Brooks, G.A., Fahey T.D. (1985) *Exercise Physiology: Human Bioenergetics and Its Application*. New York: Macmillan

KINEMATIC COMPARISON OF TREADMILL GAIT WITH BODY WEIGHT SUSPENSION BETWEEN UNIMPAIRED SUBJECTS AND SUBJECTS WITH PARKINSON'S DISEASE.

A. Joseph Threlkeld[1], Lance D. Cooper[1], Pamela M. Sprenkle[2], John M. Bertoni[2]
Biodynamics Laboratory, Creighton University, Omaha, Nebraska, USA, jthrel@creighton.edu
[1]Department of Physical Therapy, [2]Department of Neurology

INTRODUCTION

Treadmill training combined with body weight suspension (BWS) is used to improve gait in subjects with neurologic conditions including Parkinson's Disease (**PD**).(Dobkin 1999; Miyai et al 2000) A key impairment of persons with PD is diminished angular excursion of the lower extremity (LE) joints.(Morris et.al. 2001) To normalize proprioceptive input in PD gait patterns, BWS must induce kinematic patterns similar to those induced in unimpaired persons. Our purpose was to compare the kinematic responses of unimpaired and PD subjects to selected BWS levels at a single treadmill speed.

METHODS

Subjects were 7 unimpaired volunteers (**Norm** group; 2F, 5M, 25±3 yrs) and 7 volunteers with PD (**PD** group; 1F, 6M; 68±9 yrs; Hoehn & Yahr Stage 2 to 3). All subjects walked on a level treadmill at 80cm/sec at both 30% and 50% BWS suspension levels (Vigor Equipment Neuro II). The suspension level presentation order was randomized. A 4-camera 60Hz reflective marker motion capture system (MotionAnalysis Hi-Res) was used to collect 3D kinematic data. 8 to 12 strides from each subject under each condition were time normalized to percent of cycle, ensemble averaged (MotionAnalysis Orthotrak) and data from the right and left sides collapsed. Temporospatial data and sagittal plane kinematics of the LE joints were compared at critical points between conditions using two-way repeated measures ANOVA at a significance level of $p \leq .01$.

RESULTS AND DISCUSSION

The PD group took smaller steps (p=.013) but at a higher cadence (p=.032) than Norm but BWS level did not affect these factors. Average ankle dorsiflexion during singlelimb stance was unaffected by BWS (p=.017) but was greater in the PD group (p=.002). Maximum plantarflexion during swing increased with more BWS (p=.008) but was unaffected by group (p=.05). Maximum knee flexion during single limb stance decreased with more BWS (p=.002) but was unaffected by group (p=.35). Maximum knee flexion during swing was reduced with more BWS (p=.004) but was unaffected by group (p=.34). Hip flexion at footstrike was reduced by BWS (p=.004) but unaffected by group (p=.34). Maximum hip extension during stance was unaffected by BWS (p=.74) or group (p=.56).

ANKLE KINEMATICS

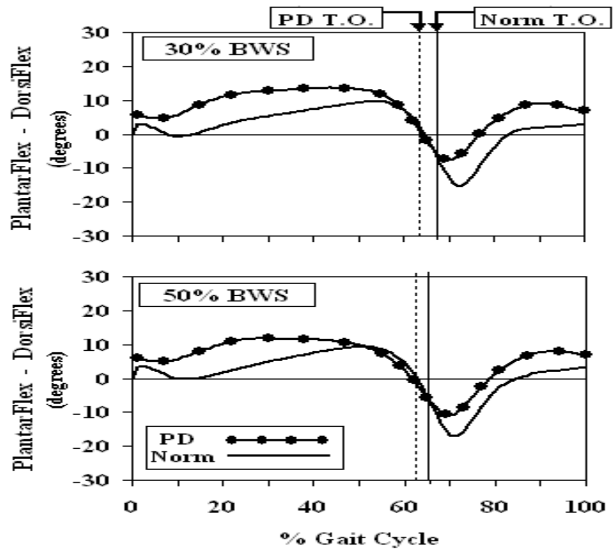

SUMMARY

There were baseline gait differences between groups but LE kinematic changes produced by BWS were comparable in both Norm and PD subjects.

REFERENCES

Dobkin, BH (1999). *Neurorehab Neural Repair*, **13**,157-65.
Miyai I et al (2000). *Arch Phys Med Rehabil*, **81**,849-52.
Morris ME et al (2001). *Clinical Biomech*, **16**,459-70.

ACKNOWLEDGEMENTS

Supported in part by Creighton HFF Grant 200256-726000

Table 1: Temporospatial and Kinematic Variables [mean (sd)] by Group with Body Weight Support Level.

	Step Length cm	**Cadence** steps/min	**Ankle DorsiFlex °** Average @ stance	**Ankle PlantarFlex °** Max @ swing	**Knee Flexion °** Max @ singlelimb stance	**Knee Flexion °** Max @ swing	**Hip Flexion °** @ footstrike	**Hip Extension °** Max @ stance
Norm 30%	56 (4)	87 (8)	7.2 (2.0)	- 13.8 (3.5)	8.5 (5.1)	54.5 (2.7)	17.8 (8.2)	-14.4 (7.3)
Norm 50%	57 (5)	86 (8)	6.8 (1.8)	- 15.8 (3.4)	6.8 (3.8)	51.6 (3.1)	15.5 (8.6)	-13.6 (8.0)
PD 30%	47 (7)	102 (18)	11.4 (1.8)	- 9.0 (2.6)	11.8 (5.4)	51.7 (6.0)	17.1 (10.6)	-16.3 (7.3)
PD 50%	46 (5)	104 (14)	9.9 (1.9)	- 12.3 (1.3)	9.1 (5.9)	49.4 (6.8)	12.5 (8.1)	-16.6 (6.6)

APOPTOSIS IN LIGAMENT AFTER A SUB-FAILURE STRETCH

Paolo P. Provenzano[1], Peter Muir[2], Zhengling Hao[2], and Ray Vanderby Jr.[1]

[1]Orthopedic Research Laboratories, Dept. of Biomedical Engineering and Orthopedic Surgery, and [2]Comparative Orthopedic Laboratory, Dept. of Veterinary Medicine, University of Wisconsin, Madison, WI, USA, email: vanderby@surgery.wisc.edu

INTRODUCTION

The aim of this study was to use immunohistochemisty (IHC) to examine the cellular response to a sub-failure ligament stretch. MMP-1 and -13 are collagenases which are important factors regulating remodeling of the extracellular matrix (ECM) of ligament and have been shown play a role in ligament healing (Hellio Le Graverand *et al*., 2000). Apoptosis (programmed cell death) is an organized physiologic process that is critical for normal development and homeostasis, while necrosis is not planned and is often associated with a traumatic event resulting in loss of cell membrane integrity. Apoptosis has been associated with rotator cuff tendon pathology (Yuan *et al*., 2001) and with increasing loads in vein grafts (Moore *et al*., 2001). Cellular necrosis precedes structural damage in sub-failure stretched medial collateral ligament (MCL; Provenzano et al., 2002). We therefore, hypothesize that a sub-failure ligament stretch will cause apoptosis and MMP-1 and -13 activation.

METHODS

Four MCLs were removed from Sprague-Dawley rats (Right leg receiving a sub-failure stretch; Left leg contralateral control). The femur-MCL-tibia (FMT) complex was harvested and kept hydrated. The FMT complex was loaded into a custom designed load frame/sterile tissue culture bath containing standard media (DMEM w/10% FBS, nonessential a.a., L-glut., pen. and strep.). In the load frame/bath the MCL was preloaded to 0.1N, preconditioned (10 cycles at 1% strain), and stretched in displacement control (10%/sec) to 4% strain (a strain which is in the linear region (~40 failure strain), and has been shown to result in cellular damage in the rat MCL (Provenzano *et al*. 2002)). Control ligament were handled in the same manner as stretched MCLs (minus stretch) with the same time from tissue harvest to incubation. After mechanical testing, MCLs were incubated for 4 hours (standard media). Tissues were fixed in Zamboni's fixative and longitudinal frozen sections (10 µm) were made. Fibroblast apoptosis was detected using the TUNEL assay. Peroxidase-labeled antidigoxygenin with DAB/cobalt/nickel staining was used to localize TUNEL-positive (+) cells. Mayer's hematoxylin was used as a counter stain. MMP staining was performed with mouse monoclonal anti-MMP-1 and -13 antibodies, 1:50 dilution, and incubated for 1hr at room temperature. Negative controls were included in both assays. The interior portions of the ligament were examined and compared in order to reduce any edge effects from harvest and handling.

RESULTS AND DISCUSSION

IHC demonstrated fibroblasts in the sub-failure stretched MCLs to be MMP-1 and -13 negative which does not support our hypothesis (not shown). Fibroblasts receiving a sub-failure stretch were TUNEL+, indicating that apoptosis was taking place, while control tissues showed almost no cells undergoing apoptosis. These results support our hypothesis (Fig. 1). This suggests that upregulation of ligament fibroblast apoptosis is an early response to sub-failure injury.

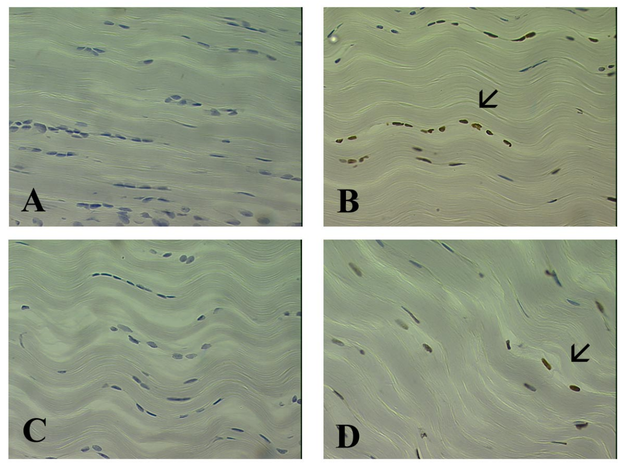

FIG. 1: Control MCLs (A & C) show normal cells (blue) while Stretched MCLs (B & D) display apoptotic (TUNEL+) cells (brown) 4 hours after a sub-failure stretch. Arrows emphasize apoptotic fibroblasts.

SUMMARY

Results of this study indicate that after MCLs undergo apoptosis but not detectable MMP-1 and -13 expression 4 hours after sub-failure stretch.

ACKNOWLEDGEMENT
This study was partially funded by NSF (grant # CMS-9907977)

REFERENCES

Hellio Le Graverand et al., *Matrix Bio*., vol. **19(5)**, 2000
Moore *et al*., *J. Biomech*., vol. **34**, 2001
Provenzano *et al., J. App. Phys*. vol. **92(1)** 2002
Yuan *et al., Trans. Ortho. Res. Soc*., vol. **47**, 2001

FACTORS RELATED TO BALL VELOCITY DURING AN INSTEP SOCCER KICK

John K. DeWitt[1] and Richard N. Hinrichs[2]

Exercise and Sport Research Institute, Arizona State University, Tempe, AZ, USA
[1]Graduate Student, john_dewitt@hotmail.com, [2]Associate Professor

INTRODUCTION

Kicking is a complex interceptive action requiring the coordination of multiple segments with the intent of obtaining maximal endpoint (i.e., foot) velocity at the time of contact with the ball. While contact is made with the foot, many segments, including the lower leg, thigh, pelvis and upper body must be coordinated throughout the motion. The peak and impact velocities of each segmental endpoint affect the velocity of the foot at impact. The purpose of this investigation was to identify those factors that are related to faster ball velocities.

METHODS

Sixteen experienced male soccer players were videotaped while kicking a stationary soccer ball as hard as possible with their right foot into a regulation goal (similar to a penalty kick). All testing was completed inside a gymnasium. The two trials for each subject that resulted in the greatest ball velocity were selected for further analysis. Video data were digitized and converted to 3D coordinates via the DLT algorithm. Data were smoothed and 3D velocities were computed. The two trials for each subject were combined into a mean trial, resulting in sixteen means values for each variable examined.

A deterministic model was developed relating the peak and impact velocities of the left hip, right hip, right knee, and foot center of mass (CM) to ball velocity. The pyramid-like model was developed to better illustrate the relation of each factor to the desired result (See Figure 1).

Resultant and component velocities were correlated to 3D resultant ball velocity. Factors found to be significantly related to ball velocity were examined until the end of the model was reached, or until no significant correlation was found. A factor was considered for further analysis if the magnitude or any component of velocity was significantly correlated with ball velocity.

RESULTS

The mean ball velocity for the group was 26.32 ± 2.47 m/s. The foot CM magnitude and downward velocity at impact and the coefficient of restitution (*e*) between the ball and the foot were found to be significantly correlated with ball velocity. Mechanical factors that were significantly correlated with ball velocity included:

- Impact (Imp) left hip vertical (V) velocity
- Decrease in the magnitude (mag) and lateral (L) velocity of the left hip from peak to Imp
- Mag and forward (F) right knee Imp velocity with respect to (wrt) the right hip
- Peak right knee mag and F velocity wrt the right hip
- Increase in right knee V velocity wrt the right hip from peak to Imp
- Peak thigh segmental angular velocity
- Mag, V, and L Imp velocity of the foot CM wrt the knee
- Mag, V and L peak velocity of the foot CM wrt the knee
- Peak lower leg segmental angular velocity

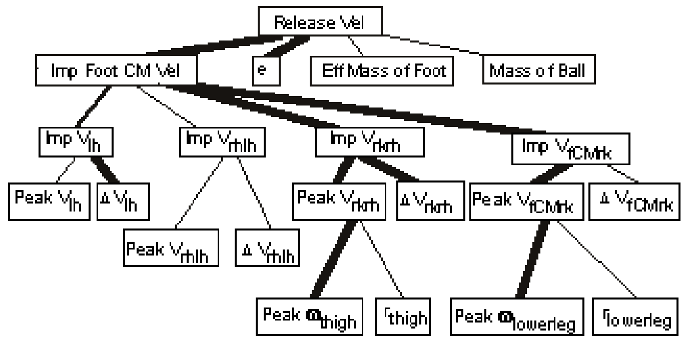

Figure 1: The deterministic model of a soccer kick. Bold lines indicate factors significantly correlated with ball velocity.

DISCUSSION

Velocity variables related to the entire body, the right knee and the right foot CM were significantly correlated with ball velocity, suggesting that approach velocity and torques created at the swing hip and swing knee are important when attempting to generate high foot velocity (and thus, high ball velocity). The significant relationship between ball velocity and *e* suggest that the quality of contact is important.

The lack of relationship between right hip variables and ball velocity suggests that the rotational velocity of the pelvis is not a contributor to ball velocity. It is possible that the role of the pelvis might be to allow the upper and lower leg musculature more time to produce forces that affect the velocity of the foot CM rather than to generate momentum itself.

The finding that greater downward velocities of the foot CM at impact were correlated with ball velocity indicates that athletes actually kick down onto the ball. This could occur to allow interception of the ball with the foot at the time that the foot CM is at its maximum velocity. The downward velocity of the foot CM at impact could trap the ball against the ground as the foot contacts the ball. This could increase the impulse applied to the ball, resulting in greater release velocities.

MUSCLE FATIGUE AND SPINAL INSTABILITY: AN ELECTROMYOGRAPHIC STUDY

Sheri P. Silfies and Andrew R. Karduna
Rehabilitation Sciences, MCP Hahnemann University, Philadelphia, PA, USA
email: silfies@drexel.edu

INTRODUCTION

The use of surface electromyographic (EMG) techniques has played a major role in our understanding of the functional activity of trunk muscles in both healthy and low back pain (LBP) subjects. Numerous studies have used EMG to identify the relationship between LBP and trunk muscle fatigue or altered motor control (Roy SH, et al., 1989; McGill SM, 1991). Specifically, shifts in EMG spectral parameters have been found to be associated with localized muscle fatigue and these parameters have been used to identify muscle impairments associated with LBP (Peach JP, McGill SM, 1998). The purpose of this study was to further investigate these effects in patients with clinical lumbar instability.

MATERIALS AND METHODS

<u>Subjects</u>-Thirty-six subjects were studied with IRB approval. Three groups of subjects were matched on the basis of age, gender and body mass index. Twelve LBP subjects were diagnosed with clinical lumbar instability (CLI) and twelve with mechanical LBP (MLBP) deemed unrelated to instability. An additional twelve healthy subjects had no history of low back pain that limited function or required medical intervention.

<u>EMG</u>-Pre-amplified surface electrodes were applied bilaterally over two extensor muscles: lumbar multifidus (LM) and the lumbar erector spinae group (LES). Data were collected at 1248 Hz, amplified and bandpass filtered (10-750 Hz).

<u>Protocol</u>-To assess extensor muscle fatigue, subjects performed a 30-second sustained isometric contraction in a standing neutral position. The target force was set at 80% of their maximum voluntary isometric (MVIC) extensor force production. Two fatigue trials were completed 5-minutes apart.

<u>Data Analysis</u>-A fast Fourier transformation (FFT) was used to perform a spectral analysis over each second of data. The median frequency (MF) was calculated for each interval. The initial median frequency (IMF) and MF slope over time were computed from linear regression analyses. Data were averaged over the two trials for analysis. Separate ANOVAs were completed for the IMF and MF slope for each muscle.

RESULTS

No significant differences were found for the IMF parameter. Results for the MF slope parameter are presented in Figure 1. Significant group differences in MF slope were found for the left LM ($p=0.011$) and the left LES ($p=0.007$). The right LM ($p=0.052$) and right LES ($p=0.092$) approached significance. *Post hoc* analysis revealed the differences existed between the CLI and control groups.

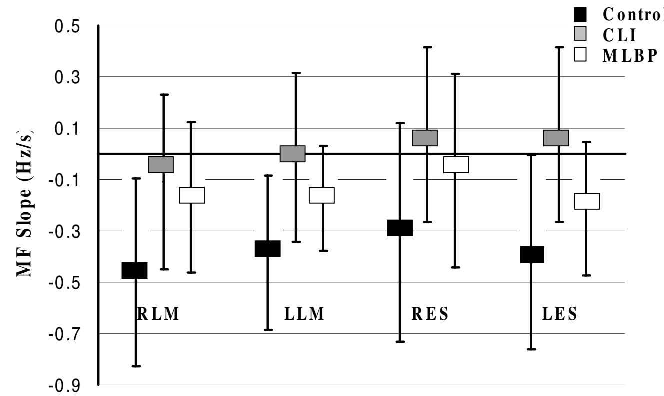

Figure 1. Mean (± SD) of MF slope values for groups clustered by muscle (i.e. RLM- right lumbar multifidus).

DISCUSSION

Based upon these data the CLI group demonstrated significantly less localized muscle fatigue than the control group. This may be secondary to alterations in neuromuscular control, muscular inhibition secondary to pain or altered muscle physiology in the CLI group. Results of this study are inconsistent with pervious research indicating subjects with non-specific MLBP fatigue more than healthy controls (Roy SH, et al., 1989; Peach JP, McGill SM, 1998). Our LBP groups are characteristically different from those previously reported in the literature in that they were painful at the time of the study and had radiographic evidence of structural changes. However, it is unlikely that our results differ due to lower MVIC effort levels from subjects with current LBP, since there were no significant group differences in extensor force production. These results indicate that LBP patients with evidence of CLI may have impairments not in muscle fatigability, but in the neuromuscular control system. Identifying the appropriate impairments in this LBP subgroup has direct relevance to clinical evaluation, rehabilitation and injury prevention.

REFERENCES

McGill, SM. (1991). *JOR*, **9**, 91-103.
Peach, JP, McGill, SM. (1998). *Spine*, **23**, 1117-1123.
Roy, SH. et al. (1989). *Spine,* **14**, 992-1001.

ACKNOWLEGDEMENTS

This project was funded by the Orthopedic Section of the American Physical Therapy Association.

H-REFLEXES IN HUMAN FOREARM MUSCLES ARE ATTENUATED DURING RHYTHMIC ARM MOVEMENT

Alain Frigon, David F. Collins and E. Paul Zehr
Neurophysiology Laboratory, Faculty of Physical Education & Recreation and Centre for Neuroscience,
(afrigon@ualberta.ca), University of Alberta, Edmonton, Alberta, CANADA.

INTRODUCTION

Transmission along the group I afferent pathway to motoneurons of homonymous leg muscles in humans is extensively gated according to the task performed (for review see Brooke et al. 1997). This is demonstrated experimentally as an attenuation of the magnitude of electrically-evoked Hoffmann (H-) reflexes in the soleus muscle during tasks such as walking and cycling, compared to static control values. Soleus H-reflexes are also modulated according to the phase of such rhythmic tasks. Thus, the afferent pathway to leg motoneurons is gated both between and within tasks. Whether a similar control is exerted over group I pathways to upper limb motoneurons is unclear. There is evidence that the control of cutaneous reflex pathways is similar for the upper and lower limb (Zehr and Kido, 2001). The present experiments test the hypothesis that during rhythmic arm movements, transmission through group I reflex pathways to wrist flexor motoneurons is attenuated compared to stationary controls and is modulated according to the movement phase.

METHODS

Nine subjects participated with informed consent. Muscle activity (EMG) was recorded using surface electrodes placed bilaterally over flexor carpi radialis (FCR) and other muscles controlling the wrist, elbow, and shoulder. H-reflexes were evoked in the wrist flexors by electrical stimulation (1 ms pulse width) delivered through surface electrodes placed over the median nerve ~2 cm proximal to the elbow. Seated subjects performed rhythmic arm cycling movements on a custom-made hydraulic ergometer situated at shoulder height in front of them. The position of the stimulated (right) limb is described relative to the clock face with 12'oclock at the top and the movement proceeding in a clockwise direction. Reflexes were sampled at 12, 3, 6 and 9 o'clock of the movement cycle. Static control reflexes were collected at each position while subjects were stationary and maintained a tonic contraction of the wrist flexors. For each condition, 75 reflexes were collected over a range of stimulation intensities from below motor threshold to that which evoked a maximal motor (M wave) response (M_{max}) and M/H recruitment curves were constructed. Mean values of ~10 reflexes were calculated at three places (ascending, descending limbs and H_{max}) on each recruitment curve. Repeated measures analysis of variance tests were used to identify significant differences between data taken from the selected regions of the M/H curves. The data presented in this abstract are taken from the ascending limb.

RESULTS AND DISCUSSION

Figure 1 shows attenuation of H-reflex amplitude across the range of stimulus intensities studied for stimulation at the 3 o'clock position. For the group, there was a 39% decrease (p=0.007) in mean reflex amplitude during cycling compared to control. The attenuation was significant at each of the four phases of the movement studied, but the amount of attenuation did not depend on the phase of the movement cycle (p=0.18). For all comparisons there were no significant differences in M wave amplitude. These results demonstrate a task-dependent gating of the pathway from group I afferents to alpha motoneurons of the upper limb similar to that show for the

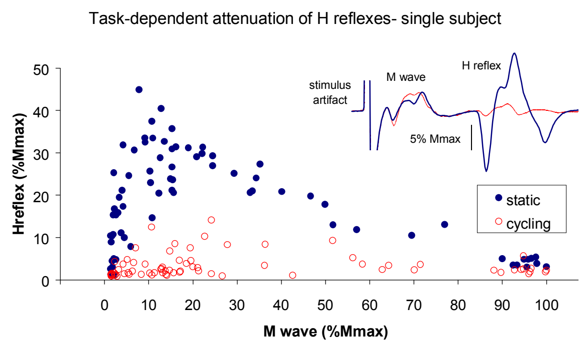

lower limb. However, unlike in the lower limb, reflex amplitudes were not modulated according to movement phase.

Figure 1: M/H recruitment curve for data recorded at the 3 o'clock position. The inset shows averaged data taken from single sweeps on the ascending limb of the curve.

SUMMARY

Rhythmic arm movement suppresses forearm H-reflexes therefore a similar task-dependent control strategy exists for regulating transmission through group I pathways in the arms and legs. However, the lack of phase-dependent modulation implies subtle differences between the neural control of reflex pathways from muscle afferents in the arms and legs.

REFERENCES

Brooke JD. et al. (1997). *Prog. Neurobiol.* **51**:393-421.
Zehr EP, Stein RB. (1999). *Prog. Neurobiol.* **58**:185-205.
Zehr,E.P., Kido,A. (2001). *J. Physiol.* **537,** 1033-1045.

ACKNOWLEDGEMENTS

Supported by NSERC and AHFMR.

AN *IN VIVO* EXPERIMENT-BASED GROWTH MODEL FOR INTIMAL HYPERPLASIA IN RAT VEIN GRAFT

Dalin Tang[1], Chun Yang[2] and Shu Q. Liu[3]
[1]Mathematical Sciences Department, Worcester Polytechnic Institute, Worcester MA USA 01609, dtang@wpi.edu
[2]Mathematics Department, Beijing Normal University, Beijing, China
[3]Biomedical Engineering Dept., Northwestern University, Evanston, IL USA 60208

INTRODUCTION. Vein grafts are commonly used to replace malfunctioned arteries. However, vein graft failure often occurs due to intimal hyperplasia. Blood flow and fluid shear stress have been shown to affect the formation and growth of vein graft neointima. While extensive studies have been carried out, the mechanisms of intimal hyperplasia remain un-resolved. Recent studies have shown that vortex blood flow and reduced shear stress are associated with neointima formation and an elimination of vortex flow by using an engineering approach prevents these pathological changes (Liu, 1998). In this paper, a computational growth model based on Liu's experimental data is introduced and solved to simulate the formation and growth of vein graft stenosis and to better understand the factors involved in the process.

METHOD. The geometry, blood flow rate, and mechanical parameters of vein grafts and host arteries, presented in previous reports, are used here (Tang et al, 2001; Liu, 1998). A nonlinear axisymmetric thick-wall model with fluid-wall interactions is introduced to simulate wall deformation, wall stress/strain distributions, and viscous flow in a vein graft to quantify wall tensile stress and flow conditions which may affect the restenosis process. The flow is assumed to be laminar, Newtonian, viscous and incompressible. The Navier-Stokes equations are used as the governing equations. Both host artery and vein graft are assumed to be elastic, homogeneous, isotropic and nearly incompressible. An incremental linear elasticity approach is used to implement the nonlinear elastic properties of the materials. A numerical method using generalized finite differences with staggered grids and upwind techniques for the fluid model, a finite element method for the wall model, and an incremental boundary iteration method for the fluid-wall interaction is introduced to solve the full FSI model. A growth function which related the growth rate of intimal hyperplasia to fluid shear stress is introduced to adjust the inner wall thickness. The wall and fluid models are solved iteratively, with wall thickness adjusted periodically according to shear stress distributions. Numerical results are compared with experiments and the growth function is adjusted so that numerical results become consistent with experimental measurements.

RESULTS AND DISCUSSION. The geometry of the vein graft and the mesh used in our computations are given in Fig. 1. The growth function is chosen so that no growth would take place if shear stress is greater than 10 dyn/cm^2, and would increase linearly as shear stress decreases from 10 dyn/cm^2 to 0 (direction ignored). Fig. 2 shows the circumferential stress distribution in the artery and the graft. Fig. 3 gives the vector plot of flow velocity in the graft region, showing the presence of eddy flow, in conjunction with reduced fluid shear stress, and focal neointima. Fig. 4. plots shear stress along the inner artery wall, showing a nonengineered graft is associated with a near zero shear stress, which creates favorable conditions for hyperplasia. Fig. 5 gives the tube shape with neointima growth at days 0, 6, 12, 30 which are consistent with experimental observations (Liu, 1998).

CONCLUSION. Shear stress plays an important role in neointima formation in experimental in vein graft. Engineering techniques can be used to modulate the distribution of fluid shear stress, prevent focal neointima formation and reduce the risk of graft failure.

ACKNOWLEDGMENT This research was supported in part by NSF grant DMS-0072873

REFERENCES

Liu, S. Q. (1998), *Atherosclerosis*, **140**, 365-377.
Tang, D. et al (2001), *J. Biomech. Engng.*, **123**, 548-557.

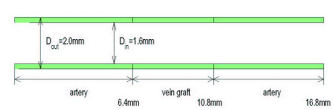

Fig. 1. Geometry of Vein Graft.

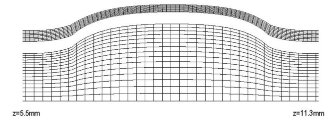

Fig. 2. Non-uinform Mesh.

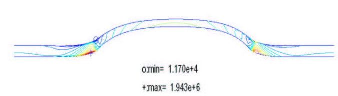

Fig. 3. Circumferential Stress Distribution in the wall.

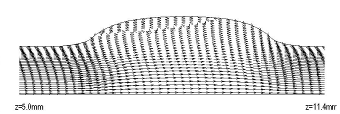

Fig. 4. Flow velocity plot Showing eddy flow.

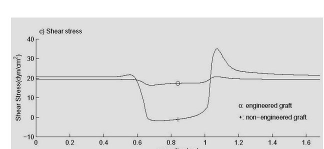

Fig. 5. Shear stresses along Inner artery and graft wall.

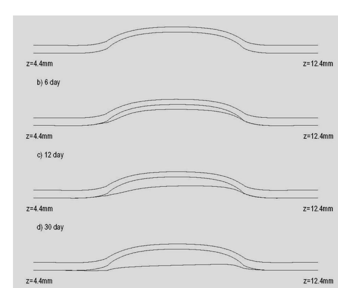

Fig. 6. Intimal hyperplasia Growth at 6, 12, 30 days.

CAN INVERSE DYNAMICS BE COMPUTED WITH A RIGID BODY MODEL

H. Böhm, H. Ruder

Institute of Astronomy and Astrophysics,
Department of Theoretical Astrophysics & Computational Physics,
Eberhard Karls University, Tübingen, Germany

INTRODUCTION

Inverse dynamics computation of resultant muscle torques in dynamical movements often lead to improper peaks in the joint torques which can not be generated from the human body in short times (van den Bogert 1996). One reason for these peaks can be found in deficiencies during the measurements. The more important problem is that the inverse computation is done with input data measured on complex real biosystems. These biosystems are incompatible with the rigid body model used for computation. For example the markers fixed on one segment of the human body do not fulfill the rigid body assumptions, because the distances between the markers are not constant during the movement. One solution to obtain a better result in the resultant joint torques can be found in (Chao et al. 1973). The authors forward simulated the movement and optimized the resultant joint torques till the marker movement was reproduced. The disadvantage of this method by Chao et al. is the high computationally cost.
The aim of this study is to demonstrate an effective method to generate joint coordinates compatible with the rigid body model used for inverse computation.

METHODS

The rigid body model in three dimensions used in this study consists of 14 segments connected by revolute joints Segment mass, inertia and joint positions are taken from regression formulas (NASA 1978). In a standing trial the marker positions on the human body are recorded and the marker positions are assigned to the local coordinate system of the respective segment of the rigid body model. Spring damper elements are attached between the marker points defined in the local body coordinate system and the global marker positions. During the movement the spring damper elements are pulling the model through space along the unfiltered marker trajectories. This requires a forward dynamical computation of the movement for which the equations of motion are formulated with a recursive Newton Euler method (Shabana 2001). With this procedure the rigid body constraints are maintained throughout the movement. The changes due to wobbling of the markers do not directly result in changes in the joint angles, they are compensated by the spring damper elements. The joint angles of the rigid body generated during the movement are therefore in agreement with the mass and inertia properties of the model. To compare this method with those commonly used in inverse dynamics (van den Bogert 1996) the joint angles are calculated from the 15 Hz low pas filtered marker coordinates (Spoor 1980). The joint angles obtained from the two methods and the unfiltered ground reaction force data are taken to inverse dynamically calculating the resultant joint torques. Calculated is a running trial with a running speed of three m/s. To test whether the obtained resultant joint torques from the two methods are in agreement with the model, the running movement is forward dynamically simulated using the calculated joint torques.

RESULTS AND DISCUSSION

Compared to the common method, the resultant joint torques calculated using the spring damper elements show smooth joint torque curves at touch down. Due to the smoothness of the data the resultant joint torques can be successfully used for the forward simulation of the movement. It was not able to simulate the movement with the joint torques obtained with the common method.
The joint torques calculated with the spring damper method are similar to those described by (Chao et al. 1973), but the spring damper method is computationally more efficient because the movement is only simulated once. Whether this approach leads to realistic joint torques of the real biosystem could not be answered and is a question of the model used to describe the human body. For a rigid body model it is a very efficient and robust method to compute inverse dynamics in highly dynamic movements.

REFERENCES

Chao, E.Y., and Rim, K., 1973, “Application of optimization principles in determining the applied moments in human leg joints during gait”, J. Biomech., 6, pp 497-510.
Van den Bogert, and A. J., Konig, J. J., 1996, “On optimal filtering for inverse dynamics analysis”, Proceedings of the Biennial Conference of the Canadian Society for Biomechanics, Vancouver, pp 214-215.
NASA Reference Publication, 1978, Tech. Rep., 1024, NASA, Springfield.
Shabana, A. A., 2001, “Computational Dynamics” , John Wiley, NY.
Spoor C. W. and Veldpaus, F. E., 1980, “Rigid body motion calculated from spatial co-ordinates of markers”, J. Biomech. , 13, pp 391-393.

ASSESSMENT OF SINCERITY OF EFFORT DURING ISOMETRIC STRENGTH TESTING

John H. Challis[1] and H.J. Sommer III[2]

[1]Biomechanics Laboratory, Department of Kinesiology, The Pennsylvania State University, University Park, Pennsylvania, USA
Email: jhc10@psu.edu
[2]Department of Mechanical and Nuclear Engineering, The Pennsylvania State University, University Park, Pennsylvania, USA

INTRODUCTION

Assessment of muscle strength is often an important part of clinical assessment, for example post anterior cruciate reconstruction surgery. The assessment of muscle weakness, by comparing one limbs strength with the other, or with a norm is used in legal cases concerned with personal injury. Isometric strength curves are estimated by having subjects perform exertions at a range of joint angles. Irrespective of the use made of muscle strength tests it would be useful to be able to assess the sincerity of effort of the participant.

Previous attempts to assess sincerity of effort under isometric conditions have focussed on factors such as the gradient of the rise of the time-moment curve, and the variability of the plateau (e.g. Gilbert and Knowlton, 1983; Saunders and Bohannon, 1991). These approaches have not been able to reliably distinguish between maximum and sub-maximal efforts. The purpose of this study was to examine two new methods for assessing the sincerity of effort during isometric strength testing.

METHODS

Sixteen subjects (eight female) gave informed consent to participate in this study (age - 24.4 years ± 5.3, mass - 74.9 kg ± 12.3, height - 1.711 m ± 0.110). After appropriate warm-up the subjects performed a series of static knee extensions using a Biodex dynamometer (model III), with the knee at 90 and the hip at 105 degrees of flexion. The subjects were secured to the dynamometer to eliminate any effects of extraneous movements on the results. The dynamometer position was manipulated so the axis of rotation of the knee joint was aligned with the axis of rotation of the dynamometer. Each subject was asked to perform three maximum isometric knee extensions, and three faked maximum efforts. Each trial lasted five seconds with two minutes rest between all trials.

The output from the tests were time-moment curves, these were assessed using two procedures,

Procedure A - the plateaus of the curves were identified and analyzed using a random walk analysis (Peng et al., 1994).

Procedure B - the time-moment curves were assessed using the approximate entropy (***ApEn***) algorithm described by Pincus (1991). ***ApEn*** is a measure of the regularity of a data set. It takes sequences of ***m*** data points and determines the logarithmic likelihood that this sequence is similar to other sequences of data points. If the data set is regular then ***ApEn*** has a small value; conversely ***ApEn*** increases in value with increasing irregularity of the data set. A parameter ***r*** is used to determine the closeness of data sequences, which effectively filters out sequences which are not close. For the comparisons made in this study ***m*** was set to 2, and ***r*** was set at the measurement precision of the Biodex dynamometer.

Each sampled data set was normalized with respect to its peak moment. The reason for this normalization was to remove any bias, due to the signals absolute magnitude, in identifying the maximum from the faked maximum trials.

RESULTS

Peak moments recorded for the faked maximums had a mean value of 59% of the maximum efforts peak moments. The scaling exponent from the random walk analysis was higher in the maximum condition than in the faked maximum for 69% of trials. This analysis indicated the data sets were representative of brown noise. The ***ApEn*** in 88% of trials indicated the maximum trials were more irregular than the faked maximum trials. If both criteria are used then 94% of the maximum trials could be identified.

DISCUSSION

Assessing the time-moment curves using both a random walk analysis and computation of the signals approximate entropy was successful in identifying maximum from sub-maximum isometric strength test efforts. It was possible that the subjects did not all produce maximum efforts during the testing. In this case these results indicate the analysis can distinguish efforts of different intensities, not just between sub-maximum and maximum efforts. This approach warrants further examination for other joints, an older populations, and subjects recovering from surgery.

REFERENCES

Gilbert, J.C., Knowlton, R.G. (1983). *Am J Phys Med*., **62**, 135-144.
Peng, C.K., et al. (1994). *Phys Rev E.*, **49**(2), 1685-9.
Pincus, S.M. (1991). *Proc Natl Acad Sci.,* **88,** 2297-2301.
Saunders, N., Bohannon, R.W. (1991). *J Hum Muscle Perform.* **1**, 16-24.

ACKNOWLEDGEMENTS

This research was in part supported by a grant from The Whitaker Foundation.

EFFECT OF POLYETHYLENE THICKNESS ON STRESSES OF AN ANKLE JOINT IMPLANT

Karol Galik[1], Mark C Miller[1,2] and Patrick J Smolinski[1]
[1]Mechanical Department, University of Pittsburgh, PA, karolgalik@yahoo.com; [2]Duquesne University, Pittsburgh, PA

INTRODUCTION

Wear of the polyethylene components in total joint replacements can lead to osteolysis and aseptic loosening of the implants. The amount of wear is associated with the magnitude of contact stresses at the articulating surfaces. Previous studies showed a significant decrease of contact pressure for polyethylene thicknesses greater than 4 mm for nearly conformal surfaces (Bartel, 1985) and for thicknesses greater than 8 mm for non-conforming surfaces (Bartel, 1986). However, these studies were based on calculations of contact pressure for which no upper limit was defined by the yield strength of the material. The present study analyzed stresses in polyethylene based on the von Mises failure criteria with specific application to ankle arthroplasty with nearly conformal cylindrical articulating surfaces.

METHODS

Three models were used in the study. First, an analytical solution assuming plain strain conditions was derived for a rigid cylinder contacting compliant polyethylene of finite thickness. Secondly, a full 3-D FEM model of the ankle implant including the tibia and fibula was created and the mesh in the contacting areas was refined using submodeling techniques (Fig. 1). Finally, because a 2-D analysis may approximate the geometry of conformal concentric cylinders, a 2-D FEM model was created. In all models, a load of five times body weight (3,337 N) was applied. The polyethylene was modeled as elastic, with υ=0.46 and E=567 Mpa, for the analytical solution and as elasto-plastic (DeHeer, 1992) for the other two models. All materials were isotropic. The talar component was modeled as rigid.

RESULTS AND DISCUSSION

No significant contact pressure decrease was found with thickness greater than 5 mm for the 3-D FEM analysis. The analytical solution showed the same trend with smaller magnitudes. However, the von Mises stress (Fig 2b) showed the opposite trend, in that these stresses increased with increasing thickness. Investigation of all components of stresses revealed that the difference between the components increased even though all three components decreased in value. The equation for von Mises stress (see below) is a function of these differences rather than of the absolute values.

$$\sigma_m = \{0.5[(\sigma_1 - \sigma_2)^2 + (\sigma_2 - \sigma_3)^2 + (\sigma_3 - \sigma_1)^2]\}^{0.5}$$

From Figure 2 it is also evident that contact pressure could be estimated using simple analytical solutions. The 2-D model predicted the same contact pressure as the 3-D model. However, von Mises stress strongly depended on the overall shape of the model. There was also a difference in the von Mises stress between the 3-D and 2-D model, which can be attributed to the fact that the plain strain conditions were violated as the polyethylene thickness increased.

SUMMARY

Results showed that with increased thickness, under plain strain conditions, the contact pressure decreased while von Mises stress increased. Contact pressure was less sensitive to the changes in the shape outside of the sagittal plane than was the von Mises stress. The 2-D FEM model was a good approximation of a full 3-D model if plain strain conditions were satisfied.

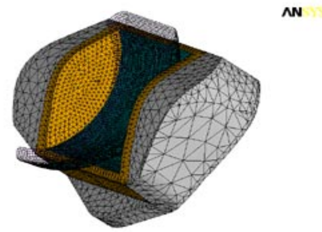

Figure 1: Submodel of the 3-D FEM model

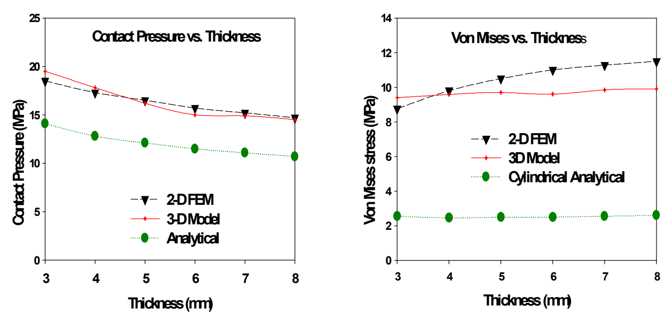

a b

Figure 2: Contact pressure and von Mises stress as a function of the polyethylene thickness

REFERENCES

Bartel, D. L. et al. (1986). *Clinical Orthopaedics and Related Research* **68-A**(7): 1041-1051.
Bartel, D. L., et al. (1985). *Journal of Biomechanical Engineering* **107**: 193-199.
DeHeer, D. C. and B. M. Hillberry (1992). *38th Annual Meeting of the ORS*: 327.

DYNAMIC GEARING AT THE LIMB JOINTS OF JUMPING DOGS

Colin Gregersen and David Carrier[1]
Department of Biology, University of Utah, Salt Lake City, Utah, U.S.A.
[1]carrier@biology.utah.edu

INTRODUCTION

If an animal were to rely on actively shortening muscles, jumping performance could be enhanced if the gear ratios of the muscles increased throughout the jump (Carrier *et al.*, 1994; Carrier *et al.,* 1998). Because the force produced by muscle fibers declines in a hyperbolic fashion as shortening velocity increases, there exists an optimal shortening velocity at which power production is maximized. However, the gear ratio of a muscle that shortens at a constant rate must change if the muscle is to contribute to acceleration of the animal. Specifically, the ratio of the ground force to muscle moment arms of an extensor muscle would have to increase as the joint extends.

To determine if this type of gearing occurs in jumping dogs we 1) calculated the gear ratios of the extensor muscles at the limb joints, 2) measured the changes in length of an extensor muscle of a joint that exhibited an increasing gear ratio pattern, and 3) calculated the relative contribution of the joints with an increasing gear ratio to the total external work produced during jumping.

METHODS

The ground reaction force moment arm was computed during jumping in three dogs utilizing a sagittal plane analytic model. The model assumed that the limbs remained in the sagittal plane during jumping and that the mass and inertia contributions of the limb segments were zero. By convention, a positive joint moment indicated that the ground reaction force acted to flex the joint. The gear ratio calculations utilized the same convention. Sonomicrometry was used to measure length changes in the vastus lateralis muscle.

RESULTS

Four of the six joints examined (wrist, elbow, ankle and hip) exhibited a decrease in extensor gear ratio during jumping. In contrast, the gear ratios at the shoulder and knee joints started out negative and increased linearly throughout the jump (Fig. 1). The gear ratio became positive midway through support at both joints.

During jumping, the average shortening of the vastus lateralis muscle ranged from 17 to 29.5% of standing length (Fig. 1). The shortening velocity for the muscle was generally constant throughout the jump as illustrated in Figure 1, and ranged from 2.7 to 3.9 muscle lengths per second.

The knee extensors produced very little negative work, but produced a significant amount of positive work. The knee extensors produced 34% of the positive external work of the hind limb, and 26.6% of the total positive external work.

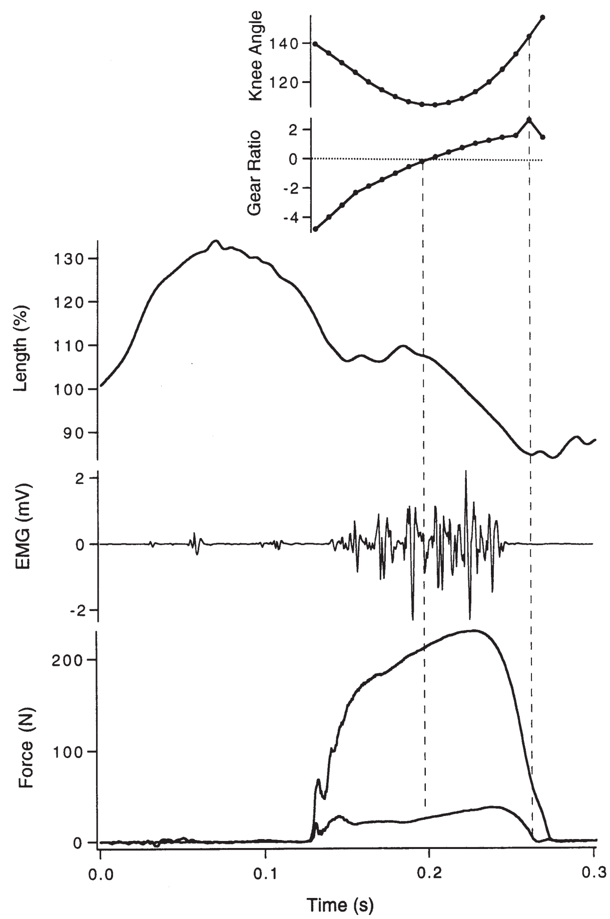

Figure 1. Sample recording of the length changes and electromyography from the vastus lateralis muscle plotted relative to recordings of knee angle, gear ratio, and ground forces.

SUMMARY

The shoulder and knee joints exhibit a pattern of increasing gear ratio that could facilitate maximum power production of their extensor muscles. Consistent with the dynamic gearing hypothesis, the pattern of shortening of the vastus lateralis muscle indicates that the knee extensor muscles shorten at a velocity near that which produces peak muscle power. Additionally, the extensor muscles of the knee produce 26.6% of the total positive work of a jump. These results suggest that dynamic gearing at the knee joint is an important factor in the mechanics of jumping dogs.

REFERENCES

Carrier, C. R., Gregersen, C. S., Silverton, N. A. (1998). *J. Exp. Biol.* 201, 3185-3195.

Carrier, D. R., Heglund, N. C., and Earls, K. D. (1994). *Science* 265, 651-653.

THE DEVELOPMENT OF A KEYBOARD FORCE PLATFORM

Theodore Becker[1] Peter Johnson[2] and Jack Tigh Dennerlein[1]
[1]Harvard Occupational Biomechanics, Harvard School of Public Health, Boston, MA.USA
[2] Department of Environmental Health, University of Washington, Seattle, WA USA

INTRODUCTION

As a person uses a computer there are many forces that act on their body. Many factors, such as the types of keyboard, mouse, computer workplace design being used, and the anthropometrics of the person will contribute to the type and magnitudes of the forces acting on the fingertips. Understanding the relationships between these factors and the applied forces can guide manufactures and researchers to design more ergonomically friendly computer keyboards, as well as the associations between computer keyboard use and musculoskeletal disorders. In order to better understand the forces experienced during typing we developed a force sensing system that allows us to test the magnitude and location of force on a keyboard, during use without significantly altering the height or position of the keyboard. The design will be used at people's own workstations and therefore must be minimally invasive. We are using this system as part of a larger study to determine the musculoskeletal exposure a person encounters during typical computer use activities.

MATERIALS & METHODS

The keyboard force sensing system (Figure 1) is comprised of a rectangular aluminum plate 3.18 mm thick and accepts most commercially available standard and alternative keyboards. Four, 5 lb. Entran load cells, model ELFS-B3-5L, are mounted to the underside of the aluminum plate in a trapezoidal arrangement to decrease the level of vibration. The load cells are mounted in shallow cuts into the surface of the plate. The wires from the load cells are mounted in grooves and lead to the rear of the plate and then to the keyboard amplifier and then onto the data collection computer through a National Instruments A/D board at 200 Hz. The force data was digitally low pass filtered with a cut-off frequency of 20 Hz.

Figure: The keyboard force platform design.

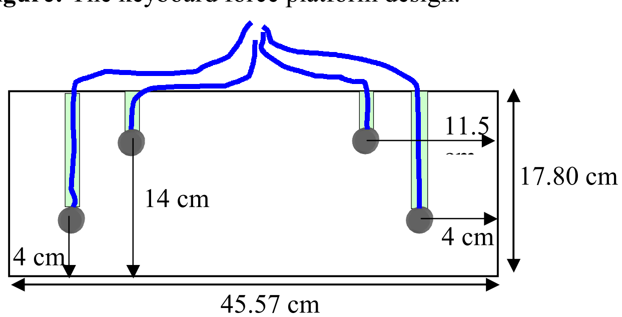

The keyboard platform was tested for load and position accuracy, both statically and dynamically. For the static tests three weights (1.0N, 3.0N and 6.0N) were placed on the platform in a grid with 41 points located 6 cm apart. For the dynamic tests five points on the platform were tapped five times each with a 0.25N weight dropped from a height of 3cm. This was done with no weight on the platform and then with a 1.0N weight over each load cell to mimic the weight of a keyboard resting on the platform. The centroid for the tapping experiments was calculated using the mean force during the tap.

RESULTS AND SUMMARY

As the weight on the point being tested is increased the platform becomes more accurate for both the static and dynamic experiments (Tables 1 and 2). The location algorithm contains the total force in the denominator. As a result, a small signal to noise ratio will increase the noise in the location prediction. For the dynamic tapping, the noise may be due the platform not resting on the table evenly and a rocking between supports may occur. With the weight of standard keyboard spread over the entire platform the platform becomes more stable. The precision of the key was increased with the 1.0N weight over each load cell. The area of a single keyswitch is approximately 2.25 cm^2. The standard deviations of the forces are more than acceptable for measuring forces on the keyboard. One limitation to this force platform is that it is only able to measure single keystrokes. For example if a person were to hold down two keys at the same time the resultant force would be measured somewhere between the two keys.

Table 1 Static Force

Wt.	Distance Err (cm)	
	Mean	Stdev.
1.0N	0.445	0.278
3.0N	0.178	0.112
6.0N	0.148	0.074

Table 2 Dynamic Tapping

Wt.	Distance Err (cm)	
	Mean	Stdev.
0.0N	3.936	0.703
4.0N*	0.651	0.376

*1N over each sensor.

In summary, the keyboard force platform is a useful tool for measuring the dynamic forces on a keyboard during typing. A single key strike on a keyboard requires approximately 1.5 N of force (Rempel, 1994), combined with the weight of the keyboard creates enough stabilizing force to make the force platform's accuracy and precision errors acceptable for use in research.

REFERENCES

(Rempel, J. Biomechanics, 27(8): 1101-1104, 1994)

ACKNOWLEDGEMENTS:

Microstrain, Burlington Vermont
NIOSH RO1 OH03997-01

DEPENDENCE OF VISCOELASTIC PROPERTIES ON COLLAGEN ECM MICROSTRUCTURE

Alaina M. Pizzo[1], Blayne A. Roeder[1], Klod Kokini[1,2], Jennie Sturgis[3], J. Paul Robinson[2,3], Sherry L. Voytik-Harbin[2,3]

[1] School of Mechanical Engineering
[2] Department of Biomedical Engineering
[3] Department of Basic Medical Sciences
Purdue University, West Lafayette, Indiana, USA

INTRODUCTION

One of the most critical aspects of functional tissue engineering is the ability to mimic the structural-mechanical properties of extracellular matrix (ECM) scaffolds that naturally serve to organize cells and regulate their behavior. Unfortunately, the tremendous diversity of ECM components and their complex organization *in vivo* make it difficult to decipher the contribution of individual molecules to its structural-mechanical behavior. Numerous mechanical studies have established that tissue explants and collagen-based scaffolds are viscoelastic and exhibit time-dependent mechanical properties. For example, model tissue, consisting of type I collagen and fibroblasts, exhibited nonlinear stress-strain responses after strain cycling (Wagenseil et al., 2001). However, the relationship between viscoelastic properties and 3D microstructure has not been defined. Previously we have shown that adjustment of collagen polymerization conditions, including collagen concentration and pH, provides a convenient means of producing collagen ECMs with distinct 3D micro-structures (Roeder et al., 2002). Using this model system, the dependence of viscoelastic properties on the 3D microstructure of collagen fibrils was determined.

METHODS

Native type I collagen prepared from calf skin (Sigma Chemical Co., St. Louis, MO) was dissolved in 0.01 M hydrochloric acid to achieve desired concentrations. To prepare 3D collagen ECMs that varied in fibril density, solutions of collagen were neutralized to achieve final collagen concentrations of 0.5 to 3 mg/ml while maintaining the same total phosphate content, ionic strength (0.14 M), and pH (7.4). To produce collagen ECMs that varied in fibril diameter and length, collagen solutions were neutralized with 10X PBS buffers with altered ratios of Na_2HPO_4 and KH_2PO_4 to produce pH conditions ranging from 6 to 9. Neutralized collagen solutions were then polymerized in "dog-bone" shaped molds in a humidified environment at 37^oC. Viscoelastic properties of the 3D collagen matrices were measured using a modified Minimat 2000 miniature materials tester (Rheometric Scientific, Inc., Piscataway, NJ). Specimens were maintained in an aqueous environment representing physiological temperature, composition, and pH during mechanical testing. The viscoelastic behavior of the 3D collagen ECMs was characterized by determining (1) the time dependent decrease in stress upon application of fixed strain (stress relaxation), (2) the effect of cyclic loading and unloading (preconditioning), and (3) the time dependent decrease in strain with a fixed stress (creep).

RESULTS AND DISCUSSION

Previously, we have demonstrated that the 3D microstructure of a collagen matrix is an important determinant of its quasistatic mechanical behavior, including linear modulus and failure stress (Roeder et al., 2002). Results of this study establish the relationship between the viscoelastic properties of a 3D collagen ECM and its microstructure. For example, Figure 1 shows the effect of preconditioning (cyclic loading and unloading) on 3D collagen matrices polymerized at pH 7.4 and pH 6.0. Collagen fibrils formed under acidic conditions were shorter and thicker while those formed under basic conditions were longer and thinner (Roeder et al., 2002). In both cases, the first cycle had the greatest hysteresis loop with less hysteresis at successive cycles. The maximum stress decreased between successive cycles, and was an order of magnitude lower at the first cycle for pH 6.0 (0.6 kPa) versus pH 7.4 (4 kPa). Between the first and fifth cycles, the maximum stress was reduced by 47% and 35% for the pH 7.4 and pH 6.0 collagen matrices, respectively. In summary, the results of this study provide fundamental information that will ultimately contribute to the establishment and prioritization of design criteria for engineering ECM–like scaffolds to be used clinically to guide tissue repair and replacement.

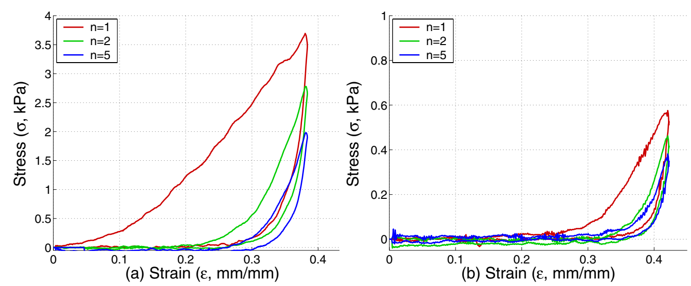

Figure 1: Stress-strain curves for a 2.0 mg/mL collagen ECM at 10 mm/min strain rate after n=5 cycles for (a) pH 7.4 (b) pH 6.0. *Note that y-axes have different scales.*

REFERENCES

Roeder, B. A. et al. (2002) In Press. *Journal of Biomechanics*. **124**.
Wagenseil, J.E. et al. (2001). *Proceedings of the ASME Bioengineering Conference*. 551 – 552.

ACKNOWLEDGEMENTS

This research was funded in part by NSF Integrative Graduate Education and Research Training (IGERT) Program in Therapeutic and Diagnostic Devices Grant DGE-99-72770 Purdue University V.P. Academic Reinvestment Initiative "Comprehensive Cell Biology Imaging and Analysis Facility." Alaina Pizzo and Blayne Roeder are NSF/IGERT Fellows.

THE BIOMECHANICS OF DART THROWING: CHANGES DURING PRACTICE.

Jennifer J. Jeansonne, Li Li and Richard A. Magill
Department of Kinesiology, Louisiana State University, Baton Rouge, Louisiana USA. jjeans@lsu.edu

INTRODUCTION

Coordination changes can best be evaluated in the manner described by Bernstein (1967). As the learner determines the most efficient or effective way to perform a skill, changes in the person's movement coordination pattern occur. How this coordination changes from one point in time to the next provides critical information about how the learner adapts a movement to produce skilled activity. More specifically, coordination describes how the joints are positioned at a specific moment of time, and how those positions change across several moments of time. This adaptation of specific components of the limbs throughout the learning of a complex motor skill is referred to as coordination changes. As the beginner performs a new task, he/she typically tries to reduce the number of degrees of freedom that must be controlled by constraining the body or multiple body segments. This "freezing" of degrees of freedom at the initial stages of learning is eventually followed by an "unfreezing" of degrees of freedom toward the later stages of learning. During the progression of skill learning, the degrees of freedom are released gradually, allowing the learner to use more degrees of freedom in adaptable ways as the skill level increases. Unfortunately, the research literature contains limited biomechanical information describing the coordination changes that occur when people learn a new motor skill. This study provides a description of those changes throughout the course of learning to throw a dart to a stationary target.

METHODS

Novice dart throwers were instructed to stand in a comfortable position at a specified location and told to throw the dart to a circular target that would appear on a cardboard screen in front of them at approximately eye level. The dart was removed after each throw so that subjects would start each practice trial with an uncluttered target. Each subject performed 150 throws per day for four days. Subjects were told only the goal of the task; no instructions were given about how to throw the dart. At the beginning of each trial the target circle would appear on the screen. After each throw of the dart, the X, Y coordinates of its location on the target were recorded. Kinematics was recorded on every 15 throws. Reflective markers were placed on the hand (FIN), wrist (MED, LAT), elbow (LAT), shoulders, head, chest (STERN, CLAV), back (C7, T10), waist (LASI, RASI, LPSI, RPSI) and dart. Kinematic data were collected using the VICON eight-camera motion system.

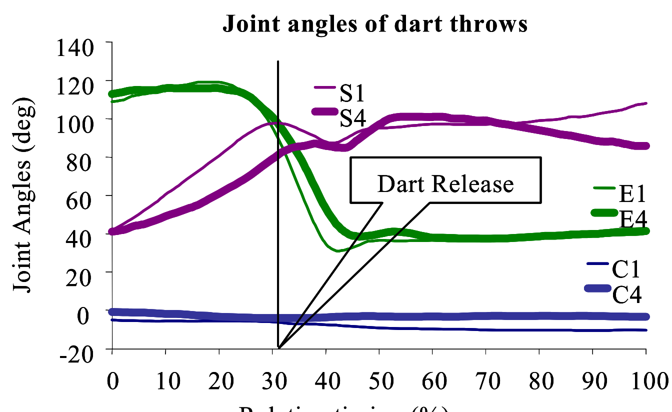

Figure 1. Exemplar Chest (C), shoulder (S), and elbow (E) angles for day 1 and day 4. Horizontal axis presents relative time starts from the beginning of the throwing motion to the end of follow through. Dart release occurred at 31% of the presented data range.

RESULTS AND DISCUSSION

Analysis of the position, velocity and acceleration of the wrist, elbow, shoulder and thorax provided evidence of the changes in coordination that occurred as novices learned this task. Early in practice the observed pattern was to increase the angles at the shoulder and elbow, followed by a large change in the chest angle (figure 1). This residual movement by the chest, which occurred after release, indicated that the subject was using the upper body to move the arm to throw the dart. This indicates a freezing of degrees of freedom at the chest, shoulder, and elbow early in practice. The pattern later in practice was to stabilize the elbow at ~120^0 prior to release and follow through with the forearm to an elbow angle of ~30^0. The magnitude of change in elbow angle was much smaller later in practice compared to day 1. This observation suggests that the subject released the degrees of freedom at the shoulder and chest throughout practice. Additional support for the freeing of degrees of freedom was observed in the changes in velocity of the elbow and wrist. Early in practice there was an increase in elbow velocity and a decrease in wrist velocity, while later in practice there was a decrease in elbow velocity and an increase in wrist velocity. These changes suggest that with practice, the subjects began to use their wrist and elbow independently from their shoulder and upper body.

SUMMARY

Novice dart throwers practiced throwing a dart at a stationary target for 600 trials. Kinematic analysis showed that early in practice, subjects constrained their chest, shoulder, and elbow to act as a single unit throughout the throw. But, with increasing amounts of practice they began to use the wrist more and decrease the movements at the chest and shoulder. The results of this experiment provide evidence that to control multiple degrees of freedom when performing a complex skill, novices will "freeze" certain degrees of freedom to enable them to achieve the goal of the skill. As novices acquire more experience, they begin to release these degrees of freedom to increase their skill performance capabilities.

REFERENCES

Bernstein, N. (1967). *The co-ordination and regulation of movements*. Pergamon Press: Oxford.

THE EFFECT OF BONE QUALITY ON INTRA-MEDULLARY FIXATION OF THE PROXIMAL HUMERUS USING A RETRO-GRADE NAIL

P Manning , M B Rajesh, L Neumann, M Parry , W A Wallace.
The Institute of Biomechanics, The University of Nottingham, UK
Angus.Wallace@rcsed.ac.uk

INTRODUCTION

The integrity of the rotator cuff is maintained in retrograde nailing of the humerus offering a potential benefit over conventional ante-grade nailing, where there is a significant incidence of post-op poor shoulder function. The proximal locking of retrograde nails has proved troublesome. The new Halder humeral nail allows cancellous bone fixation using a trio wire. It is not known whether bone quality affects the function of this trio wire.

METHODS

Ten fresh frozen adult humeri were obtained at post-mortem and stored according the "SAE" protocol for the preservation of human surrogates for biomechanical testing. All specimens underwent standard morphometrical measurements. Each specimen was assessed for bone quality using a Lunar- Expert DXA scanner. Each specimen was instrumented with the correct size retrograde nail under image intensifier control by the same specialist shoulder surgeon. A standardised osteotomy recreated a proximal humeral fracture.

Each specimen was tested for failure of the trio wire in rotation using a certified universal-testing applying pure torque, through the axis of the nail, within the bone. The testing protocol allowed for assessments of torque hold at 10, 20 and 30° rotation. In the event of torque maintenance at 30°, the specimen was rotated further to failure. Failure of torque hold was defined as a 10% drop in measured pure torque.

Proximal humeral fracture

RESULTS AND DISCUSSION

For two specimens technical problems resulted in them being unsuitable for testing. Eight were tested to full failure at the proximal end. The mean failure of torque hold for the nail was 1.25Nm ± 0.14, median 1.2Nm. The mean rotation observed at failure was 29.2°± 17.43, median 34.3°. In sub-failure testing to 10° rotation a mean recoil of only 54% was observed, with significant deformation of the trio wire, similarly at 20°, 50.5% and at 30°, 38%.

There was no significant correlation at the 5% ($p<0.05$) level between the observed bone mineral density of either the humeral head, neck, tuberosity or total proximal bone mineral density and the observed torque hold at failure.

Distally, no failures of the fixation were observed. Reproducibility of the tests was proven with strong correlation observed between failure torque at 10, 20 and 30°s.

SUMMARY

It would appear that proximal humeral bone quality is not important in determining the suitability for a retrograde nail with a trio wire. The nail would appear to function equally well in poor quality bone or good bone, possibly due to the radial force imparted by the trio wire to the cortex. This implies that the nail can be used in patients with marked osteoporosis.

The mean failure of torque hold is low when the nail is compared to other fixation devices. There is significant deformation of the trio wire on rotation even when there is no failure of torque hold. However the nail does offer significant advantages over ante-grade nails in preserving the rotator cuff. It would seem important that if the nail is used, patients should have their arm immobilised for rotation until bony union is underway.

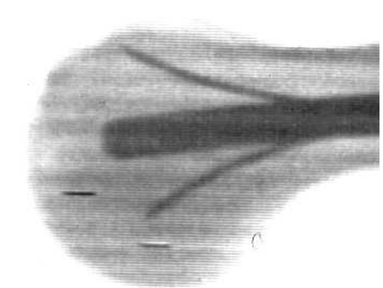

Retrograde Nail in Situ

A BIOMECHANICAL ANALYSIS OF INTERNAL FIXATION OF TRANSVERSE ACETABULAR FRACTURES

Alyssa L. DeMarco[1], Kent N. Bachus[2], Daniel S. Horwitz[3]
[1]MacInnis Engineering Associates, Richmond, British Columbia, Canada
[2]Orthopaedc Bioengineering Research Laboratory, University of Utah, Salt Lake City, Utah, USA
[3]Department of Orthopedics, University of Utah School of Medicine, Salt Lake City, Utah, USA

INTRODUCTION

The surgical stabilization of transverse acetabular fractures remains controversial in terms of approach and method of fixation. The three most frequently used methods of internal fixation are i) dual posterior column plating (2PP), ii) single posterior column plating with placement of a posterior to anterior "homerun screw" down the anterior column (PP&HS), and iii) single posterior column plating with single anterior column plating (PP&AP). Plating of both columns (PP&AP) is generally reserved for widely displaced, unstable fractures, while the other two techniques are more often used when the anterior column is minimally displaced. The purpose of this study was to evaluate the biomechanical stability of these three fixation modalities when applied to a reproducible transverse acetabular fracture model in human cadaveric pelves. The hypothesis tested was that the PP&AP and the PP&HS methods of fixation would be similar in stability and significantly more stable than the 2PP method.

METHODS

Transverse acetabular fractures were simulated by a single orthopedic surgeon (DSH) with the use of a hand held thin blade oscillating saw (System II Sag Saw, Stryker, Kalamazoo, MI, USA) and a custom cutting jig which allowed the simulated fracture to consistently be made 2 cm below the superior lateral rim of the acetabulum at a 458 angle superior to the horizontal position. Seven joints from nine pelves were tested. The fractures were reduced and instrumented three times (in random order), each time with a different construct. All screw plate constructs utilized 3.5mm pelvic reconstruction plates and the homerun screw was a fully threaded 4.5mm cortical screw. Each joint was loaded through simulated abductor muscle contraction (Bay et al, 1997) to a joint reaction force of approximately body weight. During loading, motion was measured along the plane of the osteotomy using a high-resolution differential variable reluctance transducer (DVRT, Microstrain, Burlington, VT, USA). Motion was compared between methods using an ANOVA with a Fisher's PLSD post hoc test ($\alpha < 0.05$). The variance of each method was compared using an F-ratio test.

RESULTS AND DISCUSSION

Means and standard deviations of the measured displacements during simulated partial weight bearing for the 2PP, the PP&HS, and the PP&AP were 0.641 ± 0.656 mm, 0.452 ± 0.445 mm, and 0.145 ± 0.089 mm, respectively (Figure 1) and were not significantly different. From the Fisher's PLSD test, the displacements measured for the three fixation methods were not found to be statistically different: 2PP versus PP&HS ($p = 0.454$), 2PP versus PP&AP ($p = 0.06$), PP&AP versus PP&HS ($p = 0.229$). The variances between 2PP versus PP&AP ($p = 0.001$) and PP&AP versus PP&HS ($p = 0.001$) were found to be significantly different. The variances between the 2PP and the PP&HS ($p = 0.368$) were not found to be significantly different.

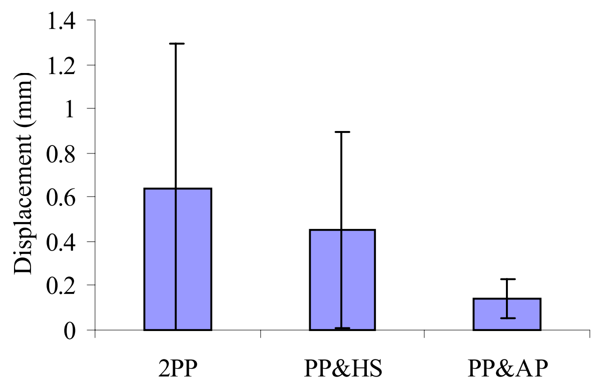

Figure 1: Means and standard deviations of the displacement during loading of the hip joint for each fixation modality.

SUMMARY

When treating transverse acetabular fractures there are three methods commonly used 2PP, PP&HS, and PP&AP. The results from this study suggest that, under ideal surgical conditions, the degree of stabilization achieved using the PP&AP method is predictable and relatively unaffected by differences between specimens whereas the other two methods are not. The stability achieved through the 2PP and the PP&HS methods was found similar in its unpredictability.

REFERENCE

Bay BK et al (1997). *J. Biomech*., **30**, 193-196.

ACKNOWLEDGEMENTS

The authors acknowledge the Department of Orthopedics, University of Utah School of Medicine for funding this project and Synthes for their donation of the plates and screws used in this study.

THEORETICAL CONSIDERATIONS FOR THE INFLUENCE OF ARM SWING ON VERTICAL JUMP TAKE-OFF VELOCITY

Nebojsa Wrbaskic and James J. Dowling
Department of Kinesiology, McMaster University, Hamilton, Ontario, Canada

INTRODUCTION

There are many instances when body segments can be manipulated in order to make movements more efficient or to improve performance. One such situation involves the use of arms during vertical jumping. Hochmuth (1984) showed that when a vertical jump is performed with an arm swing, a greater take-off velocity is achieved by prolonging the time in which the legs can produce force. Furthermore, the deceleration of the arms prior to take-off causes a reaction force which further accelerates the rest of the body by adding to the force being produced by the muscular contractions of the leg muscles. For the sake of simplicity, Hochmuth's simulation assumed that the force curves for the legs and arms were constant. The purpose of this simulation was to introduce a more physiological based model to examine the role of arm swing during vertical jumping.

METHODS

The current simulation used the same assumptions as those of Hochmuth's and are as follows: 1) the acceleration path of the arms and hands = 0.785 m; 2) the acceleration path of the residual body = 0.5 m; 3) the velocities of the residual body and that of the arms and hands must be the same at the instant of take-off. The equations for the force-velocity curves that were used for the residual body or, in other words, for the legs were taken from Alexander (1995) and are as follows:
$F_m = F_{m,iso}\,[1.8 - 0.8(v_{max} - v)/(v_{max} + 23v)]$ for $v < 0$ and
$F_m = F_{m,iso}\,(v_{max} + v)/(v_{max} - 3v)]$ for $0 < v < v_{max}$, where F_m = muscular force; $F_{m,iso}$ = isometric muscular force; v = shortening velocity; v_{max} = max shortening velocity (10 m/s). The timing of the arm swing was manipulated by selecting a range of start times of the deceleration phase relative to the time of take-off (Δt) from 0 to –0.3 seconds. The vertical velocity at the instant of take-off was the dependent variable.

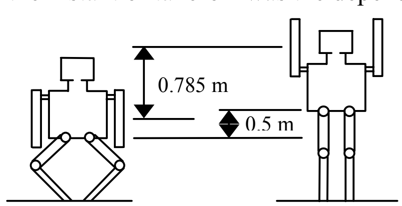

Figure 1: Schematic of model showing movement paths for the residual body (0.5 m) and arms and hands (0.785 m).

RESULTS AND DISCUSSION

The results indicated that there was an optimal time at which the arms should begin to decelerate in order for the body to achieve its maximum take-off velocity. Figure 2 shows that the maximum take-off velocity occurs when the arms start to decelerate 0.084 seconds before take-off occurs.

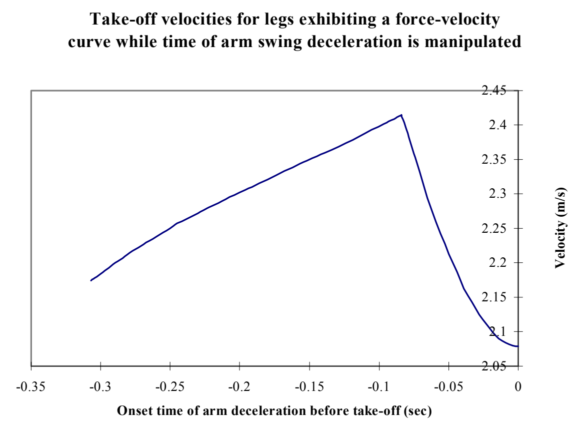

Figure 2: Depicts range of take-off velocities after manipulating time of arm deceleration prior to take-off.

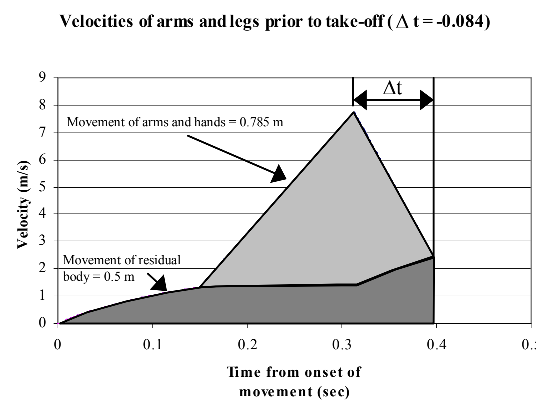

Figure 3: Depicts velocities of arms and hands and that of the residual body for the optimal take-off velocity.

SUMMARY

Compared to Hochmuth's simulation, the take-off velocities from this physiological model are much lower and the time the arms and hands should start to decelerate in order to achieve the maximum take-off velocity is of greater importance.

REFERENCES

Alexander, R. McN. (1995). *Phil. Trans. R. Soc. Lond.* B, 235 – 248.

Hochmuth, G. (1984). *Biomechanics of Athletic Movement.* Sportverlag, Berlin.

THE IMPACT OF ANTERIOR CERVICAL FUSION UPON CERVICAL SPINE RANGE OF MOTION AND OVERALL NECK FLEXIBILITY

John H. Thinnes[1], Sorin Sigler[1], Alan S. Hilibrand[2], Scott Daffner[2], Alexander R. Vaccaro[2], Todd J. Alberts[2]
[1]Biomechanics Laboratory, Drexel University, Philadelphia, PA, USA jthinnes@drexel.edu
[2]Rothman Institute of Orthopedic Surgery, Philadelphia PA, USA

INTRODUCTION

Anterior decompression and stabilization (fusion) of the cervical spine is a common surgical treatment for spondylotic radiculopathy and myelopathy (Ref). This surgery involves fusion of two or more vertebrae. There is a clinical concern that this surgery compromises the functional ability of the patient by reducing his/her neck's range of motion (ROM) and flexibility. Therefore, this study was conducted to quantify, *in vivo*, the effects of Anterior Cervical Fusion (ACF) on the overall ROM and flexibility. It is our hypotheses that 1) following surgical stabilization involving two or three vertebrae a majority of the range of motion lost at the stabilized levels is accommodated in the upper cervical spine with little impact upon the overall ROM and flexibility. However, 2) surgical stabilization involving four or more vertebrae causes a significant reduction in overall ROM and flexibility, which may affect the functional ability of the patient.

METHODS

In order to accomplish the goals of this study and test the validity of its hypotheses, the ROM and flexibility of the cervical spine was measured, *in vivo*, in four groups of subjects. The first group consisted of ten healthy, asymptomatic adults. Data obtained from this group served as the reference to which the patient groups were compared. The second, third and fourth groups consisted of patients who underwent surgical stabilization of two, three or five vertebrae correspondingly. All patients were tested pre and post surgically.

The passive ROM and flexibility of the cervical spine was measured using a specially designed device – the Neck Flexibility Tester (NFT). This device, shown schematically in Figure 1, was developed and validated in the past (Ref). The device consists of a linkage attached across the subject's neck (between torso and head) which measures the motion of the head produced in response to moments applied manually by an operator. Both the motion and the applied loads are recorded continuously on a computer. The testing procedure consists of a passive ROM measurement followed by flexibility measurements in which the neck is loaded in various directions and the motion and applied load are recorded. A complete series of test consisted of ROM and flexibility measured in axial rotation, lateral bending and flexion.

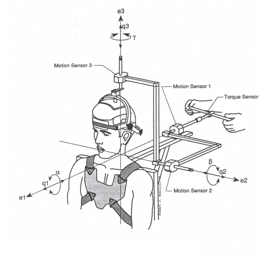

Figure 1: Neck Flexibility Tester

RESULTS AND DISCUSSION

ROM values in degrees and flexibility values in degrees per Newton meter are summarized in table 1. The first number in any field is the average of the group and the second, in parenthesis, is the standard deviation. All three patient groups preoperatively and postoperatively exhibit less ROM than the asymptotic controls. Also, all patients displayed less flexibility in lateral bending and flexion than the normal control. Surgery caused a decrease in ROM in axial rotation in all patients and an increase in ROM in lateral bending. In flexion, groups 2 and 3 showed an increase and group 4 displayed a decrease. Surgery had little effect on the neck in lateral bending and flexion. In axial rotation the largest effect of surgery was observed in patients in group 4.

SUMMARY

Fusing two or three vertebrae has little effect on the overall ROM and flexibility of the neck. Some limitation was observed in patients with five fused vertebrae.

REFERENCES

McClure P, et al: Three Dimensional flexibility characteristics of the human cervical spine. *Spine* **23**: #2, 1998

Truumees E, Herkowitz, H: Cervical Spondylotic Myelopathy and Radiculopathy. AAOS Instructional Course Lectures, **49**: 2000.

Table 1: ROM and Flexibility values for all four groups

Parameter	Normal (n = 10)	2 Fused Vertebrae (n = 5) Preop	Postop	3 Fused Vertebrae (n = 4) Preop	Postop	5 Fused Vertebrae (n = 3) Preop	Postop
ROM Right Lateral Bending	43.2 (27.0)	32.7 (9.07)	34.3 (5.3)	29.3 (6.1)	34.0 (6.3)	26.8 (11.8)	32.3 (3.2)
ROM Flexion	71.1 (12.0)	55.4 (7.8)	57.67 (12.0)	43.0 (6.7)	54.7 (17.2)	51.0 (12.6)	46.3 (9.1)
ROM Left Axial Rotation	88.6 (14.0)	67.1 (11.3)	59.5 (8.8)	59.1 (19.0)	51.1 (17.6)	63.27 (20.7)	48.4 (5.9)
ROM Right Axial Rotation	91.5 (20.3)	69.7 (17.7)	65.3 (12.0)	66.2 (7.38)	56.2 (13.6)	51.3 (18.8)	46.0 (5.3)
Flexibility Right Lateral Bending	9.2 (5.8)	7.0 (1.7)	7.0 (0.9)	6.9 (2.3)	6.3 (1.1)	6.0 (0.8)	5.7 (.9)
Flexibility Flexion	18.6 (14.8)	10.2 (2.6)	11.9 (2.05)	10.4 (1.7)	12.8 (2.6)	8.6 (2.1)	7.4 (0.3)
Flexibility Left Axial Rotation	90.2 (44.7)	158.8 (122.0)	185.8 (132.85)	84.2 (24.8)	61.3 (9.2)	90.2 (27.4)	75.1 (8.5)
Flexibility Right Axial Rotation	88.0 (31.2)	125.5 (96.4)	153.6 (75.0)	147.8 (49.8)	71.9 (24.1)	114.3 (103.1)	65.1 (9.3)

THE GEOMETRY OF GALLOPING

Michael T. Butcher, John E. A. Bertram and James R. Usherwood
Department of Nutrition, Food and Exercise Science, Florida State University, Tallahassee, Florida USA
e-mail: jbertram@garnet.acns.fsu.edu

INTRODUCTION

Many quadrupeds use galloping gaits for high-speed locomotion. Galloping gaits have traditionally been described in terms of footfall timing patterns and limb phase relationships (Hildebrand, 1977). To date however, no compelling mechanistic explanation of galloping has been reported. Recently, it was suggested that galloping involves a combination of pendular and spring-based mechanisms akin to the bipedal skip (Minetti, 1998). Though interesting, this explanation fails to account for the observed pattern of limb phase relationships. An alternative mechanical strategy is described as the basis of the gallop, one that functions through minimizing collisional energy loss. We use this model to describe the basic mechanics behind galloping and compare it to horse locomotion.

METHODS

Under almost all circumstances, a limb coming in contact with a surface will involve a mechanical collision; that component of the animal's velocity aligned with the contact limb will be lost. Collisional energy losses can be reduced if a smaller proportion of the velocity vector is oriented parallel to the limb. The remaining velocity (perpendicular to the limb) will be redirected. It is possible to recover substantial velocity even when only inelastic collisions are considered.

The model (geometric deflection) describes the path of the CoM as it is cyclically redirected from the last flight phase to the following. Although the motion appears to involve bouncing, there need not be any springs involved (Ruina and Bertram, in prep.). This motion is much the same as a stone skipping on a pond, in this case there is an obvious bouncing motion but there is no storage and recovery of strain energy.

To test the validity of the model, experimental ground reaction force data of horses galloping at a canter (slow gallop) from Merkens et al. (1993) were compared to the footfall and limb collision orientation pattern predicted by a three-limbed geometric deflection model. A three-limbed model is appropriate for analysis here because the canter is considered a "three-beat gait" where the leading hind limb and the trailing forelimb contact the ground nearly simultaneously and thus apply force to the surface in unison.

RESULTS AND DISCUSSION

The simple geometric deflection model is in accord with experimentally determined ground reaction force orientation, and also footfall sequence of cantering horses. Neural-based models can describe observed footfall patterns but they lack a mechanical justification. Spring-based models account for energy oscillations, but do not explain limb phase relationships. Both of these are explained by minimizing collisional losses. The model is simple, but differs substantially in its perspective. This approach may explain the limb coordination strategy in the gallop and how it provides for high-speed locomotion beyond the spring-based limitations of the bouncing trot gait.

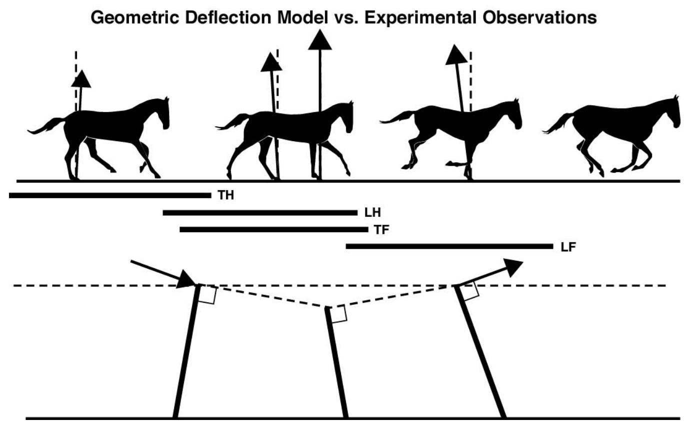

Figure 1: The canter gait of a horse with orientation of mean ground reaction force vectors (above) compared to collision geometry predicted by the geometric deflection model (below). Mean orientation matches well with the collision geometry predicted from the model. Vectors are drawn to scale based on mean vertical and horizontal force magnitudes over the limb's stance duration.

SUMMARY

The mechanics behind galloping remain elusive. A model that focuses on collisional losses at foot contact suggests that the gallop may simply involve the 'geometric deflection' of available velocity. The model is shown to predict the footfall pattern and reaction force orientation of a canter.

REFERENCES

Hildebrand, M. (1977). *J. Mammology*, **58,** 131-156.
Merkens, H. W. et al (1993). *Am. J. Vet. Res.*, **54,** 670-674.
Minetti, A. E. (1998). *Proceedings of R Soc Lond B Biol Sci'98*, 1227-1235
Ruina, A., Bertram, J. E. A. (In Preparation)

TRAINGING-INDUCED CHANGES IN KNEE STABILIZATION STRATEGIES AFTER ACL RUPTURE

Terese L. Chmielewski and Lynn Snyder-Mackler
Department of Physical Therapy, University of Delaware, Newark, Delaware, USA
http://www.udel.edu/PT

INTRODUCTION

Patients with anterior cruciate ligament (ACL) rupture selected by a screening mechanism (potential copers) use strategies to dynamically stabilize their injured knee that are superior to those used by patients who experience knee instability (non-copers) (Fitzgerald, 2000a; Chmielewski, 2001). Potential copers who receive training with perturbation of support surfaces are more likely to return to sports without knee instability, suggesting improved knee stabilization strategies post-training (Fitzgerald 2000b). Perturbations applied during gait provide a method to challenge the knee stability of patients with ACL rupture; therefore, the purpose of this study was to compare the knee kinematics of potential copers and uninjured subjects during unperturbed and perturbed gait, before and after a training program, to gain insight into training-induced changes in dynamic knee stabilization strategies after ACL rupture.

METHODS

Subjects with an ACL rupture, classified as potential copers by a screening examination, were enrolled in this study. Age- and sex-matched control subjects were also recruited. All subjects participated in a 10-session training program including perturbation of support surfaces (Fitzgerald, 2000b). Gait analysis was performed before and after the training program. Six trials of free-speed walking (unperturbed trials) were collected, followed by 6 trials each in which a custom-built platform translated horizontally in an anterior or lateral direction (5.8 cm at 40 cm/s) at heel contact (perturbed trials).

In each condition, the sagittal plane knee angle at initial contact (KAIC), peak knee flexion angle during weight acceptance (PKFA), peak knee extension angle at mid-stance (PKEA) and duration of weight acceptance (DWA; time from initial contact to peak knee flexion) were analyzed.

RESULTS AND DISCUSSION

Complete pre- and post-training data have been collected on 5 potential copers and 3 control subjects. A total of 10 subjects will be recruited in each group for this study.

Preliminary pre-training results show less knee flexion at initial contact, a reduced peak knee angle during weight acceptance, greater knee flexion at mid-stance and a longer duration of weight acceptance in potential copers compared to uninjured subjects across all conditions. After training, the knee angle at initial contact and the duration of weight acceptance were more similar between groups across all conditions. Potential copers' post-training peak knee angle was increased in the unperturbed condition and lateral perturbed condition (Table 1). Although the potential copers' post-training peak knee angle did not change in the anterior perturbed condition, uninjured subjects had less knee flexion, minimizing differences between groups. The post-training knee angle at mid-stance remained more flexed in potential copers compared to uninjured subjects in all conditions.

Comparing the different conditions, potential copers' peak knee angle was the lowest, and the duration of weight acceptance the longest, in the pre-training anterior perturbation condition. This may indicate a strategy to prolong hamstring activity to counter the effects of quadriceps activity, producing co-contraction to stabilize the knee.

SUMMARY

The preliminary results of this study show that: 1) Prior to perturbation training, potential copers have different knee kinematics compared to uninjured controls, 2) Training appears to allow potential copers to use knee kinematics similar to uninjured subjects during weight acceptance, but does not alter the knee angle at mid-stance, and 3) Anterior perturbations appear to be the most destabilizing to untrained potential copers.

REFERENCES

Fitzgerald, G.K. et al (2000a). *Knee Surg. Sports Traumatol. Arthrosc.,* **8**, 76-82.
Fitzgerald, G.K. et al (2000b). *Phys. Ther.*, **80**, 128-140.
Chmielewski, T.L.et al (2001). *Clin. Biomech.*, **16**, 566-591.

ACKNOWLEDGEMENTS

Funding was received from the NIH, Sports Section of the APTA, and the Foundation for Physical Therapy.

Table 1: Potential Copers' Average Knee Kinematics Pre- and Post-Training

	KAIC (°)		PKFA (°)		PKEA (°)		DWA (ms)	
	Pre	Post	Pre	Post	Pre	Post	Pre	Post
Unperturbed	5.7	5.6	20.3	22.5	7.7	7.9	163	152
Perturbed-Anterior	6.4	5.8	17.6	17.6	7.7	7.4	200	179
Perturbed-Lateral	6.3	7.1	20.3	21.9	7.8	7.5	154	146

WHOLE BODY BIOMECHANICS OF RESPONSES TO SLIPS

Rakié Cham[1] (chamr@msx.upmc.edu), Brian Moyer[1] and Mark S. Redfern[1,2]
[1]Department of Bioengineering and [2]Department of Otolaryngology
University of Pittsburgh, Pittsburgh, PA, USA

INTRODUCTION

Accidental injuries and deaths are often the result of slips/falls. Previous slip/fall studies, critical to the understanding of the relationship between gait and falls, have focused on the dominant role of the leading (sliding) leg (Redfern et al., 2001). However, the trailing foot may be of importance as well. Thus, the goal of this paper is to describe whole body biomechanics following a slip, including bilateral postural adjustments of the upper/lower extremities, head and trunk, as well as corrective moments generated at the joints.

METHODS

Five healthy male subjects, aged 35 years or less, were screened for neurological, vestibular and orthopedic abnormalities prior to their recruitment in the study. Subjects were equipped with a safety harness and LEDs, and instructed to walk naturally across a vinyl tile walkway instrumented with two Bertec force plates (FP). Ground reaction forces and whole body motion (2 Optotrak-3020 motion measurement systems) were recorded bilaterally at 60 Hz. Subjects were informed that the first few trials would be dry to ensure natural gait. Then, a soap solution was applied to the left FP without the subject's knowledge. Data processing included the derivation of foot kinematics (linear/angular position, velocity and acceleration), whole body joint angles and joint moments. The foot and body kinematics are reported here.

RESULTS , DISCUSSION AND CONCLUSIONS

The flexion reactions at the leading leg previously reported by Cham & Redfern (2001) during a slip were confirmed here (Fig 1). Those responses are apparent approximately 200 ms after heel contact (HC) with the slippery surface (Fig 3). In addition, the swing phase of the trailing leg during a slip was interrupted (Fig 1). The subject rotated the swing foot down such that the toe contacted first while the leading foot was sliding (Figs 2 and 3). This interruption of the trailing leg's swing phase began at 300 to 400 ms after HC with the slippery surface. Thus, the results reported here suggest that the trailing leg indeed plays a role in the biomechanics of slips.

Other results showed evidence of neck flexion, shoulder/elbow flexion as well differences in the moments generated at the right/left leg joints during slips. In conclusion, this study is a step forward towards the goal of identifying the role of body segments during slip-initiated recovery reactions.

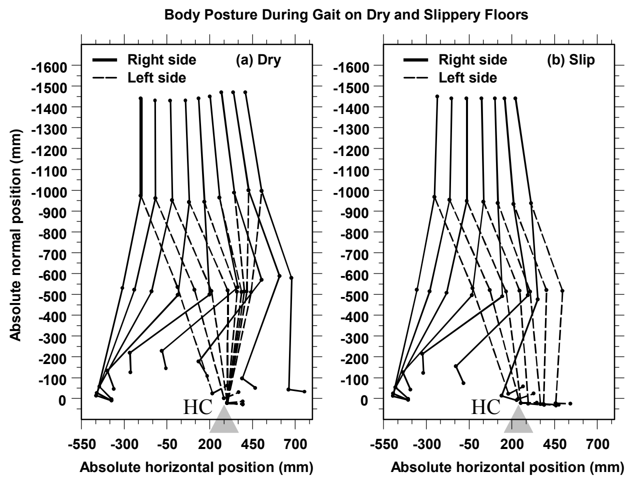

Figure 1: Posture on (a) dry, (b) slippery floors. Δt ~67 ms.

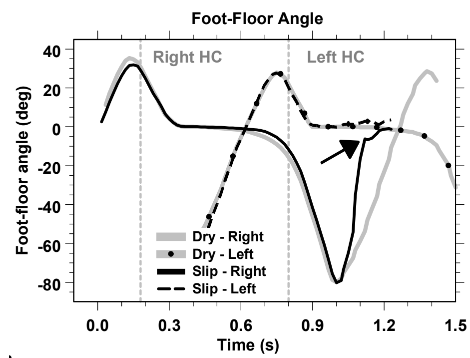

Figure 2: Foot-floor angle on dry/slippery floors. The trailing foot assists in recovery responses as it reversed its rotational motion to land toe first (arrow), attempting to stop slipping.

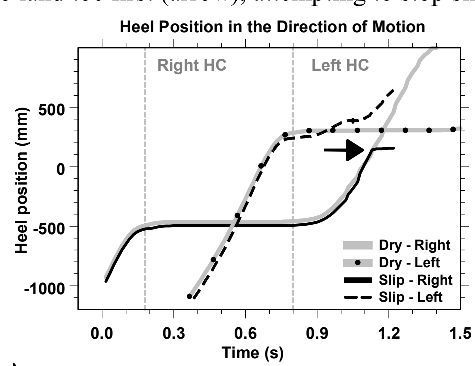

Figure 3: Heel position in the Direction of motion.

REFERENCES

Redfern, M.S. et al (2001). *Ergonomics,* **44** (13), 1038-1166.
Cham, R. & Redfern, M.S. (2001). *J Biomech*, **34**, 1439-1445.

TRAP MAY CONTRIBUTE TO ALTERED MECHANICAL PROPERTIES IN LIGAMENT AFTER CHEMICAL SYMPATHECTOMY

Kelley W. Dwyer[1], Paolo P. Provenzano[1], Peter Muir[2], Ray Vanderby, Jr[1].
[1]Orthopedic Research Laboratories, Dept. of Biomedical Engineering and Orthopedic Surgery, and [2]Comparative Orthopedic Laboratory, Dept. of Veterinary Medicine, University of Wisconsin, Madsion, WI, USA (vanderby@surgery.wisc.edu)

INTRODUCTION

The extracellular matrix (ECM) of ligaments undergoes continual remodeling (ECM degradation, biosynthesis, and matrix assembly). The peripheral nervous system (PNS) plays an effector role in ligament homeostasis and healing (Schaffer, 1998; McDougall, 1997). Previously, we have shown that chemical sympathectomy (inhibition of the sympathetic nervous system) through treatment with guanethidine leads to a reduction in mechanical strength of the rat MCL (Provenzano, 2002). The purpose of this study was to 1. further quantify the mechanical changes caused by sympathectomy and 2. determine agents that are responsible for ligament degradation in guanethidine treated rats.

METHODS

Eight Wistar rats were infused with guanethidine (40mg/kd/day) via subcutaneously implanted osmotic pumps (Alza Corp.). Eight addition control rats were infused with 0.9% saline in a similar manner. Following 10 days of infusion, the rats were euthanized. For mechanical testing the femur-MCL-tibia complex was carefully harvested and cross-sectional area measured. Tissues were inserted into our custom testing system, preloaded to 0.1N, preconditioned (10 cycles at 1% strain), and pulled to failure in displacement control (10%/s). Strain was optically measured on the ligament and synchronized with force measurements. Values compared were ultimate stress, strain at failure, and elastic modulus. An unpaired t-test was used to analyze the data. Differences were considered significant at $p < 0.05$. For histology, contralateral ligaments were harvested *in toto* (4 treated, 4 controls), fixed in Zamboni's fixative, flash frozen at $-70^{o}C$, sectioned (6μm), and mounted on slides. Slides were incubated in reaction solution, consisting of equal parts tris-maleate buffer and hexazonium parasaniline buffer with 50mM sodium-potassium tartrate, for two hours. Following incubation, slides were washed, dehydrated, coverslipped, and investigated for the presence of tartrate resistant acid phosphatase (TRAP), a collagenolytic enzyme (Oddie, 2000).

RESULTS AND DISCUSSION

All guanethidine treated animals developed ptosis (indicative of sympathectomy) by the second day of treatment, which persisted throughout the treatment period. Significant differences between ultimate stress, strain at failure, and elastic modulus were seen between guanethidine treated rats and controls (Table 1). Additionally, histological techniques demonstrated the presence of TRAP in guanethidine treated rats (Figure 1), but not in controls. To our knowledge, no other studies show TRAP in ligament tissue.

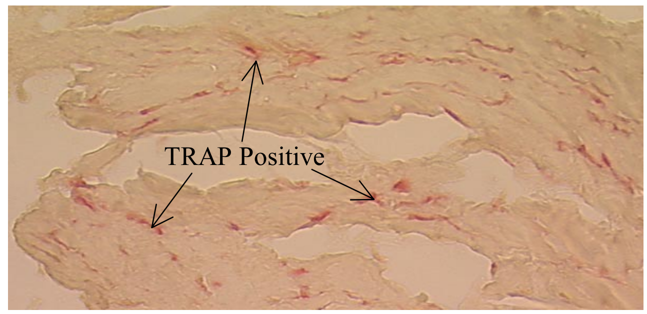

Figure 1: Active TRAP (red) in guanethidine treated rat MCL. Active TRAP was not seen in controls.

SUMMARY

Inhibition of the sympathetic PNS through guanethidine treatment leads to a reduction in ligament strength and changes to strain at failure and modulus. Guanethidine treatment also leads to the presence of active TRAP in many areas of the ligament. The presence of active TRAP suggests a role for this enzyme in ligament degradation following the inhibition of the PNS.

REFERENCES

Oddie, G.W. *et al.* (2000) *Bone*, **27**, 575-584.
Provenzano, *et al.* (2002) *Trans. Ortho. Res. Soc.*, **27**.
Schaffer M., *et al.* (1998) *Arch. Sur.*, **133**, 1107-1116.
McDougall J.J, *et al.* (1997) *Amer. J. Physiol.*, **503**(Pt2), 435-443.

ACKNOWLEDGEMENTS

This study is based upon work supported under a National Science Foundation Graduate Research Fellowship.

Table 1: Ultimate Stress, Strain at Failure, and Modulus for Guanethidine Treated Rats

Group	Ultimate Stress (MPa)	Strain at Failure (%)	Modulus (MPa)
Guanethidine	38.4 ± 4.9	8.1 ± 0.4	1090.9 ± 60.0
Control	69.8 ± 5.2	10.3 ± 0.7	598.4 ± 77.0

INVESTIGATION OF STRUCTURE-PROPERTY RELATIONSHIPS IN HUMAN FEMORAL TRABECULAR BONE

Steven Hsu[1]; Donna Ebenstein[1]; Ahi Issever[3]; Lisa Pruitt[1,2]; Sharmila Majumdar[1,3]
[1]UCB-UCSF Joint Bioengineering Graduate Group, University of California at Berkeley, Berkeley, CA, USA.
[2]University of California at Berkeley, Bioengineering Department, Berkeley, CA, USA, lpruitt@newton.me.berkeley.edu
[3]University of California at San Francisco, Radiology Dept., Magnetic Resonance Science Center, San Francisco, CA, USA.

INTRODUCTION

The goal of this study was to investigate correlations between the local biochemical composition, mechanical properties, and structural parameters of trabecular bone. Nanoindentation was used to measure mechanical properties, Fourier Transform Infrared (FTIR) spectroscopy to characterize bone mineral composition, and microcomputed tomography (μ-CT) to evaluate trabecular bone structure.

METHODS

Femoral head specimens were obtained from 3 patients undergoing surgery for bone disorders and stored in formalin. Cylindrical cores were drilled from the superior, inferior, and side poles of each head, dehydrated, and embedded in polymethyl methacrylate (PMMA) for slicing. Cores then underwent μ-CT scans to obtain structural properties using 3-D imaging at a resolution of 26 μm. Properties measured included: bone volume fraction (BV/TV), trabecular thickness (Tb.Th.), trabecular number (Tb.N.), trabecular separation (Tb.Sp.), and trabecular connectivity (Conn.D.).

Five embedded cores were sliced transversely into 1 mm thick cross-sections. Every other cross-section was then subjected to nanoindentation, while the complementary surfaces on adjacent slices were subjected to FTIR spectroscopy. The remaining 8 cores were each sliced longitudinally into half-cylinders, with one side being sliced into 2-4 mm sections for FTIR analysis. Nanoindentation was performed on the complementary unsectioned surface.

The characterization of mechanical properties was performed using the Hysitron TriboIndenter (Hysitron Inc., Minneapolis, MN). Samples were stained with alizarin red to allow for visualization of trabecular bone tissue. At least 25 specific indentation points were then chosen using the optics attached to the indenter. A trapezoidal loading curve was applied to each site with a loading rate of 40 μN/s, a 10 second hold at 400 μN, and an unloading rate of 40 μN/s. Using the Oliver and Pharr method (Oliver and Pharr, 1992), the reduced modulus (E_r) and hardness (H) at each point were determined.

FTIR analysis was performed using a Nicolet Avatar 360 (Madison, WI) spectrometer with an ATR accessory. Spectra were collected for 64 scans with a 4 cm^{-1} resolution for each sample. After baseline correction, normalization to scale, and subtraction of the pure PMMA spectrum, spectra were analyzed from 675-4000 cm^{-1}. Mineral:matrix ratios were then determined from the ratio of phosphate absorption (900-1200 cm^{-1}) to collagen amide I absorption (1585-1725 cm^{-1}), while carbonate:mineral ratios were calculated from the ratio of carbonate absorption (840-890 cm^{-1}) to the phosphate band. The 1020/1030 ratio was also determined to serve as an indicator of crystallinity, with lower values corresponding to higher crystallinity.

RESULTS AND DISCUSSION

Representative data from 3 slices of a single core are summarized in Table 1. As seen in the table, mechanical and biochemical properties tend to vary over a small range, while some structural parameters display a greater variability. From the data obtained, no obvious structure-property relationship appears evident within the individual slices of a single femoral bone sample or as a function of depth in the core. Data was then averaged for each core, and for each entire bone specimen. No trends were apparent in local mechanical and biochemical properties between cores or specimens. Instead, the results suggest that trabecular bone bulk mechanical property variation may be more dependent upon structural parameters than biochemical and mechanical properties.

Table 1: Representative structural, mechanical, and biochemical properties of three slices from a single core.

Property	Slice 4	Slice 10	Slice 14
Slice Depth	6 mm	14 mm	19 mm
Conn. D. ($1/mm^3$)	10.24	14.76	21.78
BV/TV (%)	48.69	45.33	71.19
Tb. N. (1/mm)	2.83	2.73	3.73
Tb. Sp. (mm)	0.33	0.38	0.21
Tb. Th. (mm)	0.25	0.25	0.35
E_r ± St.D. (GPa)	7.88±4.25	10.15±5.01	7.58±2.20
H ± St.D. (GPa)	0.30±0.22	0.47±0.32	0.39±0.16
mineral:matrix	4.64	4.11	4.30
carbonate:mineral	0.061	0.046	0.042
1020/1030	1.00	1.01	0.98

REFERENCES

Oliver, W.C., Pharr, G.M. (1992). *J. Mat. Res.,* **7**, 1564-1583.

INCREASING AGE SLOWS RECOVERY OF FUNCTION FOLLOWING ACHILLES TENDON INJURY IN THE RAT

Lori Vogelpohl, Donald D. Anderson, Joseph E. Hale, Stefanie D. Stangier, and Carlos A. Guanche
Biomechanics Laboratory, Minneapolis Sports Medicine Center
Minneapolis, MN, e-mail: ander284@umn.edu

INTRODUCTION

The application of exogenous insulin-like growth factor-I (IGF-I) has been shown to improve healing in muscle (Menetrey et al, 2000), stimulate bone remodeling (Chihara and Sugimot, 1997) and speed recovery after tendon injury (Kurtz et al, 1999) in young healthy animals. These findings may have broader implications in the treatment of populations with impaired healing capacity. Increasing age negatively influences the rate at which wounds heal (Eaglestein, 1989) and impairs tendon metabolism, in particular (Almekinders and Deol, 1999). Reduced bioavailability of IGF-I with aging previously reported (Adams and Moore, 1995) might well explain altered healing rates in the aged population. By supplementing the native IGF-I supply we aim to accelerate healing following muscle / tendon injury in the aged.

As a first step towards this end, we performed experiments in rats to establish whether or not age influences the rate of functional recovery from surgically induced tendon injury.

METHODS

Eighteen Sprague-Dawley rats, six in each of three different age groups (4, 11, and 19 months old), were studied. These ages were chosen to represent young, middle, and old age, based on growth and survival curves provided by the animal vendor. During a one week period of acclimatization, rats were trained for functional evaluation of their locomotion.

At surgery, rats were anesthetized using pentobarbital and subjected to sharp transection of their left Achilles tendon using techniques previously described (Kurtz et al, 1999). Following surgery, animals were returned to their cages and allowed food and activity ad libitum.

Rats were evaluated to characterize locomotor function in terms of the Achilles Functional Index (AFI), derived from rat pawprints (Kurtz et al, 1999). Deficits in Achilles tendon function following transection produce alterations in the rat's gait, reflected by decreased AFI values compared to baseline. Rats were walked pre-operatively to establish a baseline, and they were then walked on post-operative days 1, 2, 3, and subsequent odd-numbered days until post-operative day 15.

Linear regressions of AFI values vs. the number of days after injury were performed for averages within each of the three age groups, allowing comparison of the rate at which Achilles function was recovered between ages.

RESULTS AND DISCUSSION

Two of the oldest aged rats died of post-operative complications associated with anesthesia; one the day of surgery, and the other two days after surgery. The mean AFI values obtained for the three age groups are shown below in Figure 1. Linear regressions of the AFI (R^2 • 0.89) showed a nearly two-fold difference in the rate of functional recovery between the youngest age group and the two older age groups as measured by the slope of the linear fit.

One limitation of this study is the relatively small sample size, although in previous study, groups of six animals provided sufficient power to detect a 25% difference in the AFI at an 85% confidence level. Future testing will involve a larger sample size (replacing animals lost to complications) and further statistical analysis.

REFERENCES

Menetrey J. et al (2000). *J Bone Joint Surg*, **82B**:131-7.
Chihara K., Sugimot T. (1997). *Horm Res,* **48S5**:45-9.
Kurtz C. et al (1999). *Am J Sports Med*, **27**:363-9.
Eaglestein W.H. (1989). *Clin Geriatr Med*, **5**:182-8.
Almekinders L., Deol G. (1999). *Am J Sports Med*, **27**:417-21.
Adams S., Moore J. (1995).*Prog Growth Factor Res*,**6**:347-55.

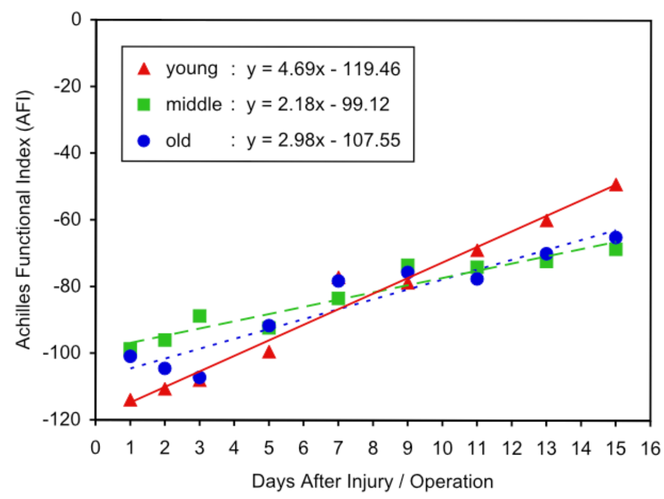

Figure 1: Linear regressions of AFI values following surgically induced Achilles tendon injury. The youngest rats experienced a slightly greater functional deficit immediately following the injury, but recovered function at a faster rate than did the older animals.

STABLE FORWARD DYNAMIC SIMULATION of BIPEDAL GAIT USING SPACE-TIME ANALYSIS

K.P. Granata[1], D.Brogan[2] and P.N. Sheth[2]
Motion Analysis and Motor Performance Laboratory, University of Virginia, Charlottesville, VA.
[1]Depts Orthopaedic Surgery and Biomedical Engineering, [2]Dept Computer Science [3]Dept Mechanical and Aerospace Engineering

INTRODUCTION

Bipedal walking is a highly sophisticated form of legged locomotion requires limit-cycle stability despite the fact that a significant part of the walking cycle violates in static equilibrium. Forward-dynamic simulations of compass-like bipedal gait are useful for the study of walking stability but have been limited to numeric solutions methods (Goswami 1996). Consequently, forward-dynamic walking models are often limited by assumptions regarding controlling activation and/or initial state configurations. The goal of this study was to document a method for determining optimal movement trajectory based upon the constraint that the repetitive gait pattern must be dynamically stable.

METHODS

A 2-D knee-less walker was simulated with a revolute hip joint at the HAT mass (McGeer 1993). Non-linear second-order equations of motion are well established (Goswami 1996) and demonstrate the movement trajectory is determined by the ground slope γ, the mass ratio m_{Leg}/M_{HAT} and mass distribution. Foot-strike was assumed plastic and the transition stage at foot-strike instantaneous, i.e. no double-support period. The state vector following foot-strike is related to the pre-impact state by algebraic relations describing conservation of momentum (Hurmuzlu 1992).

The governing equations were implemented using an ordinary-differential equation solver (MathWorks, Natick MA) to integrating forward in time. Differential equations were assumed homogeneous, i.e. passive walker. Limit-cycle stability was determined from numerical eigenvalue analyses of perturbed trajectories (Garcia 1998). Initial conditions generating stable solutions can only be determined through linear-approximation or by trial-and-error estimation.

The model was also implemented using space-time methods (Witkin 1988) to restrict the solution to dynamically stable trajectories. Movement trajectories were represented through piece-wise linear segmentation; using n=35 time increments to represent 0.6 sec the gait cycle. The entire movement trajectory was established with an angle vector $\boldsymbol{\theta}_t$ at every time increment t=1..n and associated torque vector $\boldsymbol{\tau}_t$. Forward-integration is not required as the differential equations are represented as piece-wise linear functions of the angle trajectory (see Witkin 1988). Using optimization techniques the entire movement trajectory $\boldsymbol{\theta}_i$ was determined by minimizing $\Sigma\boldsymbol{\tau}_t^2$/(step length). Movement trajectory end-points were constrained to satisfy the algebraic transition behavior, i.e. conservation of momentum. Most importantly the movement trajectory was constrained such that system dynamics must satisfy limit-cycle stability, i.e. the solution method will produce only trajectory with stable gait behavior

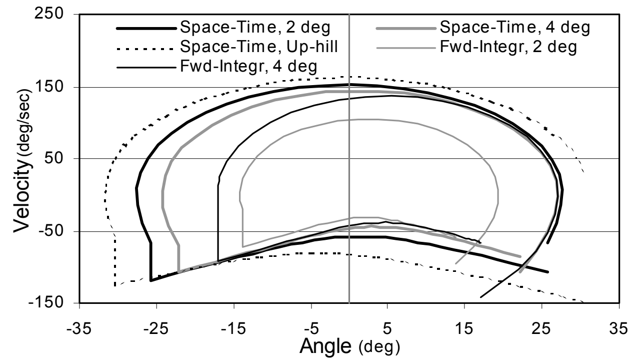

Figure 1. Movement trajectories of the walker at 2 down-hill slopes from the forward-integration and space-time methods. Up-hill walking is also illustrated for the space-time analyses.

RESULTS AND DISCUSSION

Phase-plane representation of movement trajectories are illustrated for ground slopes $=2^0$, 4^0 (FIGURE 1). Similar movement behaviors were achieved from the two simulation methods with longer step lengths from the space-time method because the optimization criterion was penalized by short step lengths. Actuator torques determined by the space-time method converged to zero for all time increments during down-hill walking; identical to the forward-integration results wherein homogeneous solution was prescribed, i.e. a passive walker (McGeer 1993). Although stable solution to uphill walking does not exist for homogeneous forward-integration methods the constrained search technique readily identified the movement trajectory and activation torques necessary to establish stable uphill walking.

SUMMARY

Methods of constrained search can be used to identify movement trajectories based upon the premise that the bipedal walking behavior must be dynamically stable. Pathologic disturbance to normal walking behavior will result in a compensatory movement trajectory only if the modified behavior is stable. This simulation method may permit determination of stable pathologic walking behavior

REFERENCES

Hurmuzlu Y, Chang T (1992) *IEEE Trans. SMC* **22**, 964-971
Garcia et al (1998) *J.Biomech.Eng.* 120, 281-288
Goswami A, Thuilot B, Espiau B. (1999) INRIA report #2996
McGeer T (1993). *J.Theor.Biol.* **163**, 277-314
Witkin A, Kass M (1988) *SIGGRAPH*, **22**, 159-168

THE EFFECTS OF HYDRATION TIME ON LIGAMENT VISCOELASTICITY

Eugene Manley[1], Paolo Provenzano[1], Roderic Lakes[2], and Ray Vanderby, Jr.[1]
[1]Department of Biomedical Engineering and Department of Orthopedic Surgery
[2]Department of Engineering Physics and Department of Biomedical Engineering, vanderby@surgery.wisc.edu
University of Wisconsin, Madison, Wisconsin, USA

INTRODUCTION

Ligaments are soft connective tissues that display viscoelastic behavior. Researchers have studied the effects of hydration on ligament and tendon using various solutions (Chimich, et. al. 1992; Hannafin and Arnockzy 1994; Thornton et. al 2001), but have not studied the role of hydration in individual ligaments subjected to repeated viscoelastic testing and recovery in a single solution. It has been shown that cyclic loading of ligaments causes a reduction in water content and that ligaments with greater water contents relax faster than those with less water (Chimich, 1992). Ligaments that are cycled may lose water due to a ringing out effect. This led us to hypothesize that if a ligament is tested and allowed to recover in physiologic saline for ten times the testing time, that when the ligament is retested it will creep at a faster. Studies have shown that 10 times the testing time is adequate for recovery of tissue gage length (Provenzano, 2001; Turner, 1973).

METHODS

The methodology was adopted from Provenzano et. al (2001). There were two exceptions. The male Sprague-Dawley rats used were 310±40g. The rats were divided into two groups:
Group 1 (n=9 ligaments) consisted of MCLs subjected to 1000s creep after harvest, then allowed ten times (10,000s) recovery time in phosphate buffered saline (1x), and retested at the same load. Care was taken to ensure the tests were started at the same preload (0.1N). Group 2 (n=8 pairs of ligaments) consisted of one leg subjected to creep for 1000s after dissection, while the contralateral leg was hydrated in physiologic PBS for 10 times the testing time, then subjected to creep for 1000s.

The data analysis was done by fitting data with a power law formulation (At^n), where n is the rate of creep. The power law formulation has been shown to describe this type of data well (Provenzano et. al 2001). The data was analyzed with a 2-tailed paired t-test. The null hypothesis is that hydration will not affect viscoelastic behavior.

RESULTS AND DISCUSSION

For Group 1 there was a significant difference in rates of creep between samples that were tested immediately after harvest (time zero) and retested after hydration for 10000 sec (0.0203±0.0012) and (0.0142± 0.0006), respectively. The p value was 0.043, which accents the difference between testing states and rejects our hypothesis (Fig. 1). This shows that hydration affects the rate of creep when a single ligament is subjected to repeated testing. This decrease in creep rate may be due to a decrease in the space between the collagen fibers and exudation of water from the ligament. Group 2 (data not shown) showed no significant difference between contralateral legs for the rate of creep (0.0248±0.006) and (0.0251±0.0058), respectively. This is may be explained by the fact that since the contralateral legs were never initially subjected to creep there was never any water loss. In addition, duplicating exact testing configuration in contralateral ligaments is difficult, adding to noise in the data.

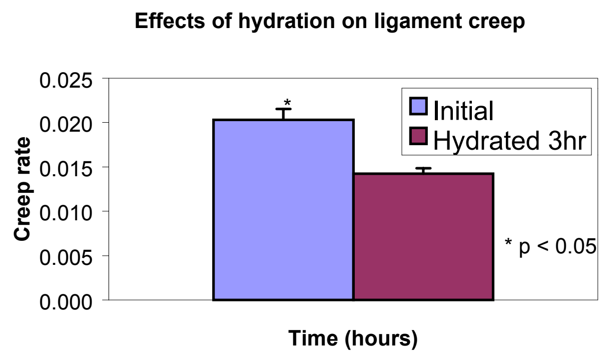

Figure 1: Changes in the rate of creep associated with hydration. There is a significant difference between specimens tested after harvesting and tissues retested after recovery in physiologic solution. * Indicates significant diff.

SUMMARY

These studies show that repeated creep testing of ligaments results in a decrease in the rate of creep with hydration time. This result was not demonstrated in contralateral legs, but may be due to different load histories before hydration. Also this could be a result of differences with the mounting of the specimen or signifies that it is not hydration alone that affects ligament behavior.

REFERENCES

Chimich, D. et al. (1992). *J. Biomech*, **25**(8), 831-837.
Hannafin, J. A., Arnockzy, S.P. (1994). *J. Orthop Res,* **12**, 350-356.
Provenzano, P. et. al. (2001). *Ann Biomed. Eng*, **29**: 908-914.
Thornton, G.M. et al. (2001). *J. Orthop Res,* **19**, 845-851.
Turner, S. (1973). Creep in Glassy Polymers. In: The Physics of Glassy Polymers. New York.

METABOLIC COST OF LATERAL LEG SWING IN HUMAN WALKING

David Shipman[1], J. Maxwell Donelan[2], Rodger Kram[3], and Arthur D. Kuo[4]
[1] Dept. of Integrative Biology, University of California, Berkeley; [2] Dept. of Physiology, University of Alberta, Edmonton;
[3] Dept. of Kinesiology and Applied Physiology, University of Colorado, Boulder;
[4] Dept. of Mechanical Engineering, University of Michigan, Ann Arbor; email contact: david.shipman@alum.mit.edu

INTRODUCTION

We have previously demonstrated that walking with narrow steps requires more metabolic energy than normal walking (Donelan, et al., 2001). One possible reason is that, with narrow walking, people must move their swing leg laterally to avoid colliding with their stance leg. We tested this hypothesis by inducing subjects to walk with increasing amounts of lateral leg swing and measured the associated metabolic cost.

METHODS

Ten healthy adults (6 male, 4 female) participated in the study after providing informed consent. We asked the subjects to follow lines marked on a treadmill belt to enforce their previously determined preferred step width (mean 10.7 cm, s.d. 2.3 cm), and used a metronome to enforce their previously determined preferred step frequency. Subjects walked at 1.25 m/s.

We constructed a device to enforce minimum foot separation at mid-swing during walking (see Fig. 1). The device consists of modified commercial ankle brace. We attached blades medially to enforce a minimum distance between the walker's feet when the swing leg passes the stance leg during walking.

Subjects performed trials with three different blade sizes, along with a baseline trial in which the blades were placed on the lateral surfaces of the ankle braces. The blade sizes used were one-half of the subject's preferred step width, and 1 cm wider and narrower.

We determined metabolic cost by analyzing the gas content of expired breaths. We calculated metabolic power (Watts) for each trial and subtracted the metabolic power for standing from all walking values. Finally, we computed the added metabolic cost as a percent of the baseline trial. We measured net ground reaction forces and moments along 3 geometric axes

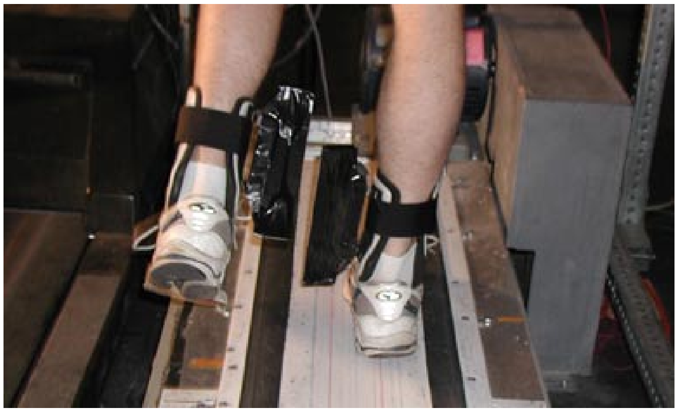

Figure 1: Device for enforcing minimum swing width

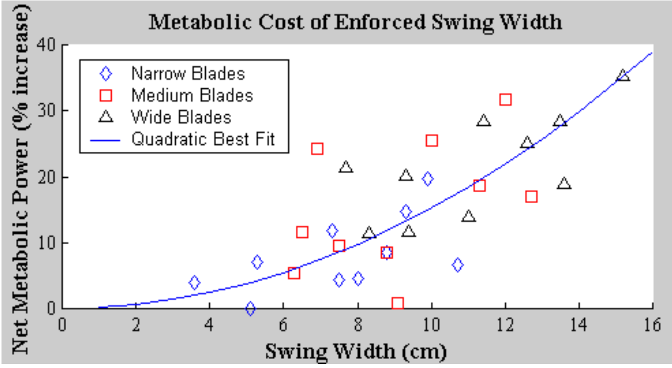

Figure 2: Metabolic costs associated with lateral leg swing

as subjects walked on a force treadmill (Kram, et al., 1998). We then calculated actual step widths from these values.

RESULTS AND DISCUSSION

Despite prior familiarization training, subjects sometimes had difficulty following the target step width lines, typically using a somewhat wider step width than specified. We calculated the actual step widths used and then computed the associated *swing width*. This swing width is the amount of lateral diversion the swing foot experiences in swinging around the stance foot. We had selected the medium blade width so as to require the same swing width as is experienced when walking without blades at zero step width. Figure 2 shows the added metabolic cost associated with increasing swing width. Under the assumption that power is proportional to amplitude squared, we have plotted a quadratic best fit line proportional to swing width squared (factor 0.15%/cm^2). For our subjects, zero step width walking is associated with a mean swing width of 10.7 cm, corresponding to an added metabolic cost of 17%.

SUMMARY

Consistent with our hypothesis, we found that metabolic cost increased substantially with increases in lateral limb swing such as are required during walking at narrow step widths.

REFERENCES

Donelan JM, Kram R & Kuo AD (2001) *Proc. Roy. Soc. Lond. B* **268**: 1985-1992

Kram R, Griffin TM, Donelan JM & Chang YH (1998) *J. Appl. Physiol.* **85**: 764-769

ACKNOWLEDGEMENTS

This research was supported in part by an NSERC fellowship to J. M. Donelan, NIH grant AR4468801 to R. Kram, and NIH grant DC0231201A1 to A.D. Kuo

ACTIVE MOVEMENTS OF THE SHOULDER GIRDLE IN HEALTHY SUBJECTS: A VALIDITY STUDY

Sylvie Nadeau[1-2], Stéphanie Kovacs[1-2], Denis Gravel[1-2], Hélène Moffet[3], France Piotte[1-2], Denis Gagnon[4], Luc J. Hébert[5]
[1]École de Réadaptation, Université de Montréal, Montréal, Québec, Canada, [2]CRIR, Site IRM,
[3]Université Laval, [4]Université de Sherbrooke, [5]Défense Nationale du Canada.
E-mail at: Sylvie.Nadeau@Umontreal.CA

INTRODUCTION

Global shoulder girdle (SG) movements are defined as elevation, depression, protraction and retraction (Lehmkuhl & Smith, 1983). These movements involve four bones and three joints: the scapula, clavicle, sternum, the first rib, and the acromio-clavicular, sterno-clavicular and scapulo-thoracic joints (Kapandji, 1997). The SG is an important part of the shoulder complex and arm movements depend on adequate ROM and muscle function in this area. Since several disorders involve the SG area, there is a need to develop objective and rigorous methods to assess the global SG active movements. The purpose of this study was to determine the concurrent validity of active range of motion (AROM) of the SG elevation, protraction and retraction as measured with a goniometer and a tape measure. These simple clinical measurements were compared to those computed from infrared markers placed over specific bony landmarks on healthy subjects.

METHODS

A sample of convenience of thirty healthy subjects, 15 females and 15 males, with a mean age of 45.3 (±11.5) years, participated in the study. Each subject was assessed by two physiotherapists having 5 and 15 years of clinical experience. AROM of the SG was measured in a sitting position, arms hanging aside the body, using the two clinical methods: goniometry and tape measure. The same movements were then evaluated with a three-dimensional (3D) movement analysis system (Optotrak 3020). Markers were placed on the subjects' head, shoulders, manubrium, scapula, cervical and thoracic spines. The location of some markers was readjusted at the end of the movements to reduce any potential error associated with overlying skin movement during scapular motion (van der Helm & Pronk, 1995). For each SG movement, the Pearson correlation coefficient (r) was calculated to evaluate the concurrent validity between goniometer and the 3D angular data as well as that between tape measure and 3D linear data obtained using the Optotrak analysis system.

RESULTS AND DISCUSSION

AROM was much greater in elevation than in the other movements (Table 1). For each movement, the differences between sides were less than 3° or 0.3 cm. Elevation was the most valid movement, with the tape measure ($r = 0.74$-0.84, $p<0.01$) and the goniometer ($r = 0.74$-0.80, $p<0.01$). With this latter method, measurements performed on the dominant side of the subjects by the examiner with less experience had poorer concurrent validity ($r=0.63$, $p<0.01$). Concurrent validity was lower but still acceptable for retraction measured with the goniometer, especially on the dominant side ($r = 0.55$-0.60, $p<0.01$). It was poor for retraction on both sides with the tape measure, ($r = 0.34$-0.43, $p<0.05$) and for protraction, with both measurement methods ($r = 0.10$-0.43, $p<0.05$). The goniometer used in clinical setting allowed the measurement of movement in one plane of motion. With SG protraction and retraction, a certain amount of elevation was observed for many subjects. This combined motion, which has also been reported by Conway (1961), made it difficult to maintain the goniometer in the plane of motion especially during protraction measurements. Consequently, examiners reported problems keeping the body of the goniometer aligned with the sternal notch and the arms, parallel to the sternum and the clavicle. During retraction and protraction, parallax errors may also have occurred due to the location of the body of the goniometer in the transverse plane, under the subject's chin. In protraction, occasional forward motion of the subject's head probably added to these reading problems. Moreover, examiners also mentioned difficulties in localizing the medial angle of the scapula at the end of these movements with the tape measure. It is believed that these factors might have decreased the concurrent validity of the protraction and retraction movements.

SUMMARY

The results of this study demonstrated the validity of the goniometer and tape measures for SG elevation. Concurrent validity was acceptable for retraction with the goniometer, especially on the dominant side. It was poor to fair when assessed with the tape measure. Future research is needed to improve the clinical assessment of AROM in protraction and retraction.

REFERENCES

Conway AM. (1961) *Phys Ther Rev* , 41: 421-432.
Kapandji, IA. *Physiologie articulaire,* Malouine, Paris, 1997.
Lehmkuhl LD, Smith LK*, Brunnstrom's clinical kinesiol*, 1983.
van der Helm FC, Pronk GM. (1995*) J Biomech Eng* , 27-40.

ACKNOWLEDGEMENTS

The project and S. Kovacs received financial support from REPAR, a network of FRSQ. Dr Nadeau is supported by the CIHR. The authors would like to thank P. Desjardins for his technical support.

Table 1: Mean (SD) AROM of the shoulder girdle movements

METHODS	Dominant side			Non-dominant side		
	Elevation	Protraction	Retraction	Elevation	Protraction	Retraction
Goniometry (°)	28.6 (5.1)	17.9 (3.9)	15.8 (5.1)	27.8 (5.2)	18.0 (4.4)	17.5 (5.9)
Tape measure (cm)	9.5 (2.1)	3.7 (0.9)	4.8 (1.2)	9.4 (2.1)	3.9 (0.9)	4.7 (1.2)
Optotrak (angular)	25.8 (6.5)	16.6 (7.6)	17.1 (6.8)	25.2 (6.9)	14.0 (6.4)	17.0 (5.4)
Optotrak (linear)	7.9 (2.2)	3.6 (0.8)	4.6 (1.6)	7.7 (2.1)	3.6 (1.0)	4.5 (1.7)

MEASURING CENTER OF MASS DISPLACEMENT DURING GAIT: WHOLE-BODY KINEMATIC MODEL VS. GROUND REACTION FORCE CALCULATION

Elena M. Gutierrez[1,2], Åsa Bartonek[2], Yvonne Haglund-Åkerlind[1,2], Helena Saraste[1,3]
[1]Dept. of Surgical Sciences, Karolinska Institute, [2]MotorikLab, Karolinska Hospital,
[3]Spine Division, Huddinge University Hospital, Stockholm, Sweden
Lanie.Gutierrez@kirurgi.ki.se

INTRODUCTION

Center of Mass (CM) displacement measurement in gait analysis has mainly been limited to either an assumption of a fixed position with the pelvis or as displacements derived from ground reaction forces (GRF) according to

$$\iint \frac{\vec{F}_{CM} - m\vec{g}}{m} dt^2 = \iint \vec{a}_{CM}\, dt^2$$

and applying integration constants based on assumptions of similar initial and final positions and constant velocity. A typical gait lab has 2 force platforms to measure GRF, making it difficult to collect GRF under both feet from one stride cycle. Numerical adjustments to estimate two phases of double-support time can be made (Whittle, 1997). Measuring CM displacement using GRF from 2 force platforms has disadvantages: 1) Subjects must walk over the platforms in the required fashion, 2) Displacement, not position, of the CM is measured, 3) No information of joint movement is gained, 4) Results are sensitive to small deviations in mass estimates and integration constants.

In modern 3-D gait analysis, a readily-available whole-body model is feasible and routinely available. CM displacement derived from a kinematic model would enable analysis of specific movements on the CM displacement as well as estimate the position of the CM anatomically.

METHODS

Model: 3-D gait analysis using 34 retro-reflective markers was performed (Vicon® 512) at 50 Hz. A 15-segment model (head, trunk, 3-segment arms, pelvis, and 3-segment legs) is used in which the CM is defined as the centroid of the system. The model is a standard install with a common motion analysis system (Plug In Gait, Vicon Motion Systems®, Oxford, England) but has not yet been validated as a whole-body model. The lower body model is well documented (Kadaba et al, 1990).

Subjects and procedure: 14 children (ages 5-12, mean 10.7 years) with no physical disability and 28 children with myelomeningocele (MMC, ages 6-17, mean 10.4 years, with varying muscle paresis) were tested in 3-D gait analysis at a self-selected speed. CM trajectory was determined as the centroid of the 15-segment model and was distinguished into vertical and lateral displacements.

GRF in 3 directions was measured simultaneously at 1000 Hz using 2 force platforms (Kistler®). Mass was measured first from a digital scale, then for comparison as the average vertical GRF in the stride cycle. When the required platform support was observed, a double second-order numerical integration was performed twice (using Matlab® software) using appropriate integration constants.

Peak displacements from the two methods were compared in both lateral and vertical directions for a subgroup of 14 MMC and 8 normal stride cycles. In 7 trials, a correlation coefficient between the methods was calculated. A sensitivity analysis of mass estimation will be performed on both methods as well as a thorough correlation comparison.

RESULTS AND DISCUSSION

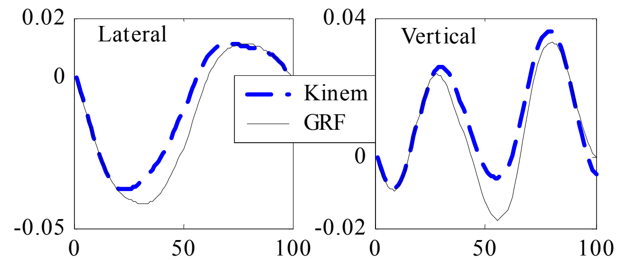

Figure 1: CM displacements from the 2 methods in one MMC subject in one stride.

Comparison of the two methods of calculating the CoM displacement showed that the GRF integration yielded higher peak displacements: 4.0% lateral and 21.4% vertical than the centroid method. The general agreement between the methods was much better in the lateral direction than in the vertical: the correlation in a sub-group of 7 trials showed r^2=.98 lateral and r^2=.77 vertical. Small changes in mass estimation resulted in large changes in both the vertical CM trajectory and in the peak displacement: up to 10% better agreement was observed when mass was calculated from the GRF during walking, though the masses varied by less than 1%. Due to the GRF method's sensitivity to mass estimation and integration constants, we are wary of its accuracy. While the kinematic model is sensitive to errors in segment parameters and is not applicable in all situations, it shows value in providing at least relative estimations of CM position and displacement and has the major advantage of simultaneous joint motion collection.

REFERENCES

Kadaba M.P. et al (1990). *J. Orthopaedic Research*, **8**,383-92.
Whittle M.W. (1997). *Human Movement Science*, **16**,347-355.

MUSCLE FORCE NOT WORK DEFINES MUSCLE CONTRIBUTIONS TO FORWARD PROGRESSION

R. R. Neptune[1, 2], S.A. Kautz[1, 3] and F.E. Zajac[1, 3, 4]
[1] Rehabilitation R & D Center, VA Palo Alto HCS, Palo Alto, CA
[2] Department of Mechanical Engineering, University of Texas, Austin, TX
[3] Departments of Functional Restoration and [4] Mechanical Engineering, Stanford University, Stanford, CA
Email: rneptune@mail.utexas.edu

INTRODUCTION

The uniarticular, and not the biarticular, ankle plantar flexors were previously shown to contribute significantly to trunk forward progression from mid stance into pre-swing (late stance) (Neptune et al., 2001). However, other muscles (specific muscles not identified in that study) also contributed to forward progression both in early stance into single-leg support (beginning of stance) and in late stance. We hypothesized that these other muscles contribute to trunk forward progression by redistributing segmental energy by decelerating the leg and accelerating the trunk through active concentric, isometric and eccentric force generation. That is, it is force generation per se that is critical to segmental energy redistribution, irrespective of whether that muscle performs positive work, no work at all, or even negative work.

METHODS

To assess this hypothesis, a forward dynamical simulation that emulated observed walking kinematics and kinetics of young adult subjects was analyzed to quantify the muscle induced-energetics of the trunk and leg segments. Those muscles contributing to trunk progression (i.e., forward acceleration of the trunk) were identified. The musculoskeletal model and simulation were developed using SIMM/Dynamics Pipeline (MusculoGraphics, Inc.) and consisted of the trunk, right and left legs. Each leg consisted of the thigh, shank, foot and fifteen individual Hill-type musculotendon actuators. The trunk was allowed to translate and rotate in the sagittal plane, while the hip, knee and ankle joints were frictionless revolutes. The model's dynamical equations-of-motion were derived using SD/FAST (PTC, Inc.). The contact between the foot and the ground was modeled with discrete visco-elastic elements located on the bottom of the foot. The individual muscle excitation patterns were modeled as block patterns and an optimization framework systematically varied the muscle controls to replicate the experimental data.

RESULTS AND DISCUSSION

The uniarticular knee extensors (vasti, VAS) contributed to trunk progression in the beginning of stance by redistributing segmental energy between the legs and trunk (Fig. 1A). VAS decelerated the leg segments (Fig. 1A, dashed line is negative), causing them to lose energy, and accelerated the trunk forward (as well as upward) through its contribution to the hip intersegmental force (Fig. 1B), causing the trunk to gain energy (Fig. 1A, dotted line is positive). VAS provided this mechanism for the redistribution of energy from the leg to the trunk even though its activity was eccentric, isometric and then concentric (Fig. 1A, solid line is initially negative, momentarily zero, then positive). The concentric uniarticular hip extensors acted co-functional with VAS in early stance by also decelerating the leg and accelerating the trunk. The eccentric rectus femoris (RF) in late stance also redistributed segmental energy to accelerate the trunk forward by acting to accelerate the knee and hip into extension, made possible through dynamic coupling of the body segments. Other muscular contributions to trunk progression, besides from the previously identified plantar flexors, were negligible (e.g., RF in beginning of stance, biarticular hamstrings, hip flexors).

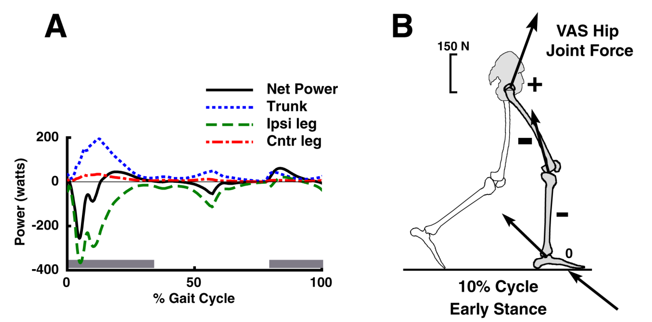

Figure 1: A) Musculotendon mechanical power output by VAS (*Net Power*) and the distribution of this power to the ipsilateral (*Ipsi leg*) and contralateral (*Cntr leg*) leg segments and trunk (*Trunk*) over the gait cycle. Solid horizontal bars indicate muscle excitation timing. B) Contribution by VAS in Early Stance (10% gait cycle) to the intersegmental joint forces and the trunk and leg segmental energetics. The summed hip intersegmental force from both hips accelerates the trunk segment's center-of-mass upwards and forward, causing the trunk to gain energy ("+"). The intersegmental joint forces by VAS decelerate forward motion of the thigh and shank causing them to lose energy ("-").

SUMMARY

The redistribution of segmental energy by the uniarticular hip and knee extensors in the beginning of stance and by RF in late stance contribute significantly to trunk forward progression to complement the late-stance contributions of the ankle plantar flexors. We conclude that muscle force generation is the determining factor in how individual muscles contribute to forward progression, rather than muscle work, since concentric, isometric and eccentric muscle action can all act to accelerate the trunk forward.

REFERENCES

Neptune, R.R. et al. (2001). *J Biomech* **33**:155-64.

ACKNOWLEDGEMENTS

This work was supported by NIH grant NS17662 and the Rehabilitation R&D Service of the Department of Veterans Affairs (VA).

MECHANOMYOGRAPHIC SIGNALS OF THE FIRST DORSAL INTEROSSEUS MUSCLE DURING ISOMETRIC VOLUNTARY CONTRACTIONS

Cíntia de la Rocha Freitas[1]; Marco Aurélio Vaz[1]; Milton Antônio Zaro[2]; Luciano R. Maciel da Silva[2] and Antônio C. S. Guimarães[1]
[1] Exercise Research Laboratory, School of Physical Education, Federal University of Rio Grande do Sul, Brazil
[2] Mechanical Measurements Laboratory, Faculty of Mechanical Engineering, Federal University of Rio Grande do Sul, Brazil
marcovaz@esef.ufrgs.br

INTRODUCTION

Muscle vibrations have been associated with force oscillations due to the unfused contraction of motor units (MUs – Vaz et al., 1996). If so, then recruitment of larger MUs should increase the magnitude of these vibrations, whereas increasing firing rates should increase tetanic fusion and decrease the magnitude of muscle vibrations. It is well known that muscles of the hand (small muscles) recruit Mus up to 50% of the maximal voluntary contraction (MVC), and increase force by increasing the firing rates of MUs from 50 to 100% MVC (Milner-Brown et al., 1973; Kukulka and Clamann, 1981; Basmajian and De Luca, 1985). Therefore, an increase in the magnitude of the mechanomyographic (MMG) signal should be observed with recruitment, while a decrease should be observed with increasing MU firing rates. The purpose of this study was to test the hypothesis that the amplitude and frequency content of the MMG signal are related to the muscle´s recruitment strategies.

METHODS

MMG signals were obtained from the first dorsal interosseus of 12 male and 3 female subjects (age 19 to 50 years) during different levels of voluntary isometric contraction (10% to 70% MVC, with a 5 minute interval between trials) using a miniature accelerometer (Entran, EGA-10D) attached to the skin with double-sided adhesive tape. Abduction of the index finger was performed against a load cell (Alfa Instruments, 5Kgf) attached to an aluminium plate designed for the experiment and mounted on a concrete table. The different levels of voluntary effort were displayed on an oscilloscope to provide the subjects with visual feedback. MMG signals were extracted for segments of 4 seconds from the middle of the trials to ensure that transient signals at the beginning and end of the contraction were excluded. Root mean square (RMS) values were obtained from the raw MMG signals. Signals were band-pass filtered with cut-off frequencies of 4 and of 262 Hz. Median frequency (MDF) was calculated from the power frequency spectrum which was obtained through an FFT algorithm.

RESULTS AND DISCUSSION

RMS values increased with increasing voluntary effort up to 50% MVC and remained about constant from 50% MVC to 70% MVC (Figure 1). Our results do not agree with the results of Stokes and Cooper (1992), who showed an increase in RMS with increasing voluntary effort for the adductor pollicis muscle, but are similar to the results of Madeleine et al. (2001) for the first dorsal interosseus muscle. It appears that the reported increase in MU recruitment for this muscle is responsible for the observed increase in MMG amplitude, whereas the leveling off from 50 to 70% MVC might be related with increases in MU firing rates. MDF of the MMG signal tended to decrease with increasing voluntary effort (Figure 2). The frequency content of the MMG signal has been related to both MU firing rates and the contractile properties of the active MUs (Orizio, 1993). Increases in the firing rates of MUs, therefore, should produce an increase in the MDF of the MMG signal with increasing voluntary effort. Our results do not agree with this relation between the MDF and MU firing rates. It appears that the frequency contents of the MMG signal are related with changes in the mechanical behavior of MUs, but not with MU firing rates.

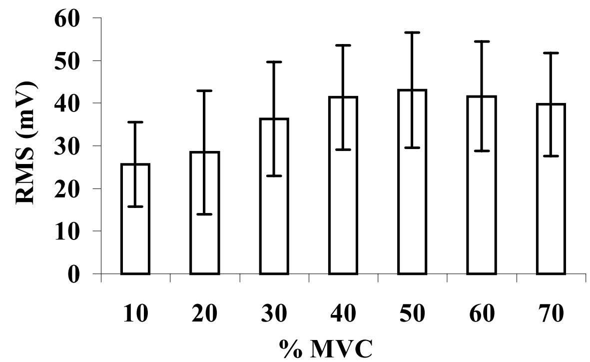

Figure 1. RMS values (mean + SD) of the MMG signal as a function of voluntary effort.

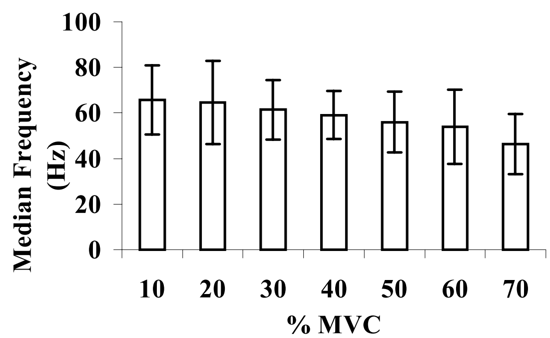

Figure 2. MDF values (mean + SD) of the MMG signal as a function of voluntary effort.

REFERENCES

Basmajian, J.V.; De Luca, C.J. (1985). *Muscles Alive.* Baltimore, Williams & Wilkins.
Kukulka, C.G.; Clamann, P.H. (1981). *Brain Res.* **219**:45-55.
Lammert, O. et al. (1976). *Biomechanics V-A.* Baltimore, University Park Press.
Madeleine, P. et al. (2001). *J. Electrom. Kinesiol.*, **11**:113-121.
Milner-Brown, H.S. et al. (1973). *J. Physiol.* **228**:285-306.
Orizio, C. (1993). *Crit. Rev. Biomed. Eng.*, **21**:201-243.
Vaz et al. (1996). *Muscle & Nerve*, **19**:774 –776.

VISUO-LOCOMOTOR CONTROL DURING ANTICIPATORY LOCOMOTOR ADJUSTMENTS

Lori Ann Vallis[1, 2], Bradford J. McFadyen[1, 2] and Martin Gérin-Lajoie[1, 2]
[1]Center for Interdisciplinary Research in Rehabilitation and Social Integration (CIRRIS), Québec, Canada
[2]Faculty of Medicine, Laval University, Québec, Canada G1K 7P4

INTRODUCTION

Successful navigation of cluttered environments is critical for maintaining independence and an acceptable standard of living. The appearance of gait as an 'automatic' motor skill misrepresents the levels of control that are required, specifically transmitting and interpreting available sensory information as well as planning and executing successful locomotion. The purpose of this study was to investigate body segment coordination strategies used for walking around a vertical obstacle placed in the travel path.

METHODS

Five healthy subjects (3 female and 2 male; age 26.6 ± 3.2 years, height 174.11 ± 11.12 cm, weight 77.84 ± 8.00 kg) volunteered for the study. Experimental protocol was approved by the ethics committee of the Québec Rehabilitation Institute and informed consent was given by all participants. Exclusion criteria included any self-reported neurological, musculoskeletal or visual impairment. Data shown is part of a larger study and only kinematic data will be discussed in this abstract.

Fourteen infrared markers, three on the feet, pelvis, trunk, and head, and one on each wrist, were tracked using the Optotrak motion analysis system (60 Hz; Northern Digital Inc, Canada). Certain anatomical points were also probed in relation to these markers to allow the calculation of principle axes and the creation of virtual marker movement (e.g., heels). Eye movement (not reported here) was captured with the ISCAN system (120 Hz) mounted on a baseball cap.

Participants walked at their natural self-selected pace along a 9-m path. Five unobstructed (control) trials were collected first. Then subjects were required to avoid a cylindrical obstacle (height 2-m, circumference 73.85-cm). No instructions were initially given as to left or right deviations. However, once five trials of walking in one direction were collected, participants were asked to walk in the other direction to ensure an equal number of trials in each direction.

In this preliminary study, data analyzed were step length, step width, yaw (transverse plan) angles of the head and trunk, roll (frontal plane) angle of the trunk, and medio-lateral centre of mass displacement. =The onset of changes in the variables was measured as the point in time when data started to deviate from the average control profile, providing the deviation continued beyond one standard deviation of the average control data. Onset times were calculated as the time before the COM crossed the obstacle in the direction of progression.

RESULTS AND DISCUSSION

Preliminary analyses indicate that there was no use of trunk roll and no significant differences between onset of M-L center of mass deviation (1.84 s), head yaw (1.91 s) and trunk yaw (1.89 s) prior to crossing the obstacle in the direction of progression. However, sequencing of body segment reorientation was variable and the head segment did not systematically anticipate change in direction of locomotion before the rest of the body as reported in steering literature (Hollands *et al.*, 2001; Patla *et al.,* 1999). This may be due, in part, to the fact that reorientation of the head to establish a new frame of reference is not required as the goal of the current task is to continue walking in the forward direction after crossing the obstacle.

Translation of the COM in a new direction of travel can be achieved both through alternate placement of the contralateral foot prior to the turn step and use of a hip strategy, illustrated by trunk roll (Hollands *et al.,* 2001; Patla *et al.*, 1999). Kinematic data from the current study indicate no modifications in trunk roll, the COM trajectory is altered through contralateral foot placement (100% of trials).

SUMMARY

Anticipatory adjustments of body segment orientation are initiated by the central nervous system to ensure safe obstacle avoidance. These locomotor adjustments require a different control strategy for deviation of the COM trajectory than observed in steering tasks. Analyses of eye movement amplitude and timing are currently underway.

REFERENCES

Hollands et al. (2001). *Exp Brain Res*, **140**: 223-233.
Patla et al. (1999) *Exp Brain Res*, **129**: 629-634.

ACKNOWLEDGEMENTS

Financial support from CIRRIS (LAV) and NSERC (BJM). We acknowledge technical assistance of Mr. Guy St-Vincent, Mr. Francois Comeau & Mr. Claude Simard.

VARIABLES ASSOCIATED WITH THE INCIDENCE OF LOWER EXTREMITY STRESS FRACTURES

I. McClay Davis [1,2], R. Ferber[1], T.A. Dierks[1], R.J. Butler[1], J. Hamill [3]

[1]Department of Physical Therapy, University of Delaware, Newark, DE, USA 19716 email: McClay@udel.edu
[2]Joyner Sportsmedicine Institute, Harrisburg, PA
[3] Department of Exercise Science, University of Massachusetts, Amherst, MA

INTRODUCTION

Overuse injuries are common among competitive runners with stress fractures (SF) being one of the most serious overuse injuries. SF are among the top 5 cited running-related injuries and females are twice as likely to experience a SF as their male counterparts. The etiology of SF is multifactorial in nature but is related, in part, to some combination of bone structure, peak forces, loading rates, as well as lower extremity running mechanics. Therefore, the purpose of this investigation was to examine differences in ground reaction force (GRF), tibial acceleration, bone structure, and kinematic variables between competitive female distance runners who had sustained a previous lower extremity SF and uninjured control subjects. It was hypothesized that peak tibial acceleration, vertical GRF loading rates, and lower extremity stiffness would be greater in the injured runners and area moment of inertia of the tibia and knee flexion excursion would be lower. In addition, those variables which were different would contribute significantly to the prediction of which runners had sustained a SF.

METHODS

Subjects consisted of 8 females with a history of at least one lower extremity SF and 8 females with no SF history who served as a control group (CON). All subjects were between ages 18-35 and ran between 30-80 miles per week. These subjects are part of a larger ongoing study investigating factors associated with SF in women runners. GRF and tibial acceleration data were recorded from 5 running trials. Three radiographs of the distal lower extremity were used to calculate the tibial area moment of inertia (Milgrom et al., 1989). Variables of interest included peak positive tibial acceleration (PPA), peak vertical GRF (VGRF), instantaneous loading rate (ILR), stiffness (STF), knee flexion excursion (KFlex) and tibial area moment of inertia in the anterior/posterior plane (I_{AP}). Independent t-tests were used to assess differences between groups. A backward, stepwise statistical regression analysis was used to determine the factors that best predicted which subjects had previously suffered a SF.

RESULTS AND DISCUSSION

Of the 8 total SF, 5 were tibial, 2 were fibular and 1 was metatarsal. Results indicated that both PPA and ILR were significantly ($p<0.05$) greater in the SF group (Table 1). Although not significant ($p>0.05$), a trend towards greater stiffness and reduced knee flexion excursion in the SF group was also observed (Table 1). Williams et al. (2001) also reported a significantly higher load rate and great stiffness in a group of runners with high arch feet and a greater incidence of stress injuries. However, Crossley et al. (1999) reported no significant differences in GRF variables between SF and control subjects.

Other investigations have reported that bone geometry was significantly different between SF and control groups (Crossley, 1999; Milgrom, 1989). However, in the present investigation, the SF group exhibited similar tibial I_{AP} values as compared with the control group (Table 1). A small subject population may account for discrepancies between previous studies and the results of this investigation.

The results indicate that PPA and ILR explained 46% of the variance ($p=0.01$) in predicting subjects who had previously suffered a SF. ($y = 3.50 + -0.12PPA + -0.01ILR$). None of the remaining variables entered into the regression equation. However, it is possible that these results may change as more subjects are analyzed during this ongoing study.

SUMMARY

These data suggest that 1) subjects who had previously suffered a lower extremity SF demonstrated greater GRF loading rates, shock, and stiffness and reduced knee flexion excursion as compared with noninjured controls and 2) kinetic measures can be used to predict which subjects had previously sustained a SF.

ACKNOWLEDGEMENTS

This study was funded by the Department of the Army (#17-00-1-0515).

REFERENCES

Crossley, K. et al. (1999). MSSE, **31**(8), 1088-1093
Hennig, E.M. et al (1993). J App Biomech, **9**, 306-314
Matheson, G.O. et al. (1987). AJSM, **15**(1), 46-58
Milgrom, C. et al. (1989). J Biomech, **22**(11/12), 1243-1248
Williams D.S. et al. (2001) Clin Biomech, **16**(4), 341-347

Table 1: Mean (SD) and p-values of selected variables for SF and CON groups.

	PPA (g)	ILR (BW/s)	STF(kN/m)	KFlex (°)	I_{AP}
SF	8.23 (1.08)	119.20 (27.97)	9.32 (1.53)	29.76 (5.70)	11016 (3175)
CON	6.50 (1.56)	90.44 (15.28)	8.30 (0.54)	33.40 (3.91)	11457 (4098)
p value	0.02	0.04	0.09	0.14	0.81

BONE RESORPTION IN SHOULDER SURFACE REPLACEMENT ARTHROPLASTY

Ulrich Hansen and Andrew Hopkins

Biomechanics Section, Department of Mechanical Engineering, Imperial College, London, UK.
u.Hansen@ic.ac.uk

INTRODUCTION

Surface replacement prostheses have several important advantages over stemmed implants. During the surface replacement procedure only the cartilage and a thin layer of underlying bone is removed. Therefore, should the implant ever become lose there will be plenty of bone stock for a more traditional stemmed arthroplasty. Over the last decade the importance of incorporating the natural anatomy in the design of shoulder prostheses has become apparent. As the geometry of the humeral bone is largely maintained the surface replacement is easily placed in the correct anatomical position.

Despite these advantages the surface replacement prosthesis is not the choice of most surgeons. This probably stems from associations to the generally recognised failure of surface replacements in hip arthroplasty. These failures have been attributed to; avascular necrosis, bone resorption under the spherical cap due to stress shielding or accelerated wear. The present work tries evaluate if bone resorption is an issue in surface replacement arthroplasty of the shoulder.

METHODS

A 3D finite element mesh of the bone and implant was created (Figure 1). Material properties were assigned to the model using interpolation between greyscale value, apparent density and Young's modulus (Rice et al. 1988, Schaffler & Burr 1988). Distributed pressure representing the joint load as well as muscle forces representing the deltoid and the rotator cuff muscles were applied while the distal end of the humerus was rigidly fixed. Bone remodelling is predicted on the basis of the difference between local strain energy density pre and post implantation (Huiskes et al., 1987).

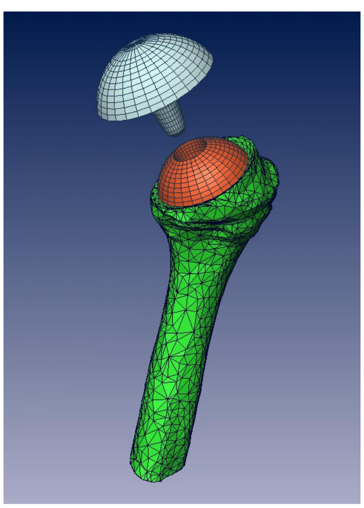

Figure 1: Finite element mesh of implant and humeral bone. Orange section is humeral bone reshaped to fit the implant which simulates the surface cutter action during surgery.

RESULTS

Figure 2 shows the predicted strain energy density in a cross section through the humeral head of two simulations. The figure compares the strain energy density from a simulation of the natural shoulder with the results of a simulation including and implant. In the figure relating to the natural shoulder the area corresponding to the implant have been removed to facilitate comparison between the two simulations. Figure 2 shows reduced strain energy density levels under the cup and increased levels under the peg indicating a potential for bone resorption and bone failure under the cup and peg, respectively.

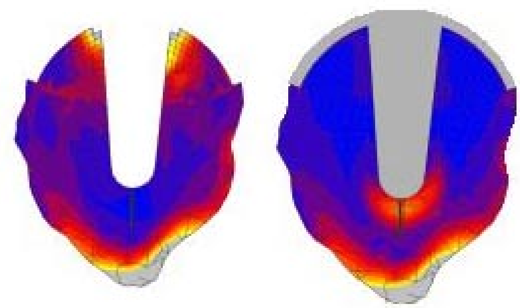

Figure 2: Strain energy density predictions. Natural shoulder (left) and shoulder with implant (right).

SUMMARY AND DISCUSSION

The strain energy densities are reduced below the lazy zone of the bone remodelling signal, hence, bone resorption would be expected. However, the design and loading of this cementless implant will encourage relatively large interface micromotions at the distal end of the cup. If this interface micromotion is large enough to cause the deposition of a soft interlayer at the distal interface this is likely to cause higher energy density levels under the cup and hence less or no resorption under the cup. Therefore, the simulations are being extended to include interface micromotion and interface failure.

REFERENCES

Huiskes, R. et al (1987). J of Biomech., **20**, 1135-1150.
Rice et al. (1988) J. Biomech., 155-168.
Schaffler and Burr (1988) J. Biomech., 13-16.

CAN INERTIAL FORCES ALONE CAUSE LIMB FOLDING DURING PROTRACTION?

Danielle F. Preedy[1] and Jeremy F. Burn
Comparative Morphology Center, University of Bristol, Southwell Street, Bristol. BS2 8EJ. UNITED KINGDOM.
dani.preedy@bristol.ac.uk[1]

INTRODUCTION

Repositioning of the limb during the swing phase is an inherent requirement in a limb-based system for locomotion. Animals that have evolved to be cursorial, such as the ungulates, have musculo-skeletal adaptations that have reduced the mass of the distal limb segments. This study uses a link-segment model of the forelimb to investigate the hypothesis that folding of the forelimb during the first part of swing is a consequence of inertial forces alone, without digital and carpal flexor muscle activity.

METHODS

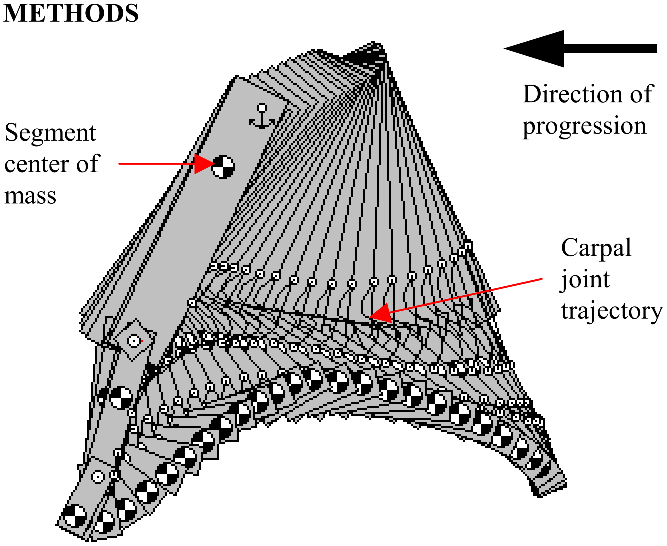

Figure 1: Model output sequence for protraction at 2 m/s

A three-segment link segment model, representing the radius, metacarpus and digit, was constructed from published morphometric data using a dynamic simulation package (Working Model 2D, Knowledge Revolution, USA). Constraints over the flexor side of the 'carpal' and 'metacarpophalangeal' joints prevented hyperextension. The center of mass of the proximal segment was given time dependent velocities from experimental data collected from horses. Limb protraction during locomotion at velocities of 1.8 to 12 m/s, was simulated using the model and compared to experimental data. The 'carpal' joint angle was used as a quantitative measure of limb folding and ANOVA were used to compare the output from the model with experimental data.

RESULTS AND DISCUSSION

Folding of the limb around the carpus due to inertial forces was dependent on subject velocity both in the simulation and in the experimental data ($p<0.001$). At high velocities the model consistently overestimated the amount of folding seen in vivo.

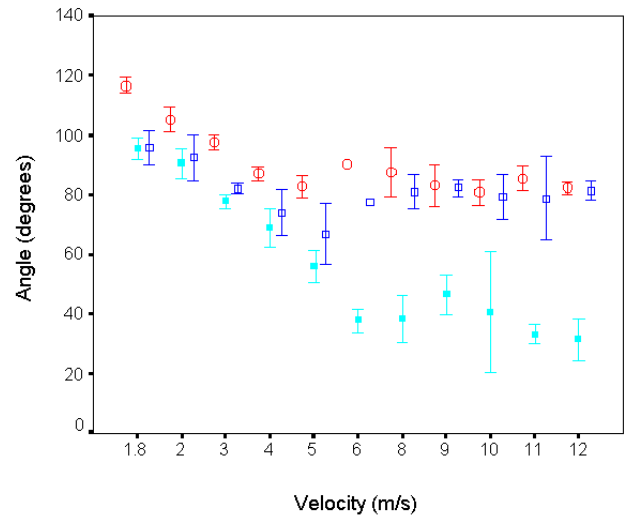

Figure 2: Scatter graph of carpal joint angle against subject velocity to compare the amount of folding of the limb in the experimental data and the simulation as velocity increased during an incremental exercise test. O minimum carpal angle achieved in the experimental data, ■ minimum 'carpal' angle achieved in the model □, 'carpal' angle in the model at the time when experimental joint angle was at its minimum.

At speeds above 4 m/s the limb did not completely unfold during the second half of the swing phase. The overfolding demonstrated by the model suggests that significant extensor muscular effort may be required during the second part of swing and during limb placement at the beginning of stance. These data suggest that carpal folding during protraction may occur entirely due to the inertia of the distal segments alone, which would act to reduce the mechanical cost of limb protraction. The model will be developed further to include the effect of carpal ligaments and connective tissue.

SUMMARY

The data presented suggest that work by the extensor muscles is important, particularly during reversal of the limb prior to impact. The results from this study support the hypothesis that the folding of the distal limb during swing is a passive event that is dependent on the motion of the proximal segments and inertial forces alone. Passive folding during protraction may be an energy saving mechanism that reduces the metabolic cost of repositioning the limb.

SURFACTANT ATTENUATION OF GAS EMBOLISM-INDUCED THROMBIN PRODUCTION

David M. Eckmann[1,3] and Scott L. Diamond[2,3]
Departments of Anesthesia[1] and Chemical Engineering[2] and
Institute for Medicine and Engineering[3], University of Pennsylvania, Philadelphia, Pennsylvania
deckmann@mail.med.upenn.edu

INTRODUCTION

There are many causes of cerebrovascular gas embolization including cardiopulmonary bypass and decompression illness. Neurologic injury can develop from thromboinflammatory responses including microthrombi formation provoked by intravascular gas bubbles. We hypothesized that addition of a surface active compound targeted to air-liquid interfaces would reduce the activation of thrombin formation precipitated by blood exposure to bubbles. We tested this hypothesis in an *in vitro* controlled-shear environment using fluorometric assays of thrombin production in gas embolized human blood.

METHODS

With Institutional Review Board approval, whole blood was drawn from four healthy volunteers (n = 4) on each of three occasions. Citrated blood was equal-volume diluted into calcium-free HEPES buffered saline. The Factor IIa (thrombin) specific fluorogenic substrate Boc-VPR was added in 50 μM concentration. Blood samples were assigned to four groups: sparging (controlled gas embolization) in the presence of surfactant; sparging in the absence of surfactant; surfactant added but no sparging; and no surfactant, no sparging. Samples were recalcified with $CaCl_2$. Surfactant (Dow Corning Antifoam 1510US), if called for, was added at 1.5 Volume %. Samples were allowed to sit for one minute or were sparged for one minute with air microbubbles. Samples were placed onto silanized coverslips and sheared at 100 (low) and 500 (high) sec^{-1} for 5, 10, and 20 minutes at 37 °C with a cone-plate viscometer and then placed into excess stop buffer (50 mM EDTA). Samples were evaluated by fluorimetry with excitation and emission wavelengths set to 352 and 470 nm, respectively (Figure 1). Baseline fluorimetry measurements of EDTA, surfactant and fluorogenic substrate were also acquired for offset of the experimental data. Mean values and standard deviations of the fluorescence intensity data were calculated for each treatment group and compared using analysis of variation. Differences between groups were considered significant for $p<0.05$ using the Bonferroni correction.

RESULTS AND DISCUSSION

Increasing the shear rate increased total thrombin production at each time point. Increasing the duration of shear exposure increased thrombin production at each level of imposed shear. Surfactant addition without sparging had no effect on thrombin production compared to baseline. Thrombin production further increased over time as a result of both level and duration of shearing following sample sparging. Thrombin production was elevated more than 3.6 fold after 20 minutes of high shear ($p<0.005$ compared to baseline) with sparging (Figure 2). Thrombin production was also increased with sparging in the presence of surfactant (2.45 fold, $p<0.005$ compared to baseline), but there was 44% less thrombin formed than if sparging proceeded without surfactant treatment ($p<0.01$).

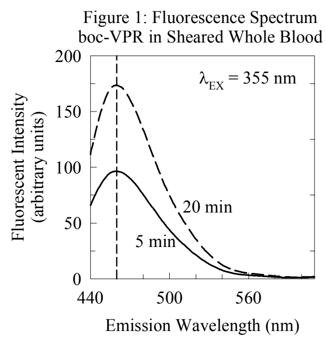

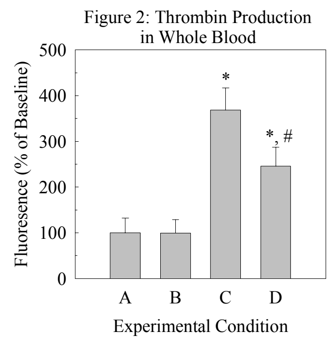

Figure 1: Fluorescence spectrum of thrombin-specific fluorogenic substrate. **Figure 2**: Relative fluorescence intensity after 20 minutes of shearing at 500 sec^{-1}. Sample preparation was A) no sparging, no surfactant, B) no sparging with surfactant, C) sparging without surfactant, and D) sparging with surfactant. * $p<0.005$ compared to A, # $p<0.005$ compared to C.

SUMMARY

These findings demonstrate that sparging (gas embolization) of whole blood increases thrombin production. The degree of increase of activation of clotting is both shear-rate- and time-dependent. The addition of the surfactant prior to sparging and shearing significantly reduces thrombin production. This experiment suggests surfactants may have a clinical application to attenuate blood activation caused by gas embolization.

ACKNOWLEDGEMENTS

Supported in part by NIH R01 HL60230 and the Department of Anesthesia, University of Pennsylvania. Ms. Rosy Jain and Mr. Feras Mardini helped conduct these experiments.

TIBIOFEMORAL KINEMATICS AND CONTACT PATTERNS ARE ALTERED DUE TO WEAKNESS OF THE SEMITENDINOSUS AND GRACILIS MUSCLES

Michael R. Torry[1], Takashi Yanagawa[1], Kevin Shelburne[1], J.R. Steadman[2], W.I. Sterett[2]
Steadman♦Hawkins Sports Medicine Foundation[1] and Clinic[2], Vail, Colorado, mike.torry@shsmf.org

INTRODUCTION

Hamstring function is vital to normal knee kinematics (Kwak et al., 2000). About 21% of all ACL reconstructions use the combined semitendinosus and gracilis tendons (STG) as the graft of choice for correction of ACL deficiency (Campbell, 1998). Long-term graft harvest site morbidity of this surgical technique is controversial. Some investigators contend that the tendons regenerate (Simonian et al., 1997), others report the regeneration is incomplete (Yasuda et al., 1995). Some have reported no significant strength changes due to the harvest (Simonian et al., 1997), while others have reported a 5-20% flexor torque decrease (Yasuda et al., 1995). The only consensus is that the early rehabilitation period is characterized by a general decrease in flexor-extensor strength. We sought to understand the functional consequences of the STG ACL reconstruction on the kinematics and articular contact patterns of the knee during isometric exercises. Since it is unclear *if* or *to what extent* the strength of the STG muscles are affected by graft harvest, we simulated various levels of strength deficit of the STG muscles using a mathematical model of the knee. We hypothesized that a weakened STG muscle complex would alter knee joint kinematics and articular contact points from the baseline (full-strength STG) condition.

METHODS

The musculoskeletal knee model has been described in detail (Pandy and Sasaki, 1998; Pandy et al., 1998). The model includes the patella, tibia, and femur; 13 non-linear springs representing the major tibiofemoral ligaments; 13 muscle-tendon units spanning the tibiofemoral joint; and a model of articular cartilage (Fig. 1). Maximum isometric contractions of the hamstrings were simulated at knee flexion angles from 0° - 90° in 15° increments. Muscle weakness relative to this baseline condition was simulated by decreasing the gracilis and semitendinosus muscle activation to 90%, 75%, and 50% of baseline. Changes in tibiofemoral contact point locations, tibial rotation angle, and anterior tibial translation as a function of STG activation level are reported.

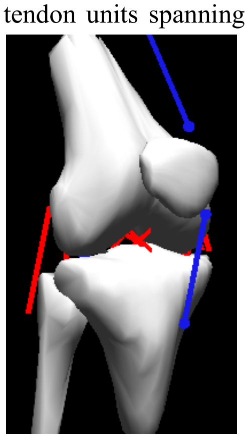

Figure 1. 3-D model.

RESULTS AND DISCUSSION

The tibia tended to rotate externally relative to the femur as the knee flexed (Fig. 2). The difference in rotation between the baseline and reduced strength conditions was more pronounced at greater flexion angles. The tibia also moved posteriorly as flexion increased. At each flexion angle, this posterior motion was reduced when the STG muscles were weaker. The combined result of the translation and rotation of the tibia caused the medial tibiofemoral contact point to move posteriorly, while the lateral contact point moved anteromedially with increasing flexion. When the STG muscles were weakened, the medial contact point was more posterior. The STG muscles assist in internal rotation of the tibia, so weakness in these muscles reduced the internal rotation moment on the tibia.

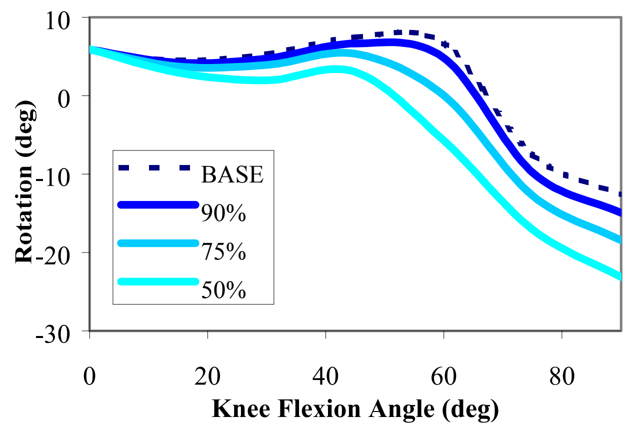

Figure 2. Internal rotation of the tibia relative to the femur in the baseline and reduced activation conditions.

SUMMARY

Reducing the STG muscle strength has little effect on tibial kinematics at small flexion angles because these muscles primarily pull the tibia proximal relative to femur at these angles. As flexion increased, the effects of reduced muscle strength were more pronounced. The aberrant kinematics seen at larger flexion angles may adversely affect STG graft patients who use more knee flexion range of motion in their daily lives.

REFERENCES

Kwak, S.D. et al. (2000) *J. Orthop Res.*, **18**, 101-108.
Campbell, J.D. (1998) *Am. J. Knee Surg,* **11**, 2:1-8.
Pandy, M.G., Sasaki, K. (1998) *Comput Methods Biomech Biomed Eng,* **1**, 265-283.
Pandy, M.G. et al. (1998) *Comput Methods Biomech Biomed Eng,* **1**, 87-108.
Simonian et al. (1997) *Am J Knee Surg*, **10**, 54-59.
Yasuda, K. et al. (1995) *Am J Sports Med*, **23**(6), 706-714.

COMPARISON OF QUANTITATIVE MEASURES OF TREMOR AS PREDICTORS OF SURGICAL OUTCOME

Duane Morrow[1], Joseph Matsumoto[2], Ann Rabatin[1] and Kenton Kaufman[1]
[1]Motion Analysis Laboratory, Division of Orthopedic Research and [2]Department of Neurology
Mayo Clinic, Rochester, MN 55905 USA

INTRODUCTION

The lasting effect of stereotactic neurosurgery in abating cerebellar tremor has not been definitively decided. It has been suggested that surgery is more effective in patients with minimal ataxia in the tremulous limb, but this is difficult to establish clinically (Alusi, 1999). While other studies have studied the frequency of tremor to classify pathologies (Spyers-Ashby, 1999), we contend that the severity or magnitude of the tremor is also necessary to predict potential surgical efficacy. The purpose of this study is to use pre- and post-surgical evaluations of three different methods used to objectively quantify tremor to assess their potential to predict surgical outcomes.

METHODS

Nine patients with clinically definite multiple sclerosis (MS) were studied. Each patient was evaluated pre- and at 3-months post-surgery using the Box and Blocks test (BB), the Clinical Tremor Rating Scale (CTRS), and Quantitative Movement Analysis (QMA). The BB test is a timed dexterity test in which the subject attempts to manipulate small blocks from one side to another of a divided box (range 0-25, worst to best). CTRS quantifies tremor amplitude as scored visually by a neurologist (range 0-26, best to worst). Developed in our laboratory, QMA quantifies tremor severity using electromagnetic sensors recording hand positions during simulated activities of daily living. QMA scores are derived from the power spectral density of hand velocity (range, 0-6, best to worst). Along with these quantified measures, a neurologist's general assessment of the surgical outcome as Excellent, Good, or Poor was recorded.

RESULTS AND DISCUSSION

Results are summarized in Figure 1 below. The pre-surgical baseline scores are plotted against their respective post-surgical improvement reflected by the change in scores.

Results of the BB test (Fig. 1A) demonstrate the severity of the tremor (few subjects could manipulate any block prior to surgery). Patients deemed to have Excellent outcomes generally showed the largest improvement in BB scores, but clearly no predictive ability exists in this test. A trend in improvement versus baseline impairment begins to be seen in the CTRS results (Fig. 1B). However, the Good and Excellent outcomes are mixed, and not clearly separated. Outcomes groups become more clearly delineated in the results of the QMA analysis. As Figure 1C) indicates, baseline values of greater than 4.25 lead to a greater reduction in tremor post surgery. It should be noted that the Poor outcome which had a baseline QMA > 4 was the result of an incomplete surgery which is included for completeness.

SUMMARY

While all three tests are useful in guiding clinical decision-making, only QMA seems to be able to predict surgical efficacy. While further studies need to be performed to confirm these findings, there appears to be a threshold in tremor severity, as measured by QMA, above which the attempt at surgical reduction of tremor is warranted.

REFERENCES

Alusi, S.H. et al, (1999). *J. Neurol Neurosurg Psychiatry*, **66**, 131-134.
Spyers-Ashby, J.M. et al, (1999). *Med Eng Phys* **21**, 713-723.
Matsumoto, J. et al (2001). *Neurology,* **57**, 1876-1882.

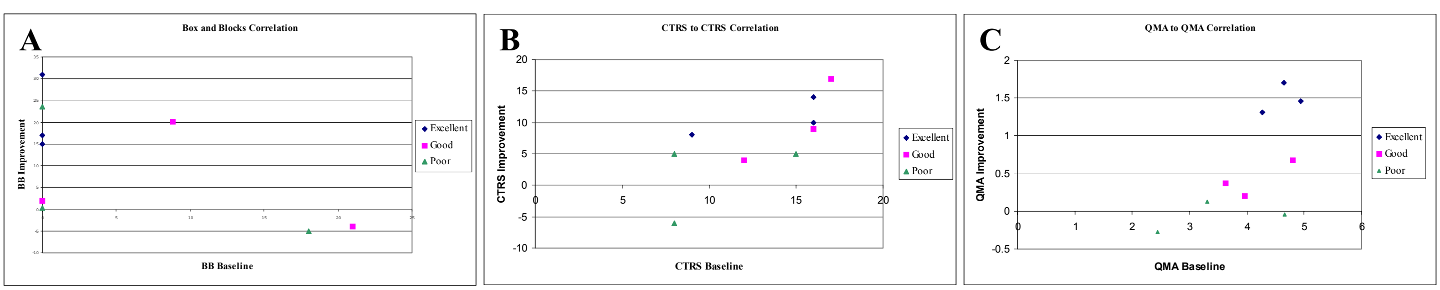

Figure 1. Pre- and post-operative correlation for the Box and Blocks (A), CTRS (B), and QMA (C) evaluations. Correlations are further separated into the global classifications of Excellent, Good, and Poor, as determined by a neurologist.

EXPERIMENTAL QUANTIFICATION OF MUSCLE CONTRIBUTIONS TO WHOLE LIMB STIFFNESS AND STABILITY

Eric J. Perreault and Thomas G. Sandercock
Department of Physiology, Northwestern University Medical School, Chicago, IL, USA
e-perreault@northwestern.edu

INTRODUCTION

In many motor tasks, muscles act to control the limb endpoint. Successful task completion requires strength to counter external forces and stability to maintain limb posture. These simultaneous requirements can be at odds with each other. McIntyre et al. (1996) demonstrated that reaction forces directed towards the joints (e.g. ground reaction forces pointing towards the hip) interact with limb geometry to reduce limb stability. Net stability is due to these external force effects combined with the stability provided by muscles resisting these forces. The dual constraints of force and stability in 3D space may thus have important implications for the claim that vertebrate motor systems are highly redundant. There are many more muscles than degrees of freedom, and determining how muscles are selected for a particular motor task remains one of the fundamental challenges to understanding normal motor behavior (Bernstein 1967).

This study seeks to quantify the contributions of cat hindlimb muscles to the 3-dimensional force generation and stability properties of the entire limb. Our hypothesis is that anti-gravity extensors must be co-activated in with flexors to counter the destabilizing effects of ground reaction forces. The need for endpoint stabilization may explain the widespread extensor-flexor co-activation at the onset of the locomotor stance phase.

METHODS

Experiments were performed on the left hindlimb of deeply anaesthetized cats. Limb stability was quantified by endpoint stiffness: the relation between imposed limb displacements and the opposing endpoint forces (Perreault, et al. 2001). The "endpoint" was defined as the middle of the foot at the end of the metatarsals. Stiffness was estimated using a 6 DOF robot (Staubli, Inc.) and load cell (JR3), allowing characterization limb mechanics in all 6 DOF relevant to normal function. Results for only the translational DOF are presented here. Preliminary data was collected for 3 experimental conditions: passive, electrical stimulation of the triceps surae (TS) on its own, and in conjunction with the hamstrings (HAM).

RESULTS AND DISCUSSION

Figure 1 shows results for one cat. (A) shows stiffness ellipsoids and endpoint forces for all three experimental conditions. These ellipsoids depict the 3D endpoint stiffness. The long axis shows the direction in which the limb is most resistant to external perturbations of posture. For all conditions the maximal stiffness was oriented along the tibia. Stiffness magnitude increased as additional muscles were stimulated. The stiffness of the HAM could not be measured in isolation, as HAM stimulation produced strong knee abduction, precluding comparison with the passive and TS trials. Nevertheless, limb posture was constant during HAM+TS stimulation, allowing HAM stiffness to be estimated by subtraction. HAM stiffness was unstable, as depicted in (B). This shows the endpoint force response to unit displacements in different directions (black arrows) and the ground reaction force orientation due to hamstrings activation (blue arrow). Note that the hamstrings assists endpoint displacements oriented towards the contralateral hip. These preliminary results support our hypothesis that muscles generating downward forces (leg extensors) decrease limb stability.

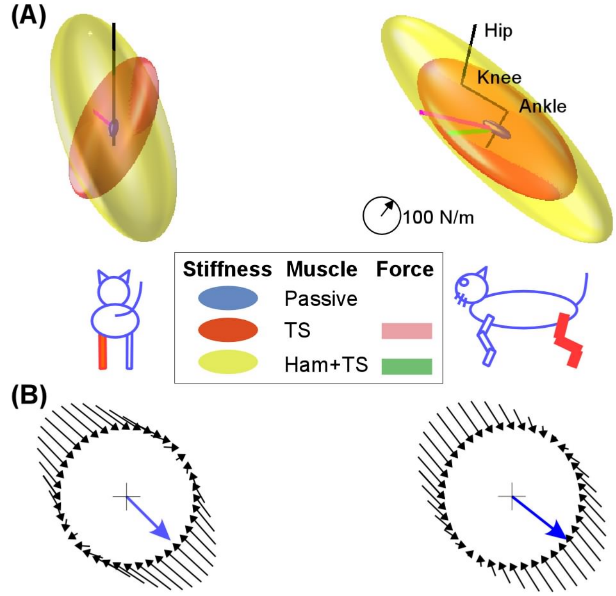

Figure 1: (A) Two views of the 3D stiffness ellipsoids and endpoint forces measured during each experimental condition. (B) Endpoint instability caused by activation of hamstrings.

REFERENCES

Bernstein, N. (1967). *The Co-ordination and Regulation of Movements.* Oxford, Pergamon Press.
McIntyre, J et al. (1996). *Exp Brain Res* **110**: 248-264.
Perreault, EJ et al. (2001). *Exp Brain Res* **141**(3): 312-23.

ACKNOWLEDGEMENTS

This work was supported by NIH grant 5R01AR41531-07, NIH Training Grant 5 T32 HD07418, and a National Science Foundation grant awarded in 2001 to EJP.

EMBOLISM BUBBLE ADHESION FORCE IN EXCISED PERFUSED MICROVESSELS

David M. Eckmann[1] and Akira Suzuki[2]
[1]Department of Anesthesia and Institute for Medicine and Engineering, University of Pennsylvania, Philadelphia, Pennsylvania
[2]Department of Anesthesia, Hamamatsu University, Hamamatsu, Japan
deckmann@mail.med.upenn.edu

INTRODUCTION

Cerebroarterial gas embolism occurs frequently in cardiac surgery and decompression sickness. Embolism bubbles lodge in 50-200 μm diameter vessels (Branger & Eckmann, 1999), and there is no readily available clinical therapy. Determining the mechanism of binding interactions between the bubble surface and the vessel wall causing bubble adhesion is critical to the development of a specific therapy to promote dewetting (Eckmann et al, 2001), bubble dislodgement (Cavanagh & Eckmann, 1999) and accelerate reperfusion through embolized vessels (Branger & Eckmann, 2002). We measured the force required to displace bubbles lodged in excised, perfused microvessels and characterized the net adhesion force per unit surface area of bubble contacting the vessel wall.

METHODS

With Institutional Animal Care and Use Committee approval, 2nd order mesenteric arterioles were removed from adult Wistar rats. Vessels were mounted between micropipettes in a perfusion chamber (Living Systems, Burlington, VT) placed on an inverted microscope (Nikon Axiovert) connected to a CCD camera. Vessels were bathed in Ringers solution and perfused with either Ringers solution (n = 6) or Ringers solution containing 5% bovine serum albumin (BSA) (n = 6). The bath fluid and perfusate were kept at 37 °C and equilibrated with 5% CO_2, 21% O_2 and balance N_2. Preservation of endothelial- and smooth muscle- mediated vascular responses was confirmed by topical application of phenylephrine and acetylcholine. Flow through the vessel was stopped and an air microbubble (3-4 nl) was injected using a Drummond Nanoject instrument via a 10 μm diameter micropipette placed through the vessel wall (Figures 1 & 2). The bubble was allowed to reside intravascularly for 1, 10 or 20 minutes at which time the pressure on the perfusate inflow side was raised until the bubble dislodged. The differential pressure across the bubble, ΔP, was recorded at the moment of bubble movement. Bubble length, L, and vessel internal diameter, D, were determined from videomicrometry. The bubble adhesion force per unit surface area, κ, was calculated to be $\kappa = \Delta PD/4L$.

RESULTS AND DISCUSSION

Table 1 shows results for κ, the adhesion force per unit area, at different durations of embolization. κ remained uniform over time in the absence of BSA but it increased with time in the presence of BSA. At any particular time point, κ was greater in the presence of the protein than without it. This was statistically significant ($p < 0.05$, Students t-test) at 10 and 20 minutes.

Table 1: κ, adhesion force/unit area (mean ± SD, dyne/cm^2)

Perfusate	1 min	10 min	20 min
Ringers	957±158	968±147	977±232
Ringers+BSA	1398±372	1897±358	2047±391

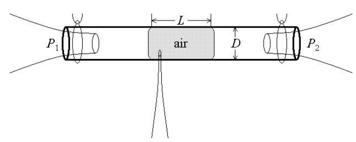

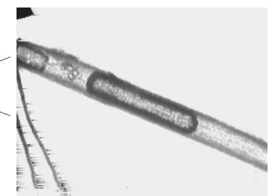

Figure 1 **Figure 2**

Figure 1: Cartoon of excised, embolized microvessel.
Figure 2: Microscopy image of excised, embolized microvessel.

SUMMARY

The magnitude of and temporal development of the adhesion force of microbubbles to the vessel wall is highly dependent on the presence of a protein in the perfusate. This suggests an adhesive interaction between the endothelium and proteins that have adsorbed to the gas-liquid interface.

REFERENCES

Branger, A.B., Eckmann, D.M. (1999). *J. Appl. Physiol.*, **87**, 1287-1295
Branger, A.B., Eckmann, D.M. (2002). *Anesthesiology*, In Press
Cavanagh, D.P., Eckmann, D.M. (1999). *J. Fluid Mech.*, **398**, 225-244
Eckmann et al (2001) *J. Colloid Interface Sci*. **242**, 386-394

ACKNOWLEDGEMENTS

Supported in part by NIH R01 HL60230, the Department of Anesthesia, University of Pennsylvania and the Department of Anesthesia, Hamamatsu University.

SHOCK ABSORBING POTENTIAL OF THE UNGULATE DIGITAL CUSHION

Justine Robilliard and Jeremy F. Burn[1]

Department of Anatomy, University of Bristol, Southwell Street, Bristol, BS2 8EJ
[1]Corresponding author: J.F.Burn@bris.ac.uk

INTRODUCTION

Metatarsal and heel pads in plantigrade and digitigrade animals play an important role in isolating the limbs from potentially damaging impact forces during locomotion. In ungulates, the digital cushion within the hoof capsule is thought to be an analogous structure but there is no scientific evidence to support this hypothesis. For the digital cushion to function as a shock absorber it must have a significant mechanical interaction with surrounding structures. Shock isolation could be provided either by visco-elastic properties of the digital cushion or by surrounding visco-elastic structures if the digital cushion were to act as a force transmitter. The aim of this study was to determine the degree to which the equine digital cushion interacts mechanically with surrounding structures and to determine its material properties.

METHODS

Cyclic loading was applied to the distal sections of five cadaveric equine limbs using a servo-hydraulic materials testing machine. The magnitude and rate of the applied load were chosen to produce limb kinematics that were equivalent to published *in-vivo* data for horses at 8m/s canter. Pressure within the digital cushion was recorded using a 2mm diameter pressure measuring needle inserted via the heels into the geometric centre of the lateral lobe of digital cushion. Force, displacement, and intra digital cushion pressure were recorded simultaneously at 200samples/sec. using a PC-based data logger.

Cylindrical specimens of digital cushion 1cm diameter and 1.5cm in length were cut from the medial and lateral lobes of five digital cushions. The specimens were loaded in axial compression using the same materials test machine both with, and without constraint on the lateral expansion of the specimens. The load applied to the specimens was derived from the pressure recorded during previous loading of the cadarveric limbs.

RESULTS AND DISCUSSION

Intra digital cushion pressure increased significantly as the limb was loaded (figure 1). The increase was non-linear and showed hysteresis between loading and unloading. The pressure rise was functionally significant and implies that the digital cushion may be involved in shock prevention.

The unconstrained isolated specimens compressed to a fraction of their original length with negligible applied stress after which stress increased with negligible decrease in the length of the specimen. This suggested the material was behaving as a liquid within its physiological strain range.

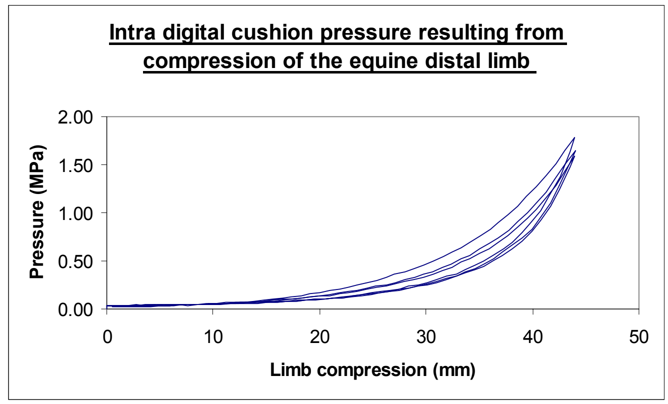

Figure 1:

The constrained samples showed a small decrease in volume for applied pressures of up to five times greater than the those recorded in the loaded cadaveric limbs. There was no apparent hysteresis between loading and unloading the constrained specimens. This indicates that the digital cushion acts hydrodynamically to transmit pressure to surrounding structures. It would further suggest that the visco-elastic behaviour observed in pressure measurements from the cadaveric limb was due to the properties of surrounding material and not the digital cushion. Further work is required to determine whether expansion of the hoof wall would account for these observations.

SUMMARY

The study investigated the potential for the ungulate digital cushion to act as a shock absorber during locomotion. Significant positive pressures were measured within the equine digital cushion during in-vitro limb loading. Materials testing of digital cushion specimens indicates that pressure is transmitted to surrounding structures which may act to prevent shock transients during locomotion from being propagated proximally through the limb.

REGIONAL DIFFERENCES IN CELLULAR DENSITIES IN HUMAN AND OVINE MITRAL VALVES

Kristina T. Jensen, Karyn S. Kunzelman, Kelley W. Dwyer, David W. Quick, Richard P. Cochran

Cardiothoracic Surgery and Biomedical Engineering Department, University of Wisconsin, Madison, Wisconsin, USA
karynk@surgery.wisc.edu

INTRODUCTION

Our prior work has demonstrated that procollagen and heat shock protein expression is altered in mitral valves subject to mitral regurgitation (MR) (Quick, 2001). However, little research has been done to examine the cellular distribution within the mitral valve that is responsible for this protein expression. A better understanding of the cellular distribution will lend further insight into how mitral valve remodeling occurs and how to prevent detrimental remodeling. The goal of this study was to determine if there are regional differences in cellular densities within human and ovine mitral valves.

METHODS

Mitral valves were excised from explanted human hearts from transplant recipients (n=7) and non-diseased hearts (n=2), and from sheep in a study comparing normal hearts to hearts that were surgically altered to mimic heart diseases (n=28). The anterior leaflets were trimmed of excess muscle and chordae tendineae, sectioned, mounted on microscope slides, and stained for nuclei with a standard hematoxylin protocol.

A digital image analysis system (Quick, 1999) was utilized to examine the histologic sections. At three locations along the valve (annulus, middle, and free edge), the number of nuclei and the area were determined for a two-millimeter long segment (Figure 1). From this information, the cellular density (number of nuclei per unit area) was determined for each location. Paired t-tests were done to statistically compare different locations. A significance level of $p < 0.05$ was used.

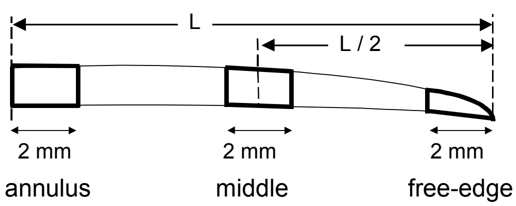

Figure 1: Three 2-mm long segments were analyzed for nuclear presents in each specimen.

RESULTS AND DISCUSSION

In the human valves, the cellular density at the free edge was significantly larger than in the middle section ($p < 0.002$) and annulus ($p < 0.001$). In the sheep valves, cellular density at the free edge was significantly larger than the middle section ($p < 0.001$) and annulus ($p < 0.001$), and the cellular density at the middle was significantly larger than the annulus ($p < 0.001$) (Figure 2).

The fibrosa, consisting of mainly collagen, is dominant at the annulus and tapers toward the free edge of the valve where the spongiosa layer (mainly GAGs) is dominant. The majority of the anterior leaflet is under tension. In contrast, the free edge of the valve, where the anterior leaflet coapts with the posterior leaflet, is mainly under compression. As a result of coaptation, which allows stress sharing between the leaflets, this region of the valve is under lower stress (Quick, 1999).

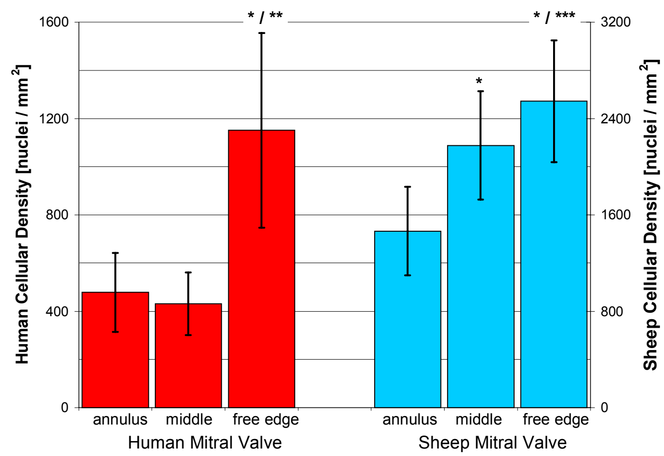

Figure 2: Cellular densities for human and ovine anterior leaflet of the mitral valves at the annulus, middle, and free edge. *$p < 0.001$ compared to annulus, **$p < 0.002$ compared to middle, ***$p < 0.001$ compared to middle.

SUMMARY

The mitral valve is a very complex apparatus. The mechanisms for valve remodeling in response to stress have not been determined. Prior research has shown that protein concentrations change with altered stress (MR) (Kunzelman, 1998; Quick, 2001). This study suggests that regional differences in cellularity may be another possible mechanism for valve adaptation.

REFERENCES

Kunzelman, K.S. et al (1998). *Ann Thor Surg* **66**(6 Suppl): S198-S205.
Quick, D.W. et al. (2001). *J Surg Res*, submitted, December, 2001.
Quick, D.W. et al (1999). *Int'l Soc Optical Eng*. 118-128.

ACKNOWLEDGEMENTS

This study is based upon work supported under a National Science Foundation Graduate Research Fellowship and a grant from the National Institutes of Health.

LOGISTIC TIME CONSTANT OF ISOVOLUMIC RELAXATION PRESSURE-TIME CURVE IN THE LEFT VENTRICLE

Junichi Araki[1], Hiromi Matsubara[2], Hiroyuki Suga[3] and Fumihiko Kajiya[1]

[1]Department of Cardiovascular Physiology, Okayama University Graduate School of Medicine and Dentistry, Okayama, Japan
[2]Department of Cardiovascular Medicine, Okayama University Graduate School of Medicine and Dentistry, Okayama, Japan
[3]National Cardiovascular Center Research Institute, Suita, Osaka, Japan

INTRODUCTION

Weiss et al originally determined the time constant by fitting a monoexponential model to left ventricular (LV) pressure decrease during isovolumic relaxation after the time of peak negative value of the first derivative of LV pressure (dP/dt). The time constant derived from the monoexponential model has been widely used as an index of LV relaxation rate or lusitropism in both experimental and clinical studies, although this model has several well-recognized problems. In the present study, we proposed a logistic model and derived a "logistic" time constant (T_L) as a better alternative to the conventional "monoexponential" time constant (T_E).

METHODS

A total of 189 beats (147 isovolumic and 42 ejecting beats) were investigated in seven canine excised cross-circulated heart preparations. The conventional monoexponential model was given by

$$P(t) = P_0 \exp(-t/T_E) + P_{asymptote}$$

where P(t) is an observed LV isovolumic relaxation pressure-time curve, P_0 is an amplitude constant, $P_{asymptote}$ is a nonzero asymptote, t is time after peak negative dP/dt, and T_E is the time constant of exponent that has conventionally been used as the time constant monoexponential function. Our proposed logistic model was given by

$$P(t) = P_A/(1 + \exp(t/T_L)) + P_B$$

where P_A is an amplitude constant, P_B is a nonzero asymptote, t is time, and T_L is the time constant of the exponent. We designated T_L as a logistic time constant to distinguish it from the T_E. We compared the goodness of fit of the logistic curve to the same P(t) curve.

RESULTS AND DISCUSSION

We found that the logistic model fitted much more precisely all the observed LV isovolumic relaxation pressure-time curves than the monoexponential model ($P<0.05$). The logistic model also fitted well both the time curve of the first derivative of the observed P(t) (dP/dt) and the dP/dt-P(t) phase-plane curve. Like T_E, T_L indicated that volume loading depressed LV lusitropism and that increasing heart rate and ejection fraction augmented it. T_L was independent of the choice of cutoff point defining the end of isovolumic relaxation; T_E was dependent on that choice (Figure 1).

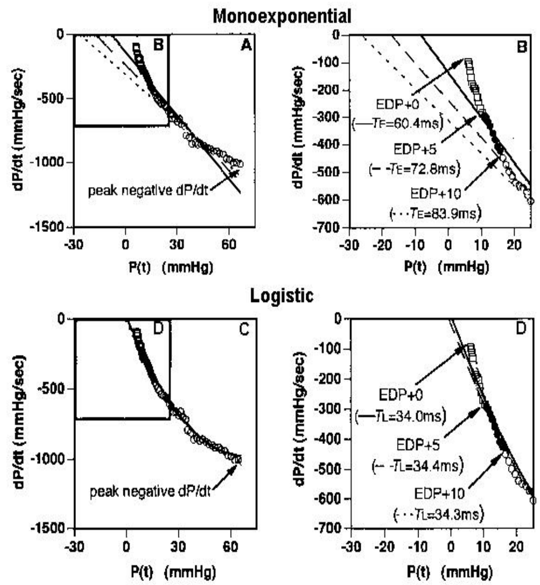

Figure 1: Representative plots of observed dP/dt vs instantaneous LV P(t) (phase-plane diagram). Observed data points from the time of peak negative dP/dt to the time when P(t) reached the three different relaxation pressure levels. B and D are close-ups of rectangular areas in A and C.

CONCLUSIONS

We conclude that the logistic model provides a better curve fit to the LV pressure decrease during isovolumic relaxation in both isovolumic and ejecting contractions. T_L can more reliably characterize the rate of LV relaxation or lusitropism than T_E. We therefore propose T_L as a better alternative to T_E for evaluating LV lusitropism.

REFERENCES

Weiss, J.L., Frederiksen, J.W., Weisfeld, M.L. (1976). *J Clin Invest*, **58**, 751-760.
Frederiksen, J.W., Weiss, J.L., Weisfeld, M.L. (1978). *Am J Physiol*, **235**, H701-H706.
Sys, S.U., Brutsaert, D.L. (1989). *Am J Physiol*, **257**, H1490-H1497.
Matsubara, H., Takaki, M., Yasuhara, S., Araki, J., Suga, H. (1995). *Circulation*, **92**, 2318-2326.

NUTRIENT DIFFUSION AND FLOW-INDUCED NUTRIENT TRANSPORT IN 3-D CELL-SCAFFOLD COMPOSITES

Edward A. Botchwey[1,2] , Cato T. Laurencin[2], Elliot M. Levine[3], and Solomon R. Pollack[1]
[1]Department of Bioengineering, University of Pennsylvania, Philadelphia PA, email: botchwey@seas.upenn.edu
[2]Center for Advanced Biomaterials and Tissue Engineering, Department of Chemical Engineering, Drexel University
[3]The Wistar Institute

INTRODUCTION

Studies in our laboratory have shown that the passive diffusion of nutrients within 3-D scaffolds used for *in vitro* tissue engineering of bone may be insufficient to maintain cell viability beyond 300microns. Therefore, we designed new microcarrier scaffolds for bone tissue engineering in a rotating bioreactor(Botchwey, et al. 2001). The purpose of this study was 1) to characterize the efficiency of passive nutrient diffusion to bone cells within our 3-D scaffolds under static culture conditions and 2) to quantify internal fluid perfusion and flow-induced nutrient transport to cells within the scaffolds during bioreactor rotation.

METHODS

We have developed a one-dimensional model to evaluate glucose diffusion within our cylindrical 3-D microcarrier scaffolds. In the absence of flow, diffusion within the scaffold is given by:

$$D\sigma \frac{\partial^2}{\partial x^2} C(x) = Q(x), \ (1) \quad \text{where } Q(x) = \frac{N\hat{R}}{nL}, \ (2)$$

Q(x) is the rate of glucose consumption as a function of pore length x and all other terms are defined in Table 1 along with their sources. The boundary conditions are given by:

$$C_0 = C(0) \text{ and } \frac{\partial}{\partial x} C\left(L/2\right) = 0, \ (3)$$

C_o represents media glucose concentration at the exterior boundary of the scaffold. Symmetry of glucose concentration within the pores results in the 0 value of the derivative. The solution to the boundary value problem is given by:

$$C(x) = C_0 - \frac{N\hat{R}}{2Dn\sigma L}\left(Lx - x^2\right), \ (4)$$

Fluid flow rate through the pores during bioreactor rotation was calculated using Darcy's law, given by:

$$U = -\left(\frac{K}{\eta}\right)\frac{\Delta P}{L}, \ (5) \quad K = \frac{\varepsilon\delta^2}{96\eta\tau^2}, \ (6)$$

where K is Darcy's permeability for the scaffold. Assuming uniform cell density within the pores, the decrease in nutrient concentration per incremental length, Δx, is given by:

$$Q(\Delta x) = \frac{N\hat{R}\Delta x}{\sigma U}, \quad (7)$$

Parametric analysis of fluid perfusion through the scaffold was performed as a function of pore size, pore volume, and pore channel tortuosity.

RESULTS AND DISCUSSION

Based on the geometry and pore architecture of 3-D scaffolds used for tissue engineering of bone by our laboratory and others(Ishaug-Riley, et al. 1998; Botchwey, et al. 2001; Botchwey, et al. 2002), our results showed that passive glucose diffusion was insufficient to maintain minimum glucose concentration beyond a depth of 300 μm within the pores of the scaffold. This result is consistent with experimental observations of osseous tissue ingrowth within 3-D scaffolds proposed for bone tissue engineering. Values of internal fluid perfusion within 3-D microcarrier scaffolds were calculated based on scaffold properties (Table 1) and motion analysis previously reported(Botchwey, et al. 2001). Internal flow rate increased linearly with pore volume from a maximum of approximately 0.01m/s to 0.001 m/s. Variation in pore diameter in the range required for tissue ingrowth, namely 100 to 300 μm, produced a range of internal fluid flow rates from 0.002 to 0.011 m/s respectively. In the range of tortuosity (τ = 1-3) describing most porous materials, internal flow rates ranged from 0.008m/s to 0.002 m/s. Flow-induced glucose transport with uniform consumption by N cells (as above) within pores indicates that a minimum internal flow rate of $3.1\text{x}10^{-4}$ m/s is required to maintain minimum concentration within the pores of the scaffold. Our studies of tissue ingrowth within these microcarrier scaffolds in the rotating bioreactor have shown no depth limitations to tissue ingrowth. In our ongoing studies, we are examining the effect of flow induced nutrient transport on glucose metabolism in culture. These studies will also examine the effects of both 3-D culture and media flow on gene expression and mineralized matrix synthesis *in vitro.*

Table 1. Physical Data and Nomenclature

D = 6.6e-10	Diffusivity of glucose (m^2/s) [3]
$\hat{R}$ = 1.6e-14	Single osteoblast rate of glucose consumption (g/s) [4]
L = .0025	Length of the cylindrical scaffold (m) [1]
N = 10000	Total number of cells within the scaffold [1]
η = 0.799e-3	Dynamic Viscosity (kg m-1 s-1) [2]
ΔP/L = 7.9e4	Pressure gradient across the scaffold (N m) [2]
n	Total number of cylindircal pores [1]
σ	Cross-sectional area of an individual pore [2]
ε	Fluid volume fraction of the Scaffold [2]
δ	Median pore diameter of the Scaffold[2]
τ	Tortuosity (pore path length per unit scaffold thickness) [2]

SUMMARY

This model provides an excellent vehicle for the study of *in vitro* bone tissue synthesis under physiologically relevant 3-D flow conditions.

REFERENCES

Botchwey, E. et al. (2002) *Biorheology,* **Accepted**
Botchwey, E. et al. (2001). *J Biomed Mat Res,* **55,** 242-253
Ishaug-Riley, S. et al. (1998). *Biomaterials,* **19,** 1405-1412
Petrov, N. et al. (2002). *Biorheology*, **Accepted**.

THE EFFECT OF PLATE DESIGN, ENDPLATE PREPARATION AND BONE MINERAL DENSITY ON IMMEDIATE STABILIZATION IN AN ANTERIOR CERVICAL PLATE FIXATION MODEL

Marcel Dvorak[1], Tobias Pitzen[2], Qingan Zhu[1], Jeff Gordon[1], Charles Fisher[1], Thomas Oxland[1]

[1]Department of Orthopaedics, University of British Columbia, Vancouver, British Columbia, Canada, toxland@interchange.ubc.ca

[2]Department of Neurosurgery, University of Saarland, Homburg, Germany

INTRODUCTION

There are two conceptual anterior plate designs in the cervical spine: a ‘rigid’ screw-plate design and a ‘dynamic’ design that allows sliding between the screw and plate. The effect of these different plate designs on spinal flexibility has not been analyzed in a cadaveric model (Brodke 2001), particularly with reference to the effects of variables such as endplate preparation and vertebral bone density. The objective of this study was to evaluate spinal stabilization provided by the two different plate designs. Endplate preparation for bone graft fusion and load shared by the plate were also considered in the present study.

METHODS

Nine cadaveric cervical spines were dissected into twenty-four functional spinal units. Bone mineral density of vertebral bodies was measured using DEXA. All specimens were randomly divided into four groups according to the combination of anterior plates (CSLP plate by Synthes and ABC plate by Aesculap) and endplate preparation (with and without endplate). Each specimen was injured by dissection of all posterior elements followed by anterior plate fixation with bone graft. A strain gauge was glued onto the plates and calibrated under an isolated pure bending moment. Flexibility testing was conducted in flexion-extension, lateral bending and axial rotation on each specimen for the intact and anterior plate condition by the application of a pure moment at 1°/sec to a maximum of 1.5Nm. Ranges of motion (ROM) and neutral zones (NZ) were calculated to compare the cervical spine fixations. A general linear model with multi-ANOVA was used to analyze effect of plates and endplate preparation, and load sharing between the two plates.

RESULTS AND DISCUSSION

There was no significant effect of plate design on flexibility except in extension, where the ABC plate reduced ROM compared to CSLP ($p=0.03$, Figure 1). There was no significant difference in the NZ or ROM between the two endplate preparation techniques in any direction. ABC shared 13% of bending moment, which is less than 39% shared by CSLP plate in flexion-extension. ROM correlated significantly with BMD in flexion and axial rotation, and NZ in flexion-extension and axial rotation (Figure 2).

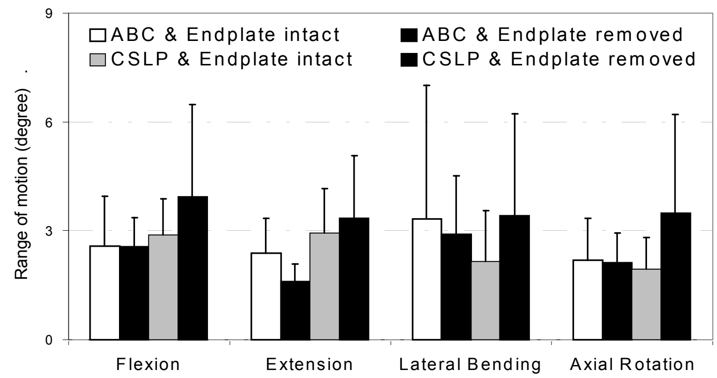

Figure 1: Effect of plates and endplate preparation on ranges of motion.

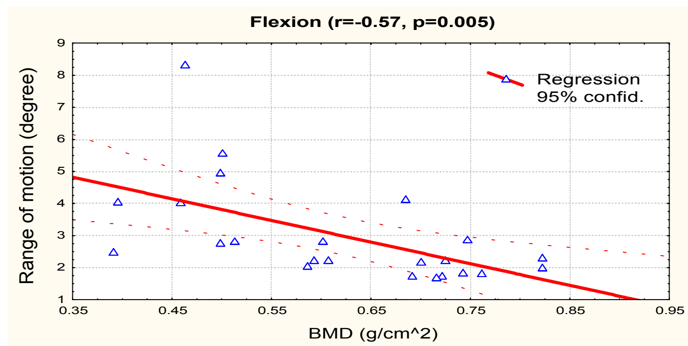

Figure 2. Correlation between bone mineral density and the range of motion in flexion.

SUMMARY

The two different designs of anterior plates in the cervical spine provided similar stabilization to the spine with the sole exception being the enhanced stabilization from the ABC plate in extension. Possibly, this was an effect of the increased load sharing role of the interbody bone graft, which was a clear difference between the two designs. The bone mineral density was clearly an important factor in the degree of stabilization achieved, regardless of the method of fixation.

REFERENCES

Brodke DS et al (2001). *Spine*, **26**:1324-9

ACKNOWLEDGEMENTS

The authors are grateful to the Rick Hansen Institute and the Natural Sciences and Engineering Research Council of Canada (NSERC) for research funding and to Aesculap AG and Synthes Canada for donation of the implants.

SOCKET COMFORT AND PERCEIVED FUNCTIONAL ABILITY IN UNILATERAL TRANSTIBIAL AMPUTEE PATIENTS USING PLASTER-CAST AND CAD/CAM MANUFACTURED SOCKETS

M. Alvarez[1], JL. Ronsky[2], R. Aggarwala[3], J. Harder[4], RF. Zernicke[1]
Human Performance Laboratory, University of Calgary, Calgary, Alberta, Canada
[1]Human Performance Laboratory, Faculty of Kinesiology, mjalvare@ucalgary,ca, [2]Department of Mechanical & Manufacturing Engineering, [3]Department of Mathematics & Statistics, [4]Department of Surgery, Alberta Children's Hospital, Calgary, Alberta

INTRODUCTION

Quality of life for a transtibial amputee is partially dictated by the way a prosthesis limb allows them to perform normal daily routines and sustain self-sufficiency. Problems with fit and ultimately comfort have impeded acceptable daily functioning and accentuated physical disability (Burgess, 1981; Sanders, 1986). Legro and colleagues (1999) found that lower limb amputees rated the ability to walk and proper fit as the most important function and characteristic of a prosthesis. The objective of this research study was to assess quality of life and functional levels of Canadian unilateral transtibial amputees and evaluate whether they were a function of socket manufacturing techniques. These objectives were met through a questionnaire developed at the University of Calgary.

METHODS

This research study is a descriptive study involving a cross-sectional survey of the adult unilateral transtibial amputee population. Nonprobability sampling was used to recruit subjects. Purposive sampling from 10 sites across 6 provinces was the primary method of subject recruitment. Subjects were assigned to one of three groups based on method of socket manufacturing: (1) Always used plaster-cast method; (2) Always used CAD/CAM method; and (3) Switched from plaster-cast to CAD/CAM method. The inclusion criteria specified that participants had to: (1) be at least 18 years of age; (2) have a unilateral transtibial amputation one or more years earlier; (3) have no other major physical limitations; and (4) provide informed consent. Each subject completed two quality of life questionnaires during two separate telephone interviews, the SF-36 and the Selected Aspects of Quality of Life for Canadian Unilateral Transtibial Amputees developed at the University of Calgary.

RESULTS

Of the 102 patients who completed both questionnaires, 35 were assessed in the Always Plaster-cast group, 7 in the Always CAD/CAM group, and 11 in the Plaster to CAD/CAM group. The mean age of the total sample was 57.40 (+/-14.44). Seventy-nine percent of the total sample was male.

One-way ANOVA revealed there were no significant differences between groups in their satisfaction with comfort while walking ($p=0.56$), comfort while running ($p=0.62$), and appearance of their gait ($p=0.37$). All subjects in the Always CAD/CAM group reported that they did not run with their prosthesis. Sixty-four percent of the total sample responded similarly.

Participants who only used a CAD/CAM socket reported significantly lower scores compared to those who only used a plaster-cast socket in terms of their perceived ability to walk inside their home, walk outside on uneven ground, walk on slippery surfaces, use an escalator, stepping up a sidewalk curb, and go up a few steps without a handrail ($p<0.05$). Amputees who switched from plaster-cast sockets to CAD/CAM sockets reported significantly higher scores than those who only used a CAD/CAM socket in the areas of walking inside their home, walking in crowded rooms and narrow spaces, walking outdoors on uneven ground and slippery surfaces, stepping up a sidewalk curb, going up and down steps without a handrail, and walking as quickly as they needed to ($p<0.05$). There was no significant difference between the three groups in the areas of walking outside on even ground, going down a few steps without a handrail, and stepping down a sidewalk curb. No significant difference was found between the Always Plaster-cast group and the Plaster to CAD/CAM group (Figure 1).

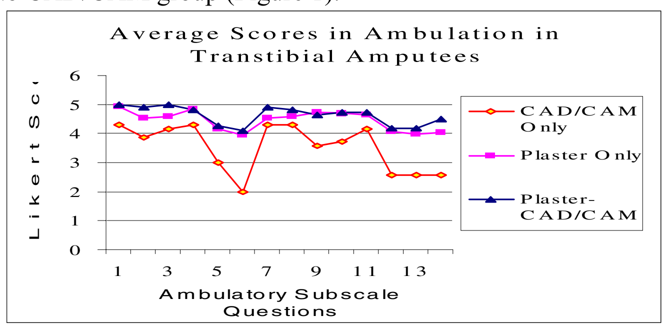

Figure 1. Subscale scores of perceived functional ability for three groups of transtibial amputees ($\alpha<0.05$). Walking items: 1=inside home, 2=crowded room, 3=narrow spaces, 4=outside, even ground, 5=outside, uneven ground, 14=walk as quickly as needed. Balance items: 6=slippery surfaces, 7=up steps with rail, 8=down steps with rail, 9=escalator, 10=step up curb, 11=step down curb, 12=up steps, no rail, 13=down steps, no rail.

Stepwise linear regression analysis revealed that walking capacities could significantly predict success with activities related to balance such as climbing stairs ($r^2=0.59$).

CONCLUSIONS

Preliminary results showed that amputees who had always used a CAD/CAM socket seemed to have lower perceived locomotor functional abilities than persons who currently use or have used plaster-cast sockets. Since five out of the seven persons in this group were greater than 65 years of age, this may have been related to age.

REFERENCES

Burgess, E.M. (1981). *Atlas of limb prosthetics*, CV Mosby.
Legro, M.W. et al. (1999). *J Rehabil Res Dev,* **36**, 155-163.
Sanders, G. (1986). *Lower limb amputations*, FA Davis Co.

ACKNOWLEDGMENTS

Funded in part by the Alberta Worker's Compensation Board.

INFLUENCE OF SEGMENT RIGIDITIES ON GROUND REACTION FORCES DURING LANDING

Rhonda L. Boros and John H. Challis
Biomechanics Laboratory, Department of Kinesiology, The Pennsylvania State University, University Park, Pennsylvania, USA
E-mail: rlb248@psu.edu

INTRODUCTION

Vertical ground reaction forces (VGRF) realized during landing from a drop range in magnitude from 2 to 14 times bodyweight, depending on the height dropped and point of initial contact (e.g. on toes or heels). Dissipation of energy has typically been attributed to shoe and heel pad material properties and joint kinematics/kinetics. Landing impact, locomotion, and jumping studies have traditionally utilized a rigid-body model in determining joint kinetics and material deformation properties of the heel pad, substantially increasing the potential for error in estimates of joint loading (Gruber et al., 1998).

The influence of soft tissue motion on VGRFs during landing however is still being explored, and only recently have wobbling mass models appeared in the impact biomechanics literature. Few however account for accurate distribution of the segmented soft tissue (e.g. greater skeletal mass than soft tissue mass in the thigh). The initial point of impact during many footfalls is the heel pad, yet to date studies have tended to ignore these properties therefore eliminating force dissipation effects below the ankle. The purpose of this study was to design a wobbling mass model to predict VGRF profiles obtained experimentally during landing from a drop, and to use this model to explore rigid and soft tissue contributions to the VGRF.

METHODS

A wobbling mass model was formulated in Working Model 2D (version 5.0, Knowledge Revolution, San Mateo, CA) in an effort to predict VGRF trace profiles obtained experimentally from a single subject landing from a 0.4m drop. The heel pad, foot, shank, thigh, torso and 6 wobbling masses were modeled as various mass-spring-damper systems.

A single female subject, (height-1.59m, mass–65.2kg), performed five flat-footed landings from a hanging position, landing with both feet simultaneously on a force platform (720 Hz). Knee, hip and arm motion was not constrained once the subject released from the bar, and the subject was instructed to maintain a relatively upright posture (e.g. head up watching the wall). Anthropometric measures were obtained and segmented soft tissue and skeletal masses for head/trunk/arms, thigh, and shank/foot were determined (Clarys and Marfell-Jones, 1986), and a visceral mass estimate of 9 kg (Minetti and Belli, 1994) served as inputs into a wobbling mass landing model. Time-frequency analyses of experimental and model predicted VGRF traces were performed in MATLAB 5.3.

RESULTS

The experimental mean peak VGRF was 6.7±0.2 body weights (BW), with peak forces occurring 0.0183±0.0081 s after initial impact. Power spectral density analysis of the VGRFs revealed 95% of the signal power occurred below a frequency of 23.5±3.5 Hz. Analysis of the first 40 ms only revealed signal power several orders of magnitude greater (mean and 95% frequencies of 39.7 and 229.4 Hz).

Wobbling mass simulations replicated mean peak VGRF within one standard deviation (6.5 BW). Power spectral density analysis of the simulated VGRF revealed a peak frequency of 8.1 Hz, with 95% of the signal power lying below a frequency of 13.2 Hz. Analysis of the first 40 ms of the simulated signal revealed a mean frequency of 83.4 Hz and substantial signal power up to 314.4 Hz. The rigid feet (57.1 and 289.2 Hz) and torso (24.3 and 170.4 Hz) elements had mean and 95% frequency components nearest to the experimental data (39.7±17.6 and 229.4±56.1 Hz) for the first 40 ms of landing impact. The motion of these model components is therefore considered to substantially contribute to the high frequency "impact" portion of the VGRF curve. Frequency components for the wobbling masses for the first 40 ms of impact were similar, ranging from 59.9 to 131.9 Hz (mean) and 294.0 to 333.6 Hz (95%), however were out of phase with the rigid model components.

DISCUSSION

The data indicate 37.5% of modeled total mass was associated with soft tissue components. Combining all of the mass into "rigid" segments resulted in a 4.4% increase in peak VGRF and a slight shift in the time frequency plot. Considering that the mean frequency content for the rigid and wobbling mass segments were similar, and peak VGRF was greater without the wobbling masses, it can be argued that in vivo the relative motion of the rigid and wobbling masses is opposite in phase and therefore the combined rigid/soft tissue motion is conducive to force attenuation, not just for VGRF but also joint loads.

REFERENCES

Clarys, J.P., Marfell-Jones, M.J. (1986). *Human Biol.*, **58,** 761-769.
Clarys, J.P., Marfell-Jones, M.J. (1986). *Human Biol.*, **58**, 771-782.
Gruber, K. et al. (1998). *J. Biomech.*, **31**,439-444.
Minetti, A.E., Belli, G. (1994). *J. Biomech.*, **27**,97-101.

THE EFFECT OF A NOVEL CAGE DESIGN ON STABILIZATION IN THE LUMBAR SPINE

Michael Johnson[1], Qingan Zhu[1], Andy Sennett[2], Marcel Dvorak[1], Charles Fisher[1], Thomas Oxland[1]
[1]Department of Orthopaedics, University of British Columbia, Vancouver, British Columbia, Canada, toxland@interchange.ubc.ca
[2]Cortek Inc. Boston, Massachusetts, USA

INTRODUCTION

Spinal interbody cages provide good stabilization to the lumbar spine, but their ineffectiveness in extension has been noted (Lund 1998, Oxland 2000). To address this point, a novel interbody cage has been developed with a dovetail feature to "lock" adjacent vertebral bodies, particularly in distraction. The objective of this study was to determine if the design modification of a dovetail results in improved immediate three-dimensional spinal stabilization, compared to an identical cage without the dovetail.

METHODS

Eight cadaveric specimens (L4-L5) were used. Each specimen was subjected to a flexibility test in flexion-extension, lateral bending and axial rotation with pure moments (±5.0Nm). The test was performed for the intact specimen and after anterior Dovetail and non-Dovetail interbody cage insertion (Cortek, Boston, MA) (Figure 1). The positions of the vertebral bodies were monitored using an optoelectronic camera system (Optotrak 3020, Northern Digital, ON). Neutral zone (NZ) and range of motion (ROM) were calculated. Paired Student's t-test was used to determine the effect of cage design on the spinal stabilization.

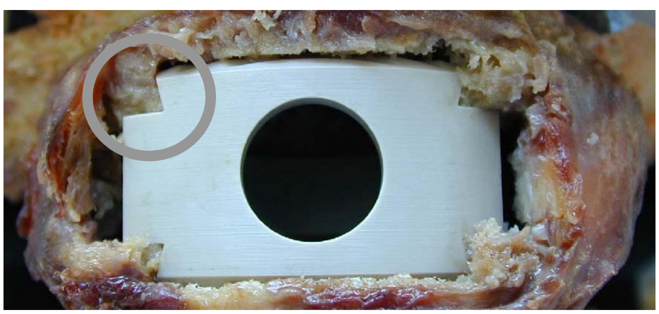

Figure 1: Anterior view of the dovetail implant in a specimen. Note the "dovetail" feature against the vertebra within the grey circle.

RESULTS AND DISCUSSION

The ROMs decreased significantly following Dovetail or non-Dovetail cage fixation in all directions, as well as NZ in lateral bending. The ROM ratios to intact with Dovetail and non-Dovetail fixation were 0.73 and 0.80 in flexion, 0.72 and 0.73 in extension, 0.46 and 0.54 in lateral bending, and 0.71 and 0.80 in axial rotation, respectively, with the only significant difference being in lateral bending (p=0.038) (Figure 2). The NZ ratios to intact with Dovetail fixation were close to those with non-Dovetail fixation.

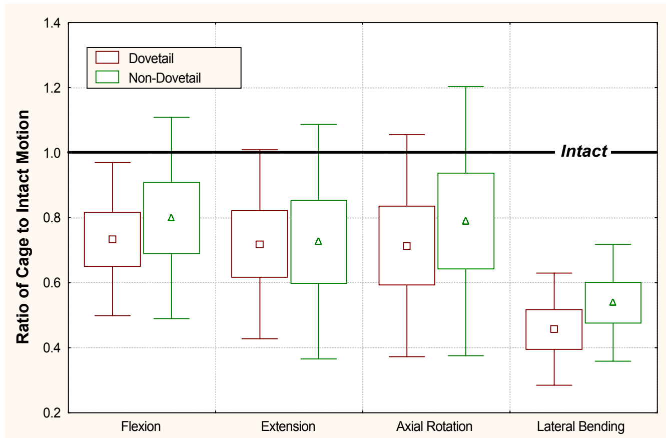

Figure 2: Ranges of motion of L4-L5 segment with Dovetail and Non-Dovetail cage.

SUMMARY

Recent questions regarding spinal stabilization with various interbody cage designs, especially in extension, have been raised from biomechanical testing. It was noteable that the Dovetail design feature did not reduce motion in extension more than the non-Dovetail cage. Of interest was that the degree of stabilization in extension for both cages was better than the intact spine, which has not been observed previously [Lund 1998, Oxland 2000]. Of note was that Dovetail cage provided more stabilization to the spine in lateral bending.

REFERENCES

Lund T et al (1998). *J Bone Joint Surg. (Br)*, **80**:351-359.
Oxland T et al (2000). *J Bone Joint Surg. (Am),* **82**:383-393.

ACKNOWLEDGEMENTS

The support in the form of a research grant from Cortek Inc., Boston MA USA, is gratefully acknowledged.

HUMAN PERFORMANCE-BASED PEDIATRIC WHEELCHAIR PRESCRIPTION

Jeremy Carrle and Dave Hawkins[1]

Human Performance Laboratory, University of California, Davis, CA, USA
[1]email: dahawkins@ucdavis.edu

INTRODUCTION

Mobility impaired children need appropriately designed and configured wheelchairs. Configuration guidelines exist for adults but little work has been done to establish appropriate guidelines for children (Brubaker, 1986). It was hypothesized that the propelling capabilities of pediatric wheelchair users could be predicted and improved using biomechanical analysis and testing. Wheelchair wheels were tested to determine the forces required to initiate movement of a pediatric wheelchair. A static mathematical model and experimental testing techniques were utilized to identify the required joint torques in the initial pre-movement phase of the push. A model that evaluates the force produced in various seating positions is being developed based on results from these analyses and validated with human subjects.

METHODS

The forces required to initiate movement of a pediatric wheelchair were experimentally measured and validated for 6 wheels on 3 surfaces (described previously Carrle and Hawkins, 2001)

A static model of a pediatric wheelchair and child was developed to assess a child's ability to self-propel and to determine the optimal wheelchair configuration for that child. The model uses child-chair specific data (body segment lengths, wheel type, ground material, age, weight, and maximum voluntary contraction (MVC) joint torques) to predict the force required to initiate movement, to determine the maximum force that the child can produce on the handrim, and to identify the effect variations in model parameters (force direction, hand position, torso angle, and the distance from the hip to the wheel hub)) have on the child's ability to produce this force. Relative information regarding seat position is extracted based on the average force produced over a range of hand positions and torso angles. The validity of the model is being tested using pediatric subjects (5 wheelchair users and 5 able-bodied), ages 3-7. Forces on the handrim of a simulated-stationary wheelchair and joint positions are recorded for each trial using a force plate and a video-based motion analysis system respectively.

The final aspect of the project involves the development of guidelines and/or software to assist in pediatric wheelchair prescription. Guidelines will be evaluated with the help of pediatric wheelchair specialists.

RESULTS AND DISCUSSION

Model predictions of optimal seating configuration are consistent with common practice of wheelchair dealers and are being compared to experimental results. The maximum force that can be applied at the handrim is highly dependent on the direction of the force and the hand position on the handrim. Regardless of seat and torso position, some hand positions and force directions make it difficult to impart a force tangential to the handrim without putting a large moment on the shoulder. The model predicts that seat positions that are lower and farther behind the traditional seat position tend to increase the child's ability to produce handrim force. Physical therapists that perform wheelchair evaluations agree that forward configurations are better in situations with small children. The elbow and shoulder limit force production in most positions, except when the shoulder and elbow are directly in line with the force vector.

Preliminary results from testing three children in 6 to 10 seat positions indicate that the maximum joint torques attainable, during a simulated-static wheelchair test, can be predicted with the MVC strength tests. The average torques measured during the simulated-static wheelchair test were 97% of max values (standard deviation of 36%).

Model results (propelling force at the handrim) were on average 41N different than the model values. The differences are largely due to the disproportionately greater error in the forward-wheel configuration. Efforts are being undertaken to understand this difference and improve the model.

SUMMARY

A new approach is being developed to facilitate pediatric wheelchair prescription by determining a child's ability to self-propel and by identifying an appropriate style of wheelchair and seating configuration based on the child's anatomy and joint strength.

REFERENCES

Brubaker, C., (1986) *Journal of Rehabilitation Research and Development,* **23(4)**:19-26.
Carrle, J., Hawkins, D., (2001) *25th Annual Meeting of the American Society of Biomechanics*. **165**:383-384.

ACHKNOWLEDGEMENTS

NSF support, Grant BES-9813634

INVESTIGATION OF CEMENTLESS CUP MICROMOTION AND STABILITY AFTER TOTAL HIP ARTHROPLASTY

Luke Aram[1], Andy Lehman[2], Paul Lewis[3], Todd Render[3], Jorge Ochoa[3], Farid Amirouche[1], and Mark Gonzalez[2]

University of Illinois at Chicago, Dept of Mechanical Engineering[1] and Orthopaedic Surgery[2], Chicago, IL, USA amirouch@uic.edu
DePuy Orthopaedics, Warsaw, Indiana, USA

INTRODUCTION

The objective of this study is to investigate the initial stability of cementless cup hip prosthesis as a function of the patients bone density and body weight in a cadaver model. The main focus is to address the combined axial and torsional loading of the artificial hip in relation to the joint stability and the patient's bone density.

Initial implant fixation is essential to the success of a total joint. Basic functions like climbing stairs and standing from a chair can eccentrically load the hip prosthesis and produce a torque on the acetabular cup (Dennis, Komistek, et. al. 2001). This torque results in a shear force across the bone prosthesis interface that produces hip micromotion (HMM). Micromotion greater than 50 to 100 microns is known prevent bone ingrowth into a porous cup (Jasty, Bragdon, et.al. 1997). The obvious and most common solution to this is to use an adjunctive screw to affix the cup to the acetabulum. However, screw holes are direct pathways for polyethylene wear particles to enter the bone-cup interface. These particles are phagocytosed by macrophages that in turn release an array of cellular mediators that are capable of inducing cell proliferation, promoting osteoclast formation, and resorption of adjacent bone.

METHODS

Seven fresh-frozen cadaver pelvises were cleaned of all soft tissues. The femoral necks were then chosen for DEXA scans. Next, uncemented cups were placed into each of the acetabula with 2mm of underreaming in relation to the cup. Pinnacle cups were then chosen. The acetabulum was then potted in a metal box, eliminating viscoelastic deformation of the pelvis relative to the sensors.

A custom jig was designed that applies both torque and axial force to the prosthesis similar to that produced inside the body. A lever arm was set to 2-cm, simulating an impingement on the rim of the cup 2-cm from the center. One hundred cycles of loading at 200-N and 4-N/m was applied to each pelvis. The loading was incremented by 100-N and 2 N-m until the interface failed. Six LVDT displacement sensors were arranged around the cup in order to measure HMM in five degrees (3 displacements and 2 rotational). The LVDT sensors measure linear motion with 1-micron repeatability. Each sensor was calibrated with a 25-micron gap gauge.

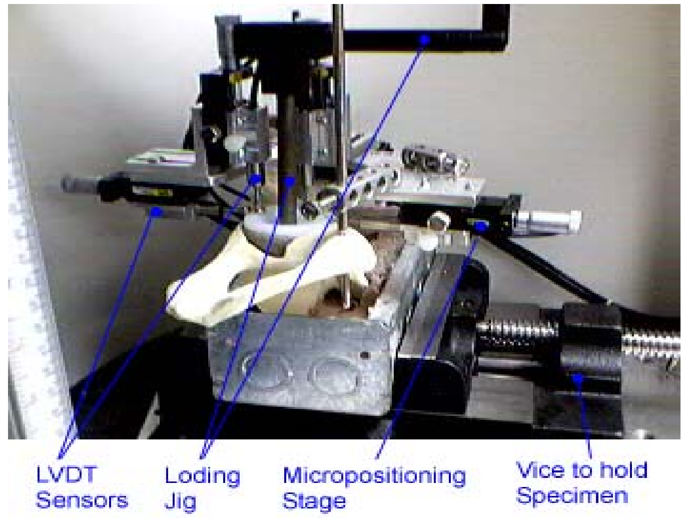

Figure 1: A photograph of the experimental setup used to both load the hip and record micromotion.

RESULTS AND DISCUSSION

The amount of torque necessary to create micromotion of 50 and 100 microns was then recorded. Also between 150 and 250 microns, we noticed a failure of the interface. At this point, plastic deformation was evident. Permanent deformation was noticeable, as the prosthesis did not return to its original position. Also, a constant loading cycle produced an increasing deformation until the interface failed. The force and torque at failure was also recorded.

SUMMARY

Most surgeons agree that if the bone quality is good enough, a press-fit prosthesis without adjunctive screw is the optimal approach. However, most surgeons cannot make a bone quality assessment until the prosthesis is already in place. Therefore, uncemented prosthesis with adjunctive screw holes still remains popular.

The purpose of this project is to correlate resistance to shear of the interference fit with the bone density of the acetabulum. This data is useful when addressing shell / bone interface and the need of future fixation such as adjunctive screws.

REFERENCES

Dennis DA, Komistek RD, Northcut EJ, et al. J Biomech. 2001 May;34(5):623-9.
Jasty M, Bragdon C, Harris WH, et. al. J Bone Joint Surg Am. 1997 May;79(5):707-14.

AN ANALYTICAL DESCRIPTION OF KINEMATIC CROSSTALK

Scott Landry and Kevin Deluzio
The Dynamics of Human Motion Laboratory, School of Biomedical Engineering, Dalhousie University, Halifax, Canada
Communicating author, landrys@is2.dal.ca

INTRODUCTION

Kinematic crosstalk is a form of error associated with the measurement of joint angles and it occurs when the chosen joint coordinate system is not aligned with the true rotation axes of a joint. In the knee for example, misalignment of the flexion axis or joint coordinate axes results in significant ab/adduction and int/external rotation angle error. Kadaba et al (1990) and Piazza et al (2000) have made reference to this error and stated that the error was related to the amount of axis misalignment and the degree of flexion. Kinematic crosstalk has also been revealed through correlation between the measured joint angles. Deluzio (2001) proposed using principal component analysis (pca) with a mechanical model to eliminate crosstalk and identify the true joint axes of rotation. No study, however, has been able to determine an analytical description of this crosstalk-induced error.

The purpose of this study was to use simulation to: i) create a numerical model capable of introducing crosstalk, ii) find an analytical equation to describe the resulting measurement error caused by crosstalk and iii) investigate the use of pca in eliminating the effects of crosstalk.

METHODS

A numerical model was created to simulate kinematic crosstalk through misalignment of a fixed coordinate system (MatLAB). A joint coordinate system was established for both a fixed and moving body, with the moving body undergoing rotation from -180º to 180º about a true flexion axis. Due to the order dependence of calculating Cardan angles, misalignment of the flexion axis has the greatest effect on crosstalk. To misalign the flexion axis anywhere in space, two ordered rotations were performed (Figure 1). Each rotation was chosen in increments from ±15º in 5º steps and once positioned, the misaligned joint coordinate system was used to calculate the three crosstalked Cardan angles for the known motion.

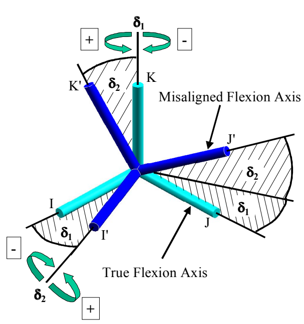

Figure 1: Misaligning flexion axis to a desired orientation using ordered rotations of δ_1 and δ_2 about the K and I' axes, respectively.

A principal component analysis of the three crosstalked angles (Deluzio, 2001) was performed to determine if the orientation of the true flexion axis could be found using the first eigenvector, thereby eliminating the effects of crosstalk.

RESULTS

Misalignment of the fixed body joint coordinate system with respect to the true flexion axis of the model resulted in kinematic crosstalk. The introduced angle measurement errors were observed to be sinusoidal in nature and dependent on the degree of axis misalignment and flexion angle. The analytical functions describing the crosstalk errors for ab/adduction and int/external rotation were found to be:

$$error_{\text{ab/adduction}} = \delta_1 \times \sin(\theta) - \delta_2 \times \cos(\theta)$$
$$error_{\text{int/external rotation}} = -\delta_2 \times \sin(\theta) - \delta_1 \times \cos(\theta)$$

where: δ_1 - misalignment of axis in transverse plane (°)
δ_2 - misalignment of axis in frontal plane (°)
θ - flexion angle (°)
errors - difference between true and crosstalk angles

The application of pca to the crosstalked angle measurements was able to identify the single degree of freedom motion. Also, for small symmetrical flexion/extension angles (i.e. $\sin\theta \approx \theta$) pca was able to determine the orientation of the true flexion axis with respect to the misaligned axis.

DISCUSSION

While the dependence of crosstalk error on flexion angle and axis misalignment has previously been stated (Kadaba et al, 1990 and Piazza et al, 2000), this study represents the first time that an analytical model has been described to explain this error. The analytical solution describes the error in ab/adduction and int/external rotation in terms of the flexion angle and the amount of axis misalignment in both planes. The technique of pca also proved to be effective, with the analytical model explaining some of the limitations of using pca to correct for crosstalk error.

This analytical description for crosstalk-induced angle measurement error completely specifies the effects of this error and offers the potential for the development of techniques to correct for it.

REFERENCES

Deluzio, K.J. (2001). *Proceedings of ISB2001*, Zurich, Ch.
Kadaba, M.P. et al (1990). *J. Orthop. Res.*, **8**(3), 388-392.
Piazza, S.J. et al (2000) *J. Biomech.*, **33**, 1029-1034.

IN VIVO INTRACARDIAC HEMODYNAMICS: DOES FLOW INFLUENCE MORPHOLOGY?

Jay R. Hove, Reinhard W. Köster, Arian S. Forouhar, Gabriel Acevedo-Bolton, Scott E. Fraser and Morteza Gharib
Correspondence should be addressed to jhove@caltech.edu
Bioengineering and Biology Options, California Institute of Technology, Pasadena, California, USA

INTRODUCTION

In vitro studies on cultured cardiac endothelial cells have shown that fluid-mechanical forces induce changes in cellular morphology through cytoskeletal rearrangement as well as changes in the gene expression profile. To link these *in vitro* data to the intact heart, a quantitative *in vivo* analysis of intracardiac flow forces is necessary. In this presentation we will describe real-time *in vivo* imaging of intracardiac blood flow within the beating hearts of living zebrafish embryos and describe the development of hearts where the natural hemodynamic milieu has been experimentally altered.

METHODS

Two embryonic stages of the zebrafish (*Danio rerio*) were chosen for their distinct heart morphologies: 4.5 days post fertiliztion (dpf) and 37 hours post fertilization (hpf). Pigment-blocked zebrafish embryos were lightly anesthetized and immobilized in ultra-low gelling agarose.

Gross cardiac dynamics were defined using high-speed transmitted light microscopy with valve dynamics visualized through high-speed laser-scanning microscopy on transgenic embryos expressing GFP. Blood flow patterns were identified by fluorescent labeling of blood serum (Bodipy-Ceramide) and observing the trajectories of dark, streaking erythrocytes. Fluid forces were more precisely quantified using real-time cine imaging of the flow at 440 frames$\cdot$sec^{-1} and digital particle image velocimetry (DPIV) to calculate the velocity vector fields and circulation patterns generated by moving red blood cells.

To test the possible influences of flow through the heart on its development, we implanted 50 μm glass beads into the inflow/outflow tracts of 57 hpf embryos and examined the resulting cardiac development.

RESULTS AND DISCUSSION

In the valved 4.5 dpf embryos we discovered a highly dynamic flow environment with high-speed (0.5 cm$\cdot$s^{-1}) jets and swirling vortices (Fig. 1). Ejection fractions were calculated at nearly 60%, surprisingly close to that of the adult human left ventricle. Viscous flow at these speeds, within such small structures yields enormous wall shear stresses (>75 dyne$\cdot$cm^{-2}). Valveless 37 hpf hearts showed jets with velocities approaching 1.5 mm$\cdot$s^{-1} yielding wall shears of 2.5 dyne$\cdot$cm^{-2}. Blockage of the inflow tract (in front of the sinus venosus) or outflow tract (ventriculo-bulbal constriction) showed severe regurgitation of blood inside the heart with shear forces reduced 8-10 fold over controls. Among the more striking effects of the procedure was retarded cardiac looping and malformation of the third chamber (bulbus arteriosus).

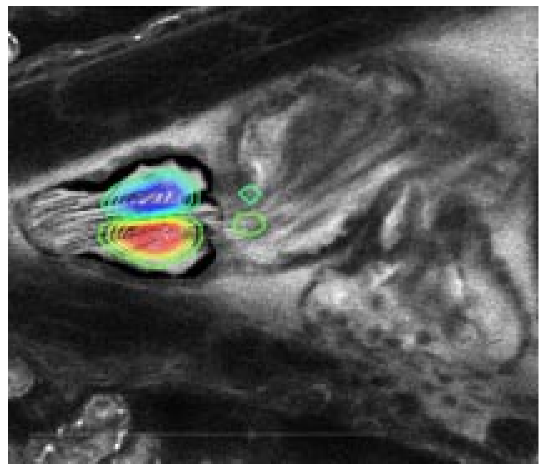

Figure 1: High-velocity circulation and blood jet Generated in the 4.5 dpf embryonic zebrafish heart during ventricular systole. Contour colors are indicative of vortical strength and direction of rotation.

SUMMARY

We conclude that the physiology and development of the embryonic heart is linked by hemodynamics. We have shown that intracardiac wall shear stress reaches significant levels above cellular sensitivity even at primitive heart stages early in embryogenesis. Interference with intracardiac hemodynamics through physical blockage results in severe cardiac malformations. Our findings underscore the importance of examining the interplay between genetics and epigenetic factors in analyzing pathogenesis of embryonic vascular defects and cardiovascular disease.

APPLICATION OF A NONLINEAR MODEL TO DESCRIBE LIGAMENT BEHAVIOR

Paolo P. Provenzano[1], Roderic S. Lakes[2], David T. Corr[1], Ray Vanderby Jr.[1]

[1]Orthopedic Research Laboratories, Dept. of Biomedical Engineering and Orthopedic Surgery, [2]Dept. of Biomedical Engineering and Engineering Physics, University of Wisconsin, Madison, WI, USA, vanderby@surgery.wisc.edu

INTRODUCTION

Recent experiments in rat medial collateral ligament (MCL) revealed that the rate of stress relaxation is strain dependent (Provenzano *et. al.* 2001). This nonlinear behavior requires a more general description than the separable quasi-linear viscoelasticity (QLV) theory commonly used in tissue biomechanics since QLV will predict the same relaxation rate regardless of strain magnitude. The purpose of this study was to determine whether the nonlinear Modified Superposition formulation (often called nonlinear superposition) could adequately model the strain dependent stress-relaxation behavior of ligaments.

ANALYSIS

The single integral formulation of the Modified Superposition method (Findley *et al.* 1976) allows the relaxation function to depend on strain level:

$$\sigma(\varepsilon,t)=\int_0^t E(t-\tau,\varepsilon(\tau))\frac{d\varepsilon(\tau)}{d\tau}d\tau. \qquad (1)$$

The form of the relaxation function will be chosen as a strain-dependent power law: $E(\varepsilon, t)= At^{B(\varepsilon)}$. The function $A(\varepsilon)$ represents the initial modulus (E_0), obtained from a stress-strain or isochronal curve describing the nonlinear elastic behavior. The function $B(\varepsilon)$ describes the strain dependent rate of relaxation and can take the form $B(\varepsilon) = g(\varepsilon)n_0$, where n_0 is some initial relaxation rate and $g(\varepsilon)$ accounts for strain dependent nonlinearity in rate. Considering the strain history to be controlled by a Heaviside step Eq 1. becomes : $\sigma(\varepsilon, t) = E_0\varepsilon t^{g(\varepsilon)n_0}$. In addition, a more complex strain history function will be examined. A sinusoidal strain history of the form: $\varepsilon(t) = 0.5\varepsilon_0[1-\cos(\alpha\pi t)]$ (ε_0 = strain amplitude and α = 2X frequency). The resulting form of Eq. 1 is:

$$\sigma(\varepsilon,t)=\frac{\pi\alpha\varepsilon_0}{2}\int_0^t A(\varepsilon)(t-\tau)^{B(\varepsilon)}\mathrm{Sin}(\alpha\pi\tau)d\tau\ . \qquad (2)$$

The model will be fit to experimental data from Provenzano et al., 2001. To the authors' knowledge no tests exist revealing strain dependent relaxation behavior during cyclic testing. Hence, Equation 2 demonstrates model behavior only.

RESULTS AND DISCUSSION

Modified superposition theory fits the data well for all strain levels (Fig. 1). Application of the model resulted in σ_0 values of 1.45, 5.72, 10.10, and 15.25 MPa for 0.82, 1.74, 2.38, and 3.74% strain, respectively, capturing elastic nonlinearity. The rate term, $B(\varepsilon)$, decreases as strain increases (-0.14, -0.054, -0.026, and –0.012 for 0.82, 1.74, 2.38, and 3.74% strain, respectively) capturing nonlinearity in the rate of relaxation.

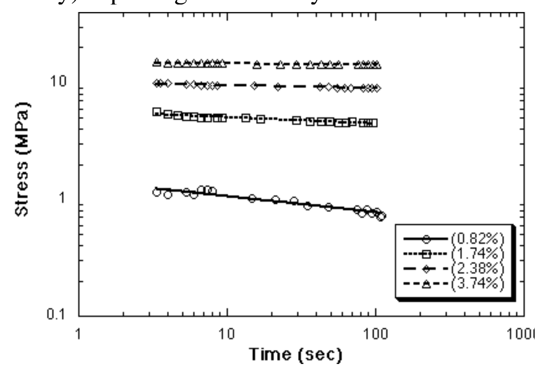

Fig. 1: Application of Modified Superposition (lines) to experimental stress relaxation (points) for testing at various strain levels in a single rat ligament. R^2 = 0.91, 0.91, 0.96, and 0.95 for ε=0.82%, 1.74%, 2.38% and 3.74%, respectively.

For Eq. 2 the function $A(\varepsilon)$ was determined from a typical σ-ε curve and $B(\varepsilon)$ was obtained by fitting rate data over a range of strains (~0.25-5.0%). The peak stresses at a constant frequency factor display strain-dependent behavior, although to a lesser extent than seen with constant strain (Fig. 1). When examining model behavior over one order of magnitude of frequency (α = 0.1 to 1.0), initial stress increased. Relaxation rate, increases with increasing frequency. Hence, the model predicts that relaxation rate is both strain and frequency dependent.

SUMMARY

Modified superposition theory describes nonlinear stress relaxation behavior well and allows a single modulus to account for differences in relaxation rate with strain.

REFERENCES

Findley et al., Creep and relaxation of nonlinear viscoelastic materials, Dover, New York, 1976.
Provenzano et al., *Ann. Bio. Eng* 29:908-914, 2001

ACKNOWLEDGEMENTS

NASA (grant # NAG9-1152) and N.S.F. (grant # CMS-9907977) provided funding for this work.

MECHANICAL PROPERTIES OF CARTILAGE SPECIMEN IN RATS – SMALL SCALE INDENTER TESTING APPLIED TO TYPICAL LAB ANIMALS

Uwe G. Kersting[1], Anja Niehoff[2], Michael M. Morlock[3], Horst Michna[4], Gert-Peter Brueggemann[2]

[1] Department of Sport and Exercise Science, University of Auckland
[2] Department of Biomechanics, German Sport University Cologne
[3] Biomechanics Section, Technical University of Hamburg-Harburg
[4] Department Morphology and Tumor Research, German Sport University Cologne

INTRODUCTION

Indenter testing has been demonstrated as a valid method to characterise material properties of cartilage specimen (Sakamoto et al., 1996). Rather large species have been investigated in most cases which require an extensive expenditure on animal keeping. In this study a down-scaled testing procedure is proposed and applied to Sprague-Dawley rats as typical lab animals.
The aim of this study was to develop and apply a miniature testing apparatus to investigate full thickness cartilage specimen by a small indenter. The procedure described was applied to a sample of animals experiencing running exercise of different amounts for four, eight and 12 weeks.

METHODS

Animals were decapitated and the legs were detached at the hip joint. The knee joint was dissected carefully in custom made preparation pool with grip screws under TBS. The left leg was frozen at –80 °C immediately after dissection and stored until mechanical testing. A relaxation test was performed using a solid spherical (0.5 mm diameter) indenter in a TBS bath on a material test machine (Z2.5/TN1S, Zwick; Fig. 1 and 2A). By use of a microscope with angular scale, specimens were orientated in a way that the indenter approached the cartilage surface perpendicularly. A ramp load of 300±5 mN (Fmax) was applied and the achieved deformation held constant for 250 s. Stiffness, short and long term relaxation were quantified by calculation of the rise time (tr), and times where the load had decreased to ½ (t1/2) or 1/e (t1/e) of the Fmax and the final load (Fend) after 250 s (Fig. 2B).

Indenter Test Setup

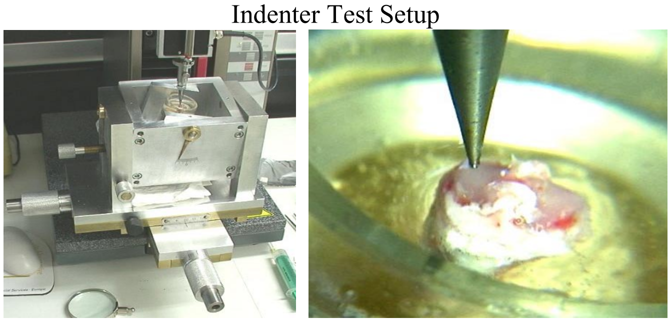

A B

Figure 1: A: Adjustable specimen positioning desk B: Indenter orientation (TBS solution removed for illustrative reasons)

Ninety female Sprague-Dawley rats (starting age three weeks) were fed and watered ad libitum. The sample was split into nine groups of ten animals each, which were killed after four, eight or 12 weeks of training. Three groups served as sedentary controls (C1 – C3). Six groups were kept in custom

Dimensions of apparatus and data analysis

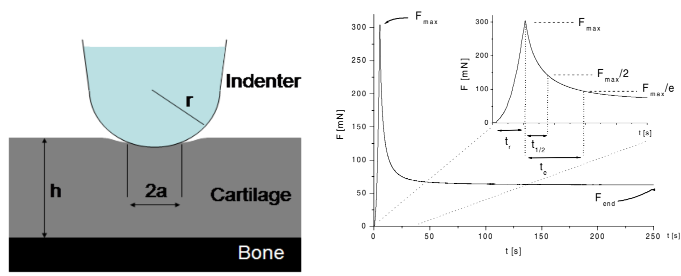

A B

Figure 2: A: Sketch of the cartilage dimensions, h = cartilage thickness, a: radius of contact area, r: radius of indenter B: Example of a force reading. Parameters described in text.

made devices containing an ordinary cage connected to a running wheel; three groups had unlimited access to the wheel (..1) while the other three could only train for half of their time (..2; T11 – T32). Running distance was counted by a magnetic switch at each wheel, monitored by a computer system.

RESULTS AND DISCUSSION

The dimensions of the apparatus correspond to recommendations from analytical studies (Sakamoto et al., 1996). Fig. 3 demonstrates that age and different training regimes produce systematic changes in mechanical properties of the rat knee joint.

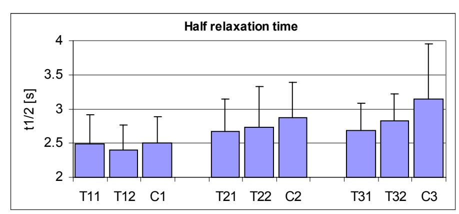

Figure 3: t1/2 for nine training groups

SUMMARY

A miniature cartilage testing apparatus was introduced which matches technical requirements given by analytical studies. Systematic differences were demonstrated with respect to training regime. The approach provides a great potential for controlled studies on cartilage adaptation.

REFERENCES

Sakamoto, M., Li, G. Hara, T., Chao, E.Y.S. (1996). J Biomechanics, **29,** 679 - 685

FUNCTIONAL ADAPTATION OF THE DORSIFLEXOR TORQUE-VELOCITY RELATION

Viviane Bortoluzzi Fração[1, 2], Henrique Marquardt Lammerhirt[1], Marco Aurélio Vaz[1]
[1] Exercise Research Laboratory, School of Physical Education, Federal University of Rio Grande do Sul, Brazil
[2] Faculty of Physical Therapy, Lutheran University of Brazil
marcovaz@esef.ufrgs.br

INTRODUCTION

Muscle excursion is important in regulating sarcomere number. Evidences in support of this idea have been shown in animal studies, where rabbits submitted to surgical procedure increased muscle excursion in 40% and in series sarcomere number in 22% (Koh and Herzog, 1998). In humans, increased excursion due to training may produce similar adaptation. Ballet dancers, for example, show increased ankle plantar flexion (Hamilton et al., 1992; Fração et al., 1999) compared to normal population, causing an increase in dorsiflexor (DF) muscle excursion. Volleyball players show an ankle joint range of motion similar to normal population, and work in a more DF position. Muscle adaptation due to these different types of joint demands might be responsible for modifying the torque-velocity relation. The purpose of this study was to compare the torque-velocity (T-V) relation of DF muscles and the electromyographic (EMG) activity of tibialis anterior muscle (TA) of classical ballet dancers and volleyball players.

METHODS

Twenty five female subjects (ballet dancers n=10; volleyball players n=15) participated in the study. DF muscles peak torque (T_{max}) was evaluated during maximal concentric voluntary contractions in different angular velocities (60, 120, 180, 240, 300, 360, 420°/s) using a Cybex Norm isokinetic dynamometer. EMG signals were obtained from the TA muscle by means of surface electrodes in a bipolar configuration. Root mean square (RMS) values were calculated from the raw EMG signals. T_{max} and RMS values were normalized for each subject. A two-way analysis of variance for repeated measures was used to evaluate possible statistical difference for each measured parameter (torque, RMS, velocity, group), as well as to test for interaction. The level of significance adopted was 0.05 for all tests.

RESULTS AND DISCUSSION

The torque behavior as a function of angular velocity was similar between the two groups (p=0,1766). An inverse hyperbolic relationship, similar to the classical relation described by Hill (1938), was observed for the two groups. However, the ballet dancers normalized torque was higher compared to the volleyball players for all angular velocities (p=0,0001; Figure 1). The normalized EMG RMS values were similar between the two groups among the different angular velocities (p=0,4467; Figure 2), showing that muscle activation was not responsible for the observed differences in torque production. Intrinsic adaptation of the ballet dancers DF muscles (i.e. increase in serial sarcomere number due to increased muscle excursion) seems to be responsible for the observed torque results. These ideas are similar to the ones proposed by Lieber (1992) where larger fibers should produce higher forces at higher shorting velocities. Another possibility would be that ballet dancers have a higher percentage of fast twitch fibers in this muscle when compared to volleyball players. Although biopsy was not obtained to clarify this point, a higher percentage of fast twitch fibers in the ballet dancers does not seem reasonable as volleyball players show higher power demands in their activities than the ballet dancers.

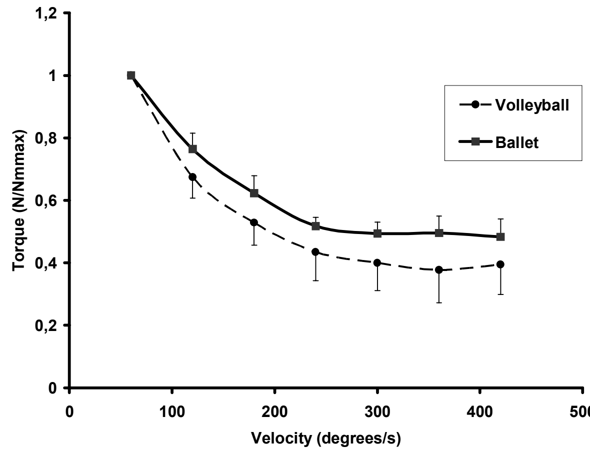

Figure 1. Normalized DF torque-velocity relation (mean ± standard deviation).

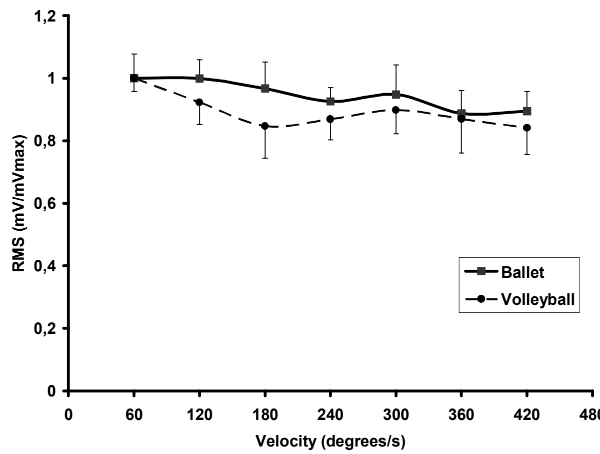

Figure 2. Normalized RMS values of TA in the different angular velocities (mean ± standard deviation).

REFERENCES

Hamilton W. G. (1992). *Am. J. Sports Med.*, 20:267-273.
Koh TJ; Herzog W. (1998). *J. Physiol.*, 508:267-280, 1998.
Fração V.B. et al. (1999). *Movimento*, 11:3-15, 1999/2.
Hill A.V. (1938). *Soc. Lond.*, 126:136-195.
Lieber L.R. (1992). *Skeletal Muscle Structure and Function*. Williams and Wilkins, Baltimore.

ACKNOWLEDGEMENTS

The authors would like to thank CNPq-Brazil and UFRGS-Brazil for the financial support, and Drs. Dilson J.E. Rassier and Walter Herzog for helping in different parts of this study.

CONTACT AREAS AND LIGAMENT LENGTHS ARE ABNORMAL IN PATIENTS WITH MALUNITED DISTAL RADIUS FRACTURE DESPITE NORMAL RADIOULNAR KINEMATICS

G.E. Marai[1], D.H. Laidlaw[1], C. Demiralp[1], C. M. Grimm[3], J.J. Crisco[2,4], D.C. Moore[4], E. Akelman[4]
[1] Department of Computer Science, and [2] Division of Engineering, Brown University, Providence, RI
[3]Department of Computer Science, Washington University, St. Louis, MO
[4] Department of Orthopaedics , Brown Medical School/Rhode Island Hospital Providence, RI
E-mail: gem@cs.brown.edu

INTRODUCTION

Altered kinematics of the distal radioulnar joint (DRUJ) and/or bone impingement are considered causes of long-term complications associated with malunited distal radius fractures. However, a recent CT image-based *in vivo* study of patients with malunited distal radius fractures found that malunion did not alter forearm kinematics and that limitations of pronosupination were not caused by bony impingement (Moore et al., *in press*). In this study, data from the previous study was reanalyzed to explore focal changes in the articulation at the DRUJ (location and area of bone contact) and potential soft tissue constraints ('length' of the dorsal and palmar radioulnar ligaments).

METHODS

The bony surfaces and kinematics of both radii were obtained from the CT image volumes of nine volunteers with unilateral distal radius fractures (3M, 6F, age 55 ± 15.4 yrs.) scanned in neutral and multiple positions of supination and pronation (Moore et al., *in press*). The dorsal angulation and radial shortening of the injured wrists averaged 20.9 ± 5.8 degrees and 4 ± 3 mm, respectively. Focal changes in the articulation of the distal radius and ulna were assessed by comparing the area and location of bony contact. Contact area was estimated using a distance field representation thresholded to distances less than 5 mm. The location of the centroid of the contact area was described in a coordinate system with the origin at the ulna-carpal surface and positive in a proximal direction. Potential soft tissue constraints were assessed by calculating the 'length' of the dorsal and palmar radioulnar ligaments, defined as the shortest paths between insertion points constrained to avoid bone penetration. Paired Student's t tests were used to compare the uninjured and malunited DRUJs. P values ≤ 0.05 were considered to be statistically significant. The data reported here are for the neutral positions.

RESULTS

Ulna contact area was smaller and was located more proximally in the malunited forearms than in the uninjured contralateral forearms (Figure 1, Table 1). The length of the dorsal radioulnar ligament paths was on average 27% longer in the malunited forearms; the palmar ligament path lengths did not differ. In seven of the nine malunited forearms, the dorsal radioulnar ligament curved around the head of the ulna as it passed from the ulna to the radius. The average deflection of the dorsal radioulnar ligament in the malunited forearms was 0.65 mm. No dorsal deflection was found for uninjured forearms.

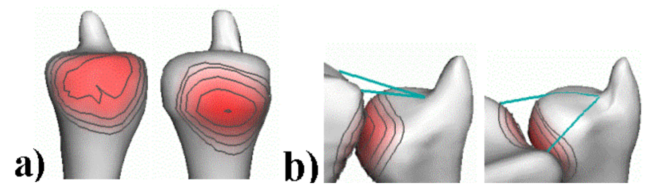

Figure 1. a) Contact areas on both ulnas from a single volunteer. The shading and contours (1 mm apart) show distance to the radius. Note proximal shift and decreased size for malunited (right). **b)** Ligament paths for two forearms, same volunteer. Note ligament deflection for malunited (right).

Table 1. Contact area (5 mm threshold), location of the centroid of the contact area, and dorsal and palmar ligament lengths in neutral pronosupination.

	Uninjured	Malunited	P < 0.02
Contact Area (mm^2)	208.1 ± 46.8	170.4 ± 43.0	Yes
Centroid location (mm)	3.7 ± 0.8	5.3 ± 0.4	Yes
Dorsal lig. length (mm)	12.1 ± 1.9	15.4 ± 2.1	Yes
Palmar lig. length (mm)	14.8 ± 1.2	15.0 ± 2.8	No

DISCUSSION

Although Moore et al. found no significant differences in the pronosupination kinematics of the malunited and uninjured wrists evaluated, this study found significant differences in the size and location of the joint contact area, and in the soft tissue constraints of the DRUJ. The significant change in the dorsal radioulnar ligament length, but not in palmar ligament length, is consistent with the original malunion (all tilted dorsally). The proximal shift in the location of the centroid of the contact area is consistent with the radial shortening. The changes reported here present a possible etiology for the development of degenerative joint disease, and the change in ligament length may be one mechanism for the limitation of pronosupination.

REFERENCES

Moore et al., *J Hand Surgery* (*in press*)

ACKNOWLEDGMENTS

Funded in part by NIH AR44005 and NSF CCR0093238.

NANOMECHANICAL AND BIOCHEMICAL PROPERTIES OF DISEASED ARTERY TISSUE

Donna Ebenstein[1], Joan Chapman[2], Cheng Li[2], Dezba Coughlin[1], Joseph Rapp[3], David Saloner[1,4], and Lisa Pruitt[1,2]

Medical Polymers and Biomaterials Group, University of California, Berkeley, California, USA
[1]UCSF/UCB Bioengineering Graduate Group, [2]Bioengineering Department lpruitt@newton.me.berkeley.edu
[3]Department of Vascular Surgery, [4]Department of Radiology, University of California, San Francisco, California, USA

INTRODUCTION

Atherosclerosis is associated with the accumulation of abnormal materials such as lipid, hematoma, and calcifications in artery walls. Structure-property relations of diseased artery consituents are essential for accurate modeling of disease progression and treatments. A study of formalin-fixed plaques using nanoindentation and Fourier Transform Infrared spectroscopy (FTIR) suggested that the stiffness of tissue samples increased as their mineral content increased (Ebenstein, 2002). In this study, the same approach is extended to the analysis of frozen and fresh tissue samples.

METHODS.

Five carotid bifurcation endarterectomy specimens were used in this study. Three of the samples were fixed in formalin prior to mechanical analysis, one was frozen at –20° C, and one was tested fresh. All were tested after equilibrating in physiological saline at 25° C. Plaque samples were dissected into regions of relatively uniform composition. The regions were then potted in dental cement for mechanical testing.

Mechanical testing was performed using the Hysitron TriboIndenter (Minneapolis, MN). A trapezoidal loading curve was applied to 5-10 sites in each region, with peak loads ranging from 40 to 600 µN. Reduced modulus values (Er) were calculated from the unloading curves following the method of Oliver and Pharr (Oliver and Pharr, 1992). After mechanical analysis, all samples were fixed in formalin and transferred to water for FTIR analysis.

FTIR was performed using the Nicolet Avatar 360 (Madison, WI) equipped with the ATR accessory. Spectra at 1-4 sites in each tissue region were collected for 32 or 64 scans at 4 cm^{-1} resolution. After standard corrections and water subtraction, Mineral:Matrix ratios were calculated by dividing the area under the phosphate peak (1200-900 cm^{-1}) by the area under the collagen amide I peak (1720–1585 cm^{-1}).

RESULTS AND DISCUSSION

Reduced modulus and Mineral:Matrix ratios for tissue regions from three formalin-fixed plaques, one frozen plaque, and one fresh plaque are summarized in Table 1. Under all treatment conditions, increases in Er between tissue categories was associated with increases in the Mineral: Matrix ratio, with hematoma being the softest and having the lowest mineral content, and calcification being the stiffest and having the highest mineral content. Further, the reduced modulus of formalin-fixed fibrous tissue is 4-fold higher than the values for fresh and frozen tissue, as expected due to the cross-linking effects of formalin.

SUMMARY

Using nanoindentation and FTIR, trends in tissue stiffness can be correlated to changes in tissue composition. In particular, increased reduced modulus values are associated with increased calcification content in the tissue. Further, differences in stiffness between fresh and formalin-fixed fibrous tissue are detectable using nanoindentation.

REFERENCES

Ebenstein, D.M. et al (2002). *Proeedings of the 2001 Materials Research Society Fall Meeting*, in press.
Oliver, W.C., Pharr, G.M. (1992). *J. Mat. Res*., **7**, 1564-1583.

Table 1: Reduced moduli and Mineral:Matrix ratios for diseased artery tissue tested fresh, after freezing, or after formalin-fixation. Data for fresh and frozen samples were collected from one specimen each; formalin-fixed data were averaged over three specimens.

Tissue Category	Property	Formalin-fixed	Frozen	Fresh
Hematoma	**Er** [MPa] *(Range)*	**1.15** *(0.10-2.60)*	**0.10** *(0.07-0.14)*	**0.27** *(0.15-0.50)*
	Mineral:Matrix	2.60 *(1.53-3.29)*	0.21 *(0.20-0.21)*	0.20 *(0.20-0.20)*
Fibrous Tissue	**Er** [MPa] *(Range)*	**1.31** *(0.06-21.5)*	**0.22** *(0.18-0.30)*	**0.31** *(0.12-0.98)*
	Mineral:Matrix	2.83 *(0.91-7.36)*	0.75*(0.63-0.86)*	0.43 *(0.20-0.73)*
Partially Calcified Fibrous Tissue	**Er** [MPa] *(Range)*	**259** *(0.10-6104)*	**1.48** *(0.08-8.10)*	**7.78** *(0.72-34.6)*
	Mineral:Matrix	3.84 *(2.51-7.90)*	1.00 *(0.99-1.00)*	1.04 *(0.24-1.50)*
Calcification	**Er** [MPa] *(Range)*	**1890** *(0.18-21300)*	**1390** *(0.10-21000)*	**174** *(9.04-300.3)*
	Mineral:Matrix	10.7 *(7.10-14.11)*	3.51 *(3.51-3.51)*	3.21 *(1.45-4.97)*

MATERIAL CLASSIFICATION OF BIAXIAL SOFT TISSUE RESPONSE

D. Claire Gloeckner[1*], Michael B. Chancellor[2] and Michael S. Sacks[1]
[1]Departments of Bioengineering and [2]Urology, University of Pittsburgh, Pittsburgh, Pennsylvania, U.S.
dcgst11@pitt.edu

INTRODUCTION

A disadvantage in the use of phenomenological models is the requirement of choosing the model before the material classification is made. Hence, the procedure becomes an arbitrary operation; if the data does not fit the model, then the assumption of material classification is incorrect and another model chosen. Other methods used to determine material classification require complex strain-based protocols that may not be physiologic (Sacks 2000). Herein we describe a generalized method for material classification.

To demonstrate this method, we examined the differences in rat urinary bladder wall mechanics in normal and spinal cord injury in a rat model. Mechanically, the absence of neural control leads to changes in the function of the bladder (German, Bedwani et al. 1994; Kruse, Bennett et al. 1994). We have observed the phenomenon of quasi-isotropy in both normal and spinal cord injured bladder, complicating modeling. Incorporation of mechanical data into a predictive model is required for organ-level simulations that can aid in designing pharmaceutical and surgical interventions.

METHODS

Normal (n=12) and ten days post spinal cord injury (n=8) rat urinary bladder wall was obtained and biaxially cycled to obtain five protocols. Details of the testing and results can be found in (Gloeckner, Sacks et al. 2002). Each axial stress was fit separately to the following interpolation function with an r^2 of >0.99.

$S_{ii} = \frac{c}{2}\exp(Q)\frac{dQ}{dE_{ii}}$ where

$$Q = a_1E_{11}^2 + a_2E_{22}^2 + 2a_3E_{11}E_{22} + a_4E_{11}^2E_{22} + a_5E_{22}^2E_{11} + a_6E_{11}^2E_{22}^2 + a_7E_{11}^4 + a_8E_{22}^4$$

All parameters and experimental strains were used to generate a square mesh of stress values in both material directions.

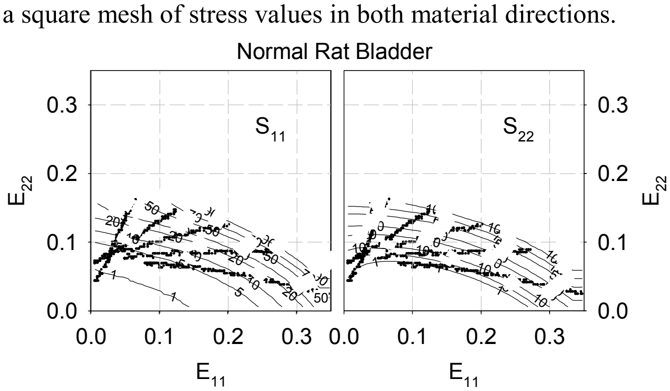

Figure 1: Stress contours overlaid with complete strain data of representative normal rat bladder wall.

RESULTS AND DISCUSSION

A representative normal sample is shown in fig 1. This normal specimen is clearly anisotropic with greater stretch in the x_1 axis. In contrast, the spinal cord injured example shown is close to isotropic (fig 2). Based on this information we then chose two appropriate models. As predicted, the isotropic model was insufficient for the normal data, but adequate for the spinal cord injured data (table).

The application of this method successfully allowed physiologic stress-based testing protocols to guide the form of the constitutive model without a priori assumptions.

4-parameter: $S_{ii} = \frac{c}{2}\exp(Q)\frac{dQ}{dE_{ii}}$ where $Q = a_1E_{11}^2 + a_2E_{22}^2 + 2a_3E_{11}E_{22}$

Isotropic: $W = c_1\left[\exp\left(c_2(I_1 - 3)\right) - 1\right]$

Table 1: Mean parameters and r^2 values for two models.

	4-parameter					Isotropic		
	C	A_1	A_2	A_3	R_2	C_1	C_2	R_2
Normal	1.75	28.0	39.9	27.1	0.86	6.65	5.03	0.58
SCI	0.85	42.4	45.4	-6.7	0.94	0.92	4.66	0.84

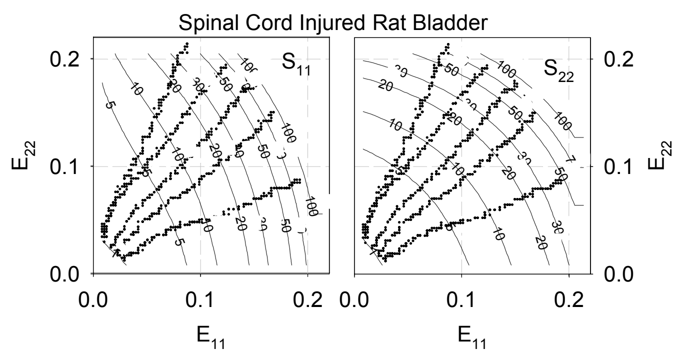

Figure 2: Stress contours overlaid with complete strain data of representative spinal cord injured rat bladder wall.

REFERENCES

German, K., J. Bedwani, et al. (1994). *Br J Urol* **74**(6): 744-8.
Gloeckner, D. C., M. S. Sacks, et al. (2002). *J Urol* **167**.
Kruse, M. N., B. Bennett, et al. (1994). *J Urol* **151**(4): 1088-91.
Sacks, M. S. (2000). *Journal of Elasticity* **61**: 199-246.

ACKNOWLEDGEMENTS

This study was funded by the National Institutes of Health grant PO1 HD39768-01A1.

DYNAMIC TESTING OF RAT ACHILLES TENDONS

Stefanie D. Stangier, Joseph E. Hale and Donald D. Anderson
Biomechanics Laboratory, Minneapolis Sports Medicine Center
Minneapolis, MN, e-mail: stan0320@tc.umn.edu

INTRODUCTION

The viscoelastic nature of tendons and similar soft tissues has long presented a challenge to researchers, as many variables affect the mechanical properties measured. In the past, often only failure properties were studied (e.g. Kurtz, 1999). However, in real life, a tendon rarely sees conditions that are anywhere near failure (Fung, 1993).

The dynamic, sub-failure properties are of more interest. In light of the many possible tests conducted, it could then be argued that the best choice for the frequency of loading for a tendon specimen is close to a typical physiological value. In order to separate the elastic from the viscous effects, it has been proposed to test materials at frequencies much higher than these physiological values (Cooke, 1996). The aim of this pilot study was to determine whether the results of dynamic material testing of rat Achilles tendons are dependent on the testing frequency. The observations serve to streamline the dynamic testing procedure for use in future research.

METHODS

Two groups of rat Achilles tendons from various sources were subjected to a cyclic uniaxial testing protocol using the EnduraTEC ELectroForce™ (ELF) 3200 testing system. The recovery period for all specimens between tests was ten (10) minutes. For the first group of tendons, the test frequencies were 0.5, 1.0, 2.0, 5.0, 10 and 100 Hz respectively. The 0.5 Hz test served as preconditioning cycle. The sequence of the remaining five frequencies was random. The second group of tendons was subjected to preconditioning at 0.5 Hz for 10 cycles, followed by the actual testing at 0.5, 1.0, 2.0, 5.0, 10 and 50 Hz. Again, the sequence of the tests was randomized.

The tendons were held by a low temperature tissue grip at the muscle end, while the calcaneus was potted in bone cement at a 45º incline. The bracket holding the potted end permitted two degrees of freedom. A tensile pre-load of 2 N was applied. Tests were performed at room temperature, with specimens covered by moist gauze between tests. Following dynamic testing, the tendons were pulled to failure at 0.167 mm/s.

RESULTS AND DISCUSSION

The Dynamic Material Characterization (DMC) software that works with the WinTest system from EnduraTEC is based on the Voigt model of viscoelasticity: a spring in parallel with a damping element. The storage, loss and dynamic stiffness were computed from the force, displacement and phase angle.

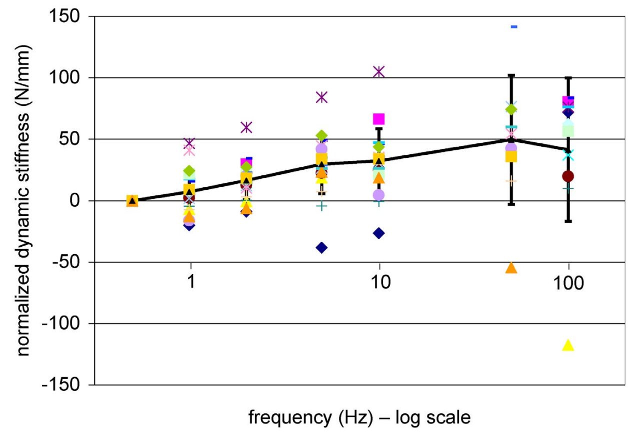

Figure 1: Normalized dynamic stiffness in relation to the frequency of loading. The line represents mean values, while the symbols depict the results across all specimens..

Figure 1 (above) shows the dynamic stiffness for all tendons along with the mean and the standard deviations at each frequency tested. Values were normalized with respect to values at 0.5 Hz for each specimen, since the changes in stiffness were of more interest than the absolute values. The dynamic stiffness at 0.5 Hz was 157.4 (± 67.9) N/mm [mean ± standard deviation]. Failure loads averaged 77.8 ± 11.8 N across the specimens tested, with the majority of failures occurring at the Achilles / calcaneal junction.

The dynamic stiffness reported is the complex composite of the storage stiffness and the loss stiffness. The storage stiffness is that associated with the purely elastic response of the tendon, while the loss stiffness accounts for the viscous portion. These values can alternatively be converted to the moduli more commonly used in the viscoelasticity literature.

REFERENCES

Johnson, GA et al (1994). *J Orthop Res* **12**, 796-803.
Kurtz C et al (1999). *Am J Sports Med* **27**, 363-369.
Cooke F et al (1996). *Biomaterials Science*. Acad. Press, 19-20.
Fung YCB (1993). *Biomechanics: Mechanical Properties of Living Tissues. 2nd ed.* Springer-Verlag. 261.

ACKNOWLEDGEMENTS

Thank you to EnduraTEC Corporation for the use of the ELF 3200 system and the DMC software. Special thanks also to the Midwest Orthopaedic Research Foundation for their hospitality.

EFFECT OF OSTEOPOROSIS IN A DISC-DEGENERATED LUMBAR SPINE

Ravikumar Varadarajan[1], Dr.F.M.L. Amirouche[1], Dr.Franklin C Wagner[2], Dr.Kern Guppy[2]
[1] Biomechanics Research Laboratory, University of Illinois at Chicago, rvarad1@uic.edu
[2] Department of Neurosurgery, University of Illinois at Chicago

INTRODUCTION

Disc Degeneration leads to various spinal disorders like Spondylylosis, Stenosis and Osteophyte formation and Osteoporosis leads to endplate fracture. Biomechanical investigation of Disc Degeneration and Osteoporosis has been studied separately by many researchers(1,2). But there is not enough data on the combined effect of Osteoporosis and Disc Degeneration. This study focuses on effect of Osteoporosis in a Disc Degenerated Lumbar Spine.

METHODS

Five 3D Finite Element models of L4-L5 FSU:

1. Intact
2. Grade(I) Degenerated
3. Grade(I) Degenerated with Osteoporosis
4. Grade(II) Degenerated and
5. Grade(II) Degenerated with Osteoporosis

were used in this study. FE Model of intact was developed using ANSYS-v5.7. Geometric data of the Vertebrae, Facet joint and Intervertebral Disc were based on recent studies(3,4). Cortical bone,Cancellous bone, Annulus Ground Substance and Posterior Elements were modeled as 3D Isoparametric 8 node elements. The Intervertebral Disc was modeled similar to recent studies(5). Facet Contact was modeled as 3D point-to-point contact elements. All Ligaments were modeled as Tension only spar element and all material properties are based on (5,6). The Model is validated with recent literature(5).

Grade(I) Disc degeneration(Dehydrated Nucleus) was simulated by using stiffer solid elements for the Nucleus with Young's Modulus twice that of Annulus ground substance.
Grade(II) degeneration was simulated by doubling the young's modulus of annulus ground substance and reducing the annulus fiber volume by 25%(5).
Osteoporosis of the vertebrae was simulated by reducing the young's modulus of Cancellous bone by 50%.
Axial Compression load of 405N was applied as uniform Pressure on the superior surface of L4 Vertebra. All Nodal points in the inferior surface of L5 vertebra were fixed in all directions.

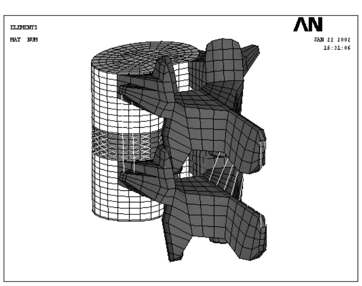

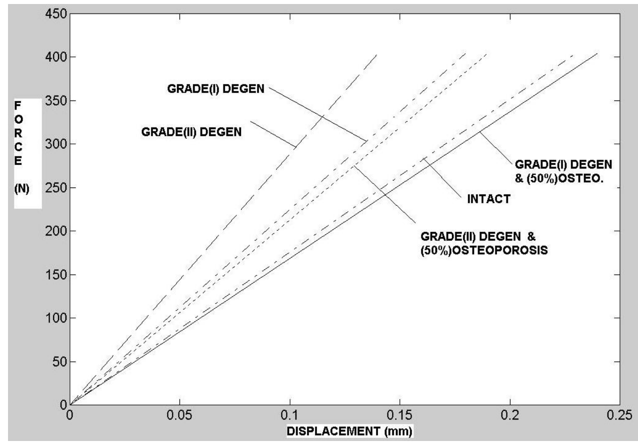

RESULTS AND DISCUSSION

As the Degeneration level increases stiffness of the FSU increases but Osteoporosis reduces the stiffness. Intervertebral Disc bulge and stress in Annulus ground substance decreased with increase in degeneration level. There was no considerable change in Disc Bulge in the Degenerated Model with Osteoporosis.

Stresses in Pedicle decreased in normal degenerated model but increased in osteoporotic degenerated model

Disc degeneration reduced the contribution of cancellous bone. This reduction was larger in normal than in osteoporotic bone. Cortical bone stress increased with increase in degeneration level. This increase was larger in osteoporotic(20%) bone than in normal bone.

Endplate stresses increased as the degeneration level increases. Osteoporosis further increases the endplate stresses.

REFERENCES

(1). Kim Y, Goel V.K, James Weinstein(1991), Spine, 16(3), pp 331-335
(2). Mizrahi J, Silva MJ, Keaveny TM(1993), Spine, 18(14), pp 2088-96
(3). Panjabi M.M., Goel, V.K, Takata K,Krag M (1992) – Spine, 17, pp 299-306
(4). Panjabi M.M., Goel, V.K, Takata K,Krag M Spine, 18(10), pp 1298-1310
(5). Kim Y, Vanderby R (2000), Spine, 3(4), pp257-272
(6). Goel V.K, Kim Y, Lim T.H(1988), Spine, 13(9), pp 1003-1011
(7). Ghosh P, Biology of Intervertebral Disc. Boca Raton, FL: CRC Press: 1988

THE BIOMECHANICS OF THE SHOULDER DURING WHEELCHAIR PROPULSION UP RAMPS

Michelle B. Sabick[1] and Kai-Nan An[2]
[1]Steadman♦Hawkins Sports Medicine Foundation, Vail, CO, USA, Michelle.Sabick@shsmf.org
[2]Biomechanics Laboratory, Department of Orthopedics, Mayo Foundation, Rochester, MN, USA

INTRODUCTION

The incidence of shoulder pain among manual wheelchair users is as high as 51% (Nichols *et al.*, 1979). Because wheelchair users rely on their upper extremities for mobility, shoulder injuries have detrimental effects on independence and quality of life. The joint forces generated during wheelchair propulsion are thought to cause chronic shoulder overuse injuries (Nichols *et al.*, 1979). One demanding and often painful task is negotiating a wheelchair up a ramp (Subbarao *et al.*, 1995). In tests where subjects used a variety of mobility aids to ascend ramps varying in grade from 1:20 to 1:8 (rise:run), manual wheelchair users had the most failures (Sanford *et al.*, 1997). Even though manual wheelchair users had difficulty, the authors suggested that the standards for ramp grade not be changed from their current values (a 1:12 maximum grade over a 9.1 m length and a 1:8 maximum grade for a 16.2 cm rise) (Sanford *et al.*, 1997). However, it is not clear whether consistently propelling a wheelchair up such ramps may cause damage to the shoulder over time. The aim of the current study was to quantify the effect of ramp grade on shoulder joint mechanics in light of the potential for injury.

METHODS

Sixteen paraplegic subjects propelled their wheelchairs up a 3.7 m adjustable grade ramp. Thirteen reflective markers were placed on each subject (Figure 1). The 3-D coordinates of the markers were collected at 60 Hz using a commercial six-camera motion capture system. Kinematics of the trunk, shoulder, elbow, and wrist were computed from the locations of the reflective markers using Euler angles. The subject's wheelchair wheels were replaced with instrumented wheels to record the force and moment applied to the wheelchair handrim at 100 Hz. The resultant forces and moments at the wrist, elbow, and shoulder were calculated using inverse dynamics. Each subject propelled his wheelchair up four ramp grades (level, 20:1, 12:1, 8:1) five times each in random order. Data were normalized in time to facilitate comparisons. Repeated measures ANOVA were performed to determine differences. In the case of a significant ANOVA, post-hoc Bonferroni/Dunn pairwise comparisons were performed.

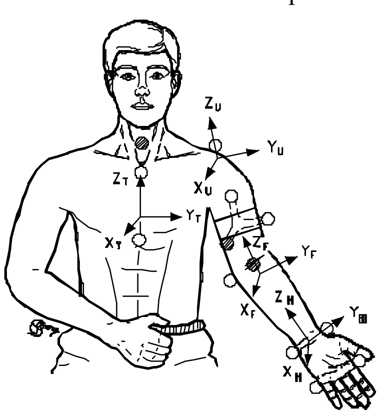

Figure 1. Marker placement for kinematic data collection.

RESULTS AND DISCUSSION

Peak shoulder joint moments in all three planes increased significantly for all the ramps compared to level ground. The largest shoulder moment was a flexion moment (Figure 2), which ranged from 14.3 ± 6.2 Nm on level ground to 46.7 ± 18.5 Nm on the 8:1 ramp ($p<.0001$) and peaked during the propulsion phase. Shoulder forces during propulsion were directed in the anterior, medial, and inferior directions. All of these values increased significantly from the level baseline condition to the ramps ($p<.0001$).

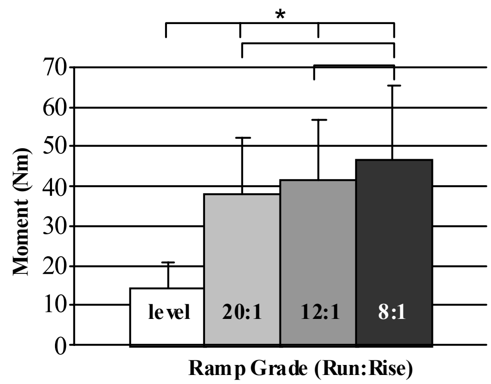

Figure 2. Mean (± SD) shoulder flexion moment as a function of ramp grade (*$p<0.003$).

Peak shoulder flexion moment increased 225% from level ground to the 8:1 ramp. Peak anterior and inferior components of shoulder joint force increased 130% and 744%. The large increase in inferiorly directed force suggests that the shoulder is at greatest risk of compression injuries during wheelchair propulsion up ramps. Compression of the subacromial structures can occur if the humerus migrates superiorly and decreases the amount of subacromial space (Kulig *et al.*, 1998).

SUMMARY

Increasing ramp grade leads to dramatic increases in shoulder forces and torques. The shoulder compression force showed the greatest increase with ramp grade. Even relatively "easy" slopes significantly increase shoulder joint kinetics. The compressive forces generated during propulsion up ramps may lead to the common problem of subacromial impingement.

REFERENCES

Kulig, K. et al. (1998). *Clin Orthop,* **354**, 132-43.
Nichols, P.J. et al. (1979). *Scand J Rehabil Med,* **11**(1), 29-32.
Sanford, J.A. et al. (1997). *Assist Technol*, **9**(1), 22-33.
Subbarao, J.V. et al. (1995). *J Spinal Cord Med,* **18**(1), 9-13.

INVESTIGATION OF STRESSES AND MICROMOTION BETWEEN THE LINER AND THE ACETABULAR CUP IN TOTAL HIP REPLACEMENT IMPLANTS

Francisco Romero[1], Farid Amirouche[1], Mark Gonzalez [2], Paul Lewis[3], Todd Render[3], Jorge Ochoa[3]
[1] University of Illinois at Chicago. Biomechanics Research Laboratory. fromer1@uic.edu
[2] University of Illinois at Chicago. Medical Campus. [3]DePuy Orthopedics, Warsaw, Indiana, USA

INTRODUCTION

The proposed research focuses on the liner and acetabular cup of a THR implant when subject to dynamic loading conditions. The objective of this paper is to address both the normal loading with the femur head in the socket joint and the effect of eccentricity and femur head dislocation. The latter reflects the induced torques responsible for liner instabilities and joint unbalance or misalignment.

METHODS

A three-dimensional 3595 element FE model (Figure 1a-, 1b-) of the femur head, liner and acetabular cup was developed using ANSYS/LS-DYNA with 8 nodes hexahedron elements (Solid 164), positioned with 45° inclination and 25° anteversion.

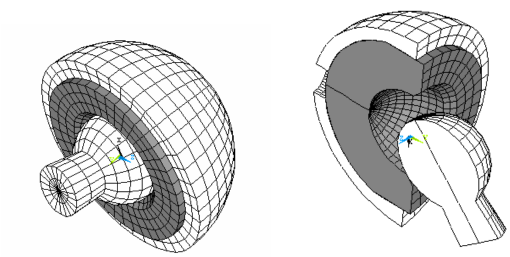

a) b)

Figure 1: FE models for a) Gait loading, b) dislocation

A rigid material type was chosen for the titanium components and a Plasticity bilinear material for the UHWMPE component. A linear contact between implant components was modeled using a surface-to-surface contact (STS) with an experimental friction coefficient between titanium and UHMWPE of μ=0.038. The acetabular cup was fully constrained; the femur head was constrained in the rotational degrees of freedom while the UHMWPE liner was fully un-constrained. Two dynamic loading cases were considered using LS-DYNA. In the first loading case the femur head is perfectly aligned in the liner socket and gait forces obtained from an in vivo instrumented prosthesis were applied. Muscles force data as depicted by Bergmann et al. were converted to the coordinate system shown in Figure 1.a-. The final applied loads are shown in table 1. In the second loading case an eccentricity was applied to the femur head (ecx=10mm, exy=4mm in shown CS).

A maximum peak force of 2132 N was applied at an angle of 23.4° lateral and 5.7° posterior over the dislocated femoral head as shown in Figure 1.b. The maximum stresses (Mpa) and relative micromotions (mm) between the acetabular cup and liner were measured in both loading case conditions.

RESULTS AND DISCUSSION

The maximum displacement data for each loading case is represented by vectors as shown in Figure 2a-, 2b-. The maximum values are found to be 172 µm (t=0.77sec) for gait loading case and 680µm (t=0.02 sec) during the dislocation loading case.

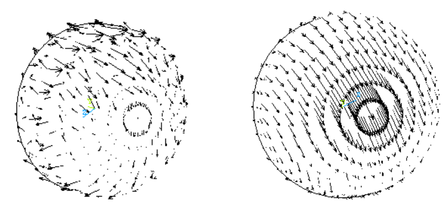

a) b)

Figure 2: Max. displacement a) Gait loading, b) dislocation

The maximum stress achieved in both cases remains under UHWMPE Yield Stress limit with maximum values of 6.6 MPa in the first loading case and 21.9 MPa during impact in the dislocation analysis. Due to the range of values obtained, instabilities caused by micromotions and UHMWPE degradation are found to be minimal.

SUMMARY

An explicit dynamic study using Finite Elements that represents a more realistic testing procedure of THR components behavior is being developed. The latter will be validated against an experiment being developed by L. Aran et al.

REFERENCES

Bergmann, G., Graichen, F., and Rohlmann, A. (1993) J. Biomech., 26:969-990.
Kuiper, J. H., and Huiskes, R. (1996) J. Orthop. 14:36-43.
L. Aram et al. (2002). World conference of biomechanics.

Table 1: Hip joint forces during gait.

Time (sec)	0.0	0.1	0.2	0.3	0.4	0.5	0.6	0.7	0.8	0.9	1.0
Fx (N)	16.94	225.4	419.6	901.1	735.4	647.7	581	450.5	168.4	101.8	64.15
Fy (N)	62.03	-225.4	-482.3	-1623	-1700	-1607	-1494	-1082	-372.7	-123.6	-26.04
Fz (N)	-44.32	0	-55.84	-414	-423.6	-281	-125	-173.2	-67.37	-42.37	-57.8

TOOLS FOR COMPUTER-AIDED SURGERY: DISPLACEMENT AND VELOCITY WORKSPACES OF THE HUMAN KNEE

John E. Fuller[1], Michael C. Murphy[2] and Gregory A. Brown[3]

[1]Schlumberger Reservoir Completions, Rosharon, TX, U.S.A.
[2]Dept. Of Mechanical Engineering, Louisiana State University, Baton Rouge, LA, U.S.A.
[3]Regions Hospital, St. Paul, MN, U.S.A.

INTRODUCTION

Quantitative comparisons of the kinematic outcomes of different joint reconstructions or total knee replacements would be an invaluable aid to surgeons in the design of successful treatment strategies. Workspace concepts developed in the field of robotics were applied to the study of the kinematics of the knee (Fuller, 2001). Fixed orientation displacement workspaces (FODW) are a map of all possible translations of the joint in a specified orientation and correspond clinically to the laxity of the joint. Each point on the surface of the FODW represents a constraint configuration, consisting of active ligament bands and surface contacts. At any point in a FODW, there are three sets of instantaneous helical axes (IHAs), corresponding to motions that do not change the constraints, motions that relax the constraints, and motions that violations of the constraints.

METHODS

Ligament lengths, ligament insertion sites, and articulating surface geometries were obtained from a matched pair of human cadaver knees through the use of computed tomography (CT) in the presence of titanium markers at ligament insertions and for reference coordinate systems. The specimens were scanned with the knee capsules undisturbed and reference markers implanted in the tibia and femur. The left knee was disarticulated and the insertions of the four major ligaments into the tibia and femur were marked and the specimen was rescanned. The resulting sets of images were correlated through the reference markers, yielding articulating surface and ligament geometries for the intact, left human knee specimen. Triangular facets were fitted to the surface data while ligaments were modeled as single filaments connecting insertion site centers. The fixed orientation displacement workspace was computed based on rigid body approximations for the articulating surfaces and inextensible link representations for each of the major ligaments

A constraint configuration was determined by studying the FODW of a model of the human knee near full extension (Fuller, 2001). Ligaments were modeled as single filament elements, inserting as spherical joints into the bone surfaces. Capable of supporting only tensile loads, ligament wrenches simplified to zero pitch wrenches, or pure force wrenches. Similarly, contact forces were modeled as point forces, considering the articulating surfaces as virtually frictionless. The resulting constraints contributed by surface contacts were also zero pitch wrenches. A basis for the velocity workspace boundary, consisting of the set of all twists reciprocal to the constraint wrenches, was computed using well-known techniques of linear algebra. A basis for the velocity workspace interior, defined by all twists not contrary to any constraint wrench, was computed using techniques of convex analysis.

RESULTS AND DISCUSSION

Figure 1(a) shows a FODW for the knee near full extension. The outer surface of the FODW is defined by the actions of different ligament bands and the surface contacts. The primary constraints are labeled on the surface of the workspace. The two twist (IHA) basis for the reciprocal velocity workspace is shown in Figure 1(b) for one point in the FODW with all four ligaments active. All four constraint wrench axes intersect the IHA corresponding to the flexion-extension axis.

SUMMARY

Workspaces have the potential to provide a quantitative tool for assessing the kinematic outcomes of surgery and providing insight into joint function.

(a) (b)

Figure 1. (a) FODW near full extension; (b) Reciprocal velocity workspace basis for point with four ligaments active.

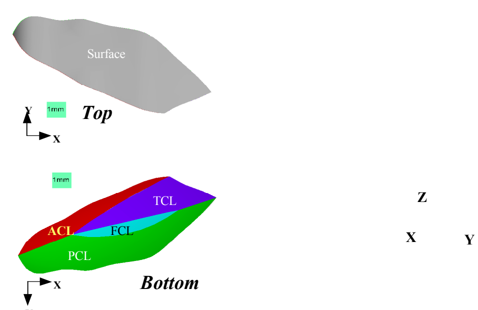

REFERENCES

Fuller, J. E. (2001). "Development and Characterization of Velocity workspaces for the Human Knee," PhD, LSU , Baton Rouge, LA

ACKNOWLEDGEMENTS

This work was supported by a State of Louisiana Board of Regents Doctoral Fellowship and the LSU Department of Mechanical Engineering.

ABILITIES OF YOUNG AND OLD ADULTS TO ADJUST MEDIO-LATERAL STEP LOCATION DURING A FORWARD FALL

Darryl G. Thelen[1], Cécile Smeesters[3], James A. Ashton-Miller[2,3], Shana Bailey[1], Rhadika Rapasinghe[1] and Neil B. Alexander[4]
[1]Engineering Program, Hope College, Holland, MI; [2]jaam@umich.edu
[3]Mechanical Engineering Department, [4]University of Michigan, Ann Arbor, MI, USA

INTRODUCTION

Old adults with a history of falls have greater difficulty with lateral stability than non-fallers (Lord et al., 1999) and hip fractures are frequently associated with falls to the side (Hayes et al., 1993). Thus, the ability to maintain and/or recover medio-lateral (ML) balance may be important in avoiding falls and fall injuries. Because the center-of-mass (COM) is typically outside the narrow base of single-support (Lyon and Day, 1997), stepping responses to recover balance require coordinated control and positioning of the ML step location relative to the trajectory of the COM. The objective of this study was to compare the ability of young and old adults to adjust their ML step location during induced forward falls. Due to age-related slowing in reaction time and rapid strength development (Thelen et al., 1996), we hypothesized that old adults would demonstrate a reduced ability to adjust their ML step location. We further hypothesized that inadequate ML adjustment of the COM would underlie this decreased ability.

METHODS

Twenty-two young (18-30yrs) and 24 old (65-85yrs) healthy adults participated. Forward falls were induced by releasing subjects from forward leans of 8º and 16º. Prior to each trial, subjects were instructed to recover balance by taking a single step with the right foot into one of three 16cm wide zones located directly in front of them (Figure 1). Two attempts were made for each zone and trials were presented in a random order. A successful trial involved stepping completely into the zone and not taking any additional steps. Success rates equaled the number of successful trials divided by the total number of trials. The time history of the COM trajectory was computed by double numerical integration of the foot-floor reactions (Lyon and Day, 1997). A rm-ANOVA was used to determine the effect of age on the toe-off (TO) time and ML motion of the COM prior to TO.

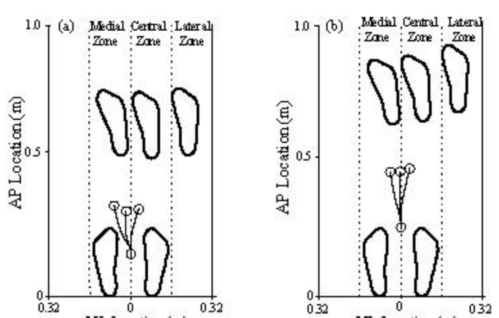

Figure 1: Mean step locations and COM trajectories of young males when they successfully stepped into the each of the three zones for 8º (a) and 16º (b) leans. Medio-lateral (ML), anterio-posterior (AP).

RESULTS

Young adults demonstrated greater success rates than old adults in stepping into the specified zones (Table 1). The medial zone proved to be the most difficult for all subjects to step to. TO times were similar for the young and old adults, except for slower ($p<0.05$) TO for old adults when stepping to central and lateral targets at the 16º lean (Figure 2). Old adults generated less ($p<0.05$) medial motion of the COM prior to TO when stepping to medial and central targets (Figure 2).

Table 1: Success rates (%) achieved by young (Y) and old (O) adults in stepping into specified target zones.

Lean	Medial		Central		Lateral	
	Y	O	Y	O	Y	O
8º	75	29	98	82	88	73
16º	38	0	82	47	75	23

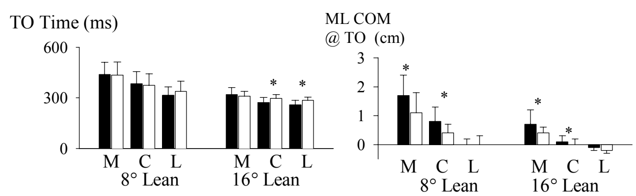

Figure 2: TO times and medial motion of COM prior to TO for young (solid bars) and old adults (white bars). *$p<0.05$.

DISCUSSION & CONCLUSIONS

Healthy old adults demonstrated greater difficulty in adjusting their ML step location during a forward fall than young adults. Interestingly, old adults often initiated the step as quickly as the young, particularly when stepping medially or straight ahead. However, the medial postural adjustment of the COM prior to TO was often reduced in old adults. Because the COM motion after TO is largely ballistic (Lyon and Day, 1997), the COM position and velocity at TO determine the COM location at landing. Consequently, inadequate control of the COM prior to TO, rather than a delayed stepping response, is the likely cause of the lower rates of success among old adults.

REFERENCES

Hayes, W.C., et al. (1993). *Calcif. Tissue Int.*, **52**, 192-198.
Lord, S.R., et al. (1999). *J. Am. Geriatr. Soc.,* **47**, 1077-1081.
Lyon, I.N., Day, B.L. (1997). *Exp. Brain Res.*, **115**, 345-356.
Thelen, D.G., et al. (1996). *J. Gerontol.,* **51A**, M226-232.

ACKNOWLEDGEMENTS

NIH R15 AG13759, NSF BES-9702275, NIH P30 AG08808.

ANKLE ARTICULAR CARTILAGE THICKNESS IS ACCURATELY MEASURED WITH MULTI-DETECTOR COMPUTED TOMOGRAPHY (MDCT)

Melvin J. Rudert[1], Kyle Alliman[1], Hannah Lundberg[2], George El-Khoury[1,3]Thomas D. Brown[1,2], and Charles L. Saltzman[1,2]
[1]Departments of Orthopaedic Surgery, [2]Biomedical Engineering, and [3]Radiology
The University of Iowa, Iowa City, IA 52242
jim-rudert@uiowa.edu

INTRODUCTION

Accurate measurements of *in vivo* ankle cartilage thickness are often needed for experimental analysis or clinical assessment. Conventionally, MRI has been the modality of choice for imaging cartilage, despite the well-recognized sequence-dependence of the tissue layer appearance. However, anecdotal observations from several clinical cases sensitized us to the extremely crisp cartilage rendition provided by multi-detector computed tomography (MDCT), done in concert with contrast media and air-injection.

MDCT has significant advantages over single or double slice helical CT or conventional CT. Up to four interweaving helices, generating four slices at a time and using collimators with better resolution, provide several substantial improvements. Data collection is faster, reducing patient movement artifact. Data have far improved temporal and spatial resolution and the isotropic images allow multiple image reconstructions in any arbitrary plane. Our Radiology Department has coupled MDCT with Vitrea® 3-D interpolation software, which by enabling sub-voxel computations further sharpens rendition. The visual appearance of cartilage on MDCT is so distinct as to suggest a potential for better-than-MRI geometric fidelity.

We designed an experiment to use MRI and MDCT to measure ankle cartilage at multiple articular surface locations in a series of cadaver foot/ankle specimens. The MRI and MDCT results were compared to location-matched direct physical thickness measurements.

METHODS

Four cadaver lower legs were transected perpendicular to the axis of the leg at approximately 5 cm superior to the medial malleolus. Care was taken to avoid capsule compromise so as to ensure subsequent contrast medium and air containment. Each foot/ankle specimen was mounted in neutral position in a custom fixture (entirely made of acetal plastic for MRI compatibility) that served as a drill guide and (later) as a joint distracter. With the articular surfaces apposed, a grid of 1.5 mm diameter marker track holes was drilled through the joint from the tibial side. These holes penetrated the tibial subchondral plate, the tibial cartilage, the talar cartilage, and the talar subchondral plate, respectively. After drilling, the adjustable fixture distracted the joint approximately 3 mm to allow space for contrast medium and air infusion.

Ankles were MR-scanned using the 3-D SPGR sequence to best delineate cartilage. Total scan time for this sequence is approximately 20 minutes. For the MDCT scan, the specimens were first injected with 0.5 – 1.0 ml of Hypaque-60® contrast medium, followed by a bolus of 7-12 ml of air to enhance medium penetration. The MDCT scans were then performed using 1 mm collimation and 0.5 mm reconstruction. Scan times were less than one minute. MRI and MDCT images were ported to a workstation, and, using Vitrea®, the images were searched to locate each of the marker tracts. Once located, the cartilage surface and bone interface adjacent to the tracts were cursor-delineated and used to calculate cartilage thickness at that tract location.

After MRI and MDCT scanning, the ankles were removed from the fixture and disarticulated to expose the articular surfaces. A cylindrical trephine was passed concentrically over the marker holes, removing annular cores of cartilage with their underlying bone. These plugs were then sectioned in half, longitudinally, and placed on the stage of an optical microscope. Using a superimposed optical comparator grid under 40x magnification, the cartilage thicknesses were measured adjacent to the tract holes. A single blinded observer performed all measurements.

RESULTS AND DISCUSSION

Using the described procedure, we obtained multiple, location-matched ankle cartilage thickness measurements via MRI, MDCT and direct physical measurement (the "gold standard"). Cartilage thicknesses at 58 talar and tibial articular sites on four ankles are summarized in Table 1. MDCT results were nearly indistinguishable ($p > 0.5$) from the gold standard physical measurements, whereas MRI significantly ($p < 0.005$) overestimated cartilage thickness. These results support air-injection contrast-enhanced MDCT as a technique for precise assessment of ankle articular cartilage thickness.

Table 1: Ankle Cartilage Thickness: MRI and MDCT Compared to Physical Measurement

Avg. Thickness (mm)			Avg. Error (mm)		Max. Error (mm)	
Physical	MDCT	MRI	MDCT	MRI	MDCT	MRI
1.61	1.62	1.77	0.05	0.18	0.20	0.80

PROLONGED COMPRESSION OF INTERVERTEBRAL DISCS ACTIVATES MMP-2

Adam H. Hsieh and Jeffrey C. Lotz
Orthopaedic Bioengineering Laboratory, Department of Orthopaedic Surgery
University of California, San Francisco, California, USA
e-mail: ahsieh@itsa.ucsf.edu web: carpal.ucsf.edu

INTRODUCTION

There is mounting evidence that mechanical loading plays a significant role in the initiation and progression of intervertebral disc degeneration. *In vivo* studies of load-induced disc degeneration in mice [Lotz et al, 1998, Lotz & Chin, 2000] have demonstrated that static compression results in disruption of the lamellar structure in the annulus fibrosus and in induction of fibrocartilaginous matrix in the nucleus pulposus. Since catabolic events may be important in these observed disc remodeling events, the objective of this study was to assess *in vivo* changes in active and latent (pro-) forms of matrix metalloproteinase (MMP)-2 in compressed discs.

METHODS

A degenerative phenotype was induced in coccygeal discs of 12-week old male Swiss-Webster mice (approved by the Committee on Animal Research, UCSF). Briefly, pairs of perpendicularly aligned stainless steel pins were inserted percutaneously through the diameters of the 9^{th} and 10^{th} caudal vertebrae. Pre-calibrated elastic bands were placed over these pins to apply 1.3 MPa compression. A third pair of pins was inserted through the 8^{th} caudal vertebral body but with no elastics; the disc between the 8^{th} and 9^{th} vertebrae served as a sham control. Normal discs were obtained from mice having neither pins nor loads applied. Static compression was applied to discs for 1 day, 4 days, or 7 days, and mice were sacrificed immediately after the respective treatment periods. The tail discs of interest were surgically excised, snap-frozen, and pulverized at liquid nitrogen temperatures. Samples were extracted in a 50 mM Tris-HCl buffer and centrifuged at speed. Supernatants were then used in the Biotrak MMP-2 activity assay system (Amersham Biosciences, UK) following the manufacturer's protocol. Levels of both active (without aminophenyl mercuric acetate – APMA) and total (pro- and active; with APMA) MMP-2 were quantified using a plate reader (405 nm). Absolute concentrations of MMP-2 were normalized with respect to wet weight of the disc tissue measured immediately post-surgery. To improve normality, percentage data were transformed using a modified arcsine function. Transformed data of the different experimental groups were then compared using ANOVA ($\alpha = 0.05$) with Fisher's PLSD post-hoc analyses ($\alpha = 0.05$). All data are presented as mean ± SEM.

RESULTS

No significant differences in total MMP-2 activity per unit wet weight were found between loaded and sham-treated discs for any loading duration ($p > 0.05$; data not shown). Figure 1 illustrates the time-course response of activated MMP-2. Compared with corresponding shams, there was no change in percent active MMP-2 in discs after 1 day static compression ($n = 3$). After 4 days of loading, however, discs exhibited a significant increase to nearly 50% ($n = 2$; $p < 0.005$). Elevation of active MMP-2 was sustained in discs through 7 days of loading ($n = 3$; $p < 0.05$). Sham-treated discs at all time points possessed percent active MMP-2 which were not significantly different from normal discs ($n = 3$).

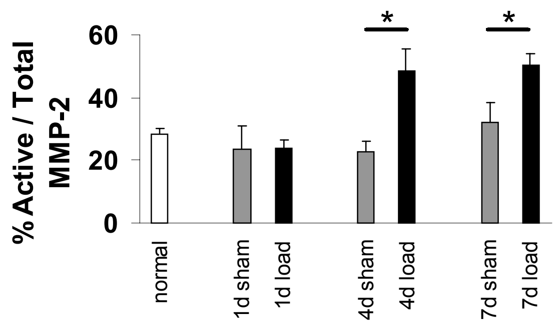

Figure 1 – Effect of static compressive loads on levels of active MMP-2 expressed as a percentage of total MMP-2.

DISCUSSION

Static compression of coccygeal discs in mice led to changes in the intradiscal distribution between active and pro- forms of the enzyme MMP-2. Specifically, while total levels of MMP-2 remained essentially constant, there was a two-fold increase in MMP-2 activation by 4 days of compression. That the elevated levels were maintained after 7 days of loading may be indicative of a shift in the basal level of MMP-2 activity in the tissue, perhaps as a remodeling response to the new stress state of the disc. Since total levels of MMP-2 were unchanged, these data also suggest that prolonged loading did not significantly alter MMP-2 synthesis on either a transcriptional or translational level. Further studies, however, are required to explore the implications of these current observations more fully. Although MMPs have long been suggested to have an important role in normal and pathological conditions in the intervertebral disc [Goupille et al, 1998], the manner in which they are involved remain unclear. This study lends insight into some of the processes that lead to degenerative changes in the extracellular matrix of the disc.

REFERENCES

Goupille, P. et al (1998) *Spine* **23**: 1612-1626.
Lotz, J.C. et al (1998). *Spine* **23**: 2493-2506.
Lotz, J.C. & Chin JR (2000). *Spine* **25**: 1477-1483.

FORCE CHARACTERISTICS FROM DROP LANDINGS ARE ASYMMETRICAL BETWEEN LEGS IN 7-11 YEAR OLD CHILDREN

Jeremy J. Bauer, Wilson C. Hayes and Christine M. Snow
Bone Research Laboratory, Oregon State University, Corvallis, Oregon, U.S.A.
email:bauerje@onid.orst.edu

INTRODUCTION

When developing exercise prescriptions for increasing bone mass, it is necessary to quantify the variables associated with osteogenesis. Given individual variations in bone responses to exercise, it is implied that there are also individual variations in the forces to which the skeleton is exposed, even in studies that use standardized loading protocols. In a recent study in which bone mass increased from drop landings, we did not observe a significant correlation between increases in bone mass at the hip and ground reaction forces (GRF's) even though GRF's ranged from 5-12 body weights (BW) (Bauer et al., 2001). One explanation for this finding is that the changes in bone were measured only at the left hip whereas the forces were measured from a two-footed landing onto a single force plate and thus, the possibility exists that the composite value does not reflect the true ground reaction forces at the left foot. If there is asymmetry in ground reaction forces between legs, then the most appropriate approach to use in the design of future studies would be to measure hip bone mass and forces on the same leg. In order to explore the symmetry question, we conducted a study to determine the degree of symmetry in ground reaction force magnitude and loading rate in children performing drop landings from 61cm. We hypothesize that, since asymmetries in GRF's have been reported in adults (Schot et al. 1994), we will observe similar findings in children.

METHODS

Fourteen children, 9.0 ± 1.2 years (6 boys, 8 girls) performed 15 drop landings onto two force plates from a height of 61cm. Vertical GRF's were collected on each leg at a sampling rate of 1000Hz. Average loading rate was defined as the slope of a line from 20% to 80% of the rising side of each force peak. A left/right difference score was determined for each variable within each subject by subtracting the left foot value from the right foot value then calculating the mean. The absolute value of the mean difference score for each subject and variable was then pooled for group description. One sample t-tests were used to compare the mean difference scores compared to zero for each variable. Statistical significance was set at $p<0.01$.

Group mean GRF's at peak1 were 2.3±0.3 (BW) and 2.3±0.7 BW for the left and right foot, respectively, and, at peak2 were 4.8±0.9 BW and 5.0±1.0 BW for left and right foot, respectively. While these group means are very similar, they do not reflect individual asymmetries (Figure 1). Loading rate at peak1 was 278±55 BW/s and 283±79 BW/s for the left and right foot, respectively and at peak2 was 349±105 BW/s and 387±122 BW/s for left and right foot, respectively.

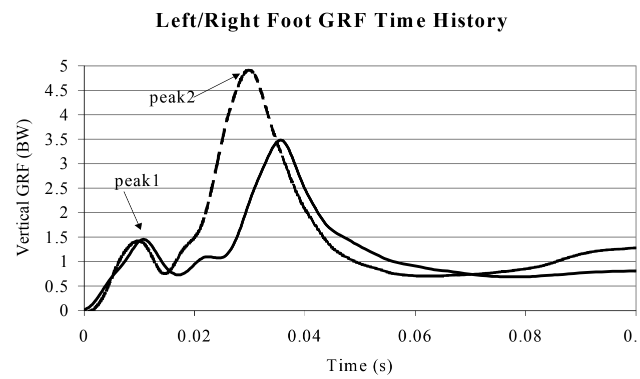

Figure 1: Ground reaction force traces on the left (broken line) and right (solid line) foot from one subject.

RESULTS AND DISCUSSION

The mean difference in GRF's at peak1 and peak2 was 0.4±0.3 BW and 0.8±0.6 BW respectively. The mean difference in loading rate at peak1 and peak2 was 47±36 BW/s and 81±68 BW/s respectively. GRF's and loading rates at both peaks were significantly different from zero ($p<.01$).

SUMMARY

The presence of asymmetries in force variables confirms that, in children, ground reaction forces and loading rates from drop landings are different between legs, supporting the need to measure forces on the same side that bone mass is assessed.

REFERENCES

Bauer, J.J., Fuchs, R.K, Smith, G.A., & Snow, C.M. (2001). *J Appl Biomech*. **17**, 142-152.

Schot, K.P., Bates, B.T, & Dufek, J.S. (1994). *Med Sci Sports Exerc*. **9**, 1153-1159.

ACKNOWLEDGEMENTS

Supported by NIH AR 45655-01

FORCE GENERATION AND STABILITY CONSIDERATIONS FOR ISOMETRIC PUSHING

B. C. Bennett, H. Kang, and K. P. Granata
Motion Analysis and Motor Performance Laboratory, University of Virginia, Charlottesville, VA
Email: bcb3a@virginia.edu

INTRODUCTION

Approximately 20% of all back injuries in the U.S. are attributed to pushing and pulling. This occurs despite the fact these tasks are thought to avoid the large compressive loads of lifting and carrying. Push studies have found co-contraction of trunk muscles. This co-contraction may be required to stabilize the spine. Unfortunately this co-contraction also increases spinal compression. This study investigates the effect of handle height and level of effort upon the moments, forces, and stability requirements on the low back during a static pushing task. A simple inverted pendulum model was used to compare spinal stability for push tasks with stability for lift tasks.

METHODS

Eleven subjects pushed on a stationary handle at three bar heights (shoulder, mid, and waist), with three levels of exertion (max, 30% and 15% of body weight). Subjects pushed with feet parallel to the push bar. Forces in three dimensions were recorded. Torso position was measured by electromagnetic sensors on T10, S1, and the sternum. The measured postures and forces were used to compute the moments at L5/S1.

The trunk was modeled as a simple inverted spring pendulum (see Figure 1). For static conditions stability requires the second derivative of the potential energy to be equal to zero:

$$\frac{d^2V}{d\Theta^2} = K - L_{cg} m_t g(\cos(\Theta)) - F L_t \cos(\Phi) = 0 .$$

The stiffness gradient (q) can be defined as the ratio of the external moment at S1 to the effective stiffness: $q = \frac{M_{ext}}{K}$.

Large q values have been associated with low stability, because the stiffness of a muscle is dependent upon its level of force production.

RESULTS

Maximum horizontal force production was larger for lower bar heights ($p<0.001$). Moments were largest at the highest bar height ($p<0.0001$) and max effort ($p<0.001$). Overall external trunk moments were in extension and were small, agreeing with published data. In addition subjects leaned forward into the bar creating a large axial (parallel to the trunk) force component without significant trunk moment.

Figure 1: Free body diagram of the trunk while pushing.

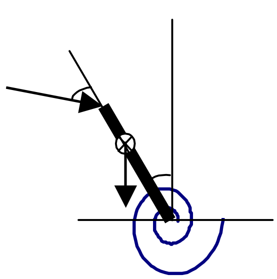

The stiffness gradients for the push trials and for equivalent lifting trials are shown in Figure 2. There was a main effect for bar height ($p<0.001$) and an interaction between effort and push vs lift ($p<0.04$). Post hoc analyses revealed a larger q (less stable) for shoulder height pushes vs. waist height pushes ($p<0.02$) and for 15% lifts vs. max lifts ($p<0.02$).

Figure 2. The stiffness gradient is larger than for pushing than for comparable lift tasks for most conditions.

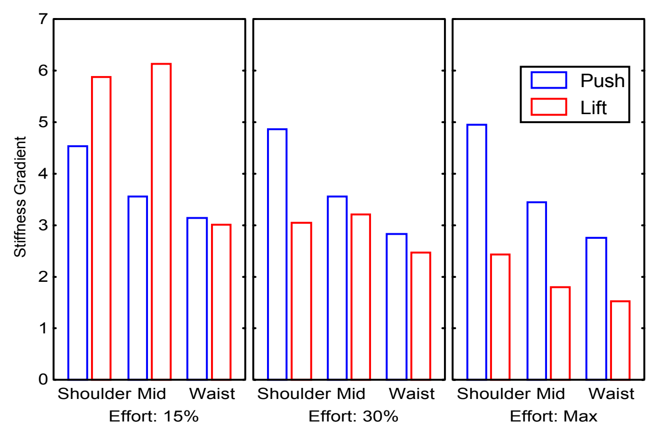

SUMMARY

The stiffness gradients indicate that the back is less stable during pushing than in lifting for all but the cases with least effort. Research on lifting (Granta & Marras, 2000) has found that trunk muscles co-contract to increase stability, suggesting this would occur in pushing. A pilot study (N=2) replicated the above tests with EMG signals recorded for the rectus abdominals, external and internal obliques, and the erector spinae muscles. These tests revealed large degrees of co-contraction of the trunk flexor and extensors for all conditions.

Taken as a whole these results reveal pushing to be a complex task where the stability of the spine is must be considered when designing or modeling pushing tasks.

REFERENCES

Granata, K. P. & Marras W.S. (2000). *Spine*, **25**, 1398-1404.

THE PROXIMAL FIBERS OF THE INTERROSSEOUS MEMBRANE CONTRIBUTES TO STABILITY IN THE RADIAL DOMINANT SINGLE BONE FOREARM

Barry P Pereira, Anam Kueh Kour and Robert W H Pho
Dearpartment of Orthopaedic Surgery, National University of Singapore, Singapore, Singapore

INTRODUCTION

The aim of this study was to investigate the allowable extent of resecting a segment of the ulna and the interosseous membrane (IOM) proximally, without compromising the stability at the proximal radio-ulnar joint (PRUJ). This work hopes to determine the portion of the IOM that contributes to stability in distraction and varus-valgus loading about the elbow, in the case of a radial dominant single bone forearm, where the distal ulna is resected.

METHODS

Forty-eight freshly-frozen upper limbs (50-70 y-o, 17 males, 7 females), disarticulated at the shoulder joint, were used in this study. They were stripped of muscles and skin leaving intact the bones, joints and ligamentous capsules. The specimens were divided into 3 test groups. In <u>Group I (n=16)</u>, the forearm was loaded in a <u>longitudinal forward direction (FD) to the length of the radius</u>. In <u>Group II (n=16),</u> the forearm was loaded in a <u>medial direction transverse to</u> the length of the radius. The failure criterion was when the forearm displaced by 45-degrees medially. This was taken as the criterion for failure in <u>varus loading</u>. In <u>Group III (n=16),</u> the forearm was loaded in a <u>lateral direction transverse</u> to the length of the radius. The specimens were loaded until the forearm displaced by 45-degrees laterally. This was taken as the criterion for failure in <u>valgus loading</u>. In all, the specimens were loaded with a continuously increasing load (5-kg-sec) with loading applied at the radius. For each loading group, four conditions (A,B, C, D) were tested assessing the contribution of the central band (**CB**) and the proximal reverse fibers (**rf**). For each condition, 4 specimens were used. Beginning with a break of the ulna at the level 20-cm from the radial head (control), segments of ulna was subsequently resected proximal together with the IOM, dividing it at the ulna attachment, in 3 sequences (Fig. 1).

RESULTS AND DISCUSSION

The mean length of the ulna for all forearms was 25.97-cm (SD, 1.59). A summary of the mean and standard deviation of load to failure for the 3 loading groups are tabulated in Table 1.

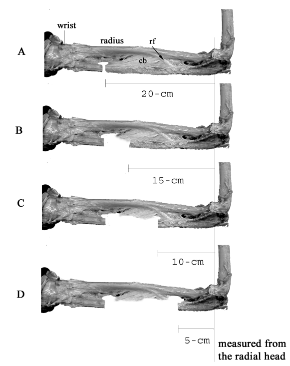

Figure 1: Four conditions (A, B, C, D) of ulna resection. **CB** =central band, and **rf** = proximal reverse fibers

In forward distraction, excision of the ulna and releasing the proximal reverse fibes (Condition D) results in a significant drop in the load to failure. In varus and valgus loading, releasing the central band (Conditions B, C) and the subsequently the proximal reverse fibers (D), resulted in significant drops in the loads to failure.

SUMMARY

The study reveals that the proximal reverse fibers plays an important secondary stabilising role in resisting further failure when the ulna is disrupted. The study provide limits to the extent of the ulna and the IOM that should be preserved if some stability in forearm distraction or varus-valgus loading is to be experienced in a radial dominant single bone forearm.

REFERENCES

Kumar V.P., Satku K., Helm R., and Pho R.W.H. (1988): *J Bone and Joint Surgery* **70B**:815.

Table 1: Mean load to failure (kg) for 4 different conditions assessing the extent of an ulna resection.

Conditions	*Group I (FD)*		*Group II (varus)*		*Group III (valgus)*	
A - (whole **CB** and **rf** intact)	52.3 (5.6)		28.3 (1.0)		19.5 (2.1)	
B - (prox ½ **CB** and **rf** intact)	52.8 (5.7)	*	17.3 (1.3)	¶	14.8 (1.0)	§
C - (only **rf** intact)	64.0 (12.4)		14.8 (1.0)		13.8 (1.3)	
D - (no IOM intact)	30.0 (5.9)		7.5 (2.1)		9.0 (2.9)	

*-, p= 0.273; ¶ -, p=0.913; § -, p = 0.147; ANOVA, post-hoc Scheffe's multiple range comparison for homogenous sub-sets.

EFFECTS OF CUSTOM ORTHOTICS ON LOWER EXTREMITY KINEMATICS, KINETICS, AND MUSCLE ACTIVITY

Anne Mündermann[1], Benno M. Nigg, and R. Neil Humble
Human Performance Laboratory, University of Calgary, Calgary, Alberta, Canada
[1]ahau@kin.ucalgary.ca

INTRODUCTION

Foot orthotics have been proposed as an effective treatment of running injuries. Their biomechanical efficacy is commonly evaluated in terms of reduction in maximum foot eversion during the stance phase of running. However, most studies found very small and non-significant differences between custom orthotic and no-orthotic conditions [1]. In a recent study, increased knee joint moments have been associated with Patellofemoral Pain Syndrome (PFPS) [2], which is the most common running injury [3]. Therefore, the main goal of foot orthotics may not solely be to reduce maximum eversion angle but also to decrease knee joint moments and to optimize muscle activity. Thus, the purpose of this study was to determine the effects of custom orthotics on lower extremity kinematics, kinetics and on muscle activity.

METHODS

21 recreational runners participated in this study (12 female, 9 male; weekly mileage: 15-40 km). All subjects were pronators and were free of injuries for at least 6 months prior to the study. Subjects were examined and casted by a podiatrist. Custom-orthotics with the goal to reduce pronation were fabricated for each subject. The control insert and the custom orthotics were placed in running sandals thereby allowing for skin marker placement directly on the heel. Kinematic and kinetic data were collected for 100 running trials (4.0 ± 0.2 m/s) per subject per condition (total: 4200 trials) during nine experimental sessions on a 30-meter runway. EMG signals were recorded from seven lower extremity muscles and root mean squares were calculated for five equal time intervals. Differences in EMG between the two conditions were detected using MANOVA ($\alpha = .05$).

RESULTS AND DISCUSSION

Foot eversion angle, knee abduction moments, external knee rotation moments and muscle activity were affected by the custom orthotics (Figure 1). When wearing the custom orthotics, foot eversion and foot inversion increased by 1.1 ± 0.3° and 2.2 ± 0.7°, respectively. Knee joint moments, reaching their maximum between 50 and 60 % of ground contact, increased when wearing custom orthotics (6.3 ± 1.4 Nm; 2.9 ± 1.1 Nm). Significant differences in muscle activity were found at times when the effects of custom orthotics on foot eversion, knee abduction and external knee rotation moments were greatest. The results of this study showed that custom orthotics can be used to alter lower extremity kinematics, kinetics, and muscle activity. However, the changes produced with the tested orthotics were opposite to the change initially attempted. Further research should assess the effect of these changes on lower extremity integrity.

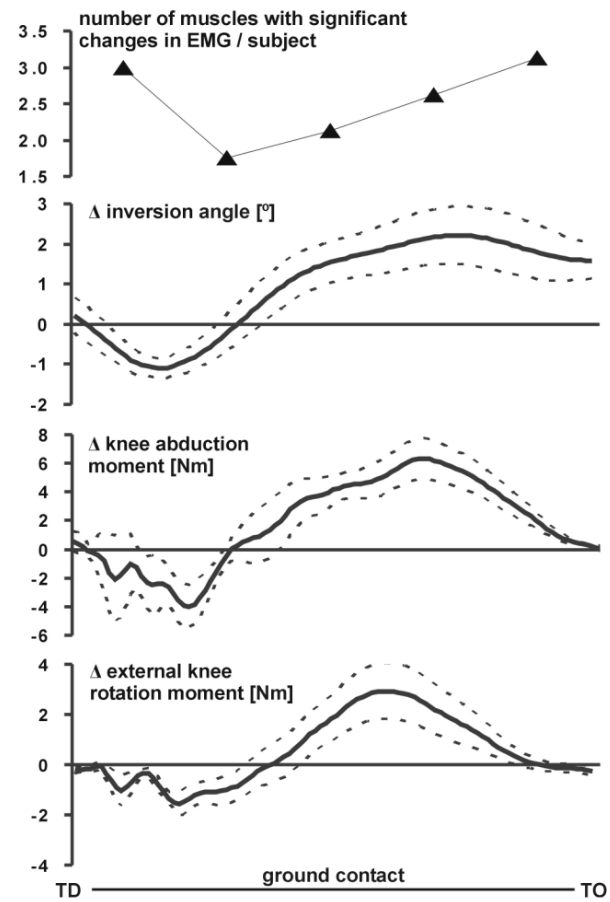

Figure 1: Mean differences (SE) in EMG, foot eversion, knee abduction and external knee rotation moments during ground contact for running in custom orthotics compared to a control condition (TD: touch-down; TO: take-off; n=8).

REFERENCES

[1] Nawoczenski, D.A. et al (1995). *JOSPT*, **21**, 317-327.
[2] Stefanyshyn, D.J. et al (1999). *Footwear Biom.*, 86-87.
[3] Clement, D.B. et al (1981). *Phys. Sportsmed.*, **9**, 47-58.

ACKNOWLEDGEMENTS

This work was supported by DFAIT (Canada), PFOLA, ISB, Paris Orthotics Ltd., and The Rockport Company. The authors would like to thank Maggie Andersen and Michelle New for their assistance in data collection.

SUBJECT-SPECIFIC FINITE ELEMENT MODELING OF THE HUMAN MEDIAL COLLATERAL LIGAMENT

John C. Gardiner and Jeffrey A. Weiss
Musculoskeletal Research Laboratories, Bioengineering Department, University of Utah, Salt Lake City, UT jeff.weiss@utah.edu

INTRODUCTION

Despite many studies of ligament function, questions remain about the precise mechanical role of some ligaments as well as the cause, effect, and optimal treatment for various injuries. This is in part due to experimental limits. The objectives of this study were to develop, analyze, and validate subject-specific finite element (FE) models of the femur, medial collateral ligament (MCL), and tibia. MCL strain distribution during valgus loading was measured experimentally and predicted using FE models. It was hypothesized that subject-specific FE models could predict experimental MCL strain.

MATERIALS AND METHODS

Eight male knees (50±7 years) underwent an experimental and computational protocol. All skin, muscle, and periarticular soft tissue was removed until only bones, menisci, and major ligaments remained and a CT dataset was obtained for each knee. 10 varus-valgus cycles were applied at flexion angles of 0, 30, and 60° to limits of 10 N-m. Joint kinematics were measured with an instrumented spatial linkage. A 3x5 marker grid allowed fiber direction MCL strain to be quantified with a 3D video system (Gardiner 2001a). After joint testing, the MCL was dissected for measurement of stress-free lengths between markers. These data were combined with in situ values to determine total fiber strain. Tensile test specimens harvested parallel and transverse to the fiber direction were used to determine subject-specific MCL material behavior (Quapp 1998).

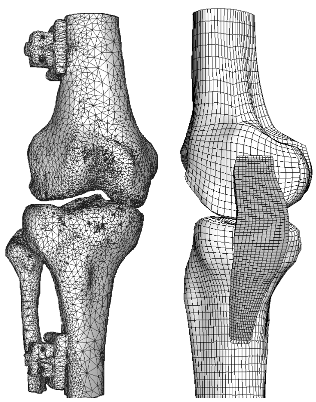

Fig 1: Polygonal surfaces and FE meshes for a single knee.

FE models were created for each knee (Fig 1). Geometry of the femur, MCL, and tibia was obtained from CT data. The MCL was modeled as transversely isotropic hyperelastic (Weiss 1996). The femur and tibia were defined as rigid allowing experimental kinematics to prescribe motions of the model. In situ strains measured during passive flexion were applied to the FE models as an initial condition (Gardiner 2001b). Regression analyses evaluated the ability of subject-specific FE models to predict experimental MCL strain.

RESULTS AND DISCUSSION

Excellent agreement was found between experimental measurements and FE predictions of regional MCL fiber strain (Fig 2). FE strain predictions significantly correlated with experimental values at all flexion angles (Fig 3) ($p<0.001$ at all angles; R^2 = 0.83, 0.72, and 0.66 at 0, 30, and 60° respectively). There was a slightly decreasing correlation between models and experiments with increasing flexion. Slope and intercept of regression lines did not indicate a constant trend toward under or overprediction by FE models.

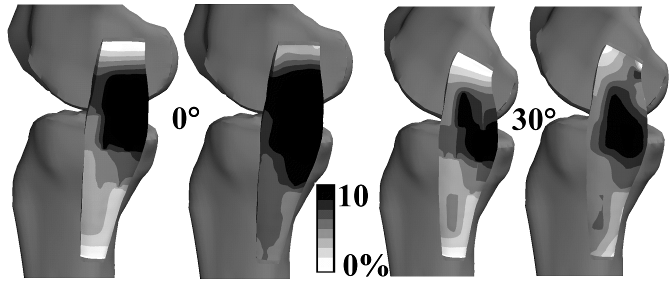

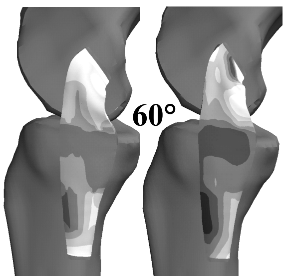

Fig 2: MCL fiber direction strain with 10 N-m valgus torque at flexion angles of 0, 30, and 60° for experimental measurements (left) and subject-specific FE models (right) for one knee. Discrete exp. values have been interpolated onto a FE mesh to generate a continuous depiction of results.

The main goal of this work was to assess the ability of FE models to predict MCL strain during valgus loading. Models with subject-specific geometry, material properties, in situ strain, and kinematics yielded good predictions of experimental strains. Numerical techniques such as the current FE models are vital to characterize complex deformations occurring in soft tissue structures such as ligaments and to quantify resultant stress and strain fields on microstructural and tissue levels. This will facilitate future studies of ligament injury, healing, and patient-specific clinical treatment.

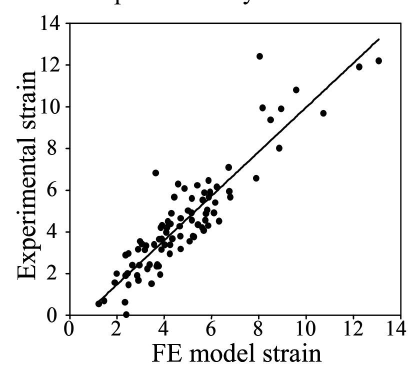

Fig 3: Scatter plot of MCL strain for FE models vs. experimental measurements during valgus load for all eight specimens at 0° flexion.

REFERENCES

Gardiner JC et al (2001a) *Clin Orthop*, **391**:266-74
Gardiner JC et al (2001b) *Proc ASME Bioen Conf*, **50**:359-360
Quapp KM, Weiss JA (1998) *J Biomech Eng*, **120**:757-763
Weiss JA et al (1996) *Comp Meth Appl Mech Eng*, **135**:107-28

ACKNOWLEDGMENTS

Supported by the Whitaker Foundation and NIH #AR47369.

CONSISTENCY OF PUTTER TRAJECTORY AND GOLF PUTTING ACCURACY

Jeff McCarty and Shirley Rietdyk
Biomechanics Laboratory, Purdue University, West Lafayette, Indiana, USA
Direct Questions to: srietdyk@sla.purdue.edu

INTRODUCTION

Accuracy in putting is vital to success in golf because 40-50% of the game is played on the putting green. Empirical studies of putting have used accuracy tests to examine the effects of such variables as the type of stance (Gott and McGown, 1988), point of visual fixation (Aksamit and Husak, 1983; Gott and McGown, 1988; Steinberg, Frehlich, and Tennant, 1995), type of putter (Gwyn and Patch, 1993), and impulse of the putting stroke (Delay, et al., 1997). However, the effects of putter trajectory on accuracy have not been examined.

METHODS

Male golfers (n=21) with USGA handicaps participated. Two groups were examined: low handicap (LH, <14) and high handicap (HH, >14). Total body center of mass (COM) was calculated for a 15-segment model, including the putter. Putter and segment motion was detected with 19 IREDs (Optotrak, NDI). Center of pressure (COP) was calculated from an AMTI force plate.

Two putting distances were observed: 2m and 4m. Radial distance from the target was calculated for 25 putts at each distance.

RESULTS AND DISCUSSION

Participants in both groups were similar in accuracy from 2m (LH mean 22.0 ± 15.2cm, HH mean 25.0 ± 17.4cm) (p=.17). Participants in the LH group were significantly more accurate from 4m when compared to HH players (LH mean 26.6 ± 14.9cm, HH mean 34.3 ± 19.1cm)(p=.001). This validates our use of handicap as a means of grouping even though other strokes are used in the determination of handicap.

Preliminary data analysis shows that highly skilled golfers (LH) have greater consistency in their putting strokes (see fig. 1). The more accurate putter must coordinate joint and segment angles to produce a consistent putter trajectory. Future research will examine the joint and segment angles.

Instructional literature in golf putting advises players not to move during the stroke. Both low and high handicap players demonstrated movement, but COP data shows that LH players have less weight shift during putts. In combination with the accuracy results above, this supports the instructional literature. Reduced movement appears to influence accuracy in golf putting.

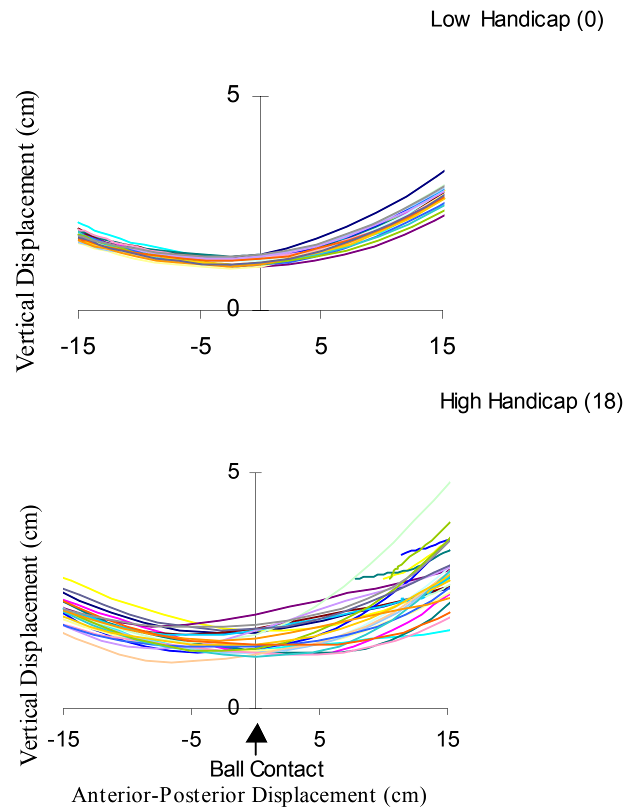

Figure 1: Putter head trajectory for 4m putts.

SUMMARY

Low handicap players are more accurate putters at greater distances. The increased accuracy may be due to greater consistency of putter trajectory and decreased weight shift during the movement.

REFERENCES

Aksamit, G., Husak, W. (1983). *Percept. Mot. Skills*, **56**, 19-22.
Delay, D., et al. (1997). *Hum. Mov. Sci.*, **16**, 597-619.
Gott, E., McGown, C. (1988). *Percept. Mot. Skills*, **66**, 139-143.
Gwyn, R.G., Patch, C.E. (1993). *Percept. Mot. Skills*, **76**, 387-390.
Steinberg, G.M., et al. (1995). *Percept. Mot. Skills*, **80**, 635-640.

ACKNOWLEDGEMENTS

The assistance of Scott Fricke, Kasey Wiley, and David Kemple was greatly appreciated.

MAXIMUM ANTERO-POSTERIOR EXCURSION OF THE CENTER OF PRESSURE DURING SIT TO STAND AND STANDING SWAY MOVEMENTS

Robyn M. Burgess and John H. Challis
Biomechanics Laboratory, Department of Kinesiology, The Pennsylvania State University, University Park, PA, USA
Email: rmb255@psu.edu, jhc10@psu.edu

INTRODUCTION

The ability to be able to perform the sit to stand (STS) is a significant determinant of independence. For certain populations, performing the STS is problematic, with for example strength being a limiting factor for some elderly subjects (Hughes et al., 1996). Measurements of postural stability in the elderly indicate that they have a greater response to perturbations to their posture; that is their stability is more affected than it is for young subjects (Nakamura et al., 2001). At the end of the STS subjects often have to stand still, that is effectively following the perturbation caused by the STS. The purpose of this study was to examine the influence of the STS on postural stability.

METHODS

Five healthy college-age subjects (3 male, 2 female) participated in this study. Subjects were asked to position themselves on a force platform (Bertec, Inc.) with the feet in a comfortable stance. Markers were placed on the FP at the toe, heel, medial, and lateral sides of the foot, and subjects were asked to reposition the feet within those marks for each trial. Trial conditions were as follows: quiet standing for 60s, standing on two feet swaying backwards and forwards as far as possible for 30s, and perform STS from a stool height of 0.45m at normal, slower than normal, and faster than normal speeds. In the STS trials once upright stance was achieved subjects had to stand still for 10 seconds. For all tasks the feet remained flat on the ground. Each condition was attempted three times by the subject. Motion analysis data were recorded for the STS to determine when upright stance occurred. All data were sampled at a rate of 240 Hz.

Antero-posterior excursions of the center of pressure were computed for sway (SW) and STS trials in the antero-posterior direction. These values are reported as a percentage of subject foot length. Anterior excursions of the center of pressure are designated positive, and posterior excursions negative.

RESULTS

Movement times reflected the instructions given to the subjects: slow STS 2.54s ± 0.46; normal STS 2.19s ± 0.44; fast STS 1.37s ± 0.33. The maximum amount of voluntary sway was +4.72% ± 0.18 and -4.05% ± 0.56. In contrast the maximum excursion of the center of pressure in the slow STS was +9.45% ± 0.69 and -24.10% ± 0.40, and +11.12% ± 0.89 and -20.10% ± 2.06 for the fast STS. Figure 1 displays these excursions relative to foot position. A time-frequency analysis of the center of pressure data once upright stance was achieved, revealed that it took longer for the amplitude and frequency of the data to attain quiet standing levels the faster the STS was performed. For example this time was twice as great for the normal speed STS trials compared with the slow speed STS trials.

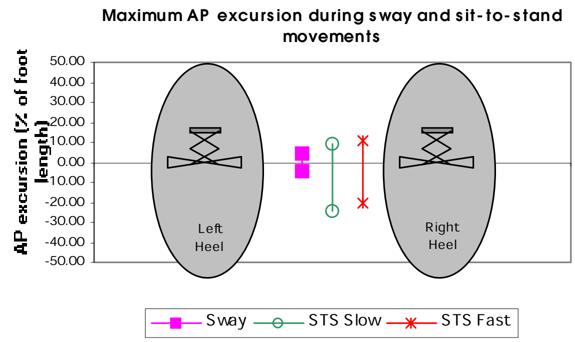

Figure 1: Maximum antero-posterior excursion of the center of pressure during standing sway trials and sit to stand movements.

DISCUSSION

These data on young healthy subjects indicate that the antero-posterior translation of the center of pressure is greater during the STS than during the maximum voluntary sway of the subjects. This indicates one of the challenges of the STS, as subjects have to be comfortable with relatively large excursions of the center of pressure. Time-frequency analysis of the center of pressure data show the time evolving properties of the center of pressure. With increasing speed of motion the time-frequency profile of the center of pressure takes longer after an upright position is obtained to return to the levels associated with quiet standing, providing evidence that the STS provides an additional challenge to the postural control system.

This study provides evidence about the challenge of the STS on postural stability after the movement. Future studies will examine these phenomena in the elderly.

REFERENCES

Hughes, M.A., et al. (1996). *J. Biomech.*, **29**, 1509-1513.
Nakamura, H., et al. (2001). *J.E. and EMG.*, **11**, 395-403.

ACKNOWLEDGEMENTS

This research was in part supported by a grant from The Whitaker Foundation.

LIGAMENT FORCES IN THE ANTERIOR CRUCIATE DEFICIENT KNEE DURING GAIT

Kevin B. Shelburne[1], Marcus G. Pandy[2], Frank C. Anderson[3], and Michael R. Torry[1]
[1]Steadman◆Hawkins Sports Medicine Foundation, Vail, Colorado, U.S.A., Kevin.Shelburne@shsmf.org
[2]Department of Biomedical Engineering, University of Texas at Austin, U.S.A.
[3]Department of Mechanical Engineering, Stanford University, U.S.A.

INTRODUCTION

The functional gait adaptations of anterior cruciate ligament deficient (ACLD) individuals have been well documented. It is generally believed that these adaptations function to reduce loading in the collateral ligaments, although direct evidence of *in vivo* ligament forces in walking is currently not available (Berchuck et al., 1990; Devita et al., 1997; Andriacchi and Birac, 1993). In this study, we tested the hypothesis that ACL insufficiency does not directly increase the forces transmitted to the collateral ligaments of the knee during gait. A theoretical approach was used to determine ligament forces in the ACLD knee during walking. Muscle forces derived from a dynamic optimization solution for normal gait (Anderson and Pandy, 2001) were used as input to a three-dimensional model of the knee (Pandy et al., 1998) to calculate ligament forces. The calculations were analyzed to describe and explain the interactions between muscle forces, anterior tibial translation, and the forces induced in the ligaments of the ACLD knee.

METHODS

The right leg was modeled using four rigid bodies: thigh, shank, hindfoot, and metatarsals. All joints were represented as described by Anderson and Pandy (2001), except the knee, which was modeled as a six degree-of-freedom joint. The geometry of the distal femur, proximal tibia, and patella was based on cadaver data reported for an average-size knee. The contacting surfaces of the femur and tibia were modeled as deformable, while those of the femur and patella were assumed to be rigid. Thirteen elastic elements were used to describe the geometric and mechanical properties of the knee ligaments and posterior capsule (Pandy et al., 1998). The model leg was actuated by thirteen musculotendinous units.

A combination of forward and inverse dynamics was used to determine the relative translations of the bones and the forces induced in the knee ligaments during walking. Joint motion, ground-reaction forces, and the corresponding muscle forces obtained from a dynamic optimization solution for gait (Anderson and Pandy, 2001) were input to the leg model. The dynamical equations of the motion for the three-dimensional knee model were then used to determine the forces induced in the knee ligaments at each instant of the gait cycle. Two simulations were performed: one with the ACL intact; the other with the ACL removed. The calculations did not include the effect of gait adaptations in the absence of the ACL.

RESULTS AND DISCUSSION

The ACL was loaded throughout the stance phase of gait in the intact knee model; peak force in the model ACL was about 344 N just after opposite-toe-off (Fig. 1). In the ACLD model, peak MCL force increased to about one half of that calculated for the ACL in the intact joint. Anterior tibial translation increased throughout the stance phase in the ACLD knee with a maximum difference of 9mm. An increase in anterior tibial translation in the ACLD knee decreases the angle of the patellar tendon relative to the tibia, and this in turn reduces the anterior pull of the patellar tendon on the tibia. Thus, there is no substantial increase in the forces transmitted to the secondary ligaments, since the anterior shear force applied to the tibia drops when the ACL is absent. Peak anterior shear force applied by the patellar tendon was 297 N in the intact model and just 117 N when the ACL was removed.

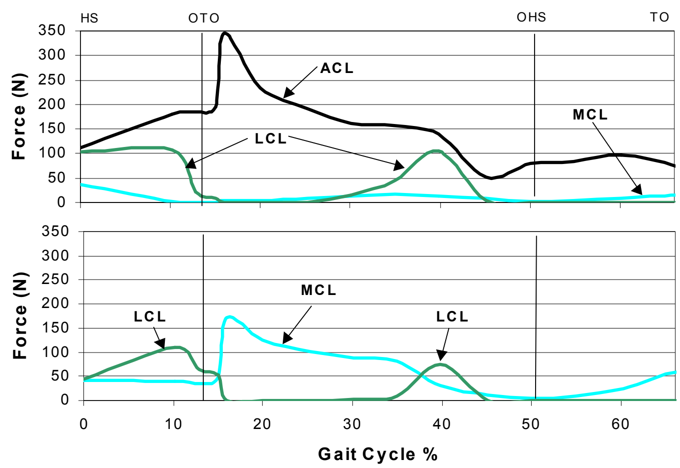

Figure 1: Ligament forces during the stance phase of gait for the intact knee (top) and ACL-deficient knee (bottom).

SUMMARY

The model results indicate that there is only a modest increase in ligament forces during ACLD gait. The collateral ligaments are naturally protected by the increase in anterior tibial translation that occurs when the ACL is absent, since this reduces the anterior pull of the patellar tendon on the tibia.

REFERENCES

Anderson, FC, Pandy, MG (2001). J Biomech Eng **123**(5): 381-90.
Andriacchi, TP, Birac, D (1993). Clin Orthop (288): 40-7.
Berchuck, M, et al. (1990). J Bone Joint Surg Am **72**: 871-7.
Devita, P, et al. (1997). Med Sci Sports Exerc **29**(7): 853-9.
Pandy, MG, et al. (1998). Comput Methods Biomech Biomed Engin **1**(2): 87-108.

INVESTIGATION OF GOLF CLUB INERTIAL PROPERTIES VIA BIOMECHANICAL MODELING

Darrin R. Richards and Gary T. Yamaguchi

Department of Bioengineering, Arizona State University, Tempe, AZ 85287-9709, USA

INTRODUCTION

It is very important for golfers to swing all clubs similarly (*i.e.* to have all clubs come square at impact given the same muscular actions). This is because a golfer cannot perform multiple swings, and adjust to the inertial characteristics of a particular club. The industry standard is to match golf clubs via "swingweights", which is a static measurement of weight distribution. However, the golf swing is a very dynamic activity involving large inertial and centrifugal forces. In addition, the advent of increasingly light and longer graphite shafts have made the swingweight scale ineffective.

It has been proposed that the static method of quantifying the mass distribution in a golf club should be replaced by a technique which accounts for the dynamic properties of golf clubs. Cochran and Stobbs (1969) suggested that a better way to balance clubs would be to balance the moments of inertia. In this study, a 3D model was developed to quantitatively investigate the feasibility of doing this.

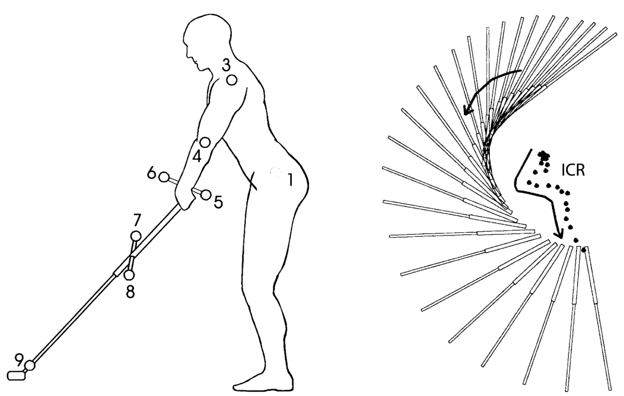

Figure 1: Marker positions (L), and ICR pathway of club (R).

METHODS

Kinematic data was collected from expert golfers using the MacReflex system (Qualisys, East Windsor, CT). Four cameras sampled marker positions at 120 Hz to submillimeter resolution. Nine markers were affixed to the subjects' body segments and clubs (Figure 1L). Kinematic changes to the body segmental angles, or to the club, caused by introducing slight weighting differences to the clubs were not detectable by our experimental measurement system. However, the instantaneous center of rotation data (Figure 1R) proved to be useful for defining the best measure of club moment of inertia.

A 6 degree-of-freedom, 3D, forward dynamic model driven by joint moments was derived and programmed using Kane's method (Yamaguchi, 2001). The model predicted kinematic variables as functions of time based on joint moment inputs, and was useful because it could quantify small kinematic changes that were too minute to measure experimentally. Baseline joint moments derived from an inverse dynamic analysis of a Nike Tour pro's swing were used as initial inputs, and modified until the model reproduced essentially the same swing in forward dynamic mode as the tour pro. The model delivered a peak clubhead velocity of 52 m/s at 290 ms, and a peak club angular velocity of 39.8 rad/s.

To measure the effect of small changes to the mass distribution of the golf club, the masses, lengths, centers of mass, etc., were altered slightly by changing inertial parameters in the modeled golf club. Three situations were investigated: (i) a 5 cm shorter, 4.1 g heavier "unbalanced" club; (ii) a "swingweighted" version of the unbalanced club; and (iii) a "dynamically balanced" club. The dynamic balancing was accomplished by matching the moments of inertia of the original club and the dynamically balanced club about a point 33.9 cm from the butt end of the club. This point is related to the "average" ICR of the club during the latter portion of the swing, and was determined through trial and error.

RESULTS AND DISCUSSION

Table 1 summarizes the results obtained by the dynamic simulations. The path of the clubhead remained quite stable in all simulations. However, the angle of the clubface at impact and the time at impact changed dramatically. Clubface angle determines the amount of sideways curvature and adversely affects ball flight and distance. As shown, the unbalanced club produced a 3.65° slice, and the swingweight technique overcorrected the clubface angle to produce a 2.38° hook. Balancing the moment of inertias of the two clubs greatly improved the result.

Table 1: Summary of results during simulated golf swings.

Modified Variables	**Unbalanced Club**	**Swingweight Balanced**	**Dynamically Balanced**
Δ Velocity	-1.56 m/s	-2.39 m/s	-2.05 m/s
Hook/slice	3.65° slice	2.38° hook	0.06° slice
Push/pull	0.30° push	0.23° pull	0.00°
Toe-up/Toe-down	0.22° toe-down	0.26° toe-down	0.21° toe-down
Δ Elevation Angle	-3.46°	-2.07°	0.20°

REFERENCES

Cochran, A. and Stobbs, J. (1969) *The Search for the Perfect Swing*. Heinemann, London, England

Yamaguchi, G.T. (2001) *Dynamic Modeling of Musculoskeletal Motion - A Vectorized Approach for Biomechanical Analysis in Three Dimensions*. Kluwer.

RUNNING ON ARTIFICIAL HIP JOINTS - IS IT WISE ? A HIP SIMULATOR STUDY

John G. Bowsher[1], Jim Nevelos[2], Jenny Pickard[2], Julia C. Shelton[1]
[1] IRC in Biomedical Materials, Queen Mary, University of London, London, UK, mail@johnbowsher.com
[2] Corin Medical, Cirencester, UK

INTRODUCTION

The question whether today's artificial joints are suitable for patients who undergo high-impact sports is yet to be fully understood. Although a small number of hip arthroplasty patients have shown continued clinical success while running marathons, performing down hill skiing (1), martial arts etc, the relationship between patient activities and implant failure have not been fully estimated. As hip joints are being implanted in younger and more active patients, coupled with the introduction of much lower wearing 2nd generation hip implants, it is therefore timely that laboratory investigations account for such high activity conditions. Also, it is very possible that alternative bearing combinations and novel coatings may offer further improved wear performances for active patients compared to today's prostheses.

A previous laboratory study has reported that simulated jogging did not generate excessive wear of lightly-crosslinked UHMWPE/CoCrMo implants (2), with the results showing only a 40% increase in jogging wear compared to normal walking. In terms of wear debris production, this result implies that for most patients, short periods of impact sports will not greatly reduce the survival of crosslinked polyethylene implants. Additional wear studies have also shown that the introduction of small areas of femoral damage during simulated jogging tests did not generate excessive polyethylene wear, Table 1, and may explain why many active patients have experienced good clinical success.

For metal-on-metal implants, the influence of high patient activities has yet to be investigated; thus the aim of this study was to quantify the influence of patient activity level on metal wear debris generation.

EXPERIMENTAL METHODS

A wear study was undertaken using two 40 mm diameter resurfacing bearings (cast CoCrMo alloy to BS7252-4), supplied by Corin Medical, UK. All wear tests were performed using an 8-station hip joint simulator (MTS Systems, USA), which applies a ±23° biaxial rocking motion. All test specimens were positioned physiologically, and were run in 25% bovine calf serum (17 mg/ml protein content) as a lubricant. Normal and simulated jogging tests were undertaken at 1 Hz and 1.75 Hz respectively, with maximum forces of 2450 N and 4500 N. Volumetric wear was measured gravimetrically, and was corrected using unloaded controls.

RESULTS AND DISCUSSION

The walking and jogging wear results for the metal-metal joints are shown in Table 1. This study offers continuing experimental evidence that higher patient activities, such as fast jogging, do not lead to excessive wear of 2nd generation hip implants. During simulated jogging, the maximum levels of frictional torque were generated at the point of contact after joint separation, typically 0.5 to 1.2 Nm, and 0.2 Nm without separation. These results are very encouraging for demanding and younger patients, as it would seem that a much higher level of patient activity can be withstood by modern implants than previously thought. Although it's strongly advised that hip arthroplasty patient avoid activities which may lead to large collisions and falls, the results from this study suggest that activities like jogging are well within the normal performance of most implants. In light of this result, further wear studies are currently underway, investigating alternative patient activities and implant bearing materials.

REFERENCES

(1) Kloen, P., et al. (2000). *Hip International*, **10(2)**, 77-82.
(2) Bowsher, J.G., Shelton, J.C. (2001). *Wear*, **250**, 167-179.

Table 1: Summary of median wear rates ($mm^3/x10^6$ cycles) and wear factors (*k*) (mm^3/N m $x10^{-6}$) generated by normal walking and jogging tests for UHMWPE-on-CoCrMo & CoCrMo-on-CoCrMo hip joints, under smooth and varying degrees of femoral damaged.

	28 mm 5 Mrad-Gamma/N^2-crosslinked-UHMWPE-on-CoCrMo					Metal-on-Metal
		Rough Femoral Conditions - Damage Area & Topography				(40 mm dia.)
Patient Activities	Smooth Femoral Conditions	180 mm^3 R_a = 0.2 μm R_p = 1.2 μm	180 mm^3 R_a = 0.5 μm R_p = 1.3 μm	180 mm^3 R_a = 0.8 μm R_p = 1.8 μm	1230 mm^3 R_a = 0.38 μm R_p = 3.0 μm	Smooth Femoral Conditions
Normal Walking (1 Hz)	15 *(k) = 0.8*	–	–	–	140 *(k) = 7.7*	0.25 *(k) = 0.010*
Fast Jogging (1.75 Hz)	23 *(k) = 0.6*	48 *(k) = 1.2*	59 *(k) = 1.4*	92 *(k) = 2.3*	2230 *(k) = 55.0*	0.8 *(k) = 0.014*

ADAPTATIONS IN LOWER EXTREMITY JOINT KINETICS TO INERTIAL ASYMMETRIES DURING WALKING

Philip E. Martin[1], Jeremy D. Smith[1], and Todd D. Royer[2]
[1]Exercise and Sport Research Institute, Arizona State University, Tempe, Arizona (email: philip.martin@asu.edu)
[2]Department of Exercise and Sport Sciences, University of Delaware, Newark, Delaware

INTRODUCTION

Modeling the lower limb as a forced driven harmonic oscillator (FDHO; Holt et al., 1990; Kugler & Turvey, 1986), walking stride time can be predicted as a function of lower limb mass distribution properties. When leg inertial properties are increased symmetrically, stride time increases in a manner consistent with FDHO predictions (Holt et al., 1990). Asymmetrical inertial manipulation disrupts temporal and kinematic symmetry such that the weighted limb reflects a longer swing time and shorter stance time (Royer & Martin, 1999). Further, actual stride time is intermediate to FDHO predicted stride times for the unloaded and loaded legs. Adaptations at the muscle and joint kinetic level underlying these temporal changes have received limited attention. The purpose of this study was to investigate these adaptations by examining net joint moment profiles about the ankle, knee, and hip under asymmetrical lower extremity inertial conditions.

METHODS

Twelve healthy young adults, free of notable gait and structural asymmetries, served as subjects. Sagittal plane video (60 Hz) and ground reaction force (480 Hz) data were collected as subjects walked at 1.57 $m \cdot s^{-1}$. Subjects completed trials under a symmetrical, unloaded condition (Sym-NL) and asymmetrical inertia conditions (0.5, 1.0, or 2.0 kg masses added to one foot only). Net joint moments at the ankle, knee, and hip were computed from inverse dynamics. Segment inertial properties were predicted using methods of deLeva (1996). Moments were normalized temporally (100% stride) and to body weight and leg length to yield dimensionless expressions (Hof, 1996).

RESULTS AND DISCUSSION

Adaptations in the net ankle, knee, and hip moments (Figure 1) to asymmetrical loading occurred in both the unloaded (Asym-0 kg) and loaded (Asym-2 kg) legs when compared to the fully unloaded condition (Sym-NL), and increased systematically with increasing inertial asymmetry. Temporal shifts in the moments consistent with a shorter stance time and longer swing time were especially notable in the loaded limb (Asym-2 kg) during the second half of stance. Adaptations in joint moment amplitude were also apparent, particularly at the knee and hip. In the first half of stance, knee extensor function was greater and hip extensor function lower in the loaded leg. In later stance, the loaded limb reflected lower knee flexion and higher hip flexion actions. Swing phase asymmetry was most apparent at the end of swing with the loaded leg reflecting higher knee flexor and hip extensor moments.

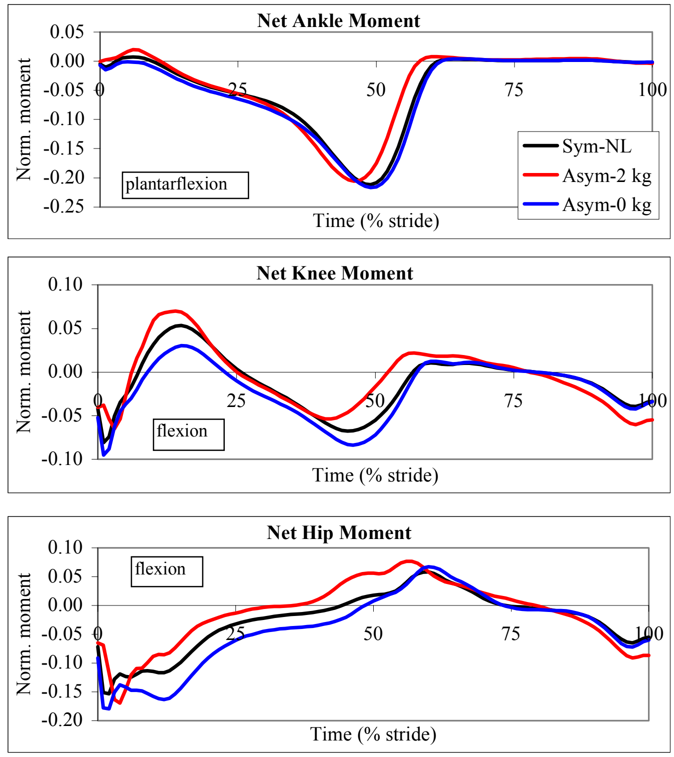

Figure 1. Average ankle, knee, and hip moments for Sym-NL and the most extreme asymmetrical inertia condition (Loaded leg: Asym-2 kg; unloaded leg: Asym-0 kg).

SUMMARY

The neuromuscular system, as reflected by net joint moments, adapts asymmetrically to imposed inertial asymmetries. This adaptation presumably is an attempt to retain as much symmetry temporally and kinematically as possible, even though both temporal and kinematic asymmetries emerge with increasing inertial imbalance.

REFERENCES

DeLeva, P. (1996). *J. Biomech.*, **29**, 1223-1230.
Hof, A.L. (1996). *Gait Posture*, **4**, 222-223.
Holt, K.G. et al. (1990). *Hum. Move. Sci.,* **9**, 55-68.
Kugler, P.N., Turvey, M.T. (1987). *Information, Natural Law, and the Self-Assembly of Rhythmic Movement*. Erlbaum
Royer, T.D. Martin, P.E. (1999). *Proceedings Gait and Clinical Movement Analysis Society*

THE TESTING AND VALIDATION OF A FAST RESPONSE INCLINOMETER

Peter W. Johnson [1], Chris Townsend [2] and Steve Arms [2]
[1] Department of Environmental Health, University of Washington, Seattle, WA, petej@u.washington.edu
[2] Microstrain, Inc., Burlington, VT

INTRODUCTION

The development of an ambulatory postural measurement tool with dynamic response may have widespread application in the field of biomechanics. Inclinometers have been primarily used for ambulatory posture measurement; however, these devices have a very slow response and typically cannot accurately measure dynamic movements. Therefore, the goal of this preliminary study was to test and characterize the performance of a prototype device, called a Flexion Angle Sensor with Gyro (FAS-G), for accurately measuring both static and dynamic movements.

METHODS

The prototype device (FAS-G; Microstrain, Inc; Burlington Vermont) was built and consisted of two accelerometers (inclinometers) and one piezo-ceramic gyro packaged in a 1.7 cm x 4.1 cm x 2.7cm plastic housing. The gyro has excellent rate response but poor signal stability over time (drift), whereas the inclinometers have great stability but poor rate response. By combining the output of the inclinometers with the gyro, the intension was to utilize the combined response of both sensors, that is, switching between the fast acting gyro signal during dynamic movements and the stable inclinometer signal during slow movements.

To test the device, the FAS-G was connected in series to an potentiometer (Model 157; Vishay Spectrol; Malvern, PA) and three tests were performed: 1) a static angle measurement tests where the FAS-G was placed in 0°, ± 30°, ± 60° and ± 70° of pitch and rotated at a slow rate between 0° and 360° of roll; 2) a dynamic swing test where the FAS-G was connected to a pendulum and subjected to swinging movements of up to 400°/s; and 3) a highly dynamic impulse test where the FAS-G was abruptly stopped in the middle of a pendulum swing. During the tests, the signals from the FAS-G, and potentiometer were collected and stored at 1000Hz using a portable computer instrumented with a data acquisition card (Model AI-16E-4; National Instruments; Austin, TX). The output between the FAS-G, inclinometers (accelerometer outputs from the FAS-G) and potentiometer (gold standard) were compared.

RESULTS AND DISCUSSION

Static Tests. Angle-angle plots comparing the outputs from the FAS-G and potentiometer demonstrated that the FAS-G accurately measured angles over 360° of roll with an average absolute error of 2.8°, 4.8°, 4.5° and 7.4° at 0°, ± 30°, ± 60°, ± 70° of pitch respectively.

Dynamic and Impulse Tests. Figures 1 and 2 show typical results from the pendulum and impulse tests.

Figure 1: Comparison of outputs between the potentiometer, FAS-G and inclinometer during a typical pendulum test. The left graph is the full test and the right graph is the first 3 seconds. The FAS-G virtually tracked the dynamic swinging

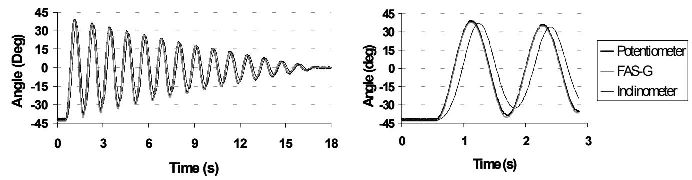

movements as measured by the potentiometer (gold standard) whereas the conventional inclinometer both lagged and underestimated the magnitude of the movements. The absolute average error over the test was 0.6° for the FAS-G and 6.9° for the inclinometer.

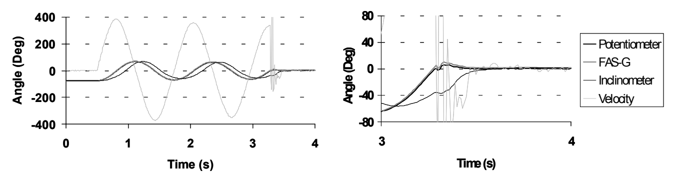

Figure 2: Comparison of outputs between the potentiometer, FAS-G and inclinometer during a typical, highly dynamic, impulse test. The pendulum was rapidly stopped at roughly 3.3 seconds. The left graph is the full test and the right graph is the last second. The FAS-G tracked the movement during the highly dynamic impulse quite well, whereas the inclinometer both lagged and took a greater amount of time to settle after the abrupt stop.

SUMMARY

Preliminary tests indicated that the FAS-G performed well for both static and dynamic angle measurement. Movements with velocities up to 400°/s were accurately measured. In addition, the impulse tests indicated that very abrupt movement changes may be accurately measured. As a result, the highly dynamic response of the FAS-G should allow the measurement of limb positions during both slow and fast movements. Unlike conventional inclinometers, the dynamic response of the FAS-G will allow the calculation of limb velocities and accelerations. Future testing will include the study of the FAS-G for measuring more rapid and random movements in order to determine the upper limits of dynamic measurement.

MECHANICS OF APE SWINGING (PASSIVE DYNAMIC BRACHIATION)

Mario Gomes (mwg1@cornell.edu) and Andy Ruina
The Human Power, Biomechanics, and Robotics Laboratory, Cornell University, Ithaca, NY, USA

INTRODUCTION

Long armed apes are able to move very rapidly through the treetops in a remarkably smooth manner. Are there some simple mechanical ideas which help explain how they achieve this type of locomotion with such apparent ease? In this work we examine the dynamics of several simplified rigid body models with a focus on energy conservation. Is it possible for the apes in our models to "brachiate" with *zero* energetic cost? To answer this, we would need to find periodic motions in the models which conserve energy.

Long armed apes have two distinct brachiating "gaits": 1) a continuous contact gait where one hand is always in contact with the overhead support and 2) a faster ricochetal gait with a period of free flight between handholds. Both of these motions are very smooth and at times resemble the motion of a simple pendulum (Fleagle,J). Further, the hands don't make jarring impacts when grabbing a new support. Given these observations and the obvious necessity for energy efficiency, we hypothesized that perfectly efficient passive-dynamic motions could be found in these models. To test this hypothesis we examined a series of two dimensional, passive rigid body models for energy conserving, periodic motions.

METHODS

All of the models we examined consist of linked rigid bodies. We "cheat" slightly by assuming that there is a non-passive hand that can grab onto and release from a handhold, with which it is coincident at appropriate times. The grabbing and releasing of the hand does not produce or absorb any mechanical work so we simplify things by neglecting the energy required to grasp and release the handhold. There are no other actuators or springs. Thus the only way for energy to leave the system is in a collision with an impact of the hand with the handhold. The key to our models is finding motions where the hand collides with a new support at a relative velocity of zero, thus dissipating no energy when the hand contacts the support.

The first model examined is a single rigid body with inertia and massless arms, an extension of the point mass model of Bertram et al. Next, we examined a model consisting of arms with inertia and a point-mass body, i.e. two rigid bodies connected at a massive hinge joint. Lastly, we examined a three-link model with two arm links and a torso-leg link, i.e. three linked rigid bodies. For each model we considered both continuous contact and ricochetal brachiation. Numerical integration of the nonlinear equations of motion was the main tool of our study.

RESULTS AND DISCUSSION

For each of the models, not only were we able to find *a* collisionless periodic motion, but we found that a whole family of solutions exists for each set of model parameters.

In the third model, for example, the arms swing passively from handhold to handhold making smooth contact at the grab. Meanwhile, the body swings underneath in a manner reminiscent of actual gibbon brachiation as shown in figure 1.

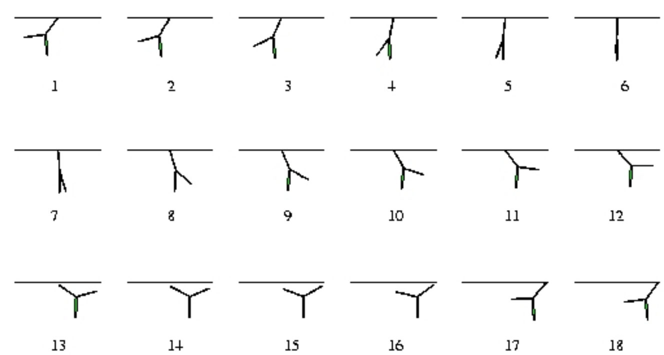

Figure 1: A collisionless ricochetal motion for the three-link model

SUMMARY

Perfectly energy efficient brachiation is possible with a rigid body model. If it is possible for the "apes" in these models to brachiate without using any energy, then actual apes might exploit this to their benefit when coordinating their quick and smooth movements in the treetops. These results support the idea that energy efficiency may be a large factor in determining the coordination strategy used by brachiating apes and that passive-dynamic mechanisms are used to achieve this efficiency.

REFERENCES

Bertram et al (1999). *J. of Experimental Biology*, **202**, 2609-2617.

Fleagle, J. (1974). *Nature*, **248**, 259-260.

ACKNOWLEDGEMENTS

This work was partially funded by an NSF biomechanics grand and NSF IGERT program. We thank John Bertram for his conversations about gibbon brachiation as well as for the video images used to make comparisons with the dynamic models. We also appreciate the insightful comments and editing help of Dave Cabrera, Manoj Srinivasan, Mike Coleman, Steve Collins, and Carmel Majidi.

CERVICAL SPINE KINEMATICS FOLLOWING SEQUENTIAL SECTIONING: NOVEL IMPLICATIONS FOR EXTENSION TYPE INJURIES

Klane K. White[1], Catherine M. Robertson[1], Andrew T. Mahar[2], Peter O.Newton[2], Mark A.Gomez[1]

[1] Department of Orthopedics, University of California San Diego, San Diego, CA
[2] Department of Orthopedics, Children's Hospital – San Diego, San Diego, CA

INTRODUCTION

Current clinical understanding of cervical spine kinematics in the intact and injured spine is based on well-referenced publications[1, 2]. Previously, Gomez et al. reported the use of a specially designed rig which induced an applied moment with a coupled vertical shear load.[3] They found significantly greater angular changes than those referenced,[1,2] as well as translation up to 5 mm in an intact motion segment. That study was limited to an examination of applied flexion moments with sequential cutting of soft tissue structures from posterior to anterior. The purpose of the present study is to examine the kinematics of individual motion segments in extension with sequential cutting of soft tissue structures from anterior to posterior.

METHODS

Cervical spines were harvested from seven fresh frozen human cadavers (ages 31-45) and sectioned into C2-C3, C4-C5 and C6-C7 motion segments. A loading rig fixed the lower vertebra to a sliding plate. The upper vertebra was fixed to a pulley system via 3.5 mm smooth pins: one through the center of the vertebral body and the other through the posterior arch. (Figure 1)

Figure 1: Loading rig for cervical testing.

A constant moment of 2 Nm with a coupled vertical shear load of 155 N (≈25% body weight) was applied to each motion segment. The linear translation of the sliding plate and the angular rotation of the pulleys were measured at two minutes with linear and rotatory variable differential transformers. Data were collected for intact segments, followed by serial transection of: (1) the anterior longitudinal ligament (ALL), (2) the anulus fibrosus (ALL+disc) and (3) the facet joint capsular ligaments (ALL+disc+facets). Linear and angular displacement values were measured after each transection. Repeated measures ANOVA ($p<0.05$) and *post hoc* difference contrast tests for multiple comparisons were used to compare differences after serial sectioning and among the three motion segment levels.

RESULTS AND DISCUSSION

There was an significant ($p<0.001$) increase in linear translation with sequential soft tissue transection. A significant sequential increase in angular rotation was also noted ($p<0.001$). There was no significant difference among motion segments in either linear translation ($p=.25$) or angular rotation ($p=.20$).

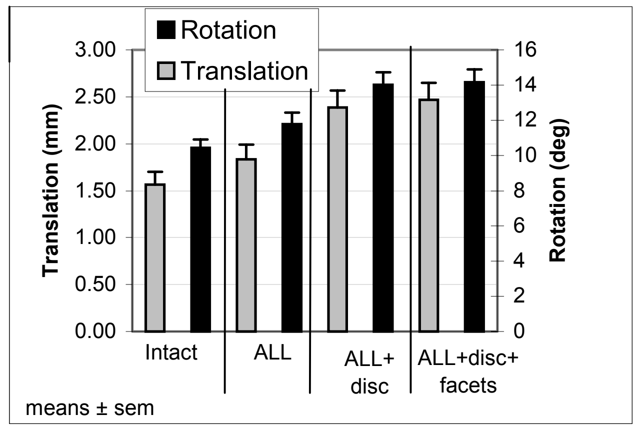

Figure 2: Data for translation and rotation.

On average, the findings of increased linear translation agree with previous data[1,2] with means less than 2.7 mm in all groups. The angular changes seen in this study were greater than those previously described [1,2]. The maximum angular change in this study was 17.8° for an intact specimen (range 5.7 – 17.8). Current recommendations for suspected cervical spine instability are angular deformity >11° relative to adjacent motion segments on static lateral radiographs, or >20° of sagittal plane rotation on dynamic radiographs.[4] Many of the intact segments surpassed these parameters.

SUMMARY

This study of cervical spine motion segment kinematics found greater cervical spine motion than reported previously [1,2]. The current test rig may better simulate physiologic cervical spine kinematics by applying a constant moment with a coupled vertical shear load. These data indicate that current recommendations for diagnosing cervical spine instability may be conservative, warranting further investigation.

REFERENCES

1. Panjabi, et. al. J Biomechanics, 1975, 8:327-336.
2. White AA, et. al. Clin Orthop, 1975, 109:85-95.
3. Gomez M, et. al., Trans Orthop Res Soc, 1993, 18:402.
4. White AA, Panjabi MM. Clinical Biomechanics of the Spine, 2nd Ed., 1990.

HAMSTRINGS ACTION ALONE CANNOT LIMIT ANTERIOR TIBIAL TRANSLATION IN ACL-DEFICIENT GAIT

Kevin B. Shelburne[1] and Marcus G. Pandy[2]
[1]Steadman◆Hawkins Sports Medicine Foundation, Vail, Colorado, U.S.A., Kevin.Shelburne@shsmf.org
[2]Department of Biomedical Engineering, University of Texas at Austin, U.S.A.

INTRODUCTION

Numerous studies have suggested that increased activation of the hamstrings muscles may compensate for the loss of anterior tibial restraint in the ACL deficient (ACLD) knee (Solomonow, et al., 1987; Liu and Maitland, 2000). Virtually no data are available, however, for the amount of hamstrings force needed to keep the ACLD knee stable in any activity. In this study, we used a three-dimensional model of the lower limb to calculate anterior tibial translation (ATT) in ACLD walking. The model was also used to calculate the amount of hamstrings force needed to limit ATT and keep the ACLD knee stable during the gait cycle. The margin of stability was defined as the amount of ATT calculated for maximum isometric contractions of the quadriceps in the ACL-intact knee (Pandy and Shelburne, 1997). We hypothesized that hamstrings muscle action alone is sufficient to stabilize the knee throughout the stance phase of ACLD gait.

METHODS

A theoretical approach was used to find the relative positions of the bones and the forces induced in the ligaments during ACLD gait. The right leg was modeled using four rigid bodies: thigh, shank, hindfoot, and metatarsals. All joints were represented as described by Anderson and Pandy (2001a), except the knee, which was modeled as a six degree-of-freedom joint. The geometry of the distal femur, proximal tibia, and patella was based on cadaver data reported for an average-size knee. Thirteen elastic elements were used to describe the geometric and mechanical properties of the knee ligaments and capsule (Pandy et al., 1997). The model leg was actuated by thirteen musculotendinous units.

Joint motion, ground-reaction forces, and the corresponding muscle forces obtained from a dynamic optimization solution for normal gait (Anderson and Pandy, 2001a) were input to the leg model. The dynamical equations of the motion for the three-dimensional knee model were then used to determine the relative positions of the bones at each instant during the stance phase of ACLD gait. Three simulations were performed: (1) hamstrings force was calculated for normal walking with the knee intact; (2) the model ACL was removed before calculating the amount of hamstrings force needed to limit ATT to the level predicted for the intact model; and (3) the ACL was removed before calculating the amount of hamstrings force needed to limit ATT to the level predicted for maximum isometric contractions of the quadriceps.

RESULTS AND DISCUSSION

The model calculations showed that hamstrings muscle action cannot limit ATT to the level calculated for the intact knee during normal gait (Fig. 1). Although less hamstrings force was needed to keep the knee stable in ACLD gait, this amount is still far greater than that developed in normal walking with the knee intact (Anderson and Pandy, 2001b). The inability of the hamstrings to limit ATT in ACLD gait is explained by the dependence of the geometry of these muscles on the flexion angle of the knee. When knee flexion angle is less than 15 degrees, as it is for much of the stance phase of walking, the angle between the line of action of the hamstrings and the long axis of the tibia remains small. In this case, hamstrings cannot exert a large enough posterior pull on the tibia to limit ATT in the stance phase of ACLD gait (Pandy and Shelburne, 1997).

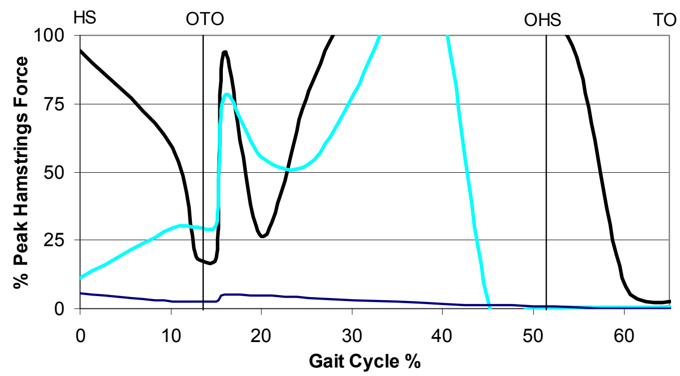

Figure 1: Percent of peak isometric hamstrings force needed to limit ATT to the level calculated for the intact knee (black line) and to keep the ACLD knee stable (gray line). Also shown is the amount of hamstrings force predicted for normal gait (thin black line) (Anderson and Pandy, 2001b).

SUMMARY

Hamstrings co-contraction force needed to stabilize the knee in ACLD gait is far greater than that evident in normal walking. The ineffectiveness of hamstrings muscle action in ACLD gait is explained by the geometry of these muscles at the knee and by the fact that knee flexion angle remains relatively small in the stance phase of walking.

REFERENCES

Anderson, FC, Pandy, MG (2001a). J Biomech Eng **123**(5): 381-90.
Anderson, FC, Pandy, MG (2001b). J Biomech **34**:153-161.
Liu, W, Maitland, ME (2000). J Biomech **33**(7): 871-9.
Pandy, MG, et al. (1998). Comput Methods Biomech Biomed Engin **1**(2): 87-108.
Pandy, MG, Shelburne, KB (1997). J Biomech **30**(10): 1015-24.
Solomonow, M, (1987). Am J Sports Med **15**(3): 207-13.

ANTERO-POSTERIOR MEASUREMENTS OF THE LAMELLIPODIUM MECHANICAL PROPERTIES IN THE MIGRATING KERATOCYTE

Valérie Laurent[1], Sandor Kasas[2], Alexandre Yersin[2], Tilman Schaeffer[4], Stefan Catsicas[2], Giovanni Dietler[3], Alexander Verkhovsky[1] and Jean-Jacques Meister[1]

[1]Cellular Biophysics and Biomechanics Laboratory, Swiss Federal Institute of Technology, Lausanne, Switzerland
valerie.laurent@epfl.ch
[2] Institut de Neurobiologie Cellulaire, Swiss Federal Institute of Technology, Lausanne, Switzerland
[3] Institut de Physique de la Matière Condensée, Université de Lausanne, Switzerland
[4] Department of molecular biology, Max-Planck-Institut for Biophysical chemistry, Goettingen, Germany

INTRODUCTION

Cell locomotion is implicated in many biological processes such as embryogenesis, inflammatory response, wound healing. The mechanism of cell locomotion is commonly divided into three steps : formation of a lamellipodial protrusion, adhesion of the lamellipodium to the substratum and translocation forward of the cell body. The first step has been extensively studied in term of the molecular basis of force generation but little is known about the mechanical properties of moving cells, especially the properties of the lamellipodium which plays a crucial role in cell locomotion. By using the Atomic Force Microscopy (AFM), we presently analysed the elastic modulus of the lamellipodium of fish epidermal keratocyte, a fast moving cell (velocity ~ 15 µm/min) characterised by high persistence and stability of shape during movement. The use of AFM allows us to locate cellular areas with different elastic properties and correlate them with the topography of the keratocyte.

METHODS

Keratocyte Culture: Black Tetra keratocytes were cultured in DMEM (Hepes modification; Sigma Immunochemicals) supplemented with 20 % FBS and antibiotics. Fish scales were extracted with tweezers, placed on dry coverslips and allowed to adhere for 30-60s to prevent floating. Culture medium was then added and the scales were kept at 30°C overnight to allow for migration of keratocytes onto the coverslip. Colonies of migrated cells were treated with 0.2 % trypsin and 0.02 % EDTA in PBS for ~30-60s and cells were allowed to recover 1-3 h in fresh medium before AFM experiments.
Atomic Force Microscope (AFM): A commercial AFM (Bioscope, Digital Instruments) combined with an inverted microscope was employed for this study. This combination allowed positioning of the AFM tip on the sample to micrometer precision. Soft silicon nitride cantilevers (force constant of 10 µm/N) were employed.
Data acquisition and analysis: The elastic modulus E can be calculated from the force curves, that correspond to the deflection of the AFM cantilever which is continuously monitored as it approaches the sample. As the cell moves at almost constant speed, the force curves are continuously recorded at a fixed point which is localised on the course of the cell and more precisely on the course of one cellular lobe. This method allows to obtain an analysis of E and of the cellular true height H along a line which is perpendicular to the leading edge of the cell and which crosses the lamellipodium. To calculate E and H from the force curves, we employed the Hertzian model for a purely elastic indentation in a flat and soft sample by a stiff cone (Radmarcher, Fritz et al., 1996).

RESULTS AND DISCUSSION

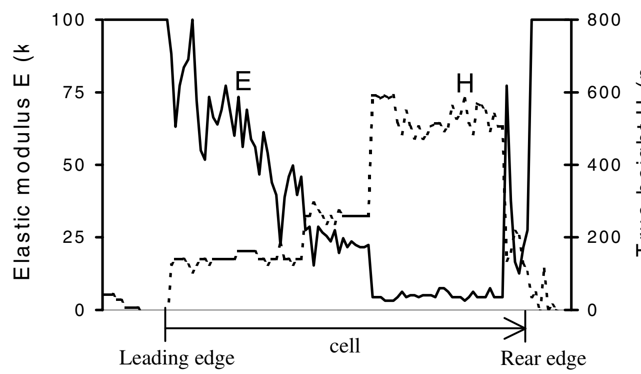

Figure 1: Variations of the elastic modulus E and the true cellular height H of a migrating keratocyte along a scan line perpendicular to the leading edge of the cell.

These preliminary longitudinal assessments of the mechanical response of the migrating keratocyte show that the motile state of the cells is not disturbed by the AFM measurements. Concerning the profile of the elastic properties, it appears that the lamellipodium is more rigid at the leading edge than at the rear: E decreases from ≈ 75 kPa on the leading edge down to ≈ 5 kPa on the rear edge (Fig. 1). Moreover, the variations of E do not appear to depend on the lamellipodium thickness H, i.e., in the first part of the curve, the true height is approximately constant (≈ 75 kPa) while the elastic modulus decreased from about 50%. These results confirm that the variations in elastic modulus are not caused by the influence of the underlying substrate. On the other hand, these mechanical properties, which are believe to reflect the underlying actin network properties (Hofmann, Rotsch et al., 1997), are consistent with the reduction of actin filament density from the front to the rear edge of keratocyte lamellipodia and with the dynamic network contraction model of keratocyte locomotion (Svitkina, Verkhovsky et al., 1997).

REFERENCES

Hofmann, U.G., Rotsch, C. et al. (1997). *Journal of Structural Biology*, **119**, 84-91.
Radmacher, M., Fritz, M. et al. (1996). *Biophysical Journal*, **70**, 556-567.
Svitkina, T.M., Verkhovsky, A. at al. (1997). *The Journal of Cell Biology*, **139**(2), 397-415.

PHYSIOLOGICAL FLOW IN A STENTED CORONARY BIFURCATION

V. Deplano[1], C. Bertolotti[1]

[1]IRPHE / ESM2 Technopôle de Château Gombert 13451 Marseille cedex 20, France, deplano@esm2.imt-mrs.fr

INTRODUCTION

When the coronary presents a partial occlusion, the myocard, depending on the degree of the occlusion severity, is no more sufficiently perfused. One of the solution consists of introducing a stent at the stenosis location. When multiple stenoses occur for example one in the coronary and one in its colateral, the cardiologists introduced two stents. However, in order to minimize the perturbations induce by the stent cell at the bifurcation, the cardiologists break the cell by inflating the balloon. This technique, cardiologist dependant, is aleatory. In addition, to the authors knowledge, no hydrodynamic studies in the literature analyze the stents influence on the flow patterns in a bifurcated artery. Therefore the goal of this numerical work is to provide informations of the perturbations induced by the presence of two stents in a bifurcated coronary with or without cell at the bifurcation position.

METHODS

The geometrical models are constituted of a 90° intersection of two cylinders. The first stent is located at the bifurcation and the second one in the colateral coronary. Several configurations have been investigated: 1) without stent in order to provide a reference flow features, 2) with two stents, 3) the stent cell located at the bifurcation is broken. The others cases represents a aleatory broken cell (4 and 5 case).

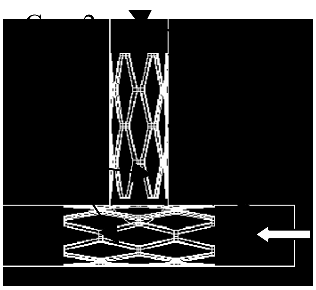

The shape of the stents is provided by a real deformed Palmaz stent issued from Abaqus code. The Navier Stokes equations are numerically solved using a volume finite package named Fluent. The viscosity is the blood viscosity ν=3.6e^{-6}m^2/s. The density , ρ is equal to 1050kg/m^3. The mesh, including the two stents, is constituted of 125335 tetrahedral elements.

RESULTS AND DISCUSSION

The figures 1 and 2 show the velocity vectors for respectively the Z=0 plane and the Y=2,96mm plane. a) represents the case 2 and b) a broken cell case.

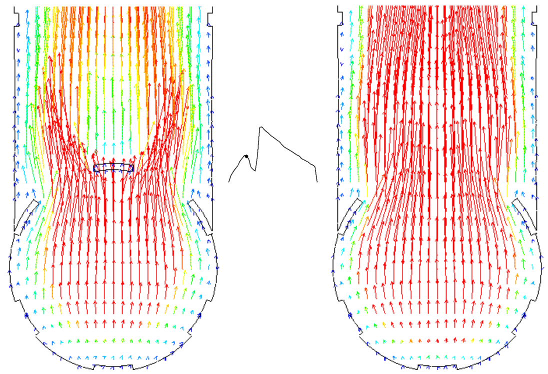

a) b)

Figure 1 : velocity vectors in Z=0 plane

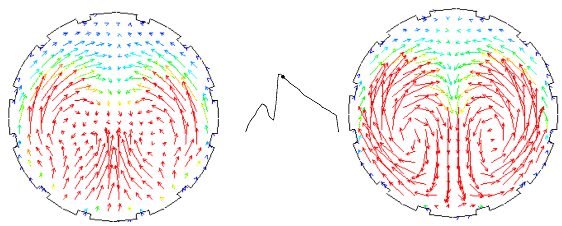

a) b)

Figure 2 : velocity vectors in Y=2.96mm plane

We observe (case 2, fig. 1a) two lateral jets and the occurrence of stasis areas downstream from the cells. In opposition the case 4 (fig. 1b) presents a large central jet. Therefore, the flow features depend on the cell overture. Figures 2a and b highlight the secondary structures differences. The well known counter rotative vortex are present for case 4 (fig. 2b) when for the case 2 (fig 2a), the motion induced by the jets through the cells modifies the classical counter rotatives vortex. The radial pressure gradient dominates the centrifugal force and stops the vortex formation.

SUMMARY

When two stents are introduced at bifurcation, the cell overture of one of them is so cardiologists dependent and the flow features so cell overture dependent that it would be reasonable to consider a specific stent design for a bifurcation implantation.

REFERENCES

Fluent Inc, Lebanon LH
Abaqus HKS, Inc

MODIFICATION IN THE POSTURAL CONTROL DURING LONG-TERM STANDING

Luís A. Imbiriba[1], Cíntia R. Cruz[1], Míriam R. M. Mainenti[1], José Magalhães[1], Marco A. C. Garcia[1]
Líliam F. Oliveira[1] and Jurandir Nadal[2]

[1]Laboratory of Biomechanics, EEFD, Federal University of Rio de Janeiro, aurelio@eefd.ufrj.br
[2]Biomedical Engineering Program, COPPE, Federal University of Rio de Janeiro, jn@peb.ufrj.br

INTRODUCTION

Stabilometry is an useful tool for studying postural balance control and also for clinical purposes. Although the test protocol is not well defined yet, it is recommended short term tests to minimize any effect due to fatigue (Le Clair et al, 1996 and Carpenter et al, 2001). Nevertheless there is no conclusive evidence of the fatigue process related to the test duration. The objective of this study is to identify modifications in some stabilometric parameters in long-term tests to help clarify this question.

METHODS

24 healthy volunteers, divided in two groups of 12 subjects (6 males e 6 females), were submitted to stabilometric tests. All subjects gave their consent. Subjects stood on a force platform, barefoot, with feet together. The session lasted for a total time of 31 minutes, with the register of seven trials of one minute in each 5 minutes. Between registers, group 1 (G1) sat on a chair , keeping the feet at the same place and group 2 (G2) continued standing on the platform.
In each trial, the subject had to choose a value at the Borg's scale that qualifies his sensation of tired and discomfort.
The analyzed stabilometric parameters were mean velocity, mean power frequency, mean position and the standard deviation of the center of pressure (COP) in lateral and anterior-posterior directions, as well as the elliptic area (Oliveira et al, 1996). It was used a 12 bits A/D converter with a sampling rate of 50 Hz and a filter anti-aliasing at 5 Hz. Two-way ANOVA for repeated measurements and Tukey's HSD post-hoc analysis were employed to compare groups (G1 and G2) and trials (seven levels).

RESULTS AND DISCUSSION

Figure 1 shows the results for Borg´s scale between the groups. There was a statistic difference from the trial 5 (approximately 20 minutes) to the end of the test, where the group 2 related higher values on the scale (p=0.000001). The stabilometric parameter witch followed this tendency was the standard deviation of COP in the lateral direction (Figure 2) where the statistic difference between groups also appeared at the trial 5 (p=0.002).
Standard deviation and mean velocity in the anterior-posterior direction and the elliptical area were statistically different between groups from trial 4 (15 minutes) to 7 (30 minutes), except for trial 5, interestingly at the same trial the Borg´s scale value differed statistically. Mean position, mean velocity and mean frequency of the lateral displacements were not different between groups at any moment of the test duration. Mean frequency at the anterior posterior direction show a tendency to reduce during the test for both groups, although not significant (p=0.162).
This results shows that for the analysis of stabilometric parameters used, there is no evidence for short term test recommendation. Borg's scale, although not used here for its primarily purpose, could be a helpful tool in detecting fatigue sensation in stabilometric tests. Future studies will use electromiography to help identifying muscular fatigue process.

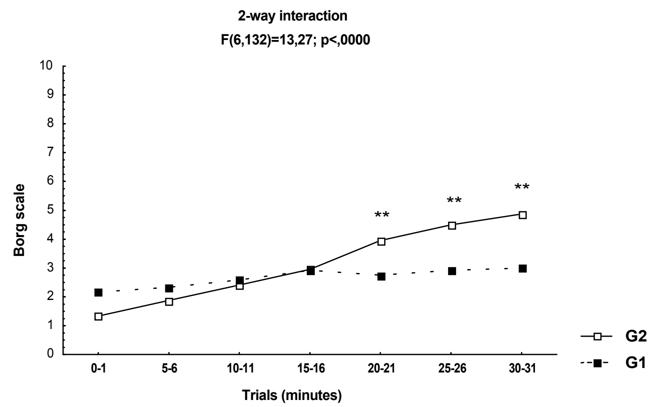

Figure 1: Perceived exertion changes (Borg's scale) in time.

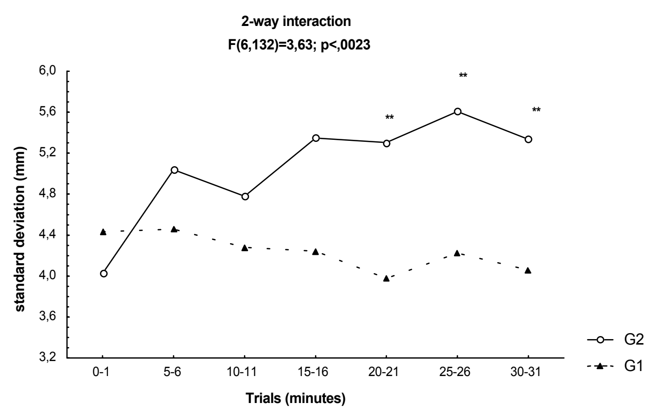

Figure 2: Standard deviation of COP, lateral direction, through the trials.

REFERENCES

Carpenter, M.G. et al (2001). *Gait and Posture*, **13**, 35-40.
Oliveira, L.F. et al (1996). *Physiol Meas*, **17**, 305-312.
Le Clair, K., Riach, C. (1996). *Clin. Biomec.*, **228**, 75-78.

ACKNOWLEDGMENTS

This work has been supported by Brazilian Research Council (CNPq) and José Bonifácio Foundation (FUJB/UFRJ).

AUTOMATED SUBJECT-SPECIFIC SCALING OF SKELETONS TO MOTION-CAPTURED MARKERS

Victor Ng-Thow-Hing[1] and Jianbo Peng[2]
[1]Fundamental Research Laboratories, Honda R&D Americas, Inc. vngthowhing@hra.com
[2]Media Research Lab, New York University

INTRODUCTION

Simulations using generic musculo-skeletal models enable qualitative insights to be made about human motor tasks (Zajac, 1993). However, simulations using subject-specific skeletons can aid in making more quantitative comparisons of a simulated model with its real human counterpart. We have developed a flexible optimization framework for the automated scaling of subject-specific human skeletons from motion-captured data. The resulting skeleton can then be used for the simulation and analysis of musculo-skeletal function. The computation of joint centers from different gait models has yielded inconsistent results (Tabakin and Vaughan, 2000). Therefore, we avoid reconstruction of joint centers based solely from a single, static pose and we scale bones using direct information from marker positions rather than distances between derived joint centers (Musculographics, 2001). The purpose of this study is to compare the performance of two different optimization strategies for subject-specific skeleton fitting.

METHODS

The framework is based on a least squares minimization of the distance between recorded marker positions and virtual markers placed on a generic, scaleable human model. A constrained nonlinear optimization is used to simultaneously adjust joint and bone scaling parameters, producing a scaled skeleton with joint angles that fits the marker data.

The parameters, **x**, of the optimization are partitioned into joint degrees of freedom, $\mathbf{x}^J$, and bone scale factors, $\mathbf{x}^B$. The optimization's objective function is a weighted sum of squared differences between the marker locations and their transformed counterparts on the generic model:

$$f(\mathbf{x}) = \sum_{s \in S} \sum_{m \in M_s} w_i \left\| T_s(\mathbf{x}^J) D_s(\mathbf{x}^B) v_m - m \right\|^2,$$

where S is the set of all segments in the skeleton and M_s is the set of markers associated with a segment s. The virtual marker, v_m, is the corresponding marker located on the generic human skeleton and is transformed by a matrix $T_s(\mathbf{x}^J)$, specifying the position and orientation of a bone segment s, and a nonuniform scaling matrix, $D_s(\mathbf{x}^B)$. Scale factors are constrained to be within anthropometric limits. The weights, w_i can be modulated to produce a stronger fit to selected markers and control rates of convergence to a solution.

Two different optimization strategies were implemented. The first method simultaneously optimizes all parameters **x** of the skeleton. The second method solves a series of smaller optimizations where each optimization solves a subset of **x** corresponding to the joint and scaling parameters of a local region of the skeleton's segments. For each frame of a motion-captured walking sequence, the optimization procedure was applied to fit the skeleton to the marker configuration of the subject's pose. The bone's scale factors over the entire motion sequence were averaged and fixed for a second optimization pass over the motion sequence that adjusts only $\mathbf{x}^J$. This prevents the bones from changing shape during the motion sequence because of inter-frame marker noise.

RESULTS AND DISCUSSION

Figure 1: Image from a motion-capture session is compared with the corresponding fitted skeleton.

Figure 1 displays a fitted skeleton from a walking motion sequence from which joint angle trajectories can be obtained. Although the second optimization method was four times faster, the first method produced a 20% average reduction in the fitting error over all frames of the motion sequence. We suggest the second method can be used to quickly find a good initial guess to accelerate convergence of the first method.

SUMMARY

A framework for automated fitting of a generic human skeleton to subject-specific anthropometric markers has been described. We are planning sensitivity analyses to investigate the robustness of the algorithm to noise and errors in marker placement.

REFERENCES

Zajac, F.E. (1993). *J. Biomechanics*, 26 Suppl. 1, 109-124.
Tabakin, D.R., Vaughan, C.L. (2000). *6th International Symposium on the 3D Analysis of Human Movement*, 98-101.
Musculographics Inc. (2001). *SIMM 3.1User Guide*.

SPINAL CANAL OCCLUSION IN FLEXION-COMPRESSION : THE EFFECT OF INJURY MECHANISM IN AN UPPER THORACIC SPINE EXPERIMENTAL MODEL

Thomas Oxland[1], Qingan Zhu[1], Randy Ching[2], Chris Lane[1], Charles Fisher[1], Marcel Dvorak[1]
[1]Department of Orthopaedics, University of British Columbia, Vancouver, British Columbia, Canada, toxland@interchange.ubc.ca
[2]Department of Orthopaedics, University of Washington, Seattle, Washington, USA

INTRODUCTION

Spinal canal occlusion (SCO) has been measured during burst fractures in the thoracolumbar and cervical spine [Chang 1994, Panjabi 1995, Ching 1997, Carter 2000] and dynamic SCO was significantly higher than post-injury SCO. However, there is virtually no information on SCO along the spinal canal, and specifically no reports of SCO for different injury mechanisms of the spine. Therefore, the objectives of the present study were to contrast the dynamic SCO for different flexion-compression spinal injuries, specifically comparing dynamic and post-injury SCO and determining how these occlusion levels varied along the spinal canal.

METHODS

Nine cadaveric spine specimens (T1-T4) were used. A custom designed spinal canal occlusion transducer was used to measure the cross-sectional area of the spinal canal, based on the changing electrical resistance of saline water under a constant current between eight discrete segments along the canal [Raynak 1998]. A known compressive displacement was applied to the upper vertebra at 500mm/sec, at 10cm anterior to the balance point of the specimen. In six specimens, the anterior translation of T1 was constrained while it was allowed to translate freely in three specimens. For the constrained test, the initial displacement was 5mm, and was followed by displacements of 10mm, 15mm, 20mm, and finally 25mm. These displacements were 10, 20, 30, 40, and 50mm for the unconstrained cases. The maximum SCO during compression was defined as the dynamic SCO. The SCO immediately after the applied compression was defined as the post-injury SCO. The dynamic and post-injury SCO for the constrained and unconstrained cases were compared with a Mann-Whitney U-test.

RESULTS AND DISCUSSION

For the constrained specimens, the general fracture pattern was a fracture-dislocation at T2-T3, while the fracture pattern of the unconstrained specimens was distractive injury at T4. The dynamic SCO for the constrained cases was significantly greater than for the unconstrained at equivalent axial displacements ($p=0.023$; Figure 1). For the constrained cases, the occlusion along the spinal canal with progressive compression demonstrated that the maximum dynamic SCO occurred in the T2 region with a 2cm extent (Figure 2). The dynamic SCO was greater than the post-injury SCO, decreasing significantly from 10mm compression compared to the intact spinal canal area.

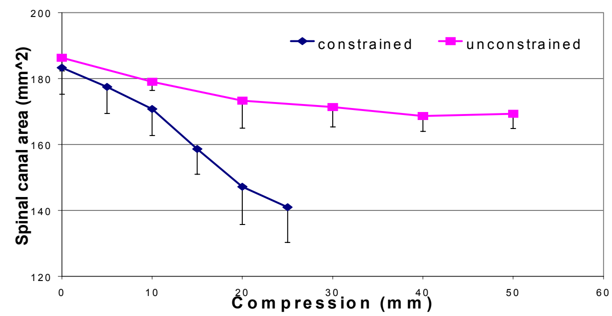

Figure 1: Effect of translational constraint on the dynamic spinal canal area with incremental compression. Note that an area of 140mm^2 represents 100% occlusion.

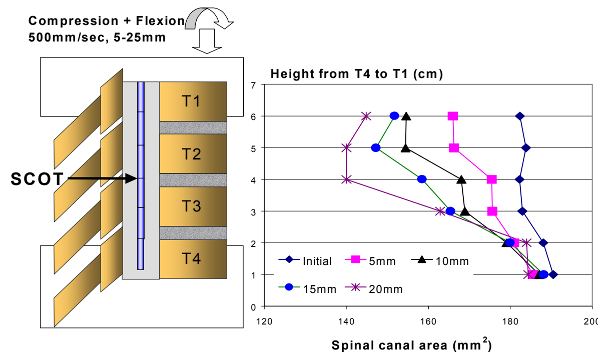

Figure 2: Dynamic spinal canal area from T1 to T4 with the progressive compression for the constrained cases.

SUMMARY

There was a clear effect of spinal column injury mechanism on the SCO. Constrained conditions led to a fracture-dislocation, which caused substantial SCO, extending at least over 2cm for the most severe injuries. Peak dynamic occlusion was higher than the post-injury occlusion which was consistent with the literature. These early findings will be extended to other injury-types in the spine and may have implications for experimental models of spinal cord injury.

REFERENCES

Chang D et al (1994). *Spine*, **19**:973-980; Panjabi M et al (1995). *J Spin Disorder*, **8**:39-48; Ching RP et al (1997). *Spine*, **22**:1710-1715; Carter JW et al (2000). *Spine*, **25**:46-52; Raynak GC et al (1998). *J Biomech Eng,* **120**:787-91

ACKNOWLEDGEMENTS

Financial support from the Natural Sciences and Engineering Research Council of Canada is gratefully acknowledged.

JOINT KINEMATICS OF POSTURAL SWAY RESPONSE TO SINUSOIDAL GALVANIC VESTIBULAR STIMULATION

L. Daniel Latt[1] and Mark S. Redfern[1,2]
Human Movement and Balance Laboratory, University of Pittsburgh, Pittsburgh, PA
Departments of Bioengineering[1] and Otolaryngology[2]
Address correspondence to: lattld@msx.upmc.edu

INTRODUCTION

The postural control system is responsible for integrating visual, somatosensory, and vestibular sensations and producing an appropriate response to maintain balance. One approach to studying this system is to perturb the system and measure its response. This response may involve rotations at multiple joints. It has been well characterized for the response to a platform perturbation (Horak, 1986), which stimulates both somatosensory and vestibular sensations. The response to a purely vestibular stimulus, such as, galvanic vestibular stimulation (GVS, an electrical current applied to the skin behind the ears, which elicits sway in standing subjects, Coats, 1972) has not been fully characterized. The goal of this project was to determine the differences in joint kinematics in the response to sinusoidal GVS that result from changing the stimulus frequency. It was hypothesized that lower frequency stimuli, would elicit a simple response about the ankles, whereas higher frequency stimuli would elicit a more complex (multi-joint) response.

METHODS

Binural-bipolar GVS was applied to the skin overlying the mastoid processes of 10 subjects while they stood with their eyes closed. The position in the frontal plane of each of the segments of the body (head, thorax, pelvis, thigh, and shank) was monitored with a magnetic position tracking system. The stimulus conditions included 4 frequencies (0.1, 0.25, 0.45, and 1.1 Hz) at various amplitudes from 0.05 to 1.0 mA. Five trials were conducted at each frequency; the order of presentation was randomized. A minimum of 10 cycles or 30 seconds of each stimulus was presented in each of the trials. The response power was calculated as the sum of the Fourier coefficients at or near (+/- 0.025 Hz) the stimulus frequency.

RESULTS AND DISCUSSION

As the frequency of the stimulus was increased, the response power at all joints decreased (Figure 1). Additionally, the relative distribution of power across the joints changed such that power at the ankle decreased, while power at the hip, back and neck increased. Thus, the predominant mode of the response changed from simple rotation about the ankle to compound rotation at the hips, back, and neck. This shifting of modes with stimulus condition has been described in the response to sagittal plane platform perturbations (Horak, 1986). One potential reason for the change in response mode is that while movement about the ankles is very effective in translating the center of pressure, the large inertia of the body prevents such changes from occurring rapidly. Thus sway about the ankles cannot play as large a role when rapid movements are required.

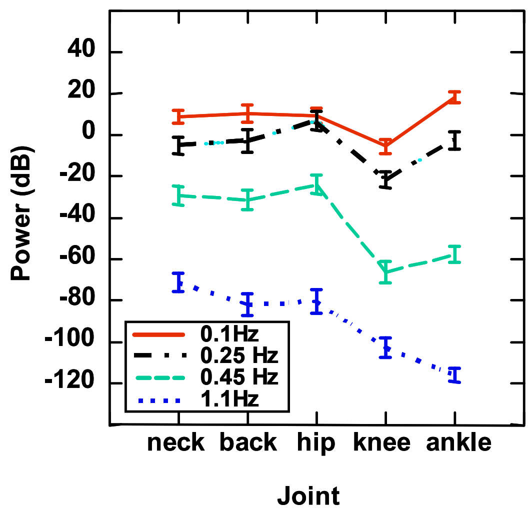

Figure 1: Response power mean and standard error by joint and stimulus frequency.

SUMMARY

The postural sway response to GVS in the frontal plane occurs at the hips, back, neck and ankles. The relative contribution of each of these joints to the response depends upon the frequency of the stimulus. A low frequency stimulus elicits a response that is primarily about the ankles, whereas the response to higher frequency stimuli involves the hips, back, and neck more than the ankles.

REFERENCES

Horak, F. B., Nashner. L. M. (1986). *J. Neurophys.* 55, no. 6, 1369-81

Coats, A. C. (1972) *Acta Oto-Laryngologica* 74, no. 3, 155-62

ARE THE ARTICULAR CONTACT STRESSES IN THE KNEE JOINT DURING DEEP FLEXION CRITICAL?

Ashvin Thambyah, James Goh, Shamal Das De

Department of Orthopaedic Surgery, National University of Singapore, SINGAPORE.

INTRODUCTION

Accurate and functionally relevant intra articular contact stresses in the natural knee joint is difficult to measure in particular those that result from walking and squatting. Given the evidence that osteoarthritis and cartilage damage can occur in the knee as a result of frequent, abnormal and high contact stresses (Swann and Seedham 1993, Dekel and Weissman 1978), the relevance in measuring the functional stresses (Jurman 1977) becomes especially significant for populations (such as Asian) where cultural and social habits commonly include high weight-bearing daily activities of deep flexion such as squatting and kneeling. The role of the entire meniscus, cartilage and soft tissue to neutralise high stresses become increasingly diminished in larger flexion angles where the tibiofemoral contact is largely reduced (Hefzy et al 1998). In this study, contact stresses are measured for the natural knee in various degrees of flexion simulating walking and squatting. It is the aim of this study that by determining the contact stresses in the natural joint, insight would be provided on the associated risks on the weight-bearing structures when an individual performs functional activities such as walking and squatting.

METHODOLOGY

The following description summarises the methods used in obtaining the input parameters for the simulation in the experimental model. Motion analysis of a healthy 60-year-old male was performed for level walking and squatting. From this, kinematic and kinetic data was obtained. X-rays of the subject were also taken in standing and squatting to obtain estimates of bone morphometry and soft tissue insertion positions. Loading conditions and the respective knee joint orientation in various phases of walking and squatting were derived and applied to quasi-static biomechanical testing on 5 cadaver knees in which pressure transducers were inserted in the articulation to measure contact stresses in these various phases.

<u>Five Loading conditions were prescribed</u>:
Heel Strike (HS) - 5.5° flexion up to 2.25 x body weight (BW)
Single Limb Stance (SLS) - 15.5° flexion up to 3.5 BW
Toe-off (TO) - 4.5° flexion up to 1.85 BW
Deep Flexion 1 (DF1) - 90° flexion up to 4 BW
Deep Flexion 2 (DF2) - 120° flexion up to 5 BW

During testing, the contact stress in each specimen was measured in real time using sensors that were inserted into the joint and between the articulating surfaces of the tibia and femur. The pressure (contact stress) measurement system consisted of a thin (0.1mm) plastic pressure sensor (K-Scan sensor and software from Tekscan Inc, Boston, USA) interfaced with a desktop PC, running software that displayed in real time and recorded the force and pressure values from the sensor. Data was streamed into an output file for statistical analysis and graphical organisation. P-values were calculated to test for significance (<0.05) in differences between means.

RESULTS

During the loading conditions that simulated the selected points of interest in stance phase of gait (HS, TO, SLS) average contact stresses in the cadaver knee joints were 14.1 MPa ($\pm$ 2.5) with little variation. However, these stresses were significantly ($p<0.05$) larger in the deep flexion and squatting loading conditions (DF1, DF2) where it increases by over 80% to 26.6 MPa ($\pm$ 7.1).

DISCUSSION

The stresses observed in the cadaver knees in deep flexion come very close to crossing the limit of 25 MPa for cartilage where fissures and lacerations have been shown to occur (Haut 1989). The reduced contact area when the knee was flexed at 90° and 120° was most likely the cause for the increase in the pressure reading.

CONCLUSION

Weight-bearing deep flexion results in critically high contact stresses in the natural knee which may in turn predispose one who does it often enough to a higher risk of primary osteoarthritis of the knee, given the premise that unduly high and frequent contact stresses in the joint is one of the causes of the disease.

REFERENCES

Dekel S., Weissman S.L. (1978) *Acta Orthop Scand*. Dec;**49(6)**:519-28.
Haut R.C. (1989) *J Orthop Res.* ;**7(2)**:272-80.
Hefzy M.S., Kelly B.P., Cooke T.D. (1998) *Med Eng Phys.* Jun; **20(4)**:302-7.
Jurman R.D. (1977) *Am J Phys Anthropol*. Mar;**46(2)**:353-65.
Swann A.C., Seedhom B.B. (1993) *Br J Rheumatol.* Jan;**32(1)**:16-25.

COMPENSATORY CORRECTIVE RESPONSES INDUCED BY CUTANEOUS NERVE STIMULATION IN THE HAND AND FOOT DURING WALKING

Carlos Haridas and E. Paul Zehr

Neurophysiology Laboratory, Faculty of Physical Education & Recreation and Centre for Neuroscience
University of Alberta, Edmonton, Alberta, CANADA (charidas@ualberta.ca)

INTRODUCTION

Previous studies indicate that electrical stimulation of a cutaneous nerve innervating the dorsum of the foot (superficial peroneal; SP) elicits a stumble corrective response in the lower extremity muscles of the stimulated leg during swing (Van Wezel et al., 1997; Zehr et al., 1997). It has also been shown that reflexes are evoked in the foot with electrical stimulation of a cutaneous nerve in the hand (superficial radial (SR); innervates the dorso-lateral surface) during a static task (Zehr et al., 2001). The purpose of this study was to investigate reflexly evoked kinematics at the ankle with electrical stimulation of the foot and hand during walking.

METHODS

Sixteen subjects were recruited with informed written consent to walk on a treadmill. Cutaneous reflexes were evoked with trains (5 × 1.0 ms pulses @ 300 Hz) of electrical stimulation delivered at non-noxious intensities pseudorandomly to the right SP and SR nerves. Kinematic data was recorded from both ankles, and was analyzed in a 120-200 ms window post-stimulus. Electromyographic (EMG) data was recorded from the lower and upper extremity muscles bilaterally. Step cycle information was collected using insole force-sensing resistors. Each step cycle was divided into 16 portions. Changes in angle with stimuli occurring in the same portion of the walking cycle were averaged together, and reflexly induced changes in ankle angle were determined by examining the kinematic data from which the control kinematic data was subtracted.

RESULTS AND DISCUSSION

Significant ($p < 0.05$) reflexly induced changes in joint angle were observed at both ankles during the stance-to-swing transition with either SP or SR stimulation. The mean response during the stance-swing transition for the right ankle was an increase in plantarflexion (PF) during SP stimulation, which reversed to an increase in dorsiflexion (DF) during SR stimulation (Figure 1, left side). SP and SR stimulation also resulted in an increase in DF in the left ankle during its stance-swing phase.

The SP-induced PF in the right ankle at the swing-stance transition may reflect a stumbling corrective response, which could allow for the foot to drag itself over an obstacle while entering the swing phase. Increased DF in the left ankle during the swing-stance transition could retard forward progression of the leg, allowing for a longer duration of stance, which could assist in maintaining balance while the opposite foot is being perturbed.

For SR stimulation, while the right leg is at the stance-swing transition, there was increased DF (Figure 1, right side), which

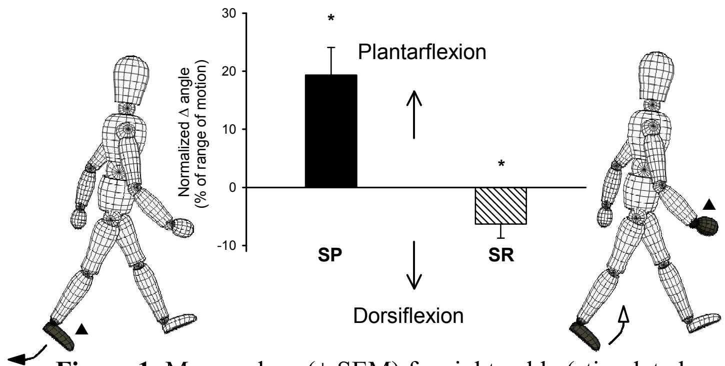

Figure 1: Mean values (± SEM) for right ankle (stimulated side) angle changes with SP and SR stimulation (*, difference from zero at $p < 0.05$). ▲ indicates site of stimulation.

may serve to retard forward motion. At this point in the step cycle, the right wrist is in front of the body, so this response may prevent forward progression into the obstacle. Increased DF in the left ankle with SR stimulation was also observed while it was in the stance-swing transition.

SUMMARY

A reversal in ankle angle direction was seen in the right ankle at the stance-swing transition point in the step cycle between SP (PF) and SR (DF) stimulation. No difference was seen in the left ankle during its stance-swing transition point with different nerve stimulation. The results suggest nerve-specific responses, which also differ according to where the ankle is in the step cycle (Komiyama et al., 2001; Van Wezel et al., 1997). This study suggests that nerve-specific responses also extend to non-stimulated limbs. Finally, the findings also suggest a behavioural relevance for the kinematic responses

REFERENCES

Komiyama et al. (2000). *Exp. Brain Res*., **133**, 267-272.
Van Wezel et al. (1997). *J. Neuroscience*, **17**, 3804-3814.
Zehr, E.P. et al (1997). *J. Neurophysiol.,* **77**, 3310-3325.
Zehr, E.P. et al (2001). *Exp. Brain Res.,* **140**, 495-504.

ACKNOWLEDGEMENTS

This work was funded by NSERC and AHFMR grants to E. P. Zehr. C. Haridas was supported by a studentship from the Alberta Paraplegic Foundation.

MATERIAL PROPERTIES OF THE HUMAN CALCANEAL FAT PAD: VALIDATION EXPERIMENTS

Janice E. Miller-Young[1] and Neil A. Duncan[2]
University of Calgary, Calgary, Alberta, Canada
[1]Human Performance Lab
[2]Dept of Civil Engineering

INTRODUCTION

Finite element (FE) models of the foot have been used to analyse calcaneal stress distributions (Giddings et al., 2000) and the influence of shoe design on pressure and stress in the plantar soft tissues (Lemmon et al, 1997; Thompson et al., 1999). However, the predictions of an FE model are critically dependent on realistic geometry and material properties. Although a material model of the heel fat pad has been developed from isolated fat pad samples, the ability of this model to predict behaviour of the intact fat pad using the FE formulation must be assessed. The purpose of this study was to obtain heel pad compression data that could be used to evaluate the quality of the heel pad material model.

METHODS

Five cadaveric feet were obtained from 3 males and 2 females (ages 63 – 72). Sagittal plane X-rays were obtained. Each foot was fixed into a stainless steel clamp with three bolts that screwed into the calcaneus, and the heel fat pad was exposed by removing the skin from the plantar surface of the heel.

Heel indentation tests were performed in an MTS machine (MTS Systems Corporation, Eden Prairie, Minnesota, USA). The foot clamp was bolted to the MTS table (with the exposed heel pad facing up) and a 2 cm diameter indentor was attached to the load cell and actuator above. Based on the range of impact velocities that occur in locomotion and the capabilities of the MTS machine, indentation tests were performed at rates of 175 and 350 mm/s, 3 trials each. Each test was performed to approximately 50% of the thickness of the fat pad (estimated from X-rays).

At the end of the "intact" experiments, the heel fat pad was dissected from the foot and refrozen so that it was hard enough to permit a cylindrical plug to be cut. An 8 mm biopsy punch was used to cut cylindrical samples from the center of the fat pad with the long axis of the cylinder corresponding to the direction perpendicular to the skin surface. Unconfined compression tests were performed on the individual cylindrical plugs at 175 and 350 mm/s, and stress relaxation tests held for 1 minute, all at approximately 50% deformation. The results of these tests can be used to determine material parameters of a hyperelastic, viscoelastic constitutive equation for the heel fat pad (Miller-Young and Duncan, 2001).

RESULTS AND DISCUSSION

On average, the forces measured during the intact heel pad indentation tests were 1.9 times higher than those measured during the cylindrical plug compression tests for the same foot (figure 1). The standard deviations were too small to show on the curves for the cylindrical plugs (max 4.4 and 6.7 kPa for 175 and 350 mm/s tests, respectively). It is speculated that the difference between plug and intact fat pad results is due to the differences in boundary conditions between the two tests.

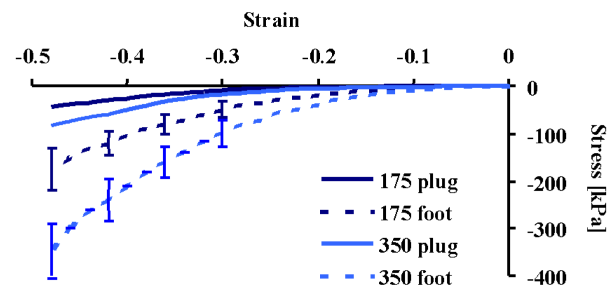

Figure 1: Variable-rate compression results (mean and SD) for cylindrical plug material tests and intact fat pad indentation tests for one foot (age = 63).

A material model will be derived from the material tests of the cylindrical plug and evaluated using a 2D FE model of the indentation experiment on the corresponding foot. The geometry of the calcaneus will be obtained from the X-rays of each foot, and several meshes will be developed in order to test the mesh density required to obtain a converged solution.

REFERENCES

Giddings et al. (2000) *Med.Sci.Sports Exercise* **32(3)**, 627-634.
Lemon et al. (1997) *J. Biomech.* **30(6)**, 615-620.
Miller-Young, J., Duncan, N. (2001) *Proceedings of ISB International Symposium on Computer Simulation in Biomechanics*, 85-90.
Thompson et al. (1999) *Proceedings of XVIIth ISB Congress*.

ACKNOWLEDGEMENTS

Kent Paulson for MTS assistance; da Vinci Foundation and adidas Int'l for financial support.

A FAST CIRCLE FINDING TECHNIQUE FOR DIGITAL RSA

P. Thistlethwaite[1], J.L Ronsky[1], H.S. Gill[2]
[1]Department of Mechanical and Manufacturing Engineering, University of Calgary
[2]University of Oxford, Nuffield Department of Orthopaedic Surgery/OOEC

INTRODUCTION

A fundamental component of the RSA technique is identification of radio-opaque markers. In a digital RSA system this identification process can be automated by employing a circle finding technique to an edge detected image. Usually, for this task, some variation of the Hough circle transform (Duda, R.D., Hart, P.E. 1972) is used. This process can be very computationally expensive and represents the bulk of time an automated digital RSA process will require to compute 3D positions (95% - Vrooman, H.A. 1998). Similar results to the Hough transform can be achieved with a convolution-based method while drastically decreasing the computation time. This study investigated the performance of this convolution-based circle finding method.

METHODS

To evaluate the performance of the convolution-based technique it was compared to the discrete Hough circle transform quantitatively for computational time and qualitatively for response. Ten 361x361 pixel, 8-bit grayscale test images acquired from RSA study radiographs were edge detected and used as starting points for both techniques (Figure 1). One of these test images was placed on backgrounds ranging from 316 to 1061 pixels square (15 images) and these were also used as a basis for comparison. The images contain circles of three different radii: 20, 16 and 4 pixels. These correspond to background and foreground calibration markers, and reference markers respectively.

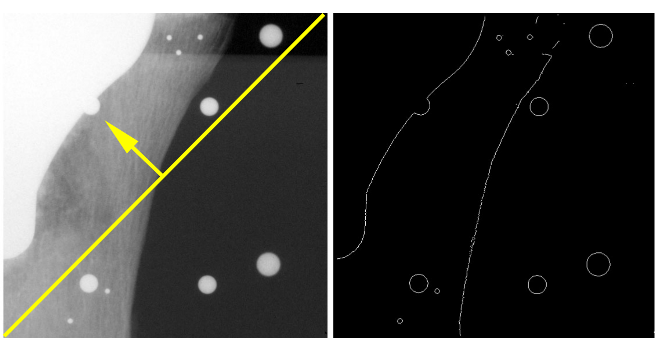

Figure 1: Example original and edge image. The line and arrow show the plane and viewing direction for the example response projections shown in Figure 2.

Table 1: Computational times for circle finding using Hough transform and convolution method

	Part 1: Number of Edge Pixels				Part 2: Image Size			
Computation Time (s)	Min	Max	Average	Std Dev	Min	Max	Average	Std Dev
	417	1673	1050	432	361	1061	711	224
Convolution (4 pixel radius)	0.031	0.034	0.0326	0.0011	0.0248	0.1770	0.0895	0.05
Convolution (16 pixel radius)	0.0545	0.0744	0.0638	0.0068	0.0499	0.2150	0.1145	0.0504
Convolution (20 pixel radius)	0.0701	0.1026	0.0857	0.011	0.0673	0.2186	0.133	0.0496
Hough (4 pixel radius)	13.1978	40.0813	26.6566	9.235	13.5477	79.4869	42.2006	20.9517
Hough (16 pixel radius)	13.1771	40.2068	26.7935	9.2931	13.6939	78.4491	41.8688	20.637
Hough (20 pixel radius)	13.1931	40.2827	26.8404	9.3139	13.6657	78.5727	41.806	20.6224

RESULTS AND DISCUSSION

In both methods a calculation must be performed to search for each circle radius independently. The total circle finding computational time is the sum of times for each radius. A clear computational advantage is provided with the convolution method in all test situations (Table 1). The computational time for the Hough transform varies linearly with the number of edge pixels in the image while the convolution method is invariant to this change (Table 1 – Part 1). Increasing image size increases the computational time for both methods but also increases the computational advantage of the convolution method (Table 1 – Part 2). The response of the two methods is very similar (Figure 2) although the background response appears slightly higher in the convolution method. The peak response of the convolution method is more tightly grouped which should allow it to be easily thresholded.

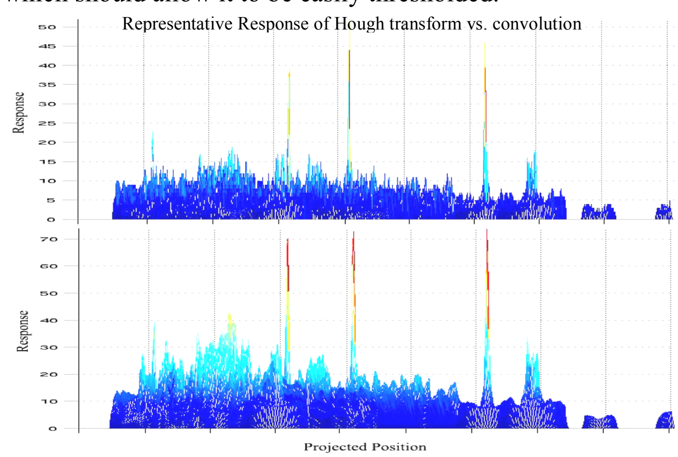

Figure 2: Representative 2D projections of response for the Hough transform (top) and convolution method (bottom)

SUMMARY

The convolution-based circle finding method can provide similar response to the Hough transform method while providing drastically reduced computation times.

REFERENCES

Vrooman, H.A. et al (1998) J. Biomechanics **31**, 491-498
Duda, R.D., Hart, P.E. (1972) Communications ACM **15**, 11-15

ACKNOWLEDGEMENTS

NSERC, the McCaig Fund, PetroCanada

A MODEL FOR EMULATION OF WRIST JOINT IMPEDANCE

Amanda M. Laslo and Theodore E. Milner*
School of Kinesiology, Simon Fraser University, Burnaby, B.C., V5A 1S6, Canada
*Corresponding author tmilner@sfu.ca tel: 604 291 3398, fax: 604 291 3040

INTRODUCTION

Models of mechanical impedance have been previously used as control schemes for electromechanical emulators (Abul-Haj and Hogan, 1987). In this study, we have developed a model of mechanical impedance based on the torque measured during imposed, bidirectional rotations of the wrist. The objective was to improve the ability of an artificial joint to emulate the impedance of an intact human joint. Unlike other linear models of mechanical impedance (Kearney and Hunter, 1982), the present model reveals that damping (***B***) is independent of torque, and that torque due to damping is small compared to torque due to stiffness (***K***). In addition, there is an initial high-slope region of the torque vs. displacement curve for which the parameters are different than the remaining cycles.

METHODS

Wrist torque was measured during imposed, bidirectional rotations of the wrist joint. A torque motor was used to generate an extensor moment, τ, which the subject matched by applying an equal and opposite flexor torque that was maintained throughout each of the trials. The investigator displaced the wrist using a sinusoidal motion while torque, T, position, θ, and velocity, $\dot{\theta}$, were measured and recorded. Four different trial conditions were tested at activation levels corresponding to flexor torques of 0, 1, 2, and 3 Nm. The displacement frequencies and amplitudes used were 2.4 Hz and 1.2 Hz, and 20 degrees and 10 degrees, respectively.

Torque vs. position graphs were plotted for each trial to investigate the shape of the hysteresis. At torques greater than 0 Nm, a drift in the central position of the hysteresis loop over time was detected and taken into account by including a correction term, ct, in the model:

$$T - I\ddot{\theta} = (K_0 - K_1\tau)(\theta - \theta_0) + B_0\dot{\theta} + ct + T_0$$

where I is the moment of inertia, t is time, and K_0, K_1, B_0, c and T_0 are constant parameters.

The data were separated into an initial high-slope region and the remaining cycles. Multiple linear regression analyses were conducted to determine parameters for each region.

RESULTS AND DISCUSSION

Regression analysis of the initial high-slope region of displacement showed that two parameters, K_0 and K_1, were sufficient for an accurate model of mechanical impedance.

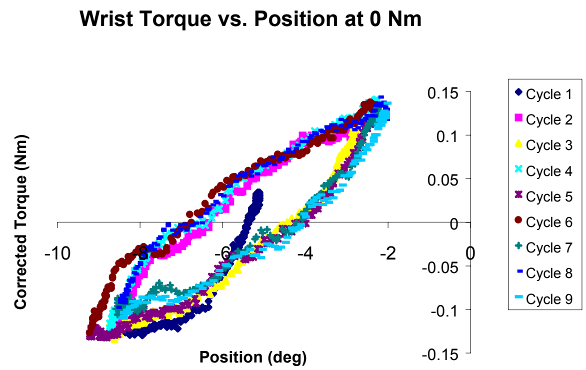

Figure 1: Data for one trial at 0 Nm. One cycle consists of wrist rotation in one direction through the displacement range.

Including the K_1 parameter increased the R^2 value from 0.58 to 0.95, indicating a large effect of torque on stiffness. Including B_o in the regression had a minimal effect on the overall fit of the model, increasing the R^2 value by only 0.008. Furthermore, since the B_o parameter was slightly negative it was eliminated from the model.

Regression performed on the remaining displacement cycles revealed that damping had a greater influence on the accuracy of the model than for the initial high-slope region. Including the B_o parameter improved the R^2 value from 0.93 (with K_0 and K_1) to 0.96. However, damping was found to be independent of torque, as the addition of the B_1 parameter had no effect on the fit of the model (R^2=0.96).

The K_0 parameter was greater in the high-slope region (51% difference), whereas the K_1 parameter was lower (6% difference), than during the remaining displacement cycles.

SUMMARY

The results of this study show that in the initial portion of a displacement, the wrist behaves like a pure spring with torque dependent stiffness, whereas once the muscles have been stretched beyond the high stiffness region, it behaves like a torque dependent spring of lower stiffness with a small amount of damping.

REFERENCES

Abul-Haj, C.J., Hogan, N. (1987). An emulator system for developing improved elbow-prosthesis designs. *IEEE Transactions on Biomedical Engineering*, **9**, 724-736.

Kearney, R.E., Hunter, I.W. (1982). Dynamics of human ankle stiffness: Variation with displacement amplitude. *Journal of Biomechanics*, **15**(10), 753-75

ARE SPINAL FACET LOADS INFLUENCED BY THE FIXATION METHOD?

Qingan Zhu[1], Youngbae Park[2], Jeff Gordon[1], Simon Sjovold[1], Michael Johnson[1], Charles Fisher[1], Marcel Dvorak[1], Thomas Oxland[1]
[1]Department of Orthopaedics, University of British Columbia, Vancouver, British Columbia, Canada, toxland@interchange.ubc.ca
[2]Department of Mechanical Engineering, Korea Advanced Institute of Science and Technology, Taejon, South Korea

INTRODUCTION

It is well-established that spinal fixation reduces intervertebral motions, and that there is variation in the rigidity of different methods such as pedicle screw fixation or interbody cage stabilization. It has been hypothesized (Oxland 2000) that some of these changes, particularly with interbody cages, are due to modification of the contact in the articular facets. A non-invasive method for determining facet loads has been used in vivo and in vitro in the canine lumbar spine (Buttermann 1991,1992). The technique models the inferior articular process as a cantilevered plate and determines the facet load and its location using extraarticular strains on one facet (Luo 1996). In the present study, a modification of this noninvasive technique was used to evaluate the facet load in a cadaveric lumbar spine model to determine the effect of different spinal fixation techniques, specifically interbody cage and pedicle screw fixation.

METHODS

Eight cadaveric specimens (L4-L5) were used. Eight uniaxial strain gauges (Tokyo Sokki Kenkyujo, Tokyo, Japan) were bonded to the posterior aspect of the left and right inferior facet of L4. Flexibility testing in flexion-extension, lateral bending and axial rotation with pure moments (±5.0Nm) was performed for each specimen in the intact state, after pedicle screw fixation (USS, Synthes Spine), and after interbody cage insertion (Dovetail, Cortek, Boston, MA). The L4-L5 level was transected following the flexibility test and the L4 vertebra was secured for calibration of the facets. In the calibration, known forces were applied to the facet surface and the corresponding strains recorded. The relationship between the eight strains ($\boldsymbol{\varepsilon}$), the facet forces (F_L, F_R), and the force location ((x_L, y_L), (x_R, y_R)) was assumed to be of the form:

$$\boldsymbol{\varepsilon} = \mathbf{f}_L(x_L, y_L)\,F_L + \mathbf{f}_R(x_R, y_R)\,F_R$$

A least squares method was used to determine the facet forces during the flexibility testing, based on the recorded strains. A repeated measures ANOVA was used to compare the peak facet loads and thereby determine the effect of the different fixation techniques on facet loads.

RESULTS AND DISCUSSION

The loading pattern between the left and right facets was generally symmetric in all directions for the intact specimen (Figure 1). Interbody cage insertion had little effect in flexion loading, but increased facet compression significantly in extension. Pedicle screw fixation slightly increased facet compression in flexion ($p=0.001$) and decreased facet compression in extension ($p=0.035$). The facet load changed

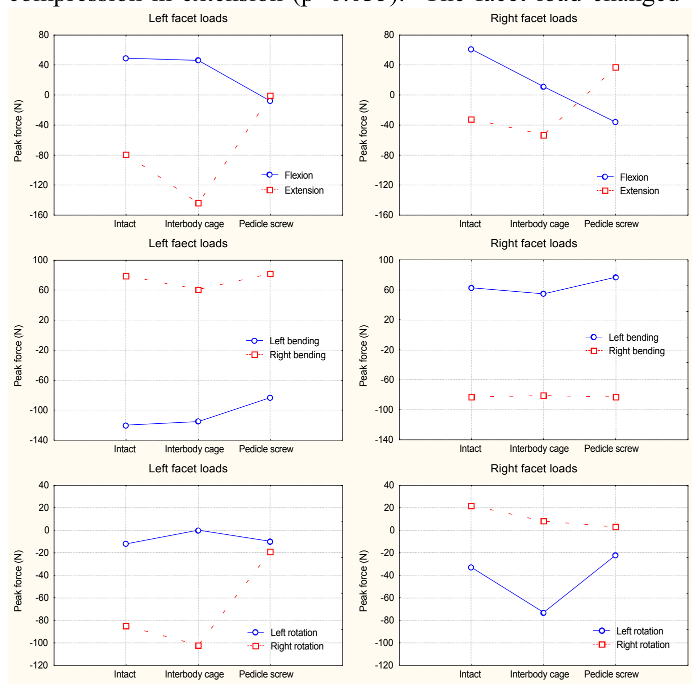

little in lateral bending after both fixation types. In axial rotation, the interbody cage increased the compression on one facet, while pedicle screw fixation reduced the facet loads.

Figure 1: Left and right facet loads in flexion, extension, left and right lateral bending and left and right axial rotation.

SUMMARY

A noninvasive technique using extra-articular strains was used to measure in vitro facet loads in the cadaveric lumbar spine. The fixation methods of interbody cage stabilization and pedicle screw fixation each affected the facet loads significantly in different directions. The clinical significance of these findings is unknown.

REFERENCES

Buttermann G.R. et al (1991). *J. Biomech. Eng,* **113**,375-386
Buttermann G.R. et al (1992). *Spine*, **17**, 81-92
Luo Z.P. et al (1996). *J. Biomechanics*, **29**, 785-790
Oxland T et al (2000). *J Bone Joint Surg. (Am),* **82**:383-39

ACKNOWLEDGEMENTS

The support in the form of a research grant from Cortek Inc., Boston MA USA, is gratefully acknowledged.

STRUCTURAL TESTING FOR SYMMETRY OF THE HIPS BY VIBRATION TECHNIQUE

Kevin Kwong[1], Xiaolin Huang[1] and Jack Cheng[2]

[1]Department of Rehabilitation Sciences, The Hong Kong Polytechnic University, Hong Kong SAR, China
[2]Department of Orthopaedics and Traumatology, The Chinese University of Hong Kong,, Hong Kong SAR, China

INTRODUCTION

A vibration technique, which provides a practical structural testing for bony symmetry of the hips, has been developed. The results of this study offer a baseline for further acoustical investigations in orthopaedics for conditions such as developmental dysplasia of the hip, degenerative osteoarthritis and loosening of hip arthroplasty, which associate with asymmetrical structure of the bone and joints.

METHODS

From an excitation system, a signal generator delivered a pink noise, which was then fed to a power amplifier, to drive an electrodynamic exciter. A vibratory force (< 1 N, RMS) was applied at the sacrum through a plastic probe, and a hand-held exciter was used instead for tests on pre-school children and neonates. The transduction system comprised of a pair of identical microphones installed separately in the tubes of two stethoscopes, forming the stethoscope-microphone assemblies, which were placed over the greater trochanters and secured by a 2.5 cm wide rubber band wrapped round the pelvis. The data acquisition system was a dual-channel signal analyser, which acquired the acoustic signals and processed the relative acoustic response by digital filters in 1/3 octave frequency bands. The coherence assessed the degree of linear relationship between the sound signals and the discrepancy evaluated the degree of structural asymmetry between bilateral hips, according to the following equation, where, Output (L) and Output (R) were acoustic signals picked up respectively from the left and right hips.

$$Discrepanc\,y = Abs\left(20\log\left[\frac{Output\,(L)}{Output\,(R)}\right]\right)dB$$

It was hypothesized that there would be equal acoustic transmission through symmetrical bony structure of normal subjects. Any asymmetry in the bone and joints would result in a difference in the acoustic response measured at both hips. The discrepancy was therefore an objective measure of structural asymmetry of the hips. Three groups of normal subjects: 27 adults, 20 pre-school children and 24 neonates were tested.

RESULTS AND DISCUSSION

For the adult group, the coherence was above 0.9 and the discrepancy between the two hips was < 3 dB in the frequency range of 160 to 400 Hz. For the pre-school children, the coherence was slightly lower and the discrepancy was less stable. This was due to the difficulty in keeping a stable position for the pre-school children during the testing. The lowest discrepancy was found to be < 2dB in the frequency range of 200 to 315 Hz. For the normal neonates, the lowest discrepancy was found to be < 1.25 dB in a wider frequency range of 160 to 315 Hz, where coherence > 0.96. However, these results cannot help identify the specific cause of the discrepancy. Discrepancy due to natural differences between both sides of the body is highly possible.

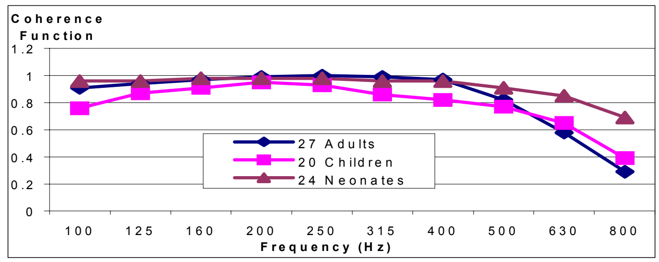

Figure 1. Coherence

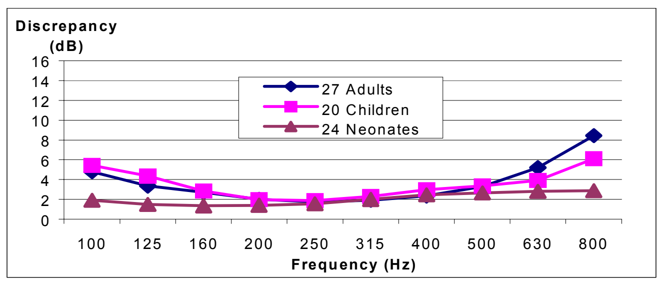

Figure 2. Discrepancy

SUMMARY

The optimal frequency range for test of structural symmetry of adult hips is 160 to 400 Hz, where the discrepancy is below 3 dB. The neonates show a smaller discrepancy (< 1.25 dB) in a wider frequency range (100 to 400 Hz). The results for pre-school children were less satisfactory by referring to the lower coherence and greater discrepancy when compared with the other two groups. Results of this study could be considered as baseline discrepancy for normal hips. Discrepancy bigger than the figures quoted about could be suggestive of structural asymmetry of the hips.

ACKNOWLEDGEMENT

This work was supported by the Research Grants Council of The Hong Kong SAR, China.

RUPTURE PROPERTIES OF THORACIC AORTIC ANEURYSMS USING PRESSURE-IMPOSED EXPERIMENT

Toshiro Ohashi[1], Syukei Sugita[1], Takeo Matsumoto[1], Kiichiro Kumagai[2], Hiroji Akimoto[2], Koichi Tabayashi[2], and Masaaki Sato[1]

[1]Graduate School of Mechanical Engineering, Tohoku University, Sendai, Japan
[2]Graduate School of Medicine, Tohoku University, Sendai, Japan

INTRODUCTION

Thoracic aortic aneurysm is a crucial disease because its diameter will grow until rupture, usually accompanied with fatal consequences. At present, the aneurysm is replaced with aortic prostheses when its diameter exceeds 5.5 cm to avoid rupture. However, some aneurysms rupture at a diameter smaller than 5.5 cm. This empirical knowledge is not a sufficient criterion. A reliable predictor would be necessary in assessing potential for aneurysm rupture. Although uniaxial tensile test has been performed on abdominal aortic aneurysm to obtain ultimate strength (Raghavan et al., 1996), rupture properties should be evaluated by pressure-imposed test from a physiological standpoint.

In this study, we measure rupture properties of thoracic aortic aneurysms using pressure-imposed test. An experimental setup is newly designed to rupture rectangular specimens excised from aneurysms.

METHODS

Ten square specimens were obtained from human thoracic aortic aneurysms (68 ± 9 years, mean ± SD) during aneurysmectomy. All procedures were carried out in accordance with permission for experimental use of the Tohoku University. Experimental setup of pressure-imposed test is schematically shown in Figure 1. The square specimen (20 mm x 20 mm) was fixed between two metal plates with a hole of 15 mm in diameter. Air pressure was applied into a rubber balloon to inflate the specimen at a rate of 10 mmHg/s until rupture occurred. Deformation process was observed through two CCD cameras and a high-speed camera. Breaking stress and strain were estimated from the specimen geometry considering incompressibility. The high-speed camera was used for detailed observation of ruptured site (data not shown).

RESULTS AND DISCUSSION

Four specimens did not rupture even at a maximum pressure of around 5000 mmHg while six specimens finally ruptured. One would expect rupture to occur longitudinally in normal aorta, whereas any tendency in the direction of aneurysm rupture was not observed. Breaking stress and strain for ruptured specimens are summarized in Table 1. Data for unruptured specimens are expressed as maximum stress and strain at the maximum pressure and also shown in the table. Groenink et al. (1999) investigated breaking stress of normal human thoracic aorta using pressure-diameter test in relation to age and showed that mean breaking stress was 0.80 MPa at 60 years. Our data were slightly higher than their results. It is interesting that strains are quite different between ruptured and unruptured groups at the similar stress. Further study is needed to elucidate a patient-specific histology to examine the relationship between rupture properties and wall structure.

SUMMARY

We have measured rupture properties of human aneurysms using pressure-imposed test. Breaking stress of aneurysms was 0.97 ± 0.39 MPa (mean ± SD), showing slightly higher value than that for normal aorta. This may be a rationale for further studies concerning a reliable criterion for elective repair.

REFERENCES

Groenink, M. et al. (1999). *Cardiovascular Research*, **43**, 471-480.

Raghavan, M.L. et al. (1996). *Annals of Biomedical Engineering*, **24**, 573-582.

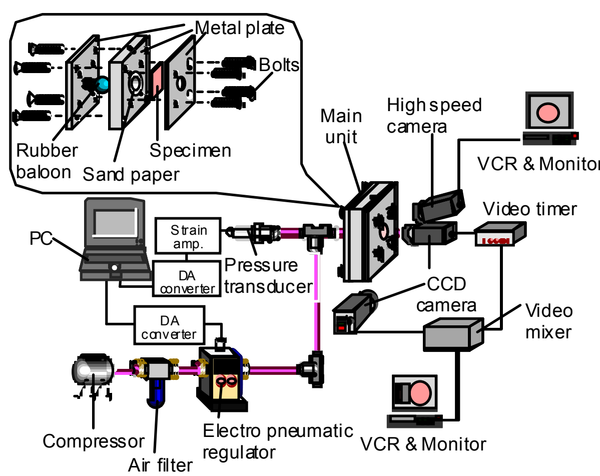

Figure 1: Schematic diagram of experimental setup.

Table 1: Mechanical properties of ruptured and unruptured aneurysms.

Ruprured			Unruptured		
Specimen	Stress (MPa)	Strain	Specimen	Stress (MPa)	Strain
H0104A	1.22	0.69	H0113a	1.06	0.24
H0108	0.64	0.55	H0115	1.88	0.47
H0109	0.37	0.72	H0122A	1.67	0.41
H0116a	1.37	0.48	H0122B	1.59	0.39
H0119a	1.22	0.71			
H0123	1.01	0.68			
mean } S.D.	0.97 ± 0.39	0.64 ± 0.10	mean } S.D.	1.55 ± 0.35	0.38 ± 0.10

LOWER LIMB KINEMATICS OF ICE HOCKEY FORWARD SKATING

Ryan Chang[1], Rene Turcotte[1], Richard Lefebvre[2], David Montgomery[1], David Pearsall[1]
[1]Department of Kinesiology and Physical Education, McGill University, Montréal, Québec, Canada
[2]Bauer Nike Hockey, St. Jérome, Quebec, Canada

INTRODUCTION

The sparsely existing quantitative kinematic research in ice hockey is likely, in part, a result of the obstacles in gathering such data. The stride traverse is long while the movements are highly three-dimensional. This study attempts to quantify kinematics of the lower limb during forward ice hockey treadmill skating.

METHODS

Joint kinematic data at the hip, knee and ankle were acquired through electrogoniometry at a sampling rate of 1KHz. The five (n=5) subjects were varsity level ice hockey players, each having been well trained on the skating treadmill.

Forward skating was analyzed at 3 randomly ordered velocities: 3.33 m/s, 5.00 m/s and 6.67 m/s. Foot strike was identified to the activation of the vastus medialis muscle. Twenty strides were used for the calculation of the average at each velocity. Data were smoothed by a 4th order Butterworth filter at a cut-off frequency of 10 Hz and normalized to the subjects standing position.

RESULTS AND DISCUSSION

Typical movement patterns of the hip, knee and ankle for one subject are presented (Figures1-3).

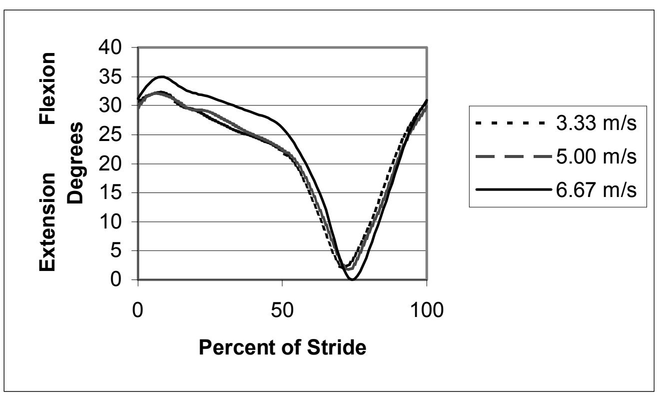

Figure 1: Local flexion/extension data at the hip for three forward skating velocities.

The data reveals a push-off phase consisting of extension at the hip and knee and plantarflexion at the ankle. This particular subject shows a trend of increasing range of motion at the knee with increased velocity. However, the same trend is not observed in the ankle data. Greatest range of motion is seen in the fastest velocity at the hip also.

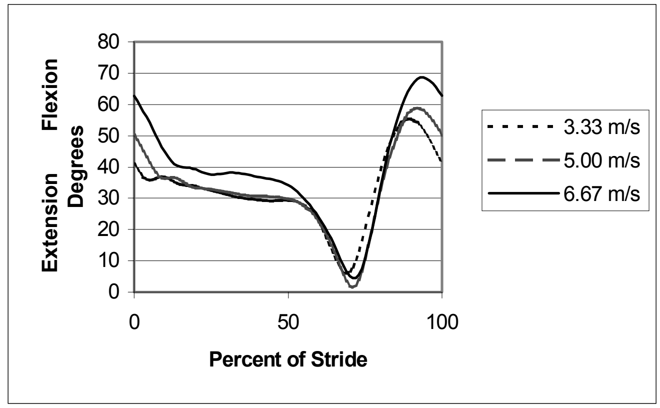

Figure 2: Flexion/extension data for the knee during three forward skating velocities.

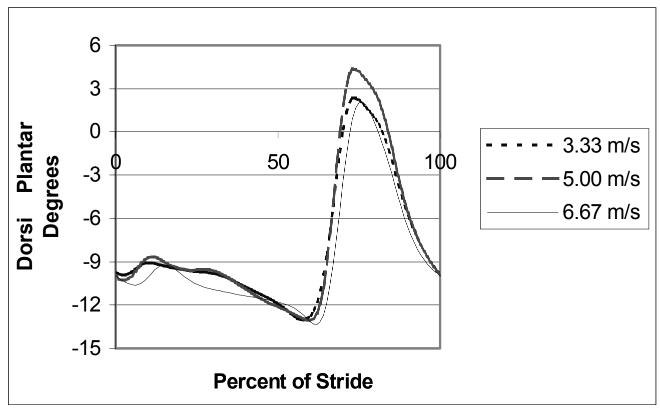

Figure 3: Plantar/dorsiflexion of the ankle during the forward skating stride for three different velocities.

As seen in this set of data, preliminary analysis reveals a longer push-off phase with a shorter swing time when strides are normalized. Further interpretation and analysis is in progress.

SUMMARY

The study demonstrates the feasibility of using goniometry to quantify lower limb kinematic patterns while skating in ice hockey. Adopting this approach, issues of skating techniques and the mechanics of other skating skills (e.g. starts, stops, backwards, pivots, cross-overs) can be examined. Information thus collected can be applied to directly to coaching, injury rehabilitation and equipment design.

ACKNOWLEDGEMENTS

National Science and Engineering Research Council (NSERC) of Canada and Bauer-Nike Hockey Inc.

FORWARD ICE HOCKEY SKATING: COMPARISON OF EMG ACTIVATION PATTERNS AT THREE VELOCITIES

R. Goudreault, D. Pearsall, R.Turcotte, D. Montgomery, R. Lefebvre
McGill University, Montréal, Québec, Canada

INTRODUCTION

Ice hockey is a sport that requires a combination of numerous skills including skating, puck handling, shooting, and checking skills. Though a popular sport, to date research on the biomechanical evaluation of the ice hockey skills have been limited to a few studies regarding the stick and forward mechanics of skating (Marino 1977). Given the limited specific ice hockey research, our best understanding of forward skating mechanics may be drawn from research focused on speed skating. Interpretation of speed skating mechanics can be useful for identifying the general movement patterns similar to ice hockey; however, fundamental differences in equipment, skill, repertoire, and play context preclude suggesting a direct transfer of speed skating to ice hockey skating (Marino, 1977). The purpose of this study is to compare the EMG activity of the lower limb in forward skating at three different speeds using the skate treadmill.

METHODS

Seven varsity hockey players from McGill University (age = 22.1 ± 1.2 years, height = 1.8 ± 0.1m, weight = 82.1 ± 8.5 kg) participated. Testing was done using a skate treadmill. Skin was shaved of hair, abraded and cleaned at the area of the electrode placement on the right leg. Disposable bipolar differential electrodes (Meditrace) were placed 1 cm apart on the vasttus medialis (VM), adductor magnus (Add), biceps femoris (BF), gluteus maximus, tibialis anterior (TA), peroneus longus (PL), and lateral gastrocnemius (GL).

The EMG signals were measured using a portable data logger, the Multi Signal System ME3000P8 muscle tester unit (Biomation Inc, Ottawa, Canada). Subjects skated at 12 km/hr, 18 km/hr, and 24 km/hr, with a two-minute rest between trials. Twenty strides measures per subject of muscle activity were parsed, rectified, and then processed using a 4^{th} order Butterworth filter. The individual strides were segmented and normalized to 100% stride, equivalent to stride time duration (blade contact to blade contact). The EMG magnitudes were normalized to 100% of the maximum value obtained during dynamic contraction for each subject when skating at 24 km/hr (MDC_{24}). An ensemble average was calculated following intrasubject calculations of 20 strides per subject.

RESULTS AND DISCUSSION

Significant differences can be seen in the amplitude of muscle activation for most muscles, as well as a few temporal differences. There were often significant increases in the peak amplitude at 24 km/hr when compared to 12km/hr.

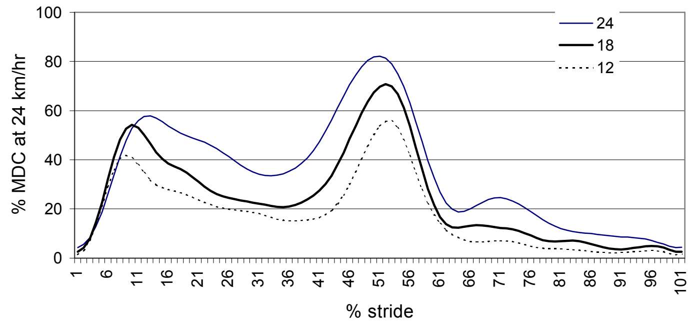

Figure 1: m. vastus medialis: EMG patterns of forward skating at three velocities: 12, 18 and 24 km/hr

Generally, as expected, it can be seen that as speed increased so does the level of activation. In most cases EMG activity at 24km/hr was significantly higher than the speed of 12km/hr. The medium speed of 18 km/hr showed few significant differences from the slow and fast speeds. This may be accounted for by the level of standard deviation found in EMG, which at 18km/hr could range close to the values found at 12 and 24 km/hr.

Skating locomotion is similar to walking in that both skills have similar single and double support phases. Likewise, increase in speed in walking produces similar augmentation in EMG amplitudes. For instance, Winter (1983) presented EMG patterns of five muscles at three speeds of walking on a treadmill. His results show that the pattern shapes remain essentially the same with the exception of the amplitude, which increases with speed. This interaction is identical to the effect found in the current forward ice skating study.

There were few significant differences in temporal values. The 1^{st} peak during the glide phase, the VM and TA were significantly ($p<0.05$) later at speed 24 km/hr. At the end of deactivation after the 2^{nd} peak at push-off, the Add and GL were significantly later at speed 24km/hr. The peak of the Add and GL at the push-off was significantly higher than both speeds of 12 and 18 km/hr. The lack of differences in temporal effects could be accounted by the fact that as speed increased, the stride rate increased, not the stride length. The skater was taking more steps, and essentially the muscle coordination pattern remained constant.

In conclusion, this study has shown that an increase in velocity results in an increase in the amount of muscle activation, but the muscle coordination patterns remain the same.

REFERENCES

Marino GW. Res Quart 48(1):93-97,1977.
Winter DA. J Motor Behav 15(4): 302-330, 1983.

GAIT ADAPTATIONS TO TRANSVERSE SLOPES

M. Nicolaou, D. Pearsall
Department of Kinesiology & Physical Education, Montréal, Québec, Canada

INTRODUCTION

Humans encounter the challenge of slopes or grades of various orientations and combinations on a daily basis. Gait adaptations to graded slopes such as inclines and declines have been studied [1,2,3]. However, little research has been conducted on the effects of banked, crowned or side (transverse) sloped terrains on walking, particularly with respect to identifying the functional adaptive asymmetries produced [4,5]. Thus, the purpose of the study was to identify the lower limb kinematic adaptations in normal gait to accommodate to static transverse slopes (0%, 5% and 10%).

METHODS

Five male subjects were recruited (age: 24 ± 3.2 years; height: 175 ± 12.6 cm, mass: 72.8 ± 0.1 kg). An electromagnetic tracking device, the Ultratrak® (Polhemus Inc., Burlington, VT, USA) was used to collect the kinematic data at 60Hz while the subjects performed the walking trials at a self-selected pace. Filmbox® software (Kaydara, Montreal, CAN) was used to control the Ultratrak® data recording. The wooden platform was elevated to the 5% and 10% slope conditions by additional wooden supports. Angular kinematic profiles of the ankle, knee and hip were calculated.

RESULTS AND DISCUSSION

Significant ($p<0.05$) joint angle changes occurred in both the uphill (UH) and downhill (DH) lower limbs. Specifically, the UH ankle (Fig 1a) was more dorsiflexed throughout the gait cycle at both the 5% and 10% slope in comparison to level, where as, the DH ankle exhibited increased plantarflexion. With respect to the knee (Fig 1b), the UH side was more flexed than at level. The DH knee was significantly more extended on both 5% and 10% slope. The sagittal plane hip kinematics were primarily affected in the DH limb (Fig 1c). Extension was greater at both the 5% and 10% slope conditions. The UH limb was relatively unperturbed in flexion/extension.

SUMMARY

Gait adaptations occur in both the UH and DH lower limbs on transverse slopes. Asymmetric changes in limb kinematics in part compensated for the unlevel surface. The adjustments appear to functionally shorten the UH limb for clearance of the walkway and to lengthen the DH limb to ensure stable ground contact.

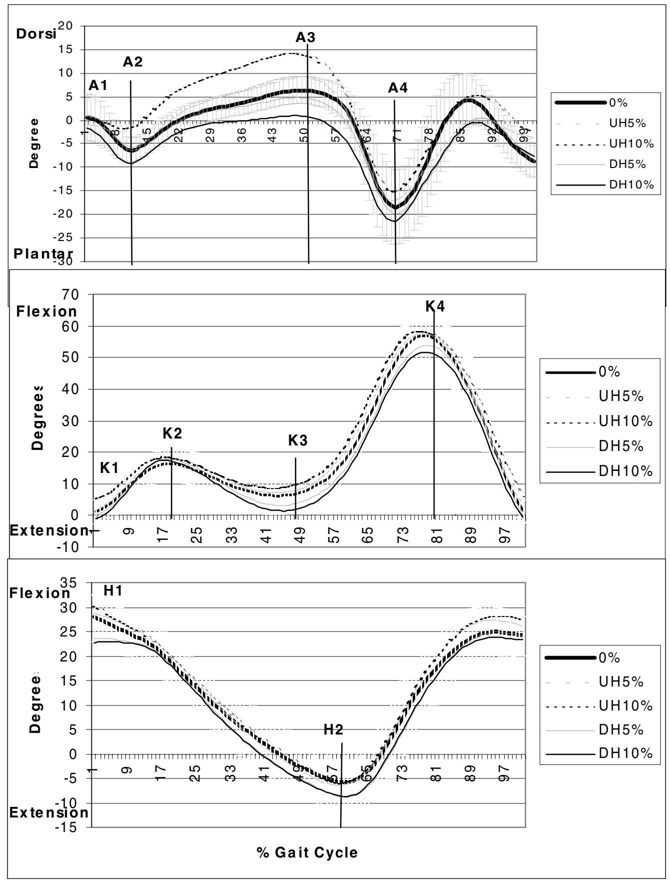

Figure 1. Mean (±SD) ankle (a), knee (b) and hip (c) kinematics during level (0%) walking in comparison to the uphill and downhill (5% and 10%) grades

REFERENCES

1. Kawamura K, Tokuhiro A, Takechi H. *Acta Med Okayama* 1991; 45(3): 179-184.
2. Gu MJ et al. *J Biomech* 1996; 29(3): 319-329.
3. Leroux A, Fung J, Barbeau H. *Exp Brain Res* 1999; 126: 359-368.
4. Fujii K et al. *Proc XVIIth ISB Cong*, Calgary, Canada. 8-13 August, 1999: 757.
5. DeGarie L, Pearsall DJ. *XXVth Cong Can Soc Biomech*, Montreal, Canada. 23-26 August, 2000: 111.

ACKNOWLEDGEMENTS

Research grant support from National Science and Engineering Research Council (NSERC) of Canada.

DESIGN METHOD OF POROUS SCAFFOLD MICROSTRUCTURE USING COMPUTATIONAL SIMULATION FOR BONE REGENERATION

Taji Adachi[1,2], Yuji Kawano[1], Yoshihiro Tomita[1,2], and Scott J. Hollister[3]
[1]Solid Mechanics Laboratory, Department of Mechanical Engineering, Kobe University, Kobe, Japan, adachi@mech.kobe-u.ac.jp
[2]Division of Computer and Information, The Institute of Physical and Chemical Research (RIKEN), Wako, Japan
[3]Departments of Biomedical Engineering, Surgery, and Mechanical Engineering, The University of Michigan, Ann Arbor, MI

INTRODUCTION

In bone regeneration using a biodegradable scaffold, geometry of porous scaffold microstructure is a key factor to control properties of regenerated bone as well as regeneration process (Hollister, *et al*. 1999). In this study, a framework of a new design method for porous scaffold microstructure is proposed using computational simulation for bone regeneration.

METHODS

By solving degradation of scaffold and formation of new bone in the same time frame, bone regeneration process was simulated (Adachi *et al*. 2001). Degradation of the scaffold was expressed as decrease in its stiffness, Young's modulus E_s, that is assumed to decrease proportionally to the molecular weight whose rate is related to the local water contents governed by the diffusion equation. New bone is assumed to form on the surfaces of old bone and scaffold, in which a rate equation of the trabecular surface remodeling (Adachi *et al*. 1997) was modified to express the new bone formation. Pixel/voxel finite element method was applied to simulate the bone regeneration process in bone-scaffold system.

Two-dimensional porous scaffold (Fig.1) was used in this case study, where the pore radius r was considered as a design valuable. Assuming periodicity of micro-structure, a unit cell (Fig.2(b)) was analyzed under uniaxial compressive loading. The unit cell was discretized into 25 x 50 pixel elements with size of 20 μm. Material properties were set as E_s = 10 GPa, ν_s = 0.3 for scaffold and E_b = 20 GPa, ν_b = 0.3 for bone.

RESULTS AND DISCUSSION

Bone regeneration process for the case of r = 300 μm is shown in Fig.2(a), where functional transition from scaffold to bone as a load-bearing component was represented. For the cases of r = 100 to 400 μm, changes in total strain energy of bone-scaffold system are plotted in Fig.2(b), showing that the mechanical function in regeneration process depends on initial pore radius r. From the mechanical viewpoint, stiffness as a bone-scaffold system is required to keep at the desired value during and after the process.

To evaluate mechanical function in the regeneration process, change in strain energy of a bone-scaffold system was calculated. Thus, the design problem was formulated to find an optimal initial pore radius of the scaffold microstructure that minimizes the objective function.

$$\Phi(r) = \int_0^T |U(t) - U_b| \, dt \quad , \tag{1}$$

where U_b is for an ideal bone and T is the completion time of bone regeneration. From regeneration simulation for 50 μm < r < 400 μm, the optimum radius was found depending on the desired strain energy U_b, that is stiffness of the desired bone.

For further application to design three-dimensional scaffold microstructure, characteristics of scaffold degradation and new bone formation have to be clarified experimentally which give us more appropriate rate equations in the bone regeneration process. Extension to a three-dimensional scaffold design with complex microstructures is necessary to apply to *in vivo* study.

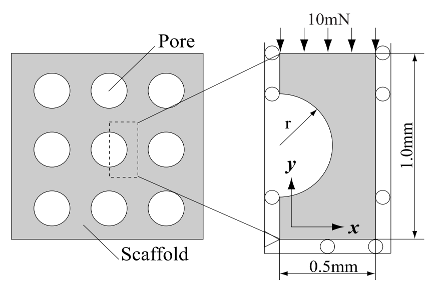

Figure 1: Simulation model of porous scaffold structure

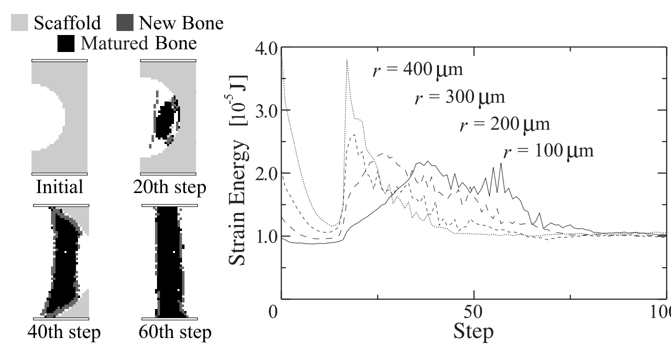

(a) Bone regeneration process (b) Change in strain energy

Figure 2: Simulation of bone regeneration process

REFERENCES

Hollister, S. J., *et al*., (1999). *IUTAM Symposium on Synthesis in Bio Solid Mechanics*, (Pedersen, P. and Bendsoe, M. P. Eds.), Kluwer Academic Publishers, 163-174.

Adachi, T., *et al*., (2001). *2001 Bioengineering Conference,* (Kamm, R. D., *et al*. Eds.), ASME, BED-**50**, 545-546.

Adachi, T., *et al*., (1997), *JSME Int. J*., **40**C-4, 782-792.

POSTURAL ESTIMATES FROM DIGITAL IMAGES: INTER- AND INTRA-TESTER RELIABILITY

Timothy K. Woo and David J. Pearsall,
Department of Kinesiology & Physical Education, McGill University, Montréal, Québec, Canada

INTRODUCTION

The present investigation was designed to assess the ability of examiners to reliably place reflective anatomical markers over well-established skeletal landmarks: specifically, intra- and inter-tester (within and between) examiner consistency.

METHODS

Three examiners evaluated 12 subjects (6 male, 6 female; age=22.7±4.6 and 25.8±10.2, respectively). Prior to the assessment, examiners were trained on designated marker placement for approximately one hour, one week prior to testing. Examiners evaluated each of the experimental subjects on two separate days. Evaluations involved the palpation of anatomical landmarks and the placement of 32 reflective markers. Four digital images (Epson, 1024x768 pixels) were recorded against a calibrated backdrop, and then processed (Biotonix software) to provide 30 biomechanical measures of body segments in three planes: anterior, posterior and lateral. Comparison within and between testers was done by using inter-class correlation coefficients as outlined in Portney and Watkins (2000).

RESULTS AND DISCUSSION

A high degree of intra-rater reliability was found when comparing the measures for the two different measurement days (Table 1). With the exception of three measures, the measures demonstrated repeatability in marker placements (ICC=0.76 to 0.96). High inter-examiner reliability also was observed (ICC=0.61 to 0.97) for 27 of 29 parameters. Low consistency was associated with marker placements overlying pelvic and upper leg locations (and the measures generated from these marker placements). In particular, the markers placed over the superior border of the upper leg (greater trochanter) gave rise to the lowest inter-rater correlation values (i.e. 0.33, 0.45). Moderate correlations were associated with markers placed over the ankles, back of the knees and posterior pelvis.

SUMMARY

High inter- and intra-examiner reliability was found in the ability of examiners to place markers over anatomical markers that define optimal posture. Some locations appear to be more difficult than others to reliably place markers, and additional attention to training is warranted.

Table 1 Intra and inter-tester ICCs of the postural measures.

		INTRA	INTER
Anterior view	Shoulders	0.95	0.97
	Pelvis	0.82	0.82
	Knees	0.82	0.85
	Forehead	0.91	0.93
	Shoulders	0.91	0.96
	Umbilicus	0.91	0.92
	Pelvis	0.89	0.87
	Knees	0.80	0.75
	Toes	0.63	0.81
Posterior view	Shoulders	0.93	0.92
	Pelvis	0.78	0.70
	Knees	0.77	0.74
	Left foot	0.73	0.64
	Right foot	0.76	0.61
	Shoulders	0.81	0.79
	C7	0.82	0.76
	5T	0.82	0.70
	Pelvis	0.94	0.80
	Knees	0.90	0.71
	Ankles		
Lateral view	Head to shoulders	0.96	0.95
	Shoulders to pelvis	0.93	0.96
	Pelvis to hips	0.82	0.33
	Hips to knees	0.81	0.45
	Knees to feet	0.93	0.88
	Head	0.96	0.95
	Shoulders	0.71	0.77
	Pelvis	0.92	0.93
	Hips	0.88	0.69
	Knees	0.96	0.87
	Mean	0.85	0.79

REFERENCES

Portney, L.G., Watkins, M.P. (2000). *Foundations of clinical research: applications to practice (2nd ed.),* Prentice Hall

NECK MUSCLE STRAINS IN WHIPLASH INJURY

Anita N. Vasavada[1], John R. Brault[2], and Gunter P. Siegmund[2,3]

[1]Department of Biological Systems Engineering, Washington State University, Pullman, WA, USA; vasavada@wsu.edu
[2]MacInnis Engineering Associates, Richmond, BC, Canada
[3]School of Human Kinetics, University of British Columbia, Vancouver, BC, Canada

INTRODUCTION

Considerable uncertainty exists regarding the role of neck muscles in whiplash injury. Neck muscle forces affect head and neck kinematics, and neck muscles may contribute to the injury of other neck tissues or may themselves be injured due to imposed lengthening. Thus, it is important to know neck muscle strains, forces and torques in order to understand mechanisms of whiplash injury. The purpose of this study was to examine strains in neck muscles by using a biomechanical model of the neck musculature together with the experimental kinematics of subjects exposed to low-speed rear-end impacts.

METHODS

A model of the head and neck musculoskeletal system of a 50th percentile male was used for this analysis (Vasavada et al., 1998). The model was implemented in Software for Interactive Musculoskeletal Modeling (Musculographics, Inc., Santa Rosa, CA) and incorporated 19 muscle pairs and muscle force-generating parameters. The sternocleidomastoid (SCM) muscle was represented by three segments: sterno-mastoid (sm), cleido-mastoid (cm), and cleido-occipital (co); whereas splenius capitis (SPL) and semispinalis capitis (SEMI) were each represented by one segment. Kinematic data from 11 male subjects (height ±3cm of 50th percentile) exposed to rear-end collisions at a speed change of 8 km/h were used in this study (Siegmund et al., 1997). The head and neck dimensions of the biomechanical model were within one standard deviation of the subject data. The translation and rotation of the head relative to the torso were imposed on the biomechanical model and the time histories of musculotendon length and strain were calculated.

RESULTS AND DISCUSSION

The initial motion of the head relative to the torso was retraction (posterior translation) and extension, followed by protraction (anterior translation) and flexion during forward rebound off the head restraint. The model predicted that the sterno-mastoid and cleido-mastoid segments of SCM lengthened less than 2%, but that the cleido-occipital segment experienced up to 4% strain during retraction (Figure 1). The small length changes for the sterno-mastoid and cleido-mastoid segments are consistent with their less effective line of action to resist head retraction, despite being active during this interval (Brault et al., 2000). SPL and SEMI initially shortened as much as 25%. In the final protracted posture, SEMI remained shorter than its initial length, whereas SPL was 10% longer than its initial length. After the initial shortening, the total lengthening in SPL was 35% of initial length. The large strains in SPL in the protraction phase indicate that injury to this muscle may be a mechanism of whiplash injury. Further, if tendon stiffness is relatively high, strains in muscle fibers will be considerably greater than the computed musculotendon strains.

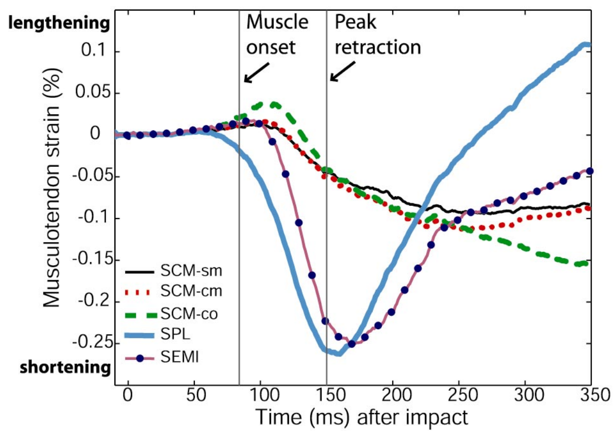

Figure 1: Musculotendon strain in three segments of SCM, SPL and SEMI. Average muscle onset occurred at 84 ms and peak retraction at 150 ms post impact.

SUMMARY

Based on this analysis, the induced kinematics that occur during whiplash loading are potentially injurious to the neck muscles and ligaments. We found that SCM underwent 2-4% lengthening during the retraction phase of whiplash, while SPL lengthened 35% in the final protraction phase. These results were consistent with a higher frequency of posterior than anterior neck pain in whiplash patients (Ryan et al. 1993). Future studies should address two issues: (1) loads and strains in shorter neck muscles and ligaments due to the induced intervertebral kinematics in protracted and retracted postures; and (2) the ability of SCM to resist head retraction.

REFERENCES

Brault JR et al. (2000). *Clin Biomech,* **15**, 426-435.
Siegmund GP et al. (1997). *41st Stapp Conf.*, pp. 357-385.
Ryan et al. (1993). *Med J Aust* **159**, 651-656.
Vasavada AN, Li S, Delp SL. (1998). *Spine*, **23**, 412-422.

DYNAMIC BEHAVIOR OF ACTIN FILAMENTS IN CULTURED ENDOTHELIAL CELLS DURING EXPOSURE TO SHEAR STRESS

Toshiro Ohashi, Kei Tsuyuki, Tsugumasa Yamamoto, and Masaaki Sato
Biomechanics Laboratory, Graduate School of Mechanical Engineering, Tohoku University, Sendai, Miyagi, Japan

INTRODUCTION

We have been interested in the mechanism of mechanical responses of endothelial cells, especially the roles of actin filaments (Kataoka et al., 1998: Sato et al., 2000). It has been pointed out that actin filaments may be moved around, form stress fibers and finally locate at the desired positions during endothelial exposure to flow (Davies, 1995). In this process integrins are expected to play important roles to decide the positions of actin filaments and/or stress fibers (Urbich et al., 2000). Dynamic process of actin filament behavior is not observed in ordinary method, because cell must be fixed and the actin is stained. However, we can utilize recent advances techniques using GFP (green fluorescent protein) combined with actin to observe the dynamic behavior in living cells.

We would like to report the detailed moving process of actin filaments in endothelial cells during exposure to shear stress and discuss the mechanisms.

METHODS

A plasmid encoding GFP fused to the amino terminus of actin (the vector was cordially provided by Dr. G. Marriott, Max-Planck-Institute for Biochemistry, Germany) was transfected into cultured bovine aortic endothelial cells (BAECs) using a liposomal method. Cells were plated on a specially ordered 35 mm glass-base dish (Asahi Techno Glass). An I/O unit was set in the dish to compose a flow chamber with flow section of 0.5 mm in height. All experiments were performed with confluent monolayers of cell. Cells expressing GFP-actin were observed in flow condition. Fluid shear stress of 2 Pa was applied using the parallel plate flow chamber. Distribution and dynamic behavior of actin filaments in a cell were observed under a confocal laser scanning microscope and the images were recorded on a computer through a high resolution digital CCD camera.

RESULTS AND DISCUSSION

A typical example of time course of changes in structure of actin filaments is shown in Figure 1. It was already confirmed by separate experiments that localization of GFP-actin coincided with the F-actin filaments stained by rhodamine-phalloidin in ordinary method. Before exposure to shear stress, actin filaments were observed as star-like configurations around upstream side (lower side of a cell in Figure 1). After exposure to shear stress, the star-like structure disappeared, development of actin filaments was observed around upstream side, and the cell elongated slightly at 60 min. Actin filaments then developed around downstream side of within 120 min. At around 180 min, the more elongated cell was observed. The shape index value of the cell reduced from 0.76 (0 min) to 0.59 (180 min). Since the focal adhesion proteins, integrins, should play important roles in re-organization of actin filaments, we need to simultaneously observe the dynamic movements. At present, we also need more examples to conclude general moving process of actin filaments in shear stress condition.

SUMMARY

We observed the dynamic process of actin filament movement in endothelial cells expressing GFP-actin during exposure to flow. Actin structure was changed at upstream side within 60 min and at downstream side within 120 min. A cell started to elongate at around 60 min.

REFERENCES

Davies, P.F. (1995). *Physiological Review*, **75**, 519-560.
Kataoka, N., et al. (1998). *Medical & Biological Engineering & Computing*, **36**, 122-128.
Sato, M., et al. (2000). *Journal of Biomechanics*, **33**, 127-135.
Urbich, C., et al. (2000). *Circulation Research*, **87**, 683-689.

ACKNOWLEDGEMENTS

We thank Professor T. Nishino, Department of Biomolecular Engineering, Tohoku University, for his technical assistances to do the experiments. This work was supported in part by a research grant from the Ministry of Education, Culture, Sports, Science and Technology, Japan (#12480257).

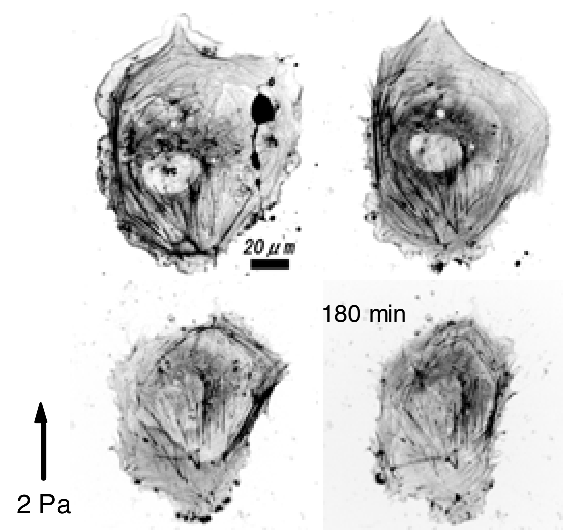

Figure 1: Time course of changes in actin structure in a cultured endothelial cell exposed to shear stress of 2 Pa. The contrast of these images is inverted.

MEDIAL-LATERAL COP VELOCITY DURING STANDING RELATES TO ASYMMETRY AND FUNCTIONAL BALANCE IN INDIVIDUALS WITH STROKE

Daniel S. Marigold[1,3], Janice J. Eng[2,3], Kelly S. Chu[2,3], and C. Maria Kim[2,3]

Graduate Program in Neuroscience[1] and School of Rehabilitation Sciences[2], University of British Columbia
Rehab Research Lab[3], GF Strong Rehab Centre, Vancouver, British Columbia, Canada, www.rehab.ubc.ca/jeng

INTRODUCTION

Impairments such as muscle weakness, pain, spasticity, visual disturbance, contractures, and sensory dysfunction contribute to poor balance and a high rate of falls in individuals with stroke (Kanis et al., 2001). Although force plate measures are commonly used to assess standing postural control in older adults, the reliability and validity of these measures are not well established for individuals with stroke. The purpose of this study was to 1) determine the test-retest reliability of standing postural sway measures, 2) establish the relationship between postural sway and weight-bearing asymmetry, and 3) determine the relationship between postural sway and clinical balance scores in individuals following stroke.

METHODS

Twenty-eight individuals with chronic stroke (age of 62.0 ± 8.6 years, height of 166.9 ± 11.3 cm, duration of injury of 4.1 ± 2.7 years, Berg Balance score of 44.8 ± 5.5 points, 12 left cerebrovascular accident [CVA], and 16 right CVA) participated in this study. Participants performed two quiet standing conditions, eyes open and eyes closed, on two separate test days. Force plate data (Bertec) was collected for 30 seconds and variables calculated included RMS centre of pressure (COP) displacement (disp.) and velocity in both the medial-lateral (M/L) and anterior-posterior (A/P) directions. The vertical force asymmetry between the paretic and non-paretic limb was also calculated (Robinson et al., 1987), where a higher asymmetry index represented greater weight-bearing on the non-paretic limb relative to the paretic limb. The 14-item Berg Balance score was used to provide a clinical measure of functional balance. Intraclass Correlation Coefficients (ICCs) assessed the reliability between the two test sessions. Pearson Correlations quantified the relationship a) between standing asymmetry and postural sway and b) between the Berg Balance score and postural sway.

RESULTS AND DISCUSSION

High test-retest reliability was found for the A/P COP displacement and velocity and M/L COP velocity (ICCs = 0.73-0.90). M/L COP displacement with eyes open and closed demonstrated moderate reliability (ICCs = 0.63-0.66). Further analyses used the means of the two test sessions (Table 1).

Table 1: Postural sway measures (mean ± SD), N=28.

Sway Measure	Eyes Open	Eyes Closed
M/L COP (cm)	0.178 ± 0.052	0.241 ± 0.088
M/L COP Velocity (cm/s)	0.887 ± 0.308	1.399 ± 0.566
A/P COP (cm)	0.360 ± 0.093	0.503 ± 0.160
A/P COP Velocity (cm/s)	1.737 ± 0.609	2.985 ± 1.240

Interestingly, it appears that an increase in weight-bearing asymmetry results in less M/L sway velocity in the eyes open condition (Table 2). It is possible that individuals who load their non-paretic limb more may choose a strategy, which relies on lateral ligamentous support from the hip and knee to "lock" the limb and reduce sway.

Table 2: Correlations between COP measures, asymmetry and the Berg Balance score.

COP measure	M/L disp.	M/L velocity	A/P disp.	A/P velocity
Eyes open				
Asymmetry	-0.29	-0.49**	-0.004	-0.20
Berg	-0.16	-0.59**	-0.21	-0.42*
Eyes closed				
Asymmetry	-0.16	-0.23	0.09	-0.08
Berg	-0.17	-0.43*	0.04	-0.09

* Significant at $p < 0.05$ ** Significant at $p < 0.01$

With the eyes closed, the relationships between asymmetry and sway measures were not significant, suggesting that visual input plays a key role in controlling sway in individuals with stroke. Lastly, a decrease in postural sway velocity (particularly in the M/L direction) was related to greater functional balance (i.e. Berg Balance score). This observation concurs with previous reports (Niam et al., 1999; Stevenson & Garland, 1996).

SUMMARY

This study demonstrates that COP velocity is a reliable measure to assess postural sway in individuals with chronic stroke. Clinicians should be aware that the extent of weight-bearing asymmetry will influence postural sway and very low sway values could indicate minimal loading on the paretic limb. Further research on the mechanical influence of asymmetry on postural sway is recommended.

ACKNOWLEDGEMENTS

This study was supported by the BC Health Research Foundation, a grant-in-aid from the Heart and Stroke Foundation of BC and Yukon and a studentship from NSERC, Canada.

REFERENCES

Kanis, J., et al. (2001). *Stroke*, **32,** 702-706.
Niam, S., et al. (1999). *Arch Phys Med Rehabil*, **80**, 1227-1233.
Robinson, R.O. et al. (1987). *J Manipulative Physiol Ther*, **10**, 172-176.
Stevenson, T.J., Garland, SJ. (1996). *Arch Phys Med Rehabil*, **77**, 656-662.

FAILURE LOAD FOR SINGLE SCREW VERSUS SINGLE SCREW PLUS STAPLE CONSTRUCTS IN THE PEDIATRIC THORACIC SPINE: DIFFERENCES BETWEEN "PLOWING" AND "LEVERING"

Andrew Mahar, Richard Oka, David Brown, Peter Newton
Department of Orthopedics, Children's Hospital, San Diego, CA

INTRODUCTION

Anterior spinal instrumentation systems for correction of scoliosis require comparison between vertebral body screws. Prior tests have applied tensile loads parallel to the screw axis (pullout). However, pullout tests do not represent the only clinical failure mode. Intraoperatively, loads are applied at the screw/bone interface in a direction orthogonal to the screw axis. While the failure is commonly described as "plowing" (translation of the screw through the bone); failures may also be described as "levering" (pitching of the screw within the bone). This difference in mechanical loading is not well described in the literature. To improve the fixation of the screw/bone interface, screws may be augmented with staple. There is little biomechanical data describing the differences in "levering" or "plowing" failure modes. The purpose of this study was to examine differences between a single screw versus a single screw plus staple when tested to failure by both "plowing" and "levering".

METHODS

Commercially available polyurethane foam (Pacific Research Laboratories, Vashon Island, WA) of 7-lb./ft^3 density was selected to simulate the cortico-cancellous bone of the vertebral body. The foam was cut to the anatomic dimensions of pediatric thoracic vertebral bodies (H = 2.5cm, W =3.0cm, L = 3.0cm). The 5.0 Moss-Miami anterior instrumentation system from Depuy Acromed was used for each test. The inclusion of the staple was randomized across specimens. All screws (6.0mm diameter) were inserted transversely across the "anterior vertebral body". The anterior portion of the foam block was unsupported during mechanical testing to simulate a vertebral body after adjacent discectomies. Each body was inserted to a rigid fixation device inside a MTS 858 servohydraulic testing machine. A 5.0mm stainless steel rod was then placed in the screw head and bent to 90 degrees to allow insertion to the piston actuator (Figure 1). For "plowing", the screw was rigidly fixed to the rod with inner and outer nuts, maintaining the screw rod interface at 90 degrees. For levering, the rods were fixed to the screw via the inner and outer nuts, but not tightened, to allow rotation of the rod and changes to the screw-rod orientation. Each mode of failure was tested parallel to the longitudinal axis of the spine. Displacement (mm) and force (N) were sampled at 100Hz for the duration of each displacement control test. Screws were driven to 10mm of displacement and failure was recorded as the maximum force recorded during the test. The average failure load for "levering" and "plowing" were analyzed with a two-way ANOVA ($p<0.05$) to determine differences in failure mechanics. The presence of the staple was also a dependent variable.

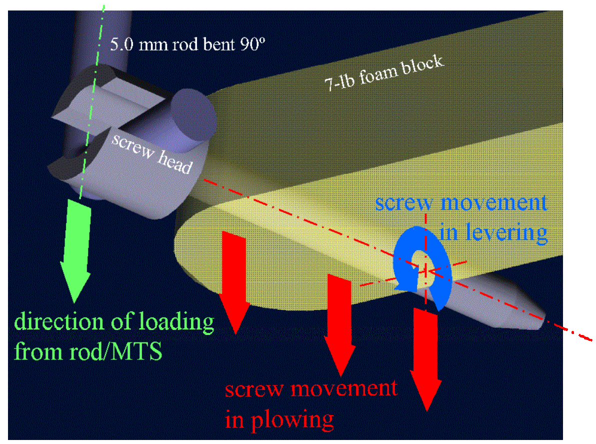

Figure 1: Schematic describing directions for plowing and levering during failure testing (without inner/outer nuts).

RESULTS AND DISCUSSION

Table 1: Screw/Bone Interface Failure Loads (N)

	Mean	Std. Deviation
Levering		
With Staple (n=8)	**123.10**	8.11
Without Staple (n=8)	**104.19**	9.12
Plowing		
With Staple (n=8)	**211.39**	44.50
Without Staple (n=8)	**170.69**	46.57
(interaction term = 0.5)		

The increased failure force for the "plowing" conditions was statistically greater ($p<0.0000$) than the failure force for "levering". For the "levering" condition, the presence of the staple significantly increased the failure force ($p<0.0011$). For the "plowing" condition, the presence of the staple increased the failure force, but this was not statistically significant ($p<0.3$).

CONCLUSION

"Plowing" and "levering" represent two distinct scenarios for bone-screw interface loading/failure. Anterior scoliosis correction may involve both "plowing" and "levering" during different phases of compression between screws. These data suggest a greater influence of the staple in the "levering" mode of loading. The differences in load magnitude under these scenarios may provide insight into fixation failures and vertebral body fractures intraoperatively.

TRANSIENT FOOT GROUND REACTION FORCES AND PROSTHETIC PYLON ATTENUATION DURING GAIT

Glenn K. Klute[1,2], Jocelyn S. Berge[3], Joseph M. Czerniecki[1,4]
[1]Dept. of Veterans Affairs, Puget Sound Health Care System, Seattle, WA (gklute@u.washington.edu)
Depts. of Electrical Engineering[2], Bioengineering[3], and Rehabilitation Medicine[4], University of Washington, Seattle, WA

INTRODUCTION

It is widely believed that transient forces generated at initial contact during locomotion are responsible for degenerative joint disease, residual limb blisters and ulceration, muscle tears, stress fractures, and chronic low back pain (Whittle, 1999). For the lower extremity amputee with only residual capacity to attenuate transient forces, prosthesis manufacturers have designed and marketed shock-absorbing pylons. Our interest is to (1) measure these transient forces in a unilateral transtibial amputee sample population and (2) determine if a shock-absorbing prosthetic pylon can attenuate these forces.

METHODS

Unilateral transtibial amputees (n=5) were fit with a prosthesis able to accommodate both a rigid pylon and a shock-absorbing pylon (Total Torsion, Blatchford, UK). After a three-week acclimation period, subjects walked at their self-selected speed (3-5 repeated trials) across a force plate (f_s=600Hz, f_c=100Hz; Kistler, SWE). The subjects were then fit with the other pylon (random order) and the acclimation and test protocols were repeated. All provided informed consent. Transient forces, by their very nature, decay during the sample period and hence do not contribute significantly to the magnitude of Fourier series coefficients. Our approach used a stationary wavelet discrete transform with a least asymmetric wavelet (width 8) to preserve both time and frequency content. The least asymmetric wavelet was selected to minimize sidelobes outside the nominal pass-band (Percival and Walden, 2000). The multi-resolution analysis included pass-bands from 9 to 18 Hz (pb1), from 18 to 38 Hz (pb2), from 38 to 75 Hz (pb3), and from 75 to 100 Hz (pb4). Peak vertical foot ground reaction force magnitudes within each pass-band were averaged for each pylon condition. A repeated measures analysis of variance was performed with an *a priori* alpha of $p<0.05$.

RESULTS AND DISCUSSION

The multi-resolution wavelet analysis of the vertical foot ground reaction force for a unilateral transtibial amputee walking with a rigid and a shock-absorbing pylon revealed surprisingly large transient forces that decay within the first 100 msec after initial contact (Figure 1). The mean peak vertical foot ground reaction forces generally decrease in magnitude with increasing pass-band frequencies (Figure 2). All but the 19 to 38 Hz pass-band (pb2) showed reduced magnitude transients for the shock-absorbing pylon when compared to the rigid pylon but none were statistically significant [pb1: $F(1,4)=2.22$, $p=0.21$; pb2: $F(1,4)=0.25$, $p=0.64$; pb3: $F(1,4)=5.69$, $p=0.08$; pb4: $F(1,4)=5.67$, $p=0.08$].

Figure 1: Typical foot ground reaction force observations and multi-resolution wavelet analysis pass-bands (pb2 and pb3 only) for an amputee with a rigid and a shock-absorbing pylon.

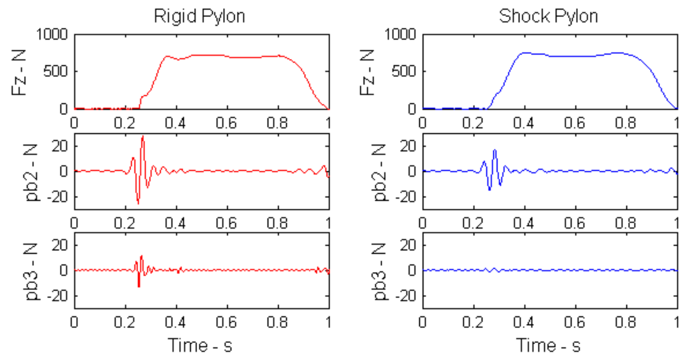

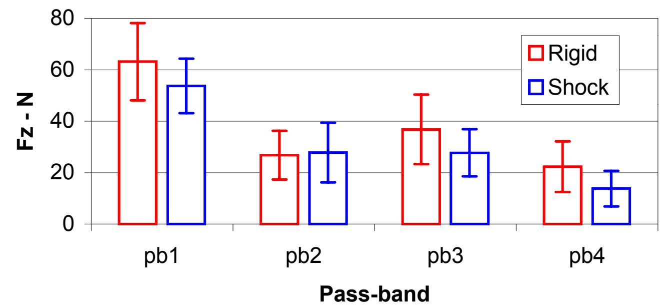

Figure 2: The peak vertical foot ground reaction force (Fz) at observed in each pass-band (n=5, mean ± s.d.).

SUMMARY

Antonsson and Mann (1985) report negligible foot ground reaction force magnitudes above 15 Hz (fast Fourier transform). Our wavelet-based approach demonstrates substantial transients exist at much higher frequencies (up to 100 Hz) in the first 100 msec following initial contact. Shock-absorbing pylons appeared to have smaller transients than rigid pylons in 3 of 4 pass-bands (9-18, 38-75, and 75-100 Hz) but were not statistically different. It remains to be determined if this lack of difference is clinically relevant.

REFERENCES

Antonsson E.K., Mann R.W. (1985). *J. Biomech.*, **18**, 39-47.
Percival, D.B., Walden, A.T. (2000). *Wavelet Methods for Time Series Analysis*. Cambridge University Press.
Whittle, M.W. (1999). *Gait and Posture*, **10**, 264-75.

The Department of Veterans Affairs, Veterans Health Administration, Rehabilitation Research and Development Service, Merit Review A2448R, supported this research.

DESIGN OF AIR SEAT CUSHION ORTHOSIS FOR PLEGIA

Jung Hwa Hong[1], Gyoo Suk Kim[1], Jong Kwon Kim[1], Mu Seong Mun[1], Jei Cheong Ryu[1], In Huk Lee[2], and Jong Keun Lee[2]
[1]Korea Orthopedics & Rehabilitation Eng. Ctr., 47-7 Koosan-dong, Pupyung-gu, Inchon 403-120, Korea (jhhong@iris.korec.re.kr)
[2]IPS International

INTRODUCTION

The use of seat cushion orthosis is required for various plegic patients and the elderly to prevent pressure sore. To design of an air seat cushion for prevention of decubitus ulcer, interface pressure characteristics between the buttock and cushion are important. The main design factors could be the distribution of interface pressure, the minimization of mean and peak interface pressure values, and the reduction of interface shear force and pressure gradient. Thus, a suitable design of the cushion satisfying all requirements is a difficult problem. To develop an air seat cushion orthosis, an appropriate and effective numerical tool is required. The purpose of the study was to develop an air seat cushion orthosis having optimized air cells representing evenly distributed and lower interface pressure between the buttock and cushion surface. For the purpose, advanced finite elements (FE) of cushion and human buttock models were utilized.

METHODS

Since the interface pressure, as well as deformation behavior of air cell in the cushion were concerns, an air cell was modeled using the airbag model in PAM-SAFE (ESI, France). Figure 1 was the base FE model of air cell. The material of air cell was the chloroprene rubber that is mostly used in the air cushion
orthosis. Since the inflating behavior of air cell in the service range, the material behavior is assumed to be linear. The material properties were obtained from experiments using the chloroprene rubber specimens. The inflating behavior of air cell model was checked by experiments. The completed base FE seat cushion model showed in Figure 2.
The human buttock model was constructed using dimensional data from CT scanning of a plegic patient. The material properties of hard and soft tissues were obtained from previously developed the H-model (IPS International, Korea).
The analysis is composed of two procedures. Firstly, the inflating simulation of the seat cushion up to the service air cell pressure was performed. Then, the human model was seated on the orthosis model to obtain the interface pressure characteristics. Figure 3 was the simulation configuration using the orthosis and human model.
To obtain appropriate, or near optimum design of the orthosis, a design procedure was applied using a sensitivity analysis. The design factors were the height of air cell, the number of rib of air cell on the transverse plane, and the density of air cell in the orthosis. For all cases, the sensitivity analyses were performed to obtain a near optimal design of the orthosis.

RESULTS AND DISCUSSION

Figure 4 shows the comparisons of air cell behavior form the experiment and simulation. The expansion curves of air cell shows a reasonable agreement. Figure 5 shows the interface pressure distributions from the test (left) and simulation (right). For the sensitivity analyses, an optimum height of air cell minimizing interface shear force and maximum pressure was 60 mm (Figure 6 and Table 1). An optimum number of rib of the air cell was 8 based on the strain distribution (Figure 7). The density of air cell was selected as a medium density. After optimizing, the interface pressure characteristics were significantly improved compared to those of the base orthosis model (Figure 8).

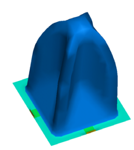

Fig. 1

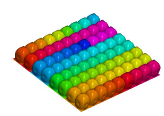

Fig. 2

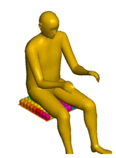

Fig. 3

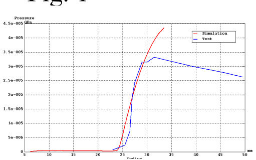

Fig. 4

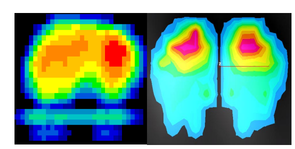

Fig. 5

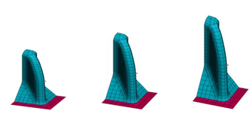

Fig. 6

Cell	40 mm	60mm	80mm
Shear	12.3 N	9.5 N	32.0 N
Max.	15.6	12 kPa	13.2

Table 1

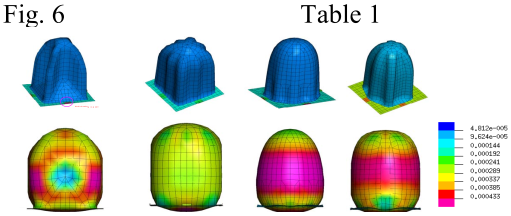

Four Eight None Six

Fig. 7

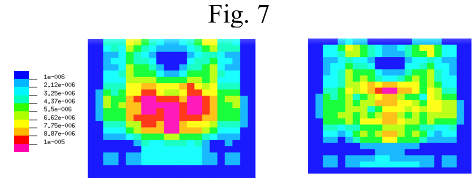

Base Optimized

Fig. 8

THE EFFECT OF BRACING ON PATELLAR ALIGNMENT AND PATELLOFEMORAL JOINT CONTACT AREA IN PERSONS WITH PATELLOFEMORAL PAIN

Li-der Chan[1], Samuel R. Ward[1], Yu-jen Chen[1], Michael S. Terk[2], Christopher M. Powers[1,2]
[1]Musculoskeletal Biomechanics Research Laboratory, University of Southern Calif., Los Angeles, CA. lidercha@usc.edu
[2]LAC/USC Imaging Science Center, Dept. of Radiology, Keck School of Medicine, University of Southern Calif., Los Angeles, CA.

INTRODUCTION

Bracing is commonly used in the management of patellofemoral pain (PFP), however, the mechanism by which braces influence symptoms has not been clearly elucidated. One thought is that bracing changes patellar alignment thereby altering the magnitude and/or location of the patellofemoral joint contact area. To date, this hypothesis has not been tested. The purpose of this study was to examine the influence of two braces on patellar alignment as well as the magnitude and location of patellofemoral joint contact area.

METHODS

Eleven subjects with a diagnosis of PFP participated (mean age 31.2± 6.7, height 164.2± 5.2 cm, weight 56.4± 5.4 kg). Subjects were included if they reported pain reduction with at least one of the braces evaluated. Axial MR images of the patellofemoral joint were obtained at 0, 20, 40, and 60º of knee flexion against a resistance of 25% body weight (Ward, 2001). Imaging was performed under three conditions: 1) dynamic patellar orthosis (Breg Inc.), 2) elastic sleeve brace (Don Joy Inc.), and, 3) no brace. Using previously described methods, measurements of patellofemoral joint contact area (medial facet, lateral facet and total area) were made (Ward, 2001). In addition, medial/lateral patellar displacement and patellar tilt were quantified at each knee flexion angle (Powers, 1998). Separate two-way ANOVA's with repeated measures (brace condition x knee angle) were performed for each dependent variable.

RESULTS AND DISCUSSION

When collapsed across all knee flexion angles, no significant differences in patellar alignment were noted between the elastic sleeve brace and non-braced conditions, however, the dynamic orthosis resulted in a small but significant decrease in lateral displacement compared to the non-braced condition (62±0.2% vs. 60±0.2% of the patella lateral to midline; p=0.041). Both the dynamic orthosis and elastic sleeve braces increased total contact area compared to the non-brace condition (non-braced: 250.3±13.3 mm^2, dynamic orthosis: 293.8±18.3 mm^2, elastic sleeve brace: 303.5±20.0mm^2, p=0.004)(Figure 1). Both braces significantly increased lateral facet contact area compared to the non-brace condition (non-braced: 197.8±9.8 mm^2, dynamic orthosis: 232.1±11.9 mm^2, elastic sleeve brace: 227.5±12.8 mm^2, p=0.007), however, only the elastic sleeve brace provided significantly greater medial facet contact area when compared to the non-braced condition (non-braced: 52.5±6.7 mm^2, elastic sleeve brace: 76.1±9.8 mm^2, p=0.005).

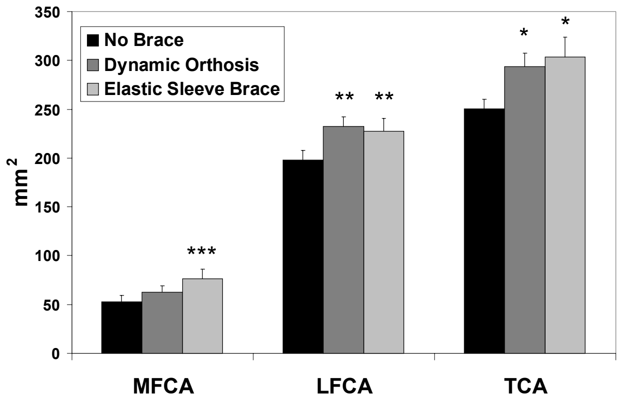

Figure 1: Changes in medial facet contact area (MFCA), lateral facet contact area (LFCA), total contact area (TCA). *p=0.004, **p=0.007, ***p=0.005. (Data collapsed across all knee flexion angles)

SUMMARY

Both the dynamic orthosis and elastic sleeve brace significantly increased total contact area over the non-braced condition by 17.4 % and 21.3 % respectively. The increase in total contact area observed with the elastic sleeve brace was achieved through significant increases in medial and lateral facet contact area, while the increase in total contact area with the dynamic orthosis was achieved through a significant increase in lateral facet contact area. Changes in contact area following bracing likely occurred as result of direct compression as changes in patella alignment were minimal. Alterations in the magnitude and location of contact area may have implications with respect to pain and stress relief in the PFP population.

REFERENCES

Powers, C.M. et al (1998). *JMRI*, **8**, 724-32.
Ward, S.R. et al (2001). *Trans ORS.*

ACKNOWLEDGEMENTS

This study was supported by the unrestricted grants from Don Joy and Breg Inc.

METHOD TO MEASURE SUSTAINABLE LOADS IN SUTURED URETHRAL TISSUE

William Baker, Kris Okumu, Michael Drews, R. Bruce Martin

Department of Urology and Orthopaedic Research Labs, University of California, Davis Sacramento, California
Corresponding Author: William.Baker@med.va.gov

INTRODUCTION

Vesicourethral anastamosis stricture affects 20% of men following radical prostatectomy. A review of literature shows that many factors contribute to stricture formation but the pathophysiology has not been well studied. Little attention has been paid to the mechanical properties of suture materials and the stresses that they have to bridge to produce a sound anastamosis. After removal of the prostate gland, a 3 – 6 cm gap between the bladder and urethra must be closed. Dynamic forces cause traction in opposite directions. Properties of suture material have been documented in literature but there is little agreement with regard to the best suture material for specific purposes. We have developed a method to measure the force at tissue failure in sutured bovine urethra for monofilament and braided suture of differing gauge.

METHODS

Eight, entire bovine urethra from freshly slaughtered bulls, including the bladder neck, were cleaned of investing tissue. The cylinders of tissue were trisected longitudinally into rectangles and secured in a U-shaped clamp designed in our lab. The tissue was sutured 6 mm from the open end and a 12 cm loop formed by tying the free ends of suture. The tissue holder was attached to the moveable stage of an Instron Tensiometer Model 1122 (Instron Instruments, Canton MA) and the suture looped around a hook secured to the fixed, lower stage. The sutured tissue was distracted at 20 mm/min and a load-displacement curve recorded on a PC using ASYST software (ASYST Technologies, Santa Clara, CA). Yield load was recorded as well as maximum load at tissue failure. Yield load was defined as:

$$\Delta F / F_{predicted} > 5\%$$

where

$$\Delta F = F_{predicted} - F_{actual}$$

To measure the maximum load sustainable by suture material itself, 12 cm loops of suture were distracted at 20 mm/min until failure.

RESULTS AND DISCUSSION

Yield load and maximum load in sutured tissue were directly proportional to suture gauge and were higher with monofilament compared to braided suture. Yield load in tissue with 0 gauge monofilament suture was 111% greater than with 4.0 gauge suture. Yield load in tissue with 0 gauge braided suture was 79.6% greater than with 4.0 gauge suture. The maximum load in tissue with 0 gauge monofilament suture was 71% greater than with 4.0 gauge suture. The maximum load in tissue with 0 gauge braided suture was 34% greater with 4.0 gauge suture. The loops of suture material failed at maximum loads higher than loads sustained by sutured tissue. Since suture failed at loads much higher than that of tissue failure, these results show that in this model, the mechanical properties of tissue are of primary importance. Thus, from a purely mechanical perspective, monofilament suture of large gauge is superior for suturing urethral tissue. Nevertheless, other factors must be considered in selecting appropriate suture. Monofilament suture offers excellent glide characteristics and causes minimal tissue trauma. This decreased tissue trauma may explain the higher sustainable loads in sutured tissue. However, monofilament suture, especially of larger gauge, is difficult to manipulate. Braided suture is easier to handle and has superior knot tying strength compared to monofilament suture. In vivo, however, braided suture loses tensile strength faster than monofilament suture and provides better media for bacterial colonization.

REFERENCES

Morris, M.C. et al (1986). *J. Urology,* **135(3)**, 602.
Debus, E.S. et al (1997). *Eur. Surg. Res.,* **29(1)**, 52-61
Outlaw, K.K et al (1998). *Am. Surg.,* **64(4)**, 348-354.
Framz, D.A. et al (1995). *Orthopaedics* **June**, 555-8.

Gauge	0	2.0	3.0	4.0
Load	105.09±14.56	45.45±5.94	40.04±5.24	29.66±4.94

Table 1. Max. Load (N) monofilament suture failure, N=3

Gauge	0	2.0	3.0	4.0
Load	97.20±1.58	75.30±1.25	44.29±1.79	32.16±0.91

Table 2. Max. Load (N) braided suture failure, N=3

Gauge	0	2.0	3.0	4.0
Load	105.09±14.56	45.45±5.94	40.04±5.24	29.66±4.94

Table 3. Yield Load (N) urethra, monofilament suture, N=3

Gauge	0	2.0	3.0	4.0
Load	7.65±1.45	7.28±3.73	5.68±3.94	4.26±1.37

Table 4. Yield Load (N) urethra, braided suture, N=3

Gauge	0	2.0	3.0	4.0
Load	19.11±10.17	14.27±1.13	12.40±3.59	11.17±4.33

Table 5. Max. Load (N) urethra, monofilament suture, N=3

Gauge	0	2.0	3.0	4.0
Load	15.40±1.24	13.58±4.66	11.49±4.23	9.6±2.54

Table 6. Max. Load (N) in urethra, braided suture

EMG CHANGES IN PARASPINAL MUSCLE OF SCOLIOSIS PATIENTS AFTER SPINAL FUSION

W W. Lu[1], Yong Hu[1], K D K Luk[1], Qiu Guixing[2], J C Y Leong[1]
[1]Department of Orthopaedic Surgery, The University of Hong Kong, China
[2]Dept of Orthopaedic Surgery, The Peking Union Medical College Hospital, Beijing China

INTRODUCTION

Adolescent idiopathic scoliosis is the most common spinal deformity, and surgical correction followed by spinal fusion is the basic method of treatment with a Cobb angle of greater than 40^o. However, previous studies have noted incidences of developing pseudarthrosis, low back pain, spinal stiffness and instability following spinal fusion. The function of the paraspinal muscles after spinal fusion is still unknown. The purpose of this study was to compare spinal muscle function in normal subjects and scoliotics pre- and post-fusion, with particular attention on the effects of long term follow up.

MATERIALS AND METHODS

Fifteen healthy subjects (mean age 19 years) and 19 patients (mean age 18 years) with adolescent idiopathic scoliosis were evaluated. All the patients had right-side thoracic curves with a mean Cobb angle of 56^o(8 degrees. They received posterior spinal fusion from T2-T5 to T12 and were followed up for a minimum of 2 years after surgery.
EMG signals were collected from healthy subjects and patients before surgery and two years after surgery. Six pairs of surface electrodes were placed along the paraspinal muscles over the left and right side of upper (T3-4), lower thoracic (T10-11) and lumbar (L2-3) regions respectively. In spinal fusion cases, the thoracic electrodes were placed inside the fusion range and the lumbar electrodes were placed on the non-fused region. Each surface EMG electrode (bipolar Ag-AgCL Disc electrodes, (=2cm) was applied to the cleaned skin. EMG signals were differentially amplified 1000 times and filtered using a band-width of 10 to 1000 Hz. The raw EMG signals were digitized at a sampling rate of 1000 Hz using a BTS EMG system (BTS Inc, Milan, Italy).

Two trial EMG signals were recorded in a relaxed upright standing posture. Then three tasks (forward, right, and left lateral bending) were carried out. Each subject performed two trials for each task. After removing DC components, the root mean square value (RMS) and the median frequency (MF) of each interval was calculated. ANOVA was used to compare functional changes between the groups and tasks.

RESULTS

The ANOVA analysis showed significant differences between control, pre- and post-operative groups, both in RMS and MF ($p<0.01$ in both cases). During upright standing, pre-operative scoliosis patients showed higher RMS activities in the thoracic region than the normal control group. After spinal fusion, the RMS in the thoracic region decreased but was still higher than that of the control group. In contrast, the RMS over the lumbar region of post-operative patients significantly increased in comparison to pre-operative patients ($p<0.01$). In lateral

bending, normal subjects showed a higher RMS on the bending side so that the RMS is greater on the left side during left lateral bending, and vice versa. However, both pre- and post-operative scoliosis patients, did not show such contraction patterns.

Observing the changes in EMG spectra following spinal fusion, the MF showed increase in the thoracic region, but decrease in the lumbar region. In comparison to normal subjects, the pre-operative scoliosis patients showed lower MF in thoracic region and higher MF in the lumbar region, especially in upright standing. After spinal fusion, this trend in MF was diminished.

DISCUSSION & SUMMARY

Previous long-term follow-up studies have reported adjacent disc degeneration syndrome after spine fusion. However, the causes of these complications after spinal fusion have not been clearly investigated. Changes in the biomechanical properties of the trunk following fusion are likely to cause change in the paraspinal muscle functions. Muscle disuse and localized atrophy may be found in some regions. In this study, EMG activities were compared between normal subjects and scoliotics before and after spinal fusion. Significant differences were found. The paraspinal muscles in the thoracic and lumbar regions showed significant differences in fused spines. The thoracic paraspinal muscles were found to be less active after spinal fusion, probably due to atrophy. Paraspinal muscles in the lumbar region showed a higher EMG activity, suggesting increased muscle activity.

REFERENCES

1. Luk, KDK, Leong, JCY, et al. Spine. 1987. Vol.12: 996-9
2. Roy SH, De Luca CJ, Casavant DA. Spine 1989 Sep;14(9):992-1001

ACKNOWLEDGEMENTS: This study was supported by The Society For The Relief Of Disabled Children Committee and HKRGC 475/96M.

FATIGUE AND WEAR EVALUATION OF A NOVEL ARTIFICIAL FINGER JOINT

S.P.Chow[1], Y Cao [1,2], Ian Gibson[3], Peter Chiu[1], Terence Lam[1,3], Henry Ho[1] , WY Ip[1], William Lu[1]
[1]Department of Orthopaedic Surgery, The University of Hong Kong
[2]Engineering Research Center for Biomaterials, Sichuan University
[3]Department of Mechanical Engineering, The University of Hong Kong

INTRODUCTION:

It is estimated that arthritis affects 355 millions of patients all over the world, causing pain, deformity, stiffness, and incapacity. When the joints are destroyed, artificial joint replacement of the hip, knee, shoulder, and elbow has provided excellent result in most cases. In the case of the finger joints, results are unsatisfactory. The initial design of various hinge prosthesis led to loosening, breakage, and erosion through the bone. A series of two components prosthesis did not lead to better results. Ceramics have favorable characteristics as a biomaterials and has been used in joint replacement. The purpose of this study was to evaluate the wear and fatigue properties of a novel ceramic finger joint(CFJ).

MATERIALS AND METHODS

Seven sets of CFJ were tested , three were zirconia (100% ZrO_2) and four sets were alumina (Al_2O_3+ ZrO_2). Both the male and female parts were made of the same material. The test was carried out using a finger wear simulator with 3 stations (self designed). The whole test lasted 5 millions cycles, which represent a clinical follow-up of five years. The male and female parts were fixed to a polyurethane holder in the wear simulator. The experiment was conducted in 50 percent bovine serum (SIGMA Lot 29H8401) with 50 percent distilled water as lubricant under room temperature of 23 ºC. The lubricant was replaced from the station every one million cycles, and the cleaned CFJ was weighted at each stop-weigh measurement. The test was restarted with fresh bovine serum solution.

The axial compression of 20N was applied during the testing and the range of motion was 60° (flexion-extension) with frequency of 2 Hz. The amounts of worn particles from the CFJ to lubricant were measured by inductively coupled plasma atomic emission spectrometry (ICP) (ZEISS, Plasmaquant 110). 5ml lubricant was acquired with1ml 10% Nitrc-acid added, and before testing, additional 25 ml distilled water was added. A gravimetric or weigh loss method was chosen for wear assessment. The weigh loss of the CFJ was measured using a balance (Denver Instrument M-220) with accuracy of 0.1mg.

SEM and EDX (Cambridge SEM 440, made in Britain) were used for observing the surface morphology and composition of the CFJ after 5 million cycles.

RESULTS

The size of particles is about 1-10 μm for the alumina CFJ and the particles were melted and contacted tightly together observed by SEM. The mainly composition is Al_2O_3 (>90%) with other element (Ca, Si, Zr) defined by EDX. After five million cycles, the bearing surface was slightly worn, but no cracks were observed. The average weigh loss was 1.9mg per million cycles and wear rate was 3.9μm per million cycles. The particle size of Zirconia CFJ was about 1μm and the composition was ZrO_2 only. Cracks were found on the surface of the CFJ before wear testing. After four million cycles, the length and depth of cracks were significant increased and the tests were stopped. The average weigh loss was 0.332 mg per million cycles and the wear rate was 0.46 μm per million cycles (Table 1).

DISCUSSION

Many biomaterials have been used for finger prostheses, metal to metal, titanium, silicone, metal to plastic. However, most of these implants developed fractures within few years. Ceramics have many favorable biomaterial characteristics, such as strong corrosion resistance, good chemical, dimensional stability, and very good mechanical strength. Although ceramics are brittle, an optimal techniques by combining zirconia and alumina may enhance the brittleness

REFERENCES

1. EW Brannon, G Klein. *J Bone Joint Surg* 41-A: 1:87-102, 1959.
2. S Affatato,M Testoni, G L cacciari, et al.*Biomaterials* 20: 971-975, 1999.

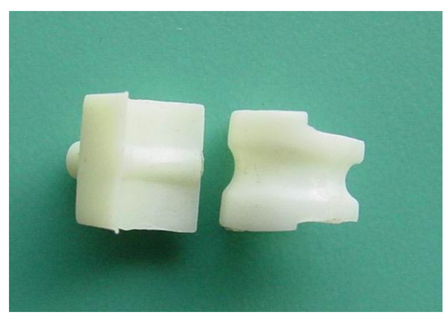

Table 1. The weigh loss and wear rate of ceramic finger joints

Alumina (million cycles)	1	2	3	4	5
Weigh loss (mg)	1.7	3.4	5.2	6.8	8.4
Depth loss (μm)	3.6	7.0	10.8	14.2	17
Ziconia (million cycles)	1	2	3	4	
Weigh loss (mg)	0.4	0.9	1.1	1.3	
Depth loss (μm)	0.6	1.3	1.6	1.8	

Fig.1.The ceramic finger joint sample

KNEE LOADING IN A MENISCECTOMY POPULATION: A RISK FACTOR FOR OSTEOARTHRITIS?

Daina L. Sturnieks[1], David G. Lloyd[1], Thor F. Besier[1] and Ken F. Maguire[2]

[1]Deptartment of Human Movement & Exercise Science, University of Western Australia, www.hm.uwa.edu.au
[2]Perth Orthopaedic and Sports Medicine Centre

INTRODUCTION

Mechanical factors are believed to contribute to the development of knee osteoarthritis (OA). The incidence and severity of knee OA has been associated with knee adduction moments during stance phase of gait (Sharma et al., 1998). As the loading of the medial and lateral tibiofemoral joint is largely determined by the adduction moment, it is considered a possible factor in the development of knee OA. Gait adaptations following knee trauma may alter loading of the knee joint, and contribute a possible mechanism for the increased risk of knee OA following meniscectomy (Sommerlath et al., 1991). The purpose of this study is to compare gait patterns in young, pre-osteoarthritic adults who recently underwent partial meniscectomy, to a control group with no history of knee injury or disease.

METHODS

Preliminary data from 45 meniscectomy patients (~6 weeks post-surgery) and 20 controls has currently been analysed from a larger cohort of 180 people. Subjects were aged 20 to 45 years and screened for existing knee OA, previous or current knee joint pain, stiffness, laxity, disease, injury (excepting meniscus tear in patient group), or any other pathology that may affect gait. Three-dimensional gait analysis was performed using a 50 Hz, six-camera VICON motion analysis system, with AMTI force platforms. Joint kinematics and kinetics were calculated using a custom seven-segment lower limb model. External knee moments were normalised to individual's height and mass, and analysed over stance. Data was statistically tested using two-way repeated measures ANOVA, Bonferroni corrected for multiple comparisons, and with the p value for significance set at <0.05.

RESULTS AND DISCUSSION

The meniscectomy group display larger knee adduction moments over stance (p<.05), compared to the control group (see Figure 1.). These findings suggest that a post-meniscectomy population load the medial compartment of the tibiofemoral joint with more force during stance phase of gait, and may therefore be predisposed to degenerative joint changes within that compartment.

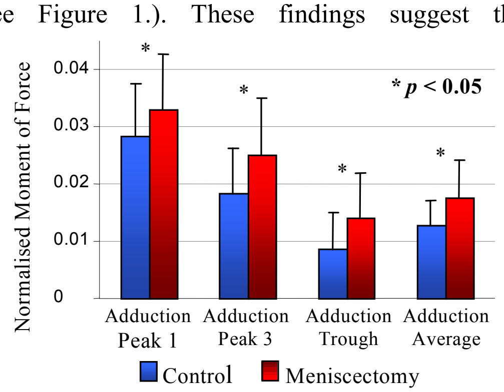

Figure 1: Knee adduction moments during stance

Based on the average knee adduction moment, 'high' and 'low' loading categories were determined as greater than and less than one standard deviation away from the mean of the control scores, respectively. Subjects were categorised as high, normal or low loaders (see Table 1).

Table 1: Percentage of subjects in different loading categories

Loading Category	Control	Meniscectomy
Low	21%	5%
Normal	68%	42%
High	11%	53%

A greater proportion of the meniscectomy group was classified as a high loader. This increased proportion of high loaders in the patient group may relate to the greater proportion of meniscectomy patients developing knee OA in the long term.

Knee flexion moments did not differ between groups, although the meniscectomy group showed significantly reduced flexion (92%) and extension (82%) moments on the meniscus leg (p<0.01). A similar unloading pattern was noted between the meniscectomy and contralateral legs for the adduction moments within the patient group. Overall, the meniscectomy group experience greater adduction moments at the knee joint yet appear to have an altered gait strategy to unload the involved knee. This may be a residual gait pattern from that adopted due to the pain associated with the initial injury.

SUMMARY

The knee adduction moment loads the medial tibiofemoral joint. If experienced at magnitudes beyond that of the coping threshold of the joint, this loading may give rise degenerative changes and the development of knee OA. This study has identified larger than normal knee adduction moments in a pre-osteoarthritic meniscectomy population, a large proportion of which will develop knee OA. Further studies prospectively investigating the development of knee OA within different loading groups will elucidate this question of cause and effect.

REFERENCES

Sharma L, et al. (1998). Knee adduction moment, serum hyaluronan level, and disease severity in medial tibiofemoral osteoarthritis. *Arthritis Rheum.*, **41**, 1233-40.
Sommerlath K, et al. (1991) The long-term course after treatment of acute anterior cruciate ruptures. *Am. J. Sports Med.*, **19**, 156-162.

BIOMECHANICAL ANALYSIS OF SIDE-STEP CUTTING: ARE FEMALES AT GREATER RISK FOR ACL INJURY?

Susan M Sigward and Christopher M Powers
Musculoskeletal Biomechanics Research Laboratory, University of Southern California, Los Angeles, CA

INTRODUCTION

Non-contact anterior cruciate ligament (ACL) injury rates are 3-8 times greater for female athletes than their male counterparts (Griffin 2000). A large number of non-contact ACL injuries occur during the deceleration phase of a cutting maneuver (i.e. following foot strike) when a rotation torque is applied to the slightly flexed knee (Delfico 1998, Kirkendall 2000). This mechanism of injury concurs with in-vitro studies that have demonstrated that the combination of knee rotation and varus/valgus moments place the highest strain on the ACL when applied between 0 and 30 degrees of flexion (Markolf 1995, Dürselen 1995). Evaluation of gender performance differences, as measured by kinematic and kinetic variables, during common athletic maneuvers may provide insight into loading patterns that put the female athlete "at risk" for and ACL injury. Previous studies comparing males and females performing athletic maneuvers have focused primarily on kinematic and EMG data and have not addressed moments or torque experienced at the hip or knee. The objectives of this study are to: 1) quantify gender differences in hip and knee kinematics and moments during a side-step cutting maneuver 2) identify performance patterns that put females at increased risk for ACL injury.

METHODS

Twelve subjects (6 male and 6 female; ages 21-32) with no history of ACL injury or current lower extremity pathology participated in the study. Subjects performed four trials of a side-step cutting maneuver. Each participant ran at a speed of 6-7.0 m/s, planted their right foot on the force plate and changed direction to the left at a 35-60 degree angle. Anthropometric data, 3-D knee kinematics (VICON Motion System, 120 Hz), and ground reaction forces (AMTI force plate, 600 Hz) were used to calculate moments in all three planes at the hip and knee (inverse dynamics equations). Peak angles and moments (external) were identified during the early deceleration phase (20% of the cut cycle). Gender differences were evaluated with paired t-tests ($p<0.05$).

RESULTS

During the first 20% of the cut, females demonstrated greater hip adduction angles and moments compared to males (Figure 1). In addition, females demonstrated greater knee valgus angles and experienced larger knee varus moments (Figure 2). Both groups demonstrated similar knee flexion angles, knee internal rotation moments, and knee internal rotation motion.

DISSCUSION

These data suggest that males and females demonstrate different kinematic and kinetic profiles at the hip and knee

Figure 1
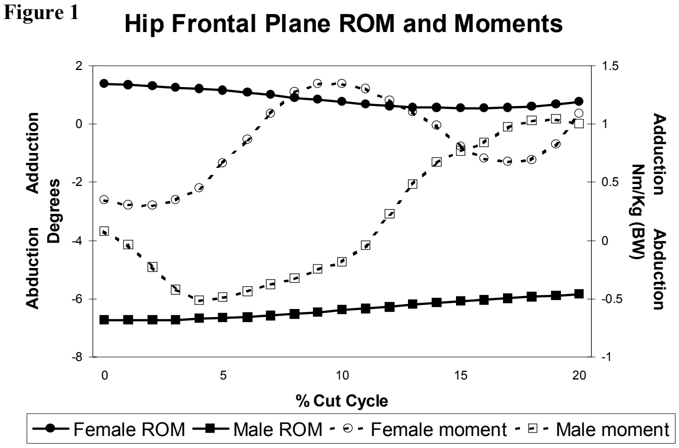

Figure 2
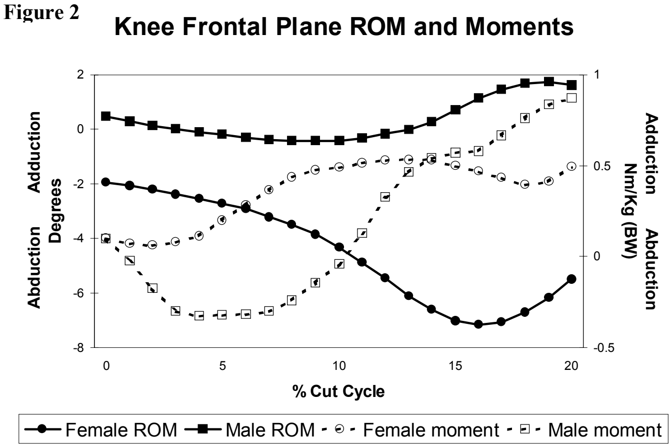

during side step cutting. Differences were found in the early deceleration phase, at time at which the knee is in a less flexed, more vulnerable position. The female athletes demonstrated a profile in which increased hip adduction translated into increased valgus at the knee. Knee valgus and internal rotation combined with a larger varus moment knee could place greater tension on the ACL (Markolf). These gender differences may place females at greater risk for injury.

REFERENCES

Delfico, A.J., Garrett, W.G.(1998). *Clinics in Sports Medicine,* 17(4), 779-785.
Dürselen, L. et al (1995). *American Journal of Sports Medicine,* 23(1), 129-135.
Griffin, L.Y. et al (2000). *Journal of the American Academy of Orthopaedic Surgeons,* 8(3), 141-150.
Kirkendall, D.T., Garrett, W.G.(2000). *Clinical Orthopaedic and Related Research,* 372, 64-68.
Markolf, K.L. et al (1995). *Journal of Orthopaedic Research,* 13, 930-935.

THE COMBINED EFFECTS OF DISUSE AND GONADECTOMY ON BONE MECHANICS IN MALE AND FEMALE RATS

Vanessa Yingling[3], Marybeth Brown[1], Jennifer Taylor[4], Wendy Kohrt[5], Matthew Silva[3], Jonathan S. Fisher[4], Eileen M. Hasser[2]
[1]Physical Therapy Department & [2]School of Veterinary Medicine, University of Missouri, Columbia MO, [3] Orthopaedic Surgery and [4]Program in Physical Therapy and [5]Division of Geriatirics and Gerentology, Washington University School of Medicine, St. Louis,

INTRODUCTION

Both decreased steroidal hormones and activity levels may lower bone mass in the elderly increasing their risk of fracture. Reduced estrogen in female rats accelerates the decline in bone mass in the proximal tibia and the vertebrae and decreases bone strength (Wronski et al, 1989, Peng et al, 1994). Increased activity of both osteoblasts and osteoclasts throughout the skeleton are responsible for the lower bone mass. On the other hand, rat models of hind limb unweighting resulted in decreased trabecular bone volume and tibia bone mineral density (BMD) through decreased bone formation. Decreases in the number of osteoblasts with no effect on bone resorption were reported from unloaded rat models (Halloran et al., 1986, Dehority et al, 1999). The purpose of this study was to investigate the interaction of these two mechanisms of bone loss in the cortical tibial diaphysis of mature male and female rats.

METHODS

Male and female rats (6-7 mo) were randomly assigned to four groups: control (C), ovariectomized/orchiectomized (OVX/ORC), hind-limb unweighted (HLU), ovariectomized/orchiectomized and hind-limb unweighted (OVX/ORC-HLU). Eight OVX female rats were injected with estradiol benzoate on days 7, 14, and 21 days post-surgery (OVX-E2). After bilateral removal of ovaries and testes using aseptic surgical technique and following a two week recovery period, the OVX/ORC-HLU groups were then tail suspended. The tail suspension method was used to unload the hind limbs of rats in both the HLU and OVX/ORC-HLU groups. The animals were suspended at an angle that allowed free movement in their cages on their forelimbs. A five-day adaptation period preceded the 2-week unloading period. After sacrifice the tibiae were harvested for density and mechanical measurements. Bone mineral content (BMC) (g) and bone mineral density (BMD) (g/cm^2) were measured using dual energy x-ray absorptiometry (Hologic QDR-1000). Torsional testing was used to assess the structural properties of the tibial diaphysis. The tibiae were internally rotated under rotational control to failure at a rate of 1 deg/sec. (Instron 8500R, Instron Corp., Canton, MA). The following parameters, maximal torsion, rotation to failure, stiffness and energy absorbed to failure were compared between groups. Cortical wall thickness was measured on 9 points of 4 cross-sections of the tibia diaphysis. A two-way Anova was used to determine interactions of HLU and OVX/ORC. Tukey post hoc tests were performed ($p < 0.05$). Bone strength variables were evaluated using an ANOVA with co-variates of cortical wall thickness and body weight.

RESULTS AND DISCUSSION

The body weight at sacrifice of the OVX group was significantly higher than all groups in the female rats. The bone mineral density (BMD) was lower in the OVX group compared to control (C) animals and (OVX+E2) animals (Table1), consistent with previous results of ovariectomized rats (Wronski et al, 1989). HLU and OVX-HLU resulted in BMD values lower than OVX values (Table 1). The combined effect of HLU and OVX did not result in any further decrease in BMD compared to HLU alone. The decrease in BMD did not translate into decreased mechanical variables or a decrease in cortical wall thickness (Table 2). The periosteal circumference of these animals was maintained that preserved the mechanical tolerance of the tibial diaphysis. The decrease in BMD that occurred in the tibia may have been at the trabecular sites of the proximal tibia. Similar trends in BMD and torsional strength were found in male rats, however these were not significant.

Table 1: Bone Mineral Density (g/cm^2) values.

Group	Male	Female
Control	0.180 (0.009)	0.160 (0.005)
OVX+E2		0.157 (0.005)
ORX/OVX	0.175 (0.0045)	0.153 (0.010)
HLU-F	0.173 (0.0089)	0.140 (0.005)$^{*\#}$
OVX+HLU	0.173 (0.005)	0.138 (0.003)*

- Different from OVX group. $^{\#}$ Different from control

Table 2: Maximum Torque (kN*degree) values.

Group	Torque (kN*deg)	
	Male	**Female**
Control	0.379 (0.051)	0.225 (0.036)
OVX+E2		0.277 (0.057)
OVX/ORX	0.393 (0.069)	0.220 (0.034)
HLU-F	0.353 (0.134)	0.238 (0.056)
OVX+HLU	0.312 (0.122)	0.219 (0.023)

SUMMARY

The duration of the unloading may have been too brief to manifest cortical bone changes in aged rats. Older bone is less affected by mechanical loading and may be less responsive to an absence of loading.

REFERENCES

1. Dehority et al, 1999
2. Halloran et al., 1986
3. Peng et al, 1994
4. Wronski et al, 1989

ACKNOWLEDGEMENTS

This study was supported by grants AG00585 and AG51262 (MB).

IS PERMANENT ARTERIAL FILTRATION POSSIBLE? IN VIVO ASSESMENT OF A FILTRATION DEVICE FOR EMBOLIC STROKE PREVENTION

Ygael Grad[1], Boaz Nishri[1], David Tanne[2], Shmuel Einav[3], Bruch B Lieber[4], Ofer Yodfat[1]

[1] MindGuard Medical Devices Ltd., Alon Hatavor 1 Caesarea Industrial Park, Israel 38900, ygael@mindguard.net
[2] Stroke Unit, Dept. of Neurology, Sheba Medical Center, Tel Hashomer, Israel 52621
[3] Dept. of Biomedical Eng. Tel Aviv University, Ramat Aviv Tel Aviv, Israel 69978
[4] Center for Neurovascular Surgery and Stroke Research, University of Miami, FL. 33124

PURPOSE

A new permanent arterial filtering device (***the Diverter***) was designed for implantation at the carotid bifurcation (CCA to ECA, thus filtering the ICA ostium, Fig. 1). The filter prevents thrombi originating proximal to it from reaching the intracranial circulation and inducing an embolic stroke. Our aim in this study was to test the patency of the permanent arterial filter in the illio-femoral bifurcations of swine.

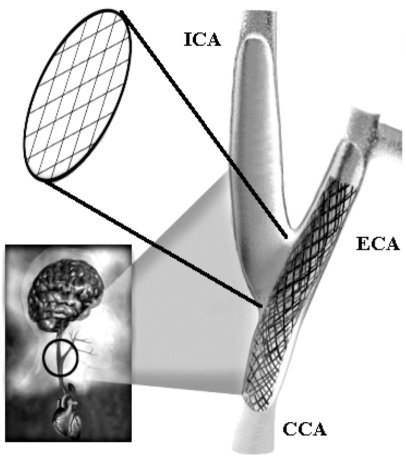

Fig. 1, *The Diverter* implanted from the CCA to the ECA in the carotid bifurcation. The filtered ICA ostium (top left) prevents emboli from reaching the brain (bottom left)

MATERIALS AND METHODS

A total of 29 Diverters, composed of multiple fine wire meshes, were implanted in illio-femoral bifurcations of 45kg female swine. The bifurcations carrying the implants were harvested at intervals of 2,4,9 and 18 weeks post device implantation for evaluation. The patency ratio of the filtered ostium, defined as ratio of the patent over total area of the ostium, was calculated using microscopy and computerized image processing morphometry.

RESULTS

Angiography and ultrasound Duplex scanning prior to animal sacrifice found the Diverter open to flow without occlusion or discernable stenosis up to 18 weeks post implantation in all devices except for 3 mechanical failures. On average, the Diverter mesh covered a lumen of $23mm^2$ at the bifurcation while the average cross sectional area of the filtered artery one diameter distal to the bifurcation was $11mm^2$. The non-filtering part of the Diverters were fully covered by a neointima 4 weeks post implantation. Morphometry and microscopy showed that the majority of the filtered area (90% on average) of the 26 specimens remained patent, as shown in **Table 1**. A small number of the filtering wires, mainly at the rim of the filtering mesh area, were covered by fibrin containing deposition in some of the diverters.

Table 1, Filtered area patency results

Harvesting week	Implanted specimens	Implantation mechanical failure	Harvested specimens	Patency ratio [%]
2	4	1	3	93
4	6	1	5	92
9	5	1	4	72
18	14	0	14	93
-	(Total=29)	(3)	(26)	-

CONCLUSIONS

Implantation of a permanent arterial filtration device is feasible. In the swine model, all implanted devices (n=26) remains patent with no deleterious encroachment of tissue on the filtering portion of the diverter up to 18 weeks. Our preliminary findings suggest that a novel therapy by the Diverter is feasible for patients at high risk of embolic stroke from proximal sources.

REFERENCES

Feinberg WN et al., 1995; *The prevalence of atrial fibrillation: analy. & implicat*. Arch Intern Med **155**: 469-473
French Study of Aortic Plaques in Stroke Group, 1996; Ath*erosclerotic disease of the aortic arch as a risk factor for recurrent ischemic stroke*. N Engl J Med **334**:1216-1221
Heart and Stroke Statistical Update, 2001 Dallas, Tex, AHA.
Sacco et al, 1989; *Infarcts of undetermined cause: the NINCDS Stroke Data Bank*. Ann Neurol **25**: 382-390
Williams GR et al., 1999; *Stroke* **30**: 2523-2528
Wolf et al., 1987; *Atrial fibrillation: a major contributor to stroke in the elderly*. Arch Intern Med **147**: 1561-4.

MOTOR LEARNING PROTOCOL OF THE HIP WALKING STRATEGY IN INDIVIDUALS WITH DIABETIC PERIPHERAL NEUROPATHY

Karen L. Perell PhD, RKT[1] and Janice Roper PhD, RN[2]

VA Greater Los Angeles Healthcare System
[1] Director, Physical Medicine & Rehabilitation Gait Laboratory, [2] Director, Nursing Research and Education

INTRODUCTION

Mueller et al. (1994) used gait training to reduce high foot pressures in patients with diabetic peripheral neuropathy, but have failed to study the "learning" by classical motor learning theories. While all subjects reduced their forefoot plantar pressures, no follow-up retention tests were utilized or feedback necessary to elicit the desired motor pattern discussed. Sanderson & Cavanagh (1990) suggest that proprioception plays an integral role in the use of feedback to develop error-detection mechanisms by integrating visual feedback and kinesthetic variables. In the diabetic peripheral neuropathy population, proprioception and kinesthesia may be compromised. To date, no studies have demonstrated whether individuals with diabetic peripheral neuropathy can "learn" a motor task (e.g. demonstrate follow-up retention of a changed motor pattern over days or weeks). The purpose of this study is to compare plantar pressures following a short-term gait training program in subjects with type II diabetes and peripheral neuropathy immediately, 1 week and 1 month post.

METHODS

Twenty subjects (age 50-80 years old) with a history of type II diabetes and peripheral neuropathy are randomized into a feedback group and a no-feedback group. All subjects receive instruction regarding using a "hip" strategy (pull their leg forward from the hip) rather than an "ankle" strategy (push off from the ankle) gait and asked to practice following the training until the follow-up testing. The feedback group receives summary feedback at the end of each trial regarding performance, while the no-feedback group receives no feedback. Baseline gait analysis (5 trials) prior to any instruction, training (15 trials), and immediate retention (5 trials) testing are done on the same day. Additional retention testing (5 trials) is done at 1 week and 1 month. EMED Pedar (Novel Electronics, St. Paul MN) insoles are worn within the subject's shoes. Peak plantar pressures across the metatarsal heads are compared across time points and groups.

RESULTS AND DISCUSSION

Preliminary data from the feedback group demonstrate significant reduction in plantar pressures under the 2nd/3rd metatarsal heads remained at the 1 week retention (Figure 1). The reduction demonstrated under the 4th/5th metatarsal heads immediately following training was not maintained statistically at the 1 week retention test (Figure 2).

Similar to Mueller et al (1994), we observed that individuals with diabetic peripheral neuropathy can change their walking pattern from an "ankle" strategy to a "hip" strategy with little training with consequential reduction in forefoot plantar pressure. We demonstrate that this change can be maintained over the course of at least 1 week, specifically in areas of greatest pressure (2nd/3rd metatarsal heads).

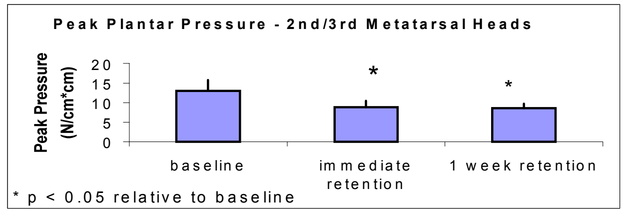

Figure 2: Mean ± standard deviation of baseline, immediate retention, and 1 week retention peak plantar pressures under the 2nd/3rd metatarsal heads for the preliminary data of the feedback group.

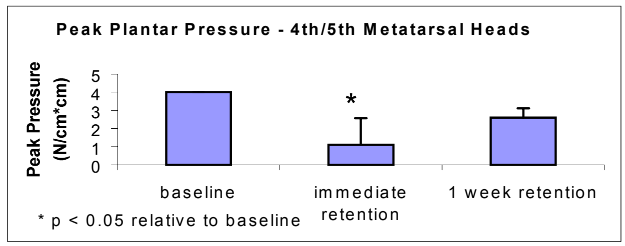

Figure 3: Mean ± standard deviation of baseline, immediate retention, and 1 week retention peak plantar pressures under the 4th/5th metatarsal heads for the preliminary data of the feedback group.

SUMMARY:

Individuals with diabetic peripheral neuropathy are at high risk for foot ulceration due to walking patterns, which facilitate increased plantar pressures. Foot ulceration often leads to lower limb amputation with high finacial and quality of life costs for the indivdiual and the healthcare system (Ollendorf et al. 1998). Consequently, gait training strategies to create long-lasting changes in gait patterns which reduce plantar pressures may have important effects on ulceration and amputation rates. While this study cannot assess ulceration rates within its design, ultimately, it will provide the first step in understanding the effect that altered motor patterns have on plantar pressures and ulceration rates. The key component, however, is that subjects with diabetic peripheral neuropathy can improve and retain motor patterns which facilitate reduced plantar pressures.

REFERENCES

Mueller et al. (1994) *Arch PM&R* 75:1196-1200
Ollendorf et al. (1998) *Diabetes Care* 21:1240-1245
Sanderson & Cavanagh (1990) *Can J Spt Sci* 15:38-42

ACKNOWLEDGMENTS

This study was supported by funds from a Career Development Award (A 0703 CD) to Dr. Perell from the Departments of Veterans Affairs Rehabilitation Research & Development Division

In vivo MEASUREMENT OF MUSCLE FIBER BEHAVIOR IN THE TRICEPS SURAE MUSCLE DURING TENSIONAL SUMMATION

Toshiaki Oda, Kentaro Chino, Toshiyuki Kurihara, Yasuo Kawakami and Tetsuo Fukunaga
Department of Life sciences (Sports Sciences), University of Tokyo, Japan, *cc16712@mail.ecc.u-tokyo.ac.jp*

INTRODUCTION

Tensional summation induced by increment of neuro-stimulation number results from fusion of twitch in skeletal muscle. Little is known about the muscle behavior during tensional summation *in vivo*. In the present study, we directly measured the fascicle length to investigate the muscle behavior in tensional summation.

METHODS

Five healthy male volunteers, aged 24 –30, participated as subjects. The subject was seated with knee joint and ankle joint at 180 deg and 90 deg, respectively. The twitch and the tensional summation were evoked by percutaneous supramaximal electrical stimulation of the tibial nerve at 1-3 times (frequency was 30Hz). The ultrasound apparatus (SSD-5500, Aloka, Japan) having a 7.5 MHz linear-array probe was used and the sequence of longitudinal ultrasonic images (78Hz) of medial gastrocmemius (MG) and soleus (Sol) at the level of 30 % of the lower leg length were recorded and synchronized with the torque (TRQ) data. Fascicle length from the image was measured using image analysis software (NIH Image, National Institute of Health, USA). Contractile velocity was calculated to differentiate the fascicle length change by time.

RESULTS AND DISCUSSION

It was shown that fascicles of MG and Sol dynamically changed their length (Fig. 1) and hence contractile velocity, even during twitch contraction. The peak TRQ became larger when stimulus number increased. The increment of peak TRQ were significantly correlated to the amount of the maximal fascicle shortening (Figure 2 A). The length change of MG was larger than that of SOL. In addition, MG showed higher mean contractile velocity in the shortening phase compared with Sol (Figure 2B). Interestingly, the mean velocity of both muscles became faster at higher contraction levels, even at the same stimulation frequency.

This study clearly indicated that MG and Sol *in vivo*, although having a common tendon, behave differently during twitch contractions. This difference might have been caused by differences in fiber types and series elasticity.

Figure 1: An example of time course of fascicle length. The

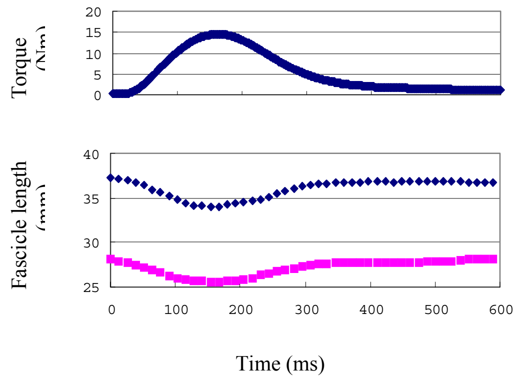

graph shows mean value of all subjects for a single twitch. Time zero corresponded to the instance of electrical stimulation.

Figure 2:

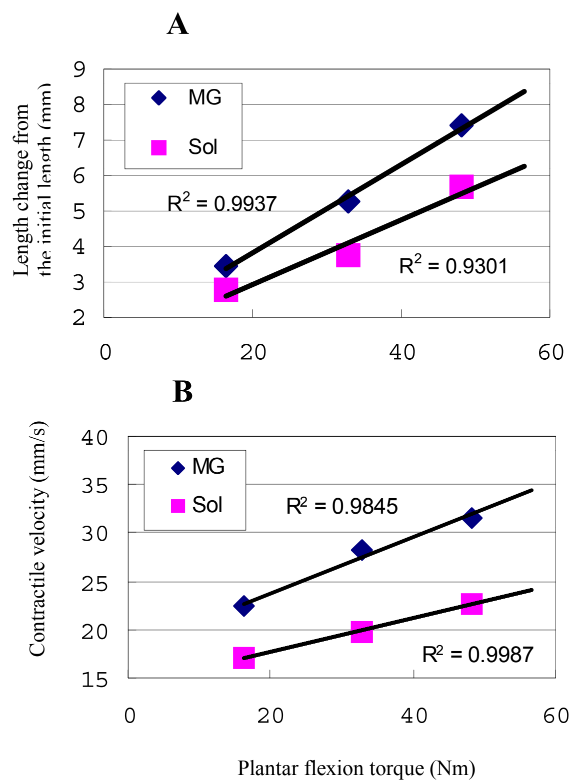

A The relationship between fascicle length change from the initial length and plantar flexion torque.
B The relationship between mean contractile velocity and plantar flexion torque.

GLOBAL OPTIMIZATION FOR RECOVERING THE POSITION AND ORIENTATION OF FREE-FORM OBJECTS IN MEDICAL IMAGING REGISTRATION USING A NEW SMOOTHING APPROACH

Mohamed Mahfouz[1,2], William Hoff[2], Robert Underwood[2], Richard Komistek[1], Douglas Dennis[1]
[1]Rocky Mountain Musculoskeletal Research Laboratory, Denver, Colorado, mmahfouz@rmmrl.org
[2]Colorado School of Mines, Golden Colorado

INTRODUCTION

Intensity-based three-dimensional to two-dimensional (3D-2D) image registration requires finding the projective transformation (i.e., a composition of rigid displacement and perspective projection), which maps a 3D object onto a 2D image of this object (Penney, 1998). The objective of this study was to develop a 3D-2D registration that can be used to determine the kinematics of total joint arthroplasty (TJA) implants, and non-implanted (normal) joints using 2D video fluoroscopy images (Mahfouz, 2002).

METHODS

An objective function is used that directly compares the input 2D image to a predicted image, generated by rendering the 3D object in a hypothesized pose. By adjusting the hypothesized pose until the objective function reaches a minimum, we can determine the pose of the object. However, the objective function usually contains large numbers of local minima due to the noise in X-ray images and hence, it will be generally too expensive to solve registration problems directly on the objective function. We present a novel method for determining the rigid body transformation that uses a new coarse-to-fine approach. Our method transforms the problem from the objective function space to image space. We apply a spatial averaging filter to smooth the X-ray image, which removes the shallow local minima. The method performs unconstrained optimization using variable metric (quasi-Newton) methods, which are gradient-based algorithms that require fewer function evaluations. By selecting different smoothing filters, images with different degrees of smoothness can be derived.

The intent is to first solve the global optimization problem on very smooth images, and then use this solution to gradually solve the problem on less smooth images and ultimately the original, unsmoothed image (Figure 1).

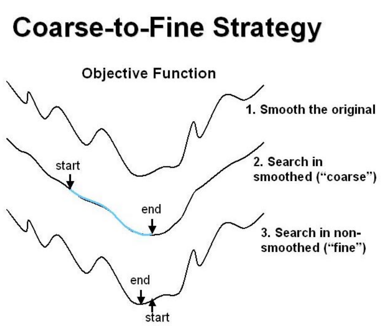

Figure 1. Course-to Fine Strategy

RESULTS AND DISCUSSION

Experimental results for 3D surface to 2D projection matching are presented for real data (Table 1). The combination of spatial averaging smoothing of the image with variable metric optimization technique results in a method that solves the 3D-2D for arbitrary anatomical and implant shapes accurately and quickly (Figure 2).

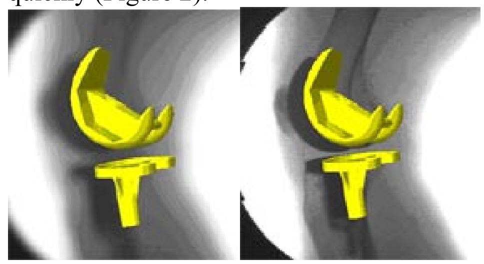

Figure 2. Smoothed Image Space (left), Non Smoothed Image Space (right).

SUMMARY

This study has described a new method for measuring the kinematics of TKA knees from single plane fluoroscopy images. This method is robust with respect to image noise, occlusions, and low object-to-background contrast. We use a direct image-to-image similarity measure, taking advantage of the speed of modern computer graphics workstations to quickly render simulated (predicted) images. As a result, we do not require an accurate segmentation of the implant silhouette in the image (which can be prone to errors). We avoided the large number of local minima by smoothing the image space and applied unconstrained optimization using quasi-Newton methods that require fewer iterations. The results from this study has revealed significant advantages over previously described methodology. (Banks, 1996)

REFERENCES

Penney, G., Weese, J., Little, J., et al., *A comparison of similarity measures for use in 2-D-3-D medical image registration* IEEE Trans. on Medical Imaging, Vol. 17, No. 4, pp. 586-595, 1998.

Mahfouz, M., Hoff, W.A., Komistek, R.D., et al, (submitted 2002). *A robust method for registration of three-dimensional knee implant models to two-dimensional fluoroscopy images.* IEEE Transactions.

Banks, S.A., Hodge, W.A. (1996) *Accurate measurement of three-dimensional knee replacement kinematics using single-plane fluoroscopy*, IEEE Trans Biomed Eng, **43:**638-49.

Table 1 Shows the mean and standard deviation (20 random trials).

	Mean	Std Deviation
X translation (mm)	0.090796	0.107635
Y translation (mm)	0.090267	0.112354
Z translation (mm)	3.636619	4.738106
X rotation (deg)	0.10822	0.136575
Y rotation (deg)	0.237305	0.302742
Z rotation (deg)	0.420159	0.524019

CFD ANALYSIS OF FLOW THROUGH MECHANICAL HEART VALVES

Idit Avrahami, Moshe Rosenfeld,

Department of Biomedical Engineering, Faculty of Engineering, Tel-Aviv University, Tel-Aviv, Israel. idita@eng.tau.ac.il

INTRODUCTION

Newly developed artificial heart pumps commonly use mechanical heart valves (MHV) such as tilting disk or bileaflet valves. The fluid dynamics associated with MHV plays a critical role in determining the longevity of these devices. The present study simulates numerically the flow across MHV in the mitral position, in order to establish the time dependent global flow field for several typical cases. The analyses used models of tilting disk and bileaflet valves in a straight channel and in realistic left-ventricle (LV) geometry.

The objectives were to study the effect of unsteadiness, the significant of the third dimension, the effect of model geometry and the motion of the valve on the flow field as well as to investigate the possibility of cavitation.

METHOD

Numerical analyzes were performed to investigate the flow through 2-D and 3-D models of tilting disk and bileaflet valves placed in a straight channel and in simplified models of the natural left ventricle (LV). A commercial CFD package (FIDAP, Fluent Inc, Evanston) was used. Cases with constant and pulsatile inflow conditions and cases with fixed and moving valves were analyzed. Four different fluid-structure interaction (FSI) methods were developed and used to couple the motion of the valve with the calculated flow field in the moving valve cases: (a) strong FSI coupling (every time step), (b) interaction at the end of several time-steps, (c) interaction at the end of each pulse and (d) interaction after several cycles.

RESULTS AND DISCUSSION

The valves, even in their fully open position, posed a significant obstruction to the flow. The jets generated between the valve tips and the walls, created a vortical flow consisting of large vortices next to the valve and a row of vortices along each wall. Major difference was found between the constant and the pulsatile inflow conditions. However, the simulations with fixed valve and physiological incoming flow consistently results in safe estimations of several critical quantities such as the axial force or the maximal shear stress on the valve or the transvalvular pressure drop.

In the 2D cahnnel model with moving valve case, all algorithms converged to the same valve motion and flow behavior. The algorithm with cycle-wise interaction (algorithm c) had the best overall convergence rate. Algorithm (b) needed 12,240 time steps (=6 pulses) for full convergence while algorithm (c) required only 6,800 time-step calculations (=10 pulses) for full convergence. No advantages were found for the algorithm (d) with interaction after several cycles. Typical results are shown in Figure 1.

Because of the relatively high Reynolds number (Re=3000), the flow in the more complex models of MHV in realistic left ventricle (LV) geometry did not converge into a simple pulsating flow, and the motion of the valve did not repeat itself every cardiac cycle, although the variations were in a limited range. It was also shown that vortices created in the instance of valve closure decreased the pressure significantly and thus might increase the possibility of cavitation.

(a) **(b)**

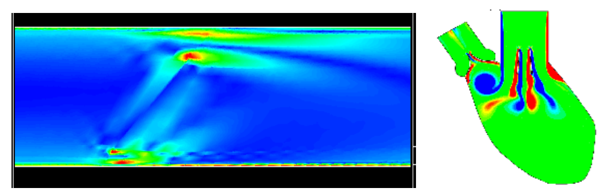

Figure 1: vorticity contours of the flow across models of (a) 3D fixed tilting disk valve in a tube and (b) 2D moving bileaflet valve in LV.

SUMMARY

The flow field across the MHV was strongly influenced by the valve type and the inflow conditions. The model geometry, the third dimension and the motion of the valve hardly affected the global features of the flow in the fully open phases. Cycle-wise FSI algorithms had clear advantage over strong FSI algorithms because of the periodic nature of the flow.

REFERENCES

[1] Rosenfeld, M., Avrahami, I. and Einav, S., "Unsteady Effects on Flow Across Tilting Disk Valves" Journal of Biomechanical Engineering, Feb. 2002

[2] Avrahami, I., Rosenfeld, M., Einav, S., Eichler M. and Reul H., "Can Vortices in the Flow Across Mechanical Heart Valves Contribute to Cavitation?" Medical & Biological Engineering & Computing, 2000; 38: 93-97.

ACKNOWLEDGEMENTS

This research was partially supported by a grant from G.I.F., the German-Israeli Foundation for scientific Research and Development and by Israel Science Foundation.

A COMPARISON OF BI-LATERAL DEFICIT IN ELITE ENDURANCE AND ELITE POWER ATHLETES DURING DROP JUMPS

Matthew Pain and Masayuki Koitabashi

Department of PE, SS, & RM, Loughborough University, Loughborough, Leics, LE11 3TU, UK
m.t.g.pain@lboro.ac.uk

INTRODUCTION

Bilateral deficit can be described as the inability to produce a maximal voluntary force in both limbs simultaneously (Taniguchi, 1998, Challis 1998). The most often cited reason for bilateral deficit is a lesser activation of fast twitch motor units (Kawakami et al. 1998).

Drop jumps are a stretch-shorten cycle activity characterized by high muscular forces and velocities. Drop jumps can produce greater jump heights than conventional jumps, however after a certain threshold landing velocity there is a decrease in jump height. Consideration of this factor needs to be kept in mind when comparing drop jumps of different heights as the mechanism for performance modulation is not fully known.

Drop jump ability is greatest amongst power athletes, who are considered to have a greater percentage of fast twitch motor units (Viitasalo et al., 1998). It is hypothesized that although elite power athletes will have greater jumping ability than elite endurance athletes, the power athletes will exhibit a greater degree of bilateral deficit in drop jumps due to a higher level of fast twitch motor units.

METHODS

Five elite endurance athletes and five elite power athletes, performed a series of 1 legged and 2 legged drop jumps from three heights; 15cm, 30cm and 60cm (two legged only). These heights were chosen to compare 1 legged and 2 legged performances in terms of: equal energy and impulse absorbed per leg during the eccentric phase, and equal drop height.
Jumps were performed without arm swing and with instruction to minimize the free leg usage in 1 legged jumps. Force and 3-D movement data were recorded at 800 Hz using a Kistler force plate synchronized with a CODA mpx30. Motion data were reduced to a planar motion for subsequent analysis. EMG data were recorded for 4 athletes, 7 muscles per leg, for further analysis.

Bilateral deficit was calculated using dominant and non-dominant leg jump heights.
BD = 100 – 100(bilateral height / (left height + right height))

RESULTS AND DISCUSSION

As expected the power athletes performed significantly better ($p<0.05$). They jumped 35 to 50% higher than the endurance athletes. They had significantly shorter contact times, higher ground reaction forces, less range of joint motion and higher concentric power. They also exhibited a much larger degree of bilateral deficit in all combinations of drop height (Table 1).

Table 1. Bilateral deficit for all combinations of drop height
b = 2 legged, md = dominant leg, mn = non-dominant leg

Jump height combinations	% deficit Power	% deficit Endurance
60b vs. 30md + 30mn	4.9	0.8
30b vs. 15md + 15mn	14.9	2.4
60b vs. 15md + 15mn	11.6	0.8
30b vs. 30md + 30mn	8.4	-5.2
15b vs. 15md + 15mn	13.8	8.1

Although the results support the hypothesis it is important to note that the 30cm single leg drop jumps appear to be above the performance enhancing height. It may be the 15cm drop height was too great for the endurance athletes as well. Selection of drop height is critical to allow fair comparisons in drop jumps.

Preliminary examination of EMG data show a similar deficit pattern in iEMG but also show different activation patterns between power and endurance athletes when going from 2 legged to 1 legged jumps. This change in pattern could also be a contributing factor to bilateral deficit.

SUMMARY

Power athletes, with a higher proportion of fast twitch motor units, exhibit much higher degrees of bi-lateral deficit in drop jumps, than endurance athletes. This could indicate that bi-lateral deficit is caused by inhibition of these motor units.

REFERENCES

Challis, J.H. (1998). *Human movement science*, **17**, 307-325
Kawakami, Y et al. (1998). *Eur j app Physiol,* **77**, 212-216.
Taniguchi, Y (1998). *Eur j app Physiol*, **78**, 226-230
Viitasalo, J.T. et al. (1998)). *Eur j app Physiol*, **78**, 432-440

EVALUATION OF A MAGNETIC TRACKING DEVICE FOR ESTIMATING CUMULATIVE LOW BACK COMPRESSION

Agnew, M.J.[1], Andrews, D.M. [1], Callaghan, J.P.[2], and Potvin, J.R.[1]

[1] Faculty of Human Kinetics, University of Windsor, Windsor, Ontario, Canada, dandrews@uwindsor.ca
[2] Department of Human Biology & Nutritional Sciences, University of Guelph, Guelph, Ontario, Canada

INTRODUCTION

Recent investigations regarding the measurement of cumulative loading in the low back have used video based data as a means of measuring cumulative load. Although the technique employed by Callaghan et al. (2001) proved to reduce the amount of data required to estimate cumulative load with little relative error, the recording and digitization of video data still requires a significant amount of time dedicated to data analysis. Through the use of a magnetic tracking device, positional data can be collected instantaneously without the time consuming task of digitization. The purpose of this study was to evaluate the use of a magnetic collection device as a means of measuring cumulative compression at the L5/S1 joint of the spine.

METHODS

Five male subjects performed a total of 27 sagittal plane lift/lower trials of varying conditions (3 lifting tasks x 3 load masses x 3 repetitions). The three lifting tasks were as follows: lift and place from the floor to a shelf at shoulder height (135 cm), lift and place from the floor to a tabletop at knuckle height (76 cm), and lift and place from the floor over a 88 cm barrier to a table top (76 cm). The three load masses chosen for this study were 2.5, 7, and 15 kg. Two-dimensional kinematic data were collected using reflective joint markers and a magnetic tracking device (Fastrak™, Polhemus Technologies). Reflective markers were placed at the hand, ankle, and from two fins attached at the C7/T1 and L5/S1 joints. Fastrak™ sensors were placed at the hand, ankle and on the skin at the site of the C7/T1 and L5/S1 joint centers. In order to synchronize the two collection devices, a signal light was placed in the field of view to indicate the start/stop of the collection period. Video data were digitized using motion capture software (Ariel Technologies) at a sample rate of 30 Hz. Data acquired from both collection methods were input into a regression-based biomechanical model (Potvin, 1997). This model calculated lumbosacral compression through the NIOSH (1991) inputs of H and V, as well as trunk angle, subject mass (kg), and gender. Cumulative estimates of L5/S1 compression were estimated for both collection methods through rectangular integration of the compression/time histories (Figure 1).

RESULTS AND DISCUSSION

The cumulative compression estimates generated from both measurement methods proved to be significantly different ($p<0.05$). The magnetic tracking device tended to overestimate the amount of cumulative compression present in general, with a relative, mean difference of 3.5% when collapsed across all subjects, tasks and loads. Although this relative difference exists, the estimates of the two measurement devices are highly correlated ($r = 0.97$). Further analysis of the relative error present between collection methods revealed that the lowest error occurred in the shoulder height and tabletop lift conditions (1.8% and 1.2%, respectively) and that the highest amount of relative error existed in the "bin-reach" task (7.2%). Due to the long reach required for this task and given the accuracy range of the tracking device it may be that the relative error in this condition is due to an incorrect estimation of the 2-D location of the hand by the tracking device.

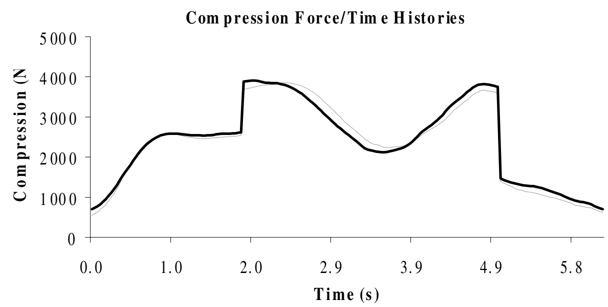

Figure 1: Time history displaying differences between the Video (thin line) and Fastrak™ methods (thick line).

SUMMARY

The results of this study indicate that a magnetic tracking device can be used as a means of collecting cumulative compression experienced in the low back during the execution of a materials handling task. The use of such a device significantly reduces the amount of data processing required to measure cumulative compression in the low back. As such, this measurement protocol could prove to be useful in further investigations of cumulative loading in the low back in a laboratory setting.

REFERENCES

Callaghan, J.P. et al (2001). *Ergonomics*, **44**, 825-837.
Potvin, J.R. (1997). *Ergonomics*, **40**, 697-707.
Waters, T.R. et al (1993). *Ergonomics*, **36**, 749-776.

ACKNOWLEDGEMENTS

This work was funded as part of the AUTO21 Network of Centres of Excellence.

OPTIMIZATION OF A NEW BLOOD FILTRATION DEVICE FOR EMBOLIC STROKE PREVENTION

Ygael Grad[1], Boaz Nishri[1], David Tanne[2], Shmuel Einav[3], Bruch B Lieber[4], Ofer Yodfat[1]

[1] MindGuard Medical Devices Ltd., Alon Hatavor 1 Caesarea Industrial Park, Israel 38900, ygael@mindguard.net
[2] Stroke Unit, Dept. of Neurology, Sheba Medical Center, Tel Hashomer, Israel 52621
[3] Dept. of Biomedical Eng. Tel Aviv University, Ramat Aviv Tel Aviv, Israel 69978
[4] Center for Neurovascular Surgery and Stroke Research, University of Miami, FL. 33124

INTRODUCTION

Implantable devices that permanently filter arterial blood flow have not been previously reported to the best of our knowledge. Filtration of blood can prevent emboli originating proximal to the filter from entering the cerebral circulation and could significantly reduce the burden of embolic stroke. Hemodynamic related shear stresses, however, resulting from the introduction of an arterial filter, may induce platelet activation, aggregation, and provoke the coagulation cascade. Our aim was to study the hemodynamic parameters governing blood filtration in-vitro, and then test a new hemodynamically optimized arterial filtering device (the ***Diverter***) in-vivo.

METHODS

Continuous Digital Particle Image Velocimetry (CDPIV) was employed to map the flow field and interrogate flow disturbances induced by various filtering meshes in a compliant transparent model (Fig. 1, Fig. 2) of the carotid bifurcation under physiological flow conditions. The local flow field around of one filtering filament was studied as well. Shear stresses (Fig. 3) and residence times were calculated and the Activation parameter (AP) was assessed by time integration of shear stress multiplied by the residence time. An in vivo swine model was applied to assess the validity of the in-vitro results, by testing the patency of 30 harvested filtering devices implanted in arterial bifurcations.

RESULTS

A structure based on thin filaments was found to be hemodynamically superior, inducing very low local Reynolds numbers. The blood activation parameter (in terms of shear stress and residence time) for such structure was found to be about 2 orders of magnitude lower than the threshold known to activate the hemostatic system. The global flow field generated in the Diverter's wake depends on mesh geometry, and was designed to minimize flow disturbances. A filtering device designed based on the above parameters, and implanted in arterial bifurcations of a swine model, remained patent upon sacrifice up to 18 weeks post implantation.

CONCLUSIONS

Permanent arterial filters can be optimized based on hemodynamic considerations derived in-vitro by CDPIV. A thin filament based design was found to minimize hemodynamic disturbances and the AP. An arterial filter designed based on the in vitro findings remained patent in a swine model and did not invoke occlusive thrombi. These findings serve as the basis for a novel vascular interventional approach for treatment of embolic disease.

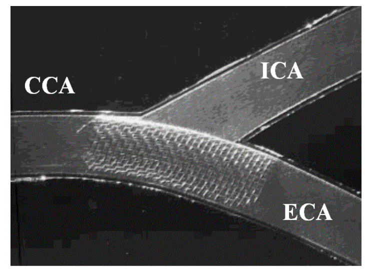

Fig. 1, The ***Diverter*** implanted from the Common Carotid Artery (CCA) to the ECA at the in-vitro carotid bifurcation CDPIV model. The filtered ICA ostium prevents emboli from reaching the brain

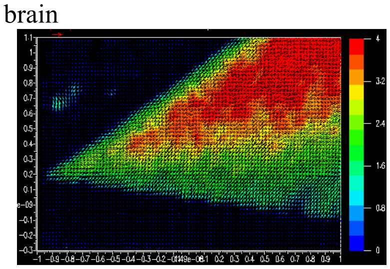

Fig. 2, Velocity vector field in the ICA wake, calculated out of the CDPIV results as depicted in Fig. 1.

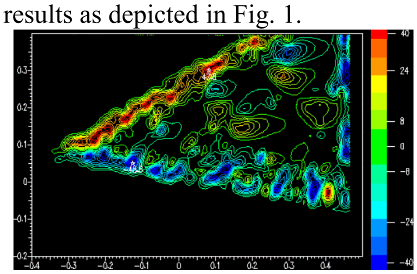

Fig. 3, Vorticity field calculated out of the vector field in Fig. 2

REFERENCES

Amarenco P, et al, 1994; *Atherosclerotic disease of the aortic arch and the risk of ischemic stroke* N Eng J Med 331: 1474-9.
Bluestein, D. et al., 1997; Fluid Mechanics of Arterial Stenosis: Relationship to the Development of Mural thrombus. *Ann. Of Biomed. Eng.* 25, 344-356
Diran et al. 1977;"Coagulation on biomaterials in flowing blood: some theoretical considerations." Biomaterials, 1517-1522, vol 18 No. 23

MECHANICS OF PLASMA MEMBRANE VESICLES

Tadashi Kosawada[1], Geert W. Schmid-Schönbein[2]

[1]Department of Mechanical Systems Engineering Yamagata University, Jonan 4-3-16, Yonezawa 992-8510, Japan
[2]Department of Bioengineering, University of California San Diego, La Jolla, CA 92093-0412, U.S.A.
gwss@bioeng.ucsd.edu

INTRODUCTION

Most cells have internal membrane structures with regions of high membrane curvatures, which may be subject to large deformation and shape changes during cell activities such as migration, endo- or exocytosis, or cell division. One of the remarkable features in this respect are local plasmalemmal membrane regions with high curvature, such as caveolae (plasmalemmal vesicles) and clathrin coated pits. Vesicles are between 50 to 100 nm in diameter with a membrane thickness of about 5 nm. Vesicles are enriched with membrane proteins, cholesterol and membrane signalling molecules to a level not found in the outer membrane domain of the plasmalemmal membrane [1]. However, little is known about the mechanics of highly bend membrane structures, such as caveolae. We examine here the membrane structure of caveolae with high curvature subject to membrane tension.

METHODS

The vesicles are assumed to consist of a flat outer membrane and a curved inner membrane with constant curvature in the unstressed state [2]. The membrane properties are uniform and support bending stress and in plane membrane shear stress. The membrane area is assumed to be constant. A strain energy functional for the membrane was formulated, including the effects of bending and in-plane shear strain energy [3]. A variational principle was used to derive a set of Euler equations that were solved numerically in form of simultaneous, nonlinear differential equations [2].

RESULTS AND DISCUSSION

Attachment of a flat outer membrane to the curved inner membrane yields a stable membrane structure with a neck typical for caveolae seen on electron micrographs [4]. The membrane tension required to unfold the vesicles is relative insensitive with respect to the exact shape of the vesicle, unless it becomes fully unfolded and approaches a relative flat membrane. Upon stretch of the outer membrane, the caveolae dramatically change shape. The vesicle neck disappears abruptly leading to membrane shapes that consist of curved indentations. While the resting shape of vesicles is predominantly affected by membrane bending energy, the membrane shear elasticity makes a significant contribution as the vesicle is subject to stretch and unfolding. Membrane shear elasticity (for a range of values recorded in the red cell membrane) serves to modify the detailed membrane shapes of vesicles but does not interfere with the fundamental structure of vesicle shapes. The shear elasticity has a significant effect on the equilibrium shape of the vesicle, particularly in the vicinity of its neck region where curvature changes sharply [5]. An increasing membrane tension is required to unfold vesicles with smaller initial radius, in agreement with experimental evidence [6].

SUMMARY

The current model for caveolae assuming two domains, an inner membrane domain with high curvature and an outer domain with flat shape without attachment to cytoskeletal fibers, yields mechanically stable and realistic shapes seen on endothelial cells. The unbending of curved membrane structures may make an important contribution to the cortical tension encountered in many cells [6].

REFERENCES

[1] Schnitzer, J.E., Oh, P., Jacobson, B.S., and Dvorak, A.M.,1995,"Caveolae from Luminal Plasmalemma of rat Lung Endothelium: Microdomains Enriched in Caveolin, Ca2+-ATPase, and Inositol Trisphosphate Receptor," Proc. Nat. Acad. Sci. Vol.92, pp.1759-1763.
[2] Kosawada, T., Sanada, K. and Takano, T., 2001, "Large Deformation Mechanics of Plasma Membrane Chained Vesicles in Cells," JSME International Journal, Series C, Vol.44-4, pp.928-936.
[3] Kosawada, T., Skalak, R. and Schmid-Schönbein, G.W. , 1999, "Chained Vesicles in Vascular Endothelial Cells," ASME J. Biomechanical Engineering, Vol. 121-5 , pp.472-479.
[4] Palade, G.E. and Bruns, R.R., 1968, "Structural Modulations of Plasmalemmal Vesicles," The Journal of Cell Biology, Vol.37, pp.633-646.
[5] Kosawada, T., Yoshida, O., Skalak, R. and Schmid-Schönbein, G.W. , 1999, "Generation Mechanism of Vascular Endothelial Chained Vesicles and Transendothelial Channel," JSME International Journal, Series C, Vol.42-3, pp.796-803.
[6] Schmid-Schönbein, G.W., Kosawada, T., Skalak, R. and Chien, S., 1995, "Membrane Model of Endothelial Cells and Leukocytes. A Proposal for the Origin of a Cortical Stress," ASME J. Biomechanical Engineering, Vol. 117-2 , pp.171-178.

ACKNOWLEDGEMENT

We thank Messrs. Akira Watanabe and Tomokazu Takahashi, graduate students of Yamagata University, for their effective assistance with the numerical computations. Supported in part by the Ministry of Education, Science, Sports and Culture, Japan, Grants-in-Aids for Scientific Research (B), Nos. 09558111, 12450093, the Suzuken Memorial Foundation, and NIH Grant PO1 HL 43026.

COORDINATION OF CAT GASTROCNEMIUS AND SOLEUS DURING LOCOMOTION BASED ON DIRECT MEASUREMENT OF IN VIVO MUSCLE FORCES AND EMGS.

Motoshi Kaya, Tim Leonard, and Walter Herzog

Human Performance Laboratory, University of Calgary, Calgary, Alberta, Canada
motoshi@kin.ucalgary.ca

INTRODUCTION

Previous studies on cat locomotion suggested that the medial gastrocnemius (MG) forces and activities increased with increasing speeds and intensities of walking, while the soleus (SOL) forces and activities remained nearly constant for a wide range of walking speeds (1, 2, 3). Therefore, MG forces and activities increase as external demands increase. For SOL, several mechanisms have been proposed to account for the lack of increase in force with increasing demands: 1) SOL was said to be fully activated at low demands, therefore SOL forces were thought to primarily depend on the contractile conditions (1), 2) Increases in SOL activity were thought to be offset by speed-dependent inhibitory effects from cutaneous and rubrospinal inputs (2), and 3) SOL activity was said to be inhibited by increasing MG forces through force-dependent inhibitory pathways (4). None of these mechanisms has been tested rigorously for in vivo movement tasks. The purpose of this study was to determine the coordination of SOL and MG during a variety of walking conditions and to test these proposed mechanisms.

METHODS

Six adult male cats were trained to walk on slopes of 30 deg downhill, level, 30, 45, and 60 deg uphill, and at different speeds on a motor-driven treadmill (0.4-1.2 m/s), running, and landing on the ground. The kinematics of the cat hind-limb were assessed by high-speed video analysis. Forces in SOL and MG were measured using buckle-type force transducers (1). EMG activities were measured using indwelling, bipolar fine wire electrodes (3). Muscle lengths were estimated using kinematics and muscle moment arm measurements.

RESULTS AND DISCUSSION

SOL peak forces and root mean square (RMS) values of SOL EMGs for all experimental conditions were not related (Fig.1a), while MG forces and EMGs showed a strong linear relationship. During uphill walking, SOL EMG was similar and SOL forces were smaller than the corresponding values for level or downhill walking. The lack of increase in EMG activity would have been interpreted by (1) as a saturation of activation. However, activation preceding landing movements was substantially greater than that for all walking conditions (Fig.1a, encircled values) indicating that SOL was not fully activated during the walking conditions. Hodgson (2) argued that SOL is inhibited in a speed-dependent way, however, walking at different speeds gave similar SOL EMG values. In order to test whether SOL forces were primarily dependent on the contractile conditions, we determined the speed of SOL contraction at the instant of peak force. Speeds of muscle shortening were greatest for uphill and lowest (negative, eccentric contraction) for downhill walking (Fig.1b). In accordance with the force-velocity relationship (and the similar activation levels across conditions), SOL forces were greatest for the smallest shortening speeds and were smallest for the greatest shortening speeds (Fig.1b). Finally, we found a negative relationship between peak MG and SOL forces, suggesting that MG may inhibit SOL forces, as proposed by (4) for decerebrate cats. However, there was no negative relationship between MG and SOL activation. Therefore, the negative relationship between peak MG and SOL forces could not be explained by reciprocal inhibition (4), but was likely associated with the SOL contractile conditions.

SUMMARY

Our results did not support any of the mechanisms previously proposed for SOL force control. It seems that SOL is not fully activated at slow speeds of walking, as proposed by (1), and that SOL is not inhibited in a speed-dependent manner, as suggested by (2). Finally, reciprocal inhibition from MG to SOL, as proposed by (4) also does not appear to hold in the freely walking cat. Rather, it appears that SOL is activated in a fairly constant (but not maximal) manner during locomotion, and that changes in SOL force can be explained to a great degree by changing contractile conditions. The constant SOL activation might be governed through the spinal pattern generator known to operate in cats.

REFERENCES

1. Walmsley, B. *et al*. (1978). *J. Neurophysiol*., **43**, 612-620.
2. Hodgson, J. A. (1983). *J. Physiol*., **337**, 553-562.
3. Herzog, W. *et al*. (1993). *J. Biomech*., **26**, 945-953.
4. Nichols, T. R. (1999). *J. Neurophysiol*., **81**, 467-478.

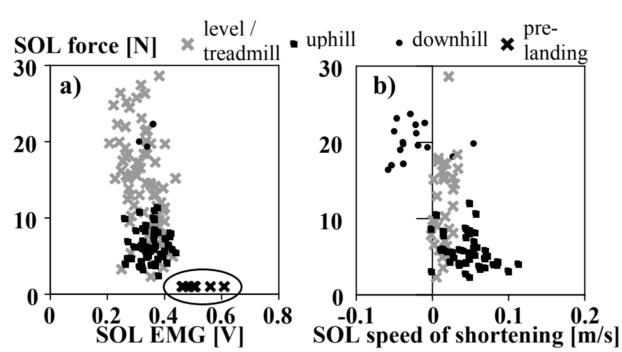

Figure 1: Relationships between a) SOL force and EMG, b) SOL force and muscle shortening speed for one cat.

ANKLE KINEMATICS USING ONE AND TWO SEGMENT FOOT MODELS

Bryan Heiderscheit[1], David Tiberio[2], Sarah Houger[1], Shane Jackson[1], Brian Malone[1] and Tim Vander Wilt[1]

[1]Human Performance Laboratory, Des Moines University, Des Moines, IA, USA, bryan.heiderscheit@dmu.edu
[2]Department of Physical Therapy, University of Connecticut, Storrs, CT, USA

INTRODUCTION

The accurate measurement of three-dimensional foot and ankle motion remains a difficult problem. Most often, the foot is considered a rigid segment (Kadaba et al., 1990; Areblad et al., 1990). Measurements of foot motion based on calcaneal markers ignore the motion occurring in the distal foot segments, while methods using a combination of calcaneal and forefoot marker placement may not accurately measure motion of the subtalar joint (Reischl SF et al., 2000). Additional investigations have employed multi-segment models of the foot to improve the understanding of foot kinematics during locomotion (Arampatzis et al., 2002; Leardini et al., 1999). The purpose of this study was to compare calculated foot and ankle angles when the foot is treated as a single rigid segment as opposed to two (forefoot and rearfoot).

METHODS

Twenty non-impaired subjects (aged 23-30) provided consent to participate in the investigation. Three-dimensional kinematic data were recorded (60Hz) bilaterally using a seven-camera (Falcon Hi-Res) Motion Analysis system (Motion Analysis Corporation, Santa Rosa, CA) during 15 trials of barefoot walking. Reflective marker triads were securely placed on the posterior surface of the leg and calcaneus, with a third attached to the dorsal surface of the first cuneiform. Each triad defined a separate rigid body (i.e. leg, rearfoot and forefoot). In addition, markers attached to the head of the 5th metatarsal and lateral malleolus were used in conjunction with the most distal calcaneal marker to evaluate the entire foot as a rigid segment.

Three-dimensional segment and joint angles were calculated using a joint coordinate system approach in reference to a static standing trial. Ankle angles were calculated using the leg and rigid foot configuration (one segment), as well as the leg and the rearfoot (two segment). Resulting ankle motions from the two approaches were compared within each subject using cross correlations and RMS values, with 95% confidence intervals (CI) reported.

RESULTS AND DISCUSSION

Table 1: One and two segment model comparison (95% CI).

Motion	RMS (°)	r
Flexion/extension	(3.1, 3.6)	(0.93, 0.98)
Inversion/eversion	(3.9, 4.7)	(0.47, 0.82)
Abduction/adduction	(3.6, 4.4)	(0.39, 0.78)

The two models demonstrated the greatest pattern similarity with least magnitude difference during flexion/extension.

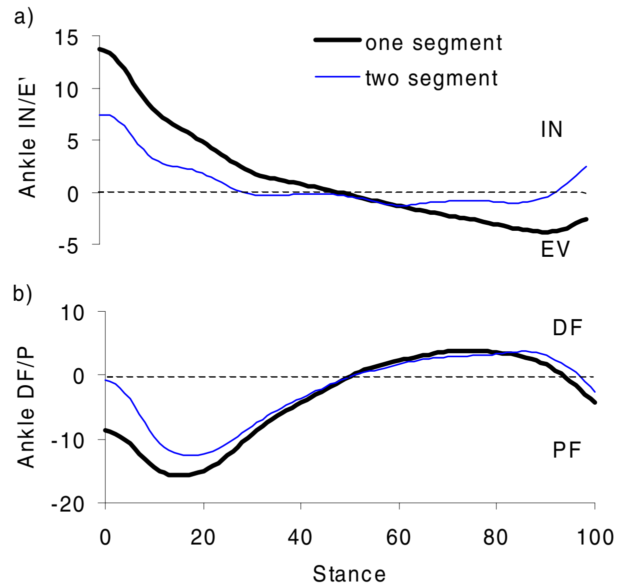

Figure 1: Ankle a) inversion (IN) & eversion (EV) and b) dorsiflexion (DF) & plantarflexion (PF) calculated from the one and two segment approach.

The one segment foot model resulted in greater total range of motion during all motions analyzed. Specifically, distinct differences in calculated ankle angles were observed at the beginning and end of the stance phase (Figure 1). At heel-strike the one segment model demonstrated an inverted position twice that of the two segment model, with greater inversion observed until mid-stance. During walking and running analysis, much emphasis is placed on the foot and ankle motion during the loading portion of stance. Whether a one or two segment model is used during the analysis will influence the interpretation.

SUMMARY

The ankle angles calculated using one and two segment foot models produced distinct differences in each plane of motion. The one segment model resulted in increased total range of motion, with most differences present during the initial 40% and final 20% of stance.

REFERENCES

Arampatzis et al. (2002). *Med Sci Sports Exerc* **34**, 130-138.
Areblad et al. (1990). *J Biomechanics*, **23**, 933-940.
Kadaba et al. (1990). *J Orthop Res*, **8**, 383-392.
Leardini et al. (1999). *Clin Biomech*, **14**, 528-536.
Reischl et al. (2000). *Foot Ankle Int,* **20**, 513-520.

A STOCHASTIC MODEL OF FATIGUE DAMAGE DEVELOPMENT IN BONE CEMENT

S. L. Evans
School of Engineering, Cardiff University, PO Box 925, The Parade, Cardiff CF24 0YF, UK

INTRODUCTION

PMMA bone cement is widely used in hip and knee replacement with excellent clinical results. However, in the long term, failure of the cement may result in loosening and may provide a path for wear particles or fluid pressure from the joint capsule to reach the bone and cause resorbtion. An better understanding of cement fatigue could lead to improvements in long term clinical results.

Although bone cement fatigue has been widely studied, at present it is not possible to model or predict failure *in vivo*. The failure process involves several stages, including crack initiation from voids or other defects, accumulation of damage through the growth of microcracks, the concentration of damage in a dominant crack, the propagation of this crack in the long crack regime and finally fast fracture. Each stage may occupy a different proportion of the total life, depending on factors such as geometry, stress level, defect distribution and the loading spectrum, and tests on specimens may not accurately weight the relative importance of each stage.

This paper presents a computational simulation which is intended to allow these factors to be evaluated, and to provide a framework for further development, including more detailed representation of damage development and a finite element representation of the *in vivo* geometry and stress distribution. The model is stochastic, incorporating random variations in defect distribution, allowing some evaluation of the effects of variation between specimens.

METHODS

Following Taylor et al. [2001], the model was based on a direct fracture mechanics representation of individual defects, rather than a damage accumulation approach. This allows the various mechanisms of damage accumulation to be modelled. An array of randomly distributed was generated and their growth was simulated on a cycle- by- cycle basis using a Paris Law model. Variable amplitude loads represented different activities and overloads. Initially it was assumed that spherical voids are present with normally distributed diameters, and that cracks initiate from these voids on first loading, as found by Lennon et al [2001]. The transition between the early stage where the crack is much smaller than the void, and the development of a circular crack much larger than the void, was modelled by interpolation based on previous boundary element models [Evans, 2001]. A three point bend configuration was modelled, using an analytical solution for the stresses in the specimen. An uncoupled analysis was used with each crack assumed to grow without affecting the stresses or other cracks. Possible endpoints include fast fracture, growth of a crack to the exterior surface and the approach of one crack to another.

RESULTS

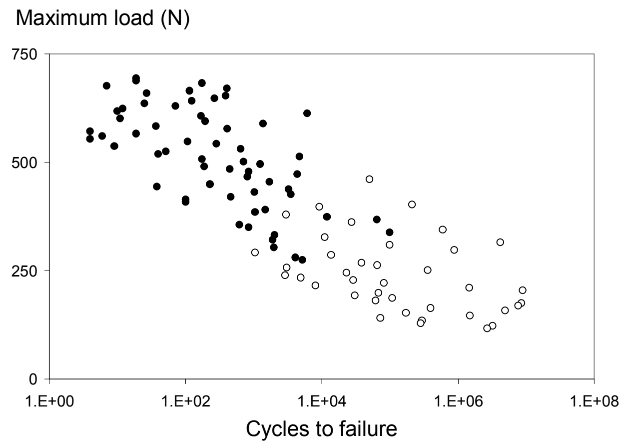

Figure 1. *Typical results for 100 runs*.

Fig. 1 shows an S-N curve for 100 simulations at various loads. The results exhibit typical S-N behaviour, but the endpoint changed from fast fracture (closed circles) to cracks reaching the surface (open circles).

DISCUSSION AND CONCLUSIONS

Initial results predict the observed fatigue behaviour reasonably well at high stresses, but at low loads the cracks become excessively large before failure. In the high cycle fatigue regime, it would be necessary to represent the dominant cracks in a coupled model, and a simulation based on accumulation of many small microcracks may be inappropriate. Laboratory tests under high, constant amplitude loads may not lead to the same type of failure as the gradual accumulation of damage under lower, variable amplitude loads in a thin cement mantle *in vivo*. For failure to occur over many years, either crack growth rates must be extremely low or failure must occur as a result of very unusual overloading, and neither of these is normally represented in laboratory fatigue tests.

REFERENCES

Taylor, D. *et al.* (2001) Damage accumulation in bone: theory and practice. *5th Int Symp Comp Meth Biomech Biomed Eng*, Rome.

Lennon, A.B. *et al.* (2001) Fatigue damage accumulation in PMMA for tensile and compressive loading regimes: development of a constitutive model from experimental observations. *5th Int Symp Comp Meth Biomech Biomed Eng*, Rome.

Evans, S.L. (2001) A computational fracture mechanics approach to the fatigue of PMMA bone cement. *5th Int Symp Comp Meth Biomech Biomed Eng*, Rome.

POSTURE DEPENDENT TRUNK STRENGTH AND EMG ACTIVITY

Amy L. Roy and Tony S. Keller
Musculoskeletal Research Laboratory, University of Vermont, Burlington, Vermont, aroy@emba.uvm.edu

INTRODUCTION

Low back pain is a common occurrence that 80% of the population will experience in their lifetime (Gomez et al 1991). The direct cause of chronic low back pain (LBP) is unknown, yet it is believed that trunk muscle function plays an important role. Current studies indicate a possible gender-specific difference in muscle strength and activation patterns. However, the majority of experiments that evaluate trunk muscle strength and EMG activity include only healthy male subjects. In addition, other studies have compared trunk muscle EMG activity and extension torque using only a small range of flexion angles (Shultz et al 1982, Shultz et al 1987, Seroussi et al 1987, Zetterberg et al 1987). As a result, the postural relationship between trunk extension strength and EMG activity over a large range of sagittal postures has not yet been quantified. The current study was designed to evaluate the relationship between sagittal plane posture, trunk muscle extensor activity, and isometric trunk extension torque, while emphasizing gender-specific differences.

METHODS

Twenty healthy adult subjects, 10 male and 10 female, having no previous history of back pain participated in this study. Each subject was positioned and restrained in a tri-axial trunk dynamometer. A series of isometric flexion (F) and extension (E) tasks were performed at 10-degree increments over a 70° range-of-motion (50° F to -20° E). Myotrace 10 electromyographic amplifiers were used to condition and linear-envelope raw EMG signals from the left and right erector spinae muscles at the L3 level during each of five trials. EMG signals and isometric trunk extension torque were recorded using a Biopac MP100 16-bit data acquisition system and Acknowledge software. Peak extension torque and EMG amplitude were determined at each posture.

RESULTS AND DISCUSSION

Trunk muscle EMG activity during isometric extension tasks increased with increasing flexion angle, and differed appreciably at the various sagittal plane trunk posture angles examined. The mean isometric trunk extension torque at a flexion angle of 40° was 64% and 71% greater than that at upright for the female and male groups respectively. Differences between left and right side EMG output were most marked at extended postures for the male subjects and at more flexed postures for the female subjects (Table 1). Significant differences were found between male and female isometric trunk extension torque at all angles except –20 degrees. Linear regression of the normalized torque (T_n) and EMG data for each of the subject groups revealed a significant positive correlation between the two parameters, as did the correlation for the combined group (Figure 1). This finding is consistent with several previous studies (Lavender 1994, Tan 1993).

Table 1. Left and right side peak EMG and extension torque values (both normalized to upright) for male subjects (n=10) and female subjects (n=9). *Indicates a significant difference between the male and female groups (p<0.01). +Indicates a significant difference from upright (p<0.01).

	FEMALES			MALES		
Angle (degrees)	EMG (right side)	EMG (left side)	Extension Torque	EMG (right side)	EMG (left side)	Extension Torque
-20	+0.78	0.79	+ 0.57	+0. 59	0.88	+ 0.45
-10	0.95	0.91	+*0.70	+0. 73	0.91	+*0.68
0	1.00	1.00	*1.00	1.00	1.00	*1.00
10	1.02	0.97	+*1.22	1.05	1.10	+*1.22
20	1.17	1.02	+*1.37	1.07	1.08	+*1.41
30	1.25	1.13	+*1.48	1.12	1.15	+*1.62
40	1.39	1.24	+*1.64	1.19	1.18	+*1.71
50	1.51	1.16	+*1.78	1.31	+1.38	+*1.73

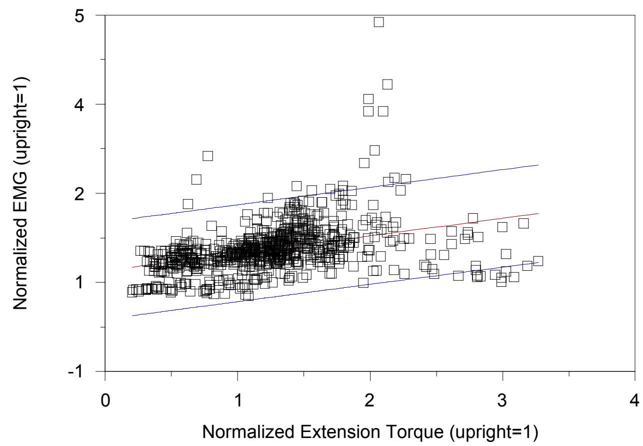

Figure 1. Relationship between erector spinae EMG and isometric trunk extension torque (both normalized to upright) combined for all subjects. Linear regression results: y = 0.293x + 0.696 (R^2 = 0.14, p-value <<0.001).

SUMMARY

In order to increase the knowledge of trunk muscle function and its role in low back pain, researchers must include both men and women subjects in their studies, and should extend their focus to include subjects who suffer from chronic LBP. Results of this study indicate that experiments should incorporate the entire range-of-motion and gender-specific differences for studies that use EMG activity to model trunk muscle activation patterns.

REFERENCES

Gomez T. et al (1991). *Spine,* **16**, 15 – 21.
Lavender S. et al (1994). *Spine,* **19**, 771 – 778.
Schultz A. et al (1982). *Spine,* **7,** 390 – 7.
Schultz A. et al (1987). *JOR,* **1**, 77 – 91.
Seroussi R. E. et al (1987). *J Biomechanics,* **20**, 135 – 46.
Tan J. C. et al (1993). *Spine,* **18**, 2480 – 2490.
Zetterberg C. et al (1987). *Spine,* **12**, 1035 – 40.

KNEE LOADING DURING GAIT AND EARLY SIGNS OF KNEE OSTEOARTHRITIS IN A MENISCECTOMY POPULATION

Daina Sturnieks[1], David Lloyd[1], Thor Besier[1], Gwidon Stachowiak[2], Pawel Podsiadlo[2], Karl Stoffell[2] and Stephen Davis[3]

[1]Deptartment of Human Movement & Exercise Science, University of Western Australia, www.hm.uwa.edu.au
[2]Deptartment of Mechanical and Materials Engineering, University of Western Australia
[3]Perth Radiological Clinic, Western Australia

INTRODUCTION

Knee osteoarthritis (OA) is the cause of more disability than any other joint condition, imposing large social and economic costs (Guccione et al., 1994). The risk of developing knee OA is considerably increased following meniscectomy (Sommerlath et al., 1991). Understanding the mechanisms contributing to the development of knee OA is an important first step for prevention and moderation of disease. The purpose of this study was to examine differences in gait patterns and knee radiographic features in young, pre-osteoarthritic adults who recently had a partial meniscectomy.

METHODS

Preliminary data from 45 meniscectomy patients (~6 weeks post-surgery) and 20 controls has currently been analysed from a larger cohort of 180 people. Subjects were aged 20 to 45 years and screened for previous or current knee joint pain, stiffness, laxity, disease and injury (excepting meniscus tear in patient group). AP weight-bearing knee radiographs were taken in normal standing and 30 degrees flexion positions. An experienced orthopaedic surgeon assessed radiographs according to a validated OA scoring system (Derek et al. 1999), using a published OA atlas (Burnett et al., 1994). Subjects were categorised as positive (+ve) or negative (–ve) to pathologic radiographic features. The +ve group were further categorised by the grade of change in joint space narrowing (JSN) and/or grouped bony changes (BC) (i.e. osteophytes and tibial erosion), in medial and lateral compartments. Subjects with greater that grade 2 changes were excluded from the study. Remaining +ve group subjects were considered free of knee OA due to the absence of pain and stiffness, precluding the clinical diagnosis of knee OA. Three-dimensional gait analysis was performed using a 50 Hz, six-camera VICON motion analysis system, with AMTI force platforms. Joint kinematics and kinetics were calculated using a custom seven-segment lower limb model. External knee moments were normalised to individual's height and weight, and analysed over stance. Data was statistically tested using two-way repeated measures ANOVA, Bonferroni corrected for multiple comparisons, p value for significance set at <0.05.

RESULTS AND DISCUSSION

Compared to controls, the meniscectomy group was more likely to have +ve radiographic features indicative of early degenerative joint changes (see Figure 1.). This increased proportion was true for lateral and medial compartment joint space narrowing (LatJSN and MedJSN, respectively), and bony changes in medial and lateral compartments (LatBC and MedBC, respectively), of the tibiofemoral joint. However, the only difference to reach statistical significance was bony changes in the medial compartment ($p<0.05$).

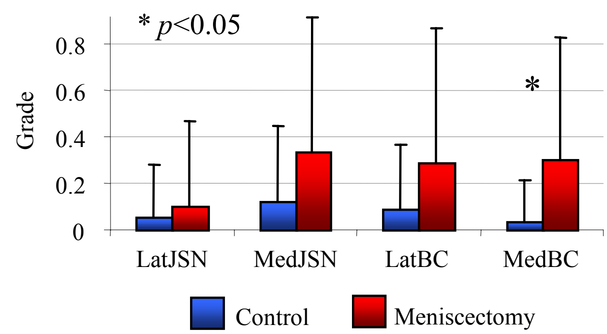

Figure 1: Radiographic changes between groups

Analysis of gait data revealed that the meniscectomy group had larger knee adduction moments (x=0.032), when compared to the control group (x=0.027) ($p<0.05$). The knee adduction moment loads the medial tibiofemoral joint and may account for the significant difference in MedBC between groups.

SUMMARY

Radiographic features indicative of degenerative joint changes were more commonly noted in the meniscectomy group. Furthermore, larger than normal knee adduction moments were experienced by the meniscectomy group. It is anticipated that inclusion of data from the remainder of the cohort will provide power for regression analyses to determine whether a relationship exists between these variables. Furthermore, examining progression of knee OA and changes in gait is suggested.

REFERENCES

Guccione A, et al. (1994). The effects of specific medical conditions on the functional limitations of elders in the Framingham study. *Am J Public Health*, **84**, 351-7.
Sommerlath K, et al. (1991) The long-term course after treatment of acute anterior cruciate ruptures. *Am. J. Sports Med.*, **19**, 156-162.
Burnett S et al. (1994). *A radiographic atlas of osteoarthritis*. London Springer Verlag.
Derek T, et al. (1999) Radiographic grading for knee osteoarthritis. *J Rheumatol*. **26**, 641-4.

EXPERIMENTAL ANALYSIS OF FLOW THROUGH TILTING DISK VALVE

Sagi Raz, Idit Avrahami, Uri Zaretsky, Moshe Rosenfeld and Shmuel Einav
Faculty of Engineering, Tel-Aviv University, Tel-Aviv, Israel. sagiraz@eng.tau.ac.il

INTRODUCTION

Tilting disk mechanical heart valves (MHV) are commonly used in new developments of artificial heart pumps. The fluid dynamics associated with tilting disk MHV plays a critical role in determining the longevity of these devices. The present study simulated experimentally the flow across tilting disk valves in a straight tube. The objectives were to establish the time dependent global flow field for several typical cases, to track down time histories of individual platelets, to locate the regions where activated platelets might be found, and to evaluate the significant of the third dimension on the flow.

METHOD

The experimental method was based on the *continues digital particle image velocimetry* (CDPIV) method. This optical method uses visualization techniques to measure quantitatively the velocity field.

CDPIV methods were used to map the flow field in time for two models of tilting disk MHV: the first was a 3D model of Bjork-Shiley MHV (Ø28 mm) installed inside a cylindrical glass tube. The second model was a two dimensional Perspex channel (size 10X60X2.8cm) with glass windows. A glass leaf connected to a hinge modeled the 2D tilting disk. Mitral inflow conditions were imposed using computer controlled pump, keeping both Reynolds and Womersley dimensionless numbers as in the physiological flow conditions.

For the 2D model, a case with constant inflow of Re=3800 and fully opened valve ($\theta = 57°$) was analyzed. For the 3D, model three flow conditions were measured: (a) Constant inflow with Re=4300 (at fully opening angle of $\theta = 57°$);(b). Constant inflow with Re=800 (at opening angle of $\theta = 23°$); and (c) pulsating flow with moving valve, according to the mitral physiological waveform.

RESULTS AND DISCUSSION

Continuous visualizations of the flow field in all cases through the different models were captured. The flow downstream the valve was calculated using DPIV software. Velocity, vorticity and shear rate contours of the time-dependent flow were extracted and compared with numerical simulations. In the pulsatile case, the motion of the valve was measured and compared to previous results. Pertinent trajectories of the particles were established from the CDPIV measurements and their shear stress histories computed to evaluate the platelets level of activation.

Figure 1 exemplify typical vectors plot (a) and shear rates contours (b) as obtained for peak flow through the 3D model.

(a) (b)

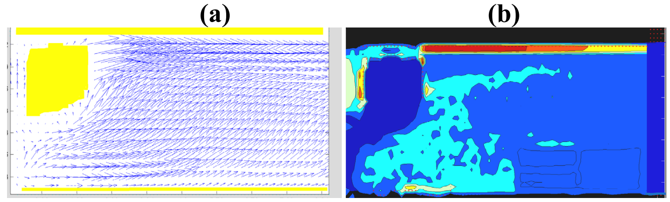

Figure 1: flow field calculated in 3D model, peak inflow (a) vectors plot (b) shear rate contours

The flow through the tilting disk valve was characterized with two high velocity jets that are passing through the valve orifices, causing two shear layers that roll into counter-rotating vortices near the valve.

As the valve opened, the large vorticity created by the upper orifice jet was shed downstream and the flow coming from the lower orifice dominated the flow near the valve. As the incoming flow decreased, the vortices were more pronounced. With the closing valve, the flow field near the valve directed backward and the flow was still until a new cycle started. Excessive high shear stresses regions were found downstream the disk, and for some particle trajectories in the flow field along the cycle, platelets level of activation reached critical values.

SUMMARY

The results of the present study indicate two regions of high shear stress and a very disturbed flow downstream the valve. The secondary flow of the third dimension strongly affects the flow in the high Reynolds velocities.

The comprehension of the global flow field across 2D and 3D models of valve in a straight channel can assist in studying several hemodynamical and clinical aspects of the flow across valves inside heart assist devices.

REFERENCES

[1] Rosenfeld, M., Avrahami, I. and Einav, S., "Unsteady Effects on Flow Across Tilting Disk Valves" Journal of Biomechanical Engineering, Feb. 2002

[2] Y. Grad and S. Einav. "Time-Dependent Vorticity Field In Vascular Junctions". 1st Joint Meeting of BMES & EMBS Oct 13-16 1999 Atlanta, GA, USA.

ACKNOWLEDGEMENTS

This research was supported by Israel Science Foundation.

MECHANISMS FOR CELL ACTIVATION IN THE CARDIOVASCULAR SYSTEM DURING PHYSIOLOGICAL SHOCK

Geert W. Schmid-Schönbein, Erik Kistler, Hiroshi Mitsuoka, Tony Hugli*
Department of Bioengineering, University of California San Diego, La Jolla, CA.
*The La Jolla Institute for Molecular Medicine, La Jolla, CA.
gwss@bioeng.ucsd.edu

INTRODUCTION

Physiological shock is one of the most life threatening condition. In shock the level of cell activation in the cardiovascular system dramatically raises within a few hours [1]. The cell activation can be detected by a wide variety of cell activities, including actin polymerisation with changes in cell shape and cytoplasmic stiffness, expression of membrane adhesion molecules, production of oxygen free radicals, a reduction of muscle contraction as well as eventual cell death. Under shock conditions the transport in the microcirculation and the biomechanics of cells is fundamentally altered.

In the past it has been hypothesised that cell activation in shock is due to intestinal bacteria and their products (endotoxin) after transport from the lumen of the intestine into the circulation. But there is no agreement whether this mechanism is the primary cause for cell activation in human or experimental forms of shock. The source and mechanisms of the powerful cell activation encountered in shock remains an important unresolved problem. In this communication we present a selected set of experiments designed to examine the origin of humoral cell activators in experimental shock.

LOCALIZATION OF THE CELL ACTIVATORS

Humoral cell activators in shock can be detected by incubation of plasma from central arteries with naive donor cells (e.g. leukocytes, platelets). The cell activators are already detectable within 1 hour after occlusion of the superior mesentery artery, indicating that no significant new protein synthesis of these mediators is required. We prepared tissue homogenates from a variety of different organs and exposed naive leukocytes to their supernatants after centrifugation. While all organ homogenates produced relatively low levels of leukocyte activation (less than 20%), the *pancreatic* homogenates generated a level of cell activation that reached close to 100%. Remarkably, organs with low levels of cell activation also started to produce high levels of cell activation after addition of pancreatic enzymes, especially serine proteases [2]. Administration of pancreatic homogenate into the circulation of rats produced not only leukocyte adhesion to the endothelium, but also parenchymal cell apoptosis [2] and high levels of mortality [3]. This evidence indicates that the reaction of digestive enzymes with autologous tissue serves to produce a set of powerful cell activators.

THE CENTRAL ROLE OF DIGESTIVE PROTEASES

Since pancreatic enzymes after discharge from the pancreatic duct become fully activated in the small intestine as part of normal digestion, we examined the hypothesis that these enzymes may be involved in the generation of activators during intestinal ischemia. The *lumen* of the small intestine was continuously perfused with saline containing a broadly acting pancreatic protease inhibitor (ANGD, 0.37 mM) before and during ischemia of the small intestine by splanchnic artery occlusion [4]. This procedure served to inhibit activation of circulating leukocytes during occlusion and reperfusion. It also prevented the appearance of cell activators in portal venous and systemic artery plasma and served to attenuate symptoms of multiple organ injury in shock. Intestinal tissue produces only low levels of activators in the absence of pancreatic enzymes while in the presence of enzymes, activators are produced in a concentration and time dependent fashion. The significant protection provided by blockade of digestive enzymes in the lumen of the small intestine can also be achieved with other pancreatic protease inhibitors [5].

SUMMARY

These surprising results indicate that pancreatic digestive proteases in the ischemic intestine serve as an important source for cell activation, inflammation, and multiple organ failure. While the pancreatic enzymes, capable to digest human tissues, are restricted to the lumen of the intestine by the epithelial mucosal barrier, this barrier may be compromised in shock. Escape of pancreatic enzymes into the wall of the intestine leads to the production of significant levels of cell activators, which are then transported via the intestinal microcirculation and lymphatics into the central circulation [6]. The presence of high levels of digestive enzymes in the intestine compared to other organs may be the reason for the central role of the intestine in shock recognized in the past.

REFERENCES

[1] Barroso-Aranda, J., Zweifach, B.W., Mathison, J.C., Schmid-Schönbein, G.W.: Cardiovasc. Pharmacol., 25:S23-S29, 1995.
[2] Kistler, E.B., Hugli, T.E., Schmid-Schönbein, G.W.: Microcirculation, 7:183-192, 2000.
[3] Kistler, E.B., Lefer, A.M., Hugli, T.E., Schmid-Schönbein, G.W.: Shock, 14:30-34, 2000.
[4] Mitsuoka, H., Kistler, E.B., Schmid-Schönbein, G.W.: Proc. Nat. Acad. Sci. U.S.A., 97:1772-1777, 2000.
[5] Mitsuoka, H., Kistler, E. B., Schmid-Schönbein, G.W.: Shock, in press, 2002.
[6] Schmid-Schönbein, G.W., Kistler, E.B., Hugli, T.E.: Biorheology, 38:185-202, 2001.

ACKNOWLEDGEMENT

Supported by NIH Grant HL 67825 and the Max Kade Foundation.

RESIDUAL STRESSES ANALYSIS AT THE INTERFACE BETWEEN HYDROXYAPATITE COATING AND TITANIUM SUBSTRATE

B.Cofino, P. Fogarassy, P. Millet, R. Taiar, A. Lodini

INTRODUCTION

Hydroxyapatite coatings on titanium alloy Ti-6Al-4V have shown for several years a great interest for implantology. Ti-6Al-4V presents good mechanical properties and is biocompatible. Hydroxyapatite has low mechanical strength, but very good osteointegration and biocompatibility. The use of plasma sprayed hydroxyapatite coatings on titanium substrates leads to a structure which has good mechanical strength and good osteointegration properties at the surface. However, the porous structure of the coatings gives failures in the implantation and it appears that the problem happens at the interface between the ceramic and the metal. These failures could be due to stresses created in the materials at the interface during plasma deposition **[1]**. Knowledge about these residual stresses is very important to predict the location of the failure.

To determine the residual stresses induced, both in the substrate and in the coating during the plasma thermal spraying process, some samples were prepared, as presented in figure 1.

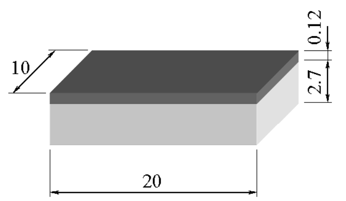

Figure 1 : Samples dimensions (mm)

High purity hydroxyapatite (HA) powder with particle sizes between 80 and 160 µm was used for the plasma spraying coating. Plates of Ti-6Al-4V alloy, 2.7 mm thick, were used as substrates and pure titanium powder with particles sizes between 25 and 75 µm was used as porous bondcoat.

In this study, two techniques have been used to determine the residual stresses near the interface between plasma sprayed hydroxyapatite coatings and titanium substrates, a numerical and an experimental method.

RESIDUAL STRESSES EVALUATION BY SYNCHROTRON RADIATION

The experimental technique is based on X-rays diffraction with a synchrotron radiation. These X-rays, with high energy (40 keV), can enter deeply into the material (0.5mm) and the diffraction gauge volume can have very small dimensions, down to 10µm with synchrotron radiation compared to 300µm for neutrons. Synchrotron radiation, using Beamline BM16 at the European Synchrotron Radiation Facility (Grenoble, France), has been used to determine residual stresses near the interface [2]. Now it is possible to determine very local thermal induced residual stresses near the interface between hydroxyapatite and titanium by synchrotron radiation measurements.

RESIDUAL STRESSES DETERMINATION BY FINITE ELEMENT ANALYSIS

During plasma spraying, molten particles cool down to the metal temperature within a few milliseconds. The thermal contraction of the particles is constrained by their bond to the substrate resulting in tensile stresses in the coating. If this contraction is totally inhibited, higher stresses than the ultimate tensile stress should develop. So a microcracking causes a stress relaxation in the ceramic coatings. There are two origins for the stresses : the speed of cooling to the substrate temperature (primary cooling), the thermal properties mismatch of the materials during cooling to the room temperature (secondary cooling).

The simulation by finite elements determines the residual stresses near the interface between titanium and hydroxyapatite induced by the plasma spraying process considering the primary and the secondary cooling during a layer by layer deposition.

RESULTS

The results are presented in figure 2 below.

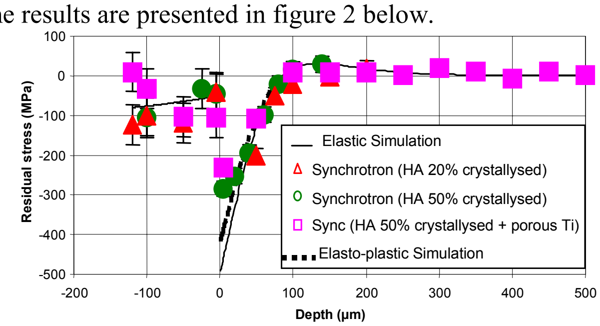

Figure 2 : residual stresses analysis

Compressive residual stresses exist in the substrate near the interface and also in the coating. The compressive residual stresses are weak after 100µm in the substrate. Plasma spraying and important cooling rates cause residual stresses near the interface. The thermal properties mismatch of the materials with a higher thermal conductivity for Ti-6Al-4V creates compressive residual stresses near the interface in the substrate and in the coating. The elasto-plastic simulation is comparable with the experimental results obtained with synchrotron radiation.

ACKNOWLEDGMENTS

The authors express appreciation for assistance from Dr. A. FITCH, European Synchrotron Radiation Facility (Grenoble, France).

BIBLIOGRAPHY

1 Elsing R., Knotek and Balting U. : Calculation of residual thermal stress in plasma sprayed coatings : the effect of substrate temperature, *Surf. and Coat. Techn.*, 1990, **43/44**, 426-435.

2Cofino B., Braham C., Millet P. and Lodini A. : Use of synchrotron radiation in the analysis of strains near the interface between a plasma sprayed hydroxyapatite coating and a Ti-6Al-4V substrate, 2001, *Journal of Neutron Research*, **9**, Issue 2-4, 243-247.

A BIOMECHANICAL STUDY COMPARING CORTICAL ONLAY ALLOGRAFT STRUTS AND PLATES IN THE TREATMENT OF PERIPROSTHETIC FEMORAL FRACTURES

Darrin Wilson, David J. Dunlop, Kuros Gadareh, Hanspeter Frei, Bassam A. Masri, Nelson V. Greidanus, Donald S. Garbuz, Thomas R. Oxland, Clive P. Duncan.
Department of Orthopedics, University of British Columbia, Vancouver, British Columbia, Canada, toxland@interchange.ubc.ca

INTRODUCTION

Fracture around the femoral component of a total hip arthroplasty is a serious complication. The frequency of these fractures is increasing as more procedures, particularly revision operations with loss of bone stock are performed. Internal fixation is the recommended management of a periprosthetic fracture adjacent to the tip of a well fixed femoral component (Wilson 2001). The purpose of this investigation was to compare the interfragmentary motions of six different fixation methods in a cadaveric model.

METHODS

A cemented femoral hip prosthesis was implanted in to six cadaveric femora. A fracture adjacent to the tip of the prosthesis was simulated by a transverse osteotomy, which is possible the “worst case” scenario around a well fixed femoral prosthesis.

The simulated transverse fracture was fixed with the following six constructs in a randomized sequence (Figure 1):

1. Lateral plate with 4 proximal cables and 4 distal bicortical screws plus anterior 20cm strut graft and 4 distal cables.
2. Lateral plate with 4 proximal cables, 2 proximal unicortical screws and 4 distal bicortical screws plus anterior 20cm strut graft and 4 distal cables.
3. Lateral plate with 4 proximal cables and 4 distal bicortical screws.
4. Lateral plate with 4 proximal cables, 2 proximal unicortical screws and 4 distal bicortical screws.
5. Two 20cm strut grafts lateral and anterior held with 8 cables, cables uniformly positioned, equal separation, four above and four below the fracture level.
6. Two 12cm strut grafts lateral and anterior held with 8 cables, cables uniformly positioned, equal separation, four above and four below the fracture level.

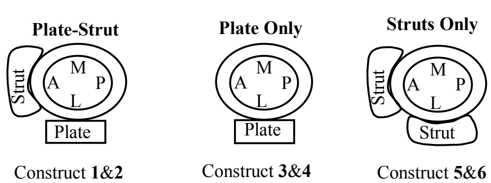

Figure 1. Schematic drawing of the different fixation constructs (A: anterior, P: posterior, M: medial, L: lateral).

One hundred cycles of a craniocaudal (1Hz) and anterioposterior (0.5Hz) sinusoidal load at 1.5 and 0.3 times body weight respectively were applied. The interfragmentary motions at the fracture site were measured using an optoelectronic camera system. Offset and amplitude of the rotation about the helical axis and the length of the translation vector were averaged for each specimen between the 93rd to the 97th cycle. The constructs were compared using non-parametric Friedman ANOVA. For individual comparison a Wilcoxon matched paired analysis was used.

RESULTS AND DISCUSSION

In general, the plate-strut constructs had less interfragmatry motions compared with the others. This was significant for the rotation amplitude compared with the plate only and struts only constructs. Significantly higher rotational offset was found for the plate-only constructs compared with the plate-strut constructs . The translation offset of strut-plate construct with two proximal screws (**2**) was significant lower than the plate-only and strut-only constructs. A significantly lower interfragmentary rotational amplitude of the two 12mm struts (**6**) compared with the plate only constructs was found.

There were no significant differences in interfragmentary motion between the different plate-strut constructs, the plate only and the struts only constructs with one exception. The plate-only construct with two proximal screws had a lower interfragmentary translation amplitude compared with the plate without the proximal screws.

SUMMARY

Internal fixation is the recommended treatment of a periprosthetic fracture around a well fixed femoral component. Six different fixation methods were compared using a transverse fracture model in cadaveric femurs. Interfagmentary motions were measured under physiological loads. The results support the use of a combined plate and strut construct rather than a single plate or a two-strut construct.

REFERENCES

Wilson D, Masri BA, Duncan CP (2001). *Orthopedics*, **24** (9):869-70

ACKNOWLEDGEMENTS

A research grant from the UBC Zimmer Research fund is gratefully acknowledged.

CENTER OF MASS ESTIMATION BASED ON ZATSIORSKY-SELUYANOV AND DEMPSTER DATA DURING POSTURE ANALYSIS.

Danik Lafond and François Prince

Laboratoire du mouvement, Centre de réadaptation Marie-Enfant, Hôpital Ste-Justine, Quebec, CANADA.
Department of Kinesiology, University of Montreal, P.O. Box 6128, Downtown Station Montreal, Quebec, CANADA, H3C 3J7

INTRODUCTION

To determine the body's COM, the segmental method is a the more accurate approach (Eng and Winter, 1993). The precision of the COM location is then lying on the validity of the segment inertia parameters (SIP). The segmental method requires the knowledge of the segment's COM location relative to specific bony landmarks. The SIP most widely used in balance studies are derived from cadavers' data. The major limitation of these cadavers' data is that they were gathered from only few older frozen specimens. Zatsiorsky and Seluyanov (1990) used gamma-scanning techniques to determine the SIP from 115 young caucasian adults. These SIP may provide a better estimation of COM because of the technique used and the sample of living subjects. The objective of this study is to compare the Zatsiorsky-Seluyanov's data and the Dempster's data on the COM position during quiet standing.

METHODS

Twenty five young adult subjects (8 males and 17 females) participated in this study. An OPTOTRAK® position sensor (Northern Digital, Waterloo, Ontario, Canada) was used to collect kinematic data of the 21 infrared emitting diodes positioned on specific bony landmarks. During the data collection, the participants were instructed to keep their arms hanging at their side and to focus on a fixed target located at eyes height. The experimental session was composed of 120 seconds standing trials with a 120 seconds seated rest period. The segmental method was used to estimate the body's COM based on 14 segments (COM14), 8 segments (COM8), 6 segments (COM6) and 3 segments (COM3). The COM location and mass fraction of body segments used to define COM-models are presented in an accompanying paper. For instance, the Dempster's data was selected from Winter's table (Winter, 1990) and the Zatsiorsky-Seluyanov's data was selected from the paper of de Leva (1996). The RMS error was used to evaluate the difference between the COM calculated from Dempster and from Zatsiorsky-Seluyanov.

RESULTS AND DISCUSSION

The RMS error values in antero-posterior (AP) and vertical are presented in Figure 1 for both genders. In AP direction, the global average difference is 12.3mm (±1.3) and 3.4mm (±0.6) for male and female respectively. In vertical direction, the average difference is 14.4mm (±7.3) for male and 29.0mm (±9.9) for female. The results for ML direction are not presented because the segments COM longitudinal location do not affect very much the ML body's COM position (global RMS error < 0.7mm).

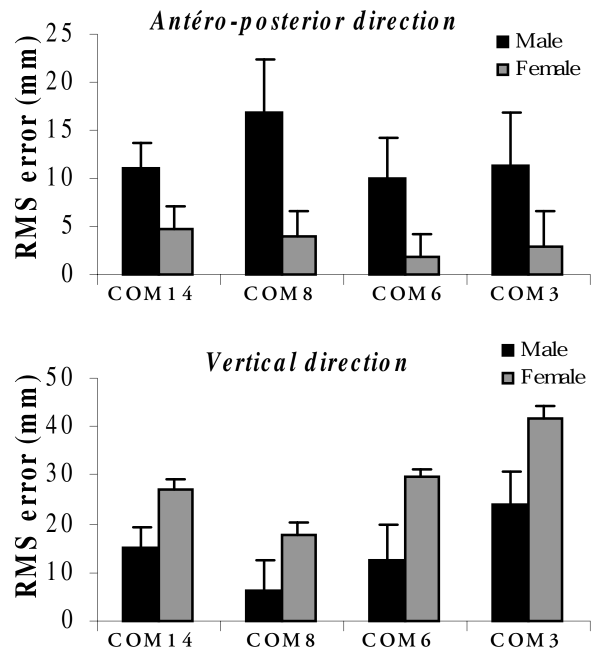

Figure 1. RMS error of Dempster's compared to Zatsiorsky-Seluyanov's parameters in AP and vertical direction.

Using a precise reaction board, de Leva (1993, 1996) found an error of 53 mm (±18 mm) and 38 mm (±13 mm) along the longitudinal axis in young male and female subjects respectively. However, Zatsiorsky-Seluyanov SIP showed a smaller average error of 16 mm (±17 mm) and –4 mm (±13 mm). Our results agree with those of de Leva (1993). We conclude that the Zatsiorsky-Seluyanov SIP provide a better estimation of the body's COM location than cadavers based SIP for young adult subjects.

REFERENCES

Corriveau, H. et al. (2000). *Diabete Care*. 23; 1187-1191.
de Leva, P. (1993). *Proceeding of International Society of Biomechanics XIVth Congress*. 318-319.
de Leva, P. (1996). *Journal of Biomechanics.* 29; 1223-1230.
Winter, D.A. (1990). *Biomechanics and motor control of human movement* (2nd Ed). New York: Wiley.
Zatsriosky, V.M. et al. (1990). *Contemporary problems in Biomechanics*. Boca Raton: CRC Press. 272-291.

ACKNOWLEDGEMENTS

D.L. and F.P. are grateful for scholarships from the FCAR and FRSQ respectively and the financial support of NSERC (FP).

SEGMENTAL MOBILITY OF LUMBAR SPINE DURING A PRONE PRESS-UP MANEUVER IN SYMPTOMATIC AND ASYMPTOMATIC SUBJECTS: ASSESSMENT USING DYNAMIC MRI

Kornelia Kulig[1] ,(kulig@usc.edu) Christopher Powers[1], Robert Landel[1], Hung Wen Chen[1], Michael Fredricson[2], Marc Guillet[2] and Kim Butts[2]

[1]Department of Biokinesiology and Physical Therapy, University of Southern California, Los Angeles, California, USA

[2]Departments of Radiology, Athletic Medicine and Physical Therapy, Stanford University, Palo Alto, California, USA

INTRODUCTION

Altered spinal mobility is thought to be contributory to low back pain. With the advent of dynamic MR imaging methods and open bore systems; the study of spine kinematics *in-vivo* is now possible (Harvey 1998; McGregor 2001). The purpose of this study was to quantify the amount of lumbar extension during a passive voluntary maneuver in a prone position (press-up). We hypothesized that the quantity of voluntary motion in the sagittal plane would differ between symptomatic and asymptomatic subjects.

METHODS

Twenty pain-free and 45 symptomatic individuals (ranging in age from 19 to 45) consented to participate in this study. Dynamic imaging of the lumbar spine was performed using a vertically open MR system (0.5 Tesla, Signa SP, General Electric Medical Systems, Milwaukee, WI, USA). Images were obtained at a rate of 1 Hz using the following parameters: repetition time (TR): 200ms; echo time (TE): 18 ms; number of excitations: 1.0; matrix: 256 x 256; field of view (FOV): 28 x 21 cm; and a 7 mm section thickness with an interslice spacing of 1 mm. Subjects were positioned with their lumbar spine centered within the magnet. A surface coil was secured to the anterior and posterior lower torso. The subjects were instructed to do a prone press-up (i.e., arch the back into extension) "as far as you are able to, without causing additional pain". Extension of each lumbar segment was quantified using the intervertebral angle (defined as the angle formed by lines delineating adjacent vertebral endplates). Segmental lumbar motion was defined as the difference between the inter-vertebral angles measured from the resting and the end-range extension image. The same investigator made all measurements. Intra-tester reliability of the measurements was performed on repeated measurements on 5 healthy volunteers. Intraclass Correlation Coefficients (ICC; 3,1) were found to be excellent, (0.95 to .99). The standard error of measurement was determined to be 0.9 degrees.

RESULTS AND DISCUSSION

A sagittal image of the lumbar spine at rest and during a press-up is presented in Figure 1. Total and segmental spine motions, as well as contribution of the individual segments to total mobility [%], are presented in Table 1. There was no difference in the mean total mobility between symptomatic and asymptomatic subjects, however the symptomatic subjects demonstrated greater relative extension at L4-L5 and less relative extension at L3-L4.

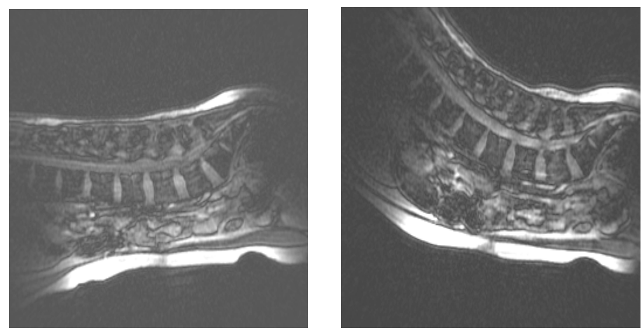

Resting *Press-up*

Figure 1: Sagittal plane MRI images of the spine during rest (left) and during a press-up (right) maneuver.

SUMMARY

These data provide unique insight into the in-vivo spinal kinematics during a voluntary press-up maneuver. Although total spine extension did not vary between symptomatic and asymptomatic subjects, a difference in individual segment mobility was observed. It is possible that the increase in segmental extension observed at L4-L5 in the symptomatic group was to compensate for diminished segmental extension evident at L3-L4. Further research is necessary to determine how altered spine mechanics relate to the development of pain.

REFERENCES

Harvey S.B., Smith F.W., Hukins D.W. (1998) *Investigative Radiology*. **33**, 439-43.

McGregor A.H. Wragg P., Gedfoyc W.M.W. (2001). *Clin Biomech* , **16**, 926-929.

Table 1: Lumbar sagittal motion; total and segmental in degrees and segmental contribution to total motion (percent, in parenthesis).

	Total	L1-L2	L2-L3	L3-L4	L4-L5	L5-S1
Asymptomatic subjects	21.0^0 (100%)	3.5 (16.6)	4.2 (19.9)	4.6 (21.9)	4.1 (19.3)	4.7 (22.4)
Symptomatic subjects	23.0^0 (100%)	4.4 (19.4)	4.9 (21.5)	4.0 (17.6)	5.4 (23.9)	4.3 (18.9)
t-test	NS	NS	NS	P<0.05	P<0.05	NS

UNDERSTANDING THE RELATIONSHIP OF MASS PROPERTIES TO THE METABOLIC COST OF LOAD CARRIAGE: MOMENT OF INERTIA

Karen Norton[1], Leif Hasselquist[1], Jeffrey M. Schiffman[1], John P. Obusek[2], Michael LaFiandra[2], Louis Piscitelle[1], Carolyn Bensel[1]
[1]U.S. Army Natick Soldier Center, Natick, MA 01760-5020, USA; E-mail: Karen.Norton @Natick.army.mil
[2]U.S. Army Research Institute of Environmental Medicine, Natick, MA 01760-5007, USA
[1,2]Center for Military Biomechanics Research, Natick, MA

INTRODUCTION

Soldiers are required to perform many actions that involve linear and angular accelerations while carrying backpack loads. The inertial properties of loads may have an effect on the energy expenditure of individuals and their ability to maneuver (Hinrichs et al., 1982). Previously, our lab found a relationship between the sagittal plane location of the center of mass (COM) of a loaded backpack and the metabolic cost of walking while carrying a heavy load (Obusek et al., 1997). The influence of backpack moment of inertia (MOI) on metabolic cost was not determined. The purpose of this study was to examine the system (torso & pack) MOI in relation to 9 COM positions and the metabolic cost of walking while carrying the loaded backpack.

METHODS

A custom external frame backpack (35 kg) was constructed. Within the backpack, a 24.9-kg lead brick could be placed in 3 horizontal positions (close, central, and away) and 3 vertical positions (high, intermediate, and low) relative to the trunk, for a total of 9 different COM positions. COM position 1 represents high and away and position 9 represents low and close (Fig. 1). Twelve soldiers (Mean ± SD: 22.1 yrs, 79.4 ± 13.6 kg, 1.73 ± 0.1 m) walked on a level treadmill at 5.6 km/hr for 5 minutes while wearing the pack in each of the 9 COM positions. Rate of O_2 consumption was found while walking (Obusek et al., 1997).

An MOI Instrument (Model XR250, Space Electronics, Inc.) was used to determine the MOI for the pack's 9 COM positions. The backpack was placed in a holder to stabilize it. The composite's (pack & holder) COM was centered over the axis of rotation of the MOI device for each plane. Subtracting the MOI of the holder and applying the parallel-axis theorem, the MOI of the backpack itself was determined for the 9 COM positions. Male cadaver torso COM and MOI data (Chandler et al., 1975) represented the soldier's COM and MOI. The torso data were combined with the backpack COM and MOI to estimate the system COM and MOI about the principal axes for the 9 COM positions by applying parallel-axis theorem.

RESULTS AND DISCUSSION

The system (torso & pack) MOI results indicate that COM position 7 (low and away) had the highest overall MOI about the principal axes and position 3 (high and close) and position 6 (intermediate and close) had the lowest (Fig. 1). In parallel with these findings, position 7 resulted in the highest metabolic cost per unit mass and position 3 resulted in the lowest (Table 1). Positions 2 and 5 were also associated with relatively low MOI values and low metabolic costs. These findings indicate that the region encompassing COM positions 3, 6, 2, and 5 may be one in which soldiers should strive to keep their backpack COM to achieve low MOI and low energy cost.

Table 1: Mean Metabolic Cost/Total Mass (ml/min/kg) ± SD by COM location.

1	2	3	4	5	6	7	8	9
16.49 ±2.05	15.69 ±1.01	15.38 ±0.91	16.82 ±1.80	15.75 ±1.03	15.80 ±0.56	18.73 ±1.29	16.65 ±1.25	16.29 ±1.16

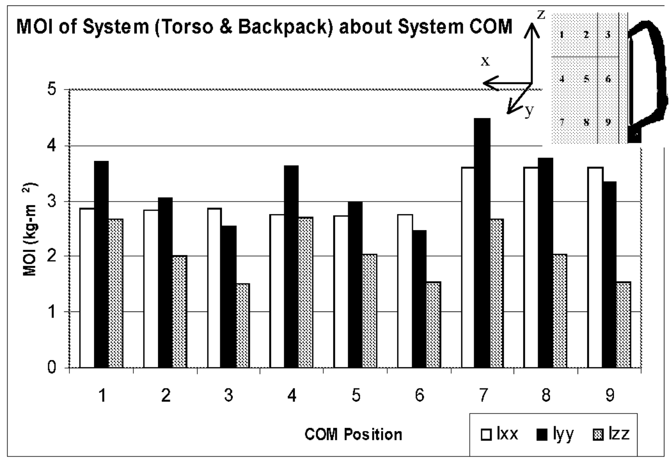

Figure 1: MOI of system about system COM.

SUMMARY

Lower system MOI values appeared in the same region of COM positions that shared lower energy cost. The findings indicate that soldiers should strive to keep backpack COM high and close relative to the torso to achieve the lowest metabolic cost and the smallest MOI values while carrying the backpack. Future research will manipulate MOI while holding a pack's COM constant to further elucidate the relationship between load carriage mass properties and energy cost.

REFERENCES

Chandler, R.F. et al. (1975). *Tech. Rep. AMRL-TR-74-137.*
Hinrichs, R.N. et al. (1982). *Tech. Rep. NATICK/TR-82/023.*
Obusek, J.P. et al. (1997). *Med Sci Sport Exerc*, 29, 5, S205.

ACKNOWLEDGEMENTS

Special thanks to Michael Holthe, Everett Harman, Peter Frykman, Christopher Palmer, Randy Bills, and Ray Spring.

THE VISCOELASTIC BEHAVIOR OF MOUSE EXTENSOR DIGITORUM LONGUS SINGLE CELLS

Jennifer Davis, Sameer Shah, and Richard L. Lieber
University of California, San Diego and The VA Medical Center, San Diego
Email: rlieber@ucsd.edu

INTRODUCTION

Skeletal muscle fibers are inherently viscoelastic. While much is known about active muscle viscoelasticity, until recently, little had been known about the mechanical behavior of passive skeletal muscle. Magid and Law (1985) showed that myofibrillar structures are the source of elasticity at physiologic lengths and that the sarcolemma and extracellular connective tissue are responsible for passive tension only in highly extended muscles. Previous studies in rat, rabbit, and frog have shown that upon stretching, a single fiber exhibits viscoelastic behavior (Katz, 1939; Wang et al. 1993, Mutungi and Ranatunga, 1996; Minajeva et al. 2001). No one has characterized the passive mechanical properties in mouse muscle. Thus the purpose of this study was to quantify the viscoelastic behavior of mouse extensor digitorum longus (EDL) cells, especially in light of the powerful studies that are possible when performed on transgenic animals.

METHODS

The EDL muscle was slightly skinned in 30% glycerol storage solution incubated with a protease inhibitor. The EDL was submerged in relaxing solution and single fibers excised from the preparation. A single fiber was transferred into an apparatus containing relaxing solution at room temperature (~25° C). The fiber was mounted between a force transducer (400A, Aurora Scientific, Ontario, Canada) and length controller (318B, Aurora Scientific, Ontario, Canada). Sarcomere length was monitored during the course of the experiment by measuring first order diffraction patterns from a He-Ne Laser (LHR-007, Melles-Griot, Irvine, CA.).

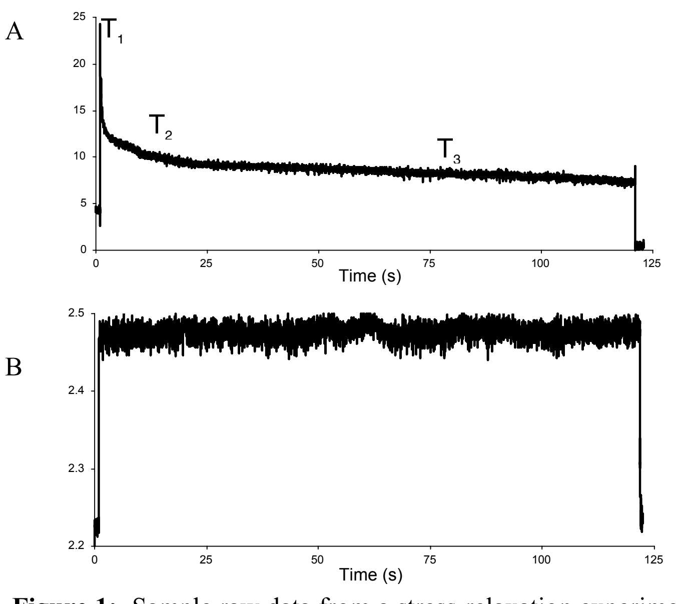

Figure 1: Sample raw data from a stress-relaxation experiment. (A) Muscle fiber force after 30% deformation, (B) Sarcomere length (SL). T_1, T_2, T_3 represent decay time points measured.

Motor length, force, and sarcomere length were recorded via a 610E series DAQ board in the LabView environment (National Instruments, Austin, Texas). Every 4 minutes, fibers were stretched to 10, 20, and 30% strain within 30 ms. Stretched fibers were held for 2 minutes and released to the initial starting position.

RESULTS AND DISCUSSION

The time points measured (T_1, T_2, T_3) represented the peak force, middle decay, and steady state force of the stress-relaxation curve (Fig.1). The average force at each strain was expressed as a function of sarcomere length for T_1, T_2, and T_3 (Fig. 2). Despite the large decay in force, sarcomere length clearly remained constant throughout the entire duration of the stretch. A 2x2 two-way ANOVA revealed a significant effect of strain on force and sarcomere length ($p<0.0001$), but the effect of time and interaction between time and strain were not significant. The source viscoelastic behavior of mouse muscle is still unresolved and that future investigations could lead to a complete characterization of mouse EDL passive mechanical properties.

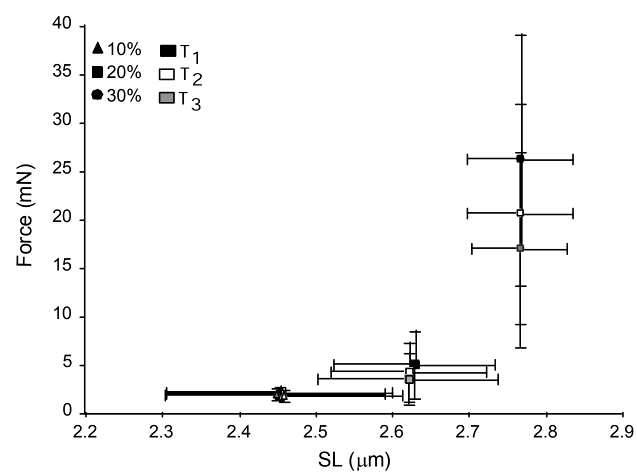

Figure 2: Relationship between sarcomere length and force for three strains (symbols show strains) and three times (shadings show times) for mouse EDL fibers.

REFERENCES

Katz, B. *J.* (1939). *Physiol. (Lond.)* **96**:45-64.
Magid, A., and Law, D.J. (1985). *Science,* **230**:1280-1282.
Minajeva, A. et al. (2001). *Biophys. J.* **80**, 1442-1451.
Mutungi, G. & Ranarunga, K. (1996). *J. Physiol.* **496**, 867-836.
Wang, K et al. (1993). *Biophys. J.* **64**:1161-1177.

ACKNOWLEDGMENTS

Support from NIH AR40050, the V.A. Rehab R&D Service and the Swedish Medical Research Council.

WHOLE-BODY POSTURAL CONTROL and TRUNK STABILITY DURING SUDDEN HAND LOADING PART 2: LOADS CAUSING COUPLED LATERAL BEND AND FORWARD FLEXION MOMENTS

Monica Haumann, Stephen Brown and Jim Potvin

Faculty of Human Kinetics, University of Windsor, Ontario, Canada
jpotvin@uwindsor.ca

INTRODUCTION

During activities of daily living, unpredictable circumstances results in challenges of equilibrium, including those that affect medial-lateral stability. The purpose of this study was to investigate the control of whole-body equilibrium, in coordination with spinal stability, in anticipation and response to sudden, asymmetric perturbations at the hands.

METHODS

Seventeen females volunteered for this study. Subjects were instrumented with EMG electrodes over 6 bilateral muscles pairs: lumbar and thoracic erector spinae (LES and TES), external and internal obliques (EO and IO), biceps femoris (BF), soleus (Sol) and the right tibialis anterior (TA). Subjects were situated on a force plate to measure Centre of Pressure (CoP) in the anterior-posterior (CoP_{AP}) and medial-lateral (CoP_{ML}) directions. CoP values were calculated with the vertical force and moments recorded on the force plate. These data were sampled at 1000Hz and dual low-pass filtered (10Hz). EMG signals (1000Hz) were rectified, low-pass filtered (3Hz) and normalized to MVC.

Subjects were asked to maintain an upright posture while holding a box with arms extended comfortably and handles at waist height. A curtain was placed in front of the subject so that they could not see the load or the box. A 6 kg load was delivered to the subject via a pulley system that applied the load into the center (Symmetry) or right side (Asymmetry) of the box. The current paper will focus on the data from the Asymmetric trials. For the purposes of this paper, data were collected under two experimental conditions: 1) asymmetrical load, with expected timing in which the experimenter counted down from 5 to 1 and released the load into the right side compartment of the box on the count of one; 2) asymmetrical, unexpected loading in which the load was dropped to the right side after random intervals with no prior warning to the subjects. Subjects performed 10 repetitions for each condition

For each condition the following dependent variables were calculated: 1) pre-average: average amplitude of the CoP_{AP} and EMG from each muscle, for the 15 ms prior to sudden load onset, 2) anticipatory response: change in amplitude from the baseline levels, averaged from 150 ms to 15 ms prior to loading, to the pre-average levels and, 3) peak response: maximum increase from the pre-average level to the peak amplitude during the first 500 ms following load onset. Averages were calculated with each of the 10 trials performed within each condition. A three-way ANOVA was performed with repeated measures (side, load placement and timing) to determine experimental effects. Significance was evaluated at $p<0.05$.

RESULTS AND DISCUSSION

The anticipatory response of the CoP_{ML} was not significantly affected by the lateral load placement or timing conditions. Absence of a lateral anticipatory postural adjustment was attributed to the substantial challenge to whole-body stability that the asymmetric perturbation evokes.

The right BF was the only leg muscle to show a significant anticipatory response prior to the asymmetric load onset. Recruitment of the BF may be indicative of the 'hip strategy', which is evoked in response to large, unpredictable perturbations (Horak and Nashner, 1986). In response to the asymmetric perturbation those leg muscles ipsilateral to the load placement (right BF, Sol, TA) were activated significantly higher than the contralateral leg muscles. It is concluded that, in response to the asymmetric perturbation, the shear forces acting at the surface were altered to regain whole-body equilibrium.

Lateral agonists of the trunk (left LES, EO) and lateral stabilizers (right TES, IO) each showed significantly higher pre averages to the asymmetric load onset. Similarly, significant asymmetries were noted for the activation of the lateral agonists (right LES, EO) and the lateral stabilizers (left TES). Co-activation of the lateral agonists and lateral stabilizers served to increase lumbar stiffness and compression acting on the spine. It was also found, in a case study of a completely unanticipated/suprise asymmetric perturbation, that the TES and IO were recruited to serve as lateral agonists as opposed to providing solely a stabilizing function. A plausible explanation for these asymmetrical stabilizers to be recruited to counter and resist the asymmetric perturbation was the degree of postural instability, given the unpredictability of the surprise perturbation.

SUMMARY

The observed increased in the ipsilateral leg muscles were concluded to control the displacement M-L CoP and prevent the lateral collapse of the trunk. Trunk stability observed increase in antagonistic co-activation, suggesting greater neuromuscular control is necessary to maintain medial-lateral stability.

REFERENCES

Horak, F.B., Nashner, L. (1986). *J. Neurophys.*, **55,**1369-1381.

PILOT STUDY OF INTRACELLULAR SIGNALING IN POST-OPERATIVE TENDONS

Jeng-Yu Lai[1], Krishna V Gumidyala[2], Aletta P. Houwink[2], Chunfeng Zhao[2], Peter C. Amadio[2], and Kai-Nan An[2]
Departments of Dermatology[1] and Orthopedics[2], Mayo Clinic, Rochester, MN, USA

INTRODUCTION

Early mobilization is necessary after tendon surgery to regain maximal function of the tendon. Studies suggested that soft tissues may require proper stimulation to maintain their integrity at the tissue as well as cellular level.

At least part of the signal transduction pathway that mediates responses to mechanical forces is coupled to activation of extracellular signal-regulated kinases (ERK) and c-Jun N-terminal kinase (JNK) which, in turn, regulate downstream transcription factors and nuclear events linked to specific cell responses (Banes *et al,* 1999; Xia *et al,* 1995; Yamauchi *et al,* 2001). Surgery should enhance JNK activation, which is a stress activated protein and whose activation leads to apoptosis. We hypothesize that the ERK and JNK activation after surgery may have an effect on the results of early motion therapy, specifically that therapy may affect ERK and JNK levels differentially, altering the balance between mitosis (ERK) and apoptosis (JNK). As a prelude to testing this hypothesis, we wished to determine if intratendinous ERK and JNK were affected by tendon surgery, and if so, when.

METHODS

Dogs were anesthetized for tendon surgeries. The surgical forepaw was immobilized by a combination of radial neurectomy and external casting. The contralateral paw served as a mobile, normal control. The side of immobilization was randomized. On the immobilized paw 2 tendons were used. The first was lacerated (Lac) and then repaired with a modified Kessler repair suture technique. The other was surgically approached in the same manner as the Lac tendon, but no laceration or repair was performed (Sham). Tendon within 7 mm proximal and distal to the operated site was discarded. Tendons were harvested at 1, 3, 5, or 7 days (3 dogs each group) after surgery and fresh frozen in liquid nitrogen before being stored.

Tendons were weighed and ground with Trizol. Proteins were dissolved in MAPK solution (Auclair *et al,* 1999), loaded onto a 12% polyacrylamide gel for electrophoresis, and transferred to a nitrocellulose membrane. The membrane was blotted against activated ERK 1/2, total ERK 2, and phospho-JNK.

The images were scanned and measured by Scion Image software. All the signal intensities were calibrated based on intensity and band area of total ERK from the normal tendon. The changes in expression were calculated against the amount of expression in the normal tendon of the contralateral limb.

RESULTS AND DISCUSSION

Since the image software determined the amounts of protein by measuring the pixel number in the band area, exposure of the film and size of the scanned image would affect the reading. Therefore, the results were presented as ratios to the control tendon**.**

The ERK expression is shown in Figure 1. ERK expression decreased after 3 days in the Sham tendons. However, ERK expression was relatively unchanged, as compared to controls, in the Lac tendons**.** However, the expression of JNK was not consistent, possibly due to technical difficulties**.** We had intended to examine and compare the expressions of ERK and JNK as an indicator for post-operative rehabilitation. However, our intention was hindered by the difficulties in preserving phospho-groups during protein extraction and photo imaging.

Nevertheless, this study presents an initial effort to design a rehabilitation protocol for tendon surgeries based on cellular signaling.

A larger sample size may be needed to demonstrate statistical differences. Also, technical improvement in the extraction process is needed. Phosphorylation is unstable unless the protein is stored in a reducing agent, which was not achievable with MAPK buffer. Therefore, some activated ERK and JNK might have lost in the process. Finally, a better imaging system could greatly increase the accuracy of the measurements.

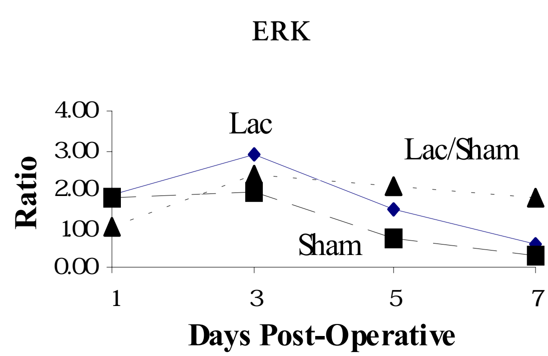

Figure 1. ERK expression..

REFERENCES

Auclair M *et al. J Clin Endocrinol Metab* 84: 3197-206., 1999
Banes AJ *et al. Osteoarthritis Cartilage* 7: 141-53., 1999
Xia Z, Dickens M, Raingeaud J, Davis RJ and Greenberg ME. *Science* 270: 1326-31., 1995
Yamauchi J *et al. Biochem Biophys Res Commun* 288: 1087-94, 2001

ACKNOWLEDGEMENTS

This project was supported by NIH grants AR 44391 and T32 HD 07447.

DETERMINATION OF THE OPTIMAL FOREARM MUSCLES TO MONITOR WITH EMG IN ERGONOMIC STUDIES

Matt MacPherson, Diane Grondin and Jim Potvin

Faculty of Human Kinetics, University of Windsor, Windsor, Ontario, Canada,
jpotvin@uwindsor.ca

INTRODUCTION

Jobs that require large grip forces and repetitive handgrips are linked to the occurrence of tendon-related disorders (Mital & Kilbom, 1992). Therefore, it is important to quantify the forces required by the muscles of the forearm during work. However, no efforts have been made to indicate which muscle(s) of the forearm best represent the demands on the hands. Also, many gripping studies do not even specify which muscles of the forearms were monitored. Many portable EMG systems used in ergonomics allow for the monitoring of only four muscles. The purpose of this study was to determine if one forearm flexor and one extensor muscle were sufficiently active during a wide variety of hand exertions to warrant the monitoring of only two EMG channels, bilaterally, when wanting to represent overall hand demands during work activities.

METHODS

Six male and four female subjects volunteered to participate in the study. Pairs of Ag/Cl bipolar surface electrodes were placed over three forearm flexors: flexor carpi ulnaris (FCU), palmaris longus (PL) and flexor carpi radialis (FCR), and three forearm extensors: extensor carpi ulnaris (ECU), extensor digitorum (ED) and extensor carpi radialis brevis (ECRB). EMG data were collected at 1024 Hz and the signals were amplified (x500) and full-wave rectified. Maximum voluntary contractions (MVCs) were obtained for each flexor and extensor muscle. The experimental trials consisted of five different hand exertion types often observed in work environments (pinch grip, lateral key grip, power grip, thumb press and finger press), with each held in three different wrist postures (flexed, neutral and extended). Trials lasted 20s with five cycles, each cycle consisting of 2 s of a maximum exertion and 2 s of rest. EMG signals were low-pass filtered using a second order Butterworth filter (f_C= 2.5 Hz) and then normalized to MVC amplitudes. The average EMG amplitude was calculated for each muscle/trial combination. In addition, each flexor was renormalized to the highest mean of the three for each trial. The same was done for the extensors. Three-way ANOVAs with repeated measures (3 muscles, 5 hand exertions, 3 postures) were calculated for the normalized and renormalized EMG amplitudes for both the flexor and extensor groups (significance at $p<0.05$).

RESULTS AND DISCUSSION

When the EMG data were pooled across postures and hand exertion types, the ECU and FCU were the extensor and flexor muscles, respectively, with the highest average amplitudes ($p<.05$ for both, Figure 1). Interestingly, the extensor activity

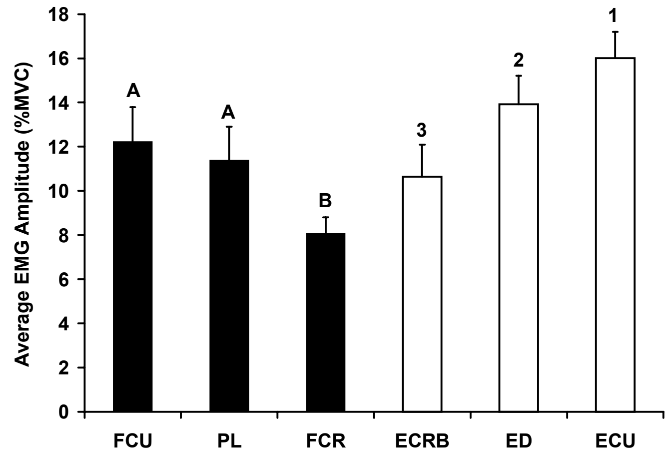

Figure 1: Pooled average EMG amplitudes, with standard error bars (n=150). Different letters or numbers indicate significant differences within flexors or extensors ($p<0.05$).

was generally higher than the flexor activity, with the most active extensor (ECU) being approximately 31% higher than the most active flexor (FCU). Moreover, for the significant Grip*Posture*Muscle interaction of the extensors, the ECU was the highest extensor in 11 out of 15 conditions, and was at least 85% of the highest extensor muscle in the other four conditions. With the renormalized data, the ECU was an average of 90% of the ultimate maximum over the 15 conditions. The FCU was higher than, or equal to, the other flexor muscles in 13 of 15 conditions, and was at least 80% of the highest muscle in the other two conditions. With the renormalized data, the FCU was an average of 89% of the ultimate maximum over the 15 conditions.

SUMMARY

It was concluded that it sufficient to collect surface EMG from only the ECU and FCU muscles when monitoring the hand and forearm demands in occupational tasks. These muscles were almost always the most active, or nearly the most active, for the 15 combinations of posture and hand exertion type. Given the higher activation levels of the forearm extensor muscles, it is important to note that these muscles cannot be ignored, even when the dominant hand motion seems to be in flexion. The extensor muscles of the forearm likely have an important stabilizing role during hand exertions and are, consequently, very important to monitor in ergonomic studies.

REFERENCES

Mital, A., Kilbom, A. (1992). *International Journal of Industrial Ergonomics,* **10**, 7-21.

THE EFFECTS OF BACKPACK LOADS ON PELVIS AND UPPER BODY KINEMATICS OF ADOLESCENT FEMALES DURING GAIT

Chriss Stanford[1], Peter Francis[2], and Hank Chambers[1]

[1]Motion Analysis Laboratory, Children's Hospital, San Diego, California, cstanford@chsd.org
[2]San Diego State University, San Diego, California

INTRODUCTION

Children carry schoolbag loads of 15% to 25% of their bodyweight (BW)[1]. Though carrying 20% BW has been associated with increased symptoms of back pain in schoolchildren[2], few studies have examined the specific effects of backpack carrying on posture and gait characteristics in children. The purpose of this study was to examine the kinematics of the pelvis, trunk, and upper extremities in the adolescent female during loaded gait.

METHODS

Reflective markers were attached to the skin overlying the feet, pelvis, trunk, shoulders, and elbows of ten healthy females, aged 13-15 years. Subjects walked down a 10 m runway, while carrying each of five randomized loads, listed in Table 1. Positions of the markers were captured using an 8-camera Motion Analysis System (Motion Analysis Corp., Santa Rosa CA), sampled at 60 Hz.

Table 1: Description of load conditions

BW	Unloaded/no backpack
D10	10% BW load carried with both shoulder straps
D20	20% BW load carried with both shoulder straps
S10	10% BW load carried on the right shoulder
S20	20% BW load carried on the right shoulder

Trunk and pelvis motion were calculated relative to a global coordinate system. Pelvis kinematics were measured in the coronal and transverse planes only, as the presence of the backpack on the dorsal surface of the pelvis prevented accurate analysis of sagittal plane motion. Shoulder motion was measured in the sagittal plane, relative to the trunk.

For each subject, data were normalized as a percentage of the gait cycle. Mean angle and range of motion (ROM) were compared across load conditions using repeated measures ANOVAs, with a Bonferonni correction. For each comparison, $p<.007$ was considered significant.

RESULTS AND DISCUSSION

Figure 1 displays mean trunk and pelvis kinematics throughout the gait cycle for BW, D20, and S20. Load carriage using a single shoulder strap induced a significant trans-planar adjustment in posture, including increased lateral tilt and rotation of the trunk in the opposite direction to the load-bearing shoulder. Increased obliquity of the ipsilateral hemipelvis and increased pelvic internal rotation was also observed when carrying as little as 10% BW on one shoulder. These changes appear to represent a strategy to center the load over the hips in an attempt to preserve the normal gait pattern. Assymetry in arm swing was also observed: a significant increase in left shoulder ROM and decrease in right shoulder ROM was observed with S10 and S20.

An increase in forward lean was the only observed significant difference between D10 and unloaded walking. This finding was not previously observed in boys[3], suggesting that the flexion response may be more pronounced in girls.

D20 significantly increased trunk flexion, reduced pelvic rotation, and increased right and left shoulder flexion, relative to unloaded walking.

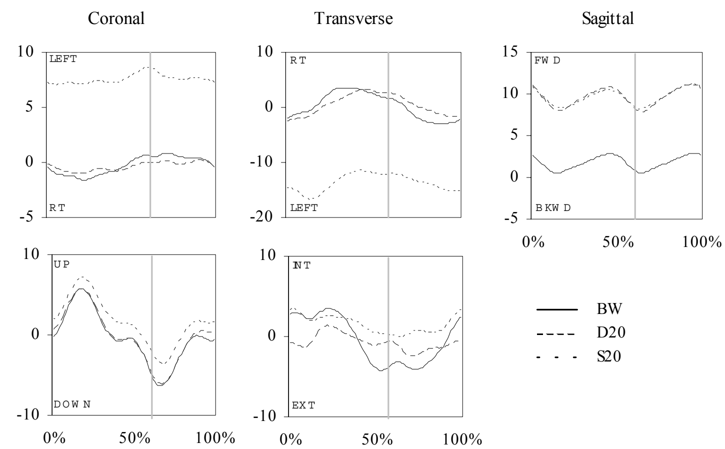

Figure 1: Trunk (top row) and pelvis kinematics (bottom) during the gait cycle for BW, D20, and S20.

SUMMARY

The results of this investigation indicate that carrying 20% BW poses additional postural consequences over 10% BW in female adolescents. Changes in posture were most evident when the load was asymmetrically distributed in the coronal plane. The resulting internal moments acting to stabilize the trunk through this mode of carriage may be of concern in the development of injuries, particularly in teenage females.

REFERENCES

Negrini, S. et al (1999). *The Lancet*, **354**, 1974-1975.
Viry, P. et al (1999). *Revue Du Rhumatisme*, **66**, 381-388.
Hong, Y., Brueggemann, G.P. (2000). *Gait and Posture*, **11**, 254-259.

MUSCLE DEMANDS AND TORQUE REACTIONS ASSOCIATED WITH AIR AND ELECTRIC HAND TOOLS

Jim Potvin[1], Mike Agnew[1], Cherrie Ver Woert[2]

[1]Faculty of Human Kinetics, University of Windsor, Ontario, Canada, jpotvin@uwindsor.ca
[2]Ford Motor Company, Dearborn, Michigan, USA

INTRODUCTION

Recently, electric (or DC) tools have been introduced as a potential replacement for pneumatic (or air) tools in manufacturing environments. While DC tools can be transducerized and programmed with many variables to improve the torque reactions during drilling, they do have a potential ergonomic liability of being heavier than air tools. Thus, the purpose of this study was to determine if differences exist between the ergonomic demands and injury risks associated with air and DC pistol grip hand tools during the run down of horizontal joints.

METHODS

Data were collected from 15 male and 15 female subjects. Each subject was instrumented with 7 pairs of surface EMG electrodes on the right arm: flex. carpi uln. (FCU), flex. carp rad. (FCR), ext. carpi uln. (ECU), ext. carpi rad. longus (ECR), biceps brachii (BB), ant. deltoid (AD) and trapezius (Traps). A triaxial accelerometer was also attached to the hand. Each subject performed drilling with five pistol grip tools from two tool suppliers. This resulted in two air tools, one non-transducerized electric (NTDC) and two transducerized (TDC) electric tools. Three types of joints were simulated: 1) 2 Nm, 720 degrees, 2) 7 Nm, 720 deg and 3) 7 Nm, 30 deg. For each of the 15 combinations of tool and joint, subjects were asked to drill five joints to completion within a 60 second period, and to repeat this 5 times for each condition (5 minutes). The order of joint and tool presentation was randomized. Each signal was sampled at 1000 Hz. The EMG signals were digitally full wave rectified, low pass filtered with a Butterworth filter (f_C =2 Hz) and normalized to MVC. A resultant acceleration was calculated from the triaxial accelerometer and this was converted into an angular acceleration based on the moment arm to the tool joint axis.

EMG and acceleration time-histories were truncated to represent drilling periods. Median and Peak (90^{th} %ile EMG, 99^{th} %ile acceleration) values were calculated for each signal time-history, but only the peak data will be presented here. A 2 factor ANOVA with repeated measures was run to determine the effects of joint and tool type.

RESULTS AND DISCUSSION

In general, the 7 Nm/720 degree joint was shown to result in the highest demands for all muscles monitored in this study, with the ECU having the highest overall demands for each condition studied. Muscle demands were similar for the other two joints. The effect of tool type could be divided into two groups: 1) the four forearm muscles monitored, 2) the biceps, shoulder (AD) and neck (Traps) muscles. For the forearm muscles, the activation levels were observed to be significantly lower in the non-transducerized and transducerized DC tools, when compared to the two air tools. However, given the greater weight of the DC tools, the BB, AD and Traps showed slightly higher amplitudes in the DC compared to the air tools. It should be noted that the highest demands were observed in the forearm ECU, ER and FCU muscles.

With regards to the hand acceleration (torque reaction) data, there was a significant interaction between tool type and joint (Figure 1). Generally, the DC tools always had lower torque reactions than the air tools, although these differences were larger for certain joints. For example, one air tool resulted in particularly high accelerations for the 7 Nm/30 deg (hard) joint.

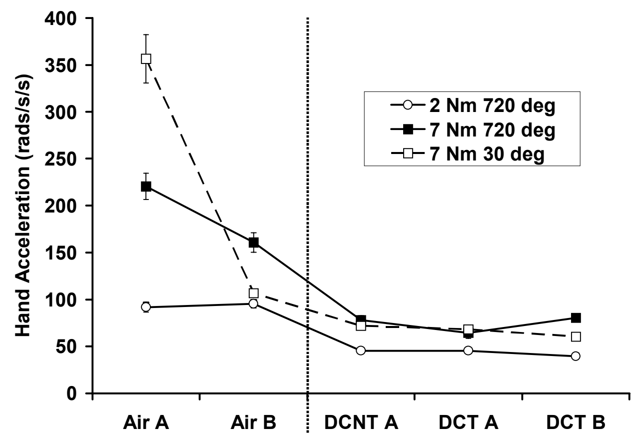

Figure 1: Joint x Tool interaction for Peak acceleration. Standard errors are indicated. (n=30)

SUMMARY

It was concluded that, although DC tools are heavier, they actually result in a decrease in the risk of cumulative trauma disorders of the upper limb. They result in a significant decrease in the demands on the highly challenged forearms, a substantial decrease in the torque reaction at the end of the joint run-down and only a slight increase in the demands on the less challenged upper arm, shoulder and neck muscles.

EFFECTS OF MECHANICAL COMPRESSION ON ANABOLIC AND CATABOLIC GENE EXPRESSION IN A RAT TAIL MODEL

CR Lee[1,2], JJ MacLean[1], S. Grad[2], K. Ito[2], M. Alini[2], and JC Iatridis[1]
[1]Department of Mechanical Engineering, University of Vermont, Burlington, VT, USA, cyndi_lee@alum.calberkeley.org
[2]AO Research Institute, Davos, Switzerland

INTRODUCTION

Mechanical loads influence the health of the intervertebral disc (IVD) in large part due to the influence of physical forces on IVD cells. To elucidate the relationship between mechanical loading and IVD cell metabolism, the current *in vivo* study evaluated the IVD cell expression of anabolic (collagen I, collagen II and aggrecan) and catabolic (stromelysin and collagenase) genes after cyclic compression.

METHODS

Animal Model: Tails of 28 skeletally mature Wistar rats were instrumented with an Ilizarov-type device spanning caudal disc level 8-9 (i.e. instrumented level). Animals were separated into 4 groups as follows:

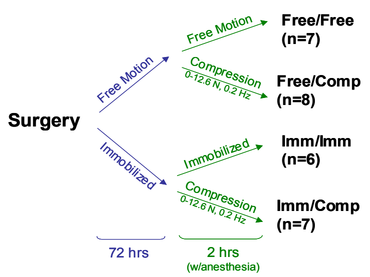

Real-time PCR Analysis: Instrumented (caudal level 8-9) and uninstrumented (i.e. internal control levels 6-7 & 10-11) discs were isolated and separated into annulus and nucleus regions, followed by mRNA extraction and reverse-transcription to cDNA. The relative expression of types 1 and 2 collagen, aggrecan, stromelysin (MMP3) and collagenase (MMP13) mRNA was measured with real-time PCR.

Statistical Analysis: Levels of mRNA in instrumented discs were normalized to the average levels measured in the 2 uninstrumented discs. Data are presented as mean ± IQ range and 95th percentiles. A t-test was used to determine effects of surgery and loading. ANOVA and SNK post-hoc testing were used to evaluate differences among loading groups.

RESULTS

Immobilization (imm/imm) resulted in a slight decrease in relative mRNA levels of collagen 1 and 2 (2- to 3-fold) in the annulus (Fig 1a) and a marked increase in MMP3 mRNA (10-fold) in the nucleus (Fig 1d). Annular collagen 1 and 2 mRNA levels were also significantly reduced in discs that were immobilized for 72 hrs and then cyclically loaded at 1 MPa for 2 hrs (imm/comp; Fig 1a). The increase in nucleus MMP3 with immobilization was down-regulated back towards control levels with 2 hrs of cyclic loading (imm/comp), while cyclic loading applied to free discs (free/comp) up-regulated nuclear MMP3 (3-fold increase; Fig 1d). The imm/comp condition moderately up-regulated relative mRNA levels of MMP3 and MMP13 (2.5- and 4-fold, respectively) in the annulus (Fig 1b).

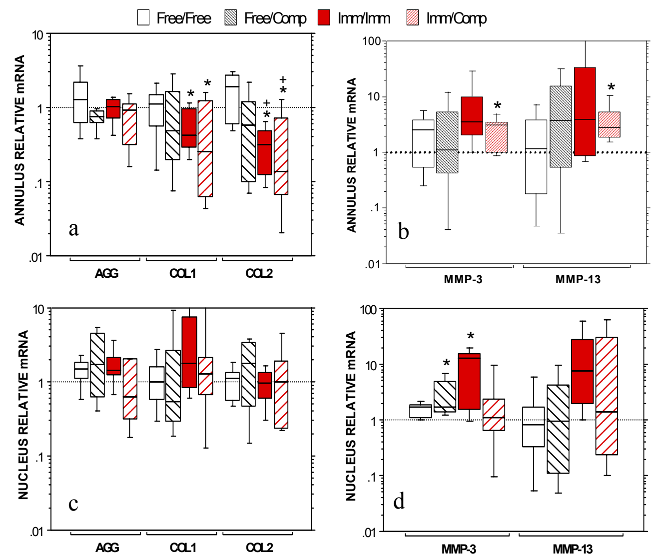

Fig. 1: Relative mRNA levels in annulus (a,b) and nucleus (c,d) of anabolic (a,c) and catabolic (b,d) genes. Data presented as mean ± IQ and 95th percentile. (*t-test $p<0.05$; +SNK vs free/free $p<0.05$)

DISCUSSION

Immobilization of the motion segment led to a decrease in collagen 1 and collagen 2 gene expression in the annulus and an increase in MMP3 (stromelysin) expression in the nucleus. Immobilization plus cyclic compression (1MPa @ 0.2Hz for 2 hrs) down-regulated collagen 1 and 2 expression while up-regulating MMP3 and MMP13 expression in the annulus. Two hours of cyclic loading offset the MMP3 up-regulation in the nucleus that was induced by immobilization. Further work is necessary to determine the magnitude, frequency, and duration of cyclic loading that stimulate anabolic and catabolic responses of the disc cells.

ACKNOWLEDGEMENTS

Funded by NIH-K01AR02078 and AO Research-Commission.

GROUND REACTION FORCES TRANSMITTED TO THE UPPER EXTREMITY DURING THE YURCHENKO VAULT AND FLOOR EXERCISE

Matt Seeley and Eadric Bressel
Biomechanics Laboratory, Utah State University, Logan, UT, USA, sl63n@cc.usu.edu

INTRODUCTION

Women's gymnastics has increased in popularity, and injury rates within the sport have also increased. Female collegiate gymnasts consistently maintain injury rates similar to collegiate football players, and elite gymnastics injury rates are higher than all other levels of gymnastics (Meeusen, 1992). Research indicates upper extremity injuries may be more prevalent during the vault than during other gymnastic skills (Caine et al., 1992; Roy et al., 1985). Previous research has not quantified ground reaction forces (GRF) transmitted to upper extremities during the vault. The Yurchenko vault is a relatively new round-off entry vault involving increased risk. The purpose of this study was to observe peak vertical GRF transmitted to the upper extremity of high-level gymnasts during the round-off phase (the round-off just before the gymnast strikes the springboard) of the Yurchenko vault.

METHODS

This study observed one independent variable, the round-off, comprised of two conditions: (a) the round-off phase of the Yurchenko vault, and (b) the floor exercise round-off. Values for the Yurchenko vault were compared to the floor exercise round-off, an activity normally associated with fewer upper-extremity injuries. Peak vertical GRF served as the dependent variable. Fifteen high-level gymnasts ($M_{age} = 18 \pm 2.58$; $M_{height} = 159 \pm 6.22$ cm; $M_{mass} = 56.4 \pm 5.87$ kg) volunteered to participate in the study. Participants performed three trials of the Yurchenko vault and floor exercise round-off in randomized order, placing the trail hand on a 40 X 60 cm force platform. GRF values were collected at a sampling rate of 500 Hz and recorded GRF values were normalized to body weight (BW). The Yurchenko vault and floor exercise round-offs were performed in dimensions identical to a competition environment, which included a sting mat placed over the force platform. A paired t-test was used to examine the effect each round-off condition had on the dependent variable with the p-value set at .05.

RESULTS AND DISCUSSION

Mean peak vertical GRF during the round-off phase of the Yurchenko vault were $2.39 \pm .25$ BW (Figure 1) and were significantly greater ($p < .05$) than peak GRF values recorded during the floor exercise round-off (Figure 1).

GRF values during the round-off phase of the Yurchenko vault and floor exercise round-off were greater than GRF values observed by Markolf et al. (1990) during the pommel horse, an activity commonly linked to chronic upper extremity injury (Figure 1). Peak GRF values during the round-off phase of the Yurchenko vault were also greater than values reported by McClay et al. (1994) and Cavanagh and LaFortune (1980) during the impact stage of running at speeds of 3.8 m/s (1.9 BW) and 4.5 m/s (2.2 BW) respectively (Figure 1). Each of the activites mentioned have been linked to overuse injury. Because upper extremities are poorly fit for weight bearing activities (Tuttle, 1969), peak GRF observed in this study may be a factor in upper extremity injury in gymnastics.

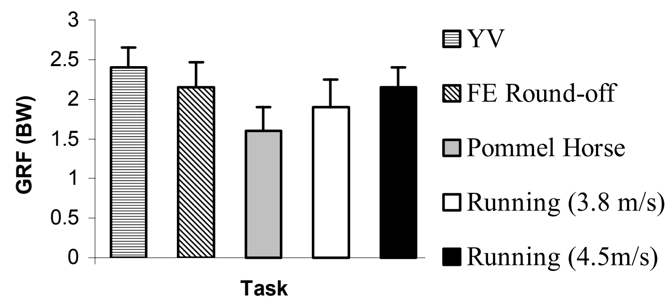

Figure 1: Mean peak vertical GRF values normalized to body weight. Yurchenko vault (YV), floor exercise (FE) round-off, and pommel horse show peak vertical GRF transmitted to upper extremities.

SUMMARY

Peak GRF values during the round-off phase of the Yurchenko vault were 2.39 BW and were significantly greater ($p < .05$) than peak GRF transmitted to the upper extremity during the floor exercise round-off (Figure 1). Peak GRF values during the round-off phase of the Yurchenko vault may be reduced through the implementation of safety equipment and/or a change in vaulting technique. Research conducted to decrease peak GRF transmitted to the upper extremities during the round-off phase of the Yurchenko vault may decrease the incidence of upper extremity injuries suffered by high-level gymnasts.

REFERENCES

Caine, D. et al., (1992). *Am J Sports Med,* **20,** 290-298.
Cavanagh, P.R., LaFortune, M.A. (1980). *J Biomech,* **13,** 397-406.
Markolf, K.L et al., (1990). *J Biomech,* **23,** 1001-1011.
McClay, I.S. et al., (1994). *Journal of Applied Biomechanics,* **10,** 222-236.
Meeusen, R., (1992). *Sports Med,* **13,** 338-356.
Roy, S. et al., (1985). *Am J Sports Med,* **13,** 301-308.
Tuttle, R.H., (1969). *Science,* **166,** 953-961.

EFFECTS OF EXPECTATION DURING SUDDEN UNDLOADING OF THE HANDS
PART 1: ANTICIPATORY POSTURAL ADJUSTMENTS

Stephen Brown, Monica Haumann and Jim Potvin

Faculty of Human Kinetics, University of Windsor, Windsor, Ontario, Canada
jpotvin@uwindsor.ca

INTRODUCTION

In whole-body control, anticipatory postural adjustments (APAs) are utilized to counteract the effects of an oncoming perturbation (Massion, 1992). These APAs appear to be more significant under self-triggered, rather than externally triggered, perturbations (Aruin & Latash, 1995). This study examines the anticipatory and responsorial whole-body adjustments made during sudden unloading of the hands with various expectancies

METHODS

Eleven male subjects volunteered for this study. All measurements were made using an EMG system and force plate. Surface Ag/AgCl electrodes were used to detect the activity of four muscles on the right side: biceps femoris (BF), rectus femoris (RF), soleus (Sol), and tibialis anterior (TA). Trunk muscles were also examined but will be dealt with in a separate abstract. Forces plate data were used to calculate anterior-posterior centre of pressure (CoP_{AP}) time-histories.

The experimental procedure was as follows: the subject stood upright on the force platform, with feet separated at shoulder width, holding a box at waist height with handles at shoulder width. A 6.8 kg load was placed in the center of the box. Three experimental conditions were examined: a voluntary timing (VT) condition in which the experimenter counted down from 5 to 1 and then the subject dropped the box; a known timing (KT) condition in which the experimenter counted down from 5 to 1 and rapidly removed the load from the box via a pulley system; and a random timing (RT) condition in which the load was rapidly removed from the box with no countdown. Ten repeat trials collected for each condition. The order of each timing condition was randomized.

Raw force plate signals (1000 Hz) were dual low-pass filtered (10 Hz). Raw EMG signals (1000 Hz) were rectified, low-pass filtered (3 Hz) and normalized to MVCs. The following statistics were calculated for each EMG amplitude and the CoP_{AP}: 1) preparatory adjustment: the change in amplitude from baseline levels to the level just preceding the load removal or drop and, 2) dominant response: the maximum increase or decrease in amplitude from the pre-perturbation level to the post-perturbation level (within 500 ms). Averages were taken across the 10 trials for each subject. A one-way ANOVA, with repeated measures, was used to determine the effect of expectancy for each dependent variable ($p<0.05$).

RESULTS AND DISCUSSION

The magnitude of the CoP_{AP} APA was highest in the VT condition. The lack of significance between the KT and RT conditions indicates that knowledge of when the unloading will occur may not have a large effect on APAs, if the perturbation is externally triggered**.** The dominant CoP_{AP} response was observed to become more negative with an increase in uncertainty of the perturbation timing (Figure 1). The BF was the only muscle to show significantly larger preparatory adjustments in the VT compared to both the KT and RT conditions. The dominant responses of the BF, Sol and TA each significantly increased from the VT to KT to RT conditions ($p<0.05$).

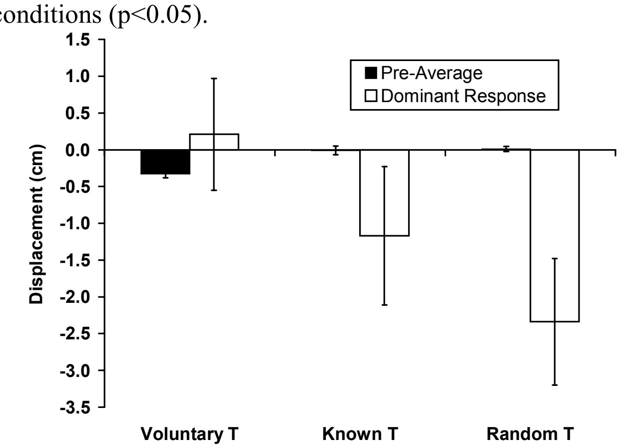

Figure 1: Responses of the CoP_{AP} for the three experimental conditions. Positive values represent displacements in the anterior direction. Standard error bars are indicated. (n=11).

SUMMARY

As knowledge of the timing of unloading increased, subjects were better able to adjust their CoP_{AP} to prepare for the perturbation. This resulted in smaller CoP_{AP} displacements in response to the unloading. The BF was the monitored muscle most responsible for adjusting the CoP_{AP} in the posterior direction prior to unloading. This adjustment seemingly enabled the BF, as well as both anterior muscles (Sol and TA), to respond to the perturbation with lower activation levels as knowledge of the timing of the unloading increased.

REFERENCES

Aruin, A.J., Latash, M.L. (1995). *Exp. Brain Research.*, **106**, 291-300.
Massion, J. (1992). *Prog. Neurobiol.*, **38**, 35-56.

HEAD, TRUNK AND PELVIS KINEMATICS DURING RAPID HEAD TURNING IN STANDING AND WALKING

Caroline Paquette , Sunil Garg, Nicole Paquet, Joyce Fung
Jewish Rehabilitation Hospital Research Center and McGill University, Montreal, Quebec, CANADA (caroline.paquette@mail.mcgill.ca)

INTRODUCTION

Maintaining balance in quiet stance is not a trivial task as it requires complex coordination of all body segments. The task can be more demanding during walking as it also requires the accurate synchronization with voluntary anterior disequilibrium to allow forward progression (Winter, 1995). The demands increase when a voluntary movement, such as an arm or head motion, is executed simultaneously. Our purpose was to evaluate the impact of a rapid head turn on the kinematics of the trunk and pelvis segments during step stance and walking.

METHODS

Six young healthy subjects (22 to 30 years) walked at their naturally preferred speed across a 10-meter walkway. They were instructed to turn the head as quickly and as fast as possible in the direction indicated by an illuminating arrow (right, left, up, down or none, randomly presented), during step stance or walking. Head turning was maintained with the aid of visual targets. A full body model (38 markers positioned over head, trunk, pelvis, arms and legs) was used to record and analyze body motions in 3-D with a 6-camera Vicon 512 system.

Paired t-tests were used to compare horizontal and sagittal excursions of the trunk and pelvis with and without head turning.

RESULTS AND DISCUSSION

Subjects responded to the arrow signal (reaction time) faster during standing as compared to walking (225±43 vs. 323±28 ms). The reaction time was similar within the different head turn directions and did not interact with standing and walking. Head movement amplitude was larger during walking as compared to standing (75±16 vs. 60±12º). The amplitude of head motion was significantly larger in horizontal movements as compared to up-down motions (78±11º vs. 57±13º). However, in the up direction there was no significant difference between standing and walking (53±11º vs. 50±11º, significant interaction effect). These head motions were executed at high velocity in both standing and walking, on average 408±144º/s. Velocities were significantly different within head turn direction: 516±119º/s horizontal vs. 300±62º/s sagittal.

Figure 1A shows that when a head turn was executed during standing or walking, trunk rotations occurred in the same direction of the head turn. The excursions were markedly larger in walking as compared to standing.

Figure 1B shows that in standing, there was very little pelvis motion associated with head turn. However, in walking, pelvis rotation is executed in the direction opposite to the head and trunk rotation.

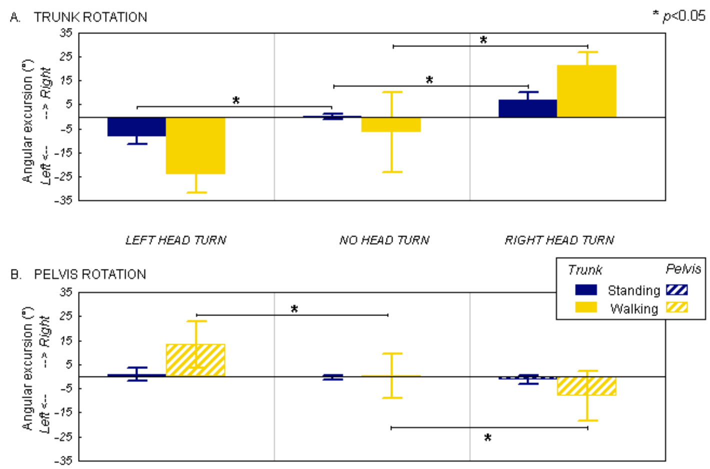

Figure 1: Maximum horizontal angular excursions of the A) trunk and B) pelvis in walking and standing for with and without head turns.

The differences observed between step stance and walking might be due in part by relative target location, since the angle separating the subject's gaze with the target was continuously increasing as the subjects were moving forward. This is consistent with the head movement amplitude difference reported between standing and walking.

Analyses for the flexion-extension motions of the trunk and pelvis revealed that they were not influenced by up-down motions of the head during walking. However, a small but significant trunk flexion accompanied a head-down movement during standing as compared to no head turn (4±5º vs. 1±2º), whereas pelvis extension occurred with head-up movement (3±2º vs. 0±1º).

SUMMARY

When a horizontal head turn is executed during walking, the trunk follows the motion of the head, whereas the pelvis moves in the opposite direction. This kinematic strategy is likely used to maintain a straight trajectory while looking to the side. This strategy is not used when head turn is executed during a similar posture in quiet stance, when trunk and pelvis stability is paramount to maintain balance.

REFERENCES

Winter D.A. (1995). *A.B.C. (Anatomy, Biomechanics and Control) of balance during standing and walking*. Waterloo, Ont.: Waterloo Biomechanics.

DETERMINATION OF ELASTIN AND COLLAGEN CONTENT IN PORCINE AORTA

Namrata Gundiah[1], Kim Dao[2], Karen King[23], Lisa Pruitt[12]
[1]Dept. of Mechanical Engineering, lpruitt@newton.berkeley.edu
[2] Dept. of Bioengineering, University of California Berkeley, Berkeley, CA 94720
[3] Dept. of Medicine, University of California San Francisco, San Francisco, CA 94143.

INTRODUCTION

Elastin and collagen are the primary passive components of arterial wall and their relative amounts contribute to the highly nonlinear stress-strain behavior of elastic arteries (Wolinsky, 1967). Because arterial diseases like atheroscleroses and aneurysms directly correlate with changes in the amounts vessel wall constituents, it is important to develop methods to quantify their amount and study their architecture. In this study, we use biochemical analyses to quantify the relative amounts of collagen and elastin in porcine arteries and study their architecture using histological methods.

MATERIALS AND METHODS

Thoracic aortae from two healthy female sows were harvested from UCSF and rings from each were stored in methanol for collagen content determination, saline for elastin isolation, and formalin for histology respectively. ***Collagen Content***: Hydroxyproline (Hyp) makes up 14% of total collagen content in porcine tissue (Gosline, 1996). Hyp content was determined using the Chloramine-T assay. The sample was hydrolyzed in 6M HCl for 20 hours in a 2 ml. sealed glass tube. Hyp was then oxidized and reacted with p-dimethylamino benzaldehyde to form a chromophore, detected using a spectrophotometer at 550 nm (Stegemann, 1967). ***Elastin Isolation***: Elastin was isolated by repeated autoclaving of the tissue followed by treatment in 6M guanidine hydrochloride (Lillie, 1990). ***Histology***: Samples were embedded in OCT, cryo-sectioned into 8 µm sections and stained using three methods. (i) Hematoxylin & Eosin (H&E) was used for the detection of nuclei (stained purple) and fibers (in pink). (ii) Masson's trichrome was used to stain collagen (blue) and muscle cells (red). (iii) Verhoeff stain counterstained with picroponceau was used to identify elastin (brilliant blue-black) and collagen (red).

RESULTS AND DISCUSSION

Trans 4 hydroxy L Proline was used to obtain the standard curve for Hyp concentration. Standard concentrations in excess of 0.03 mg saturated the absorbance curve (Reddy, 1996). A linear fit of the standard curve (Fig 1a) was used to estimate the Hyp concentrations in the sample. Based on this and data from all samples in the study (Fig 1b), we obtained % collagen of 9.52 (± 3.33) for the first animal and 17.16 (± 5.31) for that of the second animal. Elastin content for the first animal was 81.51% and that for the second animal was 63.5%. The histological images show that the elastin isolation procedure eliminates collagen and smooth muscle cells from the tissue samples.

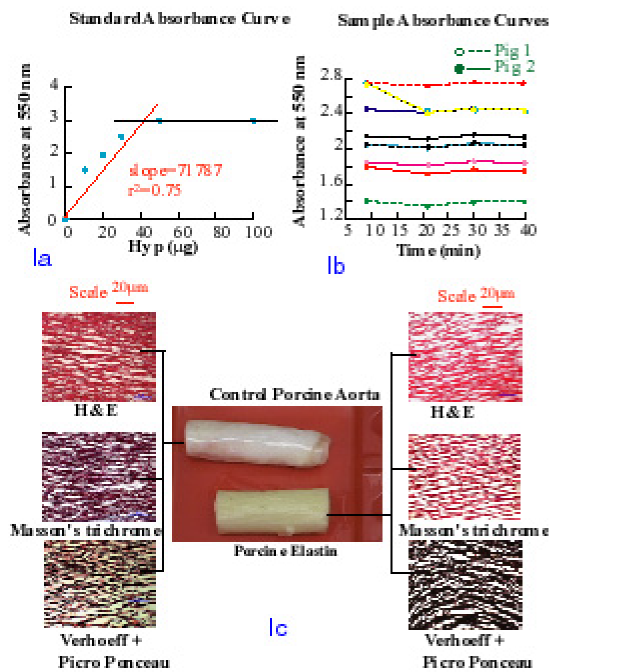

Figure Ia: Standard Absorbance curve.
Figure Ib: Absorbance curves for all samples in study.
Figure Ic: Histology of control (left) and purified elastin (right)

The amount of elastin decreases away from the aortic arch while collagen content increases. The relative differences in the amounts of elastin and collagen from the two specimens in our study may occur since the samples originate from different regions of the thoracic aorta.

SUMMARY

We evaluated methods to quantify the amounts and architecture of elastin and collagen in arterial walls. These techniques will be combined with mechanical tests of elastase and collagenase digested arteries to study their biomechanical role in healthy and diseased arteries.

REFERENCES

[1] Wolinsky *et. al.*, *Circ. Res.,* **20**: 99-111 (1967).
[2] Gosline *et. al., J. Exp. Biol.*, **199**: 985-997 (1996).
[3] Stegemann *et. al., Clin. Chim. Acta*, **18**: 267 (1967).
[4] Lillie *et. al.*, *Biopoly*., **29**: 1147-1160 (1990).
[5] Reddy *et. al.*, *Clin. Biochem*., **29**: 225-229 (1996).

ACKNOWLEDGEMENTS

Thanks to Mr Ron Baireuther, UCSF for providing study samples. This work was supported by NIH grant # NHLBI 1RO1 HL61823.

EFFECT OF SHEAR STRESS ON THE ACTIVATION OF THE PEROXISOME PROLIFERATOR-ACTIVATED RECEPTORS (PPARs)

Kitty Formentin, LingFang Zeng, Andre P Morgan, and John Y.-J. Shyy
Division of Biomedical Sciences, University of California, Riverside, CA, USA, 92521-0121.
Email address: kitti.formentin@ucr.edu

INTRODUCTION

Located at the interface between the vessel wall and the circulating blood, the vascular endothelial cells (ECs) are constantly subjected to hemodynamic forces. Ample evidence has shown that shear stress, the frictional force of the flowing blood, plays an important role in atherosclerosis through the activation of many signaling pathways. PPARs, belonging to the superfamily of nuclear transcription receptors, are now emerging as potential key players in metabolic disorders leading to atherosclerosis. Therefore, the aim of this work is to study the effect of shear stress on the activation of different nuclear receptors such as PPARγ, PPARα, RXR and LXR.

METHODS

Monolayers of ECs cultured on glass slides coated with 2% gelatin were subjected to a laminar shear stress of 4 or 12 dynes/cm^2, using a parallel-plate flow chamber as described previously (1).

To measure the effect of shear stress on the activation of various nuclear receptors, the plasmid constructs pCMX-GAL-L-hRXRa, pCMX-GAL-L-mPPARα, HN-GAL-L-PPARγ, or CMX-GAL-L-hLXRα were co-transfected with 5Gal-luciferase reporter construct, using the Fugene reagent (Roche). Twenty-four hours after transfection, the EC monolayers were subjected to shear stress or kept under static conditions for 6 hr. The cells were then trypsinized and resuspended in a buffer containing 0.6% NP-40, 0.1 M NaCl, 10 mM Tris-HCl, pH 8.0, 1 mM EDTA and incubated on ice for 20 min. After a further centrifugation, the luciferase activity was measured.

Nuclear extract and gel electrophoresis mobility shift assays were performed as previously described (2). The nucleotide sequence of the probe is as follow: 5'-GGGGTCAGTAAGTCAGAGGCCAGGGA-3' that contains the core PPARγ responsive element (PPRE) in CD36 promoter. The binding level was quantified by scanning the autoradiograph, followed by densitometric analysis.

RESULTS AND DISCUSSION

We transfected ECs with plasmids containing the specific sequence of various ligand binding domains (LBDs) of PPARγ, PPARα, RXR, and LXR. Unidirectional shear stress of 12 dynes/cm^2 induced a 0.3-fold increase in the activity of the LXR LBD, 2.2-fold increase in the RXR-LBD, 1.6-fold increase in PPARα LBD and 121-fold increase in the activity of the PPARγ LBD, compared to static controls. Moreover, gel shift mobility assay demonstrated that the binding activity of nuclear extracts to the CD36 PPRE sequence, a specific binding site for PPARγ, was already increased 2 hr after EC exposure to a unidirectional flow (4 dynes/cm^2) and the increased binding lasted for at least 24 hr. Taken together, these results suggest that unidirectional flow increases the production of ligands for PPARγ in ECs, thus enhancing the expression of the PPARγ-mediated genes such as CD36.

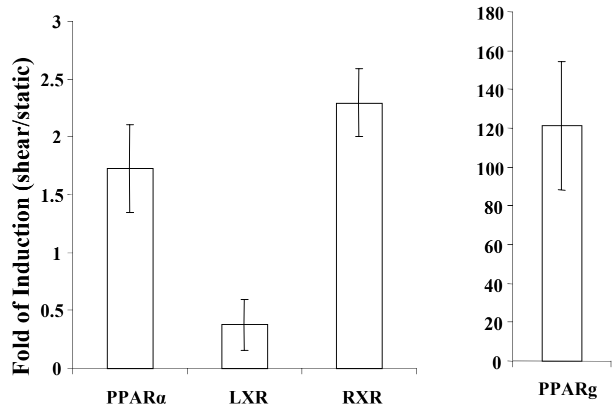

Figure 1: Laminar shear stress (12 dynes/cm^2) induces the activation of the ligand-binding domain (LBD) of PPARγ, PPARα, RXR, and LXR (n=6).

SUMMARY

In this study, we find that laminar flow, the flow pattern characteristic of atherosclerotic plaque-free regions, highly increases the PPARγ LBD activity with concurrent increased PPARγ-mediated transcription activity. These results suggest the release of specific PPARγ ligands in ECs induced by this flow pattern. The role of the unidirectional flow-activated PPARγ in vascular biology remains to be determined.

BIBLIOGRAPHY

1. Frangos, J.A., Eskin, S.G., McIntire, L.V., and Ives, C.L. 1985; 227:1477-1479
2. Graves, R.A., Tontonoz, P., and Spiegelman, B.M. 1992, Mol. Cell Biol. 12, 1202-1208

ACKNOWLEDGEMENTS

This study is supported in part by a grant from Swiss National Foundation and HL56707 from the NHLBI.

A NON-INVASIVE APPROACH FOR MEASURING SAGITTAL BALANCE OF THE SPINE

Chriss Stanford, Michelle Marks, and Peter Newton
Motion Analysis Laboratory, Children's Hospital, San Diego, California
cstanford@chsd.org

INTRODUCTION

Accurate measures of spinal alignment are vital in making proper treatment decisions and evaluating surgery outcomes. Postural deformities such as adolescent idiopathic scoliosis (AIS) are often classified based on regional measurements, including kyphosis and lordosis. Global measures of spinal alignment, such as the sagittal vertical axis (SVA) are also necessary for thorough assessment of spinal balance. Though researchers have investigated non-invasive measurement methods for spinal curvature[1], no attempts have been made to develop a technique for measuring SVA without the use of a radiograph. The purpose of the present investigation was to validate a non-invasive procedure for estimating SVA.

METHODS

Fifteen adolescent females without spinal deformity received standing lateral radiographs, while the positions of markers on the skin overlying the spinous processes of C7 and L4 were monitored using an 8-camera motion capture system (Motion Analysis Corp., Santa Rosa, CA). SVA was measured on radiograph as the horizontal distance between the posterior superior corner of the sacrum and a vertical plumb line through the center of the C7 body. SVA was also calculated using the difference between coordinates of the markers in the anteroposterior direction ($SVA_{virtual}$), and anthropometric corrections ($C7_{correction}$, $L4_{correction}$) between the markers and anatomical points used for SVA measurement obtained on radiograph, as shown in Figure 1. For each subject, SVA was estimated with the following equation, using mean correction values for all subjects:

$$SVA = SVA_{virtual} \times MF + C7_{correction} - L4_{correction}$$

MF is the magnitude of image magnification on radiograph.

Predicted and measured SVA values were compared using a Pearson's correlation and intraclass correlation coefficient (ICC).

RESULTS AND DISCUSSION

Subjects had a mean age of 12.09 $\pm$ 1.9 years, a height of 156.6 $\pm$ 10.8 cm, and a mass of 45.0 $\pm$ 9.8 kg. Mean predicted SVA was –4.23 $\pm$ 2.4 cm, and mean SVA, measured on radiograph, was –4.18 $\pm$ 2.3 cm. There was a strong relationship ($r = 0.86$) and good agreement (ICC = 0.93) between measurement techniques. The average difference between predicted and measured SVA was 0.95 cm, with a range of 0.0 to 2.7 cm.

Mean difference in SVA between radiographic measurement and non-invasive estimation was less than 1 cm, despite considerable variability in subjects' height and mass. Though variability in anthropometric corrections was low between subjects, this technique was most accurate in estimating SVA in ectomorphic subjects. Thus, the non-invasive procedure may be particularly useful in the AIS population, where most female patients tend to be slender and repetitive radiographs are indicated.

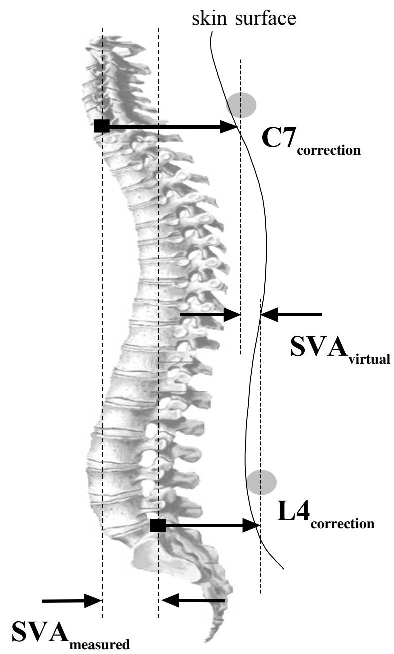

Figure 1: Estimation of Sagittal Vertical Axis (SVA).

SUMMARY

Lateral radiographs must be obtained with the patient in an unnatural standing position, to allow for adequate visualization of the spine. This introduces variability in measurement of SVA[2]. SVA can be effectively estimated using the non-invasive technique, as indicated by high correlations between calculated SVA and radiographic measures of SVA. The proposed method may be useful in reducing the number of repeated radiographic follow-up evaluations and allows a measure of SVA to be obtained with the patient in a functional position.

REFERENCES

Leroux, M.A. et al (2000). *Spine*, **25**, 1689-1694.
Van Royen, B.J. et al (1998). *European Spine Journal*, **7**, 403-412.

EFFECTS OF BOTULINUM TOXIN A AND MUSCLE STRENGTHENING ON GAIT

Ayodeji K Badejo[1], Jefferson W. Streepey, M.S.[1], Rosa M. Angulo-Kinzler, Ph.D.[1], Edward A. Hurvitz M.D.[2], Patrick Brennan, M.D.[2], Sherry Herman-Hilker, M.P.T.[2]

[1]Center for Human Motor Research, University of Michigan, Ann Arbor, Mi 48109-2214, USA
[2]Department of Pediatric Physical Medicine and Rehabilitation, University of Michigan Hospital, Ann Arbor, Mi 48109-0230, USA

INTRODUCTION

Spasticity, one of the most common motor impairments associated with cerebral palsy, alters gait patterns in children with cerebral palsy, and, as the children age, gait degenerates (Johnson et. al., 1997). Treatments of botulinum toxin injections alone or strength training alone have previously shown to have positive impacts on gait in children with spastic cerebral palsy (Yang, 1999; Damiano & Abel, 1998). However, the effect of the two interventions coupled together has not been tested. The goal of this study is to contrast the effects of a combined botulinum toxin and strength training intervention versus strength training alone on the gait patterns of children with cerebral palsy

METHODS

A sample of six children (7-13 years) with spastic diplegic cerebral palsy who ambulate independently were selected for these preliminary results. Each child had at least 20 degrees of knee flexion bilaterally, with popliteal angles of no less than 40 degrees (first catch), and with no contraindication to botulinum toxin injections. Subjects were randomly assigned to the botulinum toxin plus strengthening group (BTX, 4 subjects) or to strengthening alone (STR, 2 subjects). For subjects in BTX group, injections were performed in the hamstring muscles using 8 units per kilogram, 60% to the medial hamstring and 40% to the lateral. Two weeks after initial data collection, all subjects were instructed in a program of wall slides for strengthening. All subjects received weekly phone calls to encourage compliance.

Clinical assessments of the children were obtained pre-intervention, at two weeks, and at completion of intervention (8 weeks) by a physical therapist who was blinded to group assignment. These measures included: (1) spasticity, determined through a Modified Ashworth Scale (MAS), (2) range of motion (ROM) at the hips, knees, and ankles, and (3) strength in the flexor and extensor muscles of the hips, knees and ankles using a dynamometer. Furthermore, prior to intervention and at the completion of intervention, gait kinematics were recorded in each of the subjects as they walked at their preferred speed four times along a 3.66m walkway. A six-camera (60Hz) Peak Performance Motion Motus Analysis System was used to capture the kinematic data, and sagittal plane hip and knee angles were calculated and filtered using a quintic spline. Further gait kinematic parameters, including step length and walking speed, were determined using a 60Hz GAITRite walkway mat.

RESULTS AND DISCUSSION

All subjects complied with the exercise program. Preliminary results suggest that subjects generally improved in knee extension strength (average 1.2 Kg), MAS (average .67) and ROM (average 3.2°) but there were no significant differences between groups. Gait speed increased for all subjects in the BTX group (average $15.0 \pm 9.1\%$) while in the STR group, one subject increased and one decreased speed (Table 1). Step length increased in 7/8 legs in the BTX group (average $11.7 \pm 26.7\%$). In contrast only one leg in the STR group showed improvements the step length.

	BTX1	BTX2	BTX3	BTX4	STR1	STR2
Speed	2.2	15.0	22.1	20.8	-29.8	1.3
Length	2.8	9.3	22.8	11.9	-18.0	0.4

Table 1. Percent change in walking speed and step length.

For subjects in BTX group, there was a decrease in toe-off variability (6/8 legs), increase in amplitude of hip and knee angle trajectory (4/8 legs), and decrease in variability of the hip angle trajectory during stance and around toe-off (6/8 legs). None of the legs in the STR group showed changes in these parameters. For the knee angle, results were equivocal.

Compared to the STR group, the BTX group generally showed improvement in their gait measures. Previous research has implicated step length as a constraint on walking speed (Abel & Damiano, 1996). This relationship is illustrated in our results by increases in both walking speed and step length. Furthermore, reduction in variability of both hip angle trajectory and toe-off timing are an indication of greater consistency in the gait patterns. The reduction in variability along with the increase in the amplitude of angle trajectories are generally viewed as positive outcomes of therapeutic interventions for treating cerebral palsy.

SUMMARY

Strengthening of knee extensors combined with botulinum toxin injections to the hamstrings appeared to improve gait parameters to a greater extent than strengthening alone. Strength, ROM, and MAS did not show significant changes between groups in this small initial sample.

ACKNOWLEDGMENTS

This study received funding from ALLERGAN.

REFERENCES

Abel, M., Damiano, DL. (1996). *J. Pediatr Orthop*. **16**, 753-8.
Cosgrove et al. (1994). *Dev. Med. Child Neuro.***36**, 386-96.
Damiano DL, Abel, M. (1998). *Arch Phys Med Rehabi.*, **79**, 119-25
Johnson et al. (1997). *J Pediatr Orthop.* **17**, 392-6.
Yang et al. (1999). *J Formos Med Assoc*. **98**, 832-6.

EFFECT OF EXPRESSIVENESS ON THE KINEMATICS OF ARM GESTURES

Teerin T. Meckmongkol[1] and M. Melissa Gross[1,2]

[1]Movement Dynamics Laboratory, Division of Kinesiology, and [2]Institute of Gerontology
University of Michigan, Ann Arbor, Michigan, USA, mgross@umich.edu

INTRODUCTION

Body movements can communicate emotions while serving other demands of motor tasks. Point light displays of body movements are sufficient for observers to detect differences in affect during walking (Montepare and Zebrowitz-McArthur, 1988), arm gestures (Pollick et al., 2001), and dance movements (Dittrich et al., 1996; Brownlow et al., 1997). Although researchers have shown that information about emotions is conveyed in body movements (Walbott, 1998), how task kinematics are modified by emotion is virtually unknown.

The purpose of this study was to determine how expression affects the kinematics of arm gestures. Ballet arm gestures were studied because they can be performed precisely and reproducibly by skilled dancers, thus minimizing kinematic differences not related to expression. To ensure that dancers performed the movements with different expressions, other participants assessed the expressive differences between randomized pairs of the dancers' performances.

METHODS

After obtaining informed consent, eight professional-level female ballet dancers (mean age 24 yrs) were asked to perform two arm movements that are well-defined in ballet repertoire (port de bras to arabesque and to second position) with two different performance styles: technical and expressive. Video data were collected at 60 Hz from reflective markers placed over trunk and upper extremity landmarks. Kinematic data were filtered (4 Hz) and 3-D angular displacements were calculated for the head, upper spine, lower spine, shoulder, elbow and wrists. Paired Student's *t* tests were used to detect differences in performance style for each of the arm gestures.

An additional 36 participants (24 female, 12 male; 20-50 yrs) viewed a videotape prepared from the same trials used in the kinematic analysis. The videotape consisted of 16 randomized pairs of expressive and technical performances (two from each dancer). Participants were asked to decide if the pairs were performed in the same or different styles (i.e., technical or expressive). Analysis of variance was used to detect differences in accuracy among observers and gestures.

RESULTS AND DISCUSSION

In general, joint range of motion increased with expressiveness. However, the specific body segments affected by expression depended on the arm gesture. For the port de bras to second, head tilt and head rotation increased 48% and 19%, respectively, in the expressive compared to the technical performances (Fig. 1). The upper spine range of motion in the frontal plane also increased with expression (26%). In contrast, range of motion increased with expression for the lower spine and shoulder, but not the head and upper spine, in port de bras to arabesque. Lower spine range of motion in the frontal, sagittal, and transverse planes increased 27%, 61%, and 59%, respectively. Shoulder abduction also increased with performance (25%). Although relative changes in joint range of motion with expression were large (19-61%), the absolute differences in range of motion were quite small, varying from less than 5 degrees for the spine to 18 degrees for head rotation. Elbow range of motion did not depend on expressiveness for either movement.

Head Tilt During Port de Bras to Second Position

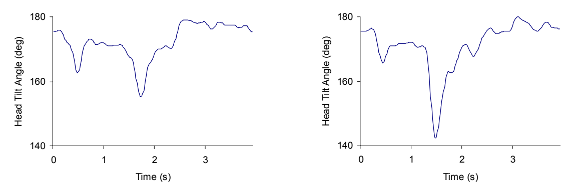

Figure 1: Head tilt increased in expressive (right) compared to technical (left) performance. Data are from one participant.

Observers were able to discriminate accurately between performances of paired arm gestures with an accuracy rate (75%) that greatly exceeded chance (41%). Accuracy among observers ranged from 43% to 93% and was similar for dancer (n=6) and non-dancer (n=30) observers.

SUMMARY

Task kinematics were modified in characteristic ways when dancers performed ballet arm movements with expression. Although the magnitude of the kinematic changes with expression was small, the differences were statistically significant and were detected by observers.

REFERENCES

Brownlow, S. et al (1997) *Psychological Record*, **47**, 411-421.
Dittrich, W. et al (1996). *Perception*, **25**, 727-738.
Montepare, J., Zebrowitz-McArthur, L. (1988). *J. Personality and Social Psychology*, **55**, 547-556.
Pollick, F. et al (2001) *Cognition*, **82**, B51-B61.
Walbott, H. (1998) *Eur. J. Social Psychology*, 28, 879-896.

ACKNOWLEDGEMENTS

Partial support was provided by a grant from the University of Michigan Center for Education for Women to T.M.

BIOMECHANICAL ANALYSIS OF FIXATION OF SPLIT-DEPRESSION FRACTURES OF THE TIBIA PLATEAU

Mark J. Blyth, S.D. Deo, Hanspeter Frei, Peter O'Brian, Piotr A. Blachut, Thomas R. Oxland
Department of Orthopedics, University of British Columbia, Vancouver, British Columbia, Canada, toxland@interchange.ubc.ca

INTRODUCTION

Tibial plateau fractures comprise 1% of all fractures. They occur across the age spectrum, but pure joint depression fractures tend to occur in the older, more osteoporotic age group (Koval 1995). The main indication for operative treatment of tibial plateau fractures are significant depression or displacement of the joint surface by more than 10mm and/or joint instability. Traditionally the depressed articular portion of the fracture is elevated and reduced and fixed with a 4.5mm periarticular plate system. The 3.5mm plate system was developed to reduce the soft tissue irritation caused by the higher profile of the 4.5mm plate, but the quality of this fixation has not been established. Therefore the purpose of this study was to compare the strength of fixation of the 3.5mm with 4.5mm periarticular plate system.

METHODS

In five cadaveric tibial pairs, a split-depression fracture was simulated surgically (Figure 1). The articular fragment was fashioned by creating a block allowing it to sit evenly distributed over two screws of the 4.5mm plate and three screws of the 3.5mm plate (Figure 1). In addition a metaphyseal defect was included in the fracture model. The fractures were fixed with either the 3.5mm or 4.5mm periarticular plate system (Zimmer, Warsaw, IN, USA). A ramp load up to 150N was applied to the articular fragment by a servohydraulic testing machine, followed cyclic loading for 5000 cycles with an amplitude of +/- 100N. The axial fragment displacement was measured by a precision optoelectronic camera system and analyzed after the initial ramp and after cyclic loading. Wilcoxon matched paired test was used to compare the two fixation methods.

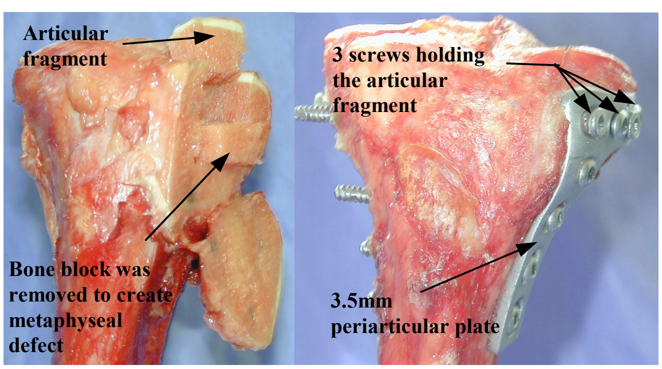

Figure 1: Left: Simulated split-depression fracture. Right: Fracture is fixed wit a 3.5mm periarticular plate with three screws holding the articular fragment.

RESULTS AND DISCUSSION

There were no differences in the axial displacement of the articular fragment after the initial ramp loading between the two plates. After 5000 cycles the displacement of the fragment was significantly greater with the 3.5mm compared with 4.5mm plate. The results are summarized in Table 1.
The depression of the articular fragment occurred by failure of subchondral bone at the level of the screws by a cheese-wire effect in all cases.

Table 1: Displacement of the articular fragment at 150N and after 5000 cycles.

	Displacement @ 150N [mm]		Displacement after 5000 cycles [mm]	
Specimen	**3.5mm**	**4.5mm**	**3.5mm**	**4.5mm**
A	1.9	2.3	6.6	5.5
B	2.2	2.9	5.4	5.1
C	3.3	1.8	16.4	13.7
D	1.4	1.7	12.3	6.6
E	1.7	1.1	8.4	3.2
Median	**1.9**	**1.8**	**8.4**	**5.5**
Min/Max	1.4 / 3.3	1.1 / 2.9	5.4 / 16.4	3.2 / 13.7

SUMMARY

The purpose of this study was to compare the strength of fixation of the 3.5mm or 4.5mm periarticular plate system in a tibial split-depression fracture model. Compressive loads were applied to the articular fragment of the model and the axial displacements measured. The displacement of the articular fragment observed after cyclic loading was significantly greater with the 3.5mm plate. No differences between the two plates were found after the initial ramp loading. In each case depression of the articular fragment occurred by failure of subchondral bone at the level of the screws by a cheese-wire effect.

REFERENCES

Koval KJ, Helfet DL (1995) *J Am Acad Orthop Surg*, **3**:86-94.

ACKNOWLEDGEMENTS

A research grant from the UBC Zimmer Research fund is gratefully acknowledged.

MAXIMUM TOE FLEXOR MUSCLE STRENGTH IN HEALTHY YOUNG AND OLDER ADULTS

Mari Endo, B.S.E.[1], James A. Ashton-Miller, Ph.D.[1-3], and Neil Alexander, M.D.[3-4]

[1]Department of Mechanical Engineering, [2]Department of Biomedical Engineering, [3]Institute of Gerontology, [4]Department of Internal Medicine, University of Michigan, Ann Arbor, Michigan, USA, marichan@engin.umich.edu

INTRODUCTION

The maximum strength of the toe flexor muscles determines the forward extent of the functional base of foot support (FBOS) while balancing on one or two feet. Maximum toe flexor strength (S) is therefore important in preventing forward falls in forward leans and reaches, and when stopping abruptly to avoid a collision during gait. We could find no published data on S, or on whether it is affected by age or gender. The FBOS is known to decrease by 16% per decade for persons over 60 years of age (King et al., 1994), but the underlying reason has not been elucidated. In Study 1 we therefore tested the (null) hypothesis that neither age nor gender affects the single-equivalent maximum isometric toe flexor strength (S), developed by all five toes about a reference axis through the first metatarsal joint (MTJ). In Study 2, we quantified the individual contributions of each toe to S in young adults (YA).

METHODS

Study 1: 40 healthy adults (20 YA, age: 22.8 yrs; 20 older adults (OA), age: 73.2 yrs.) participated. S was measured for each foot in 3 trials. The subject reached towards, but did not touch, a force-sensing target (T) while standing unipedally on a force plate (FP, Fig. 1). Subjects were instructed to maximize S with each successive trial by moving their center of reaction (R) as far forwards as possible, using visual feedback (VF).

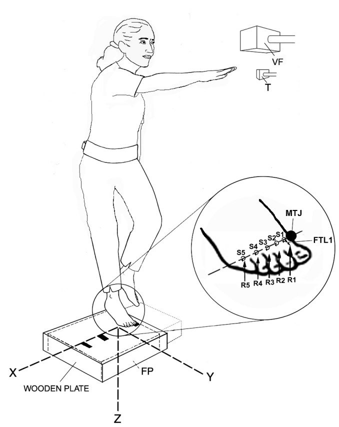

Figure 1: Set-up

Study 2: Using similar methods and gender-matched groups of 10 healthy YA (age: 24.1 yrs.), we measured the maximum individual moment contributions of each toe to S about an axis through the first MTJ. The entire foot, with the exception of the toe to be measured, was supported on a flat horizontal support plate mounted just above, but not in contact with, the FP. A short rigid column, whose diameter was the width of the toe to be measured was interposed between the toe and the FP, and constrained by a vertical low-friction hole in the support plate. Using this set up, we measured the maximum flexor moment developed by each toe about its MTJ, as well as the first MTJ (denoted S1: large toe to S5: small toe, see inset Fig. 1).

RESULTS AND DISCUSSION

Study 1: There was not a significant bilateral difference in S (p=.228), so only dominant foot data are reported. The hypothesis was rejected in that OA had 28.9% smaller S than the YA (p=.008), and the females had 39.1% smaller S than the males (p<.0005). However, after normalizing S by a measure of body size (body weight [N] x height [m]), the gender difference was no longer significant, but the age difference remained significant. Hence, S is proportional to body size irrespective of gender. Three young females performed the test on two separate days and the test-retest differences lay within 10%. The functional toe length (FTL), the maximum distance the subject could move R forward of the MTJ, was 29.6 % smaller in OA than YA (Table 1).

Table 1: Mean (SD) S and FTL on the Dominant Foot

	Men		Women	
	Young, n=10	**Older**, n=10	**Young**, n=10	**Older**, n=10
Absolute S [Nm]	24.3 (4.9)	16.1 (6.6)	13.8 (3.5)	10.8 (3.3)
Normalized S	0.017 (0.003)	0.012 (0.005)	0.014 (0.004)	0.010 (0.004)
FTL [mm]	31 (6)	21 (9)	23 (7)	18 (5)

Study 2: The gender difference in the individual (percent) contributions of each toe to S were not significant. The large toe contributed the most, 61.0%, to S (Fig. 2). The clinical significance is that individuals with amputated or impaired large toes should be advised that they might be at an increased risk for forward falls.

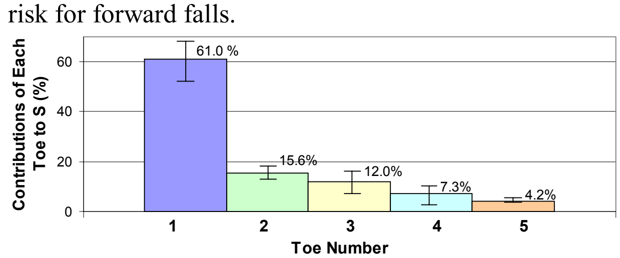

Figure 1: Individual Contributions to S: YA, n=10

SUMMARY

(1) A new method is presented for measuring toe flexor strength. (2) S decreases by 29% with age. (3) S is proportional to body size in healthy males and females. (4) The large toe contributes 61% of S in healthy young adults. (5) The age-related decline in S helps explain the age-related decline in FBOS with age.

REFERENCES

King, M.B. (1994). *J Gerontol Med Sci*, **49(6)**, M258-M263.

ACKNOWLEDGEMENTS

PHS Grants PO1 AG10542 and P60 AG08808.

MOVEMENT SYNERGY BETWEEN THE ANKLE AND HIP JOINTS DURING SINGLE LEG STANCE

Wen Liu, Kevin McIntire, Kari Bowman, Stacia Noland, Sarah Spurlock, Carrie Thompson
Dept. Physical Therapy and Rehabilitation Science, University of Kansas Medical Center, Kansas City, Kansas
Email contact: wliu@kumc.edu

INTRODUCTION
Patterns of postural response to disturbances have been observed despite the fact that postural control in upright stance requires a complex interaction of musculoskeletal and neural systems. Many studies on the postural control during two-leg stance have reported an ankle strategy for a small perturbation (Nashner, 1977), a hip strategy when feet are constrained (Horak and Nashner, 1986), and a stepping strategy if there is no constrain (McIlroy and Maki, 1993) for a large perturbation. However, very few studies examined patterns of postural control during single leg standing (Gauffin et al., 1993), and it is not know how the hip and ankle joints may contribute to the balance of single leg stance. The purpose of this study was to examine three-dimensional motions of the hip and ankle joints during signal leg standing tasks under various conditions in a group of healthy young subjects. Results of this study will help future researchers in better understanding balance deficit due to joint injuries (hip or ankle joint) or neurological diseases.

METHODS
A total of 8 healthy young subjects participated in this study (8 females, age: 22 to 24 years old). None of the subjects had a history of severe ankle, knee, and/or hip injury. Prior to participation, each subject signed an informed consent.

A three-dimensional motion analysis system (OPTOTRAK, Northern Digital Inc., Waterloo, Ontario) was used to measure marker coordinates during balance tasks. Three active markers were fixed with double sided adhesive tape on each of four body segments of the right side: the calcaneous, shank, thigh, and pelvis. In addition, 6 bony landmarks were digitized using the OPTOTRAK digitizing probe in order to established joint anatomical coordinates system for the hip and ankle, using the system recommended by the International Society of Biomechanics. The Biodex Stability System (Biodex Medical Systems, Shirley, NY) was used to provide unstable standing condition for subjects. The movable balance platform provides up to 20 degrees of surface tilt in a 360-degree range. An actuator is used to pre-set the degree of platform instability, ranging from a completely fixed surface to a very unstable surface.

The testing protocol is based on a previous study using the Biodex Stability System (Rozzi et al., 1999). To familiarize subjects with the Biodex, a 20 second practice trial of each test condition was allowed. The subject performed a total of 5 trials for each of 4 conditions: 1) Eyes open fixed platform (EOFP), 2) Eyes closed fixed platform (ECFP), 3) Eyes open level 8 (EOL8), 4) Eyes closed level 8 (ECL8). The level 8 is the least unstable level of movable platform. The conditions were chosen in a random order. Subject balanced for 20 seconds during each trial. The OPTOTRAK system recorded 3D coordinates of markers. An RMS of joint angular motions at the ankle and hip were calculated for each trial.

RESULTS AND DISCUSSION
Internal/external rotations at the ankle and hip joints were observed to go opposite direction with similar magnitudes (Fig. 1). This is confirmed by similar group means of RMS data for the int./ex. rotation for both joints under all four conditions (Fig. 2). Significant differences were found in group mean of the RMS of 3D joint motions of the ankle and hip between the eyes open and eyes closed conditions, and between the fixed and unstable platform conditions. Results of this study demonstrated first time a consistent movement synergy in axial rotations between the ankle and hip joints during single leg stance, under various conditions where joint motions varied significantly. Gauffin et al. (1993) examined only motions of the ankle during single leg stance.

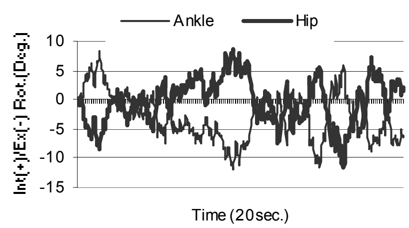

Fig. 1 Internal (+)/external (-) rotations of the hip and ankle joints shows opposite direction with same amplitude.

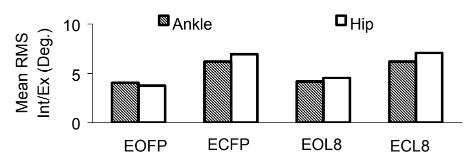

Fig. 2 Group mean of RMS of int./ex. rotations of the hip and ankle joints in four conditions

CONCLUSION
This preliminary data appears to show an equal but opposite axial rotations between the ankle and hip joints to maintain balance during single leg stance. Future research is required to examine the risk of losing standing balance when this synergy is lost due to joint injuries, such as an ankle sprain.

REFERENCES
Gauffin H,Areblad M,Tropp H. (1993) Cli Biomech 8:307-314.
Horak FB, Nashner LM. (1986) J Neurophysiol 55:1369-1381.
McIlroy W, Maki B. (1993) Neurosci Lett 164:199-202.
Nashner LM. (1977) Exp Brain Res 30:13-24.
Rozzi SL, Lephart SM, Sterner R, Kuligowski L. (1999) J Orthop Sports Phys Ther 29:478-486.

REPROGRAMMING SIT-TO-STAND AND SIT-TO-WALK MOVEMENT SEQUENCE UNDER DIFFERENT TEMPORAL CONSTRAINTS

Renato Moraes[1], Fariba Bahrami[2] and Aftab E. Patla[1]
rmoraes@ahsmail.uwaterloo.ca
[1] Gait & Posture Laboratory, University of Waterloo, Waterloo, Ontario, Canada
[2] Department of Electrical and Computer Engineering, University of Tehran, Tehran, Iran

INTRODUCTION

The study of whole body movement sequences and on-line modifications in these actions have received little attention by researchers in biomechanics and motor control areas. Magnan, McFayden and St-Vincent (1996) studied the sit-to-stand (STS) movement when gait initiation was added. They found that sit-to-walk (STW) and STS were similar until the seat-off event. Further, postural control is the most important aspect to be considered during the transition between STS to gait initiation. The question that we examine in this study is how the nervous system reprograms STS for example to a STW movement and vice-versa under different temporal constraints. The focus is on the center of mass (COM) trajectory when subtly an initial task must be modified (STS to STW or STW to STS).

METHOD

COM of the three participants (22-25 yr) was calculated using a model with 7 segments (2 feet, 2 legs, 2 thighs and HAT). A light device with two colors (red and green) was placed in front of the participant. Participants were asked to initiate the task when one of the two lights was on. Red light cued participants to perform STS while green light corresponded to STW. In some trials the light changed at seat-off or 100 ms after the seat-off. When this change happened participant must perform the new behavior indicated by the light color. Participants performed 40 trials in each control condition (STS and STW) and 5 trials in each condition when the light changed (STS to STW cue at seat-off, STS to STW cue at 100 ms after seat-off, STW to STS at seat-off, STW to STS at 100 ms after seat-off). Trials were completely randomized.

RESULTS AND DISCUSSION

In most trials participants were not able to adjust the behaviour under the time constraints when light changed (see Table 1). Failure was most pronounced in the conditions where participants must change from STS to STW; participants first completed STS and after that began to walk. On the other hand, the main reason for STW to STS transition failure was the need to take a step before final postural equilibrium.

Table 1: Failure proportion in each condition (n = 15)

Condition	Failure proportion (%)
STS to STW (seat-off)	80.0
STS to STW (100 ms)	86.0
STW to STS (seat-off)	53.3
STW to STS (100 ms)	73.3

COM vertical displacement was similar in all participants in all conditions tested. However, COM horizontal displacement differed between STW and STS to STW as we can observe in Figure 1. When performing STW the COM horizontal displacement was almost linear after seat-off. On the other hand, COM horizontal displacement in the STS to STW transition has a sigmoid shape after seat-off. When STS to STW transition was performed the COM horizontal displacement after seat-off was reduced in comparison to STW. In this case, participants finished the first task (STS) and then performed the second task (e.g., walk).

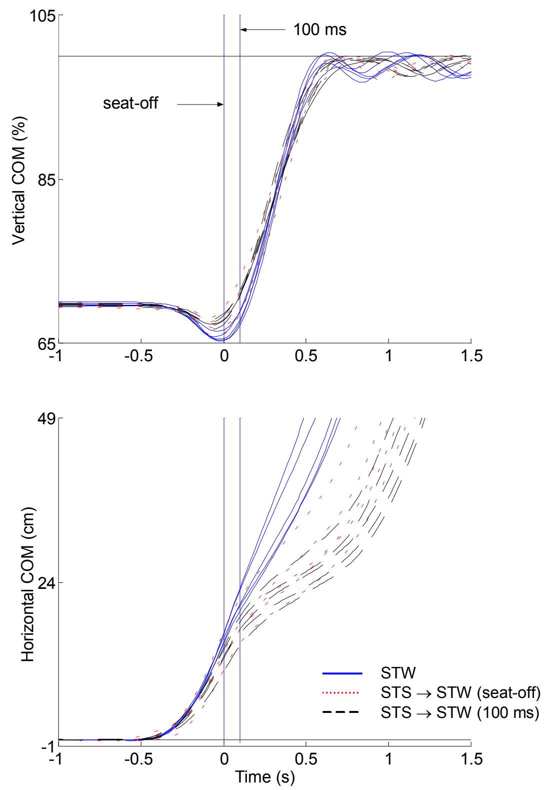

Figure 1: COM profiles during reprogramming of STW movement sequence.

SUMMARY

These findings clearly illustrate the difficulties associated with reprogramming common functional tasks (STS or STW) under temporal constraints. Postural control is severely compromised under these circumstances and could lead to a fall.

REFERENCES

Magnan, A.; McFadyen, B.J.; & St-Vincent, G. (1996). *Gait & Posture*, 4, 232-241.

ACKNOWLEDGEMENTS

Financial assistance provided by NSERC/Canada and CAPES/Brazil.

SOMATOSENSORY INPUT IN THE CONTROL OF HUMAN POSTURE IN PATIENTS WITH MORBUS PARKINSON

Beate Prätorius, Stefan Kimmeskamp & Thomas L. Milani
University of Essen, Department of Human Locomotion
45131 Essen, Germany; thomas.milani@uni-essen.de

INTRODUCTION

Postural instability is a major symptom of the Parkinson's disease and is considered to be responsible for frequent falls in Parkinson patients. Posturographic measurements with sensory perturbations are often used to investigate the physiology of the underlying mechanisms of postural instability. However, studies investigating the sway characteristics of PD patients and healthy adults have often led to a variety of different, sometimes even contradictory results. On the other side, it has been shown that somatosensory input information has a major influence in the control of human balance. Studies have focused on the specific role of vestibular, visual or muscular sensory information, but only little research has been performed so far to study the role of cutaneous sensibility from the foot soles (2). The purpose of this study was to determine the influence of somatosensory input on balance control in Parkinson patients.

METHOD

30 patients (pa) with Parkinson disease (age: 67 SD: 6,8) and 20 age matched healthy subjects (co) (age: 64 SD: 4,2) participated in this study. Subjective sensibility thresholds under five foot structures (heel, midfoot, I. & V. metatarsus head and Hallux) for different mechanoreceptors (intensity – Ruffini corpuscles, vibration – Meissner corpuscles) were determined by using a vibration exciter (30 Hz) and Semmes Weinstein-microfilaments. The sensitivity of intensity mechanoreceptors were analysed by using a 4-2-1-algorithm as described in (1). Control of human posture was measured by pressure sensitive insoles (Novel GmbH, Munich). The balance task included parallel stance, tandem stance, single limb stance and functional lean forward. Center of Pressure (COP) data were collected over a maximum period of 30 seconds for all balance tasks. The COP-data were collected at a frequency of 50 Hz for the left and the right insole. The raw data were smoothed with a fourth-order, zero-phase shift low-pass filter (Butterworth) with a cut-off frequency of 6 Hz. Based on the COP-data of left and the right foot the COP_net was calculated as described by Winter (1995). Prior to the measurements a neurological examination was undertaken to classify the motor impairment according to the UPDRS-Score. Sensitivity thresholds and balance data were averaged and analyzed with inferential statistics (t-test). A sensitivity parameter for each subject was determined by averaging vibration resp. intensity thresholds of five foot locations. Sensitivity variables and balance control variables were compared by regression analyses.

RESULTS & DISCUSSION

For healthy adults significant differences between the five foot regions were evaluated in intensity as well as vibration threshold data. For the Parkinson group, however, this result could not be confirmed. Furthermore, sensitivity parameter revealed significant differences between Parkinson patients (pa) and healthy subjects (co) (Fig.1).

Healthy adults show highly significant lower sensitivity thresholds for intensity ($p<.01$) as well as vibration ($p<.0001$) stimuli. In addition, a highly significant relationship ($p<.01$) was observed between UPDRS-scores and vibration sensitivity in Parkinson patients. Lower vibration sensitivity of the foot sole is related to higher scores respectively increasing level of disease. High UPDRS-scores are highly related to the risk of falls in Parkinson patients. These results confirm the hypothesis that somatosensory information from the foot sole may play an important role in stabilizing human balance. Furthermore,

Figure 1: Vibration threshold differences

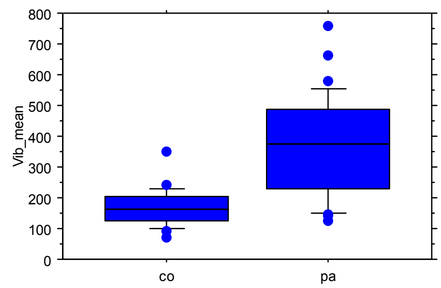

Figure 2: Regression UPDRS versus vibration threshold

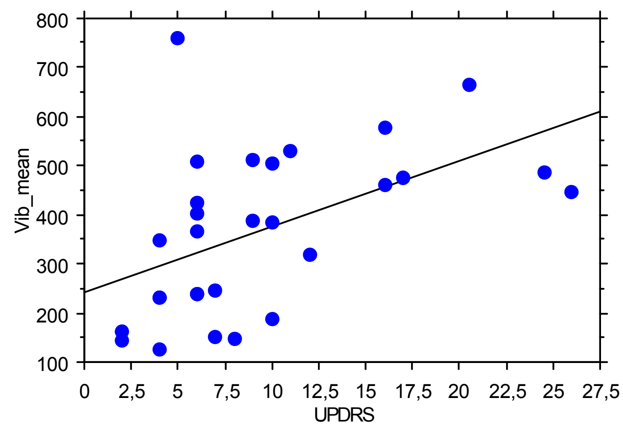

Y = 241,028 + 13,394 * X; R^2 = ,254

reduced foot sole sensibility in Parkinson patients seems to be a further risk factor to fall. Therefore, foot sole sensitivity should be considered for rehabilitation purposes and Parkinson's disease research.

REFERENCES

1. Kavounoudias, A. et.al., 1998. 9(14): p. 3247-52.
2. Dyck, P.J., et al. Neurology, 1999. 43: p. 1508-1612.
3. Winter, D.A.1995. ABC of balance during standing and walking. Waterloo Biomechanics.

INFLUENCE OF GLUCOCORTICOID PRETREATMENT ON DE-REPRESSION OF GENE EXPRESSION IN MENISCIAL EXPLANTS AFTER REMOVAL FROM BIOMECHANICAL LOADING

Takashi Natsu-ume, Alison Kydd, Helen Tsao, Cyril B. Frank, Nigel Shrive, and David A. Hart
McCaig Centre for Joint Injury and Arthritis Research, University of Calgary, Calgary, Alberta CANADA T2N 4N1
hartd@ucalgary.ca

INTRODUCTION

Recent studies using both ligament (Majima et al., 2000, 2000a) and meniscal (Natsu-ume et al., 2002) explant systems have revealed that removal of these tissues from the rabbit knee leads to the rapid de-repression of a subset of genes (MMPs, TIMPs, cytokines, enzymes) which could contribute to tissue turnover/degradation. This de-repression could be blocked by in vitro intermittent cyclic loading protocols (1 MPa, 0.5 Hz, 1 min on/14 min off for 4 hr). Many of the involved genes affected by mechanical loading have AP-1 sites in their promoter regions, and therefore, can be effectively transrepressed by glucocorticoid treatment. Therefore, the present study was undertaken to determine whether pretreatment of rabbits with glucocorticoids would prevent the subsequent de-repression of these genes in explants of intact menisci following short-term in vitro culture under non-loading conditions .

METHODS

Skeletally mature female NZW rabbits received either diluent (N = 4) or an optimal dose of DepoMedrol (10mg/kg) (N = 4) via the IM route into the hindlimbs 24 hr prior to sacrifice. At the time of sacrifice, the medial and lateral menisci of each knee were immediately removed and those from one leg immediately frozen in liquid nitrogen to serve as the Time Zero controls. The menisci of the other leg were cultured in the absence of mechanical stimulation for 4 hr in vitro under established conditions (Natsu-ume et al., 2002). At the end of 4 hr, the menisci were immediately frozen in liquid nitrogen and served as the Unloaded Experimentals. Total RNA was isolated from individual menisci, quantified, and all samples were subjected to reverse transcription (RT) at the same time. mRNA levels for specific genes were then assessed in the RT samples using semiquantitative PCR, again all at the same time, using validated rabbit-specific primer sets. All assays were in the linear range of the PCR amplification and the image analysis system used to assess the density of the amplicons. Values for individual genes were normalized to beta-actin mRNA levels to yield a semiquantitative assessment. Statistical analysis was performed using ANOVA.

RESULTS AND DISCUSSION

Comparison of mRNA levels between the Time Zero samples from the diluent treated and DepoMedrol treated animals indicated that mRNA levels for MMP-1,-3 and -13 were significantly depressed in the DepoMedrol treated samples, but values for TIMP-1, IL-1, IL-6, collagens and proteoglycans were not depressed. Thus, expression of the MMPs in menisci is very sensitive to systemic in vivo glucocorticoid treatment as predicted from the literature. Results for the medial and lateral menisci were very similar.

Comparison of untreated Time Zero controls vs 4 hr of unloading revealed that mRNA levels for MMP-1 and -3 were elevated, as were levels for TIMP-1, iNOS, IL-1, and IL-6. These results are consistent with previous studies (Natsu-ume et al., 2002). Similar comparisons for the cultured DepoMedrol treated samples vs Time Zero controls revealed that mRNA levels for MMP-1 and -3 were significantly elevated, as were levels for TIMP-1, IL-6 and iNOS. Values for IL-1 were not affected by unloaded conditions in the treatment group.

The results presented indicate that pretreatment of animals with glucocorticoids has an impact on tissue mRNA levels for some, but not all molecules in menisci. However, such pretreatment did not overtly influence the de-repression of mRNA levels following unloading the tissue in vitro for nearly all of the molecules assessed in the study (with IL-1 a notable exception).

SUMMARY

While glucocorticoids are effective in depressing gene expression in vivo for several relevant molecules, the response to unloading conditions for nearly all of the affected molecules was unaltered. Therefore, it is likely that the mechanobiology signal transduction systems involved either do not use the same mechanisms as glucocorticoids to repress gene expression, but can override them, or they can effectively compete for the same promoter sites and negate the influence of the drugs. Current studies are designed to distinguish between these possiblities, and to further characterize the molecular mechanisms associated with biomechanical loading at the cell and gene levels.

REFERENCES

Majima T, et al. J Orthop Res 18:524-531 (2000)
Majima T, et al. J Orthop Sci 5:503-510 (2000a)
Natsu-ume T, et al. In vitro cyclic hydrostatic pressure influences MMP-1, -3, and iNOS mRNA expression in the rabbit meniscus. 2002 Orthop Res Society Meeting.

ACKNOWLEDGEMENTS

These studies were supported by grants from the Canadian Arthritis Network and the Canadian Institutes for Health Research.

DYNAMIC, BIOMECHANICAL CHARACTERISTICS OF HUMAN ANKLE LIGAMENTS

R.Hopcroft[1], C.Oakley[2], S.Suman[2], P.Manning[1], R.Lowne[2], W.A.Wallace[1]

1.Institute of Biomechanics, University of Nottingham, England
mszrwh@gwmail.nottinham.ac.uk
2.Transport Research Laboratory, Berkshire, England

INTRODUCTION

Improved techniques in finite element modeling are playing an increasingly important role in predicting injury. At present, biomechanical knowledge regarding the characteristics of human ankle ligaments is limited.

This study reports the results of tests performed to investigate the dynamic nature of these properties and quantify them for the ankle.

The ligaments deemed critical to ankle joint stability are:

- Deltoid
- Calcaneofibular
- Anterior talofibular
- Posterior talofibular

METHOD

Twenty-four ligaments from six donated post mortem human surrogates were isolated for testing. Morphometry of length, width and thickness were measured in situ and again after removal from the specimen. This enabled calculation of elastic modulus and load under static in situ conditions in the anatomical position. Each ligament was tested to a sub injury level over a spectrum of applied loading rates and lengths of stretch. After each high load rate a pseudo-static test was performed as a control to confirm no injury had occurred.

Fig 1. Loading Rig

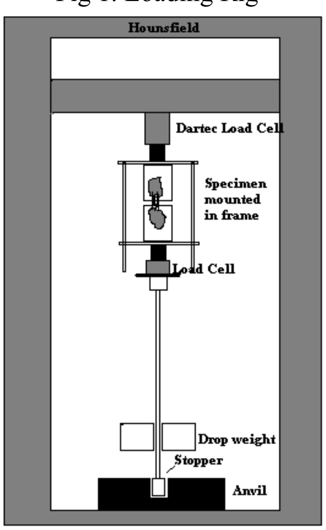

It was recognized that the deltoid ligament exists anatomically as distinct superficial and deep parts. These were tested together as a complex. In the clinical setting, each part does not have a role significantly different from the other in terms of overall stability.

The load was applied via a drop weight rig (fig 1). The length of stretch was predetermined before each test to ensure a sub-injury test when required. The mass of the drop weight was sufficiently great to ensure any loss of kinetic energy was insignificant over the length of stretch. Thus a uniform rate of loading was produced throughout each individual test.

RESULTS

This method of testing has been validated for reliability and repeatability before embarking on the main program. The analysis of twenty-four ligaments will be presented. The early data clearly demonstrates the dynamic response of these visco-elastic structures. The analysis of the test program, qualifying the ligament's characteristics at high loading rates will be presented.

DISCUSSION

The analysis presented offers a valuable insight into the biomechanical properties of ligaments at the rates of loading encountered during injury caused by high-energy impacts. This biomechanical data is vital to develop future finite element models.

ACKNOWLEDGEMENTS

Mr. J.McMaster – Rig Design
Mr. M.Parry – Institute of Biomechanics, University of Nottingham, England.

DEVELOPMENT OF A NOVEL TYPE OF OESOPHAGEAL STENT BASED ON DEPLOYABLE TUBULAR STRUCTURES

Kaori Kuribayashi, Stephen Jordan and Zhong You

Department of Engineering Science, University of Oxford, Oxford, OX1 3PJ, UK
e-mail: zhong.you@eng.ox.ac.uk

INTRODUCTION

Stent treatment has been shown to improve the quality of life in patients with inoperable malignant oesophageal cancer by allowing patients to swallow and maintain oral nutrition (Song, 1991). However, the currently used mesh stents have many problems, e.g., tumours ingrowth through the mesh, less compact folding and migration problems associated with the covered stents, etc. In addition, the cost of the stents is very high. As a result, plastic rigid tubular stents are still used. In this paper, we present a new type of oesophageal stent with an integrated cover. The concept is based on the knowledge of deployable structures and ancient origami technique.

A NEW HELICAL OESOPHAGEAL STENT

As opposed to the mesh stent, the new type of the stent is a tubular thin wall structure. To achieve foldability, the rigid wall is divided into a number of semi-rectangular units. Within each unit and in between neighbouring units, folds are introduced, so that the stent can be folded both longitudinally and radially (Kuribayshi, 2001). A schematic diagram is given in Fig. 1 in which the major folds *A* and *B* form two separate sets of helices orthogonal to one another. As shown in Fig. 1(b), the helical line *B* is around the tube, therefore the folding and expanding processes are synchronised between units. This makes the stent easy to deploy in the oesophagus.

OPTIMUM GEOMETRY

The optimum geometry of the stent, i.e., the optimum locations for the folds, is defined by the angle α. When a perfect thin-walled tube is under torsion, it will lose stability and a wavy buckling pattern will form giving valley and peak folds. Such a pattern is utilised to define the location of helices to achieve the easiest folding.

Geometrically, for the arrangement of folds shown in Fig. 1,

$$\alpha = \frac{\pi}{2} - \tan^{-1}\left(\frac{b_1 b_2}{a_1 b_2}\right) = \frac{\pi}{2} - \tan^{-1}\left(\frac{2}{2m+1}\right)$$

in which m is the number of units in circumference direction where $m > 3$. Comparing both m and α with that obtained from buckling analysis using Donnell's formula (Timoshenko, 1961) yields the optimum number of folds and their angles. For instance, for a 60 mm long and 25.4 mm diameter tube, when the thickness of the tube is 0.025 mm, m = 8 and α = 82.4°, while the thickness of 0.08 mm gives m = 6 and α = 79.7°.

FABRICATION

The novel stent can be made of the same biocompatible materials as the existing mesh stents, i.e. the stainless steel or shape memory alloys. A sheet of these materials is chemically etched to produce folding patterns. After that, the sheet is rolled and joined together forming a tubular stent. Figure 2 shows a model of the stent based upon the above design. It was made from a stainless steel sheet of 0.10 mm in thickness. The thickness was halved in the locations of the folds by etching. Folding of the stent was easily accomplished. The proposed concept has been proven useful for future stent designs.

FUTHER WORK

The automatic expansion technique for the stainless steel stent is currently under development. In parallel, we are also investigating the use of shape memory alloy sheets to produce self-expanding stents.

REFERENCES

Song, H., et al (1991). *Radiology*, **180**, 349 - 354
Timoshenko, S., Gere, J. (1961). *Theory of Elastic Stability*.
Kuribayashi, K., You, Z. (2001). *British Patent* No: 0107910.2

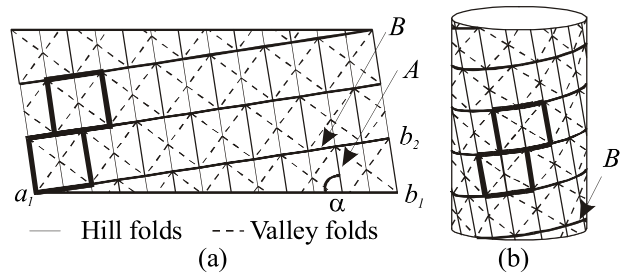

Figure 1 A helical foldable cylindrical tube.

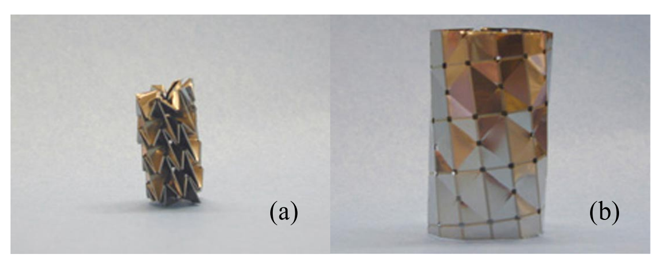

Figure 2 Photographs of a stainless steel stent (a) in its fully folded (diameter: 12 mm) and (b) fully expanded (diameter: 23 mm) configurations.

EFFECT OF AGE ON ABILITY TO BRAKE A FALL WITH THE OUTSTRETCHED HANDS

Paula J. Stotz, Sarah C. Normandin, Stephen N. Robinovitch

Injury Prevention and Mobility Laboratory, School of Kinesiology
Simon Fraser University, Burnaby, B.C., Canada, stever@sfu.ca

INTRODUCTION

Evidence suggests that an elderly individual's risk for hip fracture in the event of a fall depends on his or her ability to "brake the fall" with the outstretched hands. For example, studies have shown that risk for hip fracture during a fall is reduced approximately 3-fold if impact occurs between the ground and one or both hands (Schwartz et al., 1998; Nevitt and Cummings, 1993). Studies have also shown that, in the event of an unexpected sideways fall, young individuals tend to avoid hip impact by rotating the body forward during descent, and impacting the ground with both outstretched hands (Hsiao and Robinovitch, 1998). Ability to achieve this depends in part on one's ability to move the hands into an appropriate position during the descent stage of the fall, in preparation for impact. In this study, we examined whether differences exist between young and elderly women in this ability during simulated forward and sideways falls.

METHODS

A total of 18 young (Y) women (mean age 22 ± 3 yrs) and 18 elderly (E) women (mean age 78 ± 6 yrs) participated in the experiment. During the trials, the subject stood facing or sideways to shoulder-height padded targets, and was instructed to contact the targets "as quickly as possible" after hearing an aural cue. For both orientations, the target distance was adjusted so impact occurred with the elbows flexed at 45 degrees. Force plates (MU2535, Bertec Corp) mounted behind the targets acquired contact forces at 960 Hz, and a 60 Hz seven-camera motion measurement system (ProReflex, Qualisys Inc) acquired the 3D positions of various skin surface markers. Subjects performed ten trials in the forward direction and 10 trials in the sideways direction, in a randomized sequence. Data were analyzed to determine: (a) the time between the go cue and the onset of hand movement (reaction time (RT)), and (b) the time between the onset of hand movement and contact of the target (movement time (MT)). We used independent sample *t*-tests to determine whether differences in these parameters existed between Y and E. Reported values are for the dominant hand.

RESULTS AND DISCUSSION

We observed age-related slowing in MT but not RT. There were no differences between Y and E in mean RT for forward trials (mean Y value = 225 ± 36 ms; mean E value = 241 ± 50 ms; $P = 0.3$) and sideways trials (mean Y value = 233 ± 36 ms; mean E value = 274 ± 77 ms; $P = 0.05$). However, mean MT was significantly slower for E than Y in forward trials (mean Y value = 292 ± 36 ms; mean E value = 371 ± 77 ms; $P < 0.001$) and in sideways trials (mean Y value = 410 ± 62 ms; mean E value = 537 ± 144 ms; $P < 0.001$).

Strict time requirements exist for braking a fall with the outstretched hands. Previously, we found that the time interval between the onset of a destabilizing perturbation and contact between the hands and the ground during a fall averages 680 ± 116 ms (Hsiao and Robinovitch, 1998). This is close to the mean total contact time (sum of RT and MT) observed in the current study for Y in forward trials (517 ± 59 ms), Y in sideways trials (642 ± 79 ms), E in forward trials (613 ± 86 ms), and E in sideways trials (810 ± 166 ms).

Total contact time was determined more strongly by MT than by RT (Fig. 1). For both Y and E, there was greater between-subject variability in MT than in RT, and no correlation between these two variables ($P = 0.5$ for forward trials, and $P = 0.2$ for sideways trials).

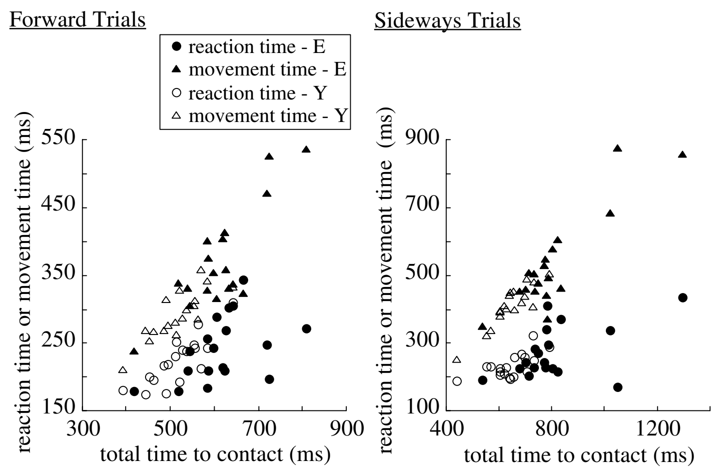

Figure 1: Reaction time and movement time components of contact time for forward and sideways trails.

SUMMARY

Strict time requirements exist for braking a fall with the outstretched hands. Age-related declines in ability to perform this task appear to be due more to slowing of movement time than reaction time.

ACKNOWLEDGEMENTS

This research was supported by grants from the CDC (R49CCR019355), NIH (R01AR46890), CIHR, and MSFHR.

REFERENCES

Hsaio, E.T., Robinovitch, S.N. (1998). J. Biomech., **31**, 1-9.
Nevitt, M.C., Cummings, S.R. (1993). *J. Am. Geriatr. Soc.*, **41**, 1226-1234.
Schwartz, A.V. et al (1998). *Osteoporos Int.*, **8**, 240-6.

FINGERTIP PULP MECHANICS DURING VOLUNTARY TAPPING

Devin L. Jindrich, Theodore Becker and Jack Tigh Dennerlein (jax@hsph.harvard.edu)
Harvard Occupational Biomechanics, Harvard School of Public Health, Boston, MA.USA

INTRODUCTION

Increased use of computer keyboards is associated with increased incidence of musculo-skeletal disorders (MSDs) of the upper extremity. Epidemiology studies indicate that one possible risk factor for the development of MSDs is the mechanical load to the soft tissues. To understand and predict the mechanical load on the soft tissues of the hand and arm during tapping activities, we seek to build a lumped parameter model of the finger, hand and wrist. We first chose to characterize the mechanics of the fingertip pulp during tapping because forces at the fingertip must be transmitted to more proximal segments through the fingertip pulp.

The mechanics of the fingertip pulp has been modeled during static and dynamic loading using sinusoidal and ramp inputs (Pawluk and Howe, 1999; Serina *et al*., 1997). However, tapping movements contain high-frequency components that may not be well characterized by existing models (Pawluk and Howe, 1999). We therefore conducted experiments to determine whether a simple model of the fingertip pulp adequately describes its mechanical behavior during dynamic tapping tasks similar to those experienced during typing.

MATERIALS & METHODS

We measured vertical force at the fingertip using a stiff force sensor, and position of the fingertip using an optical measurement system and a light-emitting diode glued to the fingernail (Figure 1). Eight subjects tapped on the force sensor while fingertip position was measured. Subjects were instructed to minimize contact time for each tap and tap once per second. Position signals were filtered and differentiated to yield velocity and acceleration.

Figure 1. Experimental apparatus used to measure tap mechanics.

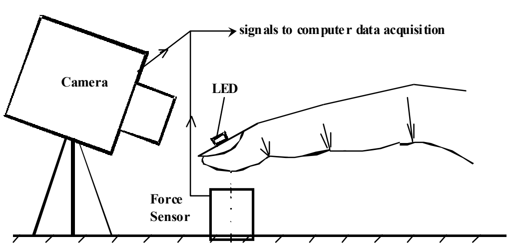

A simple dynamic model was fit to the resulting force and position data. Following Pawluk (1999), functions for the instantaneous elasticity $T^{(e)}(x)$ and relaxation $G(t)$ were used to characterize the behavior of the fingertip pulp.

Force caused by instantaneous elasticity was modeled as an exponential function of position $T^{(e)}(x) = \frac{b}{m}\left[e^{mx} - 1\right]$, and force change due to relaxation was modeled as an exponential function of time $G(t) = c_0 + c_1 e^{-vt}$.

RESULTS

When subjects were instructed to tap on the force sensor in a comfortable manner, with the rest of the hand relaxed, the fingertip pulp was rapidly compressed during the first 10 ms of the tap, then maintained relatively constant amount of compression (Figure 2).

Figure 2. Pulp compression over time for a representative tap.

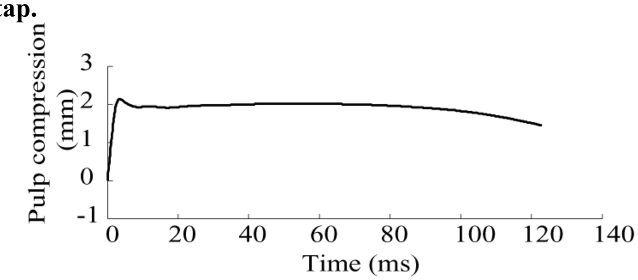

Force production was characterized by an initial force peak, corresponding to the compression of the fingertip, followed by a decrease in force caused by rapid relaxation of the fingertip pulp (Figure 3).

A simple model of fingertip pulp mechanics exhibiting instantaneous elasticity and rapid relaxation was able to re-construct the mechanical behavior of the fingertip pulp to root-mean-squared errors of 10% (Figure 3). These errors are similar to the 4-10% errors achieved for simpler inputs (Pawluk and Howe, 1999).

Figure 3. Measured and re-constructed force over time.

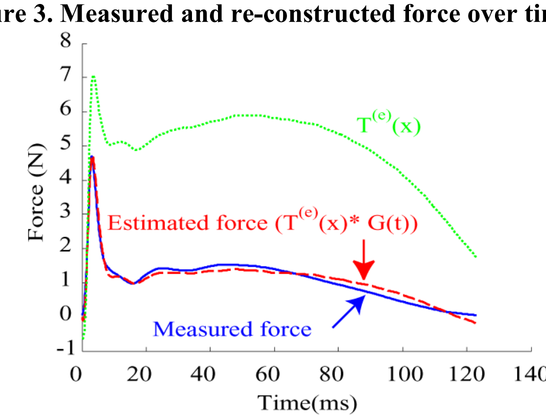

REFERENCES

Pawluk, D. T. V. and Howe, R. D. (1999b). *J. Biomechanical Engineering.* **121,** 178-183.
Serina, E. R., Mote, C. D. and Rempel, D. (1997). *J. Biomechanics* **30,** 1035-1040.

ACKNOWLEDGMENTS

This project is supported by the Whitaker foundation. We thank Yanhong Zhou for experimental work and Dianne Pawluk for assistance with modeling.

FITTING MUSCLE PROPERTIES

Tobias Siebert[1], Heiko Wagner[1], Richard Marsh[2] and Reinhard Blickhan[1]

[1]Institute of Sports Science, Friedrich Schiller-University, Jena, Germany
tobias.siebert@uni-jena.de
[2]Department of Biology, Northeastern University, Boston, USA

INTRODUCTION

Muscle properties specified for example by the force-length-, force-velocity relationships, and the stiffness of the series elastic element can be either determined separately in rather specialized experiments or by fitting a model to dynamic experiments. The two approaches are compared in an experiment on a frog M. dorsal semitendinosus. Fitting to a family of dynamic (kinetic) measurements saves time and gives acceptable results.

METHODS

The M. dorsal semitendinosus (*Rana pipiens*) was dissected. The muscle was connected with a lever arm system (Cambridge technologies 300B), which allows static and dynamic investigation of force and length with supramaximal stimulation. A series of isometric experiments was performed to measure the force-length dependency. The stiffness of the series elastic component and the force velocity relationship was measured by step-release isokinetic experiments (Curtin 1998). Isokinetic experiments started at L0 and were performed with different shortening velocities.

Muscle model: We describe the muscle with a Hill-type muscle model consisting of a force-velocity relation, a force-length relation and a linear series elastic component. The properties of the muscle model can be determined using a non-linear regression method. In order to enhance the precision of the fitting method, we used a software package (JOP kinematics) which allows to fit up to eight different data sets simultaneously with a single set of muscle properties. The fitting of 4 isokinetic frog data results in one set of muscle properties.

RESULTS AND DISCUSSION

The model calculations performed with one parameter are consistent with the isokinetic experiments (Fig. 1a). Isokinetic experiments were performed on the ascending limb of force-length relationship, therefore we obtain high correlation for this part (Fig. 1c). Deviation of 15% maximum force are found in lower part by fitting a parable function. Difference in descending limb of force length relationship are due to description of the asymmetric force length curve by a parable. A higher correlation in descending part may be possible by performing isokinetic experiments on the descending limb and usage of asymmetric force-length function. Differences in force-velocity relationship are found in the region of high velocities (Fig. 1b). They depend on the quality of force-length description. Stiffness of the series elastic component is determined as k=828N/m (experimental) and k=894N/m (fitting, Fig. 1d). Parallel elasticity was neglected.

This method was used to determine muscle properties of another muscle (M. triceps brachii of *Rattus norvegicus*) by fitting 8 isokinetic traces. Stiffness of series elastic component is 25.6 kN/m, v_{max} = 0.2m/s F_{max} = 37 N and P_{max} = 0.56 W.

SUMMARY

It is possible to obtain a suitable set of muscle properties by fitting a hill type muscle model to isokinetic data. This strongly reduces the experimental effort.

REFERENCES

Curtin, N.A. et al (1998). *J exp Biol*, **201**,103-114
Siebert, T et al (2001). *Motion Systems 2001"*, Shaker, 76-80

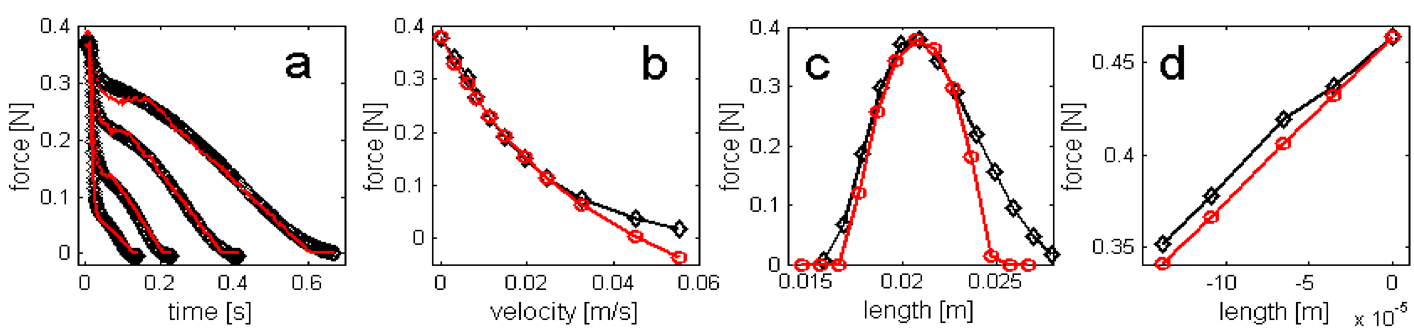

Figure 1: (a) Force traces of 4 isokinetic experiments (black line) and model calculations (red line). Force-velocity curve (b), force-length curve (c) and stiffness of the series elastic component (c). Black line (diamond): experimental results. Red line (circle): muscle properties from the fitted isokinetic data

LOWER LIMB ENERGETICS OF NORMAL AND MODERATE OA SUBJECTS

J.W. Kozey,[1] S.L. Offman, [1] K.J. Deluzio, [2], C.L. Hubley-Kozey, [3]
J.J. Chu[4] , G.E. Caldwell[4] AND W.D. Stanish [5]
[1] Schools of Health and Human Performance, [2] Biomedical Engineering, and [3] Physiotherapy, Dalhousie University, NS,
[4]Department of Exercise Science, University of Massachusetts, MA and [5] Faculty of Medicine, Dalhousie University NS.

INTRODUCTION

Osteoarthritis (OA) is a degenerative joint disease that negatively affects the integrity of articular cartilage and underlying subchondral bone. It has been suggested that OA exists in 80% of the individuals over the age of 55 (Altman, 1987). It is a particularly debilitating disease when it affects the knee, as its symptoms inhibit basic daily activities such as walking. Gait analysis has proven to be a vital tool for understanding the effects of QA on functional tasks. However, it may also be a valuable adjunct in understanding the etiology, diagnosis and treatment of knee OA as well. The present study reports the preliminary results on the use of gait analysis for individuals with OA through the calculation of muscle power and mechanical work values of the lower limb. The analysis was restricted to a 2-D sagittal plane analysis of the lower limb during a fast pace (150% preferred speed) walk. It was hypothesized that there would be alterations in the lower limb energetics in patients with moderate OA of the knee compared to normal. Specifically, we conjectured that OA might cause a redistribution of relative work contributions (RWC) among joints in the lower limb.

METHODS

All subjects completed informed consent and SF-36 health survey forms, and the OA subjects completed the WOMAC prior to the completion of any test trials. Each subject performed, in random order, five trials of their normal preferred speed (C1), and a fast walk (C2) (150% of the normal speed). All OA subjects were diagnosed as either a 1 or 2 on the Kellgran & Lawerence scale prior to participating in the study. The *Qualisys* Pro-reflex motion capture system and a *Kistler* force plate were used to record the kinematic and ground reaction force data for 7 (Norm) and 4 (OA) subjects. The mechanical work and powers were calculated for the sagittal plane motion of the entire stride using BIOMECH software for the five walking trials. Standard link segment marker locations and data smoothing techniques (Butterworth low-pass digital filter @ 6 Hz) were used. Muscle powers (W/kg) and the work (J/kg) done at the hip, knee and ankle were calculated for each trial. Work at each joint was expressed as a percentage of the total work done in the lower limb for the gait cycle. The within subject average value for the five trials were used in an ANOVA to test for between group differences.

RESULTS

There was no significant difference in the walking speeds of the two groups for the C1 and C2 conditions (Table 1). Shown in Table 2 is the RWC for each joint expressed with respect to the total lower limb work (the summed positive and negative work accumulated over the entire stride) for the C2 condition. There were statistically significant differences for the RWC at the hip ($F=104.9$, $df=1,3$, $p = 0.002$) and the knee ($F=22.69$, $df=1,3$, $p=0.018$) between the two groups. The OA group performed less work (37.8% vs 46.8%) at the knee than the controls and an increase in the work (29.6% vs 23.4%) at the hip.

Table 2: Relative work done (%) at each joint (C2 condition).

	Positive Work		**Negative work**		**Total Work**	
Joint	*Norm*	*OA*	*Norm*	*OA*	*Norm*	*OA*
Hip	31.7	35.2	13.3	20.6	23.4*	29.6
Knee	23.2	22.2	75.4	63.0	46.8*	37.8
Ankle	44.9	42.6	11.3	16.4	29.8	32.5

DISCUSSION

Subjects with moderate OA tend to be active individuals who exhibit locomotor patterns that temporally and kinematically, appear quite “normal”. The purpose of this pilot work was to compare the kinetic patterns of the lower limbs during fast walking. Although there was no difference in the speed of walking the muscle energetics information from the lower limb suggests that the OA group did perform the task employing a strategy to reduce the work done at the affected joint. The OA knee experiences a reduction in the mechanical work done during the first three major power phases of the knee during the gait cycle. Initial outcomes from this study suggest that employing a kinetic analysis of the gait pattern may be a sensitive technique to discriminate between normal and OA subjects.

CONCLUSION

There is a redistribution of the total work done among the joints in the lower limb during the entire gait cycle for individuals with OA of the knee. The key change appears to be a 9.0% decrease in the total RWC in the OA knee. This change is reflected in the form of absorption compared to the normal knee and a redistribution of work to the hip.

REFERENCES

Altman R. (1987), Overview of Osteoarthitis, Amer. J. of Med., 83, pp. 65-69.

ACKNOWLEDGEMENTS

The authors wish to acknowledge the contributions of Andrew Horne, Scott Landry and Jennifer McNutt with the data collection. As well we wish to acknowledge the financial and other contributions of the CORF, ISB, the CLFL of the QE II Health Science Centre and Faculty of Health Professions, Dalhousie University.

Table 1: Descriptive statistics and summary information of the subjects.

Group	M/F	Height m.	Mass Kg.	Age yrs	Sf36	WOMAC	C1 m/s	C2 m/s
Norm	4M3F	1.76(.09)	74.6(10)	43.6(9)	106-115		1.4 (.2)	2.0(.2)
OA	3M1F	1.74(.08)	83.5(11)	57.8(14)	95-111	89-113	1.4 (.2)	2.0(.2)

TECHNIQUES FOR AVOIDING HIP IMPACT DURING UNEXPECTED SIDEWAYS FALLS

Jessica Maurer, Brady Warnick, Lisa Inkster, and Stephen N. Robinovitch
Injury Prevention and Mobility Laboratory, School of Kinesiology, Simon Fraser University, Burnaby, B.C., Canada, stever@sfu.ca

INTRODUCTION

Falls are the underlying cause of 90% of all hip fractures in the elderly (Grisso et al., 1991). Considerable evidence now exists that the configuration of the body at impact is a stronger predictor of hip fracture risk than bone density (Greenspan et al., 1994; Nevitt et al., 1993). Of particular importance is whether impact occurs to the hip, which increases fracture risk 30-fold. Our previous studies suggest that young individuals tend to avoid hip impact during a sideways fall by rotating forward and braking the fall with the outstretched hands (Hsiao et al., 1998). Presumably, an alternate technique for achieving this is to rotate backward to land on the buttocks. In this study, we examined whether these two strategies are equally effective in allowing subjects to avoid hip impact during an unexpected sideways fall.

METHODS

Fourteen women between the ages of 18 and 35 (mean age 24 ± 6) participated in the study. In all trials, a sideways fall was initiated by suddenly releasing a tether, which supported the subject at a 15 deg lean (Fig. 1). This caused the subject to fall unexpectedly onto a soft gymnasium mat. Subjects were instructed to try to “land as softly as possible” and to “avoid impacting the hip” by either rotating forward to land on the knees and outstretched hands (FR trials), or rotating backward to land on the buttocks (BR trials). Subjects were also instructed to keep their knees extended during descent. Three trials were acquired for each condition in a randomized sequence.

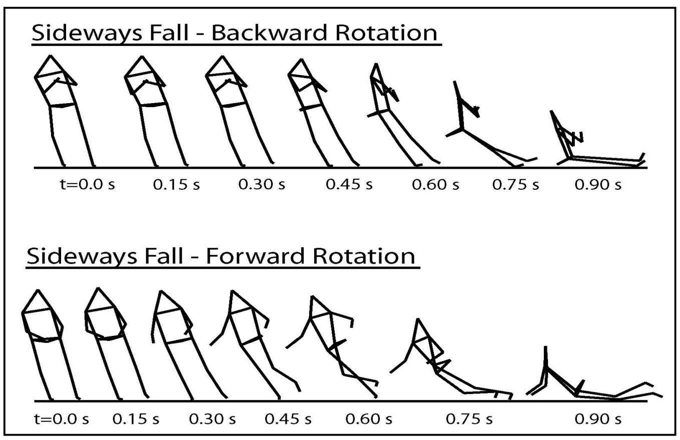

Figure 1: Stick figure image of sideways falls

We used a 6-camera, 60 Hz motion measurement system (MacReflex, Qualysis Inc) to acquire from each trial the 3D positions of 22 skin surface markers. From these data, we determined values of the following variables at the instant of pelvis impact: (1) hip proximity angle, (2) pelvic tilt angle, (3) vertical hip velocity, and (4) whole-body kinetic energy. The hip proximity angle (α) reflects how near the site of pelvis impact is to the lateral aspect of the hip (Fig 2). The pelvic tilt angle (β) indicates how near the pelvic ellipse is to being parallel to the ground at impact. Paired t-tests were used to determine if there were differences in these variables between FR and BR trials.

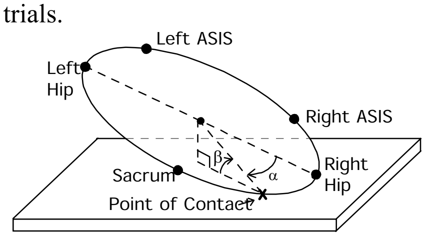

Figure 2: Pelvic contact angles

RESULTS AND DISCUSSION

There were no differences between FR and BR trials in mean values of hip proximity angle, vertical hip velocity, and kinetic energy at impact (Table 1). However, pelvic tilt angle was significantly greater in FR than in BR trials.

This suggests that individuals can avoid impact to the hip during a sideways fall by rotating backward during descent (to impact the buttocks) or by rotating forward (to impact the knees and hands). Previous evidence of a tendency for forward rotation (Hsiao et al., 1998) may reflect subjects’ desire to coordinate landing by visualizing the impact surface. However, it is likely that a range of environmental, intrinsic, and situational variables affect the feasibility and utilization of the FR and BR strategies.

Table 1: Fall severity indices from forward rotation (FR) and backward rotation (BR) trials (mean ± SD)

	FR value	BR value	*P* value
Hip Prox Angle (deg)	68.6 ± 12.5	61.5 ± 17.9	0.533
Pelvic Tilt (deg)	64.1 ± 8.6	26.2 ± 9.5	< 0.001
Hip Velocity (m/s)	3.02 ± .35	-3.26 ± .29	0.091
Kinetic Energy (J)	358 ± 216	282 ± 78	0.168

SUMMARY

During an unexpected sideways fall, young females can avoid hip impact by rotating forward or backward during descent.

ACKNOWLEDGEMENTS

Supported by operating grants from the CDC (R49CCR019355) and NIH (R01AR46890), and salary support awards from CIHR and MSFHR.

REFERENCES

Greenspan, S.L. et al. (1994). *J Am Med Assoc*, **271**, 128-33.
Grisso, J.A. et al. (1991). *N Engl J Med,* **324**, 1326-31.
Hsiao and Robinovitch (1998). *J Biomech*, **31**:1-9.
Nevitt and Cummings (1993). *J Am Geriatr Soc,* **41**, 1226-34.

DIFFERENCES IN PROPULSION KINETICS BETWEEN WHEELCHAIR DEPENDENT AND NON-WHEELCHAIR DEPENDENT USERS

W. Mark Richter[1, 2], Peter W. Axelson[2], Rory A. Cooper[3]

[1]Stanford University, Stanford, CA (wrichter@stanford.edu) [2]Beneficial Designs, Inc., Minden, NV
[3]Human Engineering Research Laboratories, Highland Drive VA Medical Center, Pittsburgh, PA

INTRODUCTION

Investigation of handrim kinetics during manual wheelchair propulsion provides insight into the demands on the wheelchair user and may ultimately serve to prevent the development of overuse injuries of the upper extremity. Studies enlisting the participation of non-wheelchair dependent users risk drawing conclusions that are not relevant to the wheelchair user population.

In a comparison of the metabolic demand of wheelchair dependent (WD) users and non-wheelchair dependent (NWD) users, Brown et al. found that WD users used less metabolic energy to complete the same propulsion task. In a study comparing propulsion kinetics of WD and NWD users, Robertson et al. found WD users tended to have lower peak tangential and vertical forces as well as longer times to reach those peak values. The researchers concluded that WD users might have developed these propulsion techniques to reduce the stress on the upper extremity. This study reevaluates the kinetic differences between WD and NWD users.

METHODS

Five WD and five NWD subjects participated in the study. Subjects propelled a wheelchair on a stationary dynamometer at a steady state target velocity of 3 m/s. The resistance of the dynamometer was set to simulate propulsion up a 2% grade. WD subjects used their own wheelchair in an unaltered configuration. NWD subjects used a Quickie Carbon wheelchair (Quickie, Fresno, CA). Handrim kinetics were measured using a SMART^{Wheel} instrumented wheelchair wheel (Three Rivers Holdings, Scottsdale, AZ).

Kinetics during ten consecutive pushes from each trial were used in the analysis. Handrim forces were normalized by subject body weight (bw) to remove subject weight as a factor in the results. The force components in the plane of the wheel were transformed from an inertial lab frame to a wheel fixed frame such that the resulting components were radial (Fr), tangential (Ft), and axial (Fa). Peak force components over the entire push and the average rate of force application (dF/dt) over the first ten percent of each push were determined and averaged. Results for each subject group were compared using a two-tailed paired samples t-test and considered to be statistically significant for $p<0.05$.

RESULTS

Resulting values of peak force and initial rate of force application are given for the WD and NWD groups in Table 1. The general trend in the data suggests that the WD users tend to exhibit larger peak forces and a higher rate of force application than the NWD users. Statistically significant differences were seen in the rate of force application in the radial and axial directions. The WD users applied force components 101% and 115% faster than the NWD users in the radial and axial directions, respectively. While propulsion velocity tended to be less for the WD users, the difference was not statistically significant. Had the propulsion velocity been higher for the WD users, it would have provided a possible reason for the trend in increased force on the handrim.

Table 1: Propulsion kinetic characteristics for wheelchair dependent (WD) and non-wheelchair dependent (NWD) users

Parameters	WD	NWD	Significance (p)
Velocity (m/s)	2.68	3.09	0.053
Push Frequency (Hz)	1.15	1.09	0.697
Peak Fr (bw)	0.112	0.081	0.070
Peak Ft (bw)	0.072	0.064	0.435
Peak Fa (bw)	0.047	0.040	0.305
Avg Initial dFr/dt (bw/s)	2.070	1.030	**0.035***
Avg Initial dFt/dt (bw/s)	0.434	0.389	0.725
Avg Initial dFa/dt (bw/s)	1.012	0.470	**0.034***

DISCUSSION

While the results of this study appear to be in contradiction to those found by Robertson et al., the two studies are not directly comparable. The variation in results found by Robertson et al. may be explained by the use of non-body weight normalized forces. Body weight of WD users tends to be less than NWD users due to lower extremity atrophy, which would likely result in a reduced net force required propel the wheelchair.

The decreased rate of force application in the NWD users is believed to be the result an actively positioned and stabilized trunk. This conclusion may be supported by results of the Brown et al. study. Metabolic demand of NWD users would be expected to be greater than WD users due to the use of the large muscle groups of the trunk being used during propulsion. Results of this study indicate that kinetic propulsion characteristics of WD users are different than NWD users and as a result, future propulsion biomechanics studies should restrict participation to WD users.

REFERENCES

Brown, D.D., et al. (1990). *European J Appl Physiology*, **60**, 179-182.

Robertson, R.N. et al. (1996). *Arch Phys Med Rehabil*, **77**, 856-864.

ACKNOWLEDGEMENTS

Research funding was co-provided by the National Institute of Child Health and Human Development at the National Institutes of Health, and the National Center for Injury Prevention & Control (NCIPC), Centers for Disease Control and Prevention (CDC) through SBIR Phase I grant # 1 R43 HD36533-01.

CONTRIBUTIONS TO FORWARD PROPULSION IN HUMAN GAIT

Frank L. Buczek, Ph.D., James O. Sanders, M.D., M. Cecilia Concha, B.S., Kevin M. Cooney, P.T.
Motion Analysis Laboratory, Shriners Hospitals for Children, Erie PA, USA
fbuczek@shrinenet.org

INTRODUCTION

In clinical gait analysis, we strive to identify movement strategies that result in propulsive (anterior) ground reaction forces (*Fx*). We feel this framework better prepares us to answer treatment questions from referring physicians. We have found two prominent opinions regarding the source for *Fx*: the position of the body's center-of-mass (COM) forward of its base of support (a clinical interpretation advocated by Perry, 1992), and the use of mechanical power at joints of the lower extremities to perform work on the body, causing changes in its mechanical energy (an engineering interpretation after Winter, 1991). We hypothesized that COM position alone would be insufficient to explain *Fx*.

METHODS

Because the theory suggested by Perry (1992) essentially models the body as an inverted pendulum, we simulated a shaft of negligible mass and a load at its tip. By summing moments in the XY-plane (X anterior, Y vertical), and noting that the moment of inertia I about the pivot equals mr^2, we derived an expression for the angular acceleration α of the pendulum:

$$\alpha = \left(-g\cos\theta\right)/r\,, \qquad (1)$$

where g is the acceleration due to gravity, θ is the pendulum inclination angle, r is the radius from pivot to COM, and m is the mass of the load. Using polar coordinates and summing forces in the X direction, we derived an expression for Fx at the pivot:

$$Fx = -mr\left(\omega^2\cos\theta + \alpha\sin\theta\right), \qquad (2)$$

where ω is the angular velocity of the pendulum shaft. To illustrate these relationships, we simulated pendulum mechanics by numerical integration of Equation (1), and substitution of results into Equation (2). To best simulate the initiation of gait within the context of this theory, initial conditions included $\theta = 89°$, $\omega = 0$ radians/s, and $\Delta t = 0.017$ s. We simulated three pendulum radii (0.660, 0.825, 0.990 m) paired with three pendulum masses (25, 45, 65 kg), chosen to approximate 50th percentile anthropometry for a 7 yr old child, a 12 yr old girl, and an 18 yr old boy, respectively. Anterior translational velocities were obtained ($v = \omega r \sin\theta$), and simulations were terminated at $\theta = 60°$, approximating opposite foot contact. For comparison, *F*x data were obtained from our normal database for a subject whose pendulum radius and mass (0.910 m and 63 kg) matched the 18 yr old simulation.

RESULTS AND DISCUSSION

Inverted pendulum simulations produced maxima in v, Fx (N), and Fx (% bodyweight) comparable to normative data (Kadaba et al., 1989; Winter, 1991). However, the time Δt_{max} (from onset of positive Fx to its maximum value) was greater for the simulations than for our representative normal subject (Table and Figure). Although this limitation in Perry's model may be partially overcome by using an initial ω as in steady-state gait (future tests), there remain no mechanisms to change walking velocity (α is dependent upon r which is largely dictated by stature), nor to achieve swing phase. Input of mechanical energy seems necessary as suggested by Winter (1991).

Table: Simulation results compared to representative normal

	v_{max} (m/s)	Fx_{max} (N)	Fx_{max} (%bw)	Δt_{max} (s)
Sim1	1.10	75.7	30.9	1.05
Sim2	1.27	136	30.8	1.17
Sim3	1.36	196	30.8	1.27
Nrml	1.39	142	22.9	0.183
KEY	Sim1: r = 0.660 m, m = 25 kg; Sim2: r = 0.825 m, m = 45 kg; Sim3: r = 0.990 m, m = 65 kg; Nrml: r = 0.910 m, m = 63 kg			

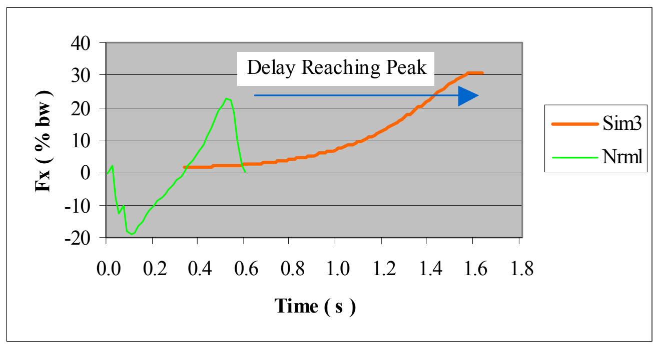

Figure: Positive *Fx* values begin at 0.33 s for normal and simulation graphs; the former peaks at 0.52 s, the latter at 1.60 s.

SUMMARY

Center-of-mass position alone, as simulated using an inverted pendulum, is insufficient to fully explain *Fx* during gait.

REFERENCES

Kadaba, M.P., et al. (1989). *Journal of Orthopaedic Research*, **7**, 849-860.
Perry, J. (1992). *Gait Analysis: Normal and Pathological Function,* SLACK, Thorofare NJ, USA.
Winter, D.A. (1991). *Biomechanics and Motor Control of Human Gait, 2nd ed.,* University of Waterloo Press.

EFFECT OF HAMSTRINGS INCLUSION ON CALCULATION OF JOINT CONTACT FORCE AND STRESS

Janet Ronsky and Nicole Baker

Department of Mechanical and Manufacturing Engineering, Human Performance Laboratory
University of Calgary, Calgary, Alberta, Canada, jlronsky@ucalgary.ca

INTRODUCTION

A method for non-invasively quantifying human patellofemoral (PF) joint contact stress has been developed (Ronsky, 1994). Load applied at the heel during a magnetic resonance (MR) scan is used as input to a mathematical model to estimate PF joint contact force and stress. Previous work neglected the hamstrings contribution to joint contact force. In the ACL-deficient knee, hamstrings may be more active than in healthy knees to provide joint stability (e.g. Solomonow et al., 1987). The purpose of this work is to quantify hamstrings forces during the MR rearfoot loading task and to compare joint contact force and stress calculated with and without hamstrings forces.

METHODS

Five female subjects (age = 25.4 ± 4.3 years, height = 164.4 ± 4.3 cm, weight = 56.6 ± 10.9 kg) with no knee injury history or knee pain volunteered for this study and gave informed consent. Knee health was verified by an orthopaedic surgeon. All experimental procedures were approved by the University of Calgary Conjoint Faculties Research Ethics Board.

Muscle forces were estimated using an EMG-force calibration procedure (Kellis and Baltzopoulos, 1997). Standard surface EMG protocol was used to record muscle activation patterns of the medial and lateral hamstrings (MH and LH) of right limbs. Each subject performed maximal and sub-maximal isometric knee flexion contractions on a Biodex dynamometer (Shirley, NY) at flexion angles of 15°, 30° and 45° (0° = full extension). Root mean square EMG values were normalized to MVC. Total knee flexor force was partitioned into MH and LH groups based on relative physiologic cross-sectional areas (e.g. McGill and Norman, 1986). A 2nd-degree polynomial was fit through the corresponding EMG-force data points.

Direct acquisition of surface EMG during the MR scan was not possible because the electrode leads caused image distortion. With EMG electrodes maintained in the same positions, MH and LH activity was recorded in the laboratory using a mock-up of the MR rearfoot loading device. The exercise is a supine leg press performed at approximately 7% MVC. Three repeat trials (right limbs only) were performed on three separate days. A confidence interval of muscle force magnitudes was calculated from the repeated measurements.

A 2D sagittal-plane model of the lower leg and PF joint was used to calculate joint contact force based on rearfoot loading quantified during imaging. Internal joint geometry and lines of action of patellar and hamstrings tendons were digitized directly from MR images (4 subjects, both limbs). Muscle forces estimated from right limbs were assumed to be valid for use in the left limb model of the same subject. PF articular surfaces were digitized from MR images and reconstructed using a thin plate spline (Boyd et al., 1999). Contact area was determined using a surface proximity threshold. Average PF contact stress was calculated as contact force divided by area.

RESULTS AND DISCUSSION

The predicted hamstring forces during the MR loading task ranged from 0-59 N (10% MVC) for LH and 0-45 N (6% MVC) for MH. The inclusion of hamstrings forces resulted in an average increase of 25 ± 18% in contact force and stress magnitudes. This is an increase of 21 ± 6 N for contact force and 0.09 ± 0.04 MPa for contact stress (Figure 1).

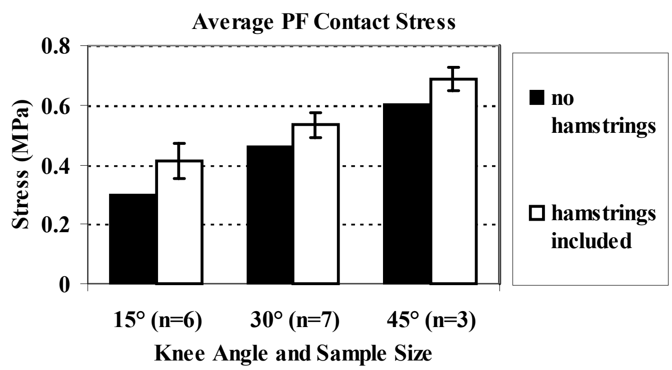

Figure 1: PF joint contact stress calculated without and with estimated hamstrings forces. Bars represent the average 5-95% confidence interval of hamstrings forces based on repeat tests. Sample sizes vary depending upon availability of MR images.

This method may be used to non-invasively estimate subject- and knee angle-specific muscle forces without having to assume a value for muscle stress. Future application of this work will be to compare PF contact characteristics between normal and ACL-deficient knees using this method to quantify hamstrings forces for input to the PF joint contact force model.

REFERENCES

Boyd, S.K. et al. (1999). *J. Biomech. Eng.*, **121**, 525-532.
Kellis, E., Baltzopoulos, V. (1997). *Eur. J. App. Physiol.*, **76**, 253-259.
McGill, S.M., Norman, R.W. (1986). *Spine,* **11**, 666-678.
Ronsky, J.L. (1994). *Ph.D. Dissertation*, U. of Calgary Press.
Solomonow, M. et al. (1987). *Am. J. Sports Med.*,**15**, 207-213.

ACKNOWLEDGEMENTS

Financial: NSERC, CHR, CRCP. Technical: E. Suter

TECHNIQUES FOR SAFE LANDING DURING AN UNEXPECTED FALL: MODULATION OF IMPACT VELOCITY VIA THE "SQUAT RESPONSE"

Stephen Robinovitch, Leslie Torburn, Lisa Inkster, and Rebecca Brumer

Injury Prevention and Mobility Laboratory, School of Kinesiology
Simon Fraser University, Burnaby, B.C., Canada, stever@sfu.ca

INTRODUCTION

Falls are the number one cause of accidental injuries in the elderly, including 90 percent of hip fractures (Grisso et al., 1991). One's risk for hip fracture in the event of a fall depends on bone strength, and on the force applied to the bone at impact. The latter depends, in turn, on the configuration and velocity of the body as it contacts the ground. Previous studies (Hsiao and Robinovitch, 1998) suggest that young subjects utilize specific protective responses to avoid injury during a fall. These include absorbing energy in the lower extremity muscles during descent (as occurs during squatting or sitting), and braking the fall with the outstretched hands. The purpose of this study was to test whether, during an unexpected backward fall, the utilization or inhibition of these responses affects the velocity of the hip and the kinetic energy of the entire body at the moment the pelvis strikes the ground.

METHODS

Seventeen women between the ages of 18 and 35 (mean age 23.58 ± 5.62) participated in the study. In all trials, a backward fall was initiated by suddenly releasing a tether (Fig 1), which supported the subject at a 5 deg lean. This caused the subject to fall unexpectedly onto a soft gymnasium mat. Four series of trials were acquired with each subject (Table 1). In all series, subjects were instructed to "land as softly as possible" and to "avoid impacting the hip." However, the series differed in whether the subject was further instructed to utilize or inhibit (i) braking the fall with the outstretched hands, and (ii) absorbing energy in the lower extremity muscles and tendons during descent ("squat response"). Throughout the session, the series (i.e., instruction) was randomized, with the constraint that 3 trials were acquired for each of the four series.

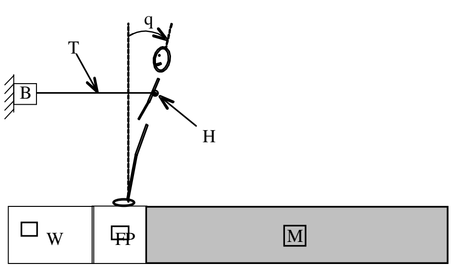

Figure 1. Tether-release falling experiment. M = gym mat; FP = force plate; W = walkway; H = harness; T = tether; B = brake. The lean angle before release was $\theta = 5$ deg.

In each trial, we used a 6-camera, 60 Hz motion capture system (Qualysis Inc) to acquire the 3D positions of 22 skin surface markers. We then used custom routines (MATLAB) to calculate from these data the vertical velocity of the right greater trochanter and the kinetic energy of the entire body at the moment the pelvis impacted the mat. We used repeated-measures ANOVA (with alpha = 0.05) and post-hoc paired t-tests (with alpha = 0.008) to determine if there were differences in outcome parameters between the series.

RESULTS AND DISCUSSION

Use of the squat response caused a decrease in hip velocity and whole-body kinetic energy at impact. When compared to Series D (no squat, no hands), Series B (squat, no hands) involved smaller hip impact velocities (21 ± 13 percent decline, on average; $P = 0.001$), and smaller kinetic energies at impact (41 ± 26 percent decline, on average; $P < 0.001$). When compared to Series C (no squat, hands), Series A (squat, hands) involved smaller kinetic energy at impact (29 ± 19 percent decline, on average; $P < 0.001$).

On the other hand, braking the fall with the outstretched hands did not affect hip velocity or kinetic energy at impact. There were no differences between Series A and Series B in hip impact velocity ($P = 0.21$) or kinetic energy ($P = 0.84$), or between Series C and Series D in hip impact velocity ($P = 0.81$) or kinetic energy ($P = 0.05$).

Table 1. Impact velocities and kinetic energies (means ± SD).

	Series A: Squat, use hands	Series B: Squat, no hands	Series C: No squat, use hands	Series D: No squat, no hands
Velocity (m/s)	2.96 ± 0.71	2.74 ± 0.33	3.51 ± 0.99	3.58 ± 0.94
Kinetic energy (J)	176 ± 52	172 ± 59	262 ± 87	312 ± 116

SUMMARY

During an unexpected backward fall, use of the "squat response" during descent can decrease hip impact velocity by up to 21 percent and kinetic energy at impact by up to 41 percent. Braking the fall with the outstretched hands has little effect on pelvis velocity or kinetic energy during a backward fall. It may, however, influence these variables during a sideways or forward fall, and affect risk for head impact.

ACKNOWLEDGEMENTS

Supported by operating grants from the CDC (R49CCR019355) and NIH (R01AR46890), and salary support awards from CIHR and MSFHR.

REFERENCES

Grisso, J.A. et al. (1991). *N Engl J Med,* **324**, 1326-31.
Hsiao E.T., Robinovitch S.N. (1998) *J Biomech,* **31**,1-9.

DEVELOPMENT OF 3D MODULAR DENTURE FE MODEL

YU Li-niu[1] , ZHANG Fu-qiang[2] , WANG Cheng-tao[1]

£¨1. School of Mechanical Engineering , Shanghai Jiaotong University , Shanghai, 200030, China;
2. School of Stomatology ,Shanghai Second Medical University , Shanghai ,200011, China£©

INTRODUCTION

The geometric complexity of denture in oral cavity prolongs the process of 3D finite element modeling and lowers the efficiency of the whole solution if geometrical comparability is required in finite element analysis of denture. Generally, the procedure of model building consists of selecting specimen, extracting geometrical information of specimen (for example ,using CT-scan), inputting it into software and reconstructing 3D model in computer .Every step is time consuming. However, the number of analyses to be performed is limited due to the case by case modeling method. Cutting short of the model building time is an effective way to improve the efficiency of the finite element analysis. Model modularization is implemented in this study to facilitate the generation of 3D denture finite element model; and this has found practical applications in oral rehabilitation.

METHODS

A skull sample with good occlusion and a healthy denture was selected and scanned by CT. The geometrical information in The CT images was extracted and the wireframe model of the denture was exported. Using FE software (ANSYS), a new solid model was created. Then whole denture solid model was divided into several separated parts, including the dental crown, root, periodontal ligament, alveolar bone. A single model unit was constituted with all the coherent parts of each tooth. Every model for each tooth was exported and saved in IGES format. A set of denture model library with normal physiological condition was established. Based on it, the new model library about alveolar bone absorption and tooth looses were created.

RESULTS AND DISCUSSION

The 3D modular models can be used in various combinations based on needs to build a specific FEA model rapidly for oral rehabilitation. The 3D modular denture FE model can be clinically applied to 3D FEA of fixed-partial and removable partial restoration:
(1).when all or some of abutments suffered from alveolar bone absorption of different degree;
(2).when all or some of abutments were loosen in different degree;
(3).some abutments were loosen while others have alveolar bone absorption.

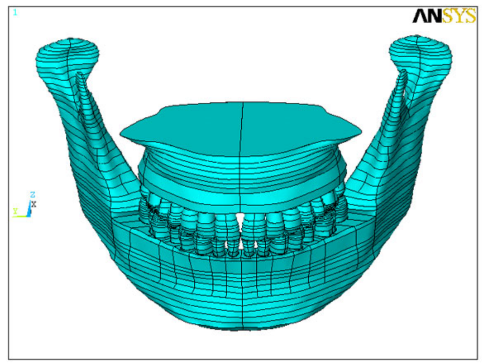

Fig.1 Solid model of mandible with denture

Modularization of denture FE model proves to reduce the modeling time from several weeks to several hours. At the same time, the large number of analyses can be performed in a short time frame. The 3D modular denture FE model will retain the same precision of material, load and constraint as convention methods. The 3D modular denture FEA model makes it possible for FEA to be widely accepted as a useful tool for oral rehabilitation due to its efficiency and convenience.

General questions, contact: Yu liniu, Tel: 86-21-62932905 or email:ylnmail@21cn.com

REFERENCES

Liu S, Ma W. (1999). *Computer-aided Design*, 31, 485-540.
Korioth TW, et al (1994). *J Dental Research*, 73, 56-66.

CYCLIC STRETCH INCREASES GENE TRANSFER AND EXPRESSION IN ALVEOLAR EPITHELIAL CELLS

David A. Dean[1,2], Winna Taylor[1], Kerimi E. Gokay[1], Chris Capaccio[3], and Matthew R. Glucksberg[3]

[1]Division of Pulmonary and Critical Care Medicine, and [2]Department of Microbiology and Immunology, Northwestern University Medical School, Chicago, IL 60611 dean@northwestern.edu and [3]Department of Biomedical Engineering, McCormick School of Engineering and Applied Science, Northwestern University, Evanston IL 60208

INTRODUCTION

Mechanical stretch induces numerous biological responses in cells, including alterations in the cytoskeleton, activation of cell signaling pathways, and upregulation of transcription factors. Intriguingly, these responses are directly related to the process of gene delivery to cells and tissues. Exogenous DNA, either viral or non-viral, must cross the plasma membrane into the cell, travel through the cytoplasm and the cytoskeletal networks, enter the nucleus, and be transcribed for gene transfer to be successful. Using a system to apply equibiaxial stretch to cultured alveolar epithelial cells, we investigated the effects of cyclic stretch on gene delivery.

METHODS

Human A549 cells (derived from an alveolar epithelial carcinoma) were grown on laminin-coated BioFlex stretch plates to 60% confluency and transfected with two plasmids, one expressing luciferase and the other expressing green fluorescent protein (GFP). The cells were either unstretched before and after transfection, stretched for 24 hours prior to transfection and left unstretched afterwards, unstretched before transfection and stretched immediately following DNA addition, or stretched both prior to and after transfection. All cells were stretched at 1 Hz at a 10% area strain using the Flexercell 3000FX with loading posts for equibiaxial strain.

Transfections were carried out using lipoplex (Lipofectin-complexed plasmid) or by electroporation of the adherent cells. Lipoplex transfections were carried out under standard conditions. For electroporations, 10 µg of DNA in 1 ml of serum-free medium was added to washed cells and one 20 msec square wave pulse of 100V/cm was applied to the cells using a Petri Pulser Electrode (Genetronics, San Diego, CA). Serum-containing medium was added back to the cells 10 minutes later. Cells were removed from the stretch device for no more than 5 minutes to perform the transfections. Twenty-four hours post-transfection, the cells were observed for GFP expression, and subsequently lysed for measurement of luciferase activity and protein levels.

RESULTS AND DISCUSSION

When cyclic stretch was applied immediately following lipoplex- or electroporation-mediate transfection, gene transfer and expression were greatly increased (Figure 1). Observation of GFP expression indicated that both the number of cells expressing gene product and the amount of gene expression in individual cells were increased with stretch. Stretching the cells prior to transfection had no effect on gene transfer and/or expression. Only when stretch was applied after DNA addition did the stimulation become evident. To determine whether prolonged exposure to stretch was needed for this enhancement, the cells were stretched for 30 minutes immediately following transfection and then grown statically for 23.5 hours or stretched for 24 hours. We found that only short periods of cyclic stretch were needed following transfection in order to observe maximal enhancement of gene transfer and expression (Figure 2).

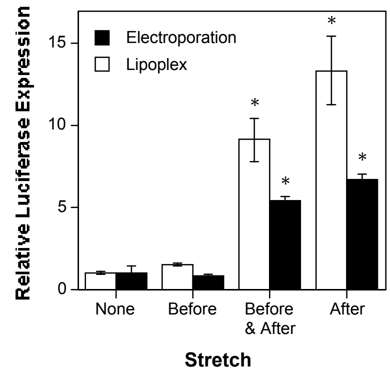

Figure 1. Cyclic stretch applied immediately following transfection greatly increases gene transfer. p<0.02

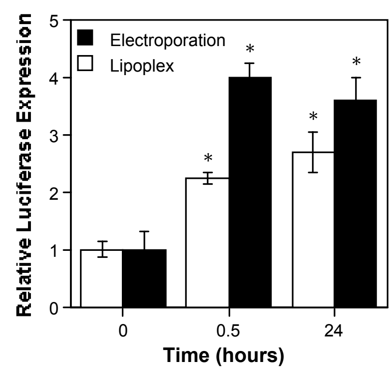

Figure 2. Short-term application of stretch post-transfection is sufficient for maximal enhancement of gene transfer. p<0.01

Because enhancement of gene transfer by stretch is seen with lipoplex and electroporation-mediated transfection, it is unlikely that stretch is exerting its effects at the plasma membrane. It is also unlikely that the enhancement is due to increased transgene transcription because stretch prior to transfection had no effect whereas stretch for 30 min after transfection did. Our continued experiments will focus on the ability of stretch to alter cytoplasmic movement of the incoming plasmids and their nuclear import.

ACKNOWLEDGEMENTS

Supported in part by a grant from the Institute for Bioengineering and Nanoscience in Advanced Medicine.

REARFOOT MOTION & TIBIAL ACCELERATION IN THE RUNNING ATHLETE

Neil Manson[1], William Stanish[1,2], Kelly McKean[2] and Andrew Milne[3]
[1]Division of Orthopaedic Surgery, Dalhousie University
[2]Orthopaedic & Sports Medicine Clinic of Nova Scotia, Halifax, NS, kmckean@tupdean2.med.dal.ca
[3]Department of Medicine, Dalhousie University

INTRODUCTION

Musculoskeletal injury is extremely prevalent in the running athlete causing significant pain and severely limiting performance. The knee has been identified as the most common site of injury (Macintyre et al., 1991), however a new pattern is emerging suggesting impact loading injuries to the lower leg are the most prevalent. Alterations in gait biomechanics and muscle stimulation (Nigg & Liu, 1999) have been hypothesized in reducing impact forces, however the mechanisms are not well understood. Higher impact forces have been documented with medial shoe inserts, to decrease pronation angle, in a healthy population (Perry & LaFortune, 1995). However, the correlation between tibiocalcaneal motion and the shock attenuated by the lower segment of the musculoskeletal system has not been documented in relation to specific injuries. Furthermore, it is unclear whether biomechanical parameters are predictive of injury or, conversely, are the result of injury. In order to design effective footwear and orthotic treatments this cause and effect relationship must be examined.

The purpose of this study is to determine the relationship between rearfoot motion and tibial acceleration according to prospective and retrospective injury frequencies.

METHODS

Forty-two well-trained, intercollegiate running athletes (males = 24, females = 18) were monitored through biomechanical analysis, retrospective and prospective survey data and physician assessment. Biomechanical data was collected at the onset of the study. Markers were placed on the rear tibiocalcaneal segments (Nigg, 1986). A skin mounted accelerometer was attached to the anteromedial surface of the right tibia (Lafortune et al., 1995). Subjects ran on a treadmill at 3.8m/s in a fatigued state. Measurements included i) rearfoot motion in the coronal plane using 2D video (60Hz), ii) shock transmission at the tibia using uniaxial accelerometers (1000Hz) and iii) retrospective injury frequencies. Athletes reported injury, location and associated factors for a 1 year follow up period. A CASM qualified physician corroborated diagnosis. Peak tibial acceleration and average range of rearfoot motion were quantified for each athlete. Correlation analysis was used to determine the relationship between these two biomechanical variables based on injury reports.

RESULTS

Retrospective data revealed an injury rate of 79% (33/42). Injury to the lower leg (i.e. shin splints, stress fractures) comprised 18% (6/33) of all injuries. A negative correlation between peak tibial acceleration and average range of rearfoot motion was found in this group (r^2= .63). Such a mechanism was not apparent in athletes not reporting injury (r^2= 0.01).

Prospective analysis revealed an injury rate of 62% (26/42). The lower leg was the most prevalent injury location comprising 31% (8/26) of injuries. No correlation was found between biomechanical parameters for either group based on prospective injury data.

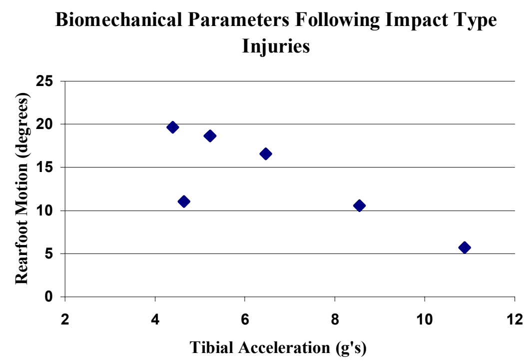

Figure 1: Rearfoot motion and tibial acceleration in a group of competitive runners following lower leg injury (r^2 =.631).

DISCUSSION & CONCLUSIONS

This important correlation between rearfoot motion and tibial acceleration has not previously been documented in the injured athlete. Increasing the angle of the calcaneus relative to the shank during the stance phase may aid in redistributing impact forces and ultimately alleviating pain. Altered biomechanics may be implicated as a compensatory mechanism opposed to a predictive measure. These findings have important implications in the design of shoe and orthotic devices to treat this new focus of running injuries.

REFERENCES

Lafortune, M.A. et al., (1995). *J Biomech*, 28, 989-993.
Macintyre, J.G. et al., (1991). *Clin J of Sport Med*, **1**, 81-87.
Nigg, B.M., Liu, W. (1999). *J Biomech*, **32**, 849-856.
Nigg, B.M., (1986). *Biomechanical Aspects of Running*. Human Kinetics Publishers.
Perry, S.D., Lafortune, M.A. (1995). *Clin Biomech*, **10**, 253-257.

ACKNOWLEDGEMENTS

A research grant was provided by the Nike Sports Research Laboratory, Beaverton, Oregon.

DYNAMIC STABILIZATION OF RAPID HEXAPODAL LOCOMOTION

Devin L. Jindrich

Department of Integrative Biology, University of California at Berkeley, dljindrich@yahoo.com
Current address: Harvard Occupational Biomechanics, Harvard School of Public Health, Boston, MA.USA.

INTRODUCTION

Simple mechanical models are capable of describing the sagittal-plane mechanics of constant average speed walking and running (Blickhan and Full, 1993). However, much less is known about the mechanics of changing the speed or direction of movement. If movement is altered by an external perturbation, animals must stabilize themselves to continue moving at a desired velocity by generating forces appropriate to overcome the effects of the perturbation.

Two (non-exclusive) mechanisms which legged animals use to stabilize rapid locomotion are 1) changing the placement of the foot relative to the body at the beginning of a step, and 2) altering the forces generated by the legs during stance. During slow movements, the nervous system can act to change leg placement or continuously alter force production. However, during rapid locomotion, neural control of stability may become increasingly difficult because of neural feedback delays (Hogan, 1990). As stance periods decrease, continuous modulation of forces by neural mechanisms may become less advantageous. However, intrinsic properties of musculo-skeletal systems, termed 'preflexes' (Brown and Loeb, 2000), may contribute to stability during high-speed movements.

This study sought to test two hypotheses: 1) changes to foot placement at step transitions are necessary to stabilize rapid locomotion, and 2) musculo-skeletal 'preflexes' contribute to dynamic stabilization of rapid locomotion. To test these hypotheses, I directly measured stabilization of rapid locomotion in a hexapod, the cockroach *Blaberus discoidalis*.

MATERIALS & METHODS

Stable locomotion may be described as a pattern of positions and velocities over time, which repeats with a characteristic frequency such as the stride frequency, to which an animal returns following a perturbation. To measure the stabilization mechanism used by cockroaches during running, I perturbed the animals by subjecting them to a brief (< 10 ms), laterally-directed force impulse 80% of the magnitude of the animals' forward momentum at their preferred speed. A miniature cannon was attached to the back of the animals (Figure 1 A).

Figure 1. A. The perturbation apparatus. B. Center of mass velocity (blue arrow) 10 ms before and 10 ms following a perturbation to the left.

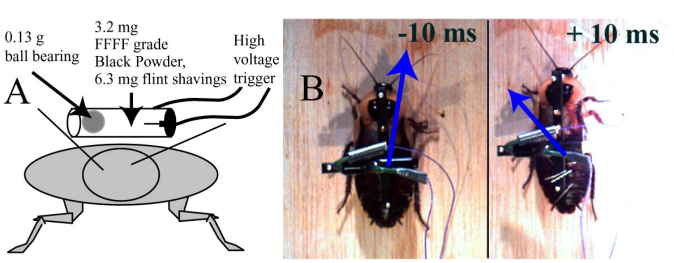

As the animals ran forward at constant average speed, the cannon was fired, and the reaction force due to accelerating the projectile perturbed the animal (Figure 1 B). Three-dimensional video analysis recorded the movements of the animal following the perturbation. Movement kinematics from perturbed trials were compared to reference trials.

RESULTS

Hypothesis 1. Cockroaches did not require changes in leg placement at step transitions to recover from lateral perturbations of 80% of their forward momentum (Figure 3). In all trials where the perturbation occurred in the first half of the stance phase of a tripod of stepping legs, lateral velocity recovered to within unperturbed values before the touchdown of the following tripod.

Hypothesis 2. Lateral velocity began to decrease (indicating that a force generated by the legs in stance acted in the opposite direction) 13 ± 5 ms following the perturbation. This time period is comparable to the fastest neural reflexes measured in cockroaches, supporting the hypothesis that musculo-skeletal 'preflexes' contribute to stabilizing rapid locomotion.

Figure 3. Lateral velocity (relative to unperturbed velocity) following perturbation for a representative trial. The perturbation occurred early in the stance period of the left front, right middle, and left hind (LF,RM,LR) legs. Lateral velocity returned to the reference velocity before the legs of the alternate tripod touched down**.**

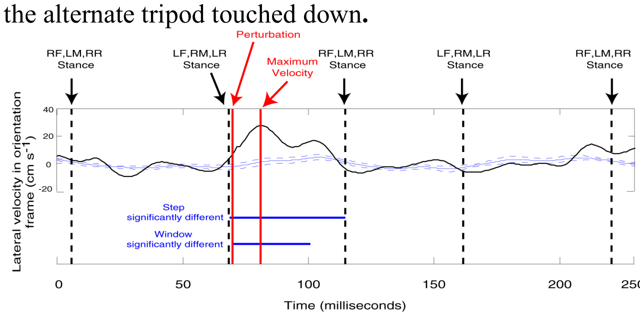

REFERENCES

Blickhan, R. and Full, R. J. (1993). *J. comp. Physiol. A* **173,** 509-517.

Brown, I. E. and Loeb, G. E. (2000). In *Biomechanics and Neural Control of Posture and Movement* (ed. J. M. Winters and P. E. Crago). New York: Springer-Verlag.

Hogan, N. (1990). In *Multiple muscle systems : biomechanics and movement organization* (ed. J. Winters and S.-L. Woo), pp. 149-164. New York: Springer-Verlag.

ACKNOWLEDGMENTS

This project was supported by DARPA/ONR N00014-98-1-0747. Thanks to Robert J. Full, Dan Koditschek and Claire Farley for contributing to this project.

THREE DIMENSIONNAL RECONSTRUCTION OF THE KNEE FROM BIPLANAR X-RAYS.

S. Laporte[1], W. Skalli[1], J.A. de Guise[2], D. Mitton[1]
[1] Laboratoire de BioMécanique, ENSAM / CNRS UPRESA 8005 / Paris, France
[2] Laboratoire de recherche en Imagerie et Orthopédie, ETS / CRCHUM / Montréal, Canada

INTRODUCTION

Three dimensional accurate reconstructions of the knee are the principal prerequisites for computer assisted surgery or personalized biomechanical finite element models (4). Currently these models are obtained from CT-Scan reconstructions with millimeter slices; nevertheless this method is quite irradiant for the patient.
The purpose of this study is to propose an alternative 3D reconstruction method for the knee based on identifiable 2D contours from biplanar radiographs (1,3) with accuracy close to the CT-Scan models.

METHODS

Technical prerequisites to the method are a calibration of the biplanar radiographic environment and a surface generic object representing the structure to be reconstructed (femur, tibia and patella). The method principle is to deform an initial solution of the structure to reconstruct, in term of shape an location, in order to make it coherent with projected 2D contours and information in the X-Ray images.

The method was applied to 8 dry femurs (5 left, 3 right). Two calibrated X-Ray films of each femur (postero-anterior (PA) and lateral (LAT)) were acquired at the Saint-Vincent de Paul Hospital using the Explicit Linear Calibration protocol (ELC) (1). A generic model of the distal femur defined by 556 points and 1100 triangular surfaces was used for reconstruction.

The obtained models were compared with those obtained from 3D computerized millimetric tomography with an overall accuracy of 1 mm (2). These models were superimposed by using geometrical transformations (rotations and translations) and a least square matching method. The quantitative comparison of the shapes between the two models was made using the point to surface distance with the CT-Scan models as reference (3). The mean errors, RMS (Root Mean Square) and maximum errors were calculated for the whole set of 556 points and for the 225 points of the articular surface.

RESULTS AND DISCUSSION

Quantitative comparisons between the CT-Scan and the biplanar reconstructions using the point to surface distance for the 8 femurs are given in table I.

Table I: Shape errors (Point to surface distances, mm) for the 8 reconstructed femurs by NSCC versus CT-Scan reconstructions.

	Global Surfaces (556 points)		
Errors (mm)	**Mean**	**RMS**	**Max**
	1.0	***1.4***	***5.0***
Errors (mm)	**Articular Surfaces (255 points)**		
	0.9	***1.1***	***4.2***

The given results indicate that the proposed method is close to CT-Scan reconstruction with less irradiation (i.e. only two radiographs).

The equivalent study is currently conducted to evaluate accuracy on 6 dry tibiae and 6 patellae.
A study is also in progress to evaluate the method feasibility in in vivo situation.

SUMMARY

This paper presents a method for accurate 3D reconstruction of the knee from biplanar X-Ray images using 2D contours extracted from the radiographs.
This technique appears to be an interesting alternative to CT-Scan 3D reconstruction, with the advantage of low radiation. Once fully validated, it will be of great usefulness for clinics and 3D applications such as finite elements studies.

REFERENCES

1. D. Mitton, W. Skalli et al. (2000), *proceedings of The 2000 Meeting of the IRSSD, Clermont-Ferrand, France, May 26-30 2000*.
2. J.A. de Guise, Y. Martel (1988), *3D biomedical modeling: merging image processing and computer aided design in IEEE EMBS 10th International Conference, New Orleans,* 426-427.
3. D. Mitton, J. de Guise et al (2000), *Medical & Biological Engineering & Computing,* **38**, *133-139*.
4. B. Fréchède, W. Skalli et al.(2001), *XVIIIth Congress of the International Society of Biomechanics, ETH Zürich, Switzerland, july 8-13 2001.*

ACKNOWLEDGEMENTS

The authors acknowledge Pr. Lassau for providing the dry bone specimens and Biospace company for the financial support.

COMMON FUNCTION OF FOREARM MUSCLES DURING GRIPPING

Peter J. Keir, PhD and Jeremy P.M. Mogk

School of Kinesiology and Health Science, York University, Toronto, Ontario, Canada
Webpage: http://www.yorku.ca/kahs/pjkeir Email: pjkeir@yorku.ca

INTRODUCTION

Understanding the biomechanics and motor control of the hand and wrist are complicated by the redundancy of the forearm musculature. Issues regarding co-contraction, common neural drive and crosstalk all play a role in our ability to examine function. This complicates the process of modeling the function and actions of these muscles. As part of a larger study examining the muscle activation levels associated with gripping in numerous postures, we examined the common signal in the muscles of the forearm using the cross-correlation function.

METHODS

Ten healthy volunteers participated in this handgrip study (5 men, 5 women, mean age 24.1 years). Maximum voluntary power grasp efforts were performed with a neutral wrist and forearm using a grip dynamometer (MIE Medical Research Ltd., Leeds, U.K.). Maximum EMG levels for each muscle were obtained through a series of isometric maximal efforts.

Target grip forces of 5, 50, 70, and 100% MVC and 50 N were performed in nine postures. Three wrist angles (flexed 45°, straight, extended 45°) and three forearm postures (pronated, neutral or mid-prone, and supinated) were used.

Bipolar surface electrodes were affixed over six forearm muscle bellies. These included flexor carpi radialis (FCR), flexor carpi ulnaris (FCU), flexor digitorum superficialis (FDS), extensor carpi radialis (ECR), extensor carpi ulnaris (ECU), and extensor digitorum communis (EDC). Raw EMG and force data were collected at 1000 Hz. All trials were videotaped in two planes. Normalized cross-correlation functions were calculated between each muscle (Winter et al, 1994).

RESULTS AND DISCUSSION

Participants were unable to accurately repeat target force levels of 70 and 100%, especially in the flexed and pronated posture, therefore we have limited our comparisons to the 5 and 50% target forces. Initial examination of EMG indicated that the extensors had higher activation levels than the flexors at both target forces. Although co-contractions between the flexors and extensors were quite obvious, the raw EMG signals were not correlated. The R_{xy} (t=0) values were highest for the wrist flexors (FCR-FCU), followed by the wrist extensors (ECR-ECU). Cross-correlations were significantly higher for the 50% target force ($p = 0.0002$), mainly due to an increase in the correlations between flexors. The increase was not seen in the extensor muscles. A comparison of the wrist flexor correlations at 5% and 50% demonstrates this well (Fig. 1). It was thought that, if common neural drive was present, it may result in high R_{xy}. We had already determined that electrode pairs within 3 cm result in correlations of approximately 0.6, while at 6 cm they dropped to 0.3 (i.e. explained variance under 10%). From this we can attribute the R_{xy} values to common signal and not to crosstalk between muscles due to the spacing between electrode pairs.

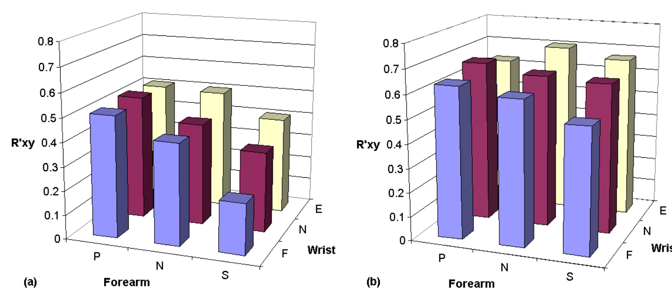

Figure 1: Cross-correlations (at t=0) between FCR and FCU in each of the nine postures. a) 5% MVC, b) 50% MVC.

SUMMARY

As part of a larger study, we analyzed the magnitude of EMG signals and the cross-correlations between each of six muscles in the forearm. We found that although co-contractions were present, only the two wrist flexors showed correlated raw EMG signals explaining upwards of 50% of the variance, suggesting the presence common neural drive. Evaluation of muscular control (and common neural drive) of the forearm may be furthered by the use of more detailed analysis techniques (e.g. Nordstrom et al, 1992; Schmied et al, 1993) and the muscular response to fatigue.

REFERENCES

Nordstrom et al (1992) *J. Physiol.* **453**, 547-574.
Schmied et al (1993) *Exp. Brain Res* **97**, 159-172.
Winter et al (1994) *J Electromyogr. Kinesiol.* **4**(1), 15-26.

ACKNOWLEDGEMENTS

Study funded by an NSERC operating grant to P.J. Keir.

ELECTRICAL CONDUCTIVITY OF LUMBAR ANNULUS FIBROSIS

MA Justiz, H Yao, A Vega, WY Gu
Tissue Biomechanics Laboratory, Department of Biomedical Engineering
University of Miami, Coral Gables, FL, USA. wgu@miami.edu

INTRODUCTION

Specific electrical conductivity is one of the material properties of intervertebral disc (IVD). Its value depends on ion concentrations and ion diffusivities within a tissue (Chammas et al, 1994; Hellferich, 1962), which in turn are functions of tissue composition and structure. Investigation of the electrical conductivity of IVD and understanding of its relationship with tissue water content and fixed charge density will provide insights into electromechanical phenomena (e.g., streaming potential) (Gu et al, 1999). The objective of this study was to measure the electrical conductivity of IVD tissues and to study the effects of tissue water content and fixed charge density on the electrical conductivity of annulus fibrosis (AF) in physiological saline. The measured results are also important for understanding strain-dependent ion transport in IVD.

METHODS

A total of 35 porcine lumbar AF specimens were divided into two groups: one control group (n=10) and one trypsin-treated group (n=25). The specimens in the control group were subjected to one dimensional free swelling in PBS, and their electrical conductivity and porosity were measured over time for a period of about 45 minutes. The specimens in the treated group were immersed in a trypsin solution (372 U / ml PBS) for 45 minutes at room temperature and the electrical conductivity and porosity were measured after treatment. Electrical conductivity was correlated to tissue porosity for control and treated specimens. The influences of porosity and fixed charge density were studied.

Conductivity measurement. An apparatus for measuring the conductivity of hydrated soft tissues in the condition of zero fluid flow (no convection) was previously developed (Justiz et al, 2001). Briefly, the apparatus consisted of two (stainless steel) current electrodes, two (Ag/AgCl) voltage sensing electrodes, a specimen chamber, a Keithley sourcemeter, and a current-sensing digital micrometer (for height measurement). The apparatus was calibrated using a conductivity standard and found to be accurate (less than 5% nonlinearity) for specimen height in the range of 2.2 – 6.0 mm. The conductivity of specimens was measured with constant direct current of 3 μA (density: 0.015 mA/cm^2) at room temperature (22 ± 1ºC). Following electrical conductivity measurement, specimens were lyophilized to determine their water content.

RESULTS AND DISCUSSION

The average value for control specimens was 5.60±0.89 mS/cm (mean±SD, n=10) before swelling and 9.11±0.90 mS/cm (mean±SD, n=10) after swelling, while tissue porosity was increased from 0.74±0.03 (mean±SD, n=10) before swelling to 0.83±0.02 (mean±SD, n=10) after swelling. These results were similar to those for cartilage (Chammas et al, 1994; Hasegawa et al, 1983; Maroudas, 1968). The trypsin treatment reduced AF porosity by 3.6% ($p<0.05$) and conductivity by 13% ($p<0.05$) compared to those for control specimens after swelling. However, the conductivity values for treated specimen were similar to those for control specimens of similar water contents. There was a significant, linear correlation between conductivity and water content for control AF specimens ($R^2 = 0.87$, 86 measurements).

Ion diffusivities increase with increasing tissue water content (e.g., Mackie and Meares, 1955). This is believed to be responsible for the linear correlation of conductivity with tissue water content observed for AF specimens in this study. The trypsin treatment reduces both fixed charge density and tissue porosity. The average decrease in conductivity for treated group compared to control group after swelling is mainly due to the decrease in ion diffusivities. The result indicates that the fixed charge density does not significantly affect measured conductivity for AF specimens in PBS. This agrees with the finding for cartilage (Hasegawa et al, 1983).

REFERENCES

Chammas, P. et al (1994). *J. Colloid and Interface Science*, **168**, 526-538.
Gu, W.Y. et al (1999). *J Biomech*, **32**, 1183-1189.
Hasegawa, I. et al (1983). *Clinical Orthop Res*, **177**, 283-288.
Helfferich F. (1962). *Ion Exchange*, McGraw Hill, New York.
Justiz, A.M. et al (2001). *Trans Orthop Res Soc* **26**, 883.
Mackie, J.S., Meares, P. (1955) *Proc Roy Soc*, **A 232**, 498-509.
Maroudas, A. (1968) *Biophys J*, **8**, 575-595.

ACKNOWLEDGEMENTS

This project was supported by a grant from the NIH (AR46860).

NUMERICAL SIMULATION OF SICKLE CELL BLOOD FLOW IN THE TRANSVERSE ARTERIOLE – CAPILLARY NETWORK

Brian Carlson[1] and Stanley Berger[2]

Department of Mechanical Engineering, University of California at Berkeley
[1]Postdoctoral Researcher, bcarlson@me.berkeley.edu
[2]Professor of Mechanical Engineering and Bioengineering, saberger@me.berkeley.edu

INTRODUCTION

Sickle cell crisis, a recurrent symptom of sickle cell disease, has been hypothesized to result from inadequate oxygen supply to the tissues, a consequence of microvascular stasis. Microvascular networks are numerically simulated for sickle and normal blood to observe differences in capillary flow characteristics as a function of driving vascular pressure. The motivation is to understand the relationships between the network driving pressure, network geometry, and the dynamics of sickle oxygen transport.

METHODS

Ten randomly generated microvascular networks are calculated for normal and sickle blood flows over a range of network input pressures. For sickle cell blood, two input oxygen concentrations are used: with and without precapillary oxygen loss. Network exit pressure is held constant.

The skeletal muscle microvascular networks are represented using a Strahler scheme of vessel ordering based on values obtained for the rat spinotrapezius muscle (Engelson et al, 1985). Hematocrit values in the network vessels are heterogeneous and described as a function of vessel diameters, input hematocrit, and fractional volumetric blood flow at each bifurcation (Pries et al, 1990). Effective relative blood viscosity also varies from vessel to vessel and here the '*in vivo* viscosity law" (Pries et al, 1994) is used.

In the arterioles, flow is assumed to be Poiseuille while in the capillaries a Lighthill lubrication theory and Krogh cylinder analysis are used to model the blood flow and oxygen transport (Berger and King, 1980). Continuity of volumetric blood flow and red cells at each bifurcation leads to a system of nonlinear equations. These are solved using a Steepest Descent algorithm coupled with a simple Newton solver.

RESULTS AND DISCUSSION

The average total volumetric flow through the simulated networks in both cases of sickle blood is 37 to 52% greater than in the normal blood case. This agrees with higher cardiac outputs observed in patients with chronic anemia (Roy et al, 1963). The anemia inherent to the sickle cell disease, on the other hand, decreases the red cell flux through the networks and 16 to 24% lower cell fluxes are observed in the simulated networks with sickle blood as contrasted to normal blood.

The ability of the network effects to compensate for reduced flow is insufficient to sustain flow in all capillaries in the case of sickle blood while with normal blood no blockages are observed even with a 18% drop in input driving pressure. In both sickle blood cases at full network driving pressure average capillary blockage percentages vary from 8 to 10%, while with an 18% drop in the input driving pressure, 32 to 36% of the capillaries become blocked (Figure 1).

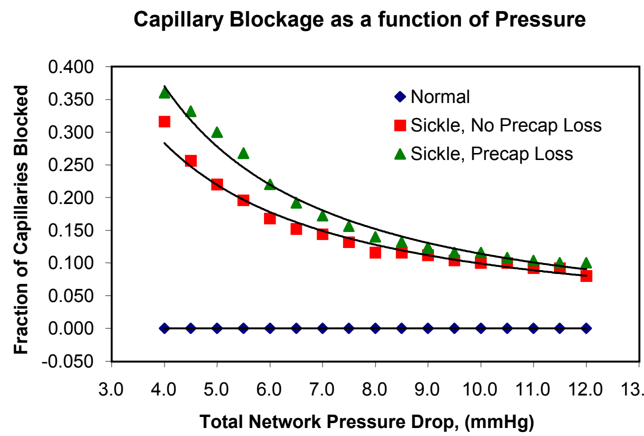

Figure 1: Fraction of capillaries blocked as a function of total network pressure drop across simulated networks. Blocked capillary fraction is the average value for the 10 networks.

SUMMARY

Network effects are inadequate to prevent capillary stasis in sickle cell disease even at full network driving pressures. Normal blood continues to flow in all vessels at all network input pressures. Vasodilation may be useful to minimize or prevent capillary blockage in sickle cell disease.

REFERENCES

Berger, S.A., King, W.S. (1980). *Biophysical J*, **29**, 119-148.
Engelson, E.T. et al (1985). *Microvasc Res*, **30**, 29-44.
Pries, A. R. et al (1990). *Circ Res*, **67**, 826-834.
Pries, A. R. et al (1994). *Circ Res*, **75**, 904-915.
Roy, S. B. et al (1963). *Circulation*, **28**, 346-356.

SIMULTANEOUS STRAINS AND DISPLACEMENTS ANALYSIS OF IMPLANTED FEMURS BY IN VITRO STUDY AND FINITE ELEMENT MODELLING

Amadou Diop[1], Nathalie Maurel[1], Arnaud Besson[2]

[1]Ecole Nationale Supérieure d'Arts et Métiers, 151 bd de l'Hôpital, 75013 PARIS, amadou.diop@paris.ensam.fr
[2]Hôpital Roger Salengro. CHR B, 59000 LILLE

INTRODUCTION

In order to implement and validate a finite element model of femurs including bone remodelling aspects around prostheses, it is necessary to first validate such a model on immediate postoperative situation. For this, in vitro tests were carried out on fresh cadaveric femurs implanted with ABG prosthetic stem and corresponding models are in progress.

METHODS

Six fresh human cadaveric left femurs issued from 4 males and 2 females (66 to 86 years) were included. For each femur, an ABG cementless stem with adapted size was implanted and CT scans were performed before testing.
For mechanical tests, the femurs were embedded at mid-length and were oriented 12° frontally, then 30° sagittally. Successive loads with increasing magnitudes were applied on the head of the prosthesis using an universal testing machine: 600N (450N for the first femur), 800N, and loading until failure.
Global medial and lateral displacements of the head of the prosthesis were measured using linear transducers, while the vertical one was directly given by the machine cross-head motion. Axial rotation between femur and prosthesis was measured using a CCD camera and 2 plates (one fixed on the bone and one fixed on the femur). Axial and transversal linear micro-motions between femur and prosthesis were obtained using a CCD camera provided with a zoom, one metallic ball fixed on the bone and one other fixed on the prosthesis.
Six strain gages (45° rosettes) were stuck on femurs. 2 were placed distally (R1:anterior, R2:lateral) and 4 were placed proximally: (R3:anterior, R4:lateral, R5:posterior, R6:medial). Principal strains ($\varepsilon 1$,$\varepsilon 2$) and their direction were then obtained.
Using the data issued from CT scans and the geometry of the prosthesis, personalised finite element models of two of the tested femurs were developed (8-nodes hexaedric elements were used). The same boundary conditions as for experiments were introduced. Different parameters were tested (bone materials, modelling of the bone-implant interface).

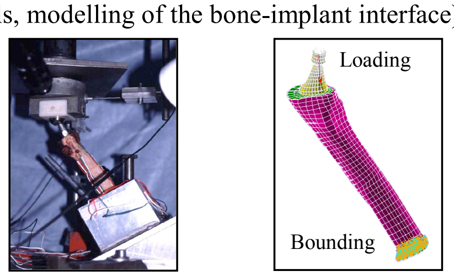

Figure 1: Experimental set-up and finite element models of an implanted femur.

RESULTS

The medial displacement was negligible comparing with the vertical and anterior ones. Except for one femur, which failed during the test, the axial micro displacements were always lower than 100µm and the axial rotations were comprised between –0.3° and +1° (at 800N). The maximal strains were recorded for the anterior distal gage and were tensile ones.
Results of models were coherent with those issued from the experiments but still need to be improved to obtain reliable validation simultaneously for all the experimental measurements.

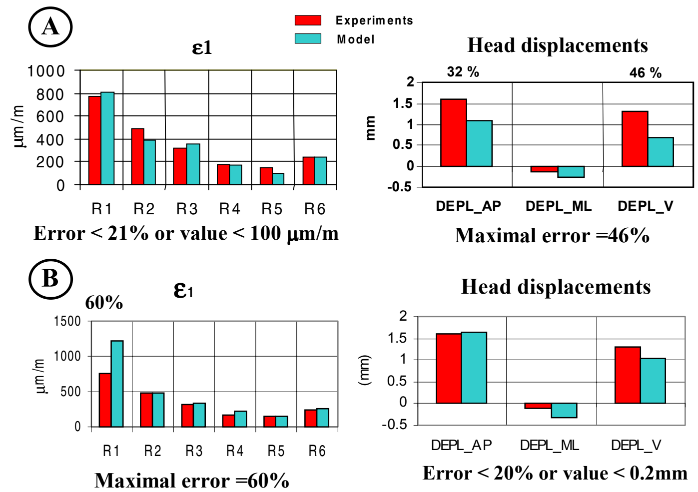

Figure 2: Model versus experimental results for two different models of the same femur, loaded at 450N. A: two distinct materials (Ecortical=20000MPa;Espongious=800MPa); B: non homogeneous bone (data from CT scan grey levels).

DISCUSSION - CONCLUSION

The main interests of this study are to combine in vitro tests and finite element analysis and to deal with global information (displacement of the head) and local information (main strains on 6 locations, micro motions and rotations between the prosthesis and the femur). The importance to use simultaneously these two kinds of information appeared during the validation of our first finite element models. Indeed, a model can be well validated regarding one parameter but can present great differences with experiments when analysing others (figure2).

ACKNOWLEDGEMENTS

We thank Benoist-Girard SAS Homedica Stryker for its financial support and for supplying the implants.

ZATSIORSKY-SELUYANOV'S SEGMENT INERTIA PARAMETERS FOR POSTURE ANALYSIS.

Danik Lafond and François Prince
Laboratoire du mouvement, Centre de réadaptation Marie-Enfant, Hôpital Ste-Justine, Quebec, CANADA.
Department of Kinesiology, University of Montreal, P.O. Box 6128, Downtown Station Montreal, Quebec, CANADA, H3C 3J7

INTRODUCTION

Zatsiorsky et al. (1990) used gamma-scanning techniques to determine segment inertia parameters (SIP) in young healthy adults. To the authors' knowledge, even though these data are available since 1990, the Zatsiorsky-Seluyanov segment inertia parameters (SIP) have not been widely used to estimate body's center of mass (COM) location during posture or balance studies. This situation may be explained by the following reasons; a) the error associated with the use of the cadavers SIP is underestimated and b) the Zatsiorsky-Seluyanov's SIP can't be applied to a simplified COM-model. A paper from de Leva (1996) reported Zatsiorsky-Seluyanov SIP related to joint centers. However, for posture and balance studies, it is useful to report the SIP relative to easily palpated bony landmarks instead of joint centers. In addition, SIP from combining segments like total arm or total leg, which help to reduce the number of segments to estimate COM, are not available. The purpose of this study is to report a complete table of the mass fraction and COM location of the several segments often used in posture analysis.

METHODS

Using the anthropometric data from de Leva (1996) and Zatsiorsky et al. (1990), we have defined the adapted COM location of several segments (see Table 1). This general formula was used to define combined segments COM:

$$\overline{P}_j = \sum_{i=1}^{N} \bar{l}_{CoM_i} \cdot m_i \Big/ \sum m_i$$

where $\overline{P}_i$ is the mean proximal longitudinal distance of the segment's COM, m_i = subsegment mass fraction, $\bar{l}_{CoM_i}$ = mean subsegment COM longitudinal position relative to the new proximal bony landmark position

RESULTS

The mass fraction and the proximal COM location of simple and combined segments are presented in Table 1. An exemple of a combined segment is the HAT. The HAT segment is composed of the head, total trunk and arms. The COM proximal location of this segment is related to the acromion (ACR) and greater trochanter (GTRC) landmarks. Using this table, researchers may use simplified segment model to estimate body's COM instead of a 16-segments model if they use de Leva (1996) SIP. For example, a 3-segment model is defined by the HAT and total arms segments.

REFERENCES

de Leva, P. (1996). *Journal of Biomechanics.* 29; 1223-1230.
Zatsiorsky, V.M. et al. (1990). *Contemporary problems in Biomechanics*. Boca Raton: CRC Press. 272-291.

ACKNOWLEGMENTS

D.L. and F.P. are grateful for scholarships from the FCAR and FRSQ respectively and the financial support of NSERC (FP).

Table 1

Segment	Endpoints	Male		Female		Segment	Endpoints	Male		Female	
		Mass	COM	Mass	COM			Mass	COM	Mass	COM
Head *	Ear canals	0.069	1.000	0.067	1.000	**Forearm, hand**	EJC / USTYL	0.022	0.680	0.019	0.680
Upper trunk *	Suprasternale / Xiphoid	0.160	0.300	0.155	0.208	**Total arms 1**	SJC / USTYL	0.049	0.564	0.045	0.532
Lower trunk *	Xiphoid / Navel	0.163	0.450	0.147	0.451	**Total arms 2**	ACR / USTYL	0.049	0.571	0.045	0.560
Pelvis 1 *	Navel / HJC	0.112	0.612	0.125	0.492	**HAT 1**	ACR / GTRC	0.603	0.399	0.582	0.353
Pelvis 2	ASIS / GTRC	0.112	0.107	0.125	0.088	**HAT 2**	SJC / HJC	0.603	0.362	0.582	0.309
Trunk 1 *	Suprasternale / HJC	0.435	0.449	0.426	0.415	**Thigh 1**	GTRC / KJC	0.142	0.405	0.148	0.356
Trunk 2 *	SJC / HJC	0.435	0.431	0.426	0.378	**Thigh 2** *	HJC / KJC	0.142	0.410	0.148	0.361
Trunk 3	ACR / GTRC	0.435	0.475	0.426	0.459	**Shank** *	KJC / LMAL	0.043	0.446	0.048	0.442
Upper arm 1 *	SJC / EJC	0.027	0.577	0.026	0.575	**Foot**	LMAL / HMET II	0.014	0.287	0.013	0.236
Upper arm 2	ACR / EJC	0.027	0.623	0.026	0.622	**Total leg 1**	GTRC / LMAL †	0.199	0.371	0.209	0.342
Forearm *	EJC / USTYL	0.016	0.461	0.014	0.459	**Total leg 2**	HJC / LMAL	0.199	0.377	0.209	0.344
Hand *	USTYL / KNU3	0.006	0.795	0.006	0.753						

* ***from de Leva (1996)***

Mass = mass fraction of the segment relative to subject's mass. COM = proximal location of the segment COM relative to specific bony landmarks. HAT= head, trunk & arms; HJC = hip joint center; KJC = knee joint center; SJC = shoulder joint center; EJC = elbow joint center; GTRC = greater trochanter; ACR = acromion; USTYL = ulnar styloïd; LMAL = lateral malleolus; HMET = head metatarsal; KNU3 = 3rd knuckle of the 3rd finger.

EFFECT OF SWELLING PRESSURE ON DYNAMIC COMPRESSIVE STIFFNESS OF LUMBAR ANNULUS FIBROSIS

H Yao, MA Justiz, D Flagler, WY Gu

Tissue Biomechanics Laboratory, Department of Biomedical Engineering
University of Miami, Coral Gables, FL, USA. wgu@miami.edu

INTRODUCTION

The intervertebral disc (IVD) is subjected primarily to compressive loading in vivo. It has been hypothesized that the compressive mechanical load on the normal IVD is mainly supported by the fluid through a high osmotic pressure and/or a fluid pressurization effect (e.g., Mow et al, 1998; Soltz and Ateshian, 2000; Urban and McMullin, 1988). It is not clear, however, how the osmotic pressure affects the dynamic behavior of the IVD tissue in compression. The objective of this study was to investigate the effect of swelling pressure on the compressive stiffness of IVD tissues under dynamic loading conditions. In this study, the swelling pressure, equilibrium and dynamic moduli, hydraulic permeability, water content, wet tissue density, and dry tissue density of control and trypsin-treated annulus fibrosis (AF) were determined to further delineate the load supporting mechanisms in the IVD under compression (Iatridis et al, 1998).

METHODS

Specimen preparation. A total of twenty-two paired specimens (5mm diameter) were prepared from all regions of annulus fibrosis (AF), harvested from the lumbar discs of a 85 kg domestic pig. Eleven specimens (thickness: 1.930±0.146 mm) were used as the control group while the other eleven (thickness: 2.074±0.090 mm) were treated with the trypsin enzyme. For the treated group (n=11), each of the specimens was immersed in a solution containing 372 units of trypsin per 1 ml of phosphate buffer saline (PBS, pH7.4) at room temperature (21°C) for 1 hour. For the control group, the specimens were immersed in PBS (without trypsin) for the same period of time.

Mechanical Testing. All mechanical tests were performed in PBS (pH 7.4) using a Perkin-Elmer Dynamic Mechanical Analyzer (DMA). A uniaxial, confined compression mode was used in this investigation. A Swelling pressure test, dynamic scan test (0.01-5.0 Hz), creep test, and free-swelling test were performed for each of the specimens.

The free swelling strain, swelling pressure, equilibrium and dynamic compressive moduli were directly obtained from the above tests. The hydraulic permeability was obtained by curve-fitting creep data to the biphasic theory (Mow et al, 1980). The tissue hydration, wet and dry tissue densities of control and trypsin-treated AF specimens were determined after mechanical testing using a method described in the literature (Gu et al, 1996).

RESULTS AND DISCUSSION

The trypsin treatment reduced the tissue swelling strain (−22%), swelling pressure(−66%), equilibrium (−57%) and dynamic moduli, and water content (−3%), but increased hydraulic permeability (88%) and phase angle shift significantly. There was a significant positive correlation (R^2=0.82, n=22) between swelling pressure and equilibrium modulus of the AF specimens. No significant differences in wet tissue and dry tissue densities were found between the control and the treated groups. The dynamic compressive stiffness of the AF specimens increased with increasing loading frequency in the range tested (0.01 – 5 Hz). This result was similar to that for cartilage (Lee et al, 1981). The magnitude of the dynamic stiffness was found to be proportional to the square root of the ratio of equilibrium modulus to hydraulic permeability at each of the loading frequencies tested.

Fluid pressurization is responsible for the increase in dynamic stiffness of AF in compression (Soltz and Ateshian, 2000). The dynamic stiffness is related to the equilibrium modulus of the tissue (Lee et al, 1981; Soltz and Ateshian, 2000). The fact that aggregate modulus linearly correlates with swelling pressure suggests that the swelling pressure plays a significant role in supporting mechanical compressive loads not only in static cases (Urban and McMullin, 1988), but also in dynamic cases.

REFERENCES

Gu ,W. et al (1996). *ASME Adv Bioengng*, **BED-Vol. 33**, 89-90.
Iatridis, J.C. et al (1998). *J Biomech*, **31**, 535-544.
Lee, R.C. et al (1981). *J Biomech Eng*, **103**, 280-292.
Mow, V.C. et al (1998). *Int J Soli Struct*, **35**, 4945-4962.
Solts, M., Ateshian, G.A. (2000). *Ann Biomed Eng*, **28**, 150-159.
Urban, J.P.G., McMullin, J.F. (1988). *Spine*, **13**,179-187.

ACKNOWLEDGEMENTS

This project was supported by a grant from the NIH (AR46860).

AN INVESTIGATION OF THE EFFECT OF CALCIUM ON THE MECHANICAL FUNCTION AND STRUCTURE OF AORTIC MICROFIBRILS IN THE LOBSTER *HOMARUS AMERICANUS*

Chantal T. Bussiere[1], M. Edwin DeMont[2] and Glenda M. Wright[3]

[1]School of Biomedical Engineering, Dalhousie University, Halifax, Nova Scotia, Canada
[2]Department of Biology, St. Francis Xavier University, Antigonish, Nova Scotia, Canada, edemont@stfx.ca
[3]Department of Anatomy and Physiology, University of Prince Edward Island, Charlottetown, PEI, Canada

INTRODUCTION

Fibrillin-based microfibrils serve as important structural elements in connective tissue. Mutations affecting the calcium-binding domains of fibrillin result in structural changes in the microfibrils. Marfan syndrome, a connective tissue disorder affecting the cardiovascular system is caused by these mutations (Dietz *et al*., 1991). Calcium also has a marked effect on microfibrillar structure and mechanical properties (Eriksen *et al*., 2001) Mechanical testing and characterization of arteries from Marfan tissues is limited by elastin, the insoluble protein that binds to a microfibrillar scaffold. Lobster arteries possess a high density of microfibrils, and like all invertebrates, have no elastin (Davison *et al*., 1995). These vessels have non-linear stress-strain curves, similar to those of vertebrate arteries containing elastin and collagen (M^c^Connell *et al*., 1997). Our lab has recently found that lobster arteries containing only microfibrils can be isolated by guanidine/collagenase digestions. In this study we have investigated the effect of calcium on the mechanical function and structure of lobster microfibrils.

METHODS

Lobsters were euthanised by injection of KCl solution (100 mg /100 g lobster). The abdominal aorta was sectioned into 2 mm rings. Wall thickness was measured from 40 μm thick frozen sections. The mechanical properties of fresh and guanidine/collagenase digested aorta equilibrated in calcium-based solutions (1mM Ca^{2+}, 13mM Ca^{2+} (physiological) and 30mM Ca^{2+}) were measured. The samples were mounted on two u-shaped tungsten hooks, which were fastened to the base of a bathing tank and to the lever arm of a dual mode motor lever system (300B-LR Model, Aurora Scientific). Motion of the lever arm was controlled from a function generator, displacement and force data were collected with a PC and BioBench Data Acquisition software. Stress relaxation tests were performed at low (0.1), moderate (0.6), and high (1.25) strains. Cyclic uniaxial testing involved imposing a sinusoidal oscillation of 0.8 Hz and dynamic strain amplitude of 0.1. Displacement and force data were converted to strain and stress using a custom built LabVIEW program. Fresh and chemically digested samples were subjected to amino acid compositional analysis after hydrolysis in 5.7 M HCl for 24 h at 110°C under vacuum. Samples at each calcium concentration were processed for transmission electron microscopy using either osmium tetroxide-glutaraldehyde or glutaraldehyde-osmium tetroxide fixation sequences. Thin sections were analyzed and photographed using an electron microscope operated at 80 kV. Measurements of microfibril periodicity and bead diameter were made from the micrographs. Mean and standard deviation were calculated and compared using a one-way ANOVA ($p=0.05$). Where appropriate, Tukey's test ($p=0.05$) was performed.

RESULTS AND DISCUSSION

The results show that fresh vessels were significantly stiffer than digested when tested at low calcium concentrations and strains of 0.6. At strains of 1.25, fresh vessels with intermediate calcium concentrations were significantly stiffer than fresh vessels at low calcium concentrations. Testing at low strains (0.1) showed no significant differences between fresh or digested vessels at any of the tested calcium levels. As expected amino acid compositional analysis displayed significant differences between fresh and chemically digested samples. Amino acid comparisons between digested samples and human fibrillin showed compositional similarity. Ultrastructural differences were also found between groups. The periodicity of fresh and chemically digested vessels incubated with physiological or high calcium concentrations was significantly larger than those vessels incubated with low calcium. These results show that solution based changes in calcium concentration do affect both the protein structure and mechanical behavior of lobster microfibrils. We have also demonstrated amino acid compositional similarity between isolated lobster microfibrils and human fibrillin. These similarities suggest that the structural and mechanical changes occurring in lobster based microfibrils are good approximations of those in Marfan based tissues.

SUMMARY

This study has shown that calcium has a significant effect on the structural and mechanical properties of microfibril-based tissue. This information will help to quantify and further understand the changes that occur in Marfan syndrome patients.

REFERENCES

Eriksen, T.A. *et al.* (2001). *Proteins*, **45(1)**, 90-95.
Dietz, H.C. *et al*. (1991). *Nature,* **352**, 337-339.
Davison, I.G. *et al.* (1995). *J. Exp. Biol.*, **198**, 2185-2196.
M^c^Connell, C.J. *et al.*(1997). *J. Physiol.*, **499**, 513-526.

ACKNOWLEDGMENTS

This work was funded by a C.I.H.R. grant to M.E.D. and G.M.W.

A PRELIMINARY EVALUATION OF A LIMB-SEGMENT MODEL FOR LIFTING TASKS

Pei Lai Cheng, Angela J. Tate, Delphine Périé, and Geneviève A. Dumas

Human Mobility Research Center, and Department of Mechanical Engineering, Queen's University, Kingston, Ontario, Canada.

INTRODUCTION

Limb-segment models have been used to estimate the loads at lumbosacral level (L5/S1) for lifting tasks. Previous models (Plamondon et al. 1996, Lariviere and Gagnon 1998) used motion data measured by optical-electronic motion analysis systems and anthropometric data obtained by regression equations. The optical-electronic system is limited to simple tasks in which markers can be seen by all cameras. The regression equations of the anthropometric data are limited to a small population. We developed a limb-segment model using kinematic data recorded by an electromagnetic motion tracking system (Motion Star®, Ascension Technologies) and individualized anthropometric data. Therefore, it can be used for complex tasks and for a larger group of population. The objective of this paper is to report a preliminary evaluation of the performance of the model for different lifting tasks.

METHOD

The whole body model, involving 11 segments, was divided into a hands-down and a feet-up models, which were separated at L5/S1. The hands-down model involves 7 segments, upper trunk, middle trunk, four upper limb segments and the load in the hands. The feet-up model has 5 segments, the lower trunk and 4 lower limb segments; it also includes the ground reaction force measured at a force platform.

One male subject (24 years, 196cm, 71.2kg), participated with written consent, and performed 4 freestyle lifting tasks (lifting a 12kg box from the floor to a shelf 83cm high). The 4 tasks included symmetrical and asymmetrical (90° to the right) lifts at slow and fast speeds. Each task was recorded 3 times. The anthropometric parameters of the subject were determined using an individualized photogrammetric method (Jensen 1978).

The body motion and ground reaction forces were recorded by the Motion Star® at 86.1Hz, and a AMTI force plate at 86Hz. The data were processed by a calibration procedure (Day et al. 2000) and filtered at 2.5Hz. The forces and moments at L5/S1 from both models were calculated using inverse dynamics. To evaluate model performance, the mean and peak differences of the forces and moments at L5/S1, and correlation coefficients between the hands-down and feet-up models results were calculated within a lifting cycle.

RESULTS

The average results of three recordings for each task are given in Table 1. Most differences of the force and moment components are below 15N and 15Nm with largest values of 18.8N and 20.4Nm for peak differences.

Table 1. The average difference of force (N) and moment (Nm) at L5/S1 between hands-down and feet-up models, f for fast, s for slow, 0 for symmetrical, 90 for asymmetrical, x forward, y upward and z to the right.

		Fx	Fy	Fz	Mx	My	Mz
Mean Difference	f0	6.8	6.4	-3.4	0.4	-2.9	18.6
	s0	16.6	-14.5	-1.9	6.9	-4.3	11.0
	f90	6.1	-1.2	-3.7	5.5	-4.0	17.3
	s90	16.7	-10.6	-1.1	-0.6	-3.0	14.0
Peak Difference	f0	-3.9	-2.4	-5.6	4.8	-2.8	-1.6
	s0	5.7	-0.4	-3.3	14.0	-1.3	4.8
	f90	-6.3	-18.8	0.7	15.6	-3.0	-20.4
	s90	5.7	7.0	-0.4	-2.9	-4.3	9.5
Correlation Coefficient	f0	0.96	0.82	0.99	0.92	0.85	0.85
	s0	0.98	0.91	0.97	0.75	0.95	0.91
	f90	0.98	0.94	0.98	0.86	0.97	0.94
	s90	0.98	0.91	0.99	0.85	0.78	0.71

DISCUSSION

The magnitudes of the mean and peak differences between the hands-down and feet-up models are similar to previous results (Lariviere & Gagnon 1998).

Paired T-tests results of the mean, peak difference and correlation coefficient show that there is no significant difference ($P>0.05$) between fast and slow lifting, and between symmetrical and asymmetrical lifting, which indicates that the model performance is consistent for different speeds and orientations of lifts. The mean correlation coefficient over all tasks is 0.91 (SD 0.07) in the range from 0.71 to 0.99, indicating that the curves have very good agreement between the two models.

In conclusion, this preliminary evaluation indicates that a model with individualized anthropometric data and using motion data recorded by an electromagnetic motion tracking system is generally acceptable for estimating the loads at L5/S1 during lifting tasks. Since this model is intended for use in a larger project, a more comprehensive validation of the model with more subjects needs to be performed.

REFERENCES

Plamondon et al. (1996), *Clinical Biomech*, **11**, 101-110.
Larivière C., Gagnon D. (1998), *Clinical Biomech*, **13**, 36-47.
Jensen R.K. (1978), *J Biomech*, **11**, 349-358.
Day J.S. et al. (2000). *J Biomech*, **33**, 1039-1045.

ACKNOWLEDGEMENTS

This study was supported by WSIB and NSERC.

MODELING LOCOMOTION IN CRUSTACEAN LARVAE

Matthew D. Ford and M. Edwin DeMont

Biology Department, Saint Francis Xavier University, Antigonish, Nova Scotia, Canada, edemont@stfx.ca

INTRODUCTION

The early life cycle of most crustaceans involves a free-swimming planktonic larval stage, which use pairs of reciprocating appendages to produce thrust. Most work on modeling crustacean dispersal has assumed that individual larva move passively following the ocean currents but actively maintaining themselves in the water column until a suitable habitat has been found. We are studying the dynamic swimming mechanics of crustacean larvae at intermediate Reynolds numbers using a combination of direct force measurement, flow visualization and computer programming. The ultimate goal is a complete understanding of the forces being produced and acting on a swimming larva. To broaden the relevance of the project the differences in swimming abilities between species that use different numbers of paired swimming appendages is also being considered.

METHODS

The equation of motion developed for the swimming larvae balances the thrust and unsteady forces produced by the appendages with the drag and unsteady force of the body. In order to solve the equations of motion the kinematics of the appendage angles and body are required and were collected at 250 fps in a small tank using a Redlake™ high-speed motion scope. The fluid force coefficients on the oscillating appendages are also required to solve the equation of motion. To measure these fluid force coefficients geometrically scaled up physical models of the appendages were built. The models were built from plastic and then oscillated and translated in a tank of glycerin while maintaining the same Reynolds number and Strouhal number as the free swimming larvae. Fluid forces were measured by attaching strain gages on each model appendage. With this information a numerical solution was produced using a fourth order Raunge-Kutta method, which was programmed in Matlab. The computer model was based on work by Williams (1994b) which examined swimming in *Artemia* (one pair of swimming appendages). Our work expanded this to encompass both the green crab (two pairs of swimming appendages) and the lobster (five pairs of swimming appendages).

RESULTS AND DISCUSSION

The swimming appendages of both the lobster and green crab larvae beat in a specific coordinated pattern. For example, the green crab moves one appendage completely through the power stroke with the second appendage not beginning the power stroke until the first has finished. The appendages are coupled on the recovery stroke. The drag coefficients measured on the models are in agreement with those measured by Williams (1994a) on the *Artemia* and when applied to the computer model match the measured velocity of the green crab within acceptable error (figure 1).

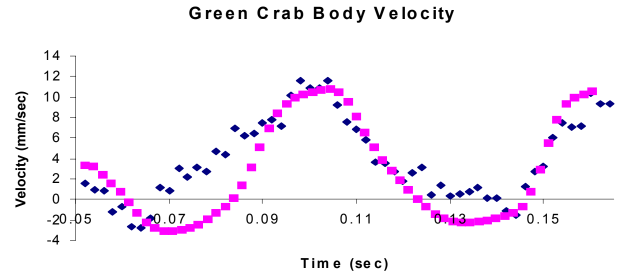

Figure 1: Comparison of measured body velocity (♦) to that predicted by the computer model (■).

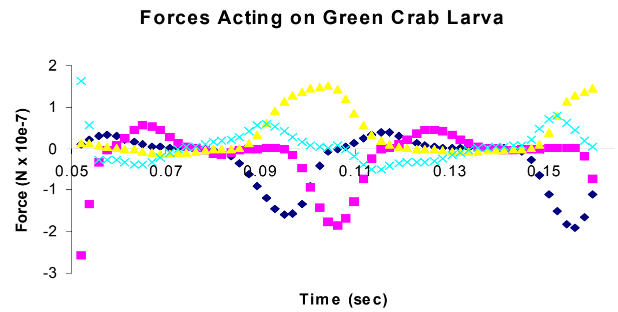

Figure 2: The forces acting on a green crab larva during locomotion include thrust force generated by front appendage (♦), thrust generated by back appendage (■), body drag (▲) and the unsteady force on the body (x).

Improvements made over previous work (Williams, 1994b) include approximating the appendage angle kinematics as a Fourier series and more rigorous calculations of the body morphometrics. The computer model also calculates all the forces acting on the swimming larva (figure 2).

SUMMARY

This work will lead to a better understanding of larval dispersal in crustaceans. This work will also enhance knowledge of the often neglected but biologically important realm of intermediate Reynolds number swimming mechanics, in which many marine organisms move.

REFERENCES

Lauder, G.V. (2001). *Nature*, 729-733.
Williams, T.A. (1994a). *Biological Bulletin*, 156-163.
Williams, T.A. (1994b). *Biological Bulletin*, 164-173.

ANTERIOR-CRUCIATE LIGAMENT FORCES IN THE INTACT KNEE DURING NORMAL GAIT

Kevin Shelburne[1], Marcus Pandy[2], Frank Anderson[3], and Mike Torry[1]

[1]Steadman-Hawkins Sports Medicine Foundation, Vail, Colorado, U.S.A. kevin.shelburne@shsmf.org
[2]Department of Biomedical Engineering, University of Texas at Austin, U.S.A.
[3]Department of Mechanical Engineering, Stanford University, U.S.A.

INTRODUCTION

Few researchers have described knee ligament function in walking despite the many clinical investigations which show that knee ligament injuries, particularly injury to the anterior cruciate ligament (ACL), are the source of persistent neuromuscular adaptations in gait. Furthermore, most rehabilitation protocols following knee ligament injury and repair require normal kinematic and muscle activation patterns during ambulation before the patient may return to full activity. Understanding how the ACL is loaded during normal walking may help to establish more focused and efficient exercise regimens for rehabilitation following ACL injury.

To our knowledge only Morrison (1970) and Collins and O'Connor (1991) have reported ACL forces during gait. The paucity of data on ACL loading is due to the difficulties inherent in the measurement and calculation of muscle and ligament force *in vivo*. In this study, muscle forces obtained from a dynamic optimization solution for normal walking (Anderson and Pandy, 2001) were used as input to a three-dimensional model of the knee (Pandy et al., 1998) to determine knee-ligament forces during gait. The model calculations were analyzed to explain the pattern of ACL loading predicted for gait. Peak ACL force for walking was compared to estimates of ACL force obtained for rehabilitation exercises performed subsequent to ACL injury and repair.

METHODS

The right leg was modeled using four rigid bodies: thigh, shank, hindfoot, and metatarsals. All joints were represented as described by Anderson and Pandy (2001), except the knee, which was modeled as a six degree-of-freedom joint. The geometry of the distal femur, proximal tibia, and patella was based on cadaver data reported for an average-size knee. The contacting surfaces of the femur and tibia were modeled as deformable, while those of the femur and patella were assumed to be rigid. Thirteen elastic elements were used to describe the geometric and mechanical properties of the knee ligaments and capsule. Details of the knee model are given by Pandy et al. (1998). The model leg was actuated by thirteen musculotendinous units.

A combination of forward and inverse dynamics was used to determine knee-ligament forces in the model. Joint motion, ground-reaction forces, and the corresponding muscle forces obtained from the dynamic optimization solution for gait derived by Anderson and Pandy (2001) were input to the leg model. The dynamical equations of the motion for the three-dimensional knee model were then used to determine knee-ligament forces at each instant during the gait cycle.

RESULTS AND DISCUSSION

Figure 1 shows the calculated ligament forces for a complete cycle of gait, beginning at heel strike. The simulation results predict that the ACL is loaded throughout the stance phase of gait. The ACL is loaded throughout stance because the net shear force applied to the tibia is directed anteriorly during this time. Furthermore, the net shear force applied to the tibia is due mainly to the anterior pull supplied by the patellar tendon (not shown). The predicted peak ACL force during gait (344N) is similar to that found for maximum isokinetic knee extension at 300 deg/sec (340N, Serpas et al., in press) and is roughly twice as large as that reported for the leg lift exercise (160N, Shelburne and Pandy, 1997).

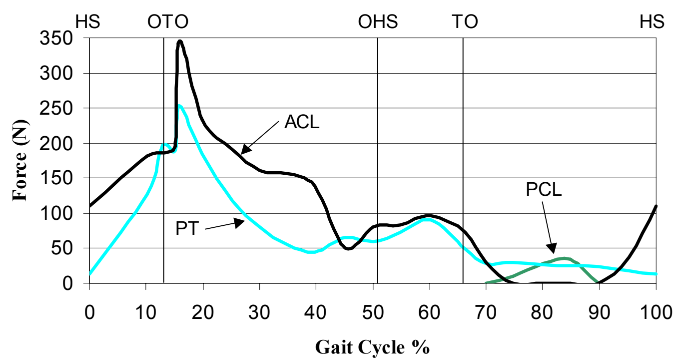

Figure 1: Force in the ACL and PCL during gait shown with the anterior tibial shear force applied by the patellar tendon.

SUMMARY

Our calculations show that the ACL is loaded throughout the stance phase of walking, and that the force transmitted to the ligament rivals that predicted for maximum knee-extension exercise performed at high speed.

REFERENCES

Anderson, FC, Pandy, MG (2001). J Biomech Eng **123**(5): 381-90.
Collins, JJ, O'Connor, JJ (1991). Proc Inst Mech Eng [H] **205**(1): 11-8.
Morrison, JB (1970). J Biomech **3**(1): 51-61.
Pandy, MG, et al. (1998). Comput Methods Biomech Biomed Engin **1**(2): 87-108.
Serpas, F, et al. (in press). Comput Methods in Biomech Biomed Engin
Shelburne, KB, Pandy, MG (1997). J Biomech **30**(2): 163-76.

ASSESSMENT OF CROSSTALK IN SURFACE EMG OF THE FOREARM

Jeremy P.M. Mogk and Peter J. Keir, PhD

School of Kinesiology & Health Science, York University, Toronto, Ontario, Canada (pjkeir@yorku.ca)

INTRODUCTION

Given the proximity and functional redundancy of the forearm muscles, crosstalk is of concern in EMG studies. Further complicating this issue is the potential for muscle movement relative to the electrodes with forearm rotation, which may alter which muscles are recorded. The amount of common signal (or crosstalk) between recording sites may be assessed by means of the cross-correlation function (Winter et al., 1994). The purpose of this study was to evaluate the magnitude of common signal between electrode pairs placed around the proximal forearm. The effects of recording site distance, forearm rotation, grip force level and grip type were examined.

METHODS

Eight healthy male volunteers participated in this study (mean age: 23.7 years; range: 22 – 25 years). Maximum voluntary pinch and power grasp efforts were performed with a neutral wrist and forearm posture using a grip dynamometer (MIE Medical Research Ltd., Leeds, U.K.). Pinch and grasps at 25, 50, 70, and 100% MVC were performed in neutral (mid-prone), fully pronated and supinated forearm postures. Seven electrode pairs were placed circumferentially around the upper third of the right forearm (Figure 1). A landmark electrode pair was placed over FCR, and the remaining six at 3 cm increments medial and lateral to the landmark pair. Cross-correlation functions were calculated using the raw EMG between each electrode pair and the three channels on either side, where applicable, without crossing the ulnar border. An additional cross-correlation was calculated between channels on either side of the ulnar border (channel 1 vs. 7). Raw EMG and force data were collected at 2000 Hz. All trials were videotaped for feedback and analysis.

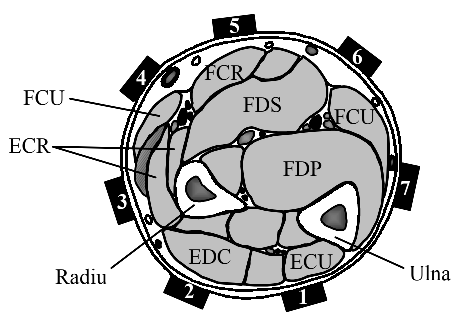

Figure 1. Cross-section of the right forearm indicating approximate location of the seven electrode pairs.

RESULTS AND DISCUSSION

Peak cross-correlation magnitude (R'xy) decreased as the distance between electrode pairs increased, with similar values between grip types (Table 1). While channels 1 and 7 appeared to have similar AEMG amplitudes, virtually no common signal was present ("Ch. 1 vs. 7" – Table 1), suggesting no crosstalk between the flexor and extensor muscle compartments across the ulnar border. This was further evaluated by calculating "crosstalk" ratios using EMG amplitudes (Perry et al., 1981). Individual variability was much greater with the ratios and difficult to interpret. Forearm rotation did not significantly alter R'xy, mainly due to the large variance observed between participants, particularly in the flexors. This variance may indicate greater movement of the flexor muscles than the extensors with forearm rotation.

Table 1. Mean peak cross-correlation (R'xy) and explained variance (R^2) for each electrode spacing, pooled across effort level.

Electrode Spacing	Pinch		Grasp	
	R'xy	R^2	R'xy	R^2
3 cm	0.601	0.361	0.623	0.388
6 cm	0.307	0.094	0.314	0.099
9 cm	0.182	0.033	0.152	0.023
Ch. 1 vs. 7	0.111	0.012	0.089	0.008

SUMMARY

This study has provided insight into electrode placement on the human forearm. Almost 40% common signal may be expected from recording sites 3 cm apart, but less than 10% is expected at 6 cm. In our grasping tasks, activation levels were similar on either side of the ulnar border, however, the correlations indicated that only about 1% of the signal was common. These findings were consistent regardless of forearm posture. Using standard EMG sites, signal contamination due to crosstalk can be minimized in studies of forearm EMG.

REFERENCES

Perry, J., et al. (1981). *Phys Ther*, **61(1)**, 7-15.
Winter, D.A., et al. (1994). *J Electromyog Kines*, **4(1)**, 15-26.

ACKNOWLEDGEMENTS

Funded by an NSERC operating grant to P.J. Keir.

Segmental Power During Propulsion in Wheelchair Users with Greater Evidence of Shoulder Injury Overtime

Alicia M. Koontz[1,2], Michael L. Boninger[1-3], Rory A. Cooper[1-3], Jeffrey D. Towers[3], Lin Ma[1,2]
[1]VA Pittsburgh HealthCare System, Human Engineering Research Labs, Pittsburgh, PA 15206, www.herl.pitt.edu
[2]Department of Rehabilitation Science and Technology, University of Pittsburgh, Pittsburgh, PA 15260
[3]Department of Physical Medicine and Rehabilitation, University of Pittsburgh, Pittsburgh, PA 15213

INTRODUCTION

Propelling a wheelchair is an arduous task and has been implicated in the development of shoulder pain and injury. Up to 54% of individuals with a spinal cord injury (SCI) complain of shoulder pain that adversely affects their mobility and independence (Pentland, 1994). The aim of this study was to follow a group of wheelchair users with paraplegia over a period of two years to track the progression of shoulder injury and determine if segmental power generated and absorbed during propulsion is related to an increased risk of injury.

METHODS

Protocol: Eight men and six women with a SCI between the levels of T3 and L5 provided informed consent prior to participation. Their average age and years post injury at the start of the study were 32.8 $\pm$ 8.8 and 10.4 $\pm$ 6.7, respectively. A standardized magnetic resonance imaging (MRI) exam designed for detection of rotator cuff abnormalities was conducted on both shoulders, at baseline and at a two-year follow-up visit. All images were read by a musculoskeletal radiologist blinded to the subjects' characteristics and biomechanical data. For the biomechanical analysis, subjects' personal wheelchairs were fitted bilaterally with SMART^{Wheels}, force and torque sensing pushrims (Three Rivers Holdings). Skin-mounted markers of the Opto*TRAK* 3D motion analysis system (Northern Digital, Inc.) were placed on prominent locations of the upper extremities and chest. Wheelchairs were secured to a dynamometer and a video monitor was used to display the propulsion speed. After an acclimation period of five minutes, subjects were instructed to propel at a steady-state target speed of 0.9 m/s (2mph) for about a minute before 20 seconds of three-dimensional kinetic data (sampling rate of 240Hz) and kinematic data (60 Hz) were collected.

Data Analysis: Shoulder MRI findings were assessed at baseline and at the two-year follow-up visit using a modified grading scale of pathology based on accepted radiological criteria. Distal clavicle edema, acromioclavicular (AC) joint degenerative disease, AC edema, acromion edema, osseous spur formation, coracoacromial (CA) ligament edema, and CA thickening were scored from 0-3, where 0 is normal, 1 is minimal, 2 is moderate, and 3 is marked. MRI pathology scores for each individual, on both left and right sides, were totaled to produce a single summary variable for each visit. The differences between total scores at the two visits were then calculated. A positive value indicated a greater number of abnormalities. Segmental power was determined by first calculating the segment's, *s*, total mechanical energy, *E*, (Robertson, 1980) and solving the difference equation:

$$P(s,t_1) = \dot{E}(s,t_1) = [E(s,t_2) - E(s,t_0)]/2\Delta t$$

Power data were normalized by dividing by the subject's hand, forearm, and upper arm segment masses in kilograms. All calculations were implemented in MATLAB (Mathworks Inc.). Peak generated (positive) and absorbed power (negative) were averaged over five push cycles. Because of high correlation, the left and right sides were combined. The power data obtained from the baseline measure of propulsion was used in the analysis.

Statistical Analysis. Subjects were divided into two groups based on differences in total MRI scores at baseline and at two-year follow-up. Chi-square analysis was used to compare the groups with respect to gender and MRI score. An independent samples t test was used to determine if differences existed between MRI+ and MRI- groups with respect to age, body mass index, years from SCI, and power data. The significance level for all tests was set at 0.05.

RESULTS

Seven subjects showed an increase in MRI abnormalities (MRI+) (mean +8.14 points) and seven subjects showed little change or improvement (MRI-) (mean –1.00 point); p=0.002. There was no significant difference in age, body mass index, or years from SCI. There were significantly more women in the MRI+ group (MRI+: 6 women, MRI-: 0 women); p=0.001. The MRI+ group generated and absorbed more segmental power during propulsion at baseline with the largest relative difference noted for the upper arm (p=0.07) although none of the group comparisons were statistically significant (Table 1).

DISCUSSION

The findings of this study suggest that wheelchair users who generate and absorb more segmental power during propulsion may be more likely to develop shoulder abnormalities overtime. This was not too surprising as results from a previous analysis showed that the MRI+ group pushed their wheelchairs with pushrim forces greater than 5% of their body weight (Dicianno, 2000). The reasons for this remain unclear but are likely related to wheelchair set-up, rolling resistance and technique. The fact that 6 of the 7 subjects in the MRI+ group were women indicate that women may be a greater risk for developing shoulder injuries and that preventative interventions should target this population of wheelchair users.

REFERENCES

Pentland WE, Twomey LT. (1994). *Paraplegia*, **32**, 219-224.
Robertson DG, Winter DA. (1980). *J. Biomech*, **13**, 845-854.
Dicianno et al. (2000). *Abstracts of the Annual AAP Meeting*.

ACKNOWLEDGEMENTS: Funding support for this study was provided by: NIH (K08 HD01122-01), NCMRR (5 P01 HD33989), VA (B689-RA).

Table 1: Segmental power data, mean (SD), in **W/kg** for both groups

GROUP	Gen. Power Hand	Gen. Power Forearm	Gen. Power Up Arm	Abs. Power Hand	Abs. Power Forearm	Abs. Power Up Arm
MRI-	3.64 (1.80)	0.81 (0.39)	**0.31** (0.22)	5.49 (0.96)	4.52 (0.51)	1.84 (0.28)
MRI+	4.18 (1.65)	1.20 (0.62)	**0.66** (0.37)	5.80 (1.11)	4.69 (1.11)	2.24 (0.56)

OPTIMIZATION OF SIMPLE THROWING MODEL EXPLAINS SOME OF THE COORDINATION OF THROWING

Manoj Srinivasan[1] and Andy Ruina
Theoretical and Applied Mechanics, Cornell University, Ithaca, NY, USA
[1] Email : ms285@cornell.edu

INTRODUCTION

Some studies of the coordination strategies for maximal-range human throwing have used models of the hand with two or three links, actuated by muscles with some bounds on the forces produced (e.g., a force-velocity relation) Alexander (1991, 1997), Herring & Chapman 1992, Chowdhary & Challis (2001). It is usually assumed that the throwing motion (for the 2-link hand model) consists of a few phases – with either one or more muscles being fully activated. Under such an assumption, these works show the need for a positive optimal delay between the activation of the proximal muscle and that of the distal muscle to maximize velocity, corroborating the ubiquitous proximal-distal sequencing in animal coordination.

To better understand this sequencing and to test the validity of the bang-bang assumption, we construct an extremely simple model of throwing – one that is perhaps too simple for experimental comparison, but one that is amenable to solution without simplifying assumptions on the nature of the optimal strategy, so that it may guide understanding of models with greater realism.

PROBLEM FORMULATION

The model consists of two masses m_1 and m_2, the proximal and distal body parts respectively. F_1 and F_2 are forces produced by "muscles", acting on the masses as shown in Fig. 1.

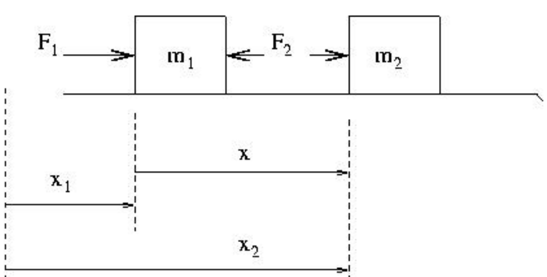

Figure 1: A one-dimensional throwing problem. It is close to the shot-putting model of Alexander (1991) but is also partially analogous to a segmented arm.

The model is formally identical to a 2D model of a throwing arm if all the mass is concentrated in the elbow and hand and if small angles are assumed. We seek the strategy – time history of the two forces, not necessarily piecewise constant or maximal – that leads to the maximum possible velocity of the second mass, subject to the following constraints (in non-dimensionalized form, with m_1=1): $F_1 \le 1$, $F_2 \le F_2^{max}$, $0 \le x_1 \le 1$, $0 \le x \le x^{max}$. That is, the forces and ranges of motion have given bounds and can only push in one direction.

METHODS AND SOLUTION

The problem is not accessible to the Pontryagin maximum principle directly because of the state-variable constraints. So we solve it numerically – by using piecewise linear forcing functions and solving the resulting linear programming problem. We solved this optimal control problem for all relevant parameter ranges. Guided and confirmed by numerical simulations, we have obtained the exact closed-form expressions of the optimal solutions for all parameter ranges. It turns out that the bang-bang solution, with the proximal-distal sequence is an optimal solution for a large parameter range, however *not* the only optimal solution. A whole family of solutions produce the same optimal value as that as the bang-bang solution. In another parameter range, the *distal* muscle needs to be fully active for all time, while the proximal does not. Again the solution is not unique. One feature of all the solutions is that when the maximum velocity is reached, x reaches x^{max} – surprisingly the same is true of x_1 in only 3 out of 5 parameter ranges. Muscle reversal is not used in any of the optimal solutions, even when allowed.

DISCUSSION

We hoped that complete understanding of this simple problem would help us deal with more realistic models. Research in progress indicates that some of the results from this model carry over to a model with two links and torque-bounds. One such is the inherent non-uniqueness in the solutions. So the lowest order approximation, a model like this, predicts that optimal coordination strategies are not tightly constrained. And a natural prediction is that much more complex models should have shallow, and perhaps multiple, local optima.

REFERENCES

Alexander, R. McN. (1991) *J. theor Biology*, **150**, 349-372
Chowdhary A. G., Challis, J. H. (2001) *J. theor Biology*, **211**, 39-53
Alexander, R. McN. (1997) *J. theor Biology*, **184**, 187-201
Herring, R. M., Chapman, A. E. (1992) *J. Biomech*, **25**, 1173-1184

ACKNOWLEDGEMENTS
The authors are grateful for fun discussions with Dave Cabrera, Mario Gomes, Mike Coleman and Steve Collins.

PROTOCOL FOR IN VIVO OPTOELECTRONIC KINEMATICS ANALYSIS OF SHOULDER

Amadou Diop[1], Nathalie Maurel[1], Jean-Luc Nephtali[2], Jean Grimberg[3], Louis-Denis Duranthon[4], Jérôme Allain[5], Olivier Gagey[6]

[1]Ecole Nationale Supérieure d'Arts et Métiers, 151 bd de l'Hôpital, 75013 PARIS, amadou.diop@paris.ensam.fr
[2]Cabinet de kinésithérapie, 11 rue Bachelet, 75018 Paris
[3]Centre Hospitalier de Meulan, 1 rue du Fort, 78250 Meulan
[4]Hôpital Européen Georges Pompidou, 20 rue Leblanc, 75015 Paris
[5]CHU Henri Mondor, 51 av. du Maréchal de Lattre de Tassigny, 94000 Créteil
[6]CHU de Bicêtre, 78 rue du Général Leclerc, 94270 Le Kremlin Bicêtre

INTRODUCTION

We undertook to implement a protocol for a multicentric in vivo kinematics analysis of the shoulder in order to better understand the behaviour of this articulation and to get a standardised clinical evaluation tool providing quantitative data for normal or pathologic subjects and for patients after prosthetic surgery.

METHODS

Flexion, abduction in the "scapular plane" (30° from the frontal plane) and external rotation were studied using the Vicon optoelectronic system provided with 6 cameras. For this, due to the great relative motions between bone and skin, two kinds of movements were analysed:
- Global movements of the arm to define the maximal global amplitudes of the shoulder;
- Static positions of the arm (at 0, 30°, 60°, 90°, 120° and 150° for flexion and abduction or at 0°, 15°, 30° and 45° for external rotation) to define, in each case, the angular positions of the different bones of the shoulder.

The subject was positioned using rests at feet, head and hip. For flexion and abduction the subject was up and for external rotation the subject was sitting.
Flexion was performed in a plane parallel to the sagittal plane and abduction in a plane oriented at 30° from the frontal plane. These two planes go through the antero-external angle of the acromion. They were materialised using a bar in rotation around an axis which was perpendicular to each of these planes and which went through the antero-external angle of the acromion. This bar can be fixed at wanted positions for static studies. The movements were produced with the arm in active extension using a handle positioned on the bar.
External rotation was performed with the forearm put on a plane perpendicular to an axis oriented at 10° from a vertical axis in the frontal plane. This axis went through the antero-external angle of the acromion. The plane of rotation was materialised using a bar in rotation around this axis.
For global movements, the mobility of the arm was determined using 2 markers fixed on the guiding bar.
For static positions of the arm, positions of scapula, clavicle and sternum were recorded using personalised palpators. The principle of palpation was described and used by Van der Helm and al. We adapted it to optoelectronic measurements (figure 1). Each palpator was provided with 3 reflective markers during measurements and with 6 reflective markers for their calibration. For the humerus, in flexion and abduction, a fixed palpator was positioned using the two gutters around the olecran to determine two anatomical points. In external rotation the position of the epicondyle and epitrochlee were calculated from their initial position, from the immobile position of the olecran obtained using a probing system and from the angular position of the mobile bar. The third point necessary for the spatial determination of the position of the humerus corresponded to the centre of the humeral head calculated as described by Meskers et al.
The kinematics calculations were performed using the sequence proposed by the ISG.

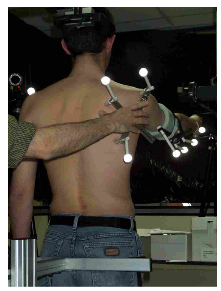

Figure 1: Palpation of scapula during flexion.

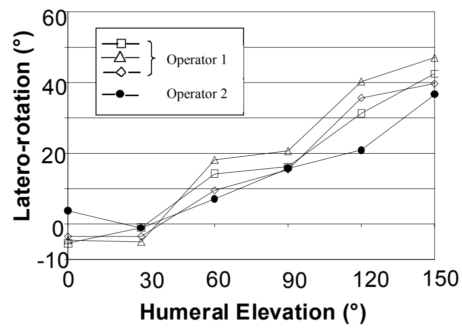

Figure 2: Latero-rotation of scapula during abduction in scapular plane (repeatability measurements with different operators)

RESULTS

The first tests were performed on normal subjects. The results seem to be coherent (in physiological point of view and in comparison with literature), and precision and repeatability evaluations are in progress (figure2).
Once validated, this protocol should be applied to a great number of normal subjects (in order to get a reference data basis), to pathologic patients and finally to patients with prostheses.

REFERENCES

Meskers C.G.M. et al (1998a), *Clinical Biomechanics*, 13, 280-292.
Meskers C.G.M. et al (1998b), *Journal of Biomechanics*, 31, 93-96.
Pronk G.M., et al (1991), *Journal of Medical Engineering & Technology* ,15(1), 15-20.
Van der Helm F.C.T. et al (1995), *Journal of Biomechanical Engineering* , 117, 27-40.

THE EFFECT OF ANALYSIS METHOD AND CALIBRATION CAGE GEOMETRY ON THE SPATIAL VARIATION OF RSA RECONSTRUCTION ACCURACY

Anthony M.T. Choo and Thomas R. Oxland
Departments of Orthopaedics and Mechanical Engineering
The University of British Columbia, Vancouver, British Columbia, Canada
amchoo@interchange.ubc.ca

INTRODUCTION

Traditional roentgen stereophotogrammetric analysis (RSA) solves for the stereo parameters in separate steps using fiducial and control planes (FCP) (Selvik, 1989). The direct linear transformation (DLT) is popularly used in camera and video photogrammetry to solve for these parameters in a single optimization (Abdel-Aziz and Karara, 1971).

In addition, the typical calibration cages used are asymmetric (Figure 1). The projective cage (PC) is skewed and the biplanar cage (BC) has a smaller control than fiducial plane. Finally, PC reconstruction involves extrapolation beyond the calibrated volume.

The objectives of this study were to quantify the behaviour of the reconstruction accuracy over a range of object positions. Specifically to assess its dependence on:

1. FCP and DLT analysis methods
2. calibration with PC and BC geometries examining the effect of calibration marker distribution

METHODS

Simulations were conducted in Matlab (v.5.0, The MathWorks Inc., Natick, MA). Calibration with PC and BC were modeled. The target object consisted of nine points distributed at the corners of a 10-cm sided cube and a single point at the cube's centroid. Normally distributed random errors were used to model manufacturing inaccuracy (0.01-mm) and radiographic measurement error (0.24-mm). In addition three hypothetical biplanar-type cages of varying asymmetry were used to probe the interaction between analysis method and cage geometry.

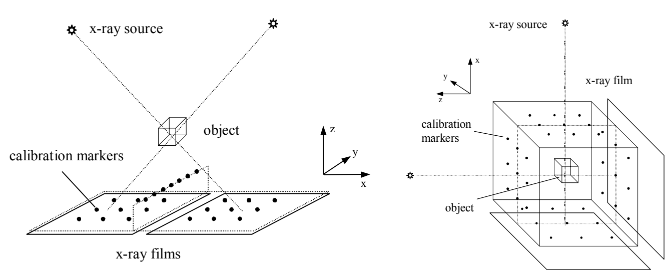

Figure 1: a) projective cage (PC) - object outside calibrated space; b) biplanar cage (BC) - object within calibrated volume

RESULTS AND DISCUSSION

For PC, the transverse errors ranged from 0.24-mm to 1.1-mm from 35-cm to 110-cm positions above the calibration cage. Axial errors ranged from 1.7-mm to 5.8-mm. The error magnitudes were the same regardless of analysis method. For BC, the errors were lower and ranged from 0.14-mm at the cage centre to 0.48-mm at the cage boundary. In addition, differences between FCP and DLT were now perceptible.

Further investigation with the hypothetical cages showed it was the even distribution of calibration markers that enabled DLT to be more accurate. By solving for the stereophotogrammetric parameters simultaneously, the method of least-squares was able to balance all measurement errors. The separated solution in FCP limits error balancing producing a sub-optimal solution.

Whereas FCP utilized strictly planar calibration markers, DLT was able to use markers from all planes. The effect of this "full" DLT method combined with a symmetric marker distribution was an improvement of up to 62% (Figure 2).

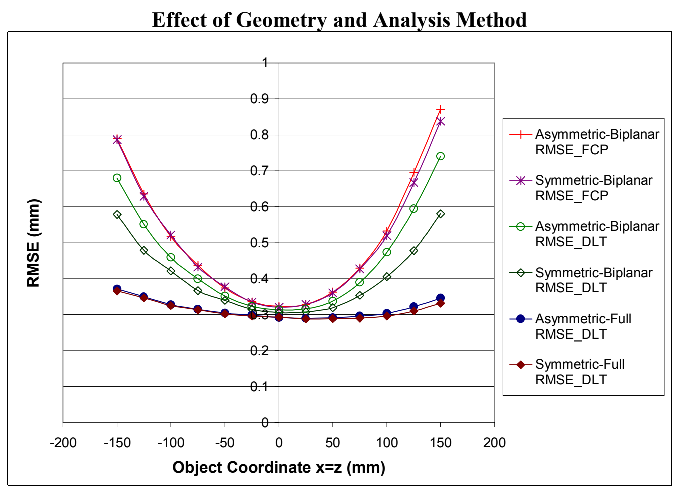

Figure 2: Accuracy was improved by using all calibration points of a perfectly symmetric cage.

SUMMARY

This study elucidated some of the subtle differences between FCP and DLT. The most accurate reconstruction is achieved using DLT with a symmetric distribution of calibration markers surrounding the volume of interest. This has implications in the utilization of RSA for motion analysis over a general unconstrained region of interest.

REFERENCES

Selvik, G. (1989). *Acta Orthop Scand Suppl*, **60**, 1-51.
Abdel-Aziz, Y.I., Karara, H.M. (1971). *Proc ASP Symp on Close Range Photogrammetry*, Falls Church.

A SIMULTANEOUS ANALYSIS OF MULTIPLE WAVEFORM AND CONSTANT GAIT MEASURES: APPLICATION TO KNEE OSTEOARTHRITIS

J.L. Astephen[1], K.J. Deluzio[1,2], U.P. Wyss[2]
[1]School of Biomedical Engineering, Dalhousie University, Halifax, Canada
[2]Department of Mechanical Engineering, Queen's University, Kingston, Canada

INTRODUCTION

Knee Osteoarthritis (OA) is a common, debilitating musculoskeletal disease process whose pathology is linked to multiple correlated biological and mechanical factors. The interrelationships between these factors, which have been largely ignored in previous gait analysis studies, house important information about the OA disease process. Deluzio (2001) recognized the temporal correlation structure within individual time-varying kinematic and kinetic gait measures and determined discriminatory features between normal and OA waveforms. More powerful discrimination of gait patterns is possible by recognising the multidimensionality of the problem. Multiple waveform gait measures (i.e. the adduction moment), constant gait measures (i.e. stride characteristics) and OA-related parameters (i.e. alignment) are important to OA and are correlated. In a review of gait analysis techniques, Chau (2000) recognised the current need for interpreting multiple gait signals and quantitatively comparing gait waveforms.

The objective of this study was to develop a multivariate discrimination technique that simultaneously considered multiple constant and time-varying measures to detect differences in normal and OA gait patterns.

METHODS

Three-dimensional gait analysis was performed on a group of 54 elderly patients with severe knee OA and a group of 63 elderly asymptomatic subjects. Three components of knee joint angles, moments and forces were calculated with the QGAIT gait analysis system. (Costigan, 1992) For each subject, the static Hip Knee Ankle (HKA) angle, the standing knee flexion angle, and the medial and lateral condyle joint spaces were measured with a standardized X-ray technique called QPR. (Siu, 1991) Body Mass Index (BMI) was also calculated. The full gait cycle data of the 9 waveform gait measures and the 5 constants were simultaneously included in a principal component analysis (PCA). PCA is a statistical analysis technique that exploits the correlation in the data in extracting important features (PCs) that explain a maximal amount of the variability in the data. A stepwise linear discrimination procedure used a subset of the features extracted with PCA to: (i) define the multidimensional hyperplane that optimally separates the 2 groups and (ii) determine the discriminatory power of each feature. The most discriminatory PCs were interpreted in terms of the relative contribution of each of the 9 waveforms and 5 constants, and the relative importance of each percentage of the gait cycle.

RESULTS AND DISCUSSION

The multidimensional technique was successful in discriminating between OA and normal gait patterns, with a misclassification error <8%. A hierarchy of discriminatory power among the features was established through inspection of the linear discriminant function. The most discriminatory feature (PC1) described an alignment difference between the 2 groups; the next most discriminatory feature (PC20) described a difference in the loading response phase of the gait cycle. (Figure 1a)

We were able to interpret the features by: (i) determining the relative contribution of each of the 9 waveform gait measures and the 5 constants to each feature, and (ii) determining the relative contribution of each percentage of the gait cycle to each feature. Figure 1b describes the former interpretation for PC1. Dominant contributions come from the adduction moment, the lateral-medial bone-on-bone force and the HKA angle, all considered related to alignment and OA. The measures were weighted more equally in PC20, but as Figure 1a shows, this feature isolated a unique portion of the gait cycle corresponding to loading response, previously hypothesized to be important to knee OA. (Radin, 1991)

Identifying 2 major features important to knee OA, this study confirmed the power of exploiting the interrelationships between measures in the analysis of gait data and the utility of including parameters in the analysis.

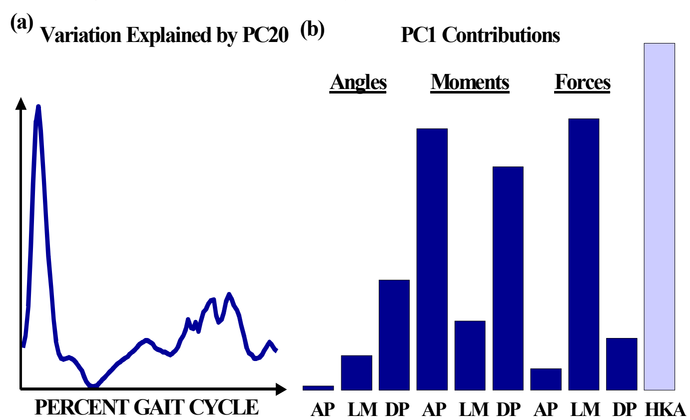

Figure 1: (a) PC20 describes loading response gait phase (b) Relative contribution of factors to PC1.

REFERENCES

Chau, T., (2001). *Gait and Posture*, **13**, 102-120.
Costigan, P etal (1992) *Med.&Biol.Eng &Comp*, May, 343-50.
Deluzio, K.J. et al (2001). *ISB Conference Proceedings*.
Radin, E.L. et al (1991). *J. Orthop Research*, **9**, 398-405.
Siu, D. et al (1991). *Investigative Radiography*, 26, 71-77

INFLUENCE OF METATARSOPHALANGEAL JOINT BENDING AND SHOE SOLE LENGTH ON JUMP HEIGHT PERFORMANCE

Jean-Pierre R. Roy and Darren J. Stefanyshyn

Human Performance Laboratory, University of Calgary, Calgary, Alberta, Canada (jproy@kin.ucalgry.ca)

INTRODUCTION

Energy implications during physical activity play an important role on performance. It has been shown that mechanical energy is dissipated at the metatarsophalangeal (MP) joint during running, sprinting and jumping (Stefanyshyn and Nigg, 1997, 2000). Stefanyshyn and Nigg (2000) also showed that performance in vertical jumping could be improved by decreasing the energy that the MP joint dissipated. This was achieved by reducing the amount of bending of the shoe. In the present study we hypothesized that by eliminating the energy dissipated at the MP joint and increasing the resultant moment or angular velocity at the ankle joint, the subject would show improved vertical jump heights. The purpose of the study was twofold: to investigate the effects that eliminating the bending of the MP joint will have on vertical jump height and to examine the effects that an increased shoe sole length will have on vertical jump performance.

METHODS

Seven male subjects were recruited for the study (mean age 23.7 ± 1.1 yr, mean height 181.2 ± 3.5 cm and mean mass 79.8 ± 5.5 kg). A total of fifteen trials were collected for each subject, five trials for each of the three shoe conditions (control, stiff (C2) and stiff with anterior extension (C3)).

The subjects performed a maximal effort standing counter movement jump while standing on the force plate. The order each subject received the various shoe conditions was randomly assigned to avoid any learning effect. Kinetic data were collected with a force platform (Kistler, Winterthur, Switzerland) sampling at 1000 Hz. Vertical jump heights were measured using a Vertec height measurement system (Sports Import, Columbus, Ohio). A one-way repeated measures ANOVA was used to compare the dependent variables between the conditions (alpha = 0.05).

RESULTS AND DISCUSSION

The results for all shoe conditions are found in Table 1. This table represents the ensemble mean of each subjects maximal value attained for a given shoe condition. The results show that shoe C2 increased vertical jump height and impulse by 1.1 cm and 2.65 Ns respectively over the control shoe. Furthermore, peak force values were greatest for shoe C3, increasing by 38.79N over the control shoe. However, these differences were not significant, and could be due in part to the limited sample size. It can also be speculated that the lack in significant results may be partially due to the subject's inability to generate the additional plantar flexor force necessary to achieve a greater resultant moment when jumping in the test shoes.

Supplementary data, such as high speed video and EMG will shed more light on these speculations, and on the results found. Centre of pressure data were collected during this study, the analysis of which will be completed in future work.

The product of resultant joint moment and joint angular velocity determines the joint's mechanical power. The authors in this study speculated that by increasing the moment arm about the anterior aspect of the ankle (by modifying the sole characteristics of the shoe), a greater resultant moment would be generated by the plantar flexors and hence greater mechanical power production at the ankle. Although this added mechanical power was not directly quantified, it was indirectly gauged by increased vertical jump heights.

With a greater sample size and additional data, the hypothesis that footwear may be capable of generating a greater resultant plantar flexor moment in the human ankle, may be supported.

REFERENCES

Stefanyshyn, D.J., Nigg, B.M. (2000). *Med. Sci. Sports Exerc*., **23**, 471-476.
Stefanyshyn, D.J., Nigg, B.M. (1997). *J. Biomechanics*, **30**, 1081-1085.

Table 1: Mean (SD) of the maximum vertical jump height, peak force and impulse.

	Control	C2	C3
Max Jump Height (cm)	298.09 (6.76)	299.19 (6.00)	299.00 (6.83)
Peak Force (N)	1986.64 (160.44)	1976.87 (215.66)	2025.43 (222.30)
Max Impulse (Ns)	919.40 (139.81)	922.05 (152.30)	885.98 (133.46)

THE LOADING RESPONSE PHASE OF THE GAIT CYCLE IS IMPORTANT TO KNEE OSTEOARTHRITIS

J.L. Astephen[1] and K.J. Deluzio[1,2], U.P. Wyss[2]
[1]School of Biomedical Engineering, Dalhousie University, Halifax, Canada
[2]Department of Mechanical Engineering, Queen's University, Kingston, Canada

INTRODUCTION

The pathogenesis of knee osteoarthritis (OA) is complex and involves many correlated biological and mechanical factors. Modern gait analysis is used to calculate mechanical measures such as knee joint loading and orientation, which play a substantial role in the progression of OA. Previous studies have reported several differences in gait measures with knee OA, such as higher adduction moments (Kaufman, 2000) and lower ranges of motion in the sagittal plane. (Deluzio, 2001) However, these studies can be difficult to interpret due to the numerous individual measures reported. (i.e. joint angles, moments, stride characteristics) There are interrelationships between the time-varying and constant gait variables measured, as well as with other parameters related to knee OA. (i.e. obesity) Important biomechanical features of OA may lie in the relationships between these variables, undetectable in univariate analyses.

The objective of this study was to detect biomechanical factors of knee OA using a multidimensional analysis technique that simultaneously considered multiple time varying and constant gait measures, and other parameters important to knee OA.

METHODS

Three-dimensional gait analysis was performed on a group of 54 elderly patients with severe knee OA, and a group of 63 elderly asymptomatic subjects. Three components of knee joint angles, moments and forces were calculated with the QGAIT gait analysis system. (Costigan, 1992) For each subject, the static Hip Knee Ankle (HKA) angle, the standing knee flexion angle, and the medial and lateral condyle joint spaces were measured with QPR, a standardized X-ray technique (Siu, 1991). Body Mass Index (BMI) was also calculated. The full gait cycle data of the 9 waveform gait measures and the 5 constants were simultaneously included in a principal component analysis (PCA). PCA is a statistical analysis technique that exploits the correlation in the data in extracting important features (PCs) that explain a maximal amount of the variability in the data. A stepwise linear discrimination procedure used a subset of the features extracted with PCA to: (i) define the multidimensional hyperplane that optimally separates the 2 groups and (ii) determine the discriminatory power of each feature. The most discriminatory PCs were interpreted in terms of the relative contribution of each of the 9 waveforms and 5 constants, and the relative importance of each percentage of the gait cycle.

RESULTS

The multidimensional analysis technique successfully identified discriminatory gait features, with a misclassification <8%. A hierarchy of the features was determined through inspection of the linear discriminant function.

The second most discriminatory feature, PC20, was a low-variance feature that described an important OA gait pattern difference. Early stance, or loading response, was completely isolated as the portion of the gait cycle important to PC20. (Figure 1) The feature consisted of relatively equal contributions from most of the 9 gait measures, as well as BMI.

DISCUSSION

The shock absorbency required during loading response can be compromised by such things as knee instability, muscle weakness or obesity, all characteristics of an OA population.

Although it has been previously speculated (Radin, 1991), this is the first time that loading response has been quantitatively identified as important to knee OA. This is largely because the difference is not isolated to one variable; it lies in a combination of many variables during this single phase of the gait cycle. With contributions from multiple variables, PC20 describes a multidimensional gait phenomenon during loading response, and required the power of a simultaneous technique for its detection. The importance of BMI, a relative obesity measure, to the feature also confirmed the utility of including parameters in the analysis.

In this same phase of the gait cycle, Radin (1991) identified an impulsive foot-ground reaction at the instant of heel strike in subjects with mild knee pain, presumably consistent with pre-OA. In recent work, we also found different muscle activation patterns during loading response of a moderate-OA group of subjects. We believe that this combination of variables involved during loading response may be important to the onset and development of knee OA.

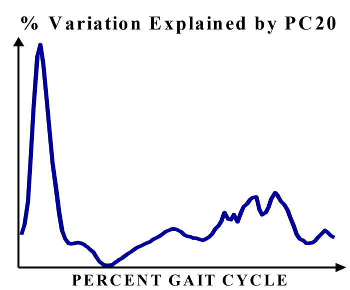

Figure 1: PC20 isolates the loading response phase of gait.

REFERENCES

Chau, T., (2001). *Gait and Posture*, **13**, 102-120.
Costigan, P etal (1992) *Med.&Biol.Eng &Comp*, May, 343-50.
Deluzio, K.J. et al (2001). *ISB Conference Proceedings*.
Kaufman, K.R. et al (2000). *Jbiomech*, **34**, 907-915.
Radin, E.L. et al (1991). *J. Orthop Research*, **9**, 398-405.
Siu, D. et al (1991). *Investigative Radiography*, 26, 71-7.

AN ANNULAR STRAIN ENERGY FUNCTION WITH A PHYSIOLOGIC BASIS

Diane R. Wagner[1,2] and Jeffrey C. Lotz[1]
[1]Orthopaedic Bioengineering Laboratory, University of California, San Francisco CA, jlotz@itsa.ucsf.edu
[2]Department of Mechanical Engineering, University of California, Berkeley CA

INTRODUCTION

The physical properties of the annulus fibrosus are critical to the intervertebral disc's biomechanical function: alterations with degeneration and aging can contribute directly to joint dysfunction and pain. A prerequisite for understanding disease etiology and progression is a constitutive model that links tissue architecture to material properties. To this end, we have developed a strain energy function with individual terms that represent specific tissue features. We applied this strain energy function to data from a wide range of experimental protocols to develop a comprehensive formulation for the multiaxial annular elastic behavior.

METHODS

We chose a Cartesian basis where the 1, 2, and 3 directions are aligned with the anatomic radial, circumferential, and axial directions, respectively. We assumed that there are two mechanically equivalent fiber families which are coplanar and oriented at $\pm\Phi$ from the axial direction. With these assumptions, Spencer (1984) showed that the strain energy W can be expressed as $W = W(I_1, I_2, I_3, I_8, I_9, I_{10}, I_{11}, \cos^2 2\Phi)$.

In the current study, we assumed that the annulus derives its material properties from three components: the proteoglycan matrix, the collagen fibers, and the collagen cross-links. We therefore considered a strain energy function consisting of a sum of separate terms: $W = a_1(I_3 - 1/I_3) + a_2(I_1 I_3^{-1/3} - 3) + a_3(\exp(b_3(I_9 - 2)) - b_3 I_9) + a_4(\exp(b_4(I_{11} - I_9^2 + 2I_{10})))$. The 1st and 2nd terms represent, respectively, the spherical and deviatoric responses of the matrix. The 3rd term models the collagen fibers with a mechanical response that is stiffer in tension than in compression. Finally, we assumed that the primary function of the collagen cross-links is to constrain the collagen fibers from sliding past one another. Consequently, the 4th term of W is a function of the shear strain along the fiber direction and represents the contribution of the cross-links.

We derived appropriate stress-stretch relations for each experimental protocol, including both zero-stress responses associated with the traction free faces in the uniaxial experiments (Mathematica). The data to which we applied this strain energy function included: radial and axial confined compression (Klisch and Lotz, 2000), radial tension (Fujita et al, 1997), circumferential tension and compression (Wagner and Lotz, 2002), axial tension (Duncan and Lotz, 1998), and biaxial tension (Bass, 1999). We limited the biaxial data to the axial stress response with circumferential strain held at 0%.

Because the stress in any direction is dependent on the stretch in every direction, we had to define the 3 principal stretches in the uniaxial experiments, even though they were not all measured. We estimated ν_{12}, ν_{13}, ν_{21} and ν_{31} to be 0.18, 0.18, 0.25 and 0.25. Because a preliminary analysis indicated that the results of the fit were very sensitive to the Poisson's ratios ν_{23} and ν_{32} and to Φ, we considered these parameters to be best found through the statistical non-linear fitting algorithm.

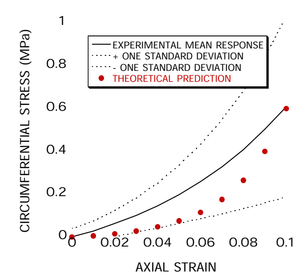

Fig 1: theoretical prediction versus experiment for circumferential response in biaxial tension.

To determine the values of the material parameters $\{a_1, a_2, a_3, b_3, a_4, b_4, \nu_{23}, \nu_{32}, \Phi\}$, we conducted a non-linear regression to the mean response of the stress versus stretch data from the experimental datasets (PV-Wave). To validate this constitutive formulation, we compared the predicted circumferential stress-stretch response in biaxial tension (circumferential strain held at 0%) with the corresponding experimental data.

RESULTS

The best fit values for the nine material parameters were {0.126, 0.00394, 0.000169, 28.9, 0.00111, 10.1, 1.65, 0.40, 55.9°}. These coefficients resulted in stress-stretch curves that lie within one standard deviation for all experimental deformations. Additionally, the theoretical prediction for the circumferential stress-stretch response in biaxial tension matched the experimental data well (Figure 1).

DISCUSSION

We have developed a strain energy function that accurately predicts the mean stress response to multiple experimental deformations. Since the terms are meant to represent separate contributions from annular constituents we hope that this formulation may be used in the future to elucidate structure-function relationships of the annulus and the pathomechanics of aging and degeneration in the intervertebral disc.

REFERENCES

Bass E.C. (1999). Ph.D. dissertation, UC Berkeley.
Duncan N.A., Lotz J.C. (1998). *Computer Methods in Biomechanics & Biomedical Engineering-2*, pages 527-34, Gordon and Breach Science Publishers, Middleton et al, Eds.
Fujita Y. et al (1997). *J Orth Res* **15**, 814-819.
Klisch S.M., Lotz J.C. (2000). *J Biomech Eng*, **122**, 180-8.
Spencer A.J.M. (1984). Springer-Verlag.
Wagner D.R., Lotz J.C. (2002). *Trans Orthop Res Soc.*

DISEASED HUMAN CAROTID BIFURCATIONS: HISTOLOGICAL CORRELATIONS TO HEMODYNAMIC FACTORS

M.R. Kaazempur-Mofrad[1], H.F. Younis[1], A.G. Isasi[1], R.C. Chan[2], D.P. Hinton[3], G. Sukhova[4], R.T. Lee[4]
and R. D. Kamm[1]
[1]Department of Mechanical Engineering and Division of Bioengineering and Environmental Health
Massachusetts Institute of Technology, Cambridge, MA
[2]Boston Heart Foundation, Harvard/MIT Division of Health Sciences and Technology, Cambridge, MA
[3]NMR Center, Massachusetts General Hospital, Charlestown, MA
[4]Cardiovascular Medicine, Brigham & Women's Hospital, Boston, MA

INTRODUCTION

Atherosclerosis is an inflammatory disease characterized by endothelial dysfunction, monocyte infiltration/differentiation, smooth muscle cell (SMC) proliferation, lipid deposition, elevated wall permeability to macromolecules, and arterial wall remodeling (Ross, 1999). The localized nature of these processes points to hemodynamics as a major contributing factor. The objective of this study is to provide a rigorous assessment of possible correlations between different hemodynamic factors and the progression of atherosclerosis.

MATERIALS AND METHODS

MRI-based *in vivo* Geometry. *In vivo* carotid bifurcation geometries were obtained in four patients P1-P4 (ages 61-73) using multi-slice black blood spin echo magnetic resonance imaging (MRI) with 2mm thick slices and 0.39mm in-plane resolution. An in-house edge detection protocol was used to convert the MRI data to a series of 2D vessel boundaries. Lofting across these 2D cross-sectional structures at each level of the carotid bifurcation was carried out using a solid modeling software SolidWorks (Concord, MA). Interpolation across the outer contours of these slices produced the external 3D solid body, while the 3D structure that results from interpolating across the inner contours gave the 3D fluid volume. Subtraction of these two yielded the 3D vascular structure (not used in the simulations, but used later in matching the histological slice location to the histology specimen).

FEM Model. Given the 3D fluid geometry, as well as the velocity profiles at the inlet (common carotid) and the outlet of internal carotid, obtained based on fully developed Womersley profiles with centerline velocities from ultrasound measurements, a computational model was developed employing a commercially available finite element package (ADINA, Watertown, MA). Blood was treated as an incompressible, Newtonian fluid and the flow was assumed laminar. The arterial wall motion was neglected considering that the plaques in diseased arteries significantly reduce strain levels. The lumen was then meshed using unstructured tetrahedral elements of edge size 0.4 mm.

Histological Processing. Histology specimens (advanced plaques) from diseased arteries were harvested from the same patients after carotid endarterectomy. Regions containing macrophage, SMC, lipid and collagen, each characteristic of the inflammatory/remodeling process, were correlated with the fluid mechanical parameters of importance, namely average wall shear stress (WSS), oscillatory shear index (OSI), and maximum wall shear stress temporal gradient (WSSTG). Stringent criteria ($p < 0.1\%$) were used to identify a correlation highly statistically significant. Correlations with $p>5\%$ were not recorded.

RESULTS AND DISCUSSION

Strong correlations existed in the vicinity of the carotid bulb, immediately downstream of the observed stenosis, although the sign of the correlation coefficient depended on the severity of the stenosis. Two patients (P1 and P2) had non-constricting (< 50%) stenoses. The results showed that the WSS (OSI) downstream of the stenosis of P1 generally exhibited strong negative (positive) correlations with presence of SMC, lipid and collagen, but no significant correlation with macrophage presence. Interestingly, P2 exhibited the opposite tendency at the same location, showing strong correlations with macrophage density but no significant correlation with the other parameters. This suggests that the inflammatory process, although at different stages in each case, is localized to downstream of the stenosis. In P3 with an 80% stenosis, the WSS at that location correlates positively with lipid, macrophage and collagen. The difference is believed to be due to the extensive re-modeling and the advanced stenosis present. No statistically significant correlations were found in P4.

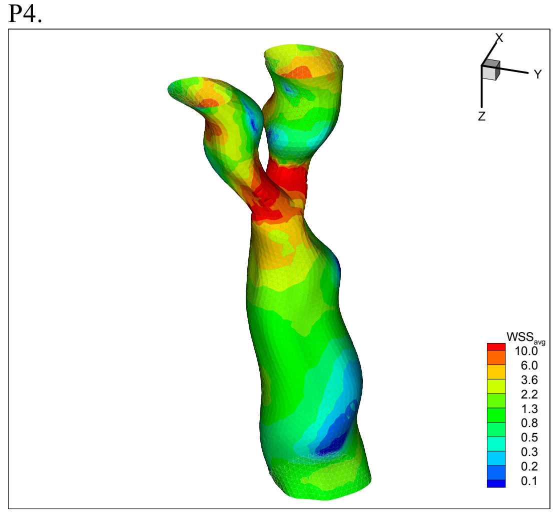

Fig. 1*: Average WSS(Pa) over the cardiac cycle in Patient P3.*

REFERENCE

Ross, R. (1999) *Atherosclerosis--an inflammatory disease*. *N Engl J Med* **340**, 115-26.

BIOMECHANICAL PROPERTIES OF ACELLULARIZED HEART VALVES AS BIOSCAFFOLDS

Toshia Fujisato[1], Seiichi Funamoto[1], Masamitsu Hasegawa[1],
Satoshi Numata[2], Kazuo Niwaya[2], Takeshi Nakatani[1], Soichiro Kitamura[2]

[1]Depertment of Surgical Research, fujisato@ri.ncvc.go.jp
[2]Depertment of Cardiovascular Surgery
National Cardiovascular Center, Suita, Osaka, Japan, www.ncvc.go.jp

INTRODUCTION

Valve homografts are superior to mechanical valves in hemodynamics, anticoagulation, and resistant to infections. However, they are still required to have more durability with potential growth and invisible immunogenicity. Tissue-engineered heart valves with autologous cells keeping intact tissue structure and biomechanical properties may provide these advantages. We are investigating efficient processes of acellalization of heart valves to have baioscaffolds made of native collagen, elastin, and basal membrane by detergents and/or other cell lysation methods. In this paper, our recent study on biomechanical properties of acellalized porcine heart valves both in vitro and in vivo was reported.

METHODS

For the in vitro study, porcine hearts were isolated and stored at 4 °C immediately. The pulmonary valves were excised and washed with Hank's balanced salt solution. The valves were then immersed in a 1% of tert-octylphenyl-polyoxyethylen (Triton® X-100) with 0.02% EDTA, 20 µg/ml of RNase A, and 0.2 mg/ml of DNase I in phosphate buffered saline (PBS) free of Ca^{2+} and Mg^{2+} (Bader A, et al, 1998). They were maintained in a 37 °C incubator equilibrated with 5% CO_2 and 95% air atmosphere under gentle shaking. After a predetermined period of time, they were rinsed with PBS and subjected to light microscopy, scanning electron microscopy, and mechanical property measurement. For the in vivo study, minipig (Nippon Institute for Biological Science) pulmonary valves were excised and acellularized as mentioned above. They were washed in PBS for 3 weeks and then replaced by minipig native valves. They were explanted 1 month after transplantation and examined histologically and mechanically.

RESULTS AND DISCUSSION

H.E. staining of porcine valves treated with Triton showed that the structure across the whole thickness of the leaflet after 6 hrs of incubation was completely cell free. However, nuclei of surrounding tissues located more than 1 mm in depth from the surface were stained even after 48 hrs of incubation. In scanning electron microscopy, gaps between endothelial cells were observed in more than 3 hrs of incubation, however residues of endothelial cells on collagen fibers were still attached even after 48 hrs of Triton treatment. The mechanical measurement showed increases in both of tensile strength and Young's modulus of the acellularized leaflets (Figure 1), however they had no bad effects on the valve replacement. This was supported from elastica-van Gieson staining which showed collagen and elastin fibers were well maintained in the bioscaffold tissue. The grafts were well functioning and their surfaces were recellularized after 1 month of transplantation. They were showed endothelial cells by the anti-vWF immunostaining (Figure 2). The leaflets transplanted had no significant changes of biomechanical properties.

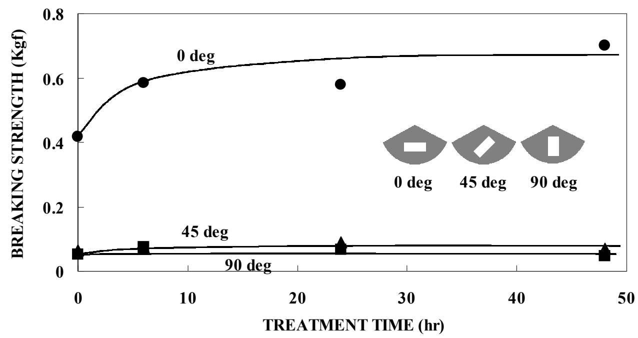

Figure 1: Breaking strength of the porcine pulmonary valve leaflets treated with 1% Triton X-100.

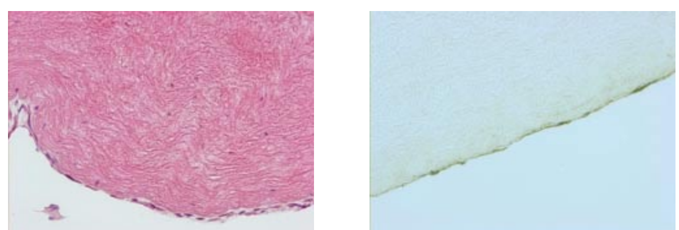

Figure 2. H.E. staining (left) and anti-vWF immunostaining (right) of the acellularized pulmonary valve tissue transplanted into minipig for 1 month.

REFERENCE

Bader A, et al (1998). *Euro J Cardio-Thorac Surg*, **14**,279-84.

ACKNOWLEDGEMENTS

This study was supported by the Research Grant from the Japanese Ministry of Health, Labour and Welfare (H12-saisei-005 and 13kou-1).

METABOLIC COST OF GENERATING HORIZONTAL FORCES DURING WALKING

Jinger S. Gottschall and Rodger Kram

Locomotion Laboratory, Department of Kinesiology and Applied Physiology
University of Colorado, Boulder, Colorado, USA
gottscha@ucsu.colorado.edu

INTRODUCTION

During steady-speed locomotion, the need to generate muscular forces creates a metabolic demand. Kram & Taylor (1990) and Farley & McMahon (1992) found proportional relationships between vertical force and the rate of oxygen consumption during running. Previously, Pugh (1971) demonstrated that generating horizontal forces to overcome an external horizontal force, such as a head wind, proportionately increases the metabolic cost of treadmill running. More recently, Chang & Kram (1999) quantified that generating propulsive horizontal forces accounts for more than one third of the metabolic cost of normal human running. The purpose of this study was to determine the metabolic cost of generating horizontal forces during normal human walking.

When comparing the peak ground reaction forces of running and walking, the peak vertical force in running is roughly two times that of walking. In contrast, the peak horizontal force in running and walking are similar. The metabolic cost of generating propulsive forces during walking has not been previously determined, and in fact there is little consensus as to which muscles are primarily responsible for propulsion (Neptune, et.al., 2001). Thus, our two aims were: to determine the portion of the metabolic cost of walking required to generate horizontal forces and to analyze the propulsive function of the ankle muscles.

METHODS

Participants (n=10) walked at 1.25 m/s normally and with either aiding or impeding applied horizontal forces (AHF), at the waist, equal to 0, 5, 10, and 15% body weight. The waist belt was connected in series with spring elements stretched over a series of low friction pulleys. We monitored the applied horizontal force via the digital readout of a force transducer. We measured net (gross - standing) rates of oxygen consumption (VO_2) and recorded ankle muscle EMG activity (anterior tibialis, medial gastrocnemius, and soleus).

RESULTS AND DISCUSSION

With an aiding AHF of +10%, VO_2 decreased by 53% $\pm$ 6.5 (mean $\pm$ SD) compared to normal walking. From these data, we infer that generating horizontal propulsive forces constitutes at least 50% of the metabolic cost of normal walking. In contrast, with an impeding AHF of -10%, VO_2 increased 150% compared to normal walking, presumably because of the extra mechanical work involved.

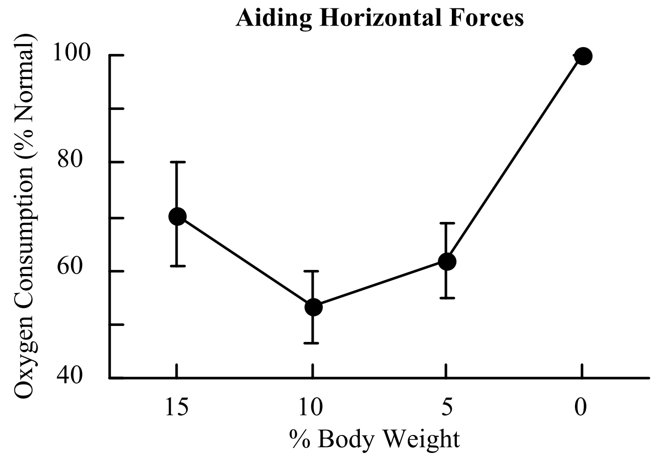

Figure 1. Rates of oxygen consumption (mean $\pm$ SD) with an aiding, applied horizontal force.

Running and walking differ substantially in terms of the fraction of energetic cost due to propulsive forces. Specifically, generating horizontal propulsive forces during running constitutes 33% of the total metabolic cost, while during walking these same forces constitute 53% of the total. Further, oxygen cost during running continued to decrease with aiding forces greater than +15%. In contrast, during walking, oxygen cost decreased to a minimum with an aiding force of +10% and increased to 70% of normal with an aiding force of +15%.

SUMMARY

By applying various amounts of aiding horizontal force, our data suggest that generating horizontal propulsive force constitutes about half of the metabolic cost of human walking.

REFERENCES

Chang, Y-H., Kram, R. (1999). *J. Appl. Physiol*, **86**,1667-1672.
Farley, C.T., McMahon, T.A. (1992). *J. Appl. Physiol,* **73**, 2709-2712.
Kram, R., Taylor, C.R. (1990). *Nature*, **346**, 265-267.
Neptune, R.R., Kautz, S.A., Zajac, F.E. (2001). *J. Biomech,* **34**, 1387-1398.
Pugh, L.G. (1971). *J. Physiol*, **213**, 255-276.

ACKNOWLEDGEMENTS

This work was supported by National Institute of Health Grant AR44688 (to R. Kram).

COMPRESSIVE BIOMECHANICS OF FRACTURE AND NEUROLOGIC INTEGRITY IN THE PEDIATRIC SPINE

David Nuckley, Suzanne Hertsted, Christopher Tainter, and Randal Ching

Applied Biomechanics Laboratory, University of Washington, Seattle, Washington, USA
Contact: dnuckley@u.washington.edu

INTRODUCTION

The majority of spinal cord injuries occur due to compressive injury mechanisms. Studies have been conducted to determine the failure tolerance for the adult cervical spine under compression [Sances, 1984; Yoganandan, 1990]. In addition, transient spinal canal integrity has been investigated to assess the potential neurologic injury tolerance associated with compressive spinal impacts [Carter, 2000]. Although these studies provide important tolerance data for the adult spine, very little data are available on the pediatric spine.

In order to develop useful safety measures for children, the biomechanical effects of maturation must be carefully studied. This experimental study measured the compressive mechanical and neuro-protective response of the cervical spine to examine age-related injury tolerance.

METHODS

Twenty-two fresh cadaveric baboon cervical spines were obtained through the Washington Regional Primate Research Center. The male specimens ranged in age from 1 to 30-human equivalent years based upon radiographic assessment of their skeletal maturity. Each specimen was dissected free of all musculature, then sectioned into two functional spinal unit segments: Occiput-C2, C3-5, and C6-T1. These were then wired and embedded in polymethylmethacrylate to ensure even load distribution. A spinal canal occlusion transducer replaced the spinal cord and dura to monitor the mid-sagittal diameter of the spinal canal [Raynak, 1998].

Compressive inputs were provided by a servohydraulic testing frame (Model 810 Bionix, MTS Corp., Eden Prairie, MN) at rates of 1.0 ±0.2-m/sec of haversine displacement to 70% strain. An inferiorly mounted six-axis load cell measured the force/moment response and the displacement was recorded using a LVDT. These data and the spinal canal mid-sagittal diameter were recorded at 40,000-Hz and filtered with a CFC 1000 (Butterworth low pass 1650-Hz cutoff) digital filter. The failure load was defined as the first reversal in the compressive load, and occlusion data were referenced to this failure event.

RESULTS AND DISCUSSION

These experiments revealed significant changes in the compressive failure load in developing spinal tissues (ANOVA $p=0.003$). The failure load increased with increasing maturity (Figure 1) and also demonstrated differences between the spinal levels tested. The C3-5 functional spinal units had larger failure loads than the Oc-C2 and C6-T1 levels. The level most susceptible to injury was the C6-T1 in adolescent and adult tissues and the upper C-spine in the very young.

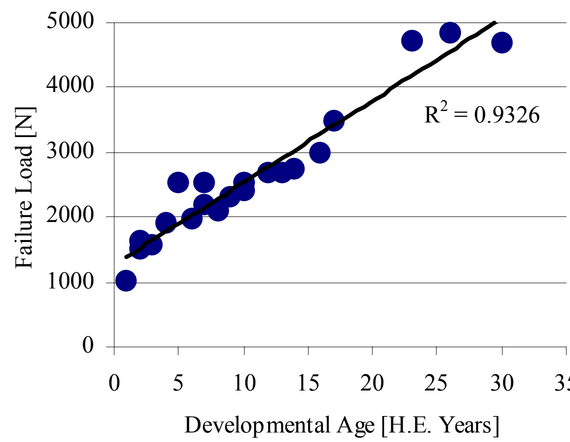

Figure 1: *Compressive Failure Load as a Function of Spinal Development. Decreased susceptibility to injury occurs with increasing maturity (2nd order polynomial).*

Concomitant with these compressive failures, the spinal canal mid-sagittal diameter was occluded by up to 90% from intact and demonstrated different occlusions for each spinal level investigated. Further, developmental differences were observed which affect the potential for spinal cord injury.

SUMMARY

Developmental processes affect the failure tolerance of individual spinal segments. These mechanical failures generate a significant potential for spinal cord injury as well as instability of the spine. The relationship between mechanical failures and the potential for spinal cord injury will be elucidated by the complete examination of this data set. Future comparison with human adult data will validate this model and support property scaling which will facilitate the use of these data. Further, size and material properties will be evaluated across maturation for their contribution to compressive tolerance. Ultimately, these data will support modeling efforts and the development of injury prevention schemes to minimized these compressive injuries to children.

REFERENCES

Carter, JW, et al. (2000) *Spine*, **25**, 46-54.
Raynak, GC, et al. (1998) *J. Biomech Eng*, **120**, 787-91.
Sances Jr., A, et al. (1984) *Crit Rev Biomed Eng,* **11**, 1-76.
Yoganandan, N, et al. (1990) *Spine*, **15**,1031-9.

ACKNOWLEDGEMENT

National Center for Injury Prevention and Control, CDC.

EFFECT OF REDUCED RANGE OF MOTION ON THE ACCURACY OF THE FUNCTIONAL METHOD OF HIP JOINT CENTER LOCATION

Stephen J. Piazza[1,2,3,4], Nori Okita[8], Ahmet Erdemir[1,2], and Peter R. Cavanagh[1,2,4,5,6,7]

[1]Center for Locomotion Studies and [2]Departments of Kinesiology, [3]Mechanical Engineering, [4]Orthopaedics and Rehabilitation, [5]Bioengineering, [6]Biobehavioral Health, and [7]Medicine, The Pennsylvania State University, Univ. Park, PA and Hershey, PA, USA
[8]Balance Disorders Laboratory, Neurological Sciences Institute, Oregon Health & Science University, Beaverton, OR, USA
e-mail: *steve-piazza@psu.edu* www: *http://www.celos.psu.edu*

INTRODUCTION

Motion analysis often requires a determination of the location of the hip joint center (HJC). Errors in HJC location that are as small as 3 cm may lead to substantial inaccuracies in inverse-dynamic hip joint moment calculations (Stagni et al., 2000). Cappozzo (1984) described a functional method for HJC location in which the center of rotation between thigh and pelvis is determined from the segments' relative motion. This method may, however, be susceptible to errors when the range of motion (ROM) is limited, though this was not found to be the case in a mechanical linkage (Piazza et al, 2001). The purpose of the present study was to assess the accuracy of HJC location performed using special motion trials in which the hip ROM in healthy subjects was limited and to investigate whether the HJC could be determined from data collected during four common activities.

METHODS

Twenty-two healthy female volunteers participated in the study. Twelve of these were young adults (21-29 y) and 10 were elderly (70-78 y). A Vicon 370 motion analysis system (Oxford Metrics) recorded the locations of pelvis- and thigh-fixed markers as the subjects descended stairs (SD), ascended stairs (SA), rose from a seated position to standing (STS), walked overground (OGW), and performed a special hip motion sequence that incorporated flexion, extension, abduction, and circumduction.

The HJC was determined by finding the points in the pelvis and thigh frames that were separated by the smallest distance as determined in a least-squares sense. A preliminary analysis of the separation between the pelvis- and thigh-fixed HJCs suggested that the average HJC location error found using the hip motion trial was at most 18 mm, consistent with previous reports (Leardini et al., 1999). The HJC determined using this trial was used to evaluate additional errors resulting from flexion-extension (FE) or ab/adduction (AA) ROM in the special hip motion trial being reduced by half (or both being reduced) and from data collected as subjects performed the various activities. ROM reductions were achieved by omitting data frames for which certain hip angles were exceeded. Two-way ANOVA and subsequent corrected pairwise mean comparisons were performed to test for differences in HJC location error and frontal- and sagittal-plane ROM that were related to age (two levels: young and elderly) and type of trial used to determine the HJC (seven levels: FE, AA, FE and AA, SD, SA, STS, and OGW).

RESULTS AND DISCUSSION

No age-related differences were found in HJC location error or ROM, suggesting that the functional method performs equally well for young and healthy elderly subjects. Hip centers calculated from special hip motion trials in which the ROM was artificially reduced were significantly more accurate than those calculated from data collected during the activities (all $p < 0.001$) (Fig. 1). Except for one case, there were no differences within ROM limitations or activities.

These results suggest that the functional method has the potential to be reasonably accurate (within 2.5 cm worst case) and comparable to that found for regression methods (Leardini et al., 1999) even when hip ROM is limited. Use of the various activity trials, however, resulted in HJC location errors that were unacceptably large (greater than 5 cm worst case), suggesting that special motion trials are indeed required for accurate functional HJC determination.

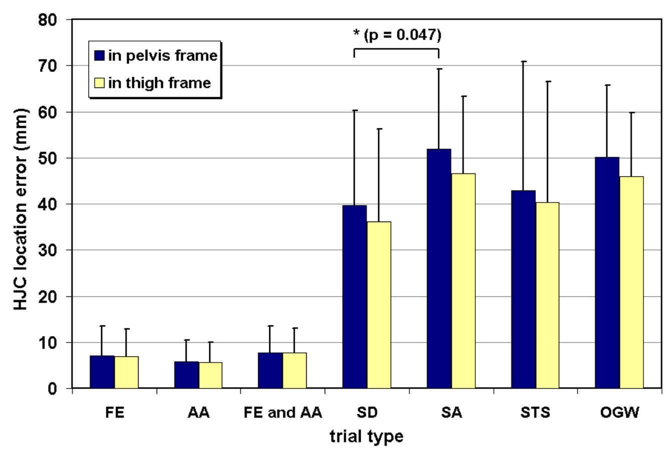

Fig. 1: HJC location errors resulting from different motion trials being used in the least-squares optimization (mean, sd of all subjects). See text for a listing of motion trial types.

REFERENCES

Cappozzo, A (1984) *Hum. Mov. Sci.*, **3**, 27-50.
Leardini, A et al. (1999) *J. Biomech.*, 32, 99-103.
Piazza, SJ et al (2001) *J. Biomech*, 34, 967-973.
Stagni, R et al. (2000) *J. Biomech.*, 33, 1479-1487.

ACKNOWLEDGMENTS

The authors wish to thank Sicco Bus, MS.

AGE-RELATED EFFECTS ON MOMENTUM GENERATION AND MUSCLE ACTIVITY DURING GAIT-INITIATION

Carrie Laughton,[1] Mary Slavin,[2] Denise Gravelle,[1] Lew Lipsitz,[3] and Jim Collins[1,4]

http://cbd.bu.edu/abl/
[1]Center for Biodynamics and Department of Biomedical Engineering, Boston University, Boston, MA, USA
[2]Sargent College of Health at Boston University, Boston, MA, USA
[3]Hebrew Rehabilitation Center for Aged, Beth Israel Deaconess Medical Center, and Harvard Medical School, Boston, MA, USA
[4]Department of Physical Medicine and Rehabilitation, Harvard Medical School, Boston, MA, USA

INTRODUCTION
Older adults utilize different strategies to develop forward momentum during gait-initiation compared to young adults (Polcyn et al., 1998; McGibbon and Krebs, 2001). This may put older adults at increased risk for falling. The aim of this study was to assess whether older adults who have had a history of unexplained falls demonstrate impaired gait-initiation dynamics compared to healthy older adults.

METHODS
Sixty-three ambulatory community-dwelling older adults and fifteen young adults (7 male, 8 female; mean age 27±3yr) volunteered for this study. Thirty-one of the older adults had a history of two or more unexplained falls in the previous year and were classified as fallers (6 male, 25 female; mean age 75±7yr). Thirty-two of the older adults did not have a history of falls and were classified as non-fallers (11 male, 21 female; mean age 76±5yr). Informed consent was obtained from all participants prior to participation. Electromyographic (EMG) data were collected from the tibialis anterior (TA) and soleus (SO) bilaterally. The subject stood on a force plate in a comfortable stance and initiated gait upon hearing an auditory cue. Five gait-initiation trials were collected at three self-selected speeds: slow, normal, and fast. Force-plate and EMG data were sampled at 1500Hz. Momentum was computed by integrating the ground reaction force in the anteroposterior (AP) direction and normalized to subject lower limb length and body mass. The integral of the AP center of pressure (COP) displacement normalized to leg length was regressed against the forward momentum to provide information on gait-initiation dynamics.

RESULTS AND DISCUSSION
Normally, a muscle activation pattern of SO inhibition followed by TA activation occurs during effective gait initiation (Crenna and Frigo, 1991). Elderly fallers and elderly non-fallers demonstrated similar frequency of use of this pattern (42±39% and 39±37% of the trials, respectively). Compared to the young subjects, the elderly subjects demonstrated the SO inhibition TA activation pattern less frequently (41±38% and 82±29% of the trials, respectively) and had greater tibialis anterior activation prior to toe off. On average, similar amounts of forward momentum generation were found between the elderly fallers and elderly non-fallers (0.55±0.17 sec^{-1} and 0.57±0.16 sec^{-1} respectively). However, when a subset of the older subjects were classified according to performance on the Dynamic Gait Index (Shumway-Cook and Wollacott, 1995), those demonstrating clinical impairments also demonstrated a decreased slope for the COP displacement versus momentum profile. This finding indicates that in the gait impaired, less momentum is developed for each incremental change in COP displacement (Fig.1). Furthermore, compared to the young, the elderly also demonstrated a decreased slope for the COP displacement versus momentum profile.

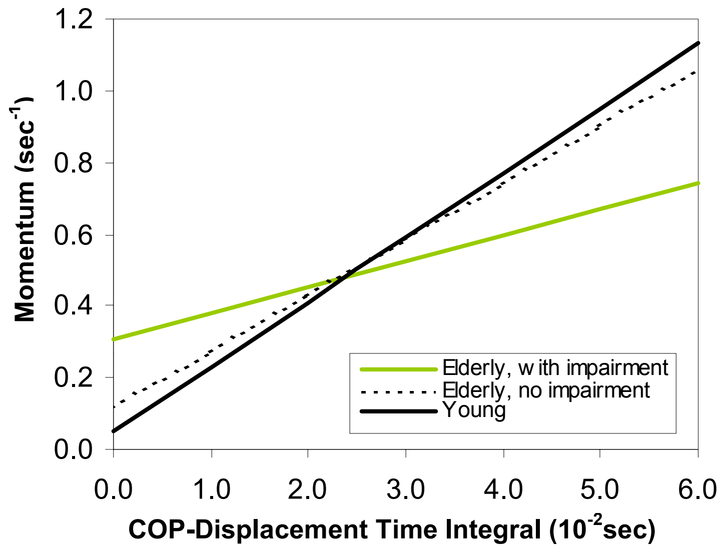

Figure 1. Clinical gait status and age-related changes in functioning of the gait-initiation motor program: group mean regression lines computed for forward momentum versus AP COP displacement time integral. Elderly, with impairment: R=0.68, Elderly, no impairment: R=0.95, Young: R=0.97.

SUMMARY
Grouping individuals by fall status did not discern differences in gait-initiation dynamics between elderly fallers and non-fallers; however, grouping by clinical gait impairment did. A decrement in the gait-initiation motor program and increases in muscle activity levels were found in the elderly subjects compared to the young subjects. This may be due age-related decrements in muscle strength and increased ankle stiffness due to co-activation of antagonistic muscles at the ankle.

REFERENCES
Polcyn, P.A., et al. (1998) *Arch Phys Med Rehabil*, **79**, 1582-1589.
McGibbon, C.A., Krebs, D.E. (2001) J Neurophysiol, **85**, 1923-1931.
Crenna, P., Frigo, C. (1991) *J Physiol*, **437**, 635-653.
Shumway-Cook, A., Wollacott, M.H. (1995) *Motor Control: Theory and Practical Applications.* Williams & Wilkins.

ACKNOWLEDGEMENTS
This research was funded by NIA Grants #PO1 AGO4390 and #AG08812.

SHEAR STRESS STIMULATES OXIDANT PRODUCTION IN HUMAN CARTILAGE EXPLANTS

James Martin and Anneliese Heiner
Department of Orthopaedic Surgery, University of Iowa, Iowa City, IA, USA
james-martin@uiowa.edu

INTRODUCTION

Cartilage is sensitive to damage caused by reactive oxygen species (ROS). ROS degrade the cartilage matrix, suppress matrix synthesis, and can cause sufficient damage to chondrocytes to provoke cell cycle arrest (senescence) or apoptosis (Tiku et al., 1999; Michel et al., 1992). Chondrocytes can generate high local ROS concentrations, and ROS production is induced by some forms of mechanical stress, suggesting that oxidative damage mediates some of the adverse effects attributed to excessive mechanical loading *in vivo*. However, these findings are based on *in vitro* studies which used stress conditions (unconfined axial compression or fluid shear) unlike those experienced by cartilage *in vivo* (Das et al., 1997; Fermor et al., 2001).

We have developed a cartilage culture device – a triaxial compression vessel – capable of recreating lifelike stress conditions. The device modulates matrix deformation, fluid flow, and hydrostatic stresses by simultaneously and independently controlling both axial compression and transverse compression (Fig. 1). Previous studies have shown that cartilage matrix synthesis is suppressed by high shear stress (Heiner & Martin, 2001). We hypothesized that the suppressive effect of high shear stress on matrix synthesis was mediated by ROS release.

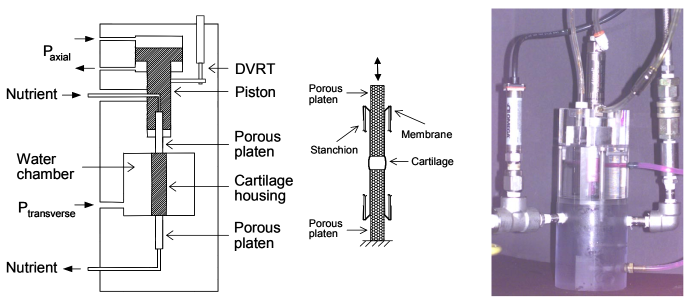

a) b)

Figure 1: a) Schematic (insert = cartilage housing) and b) physical appearance of triaxial compression vessel.

METHODS

Human cartilage explants (4 mm diameter cylinders) were harvested from a normal ankle joint and cultured in a 5% O_2 atmosphere to minimize oxidation. Dihydroethidium (DHEt) (a probe that fluoresces when oxidized) was added to the culture medium before stress treatment. Explants were randomly assigned to high shear stress (n=4) or low shear stress groups (n=4). Two explants from each group were also treated with n-acetyl cysteine (NAC), a potent antioxidant. After exposure to high shear stress (2 MPa axial compression) or low shear stress (2 MPa axial compression + 2 MPa transverse compression) for 15 minutes at 1.0 Hz, the explants were prepared immediately for cryosectioning. Ten µm-thick sections were examined using epi-fluorescent optics. Six images were recorded for each explant and analyzed using NIH Image (Martin et al., 2002). Statistical analysis was performed using repeated measures analysis of variance on ranks with Dunn's method for multiple comparisons (α=0.05).

RESULTS

DHEt fluorescence was significantly increased by high shear stress versus low shear stress, and was significantly decreased by NAC treatment under both stress conditions (Figs. 2, 3).

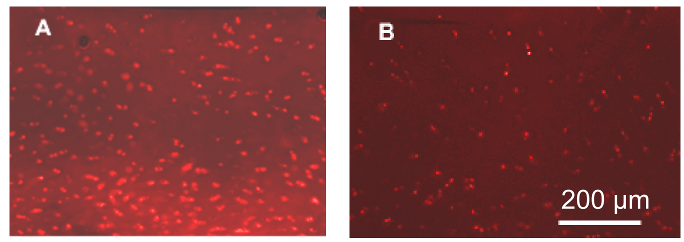

Figure 2: Micrographs showing DHEt oxidation (bright spots) after axial stress (A), and after axial + transverse stress (B).

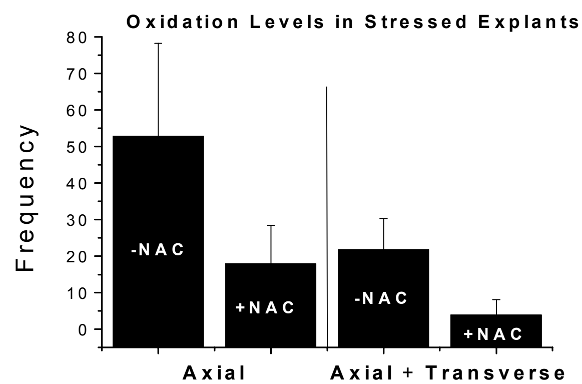

Figure 3: Mean frequency of fluorescent cells in six 0.04 mm^2 fields after axial stress or axial + transverse stress (-/+NAC).

DISCUSSION

High shear stress stimulated significantly higher oxidation levels than did low shear stress, and anti-oxidants blocked this effect. These data indicate that ROS are produced by chondrocytes in response to shear stresses which are closer to physiologic conditions than those used by other investigators.

REFERENCES

Das et al. (1997). *J Orthop Res,* **15(1)**, 87-93.
Fermor et al. (2001). *J Orthop Res,* **19**, 729-737.
Heiner & Martin (2001). *4th Comb Orthop Res Soc* #141.
Martin et al. (2002). *Osteoarthritis Cartilage,* submitted.
Michel et al. (1992). *Free Radic Res Commun,* **17**, 279-289.
Tiku et al. (1999). *Free Radic Res,* **30**, 395-405.

COLLISION LOSSES DURING BRACHIATION: WHY GIBBONS HAVE LONG ARMS

James Usherwood and John Bertram
Food, Nutrition and Exercise Sciences, Florida State University, Tallahassee, Florida, 32306.
jbertram@garnet.acns.fsu.edu

INTRODUCTION

Gibbons are able to brachiate effectively through complex environments: impressive acceleration, maneuverability and climbing are possible with support only from arms. Mistakes, however, do occur (Schultz, 1944), and are likely to be costly. Energetic costs of brachiation appear to be dominated by inelastic collisions at contact with a new handhold, analogous to the 'jerk' felt by a child falling on a swing after the chain has become loose. Minimizing energetic costs, while avoiding falling, may provide constraints on the paths available to a brachiator, and could explain some of the observed details of brachiation.

METHODS

A simple point-mass model of brachiation (following Bertram et al., 1999), with a pendular swinging phase and a ballistic flight phase, was developed, and programmed in LabVIEW 5.0. Controlled variables were: length from hand to center of mass, energy of the mass at the bottom of the first swing, and hand-hold spacing. Potential flight paths were then derived given a range of release angles, and the enegetic consequences of inelastic collision at contact of the 2nd hand-hold calculated.

Modeled kinematics were compared with video (100Hz after de-interlacing) of gibbons brachiating at a range of speeds and handhold spacing. Observed flight-paths and behaviours were assessed within an energetic context.

RESULTS AND DISCUSSION

Despite an infinite number of potential flight paths for a given initial kinetic energy, there is only a limited range of paths that minimize energetic loss due to collision. The energetic cost of missing an 'ideal' path may be considerable, and depends both on the collision geometry and the kinetic energy at collision; even a total loss of kinetic energy, due to a velocity parallel to the arm at contact, may be negligible if the body is high and slow, and potential energy dominates.

Observed kinematics of gibbons show that the theoretical zero-collision-loss paths are often missed. If the power requirements of gibbon locomotion are dominated by collision losses, this observation suggests that something limits the exploitation of no-loss paths. Adaptive paths may show a compromise between modest losses for overshooting a handhold, and the substantial costs for undershooting, missing the handhold, and falling.

Long arms and the use of a 'double pendulum' mechanism allow gibbons to reduce the energetic cost of collision (Fig.1): longer arms L improve the geometry of collision for a given 'overshoot' e, while the double pendulum allows some of the energy that would have been lost in collision to be transferred to kinetic energy of rotation about the shoulder joint (supported by Bertram et al., 2001).

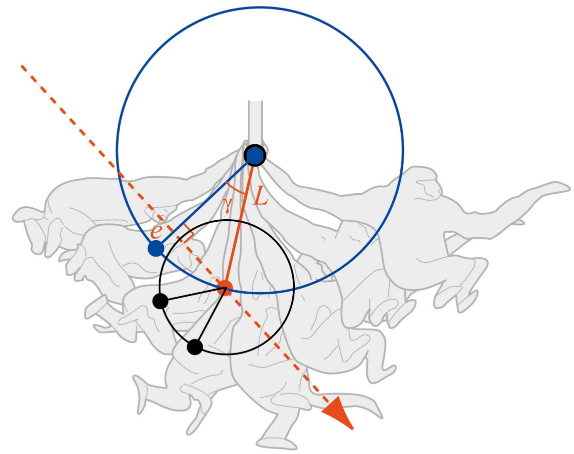

Figure 1: Gibbon during contact at a handhold while brachiating at speed. Tension occurs well after initial contact, and may show the compromise between the energetic costs of collision, and the consequences of falling. The 'Double pendulum' rotation of the hips about the shoulder (small circle) may reduce the cost of 'overshooting' the no-loss arc (dotted line through large circle).

SUMMARY

Many aspects of gibbon brachiation, including the use of long arms and a 'double pendulum' mechanism, are understandable within a context of minimizing energy losses due to collision, while avoiding the potentially lethal costs of missing a handhold.

REFERENCES

Bertram, J.E.A and Chang, Y.-H. (2001). *Am. J. Phys. Anthropol.* **115**, 319-326.
Bertram, J.E.A., Ruina, A., Cannon, C.E., Young Hi, C. and Coleman, M.J. (1999). *J. Exp. Biol.* **202**, 2609-2617.
Schultz, A.H. (1944). *Am. J. Phys. Anthropol.* **2**, 1-129.

ABSOLUTE HEEL SENSITIVITY IS NOT RELATED TO THE DISCRIMINATION OF INITIAL IMPACT LOADS TYPICAL OF HEEL-TOE RUNNING

Ben L. Patritti[1], Mark J. Lake[1] and Carine van Schie[2]

[1]Research Institute for Sport and Exercise Sciences, Liverpool John Moores University, UK, www.livjm.ac.uk
[2]Diabetes Foot Clinic, Disablement Services Centre, Withington Hospital, Manchester, UK.

INTRODUCTION

The cutaneous receptors of the footsole provide a source of sensory feedback to the body during the ground contact phase of locomotion. Sensitivity of the plantar surface of the heel has been quantified using absolute thresholds (ATs) to perceptible vibration and pressure stimuli (e.g. Nurse and Nigg, 1999). The foot is continually loaded during daily activities at levels substantially above ATs of mechanical stimuli and, as such, AT measurements may not provide a useful indication of our ability to discern much higher locomotor type loads. This sensory faculty can be characterised by difference thresholds (DTs) of the mechanical inputs and is likely to have a greater functional significance to the modification of loads and movement patterns during locomotion. Individual differences of ATs of the footsole (Nurse et al., 1998) and DTs of mechanical inputs of impact loads typical of locomotion (Patritti et al., 2001) have been observed, but it remains unclear whether differences in normal ATs of the foot partly explain differences in impact DTs. Therefore, the aim was to determine whether ATs of the heel for pressure and vibration stimuli bore a relationship to DTs of mechanical inputs of impact loads to the heel.

METHODS

A group of 22 male subjects experienced controlled barefoot impacts onto a range of 9 EVA mats of different density using a human pendulum. Impact severity was characterised by external impact force and shock to the shank measured by a wall mounted force platform and skin mounted accelerometer, respectively. The perceived impact severity of each condition was rated against a central standard using a 2 alternative forced choice (2AFC) paradigm for 20 presentations each in a mixed order. DTs of the mechanical inputs were determined from cumulative normal distribution curves fitted to the psychometric data. Pressure ATs were determined using a set of 10 Semmes-Weinstein monofilaments and a 2AFC protocol. Vibration ATs were determined using 3 devices: a CASE IV using a 4, 2, 1 stepping algorithm, a Neurothesiometer using a method of limits protocol, and a Vibratron II using a 2AFC protocol. All stimuli were applied to the centre of the heel pad. Relationships between ATs and DTs were evaluated using Pearson moment correlation coefficients.

RESULTS AND DISCUSSION

Large differences in both ATs and DTs were observed between individuals (Figure 1), with individuals most sensitive to changes in the rates of loading (ROL) of the mechanical inputs of impact (Patritti et al., 2001). All correlations between ATs and DTs of the ROLs were non-significant (Table 1) suggesting absolute heel sensitivity does not substantially contribute to the discrimination of impact severity in a normal population.

Table 1: Pearson correlation coefficients between pressure and vibration ATs and DTs of the mechanical input ROLs.

AT Test	Force DT	Shock DT
Vibratron II	0.19 (Fig. 1)	0.19
Neurothesiometer	0.33	0.36
Case IV	0.27	0.15
Monofilaments	0.09	0.02

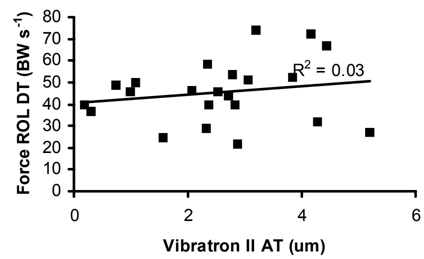

Figure 1: Typical scatterplot of vibration AT of the heel and force ROL DT for heel impacts.

This lack of association between ATs of heel sensitivity and DTs of impact indicates that ATs may not be appropriate in characterising the sensory capabilities of the foot to loads typical of locomotion. The poorer sensitivity of the heel to tactile pressure and vibration relative to other sites on the plantar surface and body (Cavanagh, 1999; Nurse and Nigg, 1999) may help to explain the present findings. Cavanagh (1999) suggested that the elevated thresholds of the foot may reflect the setting of the sensitivity of the cutaneous receptors to a higher level as a function of the residual loading experienced almost always during daily activities. Further work investigating DTs of mechanical stimuli during actual locomotion may lend support to this speculation.

REFERENCES

Cavanagh, P. R. (1999). *Proc. of ISB'99*, 18.
Nurse, M. A. et al. (1998). *Proc. of NACOB'98*, 145-146.
Nurse, M. A. and Nigg, B. M. (1999). *Clinical Biomechanics*, **14**, 667-672.
Patritti, B. L. et al. (2001). *Proc. of 5th ISB Footwear Symposium*, 68-69.

ACKNOWLEDGEMENTS

This work was supported by an ORS Award.

COMPUTATIONAL MODELING OF FLOW AND MASS TRANSPORT IN A MICROFABRICATED ARRAY BIOREACTOR FOR PERFUSED 3-D LIVER CULTURE

M.R. Kaazempur-Mofrad,[1,2] A. Sivaraman,[1,3] A. Upadhyaya,[1,2] K. Domansky,[1,3] M.J. Powers,[1,3] R.D. Kamm,[1,2] and L.G. Griffith[1,3]
[1]Division of Bioengineering & Environmental Health,
[2]Department of Mechanical Engineering, [3]Department of Chemical Engineering,
Massachusetts Institute of Technology, Cambridge, MA

INTRODUCTION

Under standard *in vitro* cell culture conditions, hepatocytes rapidly lose their liver-specific metabolic and biosynthetic phenotype. This has led to development of a variety of culture techniques, none of which, however, yet replicates a comprehensive environment for the important functions of liver. The overall goal of this work is to develop a 3-D perfusion culture, providing a suitable scaffold for tissue morphogenesis and a homogeneous distribution of flow and mass transfer to meet the metabolic demands of the cells. Detailed analysis of the fluid flow and transport patterns in the reactor is required in order to ensure that the cells enjoy metabolically sufficient oxygenation and physiologically relevant shear stresses.

MATERIALS AND METHODS

Reactor Design. A cross-flow perfusion reactor that addresses these constraints was designed and fabricated, as described in Powers et al. (2002). At the heart of the reactor is the cell scaffold, comprised of a thin (<250 mm) silicon sheet permeated by a regular array of channels and seated atop a microporous filter. The scaffold is maintained between the upper and lower chambers of a flow-through housing. The functional unit of the bioreactor system is an individual channel, attempting to mimic a single capillary bed as the functional unit of liver. The current design allows repeated *in situ* observation of cells via light or 2-photon microscopy during culture of the 3D perfused tissue structures. Further description of the design and the corresponding morphological behavior of primary hepatocytes maintained under perfusion is given in Powers *et al.,* 2002.

Computational Model for Fluid Flow. A computational fluid dynamic (CFD) model was developed to estimate shear stress magnitudes the cells experience under the influence of bulk flow at the surface of the chip and perfusion flow in the micro-channels. The CFD model involved a finite element solution of the full 3-D Navier-Stokes equations using commercial software (ADINA, Watertown, MA). The Reynolds number, based on the width of the upper chamber and the diameter of the tissue flow-channels, respectively, was of order one in the interior of the upper chamber and of order 0.1 within the scaffold micro-channels for finite cross-flow. Boundary conditions for the micro-channel regions in the scaffold were set to reflect the extremes of either zero cross flow rate or experimental values of cross-flow with open channels.

RESULTS

Shear stress in the region near the center of the scaffold is approximately 0.01-0.02 Pa and that near the sidewalls of the reactor is about 0.005-0.01 Pa. The cells in channels closest to the inlet and outlet ports experience shear stresses of about 0.02--0.035Pa, the maximum observed. Shear stress distributions at the chip surface for the extreme case where cells have completely plugged channels were not significantly different in value and had no additional features. Various perfusion flow rates were examined, and the corresponding hepatic function was correlated to the computationally determined values of maximum shear stress on the hepatocyes. The results were suggestive of 0.1Pa as the maximum shear stress under which hepatocytes maintain their physiologic phenotype. The effects of fluid flow inside single tissue-filled microchannels within the silicon scaffold were investigated by defining the channel cross-sectional geometries to reflect the representative geometries of void spaces within the tissue structures observed experimentally. One characteristic model geometry of the flow path was a cylinder of ~100μm diameter. Fluid dynamic forces in the reactor were not sufficient to cause flow induced deformation of the tissue, and thus the surface was assumed to be rigid with no slip between the fluid and tissue. Flow fields were studied inside a single channel, where tissue ringed the channel leaving a 100μm diameter cylindrical void at the center of the scaffold. The shear stresses at the walls were about 0.07 Pa.

Analytical and computational analysis was performed to ensure that the hepatocytes receive sufficient oxygen for metabolic purposes, even under the most stringent conditions of no perfusion, i.e. in case where all nutrient transport into the channels is via diffusion from fluid in the upper and lower chambers.

SUMMARY

Initial characterization of the present 3-D perfused bioreactor for liver tissue culture proves that this system approximates the perfusion conditions present in vivo, ensuring a physiologically relevant environment for hepatic tissue.

Fig. 1: *Wall shear stresses (in [Pa]) at the chip surface.*

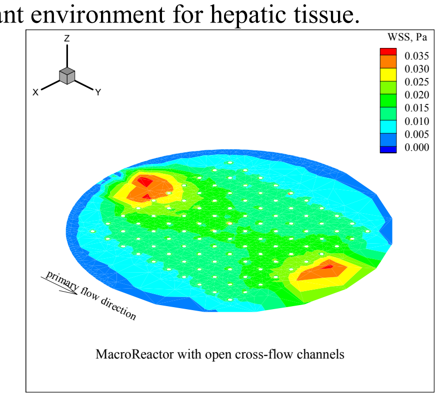

REFERENCE

Powers MJ *et al. A Micofabricated Array Bioreactor for Perfused 3D Liver Culture. Biotech. & Bioeng*. (In press).

QUANTIFYING THE CONTRIBUTION OF INDIVIDUAL MUSCLES TO LUMBAR SPINE STABILITY

Natasa S. Kavcic, Stuart M. McGill
Occupational Biomechanics Laboratory, University of Waterloo, Waterloo, Ontario, Canada
Contact: nkavcic@ahsmail.uwaterloo.ca

INTRODUCTION

Clinically, stabilization exercises are thought to train muscle patterns that ensure spine stability. Co-activation of the global muscles increases the compressive loads on the spine, which has motivated some (for example Richardson and Jull,1995) to suggest that global muscle activity should be minimized during exertion tasks. However, Granata and Marras (2000) believe the benefit to stability from global co-activation overrides the compressive loading costs. Presently, insufficient research exists which quantifies the integrated roles of both the local and global muscles in stabilizing the spine under different loading conditions. The purpose of this research is to identify which torso muscles stabilize the spine during different loading conditions imposed by different stabilization exercises.

METHODS

The stabilization exercises measured in this study are four-point-kneeling with a leg lift, back bridging, side bridging and sitting on a gym ball. Each stabilization exercise was performed statically for a period of 2 seconds. Spine kinematics and 14 channels of torso EMG were recorded. Reaction forces were measured from the upper body segments that were in contact with the ground.

Data was input into a stability model of an in vivo lumbar spine described by Cholewicki and McGill (1996). In order to determine the stabilizing potential of each single torso muscle, the EMG signal for the muscle of interest in the control trial, was replaced bilaterally by a sinusoid with a cycle duration extending over the entire trial, and an amplitude from 0 to 100% MVC. For these experimental trials, all other input measures were kept constant. The maximum change of the stability index occurring in the experimental trial (E) was expressed as a percentage of the maximum change in the control trial (C).

$$\%change = \left(\frac{E - C}{C}\right) \times 100$$

RESULTS AND DISCUSSION

The muscles that produced the greatest changes in the stability index were dependent on the exercise tested and in turn, the loading applied to the spine. As well, the magnitude of the change in the stability index varied across exercises (Table 1).

In a task requiring minimal muscle activity, such as the sitting trial, the multifidus had a 9-fold effect over the next major contributor. In contrast, in a more demanding task, such as the four-point-kneeling exercise, the internal oblique was the major contributor to stability with an almost 2-fold effect over the next important muscle, being quadratus lumborum. Clearly, when a variety of tasks are quantified, the relative importance of each stabilizing muscle is dependent on the total level of spine stability created while performing the exercise. For the ball trial the stability index is much lower that that of the other trials, therefore, a single stabilizer muscle has a larger effect on the total stability of the spine.

The idea that different torso muscles function as stabilizers depending on the loading condition has not been shown in previous research. Quint et al (1998) showed that both the psoas and multifidus stiffen the spine during different bending moments, however as with many in vitro studies, only a few muscles were modeled and as a result the interplay of the all the torso muscles were unable to be assessed.

Table 1: The percent difference between the maximum change in the control trial (C) versus the maximum change in the experimental trial (E). The last column is the stability index for the C trial.

	FPN	Bridge	Side Bridge	Sitting
Rectus Abdominis	119.38	176.51	141.45	222.10
External Oblique	1396.12	3184.31	835.55	0.00
Internal Oblique	2624.81	2122.67	642.74	7367.98
Latissumus Dorsi	345.74	764.76	166.30	793.09
Pars Lumb.	431.01	281.90	590.90	16551.10
Iliocostalis Lumb.	353.49	0.00	1313.41	33793.09
Longissimus Thor.	146.12	173.33	1127.68	24912.43
Quadratus Lumb.	1562.79	1205.71	1074.91	12886.74
Multifidus	314.73	41.90	1325.22	281553.31
Stability Index	6.28E-08	3.65E-06	6.88E+00	6.34E-16

SUMMARY

Clinical recommendations to focus on a single muscle to ensure a stable spine is not justified by the data presented here. Depending on the loading condition imposed on the spine, an understanding of the interplay between both the local and global muscles is necessary to reduce the risk of instability. Training neuromuscular patterns for sufficient stability should focus on loading the spine to involve all muscles that coordinate their roles to ensure a stable spine.

REFERENCES

Richardson, Jull. (1995). *Man Ther.,* **1**, 2-10.
Cholewicki, McGill. (1996). *Clin Biomech*.,**11(1)**, 1-15.
Quint et al (1998). *Spine*, **23(18)**, 1937-1945
Granata, Marras (2000). *Spine*, **25 (11),** 1398-1404.

KNEE JOINT KINEMATICS AND KINETICS IN PATIENTS WITH MODERATE OSTEOARTHRITIS

K.J. Deluzio[1], C.S.N Landry[1], J.J. Chu[2], C.L. Hubley-Kozey[3], J.W Kozey[1], G.E. Caldwell[2], W.D. Stanish[4]

[1]School of Biomedical Engineering, Dalhousie University, Halifax, Canada, kevin.deluzio@dal.ca
[2]Dept. of Exercise Science, University of Massachusetts. Amherst, USA.
[3]School of Physiotherapy, Dalhousie University, Halifax, Canada
[4]Dept. of Surgery, Dalhousie University, Halifax, Canada

INTRODUCTION

The pathomechanics of knee osteoarthritis (OA) are not well understood, nor are the causes for it to progress more rapidly in some individuals than others. Modern gait analysis offers a unique means to measure the biomechanical response to diseases of the musculoskeletal system during activities of daily living. Identifying the mechanical factors of gait associated with knee OA is important in understanding the initiation and progression of OA as well as in planning therapeutic interventions.

The objective of this on-going study is to quantify the knee joint kinematics, kinetics and neuromuscular function of a group of patients with moderate knee OA. This report will focus on the kinematics and kinetics aspects of the study.

MATERIALS AND METHODS

We collected 3-D motion, ground reaction force, and electromyographic data from 7 normal subjects and 5 subjects with moderate knee OA. The moderate OA group was selected from the waiting list for arthroscopies at a local sports medicine clinic. The normal subjects were recruited from the general population and were asymptomatic, without evidence or history of arthritic disease or record of surgery to the lower limbs. Subjects performed, in random order, five trials of their normal selected speed, and a fast walk (150% of the normal speed). A computer timer during the test trials monitored both. All subjects gave their informed consent to this protocol, which passed our internal ethics review board.

Three-dimensional motion and force data were used to calculate three dimensional joint angles, moments and forces. The joint angle waveform data was analysed using principal component analysis (PCA) as described in Deluzio et al. (1997). In this approach each kinematic and kinetic time series for each subject was transformed into a set of three principal component (PC) scores that correspond to the major features of that waveform.

RESULTS

All subjects were within 6.2% of their normal velocity and 7.5% of the 150% condition. There were no differences in stride characteristics (walking speeds, stride lengths, or stride times) between the two groups (Table 1).

The moderate OA patients walked with normal knee joint kinematic patterns. This was determined by comparing the moderate OA gait data both to the control group, and to historical data of 60 normal subjects. There were no differences in knee angle patterns between the moderate OA group and the control group at either of the walking speeds ($p > 0.6$).

In contrast, we found differences in knee joint kinetics between the moderate OA subjects and the normal control subjects. The magnitude of the adduction moment during stance (PC1) was larger for the moderate OA patients at both walking speeds ($p<0.05$). The PCA identified differences in the pattern of the flexion moment, but only at the higher walking speed ($p<0.05$). This difference was found in the second principal component (PC2), which measured the overall amplitude of the flexion moment waveform (the biphasic shape) (Figure 1).

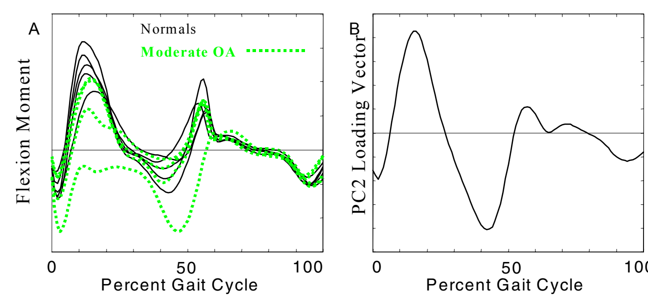

Figure 1. The flexion moment data (A), PC2 loading vector (B)

DISCUSSION AND CONCLUSION

The moderate OA patients walked with a visibly normal gait as measured by stride characteristics and joint angles. However, differences were detected in the joint kinetics, particularly at the higher walking speed. Gait analysis can provide insight into the mechanical factors of knee osteoarthritis (OA) by quantifying the dynamic loading and alignment of the knee during activities of daily living. The PCA technique was able to extract features of gait waveform data that have high discriminatory power.

REFERENCES

Deluzio,K.J.; et al. (1997) *J. of Hum. Mov. Sc.* 16: 201-217.

Table 1 Mean (SD) stride characteristics between groups for the normal walking speed condition and the fast walking speed condition (150% of normal walking speed). No significant differences ($p>0.05$) were found between groups.

	Walking Speed (m/s)		Stride Length (M)		Stride Time (s)	
Speed Condition	Normal	Fast	Normal	Fast	Normal	Fast
Normal	1.42 (0.20)	2.01 (0.17)	1.50 (0.17)	1.78 (0.14)	1.1 (0.08)	0.9 (0.06)
OA	1.41 (0.19)	1.99 (0.22)	1.53 (0.20)	1.81 (0.28)	1.1 (0.09)	0.9 (0.10)
P-value	0.9	0.7	0.6	0.6	0.22	0.3

KINEMATIC MEASUREMENTS OF SNOWBOARDERS' ANKLES

Sebastien Delorme[1,2], Mario Lamontagne[2,3] and Stavros Tavoularis[2]

University of Ottawa, Ottawa, Ontario, Canada
[1] sdelo005@uottawa.ca, [2] Dept. of Mechanical Engineering, [3] School of Human Kinetics

INTRODUCTION

In 1989, there were 1.5 million snowboarders worldwide, 40% of which were in North America. In 2001, it was estimated that Snowboarders made up to 28.5% of those using the slopes. The incidence of trauma from snowboarding is 4 to 6 for every 1000 medical examinations, which is comparable to that of alpine skiing. Compared to injury patterns in alpine skiing, snowboarders are more prone to ankle injuries than alpine skiers (Bladin, 1993; Shealy, 1993). Also, snowboarders with soft boots have more ankle injuries than snowboarders with hard boots (Kirkpatrick, 1998; Pino, 1989). The goal of this project was to design an experimental protocol to measure the kinematics of the ankle during regular snowboard maneuvers.

METHODOLOGY

An electromagnetic motion tracking system (Fastrak, Polhemus, VT, USA), with four 6-degree-of-freedom position sensors, was converted into a fully portable system operating on two 12-volts batteries and connected to a laptop computer. The sensors were attached to the shanks (antero-medial surface of the tibia) and feet (posterior surface of the calcaneus) of the snowboarder. The electromagnetic source was mounted on the snowboard between the two bindings, thus defining the global coordinate system rigidly attached to the snowboard. The bindings were adjusted at 21° and 6° rotation for the forward and backward leg respectively. The motion tracking system control box, batteries and laptop computer were carried by the snowboarder in a 20-pound backpack.

An anatomical calibration procedure was performed to calculate the spatial relationship between each sensor and a coordinate system defined on its corresponding anatomical segment (Della Croce, 1999). Bony landmarks on the shank and foot were palpated and measured with a Fastrak stylus through strategically located holes in the boots.

The trials consisted in snowboarding down a course of 10 turns and performing a sideways stop, on an intermediate-level slope of groomed snow. Each snowboarder was asked to perform 3 trials on a freestyle board with strap bindings and soft boots. The trials were measured with the motion tracking system at 120 Hz (30 Hz per sensor).

The recorded motion signals were smoothed using a two-pass second-order Butterworth filter. The rotation of the ankle through time was expressed in Euler angles with the feet considered as fixed in space.

RESULTS AND DISCUSSION

The analysis of the preliminary data obtained with two subjects showed consistent ankle range of motion in the frontal and sagittal planes. The inversion of the forward ankle and the eversion and dorsiflexion of the backward ankle (Figure 1) allow the snowboarder to shift his weight towards the tail of the snowboard. Radically different ankle range of motions were observed in the transverse plane. One subject had his forward ankle adducted (Figure 1) while the other had it abducted. Since the same standard binding rotation was imposed to all subjects, one might interpret this rotation as a shift of the shanks towards a more natural feet orientation in the transverse plane, which may differ between subjects.

The experimental method has proven successful and will be used to measure the effect of different types of snowboard boots and bindings on the ankle range of motion.

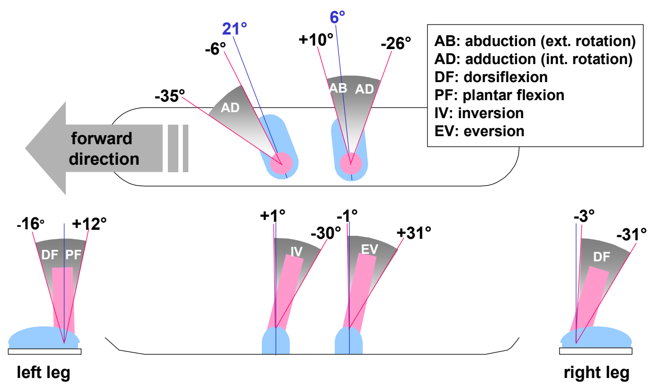

Figure 1: Range of motion of the ankle during snowboarding for one typical subject.

REFERENCES

Bladin, C., et al (1993). *Am J Sports Med*, **21**, 701-4.
Della Croce, U. et al (1999). *Med & Biol Eng & Comput*, **37**, 155-61.
Kirkpatrick, D.P., et al (1998). *Am J Sports Med*, **26**, 271-7.
Pino, E.C., et al (1989). *Am J Sports Med*, **17**, 778-81.
Shealy, J.E. (1993). *Skiing Trauma and Safety*, **9**, 241-54.

ACKNOWLEDGEMENTS

This research was funded by FCAR and the Development Fund of the Faculty of Health Sciences of the University of Ottawa. The authors would like to thank Dany Lafontaine, Robert Joncas, Station de ski Bromont and Mont Tremblant for their collaboration.

INFLUENCE OF MULTIPLE STENOSES ON DIAGNOSIS OF PERIPHERAL DISEASE

Christine Bertolotti[1], Zhao Qin[2] , Louis-Gilles Durand[2], Gilles Soulez[3] and Guy Cloutier[3]
[1] Laboratoire de biomécanique cardiovasculaire, ESM2/IRPHE CNRS6594, Marseille, France, christine.bertolotti@esm2.imt-mrs.fr,
[2] Laboratoire de génie biomédical, Institut de recherches cliniques de Montréal, QC, Canada
[3] Laboratoire de biorhéologie et d'ultrasonographie médicale, Département de radiologie, Hôpital Notre-Dame, Montréal, QC, Canada

INTRODUCTION

Atherosclerosis is the most common occlusive disease of the lower limbs, which can lead to intermittent claudication, and sometimes amputation at a late stage. Angiography morphological diagnosis is often completed with the assessment of the perfusion dysfunction by means of two parameters across the constriction(s): the pressure drop ΔP and the peak systolic velocity ratio PSVR. However, the accuracy of Duplex ultrasound and the dilution of the contrast agent are the main clinical limitations in evaluating the impact of stenoses, especially in the presence of distributed disease. The present study is intended to model the complex 3D flow field in pathological femoral segments to determine whether these hydrodynamic indexes are influenced by the multiplicity of the stenoses.

METHODS

Numerical and experimental models of flow are performed in idealized models of multistenosed femoral artery (Figure 1). The influence of varying the interstenotic distance, the distal stenosis severity and the inlet flow rates upon ΔP and PSVR are specifically analyzed. The Navier-Stokes equations are numerically solved with finite element method using the FIDAP package (Fluent Inc, Lebanon, NH). Lower limb arteries are often submitted to flows at peak Reynolds numbers above 400. As transition to turbulence may be observed even at such low flow rate, the turbulent two-equation Wilcox model is implemented after testing laminar models. In this model, through dimensional analysis, the turbulent velocity and scale are related to the kinetic energy and turbulent frequency respectively by: $u_t \propto \sqrt{k}$ and $\delta_t \propto \sqrt{k}/\omega$, the turbulent dissipation being expressed by $\varepsilon = k\omega$.

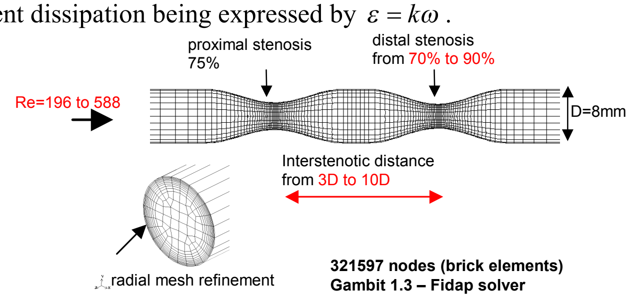

Figure 1: Exemple of a double stenose mesh.

In vitro experiments are performed on a mock flow bench including a wall-less vascular phantom of the simulated artery (made of agar gel), and a pumping system (Micropump, Cole-Parmer). Duplex ultrasonic velocity measurements and pressure tapes furnish respectively PSVR and ΔP clinical indexes.

RESULTS AND DISCUSSION

The pressure losses ΔP are showed to be mainly influenced by the most severe stenosis. Moreover, the presence of a double stenosis does not affect markedly this index (ΔP=24mmHg for a single 90% stenosis at Re=588 versus ΔP=26mmHg for a double stenosis 75%-90%). On the contrary, the PSVR is demonstrated to be more sensitive to interstenotic distance, flow rate and stenosis severity. Finally, differences between numerical and experimental results are noticed especially with axisymmetric (i.e. 2D flow) numerical assumptions. In contrast to Ang et al. (1995) or Pincombe et al (1999), successive deflections of the post-stenotic jet through double stenoses are observed, even at low Reynolds number (see Figures 2 and 3) that confirm the unstable and transient nature of such flows.

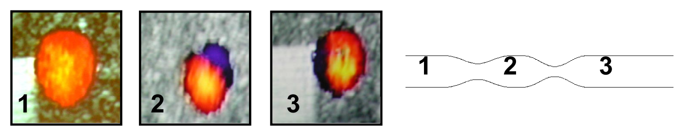

Figure 2: Duplex color longitudinal velocity in cross-planes.

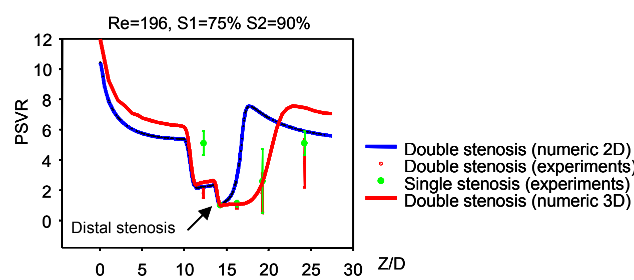

Figure 3: Longitudinal evolution of PSVR with an interstenotic distance of 3 diameters. Comparison between experiments and 2D/3D numerical values of PSVR.

SUMMARY

By altering the value of PSVR, the presence of multiple stenoses may influence the diagnosis of the peripheral disease.

REFERENCES

Ang, K. et al. (1995) *Australas Phys Eng Sci Med*, **18**, 89-94.
Pincombe, B. et al. (1999) *Med Biol Eng Comput*, **37**, 595-9.

ASSESSMENT OF A NOVEL FEMORAL COMPONENT REMOVAL TECHNIQUE FOR REVISION SURGERY

M. Browne[1], M.C.Mowlem[1], J. Mountney[2], S. Kulkarni[2] and D.S. Barrett[2]

[1]School of Engineering Sciences, University of Southampton, Southampton, SO17 1BJ, UK, doctor@soton.ac.uk
[2] Orthopaedic Dept, Southampton University Hospitals Trust, Southampton, SO16 6YD, UK

INTRODUCTION

In total knee replacement revision surgery, the femoral component may be found to be rigidly fixed to the bone. Careful and patient use of an osteotome in conjunction with a suitable extraction device may be required to loosen and remove the component. A novel technique has been developed, which has proven to be quick, simple and effective for removing a solidly fixed femoral component with minimal bone loss. In this procedure, the surgeon and the assistant each place an osteotome on the cement-metal interface at symmetric positions, directly opposite each other on the medial and lateral sides. They deliver synchronous blows with a mallet at positions around the interface until the cement fractures. The femoral component can then be removed easily.

The present research examines the events that occur during the traditional (single) and novel (double) osteotome techniques, and explains the effectiveness of the new technique in terms of the impact processes and energy absorption mechanisms experienced by the implant.

METHODS

Polyurethane mouldings, representing a suitable substrate for cementing metal components, were fixed onto a steel rod, of similar weight and length to a lower leg. Stainless steel discs (40mm diameter x 4mm thickness) were cemented onto the polyurethane substrate to form a representative model of an attached implant. The discs were instrumented to allow recording of the mechanical processes caused by the double extraction technique, and to allow comparison with the single osteotome extraction technique. Two accelerometers were used; one mounted on the top of the implant and one on the side. Therefore, the lateral and vertical acceleration of the implant could be monitored. Ten extractions using each technique (20 in total) were performed.

RESULTS AND DISCUSSION

A typical record of a blow from the single extraction technique can be seen in Figure 1. Large amplitude vibrations are seen at a frequency of approximately 15kHz; lower frequency components are also present and show a good deal of movement at the top of the implant. This blow did not result in the extraction of the implant. The double extraction technique shows a small delay between the striking of the two initial blows (Figure 2). This delay is large enough to allow the near complete decay of the high frequency components in the acceleration of the model. A third blow is also observed on the record of the lateral acceleration. The magnitude of the accelerations produced by the first blow is very similar to that

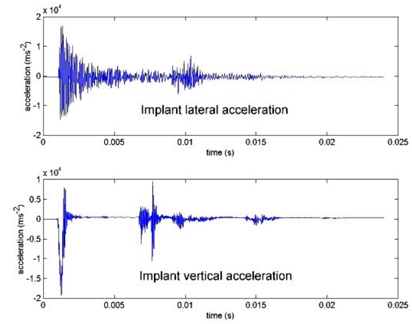

Figure 1 Typical record of the traditional extraction technique

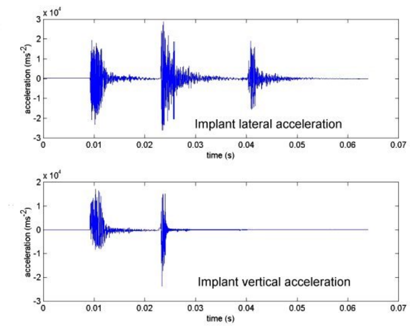

Figure 2 Typical record of the novel extraction technique

observed when using the traditional technique. The accelerations caused by the second blow however, are significantly greater in magnitude. This is caused by the movement of the implant towards the osteotome that inflicts the second blow. The third blow is a result of a reverse in the direction of motion of the implant following the second blow, and as a consequence it contacting with the osteotome that inflicted the first blow again. The maximum lateral movement is reduced by this technique. This results in less energy loss. Accelerations caused by the first and second blows are experienced by the implant; however, the third blow causes no acceleration, as by this time the implant has been extracted.

SUMMARY

The methodology described has successfully demonstrated that the double osteotome technique increases the contact force of the second blow. When the synchronous blows are delivered, less energy is expended in the movement of the tibia and more is contributed to the removal of the component. In many instances a third blow is also noted; this will be a factor in the easier extraction observed in revision procedures.

REFERENCES

Insall, J., (2000). *Surgery of the knee*, Churchill Livingstone.

ANALYSIS OF SAGITTAL BALANCE OF THE SPINE DURING VARIOUS STANDING POSITIONS AND GAIT

Michelle Marks, Chriss Stanford, Andrew Mahar, and Peter Newton

Motion Analysis Laboratory, Children's Hospital, San Diego, California
mmarks@chsd.org

INTRODUCTION

Global sagittal spinal alignment is described by the sagittal vertical axis (SVA), and is measured on a lateral x-ray by the horizontal distance from the posterior superior corner of the sacrum to the plumb line dropped from the center of the body of the C7 vertebra.[1] Measurement of SVA on a lateral radiograph can change with subtle variations in posture.

Numerous positions for lateral x-rays are utilized in the literature[2], but there is no universally accepted position. Acquisition of a standing x-ray that allows visualization of the spine requires flexion of the shoulders, preventing the patient from assuming a functional position. The purpose of this study was to examine differences in SVA during relaxed standing and walking to SVA during positions assumed during x-ray acquisition.

METHODS

Fifteen healthy females, ages 10-14 years were enrolled in this study. Reflective markers were attached to the skin overlying the spinous processes of C7 and L4, and on the right heel. Positions of the markers were captured by an 8-camera Motion Analysis System (Motion Analysis Corp., Santa Rosa, CA) at 60 Hz during simultaneous acquisition of a standing lateral radiograph, with each subject positioned with 45° of shoulder flexion. The horizontal distance between the C7 and L4 markers was measured using motion capture data. Distances between the markers and landmarks used for SVA measurement were also measured on each x-ray. A correction was developed to match SVA values between measurement techniques. This allowed for measurement of SVA during experimental positions (Table 1) without subsequent exposure to radiation. Mean SVA for each position and during the gait cycle were compared using a repeated measures ANOVA (α=0.05). Relaxed standing was chosen as a basis for comparison because it is an easily assumed and functional position.

RESULTS AND DISCUSSION

SVA means and standard deviations for the various postures are displayed in Figure 1a. Positive SVA values indicate a forward positioning of the seventh cervical vertebrae over the posterior aspect of the sacral endplate. Results of the ANOVA indicate that SVA measures for positions 2 and 4 were significantly less ($p<.01$) than for relaxed standing. Flexion of the shoulders causes C7 to shift posterior relative to the pelvis, suggesting a postural compensation by the trunk to maintain upright posture. In contrast, flexion of the knees exerts a positive influence on SVA, though it does not effectively balance SVA when combined with shoulder flexion.

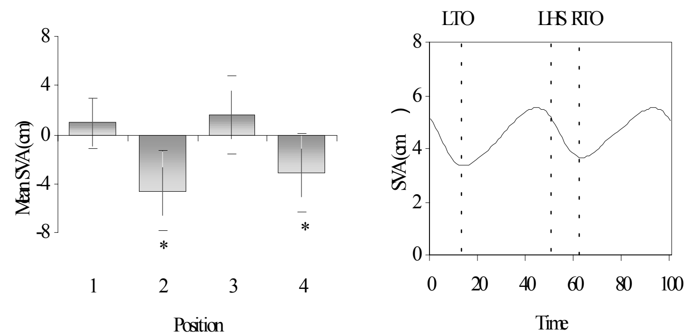

Figure 1a-b: Mean SVA for standing positions 1-4 (a) and during the gait cycle (b) for 15 subjects.

Figure 1b displays mean SVA throughout the gait cycle. Mean SVA during gait exhibited a significant increase, compared to relaxed standing ($p<.01$). SVA during the gait cycle displays a pattern similar to sagittal plane trunk motion[3], with maximum forward alignment occurring prior to heel strike.

SUMMARY

Adolescent females have a positive SVA during relaxed standing and walking. Sagittal balance of the spine may not be assessed effectively on a lateral radiograph, as positions required for visualization of the spine are not representative of functional postures.

REFERENCES

Gelb, D. (1995). *Spine* ,**20**, 1351-1358.
Weinstein, S. (2001). *The Pediatric Spine: Principles and Practice* 1: 355.
Vogt, L. & Banzer, W. (1999). *Gait and Posture* ,**9**, 18-23.

Table1: Descriptions of the four standing positions.

Position #1	Standing relaxed with arms at the side, knees at 0º
Position #2	Standing with the arms elevated 45° anteriorly, knees at 0º; this institutions typical x-ray standing position.
Position #3	Standing with 10° of knee flexion, arms at side
Position #4	Standing with the arms elevated at 45° of forward flexion, knees at 10° of flexion.

COMPARISON OF MODELS FOR THE STRESS-STRAIN RELATIONSHIP OF SOFT TISSUE

Cara L Lewis, Mary K Hastings, Joe W Klaesner, Dequan Zou, Michael J Mueller[1]

[1]Movement Science Lab, Program in Physical Therapy, Washington University School of Medicine, St. Louis, MO, USA
clewisa@artsci.wustl.edu

INTRODUCTION

Multiple models have been used to characterize the material properties of soft tissue. Common models include the use of a first order or second order exponential or the Voigt model. A parallel three-element model can also be used to quantify soft tissue stiffness with a nonlinearly elastic component (Klaesner et al 2002). The purpose of this study is to model the stress-strain relationship of the soft tissue under the 3rd metatarsal head using an exponential model, the Voigt model, and the parallel three-element model, and to determine the model with the best fit.

METHODS

Data: Force-displacement data from the soft tissue under the 3rd metatarsal head were collected on 40 subjects (age 55.56 ± 10.08 years; 28 male, 12 female) using a force transducer mounted to a three-dimensional measurement device (Klaesner et al 2001). Only trials with a consistent velocity (R^2>.95) over the force range from 2 to 9 N were accepted. Force and position data for 3 trials were collected and analyzed using software developed in the lab. Data were then converted to stress-strain data. Stress (σ) was determined by dividing the obtained force by the area over which that force was applied (i.e. the tip of the indentor device). Strain (ε) was determined by dividing the displacement by the initial thickness of the soft tissue as measured using a CT Scan.

Modeling: Exponential model: MATLAB software was used to determine the appropriate constants to produce an exponential model to fit the data. A first degree polynomial, fitting the strain to the natural log of the stress ($\ln \sigma = p(\varepsilon)$), was used to produce coefficients p_1 and p_2. The first order exponential formula, as listed in Table 1, was used to predict the stress at each data point using the obtained strain. The data were then fit with a second degree polynomial, again using MATLAB. This produced coefficients q_1, q_2, and q_3 from which the stress at each data point was predicted using the obtained strain. *Voigt model:* The Voigt model is composed of a spring and dashpot in parallel. The spring constant K and coefficient of viscosity C were computed, and these constants were used to predict the stress at each strain level. *Parallel three-element model:* The parallel 3-element model quantifies soft tissue stiffness using a single linear spring element in parallel with the Voigt model. During the initial displacement, X_s, the stress is modeled as linear elastic behavior, engaging only the single spring. After the initial displacement, the Voigt model portion, consisting of a linear spring in parallel with a dashpot, engages. A computer program developed in the lab was used to determine X_s and the constants, K_1, K_2, and C for this model. Using the constants and the formulas listed in Table 1, the stress at each data point was predicted.

Analysis: The unbiased standard error was calculated for each model for each trial and averaged over the three trials and 40 subjects. The correlation coefficient (R^2) between the predicted and obtained stress was also calculated for each trial and subject, and averaged for each model.

RESULTS AND DISCUSSION

As indicated in Table 1, the Parallel 3-element model has the least error and the highest R^2. We propose that the parallel 3-element model has the added advantage of having a physiological basis. We speculate that K_1 represents the initial stretching of collagen fibers in the plantar soft tissue, while K_2 is attributed to compression of soft tissue and the constant C to fluid displacement.

SUMMARY

Although all methods resulted in low error, the parallel 3-element model produces the best fit for the stress-strain data. Accurate representation of the material properties of soft tissue is essential for finite element modeling of the foot.

REFERENCES

Klaesner J.W. et al (2002). *Arch Phys Med Rehabil.* In press.
Klaesner J.W. et al (2001). *IEEE Trans Neural Syst Rehabil Eng,* **9**, 232-240.

Method	Formula	Error (N/mm)	R^2
1st order exponential	$\sigma = \exp(p_1 * \varepsilon) * \exp(p_2)$	0.027	0.923
2nd order exponential	$\sigma = \exp(q_1 * \varepsilon^2) * \exp(q_2 * \varepsilon) * \exp(q_3)$	0.020	0.971
Voigt model	$\sigma = K\varepsilon + C(\varepsilon')$	0.022	0.952
Parallel 3-element model	$\sigma = K_1\varepsilon$ for $0 \le X \le X_s$ $\sigma = K_1\varepsilon + K_2(\varepsilon - \varepsilon_s) + C\varepsilon'$ for $X_s < X \le X_{max}$	0.014	0.994

Table 1: Formula, error and correlation coefficients (R^2) for each method.

NUMERICAL MODAL ANALYSIS OF CEMENTED FEMUR COMPONENT OF TOTAL HIP REPLACEMENT

Gang Qi[1] and W. Paul Mouchon

Department of Mechanical Engineering, The University of Memphis, Memphis, TN, USA
[1]gangqi@memphis.edu

INTRODUCTION

A technique of vibration analysis has been utilized to study loosening of total hip arthroplasties (THA) [Georgiou,2001; Li, 1995]. However, the potential capabilities of this technique on this particular application was not demonstrated clearly in those studies due to the complexity of the problem. The aim of this work is to explore its capabilities using finite element method (FEA) evaluating the femoral component loosening.

METHODS

Various ideal interface failure models were constructed. Each model was composed of four components: bone, cement mantle, interface, and implant stem. The only difference of the models is the failure sizes and locations at the cement-stem interface. The models were constructed in the following manner. A human femur cadaver was first measured. The model was constructed from representative cross sections of the femur. Using these sections, the configuration of the femur was created by the advanced feature generation of a computer aided design (CAD) package, Pro/Engineer (Parametric Technology Corp, Waltham, MA). An uncollard straight stem was selected and modeled. The cement mantle was generated accordingly to fit the shape of the stem and the bone. A minimum of 4 mm wall thickness of the cement was maintained. A thin interface layer of 0.2 mm thickness was generated between the stem and cement mantle. The four components were then assembled automatically using the same CAD package (Fig.1). An Algor (Algor Inc., Pittsburgh, PA) FEA package was used to conduct the study.

RESULTS AND DISCUSSION

The fundamental frequency of the control model was 115.750 Hz. In comparison with the clinical data (102.3 Hz [1]), and with the in vitro result (110-115 Hz [2]), the presented results were close.The model used in this work is a fair representation of the reality. There was no significant difference of the first two natural frequencies between the control model and models with various interface failures. However, these differences became significant at harmonics above the 3rd natural frequencies. The differences increased as the magnitude of the natural frequencies increased. Also, it is observed that the proximal interface failures effected the natural frequencies greater than distal interface failures. Fig.2 shows the first seven natural frequencies compared with the control model. These modal changes revealed a mechanism of the THA construct softening due to the interface failure. Preliminary runs or FEA with varying data indicate the present finding can be extended to varying THA construtions.

CAD model of THA

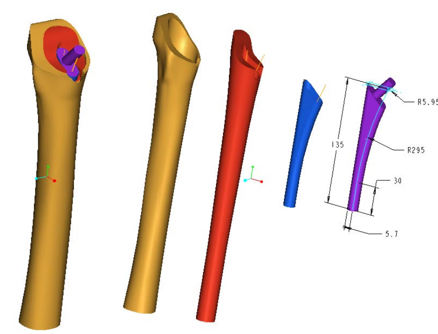

Fig.1: The real THA model generated by ProEngineer. Left: assembled model; Right: exploded view of the THA model. Dimensions are all in mm.

Differences in the Natural frequencies

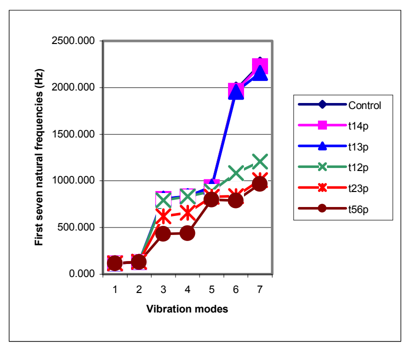

Fig.2: Effects of the failure size on first seven natural frequenices when the interface failure were at the proximal area, where control, t14p, t13p, t12p, t23p, and t56p were the data of control 1/4, 1/3, 1/2, 2/3, and 5/6 stem proximal interface failed, respectively.

SUMMARY

The traditional vibration modal analysis could be used to identify THA loosening. This technique will be more sensitive at high frequency range. However, direct modal analysis failed when the failure length was less than 1/6 of the stem length.

REFERENCES

Georgiou AP, Cunningham JL. Clin Biomech 2001;16(4):315-23.
Li PL, Jones NB, Gregg PJ. JBJS 1995;77B(4):640-4.

COMPUTER SIMULATION OF VIBRATIONAL DIAGNOSIS OF THA LOSSENING

Gang Qi[1] and W. Paul Mouchon

Department of Mechanical Engineering, The University of Memphis, Memphis, TN, USA
[1]gangqi@memphis.edu

INTRODUCTION

A numerical modal analysis provides information regarding THA loosening in terms of the magnitudes of the natural frequencies. However, indicators are needed in order to quantify the characterization of the acquired signals. The aim of this work is to conduct a computer simulation using synthesized vibration data to demonstrate a method to diagnose the THA loosening due to cement-stem interface failures.

METHODS

The multi-harmonic sinusoidal signals were synthesized according to the modal analysis. These signals represented the ones acquired by an accelerometer in a real test. Considering the fact that high harmonics may not be detectable, only the first ten natural frequencies were used in the synthesis. To count for unknown interference on the signals, random numbers were generated to emulate the real time white noise and were added to the signals. As an example, the signals of control and 1/5 proximal interface failure models were synthesized. The FFT and wavelet analysis were employed [Qi, 2000]. The phase angle and histograms of the signal wavelet decomposition components were used to illustrate the methodology of signal characterization.

RESULTS AND DISCUSSION

Fig.1 shows the spectra of three synthesized signals. It was observed that the spikes of higher harmonics indicated THA softening due to interface failure. A trend of higher harmonics shifting from right to left of the abscises indicated THA structural softening due to the interface failure.

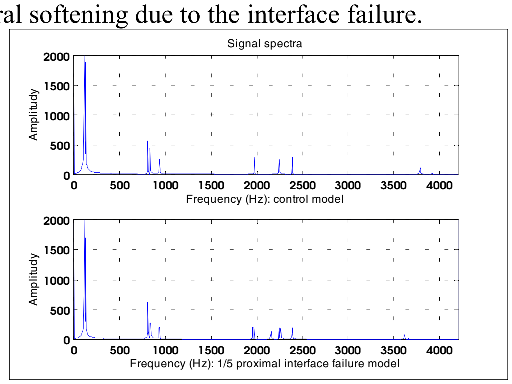

Fig.1: Spectra of synthesized signals of control (top curve) and 1/5 proximal interface failure (bottom curve).

The phase angle of the spectra can also be used as an indicator to quantify the loosening as shown in Fig.2.

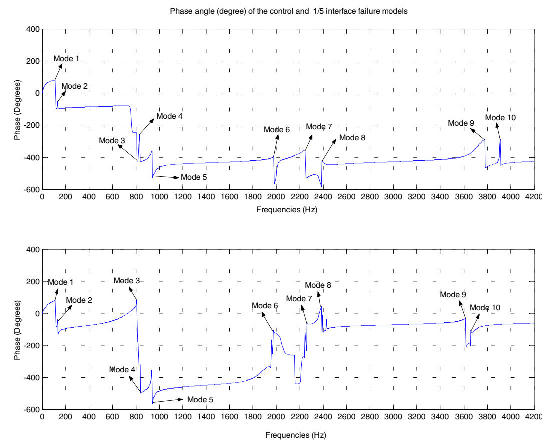

Fig.2: Phase angles of the spectra of the previous figure

Because the difference between the control and 1/5 model was not significant especially at lower frequency range, the wavelet decomposition was employed. Table 1 shows the histograms of the detail coefficients. The mean and maximum values of the decomposed wavelet coefficients provided another potential indicator that could be used to characterize the THA loosening.

Statistical characteristics		Mean	Maximum	Standard Deviation
Control Model	Detail level 1	1.765×10^{-4}	0.1218	0.04183
	Detail level 2	5.001×10^{-4}	0.3394	0.1169
	Detail level 3	14.24×10^{-4}	0.7943	0.3149
1/5 proximal interface failure	Detail level 1	1.112×10^{-4}	0.12	0.04154
	Detail level 2	3.146×10^{-4}	0.3338	0.1161
	Detail level3	8.9×10^{-4}	0.9106	0.313

Table 1. Wavelet coefficient histogram

SUMMARY

A computer simulation of vibrational diagnosis of THA loosening was conducted. The number of higher harmonics, phase angle, and wavelet coefficients can be used as indicators to quantify the severity of the loosening.

REFERENCES

Qi, G., (2000) *J. Biomed Mat Re.*Vol. 52(1): pp148-156,

Qi, G. and Ng, E. T. (2000). *J. Mat Sci.*Vol 36(10): pp 2483-2489.

STRAIN RATE SENSITIVITY OF LIGAMENTS DIMINISHES AT TRAUMATIC LOADING RATES

Joseph J. Crisco[1,2], Douglas C. Moore [1], Robert D. McGovern[1]
[1] Dept. of Orthopaedics, Brown Medical School/Rhode Island Hospital and [2] Div. of Engineering, Brown University, Providence RI
E-mail: joseph_crisco@brown.edu

INTRODUCTION

Creep, stress relaxation, and load-displacement tests have provided insight into the viscoelastic properties of ligaments at relatively low rates of loading (e.g. Woo et al., 1981). However, the existing data does not adequately address how ligaments behave when they are loaded at high rates of strain, such as those seen in sports induced trauma or in motor vehicle accidents. This study was performed to determine whether ligaments behave viscoelastically at 'traumatic' loading rates. To do so, 1) the structural and failure properties of ligaments tested via impact were compared to the properties of ligaments tested quasi-statically, and 2) the properties of two impact tests were compared.

METHODS

After approval by our institution's Animal Welfare Committee, both hind limbs were harvested from twenty-seven skeletally mature New Zealand white rabbits and all muscular and ligamentous structures crossing the knee joint were carefully removed, with the exception of the medial collateral ligament (MCL).

Quasi-static Testing. One randomly selected MCL from each pair was tested to failure at 0.167 mm/s (10.0 mm/min) with the knee positioned in 90 degrees of flexion.

Impact Testing. The second MCL from each pair was tested to failure with a drop-mass impact device. To do so, the femurs were attached to a fixed piezoelectric load cell, and a 5 kg mass was dropped down a thin (1.6 mm dia.) guidewire suspended from the tibia. During testing, displacement and acceleration of the tibia was recorded with a fast response (35 μsec) LVDT and piezoelectric accelerometer, respectively. Twelve ligaments were failed by releasing the drop mass from a height of 10 cm, and fifteen ligaments were failed by releasing the mass from a height of 70 cm.

Data Analysis. The load-displacement-time data from both the quasi-static and the impact tests were processed to yield values for displacement rate, loading rate, stiffness, failure load, displacement at failure, time to failure, and energy to failure. Paired Student's t-tests were used to compare the results generated via quasi-static and impact testing, and unpaired t-tests were used to compare the two impact tests. P values ≤ 0.05 were considered to be statistically significant. Five MCL pairs were excluded from the analysis due to technical problems during testing.

RESULTS AND DISCUSSION

The displacement and loading rates of the impact-tested groups were significantly different than one another, and significantly greater than those of the quasi-statically tested specimens (Table 1). Accordingly, failure occurred more quickly in the 70 cm impact tests (1.8 ± 0.2 msec) than in the 10 cm impact tests (5.6 ± 0.9 msec), which in turn failed much more quickly than in the quasi-static tests (16.9 ± 6.3 sec). Despite dramatic increases in displacement and loading rate with impact testing, failure load and stiffness increased only nominally over quasi-static testing; there were no detectable differences in failure displacement (Table 1).

There were no differences in the structural or failure properties of the two impact-tested groups (Table 1). This was surprising, considering the displacement and loading rates of the 70 cm impact tests were nearly four times faster than the rates for the 10 cm impact tests .

SUMMARY

Our results suggest that ligaments are only minimally strain rate sensitive, since an increase in loading rate of several orders of magnitude produced no more than a 40% change in its mechanical properties. Furthermore, an incremental increase in impact loading rate did not lead to corresponding changes in ligament structural and failure properties. Taken together, these findings suggest that the strain rate sensitivity of the rabbit MCL diminishes at traumatic loading rates.

REFERENCES

Woo, S.L. et al. (1981). *J Biomechanical Eng*, **103**, 293-298.

ACKNOWLEDGMENTS

This work was funded by the RIH Orthopaedic Foundation and University Orthopaedics, Inc.

Table 1: Structural and failure properties of rabbit medial collateral ligaments tested quasi-statically and at two impact rates. *Significantly different than Quasi-static at $p < 0.05$. †Significant difference between Impact groups at $p < 0.05$.

Test Method (n)	Disp. Rate (mm/s)	Loading Rate (N/s)	Failure Load (N)	Failure Disp. (mm)	Stiffness (N/mm)	Energy (N-mm)
Quasi-static (22)	0.17 ± 0	18.9 ± 3.8	320 ± 118	3.4 ± 0.9	113 ± 23	556 ± 294
10 cm Impact (10)	640 ± 160*†	90,000 ± 13,000*†	434 ± 91*	3.1 ± 0.9	145 ± 30*	653 ± 340
70 cm Impact (12)	2,500 ± 270*†	353,000 ± 97,000*†	443 ± 154*	3.1 ± 0.7	136 ± 29*	635 ± 282

TIME DEPENDENT DEFORMATION DURING NANOINDENTATION TEST ON OSTEONIC LAMELLAE IN A HUMAN CORTICAL BONE

Zaifeng Fan and Jae-Young Rho

Department of Biomedical Engineering, ET330, University of Memphis, Memphis, TN 38152, USA
jrho@memphis.edu

INTRODUCTION

Nanoindentation has been utilized to investigate mechanical properties of bone at the microstructural level [4]. Although viscoelastic deformation was apparent in the creep displacements observed during the constant load hold period at peak load, most experiments were not evaluated viscoelasticity of bone. In the present study, the relationship between strain rate and elastic modulus was investigated to reveal time dependent deformation during nanoindentation test on osteonal lamellae in a human cortical bone.

METHODS

A bone sample was obtained from the midshaft of one human tibia (52 years old) with no bone disease. A Triboindenter (Hysitron, Inc. Minneapolis, MN) was utilized to conduct all the indentation tests. The Oliver-Pharr method [3] was used to determine the elastic modulus. Two load-time functions were used in this study:

A. Simple loading unloading (with different loading rates and same peak load)

B. Loading unloading three times in succession followed by a final loading and then a holding period applied before final unloading (with different loading rates and same peak load).

The loading rates of 10μN/s, 30μN/s, 50μN/s, 100μN/s, 300μN/s, 500μN/s and 1000μN/s were used to produce varied strain rates for each load function. All the indents were conducted in osteonic lamellae with roughly equal radial distance to Haversian canals [4]. For a geometrically similar indenter, such as Berkovich indenter, the indentation strain rate is typically defined as $h^{'}/h$, which is the instantaneous change in displacement divided by the instantaneous displacement at the respective time point [2]. The load-displacement curves obtained from the two load functions are shown in Fig 1.

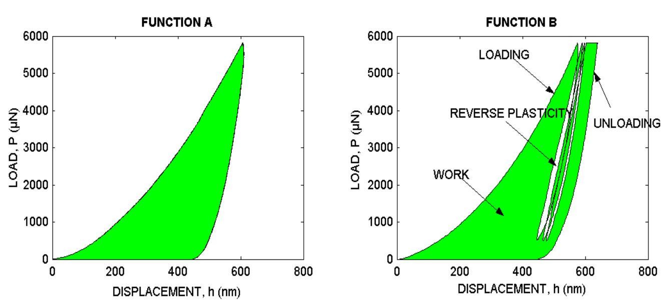

Figure 1: The load-displacement curves obtained from load function A and B

The shaded area (work) in-between the first loading and the final unloading curve reflects the plastic deformation.

RESULTS

In results from load function A, the elastic modulus and strain rate are found to hold the relationship as

$$E = 48.93\left(\dot{\varepsilon}\right)^{0.100}, \quad R^2 = 0.70$$

where E is the elastic modulus and $\dot{\varepsilon}$ is the strain rate.

The ANOVA test result (P<0.0001) indicated that significant differences existed in the works among the different loading rates. For load function B,

$$E = 37.74\left(\dot{\varepsilon}\right)^{0.059}, \quad R^2 = 0.94$$

The ANOVA test results ($P=0.24$) indicated that no significant differences existed in the works for all loading rates.

DISCUSSION

It has been assumed that the unloading data are fully elastic recovery for quasistatic indentation measurement. The Oliver-Pharr method [3] is based on this assumption. The reason for performing multiple loading unloading was to examine the reversibility of deformation and thereby make sure that the unloading data used for analysis purposes were mostly elastic. The holding period performed at maximum load allows any final time dependent plastic effects to be diminished. In the results from load function B, the works for all different loading rates are found no statistic significance, which indicates that the plasticity variations are mostly diminished by multiple loading unloading and holding period at maximum load. The unloading curves are mostly composed by elastic portion. Interesting, the relationship between elastic modulus and strain rate was similar to that of the previous study [1]. However, the result from load function A was not consistent with the previous observation. The present study suggests that nanoindentation properties of bone should be obtained with carefully designed experimental procedures since it shows time dependent deformation during nanoindentation test on bone.

REFERENCES

[1] Carter, D.R., Hayes, W.C. (1976). *Science*, **194**, 1174-1184. [2] Lucas, B.N., Oliver, W.C. (1999). *Metall. and Mater. Trans. A*. **30A**, 601-610. [3] Oliver,W.C., Pharr, G.M. (1992). *J. Mater. Res*. **7**, 1564-1583. [4] Rho, J.Y., Zioupos, P. Currey, J.D., Pharr, G.M. (1999). *Bone*, **25**, 295-300.

MUSCLE ACTIVATION LEVELS DURING RUNNING IN VARUS, VALGUS, AND NEUTRAL WEDGED SHOES

Kristian O'Connor[1], Thomas Price[2], and Joseph Hamill[1]

[1]Biomechanics Laboratory, University of Massachusetts, Amherst, MA, koconnor@excsci.umass.edu
[2]Department of Diagnostic Radiology, Yale University School of Medicine, New Haven, CT

INTRODUCTION

Nigg (2001) proposed that altering the motion of the foot from a preferred movement pattern would increase muscle activity. The extrinsic muscles of the foot contribute to supination of the foot and may apply a significant force to control foot pronation in the support phase of running. Altering the boundary conditions of the foot may lend insight into the role of these muscles. Functional magnetic resonance imaging has been used to detect changes in muscle activity post-exercise for static and dynamic resistance tasks (Price et al., 1998). It can also be used to detect differences in specific muscles. The purpose of this study was to use functional MRI to determine the changes in muscle activation caused by running in varus, valgus, and neutral wedged shoes (Milani et al., 1995).

METHODS

Six men performed five-minute running bouts in each of the three shoe conditions. The three conditions were presented in a random order. Subjects ran on a motorized treadmill at 3.6 m/s. MRI scans of the mid-calf were performed before and immediately after each running bout (< 2 minutes). The muscle activation levels were estimated by assessing the transverse relaxation time (T_2) of each muscle. This parameter has been shown to correlate with exercise intensity with higher workloads yielding higher T_2 measurements (Price et al., 1998). T_2 values before and after each running bout were calculated for the tibialis anterior (TA), tibialis posterior (TP), the peroneus (Per), medial (MG) and lateral (LG) heads of the gastrocnemius, the extensor digitorum (ED), and the soleus (Sol) (Figure 1).

Selected Muscles

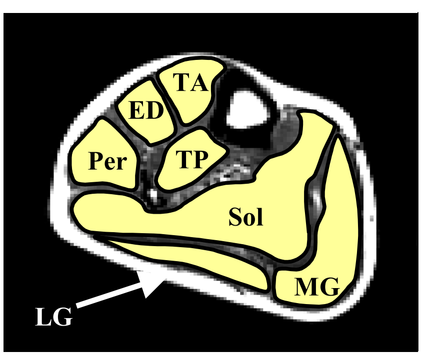

Figure 1. Illustration of the selected muscles.

RESULTS AND DISCUSSION

A five-minute run increased the T_2 in most of the muscles examined (Figure 2). The soleus only increased minimally when compared to the rest condition. These six subjects did not demonstrate a systematic change in muscle activation levels in the three shoes.

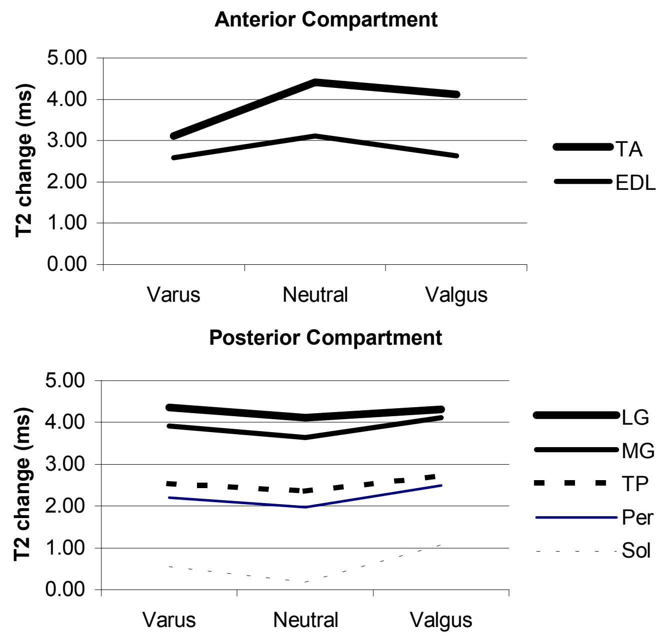

Figure 2. T_2 changes for each muscle across conditions.

SUMMARY

No differences in T_2 were detected between shoes. These results indicate that there is little change in muscle activation patterns in the muscles that control foot motion when a perturbation is applied to the foot. Thus, it appears that the neuromuscular system may not need to alter control signals in response to these comparatively small perturbations.

REFERENCES

Milani, T.L., Schnabel, G., & Hennig, E. (1995). *J Appl Biomech*, **11**, 177-187.
Nigg (2001). *Clin J Sport Med*, **11**, 2-9.
Price, T.B., Kennan, R.P., & Gore, J.C. (1998). *MSSE*, **27 (10)**, 1421-1429.

MEASUREMENT OF RESIDUAL STRESS DUE TO VOLUMETRIC SHRINKAGE IN BONE CEMENT

A. Roques[1], A. New[1], A. Taylor[2], D. Baker[3] and M. Browne[1]

[1]School of Engineering Sciences, University of Southampton, Southampton, SO17 1RY, UK, a.roques@soton.ac.uk
[2]Finsbury (Development) Ltd., Leatherhead, Surrey, KT22 0BA, UK
[3] DePuy CMW Ltd., Blackpool, Lancashire, FY4 4QQ, UK

INTRODUCTION

The mechanisms leading to loosening of cemented hip replacement and the role played by the polymethylmethacrylate (PMMA) bone cement in the failure process are not fully understood. Bone cement is believed to be one of the weak components of the cemented construct. Volumetric shrinkage during bone cement curing, due to the polymerisation process (the PMMA polymer is more dense than the MMA monomer), has drawn increasing attention, as it has been reported experimentally to be as high as 8% in volume and therefore a potentially significant source of porosity (Gilbert, 2000). It could also account for weaknesses within the cement, which could provide a path for cracks, resulting in crack deviation as observed by Topoleski et al. (Topoleski, 1993). This research aims to measure the residual stresses due to shrinkage in simulated in vivo conditions for further input into Finite Element (FE) models and experimental work.

METHODS

Two self-compensated strain gauges were fixed on a stainless steel rod of 120mm length and 12mm diameter. This allowed measurement of the hoop stresses at the surface of the stem (in contact with polymerising cement). Radiopaque CMW1 bone cement was mixed and syringed into a hollow cylinder made from Tufnol™ of 16mm internal diameter. The rod was introduced into the polymerising cement using a servohydraulic Instron machine, and held steady. A thermocouple was used to monitor the temperature in the cement mantle and the hoop strains at the interface were measured until at least 40 minutes after first contact of the liquid monomer with the powder.

An axisymmetric FE model of the experimental setup was generated. A quasi-thermal technique was used to model shrinkage of the cement. By assigning an artificial linear coefficient of thermal expansion of 0.02, the required volume change (6%) in the cement could be induced by reducing the temperature by 1°C. The cement was assumed to be fully bonded to both implant and mould; this is likely to give an upper-bound estimate of curing induced residual strains.

RESULTS AND DISCUSSION

Using the FE model, the coefficient relating the strains at the interface and the stresses in the cement was obtained (Fig 1) and used to convert the experimental strains (Fig. 2) into interfacial residual stresses of around 10MPa in the cement. The curve shown in Fig 2 also shows stress relaxation of the cement following the polymerisation peak, which is thought to be possibly due to creep or microcracking. The measured strains were much lower than the value obtained from the FE model. This discrepancy was thought to be due to (i) the level of porosity in the cement - porosity has been thought to 'compensate' for shrinkage (Gilbert, 2000) and (ii) possible cracking in the cement. For the present experiment any temperature effect on the gauges is believed to be negligible because the cement mantle was thin (2mm), and did not produce a significant temperature increase due to the heat sink effect of the rod.

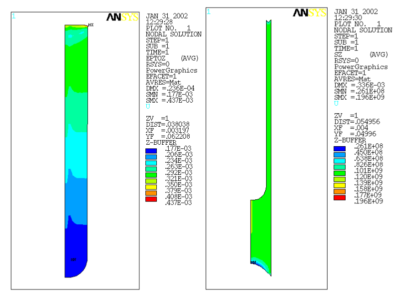

Figure 1: Implant strains (left) and cement stresses, Pa (right).

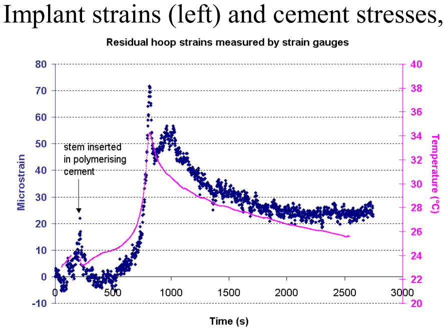

Figure 2: Residual strain measurement during polymerisation

SUMMARY

A combined experimental and analytical method has been developed to estimate residual stresses in the cement mantle. Residual stresses due to shrinkage were found to be as high as 10MPa at the interface between the cement and the stem. Further FE analysis will attempt to develop the material model to more accurately describe the residual strain development, and predict initial stress levels in the cement.

REFERENCES

Gilbert, J. K. et al. (2000). *Journal of Biomedical Materials Research* **52**(1): 210-218.
Topoleski et al. (1993). *Biomaterials* **14**(15): 1165-1172.

A MODEL FOR THE DEVELOPMENT OF INTIMAL HYPERPLASIA

N.A. Hill[1], M.K. Spendiff[2] and S.L. Jamieson[2]

[1]Department of Mathematics, University of Glasgow, Glasgow, G12 8QW, Scotland, U.K. N.A.Hill@maths.gla.ac.uk
[2]Department of Applied Mathematics, University of Leeds, Leeds, LS2 9JT, England, U.K.

INTRODUCTION

The interaction between blood flow and the transport of cholesterol through the arterial wall is critical in the formation of atherosclerosis in large arteries. A mathematical model has been developed to describe the early stages of the disease (intimal hyperplasia) and the evolution of fatty streaks which are the precursors to the formation of atherosclerotic plaques.

MODEL

The arterial wall is modelled by two layers, the intima and the media, through which cholesterol is transported. In the intima, cholesterol is converted to oxidised cholesterol that is consumed *in situ* by macrophages, which bind to the substrate and turn into fatty foam cells. These processes are described by

$$\frac{\partial c_L}{\partial t} = -\nabla . j_I - kc_L \quad \text{and} \quad \frac{\partial c_{LO}}{\partial t} = kc_L - \gamma c_{LO} \, ,$$

where c_L and c_{LO} are the concentrations of native cholesterol (*L*) and oxidised cholesterol (*LO*) in the intima. k is the rate of conversion to *LO* and γ is the constant background decay rate for *LO*. j_I is the flux of *L* in the intima and is given by

$$j_I = -D_I . \nabla c_L - c_L U \chi_I \hat{z},$$

where D_I is a diffusion tensor, χ_I is the slip coefficient (the mean velocity of the molecule relative to that of the fluid), $-Uz$ is the mean fluid velocity through the vessel wall, which is taken to be constant. No conversion takes place in the media which has relatively low diffusion and advection coefficients and thus acts a barrier to the transport of cholesterol so that the governing equation is

$$\frac{\partial c_M}{\partial t} = -\nabla . j_M \, ,$$

where $j_M = -D_M . \nabla c_M - U \chi_M \hat{z}$, c_M is the concentration of *L* in the media, D_M is a diffusion tensor and χ_M is the slip coefficient.

The key concepts are that the permeability, κ, of the endothelial layer (which lines the artery) to cholesterol in the blood depends on the local wall shear stress due to the flow of blood, and that the presence of *LO* in foam cells leads to swelling of the arterial wall and changes the flow producing a feedback mechanism. Specific functional forms need to be specified for these two processes. As a first step, the permeability of the endothelial cells is given by the quadratic formula

$$\kappa = \kappa_0 (\tau - \tau_0)^2 + \kappa_{\min} \, ,$$

where τ_0 is the value of the wall shear stress giving the minimum enodothelial permeability, and τ is the wall shear stress. This functional form gives high permeability at both low and very high wall shear stresses but in most of our simulations $\tau < \tau_0$. The swelling of the arterial wall is described by a simple first order process in which the increase in the height of the endothelium is made proportional to the excess of *LO* in the intima below it i.e.

$$h(x,t) = \eta \int_{-H_I}^{h} \left[c_{LO}(x,z,t) - c_0(x,z,t) \right] dz$$

when the integral is positive and $h = 0$ otherwise. Here η is a constant, h is the height of the endothelial layer above the mean height $z = 0$, H_I is the depth of the intima, and c_0 is the background concentration of *LO* within the intima.

RESULTS

Both steady and pulsatile flows have been simulated in a 2D channel, using standard asymptotic results for high Reynolds number flows [1,2], together with steady flow in a 3D model. The results confirm that changes in the structure of the wall with age increase the likelihood of the incidence of atherosclerosis, and show a good correlation between the most common sites of atherosclerosis in man and the persistence of fatty streaks when we use the physiological parameter values for those sites in our model. We also find an unexpected connection with the early stages of the formation of another important arterial disease — abdominal aortic aneurysms.

REFERENCES

Smith, F.T. (1976). Flow through constricted or dilated pipes and channels: part 2. *Quarterly Journal of Mechanics and Applied Mathematics*, **29**, ' 365-376

Duck, P.W., (1978). Oscillatory flow through constricted channels and axisymmetric pipes. *Proceedings of the Royal Society of London*, **A363**, 335-355

DETERMINING NEUROMUSCULAR CONTRIBUTIONS TO ACL INJURY RISK VIA COMPUTER SIMULATION

Scott McLean[1], Anne Su[1] and Anton J van den Bogert[1]

Department of Biomedical Engineering, The Cleveland Clinic Foundation, Cleveland, USA
mcleans@bme.ri.ccf.org, http://www.lerner.ccf.org/bme/

INTRODUCTION

During a number of sporting postures, the knee joint may be subjected to complex dynamic motions (eg., cutting and pivoting), generating large loads that have the potential to cause anterior cruciate ligament (ACL) injury. Cadaveric studies have provided some insight into potential mechanisms of ACL injury (Markolf et al., 1995). However, research of this type cannot reproduce the muscle forces and whole body dynamics typical of in vivo motion in young healthy individuals. The *in vivo* mechanical response of the ACL has been investigated via instrumentation for non-hazardous movement and load conditions (Beynnon et al., 1997). These data cannot be extrapolated, however, to understand injury mechanisms. With proper validation, computer simulation offers the potential to quantify ACL loads during potentially hazardous dynamic motion, while controlling all aspects of neuromuscular control. The purpose of the current study was to simulate the effects of variability in neuromuscular control (NMC) parameters during sidestepping on ACL load and hence, determine their relative contributions to ACL loading and the subsequent risk of injury.

METHODS

A previously described and validated 3D lower limb model capable of estimating ACL load during the stance phase (0-200ms) of a sidestep (McLean et al., 2001) was used in the current study. Model inputs were obtained from initial contact 3D linear and angular kinematic positions and velocities, and GRF data measured across 10 sidestep trials in a single subject. Excitation patterns for each muscle group (n=11) were described by five optimized (simulated annealing) parameters, specifying the level of muscle stimulation at fixed (50 ms) increments from initial ground contact (t=0). ACL force for the optimized system was derived from the A-P constraint force between the tibia and femur, combined with the quadriceps and hamstrings muscle forces acting across the joint. Monte Carlo simulations (N=50000) were performed to determine the effect of measured variability in pre-impact body segment positions and velocities, and variability in quadriceps and hamstring activation on peak ACL force. Data were then submitted to a stepwise linear regression analysis to determine the relative contributions of each of the control variables (9 positions, 12 velocities and 2 activations) to peak ACL load.

ACKNOWLEDGEMENTS
Funded by NIH (AR47039)

RESULTS AND DISCUSSION

Monte Carlo simulations produced a mean peak ACL force of 132 ± 168N, with 101 of these simulations demonstrating a peak ACL force of greater than 800N (Fig 1). Regression results revealed that 65% of the control variables had a significant effect on peak ACL load (P<0.005), with quadriceps and hamstring activation and knee angle having the greatest influence (Table 1, Fig 2). The current method presents a means of quantifying the relative contributions of key NMC input variables to ACL force, while concurrently incorporating the effects of dynamic body motion. Computer simulation further enables the impact of each variable on ACL injury risk potential to be identified. Work in progress involves the incorporation of "out of plane" (varus-valgus and internal-external) external torques into the model, in order to provide a more realistic estimate of ACL force.

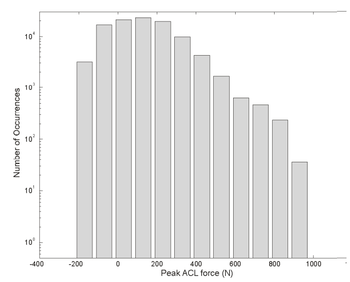

Figure 1: Effects of variability in NMC on peak ACL force.

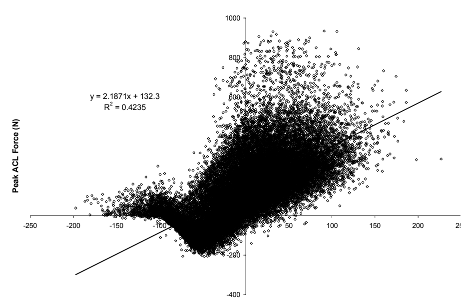

Figure 2: Peak ACL force versus % variation from optimized quads activation level during a simulated sidestep.

Table 1: Stepwise linear regression of the relative contributions of key NMC variables to ACL loading. The coefficients indicate the sensitivity of peak ACL force average (in N) to one unit change in input variable.

Input Variable	Coeff	T-Value	P
Quad Activation	216.9	174.46	0.000
Hams Activation	-160.3	-127.83	0.000
Knee Angle	731	52.32	0.000

REFERENCES

Markolf et al., (1995) *J Orthop Res* **13**:930-935.
Beynnon et al., (1998) *J Biomech* **31**:519-525.
McLean et al., (2001). Submitted for review, *J Biomech Eng*.

A GENERAL WEIGHTED LEAST SQUARES METHOD FOR INVERSE DYNAMIC ANALYSIS

Anne Su and A.J. van den Bogert, bogert@bme.ri.ccf.org
Department of Biomedical Engineering, The Cleveland Clinic Foundation, Cleveland OH

INTRODUCTION

Results of the conventional recursive method for Newton-Euler inverse dynamics (Winter, 1979) depend on the order in which the linked model is traversed. Kuo (1998) proposed an alternative method, solving joint moments from the overdetermined system of motion equations for the entire system while satisfying the boundary conditions for a postural control model. The method finds a set of joint moments that best agrees (in the least squares sense) with available measurements that have a known error variance. Having redundancy in the system of equations is attractive when certain measurements are unreliable, or even unavailable such as in instrumented treadmills with only vertical force transducers. With complete data, Kuo demonstrated about a 30% noise reduction compared to the conventional analysis. We have further developed this least squares inverse dynamics (LSID) method to be no longer restricted to systems with one fixed segment, which necessitated a new method to derive optimization weights using Monte Carlo simulations. The method was implemented as a general software tool that allows arbitrary 3-D or 2-D models to be defined, and generates and solves the equations automatically.

METHODS

The general computational method is as follows. A kinematic model is set up in Mocap Solver (Motion Analysis Corp., Santa Rosa CA), which solves generalized coordinates $\mathbf{q}(t)$ from marker trajectories. First and second derivatives of $\mathbf{q}(t)$ are obtained using smoothing splines (Woltring, 1986). From Mocap Solver the model is exported as an input file for SD/FAST (PTC, Needham MA), which was used to generate the dynamic equations of motion in the following form:

$$\mathbf{M}(\mathbf{q})\ddot{\mathbf{q}} = \mathbf{A}(\mathbf{q})\cdot\boldsymbol{\tau}_{\mathbf{u}} + \mathbf{B}(\mathbf{q})\cdot\boldsymbol{\tau}_{\mathbf{k}} + \mathbf{c}(\mathbf{q},\dot{\mathbf{q}}) \qquad (1)$$

where $\boldsymbol{\tau}_{\mathbf{u}}$ are all unknown forces and moments, typically the joint moments, and $\boldsymbol{\tau}_k$ are all known forces and moments, typically the force platform data. The number of unknowns in $\boldsymbol{\tau}_{\mathbf{u}}$ is usually smaller than the number of equations (degrees of freedom), and a weighted least squares solution can be obtained by solving the overdetermined system:

$$\mathbf{A}\cdot\boldsymbol{\tau}_{\mathbf{u}} = \mathbf{b} \quad \Rightarrow \quad \text{minimize} \left[(\mathbf{A}\cdot\boldsymbol{\tau}_{\mathbf{u}} - \mathbf{b})^{\mathbf{T}}\mathbf{W}(\mathbf{A}\cdot\boldsymbol{\tau}_{\mathbf{u}} - \mathbf{b})\right] \qquad (2)$$

with a weight matrix $\mathbf{W}$ that is the inverse of the error covariance matrix. A Monte Carlo simulation of error propagation is used to compute $\mathbf{W}$ from assumed error levels in marker coordinates and force plate signals. The unknown forces and moments $\boldsymbol{\tau}_k$ are solved from (2) using QR decomposition (Golub and Van Loan, 1989).

The method was evaluated using force plate and kinematic data generated by a 2-D forward dynamic rigid-body walking model (Gerritsen *et al.*, 1998) with known joint moments. Noise of 2.0 mm was added to the marker data and 200 N in the horizontal ground reaction force data. Joint moments were solved using the LSID software, for three cases: (1) using all available data and a 9-DOF model; (2) using only movement data (equivalent to top-down conventional approach); (3) using only lower extremity movement and ground reaction force (equivalent to bottom-up conventional approach). All data were low-pass filtered (10 Hz) before processing.

RESULTS AND DISCUSSION

Figure 1 shows the joint moments calculated from Case (1), which represents the best results attainable using the LSID method. Results were quantified using root mean square (RMS) values as an indication of how close the calculated joint moments are to the actual joint moments. Table 1 shows a comparison of the RMS values for all cases.

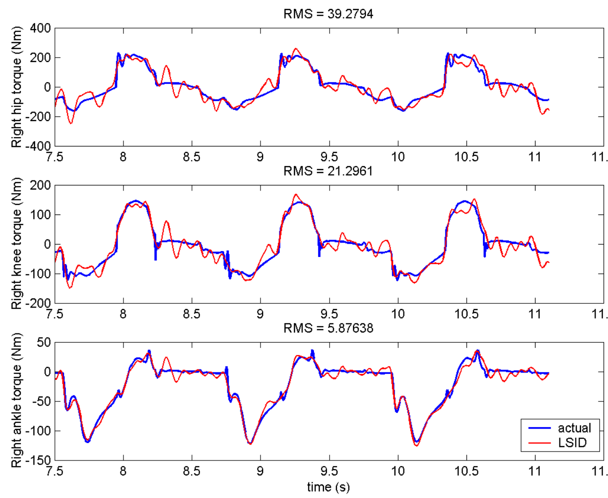

Figure 1: Actual joint moments and LSID results (whole body model).

Table 1: Comparisons of errors in joint moments, using different methods.

	RMS error (Nm) for right stance phase		
method	hip	knee	ankle
whole body model, LSID	39.279	21.296	5.876
whole body model, no force data	80.753	102.153	124.881
lower extremity model, conventional method	60.909	32.790	7.892

It is concluded that the LSID method provides the best estimate of joint moments in the presence of imperfect measurements when compared to the conventional top-down method and conventional bottom-up methods.

REFERENCES

Kuo AD (1998) *J Biomech Eng* **120**, 148-159.
Gerritsen KGM (1998) *Motor Control* **2**, 206-220.
Golub GH, Van Loan CF (1989) *Matrix Computations*. Johns Hopkins University Press.
Winter DA (1979) *Biomechanics of Human Movement*, Wiley.
Woltring HJ (1986) *Adv Eng Softw* **8**, 104-107.

ACKNOWLEDGEMENT

Supported by NIH (HD036645)

LIGAMENT STRENGTH DOES NOT DECREASE WITH SUBFAILURE STRETCHES

Joseph J. Crisco[1] and Manohar M. Panjabi[2]

[1] Department of Orthopaedics and Division of Engineering, Brown Medical School/Rhode Island Hospital Providence, RI
[2] Department of Orthopaedics and Rehabilitation, Yale University School of Medicine, New Haven, CT
E-mail: joseph_crisco@brown.edu

INTRODUCTION

Sprains or incomplete injuries comprise 85% or more of all ligament injuries and can lead to degenerative joint disease. Despite this prevalence, there is a paucity of information on ligament sprain injuries. Previously, in an *in vitro* biomechanical experiment we found that stretching the rabbit ACL to 80% of the failure deformation (about 16-20% ligament strain) subsequently increased laxity, but had no effect on failure load and deformation (Panjabi et al., 1996). We define a prior ligament stretch that is less than failure deformation as a subfailure stretch. The purpose of this study was to develop a phenomenological mathematical model of subfailure ligament injury in an attempt to better understand these experimental findings and ligament sprain injury mechanisms.

METHODS

The ligament model was composed of 250 (*n*) parallel fibers. Each fiber was ideally elastic with two distinct linear phases fully characterized by four parameters: initial stiffness K1, toe deformation D_T, final stiffness K2, and failure deformation D_F. Both K1 and K2 were assumed constant for all fibers, and had values of 0.001% and 1.0%, respectively, of the total ligament stiffness. In contrast, the deformations D_T and D_F were randomly selected from normal distributions of 40% ± 10% and 110% ± 30%, respectively.

All load and deformation values are defined as a percentage of the failure (peak) load (100%) and deformation at failure (100%) of the intact ligament model, i.e. the model without a subfailure stretch.

Subfailure stretches of 20, 40, 60, 80, and 100% were modeled and their effects on the load-deformation (L-D) curve of the intact model were studied. L-D curves were calculated by incrementally increasing the deformation D, determining the load each fiber *i* generated (l_i), and then summing the *n* fiber loads to determine the load generated by the total ligament (L):

$$L = \sum_{i=1}^{n} l_i = D \sum_{i=1}^{n} K(D).$$

For each fiber *i*, the stiffness K was a function of D, such that

$$K(D) = K1, \text{ if } D < D_T,$$
$$K(D) = K2, \text{ if } D_T < D < D_F,$$
$$K(D) = 0, \text{ if } D_F < D.$$

In the subfailure models, fibers that had failed with subfailure stretch were identified and their stiffnesses set to zero. The complete L-D curve was then recalculated from a zero deformation.

RESULTS

Failure load did not decrease even when the subfailure stretch reached 100% (Table 1). Ligament laxity (deformation at 5% failure load) increased for stretches beyond 40%, while fiber failure increased continuously in an exponential manner.

Table 1. Although fiber failure increased continuously, failure load was not affected by subfailure stretches (stretches less than 100%). Increases in ligament laxity initiated at about 40%. Subfailure stretch is the percentage of the deformation at failure (peak) load of the intact model. Failed fibers are a percentage of the total number of fibers, failure loads are a percentage of the intact failure load, and laxities are listed as deformation at 5% of intact failure load.

Subfailure Stretch	Failed Fibers (%)	Failure Load (%)	Laxity (%)
20 %	0.4	100	32.5
40 %	2	100	32.5
60 %	8	100	33.3
80 %	15	100	34
100 %	34	100	36.8

DISCUSSION

The model of subfailure stretches predicted unchanged ligament strength with some increase in ligament laxity. This finding of no change in failure load is in agreement with previous experimental work (Panjabi et al., 1996). One interesting finding was the small effect on the L-D curve due to subfailure stretches less than 80% deformation, despite failure of 15% of the fibers. We postulate that low magnitude subfailure stretches may be a mechanism for stimulating biological maintenance and repair of a ligament. In the future, this finding may be validated by *in vivo* studies which would correlate a biological/inflammatory response to a low-grade subfailure injury.

REFERENCES

Panjabi, M.M. et al. (1996). *J Orthopaedic Res.* **14**:216-222.

ACKNOWLEDGMENTS

This work was funded in part by the RIH Orthopaedic Foundation and University Orthopaedics, Inc.

A THREE-DIMENSIONAL MATHEMATICAL DYNAMIC SIMULATION OF THE KNEE EXTENSION EXERCISE: EFFECTS OF ANTERIOR CRUCIATE LIGAMENT INJURY

Dumitru I. Caruntu and Mohamed Samir Hefzy

Biomechanics Laboratory, Department of Mechanical Industrial and Manufacturing Engineering,
The University of Toledo, Toledo, U.S.A., mhefzy@eng.utoledo.edu

INTRODUCTION

Most of the anatomically based models of the knee joint are either for the tibio-femoral joint (TFJ) or the patello-femoral joint (PFJ). Also, most of these models are static or quasistatic. The only dynamic anatomical model that includes both joints is two-dimensional (Tumer and Engin, 1993). The only 3-D anatomical dynamic model available in the literature is for the TFJ and allows only for rigid contact (Abdel-Rahman and Hefzy, 1998). This paper presents a 3-D anatomically based dynamical model of the knee joint including both TFJ and PFJ. The model allows for deformable articular contact and for the wrapping of the quadriceps tendon around the femur at large flexion angles. Simulations were conducted to study the knee response during a knee extension exercise following an anterior cruciate ligament (ACL) injury.

METHODS

In the analysis the femur was fixed, while both tibia and patella underwent a general 3-D motion due to a forcing function applied to the quadriceps tendon. The twelve degrees of freedom describing TFJ and PFJ motions were defined using two joint coordinate systems (Abdel-Rahman and Hefzy, 1998, and Hefzy and Yang, 1993) and include 3 rotations and 3 translations for each of the tibia and patella. A simplified contact theory was used to allow for deformable contact at the articular surfaces.

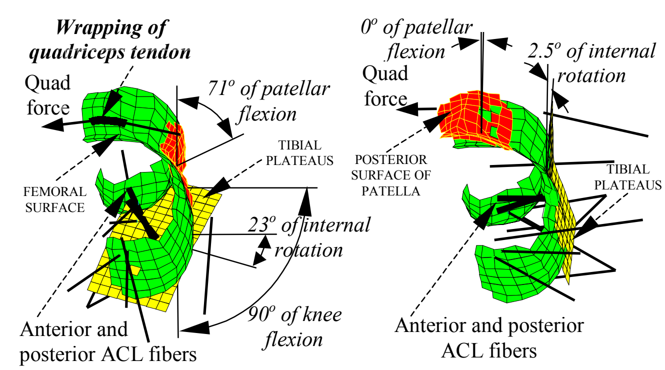

a. Initial position *(90° flexion)*

b. Final position (*full extension)*

Figure 1: Initial and final positions

Along with the posterior capsule, the lateral and medial collaterals, and the anterior and posterior cruciates were modeled using 12 nonlinear spring elements (Abdel-Rahman and Hefzy, 1998). The patellar tendon was modeled as a linear spring. Coons' bicubic surface patches were employed to allow for piecewise mathematical representation of the femoral, tibial and patellar articular surfaces (Hefzy and Yang, 1993). The dynamic response was obtained by solving a system of nonlinear differential algebraic equations using DASSL, a solver developed by Lawrence Livermore National Laboratory. Model calculations were conducted to simulate a knee extension exercise and to predict the effects of ACL injury. The quadriceps force was specified using Grood, *et al.*'s (1984) experimental data where its value increased from 75 N at 90° of flexion to 200 N at 50°, remained constant to 10°, and then increased rapidly to 350 N at full extension.

RESULTS AND DISCUSSION

Figures 1.a and 1.b show the specified initial positions and the predicted final positions, respectively, of the tibia and patella as they moved along the femur during the dynamic simulation for an intact knee. When both fibers of the ACL were cut, the anterior tibial displacement increased between 2.2 mm and 3.5 mm in the last 30° of knee extension, which is in agreement with Grood, *et al.*'s (1984) data. The maximum increase of 3.5 mm occurred at 15° with an increase of 2.4 mm at 0° flexion. This is in agreement with Shoemaker and Markolf's data (1985) reporting that the anterior laxity at 20° of flexion was somewhat greater than that seen at full extension.

SUMMARY

Since most injuries to the knee involve dynamic loads, this comprehensive 3-D mathematical and anatomically based dynamic model provides a valuable tool to study the underlying mechanisms for different knee injuries. The model was tested by simulating the knee extension exercise, a common rehabilitation regiment. The predicted significant anterior laxity in ACL-deficient knees during terminal extension suggests that this exercise may be detrimental. Keeping in mind that such an activity involves large joint compressive force, secondary ligament restraints may be stretched and/or the joint's articular cartilage could be damaged. Further simulations need to be conducted to determine the effects of extending intact and ACL-deficient knees with resistive weights placed at the foot.

REFERENCES

Abdel-Rahman, E.M., Hefzy, M.S. (1998), *Med. Engr.& Physics*, **20**, 276-290.
Grood, E.S. *et al*. (1984), *J. Bone Joint Surg.* **66A**, 725-733.
Hefzy, M.S., Yang, H. (1993), *J. Biomed. Engr.* **15**, 289-301.
Shoemaker, S.C., Markolf, K.L. (1985), *J. Bone Joint Surg. [Am],* **67A**, 136-146.
Tumer, T., Engin, A. (1993). *J.Biomech. Engr.*, **115**, 350-356.

ACKNOWLEDGMENTS

This work was supported by grant BES-9809243 from the Biomedical Engineering Program of the National Science Foundation.

CENTER OF MASS DISPLACEMENT DURING GAIT: NORMAL AND MYELOMENINGOCELE

Elena M. Gutierrez[1,2], Åsa Bartonek[2], Yvonne Haglund-Åkerlind[1,2], Helena Saraste[1,3]
[1]Dept. of Surgical Sciences, Karolinska Institute, [2]MotorikLab, Karolinska Hospital,
[3]Spine Division, Huddinge University Hospital, Stockholm, Sweden
Lanie.Gutierrez@kirurgi.ki.se

INTRODUCTION

The Center of Mass (CM) motion represents the movement of the body as a whole in a kinematic strategy and can provide information about mechanical work required in forward propusion. CM analyses in gait have often been limited to displacements, not position, and CM has at times been assumed as stationary in the pelvis (Inman et al, 1981). An understanding of the effects weakness and compensatory mechanisms have on the CM movement can provide information about strategies to optimize forward progression.

METHODS

In this study, 28 self-ambulating subjects with myelomeningocele (MMC, 6-17 years, mean age 10.4 years) and 14 healthy controls (5-12 years, mean age 10.7 years) were tested in 3-D gait analysis and strength was tested with a Manual Muscle Test. The subjects were divided into 5 muscle strength groups with Group 5 having the least muscular weakness (plantarflexors only) and Group 1 the most (below knee plus hip abductors and extensors). Distribution was as follows: Group 5: N=9, Group 4: N=6, Group 3: N=3, Group 2: N=6, Group 1: N=4. Gait analysis with a full-body (15 segment) marker set was performed (Vicon® 512, Plug in Gait Model). The CM was defined as the centroid of the segments. Five stride cycles for each subject were analyzed. Peak-to-peak movement of the CM in the medio-lateral and vertical directions was determined and normalized by each individual's average leg length, and mean displacements were compared for the different muscle-strength groups.

The CM transverse movement within the pelvis was calculated as the CM position relative to the midpoint between hip joint centers and rotated by the pelvic rotation angle, and was normalized to each subject's inter-hip joint center distance. A ensembled average of 5 strides was calculated for each subject.

RESULTS AND DISCUSSION

Medio-lateral CM displacement was larger in the MMC subjects as compared to normal and increased with muscle weakness (Figure 1). Vertical CM displacement displayed a non-linear relationship to muscle strength group and was greatest in Groups 3 and 4. The CM was observed to travel much further within the pelvis in the transverse plane in MMC subjects than in controls and varied both in distance traveled and in overall position (Figure 2).

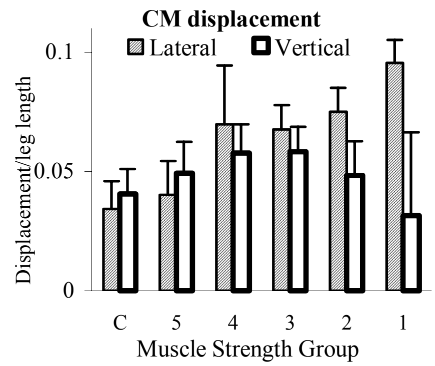

Figure 1: Peak medio-lateral and vertical CoM displacement (+ 1 SD) as a function of decreasing muscle strength groups.

The ability to displace CM minimally during gait is sacrificed in MMC due to compensatory movements resulting from muscle paresis. The increase in medio-lateral CM movement in MMC results from excessive lateral trunk and pelvis motion. The vertical CM displacement in MMC is increased in Groups 3 and 4, probably due to weak plantarflexors and lack of loading response, and is decreased in Groups 1 and 2, likely due to reduced sagittal plane motion. The strategy with weak hip abductors and extensors is for a less anteriorly-positioned CM in which, due to large pelvic rotations, forward progression is enabled through lateral movements. There is, furthermore, little doubt that the CM cannot be assumed stationary in the pelvis during gait in persons with MMC.

REFERENCES

Inman, VT et al (1981). *Human Walking*, Williams & Wilkins, pp. 2-22.
Kadaba M.P. et al (1990). *J. Orthopaedic Research*, **8**,383-92.

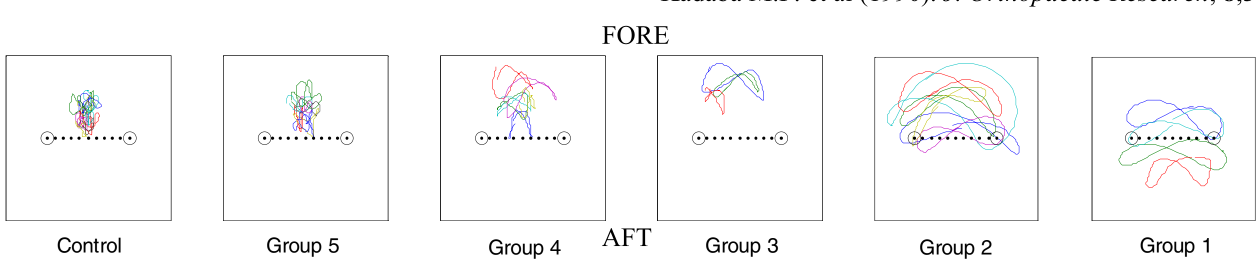

Figure 2: CM trace in transverse plane within pelvis for Controls and 5 MMC groups, ranked in decreasing muscle strength in the lower limbs (hip centers shown)

DIFFERENCES IN ANKLE AND KNEE JOINT STIFFNESS BETWEEN STRENGTH-TRAINED AND AEROBIC-TRAINED ATHLETES WHEN HOPPING AT A PREFERRED FREQUENCY

Gary D. Heise, Michael Bohne, Cheng-Tu Hsieh

School of Kinesiology and Physical Education, University of Northern Colorado, Greeley, CO 80639
E-mail: gary.heise@unco.edu

INTRODUCTION

McMahon and colleagues modeled the leg(s) in contact with the ground during hopping and running as a simple linear spring (Fig. 1). Leg stiffness (k_{leg}), the ratio of maximum force during foot contact to ΔL, has been linked to athletic performance. Mero and Komi (1986) found differences between top sprinters and less-skilled sprinters. Chelly and Denis (2001) showed a relationship between k_{leg} and maximal running velocity in a group of young, team handball players. In addition, Arampatzis et al. (1999) suggested knee joint stiffness plays an important role in efficient running.

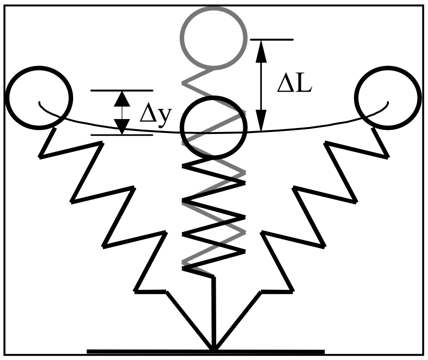

Fig 1: Leg spring model (adapted from McMahon & Cheng, 1990).

In light of the aforementioned links to sprinting, an anaerobic activity, we investigated the difference in leg spring characteristics between two groups of athletes during hopping. Specifically, we hypothesized that leg stiffness and joint stiffnesses of the lower extremity would be higher in strength-trained athletes when compared with aerobic-trained athletes.

METHODS

Three strength-trained athletes and three aerobic-trained athletes volunteered as subjects. Each subject attended one test session which included a warm-up and preferred frequency hopping for 3 min. Ground reaction force (GRF) data and sagittal plane video records of hopping were collected.

Hopping frequency and k_{leg} were determined from force platform data (Farley et al, 1991). Joint stiffnesses were calculated from an inverse dynamics analysis. Kinematic data were synchronized with force data to produce net joint forces and torques (NJT) at the ankle, knee, and hip. Joint stiffness was defined as the ratio of the change in NJT to joint angular displacement (Farley et al., 1998). Statistical comparisons were made with t-tests.

RESULTS AND DISCUSSION

NJT and angular displacement showed linear relationships at the ankle and knee joints, however, the hip joint did not and thus hip joint stiffness was not included in our analysis. Leg stiffness, ankle joint stiffness, and knee joint stiffness were 1.6-2.0 times higher in strength-trained athletes when compared with aerobic-trained athletes (Table 1). Hopping frequency and stiffness values were similar to those previously reported (Farley et al., 1998).

When comparing apparent spring constants, Luhtanen and Komi (1980) showed differences between trained long jumpers and untrained athletes while running. The differences found in the present study are also consistent with those who have identified a correlation between leg stiffness and sprinting performance, an anaerobic activity (Chelly & Denis, 2001; Mero & Komi, 1986). It remains to be seen, however, whether the difference in leg stiffness between groups is influenced more by the change in muscle activation or by the adaptation of muscle and tendon brought about by different forms of chronic exercise.

REFERENCES

Arampatzis, A et al. (1999). *J. Biomech.*, **32**, 1349-1353.
Chelly, SM, Denis, C (2001). *Med. Sci. Sports Exerc.*, **33**, 326-333.
Farley, CT et al. (1991). *J. Appl. Physiol.*, **71**, 2127-2132.
Farley, CT et al. (1998). *J. Appl. Physiol.*, **85**, 1044-1055.
Luhtanen, P, Komi, PV (1980). *Eur. J. Appl. Physiol.*, 44, 279-289.
Mero,A, Komi,PV (1986). *Eur. J. Appl. Physiol.*, 55, 553-561.
McMahon, TA, Cheng, GC (1990). *J. Biomech.*, **23** (Supp), 65-78.

ACKNOWLEDGEMENTS

Funding provided by the University of Northern Colorado Summer Graduate Research Assistantship Program.

Table 1: Mean Leg Spring Model Characteristics and Joint Stiffnesses Between Groups (± SD).

	Hopping Frequency	Leg Stiffness (p=.08)	Ankle Stiffness (p=.13)	Knee Stiffness (p=.11)
Strength-Trained	2.2 + 0.2 Hz	25.9 ± 7.7 kN m^{-1}	465 ± 237 N m rad^{-1}	792 ± 392 N m rad^{-1}
Aerobic-Trained	2.2 + 0.2 Hz	16.0 ± 5.1 kN m^{-1}	259 ± 99 N m rad^{-1}	393 ± 211 N m rad^{-1}

USE OF AN INTER-SEGMENT FOOT MODEL TO DESCRIBE KINEMATIC COUPLING BETWEEN THE FIRST METATARSAL PHALANGEAL JOINT AND THE REARFOOT IN NORMAL AND EXCESSIVELY PRONATED FEET

Deborah A. Nawoczenski[1], Jeff R. Houck[1] and Esther Barnes[2]
[1]Movement Analysis Laboratory, Ithaca College - University of Rochester Campus, Rochester, New York, USA
dnawoczenski@ithaca.edu
[2] Department of Biomedical Engineering, Northwestern University, Chicago, Illinois, USA

INTRODUCTION

Excessive subtalar joint (STJ) pronation has been linked to a progressive loss of motion in the first metatarsophalangeal (MTP) joint, referred to as hallux limitus or rigidus (Shereff, 1998). Although not demonstrated through previous motion analysis investigations, a transient restriction in motion at the 1st MTP joint resulting from excessive or prolonged STJ pronation, coupled with inadequate first metatarsal plantarflexion have been theorized to occur during normal gait (Roukis, 1996). Treatments aimed at minimizing the potentially detrimental effects associated with these abnormal movement patterns include foot orthotic therapies, special footwear and surgeries. In spite of the financial implications associated with these therapies, the kinematic relationships have not been verified through inter-segment foot analysis studies. The purpose of this study is to identify differences in kinematic coupling between hallux-first MTP joint dorsiflexion, calcaneal eversion and first metatarsal translation between normal and excessively pronated feet during the stance phase of walking.

METHODS

Fifteen subjects (8 females, 7 males) with a mean age of 22 years (range 19-24), and no history of first MTP joint pathology participated in the study. Eight subjects were classified as having "normal" foot structure; 7 subjects were defined as pronators based on a clinical orthopaedic examination. The Optotrak motion analysis system (Optotrak, Northern Digital, Inc) was used to collect three-dimensional position and orientation data of four modeled rigid body segments (hallux, first metatarsal, calcaneus, and tibia) during the stance phase of walking (Leardini, 1999). A minimum of ten walking trials were collected. Transformation matrices were generated that related the assumed constant orientation of the sensors to the anatomically based local coordinate systems established for the hallux, first metatarsal, calcaneus and tibia. A Cardan angle system of three ordered rotations (Z-Y-X) was used to extract angular information of the hallux relative to the first metatarsal (dorsiflexion/plantarflexion, Z-axis), the calcaneus relative to the leg (inversion/eversion, Y-axis) and the vertical translation (y-axis translation) of the distal metatarsal relative to the global coordinate system. Our findings challenge current theories regarding the link between excessive STJ pronation and the loss of first MTP dorsiflexion joint motion during gait. See Figure 1. Greater MTP dorsiflexion was demonstrated in the group of pronators.

In addition, metatarsal y-axis translation and peak values for calcaneal eversion were similar for both the normal and pronated feet.

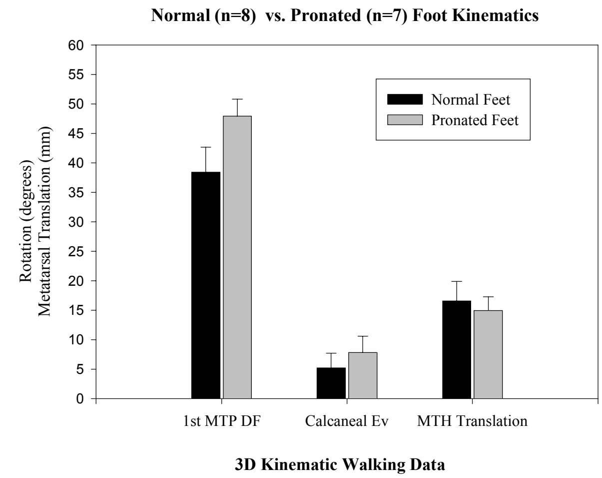

Figure 1. Mean and standard deviation values for first MTP dorsiflexion (DF): pronators: 47± 3 degrees, normals: 38 ± 4 degrees; Calcaneal eversion: pronators: 7.8 ± 3, normals:5.3 ± 2.5; Metatarsal head (MTH) translation: pronators: 15 ± 2mm, normals: 16 ± 3mm.

SUMMARY

Our findings in a group of young adult pronators suggest that motion in the first MTP joint may be excessive, rather than restricted during normal walking gait. It is unknown whether these movement patterns may precipitate arthritic joint changes or if they vary with the aging process. Additional studies are warranted to further test movement patterns across the life span and re-evaluate the goals of current therapies for abnormal pronation in the young adult foot.

REFERENCES

Shereff, M.J., Baumhauer, J.F. (1998). *J Bone Jt Surg*, **80-A,** 898-908.
Roukis, T.S. et al (1996). *J Am Podiatr Med Assoc,* **86,** 538-546.
Leardini, A. et al (1999). *Clin Biomech* **14**, 528-536.

ACKNOWLEDGEMENTS

This work was supported in part by the RUBI Program - Research for Undergraduates in Biomechanics and Imaging (NSF-REU # EEC-0097470).

MECHANICAL ASPECTS OF PLAQUE REDISTRIBUTION DURING ANGIOPLASTY: POSSIBLE CONSEQUENCES ON VULNERABILITY

Adrian Ranga[1], Rosaire Mongrain[1,2], Jean Brunette[2] , Jean Claude Tardif[2]
[1]Mechanical Engineering, McGill University, Montreal, Canada
[2]Montreal Heart Institute

INTRODUCTION

Rupture of atherosclerotic plaque is considered to be the principal initial cause of acute coronary syndromes. The biomechanics involved in plaque rupture are not fully understood, however it has been shown that mechanical stresses applied on different plaque constituents play an important role. Previous approaches have emphasized the direct relation between high stress concentrations on lipid pool boundaries and an increased probability of plaque rupture at the associated locations (Lee et al. 1993). Using 3D reconstructions from *in vivo* intravascular ultrasound (IVUS) clinical data, we present a study of the redistribution of non-ruptured plaque inclusions after angioplasty. The hypothesis is that certain reconfigurations could play a role in plaque vulnerability. For example, lipid extrusion and infiltration within the plaque could lead to a more inflammatory condition, and rearrangement of constituents may affect global structural integrity.

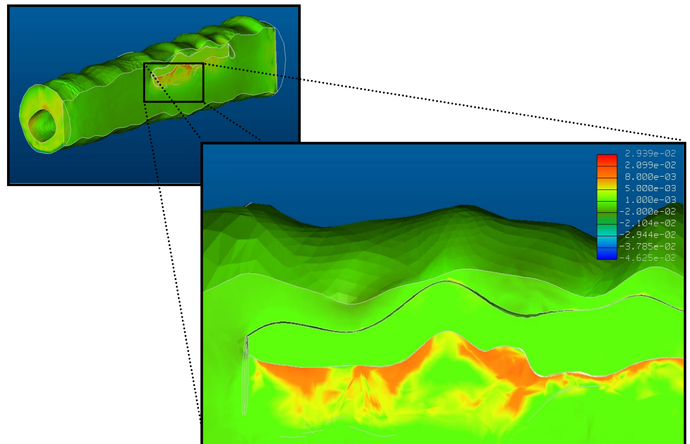

Figure 1: Fringe plot showing maximum principal stress on the boundary between inclusion and arterial wall.

METHODS

Clinical cases with pre-angioplasty, post-angioplasty and 6-month follow-up data were selected. Segmentation of *in vivo* sequences from IVUS images was manually performed to obtain geometrical contours for the vessel wall and plaque architecture. The contour data was processed in Matlab and exported to Pro/Engineer CAD software to generate a realistic 3D model of the wall and intraplaque complex structure. Mechanical properties of the different constituents (from existing literature), boundary conditions and load due to blood pressure were then incorporated into the model, and structural analyses were performed using Pro/Mechanica. Stresses, strains, and other mechanical measures around boundaries between different constitutents were obtained, and regions of high stress concentrations were identified. Post-intervention geometries and locations of maximal stresses, which are possible indicators of increased vulnerability, were compared to those obtained in pre-intervention models.

RESULTS AND DISCUSSION

The 3D reconstructions have introduced an element of perspective to commonly used IVUS 2D visualization methods, and have been useful in determining a global picture of plaque geometry.

Cases with differing geometric configurations and plaque materials were selected to permit a wider range of exploration. Results have indicated that plaque reconfiguration does indeed occur in a manner consistent with previously published results (Baptista et al. 1996), with radial compression forces leading to circumferential extrusion. Initial stress analysis results lead us to believe that there is indeed a relation between regions of high stress in plaque constituents and their increased propensity to displace within the plaque at specific sites. Work currently being carried out seeks to establish whether post-angioplasty stresses in newly reconfigured constituents are higher than pre-angioplasty ones. For lipid pools, this would be expected, as evidenced by results from simplified geometric models. Extrusion of lipid constituents into adjoining tissue may be indicative of lower load-bearing ability, and infiltration may increase the occurrence of inflammatory reaction; both mechanisms could be factors in increased plaque vulnerability.
The ongoing work currently being done suggests that it is possible that the redistribution of plaque during angioplasty may lead to local increases in stress around inclusion boundaries, therefore potentially increasing plaque vulnerability.

REFERENCES

Baptista, J. et al (1996). *Am J Cardiol*; **77** :155-121
Lee, R.T. et al (1993). *J Am Coll Cardiol*; **21**: 777-82
Holzapfel, G.A. (2000). *BioMech Preprint Series*. Institute for Structural Analysis,Graz University of Technology

THE CONTRIBUTION OF ELASTIN AND COLLAGEN TO RESIDUAL STRAIN IN PORCINE AORTA

Jingli Wang[1], Namrata Gundiah[2], Lisa Pruitt[1,2]

Medical Polymer and Biomaterials Group, University of California, Berkeley, U.S.A
[1]Bioengineering Graduate Group, UCB/UCSF
[2]Mechanical Engineering Department, U.C. Berkeley, lpruitt@newton.berkeley.edu

INTRODUCTION

Arteries are composite structures with elastin and collagen as the two main load-bearing constituents. Arterial aging and diseases result in altered elastin and collagen content. In its unloaded intact state, an artery is not stress free: an unloaded artery ring springs open and becomes a sector when it is cut longitudinally along the vessel wall. Residual strain helps to reduce the stress and stress gradient across the wall (Chuong, 1986). The purpose of this study is to establish the contribution of elastin and collagen to residual strain using a porcine model. The characterization of residual strain as a function of arterial composition is crucial for future studies modeling arteries using strain energy functions.

METHODS

Porcine thoracic aortas were harvested and stored in physiological saline solution with papaverine (PSS). The aorta was cut into 2mm-thick rings. The rings were divided into groups of four rings each. One ring in each group served as untreated reference; the other three were to be digested with enzymes. Three groups were digested with 10 unit/ml of porcine pancreatic elastase buffered in PSS solution at pH 7.4 for 20, 40, and 60 minutes at 37 °C after an 1-hr immersion in the same solution at 4 °C. Another three groups were digested with 400 unit/ml of collagenase buffered in PSS solution at pH 7.4 for 45, 90, and 135 minutes at 37 °C after an 2-hr immersion in the same solution at 4 °C. After the specified digestion interval, the rings were opened by a single cut placed longitudinally along the vessel wall.

Elastin was isolated from another aorta by repeated autoclaving, treating in 6M guanidine hydrochloride and more autoclaving cycles. The purified elastin was then sectioned into 3 2-mm thick rings, which were immersed in a 37 °C PSS bath and cut open

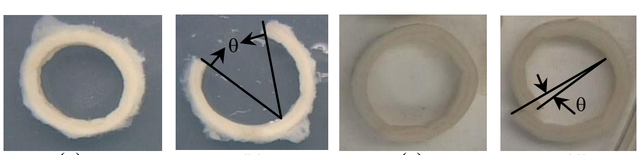

(a) (b) (c) (d)

Figure 1: (a) elastase digested: intact state; (b) elastase digested: zero-strain state; (c) elastin ring: intact state; (d) elastin ring: zero-strain state.

The opening angle θ, a measure of the residual strain in arteries, was determined from the direct measurement of the angle in the stress-free state (Figure 1).

RESULTS

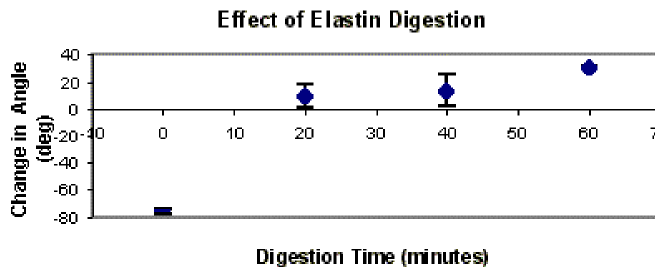

Figure 2: Difference in opening angle between elastase

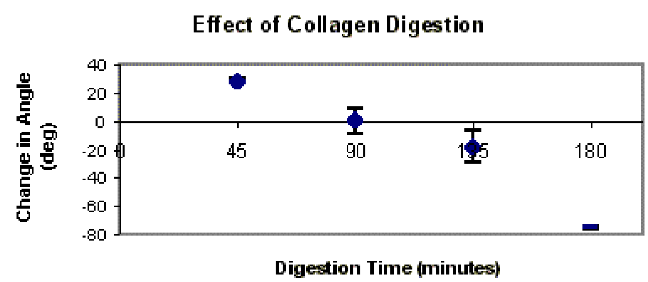

digested rings and reference rings vs. digestion time. Measurement for purified elastin ring is plotted at time = 0.
Figure 3: Difference in opening angle between collagenase digested rings and reference rings vs. digestion time. Measurement for purified elastin ring is plotted at time = 180 minutes.

As elastin is removed, the opening angle increases with respect to the reference ring and departs further away from that of purified elastin rings. As collagen is removed, the opening angle deceases with respect to the reference ring, moving it closer to the behavior of purified elastin.

SUMMARY

This study shows that the presence of elastin reduces the opening angle while the presence of collagen increases the opening angle for porcine aortas.

REFERENCES

Chuong, C.J., Fung, Y.C. (1986). *J. Bio. Eng.*, **108**, 189-192

THE EFFECTS OF A HOME-BASED FORCED-USE INTERVENTION ON INDIVIDUALS WITH CEREBROVASCULAR ACCIDENT

K. Mitchell[1], M. Barber, J. McGruder, G. Tomlin, M. Horger and J. Abendroth-Smith[2]
[1]University of Puget Sound Tacoma, WA [2]Willamette University, Salem OR

INTRODUCTION

There are approximately 550,000 strokes each year in the United States that result in 150,000 deaths and 300,000 survivors left with significant disabilities (Bartels, 1998). Of these survivors most learn to walk again, but 30% to 60% never regain the full use of their affected upper extremities (UE) (van der Lee et al., 1999). Many rehabilitation strategies are designed to improve functional return after UE hemiparesis.

A more recent therapy, called forced use or constraint induced movement therapy, began with observations of monkeys with severed sensory nerve roots of an upper extremity. Non-use of these limbs was observed, even though motor nerve pathways of the affected limbs were left intact. Because of the sensory loss, the monkeys learned that it was difficult, even painful to use their affected limbs. Because they could function adequately in their caged environment by using their other three limbs, they quit attempting to use their damaged extremities altogether. The unaffected UEs of the monkeys were then immobilized in order to alter this learned non-use behavior. Forced use of the monkey's affected limb led to improved motor function and a change from the learned non-use behavior (Taub et al., 1994). Forced use therapy has since been used with varying degrees of success in the treatment of the affected upper extremity of human cerebrovascular accident (CVA) survivors (Benevento, 1998).

The purpose of this study was to determine the potential rehabilitation effects of forced use when employed in a home environment with persons more than one year post-CVA as determined by kinematic motion analysis.

METHODS

A pretest- posttest control group design was used. A total of 6 participants that met the inclusion criteria patterned after Wolf et al. (1989) were randomly assigned to either an experimental or control group (sound limb constraint using a resting hand splint or no constraint). All participants signed a behavior contract. Five movements from the Wolf Motor Function Test were videotaped (30 hz) for each participant for both the affected and sound limbs before and after treatment, and analyzed using a 2-D motion analysis system. Pretest /posttest differences in angular positions and linear velocities were examined for each movement and compared with the sound side movements.

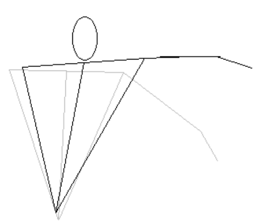

Figure 1. Abduction of the shoulder to lift the forearm and hand onto a nine-inch box.

RESULTS AND DISCUSSION

No consistent trends or differences were noted between the experimental and control groups for any of the observed movements. Individual changes were noted which could represent improvement. One of the changes of interest occurred during a movement that involved abducting the shoulder in the frontal plane thus lifting the forearm and hand onto a nine-inch box placed adjacent to the participant (Figure 1). An experimental group member's pretest demonstrated a delayed peak velocity, but the posttest and sound side peak velocity occurred at approximately the same time marker. The approximate amplitude for both pretest and posttest velocities were similar (Figure 2). This result suggests a return to a normal movement pattern for this particular movement.

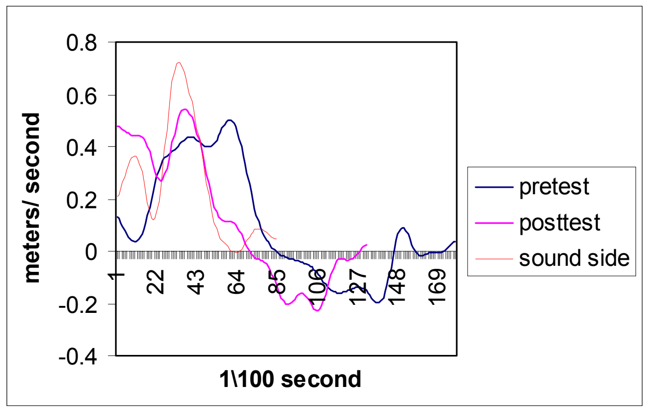

Figure 2. Vertical velocity of elbow during a movement.

SUMMARY

Past studies have shown that forced use can produce statistically significant improvements in hemiparetic patients. Results from this study show a potential trend toward normal movement patterns for some of the participants. However, these observations cannot be directly attributed to forced use. Examination of kinematic variables does allow for a more controlled examination of the relative success of movement for UE hemiparesis.

REFERENCES

Bartels, M. (1998). In G. Gillen, & A. Burkhardt, (Eds.) **Stroke rehabilitation: A function-based approach** (pp. 1-30). St. Louis: Mosby.
Benevento, A. (1998). **Oc Ther in Hth Care** *11*, 59-76.
Taub, E., et al. (1994). **J of the Exp Analysis of Behavior** *61,* 281-293.
van der Lee, H. J. et al.. (1999). **Stroke** *30*, 2369-75.
Wolf, S. L., et al. (1989). **Exp Neurology** *104*, 125-132.

THREE-DIMENSIONAL FIBER-REINFORCED FINITE ELEMENT MODEL
OF THE HUMAN ANTERIOR CRUCIATE LIGAMENT

Ashraf Ali[1] , Cy Frank[2] and Nigel Shrive[3]

McCaig Center for Joint Injury and Arthritis Research, University of Calgary, Calgary, Alberta, Canada
[1]B.Sc. Civil Engineering, afali@ucalgary.ca
[2]McCaig Professor of Joint Injury and Arthritis Research
[3]Killam Research chair

INTRODUCTION

The knee is one of the most frequently injured joints in the body. Studies estimate that 1.6 to 1.9 million patients, most between the age of 15 and 44 years, see a physician for a knee sprain each year (Butler, 1989). Among those who sustain an acute traumatic hemoarthrosis to the knee, the anterior cruciate ligament is partially or completely torn more than 70% of the time (DeHaven, 1980).
Experimental studies of ACL mechanics are technically difficult, costly, and prone to error. The emerging field of computational biomechanics (finite element (FE) method) offers a new set of tools for studies of solid and fluid biomechanics that can provide information that would otherwise be difficult or impossible to obtain from experiments (Yamamoto, 1998; Hirokawa, 2000).

METHODS

A mathematical Finite Element model for the human ACL is being developed that takes into account most of the complex characteristics of the ACL such as; three-dimensionally correct anatomical shape, helical fibre reinforcement with correct fibre alignment (angle of twist), hyperelastic stress-strain relationships, fibre recruitment, fibrer reorientation within the matrix, the role of water during ligament function (poroelastic model), a gradual change in the material properties (ligament to bone) near the insertion sites and time dependent characteristics such as creep and stress relaxation. A preliminary model is shown in (Figure 1). Accurate anatomical dimensions needed for the model will be collected from fresh cadavers.
PATRAN V.5 and ABAQUS V.6.1 are the two commercial FE packages used for data processing and analysis.

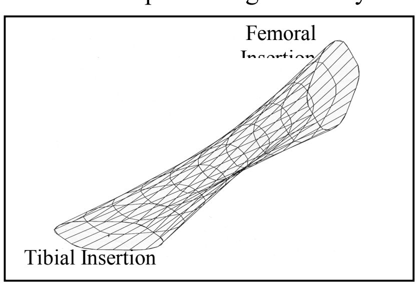

Figure 1: Three dimensional preliminary model of the human ACL with helically shaped fibres.

RESULTS AND DISCUSSION

Principal stresses (strains) in the fibres of the ligament can be obtained for different cases of external loading and/or relative deformations of the tibia and the femur. An example is shown in (Figure 2).
The ultimate goal of this modeling is to understand ACL mechanics so that reconstructed and/or synthetic ACLs can be adapted to fulfill normal mechanics more effectively, and to improve the clinical diagnosis and treatment of ACL injuries. The model may also identify means by which to prevent injuries, such as through the use of protective equipment in the case of sports-related injuries.

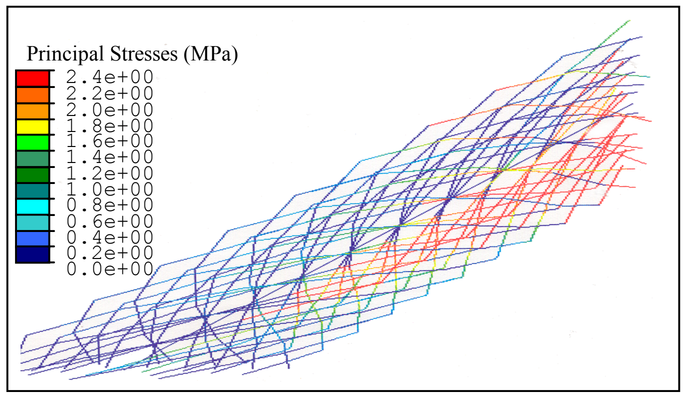

Figure 2: Principal tensile stresses caused by anterior displacement of the tibia relative to the femur by 3mm.

SUMMARY

A Finite Element model for the human ACL is being developed that considers most of its complex characteristics. The model is able to predict stresses and strains precisely within the ligament caused by different cases of loading. The model presents a new perspective for gaining a better understanding of the details of ACL function, injury mechanisms and the mechanical needs of reconstruction.

REFERENCES

Butler, D.L. (1989). *J. Orthop. Res.* **7**, 910-921.
DeHaven, K. (1980). *American J. Sports Medicine* **8**, 9-14.
Hirokawa, S., Tsurno, R. (2000). *J. Biomech.* **33**, 1069-1077.
Yamamoto, K. (1998). *Med. Engg. & Physics* **20**, 161-168.

PREDICTIONS OF RESIDUAL STRESSES IN BONE CEMENT FOR JOINT ARTHROPLASTY

Chaodi Li, Ying Wang, Steven Schmid, James Mason*

Department of Aerospace and Mechanical Engineering, University of Notre Dame, Notre Dame, Indiana, USA. *mason.12@nd.edu

INTRODUCTION

Bone cements are widely used to fix the prostheses into bones for joint arthroplasty. Residual stresses are introduced in the cement mantle as a result of curing shrinkage and constraints [Gilbert et al, 2000]. These stresses of sufficient magnitude could cause pre-load cracking and therefore could contribute to starting a damage accumulation failure scenario [Huiskes, 1993; Lennon et al, 2001]. Experiementaly determining the residual stresses in complex hip replacement systems is extremely difficult. In the present work, a finite element method was developed to predict the curing-induced residual stresses in the cements.

METHODS

The numerical predictions are based on heat transfer and sequentially coupled thermal–stress analyses.

In the heat transfer analysis, a phenomenological kinetic model was developed for the curing bone cement in which the dependence of polymerization rate and the local temperature are taken into account. This cure-dependent kinetic model has been shown to represent the polymerization behavior of the bone cement accurately for the range of temperatures expected in implant applications [Li et al, 2001]. The kinetic model was then coupled with the heat conduction equation and implemented using finite element method to predict the polymerization reaction and temperature development in the model system. Details of this method have been reported elsewhere [Li et al, 2001]. A sequentially coupled thermal-stress analysis was then performed to investigate the residual stresses in the cements. The residual stresses were determined by the stress-locked approach [Lennon et al, 2001]. In this paper, the reference temperatures for stress locking were selected from the temperatures at the end of polymerization [Lennon et al, 2001].

RESULTS AND DISCUSSION

To demonstration this finite element method, numerical analysis of a bone-cement-prosthesis system was performed with a simplified axisymmetric model, as shown in Figure 1.

Figure 1: The Bone-Cement-Prosthesis System Model

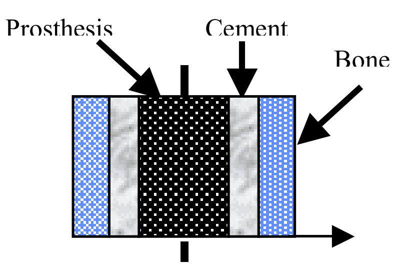

The model consists of a metallic prosthesis surrounded by a layer of bone cement that is in turn embedded in the bone. This closely models the behavior along the shank of a hip implant, where the cement is usually employed.

Figure 2(a) shows the temperature distribution in the cement at the end of polymerization. The heat transfer analyses indicate that the temperature in the middle of the cement layer increased higher than cement near the cement-prosthesis and cement-bone interfaces. The principle residual stress distribution is shown in Figure 2(b). The maximum stress is about 3.5 MPa. The built-up residual stress depends strongly on temperature developments which are related to curing history. By modifying the cure procedure, the residual stresses have been shown to be redistributed. It is expected that with careful control of curing procedure through implant design, system initial and boundary conditions, a desired low level residual stress in the critical region may be reached.

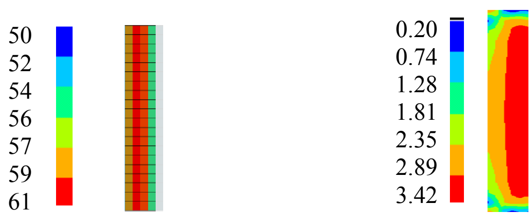

(a) Temperature (^{o}C) (b) Residual Stress (MPa)

Figure 2: Temperature (a) and Residual Stress (b) distributions in bone cement

SUMMARY

The method developed in this paper is able to predict the shrinkage residual stresses in bone cement in hip replacement systems. This method provides a numerical tool for the quantitative simulation of residual stress and for examining and refining new designs computationally.

REFERENCES

Bishop, NE. et al (1996), *J. Bone Joint Surg*, 78B(3), 349-356.
Gilbert, J. L., et al (2000). *J. Biomed Mater Res*, 52,210-218.
Lennon A. B., Prendergast, P., J. (2001). *J. Biomechanics* 0.
Li, C. et al (2001). *ASME BED-50*, 235-236.
Huiskes, R. (1993). *Current Orthopaedics*, 7, 239-247.

ACKNOWLEDGEMENTS

This research is supported by the 21st Century Research and Technology Fund, the State of Indiana, USA. The authors also thank Zimmer Inc. for it’s support.

MECHANISM OF INTRA-ARTICULAR CALCANEAL FRACTURES: THE EFFECTS OF ACHILLES TENDON LOADING

Susan E. D'Andrea, Gail P. Perusek, S. Solomon Praveen, Jennifer J.E. Kuznicki and Brian L. Davis
Department of Biomedical Engineering, The Cleveland Clinic Foundation, Cleveland, OH
Contact information: dandreas@bme.ri.ccf.org, http://www.bme.ri.ccf.org

INTRODUCTION

Calcaneal fractures are serious, debilitating injuries which are difficult to treat and rehabilitate. The severity of the injury is dependent on the type of fracture. The most difficult to manage are the intra-articular fractures which occur in seventy five percent of all calcaneal fracture cases (Colburn et al., 1989). The mechanism of the intra-articular calcaneal fracture has been attributed to two major factors the magnitude of the angle of Gissane (Essex-Lopresti, 1952) and the eccentric loading of the sustentaculum tali (Burdeaux, 1983). The current study focuses on these two mechanism with regards to calcaneal strain. By examining the influence of foot angle and muscular force on the calcaneal strain, an understanding of the interplay between lower limb configuration and intra-articular fracture can be determined.

METHODS

Experiments were performed on unembalmed human cadaveric legs dissected at the distal third of the tibia. Delta rosette strain gages were affixed in a known orientation at the angle of Gissane and the sustentaculum tali. The foot was placed in a custom made testing apparatus with an impacting surface resting on the forefoot (Figure 1).

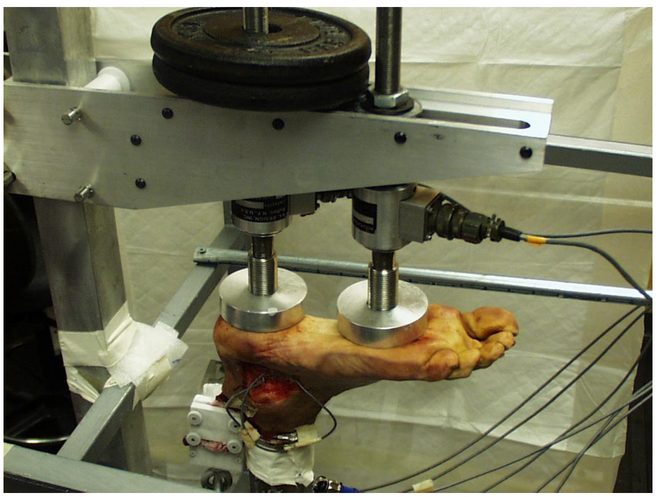

Figure 1: Experimental Testing Apparatus

A load cell was attached to the Achilles tendon in series with a freeze clamp. The Achilles tendon was loaded for two seconds in four experimental conditions: i. neutral ankle position, free-moving impactor, ii neutral ankle position, fixed impactor, iii. 10° plantar flexion, fixed impactor and iv. 20° plantar flexion, fixed impactor. Three strains signals for each rosette and Achilles force were recorded for each trial. Data were collected at 1000 Hz using a custom LabVIEW® program. Offset values were subtracted from each signal and principal strains at the angle of Gissane and the sustentaculum tali were calculated.

RESULTS AND DISCUSSION

Time series strain data showed similar patterns across trials and subjects. Principal maximum and principal minimum strains appeared as mirror images in time. Average peak maximum and minimum principals strain ranged between 400 – 900 με and -400 – -2400 με, respectively. Significant differences were present between Condition 1. Calcaneal strains were significantly related to the force in the Achilles tendon (Figure 2, $R^2 > 0.98$).

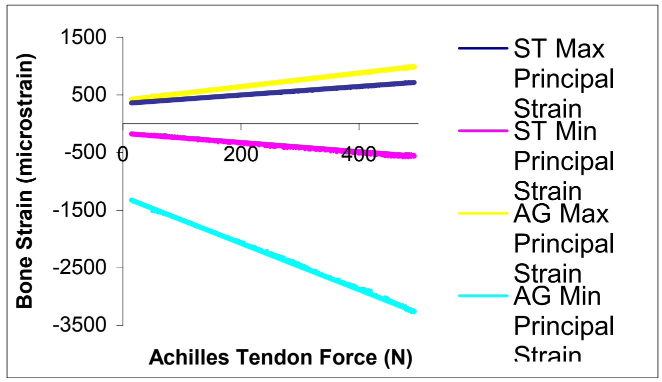

Figure 2: Principal Strains at the Sustentaculum Tali (ST) and Angle of Gissane (AG) versus Achilles Tendon Force

SUMMARY

Preliminary results show a high correlation between the load in the Achilles tendon and the subsequent strain in the calcaneus, particularly at the angle of Gissane. Further work will correlate the geometrical configuration of the calcaneus at the angle of Gissane and the sustentaculum tali to the magnitude of the principal strains. Additionally, results will allow for the direction of the principal strain to be evaluated in light of the orientation of the most common intra-articular calcaneal fracture lines

REFERENCES

Burdeaux (1983). *Clin. Orthopaedics*, 177:87-103.
Colburn et al. (1989). *J. of Foot Surgery*, 28(3): 249-254.
Essex-Lopresti (1952). *British Journal of Surgery*, 39: 395.

ACKNOWLEDGEMENTS

The authors would like to acknowledge funding from The Aircast Foundation.

ISSUES IN THE INTERPRETATION OF CONTINUOUS RELATIVE PHASE

Jeffrey M Haddad[1], Brian T. Peters[1,2], Bryan C. Heiderscheit[3], Richard E. A. van Emmerik[1] and Joseph Hamill[1]

[1]Motor Control and Biomechanics Laboratories, University of Massachusetts, Amherst, Massachusetts, USA.
[2]Wyle Life Sciences, Neuroscience Laboratories, Johnson Space Center, NASA, Houston, Texas, USA.
[3]Human Performance Lab, Des Moines University, Des Moines, Iowa, USA.

INTRODUCTION

The phase relationship between two signals has traditionally been identified as an important variable in quantifying coordination. Phase information is usually thought of as a reference phase, or the instant in time of one oscillator relative to a second at an arbitrarily chosen point. In the movement sciences this is often termed discrete relative phase (DRP) (Kelso, 1984). Recently, in an attempt to gather phase information across the entire period of a cycle, coordination was quantified utilizing a measure termed continuous relative phase (CRP) (van Emmerik et al. 1999). Whereas DRP is determined from temporal shifts at chosen events in the time series, CRP is typically calculated from position - velocity phase portraits of the component signals. Phase information calculated in this manner may be subject to artifacts if the state spaces used to calculate the phase angles are not circular (Fuchs et al. 1996). The aforementioned artifacts are not necessarily arbitrary in that the data are erroneous, but care needs to be given when interpreting the results of the CRP calculations. The purpose of this paper is twofold, namely: 1) to illustrate the traditional need for state-space normalization prior to calculating phase angles; and 2) to show that the interpretation of CRP information should be limited to describing the relationship between the individual state-spaces of the two signals and not be used to describe a relationship between their original time series data.

METHODS

CRP was calculated from two test signals with known phase and frequency properties. The test signals used were: 1) two sine waves with frequencies of $2\pi^{-1}$ Hz and $4\pi^{-1}$ Hz respectively; and 2) a skewed sinusoidal saw tooth wave. The skewed sinusoid was time shifted by 18° and 126°. CRP between the two sine waves was calculated with and without prior normalization of the state-spaces. CRP of the saw tooth waves was calculated between each phase shifted wave and a 0° offset reference wave. Phase planes were normalized by dividing the velocity by $2\pi/p$, where p is the period of oscillation. This technique maintains a consistent aspect ratio for all similar-shaped non-sinusoidal waves regardless of their period.

RESULTS AND DISCUSSION

Intuitively, the phase relationship across the cycle between the two sine waves, where one is twice as fast as the other, is a monotonically increasing line between 0° and 360°. This intuitive relationship was only observed after normalization. When no normalization was employed the phase relationship oscillated around the known DRP relationship. This oscillation was due to the elliptical shape of the phase plane of the higher frequency signal. Even without attempting to achieve a circular state-space and the intuitive monotonically increasing phase shift, without some form of normalization the CRP between 1 and 2 Hz sinusoids will not be the same as it is in a 2 vs. 4 Hz comparison. A coordination measure should be robust enough to yield an identical output when the relationship between the two inputs is identical regardless of the frequency.

The constant time lag between the non-sinusoidal saw tooth signals did not produce a constant CRP output. Moreover, the shape of the CRP pattern was not consistent between the signals with the 18° and 126° phase shifts. While other state-space normalization techniques typically used (Hamill et al., 2000) produce different CRP trajectories, none provide the constant output expected from a DRP measure. As a result of this difference between the information provided by CRP and DRP it is incorrect to state, for example, that a CRP value near 180° means that the two signals being compared are moving in opposite directions.

SUMMARY

Through simulation, we have shown that normalization is necessary to reduce the effects of frequency when using CRP to compare two signals. Additionally we have stressed that traditional CRP measures provide a relationship between the position-velocity state-spaces of two signals and therefore cannot reliably be used to describe the relationship between the two signals in the temporal domain. Caution should thus be used when interpreting CRP data and presenting its results.

REFERENCES

Fuchs, A. et al (1996). *Biol Cybern*, **74**, 21-30.
Hamill, J. et al (2000). *J. app Biomech,* **16,** 407-418.
Kelso, J.A., (1984). *Am J Physiol*, **246**, R1000-R1004.
Van Emmerik, R.E.A. et al (1999). *Arch Phys Med Rehabil*, **80**, 186-191.

CENTER OF PRESSURE MIGRATION DURING PROLONGED UNCONSTRAINED SITTING

Jason Lusk[1] and Qiong Wu[2]

Mechanical Engineering Department, University of Manitoba, Winnipeg, Manitoba, Canada
[1]M. Sc. Graduate Student
[2]Associate Professor, cwu@cc.umanitoba.ca

INTRODUCTION

The risk of developing pressure sores arises whenever tissues are exposed to excessive or prolonged mechanical loading. Although healthy, able-bodied individuals are always forewarned of excessive pressures by feelings of local discomfort, and can take the necessary corrective action, this is not the case for some populations, such as people with spinal cord injuries, diabetics and elderly. To prevent pressure sores, the idea of developing closed-loop automated seating systems, which allows for simultaneous adjustment of seating contours and measurement of the resulting pressure, has attracted much attention (Kwiatkowski and Inigo, 1993). Some studies have been carried out on understanding optimal seating (Levine *et al.,* 1990). In this work, the patterns of the pressure center migration of healthy individuals during prolonged unconstrained seating (PUS) will be studied. The main goal is to show that during PUS, specific and consistent patterns of the center of pressure migration exist. Investigations of healthy individual seating can contribute to better understanding of optimal seating.

METHODS

Fifteen healthy subjects, ten males and five females, participated in this study. Each subject was asked to sit on a force plate (Kistler 9286AA) for an interval of 30 minutes. The subjects were asked to sit in the middle of the force plate with their feet on a foot rest. They were not given any instructions on how to sit other than that once on the force plate they were required not to get off and their feet must rest on the foot rest. The subjects were allowed to adjust their posture in order to remain comfortable at all times. Each subject was allowed to converse with someone in the room, read a book, or listen to music during the data acquisition.

The data was collected using the Kistler BioWare software Version 3.21 for COP measurement. Each subject was given a few minutes to get comfortable before the data was recorded. The COP values were given in the X-Y plane, with the X direction corresponding to the anterior-posterior directions and the Y direction corresponding to the medial-lateral directions. The data was collected in 1½-minute intervals and transferred to an Excel spreadsheet, completing the 30-minute trial. Plots were then produced for both the x (a-p) and y (m-l) directions.

RESULTS AND DISCUSSION

As a result of the data acquisition it has been determined that COP migration patterns during prolonged unconstrained sitting do exist. Three COP migration patterns were found as shown in Figure 1: (1) shifting, a fast displacement of the average position of the COP from one region to another, (2) fidgeting, a fast and large displacement and returning of the COP to approximately the same position, and (3) drifting, a slow continuous displacement of the average position of the COP. Similar patterns were found in a study done on prolonged unconstrained standing (Marcos and Duarte, 2000). The following preliminary results have been obtained for a 30 minute trial PUS: shifting occurred approximately 13.3±8.8 times in the a-p direction (average amplitude of 16.6±12.3 mm) and 5.4±2.5 times in the m-l direction (average amplitude of 13.3±7.3 mm). Fidgeting occurred on average 16.1±4.3 times in the a-p direction (average amplitude of 21.7±13.3 mm) and 17.7±6.6 times in the m-l direction (average amplitude of 19.5±13.3 mm). Drifting occurred on average 1.4±1.4 times in the a-p direction (average amplitude of 13.4±8.0 mm) and 1.0±1.3 times in the m-l direction (average amplitude of 9.4±5.7 mm).

Currently, we are focusing on developing computer software to detect the COP migration patterns automatically.

REFERENCES

Kwiatkowski, R.J. and Inigo, R.M. (1993). *Journal of Rehabilitation Research*, **Vol. 30**, 393-404.

Levine, S.P., Kett, R.L., Ferguson-Pell, M. (1990). *Assistive Technology*, **1990 (2)**, 93-99.

Duarte, M., Zatsiorsky, V.M., (1999).*Motor Control*, **3**, 12-27.

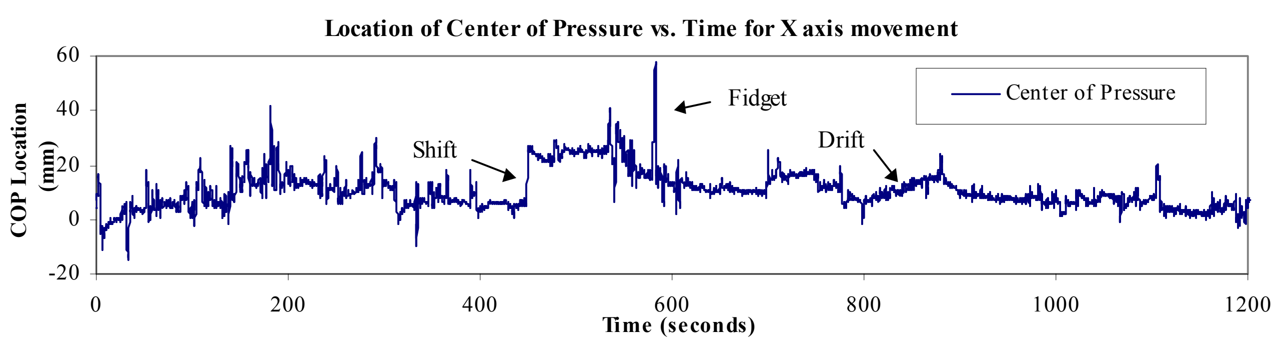

Figure 1: Three patterns found during prolonged unconstrained sitting.

EFFECT OF FATIGUE ON LEG KINEMATIC IN RUNNING TILL EXOSTION

Ales Dolenec and Branko Skof

Faculty of Sport, University of Ljubljana, Ljubljana, Slovenia

INTRODUCTION

Running is very well described by kinematic parameters. Althogh kinematic parameters are not so sensitive to fatigue as EMG parameters there are some changes in running kinematic during fatigue. The most noticeable changes in fatigue running compare to unfatigued running are stride frequency and stride length. There are changes in knee angle, too (Mizrahi et all. 2000). The aim of this experiment was to find out which kinematic parameters changed during the fatigue running compared to the unfatigued running.

METHODS

Eight well-trained middle distance runners (age 20.6 yrs ± 4.8; mass 66.4 kg ± 3.5) participated in the experiment. Running velocity (5.8 m/s ± 0.4) was 3 % lower than the velocity of their season best in 3 km run. Subjects were ordered to run as long as possible at given velocity. During the run the 3D kinematic parameters were obtained with APAS system (Ariel Dynamics Inc., USA). The running was filmed with two synchronized digital cameras, at 50 Hz frequencies. The masses and centre of gravity of the segments and the common center of gravity of the 15-segment model of the body were computed according to the anthropometric model (Dempster, 1955). Paired samples T-test was used to compare the kinematic parameters in non-fatigued and fatigued conditions.

RESULTS AND DISCUSSION

Although the running velocity during the experiment was 3 % lower than the velocity of their season best in 3 km run, only one subject was able to run 4050 m. One subject was running for 2850 m, two subjects were running for 2450 m and four subjects were running for 2050 m. This rather short distance of running is probably caused by weight of the measuring equipment (2 kg) that subjects were wearing during the run and that the experiment was done at the end of the season.

The results of the kinematic parameters are presented in table 1. The subjects were unable to sustain the running velocity constant in the last 400 m. The decrease of running velocity was small but significant. The subjects increased the contact time. This was made by increasing the leg angle at the moment of touch down and by increasing the knee angle amplitude during the contact phase. Increased knee angle amplitude during extension in fatigued conditions compared to the unfatigued conditions probably coused increase in maximal angle velocity during knee extension. Longer contact time in fatigued conditions compared to unfatigued conditions probably aloud smaller maximal angle velocity during hip contraction since this velocity is reached during the ground contact.

Table 1: Kinematic parameters in fatigued and non-fatigued conditions.

Parameters	Rest Mean ± SD	Tired Mean ± SD	p
Velocity	5.8 ± 0.4 m/s	5.4 ± 0.3 m/s	*
Contact time	168 ± 14.5 ms	188 ± 14.6 ms	*
Angle leg touch down	110.9 ± 3 deg	113.5 ± 2.7 deg	*
Ankle dorsiflexion amortization	16.2 ± 4.6 deg	19.9 ± 2.1 deg	**
Knee amplitude amortization	10.1 ± 4.2 deg	14.2 ± 3.6 deg	*
Knee amplitude extension	27.1 ± 4.9 deg	33.1 ± 4.5 deg	**
Knee angle velocity extension	399 ± 52 deg/s	440 ± 42 deg/s	*
Hip angel velocity contraction	580 ± 28 deg/s	554 ± 49 deg/s	*

* $p < 0.05$; ** $p < 0.01$

SUMMARY

The subjects changed running technique in the fatigued conditions compared to unfatigued conditions. Probably most changes were made to decrease maximal power requirements. MaMahon et al. (1989) found that these changes can increase O_2 consumption up to 50 % and so decrease the economy of running.

REFERENCES

Dempster, W. (1955). *WADC Technical report.* Wright-Patterson Air Force Base
McMahon T.A. et all (1989). J. Applied Physiol., **62**,2326-2337.
Mizrahi, J. et all (2000). *Human Movement Science*, **19**,139-151.

HEAD MOVEMENT DOES NOT CHARACTERIZE THE FAILURE OF RECOVERY FROM AN INDUCED TRIP

Mary E. Jackson[1], Tammy M. Owings[1], Michael J. Pavol[2], and Mark D. Grabiner[1, 3]

[1] Department of Biomedical Engineering, Cleveland Clinic Foundation, Cleveland, OH
[2] Department of Physical Therapy, University of Illinois at Chicago, Chicago, IL
[3] School of Kinesiology, University of Illinois at Chicago, Chicago, IL
Email: jacksonm@bme.ri.ccf.org

INTRODUCTION

Falling is a major concern for older adults, resulting in injury, restriction of activity, and even death (Nevitt et al. 1989). Identification of risk factors that predict the risk of falling is crucial to providing effective and efficient therapy that will be specifically targeted at fall reduction in older adults. Wu (2001) hypothesized that increased head movement during a backward platform acceleration may predict the risk for falls in older adults. We tested this hypothesis using a unique set of biomechanical data collected from healthy older adults on whom trips were imposed. We determined if head motion during the first 100 ms following the trip could predict the success or failure of the recovery.

METHODS

Fifty women and 29 men (age: 72 ± 5 years, mass: 76.0 ± 14.0 kg, height: 1.64 ± 0.09 m) gave written informed consent to participate in this study (Pavol et al., 1999). Subjects were screened for the presence of musculoskeletal, neuromuscular and cardiovascular exclusion factors and were required to have bone mineral density of the femoral neck of >0.65 g/cm^2.

During the protocol, subjects were tripped unexpectedly while walking (Pavol et al., 1999). The trips were induced using a concealed, pneumatically driven, mechanical obstacle. Subjects were protected from contacting the ground by a safety harness that was connected to an overhead rail. Kinematic data was collected using a six-camera motion analysis system (Motion Analysis, Santa Rosa, CA).

Recoveries were visually graded as successful or failed (i.e. falls). A load cell in the safety harness was used to identify and exclude subjects who were assisted by the harness. Sagittal plane head kinematics were determined. Head flexion and extension were quantified by the orientation of the head relative to the trunk (i.e. the neck flexion or extension angle). Five variables were extracted during the first 100 ms post-trip: maximum head flexion and extension, maximum head flexion and extension velocity, and head flexion/extension range of motion. Independent t-tests were used to determine those variables for which differences between successful and failed recovery were significant ($p<0.05$).

RESULTS

Thirty-seven older adults successfully recovered and eight failed to recover from the induced trip. None of the five variables describing post-trip head kinematics exhibited a significant difference between successful and failed recoveries (Table 1).

Table 1: Sagittal plane head kinematics for 100 ms following trip initiation (mean ± SD)

	Success	Failure	P Value
Flexion Angle	0.12 ± 0.15 rad	0.19 ± 0.17 rad	0.221
Extension Angle	0.08 ± 0.17 rad	0.16 ± 0.17 rad	0.282
Range of Motion	0.20 ± 0.08 rad	0.35 ± 0.33 rad	0.507
Flexion Velocity	0.23 ± 0.37 rad/s	0.48 ± 0.32 rad/s	0.161
Extension Velocity	0.19 ± 0.33 rad/s	0.02 ± 0.19 rad/s	0.519

DISCUSSION

We found that head motion in this group of healthy older adults was not a sensitive determinant of falling following an induced trip. This finding tends to argue against the hypothesis that head movement may be used as a measure for risks for falls. Previously, we have found that walking speed, step time, and step length could classify falling following an induced trip with a sensitivity of 70% (Pavol et al., 1999). At this time, these variables appear to be better predictors of risks for trip related falls than head movement.

REFERENCES

Nevitt, M.C. et al. (1989). *JAMA*, **261**, 2663-8.
Pavol, M.J. et al. (1999). *J. Gerontol: Med. Sci*., **54A**, M583-M590.
Wu, G. (2001). *Clin Biomechan,* **16**, 199-206.

ACKNOWLEDGMENTS

Funding by NIH-R01AG10557 (MDG)

PASSIVE ELASTIC PROPERTIES OF BICEPS; CONTRIBUTION TO LOCOMOTOR ECONOMY IN THE HORSE (*EQUUS CABALLUS*)

Watson J.C., McGuigan M.P., Wilson A.M.
Structure and Motion Lab, The Royal Veterinary College, North Mymms, Hatfield, Herts, AL9 7TA England

INTRODUCTION

Storage of elastic strain energy in the collagenous component of muscle tendon units is important in reducing the mechanical work of locomotion. This mechanism has been demonstrated in the gastrocnemius tendon of the wallaby (Biewener *et al*, 1998) , the digital flexor tendons of the horse (Wilson *et al*, 2001; McGuigan *et al* submitted) and the plantaris muscle of the human foot. Such studies have focussed on tendons that are loaded by gravitational and inertial forces during stance phase and which therefore produce a vertical displacement of the centre of mass as a spring mass system. The equine biceps has a substantial collagenous component and is strained by downward movement of the trunk at the shoulder joint. Linked flexion of the elbow joint however has the opposite effect reducing the strain in the muscle-tendon unit. Shortening of the muscle-tendon unit at the end of stance would however extend the shoulder and flex the elbow – the movement required to protract the limb. This led us to propose the hypothesis that energy stored in biceps has a role in initiating limb protraction.

METHODS

1. Biceps force was calculated during trot locomotion from shoulder joint moment and limb force using forceplate (9287BA, Kistler) and video motion analysis (ProReflex, Qualisys). Biceps moment arm was determined by radiography. The extensor contribution of biceps was estimated from measures of physiological cross sectional area (PCSA) and moment arm of the shoulder extensors.
2. Biceps muscles were harvested from horses euthanased for other reasons. Muscles were mounted in a servo hydraulic tensile testing machine (Instron) via bolts placed through the scapula and radius adjacent to muscle attachments. Each muscle was then loaded to a force of 8kN and force and deformation (via an optical system – ProReflex, Qualisys) recorded. Energy stored in the muscle was determined by integration of the force displacement curve.
3. Muscles were dissected and PCSA determined for each muscle.

RESULTS AND DISCUSSION

1. Peak extensor moment on the shoulder joint during stance phase was 8000Nm. Attributing 70% of this to biceps produces a peak muscle force of 17kN. At 85% of stance (when the heel leaves the ground) values were 1600Nm and 4.2kN.
2. Muscle tendon units were about 400mm long. Tendon strains at 8kN force were 10% and muscle tendon unit strain 4 –7%. This is similar to that recorded in other energy storage tendons at peak strain. Energy stored in the muscle at 8kN was50-57J.
3. Biceps fibre lengths were 6 to 14 mm in the lateral head and 23 to 27mm in the medial head, similar to those reported by Hermanson *et al*, 1990. The mean PCSA was 330cm^2. Taking an isometric force capacity of 30Ncm^{-2} gives an isometric force capacity of 9.9kN.

It is unclear how to relate the passive muscle properties with the potential force generation capacity of the contractile element. The force during locomotion appears to approach or exceed the passive force. Activation of the contractile element is however likely to enhance the force resisting capacity of the muscle, perhaps by as much as the predicted isometric force. This would produce a peak force of 18kN – similar that calculated *in vivo*. The tendon strain data however suggest that a muscle force of 8kN would be a reasonable maximum. It therefore appears that either our estimate of *in vivo* biceps force is too high or that biceps can resist a higher force that determined here. The energy stored in biceps at a force of 4.2kN is 18J. If the entire shoulder moment was provided by biceps at this stage of stance this would rise to 6kN and 32J. This is a significant proportion of the energy require to protract the limb. We are currently extending the data set for this study.

SUMMARY

Biceps resists high forces during locomotion and will store large amounts of elastic strain energy. The muscle fibres are relatively short compared to the length changes that occur during elastic deformation suggesting that most of the muscle's function is related to its passive properties. The energy stored within the muscle appears sufficient to make a useful contribution to initiating limb protraction.

REFERENCES

Biewener, A.A. *et al* (1998) *J. Exp. Biol*, **210**, 1681-1694
Hermanson, J.W., Hurley, K.J. (1990). *Acta Anat*, **137**, 146-156
McGuigan, P.M. and Wilson, A.M. Submitted to *J. Exp. Biol.*
Wilson, A.M. *et al* (2001) *Nature*, **414**, 895-899

ACKNOWLEDGEMENTS

We acknowledge funding from the Horserace Betting Levy Board, London.

THE EFFECTS OF LIGAMENT AND CARTILAGE PROPERTIES ON THE GLENOHUMERAL JOINT

John E. Novotny, Ph.D., Bruce D. Beynnon*, Ph.D., Claude E. Nichols, III*, M.D

University of Delaware, Dept. of Mechanical Engineering, Spencer Laboratory, Newark, Delaware, USA, novotny@me.udel.edu
*University of Vermont, Dept. of Orthopaedics and Rehab., McClure Musculoskeletal Research Center, Burlington, Vermont, USA

INTRODUCTION

An analytical model of the glenohumeral joint was developed consisting of a 3D representation of the glenohumeral joint, with linear elastic ligament elements that could wrap around the humeral head, and deformable articular contact between the humeral head and glenoid [Novotny, 2000]. Models were generated to simulate individual experimental specimens used during in vitro tests of that simulated the 'cocked phase' of throwing [Novotny 1998a; 1998b]. Experimental loading conditions were inputs. The position and orientation of the humerus relative to the glenoid that resulted in equilibrium was solved. The sensitivity of glenohumeral joint kinematics (model outputs), to the ligament and cartilage material properties (model input parameters) was investigated. This will provide insight into the effect of these structures and their properties on glenohumeral joint function, injury and surgical repairs, such as the Bankart repair.

METHODS

A sensitivity analysis of the model output to variations in its input structural and geometric constants was explored. A model of a single loading condition, with the humerus loaded with 3 Nm abduction, 3 Nm extension and a 2.5 Nm external rotation moments (cocked phase of throwing), was chosen. The model was solved, then an input parameter was changed and the model solved again. The input parameters were increased by 5% of their initial value. For each new model solution, the changes in each of six model output parameters representing the position (X, Y, Z) and Euler angle orientation (RZ, RY, RX) of the humerus relative to the glenoid were calculated [Figure 1]. The sensitivity of the model kinematics was first assessed to changes in the stiffness (K) and initial lengths (L_0) of the five ligament elements (the superior, middle and the anterior band, axillary pouch and posterior band of the inferior glenohumeral ligaments). Secondly, the aggregate modulus (S) and thickness of the articular cartilage layer (b) of the glenoid and humeral head were changed. Finally, the sensitivity of the model output to changes in the position of the glenoid ligament elements insertions was performed.

RESULTS AND DISCUSSION

Anterior-posterior translation was most sensitive to increases in the K and L_0 was. Increases in K resulted in the humeral head translating further posteriorly and inferiorly. Increasing L_0 resulted in more laxity, allowing the humeral head to translate and rotate further in the posterior-inferior direction. With an increase of b, the higher contact force and area must be balanced by increased ligament tensions, causing the humeral head to translate posteriorly. Loss of b, as typically produced by osteoarthritis, could have pronounced effects on glenohumeral translations. Posterior translation was only moderately sensitive to an increase in S. The model exhibited high sensitivity to the medial movement of the glenoid insertion of the anterior band of the inferior glenohumeral ligament. Unlike the other findings, moving the insertion affected rotations more than translations, resulting in a higher abduction angle, and less external rotation and extension. The sensitivity to rotation may indicate that changes in insertion location could be more important in controlling joint rotations than changes in the material properties of the elements.

SUMMARY

In previous experiments [Novotny, 1998b], rotations were altered after Bankart repair while translations were not, similar to the results found after moving the ligament element insertions in this study. It could be surmised that the Bankart repair may relocate the capsular insertions rather than change the initial lengths of the ligaments. The shortening of the lax capsule is often the stated goal of the Bankart repair, hopefully resulting in a reduction of anterior translation of the humerus. Constraining glenohumeral rotation is to be avoided since it limits arm function. This sensitivity analysis indicates that the maintenance of ligament insertion location during repair may be most important to avoid loss of rotational range of motion.

REFERENCES

Novotny JE, Beynnon BD, Nichols CE (2000) Modeling the Stability of the Human Glenohumeral Joint during External Rotation. *J Biomechanics,* **33**, 345-354.

Novotny JE, Nichols CE, Beynnon BD (1998a) Normal Kinematics of the Unconstrained Glenohumeral Joint under Coupled Moment Loading. *J Should Elbow Surg,* **7**, 629-639.

Novotny JE, Nichols CE, Beynnon BD (1998b) Kinematics of the Glenohumeral Joint with Bankart Lesion and Repair. *J Orthop Res,* **16**, 116-121.

PREDICTING THE INERTIAL CHARACTERISTICS OF THE HUMAN THIGH USING A GEOMETRIC MODEL

Jennifer L. Durkin[1], Laura Scholtes and James J. Dowling[2]

Department of Kinesiology, McMaster University, Hamilton, Ontario, Canada
[1]PhD Candidate, durkinjl@mcmaster.ca, [2]Associate Professor, dowlingj@mcmaster.ca

INTRODUCTION

Accurate body segment parameter (BSP) information is required to calculate the kinetics of motion. Dual energy x-ray absorptiometry (DXA) has been used to measure BSPs and provided errors of less than 3.2% (Durkin, et al. 2002). The method is rapid and safe, allowing the scanning of large numbers of subjects for both subject-specific BSP data and the development of mathematical models. Current mathematical models have been criticized for their assumption of constant density and limited application to different populations. The purposes of this study were to i) determine the mass, centre of mass location (CM) and moment of inertia about the centre of mass (I_{CM}) of the thigh segment from 4 human populations ii) create a geometric model based on the mass distribution (MD) properties of the thigh to accurately predict BSPs, and iii) evaluate the accuracy of BSP predictions from one popular source in the literature.

METHODS

20 human volunteers from 4 populations underwent a frontal plane DXA scan followed by anthropometric measurements of the thigh segment. Custom software was used to section the right and left thigh segments, retrieving mass information in elements of 0.13cm^2. The digitized mass elements were summed every 1% of segment length (SL) and normalized to 100% segment mass (SM). An ensemble average of the mass distribution plots for each group was calculated to yield the mean (±SD) % SM per 1% SL (Fig.1). A geometric solid was developed to predict the BSPs of the thigh segment based on the MD properties observed (Fig. 2). The anthropometric measurements were used in the model to calculate the BSPs. %RMS errors were calculated between the DXA measurements and model predictions and between predictions from Winter (1990) and the DXA measurements.

RESULTS AND DISCUSSION

The present model provided more accurate BSP predictions than Winter (1990), particularly for the younger populations (Table 1). The model accurately reproduced the distal half of the segment, however the proximal measurements underestimated segment mass and I_{CM} in this region. Knowledge of the MD characteristics of body segments enabled evaluation of geometric similarity between populations and allows the development and validation of a geometric model that accurately predicts BSPs for these populations. Further refining of this model and the development of other models for the remaining body segments using the MD characteristics from DXA will enable accurate BSP predictions for different populations.

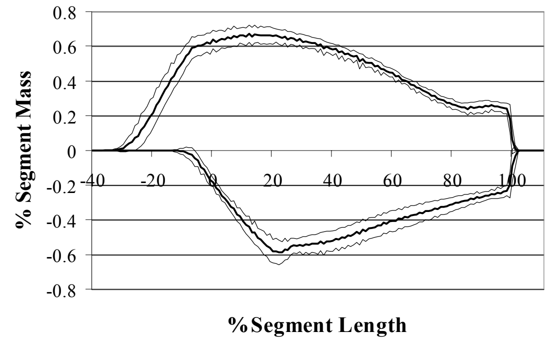

Figure 1. Ensemble average of MD properties of Males 19-30 years (Mean ± SD).

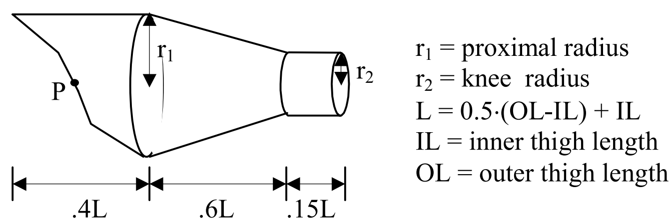

Figure 2: Geometric thigh model used to calculate BSPs.

REFERENCES

Durkin, J.L., et al. (2002). *J Biomechanics*. In Review
Winter, D.A. (1990). *Biomechanics and Motor Control of Human Movement* (2nd Ed.) John Wiley and Sons, Inc.

Table 1: %RMS Errors of Present Model and Predictions from Winter (1990) as compared to DXA Measurements.

	Males (19-30 Years)		Females (19-30 Years)		Males (>55 Years)		Females (>55 Years)	
	Present	Winter (1990)	Present	Winter (1990)	Present	Winter (1990)	Present	Winter (1990)
Mass	20.8	39.88	15.44	34.94	27.6	25.02	17.73	33.1
Length	4.08	44.9	5.41	5.41	5.65	5.65	5.59	5.59
CMx	2.2	16.94	2.29	17.01	4.96	28.77	4.04	28.92
CMy	1.06	2.08	1.79	2.78	1.18	2.07	1.82	2.99
I_{CM}	14.78	50.53	14.1	24.72	25.33	26.46	20.36	33.28

CMx = CM location from proximal joint centre along longitudinal axis. CMy = CM along mediolateral axis from segment midline.

DEVELOPMENT AND VALIDATION OF A JOYSTICK DYNAMICS MODEL TO PREDICT OPERATOR INPUT TORQUE

Michele Oliver[1], Bob Rogers[2], Phil Garland[2], Troy Gallant[2], and Ed Biden[2,3]

[1]School of Engineering, University of Guelph, Guelph, Ontario, Canada, moliver@uoguelph.ca

[2]Department of Mechanical Engineering and [3]Institute of Biomedical Engineering, University of New Brunswick, Fredericton, New Brunswick,Canada

INTRODUCTION

Over the past thirty years, North American manufacturers of off-road equipment for the construction, forestry and mining industries have gradually made a conversion from the exclusive use of lever, button and steering wheel controls to joysticks. Surprisingly, despite their widespread use, joysticks have not been studied extensively. The purpose of this work was to develop a dynamic model for hydraulic-actuation joysticks that would allow one to study the effects of joystick stiffness and speed on selected dynamic torque characteristics as a first step towards the development of a protocol for joystick design.

METHODS, RESULTS AND DISCUSSION

When an external torque due to contact from an operator's hand is present, according to Figure 1, the governing equation for the joystick becomes:

$$J\ddot{\theta} + C\dot{\theta} + M_s = mgh\sin\theta + T_{ext} \qquad (1)$$

By calculating the first four terms, the operator input torque (T_{ext}) can be determined.

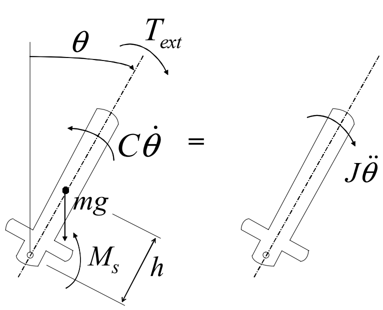

Figure 1: Free body diagram of joystick

The polar moment of inertia (J) of the rotating portion of the joystick (cam, shaft, handle, locking and connecting nuts, and one-half of the U joint) (Figure 2) can be determined experimentally by modeling the joystick as a compound pendulum. The moment (M_s) components are determined by disassembling the joystick and placing the actuator portion (Figure 2) in an Instron™ testing jig to determine actuator spring stiffnesses. Other components of M_s are determined through measurements of joystick geometry. The various θ terms (displacement, velocity and acceleration) are determined experimentally using a VICON™ motion analysis system and a pair of uniaxial piezoelectric accelerometers thread mounted to the top of the joystick. For the $mgh\sin\theta$ term, h is the distance between the U joint pivot and the centre of mass for the rotating portion of the joystick. Given that the joystick actuators contain pairs of preloaded springs, when the joystick is set into free motion, unlike a simple mass-spring-damper system, a reducing period is observed. Consequently, simple logarithmic decrement methods cannot be used to estimate the damping constant C. Therefore, C is estimated using a fourth order Runge Kutta numerical integration method using the model outlined in equation 1 (without T_{ext}) (Rogers et al., 2001). Using known values for the various model constants, and trial and error values for C, the Runge Kutta output for a given joystick is compared with experimentally obtained joystick motion time-histories. In this way, model validation is accomplished at the same time as C is estimated.

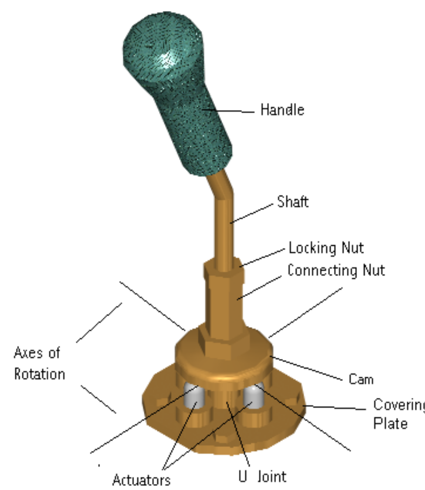

Figure 2: Joystick for hydraulic actuation

REFERENCES

Rogers, R.J., Oliver, M., Garland, P., and Gallant T. (2001). *Proceedings of the Canadian Machinery Vibration Association National Seminar*, 10.1-10.10.

ACKNOWLEDGEMENTS

The authors gratefully acknowledge the support provided by Jeremy Rickards of the Institute of Biomedical Engineering, John Deere International, the Natural Sciences and Engineering Research Council, and the New Brunswick Women's Doctoral Scholarship program.

THE EFFECT OF LIGAND DENSITY ON TETHER FORMATION BETWEEN ENDOTHELIUM AND MONOCYTES

George A. Truskey and Dora J. Levin

Department of Biomedical Engineering
Duke University, Durham, NC 27708-0281
Corresponding author: george.truskey@duke.edu

INTRODUCTION

Normal forces arising from secondary flows may play an important role in creating adhesive forces that resist detachment of monocytes from endothelium in the relatively high shear stress environment found in the arteries(Rinker et al., 2001). Cell rolling and arrest involves bond (Alon et al., 1995) and membrane tether formation (Shao et al., 1998). Tether formation influences the forces acting on cells (Shao et al., 1998). The objective of this study was to test the hypothesis that the receptor density on endothelium influenced tether formation.

METHODS

Human umbilical vein endothelial cells (HUVEC) were cultivated on microcarriers with endothelial growth media (Levin et al., 2001) and adhesion of Mono Mac 6 (MM6) cells studied using micropipet aspiration (Shao et al., 1998, Levin et al., 2001). Receptor populations were changed by incubation with 100 U/ml TNF-α for 4 h. In some cases, the TNF-α treatment was performed in the presence of cycloheximide to stabilize the number of receptors expressed. Multiple bonds were determined indirectly through observed trends in the adhesion probability, P_a. Previous studies established that adhesion probabilities > 30% suggest that multiple bonds are a significant percent of adhesive contacts (Chesla et al., 1998).

RESULTS AND DISCUSSION

TNF−α stimulation of HUVEC increased E-selectin, ICAM-1 and VCAM-1 expression. Addition of anti-ICAM-1 significantly inhibited MM6 rolling and adhesion under flow. ICAM-1 elvels were zero in control cells, $4.7 \pm 0.8 \times 10^5$ molecules per cell in cells treated with TNF-α in the presence of cycloheximide and $1.6 \pm 0.1 \times 10^6$ molecules per cell in TNF-α treated cells. In micropipet experiments, adhesion was infrequent in unstimulated HUVEC, $P_a = 8 \pm 2\%$, and was significantly higher when HUVEC were stimulated with 100 U/ml TNF-α for 4 hours with ($P_a = 48 \pm 5\%$) or without ($P_a = 51 \pm 18\%$) cycloheximide prior to testing. These results suggest that adhesion in control experiments is predominantly mediated by single bonds while multiple bonds contribute significantly to adhesion in TNF-α-stimulated cells. Multiple tethers were inferred from successive increases in MM6 velocity as it separated from HUVEC. Multiple tethers were observed in 40 ± 15% of TNF-α-treated cells, while only one multiple tether was detected in four sets of control data (8 ± 17%). Multiple tethers provide direct evidence for more than one initial bond forming.

We observed a lag period prior to tether formation that increased with TNF-α stimulation of HUVEC. The applied contact time between MM6 cells and HUVEC was held constant for all conditions tested. Prior to tether formation, the lag period increased from 0.53 sec for unstimulated HUVEC to 1.33 sec for TNF-α stimulated HUVEC ($p < 0.01$). The tether lifetime was, however, unaffected by ligand density.

SUMMARY

Increasing the receptor density on endothelial cells by TNF-α stimulation caused an increase in the probability of adhesion. Increased adhesion led to a greater frequency of single and multiple tether formation with an increase in the lag time between application of force and formation of tethers. These results indicate that multiple bond formation will produce multiple tethers but may delay the onset of tether formation by hindering the separation of cortical cytoskeleton from the cell membrane. Thus, tether formation is dependent upon both the force applied on the cell (Shao et al., 1998) and the density of receptors bound to ligand on monocytes.

REFERENCES

Alon R, Hammer DA, Springer TA. 1995. Lifetime of the P-selectin-carbohydrate bond and its response to tensile force in hydrodynamic flow. Nature 374:539-542.

Chesla SE, Selvaraj P, Zhu C. 1998. Measuring two-dimensional receptor-ligand binding kinetics by micropipette. Biophys. J. 75:1553-1572.

Levin JD, Ting-Beall HP, Hochmuth RM. 2001. Correlating the Kinetics of Cytokine-Induced E-Selectin Adhesion and Expression on Endothelial Cells. Biophys. J. 80:656-667.

Rinker KD, Prabhakar V, Truskey GA. 2001. Effect of contact time and force on monocyte adhesion to vascular endothelium. Biophys. J. 80:1722-1732.

Shao J-Y, Ting-Beall HP, Hochmuth RM. 1998. Static and dynamic lengths of neutrophil microvilli. Proc. Natl. Acad. Sci. 95:6797-6802.

ACKNOWLEDGEMENTS

This research was supported in part by NIH grants HL41372 and HL-57446.

COMPARISON OF 3 MEASURES OF GROUND REACTION FORCE: FORCE PLATE, FSCAN®, AND MULTIPLE FORCE SENSORS

Evelyn L. Morin, Susan A. Reid, J. Mikael Eklund, Joan M. Stevenson and J. Tim Bryant
Ergonomics Research Group, erg@post.queensu.ca
Queen's University, Kingston, Ontario, Canada

INTRODUCTION

The ability to measure instantaneous ground reaction forces (GRFs) generated during free gait forms an integral part of the analysis of human motion. Vertical GRFs and centres of pressure (COPs) during gait are compared when calculated from the in-shoe contact pressure measured with an FScan® to those measured by an AMTI force plate. Further study is done on the error introduced by grouping the FSRs to estimate the COP with a reduced data set size. The FSR groups are chosen based on 10 clinically significant anatomical regions.

METHODS

FScan® sensors are comprised of up to 960 force sensing resistors (FSRs). These were placed in a subject's shoe and calibrated. Data was simultaneously recorded from FScan® and the force plate at a 50 Hz sampling rate in three conditions: during various walking rates, while a stationary subject shifted their body weight, and during barefoot walking on the FScan® and force plate.

Data from the two in-shoe conditions were used to compare the vertical GRF computed by FScan® and the force plate. Data from the barefoot walking were used to compare the COP path computed from FScan® recordings and the force plate. Post hoc alignment of the data sets was necessary and done using heel-strike and toe-off as reference markers.

In-shoe FScan® data were used to develop a hypothetical grouping of FSRs, based on 10 anatomically significant regions proposed by Bhatia et al. (1999). This would reduce the data size by one order of magnitude. The sum of grouped sensor forces was used with their mean position to calculate COP. Reduction in data inputs is desirable for a portable data acquisition system and its impact on accuracy is evaluated.

RESULTS AND DISCUSSION

The Fz GRF was determined from 41 in-shoe trials. FScan® under reported Fz with a mean RMS error of 30.15%.

COP path was computed from FScan® and force plate data for 10 trials. An example of the COP trajectories can be seen in Figure 1. Mean error: 1.44 mm, STD 0.58 mm. This would cause 1–2% error in ankle moment calculations.

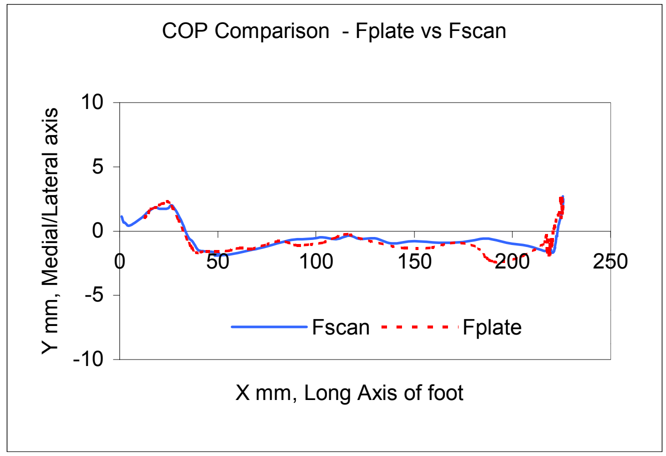

Figure 1: Force Plate and FScan® calculated COP position

Grouping FScan® sensor data into 10 regions as described by Bhatia (1999) resulted in a mean error of 2.97 mm medial/laterally and 6.85 mm anterior/posteriorly. This error in the estimate of moment arms will have a limited effect on the magnitude of joint moments. Careful placement of the FSRs can further minimize this.

SUMMARY

The FScan® system under reported the vertical GRF by 30% in this study. Furthermore, error in Fz increased with use.

It is possible to align two independent coordinate systems post hoc by aligning the lines of progression of the COP. When aligned, the FScan® sensor is capable of tracking the trajectory of the COP with a RMS error of 13% (1.44 mm).

Calculating the COP path using 10 discrete areas resulted in an RMS error of 17.26% medial/lateral variation (2.97 mm) and 4.24% anterior/posterior variation (6.85 mm). Further work will be undertaken to determine an optimum FSR size and placement to minimize the error in COP trajectory.

REFERENCES

Bhatia, M.M., Patil, K.M. (1999). *Journal of Rehabilitation Research and Development,* **36**, No. 3, 264-72, 1999 July.

ACKNOWLEDGEMENTS

This research was funded by DCIEM, DND Toronto, Canada
Special thanks to W.R. Dyck, P.Eng. DCIEM Toronto, Canada

DETERMINATION OF INERTIAL CHARACTERISTICS OF THE HUMAN FOOT USING DUAL ENERGY X-RAY ABSORPTIOMETRY

Mark R.J. Young and James J. Dowling

Department of Kinesiology, McMaster University, Hamilton, Ontario, Canada
youngmr@mcmaster.ca

INTRODUCTION

Linked segment analyses require the input of inertial characteristics to yield estimations of internal forces and moments. Modern methods of medical imaging allow accurate measurements of these characteristics in living subjects. The purpose of this study was to compare dual energy x-ray absorptiometry (DEXA) measurements of the inertial characteristics of the human foot with previous methods using cadavers and geometric shapes. (Winter, 1990; Zatsiorsky et al., 1990a; Zatsiorsky et al. 1990b)

METHODS

Twenty subjects were scanned in the sagittal plane using DEXA. Twenty-one anthropometric measurements were then taken of the foot and leg segments for use in the other predictive models.

Using custom software the DEXA foot image was analyzed for mass, centre of mass, and radius of gyration. Anthropmetric data were used to calculate mass, centre of mass, and moments of inertia using the regression equations of Winter (1990). Only mass and moments of inertia were calculated using the regression equations of Zatsiorsky et al. (1990a), and the geometrical models of Zatsiorsky et al (1990b).

Masses and moments of inertia were compared using simple linear regression. The error in the ability of Winter (1990) and Zatsiorsky et al. (1990a; 1990b) to predict the true value was quantified using root mean squared error (RMSE). Differences between the centre of mass predicted by Winter (1990) and DEXA were shown graphically.

RESULTS

The regression for the mass of the foot segment vs. DEXA yielded strong correlations for Winter, Zatsiorksy (Regression), and Zatsiorsky (Geometrical Models). The corresponding r^2 values were 0.82, 0.77, and 0.88 respectively. The RMSE of the three models was 13.2% for Winter, 11.9% for Zatsiorsky's regression equations, and 8.9% for Zatsiorsky's geometrical models.

The centre of mass, as indicated by Winter, was designated by the coordinates (50,0) along a line between the ankle and the metatarsal-phalangeal joint. DEXA showed that the true coordinates of this point could be located at (46.8, -13.7). This would indicate that the centre of mass is located more inferiorly in the foot than predicted.

Comparison of DEXA Centre of Mass Location with Predicted Winter Centre of Mass

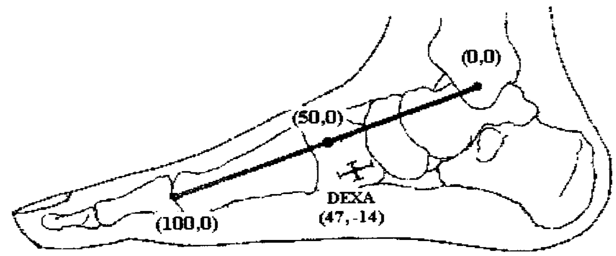

For the moment of inertia all three tested models correlated highly with DEXA. Coefficients of determination ranged from 0.81 for Winter to 0.86 for Zatsiorsky's geometrical models. However, the relationship found was not 1 to 1. The error in predicting the true values was 58% for Winter, 34% for Zatsiorsky's regression equations, and 65.2% for Zatsiorsky's geometrical models.

DISCUSSION

The errors in the ability to predict mass show little error. However, errors in prediction of centre of mass and moment of inertia show that current methods of predicting the distribution of this mass are not valid. DEXA values would enable us to more accurately estimate forces and moments at the ankle joint.

REFERENCES

Winter, D.A. (1990). Biomechanics and Motor Control of Human Movement, second Ed. John Wiley and Sons, Inc.

Zatsiorsky, V., Seluyanov, V., Chugnova, L. (1990a). In vivo body segment inertial parameter determination using a gamma-scanner method. (pp. 186-201).

Zatsiorsky, V., Seluyanov, V., Chugnova, L. (1990b). In: Cheryi, C.G., Regirer, A. Contemporary Problems of Biomechanics. Mir Publishers.

NEUROMUSCULAR FUNCTION IN ANTERIOR CRUCIATE LIGAMENT DEFICIENT AND UNINJURED PEOPLE

Glenn N. Williams, Peter J. Barrance, Lynn Snyder-Mackler, Michael J. Axe, Thomas S. Buchanan
Center for Biomedical Engineering Research, University of Delaware, Newark, DE. USA E-mail: glennwms@udel.edu

INTRODUCTION

It is estimated that 250,000 anterior cruciate ligament (ACL) injuries occur in the United States each year (Boden, 2000). Some people can cope with ACL injury and return to sports, but most cannot without surgical intervention. The annual cost of this treatment is over $1.5 billion per year (Boden, 2000). Longitudinal evidence indicates that people who sustain ACL injuries suffer early knee osteoarthritis despite successful treatment (Daniel, 1994). The inability to cope with ACL injury and the incidence of osteoarthritis following this injury may be related in part, to neuromuscular function. The purpose of this study is to compare the neuromuscular function of people with ACL deficiency (ACL-D) with that of highly active uninjured people using an experimental protocol that requires fine control of force and position.

METHODS

Five non-coping ACL-D subjects (mean age 28 $\pm$ 13 years) and 5 uninjured subjects (mean age 27 $\pm$ 6 years) have volunteered to participate in this study to date. All subjects were regular participants in high-level sports. The subjects' goal in the experimental protocol was to position a circular cursor over a narrow target that consisted of two concentric circles. The cursor moved in response to loads produced against a 6 degree of freedom (DOF) load cell to which the subjects were rigidly fixed via a cast and clamp at the distal shank. Targets appeared in random order at one of 18 positions (located at every 20° of a circle in the flexion-extension-varus-valgus plane). Seventy-two trials were performed bilaterally at each of three knee flexion angles - 50º, 70º, and 90º. Hip flexion was standardized at 90°. A load of 30% maximum force (collected prior to the trials) was required to move the cursor toward the target. Subjects were required to hold the cursor within the narrow target for 1 second before the trial was considered successful.

Electromyographic (EMG) data were collected from the medial hamstrings, lateral hamstrings, sartorius*, rectus femoris, tensor fascia lata*, gracilis*, vastus medialis, vastus lateralis, and the medial and lateral gastrocnemius during the final second in each target using either surface or indwelling electrodes (* = indwelling electrodes used). The data were later full-wave rectified, averaged, and normalized using maximum EMG data collected earlier in the session.

The specificity of muscle utilization was analyzed by calculating a specificity index for each muscle using the formula: $\Sigma(\underline{EMG_i} \bullet \underline{\lambda})/\Sigma|\underline{EMG_i}|$, where $\underline{EMG_i}$ describes the EMG magnitude in each target direction and $\underline{\lambda}$ is the unit vector in the EMG direction. Besides specificity indices, EMG magnitudes and maximum force production were evaluated. Data were broken into 4 group-limb combinations: control left, control right, ACL-D involved and ACL-D uninvolved. A two factor (group-limb, angle) MANOVA with each muscle as a dependent variable was used to test for significant differences in muscle specificity and magnitude. *Post hoc* Bonferroni-adjusted multiple comparison tests were performed. Regression analysis was used to assess the relationship between specificity and strength (peak force production).

RESULTS AND DISCUSSION

Quadriceps and hamstrings strength were similar between groups. There was a significant group-limb main effect ($p < .05$) for muscle specificity in all muscles except for the lateral hamstrings, sartorius, and gracilis. In general, the ACL-D involved limb had significantly less specificity of muscle action than the other group-limb combinations, which were usually similar. The relationship between muscle specificity and strength was insignificant. Interestingly, the mean EMG magnitude for the ACL-D involved vastus medialis and vastus lateralis were 83-100% greater than the uninjured groups' respective values. In Figure 1, mean EMG vectors at each target are plotted in polar coordinates. This figure demonstrates the decreased specificity of the vastus lateralis in the ACL-D group (note the activity in flexion in the involved limb) and that rather than quadriceps avoidance, there is a greater amount of quadriceps activity. These findings suggest that ACL injury leads to alterations in neuromuscular function and may help to explain the variable disability associated with ACL deficiency, as well as, have implications for the predisposition for early osteoarthritis following ACL injury.

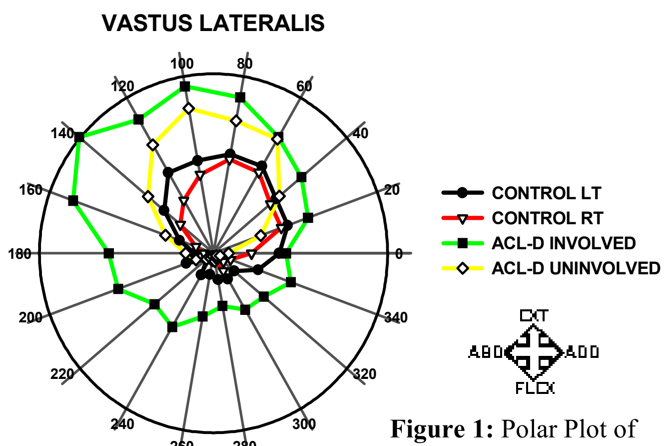

Figure 1: Polar Plot of Vastus Lateralis EMGs at 50° of knee flexion.

REFERENCES:

Boden, B.P., Griffin, L.Y., and Garrett, WE, Jr. (2000). *Phys. Sports Med.*, **28**, 53-60.
Daniel, D.M. et al (1994). *AM.J. Sports Med.*, **22**, 632-634.

ACKNOWLEDGEMENT: NIH Grant RO1AR46386

REGISTRATION OF 3D BONE GEOMETRY WITH CINE-PHASE CONTRAST MRI DATA FOR THE DETERMINATION OF IN VIVO JOINT KINEMATICS

Peter J. Barrance, Glenn N. Williams and Thomas S. Buchanan.

Center for Biomedical Engineering Research, University of Delaware, Newark, DE. USA. Email: peteb@udel.edu

INTRODUCTION

Accurate determination of *in vivo* joint kinematics has been the subject of much previous research. These investigations are important for assessing the subtle changes in joint function resulting from injury to passive or dynamic stabilizing structures. In the technique described here, 3D geometries of the articulating bones are modeled, and the motions of each are computed. Optimal trajectories of each bone are modeled to achieve correspondence with cross-sectional images and velocity data acquired in a Cine-Phase Contrast (Cine-PC) MRI study of the joint in motion. This allows accurate calculation of kinematic joint parameters, as well as estimation of areas and velocities of contact between the articular surfaces. Joint kinematics are evaluated during functional movement. This report describes an application of the method to the determination of kinematic parameters in the knee.

METHODS

MRI data is acquired using a protocol similar to that described by Sheehan et al. (1998.) Subjects perform a repetitive knee flexion/extension exercise within an MRI scanner (GE Signa LX) while lying supine. The knee angle varies between approximately 30° flexion and full extension.

Cine-PC data: A sequence of 24 frames of data is collected through the motion cycle on a user-specified sagittal image plane. Each resulting data frame yields four separate images on the selected plane; one is the usual anatomical cross-section (magnitude image), and the others are *encoded with velocity* in three orthogonal directions.

3D static scans: A sequence of high resolution axial plane MR images is acquired, centered at the subject's knee joint.

3D model reconstruction: 3D graphical models of the surfaces of the distal femur and proximal tibia are created. The periphery of each bone is traced on the 3D MR images using a digitizing tablet. Custom developed software is used to reconstruct the polygonal graphical models (Fig. 1a)

Cross-section registration: The sagittal plane MR images show lines of low signal around the edge of each bone's intersection with the image plane. An initial estimate of the location of the bone is made by intersecting the geometric model with a *virtual* cutting plane in various position and orientations. The difference between observed and virtual cross-sections is minimized computationally. Using this procedure, a region of interest (ROI) of each sagittal image is extracted which contains only points lying within the bone of interest (Fig. 1b).

Velocity tracking: Using the ROI velocity data and invoking the relationships between the motions of particles within rigid bodies, the angular and linear velocities of the bone are estimated. An iterative procedure minimizes the error between the apparent velocities produced by a modeled trajectory of the rigid body and those observed in the velocity data set.

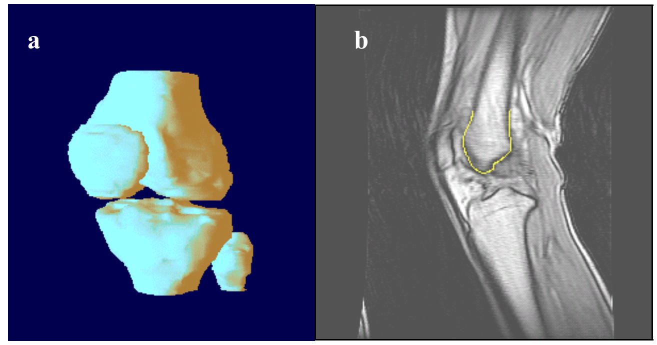

Figure 1: (a) 3D geometric models of knee joint bones. (b) Distal femur ROI of sagittal image is determined by cross-section matching.

Kinematic data: In order to quantify joint motion, anatomically based coordinate systems are fixed within each bone, and the relative motion is decomposed into rotation and translation parameters. To locate landmarks away from the joint, the surface of each 3D model is matched to a larger scale, lower resolution geometric model of the whole bone. The parameters shown here follow the convention of the knee joint coordinate system of Grood and Suntay (1983.)

RESULTS AND DISCUSSION

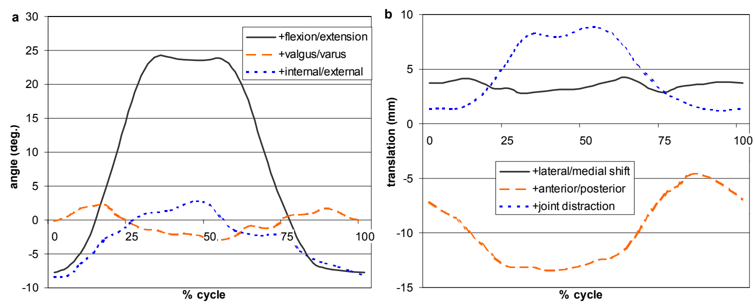

Figure 2: Grood & Suntay's joint coordinate system parameters calculated for a single knee: (a) rotations, (b) translations

Figure 2 shows an example sequence of joint parameters calculated through the knee flexion/extension cycle. As the knee is flexed, coupled internal rotation and posterior translation of the proximal tibia relative to the distal femur are observed. In an ongoing study, the current technique is being applied to quantify differences between the kinematics of normal and anterior cruciate ligament deficient knees.

REFERENCES

Sheehan, F.T. et al (1998) *J. Biomech.* **31**, 21-6

Grood, E.S. and W.J. Suntay (1983) *J. Biomech Eng.* **105**, 136-144

ACKNOWLEDGMENT

This work is supported by NIH grant R01AR46386

EFFECT OF JOYSTICK STIFFNESS AND SPEED ON SELECTED DYNAMIC TORQUE CHARACTERISTICS

Michele Oliver[1], Ed Biden[2,3], Bob Rogers[2], and Jeremy Rickards[3]

[1]School of Engineering, University of Guelph, Guelph, Ontario, Canada, moliver@uoguelph.ca
[2]Department of Mechanical Engineering and [3]Institute of Biomedical Engineering,
University of New Brunswick, Fredericton, New Brunswick, Canada

INTRODUCTION

Three actuation torque characteristics (peak torque, angular impulse, and acceleration at the hard endpoint) were chosen to provide an acute indication of the injury risk associated with using a hydraulic actuation joystick found commonly in North American excavators.

METHODS

The joystick dynamics model derived and validated in the companion WCB paper was used to quantify the actuation torque requirements for nine, untrained operators during the performance of a joystick routine which consisted of six sets, each involving a different experimental condition (slow speed-normal stiffness, fast speed-normal stiffness, slow speed-light stiffness, fast speed-light stiffness, slow speed-heavy stiffness, fast speed-heavy stiffness) of eight right-hand-side joystick motions using the excavator mock-up pictured in Figure 1. The normal stiffness condition was what would be found in an operating excavator. Subjects were instructed to move the joystick from the neutral position to one of four endpoints (forward, back, left or right) and back to neutral again. Angular displacement and acceleration were determined respectively using a three camera VICON™ motion analysis system and a pair of uniaxial piezoelectric accelerometers thread-mounted (to the top of the joystick) orthogonally to one another.

The instantaneous risk to the operator over the course of the joystick motion (not including the hard endpoint) was evaluated using the peak torque value. Peak torque at the hard endpoint of the motion could not be determined since the mathematical model did not include end-condition stiffness. Angular impulse, taken as the area under the torque time curve (not including the hard endpoint), provided an indication of the sustained exposure to torque. The third indicator, acceleration at the hard endpoint, was included to provide an indication of risk as the joystick came to a sudden stop at the hard endpoint.

RESULTS AND DISCUSSION

Based upon significance determined from analysis of variance procedures and post-hoc tests, for peak torque, fast motions to the right or left using the heavy stiffness joystick provide the highest risk to the operator. For angular impulse, slow motions forward and to the right using the heavy stiffness joystick were found to provide the highest risk. For fast speeds, where the angular impulse values were lower, there was greater risk with the forward than the right motions. Based upon the acceleration results, fast motions to the left presented the highest risk to the operator for sudden palm and/or finger compression.

Figure 1: Excavator mock-up

CONCLUSIONS

From the results obtained from the three indicators, it is safe to conclude that side-to-side motions pose the highest injury risk to an operator. Based upon the angular impulse data, slow motions pose a higher exposure risk to an operator while based upon the acceleration at the hard endpoint values, fast motions pose a higher instantaneous compression risk of the soft tissues of the fingers and palm. Golsse's (1989) finding that skilled forest machine operators make over 20,000 motions with one joystick over the course of nine hours of work indicates that dynamic joystick actuation torque requirements should be considered when designing joysticks.

REFERENCES

Golsse, J.-M. (1989). *Technical Note TN-134*, *Forest Engineering Research Institute of Canada – Wood Harvesting*.

ACKNOWLEDGEMENTS

The authors gratefully acknowledge the support provided by Maureen Tingley of the Mathematics and Statistics Department at the University of New Brunswick, John Deere International, the Natural Sciences and Engineering Research Council, and the New Brunswick Women's Doctoral Scholarship program.

FUNCTIONAL CHANGES IN KIDNEY CELLS IN RESPONSE TO SUSTAINED HYDROSTATIC PRESSURE

Julie S. Martin[1] (jspoelke@purdue.edu), Hiroki Yokota[2], and Karen M. Haberstroh[1]

[1]Department of Biomedical Engineering, Purdue University, West Lafayette, IN 47907-1296
[2]Department of Biomedical Engineering, Indiana University Purdue University at Indianapolis, Indianapolis, IN

INTRODUCTION

Pathologically elevated hydrostatic pressures have been shown to alter functions in many tissues and organs, including the kidneys (Meldrum, 2001). It is our hypothesis that changes in the cellular mechanotransduction pathway lead to such altered cell/tissue responses following exposure to an increased pressure stimulus. This study will aim to understand these complex signaling pathways by monitoring the cellular and molecular level responses of two important renal cells (specifically, tubular epithelial and inner medullary cells) under a known pathological hydrostatic pressure (60 cmH_2O; McGuire, 1981).

METHODS

Cell Culture. IMCD (cell line CRL-2123; ATCC) and LLC-PK1 (cell line CL-101; ATCC) cells were cultured under standard cell culture conditions (that is a sterile, humidified, 37°C, 5% CO_2/95% air environment) in Ham's F-12 and Medium 199, respectively, supplemented with 10% Fetal Bovine Serum (FBS) and 1% penicillin/streptomycin (P/S). All cells were used between population numbers 4 to 15 for the pressure experiments.

Pressure Experiments. Prior to the experiments, IMCD and LLC-PK1 cells were seeded (3,523 cells/cm^2) onto etched glass coverslips. After two days in culture, the standard culture media was removed and replaced with Ham's F-12 or Medium 199 supplemented with 5% FBS and 1% P/S. Kidney cells were then exposed to a sustained pressure of 60 cmH_2O for 6 hours, 12 hours, 24 hours, 3 days, or 7 days using a computer controlled pressure chamber. Control cells were maintained under 0.3 cmH_2O pressure for similar periods of time.

Cell Proliferation. Following pressure exposure, kidney cells were fixed using a 3.7% formaldehyde solution and the nuclei were stained using Hoescht 33258 (Sigma). Cell proliferation data were determined by averaging the number of cells in each of five random fields per substrate. Each experiment was run in duplicate and repeated at least three separate times. Statistical analysis was performed using student t-tests, with $p<0.05$ considered significant.

Cytoskeletal Staining. Following pressure exposure, kidney cells were fixed in a 3.7% formaldehyde solution. The microtubules were stained using a fluorescently conjugated α-tubulin antibody according to the manufacturer's protocol (Sigma); microfilaments were subsequently counter stained using rhodamine phalloidin and according to the manufacturer's protocol (Molecular Probes). Cytoskeletal elements were then visualized in the same frame using fluorescence microscopy.

RESULTS AND DISCUSSION

Results provided the first evidence that in both medullary and tubular kidney cells, exposure to hydrostatic pressures of 60 cmH_2O altered cell functions. Specifically, cell proliferation of controls (or cells maintained under 0.3 cm H_2O pressure) was increased ($p<0.05$ at 12hours and $p<0.1$ at 24hours) compared to cells exposed to pressures of 60 cmH_2O at all time points up to 24 hours. In contrast, pressure exposed cell numbers were greater than controls for the remainder of the seven day experiment. The most significant difference was observed at seven days, when, for example, the average cell counts of tubular cells under pressure increased by 25% ($p<0.01$) compared to controls. These results were intriguing and led us to question the mechanism resulting in altered kidney cell growth following exposure to hydrostatic pressure. In previous studies with other cell types, the cytoskeleton has been implicated in such signal transduction to the nucleus (Numaguchi, 1999). Our fluorescence microscopy studies supported these findings, and provided the first evidence of such time and pressure- dependent cytoskeletal alterations in kidney cells exposed to hydrostatic pressure. Specifically, the microfilaments in control cells remained elongated and in continuous fibers throughout the length of the cell. In contrast, kidney cells under 60 cmH_2O had shorter microfilament fibers that were branched throughout the cell.

Future work in our lab will be focused on understanding the molecular mediators (such as c-fos and c-jun) involved in the signal transduction pathway of renal cells to hydrostatic pressure. This information may help identify a controllable step under pathological conditions, and may aid in the design of novel, targeted drug therapies.

REFERENCES

Meldrum, K K, Hile, K, Kaefer M., Haberstroh, K.M. (2001). *Proc. 5th Ann. Int. Conf. on Cell. Eng.*, S5-6; McGuire, E.J. Woodside, J.R., Borden, T.A., Weiss, R.M. (1981) *J. of Urology*, 126, 205-209; Numaguchi, K., Eguchi S., Yamakawa T., Motley E.D., Inagami T. (1999). Circulation Research, **85**, 5-11.

ACKNOWLEDGEMENTS

The authors would like to thank the National Science Foundation Integrative Graduate Education and Research Training (IGERT) Program Therapeutic and Diagnostic Devices Grant, Grant DGE-97-72770 and Brad Goodrich for the Lab View and pressure system setup.

SOLUBLE PROTEINS RELEASED BY ENDOTHELIAL CELLS IN RESPONSE TO FLUID FLOW AFFECT SMOOTH MUSCLE CELLS

Jennifer A. McCann[1], Thomas J. Webster[1], Steven H. Frankel[2], Michael W. Plesniak[2], Lisa X. Xu[1,2], Steven T. Wereley[2], and Karen M. Haberstroh[1]

[1]Department of Biomedical Engineering and [2]School of Mechanical Engineering
Purdue University
West Lafayette, Indiana, 47907, USA
jamccann@purdue.edu

INTRODUCTION

The onset of atherosclerosis is described by the response to injury theory: endothelial cells suffer an injury resulting in altered morphology, metabolism, or other cell functions, which stimulates smooth muscle cell proliferation and migration into the lumen, ultimately causing vascular thickening and hardening (1). The objective of the present study was to determine which soluble and transferable factors, released by endothelial cells in response to laminar fluid flow, induce smooth muscle cell function indicative of atherosclerotic conditions.

MATERIALS AND METHODS

Cell Culture. Rat aortic endothelial cells (RAEC) and rat aortic smooth muscle cells (RASMC) (VEC Technologies) were maintained in MCDB-131 Complete Medium (VEC Technologies) or Dulbecco's Modified Eagle's Medium (DMEM; Hyclone) supplemented with 10% fetal bovine serum (…) and 1% penicillin/streptomycin (…), respectively. Cells were grown under standard cell culture conditions, that is, a humidified, 37°C, 5% CO_2, 95% air environment. All cells were used at population numbers five through fifteen without further characterization.

Exposure of RAEC to Laminar Flow. Prior to fluid flow exposure, endothelial cells were seeded (35,242 cells/cm^2) on etched glass cover slides previously coated with fibronectin (10 μL/mL; Sigma). Once confluent, endothelial cells were exposed to laminar fluid flow in a modified version of the parallel plate flow chamber (3) for 6 or 24 hours. The shear stress generated in this system was 11.25 dyne/cm^2.

RAEC Morphology. At the end of the prescribed time period, endothelial cell morphology was visualized using light and fluorescence microscopy. Briefly, cells were fixed with 4% formalin in a sodium phosphate buffer solution for ten minutes and stained with rhodamin phalloidin following manufacturer's protocol (Molecular Probes). Cell morphology was visualized under the light microscope and F-actin filaments were visualized using fluorescence microscopy.

mRNA Expression by RAEC Exposed to Fluid Flow. Following exposure to fluid flow, mRNA from endothelial cells was digested with Triazol (Gibco), extracted with chloroform, and precipitated with isopropanol. Reverse transcriptase-polymerase chain reaction was performed using sample RNA and the Ambio Retroscript Kit with primers (20 pmol/μL; Gibco) specific to either glyceraldehyde 3-phosphate dehydrogenase (GAPDH), cyclooxygenase-2 (COX-2), platelet derived growth factor (PDGF), or endothelial cell nitric oxide synthase (ecNOS). Electrophoresis of cDNA samples was performed in a gel casting system (Biorad) with 1X TAE buffer for 1.5 hours at 200V. The amount of cDNA in each lane was determined using a phospho imager (Biorad) and densitometry.

RASMC Proliferation Under Conditioned Medium. RASMC were seeded (3,500 cells/cm^2) onto etched borosilicate glass coverslips and incubated under standard cell culture conditions in DMEM for 24 hours. At this time, the standard media was removed and replaced with either fresh MCDB-131 medium (control) or *conditioned MCDB-131 medium* (experimental). *Conditioned medium* was collected from the laminar flow system after a 24-hour experiment; this medium contained any soluble factors released by endothelial cells upon exposure to laminar flow.

All cells were allowed to proliferate in a static environment under standard cell culture conditions for 1, 3, and 5 days. At the end of the prescribed time period, cells were fixed with 4% formalin and stained with Hoechst 33258 (Sigma) and counted.

RESULTS AND DISCUSSION

After shear exposure, endothelial cells realigned in the direction of flow, whereas cells maintained under control conditions demonstrated typical cobblestone morphologies. Furthermore, mRNA studies confirmed previous reports of increased COX-2, PDGF, and ecNOS mRNA expression (2,3) following laminar flow exposure. More importantly, our results have provided the first evidence that smooth muscle cell proliferation was altered (compared to that of cells maintained under control media) as a direct result of the soluble and transferable factors released by endothelial cells in response to fluid flow.

REFERENCES

[1.] Ross, Russell. (1992) *Endothelial Dysfunction and Atherosclerosis*. ed. Nicolae and Simionescu and Maya Simionescu. Plenum Press. [2.] Topper, J.N., et al. (1996) Proc. Natl. Acad. Sci., **93**, 10417-10422. [3.] Frangos, J.A., L.V. McIntire, and S.G. Eskin. (1988) *Biotechnology and Bioengineering*, **32**, 1053-1060.

ACKNOWLEDGEMENTS

The authors would like to thank the Showalter Foundation for funding this project, Dr. Fred Pavalko (Department of Celular and Integrative Physiology; Indiana University Purdue University Indianapolis) for supplying the flow apparatus, and Sean Peterson (School of Mechanical Engineering; Purdue University) and Karen Hile (Department of Pediatric Urology; Indiana University Purdue University Indianapolis) for technical support.

EVALUATING POSSIBLE TECHNIQUES FOR DELAYING THE WRIST RELEASE: A COMPUTER SIMULATION APPROACH

Sasho Mackenzie and Eric Sprigings

College of Kinesiology, University of Saskatchewan
sashomackenzie@hotmail.com

INTRODUCTION

A delayed wrist release during the down swing in golf is a common characteristic of golfers that develop high clubhead velocity at impact (Robinson, 1994). It has been shown that the wrist release can be delayed using a resistive wrist torque with a corresponding increase in clubhead velocity at impact. The optimal length of the delaying wrist torque was approximately 50ms (Sprigings et al., 2001). Adequately performing this technique would require precise timing from the golfer. It is possible that a phenomenon other than a resistive wrist torque is responsible for the delayed release. The purpose of this paper is to evaluate two possible techniques for delaying the wrist release. The first involves increasing the angular acceleration of the segments proximal to the wrist through increased muscular torques. The second involves applying linear accelerations to the origin of the model at the spine.

METHODS

A 2-dimensional, 3-segment mathematical model, consisting of a torso, left arm, and golf club, was developed to simulate the golf swing. Torque actuators, constrained by activation rate and muscle force-velocity properties (Alexander, 1990), were inserted at the proximal end of each of these three segments. The formulation of the equations for the model was similar to that previously published by Sprigings et al. (1998). Two separate sets of trials were conducted using the model. First, systematic increases of the trunk and shoulder torques were applied to the model. The torques were increased by adjusting the main parameters in the activation rate and force-velocity functions. The angular displacement of the arm from the right horizontal (T_A) before the relative wrist angle increased was the measured dependent variable. Second, the model's origin at the spine was accelerated linearly (A_O). The angular displacement of the arm was again used as the dependent variable. The linear displacement of the origin (R_O) was also recorded.

RESULTS & DISCUSSION

The effects of increased trunk and shoulder torques on delaying the release of the wrist are shown below (Table 1). Increasing the trunk torque alone resulted in a later release. Increasing both torques also resulted in a later wrist release. Increasing the shoulder torque alone resulted in an earlier release. A positive vertical acceleration of the model's origin resulted in a later release, while a negative vertical acceleration produced an earlier release (Table 2). The combination of a positive vertical acceleration and a 50% increase in trunk torque resulted in the greatest delayed release (172.5°), while combining a negative vertical acceleration and a 50% increase in shoulder torque produced the smallest delayed release (164.4°) (Table 3).

Table 1: Angular displacement of the arm (°) at release for various trunk and shoulder torque combinations.

Torque Increase	Trunk	Shoulder	Shoulder & Trunk
0 %	166.9	166.9	166.9
30 %	168.4	165.7	169.2
50 %	169.9	165.2	170.7

Table 2: Angular displacement of the arm (°) and translation of the origin (cm) at release for various accelerations.

A_O (m/s/s)	0	+5x	-5x	+5y	-5y
T_A (°)	166.9	165.1	166.7	168.4	164.0
R_O (cm)	0	9.2x	-11.4x	10.2y	-10.4y

Note: x – horizontal; y – vertical

Table 3: Angular displacement of the wrist (°) at release when accelerations and torque increases were applied simultaneously.

A_O (m/s/s)	50% Torque Increase	
	Shoulder	Trunk
5y	168.2	172.5
-5y	164.4	168.9

Note: y – vertical

These results suggest that the position of wrist release can be altered by manipulating the angular accelerations of the segments proximal to the wrist and by accelerating the origin of the model. Whether or not these factors play a role in an experimental setting has yet to be determined.

ACKNOWLEDGEMENTS

Natural Science and Engineering Research Council of Canada

REFERENCES

Alexander, R. McN, (1990). Phil. Trans. Royal Soc. Lond. 329, 3-10.
Robinson, R.L. (1994). Proceedings of the Third World Scientific Congress of Golf, 84-89.
Sprigings, E. et al. (1998). J. Biomech. 31, 27-35.
Sprigings, E. et al. (2001). Sports Engineering. (In press).

THE EFFECTS OF STEP UNCERTAINTY ON IMPACTS AND CONTACT KINEMATICS WHILE RUNNING ON A TREADMILL

Joshua M. Thomas and Timothy R. Derrick

Iowa State University, Ames, IA
Corresponding Author: jmt@iastate.edu

INTRODUCTION

Impacts have been implicated in overuse injuries in runners Messier et al.). They have been studied under normal environmental conditions but have not been looked at during environmental conditions that produce uncertainty in the runner. The popularity of running in society has resulted in a variety of training methods and conditions that would not be considered "ideal." These conditions are not comparable to controlled laboratory conditions. The purpose of this research was to determine the effects of step uncertainty on impacts and contact kinematics.

METHODS

Twelve experienced middle to long distance runners ran at a self-selected pace (3.30±0.24 m/s) on a treadmill under three light intensities (light ~40 foot candles, medium ~0.4 foot candles, dark ~0.02 foot candles) and two surfaces (smooth and irregular). The irregular surface was achieved by attaching wood slats (0.013 m x 0.051 m x 0.406 m) to the treadmill surface. Approximately 30% of footfalls made contact with a bump. Accelerometers were attached to the head and leg. Electrogoniometers were used to measure knee and subtalar motion. After two minutes of running the data were sampled (1000 Hz) for approximately 11 strides. Heart rate data were also collected during this period. Repeated measures analyses of variance were performed with an alpha level of 0.05.

RESULTS AND DISCUSSION

Heart rate (HR) was significantly higher during the irregular surface conditions but light intensity had no effect. Stride length (SL) did not show a significant effect of either surface or light intensity. Knee angle at contact (KNEEC) showed greater flexion with the irregular surface. Rearfoot angle at contact (RFC) was decreased during the irregular surface but it was non-significant (p=0.056). There were no significant differences in the peak head impacts (PH). Peak leg impacts (PL) increased significantly on the irregular surface but light intensity had no effect. This resulted in a nonsignificant increase in impact attenuation (ATT) during the irregular surface running.

Table 1: Kinematic variables, means and (SD).

	Smooth	Irregular	Light	Medium	Dark
HR (bpm)	151.6	153.4	152.5	152.4	152.5
	(16.23)	(16.44)	(16.57)	(16.21)	(16.27)
SL (m)	2.417	2.413	2.409	2.421	2.415
	(0.236)	(0.253)	(0.249)	(0.229)	(0.253)
KNEEC (deg)	167.1	165.6	166.1	166.8	166.1
	(10.10)	(10.10)	(10.22)	(9.97)	(9.99)
RFC (deg)	11.9	10.6	11.3	11.2	11.1
	(4.83)	(3.65)	(4.06)	(4.21)	(4.27)

Table 2: Impact variables, means and (SD)

	Smooth	Irregular	Light	Medium	Dark
PH (g)	1.52	1.60	1.55	1.55	1.57
	(0.47)	(0.41)	(0.40)	(0.46)	(0.47)
PL (g)	5.85	6.62	6.19	6.14	6.37
	(1.93)	(1.39)	(1.34)	(1.69)	(1.79)
ATT (%)	72.4	74.8	73.7	73.4	73.7
	(7.14)	(4.42)	(5.32)	(5.25)	(5.77)

Questionnaire results indicated that runners felt more anxious while running on a treadmill with bumps. In response they altered knee joint and possibly subtalar joint kinematics. Despite the small degree of change in KNEEC between surfaces, it was significant. KNEEC has been shown to cause impact forces to decrease up to 65 N per degree of change (Gerritsen et al.), however increased KNEEC also decreases the effective mass (Denoth) and therefore allows a greater acceleration of the leg. The result was greater PL accelerations and greater impact attenuation. Because the increased impacts were, at least in part, the result of a decreased effective mass, they probably did not increase injury potential. In fact, the results of Gerritsen et al. suggest the impact forces may have decreased in response to the increase in KNEEC. This kinematic adjustment may have had an associated metabolic cost. It has been shown that an increased knee contact angle can increase metabolic cost (McMahon et al.) but in this study subjects also had increased levels of anxiety while running on the irregular surface.

The irregular surface had a greater affect than light intensity. Subjects appeared to increase KNEEC to accommodate unexpected changes in terrain. They may have also decreased RFC to minimize the potential for an inversion sprain on the irregular surface. HR increased as a result of increased metabolic cost or increase levels of anxiety.

REFERENCES

Gerritsen, KGM, et al. (1995). *J Biomech*. **28**, 6, 661-668.
Denoth, J (1986). In B. Nigg (Ed.), *Biomechanics of running shoes*. Champaign, IL: Human Kinetics.
McMahon TA, et al. (1987). *J Appl Physio*. 62, 6, 2326-2337.
Messier, SP, et al. (1988). *Med Sci Sp Exer,* **20**, 501-505

EXPERIMENTAL EVALUATION OF A MODEL OF CONTACT PRESSURE DISTRIBUTION IN THE HIP JOINT

Mehran Armand[1] , Andrew Merkle[1], Theresa Sukal[1,2], and Michael Kleinberger[1]

[1]Johns Hopkins University Applied Physics Laboratory, Laurel, MD, USA http://www.jhuapl.edu
[2]Department of Biomedical Engineering, Catholic University of America, Washington DC, USA
Corresponding Author: mehran.armand@jhuapl.edu

INTRODUCTION

One major challenge in the development of finite element models of the hip is the modeling of joint contact surfaces and their contact pressure distributions. The complexity of the parameter space and the computational intensity of the finite element analysis (FEA) make them less desirable for the development of models for individual-based functional data. Discrete element analysis (DEA) (also known as rigid-body spring modeling) (Kawai, 1986; An et al. 1990, Li et al., 1997) is a simple, fast technique suitable for such data. The objective of this work was to determine whether the contact pressures on hip joints calculated using this technique could be experimentally validated.

METHODS

The 3D surface geometry of two porcine pelvis and femur bones was digitally scanned using an H40 Laser head with Nvision Faro Arm laser scanner. A computer model of the acetabular cartilage of the hip was generated from the digitized scanned data (Figure 1A). Discrete element analysis (Figures 1A and 1B) was performed for four different pelvis orientations and three sets of loads (890, 1335, and 1780 N). In order to validate the modeling results, Fuji prescale film was used to measure joint contact pressure when a preset axial force was applied from femur to the pelvis using an Instron testing machine (Figure 1C). The pelvis orientation was rotated and tested at 10^o adduction, 10^o abduction, 20^o abduction, and normal standing positions. Each pressure pattern was analyzed for location and magnitude of the maximum pressure and the percentage of joint contact surface registering above 2.5 MPa (lower limit of the film).

RESULTS AND DISCUSSION

The DEA model consistently predicted the location of the maximum contact pressure with an error of less than 10% as compared to experiments. The simulation consistently underestimated the magnitude of the maximum contact pressure. The mean underestimation was 20±6.5%. The congruency assumption for the simulated contact surface led to an overestimation of the contact area, which in turn resulted in the underestimation of the maximum contact pressure. However, the standard deviation of the difference between the model and experimental results was relatively small.

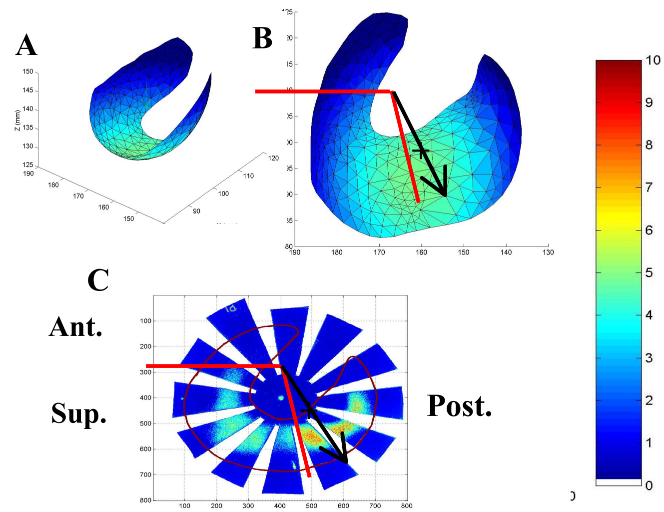

Figure1. (A) Contact pressure distribution on the surface of the acetabular cartilage. The load of the femur is 1335 N along *Z*-axis. (B) Projection of the cartilage surface into a plane. The solid lines separate anterior, superior, and posterior portions of the cartilage. The arrow and the + mark represent the polar coordinates of the maximum pressure. (C) The experimental contact pressure distribution on a rosette cut from the Fuji prescale films.

SUMMARY

DEA technique can approximate the pressure distribution within an acceptable range. This technique is at least 2 orders of magnitude faster than FEA for contact analysis. Therefore, it can be used for applications that require dynamic subject-specific models of pressure distribution in articular joints. By validating the DEA technique, this study supports the effort necessary to develop hybrid FEA/DEA techniques for analysis of stress in both bones and articular joints.

REFERENCES

Kawai, T., and Toi, Y. (1986). in *Selected papers of Emeritus Professor Dr. Kawai,* published in Japan.
An, K.N. et al (1990) *J. Biomech.*, **23**(10), 1013-1020
Li, G. et al. (1997) *J. Biomech.,* **30**(6), 635-638.

DEVELOPMENT OF A HIGH PAYLOAD TESTING SYSTEM TO STUDY JOINT KINEMATICS AND FORCES

Richard E. Debski, Shon Darcy, Jorge E. Gil, Jesse Fisk, Savio L-Y. Woo

Musculoskeletal Research Center Department of Orthopaedic Surgery, University of Pittsburgh, Pittsburgh, USA
Pittsburgh, PA. 412-648-2000, Fax: 412-648-2001, decenzod@msx.upmc.edu

INTRODUCTION

Robotic manipulators have been utilized in orthopeadic research to study joint kinematics and forces in ligaments (Livesay, Fujie et al. 1995; Fujie, Livesay et al. 1996; Rudy, Livesay et al. 1996). A new high-payload robotic/universal force-moment sensor (UFS) testing system is being developed to determine the forces in ligaments while simulating *in vivo* activities with high joint contact forces. This testing system will also reproduce joint kinematics, data imported from patients. To accomplish these tasks, the system must accurately reproduce the path of motion. Therefore the objective of this study is to evaluate position repeatability and resulting force variations measured with the high-payload robotic/UFS testing system.

METHODS

A spring model that simulated the stiffness of the knee with four linear springs was used to provide resistance to the motions of the robot (figure 1). The high-payload robotic/UFS testing system (S-900W, FANUC Robotics North America, Inc, Auburn Hills, MI) was moved through six positions in the horizontal and vertical planes. The vertical plane simulated knee flexion-extension. At each position, three points were digitized on the robotic end-effector using a MicroScribe (3DX) to determine position repeatability. The MicroScribe can digitize points with an accuracy of less than .1 mm. Force was recorded directly from the UFS (Theta Model, ATI-Industrial Automation, Garner, NC). The positions in the horizontal and vertical planes were repeated twelve times alternating between clockwise (CW) and counterclockwise (CCW), to investigate position repeatability due to backlash. This protocol causes the manipulator to approach positions different directions.

RESULTS

Transnational (Tran) and rotational (Rot) variability range from .2 to .4 mm and .1 to .4°. Force variability ranges from 1.2 to 10 N, with the average variability for the vertical and horizontal planes being 5.4 and 2.6 N. The variability in positions and forces (Forc) is calculated as the standard deviation of the 12 trials. Resultant force (FMag) measured by the UFS due to deformation of the springs ranged from 148 to 667 N. The highest percent force variability was 2.6% while the average variability for the horizontal and vertical planes was 1.5% and .7% respectively.

DISCUSSION

The high-payload robotic/UFS testing system can precisely reproduce a path of motion as demonstrated by the position repeatability, which resulted in little variation in force. Position repeatability and force variability is relatively constant for all positions and magnitudes of force examined. Therefore force variability is not affected by force magnitude. High force variability at certain positions was caused by reseating of the spring attachments in the spring model. In the future the high-payload robotic/UFS testing system will be used to evaluate clinical examination, post-operative rehabilitation exercises and provide experimental validation for computational models in response to *in-vivo* kinematics obtained from patients.

Table 1: Position repeatability and force (F) variation [Force (N), Tran (mm), Rot (deg)].

Horizontal Plane

Variability	Position 1	2	3	4	5	6	Ave
Tran	0.4	0.3	0.3	0.3	0.3	0.3	0.3
Rot	0.2	0.3	0.4	0.2	0.3	0.2	0.3
Forc	2.8	1.2	1.5	0.9	7.1	2.1	2.6
FMag	298	521	481	421	323	325	395
% F	0.9	0.2	0.3	0.2	2.2	0.6	0.7

Vertical Plane

Variability	Position 1	2	3	4	5	6	Ave
Tran	0.2	0.2	0.2	0.2	0.2	0.2	0.2
Rot	0.2	0.1	0.1	0.1	0.1	0.2	0.1
Forc	4.3	6.4	10	3.8	3.8	4.2	5.4
FMag	265	752	449	148	431	667	452
% F	1.6	0.8	2.2	2.6	0.9	0.6	1.5

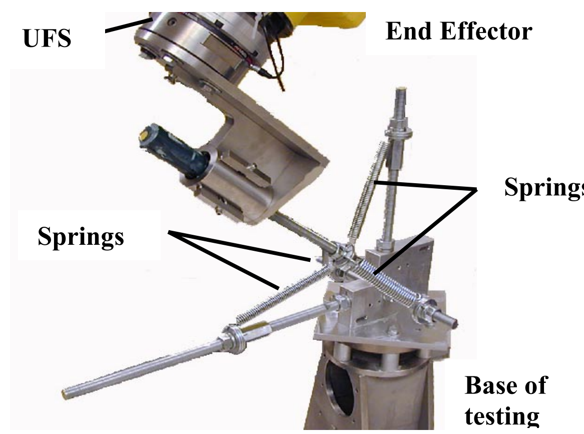

Figure 1: Spring model

REFERENCES

Fujie, H. et al. (1996). *J Biomecs* **29**(12): 1577-85.
Livesay, G. A. et al. (1995). A*BME* **23**(4): 467-74.
Rudy, T. W., G. A. Livesay, et al. (1996). *J Biomecs* **29**(10): 1357-60.

ACKNOWLEDGMENTS

NIH-Grant AR 39683

BIOMECHANICAL ASSESSMENT OF THE ANKLE AND KNEE DURING LANDING FROM A LATERAL DROP JUMP WITH A PROPHYLACTIC ANKLE BRACE

Ann L. Livengood[1], Howard J. Hillstrom[2], Michael Sitler[3]

[1]Biodynamics Laboratory, University of Kentucky, Lexington, KY, USA
[2]Gait Studies Laboratory, Temple University School of Podiatric Medicine, Philadelphia, PA, USA
[3]Biokinetics Laboratory, Temple University, Philadelphia, PA, USA
ALS97@aol.com

INTRODUCTION

Ankle sprains are one of the most common athletic injuries (Thacker et al., 1999). Stress to the lateral ligament structures occur when the ankle is inverted, plantarflexed, and internally rotated. This mechanism occurs frequently during movement from open to closed chain activities such as landing from a jump (Hume & Gerrard, 1998), coinciding with changes from ligamentous to osseous restraint of the hindfoot (Stormont et al., 1985). A prophylactic ankle brace (PAB) is frequently used to reduce the risk of lateral ankle ligament injuries (Thacker et al.). Research has shown that PABs are beneficial in preventing ankle injuries (Sitler et al., 1994).

During landing from a jump, the body's energy is converted from potential to kinetic energy, and it is through the eccentric tension of muscles that the body begins to absorb these forces (Dufek and Bates, 1990). The greatest risk of injury is at the transitional period between flight and landing. This study examines the effect PABs have on 3-D kinematics and kinetics of the ankle and knee during landing from a lateral jump.

METHODS

Ten healthy males (age 26±4 yr; height 180.3±15.2 cm; mass 85.4±28.7 kg) performed five trials of a lateral drop jump under two conditions (AirCast® Sport Stirrup PAB and nonbraced control). A wooden box with a height of 46 cm was used to standardize the landings across subjects. Kinematic and kinetic variables were collected using a five camera, 120 Hz VICON 370® Kinematic System and a Kistler® force plate. A modified Helen Hayes marker set for the lower extremity was used for data collection. Data were collected for the ankle and knee during the period from the initial forefoot contact on the force plate to the point where the sacrum reached its lowest level.

RESULTS AND DISCUSSION

The ankle and knee kinematic results are presented in Table 1, and the kinetic results are found in Table 2. The total sagittal plane range of motion (ROM) at the ankle was significantly reduced 4.11° with the PAB. The initial rate of dorsiflexion was reduced 21.1% while utilizing the PAB. A combination of a decrease in ROM and rate of loading may aid in protecting the ankle ligaments from excessive stress. The decrease in ankle sagittal plane ROM at contact resulted in an increase of 2.2° in initial knee flexion angle with the PAB. The finding of a decrease in knee internal rotation angle was associated with an increase in internal rotation moment. The decrease in valgus moment at the knee might reduce the stresses on the intrinsic structures (e.g. meniscus). The reduction in ankle internal rotation moment may be reducing stress on the lateral ligaments, which could protect them from injury. A decrease in the total ankle power absorbed was associated with no significant change in total knee power. The increases in maximum ankle inversion and knee internal rotation moments are not necessarily experienced by the lower limb. Some percentage of these loads may be borne by the PAB. Further research is needed to determine if the PAB is load sharing with the lower extremity, hence further reducing the kinetics experienced by the limb.

SUMMARY

The pilot data indicates that the lateral ankle ligaments are protected by the PAB when landing from a lateral drop jump, without deleteriously effecting the surrounding structures of the lower extremity.

Table 1: Ankle and Knee Kinematic Variables
Max = maximum; PF = plantarflexion; DF = dorsiflexion; Min = minimum;

Variable	PAB	Control
Max PF Angle (deg)	12.4±5.1***	19.7±5.4
Max DF Angle (deg)	29.2±6.0**	32.4±6.4
Initial Rate of DF (deg/sec)	1.5±0.4***	1.9±0.5
Initial Knee Flexion Angle (deg)	24.3±6.4*	22.2±7.2
Max Knee IR Angle (deg)	14.4±7.7**	22.6±8.2

IR = internal rotation; * = significance at the 0.05 level; ** = significance at the 0.01 level; *** = significance at the 0.001 level
See Table 1 for legend

Table 2: Ankle and Knee Kinetics

Variable	PAB	Control
Max Inversion Moment (Nm/kg)	0.4±1.0***	0.2±0.4
Max Ankle IR Moment (Nm/kg)	0.2±0.1**	0.3±0.1
Total Ankle Power (W/kg)	18.2±10.1*	23.3±10.8
Max Knee Valgus Moment (Nm/kg)	0.8±0.3**	1.0±0.4
Max Knee IR Moment (Nm.kg)	0.2±0.1***	0.1±0.1
Total Knee Power (W/kg)	28.1±7.5	27.9±8.7

REFERENCES

Dufek, J.S., Bates, B.T. (1990). *Med Sci Sport Exer*, **22**, 370-377.
Hume, P.A., Gerrard, D.F. (1998). *Sports Med*, **25**, 285-312.
Sitler, M. et al (1994). *Am J Sport Med*, **22**, 454-461.
Stormont, D.M. et al (1985). *Am J Sport Med*, **13**, 295-299.
Thacker, S.B. et al (1999). *Am J Sport Med*, **27**, 753-760.

IS DAMAGE DEVELOPMENT DIFFERENT IN BONES WITH A SHORTER FATIGUE LIFE?

Winson George and Deepak Vashishth

Department of Biomedical Engineering
Rensselaer Polytechnic Institute
110 8th St. Troy NY 12180, vashid@rpi.edu

INTRODUCTION Progressive damage development in the form of matrix microcracking, delamination and coalescence of microcracks causes the primary, secondary and tertiary loss of bone stiffness (Schaffler et al. 1990). However, it is unknown whether this 3-phase characteristic behavior of bone fatigue is altered with aging and disease, where a marked reduction in the fatigue life of bone is expected without any change in the imposed loading. In the current study we used modulus reduction data from two groups of bovine bone specimens demonstrating significantly different fatigue life under identical loading conditions to test the hypothesis that a reduction in fatigue life of bone is accompanied by a change in the 3-phase characteristic behavior of bone fatigue.

METHODS Twelve bovine bone cylindrical dumbbell specimens (3mm dia) were wet machined from four bovine tibiae (Age:18-24 mo.). Specimens were fatigue tested on an MTS MiniBionix System under identical loading (±50%UTS @ 2 Hz; Wet). Based on the statistical analysis of the fatigue life data the specimens were separated into long (5933±3314) and short life (643±332) groups of six specimens each. Stress-strain data collected continuously for every specimen until failure was then used to calculate tangent moduli under tension and compression in both the short life (SL) and long life (LL) groups. The reduction in moduli was plotted against fatigue life (Fig. 1) and compared within each group to determine the occurrence of the primary, secondary and tertiary phases of modulus loss (Table 1). Initial moduli and total moduli loss were also compared between the short and long life groups.

RESULTS AND DISCUSSION Although the total moduli loss was the same (*Tension*:SL=26%; LL=25%, p=0.81; *Compression*:SL=10%, LL=11%, p=0.83), the modulus degradation profiles between the groups were fundamentally different (Fig. 1). Short life group displayed the three phases of tensile modulus loss at 0-10%, 10-80% and 80-100% of the fatigue life (Table 1). In contrast, long fatigue life group showed only two phases of modulus loss at 0-70% and 70-100% of the fatigue life (Table 1). Compressive moduli degradation profiles were different from tensile moduli degradation profiles and varied significantly between the short and long life fatigue groups (not shown).

The results of this study are consistent with the occurrence of different damage mechanisms (Pattin et al., 1996: Boyce et al. 1998) in tension and compression, and demonstrate, for the first time, the role of progressive damage development in determining the fatigue life of bone. Specifically, our study shows that bones with long fatigue life do not undergo the primary phase of stiffness loss associated with transverse matrix microcracking and spend majority of their lives in the secondary phase where microcracks, parallel to the loading axis are formed (Pidaparti et al. 2002). Longitudinal microcrack formation and growth cause minimal changes in axial moduli and bone maintains its structural integrity. In contrast, bones with shorter fatigue life undergo primary phase of stiffness loss and form transverse matrix microcracks that combine more easily to cause fracture. Consequently, the secondary phase of fatigue behavior and the fatigue life itself is reduced. Thus, these data suggest that factors affecting the morphology and development of damage play a key role in determining the fatigue life of bone.

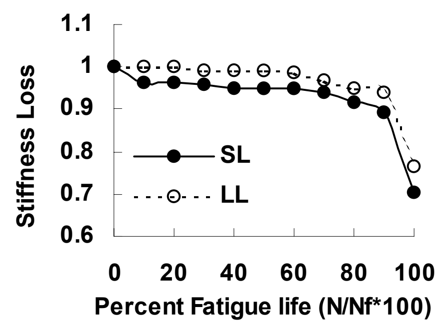

Figure 1: Average values of tensile modulus loss in short (SL) and long life (LL) groups.

Table 1: Paired t-tests were used in each group to compare the initial moduli with reduced moduli at different % of the fatigue life (10% increments). Once a difference ($p<0.05$) was detected, the new reduced moduli was chosen for futher comparisons Columns show p-values for selected load cases

% Fatigue life → ↓Fatigue Groups	10%	40%	70%	80%	100%
Short-Tension	**0.01**	0.13	0.14	**0.04**	**0.02**
Long-Tension	0.78	0.41	**0.04**	0.23	**0.01**

REFERENCES **Schaffler** et al. (1990) *Bone* 11:321-326; **Boyce** et al. (1998) *JORS* 16:322-9; **Pattin** et al. (1996) *J. Biomch* 29:69-79; **Pidaparti** et.al (2002) *JBMR* 59:282-7

ACKNOWLEDGEMENTS The Whitaker Foundation (Multiaxial Failure Characteristics of Aging Bone).

EFFECT OF STOCHASTIC ELECTRICAL JOINT STIMULATION ON BALANCE CONTROL IN OLDER ADULTS

Denise Gravelle[1], Carrie Laughton[1], Neel Dhruv[1], Kunal Katdare[2], James Niemi[2], Lewis Lipsitz[3,4], and James Collins[1]

http://cbd.bu.edu/abl/
[1]Center for BioDynamics and Department of Biomedical Engineering, Boston University, Boston, MA, USA
[2]Afferent Corporation, Providence, RI, USA
[3]Hebrew Rehabilitation Center for Aged, Beth Israel Deaconess Medical Center Gerontology Division, Boston, MA, USA
[4]Department of Physical Medicine and Rehabilitation, Harvard Medical School, Boston, MA, USA

INTRODUCTION

Diminished balance ability, seen in older adults, poses a serious health risk due to the increased likelihood of falling (Tinetti et al., 1995). Proprioceptive information is critical to balance control and the prevention of falls in older adults (McChesney and Woollacott, 2000). Recently, balance control in humans has been enhanced by applying mechanical noise to the plantar surface of the feet (Priplata et al., Submitted 2001). This noise-based technique operates by improving the detection and transmission of weak sensory signals contributing to balance control. The goal of the present study was to use electrical noise applied at the knee joint to improve proprioception and balance control in older adults.

METHODS

Thirteen healthy elderly adults (age 68-79) volunteered for this IRB approved study. Subjects were asked to perform 16 trials of single-legged stance on a slightly bent knee for up to 30 seconds while standing on a force platform. Surface stimulation electrodes were placed on the medial and lateral aspects of the stance knee, and electrical noise (zero mean, Gaussian white, SD = 0.05 mA) was applied during 8 of 16 trials in a random order. The level of stimulation was below the cutaneous sensation threshold for all subjects, ensuring a blind treatment condition. Balance improvements were measured as reductions in center-of-pressure (COP) displacement parameters when electrical noise was applied to the knee (STIM). The COP variables investigated were the standard deviations (SD) and maximum excursions in the anteroposterior (AP) and mediolateral (ML) directions, the mean radial (R) displacement, and the cumulative path length and swept area of the COP trajectory. Significant changes were noted between the STIM and non-STIM conditions using paired *t*-tests.

RESULTS AND DISCUSSION

All but one of seven traditional COP displacement parameters decreased with electrical noise, indicating an overall improvement in balance performance when electrical noise was applied to the knee (Table 1). The improvement was statistically significant for three of these measures ($p < 0.05$). Averaged across subjects, there was a 3.8% reduction in the ML COP SD ($p = 0.041$), a 5.4% decrease in the maximum AP COP excursion ($p = 0.031$), and a 3.1% reduction in the COP path length ($p = 0.041$) with application of electrical noise.

SUMMARY

Imperceptible electrical noise, when applied to the knee, can enhance the balance performance of healthy elderly adults. These balance improvements are likely related to an enhanced ability of knee joint proprioceptors to detect sensory stimuli in the presence of noise. These results suggest that noise-based devices may be effective in improving balance control in elderly people.

REFERENCES

Tinetti, M.E. et al. (1995). *J Am Geriatr Soc*, **43**, 1214-1229.
McChesney, J.W., Woollacott, M.H. (2000). *J Gerontol A Biol Sci Med Sci*, **55**, M658-666.
Priplata, A. et al. (Submitted 2001).

ACKNOWLEDGEMENTS

This research was funded by NIH Grants # AG04390, AG08812, and HD37880 and the NSF.

Table 1: COP displacement measures for non-STIM versus STIM conditions (mean ± SD).

Outcome Measures	non-STIM	STIM	% Improvement	p-value	No. of Subjects Improved
ML SD (mm)	4.63 ± 0.74	4.46 ± 0.69	3.8	0.041 *	9/13
ML Max (mm)	12.99 ± 2.22	13.13 ± 2.56	-1.1	0.712	7/13
AP SD (mm)	6.30 ± 1.28	6.06 ± 1.35	3.7	0.210	8/13
AP Max (mm)	20.04 ± 5.62	18.95 ± 5.29	5.4	0.031 *	9/13
R Mean (mm)	6.88 ± 1.05	6.66 ± 1.15	3.3	0.105	9/13
Path Length/Time (mm/s)	37.09 ± 4.97	35.93 ± 5.77	3.1	0.041 *	9/13
Swept Area/Time (mm^2/s)	88.81 ± 25.54	81.89 ± 24.74	7.8	0.054	9/13

Positive percent improvements indicate a reduction in COP displacement with electrical noise. *Indicates a significant p-value at the 0.05 level.

WALKING WITH PLATFORM SHOES – NORMAL WALKING PATTERN?

Andreas Kranzl, Nina Seirlehner, Belinda Priester, Julia Wlcek and Franz Grill
Labor für Gang- und Bewegungsanalyse, Orthopedic hospital Speising, Vienna, Austria
andreas.kranzl@aon.at

INTRODUCTION

Nowadays the young people are wearing platform shoes for fashionable reasons. But this shoes were not designed to be comfortable and healthy. They were designed to be trendy. There are some studies about platform shoes dealing with the higher injury risks caused by the increased lever arm. There are no published data's (known to us) reporting on the influence of the platform shoes onto the gait pattern. Some of the platform shoes have a small high heel component. The biomechanical influence of high heeled shoes was the topic of many research papers. So it would be interest to see the effect of this shoes and if there exists one is it compared to high heeled walking.

METHODS

The subjects for this investigation were 16 young female students. All of them had experience in walking with platform shoes and had the same shoe size. A 3-dimensional optoelectronic system (Motion Analysis Cor.) combined with two force platforms (AMTI) were used to acquire the kinematic and kinetic parameters. Physical examination were performed including ROM, force and alignment of the lower extremity. Three conditions were analyzed: walking barefoot (BF), walking with gym shoes (GS) and walking with platform shoes (PS). The analyzed order were chosen randomized. All trials were carried out at self selected speeds. The platform shoe had 10.3 cm heel height and 6 cm toe height. Statistical analysis for the kinematic and kinetic parameters were performed by using the paired t-test.

RESULTS AND DISCUSSION

Some significant differences between the three conditions were found. Table 1 shows the results for the temporal-spatial parameters. The kinematic parameters showed a reduced max knee flexion during the swing phase for the shoe conditions. No differences for the pelvic and hip motion was detected. The significant greater plantar flexion of the PS were caused by the shoe geometry. A reduced ROM of the ankle joint were found for the GS and PS. In the transverse plane a reduced foot progression angle were found for both shoe types compared to BF walking. The kinetic parameters showed a higher valgus moment for PS during second half of the stance phase compared to BF. The lowest power generation at the ankle joint was found by the PS followed by the GS and BF walking. At the frontal hip moment after loading response BF and GS walking showed a significant higher moment compared to PS.

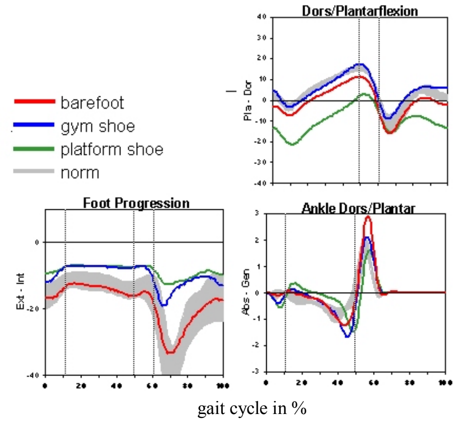

Figure 1: kinematic and kinetic results of all three conditions.

SUMMARY

The differences we found were not so big as we expected. Not all reported results for high heeled walking (Opila-Correia,K.A. 1990, Kerrigan,D.C.1998, Snow,R.E. 1994) are corresponding with our PS results. Especial the results for the pelvic and hip are not corresponding to high heeled gait pattern. The risk of injury caused by supination or pronation trauma due to the thicker sole (increased lever arm) should not be neglected.

REFERENCES

Kerrigan,D.C., Todd,M.K., and Riley,P.O.: (1998) *Lancet*, **351**:1399-1401.

Opila-Correia,K.A.: (1990) *Arch Phys Med Rehabil*, **71**:304-309.

Snow,R.E. and Williams,K.R.: (1994) *Arch Phys Med Rehabil*, **75**:568-576, 1994

Table 1: temporal-spatial parameters (* significant differences $p<0.05$)

conditions	Velocity (cm/s)	Cadence (steps/min)	step width (cm)	step length (cm)	stance phase (%)
barefoot	124.9 ± 11.5	115.2 ± 6.3	9.9 ± 1.9	64.9 ± 3.8	60.4 ± 1.0
Gym shoe	130.1 ± 11.5	112.3 ± 6.5	11.4 ± 1.7	69.5 ± 3.8	60.8 ± 1.8
platform shoe	127.7 ± 12.7	109.6 ± 6.4	11.8 ± 1.6	69.7 ± 4.4	59.6 ± 2.0
significant results			BF-GS*, BF-PS*	BF-GS*, BF-PS*	

OPTIMIZED JOINT CENTRES AND AXES OF ROTATION IMPROVE REPEATABILITY OF GAIT DATA

Thor Besier, Daina Sturnieks, Jacque Alderson, and David Lloyd
Department of Human Movement & Exercise Science, University of Western Australia, Perth, Australia
Email: tbesier@cyllene.uwa.edu.au

INTRODUCTION

Imprecise location of anatomical landmarks (ALs) has been noted as the greatest source of error during motion analysis compared to instrument error or skin movement artefact (Della Croce et al., 1997). These errors propagate to joint kinematics and kinematic 'cross-talk' and are likely to effect the repeatability of kinematic and kinetic gait data. Mathematical optimization offers a way to functionally determine joint centres and define axes of rotation, independent of ALs (OPTIM method).

The purpose of this paper was to compare the repeatability of a marker cluster model utilising either ALs alone, or ALs combined with optimized joint centres and axes or rotation.

METHODS

Gait analyses were performed on three separate occasions for ten subjects. To investigate inter and intra-tester repeatability, two different examiners administered the testing sessions. A six-camera VICON motion analysis system (Oxford Metrics, Oxford, UK) was used in conjunction with two AMTI force-plates (AMTI, Watertown, MA) to collect motion data (50 Hz) and ground reaction force data (2000 Hz), respectively. Data were collected on at least six walking trials for each limb. The kinematic/kinetic model was constructed using BodyBuilder software (Oxford Metrics, Oxford, UK).

Clusters of three retro-reflective markers were attached to lower limb segments of interest. During a series of static trials, ALs were located relative to each segment cluster (cf. Cappozzo et al., 1995). Hip joint centres were defined using either a regression equation for the AL method (Shea et al., 1997) or by using a functional method for the OPTIM marker set (cf. Piazza et al., 2001). Knee joint axes were defined by the transepicondylar line of each femur in the AL method, or by an optimal helical axis for the OPTIM method (cf. Stokdijk et al., 1999).

A Coefficient of Multiple Determination (r^2, Kadaba et al., 1989) was used to determine the repeatability of the wave form data, normalised to stride. A two-way ANOVA was then used to determine the difference in r^2 values between using the AL and OPTIM method, and to determine any differences in repeatability between and within testers.

RESULTS AND DISCUSSION

The OPTIM method had little effect on the repeatability of sagittal plane data (Table 1). However, the frontal and transverse kinematic data for the knee were more repeatable using the OPTIM method ($p<0.05$). Furthermore, there appeared to be less cross-talk between knee flexion and knee abduction/adduction using the OPTIM method (based on a correlation coefficient). The kinetic data were less effected by the method used, due to the repeatability and influence of the ground reaction force.

Table 1: Mean ± SD Coefficients of Multiple Determination (r^2) for kinematic gait data for the AL and OPTIM methods.

		Flexion Extension	*Abduction Adduction*	*Internal External Rot^n*
Hip	AL	0.980 ±0.009	0.925 ±0.036	0.547 ±0.204
	OPTIM	0.982 ±0.008	0.936 ±0.027	0.583 ±0.203
Knee	AL	0.981 ±0.011	0.736 ±0.138	0.809 ±0.130
	OPTIM	0.982 ±0.011	0.844 ±0.129	0.854 ±0.116
Ankle	AL	0.947 ±0.018	0.651 ±0.225	0.795 ±0.122
	OPTIM	0.950 ±0.016	0.630 ±0.204	0.753 ±0.159

The between-tester repeatability was expected to improve using the OPTIM method, as the examiner source of error in locating ALs is removed. However, within and between-tester repeatability was similar using both techniques. This was perhaps due to the experience of the examiners performing the tests.

SUMMARY

Repeatability of gait data was slightly improved by optimizing joint centres and axes of rotation. However, given that the optimization technique does not rely on the accurate location of ALs and is faster and easier to implement, the use of optimized joint centres and axes of rotation in a daily clinical setting should be encouraged.

REFERENCES

Della Croce, U., Cappozzo, A., & Kerrigan, D. C. (1999). *Med & Biol Eng & Computing,* **37**, 155-161.

Cappozzo, A., Catani, F., Della Croce, U., & Leardini, A. (1995). *Clinical Biomechanics,* **10**, 171-178.

Kadaba, M. P., Ramakrishnan, H. K., Wootten, M. E., Gainey, J., Gorton, G., & Cochran, G. V. (1989). *J of Orthop Res*, **7**, 849-60.

Piazza, S. J., Okita, N., & Cavanagh, P. R. (2001). *J Biomech,* **34**, 967-973.

Shea, K. M., Lenhoff, M. W., Otis, J. C., & Backus, S. I. (1997). *Gait & Posture,* **5**, 157-158.

Stokdijk, M., Meskers, C., G., Veeger, H. E., de Boer, Y. A., & Rozing, P. M. (1999). *Clinical Biomechanics,* **14**, 177-184.

ACKNOWLEDGEMENTS

We would like to acknowledge the financial support of the Australian NHMRC and Australian Football League.

DEVELOPMENT AND VALIDATION OF AN APPROACH TO RECORD AND REPRODUCE KINEMATICS

Jennifer Zeminski, Mary T. Gabriel, Maribeth Thomas, Richard E. Debski, Freddie H. Fu, Savio L-Y. Woo

Musculoskeletal Research Center, Department of Orthopaedic Surgery, University of Pittsburgh
Pittsburgh, PA. 412-648-2000. Fax: 412-648-2001. decenzod@msx.upmc.edu

INTRODUCTION

Understanding knee kinematics and *in situ* force in the anterior cruciate ligament (ACL) and replacement graft during activities of daily living is essential to efficiently diagnose injury and develop effective treatment strategies. Studies have measured these data in response to arbitrary loading conditions [Kanamori, 2000, Markolf, 1995]. However, the *in situ* force in the ACL during more realistic loading conditions needs to be determined. Therefore, the objective of this study was to develop and validate a method of recording and reproducing joint kinematics to measure external loads and the force in ligaments during more realistic activities.

METHODS

A novel method was developed to: 1) record the kinematics of a diarthrodial joint during activities of daily living or a clinical examination, and 2) reproduce the exact kinematics of the same joint using a robotic/universal force-moment sensor (UFS) testing system to determine the external loads applied to the joint and force in ligaments (**Fig 1**). To validate this method a model consisting of two plexiglas plates connected by linear springs was constructed to represent a joint (**Fig 2**). Small plexiglas cubes, or registration blocks, were attached to each plate. Points on the three orthogonal faces of the registration blocks measured by a spatial digitizer (Immersion Corporation, San Jose, CA) were fit to planes and used to define a local coordinate system for each plate [Fischer, 2001]. The top plate of the model was moved, and the relative motion of the registration blocks was determined. The forces in the spring scales were summed and used to independently record the external force applied to the model. The model was then rigidly mounted in a robotic/UFS testing system [Rudy, 1996]. The location of the registration blocks with respect to the robotic manipulator was registered. Using this information, as well as the relative motion of the registration blocks, the path of the robotic manipulator was calculated and reproduced on the model, while the force was measured by the UFS [Zeminski, 2001].

RESULTS AND DISCUSSION

For validation, the external force recorded by the springs during the original motion was compared to the force measured by the UFS when the motion was reproduced and found to be within 3 N. Similarly, the relative motion of the registration blocks that was recorded and reproduced were compared and found to be within 1.5 mm and 0.5º. An error analysis found that 0.1 mm of error in the measurements of joint motion produces over 1 mm of error in the calculated motion of the robotic manipulator. This finding is due to error propagation throughout the matrix manipulations.

A novel method to record and reproduce kinematics was successfully validated. This new approach has the unique ability to obtain *in situ* force in the ACL in response to more realistic activities rather than subjecting the knee to arbitrary external loads. The accuracy of this method is limited by error propagation throughout matrix manipulation. This method will be used to record and reproduce the kinematics of a cadaveric knee during more realistic activities such as clinical examination. The *in situ* force in the ACL as well as the external forces applied to the knee can then be determined.

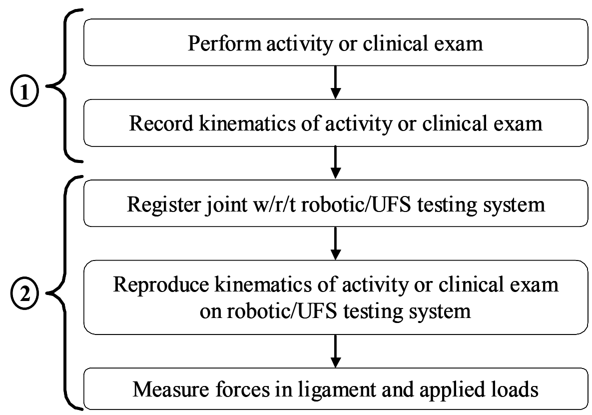

Figure 1: Novel method to determine external loads applied to joints and forces in ligaments.

REFERENCES

Fischer, K.J., et al. (2001). *J Biomech*, **34,** 377-83.
Kanamori, A., et al. (2000). *Arthroscopy*, **16,** 633-9.
Markolf, K.L., et al. (1995). *J Orthop Res*, **13,** 930-5.
Rudy, T.W., et al. (1996). *J Biomech*, **29,** 1357-60.
Zeminski, J. (2001). *University of Pittsburgh*, 112.

ACKNOWLEDGEMENTS

NIH grant #AR39683 is greatly acknowledged.

COORDINATION OF HIP AND KNEE KINEMATICS DURING REPETITIVE LIFTING

Wayne J. Albert and Cynthia Babineau

Human Performance Laboratory, University of New Brunswick, Fredericton, NB, CANADA

INTRODUCTION

Differences in neuromuscular coordination have been reported during lifting activities when individuals are required to adapt to an increasing load (Scholz, 1995). It has been speculated that differences in coordination contribute to low back pain development, but there has been little research to date that corroborates this theory. Parnianpour et al. (1988) reported an increase in asymmetric trunk rotations due to fatigue during repetitive lifting. Similarly, Sparto et al. (1997) indicated a shift from a coordinated movement of the knees and hips to a lifting motion led by knee extension as the lifting task began to cause fatigue.

The effects of adaptations in lifting technique and changes in lifting motion coordination remain unclear. This preliminary work investigates the changes in coordination during a repetitive lifting task performed by inexperienced lifters.

METHODS

The inclusion criteria for this study were healthy men and women with little manual material handling experience. Participants were instructed to lift a 25-pound box, instrumented with handles, in a freestyle manner from the floor to a table at hip height. The box was lifted and lowered at a fast rate (every 6 seconds), in order to stimulate fatiguing conditions in a short amount of time. To examine the kinematics of the lifting movement, data were collected using standard video techniques and digitised at 30Hz.

Methods outlined by Scholz (1995) were used to calculate the coordination (phase angles) of knee and hip movement during the lifting task. To do this, the phase angle of each joint is calculated as the inverse tangent of the normalized angular velocity (scaled between –1 and 1, indicating maximum flexion and extension, respectively) divided by the normalized angular position (scaled between –1 and 1).

RESULTS AND DISCUSSION

The length of time lifted varied between subjects with the average lifting duration being a half hour. Although the lift posture for initiating the lift and the trajectory of the lift were unchanged over the lifting activity, changes in back and knee motions were observed. As expected most participants demonstrated a decrease in the extension velocity of the hip (Figure 1), indicating fatiguing of the back musculature. This change in velocity was reflected in the coordination pattern between the hip and knee movements. There was no observed change in the lifting posture; a finding reported by others, however as the lifting task progressed the motion of the extension of the hip lagged behind that of the knees. Others increased the extension velocity of their knees with little change to hip extension (Figure 2). Therefore, it appears that there is individuality in the coordination accommodations in response to lifting in fatiguing conditions. Current investigations are exploring how these changes affect lumbar loading.

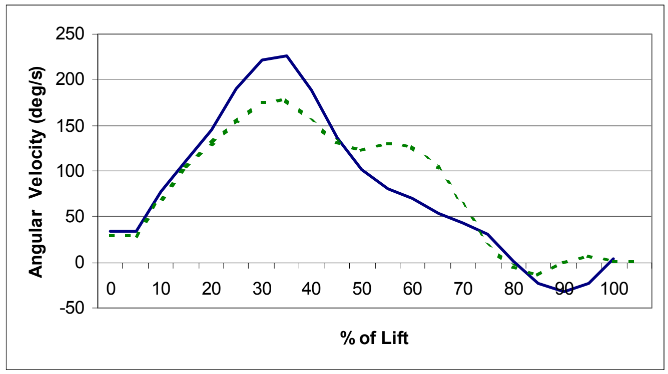

Figure 1: Observed change in hip angular velocity from early in the lifting activity (solid line) to a trial near the end of the activity (dotted).

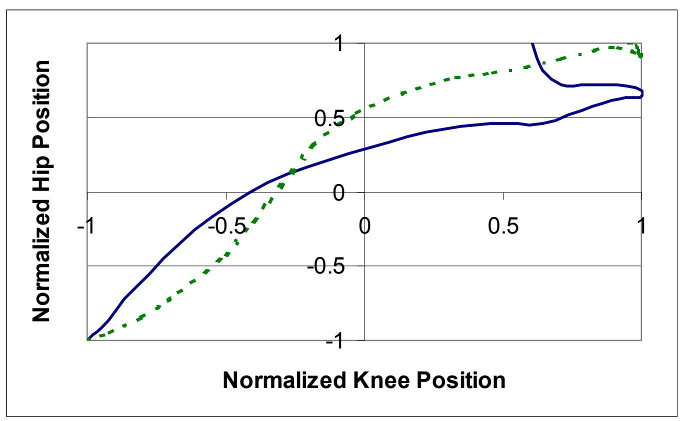

Figure 2: Change in relative phase angles from early lifting trials (solid line) to late lifting trials (dotted line).

REFERENCES

Scholz JP. (1995). *Physical Therapy*, **75(2)**: 133-144.
Parnianpour et al. (1988). *Spine*, **13(9)**:982-992.
Sparto et al. (1997). *JOSPT*, **25(1)**: 3-12.

ACKNOWLEDGEMENTS

This work was funded as part of the AUTO21 Network of Centres of Excellence whose funding is provided by the Canadian Federal Government.

VISUAL CONTROL AND LOAD EFFECTS OF FAST ROTATIONAL MOVEMENTS

Juergen Krug, Thomas Muehlbauer and Falk Naundorf

Faculty of Sport Science, University of Leipzig, Germany

INTRODUCTION

In gymnastics, diving, and figure skating rotations around the longitudinal and transversal axis are the basic skills. Airborne movements like twisting somersaults (Yeadon, 1984) are explained by mechanical principles. But there is a lack of studies to fast rotational movement's visual control and load effects. Stangl & Gollhofer (1998) reported on the spatial-dynamic precision of the vestibulo-ocular reflex. Though, the angular velocity in this experiment was relatively slow (100 deg/s). The aim of this paper was to investigate visual control and load effects of fast rotational movements.

METHODS

To analyze visual control and load effects of fast rotational movements a "Somersault Simulator" (figure 1) and a "Longitudinal Rotation Simulator" were used.

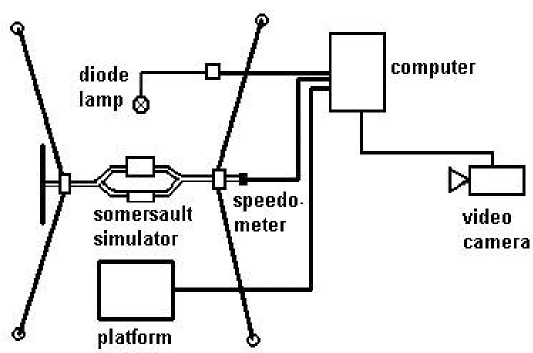

Figure 1: Measuring unit "Somersault Simulator"

In the "Somersault Simulator" the athletes were rotated by the coach using the wheel. On the "Longitudinal Rotation Simulator" the athletes rotated in a hanging position. The same measuring unit was used on both simulators.
The number of rotations and the angular velocity were recorded by computer. The diode lamp was used to test the visual control during movements. By means of a force plate (Kistler®, Typ: 9261A), the sway of the COP before and after the rotational load was analyzed. The recording time was 30 s with a sampling rate of 300 Hz.

RESULTS AND DISCUSSION

In the first study the visual control was investigated. In the "Somersault Simulator" 3 female and 3 male divers (13-15 years) trained in a 12 sessions period the visual perception of the diode lamp. Corresponding to somersaults in diving and gymnastics the angular velocity was approximately 700 deg/s. The recognition rate of the flash was significantly increased. In a replication study with 10 divers (5 female and 5 male, 12-15 years) the results could be confirmed.

In the second study the load effects of fast somersault rotations were investigated. Six divers (3 female and 3 male, 13-15 years) performed 15 somersault rotations. In a pre-post-test design the postural stability before and after these rotations was analyzed. The athletes had to go quickly to the platform for the post-test. There was a significant difference of the sway between the pre- to post-test.

In the third study the load effects of fast longitudinal rotations were analyzed. Five youth figure skaters performed ten longitudinal rotations in both directions. In a pre-post-test design the postural stability before and after rotations was investigate. There were a significant increase of the sway from pre- to post-test and a insignificant difference between the left and the right direction. In a further study to load effects of fast longitudinal rotations the differences between 6 gymnasts and non-athletes (female, 10-14 years) were investigated. There are significant differences in the postural control between both groups. The gymnasts reached a significant lower level of the sway intensity.

SUMMARY

Athletes are able for visual control in fast somersault rotations. This phenomenon could be used by diving coaches for technique training. The posturography is a suitable method to indicate load effects. The higher oscillation of the COP after rotations around the longitudinal and transversal (somersault) axis is comparable to the rotational load.

REFERENCES

Yeadon, M.R. (1984). *The mechanics of twisting somersaults.* Loughborough. Doctoral Thesis.
Stangl, W., Gollhofer, A. (1998). *BISp Jahrbuch 1997*, 119-127.

ACKNOWLEDGEMENTS

This study was supported by the BISp, Bonn, Germany.

MATERIAL PROPERTIES OF PORCINE PARIETAL CORTEX

Brittany Coats and Susan S. Margulies, Ph.D.

Department of Bioengineering, University of Pennsylvania,
Philadelphia, Pennsylvania. margulies@seas.upenn.edu

INTRODUCTION

Accurate material property descriptions are crucial to the development of biofidelic computational models of the brain. Previously we reported significant mechanical property differences between gray and white matter, and even between regions of white matter with differing degrees of neural tract alignment (Prange et al, 2002). In this study, we extend our investigation to gray matter, to examine the hypothesis that gray matter (cortex and thalamic nucleus) can be considered homogeneous.

METHODS

Adult porcine brains were collected less than 1 hour post-mortem, and transported in chilled mock-CSF solution. Rectangular samples approximately 1 mm x 5 mm x 10 mm were excised from two lateral parietal cortical locations containing predominantly (~80-99%) gray matter (N=7).

Samples were mounted in a parallel plate shear testing device described previously (Prange et al., 2002). In a humidified environment, each sample was tested using a shear relaxation protocol consisting of a rapid (60msec) ramp to 2.5% strain, and return to rest after a 60sec hold period. The test sequence continued to 5, 10, 20, 30, 40, and then 50% strain. Previously we reported that this test sequence was reproducible, and was not associated with tissue damage (Prange et al., 2001). Measurement at each strain level was preceded by two preconditioning tests at the same magnitude. All tests were completed within 5 hours post-mortem.

ANALYSIS

Data collected were fit to a modified hyperelastic Ogden model with a strain energy density function, W:

$$W = \frac{2\mu(t)}{\alpha^2}(\lambda_1^\alpha + \lambda_2^\alpha + \lambda_3^\alpha - 3)$$

where λ is the principal stretch ratio, α describes the nonlinear strain-magnitude sensitive behavior, and $\mu(t)$ is viscoelastic shear modulus expressed as a first-order Prony series. Data extracted from the hold period at 5 (time = 100, 300, 600, 1800, and 6000 msec) isochrones were used to fit parameters α and $\mu(t)$ (IGOR Pro 3.1.4). An unpaired Student's t-test was performed to determine significant difference between nonlinear shear moduli at each isochrone.

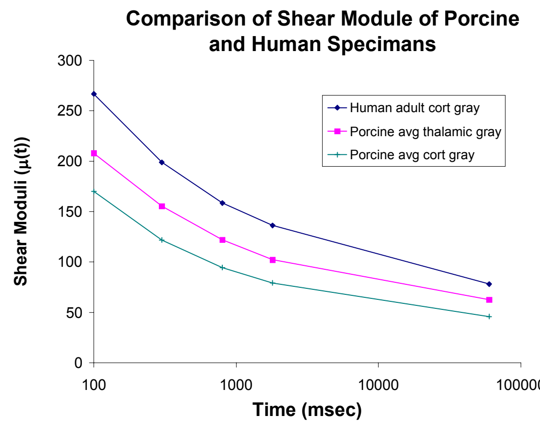

Figure 1: Shear moduli gathered from literature were compared to the average porcine cortical gray measured in this experiment. Significant difference was found between porcine cortical gray and: Human adult cortical gray ($p<.001$) and porcine average thalamic gray ($p<.01$).

RESULTS AND DISCUSSION

The properties of the two cortical regions were not significantly different, and the data was combined for further analysis. The average stiffness of the porcine parietal cortex was found to be significantly lower than that published (Prange et al, 2002) for thalamic gray matter ($p<.01$) at every isochrone. These findings may be explained by the presence of constitutive elements in the thalamus, such as the internal medullary lamina and the intralaminar nuclei, which could contribute to the increased stiffness in this region. Regardless, we must reject our hypothesis of gray matter homogeneity, and conclude that gray matter within the porcine brain is heterogeneous.

Furthermore, the average porcine parietal cortical stiffness was significantly ($p<0.001$) less stiff (38.2 to 43.9% lower) than previously published adult human temporal cortical gray matter values (Prange, et al 2002), and underscores the need for more data from fresh human brain tissue samples.

REFERENCES

Prange M.T. and Margulies S.S. (2002). *J Biomech Eng*, in press.

ACKNOWLEDGEMENTS

We are grateful to Michael Prange for his technical guidance. Support was provided by NIH-NINDS R01/NS39679 and CDC–NCIPC R49/CCR312712.

KINEMATICS OF THE GLENOHUMERAL JOINT DURING THE ANTERIOR AND POSTERIOR DRAWER TEST

Susan M. Moore, Volker Musahl, Patrick J. McMahon and Richard E. Debski

Musculoskeletal Research Center, Department of Orthopaedic Surgery, University of Pittsburgh
Pittsburgh, PA. 412-648-2000, Fax: 412-648-2001, genesis1@pitt.edu

INTRODUCTION

Clinical exams that translate the humerus with respect to the scapula are utilized to diagnose injury of the glenohumeral (GH) joint. Translations of the humeral head in response to an applied torque, without active muscle forces, have been quantified; (Harryman, 1990) however, this data has not been determined during a clinical exam. Therefore, the objective of this study was to determine the magnitude and repeatability of the translations of the humeral head during the anterior and posterior drawer test at multiple angles of external rotations (ER).

METHODS

Three cadaveric shoulder specimens (53±1 yrs.) were dissected leaving the mid-humerus, scapula, rotator cuff muscles, and the GH capsule (vented at the rotator interval) intact. The scapula and humerus were fixed in epoxy putty. The scapula was mounted vertically in a Plexiglass fixture and 13.4N was applied to the rotator cuff muscles. A 6 degrees-of-freedom magnetic tracking system (The Bird, Ascension Technologies, Inc.) determined the motion of the humerus with respect to the scapula (Debski, 1995). Anatomical landmarks were digitized to define the coordinate system for the joint motion description (Grood, 1983). For standardization, the humerus was placed at 60º of GH abduction, neutral rotation, and neutral horizontal adduction at the beginning of each exam. The clinician maximally translated the humeral head to its limit in the anterior and posterior directions at 0º, 30º, and 60º of ER and then returned the humeral head to its starting position (5 cycles). The translations for each of the 5 cycles were collected by the magnetic tracking system.

RESULTS

The magnitude and repeatability for the anterior and posterior translations are shown in Figure 1. As ER increased from 0º-60º the total anterior translation decreased by more than 60% for all specimens. During the anterior drawer test, inferior translations (coupled motion) also occurred. In contrast, superior translation occurred during the posterior drawer test and increased with ER (Figure 2). For example, in Specimen 1, during the anterior drawer test at 0º, 30º, and 60º of ER inferior translations of 1.6±1.2, 11.7±1.4, and 17.5±0.5 mm occurred, respectively. The posterior drawer test produced superior translations of 3.2±1.0, 2.2±0.4, and 9.8±0.7 mm, respectively.

DISCUSSION

The magnitude and repeatability of the translations of the humeral head were determined during the anterior and posterior drawer test. The translations in each direction were highly repeatable. Coupled motions were found in the superior and inferior directions. These findings provide further insight into the interaction of the capsular components that guide the motion and stabilization of the GH joint. Evidence of excessive coupled motions, or the lack of coupled motions may aide clinicians in diagnosing injury. Furthermore, analytical models can utilize this information to produce a more accurate representation of joint function. Future investigations will include replaying the recorded kinematics using a 6 degree-of-freedom robotic testing system to determine the in situ forces of the capsular components.

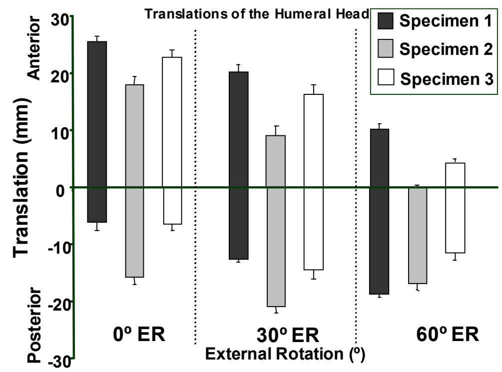

Figure 1. Maximum anterior and posterior translations of the humeral head at 0º, 30º, and 60º ER during the anterior and posterior drawer tests of the three specimens.

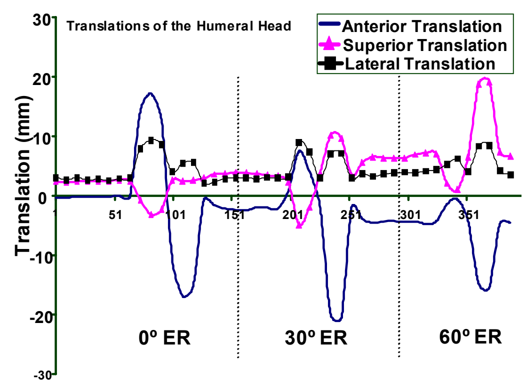

Figure 2. Representative plot that illustrates the translations of the humeral head for 1 cycle of the anterior and posterior drawer test.

REFERENCES

Debksi, R.E. et al. (1995). *J Biomech*, **28**, 869-74.
Grood, E.S., Suntay W.J. (1983). *Trans ASME*, **105**, 136-44.
Harryman, D.T. et al. (1990). *JBJS,* **72-A**, 1334-43.

ACKNOWLEDGEMENTS

The support of the Whitaker Foundation is greatly appreciated.

EFFECT OF JOINT COMPRESSION ON THE BIOMECHANICS OF THE INTACT ACROMIOCLAVICULAR JOINT

Ryan S. Costic, Rajesh Jari, Mark W. Rodosky and Richard E. Debski

Musculoskeletal Research Center, Department of Orthopaedic Surgery, University of Pittsburgh
Pittsburgh, PA. 412-648-2000, Fax: 412-648-2001, genesis1@pitt.edu

INTRODUCTION

High loads can be transmitted from the upper extremity across the acromioclavicular (AC) joint to the axial skeleton during activities of daily living and can lead to pain and early joint degeneration [Petersson, 1983]. Therefore the objective of this study was to quantify the effect of joint compression on shoulder biomechanics during application of 70N anterior, posterior and superior loading conditions.

METHODS

Fresh frozen human cadaveric shoulders (n=12) were dissected, fixed in epoxy putty and rigidly fixed to the robotic universal force-moment sensor base and arm [Debski, 2000, 2001]. After determining a joint reference position, specimens were cycled ten times under an anterior, posterior and superior load of 70N with constant 10N or 70N of joint compression. The resultant joint kinematics and *in situ* forces were recorded during the last cycle (3-DOF). The recorded paths of joint motion were repeated after sequential cutting of the inferior and superior AC capsule, conoid and trapezoid ligaments (varied). Using the principle of superposition, the vector difference in forces before and after cutting of a ligament represented the *in situ* force in that structure. Two-factor repeated-measures ANOVA was used to determine the effect of joint compression on the *in situ* forces of the AC capsule and coracoclavicular (CC) ligaments ($p<0.05$).

RESULTS

Joint compression with a 70N anterior, posterior and superior load did not significantly change primary (in the direction of loading) anterior or superior translation but significantly decreased primary posterior translation (6.6mm to 3.7mm, $p<0.05$, Figure 1). Accordingly, only two of six coupled (perpendicular to primary loading direction) translations were significantly affected by joint compression. During posterior and superior loading, coupled proximal translation decreased (2.2mm to 0.6mm) and coupled anterior-posterior translation shifted (0.5mm ant. to 0.6mm post.), respectively ($p<0.05$).

Although joint compression only affected the translation minimally, it significantly affected the *in situ* forces during all loading directions. With an applied 70N in all directions and joint compression, the *in situ* force in the superior AC capsule decreased by 10N while the force in the inferior portion remained unchanged (Figure 2). The CC ligaments were not affected by joint contact except for the 10N force increase in the conoid ligament during posterior loading. However, the joint contact force significantly increased by 20N in all loading directions with joint compression ($p<0.05$).

DISCUSSION

The effect of joint compression on the shoulder biomechanics of the intact AC joint were quantified. The decreased force in the superior AC capsule and increased joint contact force that occurred with joint compression in all loading directions suggests that the high compressive load is primarily transmitted through joint contact rather than the supporting ligaments. Therefore, common surgical techniques such as distal clavicle resection, which initially reduce painful joint contact, may adversely affect the soft tissue components of the shoulder by increasing the force transmitted through these structures. These large forces could contribute to degenerative changes in the joint and therefore the magnitude of the *in vivo* forces that are transmitted across the shoulder should be determined in the future.

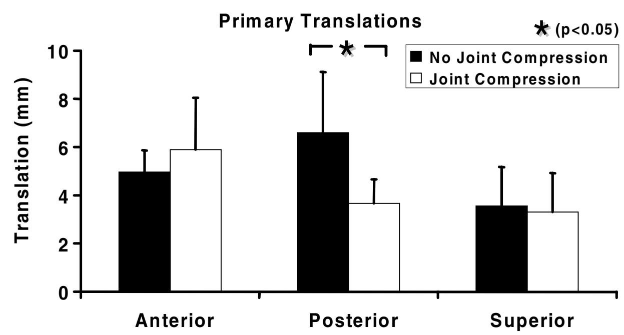

Figure 1. Translations during a 70N anterior, posterior and superior load with 10N or 70N of joint compression.

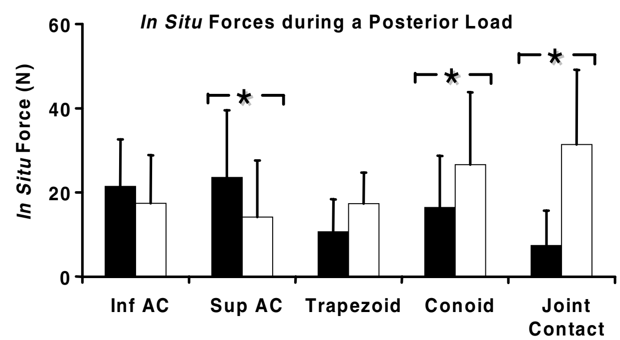

Figure 2. *In situ* force in soft tissue structures along with the joint contact force during the application of a posterior load.

REFERENCES

Debski, R.E., et al. (2000). *Annals Biomed Eng*, **28**, 612-18.
Debski, R.E., et al. (2001). *JBJS*, **83-A**, 1344-51.
Petersson, C.J., et al. (1983). *Acta Orthop Scand*, **54**, 431-3.

ACKNOWLEDGEMENTS

Support of the Aircast Foundation is greatly appreciated.

MODELLING THE SOLIDIFICATION OF AQUEOUS SOLUTIONS: A COUPLED-FIELD FINITE ELEMENT APPROACH

Richard Wan[1], Zhihong Liu[1], and Ken Muldrew[2]

[1]Department of Civil Engineering, [2]Department of Surgery
University of Calgary, 2500 University Dr., N.W.
Calgary, Alberta, Canada T2N 1N4

INTRODUCTION

The modelling of aqueous solution freezing with concomitant ice formation is of prime interest in many engineering, physical, biological problems. One of the main challenges lies in the mathematical complexity in solving a fully coupled heat-mass transfer problem. In biological tissues, the coupling results from solute diffusion and freezing processes through the freezing point depression. Any solute concentration would lower the freezing point of water, which in turn controls the growth of ice. The rate at which salt is excluded from the ice front limits its propagation. Thus, both the thermal and solute fields are strongly coupled to each other and have to be solved simultaneously in any numerical modelling endeavour.

METHOD

The mathematical treatment of a sharp discontinuity in both heat flux and solute concentration at the phase-change zone, as well as the ice front tracking in time, are two major problems that arise while solving the coupled heat and solute field equations within a Finite Element (FE) framework. In order to overcome these difficulties, we transformed both the solute concentration and temperature fields into virtual *liquidus temperature* and *freezing index* fields respectively. While these newly introduced field variables are continuous, they also facilitate the writing of a variational principle which leads to a general set of FE equations defined over the entire domain of interest for both phases. Thus, a fixed mesh approach can be used to track the ice front propagation with coupled phase change-solute diffusion. The resulting coupled non-linear FE equations are readily solved via Newton-Raphson method. A staggered iterative procedure is used to optimize the computations.

RESULTS AND DISCUSSION

The FE model was first quantitatively compared with experimental studies of solidification of aqueous solution (Korber et al, 1983). Computed transient positions of the ice front were in excellent agreement with experimental data. The simulation of a piece of cartilage tissue subjected to a cooling rate of 1^0C/min from 0^0C to -25^0C was next attempted. In Fig. 1, the distribution of solute concentration within the tissue identifies two distinct regions: one with low concentration in which planar ice front forms, and the other with highly concentrated or supercooled solution with propensity to ice lensing. The numerical computations exactly capture the essential physics of the cartilage freezing problem (Muldrew, 1997).

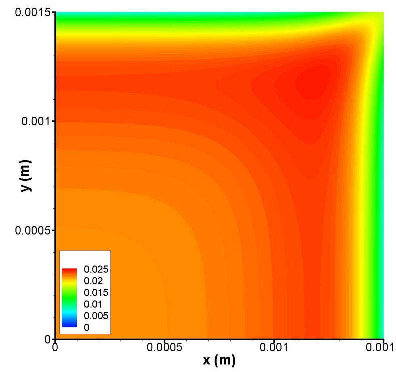

Figure 1: Solute concentration distribution in a 1.5x1.5mm cartilage tissue during freezing at 120 seconds.

SUMMARY

A FE procedure to solve the coupled phase change-mass transfer problem was developed using virtual *liquidus temperature* and *freezing index* as main variables. The effect of microstructure is readily amenable to the current model by introducing freezing point depression due to pore size. The model will be able to estimate cell survival rates under the combined effects of temperature and osmotic environment given a "cell viability criterion".

REFERENCES

Korber, Ch., Scheiwe, M. W. and Wollhover, K. (1983). *International Journal of Heat and Mass Transfer* **26** (8), 1241-1253.

Muldrew, K. (1997). *Cryobiology - A Short Course*. http://www.acs.ucalgary.ca/~kmuldrew/cryo_course/course_outline.html.

ACKNOWLEDGEMENTS

The financial support from the Whitaker foundation is acknowledged.

DETERMINATION OF PEAK LIMB FORCE FROM DUTY FACTOR

Knill, K., McGuigan, M.P., Witte, T.H. and Wilson, A.M.

Structure and Motion Lab, The Royal Veterinary College, North Mymms, Hatfield, Herts AL9 7TA England

INTRODUCTION

Ground reaction force (GRF) curves are approximately sinusoidal in running animals. Since mean limb force must equal body weight it is possible to estimate peak limb force from duty factor (the proportion of the stride that an individual limb is in contact with the ground) and the proportion of the body mass that is "supported" by that limb. This approach was used by Alexander *et al* (1979) to estimate peak limb force in the elephant and buffalo. The technique was also applied by Kram and Dawson (1998) who validated it using one kangaroo hopping over a forceplate. They found that the technique under estimated peak limb force in kangaroos by 36%. There are several possible explanations for this discrepancy: kinematic data were used for determination of foot on and off which can be inaccurate; the GRF curve may be "fatter" or "thinner" than a cosine wave of equivalent base and in multi-legged animals the weight distribution may not be as assumed. In this study we tested the hypothesis that the technique is more accurate if weight distribution is determined experimentally for similar animals.

METHODS

Accelerometers were attached to the dorsal hoof wall of the front and hind feet of horses with an orientation appropriate to differentiate heel off and toe off. Accuracy of timing of foot on and off and the error in the estimation of peak vertical GRF were determined from simultaneous forceplate recordings (Kistler 9827BA). Six horses were trotted repeatedly over the forceplate and six foot strikes recorded for each limb. Analogue accelerometer data were radio telemetered using a narrow band FM transmitter module mounted on each leg. Telemetered accelerometer data and forceplate data were recorded simultaneously at 2000 samples per second using LabView software. Horses were weighed.

The beginning and end of stance on the forceplate record were defined as the first and last samples respectively that varied from the baseline value. Peak force and vertical impulse were determined for each limb and the fore:hind ratio determined.

Peak limb vertical force (Fz) was predicted from

$$\mathbf{Fz = \pi pmg/4\beta}$$

duty factor **p**, body mass **m**, acceleration due to gravity **g** and fore:hind leg weight distribution β_f β_h (0.6/0.4 for the horse, Alexander *et al* 1979).

RESULTS AND DISCUSSION

There was an easily recognizable peak in the accelerometer signal when the foot contacted the ground. The timing of this peak was within one sample of the beginning of stance determined by the forceplate for 86% of the values and within 2 samples (1 millisecond) for 98% of values. At the end of stance it was possible to determine the time when the heels left the ground and when the toe left the ground from the accelerometer signal. Toe off was detected within 4 samples of the forceplate for 56% of values and 12 samples (6ms) of 80% of values. The error was however evenly distributed around the mean.

Application of the Alexander *et al* (1979) equation gave a mean underestimate of peak limb force of 2.7±2.7% (± standard deviation) for the forelimb and 21.8±2.0% for the hindlimb. This was assuming a fore:hind weight distribution of 0.6:0.4.

The actual weight distribution at trot for six horses (6 stance phases per horse) was 0.53:0.47 (±0.02) for peak force and 0.56:0.44 (±0.02) for vertical impulse. Calculation of the peak force using this vertical impulse distribution resulted in an underestimate by 13.3±6.9% for the forelimb and 14.1±2.2% for the hindlimb.

The error in the determination of peak vertical force from duty factor appears to be due to vertical GRF increasing more rapidly than an equivalent cosine wave. Thus peak vertical GRF occurs before the peak of the cosine wave (17±10ms in this group of horses). This rate of rise is however dependant on surface stiffness.

SUMMARY

The difference between the vertical GRF curve and a cosine wave was consistent across all the limbs of all the horses. The use of the corrected fore:hind weight distribution resulted in a similar error for the estimation of the peak vertical force in the front and hind limbs. It would be possible to apply a correction factor to the equation to partially account for the difference between GRF profile and the cosine wave and hence improve the accuracy of the estimation and its usefulness in the assessment of field locomotion.

REFERENCES

Alexander, R. McN. et al (1979) *J. Zool. Lond*. **189**, 135-144

Kram, R. and Dawson, T.J. (1998) *Comp. Biochem. Physiol. Part B* **120**, 41-49

ACKNOWLEDGEMENTS

We would like to thank the Horserace Betting Levy Board for funding this work.

A COMPUTATIONAL MODEL OF POSTOPERATIVE KNEE KINEMATICS

Elvis C. Chen[1], Randy R. Ellis[1,2,3], John F. Rudan[3], and Tim J. Bryant[2,3]

[1]Computing and Information Science, [2]Mechanical Engineering, [3]Surgery, Queen's University, Kingston, Ontario, Canada
[1]chene@cs.queensu.ca, [2]ellis@cs.queensu.ca

INTRODUCTION

Knee kinematics after Total Knee Replacement (TKR) are shown to be affected by, among other things, the design of the prosthesis and the surgical placement of prosthetic components. Based on the ligament-strain energy-minimization principle, a mathematical model of a knee was constructed for studying the passive kinematics of condylar-type total knee prosthesis. The model relied on knowledge of the prosthetic bearing surface and patient-specific ligament data, and determined the quasi-static knee kinematics by finding successive contact points of prosthetic components over a range of flexion angles.

METHODS

The goal of this study was to understand interactions between the geometry of the articular surfaces and the surrounding ligaments, and to see how such interactions affect the overall kinematics of the knee. Passive knee kinematics were computed as a quasi-static solution to energy minimization of a system with ideal single point contact. Potential energy is stored in the ligament filaments. The femoral and tibial components are assumed to be rigid in a passive model. By using patient-specific ligament data and accurate representation of articular surfaces, patient-specific kinematics were derived. Combining the quasi-static solutions from numerous flexion angles provided (a) the contact paths on the bearing surfaces and (b) the roll/slip characteristics of relative motion.

Data were collected intraoperatively from 10 consecutive patients. The neutral lengths of the ligaments were determined physically, by gently distracting the tibia until the relevant ligament were determined to be at neutral length. The articular geometries were virtually implanted to a standard position, as recommended by the manufacturer's description of surgical technique, and later validated by a surgeon, and still later were artificially deviated from that position to simulate various implantation strategies. For each flexion angle, the varus-valgus angle and internal-external rotation angle that jointly had the minimal total strain energy were selected as the orientation of passive motion, producing a total of 63 angulations of passive motion. The contact paths, relative kinematics, and ligament energies were determined for each angulation.

RESULTS AND DISCUSSION

Using previous patient ligament data, the kinematics of the AMK design were derived. This model demonstrated that general knee kinematics are a combination of spinning, rolling, and further spinning motion as the knee flexes from full extension to deep flexion. Posterior tilting/displacement of the tibia increases the range of motion, while anterior tilting/displacement of the tibia decreases the range of motion.

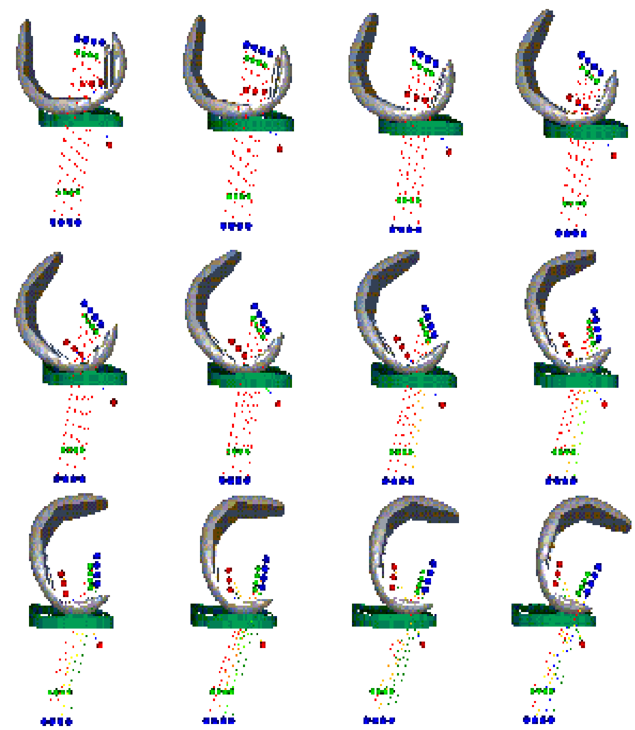

Figure 1: Knee motion is animated in 3D and demonstrates spinning, rolling, and sliding as flexion increases.

SUMMARY

A patient-specific knee model demonstrates that knee kinematics after TKR are affected by the geometry of the articular surfaces and the surgical placement of the prosthesis. Proper placement of the prosthesis can increase the range of motion with desired knee kinematics, whereas improper placement can lead to decreased range of motion and kinematics that lead to excessive tibial wear. This model provided a unique tool for evaluating the effect of different surgical implantation strategies. The model can also be used to optimize anticipated wear during the design phase of prosthesis.

REFERENCES

Chen, E. et al (2001). *Medical Image Analysis*. **5**(4), 317-330.
Martelli, S. et al (1998). *J. Arthroplasty*. **13**(2), 145-155.

EVALUATION OF TIBIOFEMORAL COMPRESSIVE AND SHEAR LOADS IN THE MEDIAL AND LATERAL KNEE COMPARTMENTS DURING ISOMETRIC KNEE EXERCISES

Takashi Yanagawa[1], Michael R. Torry[1], Kevin Shelburne[1], J.R. Steadman[2], William I. Sterett[2]
Steadman♦Hawkins Sports Medicine Foundation[1] and Clinic[2], Vail, Colorado, mike.torry@shsmf.org

INTRODUCTION

Multi-angle isometric knee extension and quadriceps sets (Qset) are often the first exercises employed to develop muscular strength in individuals who have sustained or are in recovery from surgical repair of a tibiofemoral (TF) articular cartilage lesion (Irrgang and Pezzullo, 1998; Gillogly et al., 1998). Successful rehabilitation of these injuries are predicated on 1) limiting the range of motion (ROM) to angles that do not engage the lesion, and 2) performing strengthening exercises that minimize shear load across the knee while maximizing quadriceps strength gain (Irrgang and Pezzullo, 1998). To date, clinicians have relied mostly on cadaver mechanical testing to establish ROM guidelines for selecting appropriate joint angles to conduct these exercises. However, these studies are limited as it is difficult to apply the necessary physiologic loads typical of such exercises and, most do not simulate the weakened condition of the knee muscles commonly found after this type of injury or surgery (O'Reilly et al., 1998). Furthermore, few of these studies have attempted to quantify the compressive and shear loads that may be occurring in each compartment throughout 0°-90° of knee range of motion (ROM). The purposes of this study were: 1) to assess the TF compressive and shear loads in the medial and lateral knee compartments during Qset and knee extension exercises, and 2) to determine the ROM over which either of these exercises may be beneficial in reducing compressive or shear forces.

METHODS

Isometric knee extension and Qset exercises were simulated using a 3-D model of the lower extremity. The geometry of the model bones, ligaments, muscles and the mechanics governing the dynamic performance of these tissues has been described in detail (Pandy et al., 1997). In short, the model includes: the three-dimensional geometry of the patella, tibia, and femur, 13 non-linear springs representing the major tibiofemoral ligaments and joint capsule, 13 muscle-tendon units spanning the knee that include the force-length property of muscle, and a model of articular cartilage compression between the bones of the tibia and femur. Isometric knee extension and Qset exercises were simulated at varying joint positions (0°-90° at 15° intervals). Healthy isometric knee extension exercises were simulated utilizing 100% activation of all knee extensors and 0% flexors. These simulations were then repeated altering quadriceps activation -25% to simulate decreased strength conditions (O'Reilly, et al., 1998). Isometric Qsets were simulated by balancing quadriceps activation with hamstring activation (muscular co-contraction) that resulted in zero knee joint motion.

RESULTS AND DISCUSSION

The simulations reveal that shear (Figure 1) and compressive forces in both medial and lateral compartments are highest when conducting the Qset exercises in the ranges of 0° - 45° of knee flexion. After 45°, shear and compressive forces were more pronounced for the isometric knee extension exercise. The effect of varying individual muscles or even the entire quadriceps muscle group (Weak) did not change this trend, although it did reduce the overall load being transmitted across the joint.

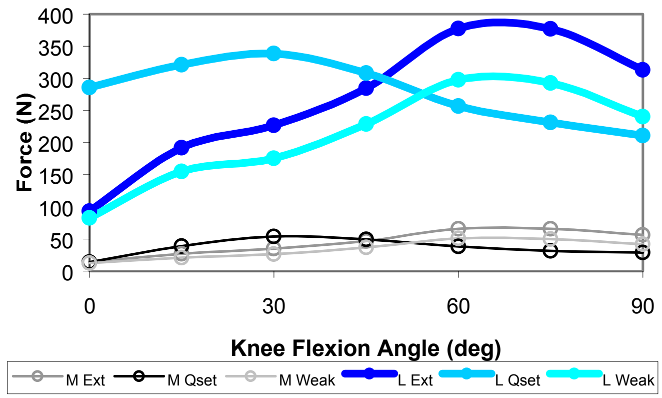

Figure 1. Shear load for medial (M) and lateral (L) compartments during knee extension (Ext) and Qsets (Qset) and under 25% decreased quads activation (Weak).

SUMMARY

These results suggest that the use of Qset and knee extension exercises is dependent upon knee angle to selectively reduce shear and compressive loads in the medial and lateral compartments of the knee joint.

REFERENCES

1. Irrgang, J.J, Pezzullo, D., (1998) *JOSPT*, **28**:4:232-240.
2. Gillogly et al., (1998) *JOSPT*, **28**:4:241-251.
3. O'Reilly, S.C. et al., (1998) *Ann Rheum. Dis*., 57:588-594.
4. Pandy, M.G. et al., (1997) *Comput Methods Biomech Biomed Eng ,* 1:87-108.
5. Pandy, M.G., Shelburne, K. (1997) *J. Biomech*., 30:1015-1024.

RELATIONSHIP BETWEEN LINEAR WRIST VELOCITY AND IMPULSE DURING FASTBALL PITCHING IN COLLEGIATE BASEBALL PITCHERS

Jeremy Smith[1], Jerry Wilkerson[2], and Brian Umberger[1]
[1]Exercise & Sport Research Institute, Arizona State University, Tempe, AZ, USA (email: jeremy.d.smith@asu.edu)
[2]Kinesiology Department, Texas Woman's University, Denton, TX, USA

INTRODUCTION

In the coaching literature there are two conflicting views as to whether a baseball pitcher should actively push off the mound while pitching. House (1983) stated that a pitcher should not "violently drive" towards home plate, but rather fall towards home plate in a controlled manner. Conversely, Ryan and Torre (1977) suggested a pitcher should drive as hard as possible towards home plate. MacWilliams et al. (1998) reported linear wrist velocity was significantly related to both anterior/posterior (AP) ($\underline{r}^2 = .82$) and vertical ($\underline{r}^2 = .74$) ground-reaction forces at the time when AP force peaked. These results tend to support a drive by the pitcher rather than a "controlled fall". Peak forces by themselves, however, do not provide a complete picture of force application by the pitcher. Quantifying impulses associated with the GRF during pitching may provide greater clarity for this issue. A positive relationship between linear wrist velocity at ball release and impulse in the AP direction of the push-off leg, provide further evidence that a pitcher drives off the pitching rubber to deliver a fastball. Therefore, the purpose of this study was to determine the relationship between linear wrist velocity at ball release and the impulses generated by the push-off leg in the three component directions of the GRF, which to date has not been reported in the literature.

METHODS

Participants were ten in-season collegiate baseball pitchers. Pitchers were allowed to warm-up until they felt comfortable enough to pitch in the first inning of a regular baseball game. Each pitcher threw five consecutive fastballs from an indoor pitching mound, which housed two force plates. The push-off force plate was oriented horizontally with the positive medial/lateral (ML) axis pointed towards third base, the positive AP axis pointed towards the catcher, and the positive vertical axis directed upward. Data from the landing plate are not reported in the present study. GRF data were collected at 1200 Hz and electronically synchronized with four 120 Hz video cameras. Video records were used to calculate 3-D resultant linear wrist velocity and identify temporal events in the progression of the pitching cycle (e.g. ball release). Since it has previously been reported that intrasubject variability in GRFs is low (MacWilliams et al., 1998), the trial that produced the highest linear wrist velocity at ball release was used in statistical analyses. GRF data were normalized by body weight and expressed relative to 100% of the pitching cycle (beginning when the ball left the glove until the ball was released). Pearson product moment correlations were used to test for significant relationships between linear wrist velocity and impulses generated in the AP, ML and vertical directions for the push-off leg.

RESULTS AND DISCUSSION

Table 1 reports the means and standard deviations for impulse and peak force in the AP, ML, and vertical directions on the push-off plate. Peak forces were consistent with previously reported data and demonstrate that substantial forces are produced in the plane of the pitch. Values for impulse in each component direction also support the "drive" theory since the largest impulses are in the AP and vertical directions. A significant relationship ($\underline{r} = .647$, $\underline{p} = .043$) existed between linear wrist velocity and AP impulse for the push-off plate, such that pitchers who generated more impulse in the anterior/posterior direction of the push-off plate threw with greater linear wrist velocity.

Table1: Push-off plate means for peak forces and impulses

	ML shear	AP Shear	Vertical
Peak Force	0.16(.08)	0.57(.08)	1.23(.10)
Impulse	0.004(.005)	0.037(.005)	0.100(.014)

Note. Peak forces are normalized to BW and impulses are normalized to BW*((height/gravity)^.5).

SUMMARY

The correlation between the linear wrist velocity at ball release and the AP impulse generated by the push-off leg, combined with the high levels of force generated on the push-off plate are evidence in support of the drive theory. Our results support the hypothesis that pitchers drive towards home plate when delivering a fastball pitch.

REFERENCES

House, T. (1983). *A Contemporary Guide to pitching a Baseball*. San Diego School of Baseball.
MacWilliams B. et al. (1998). *Am J Sports Med*, **26**(1), 66-71.
Ryan, N., Torre, J. (1977). *Pitching & Hitting*. Prentice Hall.

MEASUREMENT OF THE ENCEPHALON PHYSICAL PARAMETER WITH MRI SATURATION TRANSFER METHOD

Hideaki Obata[1], Masataka Tokuda, Tadashi Inaba, Shigeru Matsushima[2] and Yasutomi Kinosada[3]

[1]Department of Mechanical Engineering, Mie University, Tsu 514-8507, Japan, obata@bio.mach.mie-u.ac.jp
[2]Department of Radiation Oncology, Aichi Cancer Center, Nagoya, 464-8681, Japan
[3]Department of Medical informatics, Gifu University, Gifu 500-8705, Japan

INTRODUCTION

Magnetic resonance imaging (MRI) came to be used for many kind of image diacrisis recently. And it can get more useful biomechanics information by using this MRI, because it is very effective device to know the physical parameter of biomaterials. The saturation transfer method can show restricted H_2 molecular like some kind of polymer rather than amount of moisture. In this research, it was measured by the saturation transfer method which used MRI for the purpose of knowing the physical parameter of human brain.

METHODS

Nine patients, they have disease except in the head are imaged by Signa model of GE Medical Systems equipped with 1.5 Tesla clinical scanner. First, some MRI pictures to decided location are taken. Then conventional spoiled-gradient recalled acquisition in the steady state (SPGR) and also SPGR under the irradiation of ST-pulse (ST-SPGR) were obtained in the coronal plane. The off-resonance technique was adopted to achieve preferential saturation of the immobile protons and to calculate saturation transfer ratio (STR). The single ST-pulse frequency in an interval was irradiated at the frequency of 19, 5, 2, -2, and –5 ppm apart from that of water resonance.

The regions of interest (ROI) for signal intensity were measured at the same site inside of the every sample. The saturation transfer ratio (STR) values were defined as the percentage of signal loss between unsaturated (i.e., SPGR) and saturated (ST-SPGR) images according to the eq.1;

$$STR(\%) = (Mo - Ms) \times 100 / Mo \qquad (1)$$

where Mo and Ms are the signal intensity on the SPGR and on the ST-SPGR image, respectively.

RESULTS AND DISCUSSION

Figure 1 shows instances conventional (a) SPGR image and (b) ST-SPGR at the frequency offset by 5 ppm from water proton. And the calculated STR images are shown in Figure 2, (a) STR 5ppm, (b) STR 2 ppm, (c) STR -5 ppm. The conventional SPGR images were directly resulted from T_1 (longitude relaxation time)-weighted image. In the ST-SPGR images, the signal intensity was lower than that in the conventional SPGR. The ST-effect is larger, the intensity in the STR image become higher, as is demonstrated by the STR images calculated according to the eq.1.

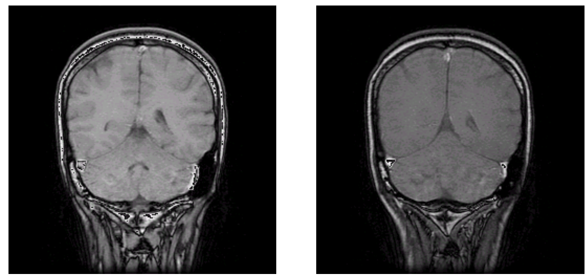

(a) (b)

Figure 1. Conventional MR Images. (a) T_1-wighted SPGR image. (b) ST-SPGR at the frequency offset by 5 ppm from water.

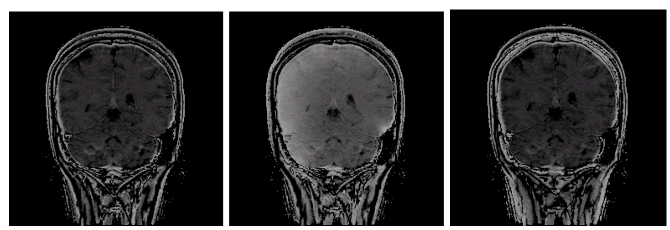

(a) (b) (c)

Figure 2. Calculated STR images at frequency offset of (a) 5ppm (b) 2ppm (c) -5ppm

In this worth pointing that the degree of reduction should be dependence upon the frequency of the ST pulse. And especially, the STR values for the human encephalon are correlated with their total water content or physical parameter.

REFERENCES

Shigeru, M. Akinori, T. et al (2000). *Polymer Journal*, **32,** 828-833

Kazuyuki, A. (1997). *Japanisch-deutsche Medizinische Berichte*, **42**, 31-44.

SCREW AND BLADE TYPE HIP IMPLANTS PRODUCE DISTINCT INSERTION FORCES

L. W. Ehmke[1]; B. Kam[2]; M.B. Sommers[1]; M. Bottlang[1]
[1]Legacy Clinical Research & Technology Center, Portland, OR; *email: mbottlan@lhs.org*
[2]Oregon Health Sciences University, Portland, OR

INTRODUCTION

Dynamic hip implants are routinely used for fixation of hip fractures (Haynes, 1997; Koval 1994). During insertion, these implants exert considerable torsional and axial forces to the femoral head (Mohan, 2000). With limited intraoperative means to constrain the femoral head during implant insertion, such forces can lead to rotational displacement and subsequent malreduction. Most recently, a novel helical blade-type implant design has been introduced, which may pose less propensity for femoral head rotation as compared to lag screws with a traditional thread design. This cadaveric biomechanical study provides a quantitative comparison of insertion forces between screw and blade-type hip implants.

METHODS

Twenty-four paired proximal femora from 7 female and 5 male fresh-frozen human cadavera with an average donor age of 76±6 years were obtained. The femoral heads were sectioned at the neck and potted into a 50-mm diameter steel shell with low melting alloy. Insertion forces of two cannulated dynamic hip implant designs were tested, one of which had a traditional thread design (DHS, Synthes), and one had a novel helical blade design (DHHS, Synthes) [Fig. 1a].

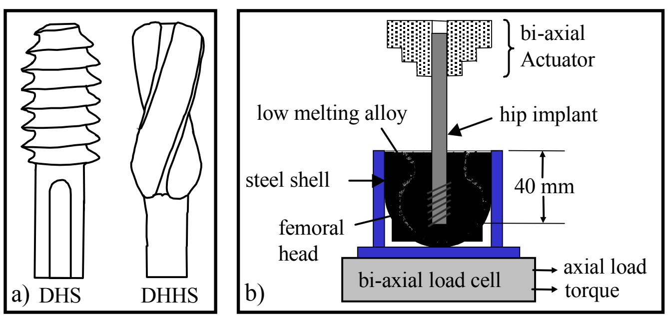

Fig. 1a) Screw and blade type hip implants, **b)** testing setup

Specimens were mounted on a bi-axial load cell and implants were attached to the bi-axial actuator of a material test system (8874 Instron) [Fig. 1b]. Implants were advanced in concurrent linear and angular displacement to precisely reflect the pitch of the implant's thread or blade. Each implant was inserted over a guide wire to a depth of 40 mm, according to the manufacturer's insertion technique, while the insertion torque and axial load were recorded. Both outcome parameters were evaluated as a function of insertion depth. Finally, the total amount of energy expended during implant insertion was computed as the area under the force-displacement curve (i.e. axial insertion energy), plus the area under the torque-angle curve (i.e. torsional insertion energy) (Heiner, 2001).

RESULTS

For all implants, insertion torque increased with increasing insertion depth [Fig. 2a]. At 40-mm insertion depth the DHHS implant exhibited an insertion torque maximum of 5.7±1.7 Nm. while the DHS implant induced a significantly higher maximal insertion torque of 8.7±3.2 Nm ($p<0.01$). Axial forces were significantly higher during insertion of the DHHS implant compared to the DHS implant ($p<0.01$) [Fig. 2b]. At 40-mm insertion depth, axial loads were 1938±906 N and 923±488 N for the DHHS and DHS implants, respectively.

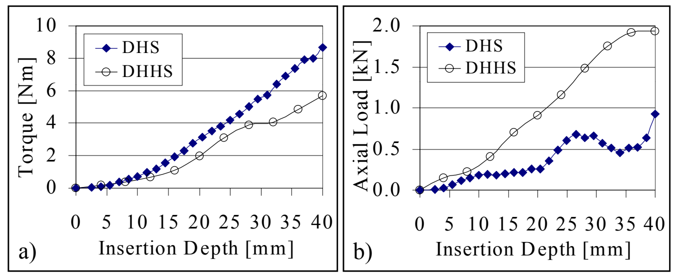

Fig. 2) Insertion forces vs. insertion depth (avg. values, n=12)

The overall insertion energy was significantly lower for DHHS implants compared to DHS implants ($p<0.01$) [Fig. 3]. DHHS implants required 41±13 J total energy with over 90% due to axial forces, while DHS implants necessitated 275±90 J total energy with over 90% due to torsional forces.

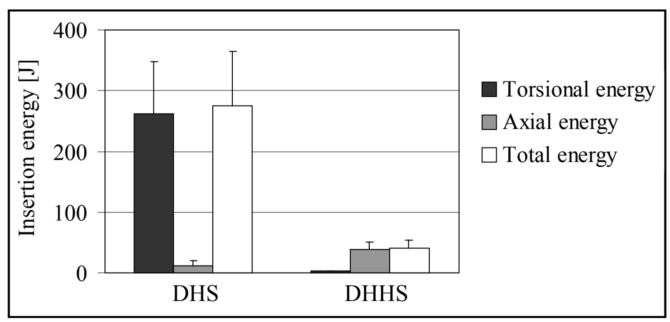

Fig. 3) Total insertion energy distribution of DHS and DHHS

DISCUSSION

The results of this study provide a quantitative analysis of the forces and energy of insertion of a novel helical-blade type implant and a traditional screw-type implant. Axial loads during implant insertion are directly supported by the acetabulum and may be well tolerated. The reported insertion torque is likely to correlate to the propensity for femoral head rotation during implant insertion. Therefore, the six fold reduced insertion energy of blade-type implants may pose a lower risk for malreduction.

REFERENCES

Haynes et al, *Medical Engr. & Phys.* **19(5)**: 446-453, 1997
Koval et al, *J Am Acad Orthop Surg.* **2(3)**: 150-156, 1994
Mohan et al, *Injury, Int. J. Care Injured* **(31)**: 697-699, 2000
Heiner et al, *J Biomech.* **(123)**: 629-634, 2001

IN VIVO MOTION OF THE SCAPHOTRAPEZIO-TRAPEZOIDAL (STT) JOINT

Joseph J. Crisco[1,2], Lana Kang[1], Sharon Sonenblum[2], Edward Akelman[1]

[1]Dept. of Orthopaedics, Brown Medical School/Rhode Island Hospital and [2]Div. of Engineering, Brown University Providence, RI
E-mail: joseph_crisco@brown.edu

INTRODUCTION

The majority of cases with wrist arthritis involve the scaphoid bone (Watson and Ryu, 1986), and a large percentage of these involve the STT joint. Altered kinematics is a potential mechanism in the etiology of degenerative joint disease, but the normal kinematics of the STT joint have been difficult to document. Recently, STT kinematics were studied *in vitro* by Moritomo et al (2000), who reported that the STT joint is a single degree of freedom joint; the motion of the trapezium and trapezoid relative to the scaphoid is the same in flexion/extension and radial/ulnar deviation. The purpose of this study was to examine this finding *in vivo*. Specifically, we measured the 3-dimensional (3-D) kinematics of the STT joint *in vivo* and we sought to determine if STT motion was the same in flexion, extension, and ulnar deviation.

METHODS

Using a computed tomography based markerless bone registration algorithm, carpal bone kinematics were determined for both wrists of ten healthy volunteers (5 male, 5 female, avg. age: 26 [range: 21-47]). After IRB approval and informed consent, both wrists were scanned simultaneously in positions of neutral, 30º and 60º of flexion and extension, and 20º and 40º of ulnar deviation. Each carpal bone, radius and ulna were segmented and registered to the neutral position. Due to the difficulty in accurately positioning the wrist, the calculated motion of the capitate was used to define wrist motion. The kinematics of the trapezium and trapezoid were determined relative to the scaphoid and described with respect to a scaphoid coordinate system (SCS) using the helical (screw) motion parameters that completely characterize 3-D kinematics by a rotation angle about and translation along a uniquely orientated and positioned axis.

A single wrist position at 40 degrees in each direction of wrist motion was analyzed and reported here. Due to the variability in defining wrist position precisely, we analyzed positions in a 10 degree bin about 40 degrees, which resulted in a sample size of n = 17, 14, and 22 for extension, flexion, and ulnar deviation, respectively. A one-way ANOVA with a Tukey-Kramer post-hoc test was used to test the difference in rotation with each direction of wrist motion. A paired Students's t test was used to compare the motion of the trapezium with the motion of the trapezoid.

RESULTS

The trapezium and trapezoid rotated more ($P < 0.01$) in ulnar deviation than in extension or in flexion (Table 1). There was no difference in the amount of rotation between extension and flexion. The trapezium and trapezoid did not move as a single unit. The trapezium rotated less ($P < 0.02$) than the trapezoid in flexion but more ($P < 0.01$) than the trapezoid in ulnar deviation.

Table 1. Rotations of the trapezium and trapezoid, relative to the scaphoid, in various directions of wrist motion. Wrist positions were defined by the capitate positions listed below.

Bone	Ext. (deg)	Flexion (deg)	Ulnar (deg)
Trapezium	20 ± 12	16 ± 6	51 ± 11
Trapizoid	19 ± 12	21 ± 8	44± 6
Capitate	-39 ± 6	42 ± 5	40 ± 5

The orientation of the trapezium and trapezoid rotation axes varied with the direction of wrist motion. In extension, the trapezium rotation axis was primarily along the Y-axis and also along the X-axis, whereas for the trapezoid it was nearly equal along the X-axis and the Y-axis (refer to Figure 1). In flexion, both bones rotated primarily about the Z-axis. In ulnar? deviation, the trapezium rotation axis was primarily along the Y-axis and also nearly equal along X-axis and Z-axis, and for the trapezoid it was primarily along the Z-axis and also along the Y-axis.

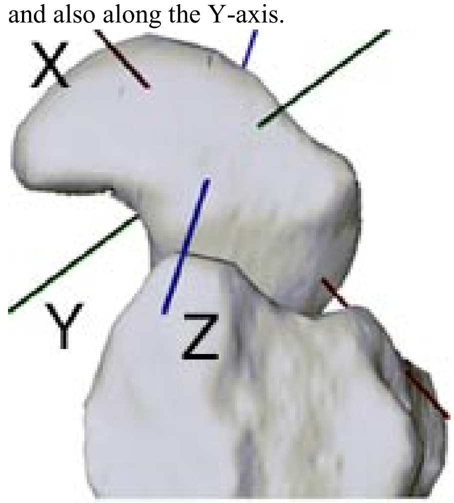

FIGURE 1: A radial view of the distal radius and the scaphoid. The X, Y, and Z axes of the scaphoid coordinate system (SCS) are shown.

SUMMARY

The *in vivo* motions of the trapezium and trapezoid varied when the wrist was in flexion, in extension, and in ulnar deviation. These findings do not support the hypothesis that the STT joint is a single degree of freedom joint; rather they suggest that the STT joint is a more mobile, complex joint than previously appreciated.

REFERENCES

Moritomo, H. et al (2000). *J Hand Surgery* **25A**(5):911-920.
Watson, H.K. and Ryu, J. (1986). *Clin Orthop* 57-67.

ACKNOWLEDGMENTS

This work was funded by NIH AR44005.

TURBULENCE INDUCED VEIN-WALL VIBRATION MAY PLAY A ROLE IN ARTERIOVENOUS DIALYSIS GRAFT FAILURE

Sang-Wook Lee[1], Francis Loth[2], Thomas J. Royston[3], Paul F. Fischer[4], Wael E.Shaalan[5], Hisham S.Bassiouny[6]

[1]Graduate Student, [2]Assistant Professor, [3]Associate Professor, Dept. of Mechanical Engineering, University of Illinois at Chicago, IL
[4]Computer Scientist, MCS, Argonne National Laboratory, Argonne, IL, fischer@mcs.anl.gov
[5] Visiting Research Associate, [6]Associate Professor, Department of Surgery, The University of Chicago, IL

INTRODUCTION

Intimal hyperplasia at the venous anastomosis of hemodialysis arteriovenous (AV) graft is often the cause of graft failure resulting in significant morbidity and cost. The AV circuit represents a unique hemodynamic environment in which transition to turbulence often occurs. Large velocity and pressure fluctuations at the venous anastomosis induce vein-wall vibration. This vibration is thought to be important in the development of intimal hyperplasia. We have established a porcine model to investigate the importance of *in vivo* vein-wall vibration on the level and activity of the ERK1/2 mechanotransduction pathway.

METHODS

Infrarenal aorta to external iliac vein 4-7 mm AV grafts were implanted in 8 male miniature swine using a standard anastomotic geometry. Volumetric flow rate was measured in the distal and proximal outflow tracts by ultrasonography. Using laser Doppler vibrometry (LDV), vein-wall vibration was passively determined at defined anastomotic regions on the vein (A, B, and C) as shown in Figure 1. Turbulence induced vibration intensity (VI) was quantified by computing the root mean squared (RMS) value of the vibration velocity amplitude in the frequency range 40-800 Hz. Western blot analysis was used to quantitate ERK1/2 levels and its activity was determined by measuring Elk1 phosphorylation with a kinase assay. The degree and cellular colocalization of ERK1/2 was assessed at 4 hours and 4 weeks using immuno-cytochemical analyses. Results were considered significant at the $P<0.05$ by a two-tailed T-test.

RESULTS AND DISCUSSION

Mean flow rate in the anastomoses was 654 ± 285 ml/min (range 350 – 1000 ml/min). High vibration regions were located just downstream of the graft-to-vein junction in the proximal venous segment (region B) as shown in Figure 2. There was close to 2.5-fold increase in vein-wall VI at region B (4.3 ± 4.94 mm/s, range 1.24 – 8.3) when compared to region A (1.6 ± 0.57 mm/s, range 0.5 – 2.71) (P = 0.0085). Correspondingly, the western blot analysis showed a 3-fold increase in ERK1/2 and Elk1 phosphorylation in region B relative to region A after four hours.

Our group has previously reported results that describe the transitional flow field present within the venous anastomosis of an AV graft [1]. Numerical simulations revealed the pressure and velocity fluctuations within the anastomosis to have frequencies consistent the vein-wall vibration frequencies measured *in vivo* (~300Hz). Thus, transitional flow or weakly turbulence flow is thought to be the cause of the vein-wall vibration. These preliminary results of vibration and ERK1/2 levels implicate vein-wall vibration as a biomechanical stimulus for the activation of ERK1/2 and intimal thickening. Further work is necessary to determine the precise relationship between AV graft failure and fluid-dynamic variables such as velocity fluctuations and wall shear stress, as well as their relative importance.

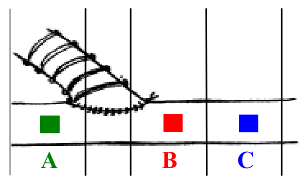

Figure 1. LDV measurement regions.

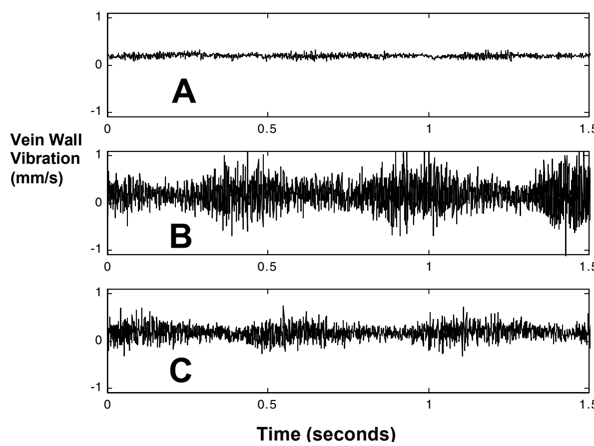

Figure 2. Vein-wall vibration velocity measured directly on the vein during surgery.

REFERENCES

Fischer et al. (2000). BED-Vol. 48, pp. 275-276.

ACKNOWLEDGEMENTS

This work was sponsored by the Whitaker Foundation and W.L. Gore & Associates, Inc.

UNSTRUCTURED HEXAHEDRAL MESH BASED ON CONDUCTION TEMPERATURE DISTRIBUTION

Seung E. Lee[1], Francis Loth[2], and Paul Fischer[3]
University of Illinois at Chicago, Chicago, Illinois, USA
[1]Graduate Student, [2]Assistant Professor, Mechanical Engineering
Argonne National Laboratory, Argonne, Illinois, USA
[3]Computer Scientist, MCS, fischer@mcs.anl.gov

INTRODUCTION

Over the past two decades, the fluid mechanics of blood flow has been shown to play an important role in arterial adaptation and disease localization (Giddens et al., 1993). For numerical studies, Milner et al. (1998) demonstrated the importance of using the true geometry of the carotid bifurcation as opposed to an idealized geometry that does not accurately represent *in vivo* curvature and variable diameter. Here, we describe a technique to generate high quality, unstructured, hexahedral meshes appropriate for spectral and finite element simulations in bifurcation geometries. This work improves upon our previous bifurcation meshing technique (Lee et al., 2000) by using thermal conduction solutions in the corresponding model domain to generate element cutting planes that are guaranteed to be orthogonal to the domain boundary and nonintersecting. This approach also automatically determines principal cutting planes that previously had to be specified by the user.

METHODS AND RESULTS

Our mesh generation technique has four main steps. First, the medical images must be processed to extract the geometry data, which is converted using Mimics (Materialise, Inc.) to a stereolithography (.stl) surface format consisting of triangles. The surface data is smoothed with a non-shrinking smoothing algorithm (Taubin, 1995). Next, the smoothed data is used to create a preliminary mesh with any meshing code (ICEM-CFD) (Fig 1a). The main objective of the preliminary mesh is to preserve the surface information, whereas the mesh quality is not as important. In the third step, three separate conduction problems are solved within the bifurcation geometry using the preliminary mesh. For each conduction problem, temperatures are specified at two branch tips with the values of one and zero, while the third branch tip is insulated. The three conduction problems are determined by a cyclic permutation of the tip boundary conditions. In all three cases, the remainder of the surface is insulated so that thermal isosurfaces are orthogonal to the domain boundary. The final step is to use these isosurfaces to generate bounding surfaces for "slabs" of hexahedral elements. Candidate isosurfaces are tessellated with quadrilateral elements, such that adjacent pairs of isosurfaces define a slab comprising hexahedral elements. Note that the isosurfaces are guaranteed to be non-intersecting. It is clear from Figs. 1b-d that a single conduction problem suffices to mesh two of the three branches. By using these isosurfaces to mesh only half of each active branch and combining the result with similarly generated meshes from the complementary problems, a symmetric approach to meshing all of the branches is obtained. The dividing surface that determines which conduction solution to use in each half-branch is taken to be the isosurface that emanates from the branch tip when that tip is insulated. Remarkably, all three of these "principal" cutting surfaces intersect in a single line such that the domain is automatically partitioned into 6 parts. Fig. 1e shows a spectral element mesh generated by this process.

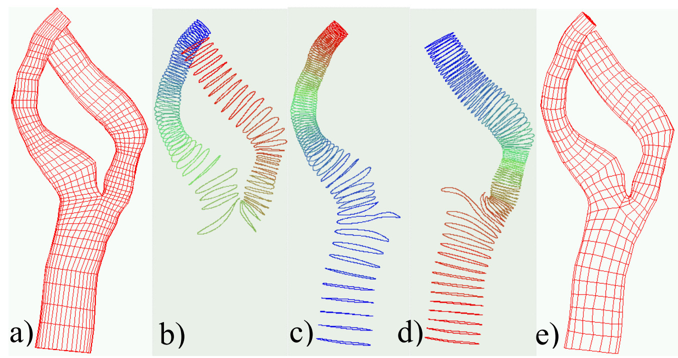

Figure 1: Meshing process of stenosed carotid shown in detail (top left branch is external carotid artery, top right is internal, bottom is common), a) preliminary mesh from commercial software, b) temperature field with ECA = 0, ICA = 1, CCA = Ins, c) ECA = 1, ICA = Ins, CCA = 0, d) ECA = Ins, ICA = 0, CCA =1, where Ins denotes 'insulation', and e) final mesh based on the temperature fields.

CONCLUSION

The solution of simple conduction problems provides a method of generating nonintersecting bounding-surfaces for coarse hexahedral elements that are guaranteed to be orthogonal to the domain boundary.

REFERENCES

Giddens, D.P. et al. (1993). *J. of Biomechanical Engineering*, **115**, pp. 588-594

Lee, S.E. et al. (2000), World Congress on Medical Physics and Bioengineering, MO-G326, Chicago, IL.

Milner, J.S. et al. (1998), *J. of Vascular Surgery*, **27**, pp. 143-156.

Taubin, G. (1995), "A Signal Processing Approach to Fair Surface Design," *Computer Graphics,* **29**, pp. 351-358

SWELLING OF ORGANOTYPIC BRAIN CULTURES AS A MODEL FOR TRAUMATIC BRAIN INJURY

Mark B. Sommers[1], Jennifer Miesch[2], Zhigang Xiong[2], Michael Bottlang[1]
[1]Legacy Biomechanics Laboratory, Portland, OR
[2]Legacy Neurobiology Laboratory, Portland, OR

INTRODUCTION

Traumatic brain injury (TBI) is the leading cause of death and disability below age 45, affecting approximately 1.5 million people in America each year [Thurman, 1994]. TBI is accompanied by diffuse brain swelling, which leads to increased intracranial pressure and reduced blood circulation by vascular congestion. A well-controlled laboratory model is essential to investigate clinically relevant traumatic brain injury and associated swelling behavior. Organotypic brain cultures can provide the basis for an attractive alternative to conventional *in vitro* and *in vivo* brain injury models. They eliminate the complexity of *in vivo* apparent systemic responses, and resemble a heterogeneous cell distribution in a physiologic matrix arrangement, unlike *in vitro* monolayer cultures.

This study quantifies for the first time the swelling behavior of organotypic brain slice cultures in response to the primary insult sustained during brain sectioning. This defined and reproducible mechanical trans-section insult induced brain swelling, which closely resembled *in vivo* apparent injury cascades. It constitutes a valuable model for investigation of TBI and consequential swelling mechanisms.

METHODS

Organotypic brain slices were obtained by a modified method of Adamchick et al. [Adamchick, 2000]. Whole brains were removed from 8-10 day old Swiss mice pubs and immersed in chilled dissecting medium. Brains were sectioned coronally into slices of 400 μm thickness on a vibrotome (Leica VT 1000). This sectioning not only yielded organotypic slices of highly accurate thickness, but also induced defined and reproducible trans-section brain injury. Subsequently, each brain slice was transferred to a culture membrane (Millipore, Millicell-CM) and maintained in 1.1ml of serum-based culture medium in a 37° humidified incubator at 5% CO2.

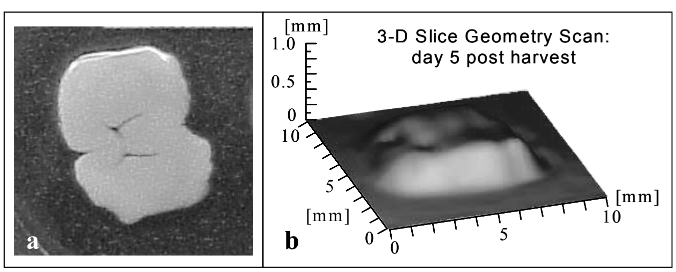

Fig. 1: a) organotypic brain culture, b) culture geometry scan.

Brain slice thickness was digitized utilizing a custom-built laser-based surface scanner (Fig. 1b). This scanner was able to scan three-dimensional surface geometries in a non-contact fashion with an accuracy of 35μm [Sommers, 2001]. Since this scanning technique terminated slice viability, slice thickness could only be measured at one time point per slice.

Thickness measurements were performed by averaging the height over a $4mm^2$ region on the center of the slice culture. Three brain slices, each from different mice, were measured immediately after sectioning, at 12 h and 24 h post-sectioning, and after 2, 3, 4, 9, 16, and 23 days in culture. Cell death was assessed by measuring the release of lactate dehydrogenase (LDH) into the slice each day from day 1 to day 7, as well as at days 9, 11, 14, 15, 20, and 25.

RESULTS

The trans-section TBI resulted in significant swelling of the organotypic brain slice. Maximum swelling to a slice thickness of 663±53 μm was detected at 48 hours post insult. The brain slice thickness increase by 70% and 87% at day 1 and day 2, respectively, was highly statistically significant ($p<0.01$) (Figure 2). After 48 hours, brain swelling declined. At day 9, the initial brain slice thickness of 400μm was recovered. Cell necrosis, as measured by LDH release, reached its maximum at post sectioning day 3, at which time it had increased by 46% compared to day 1. LDH continuously declined thereafter and became negligible 14 days after the traumatic insult.

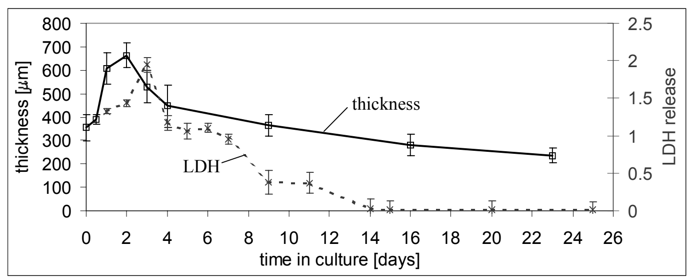

Figure 2: time history of brain slice swelling and LDH release

DISCUSSION

The reported brain swelling of organotypic slices correlates closely with clinically observed time-histories of intracranial pressure increase following TBI, and with *in vitro* studies of closed head trauma [Schneider, 1994]. The observed shift between LDH and swelling maxima may be in part caused by the requirement of LDH to diffuse into the culture medium. In conclusion, the consistent and reproducible swelling phenomena of organotypic brain slices constitutes a controlled and clinically relevant *in vitro* model for TBI. As such, it can serve as a powerful tool for the evaluation of pharmacological strategies to reduced brain swelling.

References

Thurman et al., National Center for Injury Prevention & Control, 22, 1999
Adamchik, Brain Research Prot. Elsevier 5, 153-158, 2000
Sommers, et al., ASME, BED-Vol.50, 555, 2001
Schneider et al., Acta Neurochirurgica 60, 437-9, 1994

A BIOMECHANICAL MODEL OF THE ELBOW, FOREARM AND WRIST

Rahman Davoodi, David Kleiman, Tomo Murakata and Gerald E. Loeb
A.E. Mann Institute for Biomedical Engineering and Department of Biomedical Engineering
University of Southern California, Los Angeles, CA 90089 USA; Http://ami.usc.edu; Davoodi@usc.edu

INTRODUCTION

Biomechanical models of the human arm provide a convenient and safe environment for studying the control of natural reaching movement and its restoration after paralysis. The model developed here simulates the movement of the elbow, forearm and wrist joints under arbitrary muscle excitations and external forces. It incorporates the most recent experimental data available regarding the moment arms and musculotendinous architecture of the muscles. It has been developed in a popular modeling environment for ease of sharing and future upgrades.

METHODS

The model has four segments (humerus, ulna, radius and hand), three joints (elbow, forearm and wrist), and fifteen muscles (Fig. 1). The skeleton was constructed by averaging the sizes of ten cadaver specimens reported by Murray (1997). Inertial parameters of the segments were estimated by the use of Hanavan's geometric models and experimentally measured segment densities.

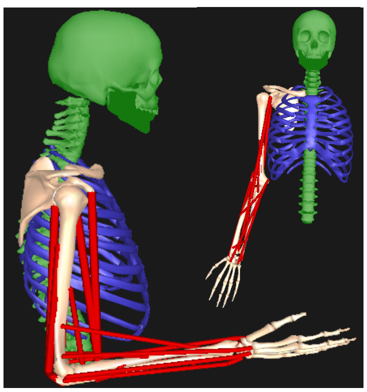

Figure 1. Anatomical model of the arm implemented in SIMM® from Musculographics, Inc.

To complete the anatomical model, the muscles were attached to the bony landmarks. Adjustments to cylindrical wrapping surfaces and muscle attachment points were used to reproduce the average experimental moment arms (Murray, 1997; Horii *et al.*, 1993; Lemay and Crago, 1996; Loren *et al.*, 1996) as a function of joint angle. The moment arms about the primary joint, where the muscle is a prime mover, were matched first. Then, additional parameters were modified to match the moment arms about the remaining joints as well as possible. The muscles' architectural parameters were selected from literature (Murray, 1997; Lieber *et al.*, 1990; Lieber *et al.*, 1992). Because the musculotendon lengths were slightly different from that of the model, the lengths of the tendons were adjusted to match the modeled and experimental operating ranges of the muscle fascicles.

Model parameters were fed to Virtual Muscle™ (Cheng *et al.*, 2000), SIMM (Delp and Loan, 2000), and MMS (Davoodi and Loeb, 2001) to build the forward dynamic model of arm that runs in the Simulink® simulation environment of MATLAB.

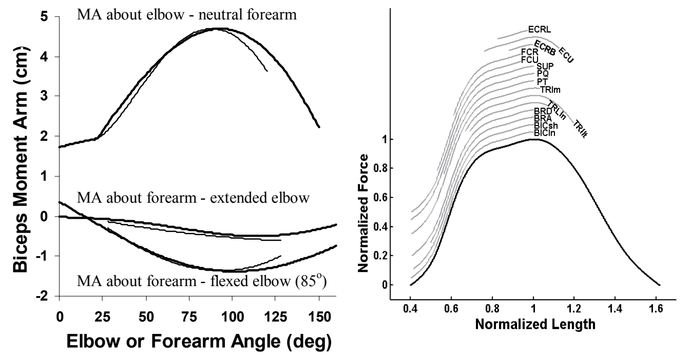

Figure 2. Biceps Brachii's modeled (thick) and experimental (thin) moment arms (left) and muscle fibers operating ranges superimposed on a normalized force-length curve (right).

RESULTS AND DISCUSSION

As an example of realistic moment arms for multijoint muscles, the modeled and experimental moment arms of the biceps muscle are shown in figure 2. Also shown are the operating ranges of the muscle fibers that are similar to those reported in the literature (Murray, 1997; Loren *et al.*, 1996).

The moment arms about multiple joints and operation of the muscle fibers in the correct region of the force length curve are key features of a realistic arm model. Further validation of the model requires moment arm data about all the joints crossed by each muscle and in different arm configuration. The data from single cadaver specimens should also be as complete as possible because there is no validated methodology for scaling the biomechanical data among specimens.

The model is being used to design neural prostheses for reach and grasp. The MATLAB software environment is slow and simulation of one second of movement requires minutes of computation time on a PC. This modeling environment is suitable for developing and testing highly accurate models that can then be simplified and converted to fully compiled versions for specific requirements.

REFERENCES

Cheng, E.J. et al (2000). *J.Neurosci.Methods* **101,** 117-130.
Davoodi,R. Loeb, G.E. (2001). Proc. of IFESS 2001, 282-284.
Delp, S.L. Loan, J.P. (2000). *Comp.Sci. Eng.* **2,** 46-55.
Horii, E. et al (1993). *J Hand Surg.* **18,** 83-90.
Lemay, M.A. Crago, P.E. (1996). *J.Biomech.* **29,** 1319-1330.
Lieber, R.L. et al (1990). *J.Hand Surg.* **15,** 244-250.
Lieber, R.L. et al (1992). *J.Hand Surg.* **17,** 787-798.
Loren, G.J. et al (1996). *J Biomech.* **29,** 331-342.
Murray, W.M. (1997). Ph.D. thesis, Northwestern University.

MATRIX BIOSYNTHESIS DUE TO EXOGENOUS STIMULI DIFFERS FOR CARTILAGE AND FIBROCARTILAGE

Imler SM[1], Hunter CJ[2], Vanderploeg EJ[1], and Levenston ME[1]

Georgia Institute of Technology, Atlanta, Georgia, USA, marc.levenston@me.gatech.edu
[1]George W. Woodruff School of Mechanical Engineering
[2]Wallace H. Coulter Department of Biomedical Engineering

INTRODUCTION

Matrix metabolism in cartilaginous tissues is regulated by a variety of environmental factors, including biomechanical stimulation and soluble growth factors. The effects of such factors on articular cartilage have received much attention in the literature. To date, however, fibrocartilages such as the knee menisci have received less attention. The menisci are critical to maintaining normal knee biomechanics, yet little is known about the role of environmental stimuli in maintaining healthy meniscal tissue. This study compared the effects of exogenous biomechanical and biochemical stimuli on animal-matched explants of articular cartilage and meniscal fibrocartilage.

METHODS

Tissue cores (4mm dia) were obtained from articular cartilage and menisci of immature bovine stifle joints and trimmed to a prescribed thickness. In each experiment, protein and proteoglycan (PG) synthesis rates were measured via radiolabel incorporation (^{3}H and ^{35}S) during the final 21 hours of culture. **Mechanical Stimulation** Explants were pre-cultured in serum supplemented medium for 3 days and then mechanically compressed for 21 hours. Explants (n=8) were placed under static compression (0%, 25%, or 50%) or oscillatory compression (10%±3% at 0.1 Hz or 1.0 Hz). **Biochemical Stimulation** Explants were pre-cultured in serum free medium plus 0.1% BSA for 3 days. Explants (n=8) were then cultured in serum free medium with 0.1% BSA or 0.1% BSA and 200 ng/ml rhIGF-1.

RESULTS AND DISCUSSION

Mechanical Stimulation In cartilage explants, both protein and PG synthesis were inhibited by static compression and stimulated by oscillatory compression (Figures 1 and 2), as previously reported (Sah, 1989). In meniscus explants, protein synthesis was also inhibited by static compression and stimulated by oscillatory compression, with synthesis per cell comparable to that in cartilage. In contrast, PG synthesis was not significantly influenced by either static or oscillatory compression. **Biochemical Stimulation** The responses to biochemical stimulation were less consistent. IGF-1 did not substantially influence protein synthesis in cartilage explants, but it significantly stimulated protein synthesis in meniscus explants (Figure 3). IGF-1 stimulated PG synthesis in both tissues, with a more dramatic effect on meniscus explants.

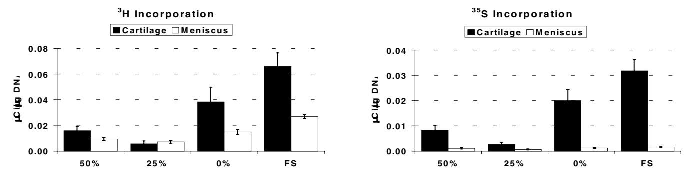

Figure 1: Static compression results

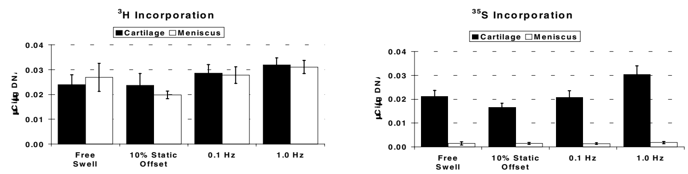

Figure 2: Oscillatory compression results

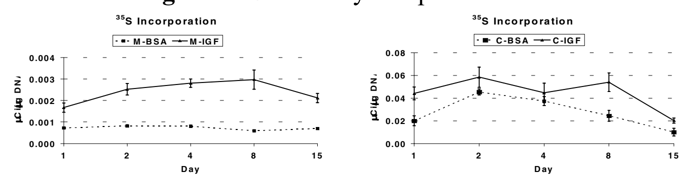

Figure 3: IGF-1 time-course results (meniscus and cartilage)

SUMMARY

This study elucidates biosynthetic differences of fibrocartilage and cartilage in response to biomechanical and biochemical stimuli. PG synthesis in meniscus explants was nonresponsive to mechanical stimulation. RT-PCR analysis indicates that the meniscal fibrochondrocytes do express aggrecan mRNA at roughly one-third the level of articular chondrocytes, indicating a potential for PG production. Indeed, IGF-1 induced sustained stimulation of meniscal PG synthesis, although the synthesis rates remained well below levels seen in cartilage. In stark contrast, regulation of protein synthesis by mechanical compression was similar for the two tissues, despite the probable difference in the predominant protein type (collagen I in meniscus and collagen II in cartilage). Effects of sustained loading on meniscal tissue remain undetermined and will give further insights into meniscal physiology.

REFERENCES

Sah, R.L-Y. et al (1989). *J Orthop Res*, **7**, 619-636.

ACKNOWLEDGEMENTS

Funded by an Arthritis Foundation Arthritis Investigator grant, the NSF-ERC under award number EEC-9731643, and by NSF and Luce Foundation Fellowships to SMI

TREADMILL SPEEDS RELATED TO SPRINTING ABILITY

Derek Kivi[1], Brian Maraj[2], and Pierre Gervais[1]
[1]Sports Biomechanics Laboratory and [2]Perceptual Motor Behavior Laboratory
University of Alberta, Edmonton, Alberta, Canada, dkivi@ualberta.ca

INTRODUCTION

Treadmill sprinting is a demanding form of speed training, requiring strength and dexterity in order to be an effective training tool. The purpose of this study was to compare the stride characteristics and lower extremity kinematics of sprinters of different abilities on a treadmill, and determine whether or not a sprinter's velocity should be a factor as to how the treadmill is used for speed development.

METHODS

Six national level sprinters (3 males, 3 females) were recruited for the study, all of whom were familiar with sprinting on the treadmill. Each subject performed runs of 70%, 80%, 90%, and 95% of their previous maximum. The treadmill was preset to a specific velocity for each individual prior to the trial; there was no acceleration or deceleration phase. A Canon 8mm video camera recorded the performance in the sagittal plane at 60Hz and a shutter speed of 1/2000. Data processing was completed using the Ariel Performance Analysis System. For each test condition three successive strides were analyzed. Data were smoothed using a low-pass digital filter with a cutoff frequency of 8 Hz. Subjects were categorized in either the highly skilled or less skilled sprint group based on the velocities selected for testing. Descriptive statistics (means (M) and standard deviations (SD)) were calculated for variables selected for analysis based on previous treadmill sprinting research (Kivi *et al*., In Press).

RESULTS AND DISCUSSION

The results are seen in Table 1 and indicate that there are differences between groups while sprinting on a treadmill, particularly at higher velocities. The highly skilled group showed faster treadmill velocities at all test conditions, however the stride frequency was similar between groups. This suggests that the differences in velocity were a result of longer stride length, as velocity is the product of stride length and stride rate. Group differences were seen in the positions achieved at the hip and knee. The highly skilled sprinters were better able to limit hip and knee extension at take-off (smaller angle) which helped reduce stance time, and were able to achieve greater angles of hip flexion (larger angle) which made leg recovery more efficient (Mann, 1985). The less skilled sprinters, in order to execute the same movements, required greater angles of knee flexion (smaller angle) through recovery to minimize the rotational inertia. These findings suggest that the differences in treadmill sprinting velocity seen between groups are a result of a lack of strength in the hip flexors, as Mann (1985) stated that excessive extension at take-off is indicative of a lack of leg strength. It is recommended that less skilled sprinters using a treamill as a speed development tool should not train at near maximum velocities until they have developed sufficient strength through the hip flexors, in order to prevent unwanted breakdown in technique. With the small number of subjects preventing adequate statistical comparison, further investigation is required.

SUMMARY

Stride characteristics and lower extremity kinematics were compared between two groups of sprinters of different abilities on a treadmill. The results suggest there are differences between groups at higher velocities, which may be the result of inadequate hip flexor strength.

REFERENCES

Kivi *et al*. (In Press). *Med. Sci. Sports. Exerc.*
Mann, R. (1985). *The Elite Athlete*. Spectrum Publications.

Table 1: Stride characteristics and lower extremity kinematics (Mean ± SD).

Variable	Highly Skilled (n = 3)				Less Skilled (n = 3)			
	70%	80%	90%	95%	70%	80%	90%	95%
Velocity ($m \bullet s^{-1}$)	8.03	9.18	10.33	10.91	6.57	7.51	8.45	8.92
Stance Time (ms)	120 ± 10	110 ± 10	100 ± 10	90 ± 10	140 ± 10	130 ± 10	120 ± 10	100 ± 10
Flight Time (ms)	140 ± 10	130 ± 10	120 ± 10	120 ± 10	150 ± 10	140 ± 10	130 ± 10	130 ± 10
Stride Frequency ($stride \bullet s^{-1}$)	1.9 ± 0.1	2.0 ± 0.1	2.0 ± 0.1	2.3 ± 0.1	1.9 ± 0.1	2.0 ± 0.1	2.2 ± 0.1	2.3 ± 0.1
Peak Hip Flexion (deg)	62 ± 6	65 ± 4	72 ± 4	72 ± 7	60 ± 7	60 ± 6	63 ± 6	62 ± 5
Hip Extension at Take-off (deg)	21 ± 1	20 ± 4	19± 4	19 ± 6	21 ± 3	22 ± 5	22 ± 6	24 ± 5
Hip Flexion Ang Vel ($deg \bullet s^{-1}$)	661 ± 36	761 ± 42	777 ± 37	769 ± 32	603 ± 30	631 ± 16	688 ± 16	687 ± 25
Hip Extension Ang Vel ($deg \bullet s^{-1}$)	545 ± 29	621 ± 49	648 ± 41	676 ± 69	500 ± 52	515 ± 36	604 ± 62	656 ± 46
Peak Knee Flexion (deg)	44 ± 5	41 ± 5	41 ± 7	44 ± 7	42 ± 5	41 ± 5	40 ± 6	40 ± 4
Knee Extension at Take-off (deg)	142 ± 3	139 ± 5	135 ± 5	136 ± 7	149 ± 4	148 ± 4	146 ± 6	147 ± 4

STIFFNESS AND POSTURAL CONTROL IN ADOLESCENT CONTROL AND IDIOPATHIC SCOLIOSIS PATIENTS

K F. Zabjek[1,2], F. Prince[1,3], M. Leroux[1], C. Coillard[1] and CH Rivard[1,2]

1. Marie-Enfant Rehabilitation Centre, Sainte-Justine Hospital, Montreal, Qc, Canada, kzabjek@justine.umontreal.ca
2. Department of Medicine, University of Montreal, Montreal, Qc, Canada
3. Department of Kinesiology and Surgery, University of Montreal, Montreal, Qc, Canada

INTRODUCTION

Idiopathic scoliosis (IS) is a complex pathology, recognized as a 3-dimensional deformation of the spine. Considerable research has focused on the deformation of the spine and thorax, with little focus on understanding the mechanisms that are responsible for postural control, and how they relate to the progression of spinal curvature. Quiet standing has been understood primarily through the Inverted Pendulum Model, where the horizontal acceleration of the Centre of Mass (COM) is proportional to the difference in amplitude between the Centre of Pressure (COP) and COM. More recently ankle muscle stiffness has been proposed to explain how the CNS controls quiet stance. The objective of this study is to apply the Stiffness model to contribute to the understanding of the mechanisms responsible for postural control in this unique pathology.

METHODOLOGY

There were 4 IS patients (age: 10, sd: 1 year) and 4 control subjects (age: 9, sd: 1years) in this study. Each subject was placed in a quite standing position with each foot on an AMTI forceplate. One Optotrak Position sensor captured the 3D position of IRED's placed on the base of support, lower and upper extremities. Four quiet standing trials were collected (120 s, 30 Hz) with adequate rest in between each trial. The following equations presented by Winter et al., 2001 were utilized to calculate in reference to the ankle joint the COM sway angle (θ_{sw}), moment (M_a) and stiffness (ka). (m= mass of the subject above the ankle joint; g = acceleration due to gravity, COP_{net} = net centre of pressure position based on COP of the right and left feet, COM= 12 segment model)

$$M_a = mg^* COP_{net} \qquad \textbf{Equation 1}$$

$$\theta_{sw} = COM/h \qquad \textbf{Equation 2}$$

$$K_a = dM/d\theta_{sw} \qquad \textbf{Equation 3}$$

RESULTS AND DISCUSSION

The stiffness, sway angle and R^2 between the sway angle and the ankle moment are presented in Table 1. The R^2 between the sway angle and ankle moment ranged between .87 to .96 for the control subjects and .93 to .97, for the scoliosis patients. This reflects how close the ankle stiffness approaches an ideal spring, and is similar to the values reported by Winter et al., 2001 for adult control subjects.

Table 1: Sway angle (θ_{sw}), stiffness (K_a), and R^2.

	Sway (θ)	**K_a (nm/rad)**	**R^2**
Control	3.1 (.4)	231 (64)	.93 (.04)
IS	3.7 (.3)	159 (54)	.96 (.04)

There was a tendency to have an increased sway, and decreased stiffness for the IS patients. Also, despite an RMS sway angle of less than 1° for all subjects, the sway angle range during the 120 s was from a minimum 1° to maximum 4° across subjects. There was a similar observation for the stiffness with a minimum range of 226 Nm/rad to a maximum range of 1244 Nm/rad across subjects during the same period. The stiffness of a typical subject is presented in Figure 1.

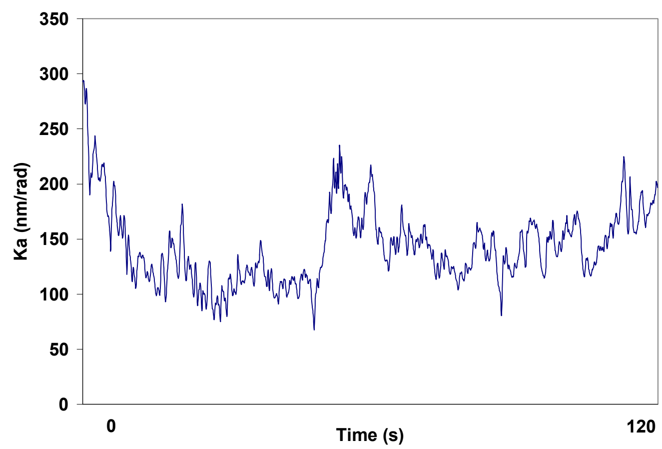

Figure 1: Ankle stiffness (K_a) of a Scoliosis patient.

SUMMARY

The control of AP sway about the ankle joint reflects a spring like mechanism that has different characteristics between IS and control subjects. The range of stiffness and sway angle over the 120 s indicates a more complex process of stiffness control than previously thought.

REFERENCES

Masso PD, Gorton GE (2000) *Spine* **25**:457-62
Winter DA et al., (2001) *J Neurophysiol,* **75**:2334-43.
Winter DA et al., (1998) *J Neurophysiol,* **80**:1211-21.

ACKNOWLEDGMENTS

The authors thank the members of the Human Movement Laboratory of the Marie-Enfant Rehabilitation Centre of Sainte Justine Hospital. As well as funding from the Hospital for Sick Children's Foundation, NSERC, and FRSQ.

ACCELERATION TRANSIENTS AND TRANSTIBIAL PROSTHETIC PYLON ATTENUATION DURING GAIT

Jocelyn S. Berge[1,2], Glenn K. Klute[1,3] and Joseph M. Czerniecki[1,4]
[1]Departments of Veterans Affairs, VA Puget Sound Health Care System, Seattle, WA (jberge@u.washington.edu)
Departments of [2]Bioengineering, [3]Electrical Engineering, and [4]Rehabilitation Medicine, University of Washington, Seattle, WA

INTRODUCTION

Repetitive high frequency transients arising from heel strike during locomotion are thought to be responsible for the deleterious effects observed on the residual limb tissue and other structures of lower limb amputees (Whittle, 1999). To ameliorate this effect, prosthetic manufactures have developed shock absorbing pylons (SAPs) to attenuate shock transients transmitted to the residual limb. To date, the performance and efficacy of SAPs is not well understood. Our focus is measure the accelerations transients transmitted to the residual limb and then access how these transients are altered by an SAP (TT Pylon, Blatchford, UK) as compared to a rigid pylon.

METHODS

Five unilateral transtibial Veteran amputees were recruited to participate, each provided informed consent. Subjects were fit with a standard prosthetic limb able to accommodate either pylon. Pylon order was randomized and after a three-week acclimation period, accelerometry data were collected while subjects walked 3-5 repeated trials at 1.2 m/s ± 10%. A lightweight accelerometer (Entran, USA) was rigidly mounted proximally on the pylon. Data were sampled from the axis parallel to the pylon (f_s = 600 Hz, f_c = 100 Hz). Subjects were then fit with the other pylon and asked to repeat the protocol sequence. The time series signals were cropped to include only one stance phase and padded, by extending the first and last values, to 512 points in preparation for the analysis. Fourier analysis determines the magnitude of a signal using the entire sample period resulting in an underestimation of damped transient magnitudes. A multilevel stationary wavelet discrete transform using a least asymmetric wavelet (width 8) (LA8) preserves both frequency and time information of the signal. The LA8 was selected to minimize sidelobes outside the pass-band (Percival and Walden, 2000). The analysis included pass-bands from 9-18 Hz (pb1), from 18-38 Hz (pb2), from 38-75 Hz (pb3), and from 75-100 Hz (pb4). Peak acceleration magnitudes within each pass-band were averaged for each pylon. A repeated measures ANOVA was performed with an *a priori* α of $p<0.05$.

RESULTS AND DISCUSSION

The wavelet analysis of accelerometry data from the rigid pylon and the SAP reveal large accelerations transient magnitudes entering the residual limb (Figure 1). For perspective, with 1 g acceleration and an assumed effective leg mass of 5 kg, a significant shock load of 50 N is transmitted. The mean peak accelerations, for the most part, decrease in magnitude with increasing pass-band frequency (Figure 2). All pass-bands showed reduced magnitude transients for the SAP compared to the rigid pylon but none were statistically significant. The attenuation could be attributed to the pylon and/or the individual loading characteristics of the amputee.

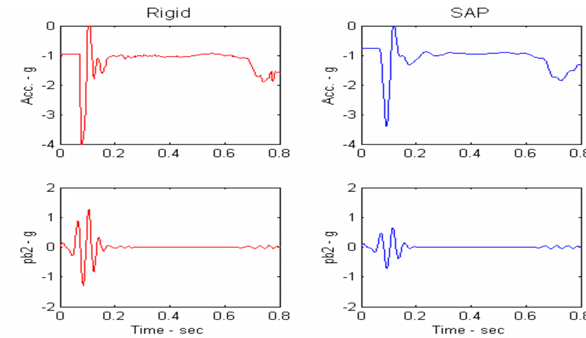

Figure 1: Illustrative accelerometry data and a multilevel wavelet analysis pass-band pb2 for an amputee wearing a rigid pylon and an SAP.

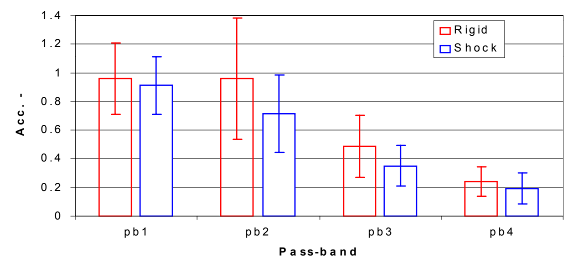

Figure 2: The means (n=5) and standard deviations of peak acceleration transients at each pass-band.

SUMMARY

Large magnitude accelerations transients were present for both pylons with decay occurring within 0.1 seconds. This wavelet approach is able to retain frequency and time information allowing for observation of possible prosthetic component differences. Reduced, but not statistically significant, mean signal magnitudes for all frequency pass-bands were observed when amputees walked on a rigid pylon versus an SAP.

REFERENCES

Percival, D.B., Walden, A.T. (2000). *Wavelet Methods for Time Series Analysis*. Cambridge University Press.
Whittle, M.W. (1999). *Gait & Posture*, **10**, 264-275.

The Department of Veterans Affairs, Veterans Health Administration, Rehabilitation Research and Development Service (grant numbers: A0806C and A2448R).

PERTROCHANTERIC FRACTURE FIXATION: EFFECTS OF IMPLANT DESIGN ON CUT-OUT FAILURE UNDER DYNAMIC LOADING

Mark B. Sommers[1], Michael Bottlang[1], Christoph Roth[2], Harry Hall[2], James C. Krieg[1]
[1]Legacy Clinical Research & Technology Center, Portland, OR; email: mbottlan@lhs.org
[2]Synthes(USA), West Chester, PA

INTRODUCTION

One of the most severe orthopaedic challenges is the rapidly rising number of over 300,000 hip fractures per year in the US [Rubenstein, 2000]. A preferred treatment option for hip fractures is the use of lag-screw implants. Despite widespread use, these implants exhibit a disturbingly high complication rate of up to 23% [Baumgaertner, 1995]. The most common failure mode is cut-out of the implant through the femoral head. The efficacy of implants to resist cut-out has been studied intensively under quasi-static loading conditions. This study investigated the fixation strength of various implants under dynamic loading.

METHODS

Four implant designs from two manufacturers (Synthes (USA), Paoli, PA; Stryker Howmedica Osteonics, Allendale, NJ) were tested (Table 1). Two lag-screws had a conventional thread design (i.e. Dymanic Hip Screw – DHS, Gamma Nail), while the other two implants featured a novel helical blade design (i.e. Dynamic Helical Hip System – DHHS, Titanium Femoral Nail – TFN).

Implant	Company	Fixation type	Implant design	
DHS	Synthes (USA)	Side Plate Fixation	Lag Screw	
DHHS			Helical Blade	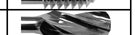
TFN		Intramedullary Nail Fixation	Helical Blade	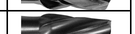
Gamma Nail	Howmedica		Lag Screw	

Table 1: Implant Specifications

Implants were tested in a femoral head/neck model, that simulated constraints characteristic of an unstable, fully collapsed pertrochanteric fracture type OTA 31-A2.1 [Fracture compendium, 1996] (Figure 1). Implants were inserted into cancellous bone surrogates (polyurethane foam, 60 MPa compressive modulus, Pacific Research Inc., Vashon, WA) with a defined posterior offset of 7 mm to simulate clinically relevant procedural imprecision of implant insertion. The shaft of the implant was affixed to a rigid base, with the implant's longitudinal axis oriented at 149° toward the horizontal plane. An electro-magnetic motion tracking system was used to record femoral head rotation around the longitudinal implant axis (α_{NECK}), and varus collapse (α_{VARUS}). A material test system (Instron, Canton, MA) was used to exercise specimens cyclically (3 Hz) to cut-out failure or up to 100,000 cycles at six distinct load levels (n=3), ranging from 0.5kN to 1.65kN.

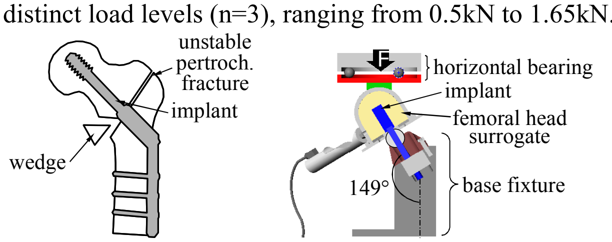

Figure 1: Fracture model and loading scenario.

RESULTS

The number of loading cycles to cut-out failure for all implants is depicted in Figure 2 in terms of fixation life curves. For a median load level of 1.2kN, implant cut-out occurred at 4 ± 1, 894 ± 430, 7850 ± 5380 and 28300 ± 4750 load cycles for the DHS, Gamma Nail, DHHS and TFN implant, respectively.

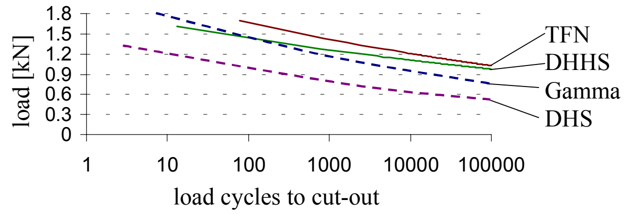

Figure 2: Fixation life curves

Implant cut-out failure was accompanied by femoral head collapse into varus (α_{VARUS}) and femoral head rotation around the implant axis (α_{NECK}) induced by the 7mm posterior offset (Figures 3, 4). After 10 load cycles at 1.0kN load amplitude, α_{VARUS} and α_{NECK} advanced on average to 64% and 89% (DHS), 35% and 58% (Gamma), 16% and 21% (DHHS) and 5% and 7% (TFN) of their maximal values, respectively.

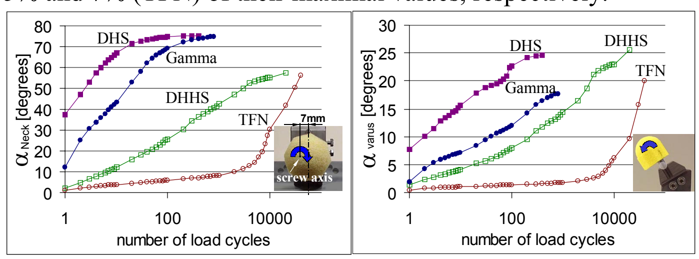

Figure 3: Femoral Head rotation versus loading cycles

Figure 4: Varus collapse versus loading cycles

DISCUSSION

The presented cut-out model allowed reproducible assessment of the implant-specific migration onset and pathway. It closely resembled clinically observed cut-out failure modes, which most frequently occur in unstable pertrochanteric fractures. It also delineated the efficacy of specific design parameters to increase cut-out resistance in a well-controlled laboratory setting. Both helical blade implants provided superior resistance to migration and subsequent cut-out failure. This suggests, that a helical blade design provides increased fixation strength compared to a conventional lag screw design.

REFERENCES

Rubenstein (2000), *New Eng J Medicine* , **343**, 1562-1563.
Baumgaertner et al. (1995), *J Bone Joint Surg*, **77**, 1058-1064.
Fracture Compendium (1996), *J Orthop Trauma*, **10:1**, pg 34.

ACKNOWLEDGEMENTS

Financial support provided by Synthes, West Chester, PA.

POSTURAL EVALUATION OF IDIOPATHIC SCOLIOSIS PATIENTS AND ADOLESCENT CONTROL SUBJECTS

K F. Zabjek[1,2], F. Prince[1,3], M. Leroux[1], C. Coillard[1] and CH Rivard[1,2]

1. Marie-Enfant Rehabilitation Centre, Sainte-Justine Hospital, Montreal, Qc, Canada, kzabjek@justine.umontreal.ca
2. Department of Medicine, University of Montreal, Montreal, Qc, Canada
3. Department of Kinesiology and Surgery, University of Montreal, Montreal, Qc, Canada

INTRODUCTION

The underlying motor control mechanisms of quiet standing have traditionally been characterized by measuring the movement in the frequency and time domains of the centre of pressure (COP) and less often the centre of mass (COM). However, Idiopathic scoliosis (IS) for example, affects spinal alignment, and ultimately the position and orientation of the pelvis, thorax and shoulder girdle during periods of rapid growth and maturation of the neuro-musclo-skeletal system. These changes may be masked by models that use only the COM or the COP. The objective of this study is to compare the segmental posture of adolescent control and IS patients during quiet standing.

METHODOLOGY

There was 5 IS patients (age: 14, sd: 2years) and 5 control subjects (age: 12, sd: 2years) who participated in this study. Each subject was positioned in a quite standing position and IRED's were placed on the base of support, pelvis, spine, thorax and shoulder girdles and captured by an Optotrak Position Sensor. Four quiet standing trials were collected (120s, 20 Hz) with adequate rest in between each trial. The parameters calculated included the anterior-posterior (A/P), and medial-lateral (M/L) shift of T1 and S1 spinous processes in reference to the base of support, as well as a relative measure between the two vertebra. The angular parameters included rotation and tilt of the pelvis and shoulders in the transverse and frontal planes. The mean and root mean square (RMS) of each trial, for each angular and linear parameter was averaged across the four trials and compared between groups.

RESULTS AND DISCUSSION

There was a significant difference between the IS and control subjects for the mean orientation of the pelvis, thorax and shoulders. (See Table 1)

Table 1: Orientation of pelvis and shoulders.

	IS	Control
Pelvis Tilt	-3±2°	0.5±2° *
Shoulder Tilt	4±1°	–0.1±2° *
Shoulder Rotation	4±2°	-0.3±2° *
Thoracic Rotation	-8±3°	. –2±3° *

*** p<0.05**

The presence of these postural asymmetries may be the consequence, or represent an aggravating facto for the evolution of IS. The lateral deviation and curvature of the spine will affect the position and orientation of the adjacent pelvis, shoulder girdle, and thorax. The direction of these asymmetries may depend on the side, level and severity of the curvature. However, in consequence this asymmetry may place un-even forces on the vertebral body, which during periods of rapid growth and development may promote vertebral deformation and progression of the spinal curvature.

There was a difference between groups (IS vs Control; $p<0.05$) for the RMS during the 120 s for the shift of T1 in reference to S1 (A/P: 3±1mm vs. 5±1mm; M/L: 1±1mm vs. 3±1mm). The control subjects demonstrated greater variability in the postural control of the trunk than the IS patients. Factors that must be considered include the phase of growth of the individual where the neuromuscular system is adapting to the changing morphology of the skeletal system, and is making continuous fine motor adjustments until a stable equilibrium is reached. The IS patients also undergo this process of maturation in addition to being challenged by greater postural asymmetries and a lateral deviation of the spine. However, changes to soft tissue (muscle fibre length and composition) and individual vertebral deformation and disorientation may contribute to the decreased mobility, and reflect greater spinal rigidity as the pathology evolves.

SUMMARY

The postural alignment and variation of IS patients does exhibit differences to adolescent control subjects. These differences and the presence of the spinal deformation will implicate unique challenges to the postural control system of the IS patients.

REFERENCES

Mannion AF et al., (1998) *Eur Spine J*; **7**:289-93.
Masso PD, Gorton GE (2000) *Spine* **25**:457-62
Wever, DJ et al., (1999) *Eur Spine J*, **8:**252-60.
Winter D, et al., (1996) *J Neurophysiol,* **75**:2334-43.

ACKNOWLEDGMENTS

The authors thank the members of the Human Movement Laboratory of the Marie-Enfant Rehabilitation Centre of Sainte- Justine Hospital. As well as funding from the Hospital for Sick Children's Foundation, NSERC, and FRSQ.

DOES VERTEBROPLASTY ALTER THE MECHANICAL RESPONSE OF OSTEOPENIC VERTEBRAE?

Dietrich von Stechow[1], Zurakowski David[2], Torres Katherine[3], SerhanHassan[3], Ron N Alaklay[1]
[1]Orthopedic Biomechanics laboratory, Beth Israel Deaconess Medical Center, Boston, MA.
[2]Orthopedic Department, Children's Hospital, Boston, MA., [3]DePuy Acromed, Raynham, MA

INTRODUCTION

Percutaneous vertebroplasty (PVP) using PMMA is rapidly gaining acceptance as an appropriate surgical treatment for age related vertebral fractures and has shown promising results with, at present, few reported complications. Although PVP significantly increases the structural compressive strength of augmented vertebrae, little is known on the efficacy of this procedure in restoring the overall structural response of failed vertebrae under complex loads.

METHODS

Nineteen thoracic and lumbar vertebrae from three spines, aged 65-78 years, were radiographed to estimate the body posterior and anterior height and their Bone Mineral Density assessed by DXA (Hologic 2000+, Hologic, MA). A custom testing jig was employed to test the vertebrae to failure using a hydraulic test system (1331, Instron, Canton, MA) under combined compression-flexion at a rate of 5mm/min. Failure was defined as 50% reduction in the vertebra anterior height or a reduction of 10% in maximum load. A 6DOF load cell (MC5, AMTI, MA) was employed to measure the resulted forces and moments and displacement to failure, measured via the material testing system, with the data acquired using LabView (National Instruments, TX) at the rate of 10Hz. The failed vertebrae were allowed to recover for 30 min, the vertebral body heights re-measured and the vertebrae re-tested. A bilateral transpedicular approach was employed to augment each fractured vertebral body using PMMA cement (Vertebroplastic, Codman&Shurtleff, MA). Augmentation was performed under fluoroscopic imaging with the procedure terminated when a complete body fill was obtained or leakage of the material was observed. The augmented vertebra was allowed to rest for two hours, vertebral body heights re-measured and the vertebrae re-tested to failure. Repeated measure ANOVA was used to test for differences in maximal failure load and stiffness estimated from the linear portion of the load–displacement curve, for each of the forces and moments (JMP, SAS, NC).

RESULTS AND DISCUSSION

For L1 levels of the specimen the mean bone mineral density ($0.54\pm0.06 g/cm^2$) suggested the spines to be osteoporotic. All of the vertebrae tested exhibited a typical anterior-flexion compressive failure. The augmented vertebrae showed a highly significant increase in compressive strength, 3552± 961N, and stiffness –741±288Nm/mm, compared to that of the failed vertebrae 1082±313N and -262±186Nm/mm, respectively ($p<0.001$). Similarly, the augmented vertebrae showed significant increases in flexion strength and both strength and stiffness parameters under anterior–posterior shear, Table 1. However, out of plane forces and moments remained relatively constant throughout the test, (Table 1).

Table 1: Mechanical parameter for fractured and augmented vertebrae

Mechanical parameter	Fractured	Augmented	Significance
Compression /N	1082 ± 313	3552 ±9 61	<.0001
C.Stiffness/$N.mm^{-1}$	-262.± 186	-741 ± 288	<.0001
Flexion./N.mm	-11 ± 4.8	-24 ± 10	<0.0001
F.Stiffness./$Nm.mm^{-1}$	4.2 ± 4.1	5 ± 2	N.S
A-P. shear/N	272 ± 103	619 ±198	<0.0001
A-P. stiffness/$N.mm^{-1}$	-74 ± 56	-125 ± 51	<0.01
Lat. Bending/Nm	-3 ± 3	-4 ± 13	N.S
L.B stiffness /$Nm.mm^{-1}$	-0.3 ± 1.4	0.7 ± 3.0	N.S
Lat. shear/N	-28 ± 41	-93 ± 167	N.S
L.shear stiffness./$N.mm^{-1}$	5 ± 9	18 ± 37	N.S
Torque/Nm	0.1 ± 0.4	-0.3 ± 0.6	N.S
T stiffness. /$Nm.mm^{-1}$	-0.2 ± 0.5	-0.1 ± 0.1	N.S

Mean ± S.D, N.S: Not significant.

This study investigated the effect of cement augmentation on the structural response of augmented thoracolumber vertebrae under compression-flexion loads. Compared to the failed vertebrae, the augmented vertebrae exhibited a significant increase in structural load carrying ability and decreased deformation, particularly in the plane of loading (Table 1). However, from the out of plane response of the augmented vertebrae, it is evident that its structural behavior was markedly different than that of the failed vertebrae. Although the desired outcome of vertebroplasty is to restore the stiffness and the strength of the vertebra to the level of non-fractured vertebrae, the observed increases in compression force (+228%) and lateral bending (+489%), may pose a risk to adjacent segments due to altered load transference.

SUMMARY

The effect of cement augmentation on the structural response of failed vertebrae was investigated. Augmentation produced a significant increase in the structural competence of the failed vertebrae whilst, at the same time, causing a significant change in the overall structural response of the failed vertebrae.

ASSESSMENT OF POSTURAL RESPONSE TO AN INTERNAL PERTURBATION

Nicolas Termoz[1,2], François Prince[1] and Luc Martin[2]

[1]L.P.L., Centre de réadaptation Marie Enfant, Hôpital Sainte Justine, Montréal, Québec, Canada
[2]Laboratoire S.P.M., U.F.R.A.P.S., Université Joseph Fourier, Grenoble, France, nicolas.termoz@ujf-grenoble.fr

INTRODUCTION

Two variables are generally used for postural studies: the Center of Pressure (COP) and the Centre of Mass (COM). Brenière et al., (1987) highlighted the existence of a linear relation between the COP-COM signal and the linear acceleration of the COM during gait initiation. Later, Winter et al., (1998) used this relation to validate the inverted pendulum model, and Rietdyk et al., (1999) expanded it to balance perturbation tasks. On the basis of this research, the objective of this study is to use this relation to quantify the efficiency of the body to respond to a self-initiated postural perturbation and returns to quiet standing.

METHODS

Eight young subjects took part in this study. An anthropometric model composed of three segments (legs, trunk, arm) was defined. A kinematic analysis was coupled to a kinetic analysis to calculate the COP and the COM for the whole body. From an initial standing position, the subjects were asked to perform an upward and downward symmetrical arm swings at three different speeds (slow (Vs), natural (Vn) and fast (Vf)). Five trials of 30 s per conditions were carried out and analysed.

The relationship linking the two variables for the sagittal plane for example, is expressed as follow:

$$\ddot{x}_{COM} = -k(x_{COP} - x_{COM})$$

where $\ddot{x}_{COM}$ is the linear acceleration of the COM, k is an inertial constant and x_{COP} and x_{COM} are the COP and COM position to the ankle joint in this plane, respectively.

To quantify this relation, the coefficient of determination (R^2) was calculated between the "error signal" (COP-COM) and the horizontal acceleration of the COM on various ranges of time: before, during and after the movement. Moreover, a mobile R^2 was calculated and compared to the R^2 measured before the movement in order to determine the instant from which the disturbance does not affect the system anymore. The R^2 was examined in a one-way ANOVA to determine the effect of the period of analysis (before, during and after the movement).

RESULTS AND DISCUSSION

The average angular velocities are Vs=1.68 rad/s (sd=0.23), Vn=2.85rad/s (sd=0.64), Vf=6.71 rad/s (sd=0.42) for the slow, natural and fast movements, respectively. The relationship between COM and COP does not seem to be affected during the movements with a slow velocity (figure1).

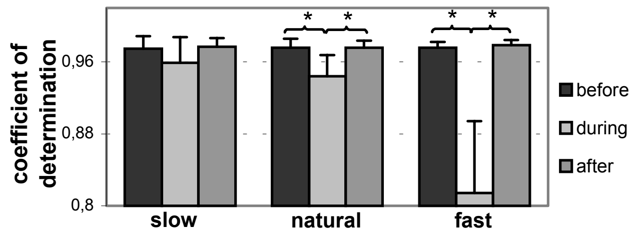

Figure1: R^2 before, during and after the movement,*significant difference at $P < 0.05$)

However, as the speed increases, the inter subject variability of the R^2 during the movement increases. This could be partly explained by the inter subject speed variability for the fast movements. Finally, in spite of a significative reduction of the R^2 for the natural and fast speed, probably explained by the intervention of another joint to counterbalance the perturbation, the relationship is always greater than .80.

Therefore, the COP remains the control variable and still maintains the COM within the base of support as suggested by the inverted pendulum model. Rietdyk et al., (1999) also found that the body controls its balance using this model for medial-lateral perturbations of the upper body during standing even though the body does not behave as a single pendulum.

The average time to recover steady state was variable from one subject to another and between the three conditions. For 80 % of the trials (slow, natural, fast) the time when the posture stops to be affected by the movement was determined to be slow=5.78±2.64 s; natural=5.46±2.24 s; fast=5.80±1.52 s. For 20% of the trials, the subjects did not return to a stable period within the data collection time. A study over a longer period should be made to evaluate this stabilization period.

SUMMARY

On the basis of the inverted pendulum model, the objective of this study was to quantify the efficiency of the body to respond to an internal perturbation such as an arm movement. Results show that the linear relation linking the COP and the COM signals to the acceleration of the COM is a valuable variable to study the control of posture following a self initiated perturbation.

BIBLIOGRAPHY

Brenière, Y., et al (1987) *J Mot Behav*, **19,** 62-76.
Rietdyk, S., et al (1999). *J Biomech*, **32,** 1149-58.
Winter, D.A., et al (1998). *J Neurophysiol*, **80,** 1211-21.

A NOVEL ALGORITHM FOR GENERATING A FORWARD DYNAMICS SOLUTION TO THE TRADITIONAL INVERSE DYNAMICS PROBLEM

Behzad Dariush
Honda R&D, Fundamental Research Labs, Mountain View, California, U.S.A. bdariush@hra.com

INTRODUCTION

In human motion analysis, the recursive "ground up" inverse dynamics analysis is a commonly used technique to estimate joint moments. The method assumes knowledge of the kinematics and ground reaction forces to recursively determine the applied moments at the joints. In an alternative approach, forward dynamics solutions using linear optimal control (Runge et al., 1995), and nonlinear optimization (Chao and Rim, 1973) have also been used for estimating joint moments. Unlike inverse dynamics analysis, optimization based methods do not require estimation of accelerations by numerically differentiating kinematic data: a notoriously difficult and ill-posed problem. However, widespread application of optimization and optimal control solutions are limited because the methods are computationally expensive, are not guaranteed to converge, and are in general too complex to implement. In this abstract, a novel recursive algorithm is developed that represents a robust 'ground up' forward dynamics solution to the inverse dynamics problem. The solution is simple to implement, fast (real time), stable, guaranteed to converge, and does not require accelerations.

METHODS

The underlying theory of the recursive algorithm is derived from concepts in tracking control and feedback linearization. The objective of trajectory tracking control is to compute a set of forces and moments that when applied to a forward simulation would result in a trajectory sequence that track (or reproduce) the measured kinematic data. The tracking proposed here is based on a feedback linearization procedure implemented at each isolated body segment of a multi-body system (see Figure 1). The required inputs to initiate the recursion equations at joint *i* include the measured kinematics (q_{i_m}), estimates of their velocities $(\hat{\dot{q}}_{i_m})$, and the joint torque and joint reaction force vector (concatenated in vector U_i). The estimated accelerations $(\hat{\ddot{q}}_{i_m})$ may also be used in noise free applications, but are not required. The output is the estimated reaction force and torque vector at joint *i+1* (U_{i+1}), which is used as the input for the next iteration. The matrices K_p and K_v represent the proportional and derivative feedback gains, respectively. They are constant, diagonal matrices whose values are selected to yield a critically damped response (Craig, 1989). The simulated states are described by $(q_i, \dot{q}_i)$ and the error between the simulated and measured kinematics is represented by the vector $e_i = q_{i_m} - q_i$. If the measurements are noise free, the parameter *a* is set to 1. In dealing with real measurements, it is suggested to exclude accelerations $(\hat{\ddot{q}}_{i_m})$ by setting the parameter *a* to zero. In both cases, the tracking error can be forced to approach zero by increasing the feedback gains.

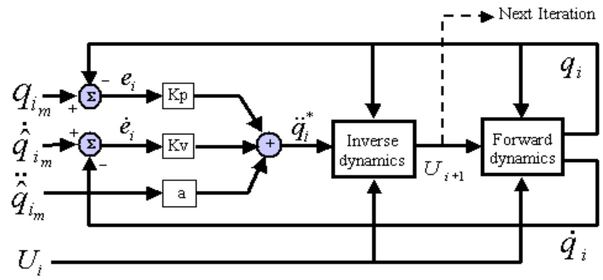

Figure 1: Recursive, feedback linearization block diagram.

RESULTS AND DISCUSSION

Extensive simulations were conducted with real motion data as well as with synthetically generated data injected with random noise. Simulations of the tracking performance for a synthetically generated rhythmic motion injected with noise is shown in Figure 2. For this motion, simulations for different values of K_p were carried out and the absolute mean tracking error was plotted for the case *a=0* and *a=1*. The simulation results of this motion, and other motions, support the theory that the tracking error using the feedback structure in Figure 1 can be forced to approach zero by increasing K_p.

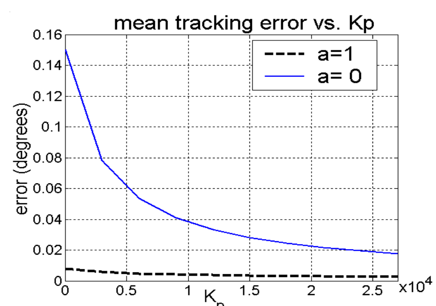

Figure 2: Tracking error is reduced by increasing Kp.

SUMMARY

A feedback linearization approach has been presented to recursively estimate the joint forces and joint moments from kinematic and ground reaction measurements. The proposed method does not require accelerations, is predictive, and represents a forward dynamics solution to the traditional 'ground up' inverse dynamics problem.

REFERENCES

Runge, C. et al., (1995). *IEEE Trans BME*,**42,12**:1158-1164.
Craig, J., (1989). *Introduction to Robotics,* 2nd ed.
Chao, E.Y., Rim, K. (1973). *J. Biomech.* , **6**:497-510.

BUFFY COAT CONCENTRATE (AGF™) WITH ALLOGRAFT IMPROVES IMPLANT FIXATION

Joan E Bechtold[1], Thomas B Jensen[1,2], Pascal Swider[3], Olivier Mouzin[1,3], Kjeld Søballe[2]
[1]Orthopaedic Biomechanics Laboratory, Minneapolis Medical Research Foundation, MN, [2]Aarhus University, Dept. of Orthopaedic Surgery, Denmark, [3]CHU Purpan, Toulouse, France. Email: becht002@tc.umn.edu

INTRODUCTION: Platelet rich plasma increases incorporation of bone *autograft (* Marx, 1998). AGF™ is a commercially available autologous platelet and white cell ultra-concentrate. We hypothesized that AGF™ mixed with morzelized bone *allograft* would increase bone formation and implant fixation.

METHODS: Eight dogs (16 implants) were followed for 4 weeks, with all animal handling and AGF™ processing approved by Institutional IACUC.
Implants: Plasma sprayed cylindrical titanium implants (6x10mm) were inserted extraarticularly in each proximal tibia, surrounded by a 2 mm gap (Jensen et al., 2002b). One gap was packed with fresh frozen bone allograft alone, and the contralateral gap was packed with allograft+AGF™.
AGF™ preparation: Under anaesthesia, immediately prior to surgery, 450 ml of blood was drawn. A cell seperator divided blood into platelet poor plasma, platelet rich buffy coat, and erythrocytes. The buffy coat (~60 ml) was isolated and further concentrated (UltraConcentrator™ Interpore-Cross) to 20 ml.
Statistics: Mean±SD are shown. With paired t-test, p-values < 0.05 (two-tailed) were considered significant.
Mechanical test: Under axial pushout, shear strength, apparent shear stiffness, and energy absorption were determined. *Histomorphometry:* Volume fractions of woven bone, allograft and non-mineralized tissue were determined using point grids: 0-900 µm (Zone 1) and 1000-1800 µm (Zone 2) from implant surface. Bone, fibrous and other tissue in contact with implant surface was estimated as % of total implant surface.

RESULTS: Mean platelet count increased from $169 \pm 58 * 10^9$/l to $1212 \pm 466 * 10^9$/l (AGF). Adding AGF to graft increased mechanical parameters (Table I; reported previously (Jensen et al., 2002a) and bone ongrowth, and decreased fibrous membrane in contact with implant surface (Table II) ($p<0.05$). Volume fractions of bone & graft in gap were unchanged with AGF (Table III): all measurements were blinded.

Table I: Mechanical parameters (mean (SD))

Group	**Shear strength (MPa)**	**Energy abs. (J/m^2)**	**Stiffness (MPa/ mm)**
Graft	1.24 (0.83)	322 (252)	5.27 (3.66)
Graft+AGF	1.88 (1.18)*	453 (265)	7.32 (5.13)

*: p<0.05 compared to allograft without AGF

Table II Contact (mean (SD)): in % of total surface

Group	**Bone**	**Fibrous**	**Other tissue**
Graft	7 (5)	25 (35)	68 (37)
Graft+AGF	11 (7)*	17 (29)*	72 (25)

*: p<0.05 compared to allograft without AGF

Table III Volume fractions of woven bone, bone graft and non-mineralised tissue, % (mean (SD))

	Woven bone		Graft		Non-mineral.	
Zone	**1**	**2**	**1**	**2**	**1**	**2**
Graft	20(7)	19(5)	6(4)	3(2)	74(10)	78(5)
Graft+AGF	20 (4)	18 (5)	5 (2)	3 (1)	75 (4)	79 (5)

No sig. diff. between AGF treated vs. non treated.

DISCUSSION: The increase seen with AGF in strength, stiffness and energy (52%, 39%, 41%, respectively) was reflected by a similar increase in the amount of bone/implant contact (57%). In contrast, there was no significant increase in bone in Zones 1 (0%) and 2 (-5%) with the addition of AGF to graft (Table III). Hence, the increase in mechanical parameters with AGF can be attributed to the increased bone found in direct implant contact. This agrees with companion theoretical mechanical studies demonstrating that the highest shear stresses are found at the implant surface, and previous experimental studies showing a similar relationship between mechanical parameters and bone in the region immediately at the implant surface (Mouzin, 2001).

SUMMARY: These results suggest that a buffy coat concentrate mixed with bone allograft may enhance early fixation and bony incorporation of implants, and suggest that this improvement is achieved by increased bone growth on the implant surface. Since bone grafting is often required in the revision of failed joint replacements (which have an inherently poor healing prognosis), application of bone stimulating agents such as AGF to the graft is of great clinical interest.

REFERENCES: Jensen T et al ., 48th ORS: 29(1): 2002a; Jensen T et al, Acta Orthop Scand.2002b (in press); Marx, RE et al. Oral Surg. 85:638-646, 1998; Mouzin O, et al., 47th ORS: 28(2):1034, 2001; Søballe K et al.,Clin. Orthop.274: 282-293, 1992.

ACKNOWLEDGEMENTS: NIH (AR4205), FRM (France, support for O. Mouzin), Biomet (plasma spray Ti implants), Interpore-Cross (AGF™ supplies).

OSCILLATORY COMPRESSION OF ARTICULAR CARTILAGE: RELEASE OF CELL SIGNALING MOLECULES AND THE EFFECT OF CONDITIONED MEDIUM ON CHONDROCYTES IN AGAROSE GEL CULTURE

Christopher J. Hunter[1] and Marc E. Levenston[2]
Georgia Institute of Technology, Atlanta, Georgia, USA
[1]Wallace H. Coulter Department of Biomedical Engineering
[2]George W. Woodruff School of Mechanical Engineering, marc.levenston@me.gatech.edu

INTRODUCTION

We previously reported the response to mechanical compression of tissue engineered cartilage in an *in vitro* repair model. Chondrocyte-seeded agarose gels were cast inside annuli of articular cartilage and cultured under mechanical compression. Both protein and proteoglycan synthesis rates were inhibited by static compression and stimulated by oscillatory compression (Fig. 1; Hunter and Levenston, 2002). We proposed that this response was due to local mechanical signals induced by compression. An alternate explanation, however, is that the repair tissue was indirectly stimulated by factors released from the tissue in response to compression. To address this hypothesis, the current study examined the influence of compression on release of TGF-β, IGF-1 and nitric oxide by articular cartilage explants and the effect of conditioned media on matrix synthesis in engineered cartilage.

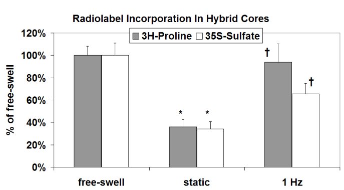

Figure 1. Radiolabel incorporation by agarose gels inside cartilage annuli. Stars: $p<0.05$ vs. free-swell. Daggers: $p<0.05$ vs. static (mean±s.e.m., n=8).

METHODS

Cartilage discs were isolated from calf femoral condyles and pre-cultured in serum-free medium for two days. Discs were then assigned to one of three compression conditions (n=5): free-swelling, static (10% of cut thickness), and oscillatory (10±4%) at 1 Hz. After 24 hours, the culture media were analyzed for TGF-β and IGF-1 via ELISA and nitrite via the Greiss assay. Chondrocytes isolated via collagenase digestion from the remaining cartilage were cast into 2% agarose gels at 10^7 cells/ml and pre-cultured in serum-free medium for two days. Gels were then cultured in 500 µl of conditioned medium from each compression condition mixed with 500 µl of radiolabeled medium (10 µCi/ml ^{3}H-proline, 5 µCi/ml ^{35}S-sulfate). After 24 hours, the gels were assayed for DNA, ^{3}H, and ^{35}S content. Data were analyzed with GLM (significance at $p<0.05$) and Tukey's test for post-hoc analyses.

RESULTS

Static compression of cartilage explants significantly decreased TGF-β release and increased nitrite in the medium, but did not significantly affect IGF-1 release. Oscillatory compression did not significantly change either TGF-β or IGF-1 release, but did increase nitrite content (Fig. 2). Levels of all three factors were higher than those in unconditioned medium containing 10% FBS. Conditioned media had no detectable effects on matrix synthesis rates by chondrocytes in free agarose gels (Fig. 3).

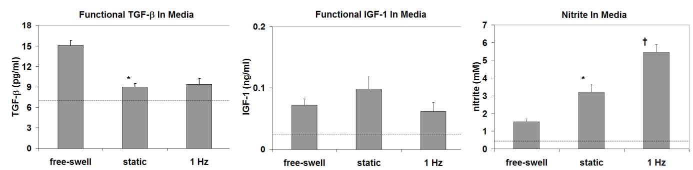

Figure 2. Analysis of conditioned culture media. Dashed lines show level in unconditioned 10% FBS medium. Stars: $p<0.05$ vs. free-swell. Daggers: $p<0.05$ vs. static (mean±s.e.m., n=8).

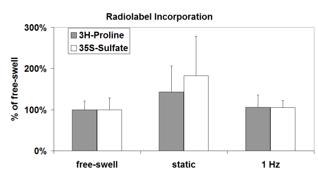

Figure 3. Radiolabel incorporation by uncompressed agarose gels treated with conditioned media (mean±s.e.m., n=5).

DISCUSSION

We previously demonstrated that mechanical compression significantly influenced matrix synthesis by engineered cartilage in a defect repair model. Compression induced changes in local mechanical stimuli, but may also have induced release of soluble biochemical factors. In the present study, we found that oscillatory compression of cartilage explants did not produce an increase in TGF-β or IGF-1 release, and that conditioned media from compressed cartilage did not stimulate synthesis by chondrocytes in agarose gels. Therefore we conclude that stimulation of matrix synthesis in the defect repair model was largely due to mechanical stimuli. These results suggest that indirect stimulation of repair tissue through soluble factors released by native tissue is minimal in comparison to stimulation by local biomechanical phenomena.

REFERENCES

Hunter C.J., Levenston M.E. (2002) *Trans ORS*, 250.

ACKNOWLEDGEMENTS

This work was supported by the ERC Program of the NSF under Award Number EEC-9731643, by the NIH under the Cellular Engineering Training Program, grant number GM08433, and by a grant from the Medtronic Foundation.

SHRINKAGE OF VACUUM MIXED CEMENT CAUSES INTERFACE GAPS AND STRESS CONCENTRATIONS IN CEMENT MANTLES SURROUNDING FEMORAL STEMS

Amos Race, Mark Miller, David Ayers and Kenneth Mann

Musculoskeletal Science Research Center, Upstate Medical University, Syracuse, New York, USA
racea@mail.upstate.edu

INTRODUCTION

Polymerization shrinkage of bone-cement has been known of for some time but has never been quantified in a stem/cement/femur construct. Gaps around femoral stems have been observed in transverse sections of stem/cement/femur constructs (Race, 2001). A greater proportion of stem/cement (s/c) interface gaps were found around grit blasted sections of stems than satin finished sections. It was not clear whether the gaps were due to air inclusion or cement shrinkage. If s/c gap formation were a shrinkage artifact then the mantles with few s/c interface gaps must manifest shrinkage elsewhere, at the c/b interface or voids. 'Mould-gaps' at a c/b interface have been described previously (Miller, 1978) but not quantified. The present study analyzed the cross-sectional area of gaps at both interfaces. We *hypothesized* 1) Total gap area was the same for all transverse sections. 2) Satin sections had greater c/b gap areas than grit sections.

METHODS

Transverse sections of 10 Charnley stem/cement/femur constructs from our previous study were processed to highlight gap areas. 5 of the stems had the standard satin finish (Ra 0.75um) and 5 were grit-blasted over their proximal 40mm (Ra 5.3um). Large gaps were filled with black modeling clay and then the sections were coated with matt black spray paint. Sections were then polished using 280 grit emery paper to remove the paint from the surface. This process left all interface gaps and voids filled with black paint, which could be conveniently digitally imaged. Gaps were visually identified and measured using Image-Pro. Gap areas for each transverse section were normalized by the area of cement in that section.

RESULTS AND DISCUSSION

There was no difference in total gap area between surface finishes (Table 1), which supports our first hypothesis. S/c gap areas were significantly greater around grit blasted sections, which was consistent with our previous finding. C/b gap areas were significantly greater around satin finished sections, which supports our second hypothesis.

Table 1: Mean gap fraction for transverse sections grouped by the local surface finish of the stem (% of cement area ± sd)

	TOTAL	S/C	C/B	Voids
Satin	3.1 ± 1.4	0.1 ± 0.4	2.3 ± 1.3	0.6 ± 1.0
Grit	3.4 ± 1.5	1.9 ± 1.7	1.0 ± 0.9	0.5 ± 0.9
	N/S	*p<0.0001*	*p=0.0001*	*N/S*

Identifying gaps at the s/c interface was straightforward, the c/b interface gaps were subjective but there were generally obvious 'mold gaps' between cement and bone (Fig. 1). The dramatic shift in gap location with a change in surface finish is illustrated in Figure 2. The total gap areas were less than the 4.8% shrinkage that is theoretically expected, it is likely that narrow but extensive c/b gaps were missed.

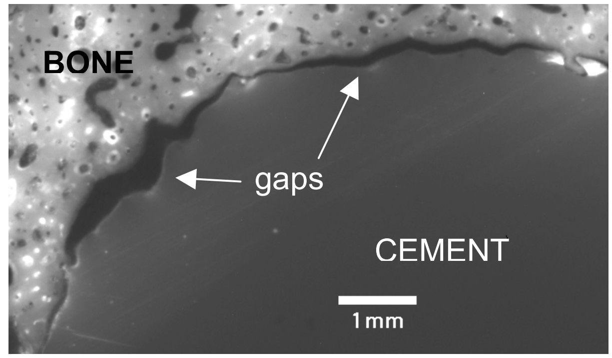

Figure 1: Transverse section of a stem/cement/femur construct showing detail of 'mould-gap' at the cement/bone interface.

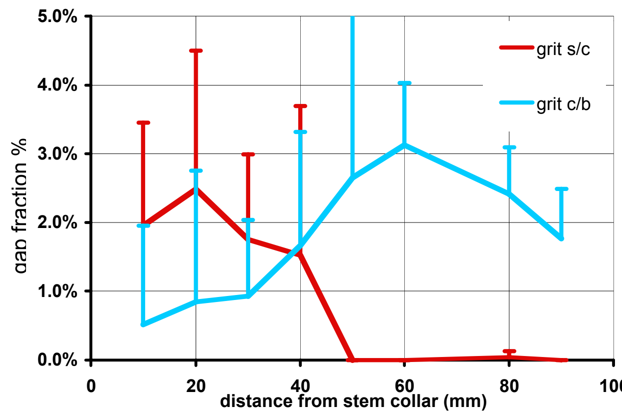

Figure 2: Graph of s/c and c/b gaps as a function of axial position for the 'grit' stems. Note that the grit blasting ended at 40mm.

It has been generally assumed that cement shrinkage manifests in a very narrow gap around the whole of the c/b interface. This study has demonstrated that cement shrinkage tends to localize into larger interface gaps. These large gaps must lead to stress concentrations, be they at the s/c or c/b interfaces. C/b gaps are potentially benign as they can fill with bone. However, it is also possible that cement will fail at the points of contact and generate debris which will hinder bone formation.

Cement shrinkage has been overlooked in recent years but is still a cause for concern.

REFERENCES

Race, A. et al (2001) *Trans ORS* **26**, 1033
Miller, J. et al (1978) *The Hip: Proc. Hip Soc.* **6**, 64-86

ACKNOWLEDGEMENTS

Support from NIH AR42017 and NIH AR47927 is gratefully acknowledged.

MECHANICAL AND METABOLIC REQUIREMENTS OF LATERAL STABILIZATION IN HUMAN WALKING

J. Maxwell Donelan [1], David W. Shipman [2] and Arthur D. Kuo [3]
[1] Centre for Neuroscience, Dept. of Physiology, Univ. of Alberta, Edmonton, mdonlean@ualberta.ca;
[2] Dept. of Integrative Biology, Univ. of California, Berkeley; [3] Dept. of Mechanical Engineering, Univ. of Michigan, Ann Arbor

INTRODUCTION

Human walking is passively unstable in the lateral direction (Kuo, 1999). Humans appear to actively stabilize lateral motion using medio-lateral foot placement (Bauby & Kuo, 1998). While this stabilization mechanism is effective, it is not without cost—precise control of the swing leg is required and variability in foot placement increases mechanical work (Donelan et al., 2001). Our purpose was to study the mechanical and metabolic requirements of active lateral stabilization in human walking. We hypothesized that external lateral stabilization would reduce the amount of active stabilization required to walk, resulting in less variability of medio-lateral foot placement and a lower metabolic cost.

METHODS

Ten healthy adults (6 male, 4 female) participated in the study after providing informed consent. They walked on a treadmill at 1.25 m/s, both with and without external stabilization (Fig. 1). To control for the effects of average step width, we instructed subjects to walk on a single line marked on the treadmill belt. We chose to enforce zero step width because our device stabilized the body about a trajectory with zero lateral movement. Subjects walked with arms crossed to prevent differences in use of arms to stabilize balance. Subjects practiced the experimental protocol prior to data collection.

The external lateral stabilizer consisted of lightweight elastic cords attached to a padded waist belt pulling in both lateral directions. The relatively long (8 m) cords insured that any non-lateral forces exerted by the apparatus were negligible. The device exhibited an effective spring constant of 1700 N/m and negligible damping (14 N-s/m).

Figure 1.

We developed a mathematical model, based on passive dynamic walking, to characterize the effect of the external stabilizer. The model predicted that the cords were sufficient to passively stabilize the body laterally, suggesting that the subject need not actively adjust medio-lateral foot placement with each step, as is normally necessary. The model therefore predicts lowered medio-lateral foot placement variability, as well as lowered metabolic cost due to the decreased active foot placement.

We measured center of pressure under the feet using a force treadmill (Kram, et al., 1998). We analyzed the first 200 steps after the subject had been walking for 150s. Step width for each step was defined as the lateral distance between consecutive centers of pressure, averaged over the single stance phase. We calculated variability in step width and length as a function of external stabilization. We also measured net metabolic power using standard methods of indirect calorimetry (Donelan et al., 2001).

RESULTS AND DISCUSSION

When stabilized, variability in step width decreased by 35% while metabolic cost decreased by 6% when compared to unstabilized walking (p= 0.0003 and 0.025, respectively). For comparison, step length variability decreased by a smaller amount (14%, p=0.01) than step width variability. Mathematical models predict this slight coupling between lateral and fore-aft dynamics. Average step width and length were not affected by stabilization (p= 0.80 and 0.69, respectively).

These results support our hypotheses that (a) lateral foot placement is used to actively stabilize walking, (b) external lateral stabilization reduces the need for this active stabilization, and (c) the reduced active stabilization results in slightly lower metabolic demand. Stability and energy consumption are concerns for groups such as amputees and the elderly. Mathematical modeling and empirical testing may lend insight into possible interventions for these groups.

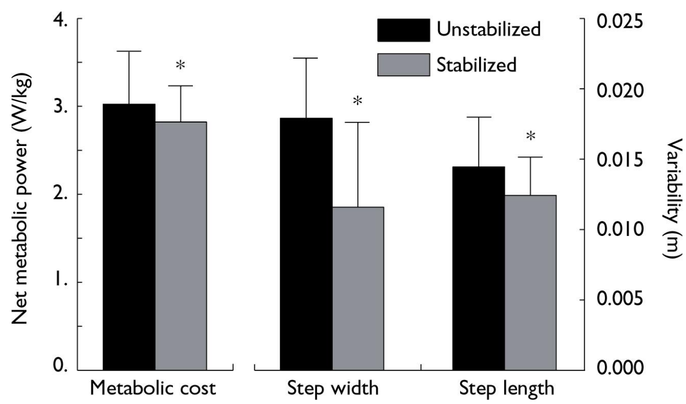

Figure 2. a) Metabolic cost, step width variability and step length variability decreased with stabilization.

REFERENCES

Bauby CE & Kuo AD (2000) *J Biomech*, **33**, 1433-1440.

Donelan JM, Kram R & Kuo AD (2001) *Proc Roy Soc Lond B* **268**: 1985-1992.

Kram R, Griffin TM, Donelan JM & Chang YH (1998) *J Appl Physiol* **85**: 764-769.

Kuo, AD (1999) *Int J Robot Res*, **18**, 917-930.

ACKNOWLEDGEMENTS

This research was supported in part by an NSERC fellowship to J. M. Donelan, NIH grant AR4468801 to R. Kram, and NIH grant DC0231201A1 to A.D. Kuo

KINEMATICS OF 90° RUNNING TURNS IN WILD MICE

Rebecca Walter
Biology Department, University of Utah, Salt Lake City, Utah, USA
walter@biology.utah.edu

INTRODUCTION

Turning is an important component of locomotion on the variable terrain which most terrestrial animals inhabit and a deciding factor in many predator prey interactions. Despite this, the kinematics and mechanics of quadrupedal turns are not well understood. This study describes the kinematics of 90° running turns in wild mice, and compares them to running turns in humans and cockroaches.

METHODS

Six adult wild mice were videotaped from below at 250 Hz as they performed ninety-degree running turns. Five markings placed along the sagittal axis were digitized to allow observation of lateral bending and body rotation throughout the turn. Ground contact periods of the fore and hindlimbs were also noted for each frame. Similar control runs were done along a straight trackway for comparison of maximum velocity and other gait parameters.

RESULTS AND DISCUSSION

During turning, mice increased their ground contact time, but did not change their stride frequency relative to straight running at maximum speed. Compared with humans running along curved trajectories (Greene, 1985), mice maintained relatively higher velocities at proportionately smaller radii (Figure 1a). One possible explanation is that being quadrupedal rather than bipedal may be advantageous for turning. Chang and colleagues (2001) found that humans are limited in their abilities to apply ground forces with the inside leg during turns. In contrast, a bounding quadruped would be simultaneously be applying forces with both inside and outside limbs and thus be less hindered by such a constraint. A second explanation for this difference lies in the more crouched limb posture of mice, which increases the mechanical advantage in horizontal relative to vertical ground force production (Figure 1b).

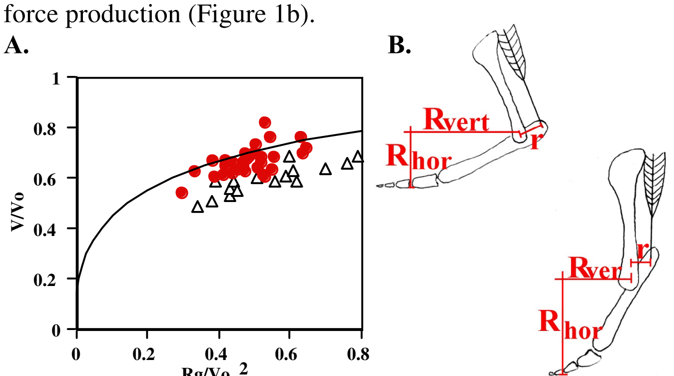

Figure 1. a) Curve shows the predicted relation between maximum speed over a curve divided by maximum speed along a straightaway (V/V_o) and dimentionless curve radius (Rg/V_o^2) (Greene, 1985). Filled circles and open triangles show mouse and human data respectively superimposed onto the curve. **b)** Comparison of the effective mechanical advantage for horizontal versus vertical force production in crouched and upright postures. Effective mechanical advantage equals r/R (Biewener, 1989) and is greater for a crouched posture in horizontal force production.

Postcranial body rotation did not occur in one continuous motion, but rather in bouts of 15-53°. These bouts were synchronized with the stride cycle, with the majority of rotation occurring during the second half of forelimb support and the first half of hindlimb support. In this phase of the stride cycle, the postcranial bodies of the mice were sagittally flexed and rotational inertia was 68% of that during maximal extension. By synchronizing body rotation with the stride cycle, mice can achieve a given angular acceleration with much lower applied torque. Head and neck rotation was smoother and less phasic than that of trunk. This may aid in visual and vestibular orientation.

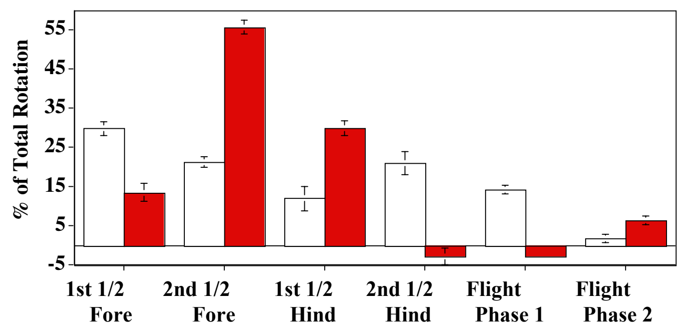

Figure 2: Percent of total head/neck (open) and body (filled) rotation occurring in each phase of the stride cycle.

Unlike in cockroaches (Jindrich and Full, 1999) postcranial body rotation preceded deflection in heading. The more sprawled limb posture of cockroaches may facilitate application of lateral ground forces, whereas the parasagittal limb posture of mice may favor production of fore-aft ground forces.

REFERENCES

Biewener, A.A. (1989). *Science*, **245**, 45-48.
Chang *et al.* (2001). Unpublished abstract.
Greene, P.R. (1985). *J. Biomech. Eng.,* **107**, 96-103.
Jindrich, D.L., Full, R.J. (1999). *J. exp. Biol.,* **202**, 1603-1623.

DIRECT AUGMENTATION RESTORES THE STRUCTURAL RESPONSE OF FAILED METASTATIC DEFECT VERTEBRAE

Ron N Alaklay[1], Dietrich von Stechow[1], Torres Katherine[2], SerhanHassan[2]
[1]Orthopedic Biomechanics laboratory, Beth Israel Deaconess Medical Center, Boston, MA.
[2]DePuy Acromed, Raynham, MA

INTRODUCTION

The spine is the most common site for skeletal metastasis with approximately 30% of bone metastasis related vertebral fractures requiring surgical intervention due to progressive spinal deformity and neurological compromise. The efficacy of Polymethylmethacrylate cement, advocated for the augmentation of vertebral bodies, in restoring the structural competence of vertebrae having a critical defect via a minimally invasive direct approach, is currently unknown.

METHODS

Twenty thoracic and lumbar vertebrae from three spines, aged 65-78 years, were radiographed to estimate the body posterior and anterior height and their Bone Mineral Density assessed by DXA (Hologic 2000+, Hologic, MA). A high-speed bur was used to create a critical defect involving 50% of the vertebral body and the vertebrae re-radiographed to verify the extent of the defect. A custom testing jig was employed to test the vertebrae to failure using a hydraulic test system (1331, Instron, Canton, MA) under combined compression-flexion at a rate of 5mm/min. Failure was defined as 50% reduction in the vertebra anterior height or a reduction of 10% in maximum load. A 6DOF load cell (MC5, AMTI, MA) was employed to measure the resulted forces and moments and displacement to failure, measured via the material testing system, with the data acquired using LabView (National Instruments, TX) at the rate of 10Hz. The failed vertebrae were allowed to recover for 30 min, the vertebral body heights re-measured and the vertebrae re-tested. A direct approach through the defect in the vertebral body cortical shell was employed to augment the failed vertebrae using 4.0-7.0cc of PMMA (Vertebroplastic, Codman & Shurtleff, Rynham, MA). The augmented vertebra was allowed to rest for two hours, the height of the vertebral body re-measured and the vertebra re-tested to failure. Repeated measure ANOVA was used to test for differences in maximal failure load and stiffness estimated from the linear portion of the load–displacement curve, for each of the forces and moments (JMP, SAS, NC).

RESULTS AND DISCUSSION

For L1 levels of the specimen the mean bone mineral density was measured at ($0.32\pm0.10 g/cm^2$). All of the vertebrae tested exhibited an anterior-flexion compressive failure preceded by buckling of the cortical shell. Compared to intact vertebrae, the failed vertebrae showed a highly significant reduction in ultimate compressive load, 1409±603N versus 2246±897N, ($P<0.001$), and a significant reduction in compressive stiffness,-250 ±130$Nm.mm^{-1}$ compared to -382±194$Nm.mm^{-1}$ ($P<0.05$). Similarly flexion strength and stiffness (58±90Nm and 9±10$Nm.mm^{-1}$), were significantly reduced, 62±26Nm and –11±5$Nm.mm^{-1}$, compared to the intact vertebrae $P>0.05$. Augmentation significantly increased vertebral ultimate compressive load and stiffness to 2606±813N, $P<0.01$, and -340±203$Nm.mm^{-1}$ respectively. Similarly, flexion strength, 66±26Nm, and stiffness, 10±4$Nm.mm^{-1}$, showed a significant increase compared to that of the failed vertebrae. However, compared to the intact vertebrae, these increases were not significant. The remaining loads and moments remained relatively constant throughout the test.

This study investigated the ability of PMMA cement augmentation to restore the structural competence of failed vertebrae having a simulated critical metastatic defect under anterior flexion-compression load. The model was successful in producing both clinically relevant defects and a repeatable combined flexion-compression fracture pattern. Compared to the intact vertebrae, the failed vertebrae exhibited a highly significant reduction in structural load carrying ability, particularly in the plane of loading. The load displacement curves, although revealing vertebral loads to exist mainly in the plane of loading, showed out of plane loads to develop on the vertebral body during the failure process. These responses combined with the complex pattern of vertebral body collapse may suggest the response to be dependent on the extent of the defect. Vertebral augmentation using PMMA was highly effective in restoring the overall mechanical competence of the vertebrae with the PMMA, in effect, masking the load response of the vertebrae. This procedure thus holds promise as an alternative for full resection of the vertebral body. Further research is needed to quantify the possible effect of the significant changes in vertebral body structural response on adjacent vertebrae and to develop predictive methods to assess its applicability.

SUMMARY

The effect of a critical (50%) metastatic defect and consequent cement augmentation on the structural response of failed vertebrae was investigated. The metastatic defect vertebrae showed a both a significant reduction in structural competence and a complex load-deformation response under combined compression-flexion loads. Augmentation was highly effective in restoring the structural competence of the failed metastatic vertebrae.

INFLUENCE OF LOADING AND LOCAL DENSITY ON BONE FRACTURE TOUGHNESS PARAMETERS

Christina L. Beardsley[1] , Helen G. Fuller[1], Yasser M. Dahab[1], and Thomas D. Brown[2,1]
Departments of [1]Biomedical Engineering and [2]Orthopaedic Surgery, University of Iowa, Iowa City, IA, USA
email: tom-brown@uiowa.edu, web: http://poppy.obrl.uiowa.edu/

INTRODUCTION

Fracture mechanics has been applied to scrutinize bone failure processes, but primarily for quasi-static loading. Dynamic fracture behavior of bone is less well understood, especially since fracture toughness (K_c) is very sensitive to loading rate. However, another fracture toughness parameter, the critical strain energy release rate (G_c), is reportedly relatively rate-independent in other viscoelastic materials (Williams, 2001). We hypothesized that, in cortical bone, dynamic G_c is less than one order of magnitude higher than quasi-static G_c, and that, furthermore, the surface produced per joule absorbed in impact tests would correlate strongly with quasi-static G_c. For brittle solids such as bone, fracture toughness parameters depend on relative material density. Various researchers have invoked power law relationships to regress fracture toughness from physical density (Gibson, 1988); we incorporated these as well.

METHODS

Segments measuring 80-mm were harvested from the mid-diaphyses of fresh frozen bovine tibiae (Fig. 1). These were subjected to a drop tower test with an impact velocity of 5.5 m/s. Helical CT data were collected from both intact specimens and fracture fragments. Using digital image analysis, the area of *de novo* fracture surface was extracted from each fractured specimen for G_c computation. The number of square millimeters of surface realized per absorbed joule was computed, and then multiplied by the normalized average Hounsfield density (H*) of the fractured specimen raised to the 1.5 power.

The H* was measured in the proximal-most 5mm of the intact segments. With this data, the dependence of the quasi-static G_c on Hounsfield density was explored. Bone in the region immediately superior to the proximal end of the impact segment was milled into three thin, ring-like (Fig. 1) specimens (one 4.5 ID/20.0 mm OD, two 1.5 ID/5.0 mm OD). Quasi-static fracture mechanics testing was conducted with a Bionix 858 servohydraulic load frame. Following pre-cycling to determine tangential and longitudinal moduli, rings were then loaded to failure in diametral compression at a rate of 0.02 cm/min. G_c was computed from the loading curves using an established protocol (Beardsley, 2002).

RESULTS AND DISCUSSION

Pre-fracture Hounsfield density, raised to the 1.5 power as suggested by Gibson (1988), was directly proportional to quasi-static G_c ($R^2 > 0.99$) (Fig. 2).

The average G_c computed from the impact test was 4406 N/m, as compared to 939.7 N/m for the quasi-static test. The pairing between quasi-static and (Hounsfield-normalized) dynamic tests showed reasonable correlation (r=0.57). In drop tower testing, fragment free surface energy resulting from an impaction event correlates strongly with absorbed kinetic energy, but demonstrates appreciable variability. The present data demonstrate that a substantial fraction of that variability is attributable to the variability of bone fracture toughness, which can be precisely accounted for in terms of Hounsfield number.

Figure 1: Specimen geometry used for (l) impact and (r) quasi-static fracture toughness testing (not to scale).

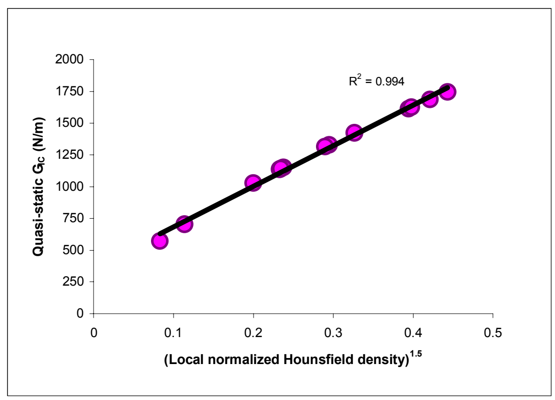

Figure 2. G_C was closely linked to a power of H* (n=12).

REFERENCES: Beardsley, C.L. et al (2002). *Trans. of 48th ORS*, 552; Gibson, L.J., Ashby, M.F. (1988). *Cellular Solids: Structure and Properties*. Pergamon Press Inc.; Williams, J.G. et al (2001). *Int J Fracture*, **107**, 259-278.

ACKNOWLEDGEMENTS: Financial support provided by EBI Inc., NIH grant #AR46601, the Arthritis Foundation, and an Iowa Fellowship. Technical consultation provided by Drs. M. James Rudert, Anneliese Heiner, and Alexander Staroselsky

TISSUE STRESS AND MODULUS CHANGES FOLLOWING VERTEBROPLASTY

Victor Kosmopoulos[1], Tony S. Keller[1], and Michael A.K. Liebschner[2]

[1]Musculoskeletal Research Laboratory, The University of Vermont, Burlington, Vermont, United States
[2]Computational Biomechanics Laboratory, Rice University, Houston, Texas, United States
keller@emba.uvm.edu

INTRODUCTION

Vertebral damage occurs when the loads applied exceed the vertebral structural capacity (force at failure). Characterization of trabecular bone tissue stresses and strains is important in understanding basic skeletal mechanics, fracture risk, damage, and fracture repair. More explicit mechanical stress-strain behavior is obtained using numerical techniques such as the finite element analysis (FEA) method. The objective of this study was to develop a structural FEA model that could be used to simulate various levels of structural damage, and show the effects of various polymethylmethacrylate (PMMA) volumes on the apparent stiffness of vertebral bodies during repair (vetrebroplasty).

METHODS

A two-dimensional (2D) osteopenic FEA model was developed from sagittal μCT scan images (83 μm/element resolution) of a T10 vertebral segment. This model was coupled with a modulus reduction algorithm derived from perfect plasticity theory [Betten, 1989]. Trabecular bone, intervertebral disc, and bone marrow tissues, are assumed to be isotropic, linear elastic materials with elastic modulus values of 10 GPa, 2.16 MPa, and 10 kPa, respectively. A Poisson's value of 0.3 is assumed and the 299 x 235 (70,265 elements) model having 4-node isoparametric elements is loaded using a uniform compressive load ranging from 50-500 N in 50 N increments. After each increment of load, the element stresses and strains were used to determine the modulus reduction (if any) for each bone element. This model was used to simulate vertebroplasty studying the effects of 6 cement (E= 2.16 GPa) volumes on apparent stiffness, and tissue stress intensity for 2 vertebral damage levels (18.7% and 91% reduction in apparent modulus).

RESULTS AND DISCUSSION

The model resulted in a non-linear stress-strain curve with a yield stress of 4.5 MPa and yield strain of 0.41%. The yield stress corresponded closely with experimental estimates of the intact strength of human lumbar vertebra [Hansson, 1977]. Trabecular bone tissue stress intensity (element stress/apparent stress) ranged from –5 to 26 for the undamaged vertebral segment. Replacement of all the bone marrow elements with PMMA cement elements ($A_f = 0.35$) resulted in an increase of apparent modulus for both damage levels (18.7% and 91%) that were well beyond the undamaged vertebral body apparent modulus (Figure 1). The 18.7% damage model reached the undamaged modulus using only a 0.25 A_f of PMMA whereas the 91% damage model required the vertebral body to be completely filled with cement (0.35 A_f).

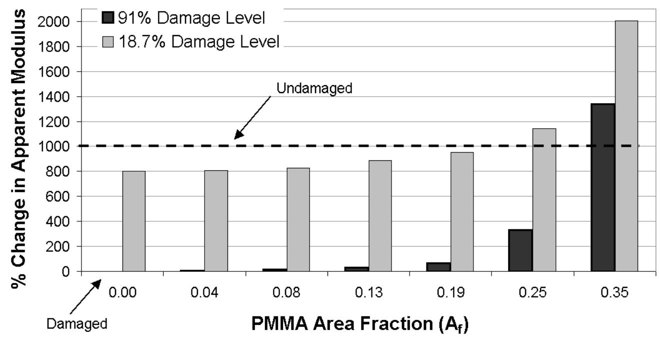

Figure 1. Change in apparent modulus with increasing PMMA following vertebroplasty for 2 damage models.

A reduction in highly stressed elements (stress intensity > 3) was found for both damage models over the range of cement A_f examined (Figure 2). The PMMA filled 18.7% damage model resulted in only 1% of the total elements having a stress intensity greater than 3 compared to a 2.7% of total elements for the 91% PMMA filled damage model.

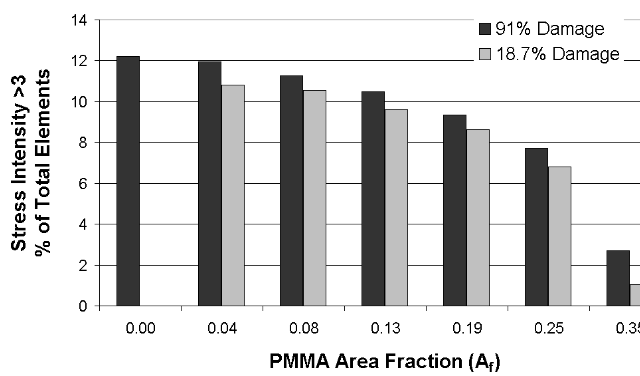

Figure 2. Stress intensity variations of the 2 damage models with increasing PMMA.

SUMMARY

In summary, the non-linear stress-strain behavior of an anatomically accurate 2D structural FEA model results reproduced experimental findings of damage in intact vertebra, and corroborates recent experimental and numerical simulations of vertebroplasty.

REFERENCES

Betten J. (1989). *European J. of Mech. A/Solids,* **8**,325-39
Hansson T. (1977) *PhD Thesis*, University of Göteborg

THE EFFECT OF BRACING ON PATELLOFEMORAL JOINT STRESS DURING FREE AND FAST WALKING

Yu-jen Chen[1], Samuel R. Ward[1], Li-der Chan[1], Michael S. Terk[2], Christopher M. Powers[1,2]

[1]Musculoskeletal Biomechanics Research Laboratory, University of Southern Calif., Los Angeles, CA. yujensch@usc.edu
[2]LAC/USC Imaging Science Center, Dept. of Radiology, Keck School of Medicine, University of Southern Calif., Los Angeles, CA.

INTRODUCTION

The etiology of patellofemoral pain (PFP) is not entirely clear, however, the most accepted hypothesis is related to abnormal patellar tracking, which increases patellofemoral stress and subsequent cartilage wear. Patellar bracing is commonly used in the conservative management of PFP. Although, it has been suggested that bracing reduces patellofemoral stress, this hypothesis has not been tested. The purpose of this study was to quantify the effects of bracing on patellofemoral stress in persons with PFP during free and fast walking.

METHODS

Ten subjects with a diagnosis of PFP took part in this study (mean age 30.6±6.8, height 163.6±5.1 cm, weight 56.0±5.0 kg). Subjects were included if they reported at least 50% pain reduction following application of an elastic sleeve brace (Don Joy Inc.). Initially, individualized patellofemoral contact area was obtained at 0, 20, 40 and 60 degrees of knee flexion using a previously described MRI method (Ward et al., 2001). Lower extremity kinematics (Vicon® motion analysis system) and kinetics (AMTI forceplates) were then obtained as subjects walked at self-selected free and fast walking velocities over a 10-meter walkway. Three trials were obtained under each gait condition. MRI and gait assessment was repeated following the application of the brace. Patellofemoral joint contact area, knee joint angle and the knee extensor moment were used as input variables into a previously described biomechanical model of the patellofemoral joint (Salem G.J, 2001), which was used to derive patellofemoral joint reaction force and stress. Data from the three trials were averaged for analysis. To compare peak patellofemoral joint reaction force, average utlized contact area, and peak stress between brace conditions, separate two-way ANOVA's with repeated measures (brace condition x walking speed) were used.

RESULTS AND DISCUSSION

Compared to the no-brace trials, peak PFJRF was greater in braced condition during both free gait (8.9±5.5 vs. 7.2±4.0 N/kg, $p=0.048$) and fast gait (13.3±6.2 vs. 10.8±4.8 N/kg, $p=0.023$). There was a significant decrease in peak PFJ stress in braced condition during fast gait (2.7±0.9 vs. 3.4±1.0 N/mm^2, $p=0.011$), however there was only a trend towards significance during the free gait condition ($p=0.10$). The utilized contact area was significantly greater with the brace compared to non-braced condition during both free (251.5±114.4 vs. 171.0±47.1 mm^2, $p=0.046$) and fast walking speeds (277.9±104.5 vs. 173.2±54.0 mm^2, $p=0.003$).

SUMMARY

Following the application of an elastic sleeve patellofemoral brace, subjects reported a 53% decrease in pain. This decrease in pain was accompanied by a 20% decrease in peak patellofemoral stress during fast walking. Decreases in peak stress were the result of increased contact area as patellofemoral joint reaction forces were significantly greater under the braced conditions. These results suggest that the mechanism by which bracing influences symptoms may be related to changes in joint stress.

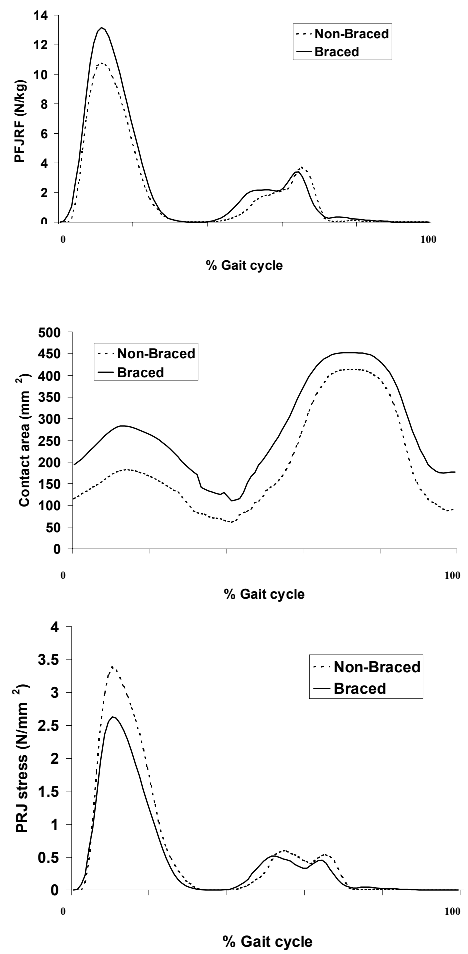

Figure 1. Mean curves (n=10) for patellofemoral joint reaction force (top), utilized contact area (middle) and stress (bottom) for fast walking.

REFERENCES

Ward S.R. et al. (2001). *Trans ORS,*
Salem G.J., Powers C.M. (2001). *Clin Biomech,* **16**, 424-430.

A COMPARISON OF ISOKINETIC STRENGTH BETWEEN SINGLE- AND MULTI-KNEE FLEXION AXIS TOTAL KNEE ARTHROPLASTY LIMBS

Kathy Simpson (ksimpson@coe.uga.edu)
University of Georgia, Department of Exercise Science, 300 River Road, Athens, GA, USA, 30602

INTRODUCTION

As many individuals who have undergone a total knee arthroplasty (TKA) had painful, compromised physical function prior to the arthroplasty, older individuals, in particular, may have less than desired quadriceps strength and/or balance. Therefore, TKA designs should provide optimal knee functioning and stability.

Some TKA patients complain of AB/ADD knee instability that occurs during the midrange of knee flexion (KF) or extension (KE) while performing daily (personal observation, O.M.M.). Most TKA designs have multiple KF/KE axes (M-AX), thus also have varying lengths of radii of rotation (ROR) that likely influence collateral ligament tension at different knee angles.

If a TKA design only has a single KF/KE axis (S-AX) and ROR, then less co-contraction muscular activity should be required to maintain frontal plane stability compared to a M-AX design. In addition, for the S-AX (Scorpio) compared to an M-AX design (Osteonics 7000®), the S-AX TKA axis is located such that its quadriceps patellar ligament moment arm is surmised to be longer, according to the manufacturer of both implants (Stryker-Howmedica-Osteonics, Inc., personal communication). Therefore, all else equal, a limb with an S-AX implant should be able to generate greater knee extensor moment than an M-AX limb.

METHOD

Bilateral implant participants (n = 9; $\underline{X} \pm$ SD: age = 73.0 $\pm$ 9.1 yr; mass = 88.13 $\pm$ 0.80 kg; min. time since last TKA = 60.4 $\pm$ 33.0 mo.) who had both arthroplasties performed by the same surgeon were recruited and medically screened. KS SF-12 scores (Insoll, et al., 1989) and morphological data, including KF ROM were obtained. Participants practiced performing the isokinetic tests during two accommodation sessions. During the actual isokinetic strength tests, EMG signals also were obtained (1080 samples$\cdot s^{-1}$) for rectus femoris, vastus medialis and lateralis, biceps femoris and semi-tendinosis. For concentric EMG, values were scaled to isometric MVC; for eccentric co-contraction data, values were scaled relative to the maximum eccentric strength values for the same knee angles (Snow, et al., 1995). Root-mean square RMS EMG data (window size equivalent to 6.6 Hz cut-off frequency) were generated. Then the RMS EMG values were averaged for each knee angle interval of 15° between 15° and 75° knee flexion angle. RM MANOVAs ($p < 0.05$) were used for the strength (LIMB) and EMG data (LIMB x KNEE ANGLE INTERVAL).

RESULTS AND DISCUSSION

As shown in Table 1, compared to the M-AX limbs, the S-AX limbs demonstrated greater ($\underline{p} < 0.05$) concentric KE peak moment and total work with similar KE RMS EMG and less concomitant KF co-contraction EMG during the 15° - 29° knee angle interval. No differences were detected for hamstrings: quadriceps ratio (0.48 and 0.55, respectively) or the angle that peak KF or KE moment occurred.

As anticipated, the S-AX versus the M-AX limbs produced greater quadriceps moment and work, but displayed similar REMG, suggesting that the S-AX's longer moment arm may have influenced the knee extensor moment. The biceps femoris activation displayed by the M-AX limbs increased for the KF angle interval of 15° to 29° during the KF concentric test. This may be due to the shift from the longer ROR to one that is more infero-posterior. Consequently, the new ROR has a reduced KF moment arm and/or creates knee instability that is compensated by increasing the BF activation.

Table 1. Means and Standard Deviations (SD) of Strength Variables.

	Peak Moment (Nm)		Angle to Peak Moment (deg)		Total Work (J)	
Limb	Mean	SD	Mean	SD	Mean	SD
Knee Extensors						
S-AX	*103.15*	44.14	66	3	*98.2*	39.2
M-AX	*88.44*	37.30	64	4	*89.1*	34.3
Knee Flexors						
S-AX	51.18	27.81	31	12	58.0	27.4
M-AX	48.33	24.42	35	16	46.4	22.5

REFERENCES

Insoll, J.N., Dorr, L.D., R. D. Scott, et al. (1989). *Clinic. Orthop.* **248,** 13-14.

Snow, C.J., J. Cooper, A.O. Quanbury, et al. (1995). *J. Electromyogr. Kinesiol*., **5,** 185-192.

ACKNOWLEDGMENTS

Financial support was provided by Stryker-Howmedica-Osteonics, Inc.

SLIP ANTICIPATION EFFECTS ON GROUND REACTION FORCES

Brian Moyer[1], Rakié Cham[1], and Mark S. Redfern[1,2]
[1]Department of Bioengineering and [2]Department of Otolaryngology
University of Pittsburgh, Pittsburgh, PA, USA

INTRODUCTION

Accidental injuries and deaths are often the result of slips/falls. Researchers have used laboratory gait analysis tools both to characterize potential slip risk (Grőnqvist et al., 2002) and to gain insight into the relationships between people and their environment. One of the many assumptions that such laboratory analysis requires is that when subjects do slip in the lab, their gait is not sufficiently altered from their normal walking style up to the point of the slip nor for subsequent trials after that slip. The goal of this paper is to investigate anticipatory effects that an initial laboratory induced slip may have on subject gait parameters for subsequent trials. In other words, once subjects experience an induced slip, do they change the way that they walk, even when instructed to walk normally for all trials?

METHODS

Five healthy male subjects, aged 35 years or less, were screened for neurological, vestibular and orthopedic abnormalities prior to their recruitment in the study. Subjects were equipped with a safety harness and motion measurement LEDs, and instructed to walk naturally across a vinyl tile walkway instrumented with two Bertec force plates (FP) in a laboratory with dimmed lights. Ground reaction forces and whole body motion (2 Optotrak-3020 motion measurement systems) were recorded bilaterally at 60 Hz for all trials. After several practice trials to ensure that subjects were walking comfortably, subjects were informed that the first few trials would be non-slippery to ensure natural gait. Then, while the subject still expected dry trials, a soap solution was applied to the left (second foot) FP without the subject's knowledge. After the resulting, unanticipated slippery trial, the soap contaminant was removed from the floor, subjects were given fresh shoes and were told that any of the subsequent trials could be slippery. Several additional dry trials were then conducted for comparison. Data processing included the derivation of foot kinematics (linear/angular position, velocity and acceleration), whole body joint angles, joint moments, and several ground reaction force related measures. Ground reaction force related measures are reported here.

Ground reaction force data were normalized to subject body weight and with respect to foot contact time from heel-strike (HS) to toe-off (TO). For both the lead foot (right) and the slip foot (left) parameters were calculated were calculated for trials before and after the first slip, including: 1) the loading rate, i.e. the slope of the normal force from heel strike (HS) to the peak normal force , 2) the magnitude of the highest peak after heel strike, and 3) the peak of the ratio of shear/normal forces. In addition, double support time, contact time and differences between the two feet were investigated.

RESULTS AND DISCUSSION

T-test analyses indicated significant differences ($p < 0.05$) for parameters measured before and after the first slip. The amount of time spent in double support increased by 1.5% and the left foot had a higher peak shear/normal ratio than the right foot after the initial slip. In addition, the slip-foot (left) total contact time decreased by about 5% and the difference between lead foot and slip foot peak normal force magnitude increased by 6.8%. Although anticipated, results did not indicate significant differences for the loading rates of normal force pre- to post- slip.

SUMMARY

Based on this pilot study, slip anticipation affects subsequent gait, even though subjects attempt to walk naturally and do not know that a contaminant is placed on the floor. The subjects in this study did change their gait in anticipation of future slips once they had experienced an initial slip. This conclusion should influence data collection protocols where multiple coerced slips are expected and should shape conclusions regarding required coefficient of friction specifications based on subjective measures. As most slips leading to injuries are likely unanticipated, measurements of gait parameters that do not take slip anticipation effects into consideration may underestimate genuine slip risks.

REFERENCES

Grőnqvist, R., Abeysekera, J., Gard, G., Hsiang, S.M., Leamon, T.B., Newman, D.J., Gielo-Perczak, K., Lockhart T.E., and Pai, C.Y.-C. (2001). *Ergonomics*, Vol 44, no 13, pp. 1167-1199.

FACTORS THAT CONTRIBUTE TO PEAK KNEE FLEXION IN NORMAL SWING: IMPLICATIONS FOR STIFF-KNEE GAIT

Saryn R. Goldberg[1,2], Frank C. Anderson[1], Marcus G. Pandy[3], and Scott L. Delp[1]

[1]Department of Mechanical Engineering, Stanford University, Stanford, California, USA, [2] saryn@stanford.edu
[3] Department of Biomedical Engineering, The University of Texas at Austin, Austin, Texas, USA

INTRODUCTION

Swing-phase knee flexion is necessary to achieve the toe-clearance required for limb advancement. In stiff-knee gait, a movement abnormality observed in persons with cerebral palsy, knee flexion during swing is diminished. This is commonly attributed to abnormal swing-phase quadriceps muscle activity. However, treatments aimed at altering the function of this muscle group only benefit some patients. Outcomes may be variable because other factors, such as low knee flexion velocity at toe-off or weak hip flexors, may limit knee flexion in some patients. To understand the relative importance of factors that could contribute to stiff-knee gait, we used a new methodology, an induced-position analysis, to quantify the contributions of individual muscles and knee flexion velocity at toe-off to peak knee flexion during the swing phase of normal gait.

METHODS

Induced accelerations describe the contribution of each force component in the equations of motion to the angular accelerations of the joints in a system (Zajac and Gordon, 1989). These components typically include forces due to muscles, gravity, Coriolis, and centripetal effects. Double integration of the induced accelerations over time yields induced positions, which quantify how accelerations due to each force component contribute to the change in position of the joint of interest during the integration time period.

Muscle forces and model kinematics for our analysis were based on the dynamic optimization solution for normal gait computed by Anderson and Pandy (2001). The induced accelerations were computed by assuming rigid contact with the ground (Anderson and Pandy, *in review*). We calculated the induced knee flexion angle from the time of toe-off to the time of peak knee flexion in swing due to each force component in the equations of motion, including all 54 muscles represented in the model. The change in knee angle due to the knee flexion velocity at toe-off was found by integrating this constant over time. The largest contributors to peak knee flexion were those factors that induced the largest change in knee angle during the time of interest.

RESULTS AND DISCUSSION

Because superposition holds for this analysis, the simulated knee kinematics can be reconstructed by summing the induced knee angle due to each factor (Fig. 1). Changes in the knee flexion angle due to gravity, Coriolis, and centripetal forces were small compared to the changes due to the initial knee flexion velocity and actuators (muscles and ligaments). The initial knee flexion velocity of the swing limb (375°/s) was the largest contributor to the peak knee flexion angle; its effect was more than double the net effect of all the actuators combined. The largest contributions to peak knee flexion made by swing-limb muscles were from the active forces in iliopsoas and the ankle dorsiflexors and from the passive forces in vasti (Fig. 2). The stance-limb gluteal muscles also made large contributions to peak knee flexion (Fig. 2).

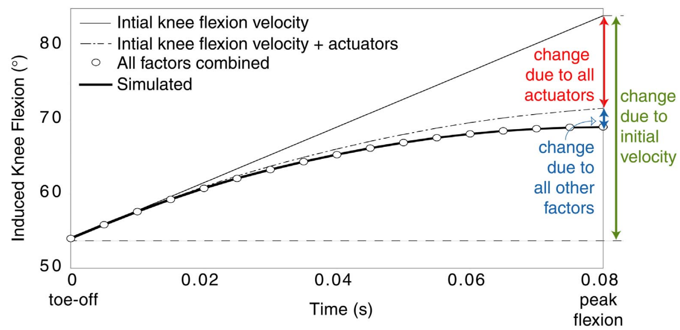

Figure 1: Induced knee angle up to time of peak knee flexion.

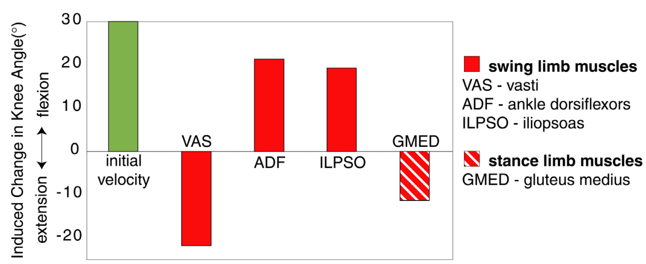

Figure 2: Largest contributors to peak knee flexion in swing.

CONCLUSIONS

These results suggest that the muscle activity that gives rise to swing-phase initial conditions may be more important than the muscle activity that occurs after toe-off in determining peak knee flexion in normal swing. This supports the possibility that low knee flexion velocity at toe-off contributes to stiff-knee gait in some patients.

REFERENCES

Anderson FC, Pandy MG (2001). *J Biomech Eng-T ASME*, **123**(5), 381-390.
Anderson FC, Pandy MG (*in review*). *Gait Posture*.
Perry J (1987). *Dev Med Child Neurol*, **29**(2), 153-158.
Zajac FE, Gordon ME (1989). *Exerc Sport Sci Rev*, **17**, 187-230.

ACKNOWLEDGEMENTS

NIH R01 HD38962, The Whitaker Foundation.

COMPARING MOVEMENTS ACROSS THREE VISUAL CONDITIONS IN A STEP AND REACH TASK

Jan M. Hondzinski, Ph.D.,
Louisiana State University, Baton Rouge, Louisiana, USA, Email: jhondz1@lsu.edu

INTRODUCTION

The effect of vision in movement control is not well understood. There is evidence to suggest that reaching errors are biased toward step and gaze directions when stepping and reaching to remembered targets (Flanders et al., 1999; Medendorp et al., 1999). This study was designed to gain a better understanding of the role of vision in whole body movement control. Thus, the purpose was to examine the relationship between final reach position and variables associated with gaze and step direction in a whole body reaching task requiring a step.

METHODS

Six healthy subjects were asked to step and reach to 9 targets. Figure 1 shows 3 target location heights approximating the shoulder, hip and knee joints (45 cm, 90 cm and 147 cm). At each height targets were located in 3 positions: central; 30 degrees right; and 20 degrees left. Radial target distance was 95 cm from the trunk. During reaches markers on head and body segments were monitored (60 Hz) using a passive marker video system (Motion Analyses Co.).

Target Location

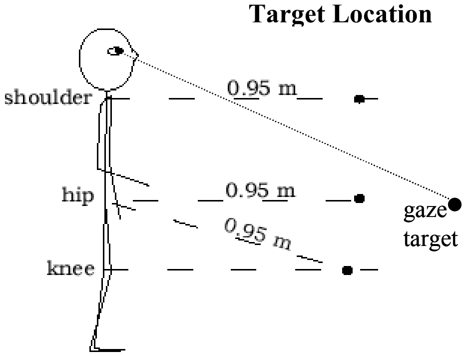

Figure 1: Experimental setup. Target location is shown from a lateral view with the subject in start position.

Reaches occurred under three visual conditions: NORMAL, where there are no alterations in the visual field and subjects gaze at the target; VIRTUAL, where the target location is remembered and subjects gaze at the remembered target position; and GAZE where an eccentric target location is noted in the subject's peripheral visual field, while gaze position is anchored elsewhere (see *gaze target*, Fig. 1).

Lateral, vertical and anterior/posterior (a/p) reaching errors (relative to an imaginary horizontal line through the midpoint between subjects toes at start and target positions) were computed. In addition, step length (length), horizontal step angle (angle) and horizontal and sagittal plane head angles (horz and sag, respectively) were calculated as movement variables. Five trials were used to compare changes in a given variable across the visual conditions and target locations for each subject using a repeated measures ANOVA (Tukey HSD post-hoc).

RESULTS AND DISCUSSION

The analyses revealed that reaching errors varied across visual conditions and target locations ($p < 0.05$). The reaching error type (lateral, vertical or A/P) was different across subjects. For example, in some subjects there was a difference found between lateral errors for the VIRTUAL and NORMAL conditions, whereas others had different vertical errors. To better understand the role of gaze and step direction contributions for whole body reaches, differences in reaching errors across visual conditions were matched to movement variables. Cases where no match was found for the given variables were identified as *none*. Each number in the table represents the number of matches identified for the given error and variable for the visual conditions. These numbers were highest (see bold, high-lighted box in Table 1) for reach error and horz, sag or none matches. Although the eyes and head are not required to move together, it is well known that head and eye movements are coupled to some degree. Thus, these data provide some evidence to suggest that people rely more heavily on gaze than step direction when reaching to targets, which require a step.

Table 1: Number of Significant Comparisons

Lateral Reach Error	length	angle	horz	sag	none	Total
NORMAL/VIRTUAL	0	0	**3**	1	**3**	6
VIRTUAL/GAZE	1	8	**16**	13	1	17
NORMAL/GAZE	3	7	**15**	13	0	15
Vertical Reach Error	length	angle	horz	sag	none	Total
NORMAL/VIRTUAL	1	0	2	4	**7**	11
VIRTUAL/GAZE	0	6	7	**9**	3	13
NORMAL/GAZE	4	10	15	**21**	0	22
A/P Reach Error	length	angle	horz	sag	none	Total
NORMAL/VIRTUAL	2	0	4	6	**7**	15
VIRTUAL/GAZE	1	4	**9**	7	0	10
NORMAL/GAZE	5	5	10	**14**	1	17

SUMMARY

Subjects were asked to step and reach to targets in three visual conditions. There were a greater number of matched changes across reaching errors and head directional variables than for reaching errors and step direction variables. It is suggested that gaze direction has a greater influence than step direction when stepping and reaching to a target.

REFERENCES

Flanders M. et al (1999). *Exp Brain Res* **126**, 19-30.
Medendorp W.P. et al (1999). *Exp Brain Res* **125**, 50-60.

ACKNOWLEDGEMENTS

Grant support: NIH NS27484. I thank Dr. M. Flanders for valuable discussions.

SIMULATION OF SCLERAL BUCKLING OPERATION ON AN EYEBALL BY USING FEM PROGRAM FOR COUPLING ANALYSIS OF HYPERELASTIC SOLID AND STATIC LIQUID

Zhi-Gang Sun[1], Akitake Makinouch[2] and Hiroo Yabe[3]
The Institute of Physical and Chemical Research, 2-1,Hirosawa,Wako-shi,Saitama 351-0198, Japan
[1]Advanced Computer Center, zgsun@postmann.riken.go.jp, [2]Integrated V-CAD System
Toho University School of Medicine, 2-17-6,Ohashi, Meguro-Ku, Tokyo 153-8513, Japan
[3]2nd Department of Ophthalmology

INTRODUCTION

Scleral buckling operation is frequently performed in clinic to treat the eyeball retinal detachment. However, the effect of the operation heavily depends on surgical experiences and it is usually difficult to obtain a desired operation effect. So the computer-added operation planning is at present greatly desired. Biomechanical simulation is a useful means to provide information for this purpose. In this study, the segmental buckling operations under different conditions were numerically simulated by employing a 2-D FEM program to qualitatively investigate the influence of factors such as buckle shape, suture width and intraocular pressure on the operation.

METHODS

To enable the simulation of the scleral buckling operation on an eyeball, a 2-D FEM program for coupling analysis of hyperelastic solid and static liquid in which the functions of the contact treatment and suture treatment are implemented was developed based on an incompressible hyperelastic program[1] which has been developed by the authors.

Total four cases of simulations were performed under the different buckle shapes, suture widths and intraocular pressures as shown in Table 1. The analysis model is shown in Fig.1. The neo-Hooke hyperelastic material model, in which the stored energy function is expressed as $W = c\ (I_1 - 3)$, was used for all the soft tissues except zinn's zonules, and the material constants are given in Table 2. The bulk modulus of 2083.3MPa was used for the liquid tissues.

As shown in Fig.2, the simulations were performed in two steps: in the first step, pressure was applied to the eyeball internal surface as a pressure boundary condition to generate its initial intraocular pressure; in the second step, a coupling analysis was performed to simulate the suture process.

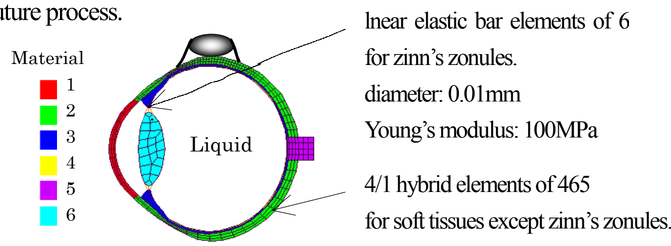

Fig.1 Analysis model for segmental buckling operation.

RESULTS AND DISCUSSION

The simulation results are shown in Fig.3. These results demonstrate that the ellipse-like buckle shape, wider suture width and lower intraocular pressure produce higher scleral buckling effects and the ellipse-like buckle shapes give relatively uniform stress distributions in the buckling sections compared to the

Table 1: Material constants for the soft tissues

	cornea-1	sclera-2	choroids-3	retina-4	optic nerve-5	lens-6
c	0.0333	0.0833	0.0083	0.0008	0.0083	16.67

Table 2: Buckling conditions in each analysis case

	buckle shape	suture width	Intraocular pressure
Case1	quadrilateral-like	8.8 mm	3.75 mmHg
case 2	ellipse-like	8.8 mm	3.75 mmHg
case3	quadrilateral-like	8.8 mm	1.50 mmHg
case 4	ellipse-like	6.4 mm	3.75 mmHg

quadrilateral-like ones. This implies that different factors would result in different operation effects, and therefore it is important to adopt suitable factors for getting the desired operation effect in the clinic. Through these results, some useful conclusions could be made. For example, in the case that an inexperienced surgery want to avoid an unexpected high buckling effect which is due to an overly strong buckling, a buckle shape with a flat bottom would be preferred, as well as a buckle shape with curved bottom can be expected to avoid the so-called fish mouth opening phenomenon that is considered to be caused by the nonuniform stress distribution of the retina in the buckling section.

SUMMARY

In this study, some useful results were obtained. It is expected that desired buckling effect would be available in the clinical operation with the aid of these results.

REFERRENCES

1. Sun, Z.G., Makinouchi,A. (2000). Proceeding of Symposium in Computational Biomechanics (RIKEN), JAPAN, 80-93

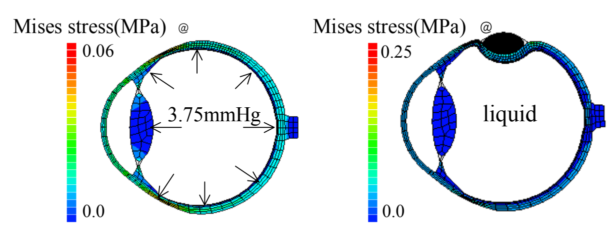

Fig.2 Calculation procedure of segmental buckling operation for case2.

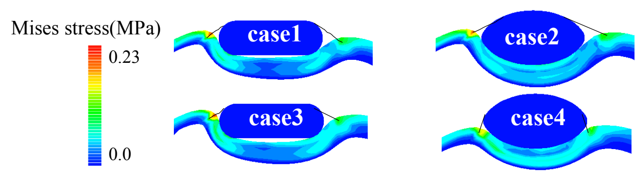

Fig.3 Simulation results of the buckling section in each case.

BONE MORPHOLOGY CHANGES IN DDH HIPS

Douglas R Pedersen, Heather Ralston, Colleen A Lamb, Stuart L Weinstein
Orthopaedic Biomechanics Laboratory, University of Iowa, Iowa City, Iowa, United States of America
poppy.obrl.uiowa.edu

INTRODUCTION

Developmental dysplasia of the hip (DDH) is a disease that leads to osteoarthritis much earlier than the population norm. After treatment, pelvis-centered anteroposterior radiographs are used to follow the progression of spherical femoral head growth and acetabular coverage that will provide natural ball-and-socket function of the hip. A group of patients with DDH, who have been treated conservatively since early infancy, are now in their fifth decade of radiographic and clinical follow-up. This combination of conservative treatment and long-term follow-up of patients afflicted with unilateral DDH constitute a unique resource to quantify the natural history of bone growth in hips with DDH. Digital methods were used to quantify radiographic changes in bone morphology, over a ten-year period, and between affected and unaffected hips.

METHODS

The thirty and forty-year follow-ups of forty-six patients with unilateral DDH are the source of clinical and radiographic data. In a recent study, a program was shown to objectively and reliably quantify hip morphology measurements on standard antero-posterior (AP) pelvic radiographs. [Lamb, 2002] The measured variables include: Sharp's angle, the center-edge of Wilberg; the articulotrochanteric distance; the acetabular depth, width and quotient; the percentage coverage of the femoral head; the femoral head-to-head ratio; and the tear drop width. Ninety-two clinical radiographs were scanned at 300 dots per inch and 8-bit (256) gray scale. A digitizing program (written in PV~WAVE Version 6.1, Visual Numerics Inc.) prompted the user to mouse-select 32 points on each digital image. A line through the distal teardrops defined the horizontal axis of the pelvis. Trigonometric and algebraic algorithms were used to exactly mimic the defined measurements of the variables by hand on clinical films.

RESULTS AND DISCUSSION

The average of 46 measured values (±1 Standard Deviation) of eight bone morphology variables are shown for both the DDH diagnosed hips and the unaffected hips at their 30-year and 40-year follow-ups (Figure 1). The DDH hips had a greater Sharp's angle than their asymptomatic contralateral hips. This is consistent with a more vertically inclined acetabular opening in dysplastic hips. The acetabulum in dysplastic hips is also wider and not as deep as in the non-affected hips. These abnormal acetabular features combine to cover only 70% of the femoral head, on average. This is an appreciable reduction from the average 85% femoral head coverage in non-affected hips. Another notable characteristic of dysplastic hips is the reduced vertical distance (ATD) from the top of the greater trochanter to the lateral margin of the articular surface. All bone morphology parameters were more consistent (smaller S.D.) for the non-affected hips than for the more irregular dysplastic hips.

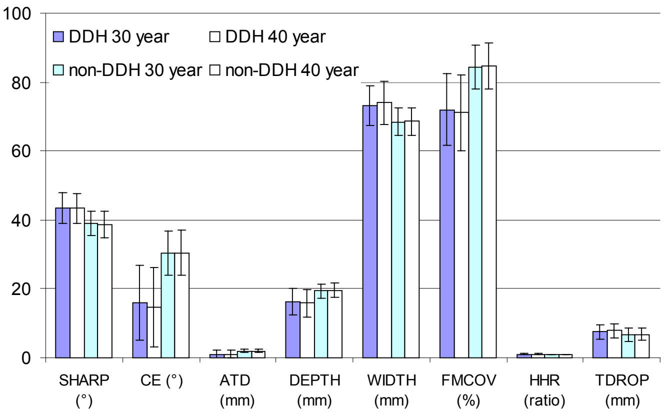

Figure 1 Digitized measurements (°, %, mm) on 30-year and 40-year films of 46 unilateral DDH patients

The non-affected hips showed almost no change during the decade between the 30 and 40-year follow-ups. Morphologic measures of the dysplastic hips quantified the erosion of the acetabulum over time (greater width, decreased depth). Combined with supero-lateral migration of the femoral head, one dysplastic hip had center-edge angle change of -35° over the 10 years between follow-ups (Figure 2).

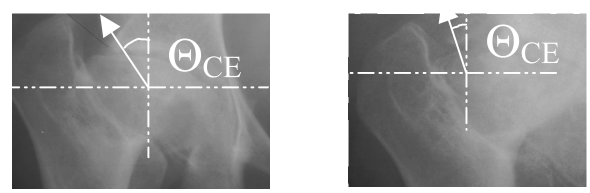

Figure 1 Radiographs of the hip at 30-year (left) and 40-year (right) follow-ups.

SUMMARY

This study demonstrates that there are measurable differences between asymptomatic hips and hips that are afflicted with DDH. Asymptomatic hips showed little change over time. However, for DDH affected hips, some measurements displayed substantial differences a decade later.

REFERENCES

Lamb, C. A. et al (2002). *Trans. of the 48th Annual Meeting of the Orthopaedic Research Society*, pp. 938.

ACKNOWLEDGEMENTS

National Institute of Health Grant: AR46601.

DYNAMIC LATERAL ARTICULATION OF THE RIGID TRUNK PRODUCES FOOT CLEARANCE IN MLKAFO GAIT

T. Adam Thrasher[1] and Brian J. Andrews[2]
[1] University of Alberta, Department of Biomedical Engineering, Edmonton, Canada
[2] University of Reading, Department of Cybernetics, U.K.

INTRODUCTION

Having no components above the waist, the medially linked knee-ankle-foot orthosis (MLKAFO) [1] allows for a unique form of gait involving unconstrained movements of the trunk. The objective of this study was to assess the feasibility of a method of lifting the feet during paraplegic gait by laterally articulating the upper body, a process that has been demonstrated in some anthropometric robots [2].

METHODS

This study consisted of human experiments and computer simulations. MLKAFO braces were custom fitted to each of three human subjects: one paraplegic with a complete spinal cord lesion at T12, and two able-bodied subjects (all adult males). While standing in the braces with knees locked in full extension, the subjects were asked to alternately lift their feet by flexing their trunks laterally. They were also asked to walk. Motion was recorded using a 4-camera Vicon 140 motion analysis system. The rocking motion was also simulated using a two-segment, two degree-of-freedom rigid body model consisting of an upper body segment and a lower body segment connected via the lumbosacral joint, which was treated as a simple pin joint spanned by abdominal oblique muscles on either side. Periodic activation signals were applied to the muscles to produce the rocking motion.

RESULTS AND DISCUSSION

The paraplegic subject was able to perform the rocking motion with and without handrails, but he could not walk. A typical trial is shown in Figure 1. The able bodied subjects performed the rocking with ease and were able to walk at speeds of 0.19 to 0.73 m/s. Two different modes of rocking were observed. In "Mode I," the upper and lower bodies rotate in opposite directions, while in "Mode II," they rotate in the same direction (relative to the frontal plane). The paraplegic subject used Mode I when using handrails and Mode II when not. The able-bodied subjects used mode I in all of the rocking trials, and in 80% of the walking trials.

The computer model was able to produce successful rocking cycles in both rocking modes. A stability criterion was found: the effective stiffness of the lumbosacral joint must be greater than approximately 120 Nm/rad.

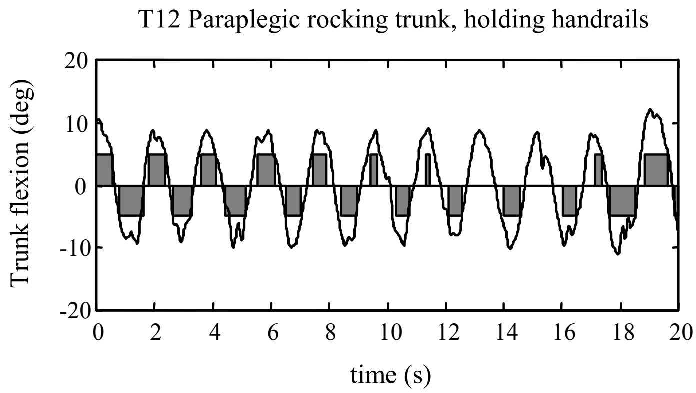

Figure 1: Paraplegic subject rocking while holding handrails (mode I). By convention, (+)ve trunk flexion is to the left. Grey rectangles indicate periods when a foot is raised: above zero indicates left foot, below zero indicates the right.

SUMMARY

This study serves as a basis for stiff-legged MLKAFO gait involving dynamic lateral trunk articulation. We demonstrated that a rocking strategy is capable of producing lower body movements that alternately lift the feet, however some additional assistance is required for paraplegic gait.

REFERENCES

[1] Andrews, B. J. et al. (1997) "Paraplegic locomotion: a linked knee-ankle-foot hybrid FES system," *Proceedings of IFESS '97*, 165-167.
[2] Li, Q. et al. (1993) "Learning control for a biped walking robot with a trunk," *Proceedings '93 International Conference on Intelligent Robots and Systems*, 1771-1777.

ACKNOWLEDGEMENTS

This study was supported by a grant from Alberta Heritage Foundation for Medical Research (AHFMR).

Table 1: Summary of rocking trials for T12 paraplegic subject (mean ± standard deviation).

Type of trial	Mode	Frequency (Hz)	Trunk flexion (deg)	Lateral translation of T1 (mm)	Duration of foot lift (seconds)
Handrails	I	0.59 ± 0.057	6.4 ± 0.87	126 ± 12	0.44 ± 0.050
no hands	II	0.46 ± 0.072	8.9 ± 1.67	178 ± 16	0.18 ± 0.103

FINITE ELEMENT ANALYSIS OF MEDIAN NERVE INSULT IN THE CARPAL TUNNEL

Christopher P. Petrie[1], Thomas D. Brown[1,2], Curtis M. Steyers[2]
Departments of Biomedical Engineering[1] and Orthopaedic Surgery[2], University of Iowa, Iowa City, Iowa, United States

INTRODUCTION

Despite its prevalence (over 600,000 new cases each year (Tanaka 1998)) and multi-billion dollar annual societal costs, Carpal Tunnel Syndrome (CTS) has received disproportionately little attention from the biomechanics research community. To date, for example, there have been no finite element (FE) analyses of the biomechanical interactions that likely lead to the development of CTS. Biomechanical research on CTS has been mostly limited to measuring 'pressure' in the tunnel. The data reported have varied widely both within and between studies (Rempel 1994, Seradge 1995). This may be due to experimental limitations or variable interpretation of terminology, or both.

METHODS

Our approach is to utilize an FE model of the wrist, including the interstitial fluid space, to conduct parametric studies of median nerve insult as a result of varying load conditions. A plane strain model currently is serving as a proof-of-concept, and as a stepping-stone on which to base the full 3-D model.

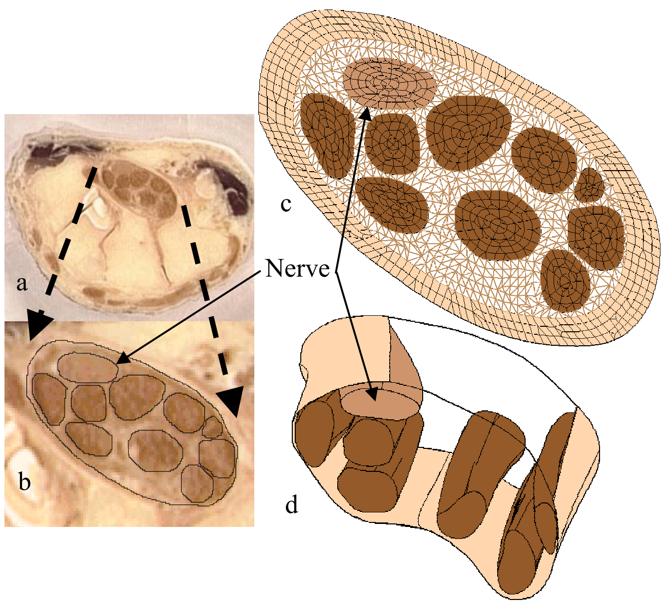

Figure 1: a) Transverse slice through wrist, b) Image in 1a with all tunnel contents and tunnel boundary sectioned, c) FE mesh of sectioned areas from 1b (includes solid and fluid mesh), d) 3-D surface model (cutaway view) of tunnel and its contents (FDS-L, FDS-R, FDS-S removed for clarity.)

The geometry for the FE model is derived from segmented high-resolution images of serial sections of a fresh-frozen cadaver. The sections are resampled into a voxel set with a voxel size of 0.247 x 0.247 x 0.247 mm. The images are segmented manually, and the segmentation data are run through a custom program that outputs the FE geometry definitions. These data are brought into ADINA v7.5 (an FE program with fluid-solid interaction capabilities), and the geometry is meshed appropriately. Figure 1a-c shows the sequence of moving from a single slice to solid/fluid mesh. Figure 1d shows a full 3-D surface model (cutaway view) of the carpal tunnel and its contents. Experimental work is ongoing concurrently, to improve on limited material property data currently existing for the flexor tendons, median nerve and the transverse carpal ligament.

RESULTS AND DISCUSSION

Figure 2 shows the computed stress distributions in the median nerve during a simulated keystroke maneuver. The dilatational stress, a reflection of the tendency for volumetric compression (presumably correlating with compromised microvascular perfusion), is shown for the nerve as the tendons approach, contact and eventually entrap the nerve against the tunnel boundary. Another insult measure is deviatoric stress, a potential correlate of shear-induced nerve tissue disruption at the cell or axonal level. These local stress measures, integrated over the tunnel-enclosed nerve, provide a basis to link median nerve insult with global limb motions or postures (Figure 3). This potentially provides a means to identify, and avoid, problematic workplace activities.

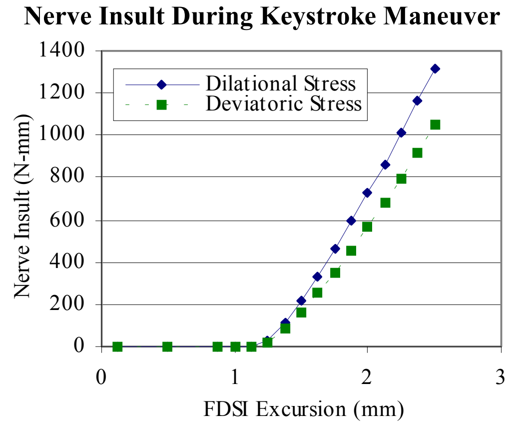

Figure 3: Nerve insult due to FDS-I excursion

REFERENCES

Rempel, D. (1994). Chapter 9 in *Repetitive Motion Disorders of the Upper Extremity*, American Academy of Orthopaedic Surgeons; Seradge H. et al (1995). *J. Hand Surgery,* **20A**, 855-859; Tanaka S. et al (1998). *Am. J. Industrial Medicine*, **27**, 451-470.

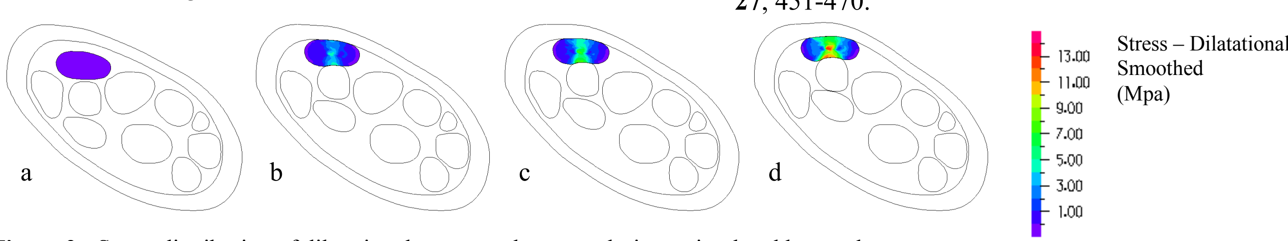

Figure 2: Stress distribution of dilatational stress on the nerve during a simulated keystroke maneuver.

IS SENSORY CONTROL OF THE LOCOMOTOR SYSTEM CRUCIAL OR NOT?

Sergiy Yakovenko and Arthur Prochazka

Centre for Neuroscience, University of Alberta, Edmonton, Alberta, Canada
sergiy.yakovenko@ualberta.ca

INTRODUCTION

It has been shown that isolated neural networks in the central nervous system can generate the basic locomotor rhythm even in the absence of sensory feedback. Furthermore, the spring-like properties of muscles provide automatic load-compensation during weight-bearing. How crucial is sensory control of the motor output, given these basic properties of the locomotor system? A biomechanical model was used to test two hypotheses. 1) Stretch reflexes are too weak and too delayed to contribute significantly to weight-bearing. 2) The important contributions of sensory input involve state-dependent processing.

METHODS

We constructed a two-legged planar locomotor model with 9 segments, driven by 12 musculo-tendon actuators with Hill-type force-velocity and monotonic force-length properties. Electromyographic (EMG) profiles of the simulated muscle groups during slow level walking served as actuator activation functions. Stability was compared in the open-loop "de-afferented" model and in models with feedback control based on either sensory-evoked stretch reflexes or finite-state rules. Spindle Ia and tendon organ Ib sensory inputs were represented by transfer functions with a latency of 35 ms and gated to be active only when the receptor-bearing muscles were contracting (Prochazka 1999). In each case, the reflex was set to contribute 15% to the net EMG profile. Together the sensory-evoked responses therefore contributed 30% of the net EMG. Finite-state rules identified in different animal species (Prochazka 1996) were used to switch between step cycle phases. Locomotor stability was assessed by parametric variations of actuator maximum forces and by mechanical perturbations during locomotion.

RESULTS

Without sensory control, the intrinsic stiffness of the muscles could provide enough weight support and flexibility to make continuous adjustments to compensate for small variations in body speed, height, and the relative positions of the limb segments (see first 2 steps in Fig. 2). However, stability was easily abolished by parametric variations such as changes in peak muscle force or cycle frequency of the CPG. When the underlying activation levels were low, stretch reflexes could provide enough additional drive to prevent a collapse (Fig. 1). However, if the underlying activation levels were sufficient to support body weight, stretch reflexes caused only a modest increase in the velocity of gait (Fig. 2). Finite-state logic considerably increased the range of kinematic and terrain variations over which gait remained stable.

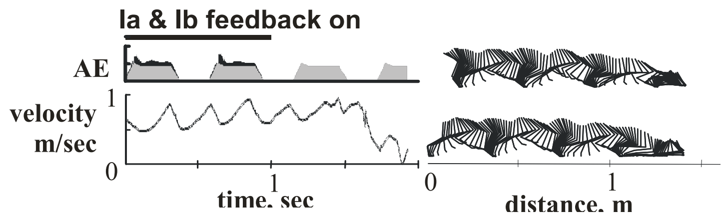

Figure 1: Model of control of locomotion with and without stretch reflexes mediated by muscle spindle Ia and tendon organ Ib afferents, when centrally generated activation levels are low. The net reflexive components of EMG are shown as black caps on top of ankle extensor (AE) EMG profile.

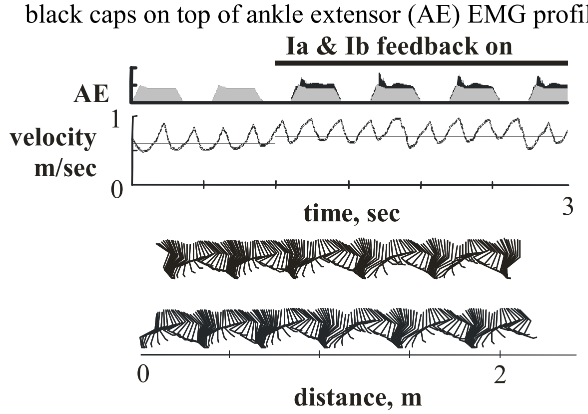

Figure 2: Contribution of stretch reflexes when actuators have high activation levels.

SUMMARY

1) In the absence of sensory control, the intrinsic stiffness of limb muscles driven by a stereotyped rhythmical pattern can produce surprisingly stable gait.
2) Contrary to hypothesis 1, the contribution of stretch reflexes can range from being modest to crucial, depending on the circumstances.
3) Finite-state control can greatly extend the adaptive capability of the locomotor system.

REFERENCES

Prochazka, A. (1996). Handbook of Physiology . *Regulation and Integration of Multiple Systems*. American Physiological Society. 89-127.
Prochazka, A. (1999). *Prog. in Br. Res.* **123**, 133-142.

EFFECTS OF VIBRATION INDUCED BY INLINE SKATING ON NEUROMOTOR FUNCTIONS COMPARISON BETWEEN VIBRATION ABSORPTION CONDITIONS

Richard Lefebvre[1], Cynthia Thompson[2], Frédéric Morin[2], Mohamed Iken[2], Marc Bélanger[2]

[1] Department of Kinesiology and Physical Education, McGill University, Montreal, Quebec, Canada, richard_lefebvre@uqtr.ca
[2] Département de Kinanthropologie, Université du Québec à Montréal, Montreal, Quebec, Canada

INTRODUCTION

Unusual sensations in the lower limbs, such as, numbness, weakness and increased difficulty in controlling the movements have been experienced after doffing the skate by people who practice inline skating. These sensations may be the results of vibration which is known to be produced by this activity (Mahar et al. 1997, Burström et al. 1999). Vibration has also been shown to alter several neuromotor functions, such as monosynaptic reflexes (Hoffmann reflex or H-reflex) (Matthews et al. 1964, Martin et al. 1986). The purpose of this study was therefore to verify the effects of vibration induced by inline skating on the Soleus (Sol) H-reflex, and to compare different vibration absorption devices on inline skates.

MATERIAL AND METHODS

Eighteen volunteer subjects (14 males, 4 females, mean age=27 years) participated in this study. In the pre-skating procedure, a minimum of 10 H-reflex responses in which the stimulus intensity was set to elicit a Motor (M) response of 10±1% of the maximal M response (Mmax) were recorded from the right Sol. The subjects were then asked to skate back and forth, at their own cruise speed, on a 200 metre section of a paved cycling path for 30 min. All subjects were recreational skaters and they all used the same four skate models (provided by a local supplier), in a randomized order. Skate 1 is a prototype inline skate, Skate 2 and Skate 3 are market available inline skates, whereas Skate 4 is a market available roller hockey skate. The four skating sessions were separated by a resting period of at least 24 hours. The frequency and amplitude of vibration were measured for the first 2 return excursions (4 lengths) using a set of 2 accelerometers positioned in different combinations; right front skate's chassis (FSC) and the middle of the medial surface of the tibia (MT); right front skate's chassis (FSC) and right front skate's boot (FSB); right rear skate's chassis (RSC) and right rear skate's boot (RSB); right front skate's chassis (FSC) and right Achilles tendon (AT). Each length of skating was timed and the subjects were asked to give the experimenter the level of numbness and fatigue felt in the lower limbs every other length, based on the 10 points Borg scale. After the skating period, the subjects returned to the lab where the H-reflex being recorded for 30 min. at a rate of one every 5 to 8 sec.

RESULTS

As a comparison base, the vibration frequencies were found to be between 105-190 Hz and 15-115 Hz. at FSC and MT levels, respectively. The vibration amplitude recorded at FSC could reach up to 5 g while that at MT went up to 2 g. Fig. 1 reveals that the H-reflex amplitude decreased significantly ($p<0.05$) after skating and this H-reflex inhibition had not recovered to the pre-skating level in all of the vibration absorption conditions. This could not be attributed to muscle fatigue since the spectral analyses of the Sol and MG EMG during the MVC, obtained from a former pilot session, showed no change between pre and post skating evaluations. The H-reflex changes were not correlated with either psychophysical test of numbness or fatigue, meaning that, the H-reflex was still inhibited while the subjects normal perception with respect to numbness or fatigue. However, Skates 1 and 2 were providing a significant faster neuromuscular recovery ($p< 0.05$) when compared to the two other vibration absorption conditions (Skates 3 and 4), as shown in Fig. 2.

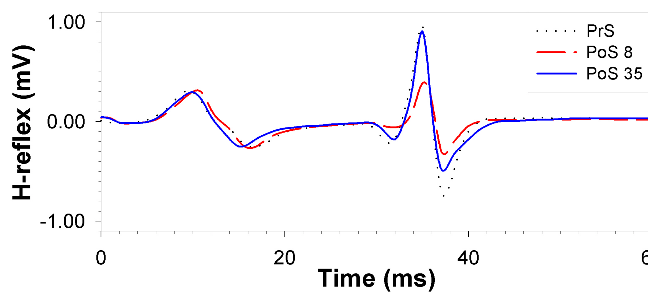

Figure 1: M-response and H-reflex (mV) in Pre-skating (PrS), Post-Skating after 8 min (PoS 8) and 35 min (PoS 35).

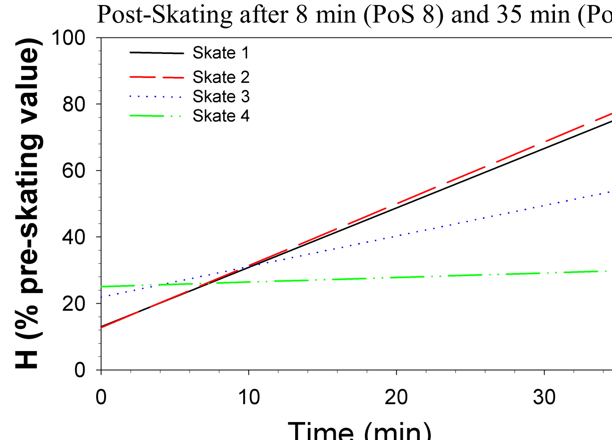

Figure 2: H-reflex (% pre-skating value) amplitude comparison between the 4 vibration absorption conditions.

DISCUSSION AND CONCLUSION

Inline skating produces vibrations that are transmitted to the lower limbs and that have some effects on the neuromuscular functions, in particular, the monosynaptic reflex. These changes will undoubtedly affect activities following skating since the effects are relatively long lasting (>30 min). It may also be attributed to a greater reliance on the skin and joint afferent information. This is supported by the relatively quick return to normal on the numbness scale.

REFERENCES

Mahar, A.T. et al. (1997). *Med. Sci. Sports Exerc.*, **29**, 1069-1075.

Burström L. et al. (1999). *SVIB*, 48-50.

Matthews P.B.C. et al. (1964). *Physiol. Rev.*, **44**, 219-288.

Martin, B.J. et al. (1986). *Aviat. Space Environ. Med.*, **57**, 681-687.

IN VIVO MUSCLE FORCE-LENGTH BEHAVIOR DURING INCLINED HOPPING IN TAMMAR WALLABIES

Craig McGowan[1]*, Russell Baudinette[2], and Andrew Biewener[1].

[1]Concord Field Station, Harvard University, Bedford, Massachusetts, USA
[2]Department of Zoology, University of Adelaide, Adelaide, South Australia, AU
*e-mail: cmcgowan@oeb.harvard.edu

INTRODUCTION

Unlike most terrestrial mammals, Tammar wallabies and other larger macropods do not experience an increase in oxygen consumption with increased locomotor speed (Baudinette *et al*., 1992) This locomotor economy has been linked to high force production with limited muscle shortening in the ankle extensor muscles, which facilitates elastic energy recovery in the large 'Achilles' tendon during steady, level hopping (Biewener *et al*., 1998). In the wild, these animals are often faced with maneuvering through more variable conditions. The goal of this study was to determine the role that the ankle extensor muscles play when the animals hop up an incline.

METHODS

Four adult tammar wallabies *Macropus eugenii* (two male and two female, ranging from 5.77-7.15kg in body mass) were trained to hop over a range of speeds on a treadmill set at 0 and 10 degrees. *In vivo* measurements were recorded from each animal at two-three speeds on the level and incline. These measurements included muscle strain and activity patterns in the Plantaris (PL) and Lateral Gastrocnemius (LG) muscles as well as forces from the Plantaris and common Gastrocnemius tendons. All trials were recorded using high-speed video (Redlake PCI-500).

Muscle strain was measured via sonomicrometry, with one pair of crystals implanted in each muscle belly aligned with the fiber trajectory. Electromyography electrodes were inserted into the muscle adjacent to crystals in to monitor electrical activity. Muscle-tendon forces were recorded by means of an 'E'-shaped buckle transducer secured to each tendon. The buckles were calibrated *in situ* post-mortem.

RESULTS AND DISCUSSION

The results of the *in vivo* strain measurements showed that in level hopping, both the LG and PL undergo little length change while producing force (LG -2.7 %; PL -4.2%; Figure 1), and therefore produce little or no net work (LG -0.03J; PL -0.01J).

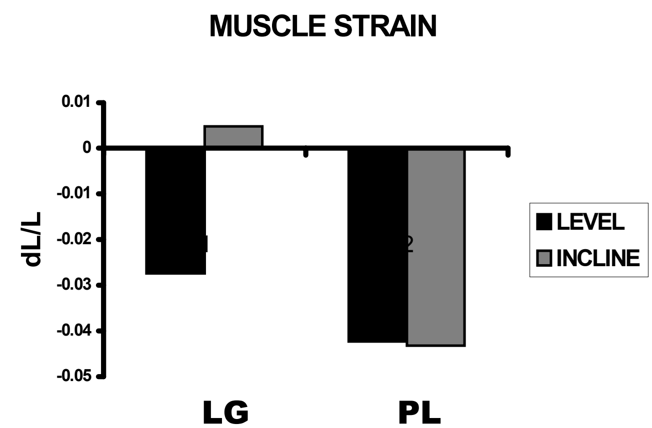

Figure 1: Average muscle strain (dL/L) in the LG and PL for steady state hopping at 4.2 m/s on level and incline.

Preliminary data suggests that there may be shift in the LG towards active shortening during inclined hopping (Figure 1), but the values for muscle strain and net work are quite small (.5% and 0.01J, respectively). The PL shows no difference in muscle strain or net work (-4.3% and -0.01J, respectively) during inclined hopping.

SUMMARY

Our data suggests that during inclined hopping, at least up to 10 degrees, there is no change in the mechanical role of the ankle extensor muscles. Such findings lead us to believe that the additional power necessary to move up a hill must be being supplied by more proximal limb muscles. Future work will explore the function of proximal muscles both in level and inclined hopping to help gain a better understanding of the mechanics of hopping.

REFERENCES

Baudinette, R.V., Snyder, G.K. and Frappell, P.B. (1992). *Am. J. Physiol*. **262:** R771-R778.
Biewener, A.A., Konieczynski, D.D. and Baudinette, R.V. (1998). *JEB*, **201**:1681-1694.

DESIGN FACTORS AFFECTING THE CONTACT STRESS PATTERNS IN A CONTEMPORARY MOBILE BEARING TOTAL ANKLE REPLACEMENT

Terence E. McIff
Orthopedic Research Laboratory, University of Kansas Medical Center,
Kansas City, Kansas, USA
tmciff@kumc.edu

INTRODUCTION

Most total ankle implants were originally developed without the aid of concerted engineering design efforts. Increasing interest in ankle arthroplasty has led to a closer examination of current ankle replacement designs in the hopes of predicting and averting any potential failure. Because of the high loads predicted at the ankle joint during normal activity (5-10X BW), there is concern that ankle implants might experience higher polyethylene wear rates that other joints. Low-constraint joint replacement prostheses, such as mobile bearing devices, are seemingly effective in reducing the shear and rotational loading believed to contribute to implant loosening. Unlike mobile bearing total knee prostheses, however, mobile bearing ankle replacements (Figure 1) have the additional advantage of maintaining complete congruency between bearing interfaces, hypothetically distributing loads more evenly and avoiding high stress concentrations implicated for higher wear rates. In previous studies, it was found that under quasi-static loading conditions uneven and unexpected contact stress distributions were observed for one of the congruent mobile-bearing total ankle devices evaluated (Figure 2), in particular, very high anterior and posterior-edge contact stresses were observed on the inferior contact surface. In this current study, design features of the polyethylene bearing were hypothesized to influence these stress patterns. This study examined the influence of several design features on the contact stress between bearing interfaces.

METHODS

A dual-contact-surface finite element model (Fig 1) was formulated for the mobile bearing device using Patran 9.0 and executed in Abaqus 5.8. The polyethylene bearing was modeled using a finite element mesh comprised of reduced-integration, 8–node Hex elements and used an elasto-plastic constitutive model. The tibial and talar components were modeled as rigid bodies. Finite sliding contact formulation was used. The FEM models were loaded with 3650 N axial force representing 5 times body weight of a 75 kg person. Once loaded, the polyethylene was constrained solely by friction and the topography of the contact surfaces. Multiple models were created wherein design features of the polyethylene bearing only were varied. A parametric study was undertaken to determine the influence of changes in these features on the contact stress distribution (both inferior and superior bearing surfaces) under static and quasi-static conditions. The independent parameters included: ant/post bevel angle, contact surface area, radius of curvature of the talar component, and mating surface conformity. Different angles of anterior and posterior bevel were modeled without altering the contact interface areas.

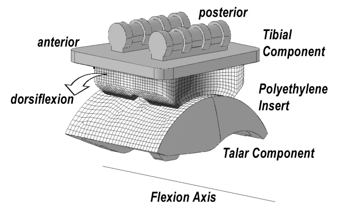

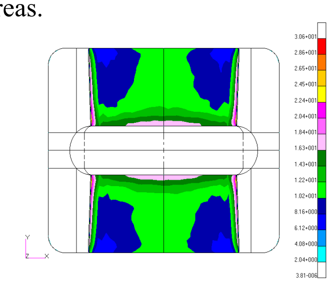

Figure 1: FE model of STAR total ankle replacement.
Figure 2: Inferior surface of the mobile bearing showing areas of high contact stress.

RESULTS AND DISCUSSION

The high stresses observed in the original design (approx. 18MPa) near the interior of the inferior bearing surface were found to result from a non-uniform curvature of the talar component. The anterior and posterior bevel angle was found to substantially influence the magnitude of the contact stress at the anterior and posterior edges. Altering of this bevel angle so that a tangent to the beveled surface is perpendicular to the surface of the talar component (Figure 3) was found to reduce the magnitude of edge stresses to the level observed over the rest of the contact area (from over 30MPa to approx. 10MPa).

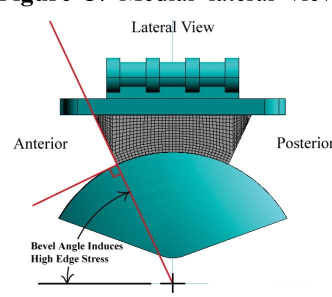

Figure 3: Medial–lateral view of the mobile bearing ankle replacement with bevel angle at a perpendicular to the surface of the talar component.

SUMMARY

Congruency of contact surfaces does not imply uniform stress distribution. Seemingly insignificant design features can substantially affect the contact mechanics of joint replacement devices. Here, the mechanisms by which a few alterable design features contribute to the disparate contact stress distributions were identified and quantified.

A NOVEL APPROACH TO MEASUREMENT OF HOOP STRAIN IN THE HUMAN MENISCUS

Cristy Richards[1], Charles J. Gatt Jr. M.D.[2], and Noshir Langrana Ph.D.[1]

[1]Rutgers University, Department of Mechanical and Aerospace Engineering, Piscataway, New Jersey, USA, crich@eden.rutgers.edu
[2]UMDNJ University Hospital, Department of Orthopaedic Surgery, New Brunswick, New Jersey, USA

INTRODUCTION

Treatment of a torn meniscus is the most common reason for knee surgery in the United States today . With a variety of treatment options, there is need for a competent means to evaluate each method to determine which serves best to restore or maintain meniscal function with the least amount of trauma to the patient. At present, however, methods for the assessment of human meniscal function involve only indirect techniques. Procedures such as casting (Walker et al 1975), and the use of micro-transducers (Walker et al 1975), Fuji Film (Baratz et al 1986), or staining (Krause et al 1976) ignore the functional means by which the meniscus bears a load. The hoop stress theory of meniscal function proposes that axial loads across the knee joint are distributed through the menisci as tension in circumferentially arranged fibers (Mow et al 1992, 1997). Therefore, only measurement of the longitudinal deformation of these circumferential fibers in response to knee joint load will allow for a direct determination of meniscal load bearing function.

METHODS

A multiple-degrees-of-freedom comprehensive testing apparatus has been designed and fabricated to simulate knee joint function under load. An Instron® mechanical testing machine is used to produce loading on the knee. Static and quasi-dynamic motion analyses are performed to assess the function of the human meniscus in response to knee joint loads, translations, and rotations. Quadriceps forces are simulated and measured by attachment of a slackening mechanism in series with a tensiometer to the patella tendon. A differential variable reluctance transducer (Microstrain® DVRT) is used for direct measurement of meniscus fiber deformation in response to axial loads across the knee joint. In addition, pressure sensitive film is used to obtain calibrated contact areas from which meniscal loading is calculated.

RESULTS AND DISCUSSION

The focus has been on the development and implementation of a new experimental protocol to evaluate meniscus strain. This involves the correlation of DVRT data with an accepted method of meniscal evaluation. Fuji film was chosen for its apparent ease and accessibility.

Three knees have thus far been tested for hoop strain with respect to external loading as given by the Instron machine and compared with coincident measurements taken with Fuji pressure sensitive film. At 1200N, result indicate strains in the mid-section of the medial meniscus of about 4.9% +/- 0.12% and Fuji film pressures of 1.5 MPa +/- 0.087 Mpa. Measurements were also taken at 800 N and 1600 N for the straight leg case. Additional data was collected for the quasi-static loading of the bent knee.

SUMMARY

Evaluation of meniscus function by means of the DVRT has been explored and compared to the widely accepted use of Fuji film. The DVRT has proven to perform with intuitive clarity over both straight and bent leg scenarios, which methods such as the use of Fuji film cannot accommodate due to the development of shear components.

By providing quantitative data combined with engineering analysis on the function of an intact, torn, partially resected, and repaired meniscus in different articular configurations, this study will allow orthopaedic surgeons to make better informed decisions regarding this common diagnosis.

REFERENCES

Walker, P.S. and Erkman, M.J., (1975). *Clin Orthop*, 109, 184-192.

Baratz, M.E. et al, (1986). *Am J Sports Med*, 14, 270-275.

Krause, W.R., et al (1976). *J Bone Joint Surg*, 58A, 599-604.

Mow, V.C., et al (1992). In: Mow, V.C., et al, eds. (1992). *Knee Meniscus: Basic and Clinical Foundations*, 4, 37-57.

WALKING AROUND STATIC AND MOBILE UPRIGHT OBSTACLES

Martin Gérin-Lajoie [1,2], Bradford J. McFadyen[1,2] , Carol C. Richards[1,2] and Lori Ann Vallis [1,2]
[1]Center for Interdisciplinary Research in Rehabilitation and Social Integration (CIRRIS), Québec, Canada
[2]Faculty of Medicine, Laval University, Québec, Canada G1K 7P4

INTRODUCTION

The ability to avoid obstacles is crucial for safe locomotion and requires pre-planned motor adaptations. Our daily activities often require that we navigate around upright static and mobile obstacles such as people standing or moving on the street or in a mall. Strategies to avoid upright static and mobile obstacles have received little attention in the literature. Studying such anticipatory locomotor strategies will provide a better understanding and assessment of locomotor ability within real world environments. The present study investigates the anticipatory strategies used to avoid static and mobile upright obstacles both with and without prior knowledge of the obstacle's movement.

METHODS

At this stage, five healthy subjects (2 females and 3 males; age 26.0 ± 3.2 years, height 1.74 ± 0.11 m, weight 64.44 ± 8.56 kg, gait speed 1.45 ± 0.23 m/s) have volunteered for the study. The experimental protocol was approved by the ethics committee of the Québec Rehabilitation Institute and informed consent was given by all participants. Exclusion criteria included any self-reported neurological or musculoskeletal impairments. A score of 20/20 on the Snell vision test was also required.

Three non-colinear infrared markers placed on the feet, legs, thighs, pelvis, trunk, left arm, left forearm and head, were tracked using the Optotrak 3020 motion analysis system (60 Hz; Northern Digital Inc, Canada). Certain anatomical points were also probed in relation to these markers to allow the calculation of principle axes and the creation of virtual marker trajectories (e.g., the heels). The obstacle used was a full-size department store mannequin mounted on an overhanging rail that crossed the walkway at a 45 degree angle. Using a remote controlled electrical motor, the mannequin could be moved at predetermined speeds, or simply placed in a set position, along the rail. Mannequin movement was also tracked using three additional infrared markers.

Subjects were asked to walk naturally, without stopping, up to a table located at the end of the walkway and to avoid the mannequin when it obstructed their path. No information was given about the direction to avoid the mannequin, but the laboratory set-up encouraged deviations to the right. For half of the trials, the action of the mannequin was revealed prior to executing the task (known), while it was unknown for the other half (uncertainty factor). Trials related to no, static and mobile obstacles, as well as to either prior or no knowledge of the obstacle's movement were randomly presented.

Dependent variables include average gait speed, lateral centre of mass displacement, forward centre of mass momentum, yaw (transverse plane) angles of the head and trunk, roll (frontal plane) angle of the trunk, and clearance of the left elbow of subject from the left elbow of the mannequin. Onsets of deviation in the variables for obstructed walking were recorded when the data began to deviate from the average control profiles and continued beyond one standard deviation of this control data. Onset times were calculated in reference to time of obstacle crossing.

RESULTS AND DISCUSSION

Preliminary analyses indicated that subjects planned their avoidance strategy in two distinct stages: 1) an early lateral deviation of the centre of mass at about 5 to 6 steps before obstacle crossing; and 2) a later more drastic lateral deviation within one stride of the mannequin. There was also a break in the forward progression of centre of mass momentum associated with the second, later, path deviation. Obstacle mobility had no effect on the centre of mass deviations, but subjects tended to reduce their average gait speed when the obstacle was mobile and when the action of the mannequin was unknown.

There was no clear upper body strategy related to head or trunk yaw movements for any condition, and head yaw was even absent for some subjects perhaps indicating a level of attention the subjects gave to the obstacle during the approach. In addition, trunk roll was non-existent for all subjects. Therefore, the data would appear to support more of a lower limb strategy to initiate changes in the lateral CM trajectories for the environmental context used here. Finally, obstacle mobility and uncertainty did not appear to affect the distance with which subjects cleared the mannequin, suggesting that subjects are not planning actual clearance distance.

ACKNOWLEDGEMENTS

Financial support from McConnel Foundation (MG-L) and NSERC (BJM). We acknowledge technical assistance of Mr. Guy St-Vincent, & Mr. Claude Simard.

NEUROMUSCULAR ADJUSTMENTS FOR HOPPING ON A HEAVILY DAMPED SURFACE

Chet T. Moritz[1], Spencer M. Greene[2] and Claire T. Farley[2]

[1]Department of Integrative Biology, Univ. of California, Berkeley, California, USA, ctmoritz@socrates.berkeley.edu
[2]Locomotion Laboratory, Dept. of Kinesiology and Applied Physiology, Univ. of Colorado, Boulder, Colorado, USA

INTRODUCTION

In the natural world, animals move over a variety of energy dissipating surfaces. Unlike running on a hard surface, to maintain a steady speed on an energy-dissipating surface, animals must produce more work than they absorb to replace the mechanical energy lost with each step. Indeed, during running on sand, humans must produce extra mechanical work and they consume more metabolic energy than on a hard surface (Lejeune et al., 1998). We hypothesized that humans hopping in place will adjust the timing of leg compression and extension and will produce extra work as surface damping increases, thereby maintaining similar center of mass dynamics regardless of surface damping. Previous work has shown that human hoppers conserve center of mass (COM) dynamics by adjusting leg stiffness on *elastic* surfaces of different stiffness (Farley et al., 1998).

METHODS

Five subjects hopped in place at 2.2 Hz on a surface supported by springs and dampers, and mounted on a force platform. For five trials, we increased surface damping from 0 to 3200 Ns/m and simultaneously decreased the spring stiffness from 30.3 to 13.3 kN/m to maintain a 6cm surface compression. We controlled for surface compression because it has a large effect on leg compression. We recorded ground reaction forces, surface compression, and sagittal plane video to determine leg compression, COM vertical displacement, and mechanical work. We determined significance ($p < 0.05$) with a repeated measures ANOVA. All values are Mean ± SEM.

RESULTS AND DISCUSSION

Hoppers maintained similar COM dynamics regardless of surface damping by altering leg mechanical work output, leg compression timing, and leg length at takeoff. The most damped surface dissipated 67±1% more of the hopper's COM mechanical energy than the elastic surface. Thus, the hopper would not have left the ground at the end of stance if the legs had behaved like springs, as they do on undamped surfaces. The legs performed increased work while maintaining similar COM dynamics by shifting the timing of maximum leg compression to offset changes in the timing of surface compression. On the most damped surface, the legs reached peak compression 33.3 ± 3 ms earlier ($p < 0.05$), and the surface reached maximum compression 46 ± 3 ms later ($p < 0.05$) than on the undamped surface. As a result, the minimum vertical position of the COM occurred at nearly the same time on all surfaces (see Figure 1).

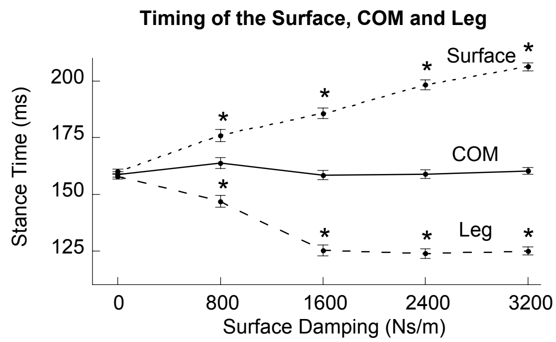

Figure 1: Surface damping vs. the time from foot contact to: (1) the minimum vertical position of the center of mass (solid), (2) the maximum surface compression (dotted), and (3) the maximum leg compression (dashed). Values are mean ± SEM and a * denotes $p<0.05$.

The legs reached peak compression earlier and absorbed 9 ± 2% less energy ($p < 0.05$) on the most damped surface compared to the undamped surface. Work output during takeoff increased by 125 ± 2% ($p < 0.05$) because the legs extended by 71 ± 4% ($p < 0.05$) more, reaching a 3.1 ± 0.1 cm ($p < 0.05$) longer length at takeoff on the most damped surface compared to the undamped surface. The remainder of the increased work was due to an increased average force during leg extension. The most damped surface was still compressed at takeoff, nearly offsetting the longer leg length and maintaining similar COM dynamics.

SUMMARY

Hoppers altered the timing of leg compression to offset differences in the timing of surface compression, thus maintaining similar COM dynamics regardless of surface damping. The legs performed net positive work to replace the energy dissipated by the damped surfaces by beginning extension earlier, and extending to a longer length at takeoff. These results show that animals can precisely adjust the timing and magnitude of leg compression and extension to maintain steady state locomotion on natural energy dissipating surfaces.

REFERENCES

Farley, C.T., et al (1998) *J. Appl. Physiol.*, **85**, 1044-1055
Lejeune, T.M., et al (1998). *J. exp. Biol.*, **201**, 2071-2080

ACKNOWLEDGEMENTS

Supported by grants from NIH (R29 AR44008) and NSF (ECS-9873474) to C.T.F

ASYMMETRIES IN THE DYNAMIC STRUCTURE OF THE CENTER-OF-PRESSURE TIME SERIES

Mark Musolino and Mark Redfern
Human Movement and Balance Laboratory, Departments of Bioengineering and Otolaryngology
University of Pittsburgh, Pittsburgh, PA, USA (markmuso@pitt.edu)

INTRODUCTION

Investigation of the center-of-pressure (COP) during quiet stance has traditionally involved the use of summary statistics (RMS, velocity, range) to quantitatively describe the COP time series collected via a single force plate. Limitations of this approach are (1) the failure of summary statistics to reflect dynamic aspects of the COP, and (2) the inability of a single force-plate to uncover any left/right asymmetries. While various metrics have recently been developed to examine COP dynamics, the issue of asymmetries in spontaneous sway remains seldom reported (Mizrahi and Susak, 1989). In light of this, *the objective of the current study was to compare dynamic measures of COP between left (L) and right (R) feet.*

METHODS

Postural steadiness was examined in five healthy adult males with no evidence or history of neurological disease or postural disorders. All subjects provided informed consent prior to testing. Each subject was asked to "stand as still as possible", in a comfortable upright posture, looking forward, with arms hanging freely at the sides, and with bare-feet placed side-by-side on adjacent, identical force plates (Model 4060, Bertec, Inc., Columbus, OH). Data were collected at 100Hz, and post-processed in Matlab (The Math Works, Inc.). Each subject performed 20 30-second trials – 10 w/ eyes open (EO), 10 w/ eyes closed (EC). EO/EC order was randomized. Numerous techniques were available to parameterize COP (Chiari et al, 2000; Newell et al.,1997; Riley et al.,1999). The stabilogram-diffusion approach of Collins and DeLuca (1993) was used because of its suitability in providing dynamic COP metrics, and because of its relative ease of application. Diffusion coefficients (D_S, D_L) and scaling exponents (H_S, H_L) were calculated for each 30 second COP time series.

RESULTS AND DISCUSSION

Visual inspection of the data and cross-correlation analysis revealed that corresponding L and R COP time series were in-phase (maximum correlation occurring at zero lag). However, L-R differences were observed in the stabilogram-diffusion parameters (Figure 1, Table 1). L values were consistently lower than R values, for all parameters – perhaps due to a R leg dominance effect. An eye condition effect was not apparent. Values for D and H were comparable to those reported by Collins and DeLuca, and indicate the existence of two distinct regions in the stabilogram-diffusion plot (Figure 1). Values for Tcrit, the transition point between "short" and "long" time interval regions, were in most cases similar for R and L; however, differences of up to 0.5 seconds were seen.

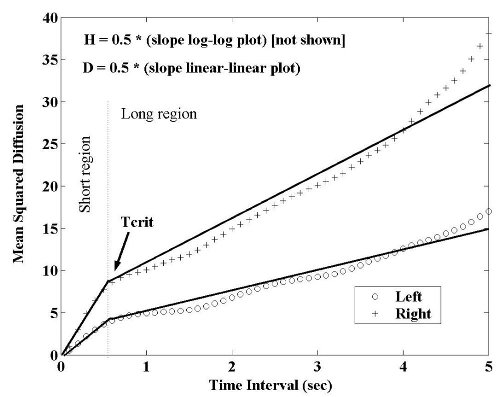

Figure 1: Stabilogram-diffusion plot shows L-R differences

SUMMARY

Noticeable differences were observed between L and R COP time series. Such asymmetries don't necessarily implicate a particular form of postural controller, but rather just indicate that R and L sides are differentially affected by the processes that are involved in spontaneous sway.

REFERENCES

Chiari et al. (2000). *Gait and Posture*, **12**, 225-234.
Collins, JJ, De Luca, CJ (1993). *Exp Brain Res*, **95**, 308-318.
Mizrahi, J., Susak, Z. (1989). *Biological Cyb*, **60(4)**, 297-305.
Newell et al. (1997). *Exp Brain Res*, **113**, 158-164.
Riley et al. (1999). *Gait and Posture*, **9**, 65-78.

Table 1: L and R values of stabilogram-diffusion parameters, D and H. Means are over a total of 50 trials (5 subjects x 10 trials). "S" subscript refers to short region, "L" to long region. See figure 1 for information on D and H calculations.

Subject Info → Age(yr): range 21-25, mean 23 | Weight(lb): range 142-250, mean 212 | Height(in): range 67-74, mean 71																
	D_S				D_L				H_S				H_L			
	EO		EC		EO		EC		EO		EC		EO		EC	
	R	L	R	L	R	L	R	L	R	L	R	L	R	L	R	L
Mean	6.4	3.4	12.7	6.4	4.2	2.3	7.4	3.1	.53	.60	.58	.56	.10	.08	.12	.09
St Dev	2.3	1.2	6.2	4.5	2.4	1.3	4.7	2.1	.21	.19	.23	.21	.02	.02	.02	.03

THE CONTRIBUTION OF THE ARM SWING TO MAXIMUM VERTICAL JUMPS

Zachary J. Domire and John H. Challis

Biomechanics Laboratory, Department of Kinesiology, The Pennsylvania State University, University Park, Pennsylvania, USA
Email: zjd100@psu.edu , jhc10@psu.edu

INTRODUCTION

When studying vertical jumping, it is common to ask subjects to perform jumps without arm swing. This simplifies analysis and reduces he amount of marker loss when performing motion analysis. It is generally accepted that not using the arms decreases jump performance. Clearly by swinging the arms the center of mass can be higher at take-off than if the arms are simply held by the side, but the motion of the arms can have other contributions to performance. The mechanisms via which arm swing can improve performance in these jumps are not fully understood. Feltner et al. (1999) proposed that a moment produced at the shoulders could oppose extension of the legs and allow for a longer period of force development and therefore an increase in jump height, others have referred to increase vertical momentum generated by arm swing (Lees et al., 2000). It is the purpose of this study to determine what effect arm swing has on the performance of a maximum jump.

METHODS

Seven healthy male subjects (age: 24 ± 2.45 years; height: 181 ± 0.075 cm; body mass: 75.1 ± 5.6 kg) each performed six maximum squat jumps. Three were performed with arm swing and three without. Force plate and motion analysis data were collected for all these jumps. Jump height was computed by computing take-off velocity from the impulse obtained by integrating the vertical force-time curve. Jump height was assumed to be the maximum vertical displacement of the center of mass once contact was lost with the ground. Time histories of the joint angles, angular velocities, and resultant moments were computed.

A direct dynamics simulation model was developed, designed to represent a typical subject. A five-link (foot, shank, thigh, trunk, arm) rigid segment model was constructed. Links were connected by frictionless hinge joints. The foot was connected to the ground by a hinge joint at the metatarsal-phalangeal joint. It had a rotational spring-damper at the heel. Inertial properties were determined from a geometric solids model of one of the subjects (1.80m and 75.2kg).

Using the model, and given for each instant throughout the jump the segment angles and angular velocities, the moments at the shoulder joint were used to estimate the accelerations these moments generate at the other joints in the model. This is referred to as induced acceleration.

RESULTS AND DISCUSSION

Jump height was 19 ± 10% higher for the jumps with an arm swing than without. This compares favorably with the results of Feltner. The kinematics and the kinetics of the tasks were similar to data presented in the literature (e.g. Challis, 1998).

The induced acceleration analysis showed arm swing causes joint accelerations away from the desired direction of motion at the knee and ankle throughout the jump, allowing the musculature at these joints longer to generate force. At the hip there is little effect until the end of the movement, when arm swing extends the hip. Figure one shows the induced acceleration at the hip, knee, and ankle throughout the jump.

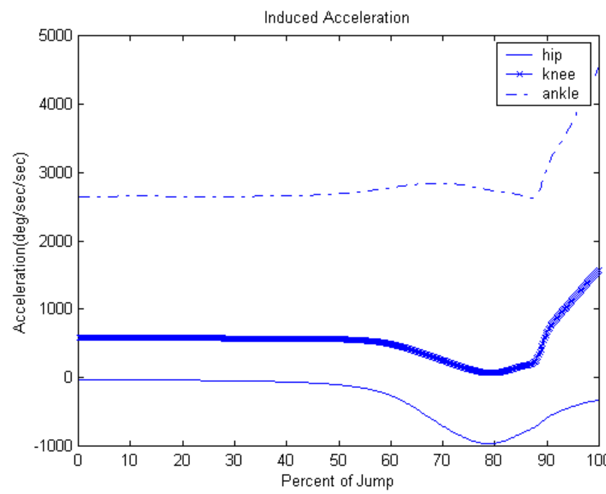

Figure (1). Induced acceleration. Extension is negative.

Bobbert et al. (1996) suggested that vertical jumps with a counter movement are higher than those with a static start because in the former there is increased time for muscle activation. The induced acceleration analysis performed here shows that a similar mechanism is at play when an arm swing is employed during a jump. It would be interesting to use this approach to analyze the influence of arm swing when subjects perform sit-to-stand, where for a phase of the movement accelerations at the knee cannot be induced as the subject is still in contact with the chair.

REFERENCES

Bobbert, M.F., et al. (1996). *Med Sci Sports Ex*., **28**, 1402-12.
Challis, J.H. (1998) *Hum Mov Sci*., **17**, 307-325.
Feltner, M.E. et. al. (1999). *J. Sport Sci.,* **17**, 449-466.
Lees, A., et al. (2000). *Ergonomics*, **43**, 1622-36

ACKNOWLEDGEMENTS

This research was in part supported by a grant from The Whitaker Foundation.

CONTROL OBJECTIVES CHANGE BETWEEN PHASES OF JUMPING AND LANDING TASKS

K. E. Costa and J. L. McNitt-Gray
Biomechanics Research Laboratory, Department of Kinesiology, University of Southern California, Los Angeles, California, USA
Communicating author: kcosta@usc.edu

INTRODUCTION

Previous investigations have shown foot position at contact and TBCM position at the time of the explosive extension during ground contact influence the redirection of total body momentum (Hodgins & Raibert, 1990; Ridderikhoff et al., 1999). The purpose of this investigation was to compare the control objectives of the trunk and leg subsystems during the landing and jumping phases of a practiced, goal-directed task.

METHODS

Sagittal plane kinematics (200Hz, NAC) were recorded while female collegiate basketball players (n=6) performed a series of rebound-like jumping and landing tasks. Subjects were asked to jump, reach a ball suspended overhead (0.4m above individual's stand and reach height), land, and jump again to reach a second ball suspended overhead (90% of max vertical jump). Ground reaction forces were recorded from the time of landing from the first jump to take-off of the second jump (Kistler, 800Hz). Subjects were asked to use their normal jumping and landing techniques. Body landmarks (DeLeva, 1996) were manually digitized (Peak Performance). Leg angle (ankle to hip), trunk segment angle (hip to C7), and TBCM position vector from ankle to TBCM position (r angle) were calculated from touch-down to take-off relative to the right horizontal

RESULTS AND DISCUSSION

Control of the lower extremity appeared to take precedence over the need to position the TBCM at contact. Within-subject, leg segment orientation at contact varied 1-2°. Whereas, r angle at contact varied on average by 11°. These results highlight the need to control the lower extremity position so that the neural system can anticipate and prepare for the mechanical demand imposed upon the lower extremity during impact. Whereas, the positioning of the TBCM appeared to determine the initiation of the explosive extension phase (figure 1). These results support the findings of Ridderikhoff et al. (1999), which identified a rotation phase preceding the explosive extension phase of maximum squat jumps. Similarly Hodgins & Raibert (1996) altered biped robot gait by adjusting the timing of the thrust according to leg position during stance. Trunk-leg subsystem control used to position the TBCM during ground contact varied across subjects. Subjects who utilized greater trunk segment motion to achieve the TBCM position prior to explosive extension utilized longer ground contact time than those using leg motion.

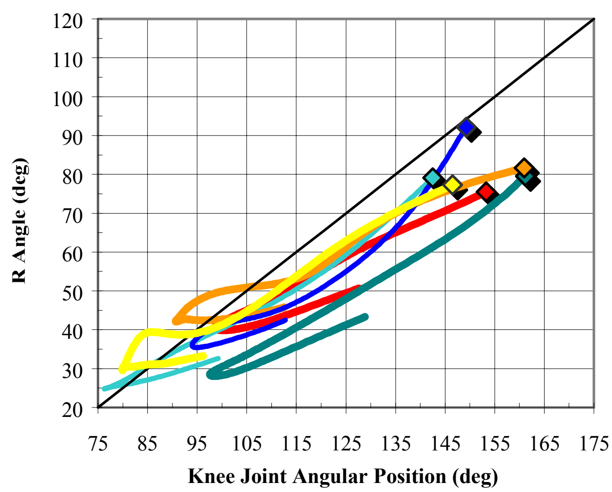

Figure 1: Angle-angle diagram of TBCM position vector (R angle) vs. knee joint angular position during ground contact. Diamonds indicate ground contact. Turning point synchronization of the variables suggests the initiation of the secondary jump task is coupled with the position of the TBCM, such that the explosive extension occurs after the preferred angular rotation of the TBCM vector.

REFERENCES

Hodgins, J.K., Raibert, M.H. (1990). Int. J. Rob. Res., 9:2, 115-31.
Ridderikhoff, A. et al. (1999). *Med. Sci. Sports Exerc.*, **31**:8, 1196-1204.

ACKNOWLEDGEMENTS

Intel, NCAA, B. Munkasy, J. Heinko, T. Smith, M. Welch

INFLUENCE OF INCREASED ROTATIONAL INERTIA ON HUMAN TURNING PERFORMANCE

David V. Lee, Rebecca M. Walter, Stephen M. Deban (sdeban@usa.net) and David R. Carrier

Department of Biology, University of Utah, Salt Lake City, Utah, USA.

INTRODUCTION

Organismal biologists have focused considerable attention on the many ways in which body size and shape influence animal locomotion, but few studies have considered the impact of rotational inertia on turning performance (Thollesson and Norberg, 1991; Evans and Thomas, 1992; Eilam, 1994; Van Den Berg and Rayner, 1995; Jindrich and Full, 1999). Given the importance of turning agility in competitive sports and athletic activities, the influence of rotational inertia on locomotor performance warrants investigation. We became interested in the effect of rotational inertia on turning performance because we were curious about the extent to which body configuration influenced the agility of theropod dinosaurs (Carrier et al. 2001). Results from that study led us to suspect that the relationship between rotational inertia and turning performance is not as simple as one might initially expect. Elevation of rotational inertia in human subjects decreased turning performance, but the effect appeared not to be in proportion to the change in rotational inertia. Thus, we quantified the effect of an elevation of rotational inertia on the turning performance of human subjects (Lee et al., 2001).

METHODS

To determine the effect of rotational inertia (I) on turning performance, we elevated I of human subjects an average of 9.2-fold above natural values and had the subjects execute maximum effort turns during vertical leaps from a Kistler 9281B SN force plate (i.e., "jump turns"). The subjects began each jump with their feet at shoulder width and their arms at their sides throughout the jump. Force plate records allowed us to measure the mean and maximum torque (T), period of torque application, total angular impulse, maximum and mean angular power (P) and angular work during the turn (Lee et al., 2001). Forces applied to the force plate were sampled at 200Hz with a BioPac Systems, Inc. (MP 100) A-D converter and a Macintosh computer. Free moments generated by the subjects during maximal jump turns were calculated from the horizontal forces and the position of the center of pressure using the methods of Holden and Cavanagh (1991).

RESULTS AND DISCUSSION

Maximum and mean T increased significantly in jumps with increased I ($P<0.001$), as did angular impulse and push-off period (Table 1). The increase in T, period, and impulse partially compensated for the increased I, and resulted in less decrease in angle turned than expected in jumps with increased I. Maximum and mean angular power were lowest in jumps with increased I, but angular work did not vary significantly among conditions. Maximum T during jumps with increased I approached isometric maximum torques (mean: 92.5±8 Nm), suggesting that turning performance may ultimately have been limited by the ability to produce torque. We suggest that there are at least two factors that contribute to the greater torque production when the subjects turned with increased rotational inertia: (1) adjustments in the pattern of muscle recruitment and (2) a reduction in muscle shortening velocity that resulted in increased muscle forces.

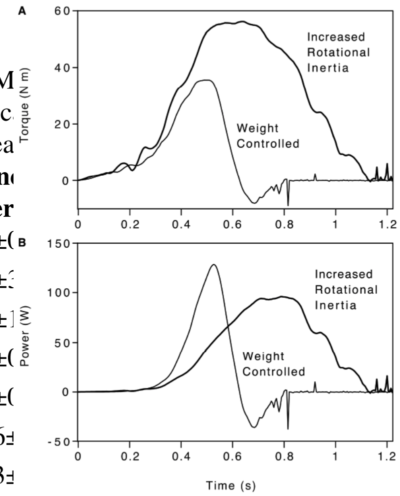

Figure 1. Sample recordings of ground reaction torque (A) and angular power (B) applied during maximum effort jump turns. Thick lines denote recording obtained when the subject turned with rotational inertia elevated 9.7-fold above that of weight-controlled turn (thin lines).

Table 1. Means and SEM conditions. Asterisk indic (P<0.001) between increa

	Unen ber		
I (kgm^2)	1.12±(		
Max T (Nm)	56.9±3		
Mean T (Nm)	21.8±1		
T period (s)	0.50±(		
Impulse (Nms)	10.8±(		
Angle turned (°)	105.6±		
Max. P (W)	242.3±		
Mean P (W)	77.7±7.7	63.4±7.7	45.2±1.9
Ang. Work (J)	37.5±3.6	35.2±3.0	35.5±2.2

REFERENCES

Carrier, D. R., et al.. 2001. *J. Exp. Biol.* 204, 3917-3926.

Eilam, D. (1994). *J. Motor Behav.* 26, 3-12.

Evans, M. R. and Thomas, A. L. R. (1992). *Anim. Behav.* 43, 337-347.

Jindrich, D. L. and Full, R. J. (1999). *J. Exp. Biol.* 202, 1603-1623.

Holden, J. P. and Cavanagh, P. R. 1991. *J. Biomech.* 24, 887-897.

Lee, D. V., et al. 2001. *J. Exp. Biol.* 204, 3927-3934.

Thollesson, M. and Norberg, U. M. (1991). *J. Exp. Biol.* 158, 19-35.

Van Den Berg, C. and J. M. V. Rayner. (1995). *J. Exp. Biol.* 198, 1655-1664.

CONFLICT BETWEEN MOMENTUM AND BALANCE CONTROL DURING LANDING

J.L. McNitt-Gray#, Philip Requejo#, and Henryk Flashner*

Biomechanics Research Laboratory, Department of Kinesiology#, Department of Mechanical Engineering*,
University of Southern California, Los Angeles, CA 90089, USA
Communicating author: mcnitt@usc.edu

INTRODUCTION

Multijoint control of moments induced by large reaction and intersegmental forces experienced during landing presents a significant challenge to the neuromuscular system prior to and during contact with the supporting surface. The set of muscles an individual chooses to control the reaction force will likely influence the mechanical loading experienced during the landing as well as their ability to position and control the momentum of the total body center of mass. The purpose of this study was to determine the source potential conflicts between momentum and balance control strategies used by individuals during landings requiring both momentum and balance control with a single placement of the feet.

METHODS

Successful landings (S: balanced without steps, n=11) and under rotated landings (UR: requiring a step forward to control balance, n=4) of flyaway layout salto dismounts performed by female gymnasts (mean height: 1.45m (.07±m); weight: 420N (62±N)) participating in the Artistic Gymnastics Competition during the 2000 Olympic Games were selected for analysis. During competition, flight and landing phase kinematics were simultaneously collected using two stationary digital cameras (200 Hz; C^2S NAC Visual Systems, Burbank, CA, U.S.A.). 3-D coordinates were derived from manually digitized 2-D coordinates using direct linear transformation (Abdel-Aziz & Karara, 1971) and filtered (15Hz, Woltring, 1986). A 2-dimensional human body model consisting of five rigid segments interconnected by frictionless revolute joints actuated by moments about the joint centers (Figure 1). The equations of motion representing the human system flight dynamics were expressed as a set of *N*-second-order differential equations of the form:

$$\mathbf{M}(\mathbf{q})\ddot{\mathbf{q}} + \mathbf{V}(\mathbf{q},\dot{\mathbf{q}}) + \mathbf{G}(\mathbf{q}) = \mathbf{Q}$$

Mechanical variables at initial contact and during the landing phase were computed and compared between successful (S) and under rotated (UR) landings.

RESULTS AND DISCUSSION

Gymnasts, able to achieve both momentum and balance control objectives (S), used multijoint strategies that allowed the CM position to come rest within their functional base of support. In contrast, gymnasts performing under rotated landings satisfied the momentum control objective using a multijoint strategy that resulted in a CM position beyond the functional base of support (Figure 1). No significant differences in CM position or velocity at contact were observed between the S and OR landings.

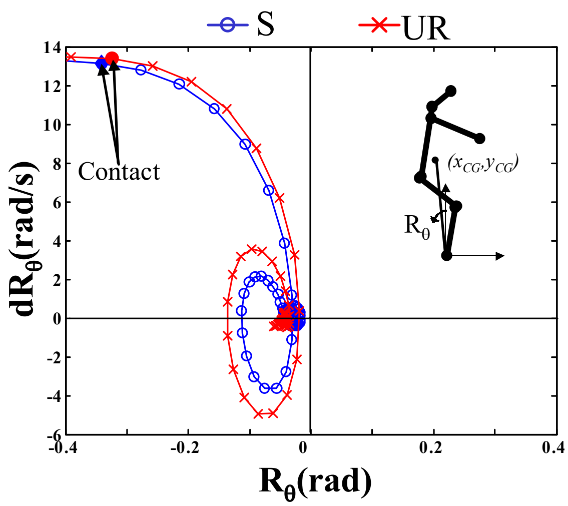

Figure 1:
Phase plane relationship between R angle and R angular velocity during the landing phase of S and UR landings. Note that the multijoint control strategy used by the individual performing the UR landing was unsuccessful in positioning their CM over the base of support.

SUMMARY

Successful landing performance requires the use of momentum control strategies that simultaneously achieve balance control objectives.

REFERENCES

Hogan, N. (1984) *IEEE Trans Auto Control* AC-29, 681-690.
Mathiyakom, W., et al. (1998). *Proceedings of NACOB'98, 439-440*
Mathiyakom, W., et al. (1999). *Proceeding of ISB'99, 167*
McNitt-Gray, J., et al. (2001) *J. Biomechanics*, 34, 1471-1482.

ACKNOWLEDGEMENTS

This project was funded in part by the IOC Medical Commission, Pfizer, Intel, and the ISB

EFFECTS OF TARGET DISTANCE AND SIZE ON REACHING KINEMATICS IN INDIVIDUALS WITH HEMIPARESIS

Patrick H McCrea[1,3] and Janice J Eng[2,3]

Dept. of Mechanical Engineering[1] and School of Rehabilitation Sciences[2], University of BC
Rehabilitation Research Lab[3], GF Strong Rehab Centre, Vancouver, Canada
www.rehab.ubc.ca/jeng

INTRODUCTION

The ability to reach with the upper extremity is critical for activities of daily living. Acute and chronic upper extremity impairment is experienced by 85% and 40% of individuals with brain injury, respectively (Parker et al., 1986).

Few formal rules in neuromotor control have the same status as Fitts' law (Fitts, 1954) with regards to its robustness and to its mathematical simplicity. The purpose of this study was to determine if the Fitts' tradeoff between speed and accuracy describes aimed reaching movements in persons with brain injury due to stroke. Secondly, we evaluated the kinematic properties of reaching to determine characteristics of reaching which may contribute to reaching performance.

METHODS

Twenty individuals with stroke (mean age=60.9±6.1 years, duration of injury=4.3±2.6 years, Fugl-Meyer upper extremity score=38±19 Ashworth=1.2±1.0) and 10 healthy age-matched controls (mean age=61±9.0 years) participated in the study. Individuals with stroke had a minimum of one year post-stroke and were able to voluntarily flex/abduct their shoulder 45° and extend their elbow 30°. Subjects were seated at a table and were instructed: "At the sound of the tone, reach to the target as fast as you can. Make sure that you touch the target." We randomized combinations of target distance (10, 20, and 40 cm) and width (2, 4, 8, 16 cm). Movements were recorded at 60 Hz with an infrared emitting diode (attached to the tip of the pointing finger) using a 3D optoelectronic system (Northern Digital) and then low pass filtered at 10 Hz.

The index of difficulty (Fitts, 1954) was determined as the logarithmic term where A is its amplitude (i.e., distance), W is the width of the target in the direction of movement, and constants a and b are experimentally determined:

$$MovementTime = a + b\log_2\left(\frac{2A}{W}\right)$$

Linear regressions were performed between movement time (representing speed) and the index of difficulty (representing accuracy) for four groups: 1) dominant arm-control, 2) non-dominant arm-control, 3) less affected arm-stroke, 4) more affected arm-stroke. MANOVAs quantified differences in kinematics (movement time, time to peak velocity, skewness, kurtosis, segmentation, and directness) among the groups. Kinematic measures were then correlated with movement time to determine factors underlying reaching performance.

RESULTS AND DISCUSSION

The relationship between movement time and index of difficulty was significant for all groups except for the more affected arm-stroke. A sub-analysis of the more affected arm-stroke group showed definitive trends towards linearity between movement time and index of difficulty for all these subjects, however, only half reached significance, suggesting that Fitts' Law was not as robust in this group.

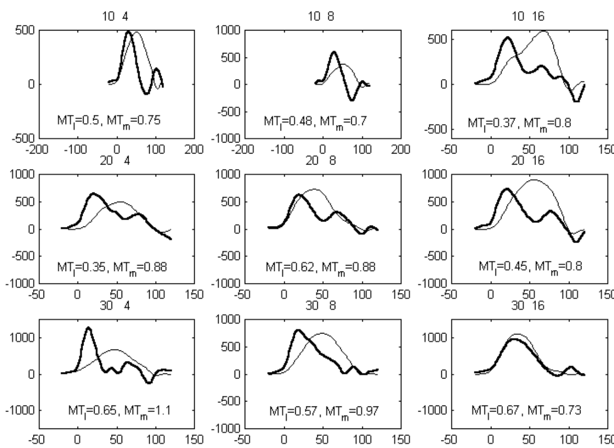

Figure 1. Typical velocity profiles normalized to movement time of the more (thick line) and less (thin line) affected arms in stroke. Plots are titled by target distance and width (in cm).
MT_l=movement time, less affected arm-stroke (sec).
MT_m=movement time, more affected arm-stroke (sec).

All kinematic measures were significantly different between the more and less-affected arm of the stroke subjects and surprisingly, between the non-dominant arm-control and the less affected arm-stroke for all measures except directness. In the more-affected arm, movement time was strongly correlated with segmentation (r=.92), skewness (r=.76), and time to peak speed (r=.89) while correlations between movement time and kinematic measures in the other 3 groups were more modest (< .50) or not significant.

SUMMARY

We suggest that the altered kinematics in the more affected arm-stroke group contributed to the weaker speed-accuracy relationship during a reaching task compared to the less affected arm-stroke group and healthy controls.

REFERENCES

Fitts, P.M. (1954). *J Exp Psych,* **47***,* 381-391.
Parker, V.M. et al. (1986). *Int RehabMed,* **8***,* 69-73.

ACKNOWLEDGEMENTS

This study was supported by the BC Health Research Foundation, a grant-in-aid and studentship from the Rick Hansen Neurotrauma Initiative.

MEASUREMENT OF THREE-DIMENSIONAL KINEMATICS OF THE GLENOHUMERAL JOINT DURING MANUAL WHEELCHAIR PROPULSION USING SKELETAL MARKERS

Tung-Wu Lu[1], Gen-Jia Li[1], Mei-Ying Kuo [1,2], Ling-Ying Chang [2], Horng-Chaung Hsu [2,3]

[1]Institute of Biomedical Engineering, National Taiwan University, Taipei, Taiwan. twlu@ccms.ntu.edu.tw

[2]School of Physical Therapy, China Medical College, Taichung, Taiwan

[3]Department of Orthopedics, China Medical College Hospital, Taichung, Taiwan

INTRODUCTION

Manual wheelchair propulsion (MWP) is an important form of mobility for people with locomotor system impairments, placing a huge mechanical demand on the glenohumeral (GH) joint. A complete understanding of the mechanics of the joint during MWP is essential for the prevention and treatment of relevant injuries. Due to the big relative movement between the scapula and the overlying skin, the motion of the GH joint has been approximated by that of the humerus relative to the trunk [1], providing only limited information of the GH motion. No study on the actual motion of the GH joint during MWP exists. The purpose of the study was to bridge the gap by measuring the 3-D kinematics of the scapula using skeletal pins.

MATERIALS AND METHODS

Five healthy male volunteers (age: 20-25 yr) participated in the study with informed consents. The experiment was approved by the Ethics Committee of the CMC Hospital. Each subject performed wheelchair propulsion in a gait lab equipped with a 7-camera motion analysis system (Vicon 370, Oxford Metrics, U.K.). The trunk and humerus were each attached with 4 retroreflective markers. Four markers attached to scapular bone-pins inserted into the acromion were used to provide the true positions of the scapula. Positions of the bony landmarks of the scapula relative to the bone-pin markers and those of the lateral and medial epicondyles relative to the humeral markers were defined using a pointer during a subject calibration trial.

Movements of the scapula were described relative to the trunk and those of the humerus relative to the scapula, giving the motion of the GH joint. The rotational movements of the humerus were defined using an Euler angle sequence consisting of the plane of elevation, amount of elevation and internal/external rotation (y-z'-y''). Rotation sequence for the scapula was internal/external rotation, upward/downward rotation and posterior/anterior tilting (y-z'-x'').

RESULTS AND DISCUSSION

The scapula moved significantly during MWP. Patterns of the scapula and GH joint motion are shown in Fig. 1. The scapula moved from 12º in protraction at initial contact to a maximum of 29º at the end of push phase and then retracted back to 12º during recovery. During the cycle, the scapula rotated downward followed by upward rotation with a range of approximately 8º and tilted anteriorly from 16º to 8º in posterior tilt and then back to 16º.

The GH joint moved from 43º in the posterior plane at initial contact and then moved progressively forward throughout the push phase and gradually reached a maximum of 9º in the anterior plane. The GH joint remained at about 40º of elevation throughout the propulsion cycle and rotated externally from 45º in internal rotation at initial contact to about 0º at the beginning of the recovery phase. These observed movement patterns differed significantly from those of the humerus relative to the trunk (Fig. 2), suggesting that traditional method of approximating GH motion by that of the humerus relative to the trunk is misleading.

The present study provided the first data on the 3D kinematics of the scapula and GH joint during MWP, which will be helpful for the improvement of the design of wheelchairs as well as the prevention and treatment of relevant injuries.

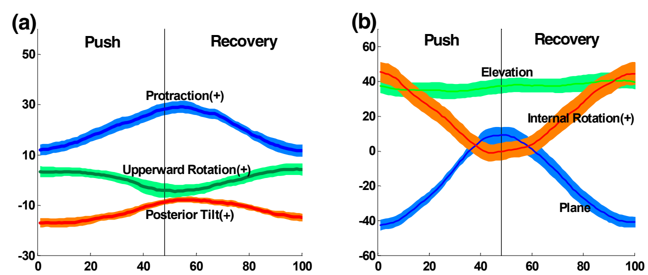

Fig. 1: Movement patterns of the scapula (a) and GH joint (b).

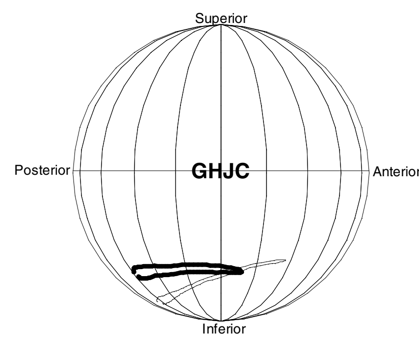

Fig. 2: Movement patterns of the GH joint from traditional method (thin curve) and the present study (thick curve).

REFERENCES

1. Davis, J.L., Growney, E.S., Johnson, M.E., and Iuliano, B.A. *Journal of Rehabilitation Research & Development*. 1998(35): 31-7.

COMPARATIVE ANALYSIS OF JOINT COMPLIANCE BY FINITE ELEMENT ANALYSIS AND ELECTRONIC SPECKLE PATTERN INTERFEROMETRY

OK Erne[1], YH Chu[1], J Miller[2], M Bottlang[1]

[1]Legacy Clinical Research & Technology Center, Portland, OR. *503-413-5489, mbottlan@lhs.org*

[2]Oregon Health & Science University, Portland, OR

INTRODUCTION

Finite Element Modeling (FEM) is a powerful method to investigate musculoskeletal structures. However, models of complex structures require validation by means of direct measurements [1]. We hypothesize, that a novel three-dimensional Electronic Speckle Pattern Interferometry system (3-D ESPI) is able to acquire full-field deformation measurements for validation of FEM models.

In this study, a 3-D ESPI system has been applied to measure tibial plateau deformation under compressive loading. This laser-based measurement technology enables acquisition of three-directional surface deformation maps in sub-micrometer resolution. For direct comparison, tibial plateau deformation was analyzed in a FEM of the proximal tibia under identical loading conditions. The results of this study demonstrate the merit of 3-D ESPI to deliver full-field experimental measurements that are directly comparable to FEM analyses of musculoskeletal structures.

METHODS

3-D ESPI Measurement: A tibia was harvested from a 78 years old non-embalmed female cadaver and transected 50 mm below the plateau. The proximal tibia section was potted with polymethylmethacrylate in a custom-made pressure chamber in a manner, that only the tibial plateau remained visible (Fig. 1a). Within this chamber, the tibial plateau was subjected to uniform pneumatic pressurization up to 200 KPa in 8 increments. The sensor of a 3-D ESPI system (Q100, Ettemeyer AG, Nersingen, Germany) was mounted over a glass cover on the chamber to record surface deformation on the tibial plateau in response to incremental pressurization.

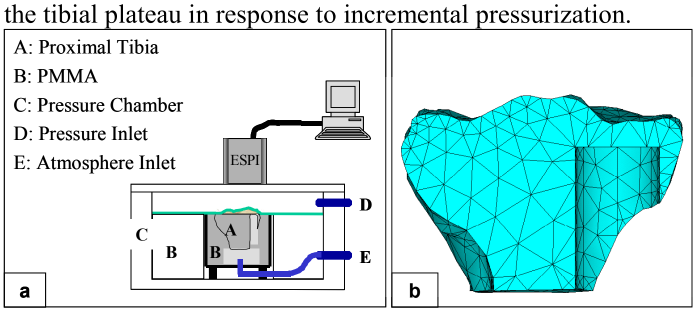

Figure 1: a) setup for 3-D ESPI measurement; b) FEM

The 3-D ESPI system generated laser speckle images on the plateau before and after pressurization. Subsequent subtraction and analysis of speckle images yielded the three-directional surface displacement over a 25 x 25 mm region of interest (ROI), which was centered over the medial tibial plateau. Three repeat measurements of the tibial plateau deformation in response to 200 KPa pressurization were obtained. Measurements were repeated after introduction of a 10 mm diameter cylindrical subchondral bone defect, centered underneath the medial plateau at 5 mm distance to the plateau.

FEM Simulation: A proximal tibia FEM was created in ANSYS (ASA IP, Canonsburg, PA) (Fig 1b). Model geometry was generated by milling the proximal tibia specimen in 1 mm coronal planes. Images of each coronal section were obtained, and the tibial surface geometry was digitized and imported to ANSYS. The FEM contained over 5,000 tetrahedral 4-node elements. Trabecular bone was modeled with linear elastic material properties, where the E-modulus of 554 MPa was estimated from DEXA bone density scanning of the specimen [2]. Equally distributed pressure of 200 KPa was applied, first to the intact FEM, and subsequently after introduction of the 10 mm diameter subchondral bone defect.

RESULTS

3-D ESPI was able to acquire full-field three-directional surface deformation reports on the medial plateau with high reproducibility. Extraction of the out-of-plane deformation component yielded a plateau center deflection of 4.05±0.45 μm in the intact specimen. After introduction of the subchondral defect, the maximum deflection increased significantly to 6.16±0.22 μm (Fig.2a). The FEM delivered center deflections of 6.34 μm and 8.45 μm for the intact and subchondral defect model, respectively.

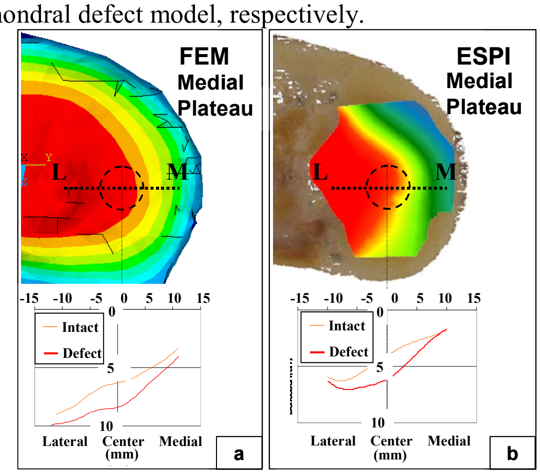

Fig. 2. Tibial plateau deflection: a) FEM, b) 3-D ESPI

DISCUSSION

This study demonstrated that the high sensitivity of 3-D ESPI allows for non-destructive evaluation of bone structure, while its three-directional displacement records are directly compatible with typical FEM output data. Since the sensitivity of 3-D ESPI is well below 0.5μm [3], differences in outcome parameters can be attributed to the limited detail and accuracy of the FEM.

REFERENCES

[1] Pistoia, W. (2001). J. Biomed. Eng.. **123**, 176-183.
[2] Hayes, W.C. (1991). Radiol Clinic N Am, **29**:1, 1991
[3] Schuetze, N.(2001). Trans 47th Orthop Res Soc, 444.

IN VIVO FUNCTION OF FASCICLES AND TENDINOUS STRUCTURES OF HUMAN GASTROCNEMIUS DURING STRETCH-SHORTENING CYCLE MOVEMENT

Sadao Kurokawa[1], Senshi Fukashiro[2], Tetsuo Fukunaga[2]
[1]Joshobi University of Art and Design, Tokyo, Japan, sadao.kurokawa@nifty.ne.jp
[2] Department of Life Sciences, University of Tokyo, Tokyo, Japan

INTRODUCTION

The purpose of this study was to investigate the *in vivo* function of human fascicle and tendinous structures during the stretch-shortening cycle (SSC) movement by observing the behavior of the muscle-tendon complex (MTC) using real time B-mode ultrasonography.

METHODS

Eight male subjects were requested to perform drop jumping (one of the typical SSC movement) from height of 0.2m (DJ). Simultaneously, ultrasonographic, kinematic, kinetic and electromyographic data were recorded during the movement.

A real-time B-mode computerized ultrasonic apparatus (SSD-2000, Aloka, Japan) was used with an electronic linear array probe of 7.5 MHz wave frequency to obtain longitudinal ultrasonic images of the gastrocnemius medialis (MG) during DJ. The probe was carefully fixed onto the tissue surface with a specially designed tool and elastic tape. During DJ, the longitudinal ultrasonic images of the MG were stored consecutively in the cine-memory of the ultrasonic apparatus set to operate at 40 frames$\cdot s^{-1}$. Fascicle lengths ($L_{fascicle}$) and Fascicle angles (α) were measured using NIH-image software.

The movements were filmed at 200Hz with a high speed digital video camera. Ground reaction force was recorded using a force platform. After synchronization of kinematic and kinetic data, instantaneous net joint moments about the ankle and knee were calculated using inverse-dynamics.

MTC length (L_{MTC}) of MG was estimated from knee and ankle joint angles (θ_k and θ_a, respectively) using the equation proposed by Grieve et al. (1978). Tendinous structure's length (L_{TS}), moment arm length (d), MG tendon force ($F_{tendon\ MG}$), MG fascicles force ($F_{fascicles\ MG}$) were calculated as follows;

$$L_{TS} = L_{MTC} - (L_{fascicle} \cdot \cos\alpha)$$
$$d = \Delta L_{MTC} / \Delta\theta_a$$
$$F_{tendon\ MG} = k_{MG} \cdot (M_{ankle} \cdot d^{-1})$$
$$F_{fascicles\ MG} = F_{tendon\ MG} \cdot \cos\alpha^{-1}$$

, where k_{MG} and M_{ankle} indicate the ratio of physiological cross sectional area of MG among plantar flexors and, the plantar flexing moments produced by single leg, respectively (see Kurokawa et al, 2001).

RESULTS AND DISCUSSION

During the down phase, MTC of MG was stretched by 4.0% relative to the length in the erect standing position. Fascicle, however, shortened by 10.6%. Consequently, the tendinous structures were stretched by 6.8%. During the following up

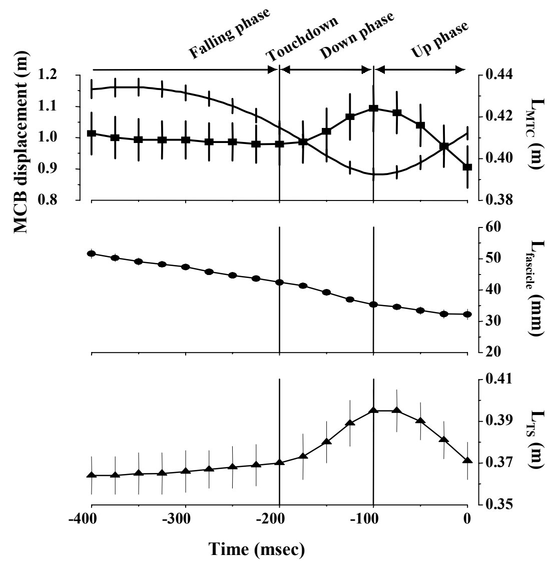

Fig. 1 Mean time histories of the displacement of mass center of body, muscle-tendon complex length, fascicle length and tendinous structures length during drop jumping. Time is expressed relative to instant of toe-off. Thin vertical bars indicate S.E.M., n=8 subjects.

phase, the fascicles continued to shorten only by 4.7% at relatively slow velocity (*i.e.*, quasi-isometric contraction of fascicle) while the MTC abruptly shortened by 6.5%. The work done by the fascicles was only 1.9 J in this phase. Elastic energy stored in the tendinous structures (7.6J ± 0.45J) during down phase was derived from the work done by the fascicles (5.0 ± 0.49J) and a part of mechanical energy change of subject between in the onset of down phase and in the end of up phase (2.6 ± 0.39J). 76% of the amount of elastic energy stored in the tendinous structures (5.8 ± 0.6J) was reutilized, and it account for 75% of the amount of mechanical work done by the MTC during up phase. It is highly probable that rapid recoil of tendinous structures allows the muscle fibers to behave quasi-isometrically during the up phase. It could be concluded that the fascicles function as a force generator operating high force region of force-length-velocity relationship, and the tendinous structures play the role of velocity generator during concentric phase, which was preceded by eccentric phase (pre-stretch) in SSC movement. And so, high power out put may be realized during this phase.

REFERENCES

Greive D.W. et al (1978). *Biomechanics IV-A*, 405-412.
Kurokawa S. et al (2001). *J Appl physiol,* 90, 1349-1358.

GENETIC VARIATIONS INFLUENCE BONE'S SENSITIVITY TO THE LOSS OF FUNCTIONAL WEIGHTBEARING

Stefan Judex, Russell Garman, Maria Squire, Clinton Rubin
Department of Biomedical Engineering
State University of New York, Stony Brook, NY

INTRODUCTION

The structure of the adult skeleton is determined, in large part, by its genome. Whether genetic variations also influence the degree of bone loss induced by bedrest, spaceflight, or aging is unknown. Using genetically distinct strains of inbred mice displaying greatly different bone mass and architecture (**Fig. 1**), we have recently demonstrated that the loss of functional weightbearing reduced osteoblastic activity in only one of three mouse strains considered while bone formation was unaffected in the other two strains. Here, we focused on the balance between bone formation and resorption and investigated whether genetic variations also control the effectiveness of mechanical disuse to alter bone quantity and quality.

METHODS

Adult (16wk) C57BL/6J (B6), BALB/cByJ (BALB), and C3H/HeJ (C3H) mice were subjected to either hindlimb suspension or free cage activity (n~10 per group) in protocols up to 3wk. Upon sacrifice, distal femurs were scanned in a micro-computed tomography (μCT) scanner (Scanco Medical AG, Switzerland) at a resolution of 11•m and fractional bone volume (BV/TV), trabecular number (Tb.N), trabecular spacing (Tb.Sp), trabecular thickness (Tb.Th), degree of anisotropy (DA), and structural model index (SMI, a measure of whether trabeculi are more plate-like or more rod-like shaped) was determined for the trabecular bone fraction.

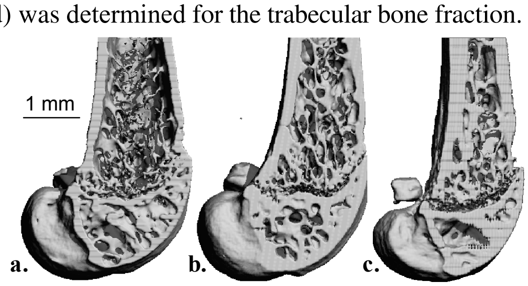

Figure 1. *Micro-computed tomography images of the distal femur, volumetrically rendered longitudinally between the femoral condyles from a 4 month old* ***(a.)*** *B6,* ***(b.)*** *BALB, and* ***(c.)*** *C3H mouse depicting the differences in trabecular and cortical bone structure associated with the differential genotype.*

RESULTS AND DISCUSSION

Fractional trabecular bone volume (BV/TV) of the distal femur was five-fold greater in BALB than in B6 mice (**Fig. 2**). Trabecular bone volume was similar between BALB and C3H mice despite the approximately 25% higher femoral bone mineral density (BMD) in C3H mice when BMD is averaged over the entire femur including both cortical and trabecular bone. The effect of hindlimb suspension on trabecular bone quantity and quality was greatly different in the three strains of mice. The loss of functional weightbearing caused a 60% reduction ($p<0.001$) in the amount of trabecular bone in BALB mice while no bone tissue was lost in C3H or B6 mice (**Fig. 2**). This large decrease in bone quantity was accompanied by compromised bone architecture in the BALB mice: connectivity density was decreased by 35% ($p<0.03$), trabecular number was decreased by 20% ($p<0.003$), and mean intercept length in the longitudinal direction was increased by 70% ($p<0.007$). The SMI increased by 80% ($p<0.0004$). In contrast, bone quality was not significantly affected by mechanical disuse in either C3H or B6 mice.

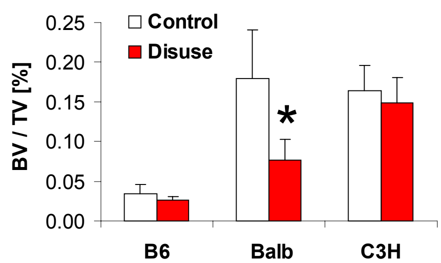

Figure 2. *Bone quantity (bone volume/tissue volume) of the distal femur was dramatically reduced in BALB but not in C3H mice (mean+SD, n~10).*

These data reveal the rapidity and severity by which mechanical unloading selectively reduces trabecular bone volume in BALB mice, but not in the similarly dense C3H strain or low bone density B6 strain. The current data are also consistent with our earlier studies in these three strains of mice which demonstrated that only osteoblasts from BALB mice responded to the loss of mechanical stimuli.

SUMMARY

We demonstrated that the efficacy of a strongly catabolic stimulus heavily relies on genetic makeup. Extrapolated to humans these data may explain the large individual variability in bone loss during bedrest, spaceflight, or aging. Our data also indicate that genetic variations may influence the effectiveness of therapeutic interventions of bone diseases. We are currently exploiting this large difference in mechanosensitivity between these three strains of mice to identify the genetic basis for this quantitative trait as well as to search for regulatory genes involved in the process by which mechanical stimuli (or lack of them) alter bone formation.

ACKNOWLEDGEMENTS

This study was kindly supported by NSBRI, NASA, and AHFMR.

ACTIVE MYOFIBER STRESS DISTRIBUTION IN PATIENT SPECIFIC MODELS OF CARDIAC MECHANICS

Liesbeth Geerts[1], Peter Bovendeerd[2], Roy Kerckhoffs[1,3], Theo Arts[1,4]
Faculties of [1]Mechanical and [2]Biomedical Engineering, Eindhoven University of Technology, Eindhoven, The Netherlands
Departments of [3]Physiology and [4]Biophysics, Maastricht University, Maastricht, The Netherlands
p.h.m.bovendeerd@tue.nl

INTRODUCTION

Mathematical models of cardiac mechanics are developing into a stage where patient specific modeling will be possible. Simultaneously, Magnetic Resonance Tagging offers the possibility of non-invasive assessment of cardiac tissue deformation. The combination of mathematical modeling and tagging may lead to a diagnostic tool, with which abnormalities in the cardiac deformation pattern can be deduced to the underlying tissue pathology. However, while some model parameters, e.g. geometry, can be assessed for each patient individually, for several model parameters, e.g. myofiber orientation, default model parameters must be used.
In this study, we assess the effect of incorporating a default myofiber orientation field in a patient specific geometry, on the model estimated active myofiber stress distribution.

METHODS

A finite element model of left ventricular (LV) mechanics (Bovendeerd et al., 1992) was used. Inner and outer LV surfaces were approximated by confocal ellipsoids. Variation between patient geometries was modeled by variation of the ellipsoid short axis/long axis ratio from 0.2 (GeoCYL) through 0.35 (GeoREF) to 0.99 (GeoSPHERE) (see Figure 1). Myofiber orientation was quantified by helix and transverse angles. Reference angle values (FibREF) were chosen to yield a practically homogeneous stress distribution in the reference geometry (Rijcken et al, 1999). Passive material was modeled nonlinearly elastic, transversely isotropic, and virtually incompressible. Active stress development was uniaxial, depending on myofiber strain, strain rate and time. LV afterload was simulated using a 3 element Windkessel model.

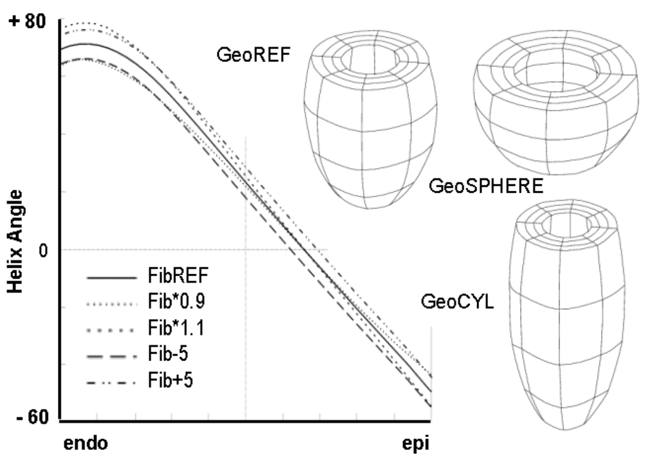

Figure 1: Geometries and helix angles in the model LV.

A complete cardiac cycle was simulated. Model predicted active stress was averaged in time over the ejection phase. Sensitivity of the equatorial transmural active myofiber stress distribution to geometry variation was assessed. For comparison, sensitivity to changes in transmural course of the helix fiber angle was determined, by changing, in the GeoREF geometry, either the slope by 10% (Fib*0.9 and Fib*1.1) or the offset by 5 degrees (Fib+5 and Fib-5) (see Figure 1).

RESULTS

Transmural stress distribution was virtually homogeneous in the GeoREF (48.1±1.5 kPa; mean±SD) geometry. Midwall stress was relatively low in the GeoCYL geometry, and high in the GeoSPHERE geometry and inhomogeneity in stress increased (GeoCYL: 45.9±5.2 kPa; GeoSPHERE: 43.2±5.5 kPa). A change in slope of the helix angle course (Fib*0.9, Fib*1.1) resulted in a redistribution of stress between midwall and superficial layers; a change in offset (Fib-5, Fib+5) gave a redistribution of stress between the subendocardial and subepicardial layers (Figure 2). For all helix angle variations SD in stress increased to about 5 kPa.

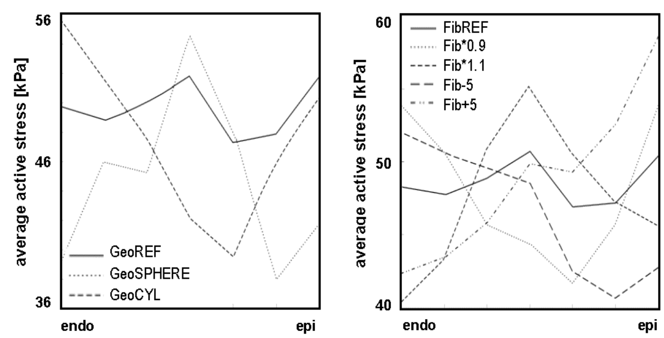

Figure 2: Equatorial time-averaged active myofiber stress, for varying geometry (left) and fiber orientation (right).

DISCUSSION AND CONCLUSIONS

Model geometry was varied over a wide range, expected to cover the majority of patient LV geometries. With the default fiber field, these geometry variations change active myofiber stress by about 10%. A similar change in stress is induced by a 10% change in slope or a 5 degree change in offset of the transmural course of the helix angle. The latter angle changes correspond to the accuracy of experimental angle data which makes the benefit of accounting for patient specific geometry questionable when using experimental fiber data. However, if fiber orientation is chosen for homogeneous distribution of active myofiber stress (Bovendeerd, 1992) or myofiber shortening (Rijcken, 1999), the optimal transmural range of the helix angle is expected to increase with decreasing short axis/long axis ratio of the ventricle.

REFERENCES

P.H.M. Bovendeerd et al. (1992). *J. Biomech.*, **25**,1129-1140.
J. Rijcken et al. (1999). *Ann. Biomed. Eng.,* **27**, 289-297.

MULTIJOINT CONTROL DURING SHORT DURATION MOVEMENTS IS SCALED USING BIARTICULAR MUSCLES

Witaya Mathiyakom, J.L. McNitt-Gray, K.E. Costa and P.S. Requejo
Biomechanics Research Laboratory, Department of Kinesiology, University of Southern California
Los Angeles, CA 90089, USA mathiyak@usc.edu

INTRODUCTION

Control and generation of large reaction forces during short duration movements presents a significant challenge to the neuromuscular system prior to and during contact with the supporting surface. In this paper, we tested the hypothesis that the multijoint control strategy used to generate impulse during short duration multijoint tasks (<0.2s) would be regulated by impedance like control as exhibited during the impact phase of landing tasks (McNitt-Gray et al., 2001). The take-off phase of Forward (forward translating, forward rotating) and Inward (backward translating, forward rotating) dives provided a set of practiced, goal directed multijoint movements to test this hypothesis. We expected that a) the set of muscles used to generate the impulse during the take-off phase of the dives would correspond with the net joint moments (NJMs) required by each task (**FW:** hip flexor and knee extensor NJM (Mathiyakom et al., 1998), IN: hip and knee extensor NJM (Mathiyakom et al., 1999) and b) the activation of biarticular muscles would be used to scale the impedance-like control between tasks.

METHODS

Eight US National Level divers (male = 5, female = 3) performed FW and IN dive take-offs (n=2) from a force platform onto a landing pit, using their competitive style. Two trials of the forward (FW) and inward (IN) rotating dive take-offs were analyzed. Sagittal plane kinematics (60 Hz), reaction force (1200 Hz) and muscle activation (surface EMG; 1200 Hz) of eight lower extremity muscles were simultaneously recorded and synchronized at plate departure. Significant between task differences in normalized EMG (20 ms bins) were tested using paired t-test ($p < 0.05$).

RESULTS AND DISCUSSION

Coactivation of muscles crossing both sides of the joints suggests that impedance-like control strategy (Hogan, 1984) was used to stabilize the joints when generating large (4-6 times body weight) impulsive forces (<0.2s) of both dives. As hypothesized, between-task differences in the activation patterns of biarticular knee-hip muscles were observed and corresponded with the specific NJM requirements of each task (Figure 1). Activation of the rectus femoris was significantly larger during the FW, whereas, activation of the hamstrings was significantly greater during the IN dive take-off. Regulation of multijoint joint control through the scaling of biarticular muscle activation may serve as a coordinative structure for short duration movements (Tuller et al., 1982). These results are consistent with rules of muscle coordination observed in other multijoint tasks (Yamashita, 1975; Wells & Evans, 1987; Prilutsky, 2000).

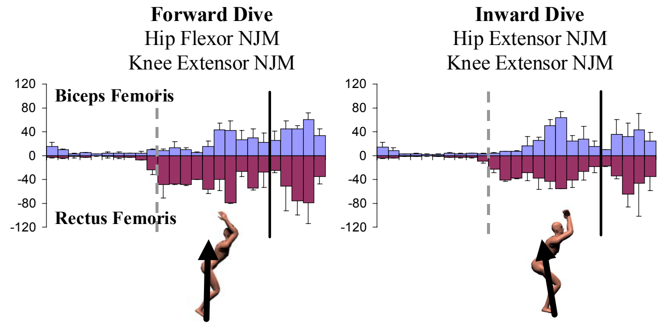

Figure 1: Activation of the primary knee and hip bi-articular muscles was scaled according to the mechanical demand imposed on the lower extremity during the take-off phase. No significant differences in trunk angular positions nor GM activation were observed between dives.

SUMMARY

Multijoint control during these short duration movements was scaled by modulating the activation of biarticular muscles. Activation of the bi-articular muscle was scaled according to the mechanical demands imposed on the lower extremity during contact. No significant differences in uniarticular hip extensor muscles, however, was observed between tasks.

REFERENCES

Hogan, N. (1984) *IEEE Trans Auto Control* AC-29, 68-690.
Mathiyakom, W. et al (1998). *Proceedings of NACOB'98, 439-440*
Mathiyakom, W. et al (1999). *Proceeding of ISB'99, 167*
McNitt-Gray, J. et al (2001) *J. Biomechanics*, 34, 1471-1482.
Prilutsky, B (2000). *Motor Control*, 4, 1-44.
Salvelberg, H, et al. (2001). *Proceeding of ISB'01*, 141-142
Wells, R., Evans, N. (1987). *Human Movement Science,* 6, 349-372
Yamashita, N (1975). *J. Human Ergol*, 4, 43-52

ACKNOWLEDGEMENTS

This project was funded in part by US Diving and Intel.

IDIOPATHIC SCOLIOSIS SIMULATION BY FINITE ELEMENT ANALYSIS WITH IMBALANCED GROWTH BETWEEN BONE AND SPINAL LIGAMENTS

Masahiro Todoh[1], Masao Tanaka[2] and Sohei Ebara[3]

Division Mechanical Science, Graduate School of Engineering Science, Osaka University, Toyonaka, Osaka 560-8531, Japan
[1]Research Associate, todoh@me.es.osaka-u.ac.jp
[2]Professor
Department of Orthopaedic Surgery, Shinshu University Medical School, Matsumoto, Nagano, Japan
[3]Senior Lecturer

INTRODUCTION

Idiopathic scoliosis develops during a rapid growth period. This suggests the growth of spinal column is one of primary causes of the idiopathic scoliosis. The etiology of idiopathic scoliosis remains to be elucidated [Lowe et al., 2000], although the spinal scoliosis simulation has been reported with local and/or asymmetric bone growth [e.g. Kawabata et al., 1988; Stokes et al., 1990]. The purpose of this study is to examine the spinal scoliotic curve from the viewpoint of imbalanced growth between the bone and surrounding ligament subsystems by computational biomechanics approach.

METHODS

A spinal column with rib cage was developed in three-dimensional finite elements by referring normal geometry and anatomy. The vertebrae were inter-connected by anterior and posterior longitudinal, intertransverse, supraspinous and interspinous, capsular ligaments and ligamentum flavum. This spine comprised of 8-node brick elements for bone and disc and the tension-only spar elements for spinal ligaments. The resultant spinal system was of 5,320 nodes and 4,646 elements.

The growth strain was applied to the bone elements of the spine model, while no growth was assumed for the ligaments, as an extreme situation. All the degree of freedom was constrained at the lower surface of L5 vertebra. The lateral translation and the rotation in sagittal plane were prescribed at C2 vertebra. The lack of symmetry with respect to the sagittal plane was considered for the asymmetric arrangement of the cardiac and arterial system, and a small disturbance was introduced at T8 level as the aortic force [Williams et al., 1989]. In this simulation, the effect of high growth rates introduced locally was also examined on the scoliotic curve pattern. The spinal deformation was simulated using ANSYS5.6 package (Ansys Inc., Houston, PA, USA).

RESULTS AND DISCUSSION

Figure 1 shows the frontal and sagittal vertebral alignments and vertebral axial rotation. Scoliotic curve was resulted by imbalanced growth between bone and surrounding ligament subsystems. The curve was of rightward convex thoracic pattern with apex at level T9. It showed the vertebral axial rotation toward the convex side of the scoliotic deflection. The scoliotic simulations with locally high growth rates represented significant influence on scoliotic deflection and rotation.

SUMMARY

The scoliosis and rotation were investigated based on the accumulation of internal stress/strain caused by the imbalanced growth between the bone and surrounding ligament subsystems. The results suggested that the imbalanced growth between bone and spinal ligaments plays a potential role in idiopathic scoliosis as a biomechanical etiology.

REFERENCES

Kawabata, H. et al (1988). *J. Jpn. Orthop. Assoc.*, **62**, 161-170.
Lowe, T.G. et al (2000). *J. Bone Jt. Surg.*, **82**-A, 1157-1168.
Stokes, I.A.F. et al (1990). *J. Biomech.*, **23**, 589-595.
Williams, P.L. et al (1989). *Gray's anatomy*. Churchill Livingstone, Edinburgh.

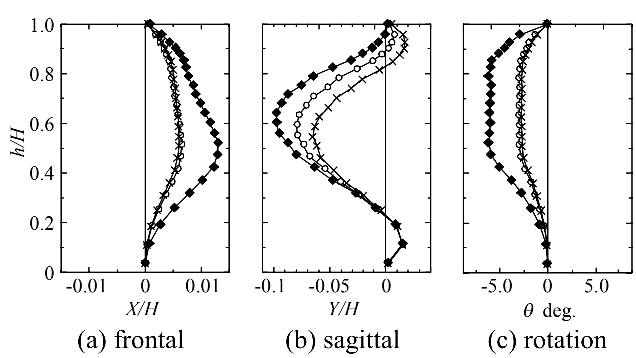

Figure 1: Frontal and sagittal vertebral alignments and vertebral axial rotation (Uniform growth rates [×], High growth rates in upper vertebrae C2-T6 [o] and in lower vertebrae T7-L5 [♦]).

FULL-FIELD STRAIN MEASUREMENT OVER ARTICULAR CARTILAGE CROSS-SECTIONS WITH ELECTRONIC SPECKLE PATTERN INTERFEROMETRY

O. K. Erne[1], L. Ehmke[1], J. Reid.[2], M. Bottlang[1]
[1]*Legacy Clinical Research & Technology Center, Portland, OR*. 503-413-5489, mbottlan@lhs.org
[2]*Oregon Health & Science University, Portland, OR*

INTRODUCTION

Quantitative assessment of strain distributions in articular cartilage is key to understand its normal function and disease mechanisms. Over the past decades, a multitude of tests were introduced to measure static and dynamic constitutive properties of articular cartilage. Within the distinct layers of articular cartilage, pronounced variations in material properties were observed and modeled (Mow, 1997; Flachsmann, 2001). Despite widespread efforts to quantify these non-linear strain distributions, no continuous full-field strain map across articular cartilage has been acquired to date. We hypothesize, that an advanced Electronic Speckle Pattern Interferometry technique (3D-ESPI) can be used to measure the strain distributions across diarthrodial joints. In this study, we employed a 3-D ESPI system to measure strain distributions on confined articular cartilage *in situ*, loaded in quasi-static compression. For comparison, we additionally obtained the strain profile across a homogeneous specimen.

METHODS

A novel 3-D ESPI system was used to measure surface strain fields on two specimens, a homogeneous fiber composite, and articular cartilage of a diarthodial joint.

A paper based fiber composite with a width of 6 mm was confined between two aluminum brackets, in a manner that the surface of the brackets and the composite were in the same plane. The cartilage specimen was harvested from a fresh frozen bovine femoral-tibial joint. The joint was sectioned in para-coronal planes using a diamond saw to obtain a 3 mm thick joint cross-section. The articular cartilage remained attached to the underlying epiphysial bone of the tibia and femur. Each specimen was loaded in uniaxial compression in displacement control to a nominal strain amplitude of 1.65% in a custom-built setup. While the composite specimen was only confined by the compression brackets, the surface of the cartilage specimen was additionally confined underneath a glass-plate to simulate apposition of the neighboring joint cross-sections. In addition, the surface of the cartilage specimen was stained with gold chloride to obtain adequate reflective properties for 3-D ESPI measurements. Compression was applied incrementally with a precision micrometer, and the resulting total displacement over each specimen was measured with a displacement transducer (LVDT LD 400-5, Omega, Stamford, CT). A laser-based quantitative 3D-ESPI system (Q100, Ettemeyer AG, Nersingen, Germany) was employed to measure the full-field surface deformation and strain on the specimen surface after each incremental load step. ISTRA software (Ettemeyer AG, Nersingen, Germany) was used for speckle pattern image analysis.

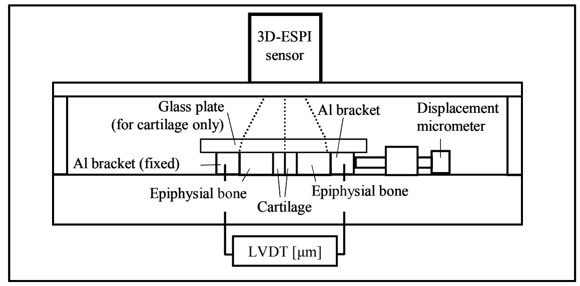

Fig. 1: Side view of test setup with cartilage specimen.

RESULTS

The 3D-ESPI system acquired continuous full-field strain maps on both specimens. The specimens demonstrated highly distinct strain distributions. The strain profile over the aluminum brackets and the composite specimen approximated a step function (Fig.2a). The average compressive strain across the 6 mm wide composite was 1.44%, and approximated the total applied compression of 1.65%. The strain profile across the joint specimen exhibited two compressive strain peaks of up to 2.23% strain. The strain peaks exceeded the predicted strain by up to 35% and were observed at the middle layers of each cartilage. Strain at the cartilage surface layer was 86% smaller as the total applied compressive strain of 1.65% (Fig.2b).

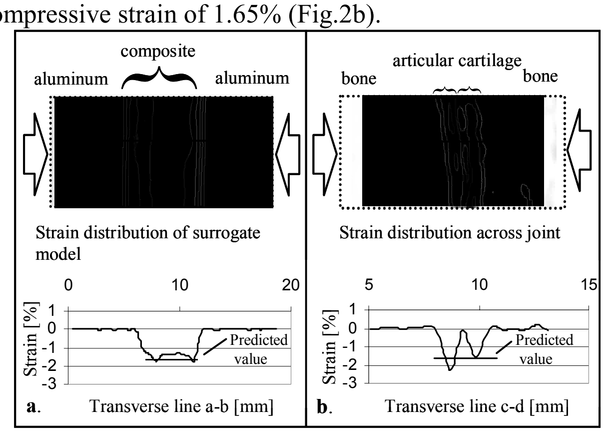

Fig.2: Strain distributions and strain profiles on a) composite specimen; and b) joint cross-section.

DISCUSSION

The results of this study demonstrate that 3D-ESPI is a powerful tool to elucidate non-linear strain distributions across diarthrodial joints. Further refinement of the experimental approach is likely to provide a unique approach to quantitative delineate normal and degenerative joint properties.

REFERENCE

Mow, V.C. et al (1980). J Biomech **102** 73-84
Flachsmann, R. et al (2001). J Orthop Res **19** 1131-1139
Narmoneva, D. et al (1999). J Biomech **32** 401-408

EFFECT OF ANKLE JOINT CONSTRAINT BY AFO ON MAINTENANCE OF STANDING POSTURE

Masao Tanaka[1], Masahiro Todoh[2] and Masanobu Ogawa[3]

Division of Mechanical Science, Graduate School of Engineering Science, Osaka Univ., Toyonaka, Osaka 560-8531, Japan
[1]Professor, tanaka@me.es.osaka-u.ac.jp
[2]Research Associate.
[3]Graduate Student

INTRODUCTION

Ankle Foot Orthoses (AFOs) have been considered useful aid for the disabled patients with gait disorder to assist standing and walking activities. Such aids primarily support and keep the ankle joint at an appreciate position by constraining the movement of ankle joint. Although the constraint of the joint movement brings some restriction in daily life activities at the same time, few studies have been reported on the effect of joint constraint. In this study, the effect of ankle joint constraints is examined in terms of different ranges of motion at ankle joint for the maintenance of standing posture under the forward translation of foot floor.

METHODS

In this investigation, six healthy male subjects participated voluntarily. The experimental set-up is shown in Figure 1. Subjects are requested to stand on the motion platform (MMS-612E2, Mitsubishi Precision) at horizontal position wearing metal column AFOs on their both limbs. The motion platform is translated in forward direction simulating the departure of vehicle such as trains or buses, in four different patterns by the combination of high and low maximal acceleration (800mm/s^2, 250mm/s^2) and short and long translation (53mm, 150mm). The metal column AFO enables us to adjust the ankle joint range of motion (ROM). By using this mechanism, five ROM conditions are employed of the experiment (Table 1).

The angular displacements of lower limb joints are recorded by the goniometers (M110/M180, P&G) mounted on the joints of right limb. The center of pressure and resultant force of foot pressure are recorded by the foot pressure sensor (Pedar standard/expert, Novel). The joint moments are calculated based on two-dimensional four-link model of human body consisting of foot, shank, thigh, and trunk. The joint stiffness is calculated for each time interval of 0.2 second as the slope of joint moment against the angular displacement.

RESULTS AND DISCUSSION

In the cases with dorsal ROM constraint (case3, case4), the angular displacements at joints were smaller than those in the cases without dorsal ROM constraint (case0, case1, case2), exhibiting the smaller body motion. It suggested us the large influence of the dorsal flexion for the maintenance of standing posture, and supported the importance of the dorsal flexion in maintenance of standing posture in sagittal plane reported [Mihelj et al. 2000]. When the dorsal ROM was constrained,

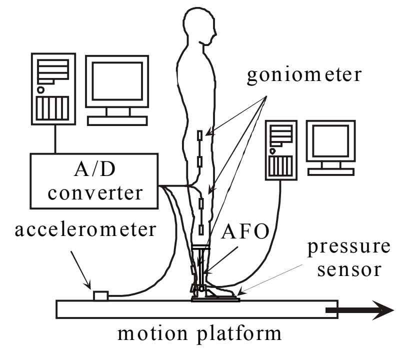

(a) Experimental set-up

(b) AFO

Figure 1 : Experimental system

Table 1 : Ankle joint constraint cases

	case0	case1	case2	case3	case4
dorsal	B	U	U	C	C
plantar	B	U	C	U	C

B: bare foot C: constrained U: unconstrained

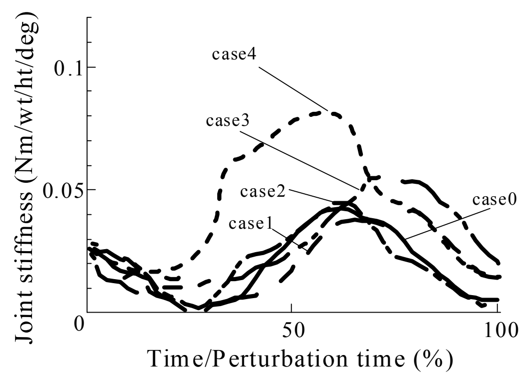

Figure 2 : Knee joint stiffness (800mm/s^2, 150mm)

the maxima of the joint moments decreased, but the joint stiffness increased (Figure 2). This showed that the smaller body motion under the dorsal ROM constraint was understood by active stiffness adjustment, by using the muscle function.

REFERENCE

Mihelj, M. et al. (2000). *Gait and Posture*, **12**, 94-104.

INFLUENCE OF SPASTICITY ON HEMIPLEGIC ANKLE JOINT MOMENT

Masao Tanaka[1], Masahiro Todoh[2], Yasushi Akazawa[3] and Hiroyuki Uematsu[4]

Division of Mechanical Science, Graduate School of Engineering, Osaka University, Toyonaka, Osaka 560-8531, Japan
[1]Professor, tanaka@me.es.osaka-u.ac.jp
[2]Research Associate
[4]Graduate Student
The Hyogo Assistive Technology Research & Design Institute, Hyogo Rehab. Ctr., Kobe, Hyogo, Japan
[3]Research Engineer

INTRODUCTION

Hemiplegia is a typical and serious pathology by cerebral stroke. Following to the initial recovery stage, locomotion is frequently disordered due to involuntary plantar flexion of ankle joint by spasticity. Ankle Foot Orthosis (AFO) is prescribed to assist such subjects keeping ankle joints at neutral or slightly dorsal position. In this context, the mechanical function of AFO closely related to spasticity in hemiplegic patients. This study examines characteristics of hemiplegic ankle joint with spasticity from the viewpoint of biomechanical ankle joint moment.

METHODS

AFOs are requested to secure the toe clearance in swing phase by resisting to the involuntary plantar flexion of ankle joint. Thus, it is the first step of AFO prescription and design to measure the plantar flexion moment at ankle joint caused by spasticity. Figure 1 shows the experimental set-up used to investigate the relation between ankle joint moment and ankle joint angle.

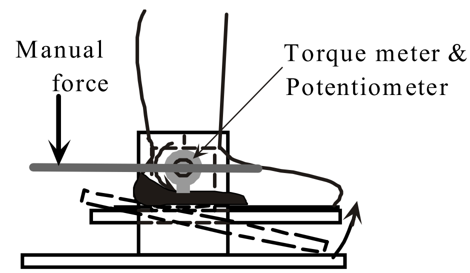

Figure 1 : Measurement set-up for ankle joint angle and moment

Simulating the manual treatment by physical therapist, subjects' ankle joints were flexed in dorsal/plantar direction passively through the operation lever. Subjects were instructed to keep upright sitting posture during the experiment. Six hemiplegia (45-77 years old) and six normal subjects (22-24 years old) participated voluntarily in the experimental measurement. All hemiplegic subjects have a capability to walk with AFO independently.

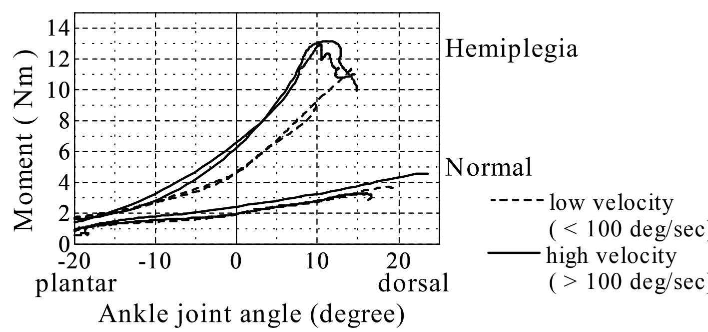

Figure 2 : Typical of ankle joint angle-moment relationship of hemiplegia and normal subjects

RESULTS AND DISCUSSION

Figure 2 shows typical examples of ankle joint angle and moment relationship of a normal subject and a hemiplegic subject. Lance et al. (1980) defined the spasticity as a motor disorder characterized by velocity–dependent increase in tonic stretch reflex. The observed relationship between ankle motion and resistant moment were dependent on the angular velocity and were larger than those of normal subjects. Under the high angular velocity over 100 deg/sec, most hemiplegic subjects exhibited moment oscillation i.e. clonus. This oscillation might be caused by hyperexcitability of a kind of the stretch reflex.

The joint moment deviation of hemiplegic subjects increased rapidly around the angular velocity of 80-120 deg/sec. During the gait motion, the range of angular velocity of hemiplegic subjects may be slower than this threshold in general. It is possible to estimate an appropriate stiffness of an AFO suitable for each patient by referring to resistant moment in this study, although these remains some possibility that factors such as mental intention happen to bring some excess joint moment over the estimated in swing phase.

REFERENCE

Lance, J. W. et al. (1980), *Spasticity: Disordered Motor Control*, *pp.485-494*, Year Book Medical Publishers

EFFECT OF PHYSICAL THERAPY AND AFFERENT STIMULATING INSOLES ON MOTOR ABILITIES IN PARKINSON PATIENTS

S. Kimmeskamp, E.M. Hennig and T.L. Milani
University of Essen, Department of Human Locomotion; 45131 Essen, Germany; stefan.kimmeskamp@uni-essen.de

INTRODUCTION

Parkinson's disease (PD) is caused by a deficiency in the neurotransmitter dopamine in the region of the basal ganglia of the brain. Parkinson patients show combined clinical symptoms of rigidity, bradykinesia or even akinesia, as well as resting tremor. They also experience disorders of posture, balance, and gait. Although there are indications of the benefit of physical therapy in PD, there is still need to identify the core elements in PD rehabilitation (1,2). In this study we compared the effects of balance training and trunk flexibility exercises on motor abilities in Parkinson patients. Parkinson patients use external cues (visual or auditory) to improve motor performance. Therefore, a second purpose of this study was to test the therapeutic effect of additional sensory input, provided by foot afferent stimulating insoles. The hypothesis behind this approach is that PD patients use the additional external information (cues) to partially compensate the basal ganglia pathology (2). It is suspected that foot sensation has a considerable influence on locomotion and posture control.

METHODS

96 Parkinson patients were randomly assigned to four different intervention groups. The first group (BN) performed balance training and wore an insole with 4 mm high nubs, evenly distributed across its surface. This insole stimulates skin receptors of the foot. The second group (BB) also trained balance, but wore a "placebo" insole with a formed foot bed (hardness: shore 36 A) and an even surface. The third group (TN) carried out trunk flexibility exercises. They also wore the stimulating insole. The fourth group (TB) also performed trunk flexibility exercises, but wore the smooth insole. The duration of the intervention period was 4 weeks. During this period the physical therapy exercises were performed daily, for 30 minutes. Additionally, the patients were asked to wear the insoles every day as long as possible. Patients with a change of medication were excluded from the study. 22 patients who were not involved in any intervention served as a control group (Co). Gait and balance analyses were performed before and after the intervention period, using a mobile pressure insole system (NOVEL GmbH, Munich). For gait and balance measurements all patients wore a simple canvas shoe. The intervention insoles were not worn during the measurements. The balance task included parallel stance, tandem stance, single limb stance and functional lean forward. Center of Pressure (COP) data were collected over a maximum period of 30 seconds for all balance tasks. Prior to the measurements a neurological examination was undertaken to classify the motor impairment according to the UPDRS-Score. Pre- and post measurements were undertaken during best medication status of the patients and at the same time of the day. The COP_net displacement as well as the characteristics of sway in anterior-posterior (A/P) and medial-lateral (M/L) directions were calculated for all balance tasks. A two way ANOVA analysis was performed to examine differences between the intervention groups.

RESULTS & DISCUSSION

For the parallel stance condition the two way ANOVA revealed a significant reduction of the COP displacement in A/P direction for the balance training group ($p<0.01$). A similar result was observed for the COP_net excursion ($p<0.05$). However, neither the trunk flexibility exercises nor any insole led to significant changes in parallel stance performance. The parallel stance results indicated that a daily performed balance training helps PD patients to achieve a greater safety during standing.

Figure 1) Changes in functional lean forward (Post – Pre)

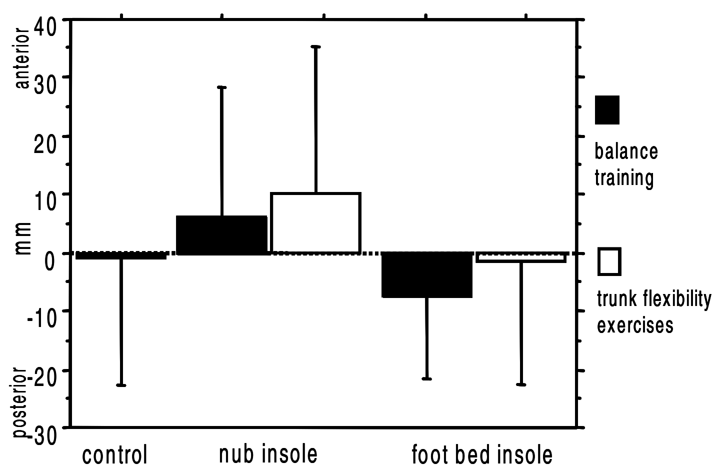

Figure 1 shows the changes in the functional lean task. This task tests the ability of PD patients to shift the COP in a parallel stance position as far forward as possible without lifting the heel from the ground. The nub insole has a highly significant ($p<0.01$) positive effect on the ability of PD patients to lean forward (figure 1). This indicates a therapeutic effect of the nub sole, resulting in an increase of the functional base of support in PD patients

REFERENCES

1) Schenkman M, et al. Exercise to improve spinal flexibility and function for people with Parkinson`s disease: a randomized, controlled trial. J Am Geriatr Soc. 1998;46:1207-1216.

2) Morris, M.E. Movement disorders in people with Parkinson disease: A model for physical therapy. Phys Ther. 2000; 578-597

RADIOGRAPHIC LANDMARKS OF THE KNEE FLEXION-EXTENSION AXIS

Martin, K[1]; Callahan, E[1]; Sommers, MB[1]; Marsh, J[2]; Bottlang, M[1]
[1]Legacy Clinical Research & Technology Center, Portland, OR; email: mbottlan@lhs.org
[2]Department of Orthopaedic Surgery, University of Iowa Hospital and Clinics, Iowa City, IA

INTRODUCTION

Articulated external fixation can be utilized to restore joint function of severely injured knee joints (Simonian, 1998). However, in a clinical scenario it is crucial to closely approximate the flexion-extension axis of the knee to maximize the attainable joint motion. No intra-operative radiographic axis detection technique has been introduced to date, which would allow for proper alignment of an external hinge to the knee. In this study, we identified landmarks to indicate the predominant flexion-extension axis of the knee on lateral radiographs. We furthermore quantified the effect of reversing the radiographic exposure direction on radiographic projections. Both of these aspects are directly applicable to increase the accuracy of hinged fixator application to the knee joint.

METHODS

Eight fresh frozen human cadaveric legs were amputated 130 mm proximal and distal to the knee joint line and mounted in a Plexiglas frame at 30° of knee flexion. Each specimen was aligned and secured such that the predominant flexion extension axis of the knee joint was oriented along the radiographic axis of a standard C-arm fluoroscope (9600 OCEM, Salt Lake City, UA). This alignment position was determined by the centers of two concentric circles fitted to the posterior 140° aspects of the medial and lateral condyles [Hollister, 1993]. Radiographic images were obtained for this 'on-axis' position as well as for 8 distinct 'off-axis' orientations: 5° and 10° each of internal and external, varus and valgus rotation. Two sets of images were recorded with (1) the radiographic source being located lateral to the specimen and (2) the source being located medial to the specimen. At all times specimens were centered between the C-arm source and receiver. All radiographs were comparatively analyzed to extract the indices which most sensitively and reliably depicted femoral on-axis alignment. Indices were quantified on each pertinent radiograph using quantitative image analysis software (PV Wave, Visual Numerics, Inc., Houston, TX) after use of gray-scale equalization and edge enhancement algorithms on the digital radiographs.

RESULTS

The accuracy of on-axis alignment on lateral radiographs (x-ray source lateral to specimen) was documented in terms of the center disparity ***CD*** of circles fitted to a 140° arc on the posterior condyles. The average center disparities in anteroposterior ($\boldsymbol{CD_{AP}}$) and proximodistal ($\boldsymbol{CD_{PD}}$) directions were 0.6±1.7 mm and –1.1 ±1.4 mm, respectively (Fig. 1a). The corresponding radii of the circles fitted to the medial and lateral condyles were 17.9±1.7 mm and 19.4±1.4 mm, respectively. The posterior arc of the medial condyle was projected inside the lateral condylar arc. Radiographs obtained with 5° and 10° internal/external femur rotations significantly increased the center disparity in anteroposterior direction ($\boldsymbol{CD_{AP}}$), while 5° and 10° varus/ valgus exposures significantly altered the center disparity in proximal distal direction ($\boldsymbol{CD_{PD}}$).

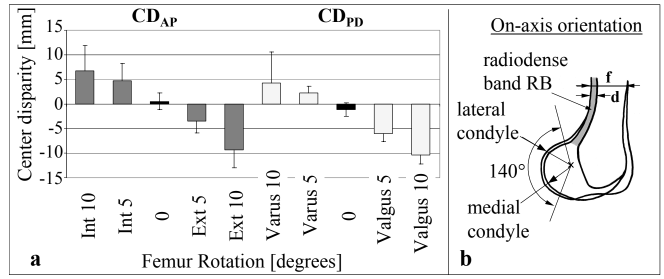

Figure 1a) Center disparity index; **b)** on-axis femur alignment

In addition to ***CD***, two further radiographic indices were determined: The ***RB*** index for internal/external rotational alignment, expressed in terms of the width of a radiodense band with respect to the femoral shaft diameter (***RB***=d/f). And the ***DR*** index for varus/valgus directional alignment, expressed in terms of the radius difference between the circles fitted to the medial and lateral condyles (Fig. 1b). On-axis radiographs were characterized by ***RB*** = 14±3% and ***DR*** = 0.9±1.9 mm (Fig. 2a, 2b).

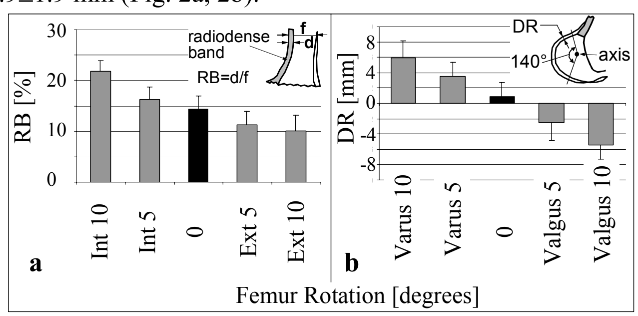

Figure 2: a) Rotation index; **b)** Varus/Valgus index

Shifting the radiographic source from the lateral to the medial side altered the appearance of the medial condylar arc relative to the lateral condylar arc, with the radii of circles changing to 18.1±1.2 mm and 17.9±1.6 mm, respectively.

DISCUSSION

While the reported CD index requires implementation of a circle-fitting algorithm, the RB, and DR indices can easily be assessed intra-operatively by linear measurement, and provide distinct sensitivity to systematically adjust femoral internal/ external, and varus/valgus rotation. Also important was the finding that if a radiograph of the knee is obtained with the x-ray source located lateral, the anatomically larger medial condylar arc is projected inside the smaller lateral arc. This is especially important since radiograph exposure with the source located laterally is routinely used in knee fluoroscopy.

REFERENCES

Simonian et al. (1998), *Am J Sports Med*, **26(4)**, 591-596
Hollister et al. (1993), *Clin Orthop Rel Res*, **290**, 259-268

TRAUMATIC BRAIN INJURY IN AN ACCELERATION-DECELERATION SCENARIO

Yung-Hua Chu[1] and Michael Bottlang[1]

[1]*Legacy Clinical Research & Technology Center, Portland, OR*. 503-413-5489, mbottlan@lhs.org

INTRODUCTION

In the United States, traumatic brain injury (TBI) is the leading causes of death and long-term disability among people below the age of 45. Evidence of diffuse axonal injury (DAI) is observed in over 35% of all TBI injuries. The objective of the present study is to model a sequence of acceleration-deceleration to the head that will induce shear strain concentrations which closely reflect clinically observed DAI. In 1989, Adams introduced a grading system for DAI, indicating *Grade 1* DAI as axonal damage limited to white matter; *Grade 2* DAI as focal lesions in the corpus callosum in addition to *Grade 1*; and *Grade 3* DAI as focal lesions in the brain stem in addition to *Grade 2*. In addition, we hypothesize that cerebrospinal fluid (CSF) can significantly reduce shear damage to the brain. Therefore, we created a finite element model (FEM) which accounts not only for distinct material properties for specific brain compartments, but which also explicitly models CSF.

MATERIAL AND MATHODS

The geometry of a para-sagittal plane of the head was reconstructed from the Visible Human Male data set, and the finite element analysis was proceeded with ANSYS™ (Fig. 1). The nonlinear viscoelastic material properties of the cerebral and cerebellar white matter were assigned with exponential decay shear modulus G_0=39.47KPa, G_∞=17.24KPa and a decay constant t=0.01s (Bandak, 1995). A constant high bulk stiffness of K=1.86GPa was implemented to simulate near incompressibility of brain tissue (Bandak, 1995). The material properties of white matter were assumed four times stiffer than those of the cerebral and cerebellar cortex and thalamus (gray matter) to account for their fibrous structure (Cotter et al., 2001). CSF was modeled as a viscoelastic solid that was assumed 10 times softer than the cerebral white matter. The skull and the cervical vertebrae were modeled as homogeneous linear elastic solids with E=6.5GPa and ν=0.2 (Bandak, 1995).

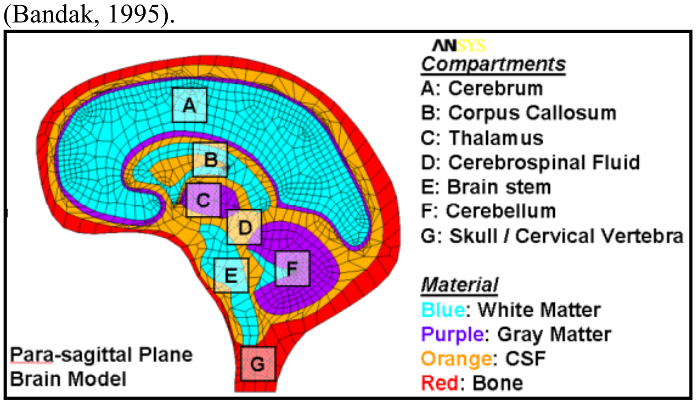

Figure 1: Finite element geometry and distinct compartments of the brain.

To simulate a moderate to sever brain injury over an acceleration-deceleration sequence of 30 ms, a 5,000N frontal step load was applied to the forehead for 15 ms, followed by a dorsal step load of –5,000N for 15 ms to the hind head. Boundary conditions enforced angular rotation of the skull around a hinge joint at the second cervical vertebra (C2). Nonlinear time-dependent transient dynamic analysis was performed to allow for large deformation, while accounting for inertial effects.

RESULTS

CSF absorbed more than 9 times the shear strain energy than any other brain compartment. During backward <u>acceleration</u> of the head, the interface between gray and white matter of the cerebellum observed shear strain concentrations indicative of *Grade 1* mild brain injury. *Grade 2* moderate DAI was initiated in the distal side of the corpus callosum. During backward <u>deceleration</u> (i.e., after application of the dorsal load step) of the head, the shear strain rate in brain compartments increased rapidly to its maximal values due the large inertial effect during load reversal (Fig.2). *Grade 3* severe DAI was predicted close to distal site of the brain stem.

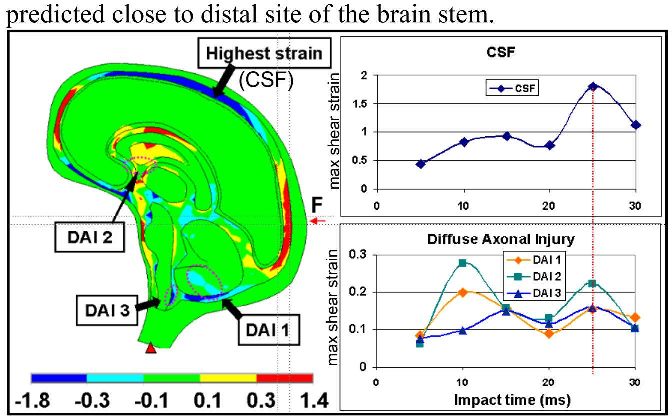

Fig. 2: Shear strain distribution during deceleration at 25 ms.

DISCUSSION

The results of this study demonstrated that CSF reduced the shear strain to brain compartments by absorbing shear strain energy. The 5,000 N focal impact load and time history realistically resembled acceleration and deceleration conditions, which are associated with *Grade 1* mild DAI, *Grade 2* moderate DAI to *Grade 3* severe DAI. The results of this study closely correlate with clinically observed diffuse axonal injury of the brain during an angular acceleration-deceleration sequence.

REFERENCES

Adams, J.H., et al., (1989). *Histopathology*, **15**, 49.

Bandak, F.A., (1995). *J. Neurotrauma*, **12**, 635.

Cotter, C.S., et al., (2001) Bioeng Conf, ASME 2001. 315.

Varney, R.N., et al., (1999). Lawrence Erlbaum Assoc., London.

REACTION FORCES INDUCED BY MUSCLES IN THE PRESENCE OF COMPLIANT CONTACT

Frank C. Anderson, Allison S. Arnold, and Scott L. Delp
Biomechanical Engineering Division, Mechanical Engineering Department, Stanford University, Stanford, CA, USA
E-mail: fca@stanford.edu Web: http://www.stanford.edu/group/nmbl

INTRODUCTION

Musculoskeletal simulations have tremendous potential to clarify the dynamical actions of muscles during movement (Zajac and Gordon, 1989). However, determining the actions of muscles during tasks that involve compliant interactions with the environment remains a challenge. Reaction forces are generated in response to muscle forces and must be taken into account to understand how individual muscles contribute to the motions of the body. In the presence of compliant contact, it is difficult to know what portion of a reaction force to attribute to an individual muscle because reaction forces are position- and velocity-dependent and do not respond to muscle forces instantaneously. We have developed a method to calculate the reaction forces induced by muscles during movement when interactions between the body and the environment are modeled using viscoelastic elements.

METHOD

Our method is applicable to forward dynamic simulations in which interactions between the body and the environment (e.g., the foot and the ground) are modeled by a set of damped springs distributed over the contact area. The objective of the method is to decompose the reaction force (F_s) of each spring into component forces that are attributable to active forces within the body:

$$F_s = F_s^G + F_s^C + \sum F_s^m \ , \qquad (1)$$

where F_s^G , F_s^C , and $\sum F_s^m$ represent the contributions to the reaction force of the forces due to gravity, Coriolis-centripetal effects, and muscles, respectively.

The force response of a damped spring results from changes in its displacement (x) and velocity (v). This force response can be expressed as a Taylor series expansion of the equations used to model the spring:

$$dF_s = F_s(x+dx, v+dv) - F_s(x,v) = \frac{\partial F_s}{\partial x}dx + \frac{\partial F_s}{\partial v}dv + O(2) \ , \qquad (2)$$

where dx and dv are changes in the displacement and velocity of the spring, respectively, and $\partial F_s / \partial x$ and $\partial F_s / \partial v$ are the instantaneous stiffness and viscosity of the spring, respectively. When $|dx| << 1$ and $|dv| << 1$, the second order and higher terms, $O(2)$ in Eq. (2), are small and dF_s can be expressed in terms of linear decompositions of dx and dv :

$$dF_s \approx \frac{\partial F_s}{\partial x}\{dx_G + dx_C + \sum dx_m\} + \frac{\partial F_s}{\partial v}\{dv_G + dv_C + \sum dv_m\} \qquad (3)$$

Hence, to decompose F_s it is necessary to determine how each force in the body contributes to changes in the displacement and velocity of the spring.

Using a Taylor series expansion in time, dx_m and dv_m can be expressed as functions of the accelerations induced by each muscle:

$$dx_m(t+dt) = v_m \cdot dt + \tfrac{1}{2} a_m \cdot dt^2 \qquad (4)$$

$$dv_m(t+dt) = a_m \cdot dt \ , \qquad (5)$$

where a_m and v_m are the acceleration and velocity of the spring induced by the muscle and dt is a small time step analogous to the integration time step used during a forward simulation. The acceleration of the spring induced by the muscle is computed from the inverse of the system mass matrix (I^{-1}), the force in the muscle (F_m), and the corresponding reaction component (F_s^m):

$$a_m = \Psi(I^{-1}\{F_m + F_s^m\}) \ , \qquad (6)$$

where Ψ is a transformation between the accelerations of the generalized coordinates of the model and the acceleration of the spring. Eqs. (2)-(5) can be combined to obtain an expression for the change in spring force that occurs during a time step due to F_m :

$$dF_s^m(t+dt) \approx \frac{\partial F_s}{\partial x}(v_m \cdot dt + \tfrac{1}{2} a_m \cdot dt^2) + \frac{\partial F_s}{\partial v}(a_m \cdot dt) \ . \qquad (7)$$

The decomposition is performed by integrating Eqs. (5) and (7) concurrent with the forward dynamic simulation:

$$F_s^m(t) = F_s^m(t_o) + \int_{t_o}^{t} dF_s^m dt \ , \quad v_m(t) = v_m(t_o) + \int_{t_o}^{t} dv_m dt \ , \qquad (8)$$

where $v_m(t_o)$ and $F_s^m(t_o)$ are initial values for the spring velocity and force induced by the muscle and t_o is the initial time of the simulation. Analogous integrations are performed for each force term.

RESULTS AND DISCUSSION

Several investigators have used musculoskeletal simulations to examine the actions of muscles during movement. In these studies, the reaction forces induced by muscles were either ignored, or were estimated using perturbed forward integrations (Neptune et al., 2001) or hard constraint techniques (Anderson and Pandy, 2001a). These approaches have important limitations. The perturbed integration method is imprecise, and it does not allow superposition of the reaction components (Eq. (1)) to be verified. Hard constraint techniques assume rigid contact between the body and the environment. To the extent that contact is not rigid, a portion of the reaction force cannot be explained. This portion can be substantial during impacts, which occur during walking and other activities. Our new decomposition method overcomes these limitations and is applicable to a wide range of biomechanical simulations. We have successfully used this method to decompose the ground reaction force for a 3D simulation of gait (Anderson and Pandy, 2001b) in which contact was modeled using damped exponential springs.

REFERENCES

Anderson FC, Pandy MG. (2001a). *Gait & Pos.*, **13**, 292-293.
Anderson FC, Pandy MG. (2001b). *J. Biomech.*, **34**, 154-161.
Neptune RR et al. (2001). *J. Biomech.*, **34**, 1387-1398.
Zajac FE, Gordon ME (1989). *Ex. Sport Sci Rev.,* **17**, 187-230.

ACKNOWLEDGMENTS

NIH R01 HD38962 and NIH R01 HD33929

VENOUS RETURN IN LOWER LIMB DURING MUSCULAR CONTRACTION

Jean-Thomas Aubert[1], Ethelle Chabran[1], Philippe Arbeille[2], Bernard Maton[3] and Christian Ribreau[4]

[1] Laboratoires Innothera, Arcueil, France, jean-thomas.aubert@innothera.com
[2] Unité Médecine et Physiologie Spatiale, CHU Hôpital Trousseau, Tours, France.
[3] Laboratoire de Physiologie du Mouvement, INSERM U483, Université Paris-Sud, France
[4] Laboratoire de Génie Mécanique Productique et Biomécanique, IUT de Cachan, France

INTRODUCTION

It is well known that in the lower limb, venous flow rate is highly affected by its environment. Indeed, movements, either body force variations or muscular contractions, act on vein and blood. The effects of such actions are not precisely quantified yet. This paper deals with the quantification of flow rate variations in the Common Femoral Vein (CFV) during muscular contractions.

MATERIAL AND METHODS

Venous flow rate was deducted from Doppler echo-velocimeter (ATL HDI 5000). The CFV cross section was measured by transverse scan, in opposition with red cells velocity measurements. Flow rate through the CFV stands for the output boundary condition of the venous network in the lower limb whereas the Popliteal Vein (usual measurement spot) drains only the shank blood (Winter et al, 2000).

The recordings were performed on 11 healthy subjects at rest and during specified movements.

The biomechanical parameters of movements that made explicit the activities of muscles were controlled by means of goniometers (Biometrics), accelerometers (Entran) and a force plate (Satel) for making sure of the repeatability of situations as well as possible and to deduce the body force distribution in blood. Moreover, 6 muscles activities were investigated by superficial EMG: 3 for thigh (Rectus Femoris, Vastus Lateralis and Biceps Femoris) and 3 for shank (Gastrocnemius, Soleus and Tibialis Anterior).

For specified movements of the lower limb, the activation of the muscles gave rise to the filling and emptying of veins. Two postures were defined for differentiating two conditions of the venous network compliance: subjects were standing or lying supine. Furthermore, loaded and unloaded limbs, with or without foot support, were investigated.

The movements involving loaded limbs in standing position were: (i) a so-called voluntary contraction of the femoral quadriceps; (ii) leaning forward with straight legs (the only ankle angle was changing); (iii) loading of the free lower limb from a monopodal position to the bipodal position; (iv) tiptoe; (v) dorsal flexion of feet in standing position.
The movements involving unloaded limbs were: (i) a so-called voluntary contraction of the femoral quadriceps and (ii) dorsal flexion of feet in lying supine position; (iii) flexion/extension of the leg on the thigh in the standing position, for a constant angle of flexion of about 45° of the thigh on the trunk.

RESULTS

Primary results (Aubert et al. 2001) show large flow rate variations due to muscular activation: from 100 mL/min to 5000 mL/min. Table 1 shows the results of this primary study realised on one healthy subject only. The communication will present the results obtained from the 11 subjects.

	Unloaded limb	Loaded limb
Knee flexion/extension	2.4	
Voluntary contraction	4.5	32
Leaning forward		13.3
Lower limb loading		13.7
Tiptoe		7.9

Table 1: Relative venous flow rate variations in the CFV due to muscular activation in standing position*100 % (Venous flow rate in the CFV in orthostatic position: 150 $mL.min^{-1}$)

DISCUSSION AND CONCLUSION

This communication presents the variations of the mean flow rate (mean-time average) in relation to the flow rate at rest for each specified movement. It shows the huge effects due to the activation of the muscles in the whole lower limb and not only the calf muscles.
Consequences on wall shear stresses may be expected. Endothelial cell physiology and endothelial cell functions should be concerned by such a study (Haond et al. 1999).

REFERENCES

Aubert J.-T. et al. (2001) Flow Rate Measurements In The Common Femoral Vein During Activities Of The Muscles In The Lower Limb. *Archives of Physiology and Biochemistry*, **109**, 85.

Haond C. et al. (1999) Laminar flow through a model of collapsed veins. Morphometric response of endothelial vascular cells to a longitudinal shear stress non uniform cross-wise. *Eur. Phys. J. AP.,* **8,** 87-96.

Winter D.A. et al. (2000) The venous pump during standing. *Archives of Physiology and Biochemistry*, **108**, 1/2, 36.

BODY FORCE DISTRIBUTION IN VEINS OF THE LOWER LIMB DURING STATIONNARY GAIT

Jean-Thomas Aubert[1] and Christian Ribreau[2]

[1] Laboratoires Innothera, Arcueil, France, jean-thomas.aubert@innothera.com
[2] Laboratoire de Génie Mécanique Productique et Biomécanique, IUT de Cachan, France

INTRODUCTION

Blood flows towards the heart through collapsible vessels: the veins. The flow equations in collapsible tubes show a strong dependence on body forces. The kinematic analysis of the stationary gait had been performed in sagittal plane in order to calculate the acceleration and its variations on every point of the 3D venous network.

BACKGROUND

Flow in collapsible tubes is governed by Equation 1:

$$\rho\left(\frac{\partial U}{\partial t}+U\frac{\partial U}{\partial x}\right)=\rho\,(G_x-M_x)-\frac{\partial p_e}{\partial x}-\frac{\partial (p_i-p_e)}{\partial x}-f_V \quad (1)$$

U	axial flow velocity
p	internal and external pressures
G_x	axial component of gravity
M_x	axial component of movement acceleration
x	flow axis
f_V	viscous force
ρ	fluid density

MATERIAL AND METHODS

In order to calculate the absolute acceleration and its variations on any point of the lower limb, the walking limb was considered as a triple pendulum in the sagittal plane (Figure 1a). The kinematic data of the stationary gait have been recorded by eight infrared cameras on one healthy subject (Aubert et al. 2001).
Absolute acceleration of each point of the venous network (in reference to the galilean referential) were computed from the data, and then expressed in the local coordinate frame of each venous trunk of the 3D venous network (Figure 1b).

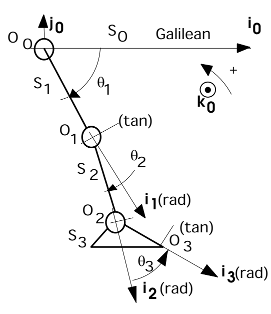

Figure 1a

Figure 1b

Figure 1: Models
a/ the lower limb; b/ a 3D venous network

RESULTS

As an example, Figure 2 shows the evolution of $\frac{\partial}{\partial t}\left(\frac{G_x}{G}-\frac{M_x}{G}\right)$ at a given node of the network.

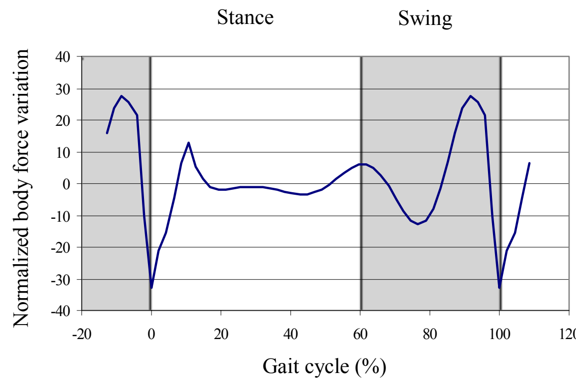

Figure 2: Variation of the normalized body forces on a distal point of the Internal Saphenous Vein for over one stride

The different results which are presented in this communication show that component peaks $[M_x]_{max}$ and $[G_x]_{max}$ can vary from [0 - 1,5 G] and [0 - 1 G] respectively. These results agree with Wu's study (Wu et al. 1996). Moreover, results present possible huge variations from 0 to 30 $G.s^{-1}$ of the body forces.

DISCUSSION AND CONCLUSION

Venous trunks are affected with large acceleration peaks M_x (greater than the gravity) and variable orientation of gravity by respect to the vessel axis. Moreover, body force variations undergone by venous trunks are not only large, but also very fast. These points, often forgotten in the modelisation of flow in collapsible tubes open a new field for future theoretical investigations.

REFERENCES

Aubert J.-T. et al. (2001) Acceleration in the venous network of the lower limb during stationary gait. A*rchives of Physiology and Biochemistry*, **109**, 86

Wu G., Ladin Z. (1996) The study of kinematic transients in locomotion using the integrated kinematic sensor. *IEEE Trans Rehabil Eng.*, **4(3)**, 193-200.

BIOMECHANICAL ANALYSIS OF THE UPPER EXTREMITY BETWEEN BADMINTON SMASH AND TENNIS SERVE

Chien-Lu Tsai, Chenfu Huang*, Der Chia Lin*, Shaw Shiun Chang,

National Taiwan Ocean University, Keelung, Taiwan
*National Taiwan Normal University, Taipei, Taiwan

INTRODUCTION

The motions of the tennis service and the badminton smash are quite similar. They are the typical techniques and the most powerful skills in the racket sports. Previous studies related to badminton, Tang, et al, 1994 he used 3D model to measure the rotation of the forearm and the wrist. And had been described the smash strokes. Elliott (1986, 1988) described the motions of the tennis serve. The purpose of this study is going to compare the kinetics variables (the net joint forces, moments and powers) on the upper extremities between tennis serve and badminton smash. In this study, we are interested in analyzing from the phase of the period before and after the point of making contact with the ball or the shuttle.

METHODS

An international world Champion elite badminton player (182cm, 74kg) in Taiwan was served as subject to perform the badminton smash technique. An elite tennis player (top 10 ranking in Taiwan, 192cm, 89kg) was served as the subject to perform the tennis serve in this study. The body segment parameters of each subject were calculated by the model of Dempster(1955). The upper extremity of the subject was separated into three segments, upper arm, forearm and racket (with fist included). A Kodak Ekta-Pro 1000 high-speed video camera (500Hz) was used to record the 2D data. The inverse dynamics solution was employed to calculate the forces, moments and powers of the upper segment joints.

RESULTS AND DISCUSSION

Table 1 shows that the initial velocity of the badminton smash (68.4m/s) is faster than the initial velocity of the tennis serve (61.4m/s). The angular velocity of tennis serve was greater than badminton smash on the wrist joint. The results showed the angular velocity of the wrist joint of the tennis serve is greater than the badminton smash. In figure 1 shows that the peak force of the upper limb joints in tennis serve were occur earlier than the peak force occur in badminton smash. The figure 2 shows the power of the upper limb joints at the contact. The joint power of the tennis serve was greater than the value in the badminton smash. We recommend that the regular training on the elbow flexor will reduce likelihood of injury due to stress the flexor through eccentric contraction during acceleration phase of the badminton smash and the tennis serve.

Table 1: The Variables Comparison Between 2 Movements

Variables	Badminton Smash	Tennis Serve
Initial Velocity	68.4m/s	61.4m/s
Wrist Contact Force	234N	227N
Wrist Contac Torque	44Nm	295Nm

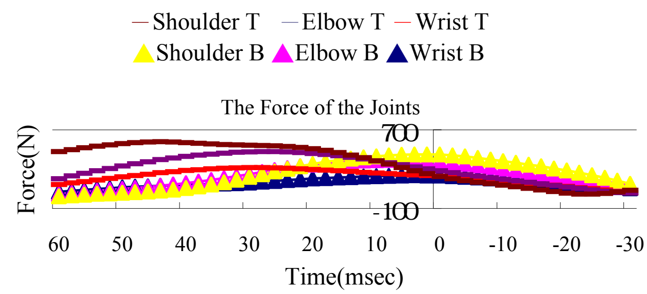

Figure 1: The Joint Resultant Force Pattern of Tennis Serve and Badminton Smash

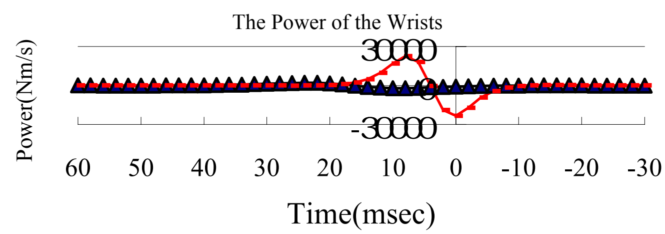

Figure 2: The Dynamical Pattern of Tennis Serve and Badminton Smash —Tennis ▲Badminton

SUMMARY

The purpose of this study is going to compare the biomechanical variables on the upper extremities between elite badminton player and elite tennis player when they were performing badminton smash and tennis serve movements. In this study, we found that the value of the joint force, moment and power of the tennis serve were greater than the badminton smash. The results showed that dynamical pattern of the three overhead strokes were different. The regular training on the wrist extensors will be necessary for reduce the risk of the injury of wrist extensors.

REFERENCES

Winter, D.A.(1990). *Biomechanics and motor control of human movement (2nd ed.)*. New York:Wiley, 103-139.

RESISTANCE TRAINING RESULTS IN AN INCREASED H-REFLEX EXCITABILITY DURING MAXIMAL MUSCLE CONTRACTION BUT NOT AT REST

Per Aagaard[1,4], Erik B. Simonsen[2], Jesper L. Andersen[3], S. Peter Magnusson[4], Poul Dyhre-Poulsen[1]
[1]Dept of Neurophysiology, [2]Anatomy Dept C, Panum Institute; [3]Copenhagen Muscle Research Centre, Rigshospitalet; [4]Team Danmark Test Centre, Sports Medicine Research Unit, Bispebjerg Hospital.
University of Copenhagen, Denmark. E-mail: p.aagaard@mfi.ku.dk

INTRODUCTION

The Hoffmann (H) reflex can be used to assess the excitability of spinal α-motoneurons, while also reflecting the transmission efficiency (i.e. presynaptic inhibition) in Ia afferent synapses (Schieppati 1987).

In the present study H-reflex measurements were performed during maximal muscle contraction and at rest to examine the effect of resistance training on spinal motoneuron function.

METHODS

Fourteen male subjects (age 25.3 ±4.7 yrs) participated in 14 wks (38 sessions) of heavy resistance training (4-10 RM loads) for the leg muscles. Evoked H-reflex and M-wave responses were recorded pre and post training in the soleus muscle during maximal isometric ramp contractions and at rest.

During maximal muscle contraction (2-s isometric ramps) an electrical stimulus (1 ms square pulse) was applied to the tibial nerve (popliteal fossa) at the instant the ankle plantar flexor moment exceeded 90% MVC. Stimulus intensity was adjusted to yield an M response of 20 ±2.5% of the maximal M-wave (M_{max}) (Dyhre-Poulsen et al. 1991, Simonsen et al. 1999, Ferris et al. 2001). In the resting muscle, the maximal H-reflex response expressed relative to M_{max} (i.e. H_{max}/M_{max}) was obtained as a measure of H-reflex excitability at rest (Voigt et al. 1998, Maffiuletti et al. 2001).

Maximal concentric, eccentric and isometric muscle strength were measured by use of isokinetic dynamometry (KinCom).

RESULTS

During maximal isometric ramp contractions, peak-to-peak H-reflex amplitude increased ($P < 0.05$) from 5.37 ± 0.41 to 6.24 ± 0.49 mV with training (± SEM). When expressed relative to M_{max}, the H-reflex amplitude increased from 0.514 ±0.032 to 0.609 ±0.025 ($P < 0.05$).

In contrast, H_{max}/M_{max} recorded at rest remained unchanged with training (0.503 ±0.059 vs 0.499 ±0.063). Also, during rest the direct M response at H_{max} did not change (0.103 ±0.024 and 0.116 ±0.021, expressed relative to M_{max}).

No change was observed in M_{max} with training (10.78 ±0.86 vs 10.21 ±0.66 mV).

Maximal muscle strength increased 23-30% ($P < 0.05$).

DISCUSSION

In the present study an increased H-reflex excitability was observed during maximal voluntary muscle contraction in response to 14 wks of heavy-resistance strength training. Consequently, the neural adaptation to resistance training appears to include increases in spinal motoneurone excitability (and/or reduced presynaptic Ia afferent inhibition). It could be speculated that the increase in H-reflex excitability was caused by reduced presynaptic inhibition of Ia afferent terminals. However, in young subjects it has been demonstrated that the amount of presynaptic inhibition is low or even fully abolished during forceful plantarflexor contraction (Butchart et al. 1993).

Lower resting H_{max}/M_{max} has been reported for endurance athletes compared to athletes trained for explosive sports (see Maffiuletti et al. 2001). It cannot be excluded, however, that these findings were the result of subject differences in muscle fibre composition, since at low stimulation intensity the evoked EPSPs will exert a stronger excitatory influence on the smallest spinal motoneurons that innervate the population of slow type I muscle fibres.

In the present study, the H-reflex response measured at rest (H_{max}/M_{max}) remained unchanged with training. In contrast, H-reflex excitability increased during active muscle contraction. Identical findings were recently reported in response to 4 wks of hopping training (Voigt et al. 1998).

Based on these findings, it is strongly suggested that training induced changes in neural motor function should be evaluated by recording of the H-reflex during actual contraction, and not rely solely on measurements obtained at rest.

REFERENCES

Dyhre-Poulsen, P., Simonsen, E.B., Voigt, M. (1991). *J. Physiol.* **437**, 287-304.
Butchart, P., Farquhar, R., Part, N.J., et al. (1993). *Exp. Physiol.* **78**, 235-242.
Ferris, D.P., Aagaard, P., Simonsen, E.B., et al. (2001). *J. Physiol.* **530.1**, 167-180.
Maffiuletti, N.A., Martin, A., Babault, N., et al. (2001). *J. Appl. Physiol.* **90**, 3-9.
Schieppati, M. (1987). *Progr. Neurobiol.* **28**, 345-376.
Simonsen, E.B., Dyhre-Poulsen, P. (1999). *J. Physiol.* 515.3, 929-939.
Voigt, M., Chelli, F., Frigo, C. (1998). *Eur. J. Appl. Physiol.* **78**, 522-532.

BIAXIAL TENSILE PROPERTIES OF AORTIC ANEURYSM TISSUES UNDER EQUIBIAXIAL STRESS

Tomohiro Fukui[1], Takeo Matsumoto[1], Toshihiro Tanaka[1], Toshiro Ohashi[1]
Kiichiro Kumagai[2], Hiroji Akimoto[2], Koichi Tabayashi[2] and Masaaki Sato[1]

[1]Biomechanics Lab., Graduate School of Mech. Engng., Tohoku Univ., Sendai, Japan
[2]Dept. of Thorac. & Cardiovasc. Surg., Graduate School of Medicine, Tohoku Univ., Sendai, Japan

INTRODUCTION

It is important to know the mechanical properties of human aortic aneurysm tissues to investigate the mechanism of their rupture. Aneurysmal walls might be stretched equibiaxially in vivo, because the radius of curvature is almost similar between the circumferential and axial directions of the aorta. Thus, it is crucial to obtain their biaxial tensile properties. While it is important to consider these properties in a physiological state, it is difficult to estimate the strain levels of each subject. It has been reported that hoop stress in a physiological state is kept constant among the aortas of various subjects (Matsumoto, 1994). Thus, mechanical properties under a physiological equibiaxial stress would be a good estimate of those in vivo. In this study, mechanical properties of aortic aneurysms and their adjacent normal tissues were measured under equibiaxial stress with a biaxial tensile tester developed in our laboratory (Tanaka, 2000).

METHODS

Fourteen 15mm square specimens were obtained from 10 thoracic aortic aneurysms of various origins and their adjacent aortas with edges aligned to the circumferential and axial directions of the aorta during aortic replacement surgery. The biaxial tensile tester has two orthogonally-arranged pairs of arms, which are pulled apart by a computer-controlled stepping motor. Each edge of the specimen was hooked with four or five clamps. They were then connected to each arm with a silk thread. A 5mm square bench mark was drawn in the middle of the specimen with black shoe polish. The specimen was stretched biaxially in the physiological saline at room temperature by widening the distance between the opposite arms at the rate of 0.2mm/sec. The tensile test was started at the point where the specimen had 0.1 to 0.2N tension in each direction. Specimens were not preconditioned because some of the specimens were very fragile. The circumferential direction of the specimen was taken as x direction as far as its directions were known clearly.

Cauchy stress in the x and y directions (σ_x, σ_y), and infinitesimal strain in these directions (ε_x, ε_y) were calculated assuming that the specimen was incompressible. Although the displacement of the arms was set equal for both directions, neither strain nor stress applied to the specimen was equibiaxial. The stress-strain curves under equibiaxial stretch were obtained by fitting measured curves with an exponential type two-dimensional strain energy function considering material anisotropy (Fung, 1979):

$$W = C\exp(aE_x^2 + bE_y^2 + 2cE_xE_y)\,,$$

where E_x and E_y are the Green's strains, and C, a, b, and c are material constants. Incremental elastic modulus in an in vivo state was obtained as the slope of the stress-strain curves under equibiaxial stress. The modulus averaged for both directions $H_m = (H_x+H_y)/2$ was used as an index of tissue stiffness. As an anisotropy index, $K_\varepsilon = |\varepsilon_x - \varepsilon_y|/\varepsilon_m$ was used.

RESULTS AND DISCUSSION

Figure 1 shows a relationship between H_m and K_ε at $\sigma_x=\sigma_y=200$kPa. In case that multiple specimens were obtained from a patient, each parameter was averaged. There was a significant correlation between the two parameters (R=0.699, P<0.03, n=10). With the progression of the aneurysm, the wall tissue may not only get stiffer but also become more anisotropic.

In this study, we evaluated the mechanical properties of aneurysm tissues in the same stress level. However, the physiological stress level might differ among aneurysms. It is necessary for the future study to estimate stress level of each aneurysm from its shape and blood pressure of each patient.

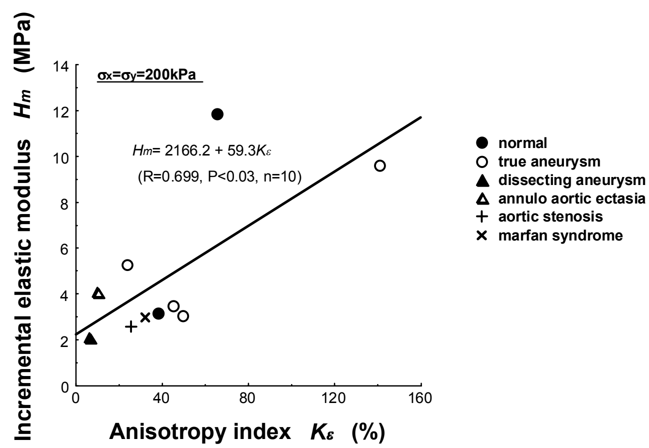

Figure 1:Relationship between H_m and K_ε at $\sigma_x=\sigma_y=200$kPa.

REFERENCES

Fung, Y.C. et al. (1979). *Am. J. Physiol.* **237**, H620–631.
Matsumoto, T. and Hayashi, K. (1994). *J. Biomech. Engng.* **166**, 278–283.
Tanaka, T. et al. (2000). *Proc. 12th Bioeng. Conf., 1999 Annual Meeting BE D/JSME*, 29–30.

MEASUREMENT OF INVERSION AND EVERSION MOVEMENTS OF THE FOOT BY USING A POSITION TRANSDUCER

Thorsten Sterzing[1], Ewald Hennig[1], David Pearsall[2]

[1]Faculty of Sport & Movement Sciences, University of Essen, Germany, thorsten.sterzing@uni-essen.de
[2]Faculty of Kinesiology, McGill University Montreal, Quebec, Canada

INTRODUCTION

Cinematography or electrogoniometers are typically used to estimate subtalar joint motion during different kinds of movement activities, e.g. walking or running. Most pieces of work focus on the relative motion between the posterior lower leg and the heel counter of the shoe. As the foot is likely to move inside the shoe no real representation of foot vs. lower leg motion can be achieved by using the traditional techniques. Previous attempts of in-shoe measurements require a modification of the footwear (Stacoff et al, 1992) or may influence subjects' movement pattern (Hennig et al, 1998). A new in-shoe electrogoniometer technique is proposed to determine the relative motion of the foot vs. the lower leg for an estimation of subtalar joint motion during different kinds of movement activities.

METHODS

A small spring loaded cable displacement position transducer was used for measuring inversion and eversion movements of the ankle during running. (*size:* 19x19x9 mm, *maximum cable displacement:* 38 mm, *weight:* 15 g). The case of the transducer was applied to the subjects' medial part of the tibia above the medial malleolus. The displacement cable was guided straight; going down across the medial malleolus, underneath the foot and then fixed to the lateral aspect of the foot. This alignment was used to avoid an influence of plantar and dorsiflexion on the inversion and eversion measurements. Prestretching of the skin was necessary to decrease skin movement disturbances of the signal. An individual calibration was taken according to each subject's anatomical range of maximum voluntary from inversion to eversion (maximum voluntary range of rearfoot motion).

Simultaneously, an external electrogoniometer was used to determine the relative motion of the lower leg vs. the heel counter of the shoe (Milani and Hennig 2000).

In the present study 10 subjects performed 5 shod heel-to-toe runs on a laboratory runway at a speed of 3.3 m/s.

RESULTS

The external measurement technique provides degree values describing the total range of rearfoot motion. The in-shoe measurement technique provides percentage values of the total rearfoot range of motion based on the maximum voluntary range of rearfoot motion.

Regression Plot: In–Shoe vs. External

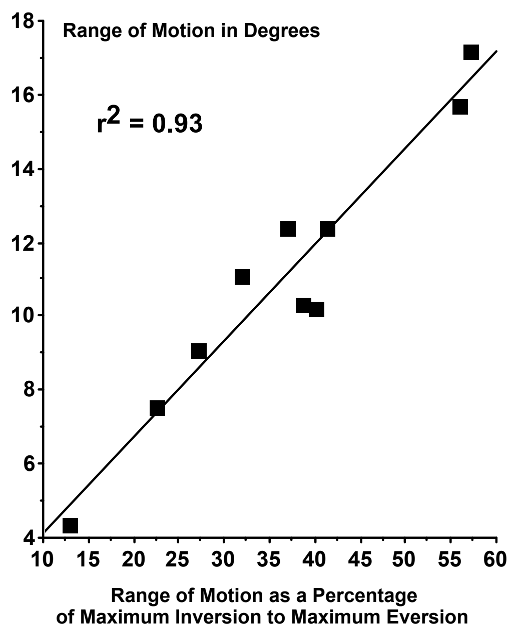

Figure 1: x-axis shows in-shoe electrogoniometer values, y-axis shows external electrogoniometer values (mean values of 5 trials per subject)

SUMMARY

The present in-shoe electrogoniometer technique provides useful values for measuring inversion and eversion movement of the foot. As it is attached on the skin directly to the lower leg and the foot, it allows a more accurate representation of rearfoot motion than traditional devices. Measurements of highly dynamic movements are possible to perform. Being independent of high-speed video cameras provides the possibility of taking laboratory experiments back to the field.

REFERENCES

Hennig, E.M. et al (1998). *Third North American Congress on Biomechanics. Waterloo, Ontario, Canada: University of Waterloo; 1998,* 323-324
Milani, T.L., Hennig, E.M. (2000). *Sportverletzung/ Sportschaden,* **14**, 115-120
Stacoff, A. et al (1992) *Med. Sci. Sports Exerc.* **24**, 695-70

ACKNOWLEDGEMENTS

Research was supported by Nike Inc., USA

STANCE LIMB CONTRIBUTES TO PREVENTION OF FALLING AFTER TRIPPING

Mirjam Pijnappels, Maarten F. Bobbert and Jaap H. van Dieën

Institute of Fundamental and Clinical Human Movement Sciences
Faculty of Human Movement Sciences, Vrije Universiteit Amsterdam, The Netherlands
m.pijnappels@fbw.vu.nl

INTRODUCTION

To prevent falling after tripping, it is essential to rapidly arrest the forward rotation, which the body gets from impact of the swing leg with the obstacle. The present study investigated whether and how push-off of the contralateral stance limb is used to reduce the forward rotation of the body after tripping.

METHODS

Twelve subjects walked over a platform of 10 meters at a comfortable walking speed. Kinematic data and ground reaction forces were measured at 100 Hz, and EMG of lower limb muscles at 1000 Hz. Based on online kinematic data, one of 21 obstacles, hidden in the platform, could be triggered to appear unexpectedly and catch the swing leg at a specific instant in mid-swing. In about 10 of 60 trials, subjects were actually tripped over an obstacle on either left or right side. A harness, attached to a ceiling-mounted rail, ensured safety.

RESULTS AND DISCUSSION

Recovery reactions appeared to be reproducible within subjects; immediately after collision the obstructed swing leg was elevated over the obstacle, while the stance limb provided prolonged push-off. After impact with the obstacle, the body rotated forward. The trunk is the main segment that contributes to body rotation. Figure 1 shows trunk rotation and angular velocity for a typical subject over the stance-phase.

Figure 1: Trunk rotation and trunk angular velocity of one subject, averages over 5 trials of normal walking (—) and of tripping (---). Trip initiation at 0 ms.

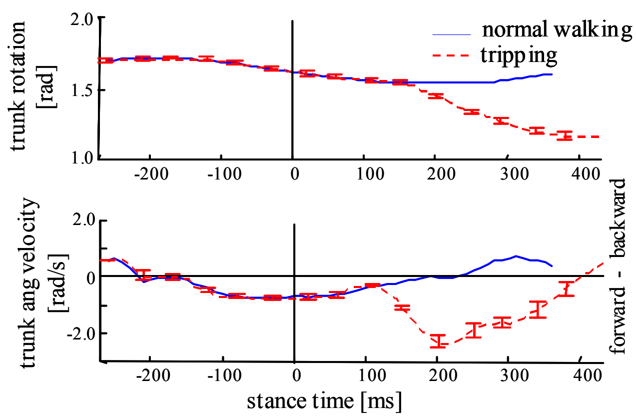

The trunk rotated forward rapidly after tripping, but its angular velocity was almost completely arrested within the push-off duration. A strategy to achieve this is reflected in an increase of the moment effect of the ground reaction forces about the body centre of mass, brought about by an increase in ground reaction forces in vertical as well as forward direction (figure 2). This results in a major contribution in the reduction of the body's forward rotation. The required push-off force magnitude and direction was generated by hamstring and gastrocnemic muscles that showed increased activity.

Figure 2: Ground reaction forces and external moment of one subject, averages over 5 trials of normal walking walking (—) and of tripping (---). Trip in contralateral swing limb at 0 ms.

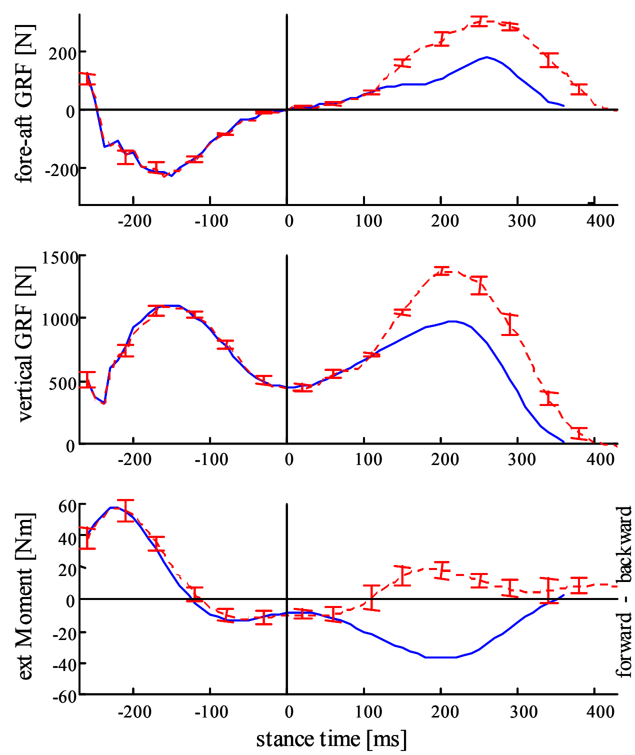

SUMMARY

After tripping, the body starts to rotate forward. The stance limb contributes in decreasing this forward rotation during push-off, by generating a ground reaction force that brings about a counteracting external moment.

SENSITIVITY ANALYSIS ON DISC BEHAVIOR IN TEMPOROMANDIBULAR JOINT

Masao Tanaka[1] , Eiji Tanaka[2], Masahiro Todoh[3], Daisuke Asai[4] and Yukiko Kuroda[4]

Division of Mechanical Science, Graduate School of Engineering Science, Osaka University, Toyonaka, Osaka, Japan
[1]Professor, tanaka@me.es.osaka-u.ac.jp
[3]Research Associate, [4]Graduate Student
Department of Orthodontics, Hiroshima University Faculty of Dentistry, Hiroshima, Japan
[2]Associate Professor

INTRODUCTION

Temporomandibular joint (TMJ) disorder is deeply related to the biomechanical condition among TMJ components. Permanent anterior disc displacement and disc derangement are typical finding in TMJ disorder. The mouth opening motion naturally induces the anterior disc displacement even in normal TMJ, and the condyle motion and disc properties are considered as the key to understand the disc displacement and stress in the disc [e.g. Solberg et al. 1979]. This study focuses the attention on the effect of disc property and condyle motion on the disc displacement and disc stress in the context of sensitivity analysis with finite element analysis.

METHODS

The biplane magnetic resonance images augmented by anatomical knowledge were used for the finite element (FE) TMJ modeling. The procedure to establish the FE model and the material property of TMJ components are the same as those in the previous work [Tanaka et al. 2001]. The major condyle movement is found in the sagittal plane, and the inferior condyle displacement is represented by a quadratic function of anterior condyle displacement. Such condyle trajectory was determined by referring to the MR images obtained at different mouth opening positions. The elastic modulus reported in the literatures scatters widely and the in vivo-experiment is impossible. The condyle positions used for the condyle path determination were not natural but artificial one for MR imaging. Thus, the anterior disc displacement and stress distribution in the disc were examined in the context of parametric study with the disc modulus ranging 1 and 100 MPa and the condyle path with variations up to 2mm at the fully open position.

RESULTS AND DISCUSSION

Figure 1 illustrates the effect of the disc modulus on the disc displacement and on von Mises stress of a normal subject. Increase in disc modulus accompanied the increase of disc displacement and the elevation of stress averaged over the disc. The image analysis of MR slices resulted the disc displacement marked by the arrow in Figure 1(a). Among the disc modulus examined, the disc modulus of 50 MPa gave the most reasonable disc displacement (Figure 1).

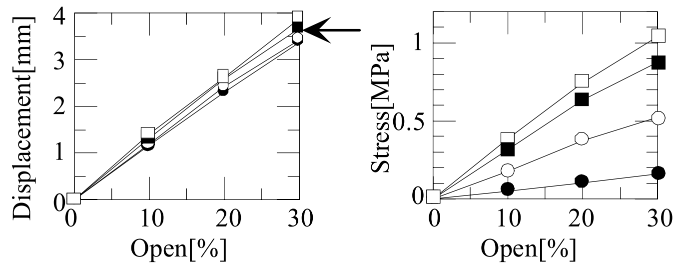

(a) Disc displacement (b) von Mises Stress

Figure 1: Parametric study on disc elastic modulus
[•:E=1, ○:E=10, ■:E=50, □:E=100MPa]

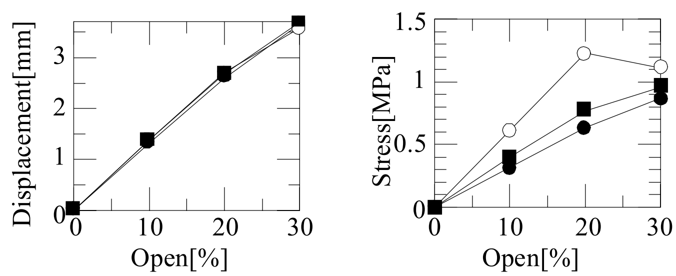

(a) Disc displacement (b) von Mises Stress

Figure 2: Parametric study on condyle path
[•:path1, ■:path2, ○:path3]

Figure 2 shows the effect of the condyle path on the disc displacement and von Mises stress. At the fully open position, the inferior displacement in path 2 is 1mm smaller than that of normal path1, and that in path3 is 2mm smaller than the normal. The von Mises stress was very sensitive to the condyle path, although the anterior disc displacement was not. These suggests us the possibility to estimate the disc modulus with the combination of MR image analysis and FE analysis based on it. However, we need some additional information to validate the condyle path that affects the stress in the disc significantly.

REFERENCES

Solberg, W.K. et al. (1979). *J. Am. Dent. Assoc.*, **98**, 70-78
Tanaka, E. et al. (2001). *J. Oral Maxillofac. Surg.,* **30**, 333-355

ALCOHOL AND OVARIECTOMY EFFECTS ON TRABECULAR BONE IN FEMALE RATS

Harry A. Hogan[1,2], Kristin L. Luthringer[1], Susan D. Bankston[1], and H. Wayne Sampson[2]

[1]Dept. of Mechanical Engineering, Texas A&M University, College Station, TX, hhogan@mengr.tamu.edu
[2]Dept. of Medical Anatomy & Neurobiology, Texas A&M University System Health Sciences Center, College Station, TX

INTRODUCTION

Alcohol consumption is a known risk factor exacerbating postmenopausal osteoporosis. The current study was undertaken to investigate these effects using the rat animal model. Recent studies with rats have shown deleterious effects due to alcohol (Turner et al., 2001; Hogan et al., 2001), but no significant effects when combined with ovariectomy (OVX) induced estrogen deficiency (Kidder and Turner, 1998). This last study did not report mechanical properties, however. The main purpose of the current study was to investigate the effects of alcohol and OVX on trabecular bone mechanical properties in adult female rats. Another important clinical issue is the relation between bone mineral density (BMD) and fracture risk or incidence. Thus, changes in BMD have also been studied and compared to corresponding changes in mechanical properties.

METHODS

Female Sprague-Dawley rats were divided into 6 groups at 9 mo. of age. Two groups were fed alcohol for 10 weeks. For each of these two groups there were two types of controls: pair-fed (which were isocaloric to the alcohol animals), and chow-fed (which received standard rat chow and water). After 10 weeks 3 of the groups were terminated and 3 were ovariectomized and then maintained on the same diets for 2.5 more weeks. The OVX groups were designated: OA (alcohol, N=12), OP (pair-fed, N=12), and OC (chow, N=8), and the other groups: A (N=8), P (N=8), C (N=8). The left femur was removed after euthanasia and 2mm long specimens were cut from the distal femoral metaphysis. The specimens were tested by reduced-platen compression (RPC), which directly loads only the trabecular bone portion (Hogan et al., 2000). Before testing, contact radiographs were made of each specimen and digitized for BMD determination. The trabecular bone compartment was isolated and density quantified through a series of aluminum step-wedges that were included in each x-ray.

RESULTS AND DISCUSSION

Alcohol generally reduced mechanical properties and BMD compared to either control group (Table 1). The combination of alcohol and OVX further reduced values of both. None of the differences were statistically significant, however. The % by which the alcohol groups were lower than controls are indicated (as %Δ), and it is clear that mechanical properties were affected more severely than BMD. Ultimate stress correlates well with BMD (Fig. 1), with R^2 values similar to those reported for rat vertebra tests (Nishikawa et al., 2000). The current study suggests, however, that BMD does not capture completely the changes in mechanical properties.

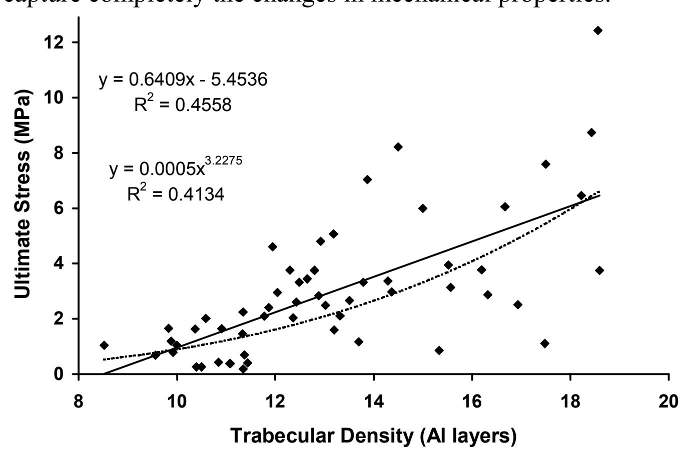

Figure 1: Correlation between ultimate stress and BMD.

REFERENCES

Hogan et al. (2001) *Alcohol Clin Exp Res* **25**:746-754.
Hogan et al. (2000) *J Bone Min Res* **15**:284-292.
Kidder & Turner (1998) *Alcohol Clin Exp Res* **22**:2159-2164.
Nishikawa et al. (2000) *Bone* **27**:647-654.
Turner et al. (2001) *J Bone Min Res* **16**:589-594.

ACKNOWLEDGEMENTS
Support provided by NIAAA AA10234.

Table 1: Mechanical properties and BMD results

	A	P	C	P-A %Δ	C-A %Δ	OA	OP	OC	OP-OA %Δ	OC-OA %Δ
Ult. Stress (MPa)	3.0±0.7	3.9±0.7	5.7±1.2	-23	-32	1.6±0.4	1.9±0.5	3.0±1.0	-20	-48
El. Modulus (MPa)	110±26	147±30	168±76	-25	-34	55±15	111±30	178±61	-50	-64
BMD (Al layers)	11.9±0.4	14.7±0.6	15.3±1.0	-18	-22	11.7±0.5	12.0±0.7	14.6±1.1	-2.3	-20

FLOW EVALUATION OF STENTS IN CAROTID ARTERY MODELS

Liepsch, D.[1], Sakurai A.[2], Schmid Th.[1], Berger.G.[3] Kleinschmidt. Th,[3]

[1]University of Applied Sciences and Institute for Biotechnik E. V. Munich, Germany, liepsch@fh-muenchen.edu
[2]Dept. of Mechanical Engineering, Kansai University, Osaka Japan
[3]Klinikum rechts der Isar der TU München, Germany

INTRODUCTION

Stroke ranks as one of the leading causes of morbidity and mortality in the western world. Atherosclerotic deposits and stenoses are among the contributing factors for catastrophic stroke. These are found in the transcerebral arteries, such as the carotid bifurcation. High- degree stenoses may be surgically approached by endarterectomy or implanted patch-plastics. In addition to these surgical procedures, stents are used for patients with high risk factors, who cannot be treated with open surgery. This procedure is not without risk as clots can be transported into the brain. We studied the influence of such stents on the flow behavior. We positioned three types of stents from the common carotid artery into the internal carotid artery and compared the flow patterns with that found in a model without stent. All three stents influenced the flow behavior significantly.

METHODS.

We studied a wall stent, a self-expanding stent (SelfX) and a covered stent. Each stent was positioned within an elastic 1:1 true-to-scale silicone rubber model of a carotid bifurcation. These models have a compliance similar to that of a real artery. The local velocity was measured at different cross sections using a laser-Doppler-anemometer (LDA). Figure 1 shows the different cross sections and measuring points. The physiological pulsatile blood flow curve was simulated with a piston pump (heart pump) which superimposed a physiological waveform on the steady flow. The flow rate ratio of the internal to the external carotid artery was 70% to 30%.

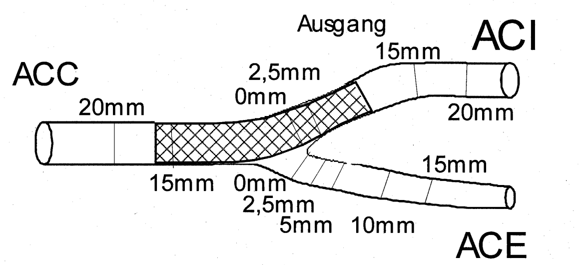

RESULTS AND DISCUSSION

The flow rate ratio is slightly changing after stent implantation,. The flow rate ratio was:

70.7 : 29.3 for the self expanding stent
70.64 : 29.36 for the wall stent
73.9 : 26.1 for the covered stent.

The flow rate change of the first two stents can almost be neglected. The covered stent showed a higher resistance towards the external carotid artery. This is caused by the design. The covered stent, however, produced a very smooth flow and formed no vortices. Some small velocity disturbances were created at the inlet and outlet only. Figure 3 shows the velocity distribution at the cross section 2.5 mm distal to the bifurcation in the external carotid artery. The empty model without a stent is compared with the three stent models during the systolic phase ωt=30°. The flow behavior in the external carotid artery is completely altered by the covered stent. At times, peak velocities are created by the stent wire.

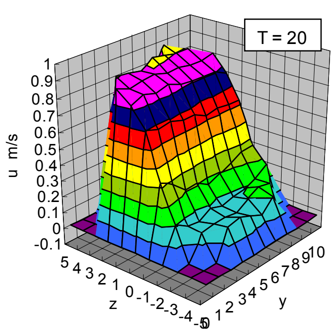

Empty model

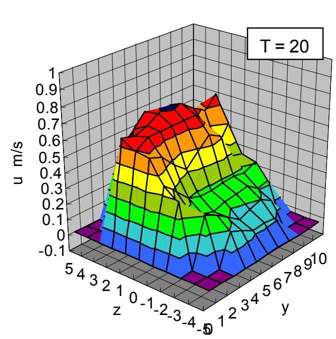

Self X

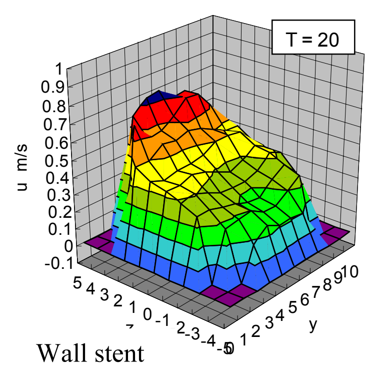

Wall stent

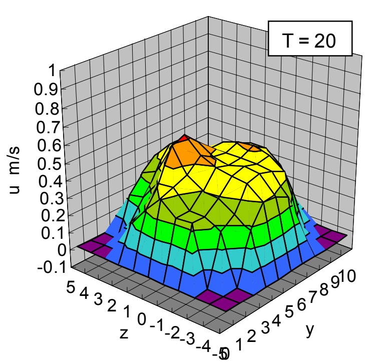

Covered stent

Re = 250, α = 3.5 (f = 62.8 b.p.m.), d = 6 mm ACI

MICRO-TENSILE TESTING OF INDIVIDUAL TRABECULAE FROM NORMAL, AGEING, AND OVARECTOMISED RAT BONES

Laoise McNamara, Patrick J. Prendergast, Kevin O' Kelly and Garrett Lyons
The Bioengineering Group, Department of Mechanical Engineering, Trinity College, Dublin 2, Ireland. mcnamalm@tcd.ie

INTRODUCTION

Cancellous bone is a porous network of interconnected rods and plates called trabeculae**.** Bone remodeling constantly adapts their structure so that cancellous bone is sufficiently strong to fulfil its load bearing function. Osteoporosis is a disease caused by altered bone remodelling due to a mismatch between bone formation and bone removal. The trabecular struts become thin and eventually fail.

A number of researchers have sought to determine the mechanical properties of the individual trabecula using 3-point bending studies (Choi et al, 1990) and micro-tensile testing (Ryan and Williams, 1989). Due to the size and shape of trabeculae a number of issues arise with respect to the accuracy of testing and reported values for the elastic modulus of an individual trabecula have conflicted, with values ranging from 0.75GPa – 20GPa.

The overall objective of this research is to measure the changes in trabecular strength from normal, aged, and osteoporotic (overectomised) rats. Questions arise as to whether or not a micro-tensile testing apparatus can be designed to eliminate errors due to misalignment and stress concentrations at the grips. If this can be done successfully then both tensile and fatigue tests of trabeculae after disease and drug treatments will be possible.

METHODS

Sections of cancellous bone were cut from the tibiae of 6 and 16-month Whistar rats and from 6 month old ovarectomised (OVX) Whistar rats. The sections were cleaned of marrow using a water jet. Using a scalpel blade and forceps individual rod-like trabeculae were excised under a stereomicroscope and stored in saline before testing.

The base test system is an MTS Tytron 250, which operates using a linear DC servomotor, and is capable of applying loads at a resolution of 0.001 N. This system has been modified, through the addition of a microscope assembly and a grip system, for use in micro-tensile testing of individual trabeculae. The main problem faced in testing of trabeculae is that of gripping them during a test. The system developed involves the use of the shafts of hypodermic needles as the grip rods. These rods were attached to the actuator and load cell of the machine. An alignment sleeve, with close tolerance fit was used to align and ensure co-axiality of the grip rods. The ends of the trabecular specimens were inserted into the hypodermic needles and affixed using a cyanoacrylate adhesive. The trabecula was aligned under the microscope, at 30X magnification, using a graticule lens as a reference for alignment. Two specimens from 6-month-old normal and osteoporotic rat bones were tested, along with 4 specimens from 16-month-old tibia. A constant displacement rate of 1 μm/sec was applied until failure. The test system software automatically recorded the force and displacement values. The cross-sectional diameter was taken under microscopy.

RESULTS AND DISCUSSION

The stress/strain relationship for seven samples of trabecular tissue have been determined, see Fig. 1. The average elastic modulus calculated for individual trabeculae excised from normal 6-month old tibia was 1.79 GPa whereas that from the normal 16-month old tibia was 1.33 GPa. The elastic modulus calculated for the OVX specimen was 4.01 GPa, but it failed at low strain. The 6 mo old normal samples sustained the highest strain before failure (Fig. 1)

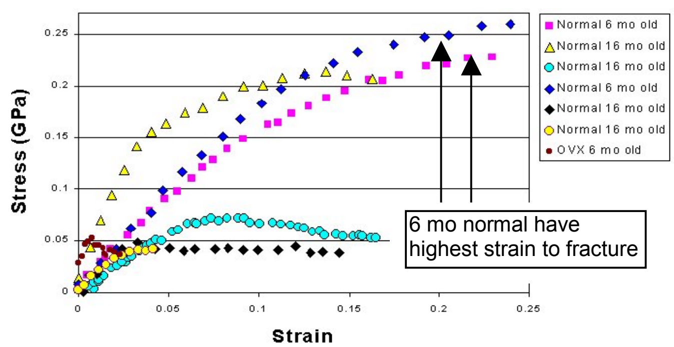

Fig 1: Stress/strain curves for individual trabeculae

SUMMARY

A method has been developed for tensile testing of individual trabeculae that ensures alignment of trabecular specimens that eliminates bending. It has proved capable of discriminating the stress/strain behaviour of trabeculae. It can now be used to compare trabecular bone tissue from both normal and osteoporotic rats. These initial results indicate that ageing of the bones results in a decrease in the stiffness of the tissue.

REFERENCES

Ryan & Williams (1989), "Tensile testing of Rodlike Trabeculae excised from Bovine Femoral bone", *J. Biomech.* **22**, pp 351-355
Choi, Kuhn, Ciarelli & Goldstein (1990), "The Elastic Moduli of Human Subchondral, Trabecular, and Cortical Bone Tissue", *J. Biomech.* **23**, pp. 1103-1113

ACKNOWLEDGEMENTS
Funded by EU Project "MIAB".

NEURAL AND BIOMECHANICAL ORGANIZATION OF ANTICIPATORY POSTURAL ADJUSTEMENTS IN FAST SYNCHRONIZED STEPPING AND ARM RISING

Yiou E. and Schneider C.

CIRRIS-Rehabilitation Research Center, IRDPQ, Quebec City, G1M 2S8 Canada, Cyril.Schneider@rea.ulaval.ca

INTRODUCTION

Many of our daily activities require combination of goal-directed arm rising task with postural support displacement. The latter requires the anticipatory postural adjustments (APAs) generating the dynamic conditions for stepping (Brenière et al. 1987). These APAs could be affected by upper limb movements (Yiou & Do 2001), since rising the arm induces an endogenous postural perturbation (Bouisset & Zattara 1988). The question is whether synchronization of arm rising with fast stepping affects the organization of APAs preceding fast stepping or highlights CNS potential for neural and biomechanical adaptation.

METHODS

Five subjects were tested 'stepping', 'arm rising' and synchronized 'stepping / arm rising'. The swing leg in stepping was the *preferential* leg. 'Arm rising' was a 90° flexion of the *contralateral* shoulder (elbow in full extension). In response to an auditory cue, subjects in quiet standing (QS) performed the tasks at maximal velocity. Biomechanical and motor features of APAs were analyzed by means of recordings from force plates (one per stance) and surface electromyographic activity (EMG) of the Deltoïdeus anterior (DA, shoulder flexors), the soleus (SOL) and Tibialis anterior (TA) (ankle plantar and dorsiflexors) of both legs. The spinal synaptic efficacy was tested by eliciting H-reflexes of swing SOL from the auditory cue to the swing foot-off (for methods, see Schneider et al. 2000).

RESULTS AND DISCUSSION

1- In both stepping tasks (Figure 1), kinetics of APAs was characterized by backward displacement of the center of foot pressure (xP) and forward acceleration of the center of mass (X''_G). These APAs were generated by cessation of SOL EMG prior to TA activation. APAs lasted from the onset of deviation in kinetic traces to the swing foot-off. Their amplitudes corresponded to the values of these deviations.
2- Duration of APAs and integrated EMG (iEMG) of the swing leg were comparable in stepping tasks. However, amplitudes of APAs and iEMG of stance TA were significantly higher in the synchronized task. **3-** Surprisingly, whilst SOL early ceased in stepping, the H-reflex reached amplitudes as high as in QS. H-reflex was then inhibited by reciprocal inhibition from TA burst and remained at minimum values throughout APAs. Conversely, the H-reflex was facilitated during APAs in arm rising. In the synchronized task, the pattern of H-modulation was the same as in the single stepping, without any significant difference in timing and amplitudes. **4-** The whole work reflects that the

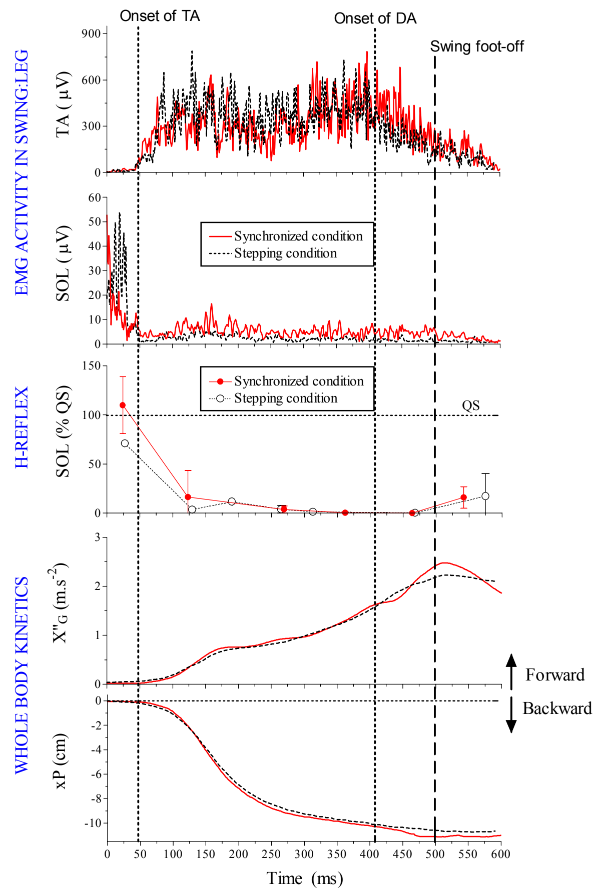

Figure 1: EMG, kinetic traces (mean, N=10) and SOL H-reflex (N=4 per symbol) of APAs in synchronized and stepping tasks.

neural and biomechanical organization of APAs in stepping was adapted to the perturbation elicited by the upper limb task, for unloading the swing leg and propelling the body forward.

SUMMARY

Biomechanical and neural techniques revealed the adaptation of the APAs of the stepping synchronized with the contralateral arm rising. Impairments of these central mechanisms may explain part of the pathophysiology of postural control.

REFERENCES

Bouisset & Zattara (1988) *Neurosci. Letters* **22** :263-270
Brenière et al. (1987). *J. Mot. Behav*. **19** :62-76
Schneider C. et al. (2000) *J. Neurophysiol*. **83** : 2881-2890
Yiou E. & Do M.C. (2001). *Exp. Brain Res*, **137** : 197-204.

ACKNOWLEDGEMENTS
Fondation pour la Recherche Médicale, Neurotrauma-CIHR

BEHAVIOURS OF MUSCLE-TENDON COMPLEX DURING ELECTRICAL STIMULATION WITH TRAINS OF LINEARLY VARYING FREQUENCY IN HUMANS.

Yasuhide Yoshitake, Yasuo Kawakami, Hiroaki Kanehisa, Tetsuo Fukunaga
Department of Life Sciences, University of Tokyo, Tokyo, Japan. ytake@idaten.c.u-tokyo.ac.jp

INTRODUCTION

The force-frequency relation frequently does not show a unique response, but appears to depend heavily on the muscle activation history. From the findings of a prior study (Binder-Macleod and Clamann 1989), stimulus trains in which the frequency varied linearly produce a tension hysteresis with a greater force production when the frequency was decreasing than when it was increasing. The exact physiological mechanisms governing such hysteresis phenomenon have not been clearly identified, but it might involve the interaction with the length changes in muscle-tendon complex throughout the muscle contractions.

Recent development in technology has made it possible to determine the kinetics of muscle-tendon complex in humans by means of real-time ultrasonography (Fukunaga et al. 1997). Using this tool we have shown that tendon elasticity plays an important role during voluntary muscle actions (Kawakami et al. 1998). The aim of this study is to quantify the length changes in the muscle-tendon complex during electrical stimulation with trains of linearly varying frequency and to investigate their effect on force production in vivo.

METHODS

Experiments were conducted on the triceps surae muscle of six male subjects with no history of neuromuscular disorders. Each subject was seated on an insulated, straight-back chair with wide belts crossing his chest and abdomen to immobilize his body and to isolate the planter flexion movement of the ankle at 90°.

The posterior tibial nerve was stimulated supramaximally (100-μs duration) to induce maximal isometric contractions of triceps surae muscle with a small surface electrode in accordance with the method described in a prior study (Yoshitake and Moritani 1999). We made a stimulation pattern on a DOS/V computer with a digital-to-analogue (D/A) converter which could control the electro-stimulator for inducing contractions. Muscles were tested with a stimulus pattern in which the frequency rose up to 20Hz (increasing frequency) and then fell (decreasing frequency) linearly (see Fig 1A-bottom). The force signals were recorded by an on-line computer system with a 13-bit analogue-to-digital converter (MacLab/16).

A real-time ultrasonic apparatus (SSD-5000, Aloka, Japan) was used to record at 30Hz continuously and simultaneously longitudinal ultrasonic images of the medial gastrocnemius muscle during stimulation. The distance which cross point of two echoes from deep aponeurosis and fascicle moved during electrically induced contractions was determined as the lengthening of tendon structures (L) as described in our previous studies (Fukunaga et al. 1997, Kawakami et al. 1998).

RESULTS and DISCUSSION

Figure 1A shows typical sets of computer outputs indicating torque curves (top) and stimulation patterns (bottom) as a function of time during stimulations. The group data of torque-frequency relation showed a marked hysteresis, in which the force enhancement occurred during decreasing frequency of stimulation (Figure 1B). The last twitch was markedly greater than the first twitch in the phase of increasing frequency of stimulation (see Fig.1A), suggesting that post-tetanic potentiation (Vandervoort et al. 1983) contributes to the appearance of hysteresis.

Stimulus trains in which the frequency varied linearly show a tension hysteresis

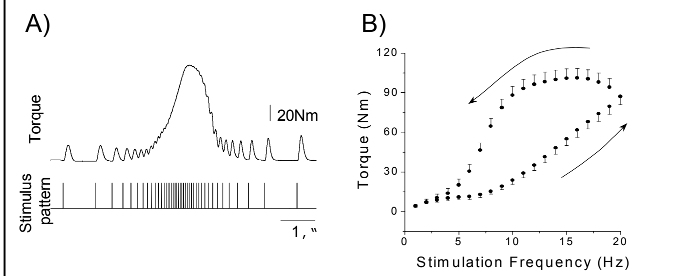

Figure1: Relation between output torque and stimulus rate.

Figure 2 represents the changes in torque and L during stimulation recorded in the same subject presented in Figure 1A. The enhanced torque and elongated tendon structure by increasing stimulation rate were "hold" even when the frequency of stimulation decreased. This indicates that alteration of muscle-tendon length may also contribute to the appearance of the force hysteresis.

Tension hysteresis might be due to resulting in an upward shift of tendon structure

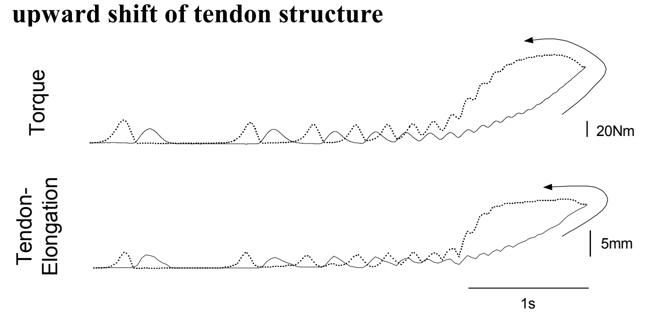

Figure 2: Torque (top) and tendon elongation (bottom) during increasing (solid) and decreasing (dot) stimulations.

REFERENCES

Binder-Macleod, S, A., Clamann, H, P. (1989) *J Neurophysiol,* **61**, 208-217
Fukunaga, T. et al (1997) *J Appl Physiol*, **82**, 354-358
Kawakami, Y. et al (1998) *J Appl Physiol*, **85**, 398-404
Vandervoort, A, A. et al (1983) *Exp Neurol*, **81**, 141-152
Yoshitake, Y., Moritani, T. (1999) *J Electromyogr Kinesiol*, **9**, 209-217

DIRECTIONAL DEPENDENCY OF SENSING CHARACTERISTICS TO MECHANICAL STIMULUS IN OSTEOBLASTIC CELL

Katsuya SATO[1], Taiji ADACHI[1,2] and Yoshihiro TOMITA[1,2]

Solid Mechanics Laboratory, Department of Mechanical Engineering, Kobe University, Nada, Kobe, Japan
[1]Depertment of Mechanical Engineering, Faculty of Engineering, Kobe University, sato@solid.mech.kobe-u.ac.jp
[2]Division of Computer and Information, The Institute of Physical and Chemical Research (RIKEN)

INTRODUCTION

It is believed that osteoblastic activities are affected by local mechanical environment in adaptive bone remodeling process (Duncan, R. L. et al., C. H., 1995). Investigation on the characteristics of sensing mechanical stimulus in osteoblasts is essential to clarify the cellular level mechanism of bone remodeling. In this study, quantitative deformation was applied to a single osteoblastic cell using a tip of glass microneedle with controlled magnitude and direction, and change in intracellular calcium ion concentration was observed as cellular response to the mechanical stimulation.

MATERIALS AND METHODS

Osteoblastic cell lines MC3T3-E1 (from RIKEN Cell Bank) were cultured in α-MEM supplemented with 10% FBS. Cells were seeded onto the glass bottom dishes at 10^5 cells per dish. After pre-culture for 3 hours, Ca^{2+} fluorescent indicator Fluo-3 was loaded for 60 min.

As a mechanical stimulus, indentation to a single cell was performed using a microneedle with a roundish tip of 10 μm in diameter (Xia, S. L. et al., J., 1992). Angle between microneedle and dish bottom was set at 40 deg. Microneedle was moved down vertically to the height of 2.0 μm from the dish bottom and held for a few seconds, and slid horizontally to apply deformation to the cell. Displacement of the tip was defined as δ (Figure 1a). The angle between micropipette and the major axis of the cell shape was defined as θ (Figure 1b), in which the major axis of the cell was determined from the ellipse fitted with the cell shape.

Change in the intracellular calcium ion concentration $[Ca^{2+}]_i$ was observed by measuring increase in fluorescent intensity using a confocal laser scanning microscope (MRC-1024/MP, Bio-Rad) in the plane at height of 2 μm from the dish bottom.

RESULTS AND DISCUSSION

By measuring change in $[Ca^{2+}]_i$, we confirmed that the cell responded to the applied deformation. At relatively small magnitude of applied deformation, δ = 2.0 to 6.0 μm, cells did not show the change in $[Ca^{2+}]_i$ as response to the stimulus. On the other hand, at δ = 8.0 to 12.0 μm, cells responded. This result suggests that there might be a threshold in magnitude of stimulus that osteoblastic cells could sense and respond. In addition, the probability of responded cells increased as the magnitude of deformation δ increased.

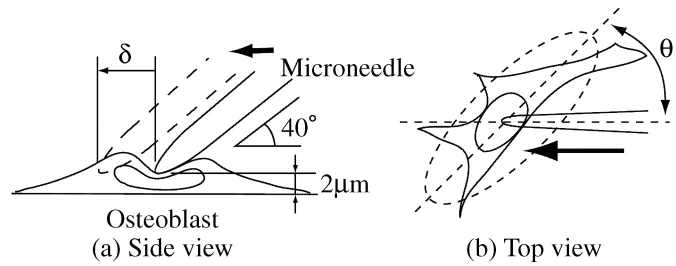

Figure 1: Definition of quantitative stimulus, (a) magnitude of deformation δ, (b) angle of applied deformation θ

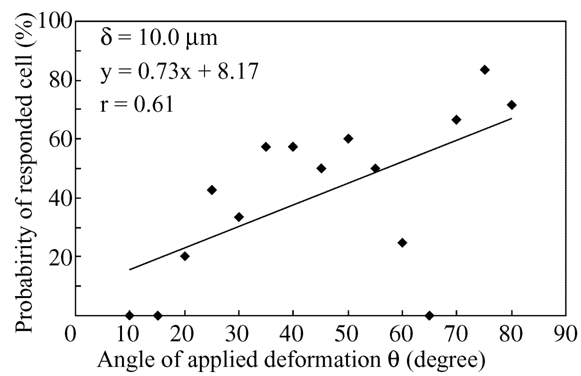

Figure 2: Directional dependency on probability of responded cells to applied deformation of δ = 10 mm

In Figure 2, dependency of the probability of responded cells on the angle of applied deformation are plotted for the case of δ = 10 μm, which was obtained by moving average within ±10 deg. at interval of 5 deg. Thus, the culuculated points were 15 from 25 experimental data. The result shows that the probability of responded cells increased as the angle of applied deformation increased. The probability of responded cells are significantly corelated with the angle of applied deformation (p < 0.05). Cells are more sensitive to applied deformation with larger angele to cell major axis. This result suggests that there is directinal dependency in sensing mechanical stimulus in osteoblstic cells.

REFERENCES

Duncan, R. L. and Turner, C. H., (1995), *Calcif. Tis. Int.*, **57**, 344-358.

Xia, S. L. and Ferrier, J., (1992), *Biochem. Biophys. Res. Commun.,* **186**, 1212-1219.

NATURAL FREQUENCIES OF FEMUR BONE AND BONEPIN

Wolfgang Potthast[1], Anton Arndt[2], G.-P.Brüggemann[1]
[1]Institute for Biomechanics, German Sport University Cologne, Cologne, Germany
[2]Karolinska Institute, Dept. Orthopedic Surgery, Huddinge University Hospital, Sweden

INTRODUCTION

Several in vivo studies exist regarding bone acceleration during different movements (Hennig & Lafortune 1991; Whittle 1999). However, the mechanics of the transition of vibrations along the bone are not yet well understood. Therefore, the purpose of this study was twofold: first to estimate the natural frequency of an instrumental setup typically used in in vivo studies (bonepin with marker array) and secondly to identify the frequencies of a vibrating femur bone by means of an accelerometer mounted to a bonepin.

METHODS

A: To identify the natural frequency of the instrumental setup (bonepin, marker array) independent of the bone, a 8 cm long steel bonepin was screwed 2.5 cm into a 9.5x6x5cm rigid plastic block. A triaxial piezoresistive accelerometer (2.5 grams, 2500 Hz) was firmly mounted at the end of the pin. An aluminium marker array with three reflecting markers was mounted on the pin 1.5 cm below its end (Fig1). , A pendulumwas used to initiate vibration of the system (Fig1).

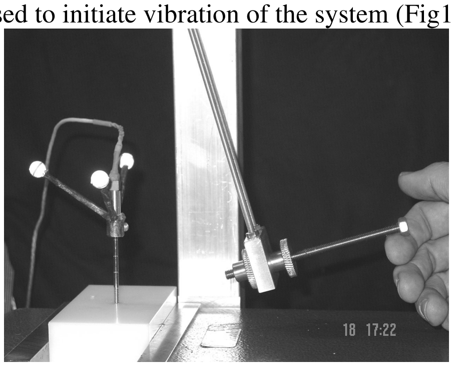

Fig1: Bonepin with marker array

B: To investigate vibrations of the femur the bone hung free with the bonepin screwed 2.5 cm into the lateral condyle (Fig2). The z-axis of the accelerometer was orientated parallel to the longitudinal axis of the femur. The vibration of this system was initiated by a manual stroke with a metal rod. The stroke was orientated approximately parallel to the longitudinal femur axis and applied centrally in the fossa intercondylaris. The direction and location of the force application was controlled by two video cameras (250 Hz).

In order to identify the occurring and superimposed frequencies in A and B the frequency spectrum was calculated using a fast fourier transformation (FFT). Due to the limitation of the sampling frequency of 2500 Hz no frequencies over 500 Hz were considered.

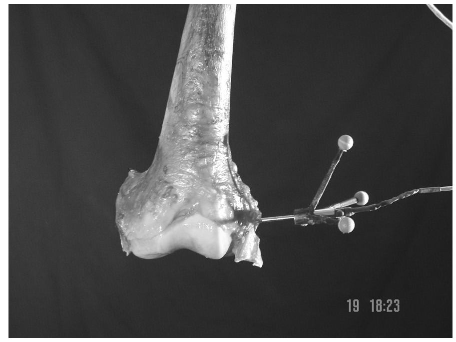

Fig2: Bonepin inserted in lateral femoral condyle

RESULTS AND DISCUSSION

Fig3 shows a typical FFT of the z-acceleration of both the bonepin in the plastic block and the bonepin mounted in the lateral femoral condyle.
The isolated bonepin shows a single sharp frequency peak located at 120 Hz which could be associated with the natural frequency of the instrumentation. A similar peak (115 Hz) can be identified in the curve for the pin mounted to the bone. An additional peak at 300 Hz occurred when the bone was activated to vibrate by a stroke located at the fossa intercondylaris. This frequency is assumed to be associated with the natural frequency of the isolated femur bone.

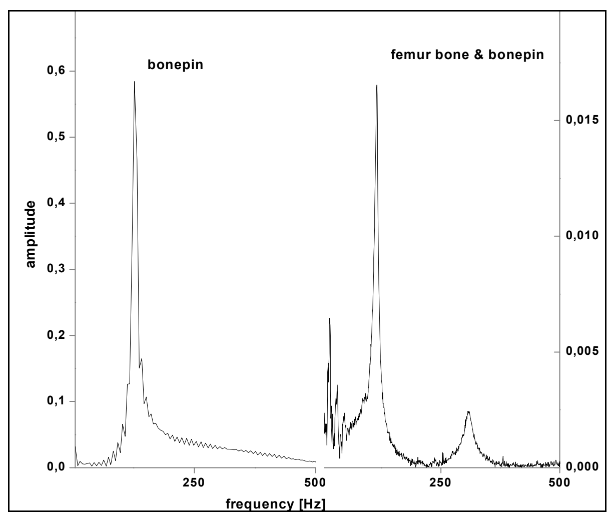

Fig3: FFT of isolated bonepin (left) and bonepin inserted in the femur (right)

REFERENCES

Hennig, E. M., Lafortune, M.A. (1991). *International Journal of Sport Biomechanics,* **7**, 303-309
Whittle, M. W.(1999). *Gait and Posture*, **10**, 264-275

ARTIFICIAL NEURAL OSCILLATORS AS CONTROLLERS FOR LOCOMOTION SIMULATIONS AND ROBOTIC EXOSKELETONS

*Daniel P. Ferris[1,2], Tiffany L. Viant[2], and Ryan J. Campbell[3]

[1]Movement Science and [2]Biomedical Engineering, The University of Michigan, Ann Arbor, MI
[3]Physics, University of Washington, Seattle, WA
*ferrisdp@umich.edu, http://www-personal.umich.edu/~ferrisdp/UMHNL.html

INTRODUCTION

Our long-term goal is to build robotic exoskeletons for human locomotion. One method for controlling the exoskeletons is to use simple models of biological central pattern generators (i.e. artificial neural oscillators). Several researchers have used artificial neural oscillators to control computer simulations of human locomotion (Taga et al. 1991; Zielinska 1996), but each simulation has been specific to one type of artificial neural oscillator and one biomechanical model. Although this approach has demonstrated the feasibility of artificial neural oscillators as legged locomotion controllers, it is unclear if the findings can be generalized to other artificial neural oscillators and other biomechanical models.

We constructed computer simulations of artificial neural oscillators coupled to simple mechanical models for two purposes. First, we directly compared two artificial neural oscillators to provide a rationale for selecting one oscillator over the other in biological simulation or robotic control. Second, we tested the hypothesis that independent neural oscillators can entrain multi-body systems in the absence of inter-oscillator connections. Countless studies have focused on the feedforward nature of biological neural oscillators, proposing complex inter-oscillator connections sufficient to generate coordinated movement. However, afferent feedback is a powerful mechanism for entraining neural oscillators to the mechanics of a system. Biological neural oscillators and artificial neural oscillators use afferent feedback to tune their neural output to the resonant frequency of the mechanical system even when the oscillator natural frequency is much lower than the mechanical resonant frequency (Hatsopoulos 1996). Thus, it seems possible that afferent feedback may also be used to coordinate the timing of muscle activity about multiple joints. To test this possibility, we built simple neuromechanical models with distributed afferent feedback and no inter-oscillator connections.

METHODS

We examined two artificial neural oscillators, van der Pol (1922) and Matsuoka (1985), and three simple models of a swinging leg: single, double, and triple pendulums. Each pendulum joint was coupled to an artificial neural oscillator via a muscle torque generator and angular position feedback.

RESULTS AND DISCUSSION

Both artificial neural oscillators were able to entrain single and double pendulums to stable limit cycles close to the primary resonant frequencies of the mechanical models. Matsuoka oscillators were also able to entrain the triple pendulum at its primary resonant frequency and the double pendulum close to its secondary resonant frequency (i.e. anti-phase) when given appropriate initial conditions. Furthermore, the Matsuoka oscillator entrained the single pendulum over a much greater range of feedback gains than the van der Pol oscillator (range: 300-fold compared to range: < 10%, respectively). The Matsuoka oscillator also displayed the unique characteristic of reducing its duty factor from 38% to 8% of the cycle period as muscle gain was raised from 2 to 100. This kept muscular impulse from rising beyond a factor of two even though muscle gain increased by 50-fold. The adjustment in duty factor kept the angular displacement steady in spite of the changes in muscle gain.

SUMMARY

A direct comparison of artificial neural oscillators revealed that Matsuoka oscillators are much more robust to changes in feedback gains and muscle gains than van der Pol oscillators. In addition, results also indicate that distributed sensory feedback is sufficient to coordinate inter-joint muscle activation patterns. Although these conclusions are based on simple neuromechanical models, the generality of the results to different mechanical systems and artificial neural oscillators supports the findings. Neural tuning to biomechanical properties is likely more important for biological neural oscillators than generating feedforward commands in the absence of sensory feedback.

REFERENCES

Hatsopoulos, N.G. (1996). *Neural Comp.* **8,** 567-581.
Matsuoka, K. (1985). Biol. Cyber. 52, 367-376.
Taga, G. et al. (1991). Biol. Cyber. 65, 147-159.
van der Pol, B. (1922). Philos. Mag. 43, 700-719.
Zielinska, T. (1996). Biol. Cyber. 74, 263-273.

ACKNOWLEDGEMENTS

NIH AR008602 & Christopher Reeve Paralysis Foundation.

DO LOWER SPINE TWISTING MOMENTS AT THE COMPLETION OF LIFT TRAINING REDUCE THE LIKELIHOOD OF BACK INJURY?

Steven A. Lavender, Eric P. Lorenz, Susan Shott and Gunnar B.J. Andersson[1]
[1]Orthopedic Surgery Ergonomics Laboratory
Rush Presbyterian St.Luke's Medical Center, Chicago, Illinois, U.S.A.
slavende@rush.edu

INTRODUCTION

Previous studies found no change in back injury incidence following training programs that have taught lifting techniques (Daltroy et al., 1997; van Poppel et al, 1998). Daltroy et al. (1997) reported that while employees conceptually understood the desirable lifting techniques, they did not use them. The purpose of this study was to evaluate a new behaviorally oriented training process that was designed to facilitate the adoption of improved lifting techniques. Our hypothesis was that those who complete the initial training with smaller spine twisting (axial rotation) moments would have a reduced likelihood of subsequent back injury relative to those with larger twisting moments or those who did not experience this training process (controls).

METHODS

Sample. Experienced employees were recruited from 17 distribution centers. These workers normally move boxes weighing between 2 and 36 kg at a rate of 160 to 180 boxes per hour. The 1,978 participants were randomized into either the "LiftTrainer" group (n=957) or the "video" control group (n=1021). The control group's participation consisted of viewing a short videotape demonstrating lifting techniques. Participants in the LiftTrainer group had the opportunity to attend 5 half-hour individualized training sessions distributed over a 10-month period. The participants in the LiftTrainer group were, on average, 33.5 years old (s.d.=9.6 yrs.), had 5.9 years of experience in the current job (s.d.=6.8 yrs). All participants were followed for up to 12 months following the completion of the initial training session.

LiftTrainer Training. A magnetic motion measurement system was used to track body movements as lifts were performed. *The LiftTrainer*^{TM} software used the movement and box weight data in a dynamic 3-D linked segment model to instantaneously calculate the 3-D moment vector acting on the spine (L5/S1). The data were sampled and the moment vector calculated at 103 Hz. The magnitude of the resultant moment vector was used as a biofeedback signal in that it controlled the pitch of a tone heard by the trainee. In addition to the continuous time-varying biofeedback, at the completion of each series of lifts the peak 3-dimensional moment components (forward bending, twisting, lateral bending) were displayed graphically.

The lifting task required the employees move four boxes at their normal pace from one pallet to another. The box weights varied across training sites between 11 and 14 kg. The training sessions started by having the employees demonstrate how they would normally complete the lifting task. At the conclusion of the half-hour session, the tone was turned off and the employee repeated the task one more time. These final lifts provided the final performance data.

Analysis. Back injury data were analyzed using survival analysis techniques in SPSS. The Kaplan-Meier procedure was used to analyze across groups based upon the value of the mean twisting moment from the final set of lifts.

RESULTS

The Kaplan-Meier tests indicated that the likelihood of back injury for those who had a final mean twisting moment less than or equal to 30 Nm was significantly lower than the video controls (p=.016) and those participating in the LiftTrainer training but had a mean twisting moment over 30 Nm (p=.001). This latter group was not significantly different from the controls (p=.10) (Figure 1).

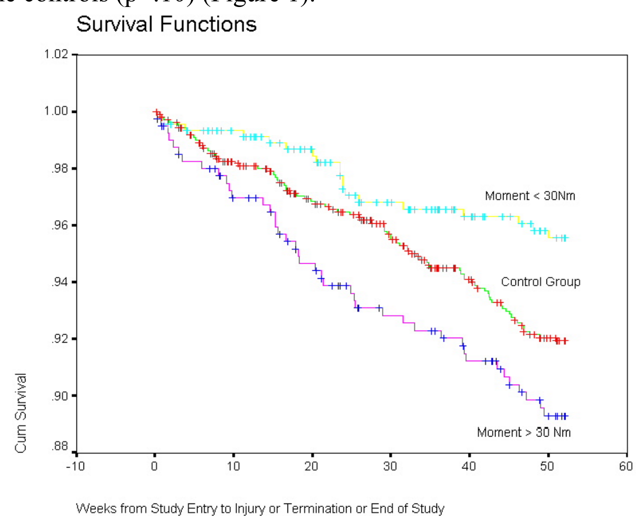

Figure 1. Survival curves for control and the two subdivided Lifttrainer groups.

CONCLUSIONS

Those that completed the initial training session with smaller twisting moments (<=30 Nm) were less likely to report a back injury in the following 12 months than LiftTrainer participants who did not achieve the same level of performance or participants who only viewed a video on lifting techniques.

REFERENCES

Daltroy, L.H. et al. (1997). *N Engl J Med,* ***337***(5), 322-8.
van Poppel, M. N et al. (1998). *Jama,* ***279***(22), 1789-94.

ACKNOWLEDGEMENTS

CDC: NIOSH R01 OH03746-02

A COMPARISON OF EMG CONTROL BETWEEN DISTAL AND PROXIMAL MUSCLES OF THE UPPER LIMB

Keith Gordon[1*] and Daniel P. Ferris[1,2]

[1] Movement Science and [2]Biomedical Engineering, The University of Michigan, Ann Arbor MI, USA, *kegordon@umich.edu

INTRODUCTION

Much of the research that has focused on myoelectrical control for assistive devices has targeted computer processing of the EMG signal. Relatively little is understood about the human motor adaptation side of myoelectrical control. Several studies have shown that humans can learn to modify their EMG patterns with audio/visual biofeedback for purposes of rehabilitation. These findings suggest that myoelectric signals will also undergo substantial adaptation when controlling prostheses and orthoses. In addition, it seems reasonable to expect differences in control accuracy and adaptation depending on which muscles are used for the EMG control signal. Muscles that control the hand are used for fine control tasks while more proximal muscles are used more for more gross motor tasks. Thus an important human factor to consider when building a proportional myoelectrical device is the muscular origin of the EMG control signal.

The purpose of this study was to compare the ability of humans to control EMG signals derived from proximal and distal muscles of the upper limb. Because of the superior motor control ability of the distal muscles, it is hypothesized that humans will have greater control over EMG signals derived from the forearm then from the upper arm.

METHODS

We created a software program to operate in real-time on dSPACE robotics hardware. The program inputs EMG signals originating from two muscle groups to control one-dimensional motion of a virtual object. The software controls the virtual object movement by applying a force proportional to EMG amplitude. One EMG signal acted as a positive force and the other as a negative force. An inertial load on the object and a viscous damping constant were set to make the positioning tasks challenging but feasible. Five male subjects, 20–27 years of age, participated in this study.

During the experiment the subjects controlled the movement of the virtual object with paired sets of EMG activity from distal musculature (forearm flexors and extensors) or proximal musculature (side biceps and triceps) on the dominant side. All EMG signals were normalized to EMG amplitude recorded during maximum voluntary contraction. Subjects performed two different positioning control tasks, a static and dynamic task, with both distal and proximal musculature. The static task consisted of the subject moving the virtual object from the 0 position to the 5 position and holding the object consistently and accurately at the target position for the remainder of the trial. For the dynamic trial the subjects were instructed to oscillate the object between two targets, 5 and –5, as fast and as accurately as possible. All trials lasted 30 seconds. Subjects performed nine sets each of the static and dynamic task while using proximal musculature and another nine sets each while using distal musculature. We analyzed data for the first and ninth trials for each task.

RESULTS AND DISCUSSION

For the static trials, subjects were able to successfully hold the virtual object at the mean target position, 5, using both the distal and proximal musculature. There were no significant differences between muscles groups to position the object during the static task. After practice, the subjects positioned the virtual object at a mean position of 5.016 ± 0.057 using the distal musculature and at 5.068 ± 0.261 when using the proximal muscles.

For the dynamic trials, subjects did not show significant differences in their ability to move the object between the two target positions using either distal or proximal musculature. After practice, subjects had mean error scores (difference between target oscillation end points 5 and –5 and the position where the subject actually changed direction) of distal: 0.025 ± 0.057. and proximal: 0.080 ± 0.261.

It was surprising that there were no differences found in the ability of the subjects to control EMG with different musculature. We hypothesized that there would be differences because the relative use to control fine motor tasks. One explanation for the lack of difference is the normalization to maximum voluntary contraction EMG amplitude. When normalized to the maximal flexion force of a muscle, there appears to be no significant difference in force control for the distal and proximal muscles of the arm (Jones 2000).

SUMMARY

Results showed that when subjects controlled movement of a virtual object with proportional myoelectrical control, there was no difference between using forearm muscles and using upper arm muscles for the control EMG signal. If this observation reflects a more general conclusion regarding proximal vs. distal musculature, then humans should be able to use EMG signals from any part of the upper or lower limb to provide accurate proportional myoelectrical devices. Our future studies will examine a greater range of musculature as potential controllers for myoelectrically controlled orthoses.

REFERENCES

Jones, L.A. (2000). *Exp Brain Res*, **130**, 269-272.

A NON-INVASIVE METHOD FOR THE BLOOD VISCOSITY DETERMINATION

Patrice Fourgeau[1], José-Maria Fullana[1] and Patrice Flaud[2]

[1]Laboratoires Innothera, Arcueil, France, Patrice.Fourgeau@innothera.com
[2]Laboratoire de Biorhéologie et d'Hydrodynamique Physico-chimique , CNRS, Université Paris 7, Paris, France

INTRODUCTION

We present a method for the non-invasive determination of the blood viscosity, valid for periodic as well as non-periodic flows. This method is based on the integral method of data inversion (Bruni, 1998). Before application, data are treated using a smoothing technique. We show on numerical data that the coupled system (smoothing plus integral method) works even for large values of noise.

METHODS

The aim of this work consists in computing the hemodynamic parameters of a stasis followed to a starting flow in a rigid cylindrical pipe. We present an inverse method to give a numerical estimation of the viscosity.
We consider a Newtonian fluid. From the Navier-Stokes equations and assuming the axial velocity profiles $w(r,t)$ are known, we can eliminate the pressure gradient and finally find an expression of the viscosity only as a function of the axial velocity profiles. The viscosity expression allows us to compute the viscosity on an optimal spatial region $[R_1;R_2]$ on the radius at each time t :

$$\nu(t) = \frac{R_2^2 \int_0^{R_1} \left(\frac{1}{r} \int_0^r r \frac{\partial w}{\partial t} \mathrm{d}r \right) \mathrm{d}r - R_1^2 \int_0^{R_2} \left(\frac{1}{r} \int_0^r r \frac{\partial w}{\partial t} \mathrm{d}r \right) \mathrm{d}r}{R_2^2\, w(R_1) - R_1^2\, w(R_2) + (R_1^2 - R_2^2)\, w(0)} \qquad (1)$$

and on an optimal temporal range $T=[t_1;t_2]$ by integration between t_1 and t_2 of the numerator and denominator of (1).

When we applied numerical inversion on experimental data we expect large variations on the solutions because inverse methods are generally ill-conditioned. Moreover in medical research the signal-noise ratio is large and in this particular application the viscosity results from a quotient of integrals. It is thus necessary to smooth the data before computing the inverse problem.
We present also a smoothing technique based on the regularization theory (Poggio et al, 1990, Hertz et al, 1991).

RESULTS

In order to evaluate the noise sensibility on the viscosity results before and after smoothing, the velocity profiles are numerically generated by integration of 2D Navier-Stokes equations. Next, we simulate the experimental data by adding a random noise to the velocity profiles. Thus, we compute the viscosity parameter for different noise values.
The first result is obtained for free-noise set to evaluate the influence of the different viscosity value, the acceleration time t_A (0.08 to 1 s), the optimal spatial region and the time range frequency f_t.

The determination of the optimal parameters and their application on numerical data allows us to test the robustness of the coupled system before experimental applications.

DISCUSSION AND CONCLUSION

Once the optimal spatial region determined, the model gives a very accurate viscosity value (Figure 1): < 3% for exact profiles, and for noised profiles < 8% at each time and < 5% for an optimal temporal region (percentage value related to the viscosity inputs ν_{input}). The highest percentages are obtained for the briefest acceleration times. For exact profiles, the optimal spatial region is confined near the wall, within the viscous boundary layer. The optimal temporal range corresponds to the time to reach a full-developed flow. If noise is present, this optimal temporal range is inferior to the acceleration time. Indeed, the level noise hides the slight differences of profile shapes when the flow is not yet full-developed. Therefore, due to the convolution effects during experimental ultrasonic acquisitions, the velocities near the wall are poorly determined (Flaud et al, 1997). So, it will be necessary to take an optimal spatial region with the radial position R_2 fixed to (1-***n***)% of the radius if the convolution size zone is less than ***n***% of the radius.

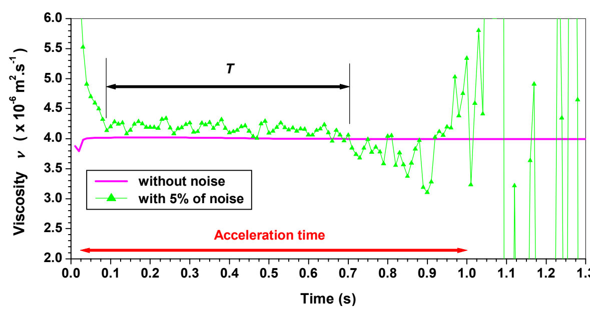

Figure 1. Viscosity determination for the optimal spatial region [0.8;0.97] for a starting flow with $t_A = 0.95$ s, $f_t = 100$ Hz, $\nu_{input} = 4\ 10^{-6}\ \mathrm{m^2.s^{-1}}$.

It is important to note that, contrary to viscometers, this approach represents a viscosity measurement method in blood vessels without modifying the rheology. Moreover the coupled system presented here is very robust and can be applied directly from instantaneous velocity profiles obtained by Doppler ultrasonic measurements.

REFERENCES

F. Bruni (1998). *PhD thesis,* Université Paris 7.
P. Flaud et al (1997). *Ultrasound Med. Biol.*, **23**, 3, 425-436.
J. Hertz et al (1991). *Introduction to the Theory of Neural Computation*, Addison-Wesley.
T. Poggio and F. Girosi (1990). *Science*, **247**, 978-982.

DEVELOPMENT OF A FLOW CHAMBER FOR STUDYING CELL BEHAVIOUR UNDER PULSATILE FLOW

Yubo Fan[1] Wentao Jiang[1] Yuanwen Zou[1] Ling Bai[1] Jinlin Song[1] Ming Zhang[2] Zonglai Jiang[3] Junkai Chen[1]

[1]Laboratory of Biomechanical Engineering, Sichuan University,Chengdu 610065,China, yubofan@yahoo.com.cn
[2]Jockey Club Rehabilitation Engineering Centre, The Hong Kong polytechnic University, Hong Kong, China
[3]Shanghai Second Military Medical University, Shanghai 20000, China

INTRODUCTION

Because of the complexity and sophistication of the in vivo environment, to systematically study the behavior of cellular response to mechanical forces has mainly relied on the use of in vitro preparations. The parallel plate flow chamber is the most common used for applying fluid shear stress to cultured cells. Most studies used parallel plate flow chambers under steady flow, and only a limited number of in vitro studies concerned with the influence of pulsatile flow. Several kinds of flow chamber were developed which can provide pulsatile flow to cells (Helmilinger et al, 1991; Ruel et al., 1995;Tacobes et al.,1998). If the flow in flow chamber similar to the in vivo arterial pulsatile flow can be applied to cultured cells, then more useful information may be achieved.

METHODS

A parallel plate flow chamber system which can simulate physiological pulsatile flow in artery was devised. The three dimensional flow field and shear stress distribution were analyzed by numerical calculation under conditions the recorded flow input/output in experiments were applied.

Calf pulmonary endothelial cells (CPECs) were cultured using the apparatus.

RESULTS AND DISCUSSION

Phenomena of CPECs was studied when cultured under steady and pulsatile flow, under different heart rates , different flow rates and different pressure levels.

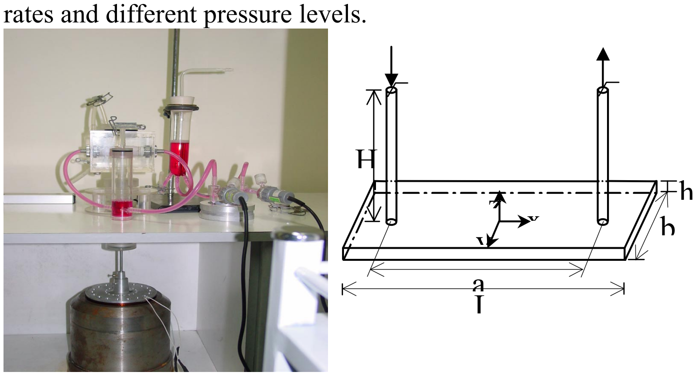

Figure 1: The flow chamber system (left), and the sketch of the flow chamber (right).

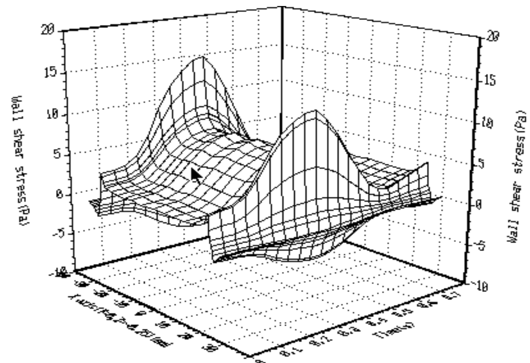

Figure 2: Wall shear stress distribution under pulsatile flow .

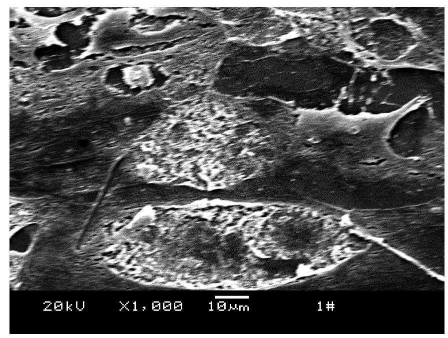

Figure 3: CPECs under pulsatile flow for 12 hours.

SUMMARY

The parallel plate physiological pulsatile flow chamber system can be used to study vascular cellular mechanical behaviors, especially combining with the computational fluid dynamics.

REFERENCES

Helmilinger, G. et al (1991), *Journal of Biomechanical Engineering*, **113**,123-131
Ruel, J. et al (1995), *ASAIO Journal* **41**,876-883
Jacobes, C.R. et al.(1998), *J. of Biomechanics*,**31**,969-976
Brown,T.D. (2000), *J. of Biomechanics*,**33**,3-14

ACKNOWLEDGEMENTS

We acknowledge the support provided by the Chinese National Science Foundation (No.10132020, No.19732003, No.19602012).

THREE-DIMENSIONAL KINEMATICS OF RIGHT VENTRICULAR SYSTOLIC CONTRACTION

Idith Haber [1,2], Dimitris N. Metaxas[3] , and Leon Axel[4]

[1]Harvard Medical School and Children's Hospital Boston, Depts. Of Cardiac Surgery and Cardiology,
Idith.Haber@tch.harvard.edu
[2]Dept. Of Bioengineering , [3]Dept. of Computer Science , [4]Dept. Of Radiology, University of Pennsylvania

INTRODUCTION

The right ventricle (RV) receives blood from the right atrium and pumps it out to the lungs. Due to its thin wall (~3-5mm), complex geometry, and large deformation, RV motion has been difficult to capture. Only recently, tagged MRI imaging combined with 3D motion reconstruction has allowed for a detailed capture of 3D motion. We present a quantitative analysis of normal RV motion, with a view towards using such data as a baseline for detecting wall motion abnormalities in diseases affecting the RV.

METHODS

ECG-gated tagged MRI cine-images of 5 normal volunteers are acquired on a 1.5T GE magnet. These images are used to reconstruct the 3D motion of the biventricular unit using a method described in (Haber, 00). The resulting dynamic finite element model of the ventricular motion is used to analyze the kinematics of RV contraction. We quantify the global motion of the RV and septum is relative to the left ventricular (LV) long axis. The finite elements also allow for calculation of the 3D strain tensor. We consider the minimum principal strain (E3), to be a measure of the greatest muscle contraction between end-diastole and end-systole. The angle ($\alpha 3$) between the E3 direction and the local circumferential direction is also considered. We define regions of the heart using anatomical landmarks: the RV outflow tract; the rest of the RV and septum are sectioned along the long axis into basal, middle and apical regions.

RESULTS AND DISCUSSION

Figure 1: Color plot of E3 on RVFW (scaled is 0 (white) to -.32). Lines indicate E3 directions in midwall. LV is shown darkly shaded

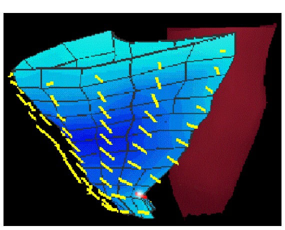

We first quantified the global displacement of the right ventricular free wall (RVFW) and found that the right ventricle exhibits the same twisting motion as the left ventricle: the base rotates counterclockwise while the apex rotates in the clockwise direction. A decreasing base-to-apex gradient (linear regression) in the axial displacement was found in the RVFW (R=0.931) and septum (R = .918). This indicates that the base of the ventricle is pulled down towards the apex during contraction. Corresponding (basal, mid, and apical) regions in the free wall showed greater axial displacement ($p<.001$) than the septum.

We calculated the principal strain directions and present the results for E3, which agreed with previous studies (Waldman, 86; Young, 94). Fig. 1 shows a typical result. Within both the free wall and septum, E3 and $\alpha 3$ were significantly smaller at the base than in other regions ($p<.005$ and $p<.05$, respectively). For the current number of subjects, no significant differences in E3 were found in corresponding regions of the RVFW and septum. However, differences in $\alpha 3$ were found (Fig. 2). These results are consistent with the fact that the muscle fiber orientations are more longitudinal in the free wall than in the septum (on average).

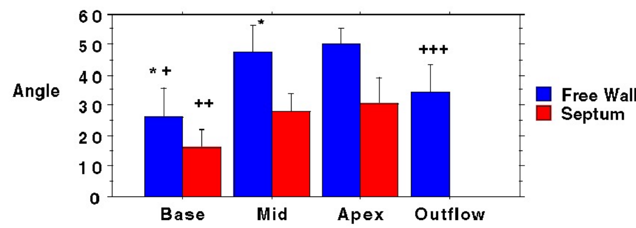

Figure 2: Angle $\alpha 3$: E3 direction vs. the circumference of RV and septum. Freewall: $\alpha 3$ was smaller (more circumferential) in the base vs. mid, apex ($^{+}p <.005$), and outflow tract($^{+++}p <.05$). Septum: smaller $\alpha 3$ in base vs. mid-ventricular and apical regions ($^{++}p<.03$). Paired t-tests between walls showed that $\alpha 3$ was significantly smaller in the base and mid-ventricle ($^{*}p <.005$). Multiple comparisons within walls were performed by Scheffe' subtesting. Values are mean +/= SD.

CONCLUSIONS

The 3D motion reconstruction allowed us to find consistent trends among 5 normal cases. We plan to perform more complex analyses of RV motion on more cases in the future.

REFERENCES

Haber, I. et al (2000). *Medical Image Analysis*, **4(4)**, 335-53.
Waldman, L.K. et al (1986). *J Biomechanics*, **29(3)**, 373-81.
Young, A.A. et al (1994). *Circulation*, **90**, 854-67.

INCREASES IN KINETIC DEMANDS OF THE SUPPORITNG LIMB DUIRNG OBSTACLE CROSSING

Shing-Jye Chen and Li-Shan Chou
Department of Exercise and Movement Science, University of Oregon, Eugene, Oregon, USA
E-Mail: chou@oregon.uotegon.edu

INTRODUCTION

Skeletal muscle strength involved in postural control and locomotion declines with age and disease. The knee extensor and the ankle plantar flexor strength of nursing home fallers were only 37 and 10%, respectively, of those of elderly community dwellers (Whipple et al., 1987). As the available strength reduced, a greater challenge will be imposed on a muscle group when performing activities of daily living. Understanding the change in joint kinetics in reaction to different perturbations during walking may provide us information to better reveal mechanisms underlying increased incidence of falling in the frail elderly. Previous studies demonstrated that significantly greater external knee flexion, hip adduction, and ankle dorsiflexion moments were generated in the trailing limb when supporting the leading limb to step over a higher obstacle (Chou and Draganich, 1997). However, limited information is available to document how the obstacle height affects the joint kinetics when the leading limb is supporting immediately after crossing the obstacle (Chou et al., 2000). Therefore, the purpose of the study was to identify any increases in joint kinetics during both supporting periods when stepping over an obstacle in healthy young adults.

METHODS

Fourteen young healthy subjects, including ten male (mean age, 25.1 years) and four female adults (mean age, 24.6 years) were recruited for this study. Subjects were instructed to walk along an 8m walkway at a comfortable self-selected speed while barefoot. Whole body kinematic data were collected from each subject using a six-camera HiRes™ system (Motion Analysis Corp., Santa Rosa, California) during unobstructed level walking and when stepping over an obstacle of height corresponding to 2.5%, 5%, 10%, or 15% of the subject's height. The order of obstacle height was randomly selected. Joint kinetics was computed using the OrthTrack™ software. Effects of the obstacle height on the joint moments of both limbs were tested with one-way ANOVA with repeated measures at $\alpha = 0.05$ level of significance.

RESULTS AND DISCUSSION

During the support of the trailing limb, the peak external hip and knee flexion moments in the early stance and the peak external ankle dorsiflexion moment in the late stance were found to increase significantly as the obstacle height increased ($p \leq 0.013$; Table 1). During the support of the leading limb, the peak external hip flexion moment in the early stance and ankle dorsiflexion moment in the late stance were found to increase significantly as the obstacle height increased ($p=0.004$ and $p<0.001$, respectively).

Effects of the obstacle height on joint moments of the trailing limb identified in this study were in agreement with those reported previously (Chou and Draganich, 1997). Greater muscular demands on extensors of the hip, knee and ankle joints of the trailing limb are required to support and elevate the whole body over the obstacle. Similarly, the hip extensor of leading limb is then challenged to accommodate a greater and faster downward movement of the whole body after crossing the obstacle during early stance. Furthermore, a greater effort from the ankle plantar flexor of leading limb is needed at the end support to regain the normal walking speed.

SUMMARY

Results of this study indicated that greater external flexion moment are generated at the hip and ankle joints of the leading limb when stepping over a higher obstacle. Greater muscular demands on the hip extensor and ankle plantar flexor during early and late stance, respectively, are required to maintain a smooth motion of the whole center of mass and to resume a normal walking speed after successfully crossing the obstacle.

REFERENCES

Chou, L.S. & Draganich, L.F. (1997). *J. Biomechanics* **20**, 331-337.
Chou, L.S. et al. (2000). *Proceedings of 24th ASB Meeting*, 93-94.
Whipple, R.H. et al. (1987). *J. Am. Geriatric Soc*. **35**, 13-20.

ACKNOWLEDGEMENTS

This work was supported by the Oregon Medical Research Foundation.

Table 1. Significant obstacle height effects on external joint moments of the trailing and leading limbs

	Trailing limb support			Leading limb support		
	Hip	Knee	Ankle	Hip	Knee	Ankle
Early stance	flexion[a] ↑	flexion[a] ↑		flexion[a] ↑		
Late stance			dorsiflexion[a] ↑			Dorsiflexion[a] ↑

[a]level of significance, $p<0.05$; ↑: Joint moment increased with the obstacle height.

THE USE OF SKIN PRE-TENSION TO MODIFY TIBIAL BONE ACCELERATION ESTIMATES

David J Pearsall[1], Ewald M. Hennig[2] Thorsten Sterzing[2]
[1.] Department of Kinesiology and Physical Education, McGill University, Montréal, QC, Canada
[2.] Biomechanik Labor, Universtät Essen, Essen, Germany

INTRODUCTION

Previous studies have demonstrated that measures taken from tibial bone-mounted accelerometers are closely related to vertical force peak loading rate (Hennig & Lafortune, 1988, 1991). Though surface-mounted accelerometers would be more practical for testing (i.e. non-invasive) the relative skin-to-bone movement has confounded their use for accurately estimating ground reaction force parameters.

METHODS

Fifteen adult subjects (mass=71.3 kg±12.7) participated in the study. A uni-axial accelerometer (Entran), oriented in the longitudinal direction, was mounted on the skin surface of distal anterior tibial shaft of each subject. To apply a constant pre-tension to the skin immediately superior to the accelerometer, two Velcro tapes strips were glued to the skin surface. A band of rubber could be adhered to these Velcro surfaces. By varying the amount of band stretch, skin tension could be induced (Figure 1). Four stretch conditions were evaluated: 0, 1-3, 4-8,10-15 mm. The tensions needed to induce these changes ranged from 4 to 15 N based on the displacement of the linear elastic rubber band. With the greatest tension, subjects expressed no great discomfort during or after testing. Subjects were evaluated while running at 3.3 m/s with running shoes within the gait lab. From a force plate (Kistler), foot strike ground reaction force measures were collected from the limb mounted with the accelerometer. Five trials of each condition per subject were collected.

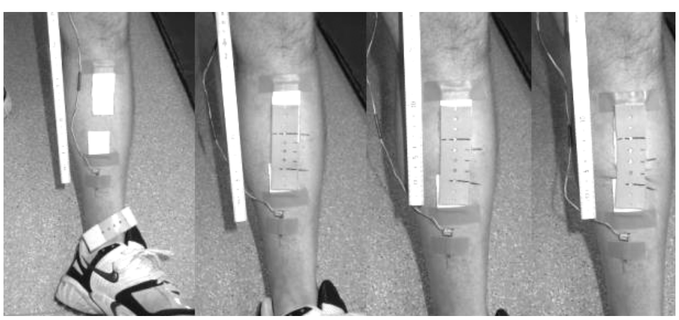

(a) (b) (c) (d)

Figure 1. Anterior view of tibial shaft with with skin deformations of 0, 1-3, 4-8, 10-15 mm induced (a-d, respectively).

RESULTS AND DISCUSSION

As reported previously (Hennig & Lafortune, 1988), elastic rebound of the skin overrepresents the acceleration of the underlying bone. In the present study the measured peak acceleration was lowered from the no stretch to the maximum stretch condition (14.0, 11.9, 8.6, 7.4 g). Bone mounted accelerometer shock measurements have a very close relationship to the peak force rate of the vertical ground reaction force (Hennig & Lafortune, 1991). With increasing skin tension an improved relationship was found between the peak force rate at ground contact (normalized to body weight) with respect to peak acceleration measures of the tibia. With no pre-tension the relation was poor (r^2=0.28) but improved incrementally with applied tension (r^2 =0.47, 0.68, 0.71).

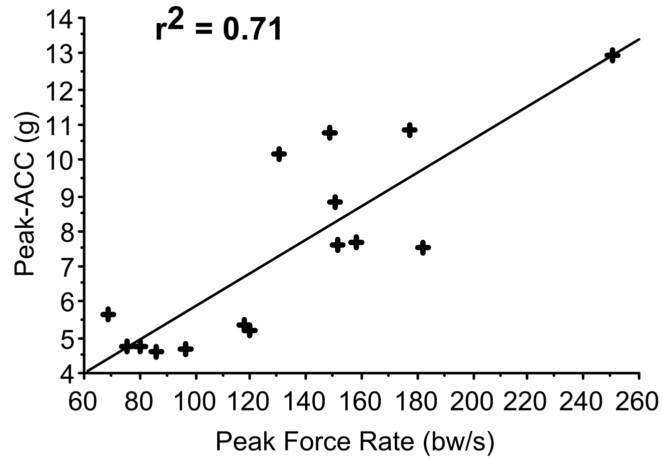

Figure 2. Peak tibial acceleration (g) vs. peak ground reaction force rate (bw/s) at maximal skin pre-tension.

SUMMARY

The skin pre-tension approach may permit the use of surface mounted accelerometers to estimate tibial bone accelerations and, in turn, ground reaction force variables. Thus, this technique creates the opportunity to explore running dynamics in number of situations where force plates cannot be utilitized.

REFERENCES

Hennig EM, Lafortune MA (1988). Vth. Biennial Conference of the Canadian Society of Biomechanics. Ottawa, 74-75.

Hennig EM, Lafortune MA (1991). *Int J Sport Biom,* 7(3), 303-309.

ACKNOWLEDGEMENTS

This Research was supported by the National Science and Engineering Research Council (NSERC) of Canada and Nike Inc. (USA).

TORSIONAL STABILITY OF TOTAL ELBOW ARTHROPLASTY

Jufang He[1], Mark E. Baratz[1], Felix Riano[1], James Rudert [3], Mark C. Miller[1, 2].

[1]Biomechanics Research Laboratory, Allegheny General Hospital, Pittsburgh PA, jhe@wpahs.org
[2]Duquesne University, Pittsburgh PA, [3]University of Iowa, Iowa City, IA

INTRODUCTION

As Total Elbow Arthroplasty is introduced to younger generations, the post-operative stability of the humeral construct is a major concern. In particular, the importance of the humeral condyles is uncertain. The presence of the condyles may increase the stability, but many surgeons remove them to reduce the duration of the procedure. Furthermore, some designs incorporate a flange and the use of a bone block that may add to the stability. This study tests the hypothesis that either condyles or bone block will increase the stiffness of the humeral construct.

METHODS

Eleven frozen cadaveric distal humerus, cut 20 cm proximal to the trochlea were defrosted at room temperature and cleaned off all soft tissue. The humeral canal was broached and the stem cemented. Specimens were mounted into a custom-made jig in a bi-axial testing machine (Bionix, MTS Inc.). Given that the torsional strength of the humerus is approximately 53N-m (Schopfer et al), loads of 10N-m and 20N-m were chosen to test the torsional stability. To avoid hysteresis effects in the structure, every specimen was pre-conditioned 10 times at both load levels. Loads were applied linearly over 10 seconds. Angular displacement and loads were recorded at 12Hz. Each specimen was tested with both condyles and bone block, then with condyles but without bone block, then without condyles and bone block, and finally with bone block but without condyles. Lastly, the specimen was loaded to failure in torsion with the bone block in place. Figure 1 shows the load and displacement curve of a typical specimen. The stiffness was defined as the slope of the best-fit line of the data points through the origin. Stiffnesses were normalized using the first test condition for purposes of comparing and repeated measures Anova was used to statistically compare the stiffnesses under different test conditions.

RESULTS

The relative stiffnesses are shown in Figure 2, in which all values are normalized by the stiffness in the first test condition. The structure with both condyles and bone block had the greatest stiffness. Although Figure 2 shows only the results for 10 N-m, the same trend was found for a 20 N-m load. Stiffnesses decreased with each test, however, statistical analysis showed no significance ($p>0.05$). The average failure load was 37.41 (± 12.51) N-m. All failures were spiral fractures of the humerus.

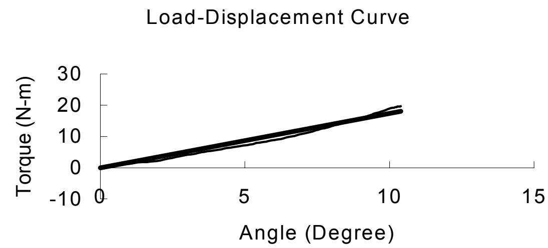

Figure 1: Load and displacement curve of a specimen at 10 N-m load.

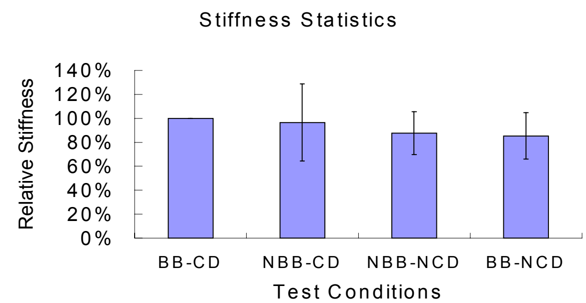

Figure 2: Normalized torsional stiffness (± S.D.) of humeral construct under different test conditions at 10 N-m load.

DISCUSSION AND CONCLUSIONS

When no condyles were present, stiffnesses with or without a bone block remained essentially the same. The largest difference appeared between the first and fourth tests ($p=0.062$), however, no significance was found. Although the sequence of test conditions was not varied, the average failure load was substantially larger than the test load. That is, the load levels were well below the failure load and no damage was believed to have affected the relative stiffnesses. This average failure load was somewhat below the results found by Schopfer et al for intact humerus, but a good cement mantle was found in all specimens.
The stability of the humeral construct was represented by the amount of torque required per unit of angular movement. A statistical analysis was performed on the tests. Results showed that the presence of either condyles or a bone block does not increase the torsional stability of the humeral construct. In conclusion, sacrifice of the condyles appears to be a viable surgical option.

REFERENCES

Schopfer A. et al (1994). *J. Orthop Trauma*, **8(5)**, 414-421
.

THE ROLE OF TORSO MUSCLES IN TRUNK TWISTING

Shrawan Kumar and Yogesh Narayan

Ergonomics Research Laboratory, University of Alberta
Edmonton, AB T6G 2G4, Canada

INTRODUCTION

Kumar (1993) and Kumar et al (1996) reported the phasic and the magnitude relationship of the external and internal obliques, rectus abdominis, pectoralis major, latissimus dorsi and erectors spinae at T_{10} and L_3 levels in an unrestricted trunk twisting at a normal velocity. These authors reported a differential in onset timing of different muscles. They found that the twisting was initiated and sustained by the contralateral external oblique, the ipsilateral latissimus dorsi. However, it is unclear if the twisting has the same (or similar) phasic and magnitude relationship in isometric and isokinetic modes. The current study reports the results of this investigation.

METHOD

Fifty normal young adults (27 male and 23 female) were placed in upright neutral seated posture in a specially designed and fabricated Axial Rotation Tester (AROT). The subjects were stabilized in the device such that only thoracolumbar region could be rotated. From the upright neutral seated posture the subjects were required to exert their 25%, 50% and 75% of previously measured maximal voluntary contraction (MVC) in bilateral twisting with visual feedback to maintain the force level. A block randomized experimental design was used. The force and EMG from erector spinae at T_{10} and L_3, external and internal oblique, rectus abdominis, latissimus dorsi and pectoralis major were recorded bilaterally at 1 kHz. The task cycle was referenced to the onset of the torque. The timings of RMS and smoothed EMG were referenced to the torque onset. The slope, normalized EMG amplitude, EMG per unit time and EMG area under the curve were calculated. An analysis of variance, Pearson's product moment correlation between the torque and EMG and the regression analysis was carried out using SPSS statistical software package.

RESULTS AND DISCUSSION

There were no significant differences between male and female subjects in EMG variables. The phasic interrelationships of external obliques, the latissimus dorsi and the erector spinae were different from other muscles ($p<0.01$). With increasing grades of contraction the latissimus dorsi and the external obliques increased their magnitude significantly ($p<0.01$) whereas that of erector spinae underwent a decrease in proportionate terms (but not in absolute magnitude) suggesting a stabilizer role for

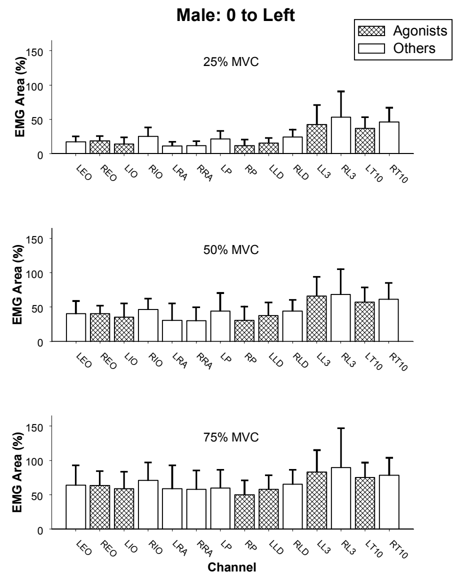

Figure 1: The magnitude contribution of different muscles in graded contractions in male samples in percent area.

them in trunk twisting. The relative timing and pattern of EMG in graded isometric contractions were significantly different from those of unresisted dynamic twisting ($p<0.01$). These variables between different grades of isometric contraction did not differ significantly. However, within the isometric graded conditions timing of different muscles were variable due to lack of any motion.

SUMMARY

The twisting of the trunk is initiated by the contralateral external oblique and ipsilateral latissimus dorsi. The erector spinae acts as a stabilizer. The phasic relationship of torso muscles in dynamic conditions is set and repeatable whereas in static condition is variable

REFERENCES

Kumar, S. (1993) Proceedings of IEEE. EMBS, San Diego, October 28-31, 93.
Kumar, S. et al., (1996) Spine, 21, 1500-1512.

ACKNOWLEDGEMENT

Financial assistance of MRC, Canada is gratefully acknowledged. The assistance of Doug Garand in data acquisition is also acknowledged.

AN EFFICIENT AND ROBUST ICP TECHNIQUE FOR SURFACE REGISTRATION

Andrea G. Cutti[1], Angelo Cappello[1], Alberto Leardini[2]

[1] DEIS – Università di Bologna, Italy, andrea.cutti@ior.it
[2] Movement Analysis Laboratory, Istituti Ortopedici Rizzoli, Bologna, Italy

INTRODUCTION

In computer-assisted surgery, a robust method for spatial registration is necessary. The Iterative Closest Point (ICP) (Besl et al., 1992) is probably the most widely used algorithm for surface rigid registration, defined as the spatial alignment between a Data Shape (DS) and a Model Shape (MS). This procedure is limited by the monotonical convergence also to local minima of the cost function, and by the computational complexity of the closest point searching when performed extensively. For the former, authors have proposed to perform the registration starting from different initial states (Besl et al., 1992). The present study is aimed at reducing the number of these states. Many solutions have been proposed also for the complexity, but these are not easy to be implemented and require extensive pre-computation (Audette et al., 2000).

METHODS

The local minimum problem was addressed in eight steps: 1) the centroid of DS and MS are initially taken to the origin of the reference system; 2) the index to discriminate global to local minima is taken as the residual distance variance at the end of the registration process; 3) a threshold for this index is empirically defined according to the specific shape of the objects and to the expected noise; 4) a preliminary registration is performed; 5) if the index value at the end of 4) is above the threshold, a set of DS initial states is obtained by uniformly sampling the rotation angle domain and applying these rotations to DS; 7) the set of these states is classified assuming that the best rotation is the one which, after only one iteration of ICP, leads to the smallest residual distance variance; 8) the registration process changes the initial state of the DS at every registration until the index is above the defined threshold. The computational complexity of the closest point searching is reduced using pre-processing based on the Delaunay Tessellation (DT) of the MS (Fortune, 1992). The DT, as dual of the Voronoi Diagram (VD), is intrinsically related to closest point problems, and it has a data structure more manageable than the one associated to VD since DT is made of simplexes. Tests were conducted using a free-form version of the Standardised Femur (Viceconti et al., 1996). For the local minimum problem, MS was set to 5000 points. 300 DS points were randomly extracted from MS, and a Gaussian noise with zero mean value and 2mm standard deviation was added. For the three erroneous local minima (Fig.1), the smallest value of the residual distance variance was found to be 19 mm^2, independently from the number of points in DS. Having also observed a 2 mm^2 residual distance variance of the registration around the global minimum, the threshold was set at 3 mm^2. The sampling rate of the rotation domain was set at 45° for all the rotations. For the closest point tests, different combinations of points for DS and MS have been tested, starting from different positions of DS with respect to MS. The DT and closest point searching implementation was taken from Matlab (The MathWorks). A highly vectorised function of the exhaustive closest point searching was implemented in Matlab.

RESULTS AND DISCUSSION

From every imposed starting state, the novel algorithm reached a registration around the global minimum. In the worst case (initial pose of 160°, 110°, 0° cardanic rotations), the algorithm imposed 40 guessing rotations to DS. Results for the closest point problem are summarised in Table 1. The starting position proved to have no influence on time performance. The pre-processing of the DT was found to have negligible computational costs ($Time_{DT}$). The data reported for the closest point searching are the mean values over 60 iterations for every combination of DS and MS points. A reduction in time from 7 to 80 times was obtained.

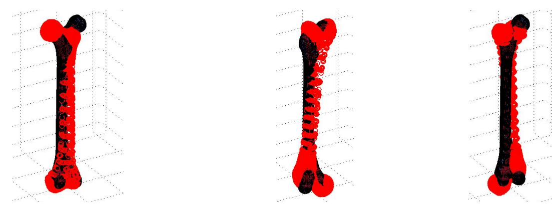

Figure 1: Opposing local minima for a femur bone.

	$Time_{DT}$	0.43	0.88	1.43	1.92	2.47
	DS \ MS	1000	2000	3000	4000	5000
DT	500	0.054	0.10	0.16	0.21	0.28
	3000			0.19	0.24	0.31
	5000					0.34
Exh.	500	0.41	0.85	1.44	2.12	2.86
	3000			8.55	12.32	16.57
	5000					27.26

Table 1: Computational performance [s] with different DS and MS points. Closest point searching using the proposed DT and the traditional Exhaustive searching are compared. Analysis was performed with an AMD 1000Mhz processor.

SUMMARY

This study enhances the convergence to the global minimum of the ICP algorithm. The proposed solution for the computational complexity of the closest point searching is simple, efficient and with negligible pre-computational costs.

REFERENCES

Audette, M. A. et al. (2000). *Med Image Anal*, **4**, 201-217
Besl, P.J. et al. (1992) *IEEE Trans. PAMI*, **14**, 239-256.
Fortune, S.(1992), Du and Hwang Ed., World Scientific.
Viceconti, M. et al. (1996). *J. Biomech*, **29**, 1241

GLENOHUMERAL JOINT LAXITY WITH AND WITHOUT ROTATOR CUFF CONTRACTION

Kevin McQuade [1,2], Anand Murthi 2, Margaret Finley [1,2]
[1]University of Maryland School of Medicine, Baltimore, MD USA
[2]Baltimore Veterans Administration Medical Health Care System, Baltimore, MD, USA
[3] Communicating Author: Kmcquade@som.umaryland.edu

INTRODUCTION

Examination of the shoulder routinely involves testing for joint laxity and stability. There have been several obstacles in developing quantitative testing for the shoulder joint under passive and dynamic conditions. These include stabilization of the scapula, appropriate location of translation points, and ability to perform tests with multiple arm configurations. McQuade et al (1999) has developed a method for quantitative assessment of the glenohumeral joint using magnetic tracking and examiner instrumented applied fore measurements. This study begins to extend previous work by using a scapular reference frame, using a humeral head center finding algorithm and including an assessment of muscular contraction effects of the rotator cuff. This pilot work presents the first three subjects using this approach.

METHODS

Three athletic female subjects between the ages of 25-30, were tested. Subject 'A' had no history of shoulder problems, Subject 'C' was previously a competitive swimmer and had a long history of shoulder problems including sublusxations. Subject 'S' was a squash player with no history of shoulder problems. Subjects were instrumented with electromagnetic tracking sensors (Flock of Birds ™) for the scapula and humerus of their dominant arm. A third sensor was attached to a small hand held plastic base that was also fixed to a small load cell . This device was held in the palm of the examiners hand and provided information as to the orientation of forces applied to the subject. The Scapula and humerus were digitized using MotionMonitor™ software (Innsport Inc , Chicago Ill). Local coordinate frames were determined for the scapula with orthogonal axes perpendicular and parallel to the body of the scapula. Humeral head sensor data was transformed with respect to the scapular reference frame. Humeral head center location was determined by using a least squares method, collecting the orientation of the humerus in ten random different configurations and predicting the zero velocity point. The RMS error (within 4mm) and the positions of the humeral center relative to the humeral sensor and the scapular sensor were used to assess the accuracy of the method. Subject's arm was placed in abduction and external rotation, clinical anterior drawer tests were performed with the subject relaxed and with the subject performing an isometric internal rotation contraction with mild resistance (5lbs).

RESULTS AND DISCUSSION

The anterior translation of the glenohumeral joint during directly applied loads under conditions of relaxation and rotator cuff contraction are shown for the three subjects in Fig 1a, 1b and 1c.

Figure 1abc

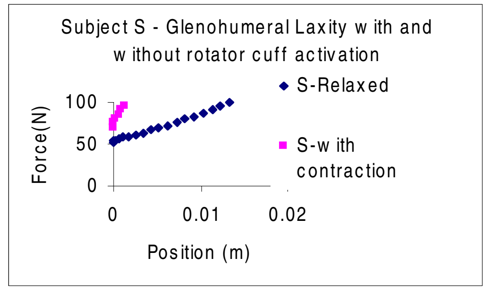

Figure 1b

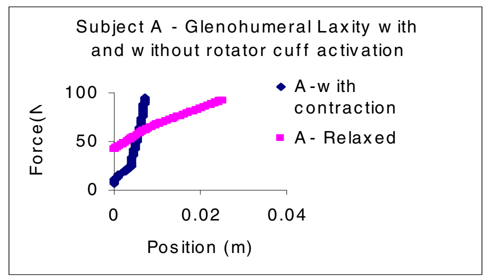

Figure 1c

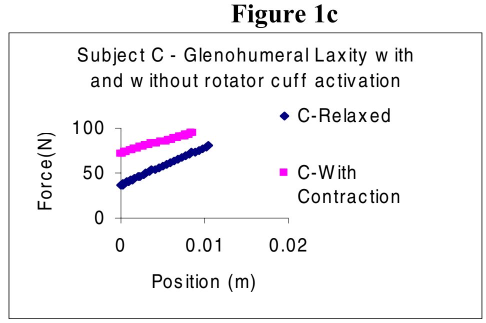

SUMMARY

Results show how stiffness of the glenohumeral joint changes with contraction primarily of the subscapularis to constrain the humeral head from anterior translation. In subjects 'A' and 'S' the stiffness increased significantly indicating an effective cuff. Subject 'C' demonstrated very little difference, indicating a dysfunctional cuff. This was consistant with her history of shoulder problems. We are continuing this study with a larger sample size and use of EMG for muscle verification and with patient populations to assess the effects of cuff surgery and rehabilitation.

REFERENCES

McQuade K. Shelly I. Cvitkovic J. Patterns of stiffness during clinical examination of the glenohumeral joint. Clini Bio. 14 (1999) 620-627

INFLUENCES ON EYE LOCATION AND POSTURE OF DRIVERS

Marion Fehren[1,2], Jan Thunnissen[1] and Klaus Nicol[2]
[1] Johnson Controls GmbH, Burscheid, Germany, marion.fehren@jci.com
[2] Laboratory of Applied Biomechanics, University of Muenster, Germany

INTRODUCTION

An accurate prediction of the driver‘s posture is important for comfort and safety. Thus, there are several models available concerning the preferred horizontal seat adjustment and eye location (e. g. Flannagan et al. 1998, Kolich 2000, Manary et al. 1998, SAE J941). Since factors such as visibility and head clearance are not considered in the models, the question was, how far they affect the drivers' joint and eye locations. Thus, posture measurements were made in a real car environment to detect the relationships indicated above.

METHODS

In a middle class car a posture study was performed with 9 volunteers (5th percentile (5th p.) females, 50th p. and 95th p. males). Backrest angle, cushion height, and horizontal seat position were adjusted by the subjects to their preference. After 5 min. of sitting, the coordinates of several palpable landmarks at head, trunk, arms and legs were recorded with a FARO arm. Seat adjusting and posture recording were performed twice for each subject. Subsequently a comfort questionnaire was applied. Then the joint coordinates were calculated according to Reed et al. (1999) and t-tests were applied to detect differences between the subgroups.

RESULTS AND DISCUSSION

The eye locations of the subgroups are shown in Fig. 1. Consistent with results of Manary et al. (1998) the locations are more rearward and upward than the SAE J941 eyellipses (a technical standard for eye location). This indicates that the SAE model is less suitable for realistic driving conditions.

Concerning the z-coordinates, in both male subgroups the eye location is significantly more upward than in the female subgroup ($p < 0,05$), but between the 50th and 95th p. males there is no significant difference in both measurements.

Surprisingly, the x-coordinates of the eye location of the 95th p. males is more forward than the ones of the 50th p. males ($p < 0,05$ in both measurements). However, analysis of the joint locations in side view do not reveal significant differences between the 50th and 95th p. males concerning torso location. Obviously, there occurs a more forward movement of the head relative to the torso for the 95th p. males compared to the 50th p. males. Concerning the reasons for this relative movement the questionnaires reveal limited head clearance and visibility (too low upper edge of windscreen). Further, questionnaires indicate restricted visibility for the 5th p. females caused by the height of the instrument panel.

Substantial differences between model and empirical data (up to 128 mm) are seen in the horizontal seat adjustment too. Inconsistencies certainly can be reduced, if visibility and head clearances are included in the models. It can be concluded that

- visibility and head clearances affect eye location and posture, so eye location and posture studies should not be performed in seat mock-ups only, but in real cars too,
- posture models should consider both, anthropometric and package variables including visibility and head clearances.

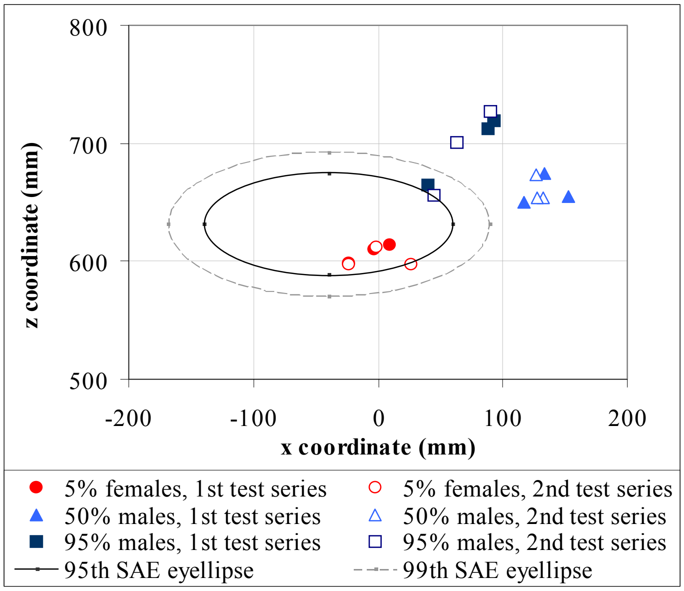

Figure 1: SAE eyellipses (for torso angle = 24°) and actually measured eye locations of volunteer drivers

SUMMARY

A posture study in a real car was performed to investigate the effect of certain package factors on joint and eye location. The results indicate substantial differences between model prediction and empirical data and lead to the conclusion that boundary conditions such as visibility and head clearance have to be considered in posture prediction models.

REFERENCES

Flannagan, C.A.C. et al. (1998). An Improved Seating Accommodation Model with Application to Different User Populations. *SAE Technical Paper* 980651

Kolich, M. (2000). Driver Selected Seat Position: Practical Applications. *SAE Technical Paper* 2000-01-0644

Manary, M.A. et al. (1998). Development of an Improved Driver Eye Position Model. *SAE Technical Paper* 980012

Reed, M.P. et al. (1999). Methods for Measuring and Representing Automobile Occupant Posture. *SAE Technical Paper* 990959

SAE J941. Motor Vehicle Drivers' Eye Locations. *Recommended Practice*. Rev. Level Jun1997

SIZE EFFECTS IN NONLINEAR VISCOELASTICITY

Anthony Escarcega, Paolo P. Provenzano, Rittu Hingorani, Roderick Lakes, Ray Vanderby Jr.

Orthopedic Research Laboratory, University of Wisconsin, Madison, WI. University of Wisconsin Hospital, Division of Orthopedic Research, 600 Highland Ave, Madison, WI 53792. vanderby@surgery.wisc.edu

INTRODUCTION

Ligaments are viscoelastic and thus, display time-dependent and load history-dependent mechanical behavior (Woo, 1982). In this study two viscoelastic properties are considered: stress relaxation and creep. In a recent study (Provenzano et al, 2001) showed nonlinear behavior in the rat MCL in which the rate of creep and relaxation is dependant upon the level of stress and strain, respectively. Since this had never been reported before in the literature, it is the goal of this study to determine if this phenomenon holds true for larger animals. This study examines rates of stress relaxation and creep at multiple levels within the physiologic range using two different sized animal models.

METHODS

Medial collateral ligaments (MCLs) from ten pairs of pig knees and six pairs of rabbit knees where used for this study. The testing for all pairs of ligaments followed the same protocol; multiple stress relaxation tests were performed on each MCL and multiple creep tests on the contralateral MCL. Between each test, the ligament was allowed to recover for at least 10 times the length of the test while remaining hydrated. The order of the tests started with the smallest strain and increased. Stress relaxation for each test lasted 100 s and had a rise time of 10 percent strain per second. The contralateral MCL was tested next in creep for 100 s and the applied load corresponded to the maximum load for stress relaxation. All tests were performed below the suspected structural damage threshold for these tissues (Provenzano, et al., 2002). Data was plotted on a log-log scale and a power law, t^n, was used to determine slopes (rate of relaxation or creep).

RESULTS AND DISCUSSION

The rates for both creep and stress relaxation were dependant upon the level of stress or strain for both the sizes of MCLs. The amount of strain varied from 0.46-5.44% for pig and 0.53-5.00% for rabbit as measured by video analysis. The rate of relaxation varied by nearly 2 times for the pig MCL with the rate being –0.0891 for 0.46% and –0.0451 for 5.06% and four times for the rabbit MCL with the rate being –0.275 for 0.87% and -.067 for 5.00% (Fig 1). In creep, the results were similar, the pig MCL rate and the rabbit MCL rate had differences of near 2 times and 4 times, respectively (Fig 2).

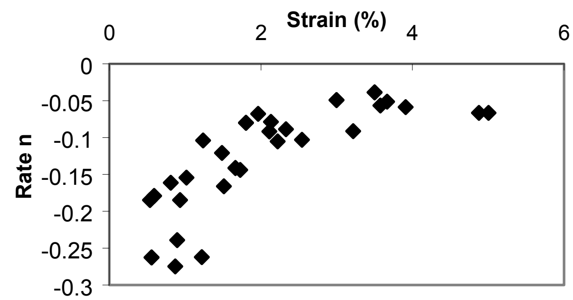

Figure 1: Change in the rate of stress relaxation for the rabbit MCL showing a decrease in rate with increasing strain.

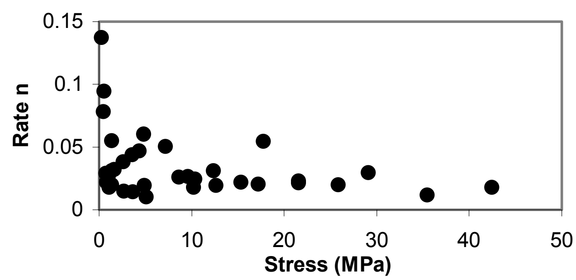

Figure 2: Change in the rate of creep for the Pig MCL showing a decrease in rate with increasing stress.

SUMMARY

The magnitudes of the values of the change in rate suggest that there is a size effect in the way the ligaments behave in stress relaxation and creep. The previous experiment in rats has shown an order of magnitude change in rate over the physiologic range, where we have shown the change to be less as the size of the ligaments increases. The mechanism behind this is not understood, but could possibly be related transport of water within the ligament.

REFERENCES

Provenzano et al., *Ann. Bio. Eng* **29**:908-914, 2001
Provenzano et al., *J. App. Phys*. **92**:362-371, 2002
Woo, *Biorheology* **19**:385-396, 1982

ACKNOWLEDGEMENTS

This work was funded in part by NSF (grant # CMS9907977)

BIOMECHANICAL MODELING OF THE SCOLIOTIC SPINE REDUCIBILITY

Yvan Petit[1,2], Carl-Éric Aubin[1,2] and Hubert Labelle[2]
[1]Biomedical Engineering, École Polytechnique, yvan.petit@polymtl.ca
[2]Research Centre, Sainte-Justine Hospital
Montréal, Québec, Canada

INTRODUCTION

The flexibility of the scoliotic spine is well recognized as an important biomechanical factor in the planning of surgical instrumentation (Kleps et al 2001). Clinical tests like the side bending or the traction tests are commonly used to estimate the possible correction and to define the spinal segment to instrument. However, none evaluate the flexibility of the spine since the forces are not known. Also, there is no consensus on the optimal test to assess the scoliotic spine reducibility. Therefore, the objective is to develop a personalized biomechanical model of the spine that will allow the design of a clinical test providing optimal estimation the reducibility.

METHODS

A flexible multi-body model of the spine (figure 1) was developed to simulate several mobility tests. Vertebrae were represented using rigid bodies. Spherical joints and generalized spring elements were used to represent the intervertebral articulations according to reported experimental data (Oxland et al 1992, Panjabi et al 1976, 1994). Postero-anterior (PA) and lateral (LAT) radiographs of a scoliotic patient taken pre- and post-operatively were used to obtain the 3-D geometry of the spine using a 3D reconstruction and modeling technique (Aubin et al, 1995). Initial conditions of the model were defined from the pre-operative geometry.

Figure 1: Flexible multi-body of the spine: a) PA and b) LAT views.

Four tests (lateral bending, fulcrum bending, traction and axial rotation of the trunk) were simulated and compared to the reducibility obtained from the pre- to post-op geometry. The reducibility of the spine was analyzed in 5 segments: 2 apical (T8-T10 and L1-L3) and 3 neutral (T4-T8, T10-L1, L3-L5). The reducibility has been defined as the rotation of the superior vertebra relative to the inferior vertebra and the metric used was the norm of the axial vector of the rotation matrix.

RESULTS AND DISCUSSION

Figure 2 shows the reducibility of the scoliotic segments measured from the 4 simulations and from the surgery. It shows that reducibility is almost uniformly distributed along scoliotic segments and also that lateral bending and axial rotation tests are the closest to surgery. However, simplifying assumptions particularly concerning mechanical properties obtained from the literature and boundary conditions may have influence the results.

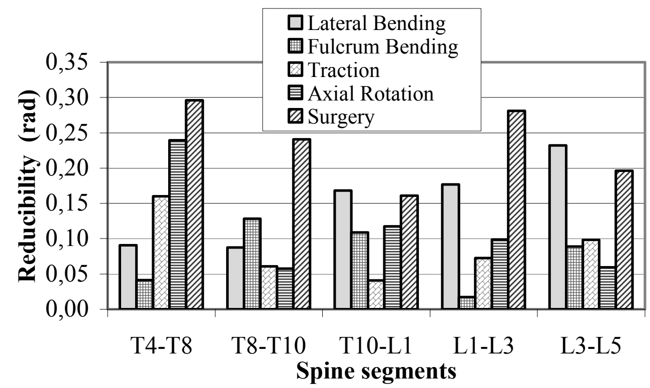

Figure 2: Simulated and measured reducibility of segments

CONCLUSION

Preliminary results show that lateral bending and axial rotation demonstrate more reducibility than other tests. Overall, these tests are the closest to that of surgery. Such results can be used to design an optimal clinical test and to define patient-specific mechanical properties for biomechanical models of the spine.

REFERENCES

Aubin C-E et al (1995). *Ann Chir* **49,** 749-761.
Kleps SJ et al (2001). *Spine,* **26**, E74-9.
Oxland TR et al (1992), *J Orthop Res*, **10**, 573-80.
Panjabi MM et al (1994). *JBJS*, **76-A**, 413-424.
Panjabi MM et al (1976). *J Biomech*, **9**, 185-92.

ACKNOWLEDGEMENTS

This research was funded by NSERC, FCAR and FRSQ.

CHONDROCYTES AND FIBROCHONDROCYTES RESPOND DIFFERENTLY TO OSCILLATORY TENSION

Vanderploeg EJ, Collier KR, Imler SM, Levenston ME
Georgia Institute of Technology, Atlanta, GA marc.levenston@me.gatech.edu

INTRODUCTION

Tissue engineering offers potential therapies for patients suffering from degenerative joint disease and complications resulting from traumatic injury. *In vivo*, articular cartilage experiences predominantly compression, while fibrocartilage tissues experience both compression and tension. Understanding cellular responses to tissue-appropriate loading regimes is crucial to developing functional bioartificial tissue replacements. Both articular chondrocytes and fibrochondrocytes are possible cell sources for tissue engineered cartilage, but limited data exist comparing their responses to mechanical stimuli. This study compared the responses of chondrocytes and mensical fibrochondrocytes (MFCs) to oscillatory tension in 3-D culture.

METHODS

Chondrocytes and MFCs were isolated from immature bovine stifle joints and seeded into fibrin constructs at 5e6 cells/mL. Constructs (n=8) were pre-cultured for 1, 7, or 14 days and then cultured for an additional 68 hours either unloaded or with an oscillatory tensile stretch (1Hz, 10% p-p). During the final 20 hours, ^{3}H-proline and ^{35}S-sulfate were added to the culture media. Six constructs were analyzed for ^{3}H and ^{35}S incorporation and total DNA content. The remaining constructs were imaged using confocal microscopy for cell viability and morphology (calcein/ethidium homodimer). Additional constructs were cultured for 1 or 7 days and imaged for F-actin filaments (Alexa Fluor® 546 phalloidin).

RESULTS

MFC Constructs Oscillatory tension had no effect on MFC protein synthesis (^{3}H) but significantly inhibited proteoglycan synthesis (^{35}S) in the 1 day pre-culture group. No effect was seen on MFC construct total DNA content. **Chondrocyte Constructs** Oscillatory tension inhibited protein synthesis (^{3}H) only in the 7 day pre-culture group but significantly inhibited proteoglycan synthesis (^{35}S) at all three time points. Tensile stretch significantly increased total DNA content; this effect was more pronounced at later time points. **Cell Morphology** Cell viability was high in all samples imaged. At all time points, unloaded chondrocytes maintained a rounded morphology (Fig.1b). Although unloaded MFCs exhibited a round morphology in the 1 day pre-culture group, by day 7 the cells had developed fine cellular projections (Fig.1a). Tensile stretch had no apparent effect on MFC morphology. In contrast, oscillatory tension induced a morphological change in a sizeable number of chondrocytes in the 7 and 14 day pre-culture groups. These cells resembled those of the 7 day MFC constructs (Fig.1a,c). Additional images of unloaded constructs revealed F-actin filaments in the cellular projections of the MFCs and showed clear cytoskeletal organization in the chondrocytes (Fig.2a,b).

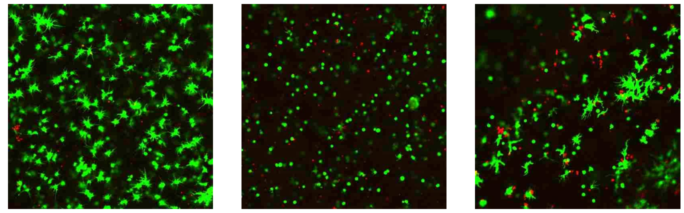

a: MFCs unloaded b: Chondrocytes unloaded c: Chondrocytes tension

Figure 1: Tension induces MFC-like morphology in chondrocytes (7 day preculture)

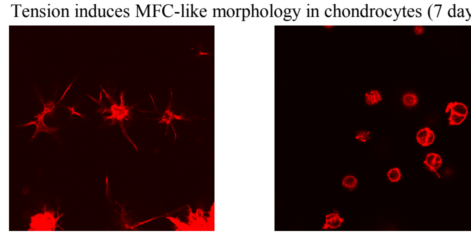

a: MFCs unloaded b: Chondrocytes unloaded

Figure 2: F-actin filaments after 7 days of preculture

DISCUSSION

The results of this study suggest that oscillatory tension causes chondrocytes to transition away from matrix synthesis and towards proliferation. In addition, the confocal microscopy images indicate that chondrocytes take on a more fibrochondrocytic morphology in response to oscillatory tension. These observations support the hypothesis that similar morphologies seen in the tensile regions of native fibrocartilage are functional adaptations to loading (Hellio Le Graverand, 2001, Errington, 1998). The spontaneous development of cellular projections by the MFCs in 3D culture raises questions regarding the stability of the adapted morphology of the chondrocytes. On-going studies are examining kinetics of cytoskeletal reorganization via confocal microscopy and specific changes in phenotype (RT-PCR) in response to tension and after its removal.

REFERENCES

Hellio Le Graverand M.P. et al (2001). *J Anat* **198(Pt 5)**:525-35. Errington R.J. et al (1998). *J Anat* **192**:369.

ACKNOWLEDGEMENTS

NSF-ERC program award number EEC-9731643, The Whitaker Foundation, and NSF graduate fellowships

DO CONSTANT-RATE RAMP TESTS REPRESENT EQUILIBRIUM BEHAVIORS IN TENDON? DETERMINATION OF TENSILE MODULUS AND POISSON'S RATIO IN TWO DIMENSIONS

Heather Anne Lynch, Jeffrey P. Wu, Andrew Jawa, and Dawn M. Elliott[1]
McKay Orthopaedic Research Laboratory, University of Pennsylvania
[1]delliott@mail.med.upenn.edu

INTRODUCTION

Tendon modulus is not highly sensitive to strain-rate under constant-rate uniaxial tensile loading (Woo, 1990). However, it is not clear that the tissue is at equilibrium even when very slow rates are used. Equilibrium behaviors, where viscoelastic effects have dissipated, represent elastic tissue properties. These properties are important for elastic modeling and for comparing tissue properties across different studies. Incremental stress-relaxation experiments have not yet been used to measure equilibrium behaviors of tendon. The purpose of this study was to determine if slow constant-rate tensile tests represent equilibrium behaviors in tendon. We hypothesize that the properties of modulus and Poisson's ratio will not be different when measured using incremental stress-relaxation compared to constant-rate ramp tests. Because three-dimensional elastic modeling is needed for tendon, we tested this hypothesis for tendon samples aligned along the fiber direction and transverse to the fiber direction.

METHODS

Sheep flexor tendons were cut into rectangular specimens (LxWxT = 9.16±1.90 x 2.41 ± 0.29 x 1.87 ±0.35mm) with the long axis either parallel (x_1: longitudinal) or perpendicular to the fibers (x_3: transverse). Uniaxial tensile loading was applied along the long axis of the specimen. Incremental stress relaxation (σ-RLX) testing of longitudinal specimens included 0.5N preload, preconditioning, and 1% strain increments with a 10-minute relaxation. For transverse specimens, a 0.005N preload and 4% strain increments were used; preconditioning was omitted. Ramp testing used the same preload and preconditioning as above, followed by a 0.01%/s, 1%/s, or 10%/s ramp to failure. Specimen images were acquired and 2-dimensional surface strain was calculated using custom Matlab and ABAQUS programs. Modulus was calculated as the slope of the linear region of the stress vs. strain curve. Poisson's ratio was calculated as $\nu_{13} = -\varepsilon_{33}/\varepsilon_{11}$.

RESULTS

There was no apparent difference between moduli for σ-RLX and constant ramp tests (FIG 1A,B) for either the longitudinal (E_1) or transverse (E_3) directions. Longitudinal moduli were approximately 2 orders of magnitude greater than transverse, consistent with previous studies (Yamamoto, 1990; Lynch, 2002; Quapp, 1998). Longitudinal Poisson's ratios (ν_{13}) were apparently strain-rate dependent (FIG 1C). The Poisson's ratios for the 1% and 10%/s ramp tests were much lower than those of σ-RLX or ramp testing. Transverse Poisson's ratio (ν_{31}) did not demonstrate strain-rate dependence for the 0.01%/s rate (FIG 1D). Poisson's ratio for the longitudinal orientation was much larger than for the transverse orientation.

DISCUSSION

In this study we measured the equilibrium anisotropic tensile properties of tendon and compared these 'elastic' properties to those of constant-rate tests. Consistent with our hypothesis, the equilibrium tensile modulus was not different from the constant ramp moduli for samples aligned parallel or perpendicular to the tendon fiber direction. Therefore, constant-rate ramp tests may represent the equilibrium elastic modulus of tendon for loading in both the longitudinal and transverse directions. However, contrary to our hypothesis, the Poisson's ratio did demonstrate strain-rate sensitivity. Poisson's ratio ν_{13} decreased as the strain-rate increased (FIG 1C), suggesting that the equilibrium volumetric loss did not have sufficient time to occur for the faster rates. We observed a loss of volume (assuming transverse isotropy of the tissue) for both the incremental stress-relaxation and for the slowest 0.01%/s constant rate tests. Volume loss may occur by fluid exudation. Thus, the values for Poisson's ratio reported here suggest that constant rate ramp tests may not represent equilibrium elastic behaviors. Additional testing is needed to show statistically significant similarities or differences between mechanical properties calculated from stress-relaxation testing and constant rate ramp testing.

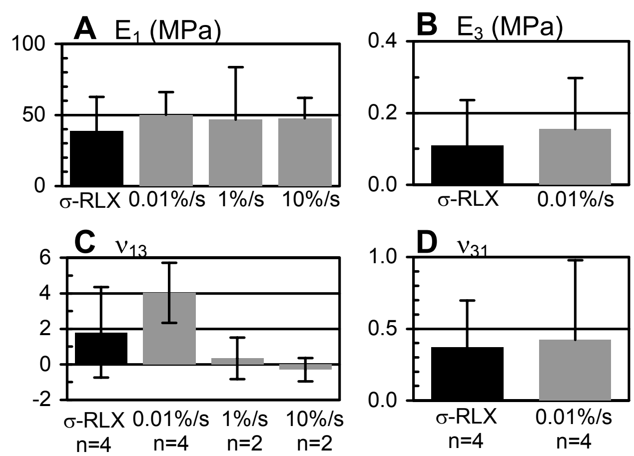

FIGURE 1. Modulus and Poisson's ratio (mean ± sd)

REFERENCES

Lynch, H.A. *et al*. (2002). *TORS*, **27**:243 .
Quapp, K.M., Weiss, J.A.. (1998). *J Biomech Eng,* **120,** 757.
Woo, S.L.-Y. *et al*. (1990). *JOR* **8,** 712-721.
Yamamoto, E., Hayashi, K., Yamamoto, N. (2000). *J Biomech Eng* **122,** 608-614.

STRENGTH PROFILE AND SWING PATTERN IN MALE AND FEMALE ELITE GOLFERS

Wen-Tzu Tang and Lawrence D. Abraham

Kinesiology and Health Education Department, University of Texas at Austin, USA

INTRODUCTION

The purpose of this study was to examine the strength profile and swing pattern of female and male golfers. The delay of the wrist uncocking action during the downswing is known to be one critical factor influencing maximum clubhead velocity at ball impact. Studies to date, however, have not compared male and female elite golfers relative to relationships among release time for uncocking, swing performance, and arm strength. Therefore, the purposes of this study are to compare male and female elite golfers in: (1) strength profile at different clubhead speeds, (2) the relationship between wrist uncocking release time and clubhead speed at ball impact (analyzed from kinematic and kinetic data), and (3) the relationship between wrist uncocking release time and the arm strength necessary to produce maximum clubhead speed.

Kinematic and kinetic data provide the basis for examining the relationship between uncocking release time, clubhead speed, and arm strength in elite male and female golfers. Strength data and kinetic data allow evaluation of the importance of joint torque limits. We hypothesize that different strength profiles in male and female elite golfers may be related to differences in the dynamic swing pattern to optimise performance and prevent injuries.

METHODS

Isokinetic testing was carried out to determine wrist, elbow, shoulder, forearm, and shoulder joint strengths at angular velocities of 30,120, and180 degrees/sec in male and female elite golfer groups. A 3-D motion analysis system was arranged to collect accurate swing data for both groups. A dynamic system model of a human swinging a golf club was developed using anthropometric measurements and calculated kinematic data. An inverse dynamics analysis was then performed to estimate torque history during the model swing.

RESULTS AND DISCUSSION

Measurements of average peak isokinetic wrist, elbow, and shoulder torques (defined here as strength) showed that distal joints (i.e., the wrist and elbow) exhibit reduced gender differences when compared with the proximal shoulder joint. Shoulder joint strength in male subjects averaged 40 - 50% more than that of female subjects. For the wrist, elbow, and forearm, strengths were about 30% greater in males. The clubhead speed at impact for male subjects was 10% - 15% more than for females, a relative reduction which was significantly less than the strength differences between genders. Duration of the wrist uncocking release time before impact was very close (0.13 - 0.14 sec) for both males and females. At the time of ball impact, female golfers exhibited maximum clubhead speed, but male golfers demonstrated the highest clubhead speed following after ball impact. Overall, female subjects had a more efficient swing, considering their strength and the timing necessary to achieve maximum clubhead speed at ball impact.

SUMMARY

Relative to male golfers, female golfers were better able to reach maximum clubhead speed at the time of ball impact. Clubhead speed is relatively higher in female subjects compared with strength differences between the genders. However, torque application in actual swings should also be compared in males and females. For further studies, dynamic analysis of actual swings and application of an optimal control model can lead to understanding of the relationships between joint strength and optimal swing patterns in different individuals and between the two genders.

REFERENCES

Lampsa MA (1975) *J. of Dynamic Systems, Measurement, and Control*, 362-367.

McLaughlin PA, Best RJ (1994) Three-dimensional kinematic analysis of the golf swing. In: *Science and golf II* (Cochran AJ, Farrally FR, eds), 91-96. London: E & FN Spon.

ACKNOWLEDGEMENTS

I acknowledge the financial support of the International Society of Biomechanics (Dissertation Award) and of the ANIMA Corporation, Tokyo.

A COMPARISON BETWEEN SINGLE-RADIUS AND MULTI-RADIUS TOTAL KNEE ARTHROPLASTIES FOR STAND TO SIT (AN EMG AND KINEMATIC STUDY)

H. Wang[1], K. Simpson[1], M. Ferrara[1], S. Chamnongkich[1], S. Casto[1], T. Kinsey[2], O. M. Mahoney[2]
[1] University of Georgia, Athens, GA. hwang@coe.uga.edu
[2] Athens Orthopedic Clinic PA, Athens, GA.

INTRODUCTION

Most total knee arthroplasty (TKA) designs are based on the classic theory that there are multiple instantaneous centers of rotation (ICR) (Frankel, et al., 1971) for knee flexion/extension (KF/KE) movements. Therefore, a traditional TKA has multiple radii (M-RAD) in the femoral component. Recently, investigators (Hollister, et al., 1993; Churchill, et al., 1998) have shown that the knee joint has only one KF/KE axis, which is fixed at approximately the femoral transepicondylar line. One TKA has been designed to have a single radius (S-RAD) in the femoral component (Scorpio™, Howmedica-Osteonics, Inc.). There are two major mechanical differences between the S-RAD and the M-RAD TKAs examined in this study. First, the KF/KE axis of the S-RAD TKA is more posterior than that of the M-RAD TKAs. As a result, the quadriceps moment arm of the S-RAD TKA is longer than that of the M-RAD TKA. Second, for an M-RAD TKA, the manufacturer of both TKAs used in this study (www.scorpioknee.com) claims that the collateral ligaments lose tension when the radius of rotation becomes shorter. This may explain why M-RAD patients experience knee joint instability during the mid-range of KF/KE (O.M.M.). The purpose of the study is to investigate the differences between the S-RAD TKA and two M-RAD TKAs for knee kinematics and electromyography (EMG) occurring during the stand-to-sit (SIT) movement. We predicted that, the S-RAD compared to the M-RAD implant would demonstrate less quadriceps activation due to less quadriceps force required, and less hamstrings muscle activation and abduction/adduction (ABD/ADD) displacement due to increased frontal plane knee stability.

METHODS

Nine healthy participants, each with an S-RAD and an M-RAD (S-7000™, Howmedica-Osteonics Inc.; and P.F.C.™, Johnson & Johnson Inc.) TKA took part in this study. Three video cameras (120 field·s^{-1}) were used to capture marker locations while the EMG signals (1080 sample·s^{-1}) were collected from vastus medialis (VM), vastus lateralis (VL), rectus femoris (RF), biceps femoris (BF), and semitendinosus (ST). Four SIT trials were conducted. Knee kinematics (Grood & Suntay, 1983) were calculated. The RMS EMG (REMG) were calculated, then averaged for each of 4 equal size angle intervals from 75° to 15° of KF (0° = KE). Doubly multivariable repeated measures with SIT time as a covariate ($\alpha = 0.05$) were used to determine the REMG and kinematics differences between the TKA limbs.

RESULTS

Compared to the M-RAD TKA limb, the S-RAD TKA limb exhibited less VM (30° to 45° KF angle interval), VL (30° to 45° and 60° to 75°), and RF (15° to 75°), but more ST (15° to 60°) REMG. The S-RAD TKA limb showed a trend to have less ABD/ADD displacement than M-RAD TKA limb ($P = 0.092$).

DISCUSSION

We first hypothesized that the S-RAD TKA limb would have less quadriceps effort than the M-RAD TKA limb. This hypothesis was supported by the current study, which showed that the quadriceps muscle groups of the S-RAD TKA limb exhibited less REMG than those of the M-RAD TKA limb. We cautiously interpret this finding to indicate that the longer quadriceps moment arm in the S-RAD TKA may have decreased the needed to produce the knee moments created to decelerate the body's downward velocity.

Our second hypothesis related to the knee joint stability was partially supported. As small sample size reduced our statistical power, we only found a tendency for greater ABD/ADD displacement for the M-RAD than the S-RAD TKA limb. However, the ST of S-RAD TKA revealed greater REMG than the ST of M-RAD TKA, which was not expected. We suggest that the role of ST is serving biarticular functions rather than a primary knee stabilizer.

REFERENCES

Frankel, VH, et al. (1971). *J Bone Joint Surg*. [AM]. **53**, 945-953.
Hollister, A. M., et al. (1993). *Clin Orthop*, **290**, 259-268.
Churchill, DL., et al. (1998). *Clin Orthop*, **356**, 111-118.
www.scorpioknee.com.
Grood, E.S., Suntay, W.J. (1983). *J. Biom. Engr*. **105**, 136-144.

ACKNOWLEDGMENTS

This research was supported by a grant from Stryker-Howmedica-Osteonics, Inc.

TIME-DOMAIN REPRESENTATION OF VENTRICULAR-ARTERIAL COUPLING AS A WINDKESSEL AND WAVE SYSTEM

Jiun-Jr Wang,[1] Aoife O'Brien,[3] Nigel G. Shrive,[2] Kim H. Parker[3] and John V. Tyberg,[1]

[1]Departments of Medicine and Physiology & Biophysics (jjwang@ucalgary.ca) and
[2]Department of Civil Engineering, University of Calgary, Calgary, Alberta, Canada
[3]Physiological Flow Studies Unit, Imperial College of Science, Technology and Medicine, London, United Kingdom

INTRODUCTION

Shape differences between central aortic pressure (P_{Ao}) and flow waveforms have never been explained satisfactorily in that the assumed explanation — substantial reflected waves during diastole — has never been demonstrated. We propose a functional, time-domain, arterial model that combines a blood conducting system and a reservoir (i.e., Frank's hydraulic integrator, the Windkessel).

METHODS

Aortic pressures, flows, and blood vessel diameters were measured in 16 anesthetized dogs (paced at ~70 bpm), so we can calculate its Windkessel pressure (P_{wk}) and thoracic blood volume (V_{wk}). The Windkessel pressure is determined by the inflow and outflow differences: $\frac{dP_{Wk}(t)}{dt} = \frac{dP_{Wk}}{dV_{Wk}} \frac{dV_{Wk}(t)}{dt} = \frac{Q_{in}(t) - Q_{out}(t)}{C}$, where $C = \frac{dV_{Wk}}{dP_{Wk}}$ is the compliance. The outflow is assumed to be driven by the difference between the Windkessel pressure and the asymptotic pressure of the diastolic exponential decay (P_∞), $Q_{out}(t)=(P_{Wk}(t)-P_\infty)/R$. R is the effective resistance of the peripheral systemic circulation. Total work performed by the LV is the area of the P-V loop. We calculated the total work performed by the LV during systole and then determined the portion of this work that was done in charging the Windkessel. The remainder, the pulsatile work, was considered to be the sum of the work done overcoming the proximal resistance and that done overcoming inertance.

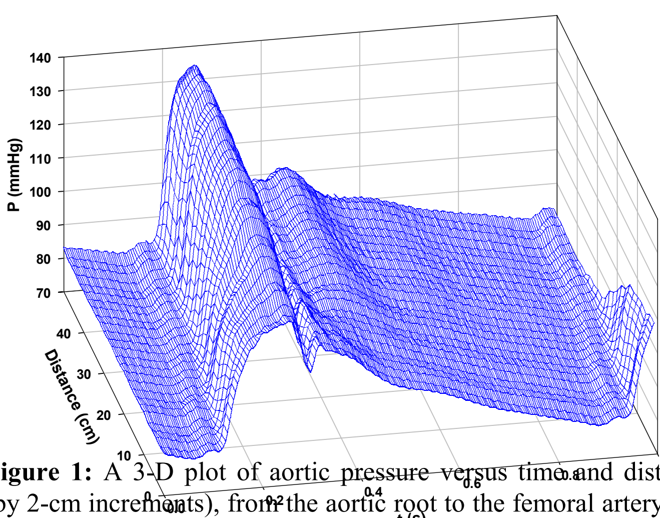

Figure 1: A 3-D plot of aortic pressure versus time and distance (by 2-cm increments), from the aortic root to the femoral artery in a single dog.

To confirm that the aortic pressure is the combination of waves and the Windkessel mechanism, a 3-D pressure-distance plot was constructed by measuring the pressure at the aortic root with 2 cm increment to the femoral artery (Fig 1).

RESULTS AND DISCUSSION

We find that P_{Wk} is proportional to thoracic aortic volume and that the volume of the thoracic aorta comprises 45.0±1.8% (SE) of total V_{Wk}. We calculated the fraction of the total LV work that is expended in charging the Windkessel (recoverable) and found it to be 86.8±1.1%, the remainder due to "pulsatile work." When we subtracted P_{Wk} from P_{Ao}, we found that the difference (excess pressure, P_{ex}) was proportional to aortic flow, thus resolving the differences between P_{Ao} and flow waveforms and implying that reflected waves were minimal (Fig 2). The ratio of P_{ex} to aortic flow is equal to characteristic impedance (from Fourier analysis), consistent with there being a resistive loss in ejecting blood into the Windkessel.

SUMMARY

We suggest that P_{Ao} is the summation of a time-varying reservoir pressure (i.e., P_{Wk}) and (primarily) forward-going waves. The majority of the total energy (~87%) was to charge the Windkessel and that would be discharged to the venous system. The waves were accounted for 13% of total energy, which used to overcome the resistance and inertance.

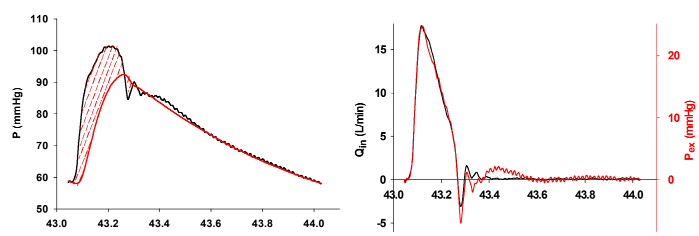

Figure 2: A. Typical aortic root pressure and calculated Windkessel pressure (red line). B. Excess pressure calculated by subtracting the Windkessel pressure from the aortic pressure (the hatched area of Fig 1A) and aortic flow (black line) plotted against time with the scales adjusted so that their peak values coincide. They appear almost identical in contour.

DETERMINATION OF THE PARAMETERS FOR THE FINITE ELEMENT MODEL OF A DEBONDED STEM-CEMENT INTERFACE PERTINENT TO HIP IMPLANTS

Natalia Nuño
Département de génie mécanique, ETS, Université du Québec, Montréal, Canada
nnuno@mec.etsmtl.ca

INTRODUCTION

During Total Hip Arthroplasty, residual stresses are generated in the bulk cement due to the cement expansion during curing. Mann et al. (1991) found that the behaviour of the push-through-stem tests and the simulated FE analysis gave the best agreement when friction as well as residual stresses was included in the numerical analysis. However, recent investigations still do not include the residual stresses (i.e., Lu and Mckellop, 1997; Norman et al., 1996). In this study, at first two parameters, the residual stresses and coefficient of friction, characterizing the debonded stem-cement interface needed in the finite element (FE) model were experimentally determined. Then, the load transfer of a cemented hip implant subjected to bending for an early post-operative situation was numerically investigated.

METHOD

Residual stresses. The residual stresses generated at the stem-cement interface after the cement curing process of an idealized stem surrounded by a PMMA mantle were experimentally determined. The normal residual stresses varied between 2.3 and 3.3 MPa.

Coefficient of friction. The static coefficient of friction between titanium alloy and PMMA was determined experimentally (Nuño et al., 2002) using a standard inclined plane (ASTM 4516-91) and a prototype computerized sliding friction tester. The influence of the contact pressures, temperature, and bovine serum was investigated.

FE Model. Figure 1 shows the idealized cemented hip stem (tapered Ti-6Al-4V stem diameter: min=10 mm, max=18 mm, 5-mm thick PMMA and 7-mm thick bone mantles). The stem-cement interface was debonded, the cement-bone interface was completely bonded and all materials were assumed to be linearly isotropic and homogeneous. The 3D FE model was solved using *Ansys 5.4*. The compressive radial residual stresses generated at the interface, due to the cement expansion during curing, were treated similar to a press-fit problem simulated by assigning an interference to the contact elements. The bending of the system was simulated by a transverse load of 600 N for the full model. The cement stress distributions were determined at the stem-cement interface.

RESULTS AND DISCUSSION

The magnitude of the residual stresses affected the cement stresses at the interface. For the case of 2.4 MPa residual stresses the maximum principal stresses, i.e. von Mises, had up to 3-fold increase compared with the stresses for the case of no residual stresses. Because there is no chemical bond at the interface between the stem and cement, the interface resistance depends on friction thus radial compressive stresses developed by the cement curing play a direct role.

REFERENCES

Lu Z, McKellop H (1997) *J. Biomed. Mater .Res.* 34, pp. 221-226.
Mann KA et al. (1991) *J. Orthopaedic Research*, 9, pp. 798-808.
Norman TL et al. (1996) *J. Biomech. Eng.* 118, pp. 399-404.
Nuño N et al. (2002) *J. Biomed. Mater. Res.* 59, pp. 191-200.

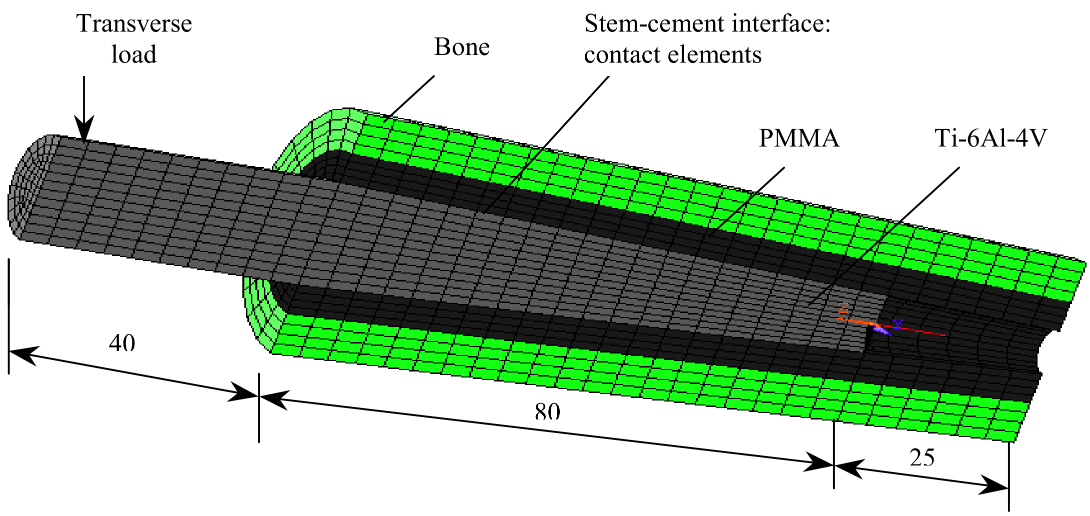

Figure 1. 3D FE mesh of the cemented hip stem. All dimensions are in mm.

ACOUSTO-OPTO-ELECTROMAGNETIC PROPERTIES OF HUMAN DENTIN COLLAGEN

M. Tabib-Azar[1], J.L. Katz[1], P. Spencer[2], A. Wagh[3], T. Namura[4], A. Scott[1], and Y. Wang[1]

[1]Case Western Reserve University, Cleveland, OH
[2]University of Missouri-Kansas City School of Dentistry, Kansas City, MO
[3]University of Memphis, Memphis, TN
[4]Niigata University, Niigata, JAPAN

INTRODUCTION

The role of collagen in providing a binding matrix in biomaterials and in interfacing with mineral particles is of great importance in understanding the strength, aging properties, and resilience of calcified tissues. The main objective of this study is to study the relationship between the mechanical, chemical, and electromagnetic properties of dentin collagen using three different scanning techniques on the same sample.

METHODS

Sample Preparation: Several samples of demineralized dentin collagen prepared from unerupted human third molars were used. Dentin slabs approximately 10 x 2 x 1.5 mm were demineralized using the following protocol. Each slab was placed in a vial containing 10 ml of 0.5 EDTA (pH 7.3) for one week. A Raman spectrum of each specimen then was acquired. The absence of spectral features associated with the mineral (P-O band at 960 cm^{-1}) indicated that the demineralization process was complete. Half of the samples were maintained as is, half were infused with Single Bond adhesive.

Experimental Techniques: Micro-Raman spectroscopy (μRS), scanning acoustic microscopy (SAM), and a GHz scanning evanescent microwave probe (SEMP) were used to study the micro-chemical, material, and electrical properties respectively of collagen both with and without Bis GMA-based polymeric adhesive-infiltration. Samples first were analyzed using μRS which determined the degree of Bis GMA polymerization as well as defining the regions of infiltration. SAM (400 MHz, nominal lateral resolution 2.5 μm) was performed over the same area studied by μRS to study the micromechanical properties. Finally, SEMP at 1 to 10 GHz has been used to measure the complex permittivity over the same area. Typical lateral resolution of the SEMP is on the order of 10 nm.

RESULTS AND DISCUSSION

Figure 1 is the SAM micrograph for the demineralized dentin collagen without adhesive infiltration. Note the uniform gray level of the collagen fibers. In Figure 2, the SAM micrograph of the demineralized dentin collagen infiltrated with Single Bond, a significant number of uniform brighter images indicate the locations where the Single Bond material has infiltrated the pores in the collagen network; this is identified by the higher acoustic impedance and correspondingly the higher elastic modulus of the Single Bond. A system of calibration curves based on a set of 13 materials including polymers, ceramics, and metals provided the following elastic moduli for the set of samples depicted below: E=1.76 GPa for the collagen alone; E=1.84 GPa for the collagen infiltrated with adhesive; E=3.4 GPa for the adhesive infiltrate.

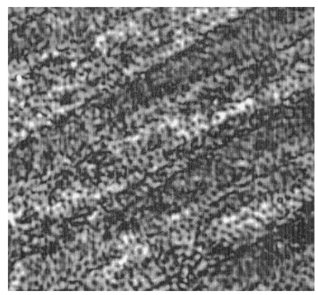

Figure 1: Demineralized dentin collagen without adhesive infiltration

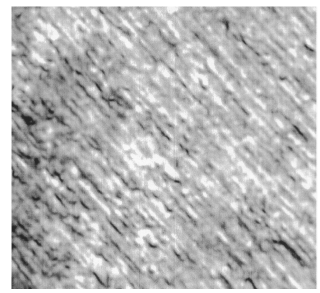

Figure 2: Demineralized dentin collagen with adhesive infiltration

SUMMARY

By combining the unique capabilities of μRS, SAM, and SEMP we can perform chemical, mechanical, and electrical characterization over the same small region of tissue-biomaterial interfaces. These complementary technologies provide direct nondestructive in situ detection of the interfacial molecular structure, micromechanics, electrical, and morphologic features of the bonded assembly. The data collected from these synergistic techniques provide added insight into the potential problems at weak interfaces, problems that may be avoided by altering the materials and/or the method of application.

REFERENCES

Spencer, P., et al (2000). *J. Dent. Res.*, **79**, 1458-1463.
Katz, J.L. et al (2001). *J. Biomed. Mater. Res. (Appl. Biomater.)*, **58**, 366-371

ACKNOWLEDGEMENTS

This research is partially supported by grant NIH/NIDCR DE 12487

IDENTIFYING THE TEMPORAL LIMITS OF VOLITIONAL GAIT ASYMMETRY

Todd D. Royer and Carolyn A. Wasilewski

Department of Health and Exercise Sciences, University of Delaware, Newark, Delaware, USA
www.udel.edu/HESC/

INTRODUCTION

Persons with a unilateral leg injury or disorder that predisposes one side to pain or instability commonly exhibit an asymmetrical gait pattern. These asymmetrical gait patterns typically result in abnormal loading of the non-affected limb. This is problematic because the non-affected limb is concomitantly made more susceptible to degenerative joint disease, specifically, osteoarthritis (Hurwitz et al., 2001). In assessing temporal gait symmetry of special populations, it is difficult to determine the severity of their asymmetry…are the between limb differences similar to the intralimb variability of healthy individuals or are they more similar to the maximum intralimb differences that can be voluntarily achieved. It is unreasonable to ask persons with unilateral leg pain to walk as asymmetrically as possible. Therefore, the purpose of this study is to assess temporal gait symmetry in healthy individuals and determine how asymmetrically they can walk by volitionally spending as little time as possible on one limb (defined as the affected limb) during stance.

METHODS

Fourteen healthy adults (4 males, 10 females; age = 22 ± 4 yrs; height = 170.9 ± 7.6 cm; mass = 69.9 ± 11.3 kg), free of neurological, cardiovascular, and lower-extremity musculo-skeletal impairments, walked overground at a self-selected walking pace to determine preferred walking speed. Footswitches were placed beneath the heel and big toe under the soles of both shoes. Footswitches of one foot (randomly assigned) were connected to an audio box that emitted a sound when either footswitch from that foot was in contact with the treadmill belt. This audio tone was used in the asymmetrical walking condition described below. Subjects walked under two randomized conditions: normal walking and asymmetrical walking. Instructions to the subject for normal walking were "walk normally and comfortably". Instructions for asymmetrical walking were "spend as little time as possible on the affected limb. When that foot is in contact with the ground an audio tone will be emitted to remind and encourage you to step onto the opposite foot as soon as possible". The treadmill operated at each subject's preferred walking speed. Subjects walked for five minutes under each condition. Footswitch data were sampled at 1000 Hz during the last minute of each condition. Stance and swing times were calculated from footswitch data. Symmetry indices (SI) were calculated to describe the relative similarity between the non-affected (N) and affected (A) limbs:

$$SI = \frac{(A - N)}{0.5(A + N)} \times 100 \qquad \text{(Herzog et al., 1989)}$$

RESULTS AND DISCUSSION

Stance and swing times are reported in Table 1. The normal walking trial resulted in stance and swing time symmetry indices of 0.9% and −1.5% respectively, indicating similar between limb temporal characteristics. Symmetry indices for the asymmetrical walking trial and results from other studies are reported in Table 2. Data from persons with a trans-tibial amputation (Mattes et al., 2000) suggest their swing time asymmetry falls substantially below the volitional asymmetry of asymptomatic adults. The addition of a 2 kg load to one foot of able-bodied adults also produced a swing time asymmetry that was much smaller than their predicted maximal asymmetry (Royer et al., 1997).

Table 1. Temporal gait characteristics.

Walking Condition	Stance time (s)	Swing time (s)
normal condition		
non-affected limb	0.64 ± 0.05	0.40 ± 0.02
affected limb	0.64 ± 0.05	0.40 ± 0.03
asymmetrical condition		
non-affected	0.66 ± 0.10	0.37 ± 0.05
affected	0.57 ± 0.08	0.46 ± 0.10

Table 2. Symmetry indices for the asymmetrical walking condition of this study and published studies.

Study	Condition	Stance SI	Swing SI
present	volitional asymmetry	−14.7 ± 7.9%	20.5 ± 9.9%
Mattes et al (2000)	unilateral trans-tibial amputation	−1.5%	8%
Royer et al (1997)	2 kg asymmetrical foot load	−6%	8%

note: negative stance SI values indicate the intact or non-affected limb was greater; positive swing SI values indicate the prosthetic or affected limb was greater

SUMMARY

Symmetry indices derived from this study represent the maximal voluntary between-limb asymmetries for asymptomatic adults. These values may be used when assessing gait asymmetries of special populations to determine whether their temporal gait pattern may be severe or mild.

REFERENCES

Herzog, W, et al (1989) *Med Sci Sports Exerc*, **21**, 110-4.
Hurwitz, D.E, et al (2001) *Cells Tissues Organs*, **169**, 201-9.
Mattes, S.J., et al (2000) *Arch Phys Med Rehabil*, **81**, 561-8.
Royer, T.D., et al (1997) *Med Sci Sports Exerc*, **29**, S113.

A METHOD FOR ASSESSING THE OVERALL IMPACT PERFORMANCE OF HELMETS USED IN CROWD MANAGEMENT INTERVENTIONS

Jean-Philippe Dionne, Ismail El Maach, Aris Makris
Med-Eng Systems, Ottawa, Ontario, Canada
Communicating author: jpdionne@med-eng.com

INTRODUCTION

Blunt impacts to the head cause differential movement of the brain relative to the skull, disrupting the neural tissue and producing concussive and other traumatic brain injuries (Ryan, 1992). To mitigate those types of injuries, riot helmets have to meet standards with specific impact energy acceptance criteria for the helmet shell and visor. The objective of this study is to introduce a comparative tool that permits the assessment of the impact performance of riot helmets.

METHODS

Riot helmets from 6 manufacturers (referred to as A, B, C, D, E and Med-Eng) were impact tested at an authorized laboratory (5 samples each). Three types of tests were carried out: the resistance of the helmet shell to frontal impact, the resistance of the helmet shell to side impacts, and face-shield deflection tests. The experimental apparatus and test protocols conformed to the NIJ standard (1984). An iterative method was used to determine what impact energy caused an acceleration of 300 g's (E_{300}). For the face-shield deflection test, the energy level of an impactor dropped from a given height was determined that would cause the face-shield to come in contact with the "nose" of the headform (E_c).

RESULTS AND DISCUSSION

The detailed results are listed on Table 1. For frontal impacts, E_{300} values ranging between 69 J and 171 J were obtained, whereas E_{300} values ranging from 102 J to 231 J were obtained for the side. The NIJ standard requirement is 111 J.

Table 1: Summary of the impact results

Helmet	E_{300} Front (g's)	E_{300} Side (g's)	E_c (J)	Frontal Area (%)
Med-Eng	152	190	95	78
Helmet A	162	176	10	68
Helmet B	69	102	18	71
Helmet C	144	165	19	75
Helmet D	171	194	46	67
Helmet E	140	231	58	73

E_c values for the various helmets were found to vary between 10 J and 95 J. For the faceshield deflection, the NIJ standard has an impact energy requirement of only 7.85 J, whereas the CSA requirement is 70 J, almost a 10-fold difference.

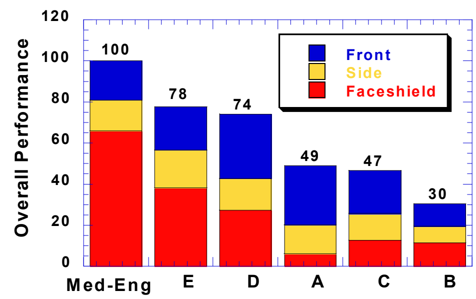

Figure 1: Global score assessed to each helmet based on the weighted balance for the three types of experiments

In order to determine a performance criterion, taking the three impact tests into account, a global score system was proposed. All impact results were first normalized with respect to the Med-Eng helmet values, used as a reference. Since it was estimated, through interaction with end users, that about 85% of the threats in a crowd management environment are frontal, a combined weight of 85% was given to the frontal impact and face-shield deflection tests, and the remaining 15% was given to the side impact tests. The 85% was then subdivided according to the percentage of frontal area occupied by the visor relative to the total frontal area. This percentage is shown in Table 1 for all helmets. The global score is thus obtained by the following formula:

$$Score = \left(\frac{E_{300}}{E_{300\,Med-Eng}}\right)_{Side} x\,15\% + \left[\left(\frac{E_{300}}{E_{300\,Med-Eng}}\right)_{Front}\left(\frac{A_{shell}}{A_{frontal}}\right) + \left(\frac{E_c}{E_{c\,Med-Eng}}\right)\left(\frac{A_{visor}}{A_{frontal}}\right)\right] x\,85\%$$

where $E_{300Med\text{-}Eng}$ and $E_{cMed\text{-}Eng}$ correspond to the E_{300} and E_c values obtained with the Med-Eng helmet respectively, A_{shell} is the frontal area occupied by the helmet shell, A_{visor} is the frontal area of the visor, and $A_{frontal}$ is the total frontal area of the helmet. The global scores obtained by each helmet are illustrated on Fig. 1.

SUMMARY

Based on this global scoring scheme, the best overall performer is the Med-Eng helmet with a score of 100.

REFERENCES

NIJ Standard for Riot Helmets and Face Shields, 0104.02 (1984). *National Institute of Justice.*

CSA Riot Helmet Standard, Z611-M86 (1986). *Canadian Standard Association.*

Ryan, G.A. (1992). *World J Surg*, **16,** 398-402.

PREDICTION OF OPTIMIZED DIAMETER OF OSTEOCHONDRAL PLUGS IN CARTILAGE REPAIRS

John Z Wu [1], Walter Herzog[2], Evelyne M Hasler[3]
[1]National Institute for Occupational Safety & Health, Morgantown, WV, USA., E-mail: jwu@cdc.gov; [2]Faculty of Kinesiology, The University of Calgary, Calgary, Alberta, Canada; [3]Sulzer Orthopedics Ltd, Baar, Switzerland

INTRODUCTION

The transplantation of autologous cartilage/bone (osteochondral) grafts offers a treatment for full thickness cartilage defects on the femoral condyle of the knee. One technical difficulty is to determine the amount of the press fit tolerance between the OC plug and the femur. If the fitting tolerance is too small, the OC plug will slide relative to the recipient hole, whereas if it is too large, the plug will induce excessive stress on the bone surrounding the plug. Further, the risk that the damage of the bone during the procedure inserting the OC plug into the recipient hole will be increased. The purpose of the present study was to predict, theoretically, the optimized diameter of OC plugs.

METHODS

The joint was assumed to be axi-symmetric with a spherical femur and tibia and a cylindrical OC graft (Fig. 1). The coefficient of friction between the plug and the recipient hole walls was assumed to vary from 0.1 to 0.5. The recipient hole was taken to be approximately 1.2 mm deeper than the height of the OC plug, so the plug was not resting on the femoral bone. The cartilage was assumed to have a constant thickness of 2 mm and biphasic material properties (Mow et al. 1980). Subchondral bone was assumed to be elastic with a much higher elastic modulus than that used for the cartilage. The press fitting was simulated using a thermal analogue. The plug was assumed to have an anisotropic thermal expansion coefficient. Expansion was assumed to only occur in the radial direction. Fitting of the plug into the recipient site on the femur was simulated numerically by increasing the temperature of the plug. The calculations of the lateral contact stress were performed assuming that the OC plug was perfectly aligned in the recipient hole (i.e., Δ=0, as shown in Fig. 1).

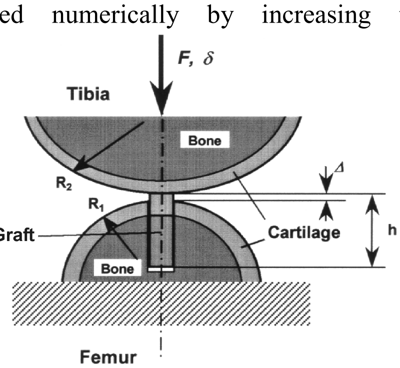

Figure 1: *Finite Element Model of Cylindrical OC Plug. (h=15 mm, R1=50 mm, R2=100 mm)*

RESULTS AND DISCUSSION

The lateral contact stresses between the OC plug and the recipient hole as a function of fitting tolerance were predicted. The sliding force of the OC plug was calculated by integration of the contact stress on the lateral contact area. Typical simulation results are depicted in Fig. 2. For a fixed size of the OC plug, the contact stress between plug and recipient hole increased approximately linearly with the press fit tolerance (Fig.2A).

Our simulations indicate that, for a fixed coefficient of friction and a fixed fit tolerance, the maximal sliding force varies with the size of the plug and reaches its maximum for a plug diameter of 5.5 mm (Fig.3). The sliding force is attributed to two factors, the fitting stress, which is associated with the frictional stress, and the contact area between the plug and the recipient hole. For a given fit tolerance, the fitting stress decreases with increasing diameter of the plug; whereas the contact area between femur and plug increases with increasing diameter of the plug. Consequently, the maximal sliding force is a nonlinear function of the diameter of the plug.

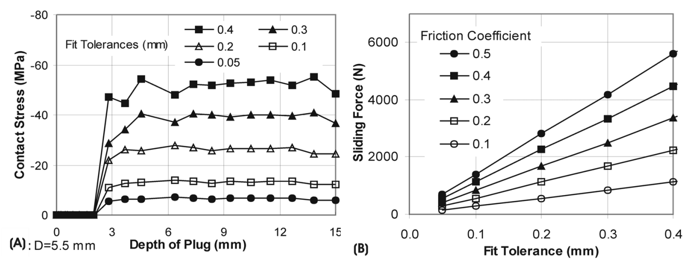

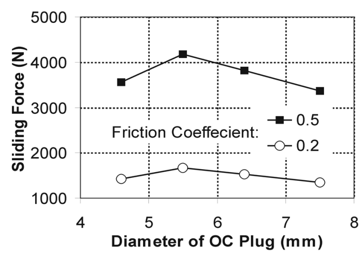

Figure 2: *(A) Typical lateral contact stress between the OC plug and the recipient wall as a function of the plug depth. (B): Typical sliding force as a function of press fit tolerance.*
Figure 3: *Sliding force as a function of diameter of OC plug.*

SUMMARY

Because of the large difference in the elastic modulus between articular cartilage and subchondral bone (2.5 MPa for cartilage vs. 2.3 GPa for subchondral bone), the primary force that keeps the plug in place comes from the frictional contact between the lateral surface of the plug and the recipient hole. The stresses in the bone are sensitive to the fit tolerance. Small variations in the fit tolerance induce great changes in bone stress. Therefore, the fit tolerance must be carefully controlled to prevent over-stressing or damaging of the bone. If the diameter of the OC plug is optimized, it would be possible to reach the maximal sliding force at a given fit tolerance, thus it would be possible to use a smaller fit tolerance and the stress in the bone surrounding the OC plug could be minimized.

REFERENCES

Mow VC et al. (1980) ASME J. Biomech. Eng., 102:73-84.

THE MATERIAL PROPERTIES OF THE SUBCALCANEAL TISSUE IN COMPRESSION

William R. Ledoux, Ph.D.[1,2], Glenn K. Klute, Ph.D.[1], Randal P. Ching, Ph.D.[1,2], Bruce J. Sangeorzan, M.D.[1,2]
[1] RR&D Center for Excellence in Limb Loss Prevention and Prosthetic Engineering, VA Puget Sound, Seattle, WA, USA
[2] Department of Orthopaedics and Sports Medicine, University of Washington, Seattle, WA, USA, wrledoux@u.washington.edu

INTRODUCTION

Computational models of the foot are becoming increasingly anatomically detailed (Thompson et al 1999; Ledoux et al 2000). The accuracy of these simulations depends on the material models of components such as the plantar soft tissue. The *structural* properties of *in vivo* subcalcaneal tissue have been studied via impact tests (e.g., Kinoshita et al 1993), while others explored *in vitro* subcalcaneal tissue with materials testing machines (Aerts et al 1995; Ledoux et al. 1999). However, *material* property data on the plantar soft tissue has not been reported. The purpose of this research was to determine the material properties of the subcalcaneal tissue.

METHODS

Subcalcaneal tissue specimens were obtained from three fresh-frozen cadaveric feet. The tissue was dissected from the calcaneus by sectioning the Achilles tendon and proceeding inferiorly and anteriorly. The soft tissue was placed on a plastic sheet and a 2cm x 2cm specimen was cut using a razor-blade punch. Each specimen was placed on a platen in an ElectroForce 3400 materials testing machine (Enduractec; Minnetonka, MN). The top platen, in series with a load cell, was lowered manually until a force of approximately 1 N was registered. The distance between the platens was measured as the initial thickness of the specimen (Table 1). An environmental chamber enclosed the specimen and platens. To simulate *in vivo* conditions, hot, moist air was circulated to keep the specimen at 37˚ C and near 100% humidity.

The target loading level for the tissue was based on normative ground reaction force data (Ledoux and Hillstrom 2002); a scale factor of 0.051 %BW/cm^2 was employed. In load control, the specimen underwent 30 sine waves from 10 N to the target load. The displacement at which the target load was reached at steady state was noted and used for the rest of the experiment. In displacement control, the tissue was preconditioned with 30 1 Hz sine waves followed with 2 quasi-static triangle waves with ramp rates of 0.5 %strain/second.

Table 1: The testing parameters for the subcalcaneal tissue.

specimen	BW (N)	target load (N)	thickness (mm)	displ. (mm)	strain (%)
foot 1	890	181	15.6	9.1	58
foot 2	623	127	10.4	5.5	53
foot 3	979	200	12.5	5.9	47

RESULTS AND DISCUSSION

The force-deformation data were normalized by the specimen area and initial thickness, resulting in a stress-strain plot (Figure 1a). To account for the difference in subject weight, we also plotted the force in %BW versus strain (Figure 1b). These data indicate a long toe region followed by a rapid increase in stress (force) with strain. Although difficult to visualize with this scale, the force increased immediately after the actuator began to move, indicating that despite the small slope in the toe region, the tissue was being loaded.

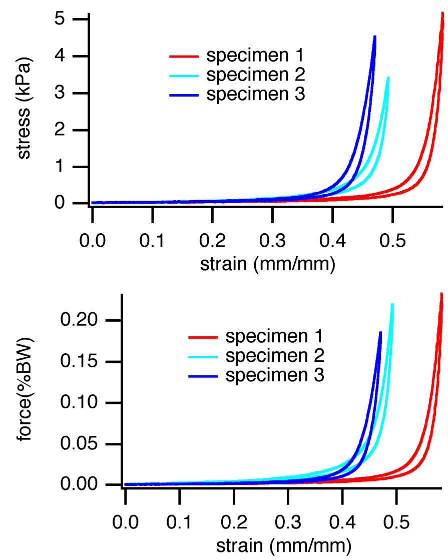

Figure 1a and b: The stress-stain and force-strain data.

SUMMARY

The data presented here represent material characteristics of the subcalcaneal tissue. We have shown that the tissue is nonlinear and viscoelastic (note the hysteresis). Furthermore, the tissue has a long toe region, after which it becomes stiff very rapidly. Also of interest are the large strains required to generate physiological loads. These properties are indicative of a material that must undergo large deformations, but still protects the underlying osseous structures.

REFERENCES

Aerts, P. et al (1995). *J. of Biomechanics* **28**, 1299-1308.
Beaugonin, M. et al (1997). Stapp Car Crash Conf, 225-237.
Kinoshita, H. et al (1993). *Int. J. Sports. Med.* **14**, 312-9.
Ledoux, W.R. et al (2000). *Cong. on Med. Phys. Bio. Eng.*
Ledoux, W.R., Hillstrom, H. (2002). *Gait & Posture* **15**, 1-9.
Ledoux, W.R. (1999). *Proceedings of ASB*, 172-73.
Thompson, D. L. (1999). *Proceedings of ISB*, 12.

ACKNOWLEDGEMENTS

Department of Veterans Affairs, grants A2362P and A0806C

MUSCLE WORK VERSUS MUSCLE FORCE: *IN VIVO* FUNCTION OF AVIAN ANKLE EXTENSORS

Monica A. Daley and Andrew A. Biewener
Concord Field Station, Harvard University, Bedford MA USA
E-mail: mdaley@oeb.Harvard.edu

INTRODUCTION

How do muscles differ in their ability to contribute to force and mechanical work during locomotion? Lateral Gastrocnemius (LG) function among different birds appears to differ substantially. The LG of running turkeys contracts nearly isometrically during level running, but can shorten more to contribute substantial positive work during incline running (Roberts et al. 1997). In contrast, the LG of mallards shortens and does work during level running, possibly increasing its cost for force production (Biewener and Corning 2001). Like turkeys, guinea fowl (*Numida meleagris*) are cursorial birds, suggesting that their ankle extensors may also contract isometrically to lower the cost of force production,. To test this, we compared *in vivo* work production by two ankle extensors of the guinea fowl during level and incline locomotion.

METHODS

We recorded muscle-tendon force, fascicle length and electrical activity from the LG and the Digital Flexor to the lateral toe (DF4) of the guinea fowl during level and 16° incline running. 'E'-type tendon buckles attached to the free tendon measured muscle-tendon force. Sonometrics^{TM} 1.0mm and 0.7mm crystals were implanted along the axis of the muscle fibers to measure muscle fascicle length. Bipolar EMG electrodes were implanted immediately adjacent to the sonomicrometry crystals. Lateral-view digital video (Redlake Motionscope PCI 500) recordings at 250 f/s were used to correlate muscle measurements with kinematics.

RESULTS AND DISCUSSION

Both the LG and DF4 substantially lengthen and shorten during active force production (Fig. 1). The timing of active strain is different for the two muscles; the LG undergoes shortening followed by lengthening, while the DF4 lengthens and then shortens. This may be due to the different joints that the muscles cross. Both muscles act at the ankle and knee, but DF4 also acts about the tarsometatarso-phalangeal (TMP) joint. The TMP flexes substantially during the first half of support, thus DF4 is stretched during this time.

Both muscles produce similar net work during running. LG produces 3.6 ± .1 and 5.6 ± 0.9 (mJ/Kg) net work per stride during level and incline running, respectively. DF4 produces 1.6 ± 2 (mJ/Kg) and 6.4 ± 2 (mJ/Kg) during level and incline running. In doing so, DF4 absorbs energy and does positive work, which sums to a small net value. LG absorbs less energy than DF4, and produces a small net positive work. Together they contribute 14% of whole-body work necessary to move up the incline. If distributed equally among extensors (based on mass), these muscles would be expected to produce about 30% of the total work.

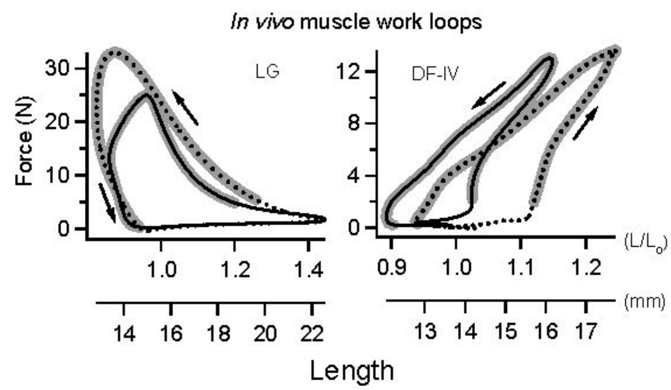

Figure 1 Representative force versus length work loops for LG (left) and DF4 (right) during level (solid line) and 16° incline (dashed line) running at 1.25 (m/s). The support phase of the stride is shaded. The work loops are positive for both muscles during level and incline running.

SUMMARY

In contrast to the near isometric function of LG in running turkeys (Roberts et al. 1997) and hopping wallabies (Biewener et al. 1998), the LG and DF4 of the guinea fowl operate at strains greater than 13%. Although they undergo substantial length change during active force development, their contribution to whole-limb work is low. This suggests that in this smaller cursorial bird, these distal muscles play a minor role in work modulation during steady level running, as well as when moving uphill, but operate primarily in force production. However, they do not operate in a manner consistent with economic force production.

REFERENCES

Biewener and Corning (2001) *J. Exp Bio.* **204**: 1745-1756
Biewener et al. (1998) *J. Exp. Bio.* **201**: 1681-1694
Roberts, T. J. et al. (1997). *Science* **275**:1113-1115.

EFFECT OF ETHANOL ON NEURONAL STRAIN TRANSDUCTION

Theresa A. Lusardi, David F. Meaney
Department of Bioengineering, University of Pennsylvania, Philadelphia, Pennsylvania, USA

INTRODUCTION

Under normal physiological motions, central nervous system (CNS) neurons exist in a 'mechanically protected' environment and experience little deformation. During traumatic injury, though, CNS neurons experience a rapid deformation that can produce lasting pathophysiological changes to neurons and cause the cell death that contributes to the long-term impairment in CNS injury.

We have shown previously that cultured hippocampal neurons experience an acute calcium transient following stretch that is both strain and rate dependent. The most prominent mechanism for this calcium increase is from influx from the extracellular space through the NMDA receptor associated channel. In this study, we consider how altering the plasma membrane properties affect the initial response of the cultured neuron to rapid mechanical stretch.

METHODS

Hippocampal cells were isolated from E17-E18 rat embryos using procedures discussed previously (Lusardi et al., in press). Cells were plated onto flexible silastic membranes (Specialty Manufacturing), allowed to mature for 10 days in vitro, and attached to a custom-designed cell stretching system (Smith et al, 1999). A rapid (20.5 ms) pressure pulse caused the underlying membrane to deform rapidly, in turn stretching the neuronal culture once at a defined rate and magnitude. All results were compared to sham experiments (0% strain) in which cultures were exposed to maximum pressure (12 psig) but no stretch.

To measure the response of the cells to mechanical stretch, we used a cytosolic calcium indicator (5 uM Fura-2am in 0.4% DMSO and 0.1% Pluronic; Molecular Probes, Inc.). Immediately prior to testing, Fura-2AM loaded cells were rinsed with control saline solution (CSS) and allowed to incubate for 10 minutes in CSS, with or without the addition of 200 mM ethanol. For these experiments, normalized peak calcium change is reported as the ratio for each cell of the peak fura ratio during the first 40 seconds following stretch normalized by the baseline (pre-stretch) ratio for that cell.

RESULTS AND DISCUSSION

As the stretch level increased, the peak calcium response in untreated cells increased. At the high stretch, the average calcium response over a five-minute monitoring period showed the cell population returning only transiently toward calcium homeostasis, with a secondary rise in calcium. At the low stretch level, the average calcium response continued to return toward baseline over 5 minutes following the stretch.

The addition of ethanol into the media did not change the peak calcium response at the highest stretch level, but did attenuate the response at the lowest stretch level. In comparison, the peak calcium response increased under ethanol treatment for a chemical agonist (100 uM NMDA). Interestingly, calcium regulation returned in the cell population at the high stretch level after treatment with ethanol.

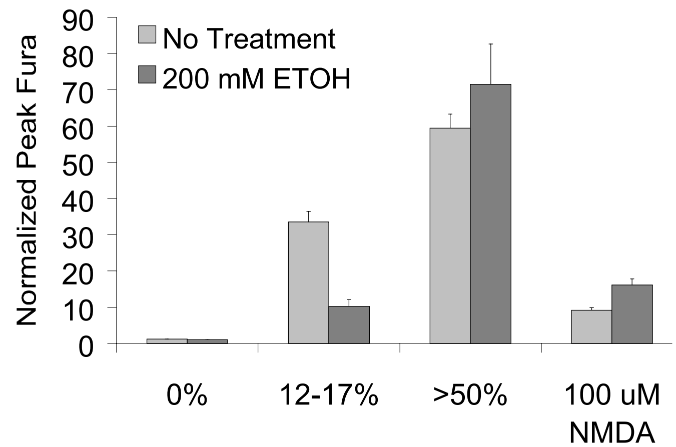

Figure 1: Ethanol pretreatment blocks the stretch response but potentiates the agonist response.

Together, these data show that ethanol has a complex effect on mechanically injured neurons. At the high stretch level, the alterations in the membrane properties appear to allow the membrane to recover more rapidly from stretch. In contrast, the attenuated response at the low stretch level suggests a direct suppressive effect of ethanol on mechanically induced receptor sensitivity.

SUMMARY

The plasma membrane is often considered merely as a holder for the more important players in signal transduction such as ion channels, metabotropic receptors, and focal adhesion complexes. However, this and other research suggest that the plasma membrane may have an active role in signal transduction, both as a modulator of ion channel properties and as a force transducer in its own right.

REFERENCES

Lusardi et al (2002), *In Press*.
Smith et al (1999). *J Neuroscience*, **19**(11), 4263-4269

ACKNOWLEDGEMENTS

Funds for this work were provided by CDC R49/CCR312712 and NIH RO1 NS 35712.

CHANGES IN H-REFLEX AMPLITUDE AFTER SPINAL MANIPULATION IN HEALTHY AND PATHOLOGICAL SUBJECTS

Esther Suter[1], Gordon McMorland[2], Walter Herzog[1]

1 Human Performance Laboratory, University of Calgary, Calgary, Alberta, Canada, suter@kin.ucalgary.ca
2 Hillhurst Chiropractic Clinic, Calgary, Alberta, Canada

INTRODUCTION

A recent study has shown that spinal manipulation of the sacroiliac (SI) joint improves quadriceps function in anterior knee pain patients (1). The exact underlying mechanisms are not known, but it has been suggested that spinal manipulation activates receptors in and around the treated joint which may help to restore afferent input. The present study was aimed at determining the reflex responses associated with spinal manipulation. Specifically, changes in soleus H-reflex amplitude was assessed after manipulation of the SI joint in healthy and pathological subjects.

METHODS

Thirteen healthy subjects (age 25±3 yr) and 15 patients with low back pain of various etiologies (age 32±11 yr) gave informed consent to participate in the present study. H-reflex of the soleus was measured using standard methodology (2). Briefly, the tibial nerve was stimulated at the popliteal fossa using an electrical pulse of 1ms duration. Soleus H-reflex was recorded using Ag-AgCl electrodes of 1cm active diameter. The gain was set at 200, and sampling frequency was 2000Hz. Recruitment curves were performed to find the optimal stimulation intensity, which was identified as maximal H-reflex amplitude with no or minimal M-wave. After establishing baseline recordings of the H-reflex, a spinal manipulation of the SI joint was conducted on the left side in healthy subjects, and on the dysfunctional side in low back pain patients as identified by the treating clinician. H-reflex was recorded immediately after manipulation for 15 minutes. In 3 healthy subjects (HB) and all 15 patients, H-reflex recordings were performed with subjects lying supine, and the SI joint manipulation performed in side-lying position. In 10 healthy subjects (HS), all measurements were done with subjects lying on the side throughout the whole procedure to test for possible repositioning artifacts in H-reflex amplitude. In these 10 healthy subjects a sham manipulation was also performed.
H-reflex amplitudes were calculated using custom-made software, and post-treatment values were normalized to baseline values for comparison between subjects.

RESULTS AND DISCUSSION

<u>Healthy subjects:</u> The HB group showed significant depression of the H-reflex amplitude following treatment. H-reflex amplitude in the HB group returned to pre-treatment values after approximately three minutes. H-reflex depression after manipulation was not evident in the HS group (Figure 1). Sham manipulation was also not associated with any changes in H-reflex amplitude.
<u>Low back pain patients:</u> H-amplitudes were largely decreased immediately following SI joint manipulation. In 6 subjects, H-reflex amplitude did not recover to baseline values over the 15-minute period measured, but remained about 20% lower. In another 6 subjects, after initial depression, the H-reflex amplitude stabilized at a higher level than baseline.

Fig 1: H-reflex amplitude following spinal manipulation with measurements performed in supine or side lying position

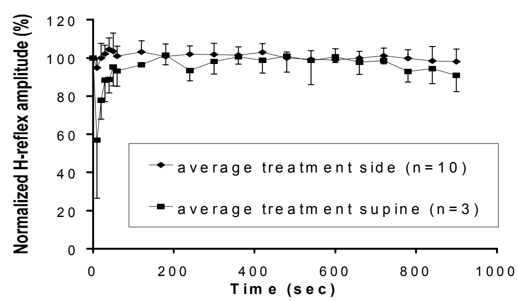

The present study confirmed a significant transient depression of the H-reflex amplitude after SI joint manipulation for all subjects that were measured in a supine position, as documented in a previous study (3). However, no depression in H-reflex amplitude was observed when the position of the subjects during the measurement procedure and the spinal manipulation was not changed. This suggests that the transient depression of the H-reflex amplitude may be a repositioning artifact rather than a direct effect of the spinal manipulation. In 12 out of 15 patients with low back pain, H-reflex amplitude remained altered throughout the post-treatment measurement period. The relationship between etiology of low back pain and changes in H-reflex amplitude after SI joint manipulation is not clear and needs further investigation.

REFERENCES:

1. Suter et al. (2000), *JMPT*, 23:307-11. 2. Hugon M. In: Desmodt JE (Ed). (1973), Karger, 1277-93, Basel. 3. Dishman JD, Bulbulian R. (2000), *Spine*, **25**:2519-25.

ACKNOWLEDGEMENTS

The study was supported by a grant from the Consortium of Canadian Chiropractic Research Centres.

ANALYSIS OF IN VIVO CARPAL BONE AND LIGAMENT KINEMATICS USING CT AND MR DATA

Anwar Upal[1], David Pichora, and Carolyn Small
Human Mobility Research Center, Queen's University, Kingston, Ontario, Canada
[1] Submit communications to upal@me.queensu.ca

INTRODUCTION

In spite of the prevalence of wrist disorders, the *in-vivo* three-dimensional kinematics of the wrist in pathological conditions is poorly understood. Many researchers have used CT data to analyze carpal bone kinematics; however CT data does not provide the required information about the attaching ligaments. MR data provides information about the surrounding soft-tissue and ligament structure, which is crucial for proper functioning of the joint. The purpose of this project was to develop easy-to-use software that calculates the distances between the carpal bones, the volume of the carpal bones, and the carpal bone displacement and rotation from both CT and MR data. This technique will allow carpal bone kinematics to be analyzed with emphasis on the surrounding soft-tissues, which are crucial for the proper functioning of the wrist.

METHODS

CT data was acquired using a GE Light Speed Plus CT scanner and MR data was acquired using a GE 1.5T MRI scanner. The voxel size was varied between 0.15mm X 0.15mm X 0.75mm and 0.75mm X 0.75mm X 1.25mm. Data was collected at 30, 45 and 60 degrees of flexion and extension; 10 degrees of radial deviation; and 30 degrees of ulnar deviation. The data includes the distal ends of the radius and ulna bones. Figure 1 shows the software validation experiment carried out using nine phantoms and one cadaver wrist. One volunteer subject's wrist kinematics were analyzed.

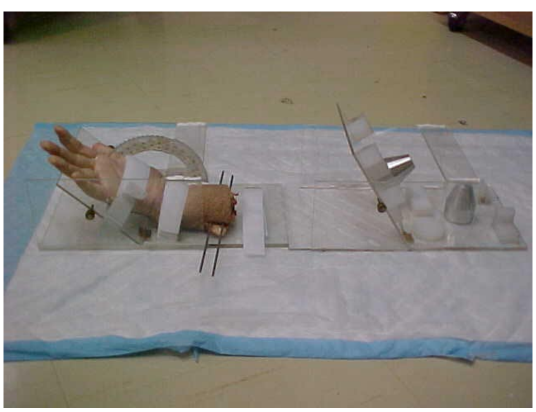

Figure 1: Validation experiment jig

The images were imported into a segmentation program to construct three-dimensional models of the Scaphoid, Lunate, Triquetrum, Trapezoid, Trapezium, Hamate, Capitate, Pisiform, and Radius and Ulna. Software with an easy to use interface was developed to quantify the movement and rotation of all the carpal bones and Radius and Ulna. The software uses principal axes analysis and describes bone motion using Screw Axis and Euler Angle kinematic parameters. One window of the carpal bone motion wizard is shown here in Figure 2.

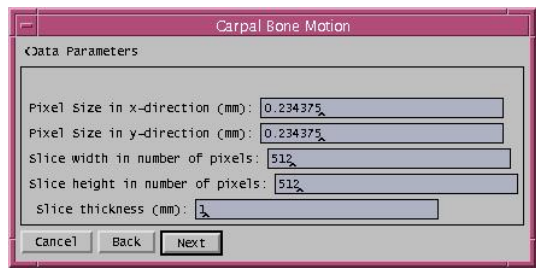

Figure 2: Carpal bone motion software interface

RESULTS AND DISCUSSION

This study has verified that both MR and CT data may be used to analyze carpal bone kinematics, and that any carpal bone kinematics may be analyzed using high-resolution CT and MR data. In our future research soft-tissues from MR data will be morphed with information about the location of the carpal bones from CT images to calculate ligamentous strains. This approach will allow analysis of carpal bone kinematics with reference to the surrounding soft-tissues providing a deeper understanding of carpal bone and ligament mechanics.

SUMMARY

A simple software tool was developed to render carpal bone meshes with the respective principal axis and to calculate the kinematic parameters for each bone relative to the radius. CT scans of one cadaver wrist and nine phantoms were used to validate the software, and CT and MR scans of one volunteer's wrist were obtained to analyze carpal kinematics. Combining CT and MR technology to look at both bone and soft-tissue mechanics may help develop better treatments for many joint disorders.

LINEAR MODEL OF RESISTANCE TO PASSIVE STRETCHING IN INDIVIDUALS WITH BRAIN INJURY: RELIABILITY & VALIDITY

Patrick H McCrea[1,3], Janice J Eng[2,3], and Antony J. Hodgson[1]
Dept. of Mechanical Engineering[1] and School of Rehabilitation Sciences[2], University of BC
Rehabilitation Research Lab[3], GF Strong Rehab Centre, Vancouver, Canada
www.rehab.ubc.ca/jeng

INTRODUCTION

Spasticity, the velocity dependent resistance to passive stretch (Lance, 1976), commonly affects the elbow flexors in individuals who have sustained a brain injury. Over 94% of health care professionals consider spasticity to be of clinical importance (Hass, 1994). Elbow flexor spasticity is quantitatively related to the magnitude of the torque response to constant velocity angular extensions (Knutsson, 1985). The mechanical response to a physical disturbance can be described in terms of stiffness and damping (eqn. 1).

$$\tau\left(\theta,\dot{\theta}\right) = k\theta + b\dot{\theta} + \tau_0 = k(\theta - \theta_0) + b\dot{\theta} \quad \text{(eqn. 1)}$$

Here k is the stiffness, b is the damping, and τ_0 is a constant; alternatively, the constant τ_0 can be expressed in terms of an equilibrium position, θ_0. The goals in this study were to determine (1) the ability of a linear spring-damper model to describe passive resistance, (2) the test-retest reliability of these parameters between days, and (3) the relationship of these parameters to a clinical assessment of spasticity.

METHODS

Nineteen individuals with stroke (mean age=61±6 years, duration of injury=4.4±2.6 years, Fugl-Meyer upper extremity score=38±18 Ashworth=1.2±.9) were tested during two sessions. We measured the velocity dependent resistance of elbow flexors of the more affected arm using a Kin-Com isokinetic dynamometer in passive mode. The arm was stabilized in a gravitationally neutral position with the shoulder abducted and flexed to 90º and 45º. The elbow was then extended through its available passive range at speeds of 30, 60, 90, 120, 150, and 180 º/sec. For each trial, the resistance-angle profile was windowed for the region of constant speed; this rotational resistance of the elbow was ensemble averaged over three trials for each speed.

The ensemble-averaged profiles for each speed were combined to create a 3-dimensional profile of the elbow flexor response to passive extensions. This profile was linearized for independent variables of angular displacement and velocity using a least-squares fit in the form of equation 1. Stiffness, damping, and equilibrium position parameters were identified for each participant as well as the value of R^2. Intraclass correlations (ICCs) were used to identify the test-retest reliability of these parameters. Stiffness, damping, and equilibrium position parameters were entered as independent variables in a multiple regression with the Ashworth spasticity scale (Ashworth, 1964) as a dependent variable.

RESULTS AND DISCUSSION

The mean R^2 value of the spring-damper models was .92. Stiffness, damping, and equilibrium position ICCs were .98, .86, and .95 respectively. Given the excellent test-retest reliability, further analyses used data from only one session.

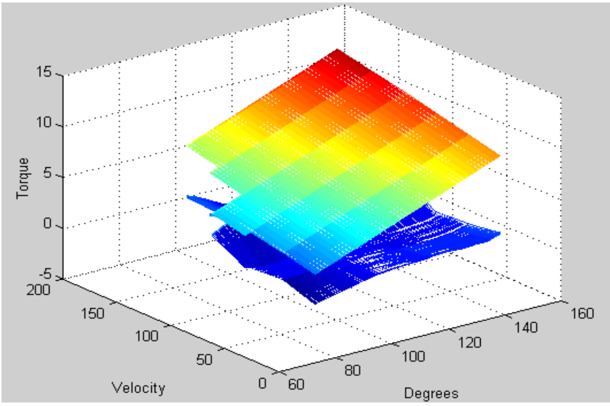

Figure 1. Passive resistance data fit to linear spring-damper model. The upper curve is the least squares fit to extensions at different speeds. Residuals are plotted on the lower curve.

Correlations of stiffness, damping, and equilibrium position with the clinical assessment of spasticity were all significant ($p<.01$). A stepwise entry of predictor variables into the regression rejected damping and position parameters. The resulting equation relating spasticity to stiffness was (eqn. 2):

$$\mathit{Ashworth\,Score} = 32.2 \times \mathit{stiffness} + .272 \;;\; R^2 = .864 \quad \text{(eqn. 2)}$$

SUMMARY

The linear spring-damper model showed excellent reliability and validity with clinical measures. Scales based on continuous measures of these parameters have potential to provide higher resolution than conventional ordinal scales.

REFERENCES

Ashworth, B. (1964). *Practitioner,* **192**, 540-2.
Hass, B.M. (1994). *Br J Ther Rehabil,* **1**, 90-5.
Lance, J.W. (1976). *Neurology,* **30**, 1303-13.

ACKNOWLEDGEMENTS

This study was supported by the BC Health Research Foundation, a grant-in-aid and studentship from the Rick Hansen Neurotrauma Initiative.

THE INFLUENCE OF NORMAL HORMONAL FLUCTUATIONS IN WOMEN ON THE BIOMECHANICS OF STEPPING AND CUTTING

HJ Yack, R Chandran, S Rao, J Wilken
Orthopaedic Gait Analysis Laboratory
Physical Therapy & Rehabilitation Science
The University of Iowa
Iowa City, IA 52242

INTRODUCTION

Normal hormonal fluctuations, that are associated with the menstrual cycle, is one factor that has been used to help explain the two to eight time higher rate of knee injuries in female athletes. Results from prospective studies that have tried to establish the link between injury and the menstrual cycle are inconsistent (Huston, 2001). Few well controlled studies have attempted to examine how performance might be affected by hormonal changes in the uninjured population. The purpose of this study was to identify biomechanical changes in performance that could be associated with hormonal variations during the normal menstrual cycle.

METHODS

Ten female recreational athletes participated in the study. The month prior to data collection subjects monitored there menstrual cycle and the timing of the luteal surge was identified. During the following month testing was started in a randomized manner to capture the three phases: follicular (days 2-4), ovulatory (LH surge, within 1 day), and luteal (6-8 days before the end of the cycle). On the day of testing serum samples were collected. Subjects warmed up by running on a treadmill for 20 minutes. Markers were placed on each subject to capture the 3-D motion of the right lower limb, pelvis and trunk. Subjects stepped off a raised (20 cm) walkway while walking at 1.8 m/s, with their right foot landing on a force platform. A directional light, triggered by the subject, randomly determined if they should continue straight ahead or cut at a 45° angle to the left or right. Five trials of each direction were collected.

Marker positions were captured in 3-D (Optotrak) at 60 Hz. and force plate data were captured at 300 Hz. Data were filtered at 6 Hz. and processed to obtain kinematic and kinetic measures using KinGait3 software.

RESULTS & DISCUSSION

Preliminary analysis of the results for three subjects demonstrate overall greater variability and a greater magnitude in the knee frontal plane (abductor) moment during the initial part of weight acceptance when subjects were in the follicular phase. This initial period of weight acceptance has been identified as being important in helping to control the knee and may be associated with give-way episodes in ACL deficient patients (Houck, 2001).

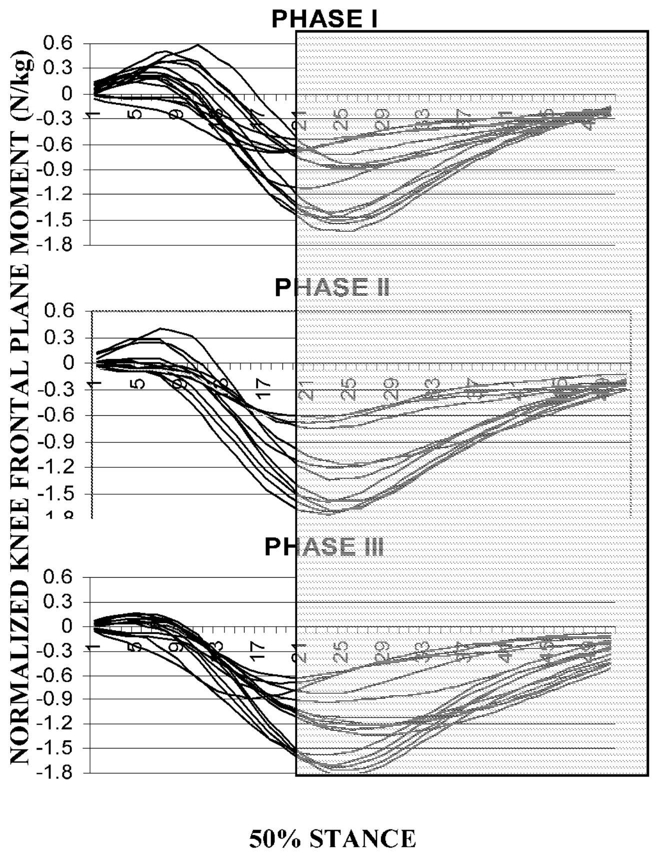

Figure1: Comparison of frontal plane moments, over the first 50% of stance, for the three phases of the menstrual cycle for five repeated trials on three subjects while performing straight ahead stepping activities. Increase variability and increased amplitude of frontal plane moment during weight acceptance (un-shaded area) is apparent during Phase I (follicular phase).

SUMMARY

An apparent association between the phase of the menstrual cycle and performance on a stepping activity was observed in the initial analysis of the data. Such an association could have implication for control of the knee that might be associated with a predisposition to injury.

REFERENCES

Houck J, Yack HJ. JOSPT 31:481-89, 2001
Huston LJ, Wojtys EM in "Prevention of Noncontact ACL Injuries", Am Acad Ortho Surg 2001

SYMMETRY IN KINETIC VARIABLES IS ACCOMPANIED BY SYMMETRY IN TEMPORAL BUT NOT DISTANCE VARIABLES OF GAIT IN PERSONS WITH STROKE

Janice J Eng[1,2] and C Maria Kim[1,2]

School of Rehabilitation Sciences[1], University of British Columbia
Rehabilitation Research Lab[2], GF Strong Rehab Centre, Vancouver, Canada, www.rehab.ubc.ca/jeng

INTRODUCTION

Gait patterns with respect to time, distance, and vertical force have been reported to be asymmetrical in pathological gait. The purpose of this study was to 1) determine whether symmetry in temporal-distance (T-D) measures is accompanied by symmetry in kinetic measures during gait, and 2) evaluate the effect of symmetry on gait speed in individuals with chronic stroke.

METHODS

Twenty-eight individuals with stroke (age of 62.5 ± 8.2 years, height of 1.68 ± 0.12 m, duration of injury of 4.4 ± 2.8 years, affected side: 14 left/14 right, sex: 20 males/8 females) participated in this study. An optoelectronic sensor was used to track infrared emitting diodes attached to the lateral malleolus and mid toe while subjects walked along an 8-m walkway over three force plates at their self-selected speed five times. Gait speed (normalized to leg length) and other T-D variables (stance time, swing time, step length) were calculated using the forward distance covered by the markers and the corresponding elapsed time. The average magnitude of the vertical ground reaction force (GRF) was measured over the stance phase of gait. A symmetry index (SI) (Robinson et al., 1987) was used to quantify asymmetries in gait:

$$SI = \frac{V_{paretic} - V_{nonparetic}}{\frac{1}{2}(V_{paretic} + V_{nonparetic})} \times 100$$

where $V_{paretic}$ is any variable recorded for the paretic limb and $V_{nonparetic}$ is the corresponding variable for the non-paretic limb. Spearman correlation was used to quantify the relationship between a) gait speed and SI for each variable and b) T-D symmetry and GRF symmetry.

RESULTS AND DISCUSSION

Concurrent with previous findings (Titianova & Tarkka, 1995), the mean symmetry indices deviated considerably from zero (i.e. perfect symmetry) (Table 1).

Table 1: T-D and GRF measures and absolute SI's (mean ± SD), N=28.

Variable	Paretic side	Non-paretic side
Stance time (s)	0.79 ± 0.20	0.89 ± 0.25
Swing time (s)	0.49 ± 0.11	0.37 ± 0.07
Step length (mm)	475.5 ± 130.3	484.8 ± 113.5
Vertical GRF (N)	537.1 ± 122.5	605.1 ± 131.0
Gait speed (s^{-1})	1.07 ± 0.34	
SI_{stance}	13.6 ± 9.1	
SI_{swing}	27.3 ± 19.8	
SI_{step}	17.3 ± 18.0	
SI_{GRF}	12.8 ± 9.5	

Correlations revealed that a) gait speed was significantly correlated with the symmetry of temporal measures and GRF and b) symmetry in GRF was correlated with symmetry in temporal but not distance measures of gait (Table 2). The significant correlation between GRF symmetry and gait speed provides some support for interventions aimed at improving weight bearing through the paretic limb to establish symmetry and ultimately increase function. Likewise, the significant relationship between GRF symmetry and temporal symmetry further supports intervention aimed to enhance symmetrical weight bearing. As a cautionary note, previous investigations have suggested that weight shifting activities must be practiced within the context of walking in order to enhance gait performance. In a controlled experimental study, Winstein et al. (1989) found that a balance retraining program that lead to a reduction in standing balance weight-bearing asymmetry did not lead to a concomitant reduction in temporal asymmetry during gait in persons with stroke.

Table 2: Spearman correlation between gait speed and symmetry indices

	Gait speed	SI_{GRF}
SI_{GRF}	-0.686** (N=25)	
SI_{stance}	-0.426* (N=26)	0.586** (N=25)
SI_{swing}	-0.567** (N=25)	0.678** (N=25)
SI_{step}	-0.321 (N=25)	0.199 (N=25)

* Significant at $p < 0.05$ ** Significant at $p < 0.01$

SUMMARY

This is the first study to report a relationship between symmetry in kinetic variables and symmetry in T-D variables of gait. A more symmetrical weight bearing between the two limbs was related to more symmetrical temporal but not distance measures during gait. GRF symmetry and temporal symmetry may be influenced by similar factors (e.g. balance) while other factors (e.g. compensatory strategies) may be more important in determining step length symmetry especially in chronic stroke survivors.

ACKNOWLEDGEMENTS

Supported by the BC Health Research Foundation, a grant-in-aid from the Heart and Stroke Foundation of BC and Yukon.

REFERENCES

Robinson, R.O. et al. (1987). *J Manipulative Physiol Ther*, **10**, 172-176.
Titianova, E.B, Tarkka, I.M. (1995). *J Rehabil Res Dev*, **32**, 236-244.
Winstein, C.J. et al. (1989). *Arch Phys Med Rehabil*, **70**, 755-762

INDUCED POSITIONS: INTUITIVE QUANTITIES FOR CHARACTERIZING MUSCLE FUNCTION

Frank C. Anderson[1,2], Saryn R. Goldberg[1], Marcus G. Pandy[3], and Scott L. Delp[1]
[1] Department of Mechanical Engineering, Stanford University, Stanford, California, USA, [2] fca@stanford.edu
[3] Department of Biomedical Engineering, The University of Texas at Austin, Austin, Texas, USA

INTRODUCTION

Even if the force exerted by a muscle during an activity is known, it can be difficult to determine the motions it generates. One reason is that a muscle accelerates all of the joints of the body, not just each joint it spans. Zajac and Gordon (1989) formulated a method for quantifying the accelerations induced by muscles. Although induced accelerations can be informative, they can also be difficult to interpret. In this paper, we extend the idea of induced accelerations by integrating them to produce induced positions. To illustrate the insight afforded by induced positions, we computed the knee flexion angle induced by muscles and other forces during the swing phase of gait.

METHODS

The dynamic equations of motion for a musculoskeletal model allow one to quantify the accelerations of the generalized coordinates ($\ddot{\vec{q}}$) in response to the forces acting on the body:

$$\ddot{\vec{q}} = \vec{I}^{-1}\{\vec{F}_G + \vec{F}_C + \vec{F}_M + \vec{F}_S\}, \tag{1}$$

where $\vec{I}^{-1}$ is the inverse of the system mass matrix, and $\vec{F}_G$, $\vec{F}_C$, $\vec{F}_M$, and $\vec{F}_S$ are vectors of generalized forces due to gravity, Coriolis and centripetal forces, muscle forces, and contact forces, respectively (Zajac and Gordon, 1989). The contact forces might be, for example, spring forces that represent ground contact. When the contact forces are viewed as reaction forces resulting from other forces within the system, they can be decomposed:

$$\vec{F}_s = \vec{F}_s^G + \vec{F}_s^C + \vec{F}_s^M, \tag{2}$$

where F_s^G, F_s^C, and $\vec{F}_s^M$ represent the contributions of gravity, Coriolis and centripetal effects, and muscles to $\vec{F}_s$ (Anderson and Pandy, *in review*). The accelerations induced by a force component i are computed from the sum of its force and the reaction forces it generates:

$$\ddot{\vec{q}}_i = \vec{I}^{-1}\{\vec{F}_i + \vec{F}_s^i\}, \quad i = G, C, M, \ldots . \tag{3}$$

Induced positions are then computed by twice integrating the induced accelerations:

$$\vec{q}_i = \iint_{t_i}^{t} \ddot{\vec{q}}_i \, dt, \quad i = G, C, M, \ldots . \tag{4}$$

If the induced accelerations of Eq. (3) satisfy superposition, then the induced positions will as well. Thus, they can be used to reconstruct the simulated generalized coordinates:

$$\vec{q} = \sum_i \vec{q}_i . \tag{5}$$

We performed an induced-position analysis based on a dynamic optimization solution for normal gait obtained by Anderson and Pandy (2001). The musculoskeletal model had 23 degrees of freedom and was actuated by 54 muscles. We quantified how muscle forces and other forces acting on the body contribute to knee flexion angle during the swing phase of normal gait. The contribution made by the initial knee flexion velocity at toe-off was computed by integrating this constant over time.

RESULTS AND DISCUSSION

If the body were acted on by no forces at all during swing, the knee would have flexed by about 150° by the time of heel strike due to the initial knee flexion velocity, which was 375°/s (Fig. 1(a)). The muscle and ligament forces that acted after toe-off extended the knee by about 125°. All other forces, but mainly centrifugal forces, were responsible for extending the knee by another 75° so that at heel strike the knee was nearly fully extended.

Stance-leg and back muscles induced 268° of knee extension. The swing-leg muscles, in contrast, induced 112° of knee flexion. In the swing leg, active forces in iliopsoas and the dorsiflexors generated large induced knee flexion angles, but these were offset by knee extensions induced by passive forces in the vasti and the plantarflrxors (Fig 1(b)).

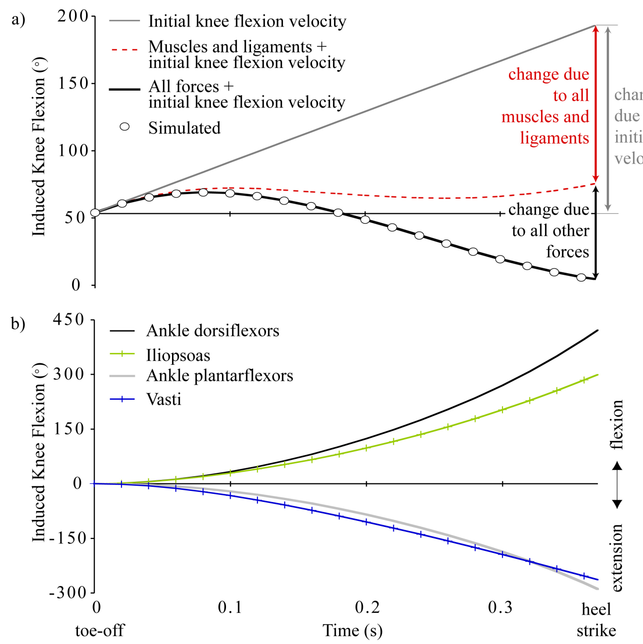

Figure 1: Knee angles induced by (a) initial velocity, muscles, ligaments, and all other forces, and (b) swing-leg muscles.

Induced positions provide an absolute measure in degrees of how muscles contribute over a time to an observed joint displacement. In contrast to induced accelerations, they are easy to interpret and allow the effects of forces and velocities on motion to be compared directly.

REFERENCES

Anderson F, Pandy M (2001). *J Biomech Eng*, **123**, 381-90.
Anderson F, Pandy M (*in review*). *Gait and Posture.*
Zajac F, Gordon M (1989). *Exerc Sport Sci Rev*, **17**, 187-230.

ACKNOWLEDGEMENTS

NIH R01 HD38962 and The Whitaker Foundation.

VISCOELASTIC CHARACTERIZATION OF ULTRA HIGH MOLECULAR WEIGHT POLYETHYLENE

Kochi Kobayashi[1,2], Makoto Sakamoto[2], Yuji Tanabe[3] and Toshiaki Hara[3]

[1]Department of Mechanical Engineering, Chiba Institute of Technology, Narashino, Japan, k_kobay@msi.biglobe.ne.jp
[2]Biomechanics Laboratory, Department of Health Sciences, Niigata University School of Medicine, Niigata, Japan
[3]Department of Mechanical and Production Engineering, Niigata University

INTRODUCTION

Mechanical characterization of ultra high molecular weight polyethylene (UHMWPE) is important to predict stress and strain distributions occurring within total joint replacements. The purpose of this study is to examine the stress-strain behavior of UHMWPE under impact compressive load. The dynamic response was modeled with the three-element viscoelastic solid as a first step toward development of the dynamic constitutive law. In addition, viscoelastic properties of UHMWPE were compared with those of compact and trabecular bone tissues, which consist of implanted joints.

MATERIALS AND METHODS

Six cylindrical specimens, 5.3mm in both diameter and length, were cored from an unused tibial insert of total knee replacement system (Axiom Standard Knee, Write Medical Technology Inc., Arlington, TN) that had been sterilized with ethylene oxide. Specimen's axis was perpendicular to the articular surface of the insert and care was taken to produce parallel ends. Impact compression tests were performed using the split-Hopkinson pressure-bar (SHPB) technique (Lindholm, 1964) to determine the dynamic stress-strain relation and to characterize viscoelastic behaviors by the method previously developed (Tanabe et al., 1994).

RESULTS

Figure 1 shows the representative dynamic stress-strain curve at a strain rate of 230/s. The stress-strain relation was almost linear and its slope determined dynamic Young's modulus, E_D. The transient response obtained from the SHPB test was modeled with the three-element viscoelastic solid consisting of a serial spring E_1 and dashpot η connected in parallel with a second spring E_2 (Fig.2). Table 1 lists the mechanical properties for UHMWPE, human tibial compact bone (Kobayashi et al., 1993) and bovine femoral trabecular bone (Kobayashi et al., 1997).

DISCUSSION AND CONCLUSIONS

The agreement shown in Fig. 2 suggests that the three-element viscoelastic solid is applicable to UHMWPE below its yield stress. The present result will allow a reliable prediction of dynamic stress and strain distributions on and within UHMWPE inserts. Further, the dynamic load transfer mechanism in implanted joints for many clinical situations can be studied with the viscoelastic parameters for bone tissues.

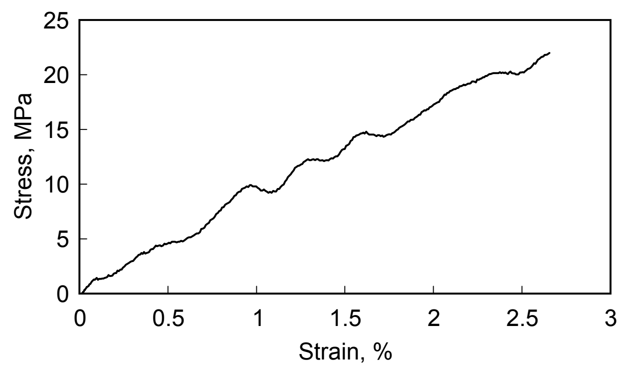

Figure 1: Dynamic stress-strain curve of UHMWPE.

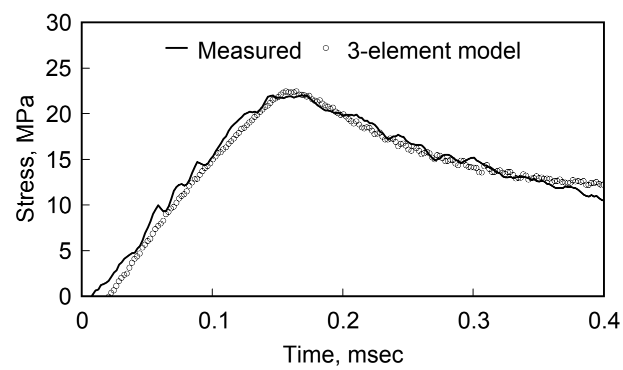

Figure 2: Comparison of measured and predicted transient responses obtained from the SHPB test.

Table 1: Values for mechanical parameters

	UHMWPE	Human compact bone*	Bovine trabecular bone*
E_D, GPa	0.84±0.11	16	2.53±0.75
E_1, GPa	1.29±0.07	19	1.97±0.58
E_2, GPa	1.38±0.07	34	1.73±1.42
η, MPas	0.44±0.19	1.9	0.94±0.73

* Longitudinal direction

REFERENCES

Kobayashi, K. et al (1993). *Theo. Appl. Mech*. **42**, 313-318
Kobayashi, K. et al (1997). *Proceedings of ICNFBE*. 295-298
Lindholm, U.S. (1964). *J. Mech. Phys. Solids*. **12**, 317-335
Tanabe, Y. et al (1994). *ASTM STP1173*, 127-141

THE CHANGE IN THE ROTATION RATE OF A BACTERIUM MOTOR CAUSES THE DIFFERENCE BETWEEN FORWARD AND BACKWARD SWIMMING SPEEDS OF *Vibrio Alginolyticus*

Tomonobu GOTO[1], Makoto ICHIBA[1], Koso NAKATA[1], Yasunari TAKANO[2], Yukio MAGARIYAMA[3]

[1] Tottori University, goto@mech.tottori-u.ac.jp
[2] University of Shiga Prefecture, [3] National Food Research Institute

INTRODUCTION

A difference in the swimming speeds between forward and backward motions has been observed for the bacterium, *Vibrio alginolyticus*, (Magariyama et al (2001)) though the cause of the difference is not illustrated yet. There are some possible reasons to count on; the deformation of a flagellum which is caused by the fluid force exerted on the flagellum, the hydrodynamic interaction between a cell and a slide, the changes in speed of revolution of a flagellar motor.

In order to investigate the cause of the difference, we measured cell body rotation rates simultaneously with swimming speeds while the cell swims forwards and backwards. The results suggested that the difference was mainly caused by the variation in the rotation rates of the flagellar motor.

METHODS

Cells of *V. alginolyticus*, each of which possesses only one flagellum, were incubated in HI broth with shaking at 30°C. The cells were harvested by centrifugation and were suspended in HG300 medium. The suspension was left at room temperature for over 30 minutes before the experiment. Then, 3μl of the suspension were sealed between a glass slide and a cover slip; the distance between them was about 10μm.

Motion of the bacteria was observed though a dark-field microscope and was recorded by a VCR. The recorded images of some wobbling cells whose flagella were at an angle to their cell bodies were chosen. Instantaneous cell body rotation rates (f) were calculated from the wobbling frequencies and corresponding swimming speeds (v) were also measured from the images.

RESULTS AND DISCUSSION

Figure 1 shows the relationship between v and f of a certain cell. The backward swimming speed is considerably bigger than the forward speed as described by Magariyama et al (2001). In addition to that, we noticed two things; one is that the swimming speed is proportional to the cell body rotation rate and the other is that the proportional constants are same in the two cases of forward and backward motions.

The former fact exhibits that the fluid motion associated with the swimming motion of the bacterium is a viscous dominated flow. In fact, the swimming speed of *V. alginolyticus* has been predicted well by using the boundary element method for creeping flows (Goto et al (2001)). This also means that the cell body rotation rate is proportional to the flagellar rotation rate.

The other fact suggests that the difference between forward and backward swimming speeds is rather due to the variation in flagellar motor rotation rates than the deformation of the flagellum.

We defined two indices I_v and I_f from a set of adjoining forward and backward swimming speeds (v_f, v_b) and a corresponding set of cell body rotation rates (f_f, f_b) as $I_v=(v_f-v_b)/(v_f+v_b)$ and $I_f=(f_f-f_b)/(f_f+f_b)$, respectively. Figure 2 shows histograms of the indices of 159 sets obtained for 35 cells. This figure entirely supports the things mentioned above for one cell, namely, that v_b is greater than v_f and the shape of the histogram of I_v is almost same as that of I_f.

SUMMARY

The speed and the cell body rotation rate of *V. alginolyticus* were simultaneously measured during both forward and backward swimming motions. The difference between forward and backward swimming speeds is mostly attributable to the variance in the rotation rate of the flagellar motor.

REFERENCES

Goto, T. et al (2001). *JSME Int. J. Ser. C*, **44**, 4, 958-963.

Magariyama, Y. et al (2001). *FEMS Microbiology Letters*, **205**(2), 343-347.

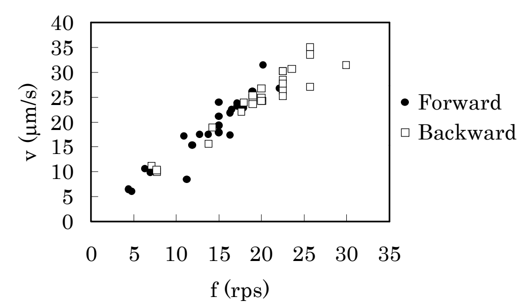

Figure 1: Instantaneous swimming speed and cell body rotation rate of a cell.

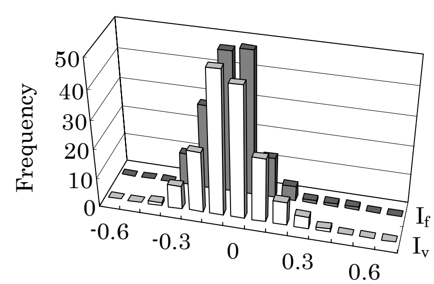

Figure 2: Histograms of indices, I_v and I_f.

RAPID MANUFACTURING OF BONE NAILS WITH IMPROVED MECHANICAL PROPERTIES

Jürgen Hoffmann[1], Ulrich Fink[2] and Klaus Friedrich[1]

[1]Institute for Composite Materials Ltd., Erwin-Schrödinger-Strasse, 67663 Kaiserslautern, Germany, http://www.ivw.uni-kl.de/
[2]AESCULAP AG & CO.KG, Am AESCULAP-Platz, 78532 Tuttlingen, Germany

INTRODUCTION

Bioresorbable implants manufactured from polymers like polylactides, polyglycolides and co-polymers slowly degrade and are reabsorbed from the human body and removal operations after fracture surgery are not necessary. Due to their limited mechanical properties, the polymer screws and pins are mostly used in the treatment of non weightbaring simple fractures. Basing on the technique of Microfibrillar Composites, a new procedure for rapid manufacturing of bone nails with higher mechanical properties by injection molding is investigated.

METHODS

Bone nails are prepared according to the technique of Microfibrillar Composites from polymer blends of immiscible partners having different melting points, T_M, like compositions of polylactides and polyglycolides (see table 1). The essential stages of the preparation with this new technique are: (i) blending, (ii) drawing and (iii) injection molding above T_M of the lower-melting component and below T_M of the higher-melting one. During drawing fibrils are created and in the subsequent injection molding step melting of the lower-melting component occurs with preservation of the fibrillar structure of the higher-melting component. It should be mentioned, that the fibrils are not added as a separate material, in fact the structure is created during manufacturing.

RESULTS

Due to the high oriented polyglycolid fibrils, the composite shows higher mechanical values than each component. A special focus is set to the drawing step to achieve a good orientation of the harder polyglycolid component and to obtain synergy effects of both materials. The polyglycolid content of the composite varies from 10 to 30 volume percent.

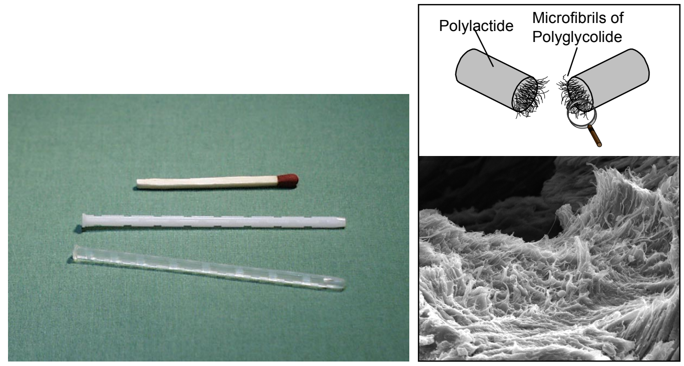

Figure 1: Photograph and cross-section of the bone nail made of a polylactide/polyglycolide microfibrillar composite.

SUMMARY

The new composite bone nail shows promising mechanical values under ambient conditions and a high manufacturing speed is possible. Regarding the processing, this technique allows a wide range of different implant forms like the conventional injection molding technique. Finally this investigations shows the possibility of producing complete degradable reinforced implants by injection molding.

REFERENCES

E. Wintermantel (1999). *Der Chirurg* **70**: 847-857.
S. Ferguson, D. Wahl, S. Gogolewski (1996). *Journal of Biomedical Materials Research* **30**:543-551.
P. Törmälä (1992) *Clinical Materials* **10**: 29-34.

ACKNOWLEDGEMENTS

The authors acknowledge the financial support of the foundation for Industry Research (Cologne, Germany) and the material support of Boehringer Ingelheim KG (Ingelheim, Germany).

Table 1: Components of the composition and their properties.

Material	Glas Transition Temp. T_G [°C]	Melting Temp. T_M [°C]	Bending Strength [MPa]
Polylactide	45	150-160	120
Polyglycolide	37	224-227	100
Injection Moulded Composite	37 and 45	150-160 and 224-227	150

ANISOTROPY OF MODULUS CHANGES IN TRABECULAR BONE FOLLOWING SHEAR OVERLOADING

Glen L. Niebur and Xiangyi Liu

Department of Aerospace and Mechanical Engineering, University of Notre Dame
Notre Dame, IN 46556, USA; gniebur@nd.edu

INTRODUCTION

When trabecular bone is damaged by overloading[1] or fatigue,[2] its elastic modulus decreases. At the macroscopic level, the decreased modulus will redistribute the applied loads and may increase fracture risk.[3] At the microscopic level, damage to the trabecular matrix will stimulate bone remodeling.[4,5] As such, damage development in trabecular bone has implications for both whole bone strength and age related bone degeneration.

It has been suggested that both microdamage and modulus reductions in trabecular bone depend on the damage loading mode.[6,7] It is complicated to evaluate the anisotropy of damage experimentally, as it requires modulus measurements in multiple loading modes on a single specimen. In this study, computational models were used to simulate damage in trabecular bone specimens in order to investigate the anisotropic damage behavior due to shear loading.

METHODS

High-resolution finite element models were created from seven bovine tibial trabecular bone specimens. The effective tissue elastic moduli for the models were calibrated from the apparent moduli in an earlier study.[8] The full apparent elasticity tensor for each model was calculated using a representative volume method.[9] Nonlinear models[8] were used to simulate apparent level damage induction by pure shear stress to 1.75% strain in an on-axis-transverse plane and in the transverse plane. An isotropic, perfectly damaging constitutive model was assumed for the tissue (Fig. 1). The damaged tissue modulus was calculated for each element Gauss point based on the maximum strain level attained.

The damaged tissue moduli were used to calculate an apparent level damaged elasticity tensor. The percentage reduction in each of the six orthotropic elastic moduli was calculated from the undamaged and damaged elasticity tensors.

RESULTS

Shear in the transverse plane caused the transverse shear modulus to decrease by more than twice as much as the two on-axis shear moduli, on average ($p < 0.01$, Fig. 2). Similarly, the two axial moduli in the transverse plane decreased by more than twice the amount that the on-axis modulus decreased after transverse shear damage.

Shear in the on-axis plane decreased the on-axis shear modulus more than the remaining five moduli ($p < 0.01$). The transverse axial modulus in the plane of shear decreased almost twice as much as the other axial moduli ($p < 0.01$), which were not significantly different from one another.

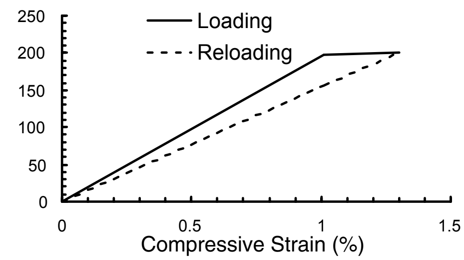

Figure 1: The tissue level damage behavior in principal strain space.

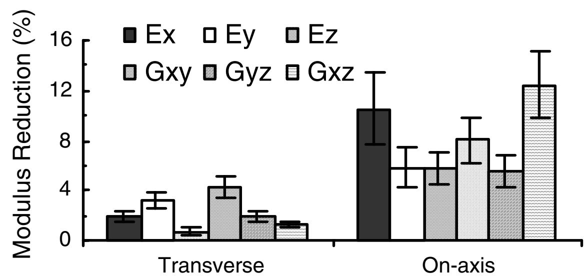

Figure 2: Reduction of orthotropic moduli due to apparent level shear damage. The XY coordinate plane is the transverse plane, and the Z axis is aligned with the principal trabecular orientation.

DISCUSSION

The on-axis modulus is the least sensitive of the six orthotropic moduli to shear loading. As such, if the bone does not fracture following a shear overload, it maintains most of its mechanical stiffness for habitual loading. For a specific strain level, the decrease following shear loading in a plane aligned with the principal trabecular orientation is more detrimental than shear loading confined to the transverse plane. The anisotropy of damage at the apparent level indicates that microdamage for a specific loading mode is localized. As such, damaged regions following off-axis loading are protected during normal loading, facilitating repair. Because of the localization, this damage repair process could result in structural adaptation of the microarchitecture.

REFERENCES

1. Keaveny, et al., 1999, JOR 17:346-53; **2**. Bowman, et al., 1998, J Biomech Eng 120:647-54; **3**. Kopperdahl, et al., 2000, JOR 18:685-90; **4**. Burr, 1993, Calcif Tissue Int S75-80; **5**. Mori and Burr, 1993, Bone 14:103-9; **6**. Zysset and Curnier, 1996, J Biomech 29:1549-58; **7**. Niebur, et al., 2001, J Biomech 34:699-706; **8**. Niebur, et al., 2000, J Biomech 33:1575-83; **9**. Van Rietbergen, et al., 1996, J Biomech 29:1653-7

SWING PHASE REDUCTION IN ABOVE-KNEE AMPUTEE RUNNING

Christiane Bohn[1], Gongbing Shan[2], Thomas Korff[3], Hagen Schaper[1], Klaus Nicol[1]

[1]Institute of sports sciences, University of Muenster, Germany
[2] Department of Kinesiology and Health Education, University of Texas at Austin, USA
[3] Department of Kinesiology, University of Lethbridge, Canada

INTRODUCTION

Since the repeal of prohibition for amputee running in 1991 the development of technical equipment is standing in the centre of interest (e.g. Knicker/Bloch 1996). But winning at a high competition level depends also on improvement of individual running technique. Therefore, the aim of this study was to improve the individual sprinting technique of above-knee amputees by computer simulation.

Previous research (Bohn 2001) shows that above-knee amputee runners often extend the knee of the prosthesis side already in the middle of the swing phase. This increases moment of inertia and thus increases flight phase and reduces running velocity. Aim of the study is to find out if it is possible to delay knee extension (to which the athlete has no direct control) by modifying hip torque (to which he has control).

METHODS

Computer simulations were conducted to analyse the influence of the hip muscles on swing phase performance on the prosthesis side. Three high performance amputee sprinters took part in the study which among others was conducted for attaining parameters for the model. In a first step, kinematic and dynamic parameters of the subject were obtained. The experimental set up included two high speed video cameras (250 Hz) and a 240 x 80 cm² segmented 3-component force platform (170 Hz). Three successive running steps were recorded at 5.7 m/s - 7.2m/s running velocity, data were filtered with a 2nd order low pass butterworth filter at 70 Hz.

In a second step, a two dimensional model with three segments (trunk, thigh and lower leg) using DADS 9.0 forward dynamic modelling software was constructed and based on the anthropometrical data of each subject. Using a procedure by Patil/Chakraborty (1991), the hip torque curve was modified in order to fit the model movement to the empirical data. In a third step the hip torque curve was modified for reducing flight phase.

RESULTS AND DISCUSSION

Simulation showed that less flexion and more extension net torques at the hip were necessary to increase knee flexion as shown in Figure 1. In this way, moment of inertia is decreased which leads to reduced swing phase duration.

It was possible for all subjects to find hip torque curves which lead to reduced swing phase and thus to higher velocity in case they manage to keep stride length constant.

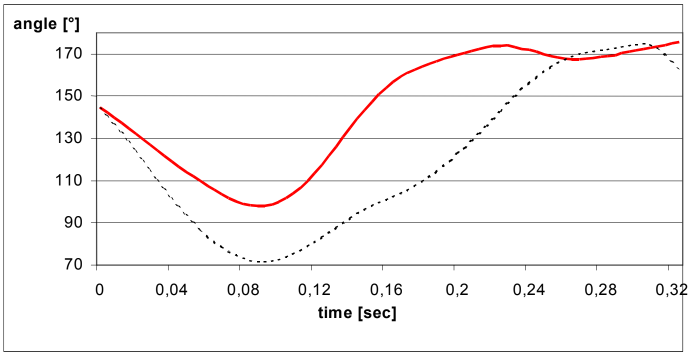

Figure 1: *Knee* angle curve of the subject during flight phase (continuous line) and simulated knee angle curve caused by modified *hip* torque (dashed line). This modification gives less moment of inertia and swing phase duration and thus possibly higher running velocity.

CONCLUSION

Simulation shows that flight phase reduction and thus possibly increase of running velocity can be achieved by reasonable modification of hip torque. Ongoing research should show whether the subjects did not produce the calculated torques due to muscle weakness, or due to deficit co-ordination. Furthermore simulation might lead to feasible modifications of the prosthetic material.

REFERENCES

Bohn, C., Shan, G.B., Korff, T.; Nicol, K. (2001). *Book of abstracts*, Zürich, 60.

Knicker, A., Bloch, O. (1996). *Forschung, Innovation, Technik*, **2**, 1 – 8.

Patil, K.M., Chakraborty, J. K. (1991). *J. of biomechanics*, **24,** 223 –233.

ACKNOWLEDGMENTS

This study was supported by the “Bundesinstitut für Sportwissenschaft”

APPLICATION OF FIBRE LASER SCANNING CONFOCAL MICROSCOPY TO STUDY OF THE BIOMECHANICS AND MICROSTRUCTURE OF ARTICULAR CARTILAGE

Jianping Wu [1], Brett Thomas Kirk [1], Peter Delaney [2], Nick Milne [3], Daniel Smolinski[1] and Karol Millar[1]
[1] The Department of Mechanical & Materials Engineering, The University of Western Australia, Australia; [2] Optiscan Pty Ltd, Australia; [3] The Department of Anatomy & Human Biology, The University of Western Australia, Australia.

INTRODUCTION

The aim of this study is to develop a fibre laser scanning confocal microscopic methodology to examine the biomechanical functions of articular cartilage in relation to the collagen matrix.

Articular cartilage has a unique structure while provides it with exceptional biomechanical properties. Articular cartilage is composed of a small portion of chondrocytes and an extracellular matrix which mainly consists of water with dissolved electrolytes, collagen fibres (mainly type II) and proteoglycans. The collagen fibres form a three-dimensional meshwork which entraps a swollen proteoglycan gel. Articular cartilage is thus provided with resilience and load capacity.

METHODS

Fibre optic laser scanning microscopy (FLSCM) uses a single mode optical fibre for transmission of the illumination and imaging signal. The FLSCM offers compact resolution and imaging capability when comparing with a conventional confocal microscope (Delaney et al, 1994). The mechanism of the FLSCM has allowed the development of potential clinical applications (Smolinski et. al, 2001). In this study, the FLSCM was modified with compression apparatus as shown in Figure 1, which incorporates a proportional pressure regulator, a pressure transducer and LVDT. Therefore, the pressure applied to the cartilage can be controlled and displayed digitally by the Pressure transducer. The displacement occurring in the articular cartilage can simultaneously be recorded using data acquisition software via the LVDT.

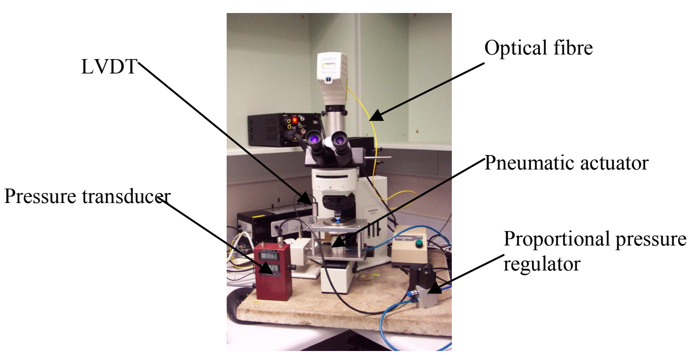

Figure 1. A modified FLSCM for study of the biomechanics of articular cartilage in relation to its internal structure.

Articular cartilage specimens attached to subchondral bone, 1.5 × 1.5 × 3 mm, were obtained from the central weight bearing region of femoral condyles of approximately two-year-old cows within twenty-four hours of slaughter. After using immunofluorescence for tracing type II collagen, the specimens were placed on the platform of the FLSCM. Using F900e software (Optiscan Pty Ltd, Australia), the three-dimensional image stacks of the collagen fibres were recorded. Using Voxblast, the image stacks were reconstructed into three-dimensional image as shown in Figure 2.

RESULTS

This study explored the three-dimensional structure of type II collagen fibres in articular cartilage. It has been confirmed that the collagen fibres in the superficial zone are parallel to the surface of the articular cartilage and predominately orientated in one direction, shown in Figure 2 (left). The collagen fibres in the transitional zone change their direction compared to the radial zone and start to become parallel to the surface of the cartilage as they approach the superficial zone, as shown in Figure 2 (middle). The collagen fibres in the radial zone are arranged predominately perpendicular to the surface of the articular cartilage as shown in Figure 2 (right).

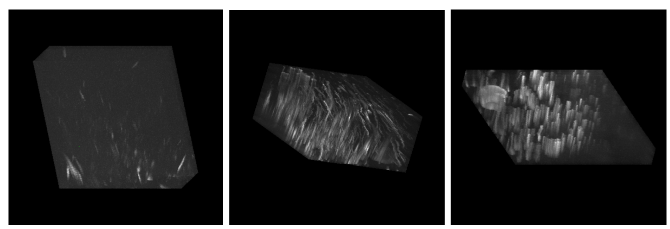

Figure 2. Three-dimensional images of the collagen fibres of bovine articular cartilage. Collagen fibres in the superficial zone (left). Collagen fibres between the transitional and radial zones (middle). Collagen fibres in the deep zone (right).

SUMMARY

In current study, based on using FLSCM, a methodology has been developed to study the biomechanical function of collagen fibres.

REFERENCE

Delaney, P.M, Harris M.R, King, R.G (1994). Fibre-optic laser scanning confocal microscopy suitable for fluorescence imaging. *Appl Opt*. **33**(4), 573-577.

Smolinski D. et al (2001). Assessment and Development of a Confocal Arthroscope. *Third Asia-Pacific Symposium on Confocal Micrscopy and Related Technologies.* Melbourne, Australia. 70.

THE IMPORTANCE OF CERTAIN DESIGN FEATURES IN A BACKPACK

Joan M. Stevenson, Susan A. Reid, J.Tim Bryant, Ronald P. Pelot, Evelyn L. Morin
Ergonomics Research Group, erg@post.queensu.ca
Queen's University, Kingston, Ontario, Canada

INTRODUCTION

There is a paucity of biomechanical studies in scientific literature for load carriage. Most designers merely use feedback from expert trekkers to develop new features ion a backpack. This purpose of this study is to show how biomechanical tools can be used to assist with the design process. To complete this research, two biomechanical tools used to develop the Canadian Forces load carriage system will be used: 1) Load Carriage (LC) Simulator (measured forces, moments, displacement and pressures); and 2) the Load Distribution Mannequin (separated and measured out the forces experienced by the upper and lower body).

DESIGN OF THE SHOULDER STRAPS

In this study, the purpose was to determine the optimal shoulder strap design to minimize forces and pressures on the torso. For this study, the Load Distribution Mannequin (LDM) was used to provided information on shoulder and lumbar forces as well as shoulder pressures. In the first study, the lower shoulder strap attachment point was moved along the vertical pack edge and horizontal belt line by reinforced D rings so that fourteen different shoulder strap angles could be created. To assess the upper shoulder straps three different shapes (A,B,C) were designed with common characteristics (width of 9.5cm and a distance of 3.5cm between the upper attachment points on the pack) and variable shapes in their radii of curvature toward the armpit;

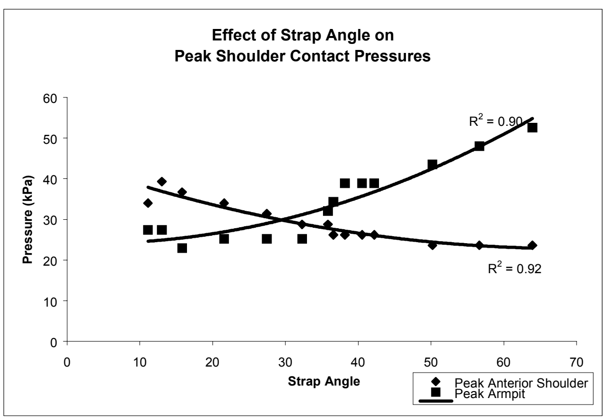

Figure 1. Effect of strap angle on peak contact pressures

A-no curvature, B-5.5cm, C-9cm. Results for the lower shoulder strap attachment point found that the shear forces were below recommended levels for all configurations, but significantly better when the strap was less than 40º from the vertical. The changing angles affected the skin contact pressure with dramatic effects in the axilla above 35º angle from the vertical. It was concluded that an attachment point 24º to 30º from the vertical would be optimal for the lower shoulder strap attachment point. For the upper shoulder strap attachment point, peak pressure, average pressure and contact area over the anterior shoulder were examined. Prototype C with the longer radius of curvature had the best force distribution, least peak pressure in the axilla and least tendency to twist.

LATERAL STIFFNESS RODS

The purpose of this study was to examine the change in load distribution characteristics associated with adding lateral stiffness elements (rods) to a rucksack. Two 3D load cells were used to determine the load applied to the shoulders and upper torso independent of the load applied to the hips and lower trunk. Position and mass of the payload (25 kg) was fixed at the centre of the volume of the rucksack and held constant during all testing. It was hypothesized that lateral rods would provide a force bridge that transfers part of the vertical load of the pack from the upper back and shoulders to the hip belt (supported by the iliac crest) thereby reducing the vertical load on the torso, and possibly reduce the horizontal reaction force that produces a shear load on the spine. Results showed that this active stiffness

Figure 2. Vertical load force for the rod / no-rod conditions.

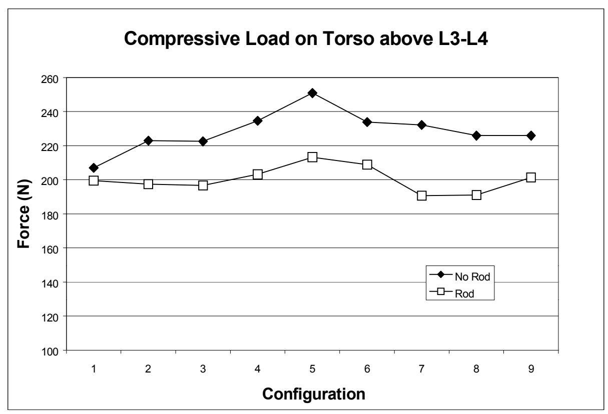

element shifted 10% of the vertical load from the upper torso to the pelvic region. Lumbar shear load remained unchanged between the rod and no-rod conditions for all combinations of shoulder strap and waist belt tension. The lateral rods also provided a greater extensor moment about the medio-lateral axis at the L3-L4 level. It was concluded that biomechanical tools can add knowledge and reduce design time and costs.

ACKNOWLEDGEMENTS

This research was funded by DCIEM, DND Toronto, Canada with special thanks to Major Linda Bossi.

DEVELOPMENT OF A TRIFILAR PENDULUM FOR MEASURING MOMENT OF INERTIA

J.Tim Bryant, Joan M. Stevenson, Rad Zdero, Lindsay Hadcock
Ergonomics Research Group, erg@post.queensu.ca
Queen's University, Kingston, Ontario, Canada

INTRODUCTION

One requirement often needed for dynamic biomechanical modeling is the location of the centre of gravity and moment of inertia of large complex objects, such as a person, prosthetic limb or a backpack. These irregular shaped objects have a heterogeneous mass distributions or awkward shapes. Numerous methods have been reported in the scientific literature, such as: photogrammetry[1], computed tomography[2], magnetic resonance imaging[3], mathematical modeling[4] and body segment pendulum methods[5]. This paper describes a tool called a trifilar pendulum that can provide this information for non-homogenous objects quickly and simply.

THEORETICAL BASIS

The trifilar pendulum consists of a round plate of a homogenous material, suspended in the horizontal plane by three cables of equal length equidistantly placed from the center of the plate (Figure 1). When the pendulum is twisted around a vertical axis running through the center of the plate, it oscillates with a period that is a function of cable length, plate radius, plate mass, local gravitational acceleration, and plate moment of inertia. This can be derived as follows:

$$I = 0.2485\, r^2 / L\, (mT^2 - m_P T_P{}^2) \quad (1)$$

Where: I = mass moment of inertia of test object [kg.m^2]
m = mass of plate/object assembly [kg]
T = period of plate/object assembly [s]
m_P = mass of plate [kg]
T_P = period of plate [kg]
r = effective radius of plate [m]
L = length of filaments [m]

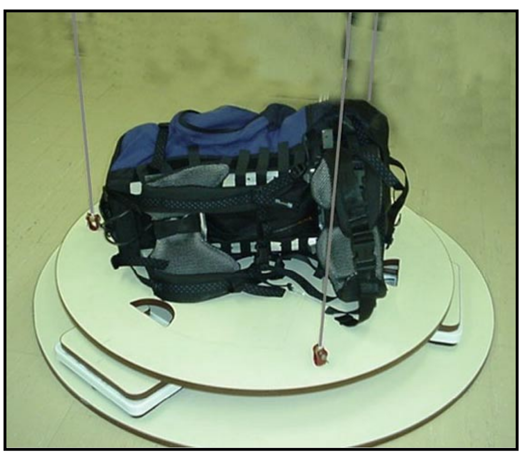

Figure 1. Trifilar Pendulum with backpack

When an object is placed on the plate such that its center of gravity (CG) is coincident with the plate CG, the resultant object/plate assembly can be treated as a new pendulum. Since all factors other than mass remain constant, the change in the period of the new pendulum is related to differences in the mass moments of inertia of the old and new pendulums. The mass can be easily measured and the moment of inertia of the object can be determined using equation (1).

CENTER OF GRAVITY VALIDATION TESTS

The purpose of this experiment was to determine the ability of the trifilar pendulum to predict the centre of gravity of a test object, a necessary requirement the correct calculation of moment of inertia as he plate centroid and object centroid must be in line. The system was calibrated at 15 distinct locations on the plate, repeated twice, using 13.6 and 45.5 kg masses. Results showed high correlations between measured (x,y) coordinates and trifilar pendulum locations (r = 0.98:1 and 0.99:1, respectively) The average absolute total error E_T is 15.5 mm (3.5 % of the radius). The accuracy of the device would improve as the weight of the object being measured increases due to the precision of the scales. The precision error is ± 0.45 kg. Thus, 13.6 and 45.5 kg objects have errors of ± 3.3 and ± 1%, respectively.

MOMENT OF INERTIA VALIDATION TESTS

The purpose of this experiment was to validate the ability of the pendulum to provide accurate physical measures, which in turn yield an accurate moment of inertia. The three test objects (3.69, 6.81 and 10.2 kg) were composed of three sets of equal mass. Each weight series was placed on the pendulum plate a three locations (0.2 m, 0.25m and 0.3m) from the centre along lines drawn from the center to the turnbuckles. The angle measurement pegs were inserted and the pendulum was rotated freely through 10 degrees 10 full rotations. Tests were repeated 10 times and results averaged. From equation (1), the moment of inertia was determined for values ranging from 0.16 to 0.95 kg.m^2. The average percent error between theoretical and measured values was 6.0 % However, accuracy improved significantly with increased mass, as the percent error reached a minimum value of 0.32 % for a 10.2 kg load located 0.25 m from the center of the plate.

REFERENCES

[1]Jensen and Fletcher, 1994; [2]Pearsall and Reid, 1994; [3]Martin et al., 1989; [4]Hatze, 1980; [5]Albery et al., 1998.

ACKNOWLEDGEMENTS

This research was funded by DCIEM, DND Toronto, Canada
Special thanks to Maj. Linda Bossi, DCIEM Toronto, Canada.

RESIDUAL STRESS AND STRAIN IN THE LAMELLAR UNIT OF THE AORTA: EXPERIMENT AND ANALYSIS

Takeo Matsumoto, Taisuke Goto, and Masaaki Sato
Biomechanics Laboratory, Tohoku University, Sendai, Miyagi, Japan
For correspondence: takeo@biomech.mech.tohoku.ac.jp (T.M.)

INTRODUCTION

If one cut a ring-like segment of an aorta radially, it usually springs open to become an arc. It has been pointed out that this happens because circumferential stress in the aortic wall distributes uniformly in the radial direction *in vivo*, and as a result, the segment at no load has compressive residual stress near the inner wall and tensile near the outer. The opened-up configuration is stress-free if the aortic wall is homogeneous. However, the wall is not homogeneous in a microscopic level: its media has a layered structure called lamellar unit which is a pair of elastic lamina (EL) and a smooth muscle rich layer (SML). Recently, we found that the EL is much stiffer than the SML (Goto, 2002). Thus, if the circumferential stress in the *in vivo* condition is the same between the two layers, residual stress of each layer in this direction should be different because the stress-strain relationships differ. Such residual stress is not released fully by radial cutting, but is released in the area close to the cut surface, causing hills and valleys on the surface due to compressive and tensile stresses, respectively. In this study, we have developed a scanning micro indentation tester (SMIT) to measure the topography and the stiffness distribution of the cut surface, and estimated residual stress and strain in the lamellar unit.

SCANNING MICRO INDENTATION TESTER (SMIT)

It is a tester to measure the surface topography and stiffness distribution of a specimen surface by pressing a cantilever tip against the surface while scanning it like the atomic force microscope in the contact mode. The cantilever was made by pulling a micro glass plate of 65mm x 1mm x 0.15mm to make its tip diameter 3–5 μm and bending it at right angle at the point 4mm from the tip. The cantilever was driven by a PZT actuator and the displacement of its tip was measured with a laser displacement meter. The specimen bath was set on a motor-driven XY stage to scan the point of measurement. The contact point was determined at the point where the cantilever began deflecting, and a stiffness index α was obtained as the initial slope of the indentaion-deflection curve. The index α was converted to elastic modulus E with the formula E (kPa)=1.88exp(2.54α) obtained by calibrating the tester with silicone elastomers with known elastic moduli.

MEASUREMENT OF SURFACE TOPOGRAPHY

Rectangular specimens of 5x10 mm (2–3 mm thick) were excised from porcine descending thoracic aortas. Macroscopic residual stresses are removed during excision. Each of the specimens was sliced with a vibrotome in the saline to obtain the surface perpendicular to the circumferential direction. The specimen with its bath was then mounted on the XY stage of the SMIT for the surface measurement. The surface of the section shows hill and valley pattern aligned with the circumferential direction (Fig. 1). The distance between the peaks and the peak height were ~25 and ~8 μm, respectively. The elastic modulus estimated from α was ~180 kPa at the peak and ~52 kPa at the bottom. On a separate study, we observed the change in thickness of EL and SML in response to radial compression and found that the elastic modulus of EL is 2.5 times higher than that of SML (Goto, 2002). Thus, we suppose the hill must be EL and the valley SML, i.e., EL may be compressed and SML stretched in the lamellar unit.

ESTIMATION OF RESIDUAL STRESS AND STRAIN

The stress distribution required to restore the hill and valley pattern to the plane where the specimen was cut corresponds to the residual stress distribution. Such distribution was estimated on a 2D simplified model based on the data shown in Fig. 1. Following assumptions were made: 1) lamellar unit is made of two layers EL and SML with uniform thickness; 2) the thickness of EL and SML are 6 and 22 μm, respectively; 3) the height of each layer is uniform and the difference between the two is 8 μm; 4) EL and SML are linearly elastic with the elastic modulus of 180 and 52 kPa, respectively; 5) residual stress is released upon cutting to the depth l_o; 6) shear stress and lateral deformations are negligible. To estimate the depth l_o, thin slices with various thickness were removed from the surface with the vibrotome while measuring surface topography with the SMIT. The height difference between hills and valleys did not decrease unless the thickness was smaller than 70μm. Thus, we roughly estimated l_o to be 70μm. The model analysis showed that the residual stress and strain increased with the decrease in l_o, and that the residual stress is at least –10 kPa for the EL and 3kPa for the SML and the residual strain is at least –6% for the EL and 5% for the SML. These values are almost comparable to those estimated to be in ring-like segments of the aortas in no load condition.

Fairly large stress may still reside in the opened-up aortic wall, which had been believed to be stress-free. Microscopic viewpoint is necessary when studying mechanical environment of the smooth muscle cells in the aortic media.

REFERENCE

Goto, T. et al (2002). *Proc 14th Bioeng Conf/JSME, in press.*

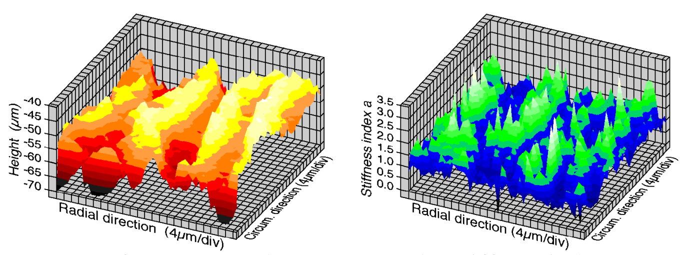

(a) Surface topography (b) Stiffness index α

Figure 1: An example of data obtained with the SMIT for a section perpendicular to the circumferential direction of a porcine thoracic aorta. Measurement area, 100μm x 100μm.

THE DEVELOPMENT OF CONFOCAL ARTHROSCOPY FOR THE ASSESSMENT OF CARTILAGE DISORDERS

Thomas B. Kirk[1] , Daniel Smolinski[1], Peter Delaney[2], Jian Ping Wu[1], Karol Miller[1], David Wood[3] and Ming Hao Zheng[3]

[1]Department of Mechanical and Materials Engineering, University of Western Australia
[2]Optiscan Pty Ltd, Melbourne, Australia
[3]Department Orthopaedic Surgery, University of Western Australia

INTRODUCTION

The internal structure of articular cartilage is critical to its biomechanical function. Cartilage is known as one of the most intricate and difficult tissues to study. The primary reason for this is that its functional characteristics depend heavily of the three dimensional microstructure of the tissue, while most microscopy methods can display only two dimensional representations of the cartilage. The sectioning requirements for most forms of examination also destroy the integrity of the tissue, making it impossible to concurrently examine the structure and function of the tissue. The development of confocal microscopy internal examination of loaded tissue for the first time, facilitating direct examination of the association between structure and function of the tissue (Guilak, 1994).

The structure/function relationship is critical to the study and the advancement of clinical treatment techniques for cartilage disorders. Osteoarthritis is characterized by severe disruption to the cartilage matrix. The emergence of autologous chondrocyte implant (ACI) therapy as a method for repairing cartilage defects has further increased interest in clinical techniques for the examination of cartilage structure and function. A confocal arthroscope has therefore been developed (7mm diameter) to facilitate clinical examination of cartilage structure (Figure 1). This, in turn, allows the functional characteristics of the tissue to be deduced.

Cartilage exhibits little intrinsic repair (Ghadially, 1983), making biopsies undesirable. Thus, with respect to cartilage in particular, the developed technologies promise to enable study to a level of detail which was previously impossible.

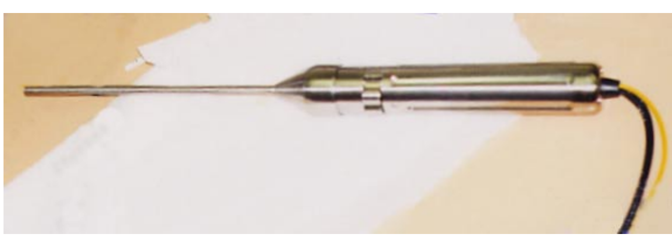

Figure 1: The prototype confocal arthroscope. Probe diameter is 7mm [Optiscan Pty Ltd]

METHODS

Bulk cartilage and bone specimens were frozen post mortem. After thawing the specimens were immersed in 0.05g/l Acridine Orange for 6 minutes. The specimens were then examined using the developed confocal arthroscope. Confocal images were recorded from various locations in the weight bearing regions of the joints. Figure 2 (left) shows an image obtained from asymptomatic tibial cartilage. Figure 2 (right) shows an image obtained from osteoarthritic cartilage.

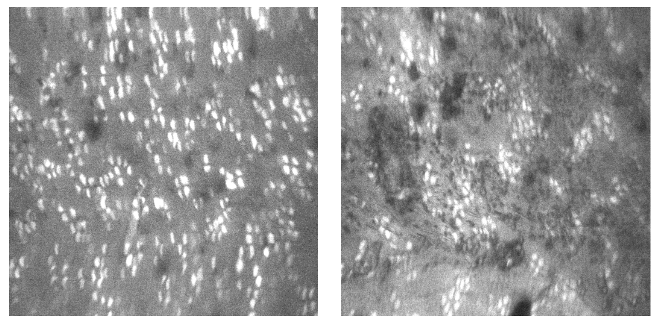

Figure 2: Confocal arthroscopic images of asymptomatic tibial (left) and ostearthritic femoral (right) articular cartilage.

SUMMARY

A confocal arthroscope has been developed and used on articular cartilage. Clear differences between asymptomatic and osteoarthritic cartilage can be seen. These differences are consistent with the histology of cartilage and the etiology of osteoarthritis. Clinical potential for the methods clearly exists for monitoring both arthritic conditions and ACI repair tissue. Further development of both equipment and methods is required before clinical trails can progress.

REFERENCES

Guilak F. (1994). *J. Microsc.*, 245-256

Ghadially F N (1983). *Fine structure of synovial joints*. Butterworth.

DEVELOPMENT OF A 3D FINITE ELEMENT MODEL OF HUMAN FOOT AND ANKLE

Ming Zhang[1], Jason Tak-Man Cheung[1], Yubo Fan[2] and Aaron K.L. Leung[1]
[1]Rehabilitation Engineering Centre, The Hong Kong Polytechnic University, Hong Kong, China, rcmzhang@polyu.edu.hk
[2]Laboratory of Biomechanical Engineering, Sichuan University, Chengdu, China

INTRODUCTION

Information on the internal stress and strain of the foot and ankle during walking is useful in enhancing knowledge on the biomechanical behaviour of the ankle/foot complex. Direct measurement of those parameters is difficult, while a comprehensive computational model can be useful. This will help to design a proper foot support. Foot model have been developed based on a certain assumptions (Chen 2001, Funk 2000, Gefen 2000, Jacob 1999). In this study, a three-dimensional finite element model of the human foot and ankle was developed using 3D actual geometry of both foot skeletons and soft tissues. The objective is to investigate the biomechanical interaction among bones, ligaments and tendons, and interaction between foot plantar and different supports under various loading conditions.

METHODS

The geometry of the FE model was obtained from 3D reconstruction of MR images from a right foot of a normal male subject. The bony structures and the soft tissue boundaries in MR images were identified and segmented using MIMICS v7.10 (Materialise). The boundary surfaces of different components obtained were processed using SolidWorks in order to form a surface model for all bones and foot surface, as shown in Fig. 1. The surface models were d meshed using ABAQUS v6.2 FE package.

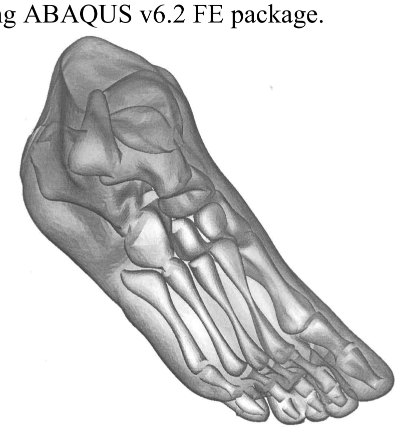

Figure 1: Bones and foot surface obtained from 3D reconstruction of MRI.

The metatarsals and the phalanges are jointed together by 1mm thick cartilage. The interaction among the metatarsals, cuneiforms, cuboid, navicular, talus, calcaneus, tibia and fibula were defined by contact surfaces, which allow more relative movement. The mesh structure for bones is shown in Fig. 2. The major ligaments were attached on the corresponding points on the bones. They were defined as tension only truss elements. The analyses can offer stresses/strains among bones and ligaments, and stress distribution between the foot and the support surface. The plantar pressure distribution can be measured to validate the finite element model.

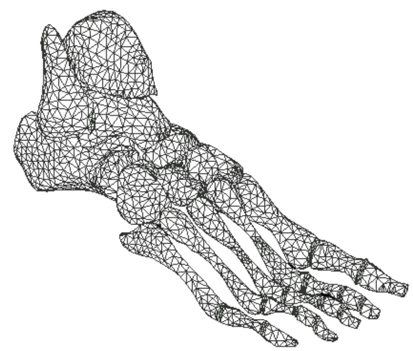

Figure 2: Mesh structure of foot bones.

RESULTS AND DISCUSSION

The present study developed a FE model and provides preliminary results on stress/strain. It can provide quantitative analysis of normal and pathological foot and ankle motion. With further improvement, correlation of various foot pathology or deformity between the corresponding biomechanical outcomes can be documented efficiently with appropriate simulation. Other potential clinical applications include studies of the biomechanical effects of varying geometrical and material factors of different structures of the foot, prediction on different surgical outcomes and orthotic performances.

SUMMARY

A 3D FE model of foot/ankle complex was developed using the actual geometry. It can offer useful information in the stress and strain among the bones and ligaments. The model can be used in clinical applications to simulate foot behaviour and to design a good foot support.

REFERENCES

Chen, W.P., *et al.* (2001). *Clin Biomech*, **16**, 614-620.
Funk, J.R., *et al.* (2000). *J Biomech Eng*, **122**, 15-22
Gefen, A., *et al.* (2000). *J Biomech Eng*, **122**, 630-639.
Jacob, S., Patil, M.K. (1999). *J Rehab Res Dev*, **36**, 252-63.

ACKNOWLEDGEMENTS
The work was supported by a research grant from The Hong Kong Polytechnic University (A/C No A-PC91).

BIOMECHANICAL ANALYSIS OF TAKEOFF TO BACK HANDSPRING AND BACKWARDS SOMERSAULT

Pia Melcher[1] and Erik B. Simonsen[2]

[1]Institute of Exercise and Sports Sciences, University of Copenhagen, Denmark (p.melcher@mai.ku.dk). [2]Anatomy Department C, Panum Institute, University of Copenhagen, Denmark.

INTRODUCTION

The body position at takeoff in gymnastics jumping (tumbling) is very important for attaining adequate height and rotation in the following jump.
Rotation can only be created during ground contact, because it requires an external force. This is a consequence of Newton's second and third laws (conservation of angular momentum).
Rotation is created if the reaction force passes outside the body's center of mass (CM). This is obtained by leaning the body either forward or backward, or by *pushing* on the ground in either forward or backward direction; which can be done by a fast hip flexion or extension.
The purpose of this study was to investigate the strategy behind the takeoff from a *round-off* to a back handspring (also called *flic flac*; FF) and from a *round-off* to a *backwards somersault* (BS). We tested the hypothesis that the body position at takeoff to the BS shows a larger inclination than the body position at takeoff to the FF and therefore a larger sagittal force. In this context, inclination is defined as when the line of action from the gravitational force falls behind the contact point of the feet.
We expected the CM to reach higher in vertical direction in the BS than in the FF. Because the mechanical energy is conserved, the peak height that the CM will reach can be calculated as $h = v^2/2g$ (v is the vertical takeoff velocity).

METHODS

Nine male elite gymnasts took part in this study (25.2yrs, 1.77m, 76.78kg). They all performed the two jumps described above.
The jumps were recorded on highspeed film (120 Hz) in the sagittal plane (2D) combined with registration of the ground reaction forces. At takeoff the subjects had one foot on the platform and the other on the floor.
The video sequences were digtised by APAS (Ariel Performance Analysis System, Ariel Dynamics Inc.). A two dimensional model with 7 segments (foot, leg, thigh, truncus, upper arm, forearm and head) was defined from the antropometric data and the video data.
Net joint moments (M) about the ankle, knee and hip joints were calculated from the ground reaction forces and the video data by inverse dynamics and normalized to body mass.
The power production (P) about a joint was calculated as the product of the joint angular velocity (ω) and the net joint moment (M).
Differences in the size of the sagittal force, Fy, jumping height and net joint moments between the two jumps were evaluated statistically by a two-tailed paired t-test. The level of significance was in all cases set to 5%. Results are given as mean ± SD.

RESULTS AND DISCUSSION

Kinetics. The force data showed that the reaction force in the sagittal direction was two times larger for takeoff to the BS than to the FF (P=0.004).

Kinematics. At takeoff to the BS the net hip moment was flexor dominated throughout the contact phase (mean peak moment 25.96 Nm/kg ± 11.27) while in the landing phase the net hip moment for takeoff to the FF initially was flexor dominated (mean peak moment 8.63 Nm/kg ± 4.50) (P=0.003), and then in the takeoff phase the moment shifted to extensor dominance. The simultaneously negative power output for the hip in BS indicated that the hip flexors worked eccentrically to keep the upper body in a more upright position at the takeoff. At the takeoff to FF the upper body extended more in the last phase of the takeoff and the power output is positive, which indicated concentrically muscle contraction in the hip extensors.
The hip joint angle changed approx. 50^o in BS (from 130^o-180^o) and approx. 80^o in FF (from 110^o-190^o), which corroborates the moment and power data.
For BS the path of CM showed a steeper rise while the path was more flat for the flic flac. In correspondance with this we saw that the jumping height was six times higher in the BS (0.50 m ± 0.07) than in the FF (0.08 m ± 0.03) (P<0.001).

Clearly, our results show that the gymnasts use different strategies in the takeoff to these two jumps although the initial movement (the *round-off*) was the same.

SUMMARY

The peak height of CM was higher in BS than in FF. The sagittal force was larger during the takeoff to the somersault than to the flic flac. The hip joint extended more in the flic flac while in the somersault the position was more upright and the angular displacement in the hip joint angle was smaller.

A METHOD FOR DETECTING THE MOMENT OF PUNCTURE USING THE FORCE PROFILE

Toshikatsu Washio[1], Kiyoyuki Chinzei[1], Hiroyuki Kataoka[2] and Kazuyuki Mizuhara[3]

[1]Institute for Human Science and Biomechanical Engineering, AIST, Tsukuba, Ibaraki, Japan, washio.t@aist.go.jp
[2]Tokyo Medical and Dental University, Chiyoda-ku, Tokyo, Japan
[3]Tokyo Denki University, Chiyoda-ku, Tokyo, Japan

INTRODUCTION

A needle insertion that is common procedure in blood sampling, biopsy and injection is one of the most popular surgical procedures. Needle insertion, on the other hand, requires high skill and much experience to stop a tip of a needle in the diseased part because a tip is not seen during needle insertion. To prevent the medical accident, especially biopsy, a needle insertion is operated with X-ray images. To avert X-ray exposure, therefore, it is necessary that a method does not depend on X-ray images to detect a moment of puncture of tissue. Generally speaking, mechanical properties of the diseased part are different from those of around the affected part. Hence, it is considered that the force profile that acts on the needle is available to detect a moment of puncture of an affected part. An objective of this study was to clarify whether the force profile was available for detection of a moment of puncture during needle insertion or not.

METHODS

The force that acted on the needle was divided into 2 parts and measured, respectively. One was the reaction force of cutting tissue by a tip of a needle. Another was friction force that acted on side of a needle during inside tissue. To measure both reaction and friction force, a load transducer consisted of 2 types of load transducer. One was the 6 axes load transducer. Another was 1 axis one (z-axis force was detected). These load transducers had same z-axis and were connected in series. Needle was divided into an inner part and an outer one. An outer part surrounded an inner one except a tip of it. An inner part was connected to 1-axis load transducer and an outer part was connected to 6-axes one. The lever of living porcine under general anesthesia was used. This experiment was approved by the Committee on Animal Experiments of Institute for Human Science and Biomedical Engineering in compliance with the Regulation for the Animal Experiment Ethics of Institute for Human Science and Biomedical Engineering. To detect a moment of puncture of tissue, video image was taken during experiment. Table 1 gives all experimental conditions.

Table 1: Experimental conditions

Insertion speed (mm/sec)	Tip types (diameters of outer needles: mm)
3 (const.)	Bevel (2), triangular pyramid (0.8, 1.2), cone (0.8, 1.2)

RESULTS AND DISCUSSION

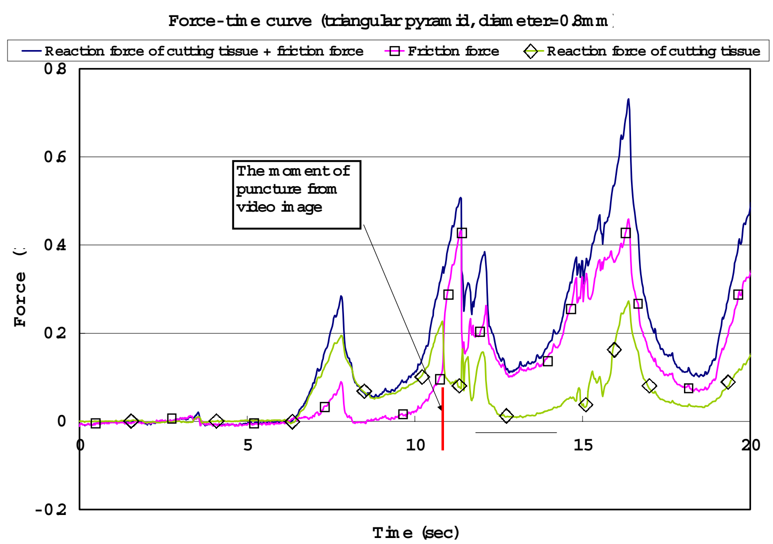

Figure 1: The force–time curve of triangular pyramid tip of needle (diameter = 0.8 mm). Vertical axis shows force (N), and horizontal axis shows time (sec). The line across the time axis shows the moment of puncture of tissue from video image.

Figure 1 shows that a force-time curve of triangular pyramid tip of needle (diameter = 0.8 mm). A reaction force decreased and a friction force increased instantaneously when tissue was punctured. These force profile patterns were shown in all experimental conditions. A whole of force that acts on needle, however, was hardly changed.

SUMMARY

In this study, force that acted on a needle during needle insertion was divided into a reaction force and a friction force and measured, respectively. As a result, it was clarified that the force profile of reaction force and friction force were available to detect the moment of puncture of tissue.

REFERENCES

Brett, P.N., et al. (1997). *Proc Instn Mech Engrs*. **211**, 335-347
Westwood, J. D., et al. (eds.) (1999). *MMVR*. IOS Press
Zivanovic, A., Davies, B. L., (2000). *IEEE Trans info tech in biomed.* **4**, 8-14

COMPARISON OF SIMULATED PROJECTILE AND BATON BLOW IMPACTS ON SHIN GUARDS USED IN CROWD MANAGEMENT INTERVENTION

Jean-Philippe Dionne, Ismail El Maach, Kevin Semeniuk, Aris Makris

Med-Eng Systems, Ottawa, Ontario, Canada
Corresponding author, jpdionne@med-eng.com

INTRODUCTION

There exists no standard procedure for testing the protection offered by shin guards used during Crowd Management Intervention (CMI). Bir *et al* (1995) investigated the impact performance of soccer shin guards, using a pendulum impactor. However, a pendulum impactor is not appropriate for generating the high level of impact energies typical of CMI. Most threats that security officers have to face in the event of a CMI can be classified into two categories: launched projectiles, and hand held blunt weapons. The Blunt Impactor (BI) and the Pitching Machine (PM) were used in the present study, to simulate these threats and assess the injury probability when subjected to blunt impacts on the leg.

Figure 1: *Blunt Impactor* (left), and *Pitching Machine* (right)

METHODS

Nine pairs of shin guards (Med-Eng Systems Inc., Canada) were tested against baseball bat blows generated by the BI and ball impacts generated by the PM (Fig. 1). The shin guards were secured to a maple wood surrogate (diameter 9cm) attached to a force platform (3 force transducers and an accelerometer). The BI uses a pneumatic system to power a baton or baseball bat. The balls used with the PM weighed 140 grams, and their velocities were measured with a radar system. Control tests were first carried out, in which the surrogate was directly subjected to the two types of threats, without any protective equipment. Tests were then performed with the protective equipment fitted on the surrogates.

RESULTS AND DISCUSSION

The forces measured are plotted against the impact energy (Fig. 2). Although injuries can occur prior to bone fracture, the force required to break bones is often used for injury thresholds. In a recent study, Porta (1996) found a higher limit of tibia fracture thresholds of 8.93 kN. Based on this threshold, it is found that much higher impact energies can be tolerated with the PM, as compared to the BI for the same impact energy, and that the shin guards provide a significant reduction in injury potential, as compared to the unprotected case.

The injury analysis presented here is conservative. The actual protection offered by the V-Top shin guard may be underestimated due to the fact that the fracture thresholds were obtained based on experiments with aged donors, soft tissues equivalent were not incorporated in the surrogate, the test surrogate was constrained, and protective equipment is designed to distribute the transmitted force over a large surface area (only a global force transmission was measured in the present study).

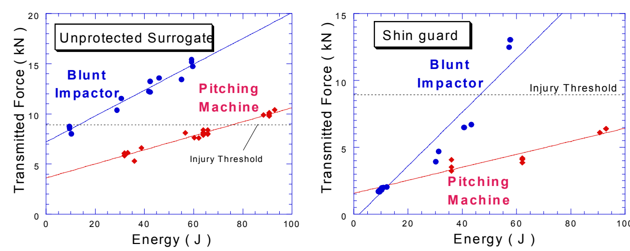

Figure 2: Peak forces for the unprotected surrogate (left) and shin guard (right) as a function of the impact energy for both threat simulators. Tibia fracture threshold shown.

SUMMARY

The above results stress the importance of wearing protection during crowd management interventions. Moreover, the large differences observed between the results obtained with the two threat simulators illustrate the large dependence on test conditions in impact tests, and the need to appropriately replicate the threats, when evaluating the protective capability of personal protective equipment.

REFERENCES

Bir, C.A., Cassatta, S.J., & Janda, D.H. (1995), *Clinical Journal of Sports Medicine*, **5**, 95-99.

Porta, D.J., (1996) The anatomy and biomechanics of experimentally traumatized human cadaver lower extremity components, Ph.D. thesis, University of Louisville

CARTILAGE DEFORMATION OF THE FELINE PATELLOFEMORAL JOINT OBTAINED FROM LASER SCANNING

Sylvain Couillard[1] and Walter Herzog[2]
Human Performance Laboratory, University of Calgary, Calgary, Alberta, Canada
[1] MSc student, Dept of Mech. Eng., sylvain@kin.ucalgary.ca, [2] Faculty of Kinesiology, walter@kin.ucalgary.ca

INTRODUCTION

It is commonly accepted that abnormal mechanical loading and subsequent articular cartilage deformation play an important role in the initiation and development of osteoarthritis (OA). We know that normal articular cartilage deforms under load, but the magnitude of this deformation in-vivo is currently uncertain. The purpose of this study was to quantify in-situ articular cartilage deformation in the feline patellofemoral joint with an improved laser scanning technique.

METHODS

To quantify articular surface deformation, two left limbs were used. A custom-built joint fixture (Couillard et al., 2000) was attached to the hindlimb before dissection. The patella and femur were then taken apart and the intact articular surfaces were scanned in 2.5 minutes with a commercially available laser scanner with a precision (2SD) below 25 µm (Couillard and Herzog, 2001). After repositioning the bones within 30 µm of their original position, the joint was statically loaded in-situ at 135 N for 4 hours and 25 minutes and chemically fixed (Hunziker et al, 1982). The bones were then separated and the deformed articular surfaces were scanned. Finally, the cartilage was removed from the articular surfaces with a bleach solution and the bone surfaces were scanned. Each surface scan comprised 57,600 data points over an area of 144 mm^2 and was repeated three times.

The median of three repeat measurements was taken, low-pass filtered, and resampled to reduce data size. The resampled surface points for the three states (unloaded cartilage, loaded cartilage, bone) were aligned using spherical ceramic bone markers. The filtered data was then modeled with interpolating thin-plate splines (Boyd et al., 1999) and subtracted along the surface normals of the unloaded surface to quantify articular cartilage surface deformation and cartilage thickness.

RESULTS AND DISCUSSION

Three-dimensional cartilage surface deformation plots were obtained and showed that cartilage from the femoral groove was compressed up to 150 µm and elevated up to 250 µm in the areas surrounding the contact (Figure 1). The contact area was 23.4 mm^2, which gives a pressure of approximately 5.8 MPa. Theses values compare well with other results obtained in-situ (Clark et al., 2002). Cartilage thickness measurements were not entirely reliable since negative values were obtained. We suspect that cartilage translucency allowed for refraction and internal reflection of the laser beam through the cartilage layer. We suggest that a thin uniform layer of reflective coating be used on the articular surface to avoid this problem. Results for the patella were difficult to obtain since the number of bone markers on the patella was insufficient to allow for three-dimensional surface alignments.

This improved laser technique, based on Haut et al. (1998), had an accuracy of 2.9 µm on an inert surface. It allowed to quantify articular cartilage surface deformation with an estimated accuracy of approximately 100 µm, and a precision less than of 30 µm. The approach developed here may prove useful when attempting to correlate cartilage mechanics to structural deformation (chondrocytes, collagen fibres), and the corresponding biosynthetic response.

REFERENCES

Boyd, S. K. et al. (1999). *J Biomech Eng* **121**: 1-8.
Clark, A.L. et al. (2002). *J Biomech* **35**(1): 53-60.
Couillard, S. et al. (2000). *Arch Phys Biochem* **108**(1-2): 179.
Couillard, S. and Herzog, W. (2001). *Proceedings of the XVIIIth Congress of the ISB* 292-3.
Haut, T. L., et al. (1998). *J Biomech* **31**(6): 571-577.
Hunziker, E.B. et al. (1982). *J Ultrastruct Res* **81**: 1-12.

ACKNOWLEDGEMENTS

Tim Leonard, Andrea Clark, Leona Barclay, Vincent Péry, Olivier Desvignes, NSERC, Olympic Oval Endowment Fund

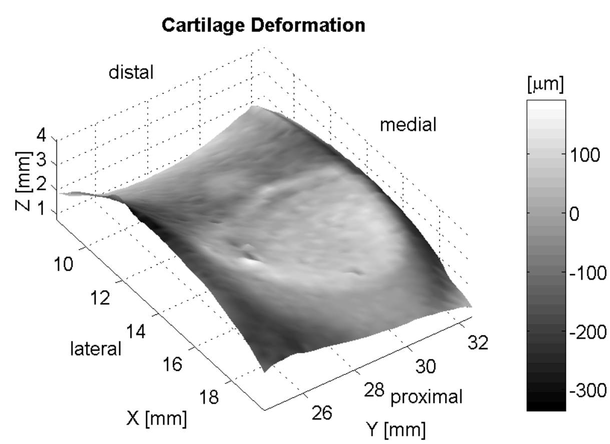

Figure 1: Articular cartilage deformation of a feline femoral groove caused by an in-situ static load of 135 N. Positive values indicate compression.

IN VIVO RABBIT PATELLAFEMORAL JOINT LOADING VIA MUSCLE STIMULATION

*Sean Craig and *Walter Herzog

*Human Performance Laboratory, The University of Calgary, 2500 University Dr NW, Calgary, Alberta Canada. T2N 1N4
Email: sttcraig@kin.ucalgary.ca

INTRODUCTION

It is generally accepted that mechanical loading of musculoskeletal tissues may cause injuries and diseases such as the tennis elbow, carpal tunnel syndrome, and osteoarthritis. However, the mechanisms underlying the relationship between loading and disease/injury are ill understood. It is not even understood why an apparently similar loading condition (for example at the work place) may cripple one person while leaving another completely unaffected. Here, we attempt to gain insight into the relationship between mechanical loading of articular cartilage and the corresponding biological (adaptive or degenerative) response. Typically, the relationship between articular cartilage loading and biological response is determined for in vitro explants. The importance of these in vitro studies for in vivo functioning is not known. Therefore, we wanted to establish a protocol to investigate the relationship between controlled, physiological joint loading and the corresponding articular cartilage response.

METHODS

Eight skeletally mature (1 year old) female New Zealand white rabbits were used. The Rabbits were anesthetized using Isoflurane and prepared for the loading procedure (both hind limbs shaved). They were then placed supine on a custom made experimental platform with the right leg secured to a force transducer bar, in order to measure the knee extensor moments produced by the quadriceps muscles (Forces were recorded using Windaq® data recording software). Mechanical loading was produced in vivo in the rabbit patellofemoral joint through knee extensor activation. Loading was created via surface electrodes controlled by a Grass S88 stimulator. The loading protocol consisted of one hour of cyclic loading. Loading was brought about by stimulating the extensors once every 30 seconds for a duration of 1 second. This was done so that 80% of maximal force was attained throughout the 1 hour. Upon completion of the 1 hour loading protocol, cartilage from the retropatellar surface and patella femoral groove (of both the experimental/right and contralateral control/left leg) was harvested, and incubated in 24-well plates in 1mL of medium (DMEM with 1% penstrep). Samples of medium were collected at 1, 8, 24, and 48 hours post loading and immediately frozen (-20 ºC). Fluid samples were then tested for the presence of Sulfated Proteoglycans (sPG's), by a known dimethylmethylene blue (DMMB) assay.

RESULTS AND DISCUSSION

In this initial study, relating the mechanical loading of a fully intact joint to the corresponding biological response, we wanted to establish a method for the non-invasive, high level, and consistent loading of the intact rabbit knee while continuously monitoring and controlling the amount of loading. We were successful with the current protocol to produce approximately 80% of the initial maximal isometric response throughout this one hour loading period (Fig. 1.)

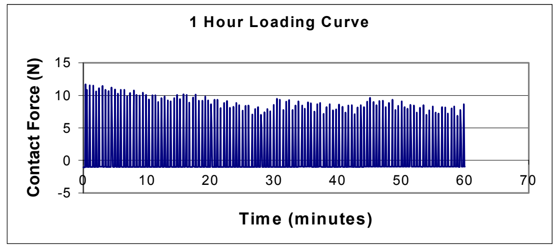

Figure 1. Sample force curve for 1 hour loading protocol

Since the forces applied to the patellofemoral joint were within the physiological range, and since the forces were applied by knee extensor contraction to the fully intact knee, we expected to see a positive loading response that would be associated with an increase in sPG production in the loaded compared to the contralateral, unloaded control cartilage. Our preliminary data, based on two independent observations per time point, do not support this hypothesis, as sPG values were similar at each time point of sample collection (Table 1.) The increase of sPG from 1 hour to the values obtained at 8, 24, and 48 hours in both, the experimental and contralateral knee articular cartilage cannot be explained at present.

In order to understand articular cartilage adaptation or degeneration, it is essential to know that biological response to physiological loading conditions. This type of research has typically been done by loading articular cartilage explants (Kurz, 2001), or by impacting joints via external devices. (Ewers, 2001) We feel that such attempts are ultimately of little relevance to what happens in an intact joint subjected to in vivo muscular loading. This study, hopefully, will be a first step towards gathering this physiologically relevant information.

Table 1. Mean data for DMMB assay.

Hours Post Loading	Experimental (ug/g of cartilage)	Control (ug/g of cartilage)
1	47 ± 25	39 ± 13
8	114 ± 24	113 ± 15
24	128 ± 24	128 ± 25
48	141 ± 25	135 ± 22

REFERENCES

Kurz, B. et al (2001). *Journal of Orthopaedic Research*, **19**, 1140-1146.
Ewers, B.J. et al (2001). *Journal of Orthopaedic Research*, **19**, 779-784

IN VIVO CHANGES IN MUSCULAR ACTIVATION BEFORE AND AFTER ANTERIOR CRUCIATE LIGAMENT TRANSECTION IN THE FELINE HINDLIMB

Meredith MacNaughton[1], Tim Leonard and Walter Herzog
Human Performance Laboratory, University of Calgary, Calgary, Alberta, Canada
[1] meredith@kin.ucalgary.ca

INTRODUCTION

Transection of the anterior cruciate ligament (ACL) in the cat knee has been established as a reliable model of osteoarthritis (OA). In the past, ACL transection models have attributed the onset of OA to the instability of the joint following ACL transection. We believe that part of the joint degeneration maybe associated with the loss of motor function in the relevant hindlimb muscles. Since there is no evidence showing long-term muscle activation patterns in any osteoarthritis model we wanted to, as a first step, establish whether muscle coordination following ACL transection might be changed. Based on preliminary data, we hypothesize that some of the muscle coordination patterns, such as that of semitendinosus, might change dramatically post ACL transection in order to compensate for the loss of the mechanical function of the transected ACL. Furthermore, some of the limb extensor muscles, such as triceps surae and rectus femoris, might be greatly inhibited and thus produce erratic EMG signals.

METHODS

One adult male cat was trained to walk on a motor driven treadmill at speeds ranging from 0.4m/s to 0.7 m/s. Under sterile conditions, indwelling, bipolar EMG electrodes with an interelectrode distance of about 5 mm were imbedded into the midbelly of eight muscles in the left hindlimb: the vastus lateralis (VL), semimembranosus (SM), semitendinosus (ST), rectus femoris (RF), soleus (SOL), medial gastrocnemius (MG), tibialis anterior (TA) and extensor digitorum longus (EDL). The EMG wires were then fed subcutaneously to the back of the cat. Here the leads were soldered to their corresponding terminals on a 50g, eight channel connector (backpack) secured by four sutures. EMG data were collected before surgical intervention, after a sham ACL transection, and post ACL transection for slow (0.4m/s) and, when possible, for fast (0.7m/s) treadmill walking. The ACL transection of the left hindlimb was confirmed *in vivo* (by anterior drawer tests). The experimental protocol was reviewed and approved by The University of Calgary Animal Research and Ethics Committee.

RESULTS AND DISCUSSION

Preliminary data show distinct changes in the activation patterns of most muscle recordings. The limb extensors, specifically, which initially manifested continuous activation patterns during the stance phase, began to exhibit sporadic bursts during the activation phase post ACL transection (Figure 1). Furthermore, we found that over time, the burst-like activation of the extensors became more normal (i.e. continuous; data not shown). Finally, we found that following the sham surgery, the activation patterns remained unchanged (i.e. continuous; data not shown) suggesting that the observed change in activation patterns post ACL transection were caused by the physical transection of the ACL and the corresponding instability of the knee, and not the surgical intervention.

CONCLUSION

Sham transection of the ACL did not cause a change in the activation patterns of major hindlimb muscles in the cat, whereas the actual ACL transection did. Specifically, the hindlimb extensors displayed an abnormal burst-like pattern post ACL transection that would likely have caused the corresponding jerk-like patterns in muscular forces, as found by Hasler et al.,(1998). These preliminary results leave open the hypothesis that loss of neuromotor control might play an important role in joint degeneration in general, and in the development of osteoarthritis, specifically.

REFERENCES

Hasler, E.M., Herzog, W., Leonard, T.R. Stano, A. and Nguyen, H. (1998). *In vivo* knee joint loading and kinematics before and after ACL transection in an animal model. *J. Biomechanics* **31**, 253-262

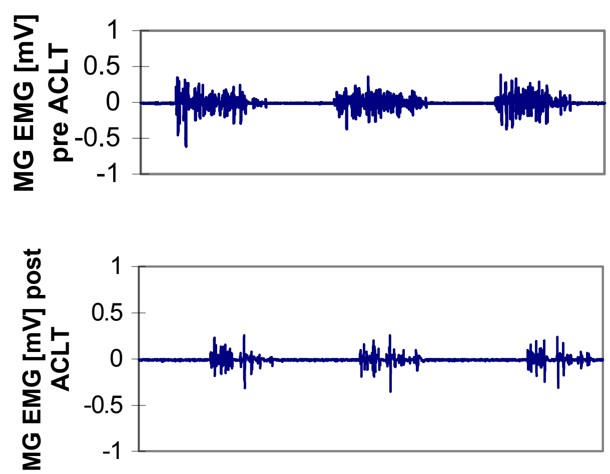

Figure 1. Medial Gastrocnemius EMG in the experimental hindlimb during consecutive step cycles before and after ACL transection . The MG EMG shows abnormal burst-like patterns post ACL transection.

WOLFF'S LAW OF CANCELLOUS BONE AS A SOLID-LIQUID TWO-PHASE BODY

Gang Qinguo[1,2] Hua Zhuxin[2] and Yang Guitong[3]

[1]Department of Kinesiology, University of Waterloo, Ontario, Canada
[2]City College, Hebei University, Baoding, Hebei Province, PRChina, 071002
[3]Institute of Applied Mechanics, Taiyuan University of Technology, Shanxi Province, PRChina

INTRODUCTION

The physiological structure of cancellous bone is composed of the trabecular architecture and the tissue fluid , which is full of the porous skeleton. Therefore, from the microscopic view, the cancellous bone is a typical solid-liquid two-phase body. The Wolff's law, which was put forward by Wolff , describes the relationship between the trabecular architecture and the principal stress in the cancellous bone. Some researchers had given the mathematical formations of this law[1-2]. But, in there papers,the cancellous bone was as the elasticity. In our paper, we will discuss the formation of the Wolff's law when the cancellous is as the solid-liquid two-phase body.

In the paper [1], the Wolff's Law is :

$$H:\sigma = \sigma : H \qquad (1)$$

H is the fabric tensor and σ is the stress tensor. This formation only showed that the direction of the principal stress in the trabecular architecture was the same as the one of the fabric tensor. In the paper [2], Turner further provided a quantitative form of the Wolff's law, which was :

$$\left|\sigma_i\right| = \alpha H_i^{\,3} \qquad (2)$$

i=1,2,3. α is a constant. σ_i and H_i are the principal stress and the principle component of H. In this paper, we consider the above formations of the Wolff's law as the relation between the trabecular architecture and the stress in the trabecular, not the stress in the cancellous bone. So, we provided an new formation according the two-phase theory.

CONSTITUTIVE RELATIONS OF MEDIA WITH POROUS

The media with porous often shows the anisotropic mechanical properties. It's constitutive equations are :

$$\sigma = E:\varepsilon \qquad (3)$$

ε is the stain tensor, and E is the elastical tensor.

The anisotropic mechanical properties of the media with porous was mainly decided by it's microscopic structure. Then, according to the knowledge in the structure mechanics, E is further expressed as :

$$E = E_1 : E_0 \qquad (4)$$

$E_0$is the elastical tensor of the component of media. E_1 is the function of the geometric structure form in the media, and called the geometric tensor in this paper. Substituted (4) into (3), we obtained:

$$\sigma = E_1 : E_0 : \varepsilon = E_1 : \sigma_0 \qquad (5)$$

σ_0 is the stress in the component of media. The relation between σ_0 and ε show the mechanical properties of the component. In the (4), the component was as the linear elasticity. If the component has the mechanical properties of liquid, the second equation in (5) is also used.

WOLFF'S LAW OF CANCELLOUS BONE

In this section, the cancellous bone was as a two-phase body. So, according to the mixture theory[3], the total stress σ is :

$$\sigma = \sigma_1 + \sigma_2 \qquad (6)$$

σ_1 is the stress in the trabecular architecture , and σ_2 is the stress in the tissue fluid . Based on the results in the last section, σ_2 can be:

$$\sigma_2 = E_2 : \sigma_{20} \qquad (7)$$

E_2 and σ_{20} are the geometric tensor and the stress tensor of the tissue fluid. Further, the decomposition of σ_{20} is :

$$\sigma_{20} = S_{20} + pI \qquad (8)$$

I is the identity tensor, p is the mean normal stress and S_{20} is the deviatoric stress tensor. With the forms (6) and (7), we obtained:

$$\sigma_1 = \sigma - \sigma_2 = \sigma - E_2 : S_{20} - \alpha_2 p \qquad (9)$$

α_2=E_2:I is a tensor. Substituted (9) into (1) and (2), it showed :

$$H:(\sigma - E_2 : S_{20} - \alpha_2 p) = (\sigma - E_2 : S_{20} - \alpha_2 p) : H$$

$$\left|(\sigma - E_2 : S_{20} - \alpha_2 p)_i\right| = \alpha H_i^{\,3}$$

(10)

which were the Wolff's law of cancellous bone as the two-phase body.

SUMMARY

The formations (10) showed that H was the functions of σ, S_{20} and p. If one of them is changed, H will change with it.

ACKNOWLEDGEMENTS

The authors would like to acknowledge the finanical assistance of the NNSF (PRChina, 39670201)

REFERENCES

[1] Cowin S.C.(1986). *Wolff's Law of Trabecular Architecture at Remodeling Equilibrium. ASME J Biomech Eng*, 108,83-88.
[2]Turner C.H.(1992). *On Wolff Law of Trabecular Architecture. J Biomechanics,* 25,1-9.
[3]R.de Boer.(2000).*Theory of Porous Media.Springer*.

MICROINDENTATION METHODS FOR EVALUATING ELASTIC AND VISCOUS PROPERTIES OF SOFT TISSUES

Narendra K. Simha[1], Namani Ravi[1] and Jack L. Lewis[2]

[1]Department of Mechanical Engineering, University of Miami, Miami, Florida, USA
[2]Department of Orthopaedic Surgery, University of Minnesota, Minneapolis, Minnesota, USA

INTRODUCTION

Microindentation offers significant advantages for mechanical characterization of soft tissues like articular cartilage (AC). It requires minimal specimen preparation, can test mm-size specimens, can provide a detailed spatial distribution of properties, and for AC, it simulates in vivo loading. However, conventional methods (Oliver & Pharr, 1992) do not account for time-dependent and large deformation behavior of soft tissues. Here, alternate model-based simulations are explored.

METHODS

Experimental details are provided in the companion paper (Lewis & Simha, 2002). Here we focus on simulations. A FEM model of the indentation contact problem was constructed using ABAQUS. Length units are in μm and 1600 axisymmetric, quadrilateral, bilinear, hybrid elements were used for the hyperelastic incompressible tissue. Indenter is rigid and contact is frictionless. Elastic parameters will be evaluated by minimizing the error between predicted and measured force-displacement curves; similarly, viscous parameters can be evaluated from creep data. Fortran minimization routines are coupled with ABAQUS simulations using the PYTHON programming language. In indentation tests, force-displacement curves are the only measurement, hence the guiding principle is to choose the simplest possible constitutive model that predicts these curves. A quasilinear viscoelastic model with nonlinear elastic and linear viscous properties will be adopted for AC. Nonlinear elasticity is modeled by Mooney-Rivlin energy density with parameters C_1 and C_2 or exponential energy with parameters B_1 and B_2. The viscous relaxation is a two-term exponential function. A procedure for evaluating model-parameters is outlined.

RESULTS

So far, FEM simulations have been performed for the large deformation Mooney-Rivlin model. Parametric studies show that varying the sum C_1+C_2 (at fixed C_1/C_2) has a stronger effect than varying C_1/C_2 (at fixed C_1+C_2). For instance, doubling (C_1+C_2) from 1 to 2 MPa causes a 100% increase in force (see Fig 1), whereas changing C_1/C_2 from 2 to 4 causes a 10% decrease in force. By examining small displacements superposed on biaxial stretch, Beatty & Usmani (1973) obtain $P=\mu\,(16\tan\alpha/\pi)(C_1+C_2)D^2$ for a conical tip with included angle 2α. However, Costa and Yin (1999) show the quadratic form is valid only for indentation depths less than 10% of the tissue thickness. Hence, quadratic fits with coefficient β to curves shown in Fig 1 for D<150μm resulted in μ=0.274 and the correlation $(C_1+C_2) = 0.297\,\beta$.

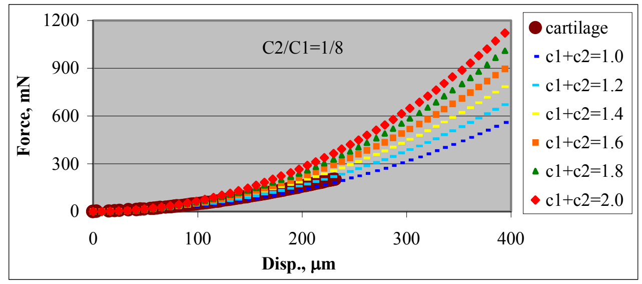

Figure 1: Force-displacement curves at fixed C_1/C_2=8

The minimization procedure to extract material properties is demonstrated by using the loading part of an indentation test with D_{max}=230μm (see Fig 1). A quadratic fit to D<150μm data and the above correlation gave (C_1+C_2)=1.2MPa. Using initial guesses of C_1/C_2 =2 and 16, the minimization procedure obtained the values C_1=0.96MPa and C_2=0.24MPa in two iterations.

Other important results from the parametric studies are: 1) The resolution for the 67° tip is $R=0.375D_{max}$ where R/2 is the radial distance at which the strain energy decreases to 1% of its maximum value. 2) The deformation beside the conical tip is primarily a shear. 3) The contact area predicted by FEM model at D_{max}=400μm is 63.4% smaller than linear elastic results (indicating need for large deformations). 4) Rounding the conical tip with a sphere of radius 53μm increases the predicted area by 28.8%

This is ongoing work; detailed results for the exponential energy and viscous parameters will be presented at the conference. These will provide a basis for finding the elastic and viscous properties of AC and other soft tissues from micro and AFM-type indentation tests. A related issue is the fracture toughness of AC. At high forces conical tips penetrate AC by tearing the surface, and new methods for fracture toughness are being developed (Lewis and Simha, 2002). A critical step involves the separation of the input work during penetration into fracture work and viscoelastic work. By providing estimates for the viscoelastic work, this study will help validate methods for fracture toughness.

REFERENCES

Beatty, M.F. and Usmani, S.A. (1975) *Quart J Mech Appl Math*. **28**: 47-62
Costa, K.D. and Yin, F.C.P. (1999) *J. Biomech. Engng*., **121**: 462-471
Lewis, J.L. and Simha, N.K., (2002) *abstract submitted to IV WCB*
Oliver, W.C. and Pharr, G.M. (1992) *J. Mat. Res*. **7**:1564-1583

SENSITIVITY OF A HILL BASED MUSCLE MODEL TO PERTURBATIONS IN MODEL PARAMETERS

Carol Y. Scovil and Janet L. Ronsky

Human Performance Laboratory and Department of Mechanical Engineering
University of Calgary, Calgary, Alberta, Canada. jlronsky@ucalgary.ca, www.ucalgary.ca/~cyscovil

INTRODUCTION

Hill muscle models are commonly used in musculo-skeletal models to predict muscles forces (Zajac 1989). The model can take several forms. In this study three common elements will be discussed. 1. The contractile element (CE) generates force, taking into account force-length (FL) and force-velocity (FV) muscle properties. 2. The series elastic element (SE) models the tendon, aponeurosis, and soft tissue stretch. 3. The parallel elastic element (PE) models the passive properties of the muscle fibers. In some studies, PE is ignored, in other models, pennation angle or viscous elements are considered. For any muscle model properties must be taken from literature. No one study includes all values necessary to describe properties of the muscle; they must be compiled from several sources. In addition, different studies have found a range of values for these parameters. There has been no evaluation of the effect the values used to create muscle models have on the resulting muscle output. The purpose of this study was to evaluate the sensitivity of the muscle model to perturbations in each of the parameters during physiological movement.

METHODS

The Hill based muscle model described in Nagano and Gerrisen (2001) was used to model the muscle forces in the forward dynamics running model of Wright et al. (1998). This model was able to match the kinematics and ground reaction forces from experimentally determined running within two standard deviations. At each timestep, the inputs for the muscle model were the lengths of the muscle (L_{MUS}) and the contractile element (L_{CE}). The outputs from the model were the force in the muscle (F_{MUS}), and the velocity of the contractile element (V_{CE}), to allow the integration of L_{CE} for the next timestep. To evaluate the sensitivity of the model, L_{MUS} and L_{CE} for the rectus femoris (RF) were taken from the running simulation, and F_{MUS} and V_{CE} were calculated throughout stance phase. This ensured a physiological range of muscle lengths. The muscle model parameters were varied from those used in the model by a factor of 0.5 to 1.5. F_{MUS} and V_{CE} were compared to the original model output, and ranked according to the amount of change observed. (Table 1)

RESULTS AND DISCUSSION

The muscle model was very sensitive to changes in L_{SEsl} and U_{SE}. V_{CE} was also sensitive to changes in L_{CEopt}, F_{ASYMP} and WIDTH. These are the parameters with which the modeler should take the most care in using values from literature. The muscle parameters summarized in Yamaguchi et al. (1990) list, for the RF, values of 0346-0.410 m for L_{SEsl}, and a range in L_{CEopt} of 0.055-0.084 m. This sensitivity analysis further emphasizes how important the choice of these parameters is. The muscle model is somewhat sensitive to F_{MAX} and SF. Variations in the parameters A_{REL}, B_{REL} and SL have little effect on model ouputs. Similar sensitivity was observed in the other muscles in the leg. The assumption that the PE does not affect forces during running is confirmed by this study. Likely, this is applicable to other movements that do not take the muscle to extreme ranges of motion. It seems reasonable that the PE could be ignored in models of locomotion.

SUMMARY

Parameters of the Hill muscle model have a varying sensitivity to small changes in their value. Care should be taken when using parameters from literature that the model is most sensitive to: L_{SEsl}, U_{SE}., L_{CEopt}, F_{ASYMP} and WIDTH. The PE may be ignored in muscle models used with locomotion.

REFERENCES

Nagano A, Gerrisen KGM. (2001) *J.App.Biomech.* **17,** 113-28
Wright, I.C. et al. (1998). *Clin. Biomech.*, **13**, 521-31
Yamaguchi GT. et al.(1990) in *Multiple Muscle Systems*, Ed: Winters JM, Woo SL., Springer-Verlag, New York. 717-74
Zajac, F.E. (1989). *Crit. Rev. Biomed. Eng.*, **17**, 359-411

ACKNOWLEDGMENTS: Dr. Gerald Cole.
Funding: NSERC, AHFMR, CEMF, University of Calgary.

Table 1: Parameters in the muscle model. Sensitivity of the model classified as: 1) None: no change due to perturbation. 2) Small: change of much less than the perturbation. 3) Linear: change of similar magnitude to the perturbation. 4) Large: change far larger than the perturbation. 5) Extreme: change in the resulting value by a factor of 50 or greater. Values marked * are specific to the RF.

Parameter	Definition	Initial Value	F_{MUS} Sensitivity	V_{CE} Sensitivity
A_{REL}	constant in hyperbolic FV equation	0.41	None	Small
B_{REL}	constant in hyperbolic FV equation	5.22 s^{-1}	None	Small
F_{ASYMP}	force where the FV curve becomes asymptotic	1.5 F_{MAX}	None	Large
F_{MAX}	maximum isometric force	*1560 N	Linear	None
L_{CEopt}	length of fiber (the CE) at F_{MAX}	*0.084 m	None	Large
L_{PEsl}	slack length of the PE	1.4 L_{CEopt}	None	None
L_{SEsl}	slack length of the SE	*0.346 m	Extreme	Extreme
SF	eccentric/concentric FV curve slopes as $V \to 0$	2	None	Linear
SL	slope of asymptote in FV curve	200 s^{-1}	None	Small
U_{PE}	force in PE at max. L_{CE} before F = 0	0.5 F_{MAX}	None	None
U_{SE}	stretch in SE at F_{MAX}	0.04	Large	Extreme
WIDTH	width of parabola in FL curve	*1.44	None	Large

EVALUATION OF 3D KNEE KINEMATICS WITH AND WITHOUT PLANTAR ORTHOPAEDIC PROCESSING

Mathieu Tremblay, Nicola Hagemeister, Michel Pelletier, Jacques De Guise

Laboratoire de recherche en imagerie et orthopédie (LIO), Centre de recherche du CHUM, Hôpital Notre-Dame, Montréal , Québec , Canada
mathieu.tremblay@umontreal.ca

INTRODUCTION

Although plantar orthoses are regularly prescribed to correct lower limb kinematics, only few studies evaluated in a quantitative and non-invasive way the effect of plantar orthoses on knee kinematics. Our research group developed an non-invasive harness allowing three-dimensional (3D) assessment of knee kinematics while limiting errors caused by soft tissue movements with respect to underlying bones[1-3]. The purpose of this feasibility study was to evaluate the capacity of the harness to detect small variations of knee kinematics following orthotic treatment of rear foot valgus.

METHODS

For a preliminary study, four female subjects aged between 16 and 54 years (m = 27.3; S = 18.0) were selected. All presented a rear-foot valgus greater than 5°. One subject was evaluated for both left and right knees. The orthoses types used were Bioptech and Biopform (Bi-Op, Joliette, Canada). The Bioptech is a semi-rigid orthosis with high control and Biopform is flexible and exerts a lighter control. The subjects were wearing standardized sandals and were asked to walk on a tread mill at comfortable speed without orthosis, with Biopform and with Bioptech. Order of testing was selected randomly before the experiment. Real time recording of the bone's space position was performed via infra-red emitting diodes which were attached non-invasively on the harness and a system of three cameras (Optotrak, Northern Digital, USA). The harness allows to measure the knee movements in the sagittal, frontal and transverse plane with an average precision of 0.4° for the abduction/adduction and 2.3° for tibial rotation movements[2].

RESULTS AND DISCUSSION

Results showed that, depending on the subject, immediate effect of foot orthotic treatment on 3D knee kinematics could vary. In 4 of 5 cases, decreased internal tibial rotation of the knee was observed when subjects walked with the orthoses compared to the walk without orthosis. In two cases, an increase of knee adduction was also observed. In one subject, however, decreased adduction was observed, which seems to be an adverse effect of the orthosis in this case. Figure 1 shows an example of a subject for whom an increase of adduction was observed with the wear of the Bioptech orthosis, whereas the Biopform orthosis had no effect.

Most observed effects are in accordance with the desired correction of orthoses as well as the work presented in the literature. For example, a study[4] using cortical pins showed a decrease of internal tibial rotation after rear-foot valgus reduction. Nevertheless, more subject must be evaluated, to be able to perform quantitative and statistical analysis of results. Altogether, 30 patients will be assessed during the study.

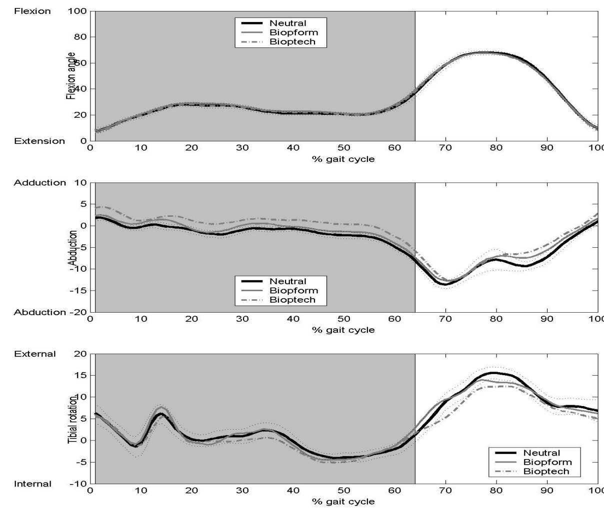

▲Figure1: 3D kinematic curves for subject #2. Black lines represent knee joint angles during gait without orthosis. Grey dotted lines give the acquisition error (mean standard deviation). Grey dotted lines represent gait with Bioptech orthosis. Grey plain lines represent gait with Biopform orthosis. Only stance phase of gait was analysed (grey part of the figure). A: Flexion/extension curve, flexion positive; B: Ab/adduction curve, Adduction positive; C: Internal/external tibial rotation, external rotation positive.

SUMMARY

This study aimed at assessing the effect of plantar orthopaedic processing on 3D knee kinematics. Preliminary results on five knees (four subjects) showed that the method allowed to detect small variations in 3D knee kinematics during gait on a tread mill when a foot orthosis was inserted in standardized sandals, compared to gait without orthosis More patients are required to perform quantitative and statistical analysis.

REFERENCES

1. SATI M ET AL. Quantitative assessment of skin movement at the knee. *Knee* 1996;3:121-38.
2. SATI M ET AL. Improving in vivo knee kinematics measurements: application to prosthetic ligament analysis. *Knee* 1996;3:179-90.
3. GANJIKIA S ET AL. 3-D knee analyser validation by simple fluoroscopic study. *Knee* 2000;7:221-31.
4. LAFORTUNE M et al. Foot inversion-eversion and knee kinematics during walking. *J Orthop Res* 1994;12:412-20.

ACKNOWLEDGEMENTS

We thank Isabelle Lévesque for her contribution to this study and Maxime Van de Putte and Gerald Parent for their assistance.

THREE-DIMENSIONAL FINITE ELEMENT ANALYSIS OF THE ACL UNDER ANTERIOR TIBIAL LOADS

Georges Limbert[1, 2], Mark Taylor[2] and John Middleton[1]

[1]Biomechanics Research Unit, University of Wales, College of Medicine, Cardiff, UK, LimbertG@cardiff.ac.uk
[2]Bioengineering Science Research Group, School of Engineering Sciences, University of Southampton, Southampton, UK

INTRODUCTION

The anterior cruciate ligament (ACL) plays an essential role in knee stability and is the most commonly injured ligament of the human body. Stress and strain distributions within the ACL are key elements for the general understanding of its mechanical behaviour and failure mechanisms in extreme conditions. Finite element (FE) analysis techniques are helpful in conducting this kind of investigation. The common assumption of mechanical isotropy of the ACL has been shown to lead to unrealistic results (Limbert and Taylor, 2001). In this study, a constitutive 3D transversely isotropic finite element (FE) model for the ACL is proposed in order to circumvent these limitations. The model is tested under simulated clinical testing procedures: a drawer test and a Lachman test.

METHODS

A 3D FE constitutive model of the ACL was implemented in the commercial FE code ABAQUS/Standard (HKS, Inc., Pawtucket, RI, USA). The ACL is assumed to be a fibre-reinforced composite material where collagen fibres are embedded in a compliant solid matrix. The constitutive law is based on the definition of an incompressible transversely isotropic hyperelastic strain energy function ψ:

$$\psi = \psi_m(I_1, I_2) + f(\lambda) = c_1(I_1 - 3) + c_2(I_2 - 3) + f(\lambda) \qquad (1)$$

where ψ_m represents the mechanical contribution from the matrix and $f(\lambda)$ that of the fibres. I_1, I_2 are the first two principal invariants of the right Cauchy-Green deformation tensor **C** and λ, the stretch in the local fibre direction, is an invariant characterizing the anisotropic properties. Structural properties of the ligaments lead to the following choice for f:

$$f(\lambda) \text{ is such that } \frac{df(\lambda)}{d\lambda} = \begin{cases} 0 & \text{if } \lambda \le 1 \\ c_3[e^{c_4(\lambda-1)} - 1]/\lambda & \text{if } \lambda \ge 1 \end{cases} \qquad (2)$$

c_i, (i=1..4) are material parameters which were determined from experimental data (Pioletti, 1997). Stress and elasticity tensors were derived from ψ (Limbert and Taylor, 2002). The geometry of the insertion sites of the ACL were obtained from a previous experiment performed on a cadaveric knee. The 3D geometry of the ACL was built by connecting these two surfaces.

Passive knee flexions were performed and the kinematics of these tests were used as displacement driven boundary conditions for the following FE analyses:

1. Lachman test: knee flexed at 30^o and then anterior tibial displacement of 4mm.
2. Drawer test: knee flexed at 90^o and then anterior tibial displacement of 4mm

These FE analyses were also repeated by considering the existence of an initial force of 135 N present in the ACL when the knee is at full extension.

RESULTS AND DISCUSSION

During knee flexion, isotropic models of the ACL generate high non physiological compressive stresses at the tibial insertion site in the posterior part of the ACL. The model proposed here was able to address this issue and has shown that the anteriormedial band of the ACL carries the maximum load during the flexion. This feature has also been observed in experimental studies (Butler et al., 1992). At 30 and 90^o of knee flexion the maximum von Mises (vM) stresses were respectively 2.68 and 6.36 MPa and were located on the anteromedial part of the ACL at the femoral insertion site. The location of maximum stress is related to clinical reports which show that injury of the ACL mostly occurs at the femoral insertion site. For the Lachman and drawer tests the maximal vM stresses were respectively 6.15 and 9.69 MPa whilst the total resultant forces within the ACL were respectively 30 and 35 N. It is now widely accepted that the ACL is composed of two main fibre bundles. These bands have different lengths and mechanical properties. This issue has not been addressed in the present model, but may have a significant influence on the pattern of deformation, and thus the stress within the ACL.

REFERENCES

Limbert, G. and Taylor, M. (2001). *Comp. Meth. Biomech. Biomed. Eng. -3*, Gordon & Breach, London, 355-360.
Pioletti, D. (1997). *PhD Thesis*, EPF, Lausanne, Switzerland.
Limbert, G. and Taylor, M. (2002). *Int. J. Sol. Struct*.
Butler et al. (1992). *J. Biomech*., (**25**) **5**, 511-518.

ACKNOWLEDGEMENTS

Prof. M.A.R. Freeman, Dr. V. Pinskerova and Dr. S. Martelli are acknowledged for providing the experimental data.

QUASI-LINEAR VISCOELASTIC MODELING OF TAIL TENDON FASCICLES FROM TRANSGENIC MICE

Dawn M. Elliott[1], Paul S. Robinson, Jon A. Gimbel, Joseph J. Sarver, Renato V. Iozzo, Louis J. Soslowsky
McKay Orthopaedic Research Laboratory, University of Pennsylvania. [1]delliott@mail.med.upenn.edu

INTRODUCTION Tendon is primarily composed of aligned type I collagen fibers in an amorphous extrafibrillar matrix of proteoglycan, glycosaminoglycan, and water. This structure and composition results in a nonlinear, viscoelastic, and anisotropic tissue. Tendon's elastic behavior is generally considered to arise from the collagen fibers, while the viscoelastic behavior is generally considered to arise from the extrafibrillar matrix. However, little quantitative data exists to formally supports these concepts. The objective of this study was to use quasi-linear viscoelastic modeling to quantitatively examine mechanical properties in mouse tail tendons with genetically engineered alterations of extracellular matrix proteins.

METHODS Tendon fascicles were prepared from the tails of three mice from each of the following genetically engineered or control groups: 8 week decorin knockout (DKO8, n=8 fascicles), 8 week reduced type I collagen (C1M8, n=9 fascicles), 3 week control (CTL3, n=7 fascicles), and 8 week control (CTL8, n=14 fascicles). Incremental stress-relaxation experiments in tension were performed as described previously (Gimbel et al, 2002). Briefly, a displacement corresponding to 0.5% strain was applied, held for a 10 min relaxation period, and repeated until failure.

The Quasi-Linear Viscoelastic (QLV) model proposed by Fung (1968) was used fit to the stress-relaxation data. This model combines elastic and time-dependent components of the stress-strain response using the convolution integral of $\sigma(\varepsilon,t)= G(t) * \sigma^e(\varepsilon)$. The reduced relaxation function (G) was defined as, $G(t)=\dfrac{1-0.577C-C\ln(t/\tau_2)}{1+C\ln(\tau_2/\tau_1)}$, and the elastic stress response as, $\sigma^e(\varepsilon)=A(e^{B\varepsilon}-1)$ (Woo et al, 1981). Each relaxation step was curve-fit using a custom-written Matlab program and the two elastic parameters (A and B) and three viscous parameters (C, τ_1, τ_2) were determined. For each fascicle, the average value of each parameter was calculated over four strain increments. A total of 7-14 fascicles were tested for each group. Between group differences were evaluated with an ANOVA followed by a Fisher's LSD post-hoc test with significance set at $p<0.05$.

RESULTS AND DISCUSSION The stress-relaxation response was well-described by the QLV model averaged over four strain increments. Significant differences between the elastic and viscoelastic parameters among the four groups existed (Table). Average parameters were used to graphically depict the elastic response (Fig 1A) and relaxation function (Fig 1B) for each group. The linear-region modulus of the four groups appears to be similar (Fig 1A), consistent with our previous findings (Robinson et al, 2001). The toe-region of the stress-strain response is shorter and extends to a lower stress for the genetically engineered DKO8 and C1M8 compared to the control groups.

The DKO8 group had the fastest relaxation response and the CTL3 had the longest relaxation time (FIG 1B). We have previously shown that CTL3 has more glycosaminoglycan (CSDS/dry weight) than the other groups (Lin et al 2002). These findings support the notion that the primary mechanism for viscoelasticity in tendon fascicles is related to the glycosaminoglycan content and likely to its associated water content. Together, these findings begin to quantify important tendon relationships of tissue composition and structure with both the elastic and viscoelastic mechanical properties.

Group	A (MPa) #	B *	C	τ_1 (s) ‡	τ_2 (s) ‡
DKO8	0.13 ± 0.01	493 ± 134	23.6 ± 48.4	0.06 ± 0.02	285 ± 231
C1M8	0.12 ± 0.01	398 ± 123	50.9 ± 88.5	0.11 ± 0.07	712 ± 601
CTL3	0.18 ± 0.10	302 ± 143	12.2 ± 16.6	0.14 ± 0.12	1085 ± 757
CTL8	0.12 ± 0.01	447 ± 60	8.1 ± 6.0	0.06 ± 0.02	495 ± 399

Table: QLV parameters for each group. Mean ± Std Dev. Significant findings: # CTL3>all others; * CTL3<CTL8 & DKO8; ‡ CTL3>CTL8 & DKO8

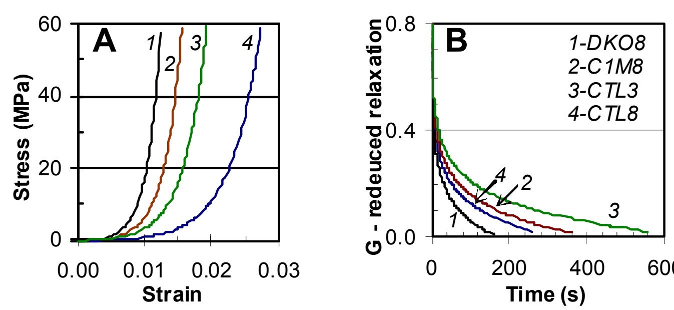

Figure 1: Elastic response (A) and reduced relaxation function (B) using mean QLV parameters

REFERENCES Fung (1968) *App Mech Rev* 21:1; Gimbel et al (2002) *Trans ORS* 27:603; Lin et al (2002) *Trans ORS* 27:45; Robinson et al (2001) *Trans ORS* 26:714; Woo et al (1981) *J Biomech Eng* 103:293

ACKNOWLEDGEMENTS NIH R01-AR45493 to LJS. Decorin knockout mice provided by RVI, Thomas Jefferson University, Philadelphia PA (NIH R01-CA39481 to RVI).

A STUDY OF BACK MUSCLE FATIGUE IN HELICOPTER PILOTS DURING REGULAR FLIGHTS

Carlos Gomes de Oliveira[1, 2] and Jurandir Nadal[2]

[1] Physical Activity Science Institute of Aeronautics – Rio de Janeiro – RJ – Brazil – CEP: 21740-000. Email: oliveiracg@yahoo.com
[2] Biomedical Engineering Program – COPPE-UFRJ

INTRODUCTION

High prevalence of backache in helicopter pilots has been reported being its etiology focused by many investigators. The constrained and asymmetric posture that the pilot adopts in-flight and the vibration are the most important causes postulated and discussed (Bonger et al., 1990). Both are accepted to induce stress in the back muscle leading to pain. Pope et al. (1986) found significant muscle fatigue as a result of the sustained static posture but not due to vibration in a simulated UH-1H cockpit (Pope et al., 1986). Nevertheless, a study conducted in UH50 helicopters during short flights (De Oliveira et al., 2001) reported very low activity in the low back muscle indicating that the pain could not be due to muscle stress but no muscle fatigue was investigated in such study. This study investigates the presence of fatigue in the low back muscle of Helicopter Pilots (HP) trough the behavior of the power spectra of the electromyography (EMG) signal during regular flights.

METHODS

Regular flights lasting 2h in average of 5 HPs were monitored. It was measured the surface EMG from the left and right Erector Spinae (ES) muscle trough electrodes placed 3 cm on both sides of the L3 vertebrae – 2.5 cm inter-electrode distance. The EMG was amplified by the ME3000P (Mega Electronics, Finland) and passed to a second stage raising a total gain of 3000 (20-500 Hz). For further filter the noise artifact in the EMG due to vibration, the latter was collected through a triaxial accelerometer 4322 and passed to a charge amplifier 5974 (both from Brüel&Kjaer, Denmark). All signals were recorded on a Digital Audio Tape PC208A (Sony, Japan). The tests were conducted in two different helicopters, BELL 412 and SK76. The data were analyzed in a PC after digitized with a sample rate of 1000 Hz. A procedure of previous study (De Oliveira et al., 2001) was performed to reduce the EKG in the EMG. Thus, windows of EMG and vibration were observed together with their corresponding spectra. Artifact in the EMG at the same frequency presented in the vibration was reduced by filtering the EMG at the corresponding frequency. Finally, consecutive FFTs were calculated over 1000 samples, averaged for each 10s and their Mean Frequencies (MF) computed. Each time series of MF was checked visually and the bias was tested by Runs Test. Failing the Runs Test the coefficient of regression was computed to verify the trend of the MF during the flight.

RESULTS AND DISCUSSION

From the 5 pilots investigated no bias in the time series of FM was evidenced by Runs Test in 2. For the remaining the coefficients of regression were either positive and very low or not significant (Table 1). Figure 1 illustrates the behavior of the time series of MF for one pilot (no bias detected).

It has been proposed that during muscle fatigue the spectrum of the EMG goes toward low frequencies causing a decrease in the MF. In this study, the trend, when present, was to slightly increase the MF indicating absence of fatigue in ES muscle during the investigated time. The EMG signals found were generally very low as observed by Hosea et al. (1986) for automobile driver and De Oliveira et al. (2001) for helicopter pilots. This could explain the lack of evidence of fatigue in the investigated muscles in this study.

Table 1: Coefficients of Regression (CR) and Pearson (r) calculated over the time series of MF for the HP whose Runs Test failed (bias detected).

	Right ES		Left ES	
HP	CR	r	CR	r
1	0.03	0.16	0.04	0.26
2	0.15	0.37	0.30	0.64
3	*	*	0.18	0.51

* Values not significant (p <0.01).

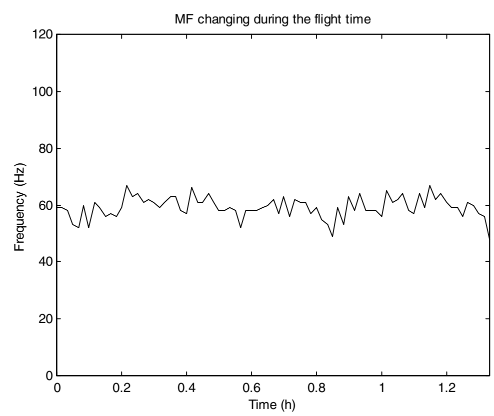

Figure 1: Time series formed by the MFs calculated over each 10 consecutive seconds for the EMG of the whole flight.

REFERENCES

Bongers, PM et al. (1990), *Ergonomics*, 33(8), 1007-1026
Hosea et al. (1986), *Spine* **11(9)**, 929-936
De Oliveira et al. (2001), *J. Biomechanics,* 34(10), 1309-1315
Pope et al. (1996), *In: Backache and back discomfort* (AGARD-CP-378, Neuily-sur-Seine), 21.1-25.9

ACKNOWLEDGEMENTS

This study was sponsored by ICAO and partially supported by the Brazilian Agency of Technology and Science (CNPq).

BONE-MUSCLE-LIMB MORPHOLOGY AND MOVEMENT DYNAMICS / ENERGETICS

Leah Dellanini and David Hawkins[1]

Human Performance Laboratory, University of California, Davis, CA, USA
[1] email: dahawkins@ucdavis.edu

INTRODUCTION

Animal movement performance, and in many cases survival, depends in part on the morphology of the animals' limbs. Limb morphology depends primarily on the size and shape of the muscle-tendon units, the bones, and the fat comprising the limb segments. Though fundamental physical and biological principles indicate that limb morphology affects joint strength, limb inertial characteristics, bone fracture strength, and the energy required to move the limbs, the interactions between these quantities has not been thoroughly investigated. Understanding these interactions is fundamental for understanding evolutionary changes and movement performance capacity.

The objectives of this study are to characterize the fundamental interactions between bone and muscle distribution, limb inertial properties, and limb movement dynamics and metabolic energy expenditure. These objectives will be achieved using musculoskeletal modeling and movement simulation.

METHODS

Five steps are required to achieve the stated objectives. First, an existing digital model of the human leg (Barr and Hawkins, 2000) was modified to include the inner bone surfaces that were not digitized in the original construction of the leg model. This step was necessary to provide data for manipulating not only muscles but the cortical bone thickness as well. Second, the Visual Basic software written by Hawkins and Barr (2001) for morphing muscle size was modified to morph bone and to accommodate the new data set. Third, a set of bone and muscle conditions were identified that provide reasonable representation of evolutionary and species variations in musculoskeletal design. Fourth, the bone and muscle conditions were simulated using the VB program and the limb inertial parameters determined and compared. Finally, the interactions between the various musculoskeletal designs and movement dynamics are being investigated using movement simulation techniques (SIMM-Musculographics, Inc.). Movement speed and the metabolic cost of movement are being compared between the different musculoskeletal designs.

RESULTS AND DISCUSSION

The first three steps of the project have been completed. The bone geometry was validated through repeat digitizing and the expansion/contraction algorithms were validated with a data set of known geometries and volumes. A variety of muscle to bone mass and thigh to shank mass ratios exist among animals. Bone size was selected to represent normal sized bones and bones with 22% larger cortical thickness, representing the size needed to prevent fracture in the absence of remodeling processes (Martin, in review). Major muscles were atrophied by 0, 20 and 40% to represent various limb ratios that are present in nature. Corresponding limb inertial parameters were quantified and described in terms of muscle and bone contributions (Fig. 1).

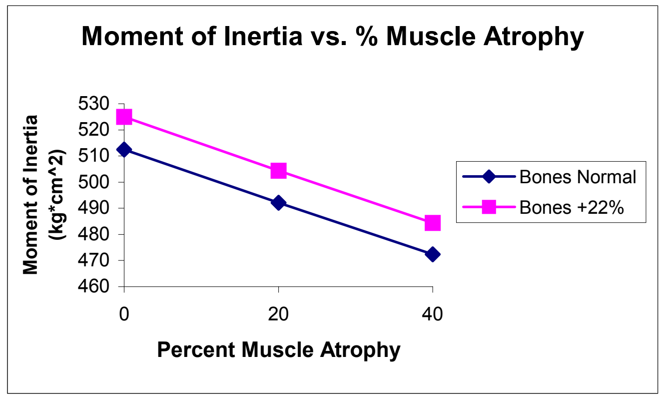

Figure 1. Shank moment of inertia for bone and muscle conditions.

It was found that increases in cortical bone thickness increase limb moment of inertia. It is hypothesized that this will result in a decrease in limb velocities achieved during a movement task. The effects of muscle atrophy are less clear. Muscle atrophy decreases muscle strength and the moment of inertia of the limb spanned by the muscle. This may lead to decreased movement velocity of the distal limb acted on by the muscle (due to strength deficits), but increases in movement velocity of the limb spanned by the muscle (due to reduced moments of inertia).

SUMMARY

The results of this study will characterize the complex interactions between bone, muscle, and limb mass distribution and the effects this mass distribution has on movement performance. Understanding these relationships will improve our understanding of movement performance as affected by evolutionary changes and tissue mass distribution.

REFERENCES

Barr, A., Hawkins, D. (2000). *Journal of Applied Biomechanics*, **16**:301-308.
Hawkins, D., Barr, A. (2001). *Computer Methods in Biomechanics and Biomedical Engineering*, **4**:399-411.
Martin, R.B. (in review). *Journal of Theoretical Biology*.

SURGICAL HAMSTRING LENGTHENING INCREASES CONCENTRIC MUSCLE VELOCITY DURING GAIT

Michael Orendurff
Gait Analysis Lab, Center of Excellence for Limb Loss Prevention and Prosthetic Engineering,
Veterans Hospital, Seattle, Washington, USA. morendurff@hotmail.com.

INTRODUCTION

In determining the indications for surgical hamstring lengthenings for individuals with cerebral palsy, physicians may assess crouch by computerized gait analysis, but also rely on physical examination to determine hamstring length and spasticity. Hamstring muscle modeling has shown normal lengths for individuals with crouch gait (Delp, et al., 1996), however improvements in knee extension are seen following surgical hamstring lengthenings (Rethlefsen, et al., 1999). The goal of this study was to evaluate physical exam measures before and after hamstring surgery and to determine if these changes are reflected in hamstring muscle velocity.

METHODS

Twenty-three individuals (40 sides) with cerebral palsy who underwent computerized gait analysis and hamstring lengthening surgery were reviewed retrospectively. All individuals underwent medial and lateral hamstring lengthenings; 22 sides also underwent adductor lengthenings, 9 sides had distal femoral derotational osteotomies, 5 sides had iliopsoas lengthenings, 4 sides underwent rectus femoris transfers, 4 sides had triceps surae lengthenings and 2 sides had subtalar fusions at the time of their hamstring surgery. Nine sides had hamstring surgery only. Physical examination of the hamstring muscle (popliteal angle) was assessed preop and about one year postop by placing the patient supine, flexing the hip to 90° and extending the knee (slow). A rapid extension of the knee was then performed to assess the velocity-dependent tone, or spasticity of the hamstrings (quick). The angles were measured with a goniometer. Gait data was collected with a 6-camera Vicon 370 system prior to and about one year following surgery. Three dimensional kinematics were calculated in Vicon Clinical Manager. Biceps femoris lengths were calculated from the kinematic data using the methods of Visser, et al., (1990). Muscle velocity data was calculated using a 3-point finite difference algorithm. Concentric (maximum) and eccentric (minimum) hamstring muscle velocities were extracted preop and postop. Maximum knee flexion in stance was calculated preop and postop. Variables were compared preop to postop using repeated measures ANOVAs. Multiple linear regression was performed to assess the relationship between quick and slow popliteal angles and hamstring muscle velocity during gait both preop and postop. An alpha level of $p < 0.05$ was chosen a priori.

RESULTS

Following surgical lengthening of the hamstring muscles, knee flexion during stance improved significantly from preop (30.1 ± 13.1°) to postop (7.6 ± 13.0°; $p = 0.0001$). The relationship between quick and slow popliteal angles and hamstring muscle eccentric velocity during gait was not significant either preop ($p = 0.551$; $R^2 = 0.033$), or postop ($p = 0.947$, $R^2 = 0.003$).

Table 1. Muscle velocities (%anatomic neutral length / %gait cycle) and popliteal angles before and after surgical hamstring lengthening. n = 40 sides (23 individuals). * indicates significance at p <0.05.

	Preop	Postop	*p*-value
Biceps Femoris			
Eccentric Velocity	0.58 ± 0.20	0.60 ± 0.17	0.4540
Concentric Velocity	-0.35 ± 0.13	-0.43 ± 0.10	0.0207*
Popliteal Angle			
Slow	-56.6 ± 12.4	-36.3 ± 16.0	<0.0001*
Quick	-86.7 ± 12.0	-55.3 ± 16.6	<0.0001*

DISCUSSION

Improved knee flexion in gait following surgical intervention in this study was consistent with other authors (Rethlefsen, et al., 1999). Accompanying this decrease in crouch gait, concentric velocity of the hamstrings (stance phase) improved significantly following surgical intervention. Contrary to expectations, eccentric velocity (swing phase) did not improve. However, the physical exam measures of slow popliteal angle and quick popliteal angle were unable to predict muscle velocity in gait with any certainty, either preop or postop. This suggest that physical exam hamstring measures have limited value to physicians deciding which individuals are candidates for hamstring lengthening. If this is the case, then were the correct candidates for surgical hamstring lengthenings chosen in the first place? If the group included those who would not benefit, then it is quite unlikely that postop these measures would have any greater success in predicting muscle velocity. Although every subject showed improvement in knee flexion in stance phase postop, 12 sides showed a worsening of concentric velocities of the hamstrings postop Excluding these twelve did not improve the statistical significance or the variance accounted for in the regression equations. It may be that there is substantial error associated with the physical exam measures, contributing to their lack of predictive power. It is quite likely that complex interrelationships between the many muscles crossing the hip, knee and ankle joints influence knee flexion in stance. Physicians are likely to incorporate a vast array of information into their decision making process, not relying on just a select few. Since all the subjects showed improvement in knee flexion, but not in hamstring muscle eccentric velocity, spasticity may not a principle cause of crouch gait.. The results do support the concept that surgical lengthening alters the concentric velocity characteristics of the hamstring muscle, but does not alter the eccentric velocity.

REFERENCES

Delp, S.L., et al., (1996) *J Orthop Res,* **14,** 144-151
Rethlefsen, S., et al., (1999) *J Pediatr Orthop B,* **8**, 75-79
Visser, J.J., et al., (1990) *Eur J Appl Physiol,* **61**, 453-460

ELECTROMYOGRAPHIC ANALYSIS OF SELECTED MUSCLES DURING A SIMULATED SOCCER GAME

Nader Rahnama, Adrian Lees, Thomas Reilly
Research Institute for Sport & Exercise Sciences, Liverpool John Moores University, Webster Street, Liverpool, L3 2ET England
HUMNRAH@LIVJM.AC.UK

INTRODUCTION

Surface electromyography (sEMG) analysis has been useful in comparing muscular activity among different sports movements and it is a valuable technique for evaluating activation, co-ordination and fatigue. Since these important variables have not been investigated during the full game in soccer, the present study aimed to make a descriptive analyses of muscle activities of major lower extremity muscles during a soccer simulation protocol with reference to running as a selected fundamental movement appropriate to soccer.

METHODS

Ten professional soccer players (age 21.40 ± 3.13 yr; height 1.77 ± 6.63 m; mass 74.55 ± 8.5 kg) volunteered to participate in this study after signing written informed consent. All participants were tested during the 2000-2001 English competitive soccer season. All tests were performed on a programmable motorised treadmill (Pulsar, HP Cosmos, Nussforf-Traunstein, Germany). The sampling frequency was set at 1000Hz. EMG activity was recorded and stored using a biopac system (MP 100 system, INC, Biopac systems INC, Santa Barbara). EMG data were analysed using custom written software. Recordings were made from the rectus femoris (RF) biceps femoris (BF) tibialis anterior (TA) and gastrocnemius (GC) muscles. Each subject performed a warm-up including some specific soccer stretching exercises and running at a slow speed on treadmill. Then the subject performed the testing protocol including walking (6 km), jogging (12 km), running (15 km) and sprinting (21 km) for duration of 10 seconds to 30 seconds in a variable order, during which the sEMG was recorded. The first recorded was taken before commencing the simulation game. The subject then performed a 45-min soccer-specific intermittent exercise protocol which consisted of the four different exercise intensities. The EMG activity was recorded after finishing the first half of simulation game. Finally, the EMG activity was recorded for the third time after finishing the second half of the simulation game. Each muscle was analysed with a 2 factor (condition × speed) repeated measure ANOVA. The level of significance on all tests was set at $P < 0.05$.

RESULTS

With regard to RF, a significant main effect ($F_{(3, 27)} = 106.35$, $P < 0.001$) was found for condition (pre-game, half-way and post-game), speed (6, 12, 15 and 21km) ($F_{(1.286, 11.577)} = 106.35$, $P < 0.001$) and interaction between condition and speed ($F_{(6, 54)} = 6.85$, $P < 0.001$). The root mean square (RMS) value was greater in pre-game than post-game and the RMS increased with increasing speed continually from 6km to 21km. For BF a significant main effect ($F_{(2, 18)} = 7.57$, $P < 0.01$) was found for condition, speed ($F_{(1.33, 11.79)} = 122.33$, $P < 0.001$) and interaction between condition and speed ($F_{(6, 54)} = 10.81$, $P < 0.001$). The RMS value was greater in pre-game than post-game and the RMS value increased with increasing speed continually from 6km to 21km. With regard to TA, a significant main effect ($F_{(2, 18)} = 4.27$, $P < 0.05$) was found for condition, speed ($F_{(1.53, 13.79)} = 101.09$, $P < 0.001$) and interaction between condition and speed ($F_{(2.60, 23.41)} = 3.53$, $P < 0.05$)). The RMS value was greater in pre-game than post-game and the RMS value increased with increasing speed continually from 6km to 21km. For GC, a significant effect was not found using for condition and interaction between condition and speed, but a significant main effect ($F_{(3, 27)} = 51.93$, $P < 0.001$) was found for speed, with the RMS value increasing with increasing speed continually from 6km to 21km.

CONCLUSION

In conclusion, the results indicated that the EMG activity in major lower limb muscles was greater before than after a simulated game. This showed that fatigue has an effect on muscle activity and is likely to be cause of reduced activity during exercise which mimicked work-rate in soccer. RMS values increased with increasing speed of running on treadmill, which revealed that muscle activity increased with increasing speed.

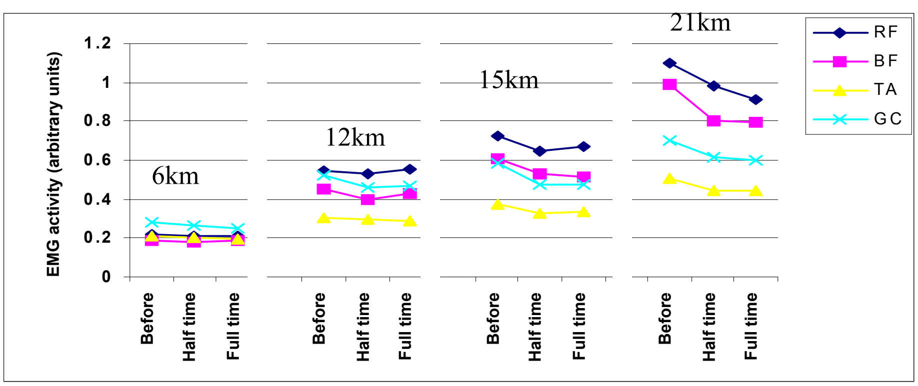

Figure 1. EMG activity with running speed during a simulated soccer game.

BACK MUSCLE FATIGUE DURING INTERMITTENT PRONE BACK EXTENSION EXERCISE

A. Plamondon[1-2], K. Trimble[2], C. Larivière[1], P. Desjardins[3],
[1]Institut de recherche Robert-Sauvé en santé et en sécurité du travail (IRSST)
[2]Laurentian University, Sudbury, Ontario, Canada
[3]Centre de recherce interdisciplinaire en réadaptation du Montréal Métropolitain (CRIR)
Email: plamondon.andre@irsst.qc.ca

INTRODUCTION

Exercise therapy is an essential component in the treatment of chronic low back pain (LBP) but there is little agreement as to which exercise programs are the most effective. There are several exercises aimed at improving the muscular function of the back. One such traditional exercise, known as the Sorensen test (Biering-Sorensen, 1984), is the prone back extension (**PBE**) exercise in which the subject's upper body is unsupported in a horizontal position against the force of gravity with arms on each side. Usually the subject maintains the horizontal position until the isometric contraction can no longer be sustained. Another way to do the exercise is to perform a large number of repetitions where there is a short period of static muscular contraction and a short period of rest (intermittent contractions). This latter form of exercise is more specific to an everyday life activity. The purpose of this study was to assess the muscular fatigue of the low back and hip extensors muscles during the performance of a dynamic-intermittent PBE exercise in males and females participants.

METHODS

Forty-one healthy students (24 males and 17 females) performed, while lying prone on a bench with the legs fixed, two maximal voluntary contractions (**MVC**) in extension, a maximum of 100 repetitions of an intermittent PBE exercise and a final MVC in extension. The PBE exercise consisted of while lying prone on a bench (10° below horizontal), repeating a task of 100 repetitions broken into four 1-s segments: (1) raising the trunk to a horizontal position; (2) holding the trunk in the static phase (10° above horizontal); (3) returning to the original position; and (4) resting on the bench. To assess the level of effort involved during the PBE exercise, electromyography (EMG) was collected to measure the level of muscle activity (erector spinae ES, gluteus maximus GT, hamstrings HA) relative to the maximum voluntary EMG (MVE). Muscular fatigue during the static phase of the exercise was estimated through the gradient change of the median frequency in time (MF_{grad}) using power spectrum analysis.

RESULTS AND DISCUSSION

Most of the subjects (34 out of 41) completed the 100 repetitions without excessive muscular fatigue according to the post exercise MVC values (decrease of 20% in male and 14 % in female). There was no gender difference in all EMG measurements. It was found that the level of muscular activation (% MVE) of each muscle group increased with the number of repetitions (figure 1: Peak activity of ES; figure 2: Average activity of ES) and the level of muscular fatigue (MF_{grad}) was greater for the ES muscles than for the GT and the HA muscles. Moreover, it was demonstrated that the subjects who did not complete the test had a higher rate of fatigue of hamstrings (MF_{grad}) than the other subjects.

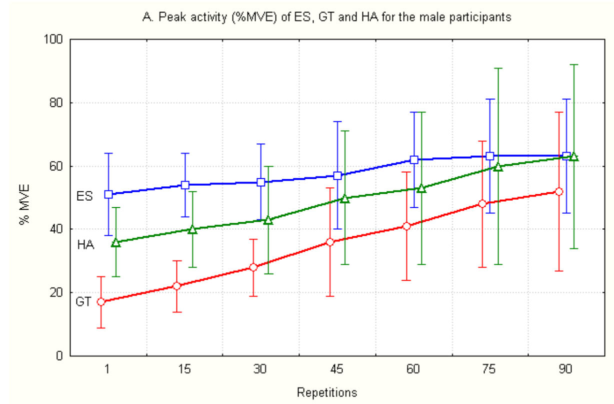

Figure 1. Peak activity of ES for male participants

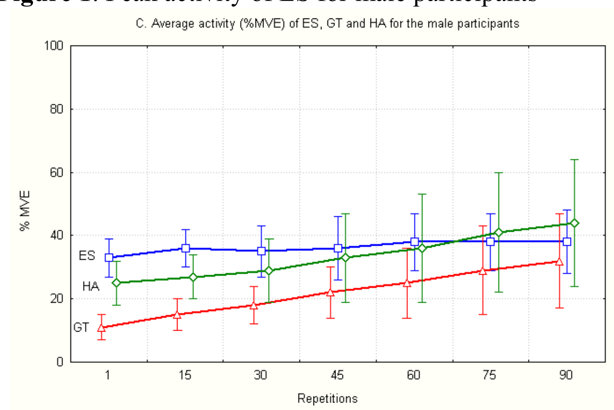

Figure 2. Average activity of ES during static phase

CONCLUSION

The PBE exercise as performed in the present study (including rest intervals) was not very strenuous for our healthy subjects but seems to be an adequate exercise to measure and to train the aerobic capacity of the back muscles. The best predictors for the subjects that did not complete the 100 repetitions were a high level of muscle activity in the HA and a low level of back muscles force.

REFERENCE

: Biering-Sorensen, F. (1984) Spine, 9, 106-119.

ACKNOWLEDGEMENTS

NSERC and IRSST

BIOMECHANICS OF PLAQUE RUPTURE IN ATHEROSCLEROTIC CORONARY ARTERIES

Jean Brunette[1], Rosaire Mongrain[1,2] and Jean-Claude Tardif[1]
[1]Montreal Heart Institute, [2]McGill University, Montreal

INTRODUCTION

Cardiovascular diseases are the leading cause of death in North America. A mechanical event is generally at the origin of a myocardial infarct, where the plaque cannot bear the different stresses anymore. This may result in a rupture of the plaque's fibrous protective cap. Exposure of the blood to the pro-aggregative content of the atheromatous gruel may result in the formation of a clot which can eventually lead to a myocardial infarct. Plaque vulnerability to rupture can be evaluated by means of a finite element analysis (FEA) over a 3D model obtained from an intravascular ultrasound imaging (IVUS) series. The mechanical properties of coronaries can be evaluated from elastography. The different stresses in conjunction with the mechanical properties of the tissues can permit the evaluation of plaque vulnerability to fissure, help to choose a proper therapeutic approach, and assess balloon size and inflating pressure during percutaneous transluminal angioplasty.

METHODS

A 3D model can be obtained from the segmentation of *in vivo* sequences of intravascular ultrasound images. The segmentation coordinates of the layers, inclusions and plaque are imported from a segmentation software to a computer aided design (CAD) package. Once the model is created, it is then exported, by means of a regular IGES format to a mesher that prepares the model for a computational fluid dynamics (CFD) solver. At this point, the mechanical properties of the artery, obtained from elastography of the intravascular images, can be incorporated into the model. Once the boundary conditions are set, velocities and shear stresses can be determined over the model. With a fluid to wall interface analysis, different stresses in the artery wall can be obtained, and their integration yields the different forces applied on the plaque and its propensity to fissure.

DISCUSSION

Three types of stresses resulting from blood dynamics can be identified along the artery wall: circumferential stress, pressure gradient stress and shear stress (see **Figure 1**). The circumferential stress has been previously described in the literature and is sometimes approximated, with some limitations, by the Laplace law. The pressure gradient stress results from the blood pressure and may create longitudinal forces on the plaque. This type of stress has been largely neglected in the literature. The third type of stress, the shear drag force results from the shear of blood circulation on the inside boundary due to blood viscosity. This shear stress can be integrated over the surface to give a longitudinal drag force applied on the plaque. This type of stress has been largely covered in the literature (Ilegbusy et al 1999), but only from a local physiological approach on the endothelium cells; however, it never has been considered under a global mechanical point of view. Fissuring results from a conjunction of the different forces applied and the mechanical properties of the plaque.

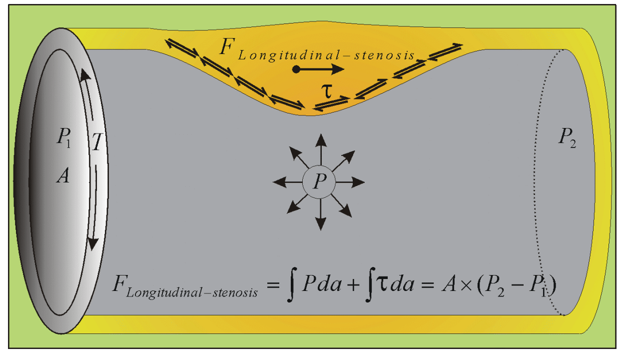

Figure 1 : Schematic of the different forces over an artery model under physiological perfusion. Three types of forces can be identified: circumferential forces (T), pressure gradient forces (P) and shear forces (τ). These forces along with the mechanical properties of the plaque (which can be determined by elastography) may result in plaque rupture, which may cause an infarct.

Plaque properties can be determined from elastography on IVUS images obtained at different blood pressures over the cardiac cycle (de Korte *et al* 1998). These mechanical properties are applied on the 3D model. Different forces calculated by CFD and FEA can be validated with a phantom in which different stress gauges can be inserted. The phantom can be made of an agar-based compound reproducing the different layers and inclusions (Brunette *et al* 2000).

SUMMARY

Plaque fissuring is at the origin of myocardial infarct. This event is a direct consequence of different blood circulation forces in conjunction with plaque mechanical properties. A 3D model can be obtained from segmentation of IVUS series, and tissue mechanical properties can be determined by elastography. The model can then be imported into a finite element solver in order to study the mechanical behavior of the coronary artery and its plaque, and to evaluate its vulnerability. This can be of great utility in a clinical environment for the evaluation of patient risk. This technique can also be useful to better determine the best therapeutic approach, and to determine balloon size and inflating pressure of percutaneous transluminal angioplasty (PTCA).

REFERENCES

Brunette J, Mongrain R, Cloutier G, Bertrand M, Bertrand OF, Tardif JC. **A novel realistic three-layer phantom for intravascular ultrasound imaging**. Int J Card Imaging 2001; **17**:371-381.

de Korte C, van der Steen AF, Cespedes E, Pasterkamp G. **Intravascular ultrasound elastography in human arteries: initial experience *in vitro***. Ultrasound Med Biol 1998; **24**(**3**):401-408.

Ilegbusi OJ, Hu Z, Nesto R, Waxman S, Cyganski D, Kilian J, Stone PH, Feldman CL. **Determination of blood flow and endothelial shear stress in human coronary artery *in vivo***. J Invas Cardiol 1999; 11:667-674.

TESTING THE RELIABILITY AND VALIDITY OF SACROILIAC JOINT ROTATIONS MEASURED WITH A MAGNETIC TRACKING DEVICE

Melanie Bussey and Toshimasa Yanai
School of Physical Education, University of Otago, Dunedin, New Zealand
mbussey@pooka.otago.ac.nz

INTRODUCTION

Measuring the motion of the sacroiliac joint (SIJ) is problematic due to the relatively small range of motion available at the joint (<10°). Most techniques for measuring the SIJ range of motion are invasive, involving the implantation of titanium markers or k-wires and requiring multiple radiographs subjecting the participant to large doses of radiation (Sturesson et al., 2000; Jacob and Kissling, 1995; Egund, 1978). The error ratio of non-invasive techniques has been considered too large to reliably evaluate such small rotations. Therefore, the aim of this study was to test the reliability and validity of SIJ rotations measured from a non-invasive palpation and digitising technique using an electro magnetic tracking device.

METHODS

Fifteen healthy subjects (11 females and 4 males) between the ages of 20 and 40 gave their informed consent to participate in this study. Each subject attended two testing sessions held on two separate days and each testing session consisted of two separate trials. SIJ rotation was generated via full hip abduction with external rotation from a secured prone position. To standardize the initial subject position a wooden frame was built to which the subject was secured. The pelvic landmarks, right and left anterior superior iliac spines (ASIS) and posterior superior iliac spines (PSIS), were palpated and digitized using the magnetic tracking device with stylus (Fastrack, Polhemus Incorporated, Colchester, VT, USA).
The mean rotational motion after four trials was calculated for both right and left SIJ and the standard deviation was calculated as the variability of the individual results from the group means. To test the reliability of the palpation and digitizing technique, a trial-to-trial comparison using Pearson correlation was performed on the average of the first trial each day and the average of the second trial each day. To test the individual subject variability in SIJ range of motion, a day-to-day comparison using Pearson correlation was performed on the average of the day one trials and the average of the day two trials. To test for significant differences in both the subject variability and the measurement variability paired t-tests (p=0.5 level of significance) were conducted. Measurement validity was tested through the use of CT scans on six randomly selected subjects.

RESULTS

The correlation coefficients of the SIJ range of motion measurements range from 0.78 to 0.84 for the day-to-day testing (Table 1) and from 0.83 to 0.90 for the trial-to-trail testing (Table 2), representing a strong correlation between the measures. Additionally, the range of error in the measurements was less than one degree and all but one paired t-test, right day-to-day, were non-significant.
The difference between the range of motion detected with the palpation and digitising method and that detected with the CT method is small, less than one degree. The correlation coefficient was high (0.9), validating the SIJ rotation measurement.

Table 1: Results of day-to-day reliability testing

SIDE	CORRELATION	MEAN DIFF. (DEG)	SD OF DIFF (DEG)	T-TEST
Left	0.80	0.27	0.82	P=0.21
Right	0.78	0.77	1.20	P=0.03
Total	0.84	0.50	1.61	P=0.24

Table 2: Results of Trial to trial reliability testing

SIDE	CORRELATION	MEAN DIFF. (DEG)	SD OF DIFF. (DEG)	T-TEST
Left	0.83	0.10	0.82	P=0.40
Right	0.80	0.14	0.80	P=0.80
Total	0.90	0.26	0.90	P=0.24

DISCUSSION AND SUMMARY

This study established the reliability and validity of SIJ rotations measured with the magnetic tracking device. The positional error for the tracking device was calculated as the mean difference between the two sets of known distances and was found to be less than 1 mm. The maximum relative error, analysed by observing the length change of the segment vectors, was 2mm, which would translate into a maximum rotational error of 1º. This measurement technique may be suitable for more quantitative clinical evaluations of the SIJ.

REFERENCES

Egund, N., Olsson, T.H., Dchmid, H., and Selvik, G. (1978). Movements in the Sacroiliac Joints Demonstrated with Rotegen Sterophotogrammetry. *Acta Radiologica Diagnosis,* **19**, 833 - 845.
Jacob, H. A. C., and Kissling, R.O. (1995). The Mobility of the Sacroiliac Joints in Healthy Volunteers Between 20 and 50 Years of Age. *Clinical Biomechanics,* **10**(7), 352 - 361.
Sturesson, B., Uden, A. and Vleeming, A. (2000). A Radiostereometric Analysis of Movements of the Sacroiliac Joints During the Standing Hip Flexion Test. *Spine,* **25**(3), 364-368.

EFFECTS OF STRETCHING AND SHORTENING ON ISOMETRIC FORCES ON THE DESCENDING LIMB OF THE FORCE-LENGTH RELATIONSHIP IN CAT SOLEUS MUSCLE.

Rachel Schachar, Walter Herzog, and Tim Leonard
Human Performance Laboratory, University of Calgary, Calgary, Alberta, Canada, raschach@ucalgary.ca

INTRODUCTION

Steady-state, isometric force enhancement (FE) following stretch and force depression (FD) following shortening, is a well-accepted property of skeletal muscle (Abbott and Aubert, 1952). The force-length (F-L) curve describes the relationship between the maximal isometric force and the corresponding muscle length. This F-L relationship is considered an important mechanical property of skeletal muscle. The textbook F-L relationship for muscle is obtained through a series of independent static contractions. The purpose of this study was to examine, through systematic tests, the effects of stretching and shortening on the isometric forces at different lengths on the descending limb of the F-L relationship.

METHODS

Ten cat soleus (SOL) were studied. Cuff electrodes were surgically implanted on the tibial nerve (Schachar, et al., 2002). Animals were secured in a stereotaxic frame. The distal insertion of the SOL on the Calcaneus was attached to a muscle puller (Schachar, et al., 2002). The F-L relationship was determined for each muscle, and the descending limb identified. Two sets of tests were performed. In the first set, the muscle was stretched at various speeds and by various amounts on the descending limb. In the second set of tests, the muscle was shortened at various speeds and by various amounts on the descending limb. Isometric reference contractions were performed at the initial and final lengths for each stretching and shortening contraction. Both force and displacement were continuously recorded. Active forces were calculated by subtracting the passive forces from the total forces.

RESULTS AND DISCUSSION

Data were collected from 120 stretching and 120 shortening contractions. Forces following muscle stretches were greater than the purely isometric forces at the initial (and therefore also the final) muscle lengths for all stretch contractions, and the maximal isometric forces following shortening were depressed compared to the corresponding isometric force (Figure 1). The total forces following muscle stretch were greater than the corresponding isometric forces at optimal muscle length. However, this could have been an artifact caused by an increase in the passive forces. In order to resolve this problem, the active (total-passive) forces were calculated, and it was found that for some stretch tests, the steady-state isometric force following SOL stretch clearly exceeded the purely isometric force at optimal length (Figure 2).

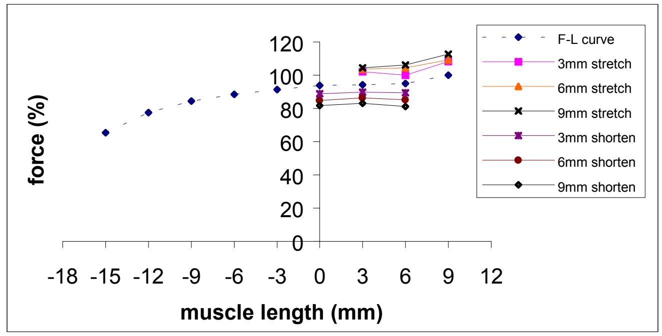

Figure 1. Example of F-L relationship and corresponding steady-state isometric F-L curves preceding dynamic stretching or shortening on the descending limb.

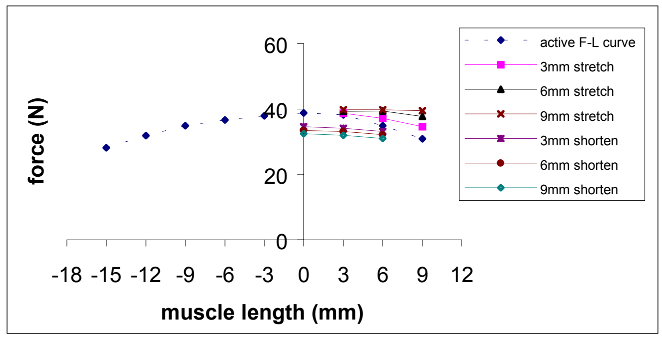

Figure 2. Example of active FE and active FD following muscle stretch.

The primary mechanism associated with FE is the "sarcomere length non-uniformity theory". According to this theory, stretch on the descending limb causes non-uniformities in sarcomere lengths, and thereby non-uniformities in the forces that can be exerted by sarcomeres. One of the conditions associated with the sarcomere length non-uniformity theory is that the steady-state forces following stretch cannot exceed the isometric forces at optimum sarcomere length. However, here, we demonstrate that such forces in excess of those observed isometrically at optimum length can be found for some stretch conditions, thereby suggesting that the sarcomere length non-uniformity theory alone cannot explain the observed results. We found that following active stretching of SOL, there was a considerable increase in passive force compared to the passive force obtained following isometric contractions or passive stretch (results not shown). This passive FE following active stretch must be analyzed carefully in the future, as it might explain the novel and unexpected results found here.

REFERENCES

Abbott, B.C., et al. (1952). *J Physiol* 117, 77-86
Schachar, R., et al. (2002). Submitted to *J Biomech.*

MOTION AND CONTACT ANALYSES OF PATELLO-FEMORAL JOINT AFTER TOTAL KNEE ARTHROPLASTY

Katsutoshi Nishino[1], Haruka Inoue[2], Youhei Takano[2], Takashi Tsurumaki[2], Naoyuki Onda[3], Go Omori[3], Yoshio Koga[1], Yasuo Nakamura[4] and Toyohiko Hayashi[4]

[1]Department of Orthopaedic Surgery, Niigata Kobari Hospital, Niigata, Japan, nishi@jkl.bc.niigata-u.ac.jp
[2]Graduate School of Science and Technology, Niigata University, Niigata, Japan
[3]Department of Orthopaedic Surgery, Faculty of Medicine, Niigata University, Niigata, Japan
[4]Department of Biocybernetics, Faculty of Engineering, Niigata University, Niigata, Japan

INTRODUCTION

In an attempt to achieve excellent surgical outcome after total knee arthroplasty (TKA), several computer-assisted systems have been developed. As one of such systems, we developed an intraoperative knee-motion monitoring system based on a photostereometry using linear CCD cameras and LED markers mounted on the TKA component (Nishino, et al., 1999). Employing this system, the femorotibial joint motions after TKA have been measured. The motion data obtained was evaluated as movement of contact area between the femorotibial components (Nishino, et al., 1998). This study aims to apply this method to motion analysis between the unresurfaced patella and the femoral component after TKA.

MATERIALS AND METHODS

The patellar surface data was obtained by digitization of the cartilage surface from magnetic resonance images. The femoral surface data was measured by means of a precise three-dimensional digitizer (BH504, Mitsutoyo, Japan). The computer model of each surface was mathematically expressed by a set of six bicubic Besier patches fitted to the surface data. The relative motion between the femoral component and the patella was measured by using LED markers mounted on them. The position of the patellar surface relative to the LEDs mounted on the patella was directly measured by means of an original digitizer with LEDs. By this registration of its measurement data and the patellar surface model, the model data could be combined with the motion data (Besl and Mckay, 1992). The motion data was visualized as the movement of the patellar model relative to the femoral component model (patella tracking). Additionally, the contact or near-contact area between the articular surfaces was calculated, and then the patello-femoral joint motion was also evaluated as the movement of the contact area. Five cadaveric knees after TKA were measured during knee flexion and extension ranging from 0 to 90 degrees. As total knee system, Genesis II cruciate retaining type (Smith & Nephew, Richards, USA) was used.

RESULTS AND DISCUSSION

It took about 50 seconds to complete the registration of the model data. Consequently, the registration error lay within 1.6 degrees and 2.1 mm in terms of the rotation and translation, respectively. In patella tracking, the patella deviated slightly from lateral side to medial side relative to the femoral component during knee flexion (Figure 1). The contact area on the patella moved proximally during knee flexion (Figure 2). This method can be assessed the movement of the patello-femoral joint high speedy and dynamically, thus it was suggested to have a potential of employing as motion analysis of the patello-femoral joint during TKA.

REFERENCES

Nishino, K., Hayashi, T., et al. (1999). *Frontiers of Medical and Biological Engineering*, **9**(4), 261-273.
Nishino, K., Hayashi, T. et al. (1998). *44th Annual Meeting Orthopaedic Research Society*, 704.
Besl, P.J. and Mckay, N.D. (1992). *IEEE Transactions on Pattern Analysis and Machine Intelligence*, **14**, 239-256.

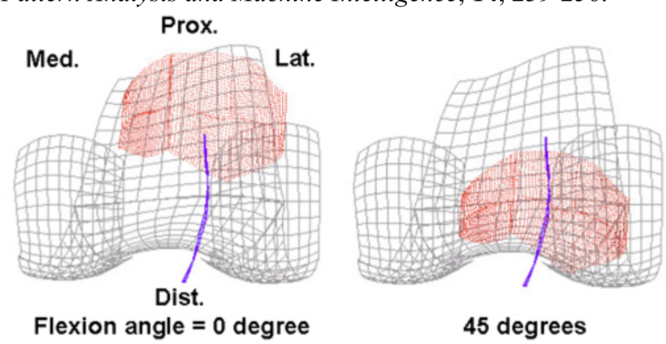

Figure 1: The patella position relative to the femoral component at 0 and 45 degrees of flexion angle.

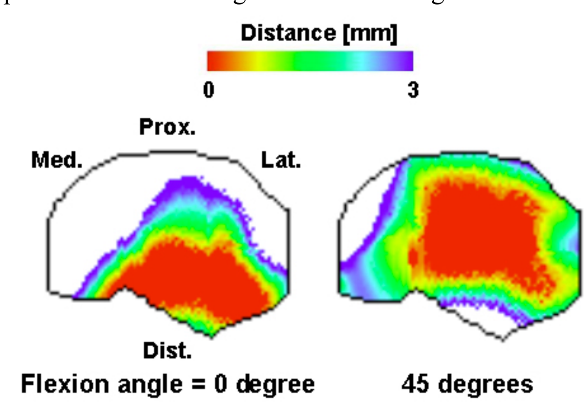

Figure 2: Visualization of the contact or near-contact area on the patellar surface at 0 and 45 degrees of flexion angle.

THE HEMODYNAMIC EFFECTS OF PARENT VESSEL INFLOW ANGLE ON A CEREBRAL SIDEWALL ANEURYSM

Yiemeng Hoi[1] BS, Amol Mulay[1] BS, Bernard R. Bendok[2] MD, Hui Meng PhD[1, 2], Kenneth Hoffman[2] PhD., Stephen Rudin[2] PhD, Adnan I. Qureshi[2] MD, Lee R. Guterman[2] PhD MD, Dale B. Taulbee PhD[1], L. Nelson Hopkins[2] MD

Hemodynamic Research Laboratory, University at Buffalo, State University of New York, USA
[1]Department of Mechanical and Aerospace Engineering
Department of Neurosurgery[2]

INTRODUCTION

The nature of flow in aneurysms depends on many factors including the complex three-dimensional geometry of the aneurysm and parent vessel. Computational fluid dynamics (CFD) allows for the analysis of hemodynamics in complex three-dimensional systems. The effect of the parent vessel inflow angle is intuitively relevant but has not been well studied. Using CFD, we examined the influence of the inflow angle in order to understand the hemodynamics factors that may lead to aneurysm rupture. Three-dimensional cerebral saccular sidewall aneurysms with various inflow angles are used in this analysis.

METHODS

In the present study, the flow is assumed to be incompressible, steady and laminar. The parent vessel is 3mm in diameter; the aneurysm size is 12mm in diameter and the sac-to-neck ratio is 3:1. Fully developed velocity profile and pressure gradients are specified at the inlet and outlet of the vessel. The pressure drop between the inlet and outlet is 50 Pa. Inflow angles of 0, 10, 20 and 40 degrees are examined.

The 3D Navier-Stokes equations are solved by commercially available package STAR-CD (Adapco, NY). The code is based on finite volume approach. We used Proam to generate approximately 120,000 of cells. The density of fluid, 1056kg/m3 and viscosity of 0.0035kgm/s were chosen in the computation. Velocity, and pressure distribution are computed numerically.

RESULTS AND DISCUSSION

The computational results show that the flow enters the aneurysm at the distal neck (inflow zone) and joins the parent vessel at the proximal (outflow zone). Vortex structure is observed inside the aneurysm. This vortex moves towards the dome as the inflow angle increases. High-pressure region is found at the inflow zone. As the inflow angle increases, the pressure at the in flow zone increases and tends to grow. As the angle of inflow increases, more rapid flow activity is observed inside the dome. Flow velocity entering the aneurysm is much faster when the inflow angle increases. However, the velocity near the dome is almost stagnant.

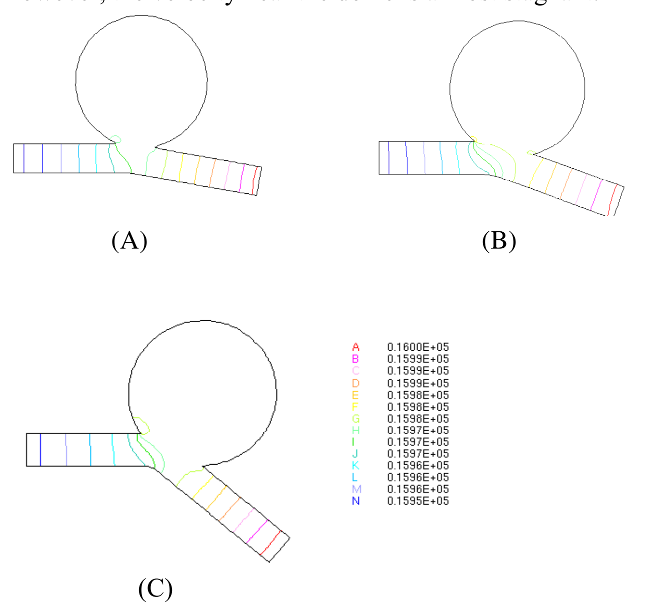

Figure 1: Relative pressure contour at the center plane for (A) 10° (B) 20° (C) 40° of the inflow angle. Flow is from right to left. As the inflow angle increases, higher pressure develops and grows in the inflow zone.

SUMMARY

Three dimensional velocity profiles and pressure distributions of a cerebral aneurysm with variable parent vessel inflow angle have been obtained. The high-pressure zone is developed at the inflow zone. As the inflow angle increases pressure in the inflow zone increases and distributes over a wider area. This phenomenon may affect aneurysm growth and rupture. Future studies will include the effect of pulsatile flow.

REFERENCES

Aenis, M., et al. (1997). *Journal of Biomechanical Engineering* **119,** 206-212.

Low, M., Perktold, K., Raunig, R. (1993). *Biorheology* **30**, 287-298.

MODELING OF FLOW IN CEREBRAL SIDEWALL ANEURYSMS: EFFECT OF ANEURYSM SIZE

Amol Mulay[1] BS, Yiemeng Hoi[1] BS, Bernard R. Bendok[2] MD, Kenneth R. Hoffmann[2] PhD, Stephen Rudin[2] PhD, Adnan I. Qureshi[2] MD, Lee R. Guterman[2] PhD MD, Hui Meng[1, 2] PhD, Dale B. Taulbee[1] PhD, L Nelson Hopkins[2] MD.
[1]Department of Mechanical and Aerospace Engineering and
[2]Department of Neurosurgery
State University of New York at Buffalo

INTRODUCTION

We present our preliminary work with the use of computational fluid dynamic (CFD) study of hemodynamics of cerebral sidewall aneurysms. Aneurysm size is known to influence rupture risk. The hemodynamic effects of aneurysm size are not clearly understood. The effect of aneurysm size on maximal velocity in the parent vessel, maximal pressure and shear force at the neck were investigated.

METHODS

The basic models consist of a tube with diameter of 3 mm representing a constant parent vessel diameter. The aneurysm size varies for each model from small (8 mm), large (12 mm) and giant (28 mm); the neck size being constant. The computational mesh is generated using Pro∗am®, a commercial code by CD-adapco. Figure 1 shows a sectional view of mesh for a large size aneurysm model.

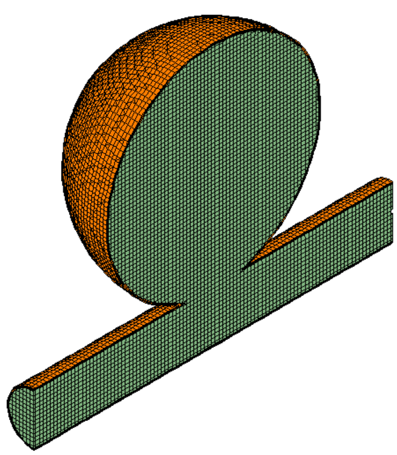

Fig. 1 - Sectional view of computational domain

The numerical simulation is carried out using StarCD®, a commercial CFD code by CD-adapco. The flow is modeled to be steady state, isothermal, incompressible and laminar. A constant pressure, 120 mm of Hg, is specified at the inlet. The mean peak value of blood velocity in large arteries is around 0.2 – 0.5 m/s (Cooney, 1976). A constant outlet pressure is specified so as to get the maximum value of flow velocity in the above range. A wall boundary condition (no slip, no penetration) is specified along the tube and aneurysm walls. The convergence of the flow solution is verified by the comparison of outlet velocity profile with parabolic velocity profile for laminar flow.

RESULTS AND DISCUSSION

The CFD results show that the flow activity inside the aneurysm is of an order of magnitude smaller than inside the parent vessel. It reveals the reversed flow (vortex flow) occurring inside the aneurysm. Table 1 gives the comparison of flow properties for three models.

Table 1: Flow dynamics for three models

Aneurysm size	Max. velocity in parent vessel (m/s)	Max. pressure at neck (N/m^2)	Max. shear force at neck (N)
Small	0.387	15990	0.3193·e-6
Large	0.3823	15983	0.2585·e-6
Giant	0.3207	15958	0.5074·e-6

SUMMARY

The effect of aneurysm size on parent vessel and aneurysm hemodynamics is complex. In this study we have attempted to analyze this effect using CFD. Many physical factors can potentially influence aneurysm hemodynamics. CFD allows for the isolation of specific factors while maintaining other factors constant. It is hence an excellent tool for deciphering cause and effect relationships in hemodynamic analyses. In summary we found that velocity in the parent vessel and maximal pressure at the neck decrease with increasing aneurysm size. Our results for maximal shear force at the neck are not straightforward. This may reflect an interesting phenomenon or may reflect limitations in our methods and calculations. Nevertheless, the ability to analyze aneurysm hemodynamics in such a manner may eventually become relevant in assessing the rupture risk of real human aneurysms.

REFERENCES

Cooney, D.O., (1976). *Biomedical Engineering Principles*, **vol. 2**, Marcel Dekker, Inc., 37-89.

Lieber, B. B. et al, (1997). *Modeling of Flow in a Straight Stented and Nonstented Side Wall Aneurysm Model.* Journal of Biomechanical Engineering, **vol. 119**, 206-212.

EFFECTS OF OSCILLATION ON ELEVATING SHEAR STRESSES

Sakhaeimanesh Ali A.
Biomedical Engineering Group, Faculty of Engineering, University of Isfahan, Isfahan, Iran, sakhaei@eng.ui.ac.ir

INTRODUCTION

In artificial heart valves, the problems of haemolysis, platelet destruction, thrombus formation, perivalvular leakage, tissue over growth and endothelial damages are directly related to the fluid dynamic characteristics of flow past artificial heart valves (Reul et al., 1993 and Yoganathan et al., 1995). Therfore, haematologically, It is highly desirable that a valve design shouldn't produce excessive turbulence, which may cause haemolysis (Yoganathan et al., 1995). In this study the effect of oscillation on elevating turbulent shear stresses through the jellyfish and St.Vincent valves has been investigated.

METHODS

Flow was driven by a servo-controlled piston pump (VSI pump) that compressed the ventricle to simulate the physiological flow. A model of the left ventricle and load was incorporated with the drive unit for testing artificial valves in the aortic position under practical flow and loading conditions. DANTEC, two-colour 5 Watt Argon-Ion laser was used to determine the velocity and turbulent components of the valve. The axial and radial mean velocities, $\overline{U}$ and $\overline{V}$, the r.m.s. of axial and radial fluctuation components, turbulent intensity, T, and the cross, $\overline{uv}$, were calculated. More details of mock circulatory system and LDA technique are given somewhere else (Sakhaeimanesh et al.,1999).

RESULTS AND DISCUSSION

Comparison between two valves revealed that at 0.5D downstream of the valves the magnitude of shear stresses in the Jellyfish valve were much higher than those of the St. Vincent valve at cardiac outputs of 4.5 and 6.5 l/min. Furthermore, at 3D and 5D downstream off the Jellyfish valve the magnitudes of shear stresses reduced dramatically to 4 and 1 N/m^2 respectively at cardiac output of 6.5 l/min. At 3 and 5D downstream of the St. Vincent valve, on the other hand, showed maximum shear stresses of the values of 49 and 16 N/m^2 respectively at the same cardiac output.

It is hypothesized that the cause of high shear stresses in close proximity to the Jellyfish valve was due to the oscillation of the membrane which in turn generated a wake downstream of the valve (in the core of valve chamber) and produced a wide region of disturbance further downstream. This resulted in further pressure drag and consequently, higher pressure drops across the valve and higher shear stresses downstream of the valve.

This idea was supported by the results of shear stress (table 1) and pressure drop measurements. Maximum and mean shear stresses at 0.5D downstream of the Jellyfish valve were about twice those of the St. Vincent valve and pressure drops across the Jellyfish valve were up to 93 % higher than those of the St. Vincent valve under steady flow rates between 10 to 26 l/min

The effect of oscillation can also be seen from the results of turbulence intensities. Maximum and mean turbulent intensities 0.5D downstream of the Jellyfish valve were as high as 723 and 255 % respectively at cardiac output of 6.5 l/min. At 3D downstream of the valve, maximum and mean turbulent intensities reduced dramatically to 17 and 8 % respectively at cardiac output of 6.5 l/min. Reduction in turbulence, and consequently in shear stress estimation in the 3D and 5D downstream measuring planes of the Jellyfish valve, indicated that the effect of the membrane oscillation decayed beyond 1D at all cardiac outputs.

REFERENCES

Reul H., et al (1993). *In vitro* comparison of bileaflet aortic heart valve prostheses- St. Jude Medical, CarboMedics, Modified Edwards-Durmedics and Sorin-Bicarbon valves. J of Thoracic and Cardiovascular Surgery, **106**, 412-420.

Yoganathan A.P., Cardiac Valve prostheses, 1995. In: J.D. Bronzino (ed), The Biomedical Engineering Handbook, CRC and IEEE presses, 1847-1870.

Sakhaeimanesh, A. A. and Morsi, Yos S., 1999. Analysis of regurgitation, mean systolic pressure drops and energy losses for two artificial aortic valves. Journal of Medical Engineering and Technology, **23(2)**, 63-68.

Table 1: Mean and maximum values of shear stresses, turbulent intensities and r.m.s of axial velocities of the Jellyfish and St. Vincent valves at cardiac outputs of 6.5 l/min at different downstream locations.

	Jellyfish valve			St. Vincent valve		
Distance, in diameter	0.5D	3D	5D	0.5D	3D	5D
Max shear stress, N/m2	143	4	1	74	21	5
Mean shear stress, N/m2	57	0.68	0.15	17.94	17.1	5.2
Max turbulent intensity, U %	723	17.7	16.6	100.2	35	30.5
Mean turbulent intensity, U %	255	8	5.5	43.7	23	15.4

BIOMECHANICAL TESTING OF AN INTRAMEDULLARY LOCKED NAILING FOR METACARPAL SHAFT FRACTURES

Gabriela Contreras[1,2], Nils Götzen[2], Michael Morlock[2], Miguel Cerrolaza[1]

[1] Centro de Bioingeniería, Universidad Central de Venezuela, Caracas, Venezuela, gabriela_contreras@web.de
[2] Biomechanics Section, Technical University Hamburg-Harburg, Hamburg, Germany, goetzen@tuhh.de

INTRODUCTION

An intramedullary locked nailing system has been developed at the Central University of Venezuela in order to allow early postoperative movement for the patient. It will be used for the treatment of diaphyseal fractures at the metacarpal bones, thus hopefully shortening the recovery time. The main goal of this study is to evaluate the mechanical behavior of the nailing system. Biomechanical testing and finite element analyses were performed to determine the ultimate strength and analyze the fatigue behavior under physiological loads.

MATERIALS AND METHODS

Experimental Study

The nail was connected by bone-screws to cylindrical clamps, made from acrylic. Four standard mechanical tests, based on standard specification for intramedullary fixation[1], were conducted to determine the ultimate strength of the nail-clamp assembly: compression test; tension test; four-point-bending test, and torque test. Three specimens were tested within each test. Additional cyclic tests were conducted to evaluate the mechanical behavior under repeating *in-vivo* loads[2]. Compression force (100N) and torque moment (100Nmm) were simultaneously applied at a rate of 1Hz for 10000 cycles Afterwards, the nail, screws, and clamps were analyzed.

Numerical Analyses

The finite element analyses were performed to evaluate the loading condition and stress distribution within the nail, the screws, and the clamps. They were also necessary to quantify the difference in the load transfer for the nail-assembly with acrylic clamps or cortical bone clamps. All static experimental tests were numerically investigated. A FE-Model, using the symmetry of the assembly and loading conditions was developed . Steel and acrylic were modeled as isotropic linear-elastic materials. Cortical bone was modeled as orthothropic linear-elastic material. Interface conditions between screws, nail, and clamps were modeled with contact elements. Physiological loads representing tip pinch were applied and transfered loads were evaluated. These loads were compared to load in the experimental setup.

RESULTS AND DISCUSSION

The obtained ultimate strength values (Table 1) are all significantly larger (factor 16 –30) than physiologically occurring loads. But all specimens showed plastic deformation after the strength test. The yield strength has to be therefore smaller. Cyclic loading showed no signs of plastic deformation in the nail or screws. All of the specimens proved to be strong enough. The numerical analyses showed that the acrylic clamps create slightly larger bending moments in the screws (Fig.1) then a cortical bone clamp would do. This is due to the larger compliance of this material. The resulting stress concentration in the screws is therefore also slightly larger.

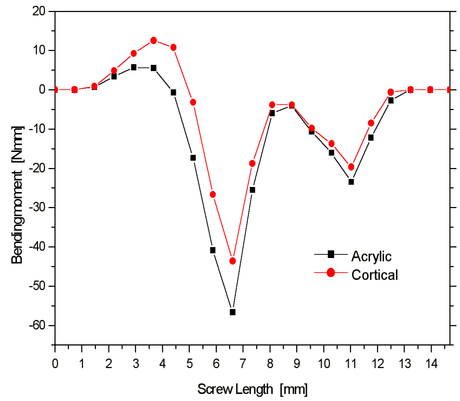

Fig.1: Bending moment in the upper screw at a compression load of 50 N.

The mechanical conditions, created in the experimental tests are very similar to the *in-vivo* loading conditions.

Table 1: Experimental strength values

Test	Strength Value
Compression	1674 ± 66 N
Tension	672 ± 42 N
Bending	6889 ± 1044 Nmm
Torsional	3270 ± 626 Nmm

The experimental and numerical studies in this investigation show clearly the sufficient mechanical strength of the nail-system.

ACKNOWLEDGEMENTS

The authors like to thank the DAAD-CONICIT, Technical University Hamburg-Harburg, Bioengineering Center of Venezuela, and Mathys GmbH for their support in this study.

REFERENCES

1) ASTM: F 1264-*99a Standard Specification and Test Methods for Intramedullary Fixation Devices*.
2) Cooney III W.P., Chao Edmund Y.S., *Biomechanical Analysis of Static Forces in the Thumb during Hand Function*, Journal of Bone And Joint Surgery, 1977 Jan; Vol. 59-A, Nº 1: 27-36.

METHODOLOGICAL CONCERNS USING INTRA-CORTICAL PINS TO MEASURE TIBIOFEMORAL KINEMATICS

Daniel Benoit [1], Dan K. Ramsey [2], Mario Lamontagne [4,5], Per F. Wretenberg [2,3], Gunnar Németh [2,3]

[1]Institution for Surgical Sciences, Section for Sports Medicine, Karolinska Institute, Stockholm, Sweden; [2]Institution for Surgical Sciences, Section for Orthopaedics, Karolinska Institute, Stockholm, Sweden; [3]Department of Orthopaedics, Karolinska Hospital, Stockholm, Sweden; [4]School of Human Kinetics, University of Ottawa, Ottawa, Canada
[5]Department of Mechanical Engineering, University of Ottawa, Ottawa, Canada
daniel.benoit@ks.se

INTRODUCTION

Currently, the most sensitive and accurate means to directly measure tibiofemoral joint motion is with the use of invasive markers implanted in the tibia and femur (Ramsey et al, 1999). To date, we have measured the skeletal kinematics of both the anterior cruciate ligament deficient and the normal knee using this technique (Ramsey et al., 2001). The purpose of this paper is to address the methodological concerns related to the femoral pin and to discuss reliable and safer insertion sites.

METHODS

The skin, subcutaneous tissue and periosteum were anaesthetised with standard anaesthetic and a 15 mm skin incision was cut. The retinaculum patellae laterale was split longitudinally approximately 25 mm. A Hoffman pin (Stryker Howmedica AB Sweden, 3.2 mm diameter, #5038-5-80) was inserted through the cortice of the femur using a manual drill. The pin penetrated the bone obliquely in a postero-medial direction from the frontal plane (Figure 1) to a depth of 10-15mm. Insertion ceased when the subject experienced discomfort. The surrounding area was then wrapped in sterile bandages. Following the surgical procedure, the subjects performed active flexion and extension movements while standing to identify whether movement restrictions were evident. If necessary, range of motion was limited. Subjects were then transported to the laboratory for data collection of the following movements: normal walking, One Legged Jumps, and lateral cut manoeuvre. Having completed the experimental protocol, subjects returned to the operating theatre to have the dressing and pins removed.

Pin Testing

A testing apparatus was designed to determine the amount of force required to permanently deform the bone pins. Pins were secured in a mechanical vice at a depth of 18 mm, approximating the average insertion depth among our subject population. Under two testing conditions, loads were applied perpendicular to the longitudinal axis of the pin at a distance of 15 mm and 20 mm respectively from the insertion sight. A regression line of the applied load was derived and the first inflexion point of the load curve was considered the point of permanent deformation of the bone pin.

RESULTS

Three of the ten subjects bent the femoral pin during activity, the result of an interaction with the surrounding soft tissue and musculature (Figure 2).

During mechanical testing of the pin, experimental load force magnitudes between 36.6–58.7N permanently deformed the pin, dependent upon where the load force was applied.

DISCUSSION

At this insertion depth (18mm) the highest load will be applied over the threaded section of the pin. In this region, the pin has a smaller cross-sectional area and thus is less resistant to bending. Customised pins with a shorter threaded section of 10-15 mm may negate bending. This would result in the threads being completely inserted into the cortice of the bone while exposing the more bending resistant area of the pin.
Alternatively, a solution may be to align the pin through the incision and have the subjects perform dynamic open chain flexion and extension movements while on the operating table. This may stretch the IT band and quadriceps tendon and may guide the femoral pin into a more optimal position prior to it being inserted into the cortex of the bone. With longer longitudinal incisions about the insertion site and by correctly aligning and inserting the femoral pin between the IT band and quadriceps tendon, impingement problems would be diminished.

REFERENCES

Ramsey DK, Lamontagne M, et al (2001). *Clin Biomech,* **16**:61-70

Ramsey DK, Wretenberg PF. (1999). *Clin Biomech,* **14**:595-611

Figure 1: Insertion of the femoral bone pin at an oblique angle of 45° from the frontal plane.

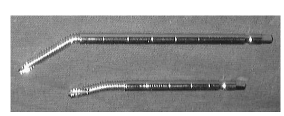

Figure 2: Bent femoral pins. (note: bend occurs in threaded portion)

FLUID STRUCTURE INTERACTION OF HEART VALVES

Gaetano Burriesci[1], Chris J. Carmody[2], Ian C. Howard[2] and Eann A. Patterson[2]

[1]Dipartimento di Meccanica e Aeronautica, University of Palermo, Palermo, Italy, g.burriesci@sheffield.ac.uk
[2]Department of Mechanical Engineering, University of Sheffield, Sheffield, United Kingdom

INTRODUCTION

The understanding of physiological function and operational mechanisms of heart valves has a fundamental role in the design process for prosthetic and, in particular, bioprosthetic substitutes. In fact bioprosthetic heart valves, realized using biological membranes, aim to offer advantages in terms of hemodynamic performances and biocompatibility over their mechanical counterparts by reproducing the behavior of natural valves.

In recent years, the use of the finite element method has led to significant contributions in the simulation of the mechanical behavior of valves. Although, the accurate modeling of these biological components is associated with a great numerical complexity, involving the coupling of non-linear deformable structures with pulsatile fluid flows. Because of these computational difficulties, the fluid and structural phenomena have been studied separately until recently. This implies that assumptions about the load distributions or the valve's instantaneous shape were necessary, introducing approximations in the analyses.

The new available computational technologies permit fluid structure interaction (FSI) to be performed with an increasing degree of confidence.

In this work, the FSI model of a natural human aortic valve is analyzed, and its fluid and mechanical behavior is studied. The model includes the full description of the flow field together with large deformation, material non-linearity and contact. Valve motion is entirely due to the inertia of a fluid moving in a physiological manner.

METHODS

An explicit finite element code with the ability to undertake fully coupled fluid-structure interaction (LS-DYNA 3D) was used to perform the analyses. Moreover, the selected package has already been successfully used to carry out analyses of large deformations of soft biological materials.

The valve geometry was based on data from Thubrikar work (1990), and the root and sinuses on data from Tindale (1984). The model considered the strong material non-linearity typical of leaflets, and included contact routines to deal with the coaption of the leaflets. The change in thickness and the anisotropy of the leaflets is not considered in the model (their effect was studied by the authors previously).

RESULTS AND DISCUSSION

This work illustrates some of the potential of FSI modeling. The predicted flow field showed the important role of the sinuses, where vortexes are produced which determine the closure initiation. Moreover, the FSI model enabled the determination of the spatial pressure distribution acting on the leaflets, which can be of possible application on simpler dry models.

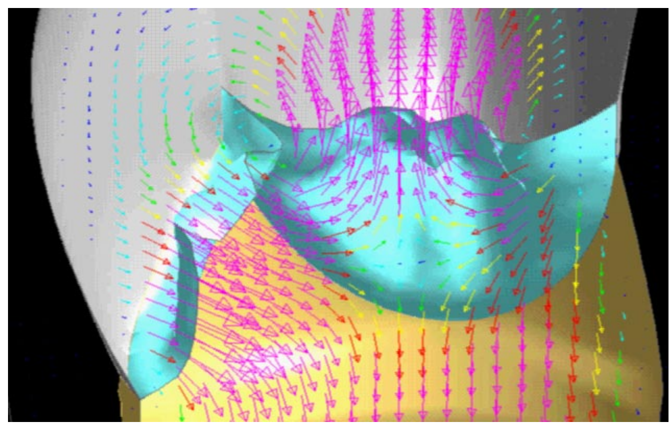

Figure 1: section of the FSI model of the aortic valve. It is possible to observe the presence of vortex in the sinuses, which determine the closure initiation.

REFERENCES

Black, M. M. et al. (1987) *Cardiovascular Reviews and Reports*, 1987, **8**, 12.

Burriesci, G. et al. (1999) *Journal of Medical Engineering & Technology*, **23**, 203-215.

De Hart, J. et al. (1998) *Journal of Biomechanics*, **31**, 629-638.

Patterson, E. A et al. (1996) *Journal of Medical Engineering & Technology*, **20**, 95-108.

Thubrikar, M (1990) *The Aortic Valve*. CRC Press.

Tindale, W. B. et al. (1984) *Experimental and Theoretical Studies of The Fluid Dynamic Performance of Heart Valve Substitutes*. PhD Thesis, University of Sheffield.

ACKNOWLEDGEMENTS

We are greatly indebted to Ove Arup & Partners for providing access to the LS DYNA software and to Dr. Brian Walker for technical assistance.

BIOMECHANICS OF ERYTHROCYTE AGGLUTINATION. DETERMINATION OF ADHESIVE SPECIFIC ENERGY

R.J.Rasia[1] , N.de Isla[2] , L.Altube[3] , J.F.Stoltz[2] and J.Valverde[3]

[1]Optica Aplicada–IFIR(CONICET-U.N.R)– Bv.27 de Febrero 210 bis – CP:S2000EZP - Rosario – Argentine rasia@ifir.ifir.edu.ar
[2] Mecanique et Ingenierie Cellulaire et Tissulaire – Bat.E (Brabois) - 54505 Vandoeuvre les Nancy – France
[3]Inmunohematol, Hemorreol e Inmunogen.–Fac.Cs.Bioq.y Farm.– U.N.R.-Suipacha 531 – 2000 Rosario - Argentine

INTRODUCTION

Measurement of the physical strength of the bonds linking circulating cells to each other or to adjacent tissue surfaces is an important prerequisite for the characterization of adhesion processes occurring in the blood microcirculation. The measurement of the energy involved in cell-cell interactions has significant implications in biological and medical sciences. Quantitative determination of the energy exchanged during immunologic agglutination of red blood cells (RBC) induced by monoclonal antibodies (MAbs) is of great importance, since it gives very useful information to estimate the quality of the antibody (Ab). The quality of an antibody is related to its affinity expressed by the equilibrium constant. The biological activity of an Ab can be estimated by the strength of antigen-antibody bridges. An optical method is proposed to estimate the specific binding energy using the dissociation behaviour of suspended RBC agglutinates in a shear flow and measuring laser backscattering. A constant increase of intensity was observed when the shear stress raises, pointing to a progressive dissociation of RBC agglutinates into smaller ones. The final break-up of two-cell rouleaux is produced at critical shear stress (τ_C), which reflects the mechanical action required to dissociate the molecular bridges between cells. The critical shear stress permitted to define the specific surface adhesive energy (Γ) by using the Derjaguin relation. τ_C provides a good way to assess the functional characterization of specific immunoglobulins, which could be very useful for Ab quality control.

MATERIALS

Blood samples. Fresh A_1, B, A_1B and O blood samples were collected from healthy donors and anticoagulated with EDTA

RBC suspensions. Blood samples were centrifuged 10 min at 2500g. RBCs were washed three times with PBS, containing 0.5% human serum albumin, and finally resuspended at 40% hematocrit in the suspending medium containing MAbs

Suspending media. A solution of Dx 70 (Dextran 70 - MW-70.000 -Sigma Chem. Co. D.1537) at 4.1% in PBS was used

Monoclonal antibodies. Anti-A (lot P47-2) and anti-B (lot P47-4B6) murine MAbs supplied by the Blood Transfusion Centre (CHU of Liege-Belgium) diluted in the suspending medium at 11.25 μg/ml. as determined by the sandwich ELISA method.

METHODS

The Erythroaggregameter (EA) is an automatic optical device built by Stoltz et al. to analyse erythrocyte aggregation, using the light backscattering theory developed by Mills and Aufrere. It measures the intensity backscattered by a thick concentrated suspension of free and aggregated RBCs confined in the gap between two relatively rotating coaxial cylinders. The internal cylinder is fixed while the external one is transparent and rotates at controlled speeds. The EA is coupled to a PC, which commands the whole instrument operation. Agglutinate suspension (1.6 ml) is poured into the gap between both concentric cylinders of the Erythroaggregameter. Samples are exposed to a rotational shear stress ($\boldsymbol{\tau}$) increasing by steps. The application of a constant shear flow in one-direction causes a slow disaggregation of agglutinates. Backscattered intensity (**r**) is recorded at each step of the applied stress ($\boldsymbol{\tau}$) showing a linear correlation with the logarithm of $\boldsymbol{\tau}$, which is calculated at each step using the shear rate (S_R) and the suspension viscosity:

RESULTS AND DISCUSSION

The complete dissociation of agglutinates is only approached asymptotically, so the final break-up of doublets is produced at critical shear stress ($\boldsymbol{\tau_c}$) which is defined by extrapolating the linear portion of the curve **r** (log $\boldsymbol{\tau}$) to $\mathbf{r_0}$ (complete dissociation). The critical shear stress τ_C acts over the upper area A_0 of the cell. R_c is the mean curvature radius of the bridging membranes. The Derjaguin relation states that the fracture energy Γ is: $\boldsymbol{\Gamma=(\tau_c A_O W) / (2\pi R_O)}$, where $W \cong 0.1$ The so obtained $\boldsymbol{\Gamma}$ value is the specific surface adhesive energy characterizing the intercellular adhesiveness (Table I). The more important conclusion is that this innovating method can help in the quality control of monoclonal antibodies and in the diagnostic of immune diseases such as Auto-Immune Hemolytic Anemias.

REFERENCES

P.Snabre, et al. *Biophys.J.*, 1987; 51: 795-807.
Derjaguin B.V., et al. *J.Coll. Interface Sci*. 1975; 53: 314-326.
Donner M. et al *Biorheology*. 1988; 25: 367-375.

Table I : Values of specific surface energy of agglutinate dissociation (Γ) obtained applying this technique.

RBC Group	A	AB	O	B	AB	O	O	O
Ab Specificity	Anti-A	Anti-A	Anti-A	Anti-B	Anti-B	Anti-B	Dx 70 (1.2%)	Dx 70 (4.1%)
Γ [10^{-7} N/m]	7.52 ± 0.60	7.95 ± 0.54	2.96 ± 0.15	9.58 ± 0.78	8.99 ± 0.83	3.17 ± 0.18	2.13 ± 0.08	3.30 ± 0.10

THE EFFECT OF VARYING FREQUENCIES ON THE STIMULATION OF THE AGGRECAN PROMOTER OF CHONDROCYTES EMBEDDED IN AGAROSE GELS

Chi S[1], Chung M[1], Hulme P[1], Doege K[2], Duncan NA[1], and Matyas JR[1]
[1]McCaig Center for Joint Injury and Arthritis Research, University of Calgary, Calgary, Alberta, Canada, jmatyas@ucalgary.ca
[2]Tampa Shriners Hospital, University of South Florida, Tampa, FL, USA,

INTRODUCTION Cartilage is composed of extracellular matrix and chondrocytes, which are responsible for synthesizing and maintaining the matrix. When isolated and cultured in a surrogate matrix of agarose, chondrocytes continue to synthesize extracellular matrix rich in type II collagen and proteoglycans (Buschmann et al., 1992). Aggrecan is the most abundant proteoglycan of cartilage and its rate of synthesis in chondrocytes embedded in agarose increases in response to dynamic compression, but decreases in response to static compression (Buschmann et al., 1995). Less is known about aggrecan gene expression in this gel system, though studies of cartilage explants suggest that aggrecan mRNA parallels aggrecan proteoglycan biosynthesis in response to load (Valmhu et al., 1998). Green fluorescent protein (GFP) is a tool that can be used to monitor the expression of genes and gene promoters in living cells. Splicing the aggrecan gene promoter to the GFP gene allows aggrecan promoter activity to be monitored by following GFP fluorescence in cells. We sought to assess how the frequency of mechanical compression influences aggrecan gene promoter stimulation in chondrocytes embedded in agarose.

METHODS Articular cartilage was harvested from the knee joints of skeletally mature dogs. Chondrocytes were isolated by digestion either: (a) sequentially with hyaluronidase, pronase, and collagenase to produce isolated chondrocytes (IC), or (b) dispase-collagenase to yield enzymatic chondrons (EC). Cells were seeded in hemi-cylindrical 4% agarose gels (4 mm x 4 mm x 2 mm) at a density of $\sim 1 \times 10^6$ cells$\cdot$mL^{-1}. The 0.9 kb promoter fragment (B18) of the aggrecan gene was cloned into a promoterless GFP vector (pTimer-1, Clontech). Cell-gel constructs were transfected using FuGENE™6 reagent and cultured in DMEM/F12 (10% FCS and 1% pen/strep/fungizone). Untransfected cell-gel constructs served as controls. On culture days 5-14, GFP fluorescence was assessed before and after compression using confocal fluorescence microscopy (Zeiss LSM 510). The constructs were compressed dynamically in a specially designed loading jig for 3 hours to a peak strain of 15% at frequencies of 0 Hz (static), 0.001Hz, 0.01 Hz, 0.3 Hz and 1.0 Hz.

RESULTS AND DISCUSSION Little or no fluorescence was observed in the cell-gel constructs prior to loading. Increased fluorescence was observed for ECs loaded at 0.01, 0.3, and 1.0 Hz (Figure 1). Fluorescence did not increase appreciably for ICs loaded at any frequency. GFP expression did not change appreciably in the unloaded condition for both ECs and ICs. These results are summarized in Table 1. The threshold frequency for stimulating the aggrecan promoter in this experimental system is between 0.001 and 0.01 Hz. Between 0.01 and 1.0 Hz, the change in the intensity of GFP fluorescence increases in parallel with loading rate.

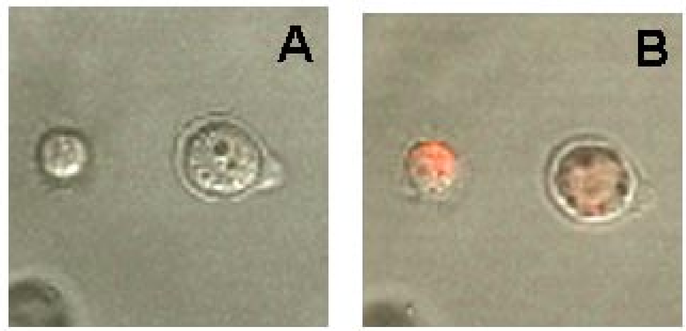

Figure 1. Representative confocal images demonstrating the changes in aggrecan-promoter driven GFP expression (red version) in chondrons before (A) and after (B) compressive loading at a frequency of 1 Hz.

	Enzymatic Chondrons		Isolated Chondrocytes	
	0 Hours	3 Hours	0 Hours	3 Hours
0 Hz (Unloaded)	-	-	-	-
0 Hz (Static)	-	-	-	-
0.001 Hz	-	-	-	-
0.01 Hz	-	+	-	-
0.3 Hz	-	++	-	-
1.0 Hz	-	++/+++	-	-

+ weak fluorescence ++ moderate fluorescence +++strong fluorescence

Table 1: Grades of GFP fluorescence (indicative of aggrecan promoter activity) for EC and IC gels compressed to 15% peak strain at various frequencies.

REFERENCES

Buschmann et al., 1992. *J. Orthop. Res.* **10**: 745-758.
Buschmann et al., 1995. *J. Cell Sci.* **108**: 1497-1508.
Valhmu et al., 1998. *Arch. Biochem. Biophys.* **353**: 29-36.

ACKNOWLEDGEMENTS Canadian Institutes of Health Research, The Arthritis Society, Shriners of North America, The Whitaker Foundation

COMPARISON OF FAILURE PROPERTIES OF SCAR TISSUES IN SKIN, PATELLAR TENDON , AND MEDIAL COLLATERAL LIGAMENT IN THE SAME RABBITS

Akira Omine[1], D. Kent Paulson[1], Gail M. Thornton[1], Nigel G. Shrive[2] and Cyril B. Frank[1]

[1]McCaig Centre for Joint Injury and Arthritis Research, University of Calgary, Calgary, Alberta, Canada
Communicating author: Cyril B. Frank, cfrank@ucalgary.ca
[2] Department of Civil Engineering, University of Calgary, Calgary, Alberta, Canada

INTRODUCTION

There is a long history of investigation into the mechanisms by which soft connective tissues from otherwise healthy normal individuals heal in the absence of any clinical intervention. Skin healing has been studied more extensively than the healing of any other soft tissue, thus providing the major database against which all other soft tissue repair can be compared. Current evidence suggests that soft connective tissues other than skin appear to heal via a similar sequence of events. However, in most studies, healing has been investigated in wounds of only one tissue from individual animals, such as skin, abdominal wall, intestine, nerve, bone, tendon or ligament. The comparison of healing in different tissues, therefore, has been based on results gained in different groups of animals or even in different species. Studies on the relationship of the rate of healing of different tissues would be more relevant if carried out on the same animal, because it would eliminate not only the heterogeneity among groups of animals but also variations in the other factors that can cause interanimal variability. The purpose of this study was to assess the healing of skin, patellar tendon (PT), and medial collateral ligament (MCL) wounds in the same rabbit.

METHODS

Eight skeletally mature 12-month-old female New Zealand White rabbits (mean body weight: 5.8 kg) were used in this study. Z-plasty wounds were created in dorsal skin, left PT, and right MCL in each rabbit. Because the PT may function under high loads compared to skin and the MCL, stress shielding (Ohno, 1993) was applied to the PT by shortening the PT length using a flexible wire and a rod. Postoperatively, all animals were allowed unrestricted cage activity. Six weeks after surgery, all rabbits were sacrificed. To standardize the width of skin to the MCL, dumbell-shaped 4 mm wide specimens were punched with scar tissues in the centre. Likewise, the patella-PT-tibia complexes were prepared by removing the medial and lateral part of the PT leaving a 4 mm wide central PT bundle. Femur-MCL-tibia complexes were prepared by mounting the knee in a MTS test system and dissecting out all structures except the MCL. All scar samples were held at 1N of tension while cross sectional area was measured, using an area caliper (Shrive, 1988). Failure tests were performed on each scar tissue at a rate of 20 mm per minute. To estimate the surface strain on scar tissues, two parallel dye lines were marked on the margin of scar tissues and tissue images were recorded with a CCD camera during failure tests. Three samples of each scar tissue were prepared for histology.

RESULTS AND DISCUSSION

Four wires used in PT stress shielding failed, so these samples were excluded from the PT data. Failure data of the skin, the PT, and the MCL scars are presented in Table 1. The skin scars showed statistically significantly lower failure load, stiffness, and faliure stress compared with the PT and the MCL scars. The skin scars had significantly higher failure strain than the PT and the MCL scars. There were no significant differences between the PT and the MCL scars in the parameters shown in Table 1. All scar samples failed in the scar region. Histologically, the skin scars showed that the extracellular matrix was disorganized and cells were not aligned in any particular orientation. On the other hand, the extracellular matrix of the PT and the MCL scars were organized and cells were aligned with the longitudinal axis of the PT and the MCL. Thus, according to these results, the skin scars were not similar to the PT and MCL scars biomechanically and histologically. These results suggest that soft tissue repair is driven more by environmental factors than genetic factors. However, dealing with structures such as skin, in which the fibres are arranged in a multidirectional way, the orientation of the fibres with respect to the load axis must be taken into consideration (Reihsner, 1998). There might be a limitation in the uniaxial test to compare skin scars with PT and MCL scars.

SUMMARY

The failure properties of skin, PT, and MCL scars in the same rabbits were investigated. Skin scars had significantly lower failure load, stiffness, and faliure stress compared with PT and MCL scars. Skin scars had significantly higher failure strain than PT and MCL scars. There were no significant differences in these properties between PT and MCL scars.

REFERENCES

Ohno, K. et al (1993). *J Orthop Res*, **11**, 592-602.
Reihsner, R., Menzel, E.J. (1998). *J Biomech*, **31**, 985-993.
Shrive, N.G. et al (1988). *J Biomech Eng*, **110**, 104-109.

ACKNOWLEDGEMENTS

We gratefully acknowledge the financial support of the Arthritis Society.

Table 1: Failure properties of skin, PT, and MCL scars (mean ± SD)

Tissues	Failure Load (N)	Stiffness (N/mm)	Failure Stress (MPa)	Deformation (mm)	Failure strain (%)
Skin (n=8)	10.31 ± 4.84 *	2.61 ± 0.87 *	1.56 ± 0.51*	0.54 ± 0.27	24.93 ± 12.18 *
PT (n=4)	210.00 ± 83.34	87.97 ± 47.31	12.99 ± 4.62	0.20 ± 0.08	8.10 ± 1.97
MCL (n=8)	135.61 ± 85.68	57.74 ± 16.65	12.85 ± 6.22	0.34 ± 0.22	8.68 ± 5.45

(* $p < 0.01$ for skin scars vs PT and MCL scars)

CLINICAL AND PLANTAR LOADING RISK FACTORS OF SUBJECTS WITH HALLUX VALGUS

Thomas W. Kernozek[1,2]. Abdulaziz Elfessi[3], Steven Sterriker[4]

[1]Stzelczyk Clinical Biomechanics Laboratory, Physical Therapy Department, University of Wisconsin-La Crosse, La Crosse, WI USA, e-mail: kernozek.thom@uwlax.edu
[2]Gundersen Lutheran Sports Medicine, La Crosse, WI USA
[3]Mathematics Department, University of Wisconsin-La Crosse, La Crosse, WI USA
[4]Private Practice, Waco, TX USA

INTRODUCTION

Previous studies (Yamamoto, et. al., 1996, Blomgren et al., 1991) have addressed some of the differences between the normal foot and the foot with hallux valgus, none have attempted to assess the strength of clinical and plantar loading risk factors in the prediction of the mild to moderate hallux valgus deformity. The present study attempts to do just that.

METHODS

Forty participants with moderate hallux valgus deformity and 51 healthy control subjects of similar age and body weight were studied. The following measurements were obtained: perceived pain while walking, seated first metatarsophalangeal (MPJ) joint range of motion of the involved limb, and resting calcaneal stance position. Plantar loading was assessed barefoot using a capacitive pressure measurement platform (EMED SF, Novel GMBH, Munich). Five trials were gathered for each participant. The intraclass correlation coefficient for stance time for all subjects across all participants was 0.84 indicating a high amount of reliability between trials.

For each pressure measurement trial, 7 plantar regions on the foot were identified: one heel region, one midfoot region, three forefoot regions, and two toe regions. The following variables calculated for each plantar region: peak pressure (PP), peak force (PF), pressure time integral (PTI), and force time integral (FTI). Based on the literature, only the medial forefoot, central forefoot and hallux region were analyzed. Force data was normalized to % body weight.

RESULTS AND DISCUSSION

A logistic regression analysis was used to predict the probability of presence or absence of hallux valgus given a set of scores on the risk factors (independent variables).

Table 1: Logistic regression results using the three clinical variables

Variable	B	Wald	p-value	odds ratio
First MPJ plantar flexion	-.15	9.32	.002	.858
Pain while walking	2.16	6.53	.011	8.69
Resting calcaneal stance position	2.27	7.96	.005	9.71

B=regression coefficient, MPJ = metatarsophangeal joint.

Table 2: Classification table using the clinical variables (overall classification=91.5%)

		Predicted	
		Normal	Hallux valgus
Observed	Normal	49(98%)	1
	Hallux valgus	5	16(76.2%)

Table 3: Logistic regression results using the three plantar variables

Variable	B	Wald	p-value	odds ratio
Hallux Region PF	-.963	8.10	.004	.382
Hallux Region PP	.059	3.03	.082*	1.06
Hallux Region FTI	3.91	5.90	.015	50.1
Central Forefoot FTI	1.01	4.78	.029	2.75

B=regression coefficient, MPJ = metatarsophalangeal joint, *=alpha < .10

Table 4: Classification table using the plantar loading variables (overall classification=93.3%)

		Predicted	
		Normal	Hallux valgus
Observed	Normal	47(94%)	3
	Hallux valgus	3	36(92.3%)

SUMMARY

High values for two (pain while walking and resting calcaneal stance position) of the three clinical variables increased the probability of being a subject with hallux valgus. High values for the three (hallux region peak pressure, hallux region force time impulse and central forefoot force time integral) of the plantar loading variables increased the probability of having hallux valgus. High values on both hallux region peak force and first MPJ joint plantar flexion increased the probability of being a normal subject. Results from this study demonstrated that the clinical and plantar loading variables are able to differentiate significantly between the two subject groups. The evidence from this research suggests the plantar loading variables had more predictive power in classifying the subject with foot deformity than the clinical variables that we chose to examine. The same variables incorrectly predicted 6% of the normal subjects as having hallux valgus (false-positive prediction). The clinical variables had a 2% false-positive prediction rate for hallux valgus.

REFERENCES

Yamamoto, H. et al. (1996) *Clinical Orthop.* **323**, 247-53.
Blomgren, M. et al. (1991) *J of Foot Surg.* **30**, 70-1.

MODEL BASED AUDITORY FEEDBACK ON THE LIFTING TECHNIQUE MAY REDUCE SPINAL MOMENTS OF WAREHOUSE WORKERS

Thomas W. Kernozek[1,2], Brian Langenhorst[3], Jessica Woodworth[1], William Haviland[1]
[1]Stzelczyk Clinical Biomechanics Laboratory, Physical Therapy Department, University of Wisconsin – La Crosse, La Crosse, WI USA, e-mail: kernozek.thom@uwlax.edu
[2]Gundersen Lutheran Sports Medicine, La Crosse, WI USA.
[3]Franciscan Skemp Healthcare, Occupational Health Department, La Crosse, WI USA.

INTRODUCTION

Exposure to physical stress has been related to low back pain and injury (Norman et al., 1998). Brophy et al. (2001) reported that the reduction of low back injuries reduces financial costs associated with low back injury and lost workdays. Auditory feedback during performance has been used effectively to reduce the peak ground reaction forces during landing from a jump and with lifting (McNair et al. 2000, Lavender & Andersson, 2000). Perhaps, coaching and performance based auditory feedback of warehouse workers can reduce the peak spinal moments during lifting/lowering. The purpose of this paper was to address this question.

METHODS

A 6-week study was completed at a local distribution center. Twenty male workers that performed a variety of warehouse tasks participated. Ten of these workers were placed into an experimental group (receiving technical and performance based auditory feedback) and 10 served as a control group. Each group was divided equally based on anthropometric data. Baseline data on the side-bending, flexor, and rotary moments at L5/S1 of each participant were collected with the Motion Monitor Electromagnetic Tracking Device (IST, Inc., Chicago, IL) during lifting scenarios for 6 lift-lowering tasks. This system uses analog scale data and X, Y, Z coordinate data of the participant to calculate the spinal moments at L5/S1 (Lavender & Andersson, 2000). On week 2, the experimental group received technique coaching and auditory feedback through the computer speakers based on the magnitude of the moments during lifting-lowering (Lift Trainer software, IST, Inc., Chicago, IL). On week 4, the experimental group received the same coaching and auditory feedback. On week 6, all participants were tested under the same conditions as during the baseline testing.

RESULTS AND DISCUSSION

A series of repeated measures analysis of variance [1 between (Group), 1 within (Time)] were performed on the average maximum moments from 6 lift/lowering cycles in all three directions: side-bending, flexor and rotary. For the side-bending and rotary moment the absolute values were used in the calculations. There was a significant group X time interactions for the side-bending moment ($p < 0.05$), the flexor moment ($p < 0.05$) but not the rotary moment ($p > 0.05$)

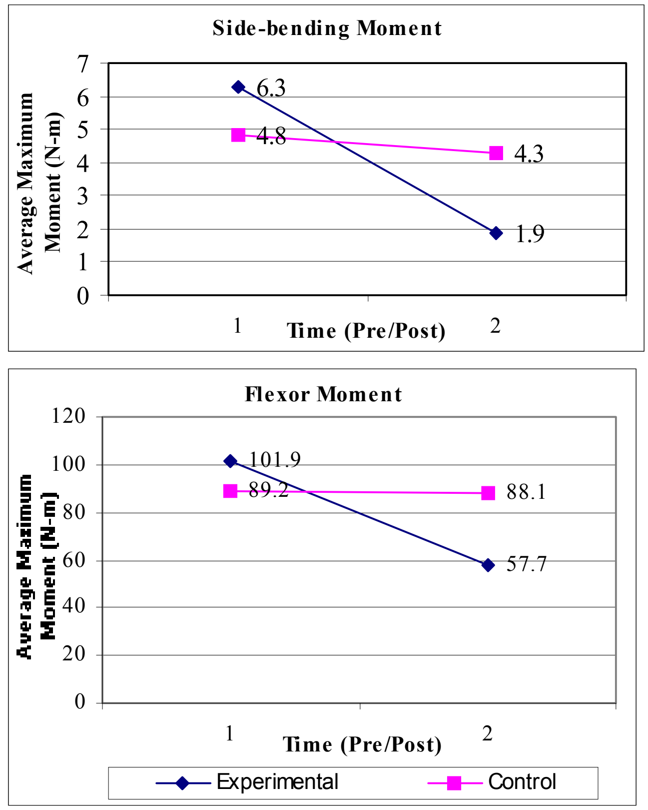

Figure 1: Average Maximum Side-bending and Flexor Moments (Average Maximum from 6 lift/lowering cycles) for Groups (Experimental, Control) over Time (Pre/Post).

SUMMARY

Coaching combined with auditory feedback during lifting/lowering may be effective in reducing the average maximum side-bending and flexor moments of warehouse workers over the short term (6 weeks).

REFERENCES

Brophy MO et al. (2001) *AIHAJ*, 62: 508-511.
Lavender S & Andersson, G (2000) *46th Meeting ORS*, 0393.
Mc Nair PJ et al. (2000) *Br J Sports Med*, 34, 293-296.
Norman R et al. (1998) *Clinical Biomechanics*, 13, 561-573

ACKNOWLEDGEMENTS – Support of the Kwik Trip Foundation, Melissa Anderson and Nick Biederwolf.

DYNAMIC Ca^{2+} RESPONSE IN VASCULAR ENDOTHELIAL CELLS SUBJECTED TO VARIOUS FLOWS

Baoguo Chen[1], Lisa X. Xu[1, 2], Steven H. Frankel[2], Karen M. Haberstroh[1], Michael Plesniak[2], Thomas J. Webster[1], Steve Wereley[2]
[1]Dept. of Biomedical Engineering and [2]School of Mechanical Engineering
Purdue University
West Lafayette, Indiana, 47907, USA
lxu@ecn.purdue.edu

INTRODUCTION

Intracellular calcium, a primary regulator of physiological functions, is involved in a variety of mechanotransduction signaling pathways in the vascular endothelium when subjected to different fluid flows. The activity of the constitutive endothelial nitric-oxide (NO) synthase is regulated by the level of Ca^{2+} binding to calmodulin, which plays important vascular physiological functions, such as regulation of blood flow, prevention of adhesion of platelets and leukocytes, etc.

METHODS

The study of Ca^{2+} dynamics in living cells has been revolutionized over the past decade by the development of dyes that exhibit fluorescent property changes upon binding Ca^{2+}. Fura-2 has been extensively used to measure endothelial $[Ca^{2+}]_i$ in individual cells and isolated vessels and organs using ratiometric fluorescence imaging. Binding to Ca^{2+} under the excitation of UV light, Fura-2 emits green light at the wavelength of 510 nm (Grynkiewicz, 1985; Haugland, 1996). The emission intensity is proportional to the calcium concentration when excited by radiation shorter than approximately 360 nm (isobestic point), and inversely proportional to the calcium concentration under the longer excitation wavelength. This allows one to take the ratio of the emission intensities excited by the source light at two different wavelengths (i.e. 340 nm and 380 nm) commonly used for Fura-2, which is directly related to $[Ca^{2+}]_i$, and independent of dye concentration, source intensity, and optical path length.

RESULTS AND DISCUSSION

Using an oil immersion lens (100x) and our Zeiss Axioskop 2 motorized focus research microscope for ratiometric imaging, fluorescence signals emitted from Fura-2-Ca^{2+} compounds can be measured under excitations of 340 nm and 380 nm. Figure 1 shows the images of vascular endothelial cells under 380 nm excitation. At the conference, we will present our measurements of the real-time Ca^{2+} in vascular endothelial cells subjected to various simulated fluid flows. We will also elucidate the interrelationship between the intracellular Ca^{2+} level with the corresponding synthesis and release of various signaling factors important to atherosclerosis development.

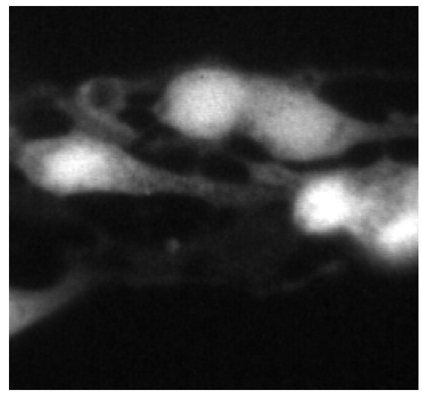

Figure 1 Vascular endothelial cells labeled with calcium sensitive dye (magnification: 1000X).

REFERENCES

1. Grynkiewicz, G, Poenie, M, Tsien, RY (1985). “A new fluorescence properties”, *J. Biol. Chem.*, **260**: 3440-3450.
2. Haugland, R (1996). **Handbook of Fluorescent Probes and Research Chemicals**, Molecular Probes, Eugene.

ACKNOWLEDGEMENTS

We are grateful to the B.F.S. Schaeffer Award and the Showalter Trust Award for funding for this work.

IN VIVO TIME-DEPENDENT TENSILE DEFORMABILITY OF HUMAN LUMBAR SPINE SEGMENTS, MEASURED IN TRACTION BATH THERAPY IN TERMS OF AGING, SEXES, WEIGHT AND HEIGHT

Marta Kurutz[1], Eva Bene[2], Antal Lovas[1], Erika Monori[3], Peter Molnár[3]
[1]Budapest University of Technology and Economics, Budapest, Hungary, kurutzm@eik.bme.hu
[2]Hungarian Institute of Rheumatology and Physiotherapy, Budapest, Hungary,
[3]Szent Imre Hospital, Budapest, Hungary

INTRODUCTION

In vivo experimental results for tensile deformability of human lumbar motion segments are presented. Elongations of lumbar segments were measured during the usual traction bath hydrotherapy of patients, where the lumbar segments are subjected to pure centric tension, and the effect of muscles can almost be excluded. The aim was to document the time and load related spinal deformations in terms of aging, sexes, body weight, body height and their combinations. Viscoelastic characteristics of segments have also been obtained. Based on the experimental results, in vivo numerical tensile model of human lumbar segments has been created.

METHODS

Weightbath therapy is applied to stretch the different parts of spinal column. The therapy has been introduced by *Moll* (1953,1956,1963), later described by *Bene* (1988), biomechanics, indications and contraindications are detailed by *Bene* and *Kurutz* (1993). The patients are suspended cervically in water for 20 minutes, loaded by extra lead weights on the ankles. The free elastic suspension in lukewarm water and buoyancy help to relax muscles and let the traction effect optimally develop. Tensile deformations are considered as the decrease of compressive deformations existing before the treatment. Deformations have been measured by using a special subaqual ultrasound measuring method developed by the authors. A mobile ultrasound instrument connected to a computer has completed the weightbath equipment. A special software has been used for analyzing the ultrasound pictures. Deformation of segments was considered as a change of the distance between the spinous processes of neighboring vertebrae. In vivo deformations of segments L3-L4, L4-L5 and L5-S1 were measured. More than 3000 ultrasound pictures of about 400 segments of 155 adult patients have been evaluated in terms of aging, sexes, body weight, body height and their combinations. 88 patients with extra lead loads, 67 patients without extra loads have been measured.

RESULTS AND DISCUSSION

Percentage of deformability of segments is illustrated in Fig. 1 during the traction bath treatment in group with extra loads, for a general lumbar segment LIII-SI, for sexes. By distinguishing the segments, for LIII-IV, the ratio of deformed segments was 52% at t=0 min, 74% at t=3 min, and 85% at t=20 min. For LIV-V it increased from 47% through 60% to 70%, for LV-SI it changed from 29% through 49% to 68%.

Figure 1 - Ratio of segment deformability during the treatment

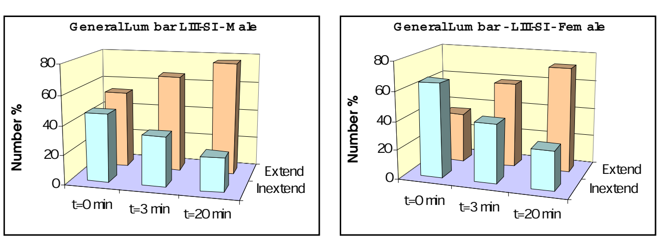

Figure 2 shows the mean elongations of each segment in the different phases of the treatment. Both the ratio and the value of tensile deformability increased during the traction treatment, with a decrease in distal direction. Just being suspended (t=0 min), due to the decompression and the buoyancy, unloading of discs and segments occur, even without any extra weights, significant elastic deformation develops (0,4-0,6 mm). At the end of the treatment (t=20 min), the mean viscoelastic elongations were 0,8-1,0 mm without, and 0,8-1,4 mm with extra weights. During the treatment, both the ratio and the value of deformability increased with a decreasing tendency in distal direction.

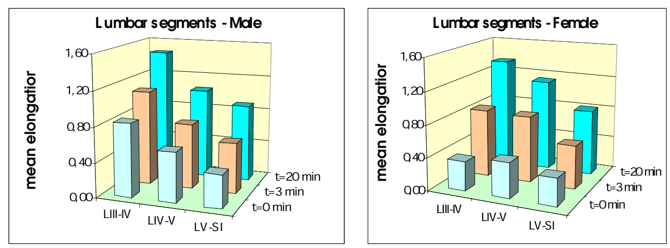

Figure 2 - Mean elongations of segments during the treatment

Correlation was found between deformability and aging. The scales of elongations with the associated mean ages demonstrate in Fig. 3 that higher deformation values occur generally at younger age.

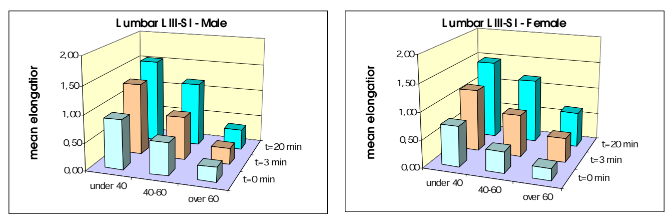

Figure 3 - Elongation decrease vs aging

SUMMARY

By means of a large-scale in vivo experimental analysis the tensile deformability of lower lumbar segments LIII-IV, LIV-V and LV-SI has been numerically documented in terms of certain biomechanical parameters. Time-, age-, sex-, weight- or height-dependence have been numerically verified for each segment. Viscoelastic numerical model was created with elastic and damping coefficients for each segments and sexes, based on in vivo measured results.

REFERENCES

Bene, E.(1988). Phys. Med. Baln. Klin. **17**, 67-71.
Bene, E., Kurutz, M. (1993). Orv.Hetil. **134**,1123-1129.
Moll,K., (1953). Orv.Hetil. **94**,292-2966.
Moll,K.,(1956). Contempl. Rheum. 97, 326-329.
Moll,K., (1963). Rheum. Balneol. Allerg. **3**, 174-177.

ACKNOWLEDGEMENTS

The study was supported by projects OTKA T-022622, T-033020, M-027469 and OM FKFP-0371/97, FKFP-0309/99.

AGE- AND SEX-DEPENDENT IN VIVO VISCOELASTIC NUMERICAL TENSILE MODELS OF HUMAN LUMBAR SPINE SEGMENTS

Marta Kurutz
Budapest University of Technology and Economics, Budapest, Hungary, kurutzm@eik.bme.hu

INTRODUCTION In vivo experimental results for tensile deformability of human lumbar motion segments are reported by *Kurutz et al* (2002a, 2002b). Based on the measured time related spinal deformations in terms of aging, sexes, body weight and height, large-scaled parameter-dependent numerical viscoelastic models of human lumbar spine segments have been created for tension.

METHODS Segment deformations were measured during the usual traction bath therapy of patients, where the lumbar segments are subjected to pure centric tension, and the effect of muscles can be excluded. Weightbath therapy of spine has been introduced by *Moll* (1956), biomechanics of the treatment by *Bene* and *Kurutz* (1993). In weightbath, patients are suspended cervically in water for 20 minutes, with extra lead weights on the ankles. Deformations of segments were measured by using a special subaqual ultrasound method reported by *Kurutz et al* (2002). Time-related in vivo deformations of segments L3-L4, L4-L5 and L5-S1 were documented. More than 3000 ultrasound pictures of 409 segments of 155 adult patients have been evaluated.

For the viscoelastic numerical model, the versions of Poynting-Thomson spring-dashpot models have been used (Figs 1 and 2). Spring constants c_1 and c_2 represent the elastic properties, damping coefficient k concerns the creep effects. From three time-related measured elongation values u_1, u_2, u_3, the elastic and damping moduli c_1, c_2 and k have been determined for all the 409 measured lumbar segments with the creep functions for both model A and B.

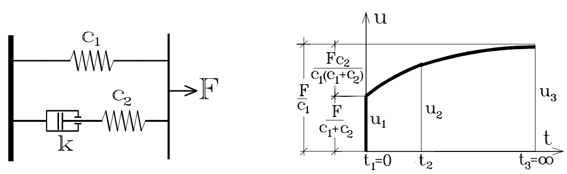

Figure 1 – Viscoelastic model A

We supposed that the last state at the 20[th] minute of the treatment concerns the steady state of the viscoelastic process. Creep functions of the lumbar segments have been obtained in terms of sexes, aging and other parameters.

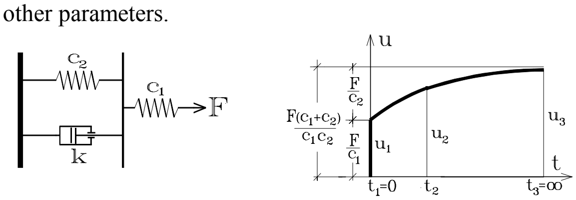

Figure 2 – Viscoelastic model B

RESULTS AND DISCUSSION At the beginning of treatment, just being suspended in water (t=0 min), due to the decompression and buoyancy, unloading of discs and segments occur, so significant elastic deformations develop. The initial elastic moduli are seen in Fig. 3, demonstrating that the rigidity of segments increases significantly with aging, and increases also in distal direction. Based on the measured time-related elongations in vivo, the creep functions of segments are obtained.

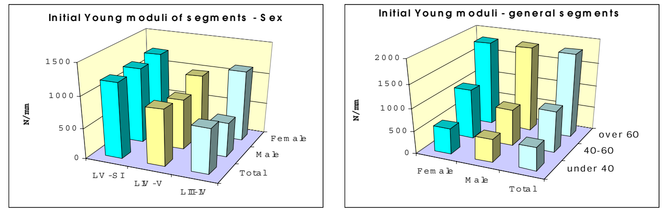

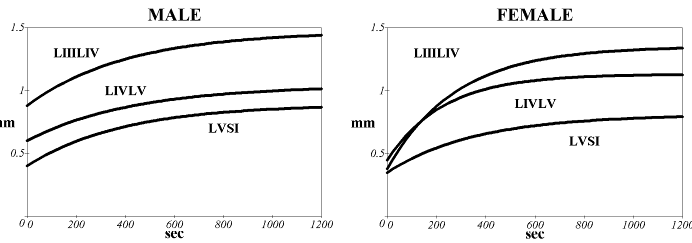

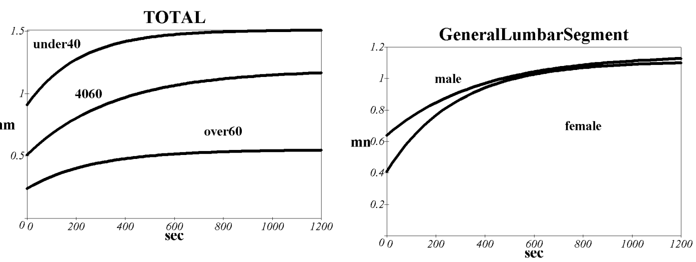

Figure 3 – Initial Young moduli vs sexes and aging
Figure 4 – Creep functions of lumbar segments
Figure 5 – Creep functions vs aging and sexes

Decreasing deformability and increasing damping can be observed in distal direction in Fig. 4. Influence of aging and sexes is illustrated in Fig. 5 for general lumbar segments LIII-SI. Due to the increasing damping with aging, the decreasing creep and deformability is numerically verified. In *Kurutz et al.* (2002a, 2002b) a difference was reported in reaction time of males and females. This observation has been verified by means the creep analysis: while males have higher instant elastic deformations, due to the smaller damping of females, the deformation propagation of women almost overtakes that of the men.

SUMMARY Based on large-scale in vivo experiments, viscoelastic tensile behaviour of human lumbar segments has been numerically verified. Numerical creep models of lumbar segments have been created in terms of several parameters. Elastic and damping moduli with creep functions have been calculated for each case. Mechanical models A and B are offered for numerical aims, to model each of the component organs of lumbar spine segments (vertebrae, discs, ligaments, etc.) in pure centric tension.

REFERENCES

Bene, E., Kurutz, M. (1993). Orv.Hetil. **134**,1123-1129.
Kurutz, M. et al. (2002a), Orv. Hetil. (in press)
Kurutz, M. et al. (2002b), WCB2002, abstract
Moll, K.,(1956). Contempl. Rheum. 97, 326-329.

ACKNOWLEDGEMENTS The study was supported by projects OTKA T-022622, T-033020, M-027469 and OM FKFP-0371/97, FKFP-0309/99.

APPLICATION OF BIO-ELECTRICAL IMPEDANCE METHOD FOR ESTIMATING THE RATIO OF EXTENSORS TO FLEXORS IN THE MUSCLE VOLUME OF THE UPPER ARM

Masae Miyatani[1], Noriko Ishiguro[1], Yoshihisa Masuo[2], Hiroaki Kanehisa[1] and Tetsuo Fukunaga[1]
[1]Dept of Life Sciences (Sports Sciences), University of Tokyo, Japan, cc07725@mail.ecc.u-tokyo.ac.jp, [2]Art Haven 9 Co., LTD

INTRODUCTION The force generation capacity of a muscle is closely related to its size. Therefore, to establish the method for quantifying muscle volume (MV) conveniently is important in sports sciences and/or clinical research fields. Recent studies indicated that bio-electrical impedance (BI) method was useful to estimate the muscle volume of the upper arm (Miyatani et al. 2001a). By the use of BI method, however, no study has tried to quantify the MV of muscle group located in either anterior or posterior sites of limbs. On the other hand, we recently found that BI method could be applied to determine the length changes in the muscle and tendon tissues of the elbow flexors (EF) while this muscle group contracted isometically (Miyatani et al.2001b). This implies that the changes in the length of EF during elbow flexion can be also detected using BI method. Hence, we tried to estimate the ratio of elbow extensors (EE) to EF in the muscle volume (V_{EE}/V_{EF}) by applying an electrical parallel-circuit model constructing the two muscle groups (Figure 1). In this model, we hypothesized five conditions. First, each the muscle volume of EE (V_{EE}) and the muscle volume of EF (V_{EF}) is constant whatever the elbow joint angle (θ) changes. Secondly, the length change of EF ($L_{EF}(\theta)$) is expressed as a function of the changes of θ. Thirdly, the changes in the BI of EE (Z_{EE}) during elbow flexion are very small in comparison with those of EF (Z_{EF}) regardless of θ, because the specific resistivity of EE ($\rho_{EE}(\theta)$) (Gielen et al. 1981) and the length of EE ($L_{EE}(\theta)$) (Murray et al. 2000) act reciprocally to cancel their influences on Z_{EE} during elbow flexion. Therefore, Z_{EE} can be considered relatively constant regardless of θ, and so the whole upper arm BI ($Z_T(\theta)$) reflects $Z_{EF}(\theta)$. Fourthly, $Z_{EF}(\theta)$ is replaced to $Z_T(\theta)$ and expressed as a function of θ and V_{EE}/V_{EF} (Figure 1, *eq.1)*. Fifthly, based on the assumptions mentioned above, V_{EE}/V_{EF} can be calculated using $Z_T(\theta)$ for two known θ conditions (Figure 1, *eq.2*). The present study aimed to examine this hypothesis by comparing the data obtained from MRI method.

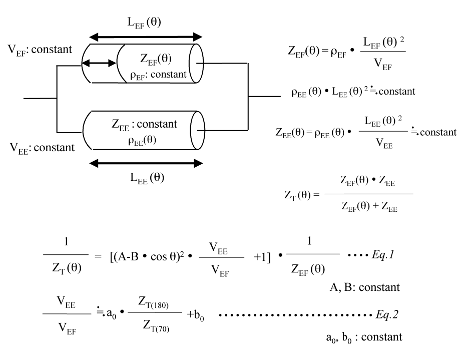

Figure 1: The principle of the estimation for the ratio of EE to EF in the muscle volume using BI method.

METHODS Subjects were thirteen healthy adult men (n=6) and women (n=7). Z_T of the right upper arm (shoulder-to-elbow) was measured at each of elbow joint angles of 180°and 70° by the use of a BI analyzer (Muscle α, ART HAVEN 9, Japan) with an operating frequency of 50KHz at 500 μ A. MRI method was used to determine the MV values of the EE and EF in the right arm. Transverse scans were carried out with 1cm thickness with no gaps, from the elbow joint to the head of humerus. By summing up the anatomical cross-sectional area of each of EE and EF along its length and then multiplying by the interval of 1cm, the MV was determined. V_{EE}/V_{EF} in the MV determined by MRI method was calculated and referred to as $V_{EE}/V_{EF\ (MRI)}$. In the case of BI method, V_{EE}/V_{EF} ($V_{EE}/V_{EF\ (BI)}$) was estimated from the relation between the ratio of Z_T at 180°($Z_{T(180)}$) to that at 70°($Z_{T(70)}$) ($Z_{T(180)}/Z_{T(70)}$) and $V_{EE}/V_{EF\ (MRI)}$.

RESULTS AND DISCUSSION $V_{EE}/V_{EF\ (BI)}$ was significantly correlated to $V_{EE}/V_{EF\ (MRI)}$ with a correlation coefficient of 0.832 ($p<0.01$, SEE=0.123:11.0%, Figure 2). This validates the electrical parallel-circuit model used in this study and implies that $V_{EE}/V_{EF(MRI)}$ can be estimated using Z_T value determined at two elbow joint angles. Since the total MV of EE and EF can be determined by dividing the right upper arm length^2 by Z_T at 180° (Miyatani et al.2001a), the MV of each of EE and EF can be estimated by using $V_{EE}/V_{EF\ (BI)}$.

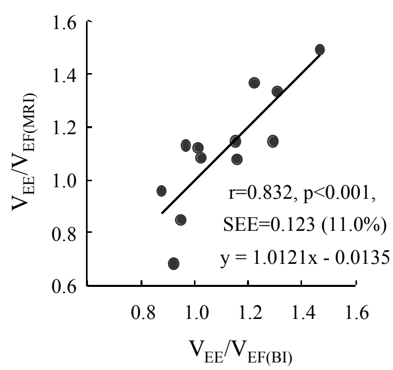

Figure 2: The ratio of EE to EF in the muscle volume measured using BI method ($V_{EE}/V_{EF(BI)}$) and MRI method ($V_{EE}/V_{EF(MRI)}$)

REFERENCES

Miyatani, M. et al. (2001a) *J. Appl. Physiol.*, **91**, 386-394.
Miyatani, M. et al. (2001b) *Proceedings of the XVIIth Congress of the International Society of Biomecanics*, 624
Gielen, F.L.H et al. (1981) *Proceedings of the Vth ICEBI*, 191-194
Murray W.M., et al. (2000) *J. Biomechanics*, **33**, 943-952

OPTIMAL ANALYSIS OF MUSCULOTENDINOUS FORCE DURING INDEX FINGER MOTION

Shigeru Tadano[1] and Kazuki Fukada[2]
Division of Mechanical Science, Hokkaido University, Sapporo, Japan
[1]Professor, tadano@eng.hokudai.ac.jp, [2]Graduate Student

INTRODUCTION

Hand-finger motion realizes fundamental activities on human daily life as pinching, gripping and holding. In the human finger, because so many muscles and tendons run to be intermixed, it is impossible to measure these forces using a bioinstrumentation as myoelectric potential. Therefore, some numerical analyses have been tried for the estimation of musculotendinous force. The aim of this work is to propose a three dimensional model of the index finger and to analyze musculotendinous forces and joint reaction forces using optimizing method of numerical analysis for an indeterminate structure.

METHOD

When a three dimensional model of index finger was constructed with eight muscles and tendons, the following assumptions were considered; no friction in joints and tendon sliding, bone as a rigid body without mass, DIP and PIP joint in one axial rotation and MP joint in two axial rotations. Each musculotendon is defined as a straight element from the origin to the insertion. Positions of the origin and the insertion were measured from X-ray CT image. The static analysis, which uses static equilibrium equations of force and moment, was applied to this model. Because twelve unknown parameters of eight musculotendinous forces and four joint reaction forces must be solved from six equilibrium equations on force and on moment in three-dimensional directions, this analysis is statically indeterminate problem of structural analysis. The SQP method (Successive Quadratic Programming Method) of optimization analysis was applied to this model. For constraint conditions, musculotendinous forces are always compression and joint reaction force at only vertical direction is always compression. The optimization process is to minimize the objective function defined as the summation of force square, taking these constraint conditions into account.

RESULTS AND DISCUSSION

The touch-typing motion was analyzed as a typical finger motion. In this case, the index finger moves in flexion-extension by three finger joints in wrist joint fixation at middle position. Vertical force to axial direction against radius was applied at the tip of index finger. Every joint angle was decided in advance. Figure 1 shows the result of touch-typing. Here muscle and tendon force at each position are expressed with nondimensinonal value divided by applied force. From the figure, every force varied with moving. For example, radial interosseus (R) decreased gradually with moving, and terminal extensor tendon (T) showed zero value to No. 3 position, and increased after that. It is clear that the total force shows the minimum value at No. 4. This position will be the optimal position at touch-typing.

SUMMARY

From X-ray CT image, a 3D musculotendinous model of index finger could be constructed in faithful to the anatomical structure. Using the SQP method of the optimizing analysis, musculotendinous forces or joint reaction forces at index finger in touch-typing motion could be calculated and an optimal posture could be confirmed.

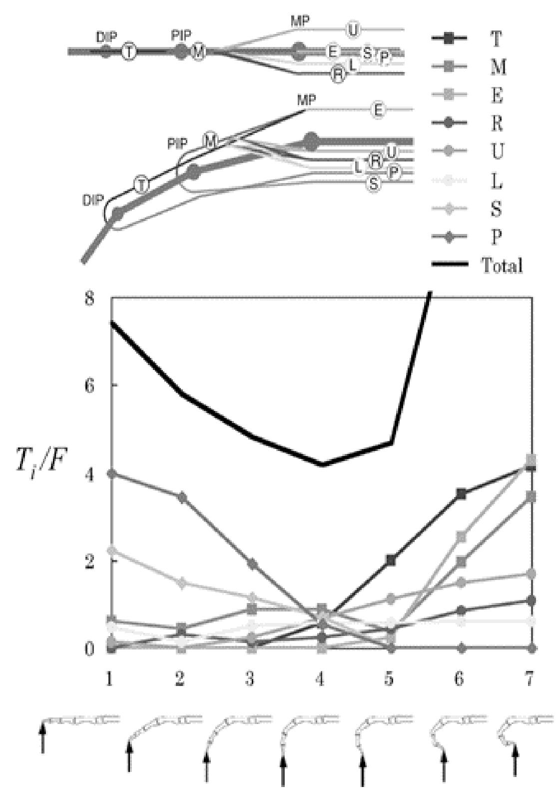

Figure 1: 3D finger model and computational result of each musculotendinous force

PREDICTION OF THE METABOLIC ENERGY CURVE DURING RUNNING AGAINST INCLINES: IMPLICATIONS FOR DELTA EFFICIENCY

Kirsten E. Bijker, Gert de Groot and A. Peter Hollander

Institute for Fundamental and Clinical Human Movement Sciences, Faculty of Human Movement Sciences, Vrije Universiteit Amsterdam, the Netherlands, K.Bijker@fbw.vu.nl

INTRODUCTION

The delta efficiency during running is much greater than the muscle efficiency. Recently, Bijker et al. (submitted) suggested that the combination of eccentric and concentric leg muscle actions, together with the large difference in their efficiency explains the great delta efficiency during running against small inclines. With running against steeper inclines, the amount of concentric contractions increases whereas the amount of eccentric contractions decreases and eventually becomes negligible (Taylor, 1994). This consequently should lead to an exponential increase in the oxygen consumption and a smaller delta efficiency. Our first hypothesis was that the delta efficiency during running against steep inclines is much smaller than the delta efficiency based on small inclines.
During level running, the horizontal component of the ground reaction force (CRF) can be divided into a braking and propulsive phase. The braking phase includes eccentric muscle actions, whereas in the propulsive phase concentric contractions dominate (Dickinson et al., 2000). Our second hypothesis was that the shape of the metabolic energy curve during running against inclines is determined by changes in braking and propulsive impulses.

METHODS

To run against steep inclines at a submaximal level, we used a reduced gravity simulator (Donelan and Kram, 2000). Seven subjects ran against inclines ranging from 0-13% at 50% simulated reduced gravity. Delta efficiencies were calculated from the regression coefficients of the regression lines, describing the external mechanical and metabolic power data. Braking and propulsive impulses were obtained by integrating respectively all negative and positive values of the GRF component parallel to the treadmill surface over the time of ground contact. Braking and propulsive impulses were divided by efficiencies of eccentric and concentric exercise (80% and 18%, Minetti et al., 1994) to obtain a metabolic measure of both muscle action types. For each incline, these concentric and eccentric metabolic measures were summed to obtain predicted metabolic energy curves in arbitrary units.

RESULTS AND DISCUSSION

With running against steeper inclines, all subjects showed an exponential increase in oxygen consumption (Fig. 1). Consequently, the delta efficiency during running was dependent on the range of inclines used. For inclines ranging from 0-5%, the mean (± SEM) delta efficiency was 59% (± 9.3), whereas for the inclines, ranging from 8-13%, the mean delta efficiency was 24% (± 1.5) ($p < 0.05$). Furthermore, with running against steeper inclines, the propulsive impulse increased, where as the braking impulse decreased. Figure 1 shows the mean measured as well as the mean predicted metabolic energy curve, which was based on braking and propulsive impulses. The correlation coefficient between both metabolic energy curves was 0.99.

Figure 1: mean measured (squares) and predicted (triangles) metabolic energy consumption for running in a 50% simulated reduced gravity situation.

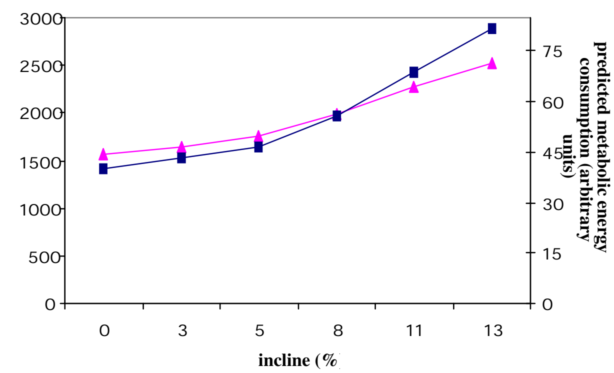

The results of the present study clearly show that the delta efficiency during running is dependent on the amount of applied load (incline). Furthermore, the results confirm our hypothesis that changes in horizontal braking and propulsive impulses determine the shape of the metabolic energy curve and consequently also the delta efficiency during running against inclines. We therefore suggest that the delta efficiency during running is mainly determined by the relative contribution of concentric and eccentric muscle actions.

REFERENCES

Bijker, K.E., de Groot, G., Hollander, AP. (submitted). Eur. J. Applied Physiol.

Dickinson, M.H., Farley, C.T., Full, R.J., Koehl, M.A.R., Kram, R., Lehman, S. (2000). Science, 288, 100-106.

Donelan, J.M., Kram, R. (2000). J. Exp. Biol. 203, 2405-2415.

Minetti, A.E., Ardigò, L.P. and Saibene, F. J. exp. Biol. 195, 211-225.

Taylor, C.R. (1994). Adv. Vet. Sci. Comp. Med., 181-215.

QUANTIFICATION OF SOFT TISSUE VIBRATION FREQUENCY IN HEEL-TOE RUNNING

Benno M. Nigg, Katherine A. Boyer, James M. Wakeling

Human Performance Laboratory, University of Calgary, Calgary, Alberta, Canada

INTRODUCTION

Impact forces in heel toe running can be characterized as an input signal with an amplitude and frequency, typically 10-20Hz. It is expected that vibrations of the soft tissue packages of the lower extremities would be initiated and that they would be substantial when the frequency of the impact force and natural frequency of the specific soft tissue package are close. Oscillations do occur but are small and of short duration indicating that the soft tissue packages oscillate in a damped manner. To avoid resonance phenomena the muscle(s) in a soft tissue package must change their mechanical properties by changing the natural frequency and/or the damping characteristics (Nigg and Wakeling, 2001). It has been shown for isometric and isotonic contractions of the leg that such changes in mechanical properties do occur through changes in muscle activity (Wakeling and Nigg, 2001). However such changes under the dynamic conditions of human locomotion have yet to be documented. Thus, the purpose of this study was to test the hypothesis that soft tissue vibration frequencies change within one step of heel-toe running. It is expected that the maximum vibration frequency of the soft tissue packages will occur shortly after the impact force peak as a protective measure to avoid coinciding with the input frequency.

METHODS

Accelerations of three soft tissue packages of the lower extremity (gastrocnemius, quadriceps and hamstrings) and ground reaction forces were measured for ten recreational runners during heel-toe running on an indoor track surface. The running speed remained constant. Data was collected for 10 steps using a remote data acquisition system. The vibration frequencies in three orthogonal planes were determined by tri-axial accelerometers mounted on the skin overlaying the selected soft tissue packages. A uni-axial accelerometer (<1g) was attached to the heel cup of the right running shoe to determine the time of first ground contact for each step. Voltage signals from both the accelerometers were transmitted to a base computer via a wireless transceiver.
The accelerometer signals were resolved into time- frequency components using wavelet techniques (von Tscharner, 2000). The mean frequency at each sampled time was then calculated.

RESULTS AND DISCUSSION

The results showed that the natural vibration frequencies of soft tissue packages change through the stance and swing phases of heel-toe running. The results from one subject are shown (Fig. 1), the vibration frequency ranges from 9Hz in the swing phase to a peak of 24Hz shortly after impact. Changes in mean frequency during each stride occurred for all three measured soft tissues. These results indicate that soft tissue packages do change their mechanical properties, specifically their mean vibration frequency, during heel-toe running. The peak natural frequency illustrated for one subject, one shoe condition, one specific speed and one soft tissue package is greater than the frequencies measured for impact forces and hence the likelihood of resonance phenomena in this example is minimal. However, it is speculated that selected soft tissue packages show more changes in vibrations for different running speeds or different shoe conditions.

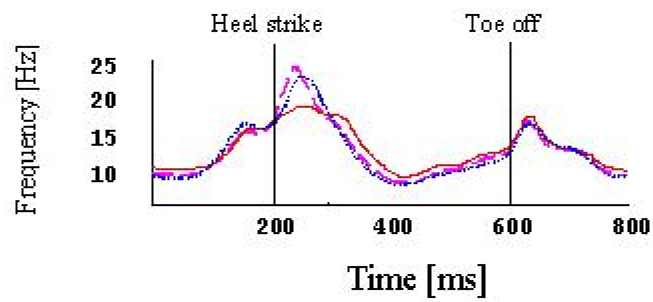

Figure 1: Gastrocnemius mean vibration frequency for axial (dashed), mediolateral (solid), and anterior-posterior (dotted) directions for heel-toe running.

SUMMARY

The results of this study show that under the dynamic conditions of running soft tissue packages do change their mechanical properties.

REFERENCES

Von Tscharner, V. (2000). *J Electromyog.Kinesiol.* **10**, 433-445
Wakeling, J.M., Nigg, B.M. (2001) *J Applied Physiology* **90,** 412-420
Wakeling et al. (2001), *J. Applied Physiology* **91**, 1307-1317

TRUNK STABILITY AND MUSCLE ACTIVITY: CHANGES IN PERTURBATION ENERGY AND PRELOADS

Gregory Slota and Kevin Granata, Ph.D.
Gslota@Virginia.edu
Motion Analysis & Motor Performance Laboratory, University of Virginia, Charlottesville, Virginia, USA
Departments of Biomedical Engineer and Orthopedic Surgery

INTRODUCTION

Low-Back Disorders (LBD) are a significant musculoskeletal problems in the United States (Bureau of Labor Statistics 1994). Spinal stability may be a primary factor in controlling LBD risk. Stability of the spine is influenced by muscle stiffness and controlled by muscle response strategies.

The control diagram (Fig.1) illustrates the interaction between the trunk stiffness (k) and perturbation invoked muscle response ($Ge^{-\tau}$). The combinations of these two factors are the key to the stability of the low-back. The trunk stiffness and reflex gain are related to the recorded EMG preparatory levels and reflex response relative peak values. The goal of this study was to quantify stiffness and muscle responses vs. trunk moment and impact energy.

METHODS

To test stability and muscle activity, an experiment was performed wherein applying static flexion loads and dynamic sudden loads were applied to the trunk. Eleven males and ten females with no history of low back pain participated after providing informed consent. Trunk and spinal motion, kinetics and trunk muscle activities were recorded during each trial. Static extension exertions (preload) required the subjects to maintain an upright posture against a horizontal flexion force of 110 N applied to the trunk. Sudden-loads were applied by applying brief (less than 10 msec) flexion perturbations of approximately 75N (1.0m drop) and 37.5N (0.5m drop) independent of the static extension exertions.

The pelvis and lower extremities were restrained while the added loads were connected to the subject via a pulley system and chest harness. EMG signals were collected from the left and right erector spinae (ES) as per Mirka (Mirka, 1991) and normalized with respect to maximum voluntary contractions.

RESULTS AND DISCUSSION

Trials, without the added preload, show significant trends wherein increased perturbational forces resulting in increased trunk deflections and increased muscle reflex responses. (Table 1)

With the addition of the preload, significant increases in the preparatory level of the erector spinae muscle groups were observed. With this increase in the muscle activity, there was a reduction in the trunk flexion displacement angles, indicating increased muscle stiffness, and a significant decrease in the muscle responses.

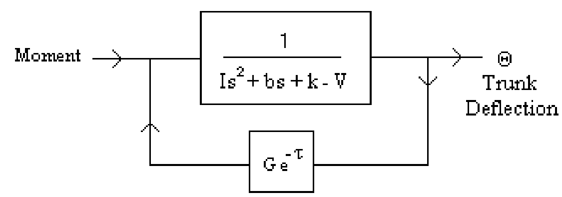

$$T/M = 1 / [Is^2 + bs + (k + G^{-t} - V)]$$

Figure 1: System control diagram

SUMMARY

To maintain the stability of the trunk when perturbed by an external moment, the combination of the trunk stiffness (k) and the muscle reflex ($Ge^{-\tau}$) must be greater than gravitational energy (V). Greater perturbations elicit increased muscle reflexes response. If the trunk stiffness is increased, then a reduced muscle response is required to maintain stability. Stability is achieved and improved upon with the addition of the preload.

REFERENCES

Bureau of Labor Statistics., 1994. *U.S.Department of Labor*. **USDL** 94-213. 1994. Washington D.C., USGPO
Mirka G.A. (1991). *Ergonomics*, **34 (3**), 343-352.

Table 1: Table of Results: Effects of preload and drop height on stability and muscle response

Loading Conditions	0.5 m Ht w/o preload	1.0 m Ht w/o preload	0.5 m Ht w/ preload	1.0 m Ht w/ preload
Trunk Deflection angle*$^{\Psi}$	11.798°	13.749°	6.919°	9.805°
Preparatory EMG (ES) *	0.03446	0.03252	0.08216	0.07931
Response EMG (ES) **	0.2728	0.3712	0.1574	0.2065

* Significant w/ preload $p<0.001$ $^{\Psi}$ Significant w/ sudden load $p<0.05$ ** Significant across all levels $p<0.02$

MARKER-BASED RECONSTRUCTION OF THE KINEMATICS OF A CHAIN OF SEGMENTS; A NEW METHOD THAT INCORPORATES JOINT KINEMATIC CONSTRAINTS

Miriam Klous[1] and A.J. "Knoek" van Soest[2]
[1]Institute of Sport Science, University of Salzburg, Salzburg, Austria, miriam.klous@sbg.ac.at
[2]Faculty of Human Movement Sciences and IFKB, Free University, Amsterdam, The Netherlands

INTRODUCTION

Several methods have been proposed (Veldpaus et al. 1988, Cappello et al. 1997) to minimize noise error in the reconstruction of kinematics based on skin marker measurements. In these studies, segments are described as independent rigid bodies. Hence, "dislocation" of the joints is generally found (Kepple et al. 1994), resulting in unreliable values of joint kinematics (Lafortune et al. 1992) and in problems in inverse dynamics modeling. The purpose of this study was to devise a new method for (1) optimal estimation of the joint positions in segmental frames of reference and (2) reconstruction of the kinematics of a chain of rigid body segments from noisy marker position data, that takes the joint kinematic constraints into account.

METHODS

The method consists of two parts: (1) a method to automatically determine the joint positions in order to minimize systematic errors in a multi-link model, (2) a method to determine the position and orientation of a chain of rigid segments, taking joint kinematic constraints into account.

Method to determine joint center positions

When analyzing a multi-link chain of segments in 2D inverse dynamics, joints are usually modeled as hinge joints. Thus, the movement of markers on a segment, in a frame of reference, fixed to an adjacent segment should be part of a circle, the center of which is the joint axis (Fig. 1). Based on Crawford (1983), an analytical method was formulated that yields the parameters of the circle that best fits the marker paths. This method was extended to 3D, where hinge joints can be generalized to ball and socket joints and a sphere is fitted.

Optimization method for reconstruction of the kinematics of a chain of rigid segments, including joint kinematic constraints

This method combines a numerical with an analytical approach. The numerical part determines the translation vector of the overall model with a least square method. The analytical part determines the orientation of all the segments. So, for any number of segments in 3D, the numerical part is concerned with finding three variables, the rest is calculated analytically.

The analytical part is based on a study of Veldpaus et al. (1988) in which a least square algorithm is described to estimate the translation vector and rotation matrix of a moving rigid body. The important characteristics of this algorithm are that the translation vector is calculated for the center P_0, which is a virtual marker calculated from the marker distribution and that the rotation matrix is calculated based on the distribution of the markers around this center. This characteristic is used to create an optimization method for a multi-link chain.

In our method the measured marker positions for any segment are first reflected in the point of rotation, so the point of rotation is the center of the marker distribution. This is also done for the modeled marker positions by reflecting the markers in the model joint position. This guarantees that the optimization routine will put the joint positions exactly on top of each other. The unaffected DOF for the optimization routine are in the rotation matrix. So, the optimal rotation matrices can be determined and the joint position will match.

To validate this method, virtual data in 3D were created for a chain of three segments with five markers each. The difference in accuracy between the optimization method for a chain of segments (OMC) and an analytical optimization method in which each segment is treated separately (OM) (Veldpaus, 1988) is analyzed by adding noise to the data. The minimized value is defined as the absolute Euclidian distance between the 'measured' coordinates and the reconstructed coordinates. This value is used to express the accuracy of the methods.

RESULTS AND DISCUSSION

The minimized value for OM and OMC as a function of the standard deviation of noise are shown in fig. 2. The results obtained with the OM follow the standard deviation of the noise as expected. In OMC, joint dislocation does not occur by definition, at the cost of a slightly higher average marker error (see Fig. 2).

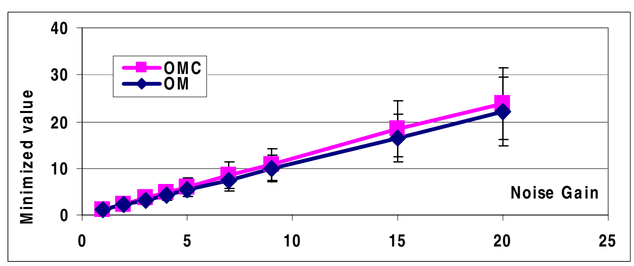

Figure 2: Minimized value for OM and OMC for different noise gain

It is concluded that OMC yields a description of kinematics that lends itself, at least theoretically, better to a subsequent inverse dynamics analysis than the classical OM method. In future work, we will establish the consequences of the assumptions made in kinematic modeling on the results of inverse dynamics calculations.

REFERENCES

Cappello, A. et al. (1997). *Hum. Mov. Science*, **16**, 259-274.
Crawford, J.F. (1983). *Nucl. Instr. and Meth.*, **211**, 223-225.
Kepple, T.M. et al. (1994). *J. of Biomechanics*, **27**, 365-371.
Lafortune, M.A. et al. (1992). *J. of Biomechanics*, **25**, 347-357.
Veldpaus, F.E. et al. (1988). *J. of Biomechanics*, **21**, 45-54.

IN VIVO MUSCLE FIBER BEHAVIOR OF THE TRICEPS SURAE MUSCLES DURING CONCENTRIC AND ECCENTRIC PLANTAR FLEXIONS

Chino K., Oda T., Kurihara T., Kawakami Y., Kanehisa H., Fukunaga T.
Department of Life Science (Sports Science), University of Tokyo, Komaba, Japan, cc16731@mail.ecc.u-tokyo.ac.jp

INTRODUCTION

Isokinetic dynamometers have usually been used to study force-velocity relationship of in vivo human muscles. In many of these studies, velocity was measured as angular speed at the joint and not as linear velocity of muscle fiber shortening and lengthening. Some studies have tried to estimate muscle shortening velocity from isokinetic data (Bobbert M. F., van Ingen Schenau G. J. 1990, Martin A. et al. 1994), but their models required a number of assumptions and approximations. In the present study, muscle fiber behavior of the gastrocnemius and soleus muscles during isokinetic concentric and eccentric actions was directly measured in vivo.

METHODS

The subject (n= 7 men) was seated on an electrical myometer with the right knee extended and performed maximal voluntary concentric and eccentric plantar flexions at four different angular velocities: 60, 120, 180 and 240deg/s. The range of motion was –15 to +35deg (0; neutral position, positive values are planter flexion angles). With the use of ultrasonography, longitudinal sections of medial gastrocnemius (MG) and soleus (SOL) muscles were visualized continuously (65 frames/s) during contraction. From the ultrasonographic images, muscle fiber lengths and pennation angles of MG and SOL were measured.

RESULTS AND DISCUSSION

From the time course of muscle fiber length (Fig.1), muscle fiber shortening and lengthening velocities of MG and SOL were calculated (Fig.2). There was almost a two-fold difference in the mean velocities between MG and SOL (Fig.3). Considering the effect of pennation angle, muscle shortening and lengthening velocity was also calculated. The difference between MG and SOL became smaller, but the change of the velocity with increasing angular velocity was larger in MG than in SOL. These results show different force-velocity characteristics between MG and SOL even during isokinetic contraction.

REFERENCES

Bobbert M. F.. van Ingen Schenau G. J. (1990) *J Biomech*, **23**: 105-119
Martin A. et al. (1994) *Eur J Appl Physiol*, **69**: 539-544

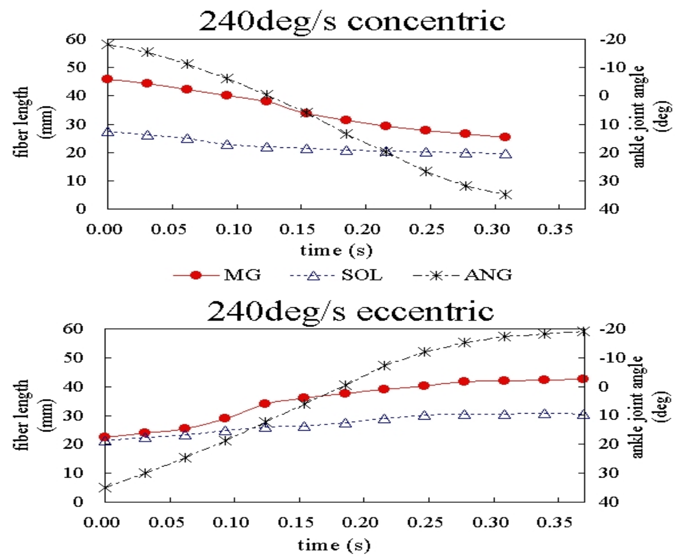

Figure 1: A typical example of time course of muscle fiber length and ankle joint angle (ANG) at 240deg/s

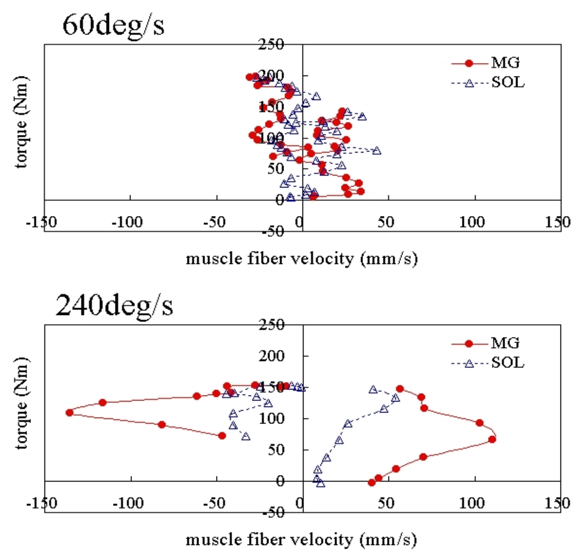

Figure 2: A typical example of the relationship between torque and muscle fiber shortening and lengthening velocity

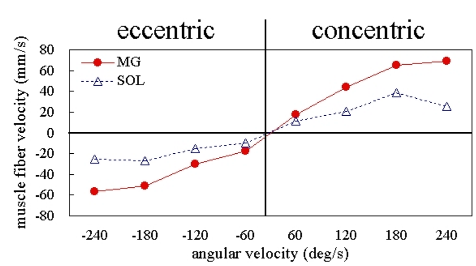

Figure 3: A typical example of the relationship between mean muscle fiber velocity and angular velocity

SIMULATING DETAILED KINEMATICS OF THE SPINE – EXTRAPOLATION OF FUNCTION FROM THE 3D FORM OF STRUCTURES DERIVED FROM THE VISIBLE HUMAN CT DATA BASE

William L. Buford, Jr., Clark E. Andersen

Orthopaedic Biomechanics Laboratory, Department of Orthopaedics and Rehabilitation,
University of Texas Medical Branch, Galveston, TX 77555-0892, wbuford@utmb.edu

INTRODUCTION

Form and function have long been synergistic in the understanding of skeletal kinematics. For example, the understanding of thumb carpometacarpal motion has been interpreted based upon the toroidal shape of the first metacarpal and trapezial joint surfaces. Resultant axes extrapolated from these shapes are two non-orthogonal, non-intersecting lines – one for flexion-extension motion running through the trapezium and the other for abduction-adduction running through the base of the first metacarpal (the AbAd axis is linked to the FE axis) [1]. Iterative adjustment of these axes with a detailed, interactive, real-time kinematic data structure assists in definition of the joint kinematics including limits in the ranges-of-motion. This becomes true for many other joints and coupled with a variety of experiments lends well to the iterative improvement of kinematic simulation [2]. Can this method be applied to kinematics of the spine? What level(s) of detail will be required? This report investigates these questions with the use of a kinematic hierarchical structure developed from the highest density CT scans available from the male Visible Human Data Set.

METHODS

The simulation development environment is a dual 700Mhz Pentium IV with Windows 2000 using Visual C++ v5.0, and OpenGl with the GLUT Library. The graphics driver is the Tornado with Evans & Sutherland's Realimage technology. In addition to mouse and keyboard interactive methods, this system utilizes pop-up menus with control widgets and 6 DOF control using a Spaceball (Spaceball model 2003, Spacetec IMC Corp., Lowell, MA). Programs developed in C++ and openGL are transferrable between NT and Unix systems with minor program modification. Use of the system for simulation of the extremities is described in [2].

Structures for the spine kinematic model are derived from axial computerized tomography (CT) slices of the NLM Visible Human (male). The frozen CT structure is used because the slices are spaced at one mm apart (maximum vertical resolution). Also, because the data set was built to maximize planar resolution, the in-plane pixel size varies from .53 to .94 mm/pixel. The images are run through the MIMICS interactive software package that creates triangular polygons representing each bone. MAGICS software (MIMICS and MAGICS are from Materialise, Inc) is used where required to edit and combine the polygonal files. Files (in .stl format) for each bone then serve as the base level structures in the openGL kinematic hierarchy.

RESULTS

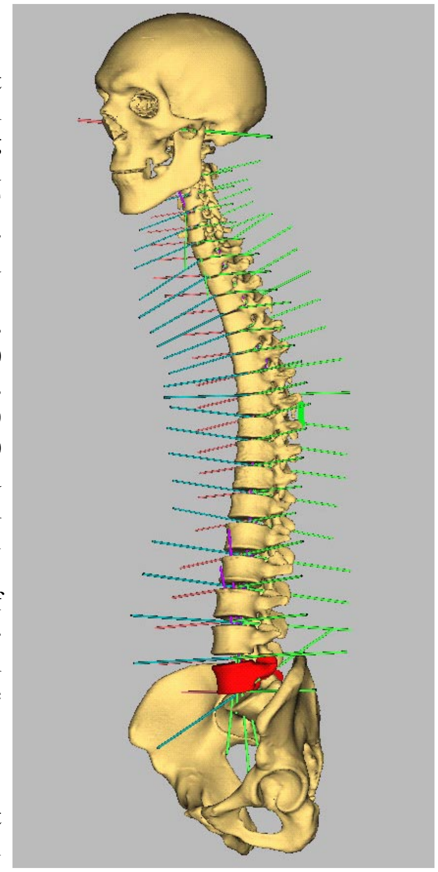

The Figure to the right is the spine simulation data structure including preliminary defined axes of motion (3DOF for all but atlanto-occipital with 2 and atlanto-axial with 1). The entire structure is nearly 500,000 triangular polygons (ranging from 6000 [C6] to 130,000 [pelvis]. 28 bones and 73 axes are linked in the hierarchical kinematic structure. Initial placement of axes and range-of-motion is based upon generalized knowledge from the literature.

SUMMARY

When viewing form at the level-of-detail represented in this Figure the structural detail derived from the NLM database is sufficient. However, since separation at the facet joints is approximately 1 pixel for most segments, optimization of the finer motions will require improved resolution (initial estimate of .25 mm, which worked quite well in the small joints of the fingers [2]). In the meantime, the simulation reported here is proving to be a provocative heuristic modeling environment. For instance, the intertransverse ligament (at T08-T09 in the Figure) experiences nearly 9% strain when the structure above T08 is rotated $\pm 2^0$ about neutral (lateral flexion).

BIBLIOGRAPHY

1. Hollister, A, Giurintano, DJ, Buford, WL, Jr., Myers, LM, Novick, A (1995) *Clinical Ortho. Rel. Res.* 320:188-193.
2. Buford, WL, Jr., Andersen, CR, Elder, KW, Patterson,RM (2001) **Proceedings**, ISB, Zurich, Jul 8-13, 2001, p 206.

ACKNOWLEDGEMENTS

Supported by the Texas Advanced Technology Program (Grant Number: 004952-0111-1999), and a research grant from Sulzer Orthopaedics, Inc., Austin, TX. Images from The National Library of Medicine Visible Human Program.

A METHOD FOR ANATOMICAL - FUNCTIONAL STUDIES OF ARTICULAR JOINTS

Sandra Martelli

Istituti Ortopedici Rizzoli, Lab. Biomechanics, Bologna, Italy
s.martelli@biomec.ior.it

INTRODUCTION

At present the relative motion of two rigid bodies or joints can be tracked in two ways. Either recording motion through reference markers attached to the two bodies (e.g RSA or spatial linkages), or recording the shapes of the surfaces as they move on each other to deduce information on the nature of the relative movements(e.g. dynamic x-rays or MRI). None of the two approaches, separately, can handle the analyses of the correlation between anatomical structures and kinematic parameters during non-static motion. In this paper we describe a new methodology for the acquisition and computer elaboration of joint anatomy and motion and the study of their correlation (E.P. 00128769.7 , Dec 30, 2000)

METHODS

The acquisition protocol consists in standard digitization of surfaces for anatomical acquisition and standard use of the electrogoniometer FARO Arm (FARO Technologies, Lake Mary, FL, USA) to record motion. In addition a fast "matching phase" has been designed and tested to allow the accurate correlation between anatomy and motion. The computer elaboration allow the 3D display of the joint state during the recorded motion, the computation of 2D sections of the digitized structures and least square fitting with lines or conics, the computation of standard kinematic models such as Euler angles and helical axis. Moreover original dynamic computations can be performed to check and quantify contact areas, tracking of points and axis during motion, relative translation and rotations of bones, user's defined anatomical landmarks or calculated objects.
An accuracy study was performed on mechanical models and through numerical analysis of the software and simulation. The method was also used for an experimental geometrical and functional analysis of the knee in order to test its practical performances (Figure 1).

RESULTS

In tests of geometric acquisition on a perspex cylinder, a perspex parallelepiped and a metal flat and in tests of sliding and rotations of the geometric models and of a 2-degrees-of-freedom hinge the method yielded the following accuracies: the anatomical structures are reconstructed with 0.3 mm precision, the kinematic features are computed with 0.3mm and 0.8° precision, and all computations concerning the use of both geometrical and kinematic data with less than 1 mm and we expect 1.5° accuracy (including tracking of numerical errors). Moreover, the error on the computed geometrical or purely kinematic results equals the acquisition error (due to equipment and experimental conditions), while the error on reconstructed motion of geometrical data could be double.

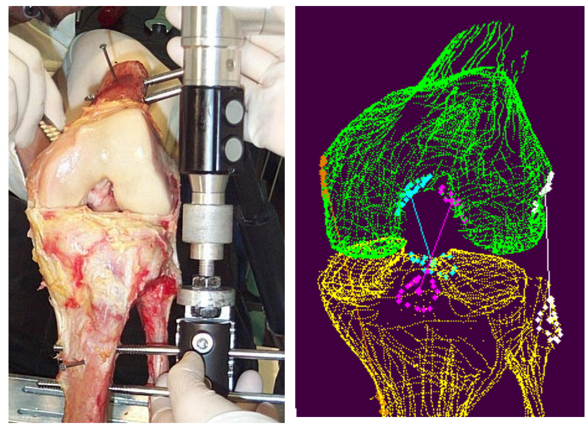

Figure 1: Use of the method to image the knee joint during the passive range of motion. On the left the acquisition phase; on the right the computer reconstruction of the joint at 90° flexion.

DISCUSSION

The main advantage of this methodology is the possibility of making fast, accurate and comprehensive analyses of individual knee behavior . It could be used easily in new computer technologies for assisted medical treatment, be particularly useful for knee model validation or to study the anatomical position of helical axes, to track instantaneous translation in diarthroid joints, such as hip or shoulder, to perform instrumented examinations instead of manual ones.
The disadvantage to the present method is that one of the two rigid bodies must be fixed and the need to expose involved structures. Therefore the method is well suitable for in-vitro studies, eventually open surgery, but difficult to use in clinical diagnosis, minimally invasive interventions or in vivo measurements.

REFERENCES

S. Martelli, S. Zaffagnini, et al., (2000). *Computer Methods and Programs in Biomedicine,* **62**:77-86

A TRANSVERSELY ISOTROPIC AND TRANSVERSELY HOMOGENEOUS MODEL OF CARTILAGE INCLUDING CHONDROCYTES AND A STATISTICAL DISTRIBUTION OF COLLAGEN FIBRES

Salvatore Federico[1], Walter Herzog[2], John Z. Wu[2], Guido La Rosa[1]

[1]Department of Industrial and Mechanical Engineering, University of Catania, Catania, Italy
[2]Human Performance Laboratory, University of Calgary, Calgary, Alberta, Canada
Corresponding Author: Salvatore Federico (s.federico@diim.unict.it)

INTRODUCTION

The mechanical properties of articular cartilage are determined by its microstructure. The arrangement of the collagen fibre network, and the distribution of the chondrocytes are such that cartilage can be modelled by a transversely isotropic and transversely homogeneous composite, the transverse plane being parallel to the articular surface and the cartilage-bone interface. In this work, the homogenisation procedure of Qiu and Weng for aligned inclusions (1990) was extended to take into account an inclusion phase in which the orientation of the inclusions follows a statistical law. This approach is used to represent collagen fibres in cartilage: collagen fibres are perpendicular to the cartilage-bone interface in the deep zone, parallel to the surface in the superficial zone, and the orientation is almost random in the middle zone. A directional averaging method for any statistical distribution of the orientation of the inclusions is proposed, in order to substitute the fibres with a phase of "equivalent aligned inclusions".

METHODS

In the Qiu-Weng method (1990), the elasticity tensor L for a mixture of $N+1$ phases (phase 0 is the matrix) is given by:

$$L = [\textstyle\sum_{r=0}^{N} c_r L_r A_r][\textstyle\sum_{r=0}^{N} c_r A_r]^{-1} \qquad (1)$$

For each phase r, c_r is the volumetric concentration, L_r is the elasticity tensor, and A_r is the average strain-concentration tensor of a single r-th phase inclusion embedded in an infinite matrix.

Neglecting the fluid phase, cartilage is modelled as a tri-phasic composite: proteoglycan matrix (index 0), cells (index c) and collagen fibres (index f). To show the proposed method, a parallelepiped cartilage sample, cut such that the top base is the cartilage surface and the bottom base is the interface with the subchondral bone, is considered. The 1-axis of the global reference frame $\{e_1, e_2, e_3\}$ is perpendicular to the bottom base. Since the morphologic properties of cartilage (cell concentration and shape, fibre concentration and orientation) change as a function of the distance from the bone-cartilage interface, all physical quantities depend on the non-dimensional distance $\xi \in [0,1]$. Substitution of the fibre phase with the "equivalent aligned inclusions" phase (indicated by the index a), is made through three steps: 1) calculation of the tensor A_f for a generic fibre whose tangent is parallel to the e_1' direction (defined by the latitude $\vartheta \in [-\pi/2, \pi/2]$ and the longitude $\varphi \in [-\pi, \pi]$, with respect to $\{e_1, e_2, e_3\}$), in the local reference frame $\{e_1', e_2', e_3'\}$; 2) calculation of A_f in $\{e_1, e_2, e_3\}$; 3) calculation of A_a for phase a via the directional average:

$$A_a(\xi) = (1/2\pi)\int_{-\pi}^{\pi}\left[\int_{-\pi/2}^{\pi/2} \gamma(\vartheta;\xi)\, A_f(\vartheta,\varphi)\, d\vartheta\right] d\varphi \qquad (2)$$

$\gamma(\cdot\,;\xi):[-\pi/2,\pi/2] \to \mathbf{R}_0^+ : \vartheta \mapsto \gamma(\vartheta,\xi)$ is a (normalized) probability distribution in the variable ϑ, having ξ as a parameter, and not depending on the longitude φ (in order to respect the restraint of having transverse isotropy). $\gamma(\cdot\,;\xi)$ is built such that: for $\xi \to 0$ (bone-cartilage interface) it is highly peaked around $\vartheta = 0$ (vertical fibres), for $\xi \to 1$ (articular surface), it is highly peaked around $\vartheta = \pm\pi/2$ (horizontal fibres), for ξ in the neighbourhood of the value 1/2 (middle zone), it is almost flat (randomly oriented fibres).

RESULTS

The predicted non-dimensional axial and transversal moduli (E_{11}/E_0 and E_{22}/E_0, where E_0 is the elastic modulus of the proteoglycan matrix) were plotted as a function of ξ, for one of the configurations studied (defined by the form of function γ, fibre concentration, cell shape and concentration).

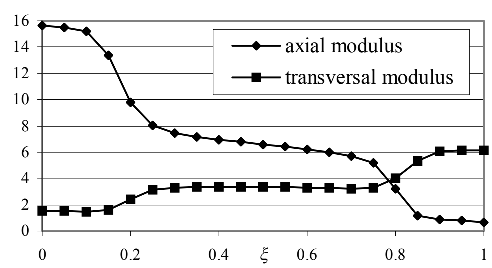

Figure 1: Non-dimensional moduli as a function of the non-dimensional depth ξ

From the deep to the superficial zone, E_{11}/E_0 decreases by a factor of about 23 (a result that agrees well with the experimental observations of Shinagl et al., 1997), while E_{22}/E_0 increases by a factor of about 4.

CONCLUSIONS

The developed method is able to simulate a variety of different configurations, whose stability can be checked by use of the thermo-dynamical restrictions on the elastic constants of the homogenised mixture. Once the configuration that best models real cartilage is found, accurate FEM models of articular cartilage, involving the fluid phase, can be created for simulation of compression tests and contact problems.

REFERENCES

Qiu, Y.P., Weng, G.J. (1990). *Int. J. Engng. Sci.* 28, 1121-37.
Shinagl R. et al. (1997). *J. Orthop. Res.*, 499-506.

AN INVESTIGATION ON THE VENTILATION OF OPERATING THEATRES

Vasco Campos; Jose CF Teixeira and Senhorinha FCF Teixeira [(1)]

School of Engineering, University of Minho, Azurem, Guimaraes, Portugal
[(1)] Corresponding author, st@dps.uminho.pt

INTRODUCTION

In the ventilation of operation theatres, it is required a constant supply of fresh air in the vicinity of the operating table. This is necessary in order to guarantee an acceptable level air quality and to mitigate the propagation of infections and bacteria. The traditional approach is to supply the fresh air from the ceiling as a laminar jet over the operating table. As the air is supplied at a lower temperature than the surrounding air, room cooling is also achieved. The difference in temperature allows the fresh air to be supplied at very low velocities, which is of great importance in terms of human comfort. However, this flow pattern is very much influenced by the presence of various obstacles in the room, particularly those which generate temperature gradients relatively to the surrounding air. Of particular interest is the room illumination and technical equipment. The complexity of the system and the required accuracy for the solution requires the use of a detailed model for the room simulation.
The present paper reports both a numerical and experimental investigation aiming at validating a simulating tool for the ventilation of an entire operating room.

NUMERICAL MODEL

In order to model the non-isothermal flow pattern inside the operating room the conservation equations for both the flow field and the temperature field have been implemented. The two dimensional time dependent equations for the mass, momentum and energy conservation are discretized using a finite volume technique upon a collocated grid. The set of equations is solved using the SIMPLE algorithm. Appropriate boundary conditions are established for the wall temperature, heat sources inside the room and mass inlet and outlet areas. In this, the best configuration for both the temperature and flow velocity can always be achieved.

EXPERIMENTAL DETAILS

In order to validate the numerical calculations, a 1:5 scale model was built. In this rig configuration, the air flow is fed through the room ceiling through a low turbulence inlet section. Upstream, the flow is cooled through a cross flow air-water heat exchanger. The model is built in plexiglass for optical access. The velocity field is measured by a two-velocity component LDA operating in backscatter. The Doppler signals are processed by two Burst Spectrum Analyzers and the resulting information is loaded to a PC for subsequent processing. Room temperature is measured across the room by a bank of thermocouples linked to a data acquisition board.

PRELIMINARY RESULTS

Figures 1 and 2 show the velocity field and the temperature contours for a symmetrical inlet at the room ceiling and four outlets.

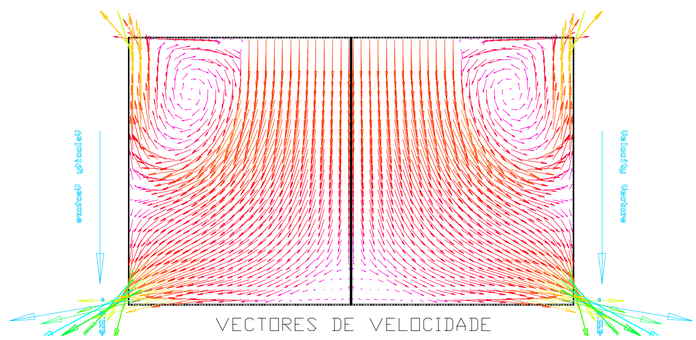

Figure 1: Velocity field.

Figure 2: Temperature contours.

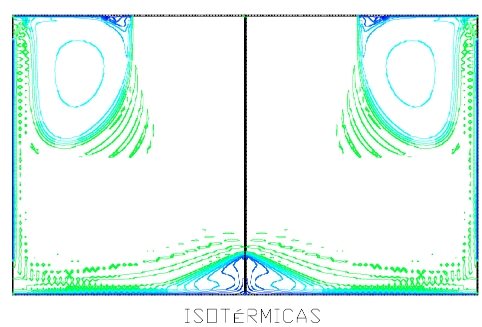

REFERENCES

Hartung, C. and Kugler J. (1998). *Proceedings of 15th International Congress of the International Federation of Hospital Engineering*

GENDER DIFFERENCES IN LOWER EXTREMITY SHOCK ABSORPTION DURING VERTICAL DROP LANDINGS

Michael J. Decker[1], Michael R. Torry[1], Douglas J. Wyland[2], William I. Sterett[2], and J. Richard Steadman[2]
Steadman♦Hawkins Sports Medicine Foundation[1] and Clinic[2], Vail, CO, USA, mike.decker@shsmf.org

INTRODUCTION

Landing from a jump is one of the primary non-contact mechanisms for ACL injury (Feretti et al., 1992; Noyes et al., 1983). Several researchers have shown that female athletes have a greater incidence of ACL injury than their male counterparts (Arendt and Dick, 1995; Feretti et al., 1992). Biomechanical performance studies reveal that females execute high-demand activities in a manner that may make them more prone to ACL injury (Colby et al., 2000; McLean et al., 1999). Specifically, reports indicate that the female knee is in a more extended position at ground contact, forcing the ACL to bear greater loads during a period of large eccentric quadriceps force. Further, hamstring activation may be less, or delayed, in females compared to males (Colby et al., 1999; Rozzi et al., 1999). This would indicate that the energy absorption strategy of the lower extremity may have a strong influence on the pre-disposition to ACL injury. However, no study, to our knowledge, has quantified or compared the energy absorption differences between genders in the entire lower extremity. The purpose of this study was to determine whether gender influences the energy absorption strategy during landing.

METHODS

Coordinates of a 13 marker body system (120 Hz, 3D) and ground reaction forces (1200 Hz) were collected from 12 healthy males and 9 females during 60 cm drop landings. All subjects were recreational athletes that were involved in jumping and landing sports at least 3 times a week. Hip, knee and ankle kinematics were calculated for the landing phase. Negative joint work values (energy absorption) were calculated during the first 100 ms after initial ground contact. An independent t-test was used to determine differences in total landing time and maximum knee flexion. A 2x3 (gender x joint) repeated measures ANOVA and Tukey post-hoc tests were used to contrast initial contact position, range of motion and energy absorption between the two groups (alpha=0.05).

RESULTS AND DISCUSSION

Both groups performed soft landings (maximum knee flexion: males, -93.0 ± 10.8°; females, -98.4 ± 10.6°) in the same amount of time (landing phase time: males, 0.191 ± 0.046 s; females, 0.209 ± 0.034 s) (both $p>0.05$). However, the females demonstrated more knee extension and ankle plantarflexion at initial ground contact, and subsequently utilized greater knee and ankle ROM (all $p<0.05$). The males demonstrated no energy absorption differences between the hip, knee and ankle, whereas the females had greater energy absorption values at the knee and ankle compared to the hip. Although both groups demonstrated the greatest amount of energy absorption at the knee, between group differences indicated that the males performed greater energy absorption at the hip, and the females greater at the knee and ankle (all $p<0.05$).

Table 1. Means and standard deviations (parentheses) for initial contact angle (deg), range of motion (deg) and energy absorption (%BW*ht).

Variable	Hip	Knee	Ankle
Cont-M	-30.8 (7.8)	*-30.0 (7.7)	*-11.3 (5.1)
Cont-F	-24.0 (10.6)	-22.8 (8.0)	-21.3 (9.6)
ROM-M	50.4 (13.0)	*63.4 (9.3)	*41.6 (6.9)
ROM-F	57.9 (13.8)	75.8 (9.1)	58.0 (7.9)
Work-M	*-4.9 (1.4)	*-6.6 (2.1)	*-4.7 (1.4)
Work-F	-3.2 (1.9)	-8.6 (2.2)	-6.4 (1.7)

*p<0.05

Although the knee was the primary functional shock absorber, the results indicate that gender does influence the energy absorption strategy of the lower extremity during landing. The males supplemented the large shock absorption role of the knee extensors with the hip extensors, whereas the females supplemented the knee extensors with the ankle plantarflexors. This muscular shock absorption strategy may indicate that the females used a smaller hip extensor, or hamstring, force for a given quadriceps force, that when combined with shallow knee flexion angles at ground contact may contribute to an increased ACL injury rate during the landing maneuver.

Soft landings are generally instructed to prevent ACL injury. Greater knee extension at initial ground contact may be required to perform progressively softer landings. It is well documented that a more extended knee provides a mechanical disadvantage to the hamstring muscles and may allow the quadriceps muscles to pull the tibia anteriorly resulting in larger values of ACL strain. Thus, instructing athletes to have greater knee flexion at contact may be an important addition to current, injury prevention training techniques for soft landings.

SUMMARY

This study provides support to the notion that the higher ACL injury rate in females during landing may be attributed to both kinematic and muscular strategies.

REFERENCES

Arendt, E., Dick, R. (1995). *Am J Sports Med,* **23**, 694-701.
Colby, S. et al. (2000). *Am J Sports Med*, **28**, 234-240.
Ferretti, A. et al. (1992). *Am J Sports Med*, **20**, 203-207.
McLean, S. et al. (1999). *Med Sci Sports Exerc*, **31**, 959-968.
Noyes, F. et al. (1983). *J Bone Jt Surg*, **65**, 154-162.
Rozzi, S. et al. (1999). *Am J Sports Med*, **27**, 312-319.

MUSCLE ACTIVATION DIFFERENCES BETWEEN THE UPPER AND LOWER SUBSCAPULARIS MUSCLES DURING ABDUCTION AND ROTATION

Michael J. Decker[1], Michael R. Torry[1], Henry B. Ellis[1], John J. Tokish[2], and Richard J. Hawkins[2]
Steadman♦Hawkins Sports Medicine Foundation[1] and Clinic[2], Vail, CO, USA, mike.decker@shsmf.org

INTRODUCTION

The broad origin of the subscapularis muscle may indicate that the upper and lower portions have different actions. Indeed several investigators have shown that the upper and lower portions of the subscapularis muscle are independently innervated (McCann et al., 1994) and activated (Kadaba et al., 1992). Recent studies (Otis et al., 1994) suggest that the upper and lower portions have different moment arms with varying positions of shoulder rotation and abduction, however, some EMG studies seem to not reflect these anatomical differences (Kadaba et al., 1992). The purpose of this study was to examine the muscle activation patterns of the upper and lower subscapularis muscles during different shoulder rotation and abduction positions.

METHODS

Applied force and EMG data were collected (1200 Hz) from 15 healthy subjects while they performed internal shoulder rotation exercises from 70˚ of internal rotation to 90˚ of external rotation at 0˚, 45˚ and 90˚ of shoulder abduction. Resistance was provided by an elastic resistance device (ERD) and applied force was monitored with a force transducer in line with the ERD. Muscle activities of the upper and lower portions of the subscapularis muscle were monitored with indwelling electrodes (Kadaba et al., 1992). All exercises were performed at a load that could only be performed for five repetitions while maintaining a pace of 54 beats per minute. A 2x3 mixed factor ANOVA was used to contrast mean, peak and average EMG activity (%MVC), and a one-way ANOVA was used to contrast peak applied force (Tukey post-hoc tests, alpha=0.05).

RESULTS AND DISCUSSION

Given the same peak applied force ($p>0.05$), the upper and lower portions of the subscapularis muscle responded differently to internal shoulder rotation across the three positions of shoulder abduction (interaction $p<0.05$). Upper subscapularis muscle activity did not change across the three shoulder abduction positions ($p>0.05$), but lower subscapularis muscle activity decreased from 0˚ to 90˚ abduction ($p<0.05$). These changes yielded greater muscle activity values for the upper subscapularis at 45 and 90˚ of shoulder abduction ($p<0.05$).

The changing muscle moment arms in abduction and rotation may assist in the functional interpretation of the muscle activation differences noted between the upper and lower subscapularis muscles. At 0˚ of shoulder abduction, both the upper and lower subscapularis muscles have similar internal rotation muscle moment arms (Otis et al., 1994), thus accounting for their similar muscle activation levels.

The upper subscapularis muscle has a greater abduction moment arm than the lower subscapularis muscle, and this moment arm is progressively greater with external shoulder rotation (Liu et al., 1997; Otis et al., 1994). Thus, upper subscapularis muscle activity may have been consistently large across shoulder abduction positions, and greater than lower subscapularis muscle activity at the 45 and 90˚ shoulder abduction positions, due to the active performance of both internal shoulder rotation and shoulder abduction.

The smaller shoulder abduction and internal rotation moment arms for the lower subscapularis muscle may indicate that its primary function is to depress the head of the humerus and only supplement internal shoulder rotation or abduction. Further, protraction and upward rotation of the scapula during arm abduction may require less inferiorly directed force from the lower subscapularis muscle. Taken together, progressively decreasing lower subscapularis muscle activity would be logically predicted with greater arm abduction positions.

Table 1. Means and standard deviations (parentheses) for peak applied force (N) and muscle activity (%MVC)

Shoulder Position	0˚	45˚	90˚
Peak Applied Force	268 (29)	268 (32)	271 (31)
Avg Upper Subscap	50 (24)	53 (41)	60 (40)
Peak Upper Subscap	85 (36)	87 (58)	91 (53)
Avg Lower Subscap	40 (28)	26 (19)	15 (11)
Peak Lower Subscap	70 (41)	51 (31)	34 (23)

SUMMARY

Previous descriptions of the muscle moment arms of the upper and lower subscapularis muscles provide support to the muscle activation differences noted during internal rotation at various abduction positions. It was concluded that larger activation levels from the upper subscapularis during greater abduction positions were due to the muscular demands of internal rotation and abduction, whereas the lower subscapularis muscle may act primarily as a humeral head depressor and only supplement internal rotation and abduction.

REFERENCES

Kadaba, M.P. et al. (1992). *J Orthop Res*, **10**, 394-397.
Liu, J. et al. (1997). *Clin Biomech*, **1**, 32-38.
McCann, P.D. et al. (1994). *J Shoulder Elbow Surg*, **3**, 94-99.
Otis, J.C. et al. (1994). *J Bone Jt Surg*, **5**, 667-676.

THE EFFECT OF TIBIAL TRAY SURFACE ROUGHNESS AND INSERT MICROMOTION ON BACKSIDE WEAR

Dwight T. Todd, Bob Jones, and Abraham Salehi
Smith & Nephew, Inc., Orthopaedic Division, 1450 Brooks Road, Memphis, TN 38116,
dwight.todd@smith-nephew.com

INTRODUCTION

Examination of the backside of retrieved tibial inserts has revealed varying degrees of polyethylene wear. Many contributing factors have been suggested including micromotion between the tibial tray and insert, tibial tray surface finish, and patient and surgical factors. The purpose of this study was to assess the effect of tibial tray surface roughness and micromotion on the backside of the insert under identical fatigue loading conditions.

METHODS

The surface roughness of five different commercially available tibial trays was measured with an optical interferometer (RST Plus, Wyko Corp.) before and after fatigue testing. Four measurements were taken from one component of each design. The components tested are designated as designs A, B, C, D, and E. Each cruciate-retaining tibial and femoral component was mounted at 20° flexion in an MTS mechanical test frame with four LVDTs (LBB-375TA-100, Lucas Schaevitz) attached to the test fixture anteriorly, posteriorly, medially, and laterally. Opposing LVDTs were placed in contact with the tray and insert to record the relative motion between the two components. A 2 Hz. compressive sinusoidal load of 222/2224 N was applied for 5 million cycles. Micromotion between the insert and tray was sampled for 20 cycles at intervals of 20,000 cycles. The backside of each insert was examined and photographed under a scanning electron microscope (SEM) before and after fatigue testing.

RESULTS AND DISCUSSION

The polished tibial trays had the smoothest surface and were significantly smoother ($p < .05$) than the roughest tray E, (Table 1). Post-fatigue measurements were taken in the wear area beneath the tibiofemoral contact area. A slight roughening effect was observed for the three smoothest trays after fatigue testing. This effect was statistically significant for tray B ($p < .05$). Conversely, a slight polishing effect was observed for the two roughest trays. The polishing effect was statistically significant for tray D ($p < .05$).

Implant	Surface Finish	Pre-Fatigue R_a (μm)	Post-Fatigue R_a (μm)
A	Polished	.052 $\pm$ .006	.086 $\pm$ .017
B	Polished	.088 $\pm$ .004	.149 $\pm$ .024
C	Satin	.417 $\pm$ .029	.440 $\pm$ .018
D	Glass-bead	1.203 $\pm$ .026	.887 $\pm$ .013
E	Grit-blast	3.782 $\pm$ .427	3.679 $\pm$ .456

Table 1: Tibial tray surface roughness

Anterior-posterior (A/P) micromotion between the insert and tray was less than 14 μm for 4 of the 5 knee systems tested (Table 2). Each of these designs has a locking mechanism that extends medially, laterally, posteriorly, and anteriorly. Insert and tray E yielded significantly more micromotion in the A/P direction than the other tibial components ($p << .01$). The locking mechanism of this tray has opposing points of contact anteriorly and posteriorly.

Implant	A/P (μm)	M/L (μm)
A	11.18 $\pm$ .1.00	8.13 $\pm$ 0.70
B	12.70 $\pm$ 1.13	10.92 $\pm$ 1.20
C	7.62 $\pm$ 0.74	10.92 $\pm$ 0.89
D	13.97 $\pm$ 3.19	1.78 $\pm$ 0.75
E	53.34 $\pm$ 1.13	4.06 $\pm$ 1.29

Table2: A/P and M/L micromotion at 5 million cycles

The prosthesis with the roughest tray surface and greatest amount of micromotion exhibited the most wear on the backside of the insert. The original machining lines of this insert were completely removed after fatigue testing (Figure 1). In contrast, the original machining lines on the backside of the inserts with polished trays were still clearly visible after fatigue testing (Figure 2).

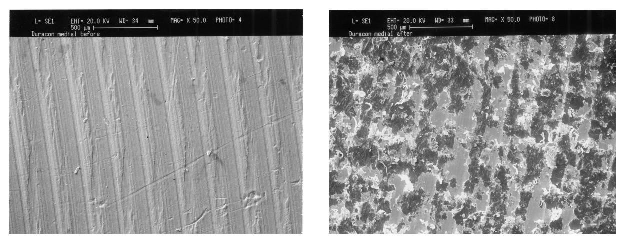

Figure 1: Backside of E insert before (left) and after (right) fatigue testing (50X)

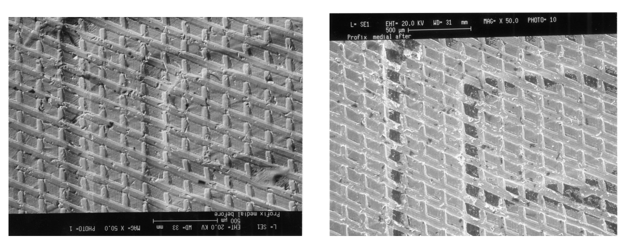

Figure 2: Backside of A insert before (left) and after (right) fatigue testing (50X).

SUMMARY

These results demonstrate that the potential for backside wear increases as the tibial tray surface roughness increases while the locking mechanism permits greater micromotion. Strong peripheral locking mechanisms can reduce but not eliminate micromotion. A polished tray surface should be considered to help reduce the potential severity of backside wear.

EFFECT OF ORTHOPAEDIC SHOES WITH ORTHOSES FOR IMPROVEING THE AMBULATION ABILITY OF DOWN'S SYNDROME CHILDREN

Saiwei Yang, Cheng-Wei Shih,
Institute of Biomedical Engineering, National Yang Ming University, Taipei, TAIWAN.
Email: swyang@bme.ym.edu.tw

INTRODUCTION

In associate with the delay development and musculoskeletal dysfunctions the Down's syndrome children (DSC) also show poor gait functions. The stance phase was longer and step length was shorter than normal subjects. And the gait pattern delays about 18 months and more in comparing to that of normal children who have their mature gait at the age of 2.

The purpose of this study was to evaluate the efficacy of new design orthopaedic shoes without or with orthoses to improve the ambulation ability by using the evaluation parameters of foot pressure and electromyography.

METHODS

Seven aged 5 years of Down's syndrome children, who could walk independently, were recruited. In addition, 24 children aged 4 to 5 years were used as the control group. Basic information and physical evaluation of entire lower extremity was done prior to the gait analysis.

Each subject was asked to walk over 8-meter distance with his own shoes. The DSC group had additional trials for a new designed orthopaedic shoes without orthosis, and followed with orthoses Plantar pressure parameters (measured by Pedar insole sensor system, Novel, Germany) and EMG pattern of anterior Tibialis, Peroneus longus (MA300, Motion Lab, USA) were analyzed to compare the difference between two groups and effect of shoes.

RESULTS AND DISCUSSION

The average cadence of normal subject was 0.85 second with stance phase of 62%. For DSC group, they were 0.95 second and 64%, respectively. The highest peak pressure of normal children of age 4 was located at the lateral calcaneus (15.34 $\pm$ 5.57 N/cm^2). For children of age 5, it was located at the hallux (13.77 $\pm$ 4.31 N/cm^2), followed by the lateral calcaneus of (13.74 $\pm$ 3.30 N/cm^2). Statistically, the two age groups showed no difference in plantar pressure measurement ($p>0.05$). The DSC with his own shoes had the maximum pressure presented at the metatarsal areas, and the minimum value at lateral toes area. Wearing the orthopaedic shoes, the maximum value shifted to the calcaneus and the minimum value was at the lateral toes and midfoot areas. The plantar pressure distribution was similar to that of normal children. Adding the orthoses the highest plantar pressure was located at 2nd metatarsal head (Fig 1). Down's children have their arch index similar to that of the normal children (0.24~0.32 for DSC, 0.20~0.32 for normal children, respectively) which may imply that the Down's children are not all pes planus.

The general pattern of Down's children was maintained at a firing level during a gait cycle. This might resulted in Down's children to be easily tired when walking. After wearing the orthopaedic shoes w/o orthoses, both could effectively control muscle activities. This effect can increase the muscle endurance and decrease the muscle fatigue.

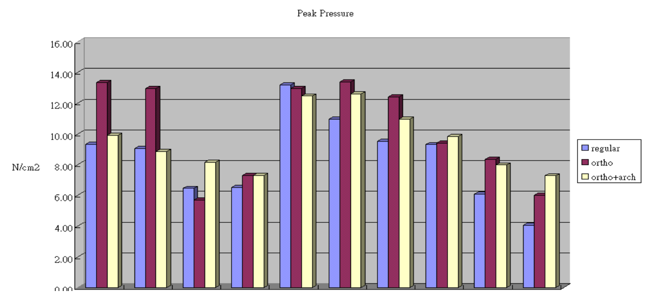

Figure 1: Peak plantar pressures with different orthoses

SUMMARY

(a) The Down's syndrome children's presented higher plantar pressure at the metatarsal heads while the normal one had their peak pressures located at heel. This result reveals the step gait pattern of DSC.
(b) This new design orthopaedic shoes seem to be good for Down's children to rebuilt their arch structure, to correct the foot alignment, to have foot pressure redistributed to normal, and to decrease the energy expenditure during walking. But the arch support may not be suitable for each individual.

REFERENCES

Parker, A.W., Bronks, R. (1980) *Archives Physical Medicine Rehabilitation*, **61**, 345-351.
Parker, A.W.,Bronks, R.,Snyder,Jr.C.W.(1986). *J Mental Deficit Research*, **30**: 93-116.
Donatelli, R.,Wolf, S.L.(1990). *The Biomechanics of the Foot and Ankle*, F.A. DAVIS CO.

ACKNOWLEDGEMENT

This study was supported by National science Council of R.O.C. (NSC90-2213-E-010-018)

SPATIAL FLOW PATTERN DIFFERNCE BETWEEN BLOOD- AND CRYSTALLOID-PERFUSED MYOCARDIUM

Takeshi Matsumoto[1], Hiroyuki Tachibana[1], Takahisa Asano[1], Mami Takemoto[1], Yasuo Ogasawara[1], Fumihiko Kajiya[1,2]

[1]Dept. Medical Engineering and Systems Cardiology, Kawasaki Medical School, Kurashiki, Japan, matsu@me.kawasaki-m.ac.jp
[2]Dept. Cardiovascular Physiology, Okayama University Graduate School of Medicine and Dentistry, Okayama, Japan

INTRODUCTION

The crystalloid perfused isolated heart model has been extensively used for characterizing myocardial function and metabolism. However, because of lower O_2-carrying capacity and higher O_2-tension than blood and without corpuscles, crystalloid perfusates will be perfused differently from blood, especially at a microvascular level. Thus, with a research hypothesis that spatial patterns of crystalloid and blood perfusion within isolated hearts differ, we measured myocardial flow distributions of isolated rat left ventricles under Tyroad and blood perfusion by quantitative digitalradiography using a molecular flow tracer, tritiated-desmethylimipramine (HDMI).

MATERIALS AND METHODS

Crystalloid perfused model Isolated rat hearts (12-14 wks) were perfused with Tyroad buffer containing 0.1%BSA at 37•C with the 100-mmHg head pressure according to the Langendorff technique. The perfusate was gassed at 95%O_2 and 5%CO_2, resulting in a pH of 7.4. Perfusion rate was measured with an ultrasonic probe in the aortic inflow line.

Blood perfused model A support rat weighing 6-700 g was anesthetized and ventilated to keep physiological arterial pH and blood gases. Both carotid arteries were connected to a 37•C water-jacketed reservoir, which supplies blood to an isolated rat (12-14 wks) heart with the 100-mmHg head pressure. The coronary effluent was conveyed to another 37•C water-jacketed reservoir and returned to the support rat via a femoral vein.

Reactive hyperemia Isolated hearts were paced at 300 bpm in both perfused models. After the heart was subjected to 30-sec global ischemia, peak reactive flow was measured.

Tracer injection and perfusion imaging HDMI (2 μCi) was injected into the perfusion line. The sample was excised from left ventricular free wall and sliced (10 μm) from subendocardium to subepicardium using cryostat microtome. Twenty-eight slices per heart were exposed to the tritium-sensitive sensor. The HDMI density, i.e., within-layer relative flow, was converted into 10-bit digital data of 100-μm pixels.

Image data analysis Two normalized indices, CV and CA, were used; CV (SD of regional flows/mean flow) is related to global flow heterogeneity and CA is given by

$$CA = [\sqrt{2}\, C(d) + C(\sqrt{2}\, d)]/(1+\sqrt{2})$$

$$C(r) = [<m_i \cdot m_j> - <m_i>\cdot<m_j>]/[<m_i^2> - <m_i>^2]$$

where C(r) is the spatial correlation function of flows in regions r μm apart; d is the pixel size; m_i is the HDMI density of the i-th pixel; < > denotes an average over all the pairs of i- and j-th pixels r μm apart. Thus, CA quantitates the degree of adjacent flow similarity. For the description of resolution-dependence of spatial flow pattern, CV and CA were computed with increasing pixel size up to 800 μm.

RESULTS

In Tyroad- and blood-perfused model, perfusion rate were 18.6±4.4 and 1.4±0.5 ml/min/g, respectively. The reactive hyperemic flow was smaller in Tyroad-perfused than in blood-perfused myocardium (11 vs. 116%). Regional myocardial flows showed lower heterogeneity (CV) and lower local similarity (CA) under Tyroad perfusion (figure 1). The increasing rates of CV and CA with reducing pixel size from 400 to 100 μm were both smaller in blood-perfused model (42 vs. 13% and 22 vs. 9%, respectively).

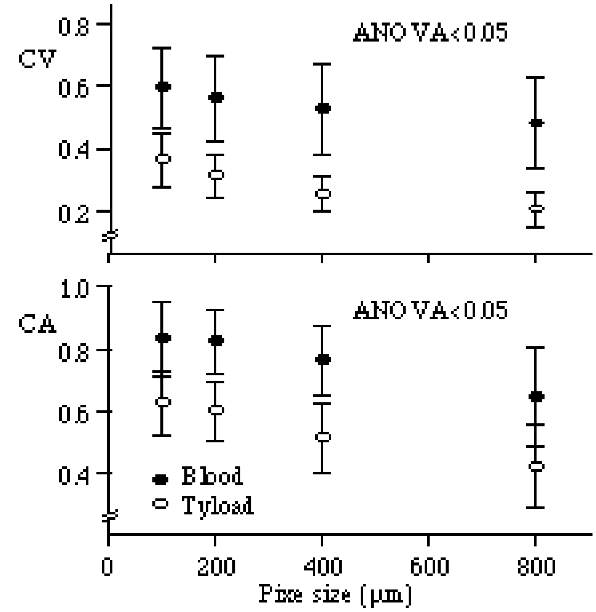

Figure 1: Myocardial perfusion heterogeneity (CV) and local flow similarity (CA) in Tyroad- and blood-perfused heart.

SUMMARY

These data suggest that the myocardial flow patterns of crystalloid-perfused isolated hearts differ from those of blood-perfused hearts. The less preserved vascular tone and lower flow resistance under crystalloid perfusion will be responsible for lower flow heterogeneity. The corpuscles may function to homogenize the flow within capillary beds.

REFERENCES

Deng, Q. et al. (1995). *J. Thorac. Cardiovasc. Surg.*, 109, 466-472.

Matsumoto, T., Kajiya, F. (2001). *Basic Res. Cardiol.*, 96, 547-552.

WAVE-FORM ANALYSIS OF ELECTROCARDIOGRAPH WITH SPECTRUM FOR SCREENING TEST

Shigehiro Hashimoto[1], Naoya Amimoto[1], Hiroshi Oku[1],
Hajime Otani[2], Hiroji Imamura[2]

[1]Biomedical Systems, Dept. of Electronics, Information and Communication Engineering,
Osaka Institute of Technology, Osaka, Japan, hasimoto@elc.oit.ac.jp
[2]Dept. of Thoracic and Cardiovascular Surgery, Kansai Medical University

INTRODUCTION

Electrocardiogram (ECG) reflects the conduction of action potential in the heart. ECG consists of several elements of electronic events in the heart. ECG was widely used for diagnostics of the heart disease as a noninvasive marker. To get enough information directly from the ECG tracings, enough training is necessary for an interpreter. Several computer-aided methods (Arthur, R.M. (1995), Kinoshita, O. (1992)) including R-R interval detection have been designed in the previous studies. To extend its use to the health-care device at home, a simple methodology with spectrum analysis to distinguish irregular conduction from normal one was investigated in this study.

METHODS

The electrocardiogram (ECG) was induced between the left ankle and the right wrist. The electrodes of disk type (diameter of 8 mm) were stuck via conductive gel on the surface near the joint-pivot to minimize intermixture of the electromyogram. After the signal was modified so that the frequencies lower than 0.08 Hz or higher than 1 kHz were cut off through the electric filter, it was converted into digital signal with the sampling rate of 256 Hz, and recorded with a personal computer. The segmented ECG data of one second between P wave and T wave were analyzed with fast Fourier transform (FFT). Data at the base line of ECG were added before P wave, when the cyclic period was shorter than one second.

Normal 30 segments of regular signal were collected from five volunteer human subjects between 21 and 25 years old at rest. Some segments of irregular signal were picked up from these measurements, and the data with compensatory ventricular premature contraction or with interpolated ventricular premature contraction were analyzed.

RESULTS AND DISCUSSION

The ECG spectrum decreases from 20 Hz to 40 Hz. The ECG spectrum can be represented with the range from 1 Hz to 60 Hz.

The data were displayed in the three-dimensional figure, when the interval of analysis was extended gradually from P wave to T wave with a step of 0.04 s. The spectrum at the time of one second shows datum at the whole cardiac cycle.

In the data from a normal ECG, the spectrum was distributed between 1 and 10 Hz during P-Q interval, while it was distributed 1 Hz and 40 Hz in the whole cardiac cycle. This is because the steepest wave occurs in QRS complex.

In the data both with compensatory ventricular premature contraction and with interpolated ventricular premature contraction, the spectrum significantly decreased between 20 Hz and 40 Hz. This is because of the extension of QRS wave width. Timing of irregular wave in the cardiac cycle did not affect the spectrum distribution.

The R-R interval analysis is useful to detect arrhythmia but is not useful to detect wave modification in a pre-excitation syndrome. The proposed method has enough availability to detect ECG wave change in heart disease, and can be applied to screening test in diagnosis for ventricular premature contraction.

SUMMARY

This paper proposes a simplified methodology to detect irregular conduction of potentials in heart during cardiac cycle using spectrum analysis of electrocardiogram.

REFERENCES

Arthur, R.M., Kavesh, N.G., et al (1995). *IEEE Trans Biomed Eng*, **42**, 29-41
Kinoshita, O., Kamakura, S. et al (1992). *Circulation*, **85**(6), 2054-2059.

ACKNOWLEDGEMENTS

This work was supported in part by a Grant-in-Aid for Scientific Research from the Japanese Ministry of Education, Culture, Sports, Science and Technology.

REFLEX RESPONSES TO THE MEDIAL KNEE LIGAMENT LOADING: EFFECT OF HIP ANGLE CHANGE

Yasin Y. Dhaher[13], Anastasios D. Tsoumanis[23], William Z. Rymer[123]
[1]Department of Physical Medicine and Rehabilitation, Northwestern University Medical School, Chicago, IL, USA
[2]Department of Biomedical Engineering, Northwestern University, Evanston, IL, USA
[3]Sensory Motor Performance Program, Rehabilitation Institute of Chicago, Chicago, IL, USA

INTRODUCTION

We have previously shown that reflex activity mediated by periarticular tissue afferents can be elicited consistently in knee muscles under the application of valgus perturbations at the human knee joint (Dhaher et al., 2002 and Dhaher et al., 2001). Considerable evidence derived from both animal and human studies suggest that signal transmission concerning hip position to the spinal cord play a significant role in modulating reflex transmission during walking and stance. It has been shown also that static hip changes are capable of modulating H-reflex excitability of distant limb muscles such as the soleus muscle (Chapman et al., 1991). There is also evidence that activation of cutaneous afferents registering changes in hip position can influence spinal reflex excitability. Furthermore, studies on decerebrate cats report that hip position is important in initiating the stance to swing transition (Hiebert et al., 1996). In the present study we investigated the effect of the change of hip angle in the modulation of the reflex response originating from periarticular tissue afferents, elicited via application of valgus positional perturbations in the human knee joint.

METHODS

The experiments performed have been described in detail previously (Dhaher et al 2001 and Dhaher et al, 2002) and will be briefly presented below. In summary, after securing the subject's leg in a single-degree of freedom servomotor system, the knee joint was pre-loaded (4° of valgus) to ensure initial stretch of passive joint tissues. The subject was asked to maintain three different knee muscle co-contraction levels as a percent of the valgus passive torque (VPT) measured at the joint's pre-loaded position: 5-10, 10-20 and 20-30% of VPT measured with a six-degree of freedom load-cell. Multiple 7° valgus perturbations were applied at the knee at two different hip flexion angles (90° and 50°) and repeated at all three co-activation levels. Surface electrodes recorded the muscle activity of a flexor, semitendinosus (ST), and an extensor, rectus femoris (RF). The normalized reflex response was then quantified as follows:

$$NR = \frac{EMG_{rms}^{reflex} - EMG_{rms}^{baseline}}{EMG_{rms}^{MVC} - EMG_{rms}^{baseline}} \qquad (1)$$

where EMG_{rms}^{reflex} is the time average of the rectified and smoothed EMG during the reflex activity period (computed from the time where the ramp input reaches its peak value and the end of the plateau period of the positional perturbation) $EMG_{rms}^{baseline}$ is the time average of the baseline activity calculated over 100 msecs before the onset of the mechanical perturbation, and EMG_{rms}^{MVC} was the time average of the EMG activity recorded over 100 msecs at maximum MVC in flexion or extension. For each muscle, the maximum NR across both hip angles and contraction levels was used to normalize all reflex intensities for the specific muscle.

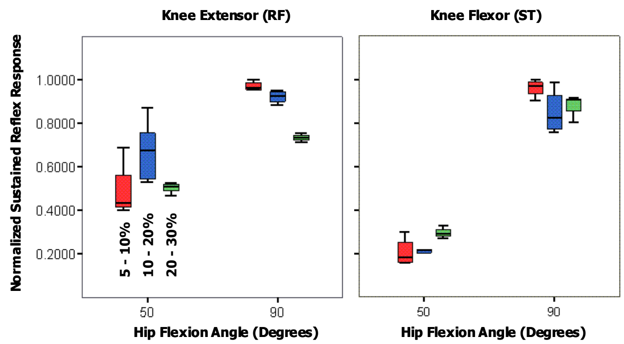

Figure 1: Normalized reflex activity as a function of hip angle and pre-activation co-contraction level.

RESULTS AND DISCUSSION

The amplitude of the reflex response of both the RF and ST muscle exhibited a statistically significant decrease ($p<0.001$) with increasing hip flexion (Fig.1). A significant trend of the reflex intensity was seen in the RF as a function of background activation at both hip angles. Specifically, a consistent decline with background activation at 90° and a modal response at 50° was observed for the RF reflex intensity ($p<0.001$). On the other hand, ST showed statistically insignificant change in the reflex intensity across all contraction levels for both hip angles.

SUMMARY

Our results show that hip extension results in decrease of the reflex response, originating from periarticular tissue afferents at the knee. The observed reduction was consistent in both flexor and extensor muscles. This effect can be attributed to one of three potential factors: 1) vestibular input, 2) hip joint proprioceptors input, and 3) input from muscle spindles of the pre-activated muscles. All these factors taken together indicate that other sensory layers derived from global sensory modalities could potentially influence the local varus/valgus-stabilizing role of reflexes deriving from the joint's periarticular tissue afferents.

REFERENCES

Chapman et al., (1991). *Electromyography and Clinical. Neurophysiology*. **31**:131-143
Dhaher et al. (2002). *Journal of Biomechanics* (*Accepted for publication*)
Dhaher et al. (2001). *Proceedings of the 23rd Annual Meeting of IEEE-EMBS*
Hiebert et al. (1996). *Journal of Neurophysiology*. **75**:1126-11

PERIODONTAL LIGAMENT BIOMECHANICS OF INTRUSIVE AND EXTRUSIVE ORTHODONTIC LOADING

Stephanie R. Toms, Jack E. Lemons and Alan W. Eberhardt

University of Alabama at Birmingham Department of Biomedical Engineering
stoms@mail.dental.uab.edu

INTRODUCTION

Previous studies of periodontal ligament (PDL) have applied relatively high stresses (>2.5 MPa) to isolated dental units to examine stress-strain behavior (Mandel et al, 1986). The mechanical properties of PDL at low stress (i.e. < 0.05 MPa) suitable for orthodontics have not been reported. In the present study, cadaveric specimens of mandibular premolars from adult donors were tested to characterize (PDL) over an orthodontic force range. We hypothesized that stress-strain behavior would be nonlinear and dependent on load direction and anatomic location.

METHODS

Cadaveric specimens of four adult mandibles were sectioned to isolate a premolar and adjacent PDL and bone. Transverse sections (n=58), approximately 0.85 mm thick, were made using a water irrigated circular saw. The sections were categorized according to anatomical location as cervical, midroot, and apex.

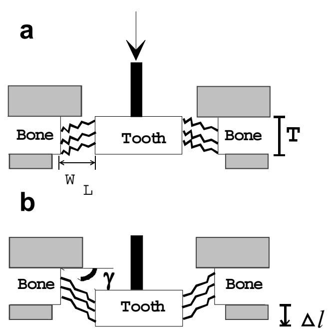

Figure 1. View of the specimen in the clamping apparatus a) before and b) after load application.

Fixtures were fabricated to clamp the bony part of each specimen firmly and allow for extrusive (out of the socket) and intrusive (into the socket) loading of the sections immersed in saline solution (Figure 1). Stress was calculated as applied force/A, where A= tooth perimeter * thickness. The tissues were preconditioned extrusively to 0.05 MPa stress for two cycles and load-displacement data was taken from the third cycle of loading. After recovery, the specimen was turned over, preconditioned, and load-displacement data was taken for intrusion loaded to 0.05 MPa stress. The student's t test was used to determine differences in calculated shear moduli (Figure 2), based on load direction and anatomic location.

RESULTS AND DISCUSSION

Distinct linear and toe regions were observed for all specimens in both loading directions (Figure 2). The average linear modulus in intrusion (1.043 ± 0.349 MPa/rad) was significantly higher (p=.001) than that for extrusion (0.688 ± 0.136 MPa/rad). No significant differences in intrusion moduli (linear and toe) comparing midroot specimens to the non-midroot (cervical margin and apex) specimens were observed. No significant difference was found for the toe modulus in extrusion. However, the linear modulus in extrusion was significantly different for the midroot and non-midroot locations (p=.0015). The extent of the toe region was smaller for intrusion (0.1060 ± 0.0778 rad) than extrusion (0.1628 ± 0.0778 rad).

SUMMARY

The current study offers unique information about the nonlinear elasticity of the PDL in the range of orthodontic forces for intrusive and extrusive loading. Less strain is needed to bring the ligament to orthodontic stress in intrusion than extrusion, and linear modulus of midroot regions is less than cervical and apex regions.

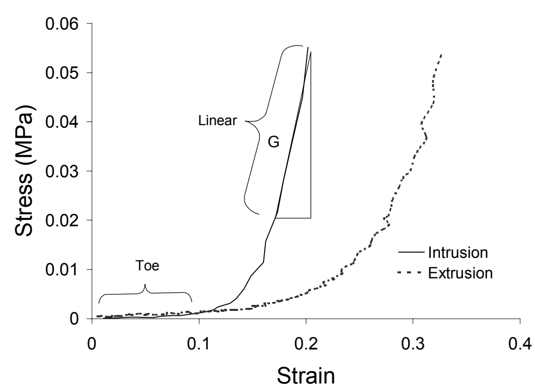

Figure 2: Example of stress-strain data of PDL for two loading directions.

REFERENCES

Mandel, U. et al, 1986.. *J. Biomechanics*, **19**, 525-526

FINITE ELEMENT ANALYSIS OF A MANDIBULAR PREMOLAR SUBJECTED TO ORTHODONTIC LOADING: EFFECTS OF PERIODONTAL LIGAMENT THICKNESS AND NONLINEAR MATERIAL PROPERTIES

Stephanie R. Toms, Jack E. Lemons, and Alan W. Eberhardt
University of Alabama at Birmingham Department of Biomedical Engineering
stoms@mail.dental.uab.edu

INTRODUCTION
Finite element analyses offer a means of determining stresses in the periodontal ligament (PDL) for a broad range of orthodontic loading scenarios. Regions of excessive orthodontic stress and potentially pathologic tooth movement can be identified. A comprehensive mathematical description for the PDL has not been reported and is a recognized weakness in computer simulations (Qian et al., 2001). The purpose of this study was to incorporate our own experimental data of PDL geometry and stress-strain relationships as input to a finite element model (FEM) to determine the influence of nonlinear and location-dependent properties on the stresses produced in the ligament due to orthodontic force.

METHODS
A two-dimensional plane-strain FEM of a mandibular premolar was constructed (Cosmos/M, SRAC, Los Angeles, CA) using anatomical data from a cadaver tooth (Figure 1). The model was an assembly of transverse sections of tooth/PDL/bone of the specimen from which nonlinear stress-strain behavior was determined experimentally (Toms et al, 2002). The model had 1674 elements and 5205 nodes, and was composed of dentin, PDL and bone. A line load equivalent of 1 N (extrusive or tipping) was applied to the midpoint of the crown occluso-gingivally. The bone was fixed at the base of the mandible.

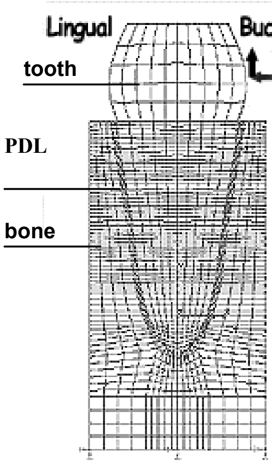

Figure 1. Finite element model of a mandibular premolar subjected to orthodontic forces on the buccal midpoint of the crown of the tooth.

Material properties for tooth, bone, and linear PDL were taken from previous FE studies (Wilson et al., 1993). Nonlinear material properties for PDL were based on experimental stress-strain data of five transverse sections of tooth/PDL/bone. Parametric analyses of the model were performed to determine the significance of PDL thickness (uniform 0.25 mm thick, and nonuniform anatomical), linear versus nonlinear elastic behavior of PDL, and consequence of load direction. Comparisons were made of the maximum principal stresses and shear stress in the PDL of the mandibular premolar.

RESULTS AND DISCUSSION
The maximum principal stress (Figure 2) and shear stress for a linearly elastic PDL did not differ significantly comparing the PDL of uniform width and the nonuniform anatomic model. In addition, predicted stresses were within the orthodontic range, i.e.<0.04 MPa (Boester and Johnson, 1974) for nearly all locations on the root for the linear models. The nonlinear extrusive model, however, revealed maximum principal stresses at the apex and cervical margins in excess of recommended orthodontic levels. Likewise, the nonlinear tipping model had excessive stresses at the cervical margin. The model suggests that the apex and cervical margin areas of PDL are vulnerable to pathologic stress levels

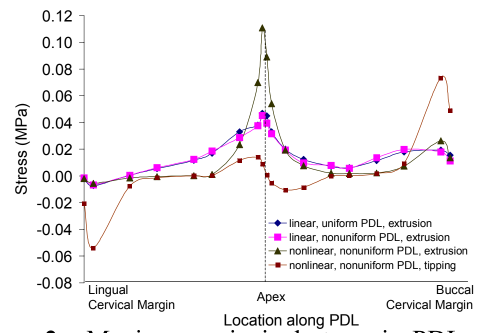

Figure 2. Maximum principal stress in PDL subject to low force on the buccal crown.

SUMMARY
This analysis suggests nonlinear material properties for PDL are required to quantify stress in PDL for orthodontic loading, and that linear material properties may underestimate the stress.

REFERENCES
Boester and Johnson, 1974. Angle Orthod, **44**, 113-9.

Qian, H. et al., 2001. *Am. J. Orthod. Dentofa. Ortho,* **120,** 272-9.

Toms, S.R., et al. (In press). *Am. J. Orthod. Dentofac. Orthop.*

Wilson, A.N. et al., 1993. *Brit. J. Orthod.,* **21**, 161-7.

RELAXATION FUNCTION AND A GENERALIZED SOLUTION FOR A NONLINEAR RHEOLOGICAL MODEL OF BIOLOGICAL SOFT TISSUES

David T. Corr[1], Ray Vanderby Jr.[2] and Thomas M. Best[2, 3]

[1]Human Performance Laboratory, University of Calgary, Calgary, Alberta, Canada, dcorr@kin.ucalgary.ca
[2]Department of Orthopedics and Rehabilitation, University of Wisconsin, Madison, Wisconsin, USA
[3]Department of Family Medicine, University of Wisconsin, Madison, Wisconsin, USA

INTRODUCTION

A nonlinear rheological model (Fig. 1) was recently developed to describe the strain-stiffening behavior displayed by many biological soft tissues (Corr *et al*, 2001). A closed-form solution had been provided for the specific case of constant-rate (iso-velocity) stretch or shortening (Corr *et al*., 2001). To extend the model's range of application, this study sought to determine a closed-form solution to constant length (hold) or stepped displacement. Additionally, the relaxation function, $K(t)$, was to be determined, leading to a generalized convolution solution according to the Boltzmann hypothesis. These solutions will broaden the model's range of applicability with respect to loading conditions, and in doing so, allow for its application to a variety of soft tissues.

SOLUTION DEVELOPMENT

By applying equilibrium, the model's (Fig. 1) force becomes

$$F(t) = c\dot{x} = k_1\delta + k_2\delta^2\,, \qquad (1)$$

where x and δ are the displacement from rest of the springs and dashpot, respectively, such that the tissue length, $L(t)$, is

$$L(t) = x(t) + \delta(t)\,. \qquad (2)$$

For the case of constant tissue length ($\dot{L}(t) = 0$) the time derivative of (2) gives the relation

$$\dot{x}(t) = -\dot{\delta}(t)\,, \qquad (3)$$

which when substituted into (1) and simplified yields

$$\dot{\delta} = \frac{-k_1}{c}\delta + \frac{-k_2}{c}\delta^2\,, \qquad (4)$$

a nonlinear first order differential equation with constant coefficients. Thus, with $a = -k_1/c$ and $b = -k_2/c$, (4) separates to

$$\frac{d\delta}{\delta(a + b\delta)} = dt\,. \qquad (5)$$

When expanded with partial fractions, simplified and integrated, (5) gives the spring displacement equation for constant whole tissue lengths,

$$\delta = \frac{Zae^{at}}{1 - Zbe^{at}}\,, \qquad (6)$$

where Z denotes the arbitrary integration constant.

For a Heaviside step-displacement at time τ, the change in tissue length, ΔL, gives the boundary conditions

$$\Delta L = \begin{cases} \delta & when \quad t = \tau^+ \\ x & when \quad t \to \infty \end{cases}. \qquad (7)$$

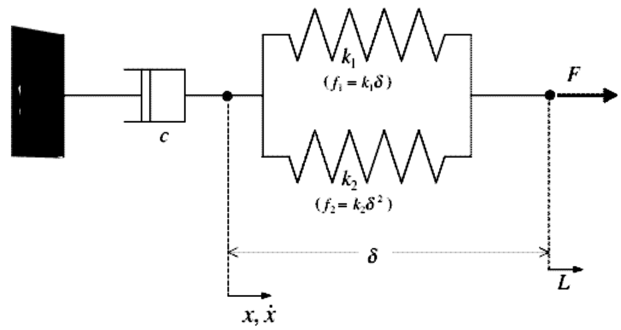

Figure 1: The nonlinear rheological model, consisting of a parallel arrangement of a linear spring (k_1) and second-order spring (k_2), in series with a dashpot (c). (Corr *et al*. 2001)

GENERALIZED SOLUTION

The tissue's force response to unit-step displacement ($\Delta L = 1$) yields the relaxation function, $K(t)$,

$$K(t) = k_1\delta(t) + k_2\delta(t)^2 \qquad (8)$$

where $\delta(t)$ is given by (6) and boundary conditions are

$$Z = (a + b)^{-1}, \qquad (9)$$

with δ=0 as time goes to infinity. Thus, for a generalized solution, the relaxation function is convolved to yield

$$F(t) = \int_0^t K(t - \tau)\frac{dL}{d\tau}d\tau\,, \qquad (10)$$

a separable, nonlinear function in time. This general solution gives the effect of numerous incremental steps, and sums their responses; a process termed nonlinear superposition, thereby allowing any arbitrary displacement function to be analyzed.

SUMMARY

These closed-form solutions grant the nonlinear rheological model the ability to interpret data from force-relaxation experiments, as well as piecewise continuous solutions for various ramp-and-hold experiments, when teamed with the previously published iso-velocity solution. Furthermore, the development of a relaxation function lead to a general solution that extends the model's range of applicability to include any arbitrary displacement function, thereby allowing a greater variety of biological soft tissue to be analyzed.

REFERENCES

Corr, D.T. *et al*. (2001) *J. Appl. Mech.*, **68**, 787-790.

IN VIVO & NONINVASIVE LOAD SHARING AMONG QUADRICEPS COMPONENTS IN PATELLAR MALALIGNMENT

Mohsen Makhsous[1-2], Amanda F. Lin[1-2], Jason T. Brizzell[4], Jason L. Koh[3], Li-Qun Zhang[1-4]
[1]Rehabilitation Institute of Chicago, [2]Department of Physical Medicine and Rehabilitation, [3]Department of Orthopaedic Surgery, [4]Department of Biomedical Engineering, Northwestern University, Chicago, IL, 60611, l-zhang@northwestern.edu

INTRODUCTION

Although unbalanced load sharing among the quadriceps components may be closely related to pathological conditions like the patellofemoral pain (PFP) with patellar malalignment[1], it is not clear how load is shared among the quadriceps components in either healthy subjects or PFP patients. In studies using cadaveric knees or computer modeling, loading of the quadriceps components has been simulated rather differently. For *in vivo* study, it is difficult and impractical to directly measure the force generated by each of the quadriceps components. The purpose of this study was to determine *in vivo* and noninvasively load sharing among quadriceps components (VL, VML and VMO) during isometric voluntary knee extension in PFP patients.

METHODS

Ten healthy subjects and ten PFP patients participated in the study. The subject was seated upright with the knee at 60° flexion and a fiberglass-tape cast was made at the ankle to attach it to a measuring device[2]. The VL, VML or VMO was activated selectively (one component at a time) using electrical stimulation using a pair of surface electrodes. The evoked M-wave from each of the quadriceps components were recorded using a second pair of surface electrodes, together with the isometric knee extension moment. The relationship between *the knee extension torque generated by an individual component* and the corresponding M-wave over different contraction levels was established for each of the three components. The subject was then asked to generate several steady levels of voluntary knee extension torque (from ~5 N·m to 50 N·m) to match a target knee extension torque displayed on a computer monitor. The *same* pair of electrodes used to record the M-wave was used to record the corresponding voluntary EMG signal.

Since exactly the same electrodes were used to record the M-wave and EMG signals for each quadriceps component during the stimulation-induced and voluntary knee extensions, respectively, it was assumed that the EMG amplitude of a quadriceps component and the torque generated by the component during voluntary contraction was similarly related as the relationship between the M-wave and knee extension torque established for each component during the stimulation test. The corresponding EMG signals during voluntary contractions were then calibrated with these M-wave-torque relationships to determine load sharing among the different components[3]. Specifically, the torque ratios of VMO/VML, VMO/VL, and VML/VL were determined and compared between the PFP and normal groups.

RESULTS AND DISCUSSION

For both normal and PFP groups, the VMO contributed less than VML to knee extension torque, and the VML generated less extension torque than the VL. The VMO and VML of the PFP patients contributed significantly less to knee extension torque than their counterparts in normal controls ($p<0.001$) (Fig. 1). In normal subjects, the combination of VML and VMO generated roughly the same amount of knee extension torque as the VL. However, in the PFP patients, VML+VMO contributed to the knee extension significantly less than the VL ($P<0.0001$). In normal group, the VML and VL contracted synergistically to extend the knee and the VML increased its relative contribution when higher knee extension torque was generated. In the PFP group, however, the VML and VMO always played minor role in generating the knee extension torque. Of note is that the remaining quadriceps components, the VI and RF, were not evaluated due to the difficulty involved, which is a limitation of the study.

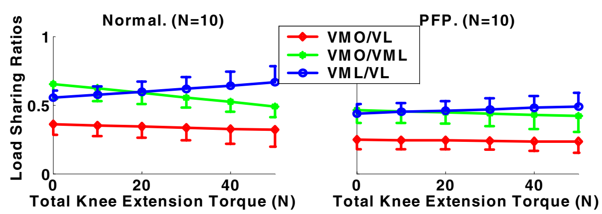

Figure 1: The torque ratios between individual quadriceps components over multiple subjects.

SUMMARY

The study provided us an *in vivo* and noninvasive way to evaluate load sharing in PFP. It was found that the VMO and VML contributed less to knee extension in PFP patients than that in normal controls.

REFERENCES

1. Fulkerson, JP Disorders of the Patellofemoral *Joint. Baltimore*, Williams & Wilkins, 1997.
2. L-Q Zhang & GW Nuber, *J. Biomech.* **33**(2): 145-154, 2000.
3. L-Q Zhang et al. *J. Biomech*. **31**(1): 71-76, 1998.

ACKNOWLEDGEMENTS

Supported by the NIH (AR45634).

INTELLIGENT STRETCHING AND EVALUATION OF SPASTIC ANKLES USING A PORTABLE DEVICE

Li-Qun Zhang[1-4], Sun G. Chung[1,2], Zach Bai[1,2], Elton M. van Rey[1,2], Thomas H. Grant[5], and Elliot J. Roth[1,2]
[1]Rehabilitation Institute of Chicago, Departments of [2]Physical Medicine & Rehabilitation, [3]Orthopaedic Surgery, [4]Biomedical Engineering, and [5]Radiology, Northwestern University, Chicago, IL, 60611, l-zhang@northwestern.edu

INTRODUCTION

Spasticity, contracture, and muscle weakness are major sources of disability following brain damages, and their development and recovery are closely interrelated. There is a strong need to treat spastic joints of the patients effectively to reduce spasticity/contracture and evaluate the outcome. The purposes of the studies were to use an innovative stretching device with intelligent control to treat spastic ankles of stroke patients and evaluate the outcome in terms of joint elastic stiffness, viscous damping, tendon reflex gain, reflex threshold, muscle force-generating capacities, and mechanical properties of the Achilles tendon (using ultrasonography).

METHODS

Twenty-four stroke patients with spastic plantar flexors (Ashworth and tendon reflex scales were 2.3±1.0 and 3.0±1.0, respectively) participated in various aspects of the study. The subject was seated (or supine when ultrasound images were taken) with the foot and leg strapped to a foot attachment and leg support, respectively (Fig. 1). The stretching device was controlled by a digital signal processor which adjusted the velocity every 0.5 ms and make it inversely proportional to the resistance torque. Near extreme ROMs, the increasing resistance slowed down the device and muscles-tendons were stretched slowly and safely. Once a peak resistance torque was reached, the joint was held statically for a period of time. In the middle ROM, the ankle was moved at higher speeds.

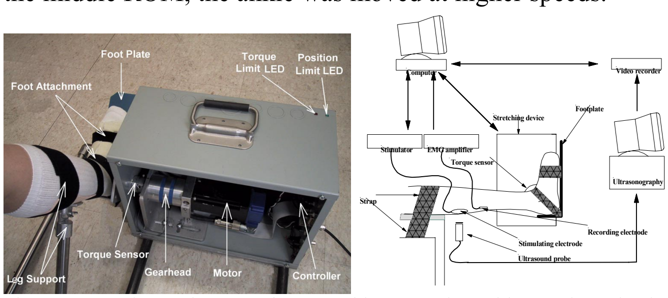

Fig. 1. Experimental setup for stretching spastic ankles and evaluating outcome.

To evaluate joint dynamic properties, the stretching device applied small-amplitude random perturbations to the ankle while the subject relaxed or maintained a steady flexion torque during a perturbation trial. Joint elastic stiffness and viscous damping were estimated from the measured position and torque using a system identification technique. Passive ROMs in dorsi- and plantar flexion were evaluated at controlled peak resistance torque in the stretching process. Additionally, under an isometric condition that minimized non-reflex contributions associated with joint movement, Achilles tendon reflex was evaluated with the tapping force and reflex torque taken as system input and output, respectively. Muscle strength was evaluated in plantar and dorsi- flexions. In 4 stroke patients and 4 healthy subjects, Achilles tendon mechanical properties (length, strain, force, stress) during stretching and triceps surae contractions were evaluated using ultrasonography (ATL HDI 5000 with a 12 MHz linear array probe).

RESULTS AND DISCUSSION

The stretching loosened the spastic triceps surae muscle-tendon unit and increased the passive dorsi-flexion ROM from 10.4±8.8° to 13.3±10.2° at 10 N·m torque ($P=0.004$ with paired t-test). Plantar flexion ROM was increase from 25.2±11.6° to 37.0±13.1° at 5 N·m torque ($P=0.036$). Joint elastic stiffness with triceps surae muscle contraction was reduced after stretching (significant at 2, 3, 7 and >9 N·m, Fig. 2(a)). Similar reduction was observed for viscous damping (Fig. 2(a)). Although some patients showed considerable reduction in tendon reflex gain, stretching-induced changes in tendon reflexes across patients were not significant.

After stretching, the patients were able to generate higher plantar flexion MVC torque (paired t-test with $P=0.005$). The increased force-generating capacity was corroborated by increased torques induced by matched electrical stimulation of the spastic muscles before and after stretching (Fig. 2(b)). It was reported that spastic muscles had elongated sarcomere length[1]. Using ultrasonography, we observed that stretching elongated the Achilles tendon in the spastic ankles, which might have put muscle fibers in a better operating range in the sarcomere force-length curves. The stretching might have also changed the abnormal rearrangement of the excessive connective tissues and atrophied muscle fibers in the spastic muscles, which would contribute to the increased force output.

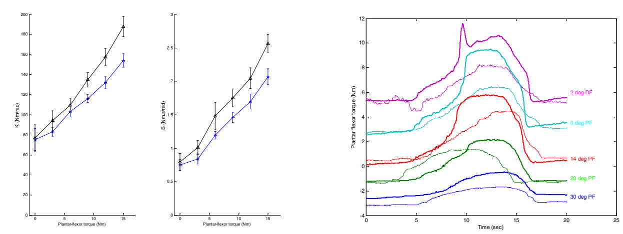

(a) (b)

Fig. 2. (a) Elastic stiffness (left) and viscous damping (right) before (black Δ) and after (blue *) stretching. (b) Plantar flexion torques induced by stimulating the gastrocnemius at constant intensity at several positions (30, 20, 14, 0, and -2° PF) before (thin lines) and after (thick lines) stretching.

In summary, the study presented a useful approach to treat spastic/contractured joints and evaluate treatment outcome in multiple aspects. Further work needs to be done to better understand the mechanisms underlying spasticity/contracture and the treatment-induced changes.

REFERENCES

1. RL Lieber & J Fridén, Spasticity causes a fundamental rearrangement of muscle-joint interaction. *Muscle & Nerve*, in press.

DOES SIMULATED DORSAL KYPHOSIS ALTER LOWER LIMB KINEMATICS, KINETICS, AND EMG PATTERNS DURING GAIT?

Joshua (Sung) You[1] , Joseph Gieck[2], and Evangeline Yoder[3]
[1,3]Department of Physical Therapy, Hampton University, Hampton, VA, U.S.A.,sung.you@hamptonu.edu
[2]Department of Kinesiology, Clinical Orthopedics & Sports Medicine, Head Athletic Trainer,
University of Virginia, Charlottesville, VA, U.S.A.

PURPOSE. The purpose of this study was to investigate the effects of simulated dorsal kyphosis on locomotor patterns in normal subjects.

SUBJECTS. Three (3) healthy males and six (6) females aged 20-43 years participated in the study.

METHODS. Using a Vicon motion analysis system, kinematic, kinetic, and electromyographic (EMG) data were collected from the L5-S1 segment, pelvis (S2), and the hip, knee, and ankle joints. Aptio-temporal data was recorded while each subject walked at a constant velocity, with and without, an orthosis, which simulated dorsal kyphosis.

DATA ANALYSIS. Descriptive analysis using means, percentages of means, and standard deviations (SD) was used to analyze the data.

RESULTS. Results are summarized in **Table 1**. Mean values for all kinematic, kinetic moment and power, and EMG values were decreased by 83%, 53%, 17%, and 76%, respectively during 'kyphotic' walking as compared to walking without the orthosis.

CONCLUSION. Results of the study suggest that kyphotic posturing causes increases in kinematic, kinetic and and EMG values, while dorsal kyphosis decreases stride length and velocity.

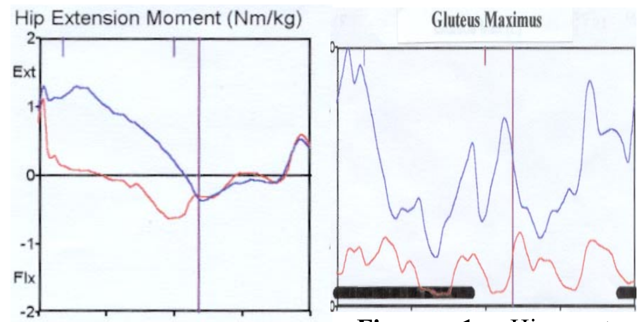

Figure 1: Hip extension moments between normal (red) vs. simulated kyphotic posture (blue).

RELEVANCE. Analysis of postural kyphosis in the elderly should be the subject of future studies to determine the possible relationships between alterations in gait determinants and falling.

REFERENCES

Winter, D. A. (1991). *The Biomechanics and Motor Control of Human Gait: Normal, Elderly and Pathological* (2nd eds.). Ontario, Canada: University of Waterloo Press.

Winter, D. A., Patla, A. E., Frank, J. S., & Walt, S. E. (1990). Biomechanical walking pattern changes in the fit and healthy elderly. *Physical Therapy*, **70**, 340-347.

ACKNOWLEDGEMENTS. I would like to acknowledge Dr. David Winter at University of Waterloo and Dr. Marilys Randolph for their critical review and insightful comments.

Table 1: Comparison of Spatiotemporal, Kinematic, Kinetic, and EMG Patterns Between Upright vs. Simulated Kyphotic (Right Side Only)

	Stride Length (cm)	Velocity (m/s)	Peak Angular Displacement in hip extension (°)	Peak moment in hip extension (Nm/kg)	Peak Power (W/kg) in hip joint	Peak EMG Amplitude (unitless) in hip extensor
Upright Gait	0.67 ± 0.11	1.03 ± 0.38	5° ± 1.5°	0.7 ± 0.1	1 ± 0.1	0.26 mv
Kyphotic Gait	0.59 ± 0.63	0.94 ± 0.21	-30° ± 4.5°	1.5 ± 0.15	1.2 ± 0.25	1.07 mv

*Please note that spatiotemporal data were acquired from all nine subjects and kinematic, kinetic, and EMG data were collected from three subjects.

MOVEMENT CHARACTERISTICS IN CHILDREN WITH LESCH-NYHAN SYNDROME (LNS)

Joshua (Sung) You[1], Linda Bunker[2], and Evangeline Yoder[3]
[1,3]Department of Physical Therapy, Hampton University, Hampton, VA, U.S.A.,sung.you@hamptonu.edu
[2]Department of Kinesiology, Motor Learning, University of Virginia, Charlottesville, VA, U.S.A.

PURPOSE
The purposes of this study were to determine in children with Lesch-Nyhan Syndrome (LNS): 1) angular accelerations required for forward reaching at the shoulder, elbow, wrist, first digit, and 2) timing characteristics during the reaching.

SUBJECTS
Two (2) ten-year right-handed male fraternal twins with LNS were subjects for the study.

METHODS
While subjects performed in sitting a right-handed forward reaching task, angular accelerations were measured at the shoulder, elbow, wrist and first digit, respectively, using the Ariel Performance Analysis System (APAS)^{TM}. **(Figure 1).**

DATA ANALYSIS
Recorded angular accelerations were analyzed in terms of: 1) movement time (MT), 2) movement units (MU), and 3) initiation, meter, and sequencing of segmental components.

RESULTS (Table 1)
As compared with healthy children**,** subject's MTs were increased by 50%, and MU's were 80% greater. Segmental movement irregularities included inconsistencies in sequencing and dysmetria.

CONCLUSION
Movement impairments in the study subjects demonstrated patterns consistent with extrapyramidal disorder.

CLINICAL RELEVANCE
Objective measurement of impairments in children with movement disorders is essential in order to document outcomes following intervention.

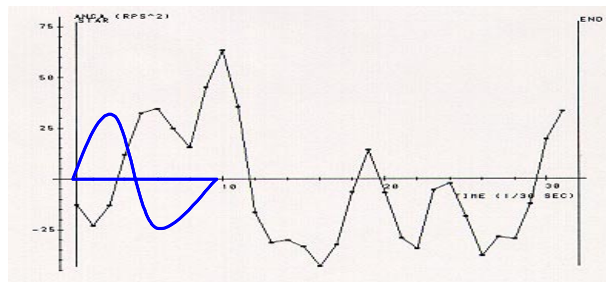

Figure 1: Comparison of movement unit derived angular acceleration profiles between normal (black) vs. LNS (blue).

REFERENCES
1. Brown, J.V. et al (1986). The accuracy of aimed movements to visual targets during development: The role of visual information. *J. Experimental Child Psychology,* **41,** 443-460.
2. Hofsten C von. (1979). Development of visually directed reaching: The approach phase. *J. Human Movement Studies,* **5,** 160-178.
3. Zernicke RF, Schneider K. (In Press). *Biomechanics and Developmental Neuromotor Control*. In: Thelen E, Lockman, J, editors. Child Development: Developmental Biodynamics: Brain, Body and Behavior Connections.

ACKNOWLEDGEMENTS
I would like to acknowledge Marilys Randolph, PT, Ph.D for her critical review and insightful comments.

Table 1: Differential Kinematic Movement Characteristics Between Normal vs. Children with LNS (Right Side Only)

Task: Reaching	Movement Time (ms)	Movement Units (in Numbers, (see Figure 1)	Interlimb Segment Coordination (sequence)
Normal Children	725 ± 109[1]	1[2]	Elbow flexion → immediately followed by shoulder flexion with maximum velocities of shoulder flexion → elbow extension[3]
Children with LNS	1454 ± 278	5	Irregularities in sequence and dysmetria

ORIGINS OF BIPEDALISM: EVOLUTIONARY MORPHOLOGY THROUGH FINITE ELEMENT ANALYSIS

Robert B. Eckhardt[1], Karol Galik[2], Brigitte Senut[3], Martin Pickford[4], D. Gommery[5], J. Treil[6],

[1]Department of Kinesiology, Pennsylvania State University, eyl@psu.edu [2]ME Department, University of Pittsburgh
[3]Laboratoire de Paléontologie du Muséum national d'Histoire naturelle & UMR 8569 du CNRS
[4] Chaire de Paléoanthropologie ed de Préhistoire du Collège de France, [5]UPR 2147 CNRS, [6]Clinique Pasteur, Toulouse

INTRODUCTION

Important fossils believed to sample the evolutionary record near the point of divergence of apes and humans have been recovered from four locations within the Late Miocene Lukeino Formation in the Tugen Hills of Kenya. Radioisotopic determinations from geological deposits underlying and overlying the fossil remains indicate an age of about 6 million years before the present, consistent with the divergence time predicted three decades ago (Eckhardt 1972). Materials recovered so far number 13 specimens, all but one collected in October and November of 2000, representing at least five individuals. Included in the sample are two mandibular fragments, six teeth, one manual phalanx, a distal humeral fragment, and three femoral fragments. Functional inferences about posture and locomotion, significant in their own right, also are critical in helping to resolve questions about the early phases of hominid phylogeny.

METHODS

Descriptive morphology is based on the most complete femoral specimen (BAR 1002'00), which comprises the left femoral head, neck, and shaft; approximately 2/3 of the intact bone is represented by the total preserved length of approximately 215 mm. The proximal portion of the bone, including the neck and head, makes direct contact with a substantial portion of the shaft across a slightly worn post-mortem break at about the level of the *trochanter minor*.

Finite element analysis in this report focuses on the shaft of BAR 1002'00. Computerized tomography was used to image 170 fossil cross-sections, on which it is possible to delineate the inner and outer boundaries of the compact bone, as well as the medullary cavity in some regions. Outlined cross-sections are transferred into an FEM program Solid model is then created, meshed with hexagonal elements. Functional inferences about posture and mode of locomotion are supported by analyzing stresses in BAR 1002'00. Optimization of cross sections for prevailing loading conditions are used to analyze mode of locomotion. Subsequently these will be compared with CT images on samples of extant chimpanzees, for the later species a model has already been created (see reference for standardized femur).

RESULTS AND DISCUSSION

The well-defined femoral head is spherical (33 mm in both antero-posterior and perpendicular diameters), with slight anterior rotation, and exhibits a moderately wide *fovea capitis*. Compared to extant humans, the head is smaller in proportion to the shaft, but is proportionally larger than in some other specimens accepted as early hominids (e.g. AL-288.1). The presence in BAR 1002'00 of an intertrochanteric groove which runs from a small, moderately deep *fossa trochanterica* to a region just above the *trochanter minor* is a feature that has been related to bipedalism (see Senut et al 2001 for further details). The femoral neck makes direct contact with a substantial portion of the shaft across a slightly worn post-mortem break. In BAR 1002'00, cortical thickness at midshaft is 5.2 mm (anterior and posterior), 7.4 mm (medial) and 5.5 (lateral). In the finite element analysis, stresses in the femur of the fossil specimen are estimated.

SUMMARY

Descriptive morphology and finite element analysis enable exploration of both details of form and inferences about features related to locomotor function in the femur of BAR 1002'00. This specimen appears to exhibit characteristics, some of which are consistent with bipedal locomotion, but on balance present an overall pattern with aspects as yet not duplicated in all details among other early hominids.

REFERENCES

Eckhardt, R.B. (1972). *Sci. Amer.* **226**, 94-103.
Senut, B. et al (2001) *C. R. Acad. Sci., Paris*, **332**,137-144
Standardized femur-http://www.cineca.it/hosted/LTM-IOR/back2net/stand_fem/stand_fem.html

ACKNOWLEDGEMENTS

The Community Museums of Kenya (E. Gitonga), the Kenyan Office of the President Funding provided by the Collège de France (Prof. Y. Coppens), Muséum national d'Histoire naturelle, Paris (Prof. Ph. Taquet) and CNRS-UMR CT images provided by the Clinique Pasteur at Toulouse (Directors : J-P Deymier, Dr F. Berthoumieu) and the staff (P. Roch; S. Charreau & A. M' Voto).

A COMPARISON OF ACL FORCE DURING SOFT AND STIFF DROP-LANDINGS

Mary A. Pflum[1], Kevin B. Shelburne[3], Michael R. Torry[3], Michael J. Decker[3], Marcus G. Pandy[2]
[1]Department of Kinesiology and [2]Department of Biomedical Engineering, University of Texas, Austin, TX
[3]Steadman♦Hawkins Sports Medicine Foundation, Vail, CO mpflum@mail.utexas.edu

INTRODUCTION

Many ACL injuries occur by non-contact mechanisms, which are often marked by sudden deceleration of the center of mass, as in the case of landing from a jump. Previous landing studies have traditionally defined landing techniques in terms of *soft* or *stiff* according to the degree of maximal knee flexion angle attained during the landing phase (Devita and Skelly, 1992). The purpose of this study was to predict and explain ACL force for soft and stiff drop-landings. ACL force during the drop-landing task was calculated using a forward dynamics computer simulation. We hypothesized that peak ACL force for a stiff landing would be higher than that for a soft landing.

METHODS

A 3D model of the body (Anderson and Pandy, 2001) was used to simulate drop-landings from a height of 60 cm. The input muscle excitation patterns for the model were based on EMG measured in vivo. Since EMG activity was not available for all the muscles in the model, the excitation patterns for these muscles were modified until the calculated joint motions and ground-reaction forces (GRFs) were found to be consistent with *in vivo* measurements of the same quantities obtained from five healthy subjects. Knee flexion angle at ground contact in the soft condition was 24° with a terminal knee angle of 92°. A second stiff landing simulation was run with a knee flexion angle at ground contact of 10° and a terminal knee angle of 33°. Time to maximum knee flexion for the stiff landing was approximately one third of that for the soft landing. The muscle forces calculated by the model were then used as input to a sagittal-plane model of the knee (Shelburne and Pandy, 1997) to determine the pattern of ACL loading during the landing phase. All surfaces in the knee model were assumed to be rigid and frictionless; thus, tibiofemoral and patellofemoral articulation were each modeled as single-point contact. Eleven elastic elements described the geometric and mechanical properties of the cruciate and collateral ligaments plus the posterior capsule.

RESULTS AND DISCUSSION

Peak ACL force was substantially higher in the stiff landing simulation (847 N) than the soft landing simulation (329 N). For the duration of the soft landing, the tibial shear force due to the resultant GRF is directed posterior relative to the tibia (Fig. 1). This posterior shear force dominates the total resultant tibial shear force during the soft landing. Thus, ACL force was highest when posterior tibial shear force due to resultant GRF was lowest (Fig. 1). Peak vertical GRF during the stiff landing was roughly 3.4 times higher than that for the soft landing. Due to the higher vertical GRF and lower knee angle, peak tibiofemoral compressive force for the stiff landing was 1.9 times higher than that for the soft landing. In the knee model, tibiofemoral compressive force results in an anterior tibial shear force due to the posterior slope of the tibial plateau. This anterior shear force dominated the total resultant shear force at the knee during the stiff landing (Fig. 2). Thus, the peak ACL force for the stiff landing depends mainly on the peak tibiofemoral compressive force and to a lesser extent on the peak vertical GRF.

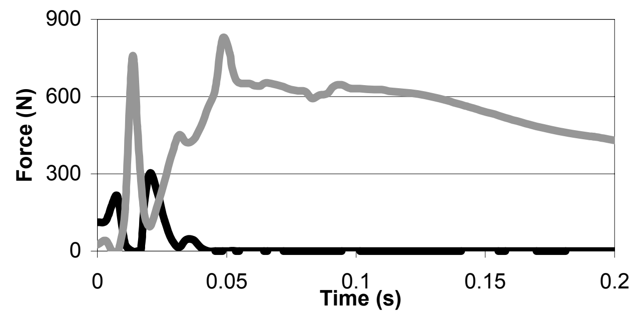

Figure 1: ACL force (black line) and the posterior tibial shear force due to resultant GRF (gray line) during a soft landing.

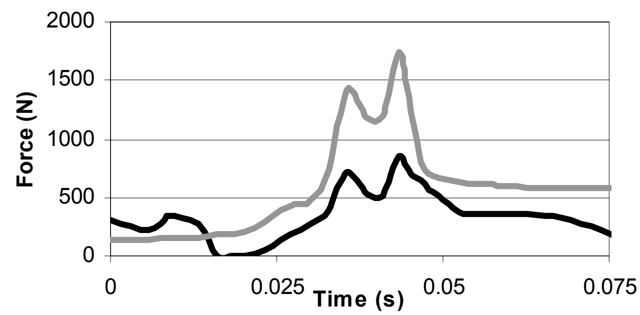

Figure 2: ACL force (black line) and anterior tibial shear force due to tibiofemoral compressive force (gray line) during a stiff landing

SUMMARY

ACL force predicted for the stiff landing was roughly 250% higher than that calculated for the soft landing. While the stiff landing increased load in the ACL, the maximum force in the ACL did not exceed the ultimate failure load required for rupture (Woo et al., 1991). This suggests that other factors, in addition to landing style, contribute to injury of the ACL.

REFERENCES

Devita P., Skelly W. (1992) *Med. Sci. Sport & Exer.*, 24:**1**:108-115.

Anderson, F.C., Pandy, M.G. (1999) *Compu Methods Biomech Biomed Engin.,* **2**:201-231.

Shelburne, K.B., Pandy, M.G. (1997) *J Biomech.*, **30**:163-176.

Woo et al., (1991) *Am J Sports Med.*, **19**:217-225.

MODELING OF ACL IMPINGEMENT USING SIMM

Mohsen Makhsous[1, 2], Amanda F. Lin[1, 2], David Fung[1,4], and Li-Qun Zhang[1-4]
[1]Rehabilitation Institute of Chicago, Departments of [2]Physical Medicine & Rehabilitation, [3]Orthopaedic Surgery, and [4]Biomedical Engineering, Northwestern University, Chicago, Illinois, 60611. m-makhsous2@northwestern.edu

INTRODUCTION

The anterior cruciate ligament (ACL) impingement on femoral intercondylar notch wall is suggested as a high risk factor of noncontact ACL injury[1]. It is very difficult to examine the impinging condition *in vivo*, although MRI may provide some indirect answers. The purpose of this study was to model/ simulate ACL impingement using Software for Interactive Musculoskeletal Modeling (SIMM)/Dynamic Pipeline based on cadaver data in which ACL impingement was measured.

METHOD

Musculoskeletal model of the knee: A cadaver knee with narrow notch (notch width index=0.22)[2] was used to establish the model. The tibiofemoral kinematics was recorded by an OPTOTRAK® system and the impinging force was detected using FlexiForce® force sensors at the ligament-notch wall-interface. ACL length-tension properties were determined along the ACL-axis (30° knee flexion) using a linear load-displacement device[3] and used in the impingement modeling. The knee was then dissected and the bone surfaces of femur and the tibia were digitized with a 3-D digitizing probe and used to build a musculoskeletal knee model in SIMM.

Simulation of the ACL impingement: Initially, each of ACL bundles (anteromedial (AM), posterolateral (PL) and intermediate (I)) was modeled as a spike cylindrical bone described by polygonal mesh representing the ACL orientation along the line connecting the origin and insertion. The contacts between the "ACL-bone" and intercondylar notch, if any, were detected using the SIMM/Dynamic Pipeline 'contact detection' function. An ellipsoid was fitted to the small surface around the contact points on the notch wall with the ellipsoid imbedded into the lateral femoral condyle. The ellipsoid was used as a wrap object to prevent the penetration of ACL into the bone. The contact points served as the wrapping tangential points. The "ACL-bone" was then replaced with the ligament object wrapping around the ellipsoid and the ACL force generated in the wrapping/lengthening was determined from the length-tension relationship obtained above. Contact force applied to the ACL by the impinging points on the notch wall was then calculated by adding the two force vectors pointing away from the impinging point to the ACL origin and insertion (Fig. 2(a), $\mathbf{F_c}=\mathbf{F_1}+\mathbf{F_2}$). Frictionless contact was assumed at the ligament-notch wall interface.

RESULTS AND DISCUSSION

ACL impingement detection: For all the kinematic trials with the combination of flexion/extension, adduction/abduction, and internal/external axial rotation, the method using "ACL-bone" successfully detected the impingement on the notch wall of the ACL AM band (Fig. 1(a) & (b)). No impingement was found for PL or I band in the simulation. The contact points found by the simulation were in the same small area as observed in the experiment (Fig. 1(c)).

ACL impinging force: The ACL-notch interface contact force predicted by the model simulation is shown in Fig. 2(b) as red dots for one of the kinematic trials during which impingement was observed with the FlexiForce® readings (solid blue line). Results show that the model prediction matches the force measured.

The impingement force of the AM bundle was found to be higher in a flexed knee with tibial abduction and external rotation. The impingement of the AM bundles is consistent with previous studies[4] that the AM bundle is tighter in flexion than the PL bundle, the latter do not show any impingement in the simulation.

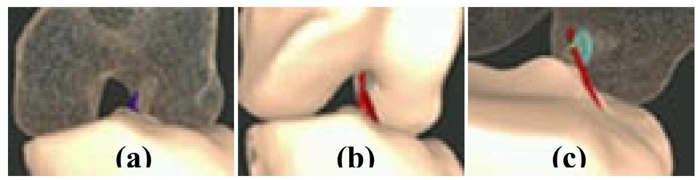

Figure 1: ACL impingement detection. A flexed left knee with tibial abduction and external rotation.

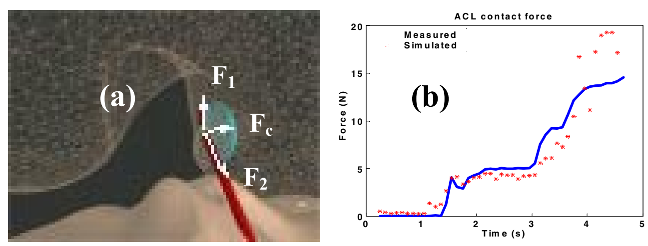

Figure 2: ACL impingement force.

SUMMARY

The method is a useful tool in analyzing/visualizing ACL impingement and it can potentially be applied to clinical problems to evaluate noncontact ACL injuries or to predict likelihood of potential injuries. Further studies are needed to identify risk factors and prevention strategies should be employed.

REFERENCES

1. Harmon, K.G. Ireland M.L. (2000). *Clinics in Sports Medicine* **19**(2): 287-302.
2. LaPrade, R.F., Burnett, Q.M. (1994). Am. *J Sports Med*, **22**(2): 198-203.
3. Woo, S.L.-Y., Adams D.J. (1990). In Knee ligaments: edited by D. Daniel, et al.: 279-89.
4. Woo, S. L.-Y., et al. (1990). In Knee ligaments: edited by D. Daniel, et al (115-34).

ACKNOWLEDGEMENT: The authors thank Krystyne Blaikie at the Musculographics Inc. for her help on contact detection using SIMM.

MATHEMATICAL MODELING OF ACL IMPINGEMENT AGAINST THE INTERCONDYLAR NOTCH WALL

David Fung[1,2] and Li-Qun Zhang[1-4]

[1]Sensory-Motor Performance Program, Rehabilitation Institute of Chicago, Departments of [2]Biomedical Engineering, [3]Physical Medicine & Rehabilitation, and [4]Orthopaedic Surgery, Northwestern University, Chicago, Illinois, Email: d-fung@northwestern.edu

INTRODUCTION

While many ACL injuries may have resulted from direct loading of the ligament, the ACL may also be injured due to its impingement against the intercondylar notch wall. A number of studies have been conducted to evaluate the relationship between the intercondylar notch width and risk of noncontact ACL injury, based on planar notch-view X-ray[1]. Considering the complex shape of the notch and oblique arrangement of the ACL, it is needed to investigate the impingement accurately in 3-D space. The purpose of this study was to evaluate ACL impingement against the notch through computer modeling based on data from individual cadaver knees in which ACL impingement was measured.

METHODS

In five cadaver knee specimens with intact ligaments, ACL impingement against the intercondylar notch was evaluated visually by moving the tibia passively relative to the femur. In one representative specimen with low notch width index (0.22), impingement was measured with paper-thin FlexiForce force sensors at the ligament-notch wall-interface. The corresponding tibiofemoral kinematics, measured in six degrees of freedom, provided details on the kinematic conditions at which impingement occurred. ACL origin (O), insertion (I), and a small patch surface representing an area around the impinging points on the medial edge of the lateral intercondylar notch wall were digitized and used in the modeling (Fig. 1).

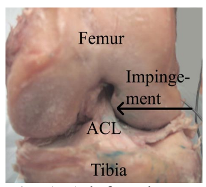

Fig. 1: A left cadaver knee in abduction and external rotation used for modeling.

ACL impingement against the notch was determined as follows. First, the small patch surface was fitted by bicubic splines with continuity up to the second derivative[2]. Positions of the anteromedial, intermediate, and posterolateral bands of the ACL during the impingement were represented by lines connecting their respective origins and insertions. If impingement of any band occurs, its corresponding line would generally intersect with the patch surface at two points, an entry point E_1 and an exit point E_2 (Fig. 2). E_1 and E_2 were determined by detecting intersection between the line OI and the small triangular polygons that were generated to represent the meshed surface. Second, using E_1 and E_2, and a third point H, the highest point along the path E_1E_2 on the fitted surface, an initial plane P_1 was generated, followed by a family of incremental planes (P_i, i=2,3,4...) rotating about an axis defined by line E_1E_2 (Fig. 2). The impinging band of the ACL should wrap around the curved notch surface in the plane that gives *the shortest ACL length*. Third, the wrapping path on each plane was determined by "crawling" on the surface from E_1 to E_2 in small steps. Starting from E_1, point C advances a small step along the Y-axis to obtain a new location on the surface. If C is off the plane, an adjustment along the X-axis will be made until C is in the plane (Fig. 3), reaching the next point on the ACL path. C then continues to "crawl" in small steps along the possible ACL path in the plane until its tangent at point C matches the slope of line OT_1. This location marks the tangential point T_1 where the impinging band makes its first contact with the curved surface (Fig. 2). From T_1, point C continues to crawl in the plane until reaching tangential point T_2 where the path's tangent matches the slope of line T_2I. The impinging band conforms to the curvature of the surface between T_1 and T_2, and connects directly between O and T_1 and between T_2 and I (Fig. 2). The deformed length of the ACL in each plane was determined by adding the linear lengths of OT_1 and T_2I, and the curved length T_1T_2.

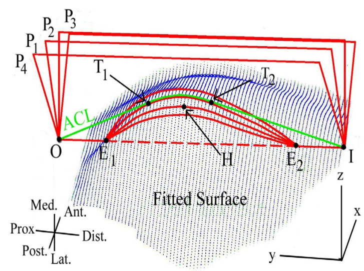

Fig. 2: Fitted surface and incremental planes.

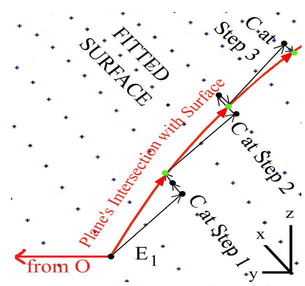

Fig. 3: "Crawling" on the surface.

RESULTS AND DISCUSSION

Since the impingement site was located on the medial side of the lateral notch wall in the specimen, impingement was induced by abduction and external rotation. At the impinging position, the AM band with an initial length was 25.5mm showed impingement bending and a deformed length of 25.7mm (OT_1=8.0mm, T_1T_2=0.4mm, T_2I=17.3 mm), and 0.78% strain. The I and PL bands showed less strain than the AM band.

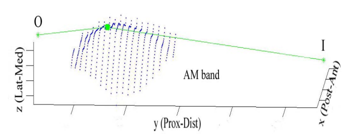

Fig. 4: Impingement of AM band shown in model

SUMMARY

The mathematical model provided a useful method to determine ACL impingement in 3-D space, including its bending, length, and strain as it wraps around the notch surface. It was shown that ACL impingement on the intercondylar notch stretched the ACL considerably. Further work needs to be done to identify the different impingement areas of the notch and to corroborate the results quantitatively with the force measurement.

REFERENCES

1. Arendt, E. (2001). *In Prevent. Noncontact ACL Injuries*. AAOS, Rosemont, IL.
2. Hayes, J.G., Halliday, J. (1974). *J. Inst. Maths Applics*, **14**, 89-103.

IN VIVO PATELLAR TRACKING IN PATELLAR MALALIGNED KNEES

Amanda Lin[1,2], Mohsen. Makhsous[1,2], and Li-Qun Zhang[1-4]

[1]Rehabilitation Institute of Chicago, Departments of [2]Physical Medicine & Rehabilitation, [3]Orthopaedic Surgery, and [4]Biomedical Engineering, Northwestern University, Chicago, Illinois, 60611 1-zhang@northwestern.edu

INTRODUCTION

Patellofemoral pain (PFP) syndrome is one of the most commonly observed physical abnormality involving the knee in sports medicine clinics, and is often associated with patellar malalignment and abnormal tracking.[1]. The purpose of the study was to study 3-D patellar tracking pattern in the PFP patients through *in vivo* and *noninvasive* method and compare it to that of the normal group. Patellar tracking was generally evaluated using cadaveric specimens, and in some cases, in vivo and invasive measurement was used[2,3]. The purpose of this study was to investigate in vivo patellar tracking non-invasively in PFP patients during selective contraction of individual heads of the quadriceps muscle and during voluntary knee extension.

METHODS

Eight PFP patients and 17 normal subjects participated in the study. Patellar tracking was evaluated with the experimental setup reported previously[4,5]. Patellar movements were described in the coordinate system shown in Fig. 1(c). For the right patella, the x, y and z axes pointed medially, proximally, and anteriorly, respectively. The patellar rotations about the x, y and z axes were defined as flexion/extension, mediolateral tilt, and mediolateral rotation, respectively. The positive directions of the rotations were flexion, medial tilt, and medial rotation, respectively. Function of each individual head of quadriceps during individual quadriceps head activation was determined by DOR and DOT described previously [4,5]. Patellar translations were normalized to the knee width of the subjects.

RESULTS AND DISCUSSION

Patellar tracking associated with knee voluntary extension shows the patella was extended 7.4±3.4° (mean±SE), medially tilted 3.2±5.6°, and little rotated during a 15° knee extension. At the same time, the patella shifted laterally, proximally, and anteriorly. Compared with previously data on normal subject[5], patellar tracking in knee voluntary extension for PFP patients in this study had almost the same pattern but with significantly more lateral tilt (Fig.1 (a)) ($p < 0.001$), and the lateral tilt continued to full knee extension.

At 20° knee flexion, the VMO mainly medially rotated the patella and shifted it medially and anteriorly. The VML extended and medially tilted the patella and shifted it anteriorly and proximally. VL laterally tilted the patella and shifted it laterally and proximally. Compared with patellar tracking at more flexed knee positions, stimulation of the VMO generated major patellar motion as extension, medial and proximal shift, and the former major motion as anterior shift at 20° knee flexion decreased to be negligible. At fully extended knees, VL changed its major motion of medial rotation to extension.

Significant differences for function of VMO were found between normal and patient groups both in the patellar translations and rotations. For normal subjects, medial shift was the only major translation generated by VMO, while in PFP group proximal shift was found as an additional major motion. Also found was that VMO did less medial tilt at full knee extension than that of normal ($p<0.001$). Similarly, substantial changes were shown in the major function of VL. For PFP group, VL laterally tilted and shifted patella more than those of normal, both at full knee extension and 20° flexion (both with $p<0.001$) (Fig. 1 (b)). The major function of VML did not change much from those of normal group.

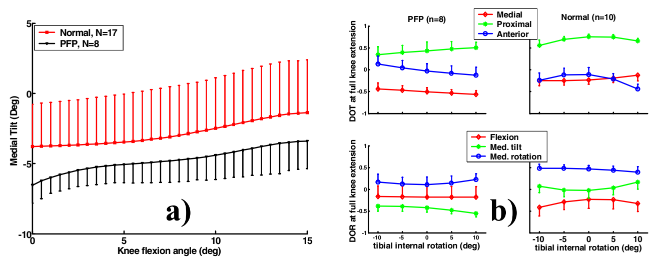

Figure 1: Comparison of the patellar tracking in normal and PFP patient.

SUMMARY

Data from PFP patients showed larger variations than that from normal subjects, possibly due to different pathological conditions among patients in this study. Abnormal patellar tracking was found in PFP patients as the more lateral tilt of patella during voluntary knee extension. Besides, significant abnormal tracking patterns were found in the function of VMO and VL between PFP and normal groups. The method presented in this study can be a quantitative 3-D tool to evaluate patellar tracking *in vivo* and non-invasively in patients with patellofemoral disorder and malalignment

REFERENCES

[1] JP Fulkerson, Williams & Wilkins,1997, Baltimore. [2] TJ Koh et al., J Biomech, 1992. **25**:637-643. [3] J Heegaard et al., Clin Orthop Res, 1994. 299:235-243. [4] G Wang et al. 3rd N. Am. Congress on Biomechanics, Waterloo, Canada, Aug. 14-18, 1998. [5] A Lin et al. Am. Society of Biomechanics Conference 2001, San Diego, Aug. 8-11, 2001

ACKNOWLEDGEMENTS

Supported by the National Institute of Health (AR45634).

BIOMECHANICAL CHANGES IN SPASTIC ANKLES OF STROKE PATIENTS

Sun G. Chung[1,2,5], Elton van Rey[1,2], and Li-Qun Zhang[1-4]

[1]Rehab Inst. of Chicago, Depts. of [2]Physical Med & Rehab, [3]Orthop. Surg., and [4]Biomed. Eng., Northwestern Univ., Chicago, IL
[5]Dept. of Rehab Medicine, Seoul National University, Seoul, South Korea, suncg@northwestern.edu

INTRODUCTION

Spasticity and contracture at the ankle are among the major sources of disabilities following stroke. Spastic hypertonia has biomechanical as well as reflex components, and contracture is directly related to biomechanical changes of the muscle tendon units. The purpose of this study is to investigate the biomechanical changes in the passive ankle of stroke patients in both the plantar and dorsiflexor muscles-tendons, including shortened muscle-tendon unit, decreased range of motion (ROM), and increased stiffness (loss of compliance).

METHODS

Twenty-four stroke survivors (15 male and 9 female, 55.3±10.1 years old) and 32 normal subjects (17 male and 15 female, 42.1±20.5 years old) participated in the study. Subjects sat with the knee at 60º flexion and the leg supported. The foot was held firmly on a footplate, which was mounted onto the shaft of a servomotor. The ankle flexion axis was aligned with the shaft of the motor by adjusting the footplate and the seat. A 6-axis force sensor was mounted between the motor shaft and the footplate. The device was controlled digitally with position/velocity and torque feedback to move the ankle into both dorsi-flexion (DF) and plantar flexion (PF) extreme ROMs. The motor moved the ankle at slower speeds as the joint was moved into extreme ROMs and the maximum speed allowed in the middle ROM was set at 300º/sec. Gravitational forces of the foot and the footplate were compensated. The DF and PF ROM were measured at the resistance torques of 10 N·m and 5 N·m, respectively. The torque-angle curves were plotted to get the hysteresis curves (Fig. 2). The slopes at 0 and 10º DF and 0 and 30º PF angles of the ascending limb of the hysteresis curves were taken as the quasistatic stiffness. The DF areas of the hysteresis curves were considered as the amount of energy lost during the passive DF stretch.

RESULTS AND DISCUSSION

Passive ROM in the normal subjects was 18.9 ± 10.5º (mean ± standard deviation) and 45.7 ± 7.8º in DF and PF, respectively (Fig. 1). The dorsiflexion ROM was similar to what was reported previously (Moseley et al. 2001). In contrast, the DF and PF passive ROMs in the stroke patients with spastic ankles were 9.3 ± 9.5º and 25.2 ± 11.6º, respectively, which was significantly smaller than their counterparts in normal controls ($P \leq 0.007$ with Student t-test) (Fig. 1(a)).

The quasistatic stiffness was significantly higher in the spastic ankles than that in normal controls at 0 and 10º DF and at 0 and 30º PF positions (Fig 1(b)). The increased quasi-static stiffness was consistent with previous studies, which evaluated the dorsiflexion stiffness bilaterally in 8 hemiplegic patients (Harlaar et al. 2000).

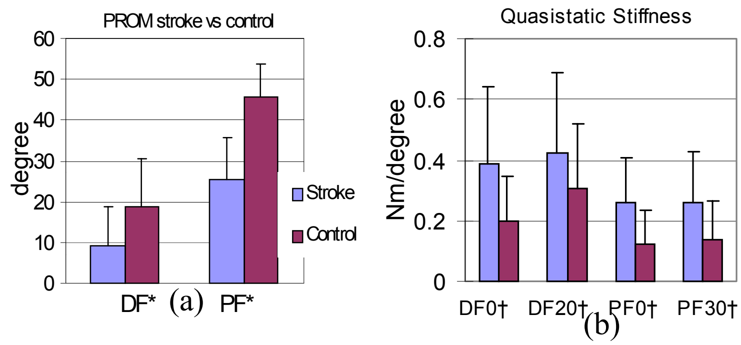

Figure 1: (a) DF and PF passive ROMs in normal and stroke subjects (*: $p<0.05$). (b) Quasi-static stiffness at several points of the hysteresis curves in normal and stroke subjects (†: $p < 0.01$).

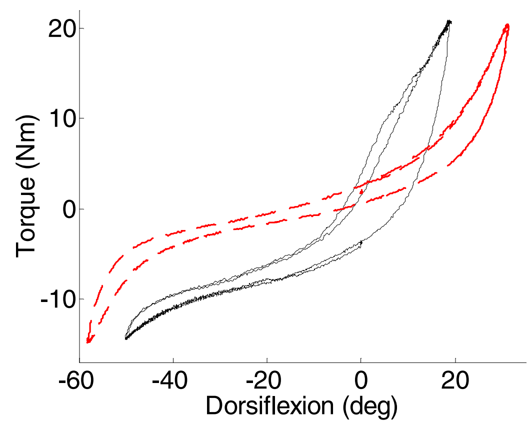

Figure 2: Typical hysteresis curves from a representative healthy subject and a stroke patient.

SUMMARY

It was shown that in both plantar flexion and dorsiflexion, the spastic ankles in 24 stroke patients showed decreased passive ROMs and increased stiffness compared to normal controls.

REFERENCES

Harlaar, J., Becher, C.J., et al (2000). *Clinical Biomechanics,* **15, 261-270**

Moseley, A.M, Crosbir, J. et al (2001). *Clinical Biomechanics,* **16, 514-52**

AGING-RELATED CHANGES IN ACHILLES TENDON REFLEXES

Elton van Rey[1-2], Sun G. Chung[1,2,6], Mark Rogers[5], and Li-Qun Zhang[1-4]

[1]Sensory Motor Performance Program, Rehabilitation Institute of Chicago, Chicago, USA, e-vanrey@northwestern.edu
Departments of [2]Physical Medicine and Rehabilitation, [3]Orthopaedic Surgery, and [4]Biomedical Engineering, [5]Physical Therapy, Northwestern University, Chicago, USA
[6]Department of Rehabilitation Medicine, College of Medicine, Seoul National University, Seoul, South Korea

INTRODUCTION

As people age, the neurological reflex properties may undergo considerable changes. Functionally, such changes may be associated with limitations in joint mobility and slower movements. Evaluation of reflexes is generally done by measuring the muscle responses (EMG recordings) and/or joint torque, each of which are net system outputs due to neuromuscular stimulation (e.g., stretching the muscles). Without adequate controls, the sensory input stimulus may vary considerably from one trial to another and lead to large variability in the response output. The purposes of this study was to evaluate reflexes while minimizing these confounding sources of variability with the reflex excitability evaluated with tendon reflex gain, contraction rate, and reflex threshold.

METHODS

Eight elderly (4 male and 4 female) and eight young (4 male and 4 female) subjects with no prior history of neurological disorders participated in the study. The age of the elderly subjects was 69.4 ± 9.7 years. The young participants' age was 26.0 ± 6.9 years. The participants were seated comfortably on a custom designed chair. The foot was placed on a footrest, knee joint positioned in 60 degree of flexion with the trunk, thigh and ankle strapped to the seat. The footplate was mounted onto a motor shaft through a torque sensor measuring the ankle flexion torque. The ankle joint was restricted at an isometric condition in order to minimize the contributions of the passive/intrinsic components associated with joint movement Four EMG-electrodes where placed on the tibialis anterior, soleus and the medial and lateral head of the gastrocnemius muscles.

The Achilles tendon was tapped by using an instrumented tendon reflex hammer, with a force sensor mounted on the head. Before tapping the Achilles tendon, the participants were asked to relax entirely and not to expect / anticipate to the tapping. The tendon tapping force, lower-leg EMG signals and the reflex torque were sampled by a computer at 500 Hz after low pass filtering at 230 Hz. To evaluate and characterize tendon reflexes, a system identification approach was used to characterize the reflex output responses and stimulus input simultaneously, which is more reliable than measuring the output responses (EMG or reflex-mediated torque) alone. Furthermore, reflex excitability was characterized as a function of the stimulus threshold measured in tapping force, which provided a usually ignored but important component of reflexes (Zhang et al. 1999).

RESULTS AND DISCUSSION

Tendon reflex gain of the younger subjects was higher than that of the elderly group (P = 0.049, 0.002 and 0.074 for 15º dorsiflexion, neutral and 15º plantar flexion, respectively), reflecting weaker reflex actions in the elderly (Angulo-Kinzler et al. 1998). Furthermore, the contraction rate in the elderly subjects was lower than that of young subjects (P = 0.053, 0.003 and 0.082 for 15º dorsiflexion, neutral and 15º plantar flexion, respectively), indicating slower contractile mechanics in the elderly. On the other hand, the reflex threshold in tapping force was higher for the elderly than that for the young subjects (P = 0.038, 0.20 and 0.027 for 15º dorsiflexion, neutral and 15º plantar flexion, respectively), indicating the need for a stronger stimulation to elicit reflex responses in the elderly subjects. In addition, the reflex-mediated output responses showed lower peak reflex torque and lower peak reflex EMG signal in the elderly group than their counterparts in the young subjects.

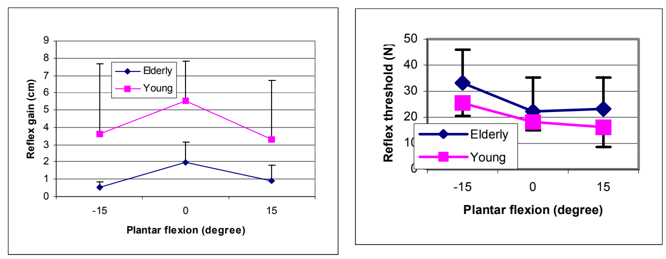

(a) (b)

Figure 1 (a). The tendon reflex gain of elderly versus young. (b) Reflex threshold in elderly and young subjects.

SUMMARY

In summary, elderly subjects showed diminished reflex excitability, as indicated by the decreased reflex gain, reduced contraction rate, and increased reflex threshold. The Achilles tendon reflex becomes hypoactive in elderly subjects, which could be due to reduced power generating capability of the muscles and decrease of sensitivity of the muscle spindles in the aged participants. The above approach provided us a simple and convenient way to evaluate aging-related reflex changes quantitatively in several aspects.

REFERENCES

1. Angulo-Kinzler et al. Gerontol: A Biol Sci Med. Sci. **53**, M120-M125, 1998.
2. L.-Q. Zhang et al. IEEE Trans. Rehab. Eng, **7**:193-203, 1999.

INTERSEGMENTAL DYNAMICS DURING MULTIJOINT ARM REACHING: IMPLICATIONS FOR CONTROL OF LIMB MOVEMENT

Gail F Forrest [1] Sue Ann Sisto[1], Quin Bond[1], Stephen Page[1], Peter Levine [1]

[1]Kessler Medical Rehabilitation Research and Education Corporation, West Orange, NJ, USA
gforrest@ kmrrec.org

INTRODUCTION

Hemiparesis is a significant clinical impairment of stroke that can precipitate functional disabilities (Gowland, et al 1992). The restrictions in voluntary movement for patients with upper limb hemiparesis may be functionally apparent but the quantitative data to explain the mechanisms related to the deficits of control of multi-joint movements is limited - particularly when the multi-joint motion is performed in 3D space. The objective of this study is to utilize inverse dynamic modeling for quantifying arm-reaching multijoint movement and compare changes in the arm intersegmental dynamics after a mental imagery intervention.

METHODS

A 56-year-old male with left hemiparesis due to stroke was tested pre and post an imagery intervention (Page et al., 2001). Testing involved 3 repeated trials of an arm-reaching task. Kinematic data were collected at 120Hz using Vicon Work Station and a 6-camera setup. A 4th order Butterworth filter with forward and reverse phase to eliminate phase delays was applied to the Cartesian 3D positional data. Residual analysis (Winter, 1990) determined the choice of cut frequencies. To analyze the motion of the arm segment, 'each limb was modeled as three interconnected planar rigid segments' (Schneider and Zernicke, 1991). Limb dynamics were calculated in the local moving plane with calculation of orientation angles for each segment relative to the right horizontal. Inverse dynamic modeling (Schneider and Zernicke, 1991) was used to quantify the net torque, gravitational and intersegmental torque and the residual term (muscle torque) for the shoulder, elbow and wrist. Net joint torque describes the joint motion. Additionally impulse values were calculated using an integration trapezoidal algorithm.

RESULTS AND DISCUSSION

After the intervention there was an increase in total net shoulder torque and impulse (pre: -0.436 ± 0.07 N.m.s; post: O.77 ± 0.06 N.m.s) and elbow net shoulder torque and impulse (pre: 0.12 ± 0.05 N.m.s; post: 0.81 ± 0.21 N.m.s) which was reflected in the increased orientation angle (with respect to the right horizontal) of the affected shoulder and elbow. The overall shoulder intersegmental impulse (pre: 1.13 ± 0.22 N.m.s; post: 2.67 ± 0.48 N.m.s) and torque were greater after the intervention. This was due to an increase in both the angular acceleration of the upper arm (i.e. acceleration torque) and the angular acceleration of the forearm - both accelerations are components that contribute to the shoulder intersegmental torque. Overall, the increase in shoulder net torque precipitated an increase in residual muscle torque that indicated an improved control following the intervention.

SUMMARY

Improved movement of the forearm, upper arm and increased shoulder muscle torque suggested an improvement in function of the arm and improved coordination. Therefore, a sensitive way to measure change of complex multi joint movement is implement to inverse dynamic techniques.

REFERENCES

Gowland, et al (1992). *Physical Therapy*, 72,624-633.
Page et al., (2001). *Clinical Rehabilitation*, **15**, 233-240.
Winter, D.A. (1990). *Biomechanics and Motor Control of Human Movement* (2nd ed) New York: Wiley-Interscience
Schneider , K., Zernicke, R.F. (1991). *Advances in Engineeering Software*, **12**,123-128

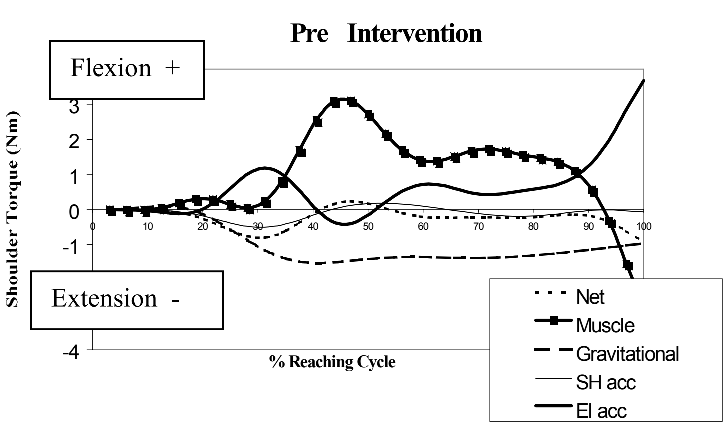

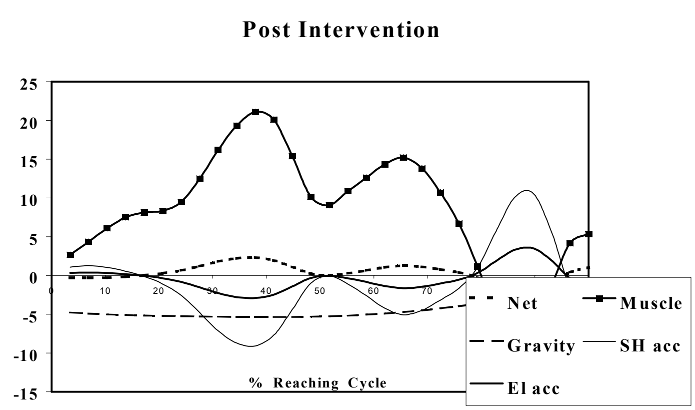

FOOT SENSATION AS A PREDICTOR FOR RESPONSE TO FOOTWEAR INTERVENTIONS

Matthew Nurse† and Benno Nigg
Human Performance Laboratory, University of Calgary, Calgary, Alberta, Canada
†Corresponding Author: manurse@ucalgary.ca

INTRODUCTION

Lower extremity muscle activity can be altered by afferent cutaneous feedback (ie Zehr et al., 1997). Sensory feedback from the plantar surface of the foot may be altered by changing the geometry, texture (Watanabe & Okubo, 1981), or density (Wu & Chiang, 1996) of materials underfoot. Footwear interventions may provide long term changes in sensory feedback from cutaneous mechanoreceptors.

Subject specific responses to footwear interventions may be due in part to the subjects' ability to discriminate changes in sensory input. It is speculated that individual differences in plantar sensitivity may play a role in the response to different footwear conditions underfoot. The purpose of this study was therefore to examine gait responses to footwear interventions as a function of subject plantar foot sensitivity.

METHODS

Sensitivity thresholds to high (250Hz) and low (10Hz) frequency vibrations were collected from 30 subjects. Each subject was tested at the heel, first metatarsal head, and hallux using a validated psychophysical algorithm (Nurse and Nigg, 2001). Subjects from the top and bottom 10^{th} percentiles in plantar sensitivity were selected to participate in this study.

Four subjects, two from each percentile, walked on a treadmill in two different footwear conditions. The control condition involved a normal, commercially available running shoe. The shoe insert was then removed and replaced with a heavily textured foam insert. The texture was noticeable enough to elicit a subjective response from all subjects. EMG measurements were obtained from the medial gastrocnemius (MG), soleus (SL), tibialis anterior (TA), vastus medialis (VM), rectus femoris (RF), and biceps femoris (BF). EMG recordings were pre-amplified (10^6), and lowpass filtered at 3Hz to obtain a linear envelope of the muscle signal. All EMG signals were time normalized, and RMS was calculated for the stance and swing phase for each of the muscles.

RESULTS AND DISCUSSION

While wearing the textured shoe insert, TA activity was lower for all subjects (Figure 1). For the highly sensitive subjects, the depression in TA activity was significant ($p<0.025$ for both subjects). Electrical stimulation of the tibial nerve, which innervates the plantar surface of the foot, has been shown to result in suppression of TA during the later portion of the swing phase (Van Wezel et al., 1997). However, electrical stimulation is usually delivered at a multiple of perception threshold, and does not account for potential differences in the subjects' ability to detect stimuli underfoot. It is speculated that the textured shoe insert increased afferent input from the foot (Watanabe et al., 1981), resulting in decreased TA activity during the swing phase.

Small and less consistent differences were observed in the other muscles of the lower extremity. It would be expected footwear effects would be most dominant during the stance phase as this is when the foot is most loaded against the shoe insert. However, contra-lateral effects of cutaneous stimulation have been demonstrated. This direction of research is ongoing, and will examine kinematic and kinetic responses, as well as EMG, to footwear interventions.

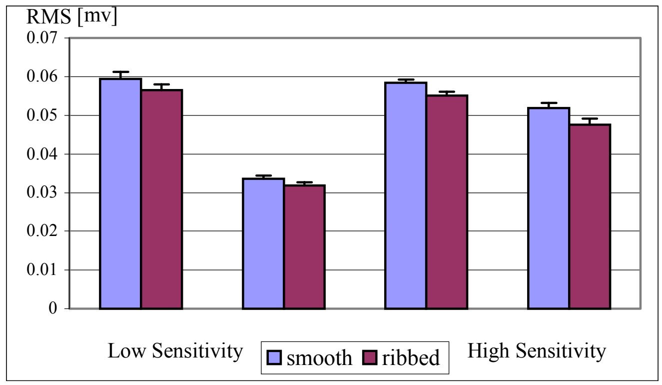

Figure 1: RMS muscle activity for TA while walking in two footwear conditions.

SUMMARY

Differences were observed in the activity of the selected muscles. Tibialis activity was suppressed in the swing phase while wearing a shoe with a textured insert, especially for subjects who were are highly sensitive to high frequency vibrations. Differences in plantar sensitivity may explain certain subject specific responses to footwear interventions.

REFERENCES

Nurse, M.A. & Nigg, B.M. (2001). *Clin Biomech* **16**, 719-727.
Van Wezel, B., et al. (1997). *J. Neuroscience* **17**, 3804-3814.
Watanabe, I. & Okubo, J. (1981). *Ann N Y Acad Sci* **374**, 855-864.
Wu, G. & Chiang, J. (1996). *Gait Posture* **4**, 122-129.
Zehr, E.P., et al. (1997). *J.Neurophysiol* **77**, 3311-3325.

ACKNOWLEDGEMENTS

This work was financially supported by the NSERC, AHFMR, and the da Vinci Foundation

TRABECULAR TISSUE STRESSES AND STRAINS IN MECHANICALLY INDUCED ANABOLIC BONE ADAPTATION: A FINITE ELEMENT STUDY

Steven Boyd[1], Stefan Judex[2], Yi-Xian Qin[2], Simon Turner[3], Ralph Müller[1], and Clinton Rubin[2]
[1]Institute for Biomedical Engineering, Swiss Federal Institute of Technology (ETH) and University of Zürich, Zürich, Switzerland.
[2]Department of Biomedical Engineering, State University of New York at Stony Brook, Stony Brook, NY, USA.
[3]Department of Clinical Sciences, Colorado State University, Ft. Collins, CO, USA.

INTRODUCTION

Mechanical stimuli play an important role in bones' adaptive processes. Recently, it has been shown that low magnitude, high frequency (<10 microstrain, >20 Hz) mechanical signals can increase bone formation in sheep (Rubin et al., 2002). This mechanical stimuli results in stiffened trabecular bone, reflected by an increase in bone density, and has a high clinical potential for the treatment or prevention of osteoporosis in patients.

To date, mechanical testing has confirmed increased stiffness of the trabecular bone (Rubin et al., 2002), however, it is remains unknown how the trabecular structure is affected. In particular, with respect to osteoporosis, it is important to understand the affect on stresses and strains, and particularly if it results in reduced peak strains. Using finite element (FE) analysis based on micro-computed tomography (µCT) data, tissue-level stresses and strains can be evaluated (van Rietbergen et al., 1999). Therefore, the purpose of this study was to quantify changes in stress and strain peaks, as well as their distributions within the adapted trabecular bone tissue.

METHODS

Twenty adult female sheep (Warhill intact ewes, 60-80kg) were randomly assigned to two groups: experimental and controls. The experimental group stood with their hind limbs on a vibrating plate (30 Hz, 0.3 g) for 20 min/d, 5 d/wk. At the end of one year, 1 cm cubes of trabecular bone were excised from the medial femoral condyles.

Cubes were scanned by µCT (nominal, isotropic resolution of 34 µm), and to reduce computational requirements for the FE analysis, the voxel data was resampled (isotropic size of 68 µm) and converted directly into a hexahedron-based FE mesh. The boundary conditions were chosen to simulate axial compression (1% strain), and FE simulations were performed for each specimen along all three axial directions (Boyd et al., 2002). Bone material properties were assumed homogeneous and isotropic: Tissue modulus = 5 GPa, Poisson's ratio = 0.3.

The FE models were solved using an iterative-based method. The stress and strain state of each element (>1,000,000/model) were sorted into histograms after normalization by the applied global stress and strain, respectively. Thus, the arbitrary tissue modulus and applied strain had no effect on the results.

RESULTS AND DISCUSSION

The apparent-level trabecular elastic modulus calculated by FE was greater in the experimental sheep in the longitudinal (17%), anterior-posterior (25%), and medial-lateral directions (44%). The resultant stresses and strains were more evenly distributed in the experimental sheep, and peak strains were reduced. Thus, more of the trabecular tissue was subjected to intermediate strains in experimental sheep than in the controls.

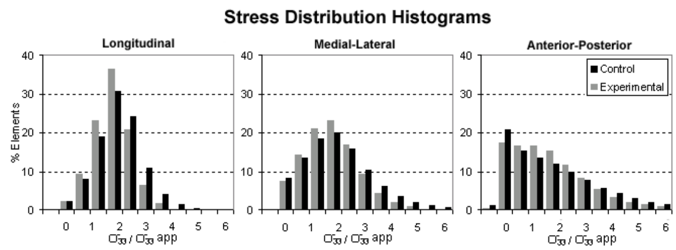

Figure 1: Histograms sorting elements by calculated stress (σ_{33}), normalized by the resultant apparent stress ($\sigma_{33\ app}$). Results for the three testing directions are shown. A ratio of 1.0 occurs when tissue stress equals resultant apparent stress.

SUMMARY

The adaptive process of trabecular bone to low level mechanical loads involves a spatial homogenization of the tissue stresses and strains, and consequently results in reduced strain gradients. The change in stiffness was greatest off-axis (i.e., other than physiological longitudinal loading direction) which may be important for prevention of fracture, particularly in a fall with lateral impact. The stiffer structure has reduced tissue strains for a given load, and is less prone to fracture.

REFERENCES

Boyd, S.K., Müller, R., Zernicke, R.F. (2002) *J Bone Miner Res*, in press.
Rubin, C., Turner, A.S., Müller, R. et al. (2002) *J Bone Miner Res*, in press.
Van Rietbergen, B., Müller, R., Ulrich, D. et al. (1999) *J Biomechanics*, **32**: 443-451.

INFLUENCE OF FLOW RATE AND AXIAL POSITION ON SHEAR STRESSES

Sakhaeimanesh Ali A.
Biomedical Engineering Group, Faculty of Engineering, University of Isfahan, Isfahan, Iran, sakhaei@eng.ui.ac.ir

INTRODUCTION

Prosthetic heart valves are commonly used for replacement of natural valves, in ventricular assist devices (VADs) and total artificial hearts (TAHs). To locate the maximum and mean turbulent shear stresses, in both time and space, and to determine how shear stresses depend on the flow rate and downstream measuring planes, this study was carried out.

METHODS

Flow was driven by a servo-controlled piston pump (VSI pump) that compressed the ventricle to simulate the physiological flow. DANTEC, two-colour 5 Watt Argon-Ion laser was used to determine the velocity and turbulent components of the valve. The axial and radial mean velocities, $\overline{U}$ and $\overline{V}$, the r.m.s. of axial and radial fluctuation components, turbulent intensity, T, and the cross, $\overline{uv}$, were calculated. More details of mock circulatory system and LDA technique are given somewhere else (Sakhaeimanesh et al.,1999).

RESULTS AND DISCUSSION

graphs of shear stress-flow rate and shear stress-axial location are presented in figure 1 to 3. All instantaneous flow rates were measured by an electromagnetic flow meter. Furthermore, as maximum shear stress and its mean absolute value of each valve occur at the same measuring plane, comparison of the mean absolute shear stresses is considered valuable, because this may reduce measurement error.

As can be seen in figure 1, maximum and mean turbulent shear stresses estimated at 0.5D downstream of the valve showed a direct relationship with flow rate both in the Jellyfish and St. Vincent valves. Our results are consistent with the finding of Schwartz *et al*. (1988). The magnitude of both mean and maximum shear stresses in the Jellyfish valve was found to be higher than that of the St. Vincent valve at 0.5 and 1D downstream of the Jellyfish valve. In figures 2 maximum and mean turbulent shear stresses are presented as a function of downstream axial distance for the Jellyfish valve. Maximum shear stresses were found in close vicinity to the valve where, highly disturbed flow with steep velocity gradients were observed. At 1D downstream of the valve, high shear stresses were also found in the valve. Further from the 1D measuring plane, flow disturbance was reduced resulting in a dramatic reduction in shear stresses in the Jellyfish valve. This was attributed to diminishing the effects of oscillation of the Jellyfish valve beyond the 1D measuring plane.

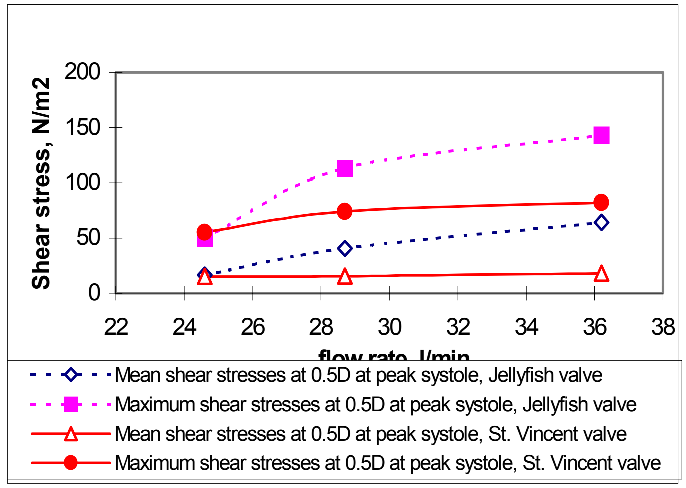

Figure 1: Mean and maximum shear stresses measured at 0.5D downstream of the Jellyfish and St. Vincent valves as a function of flow rate. Measurements were made at peak systole at cardiac outputs of 3.5, 4.5 and 6.5 l/min.

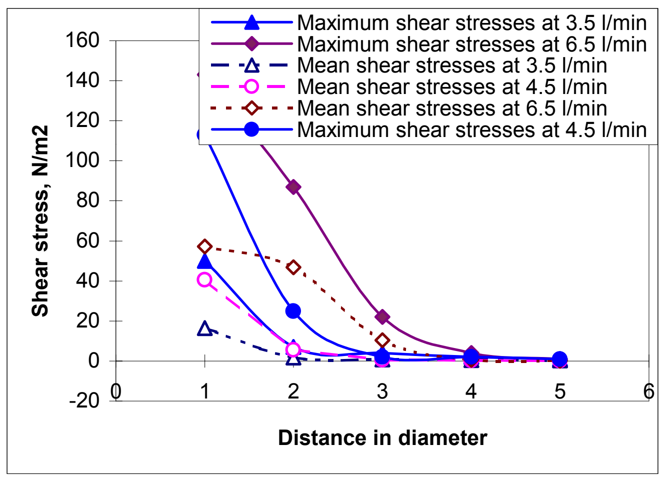

Figure 2: mean and maximum shear stresses as a function of downstream axial position of the Jellyfish valve. Shear stresses were found at peak systole at cardiac outputs of 3.5, 4.5 and 6.5 l/min.

REFERENCES

Sakhaeimanesh, A. A. and Morsi, Yos S., 1999. Analysis of regurgitation, mean systolic pressure drops and energy losses for two artificial aortic valves. Journal of Medical Engineering and Technology, **23(2**), 63-68.

Schwarz A.C., et al (1988). Influence of cardiac flow rate on turbulent shear stress from a prosthetic heart valve, J . Biomechanical Engineering, **110**, 123-129.

DYNAMIC CHARACTERISTICS OF THE JELLYFISH AND ST. VINCENT ARTIFICIAL HEART VALVES

Sakhaeimanesh Ali A.
Biomedical Engineering Group, Faculty of Engineering, University of Isfahan, Isfahan, Iran, sakhaei@eng.ui.ac.ir

INTRODUCTION

In pulsatile flow, both flow rate and pressure drop, which are a function of the time are important in judging artificial heart valve performance. Pressure drops across the valves in forward flow and the amount of backflow in the regurgitation stage is of great concern in pulsatile flow investigations (Jansen J, Ruel H, 1992 and Knott E. et al 1986).

The instantaneous relationship between pressure drop, $\Delta P(t)$, and flow rate, *Q(t),* can be obtained as a phase graph on an X-Y plane during a whole cardiac cycle. These can be regarded as dynamic flow characteristics of an artificial heart valve. This method may facilitate a more proper model of the valve in circulation simulation and provide a new way to evaluate the performance of a tested valve.

METHODS

The pulse duplicator designed by Vivitro System Inc. was used in the present investigation. The artificial heart and connecting tubes were arranged vertically and valves were mounted in their correct position in an especially moulded flexible ventricle. Flow was driven by a servo-controlled piston pump (VSI pump) that compressed the ventricle to simulate the physiological flow. More details of mock circulation are given somewhere else (Morsi Yos S. and Sakhaeimanesh Ali A. 2000).

RESULT AND DISCUSSION

The continuous monitoring of the time histories of flow and pressure revealed useful details of the complex flow as well as helping to establish location and timing of the peak parameter values. The $\Delta P - Q$ relation is presented for the Jellyfish and St. Vincent valves in figure 1 at cardiac output of 4.5.

The trace of $\Delta P(t)$ starts on the $\Delta P - Q$ graphs from a point near the negative pressure drop axis and rises to positive Q axis and develop to maximum flow rate (peak systole). This period is the acceleration (ejection) phase of heart cycle. From peak systole it turns back along flow axis and become negative after crossing pressure drop axis. This period is the deceleration phase. At this stage, pressure drop across the St. Vincent valve was higher than that of the Jellyfish valve. This shows that the occluder of the St. Vincent valve produced high resistant to forward flow, which was due to its high mass moment of inertia. When flow rate became negative, the closure phase of the valves started.

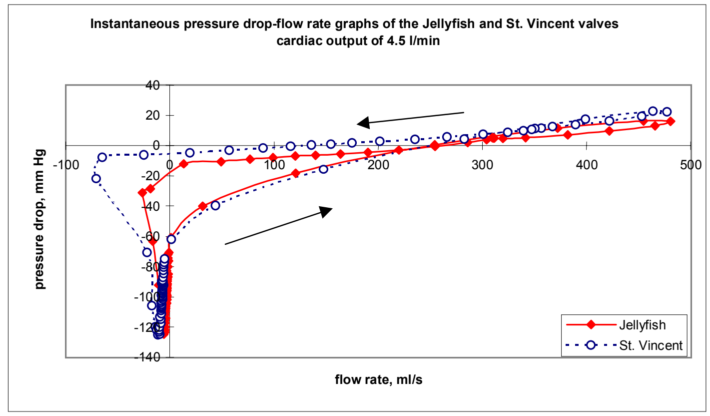

Figure 1: Instantaneous pressure drop versus flow rate during whole cycle of the Jellyfish and St. Vincent valves at cardiac output of 4.5 l/min.

High closure flow rate of the St. Vincent valve is evident in the graph. At the start of closure phase, when adverse pressure gradient across the St. Vincent valve was not enough to overcome the resistance of the valve occluder, a large amount of flow retarded to the ventricle. On the other hand, flexible membrane of the Jellyfish valve, with its low mass moment of inertia, responded to low adverse pressure gradient and closed rapidly, resulting in lower closure flow rate. At the end of closure phase (traces close to the pressure drop axis), the leakage phase of cardiac cycle started. As can be seen in the graphs, the magnitude of flow rate did not increase so much while the magnitude of pressure gradient was apparently larger than that in forward flow. This meant that leakage flow across the valve faced a larger pressure gradient than in forward flow causing high jet flow within the leakage gap. Higher leakage flow rate in the St. Vincent valve is also evident in the figure 1. The non linear phenomena of the $\Delta P - Q$ relationship which exists in pulsatile flow cannot be obtained in steady flow testing especially in backflow stage where flow rate changes a little while pressure gradient has some variation.

REFERENCES

Jansen J, Ruel H, (1992). A synthetic three leaflet valve, Journal of Medical Engineering and Technology, **16:** 27-33.
Knott E. et al (1986). Pressure drop, energy loss and closure volume of prosthetic heart valves in aortic and mitral position under pulsatile flow conditions. Life Support Systems, **4(suppl 2)**, 139-141.
Morsi Yos S. and Sakhaeimanesh Ali A. (2000). Flow characteristics past jellyfish and St. Vincent valves in the aortic position under physiological pulsatile flow conditions. Artificial Organs, Volume **24(7)**, 564-574.

ANTAGONISTIC MUSCLE ACTIVITY IN THREE-DIMENSIONAL MODELS OF THE MUSCLOSKELETAL SYSTEM

Azim Jinha[1], Rachid Ait-Haddou[2] and Walter Herzog[3]
Human Performance Laboratory, University of Calgary, Calgary, Alberta, Canada
[1]M.Sc. Candidate, Dept. Mechanical & Manufacturing Engineering, azim@kin.ucalgary.ca
[2]Post-Doctoral Fellow, Human Performance Laboratory
[3]Professor, Faculty of Kinesiology

INTRODUCTION

The control of individual muscles during skilled or repetitive movements has been of interest to researchers for a long time [Herzog, 1996]. For a given movement, a unique combination of muscle forces, typically, does not exist. One method of extracting a unique set of muscle forces is the formulation of an optimization problem [Crowninshield et al 1981, Herzog, 1996]. In most cases, the mathematical optimization problem is solved numerically for large models [e.g. Glitsch, 1997, Li et al 1999] or analytically for simple models consisting of a small number of degrees-of-freedom in a two-dimensional model [e.g. Herzog et al 1993]. These numerical approaches or analytical solutions for specific, small scale musculoskeletal models do not provide general solutions of the optimization approach that are valid independent of the geometry of the model at hand. In these cases, it was typically thought that non-linear optimization could not predict the co-contraction of a pair of single joint antagonists, but this conclusion was based on planar models of the musculoskeletal system. Recently, Li et al [1999] numerically demonstrated that non-linear optimization could predict such activity in a three-dimensional model. Therefore, the purpose of this work was to examine predictions of co-contraction between pairs of antagonistic muscles in a three-dimensional model, analytically.

METHODS

It is typically assumed that the muscles crossing a joint are primarily responsible for generating the required moment at that joint, i.e. $\boldsymbol{b} = \Sigma(\boldsymbol{r}_i \times \boldsymbol{f}_i)$, or in matrix form $\boldsymbol{A}\boldsymbol{f} = \boldsymbol{b}$, where $\boldsymbol{b}$ is the joint moment vector; $\boldsymbol{r}_i$ and $\boldsymbol{f}_i$ are the moment-arm and force vectors of the i^{th}-muscle; $\boldsymbol{A}$ is the matrix of moment-arms; and $\boldsymbol{f}$ is the vector of unknown muscle force magnitudes. To extract a unique set of muscle forces, a convex cost-function, $\phi(\boldsymbol{f})$, is minimized subject to mechanical and muscular constraints [e.g. Crowninshield et al, 1981]. Given two arbitrary antagonistic muscles in a musculoskeletal system, and using Karush-Kuhn-Tucker multipliers, the set of intersegmental moments, $\boldsymbol{b}$, for which these two muscles co-contract can be determined; unless the moment-arm vectors of the two muscles are co-linear.

RESULTS

First, we determined that the mathematical representation of a three-dimensional musculoskeletal model and a planar model having equal degrees-of-freedom are equivalent. Thus, it is possible to generalize results from two-dimensional to three-dimensional systems. Also, using Karush-Kuhn-Tucker multipliers, a set of intersegmental moment directions for which optimization predicts the co-contraction of a pair of antagonistic muscles can be found. This set of intersegmental moments is independent of the magnitude of the resultant moment, therefore, it can be represented by a set of intersegmental moment directions. Also, the region of co-contraction becomes smaller for increasing amounts of antagonism between antagonistic muscles.

DISCUSSION AND CONCLUSION

By showing that a three-dimensional model has a mathematical equivalent planar system, we were able to study the prediction of co-contraction independent of the dimensionality and geometry of the musculoskeletal system. One of the main limitations of inverse dynamics optimization models [e.g. Crowninshield et al 1981] has been the apparent impossibility of predicting co-contraction between single joint antagonists, but this limitation was found for planar systems. However, real anatomical joints are typically not planar. Therefore, it is possible to predict co-contraction of single joint antagonists, if three-dimensional joints are considered. We also show that there is a specific set of intersegmental moment directions for which optimization will predict the co-contraction of any pair of muscles, and this region becomes smaller as a pair of antagonistic muscles becomes increasingly antagonistic. Therefore, one possible method for evaluating optimization models is to determine the actual directions of movement that include the co-contraction of a pair of antagonistic muscles. Finally, we would like to emphasize that the purpose of this study was to evaluate the possibility of non-linear optimization models to predict co-contraction of antagonistic muscles, and that further experimental testing is required to validate optimization approaches.

REFERENCES

Crowninshield, R.D., Brand, R.A. (1981). *J. Biomech.*, **14**, 793–801.
Glitsch, U. (1997). *J. Biomech.,* **30**, 1123–1131.
Herzog, W. (1996). *Exercise and Sports Sciences Reviews*, **24**, 173–202.
Herzog W., Binding, P. (1993). *Math. Biosci.*, **118,** 83–95.
Li, G. et al (1999) J. Biomech. Eng., **121**, 316–322.

VARIATIONS IN THE SUPERIMPOSED TWITCH TECHNIQUE AT 100% MVC

M.A.E. Oskouei[1] and W. Herzog[2]
[1]Human Performance Laboratory, University of Calgary, Calgary, Alberta, Canada
[2]Faculties of Kinesiology and Engineering, University of Calgary, Calgary, Alberta, Canada

INTRODUCTION

The superimposed twitch technique is one of the preferred methods to determine muscle inhibition in normal and patient populations (Merton 1954, Belanger and McComas 1981). One of the limitations of this method is its variability for given contractile conditions. For example, a contraction of 50% of the Maximal Voluntary Contraction (MVC) may be associated with a variation in muscle inhibition values from 10-70% in a given subject.

Recently, we conducted an investigation aimed at determining muscle inhibition obtained using the superimposed twitch technique for contractions performed at 50% of MVC. Specifically, we tested whether potentiation, force magnitudes, or the rate of change in forces might explain the observed variations. We found that a great part of the variations could be explained with minute deviations of the force from the 50% of MVC target value. In other words, it was found that muscle inhibition values were very sensitive to whether the actual force was 47% or 53% of MVC at the instant of superimposed twitch application. The purpose of this study was to test whether variations at 100% of MVC could also be explained with small changes in the actual force.

METHODS

Eleven normal subjects (age 30 years ± 7; height 177cm ±11; mass 74kg ±12) volunteered to participate in this study. Subjects were seated on a Biodex strength dynamometer for isometric knee extensor contractions at 90 deg of knee flexion. Knee extensor stimulation was performed via percutaneous stimulation of the femoral nerve (Lee et al., 2000). Doublet stimuli (120 V, 0.8 ms, 8 ms inter-twitch interval) were given for knee extensor stimulation.

Protocol: Subjects were asked to perform ten MVC knee extensor contractions with a two minute interval between contractions. Prior to and after each contraction, three resting twitch stimuli were given for normalization of the superimposed twitch. Each MVC was sustained for 5s. After about 4s, a doublet twitch stimulus was superimposed onto the fully contracted muscle. Muscle inhibition was calculated as the percent ratio of the superimposed twitch torque divided by the resting twitch torque. The contraction that produced the greatest torque was taken as the true 100% MVC. All other contractions were expressed as a percentage of the true 100% MVC. Linear regression was used to test for statistical trends between muscle inhibition and knee extensor force.

RESULTS AND DISCUSSION

Muscle inhibition was negatively related to the amount of force produced by the knee extensor muscles (Fig. 1). Although the linear regression gave a significant result, the coefficient of variation was small (0.1043), indicating that the variations in knee extensor force accounted only for about 10% of the variations observed in muscle inhibition. Although the variations in knee extensor force were small, muscle inhibition values ranged from 0-60%. This result confirms that muscle inhibition for similar efforts varied greatly.

In our previous work we found that variations in muscle inhibition at 50% of MVC were greatly reduced when accounting for the actual knee extensor force values. We expected that the same result would hold true for contractions at, or near, 100% MVC. However, variations in muscle inhibition were great for force values ranging from 95-100% of MVC, and although there was a significant relationship between knee extensor force and muscle inhibition, the coefficient of variation was small, and variations in muscle inhibition were not greatly reduced when accounting for the knee extensor force variations. These results, imply that the variations in muscle inhibition around 50% of MVC are explained to a great degree by the corresponding variations in knee extensor force. However, this result does not seem to be correct for the variations in muscle inhibition around 100% of MVC. We conclude from these results that at 50% of MVC, muscle inhibition values give a very good account of the actual muscle force, whereas at 100% of MVC, muscle inhibition values vary greatly without an apparent cause.

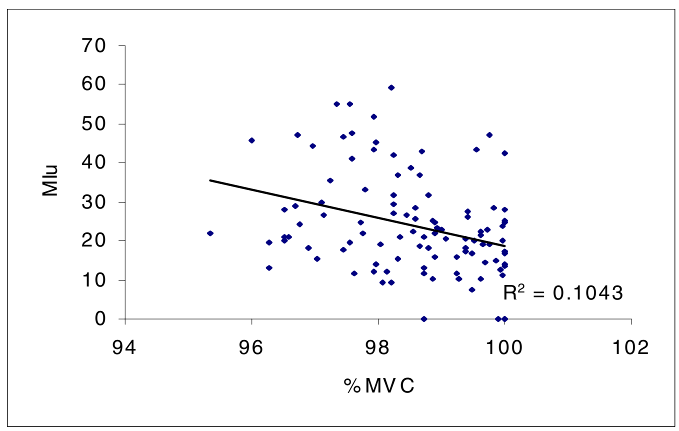

Figure 1: Muscle inhibition as a function of MVC for 11 subjects and 10 trials each

REFERENCES

[1]Belanger AY et al. J Appl Physiol 1981;51(5):1131-1135
[2]Lee HD et al. J Biomech 2000;33:917-923
[3]Merton PA. J Physiol 1954;123:553-564

ACKNOWLEDGEMENTS

NSERC of Canada and The Iranian Ministry of Health

A NEW TECHNIQUE FOR THREE-DIMENSIONAL LEG ALIGNMENT ASSESSMENT

Yoshihiro Yamazaki[1, 2], Yuji Tanabe[3], Makoto Sakamoto[1], Kazuhiro Terajima[4], and Yoshio Koga[5]

[1] Department of Health Sciences, Niigata University School of Medicine, Niigata, Japan, yoyama@clg.niigata-u.ac.jp
[2]Graduate School of Science and Technology, Niigata University, Niigata, Japan
[3]Department of Mechanical Engineering, Niigata University, Niigata, Japan
[4] Niigata University of Health and Welfare, Niigata, Japan
[5] Department of Orthopaedic Surgery, Niigata Kobari Hospital, Niigata, Japan

INTRODUCTION

Leg alignment assessment is an important key to the success of total knee arthroplasty (TKA) in orthopaedics (Robert et al., 1990). We have developed the leg alignment assessment system for the precise determination of three-dimensional coordinate system necessary for TKA by the use of bi-planar X-rays (AP and 60 degrees oblique) in combination with computed radiography (CR) system. This system enabled us to determine the coordinate system with the accuracy of angle less than 0.37 degrees with respect to all coordinate axes. However, a part of its operation was very time consuming due to the use of individual CT data. Therefore, the objective of this study is to develop an alternative technique to reduce the time of operation using a deformable bone model instead of the CT data.

MATERIALS AND METHODS

CR images were transferred to a computer. The several X-ray markers were digitized to measure the points of X-ray resources and three-dimensional space which consisted of two planes of film cassette holder was established. The origin of femoral coordinate system was the midpoint on the line A, drawn between the centers of the medial and lateral posterior femoral condyles determined as circles (Figure 1). The x-axis was laid on the line A. The line B was the connecting line from the origin to the center of the femoral head, and on the x-z plane. The z-axis crossed at right angle to the x-axis.

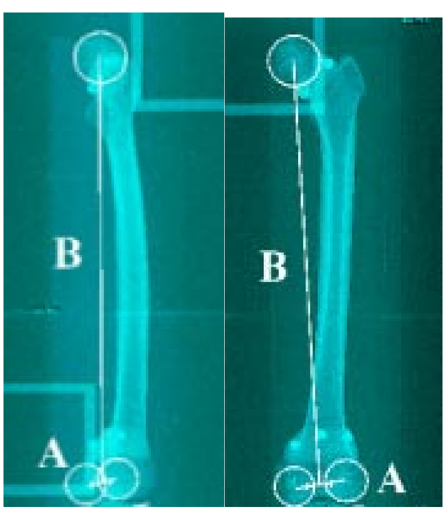

Figure 1: Femoral coordinate system

We estimated clinical parameters such as anterior bowing rate, lateral bowing rate, angle of the neck to the shaft, femoral anteversion angle and parallel to posterior peaks of condyles line using CT data of dry bones, deformable bone model and only CR data. One of the five dry bones was selected to construct a three-dimensional bone model by CT as standard, and the other four bones were used as targets for deformable bone model.

RESULTS AND DISCUSSION

No significant difference in anterior bowing rate was found between the data by CT and by deformable bone model, but the CR data yielded significantly larger anterior bowing rate than the CT data. The lateral bowing rate of deformable bone model and CR data agreed well with that of CT data. The deformable bone model showed us better results than the CR data with respect to both the angle of the neck to the shaft and the femoral anteversion angle. Thus, the deformable bone model enabled us to perform more precise assessment of the leg alignment than the CR technique (Table 1).

Table 1: Relative errors of deformable bone model and CR in clinical parameter values to the standard CT data.

	Deformable bone model (mean ± SD)	CR (mean ± SD)
Anterior bowing rate	0.03 ± 1.0 %	0.9 ± 1.3 %
Lateral bowing rate	0.3 ± 0.7 %	5.1 ± 0.9 %
Angle of the neck to shaft	0.8 ± 1.6 deg.	10.1 ±16.2 deg.
Femoral anteversion angle	0.5 ± 2.3 deg.	2.1 ± 1.6 deg.
Parallel to posterior peaks of condyles line	1.1 ± 1.6 deg.	

SUMMARY

We have developed a new method, deformable bone model, to estimate clinical parameters for three-dimensional leg alignment assessment. The deformable bone model required AP and 60-degrees CR images and deformation of the original three-dimensional CT data. We estimated the clinical parameters by CT data, deformable bone model and only CR data. The results obtained by the deformable bone model showed the accuracy within 3 degrees in the associated angle and 3 % in anterior and lateral bowing rates. It can be concluded that the proposed method should be clinically useful for assessing the leg alignment.

REFERENCES

Robert, W. W. et al. (1990). *Clin.. Ortho. Rel. Res.*, **225**, 215-227.

INVESTIGATION OF THE PERMEABILITY OF OSTEOPOROTIC BONE FOR CEMENT AUGMENTATION PROCEDURES

Gamal Baroud[1*], John Z. Wu[2], Thomas Steffen[1]
[1]Orthopaedic Research Laboratory, McGill University, Montreal, QC, Canada; *email: gbaroud@orl.mcgill.ca
[2]National Institute for Occupational Safety & Health, Morgantown, WV, USA.

INTRODUCTION

Cement augmentation (vertebroplasty) is an emerging surgical treatment for patients suffering osteoporotic vertebral compression fractures. The procedure produces significant and rapid pain relief in 80-90% of patients, although the long-term safety and efficacy remain to be proven. Vertebroplasty is still experimental, and much needs to be done to make it a reliable and safe procedure. The purpose of this study is to investigate, theoretically and experimentally, the permeability of the bone with respect to time, viscosity, shear rate, and the volumetric porosity of the cancellous bone.

METHOD

The cement flow through the permeable bone is slow, so it can be approximated using Darcy's law:

$$v = \kappa(\alpha, \eta) \cdot \nabla p \quad (1)$$

where v is the infiltration rate, κ is the bone permeability, and ∇p is the directional pressure gradient. The cement is a very thick viscous fluid, its permeability, κ, is a function of time, volumetric porosity in injection direction, and viscosity:

$$\kappa = \kappa(\alpha) \cdot \kappa(\eta) \quad (2)$$

where $\kappa(\alpha) = A\frac{\alpha}{\alpha-1}$, ($A$=0.9), the porosity dependence (Baroud, 2002), was fit to the test data (Nauman, 1999).

Cement viscosity is time, t, and shear-rate, γ, dependent. Cement viscosity was measured with respect to t and five different shear rates with a capillary rheometer. The test data were taken from Krause et al., (1982) and used to fit the dependence of the viscosity on the time and shear rate:

$$\eta = \left[a\left(\frac{t}{t_s}\right) + b\right] \cdot \left(\frac{\gamma}{\gamma_s}\right)^{\left[-c\left(\frac{t}{t_s}\right)+d\right]} \quad (3)$$

Where t_s= 1.0 min and γ_s=1.0 1/s are a characteristic time and shear rate, respectively; a, b, c, d are viscosity material parameters.

Infiltration experiments on isolated cores of osteoporotic bone, Fig 1, were performed to measure the pressure drop in response to the cement propagation through the core samples. Using an MTS testing machine, the plunger was pressed down at a constant speed of 2 mm/s, forcing the cement to flow through the interstitial space of the cancellous bone. Pressure-displacement curves were recorded. Tests were performed approximately 2.5 min after the cement mixing.
From the force-balance analysis, we obtained the relationship for the time and injection-speed dependent permeability:

$$\kappa(t) = \frac{v \cdot d}{p'(t) - \frac{2}{r}(h_0 - vt) \cdot v \cdot \eta(t)} \quad (4)$$

where v is injection speed, r is the tube radius , p' is the pressure measured at the plunger tip and is related to injection force, F, by $p'=F/\pi r^2$; h_0 denotes the initial height of cement column, and d is the thickness of the bone core.

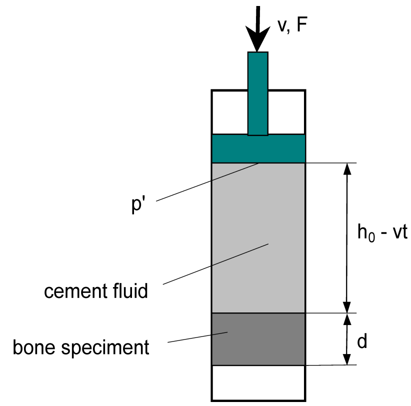

Figure 1: Experimental set-up for the determination of the permeability

RESULTS

Using the experimental data (Krause, 1982), the viscosity material parameters Eq (3) were found to be a= 590.0 (Pa*s), b= -1048.8 (Pa*s), c= 0.026, and d= 0.290. Based on these parameters and the average pressure gradient of our 10 infiltration tests, the time-dependent permeability of cement penetrating through the bone specimen has been determined, as in Fig 2. The permeability is strongly time-dependent, while the effect of viscosity through the tube wall is not significant.

Figure 2: Time-dependent permeability for different shear rate.

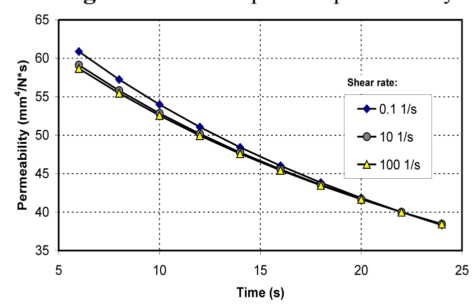

DISCUSSION

We carried out our infiltration tests using 1 cement (Simplex). However, our approach is generic and, therefore, applicable to any cement. We determined vertebral permeability only in superior-posterior direction, assuming uniformity. In reality, the bone voids are non-uniform and the porosity depends on the void location and orientation. These effects have not been accounted for.

SUMMARY

This study is first to analyze cement flow though osteoporotic bone. The findings presented would help optimizing this procedure (e.g., pressure, viscosity) for clinical practice.

REFERENCES

Baroud et al. (2002) 10th Symposium On Computational Methods in Orthopaedic Biomechanics, Dallas, TX. **Krause et al. (1982)** *Biomedical Materials Research*, Vol 16, 219-243. **Nauman et al (1999)** Biomedical Engineering, Vol 22, 517-524.

JOINT SURFACE KINEMATICS DURING WALKING IN AN ANIMAL MODEL OF OSTEOARTHRITIS

Janet Tapper[1], Shige Fukushima[2], Hiro Azuma[2], Gail Thornton[2], Janet Ronsky[1], Cyril Frank[2], Nigel Shrive[3]

[1]Department of Mechanical Engineering, [2]Department of Surgery, [3]Department of Civil Engineering

University of Calgary, Calgary, Alberta, Canada

jtapper@kin.ucalgary.ca

INTRODUCTION

The interactions of biological and mechanical factors in the pathogenesis of secondary osteoarthritis are not well understood. We have previously reported alterations in joint kinematics due to ligament deficiency in an in vivo ovine stifle joint model of osteoarthritis[1]. These kinematic changes were associated with severe cartilage degeneration 20 weeks after ligament transection. The same model has been used to investigate the hypothesis that the in vivo kinematics at the joint surface are altered following ligament transection.

METHODS

Six skeletally mature trained Suffolk sheep were studied while walking at 2mph on a standard treadmill. The in vivo kinematics were measured for thirty strides with the joint intact and at 2, 4, 8, 12, 16, and 20 weeks following combined transection of the anterior cruciate and medial collateral ligaments.

A rigid surgically implanted bone marker system was used to define the 3D positions of the tibia and femur during the in vivo motion[1]. The 3D spatial positions of the markers during gait were recorded using a 4 camera high speed (120Hz) video based motion analysis system (accuracy 0.15mm). Following euthenization, the bone markers positions were precisely digitized (±0.05mm) relative to anatomically based coordinate systems originating at the insertions of the ACL (anteromedial band) into the tibia and femur. The 3D marker coordinates were tracked and smoothed (quintic spline; f_{cutoff} 6Hz), and then normalized to percentages of the gait cycle between successive hoofstrikes. Tibial joint angles and translational positions were described using a joint coordinate system and then differentiated twice to obtain tibial velocities and accelerations. For each specimen, the in vivo kinematics of the transected joint were compared with those of the intact condition, with significance of changes in joint motion assessed using a 2-tailed students t-test ($p<0.05$). The pooled data were assessed using a t-test for paired samples ($p<0.05$).

RESULTS AND DISCUSSION

Results from four sheep show the joint flexion angle increased at 2wks after transection during the first 46% of the gait cycle ($0.007<p<0.045$). At 20 weeks normal flexion was restored throughout the gait cycle in all animals studied (Figure 1A). A plot of angular velocity vs flexion angle demonstrates that the range of flexion angular velocities was similar pre and post transection (Figure 1C).

A significant anterior tibial shift was observed in all sheep studied (Figure 1B). Anterior velocity increased prior to hoof strike and during the loading phase of initial stance ($0.002<p<0.04$), and decreased or increased in the posterior direction during the joint flexion of swing ($0.001<p<0.043$). A plot of anteroposterior velocity vs position (Figure 1D) shows the anterior tibial shift and the increased anterior tibial velocities at both 2 and 20 wks following transection. Anteroposterior acceleration remained within the range of normal variability following ligament transection.

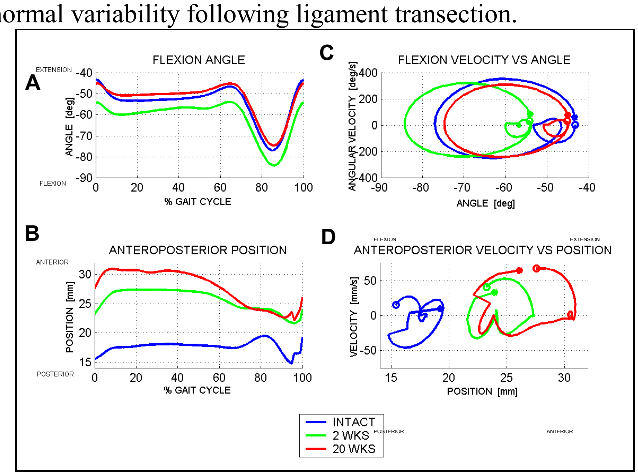

Figure 1: A) joint flexion angle
B) anteroposterior joint position
C) flexion angular velocity vs angle
D) anteroposterior velocity vs position

SUMMARY

Ligament transection alters in vivo kinematics at the joint surface. Normal flexion kinematics are restored with time. In contrast, large changes in anteroposterior position and velocity persist at 20 wks following transection. We postulate that the kinematic changes at the joint surface are important in the development of the cartilage degeneration observed in this in vivo model of osteoarthritis.

REFERENCES

Tapper, J.E. et al (2002). *Proceedings of ORS*, 665

ACKNOWLEDGEMENTS

Leona Barclay, Bryan Donnelly, Craig Good, Leslie Jacques, Linda Marchuk, and Craig Sutherland

AHFMR, CAN, CAS, CIHR, GEIODE, NSERC

HAEMODYNAMICS OF THE FONTAN CONNECTION

Keri Moyle[1], Gordon Mallinson[1], Brett Cowan[2], Chris Occleshaw[3], Tom Gentles[3]
[1]Dept of Mechanical Engineering, [2]School of Medicine,
University of Auckland, Auckland, New Zealand
[3]Green Lane Hospital, Auckland, New Zealand

INTRODUCTION

The Fontan connection is used to bypass the right side of the heart in cases of pulmonary atresia, tricuspid atresia, and univentricular hearts. Long term success is heavily dependent on the haemodynamics and the surgical nature of the connection. This study produced three dimensional, patient specific simulations of the haemodynamics within connections using a method that combines magnetic resonance imaging (MRI) data with computational fluid dynamics techniques.

METHODS

Patients who had a Fontan connection were recruited and scanned using a 1.5T Seimens Vision MRI scanner. A three dimensional Voronoi-cell based computational mesh was created specific to the anatomy of each patient using an in-house program, ModelMaker, to identify boundaries of each vessel, and reconstruct the 3D representation shown in Figure 1, and CFX-5 to create a Delaunay triangulation of the surface (Figure 2). The volume mesh was created using Dr Were's program, GENMESH.3D phase contrast MRI scans were used to measure the velocity fields at the inlets and outlets of the connections. These were used as boundary conditions and validation data for the CFD models. The CFD flow solution was obtained using an Arbitrary Lagrangian Eulerain (ALE) finite volume method that has second order spatial accuracy.

The CFD solutions are being validated by a rigorous mesh refinement study for both test configurations and for real patient data. Comparison between outflows predicted by the CFD analysis and the MRI measurements are the basis for our assessment of the validity of the numerical predictions. Structural details of the flow fields in the connections are also used as a basis for comparison.

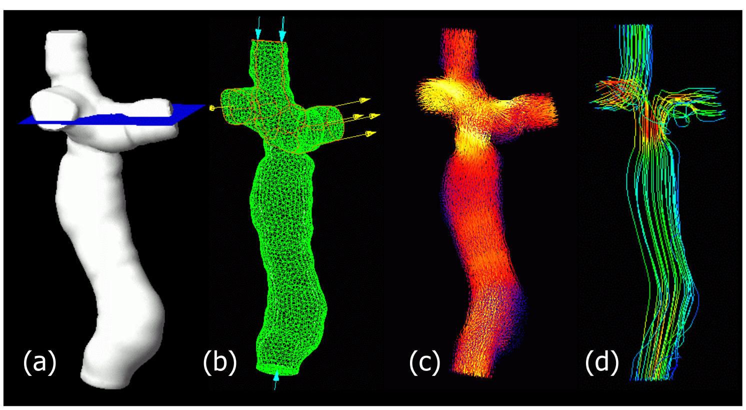

Figure 1a) Surface description reconstructed from MRI data, showing slice plane **b)** Delaunay triangulation of surface, **c)** Velocity field, **d)** Streamlines tracked through velocity field.

RESULTS

Shown in Figure 1 is the progression from reconstructed surface, to computational model, to results. This patient has a total cavopulmonary connection that baffles the inferior vena cava through the right atrium to the superior vena cava. Figure 2 shows an MRI vector field through the pulmonary arteries, and the corresponding slice through the computational model. These preliminary results show qualitative agreement, and are being assessed more rigorously for detailed flow structures and quantitative comparison.

SUMMARY

A method for the creation of three dimensional, patient specific simulations of the haemodynamics of the Fontan connection has been devised and implemented successfully. Simulation results are in general agreement with MRI data and are being further analysed.

REFERENCES

Moyle K.R., Mallinson G.D., Young A.A., Cowan B.R., Occleshaw C.J., Gentles T.L. (2001) 34th International Congress of Physiological Sciences
Were C.J., (1997) The Free–ALE Method, PhD Thesis, University of Auckland, New Zealand.

ACKNOWLEDGEMENTS

The authors thank the National Heart Foundation of New Zealand, and the University of Auckland for providing financial support for this project, and Manukau Radiology Institute.

Figure 2
a) Raw MRI velocity field through slice plane,
b) Computational velocity field through the same region.

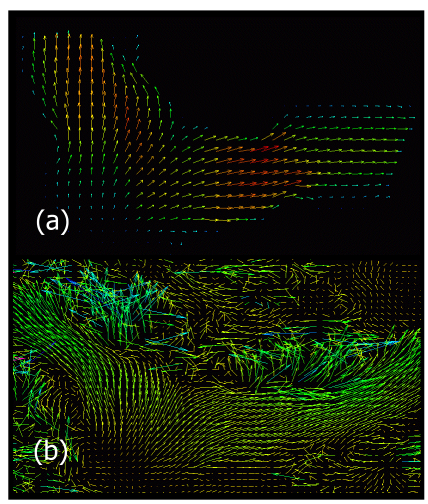

REGULATION OF MOTOR UNIT RECRUITMENT IN THE CARDIAC MUSCLE

Carmit Levy and Amir Landesberg
Department of Biomedical Engineering, Technion-Israel Institute of Technology, Haifa, Israel.
amir@biomed.technion.ac.il

INTRODUCTION

The regulation of cardiac muscle contraction is determined by coupling calcium kinetics with cross-bridge (Xb) cycling. Calcium binding to the troponin regulatory complexes regulates Xb recruitment. Our theoretical studies suggest the existence of a dominant positive feedback mechanism, denoted as the cooperativity mechanism, whereby the affinity of troponin for calcium depends on the number of force-generating Xbs.

OBJECTIVES

The suggested cooperativity mechanism leads to the prediction that there is no unique force-length relation. The generated force is determined by the bound calcium and calcium affinity. Hence, for a given sarcomere length (SL), the force should be higher when the SL is approached from longer SL and smaller when it is approached from shorter SL. To test this hypothesis we examined the force responses to SL oscillations, at constant free calcium concentration and tetanus contraction.

METHODS

Eight trabeculae obtained from rat right ventricles were studied. SL was measured by laser diffraction techniques (Resolution of 3nm). The force was measured by a silicon strain gauge (Resonance frequency of 1.3 kHz). Muscle length was controlled by a fast servomotor (rise time of 0.25msec). The fibers were tetanized using 8Hz stimulation (pulse width of 40ms) in the presence of cyclopiazonic acid ($[Ca]_0$=6mM, 25^0C). To quantify the force responses to the sarcomere length perturbations - small sinus oscillations of 40±11.02nm, at various frequencies (1, 2 and 4Hz) were imposed. The number of strong Xbs was quantified by measuring the stiffness, utilizing additional smaller (2.47±0.39nm) and high frequency (50Hz) oscillations.

RESULTS

The force response lagged the SL oscillations, for oscillation frequency smaller than 4Hz (111.87±40.98 msec at 1Hz). The oscillations of the force and the stiffness were closely aligned, suggesting that the force response was determined primarily by the regulation of XB recruitment, and not by changes in the average force per XB. A counter clockwise hysteresis was obtained between the force and the SL and for a given SL the force was higher when the SL was approached from longer SL, in accordance with the prediction. The hysteresis between the force and the SL resembles the hysteresis between the stiffness and the SL: similar direction and phase shift. The counter clockwise hysteresis implies that the muscle generated external work during the oscillations. Hence the phase delay between the SL and the force relates to delay in the regulation of Xb recruitment.

CONCLUSION

There is no constitutive unique force-length relation, and the instantaneous force depends on the instantaneous length and on the history of contraction. The counter clockwise hysteresis between the stiffness and the SL implies that the lag in the force response is due to the delay in Xb recruitment. The counter clockwise hysteresis implies also that work is done by the muscle and the hysteresis cannot be attributed to visco-elastic properties of the muscle (which will lead to clockwise hystersis). Therefore, the counter clockwise hysteresis validates the existence of the cooperativity mechanism that regulates Xb recruitment.

SIGNIFICANCE

The cooperativity mechanism provides the switching mechanism for cross-bridge recruitment in the cardiac muscle. It explains the steep force-length relation in the cardiac muscle, describes the adaptive control of energy consumption by the prevailing loading conditions and provides the molecular basis of the Frank Starling law at the whole heart level.

REFERENCES

Allen, D.G., Kentish. J. C. (1985). *J. Mol. Cell. Cardiol.* **17**: 821-840.
Chalovich, J.M., Eisenberg, E. (1982). *J. Biol. Chem.* **257**: 2432-2437.
Hofmann, P.A., Fuchs, F. (1987). *Am. J. Physiol.* **253**: c541-c546.
Landesberg, A., Sideman. S. (1994). *Am J Physiol* **266**:H1260-H1266.
Landesberg. A. (1996). *Am J Physiol* **270**: H338-H349.
Lehrer, S. S. (1994). *J. Muscle Research and Cell Motility*, **15**, 232-236.

ACKNOWLEDGMENT

This study was supported by Yegal-Allon Fellowship (LA), the Technion foundation for the promotion of science (LA) and by the “Mallat Family Fund”.

INCREASED INTRA-ABDOMINAL PRESSURE IS COUPLED WITH TRUNK MUSCLE CO-CONTRACTION DURING STEADY STATE EXERTIONS

Jacek Cholewicki, Paul C. Ivancic, and Andrea Radebold
Biomechanics Research Laboratory, Yale University School of Medicine, Department of Orthopaedics and Rehabilitation
New Haven, CT, 06520 USA jacek.cholewicki@yale.edu

INTRODUCTION

Theoretically, spinal unloading due to increased intra-abdominal pressure (IAP) is possible if the transversus abdominus and/or oblique muscles are recruited preferentially for generating IAP (Daggfeldt and Thorstensson 1997). However, Cholewicki at al. (1999) documented a significant increase in the electromyographic (EMG) activities of all major trunk muscles, in association with voluntarily elevated IAP during isometric trunk exertions. Therefore, the purpose of the present study was to investigate whether increased IAP could be achieved without elevating overall trunk muscle co-contraction and hence, without increasing spinal compression force.

METHODS

Ten subjects performed isometric trunk flexion, extension, and lateral bending exertions in a semi-seated position while generating 0, 40 and 80% of their maximum IAP or while co-contracting trunk muscles (CC) without consciously raising IAP (by keeping their glottis open). The isometric target force was set at 35% of the subject's maximum effort.

An EMG assisted biomechanical model (Cholewicki and McGill, 1996) was used to quantify trunk muscle co-contraction with calculations of spine compression force. The EMG signals were recorded from 12 major trunk muscles: left surface and right rectus abdominus, external and internal oblique, latissimus dorsi, thoracic and lumbar erector spinae.

Correlation coefficients between IAP and L4-L5 joint compression force were computed to determine the association between IAP and measures of muscle co-contraction.

RESULTS AND DISCUSSION

In parallel with increased IAP, spine compression force increased significantly ($p < 0.05$) in all isometric exertion directions (Figure 1). Increased spine compression force reflected an increase in the overall co-contraction of trunk muscles, which was accomplished with significantly greater activation of all 12 trunk muscles monitored.

None of the subjects were able to co-contract their trunk muscles without increasing IAP. They generated an average of 30 (SD=14) percent of their maximum IAP in the CC trials. The amount of trunk muscle co-contraction, quantified with spine compression force, relative to the increase in IAP was the same regardless of whether the subjects intentionally generated IAP or consciously avoided it (Figure 1). It appears that the motor control strategy of increasing IAP during steady state, physical exertions is not to reduce spine compression force, but rather to increase the stability of the spine.

SUMMARY

During steady-state exertions, it was not possible to co-contract trunk muscles without generating IAP, or conversely to generate IAP without trunk muscle co-contraction.

REFERENCES

Cholewicki J, McGill SM. (1996). *Clin Biomech,* **11**, 1-15
Cholewicki J, et al. (1999). *European Spine J,* **8**, 388-395
Daggfeldt K, Thorstensson A. (1997). *J Biomech,* **30**, 1149-55

ACKNOWLEDGEMENTS

This study was supported by a grant from the Gaylord Rehabilitation Research Institute.

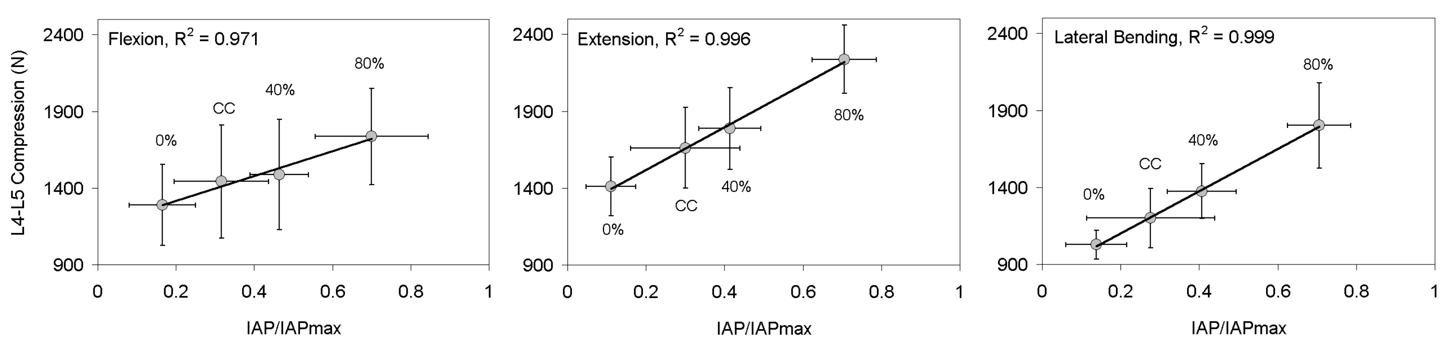

Figure 1: Regression analysis between the normalized intra-abdominal pressure (IAP/IAPmax) and the L4-L5 compression force in isometric trunk extension, flexion, and lateral bending trials. Data points represent means with standard deviation bars.

STRESS ANALYSIS ON MECHANICAL VALVE LEAFLET USING BLOOD FLOW PROFILE THROUGH THE VALVE

S. M. Rajaai
School of Mechanical Engineering, Iran University of Science and Technology, Tehran, Iran
Lecturer and Head of Biomechanics Group, s_rajaai@sun.iust.ac.ir

INTRODUCTION

In a previous research linked with this, Rajaai S. M. and Rahmani A., 1998, fifteen various valve models, with different geometrical dimensions, were studied using finite element method. From the models one of them is selected as the optimum design. The obtained model is acceptable as a result of biomechanical and spatial constraints in aorta root. In this paper, pressure distribution has been conducted on the valve leaflets applying finite element analysis in sectioning method.

METHODOLOGY

Designing of geometrical shape of leaflet of mechanical heart valve has accomplished in regard to the situation of aorta. To do this the results of H. Raul et. al.,1990 have been used. To design and select the best model, 15 models were compared on a trial & error process and the best one was selected. This comparison was held in main cross-section of aorta (Fig. 1)

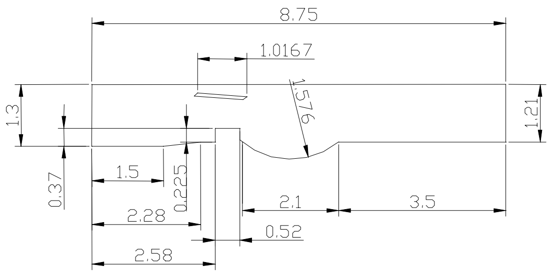

Fig.1 The dimensions of aorta(dimensions are based on centimeter)

Navier Stokes equations for viscous fluid and continuity equations considering the following assumptions have been used to analyse the blood flow around the valve.

- Blood considered as a newtonian fluid
- The blood viscosity considered equal to 3.5cp
- The flow considered as steady – state, the rhythmic nature of blood pulse has been avoided, and the aortic wall is considered rigid.

RESULTS AND DISCUSSION

Velocity equation in x direction is as follows:

$$u_x = (\beta / 4\mu).(R^2 - r^2);\ \beta = [(128.q.\mu)/(\pi.D^2)](R^2 - r^2) \qquad (1)$$

After selecting the suitable model, leaflet profile should be found by calculations. Total curve of leaflet is obtained from shear contact of surface (which has 25 degree angle) to z axis and to a cylinder with y axis, equation of this surface is as follows (The x′z′ plane is the surface of the leaflet):

$$x'^2 = R^2 - 0.821z'^2 \qquad (2)$$

To design the location of produced joint and to present the velocity profile in different cross-sections of the aorta, sectioning method has been used. The entering velocity profile of blood to aorta is gained by contact of parabolic velocity profile of fluid with crossing surface: q=20(lit/min)

$$u_x = 74.29[R^2 - (y^2 + (n.a)^2)] \qquad (3)$$

Equation 3 gives profile of entrance velocity in each cross-section, in this equation '*n*' is the number of sections and '*a*' is the distance between each cross-section. After finding velocity profile by finite element method and NISA software fluid pressure profile has been obtained and the values have been shown as contours.

Mechanical properties of the graphite layer of polycrystaline, which is covered by alloy, made of pyrolytic carbon & silicon (%10-%20 by weight) has been considered for solid analysis. Solid analysis has been performed in critical conditions, one with closed valve and the other with open valve in closed situation, the worst condition was considered with discrepancy pressure of 11 (Kpa). For analysis of critical conditions, the contact velocity has been considered up to 72 (m/s). The maximum velocity occurs between two leaflets and maximum positive pressure occurs on the edge of the leaflet against the blood flow. The maximum negative pressure occurs up site of the leaflet and around the joint.

SUMMARY

The solid analysis on mechanical valve leaflet has been carried out for two modes of open, and closed. In each case tensile stress, shear stress, main stress, VON MISES stress, and octahedral stress contours are offered on the valve leaflet. It was found out that the open state of the valve is more critical than the closed state. The most critical amount of stress is 254.3E6 (pa) related to VON-MISES stress.

REFERENCES

Rajaai S. M., Rahmani A. (1998). Artificial heart valve design, Master Thesis, Iran University of Science & Technology, Tehran, Iran

Raul H., Hirtt V. and Effort S.(1990). The geometry of the aortic root in health at valve disease and after valve replacement, *J. Biomechanics*, **23**, 181-191

SIMULATION OF ULTRASONIC WAVES' EFFECTS ON CERVIX CANCEROUS TISSUES

Farzan Ghalichi [1], Sohrab Behnia [2,3], Mehdi Ghasemi [2], and Ehsan Sadigh Rad [2]

[1] Department of Biomedical Engineering, Sahand University of Technology, Tabriz, Iran
[2] Department of Physics, IAU, Ourmia, Iran
[3] Institute for Studies in Theoretical Physics and Mathematics, Tehran 19395-1795, Iran
Communicating Author: Sohrab Behnia, behnias@yahoo.com

INTRODUCTION

The possibility of focusing ultrasonic waves at a focal zone has accelerated its use for non-invasive therapies, like extracorporeal shock wave lithotripsy and hyperthermia. This trait of ultrasonic waves makes non-invasive surgical applications feasible, using focused ultrasound to deliver intense vibrational energy to a focal zone, with no significant effect on surrounding tissues. Consequently temperature rises at the focal zone to relatively high values. This process provides a non-invasive technique with the property of destroying cancerous tissues in a well-defined target zone.

METHODS

In order to destroy cervix cancerous tissues, it is needed to gain a high level of acoustic pressure in the focal zone that can be done by an annular transducer [Table 1]. In such cases the amount of acoustic pressure can be calculated using the following equation [1,2]:

$$p(R) = \frac{\rho c}{\lambda} \int_s u \frac{e^{-(\alpha + jk)R}}{R} dS$$

Applying acoustic pressure in the following equation, radiation power at the target surface can be obtained:

$$W = \frac{1}{\rho c} \iint_s p^2 dS$$

Using the bio-heat transfer equation the rate of temperature rise in the cancerous tissue can be studied [3]:

$$\rho_t c_t \frac{\partial T}{\partial t} = \nabla.K\nabla T - W_b c_b (T - T_a) + W$$

RESULTS AND DISCUSSION

In this study, obtained results out of simulations and analytic calculations on the energy and frequency dependence during the ultrasonic waves' propagation in the cancerous tissue has been discussed.

Considering non-perfection of blood vessels in cancerous tissue and limitations of temperature rise in healthy tissues (41 ºC) and cancerous tissue (43 ºC), one of the main targets in transducer design should be increasing energy transfer rate [3]. For this purpose the relation between ultrasonic waves' frequency and the maximum energy of the focal zone has been studied [Fig.1].
According to the simulation results, it can be said that for cancerous tissues small in size, the frequency should be risen and vice versa [Fig.2].

Table 1: Transducer Specifications

1	Number of Elements	192
2	Fixed Focus	78 [mm]
3	Radius of Curvature	30 [mm]

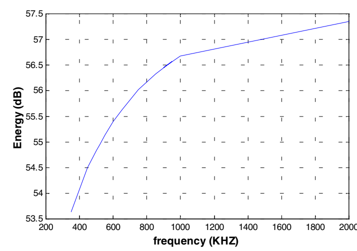

Figure 1: Maximum energy of focal zone diagram with respect to frequency.

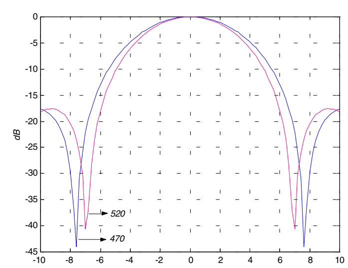

Figure 2: Comparison of beam pattern in 470 kHz and 520 kHz

REFERENCES

1. Kinsler L.E., Frey A.R., Coppens A.B., and Sanders J.V., "Fundamentals of Acoustics", John Wiley & Sons, (1982).
2. Jorgen Arendt Jensen, "Ultrasound fields from triangular apertures", Journal of the Acoustical Society of America, Vol.100 (4), October, (1996).
3. DEBICKI P. M., "A low-frequency hyperthermia system for malignant service melanoma treatment" Ph.D Thesis, Technical University of Cdansk, (1999).

ACKNOWLEDGMENTS

This work was supported in part under Biomedical Engineering Department, Sahand University of Technology and Department of Physics, IAU, Ourmia, Iran.

COMBINING MRI AND CFD FOR CAROTID BLOOD FLOW ANALYSIS: A REPRODUCIBILITY STUDY

Fadi P. Glor[1], Quan Long[1], Ben Ariff[2], X. Yun Xu[1], Simon A.McG.Thom[2], Alun D. Hughes[2], Pascal Verdonck[3]

[1] Department of Chemical Engineering, Imperial College, London, United Kingdom, fadi.glor@ic.ac.uk
[2] Department of Clinical Pharmacology, Imperial College, London, United Kingdom
[3] Cardiovascular Mechanics and Biofluid Dynamics Department, Ghent University, Gent, Belgium

INTRODUCTION

The importance of wall shear stress in the initiation and progression of atherosclerosis has been recognised for some time. A novel way to quantify wall shear stress under physiologically realistic conditions is to combine MRI and CFD. This combination of techniques has been regarded as a powerful tool for the investigation of flow in real arteries, since it is capable of providing data that are difficult to measure *in vivo*. The present study aims to investigate the reproducibility of the simulated flow by using such a combined approach.

METHODS

The right carotid bifurcations of 8 healthy subjects were scanned twice with MRI with a time-interval of at least one week. Three-dimensional geometries of the carotid arteries were reconstructed for each of the two scans and for each subject, resulting in a total of 16 carotid bifurcation models. Differences in reconstructed geometries resulting from the two scans of the same subject were evaluated using three quantitative measures, namely the centre-line distance, cross-sectional areas and shape factor. Pulsatile flows through these models were calculated with the same inlet and outlet boundary conditions to assess errors associated with the predicted flow parameters. This was done by comparing various wall shear stress indices, including time-averaged wall shear stress (TAWSS), oscillatory shear index (OSI), wall shear stress gradient (WSSG) and the wall shear stress angle deviation (WSSAD) (Hyun, 2000). Comparisons were made between the two sets of results obtained for the same subject by averaging the above-mentioned parameters on "patches" on the vessel wall. Differences in patched data between the two scans were compared using a paired Student's t-test, $p<0.05$ was considered significant.

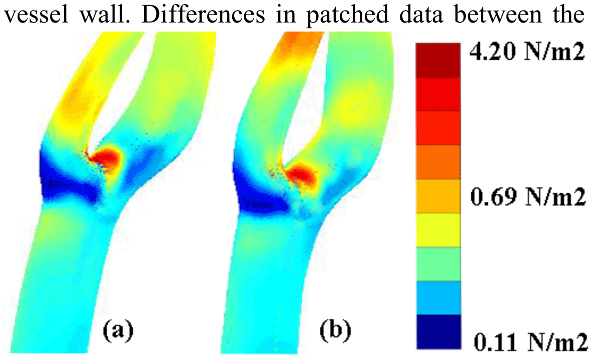

Figure 1: Time-averaged wall shear stress for the **a.** first scan; **b.** second scan. The scale is logarithmic.

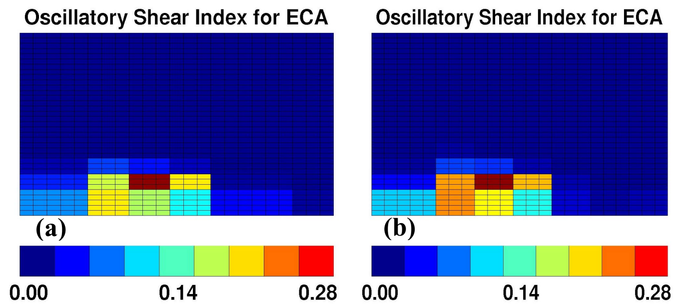

Figure 2: "Patched" oscillatory shear indices for the external carotid artery in **a.** the first scan; **b.** the second scan. Note the brown colors are patches over maximum value shown in the legend. The blood flows through the vessel from down to up in this representation of the vessel wall.

RESULTS AND DISCUSSION

Predicted TAWSS maps for two different scans of the same subject are shown in Figure 1. Differences in geometry between the models were found to be: centreline-error of 0.536 mm, shape factor errors of 6.53% (CCA), 9.44% (ICA) and 11.22% (ECA). Qualitatively, the TAWSS appears similar between scans. Figure 2 shows the colour-coded OSI distribution on the ECA vessel wall in a patched manner. All four parameters (TAWSS, OSI, WSSG, WSSAD) did not differ significantly ($p>0.1$ for all) in CCA, but the reproducibility in the ICA and particularly the ECA was less satisfactory.

SUMMARY

Reproducibility of predicted wall shear stress in the carotid bifurcation using a combined MRI and CFD method has been quantified. The overall reproducibility was found to be satisfactory although better results were obtained for the CCA than its branches. Further study will aim to correlate predicted wall shear stress errors with geometrical errors, in order to identify the most sensitive geometrical parameter that affects the predicted wall shear stress.

REFERENCES

Hyun, S. et al (2000). *Medical Engineering & Physics*, **22**, 13-27.

MOTION CONTROL SHOES REDUCE MIDFOOT RANGE OF MOTION DURING RUNNING

Richard.M.Smith[1] and Renee.L.Attwells[1]
[1]School of Exercise and Sport Science, University of Sydney, Australia

INTRODUCTION:

Excessive pronation is associated with a variety of injuries, particularly when running and this has stimulated investigation of rearfoot motion relative to the leg during running with and without footwear (eg Stacoff et al., 1991). Nigg and co-workers (cited in Clarke et al 1983) have shown that, with additional medial support in the footwear, the average pronation in subjects with over-pronation problems was reduced to below that shown in symptom free subjects. Little has been done to investigate the effect of footwear on the midfoot region of the foot. Other authors have measured significant relative motion between the forefoot and the rearfoot during the stance phase of running barefoot (Attwells and Smith, 2001). However, when wearing motion control footwear for example, the addition of midsole support may restrict the motion of the foot around the midfoot joints. The purpose of this paper was to investigate the range of motion in the midfoot region during the stance phase of heel-toe running while wearing motion control running shoes and barefoot.

METHODS:

Ten Subjects (five control and five clinically diagnosed overpronators) underwent five running trials with and without footwear. Surface markers were placed on the lower right leg and foot, and a metal shim was attached to the calcaneus. A wand marker system (Attwells and Smith, 2001) was fixed to the shim by a slot and lock mechanism. Three markers placed on the navicular, first and fifth metatarsal heads in the barefoot condition and on the surface of the shoe in the same positions for the footwear condition defined the forefoot. The three-dimensional position of these markers during stance phase of movement was captured using a seven-camera motion analysis system and the relative angles, corrected for standing eversion angle, between the forefoot and rearfoot segments calculated using a joint co-ordinate system.

RESULTS AND DISCUSSION:

A main effect of footwear was seen for dfpf ($F = 437$, $p < 0.001$) (Table 1 and Figure 1) and adab ($F = 42$, $p < 0.001$) but not for inev ($F = 3.9$, $p = 0.082$). There was no main effect of pathology for any angle. The only significant interaction between footwear and pathology was for dfpf ($F = 7.3$, $p = 0.027$) with the footwear causing a greater decrement for pronators than normals.

The shoe exhibited less range of motion around its midsole region than the foot did in the barefoot condition. Although the experiment had not measured the forefoot directly while in the shoe, the tightness of the fit of the shoe at both heel and forefoot would suggest that the shoe used in this experiment did limit the rage of motion around the midfoot during the stance phase of running. One effect of limiting dfpf in the midfoot is an increase in range of dfpf at the ankle (Attwells and Smith, 2001). The effect of limiting the other angles and possible deleterious effect on the functioning of the foot deserve further investigation.

Table 1 *Range of motion (mean SD) for the forefoot/ foreshoe relative to the rearfoot.*

	Range of Motion (deg)			
	normals		pronators	
	barefoot	shoe	barefoot	shoe
df/df	27.1 3.2	9.6 3.1	31.3 3.6	8.5 1.7
in/ev	7.2 4.0	5.3 1.6	7.8 2.5	5.0 1.9
ad/ab	7.2 4.0	3.2 0.6	11.8 4.7	2.8 1.0

SUMMARY

The motion control shoes used in his study showed a decreased range of motion about the midsole region during the stance phase of heel-toe running compared with the range of motion observed for the bare foot. If the shoe is close fitting this implies that the foot has a decreased range of motion about its midfoot region also. One outcome is a greater range of dfpf at the ankle joint. Whether this or other restrictions of range of motion are deleterious to foot function needs further investigation.

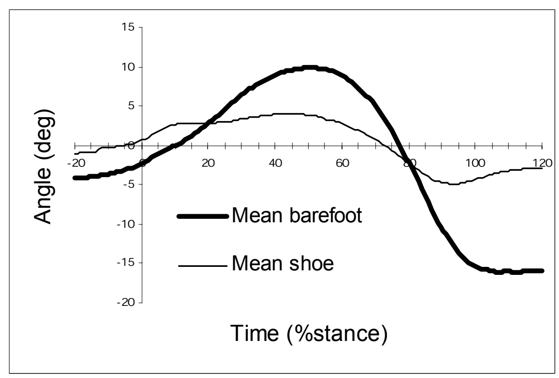

Figure 1 *Time series for dfpf for the footwear and barefoot conditions.*

REFERENCES

Attwells, R., Smith, R.M. (2001) Proceedings of the XVIIIth Congress of the International Society of Biomechanics.
Clarke TE, Frederick EC, Hamill CL (1983) Med.Sci.Sports.Exerc. 15(5) pp 376-381
Stacoff A, Kalin X, Stussi E (1991) Med.Sci.Sports.Exerc. 23(4) pp 482-490

ESTROGEN DEPLETION IS ASSOCIATED WITH CHANGES IN OSTEON MORPHOLOGY

Lanny V. Griffin , Lisa Christensen, Ryan Vandenbosch Melanie Fish, Robbie Bigley
Bioengineering Laboratory, California Polytechnic State University, San Luis Obispo, CA
lgriffin@calpoly.edu

INTRODUCTION

It is well accepted that estrogen deficiency associated with menopause increases the risk of osteoporosis and bone fragility in women. Les and coworkers have found that estrogen depletion affects the microstructure and properties of cortical bone (2001). We hypothesized that osteon morphology would also be effected by estrogen depletion.

METHODS

We obtained twelve 1.5 cm long segments of cortical bone taken from the proximal radius/ulna of six-year-old Warhall breeder sheep. At the age of 3, six of the sheep were ovariectomized (Ovx) and six were subjected to a sham surgery (Non-Ovx). The bone was kept in gauze, soaked with calcium buffered saline and frozen, except when machining. We machined 4x4x15 mm blocks from the caudal and cranial regions of each bone of using a low-speed diamond sectioning saw (Buehler Isomet 1000, Lakebluff, IL) under constant irrigation of distilled water. We set aside five 100μm thick sections from each block for each region. The sections were were lightly deburred and polished using 600 grit abrasive media moistened with calcium buffered saline, then mounted on a slide for histologic evaluation at 100x. At this magnification, approximately 20 fields were required to cover the entire section. The sections examined under polarized light to determine the collagen fiber-birefringence pattern using the osteon classification of Ascenzi (1976) and Martin (1996). We counted and recorded the diameter and type of osteon, in five of the twenty fields per section, 2 periosteal, 2 endosteal and one central field using an image analysis program (Bioquant 5.0, Nashville, TN). Volume fraction of osteon was calculated as the (area of osteon type)/(section area). Statistical analysis was conducted using a GLM procedure with volume fraction and diameter as the independent variables, with factors anatomic region, zone (periosteal/endosteal), osteon type, and Ovx/Non-Ovx. Multiple pairwise comparisons were made using the Bonferroni method and significance was reported for $p<0.05$.

RESULTS AND DISCUSSION

We found that darkfield and hooped osteons are more prevalent in the caudal and cranial regions ($p<0.0001$) and that osteons tended to be more prevalent in the endosteal portion, rather than periosteal portion of the cortex ($p<0.0001$). In the sheep we examined, there was a great deal of primary lamellar bone on the periosteal portion of the cortex, with little evidence of remodeling activity.

We found that estrogen deficiency significantly increases the volume fraction of osteon type ($p<0.0001$) with greater numbers of darkfield and hooped types of osteons being recorded.

We found that the diameters of the osteons are regionally dependent ($p<0.0001$), caudal being larger than cranial (130 μm and 100 μm, respectively). The diameter appears to be a function more of anatomic region rather than estrogen deficiency ($p=0.510$). We also found that osteons tended to be larger in the endosteal portion of the cortex (125 μm vs 100 μm). Since osteoporosis is more associated with trabecular bone, it seems reasonable that changes to cortical bone would tend to be near the inner portion of bone. Moyle and Gravens (1986) showed that the work to fracture of bovine tibia is related to osteon size and so we expect there is regional variation in the fracture properties of the sheep bone as well.

SUMMARY

We were able to demonstrate estrogen deficiency significantly effects the microstructural organization of cortical bone in a sheep model. Specifically, we found greater numbers of darkfield and hooped osteons in estrogen deficiency in bone and that most of the changes in morphology occur in the endosteal portion of the cortex.

REFERENCES

Ascenzi A, Bonucci E. (1976) Relationship between ultrastructure and "pin-test" in osteons. Clin Orthop 121:275-294

Les, C, Spence C, Plantikar S. Nakeonczny A Turner A. (2001) Estrogen depletion is associated with changes in the regional variation of compact bone density. 47th Mtg of the ORS

Martin RB, Gibson VA, Stover SM, Gibeling JC, Griffin LV (1996) Osteonal structure in the equine third metacarpus. Bone Aug;19(2):165-171

Moyle DD and Gravens AJ. (1986) Fracture properties of bovine tibial bone. J Biomech 19:919-927

ACKNOWLEDGEMENTS

This work was funded by NIH Grant RO1 DE 13579, and support from the US Army Institute of Surgical Research. We thank Dr. Les for donating the bone used in this study.

GEOMETRICALLY DEFINED 3-DIMENSIONAL COLLAGEN SCAFFOLDS FOR TISSUE ENGINEERING

Guenter Rau[1] , Ingo Heschel[2], Melanie Kuberka[1], Birgit Glasmacher[1]
[1]Helmholtz-Institute for Biomedical Engineering, Aachen University, Germany
[2]Matricel GmbH, Kohlscheid, Germany

INTRODUCTION

Tissue engineering procedures open the way to achieve living implants for a variety of medical applications. In principle, cells are yeasted from the living organism by biopsy, then expanded in culture in the laboratory. Preferably, pre-dispositioned autologous cells are used to avoid rejection of the implants after the operation.

The cells need a structure to grow on. These are e.g. biodegradable polymers, collagen scaffolds, fibrin gel or chitosan. Premature progress of differentiation has to be prevented. Cartilage repair by membrane-bound autologous implantation (MACI, VTSI Verigen Inc.) is described as state of the art in clinical approach. For enlarged defects, 3-dimensional (3D) matrices with autologous chondrocytes may be the next step. This study demonstrates how 3D-scaffolds are obtained, and that cells of different type grow into the scaffold.

METHODS

Collagen sponges are produced by freeze-drying of collagen suspensions. The porous structure can directly be controlled by the ice crystal morphology (Fig. 1) since after removal of the ice by vacuum-drying the pore structure of the collagen is a replica of the ice structure.

Homogeneous solidification of fingerlike ice formation can be obtained under almost stationary freezing conditions which is possible by applying unidirectional solidification techniques. This can be achieved by using the Power-Down-Technique to imprint a constant temperature gradient on the sample. During the freezing procedure the bottom and the top of the sample are cooled down with the same cooling rate. We investigated the variation of crystal sizes that can be adjusted by freezing parameters and composition of the collagen suspension.

Fig. 1: The porous sponge structure is determined by the ice

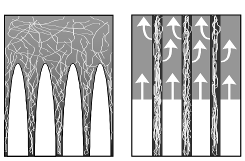

crystal-morphology in frozen collagen suspensions.

RESULTS AND DISCUSSION

The ice formation can be organized very regularly resulting in corresponding regular sponge structures as shown in Figure 2. By adding acetic acid to the collagen suspension in varying concentrations we adjust the crystal size and thus obtain pores in the range of 20 – 100 µm. The pores formed in parallel to the heat flow showed no irregularities throughout large dimensions, even up to 10 mm thickness (cf. Fig. 2).

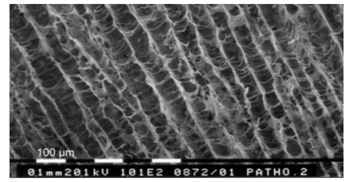

Fig. 2: SEM picture of a collagen sponge produced by directional solidification and freeze-drying according to the Power-Down technique.

It is shown for selected cell types that the cells are not only growing on the sponge surface but really penetrating the sponge. For different cell types such as chondrocytes, adipocytes, nerve cells, epithelium cells or fibroblasts, we will investigate whether the dimensions of the collagen sponge have to be "designed" individually for optimal ingrowth.

SUMMARY

3-D collagen structures can be produced as well defined and regular sponge-like scaffolds. The dimensions can be varied by selection of the process parameters and additives. The growth of different cell types indicates that viable implants can be obtained by using adequate sponges.

REFERENCES

Schoof, H., Bruns, L., Apel, J., Heschel, I., Rau, G. (1998). Einfluß des Einfrierverfahrens auf die Porenstruktur gefriergetrockneter Kollagenschwämme. *Ki-Luft und Kältetechnik* **34**, 247-252

Schoof, H., Apel, J., Heschel, I., Rau, G. (2001). Control of pore structure and size in freeze-dried collagen sponges. *J Biomed Mater Res. (Appl Biomater)* **58**: 352-357

Kuberka M., v. Heimburg D., Schoof H., Heschel I., Rau G. (2002). Magnification of the Pore Size in Biodegradable Collagen Sponges. *In J Artif Organs* **25** (1): 67-73

ACKNOWLEDGEMENTS

The studies are in part supported by Deutsche Forschungsgemeinschaft (Ra335/22-1,2) and the Interdisciplinary Center for Clinical Research in Biomaterials and Tissue-Material-Interaction in Implants (IZKF "BIOMAT."), BMBF project No. 01 KS 9503/9.

MECHANICAL BEHAVIOUR OF BASEBALLS DURING COMPRESSIVE LOADING TO BAT-BALL IMPACT LEVEL

Rochelle Nicholls[1,2], Karol Miller[2] and Bruce Elliott[1]

[1] Department of Human Movement & Exercise Science, University of Western Australia, Perth, Western Australia

[2] Department of Mechanical & Materials Engineering, University of Western Australia, kmiller@mech.uwa.edu.au

INTRODUCTION

Impact from the batted ball is responsible for 4-5 deaths per year amongst baseball pitchers (Adler & Monticone, 1996). The material properties of the ball affect the dynamics of the bat-ball interaction, and thereby the ball exit velocity and subsequent time available for the pitcher to take evasive action. During bat-ball impact, a baseball is compressed to 50% of its original diameter (Adair, 1994). Previous investigations of baseball material properties using quasi-static uniaxial compression have typically tested to 10% compression, as the force-displacement relationship is linear in this range and ball stiffness can be determined as the gradient of the curve (Hendee, Greenwald & Crisco, 1998). In order to predict baseball impact response and behaviour under maximal conditions, this research undertook compression to 50% to obtain more realistic measures of material behaviour.

METHODS

70 new baseballs from 7 models were tested, representating balls used in professional and college baseball. Uniaxial compression testing was conducted using the Instron 8501 (Instron Corp., Canton, Massachusetts). Each ball was positioned between two circular stainless steel platens: the upper platen was attached to a calibrated 100 kN load cell and lowered toward the stationary lower platen at 1 mm/s. The onset of the loading phase was indicated by the first non-zero force reading, and terminated at 50% of baseball diameter (35.86 mm). One loading cycle was completed for each ball. Force-displacement data was sampled at 5 Hz using LABTECH Notebook software. The data were normalised to 100 data points (as a percentage of maximum displacement).

RESULTS AND DISCUSSION

The nonlinear behaviour of baseballs under compression to 50% of original diameter is evident in Figure 1. The curves are concave-upward for all models, containing no linear portion from which elastic modulus can be determined.

Directional effects: The surface of the baseball is assymmetric due to its pattern of raised seams. Testing for effects of ball orientation on the force-displacement curve was undertaken using 5 orientations: 3 in which the contact points were on the ball cover (at the widest point in the xy, xz and yz planes), and 2 in which the ball was orientated on its seams. Repeated measures ANOVA for normalised force indicated no significant differences within the cover or within the seams orientations ($p=0.210$). However a distinct directional effect was evident between cover and seams orientations ($p=0.000$), with cover orientations being steeper with greater peak force (Figure 1).

Ball stiffness: Some quasi-static properties of baseballs have been previously correlated with ball impact characteristics, particularly peak force and stiffness (Hendee *et al.*, 1998).

Figure 1: Force-displacement curves for Model 2 in cover and seam orientations.

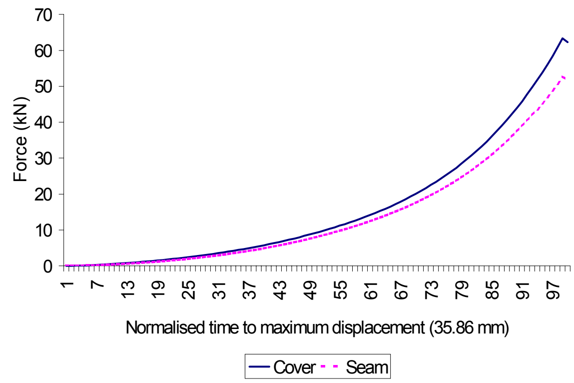

Modification of the procedure adopted by Hendee *et al.,* (1998) was used to estimate ball stiffness for compression to 50%. Data from four balls in each model were selected at random and averaged to represent that model. Linear least-squares fit was applied to the 10 (normalised) data points preceding maximum displacement for each ball model. Stiffness was determined as the gradient of this fit line (Table 1). These values are significantly higher than those reported by Hendee et al. (1998) for 10% compression (mean 2340 ± 441 N/cm, n=7) and verify the distinct directional effect.

	Cover	*Seam*
Model	**Stiffness (N/cm)**	**Stiffness (N/cm)**
A	18004	12977
B	20039	15813
C	17541	12751
D	19769	14438
E	16175	13853
F	17187	13575
G	18089	14128

Table 2: Linear fit stiffness data for all ball models

SUMMARY

Baseball stiffness during compression to 50% of initial diameter has been determined. The directional effect has implications for ball design: the reduced peak force and stiffness during compression on the seams indicates a potential control strategy for ball performance. A mathematical model to predict the behaviour during high-speed impact should be developed.

REFERENCES

Adair, R.K. (1994) *The Physics of Baseball*, Harper Collins.

Adler, R.A., Monticone,J.P (1996) In: Kyle, S. (ed.): *Youth Baseball Protective Equipment - Final Report* US Consumer Product Safety Commission, Hazard Analysis Division

Hendee,S,Greenwald,R..*et al.* (1998)*J.ApplBiomch***14**,390-400

EFFECT OF DYNAMIC COMPRESSION ON β1 INTEGRINS (CD49D, CD49E) AND CD44 ADHESION MOLECULES EXPRESSED BY ARTICULAR CHONDROCYTES.

C. Gigant-Huselstein[1], D. Dumas[1], D. Baptiste[2], WH Liu[1], X. Wang[1], S. Muller[1], P. Netter[2], E. Payan[2], JF. Stoltz[1]
e-mail : stoltz@medecine.uhp-nancy.fr
[1]Mécanique et Ingénierie Cellulaire et Tissulaire, LEMTA UMR CNRS et IFR 111, [2]Physiopathologie et Pharmacologie Articulaires, UMR CNRS 7561 et IFR 111, Faculté de médecine, 54505 Vandoeuvre-lès-nancy, France.

INTRODUCTION

In diarthrodial joints, articular cartilage experiences a variety of stresses, strains and pressures that arise during normal activities of daily living. The cartilage matrix functions to distribute relatively large loads across the bony ends. Its homeostasis is maintained in part through the chondrocyte response to mechanical stimulation.

The integrin family and the CD44 adhesion receptors appears to play a major role in mediating chondrocyte-matrix interactions.

The aim of this work was to observe, with 3D microscopy techniques, cellular dimension, the expression of β1 integrins (CD49d and CD49e) and CD44 adhesion molecules within compressed explants. A numerical simulation was also performed to determine local deformation of the cartilage under mechanical stress.

METHODS

Tissue culture and mechanical compression
Femoral heads were harvested on healthy rats. Compressive loads were applied to individual explants using a specially designed apparatus (Flexcell International). Five percent compressive strain amplitude was applied to the femoral head dynamically (Frequency=0.5 Hz) for 48 hours.

Cellular dimension and β1 integrin and CD44 receptors expression
First, images acquired by Confocal Laser Scanning Microscopy (CLSM) were used to calculate dimensional data like length, width and volume. Then, the β1 integrins and CD44 receptors were analyzed by indirect immunofluorescence assay with an Optical Scanning Microscopy (OSM) technique combined to a 3D iterative deconvolution process (CellScan EPR™) and CLSM (SP2 Leica Microsystem).

Type I and II collagen production
Types I and II collagens were analyzed qualitatively by indirect immunofluorescence assay using the CellScan system.

Numerical simulation
In order to determine local deformation of the cartilage femoral head under compression, a numerical simulation was performed. The cartilage was considered as a semi-spherical homogeneous elastic shell with a given Young's modulus. A finite element package (MARC) was used to solve the equilibrium equation of the shell under imposed displacement. This simulation allowed us to know quantitative deformation at every point of the cartilage and helped us to better understand the modification of the biological function of chondrocytes situated in different area.

RESULTS AND DISCUSSION

A series of confocal scans through the center of individual cells revealed a change from spherical to an elliptical morphology. This change was a direct consequence of a significant increase of the length (static : 11.60±1.34µm; compression : 14.91±1.85µm) and a significant reduction in width (static : 10.34±1.61µm; compression : 7.41±1.31µm). These observations included also trends for cell directional strains, confirming a role in chondrocyte metabolic response to compression [1].

The quantification with 3D fluorescence microscopy showed that dynamic compression induced an increase of CD49d and CD44 expression but any variation of CD49e adhesion molecules. Results suggest that β1 integrins and CD44 receptors could potentially act as initiators of mechanotransduction pathways under mechanical compression.

SUMMARY

Mechanotransduction events in articular cartilage may be resolved into extracellular components followed by intracellular signalling events, which finally altered cell response [2]. The aim of this study was to examine, with 3D microscopy techniques (deconvolution and confocal), the cell deformation and adhesion molecules such as β1 integrin or CD44 receptors expressed by chondrocytes within compressed explants. Results suggest that the application of compressive strain to chondrocytes in femoral head induces a number of strain events, such as cell deformation, variation of the β1 integrins and CD44 receptors expression.

REFERENCES

1. Quinn, T. et al. (1998). *J. Cell Sci*, **111**, 573-583.
2. Mow, VC. et al. (1999). *Osteoarthr Cartilage*, **7**, 41-58.

EFFECT OF RHEIN ON INTRACELLULAR IL-1? PRODUCTION AND ?1 INTEGRINS EXPRESSION IN STIMULATED CHONDROCYTES –

C. Gigant-Huselstein (1), D. Dumas (1), S. Muller (1), D. Bensoussan (1), J.F. Stoltz (1)
e-mail : stoltz@medecine.uhp-nancy.fr
[1]Mécanique et Ingénierie Cellulaire et Tissulaire, LEMTA UMR CNRS et IFR 111,
Faculté de médecine, 54505 Vandoeuvre-lès-nancy, France.

INTRODUCTION

Osteoarthritis (OA) is a degenerative disease of diarthrodial joints in which degradative and repair processes in articular cartilage, subchondral bone and synovium occur concurrently. Diacerhein is one of the proposed therapeutic agents to regulate the inflammatory process [1]. The drug and its active metabolite rhein, exerts inhibitory effects on interleukin-1 (IL-1)-induced expression of cartilage degrading enzymes [2]. However, its mechanism of action is not completely understood.

The present study was designed to quantify the receptors ?1 integrin CD49d and CD49e and the intracellular IL-1? in stimulated chondrocytes by TNF-? and *rh*IL-1?. Then, we evaluated the *in vitro* effects of rhein on intracellular IL-1? and on ?1 integrin expression.

EXPERIMENTAL METHOD

Chondrocytes cell culture

Human chondroytes monolayer were incubated for 12, 24 and 48 hours in the presence of TNF-? or *rh*-IL1?. On the other hand, we have evaluated the *in vitro* effects of rhein (10^{-5} M, Negma, France) on stimulated or no-stimulated chondrocytes.

Intracellular IL-1? production :

Chondrocytes were fixed, permeabilised and incubated with fluorescein isothiocyanate conjugated monoclonal antibody IL-1?. Then, cells were analyzed by flow cytometer and observed under an epi-fluorescence inverted microscope equipped with the CellScan EPR™ optical scanning acquisition system [3].

1 integrin CD49d and CD49e expression :

Adhesion receptor expression was determined by a direct immunofluorescence assay. The quantification of CD49d and CD49e expression was performed using Quantum Simply Cellular calibrator (Sigma, France). Calibration beads were used to transform the conventional mean fluorescence intensity obtained in flow cytometry as arbitrary units into an absolute number of antibody molecules bound per cell

RESULTS AND DISCUSSION

Flow cytometry and 3D microscopy showed that cells stimulation by TNF-? and *rh*IL-1? induced a significant increase of intracellular IL-1? production. Whereas, the addition of rhein lead to a reduction of intracellular IL-1? production.

The quantitative study of CD49d and CD49e receptors showed that normal chondrocytes expressed more strongly CD49e receptor than CD49d receptor. Moreover, stimulated cells by proinflammatory cytokines induced a significant increase of CD49e from 24 hours of incubation, suggesting a role of this receptor in transduction signal generated by rhIl-1? or TNF-?. A weak increase of CD49d receptor expression was also observed from 12 hours to 24 hours. When chondrocytes are treated with cytokines and rhein, a decrease of ?1 integrins receptors expression was observed, suggesting an action of rhein on these integrins receptors expression.

SUMMARY

Diacerhein has shown to be effective and well tolerated in the long term treatment of OA however, its precise mechanism of action on chondroprotection is unclear. The aim of this study was to estimated the intracellular IL-1? production and the expression of ?1 integrins receptors (CD49d and CD49e) on stimulated or no-stimulated chondrocytes. Then, we studied the effect of rhein, the active metabolite of diacerhein, on these parameters. From this study, it seems that rhein partially reduce cytokine-induced intracellular IL-1? production, and it has a weak action on CD49d or CD49e receptors.

REFERENCES

1. Nguyen, M. et al. (1994). *Arthritis Rheum*, **37**, 529-536.
2. Pujol, JP. et al. (2000) *Biorheology,* **37**, 177-184.
3. Dumas, D. et al. (2000) *Biorheology*, **37**, 165-176.

FORCE ENHANCEMENT IN SINGLE SKELETAL MUSCLE FIBRES ON THE ASCENDING LIMB OF THE FORCE-LENGTH RELATIONSHIP

Danny Peterson, Dilson Rassier, Walter Herzog

Human Performance Laboratory, University of Calgary, Calgary, AB, Canada

INTRODUCTION

Force enhancement following an active stretch in skeletal muscles has been associated with sarcomere non-uniformity on the descending limb of the force-length relationship (Edman et al., 1982; Morgan et al., 2000). According to this theory, during stretch, some sarcomeres elongate less than average, while others elongate more than average and produce most of their force passively as this is the region where non-uniformity develops. One of the predictions of this theory is that force-enhancement is only possible on the descending limb of the force-length relation. However, Herzog and Leonard (2002) have shown a small, but consistent force-enhancement on the ascending limb of the cat soleus muscle. This study was aimed at investigating whether force-enhancement on the ascending limb is a property of single skeletal muscle fibres.

METHODS

The experiments were performed with single muscle fibres (n=7) dissected from the flexor digitorum brevis (FDB) of the frog *Rana pipiens*. The tendons of the dissected fibres were gripped with T-shaped pieces of aluminum foil and mounted in an experimental chamber between a servomotor length controller (Aurora Scientific) and a force transducer (Sensonor). The chamber was filled with Ringer's solution and the temperature was regulated at ~7°C. Stimulation (Grass S88, Grass Instruments) was given through two platinum wire electrodes placed on either side of the muscle fibre. Following an experimentally determined force-length relationship, several isometric and stretch contractions (6 s long) were recorded along the ascending limb of the force-length relationship. Stretches were performed with a velocity of 0.8 mm/sec and an amplitude of 0.2 mm (approx. 10% of fibre length).

RESULTS AND DISCUSSION

Of the 7 fibres tested, 4 showed force-enhancement on the ascending limb of the force-length relationship. The magnitude of force-enhancement appears to increase when moving up towards the plateau of the force-length relation. The following figures show stretches beginning at the same length on the ascending limb and ending at the plateau of the force-length relationship. Figure 1 shows force traces of an experiment in which force enhancement was observed. Figure 2 shows force traces of an experiment in which force enhancement was not observed.

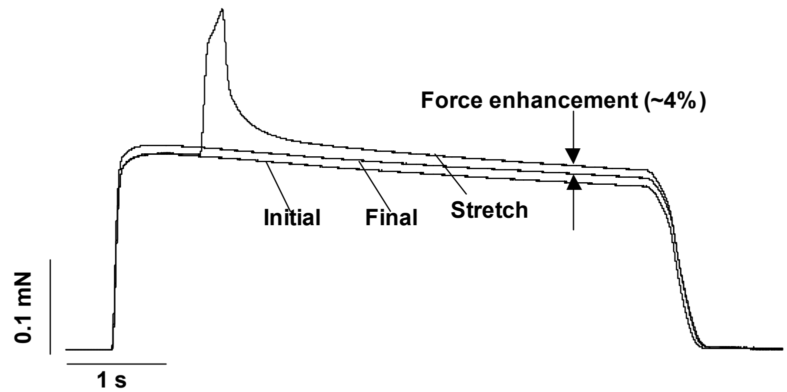

Figure 1: Fibre showing force-enhancement (~4%) on the ascending limb of the force-length relationship.

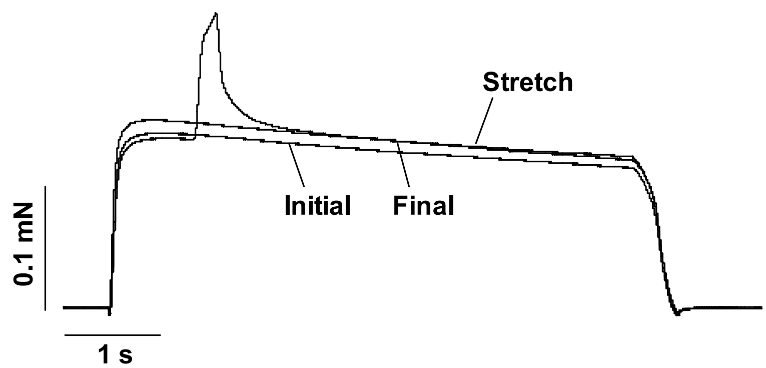

Figure 2: Fibre showing no force-enhancement on the ascending limb of the force-length relationship. However, note that forces at the initial length were not exactly the same, thus possibly hiding a small force enhancement.

We conclude that single cells may produce force enhancement on the ascending limb of the force-length relationship. If, as typically assumed, sarcomeres are stable on the ascending limb of the force-length relationship (Morgan et al., 2000), the sarcomere length non-uniformity theory cannot explain our current observations. The dichotomous results observed here may be a consequence of different fibre types in the FDB muscle.

REFERENCES

Edman, K.A.P. et al. (1982). *J. Gen. Physiol.* **80**, 769-784.
Morgan, D.L., et al. (2000). J. *Physiol.* **522.3**, 503-513.
Herzog and Leonard (2002). *J. Exp. Biol.* **205**, 1275-1283.

WALL SHEAR STRESS WITH INITIATION OF ANEURYSM AROUND ANTERIOR COMMUNICATING ARTERY IN STEADY FLOW

Ryuhei Yamaguchi[1], Susumu Kudo[1], Nobuhiko Nakazawa[1] and Hiroshi Ujiie[2]

[1]Department of Mechanical Engineering, Shibaura Institute of Technology, Tokyo, Japan
[2]Department of Nerosurgery, Tokyo Women's Medical University, Tokyo, Japan

INTRODUCTION

The aneurysm in the cerebral artery is apt to initiate around the "Circle of Willis". The anterior communicating artery (ACoA), which composes one of major part of the circle of Willis, is the most predilection artery of the aneurysm.

In the present paper, the change of flow structure such as the wall shear stress at the apex of ACoA with the initiation of aneurysm is described in steady flow. Once the early aneurysm initiates at the apex in one confluent tube with much flow rate, the distribution of wall shear stress abruptly changes around the early aneurysm. The relation between the initiation and the development of aneurysm is physiologically discussed from the viewpoint of hemodynamics.

METHODS

The flow field around ACoA is simulated by two confluent tubes joining at the angle of 60 degrees, two parallel bifurcating tubes, and the junctional tube, bypass (ACoA), connecting four tubes at normal condition. The flow model with the early aneurysm is simulated as the concave with small radius around the apex in the right confluent tube with much flow rate Q_R as shown in Fig.1. In experiment, the velocity profile is measured by LDA and the wall shear stress is estimated from the velocity gradient near the tube wall. The saturated sodium iodide NaI solution with the same refractive index of 1.49 as the channel material, acrylic plate, is employed as the working fluid in velocity measurement.

RESULTS AND DISCUSSSION

The measurement has been carried out at the Reynolds number of $Re=2R_0U/\nu=400$ and the confluent ratio of $Q_R/Q_L= 2.2$. U is the mean velocity based on the average flow rate $(Q_R+Q_L)/2$ and ν is the kinematic viscosity.

The velocity profile around ACoA is shown in Fig.1. Except for the flow field around the early aneurysm, the velocity profile around ACoA as a whole is similar to that without the aneurysm at normal condition. The velocity through ACoA is several times as large as the maximum velocity in the right confluent tube. The core flow in the right confluent tube impinges at the right apex, right medial corner. There is a small recirculating flow in the concave, aneurysm.

Except for the flow field around the aneurysm, the distribution of wall shear stress around the ACoA as a whole is also similar to that without the aneurysm at normal condition as shown in Fig.2. The wall shear stress changes around the right apex. Particularly, this change is extremely large around the concave. Therefore, this abrupt change of wall shear stress may induce the progressive development of aneurysm.

REFERENCES

Ujiie, H., Liepsch, D. W., Goetz, M, Yamaguchi, R., et al., Stroke, Vol.27(1996), 2086-2094.

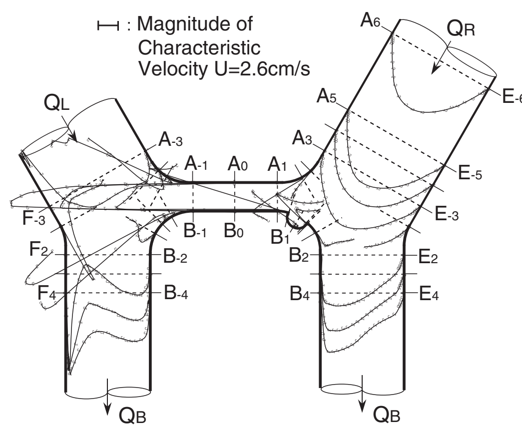

Figure 1 Axial velocity profile at symmetrical plane ($Re=400$, $Q_R/Q_L=2.2$)

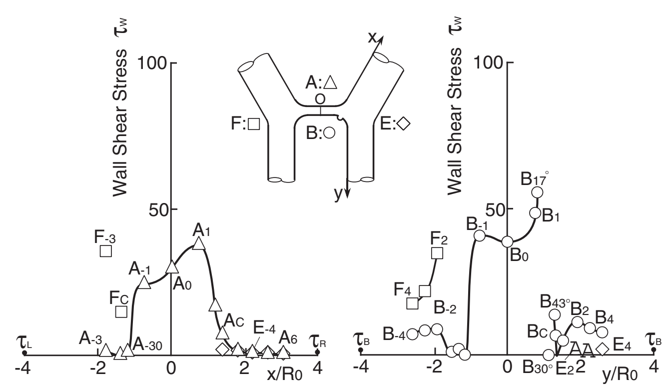

Figure 2 Distribution of wall shear stress ($Re=400$, $Q_R/Q_L=2.2$)

FOOT ROLL OVER SHAPES IN TRANSTIBIAL AMPUTEES: IMPLICATIONS FOR PROSTHETIC ALIGNMENT

T. M. Bach[1,2], G. Halford[1], D. White[1], D. Fyfe[1]
[1]National Centre for Prosthetics and Orthotics and [2]Musculoskeletal Research Centre
La Trobe University, Melbourne, Australia

INTRODUCTION

During stance phase in human walking, the ankle acts to adjust limb length, to provide shock absorption and to enable forward rotation of the leg over the fixed foot. If the ankle is fixed, it is important to compensate for lost function. In ankle foot orthoses, rocker soles are sometimes used to simulate the rocker action of the ankle. In prosthetics, this is achieved through foot design and alignment.

Hansen *et al.* (2000) introduced the concept of the foot roll-over shape (FROS) to explain the relationship between prosthetic foot design and prosthesis alignment in amputee gait. FROS was defined as the geometry of the plantar surface of the foot with respect to the leg during the single support phase of walking. Mechanical testing and "simulated" amputee gait were utilized to quantify FROS for a number of prosthetic feet.

There are three shortcomings of the study of Hansen and co-workers. Because the definition of FROS did not include terminal stance phase, it excluded the very important shape change which occurs in the anatomical foot with plantarflexion at terminal stance. The study did not measure FROS under conditions of amputee gait. Finally, the "anatomical" FROS data presented was based on a single subject reported by other investigators.

For the purposes of the present investigation, FROS was defined as the shape described by the sagittal plane projection of the center of pressure (CoP) during stance phase expressed in the local coordinate system of the leg.

The aim of this investigation was to measure FROS in a group of amputees and to compare data to able-bodied controls.

METHOD

Subjects: 11 able-bodied adults (4 female, 7 male) and nine male transtibial amputees participated in this investigation.

Apparatus: A Vicon motion analysis system and Kistler force platform were used to obtain motion and force data. Amputees wore experimental prostheses fabricated using modular componentry and Otto Bock SACH feet.

Procedures: Height and weight were measured and recorded. Reflective markers were placed on the lateral malleolus and head of fibula in normal subjects. In amputees, markers were placed on the pylon just above the distal adaptor and on the midline of the socket. Data was collected during normal velocity walking along a 10 m walkway. Trials were deemed successful if the limb contacted the force platform cleanly during stance phase. Three shod trials were collected for amputee subjects. Three shod trials and three barefoot trials were collected for able-bodied subjects.

Analysis: Marker data were reconstructed. CoP coordinates were expressed in the local coordinate of the leg with the coordinate origin at the ankle and the y axis passing through the proximal marker on the leg or socket. Data were normalised for stature, averaged across trials within subjects and across subjects within groups.

RESULTS

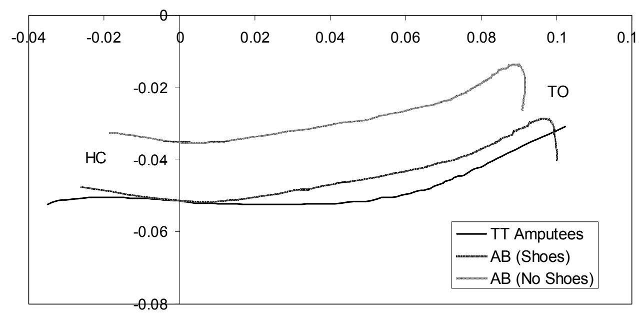

Figure 1. FROS for able bodied controls and amputee subjects. The ankle is at the coordinate origin. Heel Contact (HC) occurs at the left, Toe Off (TO) at the right.

DISCUSSION

The prosthetic FROS is different from the FROS of able-bodied controls (Figure 1). The control shape is concave throughout single support but a sharp reversal occurs as a result of plantarflexion during terminals stance. The prosthetic FROS is flat until the GRF passes the keel of the prosthetic foot. At terminal stance, the prosthetic shape appears to provide a compromise between the maximally dorsiflexed and plantarflexed points of the able-bodied FROS. It may be possible to utilise FROS information to improve bench alignment methods for prostheses. An optimisation approach could be developed to facilitate dynamic alignment. Further investigation of the FROS concept is warranted.

REFERENCES

Hansen, AH *et al.* (2000) *Pros. Orth. Int*. **24**, 205-215.

ACKNOWLEDGEMENTS

This project was supported in part by a Faculty Research Grant from the Faculty of Health Sciences, La Trobe University.

MECHANICAL ENERGY LOSS AT THE STUMP-SOCKET INTERFACE IN TRANSTIBIAL PROSTHESES

T. M. Bach[1,2], G. Halford[1] and D. Orr[3]
[1]National Centre for Prosthetics and Orthotics, [2]Musculoskeletal Research Centre
and [3]Department of Human Physiology and Anatomy
La Trobe University, Melbourne, Australia

INTRODUCTION

Reduction of energy costs for people with amputations is considered desirable. A site of possible energy loss is the interface between the prosthesis and the residual limb (Lilja *et al.* 1993). Previous x-ray studies have demonstrated differences in displacement of residual limbs within different socket designs (Narita *et al.* 1997). These differences could result in differences in energy loss but concurrent force and displacement data is necessary for definitive measurements.

The aim of this study was measure mechanical energy losses at the stump-socket interface for two socket types. A further aim was to ascertain if mechanical energy loss was related to metabolic energy cost of walking. Based on the earlier work of Narita *et al.* 1977) it was hypothesized that a PTB prosthesis would result in larger displacements, larger mechanical energy losses and higher metabolic energy costs during walking compared to a Silicone suspension system.

METHOD

Subjects: Nine male transtibial amputees participated in the investigation.

Apparatus: A Vicon motion analysis system and a Kistler force platform were used to collect motion and force data. Douglas bags and Beckman O2 and CO2 analysers were used to measure oxygen consumption during ambulation. Amputees were fitted with two prostheses: a standard PTB with cuff and a hydrostatic socket with Comfort Plus silicone liner and pin suspension. Prostheses consisted of modular components and Otto Bock SACH feet.

Procedures: Two reflective markers were placed on the thigh along a line connecting the lateral epicondyle of the knee and the Greater Trochanter. Two markers were placed on the stump with the prosthesis doffed. Data was collected while the subject flexed and extended his knee. Circles fitted to the stump marker data enabled calculation of the knee center in the local coordinate system of the thigh. Stump markers were removed, one prosthesis was donned and two markers were placed on the lateral midline of the prosthesis. Subjects marched on the spot with the prosthetic foot contacting the force platform while data was collected for 10 s. Subjects were fitted with a headpiece with a one-way valve connected to a Douglas bag. They ambulated for 300 m back and forth along a 15 m course while energy expenditure was measured. The process was then repeated for the prosthetic socket. Order of presentation was rotated between subjects.

Analysis: From the force and motion data, longitudinal displacements of the socket with respect to the knee center were calculated. Force-displacement graphs were generated and from these, energy losses for each loading cycle were computed by integration. Differences between socket conditions were analysed using t-tests for matched pairs.

RESULTS

The prosthetic coupling displayed viscoelastic properties as evident from the load displacement curves. The PTB prosthesis was associated with larger displacements (mean = 2.7cm) and mechanical energy losses (mean = 4.2 J) than the TSB silicone system (1.8 cm and 2.1J respectively). Differences were statistically significant ($p<0.05$). No differences in metabolic energy cost were found.

DISCUSSION

In this investigation, substantial energy losses were observed at the stump-socket interface. We have estimated that, for PTB sockets, these losses represent approximately 5% of the mechanical energy cost of amputee gait. Silicon liners significantly reduced pistoning of the stump within the socket and halved the energy losses. Although differences were statistically significant, they may be too small to be considered clinically significant. Measurement of metabolic energy expenditure may not be sufficiently sensitive to reliably detect the small differences in metabolic energy expenditure which may be associated with the different socket types.

REFERENCES

Lilja, Johansson & Oberg, (1993) P&O Int. Vol. 17, p21-26.
Narita, Yokogushi, Shii, Kakizawa, Nosaka, (1997) P&O Int.. Vol.21, 175-178.

ACKNOWLEDGEMENTS

This project was supported by a Faculty Research Grant from the Faculty of Health Sciences, La Trobe University.

MODELING AND VISUALIZATION OF THE MECHANICAL BEHAVIOUR OF SKELETAL MUSCLE USING A CONTINUUM APPROACH

Robson Lemos[1] , Marcelo Epstein[2], Walter Herzog[3], and Brian Wyvill[1]

[1]Department of Computer Science, www.cpsc.ucalgary.ca/~lemos
[2]Department of Mechanical Engineering, [3]Faculty of Kinesiology
The University of Calgary, Calgary, Alberta, Canada

INTRODUCTION

The purpose of this study is to investigate muscle function and deformation in whole muscle. Muscle models and geometric models have been developed to analyze the characteristics of force production [1], and to determine muscle deformation based on architecture [2][3][4]. To the best of our knowledge none of the previous models include, simultaneously, a detailed description of the three-dimensional skeletal muscle architecture, and a physically consistent model to simulate the deformation behaviour during muscle contraction. We would like to incorporate several levels of representation in a single computational model of skeletal muscle in such a way that there are basic building blocks that can be well understood and are interconnected. In this study, we present a non-linear, stand-alone computational model which contains different levels of representation of skeletal muscle using the theory of continuum mechanics and the principle of virtual work.

METHODS

For the geometric, three-dimensional representation of skeletal muscle architecture, we adopted an assembly of eight-node brick-like elements. The structural representation of the muscle architecture was obtained through the association of each brick-like element with the soft tissue information that it represents. The geometric representation of muscle architecture consists of an assembly of four main elements: muscle tissue, aponeurosis tissue, tendon tissue, and muscle fibre tissue. All these separate tissues may be considered as a particular case, represented by a unified brick-like element, which contains an underlying passive tissue matrix. In order to obtain realistic muscle deformations, we formulate a non-linear finite element analysis using the theory of continnum mechanics and the principle of virtual work. In the constitutive law for all passive tissues, we assume hyperelastic behaviour, namely the existence of a stored energy function from which the stress is obtained. In the constitutive law of the active muscle fibres we adopt a basic quadratic force-length relationship with a positive slope in the descending limb.

RESULTS AND DISCUSSION

The development of a muscle model using computational mechanics allows for the inclusion of the following features: interactive visualization techniques, full implementation of the muscle architecture, and of the behaviour arising from its complexity using a fibre bundle as the basic structural unit, application of a variety of tissue constitutive and activation/recruitment relations, and geometric constraints, such as incompressibility, that can be enforced through Lagrange multipliers.

SUMMARY

In conclusion, the model is general enough to incorporate several levels of representation of skeletal muscles. The lowest level is the muscle fibre, allowing for the full implementation and representation of the muscle architecture, and the highest level is the whole muscle allowing for the calculation of work, analysis of control phenomena, and description of generalized muscle deformation. The principle of virtual work, in the presence of geometric constraints, represents a physically consistent model to simulate the deformation behaviour of skeletal muscles.

REFERENCES

[1] Delp and Loan, Computers in Biology and Medicine, 25, 1, pp. 21-34, 1995. [2] Otten, Exercise and Sport Sciences Review, 16, pp. 89-139, 1988. [3] van der Linden *et al.*, J. of Electromyography and Kinesiology, 8, pp. 101-109, 1998. [4] Chen, Ph.D. dissertation, MIT, 1991.

ACKNOWLEDGEMENTS

CAPES – Brazil, U. of Caxias do Sul, and NSERC of Canada.

THE EFFECT OF GAIT TRANSITION ON DUTY FACTOR IN THE HORSE (*EQUUS CABALLUS*)

Witte T.H. Lichtwark G.A. Wilson A.M.
Structure and Motion Lab, The Royal Veterinary College, North Mymms, Hatfield, Herts, AL9 7TA England

INTRODUCTION

Ground reaction force (GRF) equals body weight in a standing animal. In locomotion, however, limbs must be lifted and repositioned for forward motion and can therefore only apply a vertical force for part of the stride. Averaged over the complete stride the mean GRF must still equal the body weight ie the sum of the vertical impulse applied by all the limbs must equal the product of body weight and stride time. The proportion of time a limb spends in stance is given by the duty factor; this is $T_{stance}/(T_{stance} + T_{protraction})$ The ground reaction force curve shape is cosine shaped and relatively invariant, so as duty factor drops peak limb force rises (Alexander *et al*, 1979).

In faster locomotion the leg sweeps back more quickly and despite some increase in sweep angle (Farley *et al*, 1993) a reduction in duty factor has been observed in all species studied. This results in an increase in limb force with speed. The cost of locomotion is closely related to peak limb force in a range of animals (Kram & Taylor, 1990). This relationship has been exploited to predict the energetic cost of locomotion in humans (www.fitsense.com; Weyand *et al*, 2001).

In man gait transition is complicated by changes from inverted pendulum to springing gait, but animals are able to employ several spring-like gaits; trot, canter and gallop. The deployment of limb pairs however changes from symmetrical to asymmetrical at the trot-canter transition.

Two explanations for why an animal changes gait have been proposed. Studies on horses indicate that the minimum energetic cost (expressed as J per meter traveled) coincides with the preferred speed within each gait (Hoyt and Taylor, 1981). The shape and intersections of the curves are much less distinct when expressed as actual cost of locomotion against speed. The transition from trot to canter in horses occurs not at an energetic minimum but rather at a speed appropriate to minimise limb force - weighted horses make the trot/canter transition at a lower speed than when unloaded (Farley and Taylor, 1991). This is a more convincing explanation because limb force will be mirrored by the volume of muscle activated to resist that force and because biological transducers exist (muscle spindles, Golgi tendon organs) which are appropriate to monitor the force experienced by muscle-tendon units. In this study we hypothesise that each gait transition results in an increase in duty factor as a function of speed (and hence a reduction in peak limb force).

METHODS AND RESULTS

Six thoroughbred-type horses were exercised on a high speed treadmill at speeds ranging from 1.8 to $13 ms^{-1}$. Speed was incremented with steps of $0.5 ms^{-1}$. Stance time, protraction time and duty factor were determined using radio telemetry of data from foot mounted accelerometers.

RESULTS

These data are all for the forelimbs. Limb protraction time was about 400ms at walk and slow trot, dropped to 350ms at the highest speed of trot and remained around that value for all speeds of canter and gallop. Stance time dropped in a curvilinear manner with speed from 400ms to 200ms through trot and 200ms to 110ms through canter and gallop. Sweep angle increased linearly with speed from 36 to 64 degrees. Duty factor dropped from 0.65 at walk to 0.22 at gallop. There was no effect of gait transition on the gradient of the relationship between speed and any of the parameters measured. Duty factor was 2% shorter in the lead leg than the non lead leg during canter and gallop locomotion. At canter the peak force on the lead leg of a pair (the second leg to hit the ground) is 20% lower than on the non-lead leg. (Merkens *et al* 1993). The Alexander equation does not reproduce this difference. This is because the centre of mass displacement, and hence effective vertical limb stiffness (Farley *et al*, 1993) is different during the stance of each limb.

CONCLUSIONS

There is no evidence for a change in duty factor at gait transition. Transition to canter and gallop gaits will unload one limb but at the expense of a concomitant increase in load on the contralateral limb. This may explain why lame trotting horses prefer to canter as they can unload the painful limb. Gait transition may also enable horses to achieve the higher sweep angles needed for high speed locomotion, contribute to elastic energy storage in the tissues of the spine (Alexander, 1985) and / or reduce external work on the center of mass.

REFERENCES

Alexander etal (1979). *J. Zool., London.* **189,** 135-144.
Alexander et al (1985) *J. Zool. London.* **207**, 467-482
Farley et al (1993) *J. Exp. Biol.* **185,** 71-86.
Farley and Taylor (1991) Science **253**, 306-308
Hoyt, D.F. & Taylor, C.R. (1981) *Nature* **292**, 239-240
Merkens et al (1993) Am J Vet Res **54**, 670-4
Kram, R. & Taylor, C.R. (1990) *Nature* **346**, 220-221
Weyand *et al* (2001) *J Appl Physiol* **91**, 451-8.

ACKNOWLEDGEMENTS

We acknowledge funding from the Horserace Betting Levy Board, London and the BBRSC.

HISTORY-DEPENDENCE OF FORCE PRODUCTION IN SKELETAL MUSCLE

Dilson E. Rassier and Walter Herzog

Human Performance Laboratory, University of Calgary, Calgary, AB, Canada

INTRODUCTION

When activated skeletal muscles are stretched on the descending limb of the force-length relationship, the resulting force is higher than the isometric force produced at the corresponding final length (Edman et al, 1982; Herzog and Leonard, 2000; Morgan et al, 2000). Experiments with the cat soleus have shown that muscle shortening preceding muscle stretch decreases the level of force (Herzog and Leonard, 2000), suggesting the engagement of a passive element associated with force enhancement. However, experiments with single cells from the frog show that force enhancement is not affected by previous shortening, when an interval is introduced between the length changes (Edman et al. 1982). The present study was aimed at re-evaluating the effects of shortening on the stretch-induced force enhancement in single cells, with and without intervals between length changes.

METHODS

Single cells dissected from the flexor digitorum brevis muscle of the frog were used in this study. Isometric contractions (2 s) were performed to derive a force-length relationship for each cell. Starting on the descending limb of the force-length relationship, stretch and shortening contractions were performed with amplitude of 10% of fiber length, at a velocity of 40% fiber length/s. Shortening-stretch cycles were also performed on the descending limb of the force-length relationship. These shortening-stretching cycles were done without intervals between length changes, and with intervals of 500 ms and 1000 ms between the shortening and the stretch contractions. Contractions were sustained for at least 4.5 s after the final stretch.

RESULTS AND DISCUSSION

When cells were activated, and then stretched, the steady-state isometric force following the stretch was higher than the isometric force at the corresponding final length (Fig. 1). When cells were activated, and then shortened, the steady-state force was lower than the isometric force at the corresponding final length. When muscle shortening was followed immediately by muscle stretching, the level of force enhancement was decreased (Fig. 1). However, when intervals were introduced between the shortening and stretching phases, the effects of shortening on the stretch-induced force enhancement decreased. Different amplitudes of shortening had similar effects on force enhancement (Fig 2).

In conclusion, shortening preceding stretching affects the stretch-induced force enhancement, but this effect is diminished by the introduction of intervals between the length changes. These results suggest that force enhancement is partially caused by the engagement of a passive element during an active stretch. Engagement of this passive element decreases with shortening; thus, shortening decreases force enhancement. The effects of shortening on the passive element engagement appear to decrease when the fiber is held isometrically between the shortening and stretching phases.

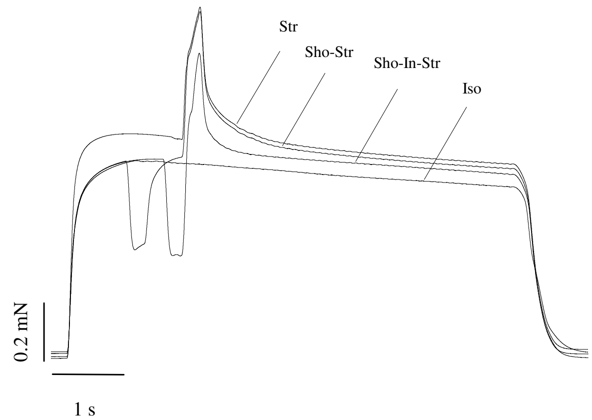

Figure 1: Force enhancement in a single muscle fiber. The traces were recorded after a single stretch (Str), and after stretches preceded by shortening with (Sho-In-Str) and without (Sho-Str) interval (500 ms). The isometric force at the final length is also shown (Iso).

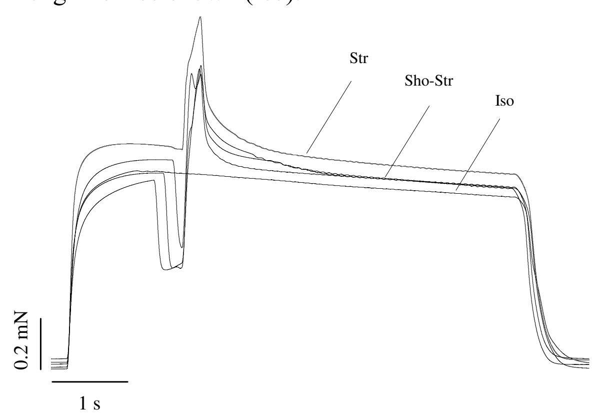

Figure 2: Force enhancement in a single muscle fiber. The traces were recorded after a single stretch (Str), and after stretches preceded by shortening of different amplitudes (Sho-Str). The isometric force at the final length is also shown (Iso).

REFERENCES

Edman, K.A.P. et al. (1982). *J. Gen. Physiol.* **80**, 769-784.
Herzog, W., Leonard, T.R. (2000). *J. Biomech.* **33**:531-542.
Morgan, D.L. (2000). *J. Physiol.* **522**:503-513.

SMELLING WITH HAIRY LITTLE NOSES: THE PHYSICAL DESIGN OF OLFACTORY ANTENNAE

Mimi A. R. Koehl

Department of Integrative Biology, University of California, Berkeley, CA, 94720-3140, USA,
http://ib.berkeley.edu/labs/koehl

INTRODUCTION

Appendages bearing arrays of hair-like structures serve important biological functions in many animals from a variety of phyla: feathery gills take up oxygen, chemosensory hairs on olfactory antennae capture odorant molecules, filamentous suspension-feeding structures catch single-celled algae, setulose appendages create ventilatory or feeding currents, and bristly legs or wings propel little animals through the surrounding water or air. To perform any of these functions, an array of hairs must interact with the surrounding fluid. We have been studying the fluid dynamics of arrays of cylinders to elucidate basic rules governing how hairy appendages work (Cheer & Koehl 1987; Koehl, 1995). The present study uses these rules to determine how the physical designs of olfactory antennae affect how they filter chemical information from the environment (Koehl 1996; 2001).

Many animals use chemical cues in the water or air around them to detect mates, competitors, food, predators, and suitable habitats. The first step in processing olfactory information, before neural filtering, is physical capture of odorant molecules from the surrounding fluid. Many crustaceans capture scents by flicking antennules that bear arrays of chemosensory hairs. We studied how the hydrodynamics of crustacean olfactory antennules flicking in turbulent odor plumes physically alters the spatio-temporal patterns of concentration arriving in the receptor area.

METHODS

We conducted high-speed video analyses of antennule flicking kinematics and SEM determination of antennule morphometrics (Goldman & Koehl 2001). Dyanmically-scaled physical models and mathematical models were used to quantify the small-scale flow fields around antennule chemosensory hairs and the diffusion of odorant molecules to hair surfaces (Koehl 2001). Planar-laser-induced flouresence was used to measure the fine-scale structure of odor plumes in turbulent water currents in a flume, and the instantaneous patterns of odorants arriving among the sensory hairs on antennules flicking in such plumes were recorded using high-speed, high-magnification video (Koehl *et al*. 2001).

RESULTS AND DISCUSSION

Lobsters and mantis shrimp flick their olfactory antennules in a critical Reynolds number range for their particular arrangements of chemosensory hairs (Reynolds number, Re, represents the relative importance of inertia to viscosity). They flick in the Re range in which the ability of water to penetrate into the hair array changes with velocity. We found that water flows through the hair array during the rapid flick, but not during the slower return stroke. In turbulent water currents, odor plumes are made up of fine-scale filaments of scent whose pattern varies with distance from the source. Water carrying these patterns of concentration penetrates into the array of chemosensory hairs only during the rapid flick, and is retained until the next flick.

SUMMARY

We used the antennules of spiny lobsters and mantis shrimp to analyze the critical first step in determining the spatial and temporal patterns of odor pulses arriving at receptors: physical interaction of the olfactory organ with an odor plume. The chemosensory hairs these olfactory antennules operate in a range of Re and hair spacings in which changes in velocity can have profound effects on the flow near the hairs, and thus on their performance in capturing molecules from the surrounding fluid. Our work has revealed how lobster olfactory antennules hydrodynamically alter the spatio-temporal patterns of concentration in turbulent odor plumes. Antennules flick: water penetrates into their chemosensory hair array only during the fast downstroke, carrying fine-scale patterns of concentration into the receptor area. Hence, because of the hydrodynaimcs of their antennules, these animals take discrete odor samples in space and time (i.e. they sniff).

REFERENCES

Koehl, M.A.R. *et al*. (2001) *Science*, **294**, 1948-1952.
Koehl, M.A.R. (2001) *Computational Modeling in Biological Fluid Dynamics*. L. Fauci and S. Gueron [eds.], IMA Series #**124,** 97-116.
Goldman, J., Koehl, M.A.R. (2001) *Chem. Senses* **26**, 385-398.
Koehl, M.A R. (1996) *Mar. Fresh Behav Physiol*. **27**, 127-141.
Koehl, M. A. R. (1995) *Soc. Exp. Biol. Symp*. **49**, 157-182.
Cheer, A.Y.L., Koehl, M.A.R. (1987). *J. Theor. Biol.* **129**, 17-39.

ACKNOWLEDGEMENTS

I thank my collaborators on various aspects of this work: A. Cheer, J. Koseff, K. Mead, T. Cooper, M. Stacey, J. Crimaldi, M. McCay, C. Loudon,T. Cooper, M. Wiley.

FAILURE ANALYSIS OF THE LOWER LIMB IN AXIAL IMPACT LOADING

R.Hopcroft[1], D. Hynd[2], C. Willis[2], P.Manning[1], A.Roberts[2], R.Lowne[2], W.A.Wallace[1]

1. Institute of Biomechanics, University of Nottingham, England
mszrwh@gwmail.nottinham.ac.uk
2. Transport Research Laboratory, Berkshire, England

INTRODUCTION

Over the last thirty years, improvements in legislation and technology have successfully reduced the number of deaths (due to head and thoracic) injuries occurring to the occupants of cars involved RTAs. However, the number of disabling lower limb injuries continues to rise.

This study was designed to enable thresholds for fractures to the calcaneus, talus and tibial plafond to be established. These fractures have been shown to result in significant long term morbidity in a large UK accident study (Taylor 1997).

Within the Instituite of Biomechanics a dedicated sled test facility has been constructed. The sled is capable of creating a validated and repeatable crash pulse. The pulse was modelled on the toe-pan recordings from a full-scale crash test using a standard mid range car in frontal impact. This sled was used to subject post mortem human surrogate (PMHS) lower limbs to dynamic frontal car impact loading. Previous work (Manning 1997) has recognized the importance of inertial loading of the lower limb and pre-impact tensioning.

METHODS

The PMHS specimens were screened to exclude prolonged pre-morbid bed rest, previous trauma or surgery. All specimens were prepared preserving the knee joint and were fresh frozen.

The sled impaction rig provided impact velocity of up to 50 Km/h with delayed application of axial loading. This delay was 50 ms after the initial deceleration of the sled, realistically simulating brake pedal intrusion. The axis of load was applied directly via a simulated brake pedal to the mid-foot in axial line with the anterior tibial border.

Realistic braking pressures were simulated by applying a plantar flexing moment at the ankle via a tension of 1KN in the achilles tendon.

Instrumentation of both the PMHS specimens and the sled rig has allowed for extensive biomechanical data collection up to and including the point of failure (fracture). Forces monitored include, direct loads applied, sled decelerations, PMHS accelerations and brake pedal intrusion.

High-speed film recording enabled additional kinematic analysis. Acoustic monitoring of the specimens provided additional data used in injury timing and to help in injury identification.

Only one impact was applied to any specimen. Specimens were randomised into one of four impact severity groups. . In 50 % of the tests, the applied loading was reduced to a sub injury impact.

At the conclusion of each test the specimens were examined for injury using X-rays and necropsy.

RESULTS

This paper presents the methodology and techniques employed in the test program.

The results from twelve PMHS specimen impacts are presented. In addition, a preliminary analysis of the biomechanical data together with detailed description of the fractures created is described. The authors put forward injury threshold levels to be considered in the drafting of future requirements for cars in legislative car crash testing.

DISCUSSION

Delaying the application of axial loading after the initial impact and sled deceleration effectively imparts momentum into the specimen preloading the foot and ankle. This increases the bracing effect, provided by the Achilles tendon tensioning.

This series accommodated the movement of hip, knee and ankle that intrusion of the foot-well and pedal mechanism may impart. There was no attempt to recreate the effect that the knee/dashboard interaction may have on ankle injuries.

A Weibull curve of injury risk against axial load was produced. The paper discusses is its significance in the prediction of injury in impact testing using dummy limbs.

REFERENCES

Taylor,A.M., et al (1997). *STAPP proceedings '97,*181-194
Manning,P.A. et al (1997).*STAPP proceedings '97,*195-206

ACKNOWLEDGMENTS

Mr. M. Parry – Institute of Biomechanics, University of Nottingham, England.

TAKE-OFF OPTIMIZATION PATTERNS IN SKI JUMPING: GENERAL VERSUS INDIVIDUAL MODELS

Frantisek Vaverka and Miroslav Janura

Dept. of Biomechanics and Engineering Cybernetics, Faculty of Physical Culture, Palacky University, Olomouc, the Czech Republic
tr. Miru 115, 771 11 Olomouc, the Czech Republic, vaverka@ftknw.upol.cz

INTRODUCTION

The designation of a model of ski-jumping take-off as optimal is a key problem in the training process. The basic question to be posed can be characterized as follows: Is there only one acceptable take-off model which should be the goal of all training efforts of both coaches and competitors, or is it possible to define several variants of a ski jumping take-off models and then work with individual models suited to individual competitors? The data so-far gathered in numerous research studies (for example Vaverka et al, 1997; Virmavirta, 2000) indicate that the degree of inter-individual variability of biomechanical characteristics is substantial for both the in-run and take-off phases of ski-jumping and that there is a very low level of statistical dependence between the in-run, the take-off and the performance in ski-jumping. In practice this means that competitors with similar individual take-off models achieve very different performance results and, conversely, competitors who perform the take-off variously have similar performance results. The solution of this problem, interesting from both the theoretical and the practical points of view, is the object of this analysis.

METHODOLOGY

This solution is based on kinematic analyses of the take-off and in-run phases of ski-jumps as performed in the Intersport tournament competitions held in Innsbruck 1991-2000. Over the course of a decade, a kinematic analysis (2D) of the take-off phase (480 analyses) and the in-run phase (940 analyses) was carried out annually on the same jumping hill, during the same events, observing the best international competitors. An analysis of the take-off in the last four meters provided us with 27 variables (course, angle, time, velocity, angular velocity), and the analysis of the in-run phase produced eight variables. The resulting jump performance was characterized by the length of the jump expressed in percentages of the critical point of the jumping hill (CLJ). The statistical analysis of biomechanical data was aimed at solving the relationship between measured variables and the resulting jumps at the level of inter-individual variability as seen in the sets of all starting jumpers (n=40-55, correlation and factor analysis), comparison of selected sets of competitors on various performance levels (best and low level of performance, n=6-10) and comparison of individuals – intra-individual variability (take-off phase, 18 jumpers, the average number of take-offs for each individual was 7.6; in-run position, 10 jumpers, analysis of variance). Further information as to the methodology used can be found in the following literature: Vaverka et al. (1997) and Janura et al. (1998).

RESULTS AND DISCUSSION

Analyses of correlational relationships between sets of biomechanical characteristics of the in-run and take-off phases and jump length proved a very low dependence between the execution of movement and jump length (in-run: 8%, take-off: 17% explained variability of the CLJ). The result of the analysis of the inter-individual variability of biomechanical variables signals a great degree of individuality in the performance of movements by jumpers. The analysis of individuals (intra-individual analysis) has proven very limited individual models of the performance of the studied ski-jumping phases. Based on the example of a comparison of five competitors of various performance levels (Fig. 1) it is evident that every athlete carries out movement in a personal, specific way.

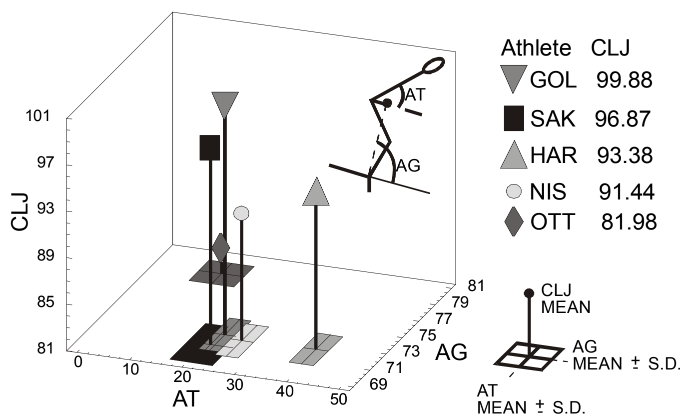

Figure 1: An example of the intra-individual variability of some selected athletes. Take-off, 0.0 m, variables: AT, AG, CLJ (criterion of the length of jump).

SUMMARY

The results of a great quantity of inter- and intra-individual analyses have indicated predominant individual variations in the in-run and take-off patterns for individuals. The resulting findings influence, in a substantial way, our opinion of the formulation of an optimal model for observed ski-jumping phases and make a significant impact on forming and correcting ski-jumping technique in training practice.

REFERENCES

Janura, M. et al. (1998). *Proceedings of ISBS'98,* 124-127.

Vaverka, F. et al. (1997). *Science and Skiing*, 61-71. E & FN Spon.

Virmavirta, M. (2000). *Limiting Factors in Ski Jumping Take-off.* Jyväskylä.

EFFECTS OF EQUIPMENT AND PERFORMANCE CHARACTERISTICS ON SKI JUMPING PERFORMANCE

Pekka Luhtanen[1] and Juha Kivekäs[2]

[1]KIHU-Research Institute for Olympic Sports, Jyväskylä, Finland
[2]Helsinki University of Technology, Espoo, Finland
[1]Senior Researcher, pluhta@kihu.jyu.fi
[2]Researcher, jkivekas@aquila.pp.fi

INTRODUCTION

The FIS rule concerning ski jumping equipment has been changed during the last years. First, the ski length was defined one's body height plus 85 cm with the unregulated toe binding location. The thickness of the suit was 8 mm, and permeability 30 l/m^2/s. Next, the rule changed to height plus 80 cm with the binding location of 57% of the ski length and the suit did not change. Last, the 146% rule and change in suits (thickness 5 mm and permeability 40 l/m^2/s) were adopted provisionally for a trial year 1998-1999. It allows jumpers taller than 173 cm to use longer skies while jumpers less than 173 cm are forced to use shorter skis than previously. The current 146% rule seems unfair to shorter jumpers.

The purpose of this study is to clarify effects of equipment and performance characteristics based on wind tunnel measurements using a 2/3 scale model and Aquila simulator.

METHODS

The equipment of the 2/3 model for the wind tunnel measurements was as follows: skis, helmet, shoes and official competition clothing. The measurements were performed in a subsonic Göttingen type closed circle wind tunnel where the cross section in the measurement area was 3.68 m^2 (Luhtanen et al., 1995). The model was attached to an overhead six-component platform-balance. The force measurement accuracy was better than 1% with the blockage ratio at most 5% and sampling rate for the force measurements 1 Hz. The force values were averaged for six seconds. The typical angle of attack range of the ski plane was 22 - 42 degrees. It was measured between each 2 degree. The relevant measurement parameters kinetic pressure, flow velocity and Reynolds number were taken into account. The drag, lift and pitching moment were transformed into dimensionless coefficients. The lift to drag ratio was calculated.

Two suit materials with the permeability of 40 l / m^2 / s were measured without and with the reference ski (length 169 cm, width at front 71 mm, at binding 65 mm and at rear 71 mm). The frontal binding of the ski location was 57%. The additional skis with the frontal binding location of 57% were in length 170, 175 and 180 cm (width at front 86 mm, at binding 78 mm and at rear 86 mm).

For simulation of jumps, the Aquila simulator was applied to Lillehammer K 120 jumping hill.

RESULTS AND DISCUSSION

The length of ski did not differentiate the polar curve clearly. It was observed that the longer the ski the higher is starting point on the polar. If the aerodynamic force production of the skis was about 40% and the difference in surface area between the shortest and longest ski was about 5% the increase in the magnitude of aerodynamic force was about 2%. It was observable that the longer skis tended to have larger range of negative pitching moment coefficient slope against incidence. The results, in the lift, drag and resultant force indicated that 60% of aerodynamic forces were acting on the jumper body and 40% on skis. With shallow incidence angles (ski plane incidence 22 degree) the drag proportion of body was about 73%. It decreased gradually when increasing incidence ending down to 57% at steep angles (ski plane incidence 42 degree). The change of lift was opposite. At shallow angles the proportion of lift on the body was about 55% and steep angles up to 60%.

SUMMARY

Concerning several jumping hills it was found that the increment of 22-29% in ski area increased about 40% in total aerodynamic forces adding jump length 9-12%. The effects of large variation in air permeability were on the drag even 7-12% and lift 12-25%. The selected averaged effects on the jump lengths in a K 120 hill due to the equipment and performance characteristics are shown in Table 1.

Table 1. The effects of relative changes (Δ p, %) in lift (Cl), drag (Cd), reference area (S), mass, friction and takeoff force on the absolute (Δ JL, m) and relative jump length (Δ JL, %) in a K 120 m hill

Variable	Δ p, %	Δ JL, m	Δ JL, %
Cl	+1	1.5	1.25
Cd	-1	0.8	0.67
S_reference	+1	0.9	0.75
Mass	-1	1.2	1.03
Sliding friction	-1	0.6	0.50
Takeoff force	+1	0.4	0.33

REFERENCES

Luhtanen, P. et al. (1995). *Book of Abstracts of the Vth International Symposium on Computer Simulation in Biomechanics*, 34-35. University Press of Jyväskylä.

HEAD RESTRAINT POSITION AFFECTS OCCUPANT RESPONSE IN REAR-END COLLISIONS

Dennis D. Chimich[1], Bradley E. Heinrichs[1], John R. Brault[1], Alyssa L. DeMarco[1], Gunter P. Siegmund[1,2]

[1]MacInnis Engineering Associates, Richmond, BC, Canada (gunters@maceng.com)
[2]School of Human Kinetics, University of British Columbia, Vancouver, BC, Canada

INTRODUCTION

Head restraints were installed in vehicles to prevent whiplash injuries at a time when the mechanism for whiplash injury was thought to be head/neck hyperextension. Although head restraints reduced the frequency of whiplash injuries, the reduction was small (<25%, Kahane, 1982). One reason proposed for this relatively small reduction was the poor vertical adjustment of most head restraints, many of which remained in the full-down position despite being adjustable (Viano and Gargan, 1995). The goal of this study was to examine the effect of vertical head restraint position on the kinematic and kinetic responses of vehicle occupants during a low-speed rear-end collision and to examine how these differences might affect injury potential.

METHODS

A BioRID II rear-impact dummy was placed in the right front seat of a 1990 Honda Accord and exposed to a series of rear-end collisions (speed change = 8 km/h; duration = 125 ms). Three head restraint conditions were studied: full up (UP), full down (DOWN) and no head restraint (NONE). Five collisions were performed for each head restraint condition and test order was randomized. Prior to each test, the position and angle of the dummy pelvis were set and the dummy's head was then positioned 4.5 cm forward of the head restraint while in the UP position. After the dummy's pre-test position was established, the head restraint condition was changed for the test. Head extension relative to T1, and retraction, defined as the rearward horizontal displacement of the head centre of mass relative to the T1 spine block in the lab reference frame, were measured using sagittal-plane high-speed video. Shear (Fx) and axial (Fz) forces applied to the head by the neck at the head/neck junction, i.e., the atlanto-occipital joint, were measured using a 3-axis upper neck load cell and reported in the head reference frame. A one-way analysis of variance was used to assess differences in the response of each dependent variable between the three head restraint conditions. Scheffé tests were used for post-hoc testing and a significance level of $p=0.05$ was used for all tests.

RESULTS AND DISCUSSION

Peak head extension was 5.3 ± 0.5º in the UP condition, smaller than in both the DOWN (8.6 ± 0.9º) and NONE conditions (45 ± 1º) ($p<0.0001$). Peak retraction was also smaller in the UP condition (6.23 ± 0.05 cm) than in either the DOWN or NONE conditions ($p<0.0001$) (Figure 1a). Peak shear force (Fx) at the atlanto–occipital joint was 119 ± 3 N in the UP condition, and was significantly lower than in either the DOWN or NONE conditions ($p<0.0001$) (Figure 1b). Peak amplitudes of the shear forces in the DOWN and NONE conditions were not significantly different ($p=0.42$), however, peak shear force occurred earlier in the DOWN condition than in the NONE condition. The tensile axial force (Fz) at the atlanto-occipital joint was 274 ± 6 N in the UP condition; 109 N lower than when in the DOWN condition ($p<0.0001$) and 139 N higher than when in the NONE condition ($p<0.0001$) (Figure 1c).

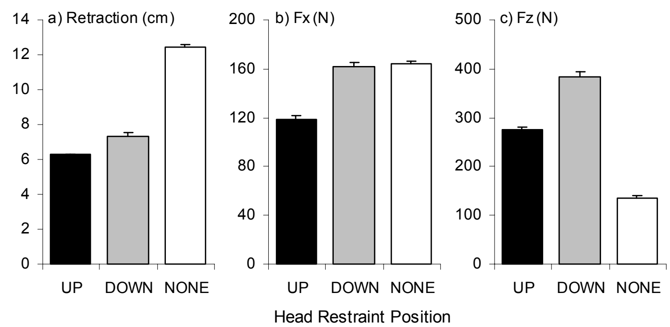

Figure 1: Mean (SD) of retraction, neck shear force (Fx) and axial force (Fz) for the UP, DOWN and NONE head restraint conditions. Fx, positive forward; Fz, positive downward.

SUMMARY

Based on the current data, head restraint position affected both the kinematic and kinetic responses of the BioRID II dummy in an 8 km/h speed change. As was the design intent, the head restraint decreased peak head/neck extension in both the UP and DOWN positions compared to no head restraint. The effect of head restraint position on peak retraction was similar. Upper neck forces, however, varied differently with head restraint position. Peak shear force at the atlanto-occipital joint was only reduced when the head restraint was properly positioned, i.e., in the UP position. Peak tensile forces at the atlanto-occipital joint were largest when the head restraint was present, but in the DOWN position, i.e., poorly adjusted. These data suggest that head/neck kinematics are sensitive to the presence of a head restraint, whereas upper neck loads are sensitive to the position of the head restraint. The larger neck loads observed with poor head restraint position may explain the marginal reduction in whiplash injury frequency observed with the introduction of head restraints.

REFERENCES

Kahane CJ (1982). Report No. DOT HS-806-108, National Highway Traffic Safety Administration, Washington, DC.
Viano DC, Gargan MF (1996). *Accid Anal Prev* 28:665-74.

ACKNOWLEDGEMENTS

The authors wish to thank Lotta Jakobsson of Volvo and Johan Davidsson and Anders Flogård of Chalmers Technical University in Göteborg, Sweden for the use of the BioRID II.

BIOENGINEERING OF AN EXPERIMENTAL BIOARTIFICIAL HEART MUSCLE.

Joseph Brackhan[1], Albert J. Banes[2], Wayne E. Cascio[1]

Department of Medicine[1], Department of Orthopeadics[2],
University of North Carolina at Chapel Hill, Chapel Hill NC, USA.

INTRODUCTION

We have devised a method using neonatal rat cardiomyocytes to create a putative 3-dimensional construct of cardiac muscle. This construct, which we designate as a BAT or bioartificial trabeculum, rhythmically contracts in culture at about a 100 beats per min. Our purpose is to develop a model system for studying the effect of mechanical loading on cardiac physiology, and we feel a 3-dimensional tissue system is an effective vehicle for studying this question.

METHODS

Rat cardiomyocytes are isolated from 1-day-old rat pups using the Worthington Cardiomyocyte Isolation Kit and a slightly modified protocol. The rat neonatal cardiomyocytes are mixed into a solution of vitrogen collagen and plated into Flexcell Tissue Train plates and placed in a 37 C incubator with 5% CO_2 for 2 Hrs before adding M199 medium with 10% FBS. The Tissue Train plates have two nylon tethers at opposite ends of each well and a flexible silicon rubber bottom. When making the BAT the Tissue Train plate is mounted over a plastic mold shaped like a trough, which runs between the two nylon tethers. Vacuum is applied and pulls the silicon bottom of the plate into the trough forming a mold that the vitrogen can be pored into. After adding medium the strand "floats" in the medium attached to flexible nylon anchor stems at each end. (See Figure 1). Pulsatile stretch can be applied to the BATs in the Tissue Train plates by using a computer controlled vacuum source and a special mount to hold the plate in place.

Results- After 4 days in culture, the heart cells migrate toward the center of the gel and form a dense cord of "tissue" that extends between the two loading posts. This strand of tissue beats in a coordinated manner that is easily observed with a low power microscope. Immunostaining with an antibody against Troponin I revealed striations characteristic of cardiac tissue and staining with an anti-Connexin 43 antibody shows cell to cell coupling through gap junctions characteristic of cardiac tissue. We have tested several stretching regimens on BATs and found that the BATs can tolerate pulseatile stretching and we plan to determine what effects stretch stimulation has on aspects such as beat rate and contractile strength.

CONCLUSIONS

Our long-term goals are to apply this system to study the effects of mechanical loading on normal cardiac physiology and to develop a model system for the study of cardiac pathologies such as congestive heart failure.

Figure 1. Flexcell tissue train plate with BATs.

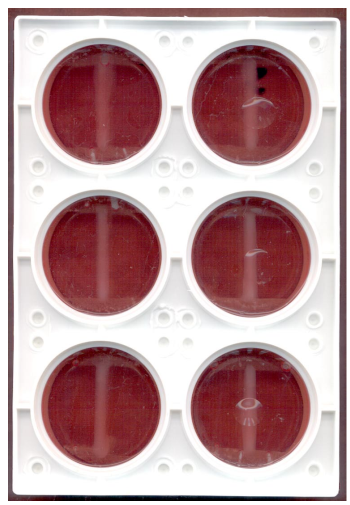

COMPUTATIONAL MODELING AND EXPERIMENTAL VALIDATION OF HUMAN EYE INTERACTION WITH HIGH-SPEED FOAM PARTICLES

Joel D. Stitzel, Erik D. Power, Joseph M. Cormier, William J. Hurst, Ian P. Herring, Stefan M. Duma
Virginia Tech, Impact Biomechanics Laboratory, Blacksburg, VA   Email: duma@vt.edu

INTRODUCTION

A recent trend in automotive interior design has the air bag placed behind a seamless module cover. During the air bag deployment process, it is possible for foam particles from the dashboard to be released at high velocities, potentially resulting in eye injuries (Duma, 2000). The purpose of this study was to validate a computational model of the human eye suitable for investigating high-speed impacts from foam particles.

METHODS

A total of five simulations were performed at a range of impact velocities to correspond with five impact experiments performed with human cadaver eyes. The model of the human eye consists of a cornea, sclera, lens, ciliary body, zonules, aqueous humor and vitreous body (Power, 2000). A total of 464 membrane elements were used for the cornea and sclera and 152 brick elements comprised the aqueous and vitreous. Nonlinear, isotropic material properties of the sclera and cornea were gathered from uniaxial tensile strip tests performed up to rupture (Uchio, 1999). Components surrounding the eye such as the bony orbit, fatty tissue and extraocular eye muscles were included in the model. Foam hardness for the simulations matched that used in the experiments. The model was generated in I-DEAS (SDRC, Milford, OH) and then material properties and geometry were imported into Madymo (TNO, Troy, MI) for dynamic impact simulations. The velocities modeled in Madymo were those attained during experimental testing.

For experimental validation, eyes were enucleated within 6 hours postmortem and refrigerated less than 48 hours postmortem prior to usage. Eyes were pressurized to normal physiological pressure prior to testing using a needle inserted tangentially at the limbus prior to testing. Foam particles with a 6.3 mm diameter, 77.5 mg mass, 192 kg/m^3 density, and 0.552 MPa hardness (at 25% compression) were projected onto the eyes. A pneumatic cannon was used to propel the foam at velocities ranging from 14 m/s to 32 m/s. The distance between the end of the pneumatic cannon and the eye was set to approximately 8 cm, as greater distances made it difficult to impact the eye consistently. All tests were recorded with high-speed digital color video at 7100 frames per second (Vision Research, Wayne, NJ). High-speed video was used to determine velocity of the foam particle, as well as globe deformation.

Additional instrumentation included ultrasound crystals that were used to measure deformation (Sonometrics, London, Ontario, Canada). Each eye was mounted in a synthetic orbit and held in place by a 10% gelatin solution designed to simulate the orbital fatty tissue. Injury analysis included fluorescein dye and ophthalmic ultrasound, as well as necropsy to further examine tissue damage.

RESULTS AND DISCUSSION

A range of five impact velocities were used with no injuries induced in any of the specimens (Table 1). Sample video frames are shown for comparison with the computational results (Table 2). The particle modeled had a velocity of 18.9 m/s as used in test number three. This value was chosen for the simulation because it represented the median value of the test velocities. Experimentally, this impacting particle caused the corneal apex to deflect 2.1 mm posteriorly, determined from the digital frames. From this simulation, the FE eye model predicted a corneal apex deflection of 2.26 mm, 7.6% greater than experimental results. From Table 2, the foam particle can be seen being deflected off the cornea after 2 ms. Both experimentally and computationally, the particle was in contact with the cornea for approximately 1 ms. Globe rupture has been shown to occur at approximately 9.5 MPa peak stress. The FE eye model in the simulation with the foam particle did not predict globe rupture, nor was globe rupture observed experimentally. The model developed will be useful as an aid to airbag design, and for other blunt impact studies such as baseballs and BB's. As the mechanisms of eye trauma are better understood, the model can be used to predict ocular trauma computationally and reduce the burden of eye injury.

REFERENCES

Duma SM, Crandall JR (2000). *J of Trauma*, 48(4): 786-789

Power ED (2001). A nonlinear finite element model of the eye to investigate ocular injuries from night vision goggles. *Masters Thesis,* Virginia Tech

Uchio E, Ohno S, Kudoh J, Aoki K, Kisielewicz LT (1999). *Br J Ophthalmol,* 83:1106-11

ACKNOWLEDGMENTS

The authors would like to acknowledge the United States Army Aeromedical Research Laboratory (USAARL) for support in developing the initial eye model.

Table 1. Foam test results with human cadaver eyes

Test	Velocity (m/s)	Displacement (mm)	Induced Injury
1	14.2	1.7	None
2	14.3	1.4	None
3	18.9	2.1	None
4	26.7	2.4	None
5	31.0	3.2	None

Table 2. Experimental and simulated results: approximately 1 ms time intervals

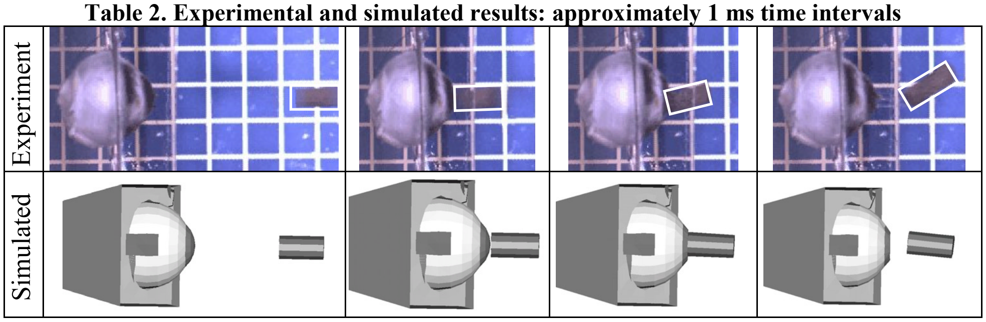

THE HIGH FREQUENCY MATERIAL PROPERTIES OF BRAIN TISSUE AS DETERMINED BY ULTRASOUND

Samuel A. Lippert[1], Elizabeth M. Rang[1] and Michele J. Grimm[2]

Bioengineering Center, Wayne State University, Detroit, Michigan, USA
[1]Graduate Research Assistant, Biomedical Engineering
[2]Associate Chair, Biomedical Engineering, grimm@rrb.eng.wayne.edu

INTRODUCTION

With the development of detailed computer models for simulating the response of the brain-skull system to impact loading, it has become vitally important to fully characterize the material properties of the brain, and thus ensure the accuracy of the models. Although brain tissue is well characterized at frequencies up to 200 Hz (Koeneman, 1966; Fallenstein *et al*, 1969; Galford and McElhaney, 1970; Wang and Wineman, 1972; Shuck and Advani, 1972; Hirakawa *et al*, 1981; Bilston *et al*, 1997; Donnelly and Medige, 1997; Arbogast and Margulies, 1998; Thibault and Margulies, 1998; and Brands *et al*, 1999), these frequencies fall short of those present in an impact event. As brain tissue exhibits viscoelastic behavior, the properties vary with respect to frequency, and thus utilizing properties obtained at lower frequencies can introduce unacceptable inaccuracies into the computer models. As mechanical rheometry is currently only possible at frequencies up to 1000 Hz, we utilized the ultrasonic wave-in-a-tube method (Lippert *et al*, 2001) to characterize the tissue at frequencies ranging from 100 kHz to 10 MHz.

METHODS

The heads of 12 lambs were obtained, 4 at a time, within 15 minutes of slaughter, from a local source. Upon removal of the brains, blunt dissection was utilized to separate the tissue white and gray matter. For each sample, the separated tissue was used to fill a tube 15.7 mm in diameter and 135 mm in length. This tube was then sealed on each end with ultrasonic transducers, and a measurement taken at each of 4 frequencies: 1 MHz, 2.25 MHz, 5 MHz and 10 MHz. Measurements at 500 kHz required use of a transducer 25.4 mm in diameter, and a correspondingly larger tube; to obtain these measurements, the tissue from 4 brains was combined, while still keeping the white and gray matter separate. The 100 kHz transducers were 50.8 mm in diameter, requiring the combination of the white and gray matter. As a general rule, the first measurement was taken within 90 minutes of the death of the animal, with the final measurement taken within 3.5 hours.

RESULTS AND DISCUSSION

Although elastic modulus, bulk modulus, Poisson's ratio as well as shear modulus can be obtained from the wave-in-a-tube technique, shear modulus is the most useful when it comes to the construction of computer models, as well as for comparison with previously reported values. Thus the shear moduli we obtained are summarized in Table 1.

Frequency	White (Avg. G*)	Gray (Avg. G*)
100 kHz	80 MPa**	80 MPa**
500 kHz	195 MPa	214 MPa
1 MHz	252 MPa	195 MPa
2.25 MHz	320 MPa	347 MPa
5 MHz	358 MPa	435 MPa
10 MHz	353 MPa	471 MPa

Table 1: Average shear modulus for various frequencies obtained by the wave-in-a-tube method. ** indicates a combined modulus for white and gray matter.

Our values for shear modulus are several orders of magnitude higher than those established previously. This is not surprising, given that our frequency of excitation was several orders of magnitude higher. This type of behavior is not uncommon with viscoelastic materials.

ACKNOWLEDGEMENTS

Primary funding for this research was provided by CDC-NCIPC grant #CCR-503534-11. Additional funding was provided by the NSF-REU program grant # EEC-9721375 and the Ford Motor Company.

REFERENCES

Arbogast, KB, Margulies, SS (1998) *J Biomech,* **31,** 801-7.
Bilston, LE et al. (1997). *Biorheology,* **34,** 377-85.
Brands, DWA. et al. (1999) *43rd Stapp Car Crash Conference*, 313-20.
Donnelly, B, Medige J (1997) *J Biomech Eng,* **119,** 423-32.
Fallenstein, G et al. (1969) *J Biomech,* **2**, 217-26.
Galford, JE, McElhaney, JH (1970) *J Biomech,* **3,** 211-21.
Hirakawa, K et al. (1981) *No To Shinkei,* **33,** 1057-65.
Koeneman, J (1966) *Viscoelastic Properties of Brain Tissue*. Case Institute of Technology.
Lippert, SA et al. (2001) *2001 Bioengineering Conference*, 313-14.
Shuck, L, Advani SH (1972) *ASME Journal of Basic Engineering,* **94**, 905-11.
Thibault, KL, Margulies, SS (1998) *J Biomech,* **31,** 1119-26.
Wang, HC, Wineman, AS (1972) *J Biomech,* **5,** 431-46.

BONE-FRIENDLY INTERVERTEBRAL CAGES

Miroslav Sochor [1], Karel Balik [2], Ladislav Toth [3], Vlasta Pesakova [4], Hana Hulejova [4], Petr Tichy [1], Jaroslav Vtipil [1] and Radek Sedlacek [1]

[1] Dept. of Mechanics, F. of Mech. Eng., Czech Technical University, Prague, Czech Republic, sochor@fsid.cvut.cz
[2] Institute of Rock Structure & Mechanics, Academy of Sciences of the Czech Republic, Prague, Czech Republic
[3] Orthopaedic Clinic, Bulovka, Prague 8, Czech Republic
[4] Institute of Rheumatism, Na Slupi 4, Prague 2, Czech Republic

INTRODUCTION

Osteosynthesis of adjacent lumbar vertebral bodies with the use of PLIF cages is a necessary procedure for degenerative spine disease. Since carbon-carbon composites exhibit good biocompatibility, stimulate ossification, are transparent for screening and can be made with mechanical properties approximating those of bone tissue, C-C components have been designed for application in the cage structure

METHODS

C-C composite samples (Torayca T800H fibres with Umaform LE phenolic resin as a matrix precursor) were prepared in various modifications: carbonised, impregnated, infiltrated and coated with PyC (pyrolytic carbon), and with PyC + pHEMA (poly[2-hydroxyethyl methacrylate]) + collagen. *The biological characteristics* of the samples were tested *in vitro* – cell adherence, proliferation, etc., and *in vivo* - C-C+PyC+pHEMA implanted into the intercondylar region of a hind leg femur of pigs, Fig.1, and Fig.2, together with comparative samples of steel, titanium, and C-C composite without coating. *The basic material characteristics* of the C-C composite were tested on the MTS 858.02 Mini Bionix Testing Machine.

Figure 1: C-C+PyC+pHEMA sample implanted in a pig hind leg femur

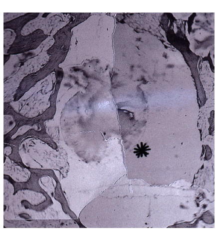

Figure 2: The trabecular bone gathers around the implant position (*)after 3 months

Based on a preliminary investigation, *two modes of cages, using a C-C composite core,* reinforced with: **A**) a titanium shell, Fig. 3; **B**) a plastic shell (e.g., PEEK), Fig. 3, were designed by the research team. With mode **A,** the C-C-core protrudes over the Ti-shell ends, thus enabling a softer contact with the bone.

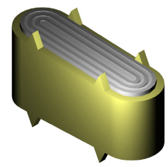

Fig. 3 Ti-shell + C-C-core

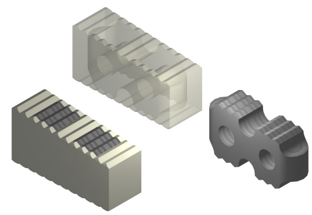

Fig. 4 Plastic-shell + C-C-core

RESULTS AND DISCUSSION

The bio tests of the C-C+PyC+pHEMA samples proved: *in vitro*- the metabolic activity of the fibroblasts shows a multiple increase and the content of inflammatory cytokines decreases; *in vivo* – better integration with the tissue than the other samples; preventing loosening of the carbon parcels, Fig.2. Mechanical compression tests of C-C composite samples, made by various technologies, served for choosing the optimal composite and together with an analysis of the L3 and L4 spine segment (based on experiments by G.Bergman - FU, Berlin), provided loading data for use in the FEM cage models, which simulated the stress distribution in the cages when implanted in the human spine.

SUMMARY

Several types of C-C composites have been developed for integration into PLIF cages, aiming at achieving a softer contact with the vertebral bodies and stimulating a better ossification process. Biological and mechanical tests proved the suitability of thematerials. Based on FEM simulation, two cage modes (Figs. 3 and 4) with C-C composite cores have been designed for use in human surgery.

REFERENCES

Sochor, M. et al (2001). *Proceedings of ASB 25th Annual Conference,* 419-420.

ACKNOWLEDGEMENT

Supported by GACR, No. 106/00/1407 and Ministry of Education, No. MSM 21000001.

DYNAMIC PARTICLE/LIQUID-LINING INTERACTIONS IN PERIPHERAL LUNG AIRWAYS

S.J. Weekley,[1] J. Rosenzweig,[2] J.R. King,[1] S.L. Waters[1] & O.E. Jensen[1]

[1]Centre for Mathematical Medicine, School of Mathematical Sciences, University of Nottingham,
Nottingham NG7 2RD, UK; Email: Oliver.Jensen@nottingham.ac.uk
[2]Centre for Computational Science, Queen Mary, University of London,
Mile End Road, London E1 4NS, UK

INTRODUCTION

A primary function of the airway liquid lining is to protect the lung from potentially harmful inhaled particles. While many previous models have sought to describe the distribution of particles that impact on airway walls throughout the lung, less attention has been paid to the details of the adhesive interaction between a particle, the airway liquid lining and the underlying epithelium. A full understanding of the dynamics of particle/liquid-lining interactions, which are controlled in part by competing surface tension and viscous forces, is important in implementing appropriate boundary conditions in aerosol inhalation simulations, and may be valuable in the development of improved inhalation therapies.

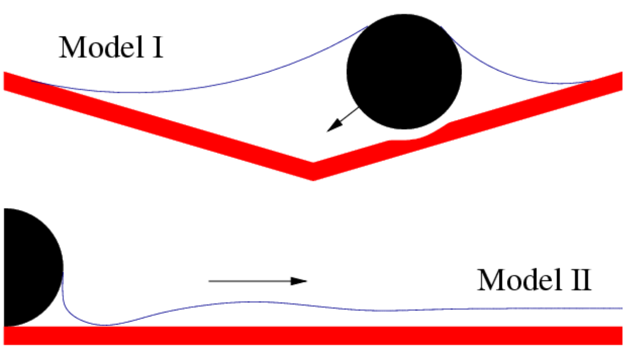

Figure 1. Model I: a particle partially immersed in a liquid pool in an alveolar corner drifts sideways under surface tension forces. Model II: a particle immersed in an initially uniform liquid layer generates an unsteady capillary wave, while trapping fluid at its base.

Schürch *et al.* (1990) have shown how surface tension, mediated by pulmonary surfactant, can pull a particle downwards into the liquid lining, indenting underlying epithelial cells. Motivated by these observations, we have investigated two model problems theoretically (Figure 1), relevant to micron-scale particles that can access unciliated peripheral airways and alveoli. Model I describes the quasi-steady normal and lateral displacement of a particle partially immersed in a laterally bounded liquid pool, as may arise in the corner of a polyhedral alveolus. We assume that, in the presence of pulmonary surfactant, the liquid wets the particle and the airway wall with zero contact angle. Model II describes the large-time unsteady response of an initially uniform airway liquid lining to the impact of a large particle.

METHODS

In both models we consider a two-dimensional geometry, recognising the potential limitations of this approximation, and represent the particle as a cylinder. In Model I, equilibrium free-surface locations are computed and are used to determine the net capillary force on a partially immersed particle. The speed of motion is controlled by viscous resistance, which is dominated by the flow in the narrow gap between the particle and the epithelium. This is computed using lubrication theory. In Model II, the unsteady evolution of the liquid lining is determined by finding asymptotic and numerical solutions of a thin-film equation of the form $h_t+(h^3h_{xxx})_x=0$, where $h(x,t)$ represents the liquid-lining thickness.

RESULTS AND CONCLUSIONS

In Model I, the particle can move either towards the centre of the pool or towards its edge, depending on the fluid volume, particle size, wedge angle and initial particle location. The particle's speed and distance of travel are influenced by non-specific surface forces and by deformability of the underlying epithelium. In Model II, an impacting particle creates a damped capillary wave that spreads outwards along the liquid layer, while a small volume of fluid remains trapped between the particle and the substrate. By computing this volume we can evaluate the dynamic adhesive force imposed by the liquid lining on the particle.

Our results demonstrate that (i) surface forces can cause slow lateral particle motion in directions that are hard to predict intuitively, and (ii) the adhesive force between a particle and a film can be controlled by long-range adjustment of the liquid layer in response to particle impact. The idealised models presented here provide a framework for the inclusion of important additional effects, such as epithelial stretching, dynamic surfactant readjustment and more realistic airway geometries.

REFERENCES

S. Schürch et al. (1990) *Resp. Physiol*. **80**, 17-32.

INSPIRATORY FLOW IN BRONCHIAL AIRWAY MODELS: BIFURCATION PLANE ROTATION

Colin Caro[1], Robert Schroter[1], Nicholas Watkins[1], Spencer Sherwin[2] and Veronique Sauret[3]

[1]Bioengineering and [2]Aeronautics, Imperial College, London, [3]Medical Physics and Bioengineering, Southampton General Hospital, UK
c.caro@ic.ac.uk

INTRODUCTION

The flow associated with non-planar branching and curvature of arteries directs attention to bronchial airway flow. In vivo and model studies indicate that characteristics of arterial flow include swirling, a relatively uniform distribution of wall shear and residence times, and inhibition of flow separation and flow disturbances (Caro *et al*, 1996; 1998; Sherwin *et al,* 2000). Model studies of flow in larger human bronchial airways have generally assumed planar geometry. Several consecutive generations of larger airway bifurcations are planar, but consecutive bifurcation planes are approximately orthogonal (Kaye and Schroter, 1993; Caro *et al*, 2002).

METHODS

The model is comprised of a straight, l/d ~ 15, inlet tube and two generations of planar symmetrical 'bronchial' bifurcations (Figure 1). Branching angle (θ) was 32.5° at 1st generation and 32.5° or 55° at 2nd. The angle of rotation of the bifurcation plane between the 1st and 2nd generations (ϕ) was 0° or 90°. Terminal resistances ensured the same volume flow in the 2nd generation daughter tubes, irrespective of θ or ϕ. The model was coated internally with litmus-containing water/starch paste. Inlet tube airflow, which carried hydrochloric acid vapour, was steady (8 l/min or 24 l/min, giving inlet tube Reynolds numbers, Re_{it}, of 600 and 1800, respectively). Acid arriving at the wall caused the litmus to redden. The local rate of change of colour indicated to approximation local relative wall shear rate, because of the effect of wall shear rate on the concentration gradient for the species between the fluid and the wall.

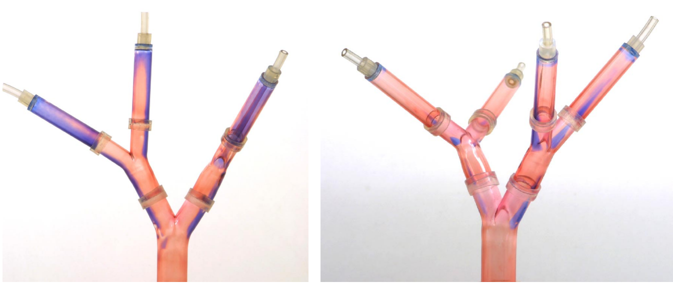

(a) *(b)*

Figure 1: (a) Residual linear blue streaks at outer walls of 1st and 2nd generations where ϕ = 0º. Reddening symmetrical at 2nd generation where ϕ = 90º (one daughter hidden but see also (b)). Reddening asymmetric where ϕ = 0º. (b) Residual linear blue streaks at outer walls of 1st generation. Residual helical blue streaks at 2nd generation where θ = 32.5°. Faster reddening and disappearance of streaks at 2nd generation where θ = 55°. ϕ = 90º at both 2nd generation bifurcations.

Experiments were done with Re_{it} = 600, θ = 32.5° at 1st and 2nd generations, ϕ = 0° or 90°; Re_{it} = 600, θ = 32.5° at 1st generation and one 2nd generation bifurcation, 55º at other 2nd generation bifurcation, ϕ = 90° at both 2nd generation bifurcations; Re_{it} = 600 or 1800, θ = 32.5° at 1st generation and one 2nd generation bifurcation, 55° at other 2nd generation bifurcation, ϕ = 90° at both 2nd generation bifurcations.

RESULTS AND DISCUSSION

The findings of this branching model included:

- Symmetrical distribution of reddening between 2nd generation daughter 'bronchi' where ϕ = 90° and asymmetrical distribution where ϕ = 0°, implying asymmetrical distribution of wall shear rate.
- Residual linear blue streaks (implying low wall shear rate) along outer walls of 1st generation bifurcation and daughter 'bronchi', and along outer walls of 2nd generation bifurcation and daughter 'bronchi' where ϕ = 0°. Residual helical blue streaks along outer walls of 2nd generation bifurcation and daughter 'bronchi' where ϕ = 90°, implying swirling flow.
- For given Re_{it}, reduction of swirl pitch and increased rate of reddening associated with increase of θ.
- For given θ, apparent reduction of swirl pitch associated with increase of Re_{it}.

Flow associated with orthogonal consecutive bifurcation planes resembles flow associated with non-planar branching. Findings are expected to have implications for all airway transport processes, including those for particles (Comer *et al,* 2000).

REFERENCES

Caro, C.G. *et al.* (1996). *Proc Royal Soc, A* **452**, 185-197.
Caro, C.G. *et al* (1998). *J Physiol,* **513.P**, 2P.
Caro, C.G. *et al*. (2002). *Proc Royal Soc, A* (in press).
Kaye, S.R., Schroter, R.C. (1993). *J Biomech Eng,* **115**, 91-96.
Sherwin, S.J. *et al.* (2000). *J Biomech Eng,* **122**, 1-10.
Comer, J.K. *et al.* (2000). *J Biomech Eng,* **122**, 152-158.

ANALYSIS OF ACROMIAL FIXATION OF GLENIOD COMPONENTS USING A 3D FINITE ELEMENT MODEL OF THE SCAPULA WITH COMPARISON TO RESULTS USING PHOTOELASTICITY

Linda A. Murphy and Patrick J. Prendergast

Department of Mechanical Engineering, Trinity College, Dublin 2, Ireland, www.biomechanics.ie

INTRODUCTION

The requirement for increased reliability and improved performance of implants necessitates rigorous pre-clinical testing. However, for the case of total shoulder arthroplasty (TSA), there is a plethora of glenoid prosthesis designs lacking this rigorous testing. Without improved pre-clinical analysis, glenoid component loosening rates will continue to be high.

This analysis will test the durability of an existing glenoid component fixation system. The hypothesis behind the design is that attachment of the glenoid prosthesis to the acromion, reduces the rate of loosening (Gagey *et al.,* 1990). Investigation of this design is carried out using a three-dimensional finite element (FE) model of the scapula (Lacroix *et al.,* 2000). Furthermore, this study will attempt to confirm the FE results where similarity of stress data will be investigated using the technique of photoelasticity.

METHODS

The 3D finite element model of the scapula was generated using CT data for geometric and material property definition [2]. The inhomogeneous nature of the material was described using 35 different Young's moduli. A model of a metal-backed acromion fixated prosthesis was inserted with bone cement and vitallium screws, see Fig. 1.The Young's modulus and Poisson's ratio for the polyethylene, metal-backing (cast vitallium), cement mantle and cancellous bone screws were taken to be 0.5 GPa, 220 GPa, 2.2 GPa, 220 GPa and 0.4, 0.32, 0.3 and 0.32 respectively. Motion between the acromion and glenoid under the action of the muscle forces analysed to determine if load sharing to the acromion occurs. Muscle and joint loads were applied for 30, 60, 90, 120, 150 and 180 degrees of abduction (van der Helm).

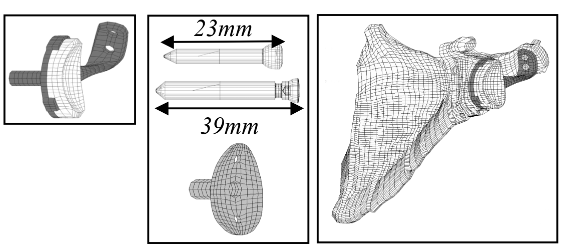

Figure 1 *Acromion prosthesis and fixation with mesh of scapula.*

For confirmation of the FE model, six scapulae were coated with a birefringent polymer using the contouring technique. The scapula was loaded using the modular head of a humeral prosthesis, see Fig. 2. The FE model of the scapula was also coated with the photoelastic material (E=2.9GPa, ν=0.36), restrained along the medial border and the glenoid was loaded parabolically to the same order of magnitudes. Plots of shear stress distributions on the experimental coating and on the finite element coating are compared.

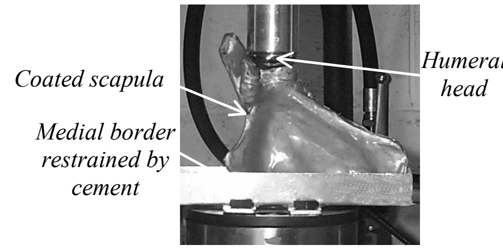

Figure 2 *Experimental set-up.*

RESULTS AND DISCUSSION

Regarding our confirmation of results, calculation of the shear stress values corresponding to regions of high stress in the FE model, we find that shear stresses in the same order of magnitude were observed. For example, for N=4, a maximum shear stress of 30 MPa was reached experimentally at the superior border. Similarly, maximum shear stresses of 25 MPa and greater were seen at the superior border of the finite element model.

In general, the stress distributions produced in the cement mantle are quite low (<3MPa). However, very high peak stresses are also reached, in the order of 20 MPa. The relative displacement between the glenoid and the acromion, under the action of the muscle loads, shows that a small but significant amount of motion occurs (~1mm). This resulted in high stresses being produced in the acromion prosthesis arm (~50 MPa). Furthermore, stresses produced in the acromion bone for this design are higher than the natural case, i.e. with no prosthesis fixation (~16 MPa higher). Since this design is recommended for cases of deficient rotator cuff function, mainly seen in rheumatoid arthrisis, problems with fracture of the acromion may occur due to these higher stresses.

SUMMARY

Results for the FE model and the photoelastic analysis are sufficiently similar, thus allowing us to use the FE model for analysis of glenoid components in TSA. Acromion fixation may prove problematic due to peak stresses seen in the cement mantle, acromion fixation bar and in the acromion bone itself.

REFERENCES

O Gagey, F Mazas (1990) Surgery of the shoulder, St. Louis, MO Mosby 282-284.
D Lacroix, LA Murphy, PJ Prendergast (2000) J Biomech Eng: 430-436.
FCT van der Helm. Muscle and joint load data file (personal communication).

ALPINE SKI RACING AND OPTIMAL CONTROL

Yoichi Hirano
Faculty of Science and Engineering, Chuo University, Bunkyo-ku, Tokyo, Japan
hirano@indsys.chuo-u.ac.jp

INTRODUCTION

In alpine ski racing it is very important for the racers to find and follow the quickest descent line between the many gates which make up the race course. Here, optimal control theory is applied to calculate the quickest line between two points on a ski slope.

SNOW RESISTANCE FORCES

During the motion of turning while skiing down a ski slope, gravitational force and snow resistance forces from the snow surface act on the skier. The equations of motion of the ski-skier system can be solved providing the resistance forces are known. Tada and Hirano determined compact snow cutting force equations by applying multiple regression analysis to experimental results, finding these forces to be functions of edging angle α and attack angle γ. These angles are respectively the angle between the ski sole and snow surface and the angle between the system velocity vector and the longitudinal ski axis.

APPLICATION OF OPTIMAL CONTROL THEORY

The objective function is the descent time t_f of a skier between two points on a ski slope. The control variable is the edging angle α, which can be adjusted by the skier, while the state variables are position (x,y) and velocity of the skier; all of which are a continuous function of time. Control and state variables, however, are discretized at time t_i ($i = 0,1,\ldots,N$), with time t_i being given by $(t_f/N)i$. The original optimal control problem can now be converted into an optimization problem in which the discretized system state variables are made to be continuous at the middle point between two consecutive time points t_i and t_{i+1}. These conditions are the equality constraints. The problem is to minimize t_f with respect to the edging angle under the equality constraints. This nonlinear programming problem is solved by Sequential Quadratic Programming (SQP) using MATLAB Optimization Toolbox software.

NUMERICAL RESULTS AND DISCUSSION

A ski slope of 15° angle is considered in which the x and y coordinate axes are taken in the steepest and horizontal direction of the slope, respectively. Calculating the quickest line between two points on the slope is now possible. The upper point is located at x = 0 m, y = 0 m and the lower point is located at x = 20 m, y = 30 m. The mass, ski length, and moment of the inertia of the system are 80 kg, 1.8 m, and 2.5 kg · m^2, respectively. The ski boot is located at 50.5% of the length of the ski starting from the top of the ski. At the upper point a skier has an initial velocity of dx/dt = 6 m/s and dy/dt = 6 m/s. The initial angle between the longitudinal ski axis and the horizontal coordinate axis on the ski slope is 30º.

In Fig. 1, curve A is the resultant quickest line with a descent time of 5.179 s, while curve B is a line obtained for comparison by considering the problem as a Brachistochrone problem. Note that in this case the decent time is only 3.283 s, being faster because only gravitational force is considered. The quickest line is a rather straight line connecting two points, which is not surprising. Figure 2 shows the control variable (the edging angle) which changes from 0.2 to 1.2 radians during descent. If many gates are taken into account, it is expected that new unexpected lines will be found; thereby suggesting that skiers follow the lines by controlling the edging angle.

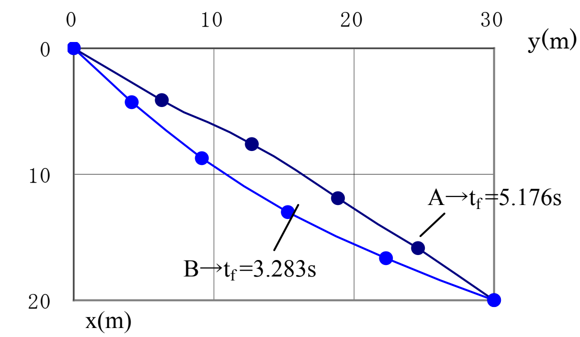

Figure 1: Quickest line between two gates on ski slope.

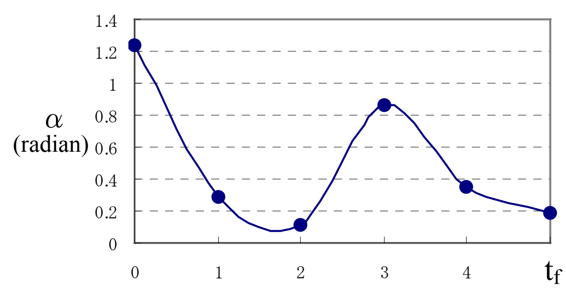

Figure 2: Control variable (edging angle) versus time.

ACKNOWLEDGEMENT

Part of the present research was done during the author's stay at Institute of Sport Science, University of Innsbruck.

REFERENCES

Hirano,Y. and Tada,N. (1996). *Medicine and Science in Sports and Exercise*, **28**, 1209–1213.
Tada, N. and Hirano, Y. (2002). *Sports Engineering*, (publication in progress).

(publication in progress).

COLLAGEN NETWORK AND MECHANICAL PROPERTIES OF ARTICULAR CARTILAGE: EXPERIMENTAL AND NUMERICAL STUDY

RK Korhonen[1], J Töyräs[1], MS Laasanen[2], R Lappalainen[1], HJ Helminen[2] and JS Jurvelin[1]

[1]Department of Applied Physics, University of Kuopio, Kuopio, Finland, rami.korhonen@uku.fi
[2]Department of Anatomy, University of Kuopio, Kuopio, Finland

INTRODUCTION

Collagen network contributes significantly to dynamic compressive and tensile stiffness of cartilage (Bader, 1992). Proteoglycans (PGs) induce swelling, controlled by collagens, and strongly determine equilibrium compressive stiffness. Nevertheless, cartilage structure-function relationships, especially the role of anisotropic collagen network, should be studied more thoroughly. Objectives of the present study were to investigate **1)** the role of collagen network in cartilage stress-relaxation under compression, **2**) the compression-tension non-linearity characteristics, **3)** the effect of superficial collagen network on the cartilage equilibrium response in different measurement geometries. For these objectives both experimental tests and numerical simulations were used.

MATERIALS AND METHODS

Sample preparation. **Group 1:** Cylindrical cartilage samples (∅=4mm) were harvested from bovine patellae. Chondroitinase ABC was used for PG digestion (44h, n=6) and collagenase for collagen degradation (44h, n=6). **Group 2:** Humeral osteochondral samples (n=6, ∅=4mm) were prepared. **Group 3:** Osteochondral samples (n=6, ∅=13mm) were drilled from bovine patellae. ***Mechanical tests.*** **Group 1:** Stress relaxation tests (12.5kPa pre-stress, 10% step) were conducted in unconfined compression. **Group 2:** Samples were glued between metallic platens and tested in unconfined compression (stepwise stress relaxation in tension and compression, strain up to ±6%). **Group 3:** Stress-relaxation tests (12.5kPa pre-stress, 4×5% step) were conducted in indentation geometry. Subsequently, cartilage (∅=4mm) was detached from the subchondral bone and measured in unconfined compression using the same protocol. ***Finite element analyses.*** Mechanical tests were simulated with finite element (FE) method (Abaqus 5.8). In axisymmetric models, cartilage consisted of 8-node quadratic poroelastic elements and nonlinear spring elements. Young's modulus of solid matrix (E, simulates mechanical role of PGs), Young's modulus of fibril network ($E_f = E_f^{\varepsilon}\varepsilon_f + E_f^0$, simulates mechanical role of collagen), and permeability (κ) were incorporated in the fibril reinforced poroelastic models (FRPE) (Li, 1999).

RESULTS AND DISCUSSION

Group 1: Experimental collagen degradation by collagenase decreased short- and long-term responses of cartilage typically by 75% and 50%, respectively (Fig. 1a). FRPE predicted the same behavior by a major decrease of E_f^{ε} (2500→750MPa), supplemented by a decrease of E (0.2→0.1MPa). The decrease in E was attributed to secondary, experimentally verified PG loss. PG digestion by chondroitinase ABC decreased short- and long-term responses of cartilage typically by 15% and 80%, respectively (Fig. 1a). FRPE predicted this behavior by a major decrease of E (0.35→0.04MPa). **Group 2:** Experimental equilibrium stress-strain behavior of cartilage was significantly different in tension than in compression, as assessed in the direction perpendicular to articular surface (Fig 1b). Contrary to isotropic model without fibril network (poroelastic (PE)), FRPE with high E_f^{ε} in axial direction (1090MPa) predicted this compression-tension non-linearity. **Group 3:** FRPE with high E_f^{ε} (5300MPa) in superficial layer (25% of cartilage thickness) simulated differences in cartilage equilibrium response in unconfined compression and indentation (Fig. 2). PE or FRPE with homogenous fibril network throughout the tissue (E_f^{ε}:430MPa) could not predict the differences.

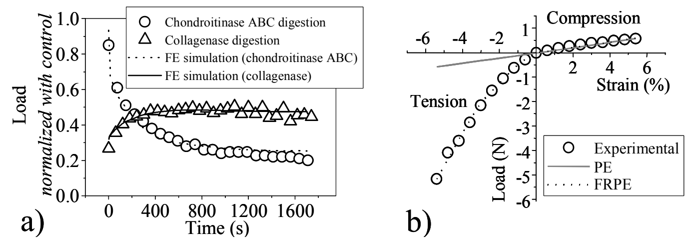

Figure 1: Typical experimental and numerical analyses: a) time-dependent behavior of cartilage after collagen or PG degradation, b) equilibrium stress-strain behavior of cartilage in compression and tension perpendicular to articular surface.

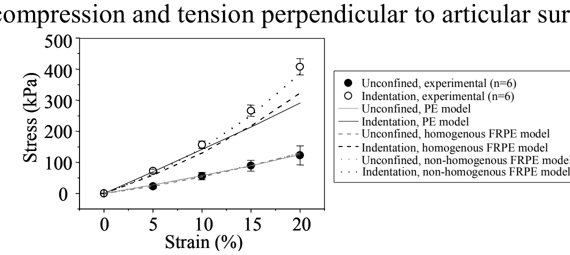

Figure 2: Experimental and numerical equilibrium stress-strain behavior of cartilage in unconfined compression and indentation.

SUMMARY

FRPE analyses with realistic values of model parameters suggest that collagen network modulates short-term response as well as contributes to compression-tension non-linearity of cartilage. Also, superficial tangential collagen network may be a predominant factor inducing differences in cartilage behavior under different loading geometries. We conclude that models comprising compression-tension non-linearity are needed to predict complex structure-function relationships in cartilage (Li, 1999; Soltz, 2000).

REFERENCES

Bader, D.L. et al (1992). *Biochim Biophys Acta*, **1116**, 147-54.
Li, L.P. et al (1999). *Clin Biomech*, **14**, 673-82.
Soltz, M.A. et al (2000). *J Biomech Eng*, **122**, 576-86.

DYNAMIC COMPRESSION INFLUENCES THE SYNTHESIS OF NITRIC OXIDE AND PGE_2 BY IL-1β STIMULATED CHONDROCYTE SUB-POPULATIONS CULTURED IN AGAROSE CONSTRUCTS

Tina T Chowdhury, David A Lee, Dan L Bader.
IRC in Biomedical Materials and Medical Engineering Division, Department of Engineering, Queen Mary, University of London, Mile End Road, London. UK. d.l.bader@qmw.ac.uk

INTRODUCTION

The structural heterogeneity of the load-bearing tissue, articular cartilage, is produced by a relatively low cell density of chondrocytes. It is well established that in vitro mechanical strain applied to 3D constructs seeded with isolated chondrocytes from full depth, superficial and deep zones, induces a range of distinct metabolic responses [1, 2]. Recently, dynamic compression at physiological frequencies was shown to downregulate the production of nitric oxide ($^{\cdot}$NO) and PGE_2 in the presence of the pro-inflammatory cytokine, IL-1β, in full depth chondrocytes [3]. The present study tests the hypothesis that dynamic compressive strain alters the synthesis of $^{\cdot}$NO and PGE_2 by IL-1β stimulated chondrocyte sub-populations.

METHODS

Superficial and deep chondrocytes were seeded in 3 % agarose (type VII), at a density of 4 x 10^6 cells.ml^{-1}, and cultured in 1 ml of DMEM + 20 % FCS for 24 hours. Constructs were incubated for a further 48 hours in radiolabelled medium containing 10 ng.ml^{-1} IL-1β, either in the presence or absence of 1 mM L-NIO, an inhibitor of NO. In a separate experiment, constructs were subjected to 15 % dynamic compressive strain at 1 Hz for 48 hours in 1 ml of radiolabelled medium containing 0 or 10 ng.ml^{-1} of IL-1β, and / or 1 mM L-NIO. Nitrite was measured using the Griess assay, PGE_2 synthesis was determined using an ELISA kit and [^{3}H]-thymidine and $^{35}SO_4$ incorporation were assessed by TCA and alcian blue precipitation, respectively.

RESULTS AND DISCUSSION

The effects of mechanical stimulation on both chondrocyte sources in terms of the synthesis of nitrite and PGE2, are shown in Figures 1A and B, respectively. It is clear that IL-1β stimulated both molecules at least twofold for superficial chondrocyte constructs, compared to a minimal induction in the deep cells.

In the absence of IL-1β, dynamic strain reduced levels of nitrite and PGE_2 production compared to unstrained controls in cells from both sub-populations. Moreover in the presence of IL-1β, the upregulation of nitrite and PGE_2 values in unstrained constructs seeded with superficial cells was reversed with dynamic compression. Similar findings were observed for deep cell constructs, although the values were significantly lower. Compression-induced inhibition of nitrite was reversed with L-NIO for superficial cell constructs. By contrast, the IL-1β induced inhibition of PGE_2 synthesis was enhanced with L-NIO for superficial cell constructs. Furthermore, nitrite and PGE_2 synthesis for IL-1β stimulated deep cell constructs subjected to dynamic compression, was not affected by L-NIO.

In untreated cells, the level of stimulation of [^{3}H]-thymidine and $^{35}SO_4$ incorporation was significantly greater in the deep cells compared to the superficial cells (data not shown). The IL-1β induced inhibition of [^{3}H]-thymidine incorporation was partially reversed with L-NIO in both cell sub-populations. By contrast, $^{35}SO_4$ incorporation was not affected by IL-1β or L-NIO under dynamic loading for both cell types.

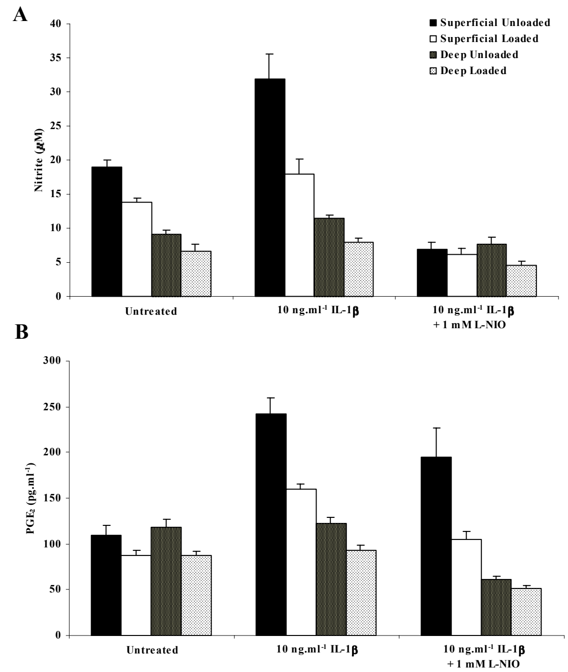

Figure 1 *Nitrite synthesis (A) and PGE_2 production (B) by superficial and deep chondrocytes, seeded in 3 % agarose Type VII and subjected to 15 % dynamic compressive strain at 1 Hz for 48 hours.*

SUMMARY

This study has demonstrated that dynamic compression, a physiologically relevant loading regime, counteracts the effects of IL-1β on superficial cells by suppressing both $^{\cdot}$NO and PGE_2 production. A similar trend was apparent in deep cell constructs although the values were significantly lower, suggesting that the superficial chondrocytes are a major source of $^{\cdot}$NO and PGE_2. The inhibition of both molecules by dynamic compression could contribute to novel strategies for the treatment of degenerative diseases of cartilage.

ACKNOWLEDGEMENTS

The work is supported by the EPSRC, UK.

REFERENCES

[1] Lee DA and Bader DL (1997) *J of Orthop Res* **15 (2):** 181 – 188 [2] Lee DA and Bader DL (1998) *J of Orthop Res* **16 (6):** 726-733 [3] Chowdhury TT *et al* (2001) *Biochem Biophys Res Comm* **285:** 1168 - 1174

INCREASING NUMBER OF INTERCONNECTED ELEMENTS IN TENSEGRITY MODELS INDUCES A STRUCTURAL SOFTENING CONSISTENT WITH CORTICAL CYTOSKELETON FUNCTION

Sylvie Wendling[1,2], Patrick Cañadas[2,3], Valérie M. Laurent[3], Emmanuelle Planus[3], Redouane Fodil[3], Patrick Chabrand[1], Daniel Isabey[3]

[1]CNRS UPR 7051, Laboratoire de Mécanique et d'Acoustique, Marseille, France, daniel.isabey@creteil.inserm.fr
[2]CNRS UMR 7052, Laboratoire de Biomécanique et Biomatériaux Ostéo-Articulaires, Créteil, France
[3]INSERM UMR 492, Fonctions Cellulaire et Moléculaire de l'Appareil Respiratoire et des Vaisseaux, Créteil, France

INTRODUCTION

Control of many cell functions including growth, motility, migration, mechanotransduction, critically depends on mechanical stress-induced alterations in global and local cell shape and structure. These functional alterations are mediated through changes in the cytoskeleton (CSK), a hierarchical and multi-modular structure of polymeric interconnected elements which constitutes multiple transmission pathways organized at different scales (Ingber, 1997). Cellular tensegrity explains how prestress, generated either at global scale (contractile apparatus), or locally (force exerted by molecular filaments), is balanced by interconnected elements compressed at various scales; e.g., microtubules (MTs) stabilize the entire cell or cytoskeletal filaments stabilize specialized microdomains of the cell surface. In the present study, we attempted to theoretically quantify the structural properties of the cortical component of the CSK (basically the actin-ankyrin spectrin network which contains a high number of slightly-dense and short actin filaments), by comparison to the internal CSK component (basically the internal CSK network of highly-dense and long actin filaments interconnected with MTs and intermediate filaments), the two CSK components being attached to the extracellular matrix through the adhesion complex. In a recent *in vitro* study, the mechanical properties of the cortical *vs* cytosolic CSK component were estimated by twisting magnetic cytometry and cortical stiffness and prestress were found smaller for the cortical than for the cytosolic CSK compartments (Laurent *et al*., 2001). In an attempt to relate these results to the specific structure of each CSK component, we studied the effect of changing the number of constitutive elements in simplified "spherical" tensegrity models including the well known 30-element tensegrity structure (Cañadas *et al*., 2001, Stamenovic *et al*., 1996, Wendling *et al*., 2000).

METHODS

We have tested four spherical models of tensegrity structures composed of a discontinuous network of quasi-rigid bars compressed by a continuous network of pre-stretched and elastic cables: (i) the *simplex*, composed of 3 bars and 9 cables, (ii) the *quadruplex*, composed of 4 bars and 12 cables, (iii) the *octahedron*, composed of 6 bars and 24 cables and (iv) the *cuboctahedron*, composed of 12 bars and 48 cables. Constitutive cables and bars are defined by their length and cross-sectional area, and their mechanical properties. Each elastic cable behaves as a pretressed linear spring. Extension forces were applied in quasi-static conditions at the 3 nodes of the superior plane (resp. 4 nodes for the *quadruplex*). The structures were all anchored to a rigid base by spherical joints at the 3 (resp. 4) inferior nodes. The overall deformation of the structure was deduced from the nodal displacement using a finite element method of resolution. The structural elasticity modulus was deduced from the stress-strain relationship of an equivalent cylinder embedding the structure at small deformation (e.g.,<5%). The apparent elasticity modulus E, the internal tension T and the length L of constitutive bars were normalized by the local properties of the elastic cables.

RESULTS AND DISCUSSION

The normalized elasticity modulus E* was expressed, for the four tensegrity models tested, as a function of three local normalized parameters, i.e., L*, T* and the number of elements N (= 12, 16, 30, 60). E* exhibits a marked negative dependence of L* (i.e., slope −2 on the logE*-logL* curve) which extends previous *octahedron's* results (Wendling *et al*., 1999). Noteworthy, E* exhibits, independently on L*, a stronger negative dependence of N, (i.e., slope ≈−2,7 on the logE*−logN curve). This result, once extrapolated, means that increasing the number of interconnected elements in a "spherical" tensegrity structure tends to soften the structure. Estimating the cellular L* and N values lead to consider that L* is 1 order of magnitude smaller and N about 2 orders of magnitude greater in cortical CSK (compared to the cytosolic), meaning that structural stiffness of cortical CSK would be smaller than the cytosolic CSK as experimentally observed. Moreover E* slightly increased with T* in the 4 models, confirming *octahedron's* results but the rate of T*-increase depended on L* and N. A rough estimate of prestress values in elastic fibers and filaments in each CSK compartment lead to consider T* values about 2 orders of magnitude smaller in the cortical compared to the cytosolic CSK which also contribute to the smaller values of structural cortical stiffness. Note that smaller rigidity and prestress measured and predicted for the cortical structure are consistent with its functional role, i.e., maintaining an intimate contact of the cell with its mechanical surrounding and sensing very local deformation forces.

REFERENCES

Cañadas, P., et al. (2001). *Arch. Physiol. Biochem*., **109**, 10.
Ingber, D.E. (1997). *Ann. Rev. Physiol.,* **59**, 575-99.
Laurent, V.M., et al. (2001). *Arch. Physiol. Biochem*, **109**, 57.
Stamenovic, D., et al. (1996). *J. Theor. Biol.*, **181**, 125-136.
Wendling, S., et al. (1999). *J. Theor. Biol*., **196**, 309-325.
Wendling, S., et al (2000). *E.P.J. Appl. Phy.*, **9**, 51-62.

ASSESSMENT OF STRUCTURAL VISCOELASTICITY OF CYTOSKELETON BY TENSEGRITY MODEL

Patrick Cañadas[1, 2], Valérie M. Laurent[1, 4], Redouane Fodil[1], Emmanuelle Planus[1], Sylvie Wendling[2, 3] and Daniel Isabey[1]

[1]INSERM U492, Fonctions Cellulaire et Moléculaire de l'Appareil Respiratoire et des Vaisseaux, BCR, 94010 Créteil, France.
[2]CNRS 7052, Laboratoire de Biomécanique et Biomatériaux Ostéo-Articulaires, EMP, 94010 Créteil, France.
[3]CNRS 7051, Laboratoire de Mécanique et d'Acoustique, MMCB, 13402 Marseille Cedex 20, France.
[4]EPFL, Cellular Biophysics and Biomechanics Laboratory,1015 Lausanne, Switzerland.
canadas@univ-paris12.fr

INTRODUCTION

Cellular deformability and transmission of mechanical forces, (e.g., from the membrane to the nucleus) are known to implicate the cytoskeleton (CSK) structure whose mechanical properties are now recognized to play a critical role for many biological functions (Ingber *et al.*, 1989). Understanding the mechanical properties of cytoskeleton is difficult because CSK is a complex tridimensional network of interconnected biopolymers (actin filaments, microtubules, intermediate filaments) which is physically linked to the extracellular matrix (ECM) through focal adhesion sites. Spatial re-arrangement of CSK-filaments, tension in viscoelastic actin filaments, compression in microtubules and in the non-flexible ECM (Wang *et al*., 2001) would all contribute to cellular prestress, stability, and CSK mechanical properties (Stamenovic *et al.,* 1996, Ingber *et al.,* 1989). Recent oscillatory cellular measurements have shown that frictional mechanical energy arises within the CSK, by coupling with elastic energy storage (Maksym et al., 2000). We presently attempted to evaluate the theoretical contribution of structural re-arrangement of CSK elements to the CSK viscoelastic response. We purposely developed a CSK model based on a previously studied tensegrity structure and analyzed the main parameters governing its viscoelastic response. Structural viscoelasticity of the cellular tensegrity model appears to satisfactorily agree with measurements of viscoelastic response in human alveolar epithelial adherent cells.

METHODS

We numerically simulated creep tests of a CSK tensegrity model composed of a continuous network of 24 pre-stretched cables which compress a discontinuous network of 6 rigid bars. By contrast to previous studied models, each cable was supposed to behave as a viscoelastic "solid" (i.e., Voigt body composed of a spring in parallel to a dashpot). The viscoelastic tensegrity model was supposed to be anchored to a rigid, non planar substratum through the four lower nodes. Elementary transient forces were externally applied to the nodes at the ends of the upper bar. Four types of loading were tested, i.e., extension, compression, shear and torsion. The creep "nodal displacement *vs* time" curve of the structure was numerically obtained from the resolution of the linearized system of differential equations using Euler's incremental formulation:

$$\{dF_i\} = [K(U_{i-1})]\cdot\{dU_i(t)\} + [C(U_{i-1})]\cdot\{d\dot{U}_i(t)\}$$

The actual force vector $\{dF_i\}$ is related to the actual nodal displacement $\{dU_i\}$ and speed $\{d\acute{U}_i\}$ vectors, via the global rigidity $[K(U_{i-1})]$ and global damping $[C(U_{i-1})]$ matrices which both reflect the spatial organization of the structure before loading. Overall time constant (τ) and elasticity modulus (E) of the tensegrity model were obtained by curve-fitting analysis via an equivalent cylindrical Voigt body embedding the entire tensegrity structure, i.e., diameter and height equal $l_{0,}$ viscosity modulus η was then calculated by $\eta=E\times\tau$. Normalized structural properties were obtained by dividing the overall viscoelastic properties of the tensegrity structure by local properties of its constitutive cables (τ_c, η_c, E_c), i.e., $\tau^* = \tau/\tau_c$, $E^* = E/E_c$ and $\eta^* = \eta/\eta_c$.

RESULTS AND DISCUSSION

Present numerical results show that values of τ^*, E^*, η^* vary with (i) local physical properties of constitutive elements, i.e., the normalized length L* and cable initial extension T^* which represents the structural prestress, and, (ii) the type of loading. While previous studies have shown that E^* exhibits a positive dependence on T* (i.e., $E^*\propto T^{*+0.5}$, Wendling *et al*., 2000), τ^*exhibits in present study a negative dependence on T^* (i.e., $\tau^*\propto T^{*-0.5}$). However, both η^* and E^* appear to follow the same negative L*-dependency (i.e., $\eta^*\propto L^{*-2}$ and $E^*\propto L^{*-2}$). Tensegrity concept predicts that a tensed structure has a faster time response than a less tensed structure, which seems to be consistent with our experimental observations showing the 'solid-like' behavior of adherent living cells by contrast to the 'fluid-like' behavior of suspended cells (Laurent et al., 2002). Moreover, the apparent viscous CSK modulus measured by different techniques in adherent cells seems to exhibit a strongly negative probe-size dependence similar to the L^{*-2}-dependency observed for η^* and E^* in the tensegrity structure. On the whole, present study provides new arguments supporting the idea that structural rearrangement of CSK-elements critically contributes to cellular viscoelasticity.

REFERENCES

Ingber, D. et al. (1989). *Cell Sh., Det., Reg, Regul. Role*, 3-31.
Laurent, V.M. et al. (2000). *Arch. Phys. Biochem*, **108**, 29.
Maksym et al. (2000). *J. Appl. Physiol.*, **89**, 1619-1632.
Stamenovic et al. (1996). *J. Theor. Biol.*, **181**, 125-136.
Wang et al. (2001). *PNAS*, **98(14)**, 7765-7770.
Wendling, S. et al (2000). *E.P.J. Appl. Phy.*, **9**, 51-62.

THE EVOLUTION OF PASSIVELY-ASSISTED HUMAN-POWERED LOCOMOTION

Alberto E. Minetti
Centre for Biophysical and Clinical Research into Human Movement, Department of Exercise and Sport Science
Manchester Metropolitan University, UK, a.e.minetti@mmu.ac.uk

INTRODUCTION

In this paper the history of passive tools devoted to improve the locomotor performance is reviewed, with particular reference to the biomechanical advantage introduced by each of them: the cross-country skis (CCS), the ice/in-line skates (S, ILS), the halteres (H), the different bicycles (Hobby Horse – HH, modern – MB). All of them were meant to increase the progression speed and/or to surpass the body limitations with respect to the motion in difficult environments.

LOCOMOTOR TOOLS

ICE/IN-LINE SKATING (3000 BC- / ca 1980)
Also used for transportation on the iced Amsterdam canals (about 14th century), the modern version of S is the fastest non-wheeled human-powered locomotion, both because of the very low friction (0.003-0.007) and because no body part has to stop with respect to the ground, even when contributing to propulsion. The lateral push while sliding allows knee and ankle extensor muscles to operate within the optimal contraction speed range. The reduced added mass and speed of limbs with respect to the body centre of mass (BCOM) implies a low mechanical internal work (W_{INT}) too.
The modern roller in-line skating, while being slower because of the higher rolling resistance, benefits from the same physio-mechanical strategy of S.

CROSS-COUNTRY SKI (2000 BC-)
Originally a mean of travel and communication in Scandinavia and Russia, CCS is today the second fastest non-wheeled locomotion because of the very low friction (0.05-0.20) and the small added mass involved. The diagonal stride (DS) and the double pole (DP) are the slower techniques mainly because the propulsion is achieved by the push of skis and poles, which stop with respect to the ground. The involved body segments has thus to be accelerated, with respect to BCOM, at the same speed of the progression one, with detrimental effects on W_{INT} and the muscle efficiency. The fastest technique in CCS is skating (SK, 1980), which adopted the ice-skating strategy for lower limbs (lowering W_{INT} and increasing muscle efficiency) and made a better use of ‘energy recovery’, i.e. the exchange between the potential and kinetic energy of BCOM (Minetti et al 2001).

HALTERES (500 - 300 BC)
The first passive tool devoted to increase the human performance in the ancient Olympics standing long-jump event, the halteres represented added hand-held loads (1.2-4.5 kg). Their role was: a) to produce a higher ground reaction force by a more efficient use of shoulder extensor muscles, and b) to alter the BCOM position at take-off (more anterior) and landing (more posterior). There are clues (Minetti 2002) that these effects increased the jump range.

BICYCLE (1820-)
The idea behind it is again an alteration of body geometry in order to escape from the rimless wheel metaphor of walking and running. By suspending the body at a fixed height from the ground, the wheels-frame structure almost completely prevents vertical displacements of BCOM, so that lower limb muscles can be used mainly to overcome rolling resistance and air drag. By progressing from the Hobby Horse (1820), where the rider pushed directly on the ground, to the High Wheeler (1870) and the modern bicycle (1890), the metabolically equivalent cruising speed, with respect to walking (1.5 m/s), increased 3.3 times (≈5.0 m/s, Minetti et al 2001). The major determinants of such a progress in locomotor economy were: 1) the decrease of the overall bicycle mass (from 24 to 16 kg), which helped to further decrease 2) the decreased rolling resistance (0.027 to 0.008), due to the transition from metal to solid and inflatable tyres, 3) the concurrent lengthening of the distance travelled per pedal revolution (2.8 to 5.5 m), which caused 4) the decrease of pedalling rate (fr) at a given speed and, consequently, 5) the decrease of W_{INT} (which in cycling depends on fr^3). In addition, the last 2 effects maximized the efficiency of knee extensor muscles at high progression speed, allowing them to keep on contracting within the optimal speed range.

MICRO-SCOOTER (1920, 1985)
This recent and fashionable device has been reintroduced mainly due to its compact size and the better rolling resistance of modern roller skate wheels. While at 1.5 m/s it is metabolically equivalent to walking, at 2.7 m/s the energy consumption corresponds to walking at 1.9 m/s (Minetti and Zamparo, personal observations). The small advantage in comparison with the other types of wheeled locomotion is due to the residual vertical excursion of BCOM and the push limb which stops with respect to the ground.

CONCLUSIONS

The increase of economy/cruising speed (or of jumping range) has been obtained by each of the illustrated passive appendices throughout a combination of the following strategies: a) the decrease of the mechanical external work, b) the decrease of the internal work, c) the modification of body configuration, and c) the maintenance of muscle performance optimization despite of the increase in speed.

REFERENCES

Minetti A. E. et al. (2001) In: Science and Skiing II, E. Müller et al Eds., Hamburg, Kovac.
Minetti A. E. (2002) 7th ECSS Congress, Athens, 2002.
Minetti A. E., J. Pinkerton and P. Zamparo (2001) *Proc. R. Soc. B* 268: 1351-1360.

MECHANICAL ENERGY TRANSFER BETWEEN ADJACENT JOINTS BY TWO-JOINT MUSCLES

Boris I. Prilutsky[1] and Vladimir M. Zatsiorsky[2]
[1]Center for Human Movement Studies, Georgia Institute of Technology, Atlanta, GA, USA
[2]Biomechanics Laboratory, Pennsylvania State University, State College, PA, USA

The goal of this presentation is to review and discuss the issues related to the energy transfer between adjacent joints by two-joint muscles. This energy transfer and its functional significance have been debated for over a century (for review, see van Ingen Schenau 1990; Prilutsky 2000; Kuo 2001).

A simple physical model of the leg (Fig. 1) can be used to illustrate the mechanism of the energy transfer between adjacent joints by two-joint muscles. This model is made of four rigid links interconnected by revolute low friction joints. The model in the squat position (left panel) has only one source of mechanical energy: the stretched rubber band, GLM, which spans only the hip joint. Nevertheless, when the model is released from the squat position, all three joints extend (right panel), and positive mechanical work is done at each joint. The mechanical energy generated by the knee and ankle joint moments during extension has its origin in the energy generated by the GLM. It has been transferred to the knee and the ankle joints by the two-joint non-stretchable ropes RF and GA, respectively, which, by themselves, do not generate any mechanical energy.

With the advent of modern methods of inverse and forward dynamics analyses, and musculoskeletal modeling, it has become possible to clearly define energy transfer by two-joint muscles in ways that allow for quantitative estimations of the transported energy (van Ingen Schenau, 1990; Prilutsky, Zatsiorsky, 1994; Jacobs et al., 1996). For example, the rate of energy transfer by two-joint muscles to or from an adjacent joint, $P_j(t)$, can be estimated from the equality

$$P_j(t) = P_j^T(t) - \Sigma_j P^M(t) \qquad (1)$$

where $P_j^T(t)$ is the power of torque at the jth joint and $\Sigma_j P^M(t)$ is the sum of powers developed by all muscles serving the jth joint. If all muscles crossing the joint are one-joint muscles, then $P_j^T(t)=\Sigma_j P^M(t)$ and $P_j(t)=0$. However, if among muscles serving the jth joint there are two-joint muscles, the rate $P_j(t)$ is not necessarily equal to zero. For example, in the push-off phase of the model on Fig. 1, $P_j(t)>0$ at the knee and ankle joints because $P_j^T(t)>0$ and $\Sigma_j P^M(t)=0$, i.e. energy comes to these joints through the action of the RF and GA. At the same time, $P_j(t)<0$ at the hip joint because $P_j^T(t)<\Sigma_j P^M(t)$, i.e. energy transported from the hip to the knee through the RF.

These new theoretical methods have also permitted assessments of the potential performance of musculoskeletal models with altered designs that prevent the transfer of energy by two-joint muscles (Pandy, Zajac, 1991; Bobbert, van Zandwijk, 1994). It has been demonstrated, for example, that maximum jump height may be increased by about 2 cm, due to the inclusion of the two-joint gastrocnemius muscle, having specific moment arm values about the ankle and knee joints (Bobbert, van Zandwijk, 1994). More accurate estimates of, and new insight into, the transfer of energy by two-joint muscles have become available following the development of methods for making in-vivo recordings of the forces exerted by two-joint muscles. By knowing the force exerted by a two-joint muscle, and its estimated rate of length change, one can calculate muscle power and, subsequently, the amount of energy transferred by the two-joint muscle (Prilutsky et al., 1996).

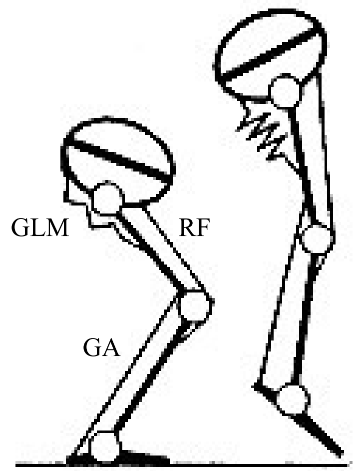

Figure 1: A physical model of the leg. A rubber band imitates a one-joint hip extensor, gluteus maximus (GLM). The two non-stretchable ropes represent the two-joint rectus femoris (RF) and gastrocnemius (GA). When model is released from a squat position (in which the GLM is stretched), all three joints extend and the joint moments in each joint do positive work, i.e. generate mechanical energy.

Estimated values of the mechanical energy transferred between adjacent joints range from 6 to 39 percent of the work done at a given joint in a variety of human and cat movements including walking, running, landing, and jumping (Bobbert and van Zandwijk, 1994; Prilutsky, Zatsiorsky, 1994; Jacobs et al., 1996; Prilutsky et al., 1996). These numbers indicate that a substantial part of energy released in a given joint can be generated by muscles that do not span it. This energy transfer appears to have important functional significance. Apart from the increase in the performance of explosive movements, it seems to allow proximal muscles (that generally have larger volumes than distal muscles, and thus have greater potential to generate and dissipate mechanical energy) to realize their work potential more fully. Because of the action of two-joint muscles, the large proximal muscles can do work on distal joints, and work done on distal joints by external forces can be partly dissipated by the proximal muscles.

REFERENCES

Bobbert, M.F., van Zandwijk, J.P. (1994) *Hum. Mov. Stud*., **13**, 697-716.
Jacobs, R. et al. (1996) *J. Biomech*., **29**, 513-523.
Kuo, A.D. (2001) In *Classics in Movement Science*, 290-315.
Pandy, M.G., Zajac, F.E. (1991*) J. Biomech*., **24**, 1-10.
Prilutsky, B.I. (2000) *Motor Control*, **4**, 1-44, 97-116.
Prilutsky, B.I. et al. (1996) *J. Biomech*., **29**, 391-403.
Prilutsky, B.I., Zatsiorsky, V.M. (1994) *J.Biomech*., **27**, 25-34.
van Ingen Schenau, G.J. (1990) *Neth. J. Zool*., **40**, 521-540.

TENSILE PROPERTIES OF THE *IN VIVO* HUMAN GASTROCNEMIUS TENDON: RELEVANCE TO FUNCTION AND LOCOMOTION

Constantinos N. Maganaris[1] and John. P. Paul[2]

[1]Centre for Biophysical and Clinical Research into Human Movement, Manchester Metropolitan University, Alsager ST7 2HL, UK, c.n.maganaris@mmu.ac.uk
[2]Bioengineering Unit, University of Strathclyde, Glasgow G4 0NW, UK

INTRODUCTION

Over the previous years, we have developed a method for *in vivo* measurement of human tendon mechanical properties (e.g., Maganaris & Paul, 1999 and 2000). The technique is based on displacement measurements of ultrasound echoes generated from the tendon, and avoids several problems associated with *in vitro*-material testing. In the present experiment we applied this *in vivo* method to obtain the tensile properties of the human gastrocnemius tendon, a high-stressed tendon suitable for spring-like action during locomotion. We sought to answer the following two questions: 1) Are the material properties of *in vivo* tendon related to its physiological function and loading. To answer this question, the results of the present study were compared with previous *in vivo* results from measurements in the human tibialis anterior tendon, which acts as force transmitter and is less highly stressed physiologically. 2) Does the spring-like action of gastrocnemius tendon contribute to the external work produced by the locomotor system during walking? To answer this question, we combined the present results with previous results of tendon behaviour and external work during walking.

METHODS

Measurements were taken in six men. The gastrocnemius tendon elongation during tendon loading–unloading induced by muscle contraction–relaxation was measured using real-time ultrasonography. Tendon forces were calculated from the moment generated during isometric plantarflexion contraction using tendon moment arm length data measured *in vivo* from Magnetic Resonance Images (MRIs). Tendon stiffness data were calculated from the slope of the tendon force–elongation curve, and were then normalized to the tendon's original dimensions, obtained from morphometric analysis of sonographs and MRIs, to estimate the tendon Young's modulus. Mechanical hysteresis values were obtained from area calculations by numerical integration.

RESULTS AND DISCUSSION

The elongation of the tendon increased curvilinearly with the force acting upon it, from 1.7±1 mm at 87.5±8.5 N to 11.1±3.1 mm at 875±85 N (Fig. 1). The tendon Young's modulus and mechanical hysteresis were 1.16±0.15 MPa and 18±3%, respectively. These values are very similar to the respective values previously obtained from *in vivo* measurements in the human tibialis anterior tendon (1.2 MPa and 19%; Maganaris & Paul, 1999 and 2000), thus indicating that the material properties of tendon are independent of physiological loading and function. Similar conclusions have previously been reached from *in vitro*-based measurements (Pike *et al.* 2000; Pollock & Shadwick, 1994). Combining the present tendon force–elongation data with previously reported data of gastrocnemius tendon elongation during walking (Fukunaga *et al.* 2001) indicates that the gastrocnemius tendon would provide ~6% of the total external work produced by the locomotor system. This estimate illustrates the contribution of passive elastic mechanisms on the economy and efficiency of walking. The contributions would be greater in more active exercise such as running.

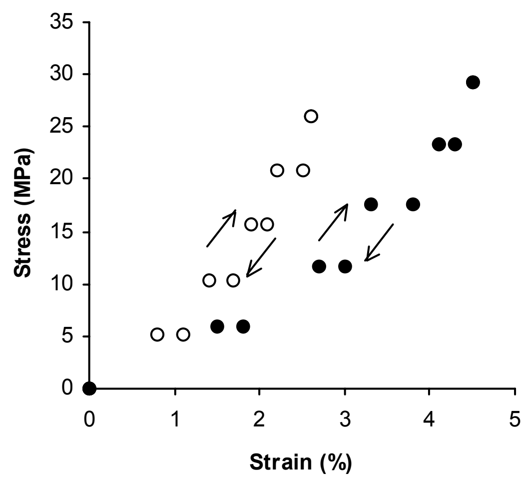

Fig. 1: Individual stress–strain relations of the tibialis anterior tendon (*open symbols*) and gastrocnemius tendon (*filled symbols*). Arrows indicate loading and unloading directions.

REFERENCES

Fukunaga *et al.* (2001). *Proc. R. Soc. Lond.* B **268**, 229-233.
Maganaris & Paul (1999). *J. Physiol.* **521**, 307-313.
Maganaris & Paul (2000). *J. Biomech.* **33,** 1723-1727.
Pike *et al.* (2000). *J. Exp. Biol.* **203**, 2187-2193.
Pollock & Shadwick (1994). *Am. J. Physiol.* **266**, R1016-R1021.

TENDON MECHANICAL PROPERTIES FOR LOCOMOTION

Robert F. Ker
School of Biology, The University of Leeds, Leeds, LS2 9JT, UK
r.f.ker@leeds.ac.uk

INTRODUCTION AND TENDON FUNCTION

Locomotion requires the co-ordinated use of numerous skeletal muscles and their tendons. Each tendon is under tension while it transmits force. It must, necessarily, have adequate stiffness, strength and resistance to fatigue for this function. Furthermore, mammalian tendons show low hysteresis loss under cyclic loading in tension. With a few exceptions, tendons bend readily and therefore buckle easily.

All tendons can store strain energy. This spring-function is made full use of in some of the ankle extensors and toe flexors of the larger mammals to save energy when running. It may also be used in other situations, such as jumping, tail-waving or wing-beating. A spring functions by stretching, but for other tendons extension can be inconvenient. For this reason, tendons differ widely in the strains and stresses to which they are subjected in life (Ker et al, 1988, Pollock and Shadwick, 1994b). The high stress of tendons used as springs is achieved by having muscles of relatively large physiological cross-sectional area. Stress and/or strain have been measured *in vivo* for a number of tendons (e.g. Komi et al., 1992; Biewener and Baudinette, 1995; Maganaris et al., 1999). For the others, we rely on assessments calculated from measurements of the areas and lengths of tendons and their muscles.

STIFFNESS AND HYSTERESIS

The elastic modulus of adult mammalian tendon in the linear region of the stress-strain curve (stress > 20 MPa) is between 0.9 and 1.8 GPa. Variations do not correlate with whether the spring-like properties of the tendon are used or with the mass of the mammal (Pollock and Shadwick, 1994a). Elastic modulus increases during growth. For low stress tendons, the effective modulus is less because these operate in the toe region. At very low stress, the modulus is effectively zero as tendons are pulled taut from a buckled condition.

The hysteresis loss is around 10%. Variations are considerable but, as with stiffness, do not seem to correlate with tendon function or animal mass.

STRENGTH

Most tendons are far too thick to be at risk of rupture from over-stretching. To put this the other way round, the muscle has much too small an area to break its tendon, typically by a factor of 5-fold. The situation with the tendons used as springs is entirely different. They probably have low safety factors, though the measurement of strength is difficult and therefore safety factors cannot the assessed with much certainty. Ultimate tensile strength is ≥ 100 MPa.

FATIGUE QUALITY

The resistance of tendons to fatigue varies by perhaps two orders of magnitude in step with the variations in stress-in-life (Ker et al., 2000). Each tendon seems to the designed to be only just good enough for its function. Being 'good enough' includes allowing for the availability, in life, of repair. It seems that all tendons must be subject to ongoing repair of fatigue damage (Wang et al., 1995; Schechtman and Bader, 1997; Ker et al. 2000). With tendons functioning as springs, because of the low safety factor, the first symptom of a lapse in the balance between damage and repair may be rupture. Rupture is a clinical problem with the human Achilles tendon and the horse superficial digital flexor tendons.

THE DESIGN OF TENDONS FOR LOCOMOTION

For most tendons, the primary need is for the correct stiffness and this is adjusted by altering thickness. The strength of the resulting tendon is more than adequate. In contrast, for spring-tendons, the first need is for sufficient strength. In each case, fatigue quality appears to be adapted to make the tendon just capable of living with its stress-pattern. In limbs, only those tendons which are maximally loaded at the mid-point of ground contact are major springs. Even with this restriction, only some of the potential is used to full advantage. In most limbs, the deep toe flexor is of relatively low stress. In many mammals, only one of the gastrocnemius and plantaris tendons of the hind limb has a strikingly high stress. Presumably, the other tendons and their muscles have functions additional to energy saving. Small mammals, do not have even one tendon of really high stress and thus seem not to take much advantage of the possibility of energy-saving. This fits in with their observed high cost of locomotion, but leaves unanswered the question as to why small mammals are designed in this way.

REFERENCES

Biewener A. A. and Baudinette, R. V. (1995) *J. Exp. Biol.,* **198**, 1829-1841.
Ker R. F. et al. (1988) *J. Zool. Lond.,* A **208**, 309-324.
Ker R. F. et al. (2000) *J. Exp. Biol.,* **203**, 1317-1327.
Komi, P. V. et al. (1992) *Clin. Sports Med.,* **11**, 521-531.
Maganaris C. N. and Paul, J. P. (1999) *J. Physiol. Lond.,* **521**, 307-313.
Pollock, C. M. and Shadwick, R. E. (1994a) *Am. J. Physiol.,* **266**, R1016-1021.
Pollock, C. M. and Shadwick, R. E. (1994a) *Am. J. Physiol.,* **266**, R1022-1031.
Schechtman, H. and Bader, D. L. (1997) *J. Biomech,.* **30**, 829-835.
Wang, X. T. et al. (1995). *J. Exp. Biol.,* **198**, 847-852.

LOSS BEFORE RECOVERY: SOME PARTIAL ANSWERS TO OLD LOCOMOTION QUESTIONS

John E.A. Bertram[1], Andy Ruina[2] and James R. Usherwood[1]

[1]Nutrition, Food and Exercise Sciences, Florida State University
[2]Theoretical and Applied Mechanics, Cornell University

INTRODUCTION

Recent advances in our understanding of locomotion using legs, stemming largely from work modeling artificial passive dynamic systems (Garcia et al., 1998; Kuo, 2001; McGeer, 1990), provide an opportunity to re-evaluate a wide range of terrestrial locomotion strategies. The key feature in this approach is to evaluate the cause of mechanical energy loss, attributed to collisional loss at foot contact, rather than the more traditional tracking of energy exchange and recovery. It is found that collisional loss so dominates the energetics of mammalian legged locomotion that remarkably simple models are able to explain the basic mechanics behind a number of misunderstood mammalian locomotion behaviors. We demonstrate this by using a common approach to two quite different examples: gibbon brachiation and the quadrupedal gallop.

METHODS

Limbs contacting the ground with non-negligible velocity will result in loss due to inelastic collision. The component of the velocity lost will depend on the orientation of the CoM velocity vector and its relationship to the contacting leg (Fig. 1). That component oriented parallel with the leg will be lost. The remainder, perpendicular to the leg, is available to continue the motion of the animal. Within the constraints of a given locomotory system, analysis of the collision geometry indicates the consequences of moving on a finite number of limbs.

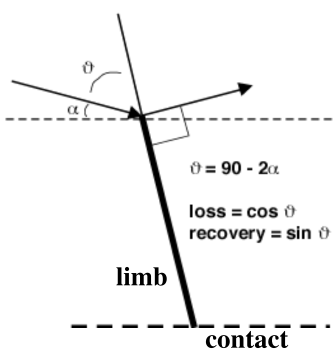

Fig. 1: Simple collision-based model of limb interaction with substrate. Vectors indicate velocity of center of mass before and after foot contact.

RESULTS AND DISCUSSION

Gibbon: Brachiation has intrigued locomotion researchers for a long time, largely due to the resemblance of brachiation to the swing of a pendulum, with the potential for mechanically efficient motion. However, pendular dynamics do not explain much of the fast moving brachiator's behavior. The gibbon inhabits an extremely complex environment and must face the challenge of adjusting sequential step lengths to match support opportunities. We demonstrate that adjusting the ballistic path of the flight phase between handholds to reduce collisional loss is a key feature of brachiation, and conclude that the energetics of brachiation relates to the skipping of a stone on a pond surface, and the pendulum model is actually quite uninformative.

Gallop: The quadrupedal gallop displays features in common with both pendular and spring-based exchange. However, the functional reason behind the details of these gaits has been elusive. We show that consideration of collision loss can account for many aspects of this gait, even without consideration of spring-based storage and recovery.

SUMMARY
Analysis of collision interaction of the support limb with the supporting substrate provides an alternate approach to understanding the function, behavior and morphological features of much of mammalian legged locomotion.

REFERENCES

Garcia, M., Chatterjee, A., Ruina, A., Coleman, M. (1998) *J. Biomech. Eng.* **120**, 281-288.
Kuo, A.D. (2001) *J. Biomech. Eng.* **123**, 264-269.
McGeer, T. (1990) *Int. J. Robot Res.* **9**, 68-82.

MECHANICAL DETERMINANTS OF THE METABOLIC COST OF WALKING: WORK, FORCE AND SWING

Rodger Kram
Department of Kinesiology and Applied Physiology, University of Colorado USA
rodger.kram@colorado.edu http://stripe.colorado.edu/~kram/

INTRODUCTION

The basic energy saving mechanism in walking is the inverted pendulum-like exchange of kinetic and gravitational potential energy. This mechanism allows nearly perfect mechanical energy exchange during the single stance phase. However, during the transition between support legs, mechanical energy is dissipated and must be replaced by the muscles. Further, metabolic energy is required to generate the forces needed to maintain the stance leg as a strut that can resist gravity. Some metabolic energy is also needed to swing the legs relative to the center of mass. My goal in this presentation is to weave together recent experiments that have quantified these major components of the metabolic cost of walking.

METHODS

To quantify the external mechanical work performed by each limb, my colleagues Max Donelan and Art Kuo developed the individual limbs method (ILM) (Donelan *et al.*, 2002). This work is needed to redirect the center of mass from a downward arc at the end of the stance phase to an upward arc over the subsequent stance leg. Two force platforms recorded the individual foot forces. The summed force signals of both platforms were used to calculate the center of mass velocity. The power performed on the center of mass was calculated as the dot product of each individual leg ground reaction force and the velocity of the center of mass. Integrating power yielded work. Donelan *et al.* (2001) measured both the ILM work and net metabolic cost for humans walking over a range of speed and stride length combinations. In all experiments described here, net rates of metabolic energy consumption (walking – standing) were measured from expired gas analysis. In a related study, Jinger Gottschall and I estimated the metabolic cost of generating horizontal propulsive forces in walking by applying an external horizontal forward pulling forces to the waists of subjects walking on a treadmill. We inferred that the reduction in metabolic cost when aiding forces were applied reflected the metabolic cost of generating the propulsive forces with muscles during normal walking. To infer the relative contributions of performing external ILM work, supporting body weight and swinging the legs Tim Griffin and I used loading experiments. Subjects walked with strips of lead (= to 0, 10, 20 and 30% of body mass) wrapped symmetrically around the waist. We calculated the cost of generating force from the active muscle volume needed to support body weight and used the inverse of contact time as a proxy for the rate of force generation.

RESULTS & DISCUSSION

The individual limbs method revealed about 33% more external work than would have been calculated using the combined limbs method. For walking at 1.25 m/sec the efficiency of performing positive mechanical work was about 21%. Knowing that and the ILM power allowed us to calculate that the work of re-directing the center of mass during double support accounted for about 60% of the net metabolic cost of walking. A similar conclusion was drawn from the horizontal aiding force experiments. When a steady external force of 10% of body weight was applied at the waist that acted to re-accelerate the center of mass, the net metabolic cost was reduced by 53%. The loading experiments showed that the net metabolic cost of walking increased in a greater than proportional manner with the load. In contrast, the ILM work increased in direct proportion to the load. Compared to the ILM work, the cost of generating force appeared to more closely parallel the increase in metabolic cost when loads were carried. The loading experiments did not alter leg swing mechanics, yet the net metabolic cost increased in greater than proportionate manner with the waist carried load. We infer that the metabolic cost of swinging the legs is likely small at 1.25 m/sec.

2002 marks the 25th anniversary of Cavagna, Heglund and Taylor's classic paper that established that legged animals use two basic mechanisms to conserve mechanical energy (Cavagna *et al.* , 1977). They described a dichotomy between the inverted-pendulum model for walking and the spring mechanism of running. Recent discoveries described above complement the classic inverted pendulum model so as to better explain the energy costs and savings involved in walking. Ultrasound recordings of calf muscle fascicle length changes during walking (Fukunaga *et al.*, 2001) and other innovative non-invasive experiments (Hof *et al.*, 2002) indicate that springs are also important in walking. A hybrid model for walking appears to be emerging.

REFERENCES

Donelan, J. M. *et al.* (2001) *Am. Soc. Biomech.,* 229-230.
Donelan, J. M. *et al.* (2002) *J. Biomech.*, **35**,117-124.
Cavagna G. A. *et al.* (1977) *Am. J. Physiol.*, **233**, R243.
Fukunaga, T. *et al.* (2001) *Proc. R. Soc. Lond. B.* **268**,229-233.
Hof, A.L. *et al.* (2002) *Acta Physio. Scand.* **174**, 17-30.

ACKNOWLEDGEMENTS

Supported by NIH AR44688.

STICKS-CONNECTED-BY-HINGES MODELS OF HUMAN WALKING: RESULTS TO DATE

Andy Ruina
Theoretical and Applied Mechanics, and Mechanical and Aerospace Engineering, Cornell University

INTRODUCTION

Robots have motors and people have muscles. What for? To guide motions and to make up for lost mechanical energy. How much guidance is fundamentally needed for repetitive tasks? How much energy needs to be supplied for what losses? One approach to understanding the need for motors and controllers is what can be done without them. Tad McGeer demonstrated (e.g., 1990) with simple computational models and with physical devices that uncontrolled human-like walking motions can be achieved with, to put it simply, sticks and hinges that walk downhill. The motions of these toy-like devices are energetically efficient (low specific transport cost) and stable (limit-cycles with linearized stability). How much can we learn from these simple devices?

METHODS

Over the past several years we (faculty, students, post-docs and visitors at Cornell) have continued the approach of McGeer using heuristic reasoning, experiments, analysis and computational models based on basic ideas in dynamical systems theory.

RESULTS

We have found that, in principle, some of these devices can walk on arbitrarily small slopes and thus approach perfect efficiency and that robot configurations that have this efficiency are reminiscent of the human design. These models can also limp (period 2), waltz (period 3), and stumble (chaos). The devices obey an energy scaling law where (gravitational) power consumption is proportional to v^4, a feature the human control system may seek to avoid. One unintuitive feature we have discoverred both in experiment and simulation, is that it is possible to have a walking machine that has no stable standing posture, yet can walk stably. Another device we have built has a more natural looking gait, we believe, than any robot ever built. The talk will be illustrated by pictures, simulations, and videos of our devices.

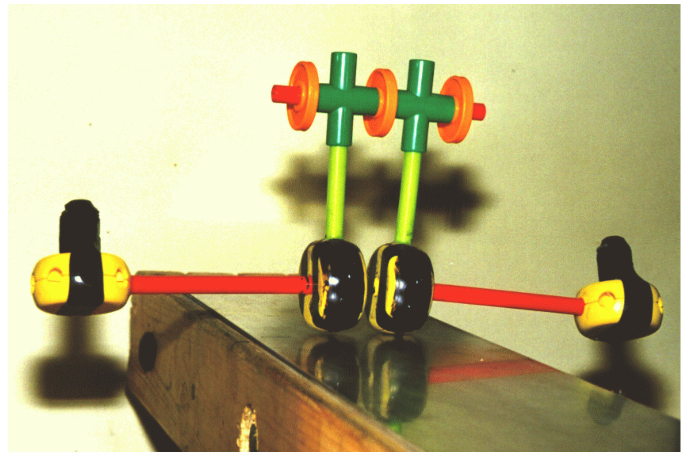

Fig. 1: A walking toy that cannot stand still.

SUMMARY

A few morals seem to be exposed: much of the coordination observed in locomotion can be understood from a purely mechanical point of view, locomotion efficiency seems to based on impacts and avoidance of impacts, and stability comes in part from utilizing the non-holonomic constraint of Intermittent contact.

See www.tam.cornell.edu/~ruina/hplab for preprints, reprints videos and photos.

REFERENCE

McGeer, T. (1990) *Int. J. Robot Res.* **9**, 68-82.

ACKNOWLEDGEMENTS

The work reported here has been done by, or aided by Michael Coleman, Steve Collins, Mariano Garcia, Katja Mombauer, Martijn Wisse, Mario Gomes, John Camp, Yan Yevmenko and other students at and visitors to the Cornell Human Power and Robotics Laboratory.

VARIABLE GEARS IN ANIMAL LOCOMOTION: EFFECTS OF SPEED, GAIT AND SIZE

Andrew A. Biewener
Concord Field Station, Department of Organismic and Evolutionary Biology, Harvard University, Cambridge MA, USA
abiewener@oeb.harvard.edu

INTRODUCTION

Animals walk, run and hop with characteristic postures. Limb posture, in turn, affects the magnitude of joint moments and muscle forces that must be exerted to support an animal's weight on the ground. Size-related differences in limb posture have been found to influence the scaling of muscle limb mechanical advantage (LMA) in terrestrial animals, enabling them to maintain uniform muscle and bone stress (constant safety factor; Biewener, 1989). By running on more upright and slender limbs, large animals reduce the magnitude of joint moments and hence, musculoskeletal force that their limbs must transmit to support ground reaction forces imposed during running. However, adjustments in limb mechanical advantage to accommodate large differences body size necessarily have an inverse gearing effect on the velocity and range of limb movements. This paper explores how limb mechanical advantage changes with speed, gait and body size. It also examines how changes in LMA affect the speed and range of limb movements in animals of different size.

MUSCLE MECHANICAL ADVANTAGE

Muscle mechanical advantage is often defined simply as the moment arm of a muscle acting at a particular joint. However, the force (F) that agonist muscles must generate to counteract external joint moments produced by the ground reaction force (G) acting on the limb is determined by the ratio of muscle mechanical advantage (r) to the mechanical advantage (R) of G acting about limb joints ($R/r = \int G/\int F$).

Fig. 1

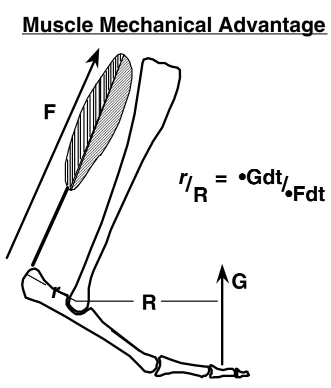

Muscle mechanical advantage at individual joints ($\int G/\int R$) can be averaged to determine overall LMA. Although this analysis ignores segmental and gravitational moments of limb segments, external moments exerted by G dominate during limb support and thus are considered here in relation to muscle force requirements for weight support and limb movement during stance.

METHODS

Different-sized mammalian species ran, trotted or hopped over a force platform with high-speed video or film recordings made from a lateral view. Muscle moment arms were determined from limb dissection or palpation. From these recordings and measurements, overall LMA was determined as a function of speed, gait and body size.

RESULTS & DISCUSSION

Except for humans, LMA of all species examined did not change significantly with running speed or change of gait (L-S regression slopes not significantly different from 0). When humans change gait from a walk to a run, however, LMA is significantly reduced (27%, $p < 0.01$), largely due to decreased $\int G/\int F$ at the knee (Biewener & Chang, 1992); associated with a more flexed posture and spring-like use of the limb (McMahon & Cheng, 1992). Changes of LMA associated with speed changes within human walking and running gaits however were not significant. The scaling of LMA (r/R) in more closely related rodents (from deer mice to capybara, 0.02 to 35 kg) $\alpha M^{0.25}$ ($R^2 = 0.84$) closely matched the more general relation for quadrupedal mammals as a whole (Biewener, 1989), indicating that adjustments of LMA also occur within more closely related taxonomic groups.

The increase in LMA with size indicates a trade-off in the speed of locomotor movements for enhanced weight support. Given that the distance ($dL\ \alpha\ Rd\Phi$) and speed of movement (dL/dt) of more distal limb segments, or the limb as a whole, depends on the rate and distance of muscle shortening (dS) in relation to the muscle's moment arm ($dS\ \alpha\ rd\Phi$), the scaling of LMA suggests $dS/dL\ \alpha M^{0.25}$. Assuming equivalent fractional shortening of muscle fibers (dS/L_f constant) in different-sized animals, such that $dS\ \alpha\ L_f\ \alpha\ M^{0.25}$ (Alexander et al. 1981), this suggests that the absolute distances of limb segment motion and rates of movement remain constant across size (dL and $dL/dt\ \alpha\ M^0$).

A similar result was obtained by Hill (1950) in his classic lecture presented to the Royal Society relating the mechanical properties of muscles to the dimensions and locomotor movements of animals. Hill's analysis assumed isometric scaling, or geometric similarity. Although terrestrial mammals scale close to isometry (Alexander et al. 1979 & 1981), they exhibit allometric patterns of muscle architecture, with larger animals having shorter-fibered, more pinnate muscles than small animals. This is matched by the scaling of LMA to predict generally similar locomotor speeds across size.

REFERENCES

Alexander, R M, et al. (1979) *J.Zool.*, **189**, 305-314.
Alexander, R M, et al. (1981) *J.Zool.*, **194**, 539-552.
Biewener, A A, (1989). *Science.* **245**, 45-48.
Biewener, A A, Chang J (1992). *J. Biomech.* **26**, 294.
Hill, A V (1950). *Sci. Prog.* **38**, 209-230.
McMahon, T A, Cheng, G C (1990). *J. Biomech* **23**, 65-78.

`WORK OR FORCE MINIMIZATION AS A CRITERION FOR THE EVOLUTION OF LOCOMOTION

R. McNeill Alexander
School of Biology, University of Leeds, Leeds LS2 9JT, UK
r.m.alexander@leeds.ac.uk

INTRODUCTION

Humans and horses tend to adjust their speeds and gaits, and humans adjust their stride frequencies, so as to minimize metabolic energy costs (Hoyt and Taylor, 1981; Minetti *et al.*, 1995). It seems likely that other animals (fliers and swimmers as well as walkers and runners) also prefer patterns of movement that minimize metabolic costs. Our understanding of locomotion could be greatly improved, if we could confidently predict how a change in a pattern of movement would affect these costs.

THE METABOLIC COST OF WORK

It is generally much easier to calculate the work done in a movement, than to predict metabolic costs from first principles. The hypothesis, that work is minimized in locomotion, has often been adopted (for example Cavagna *et al.*, 1977 on walking and running; Rayner, 1999 on flight). Such discussions tend to imply that metabolic energy costs are proportional to work. However, the efficiency of a muscle depends on the rate at which it is shortening, and muscles differ in efficiency even at their optimum shortening speeds. Also, the efficiencies with which work is performed in locomotion are much lower for small running and flying animals than for large ones (Full and Tu, 1991; Rayner, 1995).

THE METABOLIC COST OF FORCE

Muscles require metabolic energy to generate force, even when the contraction is isometric and so does no work. Roberts *et al.* (1998) have shown for mammals and birds that metabolic rate while running can be predicted by a calculation that takes account of the forces exerted, but not of the work done. It is assumed that the metabolic rate of a muscle is proportional to (force×intrinsic speed), and that the intrinsic speed (v_{max}) is inversely proportional to foot contact time.

CALCULATING METABOLIC ENERGY COSTS

Alexander (1997) and Minetti and Alexander (1997) used empirical equations that took account of both force and work to calculate metabolic energy costs for simple models of locomotion. We had some success in explaining the changes of duty factor, force pattern and stride length that humans make, as they walk or run at different speeds.

It can be shown from the equations of Alexander (1997) that the rate of use of ATP energy P of a muscle exerting force F while shortening isotonically at speeds v between 0 and $0.5v_{max}$ is given approximately by

$$P \approx 0.07Fv_{max} + 2.3Fv \qquad 1.$$

Notice that the first term on the right hand side of this equation is proportional to the force F, and the second to the rate Fv at which the muscle is doing work. Thus the metabolic rate of an active muscle may be regarded as the sum of the energy cost of exerting force, and the cost of doing work. Disappointingly, equation (1) fails to explain the low efficiency of running for small mammals.

If muscles always operated at the same value of v/v_{max}, the two terms on the right of Equation (1) would be proportional to one another, and metabolic rates could be calculated equally well from forces or from work performance. However, constant v/v_{max} cannot be assumed, in analyses such as that of Alexander (1997) that seek to predict optimum muscle properties for particular patterns of movement.

Equation (1) is based on experiments in which muscles made single isotonic contractions. However, locomotion generally involves repeated cycles of lengthening and non-isotonic shortening. The behaviour of muscle in such cycles cannot be predicted accurately from the results of isotonic experiments (Askew and Marsh, 1998). We need better understanding of the physiology of cyclic contraction, to enable us to predict metabolic costs of different styles of locomotion. There are many variables that may affect the cost of cyclic contraction, but it may be worthwhile to test the hypothesis, that the metabolic cost is simply a function of (mean force×v_{max}) and mean power output. This could be done by experiments in which the heat produced in cyclic contraction was measured (Barclay, 1994), while varying the ratio of mean force to power output by varying the timing of stimulation (Josephson, 1985).

REFERENCES

Alexander, R. McN. (1997) *J. theor. Biol.*, **184**, 253-9.
Askew, G. N., Marsh, R. L. (1998) *J. exp. Biol.*, **201**, 1527-40.
Barclay, C. J. (1994) *J. exp. Biol.* **193**, 65-78.
Cavagna, G. A. et al. (1977) *Am. J. Physiol.* R243-61.
Full, R. J., Tu, M. S. (1991) *J. exp. Biol.*, **156**, 215-31.
Hoyt, D. F., Taylor, C. R. (1981) *Nature*, **292**, 239-40.
Josephson, R. K. (1985) *J. exp. Biol.* **114**, 493-512.
Minetti, A. E., Alexander, R. McN. (1997) *J. theor. Biol.*, **186**, 467-76.
Minetti, A. E. et al. (1995) *Med. Sci. Sports Exercise*, **27**, 1194-1202.
Rayner, J. M. V. (1995) *Israel J. Zool.*, **41**, 321-42.
Rayner, J. M. V. (1999) *J. exp. Biol.*, **202**, 3449-61.
Roberts, T. J. et al. (1998) *J. exp. Biol.*, **201**, 2745-51.

TIME-DOMAIN REPRESENTATION OF VENTRICULAR-ARTERIAL COUPLING AS A WINDKESSEL AND WAVE SYSTEM

John V. Tyberg,[1] Jiun-Jr Wang, [1] Nigel G. Shrive,[2] and Kim H. Parker[3]

[1]Departments of Medicine and Physiology & Biophysics (jtyberg@ucalgary.ca)
[2]Department of Civil Engineering
University of Calgary, Calgary, Alberta, Canada
[3]Physiological Flow Studies Unit, Imperial College of Science, Technology and Medicine, London, United Kingdom

INTRODUCTION

Shape differences between central aortic pressure (P_{Ao}) and flow waveforms have never been explained satisfactorily in that the assumed explanation — the presence of substantial reflected waves during diastole — has never been demonstrated. We propose a functional, time-domain, arterial model that combines a blood-conducting system and a reservoir (i.e., Frank's hydraulic integrator, the Windkessel).

METHODS

Aortic pressures, flows, and diameters were measured in 16 anesthetized dogs (paced at ~70 bpm), so we could calculate their Windkessel pressure (P_{Wk}) and volume (V_{Wk}) which were compared with thoracic aortic volume. Windkessel pressure was determined by the difference between aortic inflow and its outflow, $\frac{dP_{Wk}(t)}{dt} = \frac{dP_{Wk}}{dV_{Wk}} \frac{dV_{Wk}(t)}{dt} = \frac{Q_{in}(t) - Q_{out}(t)}{C}$, where $C = \frac{dV_{Wk}}{dP_{Wk}}$ is the compliance. The outflow was assumed to be driven by the difference between the Windkessel pressure and the asymptotic pressure (P_∞) toward which diastolic aortic pressure decayed exponentially: $Q_{out}(t)=(P_{Wk}(t)-P_\infty)/R$. R is the effective resistance of the peripheral systemic circulation. We calculated the total work performed by the LV during systole from the area of the P-V loop and then determined the fraction of this work that was done in charging the Windkessel. The remainder, "pulsatile work," was considered to be the sum of the work done overcoming the proximal resistance and that done overcoming inertance.

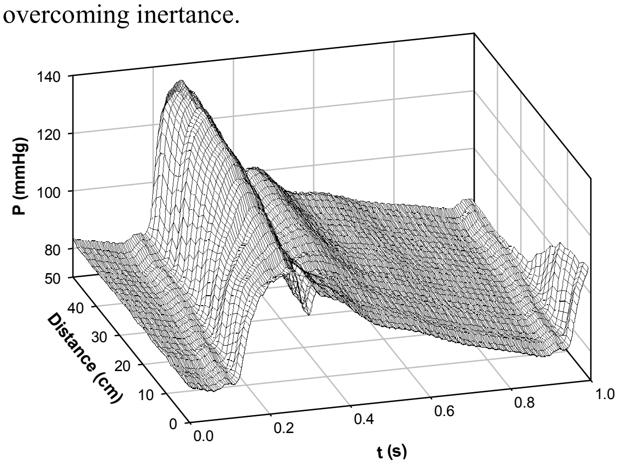

Fig. 1: A 3-D plot of aortic pressure versus time and distance (by 2-cm increments from the aortic root to the femoral artery) in a single dog. After waves have dissipated during diastole, pressures are almost equal at every location.

RESULTS AND DISCUSSION

To demonstrate that aortic pressure is the combination of the effects of waves and the Windkessel mechanism, a 3-D pressure-distance-time plot was constructed by measuring aortic pressure at 2-cm increments from the aortic root to the femoral artery (Fig. 1). During diastole, when there are no waves, pressure is distance-independent as Frank postulated.

We find that P_{Wk} is proportional to thoracic aortic volume and that the volume of the thoracic aorta comprises 45.0±1.8% (SE) of total V_{Wk}. We calculated the fraction of the total LV work that is expended in charging the Windkessel (recoverable) and found it to be 86.8±1.1%, the remainder being due to pulsatile work. When we subtracted P_{Wk} from P_{Ao}, we found that the difference (excess pressure, P_{ex}) was proportional to aortic flow, thus demonstrating that the shape differences between aortic driving pressure (P_{ex}) and flow are negligible and implying that reflected waves are minimal (Fig. 2). The ratio of P_{ex} to aortic flow is equal to characteristic impedance (from Fourier analysis), consistent with there being a resistive loss in ejecting blood into the Windkessel.

SUMMARY

We suggest that P_{Ao} is the summation of a time-varying reservoir pressure (i.e., P_{Wk}) and pressure due (primarily) to forward-going waves. Most (~87%) of the total energy is used to charge the Windkessel, which can be considered useful work because ultimately it propels blood through the peripheral resistance into the venous system during diastole. Waves account for ~13% of the total LV work, which is used to overcome (proximal) arterial resistance and inertance.

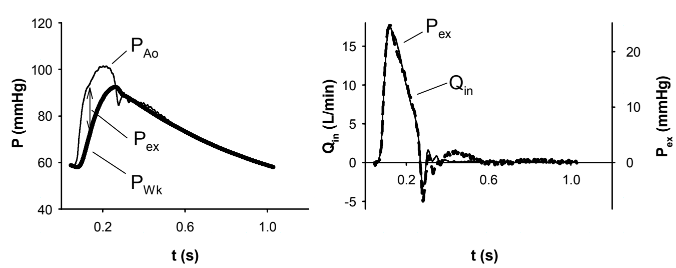

Fig. 2: Left. Typical aortic root pressure (P_{Ao}) and calculated Windkessel pressure (P_{Wk}). Right: Excess pressure (thick dashed line; P_{ex}, calculated by subtracting the Windkessel pressure from the aortic pressure) and aortic flow (Q_{in}; thin solid line) plotted against time and scaled to equalize their peak values. Their shapes are almost identical.

A NOVEL AGE-RELATED INDEX OF CARDIOVASCULAR FUNCTION

Kiyomi Niki[1], Motoaki Sugawara[1], Chang Dehua[1], Takashi Okada[2], Akimitsu Harada[2]

[1]Department of Cardiovascular Sciences, Tokyo Women's Medical University School of Medicine, Tokyo, Japan, E-mail:mniki@nora.hij.twmu.ac.jp
[2]Research Laboratory Aloka Co. Ltd, Tokyo, Japan

INTRODUCTION

The maximum values of blood flow acceleration (dU/dt) and the rate of change in diameter [(dD/dt)/D] in the carotid artery during initial ejection are higher in younger than older subjects. WID=(dU/dt)(dD/dt)/D is a modified wave intensity, which is a novel index of cardiovascular function. We hypothesized that the reciprocal of the maximum value of WID, which is defined as α = 1/Max(WID), is in proportion to age in the normal group. We evaluated α in normal subjects and patients with dilated cardiomyopathy (DCM), old myocardial infarction (OMI), and hypertension (HT).

METHODS

We studied the common carotid artery in the normal (n=126, mean age 45, range 10 - 74 years), DCM (n=40, mean age 47, range 20 – 75 years), OMI (n=14, mean age 67, range 56 – 77 years), and HT (n=11, mean age 65, range 52-76 years) groups using a specially designed wave intensity system (Aloka SSD-5500), which simultaneously measures flow velocity and diameter by Doppler and echo tracking, and provides WID, and hence α.

RESULTS AND DISCUSSION

In the normal group, α was linearly related to age with a very narrow 95% confidence interval (goodness-of-fit r^2=0.52). In the DCM group, α also increased with age (r^2=0.32). However, the slope of the regression line was significantly steeper, and the 95% confidence interval was much broader compared with the normal group. In the OMI and HT groups, α was not related to age, but α in the OMI group was significantly higher compared with a subgroup of the normal group older than 62 years (P<0.001, Dunnett's test following ANOVA with the normal, HT and OMI groups).

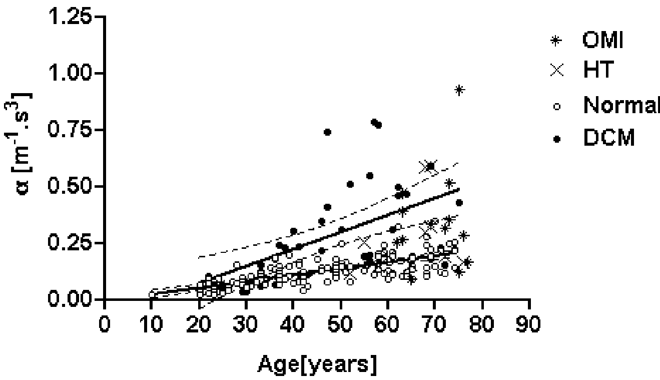

Figure 1: Relationship between α and age.

SUMMARY

α was closely related to age in the normal group, and may be a good index of youthfulness of the cardiovascular system.

REFERENCES

1. Parker KH, Jones CJH (1990) Forward and backward running waves in the arteries: analysis using the method of characteristics. ASME J Biomech Eng **112**: 322-326
2. Jones CJH, Sugawara M, Davies RH, Kondoh Y, Uchida K Parker KH (1994) Arterial wave intensity: physical meaning and physiological significance. Harwood Academic Publishers, Chur, pp 129-148
3. Ramsey MW, Sugawara M (1997) Arterial wave intensity and ventriculoarterial interaction Heart Vessels **supple 12**: 128-134
4. Harada A, Okada T, Sugawara M, Niki K (2001) Development of a non-invasive real time measurement system of Wave intensity. 2000 IEEE Ultrasonics Symposium: 1517-1520
5. Niki K, Sugawara M, Uchida K, Tanaka R, Tanimoto K, Imamura H, Sakomura Y, Ishizuka N, Koyanagi H , Kasanuki H (1999) A noninvasive method of measuring wave intensity, a new hemodynamic index: application to the carotid artery in patients with mitral regurgitation before and after surgery. Heart Vessels **14**: 263-271

WAVE INTENSITY IN THE CAROTID ARTERY IS A NEW INDEX OF LEFT VENTRICULAR SYSTOLIC AND EARLY DIASTOLIC PERFORMANCE

Nobuyuki Ohte[1], Hitomi Narita[1], Kiyomi Niki[2], Takashi Okada[3], Akimitsu Harada[3],
Motoaki Sugawara[2], Genjiro Kimura[1]

[1]Third Department of Internal Medicine, Nagoya City University Medical School, Nagoya, Japan, ohte@med.nagoya-cu.ac.jp
[2]Department of Cardiovascular Sciences, Tokyo Women's Medical University, Tokyo, Japan
[3]Research Laboratory, Aloka Co., Ltd., Tokyo, Japan

INTRODUCTION

Wave intensity (WI) is a new hemodynamic index, which is defined as (dP/dt)•(dU/dt) at any site of the circulation, where dP/dt and dU/dt are the time derivatives of blood pressure and velocity, respectively. However, pathophysiological meanings of this index have not been fully elucidated. Accordingly, we investigated the characteristics and clinical significance of WI.

METHODS

The study subjects consisted of 64 patients with coronary artery disease who underwent cardiac catheterization using a catheter-tipped micromanometer. WI was obtained at the right carotid artery using a newly developed system in which combined color Doppler for velocity measurement and echo-tracking method for acquiring vessel diameter changes (SSD-5500, Aloka, Tokyo, Japan) were applied. Using this system, vessel diameter changes were converted to pressure waves. Then, the temporal alteration of calculated (dP/dt)•(dU/dt) was automatically displayed.

RESULTS

The WI of the subjects showed two positive sharp peaks (**Figure 1**). The amplitude of the first peak during very early left ventricular (LV) ejection correlated significantly with max.dP/dt of LV pressure rise ($r=0.74$, $p<0.001$). The magnitude of the second peak at the end of ejection correlated significantly with min.dP/dt of LV pressure decay (r=□0.61, $p<0.001$) and with time constants of LV relaxation (tau from a phase loop: r=□0.77, $p<0.001$; tau from Weiss's method: r=□0.63, $p<0.001$).

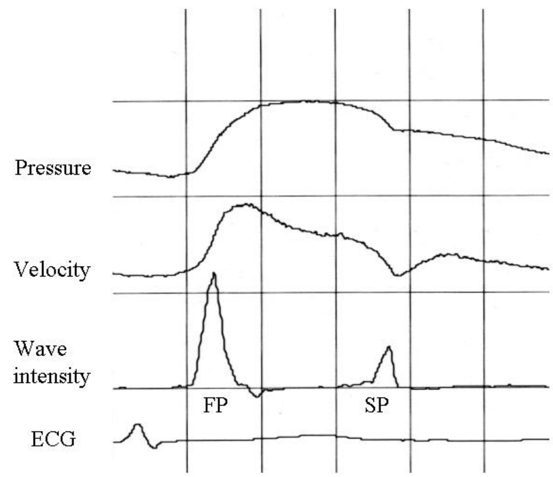

Figure 1: Representative simultaneous recordings of blood pressure, velocity, and WI waveforms at the carotid artery.
FP: first peak, SP: second peak

CONCLUSION

Using the WI at the carotid artery, hemodynamic information of LV contraction and relaxation can be obtained noninvasively. Furthermore, one can evaluate both LV systolic and early diastolic performance at the same time using this method.

REFERENCES

Jones, C.H.J., et al. (1994). *Recent Progress in Cardiovascular Mechanics.* Harwood Academic Publishers
Ramsey, M.W., Sugawara, M. (1997). *Heart and Vessels Suppl*, **12**, 128-134.
Niki, K. et al. (1999). *Heart and Vessels*, **14**, 263-271.
Sugawara, M. et al. (2000). *Heart and Vessels* **15**, 49-51.

NON-INVASIVE MEASUREMENT OF WAVE INTENSITY - REPRODUCIBILITY AND EFFECT OF GTN

Christopher J. H. Jones, Eleftherios Nicolaides, Lucy Boden, Alan Fraser and Michael Frenneaux

Wales Heart Research Institute,
University of Wales College of Medicine,
Cardiff, UK.

INTRODUCTION

The haemodynamic forces integrating arterial blood flow may be considered as elemental wave fronts, travelling forwards from the heart toward the periphery, or backwards after reflection. Wave intensity (WI), calculated simply as the product of the derivatives of measured pressure and velocity, measures the relative contribution of forward and backward wave fronts and thus separates upstream from downstream events that influence blood flow. Diameter may be substituted for pressure, allowing non-invasive assessment in man. We describe initial clinical data obtained using an ultrasound system adapted specifically for WI analysis (Aloka, Japan).

METHODS

In all studies, WI was measured in the right carotid artery in normal subjects, after 30 minutes supine rest in a temperature-controlled room. β and Ep were calculated as measures of arterial stiffness. Heart rate and BP were measured by finger cuff.

Study 1. Reproducibility: For acceptable statistical power for intraobserver, interobserver and visit-to-visit variability, WI was measured twice by 2 observers on 2 occasions 2 weeks apart in 26 subjects.

Study 2. Effect of GTN: WI was measured before and after administration of sublingual GTN or placebo in 12 subjects.

RESULTS

WI exhibited 2 positive peaks, signifying periods of dominant forward compression and expansion waves (CW and EW). Forward CW increase pressure and velocity in early systole; forward EW decrease pressure and velocity in later systole. The CW were followed by negative WI values, signifying reflections (WR) from the cerebral circulation.

Study 1. Reproducibility: Coefficients of variation for different WI measurements are shown below:

	Intra-observer (%)	Inter-observer (%)	Temporal (%)
Compression Wave	2.24	10.45	16.10
Expansion Wave	11.23	20.32	26.68
Mid-systolic reflection	14.04	19.23	28.42
Beta	11.63	10.05	14.81
E(p)	10.74	9.93	16.30

Study 2. Effect of GTN: Compared with placebo, GTN decreased diastolic BP and increased heart rate, consistent with reflex sympathetic activation. CW amplitude increased, presumably due to increased myocardial contractility. WR normalised for the CW decreased, consistent with peripheral vasodilatation. β and Ep both increased, indicating increased carotid stiffness.

DISCUSSION

WI may be measured non-invasively in real-time in man. Most WI measurements are highly reproducible during a single sitting; some measures also show acceptable variability from visit to visit. CW amplitude is an extremely stable physiological measure. WI analysis shows that GTN exerts a complex effect, causing direct microvascular dilatation and reduced backward wave travel and indirect reflex sympathetic activation with reduced diastolic BP but increased heart rate, forward wave travel and local arterial stiffness.

SUMMARY

WI analysis of non-invasively acquired data can provide a reproducible assessment of travelling wave fronts, elemental forces that govern arterial blood flow. The use of GTN, a physiologically complex intervention, demonstrates how WI analysis can resolve upstream, downstream and local influences on blood flow. WI analysis provides a clinically feasible approach to the study of intact system haemodynamics and has considerable potential as a physiological research tool.

SHEAR STRESS-INDUCED ATP RELEASE AND CALCIUM SIGNALING IN ENDOTHELIAL CELLS

Joji Ando[1], Kimiko Yamamoto[1], and Akira Kamiya[2]
[1]Department of Biomedical Engineering, Graduate School of Medicine, University of Tokyo, [2]Interdisciplinary Science Center, Nihon University, Tokyo, Japan

INTRODUCTION

Vascular endothelial cells (ECs) recognize shear stress, a mechanical force generated by flowing blood, and transmit a signal to the cell interior that leads to cellular responses involving changes in morphology, function and gene expression. Ca^{2+} signaling plays an important role in the shear stress signal transduction. Our previous studies demonstrated that shear stress activates Ca^{2+} influx into ECs via a subtype of ATP-operated cation channels, P2X4. Recently, shear stress has been shown to induce ATP release from ECs. In this study, we examined the role of endogenous ATP released in response to shear stress and flow-related Ca^{2+} signaling.

METHODS

Human pulmonary artery ECs (HPAECs) that had been cultured on a coverslip were loaded with the Ca^{2+} indicator Indo-1/AM. The coverslip was then placed in a parallel plate flow chamber, and the chamber was mounted on the stage of a confocal laser scanning microscope. The entire circuit was filled with Hanks' balanced salt solution. By changing the height of the reservoir and monitoring the flow rate using a flow sensor, the cells were subjected to stepwise increments in shear stress. Changes in intracellular Ca^{2+} concentrations ($[Ca^{2+}]i$) were monitored. The amount of ATP released in response to shear stress was determined using a bioluminescence assay and the uciferin-luciferase reaction.

RESULTS AND DISCUSSION

$[Ca^{2+}]i$ in HPAECS increased in a stepwise manner in response to stepwise increments in shear stress. When extracellular Ca^{2+} was eliminated with EGTA, the Ca^{2+} responses disappeared, indicating that the response was due to the influx of extracellular Ca^{2+} across the plasma membrane. The shear stress-dependent Ca^{2+} influx was almost completely blocked in HPAECs treated with antisense oligonucleotides targeting P2X4 receptors. Thus, P2X4 receptors probably play a crucial role in shear stress-dependent Ca^{2+} influx in HPAECs. Apyrase, which degrades ATP, significantly suppressed the P2X4-mediated Ca^{2+} influx, indicating that endogenous ATP released from HPAECs may somehow be involved in this process. We next examined whether ATP was released from HPAECs by shear stress. A stepwise increase in shear stress induced a stepwise increase in ATP release. When the HPAECs were treated with known inhiibitors of F1-F0 ATP synthase (oligomycin and angiostatin), the shear stress-dependent ATP release was markedly reduced and the shear stress-dependent Ca^{2+} influx was inhibited. These results suggest that endogenous ATP released from ECs in response to shear stress plays an important role in shear stress calcium signaling via P2X purinoceptors.

SUMMARY

We have shown that shear stress stimulates ATP release from ECs in a dose-dependent manner, contributing to Ca^{2+} signaling via P2X4. These data suggest the existence of an autocrine and paracrine ATP signaling cascade that is linked to shear stress signal transduction. Further studies are needed to clarify the shear stress-dependent mechanism of ATP release in ECs.

REFERENCES

Yamamoto K, Kamiya A, Ando J et al. Circ Res 2000; **87**: 385-391.
Yamamoto K, Kamiya A, Ando J et al. Am J Physiol Heart Circ Physiol 2000; **279**:H285-H292.
Isshiki M, Ando J, Kamiya A et al. Proc Natl Acad Sci USA 1998; **95**: 5009-50

IDENTIFICATION OF GENES REGULATED BY MECHANICAL FORCES USING MICROARRAY TECHNOLOGY IN HUMAN ENDOTHELIAL CELLS

Larry V. McIntire, E.D. Butcher Professor and Chair (mcintire@rice.edu)
Institute of Biosciences and Bioengineering, Rice University, Houston, Texas

INTRODUCTION

Two of the mechanical forces that act on vascular cells, shear stress and cyclic strain, are thought to contribute to the atherogenic properties of blood vessels. Northern blot analyses utilizing endothelial cells show that both protease activated receptor-1 and endothelin-1 gene expression are increased with cyclic strain and decreased with shear stress. This trend indicates that these mechanical stimuli may have opposing genetic influences on disease progression in the arterial system. Therefore, a comparison between the effects of these two mechanical forces on human umbilical vein endothelial cells (HUVECs) was conducted. HUVECs were subjected to shear stress at 25 dyn/cm^2 in a parallel plate flow chamber. Employing mRNA from sheared and static cells, differential expressions of over 4000 genes were evaluated simultaneously. Next, HUVECs were subjected to cyclic deformation at 10% strain, microarrays were again used for the strained, motion control and static cells. Northern blot analysis was performed on selected genes to verify the accuracy of the microarrays. Comparison between shear stress and cyclic strain data revealed differential gene expression.

METHODS

Gene microarray analysis is a powerful method for analyzing the effect of biological stimuli on gene expression profiles. We used Research Genetics microarray GF211, which contains over 4000 known human genes, to identify those regulated by fluid shear stress exposure. Message levels of genes in primary human umbilical vein endothelial cells exposed to a shear stress of 25 dyn/cm^2 or 10% cyclic strain[(1)] for 6 or 24 hours were compared with message levels in control cells. For several of the genes, Northern analysis was used to confirm the results.

RESULTS AND DISCUSSION

The microarray analysis identified many shear stress regulated genes, including genes that have been previously shown to be regulated by shear stress such as endothelin-1, monocyte chemotactic protein-1 and prostaglandin transporter. Overall the expression of 32 genes increased two fold or greater and the expression of 20 genes decreased 50% or more in response to shear stress[(2)].

The most dramatically upregulated gene expression was observed in cytochromes P450 1A1 and 1B1. Classically, the CYP gene families have been associated with cellular detoxification mechanisms. However, primary HUVECs have been shown to produce CYP1A1, and recent evidence has shown that the production of an endothelial derived relaxing factor from arachidonic acid in endothelial cells is catalyzed by CYP1A1. In addition, loss of this gene in cultured ECs correlates with dedifferentiation. No association of CYP 1B1 with ECs has been reported. It may be a factor in mammary carcinogenesis, thus associated with angiogenesis. The strong induction of these CYP genes by shear stress is consistent with the suggestion that physiological levels of shear stress are atheroprotective. The other genes, whose biological functions are known, are connected with biological systems that are regulated at least in part by shear stress. By identifying additional genes in these systems it is possible to further define the mechanisms by which shear stress controls them.

SUMMARY

Shear stress is considered by many to be the most important stimulus for NO production in EC. Several genes identified as being shear stress responsive from our DNA microarray analysis may play a role in the regulation of NO production by shear stress, and suggests exciting new pathways for shear stress regulation of NO production in endothelial cells. The use of microarray technology to study the biological effects of shear stress has the potential to expedite our understanding of the role of shear stress in vascular biology and to allow the development of new hypotheses concerning genetic networks regulated by mechanical forces.

REFERENCES

1. Nguyen, K.T., Frye, S.R., Eskin, S.G., Patterson, C., Runge, M.S., and McIntire, L.V., "Cyclic Strain Increases Protease- Protease-Activated Receptor-1 Expression in Vascular Smooth Muscle Cells", *Hypertension* **38**, 1038-1043(2001).

2. McCormick, S.M., Eskin, S.G., McIntire, L.V., Lu, C-M., Russell, C.G., and Chittur, K.K., "DNA Microarray Reveals Changes in Gene Expression of Shear Stressed Human Endothelial Cells", *Proc. Natl. Acad. Sci.,* **98**, 8955-8960 (2001).

THE ROLE OF INTEGRIN IN MECHANOTRANSDUCTION IN ENDOTHELIAL CELLS

John Y.-J. Shyy
Division of Biomedical Sciences, University of California, Riverside, CA, USA, 92521-0121.
Email address: john.shyy@ucr.edu

RESULTS AND DISCUSSION

Evidence emerging from both *in vivo* experiments using animal models and *in vitro* experiments using flow channels indicates that fluid shear stress modulates many physiological and pathological processes. In the vessel wall, vascular endothelial cells (ECs) are constantly exposed to shear stress and thus play a crucial role in maintaining vascular homeostasis. The shear stress-mediated homeostasis is maintained through the expression of proteins and factors involved in vessel constriction and dilation (e.g., nitric oxide and endothelin-1), inflammation (e.g., intercellular adhesion molecule-1 and monocyte chemotactic protein-1, MCP-1), and growth regulation (e.g., tumor suppressor p53 and platelet-derived growth factors). Mechanotransduction mechanisms by which ECs convert shear stress to biochemical signaling are responsible for these shear stress-medicated transcription events.

Integrins are a family of transmembrane heterodimers composed of α and β subunits. The extracellular domain of integrins binds to various ligands, including extracellular matrix (ECM) proteins such as fibronectin, vitronectin, and collagen. The cytoplasmic domain of integrins interacts with cytoskeletal proteins (e.g., actin filaments) and kinases (e.g., focal adhesion kinase, FAK, and c-Src) in the focal adhesion sites. The unique structural features of integrins enable them to mediate inside-out and outside-in signaling during many biological processes, including cell adhesion to ECM and migration. Inside-out signaling, which is also known as "integrin activation", modulates the affinity of integrins for extracellular ligands in response to intracellular signals. Outside-in signaling induces the intracellular signaling cascade as a result of integrin activation. Thus, integrins can function as both adhesion receptors and signal transducers to regulate cytoskeletal reorganization, intracellular ion transport, lipid metabolism, kinase activation, and gene expression. Conceptually, integrins in ECs can serve as mechanosensors by transducing the mechanical stimuli acting on the plasma membrane to ECM through inside-out signaling. Alternatively, signaling molecules associated with focal adhesions and cytoskeleton can be activated by integrins through outside-in signaling.

We and others have used flow channel system to investigate the role of integrin in mechanotransduction in ECs in response to shear stress. Results from our early studies demonstrate that shear stress modulates the expression of the MCP-1 gene in ECs, which is regulated by the mitogen-activated protein kinase (MAPK) pathways, including ERK, JNK, and p38. Using these shear stress-modulated events as readouts, we found that kinases in the focal adhesions and the Rho small GTPases, which are signaling molecules engaged in integrin activation, are all activated by shear stress in ECs. The blockade of integrins with blocking-type monoclonal antibodies (mAbs) such as LM609 anti-$\alpha_v\beta_3$ inhibits the activation of MAPKs and the MCP-1 gene by shear stress. Furthermore, the Src-homology domain-2 (SH2) containing molecules, including Shc and growth factor receptor binding protein 2 (Grb2), constitute a crucial part of the integrin-mediated signaling. Shear stress activation of Shc was subsequently used as a readout to further elucidate the dynamic nature of integrins interaction with ECM in mechanotransduction. We found that the integrin-Shc association was abolished when new integrin-ECM ligand interactions were prevented by either blocking the integrin-binding sites of ECM or conjugating the integrins to immobilized anti-bodies. These results indicate that the dynamic formation of new connections between integrins and their specific ECM ligands is critical in mechanotransduction pathways.

Sterol regulatory element-binding proteins (SREBPs) are key transcription factors regulating sterol and lipid biosynthesis. Our recent results showed that shear stress causes the maturation of SREBPs in ECs. As a result, the expression of SREBP-mediated genes such as the low density lipoprotein receptor (LDLR) are modulated. Interestingly, blocking the β1-integrin with the AIIB2 blocking-type monoclonal antibody inhibited SREBP1 activation induced by shear stress. EC attachment to fibronectin or the activation of β1-integrin in the suspended ECs by the TS2/16 monoclonal antibody was sufficient for SREBP1 activation.

In summary, research performed in our laboratory during the last few years suggest that integrins interacting with ECM is important in mechnotransduction that regulates genes important in vascular biology, including those involved in cholesterol and lipid homeostasis.

ACKNOWLEDGEMENT

This study was supported in part by research grant HL56707 and HL60789 from the National Heart, Lung, and Blood Institute of the National Institutes of Health. John Y-J Shyy is an Established Investigator of American Heart Association.

STRESSING INTEGRINS ALTERS GENE EXPRESSION

Ning Wang
Physiology Program, Department of Environmental Health
Harvard School of Public Health, Boston, MA , USA

INTRODUCTION

How are mechanical signals transduced into biochemical signals and biological responses? Although it is known that fluid shear stress and stretching result in alterations in endothelin-1 (ET-1) gene expression, it is not clear what are the initial molecular pathways that are responsible for mechanotransduction. In this study we have set out to determine if the integrin-cytoskeleton pathway is involved in stress-induced alterations in ET-1 gene expression.

METHODS

Human umbilical vein endothelial cells were plated in 60-mm dishes and grown to confluence in culture medium. The dishes were washed twice with serum-free defined medium containing 1% BSA and 2 mg of ligand-coated beads were added into each dish for 30 minutes in serum-free defined medium (average 10 beads per cell). RGD (Arg-Gly-Asp) and acetylated-low-density-lipoprotein (AcLDL) were coated onto the beads at 50 μg protein per mg beads using the manufacturer's protocols. Anti-HLA antibody was coated at 20 μg protein per mg beads as previously described. In this study, we applied constant twisting fields at 40 Gauss (equivalent to 20 dyn/cm^2) for 2 hrs with the beads remagnetized every 10 min. After mechanical stimulation of the cells, the supernatant was collected and the cells were lysed in RTL buffer. Total cellular RNA was obtained and northern analysis was performed according to the published methods. In situ hybridization was performed according to the published methods.

RESULTS AND DISCUSSION

Twisting RGD-containing-peptide-coated ferromag-netic beads (4.5 μm in diameter) increased ET-1 gene expression by more than 100%. In contrast, twisting scavenger receptors with AcLDL-coated beads or twisting HLA antigen with anti-HLA antibody coated beads did not lead to alterations in ET-1 gene expression. In situ hybridization showed that the increase in ET-1 mRNA was localized in the cells that were stressed with the RGD coated beads. Blocking stretch-activated ion channels with gadolinium or chelating calcium with EGTA inhibited stress-induced ET-1 mRNA elevation. Similarly, inhibition of tyrosine phosphorylation with genistein abolished stress-induced ET-1 mRNA elevation. Inhibiting pre-existing cytoskeletal tension (prestress) with an inhibitor of the myosin ATPase, with an inhibitor of myosin light chain kinase, or with an actin microfilament disrupter, blocked twisted-induced increases in ET-1 expression. These results are consistent with other findings that integrins are important for mechanotransduction such as stress-induced intracellular calcium elevation, protein phosphorylation, and mRNA recruitment. Our results are consistent with the hypothesis that the molecular structural linkage of integrin-cytoskeleton is an important pathway for stress-induced endothilin-1 gene expression and that stretch-activated ion channels, protein tyrosine phosphorylation, and the prestress are important in transducing mechanical signals into gene expression.

SUMMARY

We have shown that ET-1 gene expression is upregulated when integrin receptors are stressed but not when other non-adhesion molecules are stressed. This work demonstrates the importance of the specific transmembrane molecular pathway (integrins), the integrity of the cytoskeletal structure, and the prestress in mediating stress-induced gene expression.

REFERENCES

Chen, J. et al. (2000) *Am. J. Physiol. Cell*, **280**, C1475-1484.
Malek, A., Izumo, S. (1992) Am. J. Physiol. Cell, **263**, C389-C396.
Wang, D.L. et al (1993) Biochem. Biophys. Res. Commun., **195**, 1050-1056.
Wang, N. et al (2001). *Proc. Nat. Acad.Sci. USA*, **98**, 7765-7770.
Wang, N. et al (2002) *Am. J. Physiol. Cell*, in press.

ACKNOWLEDGEMENTS
This work was supported by NASA grant NAG 2-1509 and NIH grant HL33009.

THE FREE VOLUME THEORY OF MECHANOCHEMICAL TRANSDUCTION

John A. Frangos

La Jolla Bioengineering Institute
La Jolla, California, USA
http://www.ljbi.org

The ability of cells to respond to hydrodynamic stimuli is ubiquitous amongst all cells and organisms, and has been implicated in a number of physiological and pathological processes. While many of the biochemical transduction pathways have been characterized, the primary mechanoreceptor(s) remain(s) unknown. It is our hypothesis that hydrodynamic shear destabilizes the plasma membrane, leading to a decrease in membrane microviscosity, or more precisely, an increase in membrane free volume. Mechanochemical transduction is proposed to occur when membrane-associated signaling proteins are activated by the increase intramolecular mobility.

A number of studies have implicated a role of heterotrimeric G proteins in the mediation of cellular responses to fluid shear stress and stretch. Studies from our lab demonstrate that heterotrimeric G proteins are rapidly activated by hydrodynamic shear, representing the earliest known biochemical response to mechanical stimulation presented. Furthermore, both fluid shear stress and membrane fluidizing agents activate these G proteins in the absence of classical G protein coupled receptors. Using fluorescent molecular rotors it was recently shown that hydrodynamic shear increases membrane free volume. Taken together, these results demonstrate that hydrodynamic shear stress stimulates cellular responses by increasing membrane fluidity and activating heterotrimeric G proteins.

The presentation will discuss these results in the context of the membrane free volume theory of mechanochemical transduction.

CHANGES OF CAVEOLIN-1 IN HUMAN ENDOTHELIAL CELLS EXPOSED TO SHEAR STRESS

Ruijuan Sun[1,2], Xiong Wang[2], Xi Dong[1], Sylvaine Muller[2], Jean-Francois Stoltz[2]

1. China-Japan Friendship Research Institute of Clinical Medical Sciences, Beijing, 100029, China, sunrj@hotmail.com
2. Cell and Tissue Engineering and Mechanics, LEMTA-UMR-CNRS 7563, Vandoeuvre-lès-Nancy, France.

INTRODUCTION

Caveolae are special invaginated microdomains (50-100nm) at cell membrane of many cell types, such as epithelial cells and vascular endothelial cells.
Caveolins are the main structural proteins of caveolae and form a scaffold by the interaction with each other and binding to cholesterol for the attachment and assembly of many classes of signaling molecules. Caveolins can directly interact with these signaling molecules and regulate their activation (Schlegel and Lisanti 2001).
Considering that vascular endothelial caveolae could be flow-sensors converting mechanical stimuli into chemical signals transmitted into the cell, this work studied the changes of caveolin-1 expression and distribution in cultured endothelial cells exposed to laminar flow. In addition, the influence of cytokine TNF-α on caveolin-1 was also investigated.

METHODS

HUVECs were harvested from human umbilical cord veins. For shear experiments, the cells were seeded on glass slides coated with 1% gelatin. The cells of passage 2 were used in our experiments.

The slide with an endothelial monolayer was assembled to a widely used parallel rectangular flow chamber and a steady flow rate was generated by a peristaltic pump with a damping system. ECs were exposed to shear stress of 1.0 Pa for different times (4-24h). Cells cultured in static condition were considered as normal control and cells stimulated by TNF-α (100U/ml) as control of biochemical effect.

In order to observe the effect of F-actin organization on caveolin-1 distribution, certain cells were pretreated with cytochalasin-D (2μM/ml) before TNF-α stimulation.

After exposure to shear stress or stimulation by TNF-α, the cells were fixed and permeabilized. Caveolin-1 was labeled with indirect immunofluorescence method. Labeled cells were observed with a 3D optical sectioning acquisition system CELLscan. Western Blot analysis was used to evaluate caveolin-1 expression in the cells under different condition.

RESULTS AND DISCUSSION

The results showed that in control cells, caveolin-1 was primarily localized on the cell surface (Fig.1A), which corresponded to the peripheral distribution of F-actin, and presented a discrete concentrated distribution. In cells exposed to laminar flows, caveolin-1 distribution showed a time-dependent variation. After 24h of shear, we found not only more caveolin-1 in the cells, but also a local caveolin-1 concentration, in most cells, at the upstream side of cell body (Fig.1B). In contrast, TNF-α induced a decrease of caveolin-1 in the cells. F-actin organization seemed to be correlated to caveolin-1 distribution.

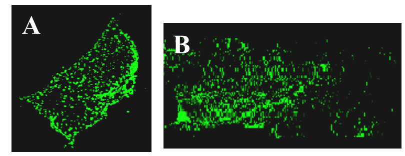

Figure 1: Distribution of caveolin-1.
A: static condition
B: 24h, 1.0Pa

If we consider the subcellular distribution of mechanical forces, an interested theoretical analysis result of the flow in the vicinity of an endothelial monolayer was found (Waché et al 2000). The distribution of mechanical forces is not uniform on the cell surface. In fact, the shear stress is maximum at the top of the cells, but the hydrostatic pressure is maximum at the upstream side of the cells; also this area has a high spatial gradient of shear stress.

CONCLUSIONS AND PERSPECTIVES

The results suggest that: 1) shear stress can sufficiently induce caveolin-1 translocation, but TNF-α down-regulates caveolin-1 expression; 2) there is a relation between the local distribution of caveolin-1 and that of hemodynamic forces (shear stress gradient and /or pressure) at cell surface ; 3) there could be a correlation between caveolin-1 distribution and F-actin organization.

However, further studies are necessary to elucidate the mechanism of these changes of caveolin-1. It would be particularly interesting to study the role of F-actin, caveolin-1 tyrosine phosphorylation and effect of cholesterol content.

REFERENCES

Schlegel A. and Lisanti M.P. (2001). *Cytokine and Growth Reviews*, **12**,41-51.
Waché P. et al (2000). *C.R. Acad. Sci Paris*, **t.328, Série IIb**: 633-638.

ACKNOWLEGEMENTS

This work was partly supported by the Association Franco-Chinoise pour la Recherche Scientifique & Technique (Program PRA B98-07), and Region Lorraine, France, and Natural Sciences Foundation of China (grant No. 30170241).

LAMINAR SHEAR STRESS INDUCES VASODILATOR-STIMULATED PHOSPHOPROTEIN CHANGE IN CULTURED HUMAN ENDOTHELIAL CELLS

Lei Wei[1,2], JingPing Ouyang[2], Sylvaine Muller[1], Jean-François Stoltz[1], and Xiong Wang[1]*

[1]LEMTA -UMR 7563 CNRS/INPL/UHP, 54500 Vandoeuvre-lès-Nancy, France, *Xiong.Wang@ensem.inpl-nancy.fr
[2]Department of Pathophysiology , Medical College of Wuhan University, Wuhan , 430071, China

INTRODUCTION

Shear stress is a tangential component of hemodynamic forces that acts mainly on vascular endothelial cells (ECs) and is now generally considered to play a role in development of some cardiovascular diseases, such as atherosclerosis. The conversion of mechanical stimulation into cells seems to be associated with cytoskeleton. But the molecular mechanisms have not yet been clearly established. Recent elucidation of the primary vasodilator-stimulated phosphoprotein (VASP) structure suggests that VASP is an potential component of focal contacts which may link to signal transduction pathways (Salazar et al. 1999). Hence, the aim of the study is to evaluate shear stress-induced changes of VASP expression in ECs.

METHODS

Cell culture: Human umbilical endothelial cells (HUVECs) were cultured according to a modified method of Marin et al. (2001).

Shear experiments: The cells were divided into three groups which would be exposed to different shear stresses (2, 10, and 15 dyn/cm^2) for duration variable from 1 to 24 hours. A conventional parallel-plate flow chamber was used to create laminar shear stresses.

Protein isolation and western blot analysis: Cells were scraped into a lysis buffer. After centrifugation, the supernatant was subjected to SDS/PAGE analysis followed by immunoblottings followed by pixel detection (HPIAS-1000 software, QianPing company, China). Primary antibody was anti-VASP serum M4.

Indirect immunofluorescence: Confluent HUVECs were fixed and permeabilized, then incubated with primary anti-VASP antibodies IE273 and secondary antibodies Alexa™ 488. Phalloidine-rhodamine was used for cytoskeleton labelling.

RESULTS AND DISCUSSION

Time course of VASP expression : Figure 1 shows OD values of VASP expression at 46kD in HUVECs stimulated by 3 different levels of shear stresses. The shear stress of 15dyn/cm^2 led to a rapid increase followed by a transient decrease of the VASP expression, accompanied by a rapid phosphorylation of VASP at 50kD (Data not shown). While a lower shear stress (2 or 10 dyn/cm^2) had slower effects on the same tendency.

Immunofluorescence staining: Figure 2 shows a double fluorescence staining of VASP and F-actin. In static HUVECs, VASP was only an weak decoration of stress fibres along their entire length (Fig.2 A). After exposure to shear (15dyn/cm^2, 24h), HUVECs presented an assembly of subplasmalemmal F-actin with thicker VASP than in control, targeted to the ends of stress fibres (Fig.2 B).

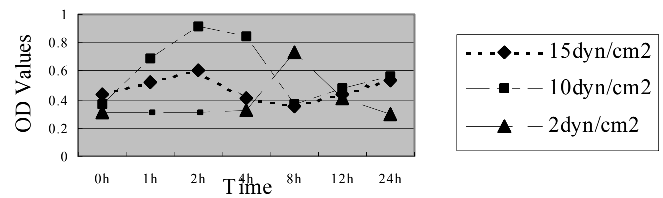

Figure 1: OD values of VASP expression in sheared HUVECs.

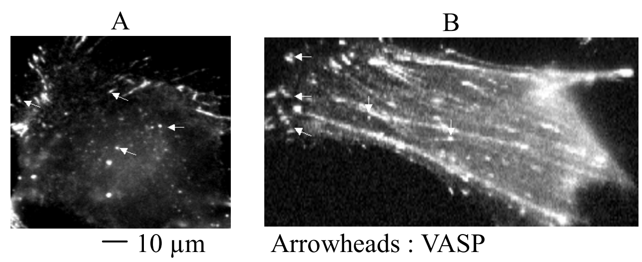

Figure 2 : Double immunofluorescence staining of F-actin and VASP in HUVECs. A : static control ; B : HUVECs exposed to a shear stress of 15dyn/cm^2 for 24 hours.

SUMMARY

Our experimental results show for the first time that shear stress induces VASP expression changes in a time-dependent manner accompanied by a rapid phosphorylation. These results suggest that VASP is an potential important component which participates in the regulation of cell actin remodelling induced by shear flow.

REFERENCES

Marin V. et al.(2001). *J. Immunol. Meth.*, **254**, 183-190.
Salazar R. et al.(1999). *Exp Cell Res*. **249,** 22-32.

ACKNOWLEDGEMENTS

This work was partly supported by the “Association Franco-Chinoise pour la Recherche Scientifique & Technique”, France (PRA B00-09) and the Region Lorraine (99/469SJE).

PREDICTION OF THREE-DIMENSIONAL ORIENTATION OF STRESS FIBERS IN CULTURED ENDOTHELIAL CELLS UNDER CYCLIC DEFORMATION

Hiroshi Yamada, Tohru Takemasa[1] and Takami Yamaguchi[2]
Department of Biological Functions and Engineering, Graduate School of Life Sciences and Systems Engineering, Kyushu Institute of Technology, Kitakyushu, Japan, yamada@life.kyutech.ac.jp
[1]Institute of Health and Sports Sciences, University of Tsukuba, Tsukuba, Japan
[2]Department of Mechatronics and Precision Engineering, Graduate School of Engineering, Tohoku University, Sendai, Japan

INTRODUCTION

To elucidate the mechanism of the orientation of intracellular stress fibers (SFs) in vascular endothelial cells, the effect of cyclic deformations on the orientation has been studied (Takemasa et al. 1998). Cyclic deformations with a constant strain range cause a reorientation of SFs in a certain direction depending on the magnitude of the strain range. Some hypotheses have been proposed to explain the two-dimensional (2D) orientations of SFs or cells along the surface of the substrate (Wang et al. 1995, Takemasa et al. 1998, Yamada et al. 2000). Three-dimensional (3D) orientations of SFs in cultured endothelial cells have also been reported under mechanical stimuli of fluid shear stress (Kano et al. 2000) or cyclic deformation (Wang et al. 2000). In this study we predicted 3D orientations of SFs under various types of cyclic deformation of a substrate on the basis of a hypothesis (Wang et al. 1995, Takemasa et al. 1998).

METHODS

The hypothesis which we used in this study was that SFs are realigned in the direction in which the strain is less than +/-5% in a maximally deformed state of a substrate. Based on this hypothesis and under an incompressibility condition of a cell, we carried out numerical simulations. Boundary conditions were (1) uniaxial cyclic loading in x direction (Cauchy stress $\sigma_y = \sigma_z = 0$; stretch ratio $\lambda_y = \lambda_z = \lambda_x^{-1/2}$), (2) uniaxial cyclic stretch in x direction ($\lambda_y = 1$, $\sigma_z = 0$; $\lambda_z = \lambda_x^{-1}$), (3) equi-biaxial cyclic stretch ($\lambda_x = \lambda_y > 1$, $\sigma_z = 0$; $\lambda_z = \lambda_x^{-2}$) where the x-y plane and z-axis corresponded to the substrate surface and its normal direction, respectively. It was also assumed that a line element with a unit length represented an initial SF and that an end of a SF was always located at the origin of the x,y,z coordinate system and the other end changed its position following a deformation of the substrate.

RESULTS AND DISCUSSION

Figure 1 shows numerical simulation results of 3D orientation in SFs under the uniaxial cyclic loading (Fig. 1 (a)), the uniaxial cyclic stretch (Fig. 1 (b)), and the equi-biaxial cyclic stretch (Fig. 1 (c)) with a strain range $\lambda_x = 1.12$. In these figures, an end of a SF is located at the origin *O* and the other end at an arc of each surface which intersects with a surface of a unit sphere. Each sector-like surface from the front to the back in Fig. 1 (a) and Fig. 1 (b) and each from the back to the front in Fig. 1 (c) correspond to the cases of SFs with a length of 0.95, 1 and 1.05 in a maximally deformed state of a substrate, respectively. These results predict 3D formation of SFs; both ends of which attach to the basal membrane (x-y plane), or one end attaches to the apical membrane and the other to the basal one, depending on the deformation type of the substrate. The result in Fig. 1 (c) qualitatively agrees with an observation of "tent-like" structure in an equi-biaxial cyclic stretch for cultured endothelial cells by Wang et al. (2000).

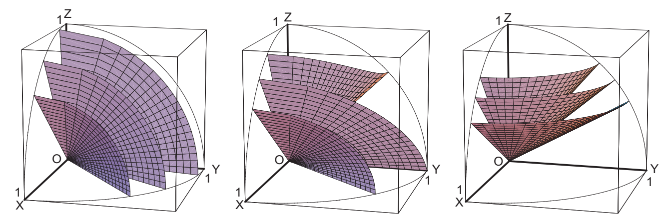

(a) **(b)** **(c)**

Figure 1: Orientations of SFs in the unloading state with a strain range $\lambda_x = 1.12$ under the boundary conditions: **(a)** $\sigma_y = \sigma_z = 0$, **(b)** $\lambda_y = 1$, $\sigma_z = 0$, and **(c)** $\lambda_x = \lambda_y$, $\sigma_z = 0$. The length of the SF is 0.95, 1 or 1.05 in a maximally deformed substrate.

SUMMARY

3D orientations of SFs were predicted theoretically under various boundary conditions of cyclic deformations. The simulation result under equi-biaxial cyclic deformation agreed with an observation of "tent-like" structure of SFs in the literature. These predictions give an insight of the formation in SFs under mechanical stimuli from a mechanical viewpoint.

REFERENCES

Kano, Y. et al. (2000). *Circ.Res.*, **86**, 425-433.
Takemasa, T. et al. (1998). *Eur. J. Cell Biol.*, **77**, 91-99.
Wang, H. et al. (1995). *J. Biomech.*, **28**, 1543-1552.
Wang, J.H.C. et al. (2000). *Cell Motil. Cytoskel.*, **46**, 137-145.
Yamada, H. et al. (2000). *J. Biomech.*, **33**, 1501-1505.

ACKNOWLEDGEMENTS

This study was supported in part by a Grant-in-Aid for Scientific Research (C) from the Ministry of Education, Culture, Science and Technology of Japan (No. 13650083).

STUDIES ON THE SINGLE BINDING FORCE OF LFA-1 AND ICAM-1

Fengyuan Zhuang[1], Hong Zhao[2],Xi Dong[2], Xiufeng Li[3]

[1]Bioengineering Department, Beijing University of Aeronautics and Astronautics, Beijing 100083,China, zhuangfy@buaa.edu.cn
[2]Research Institute China-Japan Friendship Hospital, Beijing 100029, China [3] Beijing Polytechnic University, Beijing 100022, China

INTRODUCTION

This study is to explore the properties of the binding force between a pair of ligand and receptor. LFA-1, an integrin molecule, and ICAM-1, an immunoglobulin superfamily molecule, which is a pair of adhesive molecules, and is central to many leukocyte adhesive events in inflammation, immigration and endothelium injury.

MATERIALS AND METHODS

For studies on the interaction of LFA-1 with ICAM-1, SKW-3, [kindly provided by Dr. Periasamy Selvaraj of Emory Univ. School of Medicine, (Atlanta, GA, USA)], a human T-cell leukemia cell line, which expresses LFA-1 on the membrane, and health human RBC were the carriers respectively for LFA-1 and ICAM-1. For carrying ICAM-1, first the health human RBCs were coated with CA7 (an monoanti-ICAM-1) by an improved chromium chloride, then the RBCs coated with CA7 were incubated with human plasma for CA7 to conjugate soluble ICAM-1.

SKW-3 and RBC coupled with ICAM-1 were respectively held by micropipettes with negative pressure, brought into contacting with constant contacting area, and the certain contacting duration, upon retracting the deformation of the RBC were observed for judging the happening of adhesion and measuring the adhesion force. Each pair of cells was subjected with 100 cycles for contacting and retracting.

Cells were divided into 5 groups: (1) non-stimulated SKW-3; (2) SKW-3 incubated with sLe^{a} (the ligand for L-selectin on the membrane of SKW-3); (3) SKW-3 incubated with Dreg-56 (the mAb for L-selectin);(4) SKW-3 incubated with PHA; (5) SKW-3 cells incubated with PHA and Tetramethylpyrazine simultaneously

RESULTS AND DISCUSSION

The binding force is not obviously and directly related with different groups, while the binding force were found to have an approximate linear relation with the adhesion probability (Fig.1) According to the two-dimensional receptor-ligand binding kinetics, under this range of adhesive probability, most of adhesion were between one ligand and one receptor, and were considered as a single bond of receptor and its ligand. The following hypotheses may be

Fig.1 The relation of adhesive force with the adhesive probability

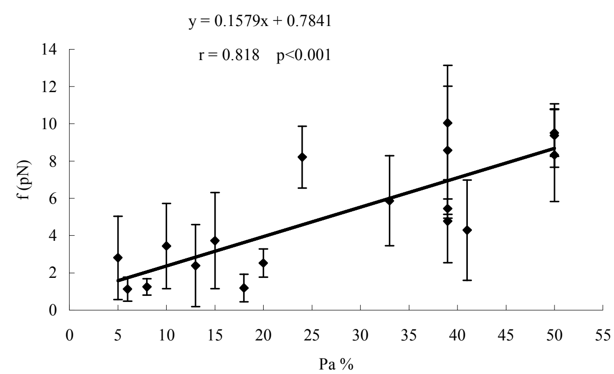

the possible reason for this relation: (1) this binding is via weak bonds, hydrogen bond and van deer Wails attraction, which bond energy are respectively about 7.0 pN.nmand 0.7 pN.nm, which is not so much larger then the thermal motion energy kT (here k is Boltzman constant, T is temperature (°K)), then the binding force is not constant and has statistical properties. (2) This binding depends on the matching of conformation of receptors and its ligands, so-called lock-key relation, this matching creates good morphological condition for many hydrogen bonds and van der Waals bonds, then one single bond of a receptor and its ligand consists of many hydrogen bonds and van der Waals bonds, during the binding the matching sites of both receptor and its ligand can have a further modification to reach a stronger binding, which is a process during the interaction of receptor and its ligand and may cause the increases of the binding force with the adhesive probability. These hypotheses and the mechanism of the linear relation of adhesion force with adhesion probability is waiting for further exploring.

REFERENCES

Chesla,S.E. et al (1998). *Biophys. J* **75**, 1553-1572
Zhao,H. et al (2000) *Clin. Hemorheol. And Microcircul.* **23**,145-151

ACKNOWLEDGEMENTS

This project was supported by National Natural Science Foundation of China (Grant No. 19872078 and 39830110).

NUMERICAL SIMULATION OF THE CARDIOVASCULAR SYSTEM : A MULTISCALE APPROACH

L Formaggia[1] , F. Nobile[1] and A. Quarteroni[1,2]
[1]Institut de Mathématiques, EPFL, CH-1015 Lausanne, Switzerland, http://dmawww.epfl.ch/Quarteroni-Chaire
[2]Dep. of Mathematics, Politecnico di Milano, v. Bonardi 9 Milano, Italy

INTRODUCTION

The mathematical modeling and the numerical simulation of blood flow in the human cardiovascular system presents many challenges. A detailed study of the local flow pattern, as well as the wall shear stress in some critical regions, such as bifurcations or stenotic arteries, may provide very useful indications to the medical researcher; yet such an analysis can't leave aside the interaction with the remaining part of the circulatory system. Indeed, local flow features may have a global effect on circulation; for instance, a stenosis caused by an atherosclerotic plaque may change the overall characteristic of the vessels involved, and consequently have significant influence on the flow in the whole system. Hence, it lays the interest to set up a numerical device that could represent accurately both local and systemic features at the same time.
In this work we propose a modeling of the cardiovascular system based on a multiscale description. On the bottom level of complexity, we consider a "lumped" parameter model (hereafter called 0D model) that provides the time evolution of averaged quantities such as mean pressures and mass fluxes in some districts of the circulatory system. Such a model is represented by a system of ordinary differential equations and is traditionally described by means of an electrical network analogue.
As an intermediate level of complexity we propose monodimensional models (hereafter 1D models) that describe arteries as monodimensional entities and provide mean pressure and mass flux at each point along the arterial axis. These models are well suited to describe pressure waves propagation and may be used to capture spurious wave reflections due to the presence of a prosthesis or a stent in a trait of artery. Simple 1D models derived for a cylindrical rectilinear artery with uniform mechanical properties have been proposed and widely used in the literature. Improvements on these models may be achieved by accounting for non-uniform (or even discontinuous) mechanical characteristics of the vessel wall, curved geometries or branching. We will present recent results on that direction.
Finally, models that provide a very fine description of the local fluid dynamics are based on a set of partial differential equations. They account at the same time for fluid flow and structure deformation and provide a fine description of fluid quantities (pressure and velocity field) as well as vessel wall deformations. At a numerical level they are the most costly in computational time and memory requirement; moreover, their discretization is not an easy task. Indeed, on one hand, fluid equations should be solved on a moving domain; this implies the development of special techniques such as the so-called Arbitrary Lagrangian Eulerian (ALE) formulation, which we have adopted in our numerical simulations. On the other hand, staggered algorithms aiming at solving sequentially fluid and structure equations are very critical regarding the stability properties of the numerical solution. A deep investigation is, thus, demanded to devise stable, accurate and efficient algorithms. We will present some theoretical and numerical results concerning finite element approximations of this fluid/structure problem.
By suitably coupling the three models we may realize a numerical device that is capable to simulate at the same time local and global phenomena. In figure 1 we show a possible application of this technique. The local fluid/structure model is used to simulate blood flow in a coronary anastomosis and is coupled with a 0D model of the circulatory system, here represented as an electric circuit. The 1D model is used to realize the transition between the local and the systemic model.

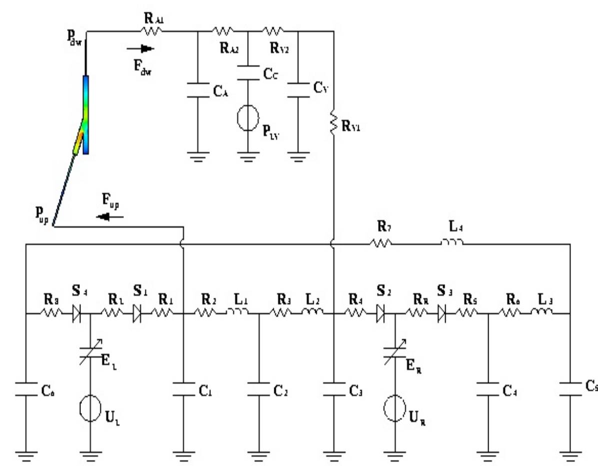

Figure 1: Example of a coupled 0D/1D/2D model for blood flow in a coronary anastomosis.

REFERENCES

Formaggia, L., Nobile, F., Quarteroni, A., (2002). *Lecture Notes in Comput. Sci. and Engrg,* **19***,* 137-153. Springer-Verlag, Berlin.
Formaggia, L., Gerbeau, J-F., Nobile, F., Quarteroni, A., (2001). *Comput. Methods Appl. Mech. Engrg,* **191**, 561-582.

WAVE PROPAGATION IN BLOOD VESSELS USING VELOCITY PROFILES BASED ON BOUNDARY LAYER THEORY

Frans N. van de Vosse
Department of Biomedical Engineering, Eindhoven University of Technology, Eindhoven, The Netherlands,
F.N.v.d.Vosse@tue.nl

INTRODUCTION

Lumped parameter models (0D), pressure and flow wave propagation models (1D) and models based on numerical solution of the full Navier-Stokes equations (3D) can give valuable contribution to answers on (patho-)physiological questions in diagnostics and treatment of cardiovascular disease. As fully 3D models are consuming too much computer time to be useful in a clinical setting, lumped parameter and 1D wave propagation models are still most suited to obtain patient specific clinically relevant information and proper boundary conditions for local 3D analyses. The non-linear nature of the equations due to the convection terms in the Navier-Stokes equations and the non-linear constitutive equations that describe the mechanical properties of the arterial wall significantly complicate models that are based on a description in the frequency domain. Moreover, wave propagation phenomena are difficult to describe with lumped parameter models. In view of the above mentioned, in this study 1D wave propagation models in the time domain are considered. One of the shortcomings of the existing 1D models is that the non-linear convection terms and the friction forces both are based on an assumed velocity profile. In this study a velocity profile is derived from boundary layer theory based on an assumed boundary layer thickness.

METHOD

In order to derive a first order approximation of the velocity profile, the vessel is decomposed in an inviscid core where a flat velocity profile is assumed and a viscous boundary layer where the velocity profile is derived from boundary layer theory. The boundary layer thickness is assumed to be proportional to the reciprocal of the Womersley parameter α. The velocity profiles obtained in this way can be integrated and provide valuable expressions for the non-linear and friction terms in the 1D wave equations.

RESULTS AND CONCLUSIONS

For limiting values of the Womersley parameter ($\alpha=\infty$, $\alpha=0$) the wave equations based on the boundary layer profiles correspond with theory based on flat and parabolic profiles respectively as derived in Hughes and Lubliner (1973).
In order to validate the velocity profiles as obtained from the boundary layer approximation, a comparison has been made with Womersley profiles for a given periodic flow pulse. As can be depicted from figure 1, a fair approximation of the velocity profiles and a perfect approximation of the wall shear stresses are obtained for single harmonic flow pulses for all values of the Womersley parameter.

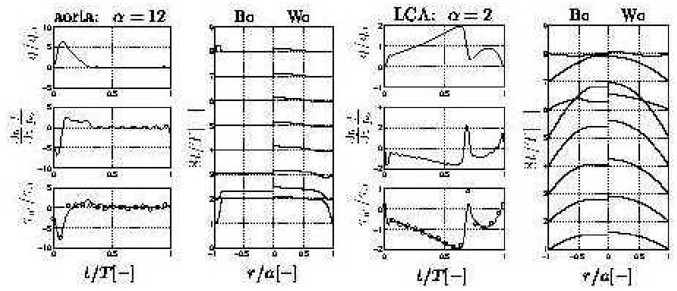

Figure 1: The flow, pressure gradient and wall shear stress and the velocity profiles for aortic and coronary flow pulses as predicted with Womersley theory (- and Wo) compared to the predictions based on the boundary layer profiles (o and Bo).

The viscous forces are found to be proportional to the flow and pressure gradient with multiplication factors c_q and c_p repectively. Figure 2 shows that excellent agreement is found with the corresponding factors based on Womersley theory.

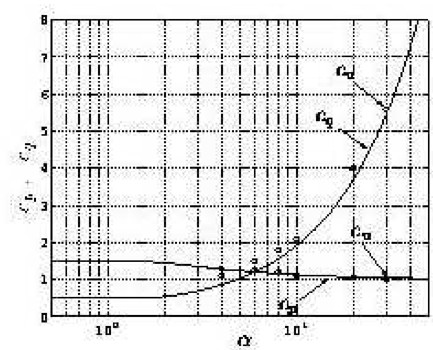

Figure 2: The parameters c_q and c_p (solid lines) as a function of Womersley parameter α compared to the corresponding values c_v and c_u of Young and Tsai (1973).

REFERENCES

Hughes, T.J.R., Lubliner, J. (1973). On the one-dimensional theory of blood flow in the large vessels. *Math. Biosciences*, **18**, 161-170.
Young, D.F., Tsai, F.Y. (1973), Flow characteristics in models of arterial stenosis II. Unsteady flow, *J. Biomech.*, **6**, 547-559.

ACKNOWLEDGMENTS

Thomas Hughes, Jing Wan and Charles Taylor at Stanford University, CA, for their contribution to this study.

INFLUENCE OF CORONARY VASCULAR BED COMPLIANCE ON THE SHAPE OF PRESSURE-FLOW WAVES

Shmuel Einav[1] and Evgeny Shalman[2]
[1]Tel-Aviv University and [2]Florence Medical Ltd., Israel

INTRODUCTION

A new parameter, PTC, for assessing stenosis severity was recently introduced[1]. PTC, or Pulse Transmission Coefficient, is the ratio of the high-frequency pressure components that are distal and proximal to a stenosis during early diastole. Clinical trials[1] have shown that PTC has high specificity and sensitivity. We developed an hemodynamic model for describing the decay of the high frequency pressure and flow component across a stenosis.

MATHEMATICAL MODEL

The hemodynamic properties of a stenosis are exhibited on a one-dimensional hydraulic model. The pressure gradient across the stenosis, ΔP, is assumed to be a quadratic function of the flow, Q. The usefulness of this model for studying coronary stenosis had been demonstrated earlier[2]. The model of a vascular bed is similar to the well-known (RCR) or intramyocardial pump models[3] which use two resistive compartments with a compliant compartment between them. We assume that a vascular bed consists of only one compartment that is both resistive and compliant. The vascular bed compliance, C, is inverse to its resistance, R: $C=k_c/R$. The systolic-diastolic change in resistance is described by step-wise functions of time. The arterial diameter and mean wall shear stress proximal to a stenosis define the flow at rest. The suggested model uses a minimal number of parameters and allows direct estimation of the influence of vascular bed compliance on the shape of the pressure wave. The obtained nonlinear stiff ordinary differential equation is solved by a CFD numerical procedure.

RESULTS

The model's calculations of coronary blood flow described the main features of the pressure signal distal to a coronary stenosis. The PTC was mainly dependent upon stenosis severity and early diastolic change in the vascular bed compliance (coefficient k_c). Calculations for a proximal pressure signal composed of the "smooth" low-frequency component and one high-frequency sinus wave were carried out, and an example of the calculation for vascular beds having various compliances is presented in the figure. A high-frequency component could be observed in the distal pressure signal when the vascular bed had low compliance (k_c=0.025). This component disappeared when the vascular bed had high compliance (k_c=0.1). The proposed model could also demonstrate an abrupt early diastolic drop in distal pressure.

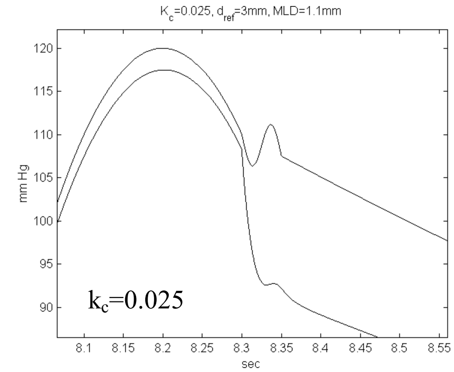

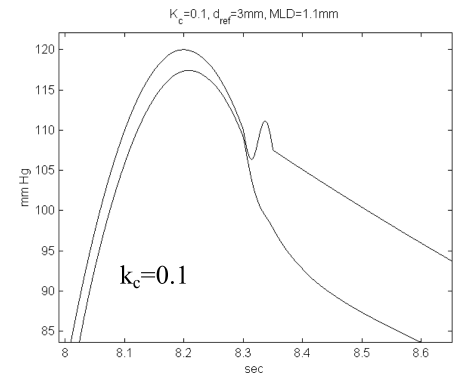

DISCUSSION

The early diastolic filling of the coronary vascular bed has a strong impact on the shape of the pressure wave distal to a coronary stenosis. The PTC allows an estimation of stenosis severity at rest. Clinical application of the PTC will enable non-hyperemic assessment of stenosis severity.

REFERENCES

1. Brosh D et al. (2001) *The American Journal of Cardiology TCT-313, 122G.*

2. Shalman et al. (2001) *Computers in Biology and Medicine,* 31, 353-363 .

3. Spaan et al. (1981) *Circulation Research, 49, 584-593.*

BLOOD FLOW SIMULATIONS FROM PHASE CONTRAST MRI DATA FOR THE MEASUREMENT OF LARGE GRADIENT ARTERIAL WALL SHEAR STRESSES

Daniel R. Karolyi [1,2], John N. Oshinski [1,3], Don P. Giddens [1,4]

[1]Georgia Institute of Technology / Emory University, Wallace H. Coulter Department of Biomedical Engineering, Atlanta, GA, USA. [2]Medical College of Georgia, School of Medicine, Augusta, GA, USA. [3]Emory University, School of Medicine, Department of Radiology, The Frederik Philips Magnetic Resonance Research Center, Atlanta, GA, USA. [4]don.giddens@bme.gatech.edu

INTRODUCTION

Hemodynamic studies have suggested that atherosclerosis is associated with areas of oscillating and low mean wall shear stress (WSS) values (Ku et al., 1985). This study investigates using velocity and geometry data from phase contrast magnetic resonance imaging (PC-MRI) to determine WSS values in symmetric stenosis geometries. The importance of using blood flow simulations is illustrated by comparing WSS values derived from computational fluid dynamic (CFD) simulations to the direct calculation of WSS from PC-MRI derived velocity profiles.

METHODS

Idealized models of common carotid arteries (6.35mm diameter) with 52.7% and 75.0% symmetric stenoses were manufactured from polyvinyl alcohol, which has MRI relaxation properties similar to arterial wall tissue. These models were placed in a clinical MRI scanner (Philips ACS-NT) and connected to a flow system containing a glycerin/water mixture with a viscosity similar to blood. This fluid was run through the models at rates equal to the average (270 mL/min) flow rates found in human common carotid arteries. Geometry and velocity data were acquired using spin-echo inversion recovery (IR) and phase contrast sequences with the following parameters: FOV = 128mm, scan matrix = 256x256, TR = 20msec, TE = 6msec, flip angle = 40 degrees, slice thickness = 2mm, 8 signal averages.

WSS values were calculated directly from the PC-MRI data by fitting quadratic curves to the near-wall velocity data. The near-wall fluid strain rates were determined from the slopes of these lines evaluated at the wall location as determined from the IR images. The IR images were also used to reconstruct the 3D geometry so that the hemodynamics through the model could be simulated using CFD (FIDAP 8.5) with the inlet boundary conditions taken from the PC-MRI velocity data. Gold standard WSS values were determined from CFD simulations using idealized geometries and idealized inlet boundary conditions.

RESULTS AND DISCUSSION

52.7% Stenosis: The maximum WSS was calculated directly from the PC-MRI derived velocity profiles as 21.6 dynes/cm^2, which was a 64.6% underestimation of the gold standard value (60.9 dynes/cm^2). The CFD simulation yielded 35.5 dynes/cm^2, which was a 41.8% underestimation.

75.0% Stenosis: The maximum WSS was calculated directly from the PC-MRI derived velocity profiles as 51.6 dynes/cm^2, which was a 73.1% underestimation of the gold standard value (192.1 dynes/cm^2). The CFD simulation yielded 148.0 dynes/cm^2, which was a 23.0% underestimation (see figures).

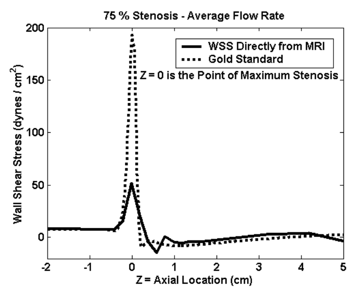

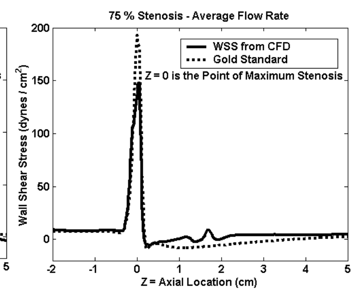

For both models, the calculation of WSS directly from the PC-MRI velocity profiles underestimated the peak WSS values more than the CFD simulations. Furthermore, the PC-MRI derived WSS values in both geometries took longer to return to baseline levels as compared to the CFD simulations. This is largely due to the low resolution of the PC-MRI data and the necessity to average velocity values over large voxels (2mm x 0.5mm x 0.5mm) to obtain acceptable signal-to-noise ratios. Large variations in WSS values at the same axial location and different angular locations were present in both methodologies. Inadequate in-plane resolution and ambiguity in wall location caused by low contrast between the PVA model and the fluid are thought to have caused the large standard deviations present in the data.

SUMMARY

CFD simulations based on PC-MRI data can better detect large WSS gradients due to higher near wall velocity resolution. Direct calculation of WSS from PC-MRI data is limited due to the large image slice thicknesses required to reduce signal noise and limited in-plane resolution. This leads to large voxels over which velocity data is averaged, effectively reducing the ability to detect large and small velocities and therefore large velocity gradients.

REFERENCES

Ku, D.N. et al. *Arterio*, **5**,293-302, 1985.
Milner J.S. et al. *J. Vasc. Sug.*, **27**,143-156, 1998.
Oshinski, J.N. et al. *J. MRI*, **5**, 640-647, 1995.
Oyre, S. et al. *MRM*, **40**, 645-655, 1998.

HEMODYNAMIC MODELING IN STENTED ARTERIES

James E. Moore Jr., Andreas O. Frank, Yong He, and Peter W. Walsh

Biomedical Engineering Institute, Florida International University, Miami, Florida, USA
james@eng.fiu.edu

INTRODUCTION

Stents are small, metallic tubes used to prop open arteries diseased with atherosclerotic plaque. While the deployment of a stent is considerably less traumatic than surgical alternatives, the procedure suffers from failure rates of 20% - 30% due to restenosis. The mechanical conditions inside the stented artery may be related to the development of restenosis. Stents are responsible for changes in flow patterns and artery wall stresses. These changes depend on the design of the stent. This research was initiated to quantify changes in arterial blood flow patterns as a function of stent design parameters. The data from flow simulations help explain the results of in vitro experiments on the role of flow patterns in restenosis development.

METHODS

Computational simulations of blood flow in stented arteries were performed using commercially available software. The artery wall was assumed to be rigid, and the stent struts protruded into the flow stream. The height of the stent struts was H = 0.15 mm. The stent strut spacing in this 2D model varied from 2.5 H to 7 H. The flow rate was specified so that the wall shear stress in the absence of stent struts would be 10 ± 5 dynes/cm^2.

RESULTS AND DISCUSSION

The patterns of flow separation and wall shear stress depended strongly on the stent strut spacing. At stent strut spacings less than 3 H, flow separation is continual from one strut to the next. For larger strut spacings, there is at least partial flow reattachment between the stent struts. The mean wall shear stress was less than 1 dyne/cm^2 between the struts for stent strut spacings less than 5H. At the largest stent strut spacing (7 H), the mean wall shear stress recovered to a maximum value of 45% of the nominal value.

SUMMARY

These results indicate that flow phenomena likely to play a role in stent restenosis. Additional in vitro experiments have demonstrated that platelet adhesion and endothelial cell regrowth are sensitive to flow conditions. Platelet adhesion is highest in regions of partial flow reattachment and low shear stress. Endothelial cell regrowth occurs fastest in regions of flow reattachment and high shear stress. These results aim to provide a more quantitative understanding of the role of flow patterns in restenosis, and to provide information that can be used to design better stents.

ACKNOWLEDGEMENTS

This work was supported by an NHLBI/NIGMS MBRS SCORE grant (S06 GM08205).

FLUID DYNAMICS AND WALL MECHANICS IN PERIPHERAL BYPASS ANASTOMOSES

Karl Perktold[1], Thomas Berk[1], Armin Leuprecht[1], Martin Prosi[1], Tanja Brandl[1],
Martin Cerny[2], Wolfgang Trubel[3] and Heinrich Schima[4]

[1]Institute of Mathematics, Graz University of Technology, Graz, Austria; perktold@matd.tu-graz.ac.at
[2]Department of Cardiothoracic Surgery, University of Vienna, Vienna, Austria
[3]Department of Vascular Surgery, University of Vienna, Vienna, Austria
[4]Institute of Biomedical Engineering, University of Vienna, Vienna, Austria

INTRODUCTION

For the improvements of patency rates following peripheral blood vessel reconstructions in which synthetic prosthesis must be used because of insufficient autologous venous replacement material, several modifications at the distal bypass anastomosis have been suggested. The long term function of such vascular reconstructions is influenced by several factors. Apart from cell biological and biochemical influences on intimal hyperplasia in synthetic vascular prostheses reactive mechanisms resulting from non-physiological flow dynamical and wall mechanical conditions play a certain role in the disease process. The present study aims to investigate the relationship between flow characteristics and mechanical stresses and post-operative intimal hyperplasia in three established types of distal end-to-side anastomoses using expanded polytetrafluoroethylene (e-PTFE) prostheses. Related to the surgical techniques the models differ in shape and structure of the graft-artery connector region (Leuprecht et al.). A significant aspect of the modification is the reduction of the compliance mismatch between the prosthetic graft and the native artery using an interposed vein patch and cuff.

METHODS

Computer simulations based on casts of femoro-popliteal bypasses implanted in sheep were performed to analyse the flow dynamics and the wall and suture mechanics in anatomically correct bypass configurations related to the surgical techniques conventional type anastomosis, Taylor-patch and Miller-cuff anastomosis. Time-dependent Navier-Stokes equations describing the flow field and a non-linear shell structure for the vessel wall were coupled using finite element methods. Experimental-surgical investigations and computer simulations were carried out, and possible relations between flow characteristics and mechanical stresses and occurring post-operative intimal hyperplasia in the anastomoses have been studied. For morphometry of the intimal thickness the implanted grafts were explanted and prepared for histological examination after six months.

RESULTS AND DISCUSSION

The simulation analysis referring to medium diameter vessel replacements demonstrates the influence of geometrical asymmetries and irregularities on the anastomotic flow and wall shear stress patterns. The stress field calculation confirms that more compliant grafts result in lower principal stresses at the suture lines. The in-vivo studies of our project demonstrate correlations to compliance mismatch to some extent, with the graft-artery junctions showing the largest amount of intimal hyperplasia in mean values. However, at detailed locations, the situation may look different, due to geometry and flow field influences. The design of a peripheral vascular bypass configuration may affect the long term patency of the reconstruction. The selection of suitable materials and the definition of suitable geometry are important features of increased performance. Intimal hyperplasia at graft-artery junctions are also affected by biochemical influences and material interactions as discussed by Kissin et al. Material characteristics and cell biological aspects are not included in the present mathematical analysis.

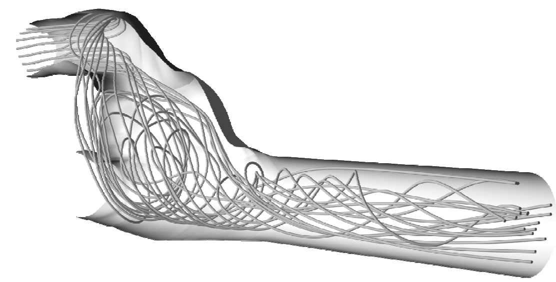

Figure 1: Miller-cuff anastomosis, anastomotic flow field.

SUMMARY

The results of this investigation confirm the advantage of modified anastomoses as compared to both other non-conventional combinations. They allow the conclusion that the long-term function of e-PTFE reconstructions with venous grafts according to Taylor and Miller (and Linton-patch, which was also included in the in-vivo study) is improved due to reduction of the compliance mismatch rather than to changes in local blood flow phenomena. The study confirms that graft-artery compliance mismatch promotes the suture line hyperplasia.

REFERENCES

Kissin, M. et al. (2000). J. Vascular Surgery, 31, 69-83.
Leuprecht, A. et al. (2002). J. Biomechanics, 35, 225-236.

ACKNOWLEDGEMENTS

Research supported by FWF, Project No. P 14 321-TEC, Vienna, and Austrian NB, Project No. 5021, Vienna.

CHARACTERISATION AND SIMULATION OF IN-VIVO PERHIPERAL DISTAL BYPASS GRAFTS

S.J.Sherwin[1], S.Giordana[1], J.Peiró[1], Y. Papaharilaou[1], D.J.Doorly[1], C. Caro[2], M. Jackson[3], C. Bicknell[3], V. Zervas[3], N.J.W. Cheshire[3]

[1]Aeronautics, [2]Bioengineering and [3]St. Mary's hospital, Imperial College, London, UK
s.j.sherwin@ic.ac.uk

INTRODUCTION

Abnormal haemodynamic conditions are implicated in the development of anastomotic myointimal hyperplasia (MIH). These conditions are difficult to determine *in vivo*, prompting research using ex-vivo idealised models. To relate the understanding gained in idealised studies to anatomically correct conditions we have investigated an approach to characterise *in vivo* distal graft anastomoses and their inter-patient variability.

METHODS

Distal anastomotic geometries were acquired in vivo by MR angiography from 10 patients undergoing infrageniculate autologous venous bypass at a median 2 weeks postoperatively. Four patients underwent repeat examinations 13 to 49 days later.

For each geometry the two-dimensional MR slice data was segmented and then approximated by smooth splines and evaluated at discrete points as shown in figure 1(a). The lumen's surface was then interpolated through the discrete points using a zero level set of an implicit function (Turk & O'Bien) as indicated in figure 1(b). The implicit function was made up of a radial basis function that minimises curvature using a variational principle which ensures smoothness. At this stage further smoothing may be applied followed by another implicit surface representation. From the lumen representation we can construct a computational mesh (Peiró et al.) to simulate flow quantities such as the wall shear stress shown in figure 1 (c).

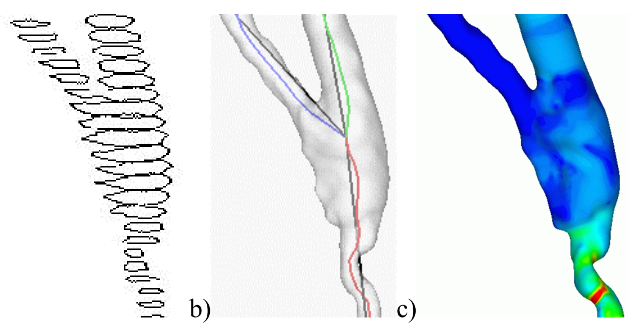

a) b) c)

Figure 1: a) segmented MRI data, b) implicit surface reconstruction and centreline representation, c) wall shear stress distribution.

Alternatively we can use the lumen representation as a starting point to characterise the geometry. A skeletonization procedure (Palagyi & Kuba) was then applied to determine a centreline approximation which approaches the medial lines of the geometry as indicated in figure 1(b). The proximal and distal host and the graft vessels were then approximated from the intersection point using a linear least squares fit using data over a range of segment lengths. The linear approximations were then used to define angles between graft and proximal host vessel (α), graft and distal host (β), proximal host and distal host (γ) and each angle was evaluated over a range of sample lengths as shown in figure 2.

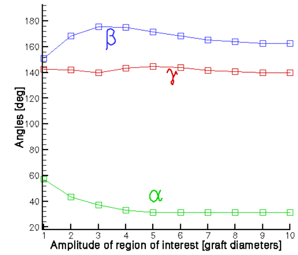

Figure 2: Variability of graft angle with inspection length normalised by the diameter.

Diameter ratios between the graft and host vessels were also calculated from the cross-sectional areas of the three vessels at the reconstructed anastomosis boundaries. A preliminary distal anastomotic planarity index (API) based on the variation of the normal to the plane containing the end points of the linear fits has been also introduced (for a planar anastomosis API=0). The data is summarized in table 1.

RESULTS

Angles	Min	Max	Mean	S.D.
α	28	101	41.6	20.3
β	144	177	163.8	9.9
γ	113	175	148.4	16.3
Diameter ratio				
Prox . - Graft	0.35	0.79	0.56	0.16
Distal - Graft	0.41	0.96	0.59	0.16
API	0.04	1.4	0.37	0.34

Table 1

Good agreement was found between the distal anastomotic angles in the initial and follow-up examinations. The differences in the angles varied between 1 and 10 degrees with a mean of 4.3 degrees.

REFERENCES

Turk, G., O'Brien, J.F., (1999), SIGGRAPH98, 335-342.
Palagyi, K., Kuba, A.,(1998), Pattern Recognition Letters **19** 7
Peiró, J., Griffith, C., Giordana, S., Sherwin S.J., (2002), *Int. J. Num Methods Fluids*, To appear.

EFFECTIVE HEMODYNAMIC DIAMETER: A PARAMETER WITH PREDICTIVE VALUE FOR PATENCY

Francis Loth[1], Shari L. Meyerson[2], Christopher L. Skelly[2], Michael A. Curi[2], and Lewis B. Schwartz[3]

[1]Assistant Professor, Department of Mechanical Engineering, University of Illinois at Chicago, Illinois, floth@uic.edu
[2] General Surgery Resident, [3]Associate Professor, Department of Surgery, University of Chicago, Illinois

INTRODUCTION

Great advancements have been made in the simulation of blood fluid dynamics due to increased computer power, improved CFD algorithms, and better *in vivo* measurements through medical imaging. One can envision that a full and accurate simulation of a patient's hemodynamic environment could be available to the physician in the years to come. Thus, we are conducting research to determine how simulations can be used to predict disease, plan surgical procedures, or to assess the effectiveness of medical treatments. Conduit size and quality are major determinants of the long-term success of infrainguinal autologous vein grafting. However, accurate measurement of the internal diameter of vein graft is surprisingly difficult given their variable wall thickness and taper. The purpose of this study was to define the "effective" internal diameter of a vein graft according to its hemodynamic properties and to determine its significance for graft patency.

METHODS

Sixty infrainguinal bypass grafts performed on 57 patients were evaluated intraoperatively. Proximal and distal graft pressure and blood flow were measured with fluid-filled catheter transduction and ultrasonic transit-time flow meter (Transonics, Inc.). Waveforms were recorded under baseline conditions and after stimulation with 60 mg of papaverine. The Womersley solution for pulsatile flow in an infinitely straight circular pipe was used to calculate a theoretical flow waveform for a range of graft diameters with fluid viscosity (3.5 cP). These theoretical waveforms were then compared with the measured flow waveforms and the best-fit diameter was chosen as the "effective hemodynamic diameter" (EHD). After a mean follow-up of 12.5 months (range, 0.1-43.9 months), patency was determined by the life table method.

RESULTS

The mean EHD was 4.1 ± 0.1 mm with a range of 2.5 to 5.7 mm. Administration of papaverine caused significant changes in the pressure difference between the proximal and distal ends of the graft as well as the blood flow rate (+71% ± 12%) as expected, but had almost no effect on EHD (+0.05% ± 0.1%). Patency of small diameter grafts (EHD < 3.6 mm: n=11) was compared with patency of larger grafts (EHD > 3.6 mm; n=36) to test a frequently espoused clinical guideline. Grafts with an EHD less than 3.6 mm exhibited significantly lower secondary patency compared with larger grafts (P=0.0001) as shown in Figure 1.

DISCUSSION

The parameter EHD was defined to provide the physician with a way to characterize a vein graft with a single number. The EHD represents the diameter of a circular tube that would have a similar flow waveform if imposed by the same unsteady proximal and distal pressure waveforms. Note that while this circular tube has the same length as the vein graft, it is of constant diameter, fully developed pulsatile flow is assumed thought the tube, and the fluid is assumed to be a Newtonian fluid. The EHD is not meant to correspond to a specific diameter measured at a point along the graft. It is the effective diameter along the length of the conduit that constrains the relationship between pulsatile pressure and flow. Since it is unaffected by papaverine stimulation, it is an inherent property of a given graft.

While the simulation technique is rather simple given the CFD resources available today, the resulting EHD does incorporate the true pressure drop associated with the *in vivo* complex 3D geometry since it is based on intraoperative measurements. Thus, any deformation, kink, or blockage due to a vein valve in the vein graft that would significantly increase the pressure drop would be reflected in a lower value of EHD. In conclusion, EHD is a unique parameter that quantifies a vein graft's resistive properties to blood flow and is predictive of graft patency.

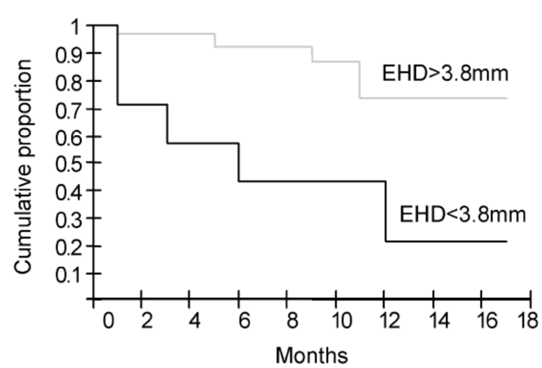

Figure 1: Effect of EHD on Secondary Patency

REFERENCES

Meyerson et al., J Vasc Surg 2000, Vol. 31, pp. 910-917.

WALL SHEAR STRESS AND ALBUMIN PERMEABILITY AT THE PORCINE AORTIC TRIFURCATION

Morton H. Friedman[1], Deborah M. Grzybowski[2], Andrew L. Hazel[3], Heather A. Himburg[1], and Jeffrey A. LaMack[1]
[1]Department of Biomedical Engineering, Duke University, Durham NC, USA; mhfriedm@duke.edu
[2]Biomedical Engineering Center, Ohio State University, Columbus OH, USA
[3]Department of Mathematics, University of Manchester, Manchester, UK

INTRODUCTION AND SUMMARY

A knowledge of the normal relationship between fluid dynamic shear stress and vascular macromolecular permeability in vivo is essential to understanding the mechanisms by which these stresses affect the localization and progression of atherosclerotic disease. Such data are difficult to obtain because the complexity and variability of arterial geometry require that colocalized shear stress and permeability data be obtained in the same vessel. We report here on a first experiment in which the albumin uptake distribution at the porcine aortic trifurcation is correlated on a site-by-site basis with a CFD calculation of the wall shear stress distribution in a computational region derived from a luminal cast of the same segment. The results suggest that the normal permeability of the vessel decreases with increasing shear stress, reaching a plateau at shear stresses ca. 40 dynes/cm^2.

METHODS

Perivascular flow probes (Transonic Systems, Ithaca NY) were placed around the exposed femoral arteries of an anesthetized 72 kg female domestic swine. Evans Blue dye (EBD), 2:1 molar with blood albumin, was administered intravenously and allowed to circulate for 90 minutes. The animal was sacrificed and a silicone rubber/glass fiber casting mixture was injected at physiological pressure into the abdominal aorta. The cast replicated the animal's infrarenal aorta and iliac-femoral arteries. Once the casting material had cured, the cast and surrounding tissue were excised from the animal. The tissue was removed with a dorsal cut; the cut line marked the surface of the cast and was subsequently used for registration purposes.

The cast was laser scanned by Product Development Technologies, Inc. (PDT, Lincolnshire, IL) to generate a 3-dimensional cloud of 150,000 points representing the luminal surface. Using a custom mesh generator, a 3-dimensional 8-node brick element mesh representation of the terminal aorta and the common internal, external and circumflex iliac arteries was created. The mesh contained a total of 135,648 volume elements and 8,352 surface elements. The flows through each branch were adjusted using terminal porous plugs to obtain flow partitions that were estimated (Henderson et al, 1999) from the flow probe measurements.

Steady, laminar flow calculations were performed using the finite-element code FIDAP (Fluent, Inc.), a uniform inlet velocity profile and a no-slip boundary condition at the rigid walls. The aortic segment was sufficiently long that a well-developed velocity profile existed immediately proximal to the trifurcation. The inlet Reynolds number was 985 and the fluid was Newtonian, with a kinematic viscosity of 3.3 cs.

The distribution of computed shear stress in the right and left external iliac arteries, from the trifurcation to the deep femoral ostia, was mapped to an en face image by a numerical transform that simulates the cutting and pinning out of the tissue, using the cut line on the cast. The transformed image was deformed to a standard template and the shear distribution was compared on a pixel-by-pixel basis (20,000 pixels total) against the optical density (OD) distribution of a similarly templated photographic image of the EBD-stained tissue removed from the cast. The technique for obtaining the OD distribution has been described elsewhere (Friedman et al, 2000). OD measures albumin uptake during the dye exposure and is proportional to local permeability.

RESULTS

The correlation of OD vs. shear stress is shown in Fig. 1. Permeability appears to decrease monotonically with shear stress until a plateau is reached at about 40 dynes/ cm^2.

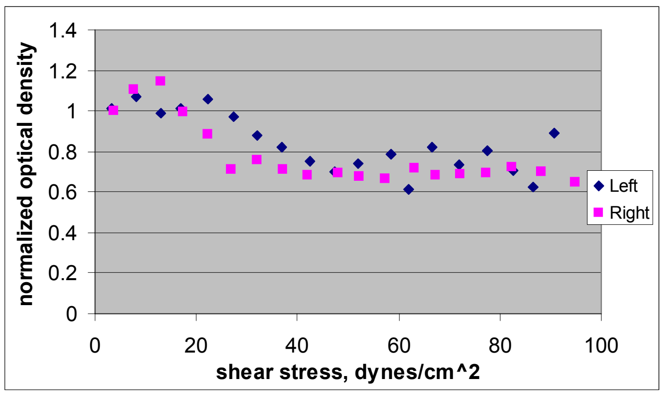

Figure 1: Normalized optical density vs. calculated wall shear stress for both external iliac arteries. For each 5 dynes/cm^2 shear stress interval, the OD's of all pixels whose shear value was in that interval were averaged and divided by the mean OD of all pixels in that segment.

REFERENCES

Friedman, M.H. et al (2000). *Biorheology,* **37,** 265-277.
Henderson, J.M. et al (1999). *Biorheology*, **36**, 257-266.

ACKNOWLEDGMENTS

Research supported by NIH Grant HL-50442. I. Tseng assisted in the data analysis.

IMAGE BASED SYSTEMATIC MODELING OF LARGE ARTERIES FOR CLINICAL CARDIOVASCULAR MEDICINE

Takami Yamaguchi[1], Daisuke Mori[1], and Tomoaki Hayasaka[2]

[1]Department of Mechatronics and Precision Engineering, Tohoku University, Aoba 01, Sendai 980-8579 Japan
The Institute of Physical and Chemical Research (RIKEN), 2-1 Hirosawa, Wako, 351-0198, Japan

INTRODUCTION

Vascular diseases including cardiovascular and cerebrovascular diseases are the leading causes of death in the industrialized world. They share a common background, atherosclerosis, and a common final event, the breakage or destruction of vascular structure. Atherosclerosis preferentially occurs at specific arterial sites, which are strongly suspected to be related with the wall shear stress (WSS) distribution. The final vascular events that induce a fatal outcome, such as acute coronary syndrome, are now strongly suspected of being triggered by the sudden mechanical disruption of atherosclerotic plaque on the coronary artery wall. Subarachnoidal hemorrhage, which is another very acute and fatal disease, is the direct result of the rupture of a cerebral aneurysm. Thus, both the onset and final outcome of fatal vascular diseases are related to mechanical events that occur on the vascular wall, probably due to alterations in blood flow. Consequently, the fluid-solid mechanical interactions between blood and the vascular wall must be analyzed in order to predict, diagnose, and prevent the fatal consequences of vascular disease. We need to use computational studies to elucidate the mechanism of such disease, to refine the diagnostic measures, and to develop therapeutic modalities, either invasive or non-invasive.

PARAMETRIC AND REALISTIC MODELING OF THE CARDIOVASCULAR SYSTEM

Fig.1 Simulated blood flow in the human aorta using an overset mesh technique.

In conventional modeling of arteries and the heart, parametric and realistic methods are regarded as different. In the former, some characteristic configuration of the vascular system is modeled using simple elemental geometrical modeling. In the latter, direct segmentation, registration, and vectorization of complex anatomical structures from medical images are carried out. We proposed the so-called differential geometrical method of modeling arterial trees as a method that combines these two methods. In our method, vascular trees are represented using their centerlines and their normal planes defined by a combination of normal and binormal vectors. Each branch is modeled separately and connected using an overset mesh technique when fluid mechanical computations are made (Fig.1).

IMAGE-BASED MODELING AND CLINICAL INTERFACES

Due to the rapid advances in invasive and non-invasive imaging technology in clinical medicine, we can now obtain images of target organs to use in computational analysis modeling. However, the resolution and reproducibility of non-invasive methods, such as magnetic resonance imaging (MRI), are still insufficient for automatic modeling. Therefore, we believe that any clinical application should fully utilize human pattern recognition and image reconstruction abilities. This is also a practical and efficient way of processing images. Consequently, we have been developing a comprehensive computational analysis support system that includes the preprocessing of medical images, segmentation, structure registration, database and human interfaces, mesh generation, and the final evaluation of the computed results (Fig. 2).

CONCLUDING REMARKS

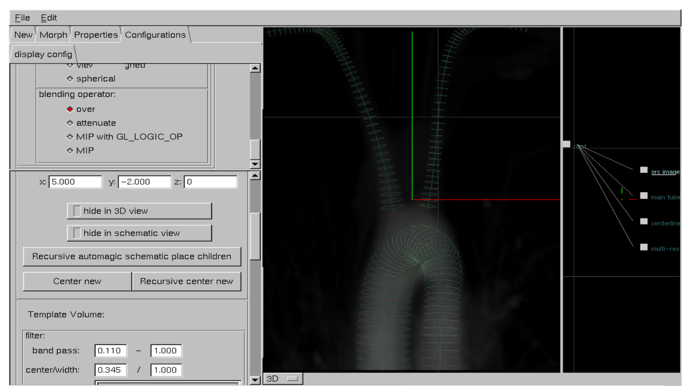

Fig.2 A clinical interface for computational analysis

We now expect that a prototype will be developed for clinical application within a few years, and that we will be able to accumulate the necessary data and experience from real patients once this system becomes available to medical practitioners.

REFERENCES

T.Yamaguchi, *Clinical Application of Computational Mechanics to the Cardiovascular System*, Springer-Verlag, Tokyo, 2000

ACKNOWLEDGEMENTS
Part of this study is supported by a grant from the JST-ACT, 01.

NUMERICAL STUDY OF HUMAN AORTIC BLOOD FLOW: A COMPARISON BETWEEN HEALTHY AND DISTURBED FLOW DISTAL TO ARTIFICIAL HEART VALVES

Armin Leuprecht[1], Karl Perktold[1], Sebastian Kozerke[2] and Peter Boesiger[2]

[1]Institute of Mathematics, Graz University of Technology, Graz, Austria, armin.leuprecht@tugraz.at
[2]Institute of Biomedical Engineering and Medical Informatics, University of Zurich and Swiss Federal Institute of Technology Zurich, Zurich, Switzerland

INTRODUCTION

Flow in the human ascending aorta is of very complex three-dimensional pulsatile behavior. During systolic acceleration blood is expelled from the heart through the aortic valve. Flow in a healthy configuration shows a significant jet in the centre of the vessel featuring essentially flat profiles. Velocity profiles downstream mechanical heart valves demonstrate substantially different patterns that depend mainly on the valve design. As such local flow disturbances have been associated with late complications it is of major interest to analyse the hemodynamic performance of artificial valves. In this study magnetic resonance imaging (MRI) and computational fluid dynamics (CFD) are used in combination to compare aortic flow patterns and related hemodynamic quantities between an individual healthy and an artificial valve configuration.

METHODS

Two volunteer individuals showing similar geometrical features and similar flow conditions have been selected for this study: a female patient with an implanted artificial heart valve (Saint Jude Medical® aortic valve) and a young, healthy, female subject. Using a Philips Gyroscan NT 1.5T whole body scanner time-resolved, three-directional phase contrast data of both geometries has been acquired (Kozerke, 2000). Within several reconstruction steps time-dependent, three-dimensional computer models of the arterial lumen have been generated for the entire pulse cycle. Cine magnetic phase contrast measurements were performed just downstream the aortic valve providing inflow velocity profiles for the computational study. The mathematical description of the pulsatile blood flow in the ascending aorta uses the incompressible Navier-Stokes equations for Newtonian fluids. With respect to the movement of the flow domain the Arbitrary Lagrangean-Eulerian technique is applied. The numerical solution procedure employs our recently developed finite element solver (Karner et al., 1999) that applies a streamline upwind stiblization scheme with respect to the highly convective flow.

RESULTS AND DISCUSSION

Especially during the systolic phase the inflow conditions differ significantly for the two configurations. During acceleration, however, the velocities develop very quickly to blunted profiles that are skewed to the inner wall of the aortic arch. In deceleration the specific shape of the inflow patterns is preserved much longer and extends to the entrance of the aortic arch. Zones of reversed flow develop at the inner wall leading to C-shaped profiles in both cases.

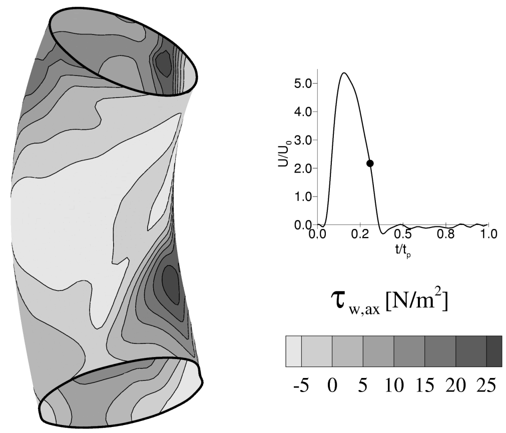

Figure 1: Axial wall shear stress distribution during systolic deceleration in the artificial aortic valve configuration.

Wall shear stress distributions during deceleration (Figure 1) demonstrate these recirculation zones and show the regurgitation at the aortic root. Due to the shorter and steeper systolic phase of the artificial valve configuration wall shear stresses are considerably higher than in the healthy vessel.

SUMMARY

A newly developed MRI velocity mapping technique enables the in-vivo measurement of blood flow patterns following the aortic root. In combination with the CFD analysis accurate prediction of blood flow in the ascending aorta can be done. This study compares blood flow distal to an artificial heart valve with undisturbed healthy flow. Further studies shall – as long term objective - contribute to optimal valve design in humans.

REFERENCES

Karner, G. et al (1999). *Computer Methods in Biomechanics and Biomedical Engineering*, **2**, 171-185.
Kozerke, S. (2000). PhD theses, Swiss Federal Institute of Technology.

ACKNOWLEDGEMENTS

This study is supported by the Austrian Science Foundation, Project-No. P 14 321-TEC, Vienna, Austria and by EUREKA, Project-No. E!2061.

EFFECTS OF VESSEL MOTION ON RIGHT CORONARY ARTERY HEMODYNAMICS

D. Zeng[1], Z. Ding[2], M. H. Friedman[3] and C. R. Ethier[1]

[1]Department of Mechanical and Industrial Engineering, University of Toronto, Canada; ethier@mie.utoronto.ca
[2]Department of Diagnostic Radiology, Yale University, New Haven, CT
[3]Department of Biomedical Engineering, Duke University, Durham, NC

INTRODUCTION

Blood flow in coronary arteries depends on 3D vessel geometry, flow pulsatility, and vessel motion due to cardiac contraction. Here our objective was to evaluate the effects of vessel motion on right coronary artery (RCA) hemodynamics.

METHODS

Biplane cineangiography was used to determine the *in vivo* motion of an RCA segment beginning ~ 1.5 cm distal to the ostium and terminating near the interventricular bifurcation (Ding and Friedman, 2000). The extracted data contained the 3D positions of 126 markers on the vessel axis at selected times during a cardiac cycle. We assumed that: (i) the cross-sectional contours of the RCA were circles of uniform radius 1.24 mm; and (ii) the contours maintained an orientation normal to the local, time-varying axis tangent direction at all times. This allowed the contours to be displaced and rotated to follow the dynamic RCA axis, from which we reconstructed the dynamic RCA lumen geometry. Inlet and outlet extensions consisting of a straight, stationary section and a flexible connector section were added to the RCA segment (Figure 1). The 3D, unsteady, incompressible Navier-Stokes equations were numerically solved on this moving geometry using a carefully validated finite element code based on an arbitrary Lagrangian-Eulerian formulation and a torsional spring mesh updating scheme. Newtonian blood rheology was assumed. To isolate the effects of RCA motion, we imposed a steady (Poiseuille) inflow with inlet Re_D = 233. The Womersley parameter based on the heart rate (75 beats/min) was 1.82. For comparison, we also simulated steady flow in a static "average" RCA model, obtained by averaging the RCA axis marker positions over one cardiac cycle.

RESULTS AND DISCUSSION

The wall shear stress (WSS) varied significantly with both axial position and time (e.g. Figure 2). The distribution of time-averaged WSS in the moving RCA model was quite similar to the WSS distribution in the static "average" geometry, suggesting that temporal variation in WSS was due to changes in local geometry (curvature, torsion), rather than inertial effects due to vessel motion. The magnitude of the temporal variation of WSS at material points on the RCA was strongly dependent on axial location. The maximum (peak-to-peak) variations in WSS magnitude were ~150% and 200% of the Poiseuille inlet value along the inner and outer walls of curvature, respectively. In contrast, some axial locations showed almost no WSS variation over the cardiac cycle.

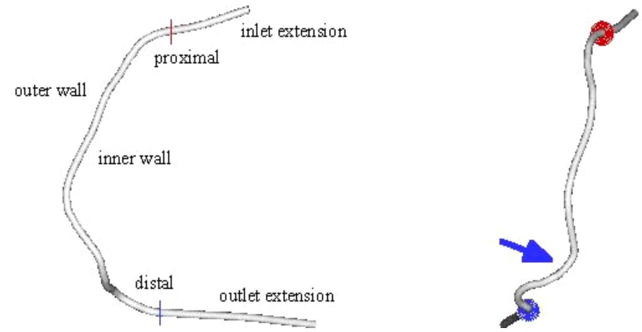

Figure 1: The RCA at time t=0. Left panel: Anterior-posterior view showing the primary curvature of the RCA and definitions of inner and outer walls. Right panel: A medio-lateral view approximately coincident with the plane of primary curvature, showing secondary curvature. Disks are the boundaries between the RCA and inlet/outlet extensions.

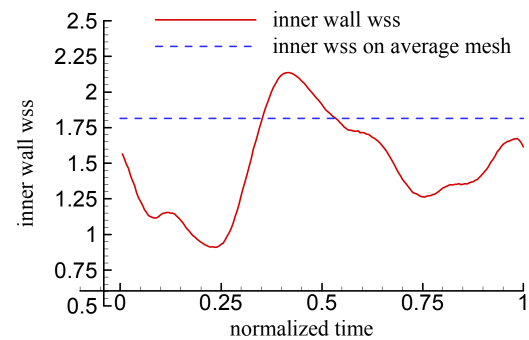

Figure 2. WSS vs. time at the location in the distal RCA shown by the arrow in Fig 1. The WSS at the same axial location on the static average mesh is shown by the dashed line. WSS values are normalized by the inlet Poiseuille WSS (41.9 dyne/cm^2), and time is normalized by the cardiac period.

SUMMARY

WSS patterns in a simplified right coronary artery model are strongly influenced by vessel motion. The large magnitude of the motion-induced temporal variations in WSS, and their strong dependence on axial location in the vessel, suggest that the role of vessel motion as a localizing factor in atherogenesis needs to be considered.

REFERENCES

Ding and Friedman (2000). *J. Biomech. Eng*, **122**, 488-492

ACKNOWLEDGEMENTS

Natural Sciences and Engineering Research Council (CRE).

COMPUTED BLOOD FLOW DYNAMICS IN AN ANATOMICALLY REALISTIC CEREBRAL ANEURYSM

David A. Steinman[1,2,*], Jaques S. Milner[1], Chris J. Norley[1], Stephen P. Lownie[1,2,3], David W. Holdsworth[1,2]

[1]The John P. Robarts Research Institute, [2]University of Western Ontario, and [3]London Health Sciences Center, London, Canada
[*]Corresponding author: steinman@irus.rri.ca, www.irus.rri.ca/~steinman

INTRODUCTION

Local hemodynamic factors such as wall shear stress, dynamic pressure, and residence time are thought to play key roles in the initiation and growth of aneurysms, and also the success or failure of interventional aneurysm therapies. To date most studies of aneurysm hemodynamics have been carried out in mathematically idealized geometries or models reconstructed from post-mortem casts. The former, while convenient, remain crude approximations to real aneurysm geometries, while creation of the latter is, as noted by Imbesi & Kerber (2001), "a tedious and technically difficult undertaking." With recent advances in computational modeling and in vivo medical imaging technologies, it is now possible to reliably simulate blood flow dynamics in a prospective, patient-specific manner. In this paper we present a computational fluid dynamic (CFD) simulation of physiologically pulsatile flow in an anatomically realistic aneurysm reconstructed from in vivo 3-D imaging of a human subject.

METHODS

Computed rotational angiography (CRA; Fahrig et al. (1997)) was used to acquire high-resolution (0.4mm isotropic) 3-D images of a 58-year-old female patient with a giant internal carotid artery (ICA) aneurysm (Figure 1a). The lumen geometry was extracted from the CRA data using the semi-automated 3-D discrete dynamic contour (DDC) of Ladak et al. (2000) (Figure 1b). Outlet branches were truncated proximal to further branches, and the resulting triangulated surface was used to generate a sufficiently resolved volume mesh composed of 213,000 quadratic tetrahedral finite elements (Figure 1c). As the patient's blood flow rates were not available, we applied fully developed velocity boundary conditions at the inlet based on an ICA flow rate waveform measured via phase contrast MRI of a 73-year-old female volunteer. Traction-free boundary conditions were applied at both outlets. CFD simulations were carried out on a Pentium workstation using an in-house solver.

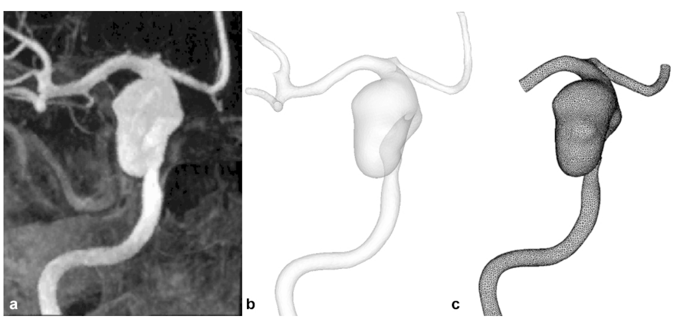

Figure 1: Stages in the construction of the CFD model (anterior-posterior view): (a) Maximum intensity projection of the source CRA data; (b) Translucent rendering of the lumen boundary extracted via 3-D DDC; (c) Finite element mesh after truncation of outlet branches.

RESULTS AND DISCUSSION

To visualize this complex flow field, we mimicked the slipstream visualizations of Imbesi & Kerber (2001) by tracking passive, non-diffusing tracers, seeded randomly within a small radius, at two locations near the model inlet, separated by 90°. As illustrated in Figure 2a, the resulting velocity field is largely free of secondary flow proximal to the aneurysm ostium, at which location the blue slipstream undergoes marked dispersion within the aneurysm sac while the red slipstream maintains its integrity as it divides between the two outlets, avoiding the aneurysm sac altogether. Cycle-averaged wall shear stresses (Figure 2b) were maximal at and distal to the narrowing of the ICA (caused by aneurysm-induced compression of the vessel against adjacent bone), and at the distal ostium, at which location flow from the parent vessel can be seen to be impacting the aneurysm wall.

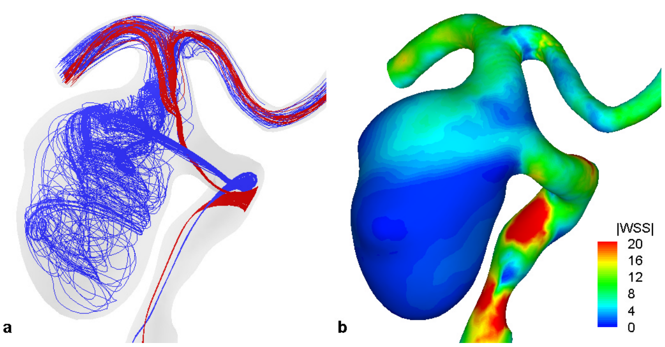

Figure 2: Physiologically pulsatile flow in an anatomically realistic aneurysm (right-anterior-oblique view): (a) Virtual slipstreams; (b) Cycle-averaged wall shear stress magnitude (in dyne/cm^2).

SUMMARY

Using computational fluid dynamics and high-resolution medical imaging, it is now possible to study, in a prospective, patient-specific manner, the complex fluid dynamics associated with cerebral aneurysms. Such techniques may be used to study the forces that predispose certain aneurysms to rupture, and also to predict the success or failure of interventional therapies that rely on altering the dynamics of flow within the aneurysm sac.

REFERENCES

Fahrig, R. et al. (1997). *Am. J. Neuroradiol.*, **18**, 1507-14.
Imbesi, S.G. & Kerber, C.W. (2001). *Am. J. Neuroradiol.*, **22**, 721-4.
Ladak, H.M. et al. (2000). *J. Biomech. Eng.*, **122**, 96-9.

THE INFLUENCE OF RESTING PERIODS ON FRICTION IN THE ARTIFICIAL HIP JOINT

Michael M. Morlock[1], Roman Nassutt[2], Markus Wimmer[3], and Erich Schneider[4]

[1]Biomechanics Section, Technical University Hamburg-Harburg, Hamburg, Germany, morlock@tuhh.de
[2]eska implants, Lübeck, Germany
[3]Department of Orthopedics, Rush Medical Center, Chicago, Illinois
[4]AO Research Institute, Davos, Switzerland

INTRODUCTION

Insufficient tribological performance of total joint components has been identified as one major cause of prostheses failure. Wear has been studied intensively using testing machines that apply continuous motions. Human locomotion, however, is not well represented by continuous motions alone. Singular events as well as resting periods are a substantial part of daily activities. Resting does influence adhesion in the artificial joint with possible effects on friction, wear, and loosening. The purpose of this study was to evaluate the effects of resting on the frictional properties of hip prosthesis components.

METHODS

Friction measurements were performed using a pin-on-ball testing device placed into an acrylic container with stabilized bovine serum (diluted to 30%, 37°C) mounted onto a biaxial hydraulic material testing machine (sinusoidal motion of 1 Hz frequency, ±20° ball rotation, contact load 1000N, Fig. 1). The testing concept consists of a pair of concave pins pressed onto a conforming ball (Wimmer et al, 1998). The pins represent the same geometric and morphologic features as original hip cups, the ball a commercially available femoral head. Static friction was defined as the maximum friction peak during motion initiation after resting periods of certain durations (0, 1, 5, 10, 30 and 60s).

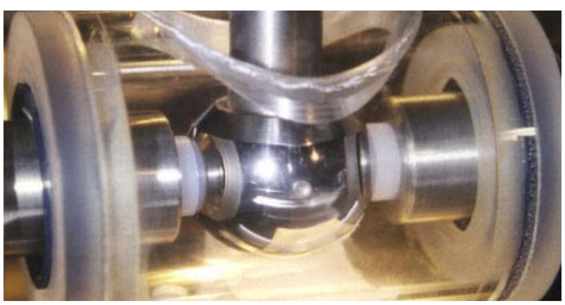

Figure 1: Pin-on-ball testing device.

Ceramic (Biolox®) and metal (Mathys Medical Ltd.) prosthesis heads were tested against pins made from UHMWPE (PolyHiSolidur). Metal pins were worked out of cups, ceramic pins sintered from BIOLOX *Forte*® and finished (polished). Five repetitions for 3 samples of each material combination were performed ans analysed.

RESULTS

The level of friction was significantly higher for metallic heads compared with ceramic heads when paired with polyethylene and also when paired with the respective hard partners at all tested load levels and for all tested resting durations (Fig. 2). For up to 10 seconds of rest, an increase in friction was observed, which then leveled out for all material combinations but not for metal-on-metal bearings, for which friction increased further with increasing resting durations (Fig. 2).

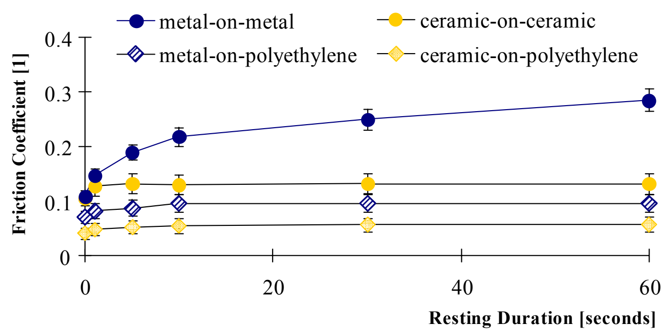

Figure 2: Frition coefficient for all resting durations and material combinations.

DISCUSSION

Static friction increased significantly with increasing resting duration. This basic relationship was pronounced for metal-on-metal bearings. The influence of resting periods on wear has not been shown yet. However, considering metal-on-metal prostheses with 48mm nominal head diameter in a patient with a body weight of 80kg and the static friction coefficient determined in this study, the calculated moment peaks reach 14.2Nm after 30 seconds of rest. These value is close to the interface strength of certain in-vitro determined press-fit cup fixations and highlights the fatigue problem which may arise during starting procedures if an unfavorable combination of parameters (high friction + large head diameter + overweight patient) coincides. The individual anatomic situation of the patient, the design of the implant, and the situation after surgery strongly affect the safety against frictional torque-induced loosening. Nevertheless, metal-on-metal articulations should be used with care in combination with big head sizes because of the friction characteristics.

REFERENCES

Wimmer M. et al. (1998) *Alternative Bearing Surfaces in Total Joint Replacement, ASTM STP 1346*, 30-43.
Clarke H et al. (1991) *J Arthroplasty* 6: 335-340.
Ma S et al. (1983) *J Bone Joint Surg Am* 65: 366-370, 1983.

DEVELOPMENT OF ORTHOPEDIC IMPLANTS - A FIELD OF TENSION BETWEEN RISK ASSESSMENT, PRE CLINICAL AND CLINICAL TESTING

Ulrich Fink
R&D, Aesculap AG & Co. KG, Tuttlingen, Germany, ulrich.fink@aesculap.de

PRESENT SITUATION

In recent years some serious systemic failures with orthopedic implants have been observed on the market. We saw for instance toxicological surface contamination on porous coated sockets (www.sulzermedica.com), we saw wear problems with highly crystalline phase modified polyethylene (Scott et al, 2000), we saw corrosion induced loosening of cemented titanium stems in hip arthroplasty (Willert et al, 1996) and we saw mechanical brake down of a PMMA bone cement due to problems with the glass transition temperature (Abdel-Kader et al, 2001).

All the above mentioned products failed despite intensive laboratory testing and the approval of regulatory or notified bodies either in the US or in Europe. That resulted on the one hand in harm to the patient, but also on the other hand affected the medical device company due to recourse claims from the patients, and in the midterm the loss of confidence from the surgeons.

In order to receive the selling permission from the certification or notified bodies, the medical device company has to document the safety and efficiency of the product as well as the reproducibility in production. For both cases it is a key feature to make a risk assessment to get an idea about the worst case scenario. Additionally several organizations for the standardization of test procedures and design features do exist. "Specialists" are consulted by these organizations in order to define the testing criteria. Nevertheless the aforementioned systemic failures still occurred. In contrast there are several restrictions for products from the government or notified bodies which the producers don't really understand, such as the restrictions on pedicle screws and on cementless joint replacements. The failures of medical devices in the past together with the key feature "risk assessment" required for the registration result in the situation, that in the best case a true evaluation can only be made for variations of existing products.

A Research and Development department has to keep in mind that the step from pre clinical lab testing into the clinical evaluation must be seriously combined with an intensive risk assessment, in which neutral experts to provide clinical outcome have to be involved. As mentioned above, the failures which showed up in the past were hardly predictable at the time the products were introduced into the clinic. During the step into the clinic evaluation the R&D departments are often too focused on the well known regulations of the registration procedure, not by the real clinical risks, which are much more difficult to identify.

This leaves the question "How to proceed ?", if the risks are not really predictable as with a completely new implant design. In this situation the only solution can be to go ahead with a well defined clinical evaluation investigating the safety and functionality of the product by statistical, relevant numbers. The obtained results must be supported by hard, objective facts as much as possible. For instance the x-ray picture in itself has nearly no value.

In the case of hip joint replacements very good survival rates of above 90% after 10 years can be called the "normal" standard today. However, in an early stage after implantation, unfortunately no signs of deterioration for the individual patient, whose prosthesis might fail earlier, are observed. This means for the statistical relevance of a clinical evaluation for a new product that either a high number of patients or more sensitive test methods are needed to predict the individual survival time. Unfortunately the clinical studies described in the literature are not reproducible in other hospitals or other situations. This is why for every new implant a new study, a new sample of patients has first to be treated to set the new standard. This requires a high input of man power, money and the feeling for the right business decisions. What can scientists do to improve this pending situation?

CONCLUSION

Every innovation with clinical relevance has to be compared with the actual outcome in the hospital. Pre-clinical laboratory testing is an absolute prerequisite for this comparison. However, the comparison can not only be made based on such laboratory tests since history showed, that many uncertainties in the risk assessment do exist. Computer models presently can also be only a hint towards the approval of a product and must in any case be validated by mechanical and/or in-vitro testing. In order to limit the effort and expenses for the regulatory work, and, more important, to provide the highest possible security for the patient, a well defined clinical procedure for the assessment of reproducible clinical outcome for standard indications has to be defined. To judge these comparative results it is necessary to develop improved measurements for the clinical outcome.

REFERENCES

Abdel-Kader, K.F. et al (2001). *J. Arthroplasty*, **16**, 811-819
Scott, D.L. et al (2000). *J. Arthroplasty*, **15**, 35-46
Willert, H.G. et al (1996). *Clin. Orthop.*, **333**, 51-75

HIP CONTACT FORCES – SOME IMPORTANT OBSERVATIONS

G. Bergmann, F. Graichen, A. Rohlmann

Biomechanics Lab., Benjamin Franklin School of Medicine, Free University of Berlin, www.biomechanik.de

PEAK FORCES

With telemeterized hip implants contact forces were measured in 7 patients over periods up to 9 years (Bergmann et al. 1993, 2001B). Average forces during normal walking of 4 patients showed peak values of 233%BW (percent body weight) (Fig.1). In other patients they were higher. Slightly disturbed muscle functions and gait patterns increase the contact forces because muscles with less optimal lever arms have then to maintain the dynamic balance of moments. During slow jogging the highest peak contact force observed was 584%BW. Antagonistic muscle activities during incidental stumbling caused forces up to 870%BW.

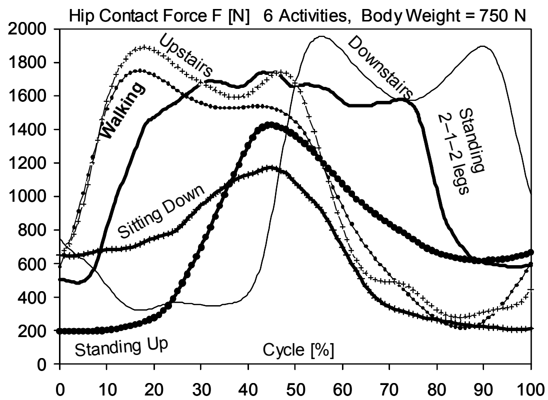

Figure 1 *Contact forces, 6 activities, average of 4 patient*

FORCE DIRECTIONS

The range of forces directions in the frontal plane of the femur is very narrow for all activities if the force is larger than about 50%BW. Typical are angles between 20° and 30° relative to the long femur axis (Fig.2). In the transverse plane the force directions approaches the anteversion angle with increasing magnitudes. The torsional moment in the transverse plane is an important factor for implant loosening. It is close to the torsion stability of the prosthesis. Implants should therefore have torque resistant cross sections.

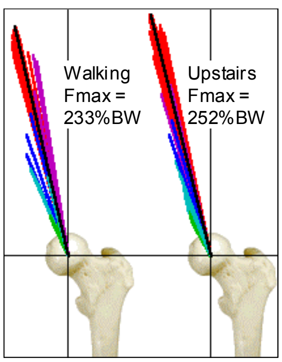

Figure 2 *Forces in frontal plane*

TEMPERATURE INCREASE

Temperature measurements in the prostheses (ceramic head, polyethylene cup) indicate that the friction induced rise of implant temperatures may be one of the factors contributing to implant loosening (Bergmann et al. 2001A). After 1h of walking the temperatures in the middle of the head rose up to 43,2°C (Fig.3). No strong correlation could be found between peak temperature and body weight. Lower forces during cycling at the same metabolic power clearly decreased the peak temperatures, however. Factors like the volume or lubricating properties of synovial fluid probably play an important role for friction induced implant heating.

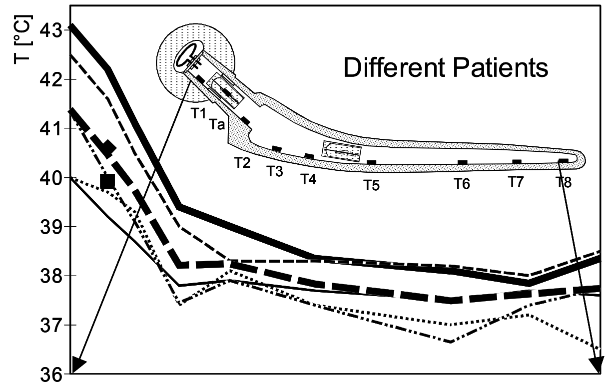

Figure 3 *Implant temperatures after 1 h of walking*

INFLUENCE OF FLOOR MATERIALS AND SHOES

During walking and jogging the contact force in the hip joint reaches its maximum shortly before the straight leg passes through the vertical position. The short force peaks, observed at the foot at the moment of heel contact, are totally damped before reaching the hip joint (Bergmann et al. 1995). This is true for soft and hard shoe and floor materials. In general the heel contact occurs too early in the gait cycle as to have any effect on the force magnitudes in the joint. In contrast, due to the higher muscular effort required to balance the movement, soft shoe or floor materials even slightly increase the maximum contact forces.

JOINT SEPARATION DURING WALKING ?

It was reported that head and cup of the implants separate during walking and abduction detrimental effects on wear and implant stability were hypothesized. Based on analyses of contact force directions (Fig.4) and on fluoroscopic images we can exclude that such an effect occurred in the patients we investigated (Bergmann et al. 2001C).

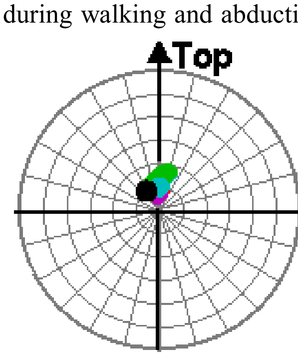

Figure *4 Areas of load transfer in cup, average patient*

REFERENCES

Bergmann et al. (1993). *J. Biomech.*, **26**. 969-990
Bergmann et al. (1995). *J. Biomech.*, **28**, 817-827
Bergmann et al. (2001A). *J. Biomech.*, **34**, 421-428
Bergmann et al. (2001B). *J. Biomech.*, **34**, 859 – 871
Bergmann et al. (2001C). HIP98. *Free Univ. Berlin (CD)*

ROBOTIC ASSISTED VERSUS MANUAL IMPLANTATION - A PROSPECTIVE STUDY IN PRIMARY TOTAL HIP REPLACEMENT

Matthias Honl[1], Oliver Dierk[1], Sebastian Dries[1], Karsten Schwieger[2], Volker Carrero[1], Reemt Rentzsch[1] , Ekkehard Hille and Michael Morlock[2]

[1]Department of Orthopedic Surgery, Barmbek General Hospital, Ruebenkamp 148, D-22307 Hamburg, Germany, honl@ortho-hamburg.de
[2]Biomechanics Section, Technical University Hamburg-Harburg, Denickestrasse 15, D-21079 Hamburg, Germany

INTRODUCTION

Robotics is a well-established method of process optimizing and quality increasing in industrial applications. The idea of using this approach in the field of orthopedic surgery originated in the USA in the early 1990s but has not yet been FDA approved. In Germany, with less strict legislation as in the USA, robots have already been used for more than 3,000 Total Hip Replacements (THR). However, no study is available demonstrating the clinical advantages of the robotic approach in comparison to the manual implantation. The purpose of this study was to compare prospectivly robotic assisted to conventional manually implanted THR.

METHODS

154 patients scheduled for THR were randomly assigned to either the manual or the robot assisted implantation of a S-ROM® prosthesis. The surgeries were carried out using the same antero-lateral approach in a side position of the patient.
The manual implantation was carried out according to the manufacturers specification whereas for the robot group the ROBODOC® was used (Figure 1).

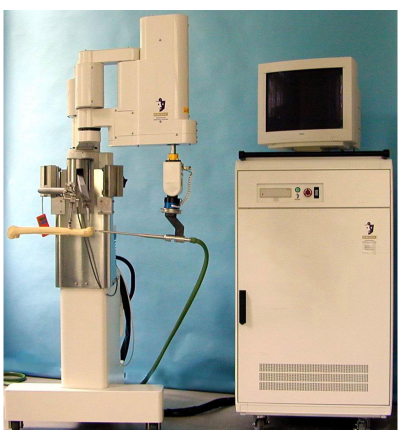

Figure 1: The control computer together with the ROBODOC® robot with 5 degrees of freedom. The pneumatic turbine with the reamers bearing sleeve is attached to the robot arm.

Pre-operatively as well as 3, 6, 12 and 24 months after surgery the scores according to Harris, Merle d'Aubigne and Mayo were determined. X-rays taken at these intervals were analyzed for prosthesis alignment, leg length discrepancy, loosening, and ossification. Maximum follow-up presently is 24 months.

RESULTS

Surgery had to be converted in 13/74=18% of the robotic procedure to manual due to failure of the system. Surgery duration was higher in the robotic group (robotic / manual: 107.1±29.1 / 82.4±23.4min; $p<0.001$). Leg length equality (0.18±0.30 / 0.96±0.93cm; $p<0.001$) and stem varus-valgus orientation (0.34±0.67 / 0.84±1.23°; $p<0.001$) were better in the robotic group. After 6 months the robotic group showed a better Mayo-score (63.6±15.0 / 56.0±16.8; $p=0.01$) and after 12 month a better Mayo- (73.1±7.3 / 62.8±14.3; $p<0.001$) and Harris-score (85.9±12.0 vs.73.2±16.9; $p<0,001$), whereas after 24 month no differences between the 2 groups of patients were found any longer. Slightly more ossifications were seen in the robotic group ($p=0.31$). In the robotic group dislocation was more frequent (11/61=18% / 3/80=4%; $p<0.001$). Recurrent dislocation and pronounced massive limping was the indication for revision surgeries in the robotic group (non-infectious etiology: 9/61=15% / 0/78= 0%; $p<0.001$). During reoperation, rupture of the abductor muscle tendon (pseudo-paralysis similar to the rupture of rotator-cuff) was observed (Figure 2).

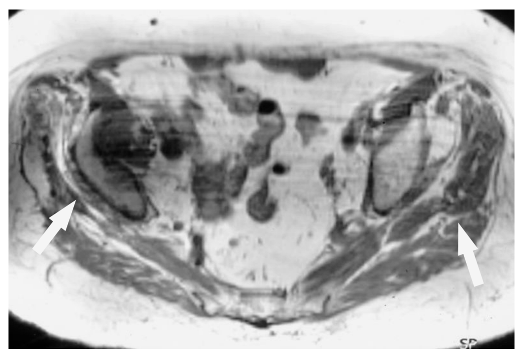

Figure 2: MRI of the abductor muscle- fatty degeneration of the medial gluteus muscle (left arrow).

DISCUSSION AND CONCLUSIONS

The robotic assisted technology showed advantages in pre-operative planning and accuracy of intra-operative procedure. Disadvantages are the un-acceptable high revision rate, which was probably caused by the amount of muscle damage and the longer surgery duration The presented study shows that with the robotic a good or slightly better result than with the manual approach can be achieved – assuming that one is prepared to overlook the very high revision rate and the excluded patients. Such this study clearly shows that the described robotic approach, in its present form, is an endangerment to the THR patient: a dislocation rate of 18% and a revision rate within two years of 15% are well below today's (and those of 25 years ago) standards for THR.

ACTIVITY PATTERN AND JOINT MOTION PROFILE OF TOTAL KNEE PATIENTS

Markus A. Wimmer[1], Markus Hänni[2], Thomas Kehl[3], Michael M. Morlock[4], and Erich Schneider[2]

[1]Department of Orthopedics, Rush Medical Center, Chicago, Illinois, USA, markus_a_wimmer@rush.edu
[2]AO Research Institute and [3]Zürcher Höhenklinik, Davos, Switzerland
[4] Biomechanics Section, TU Hamburg-Harburg, Hamburg, Germany

INTRODUCTION

Huge efforts have been undertaken to test novel cross-linked UHMWPE as a bearing surface for total joint replacement. The latter has proven outstanding wear characteristics for abrasive or adhesive wear mechanisms, which prevail at the artificial hip. At the total knee, fatigue related mechanisms are dominant, which is indicated by the analysis of failed tibial components. Since the fracture mechanical properties of cross-linked polyethylene are reduced, caution appears appropriate. For realistic knee testing protocols, basic knowledge about joint motion as well as frequency and duration of daily activities in patients after total knee arthroplasty (TKA) is required. The purpose of the study was to investigate the activity profile of TKA patients during the day and analyze motion of the artificial knee.

METHODS

37 TKA patients gave informed consent to participate in the study. The measurements were performed in the habitual environment of the patients and started as soon as after wake-up in the morning and continued until about 7 or 8 pm in the evening. The measurement time of each patient was normalized to 12 hours.

A portable measurement system was used to monitor daily activities. Two absolute inclination sensors (providing one-dimensional inclination in a global coordinate system), attached to the shank and the thigh, and an electro-goniometer were mounted along the anatomical axes of the lower extremities of the operated leg. Data were recorded at 30Hz. The system has been previously validated[1].

Using a classifying software program, frequency and duration of walking, standing, lying, sitting, stair climbing and stair descending were analyzed from each patient. Data analysis was based on a calibration protocol performed prior the measurements. In addition, the signal of the electro-goniometric sensor was processed to analyze the dynamic changes of the knee angle. Every 10 degrees, level crossings of the signal were counted (only when the knee flexion angle increased) and classified. The angular motion pattern of the ISO knee simulator served as a control, based on the generally accepted assumption that 1 million gait cycles represent 1 year of use.

RESULTS AND DISCUSSION

Three patients experienced technical difficulties, which left 34 patients for motion analysis. Their artificial joint crossed most often the 20º-level ($8.3 \pm 4.5 \times 10^3$counts), while it is the 10º-level for the knee simulator (5.5×10^3counts). Motion at knee angles beyond 50º occurred frequently in patients (e.g. for 70º: $1.8 \pm 1.9 \times 10^3$counts), however, are not employed with the knee simulator. The activity pattern has been analyzed for 24 patients. Most of the time was spent in sitting (46%), followed by standing (17%) and walking (17%). Activities like stair climbing or lying played only a minor role (Table 1). On average, 13% of the recorded activities remained unknown.

Table 1: Load bearing activities during the day

	TKA Patients	Knee Simulator
# Steps (affected side)	6609 ± 3353	2740
# Stairs (affected side)	232 ± 346	-
# Standstills (upright)	666 ± 452	-
# Sitting (up & down)	556 ± 440	-
# Lying* (up & down)	6 ± 18	-

*includes high foot resting

The most striking mismatch between patients and simulator is the difference in activity: 6609 vs. 2740 gait cycles per day. Further, there is a shift of the maximum of level crossings from 10° to 20° because most of the TKA patients did not reach full extension during the stance phase of gait. The occurrence of level crossings at higher knee flexion angles demonstrates the importance of activities like sitting down or rising from a chair. However, not all counted level crossings could be explained by known load bearing activities.

SUMMARY

Wear and failure of TKA is a function of relative motion and load. We tried to analyze patient activities and to assess relative motion with a level crossing classification. It was found that the TKA prosthesis undergoes higher demands in vivo than in vitro. Therefore, the testing protocols of knee simulators should be re-considered.

REFERENCES

[1]Morlock, M.M., et al. (2001). *J Biomech,* **34**, 873-881

THE ACTING WEAR MECHANISMS ON METAL-ON-METAL HIP JOINT BEARINGS

Markus A. Wimmer[1], Christoph Sprecher[2], Georg Täger[3], and Alfons Fischer[4]

[1]Department of Orthopedics, Rush Medical Center, Chicago, Illinois, USA, markus_a_wimmer@rush.edu
[2]AO Research Institute, Davos, Switzerland
[3]Department of Trauma Surgery and [4]Materials Science and Engineering, University of Essen, Germany

INTRODUCTION

Insufficient understanding of tribological behavior in total joint arthroplasty is considered as one of the major reasons for premature prosthesis failure. Contrary to movement profiles of hip simulators, human locomotion is of erratic shape containing motion interruptions among other irregularities. These occurring resting periods cause stick phenomena in metal-on-metal hip joints as is shown by another paper in this session. The aim of the study was to analyze the acting wear mechanisms of all-metal joints and identify in particular the interlocking bodies on in vitro and in vivo specimens.

METHODS

Twelve 28 mm commercially available CoCrMo-balls were tested against self mating concave pins with a radial clearance of 57±2 µm in a physiological fluid at 37°C under reciprocating, bi-directional sliding wear (1 Hz). The compressive load was const. 750 N (1 body weight). For two million cycles tests were carried out continuously and with periodically occurring resting periods.

In addition, 55 retrieved metal-on-metal prostheses from 18 male and 29 female patients with a complete record and regular follow-up were obtained. The implants were 11.5 years (range 1.3 … 22) in situ and none of them was removed because of excessive wear, e.g. metallosis.

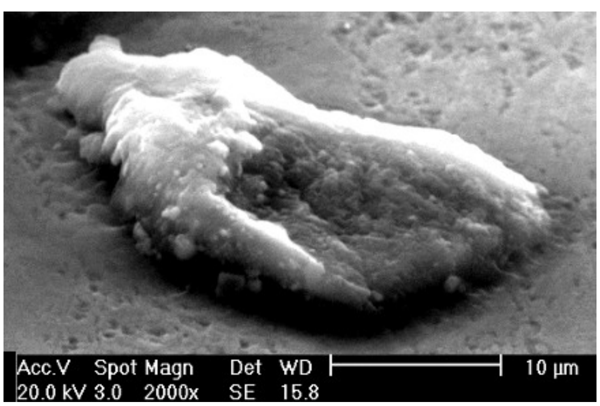

Figure: Tribochemical reaction product on the ball surface

Samples were rinsed in tap water, soaked in acetone and then ultrasonically cleaned in deionized water. The appearance of the worn simulator samples was macro- and microscopically compared to the retrieved specimens. All components were inspected without further preparation using light- and scanning electron microscopy. The latter was equipped with energy dispersive x-ray for local and area distribution analyses of metallic and nonmetallic elements. On the basis of the observed wear appearances, the acting wear mechanisms were defined and evaluated as to their contribution to the wear behavior.

RESULTS AND DISCUSSION

Besides scratches and pitting, testing pins, balls and retrieved specimens showed distinct layers, which adhered rigidly to the surfaces (Figure). These precipitates were present within and - larger in number - at the edges of contact. They consisted mainly of carbon, containing little amounts of Na, Cl, K, Ca, P, O. Their shapes varied in a wide range between hilly and compact to flat and lengthy. Some of them exhibited cracks, or were scratched.

Wear mechanism: Due to the high local contact stresses surface fatigue prevails initially. Thus, Cr- and Mo-carbides are fractured and torn off the surfaces bringing about additional surface fatigue (by indentation) and abrasion. The weight loss can be predominately attributed to these mechanically dominated wear mechanisms. In parallel, the high contacts stresses on local asperities cause flash temperatures of 70º+ as calculated using the Kuhlmann-Wilsdorf model. Hence, tribochemical reactions are initiated, which generate layers from denatured proteins. Once human or simulator motion comes to a complete stop, these layers start to adhere rigidly to the activated surfaces. This causes an interlocking phenomenon during motion re-initiation, and a frictional break-away torque is observed. While this may be interpreted negatively, the generated layers cover parts of the contacting surfaces avoiding adhesion. The wear outcome is therefore influenced by the alternating balance between surface fatigue and abrasion on the one side and by tribochemical reactions on the other side.

SUMMARY

Wear and friction are system properties rather than intrinsic material properties and are therefore affected by multiply variables. In order to understand and control the wear behavior of artificial bearings a close correlation between the microstructures of the material used and the acting wear mechanisms has to be found.

TIBIOFEMORAL CONTACT KINEMATICS DEPENDENT WEAR OF A UHMWPE TOTAL KNEE INSERT

T.S. Johnson, M.P. Laurent, and J. Q. Yao
Zimmer Research Department, P.O. Box 708, Warsaw, IN 46581-0708, USA, todd.johnson@zimmer.com

INTRODUCTION

The mechanisms of in-vivo UHMWPE wear at the tibiofemoral interface of a total knee replacement are dependent on the contact kinematics and the loading between the articulating surfaces. Previous studies have shown that a small threshold value of cross shear motion is sufficient to significantly increase the UHMWPE wear rate (Johnson et al., 2002) and that elimination of either internal/external rotation or anterior/posterior input motion significantly reduces in vitro knee simulator wear rates (Johnson et al., 2001a). The purpose of this study is two-fold: 1) to compare the contact kinematics path of motion profiles and in-vitro wear rates for two different wear protocols, standard and aggressive, implemented on a common posterior cruciate retaining (CR) knee design and 2) to analytically determine the relative tibiofemoral interfacial slip velocity v_s ($v_s = 0$ for pure rolling or no relative motion) in combination with the applied load for both protocols utilizing a wear intensity factor (WIF), where v_s was calculated using a previously described method (Johnson et al., 2001a).

MATERIALS AND METHODS

The standard walking gait protocol inputs consist of femoral extension motion from 0 to -58 degrees, -2 to 6 degrees of external tibial rotation, 5.2 mm of maximum posterior femoral displacement, and a peak load during the stance phase of 3188 N (ISO/WD, 1999). The aggressive protocol, which is based on in-vivo patient data (Johnson et al., 2001b), has femoral extension motion from 3 to –65 degrees and a heel strike sliding velocity transient with a maximum of 10.2 mm posterior femoral displacement. The external tibial rotation and load curves were identical. The tibiofemoral components were wear tested on an AMTI knee simulator as reported previously (Johnson et al., 2001b).

The horizontal low point in the medial/lateral and anterior/posterior direction for both compartments were chosen on the inserts to investigate the size and shape of the paths of motion. The wear simulator kinematics were recreated utilizing 3D CAD models of the components with the insert moving relative to a fixed femoral component, to obtain the points path of motion geometry. To gauge the combined effects of load and sliding velocity, a wear intensity factor (WIF) was calculated as WIF = $|v_s|$*P, where $|v_s|$ is the slip velocity magnitude (m/s) and P is the applied compressive load (N).

RESULTS

The paths of motion in the lateral compartment for the standard and aggressive protocols are shown in Figure 1. The corresponding total path lengths are 59 and 95 mm and the corresponding in vitro knee wear rates are 14.4 ± 2.8 and 27.9 ± 2.9 mg/10^6 cycles (± std. dev). The WIF curves (lateral compartment) for both protocols are displayed in Figure 2. Immediately after heel strike and during the terminal swing phase, the WIF is approximately three times larger for the aggressive protocol.

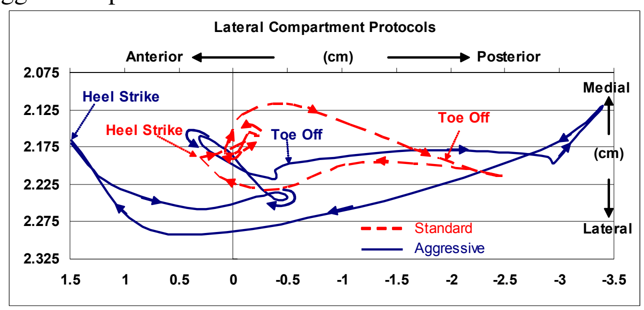

Figure 1: Paths of motion for the standard and aggressive protocols.

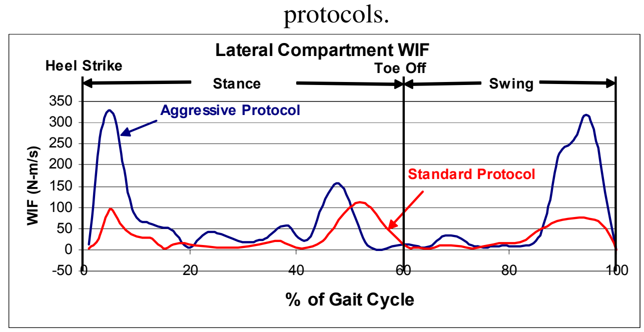

Figure 2: WIF for both testing protocols.

CONCLUSIONS

The wear rate and path length for the aggressive protocol are 94% and 61% higher, respectively, than for the standard protocol. The difference in wear rates may at least be partially due to the difference in sliding distances alone. The large differences in the WIF may provide additional insight into the actual wear mechanism. The swing phase of gait in conjunction with a heel strike transient may have important implications, not previously reported, in producing clinically relevant wear.

REFERENCES

ISO/WD (1999) *14243-3 Draft.*
Johnson, T.S. et al. (2001a). *Wear*, **250**, 222-226.
Johnson, T.S. et al. (2001b). *Soc. For Biomat., 27th Ann Mt.*
Johnson, T.S. et al. (2002). *Soc. For Biomat., 28th Ann Mt.*

THE EFFECTS OF EARLY ROLLBACK IN TOTAL KNEE REPLACEMENT ON STAIR STEPPING

Louis Draganich[1], Gary Piotrowski, Lawrence Pottenger, and John Martell
Section of Orthopaedic Surgery and Rehabilitation Medicine, Department of Surgery, University of Chicago
[1]ldragani@surgery.bsd.uchicago.edu

INTRODUCTION

Femoral rollback has been shown to increase the quadriceps lever arm in cadavera.[1-3] One of the purposes of the posterior stabilizer (PS) in total knee replacement (TKR) is to enforce rollback to increase the quadriceps extension moment (i.e., knee external flexion moment). However, the cam and post components of PS TKRs engage at different flexion angles and, therefore, enforce rollback at different flexion angles. We tested the hypotheses that a TKR that enforces sufficient rollback at a lower angle of flexion than those important to stair stepping would result in normal peak external flexion moments and that a TKR that does not enforce rollback until a higher angle of flexion than those important to stair stepping would result in reduced peak external flexion moments during stair stepping.

METHODS

There were 21 healthy control subjects. All TKRs in this study were posterior stabilized. There were 8 patients with the IBII (Zimmer) TKR, 9 patients with the Maxim (Biomet) TKR and 8 patients with the TRAC PS (Biomet) TKR. The Maxim and IBII are fixed bearing TKRs. TRAC PS is a mobile bearing TKR designed to have area contact throughout the range of motion and to maximize the quadriceps lever arm early in flexion. The posts and cams of the posterior stabilizers engage at approximately 73º for IBII, 20º to 30º for Maxim, and 8º for TRAC PS. The mean (SD) ages of the subjects were 61 years (7) for the controls, 67 years (9) for the IBII patients, 70 years (5) for the Maxim patients and 62 years (7) for the TRAC PS patients. Patients were required to have Hospital For Special Surgery Knee Scores of 85 points or more, no pain during ambulation, and be able to step on and over a step without aid. The postoperative time to testing averaged 15 months for the IBII patients (Range, 12-30 mos), 24 months for the Maxim patients (Range, 12-32 mos) and 31 months for the TRAC PS patients (Range, 25-38 mos). The protocol was approved by the Institutional Review Board and informed consent was obtained. Subjects were asked to stand, feet together, at a distance of twenty cm from the end of the subject's great toes to a 20 cm high step, step onto the step using the limb with the implant under investigation, step over the step and onto the ground with the opposite limb, step onto the ground with the implanted limb, and then walk along the walkway, all in a continuous fashion. The kinematic parameters were measured using the Watsmart (Northern Digital, Inc., Waterloo, Ontario, Canada) optical electronic three-dimensional digitizing system. Force parameters were measured with a multicomponent force platform (Advanced Mechanical Technologies, Inc., Newton, Mass.). The step was positioned on the force platform. The motion and force data were acquired at a rate of 100 samples per second. The motion and force data along with anthropometric measurements and linear and angular velocities of the segments of the lower extremities were used to compute the external three-dimensional moments at the knee joint. Statistical differences were determined with two-way repeated measures analysis of variance and Tukey's test. P levels ≤ 0.05 were regarded as statistically significant. The Greenhouse-Geiser adjustment to the degrees of freedom was used in assessing significance levels based on the overall F-test.

RESULTS

The patterns and magnitudes of knee flexion were very similar for all of the subjects. The flexion angle of the knee at foot strike on the step was between 58º and 63º. At midstance, the knee extended to approximately 30º of flexion, which was the minimum amount of flexion attained. The knee flexed to a maximum of between 91º and 97º when the foot lifted off the step. The patterns of the external flexion-extension moments on the step were similar for all subjects. There were two moment peaks. For each peak, the knees of the control subjects generated the highest peak external flexion moments, followed by those of the TRAC PS and Maxim patients. The knees of the IBII patients generated the lowest peak external flexion moments. The peak external flexion moments of the knees of the controls, TRAC PS patients and Maxim patients were not significantly different ($p > 0.05$). However, the moments generated about the knees of the IBII patients were significantly less than those of the controls for both peaks (p □0.019). Furthermore, the knee flexion angles of the IBII patients were 46º for the first peak moment and 65º for the second peak moment, which were less than 73º, the angle necessary for the post and cam to engage and enforce rollback.

DISCUSSION

These results support the hypotheses. The peak knee external flexion moments generated during stair-stepping for the TRAC PS and Maxim PS patients were not significantly different from normal. Those for the IBII patients were significantly less than normal in agreement with the literature.[4] Thus, for normal stair-stepping function, the cam and post of a posterior stabilized TKR should engage to produce sufficient rollback at a knee flexion angle lower than those occurring when the peak knee external flexion moments are generated.

REFERENCES

1. Kurosawa et al: J Biomechanics, 18:487, 1985
2. Draganich et al: J Orthopaedic Research, 5:539-547, 1987
3. Mahoney et al: J Arthoplasty, 9:569, 1994
4. Andriacchi et al: J Bone Joint Surg [Am] 64:1328, 1982

ACKNOWLEDGEMENT

We thank Biomet, Inc for partial support of this study.

KINEMATIC OBSERVATIONS ACROSS THE SPECTRUM OF TOTAL KNEE REPLACEMENTS

Scott A. Banks and W. Andrew Hodge
The Biomotion Foundation, 1411 N. Flagler Drive, Suite 9800, West Palm Beach, FL 33401, banks@alum.mit.edu

INTRODUCTION

Surgeons use total knee replacements (TKR) to relieve pain and, hopefully, provide a very long lasting reconstruction with excellent mechanical function. Knee kinematics may or may not have a large effect on pain relief, but can certainly have an effect on knee function and device longevity. The goal of this summary is to present *in vivo* observations of motion with a wide variety of TKR designs, to identify trends in motion according to design class, and to demonstrate a relationship between articular motions and patient function.

METHODS

This study was conducted at 14 venues and included patients from 21 surgeons using 25 different articular designs. 213 well functioning TKR's were studied using fluoroscopy as subjects performed a dynamic stair ascent. There were 129 cruciate retaining fixed bearing knees (13 CR designs), 44 mobile bearing knees (8 MB designs), and 40 posterior stabilized knees (4 PS designs). CAD model based shape matching was used to determine 3D knee kinematics and the locations of medial and lateral tibiofemoral contact in 22,907 fluoroscopic images. The average center of axial rotation, or pivot location with respect to the tibial plateau, was computed over the entire motion. The medial/lateral location of the center of axial rotation was normalized to the width of each tibial component, and expressed as a percentage of tibial width, -50% (lateral) to +50% (medial). A subset of 121 knees of 15 articular designs was studied as patients performed a maximum weight-bearing flexion activity with their foot placed on a 25-42cm riser.

RESULTS

Posterior stabilized knees exhibited medial pivots (+14%) while cruciate retaining (-9%) and mobile bearing knees (-19%) exhibited lateral pivots on average (Table 1). Cruciate retaining fixed bearing knees exhibited slightly more axial rotation than did posterior stabilized knees. A relatively posterior position of the femur on the tibia was significantly correlated with greater maximum weight-bearing knee flexion (Figure 1, $p<0.001$, linear regression). PS knees exhibited significantly greater posterior femoral position and maximum flexion than CR knees, which exhibited more posterior femoral position and greater maximum flexion than MB knees (Figure 1).

DISCUSSION

Since essentially all knees showed tibial internal rotation with flexion, the 'pivot' description for motion is simply a convenient parameterization describing anterior/posterior motion of the femur with respect to the tibia. Knees where the femur is forced posterior with flexion show medial pivots on average, whereas those that allow anterior translation of the femur in flexion show generally lateral pivots. The significance of this finding is in demonstrating a consistent relationship between the intrinsic anteroposterior control of the TKR and the kinematics observed during a dynamic weight-bearing activity. TKR designs that intrinsically control femoral anteroposterior position in flexion achieve greater average weight-bearing range of motion.

Table 1. Computed medial/lateral locations of the pivot point, or average center of axial rotation.

Implant Type	# Knees	# Images	Average Range of Axial Rotation (deg)	Med/Lat Center of Rotation (%)
PS	40	4133	7.9 ± 1.5	+14% ± 9%
CR	131	14646	9.3 ± 2.1	-9% ± 16%
MB	44	4128	8.6 ± 1.0	-19% ± 15%
KW-ANOVA on Ranks, Dunn's (p<0.05)			CR > PS	PS > CR > MB

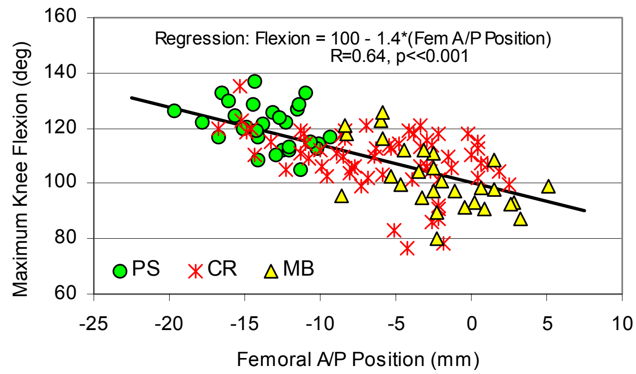

Figure 1. Maximum weight-bearing knee flexion as a function of femoral A/P position for 121 knees. Femoral posterior positions are negative, anterior is positive, and zero represents the anterior/posterior mid-point of the tibial component. Open circles represent PS knees, asterisks represent CR fixed bearing knees, and open triangles represent MB knees.

ACKNOWLEDGEMENTS

The authors gratefully acknowledge the following individuals for their participation in these studies: Anne Banks, Sherry Backus, Johan Bellemans, Leigh Breslauer, Fabio Catani, James D'Antonio, Gary Davidson, Kevin Deluzio, Lewjack Dorrance, Tomas Drobny, Silvia Fantozzi, Steven Haas, Melinda Harman, William Harris, Fraser Harrold, Anthony Hedley, Robyn Kabbaz, Ryutaku Kaneyama, Mark Kester, Richard Laskin, Alberto Leardini, Gerhard Luder, Robert Mann, Raul Marquez, Phillip Merritt, Hideshige Moriya, Urs Munzinger, Hiroyuki Nozaki, James Otis, Michael Piazza, Michael Ries, Patrick Riley, Donald Reilly, Christoph Reinschmidt, Alex Stacoff, Tohru Suguro, Jan Victor, Leo Whiteside, David Wilson, Urs Wyss.

The authors gratefully acknowledge the following companies for research support and/or the provision of computer models of the TKA components: DePuy, Encore, Howmedica/Osteonics, Nakashima Medical, Smith&Nephew, Sulzer, Wright Medical, and Zimmer.

pKNEE ROTATION IN DEEP FLEXION AND TOTAL KNEE REPLACEMENT DESIGN

Thomas P. Andriacchi and Chris O. Dyrby

Biomechanical Engineering, Stanford University, Stanford, CA 94305-4038, USA, tandriac@stanford.edu

INTRODUCTION

Current designs of total knee replacement can accommodate approximately 130 degrees of flexion (Kim *et al,* 1995). However, deeper flexion is essential for activities of daily living for Indian, Middle Eastern and Japanese cultures. Even in western cultures there is a wide range of activities (recreational and occupational) that require deep flexion. The mechanics of the knee in deep flexion is not well understood. For example, it has been reported (Hefzy *et al.* 1998) that the knee must permit rotation in deep flexion. However, the relationship between flexion and rotation has not been quantified in flexion. The purpose of this study was to examine the relationship between rotation and knee flexion knee in deep flexion.

METHODS

Twenty (10 male, 10 female) native Japanese subjects (35 ± 13 years, 1.6m ± 0.1, 588 ± 166N) were tested while moving from standing into a deep squat resting position (both legs). All subjects were selected on the basis of a history of no previous musculoskeletal injury or disease that would influence performing a deep squat.
Knee kinematics were measured using a previously described technique (Andriacchi *et al*, 1998) based on a cluster of reflective markers distributed on the segments of the lower limbs. Markers were tracked with video based optoelectronic digitizer. Six degree-of-freedom motion of the knee was analyzed. Measurements were obtained bilaterally and a single left or right observation was randomly selected from each subject for observation. The rate of change of internal-external rotation was analyzed as a function of knee flexion. Rates of change were compared using paired T-tests testing for a significance level of $\alpha < 0.05$.

RESULTS

The squat activity began in a standing position and ended with the subject having both knees flexed to approximately 150 degrees in a resting squat. As the knee initially flexed in the range between 0 and 120 degrees, the femur externally rotated at a uniform rate. There was a significant relationship between knee flexion and internal/external rotation. As the knee flexed between 0 and 128 degrees, the femur externally rotated on the tibia (Figure 1). At an average of 129 ± 10 degrees of knee flexion, the rate of change of rotation significantly increased. The total external rotation prior to this break point was an average of 16 ± 6 degrees for the first 124 ± 12 degrees of knee flexion or rate of 0.12 ± .05 degrees of rotation per degree of flexion angle. Past the break point, the knee flexed an additional 21± 10 degrees to 150 ± 11 degrees of flexion. The rate of external rotation of the femur on the tibia increased to 0.5 ± 0.2 degrees of external rotation for each degree of flexion.

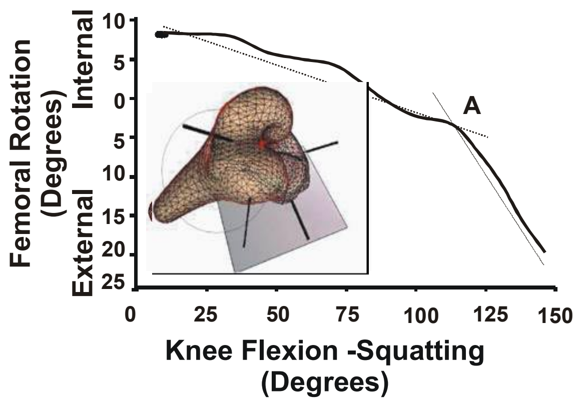

Figure 1. An illustration of femoral rotation as a function of knee flexion while going from a standing position to a squat into deep flexion. Note the rate of external rotation with flexion increases substantially after 120 degrees of flexion (Point A).

DISCUSSION

Currently, most designs of total knee arthroplasty can achieve 120 degrees of flexion. However, patients requiring deeper flexion will need the capacity for substantial rotation beyond 120 degrees of flexion.
This information is important for understanding the mechanics of the normal knee, functional activities that required deep knee flexion and providing the basis for understanding the mechanics of knee replacement for individuals requiring increased ranges of motion.

REFERENCES

Andriacchi, T.P. et al (1998). A point cluster method for *in vivo* motion analysis: applied to a study of knee kinematics. *J of Biomechanical Engineering*, **120(12)**, 743-749.
Hefzy, M.S. et al (1998). Kinematics of the knee joint in deep flexion: a radiographic assessment. *Med Eng Phys,* **20**, 302-307.
Kim, J., Moon, M. (1995). Squatting following total knee arthroplasty. *Clin Orthop* **313**, 177-186.

CHANGES IN RANGE OF MOTION IN THE CERVICAL SPINE FOLLOWING SPINAL MANIPULATION - A REVIEW.

Niels Nilsson and Rene Fejer
Institute of Sports Science and Clincal Biomechanics, University of Southern Denmark, Odense, Denmark
n.nilsson@imbmed.sdu.dk

INTRODUCTION

With increasing evidence that spinal manipulation may have an effect on some disorders and not others, it becomes important to try to elucidate the biomechanical/physiological basis for such experimental observations. It is generally assumed among practitioners that spinal manipulation somehow affects the biomechanical behavior of the spine. Most common is the assumption that spinal manipulation results in an increase in either passive or active range of motion.

At present three trials exist comparing changes in range of motion in a spinal manipulation treatment group with changes in range of motion in a control group, not receiving any form of spinal manipulation.

All three trials use a strap-on head goniometer, blinded observers for measurements and randomization of subjects. A pattern seems to be emerging.

PASSIVE RANGE OF MOTION IN SUBJECTS WITH DECREASED ROM

This trial randomized 39 patients with objectively subnormal cervical range of motion into two groups, one of which received manipulation to the cervical spine twice a week for three weeks, while the other received low-level laser to the cervical area plus massage in the shoulder girdle region twice a week for three weeks. Cervical passive range of motion was measured at the start of the intervention period and again at the end of the three week period. There were no differences pre-post between the treatment group and the control group [Nilsson, 1996]

ACTIVE RANGE OF MOTION IN NORMAL SUBJECTS

20 symptom-free subjects with cervical range of motion in the low end of the normal range were randomized into two groups. One group received cervical manipulation twice a week for three weeks, and the control group a placebo treatment (detuned activator) twice a week for three weeks. Active cervical range of motion was measured pre and post the intervention phase and no differences were found between the two groups. [Petersen, 2002]

ACTIVE RANGE OF MOTION IN SUBJECTS WITH DECREASED ROM

105 patients with objectively decreased cervical range of motion were randomized into 2 groups. After a baseline observation period, Group 2 received manipulation to the cervical spine, while Group 1 received sham manipulation. In the next trial phase, Group 1 received manipulation, while Group 2 received no treatment. This was followed by the final trial phase, in which Group 2 received sham manipulation and Group 1 received no treatment. After each trial phase, active range of cervical motion was measured with a strap-on head goniometer by 2 blinded examiners.

Following the manipulation phases there were consistent and statistically significant increases in active cervical range of motion [Whittingham, 2001]

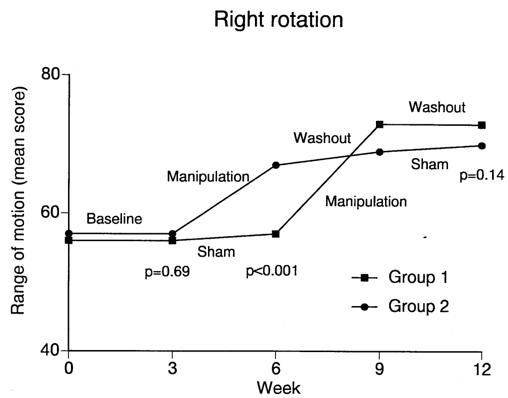

CONCLUSION

A pattern of results seems to be emerging; namely that spinal manipulation increases active range of spinal motion in those subjects who have decreased motion to start with, whereas, manipulation does not alter active motion in subjects with normal range of motion. In contrast passive range of motion is not affected.

However, more evidence is needed for any firm conclusions to be drawn.

KEY REFERENCES

Nilsson, N., H. Wulff Christensen, et al. (1996). “Lasting Changes in Passive Cervical Range of Motion following Spinal Manipulation - a Randomized Blinded Controlled Trial.” J Manipulative Physiol Ther **19**(3): 165-168.

Petersen, K., F. Rolschau, et al. (2002). Active Range of Motion following Spinal Manipulation. A Blinded Randomized Controlled Trial. (in danish). Institute of Sports Science and Clinical Biomechanics. Odense, Denmark, University of Southern Denmark.

Whittingham, W. and N. Nilsson (2001). “Active Range of Motion in the Cervical Spine increases after Spinal Manipulation.” J Manipulative Physiol Ther **24**: 552-5.

NECK LOADS DURING SPINAL MANIPULATION

John J. Triano, DC, PhD
Texas Back Institute & UT Southwestern and Arlington Joint Biomedical Engineering Program

INTRODUCTION

Manipulation (SMT) of the cervical spine has been controversial but is increasingly used for patients with neck, arm and headache complaints. This project sought to understand their mechanisms and to quantify the relative biomechanical risks.

METHODS

Healthy volunteers signed informed consent approved by the committee for the protection of human subjects. Testing was block-randomized on two variables. The first distributed procedures to be applied from the left (n=35) or right (n=31). in the absence of quantitative data, the second divided the manipulations into groups based upon the intensity of effort defined as "hard" and “soft". A "hard” procedure was the greatest intensity considered safe for the subject’s stature and age. Similarly, “soft" was the minimum to achieve treatment objectives. The four conditions; hard left & right (HL/HR), soft left & right (SL/SR); spanned the spectrum of intensity used in clinical practice. Prior to SMT, neck muscle myoelectric activity was calibrated for standardized isometric tasks. Intensities were systematically varied from 10% to 100% maximum voluntary contraction.

Subjects were positioned on a sensing table with imbedded AMTI force plate. Infrared diodes mounted on the head and thorax were monitored by a WATSMART system. Myoelectric activity was recorded as SMT was administered randomly according to group. An inverse dynamics model first evaluated the passive loads through the neck at C2/C3. An RMS-myoelectric optimization model then predicted muscle tensions and were summed to predict total loads. Values were compared to volunteer studies of whiplash simulation.

RESULTS

Load-time histories showed no differences for right vs. left procedures. Differences were observed for procedure intensity ($0.000007 < p < 0.0294$) by ANOVA. Muscle contributions were negligible. No adverse reactions were reported. Table 1 compares the maximum loads in this study with loads tolerated in volunteer subjects without injury.

CONCLUSION

Maximum loads acting on the spine during SMT procedures were within the range of those tolerated during whiplash–type stresses to the neck. Relative load amplitudes can be controlled on demand. This data is the first quantitative data on transmitted neck loads and form a basis to begin understanding the mechanisms of action.

REFERENCES

Triano .J.J. (2001). *The Spine*, **1**, 121-30.
Triano, J. J. (1998). *Biomechanical analysis of motions and loads during spinal manipulation.* University of Michigan
Triano J.J., Schultz A.B. (1997). *Spine*, **22**, 1955-64.

Table 1. Maximum moment loads (Nm), tolerated by human volunteers.

Author	Direction				Location
	Extension	Flexion	Lat Bend	Rotation	
Sauces	46.1	24.4	---	---	C0 / C1
Patrick&Choy	---	---	42.1	---	C0 / C1
Gadd&Culver	94	---	143	---	C4 / C6
Present study	32	32	65	50	C2 / C3

PARASPINAL MUSCLE SPINDLES RESPONSES TO BIOMECHANICAL CHANGES IN THE SPINE

Joel G. Pickar[1, 2], Yu-Ming Kang[2], John D. Wheeler[3]
[1] Palmer Center for Chiropractic Research, Palmer College of Chiropractic, Davenport, Iowa
[2] Iowa Spine Research Center, University of Iowa, Iowa City, IA
[3] Private Practice, Manhattan, Kansas
pickar_j@palmer.edu

OBJECTIVE

Muscle spindle activity from paravertebral muscles likely affect vertebral movement and posture because sensory feedback from muscle proprioceptors is important for motor control. Because mechanical stability of the lumbar spine requires muscle activity, studies were performed to understand how muscle spindles in lumbar paraspinal muscles respond to vertebral loading. The first study determined the effect of a static vertebral position on the sensitivity of lumbar paraspinal muscle spindles to subsequent vertebral displacement. The second study determined if lumbar paraspinal muscle spindles respond to a mechanical load whose force-time profile is similar to that of a spinal manipulation.

METHODS

Experiments were performed on 10 anesthetized adult cats anesthetized with pentobarbital sodium (35mg/kg). The L_6 dorsal root was isolated for electrophysiological recordings while leaving intact the L_6-L_7 vertebrae and associated paraspinal tissues. Single unit activity from lumbar paraspinal muscle spindles was recorded from teased afferent filaments isolated in the L_6 dorsal root. Receptive fields were in the lumbar multifidus or longissimus muscles. Controlled loads were applied at the spinous process of the L_6 vertebra using an electronic feedback control system (Aurora Scientific, Inc.).

To study the effects of static vertebral position on spindle sensitivity, the experimental protocol consisted of 4 parts: 1) muscle deconditioning, 2) muscle conditioning, 3) return to neutral position and, 4) test. Paraspinal muscles were deconditioned by rapidly extending and flexing the lumbar spine (1mm each direction, 10mm/sec). Conditioning consisted of statically holding paraspinal muscles shortened ("hold-short") or lengthened ("hold-long") for 5 seconds. After each type of conditioning the L_6 vertebra was returned to the same position (neutral position) and the sensitivity of the muscle spindles was tested by slowly displacing the L_6 vertebra (2 mm, 0.14 mm/sec) in a direction which stretched the muscle spindle.

For the second study a load simulating the force-time profile of a spinal manipulation was applied to the L_6 vertebra. The load consisted of 3 phases: 1) control (duration: 3.0s); 2) preload consisting of ramp-up (duration: 3.0s) and plateau (duration: 3.0s; force: 25% body weight); and 3) impulse (duration: 200ms, peak force: 100% body weight). Loads were applied in compressive and distractive directions with respect to the L_6-L_7 facet joint and at 2 different angles (0^0 and 45^0) with respect to the long axis of the vertebral column.

RESULTS AND DISCUSSION

Hold-short conditioning sensitized paraspinal muscle spindles to subsequent muscle stretch during the test protocol. Mean afferent discharge rate increased 25%, 23%, 11%, 6% and 6% after "hold-short" compared with "hold-long" conditioning (Table). Four of the 5 muscle spindle afferents had receptive fields in the longissimus muscle very near the L_{6-7} facet joint and one afferent's receptive field was in the multifidus muscle near the L_7-S_1 facet joint.

Table. Average muscle spindle discharge rates during the test.

Afferent Number	After hold-long Mean ±SE (in Hz)	After hold-short† Mean ±SE (in Hz)
1	14.1 ±0.4	14.9 ±0.4
2	24.0±0.8	26.7 ±0.9
3	50.7 ±1.6	62.6 ±1.6
4	40.2 ±2.1	50.2 ±1.8
5	42.6 ±0.7	45.0 ±0.8

† $p<0.07$ compared with "After hold-long".

During the spinal manipulative-like load, muscle spindle discharge rate increased more to the impulse than to the preload during 10 of the 16 manipulations. Changing the angle of the manipulation could dramatically alter the response of a muscle spindle. Distractive manipulations loaded the spindles more effectively than compressive manipulations. After 7 of these 10 manipulations, muscle spindles became silent for 1.3 ±0.6s (range: 0.1–4.3s). Six of the 16 manipulations unloaded the muscle spindles.

SUMMARY

The results from the first study indicate that vertebral position, statically maintained for a relatively brief duration, alters a paraspinal muscle spindle's sensitivity to an identical rate and amount of vertebral movement. These findings support the conclusion that spinal postures which produce sustained vertebral positions elicit proprioceptive errors. These errors could adversely affect neuromuscular mechanisms stabilizing the vertebral column.

The results of the second study demonstrate that the high velocity, short duration load delivered during a spinal manipulation can stimulate muscle spindles more than the preload. The results may indicate that spinal manipulation's distinct effect on the response of paraspinal muscle spindles may contribute, in part, to the effects of spinal manipulation.

Supported by NIH grant NS35300 on behalf of NCCAM and FCER grant on behalf of NCMIC to JGP.

NEUROMUSCULAR IMPLICATIONS OF LUMBAR VISCOELASTIC TISSUES

M. Solomonow
Occupational Medicine Research Center
Bioengineering Laboratory --- Dept. of Orthopaedic Surgery
Louisiana State University Health Sciences Center
New Orleans, Louisiana 70112 USA — **msolom@lsuhsc.edu**

INTRODUCTION

The major viscoelastic tissues of the spine consist of its ligaments, discs and facet capsules. Such tissues have some classical mechanical behaviors which are well known such as hysteresis in a stretch – release cycle, dependence on strain rate, and creep when subjected to loads over time. While such viscoelastic behavior has direct implications on the mechanical properties of the spine, it may also have profound neurophysiological implications. Since these viscoelastic tissues are endowed with diverse types of sensory receptors (1, 2) which are known to reflexive activate various muscles (3, 4), it is clear that they may also have neurophysiological functions. Reflexive activation of the muscle is known, from the control point of view, to be part of the feedback associated with the movement control system (5, 6). A property inherent to most electro-mechanical systems is relatively small zone about the resting point which is not optimally functional, e.g., a dead zone. Panjabi (5) identified such a mechanical zone in the spine and termed it "Neutral Zone"; a range of intervertebral excursions which does not impact on spinal stability. He also went on to show that muscular activity is capable of modifying the range of such Mechanical Neutral Zones (MNZ). Recent work further demonstrated that the feedback loop of the spine also has neuromuscular neutral zones, e.g., small perturbations in viscoelastic tissue status that does not elicit feedback (reflexive) activation of muscles (7, 8). It is of interest and importance to assess the impact of spinal viscoelastic tissues behavior (such as hysteresis and strain rate dependence) on the function of the spine's feedback network, e.g., the Neuromuscular Neutral Zones (NNZ).

METHODS

Anaesthetized feline specimens were used as the experimental model. Tests included linear stretch of the posterior lumbar spine into flexion at rates ranging from 17 – 100% /s (with 100% being ¾ of the physiological strain range of the ligaments) as well as single cycles of flexion – extension at frequencies ranging from 0.1 – 1.0 Hz in order to assess the response of the NNZ to velocity and hysteresis, respectively. EMG of the lumbar multifidus muscles was recorded by intramuscular wire electrodes. The range of elongation and its corresponding tension from the resting point at which the EMG was first recorded was defined as the NNZ. In the single cycle tests, the length and corresponding tension at which the muscles ceased activity in the release phase were also calculated.

RESULTS AND DISCUSSION

For linear deformation of the spine into anterior flexion, the NNZ was the smallest for the fastest rate of flexion. And gradually increased for decreasing rates. In general the elongation or tension in the viscoelastic tissues increased to above 5 – 15% of the physiological range before the muscles were reflexively recruited, and that range depends on the velocity of the movement. Faster velocities are associated with smaller NNZ.

For cycles of anterior flexion / extension, the NNZ were significantly lower in the flexion phase as compared to the extension phase. As the cycle frequency increased the NNZ became even smaller during flexion and larger during extension. The peak EMG was also dependent on the frequency of the cycle, being higher at higher frequencies.

CONCLUSION

Faster rates of movement develop higher tension in the viscoelastic tissues and trigger reflexive muscular activity earlier in the movement thus lending greater dynamic stability to the spine. This emerges due to the fact that viscoelastic tissues deformation is time dependent with respect to the tension they develop. Faster movements also elicit higher forces from the muscles which further stabilize the spinal joints. The hysteresis associated with a stretch – release cycle of the tissues, however, exposes the spine to a relatively increased NNZ at the end of extension. This period leaves the spine without muscular support especially in a fast extension, and is prone to instability and injury.

REFERENCES

1 Pedersen et al, *JBJS,* **38**:377, 1956
2 Yahia et al*, Pathol.,* **187**:936, 1991
3 Stubbs et al, J. EMG & Kinesiol., **8**:197, 1998
4 Solomonow et al*, Spine*, **23**:2552, 1998
5. Panjabi, M., Low Back Pain, Weinstein & Gordon (Eds). *AAOS*, 1996
6. Solomonow, IEEE-TBME, **31**:752, 1984
7. Eversull et al, *Clin. Biom*. **16**:102, 2001
8. Solomonow et al, *Spine*, **26**:E-314, 2001

THE SACROILIAC JOINT, INTERVERTEBRAL DISC AND MUSCLE REFLEXES

Aage Indahl[1], Allison Kaigle[2], Olav Reikerås[3], and Sten Holm[2]
[1]Kysthospitalet, Stavern, Norway, Department of Orthopaedics, [2]Sahlgrenska University Hospital, Göteborg, Sweden, and [3]National Center for Orthopaedics, Oslo, Norway

OBJECTIVE

The lumbar motion segment is a complex joint with a network of different muscles crossing it. The sacroiliac joint (SIJ) is a true synovial joint which is richly innervated. It bears tremendous loads, but has a very limited amount of motion. Numerous spinal and gluteal muscles attach to the SIJ capsule and iliac crest. Loss of mechanical stability has been in focus a a key factor in dysfunction. The function or dysfunction of spinal reflexes responsible for muscle activation are less studied. The aim was to determine if stimulation of nerve elements in intervertebral disc, the SIJ and SIJ capsule could elicit contractions in porcine gluteal or lumbar spinal muscles.

METHODS

A porcine model was used to study the interaction between the intervertebral disc, zygapophyseal joints, sacroiliac joint and the paraspinal muscles. In the first experiment twenty-three pigs were used to measure the electromyographic response in the paraspinal musculature to electrical stimulation of the anulus fibrosus of the L3/L4 intervertebral disc before and after the introduction of normal saline to the zygapophyseal joint. Motor unit action potentials were recorded using three sets of needle electrodes placed in the deepest fascicles of the multifidus, bilateral to the L¤ and L5 spinous processes, and into the central longissimus musculature, bilateral to the L4 spinous process. In the second experiment ten pigs were used to study the muscular response to electrical stimulation of nerve endings in the ventral and dorsal capsule of the sacroiliac joint. Six bipolar EMG needle electrodes were used for measuring compound motor unit action potentials (MUAPs) and inserted in the deep medial multifidus fibers lateral to L3-L5, the central belly of the gluteus medius and maximus and in the quadratus lumborum muscle lateral to L5.

RESULTS AND DISCUSSION

Stimulation of nerves within the posterolateral anulus of the disc elicited reactions in the paraspinal muscles, namely the lumbar multifidus and longissimus. Introduction of physiological saline into the zygapophysial joint resulted in a reduction in the motor unit action potential amplitude. This reduction was manifested as an immediate and constant reduction, a graded reduction, or a delayed reaction, during which the reduction occurred an average of 5 minutes after the saline injection. This effect was most likely an inhibitory stretch reflex from the capsule that stimulated inhibitory interneurons, thus inhibiting motorneurons. Inhibitory discharges from the joint capsule can explain why manipulative treatment and mobilization of the zygapophysial joint provide relief in some cases. Thus, it appears that there is a delicate interaction between the different parts of the spinal motion segments, and proprioceptive nerve endings may play a vital part in load distribution during movements.
Stimulation of nerves and mechanoreceptors in the sacroiliac joint, as well as in the joint capsule, elicited motor unit action potentials in different muscles, which revealed an interesting activation pattern. Stimulation of nerve elements in the ventral area of the sacroiliac joint produced significant contractions in muscles located more distally from the lumbar spine, namely the gluteus maximus and quadratus lumborum. However, stimulation of the SIJ capsule elicited significant responses in the medially located multifidus fascicles. These findings suggest that the SIJ is involved in activating muscles responsible for overall posture control, as well as control on the segmental level in the lumbar spine. It is possible that the different areas of the sacroiliac joint play different roles in regulating the locomotive system, and the response may therefore vary depending on the stimulation site. Disturbances in the sensory part of the joint innervation may lead to altered muscular activation and represent the true dysfunction.

SUMMARY

The functioning of the motor system is intimately related to that of the sensory system. The proper moment-to-moment functioning of the motor system depends on a continuous inflow of sensory information. The afferent input from sacroiliac joint receptors, as well as mechanoreceptors in the intervertebral disc and zygapophysial joints, may contribute to different degrees of muscle activation and may constitute an integral regulatory system.

REFERENCES

1. Indahl A, et al. *Spine* 1997;**22**:2834-40.
2. Indahl A, et al. *J Spinal Dis* 1999;**12**:325-30.

ROLE OF LOCAL BIOMECHANICS IN TEMPORAL BEHAVIORAL RESPONSES OF PAINFUL RADICULOPATHY

Beth A. Winkelstein PhD[1], James N. Weinstein DO MS[2], and Joyce A. DeLeo PhD[1,3]
Dartmouth–Hitchcock Medical Center, Lebanon, NH 03756, Beth.Winkelstein@Dartmouth.edu
[1]Department of Anesthesiology
[2]Department of Orthopaedic Surgery
[3]Department of Pharmacology & Toxicology

INTRODUCTION

Nerve root injury resulting from herniated nucleus pulposus contributes to radicular pain mechanisms. Injury magnitude has been shown to directly modulate nociceptive responses, including mechanical allodynia (MA), which is an increased behavioral sensitivity to a non-noxious stimulus (Winkelstein et al., 2001). Studies report edema and increased endoneurial pressure in injured nerve roots (Lundborg et al., 1983; Olmarker et al., 1989). Yet, the simultaneous examination of local changes in structural geometry following compressive injury and central changes linked with the onset and maintenance of persistent pain remains limited. Therefore, this study temporally characterizes local nerve root geometric changes following compressive injury in a rat lumbar radiculopathy (LR) model and examines these structural changes in the context of pain behaviors (MA) and activation of two populations of glial cells, microglia and astrocytes, in the CNS.

METHODS

Male Holtzman rats were divided into a sham group with only nerve root exposure or a ligation group with tight ligation of the left L5 nerve roots. Using image analysis, nerve root compressive strains were calculated at injury and postoperative time points (Winkelstein et al., 2001). Mechanical allodynia was continuously measured to assess behavioral sensitivity. In a subset of animals, the nerve roots were reimaged on postoperative days 1,3,5,7 to quantify local swelling. In another subset of animals, lumbar spinal cord tissue was harvested on days 1,3,7,14 for immunohistochemical analysis of changes in glial activation using OX-42 and GFAP(Colburn et al., 1999).

RESULTS AND DISCUSSION

Mean applied compressive injury strain in the nerve roots was 30.8 ± 14.5%. All postoperative tissue geometry changes were positive, indicating a relative swelling response in the nerve root (Fig. 1). Swelling was greatest at early time points following injury and then decreased over time. While the initial degree of swelling was dependent on the initial injury magnitude, swelling at later time points did not depend on injury magnitude and showed no direct relationship to MA. Likewise, microglial activation in the spinal cord showed a direct relationship with the magnitude of initial tissue injury (Fig. 2). However, the degree of astrocytic activation did not show a relationship with initial injury.

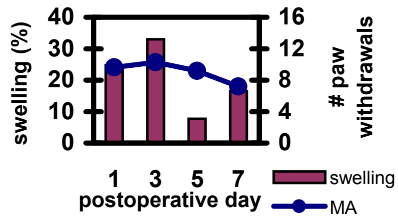

Fig. 1. Time course showing mean postoperative nerve root swelling and the corresponding mean MA for these animals at each time point.

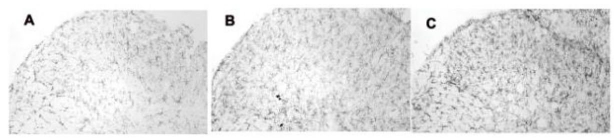

Fig. 2. Microglial activation (using OX-42) in the L5 spinal cord dorsal horns at day 7 for a normal (A), a lower injury magnitude (B) and a higher injury magnitude (C) animal, showing graded activation.

SUMMARY

While pain-associated behaviors depend on the initial magnitude of nerve root deformation in LR, they cannot be explained by the temporal nerve root swelling. Spinal microglial responses also show a relationship with injury severity, but they are not related to MA. The OX-42 antibody to CR3/CD11b is a sensitive marker of injury, yet not necessarily behavioral sensitivity. Given earlier work showing spinal cytokine mRNA levels and behaviors depend on initial injury magnitude (Winkelstein et al., 2001), it is suggested that subpopulations of activated glia and their immunologic responses upon activation may play important roles in pain *maintenance*.

REFERENCES

Colburn R, et al (1999). *Exp Neurol*, **157**,289-304.
Lundborg G, et al (1983). *J Neurol Neurosurg Psych*, **46**,1119-24.
Olmarker K, et al (1989) *Spine*, **14**(6),569-73.
Winkelstein B, et al (2001). *J Neurosci Meth*, **111**,49-57.

ACKNOWLEDGEMENTS

Grant support from NINDS NS11161, NIAMS AR44757, Bristol-Myers Squibb/Zimmer Orthopaedic Foundation.

THE ASSESSMENT OF SPINAL KINEMATICS DURING THE APPLICATION OF AN A-P MOBILISATION

Alison McGregor[1], Anthony Bull[2], Raymond Lee[3], Paul Wragg[4], Waldyslaw Gedroyc[4]

[1] Dept. of Musculoskeletal Surg., Faculty of Medicine, Imperial College of Science, Technology & Medicine, London, U.K.
[2] Department of Bioengineering, Imperial College of Science, Technology & Medicine, Exhibition Road, London, U.K.
[3]Rehabilitation Sciences, Hong Kong Polytechnic University, Hong Kong
[4]Interventional MRI Unit, St Mary's Hospital, Praed Street, London, U.K. Email contact: a.mcgregor@ic.ac.uk

INTRODUCTION

The mechanisms underpinning manual therapy are poorly understood. This is particularly true of posteroanterior mobilisation (PA) a manual physiotherapy technique that is commonly used as an examination tool and a form of conservative treatment for spinal complaints. The evolution of open MRI scanners has provided a new non-invasive method of investigating the mechanics of mobilisation therapy. Studies to date (McGregor et al 2001) have recorded static spinal kinematics during the application of a PA mobilisation, but have failed to quantify the force applied during the technique. This study sought to develop and validate a tool that was capable of measuring the force applied to the cervical spine during the administration of a course of PA manual therapy within an open MRI scanner.

METHODS

Design Criteria: The force measurement device had to be MR compatible, give the correct feel to the examiner to simulate the normal PA manipulation technique, easy to read from within the iMR suite by the examiner, calibrated for specific levels of force application, and the force values had to be recorded simultaneously with the MR images.

Device Design and Use: A water filled pressure device was designed through which the force to the cervical spine could be applied. This consisted of a rubber tube of diameter 25 mm, and length 125 mm that was connected to a clear plastic hose of internal diameter 5 mm with one end open to atmospheric pressure. The pressure applied to the rubber tube by the examiner was then equal to the pressure change measured by the height change of the column of water in the clear hose. The device was calibrated by the application of constant loads, using weights, to the rubber tube, and then marking the clear hose at the level of the column of water. The clear hose was mounted on the iMR magnet within sight of the examiner, and within sight of the video recording device within the iMR suite. This device recorded the position of the examiner, the MR images produced by the manipulation, and the height of the column of water in the pressure measuring device.

Imaging Protocol: Subjects were scanned using a General Electric Signa SP10 Interventional MRI scanner (iMR). This is an open MRI scanner consisting of 2 connected but opposing ring "doughnut" magnets. The gap between these magnets is 56 cm generating a uniform field of 0.5Tesla. Subjects were scanned in the prone position with their necks in a neutral position. An experienced manipulative physiotherapist delivered an oscillatory PA forces to be spine whilst getting feedback on the force produced. The maximum PA force applied was 140-150N (Lee & Evans 1992), and the frequency of the technique was in accordance with the iMR image acquisition rate (0.2 image per second). Each subject received 30 seconds of PA mobilisation at the spinous process of the fifth cervical vertebra level of the spine. Measurements of intervertebral rotation and translation were obtained from the sagittal images, alongside measures of soft tissue compression.

RESULTS TO DATE

Clear images of vertebral position could be obtained in each position during the application of a PA mobilisation within the open MRI scanner from which measurements of intervertebral angulation and translation could be obtained. These images suggest little or no movement of the vertebrae but marked soft tissue compression. Statistical analysis confirmed this finding on the 5 subjects scanned to date. Preliminary investigations confirm that the loads applied to the spine within the scanner are appropriate and that load can be recorded in the scanner during the technique. The load measurement system was adjusted so that the height change of fluid in the system was 1.5 metres for 145N.

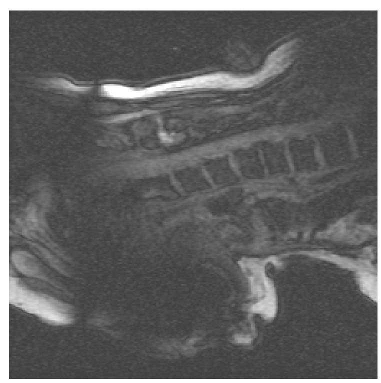

DISCUSSION

These preliminary studies confirm that mobilisation of the lumbar spine does not produce any changes in vertebral kinematics and suggest that beneficial effects may be derived from changes in the soft tissues.

REFERENCES

McGregor AH et al (2001). Clin Biomech, **16**(10):926-929.
Lee, R., Evans, J. (1992). Aus J Physiotherapy, **38**:115-23

BIOMECHANICAL EVIDENCE FOR PROPRIOCEPTIVE FUNCTION OF LUMBAR FACET JOINT CAPSULE

Partap S. Khalsa, Jonathan B. Chiu, Nicholas J. Aliberti, and Michael Sileo
Dept. of Biomedical Engineering, Stony Brook University, Stony Brook, New York, (www.bme.sunysb.edu)

INTRODUCTION

The lumbar facet joint capsule can be a pain generator in low back pain patients (Cavanaugh 1995; Kuslich et. al 1991; Revel et. al 1998; Schwarzer et. al 1994). However, its proprioceptive role is largely theoretical (cf. Pickar & McLain 1995). Histological studies have conclusively established the presence of mechanoreceptors in human facet capsule (McLain & Pickar 1998), and animal models have demonstrated that capsule mechanoreceptors respond to loading (Pickar & McLain 1995; Yamashita et. al 1990). Here we present biomechanical data supporting a proprioceptive role for facet joint capsule.

METHODS

Post. Capsule Material Properties. Bone-capsule-bone (BCB) specimens were harvested from intact, cadaveric human spines, using a university approved protocol. The BCB specimens were trimmed to a rectangular shape to facilitate uniaxial tensile testing and loaded in a uniaxial tensile testing system (Tytron 250, MTS, Inc.). Capsule geometry was measured optically, and the material testing was performed under strain control. Tensile stress was calculated from resultant force and cross-sectional area at mid-length. Following preconditioning, trials consisted of ramp displacements (1, 5, 10, or 15% strain/s) to a specified tensile strain (10, 20, 30, 40, or 50 %), which was held constant for 300 s, and then a ramp unload.

Post. Capsule Strains during Physiological Motions. Intact, human cadaveric, ligamentous, lumbar spine specimens were actuated at the L_1 vertebra (sacrum potted) with a linear, servomotor using a programmable controller and digital encoders. Motions consisted of flex., ext., and lat. bending (left & right). Vertebra angulation during motion was measured with two biaxial inclinometers fixed to the ant. vertebral bodies of the studied joints. Joint moments were calculated from the moment arm and a force transducer in series with the actuator. 9 markers were glued to each studied post. capsule, forming a 3 x 3 array. The markers were optically tracked in three dimensions using a dual-camera kinematic system. Capsule plane strains were calculated using a Lagrangian, large strain formulation.

RESULTS AND DISCUSSION

Capsule stiffness was nonlinear and anisotropic up to its yield strength, and the stiffness was larger aligned parallel rather than perpendicular to the collagen fibers (Fig. 1). No significant differences in capsule stiffness were found for the different joint levels, nor for the left or right sides of the lumbar spine. Capsule stiffness was independent of the strain rates used for ramp loading.

Plane strains (referenced from the spine's neutral vertical position) in all joint capsules increased monotonically for all motions (Fig. 2), though intra-capsule strains were inhomogeneous. On average, shear strains (ε_{xy}) were larger than axial strains (ε_{xx} or ε_{yy}), with the largest strains in flexion at L_4-L_5 or L_5-S_1 joint levels and decreasing for more cephalic levels (Table 1). During ext., strains were mirror symmetric of flex.,

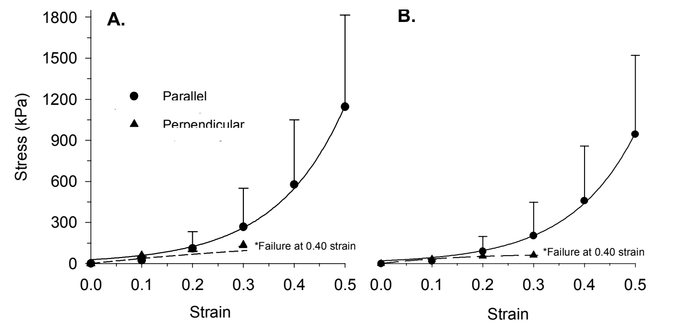

Fig. 1. Stiffness curves of human facet joint capsule parallel (n = 27) and perpendicular (n = 2) to the dominant orientation of the collagen fibers. A) Instantaneous or 'viscous' response. B) Relaxed or 'elastic' response. Error bars are std. devs.

negatively increasing for more caudal capsules, hence, indicating capsule relaxation. Mean strains during lateral bending motions were smaller than those in flex. (≲1% for L_{1-2}) and also demonstrated mirror symmetry between left & right bending (Table 1).

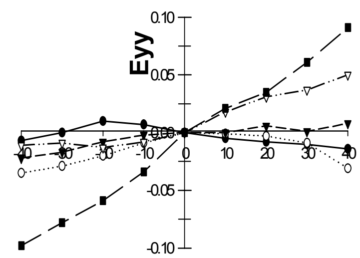

Fig. 2. E_{yy} strains at 5 capsule levels from full extension to full flexion.

Physiological motions of the in-vivo lumbar spine would likely activate capsule mechanoreceptors. Cat knee joint capsule mechanoreceptors have a mean tensile threshold of 5 kPa (Khalsa et. al 1996). At only 2% facet capsule tensile strain (from full ext.), estimated tensile stress (~21 kPa) would be over four times greater than threshold of Ruffini type mechanoreceptors (Khalsa et. al 1996), which also innervate human facet joint capsule (McLain & Pickar 1998). Hence, the biomechanics of lumbar facet joint capsule is favorably disposed to allow it to function neurophysiologically as a proprioceptive organ. A major question remains whether human facet capsule mechanoreceptors function similarly to those in other mammals & what is their threshold relative to capsule loading.

	Flexion		Extension	
Strain	L_{1-2}	L_{4-5}	L_{1-2}	L_{4-5}
ε_{xx}	-0.003	-0.014	0.027	0.089
ε_{yy}	-0.006	0.082	-0.022	-0.070
ε_{xy}	0.004	0.131	-0.005	-0.167

Table 1. Comparison of capsule strains in flx. & ext.

REFERENCES

Cavanaugh (1995) *Spine* **20**(16):1804-1809. Khalsa et. al (1996) *J.Neurophysiol.* **76**(1):175-187. Kuslich et. al (1991) *Orthop.Clin.North Am.* **22**(2):181-187. McLain et. al (1998) *Spine.* **23**(2):168-173. Pickar et. al (1995) *Spine.* **20**(22):2379-2385. Revel et. al (1998) *Spine* **23**(18):1972-1976. Schwarzer et. al (1994) *Spine* **19**(10):1132-1137. Yamashita et. al (1990) *J.Bone Joint Surg.[Am.]* **72**(6):865-870.

MODELS FOR WHIPLASH INJURY

Manohar M Panjabi
Biomechanics Laboratory, Department of Orthopaedics and Rehabilitation,
Yale University School of Medicine, New Haven, CT, USA

INTRODUCTION

Whiplash injury of the neck is usually caused by a rear impact at slow speed. Such injuries seem benign as they do not include vertebral fractures or dislocation, and are generally caused by low impact energy trauma. However, whiplash injury can result in severe pain that may last for many years. These injuries have been on the rise in recent times, due primarily to the increased traffic density. A 50% increase was noted in Sweden and a 100% in Germany in the last 20 years. The clinical symptoms associated with whiplash are well documented, but our understanding of the injury mechanism remains poor. Whiplash injuries are most commonly thought to be incomplete or subfailure soft tissue injuries of the spinal column, although, there are also hypotheses including injuries to the nervous system and muscle strains. The prevailing view of neck hyperextension causing the whiplash injury has not been supported by epidemiological studies. Understanding the mechanism of whiplash injury is important. It may help in automotive design to prevent the injury, in diagnosis to precisely locate the injury, and in treatment to make it more effective. Various models have been used to get to the mechanism of injury. These include: volunteers in cars or sleds; cadavers in sleds; cervical spine specimens with head; animal models; physical models or dummies; and mathematical models. The purpose of this communication is to present the latest findings using the cervical spine specimen model.

METHODS

Model I consisted of a human cervical spine specimen (occiput to T1, both mounted in epoxy mounts), devoid of musculature, thus allowing free access to vertebrae, discs and ligaments for monitoring during trauma (Panjabi 1998). The T1 was mounted on a mini-sled above a 6-component load cell, while the occiput was provided with a simulated head. The weight of the head was balanced by a suspension system carried on the sled. Various transducers were designed to monitor the deformations of capsular ligaments, vertebral artery, and alar ligaments during the trauma. Defining soft tissue injury was one of the primary goals. Multidirectional flexibility test was used before and after each trauma step, to quantify the resulting injury at each spinal level. The model was impacted sequentially at 2, 4, 6, 8, and 10 g. Model II, additionally, included caudally increasing compressive forces applied to vertebrae via cables approximately passing through flexion/extension centers of rotation, based upon follower load concept (Patwardhan 2000). The compressive loads increased from 60 N at C0-C2 to 240 N at C6-T1. These forces, applied on the left and right sides of the specimen, stabilized the specimen in the frontal plane. To resist the horizontal loads in the sagittal plane, anterior and posterior forces were also included in the model. This muscle force replication system simulated the expected in vivo loads and stiffness in neutral posture, and thus helped bring the in vitro whiplash model closer to the in vivo situation.

RESULTS

The hyperextension hypothesis of injury mechanism was not supported. We found a bi-phasic kinematics response of the cervical spine during whiplash trauma. In the first phase, the spine formed an S-shaped curve with flexion at the upper levels and hyperextension at the lower levels. In the second phase, all levels of the cervical spine were extended, and the head-neck reached its maximum extension. The occurrence of anterior injuries at the C5-6 level in the first phase was documented by flexibility tests and functional radiography. The largest dynamic elongation of the capsular ligaments was observed at C6-C7 level during the initial S-shaped phase of whiplash. The same was true for the maximum elongation of the vertebral artery. Whiplash using the second model showed dramatic increases in the anterior force during whiplash trauma.

CONCLUSION

The isolated spine specimen models provide significant advantages because of their openness and easy accessibility to the vertebrae, discs, ligaments and vascular and neural structures. These spinal elements can be monitored during the simulated trauma. Another, equally important advantage is the quantification of the subfailure soft tissue injuries. Such detailed information may provide truer understanding of the whiplash trauma, and may help in improving the diagnosis, treatment, and prevention of these imprecisely defined injuries.

REFERENCES

Panjabi MM et al., Spine 23 (17-24), 1998. Patwardhan AG et al., Spine 25(1548-54), 2000.

IN VIVO QUANTIFICATION OF DISC BULGING IN DIFFERENT ANNULAR REGIONS ALONG A RADIAL PATH

Greg Kawchuk[1], Allison Kaigle Holm[2], Sten Holm[2], Lars Ekström[2], Tommy Hansson[2]

[1]Faculty of Kinesiology, University of Calgary, Calgary, Alberta, Canada, kawchuk@ucalgary.ca
[2]Department of Orthopaedics, Sahlgrenska University Hospital, Göteborg, Sweden

INTRODUCTION

The intervertebral disc is a load-bearing structure comprised of a gelatinous nucleus pulposus surrounded by concentric lamellae of the annulus fibrosus. During axial compression, the most external annular layer is known to bulge. While the magnitude and direction of external layer bulging has been quantified theoretically (Shirazi-Adl) and *in vitro* (Stokes), knowledge of the load-response of the remaining internal lamellae is limited to directional information only. Given that disc bulge is influenced by several factors including simulated injury (Brinckmann and Horst), understanding regional load responses within the annulus may be of clinical significance. Therefore, the purpose of this *in vivo* study was to compare annular bulging within different annular regions along a radial path.

METHODS

Seven mature Swedish Landrace pigs were utilized in this study. Each animal was anesthetized in a prone position and the posterior muscles of the spine partitioned to permit the installation of four bone pins into the pedicles of L3 and L4. A miniaturized hydraulic loading device was then attached to these pins and suspended above the back of the animal. Through a separate, retroperitoneal approach with psoasectomy, a 10 MHz ultrasonic transducer (Acuson) was placed in the coronal plane against the lateral aspect of the L3-L4 intervertebral disc. Cyclic compression loading of the L3-L4 disc was then performed (300N, 1Hz, 10 cycles) with concurrent imaging of the disc space. Ultrasonic images at minimal and peak compression loads were collected automatically from an image capture card using a synchronizing pulse from the hydraulic device. Image pairs from each compression cycle were then analyzed digitally using customized software. Specifically, a digital line was drawn in each image that bisected the L3-L4 disc mediolaterally (Figure 1) and the signal intensities of all pixels falling on the bisecting line determined. To account for movements of the transducer with respect to the vertebrae, the bisecting line in each image was referenced to a second, intersecting line connecting the inferiolateral aspect of L3 and the superiolateral aspect of L4 (Figure 1). Graphically, lamellae were characterized along each bisecting line as regions of high pixel intensity while interlamellar spaces corresponded to regions of low pixel intensity. Phase shifting of high intensity regions between images was interpreted as translation of the lamellae along the bisecting line. The direction and magnitude of lamellar translation in the middle 1/3 and outer boundary of the annulus was determined by the sign and magnitude of the pixel phase shift.

RESULTS AND DISCUSSION

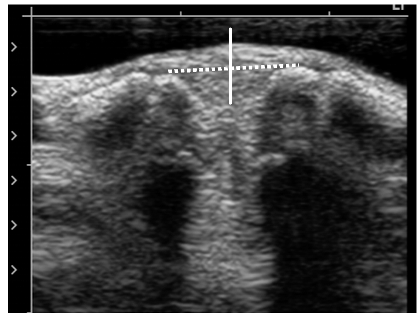

Figure 1: Coronal ultrasonic images of the unloaded L3-L4 segment showing the digital bisecting line (solid) and digital intersecting line (dashed).

The lamellae of the middle 1/3 of the annulus as well as the lamella defining the outermost boundary of the annulus were observed to bulge outward during compression loading. While all lamellae of each region were displaced in the same direction (outward), the magnitude of displacement was significantly greater in the middle 1/3 of the annulus (0.14 ± 0.10 mm) compared to the outermost boundary (0.06 ± 0.06 mm) (Wilcoxon Matched-Pairs Signed-Ranks Test $p <= 0.03$).

While other studies have described alterations in external disc bulge at different circumferential sites (e.g. anterior vs. posterolateral), to our knowledge, this study is the first to quantify regional deformations of the annulus along a radial path. These *in vivo* findings are supported indirectly by previous *in vitro* studies that have demonstrated the capability of the internal lamellae to move independently of the external lamellae along a radial path during conditions of nuclear depletion (Meakin et al., Serousii et al.). Additional investigations to confirm these findings must be performed as the impact of a variety of known variables (e.g. load magnitude, disc height) and uncontrolled variables (e.g. out-of-plane imaging and off-axial loading) is unknown.

SUMMARY

The results of this *in vivo* study suggest that at a 300 N axial load, outward deformation in the middle 1/3 of the annulus is significantly greater when compared to the lamellae of the outermost disc boundary.

REFERENCES

Brinckmann, P., Horst, M. (1985). *Spine*, **10**, 138-145
Meakin, J.R., et al. (2001). *Clin Biomech*, **16**, 121-128
Serousii, R.E., et al. (1989). *J. Ortho Res*, **7**, 122-131
Shirazi-Adl, A. (1983). *Spine*, **9**, 120-134
Stokes, I.A. (1988). *J. Spinal Disorders*, **1**, 189-193

COORDINATION OF MUSCLE ACTIVATION TO ASSURE STABILITY OF THE LUMBAR SPINE

Stuart M. McGill[1], Sylvain Grenier[1], Jacek Cholewicki[2]
[1]Faculty of Applied Health Sciences, University of Waterloo, Canada
[2]Department of Orthopaedics, Yale University School of Medicine, New Haven, CT, USA
mcgill@healthy.uwaterloo.ca

INTRODUCTION

The spine is inherently unstable since, in vitro, the osteo-ligamentous lumbar spine buckles under compressive loading of only 90 Newtons. A critical role of the musculature is to stiffen the spine in all potential modes of instability (3 rotational and 3 translational). But given the wide range of individuals and physical demands, question remain as to what is the optimal balance between stability, motion facilitation and moment generation - if stability is achieved through muscular cocontraction, how much is necessary and how is it best achieved? The intention of this presentation is to define stability and to demonstrate that spine stability results from highly coordinated muscle activation patterns involving many muscles, and that the critical patterns must continually change, depending on the task.

ON STABILITY: THE FOUNDATION

During the 1980's, Professor Anders Bergmark of Sweden, very elegantly formalized stability in a spine model with joint stiffness and 40 muscles (Bergmark, 1987). In this classic work he was able to formalize mathematically, the concepts of “energy wells”, stiffness, stability and instability using the elastic potential energy approach. The approach was limited to analysis of “local stability” since the energy wells are not infinitely deep and the many anatomical components contribute force and stiffness in synchrony to create “surfaces” of potential energy where there are many local wells. Local minima are located from examination of the derivative of the energy surface. Spine stability then, is quantified by forming a matrix where the total “stiffness energy” for each degree of freedom of joint motion is subtracted from the applied work (represented by a number, or eiganvalue). Eigenvalues less than zero indicate the potential for instability. Others have enhanced this work. The eigenvector (different from the eigenvalue) can then identify the mode in which the instability occurred while sensitivity analysis may reveal the possible contributors allowing unstable behaviour, or for clinical relevance - what muscular pattern would have prevented the instability?

SOME EXAMPLES OF MOTOR PATTERNS AND STABILITY

Several examples will be presented to demonstrate the dynamic nature of the “healthy” eiganvector that ensures stable conditions are preserved.

LOOKING FORWARD

There is no single muscle that is the best stabilizer of the spine – the most important muscle is a transient definition that depends on the task. Further, virtually all muscles work together to create the ‘balance” in stiffness needed to ensure sufficient stability in all degrees of freedom (or to maintain the appropriate level of potential energy of the spine). With the evidence supporting the importance of muscle endurance (not strength) and “healthy” motor patterns to assure stability, work must continue to: **1)** understand the role of various components of the anatomy to stability - and the ideal ways to enhance their contribution; **2)** understand what magnitudes of muscle activation are required to achieve sufficient stability; **3)** identify the best methods to re-educate faulty motor control systems to both achieve sufficient stability and to reduce the risk of inappropriate motor patters occurring in the future. Much remains to be done.

REFERENCES

Bergmark, A., (1987) Doctoral Dissertation, Department of Solid Mechanics, Lund University, Sweden.

PAIN AND MOTOR CONTROL OF THE SPINE: EFFECT AND MECHANISMS

Paul W Hodges[1, 2] and G Lorimer Moseley[2, 3]

[1]Department of Physiotherapy, The University of Queensland, Brisbane, Qld,
[2]Prince of Wales Medical Research Institute, Sydney, NSW, p.hodges@unsw.edu.au
[3]Pain Managementand Research Centre, University of Sydney & Royal North Shore Hospital, Sydney, NSW, Australia

INTRODUCTION

Numerous studies have identified changes in the trunk muscles in people with low back pain. These changes range from changes in the pattern of muscle activation (e.g. Hodges & Richardson, 1996) to deficits in strength and endurance (e.g. Roy, De Luca & Casavant, 1989). Several recent studies have highlighted changes in activity of the trunk muscles in postural tasks. For instance, during rapid arm movements the onset of activity of the deep abdominal muscle transversus abdominis (TrA) is delayed compared to control subjects (Hodges & Richardson, 1996). However, it is unknown whether these changes are the result of pain. Furthermore it is uncertain whether it is nociceptor stimulation or other elements of clinical pain, such as increased information processing demand, stress and fear that may cause changes in motor control. The postural response of the trunk muscles in association with arm movement provides a model to investigate these questions. The aim of this series of experiments was to investigate these questions.

METHODS

In the first study electromyographic (EMG) recordings of the abdominal (transversus abdominis (TrA), obliquus internus (OI) and externus (OE)) and paraspinal (deep and superficial fibres of multifidus) muscles were made in 7 healthy subjects. In standing, subjects rapidly moved the left arm in response to a light in a control trial, following the injection of isotonic (non-painful) and hypertonic (painful) saline into the longissimus muscle at L4, and during a 1-hr follow-up. Temporal and spatial parameters of EMG were measured.

In the second study the same EMG recordings were made in a separate group of 8 subjects. For this study rapid arm movements were performed in control trials, while performing an attention demanding task ('attention'; modified Stroop test); while performing the attention demanding task with negative feedback of performance ('stress'), during anticipation of randomly delivered electric shocks ('fear'); and following injection of hypertonic saline into the back muscles ('pain').

RESULTS AND DISCUSSION

In the first study, subjects reported pain of ~6/10 on a visual analog scale. The majority of muscles responded in a variable manner to hypertonic saline injection. However, the onset of TrA EMG was delayed by ~20 ms after hypertonic saline injection in 5/6 subjects for whom TrA data were collected. In addition, the amplitude of TrA EMG in the 50 ms before and after the onset of deltoid EMG was reduced. The results suggest that nociceptor stimulation and/or pain alter feedforward postural responses, but this response is not consistent across apparently synergistic muscles.

The results of the experimental pain trials in the second study were consistent with those of study one. Delayed onset of TrA EMG was identified in all subjects. This change was not replicated in the attention trials. Instead, the onsets of TrA and deep MF EMG occurred earlier relative to that of deltoid as a result of delayed reaction-time for limb movement. When the attention task was made stressful by provision of negative feedback (e.g. 'you're not performing well enough') the latency between onsets of TrA and deltoid EMG were not different to the control trials. Unlike the attention and stress trials, when the arm was moved in the fear condition the onsets of TrA and deep MF EMG were both significantly delayed and the response of TrA was not different to that reported in the pain trials. Although consistent within-subject changes were observed in OI and OE EMG in all conditions, there was marked variability between subjects.

These data suggest that the change in postural activation of TrA associated with pain is not due to the competitive attention demand of pain, but may be due in part to anxiety associated with pain.

SUMMARY

These data confirm that changes in motor control of the trunk muscles in association with low back pain may occur as a result of the pain, rather than a predisposing factor. Furthermore, the changes may not be due to nociceptor stimulation, but instead could be mediated by processes such as fear. Finally, these data confirm the specificity of these changes to the deep intrinsic spinal muscles.

REFERENCES

Hodges, P. W., Richardson, C. A. (1996). *Spine*, **21**, 2640-50.
Roy, S. H., DeLuca, C. J., Casavant, D. A. (1989). *Spine* **14**, 992-1001.

ACKNOWLEDGEMENTS

Financial support was provided by the National Health and Medical Research Council of Australia.

SPINAL STIFFNESS INCREASE WITH AXIAL LOAD: ANOTHER STABILIZING CONSEQUENCE OF MUSCLE ACTIVATION

Ian Stokes and Mack Gardner-Morse

University of Vermont, Department of Orthopaedics and Rehabilitation
Burlington, VT 05405-0084, USA, Ian.Stokes@uvm.edu

INTRODUCTION

The stiffness of motion segments, together with muscle actions, stabilizes the spinal column. The objective of this study was to compare the experimentally measured load-displacement behavior of porcine lumbar motion segments *in vitro* with and without physiological axial compressive preloads of 0, 200 and 400 N equilibrated with a physiological fluid environment to determine whether these preloads increased stiffness, hysteresis and linearity of the load displacement behavior.

METHDODS

At each preload, displacements in each of six degrees of freedom (three translations and three rotations) were imposed and the applied forces and moments were recorded, using a “hexapod” apparatus (Stokes *et al.*, 2002). These tests were repeated after removal of posterior elements. Forces at the vertebral body center were related by linear regression analysis to the displacements by a symmetric 6x6 stiffness matrix. Also, the hysteresis and linearity of the load-displacement recordings were evaluated. Six diagonal and two off-diagonal load-displacement relationships were examined for differences in stiffness, linearity and hysteresis in each testing condition.

RESULTS

Motion segment and disc load-displacement behavior was stiffer, more linear and had greater hysteresis with axial compressive preload imposed. Mean values of the diagonal terms of the stiffness matrix for intact porcine motion segments increased significantly by an average factor of 2.2 and 2.9 with 200 and 400 N axial compression respectively ($p<0.001$). Increases for disc-only specimens averaged 4.6 and 6.9 times with 200 and 400 N preload ($p<0.001$). Changes in hysteresis correlated with the changes in stiffness. The load-displacement relationships were progressively more linear with increasing preload (R^2 = 0.82, 0.97 and 0.98 at 0, 200 and 400 N axial compression respectively). The increase in stiffness with preload was slightly nonlinear for the axial stiffness ($p=0.012$).

DISCUSSION

These findings show that the elastic energy storage and energy absorption (damping) that occurs with displacements of motion segments *in vivo* increases with the magnitude of the prevailing muscle force and applied loading. This has implications for spinal stability.

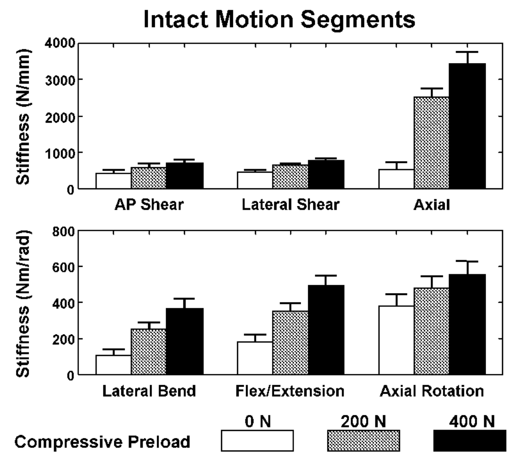

Figure 1 Mean and standard error of diagonal terms of the stiffness matrix for intact motion segments at three levels of axial compressive preload.

Preload may cause an increase in stiffness and linearity of the load-displacement behavior of the disc. Broberg {1983} predicted a doubling in stiffness for rotational degrees of freedom with increased axial preload (700 N to 3000 N) in a analytical model. Janevic *et al* (1991) demonstrated this effect experimentally. We believe that a combination of fluid flow effects and viscoelastic tissue properties were responsible for the increase in hysteresis with preload.

REFERENCES

Broberg K.B. (1983). On the mechanical behaviour of intervertebral discs. *Spine* **8**:151-165.

Janevic J., Ashton-Miller J.A., Schultz A.B. (1991). Large compressive preloads decrease lumbar motion segment flexibility. *J Orthop Res* 1991; **9(2)**:228-36.

[16] Stokes I.A.F., Gardner-Morse M., Churchill D., Laible J.P. (2002) Direct measurement of spinal motion segment stiffness matrix. *J Biomech* in press

ACKNOWLEDGEMENTS

Supported by NIH R01 AR 44119. Gary Badger and Richard Single preformed the statistical analyses. Porcine lumbar motion segments were obtained with the kind assistance of Donita Bylski-Austrow.

SPINAL STABILIZING SYSTEM: CONSEQUENCES OF A SUBFAILURE INJURY

Manohar M. Panjabi

Department of Orthopaedics and Rehabilitation, Yale University School of Medicine, New Haven, CT
manohar.panjabi@yale.edu

INTRODUCTION

Chronic spinal pain (CSP), representing collectively the low back and neck pain, is an important societal problem causing patient suffering, consuming significant health resources, and costing large amounts of funds. Although there are many possible reasons, mechanical derangement has been considered as one of the most important causes. Several studies have documented the changes in the spinal column kinematics and the spinal muscle responses of CSP patients. For example, in comparison to the controls, the low back pain patients have more erratic and widely dispersed centers of rotation, greater out-of-sagittal plane torques during flexion/extension, muscle spasm, longer muscle reaction times to external events, greater muscle co-contractions while moving through the neutral posture, and antagonistic spinal muscle activity even when the external challenge to spinal stability has been removed. The whiplash patients have been described as trapped in the neutral zone. The basic understanding of these *in vivo* observations is not clear. Subfailure or incomplete injury of the soft tissues may be the initial event in the development of CSP. The purpose of this presentation is to examine a hypothesis which attempts to relate the diverse patient observations to the subfailure injuries, within the context of the spinal stabilizing system.

HYPOTHESIS

The spinal stabilizing system can be thought of as consisting of three subsystems: spinal column, spinal muscles, and the neural control unit. The spinal column is the multi-body mechanical structure to be stabilized (Panjabi 1992). The orchestration of the spinal muscle tensions and timings to achieve the needed multi-directional dynamic stability of the spinal column is the function of the control unit. The injury to the spinal column may affect both the mechanical properties of the spinal column and the proprioception received by the control unit. The former directly affects the stability of the spinal column, while the latter affects the muscle function, and, therefore, the spinal stability to even a greater extent. The proprioception obtained from the built-in transducers within the various soft tissues of the spinal column describes the spinal loads and motions, and thus, the dynamic stability. When a subfailure injury to one or more of the soft tissues occurs, the consequences depend upon the injury severity. If the injury is less severe (i.e. little change in mechanical properties), then it may corrupt the proprioception only, while a more severe injury, additionally, may cause changes in the mechanical properties. In the case of a more severe injury, with decreased stiffness and faulty proprioception, the control unit may mobilize muscles maximally by increasing, in general, all muscle tensions all the time, leading to muscle spasm. However, with the faulty proprioception alone, the task for the control unit is more complex, and therefore, the results more varied. An example is the whiplash patients who moved with in the neutral zone like the healthy, but did not move beyond it. With finite number of pre-programmed responses, which are designed for the healthy spine, the control unit may not be able to orchestrate efficiently the multitude of the spinal muscles. The control unit may take a little longer to activate the muscles, and it may do so erratically. It is possible, that over time a more severe injury may convert itself into a less severe injury due to ligament healing, osteophyte formation and other stabilizing changes of the spinal column. Thus, the less severe injury, and the faulty proprioception it generates, may be an important cause of CSP patients.

DISCUSSION

The hypothesis presented attempts to examine the consequences of the soft tissue injury to the spinal column, and subsequent muscle dysfunction within the context of the spinal stabilizing system. Many low back pain and neck pain problems involve trauma - multiple micro traumas or a single trauma. Seen biomechanically, trauma results in tissue injury. As the spinal soft tissues not only provide stiffness and strength to the spinal column, but also proprioception to the neuromuscular control system, it is reasonable to assume that the subfailure soft tissue injury may affect the proprioception as well as the mechanical properties of the functional spinal unit. As the built in responses of the control unit are designed for the healthy spine, the control unit is not likely to function efficiently if the proprioception is faulty. This may result in various types of muscle dysfunctions which have been observed in patients. If this hypothesis can be validated by carefully performed experiments, then it may be possible to improve the diagnosis and treatment of CSP patients whose precipitating event was a soft tissue injury. This could be accomplished by re-programming the control unit by appropriate training or other means to come in synch with the altered spinal column structure and function.

REFERENCES

Panjabi MM. *J Spinal Disord* 5 (4) : 383-389, 1992.

MODELS OF NEUROMUSCULAR DISORDERS IN THE SPINE

M. Solomonow
Occupational Medicine Research Center
Louisiana State University Health Sciences Center
New Orleans, Louisiana 70112 USA — msolom@lsuhsc.edu

INTRODUCTION

The spine, a complex multi-joined structure, functions as a closed loop control system similar to the extremity joints (Solomonow, 1984, Panjabi, 1991). While many productive models describe the forward components of the spine functions and structures, (Marras, 1997, McGill, 1986), very little is known of the feedback functions, and this is the objective of this paper.

The literature points out that mechanoreceptors are located in the lumbar ligaments, discs and capsules (Yahia, 1991), and that a reflex activation of the multifidus and longissimus muscles is elicited upon stimulation of these structures (Indahl, 1995, 1997, Stubbs, 1998, Solomonow, 1998). It is of interest to describe the behavior of these feedback structures and to assess their role in low back disorders.

METHODS

An in-vivo anaesthetized feline preparation was used. Intramuscular EMG wire electrodes were inserted in the L-1/2 to L-6/7 multifidus (feline has 7 lumbars) in a bipolar configuration. The lumbar spine was loaded into moderate flexion via the L-4/5 supraspinous ligament using a MTS Bionix 858 in two conditions; displacement control and load control. Two paradigms were used to simulate repetitive and static flexion: a sinusoidal increase/decrease in force or displacement and a sustained step force or displacement of a given magnitude. The EMG, creep or tension - relaxation were measured simultaneously and stored in a computer for analysis. The loading of the spine was applied over a 20-minutes period followed by 7 - 8 hours of rest. During rest a brief 10-second tests were applied every hour to assess recovery of the muscles, ligaments, discs and capsule.

Models consisted of exponential functions, as it is the classical description of viscoelastic structures behavior. The models were applied to the mean ± SD of the EMG, creep and displacement from a group of preparations tested in the same condition. A Marquardt-Levenberg non-linear regression was performed to determine the best fit model to the data.

RESULTS AND DISCUSSION

The analysis shows that under displacement control, the tension - relaxation and EMG are described with a bi-exponential models accounting for the large difference in the proportion of elasticity and viscosity between the ligaments and the discs. The general equations are given by:

For loading: $NIEMG_{(t)} = Ae^{-at} + Be^{-bt} + R$

For rest: $NIEMG_{(t)} = C(1-e^{-cT}) + D(1-e^{-d\,(t-T)}) + R$

The equations describe the biexponential decrease in EMG to 5% of its initial value due to the tension-relaxation during loading. Conversely, a biexponential rise in EMG is described with rest, as the ligaments recover to their resting length and the fluids slowly returns to the disc's interior.

Under load control, a completely different response was obtained. The best fit models predict a single exponential decrease in EMG during the loading and a single exponential increase during rest. The model, however, also includes description of an initial hyperexcitability in the first hour and a delayed hyperexcitability peaking 6-9 hours after rest initiation. Spasms were always observed under static load control but could not be described due to their unpredictable nature. Therefore, for load control the model is:

$NIEMG_{(t)} = Ae^{-at} + R$ during loading and

$NIEMG_{(t)} = C(1-e^{-cT}) + tFe^{-ft} + (t - T)\,De^{-d\,(t-T)}$
during rest.

CONCLUSION

Static flexion of the lumbar spine seems to elicit a complex transient neuromuscular disorder that may last up to several days. The disorder consists of four components: An exponential decrease in muscle activity during flexion, spasms superimposed on the decreasing EMG, initial hyperexcitability and a delayed hyperexcitability during rest. It seems that static flexion inflicts micro-damage on the collagen structure of the viscoelastic tissues which result in spasms and initial hyperexcitability and probably pain. The inflammatory response to the micro-damage require several hours to develop and the associated pain and stiffness are observed in the "morning after" and last more than 24-hours.

REFERENCES

Solomonow, M., *IEEE-TBME*, 31:752, 1984.
Panjabi, M., *J. Spin. Disord*., 5:383, 1992
Marras, W., *J. EMG & Kin*., 7:259, 1997.
McGill, S., *Spine*, 11:666, 1986.
Yahia, L., *Pathol,* 187:936, 1991.
Indahl, A., *Spine*, 20:2652, 1995.
Stubbs, M., *J. EMG & Kin*., 8:197, 1998.
Solomonow, M., *Spine*, 23:2552, 1998.

NUTRITION OF THE INTERVERTEBRAL DISC; EFFECTS OF PATHOLOGICAL CHANGES

Deborah A. Jones, Susan R.S. Bibby, Robert B. Lee, Saj Razaq, C. Peter Winlove[2] and Jill P.G. Urban

Laboratory of Physiology, Oxford University, Parks Road, Oxford OX1 3PT, UK., jocelyn.urban@physiol.ox.ac.uk
[2]School of Physics, Exeter University, UK.

INTRODUCTION

The disc is the largest avascular tissue in the body with cells in the centre of an adult lumbar disc 6-8 mm from the nearest blood supply. In order to function and remain viable, the cells require an adequate nutrient supply, and an efficient means of removing products of metabolism such as lactate. Nutrients reach the nucleus cells by diffusing from blood vessels of the vertebral body through the cartilage endplate into the disc matrix. Even in a normal healthy disc, oxygen levels in the centre of the nucleus are low as the cells use oxygen even though metabolism is mainly anaerobic. Lactate is produced at high rates and accumulates away from the blood supply leading to a fall in tissue pH. Failure of nutrient transport and the consequent further fall in pO2 and increase in lactate level could affect cellular activity and may thus be one route to disc degeneration. Here we describe measurements of nutrient supply to human discs in vivo, and the effect of fall in nutrient concentrations on cellular metabolism.

METHODS

In vivo transport and concentrations of small solutes was measured electrochemically as described previously (1, 2). Briefly, a silver needle microelectrode was inserted into the disc during routine anterior spinal surgery with the reference Ag/AgCl electrode attached to adjacent muscle. The electrodes were driven by a computer-controlled potentiostat. Currents were measured at 0.6v and -1.3v w.r.t to Ag/AgCl and converted to concentrations of N_2O and O_2 using calibration curves measured in bovine discs in vitro. Calculated versus expected N_2O concentrations provided a measure of transport inhibition.

For measurement of the effects of metabolites on cellular activity, discs were obtained from steer (18-24 months old) tails within 24hrs of slaughter, cells extracted, embedded in alginate and cultured under 5% CO_2 in air, at pH7.4 for 48 hours. The effect of varying pO_2 and pH on cellular energy metabolism (lactate measured using a Yellow-Springs analyser, ATP by a standard luciferin-luciferase assay) and matrix turnover (S^{35}-incorporation, MMP activity by zymography and fluorescence assays) was then examined.

RESULTS AND DISCUSSION

The measurement of N_2O concentrations in the disc of patients with scoliosis (22 discs) shows that transport into these discs is inhibited, possibly by calcification of the cartilaginous endplate. Since pressure profiles in scoliosis are also abnormal (3), the blood supply to the scoliotic discs may also be affected adversely and contribute to the fall in nutrient supply to these discs. Both transport and oxygen concentration and as well as cell density were lowest and lactate concentrations greatest at the curve apex suggesting nutritional failure was involved in cell death (4).

In studies of cellular behaviour in vitro, we found that both low oxygen and acid pH affected cell behaviour markedly. Matrix synthesis rates and cellular ATP concentrations fell steeply as the extracellular pH fell below pH6.8; at pH 6.4 the rate of energy metabolism had fallen by 60% and that of sulphate incorporation by 90%. A fall in pO_2 similarly inhibited cellular activity, with both energy metabolism and rates of matrix synthesis falling steeply in a concentration-dependent manner, once pO2 fell below 5% O_2. In contrast to the fall in matrix synthesis, MMP activity under these conditions, decreased only marginally.

The results show that in some pathological conditions, nutrient supply to the disc is diminished. In these discs, regions with the lowest nutrient supply have the lowest oxygen concentration and highest concentration of lactate, confirming that metabolite concentrations in vivo are affected by a fall in supply. In vitro evidence demonstrates that cells are very sensitive to the extracellular nutrient concentrations. Thus with loss of nutrient supply and consequent changes in extracellular concentrations of lactic acid and oxygen, cells are unable to maintain normal activity.

SUMMARY

The results of these test indicate that loss of nutrient supply will lead to a fall in matrix synthesis but not in MMP activity; matrix composition will no longer be maintained and the disc will eventually degenerate.

REFERENCES

1. Bartels EM et al (1998). *Spine* **23**:1-8.
2. Urban MR et al (2001). *Spine* **26**:984-90.
3. Meir A et al (2001). SPBR meeting, Bristol.
4. Horner HA, Urban JPG. (2001). *Spine* **26**:2543-9.

ACKNOWLEDGEMENTS

This work was supported by the EPSRC and the ARC (U0511;U0508).

THE STRUCTURE AND FUNCTIONS OF ELASTIC FIBRES IN BOVINE INTERVERTEBRAL DISC

J. Yu[1], Sally Roberts[2], Jill P.G. Urban[1] and C. Peter Winlove[3]

[1]Laboratory of Physiology, Oxford University, Parks Road, Oxford OX1 3PT, UK.
[2]RJAH Orthopaedic Hospital, Oswestry, UK.
[3]School of Physics, Exeter University, UK., C.P.Winlove@exeter.ac.uk

INTRODUCTION

Water movement in the intervertebral disc is important both as a determinant of the mechanical properties of the tissue and in the context of the convective movement of solutes. The role of proteoglycans in determining the hydraulic permeability of the extracellular matrix and in generating an osmotic (swelling) pressure and that of collagen in supporting tensile loads and determining stress and strain gradients in the matrix have been extensively discussed for the disc and other load-bearing tissues. Several authors report that the disc contains elastic tissue (1-3), but its potential functions have not been considered. We hypothesise that the elastic tissue is important for the recovery of the tissue after loading either because it itself forms an extensive network or because it links the essentially inextensible collagen fibres. Such roles would regulate tissue swelling pressure and thus influence fluid movement under osmotic and pressure gradients. As an initial step in determining its role in the disc, we have quantified the amount of elastic tissue, undertaken a microscopic examination of its organisation and partially characterised its biochemical composition .

METHODS

Discs were obtained from steer (18-24 months) or calf (12 days) tails. Elastic tissue was quantified as the insoluble residue remaining after autoclaving for 1 hr and then digested in 0.1 N NaOH at 98^{o}C (4). Elastic fibre organisation, was determined in 30µm sections of snap-frozen tissue utilising orcein staining or immunostaining (rabbit anti-human α-elastin, Biogenesis). Amino-acid analyses were performed on the alkali digests and on the residues remaining after CNBr digestion (4). Selected residues and histological sections were examined by Raman microspectrometry.

RESULTS AND DISCUSSION

The alkali resistant residue and the residue after cyanogen bromide digestion of 18-24 month steer discs comprised 0.39+0.07%(n=10) and 2.45+0.38% (n=5) of the dry weight of the annulus respectively and appeared to increase with age.

Orcein and immunostaining revealed a similar pattern of fibres in the tissue sections. In the centre of the nucleus, long (>100mm), thin and straight fibrils appear to radiate from the centre. At the boundary between nucleus and annulus the orientation changes to form a lattice pattern. In the annulus fibres are densely packed in the region between the lamellae and also form bridges between the lamella. Elastic fibres, parallel to the collagen fibres are also visible within the lamellae. At the bone-disc interface the fibres penetrate the cartilaginous end plate and terminate there.

The amino acid composition of the alkali residue contained less valine than elastin. The Raman spectra contained some unidentified peaks not found in arterial elastin. The fibres seen are thus predominantly formed of elastin but the residue remaining after alkali digestion is still contaminated with other polypeptides that require characterisation.

These results show that the disc has an extensive and organised elastic fibre network. Although we found that elastin comprises a relatively small percentage of the total dry weight, our extraction procedures possibly underestimate the amount present. With respect both to the geometry of the disc and to collagen fibres the organisation of the elastin network suggests that it has a mechanical role even in the nucleus. In the annulus, where the fibres are concentrated between lamellae, we suggest that they allow relative movement and elastic recovery of collagen fibres. However, further work on the nature of the association between the two proteins is necessary to provide insights into this interaction.

SUMMARY

The presence of an elastic component in the disc matrix would influence both tissue swelling pressure and the time-dependent deformations under load and could affect fluid and macromolecule movements through the tissues. The possible role of elastin in this regard should be considered in future modelling or experimental studies on transport in the disc.

REFERENCES

1. Johnson, E.F. et al. (1984). *Acta Anat*, **118**:238-242.
2. Mikawa, Y. et al. (1986). *Arch Orthop Trauma Surg*, **105**:343-349.
3. Olczyk, K. et al. (1994). *Folia Histochemica Et Cytobiologica*, **32**:41-44.
4. Soskel N. et al. (1987). *Methods in Enzymology*, **144**:196-214.

ACKNOWLEDGEMENTS

This work was supported by the Wellcome Trust.

OCCLUSION OF VERTEBRAL ENDPLATE OPENINGS: A MECHANISM FOR INTERVERTEBRAL DISC DEGENERATION?

Lorin M. Benneker, Suzanne E. Anderson [1], Paul F. Heini [2], Mauro Alini, and Keita Ito

AO Research Institute, Davos, Switzerland
[1]Department of Radiology, University of Berne, Inselspital, Berne, Switzerland
[2]Department of Orthopaedic Surgery, University of Berne, Inselspital, Berne, Switzerland

INTRODUCTION

Much remains unknown about the etiology and pathogenesis of intervertebral disc degeneration. The nearest source of perfusion to the avascular disc, is the outer annulus and the capillary buds in the marrow contact channel (MCC) openings of the osseous endplate. With disease and age, calcification of the overlying cartilaginous endplates have been observed (Bernick & Cailliet), and it has been suggested that insufficient nutritional supply may contribute to disc degeneration (Nachemson et al). In this study, the relationship of endplate openings to disc degeneration is explored.

METHODS

39 human lumbar discs from 8 cadavers (19-86 years-old) were collected, and fresh MR images were graded. Discs were sectioned and graded according to morphological appearance (Thompson et al). Samples of nuclear and annular regions were evaluated for: water, proteoglycan (PG), total collagen, collagen-II contents, and % denatured collagen-II (Antoniou et al). After digestion with papain, endplates disc surfaces were sputter coated with Au/Pa, and imaged with backlighting. The caliber and distribution of endplate MCC openings for each disc were measured with image analysis software. Correlation between opening parameters and disc degeneration was analyzed using general linear regression models with backward elimination (10% sig. level) to identify opening size ranges of most significance.

RESULTS AND DISCUSSION

To date, only the nuclear endplate region has been analyzed. Density of all openings (# openings/endplate surface area) significantly correlated (R=0.502, p=0.001) to morphological degeneration grade (Fig. 1), and those with 20-50 µm equivalent diameter correlated most significantly (R=-0.575, p<0.001), accounting for 95% of the variability. Although the density of these openings also significantly correlated to age, it was not as strong. There was no significant correlation of % area of openings (cumulative opening area/ endplate area) to either degeneration grade or age. T2-intensity score also did not correlate to opening density. In contrast, 20-50 µm opening density significantly correlated to nuclear PG content (R=0.628, p<0.001). However all other biochemical parameters did not correlate to opening density.

Indirect correlation between 20-50 µm opening density and morphologic degeneration grade is particularly of interest as this size of opening has been shown to house capillary buds (Oki et al). Correlation to age was not as strong because of a degenerated younger spine specimen, but this illustrates that opening occlusion was not simply dependent on age. Also the % area of opening did not correlate to age or disc degeneration because of the increase in larger openings with degeneration.

Lack of correlation to T2-intensity loss may have been due to poor resolution of the scoring (3 levels), and quantitative MRI is recommended. Although correlation of biochemical degeneration descriptors to opening density was ambiguous, a strong indicator of degeneration, PG content, did correlate.

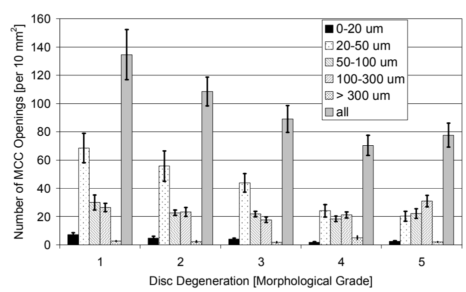

Figure 1: Endplate opening density and disc degen. grade.

SUMMARY

The results of this study support the hypothesis that occlusion of MCC opening in the vertebral endplates may deprive the cells of nutrients, leading to insufficient maintenance of the extracellular matrix and disc degeneration. However evidence of more causal relationships would be helpful to understand this mechanism.

REFERENCES

Bernick S. and Cailliet R. (1982). *Spine*, **7**:97-102. .
Nachemson A. et al. (1970). *Acta Orthop Scand*, **41**:589-607.
Thompson J.P. et al. (1990). *Spine*, **15**:411-5.
Antoniou J. et al. (1996). *J Clin Invest*, **98**:996-1003.
Oki S. et al. (1994). *J Orthop Res*, **12**:447-9.

ACKNOWLEDGEMENTS

Supported in part by the AO Foundation, Switzerland.

INTERVERTEBRAL DISC METABOLISM UNDER MECHANICAL LOAD: THE ROLE OF EXTRACELLULAR PHYSICAL FACTORS

Hirokazu Ishihara, Gen-Zhe Liu, Tadashi Handa, Hiroshi Ohshima and Jill P.G. Urban*

Department of Orthopaedic Surgery, Toyama Medical and Pharmaceutical University, Toyama, Japan, hirokazu@ms.toyama-mpu.ac.jp
*Physiology Laboratory, Oxford University, Oxford, United Kingdom

INTRODUCTION

There is general agreement that mechanical load can contribute to the development of intervertebral disc degeneration. However, the fundamental mechanism of disc degeneration in relation to changes in mechanical load is not known. Many studies indicate that mechanical load has an important influence on matrix synthesis. Mechanical load alters the extracellular physical environment of the disc matrix in a complex fashion. When load is applied to the disc, the tissue deforms, leading to a rise in hydrostatic pressure. If the load is removed immediately, the disc returns to its original conformation and pressure. If the load is maintained for any length of time, fluid is expressed and leads to a change in ionic composition and hence to a rise in osmotic pressure. Because matrix synthesis is influenced by loading, the cells in the disc are responding to some or all of these matrix changes, but their relative contributions are unknown. This study clarifies the effect of extracellular physical factors on metabolism in the intervertebral disc.

METHODS

Bovine coccygeal and human lumbar discs were used. The specimens were divided into the nucleus pulposus, inner and outer annulus fibrosus and each region of the disc was incubated in a medium containing 35S-sulphate. Proteoglycan (PG) synthesis rate was determined by radioisotope incorporation. The production of matrix metalloproteinase-3 (MMP-3) and tissue inhibitor of metalloproteinases-1 (TIMP-1) were measured by a one-step enzyme immunoassay method using monoclonal antibodies. Hydrostatic pressure was applied by a water filled specially equipped pressure vessel. The fluid content was controlled by a small-pore dialysis tube and polyethylene glycol 20,000. Medium osmotic pressure and ionic composition were changed by adding sucrose or NaCl to the medium as required. Medium osmotic pressure was measured using a freezing-point osmometer.

RESULTS AND DISCUSSION

The effect of hydrostatic pressure on PG synthesis and MMP-3, TIMP-1 production: PG synthesis rate in the nucleus pulposus and inner annulus were highest at 3 atm pressure and decreased as pressure decreased (1 atm) or pressure increased (10, 30 atm). However, hydrostatic pressures had no apparent effect on PG synthesis rate in the outer annulus. In the nucleus pulposus, MMP-3 production was stimulated at a pressure of 30 atm relative to 3 atm. The TIMP-1 production showed highest values at 3 atm pressure in the inner annulus.

The effect of water content, Na concentration and osmotic pressure on PG synthesis: In the medium, the nucleus pulposus swelled markedly and PG leached from the matrix. When 10% polyethylene glycol was added to the medium, tissue hydration was held close to that of the fresh tissues and PG synthesis rates were more than 2.5 times greater than in the medium alone. When NaCl was added to the medium, PG synthesis rate in the nucleus pulposus increased as NaCl concentrations increased; the peak in rates was found when the NaCl concentration was 200 mM. Also, PG synthesis rates increased with increase in sucrose concentration, and reached a maximum at 150 mM. Rates fell steeply as concentrations were further increased. It can be seen that the peak rate for both NaCl and sucrose occurred at an estimated extracellular osmolality of 430 mosmol.

Hydrostatic pressure and osmotic pressure levels in the disc have been found to vary with posture and activity, being lowest when lying down (3 atm, 440 mosmol) and highest when carrying weights (20-30 atm, osmotic pressure was not measured but higher than lying down). The disc slices incubated in the medium under atmospheric pressure swelled considerably and osmotic pressure was decreased (1 atm, 325 mosmol). This study clearly show that a change in extracellular hydrostatic pressure and osmotic pressure, such as might occur physiologically during daily activity, had a marked effect on matrix synthesis and breakdown.

SUMMARY

Physiological hydrostatic and osmotic pressures appear to be essential signals for maintaining the disc matrix. Pressures that are too high or too low may have catabolic effects with reduction of PG synthesis and increase of MMP production, eventually leading to PG loss and disc degeneration.

REFERENCES

Ishihara H, et al. (1996). *J Appl Physiol* **80**:839-846.
Ishihara H, et al. (1997). *Am J Physiol* **272**: C1499-C1506.
Handa T, et al. (1997). *Spine* **22**: 1085-1091.

CONVECTIVE MOLECULAR TRANSPORT IN THE INTERVERTEBRAL DISC

Stephen J. Ferguson[1], Keita Ito[2], Lutz-Peter Nolte[1]

[1] M.E. Müller Institute for Biomechanics, University of Bern, Bern, Switzerland, stephen.ferguson@memot.unibe.ch
[2] AO Research Institute, Davos, Switzerland

INTRODUCTION

The intervertebral disc is the largest avascular structure in the body, with cells in the centre of the adult disc lying as far as 8 mm from the nearest blood supply [Katz et al]. It has been suggested that a deficiency in the nutrient supply to the disc may be a contributing factor in disc degeneration [Nachemson et al]. Previous studies have demonstrated that for small molecules diffusive transport alone likely fulfils the nutritional needs of disc cells [Holm et al, Roberts et al, Urban et al]. However, it has been often proposed that fluid flow into and within the disc may enhance the transport of larger molecules [Urban et al, MacMillan et al]. A substantial volume of fluid is expressed from the disc during daily loading [MacMillan et al], which is subsequently reimbibed overnight during rest, driven by osmotic potential. With aging, changes to disc and endplate permeability [Roberts et al] likely alter the magnitude of fluid exchange in the disc, which may have implications for disc metabolism if convection contributes substantially to molecular transport. The goal of this study was to predict the influence of this load-induced interstitial fluid flow on mass transport within the intervertebral disc.

METHODS

An iterative procedure was used to predict the convective transport of molecules of physiologically relevant size within the disc. An axisymmetric finite-element poroelastic model of the disc was developed, with unique material properties for the nucleus, annulus ground substance, annulus fibres, cartilaginous endplates and bone. The diurnal loading cycle (16 hours compression, 8 hours unloaded) was discretised into fixed time steps. At each time step, the fluid flow within the disc due to compression or swelling was calculated. The overall response of the poroelastic model was validated against in vitro creep / swelling data for isolated discs.

A separate diffusion / convection model was used to calculate the influence of the fluid velocities on solute transport, with a constant concentration of solute being provided at the vascularised regions of the endplates and outer annulus. Local fluid velocities calculated by the poroelastic model were transferred to the corresponding nodal points of the mass transport model. Loading was simulated for several diurnal cycles, and the relative convective and diffusive transport was compared for solutes with molecular weights ranging from 400 Da to 40 kDa, with diffusion coefficients based on in vitro measurements of solute transport through cartilaginous tissues [Quinn et al].

RESULTS AND DISCUSSION

Due to the strain-dependent permeability of intervertebral disc tissue, fluid re-imbibition during unloaded periods occurs much more rapidly than fluid expression under compressive loading. Fluid velocities are greatest immediately following load application or removal, with fluid exchange to and from the disc occurring predominantly across the permeable endplate, rather than across the annulus boundary.

Fluid velocities of the magnitude generated by daily loading did not enhance the transport of small solutes. Fluid flow within the intervertebral disc did enhance molecular transport for large molecules. During swelling, interstitial fluid flow increased the unidirectional penetration of 40 kDa solutes by approximately 100%. Due to the biphasic nature of disc loading, however, fluid expression during compressive loading reverses the direction of convective transport and opposes the diffusive transport resulting from concentration gradients. The net effect of convective transport for large solutes over a full diurnal cycle was therefore more limited, with a 30% increase in solute penetration compared to diffusion only.

The net fluid exchange over one entire diurnal loading cycle has only a modest influence on the transport of large molecular-weight solutes. However, convective transport during swelling is substantial. Furthermore, due to the non-linear response of the disc during compression and swelling, convective transport advances the solute quickly at the beginning of swelling, whereas convective transport of solutes occurs more gradually during loaded periods. Further study is required to determine the significance of large solutes and the timing of their delivery for intervertebral disc nutrition and the regulation of cellular processes.

REFERENCES

Katz, M.M. et al. (1986). *Clin. Orthop.*, **210**:243-5.
Nachemson, A. et al. (1970). *Acta Orthop. Scand.*, **41**:589-607.
Holm, S. et al. (1981). *Connect Tissue Res.,* **8**:101-9.
Roberts, S. et al. (1996). *Spine,* **21**:415-20.
Urban, J.P. et al. (1982). *Clin Orthop* **170**:296-302.
McMillan, D.W. et al. (1996). *Ann. Rheum. Dis.* **55**:880-7
Quinn, T.M. et al. (2001). *J. Biomech.* **34**:1463-9

DETERMINANTS OF LUMBAR DISC DEGENERATION AND LINKS WITH BACK SYMPTOMS

Michele C. Battié

Faculty of Rehabilitation Medicine, University of Alberta, Alberta, Canada

INTRODUCTION

Disc degeneration is commonly attributed to the accumulation of environmental effects, primarily mechanical insults and injuries, imposed on "normal" aging changes. Yet, the activities and agents that accelerate degeneration remain largely speculative. Among the factors most commonly suspected of accelerating degenerative changes in the discs are various physical loading conditions, such as heavy occupational materials handling, postural loading, and vehicular whole-body vibration. Numerous studies have examined the relationship between these factors and disc degeneration. However, most have been plagued by methodological constraints, including inadequate control of possible confounding factors, and have resulted in mixed findings related to the presence and degree of association with disc degeneration. Until recently, detailed studies focusing on hereditary aspects of disc degeneration and rupture have been lacking. My research group's goal has been to determine the roles of constitutional, behavioral and environmental factors in the development of lumbar disc degeneration, including the examination of gene-environment interactions, using study designs that allow for a high degree of control of extraneous factors. We have investigated the role of specific degenerative findings in back symptoms, as well.

SUBJECTS AND METHODS

We conducted a series of studies investigating the influences of commonly suspected risk factors on disc degeneration and back symptoms using monozygotic (MZ) twins highly discordant for the factor of interest, who were selected from the population-based Finnish Twin Cohort. Exposures were verified and data on potentially confounding factors were gathered in an extensive structured interview. Disc degeneration was assessed both quantitatively and qualitatively from MR imaging using a 1.5 Tesla scanner. The data from these studies were aggregated to allow multivariable analysis to examine the relative effects of lifetime exposures and familial aggregation on disc degeneration. Familial aggregation represents the effects of genetic and other shared family influences (e.g., shared childhood environment). DNA analysis using a candidate gene approach also was conducted in search of genotypes associated with disc degeneration. The association between specific degenerative findings and back pain history was investigated, controlling for age and physical loading.

RESULTS AND DISCUSSION

Our findings indicate that while physical loading involving materials handling, bending, and twisting appear to influence disc degeneration, the effect size is very modest, which would help explain the inconsistent results of previous studies of occupational loading. Our investigation of MZ twins, highly discordant for lifetime occupational driving, did not demonstrate any significant differences between siblings in MRI findings of the lumbar discs, including quantitative measures of adjusted signal intensity, which should be highly sensitive for disc degeneration.

Conversely, we found disc degeneration could be explained to a great degree by familial aggregation, the combined effects of genetic and shared early environmental influences. In the multivariable analysis of the T12-L4 region, 61% of the variability was explained by familial aggregation, beyond that of age and occupational physical loading that together explained 16%. In the L4-S1 discs, physical loading and age explained 11%, which rose to 43% once familial aggregation was added to the model. Fifty-seven percent (57%) remained unexplained in the lower lumbar region. It will be important to disentangle the effects of genetic influences from those of shared childhood environments, which comprise familial aggregation, since genetic, childhood and work environmental exposures have very different implications for future research directions and prevention strategies.

Although our findings suggest that physical loading and other suspected environmental risk factors experienced in adulthood have modest effects on disc degeneration, it is possible that certain gene-environment interactions could have major importance. Our identification of two gene polymorphisms associated with disc degeneration, TaqI and FokI, each explained 6.5% of the variability in nuclear signal intensity, as well as subsequent discoveries of others, allows for the investigation of specific gene-environment interactions. The degenerative findings of outer annular tears and disc height narrowing are of particular interest because of their consistent pattern of associations with history of back-related symptoms in the study subjects.

SUMMARY

Intervertebral disc degeneration and failure and their sequelae lead the list of suspected culprits underlying back-related symptoms. The development of rational interventions is directed by knowledge of causal factors, the magnitude of their effects and possible interactions. Our study findings suggest that disc degeneration may be explained primarily by genetic influences, childhood environments and as yet unidentified factors, which may include complex interactions. Specific environmental exposures suspected of accelerating disc degeneration appear to have a more modest effect than previously believed.

EVIDENCE FOR DIFFERENCES IN MATRIX TURNOVER IN THE DEVELOPING AND DEGENERATING HUMAN LUMBAR INTERVERTEBRAL DISC

J. Antoniou[1], N. Goudsouzian[1], T. F. Heathfield[2], T. Steffen[1], A. Zahid[1], F. Nelson[2], A.Hollander[2], A.R. Poole[2], M. Aebi[1].
[1]Orthopaedic Research Laboratory and [2]Joint Diseases Laboratory, McGill University
687 Pine ave. West, Montreal, Quebec Canada, H3A 1A1.

INTRODUCTION

Degenerative disc disease, viewed by most as an inevitable consequence of aging, is believed to begin as early as the second decade of life[1]. Despite its prevalence, there is no clear distinction between what truly represents disc degeneration and normal maturation. The purpose of this study was to analyze how changes in matrix composition and matrix turnover (synthesis and degradation) varies with aging and degeneration in the human lumbar intervertebral disc. For this, we used available antibodies that recognize epitopes present either on newly synthesized proteoglycan and collagens, or epitopes exposed once type II collagen loses its triple helical configuration following cleavage by proteolytic enzymes.

MATERIALS AND METHODS

Twenty five whole lumbar spine specimens were harvested from fresh cadavers (within 18 hours of death). A total of 125 lumbar intervertebral discs were examined (five per spine). The age distribution ranged from 12 weeks up to 79 years of age (mean of 29 years). The lumbar spines (T12 to S1) were retrieved, and each segment was separated by sawing through the vertebral bodies. A 7mm thick midline sagittal slab was cut, and it was then separated into 2.5mm sections from the various defined regions of the disc (i.e., anterior annulus, anterior intermediate zone, nucleus pulposus, posterior intermediate zone, and posterior annulus). These were further cut into equally sized (2mmx4mmx7mm) sections through the use of a fine cutting block (approximately 50 mg each). Representative samples were extracted with 4 M guanidinium chloride for quantitation by immunoassay of 846 epitopes[3] (a chondroitin sulfate epitope present on newly synthesized cartilage proteoglycan aggrecan molecules, and hence a putative maker of synthesis) and of C-propeptide of type II collagen (CPII, a marker of newly synthesized type II procollagen). In addition, the content of the C-propeptide of type I collagen (CPI, reflecting type I procollagen synthesis) was also measured on the same extracts (ELISA assay kit, Metra). Adjacent tissue blocks underwent alpha-chymotrypsin and proteinase K treatment to quantitate type II collagen percent denaturation[2]. The third representative samples from each zone was dried at 110 C for 4 days to obtain the dry weight.

RESULTS

The results showed that the discs' synthetic ability, measured by the presence of the 846 epitope, the CPI and CPII contents, was at its highest in the neonatal (0-2 years) and in the juvenile groups (up to 15 years). Thereafter, the 846 epitopes and the CPII contents markedly diminished with increased age. The CPI profile showed a more dramatic drop being at its lowest content already in the 15-40 years age group. Thereafter, it remained constant, except in the oldest age-group (60-80) or in high grade disc, where a significant increase was observed.

The percent of denatured type II collagen increased two fold when comparing the neonatal discs (0-2 age-group) to the young age-group (2-15 years old). Then, similar to the disc synthetic activity, it also rapidly decreased. However, in the oldest age-group (60-80), and in highly degenerated discs (Thompson gross morphology grade), the percent of denatured type II collage was increased two fold.

DISCUSSION

This study examines the biosynthesis of type I and II procollagens, and the proteoglycans aggrecan (synthetic ability) in relationship to the denaturation of type II collagen (degradative processes) in the human lumbar intervertebral disc, with respect to growth, aging, and degeneration. The results suggest the presence of three distinct phases of matrix turn-over. Phase I is characterized by high synthetic activity of aggrecan and collagen I and II, associated with elevated levels of type II collagen denaturation, which are independent of disc degeneration (**growth phase**). Phase II features a drop in general synthetic activity along with a reduction in denatured type II collagen (**aging and maturation phase**). Phase III shows a grade dependent increase in collagen type II denaturation together with an increase in type I collagen synthesis, but not that of type II or aggrecan (**degeneration and fibrotic phase**). This identification of clearly recognizable changes in matrix turnover during growth, maturation and aging, and degeneration provide us with valuable new insight into disc pathology. This is an essential prerequisite for the identification of specific treatment modalities that may prevent or help contain excessive disc damage.

REFERENCES

1. Crock, H. V. (1991) The Adult Spine: principles and practice, J.W.Frymore, ed., Raven press Ltd. New York.
2. Hollander et al, (1994) J.Clin.Invest. 93:1722-32.
3. Rizkalla et al, (1992) J. Clin. Invest. 90:2268-77.

ACKNOWLEDGMENTS

This work was supported by a grant from the AO/ASIF and the CIHR.

DEVELOPMENT OF THE INTERVERTEBRAL DISK

Jim Ralphs

School of Biosciences, Cardiff University, Cardiff, Wales, U.K.
ralphs@cf.ac.uk

INTRODUCTION

The intervertebral disk, consisting of the outer fibrous annulus fibrosus and inner cartilaginous nucleus pulposus, has a complex developmental origin. The initial pattern of disk-vertebral body-disk along the spine is set up in association with a cascade of expression of genes involved in embryonic axial pattern formation, notably PAX genes, which ensure that sclerotomally derived connective tissue precursors arrive in the right places and form the correct structures. This results in the fundamental pattern of the early spine: repeated longitudinal arrangements of loosely arranged mesenchymal cells, which will form the vertebral bodies, and dense condensation of cells, which will form the intervertebral disks, with the notochord running centrally through both. From this point onwards, discs become organised and differentiate, at least in part under mechanical regulation. I will concentrate mostly on the annulus fibrosus, although it should be noted that behaviour of the notochord and nucleus pulposus is crucial to annulus development and its later maintenance.

EARLY DIFFERENTIATION.

Within the disk condensations there is little extracellular matrix (ECM) and a large amount of cell-cell contact. The cells deep in the condensation, close to the notochord, tend to be larger and rounder than the more peripheral ones. The first sign of overt disk differentiation is the swelling of the notochord in the centre of each disk condensation to form the early nucleus pulposus. The swelling seems to be generated by pressure from the differentiation of the cartilage of the vertebral bodies, and probably triggers differentiation in the surrounding disk condensation: at the same time the inner part of the annulus fibrosus becomes cartilaginous, and the outer part fibrous.

DEVELOPMENT OF THE ANNULUS FIBROSUS

There are two important aspects of the subsequent development of the annulus fibrosus: the nature of the ECM made by the cells, and the way in which it becomes organised to form its functional collagenous lamellae.

Matrix composition. The inner part of the annulus forms an ECM containing markers typical of cartilage – type II collagen and the proteoglycan aggrecan, whereas the outer part contains type I collagen and versican, typical of fibrous tissues. This correlates with the later composition of the adult annulus. The cartilaginous nature of the inner annulus is associated with load experienced – it receives a large compressive load from the nucleus pulposus as the spine is compressed vertically by gravity and muscle action. The outer annulus is subject to more tensile and torsional loads due to bending and twisting of the spine, and thus contains predominently tension-resisting extracellular matrix. The onset of this distribution in the embryo may also be associated with loading. The expansion of the nucleus pulposus must compress the annulus at its inside and could thus promote cartilaginous differentiation, whereas at the outer annulus, cells must also be stretched because of the increased dimensions, promoting fibrous differentiation.

Matrix organisation. The outer part of the annulus fibrosus consists of a series of collagenous lamellae; each one contains parallel bundles of collagen fibres spiralling from one vertebral body to the next. Successive layers have their collagen fibres arranged at an angle of 50-60^{o} to one another, forming a strong radial ply structure resisting pressure from the nucleus pulposus and tension and twisting from spinal movements. This structure arises at the earliest stages of disc diffentiation. In the short period in which the notochord expands to form the nucleus pulposus cells become organised in the outer annulus: cells become arranged into parallel sheets, with the long axis of the cells in successive sheets alternating in angle by 50-60 degrees as do the collagen fibres in the adult annuli; the cell layers then deposit the oriented collagenous layers. Thus matrix orientation is preceded by cellular organisation. Cellular organisation occurs within 12 hours (in rat development) and is associated with the cytoskeletal component actin – cells develop large longitudinal actin stress fibres as they elongate and orient – and actin associated cell-cell junctions (adherens junctions). The pattern of cell-cell junctions seems to be important in determining the cell layers and cell orientation within successive layers. There is evidence of direct involvement of the cytoskeleton in orientation of deposited ECM. Actin stress fibres are associated intracellularly with the fibronectin receptor alpha5 beta1 integrin, which links to fibronectin fibrils on the cell surface which can subsequently bind collagen. Thus in addition to orienting cell sheets, the cytoskeleton has the potential to organise the early ECM deposited by the cells. Once orientation is established and collagenous lamellae become prominent, the actin stress fibres disappear. In the rat annulus, the whole process from cell orientation and stress fibre formation, to matrix deposition and loss of stress fibres takes only 4 days. At this stage, we assume that cells orient to the deposited matrix, rather than having to generate their own orientation. Whilst the above is based on rat embryos, the same histological sequence of events occurs in human annulus development and the same cellular mechanisms of development are likely to apply.

ACKNOWLEDGMENTS

I am pleased to take this opportunity to acknowledge funding from the Arthritis and Rheumatism Council, UK, and the superb work produced by my former postgraduate student Dr Tony Hayes during the course of his PhD project.

THE INFLUENCE OF MECHANICAL FACTORS ON INTERVERTEBRAL DISC DEGENERATION

J.C. Lotz
Orthopaedic Bioengineering Laboratory, Department of Orthopaedic Surgery
University of California
533 Parnassus Ave., San Francisco, Ca 94143-0514

INTRODUCTION

Intervertebral disc degeneration is defined by morphologic, cellular, and biochemical changes that commonly cause joint dysfunction and pain. Given the diversity of known risk factors, and the variability in which they present in back pain patients, the etiology and natural history remain poorly understood. From an epidemiologic perspective, repetitive spinal loading (e.g. manual materials handling) has been linked to increased rates of back pain and disc degeneration. To explore mechanisms of causality, our laboratory has developed an *in vivo* model system in which dose-response relationships between spinal stress and disc degeneration can be examined while minimizing the influence of confounding factors.

MATERIALS AND METHODS

Two types of external loading device (one static, one dynamic) were used to apply compression to the 10th coccygeal disc of Swiss Webster mice. To facilitate disc loading, two 0.4 mm diameter stainless steel pins were inserted percutaneously through adjacent vertebrae in each mouse tail. The static device consisted of calibrated elastics that applied one of three compressive stresses (0.4, 0.8 or 1.3 MPa) for variable durations (3 hrs through 7 days). The second device (Figure 1) consists of a ring-shaped latex bladder placed on the distal side of the subject disc, plastic washers and a cylindrical covering with a backing.

Inflation of the latex rubber bladder imparts disc compression. When the bladder deflates, the force is removed. An electronically controlled pressure valve mounted outside the animal's cage allows control of the pressure magnitude, duration and frequency. A flexible tube and swivel bridging the pressure generator and bladder permits the mouse free range of motion.

Dynamic exposures are applied 6 hours per day for 7 days. Discs were loaded according to a square wave function, which alternated between applied stresses of 0 MPa and one of two peak stresses (0.8 MPa or 1.3 MPa) at one of two frequencies (0.01 Hz or 0.1 Hz). For the remaining 18 hours each day, no load was applied.

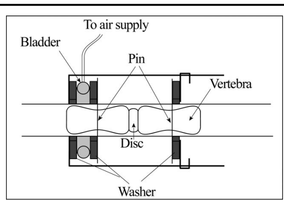

Figure 1. Dynamic loading device

Outcome measures include histology to assess disc morphology, biomechanical testing to examine structural performance, *in situ* hybridization and TUNEL assay to investigate cell function, biochemical and enzyme activity analyses to quantify matrix synthesis and degradation.

RESULTS

The results of these experiments clarify a number of dose-dependent cellular responses to spinal stress. These can be either anabolic or catabolic, depending on the specifics of the loading exposure. Importantly, the disc's viscoelastic nature leads to a complex pattern of tissue deformation. Correlation between temporal and spatial patterns of tissue deformation and cell function demonstrate that excessive tissue strain leads to cell death in both the nucleus and inner annulus. By contrast, intermediate dynamic deformations can lead to an anabolic response

Altered cell function, in turn, leads to changes in extracellular matrix and concomitant changes in biomechanical function. With excessive static compression or excessive dynamic stress, nuclear cell death leads to marked loss of disc height. At the same time, the inner annulus experiences loss of normal matrix architecture. Together, these architectural changes alter the disc's bending and compressive response leading to spinal instability.

Subsequent remodeling after load removal leads to an altered steady-state morphology that is characterized by loss of disc height, loss of distinction between the inner annulus and nucleus, and regions of fibrocartilage within the annulus fibrosus.

Dynamic loading experiments demonstrate effects of stress magnitude and frequency that are both anabolic (increased proteoglycan synthesis) and catabolic (increase cell death and enzyme activity). Interestingly, these were observed in the absence of any obvious structural damage.

DISCUSSION

This in vivo model system demonstrates that a number of morphologic features characteristic of aging and degeneration are induced by spinal stress. These occur in the absence of acute structural damage, which implies that disc remodeling is secondary to subtle load-induced changes in cell function that, over time, lead to altered tissue architecture and biomechanics. Which, if any, of these load-induced changes cause back pain remains unclear. Disc degeneration is common in asymptomatic humans, consequently, altered morphology by itself is an insensitive measure of disability. Future study is required to clarify mechanisms of discogenic pain and how these are linked to alterations in disc morphology and biomechanics.

ACKNOWLEDGMENTS

This work was supported by the NIH (AR44179).

BIOLOGICAL ASPECTS OF DISC DEGENERATION

Sally Roberts

J O'Brien Laboratory, Centre for Spinal Studies,
Robert Jones and Agnes Hunt Orthopaedic Hospital NHS Trust, Shropshire, SY10 7AG, UK.
s.roberts.keele.ac.uk

INTRODUCTION

Intervertebral discs degenerate relatively early in the life of most mammals (Miller et al 1988) and in humans this process is associated with back pain. Disc extracellular matrix, like other tissues, is produced by cells within it. These cells are at a very low density compared to other tissues, but they are still responsible, not only for producing matrix, but also for breaking it down. The study of disc matrix and cells in health and disease provides insight into the normal equilibrium and how this might be disrupted in disc degeneration.

METHODS

Histological techniques have been used to study cell proliferation and cell death, synthesis and degradation of matrix components, in addition to the organisation of that matrix. Biochemical analysis of collagen crosslinks have been used to demonstrate collagen turnover (Duance et al 1998). *In vivo* and *in vitro* systems have been used in other laboratories to monitor the cells and their biosynthetic responses to changes in loading or other environmental factors such as osmolality.

RESULTS AND DISCUSSION

Disc degeneration is characterised morphologically by changes to the fibrous architecture and increased vascularisation and innervation. Clusters of cells occur due to cell proliferation (Johnson et al 2001) but there is also increased cell death. There is evidence for the production of newly synthesised extracellular matrix components (Roberts et al 1994) which, together with cell proliferation, could represent an initial repair phase. The production of degradative enzymes is present to some extent in virtually all discs but increasingly with degeneration. These include enzymes capable of degrading collagen, the collagenases (MMPs1,8 and 13) and proteoglycans (aggrecanases and MMPs 1,2,3,7,8,9 and 13; Roberts et al 2000). The elevated levels of enzymes is likely to be responsible for the increased degraded extracellular matrix components seen in degenerate discs (Antoniou et al 1996). Many of these changes can be induced in cells *in vitro* by varying mechanical and other factors (Ishihara and Urban 1999).

Hence changes seen in degenerate discs from patients with back pain are likely to have happened via the disc cells responding to stimuli such as altered incident loading or diminished nutrient supply.

SUMMARY

Disc degeneration results from disruption of the normal homeostasis of disc cell metabolism. There appears to be an initial repair phase, when cells increase their proliferation and synthesis of extracellular matrix. This is followed by a further shift of equilibrium towards the degradative processes when degeneration supercedes synthesis. It is important to understand the cell processes involved in disc degeneration and the sequence of and extent to which they occur and identify at what stage they might be reversible. This is necessary, not only for the successful development of pharmacological therapies, but also for the new generation of cell-based treatments and biological repair.

REFERENCES

Antoniou J et al (1996). *J Clin Invest*,**98**,996-1003
Duance VC et al (1998). *Spine*,**23**,2545-2551
Johnson WEB et al (2001). *Conn Tiss Res*,**42**,197-207
Miller J et al (1988). *Spine*,**13**,173-178
Roberts et al (1994). *Histochem J*,**26**,402-411
Roberts S et al (2000). *Spine*,**25**,3005-13

ACKNOWLEDGEMENTS

We are grateful to the Arthritis Research Campaign, UK for financial support.

"FLEXIBLE" STABILIZATION OF THE SPINE - IS THIS THE FUTURE?

Thomas Nydegger

Biomechanical Analysis, Sulzer Orthopedics Ltd, Winterthur, Switzerland, Thomas.Nydegger@sulzermedica.com

OBJECTIVES OF "FLEXIBLE" IMPLANTS

For several decades the treatment of choice for degenerative spinal pathologies was the rigid fixation of the functional spinal units (FSU) to promote bony fusion. In recent years several alternative methods for dynamic stabilisation were suggested to restore and/or maintain the segmental motion to overcome certain disadvantages of fusion surgery. The main objectives for dynamic stabilisation of the spine are to eliminate donor-site morbidity, minimise stress on the adjacent segment, and to restore disc height and normal kinematics. Current concepts in the lumbar spine can be classified in three subgroups: partial disc replacement (i.e. nucleus replacement), total disc replacement and posterior dynamic stabilisation systems. The objectives of this presentation are to review current concepts, some pre-clinical data, and early clinical results with these techniques.

CURRENT CONCEPTS

Nucleus replacement: Two hydrogel concepts (Aquarelle™ Stryker Spine; PDN™ Raymedica) and a polycarbonate urethane (PCU) spiral (Newcleus™ Sulzer Medica) are currently under clinical investigation. The hydrogel concepts aim to restore disc height by swelling due to hydration, whereas the spiral implant has a selection of fixed heights.

Total disc replacement: The three different concepts for total disc replacement are composed of two metal plates with a polyethylene inlay (SB Charité III™, W. Link GmbH; Prodisc™, Spine Solutions Inc) or with a silicone elastomer core (Acroflex™, Depuy Acromed). They completely replace the inner part of the disc; usually parts of the annulus are preserved. The biomechanical properties of the instrumented segment rely on the remaining part of the annulus and on the preservation of the facet joints and ligaments.

Posterior dynamic stabilisation systems: Graf ligaments consist of bilateral pedicle screws laced by an elastic PE tension band. They aim to stabilise the FSU by applying compression to the posterior complex of the spine. Another posterior device attempts to achieve normal kinematics and disc height by repositioning degenerative segments into a neutral position, (DYNESYS™, Sulzer Medica). PCU spacers are inserted bilaterally between two pedicle screws to counteract compressive loads and PET cords are inserted through the core of the spacers and fixed in the screw heads to withstand tensile loads. This approach preserves the disc and facet joints and may unload these structures.

RESULTS AND DISCUSSION

Most of those devices have been under clinical investigation for several years and have shown promising short and midterm results [Blumenthal 2001, David 1999, Schwarzenbach 2000]. The ranges of indications of the different approaches are overlapping with each other and clearly also with current standard procedures. Nucleus replacement implants aim to address the problems occurring after herniation surgery, such as loss of disc height, increase of the annular bulge [Brinckmann 1991] as well as changes in the kinematics [Steffen 1991] and kinetics [Frei 1999] of the motion segment. Long-term results have yet to show improvement of clinical outcomes compared to the standard intervention. Total disc replacement implants have distinct benefits compared to fusion techniques. An in vitro study [Zollner 2001] has shown that after insertion of the implant, segmental mobility was restored to the intact situation. The maintained segmental motion may lead to lesser stresses on the adjacent segment, but it remains a rather invasive technique. From the posterior dynamic stabilisation devices, DYNESYS™ appears to be a promising system regarding the range of applications and clinical outcome [Schwarzenbach 2000]. Freudiger et al. reported the effectiveness of the system in the sagittal plane.

SUMMARY

Short and midterm clinical evaluations of these concepts have revealed promising results. However, scientific evidence for the long-term behaviour has yet to be shown. The often-heard analogy is that, "fifty years ago, hips were fused for degenerative problems, but the development of the low friction arthroplasty has superceded this treatment". Clearly, such a paradigm shift may be the future for the spine. In various parts of the world, "flexible" stabilisation for a number of indications is already a reality.

REFERENCES

1. Blumenthal SL., et al.; Proceedings of NASS 2001
2. Brinckmann P., Grootenboer H.; Spine 1991
3. David T.H.; RACHIS, Vol. 11 No. 4-5, 1999
4. Frei et al.; EurSpine J. 1999
5. Freudiger et al.; Arch Orthop Trauma Surg 1999
6. Schwarzenbach O.; *Proceedings of Worldspine 1, 2000*
7. Zollner et al.; Orthopäde 2001

ANTERIOR AND POSTERIOR SPINAL FIXATION – AN *IN VITRO* SUMMARY

Peter A. Cripton

Exponent Failure Analysis Associates, Biomechanics Practice
2300 Chestnut St., Philadelphia, PA, USA, 19103
pcripton@exponent.com

INTRODUCTION

Surgical stabilization of the spine is performed for a variety of clinical indications including trauma, tumor, congenital deformity and pain, or neurological pathology secondary to degenerative changes. The ultimate goal of most of these procedures is to prevent motion at one or more intervertebral joints. This causes bony fusion to occur across the intervertebral discs and/or facet joints of the stabilized levels.

A wide variety of surgical techniques and implantable devices are currently used to provide the necessary stabilization in these areas. Techniques and implants have evolved which are specific for each region of the spine (cervical, thoracic and lumbar) and indication. For many indications, new techniques and implants are proposed with some frequency, and in these areas, the “state-of-the-art,” continues to evolve.

Biomechanical testing of these surgical techniques and implantable devices is an important step in the overall evaluation of their potential effectiveness in clinical practice. *In vitro* biomechanical testing using human cadaveric specimens is often used to model the immediate post-operative situation that these devices are exposed to. In this paradigm, the geometry of the human anatomy is used directly and then loads or displacements are applied to model particular loading cases representative of those believed to occur *in vivo*. Investigators have used this type of *in vitro* testing to compare existing devices, to evaluate devices prior to clinical introduction, and in attempts to establish the basic principles of operation of a device, device type or technique.

PRESENTATION SUMMARY

In this presentation, several common techniques and devices used for surgical fixation of the spine will be presented from an *in vitro* testing perspective. Emphasis will be placed on studies, which have elucidated the basic biomechanical mechanisms behind the function of particular types of anterior and posterior devices.

ANTERIOR TOPICS

In the anterior column of the spine, the most common surgical fixation techniques consist of anterior plates and devices which are inserted between the vertebral bodies such as interbody fusion cages or bone grafts.

Cervical Spine Strut Graft Mechanics

Analyses of the basic biomechanical function of anterior devices will be presented by considering anterior strut graft procedures in the cervical spine (Cripton *et al.*, 2002). A study in which load-sharing, stability and device loosening was quantified for three-level strut grafting of the subaxial cervical spine will be presented. The results of studies without defect-spanning anterior plates will be presented and compared to similar studies, which included anterior plating. The likely consequences implied by these results with respect to the clinical performance of these techniques will be discussed and illustrated with references to the clinical literature.

Lumbar Interbody Fusion Cages

Studies focused on the biomechanical performance of posteriorly implanted lumbar interbody fusion cages (PLIF) from the perspective of compressive load bearing and multi-dimensional stability will be presented (Oxland *et al.*, 1996). Three diverse PLIF cages will be compared to evaluate the effect of cage design on biomechanical performance. The effect of cage design will be compared to other relevant parameters such as the presence of posterior instrumentation, bone mineral density and disc degeneration.

POSTERIOR TOPICS

In the posterior column of the spine, the most common surgical fixation techniques consist of rods or plates, which run longitudinally along the spine on either side of the spinous processes. These systems are usually connected to the underlying vertebra by transpedicular screws, hooks or wires.

Load-Sharing in the Stabilized Lumbar Spine

Longitudinal rods instrumented with strain gauges and intervertebral disc pressure sensors were used to study load-sharing in the stabilized lumbar spine segments (Cripton *et al.*, 2000). The results demonstrate the relative importance of specific anatomic structures to load-sharing in these systems as a function of the type of load applied.

Cross-Bracing of Posterior Fixation Systems

Cross-braces (also called transverse connectors) are available for the many contemporary posterior fixation systems. The biomechanical efficacy of these devices has not yet been definitively established. Two studies, which evaluated these devices using in vitro biomechanical techniques, will be presented (Lund *et al.*, 1998) and the application of these results within the clinical context will be discussed.

CONCLUSION

In vitro biomechanical studies have played a key role in evaluating the efficacy of contemporary spinal fixation techniques. This presentation will present several examples of the contributions made to this field using *in vitro* biomechanical techniques.

REFERENCES

Cripton P.A., *et al.* (2002) Proc. 16th N. Am. Spine Soc., 304
Cripton, P.A., *et al.* (2000), Spine. **25**, 170-9.
Lund, T., *et al.* (1998), JBJS, **80-B**, 351-9.
Oxland, T.R., *et al.* (1996) Spine. **21**, 2558-69.

BIOMECHANICAL TESTING TO QUANTIFY ADJACENT-LEVEL EFFECTS

Manohar M. Panjabi

Department of Orthopaedics and Rehabilitation, Yale University School of Medicine, New Haven, CT

INTRODUCTION

To test spinal fixation devices using spine specimens, the flexibility protocol is often used. Here independent load components are applied individually in multiple directions and the resulting three-dimensional motions are recorded (Panjabi et al 1976, Panjabi 1988). Alternatively, in the stiffness protocol, independent displacement components are applied individually in multiple directions and the resulting six load components are measured. Which of the protocols is most suitable for studying adjacent-level effects in a specimen? There are some clinical observations to help in this decision. Patients, after a solid fusion, have been found to demonstrate approximately the same range of motion as before the fusion, between the body parts surrounding the fusion level, e.g. between the head and trunk for the cervical fusion. Thus, the motion between the body parts should be the independent parameter. The stiffness protocol seems to fit the bill. But there are several important, theoretical and practical, limitations to the use of the stiffness protocol as documented in some recent studies. The purpose of this presentation is to explore a hybrid protocol, from the viewpoint of its use in quantifying the adjacent-level effects due to an intervention at one or more levels. For example, the intervention may be an injury, a fusion or a disc replacement.

METHODS

The stiffness protocol requires the application of one independent motion component, out of a total of six, to the spine specimen, and measurement of the resulting six load components in the specimen. This brings up several issues and points to the disadvantages of this protocol type. First, how to apply a single component of motion, while blocking all other five motion components? If the motion component is one of the three rotations, then how is the axis of rotation chosen and defined uniquely within the spine anatomy? It has been shown that the axis of rotation makes a significant difference to the measured load displacement curves. Similar choices must also be made for each of the three translation components. Second, how to apply a displacement component, which does not cause tissue injury? Injuries have been documented using the stiffness protocol. Third, having applied a displacement component where and how to measure the resulting six load components in the spine specimen? Finally, the human spine *in vivo* does not move with one independent motion component alone, but moves naturally, for example during the flexing of the spine, the motion includes inferior and anterior translations and flexion rotation. It is easy to see that the requirements just mentioned, makes the stiffness protocol difficult to carry out.

RESULTS

An alternative is proposed, which uses a hybrid approach. This consists of two steps. As an example, let us assume that we are interested in the adjacent-level effects due to an intervention: fusion or a disc replacement at C4-C5 in the cervical spine. Assume further, for the sake of simplicity, that we want to study flexion and extension of the neck. Step 1. Using the flexibility protocol, apply unconstraining pure flexion and extension moments to the intact spine specimen, which result in motions similar to the physiological motions observed *in vivo*. Note the overall ranges of main motions. Step 2. Apply the same moments to the spinal construct (specimen plus the simulated fusion or artificial disc implantation), but this time the magnitudes are adjusted to obtain the same overall ranges of main motions as when the specimen was intact. During both the Steps, the responses of the spinal elements of interest, e.g. the motions and strains in discs and vertebrae, are monitored. The changes in the responses between the intact specimen and spinal construct constitute the adjacent level effects due to the intervention.

DISCUSSION

One of the advantages of this approach is that there is no need to determine before hand the axis of rotation around which the rotation is applied, as the stiffness protocol would require. Being unconstrained, the rotation axis is naturally floating as a response to the externally applied pure moment. As the specimen reaches the same end point in Steps 1 and Step 2, the protocol mimics the *in vivo* clinical observations mentioned earlier. There are some specifics associated with the hybrid protocol. Firstly, to mimic the *in vivo* situation, the ideal specimen length should be the same as the *in vivo*, e.g. whole cervical spine, for the fusion at C4-C5. Secondly, the motion between the body parts has six degrees of freedom. Therefore, in an ideal protocol, all the six degrees of freedom should be match between Step 1 and Step 2. Of course, each experimental design is a compromise, which balances the ideal against the practical.

REFERENCES

Panjabi MM et al., J Biomechanics: 185-192, 1976.
Panjabi MM, Spine: 1129-1134, 1988.

IN VIVO LOADS ACTING IN THE SPINE AND IN SPINAL IMPLANTS

Hans-Joachim Wilke[1], Antonius Rohlmann[2], Georg Bergmann[2], Lutz Claes[1]
[1]Dept. of Orthopaedic Research and Biomechanics, University of Ulm, Ulm, Germany, hans-joachim.wilke@medizin.uni-ulm.de
[2]Biomechanics Laboratory, University Hospital Benjamin Franklin, Free University of Berlin, Germany, rohlmann@biomechanik.de

INTRODUCTION

In order to design spinal implants or to improve the methods to test them the load acting on the spine or in the implants during daily activities and in extreme situations have to be known. Unfortunately still few data are available.

In vivo data directly determined in the spine or indirectly with spinal implants are known from only few studies due to ethical reasons. The most known data came from intradiscal pressure measurements in the 60s and 70s (1), which were complemented with dynamical measurements only in 1999 (5). Implant loads were first measured exemplarily with an external fixator (4) and later extensively in internal fixators (2).

The objective of this paper is to summarize and compare results from these independent *in vivo* studies applying different methods to provide information about loads acting in the spine or its implants.

METHODS

The early intradiscal pressure measurements were perfomed with some twenty volunteers by inserting a stiff needle with an integrated pressure sensor into the center of the disc (1). The recent intradiscal pressure values were measured in only one volunteer with a similar technique but using a flexible transducer (5). They were recorded with a telemetry system over a period of 24 hours during daily activities, physiotherapy and manipulations, and during some sports activities.

Loads in the external fixator were measured indirectly through the deformation of the Schanz screws with strain gauges which allowed the estimation of loads in the spine (4). Internal fixator loads (three force components and three moments) were measured in the modified and telemeterized longitudinal rods of the bisegmental implant in ten patients in similar situations as above. This allowed a quantitative comparison of the pressures and the fixator loads for many different static and dynamic activities when normalized to standing (3).

RESULTS

For the pressure in the nucleus we found for lying in prone position 0.1 MPa, lying laterally 0.12 MPa, relaxed standing 0.5 MPa, standing flexed forward 1.1 MPa, sitting unsupported 0.46 MPa, sitting with maximum flexion 0.83 MPa, nonchalant sitting 0.3 MPa, lifting a 20 kg weight with round flexed back 2.3 MPa, with flexed knees 1.7 MPa, and close to the body 1.1 MPa. During the night, pressure increased from 0.1 to 0.24 MPa. 2.3MPa was the highest pressure for all situations measured. Although it is difficult to calculate spinal load directly from the pressure values they may be converted approximately by multiplying the pressure with the cross-sectional area of the disc which was 18.2 cm^2 (e.g. lifting 20 kg with back flexed creates 2.3 MPa ca. 4200N).

Implant loads differed considerably from patient to patient depending, for example, on the indication for surgery and the surgical procedure. They were altered by anterior interbody fusion. Mostly, only small differences in implant loads were found for the various lying positions. Flexion bending moments were significantly higher in upright than in lying body positions. Loads on the fixators were not higher for sitting than for standing.

The results show that fixators may be highly loaded even after fusion has occurred. A flexion bending moment acts on the implant even with the body in a relaxed lying position. This means that already shortly after the anterior procedure, the shape of the spine is not neutral and unloaded, but slightly deformed, which loads the fixators. Pedicle screw breakage more than half a year after insertion does not prove that anterior interbody fusion has not occurred. The maximum bending moments were around 10 Nm.

DISCUSSION

During many exercises the new intradiscal pressure measurements showed a good correlation with Nachemson's data, but not in the comparison of standing and sitting or of the various lying positions. These differences may be explained by the use of different transducers in this study and those from before.

The normalized values of the new intradiscal pressure values and fixator loads corresponded in most cases. Both studies showed slightly lower loads for sitting than for standing and comparable low loads in all lying positions. Different relative values for intradiscal pressure and fixator loads were found when the load was predominately carried by the anterior column, as during flexion of the upper body or carrying a weight.

These few studies provide some absolute values for the load acting in the spine and the forces and moments seen by the implant. The combination of these two methods improves the understanding of the biomechanical behavior of the lumbar spine and the results may be used to design new implants or new testing procedures.

REFERENCES

1. Nachemson A. (1964) JBJS; 46:1077-92.
2. Rohlmann A et al (1999) Spine; 25(23):2981-6.
3. Rohlmann A et al (2001) Ergonomics ;44(8):781-94.
4. Wilke H-J et al (1992) Biomed. Technik; 37(4):78-85.
5. Wilke H-J et al (1999) Spine; 24(8):755-62.

ACKNOWLEDGEMENTS

We would like to thank all the volunteers and patients for their kind cooperation.

SPINAL FIXATION FROM A CLINICAL PERSPECTIVE

Marcel Dvorak, MD, FRCSC

Combined Neurosurgical & Orthopaedic Spine Program
Vancouver Hospital and Health Sciences Centre
Department of Orthopaedics
University of British Columbia
Vancouver, BC, Canada

INTRODUCTION

Internal spinal fixation is widely used to maintain spinal alignment and facilitate a solid osseous union. Common clinical problems include degenerative conditions such as lumbar scoliosis, spondylolisthesis, and internal disc derangement. Other conditions that frequently require internal stabilization include trauma, iatrogenic spine instability, and tumors. Major deformity correction also requires stabilization.

The surgeon is faced with a number of uncertainties while pre-operatively planning the approach and technique of fixation. In vitro biomechanical studies should assist in providing guidance to the surgeon. Some of the most frequently encountered clinical questions include:

1. When is anterior column support necessary in addition to posterior fixation?
2. What degree of posterior stability is necessary to enhance osseous union?
3. When is anterior instrumentation alone inadequate?
4. How to best optimize the implant-bone interface?

METHODS

A variety of clinical case examples focused on the cervical and thoraco-lumbar spine will be presented to highlight pertinent fixation issues. The clinically relevant unresolved issues relating to spine fixation will be outlined.

RESULTS AND DISCUSSION

Cervical Spine:
Traumatic injuries to the posterior and anterior elements of the cervical spine from C3-T1 have been successfully treated by anterior or posterior instrumentation alone, as well as by combined anterior-posterior fixation. Although posterior fixation has been reported to be superior to anterior in in-vitro testing, the clinical success seen with anterior stabilization alone questions the relevance of these studies. Newer dynamic anterior plate designs further confuse the indications for anterior alone or anterior-posterior fixation, particularly in long segment anterior fusions.

Thoraco-lumbar Spine:
Following vertebrectomy, the anterior column may be stabilized using autograft, allograft, or prosthetic replacements. Anterior and posterior fixation methods may sacrifice stability if the short segment fixation relies on few anchor points, but may be plagued by adjacent segment degeneration and instability if longer constructs are used. These questions gain further relevance in osteoporotic bone.

Many fixation challenges relate to failure at the implant-bone interface, particularly in osteoporotic bone. Revision and de-novo surgery is often complicated by less than ideal fixation to bone.

Degenerative conditions in the lumbar spine have been treated with anterior 'stand alone devices', posterior fixation alone, and circumferential arthrodesis. The optimal degree of added "surgical stability" necessary in many of these conditions is debatable. Lack of correlation between the clinical outcome and radiographic osseous union continues to fuel this debate.

SUMMARY

By presenting some clinical examples of unresolved spine fixation issues, it is expected that efforts may be directed at providing guidance to clinicians in choosing fixation constructs and approaches.

The development of new products should also keep these clinical issues uppermost.

BIOMECHANICAL TOOLS TO UNDERSTAND AND PREDICT THE EFFECTS OF INTERVENTIONS IN SCOLIOSIS

C.E. Aubin Ph.D.[1,2], D. Perié D.[2], Y. Petit M.A.Sc.[1,2], J. Dansereau Ph.D.[1,2], H. Labelle M.D.[2]

1- Dept. Mechanical Engineering, Ecole Polytechnique; 2- Sainte-Justine Hospital; Montreal; carl-eric.aubin@polymtl.ca

INTRODUCTION AND OBJECTIVES

Scoliosis is a complex musculoskeletal disease requiring treatment in moderate and severe cases. To investigate correction mechanisms, it is necessary to evaluate not only the geometry from imaging techniques, but also to assess the loads acting on the trunk and how they contribute to spine correction. This paper presents some biomechanical modeling applications to study the effects of intervention in scoliosis.

BRACE TREATMENT INVESTIGATIONS

The biomechanics of the Boston brace was studied using finite element models (FEM) and experimental measurements. Pressures generated by the brace on the torso and the strap tension were measured using 192 thin pressure sensors and force cells. They were used as input into a personalized FEM built using a multi-view radiographic reconstruction technique (Aubin et al., 1995). The brace treatment was simulated: 1) by applying equivalent forces calculated from the pressures; 2) by an explicit representation of the brace and its interface (contact elements) with the torso (Fig. 1), and a 3-step simulation: 1) brace opening to include the trunk; 2) brace closing; 3) strap fastening. The simulations were compared to the geometry of the patient wearing a brace by means of several geometrical indices. Simulation results showed the feasibility and the validity of such modeling approach, and pointed out the major influence of the boundary conditions.

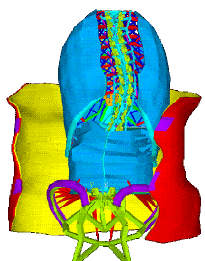

Fig 1 – FEM of the trunk and brace

The FEM also was used to investigate the coupled mechanisms between the scoliotic spine and the rib cage subjected to brace loads (Aubin et al., 1997). Coupled mechanisms were found between the spine and rib cage. For instance, loads on the posterior rib hump tends to reduce sagittal curvatures (flat back phenomenon), and to increase the coronal deformation of the thoracic curve. FEM also was used to test novel orthotic approaches. An original concept consisting in applying differently the loads on the thorax was proposed and investigated. Optimization of brace treatment was realized by Gignac et al. (2000) to find the most favourable corrective load patterns in 3D. Optimal forces were mostly located on the convex side of the curve (postero- and antero-laterally), but they differed depending on patient shape. This study pointed out the usefulness of biomechanical modeling and optimization approach to develop better individualized brace design.

SPINE SURGERY SIMULATIONS

The biomechanics of scoliosis surgeries was studied using the FEM personalized using patient's 3D reconstruction. The C-D instrumentation procedure was simulated in 4 steps, similarly as in Gardner-Morse (1994): 1) installation of hooks/screws on instrumented vertebrae (calculated using geometric transformations from the post-op to the pre-op configuration). Links between the vertebrae and the hooks/screws were considered rigid. 2) translation and attachment of the hooks/screws on the first rod on the concave side. Hooks and screws were free to rotate around the longitudinal axis of the rod. The 3D rod shape was obtained from a -90° rotation from the post-op reconstruction. 3) rod rotation (90°), hooks/screws lock up, and spring back (removal of the applied torque). 4) translation and attachment of the hooks/screws on the second rod on the convex side (idem step 1) followed with hooks/screws lock up. Good agreement was found between simulated and 3D reconstructed post-operative geometry of the spine (difference of 2° for the kyphosis, 6° for the Cobb angle). At the apical vertebra, traction loads were found in the ribs on the concave side of the curve, while on the convex side, lower compression loads were observed. Thus, the rib cage acts as a buttress on the spine leading to counteract the correction provided by the instrumentation stiffness and the surgical maneuvers. Biomechanical modeling also was used to simulate various designs of costoplasties. Gréalou et al. (2002) analyzed different procedures (side, location, length, and number of ribs to resect or to graft), to investigate their biomechanical effect and to also test corrective mechanisms involving the rib cage.

FEM has shown limitations to simulate surgical instrumenttation, especially because of the difficulty to represent a discontinuous structure and the stiffness difference within components (mechanism). A novel approach using a kinematic model including flexible elements to represent each motion segment was developed to simulate the instrumentation maneuvers (Fig. 2) (Poulin et al., '98). This model is quite equivalent to the FEM, however it allows a much better and realistic way to model the instrumentation. Good agreement also was found between the simulated and 3D reconstructed post-op geometry (< 5° for the kyphosis and Cobb angle). We also found that boundary conditions were the most influential parameters, followed by individualized mechanical properties.

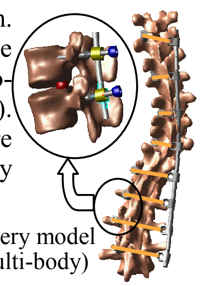

Fig 2 – Surgery model (flexible multi-body)

CONCLUSION

Biomechanical models, used under well understood conditions, are practical tools to understand and assist with orthotics and pre-operative planning, to test and build more efficient (rationalized) treatments.

REFERENCES

[1] Aubin et al, Ann Chir, 1995, 49:8, 749-61; [2] Aubin et al, Spine, 1997, 22:6, 629-35; [3] Aubin et al, Spine, 1999, 24:4, 349-54; [4] Gardner-Morse and Stokes, 1994, J. Biomech 27:177-81. [5] Gignac et al., Eur Spine J, 2000, 9:3, 185-90; [6] Gréalou et al., J Orthop. Res. (in press); 7- Poulin et al., Ann Chir, 1998, 52:8, 761-7

ACKNOWLEDGEMENTS

Research funded by NSERC and CIHR Canada. Preliminary FEM work (< 1996) done in collaboration with ENSAM-Paris.

INTERVERTEBRAL DISC STIFFNESS - PERSONALIZED VALUES AND USE IN SURGERY SIMULATION

W. Skalli[1], J. Dubousset[2], V. Lafage[1], and F. Lavaste[1]
[1]Laboratoire de Biomécanique, ENSAM, Paris, France (wafa.skalli@paris.ensam.fr)
[1] Hôpital Saint Vincent de Paul, Paris, France

INTRODUCTION

Management of scoliosis and its treatment requires a good understanding of the behavior of the intervertebral spine soft tissues (mainly discs) for two reasons: 1/ the degree of correction depends on the specific stiffness of the segments included in the fusion, and 2/ the post correction behavior is related to stiffness of the remaining unfused segments. In vitro experiments and quantified clinical analysis can yield estimation of intervertebral stiffness. Finite Elements modeling helps to quantify stiffness and to study its effect on the behavior of the scoliotic spine during surgery.

METHODS

In vitro experiments: In the Ensam Biomechanics Laboratory, quantification of three dimensional load displacements curves has been performed since 1986, for more than two hundred functional units from the cervical, thoracic and lumbar spine. Results allow us to assess the range of variation in the behavior of non-scoliotic spines. These data form the basis of a global finite elements model of the spine used for surgery simulation (Leborgne & al. 1998, Lafage & al. 2001).

Clinical analysis: preoperative bending tests are routinely performed in St Vincent de Paul Hospital prior to surgery for scoliosis. The finite elements model is used to simulate these bending tests, and then the soft tissues mechanical characteristics of the model are adapted to achieve a simulation that renders the specific vertebral motion of a given patient. A first difficulty in this process concerns the reliable quantification of 3D vertebral rotations measurements from single plane bending Xrays. But the main difficulty is in assessing the proper mechanical characteristics for a patient. In the numerous simulations we performed for many patients, we observed that a very local change in disc stiffness often results in a modified response of the whole spine. These investigations yield progressive understanding of the very complex behavior of this mechanical system. We used a detailed model to complement the understanding of these phenomena (Lafage & al. 2001): geometric modification (wedging of vertebrae and discs does not explain this modified stiffness in scoliosis, which is probably related to physical changes in the tissues.

Pre and postoperative global analysis of posture and motion of the scoliotic subject are of high interest because they provide the pattern of motion of the unfused segments, before and after surgery. Indeed, the result of surgery depends on what has been done at the fused level, but also on the situation of the remaining unfused parts: disc height, stiffness, symmetry, and hip capability to compensate a part of the lost spine motion. Considering spine 3D configuration with regard to the gravity line (Champain & al. 2001) is of particular interest, to consider spine balance and predictions of loads on the remaining discs.

Finite elements modeling is used in clinical research to understand surgery effects. Once the model is considered as representative of the patients spine, both for geometry and intervertebral stiffness, it can be used to investigate alternative possibilities of surgery correction. As an example, Figure 1 shows for a specific patient four virtual postoperative configurations resulting from alternative placement of hooks. Some of them yield undesirable global spine imbalance, or local excessive motion.

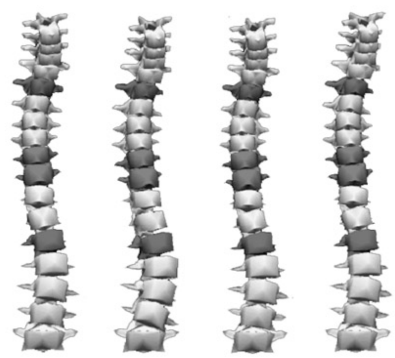

Figure 1 : Four surgical strategies for the CD virtual correction

CONCLUSION

Intervertebral soft tissues are essential in biomechanics of the scoliotic spine. The use of personalized geometric and mechanical models allows us both to investigate the behavior of these tissues, and to analyze the effect of surgical treatment.

REFERENCES

1. Le Borgne P. PhD thesis, ENSAM Paris, 1998
2. Lafage, Skalli & al, IRSSD Congress, 2000.
3. Champain, Skalli & al, ISB Congress, 2001

ACKNOWLEDGEMENTS

To J. de Guise (ETS Montreal), and D. Mitton, S. Laporte, R. Dumas, for their contribution in spine geometric modelling.

MUSCLES AND COORDINATION

A.G.Feldman, Ph.D.[1,4], M. Beauséjour, M.Sc.A[2,4], P. Garceau[2,4], C.É. Aubin, Ph.D. [2,3], P.A. Mathieu, Ph.D.[2,4]
1. Montreal Rehabilitation Institute, 2. Sainte-Justine Hospital; 3. Dept. Mechanical Engineering, École Polytechnique; 4. Biomedical Engineering Institute, University of Montréal, Montreal; feldman@MED.UMontreal.CA

INTRODUCTION

Several hypotheses relate muscle activation with the control of body posture. Some propose that differing postures of the limb are produced by vector summation of several basic force fields, attractors, or primitives [1] or are combined of memorized postures with some weight coefficients [2]. For example, consider two force fields that in the absence of external loads stabilize the limb at two different configurations. Summation of these fields will produce an intermediate configuration with zero net torques at each joint. The resulting zero torque, created by the summation of opposing torques from the two fields, implies coactivation of two opposing muscle groups. This means that many postures of the body cannot be maintained without coactivation although empirical observations show that coactivation and postural control are in principle separate. One can easily co-activate and de-activate opposing muscle groups of the arm without changing arm configuration.

CONTROL LEVELS

Thus, control levels likely reset the initial postural attractor to a new point in space, rather than combining different attractors. Such a postural resetting mechanism for movement production was postulated based on the finding [3] that EMG activity of a single muscle occurs when its length exceeds a referent (threshold) length. It has been suggested that, by appropriate tuning of the intermuscular interaction mediated by proprioceptive afferents and appropriate spinal and supraspinal neurons, the nervous system specify a single threshold configuration of the body for all skeletal muscles. This threshold configuration may be considered a virtual, referent configuration (R) with which actual body configuration (Q) is compared. The muscles will be silent at the R configuration but will generate EMG activity and forces resisting from deviations of the body from it [4,5,6]. Physiologically, this resistance results from position- and velocity-dependent muscle forces strengthened by homonymous and heteronymous proprioceptive reflexes functioning according to the spatial thresholds determined by the R configuration. Control levels may change the R configuration and thus influence the difference between the Q and R, resulting in the generation of muscle forces. The system will then move until a final body posture is reached. The R hypothesis has been used to simulates trunk motion in healthy and scoliotic subjects.

APPLICATION TO SCOLIOSIS

The λ model for multi-muscle and multi-joint systems has beenapplied to the study of recruitment patterns in scoliosis patients. A biomechanical model representing the osseo-ligamentous structures of the trunk [7] has been complemented by the introduction of 160 muscle fascicles from the main agonist and antagonist muscles involved in lateral bending movement. The model geometry is personalized to the subjects using 3D reconstructions from multi-planar radiographs. Control commands in this finite element model of the trunk were generated in accordance to the R hypothesis. Global movement involving the whole body from an initial to a final position (Q) is therefore a consequence of a change from an initial to a final R configuration, implying the modification of the 160 recruitment thresholds ($R_i = \{\lambda_{1,\ldots,}\lambda_{160}\}_i \rightarrow R_f=\{\lambda_{1,\ldots,}\lambda_{160}{}^*\}_f$) [8]. Right lateral bending test was investigated in scoliotic patients because it reflects the spine mobility in relation to thoracic scoliosis curve opening. Differences, in comparison to healthy subjects, were first observed as local disruptions in the recruitment patterns for right and left multifidus fascicles crossing the thoracic apex vertebra. Secondly, hyper recruitment was observed for left and right iliocostalis thoracis pars thoracis fascicles crossing the apex level (Figure 1). In particular, hyper-facilitation of agonists on the convex side and hyper-inhibition of antagonists on the concave side has clearly been noticed [9]. Correlation matrix analysis also revealed that the generation of central commands for healthy subjects was strongly correlated with the amplitude of the bending task (r^2 = 0.92) but the same relationship was much weaker for scoliotic subjects (r^2= 0.58). This implies that the command-position relationship complexity could depend on geometry and may indicate that position is controlled differently in scoliosis patients.

Figure 1.Recruitment patterns of the left and right illiocostalis for scoliotic (dark curves) and healthy subjects (light curves).

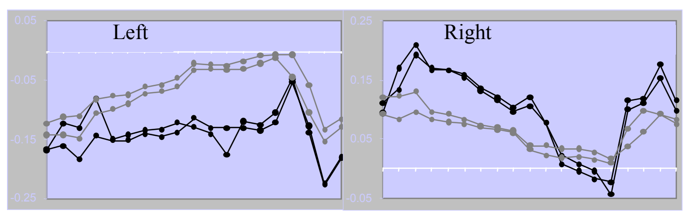

CONCLUSION

This model provides also a framework for the study of the biomechanical effects of these fascicle recruitment patterns on the spine, and the investigation of the relation between the possible resulting adverse stresses on the vertebrae and the progression of the scoliosis deformities.

REFERENCES

[1] Bizzi et al., Beh. Brain Sci., 15: 603-13, 1992; [2] Rosenbaum et al., Acta Psychol. (Amst), 82(1-3): 237-50, 1993; [3] Matthews, J. Physiol. (London), 147: 521-46, 1959; [4] Feldman and Levin, Beh. Brain Sci., 18: 723-804, 1995; [5] Feldman et al., Motor Control, 2(3): 189-205, 1998; [6] Lestienne et al., Neurosci Lett., 283(1): 65-68, 2000; [7] Aubin, et al., Ann Chir., 49(8): 749-61, 1995; [8] Beauséjour et al., IOS Press, 59: 151-3, 1998; [9] Garceau et al., IOS Press, 2002. In press.

ACKNOWLEDGEMENTS

Research funded by FCAR and NSERC Canada.

MODELING SKELETAL SHAPE CHANGES AND GROWTH IN SCOLIOSIS

Hideyuki Azegami[1], Kenzen Takeuchi[1], Ryu Sasaoka[1], Noriaki Kawakami[2]

[1]Dept. of Mechanical Engineering, Toyohashi University of Technology, 1-1 Hibarigaoka, Tempaku-cho, Toyohashi, 441-8580, Japan
[2]Meijyo Hospital, Orthopaedic Surgery, 1-3-1 Sannomaru, Naka-ku, Nagoya, 460-0001, Japan, azegami@mech.tut.ac.jp

INTRODUCTION

Idiopathic scoliosis is known as a spinal irregularity with lateral curvatures. Considering function of the spine supporting body, investigation from mechanical aspect lays the foundations for investigation of etiology and development of treatments. However, the structure of spine is not so simple. So the finite element modeling and analysis play a key role as means of the investigation. This presentation describes how to construct a finite element model of the spine, how scoliotic deformations emerge and grow, and how to reinforce the spine structure to prevent the scoliotic deformations from the purely mechanical aspect.

HOW TO CONSTRUCT SPINAL FINITE ELEMENT MODEL

The spinal finite element model was constructed using a commercial spine surface data (Viewpoint Premier, catalog num. VP2886 and VP361). The material properties of bones were assumed using data by Yamada (1970). Material properties of disks and joints were identified by comparing with the experimental results by Lucas and Bresler (1961), Markolf (1972) and Schultz et al (1974) (Takeuchi et al 2001).

HOW SCOLIOTIC DEFORMATIONS EMERGE AND GROW

Using the spinal finite element model, bucking phenomena caused by the growth of vertebral bodies were analyzed by a commercial finite element analysis program (MSC.Nastran v.70). The growth was simulated by generating initial strain (thermal strain). Displacement was fixed only on the adjacent surface with sacrum. Figure 1 shows part of the results of the fourth and the sixth buckling modes. The shapes of the fourth and the sixth buckling modes accorded with the clinical shapes of single and double curves respectively.

A simulation of the progression of scoliosis was demonstrated by the authors (Goto 2000).

HOW TO REINFORCE TO PREVENT THE SCOLIOTIC DEFORMATIONS

If the buckling hypothesis is acceptable, sensitivity function with respect to the critical growth of thoracic vertebrae on the maximization problem of buckling load with the fourth and the sixth buckling modes gives us useful information to improve and develop treatments for the idiopathic scoliosis. Figure 2 shows part of the computational results of the sensitivity function.

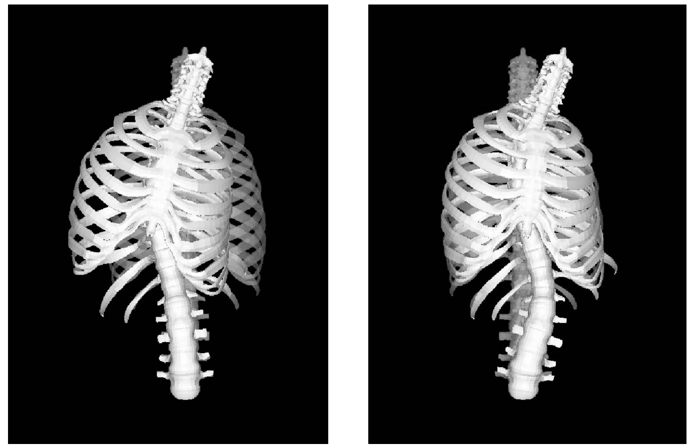

Fig. 1 Buckling modes: Fourth mode caused by growth of T4 to T10 (left) and Sixth mode by growth of T1 to L5 (right) (Takeuchi, et al. 2000).

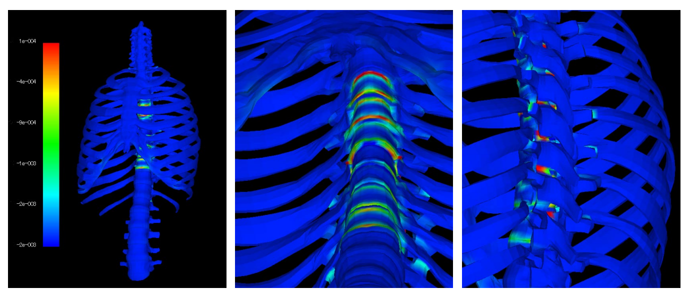

Fig. 2 Distribution of sensitivity with respect to fourth buckling mode caused by growth of T4 to T10 (Takeuchi et al 2001).

REFERENCES

Azegami, H. et al (1998). *Clinical Orthopedics and Related Research*, 357, 229-236.
Takeuchi, K. et al (2000). *Proceedings of the 34th Annual Meeting of Japanese Scoliosis Society*, 49 (in Japanese).
Takeuchi, K. et al (2001). *JSME International Journal Series C*, **44**, 1059-1064.
Goto, M. et al (2000). *Spinal Deformity, The Journal of Japanese Scoliosis Society*, **15**, 28-31 (in Japanese).

BIOMECHANICS IN IDIOPATHIC SCOLIOSIS ETIOLGY

V James Raso

Capital Health Authority, Glenrose Rehabilitation Hospital, Edmonton, Alberta, Canada
jraso@cha.ab.ca

INTRODUCTION

Biomechanical factors have been suggested to play a part in the etiology of idiopathic scoliosis and certainly play a significant role in its progression. Static mechanisms such as the constituent properties of the tissues, shape of the structure, loads on the spine or the spinal support conditions may cause a scoliosis to develop.

CONSTITUENT PROPERTIES OF THE SPINAL TISSUES

Significant differences in bone quality in patients with idiopathic scoliosis have been observed at sites that presumably are unaffected by the scoliosis, eg. the femoral neck, and so these differences may reflect an etiology rooted in the bony anatomy of the spine. Studies of soft the soft tissues suggest that joint laxity may contribute to the development of idiopathic scoliosis [2]. If general joint laxity is a primary cause of IS then a collage defect is a strong candidate as the source for the defect but Carr et al [3] found evidence against this.

ABNORMAL LOADING ON THE SPINE

Sevastik suggested that asymmetrical rib growth led to unusual lateral loading on the spine and the development of scoliosis [1]. The work culminated in a recent paper describing unilateral rib resections in the successful treatment of a scoliosis [6].

HYPOKYPOSIS AND THE DEVELOPMENT OF SCOLIOSIS

Scoliosis may develop in an otherwise normal child if the spine is hypokyphotic and the child undergoes a sharp growth spurt. Scoliosis develops when the growth of the anterior aspects of the body is greater than posterior growth [5]. In this case, the spine loses the protection of a kyphotic shape and may buckle. The direction of the collapse depends on local conditions but is often determined by the lateral pressure exerted by the aorta. Dickson provides considerable circumstantial evidence in support of his thesis. Progress of the scoliosis is controlled by the extent of asymmetry caused by the rotation of the vertebrae [4].

Although considerable effort has been directed to understanding the importance of the sagittal profile to the development of scoliosis in the thoracic spine, very little work has been done on lumbar scoliosis.

SUMMARY

The lack of a good animal model to study the mechanics of the upright spine has made it difficult to prove many of the biomechanical theories of adolescent idiopathic scoliosis. Many of the animals used to model adolescent idiopathic scoliosis will develop scoliosis in response to numerous intervention and care must taken in generalizing results based on these studies to the people.

Spinal stability as a mechanical process involves continuous re-alignment of the spine based position sensing on both a local and on a global level. There is no strong evidence to support any particular biomechanical factor in the etiology of idiopathic scoliosis. Much of the evidence is contradictory and the reviewed papers were consistently weak in statistical analysis. Conclusions drawn from animal studies are difficult to transfer to humans because of the very different nature of the relevant mechanics in the two groups. There is little scientific evidence that biomechanics plays a direct role in the etiology of idiopathic scoliosis.

REFERENCES

1. Agadir M, Sevastik B, Sevastik JA, Persson A, Isberg B: Induction of Scoliosis in the Growing Rabbit by unilateral Rib-Growth Stimulation. Spine 13(9):1065-1069, 1988.
2. Binns M: Joint Laxity in Idiopathic Adolescent Scoliosis. J Bone Joint Surg [Br] 70B(3):420-422, 1988.
3. Carr AJ Ogilvie DJ, Wordsworth BP, Priestly LM, Smith R, Sykes B: Segregation of Structural Collagen Genes in Adolescent Idiopathic Scoliosis. Clin Orthop Rel Res 274:305-310, 1992.
4. Deacon P, Archer IA, Dickson RA: The anatomy of spinal deformity: a biomechanical analysis. Orthopaedics. 10(6):897-903, 1987.
5. Dickson RA: The aetiology of spinal deformities. Lancet. 1(8595):1151-5, 1988.
6. Xiong B, Sevastik JA: A Physiological Approach to Surgical Treatment of Progressive Early Idiopathic Scoliosis. A case report. Eur Spine J;7(6):505-8, 1998.

ACKNOWLEDGEMENTS

This material was originally developed as part of a review conducted by the Etiology Committee of the Scoliosis Research Society.

ANGIOGENESIS AND HEALING IN RABBIT KNEE LIGAMENTS

Robert Bray[1], Catherine Leonard and Paul Salo
Department of Surgery, University of Calgary, Calgary, Alberta, Canada
[1] Communicating author, rcbray@ucalgary.ca

INTRODUCTION

In clinical terms, functional recovery after anterior cruciate ligament (ACL) injury is generally poorer than after medial collateral ligament (MCL) injury. In experimental studies after induction of "damage" the early phases of ligament healing require an adequate vascular response in the form of augmented blood supply (Bray et al 1996; Frank et al 1999). In this study, we hypothesized that the differences in healing properties of the ACL and MCL would be reflected in their respective vascular responses to partial injury. This study therefore examines changes in ligament vascular volume following hemisection of the ACL and MCL.

METHODS

Standardized injuries were surgically induced in adult rabbit knees ligaments: partial ACL transection or partial MCL transection. Two, 6 or 16 weeks later, the vascular volume (a measure of microcirculation capacity) of the ACL and MCL were measured using carmine red dye infusion (McDougall and Bray 1998). Ligament blood flow was also measured using coloured microspheres. The results were examined in experimentally injured, control and sham operated animals.

RESULTS AND DISCUSSION

The mean vascular index for the MCL in control animals was 5.57 ± 1.04 µl/g (n=6), while that of the ACL was 0.91 ± 0.33 µl/g (n=6). In response to hemisection, the MCL showed a large significant increase in vascular index (µl/g) that was apparent at 2wk after injury, peaked at 6wk (5-fold increase, $p<(0.001)$ and was no longer different from sham operated animals by 16wk (Figure 1). In contrast, hemisected ACLs showed a significant sustained two-fold ($p< 0.01$) increase in vascular index induced by injury (Figure 2).

The MCL showed significant increases in mass and water content 2 and 6 wk post-injury. In contrast, the water content of the ACL was unchanged from control values, and the mean mass was significantly decreased by 16 wk (Table). Results of blood flow are incomplete but will be presented.

SUMMARY

Ligament injury of the ACL and the MCL induces increased blood supply to healing tissue. The ACL and MCL show increases in vascularity in response to hemisection, but the MCL shows a much larger peak of angiogenesis during early scar formation at two to six weeks after injury. Water contents increased only in MCL tissue and paralleled the increased vascular volume observed in this structure.

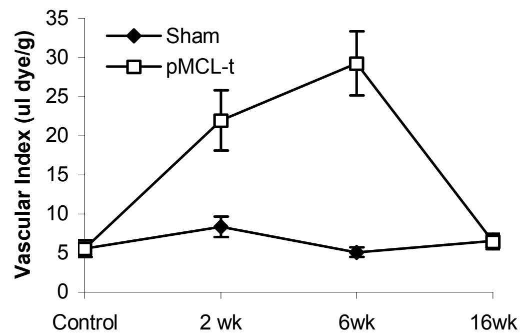

Figure 1: Vascular index of the medial collateral ligament following direct ligament injury (hemisection).

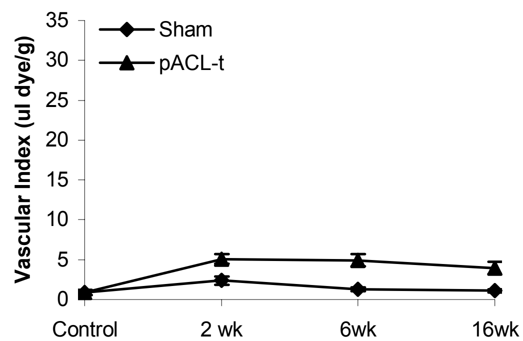

Figure 2: Vascular index of the anterior cruciate ligament following direct ligament injury (hemisection).

	Control	2 week	6 week	16 week
MCL mass (mg)	85±3	199±11	147±9	119±8
MCL water (%)	63.2±1.3	74.7±9.4	72.2±1.1	66.7±1.6
ACL mass (mg)	44±3	56±3	36±2	34±4
ACL water (%)	66.2±1.8	66.2±1.0	66.8±1.8	67.4±1.7

Table: Mass (mg) and % water content of rabbit MCL and ACL following ligament hemisection.

REFERENCES

Bray, R.C., et al (1996) *J Orthop Res*, **14**, 618-625.
Frank, C. et al. (1999) *J Sci Med Sport*, **2(3)**, 190-210.
McDougall, J.J., Bray, R.C., (1998) *Anat Rec*, **251,** 207-213.

THE EFFECT OF GROWTH FACTORS ON MECHANICAL PROPERTIES OF THE *IN SITU* FROZEN-THAWED LIGAMENT AND GENE EXPRESSION OF COLLAGEN IN EXTRINSIC FIBROBLASTS

Harukazu Tohyama and Kazunori Yasuda
Department of Medical Bioengineering & Sports Medicine, Hokkaido University School of Medicine, Sapporo, Japan,
tohyama@med.hokudai.ac.jp

INTRODUCTION

A number of studies have shown that, in the tendon autograft for ligament reconstruction, extrinsic cell infiltration occurs following intrinsic fibroblast necrosis, and that its mechanical properties are subsequently deteriorated. However, much remains unknown on the mechanism of the mechanical deterioration of the tendon autograft. Recently, many studies have reported that various growth factors regulate collagen-matrix metabolism in fibroblasts. Then, we have conducted two studies using the *in situ* frozen-thawed tendon and ligament, which have been established as idealized models of the autograft, in order to investigate the mechanism of the deterioration of the tendon autograft. The aim of the first study was to clarify the *in vivo* effect of administration of platelet-derived growth factor BB (PDGF-BB) and transforming growth factor beta 1 (TGF-beta1) on the mechanical properties of the the *in situ* frozen-thawed anterior cruciate ligament (ACL). The purpose of the second study was to elucidate the *in vitro* effect of these growth factors on gene expression of collagen in extrinsic fibroblasts derived from the *in situ* frozen-thawed patellar tendon (PT).

METHODS

Study I **(*In vivo* biomechanical evaluation):** In skeletally mature Japanese White rabbits, the in situ freeze-thaw treatment with a specially designed mini-cryoprobe was applied to the right ACL to kill intrinsic fibroblasts. Then, the rabbits were divided into three groups. In Group I, 400-ng rh-PDGF-BB was applied with 0.2-ml fibrin sealant around the frozen-thawed ACL. In Group II, 4-ng rh-TGF-bata1 was applied with 0.2-ml fibrin sealant in the same manner. In Group III, 0.2-ml fibrin sealant was applied as a control. All rabbits were sacrificed at 12 weeks after treatment. The cross-sectional area (CSA) of the ACL was determined with the optical method using a video dimension analyzer (VDA). Tensile tests for the femur-ACL-tibia complex were performed with non-contact measurement of ligament strain using a VDA.

Study II **(*In vitro* evaluation of gene expression):** In 16-week old Wistar rats, the in situ freeze-thaw treatment was applied to the right PT. At 6 weeks after the treatment, bilateral PTs were excised. Using the explant culture technique, we isolated extrinsic and normal fibroblasts from the frozen-thawed and non-treated PTs, respectively. Following the addition of rh-PDGF-BB or rh-TGF-beta1 under serum-free medium, the cell samples were collected at indicated times and total RNA was extracted. Then, Northern blot hybridization was performed to evaluate the effect of each growth factor on mRNA levels of types I and III collagens.

RESULTS

Study I: The CSA of Group II was significantly smaller than that of Group III, while there were no significant differences between Groups I and III (Figure 1-a). The elastic modulus of Group II was significantly higher than that of Groups I and III, while there were no significant differences between Groups I and III (Figure 1-b).

Study II: PDGF-BB or TGF-bata significantly increased mRNA levels of both collagens up to 36 hours. The effect of each growth factor was dose-dependent. TGF-bata stimulation significantly increased the ratio of type I collagen mRNA to type III collagen mRNA (I/III ratio) in both types of fibroblasts (Figure 2). However, PDGF-BB did not significantly affect the I/III ratio in extrinsic fibroblasts, although PDGF-BB significantly increased the ratio in normal fibroblasts.

DISCUSSION

The first study demonstrated that administration of TGF-beta1 has an significant inhibitory effect on the mechanical deterioration in the *in situ* frozen ACL *in vivo*, but that PDGF-BB does not have it. The second study showed that TGF-beta1 significantly increases the I/III ratio in extrinsic fibroblasts. In contrast, PDGF-BB does not increase the I/III ratio in extrinsic fibroblasts, although it significantly increases the ratio in normal fibroblasts. It is well known that the ratio of type I collagen to type III collagen is much lower in the scar tissue than that in the normal ligament tissue. Therefore, this study suggested that the inhibitory effect of application of TGF-beta1 on the mechanical deterioration in the *in situ* frozen ACL may be caused by an increase in the ratio of type I collagen to type III collagen, which is induced by extrinsic fibroblasts.

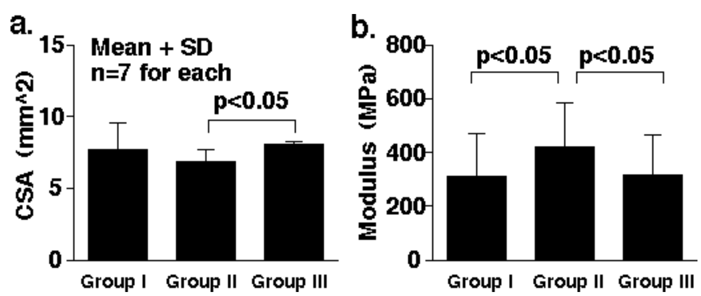

Figure 1 Cross-sectional area (a) and elastic modulus (b) of the ACL

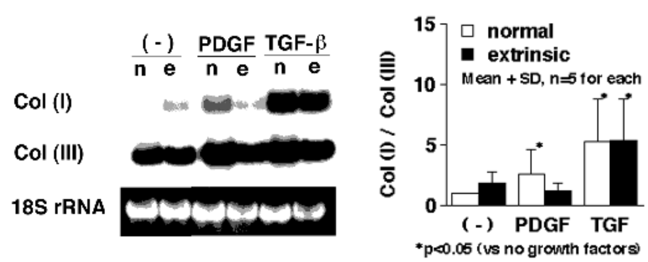

Figure 2 The effect of PDGF-BB (100 ng/ml) and TGF-beta1 (10 ng/ml) on mRNA levels of collagens at 24 hours post-stimulation in normal (n) and extrinsic (e) fibroblasts.

THE USE OF ROBOTIC TECHNOLOGY IN THE DETERMINATION OF *IN SITU* FORCES IN LIGAMENTS

Savio L-Y. Woo, Ph.D., D.Sc.

Musculoskeletal Research Center, Department of Orthopaedic Surgery
University of Pittsburgh, P.O. Box 71199, Pittsburgh PA, 15213, 412-648-2000
Email: decenzod@msx.upmc.edu Web: http://www.pitt.edu/~msrc

Ligaments in the knee and shoulder joints are frequently injured during sports activities. However, in order to understand injury mechanisms, knowledge of joint mechanics, specifically the forces in ligaments, is needed to improve surgical procedures and design better post-surgical rehabilitation protocols. We have developed a robotic/universal force-moment sensor (UFS) testing system designed to obtain the *in situ* forces in normal ligaments as well as the distribution of these forces in a non-contact manner [Fujie 1993, Rudy 1996]. Also, this methodology can be used to examine those for replacement grafts following ligament reconstruction using the same specimen, so as to eliminate the inter-specimen variation and to significantly increase the statistical power of the experimental data.

In this presentation, the results of several experimental studies will be presented. For example, there is a distribution of *in situ* forces in the ACL in response to an anterior tibial load, as its posterolateral bundle carries a different force than its anteromedial bundle throughout the range of knee flexion [Sakane 1997]. These results suggest that ACL reconstruction with a single graft may be inadequate to reproduce the function of the native ACL. The combination of axial compression and anterior tibial load can significantly reduce anterior-posterior translation as well as the *in situ* forces in the ACL. In addition, quadriceps and hamstring co-contraction protects the ACL from excessive forces. On the other hand, rotatory loads that simulate the pivot shift can cause significant increases in the anterior tibial translation and *in situ* forces in the ACL [Kanamori 2000]. A series of similar experiments on the PCL demonstrating its significant interaction with the posterolateral structures will also be shown.

We have also found both the bone-patellar tendon-bone and hamstrings grafts are effective in providing anterior knee stability during anterior tibial loads, but less so during rotatory loads [Woo 2002]. Comparison between ACL reconstructions using an anatomical double bundle with a traditional single bundle reconstruction shows the former reconstruction can more closely reproduce the knee kinematics and *in situ* forces of the native ACL.

The glenohumeral and acromioclavicular (AC) joints of the shoulder have also been assessed using the robotic/UFS testing system. For example, the *in situ* force in the superior AC ligament, in response to an anterior load, is 50% greater than all other ligaments. During posterior loading, both the superior AC and trapezoid ligaments have significant *in situ* forces [Debski 1999].

This innovative approach has provided important quantitative data on the ligaments around the shoulder and knee joints. It has many advantages suggesting that this experimental approach be adopted in future studies of the function of ligaments and tendons in other diarthrodial joints.

REFERENCES

Debski, RE, et al. (1999). *JOR,* 19, 769-76
Fujie, H, et al. (1993). *JBME,* 115,211-7
Kanamori, A., et al. (2000). *Arthroscopy*, 16, 633-9
Rudy, TW, et al. (1996). *J Biomech,* 29, 1357-60
Sakane, M, et al (1997). *JOR,* 15, 285-93
Woo, SL-Y, et al. (2002). *JBJS,* 84, 915-920

INVESTIGATIONS OF SOME POSTERIOR LIGAMENTOUS STRUCTURES OF THE KNEE

Andrew Amis, Anthony Bull, Chinmay Gupte, Ibraheem Hijazi, Amos Race, James Robinson, Takehiko Sugita

Departments of Mechanical Engineering, Bioengineering, and Musculoskeletal Surgery, Imperial College, London SW7 2BX, UK.
a.amis@ic.ac.uk

INTRODUCTION

The posterior cruciate ligament (PCL) is the largest and strongest ligament stabilising the human knee. Surprisingly, though, isolated rupture of the PCL is not usually greatly disabling, and many cases do not require surgery. There has been comparatively little work done on knee ligaments other than the cruciates, and so the objective of this talk is to describe work done recently on structures that may contribute to posterior knee stability, to help to understand why PCL deficiency is not necessarily disabling. These are: the PCL itself; the posterolateral structures such as the lateral collateral ligament (LCL) and popliteofibular ligament (PFL); the posteromedial structures such as the medial collateral ligament (MCL) and posteromedial corner complex (PMC); and the meniscofemoral ligaments (MFL).

THE PCL

The fibres of the PCL diverge widely as they pass from the tibia to the femur, and have distinct patterns of slackening and tightening as the knee flexes. This means that different parts of the PCL are working at different points in the arc of flexion. This is seen if the PCL is separated into anterolateral (aPC) and posteromedial (pPC) fibre bundles. The aPC is slack when the knee is extended, and tight in mid flexion; the pPC is tight at both extremes of the arc of motion. Since the majority of the PCL strength is the aPC, and the pPC is oriented vertically in extension, the PCL does not resist posterior tibial translation well in the functional (extended knee) posture. Selective cutting has shown that it is only a secondary restraint to tibial posterior translation near knee extension. Therefore, the role of other structures in controlling tibial posterior laxity is important.

POSTEROLATERAL STRUCTURES

The posterolateral anatomy is complex and variable. The position of the fibula varies between specimens, around the lateral and posterior aspects of the proximal tibia. This leads to differing orientation of the LCL and PFL, that both pass from the femoral lateral condyle to the head of the fibula, and to inherent difficulty for surgical reconstruction to stabilise some knees. As the knee flexes, so the orientations of these structures alters, and the LCL slackens, so it cannot then resist posterior tibial translation. This leaves the PFL as the primary restraint to tibial external rotation. These structures are ruptured by combined varus plus hyperextension injury of the knee. Simulated injuries in vitro show progression of structural damage, that later propagates into the cruciates. Reconstructions using several common surgical methods (Muller, Larson, modified Larson) all failed to restore normal knee laxity, with excessive laxity in knee extension (i.e. failure to restore knee stability) and significant overconstraint in flexion. More work on graft placement and tensioning is needed to optimise these reconstructions.

THE POSTEROMEDIAL CORNER

The medial ligaments have been described in different ways, and anatomical study suggests division into three main structures: superficial MCL (sMCL), deep MCL (dMCL) and a ‘posteromedial corner complex’ (PMC), that includes the knee capsule with various thicker bands of collagen fibres. The PMC is tight in knee extension, and slackens with flexion, while the MCL is approximately isometric. Tensile tests showed that these structures had strengths of 723N sMCL, 238N dMCL, 454N PMC, and failed at 10.7, 7.3, and 13.7 mm extension respectively. This explains the occurrence of deep ruptures of the MCL. Tests of anterior-posterior (AP) tibio femoral laxity with sequential cutting have shown how the PMC restrains posterior tibial translation, particularly in the extended knee with internal tibial rotation. At the same time, damage to these structures raises strain in the ACL (measured by DVRT), showing why they should be repaired or reconstructed at the same time as cruciate ligament surgery.

MENISCOFEMORAL LIGAMENTS

A literature review, plus our study of 85 knees, showed that at least one MFL is present in 93% of knees. The anterior MFL of Humphrey (aMFL) attaches distal to the PCL on the femur and is tight in knee flexion; the posterior MFL of Wrisberg (pMFL) attaches proximal to the PCL and tightens in knee extension. Tensile tests have found mean strengths of 301N and 303N for the a and pMFLs (n=10). This suggests that they have some load-bearing function. Selective cutting under cyclic anterior-posterior draw loading showed that the tibial posterior translation increased significantly after cutting the MFLs in PCL deficient knees. This is the first time that their role in knee stability has been shown, and suggests that they should be preserved. Their presence may help the PCL to heal close to its normal length after rupture, thus avoiding surgery.

CONCLUSIONS

The studies described all help to throw light on the behaviour of the knee under loads tending to cause posterior tibial translation/rotation, but it is clear that much more work is needed for more complete understanding of how best to deal with damaged posterior ligamentous structures of the knee.

COMPARISON OF SUBJECTIVE AND OBJECTIVE MEASUREMENTS OF BALANCE DISORDERS FOLLOWING TRAUMATIC BRAIN INJURY

Kenton R. Kaufman[1], Robert H. Brey[1], Li-Shan Chou[2], Ann Rabatin[1], and Jeffrey R. Basford[1]
[1]Mayo Clinic/Mayo Foundation 200 First Street SW, Rochester, MN 55905 USA
[2]University of Oregon, Eugene, Oregon
e-mail: kaufman.kenton@mayo.edu

INTRODUCTION

Clinicians use multiple approaches to assess balance impairment. However, these clinical measures are not sensitive to subtle changes in balance. The scientific analysis of balance is an emerging field. Objective measures of balance include posturography and gait analysis. The purpose of this study was to compare the relationship among the various measures of balance impairment.

METHODS

The study consisted of 10 patients (6 men and 4 women ranging in age from 18 to 65 years) who had a traumatic brain injury (TBI) and ten age, gender, and body mass index matched controls. The TBI designation was made on the basis of a documented TBI by physician assessment supported by additional information such as decreased Glasgow Coma Score within 24 hours of injury, documented loss of consciousness and findings on imaging. Subjects were required to be at least 3 months post injury, living in the community, and to have had normal gait and balance prior to their injury. In addition, the patients had to have current complaints of dizziness or unsteadiness when walking. Each subject's self-perception of disability due to symptoms of dizziness was measured using the Dizziness Handicap Inventory (DHI), a standardized, validated questionnaire (Jacobson and Newman 1990).

Balance impairment was objectively tested using two methods. A sensory organization test (SOT) that assessed the three components of balance (vision, proprioception, and vestibular function) was performed using computerized dynamic posturography (Equitest NeuroCom International Inc., Clackamas, Oregon). A gait study was used to quantify the displacement of the body center of mass (COM). Twenty seven reflective markers were placed on bony landmarks and an eight-camera ExpertVision® System (Motion Analysis Corp., Santa Rosa, California) was used to collect 3-D marker trajectory data. A biomechanical model consisting of 13 body segments (four upper extremity, six lower extremity, and one for the pelvis, trunk, and head) was used to compute the COM displacement.

RESULTS AND DISCUSSION

Based on the initial Glasgow Coma Score (GCS), four subjects had severe TBI (GCS< 9), two had moderate TBI ($9 \leq GCS \leq 12$), and four had mild TBI (GCS > 12). Tinetti Balance Assessments were obtained and the TBI group was not significantly different from the normal controls.

The DHI scores supported the subjects' complaints of "unsteadiness" and "imbalance". The DHI physical domain score was 10.4 (± 5.3), emotional domain score of 10.2 (± 9.6), functional domain score of 11.6 (±10.7), and total score of 32.2 (± 23.0). The subject's complaints of "dizziness" or "unsteadiness" were not detected by a clinical examination or the Tinetti balance scale score. However, the DHI indicated that this imbalance had effects on the physical, emotional, and functional aspects of individual's lives.

The SOT composite score was significantly lower in the TBI subjects (70 $\pm$ 12) compared to the normal controls (80 $\pm$ 8). Using posturography, four of the patients would be considered to have abnormal balance (SOT<70). There were correlations between the SOT and DHI. However, none of these correlations were statistically significant and all correlations were only moderate to weak. There is controversy regarding the use of posturography as a measure of balance impairment. Some authors have stated that posturography does not predict stability (O'Neill, Gill-Body et al. 1998; Evans and Krebs 1999). In contrast, Furman (Furman 1994) believes that posturography provides an indication of the impact of balance impairment on daily activities.

The displacements of the COM in the anterior and vertical direction were negatively correlated with the components of the DHI, whereas the displacement in the medial/lateral direction was positively correlated. Most importantly, there was a significant correlation of the COM peak velocity in the coronal plane with the physical, functional, and total DHI scores.

SUMMARY

The present study found that posturography test scores do not correlate with the subject's clinical symptoms. Gait analysis techniques have not been used routinely to assess clinical complaints of imbalance from patients. However, this study has demonstrated that gait analysis can be used to objectively quantify the subjective complaints of unsteadiness reported by patients with balance disorders. Moreover, gait analysis techniques quantify the dynamic aspects of balance impairment which the patient senses.

REFERENCES

.Evans, N. K. and D. E. Krebs (1999). *Otolaryngol Head Neck Surg* **120**: 164-173.
Furman, J. (1994). *Baillieres Clin Neurol* **3**: 501-513.
Jacobson, G. T. and C. W. Newman (1990). *Arch Otolaryngol. Head Neck Surg* **116**: 424-427.
O'Neill, et al. (1998). *Am Otol* **19**: 797-803.

USE OF AN INSTRUMENTED TREADMILL IN THE EVALUATION OF AMPUTEE GAIT

BL Davis[1], JE Perry[1], JD Redhead[2], KR Richards[2], C Wright[1]
Cleveland Clinic Foundation (ND20), Cleveland, USA
[1]Department of Biomedical Engineering davis@bme.ri.ccf.org,
[2]Orthotics and Prosthetics

INTRODUCTION

Traditional gait laboratories use floor-mounted forceplates to study joint kinetics and kinematics. These studies require that a patient correctly places his/her foot on a forceplate. In studies involving patients with limited walking abilities, this can often be problematic. In the current study, an instrumented treadmill was used to evaluate amputee gait patterns when prosthetic limbs of different compliance parameters were fitted to the residual limb.

METHODS

Eight subjects (mean age 45 years; mean time since amputation 65 months, 6 below-knee, 2 above-knee, 7 males) were fitted with prostheses with different cushioning. A Flex-Foot system (Fig 1) (spring cushion), a Stratus pylon (foam cushion), and a Lord Corporation pylon (polymer cushion) were tested in random order. Data were collected after initial fitting of the prosthesis and after 4 weeks of wear. Four 20s trials of force data were collected at 100Hz while walking at 3.2 km/hr on an instrumented treadmill.

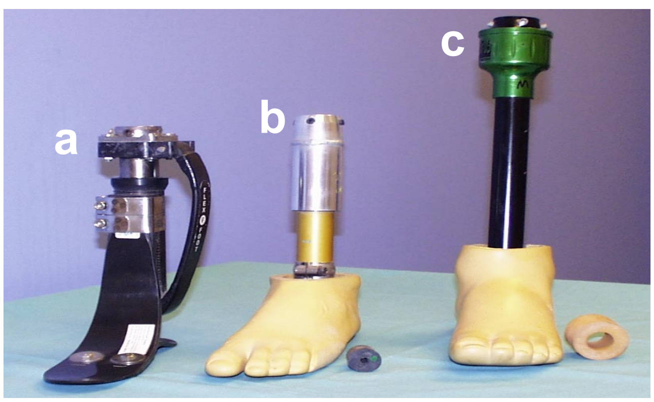

Figure 1. The prosthetic devices: (a) Flex-Foot, (b) Lord Corporation and (c) Stratus.

For each trial, eight consecutive strides (32 total) were analyzed. For the natural (N) and prosthetic (P) sides two variables were calculated: peak impact (F1) as % of bodyweight (F1_%BW) and time (F1_T) in seconds to reach F1. ANOVA and post-hoc Student T-tests were used to compare prostheses and wear time (initial vs. 4 weeks later).

RESULTS

Wear time had no significant effect on the symmetry indices but prosthetic type did. For F1_%BW, the Stratus and Flex-Foot had greater %BW borne by the prosthetic limb resulting in less symmetry than the Lord pylon. The time to reach F1 was greater for the natural leg when the contralateral limb was fitted with a Flex-Foot (Symmetry index (SI)=7.66), whereas for the Stratus and Lord it was greater for the prosthetic leg (SI=-4.78 and –3.13, respectively). The difference between natural and prosthetic legs resulted in less symmetry for the Flex-Foot compared to the Lord and Stratus.

DISCUSSION

Amputee patients typically expend less energy when walking symmetrically. In addition, recent prosthetic design trends have emphasized the need to avoid transient impact forces on the residual limb. Thus, this study evaluated gait symmetry in unilateral amputee subjects fitted with shock-attenuating prosthetic limbs.

For this subject cohort there was a rapid adaptation to wearing a new prosthesis as there was no significant change in gait symmetry due to wear time. For patients wearing the Flex-Foot system, the greater time to reach F1 for the natural leg indirectly suggests a slower rate of unloading for the prosthetic leg, which may be indicative of the Flex-Foot spring mechanism. For F1_%BW, the near perfect symmetry for the Lord device indicates equal loading on both legs.

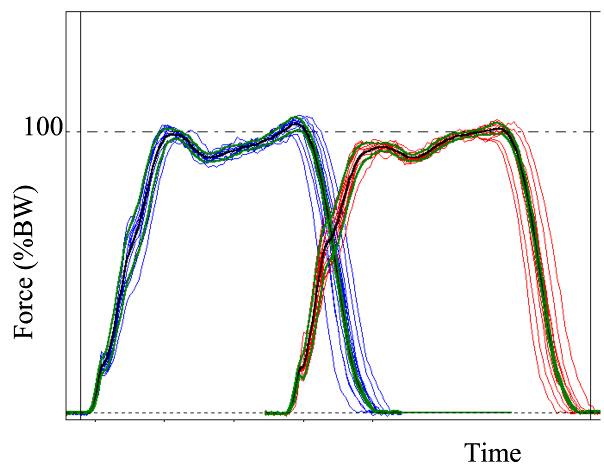

Figure 2. Vertical ground reaction forces for seven consecutive left and right strides for normal gait on the instrumented treadmill.

Finally, to alleviate concerns that (i) treadmill gait is affected by fluctuations in belt speed and (ii) friction beneath the treadmill belt affects force readings, we have performed tests to examine these effects. Results for the treadmill currently used show belt speed fluctuations less than 1% of the nominal setting and correlations between treadmill force data (e.g., Figure 2) and instrumented pylon data that exceed 0.9.

ACKNOWLEDGEMENTS

Funding for the instrumented treadmill design was provided by the NIH, support from the NSF (through the NSF REU program) covered the design of the pylon force transducer, and funding for the pylon designs was provided by the Lord Corporation. The authors have no direct or indirect interests in the Lord Corporation.

STEPPING OVER OBSTACLES DURING LOCOMOTION IN ANTERIOR CRUCIATE LIGAMENT PATIENTS

Tung-Wu Lu[1], Hsiu-Chen Lin[1,2], Te-Chang Kao[1], Horng-Chaung Hsu[2,3]

[1]Institute of Biomedical Engineering, National Taiwan University, Taipei, Taiwan. twlu@ccms.ntu.edu.tw
[2]School of Physical Therapy, China Medical College, Taichung, Taiwan
[3]Department of Orthopedics, China Medical College Hospital, Taichung, Taiwan

INTRODUCTION

Stepping over obstacles is an inevitable part of daily locomotion. Fails to negotiate successfully the obstacle will result in falls, a serious problem in the elderly [1]. A safe and successful obstacle-crossing requires stability of the body provided mainly by the stance limb and sufficient foot clearance of the swing limb. These demands may not be met in patients with anterior cruciate ligament deficiency (ACLD) that impairs both the structural stability and sensory feedback of the joint [2]. The influence of these impairments on the performance in stepping over obstacles during locomotion has not been reported in the literature. The present study addresses this issue by comparing foot clearances and knee joint kinetics between ACLD, ACL-reconstructed (ACLR) patients and normal subjects. The potential advantage of reconstruction of the ACL in stepping over obstacles was investigated.

MATERIALS AND METHODS

Three groups of subjects participated in this study: six unilateral ACLD subjects (age: 23.2±4.9 yr, height: 171.7±5.8 cm, weight: 70.8±7.1 kg), seven unilateral ACLR subjects (age: 27±8.1 yr, height: 164.2±10.5 cm, weight: 59.4±13.65 kg) and eight normal controls (age: 20±1.1 yr, height: 164.8±6.1 cm, weight: 63.3±14.3 kg). Each subject walked at self-selected pace and stepped over obstacles of three different heights (10, 20 and 30% of leg length). Twenty-eight markers were used to track the motion of both limbs. Kinematic and kinetic data were measured with a 7-camera motion analysis system (Vicon, Oxford Metrics, U.K.) and two force plates (AMTI, U.S.A.) placed on each side of the obstacle. The clearance distances of big toe, heel and lateral malleolus markers were calculated. A model of the lower limb was used to obtain the knee joint moments. Clearance distances and knee moments between limbs were compared using repeated t-test while independent t-test was used for between-group comparison. The significance level was set at 0.05.

RESULTS AND DISCUSSION

Compared to normal subjects, leading leg clearances of both affected and sound limbs in ACLD subjects were significantly smaller while in ACLR subjects those of the sound limbs were not significantly different from normal but those of the affected limbs were smaller, Fig.1. Leading leg clearances in affected limbs were significantly smaller than those in sound limbs for 20% and 30% conditions in ACLR group, and for 30% condition in ACLD group. These suggest that ACLD subjects are at higher risk in tripping over obstacles while ACL reconstruction could help to restore the subject's ability in successfully stepping over obstacles of lower heights. In ACLR subjects, the restored stability of the knee resulted in the close-to-normal clearances of the sound leading leg. The smaller obstacle clearance of the affected limb may be due to the partial restoration of the proprioception of the joint.

Trailing leg clearances were indifferent among the groups and were found to be much bigger than leading leg clearances. The bigger clearance for the trailing limb is needed to ensure safe obstacle-crossing when visual cue is not available. The results suggest that this mechanism is less sensitive to the structural and proprioceptive impairment of the ACL.

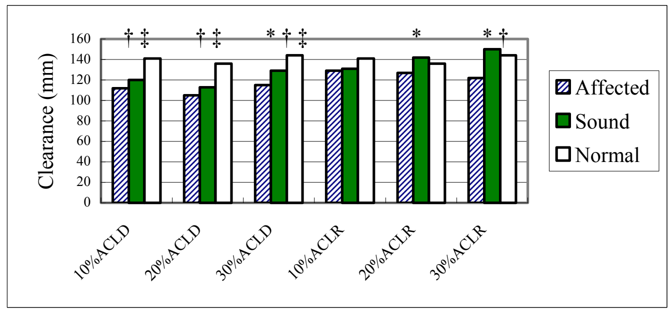

Fig. 1: Comparison of clearances in different conditions.
* Significant difference between affected and sound limbs
† Significant difference between affected and normal limbs
‡ Significant difference between sound and normal limbs

Knee extensor moments in the sound stance limbs were significantly bigger than those of the affected stance limbs when crossing obstacles of all heights in both ACLR (14.8, 5.2 Nm, $p<0.004$) and ACLD (14.1, 5.7 Nm, $p<0.029$) groups. This may be a result of muscular adaptation that tries to reduce anterior tibial translation in ACLD patients and protect the reconstructed ACL from excessive stress in ACLR patients.

Injury of the ACL affected joint proprioception and stability, resulting in insufficient information for the appropriate positioning of the leading leg and altered muscular control and force-bearing in passive structures for necessary stability of the body. The results of the present study suggest that ACLD patients are at higher risk of stumbling or falling in stepping over obstacles during locomotion and reconstruction of the ACL could reduce the risk.

REFERENCES

1. Chou, L.-S., Draganich, L. F. (1998). *Gait & Posture*, **8**, 186-204
2. Friden, T., Roberts, D., Zatterstrom, R. et al (1997). *J. Orthop. Res.*, **7**, 637-644.

RELATIONSHIP OF ANIMAL TO HUMAN METHODS FOR IN VIVO TENDON STRAIN DETERMINATION IN BIPEDAL LOCOMOTION

Rebecca B. Campbell[1,2], Michael B. Bennett[2] and Christopher L. Vaughan[1]
[1]Biomechanics Laboratory, MRC/UCT Medical Imaging Research Unit, Cape Town, South Africa
[2] Department of Anatomy and Developmental Biology, University of Queensland, Brisbane, Australia
rebecca@sports.uct.ac.za

INTRODUCTION

Most *in vivo* research to date has utilised animal models to investigate muscle-tendon mechanics due to the ethical and methodological limitations involved in human research. However, with modern techniques, the study of *in vivo* muscle-tendon mechanics in humans has been realised. The question remains: how applicable and accurate are animal models for human studies?

Chronic soft tissue injuries that occur with running are thought to result from the accumulation of damage from sub-maximal forces within the musculo-tendinous structures. Measurements of these forces *in vivo* are required, but are essentially impractical for most human studies. Such measures may be obtained for locomotion through the use of animal models.

METHODS AND RESULTS

Turkeys present an ideal model to investigate the muscle-tendon mechanics of bipedal locomotion *in vivo*, due to the presence of mineralised tendons in their lower limbs. This mineralisation permits the surgical attachment of strain gauges for *in vivo* strain measurements, providing a direct measure of the forces involved during treadmill locomotion. Such an application for humans does not exist due to higher tendon compliance and lack of mineralisation.

Turkey tendon force levels were found to increase from walking to running (Figure 1).

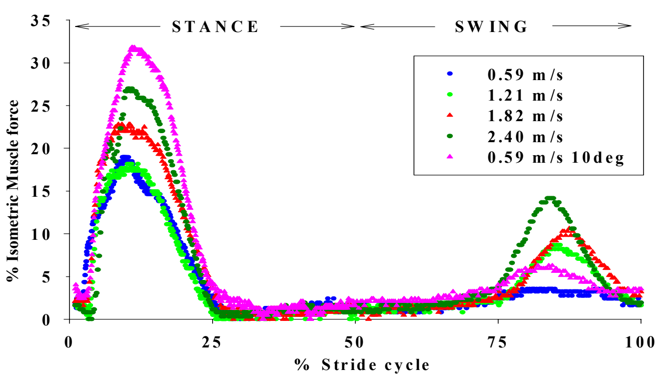

Figure 1: Example of *in vivo* tendon force (lateral gastrocnemius) for increasing speed in turkey locomotion, presented as a percent of the estimated maximal isometric muscle force, as recommended by Ker et al. (1988). Stance and swing phases are normalised so that each represents half of the stride cycle.

DISCUSSION

The data presented here show that the peak force levels experienced during level walking and running (≤1.8m/s), by the lateral gastrocnemius tendon, were less than one third of the maximal isometric force capability of the associated muscle. Treadmill locomotion on a 10° incline resulted in a dramatic increase in the forces recorded at any given speed, although peak forces were still less than 33% of the calculated isometric muscle force. These findings indicate that this muscle-tendon complex operates with a large safety factor during normal locomotion.

Early measures of tendon force in humans used force buckle transducers (Komi et al., 1987). Recent advances have used a relatively pain-free optical fibre technique to estimate Achilles tendon forces during walking (Finni et al., 1998). Finni et al. (1998) reported that the peak tensile stress for the Achilles tendon in humans during walking was 55% of the maximal isometric plantarflexion stress. The apparent large differences between gastrocnemius mechanics in humans and turkeys is probably due to a greater utilization of elastic strain energy for economical locomotion in the larger, more cursorial humans.

Accurate *in vivo* measures for muscle-tendon variables (namely moment arm lengths, fascicle lengths and pennation angles) by ultrasonography and nuclear magnetic resonance imaging (nMRI) are currently limited to isometric voluntary contractions on a plinth or during static postures (Rugg et al., 1990; Muramatsu et al., 2002). These methods are inadequate to fully describe and replicate the movement and forces involved during locomotion. Consequently, we are unable to accurately determine the function of human muscle-tendon mechanics during locomotion. Such measures do assist in the development of accurate theoretical models. The study of animal models remains an important area of research, for the determination of muscle-tendon mechanics during locomotion.

REFERENCES

Finni, T. et al (1998). *Eur J Appl Physiol* **77(3)**, 289-91.
Ker, R.F. et al (1988). *J Zool., Lond* **216**, 309-324.
Komi, P.V. et al (1987). *Int J Sports Med* **8**, 3–8.
Maganaris, C.N. et al (2001). *J Appl Physiol* **90**, 865-872.
Martin, D.C. et al (2001). *J Anat* **199(4)**, 429-434.
Muramatsu, T. et al (2002). *J. Biomech* **35(2)**, 217-223.
Rugg, S.G. et al (1990). *J Biomech* **23**, 495–501.

DIFFERENT MUSCLE ACTIVATION PATTERNS DURING WALKING AND RESPONSE TO COMMON PERONEAL STIMULATION

Jane Burridge[1], Lindsay McLellan[1], Paul Taylor[2] Duncan Wood[2]
[1]University of Southampton, School of Health professions and Rehabilitation Sciences, Southampton UK (jhb1@soton.ac.uk)
[2]Department of medical Physics and Biomedical Engineering, Salisbury District Hospital Salisbury UK

INTRODUCTION

There is a growing body of research evidence to support the use of common peroneal nerve stimulation for the treatment of spastic drop foot (Burridge1997 & Wieler 1999), yet it is not commonly used in clinical practice. There may be many reasons for this, including cost, reliability of equipment, and problems experienced by users in effective application. One reason for poor acceptance, that may also explain the varied response identified in clinical trials, may be that effectiveness is dependent on underlying neurophysiology. An understanding of which may allow more precise selection of patients. Using the experience of Knuttson (1994), this study investigated muscle activation patterns recorded during treadmill walking and related these to individual response to stimulation. The objective was to see whether response to stimulation could be predicted by certain abnormalities commonly observed in the upper motor neuron syndrome.

METHODS

Individuals with established hemiplegia (>6 months) following stroke, who had a drop foot that hindered walking, and age matched neurologically unimpaired volunteers were recruited. Individuals with hemiplegia were assessed on three occasions to establish a baseline, prior to using common peroneal stimulation, and volunteers were assessed once. Stimulation was applied using the ODFS III Pulse width 0 - 300µs (biphasic) frequency 40Hz, current 20-100mA.

EMG was recorded using Medelec surface electrodes from the calf and anterior tibial muscles - Signals were pre-amplified at source (gain x15, bandwidth 10 – 1000 Hz, common-mode rejection 100 dB at 50 Hz). Further amplification was provided, before each signal was rectified, then integrated using a low pass filter, using a 2µ2 F capacitor (time constant 13.8 seconds). Phases of the gait cycle were identified by Force Sensitive Resistor (FSR) foot-switches under the heel and 1st metatarsal heads of both feet. Digitised data were recorded on video-tape and five-second samples were retrieved for analysis at a later date. Ratios of calf and anterior tibial muscle activity during defined phases of the gait cycle were used to derive indices to describe three muscle activation patterns. a) ability to activate the anterior tibial muscles during the swing phase of walking (TAAI), b) ability to activate the calf muscles during push-off (POI) and c) inappropriate calf activity during early stance phase, described as premature calf activation, (PCAI). Spasticity of the calf was measured as response to passive stretch prior to the walking tests (Burridge 2000).

Response to common peroneal stimulation was measured as change in walking speed, and physiological Cost Index, both with and without stimulation, measured over 10m.

RESULTS AND DISCUSSION

18 hemiplegic subjects, 10 right and 8 left sided, mean age 61 years, 11 male, 7 female, mean time since stroke 3 years and 12 volunteers mean age 57 years, 5 male, 7 female were recruited and completed the study. Results were not normally distributed therefore non-parametric tests were applied and are summarised:

- A statistically significant difference between normals and hemiplegic subjects in PCAI $p=0.001$and POI $p=0.001$, but not TAAI $p=0.325$
- A statistically significant correlation between PCAI and spasticity measured as a stretch index (Spearman) 0.582 $p<0.05$ ($n=16$) prior to the walking test described in a previous publication (Burridge 2000).
- A significant correlation between PCAI and increase in walking speed with stimulation (Spearman) 0.459 $p< 0.05$
- Subjects who had premature calf activation tended to strike the ground with the toe before the heel

SUMMARY

In this small study statistical results should be interpreted with caution and validated with a larger sample of both impaired and unimpaired individuals. Nevertheless the following points could be considered:

- Patients with inappropriate calf activity may respond well to stimulation through the reciprocal inhibition mechanism
- If so, maintaining stimulation beyond heel strike may be beneficial
- There is no indication that inability to activate the anterior tibial muscles can be used to predict a good response to stimulation
- In some cases calf stimulation during the push-off phase may be useful - possibly in early rehabilitation
- A simplified version of the walking test may be useful clinically and to identify suitable subjects for future studies

REFERENCES

Burridge JH, Taylor PN, Hagan SA, Wood DE, Swain ID. (1997) The Effects of Common Peroneal stimulation o the effort and speed of walking. *Clinical Rehabilitation* **11**:201-210

Burridge JH and McLellan DL. (2000) Relation between abnormal patterns of muscle activation and response to common peroneal nerve stimulation in hemiplegia *Journal of Neurology, Neurosurgery and Psychiatry*; **69**, 353-361

Knutsson, E. (1994) Can gait analysis improve gait training in stroke patients. *Scand J Rehab Med Sup* **30**, 73-80

Wieler M, Stein R, Ladouceur M, Whittaker M, Smith,AW, Naaman S, Barbeau H, Bugarest J, Aimone E. (1999) Multi-center evaluation of Electrical Stimulation Systems for Walking. *Arch Phys Med Rehabil* Vol **80**, May

SELF-ASSEMBLING PEPTIDE SCAFFOLD PROMOTES DIFFERENTIATION AND NETWORK FORMATION IN THREE-DIMENSIONAL CULTURE OF HUMAN MICROVASCULAR ENDOTHELIAL CELLS

Daria Narmoneva, Richard T. Lee[1], Jonathan G. Gertler[2], and Roger Kamm
Department of Mechanical Engineering, Massachusetts Institute of Technology, Cambridge, MA, rdkamm@mit.edu
[1] Cardiovascular Research, Brigham & Women's Hospital, Boston, MA; [2] Vascular Surgery, Mass. General Hospital, Boston, MA

INTRODUCTION

Engineering of vascularized grafts and organs is a rapidly evolving area of current biomedical research (Vacanti & Langer, 1999). Increasing understanding of the mechanisms that govern angiogenesis opens new opportunities for manipulating this process in both clinical and tissue engineering applications (Carmeliet & Jain, 2000). Recently, a new class of biomaterials - self-assembling peptide scaffolds - has been developed, which are extremely promising for use as biological scaffolds for tissue engineering (Zhang et al., 1995, Holmes 2002). This study presents evidence that one type of the self-assembling peptide scaffolds promotes a rapid angiogenic response and long-term survival of human microvascular endothelial cells, indicating the potential of this material for tissue engineering of vascularized organs.

METHODS

Human microvascular endothelial cells were isolated from fat tissue and cultured on gelatin-coated dishes. Cells (passage 4-6) were trypsinized, seeded on the surface of the self-assembling peptide gel (peptide RADII-16, 1%, Zhang et al., 1995) and cultured for up to 3 weeks using Medium 199 (Gibco) with 10% FCS, 5% heparin, and 1% ECGS (Sigma). Cells cultured on gelatin-coated dishes were used as controls. Cell phenotype was evaluated by immunostaining for human von Willebrand Factor (DAKO). Cell proliferation and apoptosis were assessed using BrdU kit (Zymed) and TUNEL assay (Roche), respectively. To characterize capillary network formation, cell cultures were fixed in 2% paraformaldehyde for 2 hr and stained using DAPI nucleic acid fluorescent stain (Molecular Probes) or anti-actin monoclonal antibody (Chemicon). Gray-scale images of the cell networks were taken using a fluorescence microscope (Nikon) and then used to calculate a correlation function $F(\boldsymbol{R})$, where $\boldsymbol{r}$ is a position vector measured in pixels on the original image, $\boldsymbol{R}=(R,\theta)$ represents the correlation vector, $I(\boldsymbol{r})$ is image intensity at $\boldsymbol{r}$, "$< >$" denotes averaging over $\boldsymbol{r}$, I_{ave} is average image intensity,

$$F(\boldsymbol{R}) = \frac{\left\langle \left(I(\boldsymbol{r}) - I_{ave} \right)\left(I(\boldsymbol{r}+\boldsymbol{R}) - I_{ave} \right) \right\rangle}{\sigma^2} \qquad (1)$$

and σ is standard deviation for $I(\boldsymbol{r})$. The function $F(\boldsymbol{R})$ was then averaged over θ to obtain $F(R)$ as a function of distance.

RESULTS AND DISCUSSION

Within 2 hours of seeding on the peptide gel, cells attached and started to migrate toward each other. Initial structures were formed at 8 hours, and final structures were formed by 24 hours, with most cells assembled into capillary-like networks (Figure 1A). Correlation analysis demonstrated a gradual increase in characteristic size of the structures on the gel with time, while no structures were detected in control cultures (Figures 1B,C). During long-term culture, cells migrated into the gel and were actively proliferating with no significant signs of apoptosis and minimal gel degradation.

In summary, these data suggest that RADII-16 peptide gel supports endothelial cell migration, proliferation and capillary-like structure formation and survival for a period of at least 3 weeks. In contrast to other three-dimensional substrates used for studies of angiogenesis *in vitro* (Vailhé et al., 2001), this angiogenic response was observed in the absence of externally supplied angiogenic factors. These results indicate that the self-assembling peptide scaffold provides a substrate that triggers a self-sustaining angiogenic process in endothelial cell culture and therefore, is promising for *in vitro* studies of angiogenesis and engineering of vascularized organs.

REFERENCES

1. Vacanti, J.P., Langer, R. (1999) *Lancet,* 354(Suppl), 134-142. 2. Carmeliet P, Jain RK. (2000) *Nature*, 407, 249-257. 3. Zhang S, et al.. (1995) *Biomaterials*, 16:1385-1393. 4. Holmes TC. (2002) *Trends Biotechnol*, 20(1):16-21. 5. Vailhé B, et al. (2001) *Lab Invest*, 81:439-452.

ACKNOWLEDGEMENTS Support for this work has been provided by Aircast Corp.

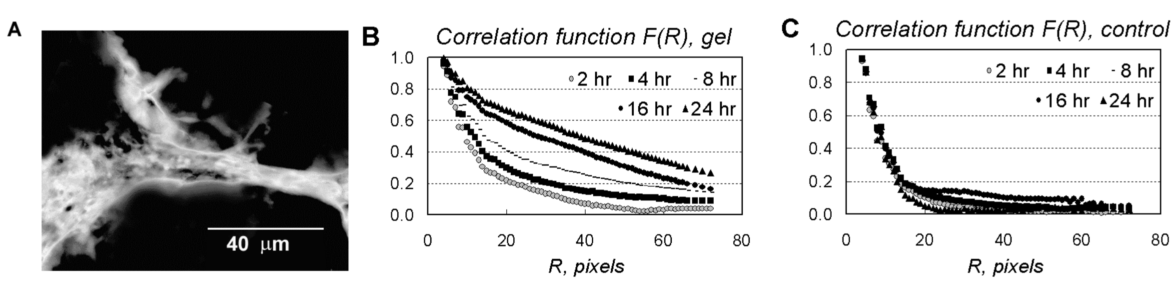

Figure 1. A – actin staining of capillary-like network formed by human endothelial cells on the peptide gel at 24 hr after seeding. B - increasing long-range correlation for cells cultured on the gel reflects network formation over time. In contrast, only short-range correlation corresponding to characteristic nucleus size is present in the control cultures (C).

COMPARISON OF SCAFFOLD DESIGNS FOR TISSUE-ENGINEERED SMALL-DIAMETER GRAFT APPLICATIONS

A. Ratcliffe[1], L. K. Landeen[1], M. Sotoudeh[1], H. G. Alexander[1], D. DalPonte[2], A. Garcia[1], L. Kleinert[2], A. Kern[1], S. Ong[1], A. Jahed[1], R. Calzo[1], S. Chien[3], Y-C Fung[3], S. K. Williams[2].
[1]Advanced Tissue Sciences, Inc., 10933 N. Torrey Pines Rd., La Jolla, CA 92037 USA (tony.ratcliffe@advancedtissue.com)
[2]University of Arizona, Biomedical Engineering Program, Health Sciences Center, 1501 N. Campbell Ave., Tucson, 85724, AZ, USA
[3]University of California San Diego, Department of Bioengineering, 9500 Gilman Dr., La Jolla, CA 92093 USA

This research was funded in part with the U.S. Government support under cooperative agreement 70NANB7H3060 awarded by NIST.

INTRODUCTION Vascular disease represents a considerable health concern, and an inadequate supply of native vessels for bypass procedures has created a significant need for clinically successful alternatives. While small-diameter synthetic vascular grafts made from expanded polytetrafluoroethylene (ePTFE), polyethylene terephthalate (PET; Dacron) or polyurethane (PU) have been used to satisfy this need, they have not matched long-term patency rates of autologous vessels. Incorporation of proteins (e.g. albumin, collagen, gelatin or elastin) or treatment with anti-thrombotic agents (e.g. heparin or hirudin) have been evaluated to improve patency. To date, long-term improvement in patency has not been achieved with these treatments. Some improvements have been achieved with endothelialization; however, there is a continued interest in new approaches for designing vascular grafts to improve biocompatibility and long-term function. Using a cell-scaffold-based approach, we have developed small-diameter (<5-mm ID) tissue-engineered vascular grafts (TEVGs) by culturing allogeneic canine smooth muscle cells (SMCs) on porous PU, ePTFE or braided PTFE tubular scaffolds, followed by endothelialization with autologous microvascular endothelial cells (MVECs). The objectives of these studies were to optimize scaffold design and endothelialization and to evaluate TEVG performance in a canine carotid artery implantation model.

MATERIALS AND METHODS Porous (63-500-µm pore sizes) aromatic polyether PU (Thermedics) tubular scaffolds (4-5- mm OD, 0.75-mm wall thickness, 7-cm length) were fabricated using solvent-casting particulate-leaching methods at 85-93% w/w ratio of salt to polymer. ePTFE scaffolds (4-mm ID, 20- or 120-µm internodal distance [IND], 6-cm length) and braided PTFE scaffolds (5-6-mm ID, 6-cm length) were obtained from Atrium Medical Corp. and Prodesco, respectively. All scaffolds were irradiation-sterilized, coated with fibronectin, seeded with allogeneic adult canine SMCs (passage 5-8) and cultured for 2-5 wk in bioreactors under low-flow (10 ml/min) or high-flow (50 ml/min) conditions in 20% FBS DMEM growth medium containing $CuSO_4$ and ascorbic acid. Autologous falciform fat-derived canine MVECs were seeded at subconfluent densities onto the TEVG lumens and cultured under low fluid shear stress (0.5-0.75 dynes/cm^2) for 3-4 d, followed by a stepped increase in fluid shear stress (3-6 dynes/cm^2) for an additional 3-4 d. All cultures were maintained in 5% CO_2, 37°C humidified incubators. TEVGs were examined for cell viability (MTT mitochondrial assay), for collagen (hydroxyproline assay) and elastin (desmosine RIA) content, and for cell identification by immunohistochemistry and SEM. Endothelialized TEVGs (4-cm lengths) (n=4 PU-based, n=6 ePTFE-based, and n=6 braided PTFE-based) were implanted interpositionally (end-to-end anastomoses) in canine carotid arteries, and implant-phase patency was monitored by ultrasonography. All dogs received daily aspirin for the course of the studies. All procedures and study protocols were reviewed and approved by the Univ. of AZ IACUC and carried out according to the *NIH Guidelines for the Care and Use of Laboratory Animals*. At explant, each TEVG and adjacent native vessel (>2 cm beyond each anastomosis) was harvested, photographed, fixed and prepared for histological, immunohistochemical and SEM assessment.

RESULTS PU scaffolds of 150-300-µm pore size and 90% w/w and cultured at 10 ml/min were found to support optimal SMC tissue. This SMC tissue contained collagen types I and III and elastin and was capable of secreting a number of endothelial-responsive growth factors including vascular endothelial growth factor (VEGF). TEVG SMCs were oriented perpendicular to flow and stained positive for the intracellular contractile proteins SM α-actin, calponin and myosin heavy chain (the latter two being characteristic of differentiated SMCs in native tissues). MVECs adhered to the SMC tissue and SEM showed an intact monolayer with the MVECs aligned in the direction of fluid flow. Patency in both implanted PU MVEC-TEVGs and contralaterally implanted control grafts (untreated ePTFE) was 25% at 6-7 weeks. Several PU MVEC-TEVGs exhibited scaffold biodegradation and aneurysm formation that may have contributed to the decreased patency observed in this experimental group.

TEVGs made using ePTFE (120-µm IND only) or braided PTFE scaffolds also showed SMC tissue formation and the ability to support endothelialization. One out of six implanted MVEC-TEVGs (for each group) occluded within 72 hr after implantation, whereas all other TEVGs remained patent. At 4 and 8 wk, one patent TEVG from each group was selected for explantation. Twelve-wk implant-phase ultrasound evaluation showed that each remaining TEVG (n=3 each) was patent with no evidence of anastomotic or mid-graft intimal thickening. Gross and histologic evaluation demonstrated the absence of aneurysm or thrombus formation, an intact endothelium on the lumenal surface, and no occlusive intimal thickening of the underlying SMC tissue.

CONCLUSION Scaffold design (90% w/w and 150-300-µm pore size for PU, 120-µm IND for ePTFE and braiding for PTFE) was important for enhancing SMC neo-media development that provided a suitable substrate for endothelial cell adherence and maturation. The selected PU was not biostable in vivo and hence impacted TEVG performance. More importantly, the results with ePTFE-based and braided PTFE-based TEVGs demonstrated moderate- to long-term patency and that a cell-scaffold-based approach to tissue engineering can be used to modify synthetic materials. This approach holds significant promise towards development of an alternative small-diameter vascular graft.

TISSUE ENGINEERED BLOOD VESSELS (TEBV) : THE FUTURE IS NOW

François A. Auger M.D. FRCP (C)
LOEX Hôpital du Saint-Sacrement
1050, chemin Ste-Foy
Québec (Québec) G!S 4L8 Canada
Francois.auger@chg.ulaval.ca

INTRODUCTION

Successful tissue engineering of blood vessels is one of the most difficult goals in this field of biotechnology. It holds great promises but has also some very demanding hurdles before true clinical success can be achieved. The replacement of small-diameter blood vessels (≤6 mm) is a clinical situation frequently encountered by vascular and cardiothoracic surgeons.

TEBV CHALLENGES

During the last decades, progress in the field of tissue engineering has allowed investigation in this area. Our laboratory was implicated in such a project and, on the basis of previously published blood vessel models composed of living cells embedded in an exogenous collagen matrix, we developed, using the self-assembly approach, the first completely biological tissue-engineered blood vessel (TEBV) constituted of living human cells in the absence of any synthetic or exogenous material.

The TEBV produced has a morphological and histological structure closely comparable to a natural blood vessel. It is composed of an endothelium lying on a sub-endothelial layer of collagen fibers, a media, and an adventitia, respectively composed of smooth muscle cells and fibroblasts surrounded by their own extracellular matrix, as in a native vessel. In the absence of culture support, this TEBV does not collapse, shows an impressive burst strength resistance (2500 mm Hg) and can be easily handled as was proven when tested in femoral interposition prostheses in dogs [24]. In light of its composition, this TEBV has the distinct advantage of being completely biological and thus, presents the possibility of being produced autologously with a wide range of inner diameters (3 mm or more), is fully biocompatible and able to renew itself over time if damaged.

Consequently, the production of these autologous TEBV conduits, even though their preparation is quite long (4 months), could be the ideal solution for most clinical situations and could possibly eliminate reinterventions and anticoagulotherapies associated with biomaterial prosthesis implantations.

Thus, the characteristies of all vascular substitutes must reach a level of mechanical properties and biological functionalities unknown in any other tissue engineered construct. This presentation will address the clinical demands on both these aspects since they set the stage for some fascinating bio engineering challenges.
According to the method of tissue engineering reconstruction chosen in order obtain these TEBV some goals will be either easier to reach or not so.

Furthermore the aspects of TEBV in vitro applications will be assessed in the present context pertaining to angiogenesis.

CONCLUSION

Thus, the field of TEBV, which was deemed to be an impossible feat a decade ago, is now the Holy Grail of tissues regeneration. It has a bright future if all the obstacles are vanquished in this pursuit.

SCAFFOLDS IN CARDIOVASCULAR TISSUE ENGINEERING – ULTRA THIN LAYER BY LAYER

Swee-Hin Teoh

Laboratory for Biomedical Engineering, Division of Bioengineering and Department of Mechanical Engineering
National University of Singapore, Engineering Drive 3, 10, Kent Ridge Crescent, Singapore 119260

INTRODUCTION

Recent publications on cardiovascular tissue engineering have shown that this is a vibrant field of research. Nerem and Selikar (2001) reviewed the vascular tissue engineering. The issues addressed ranges from stem cells technology to know-how in scaffolds manufacturing. Work by Auger's team showed that by growing the cells in sheets and then rolling them into a tube eliminates immunological mismatch and the smooth muscles cells (SMCs) re-expressed desmin, a differentiation marker known to be lost under culture conditions. Large amount of extra cellular matrices (ECM) were produced and the structural integrity maintained. However, the handling of the sheets is delicate and it is not clear if the material would survive the viscoelastic compliance mismatch in long-term in vivo physiologic environment. One of the earliest report of a human trial is a 10 mm diameter artery (Shin'oka et al 2001). Here a biodegradable poly-caprolactone (PCL)-polylactic acid (PLA) copolymer was seeded successfully with cells from the patient's peripheral vein. However for smaller diameter vessels less than 5 mm, there has not been significant breakthroughs. One major obstacle is the over SMCs proliferation. Recent work (Kaushal et al 2001) showed the role played by endothelial progenitor cells (EPCs) in inhibiting SMCs in a 4 mm vessel. It seems that the EPCs expressed nitric oxide. Similarly immobilizing dipyridalmole on surfaces of porous polyurethane 5 mm vascular prosthesis (Aldenhoff et al 2001) showed improved results as dipyridalmole is a strong inhibitor of SMCs and platelet activation.

In our present work we propose a composite layer-by-layer technique using ultra thin bioresorbable membrane. Figure 1 shows schematically the concept as applied to blood vessel and heart valve construct.

METHODS

Earlier publication described the method for producing ultra thin membrane and cells seeding (Ng et al 2001). The membrane is made by a special bi-axial stretching technique pioneered by our group using PCL of 80,000 molecular weight to a thickness less than 4 µm, a breakthrough in developing barrier membrane for tissue engineering. Human dermal fibroblasts were used as preliminary trials to see how the cells respond.

RESULTS AND DISCUSSION

We engineer the barrier membrane so thin that we hope to define the boundaries for cell proliferation and provide strength for long-term physiologic stress stimulation in vivo.

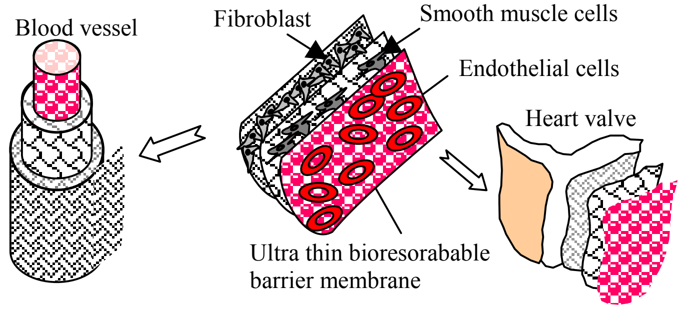

Figure 1: Schematic illustration of growing cells layer by layer on an ultra thin bioresorbable barrier membrane scaffold.

It is envisaged that the slow degradation of PCL would maintain the 3D geometry and invoke less severe host response to biodegradable products. The AFM result (Figure 2) shows that the membrane has nano-porosity. Figure 3 shows that the membrane is highly flexible but yet strong. The tensile strength is close to 50 MPa. The cells proliferate and conform to the surface morphology nicely (Figure 4).

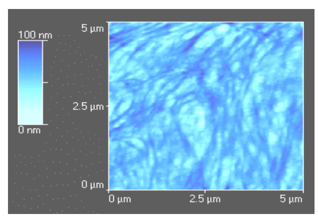

Figure 2: AFM picture.

Figure 3: Ultra thin film.

This shows good biocompatibility and potential for composite tissue engineering layer-by-layer, a strategy for more viable tissue regeneration. The surface properties of the material have a strong biophysical influence on the cell kinetics. The PCL film can be surface modified to immobilize proteins, growth factors and SMCs inhibitors. Recently we saw vascular structures penetrating the film (Schantz et al 2002).

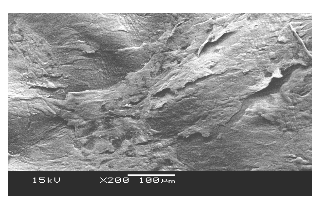

Figure 4: SEM of fibroblast on PCL after 1 day.

REFERENCES

Aldenhoff Y.B.J. et al (2001). *J. Biomed. Mat. Res.*, **54**, 224-233.
Kaushal, S. et al (2001). *Nature Med.*, **7**, 1035-1040.
Nerem, R.M., Seliktar, D. (2001) *Annu. Rev. Biomed. Eng.*, **3**, 225-243.
Shin'oka, T. et al (2001), *N. Engl. J, Med.*, **344**, 532-533.
Ng, K.W. et al (2001), *Tissue Eng.*, **7**, 441-455.
Schantz J-T. et al (2002), Int. J. Oral Max. Implants, (in press).

MECHANICAL PROPERTIES OF ELASTIN-HYBRID TISSUE ENGINEERED VASCULAR CONSTRUCTS

Joseph D Berglund, Athanassios Sambanis, Robert M Nerem
P H Petit Institute for Bioengineering and Bioscience, jdberglund@earthlink.net
Georgia Institute of Technology, Atlanta, Georgia, USA

INTRODUCTION

Collagen-based tissue engineered vascular constructs have many interesting properties and have been utilized to study various aspects of vascular biology for many years. Unfortunately, these constructs possess poor mechanical properties and are too weak to be implanted for *in vivo* studies. In addition to collagen, elastin fibers comprise a large fraction of the extracellular matrix (ECM) of native arteries and are responsible for elastic recoil during pulsatile blood flow. We have developed a method to incorporate elastin with organized structural architecture into collagen-based vascular constructs in an effort to better mimic the native arterial physiology and to improve the mechanical properties of the constructs. This study investigates some of the chemical, biological, and mechanical issues associated with these elastin-hybrid constructs.

MATERIALS AND METHODS

Intact elastin scaffolds were procured from porcine carotid arteries using a series of phosphate buffer rinses; autoclave cycles; trypsin, cyanogens bromide, and β-mercaptoethanol incubations; and ethanol washes. Purity of the elastin scaffolds were verified via immunohistochemical staining and amino acid sequencing. Hybrid constructs were formed using acid-solubilized Type I rat tail collagen and either human dermal fibroblasts (HDFs) or rat aortic smooth muscle cells (RASMs). Collagen solutions (2 mg/ml) containing suspended cells ($1x10^6$ cells/ml) were poured into tubular molds about the elastin scaffolds and gelled at 37°C. The resulting constructs were statically cultured for up to twenty-three days prior to analysis. Standard collagen constructs without elastin scaffolds were also cultured as controls.

Construct function and viability was assessed using live/dead analysis, gel compaction quantification, and Hoescht DNA assays. H&E and immunostaining was used to examine ECM organization. Mechanical strength and viscoelastic characterization was assessed using uniaxial tensile testing, creep analysis, and stress relaxation. The resulting stress-strain profiles were evaluated to obtain a number of mechanical parameters and fit to Burger's four parameter mathematical model using non-linear Newtonian regression.

RESULTS AND DISCUSSION

Concentric lamellar rings surrounded by loosely woven fiber lattices presented brightly in the isolated scaffolds when stained with the anti-elastin BA-4 antibody. Amino acid analysis of the digested scaffolds compared favorably with elastin values reported in the literature indicating a high degree of purity. While the cells were able to rapidly remodel their surrounding matrix both with and without the matrix, the collagen-based controls compacted to a greater extent than the elastin-hybrid constructs. Additionaly, HDFs compacted the gels to a larger extent than the RASMs.

Figure 1: Ultimate tensile stress mechanical parameters

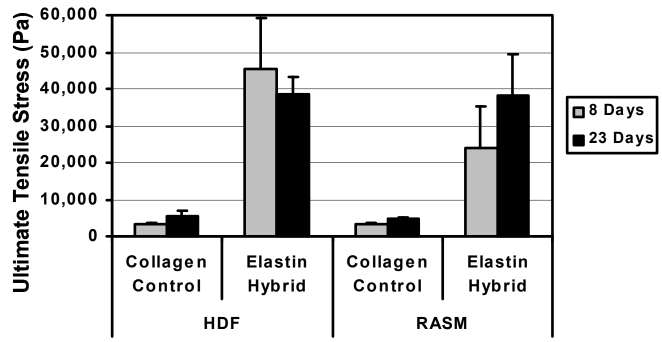

Incorporation of elastin scaffolds improved the mechanical properties of the constructs. Shown in Figure 1, the ultimate tensile stresses (UTS) were significantly higher in the elastin-hybrid constructs. The viscoelastic properties of the elastin-hybrid constructs also improved (see Table 1). The η1 parameters are of particular interest as they describe the long-term creep behaviors. No statistically significant differences were observed between days eight and twenty-three for either the elastin-hybrid or collagen control constructs.

SUMMARY

Hybrid constructs that combine intact elastin scaffolds with a cell-seeded collagen gel provide a promising approach for the development of a TE blood vessel model. These constructs remain viable for up to 23 days and exhibit improved mechanical properties compared to collagen controls. Current work efforts are focusing on optimizing the hybrid constructs in an attempt to expand our studies to *in vivo* investigations.

Table 1: Burger's model parameters of HDF constructs as determined through creep analysis (8 Days/23 Days)

	Collagen Control	Elastin Hybrid	Native Carotid
R_1 (Pa)	$4.2x10^3/1.3x10^4$	$6.3x10^4/4.0x10^4$	$1.9x10^5$
η_1 (Pa/s)	$3.7x10^6/1.7x10^7$	$1.9x10^9/1.4x10^9$	$5.8x10^8$
R_2 (Pa)	$7.2x10^3/1.5x10^4$	$4.2x10^5/2.5x10^5$	$1.9x10^5$
η_2 (Pa/s)	$2.8x10^5/1.1x10^6$	$3.7x10^6/7.1x10^6$	$2.6x10^7$

MECHANICAL FORCES AND ENGINEERED VESSELS

Laura E. Niklason and Amy Solan
Department of Biomedical Engineering, Duke University, Durham North Carolina
nikla001@mc.duke.edu

INTRODUCTION:

Blood vessels in the body are exposed to constant pulsatile physical forces due to the cardiac cycle. Native arteries are known to respond to changes in applied pressure and wall stress with changes in cellular proliferation and extracellular matrix deposition. Recently, several groups have shown that application of pulsatile physical forces in vitro can impact the development of tissue engineered arteries (Niklason 1999; Seliktar 2000). However, these effects have not been quantified in detail, and the impact of applied physical forces on engineered vessel mechanics have not been fully explored.

METHODS:

Porcine carotid vascular smooth muscle and endothelial cells were harvested from Yucatan miniature swine. Cells were cultured in Dulbecco's Modified Eagles Medium (DMEM) supplemented with fetal bovine serum, porcine serum, amino acids, copper and ascorbate. Vascular smooth muscle cells (SMC) were utilized at passage 3 to culture engineered arteries. Cells were seeded at 5×10^6 cell/ml onto polyglycolic acid mesh scaffolds that were secured in bioreactors and attached to a pulsatile perfusion system. Scaffolds were 8 cm in length, 3 mm internal diameter, and 1 mm thickness (Freed 1994). Vessels were cultured under one of three conditions: non-pulsatile, 1% distension at 90 beats per minute (bpm), 1% distension at 165 bpm. Vessel culture proceeded for 6-7 weeks, after which vessels were analyzed for cellularity, extracellular matrix composition, and mechanical properties.

Cellularity was determined from papain-digested samples that were reacted with H33258 Hoechst dye and analyzed in a spectrofluorometer at an excitation wavelength of 365 nm and an emission wavelength of 458 nm. Collagen (calculated as 10x hydroxyproline) was assayed by acid hydrolysis in 6 N HCl at 115° C for 18 hours, and reaction with p-dimethylaminobenzaldehyde and chloramine-T. Collagen covalent cross-links (pyridinolines) were assayed from acid hydrolysis samples by reverse-phase HPLC and detected by fluorometry. Matrix metalloproteinase-1 (MMP-1) and tissue inhibitor of MMP-1 (TIMP-1) were assayed using commercially available ELISA's according to manufacturer's instructions (BioRad). Vessel mechanical characteristics were measured using techniques similar to those previously described (Niklason 2001). We utilized a Canon XL1 digital video camera that is equipped with a 180 mm/3.5 F-stop lens with an effective pixel size of 20 microns to acquire images of vessels under a range of distending pressures. Data were analyzed using NIH Image software and a MacIntosh G3 computer.

RESULTS AND DISCUSSION:

Pulsatile physical forces exerted during the culture period resulted in significantly increased accumulation of insoluble collagen in engineered blood vessels. This result was noted for both the 90 bpm and the 165 bpm conditions, as compared to non-pulsed controls. While both TIMP-1 and MMP-1 tended to increase under pulsatile conditions, these increases did not achieve statistical significance. Hence, it is likely that increased rates of collagen synthesis, as opposed to changes in collagen breakdown and remodeling, were responsible for the observed changes in collagen accumulation effected by pulsatile forces.

In keeping with the key role of insoluble collagen in blood vessel mechanics, vessels that were cultured under pulsatile conditions had increased burst strengths and improved tensile moduli as compared to non-pulsed controls. However, because of a substantive lack of insoluble elastin in these engineered constructs, vessels displayed substantial creep during in vitro testing. These results show that the application of pulsatile physical forces is key to the engineering of vascular grafts having improved compositional and mechanical characteristics.

REFERENCES:

Freed, L. E., Vunjak-Novakovic, G., et al (1994). Bio/Technology **12**: 689-693.
Niklason, L. E., Gao, J., et al (1999). Science **284**: 489-493.
Niklason, L. E., Abbott, W.A., et al (2001). Journal of Vascular Surgery **33**: 628-638.
Seliktar, D., Blcak, R.A., et al (2000). Annals of Biomedical Engineering **28**: 351-362.

ENGINEERED ARTERIAL RECONSTRUCTION: INTEGRATION OF BIOMECHANICAL, GENETIC, AND STEM CELL ENGINEERING

Takehisa Matsuda
Department of Biomedical Engineering, Graduate School of Medicine, Kyushu University, Fukuoka, Japan
matsuda@med.kyushu-u.ac.jp

INTRODUCTION

The patency of an implanted vascular graft is reduced by thrombus formation in an early period of implantation and an excessive intimal hyperplasia in a later stage, both of which become more critical as an inner diameter of the graft becomes smaller. To realize small-diameter graft in clinical application, a multifaceted approach is needed for vital functioning small-diameter graft. One such an approach which has been taken over two decades is to utilize vascular cell types as active components. However, clinical application has been limited due to difficulty endothelial of cell (EC) harvesting from patients. The other major problem is compliance mismatching of artificial graft or scaffold with native arteries, which has been discussed over the years, resulting in thrombus formation and excessive intimal tissue ingrowth, both of which are quite critical especially for a small-diameter graft. In this talk, our recent approaches to engineered arterial reconstruction will be described, which include

1) biomechanical design of scaffold to exhibit compliance matching with native arteries,
2) gene-transfected fibroblasts as transient antithrombogenic cells replacing with ECs, and
3) circulating endothelial progenitor cell as a novel cell source.

1) Biomechanical design of scaffold

Our small-diameter artificial graft is a co-axial double-tubular graft with a high compliant tube inserted into a less compliant tube, both of which are made of multiply micropored thin segmented polyurethane (SPU) films. This double-tubular graft exhibited “J-curve” in the intraluminal pressure-diameter relationship, resembling that of native canine carotid arteries. After surface photoprocessing leading to formation of heparin/gelatin gel layering on the inner tube and very hydrophilic polymer gel layer on the outer tube, these grafts were implanted into canine carotid arteries. The results up to one year showed excellent patency and well-controlled neoarterial tissue formation. However due to an excess encapsulation at the outer surface of outer tube, a gradual deterioration of “J-curve” was noticed with time.

2) Genetical manipulation of fibroblasts as a transient cell source

Since fibroblasts are highly thrombogenic due to secretion of tissue factor (TF) which triggers the extrinsic pathway of coagulation cascade, in addition to no antithrombogenic bioactive machinery unlikely to ECs, fibroblasts, which can be easily harvested from patients’ skin, were gene-transfected with adenovirus encoding TFPI (tissue factor pathway inhibitor), CNP (C-type natriuretic peptide acts as multipotent tissue modulator) and/or VEGF (vascular endothelial growth factor). A tubular hybrid tissue fibroblasts inoculated collagen gel, transfected with these adenoviruses and wrapped with micropored SPU film, remarkably increased patency at one-month implantation into canine carotid arteries, and tissue remodeling proceeded well without endothelializaiton. The SEM observation showed minimal fibrin clot on the luminal surface, indicating that gene-transfected fibroblasts may be used as a luminal cell living.

3) Endothelial progenitor cells (EPCs)

EPCs were harvested and purified from monocyte fraction of circulating blood. The antithrombogenic potentials as compared with ECs were as follows: tPA (tissue plasm tissue plasminogen activator) fibrinolytic level of EPCs was almost same as that of ECs, whereas antiplatelet functional eNOs (NO synthase) and prostacylin production were almost one-half to one-third of ECs. After complete monolayering of EPCs on collagen-fiber meshes, wrapped with the micropored SPU film, exhibited very high patency as same as that of EP-lined grafts. Thus, EPC is a high choice of cell source, and an EPC-engineered graft incorporated with matrix and scaffold engineerings is a promising tissue-engineered vascular graft.

PRE-CLINICAL TESTING OF MECHANICAL HEART VALVES FOR POTENTIAL TO CAUSE THROMBOSIS: A MILK-BASED PROCEDURE AS AN ADJUNCT OR ALTERNATIVE TO ANIMAL TRIALS

Christy J.R.E., Martin A
University of Edinburgh, Edinburgh, EH9 3JL, Scotland, UK. E-mail: john@chemeng.ed.ac.uk

INTRODUCTION

Animal testing of artificial mechanical valves has for many years been the only accepted means of assessing the potential of the valve to thrombose or to cause thromboembolism. However, it is known that there are variations between species in both the chemical composition of the blood and the haemodynamics of the cardiovascular system. In addition, intra-species variations (as indeed are found in clinical practice) can lead to the necessity of extensive testing before reliable statistical data can be generated. This is especially true as valve designs improve and the differences in thrombogenic potential decrease. This is exemplified by experience in the mid 1990s of the Medtronic Parallel valve, where the valve showed no sign of thrombosis in animal trials, but thrombus formation in the region of the hinge came to light during clinical trials (Bodnar 1996).

An in-vitro procedure for assessing flow-related thrombosis, using milk as an analogue for blood (Lewis 1983, Christy 1989), has been developed to simulate the latter stages of thrombosis (i.e. the action of thrombin on fibrinogen). This procedure is reproducible, in that the enzyme, Chymosin, is added in controlled amounts to milk of known protein concentration. The test is not intended to model the activation of the clotting cascade but, in previous application to mechanical valves, comparison of milk-clotting with clinical thrombosis suggests that this is not important. In order to prove the usefulness of the technique in differentiating between valves whose potential to form thrombosis is low, we are analysing a range of valves for which incidence of clinical thrombosis is known.

METHODS

The technique originated in Edinburgh has been fully described elsewhere (Lewis 1983, Christy 1989). It uses a mixture of milk and cheese makers' rennet as the coagulable fluid in a once-through flow system in which metered, temperature-controlled streams of these components are blended shortly upstream of the valve under test. The chemical and chemical-kinetic resemblances between steps to clotting in this system and the latter stages of thrombus formation in blood have long been established (Jolles 1975). The delay before spontaneous coagulation is chosen to exceed the fluid transit time through the apparatus and the injection of calcium chloride ensures that any coagulum deposited can be made-to resemble thrombus in consistency and adhesiveness. A range of caged ball valves (Starr-Edwards silastic ball and cloth-covered strut valves), monoleaflet valves (Bjork-Shiley Standard, Bjork-Shiley Monostrut, Omniscience, and Ultracor) and bileaflet valves (St. Jude Medical and Duromedics) have been tested in our artificial heart.

RESULTS AND DISCUSSION

For the valves tested, milk clot forms in the locations for which thrombosis has been reported in clinical practice. There are, however, some instances where additional, thin films of clot form on discs or around the sewing ring which are not reportedly found with blood. However, the extent of clot deposition in such areas is generally low and is usually distinguishable by its appearance.

False positive results for clot formation may be due to a number of factors: the assumption that blood is already activated on passing through the valve, the geometry of our in-vitro test system, effects due to the presence of anticoagulants in blood and differences in properties (eg adhesion) of the two types of clot. Our model heart has a rigid ventricular chamber and the flow pulse is a modified sinusoid. For some valves this may result in modified opening dynamics and, in the case of the mitral position, recirculation zones that would not be present in-vivo. The localised effect of anticoagulants is unknown, but there is the possibility that their effectiveness will be greater around some valves than around others. We have endeavoured to match the properties of the milk clot to those of thrombus, but the relative adhesivity to different surfaces is not amenable to control.

Velocimetry studies at present are not capable of predicting thrombosis, but they can identify flow features conducive to thrombosis. Thus, whilst we are addressing the issue of haemodynamic characteristics of our test chamber, it would be possible to use this technique in its present form to act as a guide to regions for detailed flow investigation.

SUMMARY

An in-vitro milk clotting procedure is shown to result in clot formation in the same regions around mechanical valves as is thrombus in-vivo. Some evidence of additional clotting is also found. This test, perhaps conducted in conjunction with tests involving velocimetry (PIV or LDV), may provide a useful adjunct to animal trials for mechanical valves.

REFERENCES

Bodnar E. (1996) J Heart Valve Dis, **5**, 572-573
Lewis JMO, Macleod N. (1983) Cardiovasc Res, **17**, 466-475
Christy JRE, Macleod N. (1988) Cardiovasc Res, **23**, 949-959
Jolles P. (1975) Mol Cell Biochem, **7**(2), 73-85

UNDERSTANDING THE MECHANISMS OF MECHANICAL HEART VALVE CAVITATION

Keefe B. Manning, Arnold A. Fontaine[1], Steven Deutsch[1], Peter Johansen[2], Hans Nygaard[2], and John M. Tarbell

Department of Bioengineering and [1]Applied Research Laboratory,
Pennsylvania State University, University Park, PA
[2]Department of Cardiothoracic and Vascular Surgery,
Aarhus University Hospital Skejby Sygehus, Aarhus N., Denmark

INTRODUCTION

Cavitation associated with mechanical heart valve closure can damage valve materials and blood elements and remains poorly understood mechanistically. Evidence of cavitation in vivo has been noted in the form of pitting on explanted mechanical valve occluders (Kafesjian et al., 1989) and through high frequency pressure signatures (Chandran et al., 1998). In vitro cavitation studies attempt to simulate the fluid mechanical environment of valves in vivo in order to determine the mechanisms of cavitation. There are, however, aspects of the in vivo environment that have not been adequately simulated in vitro. In particular, CO_2, the most soluble blood gas, is not normally present in blood analog solutions and the gaseous nuclei present in the test fluids have not been fully characterized. The current study focuses on cavitation studies in blood analog fluids with varying nuclei content that have been supplemented with CO_2 to illustrate the influence of dissolved gas on cavitation intensity in vitro.

METHODS

To assess mechanical heart valve cavitation associated with a Bjork-Shiley monostrut valve, a “single-shot” heart valve chamber simulating the left side of a natural heart was constructed as described in Kini et al. (2000). Cavitation energy was measured in the atrial chamber utilizing a 1 MHz high fidelity pressure transducer (PCB Electronics) while in the ventricular chamber a similar high fidelity pressure transducer was used along with a Millar pressure catheter. All transducers were suspended within 4 mm of the valve’s major orifice in their respective chambers. Visual evidence of cavitation was collected through the use of a KODAK Ultra-SR high-speed video camera at an acquisition rate of 3000 frames per second. Blood analog mixtures consisted of 40% glycerin and 60% water to mimic blood’s viscosity and density. The fluid nuclei content and dissolved gas concentration were varied using tap water and distilled water supplemented with various concentrations of carbonated water to elevate CO_2 concentrations to physiologic conditions and higher. A CDI 300 blood gas monitoring system (3M HealthCare) measured CO_2 and O_2 concentrations. All analog fluids were filtered at various cutoffs in the micron range, and nuclei counts were determined through the use of a Coulter Counter. An algorithm developed by Johansen et al. (2002) was employed to calculate the cavitation energy spectrum for a range of ventricular pressure gradients (dP/dt).

RESULTS AND DISCUSSION

Cavitation may be quantified by examining the energy spectrum associated with valve closure as well as by observing cavitation bubble formation and collapse visually. The energy spectrum associated with valve closure may be separated into a deterministic part driven by vibration of the solid mechanical structure of the valve, a signature of the valve, and a non-deterministic portion associated with the cavitation events. Our results show that the cavitation energy spectrum is sensitive to changes in CO_2 concentration and nuclei characteristics. Shifts at the low and high ends of the frequency spectrum (up to 1 MHz) were noted with changes in pCO_2 in the range 0 to 100 mmHg. With increasing pCO_2, low frequencies increase in magnitude while high frequencies are attenuated. This would appear to reflect a shift in the bubble size distribution toward larger bubbles that cannot be detected readily in video images. Preliminary results also suggest that nuclei density plays a role in the cavitation energy developed, but the nuclei size distribution is not well characterized.

CONCLUSIONS

To simulate cavitation in vitro special attention should be paid to the dissolved gas content, especially the CO_2 concentration that is not normally present in analog fluids in equilibrium with room air. Dissolved CO_2 can affect the energy distribution associated with cavitation and this could have an impact on both valve material and blood damage characteristics. Gaseous nuclei also play a vital role in the development of cavitation and should be characterized carefully in vitro. The nature of cavitation nuclei in blood in vivo remains poorly understood and thus it is difficult to properly simulate this critical factor in vitro at the present time.

REFERENCES

Chandran et al (1998). *Ann Biomed Eng*, **26**, 546-556.
Johansen et al (2002). *Proc 6th Annual Heart Valve Workshop*.
Kafesjian et al (1989). *Surgery for Heart Valve Disease*. ICR Publishers, 509-516.
Kini V. et al (2000). *Ann Biomed Eng*, **28**, 4341-4441.

ACKNOWLEDGEMENTS

Supported by NIH NHLBI Grant HL 48652.

MIXED-ELEMENT ALE METHOD FOR SIMULATION OF MECHANICAL HEART VALVE FUNCTION

Yong G. Lai[1] and K.B. Chandran[2]

University of Iowa, Iowa City, Iowa
[1]IIHR-Hydroscience & Engineering, yong-gen-lai@uiowa.edu
[2]Department of Biomedical Engineering

INTRODUCTION

The numerical simulation of heart valves is quite challenging as it demands a numerical model capable of addressing several difficult issues. Two approaches are often used for heart valve simulations: The Eulerian method and the arbitrary Lagrangian-Eulerian (ALE) method. The Eulerian method uses the fixed computational mesh in space while the motion of the leaflet is incorporated using several means. One popular Eulerian implementation is the fictitious domain method of Glowinski et al (1994). The analysis was based on the finite-element formulation and the imposition of velocity constraints for the moving boundaries through Lagrangian multipliers. The major uncertainty of the method is its accuracy – inadequate mesh representation for flows near the leaflet and when leaflet is near closure. The ALE method, on the other hand, has been quite popular in the heart valve simulation. The method allows the computational mesh to deform in space in an arbitrary way to conform to the leaflet motion, thus offers an accurate and general way of treating the flow near the moving leaflet. The major drawback of the ALE method is its need to incorporate a mechanism to adapt (or deform) the mesh to conform to the leaflet motion at each new time step. Therefore, the merit of the ALE method largely depends on the mesh adaptation procedure. Most previous studies used the structured mesh and the large motion of the leaflet made the mesh adaptation quite difficult.

METHODS

In this presentation, the mixed-element ALE method is proposed for the blood flow simulation within prosthetic heart valves. The method is based on the arbitrarily shaped element method of Lai (2000) for mesh representation and the ALE method of Lai and Przekwas (1994) for the leaflet motion. As discussed, the ALE method has many advantages and is the preferred method if mesh adaptation can be carried out easily and the mesh quality can be maintained. Previous models for the heart valve simulation used the structured grids (quadrilateral elements in 2D and hexahedral elements in 3D), which severely limited the success of the mesh adaptation and often led to poor mesh quality. The proposed mixed-element ALE method is intended to overcome these difficulties by using a more flexible mesh system. The objective is that the mesh adaptation can be carried out in a much-simplified manner while the required accuracy near the leaflet and at valve closure can be maintained.

RESULTS AND DISCUSSION

The proposed method is implemented and the mechanical heart valve closure dynamics in two-dimensional space is simulated as a verification and test of the proposed method. One sample mixed-element mesh is shown in Fig. 1 in which a quadrilateral O-grid is used to represent the near-leaflet flow while the rest of the domain is filled with the triangular elements. Such a mixed mesh has several desirable features for the simulation of heart valves. Firstly, the O-grid can rotate or deform together with the leaflets easily as the O-grid is not tied to the overall mesh topology. The remaining triangular elements are known to be naturally suited to adaptation. Secondly, the proposed mixed mesh provides much needed accuracy for the heart valve simulation: finer mesh can be used in the O-grid to resolve the flow near the leaflet and when leaflet is near closure. Such flexibility has been difficult with the Eulerian method in general, and the ALE mesh often leads to mesh distortion.

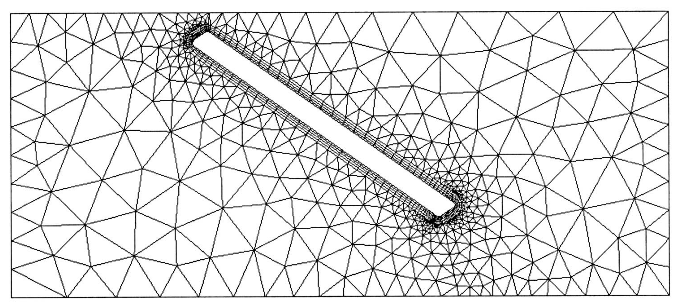

Figure 1: Mixed Element Mesh for Mechanical Heart Valves

The computed results will be compared to previously published results and the proposed method will be assessed for its success during the presentation.

REFERENCES

Glowinski, R., Pan, T.W., Periaux, J. (1994). *Computer Methods in Applied Mechanics and Engineering*, **111**, 283-303.

Lai, Y.G. and Przekwas, A.J. (1994). *Comp. Fluid Dynamics*, **2**, 19-40.

Lai, Y.G. (2000). *AIAA Journal*, **38**, 2246-2252.

HIGH-FREQUENCY PRESSURE FLUCTUATIONS MEASURED IN HEART VALVE PATIENTS

Hans Nygaard, Tina S. Andersen, J. Michael Hasenkam, Peter K. Paulsen
Department of Cardiothoracic and Vascular Surgery, Skejby Sygehus, Aarhus University Hospital, Denmark
nygaard@iekf.au.dk

INTRODUCTION

In contrast to bioprosthetic valves, mechanical heart valve patients require life-long anticoagulant therapy due to the risk of thromboembolic complications. The reason for this is still not fully understood. In vitro studies have demonstrated the presence of cavitation bubbles in the vicinity of mechanical heart valves, but not in the vicinity of bioprosthetic valves. When cavitation bubbles collapse, they release a significant amount of energy, which may damage the formed elements of the blood. Cavitation has been extensively studied in vitro and a correlation between the presence of cavitation bubbles and high-frequency pressure oscillations has been established in vitro. However, there is a lack of in vivo studies to confirm these findings thus, the aim of this study was to measure and quantify high-frequency pressure oscillations in patients with normal, bioprosthetic or mechanical aortic valves, using both invasive and noninvasive techniques.

METHODS

Measurements were performed in 10 patients with normal aortic valves after coronary bypass surgery, in 5 patients with a Carpentier-Edwards pericardial bioprosthesis implanted and 16 patients with a St. Jude Medical valve. High-frequency pressure fluctuations were measured intraoperatively using a hydrophone (B&K 8103) placed near the aortic annulus at the low aortic/left arterial junction. Simultaneously, blood pressure, heart rate, cardiac output and blood gasses (PO_2 and PCO_2) were registered. Postoperative measurements were performed on the 4th postoperative day using a specially designed "hydrophone in a water sound chamber" – transducer placed on the precordium in the left intercostal space 4, close to the sternum. The root mean square (RMS) value of the high-frequency pressure signals was calculated in the frequency range 50-150 kHz within 5 ms time windows. Data acquisition and signal analysis was performed by a dedicated LabView-program at a sampling rate of 500 kHz. The frequency distribution was evaluated with and without 50 Hz high-pass filtering using FFT.

RESULTS AND DISCUSSION

High-frequency pressure fluctuations with intensities significant above the noise floor were registered intraoperatively in the vicinity of only mechanical heart valve prostheses, and not in the vicinity of normal or bioprosthetic valves. The mean value of RMS pressure fluctuations was 2 Pa for normal aortic valves, 4 Pa for bioprosthetic valves and 61 Pa for mechanical valves. The corresponding RMS values for the postoperative measurements were 0.1, 0.2 and 3 Pa, respectively implying damping of the high frequency pressure fluctuation through the thoracic tissue of about 30 dB. Female patients with mechanical heart valves had lower postoperative RMS-values compared to the male patients – probably because the transducer (11 cm in diameter) interfered with mammae, so the membrane could not in all cases fit closely to the skin.

During the intraoperative measurements the hydrophone was handheld by different surgeons, which could introduce some variations in the magnitude of the recorded pressure signals, because the distance to the valve is important.

The RMS values of the HFPF for all three patient groups measured intra- and postoperatively disclose a significant difference between the mechanical valves and the two control groups. Indicating that there is no cavitation in the vicinity of the biological or the genuine valves. In this study, the various hemodynamic parameters and valve size are correlated to the intraoperatively measured RMS values. In vitro studies have shown that larger valves generate more cavitation by evaluating the pressure changes during the valve-closing phase. In this study a correlation may be present between RMS values and valve size if the mean values are considered, where the larger valves give a larger mean RMS values. Though, it would need further elaboration before any firm conclusions can be drawn. No relation was found in regard to blood pressure or blood gasses either.

HFPF can be due to natural mechanical resonance and cavitation. When the highest frequencies for the mechanical resonance are known, a high-pass filtering of the signal makes it possible to remove the natural resonance, extracting the signal due to cavitation. The chosen high-pass filtering in this study is 50 kHz. In vitro studies have shown that the mechanical resonance may reach frequencies above the 35 kHz that has been used in other cavitation studies. By using 50 kHz, most of the natural mechanical resonance components in the recorded signal were removed. However, as the resonance frequencies and cavitation frequencies overlap a small part of the cavitation signal would be removed as well. This study cannot with certainty establish whether the recorded signals are due to the mechanical resonance, cavitation or both. It is assumed, however, that most of the energy in the signals above 50 kHz is due to cavitation based on previous studies.

SUMMARY

High-frequency pressure fluctuations are present in the vicinity of mechanical aortic valves and can be measured in patients both invasively and non-invasively. This phenomenon is not present in patients with either normal or bioprosthetic aortic valves.

EVALUATION OF BILEAFLET MECHANICAL HEART VALVE INDUCED BLOOD DAMAGE DURING LEAKAGE FLOW USING LASER DOPPLER VELOCIMETRY AND INDICATORS OF PLATELET ACTIVATION

Brandon Travis[1], Jeff Ellis[2], Leo Hwa-liang[2], Anna Fallon[1] Steven Hanson[3], and Ulla Marzec[3], Ajit Yoganathan[3]
[1]School of Chemical Engineering, [2]School of Mechanical Engineering, Georgia Institute of Technology,
[3]Wallace H. Coulter School of Biomedical Engineering, Georgia Institute of Technology and Emory University,
ajit.yoganathan@bme.gatech.edu,

INTRODUCTION

Mechanical heart valves (MHVs) are far more durable than bioprosthetic alternatives; however, patients with mechanical heart valves are predisposed to thromboembolic disorders and must undergo lifelong anticoagulation therapy. Depite this therapy, some patients still develop thromboemobolic complications. The exact cause of these complications is unknown, but they could be due to the design of bileaflet MHVs, which includes some degree of leakage flow upon valve closure in order for the reverse flow to wash the hinge/pivot region of the valve. It is believed this reverse flow helps prevent areas of stasis and inhibit micro-thrombus formation. However, the magnitude of this retrograde flow may also give rise to unacceptable levels of blood element damage and lead to platelet activation and/or hemolysis, as a result of the increased flow velocities through the hinge region. In two separate studies, bileaflet MHVs have been evaluated using laser Doppler velocimetry (LDV) and indicators of platelet activation in blood during leakage flow through a MHV. LDV was used to analyze the blood flow patterns during leakage flow and to quantify the shear stresses and velocities of the flow. Platelet activation indicators were used to determine the effects of hinge design on platelet damage.

METHODS

For the LDV experiments, two-dimensional laser Doppler velocitometry was used to measure the velocity and turbulent shear stress fields in the hinge regions. In order to conduct these measurements, exact dimensional models of the bileaflet hinge regions were cast and/or machined from transparent plastic materials. The experiment was conducted in a pulsatile flow loop with the measurement taken at different levels within the pivot and hinge regions.

For the blood studies, a centrifugal pump was used to drive whole, human blood anticoagulated with PPACK through a circuit containing various MHVs in the closed position for the experimental runs or a MHV in the open position for the control runs. Samples were taken at set time intervals after the start of the pump. These samples were analyzed by cell counting and flow cytometry to quantify the presence of annexin V and platelet factor 4 binding. Annexin V binding indicates the presence of anionic phospholipids on cell surfaces, which indicate cell damage. By isolating the platelet population before and at various intervals during the test, it is possible to determine the percentage of platelets that are damaged throughout the experiment. In a similar fashion, platelet factor 4 indicates the degree of platelet activation.

RESULTS AND DISCUSSION

In the LDV experiments, the velocity and shear fields were animated in order to visualize the flow structures within the hinge regions. Animations at the flat level revealed that certain designs created areas of stasis throughout the cardiac cycle, while others such as the Regent valve had very good wash out. Shear stress measurements revealed that certain hinge designs caused elevated levels of turbulence (>3000 dyne/sq.cm) that could cause platelet activation and/or hemolysis.

In the blood experiments, it was found that leakage through the MP design caused 17% more secretion of platelet factor 4 and 14% more anionic phospholipid expression on platelet surfaces than the SJM Standard design after two hours of run time. The effect of pivot gap width was shown by using a SJM 27 Standard valve, High Leaker valve, and Low Leaker valve. The results were that leakage through the High Leaker valve caused 25% more platelet factor 4 secretion than the Standard valve. In addition leakage through the High Leaker valve caused 96% more platelets to be positive for expression of anionic phospholipids and significantly more anionic phospholipid exposure on platelet surfaces than leakage through the SJM Standard valve at all sampling times after 5 minutes.

The LDV studies clearly demonstrate that the actual design/shape of the hinge/pivot region influences the degree of washing, the levels of turbulent shear stresses and/or unsteadiness within the hinge. Such micro flow field studies are critical to clinical outcomes and should be conducted in the pre-clinical evaluation phase of all new MHV designs.

The blood studies indicate that bileaflet valve leakage flow causes significant platelet disruption. Also, although pivot design was not shown to result in a significant difference in secretion of platelet factor 4 or anionic phospholipid expression, gap width did have a significant effect on platelet damage. The leakage flow rate through the High Leaker is twice the leakage flow rate through the SJM Standard valve. Increasing leakage flow rate exposes more blood to the stresses encountered during leakage flow. Leakage gap width also influences the likelihood for turbulence in the jets created by flow through the pivots.

Although these studies were performed independently, the advantages of using them together is evident. LDV is able to pinpoint the locations at which Reynolds stresses exceed the limit for blood damage, and platelet activation indicators can determine whether or not blood damage has occurred.

STRETCH-AND-FOLD FRACTAL-LIKE AEROSOL BOLUS SPREADING IN THE RYTHMICALLY EXPANDING ALVEOLATED DUCT

Akira Tsuda[1], James P. Butler[1], and Frank S. Henry[2]

[1]Physiology Program, Harvard School of Public Health, Boston, MA 02115; atsuda@hsph.harvard.edu
[2]School of Engineering, City University, London EC1V 0HB, U.K.

INTRODUCTION

In current theories, transport of submicrometer aerosols in the pulmonary acinus is described as a dispersive (diffusion-like) process in the context of reversible alveolar flow. Recent experimental data, however, have questioned the validity of the basic assumptions -kinematically reversibility of acinar flow- that formed the basis of the dispersive theories. The objective of this study was to demonstrate through numerical simulation of bolus experiments that the behavior of particles in a cyclically ventilating alveolar duct and multiple alveolus is not consistent with the predictions of any dispersive theory characterized by an effective diffusivity.

METHODS

We developed a computational fluid mechanics model with rhythmically expanding and contracting multiply-alveolated walls. Geometric model: The model comprised a closed-end central circular channel around which are placed nine tori, equi-spaced in the axial direction, representing the alveoli. The duct and alveolar walls move in a perfectly kinematically reversible, simple sinusoidal manner with a specific volume excursion of 25% and a cycle period of 3 seconds. Flow solver: The flow field was defined by the full, incompressible, Navier-Stokes equations with no-slip condition on all solid surfaces, which are solved numerically on a multi-block, body-fitted, moving grid using the finite volume code CFX-4 (CFDS, AEA Technology, Harwell, UK). Lagrangian particle tracking: Approximately 16,000 massless particles were placed on radial line across the central channel midway between alveoli. Regarding these massless tracer particles as marked fluid elements, this line of particles represents the front of incoming tidal gas or a tracer bolus facing the host alveolar residual gas. The behavior of the tracer was tracked over the first few cycles.

RESULTS AND DISCUSSION

Similarly to our previous study performed in the single-alveolus model (Tsuda, et al., 1995), the results showed that the acinar flow patterns become highly complex if the walls are not stationary (i.e., expand and contract). There are stagnation saddle points near the alveolar openings that are associated with slow alveolar recirculation. Lagrangian tracking of fluid particles indicated that the fluid motion exhibited unpredictable and irreversible stretched and folded patterns, characteristic of chaotic flow (Otino, 1989). To quantify the extent of axial spreading of the tracer, we analyzed the cycle-by-cycle evolution of the variance (σ^2) of axial particle distribution. We found that σ^2 increased exponentially, rather than linearly, with increasing cycle number (i.e., time). This demonstrates that axial bolus spreading in the acinar duct does not follow the basic additive of variance, which is characteristics of classical dispersive transport theories (Taylor, 1953). Further analysis on tracer pattern showed the following remarkable phenomena. As the tracer sampled irreversible multiple alveolar fields, the shape of the tracer progressively evolved into “finger-like” protrusions located especially near the duct walls. Each protrusion consisted of complex stretched-and-folded patterns, and moreover, as the scale became finer, similar and finer stretched-and-folded patterns were revealed. Thus, the observed patterns seemed to be at least qualitatively self-similar over a wide range of length scales. Such self-similarity is characteristic of fractal geometry which is often observed in many chaotic systems (Mandelbrot, 1982). Indeed, fractal analysis with the method of box counting technique (Sommerer, 1994) revealed that the distribution of tracer particles evolved in a fractal-like manner, with a fractal dimension of $D \approx 1.2$. The fact that the tracer pattern exhibited fractal characteristics is not entirely surprising since the origin of particle irreversibility is due to chaotic alveolar flow and deterministic chaos often manifests a fractal geometry (Sommerer, 1994). It is important and remarkable, however, that the observations in these simulations are strikingly similar to findings in animal experiments. These similarities strongly suggest that the numerical simulations – though they were based on highly idealized assumptions – captured the fundamental features of the underlying mixing mechanism, namely that low Reynolds number chaotic flow in the acinus determines particle transport in the lung.

SUMMARY

The results suggest that (i) kinematic irreversibility is the origin of aerosol transport, (ii) axial transport cannot be characterizable by an effective diffusivity, and that (iii) fractal trajectories can occur, in most of the alveoli in the acinar tree. The alternative mechanism of aerosol transport that we propose here may in fact be the dominant mechanism determining deposition of submicron particles deep in the lung.

REFERENCES

Mandelbrot, B.B. (1982). *The fractal geometry of nature*. Freeman, San Francisco.
Ottino, J.M. (1989). *The kinematics of mixing: stretching, chaos, and transport*. Cambridge University Press.
Sommerer, J.C. (1994). *Physica D*, **76**, 85-98.
Taylor, G.I. (1953). *Proc. R. Soc. Lond. A.* **219**, 186-203.
Tsuda, A., F.S. Henry, Butler, J.P. (1995*). J. Appl. Physiol.* **79**, 1055-1063.

ACKNOWLEDGEMENTS

This study was supported by NIH HL54885.

AUGMENTED LONGITUDINAL DIFFUSION IN OSCILLATORY FLOW ALONG A LATERAL GROOVED TUBE IMITATED OF TRACHEA WITH UNEVEN INNER SURFACE BY CARTILAGE

Akihiro Shimizu[1], Kosuke Miyahara[2], Masashi Shimizu[2] and Saburo Ryumae[2]
[1] Department of Mechanical Engineering, Tokyo National College of Technology, 1220-2, Kunugida, Hachioji, Tokyo, Japan
shimizu@tokyo-ct.ac.jp
[2]Graduate School of Information Science and Engineering, Tokyo Institute of Technology, Ookayama, Meguro, Tokyo, Japan
mshimizu@mei.titech.ac.jp

INTRODUCTION

Respiration is attained despite small tidal volume breathing and large dead space in the trachea. Uneven inner surface configuration by cartilage of trachea may influence on the effective diffusivity. Ye had reported augmentation of diffusion by oscillatory flow of water in a lateral grooved tube. Measurements of CO_2 concentration in the oscillatory flow in tubes with several groove widths have been carried out.

METHODS

Inner diameter of the test tube was 18mm, and inner surface configuration was composed by combination of aluminum rings with rectangular cross section as shown in figure 1. Depth of the groove of each configuration was 2mm and Bottom width and top width of it are described in table 1. Total length of the test tube was 3025mm, consisting of the part from the entrance to injecting point of 1260mm and from there to sensing point of 500mm, and further 1265mm to the open end. Oscillatory flow was generated by piston(ƒÓ50) connected with a reciprocating block double slider-crank mechanism driven by AC servomotor. CO_2 gas was injected simultaneously with the lower dead point of the piston. Non-dispersive infrared analyzer measured CO_2 concentration.

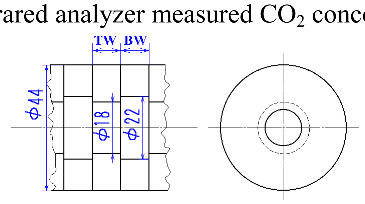

Figure 1: Inner surface configuration along the grooved tube.

RESULTS AND DISCUSSION

Values of $(D_{eff}/D_{mol}\text{-}1)/(V^2/a^6)$, where D_{eff} is effective diffusivity, D_{mol} is molecular diffusivity, V is stroke volume and a is the inner radius of the tube, are shown in figure 2. The difference between the effective diffusivity obtained and the theoretical one in the oscillatory flow in a straight tube is increasing with the increase of Womersly number. As for the bottom width of the groove, wide width of groove gives relatively large augmentation on the effective diffusivity.

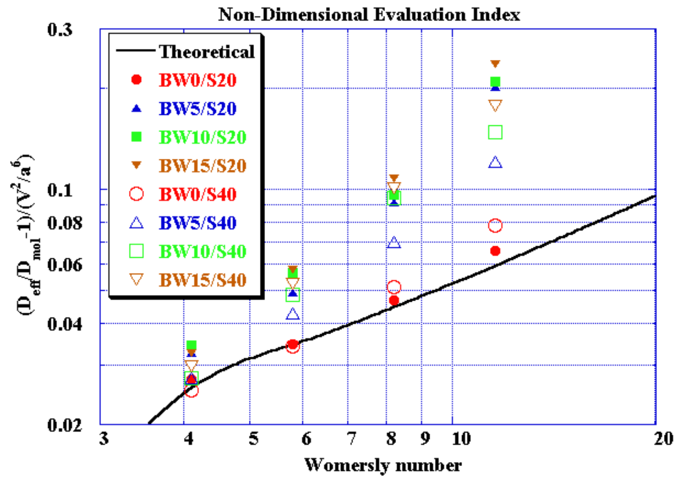

Figure 2: Evaluation index derived from non-dimensional effective diffusivity and non-dimensional stroke volume. Solid curve indicates the theoretical value for laminar flow in a straight tube.

SUMMARY

The effective diffusivity of CO_2 in oscillatory flow along tubes with the lateral grooves has been measured. The difference between the effective diffusivity through the lateral grooved tube and one through the smooth straight tube is increasing with the increase of Womersly number. The effective diffusivity is more augmented by each inner surface configuration with the increase of the width of the groove within the region of the present experimental condition.

REFERENCES

Ye Xiaofeng, Shimizu Masashi, *Augmented longitudinal diffusion in grooved tubes for oscillatory flow*, *Int. J. Heat and Mass Transfer*, **44**(2001), 633.

Watson, E. J., *J. Fluid Mech.* **133**(1983), 233.

Table 1: Piston stroke and dimension of the top and the bottom width of each lateral groove of inner surface [mm]

Item	BW0/S20	BW0/S40	BW5/S20	BW5/S40	BW10/S20	BW10/S40	BW15/S20	BW15/40
Piston stroke	20	40	20	40	20	40	20	40
Top width	10	10	10	10	10	10	10	10
Bottom width	0	0	5	5	10	10	15	15

MODELING THE INTERSUBJECT VARIABILITY OF OZONE UPTAKE INTO HUMAN AIRWAYS

Gregory Zugates[1] and James Ultman[2]

[1]Department of Chemical Engineering, Massachusetts Institute of Technology, Cambridge, MA
[2]Department of Chemical Engineering, Penn State University, University Park, PA, jau@psu.edu

INTRODUCTION

Ozone (O_3) is an inhaled air pollutant that causes decrements in pulmonary function and promotes airway inflammation. These health effects are variable among different individuals, making some people particularly susceptible to O_3 exposure (*e.g.,* McDonnell *et al.*, 1995). One source of this intersubject variability in physiological response is a corresponding variability in O_3 dose. The hypothesis of the current study was that variations in O_3 dose between subjects occur because of differences in breathing patterns (*i.e.*, frequency and tidal volume). This hypothesis was tested by comparing mathematical simulations of O_3 transport to measurements of O_3 uptake performed on human subjects under four different short-term exposure conditions.

METHODS

In the experiments, ten healthy adult nonsmokers inhaled an ozonated air mixture through an oral mask while exercising continuously on a cycle ergometer. Each subject participated in four sessions with respective O_3 concentrations, workloads, and durations as follows: A) 0.4 ppm, light, 1 hour; B) 0.4 ppm, moderate, ½ hour; C) 0.2 ppm, light, 1 hour; and D) 0.2 ppm, moderate, ½ hour. In each session, O_3 concentration and respiratory flow was continuously monitored by instruments positioned at the oral mask, and fractional uptake of O_3 (FU) was determined on a breath-by-breath basis as the ratio of O_3 uptake to the amount of O_3 inhaled. Further details can be found elsewhere (Rigas *et al.*, 2000).

In the simulations of FU, the airways were modeled as a single conduit of expanding flow cross-section and surface-to-volume ratio. Transport along the airways occurred by bulk flow and longitudinal dispersion. Lateral uptake was governed by an overall mass transfer coefficient that accounted for convective diffusion in the gas phase and reactive diffusion in mucus. Respired flow was modeled as a rectangle wave such that breathing pattern could be defined in terms of frequency and minute volume (MV). Whereas these ventilation parameters were specified from experimental measurements of each breath, anatomical and transport parameters were fixed at values previously found for this model (Bush *et al*., 2001).

RESULTS AND DISCUSSION

FU data were obtained for each subject from about 70 breaths in each of sessions A and C and 35 breaths in each of sessions B and D. These breath-by-breath FU values were then averaged for each person within each session (Fig. 1). The resulting subject-average FU values were averaged across all subjects to obtain a session-average FU and its variance (σ^2) for each of the four exposure conditions (table 1).

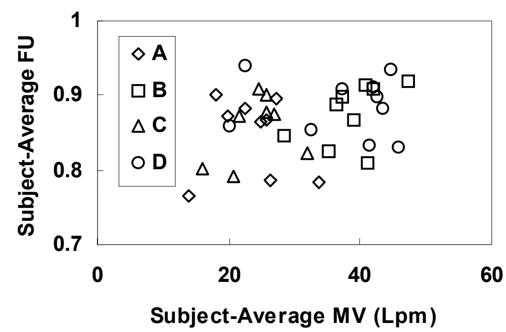

Figure 1: Intersubject Variability Grouped by Session

Simulations of FU were obtained for each individual breath and were then averaged across breaths and across subjects to obtain session-average FU and σ^2 values (table 1). In comparison to the measurements, the simulations systematically overpredicted FU by about 5%. Variances in the simulated FU induced by the breathing pattern explained about 50% of the intersubject variances observed in the data. The unexplained portion of the variances may be due to intersubject differences in anatomy and mucus chemistry not yet included in the diffusion model.

Table 1: Distribution of Subject-Average FU

Session	Ave. FU (meas.)	σ^2 (meas.)	Ave. FU (simul.)	σ^2 (simul.)
A	0.8465	0.0028	0.9053	0.0018
B	0.8754	0.0016	0.9334	0.0005
C	0.8563	0.0020	0.9132	0.0012
D	0.8849	0.0016	0.9311	0.0006

REFERENCES

Rigas, M.L., Catlin, S.N., Ben-Jebria, A., Ultman, J.S (2000). *J. Appl. Physiol.,* **88**, 2015-2022.
Bush, M.L., Zhang, W., Ben-Jebria, A., Ultman, J.S. (2001), *Toxicol. Appl. Pharmacol.* **173**, 137-145.
McDonnell, W.F., Stewart, P.W., Andreoni, S., Smith, M.V. (1995), *Am. J. Respir. Crit. Care Med.* **152**, 589-596, 1995.

ACKNOWLEDGEMENTS

This work was funded part by a National Institute of Environmental Health Sciences Grant R01-ES0675.

ANATOMICALLY BASED MODELS OF GAS FLOW AND GAS EXCHANGE IN THE HUMAN LUNG

Merryn Tawhai and Peter Hunter

Bioengineering Institute, The University of Auckland, Auckland, New Zealand
m.tawhai@auckland.ac.nz

INTRODUCTION

An anatomically based model of the human lung airways and vasculature is being defined as part of the Lung Physiome (http://www.bioeng.auckland.ac.nz/physiome/physiome.php). The airway model includes a 60,000 element description of the conducting airways, terminating in lumped parameter acinar models. The lumped parameter models are targeted to specific function, with parameters derived from simulations in anatomically detailed respiratory airway models (Tawhai and Hunter, 2001a). Similarly, the pulmonary vasculature is modeled at the whole organ scale with a branching finite element network and coupled to lumped parameter models of the capillary bed, where these are based on a detailed model of blood flow and gas exchange at the alveolar level. The airways and blood vessels are coupled to a 3D finite deformation soft tissue model of the lung parenchyma.

METHODS

The conducting airway and large blood vessel models are generated into an accurate volume mesh of a human lung, using a bifurcating-distributive algorithm (Tawhai et al., 2000). The algorithm has been customized to generate branching trees with geometric properties similar to the real lung. The pulmonary acinus is modeled as an asymmetric bifurcating mesh, with mean dimensions from Haefeli-Bleuer and Weibel (1988). The alveolar structure is modeled using a Voronoi mesh that fills a given volume, with faces removed to form alveolar ducts, alveoli, and sacs. A capillary network is texture mapped to each alveolus, using a 2D Voronoi network generated over a ¾ sphere as the generic capillary mesh.

Advective-diffusive transport equations for relatively inert gases are integrated over the cylindrical airway cross-sections (Tawhai and Hunter, 2001a), and are solved using a Lagrangian Finite Element method. This solution can be applied at the acinar level through coupling of a detailed acinar model and a symmetric conducting airway model, or at the whole lung level through coupling of the detailed conducting airway model and lumped parameter acinar models.

By embedding the conducting airways in a soft tissue deformation model of the lungs, breath-like boundary displacements of the lungs can be solved to produce mechanically-coupled pressure fields in the respiratory zone. These pressures provide boundary conditions for solution of Navier Stokes equations to describe the air distribution. Similarly, blood flow in the large vessels is described by solution of Navier Stokes equations with pressure boundary conditions at the pulmonary artery and vein, and a lumped parameter model of pulmonary capillary pressure changes.

RESULTS AND DISCUSSION

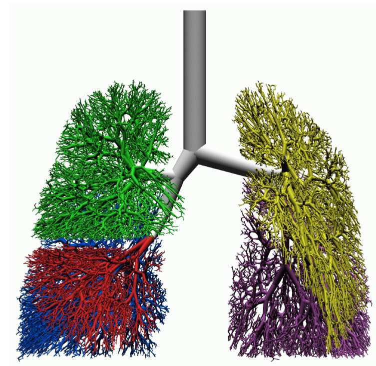

Figure 1: Asymmetric conducting airway model.

Almost all respiratory disorders result in an impairment of gas exchange, often through some effect on ventilation-perfusion matching. A predictive model that is capable of investigating these complex interactions must include detailed structural information (geometry, tissue properties) and the ability to couple different processes over a range of spatial scales (air flow, blood flow, tissue mechanics, gas exchange).

We have developed structural models based on detailed anatomy, then have identified simplified forms of the detailed models to facilitate their coupling to large-scale structural and functional models. For example, the coupled airway model has been used to investigate the effect of conducting airway asymmetry on gas mixing (Tawhai and Hunter, 2001b) utilizing a hierarchy of airway models. The study highlighted the importance of accurately representing airway structure at both the conducting and respiratory level, and the need to couple gas mixing models to accurate solutions of airflow distribution.

Models of airway and vasculature smooth muscle at both the cellular and tissue levels are being developed to include in the anatomically based lung models described above. This hierarchy of models at several spatial scales (cell, tissue and organ) has the potential to provide a link from the level of protein expression to whole organ function.

REFERENCES

Haefeli-Bleuer, B., Weibel, E.R. (1988). *Anat. Rec.*, **220**, 401-414.
Tawhai, M.H., Pullan, A.J., Hunter, P.J. (2000). *Ann. Biomed. Eng.*, **28(7)**, 793-802.
Tawhai, M.H., Hunter, P.J. (2001a). *Resp. Physiol.*, **127(2-3)**, 241-248.
Tawhai, M.H., Hunter, P.J. (2001b). *Resp. Physiol.*, **127(2-3),** 249-258.

A MODEL OF VENTRICULAR ANATOMY BASED ON STRUCTURAL MEASUREMENTS FROM PIG HEARTS.

Carey Stevens, Ian LeGrice, Bruce Smaill and Peter Hunter
Bioengineering Institute, The University of Auckland, Auckland, New Zealand
c.stevens@auckland.ac.nz

INTRODUCTION

Models of ventricular mechanics have been developed over the last 20 years to include finite deformation theory, anisotropic and inhomogeneous material properties and an accurate representation of ventricular geometry. Anatomically based models of dog and rabbit heart have been developed previously (Le Grice et al. 1997, Vetter 2000) but since the pig is now the preferred large animal model for many physiological studies we have recently measured and modeled the geometry and fibrous-sheet structure of the pig myocardium using the finite element techniques and data fitting algorithms reported in Hunter et al. (1997). Material properties were also measured using a purpose-built shear testing rig to complement earlier measurements with a biaxial rig. Stress and strain distributions throughout the cardiac cycle were then determined using the anatomical model together with finite deformation elasticity theory and ventricular pressure boundary conditions.

METHODS

A finite element model of the left and right ventricular myocardium in rectangular Cartesian coordinates was developed with tri-cubic Hermite basis functions (Hunter et al. 1997). Geometric measurements from the potassium arrested pig hearts were obtained with the cylindrical polar measurement rig described previously (Nielsen et al. 1991) and with a Faro Arm (Faro Technologies Inc) which allowed more accurate measurements around the base and apex of the heart. Fibre orientation measurements were obtained by shaving layers off the heart in the measurement rig, as previously reported for canine myocardium (Nielsen et al. 1991). Sheet orientations were obtained by cutting and drying 100µm transmural base-apex segments then using digital image analysis to quantify the sheet orientations as previously reported (Le Grice et al. 1997).

RESULTS

The model captures the anatomy of the basal and apical regions of the heart more accurately than any previous model. Figure 1 shows a crosssection of the apex and Figure 2 shows the fitted model geometry and fibre fields.

Figure 1: A sagittal cross-section of the left ventricular apex.

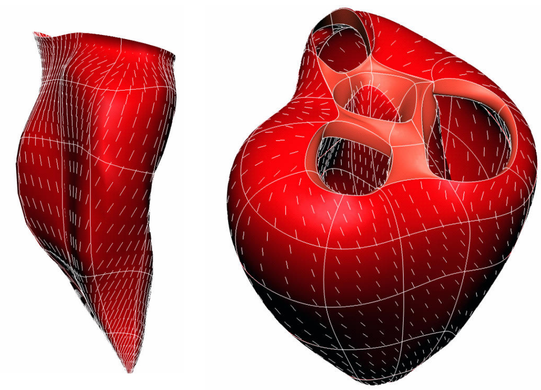

Figure 2: Fitted geometry and fibre fields. The left ventricular endocardium (left) and the complete pig heart model (right).

APPLICATION OF MODEL

The material properties of pig myocardium were also determined by mounting 5mm cubes in a purpose-built rig and loading the blocks in shear at various states of compression (Dokos, 2001). The shear behaviour was successfully fitted with the "pole-zero" law and the active myofilament properties were based on the HMT model (Hunter, McCulloch and ter Keurs 1998). The passive and active constitutive laws are referred to the anisotropic fibrous structure of myocardium and the tissue is assumed to be incompressible. Three-dimensional finite deformation, finite element analysis was used to determine the stress and strain fields during diastolic pressure loading and systolic contraction using methods reported in Nash and Hunter (2000).

REFERENCES

Dokos, S., Smaill, B.H., Young, A.A., Le Grice, I.J. (2001). *Amer. J. Physiol*., (submitted).

Hunter, P.J., Arts, T. (1997) *Analytical and Quantitative Cardiology*, Plenum Press, New York.

Hunter, P.J., McCulloch, A.D., ter Keurs, H.E.D.J. (1998). *Progress in Biophysics & Molecular Biology*, **69**, 289-331.

Hunter, P.J., Smaill, B.H., Nielsen, P.M.F., LeGrice, I.J. (1997). *Computational Biology of the Heart*, Wiley.

LeGrice, I. J, Hunter, P.J., Smaill, B.H. (1997) *Amer. J. Physiol*. **272**, H2466-H2476.

Nielsen, P.M.F., LeGrice, I.J.,Hunter, P.J., Smaill, B.H. (1991). *Amer. J. Physiol*, **260**, H1365-H1378.

Nash, M.P., Hunter, P.J. (2000). *J. Elasticity*, **61**, 113-141.

Vetter, F.J., McCulloch, A.D. (2000). *Annals of Biomed Eng*, **28**, 781-792.

ACKNOWLEDGEMENTS

We gratefully acknowledge the contributions of Jenny Hunter and Dane Gerneke to the data measurements.

STUDYING ELECTROMECHANICAL BEHAVIOR *IN VIVO* WITH MRI TAGGING AND EPICARDIAL ELECTRICAL MAPPING

Elliot McVeigh[1,2], Owen Faris[1,2], Dan Ennis[1,2], Frank Evans[1]
[1]Laboratory of Cardiac Energetics, National Heart Lung and Blood Institute
National Institutes of Health, Bethesda, MD
[2]Johns Hopkins University School of Medicine

INTRODUCTION

We have developed a system for measuring regional mechanics and spatially registered epicardial potentials in the canine heart.

METHODS

In the MR scanner, tagged cine images and nearly simultaneous electrograms and LV pressure recordings can be acquired for sinus rhythm and different pacing schemes. Unipolar electrograms are recorded at 1 kHz from an epicardial sock. MR tagging is performed on a GE Signa CV/i 1.5 Tesla scanner yielding movie sequences with a time resolution of 12-15 ms, 1.25 x 1.25 mm pixels, 7-pixel tag spacing. The trigger to begin MR scanning was delivered 40-80 ms prior to the ventricular pacing stimulus or simultaneous with the RA pacing stimulus so that the image sequence included the onset of mechanical shortening. After imaging is complete, the animals are euthanized and a T1-weighted scan is obtained in order to locate Gd-DTPA beads sewn onto the electrode sock for registration of the electrodes with the MR data.

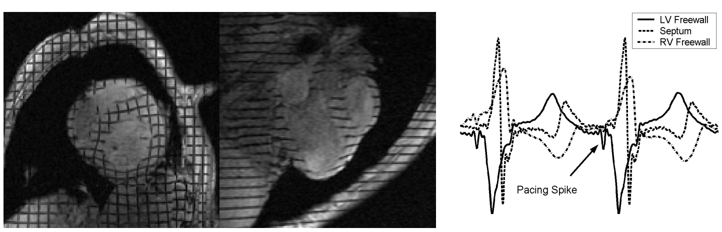

Figure 1: Example short (super-imposed stripes) and long axis images (RA pacing) showing tag deformation characteristic of asynchronous contraction, and example electrograms from the epicardial sock (LV pacing).

After imaging, hearts are excised and electrode and bead locations are digitized using a 3D digitizer (Microscribe, 3DLX). Electrograms are correlated spatially to the MR images by registration of the bead coordinates and all data is referenced in time to the pacing stimulus. Tag locations are segmented using two in-house programs: XBS[1] and Findtags [2].

The motion of the myocardium is modeled using a 4D B-spline tensor field with 7x7x7 control points in the volume containing the heart and 20 to 30 control points in time[3]. 3D strain is calculated through time over a subepicardial surface, and at points corresponding to electrode locations. Electrical activation times (minimum dV/dt) are evaluated for electrode signals from each pacing protocol and used to make maps of electrical activation.

RESULTS

The existence of the electrode sock around the heart does not interfere with the MR image quality to a significant degree. Clean electrical signals are also available even with the long cable runs from the MRI control room to the scanner. Spatially registered maps show an excellent correlation between the spatio-temporal pattern of mechanical activation and the electrical activation in the normal heart under different pacing conditions.[4] Specific definitions of “mechanical activation time” derived from the local myocardial deformation are now being explored.

CONCLUSIONS

A measurement system now exists for examination of the electromechanical behavior of the heart in vivo. The change in this relationship under different conditions is now under investigation.

REFERENCES

1. Shechter G., Ozturk C., McVeigh E., Proc. SPIE, 3976, 165-173, 2000.
2. Guttman M., Zerhouni E., McVeigh E., IEEE Comp. Graph Appl., 17(1), 30-38, 1997
3. Ozturk C., McVeigh E., Phys. Med. Biol., 45,1683-1702,2000.
4. B.T. Wyman et al. Am. J. Physiol. Heart Circ Physiol 282: H372-379 (2002).

PRINCIPAL COMPONENT ANALYSIS OF CARDIAC FUNCTION

Kevin F Augenstein and Alistair A Young
Departments of Engineering Science, Anatomy and Physiology, University of Auckland, Auckland, New Zealand

INTRODUCTION

Heart wall motion can be efficiently and accurately estimated from magnetic resonance (MR) tagged images using finite element models of ventricular shape and motion [IEEE]. However, statistical analysis of the resulting deformation fields is a unsolved problem. We show how the model parameters from a number of subjects can be directly incorporated into a principal component analysis (PCA) of the dominant modes of shape and motion. This allows a statistical characterization of subpopulations of healthy and diseased subjects and may allow further understanding of the mechanical effects of disease and remodeling processes.

METHODS

Tagged MR images of fifteen normal volunteers were analyzed with a four by four element mesh using the methods described in [1]. The model parameters were converted into 3D Bezier control points which completely describe the shape of the LV at each time point. The location of these points can be regarded as consistent between subjects due to the automated process in which the models are registered to each subject.

Let **U** be a vector of model parameters describing a subject's LV shape at end-diastole (ES) and end-systole (ES). We use a frame-wise ordering system in which all the ED parameters are followed by all the ES parameters. These vectors can be placed in a data matrix, **X**, in which each row, $\mathbf{X}_i$, of the data matrix contains a separate case at ES and ED (i.e. $\mathbf{X}_i = \mathbf{U}^t$). The difference between each subject and the mean is $\boldsymbol{\delta}_i = \mathbf{X}_i - \overline{\mathbf{X}}$ and the covariance matrix of the model parameters is $C_{ij} = \frac{1}{n}\boldsymbol{\delta}_i \bullet \boldsymbol{\delta}_j$ where n is the number of subjects in the database. The principal modes of variation are found using the eigenvalue decomposition $\mathbf{C} = \mathbf{P}\Lambda\mathbf{P}^T$ where Λ is a diagonal matrix of eigenvalues and **P** is an orthonormal matrix of eigenvectors. Assuming the modes are normally distributed about zero, each row of **P** describes the shape variation of the mode while the corresponding eigenvalue is the associated variance. The resulting (orthogonal) modes and variances describe the statistical variation present in the database. Similar formulations have been used previously in the construction of point distribution models [2].

RESULTS

The strength (variation) in each mode drops rapidly with the mode number, with approximately 6 modes containing most of the variation in the distribution. The modes obtained contain information about ED shape as well as deformation from ED to ES. To visualize the deformation separate from the initial geometry, we performed a PCA of the difference between the ED and ES parameters.

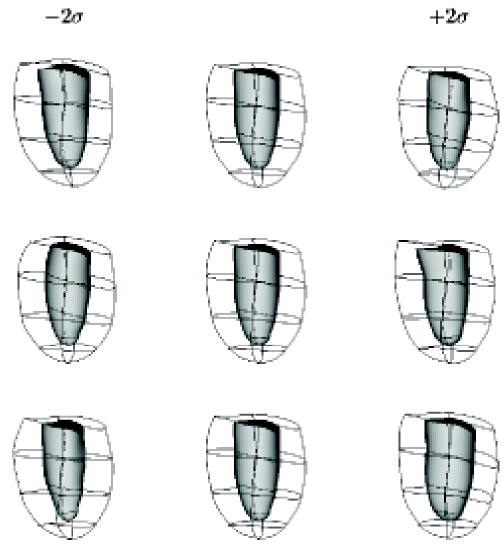

Figure 1: First three modes of variance in the ES shape after performing a PCA on the displacement parameters. The shapes have a common mean ED shape and the middle column is the mean displacement from that shape.

The first mode appears to vary the twist at the apex, the second the position of the base (i.e. longitudinal shortening) and the third mode appears to signify the size of the cavity (and therefore the ejection fraction and circumferential shortening).

SUMMARY

PCA describes heart motion with a small number of parameters (modes). Although the fitted models have hundreds of parameters, by using PCA on a training set we hope to distinguish the modes which truly differentiate the hearts, and remove the modes that are insignificant. A new heart model could be compared with the database distributions to see if statistical evidence of abnormal function exists.

REFERENCES

Young A. A., *et al.* (1995). *IEEE Trans Med Imag.* 14(3):413-421.

Cootes, T. F., *et al.* (1994). *Image and Vision Computing*, 12(6):355-66.

MODELING ELECTRICAL AND MECHANICAL ACTIVATION TIMES IN THE NORMAL HEART

Roy Kerckhoffs[1,3], Peter Bovendeerd[1], Frits Prinzen[2], Jiska Kotte[3], Karel Smits[4], Theo Arts[1,3]

[1]Department of Biomedical Engineering, Eindhoven University of Technology, P.O. Box 513, 5600 MB Eindhoven, The Netherlands
Department of [2]Physiology and [3]Biophysics, Maastricht University, P.O. Box 616, 6200 MD Maastricht, The Netherlands
[4]Medtronic BRC, Endepolsdomein 5, 6229 GW, Maastricht, The Netherlands
r.c.p.kerckhoffs@tue.nl

INTRODUCTION

Numerical models of cardiac electrophysiological and mechanical mechanisms may be of great help to understand the consequences of various pathologies related to cardiac failure. In the present study we investigated the timing between moment of electrical depolarization and onset of myofiber shortening using integrated finite element models of electrical depolarization and mechanics in the normal canine left ventricle (LV) and compared the results with measurements from literature.

METHODS

In the reference state, when transmural pressure is zero, the LV is represented by a thickwalled truncated ellipsoid (Bovendeerd, 1992) and a realistic myofiber distribution (Rijcken, 1999).

The spatial variation of electrical activation is computed by the solution of a transversely isotropic eikonal-diffusion equation (Colli-Franzone et al, 1990; Tomlinson, 2000). The calculated moments of electrical activation are used as moment of onset of active stress generation.
LV mechanics is computed by solution of the momentum equation. Passive material was modeled nonlinearly elastic, transversely isotropic, and virtually incompressible. Active stress is generated in the fiber direction, depending on myofiber strain, strain rate and time (Arts, 1982). LV afterload during ejection is computed using a 3-element Windkessel model.

RESULTS

Figure 1 shows the results of a simulation for the LV depolarization wave during sinus rhythm for a dog. The results are well in agreement with measurements of Scher et al (1953). Figure 2 shows global hemodynamics during the cardiac cycle.
Onset of myofiber shortening as a function of electrical depolarization time from simulations and measurements are plotted in figure 3. Applying linear regression, a slope of 2.5 is found from the simulations. Wyman et al (1999) found a slope of 1.06 in their MRI tagging experiments in dogs.

DISCUSSION AND CONCLUSIONS

Simulation of electrophysiological conduction and mechanics yields results, which are in agreement with experimental results. However, when linearly relating timing of electrical activation and onset of myofiber shortening, the slope in the simulation differs from the slope in the experimental results. We conclude that the coupling of electrical activation to the moment of mechanical activation is insufficiently described by the current knowledge on excitation contraction coupling, as included in the model.

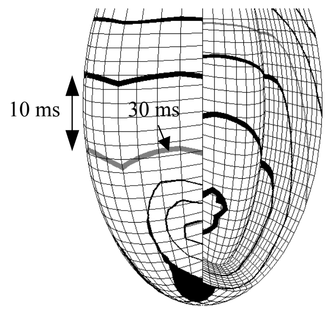

Figure 1: Electrical activation for sinus rhythm (latest activation at 56 ms)

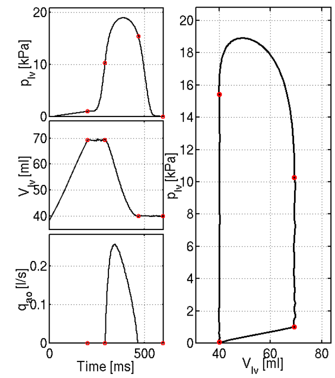

Figure 2: Global hemodynamics for normal sinus rhythm

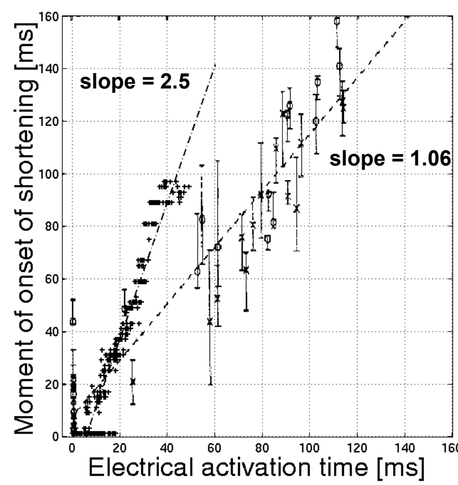

Figure 3: Onset of fiber shortening as a function of electrical activation from measurements (o,x Wyman et al, 1999) and simulations (+).

REFERENCES

Arts, T. et al (1982). *Am. J. Physiol*. **243**, H379-390
Bovendeerd, P.H.M. et al (1992). *J. Biomech.*, **25**, 1129-1140
Colli-Franzone, P. et al (1990). *Math. Biosc*. **101**, 155-235
Rijcken, J. et al (1999), *Ann. biomed. eng*. **27**, 289-297
Scher, A.M. et al (1953). *Circ. Res*. **1**, 539-547
Tomlinson, K.A. (2000), *Phd. Thesis, Univ. Auckland, NZ*
Wyman, B.T. et al (1999). *Am. J. Physiol*. **276**, H881-891

ASYNCHRONOUS ELECTRICAL ACTIVATION IN A THREE–DIMENSIONAL MODEL OF CARDIAC ELECTROMECHANICS

Taras P. Usyk and Andrew D. McCulloch
Department of Bioengineering, The Whitaker Institute for Biomedical Engineering, University of California, San Diego
La Jolla, CA 92093-0412, USA, e-mail: amcculloch@ucsd.edu

INTRODUCTION

Asynchronous electrical activation, induced by an ectopic focus or ventricular pacing, can cause abnormalities in perfusion and pump function and, when chronic, can lead to asymmetric ventricular hypertrophy. These may be caused by local abnormalities, such as heterogeneity in regional workload and shortening.

Assessing the magnitudes of regional myocardial work requires knowledge of regional myofiber stress and strain. While some variables, such as regional strains and epicardial activation patterns have been measured in the intact heart (Wyman et al., 1999), practical experimental methods for mapping three-dimensional distributions of other important variables such as stress, strain energy, or transmembrane potential are still not available.

To investigate the mechanical effects of altered cardiac activation sequence, associated with external pacing or conduction abnormalities, it is necessary to integrate the biophysics of ventricular myocytes and realistic mechanical properties of myocardial tissue into detailed three-dimensional models of the ventricular walls during the whole cardiac cycle, using realistic anatomic, morphologic, and constitutive properties of myocardial tissue.

METHODS

A three-dimensional model of canine left and right ventricular anatomy with detailed myofiber and sheet architecture was based on measurements in the canine heart (Nielsen et al., 1991). We added a model of the Purkinje fiber network as an anisotropic, non-homogeneous, two-dimensional continuum, based on measurements in the dog heart (Pollard et al, 1990; Usyk et al, 2002). Finite element equations for time-dependent excitation and recovery variables were assembled using a collocation finite element method (Rogers et al, 1994) and solved using adaptive Runge-Kutta integration with pacing from the His-Purkinje bundle, left ventricular free wall or right ventricular wall. The computed activation time was used to trigger regional mechanical contraction following constant delay. The model also included length-, time- and calcium dependent active contractile stresses with transverse active stress components. A Windkessel model for arterial impedance was coupled to ventricular pressure and volume to compute the hemodynamic boundary conditions. Ventricular cavity volume constraints were imposed during the isovolumic phases (Usyk et al, 2002).

RESULTS AND DISCUSSION

Electrical propagation velocities obtained from the model were 2.36, 0.48, 0.18 m/s along Purkinje fibers, along ventricular muscle fibers and transverse to muscle fibers, respectively, consistent with experimental measurements. Using the model to compare the mechanical effects of pacing from left and right ventricular sites, close agreement was obtained with spatio-temporal distributions of three-dimensional strain observed experimentally in dogs by Wyman et al (1999) using tagged MRI.

Computed strains show that the tissue shortened rapidly at the early activated regions and shortening was preceded by prestreching of the tissue. This prestreching was a result of passive stretching of the late-activated regions in response to the contraction of the tissue activated earlier. Contraction in the prestreched regions did not begin until a delay about 40 ms after the earliest activation time.

External work was very small (or even negative) at the pacing site and increased up to twice that normal values in regions remote from the site of pacing.

SUMMARY

These results suggest that a coupled model of ventricular electromechanics could be useful for investigating the mechanical consequences of different pacing protocols in patients with conduction abnormalities. The computational techniques developed for the model provides a foundation for more biophysically detailed models.

REFERENCES

Nielsen, P.M.F. et al (1991). *Am. J. Physiol.* **260** (*Heart Circ. Physiol*. **29**), 1365-1378.
Pollard, A.E., Barr R.C. (1990). *IEEE Trand Biomed Eng.* **37**, 1173-1185.
Rogers, J.M., McCulloch, A.D. (1994). *Transactions on Biomedical Engineering.* **41**, 743-757.
Usyk, T.P. et al (2002). *Computing and Visualization in Science*, (in press)
Wyman, B.T. et al (1999). *Am J Physiol.* **276**(**3**) (*Heart Circ. Physiol*), 881-891.

ACKNOWLEDGEMENTS

Supported by NSF, the National Biomedical Computation Resource, and the National Space Biomedical Research Institute.

CYCLE-INDUCED FLOW AND TRANSPORT IN AN ALVEOLUS FOR PARTIAL LIQUID VENTILATION

Hsien-Hung Wei and James B. Grotberg

Department of Biomedical Engineering,
University of Michigan, Ann Arbor, MI 48109-2125, USA.
E-Mail: grotberg@umich.edu

INTRODUCTION

The flow and transport in an alveolus are of fundamental importance to partial liquid ventilation, surfactant transport, pulmonary drug administration, and potential delivery of genetic material into the lung. We propose two simplified models for alveolar liquid undergoing cyclic stretching which mimics breathing motions.

METHODS

When the fluid layer is thin compared with the size of an alveolus, we model the system as a two-dimensional extensible slot. The presence of insoluble or soluble surfactants is considered. See Figure 1(a). We apply scaling analysis and asymptotic theory to describe the interface profile and surfactant distribution during the oscillation cycle for either insoluble or soluble surfactants.

We also model the case when the liquid is partially filled in the alveolus and has a comparable thickness to the size of the alveolus. See Figure 1(b). The surfactant-free case is first investigated. By assuming a spherical interface due to small capillary number, we solve the Stokes flow analytically in the toroidal coordinate system.

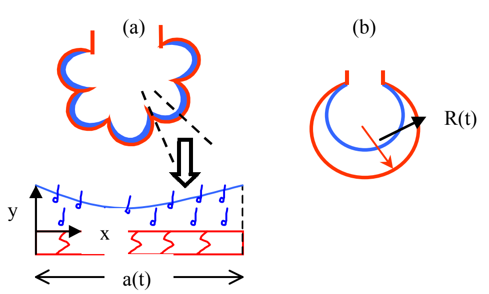

Figure1: Alveolar models for (a) thin fluid layer (b) thick fluid layer. Red lines are the alveolar walls. Blue shading indicates fluid layers.

RESULTS AND DISCUSSION

For the thin fluid layer case, Figures 2 show typical non-zero cycle-averaged flows for both insoluble (Fig. 2(a)) and soluble surfactants (Fig. 2(b)). For insoluble surfactants, the upper (lower) portion of the fluid tends to the extensible end (pinned end). However for a soluble surfactant with higher solubility, the stream pattern is different. Their turning directions near the pinned wall depend on the parameters of the system.

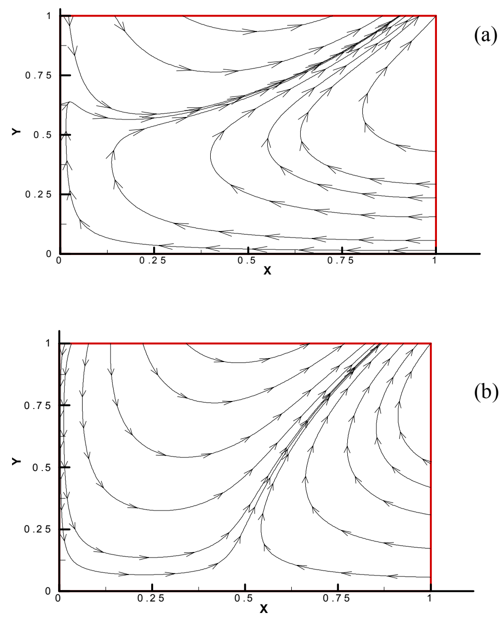

Figure 2: Cycle-averaged streamlines for thin layer model with (a) insoluble (b) soluble surfactants.

For the thick layer case, sufficiently large liquid volume the flow leads to re-circulations near the alveolar opening. This preliminary model, without surfactants, shows no steady streaming due to the reversibility of the Stokes flow. However it is anticipated that adding surfactants will lead to non-reversible Marangoni stresses that will cause steady streaming.

ACKNOWLEDGEMENTS

The research is supported by grants NASA NAG3-2196, NIH HL41126 and HL64373.

COVARIANCE AMONGST RESPONSE TERMS WILL MAGNIFY THE EXPERIMENTAL ERROR THAT IS INHERENT IN MECHANICAL TESTS ON MYOCARDIUM

John C. Criscione

Department of Biomedical Engineering, Texas A&M University, College Station, Texas, USA
http://biomed.tamu.edu/faculty/Criscione/

INTRODUCTION

In the cardiome and similar projects that try to bridge the knowledge gap between myocyte physiology and heart mechanics, it is helpful to characterize myocardium as a continuum. Toward this end and as a graduate student in the lab of Dr. William C. Hunter at Johns Hopkins, this author began a series of extension and torsion tests on papillary muscles with the hopes of further defining the constitutive properties of myocardium. Using a conventional elasticity framework (Humphrey et al., 1992), however, there was tremendous error (> 100% of the mean values) in our response function calculations with much variation amongst specimens.

Upon further analysis it became evident that conventional elasticity theories themselves are excessively sensitive to experimental error for high-strain materials. We have become accustomed to large variations in parameters for biotissues. To our surprise yet clearly present in the elasticity literature, separate batches of rubber also exhibit large variations in response function forms. In short, when conventional theories are used, small perturbations in data are greatly magnified.

Consequently, we sought and discovered a high-strain elasticity theory for rubber that was not sensitive to error (Criscione et al., 2000). This theory has response terms that are mutually orthogonal (the minimum of covariance), and we noticed that Ogden's approach is similarly orthogonal and insensitive to error. Believing that minimal covariance amongst response terms is necessary for reducing any propagation of measurement error, we subsequently developed such theories for materials with microstructures that are transversely isotropic (Criscione et al., 2001) and laminar with one family of fibers (Criscione et al., 2002) as is myocardium.

In these works and at meetings in the last 5 years, we have conjectured that covariance amongst response terms should be avoided because theories with orthogonal response terms are insensitive to error. Here we show rigorously that covariance amongst response terms will always cause a magnification of measurement error. Whereby, we can now say with certainty that constitutive theories must minimize the covariance amongst response terms or else compromise the results of tests on myocardium, soft tissue, or any other high-strain material. Currently, most elasticity theories for myocardium and high-strain materials have response terms with much covariance.

COVARIANCE MAGNIFIES ERROR

In order to mathematically define covariance amongst tensors $\mathbf{A}_1$ and $\mathbf{A}_2$, consider the covariance ratio $R_C(\mathbf{A}_1,\mathbf{A}_2)$ as follows:

$$R_C(\mathbf{A}_1,\mathbf{A}_2) = \frac{\text{abs}(\mathbf{A}_1 : \mathbf{A}_2)}{|\mathbf{A}_1||\mathbf{A}_2|} \quad .$$

where ':' denotes inner product and e.g. $|\mathbf{A}_1|=\text{sqrt}(\mathbf{A}_1\!:\!\mathbf{A}_1)$. It follows that (1) $R_C(\mathbf{A}_1,\mathbf{A}_2)\in[0,1]$; (2) $R_C(\mathbf{A}_1,\mathbf{A}_2)=1$ iff $\mathbf{A}_1$ and $\mathbf{A}_2$ are colinear; (3) $R_C(\mathbf{A}_1,\mathbf{A}_2)=0$ iff $\mathbf{A}_1$ and $\mathbf{A}_2$ are mutually orthogonal; (4) $R_C(\alpha_1\mathbf{A}_1,\alpha_2\mathbf{A}_2)=R_C(\mathbf{A}_1,\mathbf{A}_2)$ with $\alpha_{1\text{-}2}$ as scalars.

Consider a constitutive law for the true stress **t** as follows:

$$\mathbf{t} = \alpha_1\mathbf{A}_1 + \alpha_2\mathbf{A}_2 + \alpha_3\mathbf{A}_3 + \alpha_4\mathbf{A}_4 + \alpha_5\mathbf{A}_5 + \alpha_6\mathbf{A}_6$$

where $\mathbf{A}_{1\text{-}6}$ are symmetric, 2nd order, kinematic tensors and $\alpha_{1\text{-}6}$ are scalar response functions. Here we assume $\mathbf{t}=\mathbf{t}^T$ (i.e. there are no body torques). We do not assume elasticity. $\mathbf{A}_{1\text{-}6}$ and/or $\alpha_{1\text{-}6}$ could depend on strain, strain-rate, or strain-history. As new terminology, let the i^{th} term in **t** be considered as the i^{th} response term. It is necessary that **t** not depend on more than 6 response terms because there cannot be 7 linearly independent, symmetric, 2nd order tensors. Hence, linearly dependent terms could be grouped into the 6 (or fewer) linearly independent terms. For isotropic elasticity there are 3 terms. For transverse isotropy there are 5 terms. With fewer terms (i.e. < 6), our results are analogous yet easier to obtain.

For homogenous tests, **t** is the same everywhere and thus known pointwise. To obtain 6 equations to solve for the 6 response terms, separately contract $\mathbf{A}_{1\text{-}6}$ onto **t** above. These equations will be poorly conditioned (condition number large) if $R_C(\mathbf{A}_i,\mathbf{A}_j)$ is not small for all $i\neq j$. For poorly conditioned systems, small perturbations in **t** give rise to large perturbations in the solution for the response functions. Hence, unless the covariance amongst the response terms is minimized, there will be a magnification of error for homogenous tests. Inhomogenous testing further complicates matters because the **t** field is not known pointwise. Yet, as shown above, for each possible solution for **t**, locally there will be ambiguity in determining the response functions if covariance is not minimized. It follows that a large range of response functions will give nearly the same solution.

REFERENCES

Criscione, J.C., Humphrey, J.D., Douglas, A.S., Hunter, W.C., (2000). *J. Mech. Phys. Solids*, **48**, 2445-2465.
Criscione, J.C., Douglas, A.S., Hunter, W.C. (2001). *J. Mech. Phys. Solids*, **49**, 871-897.
Criscione, J.C., McCulloch, A.D., Hunter, W.C. (2002). Constitutive framework optimized for myocardium and other high-strain, laminar materials with one fiber family. *J. Mech. Phys. Solids*, In press.
Humphrey, J.D., Barazotto, R.L., Hunter, W.C. (1992) *J. Biomech.*, **25**, 541-547.

EFFECTS OF SARCOMERE LENGTH, Ca^{2+} AND STIMULATION RATE ON FORCE GENERATION OF MOUSE CARDIAC MUSCLE.

Bruno D. Stuyvers [1], Andrew McCulloch [2], Jiqing Guo [1], Hank J. Duff [1], Henk E.D.J. ter Keurs [1]

[1]: Dept of Medicine, Physiology & Biophysics, Health Sciences Center, University of Calgary, Calgary, Alberta, Canada; [2]: Dept of Bioengineering, University of California at San Diego, La Jolla, CA, USA.

INTRODUCTION

In cardiac physiology, genetically modified mice have provided unique tools to study the role of important proteins in Excitation-Contraction Coupling and helped investigators to understand molecular alterations that lead to diseases. Nevertheless, the mouse is a relatively recent animal model in cardiac physiology and little is known about underlying processes of force generation. Data published in the literature are often contradictory and, therefore, subject to controversies. We examined in mouse two fundamental relations that govern the functioning of the cardiac pump in mammalian species: 1) the force-frequency (FFR) and 2) the force-sarcomere length relationships.

METHODS

24 trabeculae (length~1mm, thickness~ 100µm) were isolated from mice hearts (~120 adult males CF-1), mounted horizontally between a force-transducer and a servo-controlled motor arm and superfused with HEPES buffer solution containing 1 mM [Ca^{2+}]. The stress (σ) was measured with a silicon strain gauge (res: ~ 0.5µN). Sarcomere Length (SL) was determined by laser diffraction technique (res: ~ 4nm). We measured, first, the force response to different stimulation frequencies (*Freq*'s) (0.07-10Hz). Second, different SLs were tested randomly between slack length and 2.3µm. Each individual value of σ was expressed in % of reference measured at 1Hz (σ_{1Hz}). Interpretation of the results required the determination of Ca^{2+} amount carried by the L-type Ca^{2+} current ($I_{Ca,L}$). The action potential (AP) and $I_{Ca,L}$ were measured in mouse ventricular myocytes using patch-recording techniques. The amount of Ca^{2+} entering the cell was calculated by integration of $I_{Ca,L}$ measured under AP clamp condition.

RESULTS & INTERPRETATION

σ and Freq followed a biphasic relationship in mouse cardiac trabeculae: from 0.1 to 1 Hz, σ decreased, whereas it increased from 1 to 5 Hz with raising *Freq* (Fig.1). Negative segment was sensitive to ryanodine (0.1µM), whereas the positive segment was abolished by nifedipine (0.1 µM). Consequently, the shape of the FFR was dictated by the combination of 2 sources for activating Ca^{2+}: 1) Ca^{2+} release function of the Sarcoplasmic reticulum (at low Freq) and by $I_{Ca,L}$ (at high Freq). This conclusion was supported by modeling the descending and the ascending branches of the FFR.

Fig.1

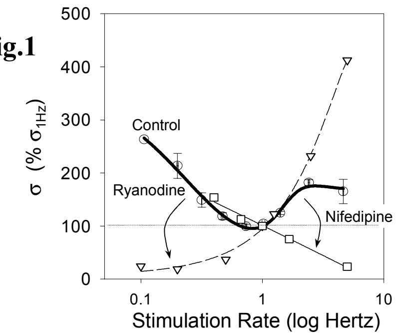

Passive σ (σ_p) increased exponentially with SL and σ_p- SL curves suggested that, like in the rat, passive properties of mouse trabeculae are dictated by titin and collagen. **Fig.2** shows that σ increased with SL and with $[Ca^{2+}]_o$. σ_{active}-SL curves measured ≥4mM superimposed showing that production of force in mouse muscles becomes independent on Ca^{2+} above 4 mM. In contrast, the force obtained using post extra-systolic potentiation at the same SL was ~50 % larger. This result suggests that Ca^{2+} load of the SR is a limiting factor for the production of force in mouse cardiac muscle.

Fig.2

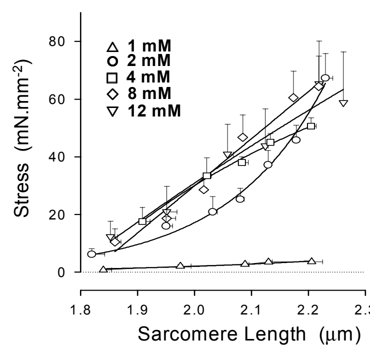

The high tolerance for Ca^{2+} seems to be a characteristic of mouse that probably relates to particularities in the SR function. Extrapolation of results obtained in other mammalian species to the mouse (genetically modified or not), therefore, requires caution.

CANDIDATE MECHANICAL STIMULI FOR HYPERTROPHY DURING EARLY VOLUME OVERLOAD

Kathryn A. Guterl and Jeffrey W. Holmes

Cardiac Biomechanics Group, Department of Biomedical Engineering, Columbia University
jh553@columbia.edu http://www.columbia.edu/~jh553/

INTRODUCTION

Pressure overload and volume overload of the left ventricle induce different gene expression patterns, cellular dimension changes and gross geometric remodeling. While systolic wall stress has been proposed as the control variable driving pressure overload type hypertrophy, Emery and Omens demonstrated that diastolic strain is a more plausible control variable for volume overload type hypertrophy (Emery 1997). Since expression of genes associated with both hypertrophic phenotypes has been demonstrated within hours of in vivo overload, hypertrophic mechanical or hormonal signals must appear early after the overload is initiated.

METHODS

All studies were performed according to the American Association for Accreditation of Laboratory Animal Care guidelines and approved by the Columbia University Institutional Animal Care and Use Committee. Sprague-Dawley rats weighing approximately 250 g were anesthetized with ketamine and xylazine (80 mg/kg and 12 mg/kg initial doses respectively, with supplemental doses as required) and ventilated with room air. The chest was opened via midline sternotomy and the heart instrumented with sonomicrometers to measure ventricular volume (Sonometrics, London ON, Canada) and a fluid-filled catheter connected to a pressure transducer (TRN050, Kent Scientific, Torrington CN) to measure ventricular pressure. The chest was loosely closed and covered with moist gauze.

Five seconds of continuous volume and pressure data were acquired digitally every five minutes at a sampling rate of 200 Hz. Following 45-60 minutes of control data acquisition, the abdomen was opened in the midline and an infrarenal aortocaval fistula was created using the method of Garcia and Diebold (Garcia 1990). Presence of a patent fistula was confirmed visually by dilation and streaming of arterial blood in the abdominal vena cava. The abdomen was irrigated with 5 ml of saline and closed. Volume and pressure data were recorded for an additional two hours and analyzed off-line to calculate minimum volume, maximum volume, mean volume, stroke volume, heart rate, and rates of volume change during at least five cardiac cycles for each sampling period.

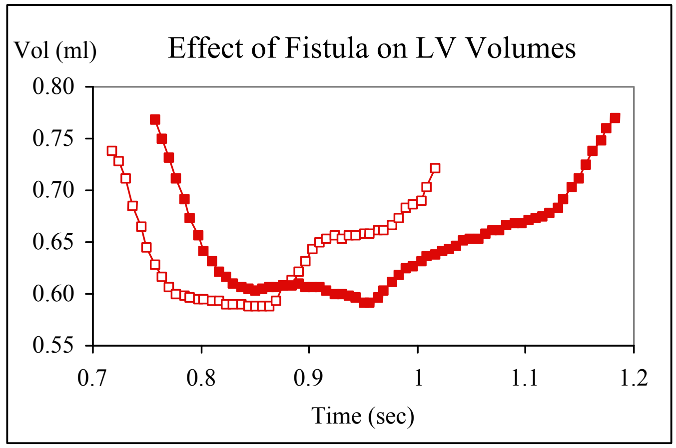

Figure 1: Left ventricular volume (including wall volume) during typical beats 40 minutes prior to (open symbols) and 40 minutes after (closed symbols) creation of an infrarenal aortocaval fistula.

RESULTS AND DISCUSSION

At the cellular level, increases in diastolic strain such as those reported by Emery and Omens might be transduced as increases in time-averaged cell length, maximum cell length, amplitude of the length variation, or rates of length change. In the present study, acutely opening an aortocaval fistula increased maximum volume (14%) more than time-averaged volume (7%). Minimum volume and rates of volume change remained stable (Figure 1). These preliminary findings appear more consistent with a role for maximum cell length or amplitude of cell length variation as stimuli for hypertrophy.

The acute response to volume overload likely includes both compensatory regulatory responses and large volume shifts. In this study, increased stroke volume was offset by a decrease in heart rate, producing an overall drop (15%) in left ventricular cardiac output. Additional study is needed to better define the subacute responses that lead to a significant increase in left ventricular mass at three days in this experimental model.

REFERENCES

Emery, J.L., Omens, J.H. (1997*). Am J Physiol Heart Circ Physiol* **273**, H1198-H1204.
Garcia, R., Diebold, S. (1990*). Cardiovasc Res* **24**, 430-432.

SHEAR PROPERTIES OF VENTRICULAR MYOCARDIUM

Ian LeGrice, Socrates Dokos, Bruce Smaill and Alistair Young

Department of Physiology, University of Auckland, Auckland, New Zealand. i.legrice@auckland.ac.nz

INTRODUCTION

Ventricular myocardium has a characteristic laminar structure (LeGrice et al., 1995a). Myocytes are organized in branching layers separated by extensive cleavage planes. The orientation of layers varies across the ventricular wall, but is relatively uniform in the midwall. At any point in the myocardium, the laminar structure may be characterized by identifing orthogonal axes aligned i) with the myocyte direction, ii) transverse to the myocyte axis within a layer, and iii) normal to the layer. Separate families of perimysial connective tissue are associated with these different material directions. Shearing between layers is believed to be important in active (LeGrice et al., 1995b) and passive (Spotnitz et al 1974) ventricular function. However, there have been few attempts to characterize the shear properties of cardiac tissue. The aim of this study was to determine the shear properties of passive ventircular myocardium with respect to its three principal material axes.

METHODS

We have developed a novel device for this purpose (Dokos et al., 2000). Simple shear deformations can be applied to isolated segments of soft biological tissue in two orthogonal directions simultaneously while resulting forces along the three associated axes are measured. Six pig hearts were arrested in diastole and perfused with 2,3-butanedione monoxime to maintain the tissue in a passive state. Three samples, approximately 3x3x3 mm with sides parallel to the principal material directions, were removed from adjacent regions of the lateral LV midwall of each heart. Because only two of the six different modes of simple shear deformation can be imposed in a single sample, the three specimens from each heart were tested in different orientations to cover all possible modes. Four cycles of sinusoidal (30 sec period) displacement were applied separately in each direction for maximum shear strains from 0.1 to 0.5. On completing sinusoidal testing, rapid 50% shear step displacements were imposed in each direction and the resultant forces were recorded for 300s.

RESULTS AND DISCUSSION

Our study demonstrates that passive myocardium has nonlinear viscoelastic shear properties at physiological levels of deformation with reproducable, directionally dependent softening as strain is increased. Shear properties were clearly anisotropic with respect to the three principle material directions: Passive venticular myocardium is least resistant to simple shear displacements imposed in the plane of the myocardial layers and most resistant to shear deformations which produce rotation and extension of the myocyte axis. Comparison of stress strain relations for the six different shear modes suggests that simple shear deformation is resisted by elastic elements initially perpendicular to the direction of the shearing motion.

REFERENCES

LeGrice IJ, Smaill BH, Chai LZ Edgar SG, Hunter PJ, Gavin JB. Laminar structure of the heart: ventricular myocyte arrangement and connective tissue architecture in the dog. Am J Physiol 269: H571-H582, 1995a.

Le Grice IJ, Takayama Y, Covell JW. Transverse shear provides a mechanism for normal systolic wall thickening. Circ Res 77: 182-193, 1995b.

Spotnitz HM, Spotnitz WD, Cottrell TS, Spiro D, Sonnenblick EH. Cellular Basis for volume related wall thickness changes in the rat left ventricle Jnl Mol Cell Cardiol 6: 317-331, 1974.

Dokos S, LeGrice IJ, Smaill BH, Kar J, and Young AA. A triaxial-measurement shear-test device for soft biological tissues. J Biomech Engr 122: 471-478, 2000.

ACKNOWLEDGEMENTS

This work was funded by Health Research Council of New Zealand and The National Heart Foundation of New Zealand and approved by The University of Auckland Animal Ethics Committee.

CYTOSKELETAL DEFECTS ALTER MYOCARDIAL MECHANICS BEFORE THE HEART FAILS

Ilka Lorenzen-Schmidt, Andrew D. McCulloch, Jeffrey H. Omens

Department of Bioengineering, University of California, San Diego, La Jolla, California, USA
jomens@ucsd.edu

INTRODUCTION

Cytoskeletal defects may play an important role in the development of dilated cardiomyopathy and heart failure [1]. Targeted deletion of the cytoskeletal protein MLP (muscle LIM protein) consistently leads to typical signs of dilated cardiomyopathy in mice greater than two weeks old. These signs include decreased ejection fraction and depressed diastolic and systolic performance [2]. It is not known, however, whether the dysfunction is directly due to the lack of MLP through a structural defect or whether it is indirectly caused by MLP deficiency. We examined diastolic and systolic behavior of papillary muscles in two-week-old MLP knockout (MLPKO) and control mice, when echocardiography showed normal cardiac function and no clear signs of heart failure.

METHODS

12-to-17-day-old MLPKO and control mice were used for this study. After anesthesia, the chest was opened, the heart arrested and excised. The left anterior papillary muscle, still attached to the wall, was placed in an apparatus that allowed muscle force measurements, continuous superfusion with oxygenated solution and motor-controlled length change of the muscle. Titanium dioxide markers were arrayed on the muscle to observe local length changes during the experiment. Diastolic and systolic length-tension relations were recorded as well as force time course and force-frequency relationship.

RESULTS AND DISCUSSION

The diastolic length-tension relations in both groups revealed that muscles from young MLPKO hearts were softer than controls (Fig. 1a), although stiffness is elevated in adult MLPKO [3]. Systolic stress was decreased in the MLPKO muscles compared to wildtypes at comparable length (Fig. 1b). Time to half relaxation was prolonged in the MLPKO, also indicating depressed cardiac function. No difference in force-frequency relation was detected between the genotype groups.

The decreased stiffness in the young MLPKO muscles is striking, since it stands in contrast to typically elevated stiffness in adult muscles in dilated cardiomyopathy. The softer properties could be caused directly by the lack of MLP and may contribute to the progression of cardiomyopathy through increased ventricular dilatation during filling. Mild cardiac dysfunction, shown by decreased systolic tension and slightly prolonged relaxation time, is already present at two weeks of age. Therefore, it is unclear whether these changes are primary or secondary effects of the disease.

a)

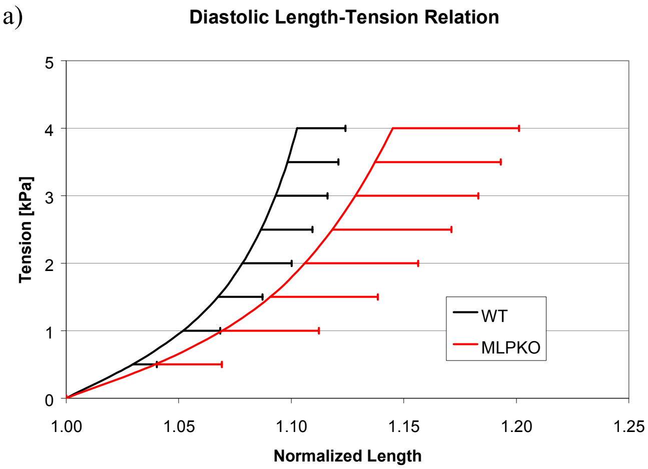

b)

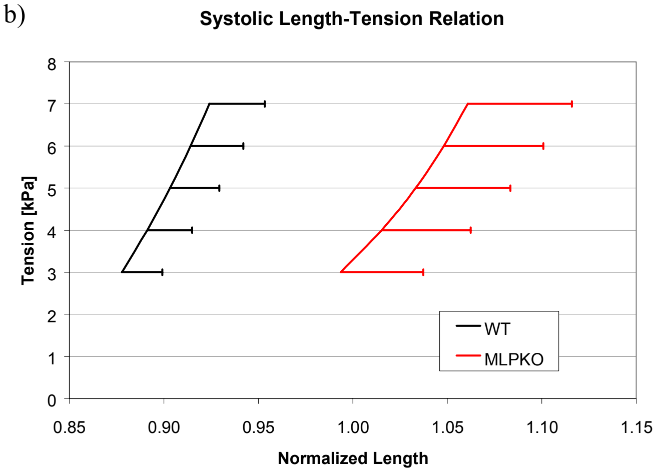

Figure 1: a) Diastolic and b) systolic length-tension relation in MLPKO and wildtype muscles. Young MLPKO papillary muscles are softer than wildtype controls and develop less systolic tension than controls at the same length.

REFERENCES

1) Chien KR: Stress pathways and heart failure. *Cell* 98(5):555-8, 1999.
2) Arber S et. al.: MLP-deficient mice exhibit a disruption of cardiac cytoarchitectural organization, dilated cardiomyopathy, and heart failure. *Cell* 88(3):393-403, 1997.
3) Omens JH et.al.: Muscle LIM protein deficiency leads to alterations in passive ventricular mechanics. *Am J Physiol Heart Circ Physiol* 282(2):H680-7, 2002.

MECHANICAL EFFECTS ON CARDIAC MYOCYTE ELECTROPHYSIOLOGY

Peter Kohl

Cardiac MEF Group, Department of Physiology, University of Oxford, Parks Road, Oxford, United Kingdom
http://www.physiol.ox.ac.uk/~pk

INTRODUCTION

Electro-mechanical regulation of cardiac myocytes consists of control (Excitation-Contraction Coupling) and feedback pathways (Mechano-Electric Feedback, MEF). The latter is much less investigated – even though there have been abundant phenomenological reports, over the past 120 years, about the mechanical induction and termination of cardiac arrhythmia by pre-cordial chest impact (Nesbitt et al 2001). The lack of insight into MEF at the cellular level is largely caused i) by the difficulty of simulating cardiac mechanical stimulation in isolated cells, and ii) by the absence, until last year, of selective blockers of underlying ion channels (Bode et al 2001). Here, we review recent advances in our understanding of the cellular basis of cardiac MEF, and highlight the role that detailed mathematical models of cardiac mechano-electrical interactions have played in the process.

EXPERIMENTAL METHODS

Studies of cardiac cellular MEF are based on electrical recordings from isolated cardiomyocytes during mechanical stimulation. Recordings are mostly made in patch-clamp, cell-attached or whole-cell mode (although sharp-electrode recordings have been performed in isolated cells and tissue). Mechanical stimulation in the patch-clamp setting is via deformation of the membrane patch under the pipette by application of a pressure gradient (pipette suction). Cell-attached and whole-cell cell studies tend to use local membrane deformation (poking, compression), cell volume changes (swelling, inflation), or axial elongation (stretch by probes attached to the cell); for review see (Kohl et al 1999).

MATHEMATICAL MODELS

Models of cardiac cellular MEF range from simple three-equation-outlines to detailed representations of mechanically-activated ion channels and their interactions with the 'standard' set of cardiac cellular electrophysiological mechanisms; for review see (Kohl, Sachs 2001).

RECENT FINDINGS

Out of the methods used to mechanically challenge isolated cardiac cells, axial stretching is best suited to reproduce patho-physiological responses like, for example, the increase in spontaneous beating rate of the natural cardiac pacemaker (Cooper et al 2000). Cell swelling, in contrast, reduces pacemaking in isolated cells (Lei, Kohl 1998). This is caused by differences in ion channel sub-populations activated by interventions that primarily affect i) cell volume (volume-activated channels) or ii) cell length (stretch-activated channels, SAC). Extrapolations from experimental findings have to take this into account (swelling is a feature of ischaemia/ reperfusion, but not of cyclical cardiac loading/contraction).

Various SAC have been described. They can roughly be divided into potassium-selective and cation non-selective channels. The former will abbreviate action potentials but have little effect in diastole, while the latter serve as potent triggers of diastolic depolarisation/excitation (Craelius 1993).

Apart from sarcolemmal ion channels, mechanical stimulation affects cellular Ca^{2+} handling; for review see (Calaghan, White 1999). Modelling suggests that Ca^{2+}-mediated stretch effects on action potential duration may be opposite to those brought about by stretch-activated channels (Kohl et al 1998), which may explain some of the contradictory findings in experimental work, particularly using the whole-cell patch clamp technique (where Ca^{2+} buffers reach the cell interior).

SUMMARY

In gross simplification: stretch of cardiac myocytes shortens action potential duration, depolarises resting cells, and promotes automaticity. Other important effects emerge only at the level of cardiac tissue, like those caused by gradients in electro-mechanical parameters, or effects on conduction.

KEY QUESTIONS

At present, it is not known how external forces reach mechano-electrical transducers at the cellular level, and whether it is primarily stress or strain that affects sub-cellular behaviour. Furthermore, the question of how SAC and Ca^{2+}-handling effects are linked is open, to the extent that we cannot confirm or reject at present, whether Ca^{2+} travels via SAC in mammalian cardiac myocytes.

REFERENCES

Bode, F. et al (2001). *Nature*, **409**, 35-36.
Calaghan, S.C., White, E. (1999). *Prog Biophys Mol Biol*, **71**, 59-90.
Cooper, P.J. et al (2000). *J Appl Physiol*, **89**, 2099-2104.
Craelius, W. (1993). *Exp Physiol*, **78**, 411-423.
Kohl, P. et al (1998). *Can J Cardiol*, **14**, 111-119.
Kohl, P. et al (1999). *Prog Biophys Mol Biol*, **71**, 91-138.
Kohl, P., Sachs, F. (2001). *Philos Trans R Soc Lond A*, **359**, 1173-1185.
Lei, M., Kohl, P. (1998). *Acta Physiol Scand*, **164**, 1-12.
Nesbitt, A.D. et al (2001). *The Lancet*, **357**, 1195-1197.

ACKNOWLEDGEMENTS

The Oxford Cardiac MEF Group is supported by grants from the Medical Research Council, the British Heart Foundation and the Royal Society, London.

POST-TRANSLATION MODIFICATION OF TITIN AND EFFECTS ON PASSIVE TENSION IN CARDIAC MYOCYTES.

Yiming Wu[1], Robert Yamasaki[1], Mark McNabb[1], Siegfried Labeit [2]and Henk Granzier[1].

[1]Dept VCAPP, Washington State University, Pullman, WA 99164. [2]Institut für Anästhesiologie und Operative Intensivmedizin, Universitätsklinikum Mannheim.
Corresponding author's Email: granzier@wsunix.wsu.edu

INTRODUCTION

Stimulation of β-adrenergic receptors on cardiac myocytes initiates complex signaling pathways that enhance contractility and accelerate relaxation. These effects are mediated by cAMP-dependent protein kinase (PKA), which phosphorylates a host of intracellular substrates, including accessory proteins on the thin and thick filaments (e.g., TnI and MyBP-C). In addition to the thin and thick filaments, striated muscles also contain a third filament system composed of the giant protein titin. Individual titin molecules span the distance between the M-line and the Z-line to form an elastic connection between the A-band and the ends of the sarcomere. As muscles are passively stretched from their slack length, titin's I-band spanning segment extends and generates an opposing force, referred to as passive tension (Granzier and Irving, 1995). In the present work, we investigated whether the β-adrenergic pathway can also modulate the properties of titin.

METHODS

Cardiac myocytes were isolated from rats. Passive tension-SL curves were measured in relaxing solution (RS) as explained in Wu et al. (2000). 1U/µl PKA was achieved by changing 200µl of RS within the experimental chamber (total volume 600 µl) with 200µl of RS containing 3U/µl PKA solution. Myocytes were stretched and released at 7 min intervals to facilitate diffusion of the kinase, and passive tension was measured after 35 min. Phosphorylation assays were carried out with myocytes as well as with recombinant fragments that represent the extensible region of human cardiac titin, see Labeit and Kolmerer (1995). Cells or protein samples were incubated in a buffer containing ATP-gamma ^{32}P and PKA. Samples were electrophoresed, stained, destained, dried and exposed to autoradiographic film.

RESULTS AND DISCUSSION

Findings indicate that PKA phsophorylates titin and causes a decrease in passive tension in skinned rat cardiac myocytes. *In vitro* phosphorylation assays with recombinant titin fragments suggest that a region of titin expressed only in cardiac titins, referred to as the N2B spring element, is the target site for PKA. The N2B spring element is a 572-residue sub-domain of titin's elastic segment that allows cardiac titins to function as adjustable springs. Our findings suggest that its phosphorylation in response to β-adrenergic stimulation can also alter titin's elasticity. Because the N2B spring element is differentially spliced into only the cardiac titin isoforms (Labeit and Kolmerer, 1995), these results suggest that like TnI and MyBP-C, titin contains a cardiac-specific domain that serves as a PKA substrate. Because titin-based passive tension is a determinant of diastolic function, our results suggest that titin phosphorylation may modulate cardiac function *in vivo*.

REFERENCES

Labeit S, Kolmerer B. Titins: giant proteins in charge of muscle ultrastructure and elasticity. *Science*. 1995;270:293-6.
Granzier, H., and T. Irving. 1995. Passive tension in cardiac muscle: The contribution of collagen, titin, microtubules and intermediate filament. *Biophysical Journal,* 68: 1027-1044.
Wu, Y., Cazorla, O., Labeit, S.Granzier H, 2000 Changes in titin and collagen underlie diastolic stiffness diversity of cardiac muscle.. *Journal of Molecular and Cellular Cardiology*, 32, 2151-2161.

ANALYSIS OF 3-DIMENSIONAL CULTURE OF CARDIAC MYOCYTES AND FIBROBLASTS THAT SIMULATE MECHANICAL CONDITIONS IN VIVO

Thomas K. Borg[1], Alexander McFadden[1], Anna McNeal[1], Andrew McCulloch[2], and Edie Goldsmith[1]
Department of Developmental Biology and Anatomy[1] http://www.med.sc.edu:89
University of South Carolina, Columbia, SC
Department of Bioengineering, UCSD[2] La Jolla, CA

INTRODUCTION

The three dimensional (3-D) organization of cardiac tissue *in vivo* is for efficient mechanical function. This organization combines the proper orientation of cellular components, cardiac myocytes and fibroblasts, with extracellular matrix (ECM) components in relation to the overall geometry of the heart. In this manner, the mechanical properties of the heart are dependent upon the ventricular fiber architecture in relation to the chamber walls. Specific receptors, integrins, link the cellular components with the ECM making a hierarchically coupled interacting 3-D structure (Ross and Borg, 2001). Experimental and mathematical models suggest that the distribution of myofiber orientations, ECM organization (patterning) and cellular alignment are all integral to maintaining uniform fiber stress and strain during the filling and ejection of the ventricles. To investigate this hypothesis, a 3-D model of cellular and ECM arrangement has been developed and subjected to various mechanical and electrical stimuli.

METHODS

Neonatal cardiac myocytes were isolated, subjected to Percoll gradients, and plated on aligned collagen (Simpson et al 1999). This method produces a cardiac phenotype that is similar to myocardium *in vivo*. Multilayers of cells and connective tissue are then layered to form laminae similar to those found *in vivo*. Multilayers, usually consisting of collagen-myocyte-myocyte-collagen, were then subjected to a variety of mechanical forces including static and cyclic stretch (Yost et al, 2000) and field stimulation. Morphological analysis was done by confocal microscopy using specific antibodies for myocytes, fibroblasts, integrins and connexins.

RESULTS AND DISCUSSION

Analysis of the multilayers showed that myocytes and fibroblasts had a similar phenotype to that observed *in vivo.* With time in culture, the collagen became modified into networks similar to the endomysium.(figs. 1). Confocal analysis showed that the fibroblasts were tightly associated with the cardiac myocyte in a non-random fashion. When multilayers were subjected to mechanical force, myocytes demonstrated increased growth. Biochemical analysis confirmed these morphological observations. Multilayer systems that were subjected to electrical pacing also demonstrated an increase in size as well as actin and myosin.

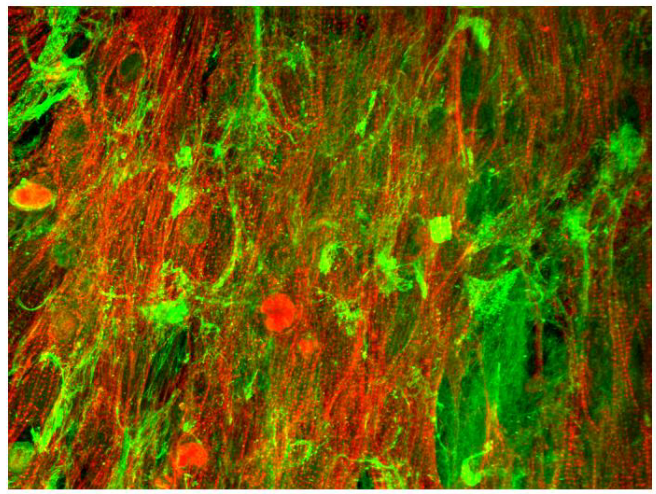

Figure 1: Multilayers consisting of collagen (FITC-Green) associated with myocytes (Phollodin-Red). The arrangement is consisted of aligned collagen-myocyte-myocyte-aligned collagen.

SUMMARY

These data demonstrated the feasibility of the culturing cardiac myocytes and fibroblasts in 3-D that showed a *in vivo* like phenotype and responded to mechanical and electrical stimulation. These procedures are suitable for morphological, biochemical and molecular analyses of the cellular and acellular components to determine how these properties are altered by mechanical stimulation.

REFERENCES

Simpson et al (1999) Circ. Res, **8**, 59-69
Yost et al (2000) Am J. Physiol, **279**, H3124-3130
Ross and Borg Circ. Res (2001), **88**,1112-1112

FORCE AND SARCOMERE SHORTENING VELOCITY IN RAT HEART

Henk EDJ ter Keurs, Nathan Deis, Mei L Zhang, Amir Landesberg*

Departments of Medicine Physiology and Biophysics, Cardiovascular Research group, Faculty of Medicine, University of Calgary, Canada. *Dept of Biomedical Engineering, Technion-Israel Institute of Technology, Haifa Israel.

INTRODUCTION

Sarcomere shortening determines ventricular ejection. The velocity of sarcomere shortening depends on the load on the cross-bridges on the one hand and the effect of shortening on the number of force generating cross-bridges on the other. Further, this interplay between load and shortening depends on the myosin iso-enzyme composition in the muscle. The myosin iso-enzyme expression varies depending on effects of prolonged loading on the heart and on the effects of thyroid hormone, especially in rodents. The maximal velocity of sarcomere shortening in muscle the rapid V1 myosin isoform exceeds that of the V3 isoform 2.5 fold. Little is known about the effect of shortening on the number of force generating cross-bridges, and on its consequences for the shape of the force velocity relationship in cardiac muscle containing different myosin isoforms. In this study we have analyzed the relationships between force and velocity in Cardiac Trabeculae from the Rat containing either V1 or V3 myosin.

METHODS

We used trabeculae from the right ventricle of 3 month-old LBN Rats. Rats were either pre-treated with propylthiouracil (PTU) 0.8g/l in their drinking water for 6 weeks or pre-treated with 30 µg Triiodo-thyronine (T3)/100g bw s.c. per day for 14 days.

Myosin isoenzyme composition was identified by non-denaturing pyrophosphate poly-acryl-amide gel electrophoresis (PPi-PAGE) using a procedure similar to that of Hoh and co-workers (Hoh et al., 1977).

The trabeculae were suspended between a silicon strain gauge and a motor arm. Sarcomere Length (SL) was measured using laser diffraction techniques. The muscles were stimulated at 0.5 Hz in $[Ca^{2+}]_o$ 1.5 mM at 26 C. The velocity of sarcomere shortening was measured at SL 2.0 µm in order to avoid effects of elastic forces opposing shortening. SL was controlled until 70% of peak force of the twitch was reached; then, a quick release was applied followed by a controlled release at constant velocity of sarcomere shortening, yielding constant force. Alternatively a shortening ramp was imposed that caused linear sarcomere shortening and biphasic decline of force. The rate force decline during the slow phase was normalized to isometric force (F_{isom}) at the same moment during the twitch and correlated with the velocity of sarcomere shortening (V_{SL}). The slope (G1) between the force deficit (ΔF) and V_{SL} was interpreted as a velocity dependent rate of weakening of the cross-bridges. The number of force generating cross-bridges was estimated independently using the modulus of stiffness at 200Hz sinusoidal length perturbations of the muscle. G1 was used to calculate the parameters a_H and b_H in the Hill's hyperbola fitted to the force velocity relations of muscles with V1 or with V3 myosin isoforms.

RESULTS

Treatment with T3 increased the V1 fraction of myosin in young rats from 90% to 100%. PTU eliminated V1 and left the muscles with only V3 myosin.

Maximal stress development at SL 2.0 µm was 98±8mN/mm^2 in V1 muscle following T3 treatment and 35% lower following PTU treatment. The maximal velocities of sarcomere shortening (V_0) were 17.6± 1.4µm/s and 8.2± 0.7µm/s for V1 and V3 myosin respectively. The Hill coefficients a and b (in %F_{max} and µm/s, respectively) calculated from the force velocity relationship were 8±2 and –1.2±0.5 and 5±0.8 and 0.6±0.6 for V1 and V3 muscles, respectively.

The normalized force deficit following sarcomere shortening ramps at varied velocity, in both T3 and PTU treated muscle increased linearly with time and was proportional to the velocity of shortening:

$$\Delta F = G1 \bullet F_{isom} \bullet \Delta t \bullet V_{SL} \bullet (1 - V_{SL}/V_o)$$

The modulus of stiffness declined during the shortening ramps and G1 was 6.15±2.1 µm^{-1} in predominantly V1 muscle.

CONCLUSION

the linear interrelationship between ΔF and V_{SL} suggest that the kinetics of weakening of both V1 and V3 cross-bridges depends on V_{SL}. The feedback of V_{SL} to the number of attached cross-bridges provides a description of the interrelationship between force and shortening in muscle with V1 and V3 iso-enzymes explaining the nature of the force velocity relationship may be used for a general description of the energetic behavior of cardiac muscle.

ENGINEERED TISSUES AS MODEL SYSTEMS FOR STUDYING MYOCARDIAL BIOMECHANICS

Eun Jung Lee, Vedran Knezevic, Jeffrey W. Holmes and Kevin D. Costa

Cardiac Biomechanics Group, Department of Biomedical Engineering, Columbia University, New York
kdc17@columbia.edu, http://www.bme.columbia.edu/research.html

INTRODUCTION

Evaluation of ventricular wall stress, which influences myocardial growth and remodeling, requires a mechanical constitutive law relating stress and strain in the tissue. Biaxial testing has been widely used to investigate the constitutive properties of passive and active myocardium [review by Costa et al., 2001]. However, due to variability in tissue structure and damage during dissection of the test specimen, several fundamental biomechanics questions remain unresolved. Tissue engineering, while not yet capable of producing fully functional myocardium [Mann and West, 2001], may be useful to design rudimentary cardiac tissues with geometry, structure and composition ideally suited to overcome some of the practical limitations of biaxial testing of myocardium. This study examines the potential of this novel approach.

METHODS

Adult rat cardiac fibroblasts (ARCF) and human foreskin dermal fibroblasts (HFF, gift from Dr. Steven Nicoll) were harvested by serial collagenase digestion of minced tissue (and 30 min panning to separate attached ARCFs from floating myocytes) and cultured in polystyrene flasks (Fisher) for several days at 37°C and 5% CO_2 in DMEM with 10% fetal bovine serum and 1% penicillin-streptomycin (Gibco BRL).

Square cell-populated collagen gels were created as detailed elsewhere [Knezevic et al., 2002]. Briefly, a suspension of 2-6x10^5 cells/ml in 2.0 mg/ml purified bovine dermal collagen type-I (Vitrogen 100, Cohesion Technologies) was mixed on ice, and 10 ml placed in a 4x4-cm square mold. Secured at the edges of the mold are 6x20x2-mm bars of hydrophilic porous polyethylene (PE, Small Parts) threaded with 5-0 monofilament suture. After 1 hour incubation, 10 ml of media was added to "float" the gels, and the sutures were either held fully constrained in both directions (FULL), or uniaxially constrained in only one direction using either single solid PE bars (UNIsolid) or PE bars cut into 3 short segments to permit lateral freedom of the gel boundary (UNIcut).

After 72 hours incubation, gels were fixed in 3.7% formaldehyde for 24 hours. The central region of the gels was then imaged at 100x magnification on an inverted phase contrast microscope (IX-70, Olympus) with a digital video camera (Sensicam, Cooke Corp). The distribution of cell orientation in each image was automatically measured on a Unix workstation (O2, Silicon Graphics Inc) using software specifically designed for quantifying alignment [Karlon et al., 1999] using circular statistics to obtain a mean and angular deviation (ANGDEV) of local cell orientation.

Biaxial mechanical testing of one UNIsolid gel was performed at 24 and 48 hours incubation by applying equibiaxial 50, 100, and 200 mg weights to the loading sutures and photographing the positions of small markers affixed to the top surface of the gel [Knezevic et al., 2002]. From the digitized marker coordinates, Lagrangian finite strains were computed in the constrained direction (Exx) and in the unconstrained direction (Eyy), as well as the shear strain (Exy).

RESULTS AND DISCUSSION

In FULL gels, cells were randomly oriented in the plane with an average angular deviation of 36.1° ± 2.3°. In UNI gels, cells became aligned parallel to the lateral free boundaries with a mean orientation within ±5° of the constrained X-axis. However, the UNIsolid gel had a broader distribution of cell orientation (ANGDEV = 18.8° ± 0.57°) compared to the UNIcut gel (ANGDEV = 14.8° ± 0.7°). Thus, by altering loading constraints at the gel boundaries, cell alignment could be regulated as random, moderately aligned, or highly aligned.

In the equibiaxial loading of a UNIsolid gel, Exx < Eyy (Exy negligible) and the degree of anisotropy increased from 24 to 48 hours of incubation (Fig. 1). This reflects mechanical anisotropy created in the tissue construct by controlling cellular alignment, with the constrained direction stiffer than the unconstrained direction.

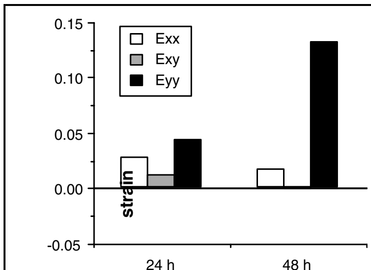

Figure 1: Strain vs. incubation time for 200 mg load.

SUMMARY

A method has been developed to generate rudimentary tissues composed of cardiac cells embedded in a three-dimensional collagen matrix, in an ideal geometry for biaxial material testing, with integrated attachment points and control of cellular alignment and mechanical anisotropy. These engineered tissues overcome some of the fundamental limitations of biaxial testing of natural heart tissue, and offer a promising new model system for interrogating fundamental aspects of myocardial biomechanics.

REFERENCES

Costa, K.D. *et al.* (2001) *Phil Trans R Soc Lond A*, **359**:1233-1250.
Karlon, W.J. *et al.* (1999) *Ann Biomed Eng*, **27**:712-720.
Knezevic, V. *et al.* (2002) *Biomech Model Mechanobiol*, (in press).
Mann, B.K, West, J.L. (2001) *Anat Rec*, **263**:367-371.

WAVE INTENSITY IN THE PULMONARY CIRCULATION

Aoife B O' Brien and Kim H Parker
Physiological Flow Studies Group, Dept. of Bioengineering, Imperial College of Science, Technology and Medicine, London, U.K. (a.obrien@ic.ac.uk)

INTRODUCTION

The pulmonary circulation is very different from the systemic circulation and has been much less extensively studied. It operates at a much lower pressure and resistance, branching distances are shorter, pulmonary arteries are thinner and more compliant allowing larger pulsation of the vessels. We studied wave propagation, in the time domain, in both directions, in the proximal pulmonary circulation using wave intensity analysis, which also allowed the determination of wave speed and vessel distensibility.

METHODS

Pressure, flow, and diameter were measured simultaneously in the main and left pulmonary arteries in anaesthetised, open chest dogs during baseline and hypoxia (>1hour, 10% O_2) and during occlusion of the right pulmonary artery. Data were analysed using wave intensity analysis. The theory is based on the 1-dimensional conservation equations and considers waves to be the resultant of successive, infinitesimal wave fronts. Wave intensity is defined as the product of the change in pressure and the change in velocity (*dI=dPdU*) across the wave front. The theory provides an analytical expression for local wave speed, c, in terms of density, ρ, and vessel distensibility, *D*, ($c = \sqrt{1/\rho D}$) and leads to the water-hammer equation, relating changes in pressure to changes in velocity $dP_\pm = \pm \rho c dU_\pm$. Thus, c can be determined experimentally from the slope of a pressure-velocity loop. This allows the separation of pressure and velocity waveforms into their forward (mainly generated by the ventricle) and backward (mainly due to reflections from bifurcations or terminal vessels) components.

RESULTS AND CONCLUSIONS

The usual forward compression and expansion waves were observed during ventricular contraction and relaxation respectively. Expansion reflections were observed in both the main and left pulmonary arteries in early systole during ejection. They had the effect of lowering pressure and augmenting flow thus assisting right ventricular ejection. This is unlike the systemic circulation where reflections are normally compressive. The time of arrival of these reflections suggests that the reflection sites must be in the proximal vessels. Compression reflections, originating from more distal and terminal sites were observed in late systole under all conditions.

During occlusion of the right pulmonary artery, the expansion reflections were abolished and compression reflections were observed in early systole. During hypoxia, expansion reflections were augmented but were of shorter duration due to the earlier arrival of compression reflections in mid-systole. These earlier and increased compression reflections were probably due to hypoxic vasoconstriction of the distal pulmonary vessels. Determination of local wave speed allows the study of vessel distensibility and thus can help to explain complex vessel behaviour, which is influenced by both mean pressure and vascular tone.

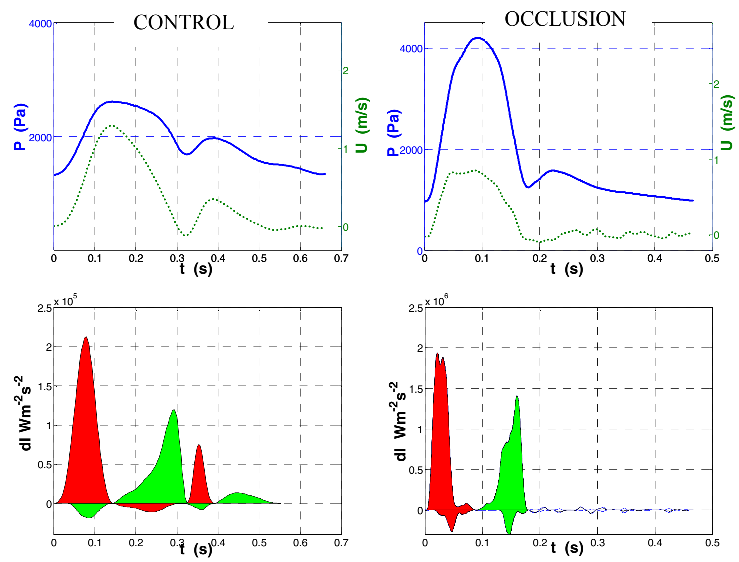

Figure 1: Pressure (—), velocity (--) and wave intensity (below) in the canine pulmonary artery during control and occlusion. (note change of scale during occlusion). Early systolic backward expansion waves (negative, green/grey) during control conditions are replaced by backward compression waves (negative, red/black) during occlusion.

SUMMARY

Wave intensity analysis, is well suited to the study of waves in the pulmonary circulation. It allows the determination of local wave speed, which is related to vessel distensibility, and, allows the separation of waveforms into their forward and backward components in the time domain. Application of the analysis to measurements in the dog show that reflected expansion waves (lowering pressure and augmenting flow) exist in the main and left pulmonary arteries in early systole during right ventricular ejection.

ACKNOWLEDGEMENTS

We acknowledge the support and hospitality of Prof. J.V. Tyberg and his laboratory, University of Calgary, Calgary, Alberta, where all the experiments were performed.

FINITE ELEMENT IMPLEMENTATION OF A STRUCTURAL MODEL FOR AORTIC VALVE TISSUE

D. R. Einstein[1], P. Reinhall[2], M. Nicosia[3], K. S. Kunzelman[3], R.P. Cochran[3]
[1]Bioengineering, University of Washington, [2]Mechanical Engineering, University of Washington,
[3]Cardiothoracic Surgery, University of Wisconsin, karynk@surgery.wisc.edu

INTRODUCTION

We extend our previous work, by demonstrating how an affine structural model for aortic valve tissue may be recast as a strain energy function with a finite number of fiber families that is readily implemented in an explicit finite element environment. Computational efficiency is achieved with a modified single-point Hughes-Liu shell. Transverse behavior is updated separately to match experimental internal shearing data.

METHODS

Constitutive Equations: Membrane behavior is adapted from a seminal structural model for aortic valve tissue by Billiar and Sacks. In terms of the 2nd Piola-Kirchoff stress:

$$\mathbf{S} = pJ\mathbf{C}^{-1} + 2J^{-2/3}\mathrm{DEV}\left[\frac{\partial \tilde{W}}{\partial \tilde{\mathbf{C}}}\right]$$

$$\frac{\partial \tilde{W}}{\partial \tilde{\mathbf{C}}} = \mu + \int_{-\pi/2}^{\pi/2} A\left[\exp\left(\frac{B}{2}\left[\mathbf{N}\tilde{\mathbf{C}}\mathbf{N} - 1\right]\right) - 1\right] R(\theta)\,\mathbf{N}\otimes\mathbf{N}\,d\theta$$

where **N** is implicitly a function of θ, and R(θ) is a Gaussian that determines fiber splay. The integral is performed discretely on 18 intervals over the domain.

Cauchy stresses for the transverse components are adapted from Carew *et al.*:

$$\sigma_{i3} = r\mu E_{i3} + sE_{i3}\left(\exp\left[tE_{i3}^2\right] - 1\right); \quad i = 1,2$$

Finite Element Formulation: The constitutive equations are implemented in a modified single-point, co-rotational Hughes-Liu shell. Our finite element formulation has been described elsewhere (Einstein, et al.). Significant additions include a Newton-Raphson search to determine the thickness strain component to accommodate nearly incompressible behavior, and a partitioning of the co-rotational deformation gradient into membrane and transverse terms.

Simulations: The following parameter values, corresponding to mean values of 4 mm Hg fixed tissue, were used: A = 25.42 kPa, B = 11.5, σ = 14.9 deg, μ = 1.4, K = 2.1E04 kPa. Simulated biaxial tests followed closely the protocol in Billiar and Sacks. The complete set consisted of seven Lagrangian membrane tension controlled tests: T_{11}/T_{22} = 10:60, 30:60, 45:60, 60:60, 60:45, 60:30 and 60:2.5 (mN/mm).

Clamped inflation simulations (10 x 10 mm) to 80 mm Hg. were performed to demonstrate the influence of transverse stiffness on membrane stresses. Parameters were: r = 5kPa, s = 2, t =5 or t =10.

RESULTS AND DISCUSSION

Results from the simulated biaxial load tests showed excellent agreement with analytic values, for all protocols, over the entire range of motion (Fig. 1). Addition of the small "linear" term, μ, had the greatest influence at low values of strain. Both experimentally observed strain reversal, and strong in-plane coupling were correctly predicted.

Peak stresses for the clamped 80 mm Hg. inflation tests were 306.0 kPa corresponding to t = 5.0, 360.7 kPa for t = 10.0 and only 199.4 kPa for a pure membrane response.

Two ultra-structural features of the aortic cusp - the presence of the compliant spongiosa and the macroscopic radial corrugations of the fibrosa - may serve to further reduce the bending moment that gives rise to the higher peak stresses seen in the two inflation tests with respect to a pure membrane solution. Neither of these features were included in the present formulation, but are a logical evolution.

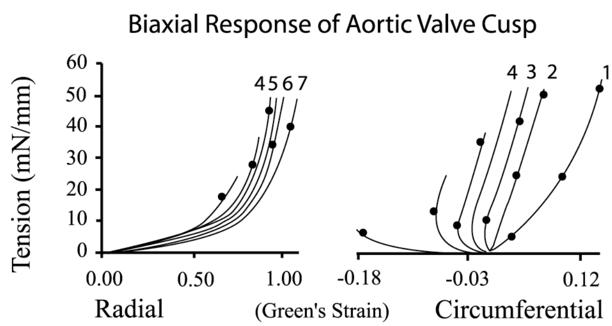

Figure 1: Results from biaxial simulations, showing correct prediction of in-plane coupling and strain reversal.

SUMMARY

We have successfully implemented a structural constitutive equation for aortic valve cusp in a computationally efficient shell. The formulation allows for the separate inclusion of an experimentally driven stress-strain equation for transverse shear. Inflation tests demonstrate the detrimental effect of greater transverse stiffness assumed to be associated with chemical cross-linking.

REFERENCES

Billiar, K.L., Sacks, M.S. (2000). *J. Biomech. Eng.*, **122**, 327-335.
Carew, E.O., et al. (1999). *J. Biomech. Eng.*, **121**, 386-392.
Einstein, D.R. et al (2002). *Submitted to: Comp. Meth. Biomech. Biomed. Eng.*
Vesely, I., J. Biomechanics, **31**, 115-

TENSILE VS. COMPRESSIVE GLYCOSAMINOGLYCAN PROFILES IN NORMAL AND MYXOMATOUS MITRAL VALVES

K. Jane Grande-Allen, Ph.D., Ivan Vesely, Ph.D.
Heart Valve Laboratory, Department of Biomedical Engineering, The Cleveland Clinic Foundation, Cleveland, Ohio, USA
grandej@bme.ri.ccf.org

INTRODUCTION

The extracellular matrix composition of heart valves is believed to be determined by the load patterns imposed during valve function, such as the varying tensile and compressive loading in the leaflets and chordae of the mitral valve. Consequently, alterations to the normal tissue loading patterns will locally affect the cellular phenotypic production of extracellular matrix (including glycosaminoglycans (GAGs) and structural proteoglycans (PGs)) and hence transform the valve morphology, mechanics, and function. PGs consist of one or more long chains of repeating disaccharides (GAG chains) that branch off central protein cores. PGs and GAGs serve several structural, regulatory, and cellular roles in connective tissues. To examine the link between GAG composition and mechanics, we measured the concentrations of the different GAG classes in leaflets and chordae from normal and myxomatous (diseased) mitral valves.

METHODS

Leaflets and chordae from normal human mitral valves (n=31, obtained at autopsy) and myxomatous mitral valves (n=71, obtained following surgical repair) were weighed and dissolved using Proteinase-K. Sample aliquots were further digested using hyaluronidase SD, chondroitinase ABC, and chondroitinase ACII. Fluorophore-assisted carbohydrate electrophoresis was then used to quantify the GAG types and the chondroitin/dermatan sulfate chain lengths (Calabro 2000). Both of these can be used to identify the type of proteoglycan.

RESULTS AND DISCUSSION

Normal chordae, which typically experience high tensile loads and contain highly aligned collagen, contained primarily the GAG dermatan 4-sulfate in chains approximately 50-60 disaccharides in length. This pattern is suggestive of the proteoglycan decorin, which binds to type I collagen fibrils. Normal leaflets, which experience a combination of tensile, bending, and compressive loads, contained mainly the GAGs hyaluronan and chondroitin 6-sulfate in GAG chains approximately 80-100 disaccharides in length, indicative of the water- and hyaluronan-binding proteoglycan versican. The relative amounts and distributions of these GAGs are consistent with the tensile and compressive loads that these tissues bear. The myxomatous tissues contained elevated concentrations of hyaluronan and chondroitin 6-sulfate as compared to normal mitral valve tissues. The makeup of these diseased leaflets and chordae thus appears to have shifted away from the tensile loading pattern. Furthermore, all differences between the myxoid and normal tissues were far more pronounced in the chordae than in the leaflets.

Figure 1: GAG classes in normal and myxoid mitral valves

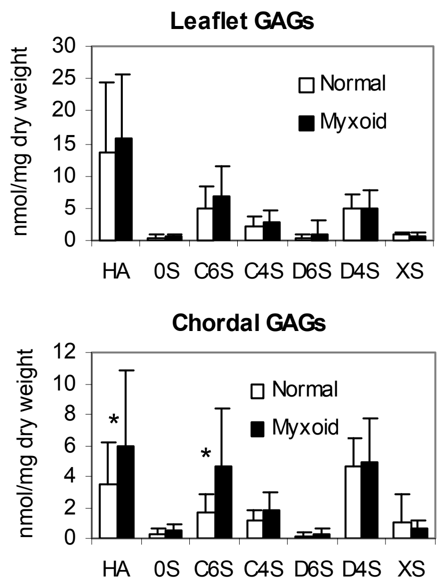

(nmol/mg dry weight). HA = hyaluronan, 0S = unsulfated chondroitin, C6S = chondroitin 6-sulfate, C4S = chondroitin 4-sulfate, D6S = dermatan 6-sulfate, D4S = dermatan 4-sulfate, XS = di-and tri-sulfated chondroitin/dermatan sulfate. *$p<0.05$

SUMMARY

These findings support reported observations that chordal rupture due to myxomatous degeneration is the leading cause of mitral valve regurgitation, and illustrate the roles of GAGs and proteoglycans in heart valve mechanics.

REFERENCES

Calabro, A., Hascall, V.C., et al. (2000). *Glycobiology*, **10**, 283-293.

IN VITRO EXPLORATION OF SYNERGIES BETWEEN FATIGUE DAMAGE AND PROTEOLYSIS IN BOVINE PERICARDIAL BIOPROSTHETIC MATERIALS

J. Michael Lee, Sean D. Marguerratt, and Rajesh A. Khanna

School of Biomedical Engineering, Dalhousie University, 5981 University Avenue,
Halifax, Nova Scotia, Canada B3H3J5 jmlee@is.dal.ca

INTRODUCTION

Most failed bioprosthetic heart valves show signs of the tearing and perforation the leaflet material; however, the mechanism behind this degeneration remains unclear. There is analytic and experimental evidence that simple fatigue can lead to local collagen disruption in regions of high bending or tensile stresses, perhaps with denaturation of the collagen triple helix [1]. Ultrastructural studies have also demonstrated the presence of host inflammatory cells in regions of collagen degeneration [2]. Moreover, it is clear that there is substantial metalloprotease activity (cellular or non-cellular in origin) in bioprosthetic heart valve materials [3]. Taken together, these observations suggest a potential mechanism whereby fatigue damage and enzyme-driven proteolysis combine to disrupt leaflet collagen. We have developed in vitro experimental methods to explore this hypothesis and have demonstrated both: (i) synergies between fatigue and proteolysis, and (ii) dependence on the nature of both fatigue loading and chemical processing of the bioprosthetic material.

METHODS

Bovine pericardium was obtained fresh from slaughter, cleaned of fat, and prepared as 10 x 10 cm anatomically oriented squares overlying the ventral surface. The tissue was then crosslinked in 0.5% glutaraldehyde (GA, pH 7.4 in 0.1 M phosphate buffer) or 1.15% by weight EDC carbodiimide solution with a 2:1 molar ratio of EDC to NHS maintained at a pH of 5.5 (without buffering). In both cases, the tissue was subject to 250 kPa uniaxial load during crosslinking to remove collagen crimp in the loading (base-to-apex) direction [4]. GA-crosslinked samples were also prepared without tensile loading to preserve crimp. In all cases, a glycine solution was used to quench any unreacted crosslinking groups.

Strip samples 16 x 4 mm were subject to 20 million loading cycles at 30 Hz (antibiotic and antiproteolytic protection) in a custom-built fatigue system. Fatigue loading included either: (i) simple refolding producing buckling as per Broom [5] or (ii) refolding alternating with tension so as to emulate systolic/diastolic loading cycles in vivo. Fatigue-damaged and non-damaged tissue strips were then incubated in (i) Tris $CaCl_2$-buffered, bacterial collagenase (20 U/ml) solution (pH 7.4) or (ii) buffer only, while being subjected to a 1 Hz sinusoidal tensile loading profile (mean 60 g, amplitude 20 g) for 48 hours [6]. Afterwards, tensile testing was performed on an MTS servohydraulic system. The incubation solution and the tissue samples were examined for hydroxyproline content as a measure of collagen content and the percent collagen solubilized during enzymatic degradation was calculated.

Fatigue Type	*Treatment Group*	*UTS (MPa)*	*% Collagen Solubilized*
Refolding only	Buffer	21.2 ± 3.8	0.02 ± 0.01
	Fatigue Only	15.6 ± 2.2	0.10 ± 0.04
	Collagenase Only	16.4 ± 1.7	0.09 ± 0.19
	Fatigue/Collagenase	6.6 ± 1.1	0.98 ± 0.19
Refolding & Tension	Buffer	17.5 ± 4.3	0.09 ± 0.02
	Fatigue Only	13.4 ± 2.3	0.15 ± 0.04
	Collagenase Only	22.2 ± 6.9	0.14 ± 0.02
	Fatigue/Collagenase	5.2 ± 1.5	0.26 ± 0.08

Table 1: Changes in Ultimate Tensile Strength (UTS) and Collagen Solubilization in GA-Treated Materials Crosslinked Under Uniaxial Stress

RESULTS AND DISCUSSION

When crosslinked under stress, the collagen crimp typically seen in juvenile bovine pericardium was lost. Cyclic refolding produced compressive buckling and bundle disruption after 20 million cycles. As seen in Table 1 above, the result was not simply a loss of tensile strength, but a synergistic susceptibility to bacterial collagenase. Use of a more complex fatigue protocol (with refolding and tension) modulated the observed results—in particular, reducing the collagen solubilized by 75%—suggesting that the loading protocol used for fatigue simulation is important. However, the synergy was preserved.

In materials crosslinked *without* stress, a similar loss of UTS was observed, suggesting that the preservation of crimp is not particularly protective against fatigue-enhanced proteolysis. Interestingly, however, EDC carbodiimide stress-crosslinking produced significantly better resistance to fatigue and the fatigue/proteolysis synergy, demonstrating the importance of the crosslinking chemistry—even with complete crimp collapse.

REFERENCES

1. Vyavahare, N. et al. (1999) *J Biomed Mater Res*, **46**, 44-50
2. Dahm, M. et al. (1995) *Ann Thorac Surg*, **60**, S348-352
3. Simionescu, A. et al. (1996) *ASAIO J*, **42**, M561-567
4. Chachra, D. et al. (1996) *Biomaterials*, **17**, 1865-1875
5. Broom, N.D. (1980) *Biomaterials*, **1**, 3-8
6. Ellsmere, J.C. et al. (1999) *Biomaterials*, **20**, 1143-1150

RATIONALE FOR BIOMECHANICAL MIMICRY IN THE DESIGN OF ARTIFICIAL HEART VALVES

Vladimir A. Kasyanov [1] and Richard T. Schoephoerster [2]

[1] Latvian Academy of Medicine, 16 Dzirciema St., Riga, LV-1007, Latvia, kasyanov@latnet.lv
[2] Florida International University, 10555 West Flagler St., Miami, FL 33199

INTRODUCTION

There are many types of prosthetic heart valves, which have achieved clinical success (Barton 2001). Nevertheless neither is a perfect solution to the problem of a suitable replacement for defective natural valves (Vesely et al. 2001; Bernacca et al., 2002; Sodian et al., 2000). Stress concentrations in bioprosthetic or tissue engineered valves typically results in tissue and cell injury with sequential calcification, tearing of the leaflets and thrombosis for polymeric valves. Soft tissue is a composite material (Kasyanov et al., 2001), and this structure is a critical factor in the biomechanics of the human natural valve. Therefore, the mimicry of natural valve structure is a keystone in the design of novel prosthetic valves (Schoephoerster et al., 2001). From this point of view the biomechanical properties and structure of individual elements of human valves were investigated, and the novel soft stent for bioprosthetic valve and polymer trileaflet aortic heart valve have been designed and tested.

METHODS

The mechanical and structural studies were carried out on human aortic and pulmonary valves (to understand implications of the Ross procedure) of individuals from 35 to 45 years old, which died not as the result of cardiovascular disease. The material was removed from the cadavers no later then 24 h after death. The valves were cut into rectangular strips and tested in a specially designed tensile testing stand. During testing, the strips were immersed in a chamber of physiological solution heated to 37^0C. All strips were 3 mm wide. The structure of the individual valve elements was studied by transmission electron microscopy using the ultrathin slice method for an accurate interpretation of the scanning and transmission electron microscopy data. A parallel study was carried out on the same material by light microscopy.

On the basis of experimental data, a novel braided soft stent for bioprosthetic valves was designed, and fatigue tests using porcine bioprosthetic heart valves with rigid and soft stents were made in a pulse duplicator.

A novel polymer composite trileaflet aortic heart valve was designed. The proposed valve design incorporates a new polymeric material, polystyrene–polyisobutylene–polystyrene (SIBS), with the thread architecture and geometry mimicking the natural valve leaflet. Reinforcement fibers in the leaflets emanate from the top of the post, and coincide with collagen bundles in the natural leaflet. Spherical and elliptical valves were manufactured. The regurgitation and pressure gradient were measured and compared with a St. Jude valve.

RESULTS AND DISCUSSION

The stress-strain curves of individual elements of valves demonstrated the typical non-linear, progressive increase in the stress as the tissue was strained. The leaflet material of valves has an anisotropy: it is stiffer in the circumferential then in the radial direction. The fibrous ring is more rigid than another areas of the aortic valve. The structure of valve elements depends on function which they perform and has specific orientation and composition in each element of the valve. All elements of the valve: leaflets, commissures, sinus wall and arched ring work together as a common construction that minimizes leaflet stress.

Morphological investigation of the porcine leaflet treated by glutaraldehyde and fixed on the rigid stent after fatigue testing showed a destruction of the collagen fibers. Structure of the leaflets on the novel soft stent was more organized and practically unchanged in comparison with the rigid stent. The soft stent in conjunction with other valve elements minimizes the tensile stress in leaflets to maintain their structure integrity.

Polymeric trileaflet valves were mounted in the aortic position of a left heart and systemic circulation simulator for acute performance evaluation of pressure gradient and regurgitation in comparison with St. Jude valve. The elliptical geometry produced equal pressure drop compared with the spherical geometry, but provided reduced backflow. Finally, for the composite elliptical valves, pressure gradients compared favorably with the St. Jude valve.

SUMMARY

The arrangement and orientation of the fibrous structure and their packing in the elements of the human valve are a function of the load acting on these elements. Biomechanical mimicry of the features of valve elements gives promising results in the design of novel heart valve prostheses. It is the main ingredient for the creation of a fully bio-integrated valve (bioprosthetic, polymeric and tissue engineered valves) with long-term durability and ideal hemocompatibility in the future.

REFERENCES

Barton, K. et al (2001). *BMSE Bulletin*, **25**, 1, 3-16.
Vesely, I. et al. (2001). *J. Heart Valve*, **10**, 4, 471-477.
Bernacca, G.M. et al. (2002). *Biomaterials*, **23**, 1, 45-50.
Sodian, R. et al. (2000). *Circulation*, **102**, 19, 22-29.
Kasyanov, V. et al. (2001). *Int. J. Cardiovasc. Medicine & Science*, **3**, 3/4, 97-104.
Schoephoerster, R.T. et al. (2001). *Proceeding of 2001 ASME Int. Mechanical Engineering Congress*, **51**, 1-2.

MODELLING THE NONLINEAR ANISOTROPIC PORCINE HEART VALVES

Jue Li[1] and XiaoYu Luo[2]
[1]School of Civil Engineering and Mechanics, Xi'an Jiaotong University, Xi'an, China, leejewel@hotmail.com
[2] Department of Mechanical Engineering, University of Sheffield, x.y.luo@shef.ac.uk

INTRODUCTION

Biotissue valves such as porcine valves are used due to their excellent hemodynamic properties. This is no need for patient to have immunosuppressive therapy as tissue is accepted by the body, unlike with mechanical valves. The main disadvantage of the biotissue valves is the durability. It was generally believed that the majority of structural failures of biotissue valves resulted from tensile stress developed during valve closure. Stress analysis using numerical modeling has been used to understand the loading of natural and prosthetic heart valves during the closing phase. Most of the modeling, however, assumes that the valves are isotropic material, with but a few exceptions. The anisotropic and nonlinear properties of porcine aortic valve leaflet have potentially significant effects on its mechanical behavior and the failure mechanisms. This paper studies behavior of porcine valves using a nonlinear anisotropic model.

METHODS

The model is based on the uniaxial experimental data of porcine aortic heart valve leaflet and the properties of nonlinear composite material. A finite element code is developed to solve this problem using the 8-node nonlinear shell elements and the update Lagrangian method. The leaflets of porcine aortic valve are reinforced with collagen and elastin fibers, and behave like the anisotropic fiber-reinforced composite. We assume that both the fiber and the matrix are isotropic and incompressible materials with the same Poisson ratio of 0.45, and that the coupling between the longitudinal and the transverse elasticity to be negligible. This allows us to determine the longitudinal and the transverse elastic moduli from the experimental data by Mavrilas & Missirlis (1991).

RESULTS AND DISCUSSION

The pattern of the stress distribution can be strongly influenced by the thickness variation of the leaflet. This is investigated by varying the thickness of the anisotropic leaflet from 0.2mm to 1.4mm. In addition, valves with stent height from 16-20mm, and stent diameter between 19-27.8mm are also studied. The results of the nonlinear anisotropic leaflet are compared with the stress contours from the corresponding linear anisotropic leaflet. It is found that the stress distribution of the non-uniform leaflet seems to be more uniform due to the non-uniform thickness. For isotropic case, the site of the maximum principal stress remains the same. However, there is a secondary maximum principal stress located at the belly of the valve when the thickness of the valve is non-uniform. This phenomenon is even more pronounced in the anisotropic case, where the peak principal stress actually locates in the belly zone, and the stress at the commissures is reduced by 43%. This is in agreement with the pathological examination of excised valves by Carpenter et al. (1976) that the leaflet's belly zone to be a common site of tissue rupture and disruption.

SUMMARY

To evaluate the model as a tool for valve assessment, valves with variable thickness, different ratios of stent height/diameter are examined both for isotropic and nonlinear anisotropic material. Compared with the isotropic valve at the same loading condition, it is found that the site of the peak stress of the anisotropic leaflet is different; the maximum longitudinal normal stress is increased, but the maximum transversal normal stress and in-plane shear stress are reduced. We conclude that it is very important to consider the anisotropic property of the porcine heart valves in order to understand the failure mechanism of such valves in vivo.

REFERENCES

Carpenter, A., Deloche, A., Relland, J., & Dubost, C., 1976, Valvular xenograft and valvular bioprosthesis: 1965-1975, The Mitral Valves: a pluridisciplinary approach, D.Kalmanson, Edward Arnold, London, 505-518.
Li, J, Luo XY & Kuang ZB, 2001, A nonlinear anisotropic model for porcine aortic heart valves. 34/10, 1279-1289, J. Biomechanics, 2001.
Mavrilas, D. & Missirlis, Y., 1991, An approach to the optimization of preparation of bioprosthetic heart valves, Journal of Biomechanics, 331- 339

BIOFLUID EFFECTS OF THERAPEUTIC ULTRASOUND ON BIOLOGICAL TISSUES

Eitan Kimmel[1, 2] and Boris Krasovitski[1]

Departments of Agricultural Engineering[1] and Biomedical Engineering[2], Technion IIT, Haifa 32000, Israel. agreita@tx.technion.ac.il

INTRODUCTION

This study has a long-term goal of utilizing therapeutic ultrasound for curing various pathologies in the cardiovascular system. It originates from experimental and theoretical studies on ultrasound-enhanced transdermal drug delivery in fish.

Micro alterations in fish epidermis, exposed to ultrasound (intensities of up to 2.2 W/cm^2, frequencies 1 and 3 MHz, continuous mode), are observed using electronic microscopy. Five seconds of exposure to 1 MHz ultrasound (1W/cm^2) result by hole formation in the membranes of the first cell layer. During longer exposures, deeper cell layers become affected and the level of damage increases as well. At the same time cells stay intact. This phenomenon is attributed to the behavior of gas bubbles near a rigid surface. Under conditions of unsteady cavitation the bubbles collapse towards the surface and high-velocity jets are formed. Interestingly, no isolated zones of damaged cells are observed. This type of cell damage is expected when bubbles are formed and collapse within an intact cell. Nevertheless, the epidermis is clearly divided by damage front, parallel to the skin, into two layers, damaged and undamaged. The front propagates inwards slowly in a diffusion-like process (Frenkel et al. 1999). The absence of damaged cells in the undamaged tissue is probably due to the fact that bubbles do not collapse in intact cells. We speculate that at first cell membrane ruptures from outside and only then cell contents change and conditions for bubble formations develop. The absence of cavitation damage from inside out in intact cells is probably due to the cell content and not its constraining size. This prediction is supported by a theoretical study of unsteady bubble collapse in semi-confined space. The bubble is located between two parallel and rigid surfaces, at equal distance from each surface. The distance is comparable to bubble size. In this case, under certain conditions, the bubble split into two parts and two high-velocity jets are formed aiming at both surfaces (Krasovitski and Kimmel, 2001). Those jets are similar in size to the jets created by bubble collapse in semi-infinite medium. Note that Chanine et al. (1982) observed similar bubble split.

Exposures to 3MHz ultrasound stimulate creation of intercellular spaces, which take place primarily between the two outermost cell layers. When exposure time increases, the number and size of spaces increase (Frenkel et al. 1999). At the same time cells stay intact. It is still unclear why intercellular spaces are formed and what is the reason they are concentrated at such a thin layer of about 10µm. One possible explanation is the formation of transverse (shear) waves at the water-epidermis interface, waves that attenuate rapidly in the cellular tissue because of high viscosity of cells cytoplasm. Another possible mechanism for induction of intercellular spaces by quasi-steady bubble pulsations is hereby discussed.

METHODS

A simulation method is developed for the shear stress induced by a spherical bubble, located near a rigid surface, when it is subjected to ultrasound field of relatively small intensity (about 0.01 W/cm^2) and pressure amplitude (20kPa). The pulsations of a bubble near a rigid surface generate steady flow field, known as acoustical microstreaming. Nyborg (1958) suggested an approximate method for estimating the velocity profile in the boundary layer from the potential flow. We solve Laplace equation for potential flow field in a domain bounded by a sphere and a plane. The boundary condition on the bubble surface is obtained by solving the bubble dynamics equation in infinite medium for a bubble that stays spherical while pulsating. The relatively complex set of boundary surfaces is then transformed into a simple square. The transformed Laplace equation is solved numerically as an asymptote of the solution of Fourier equation. The described method provides quasi-steady and oscillatory shear stresses on the tissue surface. Evolution of the bubble with time is also studied by introducing rectified diffusion – accumulative effect of the diffusion of gas in and out of the pulsating bubble.

RESULTS AND DISCUSSION

Quasi-steady shear stresses on the surface reach a peak of about 1kPa intensity (corresponding to intensity of 0.01 W/cm^2) over a region comparable to bubble size. The shape and direction of the shear distribution can be viewed as obtained by two concentric rings that touch the surface and move in the radial direction outward (the inner one) and inward (the outer one). The magnitude of the shear stress increases with ultrasound intensity and decreases with increasing distance between the bubble and the surface. For comparison, microstreaming stresses are 1000 times greater than the normal shear acting on endothelial cells in blood vessels, and as such might induce micro alterations.

CONCLUDING REMARKS

This study applies to any liquid/solid interface. It explains some of our observations in fish (water/epidermis interface) and might shed some light on the effects of therapeutic ultrasound on blood vessels (blood/vessel-wall interface).

REFERENCES

Chanine, G.L. (1982) *Appl. Sci. Res.* **38,** 187-197
Frenkel, V. et al. (1999). *Ultras. Med. Biol*. **25**, 1295-1303.
Frenkel, V. et al. (1999). *Ultras. Med. Biol*. **26**, 473-480.
Krasovitski, B. Kimmel, E. (2001). *J. Acoust. Soc. Am.* **109,** 891-898.
Nyborg, W.L. (1958). *J. Acoust. Soc. Am.* **30**, 329 – 339.

NUMERICAL SIMULATION OF CEREBROSPINAL FLUID MOTION WITHIN A HEALTHY AND DISEASED SPINAL CANAL

Wojciech Kalata[1], Seung E. Lee[1], Noam Alperin[2], Paul F. Fischer[3] and Francis Loth[4]

[1]Graduate Student, Department of Mechanical Engineering, University of Illinois at Chicago, Illinois
[2]Associate Professor, Department of Radiology, University of Illinois at Chicago, Illinois
[3]Mathematics and Computer Science Division, Argonne National Laboratory, Argonne, Illinois
[4]Assistant Professor, Department of Mechanical Engineering, University of Illinois at Chicago, Illinois, floth@uic.edu

INTRODUCTION

Cerebrospinal fluid (CSF) moves in a pulsatile manner within the spinal and cranial subarachnoid spaces (SAS) and ventricular system. This fluid cushions the brain from impact on the cranial vault walls due to sudden motions. CSF also delivers nutrients and protein to/from the brain surface along with the removal of waste products. Recent developments in non-invasive flow measurement techniques, such as phase encoded magnetic resonance imaging (PCMRI), enable *in vivo* measurement of the velocity pulsation. We have previously shown the basic velocity patterns present within a healthy SAS using 2D numerical simulations [1]. Changes in the SAS anatomy are associated with pathological conditions such as Chiari malformation and syringomyelia. Therefore, patient specific 3D hydrodynamic analysis of CSF motion is warranted since it may be used to provide an evaluation of the Chiari malformation severity before and after surgical treatment.

METHODS

The SAS geometry of a 21-year-old healthy male volunteer was obtained axially along the spinal canal using MRI. In addition, the geometry of 35-year-old male patient with Chiari I malformation was obtained pre- and post-surgically. For the three geometries, velocity measurements were obtained using PCMRI at the level of the second cervical vertebra (C2). The 3D geometries were obtained using a commercial image processing software (MIMICS, Materialise). The geometries were smoothed and meshed using MATLAB (Figure 1) as described previously [2,3]. The incompressible unsteady Navier-Stokes equations were solved using a commercial CFD code (Star-CD, adapco Inc.) with rigid walls. The inlet boundary conditions were imposed to match the CSF flow waveform (Q) obtained from PCMRI measurements.

The difference in unsteady pressure (dP) from base of the cranium to a position below C2 (25 mm) was computed from the numerical simulations for each specific geometry and corresponding Q. The unsteady flow resistance or longitudinal impedance (Z_L) was computed by the ratio of the fast Fourier transform (FFT) coefficients of dP and Q. The Z_L modulus was computed using the magnitude of the real and imaginary components for each harmonic [4].

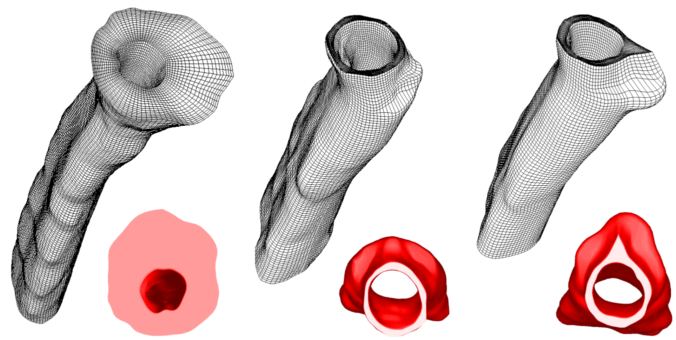

Figure 1: Healthy, pre- and post-surgical SAS geometries

RESULTS AND DISCUSSION

Peak Reynolds numbers (Re, based on hydraulic diameter) and Womersley numbers (α, based on hydraulic radius) varied with position along the SAS and between cases. The Peak Re and α values for the three cases ranged from 50 to 150 and 5 to 17, respectively for the region extending 6 cm below the cranium. The velocity profiles within these SAS regions were generally blunt and pulsatile in nature for the three cases with the exception of narrow regions in the diseased geometries. The Z_L modulus was computed for each case at different frequencies (1st - 9th harmonic). The mean Z_L modulus values for the healthy, pre-surgical and post-surgical cases were 28, 65, and 48 dynes·s/cm^5, respectively. Hydrodynamic evaluation of the SAS resistance to pulsatile CSF flow motion may provide additional information to the surgeon in evaluating Chiari malformation severity before and after surgical treatment.

REFERENCES

1. Loth et al., *J Biomech Eng*, 2001. 123: pp. 80-87.
2. Yedavalli et al., *J Biomech Eng*, 2001. 123: pp. 372-376.
3. Lee et al., *World Congress on Medical Physics and Bioengineering,* MO-G326, 2000, Chicago, IL.
4. Skelly et al., *Ann Vasc Surg*, 2001, 15(1), pp. 110-22.

ACKNOWLEDGEMENTS

This work was supported by The Labuda Foundation and by NIH Grant RR14242-01.

HORIZONTAL-TO-VERTICAL VELOCITY TRADEOFF IN HORIZONTAL JUMPING

Steven LeBlanc
School of Health and Human Performance, Dalhousie University, Halifax, Nova Scotia, Canada
Steve.LeBlanc@dal.ca

INTRODUCTION

In the long jump and the triple jump, the primary goal of the athlete is to build up horizontal velocity during the approach run and then to maintain as much of that horizontal velocity as possible while generating vertical velocity during the takeoff. Research has shown that some horizontal velocity will always be lost during the takeoffs in both long jump and triple jump. Yu (1999) examined the relationship between the loss in horizontal velocity and the gain in vertical velocity during the three takeoffs in the triple jump and found that there was a significant linear relationship between the two measures. Yu (1999) used the competitive triple jumps of elite athletes to examine this relationship. The purpose of the present study was to determine if a linear relationship could be found between the change in the horizontal velocity of the total-body centre of mass (**dVh**) and the change in the vertical velocity of the CM (**dVv**) under different jumping conditions. It was hypothesized that this linear relationship would be found.

METHODS

The study made use of two sets of data, one in a competitive setting and the other in a laboratory setting. Kinematic data for each data set was collected using standard two-dimensional video analysis techniques (60 Hz). For the competitive jumps, the best two jumps from four male long jumpers and three male triple jumpers were selected for analysis (LeBlanc, 1997). For the laboratory trials, five athletes (3 male, 2 female) performed five trials each of three- and four-step approach long jump-style takeoffs in a laboratory setting. Athletes in both sets of data were experienced non-elite jumpers.

A regression model (see Equation 1) was used to examine the relationships between **dVh** and **dVv**. It was deemed to be evidence of a significant relationship if the regression analysis resulted in a model with a large F-value, a large R^2 value, a significant p-value for **dVh**, and a negative β_1 coefficient.

$$\mathbf{dVv} = \beta_0 + \beta_1 \mathbf{dVh} \qquad \text{[Eq. 1]}$$

The regression model was applied to the two data sets separately to see if the competitive and laboratory trials differed in the relationship of **dVh** and **dVv**. A combined analysis was also performed using both data sets together.

RESULTS AND DISCUSSION

The regression analysis found that there was a significant linear relationship between **dVh** and **dVv** in the 50 laboratory trials ($F= 69.28$, $R^2= 59.1\%$, $p= 0.000$, $\beta_1= -1.23$) but not the 14 competitive trials ($F= 1.38$, $R^2= 10.3\%$, $p=0.263$, $\beta_1= -0.22$). This may have been due to technical differences between the short-approach laboratory jumps and the competitive LJ and TJ trials, particularly the TJ trials (see Figure 1). However, in both data sets a negative β_1 coefficient was found, indicating that the trend was for greater loss of horizontal velocity to coincide with greater gains in vertical velocity during takeoff. When the two data sets were combined, a significant linear relationship was found to exist ($F= 30.99$, $R^2= 26.3\%$, $p= 0.000$, $\beta_1= -0.68$). The results seem to support the notion proposed by Yu (1999) that there is a linear relationship between the loss in horizontal velocity and the gain in vertical velocity during a horizontal jump takeoff.

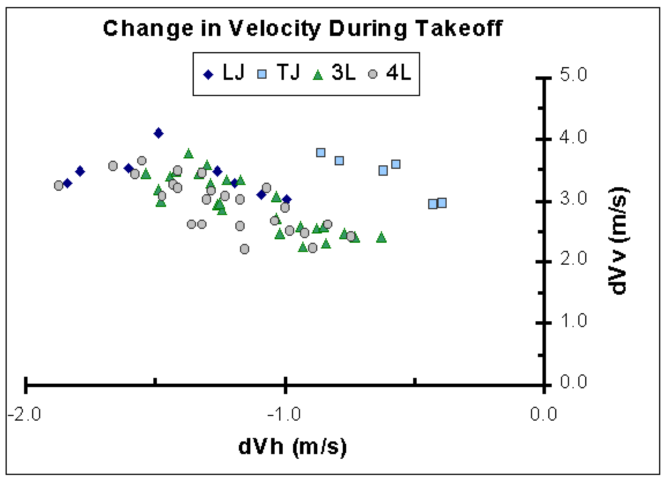

Figure 1: Change in horizontal versus vertical velocity during the takeoff in long jumps (LJ), triple jumps (TJ), 3-step approach jumps (3L) and 4-step approach jumps (4L).

REFERENCES

LeBlanc, J.S. (1997). The use of active landings in the horizontal jumps. *Biomechanics in Sports XV*, 125-131.

Yu, B. (1999). Horizontal-to-vertical velocity conversion in the triple jump. *J of Sports Sciences*, **17**, 221-229.

DEGRADATION OF DRUG TABLETS AND MIXING IN THE STOMACH USING COMPUTER SIMULATION WITH THE LATTICE-BOLTZMANN ALGORITHM

James G. Brasseur[1,3], Anupam Pal[1], Bertil Abrahamsson[2]

[1]The Pennsylvania State University, University Park, PA, USA.
[2]AstraZeneca Pharmaceuticals, Mölndal, Sweden
[3]communicating author: brasseur@jazz.me.psu.edu

INTRODUCTION

Drug release from polymer-based extended release (ER) tablets in the stomach is controlled by surface degradation due to local surface shear stress [Abrahamsson et al 1999]. Recent high resolution concurrent manometry/MRI studies [Indireshkumar et al 2000] have shown that slowed gastric emptying is confined primarily to periods of quiescence, suggesting that the primary function of antral contraction wave activity may be other than gastric emptying.

AIMS

Using numerical methods and computer simulation we seek to understand and quantify the gastric motions within the stomach in the fed state associated with dispersion of gastric content, gastric emptying, intragastric pressure variation (as measured manometrically, for example), and viscous stress. In particular, we aim to "measure" surface shear stress variation on tablets moving within the stomach and evaluate the dispersion and mixing of drugs released within the stomach.

METHODS

A sophisticated numerical code was developed based on the "lattice Boltzmann" algorithm and combined with a realistic stomach geometry model derived from MRI movies of the human stomach. Gastric fluid motions, tablet surface stresses on 1 cm diameter tablets, and drug dispersion were predicted in a simulated human stomach in two dimensions with fundic and antral contraction and pyloric opening representative of the fed state.

RESULTS

Antral contraction waves generate recirculating gastric fluid motions which create a "mixing zone" of high relative surface shear stress (figure 1). Frequency distributions of surface shear stress during tablet motion revealed 4 levels of stress: (i) low level shear stress (<1 dynes/cm^2) when tablets move within the fundus, (ii) moderate shear stress (~10 dynes/cm^2) when tablets move in the antrum between contraction waves, (iii) high shear stress (~35-50 dynes/cm^2) generated as tablets encounter antral contraction waves, (iv) very high short-lived shear stress events (>300 dyne/cm^2) as tablets are forced retrograde through advancing contraction waves. The frequency of high shear stress events from tablet-contraction wave encounters is much lower than during the moderate shear stress periods. Nevertheless, the relative contributions to overall, time-integrated, surface shear stress of the shorter-lived high stress periods vs. the longer-lived moderate stress periods were comparable. The coordination of pyloric opening with the space-time structure of antral pyloric contraction-wave activity has a significant influence on particle motion, mixing and emptying.

CONCLUSIONS

Wave-like contractile activity in the antrum of the stomach is responsible for circulatory motions that underlie mixing, viscous stress and pressure, particle degradation, and mixing. The coordination of antral contraction waves with pyloric opening history is important for emptying and details of mixing. Both long periods of moderate shear stress and short periods of high shear stress contribute to the degradation of ER tablets, albeit in different ways. Whereas the extended periods of moderate stress will continuously degrade the tablet surface, shorter-acting high shear stress events may remove larger pieces of tablet surface and contribute to uneven wear, change in tablet shape, and tablet breaking. We conclude that drug release may result from both continuous and discrete surface degradation periods.

REFERENCES

Abrahamsson , B, Roos, K, Sjögren, J. Investigation of prandial effects on hydrophilic matrix tablets, *Drug Dev. Indust. Pharmacy.* **25**: 765-771 (1999).

Indireshkumar, K., Brasseur, et al. 2000 Relative contributions of “pressure pump” and “peristaltic pump” to slowed gastric emptying, *Amer. J. Physiol.* **278**: G604-G616.

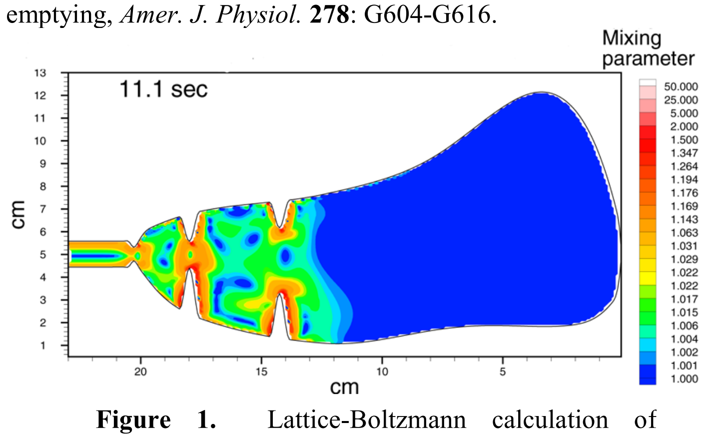

Figure 1. Lattice-Boltzmann calculation of “mixing parameter” vs. position within a simplified stomach during the progression of antral contraction waves towards and open pylorus. We observe a clear demarcation between the “mixing zone” induced by the progressing contraction waves and the poorly mixed fundus.

AQUEOUS HUMOR FLOW AND PASSIVE IRIS DEFORMATION

Jeffrey J. Heys[1], Eric C. Huang[2], and Victor H. Barocas[3]
[1]Department of Applied Mathematics, University of Colorado, Boulder, CO, USA
[2]Department of Chemical Engineering, University of Minnesota, Minneapolis, MN, USA
[3]Department of Biomedical Engineering, University of Minnesota, Minneapolis, MN USA

INTRODUCTION

Active deformation of the iris in response to available light is a well-studied and important phenomenon. Less attention, however, has been paid to passive deformation of the iris in response to changes in anterior eye geometry or aqueous humor (AH) flow dynamics. Extreme passive displacement of the iris can have pathological consequences. Anterior displacement of the iris leads to angle-closure glaucoma, in which the proximity between iris and cornea prevents AH outflow. Posterior displacement, in contrast, can lead to rubbing of the iris against the lens capsule and zonules, which in turn can lead to pigmentary glaucoma.

METHODS

The fluid-stucture problem involving AH (the fluid) and iris (the structure) has been formulated based on available anatomical and physical data; the domain is shown in Figure 1. An inflow boundary condition was specified at the ciliary processes, and the intraocular pressure was subsequently set based on the outflow at the trabecular meshwork. The cornea was treated as a section of a spherical shell of known properties (Smolek 1994). For steady-state calculation, the lens was assumed to be rigid.

Once the model was complete and tested for steady-state problems, we examined the hypothesis that AH flow due to lens motion during accommodation (shift in focus to view near objects) causes the characteristic bowing of the iris seen in pigmentary glaucoma patients. Accommodation was modeled by specifying the motion of the lens (Koretz et al. 1989).

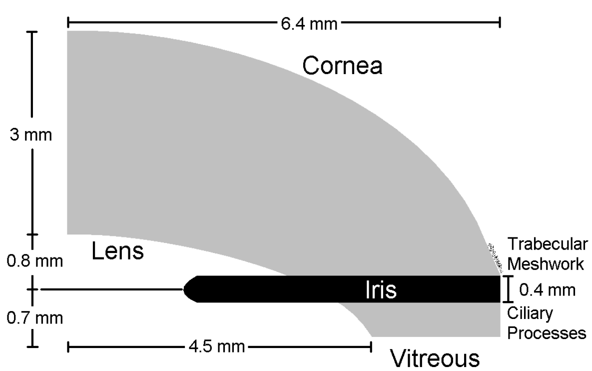

Figure 1: Domain and specifications for fluid-structure model of the anterior eye.

RESULTS AND DISCUSSION

Figure 2 shows the calculated AH velocity field at the start of accommodation and posterior bowing that results from interaction between the AH and iris. In the absence of an iris, AH displaced by the motion of the lens would flow around the lens into the space vacated by accommodation. The iris behaves like a flap valve (cf. Pavlin et al. 1996), preventing posterior flow of the AH. We found that the pressure on the anterior iris surface is in fact higher than that on the posterior surface (unlike the steady-state case). After accommodation, the system takes 3-5 minutes to re-equilibrate.

SUMMARY

Our computational model has shown that passive deformation of the iris due to AH flow during accommodation is a reasonable explanation for the posterior bowing of the iris observed during accommodation in pigmentary glaucoma patients. We have not yet elucidated the mechanism by which some people suffer from pigmentary dispersion but almost all do not, even though accommodation is a universal process.

REFERENCES

Cook , C.A. and J.F. Koretz (1991). *Appl. Opt.,* **30**:2088-2099.
Koretz, J.F. et al. (1989). *Appl. Opt.*, **28**:1097-1102.
Pavlin, C.J. et al. (1996), *Ophth. Surg. Lasers*, **27**:113-120.
Smolek, M.K. (1994). *J. Cat. Refr. Surg.*, **20**:277-286.

ACKNOWLEDGEMENTS

This work was supported by the Whitaker Foundation and the National Institutes of Health. Computations were made possible by a supercomputing resources grant from the Minnesota Supercomputing Institute.

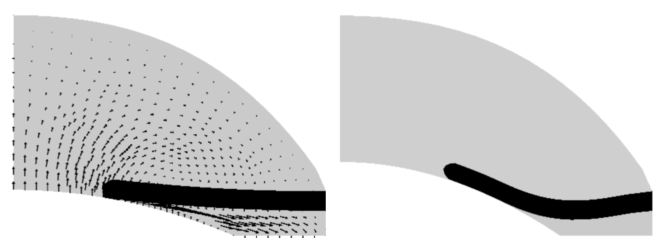

Figure 2: Anterior eye dynamics during accommodation. At the start of accommodation (left), aqueous humor is pushed forward by the lens and driven back into the iris, pinning the iris against the lens (right). The simulation shown is for a large amount of accommodation (Cook and Koretz 1991).

UTERINE BIOFLUID DYNAMICS

Osnat Eytan[1], Sarit Yaniv[2], Ariel J. Jaffa[1] and David Elad[2]

[1]Ultrasound Unit, Lis Maternity Hospital, Tel-Aviv Sourasky Medical Center, Tel-Aviv 64239, Israel, osnate@post.tau.ac.il
[2]Department of Biomedical Engeeniring, Faculty of Engineering,Tel-Aviv University, Tel-Aviv 69978, Israel.

INTRODUCTION

Uterine motility plays a central role in human conception which depends on a number of transport vehicles within the female reproductive tract. The detached ovum is transported to the fallopian tube. Spermatozoa are rapidly transported in the uterine fluid towards the ampulla where fertilization occurs. The newly born embryo is driven to the uterine cavity within four days of ovulation, and is then conveyed during another 3-5 days to an optimal implantation site in the fundal area at the upper part of the uterus. Fulfillment of these essential events within the time limits of fertilization and implantation depends on concomitant intrauterine fluid motion induced by spontaneous myometrial contractions. Myometrial contractions in non-pregnant uteri were studied from measurements of intra-uterine pressures with fluid-filled catheters and by visual observations of high-speed replaying of transvaginal ultrasound (TVUS) images of the uterus. The contractions propagate from cervix to fundus during the proliferative and secretory phases, with the direction being reversed and the contractions rate slowed during menstruation. This study presents an objective method to evaluate the characteristics of the uterine dynamics and a mathematical simulation of intra-uterine fluid transport pattern.

METHODS

Transvaginal ultrasound (TVUS) images of the sagittal cross-sections of the non-pregnant uterus were scanned with an vaginal ultrasound probe. Images at consecutive times (1 second apart) were digitized and processed by employing modern techniques of image processing (Eytan *et al*, 1999). The sets of images were compared to evaluate time variation of the fluid-wall interface in terms of amplitude, frequencies and passive width of the uterine cavity.

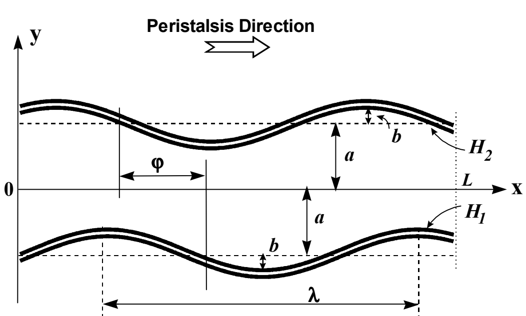

Figure 1. Description of a uniform two-dimensional channel with oscillating walls. Legend: L and $2a$ are the channel's passive length and width, b and λ are the amplitude and the wavelength of wall motility, φ is the phase between the walls.

Intra-uterine fluid flow in a sagittal cross-section of the uterus was simulated by wall-induced fluid motion within a two-dimensional channel. Fluid motion within the channel was induced by two rhythmic wall displacements that were simulated by an infinite train of sinusoidal waves that propagated along the channel walls (Fig. 1). The time-dependent fluid pattern and possible trajectories of massless particles were studied by employing the lubrication theory (Eytan & Elad, 1999). The intrauterine fluid flow pattern and trajectories of embryos were simulated for various amplitudes, frequencies, pressure gradients and phase shift between the cannel's wall.

RESULTS

Analysis of TVUS images from 25 volunteers during end proliferative phase and early secretory phase revealed that myometrial contractions are fairly symmetric and are propagated from the cervix towards the fundus at a frequency of about 0.03 Hz. The amplitudes of the fluid-wall interface during a typical contractile wave are about 0.08 mm, and the passive width of the uterine cavity is about 0.5 mm. The averaged results from the in vivo measurements were implemented in a mathematical simulation to study the intra-uterine fluid flow patterns. The paths of massless particles (embryos) were curly and the particles generally propagated towards the direction of the peristaltic wave. As the phase shift between the walls decreased from π to zero (i.e., symmetric to asymmetric), the trajectories of the particles became more tilted towards the transverse axis (y) until they were completely perpendicular to the axial axis at φ=0.

DISCUSSION

The newly born embryo is transported by intrauterine fluid motions towards the site of implantation at the fundus. The mathematical simulations showed that the embryo may reach the fundus within a few hours if uterine wall motility is normal and will stay there until hormonal conditions are suitable for its successful implantation in the endometrium. In a different situation one may imagine a case of asymmetric myometrial contractions that lock the embryo within a confined vicinity and, as a result, it cannot reach an implantation site within the allowbale time. This may provide a partial explanation for the outcome of IVF that many of the embryos transferred to the uterus fail to implant in the endometrium within the critical time limits.

REFERENCES

Eytan O. and Elad D. (1999). *Bull Math Biol,* **61***,* 221-238.
Eytan O. *et al* (1999). *Ann Biomed Eng,* **27**, 372-337.

THE ROLE OF THE PASSIVE STRUCTURES IN THE MOBILITY AND STABILITY OF THE NATURAL AND REPLACED HUMAN ANKLE JOINT

Alberto Leardini[1], John J O'Connor[2], Rita Stagni[3], Federico Corazza[4], Vincenzo ParentiCastelli[4], Fabio Catani[1], Sandro Giannini[1]

[1] Movement Analysis Laboratory, Istituti Ortopedici Rizzoli, Bologna, Italy, leardini@ior.it
[2] Oxford Orthopaedic Engineering Centre, Oxford, England
[3] Dipartimento di Elettronica, Informatica e Sistemistica, Università degli Studi di Bologna, Italy,
[4] Dipartimento di Ingegneria costruzioni meccaniche, nucleari, aeronautiche e di metallurgia - Università di Bologna, Italy

INTRODUCTION

Current unsatisfactory clinical results in ligament reconstruction and joint replacement at the human ankle joint have been related to designers' inability to restore adequately the original mechanisms which guide joint mobility and stability. Thorough experimental and modelling studies are necessary to elucidate the role played by the ankle passive structures in these mechanisms (Leardini et al., 2000). A recent extensive investigation from these authors (Leardini et al., 1999a,b, 2001b) is revealing that a close relationship between the geometry of the ligaments and the shapes of the articular surfaces is responsible for the physiological relative motion of the bones in passive conditions and for an accomplished resistance to this motion when load is applied.

METHODS

Ten skeleto-ligamentous lower leg preparations including tibia, fibula, talus, calcaneus and intact ligaments were analysed (Leardini et al., 1999a, 2001b). Motion of these bones during passive flexion, deviation tests and muscle strengthening was tracked using both optical (Elite, BTS, Milan) and roentgen stereo-photogrammetry. Geometry of ligament fibre arrangement and articular surface shapes was obtained with a 3D digitiser (FARO Technologies, Inc.). The instantaneous distance between corresponding fibre attachments was calculated. Articular contact area was estimated by modelling the surfaces as thin plate splines and setting a distance threshold (Corazza et al., 2002c).

A sagittal four-bar linkage model was formulated as formed by the tibia/fibula and talus/calcaneus bony segments and by fibres within the calcaneofibular and tibiocalcaneal ligaments (Leardini et al., 1999b). A mechanical analogue of the extensor retinaculum was devised to include the action of the main flexor and extensor muscles (Leardini et al., 2002a). The model was used also to analyse current and possible novel prosthetic designs, particularly to test the ability to reproduce the compatible mutual function between the articular surfaces and the ligaments retained (Leardini et al., 2001a). Non-conforming two-component and fully-conforming three-component designs with either flat, concave or convex tibial surfaces were analysed. A mechanical 3D model of the ankle was also devised to calculate ligament fibre recruitment and load/displacement curves at different flexion angles during a simulated anterior drawer test (Corazza et al., 2002b). Ligaments were modelled as three-dimensional arrays of fibres with non-linear stress/strain relationships from the literature.

RESULTS AND DISCUSSION

The articular surfaces and the ligaments alone prescribed joint motion into a preferred single path of multiaxial rotation. The ankle complex exhibited one degree of unresisted freedom, the ankle joint behaving as a single degree of freedom mechanism and the subtalar joint as a flexible structure. Fibres within the calcaneofibular and tibiocalcaneal ligaments remained most isometric throughout the passive range, with change in distance smaller than 1% (Stagni et al., 2002d). These two fibres must guide and all other fibres must only limit this motion. The contact area was calculated to move anteriorly and laterally with dorsiflexion on both articular surfaces.

The four-bar linkage model well predicted the sagittal plane kinematics observed in corresponding experiments. The mechanical analogue of the extensor retinaculum revealed that the displacement of the flexion axis guarantees a mechanical advantage for the muscle forces during gait. Among a large range of ankle prosthesis designs, a ligament-compatible, convex-tibia, fully-congruent, three-component showed the best features. A complete congruence over the entire range of flexion together with an acceptable degree of entrapment of the meniscal bearing were obtained while restoring exactly the original patterns of joint kinematics, ligament recruitment and tensioning and muscle lever arms. The mechanical 3D model for the drawer test elucidated the significant different response of the joint at different flexion angles, well comparing with previous experimental reports (Corazza et al., 2002b).

SUMMARY

The overall investigation is demonstrating that a profound knowledge of the changing geometry of the passive structures throughout the range of passive flexion (mobility) is mandatory for a successful mechanical analysis of the response to external load (stability). A 3D extension of the sagittal four-bar linkage model is now in progress.

REFERENCES

Leardini, A.,et al. (1999a), *J Biomech*, **32(2)**, 111-118.
Leardini, A.,et al. (1999b), *J Biomech*, **32(6)**, 585-591.
Leardini, A.,et al. (2000), *Foot & Ankle Int*, **21(7)**, 602-615.
Leardini, A.,et al.(2001a), *Med Bio Eng Comp*, **39(2)**, 168-175
Leardini, A.,et al. (2001b), *J Biomech*, **34(6)**, 805-809.
Leardini, A.,et al. (2002a), *Gait & Post*, in press.
Corazza, F.,et al. (2002b), *J Biomech*, accepted.
Corazza, F.,et al. (2002c), *Proceedings WCB 2002.*
Stagni, R.,et al. (2002d), *Proceedings WCB 2002.*

IN-VITRO REPORTS ON ANTERIOR ANKLE LIGAMENT DAMAGE AND ANKLE-JOINT LAXITY: A REVIEW OF THE LITERATURE

GMMJ Kerkhoffs, L Blankevoort, D Van Poll, Rk Marti, CN Van Dijk
Orthopaedic Research Center Amsterdam, Department of Orthopaedic Surgery, Academic Medical Center, University of Amsterdam, Amsterdam, The Netherlands.

INTRODUCTION

Diagnostic methods for inversion injuries of the ankle have remained controversial throughout the years. An instrumented test for anterior ankle-joint laxity could be a diagnostic tool for evaluation of anterior lateral ankle ligament function. The relation between ligament damage and anterior ankle joint laxity is the key to the validation of any diagnostic test. The purpose of this study was to provide a systematic review of the literature on this relationship as observed in cadaver experiments.

METHODS

An advanced electronic database search using MEDLINE and EMBASE was performed to find studies describing the correlation between lateral ankle ligament damage and ankle-joint laxity. Two reviewers assessed the methodological quality for each study and agreement was noted. Two reviewers extracted all relevant data with respect to methodology, motion constraints and laxity measurements.

RESULTS

The quality assessment resulted in 5 studies being scored as high quality and 5 as low quality, out of 19 studies that described ankle ligament cutting experiments. Different test devices were used to apply the load and measure the displacement. All in-vitro tests applied a load to the calcaneus and subsequently measured the translation of the talus and/or calcaneus relative to the tibial dome. Rotation in the transversal and frontal plane was restricted in 8 tests. After analysis of the results presented by nine different studies, the mean value of anterior ankle-joint laxity with intact ligaments is 4.2 mm. The mean laxity value after sectioning of the anterior talofibular ligament is 6.5 mm (Figure 1). The mean laxity value increases to 8.4 mm after sectioning of the calcaneofibular ligament. The mean anterior laxity value with the foot in dorsal flexion (3.1 mm) is less than the mean value with the foot in neutral position (4.5 mm) or in plantar flexion (4.7 mm). The applied load and the anterior laxity values between the different studies vary greatly.

CONCLUSIONS

Each ligament section results in significantly increased anterior ankle-joint laxity. Ankle-joint laxity can be used as a measure for damage to the anterior talofibular ligament (ATFL) or calcaneofibular ligament.

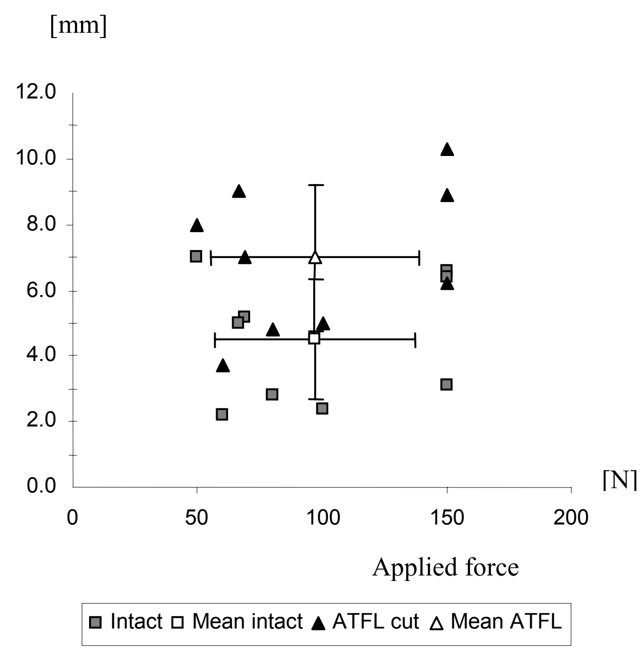

Figure 1: Scatter diagram showing anterior ankle laxity and applied force for intact and ATFL-deficient ankles from the different studies. The values represent tests with the foot in neutral flexion. This figure represents all 9 studies.

REFERENCES

Kerkhoffs GMMJ, et al (2001). Clin Biomechanics, **16**, 635-43.

ACKNOWLEDGEMENTS

This study was conducted as part of a greater project to develop an instrumented test for evaluation of ankle-joint laxity. This project is kindly sponsored by Ortomed bv, The Netherlands.

TWO INSTRUMENTED TESTS FOR ANTERIOR ANKLE-JOINT LAXITY: AN EVALUATION IN THE CLINICAL SETTING

Gino MMJ Kerkhoffs, Leendert Blankevoort, Ruby Corveleijn, Inger N Sierevelt, Mark JC Smeulders, C Niek van Dijk
Orthopaedic Research Center Amsterdam, Academic Medical Center, Amsterdam The Netherlands

INTRODUCTION

As a diagnostic tool and for postoperative follow-up studies, an objective measure for anterior ankle laxity can be obtained through the use of an instrumented tester. Two such testers were developed for the measurement of anterior laxity of the ankle joint complex. The purpose of this study was to evaluate the reproducibility of these testers and their functionality in a clinical setting.

METHODS

The two devices used for the study are a quasi-static ankle tester and a dynamic ankle tester. The test devices both comprise of a vertical construction to fixate the lower leg, a horizontal construction to apply a load to the calcaneus and to measure the amount of displacement. Movement of the footplate enables measurement of displacement in the anterior direction.

The dynamic ankle tester measures the anterior displacement of the calcaneus in relation to the tibia as a result of a hammer hitting the heel-plate. The impulse of the hammer pushes the foot forward. The resulting anterior-posterior and medio-lateral translation are measured. The load-displacement event takes place within the reflex time of the muscles, so involuntary muscle contraction cannot influence the test results. The translation values of the calcaneus in relation to the tibia as measured with the quasi static ankle tester are the result of a manually applied load up to maximally 150N.

Figure 1. Dynamic ankle tester

Figure 2. Quasi static ankle tester

Twenty-four volunteers visited the clinic twice with minimally 1 week in between. During the first visit, 2 different observers tested the patients with both instrumented tests. Stress-radiographs were made with help of the Telos® device. During the second visit, one observer performed the manual test; the second performed both instrumented tests.

Reliability coefficients were calculated to investigate inter- and intra-observer reliability. Paired t-tests were performed to determine systematical errors between the observers. Pearson correlation coefficients were determined to investigate the correlation between the two testers, manual testing and Telos® stress testing.

RESULTS AND DISCUSSION

Intra-observer reliability coefficients for the dynamic test and quasi-static test were 0.84 and 0.82 respectively ($p<0.01$). Inter-observer reliability was 0.83 for the dynamic and 0.82 for the quasi-static test ($p<0.01$). Small but significant systematical errors between the observers of 0.58 mm (6%) and 2.84 mm (12%) for the dynamic test and the static test respectively were found ($p<0.01$ for both tests)). The correlation coefficients of the two testers are shown in Figure 3. There were no correlations between the two testers on the one hand and the manual and Telos® test on the other, nor was there a correlation between the manual and Telos® test.

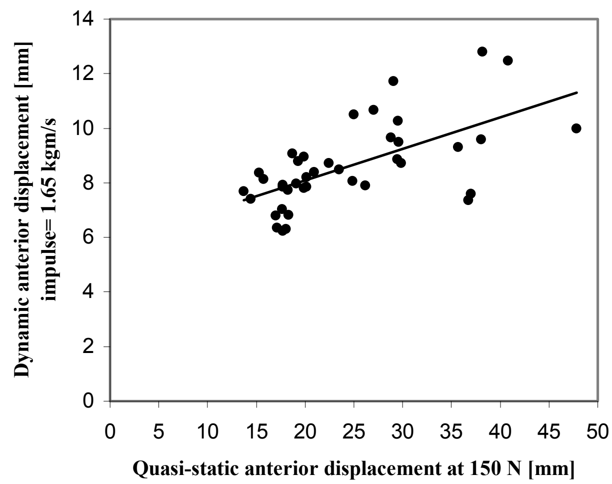

Figure 3. Comparison of displacement measurements between the dynamic and quasi-static ankle testers.

CONCLUSIONS

The reproducibility and repeatability of both test devices are good. The systematical errors represent low clinical significance but call for further improvement of the measurement procedure. Which test (device) is the best and most reliable is not yet clear. Also the manually performed test and the TELOS® test with radiographs need re-evaluation.

ACKNOWLEDGEMENTS

Ortomed® sponsored this study.

THE LEVEL OF SYMMETRY IN THE ANTHROPOMETRIC AND MECHANICAL PROPERTIES OF THE ANKLE AS DETERMINED BY A MECHANICAL/MRI TECHNIQUE

S.I. Ringleb[1], S. Siegler[1], J.K. Udupa[2], C.W. Imhauser[1], B.E. Hirsch[2,5], P.K. Saha[2], D. Odhner[2], E. Okereke[3], N. Roach[4]
[1]Department of Mechanical Engineering and Mechanics, Drexel University, Philadelphia, PA
http://www.drexel.edu/academics/engineering/departments/mem/
[2]Medical Image Processing Group, [3]Department of Orthopedic Surgery, [4]Department of Radiology
University of Pennsylvania, Philadelphia, PA
[5]Department of Anatomy and Cellular Biology, Temple University, Philadelphia, PA

INTRODUCTION

Various pathological conditions of the foot and ankle affect its morphological, architectural, and mechanical properties. These parameters have a variability among individuals, which is known to be very large. Therefore, for those conditions in which only one ankle is affected it is desirable to develop diagnostic techniques based on a comparison with the unaffected contra-lateral side. In order to do so, the level of left to right symmetry of the ankle in healthy asymptomatic individuals must be established. This was the goal of the present study.

METHODS

The morphological and architectural properties of the ankle complex consisting of the truncated tibia and fibula (i.e., based on an isoshaping procedure) (1), the talus and calcaneus were determined from three-dimensional reconstructions of MR images using the 3DVIEWNIX software system (2). This procedure included segmenting and creating a 3D representation of the bones, and calculating their morphological and architectural properties (3). These included the lengths of the principal axes within the bone and their corresponding principal moments of inertia, location of the centroids, and distance between the centroids. Kinematic parameters (i.e., centroid displacement, the direction of the equivalent axis, and the net rotation about it) representing relative bone movement under various incremental loading conditions were calculated for each load increment. To apply the loads, a non-metallic arthrometer, was used (4). The ankle was first scanned in the unloaded configuration. A 2.26 Nm inversion moment was applied, the arthrometer was locked, and the ankle was scanned. This procedure was repeated for a 133.45 N anterior drawer force.

RESULTS AND DISCUSSION

The average percent difference between the principal moments of inertia and the lengths of the principal axes for five healthy subjects are presented in Table 1. The distance between the centroids of the tibia and talus, tibia and calcaneus, and calacneus and talus yielded percent difference of 1.20±0.78%, 0.64±0.29%, and 1.07±1.02%, respectively. These anthropometric data show a high level of symmetry.

The angle of rotation and the centroidal displacement for each bone were small and close in magnitude to the level of accuracy of the MRI kinematic technique (3). Therefore the left to right symmetry in these properties were reported in absolute values. The average difference between left and right rotations and translations were calculated for the talus and calcaneus relative to the tibia. In inversion, the average difference for the calcaneus and talus were 6.28±4° and 4.94±2.89°, respectively. The average difference in displacement in anterior drawer for the calcaneus and talus were 2.82±3.13 mm and 1.19±1.63 mm, respectively. These parameters show a greater symmetry than those calculated based on external measurements (4).

SUMMARY

The level of symmetry in the anthropometric and mechanical properties of the ankle joint identified in this study established a threshold, which can be used when a diagnosis of a unilateral ankle pathology relies on comparison to the intact contra-lateral side.

REFERENCES

(1) Saha, PK, et all. SPIE Proceedings, 4684, accepted
(2) Udupa JK, et al. SPIE Proc., 2164, 58, 1994
(3) Udupa JK et al. IEEE Tr. BME, 45, 1387, 1998
(4) Chen J, et al. J Bimech. Eng., 110, 1988

ACKNOWLEDGEMETS

This research was funded by DHHS Grant AR46902.

Table 1: Average Percent Difference Between Left and Right Ankles for Moments of Inertia and Lengths of Principal Axes

Bone	I_x	I_y	I_z	L_1	L_2	L_3
Calcaneus	1.61±1.35	2.73±1.75	5.53±4.29	1.72±0.77	2.62±.2.4	5.69±6.78
Talus	1.46±0.91	3.16±3.08	1.27±0.88	2.37±1.90	2.98±3.80	5.06±2.90
Tibia	2.06±0.966	2.64±2.52	2.50±2.79	1.2±0.911	4.88±5.87	1.69±1.50
Fibula	7.1±3.01	2.28±3.13	12.01±11.42	4.40±2.09	5.79±3.24	7.2±6.52

SIMULATION BASED MEDICAL PLANNING FOR CARDIOVASCULAR SURGERY: RECENT DEVELOPMENTS

Charles A. Taylor

Departments of Surgery and Mechanical Engineering, Stanford University, Stanford, California, U.S.A., taylorca@stanford.edu

INTRODUCTION

We describe the results from a series of animal experiments used to test the accuracy of our three-dimensional and one-dimensional finite element methods for modeling blood flow by comparing predicted flow rates to *in vivo* measurements obtained using phase contrast magnetic resonance imaging (PC-MRI). Both 3D and 1D methods involve solving the governing equations of blood flow on a domain and prescribing boundary conditions to account for the vasculature downstream. A variational multiscale method to obtain boundary conditions applicable to blood flow will be discussed in the podium presentation. In this approach, a finite element method is used for the region where the governing equations are nonlinear or not amenable to analytic solution and a lumped parameter model or linear wave equation is used for the vasculature downstream.

METHODS

Experimental validation studies were performed using data collected from experiments involving eight pigs. In each animal, we created an aortic constriction, or stenosis, by tying polyester (Dacron) umbilical tape around the descending thoracic aorta to restrict blood flow and then attached a 10 mm diameter polyester (Dacron) graft to the thoracic aorta proximal and distal to the constriction to provide an alternate path for blood flow. Blood is divided between the native aorta and the bypass graft and combines downstream of the stenosis. Magnetic resonance angiography was used to acquire three-dimensional anatomic images, while phase contrast MRI (PC-MRI) was used to collect velocity data at four different locations: the proximal aorta (inlet), the mid-aorta (aorta), the graft, and the distal aorta (outlet). Numerical predictions of flow rate were compared with magnetic resonance imaging data in eight pigs.

RESULTS AND DISCUSSION

Figure 1 shows computed flow rates using 3D and 1D methods with empirically-derived stenosis and branch loss terms.

SUMMARY

We have demonstrated that both three-dimensional methods and one-dimensional methods can describe blood flow distribution in a porcine thoraco-thoraco bypass surgery.

REFERENCES

Taylor, C.A., Draney, M.T., Ku, J., Parker, D., Steele, B.N., Wang, K.C., Zarins, C.K. (1999) Predictive medicine: Computational techniques in therapeutic decision-making, *Computer Aided Surgery*, 4, 231-247.

Wan, J., Steele, B.N., Spicer, S.A., Strohband, S., Feijoo, G.R., Hughes, T.J.R., Taylor, C.A. (2001) A One-dimensional Finite Element Method for Simulation-Based Medical Planning for Cardiovascular Disease. To appear in *Computer Methods in Biomechanics and Biomedical Engineering*.

Ku, J.P., Draney, M.T., Arko, F.R., Lee, W.A., Chan, F., Pelc, N.J., Zarins, C.K., Taylor, C.A. (2001) In Vivo Validation of Numerical Predictions of Blood Flow in Arterial Bypass Grafts. Submitted to *Annals of Biomedical Engineering*

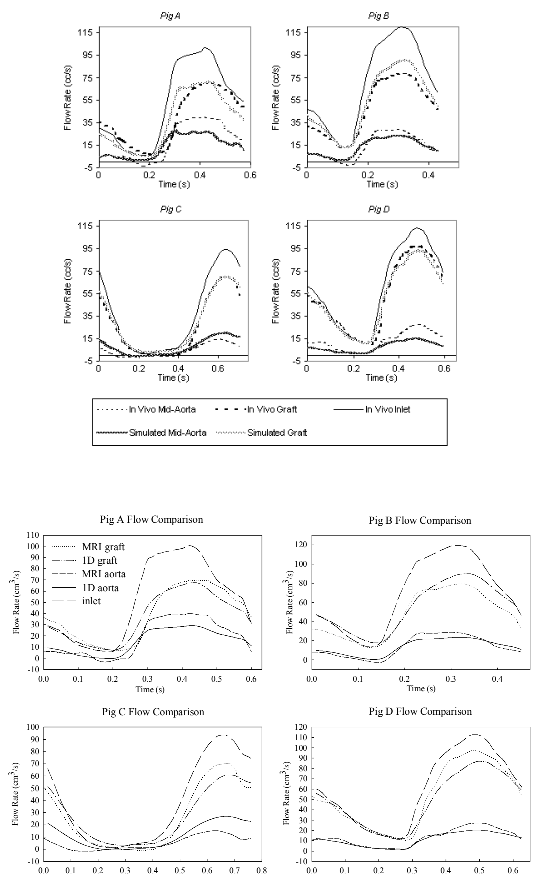

Figure 1. Results from 3D (top) and 1D (bottom) blood flow simulations for 4 pigs.

ACKNOWLEDGEMENTS

The author would like to acknowledge the contributions of Joy Ku, Brooke Steele, Jing Wan, Mary Draney, Chris Zarins and Thomas J.R. Hughes.

PROSPECTS OF MICRO- FINITE ELEMENT ANALYSES OF BONE FOR CLINICAL APPLICATION

Bert van Rietbergen

Department of Biomedical Engineering, Eindhoven University of Technology, Eindhoven, Netherlands

INTRODUCTION

Micro- finite element analysis (μFE) enables a complete and precise evaluation of cancellous bone mechanical properties as they relate to its trabecular structure as quantified by high-resolution images. A tempting application of this technique is the analyses of structure-related mechanical properties of bone in-vivo. Such analyses potentially could improve the diagnosis of bone strength reduction with osteoporosis or increase the sensitivity of osteoporotic drug treatment efficacy studies. So far, however, the clinical application of this technique has been limited by the poor resolution of clinically available imaging methods.

Recently, high-resolution pQCT and MR imaging techniques have been introduced that enable the visualization of trabecular bone in-vivo. The resolution of these images, however, is still less than that commonly used for μFE analyses and the question remains whether results of analyses based on such images are better than those of stochastic relationships based on DEXA bone density measurements, which is the most common predictive tool used nowadays.

In this paper, the results of two recent studies that addressed this question are summarized. Based on these results, the prospects of μFE as a clinical application will be discussed.

μFE FOR BONE FAILURE LOAD PREDICTION

In the first study [1], a special 3D-pQCT device that can be used for bone in-vivo was used to create μFE models of 54 cadaver arms at 165μ resolution. After imaging, the arms were compressed to failure to produce a collus' type fracture and the failure load was measured. Micro-FE analyses were used to simulate the experiments and the bone failure load was predicted from these FE results using a bone tissue failure criterion. To evaluate the predictive value of stochastic relationships structural indices were measured as well from the 3D-pQCT images and bone mass measurements were obtained from DEXA measurements.

The predicted failure loads calculated from the FE-analysis compared well with those measured in the experiments (R^2= 0.75 $p<0.001$). Lower correlations were found with bone mass (R^2=0.48 $p<0.001$) and bone structural parameters (R^2=0.57 $p<0.001$). It was thus concluded that micro-FE results significantly improved the prediction of bone failure load.

μFE FOR DRUG TREATMENT EFFICACY STUDIES

In the second study [2], high-resolution (195×195×500μ) MR-imaging was used to create 3D μFE models of a cancellous volume of interest (VOI) in the calcaneus of 56 postmenopausal women participating in a longitudinal clinical trial to evaluate the effect of idoxifene (Fig. 1). Subjects received either a placebo or the idoxifene treatment. MR-images were acquired at baseline and after one year of treatment and μFE was used to calculate changes in elastic properties of the VOI. DEXA measurements were performed at the heel as well.

Elastic moduli in the treated groups significantly differed from baseline after one year of treatment. Changes in bone mass, however, were not significant. Changes in the placebo group were not significant for any parameter. Since significant changes in moduli were obtained for the treated groups whereas no significant change in bone mass was found it was concluded that the application of these techniques may increase the clinical significance of these trials.

DISCUSSION

In both studies summarized here it was found that the results of μFE analyses could improve upon predictions based on bone density measurements. Moreover, the μFE analyses provide direct and very detailed information about (changes in) bone mechanical properties.

Some limitations should be mentioned as well. First, high-resolution in-vivo images presently can be obtained only for the peripheral skeleton and not for other important osteoporotic fracture sites such as the femur or vertebrae. Second, the results of these analyses do not reflect (changes in) the bone tissue material properties, the measurement of which would require invasive (biopsy) techniques.

Based on the encouraging results obtained so far, it is concluded here that μFE potentially could lead to more accurate predictions of bone failure load, shorter follow-up periods and smaller population sizes in clinical studies.

REFERENCES

1. Pistoia et al. (2002), Bone (accepted)
2. Van Rietbergen et al. (2002), *Clin. Biomech.*, **17**:81

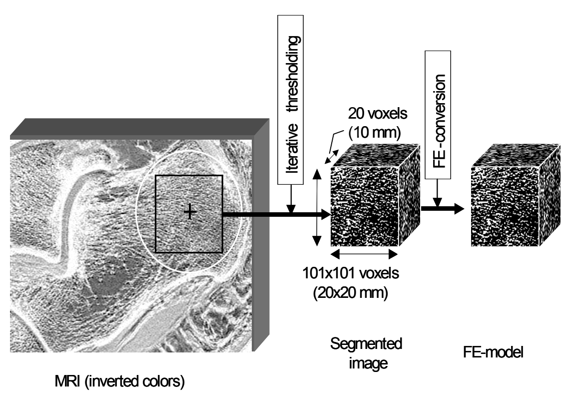

Fig. 1: Overview of the micro-FE approach used in [2]

THE MECHANISMS AND SIGNIFICANCE OF THE CORRELATION BETWEEN BONE STRENGTH AND STIFFNESS

David P. Fyhrie, Yener N. Yeni, Deepak Vashishth[+], Clifford M. Les

Bone and Joint Center, Henry Ford Health System, 2799 W. Grand Blvd., Detroit, MI 48202
[+]Biomedical Engineering Department, Rensellaer Polytechnic University, Troy, NY

INTRODUCTION

Bone stiffness is fundamental to the ability of a vertebrate to move (Wainwright 1982). Sufficient strength is also essential for the skeleton to withstand overloads (Wainwright 1982). These observations are similar but it is fundamentally more difficult to control strength than it is to control stiffness. The difference is caused by the fact that bone stiffness affects *deformation,* but strength is related to the *force* (stress) when failure occurs. Deformation can be measured and, therefore, stiffness can be controlled. Force is not directly measurable (*e.g.,* load cells measure the deformation of a calibrated structure). Therefore, strength is a property of bones that cells cannot measure and cannot directly control. This talk presents recent work on how, despite it's apparent impossibility, vertebrates still manage to control bone strength.

STIFFNESS PREDICTS STRENGTH

The key observation that suggests how cells may control bone strength is the high correlation between apparent strength and stiffness (Fyhrie and Vashishth 2000). Consequently, any ability to control bone apparent stiffness (by controlling deformation) will translate into an ability to control apparent strength. It is odd, however, that strength and stiffness correlate at the *apparent* level. Apparent strength and stiffness are calculated from volume and area averages of deformation and force. It is not obvious how a bone could know these averages. We conclude that the correlation of strength and stiffness for cortical and cancellous bone tissue derives from microstructural and ultrastructural mechanisms.

MICROMODELS FOR STRENGTH

Strain distribution in cancellous bone is strongly affected by trabecular microstructure (Hou 1998). We showed that the average and standard deviation of trabecular shear stresses are correlated (Fyhrie et al, 2000). Control of the correlation between stress statistics is a mechanism that can affect the correlation of stiffness and strength.

For cortical tissue, tensile failure is by propagation of cracks. A micromodel of collagen bridged microcracks (Yeni 2002a) can predict the apparent failure strength of cortical bone from the apparent stiffness of the tissue and the failure strain of the collagenous matrix. This model shows the importance of collagen viscoelasticity to the creation of bone strength.

The key to the model (Yeni 2002a) was the viscoelasticity and *hidden length* (Thompson 2001) of the collagen fibrils. The hidden length of a macromolecule allows it to unfold (extend) under load and to dissipate energy. Reversible bond breaking "toughens" (adds strength to) a material and is a mechanism that can correlate strength and stiffness. Energy dissipation manifests as viscoelasticity at the macroscopic level. Consequently, our observation that viscoelastic properties of bone can predict macroscopic bone strength (Yeni 2002b) may relate to reversible bond breaking in collagen.

VISCOELASTICITY AND MENOPAUSE

The correlation of apparent bone strength to bone stiffness is very good and is related to bone viscoelastic properties. Changes in bone viscoelastic properties with age or menopause may be important predictors of changes in bone strength. The dissipation of energy in ovine cortical bone (tanδ) is decreased at high frequency after three years of ovariectomy (Les 2002). This change in viscoelastic properties, along with our other observations, leads to the hypothesis that ovariectomy (and possibly menopause) reduces the strength of bone under rapid loading. Testing this hypothesis is the next goal in determining the relationship of bone stiffness to strength.

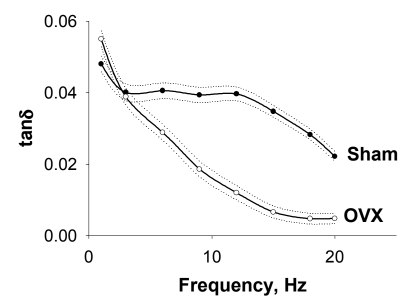

Fig. 1: Frequency dependence of energy dissipation for ovine cortical bone after three years ovariectomy.

ACKNOWLEDGEMENTS

NIH grants AR40776 and AR47434

REFERENCES

Fyhrie, D. P., S. J. Hoshaw, et al. (2000). Ann Biomed Eng **28**(10): 1194-9.

Fyhrie, D. P., D. Vashishth (2000). Bone **26**(2): 169-73.

Hou, F. J., S. M. Lang, et al. (1998). J Biomech **31**(11): 1009-15.

Les, C., Vance, J., et al. (2002). Trans. Orth. Rsch. Soc, 89.

Thompson, J. B., J. H. Kindt, et al. (2001). Nature **414**(6865): 773-6.

Wainwright, S. A., W. D. Biggs, et al. (1982). Mechanical Design in Organisms. Princeton, NJ, Princeton University Press.

Yeni, Y. N., Fyhrie, D.P. (2002a). Trans. Orth. Rsch. Soc, 18.

Yeni, Y. N., Fyhrie, D.P. (2002b). Trans. Orth. Rsch. Soc, 87.

APPLICATION OF VIRTUAL EXPERIMENTS TO THE STUDY OF TRABECULAR BONE MECHANICS

Glen L. Niebur
Department of Aerospace and Mechanical Engineering and Center for the Study of Biocomplexity
The University of Notre Dame, IN, USA gniebur@nd.edu

INTRODUCTION

The development of high-resolution imaging modalities and the high-resolution finite element technique has greatly expanded our capability to study trabecular bone mechanics through the application of "virtual experiments" (Niebur et al. '00). Computer models have been applied as surrogates for mechanical testing to formulate relationships between fabric and the elastic properties of trabecular bone (Van Rietbergen et al. '98; Zysset et al. '98). Nonlinear models have been used to study multiaxial yield behavior (Niebur et al. '01). In both cases, these virtual experiments provided additional insight into both the apparent and tissue level mechanical behavior of trabecular bone.

TISSUE CONSTITUTIVE MODELING

The degree to which a computer model will reflect a true mechanical test depends on the validity of the assumed tissue level constitutive behavior, and the accuracy with which the parameters to the constitutive law can be determined. Direct assessment of the trabecular tissue behavior is limited due to the small size of the experimental material (Choi et al. '90). Virtual experiments complemented by apparent level measurements can be used to gain insight into these tissue level properties.

For most applications, the elastic behavior of the tissue can be described by a single modulus (Kabel et al. '99) that can be calibrated (Van Rietbergen et al. '95) from accurate mechanical measurements of the apparent modulus (Keaveny et al. '97).

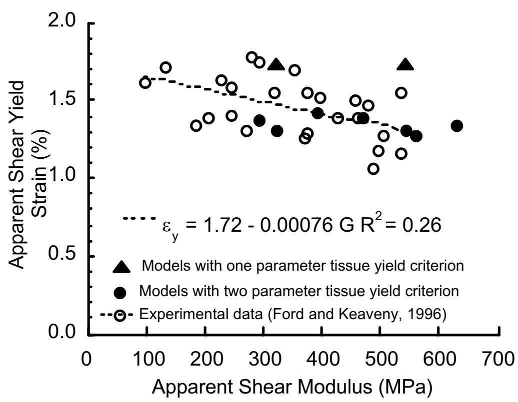

Figure 1: Apparent shear yield strains for bovine tibial trabecular bone. A one-parameter tissue yield criterion cannot accurately predict the apparent yield behavior in shear.

The yield properties of the trabecular tissue can be calibrated using a similar approach. Initial experiments demonstrated that he tissue level yield criterion must incorporate tension-compression strength asymmetry (Niebur '01) (Fig. 1), requiring at least two failure experiments to calibrate the constitutive behavior. However, aggregate tissue level yield properties can be calibrated by comparing computationally predicted apparent yield properties to mean values from mechanical measurements (Niebur '00).

MULTIAXIAL YIELD PROPERTIES

Accurate measurement of multiaxial yield properties of trabecular bone is complex. High-resolution finite element models can be used to apply arbitrary loading combinations without loading artifacts (Keaveny '97). More importantly, multiple loading conditions can be investigated for a single specimen. Thus, the general form of a multiaxial yield criterion can be considered without the confounding effects of inter-specimen heterogeneity and anisotropy (Fig. 2)

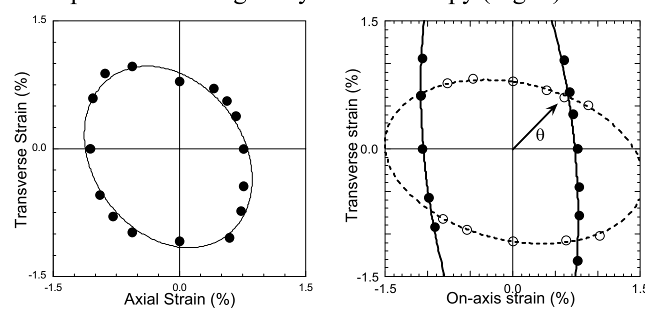

Figure 2: Complete Tsai-Wu (left) and multi-surface (right) failure envelopes characterized for a single specimen of trabecular bone using virtual experiments.

SUMMARY

Virtual experiments based on high-resolution finite element models of trabecular bone provide a powerful means to confront the issues of heterogeneity and anisotropy when studying trabecular bone mechanics. High-resolution finite element models allow data for multiple loading conditions to be obtained for a single specimen. It is thereby possible to control or isolate the effects of inter-specimen heterogeneity and anisotropy to gain improved insight into the mechanical behavior of trabecular bone.

REFERENCES

Choi, et al. (1990). J Biomech **23**(11); Kabel, et al. (1999). J Biomech **32**(7); Keaveny, et al. (1997). J Orthop Res **15**; Niebur, et al. (2000). J Biomech **33**(12); Niebur, et al. (2001). 47th Annual meeting of the ORS; Van Rietbergen, et al. (1998). J Orthop Res **16**(1); Van Rietbergen, et al. (1995). J Biomech **28**(1); Zysset, et al. (1998). J Biomech Eng **120**(5)

CREEP FORMULATION OF STRAIN ACCUMULATION DURING TENSILE FATIGUE OF CORTICAL BONE

John R. Cotton[1], Peter Zioupos[2], Keith Winwood[2], and Mark Taylor[1]

[1]Bioengineering Science Research Group, School of Engineering Sciences, University of Southampton, Highfield, Southampton, SO17 1BJ, UK. Email: jcotton@soton.ac.uk
[2]Department of Materials & Medical Sciences, Cranfield University, Shrivenham, SN6 8LA, UK

INTRODUCTION

Bone subsidence has been identified as a cause of implant failure (Taylor, et al, 1999). We wish to characterize this phenomena and use it with finite element models to predict subsidence of implanted systems. During *in vitro* fatigue tests with non-zero mean loads, strain accumulation is noticed upon unloading under a variety of loading modes. This observation has been described by various researchers as "creep" (Carter and Caler, 1983), "plasticity" (Taylor, et al, 1999), and "strain drift" (Pattin, et al, 1996). Limited work has focused on characterizing this phenomena, while a number of researchers have quantified the accompanying stiffness loss.

We examine if this strain accumulation during fatigue in cortical bone is accurately described as creep. Although several researchers (Carter and Caler, 1985; Zioupos, et al, 2001) have related in fatigue and creep cycles and times to failure, respectively, this study examines the actual rate of strain accumulation in fatigue. In cancellous bone, such a relationship has been presented (Bowman, et al, 1998).

Under constant load conditions, creep has been reported in human cortical bone. A formulation derived (Fondrk, et al, 1999) proves useful, where the rate of creep strain is determined by

$$\dot{\varepsilon}_c = \dot{\varepsilon}_{c-th}(\sigma/\sigma_{th})^N$$

An arbitrary creep rate threshold is chosen and constants of a stress threshold, σ_{th}, and power, N, determine the creep rate as a function of stress.

METHODS

Bone samples (n=29) were taken from four individuals: females age 53, 69, and 79; a male, age 55. Samples were fatigued until failure in 0-T loading over a range of stresses, (Winwood, et al, 2001). The average creep strain per cycle was calculated from 10% to 90% of the fatigue life. Creep rate was converted from equation 1 to a "per cycle" basis by substituting stress as a sinusoidal function of time, and integrating over a cycle. Thus, the constants of equation 1 were determined for the experimental data. Creep rate threshold was taken, as Fondrk, to be 10^{-5}/sec.

RESULTS

Creep strain accumulated according to the classically described "three stage creep". The portion from which creep strain rate was taken corresponded to the middle, constant rate regime (stage II creep). Creep rates per cycle were observed in the range of 10^{-10} to 10^{-4} and are shown as a function of stress in figure 1. These relationship fitted well to a power law. Resulting stress threshold values and powers were determined for the four individuals and are shown in Table 1.

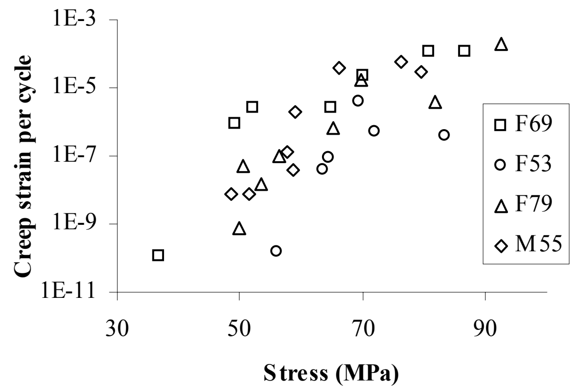

Figure 1: Creep strain per cycle as a function of stress.

	f69	f53	f79	m55	Combined
σ_{th}	56.3	74.3	65.4	60.5	64.4
N	14.5	19.6	16.3	20.0	14.8
R^2	0.86	0.58	0.85	0.83	0.62

Table 1: Results of fitted analysis.

SUMMARY

The non-zero strains accumulated at a rate well described by a stress power law used to describe creep. Constants are seen to be in the range of speculated values presented by Fondrk (σ_{th} of 68-79 MPa) and (N = 12-17), even though the creep rates are mostly lower than those seen by Fondrk, owing to the different time scales of the tests. Notable is the advanced age and gender (mostly female) of the samples.

REFERENCES

Bowman, S.M. et al. (1998). *J Biomech Eng*, **120,** 647-654; Carter, D.R, Caler W.E. (1983). *J Biomech Eng,* **105,** 166-170; Carter, D.R, Caler W.E. (1985). *J Orthop Res* **3,** 84-90; Fondrk, M.T. et al (1999). *J Biomech Eng*, **121,** 533-541; Pattin, C.A. et al (1996). *J. Biomech,* **29,** 69-79; Taylor, M. et al (1998). *J. Biomech,* **31,** 303-310; Taylor, M. et al (1999). *Journal of Materials Science: Materials in Medicine,* **10**, 841-846; Winwood, K., et al (2001). *XVIIIth ISB Congress*, P721; Zioupos, P. et al (2001). *J Theor Biol*, **210**, 389-399.

ACKNOWLEDGEMENTS

Funded by EPSRC (UK) grant GR/M59167.

A COMPUTATIONALLY EFFICIENT ALGORITHM FOR IN-VIVO BONE FAILURE PREDICTION ON THE TRABECULAR LEVEL: A COMBINED EXPERIMENTAL AND COMPUTATIONAL APPROACH

Martin Stauber, Steven K. Boyd, Ara Nazarian and Ralph Müller

Institute for Biomedical Engineering, Swiss Federal Institute of Technology (ETH) and University of Zürich, Zürich, Switzerland

INTRODUCTION

Osteoporosis is a major health disease characterized by low bone mass and micro-architectural deterioration of bone tissue. Eventually, the bone becomes fragile resulting in increased fracture risk. The fracture risk has traditionally been assessed by bone density measurements, however it is known that changes in trabecular morphology can lead to disproportionate decreases in bone strength (Goldstein, 1987). Experimentally, using image-guided failure assessment technique, Müller et al. (1998) showed that failure of individual trabeculae can lead to global bone failure. Therefore, failure prediction of individual trabeculae is important for global failure prediction.

Individual trabecular strains can be predicted by finite element (FE) analysis of high-resolution image-based models. One possibility is the use of a solid FE model (Verhulp et al., 2001), but this approach is computationally taxing, and hence is currently of limited use for clinical purposes. In this study, we propose a computationally efficient FE technique to predict local trabecular strains and displacements and validate it against real experimental dynamic failure visualization. The FE model uses beam elements derived from skeletonized micro-structural data, and may have future clinical potential for *in vivo* applications of bone failure prediction.

METHODS

A micro-compression device was used to measure unloaded and loaded porous structures (aluminum foam, whale and human vertebral bone). The specimens were step-wise compressed to 0, 2, 4, 8, 16, and 20 percent global strain, and then measured in the micro-tomographic system (μCT 20, Scanco Medical AG, Bassersdorf, Switzerland) at a spatial resolution of 68 μm. During compression, a data acquisition system recorded the displacement applied to the specimen and the corresponding load providing stress-strain curves for global modulus assessment.

The experimental approach to compute local strains was based on the six consecutively measured compression images. Each of those three-dimensional (3D) time-steps was spatially decomposed using a thinning approach leading to a homotopic skeleton of the structure (Figure 1). Corresponding elements were identified within the different time steps using a 3D correlation procedure. This method allowed us to track each trabecular element and its deformations within the structure during the compression procedure, and hence to compute the relative strain for each element.

The computational FE approach to assess local strain was based on the unloaded 3D structure. The skeletonized structure was the basis for obtaining a list of nodes and connectivities that could automatically be translated in a homotopic beam model used for subsequent FE calculations. The beam model was imported into Marc (MSC Software Corporation, Los Angeles, CA), where all material properties and boundary conditions were specified. All elements were chosen to be of the same type and same diameter (466 μm), but lengths depending on the original trabecular structure. Boundary conditions for the compression test simulated the axial compression used in the experimental approach: a plane at the bottom surface fixed the nodes in contact, and a parallel plane on the top surface displaced the nodes of the elements at increments of 0.2% global strain. As compression continued, nodes coming in contact with either plane were constrained to move within the plane in all subsequent steps.

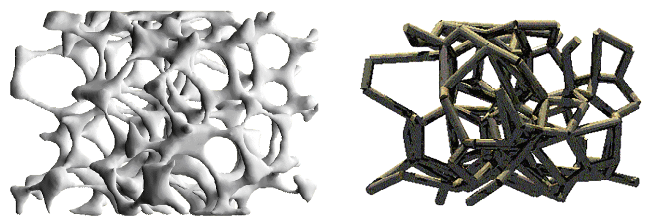

Figure 1: Porous structure measured by μCT (left) and the derived beam FE model from the skeletonized image (right).

RESULTS AND DISCUSSION

The presented method allowed spatial decomposition of trabecular structures into individual elements, thus enabling computation of local strains both from experimental data and the derived beam FE model. The advantage of this approach is the ability to directly validate the beam FE model.

Globally, the resultant stress-strain curves were in excellent agreement, but more interesting also local strains computed from the experimental approach were in good agreement with local strains computed by the FE model. Thus, it appears that this computationally efficient FE approach has the potential to predict local failure in bone, and may have future applications for risk assessment in upcoming 3D *in vivo* image data.

REFERENCES

Goldstein S.A. (1987) *J Biomech,* 20: 1055-1061.

Müller R., Gerber S.C., and Hayes W.C. (1998) *Technology and Health Care,* **6:** 433-444.

Verhulp E., van Rietbergen B., Müller R., and Huiskes R. (2001), *Computer Methods in Biomechanics & Biomedical Engineering,* in press.

SENSORY TRANSDUCTION IN AN ARTHROPOD MECHANORECEPTOR SYSTEM

Andrew S. French
Department of Physiology and Biophysics, Dalhousie University, Halifax, Nova Scotia, Canada
E-mail: andrew.french@dal.ca

INTRODUCTION

Arthropods (insects, spiders and crustaceans) have provided a variety of model systems for studying fundamental mechanisms of sensory transduction and processing of sensory information. In addition to their ready availability and relatively simple nervous systems, the arthropods possesss a class of sensory receptors, the Type I or cuticular receptors, that have their sensory neuron cell bodies located in close proximity to the sensory endings in the external cuticle. These receptors allow experiments to be performed that are currently impossible with most vertebrate mechanoreceptors.

Slit sensilla are specialized mechanorecptors that detect mechanical strain in the spider cuticle. They occur singly and in groups, called slit-sense organs. We developed a preparation of the VS-3 slit-sense organ (Barth and Libera, 1970) in the tropical wandering spider, *Cuppienius salei*, that has allowed us to make intracellular recordings from primary mechanosensory neurons and to voltage-clamp the receptor current during sensory transduction.

METHODS

Figure 1 shows the experimental arrangement used for most of our studies on the VS-3 slit-sense organ. The organ consists of 7-8 slits in the cuticle, with each slit innervated by a pair of sensory neurons. Both the neurons of each pair are mechanoreceptors but they have different adaptation properties. Glass microelectrodes of about 60 MΩ resistance were inserted into the sensory neurons allowing measurement of the membrane potential or the receptor current by the switching single electrode voltage clamp technique (Juusola et al., 1994).

RESULTS AND DISCUSSION

Tansduction occurs in the tips of the sensory dendrites that terminate in the slits. The tips are surrounded by a sodium-rich lymph, and recordings of the receptor current, including its current-voltage relationship and ion substitution experiments showed that mechanical stimulation opens sodium selective ion channels in the tips (Höger et al., 1997). Noise analysis of the receptor current indicated that there are probably a few hundred mechanoreceptor channels with comparatively small single-channel conductance (Höger and French, 1999).

The receptor current adapts with time after a step stimulus to the slits, but the adaptation is much slower than the rapid adaptation of the action potential discharge, indicating that other membrane currents control the rapid adaptation.

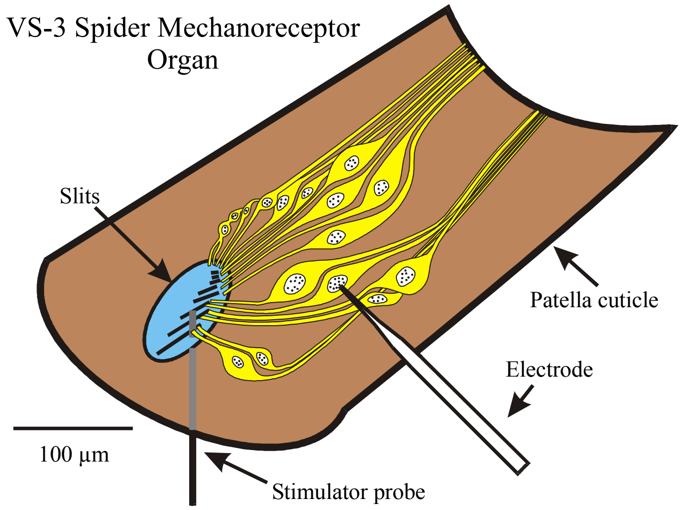

Figure 1: Mechanotransduction in the spider VS-3 slit-sense organ. The patella cuticle was dissected and the tissues removed to expose the sensory organ. Microelectrodes were inserted into neuron cell bodies while a mechanical stimulator pushed on the appropriate slit from below.

SUMMARY

The spider VS-3 organ has provided important new information about fundamental mechanisms of transduction in arthropod mechanoreceptors. Current experiments are aimed at further characterization of the receptor channels to allow comparison with families of mechanically-activated ion channels in other systems.

REFERENCES

Barth, F.G., Libera, W. (1970). *Z. Morphol. Tiere* **68**, 343-369.
Höger, U., Torkkeli, P.H., Seyfarth, E.-A. and French, A.S. (1997). J. Neurophysiol. **78**, 2079-2085.
Höger, U., French, A.S. (1999). *Brain Res.* **826**, 230-235.
Juusola, M.I., Seyfarth, E.-A., French, A.S. (1994). *J. Neurophysiol.* **72**, 3026-3028.

ACKNOWLEDGEMENTS

This work was supported by CIHR and NATO.

RECONSTITUTING A *C. ELEGANS* ION CHANNEL REQUIRED FOR MECHANOSENSATION

Miriam B. Goodman

Department of Molecular and Cellular Physiology, Stanford University, Stanford, CA., mbgoodman@stanford.edu

INTRODUCTION

The soil nematode, *Caenorhabditis elegans*, is an excellent animal for studying the molecular events that give rise to the sensation of force. Its response to force is simple: touching the animal in the head elicits backward movement and vice versa. This behavior depends on six specialized sensory neurons called touch cells, all of which can be identified in living animals and exposed for electrical recording. Genetic screens for touch insensitive animals identified twelve *mec* (*mec*hanosensory abnormal) genes needed for the function, but not the development, of the touch cells. Except for *mec*-5, which encodes a collagen protein expressed in closely apposed hypodermal cells (Du, et al, 1996), all of the cloned genes are expressed in touch cells.

The protein encoded by *mec*-4 is touch-cell specific and belongs to the DEG/ENaC superfamily of proteins that form amiloride-sensitive ion channels. The *mec*-10 gene encodes another DEG/ENaC channel subunit expressed in touch cells and four additional mechanosensory neurons. Both channel proteins are needed for touch sensitivity and can mutate to cause neuronal degeneration. MEC-4 and MEC-10 are hypothesized to form an ion channel at the center of a sensory mechanotransduction complex that includes genes encoding two additional membrane proteins (*mec-2* & *mec-6*), three extracellular matrix proteins (*mec-1*, *mec-5*, *mec-9*), and two microtubule proteins (*mec-7*, *mec-12*) (for review, see Tavernarakis & Driscoll, 1997). As a first step in reconstituting this putative sensory mechano-transduction complex, we co-expressed the DEG/ENaC proteins, MEC-4 and MEC-10, in *Xenopus* oocytes and determined how channel activity was affected by the addition of the membrane proteins, MEC-2 and MEC-6.

METHODS, RESULTS AND DISCUSSION

A long-standing question is whether the putative ion channel subunits, MEC-4 and MEC-10, form channels similar to other DEG/ENaC channels. To address this question we measured whole cell currents in Xenopus oocytes injected with cRNAs encoding the channel subunits (Goodman et al., 2002). Co-expression of the mutant or ‘d’ forms of MEC-4 and MEC-10 produced a constitutively-active Na^+ current that is blocked by amiloride with high affinity (at –60, K_i’ = 0.2±0.1 µM). MEC-2, a membrane protein related to human stomatin, increased the activity of mutant channels by approximately 40-fold and allowed currents to be detected with wild-type MEC-4 and MEC-10. MEC-6 also increased the activity of mutant channels by ~10-fold. MEC-6 has limited sequence similarity to paraoxonases, a family of arylesterases. Neither MEC-2 nor MEC-6 generated any detectable amiloride-sensitive current when expressed alone, indicating that they increase channel activity by interacting with MEC-4 and MEC-10. The picture that emerges from these functional interactions and previous evidence of interaction derived from genetic analysis is that MEC-4 and MEC-10 form an ion channel complex together with the accessory proteins, MEC-2 and MEC-6.

MEC-2 belongs to family of proteins with members expressed in bacteria, plants, and animals. The central domain of MEC-2 is highly conserved and is 64% and 46% identical to the human proteins, stomatin and podocin, respectively. To test the hypothesis that MEC-2 function is conferred by this conserved domain, we truncated MEC-2 and tested if truncated MEC-2, stomatin and podocin generated similar activities in Xenopus oocytes. While all three proteins could generate amiloride-sensitive currents when co-expressed with the ‘d’ form of MEC-4, none retained the activity of full-length MEC-2. These results suggest that the highly conserved central domain of MEC-2 is not sufficient for its function as an ion channel accessory protein.

SUMMARY

Screens for touch insensitivity in *C. elegans* have identified components of a candidate sensory mechanotransduction complex. We have taken the first steps in reconstituting this complex in Xenopus oocytes and understanding the function of its individual components. Current experiments are aimed at understanding how this channel is gated, understanding the mechanism by which the accessory proteins alter channel activity and testing whether or not this channel is necessary for transduction *in vivo*. Emerging strategies for studying channel function *in vivo* will be discussed briefly.

REFERENCES

Du, H., Gu, G., William, C. M., Chalfie, M. (1996) *Neuron*, **16**, 183-194.
Goodman, M.B., Ernstrom, G.G., Chelur, D.S., O'Hagan, R., Yao, C.A., Chalfie, M. (*in press*) *Nature*.
Tavernarakis, N., Driscoll, M. (1997) *Annu Rev Physiol*, **59,** 659-689.

ACKNOWLEDGEMENTS

Many thanks to my collaborators at Columbia University: Glen Ernstrom, Dattananda Chelur, Robert O’Hagan, Andrea Yao, and Marty Chalfie.

MYOSIN-1c IS THE HAIR CELL'S ADAPTATION MOTOR

Peter G. Gillespie[1]

Oregon Hearing Research Center and Vollum Institute, Oregon Health & Science University, Portland, OR.
[1]gillespp@ohsu.edu

INTRODUCTION

Hair cells, the sensory cells of the inner ear, transduce auditory and vestibular stimuli into receptor potentials, which initiate transmission of the sensory signal to the central nervous system. Mechanical transduction is carried out by the hair bundle, a crosslinked cluster of ~50 actin-filled stereocilia arranged in ranks of increasing height. This anatomical polarity corresponds to the physiological polarity of the bundle, so that deflections of the bundle towards the tallest stereocilia depolarize the cell, deflections towards the shortest stereocilia hyperpolarize the cell, and perpendicular deflections have no effect on the membrane potential. Hair-cell transduction is direct: bundle deflections stretch ~50 gating springs, which tug open 50-100 cation-selective transduction channels within microseconds and without second-messenger intervention. Although transduction channels open and close stochastically, changes in gating-spring tension alter the channels' open probability (P_{open}) and change the total receptor current flowing through them.

Hair cells adapt to sustained bundle deflections by adjusting the P_{open} of transduction channels back towards a resting level. Four lines of circumstantial evidence implicate myosin molecules in adaptation. First, adaptation is not merely a passive response to the stimulus; the adaptation motor actively generates force. Second, adaptation takes place within actin-rich stereocilia, and myosins are the only motor molecules known to move along actin. Third, adaptation requires Ca^{2+} and calmodulin, both of which control the activity of unconventional myosins. Fourth, ADP analogs and phosphate analogs, inhibitors of myosin activity, block adaptation. Candidates for the adaptation motor are therefore likely to belong to the extensive myosin superfamily. Although several myosin isozymes are present in hair bundles, the best-supported adaptation-motor candidate is myosin-1c (Myo1c).

METHODS, RESULTS AND DISCUSSION

To test the hypothesis that Myo1c participates in adaptation, we have applied a chemical-genetic strategy for selectively inhibiting its motor activity. We designed a mutation in Myo1c, Y61G, that greatly increased its sensitivity to inhibition by N^6-modified ADP analogs. Because the adaptation-motor complex likely consists of dozens of myosin molecules working together, immobilization of only a fraction of these molecules in an actin-bound state should be required to arrest adaptation. We therefore made transgenic mice that express Y61G-Myo1c, and found that slow adaptation is blocked when hair cells are dialyzed with N^6(2-methyl butyl) ADP (NMB-ADP).

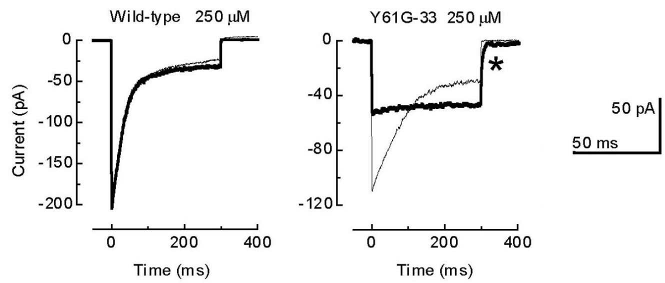

Figure 1: Block of adaptation in Y61G mice by NMB-ADP. Wild-type (left) or Y61G (right) hair cells were dialyzed with NMB-ADP; transduction and adaptation were assessed before (thin lines) and after (thick lines) diffusion of NMB-ADP to stereocilia. Asterisk, slowed closing kinetics.

SUMMARY

Myosin-1c has been proposed to mediate the slow component of adaptation by hair cells, the sensory cells of the inner ear. To test this hypothesis, we mutated tyrosine-61 of myosin-1c to glycine, conferring susceptibility to inhibition by N^6-modified ADP analogs. We expressed the mutant myosin-1c in utricular hair cells of transgenic mice, delivered an ADP analog through a whole-cell recording pipette, and found that the analog rapidly blocked adaptation to positive and negative deflections in transgenic cells but not in wild-type cells. The speed and specificity of inhibition suggests that myosin-1c participates in adaptation in hair cells.

REFERENCE

Holt, J. R, Gillespie, S.K.H., Provance, D.W., Shah, K., Shokat, K.M., Corey, D.P., Mercer, J.A., and Gillespie, P.G. (2002). *Cell* **108**, 371-381.

ACKNOWLEDGEMENTS

Thanks to my collaborators on this project: Jeff Holt, David Corey, Kevan Shokat, and John Mercer.

EXPERIMENTAL VERIFICATION OF THE ROLE OF INTERSTITIAL FLUID PRESSURIZATION IN THE FRICTIONAL RESPONSE OF BOVINE ARTICULAR CARTILAGE

Ramaswamy Krishnan and Gerard A. Ateshian[1]
Department of Mechanical Engineering, Columbia University, New York, NY 10027
[1]http://www.columbia.edu/~ga29 ateshian@columbia.edu

INTRODUCTION

Articular cartilage functions as the bearing material in joints and provides low friction and wear over a lifetime. The cartilage lubrication mechanism has not yet been fully characterized though several theories have been proposed. In previous studies (McCutchen, 1959; Forster and Fisher, 1996; Ateshian, 1997) it was hypothesized that interstitial fluid load support contributes significantly to the reduction of the frictional coefficient due to load transfer from the solid to the fluid phase of the tissue. This study provides experimental verification for a theoretical model based on this hypothesis (Ateshian, 1997; Ateshian et al., 1998). The specific aim of this study is to experimentally investigate the correlation between frictional response and interstitial fluid load support.

METHODS

Six cartilage plugs (diam. 6mm) were harvested from the femur and tibia of bovine knee joints obtained from a local abattoir. (2 joints, ages 3 & 24 months). Using a sledge microtome (model 1400; Leitz, Rockleigh, NJ), ~1mm of tissue was removed from the deep zone to produce samples 1.13±0.19mm thick, with the articular surface left intact. All specimens were stored at -20^{0}C in physiological buffered saline (PBS) solution. On the day of testing, each sample was thawed and equilibrated in PBS solution. The test protocol consisted of an unconfined compression creep test with intermittent sliding. Sliding motion was provided by a computer controlled translation stage (Model PM500-1L, Newport Corporation, CA). Normal loads were prescribed via a stepper micrometer (Model 18503, Oriel Instruments, CT) connected with a linear variable differential transformer to measure displacements (HR100, Shaevitz sensors, VA). All loads were measured with a multiaxial load cell mounted on the translation stage (Model 20E12A-M25B,JR3 Inc., CA). Fluid pressure measurements were made on the face opposite the articular surface (Soltz and Ateshian, 1998) using a microchip piezoresistive pressure transducer (NPC 1210 series; Lucas NovaSensor, CA). Data acquisition and control was performed using a personal computer equipped with a data acquisition card. The entire specimen and glass surface were immersed in 0.15M PBS solution, at room temperature, throughout the test. Cartilage-on-glass friction measurements were made under the configuration of unconfined compression creep with a prescribed load of 4.5N or 9N and simultaneous intermittent sliding over logarithmic time increments (range of translation ±2mm; sliding velocity 1mm/s). The test was terminated when the interstitial fluid pressure nearly reduced to zero. The normal force, frictional force, interstitial fluid pressure and displacement were monitored throughout this time. According to our model, the time-dependent friction coefficient μ_{eff} varies as a function of the interstitial fluid load support W^p/W as $\mu_{eff} = \mu_{eq}\left[1-(1-\varphi)W^p/W\right]$, where μ_{eq} is the equilibrium friction coefficient achieved when W^p/W =0, and φ is the fraction of the porous contact area where solid-to-solid contact occurs. Thus μ_{eff} is a linear function of W^p/W .

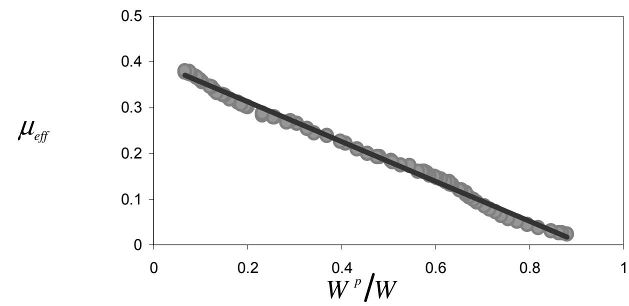

Figure 1: μ_{eff} vs. W^p/W for a typical specimen.

RESULTS AND DISCUSSION

The friction coefficient μ_{eff} was observed to increase with time, from a minimum value of μ_{min} =0.024±0.01 to a near equilibrium value of μ_{eq}=0.28±0.08, over a period of 10,600±7,500 s. Concomitantly, W^p/W decreased from a peak value of 93%±3% down to approximately 9%. Plotting μ_{eff} against W^p/W produced a linear response as shown for a typical sample in Figure 1. A linear fit to the experimental data yielded an average coefficient of determination of r^2=0.97±0.014 over all specimens. To our knowledge, this is the first study to report the measurement of interstitial fluid load support simultaneously with the frictional response of cartilage. The observed inverse linear correlation between these variables supports the hypothesis that interstitial fluid load support is a major mechanism governing the frictional response of articular cartilage. Any mechanism that compromises interstitial fluid pressurization, such as tissue fibrillation or degradation, is thus likely to adversely affect the frictional response.

REFERENCES

Ateshian, G.A. (1997). *J. Biomech. Eng.,* **119**, 81-86.
Ateshian, G.A., Wang, H., Lai, W.M. (1998). *J. Tribology,* **120**, 241-251.
Forster, H., Fisher, J. (1996). *Proc. IMechE*, **210 H**, 109-119.
McCutchen, C.W. (1959). *Nature,* **184**, 1284.
Soltz M.A., Ateshian G.A. (1998) *J Biomech,* **31**, 927-934.

ACKNOWLEDGEMENTS

National Institutes of Health, NIAMS AR43628.

BIOMECHANICAL MODELING OF ARTICULAR CARTILAGE: FROM MACROSCALE TO MICROSCALE

John Z Wu [1]and Walter Herzog[2]
[1]National Institute for Occupational Safety & Health, Morgantown, WV, USA., E-mail: jwu@cdc.gov
[2]Faculty of Kinesiology, The University of Calgary, Calgary, Alberta, Canada

INTRODUCTION

It is generally accepted that cartilage adaptation and degeneration, such as observed during osteoarthritis, is mechanically mediated. Experimental evidence suggests that cartilage deformation caused by mechanical loading is directly associated with deformation and volume changes of chondrocytes, and stress and pressure concentrations around the chondrocytes. Therefore, it is feasible to speculate that changes in cartilage loading are associated with changes in the stress/strain states of the corresponding chondrocytes, which in turn influence the in vivo biosynthetic activity of the cells, and so, regulate cartilage adaptation. Chondrocyte stresses cannot be measured experimentally, thus requiring a theoretical approach to obtain this information. The purpose of this presentation is to describe our efforts towards developing a biomechanical joint contact model, which predicts stress/strain state and chondrocyte deformation in articular cartilage under physiological loading conditions.

METHODS, RESULTS, AND DISCUSSION

Six years ago, we developed an analytical model of the static axi-symmetric joint contact mechanics with biphasic cartilage layers (Wu et al., 1996), based on an asymptotic solution by Ateshian et al. (1994). This approach extended Ateshian et al.'s model to more general cases, and could account for the interactions of curved convex and concave surfaces of different radii of curvature, and for the effects of changing articular cartilage dimensions and mechanical properties in the contact mechanics. Later, the solution for axi-symmetric joint surface geometry for static loading was generalized to account for dynamic loading (Wu et al., 1999a). In our previous joint contact models, the articular cartilage was considered to be uniform and isotropic, therefore, the deformation behaviour of chondrocytes and the effects of substructures on the global mechanical characteristics were not simulated.

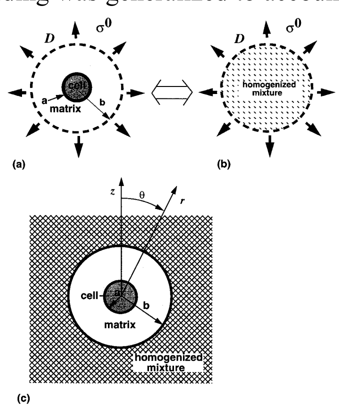

Fig. 1: *Cell-matrix composite treated as a homogenized equivalent matrix.*

In a theoretical or numerical joint contact model, it is technically intractable to take into account the effects of individual cells on the global mechanical behavior of cartilage. Therefore, we proposed a homogenization technique to account for the average effects of the distributed substructures on the global mechanical characteristics of cartilage layers. The approach involved three basic steps (Fig. 1)(Wu et al., 1999b, 2000): first, the cartilage was approximated as a macroscopically homogenized material having effective material properties; second, the mechanical behavior of cartilage in a joint was calculated using the homogenized model; and third, the solution of the time-dependent displacement and fluid pressure fields was used as the time-dependent boundary conditions for a microscopic sub-model (Fig. 1c), to obtain the average, time-dependent mechanical behavior of cells in different locations within the cartilage. In our preliminary model, cartilage was considered to be composed of extra-cellular matrix and small, spherical cells. The cartilage was assumed to be uniform, and the effects of collagen fibers were neglected. Both, cartilage matrix and cells, were treated as biphasic materials.

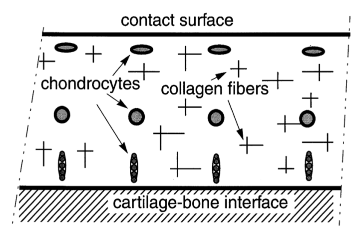

Fig. 2: *Anisotropic cartilage model*

In an improved homogenization procedure (Wu and Herzog, 2001), we tried to include the effects of anisotropy induced by the substructures in the cartilage. The articular cartilage was represented by a four-phasic composite, comprised of matrix, cell inclusion, and horizontal/vertical collagen fiber inclusions (Fig. 2). In the superficial layer, collagen fibers were assumed to be, predominantly, parallel to the contact surface; in the middle zone, 1/3 of the fibers were assumed vertical to the contact surface and 2/3 of the fibers were assumed parallel to the contact surface; and in the deep zone, collagen fibers were assumed to be vertical to the contact surface. The shapes of chondrocytes were assumed to vary from flat in the superficial zone, to spherical in the middle zone and columnar in the deep zone.

Using our analytical/numerical models, we predicted the mechanical responses of a joint to static and dynamic loading, the dynamic deformation behaviors of chondrocytes during an unconfined compression of a cartilage specimen, and the effects of microstructures on the global mechanical properties of articular cartilage.

SUMMARY

The goal of our research is to understand the growth, adaptation and degeneration of articular cartilage. However, before being able to tackle the problem of cartilage adaptation, we have to know the stress-strain states of chondrocytes and articular cartilage matrix for physiological loading conditions.

REFERENCES

Ateshian et al. (1994). *J Biomech*. 27:1347-60. Wu JZ et al. (1996). *J Biomech*, 29:1263-81. Wu JZ et al. (1999a) *J Biomech Eng*, 120:77-84. Wu JZ et al. (1999b) *J Biomech*, 32:563-72. Wu JZ et al. (2000). *Ann Biomed Eng*, 28:318-30. Wu JZ & Herzog W. (2001). Submitted to *J Biomech.*

RESPONSE OF THE CHONDROCYTE TO MECHANICAL STIMULI: PHYSIOLOGIC AND INJURIOUS COMPRESSION

Parth Patwari1[1] Moonsoo Jin[2], Michael DiMicco[4], Alan Grodzinsky[1,2,3,4]

Departments of [1]Electrical Engineering and Computer Science, [2]Mechanical Engineering
[3]Biological Engineering Division, [4]Center for Biomedical Engineering
Massachusetts Institute of Technology, Cambridge, MA 02139

INTRODUCTION

Cartilage is subjected to wide range of mechanical forces associated with joint loading *in vivo*. These mechanical forces can dramatically alter chondrocytes synthesis, assembly, and degradation of extracellular matrix (ECM). Recent studies suggest that there are multiple regulatory pathways by which chondrocytes in cartilage can sense and respond to mechanical stimuli. These pathways include upstream signaling and changes at the level of gene transcription, protein translation, post-translational modifications of newly synthesized macromolecules (Fig. 1). For example we recently observed that dynamic tissue shear deformation within the physiological range of 1-3% strain amplitude (with little macroscopic fluid flow) could stimulate synthesis of proteoglycans, total protein, and collagen relative to no-shear control explants. In addition, we found that dynamic tissue shear could activate the ERK1/2 pathway and caused an increase in mRNA levels for type II collagen and aggrecan core protein. In contrast, overload injury of cartilage can lead to chondrocyte death, direct matrix damage, and cell-mediated degradation of ECM. Interestingly, data from most in vitro models have thus far had limited success in demonstrating the steady progression of ezymatic matrix degradation that one might expect from models of osteoarthritis development. We have therefore focused on characterizing mechanical versus enzymatic degradation of ECM in conjunction with the effects of exogenous cytokines.

METHODS and RESULTS

Cartilage explants were prepared from the femoropatellar grooves of 1-2 week old calves as previously described and subjected to an injurious compression consisting of a ramp and hold compression to 50% strain at a strain rate of 1 s^{-1}.

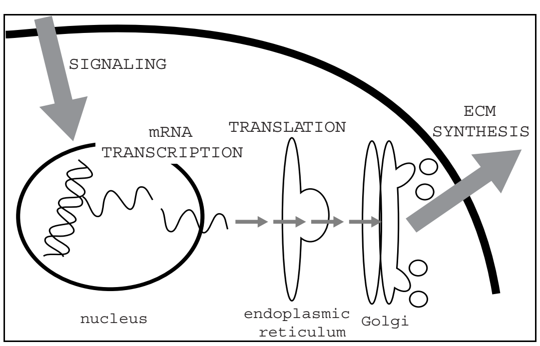

Fig. 1. Mechanotransduction pathways

After injury, explants were replaced in culture, and selected groups were subjected to addition of 1 or 10 ng/ml of human recombinant IL-1α. With no IL-1, GAG loss was slightly greater in injured tissue compared to controls by day 3. Addition of IL-1 to uninjured tissue caused a significant increase in GAG loss (Fig. 2). Explants subjected to IL-1 + injury showed significantly greater GAG loss compared to uninjured tissue with added IL-1.

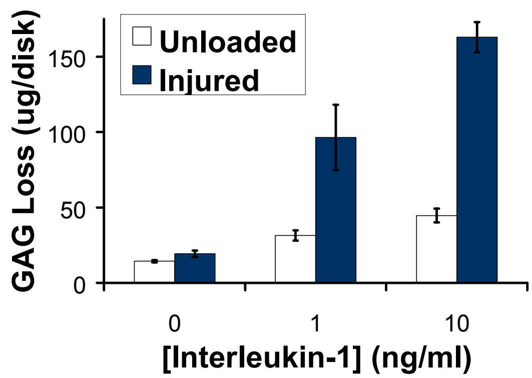

Fig. 2. Combined effects of injurious mechanical compression and addition of graded levels of IL-1α on loss of GAG from bovine cartilage explants

DISCUSSION

Chondrocyte mechanotransduction is critically important *in vivo* in the cell-mediated feedback between joint loading, the molecular structure of newly synthesized ECM collagens and proteoglycans, and the resulting functional biomechanical properties of cartilage. Here, Addition of IL-1 to injured cartilage was found to synergistically increase the loss of GAG from the tissue. It is likely that GAG release is mediated by a combination of cell-mediated processes and mechanical disruption of the ECM..

REFERENCES

Jin et al. (2002) *Trans 48th Orthop Res Soc*, p. 31.
Jin et al. (2001) *Archiv Biochem Biophys*, **395**:41-48
Patwari et al. (2001) *Clin Orthop Rel Res*, **391S**:61-71.

ACKNOWLEDGEMENTS

Supported by NIH Grant AR45779 and GlaxoSmithKline

MAGNETIC FIELD VISUALIZATION IN APPLICATIONS TO PULSED ELECTROMAGNETIC FIELD STIMULATION OF TISSUES

Maciej Zborowski[1], Ronald Midura[1], Alan Wolfman[2], Thomas E. Patterson[2], Yoshitada Sakai[1], Michael Ibiwoye[1], and Mark Grabiner[3], zborow@bme.ri.ccf.org

Departments of [1]Biomedical Engineering, ND20, and [2]Cell Biology NC10,
Cleveland Clinic Foundation, Cleveland, OH 44195
[3]School of Kinesiology, University of Illinois at Chicago, Chicago, IL 60608-1516

INTRODUCTION

Electromagnetic field visualization is important in multidisciplinary research on the molecular basis of therapeutic effects of pulsed electromagnetic fields (PEMF). We have compared classic PEMF representation by two-dimensional field lines and field magnitude contour plots (Schwinger 1998) with a field representation using three-dimensional field isosurfaces. Field simulations were performed for a clinically approved Spinal-Stim® Lite system (Orthofix Inc., McKinney, TX). The relatively simple coil system geometry and the predominantly dielectric properties of the surrounding medium (Foster 1989) allowed us to develop analytical expressions for the field and a closed-form PEMF model. Field isosurfaces, represented as three-dimensional solids, allowed for direct visualization of PEMF targeting of individual organs (lumbar spine), the extent of the therapeutic field value, and the directional field characteristics.

METHODS

The magnetic vector potential of a current-carrying loop is approximated by a sum of N finite-length current segments:

$$\boldsymbol{A}_N = \boldsymbol{A}_N(\boldsymbol{r},t) = \frac{\mu I(t)}{4\pi}\sum_{i=1}^{N+1}\frac{\boldsymbol{r}_{i+1}-\boldsymbol{r}}{\left|\boldsymbol{r}_{i+1}-\boldsymbol{r}\right|}\ln\frac{\left|\boldsymbol{r}_{i+1}-\boldsymbol{r}\right|}{\left|\boldsymbol{r}_{i}-\boldsymbol{r}\right|}\frac{\cos\varphi_{i+1}+1}{\cos\varphi_{i}+1}, \qquad \boldsymbol{r}_{N+1}=\boldsymbol{r}_1$$

where

$$\cos\varphi_i \equiv \frac{(\boldsymbol{r}_{i+1}-\boldsymbol{r}_i)\cdot(\boldsymbol{r}_i-\boldsymbol{r})}{\left|\boldsymbol{r}_{i+1}-\boldsymbol{r}_i\right|\left|\boldsymbol{r}_i-\boldsymbol{r}\right|}$$

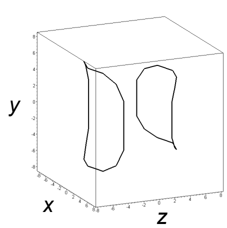

$$\cos\varphi_{i+1} \equiv \frac{(\boldsymbol{r}_{i+1}-\boldsymbol{r}_i)\cdot(\boldsymbol{r}_{i+1}-\boldsymbol{r})}{\left|\boldsymbol{r}_{i+1}-\boldsymbol{r}_i\right|\left|\boldsymbol{r}_{i+1}-\boldsymbol{r}\right|}$$

and $\boldsymbol{r}$ is the field position vector, $\boldsymbol{r}_i$ are the loop vertices position vectors, $I(t)$ is the total current intensity in the loop at time t, and μ is the magnetic permeability of the medium. The magnetic field vector:

$$\boldsymbol{B}_N = curl\ \boldsymbol{A}_N$$

RESULTS AND DISCUSSION

Results of the of the closed-form field model were compared with results of the field modeling software package for electrical engineering applications (Amperes 5.2) and was verified experimentally using a search coil (Model 49935, Magnetic Instrumentation, Indianapolis, IN) connected to an amplifier and signal integrator (Orthofix Inc., McKinney, TX) and a digital oscilloscope (Infiniium Oscilloscope Model 54810A, Agilent Technologies, Englewood, CO). Excellent agreement was obtained for $N = 14$. Momentary field lines show a pattern of a nearly-uniform field at the center of the coil system, a highly rotational field in the vicinity of the wire, and a dipolar field far from the coils, as expected, Fig. 1.

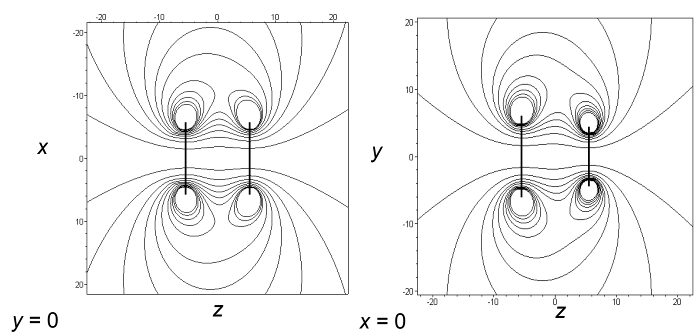

Fig. 1 Field lines of a closed-form PEMF model (flat coils).

The field contour plot of $B_N = 0.46$ mT at a peak PEMF signal was superimposed on the lumbar spine vertebrae, Fig. 2. The spinal vertebrae were modeled by circular discs. The field isosurfaces visualized well the spatial properties and the anatomical fit of the PEMF.

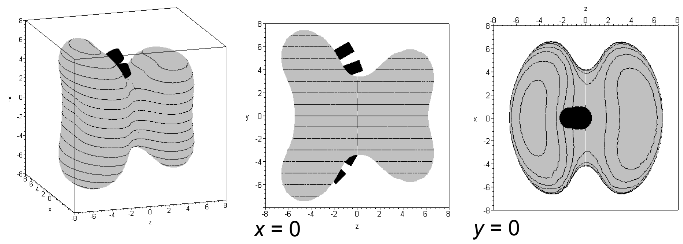

Fig. 2 Field isosurfaces of a closed-form PEMF model, fitted to lumbar spine vertebrae (curved coils configuration).

REFERENCES

Amperes 5.2, Integrated Engineering Software, Canada.
Foster K.R., Schwan H.P. *Critical Reviews in Biomedical Engineering* 17: 25-104, 1989.

ACKNOWLEDGEMENTS

We acknowledge the support of Orthofix, Inc., McKinney, TX.

PULSED ELECTROMAGNETIC FIELD-DEPENDENT STIMULATION OF PRE-OSTEOBLAST PROLIFERATION *IN VIVO*

Ronald J. Midura[1], Mark Grabiner[3], Michael Ibiwoye[1], Maciej Zborowski[1], Yoshitada Sakai[1], Thomas E. Patterson[2], and Alan Wolfman[2], midura@bme.ri.ccf.org

Departments of [1]Biomedical Engineering ND20, and [2]Cell Biology NC10,
Cleveland Clinic Foundation, Cleveland, OH 44195
[3]School of Kinesiology, University of Illinois at Chicago, Chicago, IL 60608-1516

INTRODUCTION

In double-blind studies, pulsed electromagnetic fields (PEMF) have been shown to enhance bone healing (Eyres & Kanis, 1996; Mammi, 1993; Mooney, 1990; Sharrard 1990). However, the biological mechanisms underlying this PEMF-enhanced bone healing are still not known. One hypothesis is that PEMF stimulates bone progenitor cells at the osteotomy site to enter mitosis, proliferate, and differentiate into new bone-forming cells (osteoblasts). We tested this hypothesis using a novel, bone nonunion model utilizing bilateral fibula osteotomies in 9 month-old rats. In each rat, the right hindlimb was treated with PEMF, while the left hindlimb was kept as an "in-animal" untreated control. Fibula osteotomy tissue was then assessed for the *in vivo* expression of Proliferating Cell Nuclear Antigen (PCNA).

METHODS

Osteotomy, Nine month-old, Sprague-Dawley male rats were anesthetized with Nembutal (60 mg/kg I.P.). A 5-6 mm segment was resected from the mid-fibula diaphysis using a rotary saw blade pre-cooled to 4° C with an irrigation solution. The wound was closed with sutures and a topical antibiotic then applied. ***PEMF,*** 21 days after surgery, right hindlimbs received daily 3 h treatments from a PhysioStim PEMF coil, while left hindlimbs were magnetically shielded. ***Histology,*** Fibula were fixed in 2% paraformaldehyde/TBS, pH 7.5 for 16 h at 4° C, decalcified with 300 mM EDTA in fixative solution for 4-5 days at 4° C, and cyrosectioned at 10 µm. ***PCNA staining,*** Sections were pretreated for 1 min. at 100° C in antigen unmasking solution (Vector Labs), blocked with 5% ovalbumin, treated with a 1:50 dilution of mouse anti-rat PCNA, (PC10, DAKO), and treated with a 1:200 dilution of Alexa Fluor 594-conjugated secondary antibody (Molecular Probes). Sections were mounted in Vectashield + DAPI (Vector Labs). Slides were examined using a Nikon Microphot FX epifluorescence microscope. *Cell proliferation index = % PCNA+ nuclei / total DAPI-stained nuclei.*

RESULTS AND DISCUSSION

In Vivo X-Ray Imaging – After 20-days treatment, 5 of 10 rats (50%) exhibited evidence of PEMF-dependent bone healing by longitudinal X-ray imaging (0.58 ± 0.2 mm of *new bone formed* at the PEMF-treated osteotomy versus 0.55 ± 0.3 mm *bone loss* at the contralateral untreated osteotomy). Three of ten rats (30%) showed marginal PEMF-dependent differences (0.2 ± 0.3 mm of new bone formed in PEMF-treated osteotomy versus 0.51 ± 0.4 mm bone loss on the contralateral side). Two of ten rats (20%) showed no PEMF-dependent effects on osteotomy healing by *in vivo* X-ray imaging.

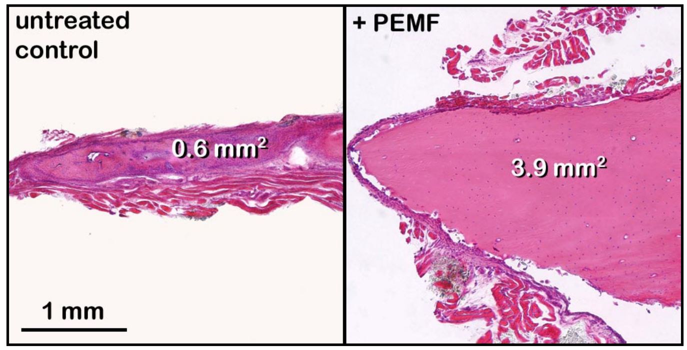

Fig. 1: H & E histology of the distal fibula osteotomy sites from a rat exhibiting a PEMF-dependent healing response.

Bone Tissue Histology – Proximal and distal fibula segments were recovered from the five rats that exhibited significant PEMF-dependent osteotomy healing, and were processed for decalcified bone tissue histology. A comparison of the mid-saggital, longitundal tissue sections from one of these rats is shown in Fig. 1; these results are typical for this group of rats. On the contralateral-untreated side, the osteotomy-end of the distal fibula appears thin and poorly stained by eosin. About 0.6 mm^2 of bone tissue area was measured within a 3 mm distance from the end of the bone. Compared to this contralateral control, the osteotomy-end of the distal fibula on the PEMF-treated side appears thicker and intensely stained by eosin. Close inspection revealed a uniform lamellar-quality bone tissue. About 3.9 mm^2 of bone tissue area was measured within a 3 mm distance from the end of the bone, which is 6.5-fold more than its respective contralateral control.

Cell Proliferation Index – Tissue sections adjacent to those shown in Fig. 1 were stained with an antibody that reacts specifically with rat PCNA. The cell proliferation index for PEMF-treated specimens (22/1945, or 1.1%) was ~20-fold higher than that for the contralateral untreated control (1/1887, or 0.05%). PCNA-positive nuclei were exclusively localized within the apical cell layers of the overlying periosteum in positions typically assigned to "pre-osteoblasts". PCNA-positive nuclei were not observed in other surrounding connective tissues or in osteocytes within the bone tissue.

REFERENCES

Eyres, KS and Kanis, JA. (1996) *Bone*, **18**, 505-509.
Mammi, GI, *et al*. (1993) *Clin Orthop.,* **288**, 246-253.
Mooney, VA. (1999) *Spine*, **15**, 708-712.
Sharrard, WA. (1990) *J Bone Joint Surgery*, **72B**, 347-355.

ACKNOWLEDGEMENTS

This work was supported by Orthofix, INC., McKinney, TX.

PULSED ELECTROMAGNETIC FIELD-DEPENDENT DIFFERENCESOF COLLAGEN PROCESSING IN PRE-OSTEOBLASTS

Thomas E. Patterson[1], Yoshitada Sakai[2], Mark Grabiner[3], Michael Ibiwoye[2], Ronald Midura[2], Maciej Zborowski[2], and Alan Wolfman[1], pattert@ccf.org

Departments of [1]Cell Biology NC10, and [2]Biomedical Engineering, ND20,
Cleveland Clinic Foundation, Cleveland, OH 44195
[3]School of Kinesiology, University of Illinois at Chicago, Chicago, IL 60608-1516

INTRODUCTION

The use of electromagnetic fields to promote healing in bone may be traced to the middle of the last century when the piezoelectric properties of dry bone (Fukada, E, 1995) and electrical properties of wet bone (Cochran, GV, et al 1968) were described. However, although evidence of altered cell activity following exposure to electromagnetic signals has been reported, the mechanisms by which electromagnetic fields are sensed, transmitted, and ultimately used by cells to influence physiologic activity have not been defined. Establishing causal linkages between responses of cells in a controlled cell culture environment and responses of cells in a complex *in vivo* organ environment is a daunting task. One common feature of cell culture and *in vivo* models is the presence of an extracellular matrix, which in osteoblast cells is composed mainly of Type I collagen. As part of a larger effort to understand the signaling pathway(s) by which cells respond to Pulsed Electro-Magnetic Fields (PEMF), we have detected a PEMF-dependent difference in the processing of Type I collagen in the mouse pre-osteoblast cell line, MC3T3-E1, subclone 30 (a non-mineralizing clone) (Wang, D, et al 1999).

METHODS

MC3T3-E1, subclone 30 was grown in α-MEM in 60 mm dishes until confluence. Cells were washed twice with Hank's Balanced Salt Solution, and grown in α-MEM supplemented with 50 μg/mL freshly prepared ascorbic acid. The next morning, at Time = 0, cells were exposed daily to 8 hours of Physio-Stim® (Orthofix, INC.) PEMF, followed by 16 hours without stimulation. Conditioned medium (CM) was collected from cultures at 0, 24 and 48 hours, protease inhibitors were added, and the Type I collagen forms were detected by Western blot after PAGE through 6% gels.

RESULTS AND DISCUSSION

Exposure of MC3T3-E1 subclone 30 cells to two, eight hour periods of Physio-Stim PEMF resulted in an approximately 2-fold reduction in the amount of Type I collagen processing intermediates in conditioned medium compared to unexposed control cells. Procollagen is proteolytically processed at both the amino and carboxy termini, and our results suggest that either the kinetics of one or both processing steps are decreased, or that the mature form of collagen is more efficiently incorporated into the extracellular matrix. We will discuss the implications of this result with respect to the collagen processing pathway.

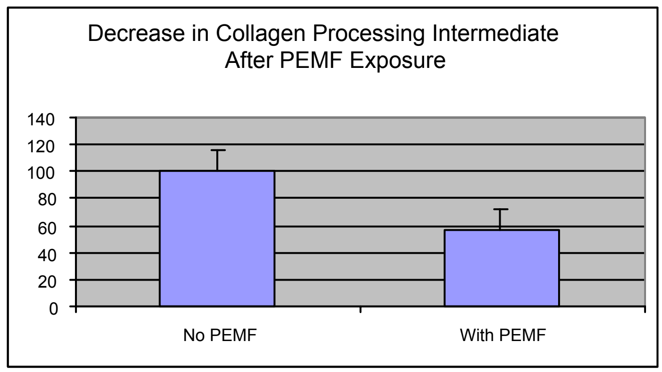

Figure 1: Effect of PEMF exposure (2 x 8 hours over two days) on amount of Type I collagen procesing intermediate in conditioned medium of pre-osteoblast cells.

REFERENCES

Fukada, E. (1995) *Biorheology*, **32**, 593-609.
Cochran GV, et al (1968) *Clin Orthop*.;**58**, 249-70.
Wang, D et al (1999) *J Bone Miner Res*, **14**, 893-903.

ACKNOWLEDGEMENTS

We acknowledge the support of Orthofix, INC., McKinney, TX

EFFECTS OF CUSTOM MOLDING AND POSTING OF FOOT ORTHOTICS ON LOWER EXTREMITY KINEMATICS

Anne Mündermann[1], Benno M. Nigg, and R. Neil Humble

Human Performance Laboratory, University of Calgary, Calgary, Alberta, Canada
[1]ahau@kin.ucalgary.ca

INTRODUCTION

Foot orthotics are frequently used as treatment of running injuries. Foot orthotics usually consist of a custom molded shell with some amount of intrinsic or extrinsic posting with the goal to align the skeleton. Their biomechanical efficacy is commonly evaluated in terms of reduction in maximum foot eversion during the stance phase of running. However, most studies found very small and non-significant differences between custom orthotic and no-orthotic conditions [1] and to date little is known about the contribution of custom molding and posting to such changes [2]. Thus, the purpose of this study was to determine the effects of custom molding and posting of foot orthotics on lower extremity kinematics.

METHODS

21 recreational runners participated in this study (12 female, 9 male; weekly mileage: 15-40 km). All subjects were pronators and were free of injuries for at least 6 months prior to the study. Subjects were examined and casted by a podiatrist. Neutral shells and custom orthotics with 6mm extrinsic varus posting were fabricated for each subject. The non-molded conditions were the control inserts (3mm EVA) and varus inserts (6mm medial wedge). The top layer of all four inserts conditions consisted of 3mm Spenco©. All inserts were placed in running sandals thereby allowing for skin marker placement directly on the heel. Kinematic data were collected for 100 running trials (4.0 ± 0.2 m/s) per subject per condition (total: 8400 trials) during nine experimental sessions on a 30-meter runway. Maximum foot eversion (β_{max}), time to maximum eversion ($t_{\beta max}$), and maximum eversion velocity ($v_{\beta,max}$) were calculated for each trial. Values for the control inserts were subtracted from values for varus inserts, neutral shell and custom orthotics for each subject and session to eliminate between-subject and between-session effects. MANOVA for repeated measures was performed to detect significant differences in the effects of the orthotic conditions (α = .05).

RESULTS AND DISCUSSION

Maximum foot eversion, time to maximum foot eversion, and maximum eversion velocity were affected by varus inserts, neutral shells, and custom orthotics (Figure 1). Maximum foot eversion decreased for the varus inserts by 1.7 ± 0.2° and increased for the neutral shells and custom orthotics by 0.8 ± 0.2° and 1.0 ± 0.3°, respectively. Wearing neutral shells or custom orthotics reduced time to maximum foot eversion by 2.0 ± 0.4% and 3.6 ± 0.6% and maximum eversion velocity by 20.9 ± 8.1°/s and 22.8 ± 9.2°/s, respectively. In contrast, wearing varus inserts increased maximum eversion velocity by 47.8 ± 9.4°/s. The results of this study showed that adding posting to neutral shells further reduces time to maximum foot eversion, however, maximum eversion velocity remains unaffected. Furthermore, extrinsic posting may have an effect on maximum foot eversion opposite to changes usually attempted. Based on the results of this study the function of custom orthotics to reduce maximum foot eversion has to be questioned. Further research should investigate the effect of custom molding and posting of foot orthotics on lower extremity integrity.

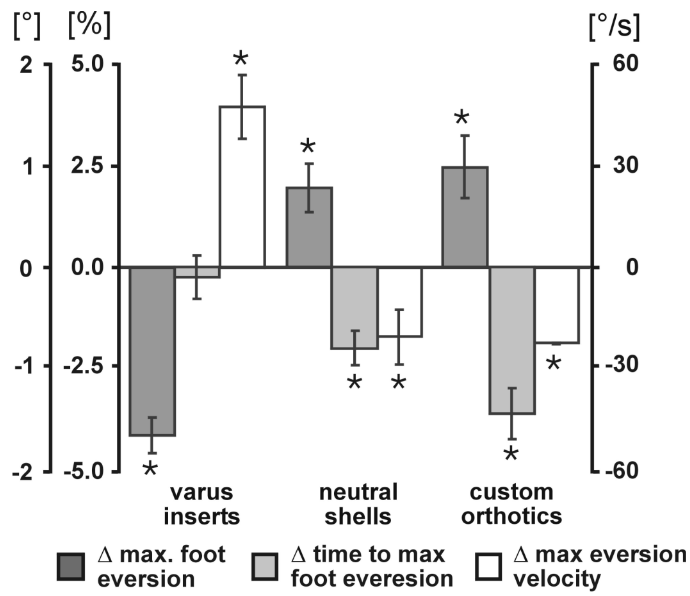

Figure 1: Mean differences (SE) in in maximum foot eversion, time to maximum foot eversion, and maximum eversion velocity of varus inserts, neutral shells, and custom orthotics compared to control inserts. * = significant difference (p < .05; n = 8).

REFERENCES

[1] Nawoczenski, D.A. et al (1995). *JOSPT*, **21**, 317-327.
[2] McCourt, F.J. (1990). *Chiropodist*, **45**, 239-243.

ACKNOWLEDGEMENTS

This work was supported by DFAIT (Canada), PFOLA, ISB, Paris Orthotics Ltd., and The Rockport Company. The authors would like to thank Maggie Andersen and Michelle New for their assistance in data collection.

FOOT FUNCTION AFTER THE SHORT TERM USE OF CUSTOM MADE FOOT ORTHOSES

Craig Payne

School of Human Biosciences, La Trobe University, Melbourne, Australia
c.payne@latrobe.edu.au

INTRODUCTION

Foot orthoses (FOs) are widely used in clinical practice for what is assumed to be biomechanical dysfunction. Many studies have previously investigated the immediate kinematic effects of FOs, but little is known about the longer term effects of FOs on foot function. The aim of this project was to determine foot function when custom FOs were first used and then again at 4 weeks.

METHODS

Consecutive patients needing rigid custom FOs at a podiatry teaching clinic were recruited for this project. Custom made FOs were made over a negative plaster cast of the foot in its defined neutral position. When orthoses were first issued, foot function was determined using the Pedar in-shoe pressure measuring system. Subjects were measured walking for approximately 10 steps in canvas shoes with and without their FOs. This was repeated again at approximately 4 weeks after the subjects had been using the FOs. Using the NovelWin software, 6 steps of each trial were averaged. Masks were created over the hallux, first metatarsal head, lateral forefoot, arch and heel areas to calculate mean pressure and the pressure tine integral in each masked area. Contact time for the averaged steps to check if velocity was consistent between trials.

RESULTS AND DISCUSSION

36 subjects were recruited (10 were lost to follow-up). The left foot of 26 subjects was used for the analysis. Mean time between baseline and follow up was 29.5 (±10.3) days. Repeated measures ANOVA showed that the velocity within subjects of each trial were consistent enough for further analysis ($p=0.31$). The results of the pressure variables are reported in Tables 1 & 2. Post hoc analysis showed, as expected, differences between the use of FOs and no FOs both at baseline and at follow up. However, no differences were found between foot function at baseline and at follow up without the use of FOs. Similarly, no differences were found in foot function at baseline and follow up with the use of FOs, indicating that no adaptation or changes occur to foot function in the parameters we measured over a 4 week period of using FOs.

SUMMARY

This study has shown that there are no adaptive changes in foot function in the short term in the parameters used. This does not rule out the possibility of longer term changes.

Table 1: Mean pressure

	No orthoses at baseline	Orthoses at baseline	No orthoses at follow up	Orthoses at follow up	ANOVA
Hallux	12.9 (±4.6)	13.7 (±4.6)	12.6 (±5.0)	13.5 (±5.1)	p=0.38
First MPJ	9.5 (±1.7)	9.2 (±2.4)	9.8 (±1.6)	9.3 (±2.1)	p=0.37
Lateral forefoot	13.1 (±1.9)	10.8 (±1.8)	13.5 (±2.1)	10.9 (±2.0)	p=0.000[a]
Arch	2.7 (±0.95)	4.2 (±1.2)	2.6 (±0.8)	4.0 (±1.3)	p=0.000[b]
Heel	11.9 (±2.0)	10.2 (±1.8)	12.3 (±1.7)	10.8 (±2.0)	p=0.000[c]

Table 2: Pressure time integral

	No orthoses at baseline	Orthoses at baseline	No orthoses at follow up	Orthoses at follow up	Repeated measures
Hallux	57.1 (±19.8)	64.6 (±19.4)	53.6 (±23.3)	65.5 (±24.8)	p=0.005[a]
First MPJ	64.4 (±15.1)	51.3 (±14.9)	64.1 (±14.7)	48.9 (±13.7)	p=0.000[b]
Lateral forefoot	87.8 (±19.8)	68.9 (±16.3)	87.7 (±19.3)	67.8 (±17.1)	p=0.000[c]
Arch	26.0 (±10.6)	39.7 (±10.6)	24.2 (±9.1)	36.7 (±10.8)	p=0.000[d]
Heel	63.1 (±10.7)	50.2 (±10.9)	60.6 (±11.0)	52.7 (±14.7)	p=0.000[e]

THE EFFECT OF FOREFOOT AND ARCH POSTING ORTHOTIC DESIGNS ON HALLUX-FIRST METATARSAL KINEMATICS DURING GAIT

Deborah A. Nawoczenski[1] and Paula M. Ludewig[2]
[1]Movement Analysis Laboratory, Ithaca College - University of Rochester Campus, Rochester, New York, USA
dnawoczenski@ithaca.edu
[2] Department of Physical Medicine and Rehabilitation, University of Minnesota, Minneapolis, MN, USA

INTRODUCTION

Although the forefoot has been implicated in foot pathologies, little is known about how forefoot kinematics, particularly hallux-first metatarsophalangeal (MTP) motion are influenced by orthotic use. A common orthotic design used to control excessive pronation incorporates the use of a medial post in the forefoot and/or rearfoot locations, with the purported goal of 'bringing the ground up to the foot' during gait. It is unknown whether this design actually restricts normal first metatarsal plantarflexion motion and hallux dorsiflexion during late stance. An alternative design is an orthotic which incorporates an elevated arch support in combination with first metatarsal plantarflexion. The theory behind this design is that normal first metatarsal plantarflexion and hallux dorsiflexion are facilitated. The purpose of this study was to examine the effect of two different types of orthotic designs on first MTP joint kinematics, and on the kinematic coupling between first MTP and rearfoot rotation during gait.

METHODS

Twenty subjects between the ages of 18 and 45 participated in the study. All subjects were classified as pronators based on a clinical orthopaedic examination. Two different orthotic designs were custom-molded using either 5/32" or 3/16" polyethylene, depending upon the subject's weight. One design incorporated an extrinsic rearfoot and forefoot post (Fig.1). The second pair had a high medial longitudinal arch without extrinsic posting (Fig.2). The Flock of Birds® electromagnetic tracking device was used to collect three-dimensional position and orientation data of three modeled rigid body segments (hallux, first metatarsal, and calcaneus, during the stance phase of walking (Nawoczenski, 1999; Umberger 1999). Transformation matrices were generated that related the assumed constant orientation of the sensors to the anatomically based local coordinate systems established for the hallux, first metatarsal, and calcaneus.

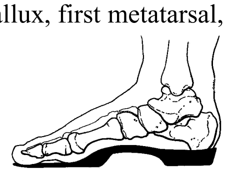

Figure 1

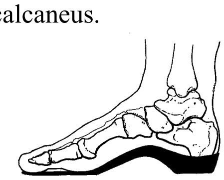

Figure 2

A Cardan angle system of three ordered rotations (x-z'-y'') was used to extract angular information of the hallux, first metatarsal and calcaneus. Subjects wore identical sports sandals for all test conditions.

RESULTS

A repeated measures ANOVA was used to assess differences between orthotic conditions: no orthotic, forefoot/rearfoot posted orthotic and arch orthotic during standing and walking. The mean of three trials was used in the analysis. Preliminary findings for peak hallux-1st MTP dorsiflexion are presented in Table 1.

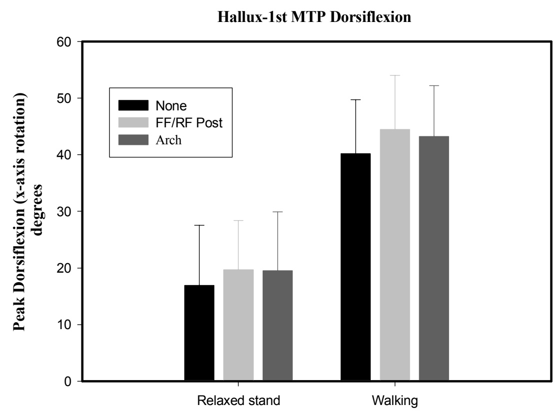

Table 1. None = no orthotic; FF/RF Post = posted orthotic and Arch = medial arch orthotic

Early findings suggest that 1st MTP dorsiflexion values increased under both orthotic conditions (mean 4°) with no differences detected between conditions. Similarities were also found for metatarsal head translations between orthotic conditions.

SUMMARY

Preliminary results indicate that an orthotic with a forefoot post does not have a negative effect on hallux-1st MTP kinematics during gait. Additional analyses are needed using a larger sample and to further test movement patterns under different orthotic conditions.

REFERENCES

Nawoczenski DA, Baumhauer JF, Umberger BR. (1999). *J Bone Joint Surg (Am)* **81**:370-376.
Umberger BR, Nawoczenski DA, Baumhauer JF (1999): *Clin Biomech* **14**:74-76.

ACKNOWLEDGEMENTS

This work was supported in part by the Orthopaedic Section of the American Physical Therapy Association.

CUSTOM AND SEMI-CUSTOM ORTHOTIC DEVICES: A COMPARISON OF REARFOOT MOTION CONTROL AND COMFORT

A.T. DeLeo[1], I. McClay Davis[1,2], R. Ferber[1]
[1]University of Delaware, Newark, DE, USA 19716 atdeleo@hotmail.com
[2]Joyner Sportsmedicine Institute, Mechanicsburg, PA, USA 17111

INTRODUCTION

The cost of custom fitted orthotic devices has led many patients to buy off-the-shelf inserts. In response to this, some orthotic laboratories have begun creating semi-custom orthotic devices as a more cost-effective solution. Semi-custom orthoses can be fabricated in several ways, but all involve matching a "mold-of-best-fit" to an individual. While the primary function of orthotic devices is motion control, comfort is an important feature for patient satisfaction and long-term use. No studies have compared the function or comfort of custom versus semi-custom devices. Therefore, the purpose of this study was to assess differences in rearfoot motion control and comfort of a between these two types of orthoses. Since this is an ongoing, double-blind randomized study, the devices cannot be differentiated. They are therefore referred to as device A and device B. It was hypothesized that there would be no difference in rearfoot peak eversion (EV), eversion excursion (EVEXC), and peak eversion velocity (EVVEL) between device A and B. Additionally, these rearfoot variables were expected to be significantly reduced from the no orthotic (NO) condition. Finally, it was hypothesized that there would be no significant differences in comfort between the two orthotic conditions.

METHODS

Six injury-free recreational runners have volunteered for the study thus far. Plaster casting of their feet was performed using a neutral non-weight bearing supine method. The casts were sent to a single orthotic laboratory where two devices were fabricated. The custom orthosis was fabricated based on the plaster casts and the semicustom orthosis was made based on foot measurements taken from the casts. Both devices were made with semi-flexible graphite and vinyl covers. Following a two week accommodation period, the subjects returned to the laboratory for data collection. Kinematic data were collected from 5 running trials for each of 3 conditions: NO, device A, and device B. Comfort was measured with a 100 mm visual analog scale (VAS) after each orthotic running condition. VAS scores for the heel, arch, edges, forefoot, and overall comfort were collected. A repeated measures ANOVA was used to compare the variables of interest between conditions ($p<0.05$).

RESULTS AND DISCUSSION

Device A provided greater rearfoot control (Figures 1 and 2) and greater comfort (Table 1) than device B. However, only EVVEL and heel comfort were significantly different. It is has been suggested by Smith et al, (1986) that EVVEL may be a more important indicator of orthotic control compared to EV or EVEXC. Device A did provide significantly greater rearfoot control than NO device for all three variables. There were no significant differences in comfort between the two orthotic conditions with respect to the overall comfort, arch, forefoot, and edges. However, device B was significantly less comfortable than device A in the heel region (Table 1).

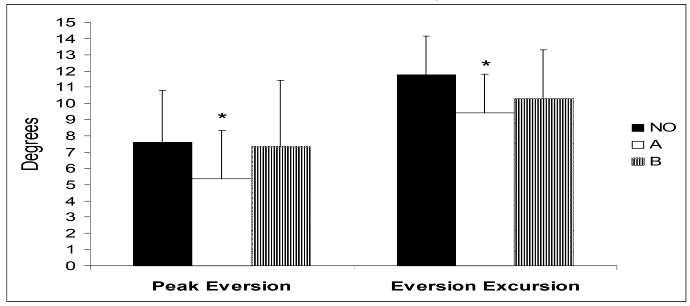

Figure 1: Peak EV and EVEXC for the three conditions. Note: *= sig. dif. from NO ($p<0.05$).

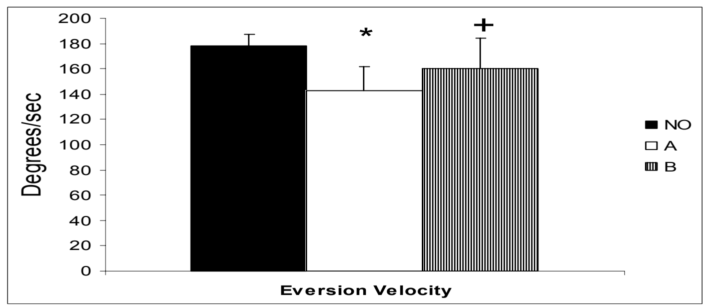

Figure 2: Peak EVVEL for the three conditions. Note: *= sig. dif. from NO; += sig. dif. from device A ($p<0.05$).

Table 1 Orthotic comfort (on 100 mm VAS)

	Heel	Arch	Forefoot	Edges	Overall
Device A	94.5	88.8	93.0	93.8	92.5
Device B	89.0*	86.6	87.0	91.0	87.6

SUMMARY

Based on these early results, there may be differences between the custom and semi-custom foot orthoses in terms of comfort and rearfoot control. These preliminary data need to be further validated with additional subjects as they are added to the study.

REFERENCES
Smith et al. (1986) *Podiat. Sports Med.*, 4, 227-233

ACKNOWLEDGEMENTS
We thank the Pauline Marshall Research and Education Foundation for funding of this project.

ARTERIAL BLOOD FILTRATION FOR THE PREVENTION OF ISCHEMIC STROKE

Baruch B Lieber[1], Ygael Grad[2],Boaz Nishri[2], David Tanne[3], Shmuel Einav[4], Ofer Yodfat[2]

[1]Center for Neurovascular Surgery and Stroke Research, University of Miami, FL. 33124
[2]MindGuard Medical Devices Ltd., Alon Hatavor 1 Caesarea Industrial Park, Israel 38900, ygael@mindguard.net
[3]Stroke Unit, Dept. of Neurology, Sheba Medical Center, Tel Hashomer, Israel 52621
[4]Dept. of Biomedical Eng. Tel Aviv University, Ramat Aviv Tel Aviv, Israel 69978

INTRODUCTION

Stroke is the third leading cause of death and the major cause of disability. In the US alone there are more than 730,000 stroke victims and 4.4 million stroke survivors annually [1]. Stroke is a syndrome of multiple etiologies. Emboli emerging from the heart, aortic arch and the large arteries, mainly carotids, account for about 60% of all stroke cases [2,3]. Atrial fibrillation (AF) is the most important precursor of embolic stroke. More than 2 million Americans have intermittent or sustained AF [4]. Protruding aortic arch atheroma (AAA), prevalent among the elderly, has emerged as an additional common cause of embolic stroke [5]. Plaques located in the aortic arch have been found in 60% of 60 years old patients with ischemic stroke. The association is particularly strong when the plaques are > 4 mm in thickness [6]. AF and AAA often coexist [7]. Currently, the treatment of choice for AF and AAA is anticoagulation with warfarin. The relative risk of stroke can be reduced by 70% in selected subgroups of patients with AF using anticoagulants [8]. However, anticoagulants are contraindicated in about 40% of patients over 65 years old [9]. Moreover, anticoagulation was repeatedly shown to be underused, about 30% of eligible patients [10], and quality of control in routine clinical practice is often poor. Carotid stenosis is a local disease accounting for 9% of stroke [2,3]. Current treatment modalities of carotid stenosis are carotid endarterectomy or carotid stenting, with or without a cerebral protection device. However, these treatments address only transient ischemic attacks and prevention of stroke attributable to carotid stenosis, but not to the prevention of stroke due to emboli originating from the heart or the aortic arch.

METHODS

A novel filtering device for stroke prevention is proposed. This permanent implant can prevent ischemic stroke by diverting proximally originating emboli that ascend in the carotid arterial system away from the anterior cerebral circulation to a non-hazardous territory, the systemic extra cranial circulation (Fig. 1). The diverter is of a tubular mesh like structure that is implanted at the carotid bifurcation traversing the common carotid artery into the external carotid artery (ECA) essentially jailing the internal carotid artery (ICA). The ECA supplies oxygenated blood to superficial extra cranial structures, an abundantly interconnected arterial network, insensitive to oxygenated blood supply. Therefore, emboli entering the ECA are typically asymptomatic and benign. In contrast, emboli entering the ICA often lodge in the middle cerebral artery or its branches, and are the main source of disabling embolic stroke in the oxygen starved brain territory within seconds.

RESULTS AND DISCUSSION

The feasibility of arterial filtration by a permanent implant without the possibility of filter-originated deleterious consequences was examined both in vitro and in vivo. The main issues with such an implant include the possibility of the filtering section being occluded, and the activation of cellular blood elements, particularly the platelets, by the implant. The preliminary in vitro results suggest that the activation parameter of the platelets is two orders of magnitude below the established customary value while the in vivo results in the swine model show that the filtering section of the implant remained patent up to four months post implantation.

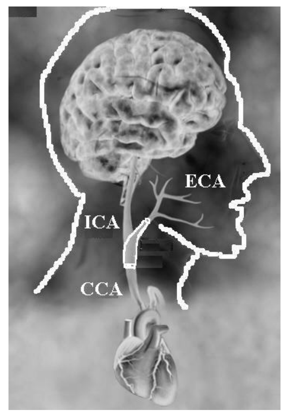

Fig. 1, Proximal emboli sources, and the carotid bifurcation

SUMMARY

Preliminary findings give hope to a novel therapy for patients at high risk of embolic stroke from proximal sources, and may serve as a new potential vascular approach for this devastating disease.

REFERENCES

1. Williams GR et al., 1999; *Stroke* **30**: 2523-2528
Heart and Stroke Statistical Update, 2001 Dallas, Tex, AHA.
2. Sacco et al, 1989,. Ann Neurol **25**: 382-390
3. Wolf et al., 1987 ;Arch Intern Med **147**: 1561-4.
4. Feinberg WN et al., 1995. Arch Intern Med **155**: 469-473
5. French Study of Aortic Plaques in Stroke Group, 1996 N Engl J Med **334**:1216-1221
6. Amarenco P et al., 1994; N Eng J Med **331**: 1474-9, 1994
7. The Stroke prevention in atrial fib. investigators committee on echocardiography, 1998. Ann Intern Med **128**: 639–647
8. Albers GW et al., 2001; Chest **119**(1 Suppl): 194S-206S
9. Bradley BC et al., 2000; Am J Cardiol **185**: 568-572
10. Gage BF et al., 2000; Stroke **31**: 822-827

ANALYSIS OF TOTAL CAVOPULMONARY CONNECTION FLUID DYNAMICS: EXPERIMENTAL STUDIES

Frakes, David H.[1], Lucas, Carol[2], Ensley, Ann E.[1], Healy, Timothy M.[1], Sharma, Shiva[3], Yoganathan, Ajit P.[1]
[1]School of Biomedical Engineering, Georgia Institute of Technology, Atlanta, GA, USA
[2]Dept. of Biomedical Engineering, University of North Carolina at Chapel Hill, Chapel Hill, NC, USA
[3]Egleston Children's Hospital, Atlanta, GA, USA

INTRODUCTION

The total cavopulmonary connection (TCPC) is a palliative surgical repair performed on children with a single ventricle (SV) physiology. The surgical procedure involves anastomosis of the superior and inferior vena cavae to the unbranched right pulmonary artery. This results in a complete bypass of the right side of the heart with the single ventricle driving blood through the circulatory system.

Much of the power produced by the univentricular pump is consumed in the systemic circulation. When power consumption is excessive, the result is decreased circulation of oxygenated blood throughout the body. Consequently the minimization of power loss in the TCPC is imperative for optimal surgical outcome. In order to achieve configurations that promote minimal power loss, underlying factors must be understood and controlled. We have performed a comprehensive fluid dynamic evaluation of the TCPC using experimental modeling and numerical simulation studies in order to elucidate and analyze these underlying factors. Information produced by this research can be used to facilitate the creation of optimal TCPC configurations in patients.

METHODS

Experimental Simulations: Custom crafted glass prototype models of the TCPC were selected with varying anastomosis geometries. Specifically models possessing different characteristics in terms of caval diameters, caval offsets, and pulmonary artery planarity were constructed. These models were used in conjunction with a steady flow loop capable of varying the total cardiac output and pulmonary artery flow ratios over a range of physiologic values. Models were investigated using pressure measurements, flow visualization, digital particle image velocimetry (DPIV), and magnetic resonance (MR) imaging. An image extracted from one flow visualization data set is displayed in Figure 1. Figure 2 displays a similar plane acquired with MR imaging.

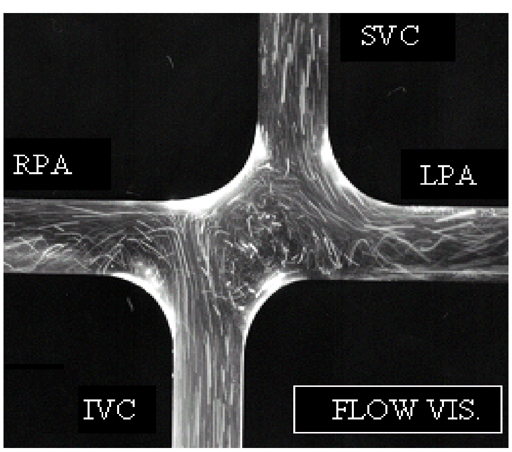

Figure 1. Flow visualization image of planar one-diameter offset TCPC model

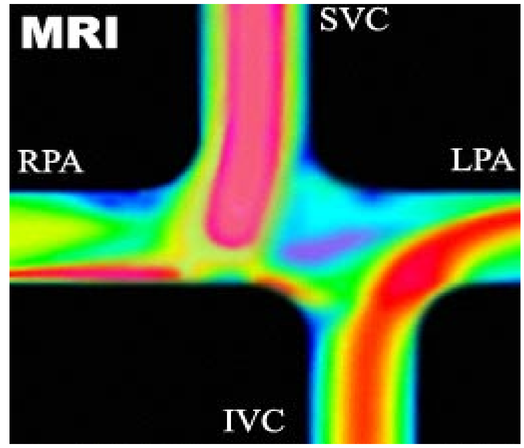

Figure 2. MR image of planar one diameter offset TCPC

Data acquired with these modalities were then used with control volume analysis to evaluate and study energy loss in TCPC model geometries. In all studies a blood analog fluid, composed of glycerine and water, with a kinematic viscosity of 3.5cSt was used.

Numerical Simulations: Numerical simulations were performed to supplement experimental data from TCPC models of varying anastomosis geometry. To this end, three-dimensional computational models were created and boundary conditions were specified to match experimental conditions. Energy loss information, obtained from control volume analysis and dissipation function analysis, was calculated and compared to experimentally determined power losses.

RESULTS AND DISCUSSION

Experimental and numerical energy losses compared well for similar TCPC models. Furthermore, velocity fields obtained from DPIV, flow visualization, and MR imaging showed similar flow patterns to those present in numerical simulations on a model-by-model basis. Based on these results conclusions regarding flow patterns deleterious to efficient circulation in the modified district could be identified and optimal TCPC design characteristics recommended. Numerical simulation combined with experimental modeling can provide an accurate prediction of flow conditions and subsequent energy losses in simple models of the TCPC. Future work will focus on continued development of the integrated methods described here, the use of more physiologic models, and further clinical interactions, all aimed at facilitating the surgical creation of optimal TCPC configurations.

LASER DOPPLER ANEMOMETRY IN THE EVALUATION OF MECHANICAL HEART VALVES' HEMODYNAMICS

Mauro Grigioni, Carla Daniele, Giuseppe D'Avenio and Vincenzo Barbaro
Laboratory of Biomedical Engineering, Istituto Superiore di Sanità, Roma, Italy
grigioni@iss.it

INTRODUCTION

Mechanical heart valves (MHVs) are nowadays very common devices in the clinical practice. This notwithstanding, they are still not free from problems (witnessed by the necessity of continuous anticoagulation therapy), which can be related mostly to their fluid dynamics: excessive turbulence shear stress levels must be avoided, in order to limit the incidence of hemolysis, platelet activation or other blood traumatic events. Laser Doppler anemometry (LDA) is, to date, the most powerful tool to investigate the finer details of a MHV's flow field and, thus, to evaluate its damage potential for blood components.

METHODS

A series of 19-mm (nominal diameter) bileaflet MHVs was tested in the aortic section of the Sheffied University pulse duplicator. A glassblown aorta, whose transparency is essential for LDA operation, was pressed against the valve's sewing ring. The tests were performed at a cardiac output of 6 l/min (exercise conditions): together with the small diameter of the valve, this constitutes the worst case for the generation of velocity gradients (and turbulence) for this kind of devices.
A two-color LDA system (Aerometrics, USA) was employed to measure the local velocity all along the width of the aorta, at four distances downstream of the valve plane.
The velocities were gate-time weighted, in order to prevent the *velocity bias* which typically affect LDA measurements. The elliptical filtering (Baldwin et al., 1993) was also used to discard occasional data corrupted by noise.
Principal stress analysis (Fontaine et al., 1995; Grigioni et al., 2000) was subsequently applied to the velocimetric data, in order to quantify the highest turbulence shear stress (TSS_{max}) in each considered point, independently from the particular TSS value $\rho\overline{uv}$ associated with the adopted coordinate system ($\rho\overline{uv}$ can obviously provide a gross underestimation of the actual mechanical load on blood particles).

RESULTS AND DISCUSSION

The highest TSS_{max} values we found are below the threshold for hemolysis which, after the data reported in Sallam and Hwang (1984) and in Grigioni et al. (1999) can be quantified to be at least 600 N/m^2. Since the limit conditions of the tests, this result underlines the good hemodynamics of bileaflet valves. Apart from hemolysis, however, some problem can still be expected from the observed turbulence levels, since also sublethal damage or platelet activation may have important clinical consequences, especially when artificial surfaces are in contact with blood. Nevertheless, the limited hemolytic potential of these devices is important, since this traumatic event, unlike other valve-related problems such as, e.g., thrombus formation, cannot be controlled pharmacologically after implantation.
The fine-scale investigation made possible by LDA enabled to bring to light some interesting features of bileaflet MHVs: it was seen for the first time, for instance, that the leaflets' curvature has a very important role in the turbulence development downstream of the valve, with a stabilizing effect with regard to the lateral jets. This effect might constitute the basis for further design improvements.
Due to the steady progress of echographic techniques, the possibility can be foreseen that turbulence measurements will be soon routinely performed also in vivo. In this view, we characterized the possibility of a monodimensional approach to the problem of determining the TSS_{max}, which is, generally, a quantity requiring three-dimensional measurements. Thus, in vivo measurements of the rms axial velocity u', together with the data obtained from our in vitro LDA measurements, could provide a simple assessment of the turbulence production and the hemolytic potential of an implanted bileaflet.

SUMMARY

The evaluation of a bileaflet heart valve is very complex, due to its hemodynamics, characterized by high velocity gradients. The use of an advanced technique such as Laser Doppler anemometry (LDA) enabled to quantify the hemolytic potential of several bileaflet valves; moreover, the effect of design features was studied, and useful parameters for future in vivo valve evaluations were proposed.

REFERENCES

Baldwin, J.T, Deutsch, S., Petrie, H.L. and Tarbell, J.M. (1993), *J. Biomech. Engng.,* **115,** 396-403.
Fontaine, A.A., Ellis, J.T., Healy, T.M., Hopmeyer, J. and Yoganathan, A.P. (1996), *ASAIO J,* **42**, 154-163.
Grigioni M., Daniele C., D'Avenio G., Barbaro V. (2000) *Ann. Biomed. Eng.,* **28**(2), 194-203
Sallam A.M. and Hwang N.H.C. (1984). *Biorheology,* **21**, 783-797
Grigioni M., Daniele C., D'Avenio G. and Barbaro V. (1999). *J. Biomech.,* **32** (10), 1107-1112.

PLATELET ACTIVATION IN FLOW THROUGH A STENOSIS MODEL: COMPARISON BETWEEN CFD AND CDPIV RESULTS

Sagi Raz*, Shmuel Einav*, Yared Alemu#, Danny Bluestein#

*Department of Biomedical Engineering, Faculty of Engineering, Tel Aviv University, Tel Aviv 69978, Israel, einav@eng.tau.ac.il
Department of Biomedical Engineering, Stony Brook University, Stony Brook, NY 11747, USA

INTRODUCTION

The activation of the hemostatic system is related to platelet activation, and may be initiated by a series of rheological and hemodynamic processes. Shear stresses and flow patterns (fluid dynamics factors), and concentration of coagulation factors and platelet agonists (biological factors) may lead to platelet activation and aggregation. As it passes through pathological geometries characteristic of arterial stenosis, a platelet is exposed to varying levels of shear stress. The cumulative effect of the shear stress level and the duration the platelet is exposed to it, will determine whether it is brought beyond its activation threshold [1,2]. Thus, time histories of individual platelets should be tracked down to locate the regions where activated platelets might be found and subsequently adhere to the wall.

METHODS

Numerical simulations (NS) of turbulent transient flow of non-Newtonian fluid through a 3D eccentric and axisymmtric models of a coronary stenosis was conducted. NS were validated by Continuous Digital Particle Image Velocimetry (CDPIV), in optically clear, scaled up (5:1) stenosis models. Turbulent trajectories of the platelets were computed using a stochastic model. The shear stress histories were quantified along the trajectories to determine their level of activation. Pertinent trajectories of the particles were established from the CDPIV measurements and their shear stress histories computed in the stenosis throat region. The experimental and numerical methods were conducted over a range of flow conditions, corresponding to the entire physiologically relevant range in coronary arteries.

RESULTS & DISCUSSION

The results indicated that platelets that were exposed to elevated stresses at the stenosis throat and then entrapped in the recirculation zone had a higher incidence of activation.

It was demonstrated that trajectories that exposed the platelets to the highest shear stress levels in the stenosis throat region, led them towards entrapment in the recirculation zone, where the shear stress levels decreased but exposure time increased. As platelet activation depends on the combination of shear stress and exposure time, this yielded higher incidence of platelet activation, compared to platelets flowing in the core flow region. The decrease in wall shear stress in the recirculation zone diminished the capacity of the geometry to embolize the deposits, allowed, at the same time for prolonged contact with the wall, and led to possible thrombus formation.

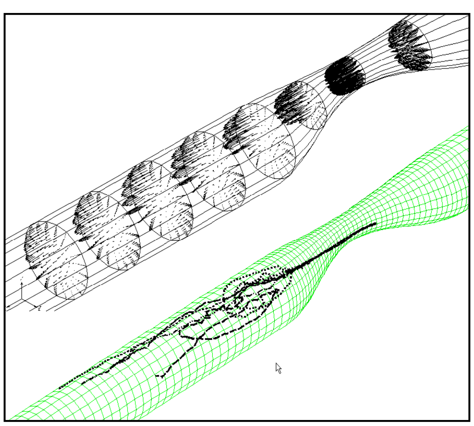

Fig. 1 Velocity vectors and turbulent platelet trajectories in a 3D model of 84% arterial stenosis (Re = 300)

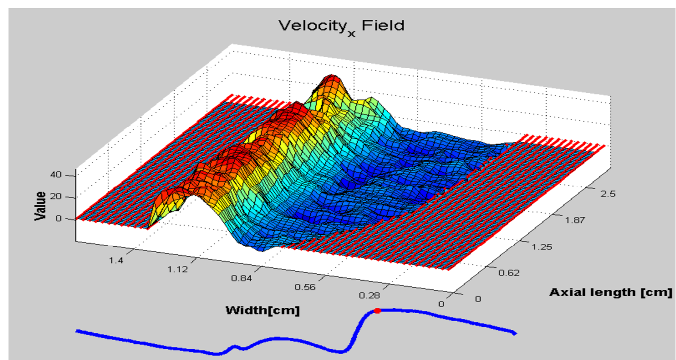

Fig. 2: The velocity field of 84% stenosis eccentric model (x-component) from CDPIV measurements, the time zone indicated on the flow waveform (Axis z is the velocity [cm/s]).

REFERENCES

1. Bluestein, D., Gutierrez, C., Londono, M. and Schoephoerster, R.T. (1999) Vortex shedding in arterial stenosis and its relevance to mural platelet deposition. *Annals of Biomedical Engineering,* Vol. 27:6, pp. 763-773.
2. Bluestein, D., Niu, L., Schoephoerster, R.T. and Dewanjee, M.K. (1997) Fluid mechanics of flow through a stenosis: relationship to the development of mural thrombus. *Annals of Biomedical Engineering*, Vol. 25, No. 2, pp. 344-356

ACKNOWLEDGMENTS

The work was supported by a grant from the United State-Israel Binational Science foundation (BSF).

FLOW PATTERNS AND PREFERRED SITES OF INTIMAL THICKENING IN END-TO-END AND END-TO-SIDE ANASTOMOSED ARTERIES

Takeshi Karino[1], Hiroyuki Ishibashi[2] and Makoto Sunamura[3]

[1]Research Institute for Electronic Science, Hokkaido University, Sapporo, Japan
[2]First Department of Surgery, Aichi Medical University, Aichi, Japan
[3]2nd Department of Surgery, Tohoku University, Sendai, Japan
karino@bfd.es.hokudai.ac.jp

INTRODUCTION

It is suspected that flow disturbances created by the geometric irregularity of the vessel wall at sites of anastomoses are responsible for post-operative narrowing and occlusion of anastomosed vessels through the development of intimal hyperplasia. However, no direct correlation has been established between the flow and the exact sites of intimal hyperplasia. Hence we have studied the relationship between the flow and preferred sites of wall thickening in vessels that have undergone various types of anastomotic procedures.

MATERIALS AND METHODS

Adult mongrel dogs weighing from17 to 45 kg were used as subjects for arterial reconstructive procedures. Under general anesthesia with Nembutal, both the left and right femoral arteries were exposed and one of the following 3 types of anastomosis was performed on both femoral arteries: (i) 90-degree or 45-degree end-to-end anastomosis, (ii) interposition with either a saphenous vein or a jugular vein, (iii) bypass grafting with either a saphenous vein or a common carotid artery. Anastomotic procedures were carried out using either a 7-O non-absorbable suture (Surgilene: a monofilament polypropylene suture, Sianamid Canada Inc., Montreal, Canada) or a 7-O absorbable suture (PDS : a monofilament polydioxanone suture, Ethicon Inc., Somerville, NJ) and the techniques of continuous over-and-over intramural stitching.

The dogs were kept alive for 3 or 6 months for recovery and healing, and then sacrificed. The vessel segments which had undergone anastomotic procedures were harvested keeping their original lengths in vivo, fixed under physiological perfusion pressure, dehydrated with ethanol, and finally rendered transparent by suspending them in oil of wintergreen (methyl salicylate) containing 5% ethanol. To visualize the flow in these vessels, dilute suspensions of 30 to 350-µm diameter polystyrene microspheres in oil of wintergreen were subjected to a steady or pulsatile flow through the vessel, and the behavior of individual tracer particles was photographed on 16-mm cine films. The developed films were subsequently projected onto a drafting table, and the movements of individual tracer particles were analyzed frame by frame to obtain detailed flow patterns and distributions of fluid velocity and wall shear rate (shear stress) in various regions of these vessels under normal physiological and altered (pathological) conditions.

RESULTS AND DISCUSSION

It was found that a definite correlation exists between the preferred sites of intimal thickening and the regions of slow recirculation flows with low wall shear stresses. In both 90-degree and 45-degree cut and anastomosed vessels, intimal thickening developed only in those vessels in which formation of slow recirculation flows was observed. It was also found that although a pronounced and localized intimal thickening developed in 45-degree anastomosed vessels, the degree of circumferential constriction caused by both surgical procedures and development of intimal thickening was much milder in 45-degree than 90-degree anastomosed vessels. In vein graft-interposed vessels, anastomotic intimal thickening was found at the distal anastomosis in saphenous vein-interposed vessels as shown in Figure 1 and at the proximal anastomosis in jugular vein-interposed vessels where, in both cases, a large recirculation zone was formed because of a sudden enlargement of the vessel lumen caused by mismatching of vessel diameters. In bypass-grafted vessels, a large recirculation zone was formed at the dead end of the partially or totally occluded host artery adjacent to the flow divider of the bypass, at the toe of the bypass graft, and the distal mouth of the host artery, where the bypass met the host artery. Intimal thickening was found at the proximal leading edge (opposite the flow divider), distal edge (toe) of the bypass, and on the floor of the host artery opposite the flow divider and the distal apex of the bypass. These areas well corresponded to the regions of slow secondary and recirculation flows where wall shear stresses were low.

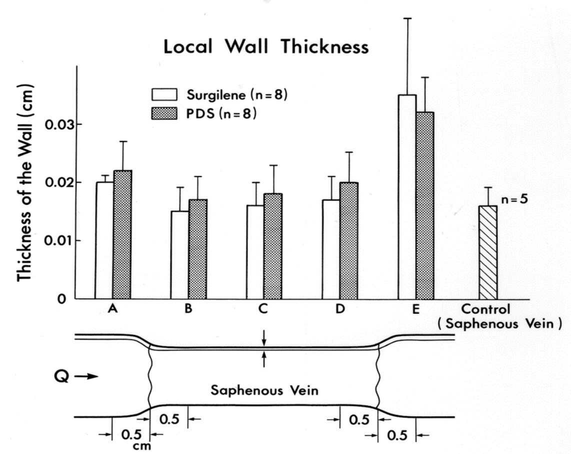

Figure 1: Distribution of wall thickness in a saphenous vein-interposed dog femoral artery.

DISSOCIATION OF PECAM-1/Gq WITH TEMPORAL GRADIENTS IN SHEAR STRESS

Laurent Loufrani[1], Charles White[1], Guang-Liang Jiang, [1] and John A. Frangos[1,2]

[1]Department of Bioengineering, University of California-San Diego, La Jolla, CA and
[2]La Jolla Bioengineering Institute, La Jolla, CA (www.ljbi.org)

As the inner lining of the vessel wall, vascular endothelial cells are poised to act as a signal transduction interface for hemodynamic forces. The molecular mechanisms of the primary force sensing elements of the cell, and the cascade of events that are involved in the mechanochemical signal pathway remain unclear. Activation of the G protein Gαq and the phosphorylation of platelet endothelial cell adhesion molecule-1 (PECAM-1) have been reported to be involved in the early events of shear-induced signaling pathways. Using immunofluorescence and co-immunoprecipitation techniques, we demonstrate here for the first time that Gαq and PECAM-1 co-localize as a complex at the cell-cell junction in primary human umbilical vein endothelial cells. Temporal gradients in shear stress lead to a rapid disassociation and re-association of the Gαq-PECAM-1 complex within 15 sec (0.65 ±0.059 ratio G□q/PECAM-1 versus sham control), whereas slowly transitioning fluid flow devoid of temporal gradients does not disrupt the complex (1.04 ±0.08 ratio Gq/PECAM-1 versus Sham control). Inhibition of protein kinases and tyrosine kinases completely eliminated impulse flow induced G□q-PECAM-1 disassociation and PECAM-1 phosphorylation. Taken to together, this data may represent a missing link between the primary force sensing elements of the cell, and the downstream mechanochemical transduction pathway.

A ROLE FOR MOLECULAR DYNAMICS OF ENDOTHELIAL CELL LIPIDS IN MECHANOTRANSDUCTION

Peter J. Butler[1], Benjamin P. Bowen[2], Neal Woodbury[2]

[1]Department of Bioengineering, Pennsylvania State University, University Park, Pennsylvania, USA
[2]Department of Chemistry and Biochemistry, Arizona State University, Tempe, Arizona, USA

INTRODUCTION

Endothelial cells (ECs) form the inner lining of the blood vasculature and are therefore exposed to shear stress (tau), the tangential component of hemodynamic forces. Shear stress exacts potent changes in EC biology, possibly via EC-membrane perturbations, with consequent influences on vascular health. The role in mechanotransduction by ECs of shear-induced changes in membrane lipid dynamics is explored.

METHODS

The cell membrane's proximity to blood flow makes it a candidate shear-sensitive system. By adapting a confocal laser scanning microscope for measurements of fluorescence recovery after photobleaching (confocal-FRAP), we made, for the first time, quantitative, two-point, sub-cellular measurements of membrane fluidity (as quantified by the lipid lateral diffusion coefficient) on the apical membrane of ECs while they were subjected to shear stress (fig. 1). Bovine aortic endothelial cells (BAECs) were grown to confluence on glass, stained with DiI C16, and exposed to step- and ramp-changes in shear (max tau=10 dynes/cm2).

We now use membrane phase-specific lipoid dyes to probe the effects of shear stress on membrane sub-domains existing in liquid or liquid-ordered phases. Confocal, molecular spectroscopic tools are used to measure fluorescence lifetimes, polarizations, and rotations of lipoid molecules (DiIs) in the membranes of confluent BAECs which are subjected to membrane-perturbing agents including shear stress.

RESULTS AND DISCUSSION

Previously, we have used confocal-FRAP to investigate the time- and position dependence of the effects of tau on EC-membrane lipid dynamics (Butler, et al, 2001a,b). We showed: (i) shear stress induces a rapid, spatially heterogeneous, and time-dependent increase in the lateral diffusion of a fluorescent lipoid probe in the BAEC membrane (fig. 1) (ii) the location, magnitude, and persistence of these shear-induced increases in membrane fluidity depend on the shear magnitude and the rate of change of shear, and (iii) shear stress elicits a secondary (7 min) increase in membrane fluidity.

We now present evidence for phase specificity of lipoid dyes (DiIs) in confluent endothelial cells using confocal molecular

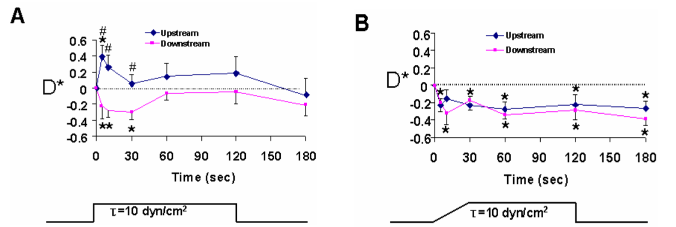

Figure 1: Effects of **A** step-shear and **B** ramp-shear on the normalized diffusion coefficient of DiI C16–stained BAEC membranes. Blue diamonds and pink rectangles represent simultaneous measurements on the portion of the cell upstream and downstream of the nucleus, respectively (from Butler, 2001b).

spectroscopy (fig. 2). Our measurements of fluorescence lifetime and polarization are consistent with the partitioning of DiI C12 (a carbocyanine dye with dual 12-carbon alkyl chains) in a liquid phase, and of DiI C18 (a carbocyanine dye with dual 18-carbon alkyl chains) in the liquid-ordered or gel phase. These properties are used to probe the spatial and temporal aspects of the effects of shear stress on membrane sub-domains.

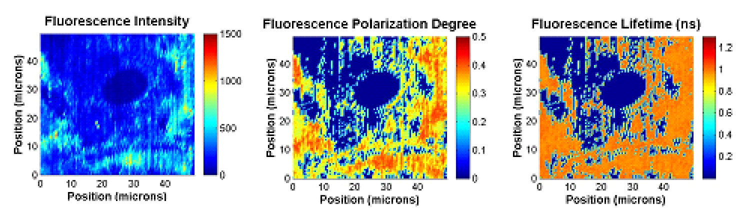

Figure 2: Spatial plots of fluorescence intensity, polarization, and lifetime of DiI C18 incorporated into BAEC membranes.

SUMMARY

Fluorescence spectroscopic tools along with membrane-phase specific lipoid dyes allow the detection of position dependence of shear effects on the EC membrane and the quantitative measurements of changes in lipid dynamics which have been correlated to changes in biochemical processes in ECs.

REFERENCES

Butler, et al., Am J Physiol Cell Physiol. 2001, 280(4): C962-9

Butler, et al., FASEB J. Dec. 14, 2001, 10.1096/fj.01-0434fje

CHANGES IN THE PROPERTIES OF THE ENDOTHELIAL GLYCOCALYX AFFECT THE DISTRIBUTION OF SHEAR STRESS AND SHEAR RATE ON ENDOTHELIAL CELLS

Wen Wang
Medical Engineering Division, Department of Engineering, Queen Mary, University of London, London, UK
wen.wang@qmul.ac.uk

INTRODUCTION

It is well established that shear stress on vascular endothelial cells, imposed by the blood circulation, plays an important role on vascular biology and pathology (e.g. Davies, 1995). Little attention, however, has been given to the function of the endothelial glycocalyx, which forms a continuous surface layer on endothelial cells, and the role it plays in these processes. As it represents the interface between the flow and the endothelium, the glycocalyx is likely to affect the permeability of the endothelium to solutes, such as plasma proteins. Changes in properties of the endothelial glycocalyx are also likely to alter the magnitudes of the shear stress and the shear rate, and more importantly, the way in which the stress is imposed on the cell membrane.

METHODS

At a microscopic level, fluid flow within the endothelial glycocalyx introduces shear stresses on luminal surfaces of the cell membrane via two different routes: 1) the stress imposed by fluid movement directly on the cell membrane, and 2) the drag force transferred by fiber-branches of the glycocalyx to the endothelial cell. To gain insight into the distribution of these contributing factors to the total shear stress on endothelial cells, we have developed a theoretical model based on a binary mixture theory and modelled the endothelial glycocalyx as a surface layer of fiber matrix (Wang and Parker, 1995; Wang and Michel, 2000). The matrix contains both solid and liquid phases and is assumed to be uniform. It has a thickness, ε, volume fraction of liquid is ϕ, the apparent viscosity of the liquid in the matrix is μ and the drag coefficient between the solid and liquid phases is κ. Mass conservation and momentum equations for the matrix are solved asymptotically. Flow and stress distributions within the matrix as well as on the cell membrane are calculated.

RESULTS AND DISCUSSION

When the structure of the glycocalyx is altered, e.g. by enzyme digestion, the thickness, ε, or the volume fraction of fibers in the matrix, $1-\phi$, or both will be reduced. From a force balance analysis, the overall (i.e. total) shear stress on the luminal surfaces of endothelial cells, τ, remains unchanged regardless of the structural alterations of the glycocalyx layer, provided that flow conditions in the vessel are kept constant. However, the stress that is imposed on the endothelial cells by the direct 'pulling' of fibre branches of the glycocalyx may be reduced significantly. This 'pulling' stress, through branches of the endothelial glycocalyx, can be expressed as $\tau_s = \lambda\,\tau$, where λ is a constant parameter which depends on the properties of the glycocalyx and the radius of the vessel, R. λ has an asymptotic expression,

$$\lambda = 1 - \phi + \phi\,(1 - \phi)\ \{1 - \cosh^{-1}(\xi) + 2\varepsilon/r\ [1 - \tanh(\xi)/\xi]\},$$

with the intermediate parameter $\xi = (\kappa/\mu)^{1/2}\varepsilon$. Shear rate at the cell membrane due to flow inside the fiber matrix can be expressed as $\gamma = \theta\ \Gamma$, where Γ is the wall shear rate in the absence of the fiber matrix and θ is a constant depending on the structure of the glycocalyx,

$$\theta = \phi\ \{\cosh^{-1}(\xi) + 2\varepsilon/R\ [\tanh(\xi)/\xi]\}.$$

To demonstrate how changes of the glycocalyx, e.g. changes in the drag parameter ξ and the volume fraction of liquid, ϕ of the fiber matrix, affect the 'pulling' stress, τ_s and shear rate, γ at the cell membrane, we present in Figure 1 variation (in contours) of the λ and θ with ξ and ϕ, respectively.

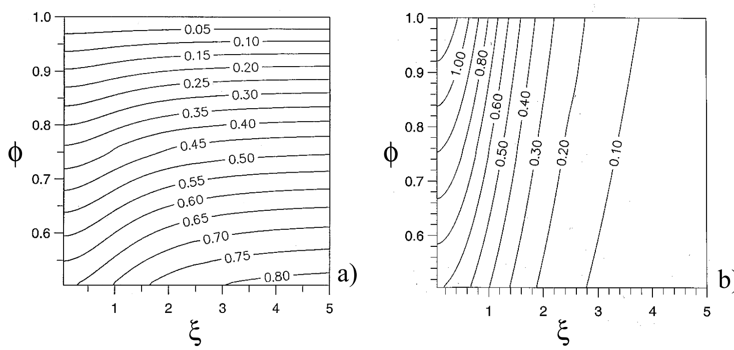

Figure 1. Variation of λ (in a) and θ (in b) against ξ and ϕ.

It is shown that, as the property of the glycocalyx changes, fluid shear rate at the endothelial membrane alters significantly (as shown in Figure 1b). In addition, there are associated changes in the stress due to pulling of the glycoproteins (in Figure 1a), despite the presence of a constant total shear stress.

SUMMARY

The model enables us to analyse how changes in the properties of the glycocalyx alter the shear rate and the "pulling" stress on the endothelial cell membrane. It may be used to interpret experiments investigating the role of the glycocalyx in shear induced responses of the endothelium.

REFERENCES

Davies, PF (1995). *Physiol Rev* **75**: 519-560.
Wang, W and Parker, KH (1995). *J Fluid Mech* **283**: 287-305.
Wang, W and Michel, CC (2000). *J Vas Res* **38** (2): 187.

ACKNOWLEDGEMENT

This work was funded by the Wellcome Trust.

THE BIOMECHANICS OF THE WEIGHTBEARING KNEE

Braden Fleming [1], Bruce Beynnon [1], Per Renstrom [2], Robert Johnson [1]

[1]McClure Musculoskeletal Research Center, Department of Orthopaedics & Rehabilitation,
University of Vermont, Burlington VT 05405; Braden.Fleming@uvm.edu
[2]Section of Sports Medicine, Division of Orthopaedics, Karolinska Hospital, Stockholm Sweden

INTRODUCTION

The musculature and articular contact forces play an active role in maintaining knee joint stability. Thus, biomechanical investigations of knee function should be performed *in vivo* where physiological loading conditions can truly be examined. Cadaver studies have shown that compressive loads on the knee reduce laxity relative to the non-weightbearing state. These studies support the popular belief that the compressive load produced by bodyweight stabilizes the knee and protects the ACL by forcing the articular surfaces together and inducing co-contraction of the hamstrings and quadriceps muscles. Although there is a reduction in knee laxity with the application of a compressive load, the cadaver model of Torzilli et al (1994) also found that there was an anterior shift of the tibia relative to the femur as the knee made the transition from non-weightbearing to weightbearing. This finding questions the protective function of weightbearing. We designed two experiments to compare the biomechanical response of non-weightbearing and weight-bearing knees *in vivo*. These experiments involved measurements of tibio-femoral kinematics in ACL-deficient and ACL-intact knees (Beynnon et al 2002), and direct measurements of ACL strain in the ACL-intact knee (Fleming et al 2001a).

EXPERIMENTS

Experiment 1: The objective of this study was to measure the A-P translation of the tibia during the transition from non-weightbearing to weightbearing in eleven subjects with a normal and a contralateral ACL-deficient knee. The subjects were positioned on a custom loading fixture with their muscles relaxed and no compressive load applied across the knee. The knee was positioned at 20^o of flexion to simulate the slightly flexed, double-legged stance position. A lateral radiograph of the knee, with the posterior aspects of the femoral condyles superimposed, was obtained to document the position of the tibia relative to the femur. A compressive load equal to 40% bodyweight was then applied to each foot, and a second radiograph was obtained to document the change in position of the tibia relative to the femur. The transition from non-weightbearing to weightbearing produced a significant increase in the mean ± 1 standard deviation of the anterior translation of the tibia relative to the femur (3.4 ± 2.6 mm) for the ACL-deficient knee. These values for the ACL-intact knee were significantly less (0.8 ± 2.2 mm; $p<0.01$).

Experiment 2: The objective of this study was to measure the ACL strain response of the ACL-intact knee during the transition from non-weightbearing to weightbearing. A strain transducer (DVRT; MicroStrain, Inc., Burlington VT) was implanted on the anteromedial band of the ACL in eleven subjects. A device similar to that used in first experiment was used to apply the compressive loads to each foot (40% bodyweight) with the knee at 20^o of flexion. A significant increase in the mean ± 1 standard deviation for the ACL strain values were observed as the knee made the transition from non-weightbearing (-2.0 ± 1.78%) to weightbearing (2.1 ± 1.78%). These values were significantly different ($p < 0.01$).

CONCLUSIONS

The application of bodyweight across the knee joint causes the tibia to shift anterior relative to the femur in the ACL-deficient knee (Beynnon et al 2002). The four-fold increase in anterior translation of the tibia for the knees with ACL tears compared to the contralateral side is a concern because it is substantially greater than the 95% confidence limits for the side-to-side differences in anterior-posterior knee laxity values that are obtained from subjects with normal knees. This observation could explain, at least in part, one of the mechanisms that could initiate damage to the meniscus and articular cartilage in subjects that have suffered an ACL tear. The direct measurements of ligament strain verify that the anterior shift of the tibia that occurs during weightbearing strains the ACL in the intact knee, at least when the knee is near extension (Fleming et al 2001a). This shift is most likely due to a combination of factors: 1) the dominance of the quadriceps muscles even though the quadriceps and hamstrings are co-contracted in this position (Beynnon et al 1995; Torzilli et al 1994), 2) the activity of other muscle groups that span the knee (i.e. the gastrocnemius muscle) (Fleming et al 2001b), and 3) the orientation of the contact force vector relative to the inclination of the tibial plateau (Torzilli et al 1994). These data have important clinical ramifications in the development of rehabilitation protocols following ACL reconstruction since the anterior shift of the tibia produces strain, or load, in the injured ACL or healing ACL graft. This mechanism has been previously thought to protect the ACL.

REFERENCES

Beynnon B.D. et al (1995). *Am J Sports Med* **23**, 24-34.
Beynnon B.D. et al (2002). *J Orthop Res* (In press).
Fleming, B.C. et al (2001a). *J Biomech* **34**, 163-170.
Fleming, B.C. et al (2001b). *J Orthop Res* **19**, 1178-1184.
Torzilli, P.A. et al (1994). *Am J Sports Med* **22**, 105-112.

ACKNOWLEDGEMENTS

These projects were supported by grants from the National Football League, Bauerfiend Corp, and dj Orthopaedics LLC.

TOWARDS UNDERSTANDING IN VIVO KNEE JOINT MUSCULOTENDON AND SKELETAL DYNAMICS

Frances T. Sheehan, Ph.D.

Mechanical Engineering Department-The Catholic University of America, Washington, D.C. USA (sheehan@cua.edu)
Physical Disabilities Branch and Diagnostic Radiology, The National Institutes of Health, Bethesda, MD. USA

INTRODUCTION

In order to achieve a greater understanding of the demands placed on the musculoskeletal system and the capabilities of tissue to withstand and adapt to these demands, we are developing an imaging and analysis package, known as virtual functional anatomy (VFA), for the quantification and visualization of 3D musculoskeletal dynamics. VFA is a tool for the creation of subject-specific, 3D total joint anatomy models, animated based on actual joint kinematics during volitional movement. In addition, this tool will quantify the loads placed on individual joint structures. The first phase of VFA development focused on adapting cine phase contrast magnetic resonance imaging (cine-PC MRI) to the non-invasive *in vivo* study of 3D musculoskeletal kinematics. After confirming the precision and accuracy of cine-PC, the kinematics of healthy knees were quantified. These data (i.e., 3D tibio-femoral-patellar kinematics and patellar tendon strain) became the springboard for ongoing studies of impaired knee joint function. For example, we have quantified altered knee joint kinematics and vasti contraction patterns in subjects diagnosed with patellar maltracking. Additionally, we have begun to define possible coping strategies after an ACL loss.

METHODS

Contrary to standard MR imaging, where subjects need to remain as still as possible, cine-PC MRI requires that subjects cyclically move the limb being studied. For the knee joint studies, subjects were placed in a supine position within a 1.5T MR imager and were asked to extend/flex their knee at a rate of 35 cycles/min from ~40° of flexion to full extension. Consistency was maintained with the aid of a metronome. Cine-PC MR images were taken in a sagittal plane, at the center line of the femur and patella (Figure 1). Anatomically based reference frames were defined using anatomical images taken in 3 axial planes during the movement. For the vasti studies, an axial imaging plane proximal to the insertion of the vasti lateralis was used. Using integration algorithms developed previously (Zhu, et al, 1996), regions were selected on the tissues of interest and tracked 3-dimensionally throughout the motion cycle. Skeletal data were then translated into 3D xyz body-fixed orientation angles. Using 3D patellar-tibial data, the strain in the patellar tendon was calculated.

RESULTS

Cine-PC MRI was shown to have an accuracy of better than 0.55mm for the 3D displacement measures and a precision of

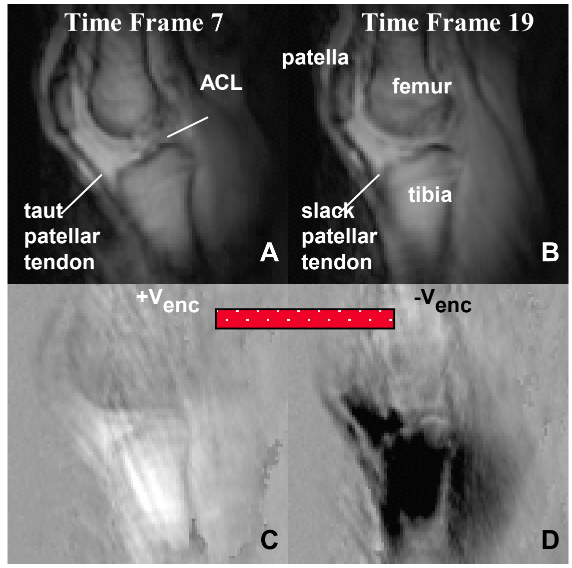

Figure 1: A/B) Sample cine-PC MR anatomic images; **C/D)** anterior/posterior (A/P) velocity images (superior/ inferior and medial/ lateral images not shown). White/ black pixels indicate maximum A/P velocity, respectively.

better than 1.1° in the measurement of orientation angles.The kinematic profiles of the unimpaired knees agreed with previous studies (Sheehan, Zajac & Drace, 1999), but the average maximum tendon strain (6.6%) was greater than typically reported. The kinematics of the impaired subjects studied were clearly altered from those of the unimpaired.

DISCUSSION

Despite the frequency of reported knee pain, especially patellofemoral, there is still a lack of specificity in diagnosing the pathology causing this pain. This leads to confusion when designing a treatment plan and to difficulty in assessing the efficacy of intervention. Broad categories such maltracking chondromalacia, and anterior knee pain are often too quickly accepted as a diagnosis without the underlying etiology being understood. VFA's ability to non-invasively measure 3D musculoskeletal dynamics *in vivo* offers us an opportunity to revisit these broad classifications in order to develop more definitive diagnoses that can be correlated with specific impairments. This in turn will allow for improved diagnosis, treatment, and eventual outcome.

REFERENCES

Zhu, *et al.* (1996) *Magn. Reson. Med.*, **35**:471-8
Sheehan, Zajac, & Drace, (1999) *J Biomech.Eng* **31:**1,21-26

INSIGHTS INTO IN-VIVO KNEE MECHANICS WITH MAGNETIC RESONANCE IMAGING

Janet Ronsky, Nicole Baker, Rebecca Moss, Richard Frayne*

Mechanical and Manufacturing Engineering, Human Performance Laboratory, *Clinical Neurosciences
University of Calgary, Calgary, Alberta, Canada, jlronsky@ucalgary.ca

INTRODUCTION

Understanding the complex relations between joint structure, dynamic joint function and joint health status have been hampered due to lack of technologies for probing the in-vivo joint under physiologic loading conditions. Magnetic resonance (MR) imaging has provided an excellent venue for non-invasively quantifying joint structures in-vivo. The assessment of MR imaging for accurate measurements has been limited and has focused primarily on the measurement of cartilage thickness and volume as an indicator of the progression of cartilage degeneration (e.g. Peterfy et al., 1994; Kladny et al, 1999). Cartilage volume and thickness have also been used to calculate cartilage deformation under load in an attempt to better understand cartilage material properties (e.g. Eckstein et al., 2000). Ronsky and coworkers (1994) assessed in-vivo contact characteristics in both intact and ACL deficient patellofemoral joints under loading with MR imaging at flexion angles ranging from 0° - 45°. However, evaluation of contact area is plagued by lack of an appropriate gold standard. Cohen et al. (1999) used MR images and digitization techniques to collect surface data to measure cartilage topography, cartilage thickness and contact area between the joint surfaces, and compared results with stereophotogrammetric measures on an unloaded knee joint. As the limits of MR imaging for joint mechanics assessments are probed, issues related to feature extraction, motion artefact, image registration and reconstruction, accuracy, and repeatability become increasingly important. Hardware and software limitations related to bore size and orientation, magnet strength, imaging coils, image resolution, partial volume effects and pulse sequences provide constraints. Additional challenges include relating in-vivo joint structures to dynamic joint loading associated with locomotion, stair climbing and other functional activities. Our recent progress focusing on quantification of error sources and accuracy in prediction of joint contact, as well as relations between anatomical structures and functional joint centres is presented.

METHODS

A method for quantifying patellofemoral (PF) joint contact stress under physiologic load, non-invasively and in-vivo has been developed (Ronsky, 1994). A T2 weighted sagittal plane FSE sequence with 2 mm thick slices and imaging time of 2 min 52 s was employed. To evaluate the influence of edge detection, image registration, surface modeling techniques and proximity threshold on joint contact location and magnitude, this technique was applied to five loaded fresh porcine joint specimens (Moss, 2001). Staining and multi-station digital photogrammtery were used for comparative analyses. In a second study, variations in muscle moment arms for determination of resultant knee joint forces were compared based on a functional joint centre location and two anatomical locations (cruciate ligament intersection and tibiofemoral contact point). Subject specific functional joint centres were obtained by determining the instantaneous helical axis (IHA) piercing point based on kinematic data, and relating this location to the joint structures visible on MR images (Figure 1).

RESULTS AND DISCUSSION

Non-Maxima Suppression semi-automated edge detection technique provided the most repeatable contact area results (intra-user coefficient of variability 0.94%) with the smoothest edge representation (0.27 pixel resolution). Contact area was sensitive to selection of proximity threshold value, with the optimal threshold of 0.2mm resulting in an uncertainty in contact area of 13%. Accuracy is specific to image sequence, MR unit and coil, and results suggest that this approach can be used for accuracy evaluations of specific experimental setups. The functional joint centre was located more closely to the cruciate ligament intersection point. While improvements in accuracy and processing time are required, this technique provides an example of integration of functional joint mechanics with MR imaging to reveal new insights into relations amongst normal and injured joint structure and function. Advances in image integration, dynamic imaging and increased image resolution through custom coils and higher strength magnets are projected to make MR imaging an integral component in monitoring joint health status and in-vivo joint mechanics.

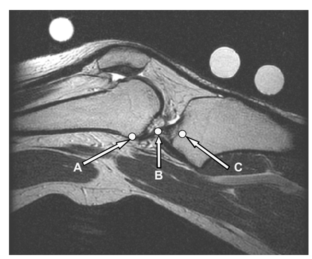

Figure 1: Sagittal MR image (30° knee flexion) showing joint centre locations calculated using: IHA piercing point (A); cruciate ligament intersection (B); tibiofemoral contact point (C).

REFERENCES

Baker, N. et al., (2001) Proc. XVIIIth ISB.O16.
Cohen, Z. et.al. (1999) *Ost. & Cart.* **7**, 95-109.
Eckstein, F. et al., (2000) *J. Biomech*. **33**, 819-825
Kladny, B. et al. (1999), *Int. Orthop*. **23**, 264-267.
Peterfy, C. et al., (1994). *Radiology*. **192**, 485-491.
Moss, R. (2001) *M.Sc. Dissertation*, U. Calgary Press
Ronsky, J.L.et.al. (1994). *Proc. 8th CSB,* 82-3.

ACKNOWLEDGEMENTS

Financial: NSERC, CHR, AHFMR, CRCP, GEOIDE.

3D KNEE KINEMATICS FROM PICTURES: HOW'S IT WORK, WHY'S IT USEFUL, AND WHERE'S IT GOING?

Scott A. Banks

The Biomotion Foundation, 1411 N. Flagler Drive, Suite 9800, West Palm Beach, FL 33401, banks@alum.mit.edu

INTRODUCTION

In the late 1980's, frustrated by the inability to use skin-mounted markers to accurately determine dynamic tibiofemoral translations and rotations, research groups sought new techniques to measure how total knee replacements (TKR) moved. Roentgen stereophotogrammetric techniques were well known at the time, but the requirement for surgically implanted fiducial markers made these techniques inappropriate for retrospective studies of patients with knee replacements. Instead, new techniques were developed based on ready availability of fluoroscopic imaging hardware in hospitals and computer geometry information from prosthesis manufacturers. Almost fifteen years later, these techniques have provided a wealth of quantitative information on the function of knee replacements, and have been adapted for a variety of other applications. The purpose of this summary is to briefly describe the principals of performing a three-dimensional pose measurement from a two-dimensional image, describe a few direct applications of these techniques, and provide an overview of the many related applications to which image derived kinematics will contribute.

MEASUREMENT PRINCIPLES

Measuring knee motion from images is a 'model and match' process. Fluoroscopic video sequences, as well as x-ray film images, are central or perspective projections of the implant components such that the shadow cast by the implants in the image are (usually) unique functions of the imaging geometry and the pose of the implants. The optical geometry of the imaging hardware, and spatial distortions, can be measured and incorporated into an image synthesis routine for projecting surface geometry of the implant components. The synthesized images can be compared to the recorded images, and an iterative process or look-up table can be used to optimize the shape correspondence. The pose of the virtual implant is taken as the estimated pose of the physical implant in 3D space.

These techniques are monocular vision (for most applications) and have highly non-uniform errors. Uncertainty for linear displacements along the optical axis can be an order of magnitude higher than for displacements parallel to the image plane. Uncertainties for angular displacements are slightly more uniform, but are more sensitive to the shape and features of the implant components. Significant sources of measurement error can include discrepancies between the physical object and the computer model used for shape matching, residual geometric distortion in the image, uncertainties in the optical parameters, motion blur, and penumbra.

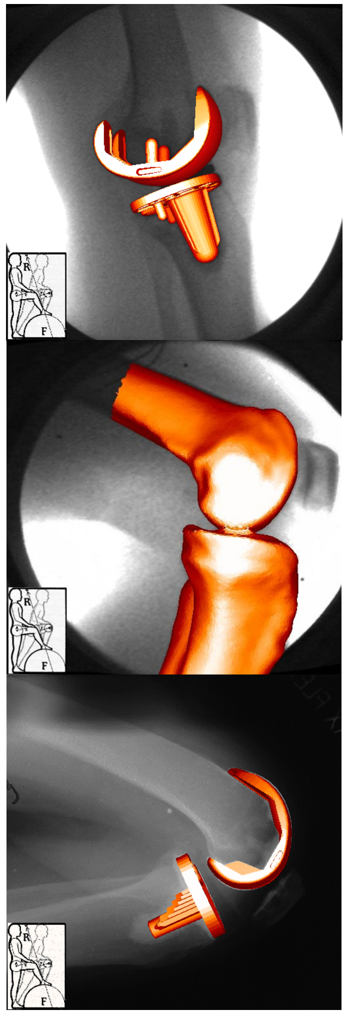

Figure 1. 3D Knee motions from pictures: fluoroscopic (top, middle) or x-ray film (bottom) images and shape models of skeletal (middle) or prosthetic structures (top, bottom) can be used for matching and pose estimation.

MEASUREMENT APPLICATIONS

Single plane fluoroscopy has been used to characterize the motions of many (>30) designs of total knee replacement during a wide variety of dynamic and static activities, e.g. stair step, deep knee bend, gait, kneeling, rising from a chair (Fig. 1). These data have contributed significantly to an improving understanding of how total knee replacements function, and towards the objective refinement of TKR designs. The identical measurement approach has been applied on a more limited basis to the anatomic knee, with shape models derived from either CT or MRI scans. The same techniques apply equally well to planar x-ray films for static studies. Model and match techniques have been used to characterize motions in other joints and have been used in bi-plane joint imaging, where the accuracy can be increased substantially.

ASSOCIATED APPLICATIONS

Although measurements of knee motions are, by themselves, interesting and useful, it is possible to use this same information to compliment a wide variety of other test, evaluation, and development methodologies. In vivo knee kinematics can be used as inputs or validation for TKR wear testing systems. Image based data can be used to better understand damage to retrieved implants or, in some cases, predict wear in implants *in situ*. In vivo data can be used to drive musculoskeletal models and tribology simulations. Fluoroscopy, marker based motion capture, forceplates and EMG can be performed simultaneously to provide extremely detailed assessments of intrinsic and extrinsic biomechanics.

SUMMARY

Kinematic data from image matching is helping to 'close the loop' in the design of improved joint replacements and assessing the efficacy of ligament reconstruction and other surgical procedures. Image based 'model and match' techniques are yet another tool in the biomechanists' toolbox that will find varied and diverse application wherever the measurement properties are appropriate to answer the questions being asked.

ACL STRAIN DURING REHABILITATION EXERCISES, IN VIVO

Braden Fleming, Bruce Beynnon, Robert Johnson
McClure Musculoskeletal Research Center, Department of Orthopaedics & Rehabilitation,
University of Vermont, Burlington VT 05405; Braden.Fleming@uvm.edu

INTRODUCTION

Disruption of the anterior cruciate ligament (ACL) has been shown to lead to the early onset of osteoarthritis (OA), and that OA may progress despite surgical reconstruction of the injured ligament. One variable that is thought to influence the outcome of ACL reconstruction is the post-operative rehabilitation program prescribed. It is through rehabilitation that the biomechanical environment of the healing graft (and articular cartilage) can be controlled. Thus, it is necessary to understand how the ACL, and hence ACL graft, will respond to different joint loading conditions and exercises. These data could then be used to design clinical studies and to develop rehabilitation programs with the goal of optimizing graft healing while minimizing OA progression. Our approach has been to measure ACL strains *in vivo* because the force balance between the ligaments, articular contact, musculature and bodyweight regulates the ACL strains. The interaction between these structures is difficult to simulate in cadavers.

EXPERIMENTS

We used a small displacement transducer (DVRT; MicroStrain, Inc. Burlington VT) that can be arthroscopically applied to the ACL to evaluate the strains produced under different muscle contraction sequences and other commonly prescribed rehabilitation exercises. All study participants had normal ACLs and were candidates for arthroscopic partial meniscectomy or diagnostic arthroscopy. We assumed that the exercises producing the greater strain values in the normal ACL would also produce greater strains in an ACL graft.

We found that contractions of the quadriceps muscles strained the ACL when the knee was between 50^o and full extension, while that hamstrings muscles did not except when the knee was near full extension. Co-contraction of the quadriceps and hamstring muscles reduced ACL strain values compared to isolated contractions of the quadriceps muscles. We also revealed that contractions of the gastrocnemius muscles strained the ACL when the knee was between full extension and 30^o flexion emphasizing the important contributions other muscle groups may have. "Closed-kinetic chain exercises" (e.g. squatting) are commonly prescribed following ACL surgery since they are thought to enhance muscle co-contraction, and utilize the tibiofemoral compressive load produced by bodyweight to increase knee stability and protect the ACL. "Open-kinetic chain exercises" (e.g. active knee extension) are thought to produce higher strains since they are quadriceps dominant and do not include the compressive load induced by bodyweight. However, direct comparisons of the peak ACL strain values produced during squatting and active knee extension found no significant differences. We have shown that this may be due to the increase in strain produced by compressive loading and/or the inability of the hamstrings to fully protect the ACL when the knee is near full extension.

Unfortunately, the strain thresholds beneficial and detrimental to ACL graft healing remain unknown. We used the strain data to design a clinical study evaluating the relationship between ACL strain and the graft and articular cartilage healing responses.

The clinical study utilized a prospective randomized design to compare two different rehabilitation programs (an "accelerated" program versus a "non-accelerated" program). The same exercises were prescribed in both programs; however, those that were found in our biomechanical studies to produce high strains were delayed by 4- to 6-weeks in the non-accelerated program. 25 patients who underwent ACL reconstruction with patellar tendon grafts were utilized. We hypothesized that the two rehabilitation programs would not produce significant differences in anterior-posterior knee laxity, patient-oriented outcomes, and "biomarkers" of articular cartilage metabolism (synovial fluid markers evaluating Type II collagen and aggrecan degradation and synthesis). Altered cartilage metabolism is thought to be indicative of OA. All outcome measures were assessed at the time of surgery and at 6-, 12-, and 24-months post-operatively.

We found that the patients who underwent the accelerated program had twice the increase in knee laxity after 24-months when compared to those in the non-accelerated rehabilitation program. However, neither program produced significant differences in any of the other outcome measures. The biomarkers of articular cartilage metabolism did not return to normal for either treatment group by 24-months.

CONCLUSIONS

Our biomechanical studies have shown that the ACL strains produced during rehabilitation exercises can be regulated. Our clinical study then revealed that a rehabilitation program that permits high strain activities in the early phases of graft healing produced greater changes in knee laxity. This may place the knee at risk for additional articular cartilage and meniscal damage. We hope that our future assessments of the biomarkers of articular cartilage metabolism and the patient-oriented outcomes in these patients will shed light on the long-term consequences of this increase in knee laxity.

ACKNOWLEDGEMENTS

These projects were supported by grants from the NIH, the National Football League, and the Arthritis Foundation.

MEASURING SPRING CONSTANTS OF THE P-SELECTIN/PSGL-1 MOLECULAR COMPLEXES BY AFM

Bryan Marshall[1], Rodger McEver[2], and Cheng Zhu[1]

[1]Schools of Mechanical Engineering and Biomedical Engineering, Georgia Institute of Technology, Atlanta, GA 30332, USA, cheng.zhu@me.gatech.edu, [2]Warren Medical Research Institute and Departments of Medicine and Biochemistry and Molecular Biology, University of Oklahoma Health Sciences Center, Oklahoma City, OK 73104, USA.

INTRODUCTION

P-selectin is a cell adhesion molecule induced on activated endothelial cells and platelets. It plays a critical role in the inflammatory and thrombotic processes. P-selectin glycoprotein ligand 1 (PSGL-1) is expressed on leukocytes, and its interaction with P-selectin mediates the flowing cells tethering to and rolling on the blood vessel wall. In this mechanically stressful environment, the P-selectin/PSGL-1 complex is subject to a wide range of forces. As such, how much it would be stretched by force is a relevant question to the function of this interaction. Also, measuring properties of a single pair of interacting molecules not only symbolizes a long-standing theoretical appeal but also represents quite a technical challenge. As such, the elasticity of P-selectin/PSGL-1 complex is of interest. Here we report molecular spring constant measurements using an atomic force microscope (AFM).

MATERIALS AND METHODS

Dimeric P-selectin and wild-type (wt) PSGL-1 were purified from human platelets and neutrophils, respectively. Monomeric soluble (s) PSGL-1 was secreted by CHO cell transfectants. P-selectin was reconstituted into a glass supported lipid bilayer cushioned with a polymer layer. Dimeric wtPSGL-1 or monomeric sPSGL-1 was coupled to the tip of an AFM cantilever via the antibody PL2. In some experiments, the AFM tip was coated with the anti-P-selectin antibody G1.

The spring constants of AFM cantilevers were measured by thermal fluctuations. The spring constants of the molecular complexes were measured by two methods. In the thermal method, the spring constants of the AFM cantilevers linked to the surfaces by molecular complexes subject to given tensile forces were measured by thermal fluctuations. These were then compared to the spring constants of the same cantilevers not linked to the surfaces to deduce the spring constants of the molecular linkages. In the stretch method, the molecular spring constants were directly measured from their force-stretch curves.

RESULTS AND DISCUSSION

Spring constants were measured by either thermal or stretch method for each of the three molecular complexes: P-selectin interacting with wtPSGL-1, sPSGL-1 and G1. These are grouped according to the number of rupture events observed as the linkage between the AFM tip and the surface dissociated. The results are summarized in Figure 1.

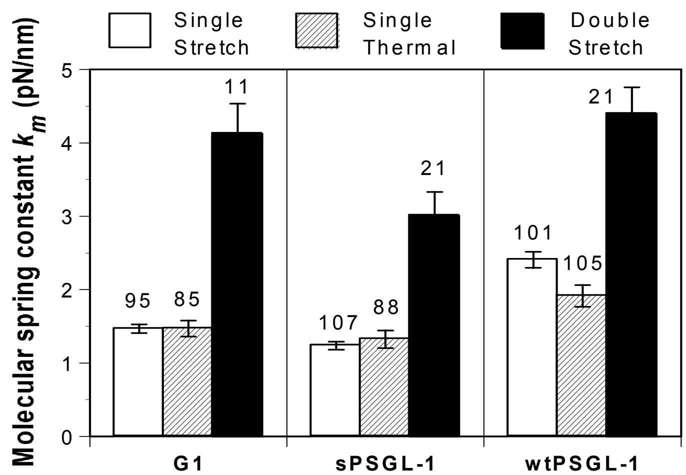

Figure 1: Spring constants for the three molecular systems were measured by the stretch or thermal method from single or double rupture events. Data are presented as mean ± standard error of N (indicated on the top of the bars) measurements.

Good agreement was found between data measured by the thermal and the stretch methods, which are indifferent to the spring constant of the cantilever used, thus imparting confidence in our methods. The spring constant of P-selectin complexed with wtPSGL-1 (which forms a dimeric bond) is about twice that of P-selectin complexed with sPSGL-1 (which forms a monomeric bond) when both were measured from single rupture events. For all three molecular systems, the spring constants measured from double rupture events are about twice those of the corresponding values measured from single rupture events. This suggests that the observed discrete the spring constant of a single molecular complex bound by a monomeric bond (for the sPSGL-1 case) or a dimeric bond (for the wtPSGL-1 case) was measured from the single rupture events. The similar values of the P-selectin/sPSGL-1 and P-selectin/G1 spring constants suggest that G1 formed single monomeric bonds with P-selectin in the single rupture events. They also suggest that most of the compliance of the molecular complex comes from P-selectin and PSGL-1 is a much more rigid molecule.

ACKNOWLEDGEMETNS

This work was supported by NIH grants AI 44902 and HL65631 and a Whitaker Foundation Graduate Fellowship (BM).

LEUKOCYTE TETHERING UNDER FLOW: MODEL FOR INTERFACIAL COMPRESSION, VISCOELASTIC TETHER EXTENSION, AND CYTOSKELETAL UNBINDING

Michael R. King[1,2], Volkmar Heinrich[3], Evan Evans[3,4], and Daniel A. Hammer[1]

[1]Departments of Chemical Engineering and Bioengineering, University of Pennsylvania, Philadelphia, Pennsylvania, USA
[2]mrking@seas.upenn.edu, Department of Biomedical Engineering, University of Rochester, Rochester, New York, USA
[3]Department of Biomedical Engineering, Boston University, Boston, Massachusetts, USA
[4]Departments of Physics and Pathology, University of British Columbia, Vancouver, British Columbia, Canada

INTRODUCTION

The formation of transient attachments between leukocytes and a sparsely-coated reactive surface under flow is a commonly used assay for measuring the dissociation kinetics of leukocyte adhesion molecules such as selectins (Alon, Hammer, and Springer, 1995). These cell tethering experiments yield rate constants which are quite different from independent measurements obtained from either dynamic force spectroscopy (DFS) or atomic force microscopy (Fritz et al., 1998). We reexamine recent tethering results (Park, et al., submitted to *Biophys. J.*) using a numerical simulation of cell tethering that incorporates new kinetic parameters and viscoelastic relations obtained from DFS for the P-selectin/PSGL-1 bond.

METHODS

Using micropipette aspiration, a biomembrane force probe (i.e., red blood cell) serves as a transducer spring to measure the force experienced by two functionalized surfaces brought into contact (Merkel et al., 1999; Evans, 2001). In contrast to cell tethering, where the bonds experience a constant tensile stress once cell motion has ceased, a steady retraction of the DFS probe produces a linear ramp in force. We measured the strength of the P-selectin/P-selectin glycoprotein ligand-1 (PSGL-1) bond using DFS. The force vs. displacement profile for the compression of unactivated polymorphonuclear (PMN) neutrophils with a glass bead was also generated for several rates of force loading.

Cell and bead tethering on a P-selectin surface under flow was numerically simulated using adhesive dynamics to determine whether DFS-measured kinetic rate constants and derived relations for cell deformation could reproduce behavior observed in prior tethering experiments, and most recently by Park and coworkers. Adhesive dynamics is a technique for simulating the adhesion of cells to surfaces by coupling a hydrodynamic calculation of one or more rigid spheres suspended in a viscous fluid interacting with a wall under an imposed flow, with a stochastic model of specific receptor-ligand adhesion (Hammer and Apte, 1992; King and Hammer, 2001). Each molecular bond between the cell and substrate is explicitly included as a linear spring with endpoints fixed on either surface. The instantaneous length and orientation of each bond determines both the total force and torque acting on the spherical cell, as well as each bond's probability for failure at that time step.

RESULTS AND DISCUSSION

The normal force resisting PMN compression was measured to be $f \sim (2\pi R P_0)\Delta x$, where R is the harmonic mean of the PMN radius and the radius of curvature of the opposing surface, $P_0 = 17$ N/m^2, and Δx is the relative displacement. The dynamics of tether extension was measured to consist of two regimes, with each regime ended by a stochastic unbinding process. The initial response obeys a linear elastic relation $f = k_{int}\Delta x$, defined by the interfacial elastic constant $k_{int} = 0.25$ pN/nm which is independent of pulling speed. The transition from the elastic regime to a plastic tether growth regime occurs due to cytoskeletal unbinding at a force f_{cl} and a rate ν_{off}:

$$f_{cl} = f_\beta \log_e(k_{int} v_{pull} t_{off} / f_\beta) \qquad (1)$$

$$\nu_{off} = (1/t_{off}) \exp(f / f_\beta) \qquad (2)$$

where $f_\beta = 15.7$ pN, $1/t_{off} = 0.5$/sec, and v_{pull} is the pulling speed. After cytoskeletal unbinding, the force approaches a plateau in a quasi exponential fashion (i.e., $f \sim 1 - \exp(-t/\tau)$). Both the plateau force f_{tg} and the relaxation time τ were determined to depend on the

$$\tau \approx 0.4 \sec(v_{pull} / \mu m/\sec)^{-0.83},$$

$$f_{tg} \approx 85\, pN (v_{pull} / \mu m/\sec)^{0.17}$$

pulling speed, as

The final event is rupture of the PSGL-1/P-selectin bond which again follows the quasi-Bell model form of eqns. (1) and (2) with $f_\beta = 17$ pN and $1/t_{off} = 0.1$/sec.

DFS of P-selectin/PSGL-1 reveals a single transition state with a significantly slower off rate and significantly larger bond interaction length than measured by tethering. When all of these refinements were included in the adhesive dynamics simulation, the tethering results of Park et al. (submitted to Biophys. J.) were accurately reproduced. This implies that the common steady-state, unimolecular interpretation of cell tethering results can produce highly inaccurate estimates of unbinding kinetics, and that more direct measurement techniques such as DFS or AFM are better suited to characterize receptor-ligand interactions at the single-molecule level.

REFERENCES

Alon, R., Hammer, D.A., Springer, T.A. (1995). *Nature*, **374**, 539-542.
Evans, E. (2001). *Annu. Rev. Biophys. Biomol. Struct.*, **30**, 105-128.
Fritz, J. et al. (1998). *Proc. Nat. Acad. Sci. USA*, **95**, 12283-12288.
Hammer, D.A., Apte, S.M. (1992). Biophys. J., **62**, 35-57.
King, M.R., Hammer, D.A. (2001). Biophys. J., **81**, 799-813.
Merkel, R., et al. (1999). *Nature*, **397**, 50-53.

ACKNOWLEDGEMENTS

D.A.H. is supported by NIH Grants HL18208 and GM54100, M.R.K. is supported by NIH National Research Service Award HL10353, and E.E. is supported by NIH Grants HL31579 and HL54700.

RHEOLOGICAL PROPERTIES OF THE BLOOD AND LOCAL HAEMODYNAMICS MODULATING LEUKOCYTE ATTACHMENT TO SELECTIN-COATED SURFACES

G.B. Nash[1], K.B. Abbitt[1], C.A. Skilbeck[1], S.M. Westwood[2], P.G. Walker[2] and T. David[2]
[1]Department of Physiology, The University of Birmingham, Birmingham B15 2TT, g.nash@bham.ac.uk
[2]Department of Mechanical Engineering, University of Leeds, Leeds, LS29JT, UK

INTRODUCTION

The local physical environment critically constrains the interaction between adhesion receptors expressed on flowing leukocytes and vascular endothelium. The rheological properties of the blood (haematocrit, red cell aggregation, viscosity) and the pattern of flow influence initial contact, formation of bonds and bond survival. Contact with the vessel wall is promoted by margination of leukocytes by aggregated, centrally flowing erythrocytes, with aggregation itself being more extensive at low shear rates. Shear rate at the vessel wall determines the velocity of leukocytes at contact and thus influences the probability of establishment of a receptor-ligand bond. Wall shear stress (the product of shear rate and fluid viscosity) applies force to cells once they have bound, and accelerates bond disruption. We examined how variation in blood rheology and characteristics of flow affected leukocyte margination and capture from flowing whole blood.

METHODS

Whole citrated blood was fluorescently labelled with rhodamine 6G and perfused at variable rate over glass surfaces coated with P-selectin, an adhesion receptor able to capture flowing leukocytes and support a rolling form of adhesion (Abbitt & Nash, 2001). We used either straight glass capillaries with rectangular cross-section (microslides), or a flow chamber which incorporated a backward-facing step. In the latter case, flow seperation occurred downstream of the step. A region of recirculating flow, a reattachment point, and a region where simple laminar flow was re-established could be distinguished (Skilbecck et al., 2001). We measured surface density of adhesion (corrected for leukocyte numbers) and rolling velocity. To quantify leukocyte margination, we used a non-adherent surface and measured flux of leukocytes near the wall and cell velocity.

RESULTS AND DISCUSSION

Manipulation of haematocrit from 10% up to 50% caused an increase in velocity of marginated leukocytes, but little change in their flux. Since volumetric flow rate was constant, this implied that the flow velocity profile became blunted and wall shear rate increased as haematocrit increased. The number of leukocytes adhering increased between 10 to 30% haematocrit, and was essentially constant thereafter. It seems that increasing red cell concentration promotes initiation and stabilisation of attachment, even in the face of increasing wall shear rate, blood viscosity and hence shear stress. To study the influence of red cell aggregation, blood was diluted to 20% haematocrit with plasma, 40kD dextran (reduced aggregation) or 500kD dextran (enhanced aggregation). Increasing aggregation correlated with increasing numbers of adherent leukocytes, and was associated with an increase in slow-flowing leukocytes near the wall. These results demonstrate that the physical properties of the blood control movement of leukocytes toward and contact with the vessel wall, and influence the initiation and outcome of adhesive interactions that follow.

Examining flow over a backward-facing step, it was evident that adhesion to a selectin-coated surface could occur either side of the reattachment point. On the upstream side, cells rolled inward towards the step. On the downstream side cells rolled away from the step and could enter regions where attachment could not occur from the main flow, presumably because shear rate was too high (>$400s^{-1}$). Thus discontinuity in the 'vessel' wall allowed adhesion in a conduit which otherwise had too high shear rate, and rolling adhesion allowed population of regions where attachment could not occur directly. The patterns of adhesion in the recirculation zone also showed that local components of flow toward or away from the wall influenced attachment, as well as the local shear stress.

SUMMARY

These studies indicate that adhesion within the circulation depends on rheological characteristics of the blood, physical interactions between blood cells, and the local patterns of shear rate and stress, as well as expression of endothelial receptors. This accords with findings that adhesion is typically restricted to post-capillary venules where shear rates are lowest. Nevertheless, mononuclear leukocytes are found within arterial atherosclerotic plaque, and adhesion may also occur in arterioles in pathological states. Adhesion in such regions might be promoted by flow separation at discontinuities in the wall, causing localised low shear and a normal component of flow.

REFERENCES

Abbitt, K.B., Nash, G.B. (2001). Br. J. Haematol., **112**, 55-63.
Skilbeck, C., Westwood, S.M., Walker, P.G., David T., Nash, G.B. (2201). Arterioscler. Thromb. Vasc. Biol., **21**, 1294-1300.

DIVALENT ION INDUCED ADHESION OF NEUTROPHILS TO ICAM-1 AND VCAM-1 COATED SURFACES

Richard Waugh,[1] Elena Lomakina, Christopher Spillmann and Philip Knauf
Department of Biomedical Engineering, University of Rochester, Rochester, New York [1]waugh@seas.rochester.edu

INTRODUCTION

The firm adhesion of neutrophils to endothelium in the complex mechanical environment of the microvasculature is a critical step in the body's response to infection or inflammation. This interaction is primarily mediated by binding of members of the β_2 family of integrins expressed on the neutrophil to ligands, principally ICAM-1, expressed on activated endothelium. Members of the β_1 integrin family, capable of binding to VCAM-1 on endothelium, are also found in smaller numbers on the neutrophil surface. Binding of integrins to their ligands occurs only when integrins are in an "activated" or high-affinity conformation. *In vivo*, this conformation is induced by signaling events within the cell, but this conformation can be induced *in vitro* by the presence of Mg^{2+} (and not Ca^{2+}) in the extracellular medium. We are using the latter approach to examine the influence of mechanical force on integrin-mediated cell adhesion to endothelial ligands immobilized on beads.

METHODS

A small blood sample was obtained by fingerprick and dispersed into sterile buffer (Hank's Balanced Salt Solution (Gibco) to which was added 4% heat-inactivated fetal bovine serum (Hyclone, Logan, UT) and either 5.0 mM Mg^{2+} or 1.5 mM Ca^{2+}, pH 7.4, 290 mOsm). The cell suspension was placed in a chamber on the stage of an inverted microscope kept at 37°C. Neutrophils were selected based on the multi-lobular morphology of the nucleus. Two micropipettes were mounted opposite each other. One was used to hold a small (4.5 μm diameter) bead (tosyl-activated, Dynal, Lake Success, NY) that had been coated according to the manufacutrer's protocol with soluble ICAM-1, VCAM–1 (R&D Systems, Minneapolis, MN) or NCAM (Chemicon, Temecula, CA). The second pipette was used to manipulate a cell into repeated contact with the bead surface. The cell and the bead were held in contact for a specified length of time (typically one minute), then separated, and the formation of an adhesive contact was noted by a deformation of the cell surface during separation. The percentage of contacts that resulted in the formation of an adhesive bond was calculated.

Flow cytometry measurements were made to estimate the number of adhesive ligands on the cells and the beads. Cells were labeled with fluorescent antibodies against CD18 (β_2 integrin) or CD29 (β_1 integrin) then fixed and the fluorescence intensity was compared to that of cells treated with isotype control antibodies. The fluorescence signal was converted to the number of antibodies bound to the surface by comparison with Quantum Simply Cellular beads (Flow Cytometry Standards, Fishers, IN).

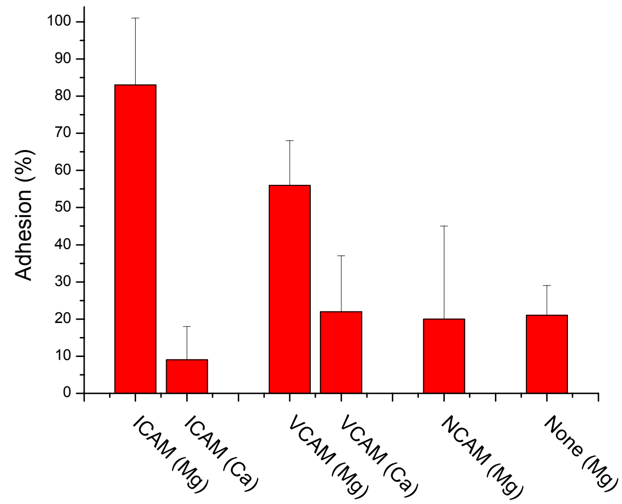

Figure 1: Adhesion probability for interaction of neutrophils with beads coated with the specified protein and in the presence of 1.5 mM Ca^2 or 5.0 mM Mg^{2+}, as indicated.

RESULTS AND DISCUSSION

The density of ICAM-1 on the bead surface was estimated to be 500 copies/μm^2 and the density of VCAM-1 was estimated to be 1000 copies/μm^2. The density of β_2 integrins on the cells was approximately 300 copies/μm^2 (~70,000/cell). Preliminary estimates of the density of β_1 integrins indicated 25 - 50 copies/μm^2 or 6,000 – 12,000 copies/cell.) In Mg^{2+}-containing media, adhesion was more likely to occur with ICAM-coated beads than with VCAM-coated beads (Fig. 1). Under conditions in which the adhesive probability for ICAM was over 80%, the probability of adhesion to the VCAM coated beads was ~60%. This high level of adhesion to VCAM was surprising, as VCAM is not thought to be a prominent ligand in mediating neutrophil-endothelial interactions. (In fact, the VCAM experiments were originally performed as a non-adhesive control for the ICAM experiments!). For both ICAM and VCAM, the frequency of adhesion was dramatically reduced when $Mg^{2+}$was replaced with Ca^{2+} in the external medium. Experiments in which cells were contacted with beads coated with NCAM showed little adhesive interaction. Interestingly, the formation of adhesive contacts was found to depend strongly on the size of the contact zone produced during impingement of the cells on the beads. For example the rate of adhesive contact formation after brief (2 s) contacts with ICAM beads was 75% when the size of the contact area was greater than 13 μm^2, but fell to less than 33 % when the contact area was less than 12 μm^2. This corresponds to impingement forces of ~400 pN and ~175 pN respectively for the two groups tested.

This work was supported by the US Public Health Service under NIH grant No. PO1 HL-18208.

THE NATURE OF MECHANICAL FORCES REGULATING SHEAR-INDUCED PLATELET ACTIVATION

Sriram Neelamegham[1] and Harish Shankaran
Bioengineering Lab., Chemical Engineering, State University of New York at Buffalo, Buffalo, New York [1]neel@eng.buffalo.edu

INTRODUCTION

Shear-induced platelet activation may occur under conditions of high blood flow, such as those encountered in stenosed arteries. This phenomenon is thought to contribute to thrombosis. The molecular mechanism controlling this process involves the binding of plasma protein von Willebrand factor (vWF) to platelet membrane receptor complex GpIb/V/IX under high shear conditions. For this process, it is speculated that fluid forces may cause conformational changes in either vWF or GpIb thereby promoting receptor-ligand interaction. In this paper, we aim to quantify the nature and magnitude of the fluid stimulus that triggers platelet activation.

METHODS

Platelets (in citrated/PPACK treated platelet rich plasma or in whole blood) were subjected to defined shear in a cone-plate viscometer. The extent of platelet activation was measured by quantifying the level of AnnexinV-FITC binding to phosphatidyl serine expressed on the activated platelet surface. Generation of microparticles and the level of platelet aggregation was also monitored over a range of fluid shear protocols. In selected experiments, human vWF was isolated from blood cryoprecipitate. This isolated vWF was subjected to hydrodynamic shear and analyzed using static and dynamic light scattering experiments, in order to assess the extent to which fluid shear may alter the macroscopic shape of vWf.

RESULTS AND DISCUSSION

In studies performed to determine a sensitive marker of shear-induced platelet activation, we observed that the binding of Annexin V to phosphatidyl serine expressed on the activated platelet surface was a more sensitive and reproducible marker of platelet activation than platelet microparticle formation and cellular aggregation. Statistically significant detection of cellular activation was observed within 10sec. of application of shear (Fig 1), and this was consistently blocked by antibodies against GpIb but not GpIIb/IIIa.

Experiments were further performed using a range of fluid shear protocols to assess the contributions of mechanical forces on the rates of platelet activation. Here, we observed that: **i)** platelet activation levels were low below a shear rate of 6000/s, beyond which they increased approximately linearly with increasing shear. **ii)** In experiments with varying cell concentrations, we observed that the extent of cell activation only doubled when we increased the cell concentration over a 30 fold range from 10 to 300×10^6 cells/mL, thus indicating that collisions between platelets is not a major contributor to shear-induced cell activation. **iii)** Experiments performed with increasing fluid viscosity further illustrated that it is fluid shear stress rather than shear rate that is the primary parameter controlling activation. In these runs, doubling the fluid viscosity by addition of high molecular weight dextran at a constant shear rate of 9600/s caused a 2.4 fold increase in cell

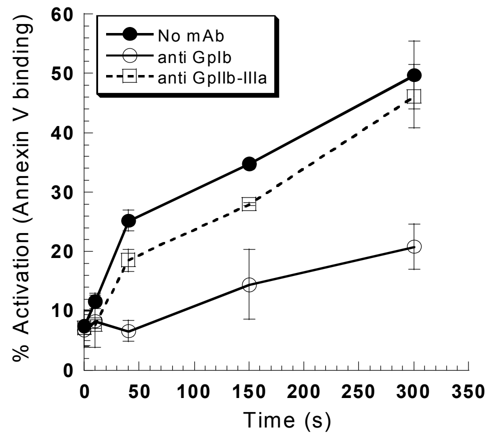

Fig 1: Citrated PRP subjected to shear at 9600/s in the presence of function blocking antibodies against GpIb or GpIIb/IIIa.

we varied the volume of our experimental sample. Recently, we have demonstrated that increasing sample volume at a constant cone rotational rate causes an increase in non-linear secondary flow in the cone-plate viscometer without markedly altering the average applied shear rate (1, 2). In these experiments we observed a ~20% decrease in platelet activation when non-linear shear was applied thus suggesting that time-varying fluid forces are not necessary for shear-induced platelet activation. **v)** Our experiments with static light scattering also revealed macroscopic changes in the shape of vWF upon application of hydrodynamic shear. Here, vWF molecules were observed to irreversibly change from a near spherical shape to an elongated conformation upon application of shear at 9600/s for 2 minutes.

SUMMARY

Our results suggest that fluid shear stress rather than shear rate, non-linear/time-variant flow or cell-cell collisions regulate platelet activation. Besides causing minor changes in the conformational domains of vwf, fluid shear can also cause dynamic irreversible changes in the macroscopic shape of vwf. Implications of our findings on our understanding of how physical forces may control GpIb/vWF function and contribute to thrombosis are discussed.

REFERENCES

1. Shankaran H., and Neelamegham, S. (2001) *Biorheology* **38**(4):275-304.
2. Shankaran, H. and Neelamegham, S. (2001) *Biophysical J.*, **80**(6):2631-2648.

OF MICE AND PIGS: THE CORONARY MICROVASCULATURE

Ghassan S. Kassab
Center for Biomedical Engineering, University of California, Irvine, CA, USA; gkassab@uci.edu

INTRODUCTION

Inbred strains of mice are being used with increasing frequency as subjects in many experimental cardiovascular studies. In particular, the strain C57BL/6 is perhaps the most widely used and hence the best known of all inbred strains. Despite the tremendous progress in the genotypic characterization of the mouse cardiovascular genome, however, the phenotypic characterization of the morphometry of the coronary microvasculature is lagging behind. The goal of the present study was to obtain a systematic set of data on the morphometry of the first several orders of the coronary microvasculature.

METHODS

Four mice (25.3±1.3 g) were pre-anesthetized to achieve requisite immobilization. The mice were anesthetized with an intra-peritoneal injection of sodium pentobarbital (40 mg/kg) and the carotid artery was cannulated for blood pressure measurement. A tracheostemy was performed and the mouse ventilated with a rodent respirator. The chest was opened with a mid-line sternotomy. The blood was heparinized with a 0.1 ml of normal saline with 200 U/ml of heparin via the carotid artery catheter. The animal was sacrificed with an injection of 0.5 ml of 3.3 M KCl via the jugular vein for diastolic arrest while the animal is deeply anesthetized. The heart was rapidly removed and cannulated via the thoracic aorta at the arch for retrograde perfusion of the coronary arteries. A solid cast of the coronary vasculature was made with elastomer that was catalyzed to solidify in 45 minutes (Kassab et al, 1993). The aortic perfusion pressure was maintained at physiologic value until the elastomer was completely hardened.

The morphometric data on the coronary arterial vessels of diameters < *50* µm was obtained from histological specimens as described in our previous studies on the pig (Kassab et al, 1993). Briefly, plugs of myocardial tissue were removed from the left ventricles of cast hearts. Each plug was mounted on a freezing microtome and serial sections of 60- to 80- µm thickness was cut. Each section was dehydrated with 100% alcohol and cleared with methyl salicylate to render the myocardium transparent and the elastomer-filled microvasculature visible in light microscopy. The distinction between arterioles and venules were made possible because of the differences in the branching pattern. The morphology of the coronary microvessels were reconstructed through optical sectioning as described previously by Kassab et al. (1993). The reconstructed vessels were ordered in accordance with the diameter-defined Straher system to obtain a relationship between the diameter, length, connectivity and the order number (Kassab et al, 1993).

RESULTS AND DISCUSSION

We found the first four orders of the mouse arterioles vessels to have diameters of 9.1±0.85, 12.4±1.1, 17.9±1.8 and 25.8 ± 3.6, respectively. The data on the diameter were not different from the corresponding orders in the pig heart. The data on the length of the first four orders of elements are shown in Fig. 1. The data is compared to the published data of the pig coronary arterioles. We found the lengths of the first four orders of vessels to be significantly smaller in the mouse heart.

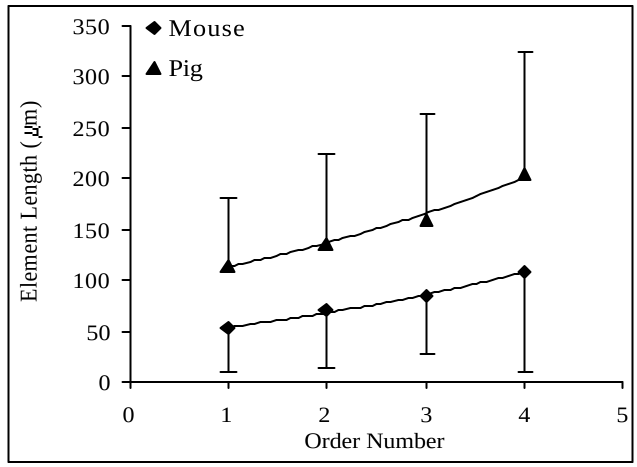

SUMMARY

Our preliminary results show that the vascular anatomy of the first several orders of vessels (microvascualture) to be very similar to those of the pig heart. The diameters of the first several orders of arterioles were found to similar to the respective orders in the pig heart. The lengths however were found to be significantly smaller in the mouse heart as shown in Fig. 1. Since the diameter is hemodynamically a more important parameter than the length, it is important to establish that the mouse is similar to the pig which is considered an excellent model for the coronary anatomy of humans.

REFERENCES

Kassab, G.S., C.A. Rider, N.J. Tang and Y.C. Fung. Morphometry of pig coronary arterial trees. *Am. J. Physiol.* ***265*** *(Heart Circ. Physiol. 34)*: H350-H365, 1993.

MORPHOLOGY OF ENDOTHELIAL CELLS UNDER FLOW ALTERATION IN VIVO

Hirotake Masuda[1], Koichi Kawamura[1], Hiroshi Nanjo[1], Masayo Komatsu[1], Tatsuo Sugiyama[1], Eiketsu Sho[1,2], Akihiro Sugita[1], Yasushi Asari[1], Mikio Kobayashi[1], Toshihito Ebina[1], Naoto Hoshi[1], Tej M Singh[2], Chengpei Xu[2], and Christopher K Zarins[2]

[1] Second Department of Pathology, Akita University School of Medicine, Akita 010-8543, Japan, masuda@med.akita-u.ac.jp, [2] Division of Vascular Surgery, Stanford University School of Medicine, Stanford, CA 94305-5642, USA

INTRODUCTION

Endothelial cells show smooth lumen surface and scanty organelles with flat nucleus. It is known that high-flow dilates blood vessel and low-flow narrows blood vessels (Thoma, 1893). Later Kamiya and Togawa (1980) showed that Thoma's principle works so as to keep wall shear stress constant in the artery and that blood vessels are in equilibrium to the flow. It is therefore considered that the endothelial cells in vivo represents the equilibrium state, if we observe blood vessels in the normal animals. However, there would be various states of endothelial cells according to the various states of flow. In this report, we show morphology of endothelial cells in flow alteration and discuss the relationship to flow.

ARTERIES IN HIGH FLOW

Arterial blood flow increases, when arterio-venous fistula (AVF) is made in the distal of the arteries (Kamiya and Togawa, 1980; Masuda et al., 1999). In the common carotid arteries of the dogs and the rats, artery dilated and endothelial cells proliferated (Tohda et al., 1992; Sugiyama et al., 1997). In the rabbit common carotid arteries (Masuda et al., 1999), artery dilated remarkably as compared to those of dogs or rats. At 2 days of AVF, endothelial cells protruded abluminally and basement membrane was degenerated. At 3 days, endothelial cells frequently attached with medial smooth muscle cells in the enlarged fenestrae of the internal elastic lamina. At 4 days, there appeared the gaps of the internal elastic lamina. The gaps of the internal elastic lamina enlarged thereafter and the artery dilated.

ARTERIES IN LOW FLOW

Increased blood flow induced by AVF was reduced by the closure of the AVF (Zhuang et al., 1997; Sho et al., 2001). In the rabbit common carotid arteries, which were dilated by the 4 weeks AVF, wall shear stress reduced remarkably near 0.1 to 0.2 Pa (control or normal, 1-2 Pa) by the closure. After closure of the AVF, endothelial cells became short (1 day after AVF closure) and became almost round (3 days after AVF closure). Number of endothelial cells decreased rapidly with apoptosis. Medial smooth muscle cells began to migrate into the intima through the gaps of the internal elastic lamina.

CAPILLARIES IN THE ELELECTRICALLY STIMULATED SKELETAL MUSCLE

When skeletal muscle is electrically stimulated, capillaries increase with angiogenesis (Hudlicka et al., 1992). We observed extensor digitorum longus of the rabbits, which was electrically stimulated for 3, 7, and 14 days (Ebina et al., 1996). Tissue blood flow increased after stimulation. At 7 days stimulation, capillary sproutings appeared nearly 4,000 per cubic mm. When, in the electrically stimulated extensor digitorum longus of the rabbits for 7 days, electrical stimulation was stopped, some capillaries disappeared (Hoshi et al., 2000). After 4 weeks, capillary density became normal.

SUMMARY

Morphologic changes of endothelial cells in the arteries and capillaries were studied under flow alteration using arterio-venous fistula or electrical stimulation. Endothelial cells under high-flow usually proliferate and induce remodeling of the blood vessels. In the arteries, the remodeling is dilatation and in the capillaries, it is angiogenesis. On the contrary, endothelial cells under low-flow usually disappeared with apoptosis and induce regression of the blood vessels. In the arteries, the remodeling is narrowing and in the capillaries, it is angio-regression. Therefore endothelial reaction to flow alteration would be summarized as "High-flow induces angiogenesis and low-flow induces angio-regression."

REFERENCES

Ebina, T. et al. (1996). *Sixth World Congress for Microcirculation.* Monduzzi Editore, Italy, pp27-31.
Hoshi, N. et al.. (2000). (Abstract) *J. Submicrosc. Cytol. Pathol.* **32**: 361.
Hudlicka, O. et al. (1992). *Physiol. Rev*. **72**: 369-417.
Kamiya, A., Togawa, T. (1980). *Am. J. Physiol.* .**239**: H14-21.
Masuda, H. et al. (1999). *Arterioscler. Thromb. Vasc. Biol.* **19**: 2298-2307.
Sho, E. et al. (2001). *Arterioscler. Thromb. Vasc. Biol.* **21**: 1139-1145.
Sugiyama, T. et al. (1997). *Arterioscler. Thromb. Vas. Biol.* **17**: 3083-3091.
Thoma, R. (1893). *Untersuchungen uber die Histogenese und Histomechanik des Gefasssystems*. Stuttgart. Enke.
Tohda, K. et al. (1992). *Arteriosclerosis and Thrombosi*s **12**: 519-528.
Zhuang, Y-J. et al. (1998). *Eur. J. Vasc. Endovasc. Surg.* **16**: 301-310.

CORONARY MICROVASCULAR RESISTANCE AS DERIVED FROM INTRACORONARY PRESSURE AND VELOCITY MEASUREMENTS IN HUMANS

Maria Siebes

Depts. of Cardiology and Medical Physics, Cardiovascular Research Institute Amsterdam
Academic Medical Center, University of Amsterdam
Meibergdreef 15, 1105 AZ Amsterdam, The Netherlands

INTRODUCTION

For the evaluation of coronary stenosis severity in the catheterization room, sensor-equipped guide wires have been developed that on the one hand serve as a classical guide wire over which, e.g., balloon catheters can be introduced in the coronary arteries, but which at the same time allow for the measurement of pressure or blood velocity distal of the lesion. Recently, wires have been developed that enable the combined measurement of these two quantities and thereby allow not only the quantification of stenosis severity but also of the resistance of the coronary microcirculation.

PHYSIOLOGICAL CONCEPTS

The evaluation of the physiological significance of a stenosis is based on concepts of the coronary circulation developed in physiology. A patient develops problems when blood supply is not sufficient to meet oxygen demand. Demand increases with exercise and hence, supply may be sufficient at rest but fails at exercise. With a sensor downstream of the lesion, one is able to quantify the response of the coronary circulation to a vasodilator as a substitute stimulus for exercise.

Until recently, only the velocity or the pressure could be measured clinically distal to a stenosis. The interpretation to the vasodilator stimulus measured by either signal is based on the same physiological concept: coronary flow reserve. The velocity-based index is simply the ratio of velocity at maximal dilation and at rest and results in CFVR. With the pressure sensor, the ratio of distal pressure and aortic pressure at maximal dilation is used as an index, FFR. This index represents the ratio of flow with a stenosis to that in the same vessel without a stenosis.

CORONARY MICROVASCULAR RESISTANCE

The problem with the traditional concepts, FFR and CFVR, is that these are based on a simplified concept of the coronary microvascular resistance. It is assumed that microvascular resistance at maximum vasodilation is independent of pressure and that it is similar between different perfusion areas of major coronary arteries in the same heart. It is therefore not surprising that these indices can result in rather conflicting outcomes in the prediction of the physiological impact of the stenosis (Meuwissen, 2001).

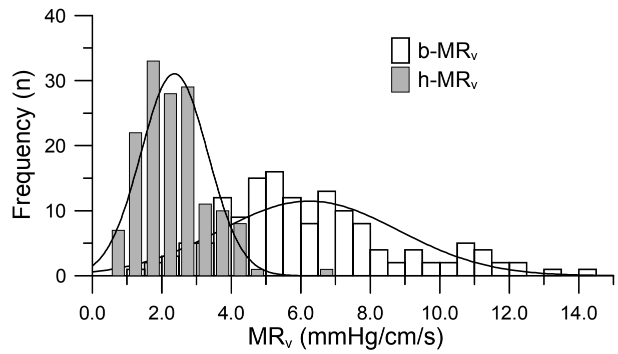

Figure 1: Distribution of microvascular resistance at rest (b-MR_v) and at maximal hyperemia (h-MR_v)

First, combined measurements of distal pressure and velocity demonstrate a rather large variation of microvascular resistance between hearts and between perfusion areas as demonstrated in Figure 1. These variations still hold when velocity-based resistance is corrected for vascular dimensions. These variations are in line with what is known about heterogeneous distribution of blood flow in animal studies, which was more recently confirmed in humans with PET (Chareonthaitawee, 2001).

FINALLY

At present we are evaluating a guide wire which has both a velocity and a pressure transducer at the tip that can be located downstream of the stenosis. In this way, information on the microcirculation can be incorporated in the clinical decision making before PTCA and/or stenting and the effect of the intervention on the microcirculatory resistance index can be evaluated.

REFERENCES

Meuwissen, M., et al. (2001). *Circulation*, **103**, 184-187
Chareonthaitawee, P., et al. (2001). *Cardiovasc Res.*, **50**,151-161

ACKNOWLEDGEMENTS

This presentation is the result of collaboration with Prof. Jan J. Piek from the Dept. of Cardiology and Prof. Jos A.E. Spaan from the Dept. of Medical Physics.

RESCUE BY TRANSPLANTATED ENDOTHELIAL CELLS FOR ISCHEMIC RENAL FAILURE -VISUALIZATION OF PERITUBULAR CAPILLARIES USING INTRAVITAL VIDEOMICROSCOPY-

Tokunori Yamamoto[1)], Eisei Noiri[2)], Tetsuhiro Tada[3)], Reiji Hashimoto[3)], Sergey V. Brodsky
Fumihiko Kajiya[4)] and Michael S. Goligorsky[5)]

Dept. of Urology, Kawasaki Medical School [1)], Dept. of Nephrology and Endocrinology, The University of Tokyo[2)],
Dept.of Electronic Eng.,Okayama, Univ of Science[3)], Dept. of Cardiovascular Physiology, Okayama University School of Medicine and Dentistry[4)],Dept. of Medicine, Physiology and Biophysics, SUNY[5)],

INTRODUCTION

The recent advent of intravital microscopy has permitted to monitor microcirculation in vivo with minimal invasion. Here we report on the first findings made with the use of a pencil-lens intravital non-invasive technology(AJP-Renal 2001) as applied to ischemic rat kidney.The aims were to clarify vizualize peritubular capillary(PTC) microcirculation contributed pathology on ischemic renal failure directly and whether does the transplantation of human umbilical venous endothelial cell(HUVEC) result hemodynamic improvement in the ischemic renal failure .

MATERIAL AND METHODS

Peritubular capillary and glomerular blood flow were monitored under basal conditions, during renal artery occlusion and immediately following release of the clamp. Erythrocyte velocity was calculated as an angle on consecutive spatio-temporal images(Methods Inf Med 2000)

After 45 minutes, the left renal artery was released, while the right renal pedicle and the right ureter were ligated and a right nephrectomy was performed. After release of the clamp, 10^6/0.2 ml HUVEC labeled with Cell Tracker (Molecular Probes) and human embryonic kidney cells(HEK), HEK/2GA(Mutant) or HEK/eNOS(Wild type human endothelial nitric oxide synthase) were injected into the right jugular vein or the aorta (through a catheter inserted into the left carotid artery) to athymic nude rats(n=5) with the ischemic renal failure.

RESULTS

RBC velocity in peritubular capillaries averaged 1069±146 um/sec (n=15). As expected, clamping the renal artery resulted in a complete cessation of blood flow accompanied by blanching of the surface and visualization of individual RBC halted within the vessels. The release of renal artery occlusion consistently resulted in an almost instantaneous recovery of blood flow. Surprisingly, within 1-2 minutes blood flow seized and showed partial recovery by 60 min. Twenty-four hours post-ischemia, peritubular capillary blood flow remained significantly diminished, representing only 1/3-1/4 of control level(Fig.1). Blood flow was uniformly orthograde under control conditions, however, it displayed retrograde direction of flow upon reperfusion. The patency of peritubular capillaries was partially compromised during early reperfusion period, but rapidly recovered. The recovery of glomerular microcirculation occurred faster than that of peritubular capillaries. HUVEC-injection kidneys displayed(Fig.2) a significant hemodynamic improvement. Microcrculatory hemodynamics was not affected by the transplantation of HEK or HEK/G2A cells. In contrast, HEK/eNOS cells afforded a significant hemodynamic protection to the ischemic kidney.

SUMMARY

We suggest that in superficial cortical microvasculature, a functional vasculopathy develops early in the course of ischemia-reperfusion. and the circulating exogenous endothelial cells could protect the kidney against ischemic injury.

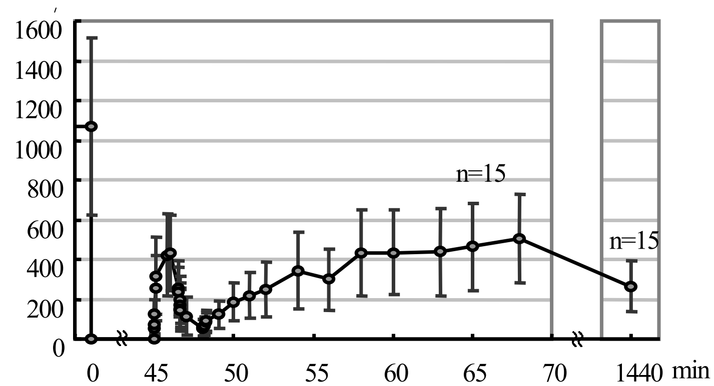

Fig.1 Erythrocyte velocities in PTC

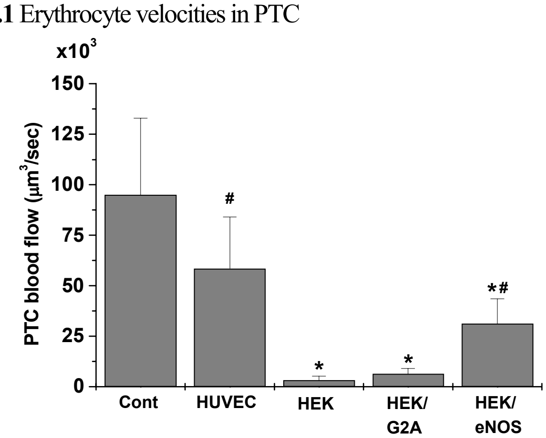

Fig.2 Blood flow in PTC of athymic nude rats

INHIBITORS OF NITRIC OXIDE SYNTHASE IN RELATION TO DISTURBANCE OF CORONARY SUBENDOCARDIAL MICROVESSELS

*Toyotaka Yada, #Fumihiko Kajiya
*Department of Medical Engineering, Kawasaki Medical School, 577 Matsushima, Kurashiki, Japan
#Department of Cardiovascular Physiology, Okayama University Graduate School of Medicine and Dentistry, 2-5-1 Shikatacho, Okayama, Japan

INTRODUCTION

It is well known that coronary risk factor contribute to the development of atherosclerosis with endothelial dysfunction. Asymmetric dimethylarginine (ADMA), an endogenous inhibitor of nitric oxide (NO) synthase is elevated in vascular endothelial dysfunction with decrease of dimethylarginine dimethylaminohydrolase (DDAH) activity, which degrades ADMA. Oxidized-LDL inhibits the DDAH activity and tetrahydrobiopterin (BH_4) in vitro (Figure 1). The subendocardium (ENDO) is more prone to ischemia than the subepicardium (EPI) in the hypertensive hypertrophic heart. However, there is no study of evaluation of the endothelium-dependent, -independent vasodilation and inhibitor of NO synthase in ENDO in the time-course of hypertension (HT).

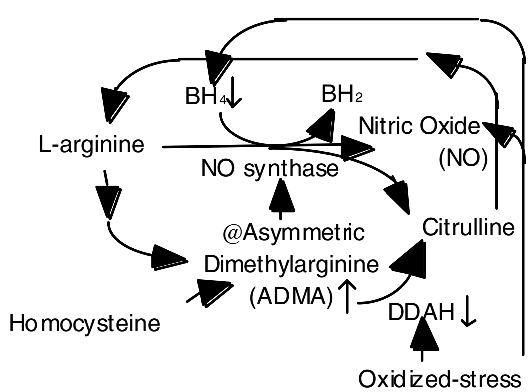

Figure 1 @NO synthase pathway

We evaluated the time sequential changes in endothelium dependent and independent vasodilator on subendocardial arterioles (Endo-A) in the renovascular hypertensive canine hearts and also evaluated ADMA, BH_4 and DDAH in both ENDO and EPI of hypertensive hearts.

METHODS

We measured the diameter of Endo-A and subepicardial arterioles (Epi-A) in renovascular hypertensive canine hearts using CCD intravital microscope. Vascular responses to acetylcholine (Ach) and papaverine (Papa) were compared in normotensive (N) and hypertensive (4th week HT, 4wHT and 12th week HT, 12wHT) hearts.

We also evaluated plasma and rat heart tissue ADMA, BH_4 and DDAH in WKY and SHR (both 14th-week). ADMA and BH_4, and DDAH were evaluated by HPLC and ELISA.

RESULTS

The mean aortic pressure were higher than those of normotensive group in both renovascular hypertensive canine model and SHR model.

Renovascular hypertensive hypertrophic canine model

Percent diameter change of Endo-A in both 4wHT and 12wHT after Ach were smaller than that of N. In Epi-A, a significant difference was observed only between N and 12wHT. The vasodilation of Endo-A in 4wHT and 12wHT was smaller than that of Epi-A. Endothelium-dependent vascular responses of Endo-A were impaired in both 4wHT and 12wHT, but only in 12wHT in Epi-A.

There was no significant difference after Papa between N and 4wHT in both Endo-A and Epi-A, while the vasodilation in 12wHT was impaired only in Endo-A. Thus, the endothelium-independent vasodilation was impaired time sequentially only in Endo-A of 12wHT.

Spontaneous hypertensive rats model

Plasma and myocardial ADMA were significantly elevated, myocardial DDAH, plasma and myocardial BH_4 were significantly decreased in SHR compared with WKY. These factors of NO synthase inhibition in ENDO is greater than that in EPI (see arrowheads in Figure 1).

CONCLUDING REMARKS

In an early stage (4wHT), the endothelium-dependent response of Endo-A was impaired. In the later stage (12wHT), both the endothelium-dependent and independent responses of Endo-A were impaired.

NO synthase disturbance in hypertension may be exacerbated by increment of ADMA, and decrease of DDAH and BH_4, causing endocardial ischemia and the advancement of ischemic heart disease.

REFERENCES

Yada, T. et al. (1997). *Circulation*., **96**, I-315.
Yada, T. et al (2001). *Jp. Circ. J.*, **65**, Suppl I-A.434

ACKNOWLEDGEMENTS

This study was supported by Grant-in-Aid 05454278 and 05557043 for General and Development Scientific Research (B) from the Ministry of Education, Science, Sports and Culture, Japan and Kawasaki Medical School Grant (4-107).

THE PATTERN OF SCAPULOHUMERAL MOTION - HOW STABLE IS IT?

Andrew Karduna[1], David Ebaugh[1], Lori Michener[3] and Phillip McClure[2]
[1] Programs in Rehabilitation Sciences, MCP Hahnemann University, Philadelphia, PA
[2] Department of Physical Therapy, Arcadia University, Glenside, PA
[3] Department of Physical Therapy, Virginia Commonwealth University, Richmond, VA
email: karduna@drexel.edu

INTRODUCTION

Scapular motion plays a fundamental role in the biomechanics of the shoulder complex. Experimental measures of scapular kinematics are important for a better understanding of shoulder function and for the development of computational models. Ever since the seminal paper of Inman et al. (1944) over a half-century ago, there have been over 50 published studies of scapular kinematics. Approximately half of these studies have examined the robustness of the scapulohumeral rhythm by looking at changes due to factors such as shoulder pathology, external load, velocity, posture, muscle fatigue, plane of elevation and rehabilitation. Recent models have only been able to account for changes in one or two factors (eg, de Groot and Brand, 2001). The purpose of this abstract is to review our experience with factors that can influence the stability of scapular kinematics.

MATERIALS AND METHODS

We have recently developed a non-invasive methodology for measuring scapular kinematics with a magnetic tracking device (Polhemus 3Space Fastrak, Colchester, VT) attached to the scapular spine and acromion process. This technique has been validated by comparison with measurements made by drilling pins directly into the scapula (Karduna et al., 2001). Additional surface mounted sensors were placed on the thorax and humerus. For each sensor, the arbitrary axes defined by the magnetic tracking device were converted to anatomic axes by digitizing bony landmarks. For each experiment, data were collected when subjects elevated their arms in the scapular plane. We have used this protocol to compare normal motion with motion under the following conditions:

- patients with impingement vs healthy controls
- patients with spinal accessory nerve palsy vs healthy controls
- effects of rehabilitation in patients with impingement
- effects of muscle fatigue in healthy subjects
- effects of external loads in healthy subjects
- active vs passive shoulder motion in healthy subjects

To help summarize the data from all of these studies, the maximum differences in the upward rotation motion of the scapula were calculated.

RESULTS AND DISCUSSION

The largest changes were observed in the two conditions in which the muscular control of scapular motion was the most affected – passive motion and nerve palsy (figure 1). Our results are consistent with the majority of studies in the literature, where differences of less than 5 degrees are observed for upward rotation with a perturbation to the system. To our knowledge, the only study reporting differences from controls in excess of 10 degrees of upward rotation was a study of patients who had sustained a stroke (Johnson et al., 1998). The implication of our results and results from the literature is that the scapulothoracic motion is a robust system, requiring substantial compromise before it exhibits dramatic pattern changes. It still remains to be seen whether the modest changes observed under most conditions are clinically or biomechanically relevant. For example, Ludewig et al. suggest that in patients with impingement syndrome, even small changes in scapular rotation may result in detrimental decreases in the clearance in the suprahumeral space (Ludewig and Cook, 2000). Additionally, although the scapula moves in a complex three-dimensional pattern, we have chosen to only report the motion about one axis here.

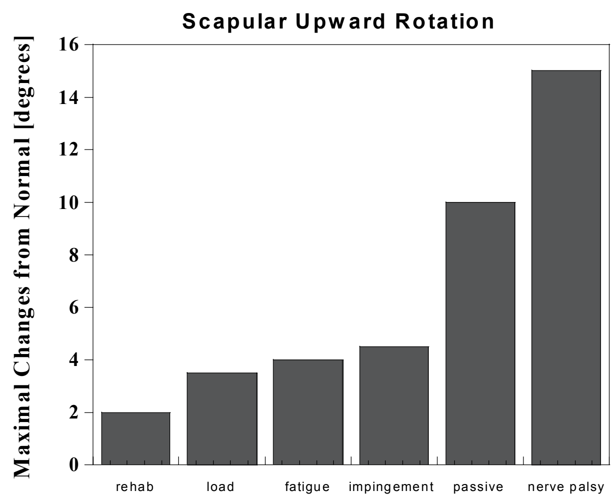

Figure 1 Maximal effects of different factors on upward rotation of the scapula.

REFERENCES

de Groot JH and Brand R, 2001, Clin Biomech, **16**, 735-43
Inman VT et al, 1944, JBJS **26**, 1-30
Johnson GR et al, 1998, Fifth International Symposium on the 3-D Analysis of Human Movement, 30-33.
Karduna AR, et al, 2001, J of Biomech Eng, **123**, 184-90
Ludewig PM and Cook TM., 2000, Phys Ther, **80**, 276-291.

ACKNOWLEDGEMENTS

Funding for this work was received from the Arthritis Foundation, Foundation for Physical Therapy and the National Institute of Occupational Safety and Health.

TOWARDS THE CREATION AND VALIDATION OF A LARGE SCALE MUSCULOSKELETAL UPPER LIMB MODEL

Germano T. Gomes[1], Garth R. Johnson
Centre for Rehabilitation and Engineering Studies (CREST), University of Newcastle Upon Tyne (UNUT), United Kingdom
[1]communicating author, G.T.Gomes@ncl.ac.uk, CREST, http://www.ncl.ac.uk/crest

INTRODUCTION

The shoulder mechanism is arguably the must complex joint system in the human body. Among the main factors that have precluded the accurate 3D measurement of movement and the development of large scale musculoskeletal models of the shoulder are: complex bone geometry allowing for a uniquely large range of movement, high number of muscles, some with very large attachment sites and with bi-articlar function, and existence of a gliding bone (scapula).

In the past 10 years these problems started to be dealt with, leading to the creation of large-scale shoulder/elbow models. Currently three of such models exist, namely the Dutch model (van der Helm, 1994), the Swedish model (Hogfors, 1989) and the Newcastle model (Charlton , 2001) to be discussed here.

METHODS

The construction of the model started with the appearance of accurate morphometric data obtained in detailed anatomical studies of the shoulder complex (Johnson at al, 1996) and from MRI and CT data from large general datasets (Visible Human Project). This has allowed the 3D reconstruction of all bone structures, identification of muscle attachment sites, subdivision of large muscles into different functional units and estimation of varying moment arms for each muscle.

The second aspect was the determination of the kinematics relations between scapula, clavicle and the humerus. Following the development of palpation techniques and instrumented linkages (Johnson, 1993) it was possible to derive 3D regression equations for both the scapula (Barnett, 1996) and the clavicle (Marchese, 2001) as functions of three angles of the humerus.

Third, an extensive database of daily activities (10 activities) directly involving the upper limb was gathered with the objective of estimating the forces/moments acting in the joints. In the process a robust upper limb marker attachment procedure and a method based in robotics for calculating joint forces/moments were developed. (Murray, 1999)

Finally, these have been integrated into an interactive shoulder/elbow model with (74 muscle elements) capable of estimating joint contact forces, joint stability, and muscle contact forces (Charlton, 2001)

Ongoing developments are towards the full integration of the model with the Matlab® environment and the development of muscle and proprioception models allowing for seamless inverse/forward dynamics control studies. Also, force/length perturbation experiments are being carried out to quantify stretch reflex for muscles crossing the elbow joint (Torres, 2002).

RESULTS AND DISCUSSION

1. The morphologic shoulder data obtained in CREST corresponds well with that obtained in other groups (Veeger, 1997) and is now part of a much larger database available to the entire biomechanics community.
2. The kinematics description of the scapula shows the same behaviour as that obtained in other groups. There is still the need to make it scalable as in the Dutch model and to increase its envelope of validity. The kinematic regressions describing movement of the clavicle agree well for 2 dof, the third (rotation) cannot be directly compared due to absence of similar data. (Marchese, 2001)
3. Our database of forces/moments during daily activities agrees with that obtained in (Cheng, 1996). Its uses are the assessment of disability, quantification of postoperative recovery and the design of rehabilitation equipment.
4. Computed moment arms agree largely with those found *in-vivo;* glenohumeral forces follow similar trends to those found in previous studies (Charlton, 2001).
5. The stretch reflex mechanism (posture maintenance) agrees well with experimental data for the cat soleus (Gomes, 2001). Transposition of methodology for elbow and shoulder remains to be considered after the model is (or can be) validated for elbow muscles.

In terms of direct and strict validation of the final model, the only two avenues currently available seem to be EMGs and, more promising, the inclusion of force sensors in shoulder prostheses. Indirectly, the use of forward dynamics can also be used to corroborate these models. Apart from these two aspects, the need for creation of individualized or highly scalable models has also been identified.

REFERENCES

Barnett, N.D. (1996). Measurement and modelling of 3D scapulohumeral kinematics. Ph.D. Thesis, UNUT, UK.
Charlton, I.W. (2001). Application of a large-scale musculoskeletal upper limb model: Analysis of forces at the glenohumeral joint ISB Congress, Zurich.
Cheng, P.L.(1996) Biomechanical study of upper Limb activities of daily living. PhD Thesis, University of Strathclyde, Glasgow, Scotland.
Gomes, G.T. (2001). The use of a cross-bridge model in closed loop simulations. ISB Congress, Zurich.
Hogfors, C. et al (1989). J. Biomech. 20,157-166.
Johnson G.R. et al (1996). J. Biomech 29, 1039-1051.
Johnson, G.R. et al (1993). Clin Biomech ;8:269-73 .
Marchese, S.S. (2000). Sterno-clavicular kinematics - a new measurement system. Ph.D. Thesis, UNUT, UK.
Murray, I.A.(1999).Upper limb kinematics and dynamics during every day tasks. PhD Thesis, UNUT, UK.
Torres, J.S (2002). A novel approach to the measurement of human stretch reflex responses. Internal report, UNUT, UK.
Van der Helm, F.(1994).Journal of Biomechanics 27,551 –569.
Veeger, H.E.J. et al (1997). J. Biomech. 30, 647 –652.

AKNOWLEDGMENTS

This work is the result of the combined effort of many people at Crest namely Prof. Garth Johnson, Dr. Nick Barnett, Dr. Ingram Murrey, Dr. Sandro Marchesse, (Dr) Ian Charlton, Jose Salazar and Andreas Kontaxis.

STRESS ANALYSIS OF THE ROTATOR CUFF: MODEL DEVELOPMENT AND VALIDATION

Mark E. Zobitz and Kai-Nan An
Biomechanics Laboratory, Department of Orthopedics, Mayo Clinic/Mayo Foundation
200 First Street SW, Rochester, MN 55905, e-mail: an.kainan@mayo.edu

INTRODUCTION

Rotator cuff injuries produce significant clinical sequelae and can impair joint functionality. Therefore, an understanding of the etiology of rotator cuff tears would be useful for devising treatment strategies that promote healing and prevent further damage. Although mechanical factors have been implicated as the initiator of rotator cuff tears, there is considerable debate whether damage is instead initiated intrinsically. Using a finite element model to predict the stress state of the rotator cuff tendons under various conditions would be useful for understanding how different variables contribute to the pathological condition. A model could also be used to predict how a cuff tear would progress from a clinically insignificant size to one that requires surgical intervention. A third utility of a model could be to simulate treatment strategies that maintain joint stability without compromising tissue integrity. Development of a representative finite element model involves three basic components: geometry, material properties, and boundary conditions. The purpose of this paper is to highlight some of the work we have done to characterize these components to help validate computer simulations.

ANALYTIC MODEL

A stress analysis of the rotator cuff was reported using a 2-D model of a coronal section through the rotator cuff (Luo, 1998). Although 2-D models have the advantage of being simple to construct, their utility is limited as the rotator cuff tendon geometry is not uniform (Halder, 2000a, 2000b, and 2001a; Itoi, 1995). Anatomic geometry of the rotator cuff can be obtained from MRI scans to produce a 3-D model. We created a 3-D surface rendering of the rotator cuff using Analyze image processing software (Mayo Foundation, Rochester, MN) to process the MRI slice data. Then, the surface information was imported into Patran (MSC Software, Santa Ana, CA) finite element software for meshing.

Proper representation of the material behavior of biological tissues is quite a challenge. Since the supraspinatus tendon is subjected to longitudinal stresses (due to muscle tension) and compressive stresses (due to acromial impingement), a material model has been described using an elastic fiber embedded within a hyperelastic extrafibrillar matrix (Luo, 1998). The elastic fiber component, which simulates the collagen fibers, is easily incorporated using the Rebar element in ABAQUS software (HKS, Pawtucket, RI).

To validate the material model, experimental test results are needed. We have measured the regional variations in tensile properties of the rotator cuff tendons (Zobitz, 2001a). In addition the compressive properties of the supraspinatus tendon were measured (Lee, 2000) and fit to a hyperelastic model (Zobitz, 2001b).

Due to the convergence of the rotator cuff tendons at the humeral insertion, force transmission is still possible in the presence of a rotator cuff defect, due to the concept of the rotator cable (Burkhart, 1993). We have undertaken a number of studies to characterize force transmission patterns through the rotator cuff in the presence of increasing supraspinatus and infraspinatus defects. In addition, we have studied how repairs using either native tissue or synthetic graft material can restore the force generating capacity (Halder, 2001b; Mura, 2002).

EXPERIMENTAL VALIDATION

Recent advances in medical imaging make the experimental measurement of the stress and strain distributions possible. The technique of magnetic resonance elastography (MRE) has shown promise for providing information on tissue properties and tension distribution under various loading conditions and identification of regions of tissue injury (Jenkyn, 2001).

Measuring tissue strain using a pattern matching technique also shows promise for characterizing regional variations in tissue strain (Bey, 2001). The method involves taking MRI images at different joint orientations and calculating the strain components of a particular region of pixels. Since regional strain values can be obtained this method could be used to validate the results predicted by the finite element model.

CONCLUSION

In conclusion, information from experimental measurements is available for establishing a reliable 3-D model for rotator cuff stress analysis. In addition, potential imaging techniques could possibly be used to validate the findings. Such models would be useful to understand the etiology and treatment of rotator cuff disorders better.

REFERENCES

Bey, M.J. et al (2001). *ASME Summer Meeting*, **50**, 45.
Burkhart, S.S. et al (1993). *Arthroscopy*, **9**, 611-616.
Halder, A. et al (2000a). *Clin Biomech*, **15**, 456-462.
Halder, A. et al (2000b). *J Orthop Res*, **18**, 829-834.
Halder, A.M. et al (2001a). *J Musculoskeletal Res*, **5**, 105-112.
Halder, A. et al (2001b). *Trans 47th ORS Meeting*, **26**, 774.
Itoi, E. et al (1995). *J Orthop Res*, **13**, 578-584.
Jenkyn, T. et al (2001). *Trans 47th ORS Meeting*, **26**, 299.
Lee, S.B. et al (2000). *Clin Biomech*, **15**, 241-247.
Luo, Z.P. et al (1998). *J Shoulder Elbow Surg*, **7**, 616-620.
Mura, N. et al (2002). *Trans 48th ORS Meeting*, **28**.
Zobitz, M. et al (2001a). *Trans 47th ORS Meeting*, **26**, 773.
Zobitz, M.E. et al (2001b). *J Biomech Eng*, **123**, 47-51.

ACKNOWLEDGEMENTS

Funding for studies performed at the Mayo Clinic was received from NIH and the Mayo Foundation.

CELLULAR RESPONSES REGULATING SIGNALING AND GENE EXPRESSION IN TENDON CELLS

Albert J. Banes [1,2,3], Joanne Archambault[4], Mari Tsuzaki[1], Michelle Wall [1,2], Joanne Garvin [1,3]. Department of Orthopaedics[1],

Biomedical Engineering[2], Curriculum in Applied and Materials Sciences[3], University of North Carolina, Chapel Hill, NC 27599; Genetics Institute[4], Boston, MA

ABSTRACT

Tendons are designed to transfer the force and are principally tensile load bearing. However, tendons may also be subjected to compression when passing through a pully or travel around bone. Tendons are also subjected to shear as they glide through sheaths, past extratendinous tissue, as collagen fibrils slide past one another during torsional bending or as fluid flows amidst cells and fibrils during load bearing. Hence, tendon cells are subjected to multifaceted mechanical loading during routine use. These load fields are changed as a consequence of traumatic injury or overuse. Our lab has focused on tendon cell responses to mechanical loading in several different models in vivo, ex vivo and in vitro. Cells in each experimental model respond to applied load by signaling, usually through an increase in intracellular calcium. Cells may also act synergistically with a ligand to increase or decrease a response to load. IL-1b can act as a positive stimulus whereas ATP can act as a negative modulator of a load response. Moreover, cells have multiple mechanisms with which to respond to load including integrin contacts with extracellular matrix, cell-cell contacts at desmosomes, intracellular contractile proteins including actin but also titin and nebulin, classically associated with muscle. We will discuss the loading paradigms as well as cellular responses in tendon cells.

REFERENCES

Banes AJ, G Horesovsky, C Larson, M Tsuzaki, S Judex, J Archambault, R Zernicke, W Herzog, S Kelley and L Miller. (1999). Mechanical load stimulates expression of novel genes *in vivo* and *in vitro* in avian flexor tendons. *Osteoarthritis and Cartilage* 7:141-153.

Banes, AJ, Weinhold, P, Yang X, Tsuzaki, M, Bynum D, Bottlang M, and Brown T. (1999) Gap junctions regulate responses of tendon cells ex vivo to mechanical loading. *Clin Orthop and Rel Res*, in press November, 1999.

Archambault J, Tsuzaki M, Herzog W, Banes AJ. Stretch and interleukin-1b induce matrix metalloproteinases in rabbit tendon cells in vitro. J Orth Res in press, 2001.

TENSILE LOAD MODULATES INHIBITION OF MMP-1 EXPRESSION IN TENDONS

SP Arnoczky, T Tian, M Lavagnino; Laboratory for Comparative Orthopaedic Research,
Michigan State University, East Lansing, Michigan 48824

INTRODUCTION

The deleterious effects of immobilization on the material properties of ligaments and tendons are well-known. Previous work in our laboratory has demonstrated a progressive and significant decrease in the tensile modulus of stress-deprived tendons in an *in vitro* system. However, this effect was inhibited by application of low level (frequency and magnitude) cyclic strain. While the exact mechanism by which stress-deprivation decreases tensile modulus is still unclear, several investigators have implicated the role of collagenase (MMP-1) in this process. It was the purpose of this study to examine the effect of various levels of tensile load on the inhibition of MMP-1 expression in rat tail tendons. It was our hypothesis that tensile load will inhibit MMP-1 expression in a dose dependent manner.

MATERIALS AND METHODS

Tendons were obtained from the tails of adult ACI rats. The tendons were maintained in DMEM media supplemented with 10% fetal bovine serum, antibiotic/antimycotic solution, and ascorbate at 37°C and 10% CO_2 for the duration of the experiments. Tendons were divided into the following groups: *Group 1 (n=20)*: stress deprived (no load) for 24 hrs; *Group 2 (n=20)* statically stressed @0.16MPa for 24 hrs; *Group 3 (n=20)* statically stressed @0.75MPa for 24 hrs; *Group 4 (n=20)* statically stressed @25MPa for 24 hrs; *Group 5 (n=20)* cyclically loaded (6% strain @0.017Hz) for 24 hrs. The 6% strain coincides with a tendon stress of 25MPa. At the end of the experimental period total cellullar RNA was extracted from the tendon cells and processed for Northern blotting. The RNA blots were hybridized with a cDNA probe for rat MMP-1 generated in our lab and a human G3PDH cDNA control probe. The exposed films were scanned and MMP-1 expression was quantified by optical density measurements and standardized as a ratio of G3PDH expression. The effect of load magnitude was evaluated using an ANOVA with significance set at $p<0.05$).

RESULTS

Stress deprivation for 24 hours resulted in a marked up-regulation of MMP-1 expression in tendon cells. Static loading resulted in a significant dose-dependent (but not complete) inhibition of MMP-1 expression (Figure 1). These loads corresponded with a progressive loss of tissue crimp and an increase in fiber recruitment (Figure 2). Cyclic loading (6% strain @0.017Hz [I cycle/minute]) for 24 hours completely inhibited MMP-1 expression.

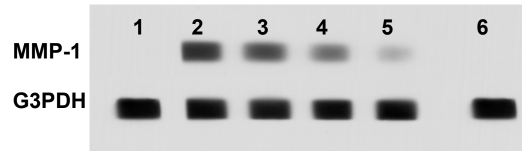

Figure 1: Northern blot showing mRNA expression of MMP-1. Lanes 1-fresh tendon (0 time); 2-no load, 24h; 3-0.16MPa, 24h; 4-0.75MPa, 24h; 5-25MPa, 24h; 6-6% cyclic strain @0.017Hz 24h.

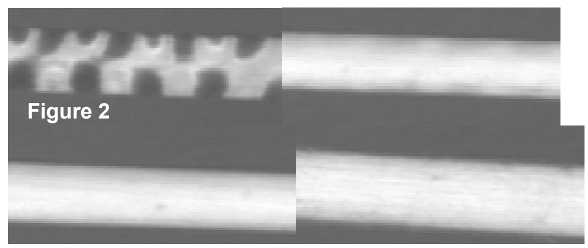

DISCUSSION/CONCLUSION

The results of this study demonstrate that stress deprivation in tendons results in an immediate (within 24 hrs) up-regulation of MMP-1 expression in tendon cells. This expression appears to be inhibited by tensile load in a dose dependent manner and coincides with the progressive recruitment of collagen fibers. The importance of cell matrix interactions in maintaining normal tissue homeostasis has been well-documented. Studies from our lab have shown that there is a significant correlation between tendon strain and cell nucleus deformation. This stress-induced deformation is probably important in the MMP-1 inhibitory mechanism in tendon cells as cytoskeletal alterations have been implicated in the regulation of MMP-1 expression in fibroblasts grown in monolayer. While static load (and cell deformation) partially inhibited MMP-1 expression, low frequency cyclic loading completely inhibited MMP-1 expression; suggesting the importance of repetitive signaling. Thus, the effect of loading history on *in situ* cytoskeletal adaptations and matrix interactions may provide a key to understanding the effect of various exercise regimes on tendon health. This is the subject of ongoing investigations in our lab.

MOLECULAR AND CELLULAR ANALYSIS OF ROTATOR CUFF TENDINOSIS IN A RAT OVERUSE MODEL

Laura Gamer[*], Kelly McDermott[#], Karen Cox[#], Maureen Mertens[+], Louis J. Soslowsky[1], Vicki Rosen[*]
McKay Orthopaedic Research Laboratory, University of Pennsylvania. [1]soslowsk@mail.med.upenn.edu

INTRODUCTION

Tendinosis, often caused by overuse, can lead to microtrauma and weaken the structural and vascular elements of tendon. As tendinosis progresses and the intrinsic reparative ability of the tendon is overwhelmed, the tissue degenerates, often leading to tendon rupture, joint instability, and/or degenerative arthritis. Little is known about the mechanisms responsible for tendinosis and this lack of knowledge has hindered therapeutic advances in treatment. The objective of this study was to use a rat overuse model [1] to begin to profile the cellular and molecular changes associated with repetitive tendon injury.

METHODS

Sprague-Dawley rats were subjected to treadmill running to model a rotator cuff tendon overuse injury [1]. Rats were sacrificed at 4, 8, 13 and 16 weeks. For histologic analysis, both left and right supraspinatus tendons from 3 rat runners and 3 cage activity controls were removed, processed for histology, stained with toluidine blue, and analyzed by light microscopy. For Northern Blot analysis, both supraspinatus tendons from 5 additional rat runners and 5 additional cage activity controls were pooled and total RNA was extracted using the TRIspin method [2]. Ten microg of total RNA was used for each group. Blots were consecutively hybridized with rat cDNA probes specific for collagen type I, collagen type III, biglycan, decorin, TGF-B1, and GAPDH.

RESULTS

Control supraspinatus tendons showed low cellularity, long spindle shaped cells, and well organized linear collagen fibers (fig 1.). Tendons from rats run for 4 weeks showed some slight changes. Tendons from 8 week rats showed more degenerative changes, potentially reflecting the progression of tendinosis. Large numbers of cells were rounded up and bunched together, with a disorganized collagen fiber network. Tendons from 13 to 16 week rats showed focal areas of damage as well as an increasing number of blood vessels in the tendon body, consistent with that seen in later stages of human tendinopathy (fig. 1). From Northern blot analysis, we found significant changes in tendons from rats run for only 4 weeks. Collagen type I, collagen type III, and TGF-B1 gene expression were downregulated while biglyan and decorin levels were unchanged (fig. 2). Similar changes were seen in tendons from 8 week rats. In tendons from 13 week rats, levels of collagens I and III remained repressed, while biglycan levels began to fall and TGF-B1 expression levels returned to that of control (fig. 2).

ACKNOWLEDGEMENTS Genetics Institute and the NIH.
*Harvard-Forsyth, #Genetics Inst., +Millenium Pharm.

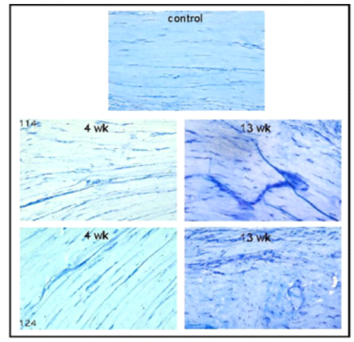

Figure 1. Histology of control, 4 and 13 week supraspinatus tendons

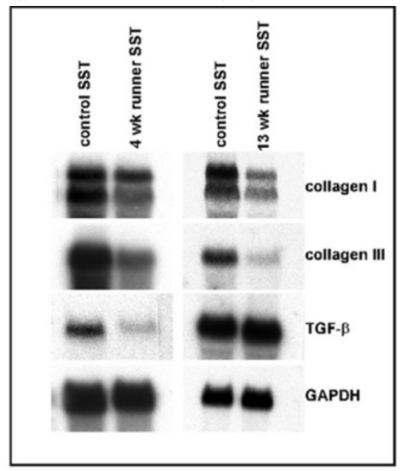

Figure 2. Northern Blot analysis of control, 4 and 13 week supraspinatus tendons

DISCUSSION

Molecular changes consistent with degeneration were present at the earliest time point studied and over time consistent with a tissue injured early in overuse and repeatedly damaged. As a result, the tissue cannot mount a successful repair response. The molecular data is consistent with previous data from this model [1] which showed decreased mechanical properties of exercised tendons between 4 and 16 weeks. In that study, exercised tendons showed an increase in the amount of tissue present over time, suggesting an increase in the production of matrix components [1]. This fact was not reflected in our gene expression analysis as most of the matrix mRNAs examined were downregulated. One explanation for this discrepancy is the limited number of genes evaluated in this initial study. Further study is necessary to identify important factors in the disease etiology/pathogenesis so that appropriate prophylactic and/or therapeutic treatment modalities can be developed.

REFERENCES 1. Soslowsky et al J Shoulder Elb Surg, 9:79-84, 2000, 2. Reno et al Biotechniques 22:1082-1086, 1997

EXTRACELLULAR MATRIX WITHIN MUSCLE AND MUSCLE CELL – ECM INTERACTIONS IN RELATION TO MECHANICAL FUNCTION

Peter P. Purslow* and Moira A. Lawson†
*Department of Biological Sciences, University of Stirling, Scotland, UK, and Department of Dairy & Food Science, Royal Veterinary and Agricultural University, Frederiksberg, Demark.

TISSUE ARCHITECTURE AND FUNCTION

The internal organisation of muscles into fascicles and fibres by intramuscular connective tissue (IMCT) is highly variable between muscles and is accepted to be a structural adaptation to the varying mechanical function of the muscles. Discussion of mechanical roles for IMCT has traditionally been limited to the passive elastic response of muscle. However, it is now clear that IMCT provides a matrix to integrate the contractile function of the whole tissue. Mechanical forces are co-ordinated and passed between adjacent muscle cells via cell-matrix interactions and the endomysial connective tissue that links the cells together. The highly compliant tensile nature of the collagen network that comprises the bulk of the endomysium easily permits changes in muscle length, but force transduction is by shear through this layer.

A mathematical analysis of the translaminar shear moduli of endomysial connective tissue networks has been constructed from composites science theory (Purslow, 2002) and shows that the efficiency of this network in transmitting force laterally between muscle fibres is only marginally dependent on the working length of the muscle.

An emerging concept is that division of a muscle into fascicles by the perimysial connective tissue is related to the need to accommodate shear strains as muscles change shape during contraction and extension. An analysis of shear between fascicles caused by muscle contraction shows that local shear strains within muscle may be considerable (Purslow, 2002). Experiments involving the deformation of rigor muscle show that fascicular boundaries, delineated by perimysial connective tissue, provide “slip planes” to relieve shear (Purslow, 1999).

CELL-MATRIX INTERACTIONS

IMCT also has a number of clearly defined roles in muscle growth and development. In developing muscles, proliferation and growth of muscle cells is stimulated and guided by cell-matrix interactions. Recent work has shown that the topography of collagen fibres is an important signal in this (Lawson et al., 2000). Muscle cells grown on fibrous collagen are more irregularly shaped than cells grown on solubilised collagen. Cells deposit talin-rich focal adhesions where they touch collagen fibrils. The timing and rates of expression of connective tissue proteins also show clear differences between muscles (Lawson & Purslow, 2001). Expression of type I collagen starts earlier and continues at a higher level in chick quadraceps than in pectoralis, a difference maintained into post-hatch maturity. Studies on tissue sections using immuno-labelling indicate that integrin linkages at the cell surface are more rapidly degraded by the calpain enzyme system than dystroglycan linkages (Lawson & Schäfer, 2002).

MECHANOTRANSDUCTION

Mechanotransduction via cell-surface integrins is implicated as a signalling mechanism in muscle development, growth, hypertrophy and turnover. Current work indicates that cyclic shearing of muscle cells adhering to matrix proteins promotes the deposition of integrin-rich focal adhesions. Alternative mechanostimulation regimes, including fluid shear, are currently under development.

REFERENCES

Lawson, M.A., Mosler, S., Gadegaard, N., Purslow, P.P. (2000) The role of collagen topography in myoblast morphology, proliferation and differentiation. Molecular Biology Of The Cell 11, 2041. Suppl. S.

Lawson, M.A., Purslow, P.P. (2001). Development of components of the extracellular matrix, basal lamina and sarcomere in chick quadriceps and pectoralis muscles. Brit. Poultry Sci., 42, 315-320.

Lawson, M.A. and Schäfer, A. (2002). Degradation of cell/membrane adhesion complexes postmortem correlate to the opening of drip channels in pork . Proc. Levnedsmidelskongres 2002, Frederiksberg, Denmark.

Purslow, P.P. (1999). Proc 45th Intl. Congr. Meat Sci. Technol. (Yokohama) 210-219.

Purslow, P.P. (2002). The structure and function of connective tissue within muscle. Comp. Biochem. Physiol., in press.

THE INFLUENCE OF AGEING AND EXERCISE ON TENDON MATRIX – HYPOTHESES FOR THE INITIATION AND PREVENTION OF STRAIN-INDUCED TENDINOPATHIES.

Smith RKW* and Goodship AE
Royal Veterinary College, University of London, U.K.

Tendon strain injuries are common in human and equine athletes. In horses, *in vitro* strain measurements at rupture are close to *in vivo* measurements at the gallop. Small decreases in matrix 'quality' will therefore increase the risk of tendinopathy substantially. Epidemiological studies in horses and man have demonstrated a close association between age and exercise, and ultrasonography has shown bilateral tendinopathy commonly in both species. Therefore progressive tendon degeneration may precede clinical tendinopathy. Our studies on the tensional region of equine digital flexor tendons have demonstrated a regional reduction in the collagen fibril crimp angle and length with exercise and age, with a synergistic effect. A higher proportion of small collagen fibrils was found in long-term exercised older horses, but not in short-term exercised, or younger, horses. This did not correlate with new collagen formation and thus may result from disassembly of larger diameter fibrils. Cartilage Oligomeric Matrix Protein (COMP) levels were low in the neonate, increased in response to loading until they peaked at skeletal maturity. Mechanical properties were related to COMP levels at this age. Levels subsequently declined which was accelerated by exercise. There was high expression of TGF-β in young equine tendon, declining after skeletal maturity, while tenocytes recovered from digital flexor tendons showed similar although reduced responses to growth factors *in vitro*. We hypothesise that tensional weight-bearing tendon can adapt to exercise during development but has poor or no ability to do so after skeletal maturity, which may be, at least in part, due to a relative lack of growth factors. Exercise accelerates the ageing effect of cumulative degeneration after skeletal maturity.

DYNAMIC CELL/SCAFFOLD INTERACTIONS:IMPLICATIONS FOR BONE TISSUE ENGINEERING

Alicia J. El Haj
Centre for Science and Technology in Medicine, School of Medicine, Keele University, North Staffordshire Hospital, Staffs, UK

INTRODUCTION

The development of tissue engineering and the reconstruction of autologous complex *in vivo* environments has been advanced by studies assessing the role of cell-cell and cell-matrix interactions following the introduction of implants. However, the role of dynamic mechanical interactions in this process has often been ignored. Our work has involved identifying key mechanotransduction pathways which can be manipulated for enhanced tissue engineering (El Haj et al 1999; Walker et al 2000). Our aim is to investigate ways by which we can regulate and augment the mechanical conditioning of bone tissue constructs both *in vitro* in bioreactors and *in vivo* following implantation by 1) design of mechanical bioreactors capable of process engineering of autologous tissue implants, 2) creation of 'mechano-active' scaffolds which augment specific load pathways previously shown to be involved in bone mechanotransudction and 3) investigate how surface modifications to biodegradable scaffolds can influence or facilitate the ability of the cell to respond to mechanical cues.

METHODOLOGY

In this report, we present our recent investigations into optimising PLLA type biodegradable materials for enhancing load transduction pathways in bone tissue engineering. Using primary human bone cells derived from tibia fracture, distraction osteogenesis (10-30 yr) patients (LREC # 1293) or the MG63 bone cell line, we report on the interactions between cells seeded on varying scaffold materials with altered surface topography, varying coatings such as collagen or tri-calcium phosphate and addition of slow release agonists of load transduction pathways. The constructs are cultured in short or long term culture using 2D four point bending or 3D compression perfusion bioreactor. The effects of using specific peptide ligands e.g. RGD or coatings such as collagen in biomaterial design on mechanotransduction pathways will also be described.

RESULTS AND CONCLUSIONS

Our results demonstrate the enhancing effects of biomechanical conditioning on bone matrix production in a compression perfusion bioreactor. By addition of chemical membrane channel agonists released from porous scaffolds, we can further enhance the production of bone. Figure 1a shows the human bone cells grown within the PLLA porous matrix following static conditioning for 3 weeks. Figure 1b show elevated mRNA expression of the bone cell differentiation factor, CBFA1, in scaffolds with and without agonist release following cyclical compressive loading.

a)

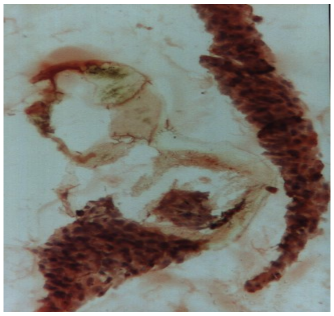

b)

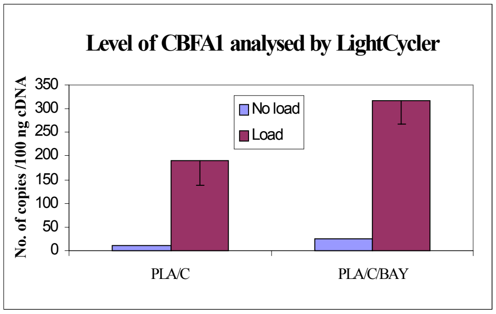

Figure 1 a) Bone cells cultured in a PLLA based porous scaffold coated with collagen type 1 after 3 weeks in static culture. **b)** Level of the bone differentiation factor,CBFA1 mRNA in cell seeded constructs cultured in a compression perfusion bioreactor. Scaffolds are PLLA with collagen type 1 coating (PLLA/C) and PLLA with collagen and slow release membrane channel agonist (PLLA/C/BAY)

In addition, surface topography and composition can effect the ability of cells to transmit the load signal which is important in considering the balance between conditioning in bioreactors and static cultures with osteoinductive materials. Furthermore, the question of whether coatings or peptide binding motifs are an important feature for improved biomechanical conditioning both *in vitro* and *in vivo* will be discussed. Work is currently in progress to determine if we can influence the sites of bone deposition by combining scaffold design with the appropriate loading environment.

REFERENCES

El Haj et al (1999) Medical Bio Eng Comp 37;403-409
Walker et al (2000) J. Cell Biochem. 79;648-661

ACKNOWLEDGEMENTS

This work is supported by EU Vth Framework programme 'BITES' #QLK3CT1999 00559.

EFFECT OF PERFUSION RATE ON CELL SEEDED 3D CONSTRUCTS *IN VITRO*

Blaise Porter, Sarah Cartmell and Robert Guldberg
Georgia Institute of Technology, Atlanta, GA 30324 robert.guldberg@me.gatech.edu

INTRODUCTION

Cell viability at the center of tissue engineered constructs in static culture may be decreased due to diffusion limitations. We have designed a 3-dimensional perfusion system (fig. 1) that has the ability to simultaneously perfuse culture media through porous cell seeded constructs, as well as apply axial mechanical loads between 0 and 25lbs. This study tested the effects of media perfusion rate on cell viability, proliferation and gene expression on cell seeded 3D bone scaffolds.

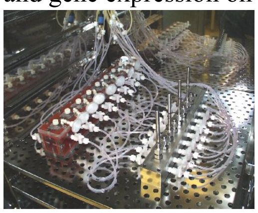

Figure 1

Figure 2

METHODS

MC3T3-E1 osteoblast-like cells were seeded onto 56 human trabecular bone cylindrical scaffolds measuring 0.25" in diameter and length. Eight constructs were perfused at each of the following flow rates: 0.01, 0.05, 0.1, 0.2 and 1ml/min for one week. Two non-perfused controls included cell seeded scaffolds in 6 well plates and cell seeded scaffolds placed into stainless steel chambers in 6 well plates (fig. 2). Media was changed on days 2 and 4consisted of α-MEM with glutamax (GIBCO), 10% fetal bovine serum, 1% penicillin/ streptomycin, 50μg/ml ascorbate, 3mM β–glycerophosphate, and 10^{-8} M dexamethasone. Laser scanning confocal microscopy was performed at one week to visualize calcein (viable cells) and ethidium homodimer (non-viable cells) staining of the scaffolds. Real-time quantitative RT-PCR using an ABI PRISM 7700 (Applied Biosystems) sequence detector was performed on 5 of the constructs at each perfusion rate. Runx2, osteocalcin (OCN), alkaline phosphatase (ALP) and bone sialoprotein (BSP) were quantified using real-time RT-PCR and were normalized to 18S. A DNA assay using Hoechst dye fluorescence was performed on scaffolds at each perfusion rate.

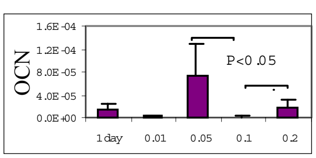

Figure 3

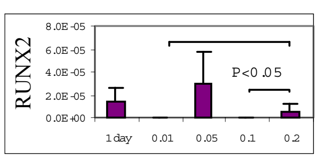

Figure 4

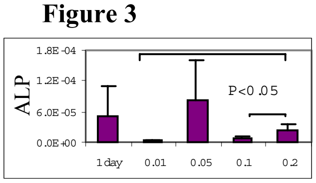

Figure 5

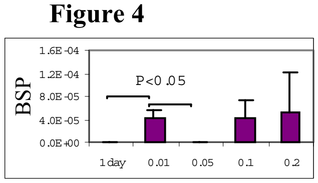

Figure 6

RESULTS

Confocal microscopy revealed that flow rates of 1ml/min showed cell necrosis, while 0.01 and 0.05 ml/min showed consistent cell viability after one week of perfusion. Real-time RT-PCR showed that cells perfused at 0.2ml/min and less produced all four genes analyzed. There was a significantly higher amount of OCN produced at 0.05ml/min than at higher flow rates (fig. 3). There was also significantly more Runx2 and ALP produced by the cell seeded constructs perfused at 0.2 ml/min than at lower flow rates (fig. 4 and 5). BSP had significantly increased at one week in the cellular scaffolds perfused at 0.01ml/ min compared to the 1 day seeded and 0.05ml/min perfused constructs (fig. 6). DNA analysis showed increased cell proliferation at flow rates of 0.01 and 0.05ml/min compared to 0.2ml/min and static controls (fig. 7). Constructs perfused at 0.01ml/min showed significantly higher cell proliferation than bone only (no cells), 1 day seeded constructs and 0.2ml/min perfused constructs.

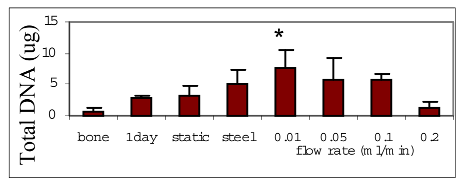

Figure 7 (* - $p<0.05$).

DISCUSSION

Altering the perfusion rate through the cellular scaffolds showed an effect on the amount of osteorelated genes produced, cell viability and cellular proliferation. This effect of media perfusion may be the result of enhanced nutrition to cells and/or flow induced mechanical stimuli. The perfusion rate must be kept relatively low to enhance cell viability. Cell proliferation was also higher at lower flow rates; however, expression of OCN, Runx2 and ALP was decreased at the 0.01ml/min flow rate compared to higher flow rates. These short-term studies suggest a perfusion rate of 0.05ml/min maybe optimal in this system for developing 3D bone constructs. Previous *in vitro* studies have shown that mineralized matrix formation on 3D scaffolds is limited to the outer 150-250μm of the scaffold[2]. A perfusion system may allow mineralization to develop throughout tissue engineered constructs. Longer-term studies to investigate matrix mineralization on 3D constructs in the perfusion system are ongoing.

ACKNOWLEDGEMENT

This work made use of ERC Shared Facilities supported by the National Science Foundation under Award Number EEC-9731643.

GROWTH FACTOR LOADED CALCIUM PHOSPHATE CEMENT FOR BONE REGENERATION

E.J. Blom[1], E.H. Burger[2] , M.A.J. van Waas[1] , J. Klein-Nulend[2]
[1]Dept. of Oral Function and [2]Dept. of Oral Cell Biology, Academic Centre for Dentistry Amsterdam,
University of Amsterdam and Vrije Universiteit,, Amsterdam, The Netherlands. e.blom@acta.nl

INTRODUCTION

Enhancement of peri-implant bone growth by growth factors may improve indication and success of implant use. Calcium phosphate as a material for implants or for coating of implants is known for it's good biological interaction with bone. A calcium phosphate implant combined with a growth factor like transforming growth factor-ß1 (TGF-ß1) might improve bone regeneration and subsequently osseointegration.

Calcium phosphate in cement[1] form can be used as a carrier for TGF-ß1 and applied as a paste in vivo to fill micro- and macroscopic bone defects. The effectiveness of a calcium phosphate cement (CPC) combined with TGF-ß1 for bone regeneration needs to be determined in a biological environment, such as cell or tissue culture experiments and animal studies. After showing its usefulness and safety in pre-clinical studies, then clinical studies can be initiated.
In a series of studies we have demonstrated the capability in bone regeneration of calcium phosphate cement (CPC) that was intermixed with TGF-ß1.

MATERIALS AND METHODS

First, a method was developed to incorporate recombinant human TGF-ß1 (rhTGF-ß1) during setting in CPC. CPC was prepared by mixing calcium phosphate powder with liquid. The liquid for rhTGF-ß1 containing CPC was mixed with HCl and albumin. A release study was performed to determine the amounts of rhTGF-ß1 released in surrounding medium.
In a subsequent study[2], two cell populations were obtained from adult rat long bones: pre-osteoblastic cells, and osteoblastic cells. After preculture the cells were plated on a layer of CPC containing 0, 10 or 20 ng rhTGF-ß1. Bone cell differentiation was analysed by measuring alkaline phosphatase (ALP) activity, as well as protein content of the cell layer.

The following study was set-up to determine the possible intervening effects of rhTGF-ß1-intermixing on the clinical compliance of two comparables CPCs by assessing their physicochemical properties. Both CPCs, with and without modification for rhTGF-ß1, were examined for setting time, compressive strength, crystallinity, Ca/P ratio, porosity, and microscopic structure.

A final study[3] was performed to examine whether the identical enrichment with rhTGF-ß1 (as *in* vitro) affected the replacement of CPC by bone (osteotransduction) in calvarial defects of adult rats. Two bone defects were filled with CPC without rhTGF-ß1 (control) at one side, and with 10 or 20 ng rhTGF-ß1 at the other side. Defects with surrounding skull were analysed histologically and histomorphometrically.

RESULTS

A gradual release was found into tissue culturing medium leading to 20% of rhTGF-ß1 of the amount added, after 24 hr.
Incorporation of 10 ng rhTGF-ß1 increased ALP activity in pre-osteoblastic cells by 3-fold, and 20 ng rhTGF-ß1 per CPC layer by 5-fold. ALP activity in osteoblastic cells was not affected by rhTGF-ß1.

Both CPCs became a dense, micro porous structure of calcium deficient apatite with a compressive strength of over 20 MPa within 24 hrs. The setting time differed greatly between the two CPCs; for slow setting CPC, 18 min at 37ºC was needed vs. 5 min for fast setting CPC. The modification for rhTGF-ß1 hardly affected the physicochemical properties.
Addition of rhTGF-ß1 to fast setting CPC stimulated bone formation as indicated by an increased bone volume of 50% and an increased bone/cement contact of 65%. In addition, rhTGF-ß1 *reduced* the remaining volume of cement, by 11 % at 10 ng rhTGF-ß1, and by 20 % at 20 ng rhTGF-ß1 in the cement.

DISCUSSION AND CONCLUSION

In a series of step by step development we have demonstrated the improved bone regenerative properties of the appropriate CPC by the addition of certain concentrations of rhTGF-ß1. The intermixed concentrations of rhTGF-ß1 in the cement were released and stimulated bone cell differentiation. Subsequently, the addition of identical concentrations of rhTGF-ß1 in fast setting cement increased the amount of bone and osteotransduction of the cement.
For bone regeneration procedures around endosseous implants, calcium phosphate cement with rhTGF-ß1 might be an appropriate combination for early osseointegration and implant use.

REFERENCES

1. Driessens, F.C.M. *et al.* Proc. Inst. Mech. Eng. 212: 427-435 (1998).
2. Blom, E.J. *et al.* J. Biomed. Mater. Res. 50:67-74 (2000).
3. Blom, E.J. *et al.* Clin. Oral Impl. Res. 12:609-616 (2001).

ACKNOWLEDGEMENT

This study was financially supported by the Netherlands Institute for Dental Sciences and the Academic Centre for Dentistry Amsterdam.

AN APPROACH FOR IMPROVING THE PERFORMANCE OF POLYMERIC MACROPOROUS SCAFFOLDS FOR *IN VITRO* AND *IN VIVO* BONE TISSUE ENGINEERING APPLICATIONS

K. Rzeszutek, D. Baksh, L. Guan, J.M. Karp, F. Sarraf, J.E. Davies
Institute of Biomaterials and Biomedical Engineering, University of Toronto, Toronto, Ontario M5S 3G9 Canada
E-mail: kathy.rzeszutek@utoronto.ca

INTRODUCTION

During the past decade, many polymeric scaffolds have been created for bone tissue engineering applications (Agrawal C.M. et al 2001; Mikos A.G. et al 2000; Holy C.E. et al 1997). Some of these materials are not only biocompatible and biodegradable, but also mimic the trabecular bone morphology, which allows efficient host tissue invasion. However, one problem with those scaffolds which permit ubiquitous 3-dimensional cell colonization is that when these materials are implanted into bony defects, they may shrink when clot contraction occurs during the early stages of the wound healing cascade. One of the strategies used to overcome the problem of contraction of polymeric scaffolds involves modification of these materials with calcium phosphates. Although such a modification often improves the physical properties of the scaffold, it also undesirably reduces the scaffold macroporosity which is essential for effective tissue ingrowth. We have recently produced a biodegradable PLGA scaffold modified with calcium phosphate (CAP) particulate which has both the required physical properties and a macrogeometry that mimics trabecular bone. We compared the geometric stability of this composite scaffold with that of the traditionally employed PLGA formulation alone, both *in vitro* and *in vivo,* and demonstrated that improvements in the mechanical properties can be attained by the addition of the CAP phase without compromising the biological requirements for optimal *in vitro* and clinical performance of the scaffold.

MATERIALS AND METHODS

Poly(lactide-*co*-glycolide) 75:25 (PLGA) was purchased from Birmingham Polymers (Birmingham, Al, USA). Dimethylsulfoxide (DMSO) was purchased from BDH Inc. (Toronto, ON, Canada). Sugar crystals were purchased from Redpath Sugar (Toronto, ON, Canada). Dicalcium phosphate anhydrous (DCPA) and tetracalcium phosphate (TTCP) were purchased from Sigma-Aldrich Inc. (Oakville, ON, Canada) and Inui Corp. (Osaka, Japan), respectively. The starting PLGA/CAP 3-dimensional scaffold blocks were prepared by dispersing an equimolar mixture of DCPA and TTCP powders with glucose crystals in a solution of 10% (wt/v) PLGA in DMSO. The sugar/polymer/calcium phosphate mixture was then placed in a Teflon®FEP-coated aluminium mould and allowed to set. Following polymer precipitation, the glucose crystals were extracted, which resulted in a 3-dimensional scaffold block having macroporous, interconnected porosity. Pure PLGA scaffold blocks were prepared as described above to function as controls. Cylindrical scaffolds were cut from the starting scaffold blocks such that the porosity was maintained to the outer margins. *In vitro* testing of the scaffolds was performed by seeding scaffolds (6.7 mm diameter and 6 mm length) with 1.9×10^5 rat bone marrow-derived cells, and culturing the cells for 4, 7, and 21 days under osteogenic and non-osteogenic conditions. Control scaffolds were exposed to the same medium conditions as their parallel experimental samples, but in the absence of cells. *In vivo* testing was done using a rat animal model. Bone defects (2.5 mm diameter) were made in the mid-diaphysis of the femurs of young male Wistar rats (Charles River, QC, Canada). At various time points, the femurs were removed and processed for histology. Sections, perpendicular to the long axis of the implant, were stained with Masson's Trichrome stain.

RESULTS AND DISCUSSION

Modification of the polymeric scaffold with a CAP phase improved the physical properties of the material without affecting the trabecular bone morphology of the resultant PLGA/CAP scaffold. *In vitro* experiments demonstrated that our PLGA/CAP scaffolds did not show a quantifiable amount of shrinkage in the presence of cells or media alone. Improved physical performance of the PLGA/CAP scaffolds was further demonstrated *in vivo*. Histological results in Figure 1 show that the PLGA scaffold contracted *in vivo*, as was expected based on our *in vitro* data; in contrast, the PLGA/CAP scaffold retained its original cylindrical shape and macroporosity throughout the implantation period, as a result of which bone tissue invasion was observed inside the macropores of this composite construct.

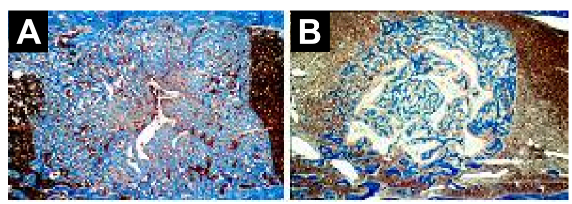

Figure 1: Transverse sections of rat femora containing scaffolds at 7 days *in vivo*: (A) PLGA, (B) PLGA/CAP. FW 2.5 mm (white areas represent the space occupied by the scaffold, blue areas are bone).

SUMMARY

Polymeric scaffolds, which mimic trabecular bone morphology, when modified with a calcium phosphate phase offer improved handling characteristics and physical performance while supporting rapid bone tissue invasion *in vitro* and *in vivo*.

REFERENCES

Agrawal C.M. et al (2001). *J Biomed Mater Res* **55**(2), 141-50.
Mikos A.G. et al (2000). *EJB Electronic J Biotech* **3**(2).
Holy C.E. et al (1997). In: *Biomaterials, Carriers for drug delivery and scaffolds for tissue engineering* (Peppas NA et al Eds.) A.I.Ch.E. Press., 272-274.

THE EFFECT OF PULSATILE BUBBLE MOTION ON SURFACTANT DISTRIBUTION DURING AIRWAY REOPENING

D.P. Gaver[1], M. Zimmer[1], D. Halpern[2], and H.A.R. Williams[3]

[1]Dept. of Biomedical Engineering, Tulane University, New Orleans, LA; donald.gaver@tulane.edu
[2]Dept. of Mathematics, The University of Alabama, Tuscaloosa, AL
[3]Dept. of Mathematics, The University of New Orleans, New Orleans, LA

INTRODUCTION

Pulmonary surfactant is a complex mixture of phospholipids with hydrophobic and hydrophilic surfactant-associated proteins that dynamically modifies the surface tension of the lung through molecular interactions and multilayer respreading during interfacial area cycling. When lung surface tension is high, as is the case with premature newborn Respiratory Distress Syndrome, mechanical stresses applied to the airway walls during ventilation can damage the airway epithelial tissue. Our goal is to analyze surfactant transport in computational models of steady and unsteady pulmonary airway opening to determine if physicochemical hydrodynamic interactions can be used to optimize this process and minimize tissue damage.

METHODS

To investigate surfactant transport behavior during oscillatory flow, we have computationally modeled the pulsatile motion of a semi-infinite gas bubble in a horizontal channel of width 2a filled with a Newtonian liquid of viscosity μ and surface tension γ. We investigate the fluid mechanical responses to a volume flux Q(t) with non-zero mean (Q_0) and an oscillatory component of magnitude Q_ω and frequency ω. Stokes equations are solved using a mixed boundary element and lubrication analysis technique and are time-stepped using a fully implicit method. The fluid dynamics are characterized by several dimensionless parameters:

- $Ca = \mu Q_0/(2a\gamma)$, a steady-state Capillary number, which represents the ratio of viscous to surface tension forces;
- $Ca_\Omega = \mu Q_\Omega/(2a\gamma)$, an oscillatory forcing magnitude, and
- $\Omega = \omega\mu a/\gamma$, a non-dimensional frequency that represents the ratio of oscillatory-forcing to viscous-draining timescales.

RESULTS AND DISCUSSION

An oscillatory forcing component superimposed over a steady-state Capillary number caused significant modifications in the air-liquid interfacial behavior as well as the surrounding fluid flow field. Multiple case analysis revealed the importance of a ‘stroke length’ parameter, $A=2Ca_\Omega/\Omega$, that describes the forced oscillatory amplitude of the system. Using systems with simple surfactant transport models, ‘optimized’ frequencies (Ω) for interfacial surfactant concentration in the bubble tip region could be found for cases of given Ca_0 and stroke length, *A*. Such a case can be seen in Fig 1.

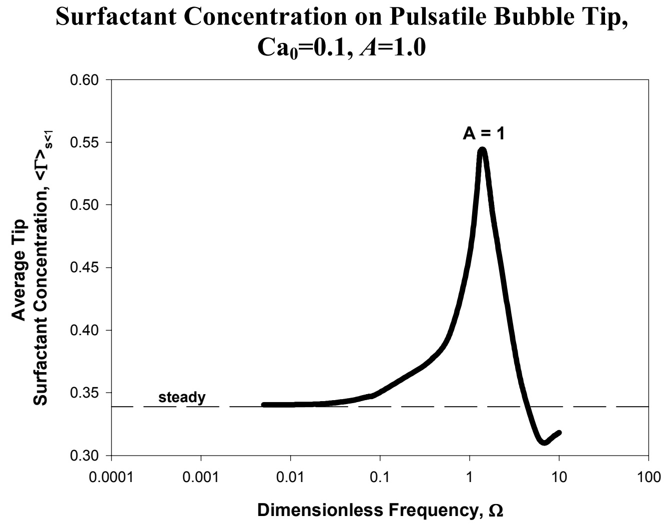

Figure 1: The effect of oscillation frequency on surfactant sorption to the bubble tip. $Ca_0 = 0.1$, A=1.0.

Additionally, analysis of multiple amplitudes, *A,* over a range of oscillatory frequencies, Ω, for a given Ca_0 provided a quantitative comparison of the relative increase in interfacial surfactant transport gained by each amplitude case as compared to the steady state Ca_0 value. We will expand these studies to investigate surfactant multi-layer dynamics.

SUMMARY

Our analysis of pulsatile pulmonary airway reopening shows that interfacial surfactant transport can be improved in comparison to the transport characteristics of similar steady-state systems. Quantitative comparisons of interfacial surfactant transport show that there exist optimized oscillation frequencies that will maximize surfactant concentrations in the bubble tip region. This increased surfactant concentration serves to lower lung surface tension, thereby decreasing necessary ventilation pressures, which should minimize ventilator-induced lung injury.

ACKNOWLEDGEMENTS

Funded by NSF grant BES-9978605, and the NASA Physical Sciences Research Division. Computational resources provided by the U.S. DOE through the Livingston Digital Millennium Center for Computational Science at Tulane and Xavier Universities, award #DE-FG-02-01ER633196.

BIOPHYSICAL AND BIOLOGICAL RESEARCH IN LUNG SURFACTANT DRUG DEVELOPMENT

Edmund A Egan, MD[1] and Robert H. Notter, MD, PhD[2]

[1]Departments of Pediatrics and Physiology, State University of New York At Buffalo, Buffalo, NY
President ONY, Inc., eegan@ony.incubator.buffalo.edu
[2]Departments of Pediatrics and Biomedical Engineering, University of Rochester, Rochester NY

INTRODUCTION:

In 1959 Avery and Mead described high minimum surface tensions on Wilhelmy balance testing of lung extracts from premature infants who had died of the Respiratory Distress Syndrome (Avery and Mead, 1959). Although this directly linked lung surfactant deficiency to disease in these infants, effective surfactant replacement therapy was not available for another 30 years. This compares to an interval of less than 5 years between the discovery of insulin deficiency in diabetes and availability of insulin replacement therapy. Difficulties linking biophysical and biologic research explain the prolonged delay in developing effective surfactant replacement therapy, and it was the eventual ability to relate biophysical and biological results that eventually allowed development of the therapy.

METHODOLOGIC CONSIDERATIONS:

Development of effective surfactant therapy was delayed because of a series of false scientific assumptions. The composition of active lung surfactant is complex, not simple; there are multiple essential biophysical properties, not one; biophysical activity is a necessary, but not sufficient standard; biologic evaluations ultimately require experimental testing in animals in vivo, not just in bioassays. Finally, since lung surfactant acts on an internalized, but ultimately exterior epithelial surface, accurate evaluation of replacement surfactants also requires assurance of adequate quantitative delivery of the material to the airspace and its appropriate deposition among the $3x10^8$ alveoli.

RESULTS

In the early 1960's, following relatively little biophysical study and virtually no biological evaluations, a clinical trial was conducted evaluating the aerosolization of dipalmitoylphosphatidylchline (DPPC, a major phospholipid component of lung surfactant) into the incubators of premature babies with RDS (Chu *et al*., 1967). The lack of success of that effort, which is now known to be due both to inadequate surface activity and inadequate delivery, was misinterpreted to imply that surfactant deficiency was not the cause of RDS.

In the 1970's, replacement studies in premature animals re-affirmed original insights about lung surfactant and RDS. However, the material complexity of lung surfactant and limitations on the parameters evaluated in biophysical testing still left unresolved conflicts in biophysical and biological research until the Enhorning Pulsating Bubble Surfactometer was introduced in the early 1980's. The ability to study a physiologically-relevant combination of adsorption and dynamic activity, and correlations between biophysical and biological testing, improved understanding of surfactant function and the crucial roles of lipid-protein interactions in activity. Effective synthetic and natural surfactant drugs for premature newborns were developed and tested in the 1980's. They have now become standard therapy.

Since the 1960's it has been assumed that surfactant has a significant role in the Acute Respiratory Distress Syndrome (ARDS) that causes respiratory failure in children and adults. Basic research has identified how lung surfactant can be inhibited (inactivated) biophysically or chemically degraded in these clinical syndromes (Notter, 2000). Development of surfactant therapy in ARDS has repeated some of the missteps of the past (Anzueto *et al*., 1996). However, basic science and clinical data exist that surfactant replacement therapy can modify the course of ARDS (Notter, 2000; Willson *et al*., 1999).

SUMMARY

Development of optimal surfactant replacement therapy for newborn infants was not achieved until biophysical and biological testing matured and complementary assessments were combined. That achievement must be replicated if it is going to be possible to develop equivalent therapy for ARDS.

REFERENCES

Anzueto A et al. (1996) *N Eng J Med* **334**,1417-21
Avery ME, Mead J. (1959) *AMA J Dis Child* **97**,517-523.
Chu J et al. (1967) *Pediatrics* **40**,709-82.
Notter RH, (2000) *Lung Surfactant*, Marcel Dekker
Willson et al. (1999) *Crit Care Med*; **27**,188-195

3D AIRWAY REOPENING: THE STEADY PROPAGATION OF AN AIR FINGER INTO A STRONGLY COLLAPSED ELASTIC TUBE

Matthias Heil [1] and Andrew L. Hazel [2]

Department of Mathematics, University of Manchester, UK
[1]M.Heil@maths.man.ac.uk; http://www.maths.man.ac.uk/~mheil
2ahazel@maths.man.ac.uk

INTRODUCTION

Many pulmonary diseases result in the collapse and occlusion of parts of the lung by viscous fluid. The subsequent airway reopening is assumed to occur via the propagation of an `air finger' into the collapsed, fluid-filled part of the airway. A complex 3D fluid-structure interaction governs this problem (a free-surface flow interacting with a strongly collapsed elastic tube), and hence the mechanics of airway reopening are still poorly understood. Previous work (e.g. Gaver *et al.* 1996, Heil 2000) has been restricted to 2D models, which fail to capture some potentially important features of the 3D system.

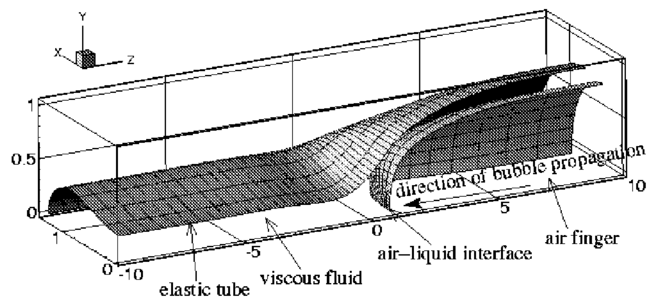

Figure 1: An air-finger propagates into a strongly collapsed elastic tube. Only one quarter of the domain is shown.

THE COMPUTATIONAL MODEL

Fig. 1 illustrates the model problem. The bubble pressure, p_b, drives an air finger at constant speed *U* into a strongly collapsed, thin-walled elastic tube of undeformed radius *R*. The collapsed part of the tube is filled with viscous fluid of viscosity ¯ and surface tension □. The air finger reopens the tube, depositing a thin layer of fluid on the walls. We assume that the flow is governed by the free-surface Stokes equations and describe the wall deformation by geometrically non-linear shell theory. The governing equations are solved by a fully coupled finite element method.

RESULTS

Fig. 2 shows a typical computational result. At small propagation speeds, the air finger `pushes' a large volume of fluid ahead of the bubble tip and a decrease in bubble pressure, p_b, is required to increase the speed of the steadily propagating finger. At larger bubble speeds, the finger tip is nearer the tube wall and an increase in bubble pressure is required to increase the bubble speed. The resulting two-branch behaviour implies the existence of a minimum pressure below which there is no steady bubble propagation. These results are surprisingly similar to those found in previous 2D models. We present a simple model for the behaviour on the `pushing' branch to explain this observation. In contrast to previous 2D models' predictions, we find that an increase in the degree of collapse *decreases* the bubble pressure required to drive the air finger at a given speed. This could have important physiological ramifications. Furthermore, the stresses that the fluid exerts on the airway walls are found to be so large that they have the potential to cause damage to the lung tissue.

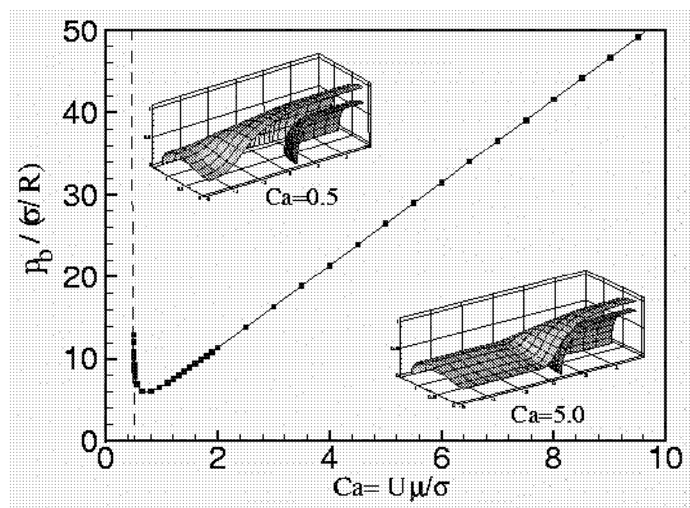

Figure 2: Non-dimensional bubble pressure p_b/(¯/R) vs. the non-dimensional bubble speed *U*□/□.

REFERENCES

Gaver, D.P. *et al.* (1996) The steady motion of a semi-infinite bubble through a flexible walled channel. *Journal of Fluid Mechanics* **319**, 25-56.

Heil, M. (2000) Finite Reynolds number effects in the propagation of an air finger into a liquid-filled flexible-walled channel. *Journal of Fluid Mechanics* **424**, 21-44.

STRUCTURAL AND FUNCTIONAL ASPECTS OF ALVEOLAR AND AIRWAY SURFACTANT

Samuel Schürch[1,2], Marianne Geiser[2] and Peter Gehr[2]

[1]Department of Physiology and Biophysics, University of Calgary, Calgary, Alberta, Canada. schurch@ucalgary.ca
[2]Institute of Anatomy, University of Berne, Switzerland

INTRODUCTION

The extracellular fluid lining the airways and alveoli exists as a continuum from the larynx to the alveolus. In the alveolus, the extracellular layer consists of a thin hypophase covered by a dipalmitoylcholine (DPPC)-rich surfactant film. In the airways it consists of sol and gel layers surmounted by a surfactant film of unknown composition. The direct demonstration of a surfactant film in the airways is relatively recent, although a surfactant film had been inferred by electron microscopic studies by Weibel and Gil about 30 years ago. Recently, non acqueous fixation techniques in conjunction with electron microscopy (EM) have demonstrated a continuous film covering the entire airway and alveolar surfaces. The film appears frequently multilaminated with a variable number of lipid layers at its surface (eg Schürch *et al*, 1998). This is consistent with studies in the captive bubble surfactometer (CBS), which indicate that the film can form a reservoir of surface active material.

The function of the alveolar surfactant film in stabilizing the gas exchange area and keeping the alveolus relatively dry has been well documented. Direct measurement of surface tension in intact lungs confirmed that the surface tensions within alveoli at lung volume levels of normal breathing are very low, varying from near zero to approximately 10 mN/m (eg Bachofen *et al* 1987). A surface tension of approximately 32 mN/m has been recorded in large airways, this suggests the presence of a surface film in large airways. This film promotes the displacement of particles into the aqueous phase (Schürch *et al,* 1990, Gehr *et al*, 1990). In small airways, where the surface tension is probably much lower, close to that in the alveolar spaces, surfactant is likely important in maintaining small airway patency. In addition a surface tension gradient will likely promote particle and fluid transport between the alveolus and the ciliated airways.

SURFACE ACTIVITY & STRUCTURE FUNCTION RELATIONS

The surface activity of pulmonary surfactant, including therapeutic surfactants, used for replacement therapy, encompasses at least three physical properties essential for normal lung function: (1) rapid film formation (within a few seconds) by adsorption from the hypophase; (2) low film compressibility (less than 0.01 m/mN) with a fall in surface tension to a value of less than 2 mN/m upon a maximum surface compression of approximately 20%; (3) effective replenishment of the surface film on expansion by the incorporation of reserve material associated with the surface. In general, rapid film formation (within 1 s) to an equilibrium surface tension between 23 and 25 mN/m is followed by a low film compressibility close to 0.005 m/mN, the value for pure DPPC, and stable minimum surface tensions around 1 mN/m on quasi-static and dynamic compression. Such film properties suggest that these films are highly enriched in DPPC formed by preferential adsorption. If such films are not compressed beyond the area at which minimum surface tension is obtained, there is negligible hysteresis upon repeated cycling between surface tensions of 25 and 1-2 mN/m.. In contrast to films formed from surfactant at relatively high phospholipid (PL) concentrations, films formed from surfactant with low PL concentrations below about 1mg/ml, may show a “squeeze-out plateau” upon area compression and thus demonstrate increased compressibility and substantial hysteresis in their surface tension-area relations. At relatively low concentration only a faint and amorphous film can be visualized by EM although the film may produce near zero surface tension upon its compression. With suspensions at higher concentrations, a more distinct film is seen. It is of variable thickness with frequent multilayer formations, consistent with the concept of the surface reservoir. These multilayers form de novo, upon film adsorption. After repeated cycling with over-compression at near zero minimum surface tension the bubble shape may become asymmetrical (non-Laplacian) after mechanical distortion. Such bubbles may revert slowly, within a few seconds into a Laplacian shape.

SUMMARY

There is “surplus” surfactant material in excess of a monolayer at the liquid- air interface upon de novo adsorption from surfactants derived from natural sources. Films from surfactants at high concentrations show high surface activity *i.e.*, very low compressibility, near zero and mechanically stable minimum surface tension obtained upon area compressions below 20%. They appear highly enriched in DPPC by preferential adsorption. Electron micrographs of such films are frequently multi-laminated. By repeated dynamic cycling, highly surface active films may show visco-elastic behavior, which may be important in vivo for clearing mechanisms.

REFERENCES

Bachofen, H., Schürch, S., Urbinelli, M., Weibel, E.R. (1987). *J. Appl. Physiol*, **62**, 1878-1887.
Schürch, S., Green, F.H.Y., Bachofen, H. (1998) *Biochim et Biophys Acta* **1408**, 180-202.
Schürch, S., Gehr, P., Im Hof, V., Geiser, M., Green, F. (1990). *Respir Physiol* **80**, 17-32.
Gehr, P., Schürch, S., Berthiaume, Y., Im Hof, V., Geiser, M.. (1990). *J Aerosol Med* **3,** 27-43.

DYNAMICS OF WOUND HEALING IN AIRWAY EPITHELIAL CELLS: GFP-ACTIN REMODELING

Christopher M. Waters[1,2,3], Leena P. Desai[1], Ashish Aryal[2], A. Nico West[1], and David Fischer[1]

Departments of [1]Physiology and [2]Biomedical Engineering
The University of Tennessee Health Science Center
Memphis, TN, USA
[3]email: cwaters@physio1.utmem.edu

INTRODUCTION

Mechanical ventilation of patients is often necessary in order to provide adequate gas exchange, but considerable damage to the lungs can occur. One of the prominent features of ventilator-induced lung injury is damage to the epithelium lining the airways. We have previously demonstrated that cyclic mechanical stretching and compression of wounded airway epithelial cells delays wound closure (Savla and Waters, 1998; Waters et al., 2001). Tracking wound closure by video microscopy demonstrated that wound closure was inhibited due to decreases in cell spreading and cell migration. Both of these processes involve remodeling of cytoskeletal components. Therefore, we sought to develop techniques to visualize actin remodeling in live cells. In this study we describe the development of a cloned cell line of human airway epithelial cells that we have stably transfected with a gene expressing a fusion protein that combines enhanced green fluorescent protein (EGFP) and human β-actin.

METHODS

We transfected a cell line of SV40-transformed human bronchial epithelial cells (16HBE14o-, from Dr. D. Gruenert, UCSF) with an EGFP-actin vector obtained from Clontech. During selection with G418, we identified individual cells that expressed the highest levels of EGFP-actin and transferred these cells to individual wells to initiate colonies. Several stable transfectants have been cloned. To visualize EGFP-actin in live cells, we grew cells in coverslip chambers and then placed the chambers on a motorized stage enclosed within a heated box. Wound closure was observed after scraping wounds across confluent monolayers.

RESULTS AND DISCUSSION

To directly visualize de-polymerization of f-actin, cells were treated with cytochalasin D (1 μg/ml) and disruption of F-actin was observed within minutes. Fig. 1 shows the progression of disruption from the initial time until 10 min later. Similar experiments were performed to demonstrate membrane ruffling, pseudopodal extensions, and cell migration in response to epidermal growth factor (EGF) and keratinocyte growth factor (KGF).

Two hours after wounding monolayers we observed formation of a strong, uniform band of actin at the wound edge that was parallel to the wound. Pseudopodal extensions emanated from this band and contained actin filaments perpendicular to the wound edge. Cells away from the wound edge were observed to remodel, elongate, and extend toward the wound front. These images can be used to measure the kinetics of actin remodeling.

REFERENCES

Savla, U., and C. M. Waters (1998). *Am J Physiol* **274**: L883-92.

Waters, C. M., M. R. Glucksberg, E. P. Lautenschlager, C. W. Lee, R. M. Van Matre, R. J. Warp, U. Savla, K. E. Healy, B. Moran, D. G. Castner, and J. P. Bearinger (2001). *J Appl Physiol* **91**: 1600-10.

ACKNOWLEDGMENTS

Supported by NHLBI/NIH grant HL64981.

Figure 1: Cytochalasin D treatment causes disruption of F-actin in live human bronchial epithelial cells.

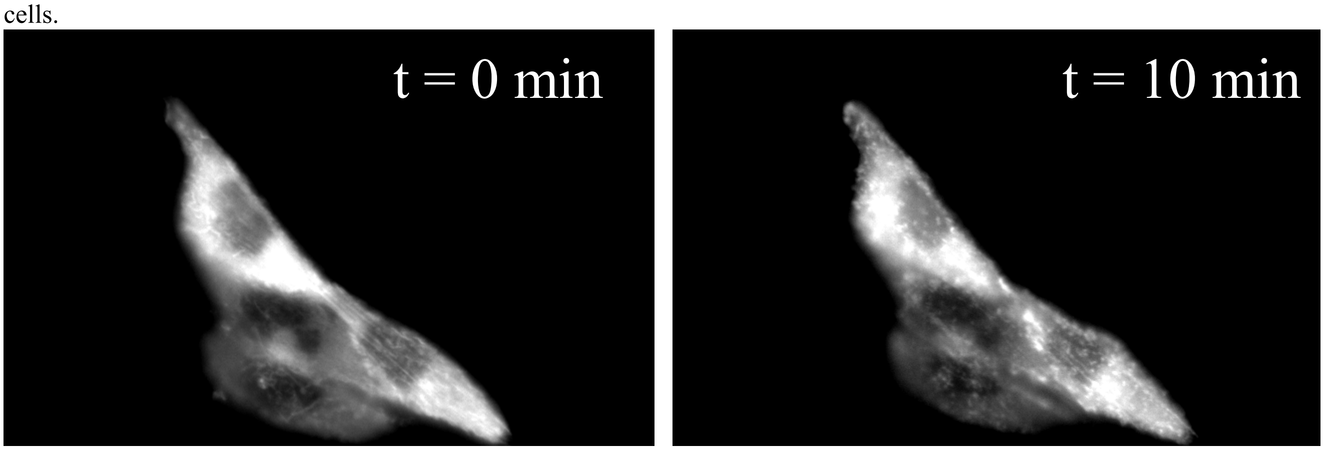

CELL-IMMERSED MICROBEADS USED AS PROBES OF CYTOSKELETON MECHANICAL PROPERTIES

Valérie M. Laurent[1, 2, 3], Sylvie Hénon[2], Emmanuelle Planus[1], Redouane Fodil[1], Martial Balland[2], François Gallet[2] and Daniel Isabey[1]

daniel.isabey@creteil.inserm.fr

[1] INSERM UMR 492, Fonctions Cellulaire et Moléculaire de l'Appareil Respiratoire et des Vaisseaux, Facultés de Médecine et des Sciences et Technologie, Université Paris XII, 94010 CRETEIL cedex, France.

[2] CNRS ESA-7057, Laboratoire de Biorhéologie et d'Hydrodynamique Physicochimique, Universités Paris VI et Paris VII, 75251 PARIS cedex 5, France.

[3] Cellular Biophysics and Biomechanics Laboratory, Swiss Federal Institute of Technology, Lausanne, Switzerland.

INTRODUCTION

Cellular mechanical properties can now be evaluated by a variety of micromanipulation techniques. These techniques implicate a variety of probes (e.g., micropipettes, beads, plates, poker, microscopic tip) of very different sizes (from nm to µm) which, in general, are physically connected to the cytoplasm through molecular junctions, the adhesion plaques. However, different types of probe-cell coupling may lead to probing of different subcellular structures, e.g., RGD-coated beads were used to measure cytoskeleton properties through the molecular linkage that integrin transmembrane mechanoreceptors constitute (Wang *et al*., 1993). In addition, the large variety of probe diameter might also contribute to the scatter of reported experimental data based on a tensegrity length scale that would fit the probe diameter (Maksym *et al*., 2000; Wendling *et al*., 1999). But some other factors may contribute to influence the cellular response. Because spherical probes are most often partially immersed, e.g., in case of bead attachment to the extracellular extremity of a transmembrane protein, the effect of incomplete bead immersion in the cytoplasm must be considered (Laurent *et al*., 2001). We presently analyze theoretically and experimentally the effects of partial bead immersion, in relation with the type of loading, e.g., a force and a torque respectively generated by two micromanipulation techniques implicating beads: Laser Tweezers (LT) and Magnetic Twisting Cytometry (MTC) .

METHOD

Theory: At equilibrium, the displacement (translation and/or rotation) of a rigid spherical bead, was calculated for various degrees of bead immersion in a homogeneous elastic medium, when submitted to either a force $\boldsymbol{F}$, or a torque $\boldsymbol{C}$, applied to its center. Assimilating the true displacement x (or rotation angle θ) of a bead (radius R) to the free displacement of the medium alone, we obtained reliable relationships describing the behavior of x (or θ) versus the elastic force $\boldsymbol{F_e}$ (or elastic torque $\boldsymbol{C_e}$) exerted by the intracellular medium, α being the half-immersion angle of the bead, i.e.,

$$x = -\frac{3}{4\pi\,\mathrm{E}}\frac{F_e}{\mathrm{R}}\left(\frac{3}{2\sin\alpha}+\frac{\cos\alpha}{\sin^3\alpha}\right), \text{ and } \theta = -\frac{3}{4\pi\,\mathrm{E}}\frac{C_e}{\mathrm{R}^3\sin^3\alpha}$$

These formulae which are used to determine the equivalent Young modulus E, are basically established at small α, but their validity extends to $0<\alpha\leq\pi/2$. Both formulae show that the degree of bead immersion, α, greatly affects the x-$\boldsymbol{F_e}$ and θ-$\boldsymbol{C_e}$ relationships, the smaller α, the larger the α-dependency, and that this effect depends on the nature of the load. Moreover, x-$\boldsymbol{F_e}$ formula takes into account the fact that a unidirectional force applied to partially immersed beads results in both translation and rotation (LT case).

Experiments: we performed specific measurements of the CSK mechanical properties in a given type of living adherent human epithelial cells with two independent bead micromanipulation techniques, the laser tweezers already described by (Hénon *et al*., 1999) and the magnetic twisting cytometry initiated by (Wang *et al*., 1993). Discrepancies between the two techniques were minimized using beads of similar sizes (∅≈5µm), i.e., silica beads for LT and ferromagnetic beads for MTC, same cellular substrate and same bead coating. We determined α from spatial reconstructions of the F-actin cytoskeleton for a representative sample of beads during MTC, while α was measured bead by bead from each bright field microscopic image during LT.

RESULTS and DISCUSSION

Direction and nature of efforts differ between the two techniques since a torque is applied during MTC while both a force and a torque are applied during LT. Analyzing the data obtained with each technique using the theory described above, shows that bead deviation angles and applied external torques get comparable but are on average larger in MTC ($\theta°$= 21-32°; C=444-1205 pN×µm) than in LT ($\theta°$=0-25°; C=0-400 pN×µm). Concerning the degree of bead immersion, we measured on average, α=62° in LT and α=67° in MTC. The values of equivalent Young modulus E obtained from above theoretical relationships appeared roughly in the same range of magnitude, i.e., E ~ 34-58 Pa in MTC and E ~ 29-258 Pa in LT. E-values in MTC appear one order of magnitude larger than those reported in previous MTC studies (Wang *et al*., 1993). Compared to LT, a number of reasons may contribute to explain the smaller E-values in MTC, including (i) heterogeneity in bead rotation already pointed out by (Fabry *et al*., 1999), (ii) reinforced non linearity and plasticity due to higher stress values in MTC possibly making inadequate the use of linear theory of elasticity. On the whole, this study is a contribution to define reliable transducers of cellular mechanical properties.

REFERENCES

Fabry, B., et al. (1999). *J. Mag. Mag. Mat.,* **194**, 120-125.
Hénon, S., et al. (1999). *Biophys. J.,* **76**, 1145-1151.
Laurent, V. M., et al. (2002). *J. Biomech. Eng*, in press.
Maksym, G. N., et al. (2000). *J. Appl. Physiol.,* **89**, 1619-1632.
Wang, N., et al. (1993). *Science,* **260**, 1124-1127.
Wendling, S., et al. (1999). *J. Theor. Biol.,* **196**, 309-325.

THE EFFECT OF PRESTRESS ON MECHANICAL PROPERTIES OF ADHERENT CONTRACTILE CELLS

Dimitrije Stamenović[1], Zhuangli Liang[1] and Ning Wang[2]

[1]Department of Biomedical Engineering, Boston University, Boston, Massachusetts, USA, dimitrij@engc.bu.edu
[2]Physiology Program, Department of Environmental Health, Harvard School of Public Health, Boston, Massachusetts, USA

INTRODUCTION

Rheological properties of cells play essential roles in various cell functions including spreading, interacting with the extracellular matrix or maintaining an appropriate tone (e.g. airway wall hysteretic properties). It is well established that rheological behavior of adherent cells can be characterized as viscoelastic. Cells exhibit creep, stress relaxation and hysteresis (cf. Sato et al., 1990; Thoumine and Ott, 1997; Maksym et al., 2000). However, adherent cells also exhibit features that characterize stress-supported structures (Wang et al., 2002). The prime feature of these structures is that their deformability is strongly influenced by pre-existing tensile stress (prestress) carried by their structural components. In the cell, the prestress is carried primarily by the actin cytoskeleton (CSK) and is generated either actively by the cell contractile apparatus or passively by cell distension on the substrate and by swelling pressure of the cytoplasm. It is not known, however, whether the origin of these two distinct types of rheological behaviors, the rate of deformation-dependent ones and the prestress-dependent ones, can be traced to common mechanisms. The goal of this study is to answer this question.

METHODS

We measured cell dynamic modulus (mechanical impedance) (G^*) and prestress (P) at different states of cell contraction. Measurements were done in cultured human airway smooth muscle cells. Cell contractility was modulated by graded dozes of histamine (0.1, 1, 10 μM) or isoproterenol (0.01, 0.1, 1, 10 μM). Measurements were done at each doze and at the baseline. G^* was measured using the magnetic oscillatory cytometry technique (Maksym et al., 2000). This technique applies an oscillatory twisting field to small ferromagnetic beads attached to integrin receptors on the cell apical surface. Integrins are physically linked to the CSK. Thus by twisting the beads, stresses and strains are induced into the CSK. Form a known applied specific twisting torque and measured corresponding angel of twisting, G^* is obtained as the complex ratio of the two. The real part of G^* is the elastic modulus (G') and the imaginary part is the frictional modulus (G''). Measurements were done at 0.1 Hz and amplitude of 6 Pa. P was measured using the traction microscopy technique (Wang et al. 2002). This method measures traction that arises at the cell-substrate interface in response to cell contraction. Since traction balances contractile stress, P can be obtained.

RESULTS AND DISCUSSION

G', G'' and P gradually increased/decreased with increasing doses of histamine/isoproterenol. At a given drug doze, G' was greater than G'' by a factor of 3-4. This, in turn, suggests that the cell behavior is predominantly elastic. Both G' and G'' increased linearly with increasing P (Fig. 1).

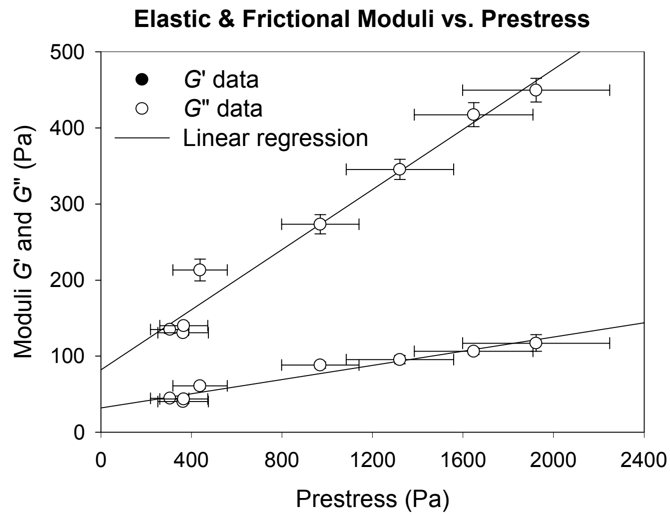

Figure 1: Elastic (G') and frictional (G'') moduli increased linearly with increasing prestress. Data, mean ± SE.

The most significant finding of this study is that both G' and G'' depend on the level of P. The linear dependence of G' on P is a known property of adherent cells and could be traced to mechanisms of stress-supported structures (Wang et al. 2002). However, the dependence of and G'' on P is a novel result. To investigate whether its origins can be traced to mechanisms of stress supported-structures, we modeled the CSK as a prestressed structure composed of linear Kelvin-Voigt bodies. The model could mimic the relationships shown in Fig. 1. However, we cannot rule other biophysical and biochemical mechanisms that may also explain the observed behavior.

SUMMARY

This study shows that rheological properties of contractile adherent cells reside within the CSK and that they can be modulated by the CSK contractile stress in a dosed-dependent manner. This behavior is consistent with the notion that the CSK is organized as a stress-supported structure.

REFERENCES

Maksym, G.N. et al (2000). *J. Appl. Physiol*. **89**, 1619-1632.
Sato, M. et al (1990). *ASME J. Biomech. Eng.* **112**, 263-269.
Thoumine, O., Ott, A. (1997). *J. Cell Sci*. **110**, 2109-2116.
Wang, N. et al (2002). *Am. J. Physiol. Cell Physiol*. In press.

ACKNOWLEDGEMENT

Supported by NIH grant HL-33009.

MICRORHEOLOGY OF THE LIVING CELL: ARE WE BUILT OF GLASS?

Jeffrey J. Fredberg[1], Ben Fabry and James P. Butler

Physiology Program, Harvard School of Public Health, Boston, MA 02115
[1] jfredber@hsph.harvard.edu

INTRODUCTION

Mechanical stresses and resulting deformations play central roles in cell contraction, spreading, crawling, invasion, wound healing and division, and have been implicated in regulation of protein and DNA synthesis and programmed cell death. If the cytoskeleton were simply an elastic body, it would maintain its structural integrity by developing internal elastic stresses to counterbalance whatever force fields it might be subject to. However, those same elastic stresses would tend to oppose - or even preclude altogether - other essential mechanical functions such as cell spreading, crawling, extravasation, invasion, division and contraction, all of which require the cell to "flow" like a liquid. A liquid-like cell, however, would be unable to maintain its structural integrity. The classical resolution of this paradox has been the idea that cytoskeletal polymers go through a sol-gel transition, allowing the cytoskeleton to be fluid-like in some circumstances (the sol phase) and solid-like in others (the gel phase). The data presented here suggest that, rather than being thought of as a gel, the cytoskeleton may be thought of more properly as a glassy material existing close to a glass transition. If so, then disorder and metastability may be essential features underlying cell mechanical functions (Fabry et al. 2001).

METHODS

We used optical tracking of ligand-coated, magnetically twisted ferrimagnetic beads that were bound to integrin receptors on adherent cells: human airway smooth muscle cells, human bronchial epithelial cells, F9 mouse embryonic carcinoma cells, J774A.1 mouse macrophages and human neutrophils. We used this system to measure the complex elastic modulus over bead displacement amplitudes ranging from 5 to 500 nm and twisting frequencies ranging from 10^{-2} to 10^{3} Hz.

RESULTS AND DISCUSSION

The complex modulus did not change with displacement amplitude, implying linear mechanical behavior in this range. Elastic stresses dominated at frequencies below 300 Hz, increased only weakly with frequency, following a power law. Frictional stresses were also weakly dependent on frequency below 10 Hz, but approached a viscous limit at higher frequencies.

Surprisingly, data for all cell types, frequencies, and interventions studied could be scaled onto universal master curves (Fabry et al., 2001). This scaling identified these cells as soft glassy materials existing close to a glass transition, with an effective noise temperature, x, of about 1.2, where trap models of glassy materials use the effective noise temperature to express the level of mechanical agitation, or noise, in the matrix relative to the depth of the energy wells in which metastable elements are trapped (Sollich, 1998).

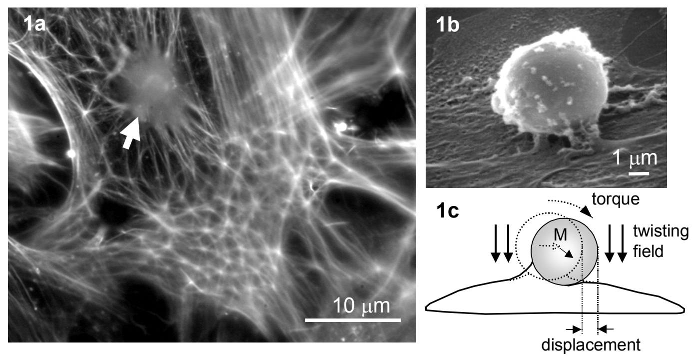

Fig. 1a: Ferrimangetic beads (arrow) bind avidly to the actin cytoskeleton (stained with phalloidin) of HASM cells via cell adhesion molecules (integrins). 1b: Scanning EM of a bead bound to the cell surface. 1c: A magnetic field introduces a torque which causes the bead to rotate and to displace. M denotes the direction of the bead's magnetic moment.

SUMMARY

These results stand in contrast to current concepts in cell rheology in that 1) relaxation processes exhibited no intrinsic time-scale, implying stress relaxation going as the power law t^{1-x}, and 2) frictional stresses did not correspond to a viscous process.

These findings support the novel hypothesis that cytoskeletal proteins can regulate cell mechanical properties by modulating the effective noise temperature of the matrix and, thereby, the ability of cytoskeletal elements to hop out of energy wells. The practical implications are that the effective noise temperature is an easily quantified measure of the ability of the cytoskeleton to deform, flow, and reorganize.

REFERENCES

Fabry, B, GN Maksym, JP Butler, M Glogauer, D Navajas, JJ Fredberg (2001). Scaling the microrheology of living cells. *Physical Review Letters*, **87(14)**:148102-1-4.
P. Sollich (1998). Rheological constitutive equation for a model of soft glassy materials. *Phys Rev E* **58**, 738.

A MODEL OF NON-UNIFORM LUNG PARENCHYMA DISTORTION

E Denny and R C Schroter

Department of Bioengineering, Imperial College of Science, Technology & Medicine, London SW7 2BX, UK
r.schroter@ic.ac.uk

INTRODUCTION

Non-uniform distortion of lung parenchyma is a ubiquitous phenomenon in lung mechanics. Important examples include parenchymal distortion around constricted airways and support of airways by surrounding parenchyma during forced expiration. It is common to model the lung as a homogeneous elastic continuum undergoing small distortions from a state of uniform inflation with a single bulk modulus and shear modulus. However this simple model of lung parenchyma undergoing non-uniform distortion is a poor description of the real case in many circumstances – distortions cannot be considered as small or be modelled using linear elastic theory. Distortion of parenchyma causes re-orientation and a change in strain distribution of the load bearing components. The parenchyma becomes physically inhomogeneous with anisotropic properties and different elastic moduli in different directions.

THE MODEL

The parenchyma is modelled as an assemblage of truncated octahedra arranged in a cuboidal block; the model is a development of our earlier work [Denny & Schroter 2000]. A finite element computer model is used to study the effect of large non-uniform distortion on the elastic behaviour. The distortion is a uni-axial stretch from an initial state of uniform pressure expansion. (Figure 1). For large distortions, the anisotropic non-linear elastic properties are described by five independent elastic moduli, each dependant on the initial pressure and degree of distortion.

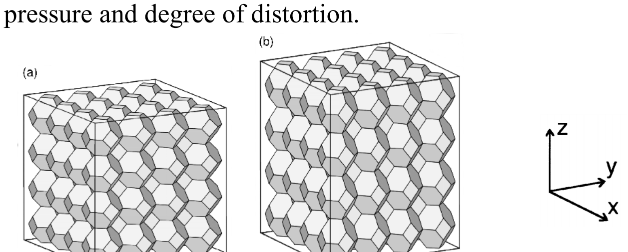

Figure 1: Alveolar assembly of 91 truncated octahedral alveoli: (a) block inflated and undistorted; (b) block uni-axially strained in the z direction.

RESULTS

When the distortion is zero, the five elastic moduli reduce to the two moduli for small distortions. The Young's modulus in the direction of stretch (E_z), increases significantly with distortion while the Young's modulus in the plane perpendicular to the stretch (E_x), is approximately constant. The higher the initial pressure, the greater the difference between the two moduli at larger distortion strains. For an initial pressure of 5 cmH_2O, E_z rises from 10.4 to 13.2 cmH_2O and E_x falls from 10.4 to 9.3 cmH_2O as the uni-axial distortion strain (ε_z), increases from 0 to 0.1. At 20 cmH_2O, E_z increases from 55 to 115 cmH_2O and E_x increases from 55 to 55.6 cmH_2O as ε_z increases from 0 to 0.05. The shear modulus (G_{xz}) is approximately independent of degree of distortion except at the highest initial pressure. At 5 cmH_2O, G_{xz} increases from 5.05 to 5.07 cmH_2O as ε_z increases from 0 to 0.1. At 25 cmH_2O, G_{xz} falls from 37.3 to 32.2 cmH_2O and as ε_z increases from 0 to 0.05. The Poisson's ratio, (ν_{xz}) is approximately constant with distortion strain for lower initial pressures, but increases significantly with ε_z at higher pressures. At 10 cmH_2O, ν_{xz} increases from 0.26 to 0.3 as ε_z increases from 0 to 0.1, but at 20 cmH_2O, ν_{xz} increases from 0.29 to 0.45 as ε_z increases from 0 to 0.05.

In general, both fibre bundle realignment and a change in strain distribution of individual fibres occur with increasing ε_z. At high inflation pressures, some individual fibres their approach maximum strain (~ 0.85) at ε_z = 0.08. Despite this, the average individual fibre strain remains virtually unchanged at ~ 0.62 as the distortion ε_z increases from 0 to 0.08 (Figure 2). However, at low to moderate inflation pressures, maximum fibre bundle strains are not reached for ε_z = 0.2 because they have lower initial strains.

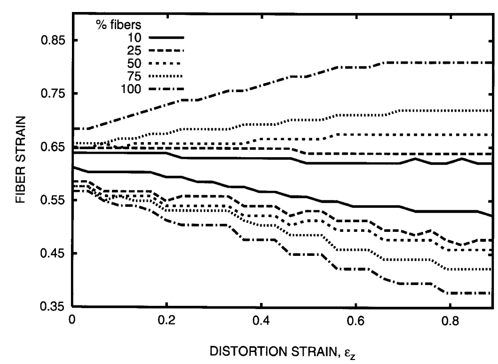

Figure 2: Effect of distortion strain on individual fibre strain distribution at an initial inflation pressure of 20 cmH_2O.

REFERENCE

Denny, E., Schroter, R.C. (2000). *ASME J. Biomech. Eng.*, **122**, 143-151

ACKNOWLEDGEMENT

We thank the Wellcome Trust for the support of E Denny on a Research Career Development Fellowship.

BIOMECHANICAL MEASUREMENTS AND DYNAMIC MODELING OF THE RHESUS MONKEY ARM

Gary T. Yamaguchi

Department of Bioengineering, Arizona State University, Tempe, AZ 85287-9709, USA

INTRODUCTION

An accurate, quantitative, dynamic model of the upper extremity is an important asset to analyses of reaching movements. The process of creating such a model involves detailed anatomical studies of the musculoskeletal system, 3D digitization, and computerized reconstruction of boney surface geometries. Adding dynamic capabilities to the anatomical model requires the definitions of reference frames, inertial parameters, joint motions, and dynamic equations. An overview of the process of model creation is given.

METHODS

Over the past decade, four young rhesus monkeys between 2.0 and 2.2 kg were dissected and used to determine typical segment lengths, muscle paths, and muscle parameters. Frozen monkey right upper extremities were pinned to a plexiglass board and digitized with an Optotrak 3D Bar (Northern Digital, Waterloo, Canada). 39 musculotendon paths were identified and measured to determine origins, insertions, and via points, muscle volumes, and fiber lengths. Left side arms were dismembered to determine weights and center of mass locations for the upper limb, forearm, and hand. To get the surface geometries, the bones were dried, mounted, and hand or laser digitized. Currently, a laser diffraction method (Lieber and Friden, 2000) is being used to measure average sarcomere lengths and optimal fiber lengths.

A seven degree of freedom (7-DOF), 3D dynamic model of the arm was constructed using vector methods as described in Yamaguchi *et al.* (1995). The shoulder was modeled as a fixed point, with the humerus revolving about the shoulder through three successive rotations. The humeroulnar joint defined elbow flexion and the proximal location of the radius. The distal radius pronates naturally about an axis drawn through the proximal radius and the distal ulna. Two additional degrees of freedom were defined for wrist flexion-extension and ulnar-radial deviation. This model features separate rigid bodies for the radius and ulna, with distinct inertial properties.

The final step of model development was to display the muscle pathways simultaneously with the bone surface geometries. Software for Interactive Musculoskeletal Modeling (SIMM, Musculographics, Inc., Evanston, IL) was used to display and adjust the results. When muscle pathways were incompatible with the surface geometries, small numerical corrections were made to improve the appearance of the model when viewed as a light-shaded, 3D surface model (Figure 1).

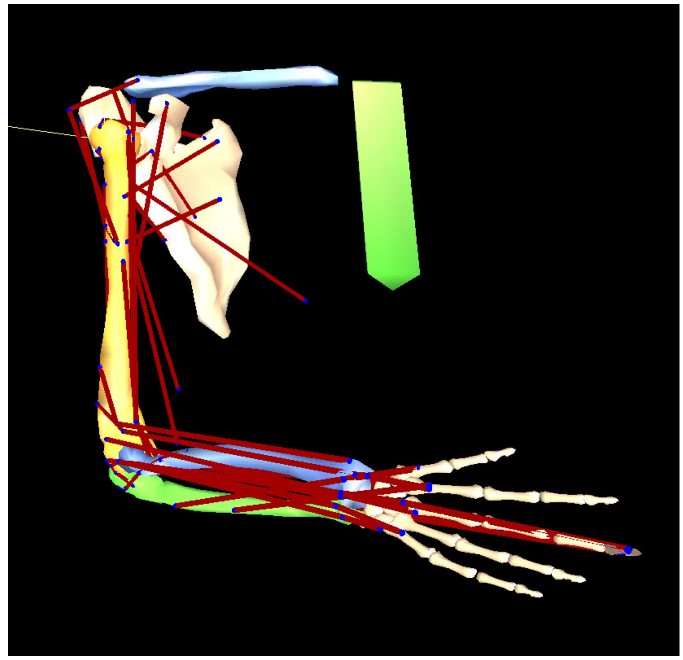

Figure 1: 7-DOF model of the monkey upper extremity.

RESULTS AND DISCUSSION

The model has been used in pilot optimal control studies to compare predicted muscle tensions with EMG and *in-vivo* force measurements. Force predictions made using the pseudoinverse optimal control method (Yamaguchi, 2001) compare favorably with *in-vivo* force measurements, but do not compare favorably with EMG (Figure 2). The latter discrepancy may be due to the optimization's preference for minimizing energy expenditure, while the monkey maximizes the likelihood of receiving a reward.

REFERENCES

Lieber, R.L. and Friden, J. (2000). Chp. 3, ***Biomechanics and Neural Control of Posture and Movement.*** Springer, 58-73.

Yamaguchi, G.T. (2001) *Dynamic Modeling of Musculoskeletal Motion -- A Vectorized Approach for Biomechanical Analysis in Three Dimensions*. Kluwer.

Yamaguchi, G.T. *et al.* (1995) *J. Biomech,*. **28**, 999-1005.

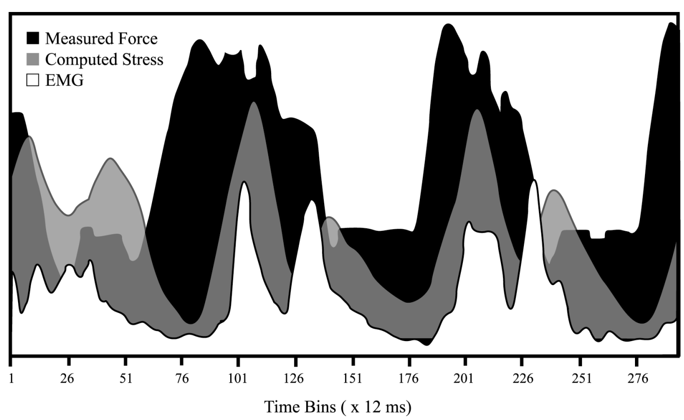

Figure 2: Predicted and measured biceps forces, and EMG.

THE DEPENDENCE OF WRIST EXTENSION MOMENT ON ELBOW AND WRIST POSITION AFTER BRACHIORADIALIS TENDON TRANSFER

Wendy M. Murray[1], Kevin L. Kilgore[2,3,4], and Michael W. Keith[2,3,4]

[1]Rehab R&D Center, VA Palo Alto HCS, Palo Alto, CA, murray@rrdmail.stanford.edu
[2]Louis B. Stokes Veteran's Affairs Medical Center, Cleveland, OH, [3]Case Western Reserve University, Cleveland, OH,
[4]MetroHealth Medical Center, Cleveland, OH

INTRODUCTION

Brachioradialis is the most commonly utilized donor muscle for tendon transfers that restore some upper extremity function after cervical spinal cord injury. Because brachioradialis shortens substantially with elbow flexion, function restored by brachioradialis transfers is thought to be weak in flexed elbow postures (Wilson 1956; Brand 1985). However, Fridén and Lieber (1998) demonstrated that surgeons frequently attach donor muscles at relatively long lengths, suggesting transferred muscles operate on the descending limb of the isometric force-length curve. If this is true, the transferred brachioradialis would produce *more* force at shorter fiber lengths (i.e., with the elbow flexed), rather than *less* force as is generally assumed.

After transfer to the paralyzed ECRB or ECRL, brachioradialis is essentially the only muscle that powers wrist extension. Thus, it is likely that differences in the wrist extension moment produced during maximal effort in different elbow positions reflect the force-length properties of brachioradialis. For example, if the wrist extension moment generated with the elbow flexed is greater than the moment produced with the elbow extended, it would suggest the transferred brachioradialis operates on the descending limb of the force-length curve (i.e., the muscle produces more force at a shorter length). Conversely, smaller moments when the elbow is flexed would imply the muscle operates on the ascending limb. The objective of this work is to determine if the isometric moment produced at the wrist increases or decreases with elbow flexion following brachioradialis tendon transfers that restore wrist extension. Because brachioradialis length also depends on wrist position after transfer, we evaluated how elbow position influences wrist extension strength in different wrist postures.

MATERIALS AND METHODS

We quantified the isometric wrist extension moment produced during maximal effort in seven individuals (eight limbs) following transfer of the brachioradialis to ECRB (n = 7) or ECRL (n = 1). Data was collected in two elbow postures (maximum elbow extension, 120° elbow flexion) and 3 wrist positions (30° flexion, neutral, 30° extension). Four trials were collected for each combination of elbow and wrist positions. The order the positions were tested was randomized across subjects. Subjects received visual feedback of the moment they produced on an oscilloscope which also displayed a target moment just beyond their capability to encourage maximum effort. All subjects provided informed consent. Results were analyzed using a 2x3 two-factor ANOVA with repeated measures on both factors.

RESULTS

The relationship between wrist extension strength and elbow position depended on the position of the wrist for the eight limbs in this study ($p = 0.01$). With the wrist flexed, the isometric moment produced with the elbow flexed was greater than the moment generated with the elbow extended (c.f., Fig. 1, black bar). On average, wrist extension moment increased by 13.7 Ncm with the elbow flexed, a 67% increase from the average moment produced with the wrist flexed and the elbow extended (20.6 Ncm). In contrast, wrist extension moment tended to decrease with elbow flexion when the wrist was in neutral (gray bar) or was extended (white bar).

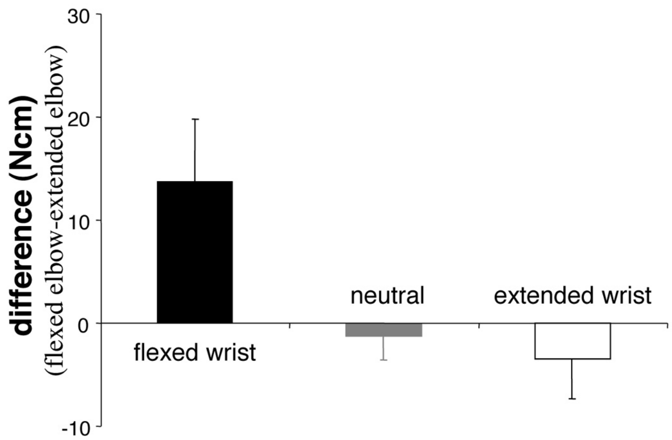

Figure 1. The difference between the wrist extension moments produced with the elbow flexed and with the elbow extended in three wrist postures. A positive difference indicates the wrist extension moment was larger when the elbow was flexed. Error bars indicate one standard error.

DISCUSSION

While few studies investigate joint moment-joint angle relationships after tendon transfer, understanding the moment-generating capability of transferred muscles can provide insight into the *in vivo* function of a single muscle. Our data indicate that the transferred brachioradialis tends to operate on the descending limb of the force-length curve when the wrist is flexed and shifts toward the ascending limb as the muscle shortens with wrist extension. These results provide direction for future biomechanical simulations aimed at improving surgical outcomes.

REFERENCES

Brand, P. W. (1985). *Clinical Mechanics of the Hand.* A. Hollister. St. Louis, Mosby Year Book, Inc.

Fridén, J. and R. Lieber (1998). *J Hand Surg* **23A**: 105-110.

Wilson, J. N. (1956). *J Bone Joint Surg* **38-A**(5): 1019-1024.

AN EMG-DRIVEN BIOMECHANICAL MODEL OF THE HUMAN ELBOW: FITTING A GENERIC MODEL TO SPECIFIC SUBJECTS

Thomas S. Buchanan, Kurt Manal and Richard Heine

Center for Biomedical Engineering Research, University of Delaware, Newark, Delaware USA
buchanan@udel.edu

INTRODUCTION

We have developed a biomechanical model of the human elbow that takes EMGs as inputs and yields estimates of joint moments in real-time as outputs (Manal et al., 2002). One factor that impacts the accuracy of the model is the relationship between the generic musculoskeletal parameters with which we begin, and the actual musculoskeletal properties of the specific subject being examined. In this abstract we will examine ways to scale (or tune) generic models so that they accurately represent specific subjects.

METHODS

EMG data from eight elbow muscles were collected during cyclic flexion-extension using fine-wire EMG electrodes. EMG data were rectified, filtered, and normalized to maximum effort. The elbow joint moment was simultaneously recorded.

The transformation from EMG to joint moment requires several steps, each of which can be described as a type of model. First, activation dynamics transforms each processed EMG signal to muscle activation, expressed as values between zero and one. Next, a model of muscle contraction dynamics transforms the muscle activation values to muscle force values. Finally, a musculoskeletal geometry model is used to transform the muscle force values to joint moment values. These can be compared with the measured value to assess the accuracy of the model

Muscle contraction dynamics is based on Hill-type models, requiring knowledge of musculoskeletal parameters such as optimal fiber length, tendon slack length, pennation angle, and maximum muscle force. It also requires values for the time varying muscle and tendon lengths, as well as muscle velocity. These come from the musculoskeletal geometry model, which, in addition, must compute the time varying (angular dependent) value of each muscle's moment arm. These parameters, as well as the parameters involved in modeling muscle activation dynamics, are the ones that must be adjusted if the model is to be tuned for a particular subject.

RESULTS AND DISCUSSION

For each subject, the parameters of the model are tuned by comparing the measured moment and the estimated moment and minimizing the differences between them. Typically, tuned parameters that are rooted in actual measurements are allowed to vary between plus or minus one standard deviation of the mean reported values used in the generic model. This allows each subject specific model the ability to accept anatomical variability without introducing parameters into the model that fall outside the normal physiological range. In Fig 1 we see the results of this tuning. Once the model has been tuned for a subject, it can be used without further tuning to predict joint moments from EMGs during novel tasks.

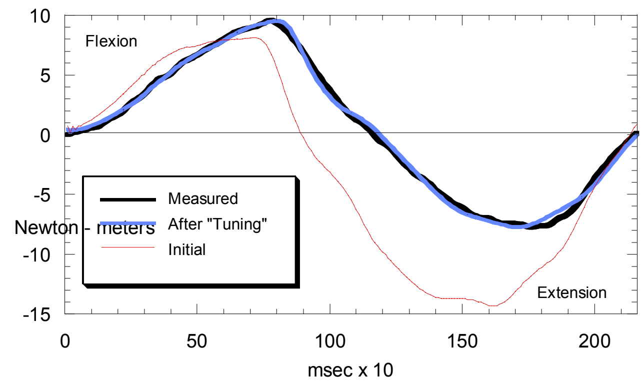

Figure 1: Elbow flexion-extension moment measured during a time varying task compared to that estimated from our EMG-driven model before and after tuning the model.

An analysis of the importance of each parameter has been performed to examine which most substantially impact the model's ability to accurately predict joint moments. The model was found to be rather sensitive to changes in the values of tendon slack length, whereas other parameters such as pennation angle were found to have little effect in joint moment estimation, even when substantially modified. This information is being used to determine the minimum number of parameters necessary to adjust in the model tuning process.

SUMMARY

An EMG-driven biomechanical model has been created to estimate muscle forces and, from these, joint moments. The model can be tuned for specific subjects by adjusting a few important anthropometrical parameters over physiological ranges and can yield very good results.

REFERENCES

Manal, K. et al. (2002) *Comp Biol Med* **32**, 25-36.

ACKNOWLEDGEMENTS

Supported by NIH grants AR40408 & AR46386.

WHEELCHAIR PROPULSION BIOMECHANICS WITH UPPER EXTREMITY IMPAIRMENT AND FATIGUE

Mary M. Rodgers and Margaret A. Finley

University of Maryland School of Medicine, Baltimore, MD USA
Baltimore Veterans Administration Medical Health Care System, Baltimore, MD, USA
Communicating Author: mrodgers@umaryland.edu

INTRODUCTION

A fatigue protocol is one model used to study the potential risks for overuse injuries in wheelchair users. Rodgers, et al (2000) has shown that several biomechanical characteristics of manual wheelchair propulsion change with fatigue. Many manual wheelchair users (MWCU) have upper extremity impairment (UEI) due to paralysis or motor control deficits, yet are functionally independent. The purpose of this study was to compare biomechanical characteristics in functionally independent MWCU, with and without UEI, during fresh and fatigued states. It was hypothesized that 1) MWCU with UEI would demonstrate different biomechanical values compared with those without UEI and 2) fatigue would magnify the differences.

METHODS

Subjects included 43 MWCU (14 with UEI, 29 without UEI, mean age = 39.1±9.1 yrs, WC use = 10.4±8.3 yrs, height 169.5+14.6cm, weight 71.6+14.8N). Diagnoses included spinal cord injury (24), spina bifida (4), cerebral palsy (3), multiple sclerosis (3), and other (9). Following informed consent and medical screening, propulsion mechanics were measured during a maximal exercise test to exhaustion (defined as volitional inability to sustain the target velocity of 3km/hr). Peak power output (POpeak) for the test corresponded to 60% of the maximal load achieved during a prior graded maximal exercise test. Three Peak 3D Charge Coupled Device (CCD) cameras and a video acquisition system (Peak Performance Tech., Colorado Springs, CO) were used to measure upper extremity and trunk movement. Temporal features of propulsion were determined from this kinematic data (60 Hz). A wheelchair ergometer instrumented with a PY-6 six-component force/torque transducer (Bertec Corp, Worthington, OH) in the wheel hub was used to measure handrim forces and moments. Orientation of the x-y-z transducer coordinates was tangential (forward+), radial (up+) and medial-lateral (into the wheel+), respectively. Peak joint angles during wheel contact and at release, temporal data and handrim data (360 Hz) were collected when the load was applied (fresh) and at exhaustion (fatigued), and averaged over three cycles. Joint kinetics were calculated using a 3-D linked segment Newton-Euler method based on body segment coordinate systems. Inputs to the model included 3-D angular displacement, velocity, acceleration and linear acceleration, handrim kinetic, temporal, and anthropometric data. A 13 item functional test called Wheelchair Users Functional Assessment (WUFA©) was used to assess level of independence (Feliciano, 1994). ANOVA was used to determine if differences existed between the groups and states ($p \leq 0.05$). ANCOVA determined differences in Mz between groups with POpeak covaried.

RESULTS

UEI demonstrated less wrist extension ($p=0.02$), elbow extension ($p=0.01$), shoulder flexion ($p=0.01$) and abduction ($p=0.01$ with a more upright trunk position at release ($p=0.04$). Contact time was shorter ($p=0.01$). Kinetically, the UEI had smaller handrim Mz ($p=0.003$) and elbow extension power ($p=0.03$). When POpeak was covaried, there was no difference in handrim Mz between the groups. Both groups had decreased radioulnar range with fatigue at contact ($p=0.04$) and release ($p=0.05$). As shown in the figure below, UEI demonstrated a greater decrease in shoulder flexion power from fresh to fatigue ($p=0.04$).

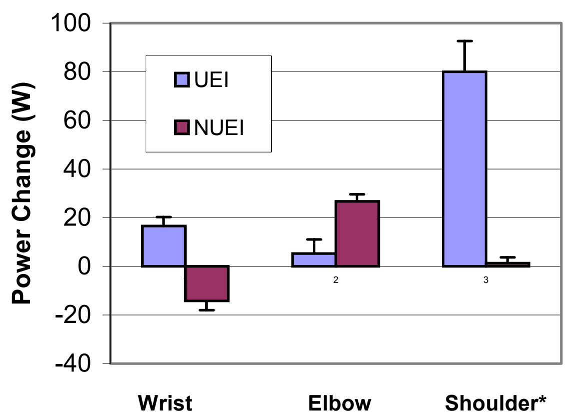

DISCUSSION

Although both groups were functionally independent, overall kinematics and kinetics were decreased for the UEI. MWCU with UEI were able to propel at the same proportion of their maximum effort as those without UEI. The primary effect of fatigue was to decrease wrist range used for propulsion for both groups. The combination of decreased joint excursion and no change with fatigue may provide UEI MWCU some amount of protection from overuse types of stresses.

REFERENCES

Feliciano, et al. (1998) APTA Sect Res Newsletter 30(3): 10
Rodgers MM, et al. (2000) *J Rehabil Res Dev.*37(3):283-295.

ACKNOWLEDGEMENTS

Funded by Veterans Affairs Rehabilitation Research and Development Service Merit Review Board Project #B2168RA

IN VIVO MEASUREMENT AND BIOMECHANICL MODELING OF THUMB CIRCUMDUCTION RANGE OF MOTION

Peter Braido and Xudong Zhang

Department of Mechanical and Industrial Engineering, University of Illinois at Urbana-Champaign, Urbana, IL, USA

INTRODUCTION

Thumb function is often regarded as accounting for 40-50% of hand usefulness (Emerson et al., 1996). A normative database along with a clear understanding of the biomechanics of thumb movement can aid in clinical evaluation of thumb functional impairment and ergonomic design of hand-held devices. Data obtained from in vitro studies (Imaeda et al., 1994) have limited applicability. This study aimed to explore the use of a contemporary motion capture system for measuring in vivo maximum thumb circumduction, and through biomechanical modeling and statistical analysis, to establish a normative database of 3D functional thumb ROM.

METHODS

Twenty-eight anthropometrically diversified subjects (14 males & 14 females) were selected according to stature through a rigorous screening process. A Vicon motion capture system (Oxford Metrics Ltd.) recorded the movement of 21 miniature reflective markers secured over the bony landmarks of the thumb and hand during the motion of right-hand maximum thumb circumductions in the counterclockwise (CCW) and clockwise (CW) directions.

A globographic representation method (Engin & Chen, 1986) implemented in MATLAB (MathWorks Inc.) was used to first calculate three best fitting concentric spheres for the metacarpophalangeal (MCP), interphalangeal (IP) and distal phalanx (DP) marker trajectories of the thumb and determine the carpometacarpal (CMC) joint center (JC). A plane was then fitted to each marker trajectory to identify a reference axis around which the thumb circumducts (Figure 1).

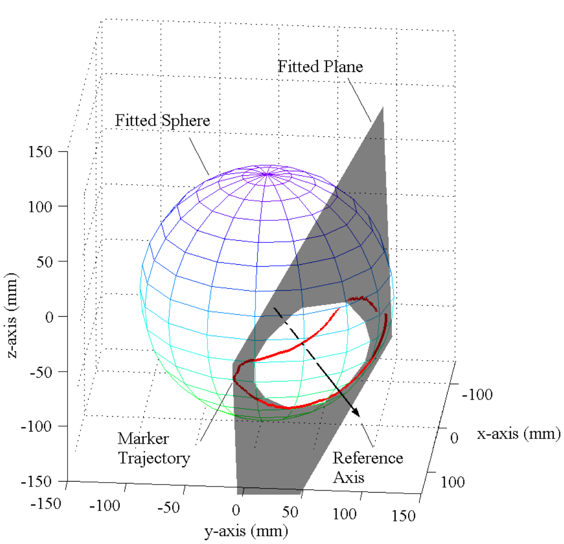

Figure 1: Fitted sphere and plane for a DP marker trajectory.

The thumb range of motion was quantified using (1) the volume that the thumb is capable of sweeping through defined by a cone with an irregular base, and (2) the included angles with respect to a reference axis, expressed as the joint sinus. To examine the effects of stature, gender and direction of circumduction on the ROM measures, two-sample t-tests and analysis of variance (ANOVA) were carried out using SAS (SAS Institute Inc.).

RESULTS AND DISCUSSION

The mean (±SD) root-mean-square-error (RMSE) between the estimated MCP, IP and DP sphere radii and marker trajectories are 1.31 (±0.50), 1.21 (±0.65) and 1.41 (±0.60) mm respectively, and the kinematic JC occurs within the thumb near the CMC joint. Gender has the most notable effect ($p<0.05$) on the JC location. Direction has the most significant effect on the orientation of the reference axis, followed by stature and gender respectively. The orientation of the reference axes of the more distal markers display a pattern that suggests an involuntary tendency to oppose the thumb to the palmer surface of the hand. The marker trajectories of thumb circumduction form a saddle shape in 3D that produces a joint sinus profile resembling a sine wave. Only direction has a significant effect on the computed angular values of the joint sinus. Anthropometry is the dominant factor in determining the cone volume, while gender and direction both have statistically significant effects.

SUMMARY

The validity of the globographic approach to quantify the maximum functional thumb ROM in vivo was supported by the low RMSE of the fitted spheres and the plausible physical location of the CMC joint center. The results of this study led to useful insight for future biomechanical modeling of thumb motion as well as implications on clinical diagnosis of impairment and ergonomic hand-tool design.

REFERENCES

Emerson, E. T. et al. (1996), *Annals of Plastic Surgery*, **36**, 180-191.
Engin, A. E., Chen, S-M. (1986), *J. Biomechanical Engineering*, **108**, 215-221.
Imaeda, T. et al. (1994), *J. Orthopaedic Research*, **12**, 197-204.

ACKNOWLEDGEMENTS

Funding provided by Caterpillar Inc.

HOW NETWORKS OF CORTICAL ACTIVITY ADAPT IN RESPONSE TO CHANGES IN THE TYPE AND QUALITY OF SENSORY INPUT DURING DYNAMIC PRECISION PINCH

F.J. Valero-Cuevas[1,2], A. Talati[3,4], M. Venkadesan[1] and J Hirsch[3,5]

[1]Neuromuscular Biomechanics Laboratory, Cornell University, Ithaca, NY. www.mae.cornell.edu/nmbl
[2]Laboratory for Biomedical Mechanics and Materials, The Hospital for Special Surgery, New York, NY.
[3]Department of Neurology and Neuroscience, Memorial Sloan-Kettering Cancer Center, New York, NY
Graduate Programs [4]Pharmacology & [5]Neuroscience, Weill Graduate School of Medical Sciences, Cornell University, New York, NY

INTRODUCTION

Effective methodologies for experimentally investigating computational principles of the brain are in short supply (Ito, 2000). Two competing demands dominate the design of experiments to study the cortical foundation of dexterous manipulation: (i) the biomechanical versatility of the hand requires that the experimental task be sufficiently constrained mechanically to reduce inter- and intra-subject variability. And, (ii) the task must be complex enough to be representative of dexterous manipulation. Functional MRI studies have shown that primary motor cortex, premotor and parietal areas are important for control of fingertip forces during static precision grip (Ehrsson, et al, 200), but we lack dynamic tasks to study sensorimotor integration during dynamic manipulation. We present a novel well-defined dynamical task to identify cortical areas involved in sensorimotor integration during dynamic precision pinch.

METHODS

Task: Ten healthy, right-hand dominant subjects (avg. age 27 yrs) used three-point pinch to repeatedly compress a slender spring that requires a specific combination of pinch force magnitude and directional accuracy to compress without buckling. In a modified version of the Strength-Dexterity test (Valero-Cuevas et al., 2001), two smooth plastic end caps flanked a 25 mm long, 10 mm diameter compression spring. The pads of the second and third digits opposed the pad of the thumb to compress the spring without buckling by simultaneously and dynamically regulating fingertip positions and forces to keep the end caps parallel and aligned (see Figure). The pinch force needed to fully compress the spring was 2.5 N, which could be repeated continuously for 50 s without fatigue in each experimental condition. We presented four experimental conditions twice at random to study cortical activity during spring compressions as we varied the presence of vision and the quality of tactile input: (1) Eyes Open (2) Eyes Closed (3) Eyes Open with Sandpaper, and (4) Eyes Closed with Sandpaper. In conditions 3 & 4 coarse sandpaper covered the smooth end caps. ***Brain Imaging:*** A 1.5 tesla Magnetic Resonance Scanner and a standard head coil (General Electric) were used to obtain T2*-weighted images (sensitive to deoxygenation accompanying neuronal activation) and conventional high-resolution T1-weighted images for anatomical reference. We collected 21 contiguous slices that covered the entire cortex for all subjects. Analysis of Variance compared the activity of brain regions that were active across all subjects and conditions (Hirsch et al., 2000).

RESULTS & DISCUSSION

Regions that co-varied significantly ($p<0.05$) with the visual input included the inferior parietal lobule (Brodmann's Area [BA] 40), inferior occipital (BA 18) and middle occipital (BA 19) gyri, the medial frontal gyrus (BA 6), and the cingulate Gyrus (BA 24, see Figure). The parietal and occipital regions showed the most activity when visual input was present. The medial frontal and cingulate gyri, in contrast, were more significantly activated when vision was occluded, perhaps reflecting a requirement for increased preparation and attention when visual feedback was unavailable. Regions that co-varied with the tactile input included the pre-central motor (BA 4), and post-central sensory (BA 1,2,3) gyri. The interaction between visual and tactile data was strongest in the inferior parietal lobule, consistent with the known associative role of this structure. These findings suggest that fine-tuned motor tasks are mediated by a network of several cortical regions where the relative contribution of these regions varies depending on the type and quality of sensory input available.

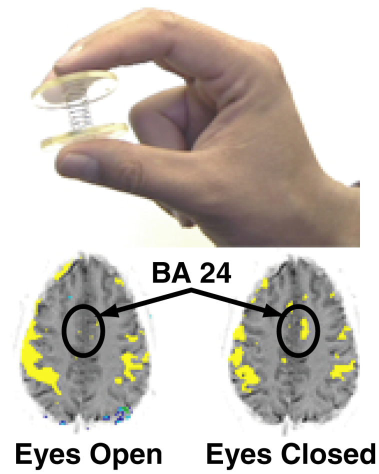

SUMMARY & SIGNIFICANCE

Part of the internal model theory predicts that the occlusion or enhancement of a sensory channel will cause a complementary enhancement or downgrading of other channels, respectively, to maintain an appropriate level of sensory feedback (Wolpert et al, 1995). Our novel dynamic manipulation task has allowed us to detect changes in associative regions (e.g., BA 24) that may reflect the cortical activity necessary for the internal model to adapt to the presence and quality of sensory input.

REFERENCES

Ehrsson, H., et al (2000) J Neurophysiol 83, 528-536. **Hirsch**, J., et al (2000) Neurosurgery 47: 711-722; **Ito**, M. (2000) Nature 403: 153-154; **Valero-Cuevas** et al. (2001). Proc. of ASB ; **Wolpert** et al. (1995) Science 269:1880-1882.

ACKNOWLEDGEMENTS: Niels Smaby, MS.

MODEL-BASED DEVELOPMENT OF A NEUROPROSTHESIS FOR HIGH CERVICAL SPINAL CORD INJURY

Robert F. Kirsch[1] and Ana Maria Acosta[2]
[1]Case Western Reserve University and Cleveland FES Center, Cleveland, Ohio, USA rfk3@po.cwru.edu
[2]Rehabilitation Institute of Chicago, Chicago, IL, USA a-acosta@northwestern.edu

INTRODUCTION

Individuals with high cervical spinal cord injury (C1-C4) are highly disabled, with all movements below the level of the neck paralyzed except for shoulder shrug. We are developing a neuroprosthesis based on functional neuromuscular stimulation (FNS) of paralyzed muscles to restore arm function to these individuals. The challenges are significant because of the sheer number of paralyzed motions and, in particular, because the shoulder complex is involved. We are making extensive use of simulations with a musculoskeletal model to develop this neuroprosthesis, beginning with an evaluation of its basic feasibility. Here we describe the minimal muscle set needed to restore a series of simple yet critical arm motions, and the minimum muscle forces needed to produce these movements.

METHODS

We used the 3D musculoskeletal model of the shoulder and elbow developed by the Dutch Shoulder Group, (van der Helm 1994). Inverse static simulations were performed at several arm postures to find the muscle forces needed to balance the weight of the arm and an external load. Shoulder and elbow input kinematics were measured on an able-bodied individual using an established method (van der Helm and Pronk 1995). Three simple tasks were chosen for simulation: arm elevation from resting to horizontal (90°) in the coronal and scapular planes, and hand movement from a tabletop to the mouth. These dynamic tasks were approximated by a series of 5-6 fixed postures along each of the 3 trajectories so that inverse static simulations could be used. Simulations were performed with no load and a 300g load attached at the hand. The algorithm illustrated in Figure 1 was used to find the minimum muscle set that allowed feasible solution of all the tasks. This algorithm iteratively removed muscles from the simulations (i.e., made the muscles "paralyzed") until one or more of the postures could no longer be maintained, taking care to determine if previously discarded muscles could substitute for the remaining muscles. This process converged to the minimum muscle set needed across all of the postures.

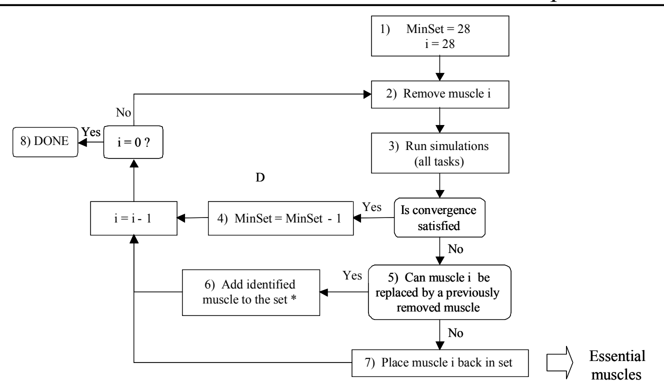

Figure 1: Algorithm for detecting minimal muscle set

RESULTS AND DISCUSSION

We found that the minimum muscle set obtained from the simulations was unique and included only six muscles: scapular head of trapezius, serratus anterior, clavicular head of deltoid, infraspinatus, subscapularis, and brachialis. Five of these were essential, i.e., no combination of other muscles could substitute for the actions of any one of them. Clavicular deltoid could be replaced by scapular deltoid plus teres minor (i.e., a larger muscle set). Of these six muscles, 5 would be paralyzed in an individual with a C3-C4 spinal cord injury, while the scapular trapezius would retain voluntary control. The muscle force magnitudes required of these muscles for the unloaded conditions were always less than 68% of maximum and typically 20-40% of maximum. For the loaded conditions, the required forces increased only modestly (less than 22%). These simulation results indicate that the minimum number of muscles that would need to be stimulated (five) to restore arm movements is well within existing FNS technology. Further, the muscle force magnitudes required for the simple tasks simulated are likely to be low enough for stimulated muscles to generate in individuals with disuse atrophy due to chronic paralysis. Thus, we believe that a neuroprosthesis to restore simple arm movements in individuals with high cervical spinal cord injuries is feasible.

SUMMARY

To evaluate the feasibility of restoring arm movements to individuals with high cervical spinal cord injuries via FNS, model-based simulations were used to identify the minimum number of muscles needed to move the arm in a set of simple tasks. We found that both the number of muscles (6) and required strength (typically less than 40% maximum) were low enough to indicate that such an approach may be feasible.

REFERENCES

Van der Helm, F.C. (1994) *J. Biomech*. 27:551-569.
Van der Helm, F.C. and Pronk, G.M. (1995) *J. Biomech. Engineering* 117:27-40.

ACKNOWLEDGEMENTS

This work was supported by the Spinal Cord Research Foundation (Grant 1826) and by the NIH Neural Prosthesis Program (N01-NS-1-2333).

A FORCE-FIELD APPROACH TO THE ADAPTIVE CONTROL AND LEARNING OF ARM MOVEMENTS

Ferdinando A. Mussa-Ivaldi, Michael A. Conditt, Jonathan B. Dingwell, Amir Karniel, Christopher D. Mah, James L. Patton, and Robert A. Scheidt

Northwestern University Medical School
Sensory Motor Performance Program, Rehabilitation Institute of Chicago, Chicago, Illinois, sandro@northwestern.edu

When we learn to move our arm and to act upon the environment, our brains become to all effects "experts in physics". How can such expertise come about from experience? What kinds of representations are used by the brain to control the arm dynamics? How can we handle objects with inherent instabilities and internal degrees of freedom? How can arm movement control be recovered after stroke? We have addressed these questions in a set of experimental and theoretical studies. The theoretical framework is based on the idea of representing a complex control function as a superposition of "basis fields" representing the action of primitive controllers. The experimental studies make use of a simple robotic device, which alters the dynamics that the brain must control in order to execute the desired movements. Taken together, these studies present a new perspective on the control, learning and recovery of multi-joint arm movements.

THEORETICAL FRAMEWORK: MOTOR LEARNING AND CONTROL THROUGH THE COMBINATION OF PRIMITIVES

Microstimulation of the spinal cord in spinalized frogs and rats provided evidence for a modular organization of the spinal cord function [1]. A spinal module is a functional unit of the spinal cord circuitry that generates a motor output by producing a muscle synergy - a specific pattern of muscle activation. The output of a spinal module can be characterized as a force field - a mapping that associates each position of the frog's limb with a corresponding force generated by the neuromuscular system. Remarkably, these studies demonstrated that the simultaneous activation of spinal sites results in the vector summation of the corresponding fields.
Arm dynamics are described by a set of nonlinear differential equations, which may be summarized as:
$D(x,\dot{x},\ddot{x}) = C(x,\dot{x},t)$, where D represents the passive (inertial, viscoelastic, gravitational) dynamics and C represents the time varying controller dynamics, which also include state-dependent terms. The finding of vector summation of spinal force fields suggests that under descending supraspinal commands, the fields expressed by interneuronal modules in the spinal cord may form a broad repertoire of control fields $C_S(x,\dot{x},t\,|\,c_\alpha)$:

$$\Gamma = \{C_S(x,\dot{x},t\,|\,c_\alpha) = \sum_\alpha c_\alpha \phi_\alpha(x,\dot{x},t)\}$$

where each element of Γ is generated by the descending neural commands selecting a group of synergies through the weighting coefficients, c_α. Following this view, the neural control system may approximate a target field implementing a desired behavior, by finding the element of Γ that is closest to the target field. We have developed experimental techniques with robotic manipulandum and human subjects to reveal the capabilities and limitations of this internal representation of the external force perturbations.

EXPERIMENTAL FINDINGS

Experimental studies of motor learning involve the mechanical interaction of subjects with a 2-joint robotic manipulandum. Typically, in these studies, subjects execute reaching movements holding the handle of the manipulandum, which applies a preprogrammed field of forces. The following main results have been obtained by our group:
1) When subjects execute arm movements against a field of forces that depend on the state of motion of the hand, they learn to compensate the field by constructing an internal representation of the perturbing field. The clearest evidence for that are the predictable erroneous movements that are observed as the field stopped unexpectedly.
2) When forces depend upon time but not upon state, a correct representation is not learned. Instead subjects tend to substitute the time-varying force with a state-dependent force, which generate similar effects on the training movements. This is in contrast to artificial systems that typically use clocks, counter and switches and not state mapping.
3) The mechanism of adaptive control may be exploited to induce the implicit learning of a desired movement as an after-effect of adaptation. This method is investigated for the design of force fields that can facilitate the recovery of motor skills lost to stroke and other disorders.
4) Time-series analysis of motor adaptation has reveled that the perturbing state-dependent field is learned based only on recent memories of the perturbation and of past performance. The same model fits both predictable and random sequences of perturbations.
5) When interacting with an object with internal degrees of freedom (such as a spring in series with a mass), subjects learn to control the kinematics of the object by forming an internal model that specified the forces that the hand must exert at the point of contact to induce a smooth motion of the object's endpoint.

REFERENCES

[1] E. Bizzi, F. Mussa-Ivaldi, and S. Giszter, "Computations underlying the execution of movement: A biological perspective," Science, vol. 253, pp. 287-291, 1991.

Further details and references are available through our lab web pages: http://www.smpp.nwu.edu/robotLab/

IMPEDANCE MODELS OF FINGER JOINTS DURING TYPING

Devin L. Jindrich and Jack Tigh Dennerlein (jax@hsph.harvard.edu)
Harvard Occupational Biomechanics, Harvard School of Public Health, Boston, MA.USA

INTRODUCTION

One possible risk factor for the development of computer work-related musculoskeletal disorders (MSDs) is mechanical load to the soft tissues resulting from extensive keying. Predicting the mechanical load on the soft tissues of the finger and hand is difficult because of the complex musculoskeletal structure and the dynamic nature of the finger during a keystroke. Simple mechanical impedance models of animal locomotion, however, have revealed principles of musculoskeletal design, and lead to specific motor control hypotheses (Farley *et al*., 1993). Our approach therefore, is to build a lumped-parameter model of the finger to test the hypothesis that joints of the finger behave like a relatively simple mechanical impedance system.

MATERIALS & METHODS

Subjects tapped with the index finger of the right hand on a computer keyswitch mounted on a bi-axial force sensor, which measured vertical and sagittal forces (Figure 1). An optical measurement system measured the position of the keyswitch using an infra-red LED glued to the side. Miniature finger goniometers (Model S720 Shape Sensors, Measurand, Inc.) placed across each joint measured joint kinematics. Output from the force, position and angle sensors were sampled at 10 KHz using a computer A/D system (National Instruments NB-MIO16E DAQ board, LabVIEW software).

Figure 1. Experimental apparatus.

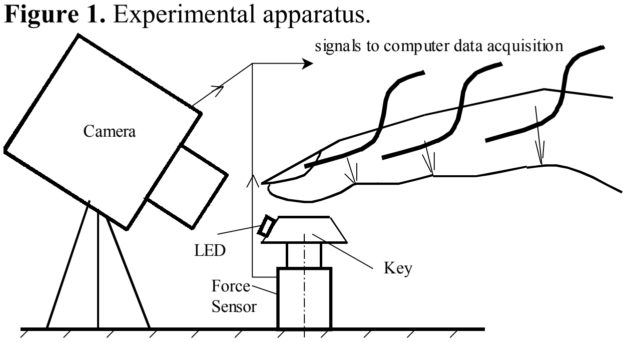

Finger segment lengths were measured, and an inverse dynamic model of the finger was used to calculate joint torques from forces and kinematics (Craig, 1989).

A linear Voight model, (linear spring and damper in parallel), was fit to the kinematic and torque data from each joint. Using the model parameters, joint angles and angular velocities over the tap, the joint torque was re-constructed and compared to the measured torque to determine the effectiveness of the model. Proportional errors were calculated as the RMS value of the difference between measured and predicted torque relative to the RMS value of the input torque signal. Three subjects have been tested to date.

RESULTS

For the subjects tested to date, the distal finger joints of the index finger acted as simple spring-mass-damper systems during the contact phase of a keystroke. Torques at the Distal interphalangeal (DIP) and proximal interphalangeal (PIP) joints were re-constructed by a linear Voight model (Figure 2) to errors of less than 20%. A linear Voight model was not able to accurately model the mechanics of the metacarpophalangeal (MCP) joint during tapping on a keyswitch, suggesting a more complex motor control pattern.

The effectiveness of viscoelastic models in describing the behavior of some finger joints may simplify the analysis and prediction of tissue loading during keying. Monitoring only a subset of joints during different typing tasks may be sufficient to understand the tendon forces, which determine the movements of, and external forces on, the finger.

Figure 2. Measured (solid black curve) and predicted (dotted blue curve) joint-torque over time for a representative tap.

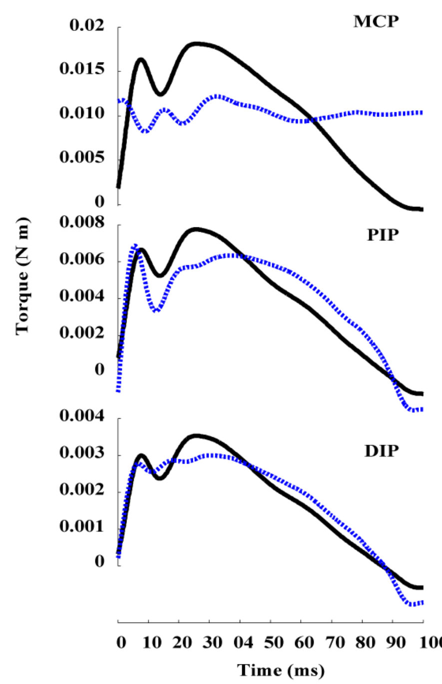

REFERENCES

Craig, J. (1989). Reading, MA: Addison-Wesley Publishing Company, Inc.
Farley, C., et al. (1993). *J. exp. Biol.* **185,** 71-86.

ACKNOWLEDGMENTS

This project is supported by the Whitaker foundation.

EFFECTS OF LOW-LOAD, HIGH REPETION MOTION ON SCAPULAR KINEMATICS

Andrew Karduna, Chao-Yin Wu, David Ebaugh
Programs in Rehabilitation Sciences, MCP Hahnemann University, Philadelphia, PA
email: karduna@drexel.edu

INTRODUCTION

Although the National Institute of Occupational Safety and Health has identified a clear epidemiological link between repetitive arm motion and shoulder disorders in the workplace (Bernard, 1997), there are few scientific data available regarding the biomechanics of this connection. On theory is that repetitive motion leading to scapulothoracic muscle fatigue may result in abnormal scapular kinematics that are potentially dangerous to a worker. There is evidence that high load, low repetitive activity is associated with muscle fatigue and abnormal scapular motion (McQuade et al., 1998). The purpose of this study was to investigate the consequences of low load, high repetition activities frequently associated with workplace shoulder disorders.

METHODS

Kinematics The Polhemus 3Space Fastrak (Colchester, VT) was used to collect kinematic data. A thoracic receiver was placed over T3 using double sided tape, a humeral receiver was placed at the deltoid tuberosity using an elastic strap, and a scapular receiver was fixed to a so-called scapular tracking device that was attached to the scapular spine and acromion process using Velcro strips. We have previously demonstrated the validly of the technique for measuring scapular kinematics (Karduna et al., 2001). Data were collected during three trials of elevation in the scapular plane, with data averaged over the three trials. Data for 3 scapular rotations were analyzed: posterior tilting, upward rotation, and external rotation.

Measurements of Fatigue Force, EMG and perceived stress data were collected in order to assess the effects of a simulated work task on fatigue. Pre-amplified surface electrodes were applied to the anterior deltoid, upper trapezius and serratus anterior. Data were collected at 1200 Hz, amplified and bandpass filtered (10-750 Hz). Force and EMG data were collected during a 5 second maximum isometric contraction. A spectral analysis of the EMG data was performed and the median power frequency (MPF) was calculated. The Borg's rating of perceived exertion scale was used to measure the subjective physical intensity of the simulated work task. This is an interval scale scored with levels ranging from 6 (no exertion) to 20 (maximal exertion).

Protocol Sixteen healthy subjects were studied with IRB approval (mean age of 27 years). The first step was to collect baseline measurement of force, EMG, perceived fatigue and kinematics. The subject then performed a simulated work task for 15 minutes. The task required the subject to reach out and grasp a bar positioned at a height that resulted in 110 degree of shoulder flexion in the sagittal plane and then return to 0 degrees of flexion. The subject performed this task at a pace of 41 cycles/minute with no load in their hand. Immediately after the completion of this simulate work task, force, EMG, perceived fatigue and kinematic data were collected again.

RESULTS

Signs of fatigue after the simulated work task were varied among the measurements. While there was no significant reduction in isometric force, the serratus anterior showed a significant reduction (10%) in MPF after the simulated work task. Also, there was a dramatic change in perceived exertion, going from 7 (extremely light) to 16 (hard). With respect to kinematics, there were no significant differences in posterior tilting and external rotation. However, there was a small but significant increase in upward rotation between 60 and 120 degrees of humeral elevation (figure 1).

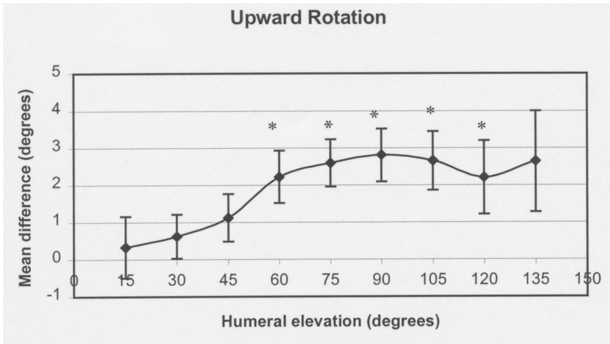

Figure 1 Mean differences in upward rotation * $p< 0.05$

DISCUSSION

Clearly, the low load, high repetition task of this study resulted in a substantial perception of fatigue as indicated by the results fom the Borg scale. However, the fact that there was only moderate fatigue in one muscle and no reduction in force production might help explain why only minimal changes in scapular kinematics were observed. Additionally the low load condition of the present study may have resulted in EMG activation levels less than 10%, which may not be high enough to elicit a shift in action potential velocity necessary for a decrease in MPF (Hagg, 1992). Other methods may be necessary for assessing muscle fatigue under these conditions. We are currently examining the effects of varying load intensity on fatigue and kinematics.

REFERENCES

Bernard, B.P (1997), NIOSH report 97-141
Hagg, GM (1992). *J Appl Physiol,* **73**, 1211-1217.
Karduna, AR et al, B. (2001). *J Biomech Eng,* **123**, 184-190.
McQuade, KJ et al. (1998). *JOSPT,* **28**, 74-80.
Melhorn, J. M. (1998). *CORR,* **351**, 107-126.

INDIVIDUAL LOAD LIMITATION OF THE GLENOHUMERAL JOINT AS A PREVENTION TOOL FOR MUSCULOSKELETAL INJURIES

Krystyna Gielo-Perczak and Tom Leamon

Liberty Mutual Research Center for Safety and Health, Hopkinton, MA U.S.A.
Krystyna.Gielo-Perczak@LibertyMutual.com
http://www.libertymutual.com/research/

INTRODUCTION

An important feature of workplace design is the creation of solutions for preventing excessive joint loading. Ergonomists apply quantitative methods during the search for optimal relationships between workers and their work environments, but these assessments are mainly based on anthropometry which often represents the main design criteria. An important need in workplace design is the creation of innovative ways to prevent excessive joint loading. The only methods for finding these different options are modeling and simulation.

METHODS

Musculoskeletal disorders of the upper extremities due to work factors are common and occur in nearly all sectors of our economy. The highest rates of these disorders occur not only in the industries with a significant amount of forceful work in high arm positions during concentric contractions, but also during eccentric contractions in arm positions of 0 to 30 degrees of abduction.

A new model of the glenohumeral joint has been proposed and investigated for its applicability to ergonomic studies (Gielo-Perczak, 1989). The most important feature of the proposed model is that the internal loading – which means the forces at the bone-on-bone contact point, or in the muscles, or in the ligaments – can be expressed as the multivariable function of its articular geometry. This method of analysis takes into account individual differences in geometry of the glenohumeral joint (GHJ) with different types of work. Central to the study is an investigation of the individual influence of joint geometry on the Maximum Acceptable Workload (MAW) applied to the hand.

The proposed model provides sets of humerus positions that are acceptable in terms of muscle and ligament strength and stresses at the bone-on-bone contact points. The maximum acceptable workload of each element of a joint can be calculated individually as a function of the external load, the geometry of the articulating surfaces, and the muscles and ligaments.

RESULTS & DISCUSSION

The load applied at the hand is a critical element in assessing individual force limitations during activities. Calculations have been performed for the different joints and loading, and the results show that when an individual pushes an object on a table, the bone-on-bone forces have the greatest influence on the MAW. In a pulling activity, if the arm is moved about 30° from the side, and the angular position of a handle is:

- 170°, then the maximum acceptable load can be 971 N;
- 160°, then the maximum acceptable load can be 414 N;
- 150°, then the maximum acceptable load can be 271 N.

The maximum weight of the pulled object depends on the geometry of a joint and position of the arm, and on the position

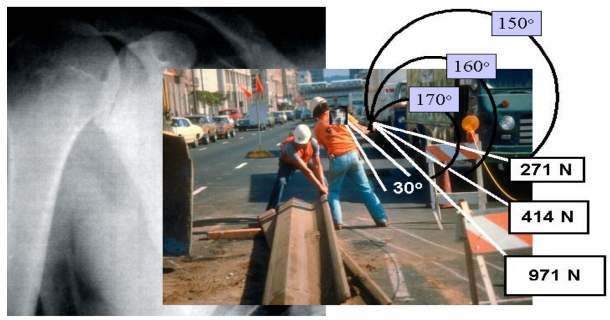

of the handle.

This method can be a useful tool for:

- minimizing incompatibilities between the capabilities of workers and the demands of their jobs,
- preventing likely shoulder injuries during work.

With this GHJ model, it is possible to reduce musculoskeletal injuries by assessing individual acceptable loads during carrying, pushing and pulling. This model can help reduce the risk of shoulder injuries during static and repetitive work, and can help researchers examine the forces in ligaments, selected muscles, and between bones for specific joint geometry.

SUMMARY

To understand human tolerance to work loads, it is necessary to calculate the stress and strain at specific points in the musculoskeletal system. Joint loading analyses, by application of computer simulation, imply the etiology of injury. The application of computer simulation can be useful for minimizing incompatibilities between the workers' physical capabilities and their job demands towards preventing work-related musculoskeletal injuries.

REFERENCES

Gielo-Perczak K. Analysis and Modeling of the Glenohumeral Joint Mechanism Structure. *SOMA- Engineering for the Human Body* **3**(3) 35-46, 1989.

Van den Helm F. Analysis of the Kinematic and Dynamic Behaviour of the Shoulder Mechanism of the Shoulder System. *J. Biomechanics* 27(5): 527-550, 1994.

CONTRACTILE PERFORMANCE OF MUSCLES THAT GENERATE POWER *VS* MINIMIZE COST/FORCE

Andrew A. Biewener
Concord Field Station, Department of Organismic and Evolutionary Biology, Harvard University, Cambridge MA, USA
abiewener@oeb.harvard.edu

INTRODUCTION

Limb muscles are recruited and contract to carry out a range of mechanical functions. Many muscles shorten while generating force to do (concentric) work and generate mechanical power (work/time), while others lengthen (eccentric contraction) to absorb energy. Still other muscles may contract isometrically to transmit force, but do no work. Different modes of locomotion (flight and swimming *vs* running), as well as differing locomotor movements (level *vs* incline and steady *vs* acceleration & deceleration), emphasize these differing roles of muscles. Furthermore, in contrast to the quasi-steady nature of a muscle's force-length and force-velocity properties, the *in vivo* performance of muscles requires that they be cyclically activated in relation to time-varying changes in length and force.

This paper compares the dynamic *in vivo* force-length behavior of muscles that function to generate mechanical power (bird flight muscle) versus those (leg muscles of hopping and running animals) that minimize cost/force (Biewener & Roberts, 2000). It examines three aspects of muscle function: 1) how muscle architecture affects muscle function; 2) whether similar features of muscle activation relative to force development and length change apply to muscles that generate power *vs* those that minimize cost/force, and 3) how changes in grade, speed and gait affect the *in vivo* contractile performance of a muscle.

METHODS

In vivo patterns of muscle activation (EMG) were recorded in relation to fascicle strain (via sonomicrometry) and muscle force (via bone strain or tendon buckle) for the pectoralis (*Pect*) of birds during flight (Biewener et al. 1998a) and the lateral gastrocnemius (*LG*) and plantaris (*Pl*) of wallabies during hopping (Biewener et al. 1998b). EMG and fascicle strain were also recorded in the biceps femoris (BF) and vastus lateralis (VF) of rats (Gillis & Biewener, 2001) and goats (unpublished) during treadmill locomotion at different grades, speeds and gaits.

RESULTS & DISCUSSION

In contrast to the pigeon *Pect*, which undergoes considerable shortening (total fascicle strain: 35-40%) while generating force to produce mechanical power to move the wing during flight, the wallaby *LG* (not shown) and *Pl* muscles both contract under nearly isometric conditions (< 5% strain; Fig. 1), similar to the *LG* of running turkeys (Roberts et al. 1997). Near isometric contractile behavior favors greater force/ATP use and may often be related to tendon elastic energy savings.

A common feature of both contractile behaviors is that these muscles are all activated near the end of passive lengthening

Figure 1.

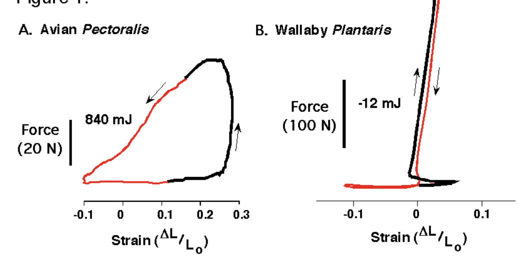

(wing upstroke or limb swing protraction), just prior to shortening. Eccentric activation of the muscles enhances both the rate and magnitude of force development, which favors both increased work and reduced cost/force.

The rate and magnitude of muscle force, and *not* muscle work, have been argued to be the main determinants of energy cost in terrestrial running gaits (Kram & Taylor, 1991). Direct experimental evidence for this relies largely on the observed isometric behavior of distal leg muscle-tendon units (Roberts et al. 1997). Measurements of muscle strain and EMG patterns in more proximal muscles of rats and goats (Fig. 2) however indicate that both the BF and VL undergo considerable strain (20 to 25%) during limb support, indicating that they play important roles in modulating whole-limb work during limb support. In general, changes in speed and gait have only subtle

Fig. 2

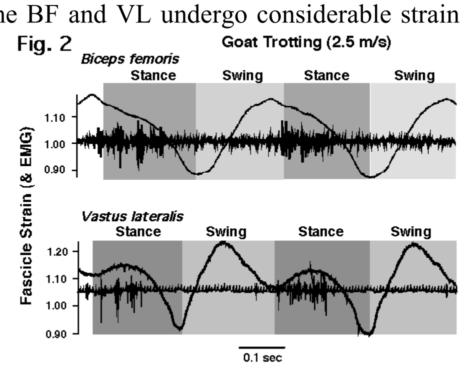

effects on the *in vivo* patterns of muscle strain and activation. In contrast, changes of grade strongly influence the contractile behavior of the BF and VL. Both muscles shorten more during incline running (VL: 9%; BF: 27%, $p < 0.01$), and the rat BF is generally 'turned-off' during downhill locomotion.

REFERENCES

Biewener, A A, et al. (1998a) *J.exp. Biol.*, **201**, 3293-3307.
Biewener, A A, et al. (1998b) *J.exp. Biol.*, **201**, 1681-94.
Biewener, A A, Roberts, T J (2000). *Exer Sport. Sci Rev.* **28**, 99-107.
Gillis, G B, Biewener, A A (2001) *J.exp. Biol.*, 204, 2717-31.
Kram, R, Taylor, C R (1990). *Nature* **356**, 265-67.
Roberts, T J, et al. (1997). *Science* **275**, 1113-15.

ELASTIC MECHANISMS IN EQUINE LOCOMOTION (*EQUUS CABALLUS*)

Wilson A.M.
Structure and Motion Lab, The Royal Veterinary College, North Mymms, Hatfield, Herts, AL9 7TA England

INTRODUCTION

Storage of elastic strain energy in the collagenous component of muscle tendon units of anti gravity muscles is important in reducing the mechanical work of locomotion (Minetti *et al*, 1999). This mechanism has been demonstrated in the gastrocnemius tendon of the wallaby (Biewener *et al*, 1998), the digital flexor tendons of the horse and the plantaris muscle of the human foot (Alexander & Bennet-Clark, 1977). These specialised muscle-tendon units have very short muscle fibres and long tendons. Short muscle fibres mean that there is limited scope for changing the length or the stiffness of the muscle tendon unit. The limb therefore acts as a passive elastic structure with fixed mechanical properties. We are interested in how the horse deploys this mechanically constrained limb under the varying requirements of locomotion.

In this talk I will summarise a series of experiments testing the following hypotheses:

1. The equine limb does not change stiffness as a result of changes in speed, gait or surface.
2. The short fibred muscles act not to control limb stiffness but as dampers of high frequency vibration within the tendons.
3. Elastic energy storage appears to also be used to initiate limb protraction.

METHODS AND RESULTS

1. We conceptually divided the equine limb into two compression springs, one extending from the elbow to the foot and the second from the scapula to the elbow. Length change was measured using video motion analysis (ProReflex, Qualysis) during treadmill locomotion. About 90% of the length change occurred in the distal portion of the limb where the highly adapted muscles lie. We speculate that the proximal limb is more involved with limb protraction.

Limb length change occurs as a result of metacarpo-phalangeal (MCP) joint extension. We used the relationship between MCP angle and limb force as a measure of limb stiffness. This relationship was almost unchanged as a function of surface properties, gait or muscle activation. Theoretical calculations indicate that the proximal limb is too stiff to make any significant contribution to changing whole limb stiffness.

2. The elastic and multi segmented nature of the equine limb make it susceptible to a secondary mode of vibration in a cranio-caudal direction – much like plucking a violin string. These oscillations are excited by foot impact, occur at a frequency of 30 – 40Hz and, we believe, are important in the development of musculo-skeletal injury. (Wilson *et al*, 2001) Such vibrations are damped by the surface and by the energy absorption properties of muscle. These oscillations can be recreated by impacting a mechanical model of the equine limb; this enables us to study the relationship between musculo-skeletal arrangement, surface properties and limb oscillation. It transpired that whilst surface stiffness is important in tuning the primary resonant frequency of the limb it has little influence on vibration magnitude or frequency. The damping properties of the surface are however critical in determining the duration of limb vibration. The very short fibred digital flexor muscles, whilst of little value in controlling limb movement, appear ideal for damping the higher frequency oscillations of the limb. When a cross bridge model is subjected to small amplitude oscillations it demonstrates peak energy absorption around 50-100Hz and there are sufficient cross bridges in the digital flexor muscles to account for the damping response seen *in vivo.*

3. It is biologically important to maximise duty factor (fraction of stride time that foot is on ground) because this will minimise peak limb and muscle stress. Muscles are not very good at generating force at high contraction velocities. In the horse the biceps muscle (which has short fibres and a substantial internal tendon) is loaded by body weight during stance phase. The length of the muscle tendon unit peaks at the end of stance at which point the leg is de-stabalised and the biceps shortens, flexing the elbow and extending the shoulder, the movements required to initiate limb protraction.

CONCLUSIONS

The equine forelimb contains a large amount of collagenous tissue which is important for storage of elastic energy in the limb. The springs are loaded by gravitational and inertial forces during stance phase and energy is returned to lift the centre of mass and accelerate the limb forwards for the next stance phase. Despite the large contribution of passive mechanisms to locomotion horses are able to demonstrate a wide range of gaits and speeds. Understanding the deployment mechanisms for the limb may be important in the design of legged robots.

REFERENCES

Alexander, R. McN. & Bennet-Clark, H.C. (1977) *Nature* **265,** 114-117

Biewener, A.A. *et al* (1998) *J. Exp. Biol*, **210**, 1681-1694

Minetti AE (1999) *J. Exp. Biol.* **202,** 2329-2338

Wilson, A.M. *et al* (2001) *Nature*, **414**, 895-899

ACKNOWLEDGEMENTS

I acknowledge funding from the Horserace Betting Levy Board, London and contribution of my co workers Polly McGuigan, Ton van den Bogert, An Su, Jo Watson, Glen Lichtwark and Tom Witte.

MECHANISMS OF FLIGHT FORCE ENHANCEMENT IN FLAPPING FLIGHT

Fritz-Olaf Lehmann
BioFuture Research Group, Theodor-Boveri-Institute, University of Würzburg,
Am Hubland, 97074 Würzburg, Germany, email: lehmann@biozentrum.uni-wuerzburg.de

INTRODUCTION

Insects display an impressive variety of flight maneuvers. Flies, in particular are capable of extraordinary aerial behaviors, aided by an array of unique sensory specializations including neural superposition eyes and gyroscopic halteres. Using such elaborate sensory input, flies steer and maneuver by changing many aspect of wing kinematics including angle of attack, the amplitude and frequency of the wing stroke, and the timing and speed of wing rotation. Conventional aerodynamic theory based on fixed-wing aircraft, however, may not explain how the flapping wings of insects control and produce flight forces that exceed twice the body mass while the animal is carrying loads or performing flight maneuvers. In addition to force production by flapping one wing, small insects such as fruit-, damsel- and butterflies may enhance total lift production and control by an interaction of both wings at the dorsal stroke reversal. The *clap and fling* is a close apposition of the two wings preceding pronation and is thought to enhance aerodynamic circulation at the beginning of the down stroke (Fig. 1). The purpose of this study was to estimate the contribution of clap and fling to total flight force production.

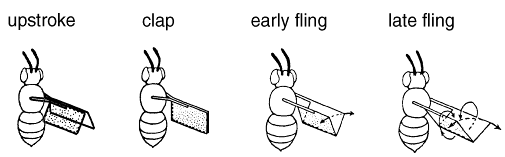

Figure 1. Kinematics of clap and fling during dorsal stroke reversal in insects (modified from Weis-Fogh 1973).

METHODS

The constraints of force measurements in the living animal can be circumvented by building a dynamically scaled robotic model of the 1.1 mg fruit fly. In this robot, the motion of the two wings is driven by an assembly of six computer-controlled stepper motors attached to the wings gearbox via timing belts and coaxial drive shafts. The 25 cm long model wings were constructed from clear Plexiglas (3.2 mm thick) to allow flow visualization on both sides of the wing. The base of the wing was equipped with a 2D force transducer consisting of two sets of strain gauges wired in full-bridge configuration. Each set measured forces parallel and normal to the wing, respectively. Wings, sensors, gearboxes and part of the coaxial drive shafts were immersed in a 1 m by 1 m by 2 m tank filled with high viscous mineral oil (density = 0.88×10^3 kg m^{-3}, kinematic viscosity = 115 cSt). The length of the model wings, their translational velocity and the viscosity of the mineral oil were chosen to match Reynolds number of 134 typical for wing motion of fruit flies.

RESULTS AND DISCUSSION

The contribution of clap and fling to total flight force varies between 3.6 and 21% of total aerodynamic force production depending on the trajectory of wing motion (Fig. 2). In fruit flies *Drosophila* the clap and fling wingbeat contributes up to 16% to total flight force at a stroke amplitude of 160 degs - a high value considering the brief duration (~10% of the stroke cycle) over which dorsal wing interaction occurs.

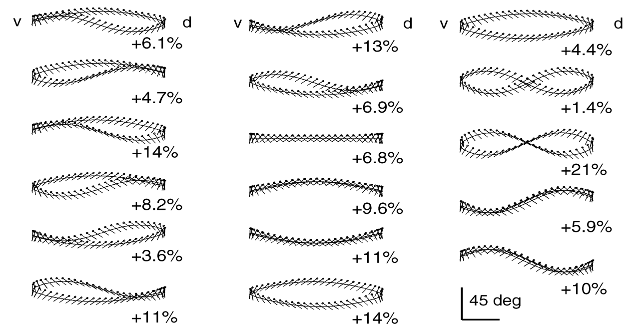

Figure 2. Force contribution of clap and fling at various types of wing kinematics. v= ventral, d= dorsal.

SUMMARY

Aerodynamic force measurements in a dynamically scaled robotic insect have revealed that the enhanced performance of a flapping insect wing results from three distinct unsteady aerodynamic mechanisms: delayed stall, rotational circulation and wake capture. In addition to force production by flapping one wing, insects may enhance total lift production through the interaction of both wings at the dorsal stroke reversal. Instantaneous measurements of aerodynamic forces during the stroke of the robotic insect suggest that in the fruit fly *Drosophila*, clap and fling significantly contributes to total force production. Reconstruction of wing movement during yaw torque maneuvers in tethered flight indicates that the neuro-muscular system of fruit flies actively modulates the timing of wing rotation during clap and fling within a 0.2 ms range, whereas angular velocity of wing rotation does not change. Fruit flies might primarily use clap and fling to modulate flight forces in order to enhance both flight stability and maneuverability.

REFERENCES

Weis-Fogh, T. (1973). Quick estimates of flight fitness in hovering animals, including novel mechanisms for lift production. *J. Exp. Biol.* 59, 169-230.

ADAPTIVE RESPONSES OF ENDOTHELIAL CELLS TO CYCLIC PRESSURE

Hainsworth Y. Shin[1], Michael L. Smith[2], Karen J. Toy[3], Mickey P. Williams[3], Mary E. Gerritsen[3], and Rena Bizios[1]
[1]Dept. of Biomedical Engineering, Rensselaer Polytechnic Institute, Troy, NY
[2]Dept. of Biomedical Engineering, University of Virginia, Charlottesville, VA
[3]Dept. of Molecular Biology and Dept. of Cardiovascular Research, Genentech, Incorporated, South San Francisco, CA

INTRODUCTION

In the vasculature, the pumping action of the heart as well as containment of blood within the blood vessel lumen exposes vascular endothelium to cyclic pressure. Although basic functions (specifically, proliferation and apoptosis) of endothelial cells are dependent on the applied cyclic pressure levels (Shin *et al*., 2002), the modulatory role of this type of mechanical force on endothelial-specific phenotype (such as barrier function and gene expression) has not been elucidated.

The present study utilized an *in vitro* cell culture model and examined select functions (specifically, transendothelial permeability and gene transcription) of human umbilical vein endothelial cells (HUVEC) after exposure to cyclic pressure. These results elucidate the adaptive responses of endothelial cells to cyclic pressure.

METHODS

Cyclic Pressure Experiments

Well-characterized populations of HUVEC (passage 4 to 6) were exposed to either 60/20 or 140/100 mm Hg cyclic pressures at 1 Hz using a custom-made cyclic pressure system and procedures previously described (Shin *et al*., 2002) for various time periods up to 24 hours. Controls were parallel cultures of HUVEC maintained under 0.15 mm Hg sustained hydrostatic pressure but, otherwise, similar experimental conditions.

Endothelial Cell Barrier Properties

Confocal microscopy and standard immunocytochemical techniques were used to assess ZO-1, VE-cadherin, and β-catenin localization using confluent HUVEC monolayers cultured on fibronectin-coated glass slides and exposed to either 60/20 or 140/100 mm Hg cyclic pressure at 1 Hz for 18 hours. The effects of cyclic pressure on macromolecular transport was investigated using confluent monolayers of HUVEC cultured on fibronectin-coated Transwell inserts (Costar) for 36 hours and, subsequently, exposed to either 60/20 or 140/100 mm Hg cyclic pressure for 18 hours. At that time, permeability of endothelial monolayers to fluorescein-conjugated bovine serum albumin (FITC-BSA) was monitored under control (0.15 mm Hg) sustained pressure conditions for 30 minutes. Concentrations of FITC-BSA transported across HUVEC monolayers were determined using fluorescence (490 nm excitation/520 nm emission) spectrometry.

Endothelial Gene Expression

Total RNA was harvested from HUVEC following exposure to 60/20 mm Hg cyclic pressure for 24 hours using procedures described in Kahn *et al*. (2000) and analyzed using Affymetrix™ Gene Chip® HuGene FL arrays according to procedures described in Jin *et al*. (2000). The results of the microarray analysis were independenty confirmed using quantitative reverse transcriptase-polymerase chain reaction following standard procedures (Kahn *et al*., 2000).

RESULTS/DISCUSSION

Select levels of cyclic pressure affected the barrier function of endothelial cells. Compared to cells maintained under control (0.15 mm Hg) sustained pressure conditions (controls), only HUVEC exposed to 140/100, but not 60/20, mm Hg cyclic pressures exhibited altered barrier properties which included changes in the localization of interendothelial junctional proteins and in transendothelial permeability.

Exposure of HUVEC to 60/20 mm H cyclic pressure at 1 Hz for 24 hours elicited an altered pattern of gene transcription. In addition to genes (such as, tissue plasminogen activator and cytosolic phospholipase A_2) known to be up-regulated in response to shear stress and cyclic strain, HUVEC exposed to 60/20 mm Hg cyclic pressure for 24 hours exhibited a gene transcription profile characterized by changes in the expression of a unique subset of cyclic pressure-sensitive genes.

CONCLUSIONS

The present *in vitro* study demonstrated that physiologically-relevant levels of cyclic pressures modulate select HUVEC functions, specifically, barrier function and gene expression. These findings provide novel insight into the fundamental importance of circulatory pressure to endothelial cell physiology.

REFERENCES

Jin, H., Yang, R., Awad, T.A. *et al*. (2000) *Circ.* **103**: 736-742
Kahn, J., Mehraban, F., Ingle, G. *et al*. (2000) *Am. J. Pathol.* **156**: 1887-1900.
Shin, H.Y., Gerritsen, M. E., Bizios, R. (in press, 2002) *Ann. Biomed. Eng.*

LEG DESIGN AND JUMPING IN SPIDERS

Reinhard Blickhan[1], Jelena Zentner[2], Andre Seyfarth[1] and Michael Karner[1]

[1]Motion Science, Friedrich-Schiller-University, Jena, Germany, reinhard.blickhan@uni-jena.de
[2]Technical Mechanics, Technical University, Ilmenau, Germany

INTRODUCTION

Jumping represents a basic locomotory behavior in animals. In spiders the ability to jump is well known for *Salticidae* however less well described for hunting spiders or other groups. There, a surprisingly flexible performance can be observed. Simplified, the leg of a spider can be approximated by three slender segments connected via two hinge joints, the femuro-patellar and the tibio-metatarsal joint. In these joints extension is provided by hydraulic (hemolymph) pressure. In order to achieve high and robust performance the animals follow kinematic and design criteria.

METHODS

Experiments were made with 42 specimens of the South American hunting spider *Cupiennius salei* (Keyserling) from juveniles of about 1 cm body length to subadult animals (donation: F. G. Barth , Vienna, E. A. Seyfarth, Frankfurt am Main). Kinematic data were obtained using a high speed video system with three cameras (CAMSYS 500, mikromak at 500 frames per second. Three-dimensional analyses were carried out by use of WINanalyze 1.3 (mikromak).

Numerical simulations (Bohmann and Blickhan, 1998) were performed using the software packages Mathematica (Wolfram) and Matlab (Mathworks).

RESULTS AND DISCUSSION

The spiders show a surprisingly flexible behavior. In unprepared jumps the animals might jump in any direction opposite to an approaching object. The remarkable flexibility in jumping directions is achieved by flexing the legs on the leading and extending them on the trailing side. In prepared jumps the spiders show characteristic leg positioning and the jumps are directed anterior. Jumping movements are initiated by a backward movement immediately before the acceleration phase. This is accompanied by a slight bending of the tibio-metatarsal joint. Only minor compression of the carapace is sufficient to generate the jump.

In simulations jumps generated by hydraulic leg extension are investigated. Reasonable jumps are only possible from a starting position similar to that observed in the animals. The backward movement in the early phases of the jump can be attributed to a lack of equilibrium in torque generated by the hydraulic pressure partly due to joint geometry and to delayed filling of the distal joint. The dimensions of the spider's leg are optimized to provide jumps within a short time. This is relevant for flight situations. The slenderness of the leg of the hunting spider is optimum for high take-off-velocities (Fig. 1).

Three segmented legs are typical for most animals. Spiders prefer C instead of Z-shaped segment arrangements (Seyfarth et al., 2000). This results in a much higher leg compliance but is a save mode of operation for legs with imbalanced and softening joints.

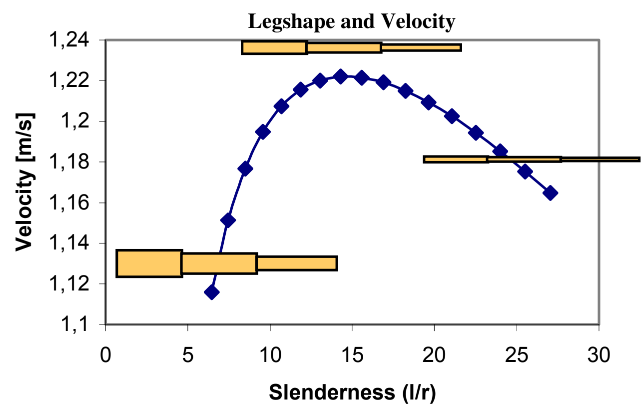

Figure 1: Legs with large diameters provide more effective area for the hemolymph pressure. However, the weight increase compensates this advantage.

SUMMARY

Jumping is the most vigorous activity of spiders. The necessary performance combined with limits imposed by the hydraulic extension mechanisms may determine to a large extent the leg design in spiders.

REFERENCES

Bohmann, L., Blickhan, R. (1998) *Z. angew. Math. Mech*. **78**, 87-96

Seyfarth, A., Günther, M., Blickhan, R. (2000). *J biol Cybern.* **84**, 365-382

ACKNOWLEDGEMENTS

Supported by the DFG Bl 236/9.

MECHANICAL FUNCTION OF LEG MUSCLES IN RUNNING BIRDS

Richard L. Marsh[1], David J. Ellerby[1], and Cindy I. Buchanan[2]

Department of Biology[1] (r.marsh@neu.edu) and Department of Physical Therapy[2]
Northeastern University, Boston, MA

INDRODUCTION

Skeletal muscle serves a variety of functions during locomotion. During some activities the primary function is clear, e.g., in swimming and flying the main function of muscle is to produce mechanical power. However, muscle function during running has remained a puzzle. During level running at constant speed, considerable energy is used, but no net work is done. Work must be done during parts of the stride to move the center of mass up and down and to accelerate it slightly in the horizontal plane. Work is also done to accelerate the segments of the body during the stride. However, the potential exists for recovering much of this energy in elastic elements, thus reducing greatly the energy required for running. These facts led C.R. Taylor and associates to suggest the major function of most muscles during running was to support the weight of the body, not to produce work. They further suggested that muscles could most economically perform this function if they operated isometrically while active.

Evaluating this hypothesis has been hampered by a lack of information on the mechanical function of individual muscles. Muscle function has most often been studied using electromyography. Muscle length has been predicted using limb kinematics measured from light or x-ray cine and video. However, the complexity of the movements and of the architecture of the limbs limits the success of this approach.

Sonomicrometry has recently provided an alternative approach to measuring length change at the level of the muscle fibers (fascicles). Using this technique combined with electromyography we are evaluating the mechanical function of the bulk of the hind limb muscles in running helmeted guinea fowl *Numida meleagris*.

METHODS

Sonomicrometer transducers and electromyography electrodes were surgically implanted in individual hindlimb muscles. The birds were run on a motorized treadmill and data acquired while simultaneously recording limb movements using high-speed video.

RESULTS AND DISCUSSION

The lateral gastrocnemius in running Guinea fowl appears to function nearly isometrically while active during ground contact. In this regard, its function matches the prediction of C.R. Taylor and colleagues, and agrees with data collected on the ankle extensors of other birds and mammals. These data suggest that the ankle extensors of terrestrial vertebrates generally may satisfy the conditions for economical force production.

In contrast to these data on the ankle extensors, none of the thigh muscles examined to date appears to operate mainly isometrically during activity. The posterior iliotibialis lateralis (PIL), the single largest muscle in the limb, is stretched during the bulk of its active period. The mechanics of the stride predict that the stretch of this bi-articular muscle (knee flexor and hip extensor) results from the co-contraction of knee flexors. Two of these flexors the flexor cruris lateralis (FCL) and the iliofibularis (IF) do indeed shorten while active. Intriguingly, the IF also shows a second period of activity during early swing phase when it is being lengthened by antagonistic muscles that produce hip flexion and knee extension. The only swing phase muscle examined so far, the iliotibialis cranialis (IC) is active mainly during shortening, but has a short period of active lengthening at the end of stance. The muscles measured represent approximately 40 % of the total mass of the hindlimb muscles.

CONCLUSIONS

A complex picture of muscle function during level steady speed running emerges from the data on guinea fowl. Some muscles function nearly isometrically to support the body weight during stance. However, many of the active muscles measured either shorten, producing work, or, conversely, lengthen, absorbing work. We hypothesize that considerably more muscle work is done during running than appears externally because active muscles absorb some work during stretch. Because the strain in the muscle fibers is large, this energy cannot be recovered elastically. We propose that this seemingly wasteful co-contraction of antagonistic pairs of muscles allows greater stability during running because the muscles that are stretched provide predictable forces against which the shortening muscles operate. The potential for instability may be greatest at the knee, which goes through a point of zero moment during ground contact. A major challenge for the future is determining the importance of the various types of mechanical activity for the overall energetic economy of running.

ACKNOWLEDGEMENTS
Supported by NIH AR39318 and AR47337.

INSIGHTS INTO THE PROCESSIVE MOVEMENT OF MYOSINS V AND VI.

Lee Sweeney. Department of Physiology, Pennsylvania Muscle Institute, University of Pennsylvania School of Medicine, 3700 Hamilton Walk, Philadelphia, Pennsylvania 19104-6085, USA.(lsweeney@mail.med.upenn.edu)

SUMMARY

We have conducted kinetic and single molecule analyses of myosin V and VI. For both motors, ADP release is the rate-limiting step of the actin-activated ATPase cycle, and both motors have high duty ratios. The duty ratios combined with the structural coupling of the heads allows these motors to move processively. Surprisingly, the motors have similar step sizes. We will present data supporting a conventional lever arm mechanism for myosin V, but a completely different mechanism for the motility of myosin VI.

MYOSIN V TRUNCATION MUTANT WITH ONLY ONE IQ MOTIF CAN PROCESSIVELY MOVE ALONG AN ACTIN FILAMENT WITH 36 NM STEPS.

Hiroto Tanaka*, Kazuaki Homma†, Atsuko Hikikoshi Iwane‡, Eisaku Katayama§, Reiko Ikebe†, Junya Saito†, Mitsuo Ikebe† and Toshio Yanagida*‡

*Single Molecule Processes Project, ICORP, JST, 2-4-14, Senba-higashi, Mino, Osaka, 562-0035, Japan, †Department of Physiology, University of Massachusetts Medical School, 55 Lake Avenue North, Worcester, Massachusetts 01655-0127, USA, ‡Department of Physiology I, Osaka University Medical School, 2-2, Yamadaoka, Suita, Osaka, 565-0871, §Department of Fine Morphology, Institute of Medical Science, The University of Tokyo, Minato-ku, Tokyo, 108-8639, Japan. (Email: yanagida@beta)

INTRODUCTION

Class-V myosin is recently found by using an optical trap to processively move along an actin filament with large (~ 36 nm) steps. Since myosin-V has two heads, each of which consists of a motor domain and an expanded neck domain (23 nm long), it is postulated to stride along the helical repeat (36 nm) of an actin filament by using its long neck domain as a lever arm. This postulation agrees the widely-accepted lever-arm model. To test this postulation, here, we measure the mechanical properties of single molecules of deletion mutants of myosin-V, which has an extremely short (one sixth of the native one) neck domain.

METHODS, RESULTS AND DISCUSSION

The results show that the size and processivity of steps of short-necked myosin-V are both similar to those of myosin-V fully equipped with a long neck domain. Thus, the long extended neck domain is critical to neither the large step nor the processivity of myosin V, presenting evidence that calls into question the lever arm model. We propose that the myosin motor domain and/or actin-myosin interface determine the processive and large steps of myosin V.

REFERENCES

Tanaka et al. The motor domain determines the large step of myosin-V.Nature 415 192-195 (2002)

OBSERVATION OF DISPLACEMENT STEPS BY SINGLE MYOSIN ID AND MYOSIN II MOLECULES

Christine Ruff[1], Danny Koehler[2], Martin Bähler[2] and Edgar Meyhöfer[1,3]
[1]Molecular and Cellular Physiology, Medical School Hannover, [2]Institute for General Zoology and Genetics, University Münster,
[3]Department of Mechanical Engineering, University of Michigan (meyhofer@umich.edu)

INTRODUCTION

Considerable evidence from structural work and single molecule experiments suggests that the displacement generated by single myosin II molecules concurrent with ATP-hydrolysis is amplified by the lever-action of the light chain binding region of myosin. Myosins constitute a large family of actin-based motors[1] which differ substantially in their structural and physiological properties. It remains unclear if the same basic chemo-mechanical transduction mechanism operates in all myosins. For example, step sizes measured from rat liver and brush border myosin I did not relate directly to the length of the proposed lever[2]. In the present study we characterized rat myosin ID, formerly known as myr 4, and compared it to myosin II.

METHODS

Using stably transfected HeLa cells we expressed three recombinant FLAG-tagged myosin ID proteins with either no, 1 or 2 light chain binding IQ-motifs and measured the single molecule step sizes of all constructs with a combined microneedle/laser trap apparatus.

RESULTS AND DISCUSSION

The step size of the myosin ID construct without IQ-motifs was 4.6 nm, while the step size of the comparable *Dictyostelium* myosin II motor is only 1.6 nm[3]. The step sizes of the two myosin ID constructs encompassing either 1 or 2 IQ-motifs increased in a linear manner, strongly suggesting that the myosin ID step size is determined by a lever mechanism. A rotation of approximately 90° about the same pivoting point as in myosin II is sufficient to explain our data. We conclude that the degree of lever arm rotation can vary considerably in different myosins. Lever arm rotation is an important determinant for the step size of myosin, and together with the length of the lever arm is sufficient to account for all reported step sizes on the basis of the same general mechanism.

REFERENCES

1. Marmell, V., P. L. Post and M. S. Mosseker (1998) Science *279*: 527-533.

2. Veigel, C., L. M. Coluccio, J. D. Jontes, J. C. Sparrow, R. A. Milligan and J.E. Molloy (1999). Nature *398*: 530-533.

3. Ruff, C., M. Furch, B. Brenner, D. J. Manstein and E. Meyhöfer (2001). Nature Structural Biology *8*: 226-229.

REGULATED ACTIN-MYOSIN INTERACTION AND SARCOMERIC STIFFNESS

Kenneth Campbell, Yiming Wu, Robert Kirkpatrick, Henk Granzier

Dept VCAPP, Washington State University, Pullman, WA 99164
cvselkbc@vetmed.wsu.edu

INTRODUCTION

Muscle stiffness is the outcome of a large number of individual actin myosin interaction events. To understand stiffness in terms of these underlying actin-myosin events, it is necessary to accept that some details of the kinetics of an individual event will be lost in the population dynamics of large numbers of these events. However, it is also reasonable to expect that some essential features will be retained. In this report, we strive to extract essential features of the underlying events from measured cardiac muscle stiffness.

METHODS

Our fundamental assumption was that the force generated by a population of parallel, linearly elastic crossbridges, XB, is given by

$$F = \sum_{i=1,n} \varepsilon N_i X_i$$

where n is the number of attached XB states, N is the number of XB in each of the i attached states, X is the average distortion among all XB in each state, and ε is the elastic coefficient for each XB.

At the outset, we assume one attached state. Then, in the presence of changes in sarcomere length, *dSL*, the stiffness of this population of attached XB may be calculated. As has been shown (Kawai et. al., 1980, 1993), the stiffness of muscle fibers is a function of frequency; putatively, as a result of the underlying kinetics of actin myosin interaction. Thus, stiffness, as a dynamic transfer function, may be written in terms of its distortion and recruitment components as

$$\frac{dF}{dSL}(j\omega) = X_0 \frac{dN}{dSL}(j\omega) + N_0 \frac{dX}{dSL}(j\omega)$$

where the zero subscripted variables represent baselines around which variations occur and the two transfer functions on the right hand side of the equation represent respectively, the frequency dependence by which XB are recruited into the attached state when there has been a change in sarcomere length, and the frequency dependence by which the average distortion among attached XB change when there has been a change in sarcomere length.

We have shown elsewhere [Campbell et. al., 2001] that the distortional transfer function, $dX/dSL(j\omega)$, takes the form of a high-pass filter. Further, the coefficients of this dynamic transfer function depend entirely on sums, products, and sums of products of kinetic coefficients regulating steps leading away from the attached XB state. Of more interest in this work is the myofilament origins of $dN/dSL(j\omega)$ and how these myofilament processes are expressed in the measured stiffness of cardiac trabecular muscle.

DISCUSSION

We can imagine three mechanisms by which XB may be recruited into attached states in response to *dSL*: 1) sliding filament mechanisms; 2) length-dependent myofilament kinetic steps; and 3) certain cooperative mechanisms by which transient changes in XB force influence the probability of state transitions. Mechanisms 1 and 2 result in **low-pass filter** type behavior in which *F(t)*, following a step increase in *SL* develops slowly and is sustained. Mechanism 3 results in a **band-pass filter** behavior in which *F(t)* following a step increase in *SL* develops slowly but eventually dissipates and is not sustained. It has been shown in cardiac muscle that mechanism 1 is a small effect. Thus, it becomes important to distinguish between the relative importance of mechanisms 2 and 3 as means for length-dependent recruitment in cardiac muscle.

Mechanisms 2 and 3 are not confined to just the kinetic steps within the XB cycle but also involve the kinetics of regulatory protein steps in the transition between permissive states that allow myosin access to the actin binding site and nonpermissive states that do not (Campbell et. al., 2001). Thus, all the regulatory mechanisms on the thick and thin myofilaments may participate in length-dependent recruitment of force-bearing XB as seen through myocardial stiffness.

Constantly-activated, rat skinned trabecular muscle was subjected to ΔSL perturbations containing a broad spectrum of frequency components. The calculated ccardiac muscle stiffness was decomposed into components representing high-pass, band-pass, and low-pass aspects of the response. The relative contributions of length-dependent kinetic steps and cooperative mechanisms in cardiac muscle length-dependence were assessed.

Kawai, M, P. Brandt. *J. Mus. Res. & Cell Motil.* 1:279-304, 1980.
Kawai, M, Y Saeki, Y. Zhao. *Circ. Res.* 73:35-50, 1993.
Campbell, KB, MV Razumova, RD Kirkpatrick, BK Slinker. *Biophys. J.* 81:2278-2296, 2001.

EVOLUTIONARY MODULATION OF TITIN GENE STRUCTURE AND FUNCTION BY LINE ELEMENT INTEGRATION

Michael Gotthardt[1], Henk Granzier[1], Siegfried Labeit[2],

[1]VCAPP, Washington State University, Pullmann, WA, 99164-6520, USA,, [2]Anesthesiology and Intensive Operative Medicine, University Hospital Mannheim, D-68135 Mannheim, Germany.

Email: labeit@embl-heidelberg.de

INTRODUCTION

Titin is a giant (up to 3,700 kDa) protein that constitutes an elastic half-sarcomere spanning filament system in vertebrate striated muscles. Titin is the major contributor to passive tension during physiological amounts of stretch in mammals such as humans, with the extracellular matrix (collagen) and the cytoskeleton playing secondary roles (Gregorio et al., 1999; Granzier and Labeit, 2002). A plethora of titin isoforms has been reported with expression that correlates with the tissue-specific diversity of myofibrillar elasticity (Freiburg et al., 2000; Cazorla et al., 2000). These differentially expressed titin isoforms have spring elements within their I-band segments that vary in composition and length. Because of titin's giant size, the molecular mechanisms that underlie differential splicing have remained unknown.

RESULTS AND DISCUSSION

To study splicing in more detail we determined titin's gene sequence in human and mouse. In both species we could identify only a single locus for titin. Titin isoform diversity results from this single gene locus by multiple splice cascades. The human titin gene contains 363 coding exons and two LINE-1 elements within the differentially spliced PEVK spring region. Their >99% similarity suggests that LINE-1 integration caused PEVK exon duplication in primates several million years ago. In mouse, one LINE element could be identified in the differentially spliced Z-disc region of the repetitive Z-repeat segment. Interestingly, a LINE integration was also recently identified in a mutant titin gene of the mdm mouse strain. This integration skips 4 exons from the N2A region and modifies splice patterns (Garvey et al., 2002). Thus, in both the mouse and human, integration of LINE elements in the titin gene has caused exon duplication and skipping events that can modify titin isoform splice patterns. This modification may influence titin's elastic properties since the PEVK exon duplication introduced additional spring elements.

SUMMARY

Significant differences between the mouse and human titin gene exist which point at recent evolutionary intragenic duplication events. These events contribute to the plethora of titin isoforms found today. Further characterization of titin isoforms expressed in different species is likely to provide molecular insights in how myofibrilar mechanics and titin structure are linked

REFERENCES

Cazorla, et al. (2000). *Circ. Res*. 86, 59-67.
Freiburg, et al. (2000). *Circulation Research,* 86(11):1114-21.
Garvey, et al. (2002). Genomics 79, 146-149.
Gregorio, et al. (1999). *Curr. Opin. Cell Biol.* 11, 18-25
Granzier, and Labeit, S. (2002). *J. Phys*., in press.

A UNIQUE SEQUENCE OF TITIN, THE PEVK-DOMAIN, IS AN ENTROPIC SPRING THAT INTERACTS WITH ACTIN

Wolfgang A. Linke[1], Michael Kulke[1], Hongbin Li[2], Setsuko Fujita-Becker[3], Ciprian Neagoe[1], Mathias Gautel[4], Julio M. Fernandez[2]

[1]Institute of Physiology and Pathophysiology, University of Heidelberg, Im Neuenheimer Feld 326, D-69120 Heidelberg, Germany, wolfgang.linke@urz.uni-heidelberg.de, webpage: http://www.physiologie.uni-hd.de/linke/
[2]Department of Physiology and Biophysics, Mayo Clinic Rochester, MN, U.S.A.
[3]Max-Planck Institute of Medical Research, Heidelberg, Germany
[4]Max-Planck-Institute of Molecular Physiology, Dortmund, Germany

INTRODUCTION

The PEVK-domain is a unique sequence within the giant muscle protein titin. The PEVK-domain, along with titin segments comprised of immunoglobulin-like (Ig) modules, earlier was shown to determine extensibility and passive-force development of skeletal and cardiac muscle sarcomeres (Linke et al., 1996). Recent results of several groups have also hinted at the possibility that PEVK-titin could interact with other sarcomere proteins. Here we studied functional properties of the PEVK-domain of cardiac titin by using a hybrid experimental approach.

METHODS

Single-molecule atomic force microscopy (AFM) was used to measure the force-extension behavior of cloned cardiac-PEVK polyproteins of the type (PEVK-Ig27)$_3$ (Fig. 1; *cf.*, Li et al., 2001).

AFM Force Spectroscopy on PEVK Polyproteins

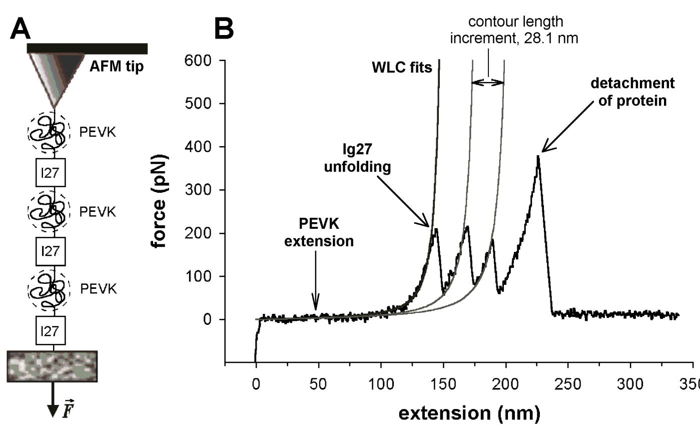

Figure 1: (A) (PEVK-I27)$_3$ construct stretched by AFM. (B) Force-extension curve and fit with wormlike-chain (WLC) model.

The AFM data obtained then were compared to the extensibility data of PEVK-titin previously established by immunoelectron microscopy in rabbit cardiac sarcomeres (Linke et al., 1999). To study whether the PEVK-domain and/or other regions of titin can interact with actin filaments, we employed the actin-myosin *in-vitro* motility assay (IVMA) (Fig. 2; *cf.*, Kulke et al., 2001).

RESULTS AND DISCUSSION

We found that the results of AFM measurements could be readily applied to explain cardiac-PEVK extensibility in the sarcomere. The analysis revealed that both *in vitro* and *in situ*, cardiac PEVK behaves as an entropic spring with the properties of a random coil. Possibly, however, the random coil exhibits mechanical conformations of different flexibility (Li et al., 2001).

Titin Constructs Tested in the IVMA

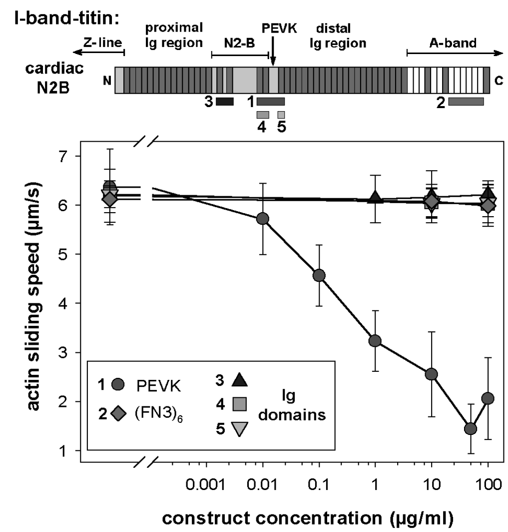

Figure 2: Results of IVMA assays with titin constructs.

Actin-titin interaction was indeed detectable in the IVMA: cardiac-PEVK constructs slowed down the sliding speed of actin filaments over myosin; in contrast, Ig/fibronectin-like titin domains had no effect (Fig. 2). Interestingly, the PEVK effect was partially reversed in the presence of physiological concentrations of Ca^{2+}. Co-sedimentation assays confirmed a weak Ca^{2+}-modulated actin-binding propensity of the cardiac PEVK-domain. In the sarcomere, the actin-PEVK interaction may give rise to a viscous force component opposing filament sliding (Kulke et al., 2001). Thus, the PEVK-domain contributes not only to the extensibility of cardiac myocytes, but also affects contractile properties.

SUMMARY

Single-molecule AFM force spectroscopy and in-vitro binding tests show that cardiac PEVK-domain contributes to titin elasticity as a random coil exhibiting entropic-spring behavior, but—via binding to actin—also modulates contractile properties of cardiac-muscle sarcomeres.

REFERENCES

Kulke, M. et al. (2001). *Circ. Res.*, **89**, 874-881.
Li, H. et al. (2001). *PNAS*, **98**, 10682-10686.
Linke, W.A. et al. (1996). *J. Mol. Biol.*, **261**, 62-71.
Linke, W.A. et al. (1999). *J. Cell Biol.*, **146**, 631-644.

TITIN INTERACTS WITH MURF-1 TO REGULATE SARCOMERIC M-LINE AND THICK FILAMENT STRUCTURE

Abigail S. McElhinny[1], Siegfried Labeit[2], and Carol C. Gregorio[1](gregorio@u.arizona.edu)
[1]Dept. of Cell Biology and Anatomy, University of Arizona, Tucson, Arizona, USA
[2]University Hospital, Mannheim, Germany

INTRODUCTION

The giant sarcomeric protein titin appears to have several essential roles in striated muscle. Recent studies have aimed to decipher titin's functions by investigating its unique ligands. Previously, a member of the muscle-specific RING finger protein, MURF-1, was found to bind titin's C-terminal A168-170 domains, located adjacent to the titin kinase domain in the M-line region of the sarcomere (Spencer et al., 2000; Centner et al., 2001). Structurally, this protein is comprised of an N-terminal RING domain, a MURF family conserved region, a B-box domain, coiled-coil domains, and an acidic tail. In this study, we aimed to investigate the functional significance of the interaction of titin with MURF-1 in cardiac myocytes.

METHODS

We expressed GFP-fusion constructs encoding defined regions of titin's M-line region and MURF-1 in primary cultures of embryonic chick cardiac myocytes. Immunofluorescence microscopy was utilized to examine potential phenotypes. MURF-1 bait constructs were used in yeast two-hybrid screens to identify novel MURF-1 binding partners.

RESULTS AND DISCUSSION

Strikingly, the majority of MURF-1 transfected cardiac myocytes exhibited severe disruption of the C-terminal region of titin compared to cells expressing GFP alone (Fig. 1). Triple labeling studies revealed that although titin's C-terminal region was disrupted in MURF-1 expressing cells, staining for titin's N-terminal region appeared in a regular, striated pattern. However, staining for myosin, myosin binding protein C (MyBP-C), and myomesin demonstrated that MURF-1 expression also perturbed thick filament structure. Unexpectedly, the structure of the actin-containing thin filaments, the I-band region of titin, and Z-line components appeared in typical striated patterns in the majority of MURF-1 transfected cells. An identical phenotype was observed in myocytes transfected with titin A168-170-GFP, but not in cells transfected with other titin M-line regions (domains M1-M2-M3 or M8-M9-M10), or with titin's Ser/Thr kinase domain.

Yeast two-hybrid screens of human heart and skeletal muscle cDNA libraries revealed that MURF-1 interacts with ubiquitin-conjugating enzyme-9 (Ubc-9) and isopeptidase-3 (ISO-T3), enzymes implicated in post-translational

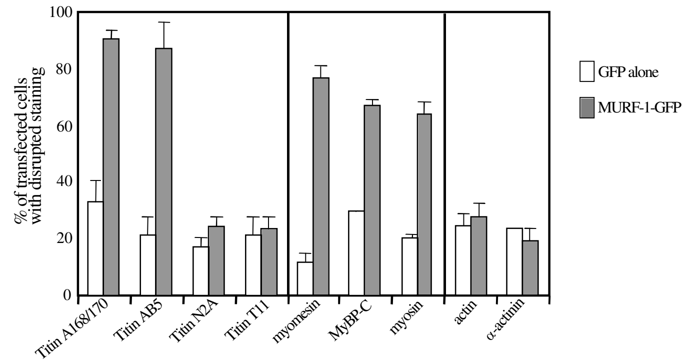

Figure 1. Quantification of MURF-1-GFP and GFP expressing myocytes exhibiting disrupted staining for various sarcomeric components. Data presented as mean percentage of total transfected myocytes (n>50 cells from >2 experiments) with disrupted staining patterns ± S.D. Titin epitopes are: A168-170 and AB5 (N-terminal), N2A (I-band) and T11 (N-terminal region.

modification pathways involving small ubiquitin-related modifier-3 (SUMO-3). MURF-1 also interacts with glucoccorticoid modulatory element binding protein-1 (GMEB-1), a transcriptional regulator. Consistent with this, a portion of endogenous MURF-1 colocalized with GMEB-1-GFP fusion proteins in some nuclei.

SUMMARY

The results from our studies suggest that the interaction of titin with MURF-1 plays an important role in the structure of the sarcomeric M-line region and the thick filaments. Additionally, while disruption of titin's C-terminal region perturbs thick filament structure, it does not appear to affect the integrity of titin's I-band or N-terminal regions, the thin filaments, or the Z-lines. We speculate that MURF-1 may link myofibril signaling pathways with nuclear functions via its interactions with titin and GMEB-1.

REFERENCES

Centner, T., et al. (2001). *J Mol Biol*, **306**, 717-726.
Spencer, J.A.., et al. (2000). *J.Cell Biol*, **150**, 771-784.

ACKNOWLEDGMENTS

We thank K. Kakinuma and H. Sorimachi for performing yeast 2-hybrid screens. This work was supported by grants from NIH HL57461 (CG), AHA 0120586Z (AM) and the Duetsche Forschungsgemeinschaft (La668/5-2) (SL).

MUTATIONS OF TITIN CAUSE DILATED CARDIOMYOPATHY

Brenda Gerull[1], Michael Gramlich[1], John Atherton[2], Mark McNabb[3], Sabine Sasse-Klaassen[1], JG Seidman[4], Christine Seidman[5], Henk Granzier[3], Siegfried Labeit[6], Michael Frenneaux[7], Ludwig Thierfelder[1]

[1]Max-Delbrück Centre for Molecular Medicine and Charité, Humboldt-University, Berlin-Buch, Germany, (b.gerull@mdc-berlin.de),[2]Dept. of Cardiology, Royal Brisbane Hospital, Brisbane, Australia, [3]VCAPP, Washington State University, Pullmann, WA, 99164-6520, USA,[4]Dept. of Genetics and Howard Hughes Medical Institute, Harvard Medical School, Boston, MA 02115, USA, [5]Cardiovascular Division and Howard Hughes Medical Institute, Brigham and Women´s Hospital, Boston, MA 02115, USA, [6]Anesthesiology and Intensive Operative Medicine, University Hospital Mannheim, D-68135 Mannheim, Germany,[7]Dept. of Cardiology, University of Wales College of Medicine, Cardiff, UK

INTRODUCTION

Congestive heart failure (CHF) can result from various disease states with inadequate cardiac output. CHF due to dilated cardiomyopathy (DCM) is a familial disease in 20-30% of cases and associated with mutations in genes encoding cytoskeletal, contractile or inner nuclear membrane proteins (Seidman & Seidman, 2001). DCM is the most frequent indication of heart transplantation in young patients. We show that mutations in the giant muscle filament titin cause autosomal dominant DCM linked to chromosome 2q31 (*CMD1G,* Siu et al.,1999). The giant muscle protein titin serves several important functions in striated muscles: it directs assembly of contractile filaments, provides elasticity by its serial spring elements and, based on the presence of a C-terminal kinase domain, has a role in cell signaling. Furthermore a lot of splice isoforms in skeletal and cardiac muscles are known (Gregorio et al., 1999).

RESULTS AND DISCUSSION

Affected members of two large DCM kindreds (family A1, family MAO) suffer from autosomal dominant DCM with CHF of variable age of onset but absence of cardiac conduction defects or clinically detectable skeletal muscle disease. Linkage and haplotype analyses of DCM in both families revealed a 7.7 cM disease gene interval on chromosme 2q31. Among the more than 70 transcripts of the chromosome 2q31 DCM disease gene locus the gene for the giant muscle protein titin was considered an excellent candidate for DCM due to its high cardiac expression and central physiologic role in muscle assembly and function. On this base we deliberately chose titin and screened 313 of the 363 exons known to be expressed in cardiac muscle by direct sequencing of PCR amplified genomic fragments in both families.

In family A1, a segregating 2bp insertion mutation in titin exon 326 causes a frame shift, thereby truncating A-band titin. The truncated 2 mD protein is expressed in skeletal muscle but Western blot studies with epitop-specigic antibodies suggest its proteolytic processing into a 1.14mD subfragment by site-specific cleavage C-terminaly of the N2A domain, presumably within the PEVK domain. Interestingly, the N2A segment has been shown to interact with calpain 3 (Sorimachi et al., 1995). Our data raise the possibility that the calpain 3 /titin complex may indeed cleave the titin polypeptide under specific circumstances, such as if the titin filament is damaged as in our case.

In another family (MAO) a titin missense mutation (2920T→C) was found in all affected family members. This mutation results in the substitution of a highly conserved tryptophane by an arginine at amino acid position 930 within an immunoglobulin domain (Ig-Z4) located near the Z-disc/I-band transition zone. The functional consequence of this mutation is unknown, it is likely that the ß-sandwich structure of the Ig-Z4 domain is disrupted. Possibly, Ig module Ig-Z4 is a key domain for organizing the Z-disc, maintaining I-band elasticity or has other yet unknown functions.

SUMMARY

We have shown that mutations in the giant muscle filament titin (*TTN*) cause autosomal dominant dilated cardiomyopthy linked to chromosome 2q31. The identification of titin mutations should provide further insights into the pathogenesis of familial forms of congestive heart failure and myofibrillar titin turnover.

REFERENCES

Seidman, J.G. & Seidman, C. (2001). *Cell* **104**, 557-567.
Siu, B.L. *et al.* (1999). *Circulation* **99**, 1022-1026.
Gregorio, C.C., Granzier, H., Sorimachi, H. & Labeit, S. (1999) *Curr. Opin. Cell Biol.* **11**, 18-25
Sorimachi, H. *et al.* (1995). *J. Biol. Chem.* **270**, 31158-31162.

CHARACTERIZING TRANSIENT LOWER EXTREMITY KINEMATICS DURING THE IMPACT PHASE OF RUNNING

Mark Lake
Research Institute for Sport and Exercise Sciences, John Moores University, Liverpool, United Kingdom.
Email: M.J.Lake@LIVJM.AC.UK

INTRODUCTION

Transient loading of the lower limb during running ground contact has been implicated in many overuse-type injuries although the mechanism of load attenuation during impact remains to be established. Adequate characterization of impact transients can help further our understanding in this area. Rapid loading during running can be readily detected using a force platform and examining the rate of increase in the ground reaction force. But also detected from this data are oscillations in the trace which correspond to rapid movement phenomena occurring during the initial 10-30 ms (Lees, 1998). Undulations in the Fz curve are seen in a wide variety of published literature and several peaks are usually obtained in the initial portion of the continuous differential of Fz. These biological vibrations occurring during force loading are the focus of the present discussion.

METHODS

We have examined the oscillations by tracking high frequency movements of individual body segments using high speed displacement data (1000 Hz) and three dimensional accelerometry (e.g. Lake et al., 2001). Damped high frequency oscillations of 30-45 Hz were detected in the angular acceleration of the shank. These were typically damped within 100 ms of ground contact and were significantly modified by footwear. Using displacement data sampled simultaneously at 240 Hz and established data processing techniques (low pass butterworth filtering followed by numerical differentiation) to obtain movement velocities and accelerations, no oscillations in segmental motion were detected. In addition, the peak magnitudes of these lower limb movement transients were substantially attenuated. Filter cut-off frequencies (determined using residual analysis) were 15 Hz and 50 Hz for the 240 Hz and 1000 Hz displacement data, respectively. Therefore, it is not surprising that higher frequency signal above 30 Hz was completely removed from the 240Hz information. For analysis of high-frequency loading, such as impact or vibration, improved data processing techniques in the time-frequency domain have been proposed (e.g. Giakas et al., 2000). By adjusting filtering parameters according to the frequency content over time higher frequencies can be maintained in the derivatives of displacement data without sacrificing the signal to noise ratio.

VIBRATION DAMPING AND JOINT STIFFNESS

Oscillations and higher magnitudes of movement transients influence the calculation of joint kinetics using the traditional inverse dynamics procedure. To evaluate movement adaptation to loading conditions during locomotion, joint ‘stiffness’ has often been quantified by assuming a linear relationship between joint moment and angular displacement. We have found highly non-linear vibrations in such joint stiffness measures during running. To adequately determine the control and damping of these high frequency vibrations, improved calculations of dynamic joint stiffness are required that are frequency dependent. Frequency domain sinusoidal models of muscle-tendon-mass systems have recently been used to predict the damping of limb vibration during hoof impact in horses (Wilson et al., 2001). Such approaches should enhance our understanding of natural shock attenuation mechanisms to protect the body from injury and how we adapt to changes in external loading conditions during running.

SUMMARY

High frequency oscillations of the lower limb have been found during the impact phase of running. They are modified by external loading conditions and characterise movement adaptation to the severity of foot-ground impact. Methodological considerations needed to adequately capture these spring-like joint vibrations include suitable sampling frequency and/or processing of the kinematic data. Developments in the calculations of vibration damping and joint stiffness setting during running are likely to occur in the frequency domain.

REFERENCES

Lake, M., Coyles, V., Lees, A. (2001) ISB Congress Proc., pp. 200-201, Zurich.
Lees, A. (1998). ICB Seminars, Warsaw, 116-123.
Giakas, G., Stergioulas, L.K., Vourdas, A. (2000). Journal of Biomechanics **33**, 567-574.
Wilson. A. et al. (2001). Nature, 414, 895-899.

ACKNOWLEDGEMENTS

The contributions of Virginia Coyles, Adrian Lees and Ben Patritti are warmly acknowledged.

SPRING-LIKE FORCE GENERATION BY THE LEG IN RUNNING

Claire T. Farley[1] and Cassie Shigeoka[2]
[1]Dept. of Kinesiology and Applied Physiology, Univ. of Colorado, Boulder, Colorado, USA. Claire.farley@colorado.edu
[2]Department of Integrative Biology, Univ. of California, Berkeley, California, USA.

INTRODUCTION

When humans and other animals use running gaits, their legs generate force in a spring-like pattern during the ground contact phase. The leg is often modeled as a linear spring because a simple spring-mass model, consisting of a linear "leg spring" that represents leg behavior and a point mass that represents the runner's body mass (McMahon & Cheng, 1990), mimics the *pattern* of movement of the center of mass in many quadrupedal and bipedal mammals, including humans (Farley et al., 1993). Indeed, a runner's leg exhibits a spring-like force-displacement relationship. Although the model's leg spring is passive, the muscles in a runner's leg generate force actively to produce the spring-like behavior. Thus, the leg's spring-like force-displacement relationship can be interpreted as representing a rule for the control of leg force generation.

Because this force-displacement relationship is produced by active muscles, humans can modulate its slope (i.e., "leg stiffness") to control running dynamics. For example, when runners use faster stride frequencies or encounter softer surfaces, they increase leg stiffness dramatically (Farley & Gonzalez, 1993; Ferris et al., 1998). As a result of leg stiffness adjustment, the series combination of leg and surface stiffness remains the same regardless of surface stiffness. Thus, by controlling the force-displacement relationship of the leg, runners adjust the their dynamics.

The qualitative similarity between the movements of a runner and a spring-mass system inspired the development of a spring-mass model for running (McMahon & Cheng, 1990). Our goal was to quantify the accuracy of a spring-mass model's prediction of the trajectory of a runner's center of mass. This information will allow us to assess whether a spring-mass model provides a rigorous quantitative framework for understanding the rules underlying the control of running.

METHODS

Ten subjects (body mass = 55.5 ± 5.6 kg, mean ± S.D.) ran at 3.7 m/s on rubberized foam surfaces covering two force platforms while being videotaped in sagittal view. We used three surfaces: a continuous "hard" foam surface ($k_{surface}$ = 505.6 kN/m), a continuous "soft" foam surface ($k_{surface}$ = 37.3 kN/m), and a surface comprised of alternating hard and soft sections sized so that. a runner's footfalls alternated between hard and soft sections. We determined the trajectory of the center of mass (COM) by double integration of its acceleration derived from the vertical and horizontal components of the ground reaction force.

We used Matlab to simulate the spring-mass model. We input body mass, leg length, COM velocity at touchdown, and leg angle at touchdown. We iteratively found the leg spring stiffness value that predicted the COM trajectory with the least error. We quantified the error by expressing the average difference between the predicted and actual COM vertical displacement for all the timesteps in a trial as a % of the actual vertical displacement.

RESULTS AND DISCUSSION

On each surface, the spring-mass model predicted the center of mass trajectory with remarkable accuracy. The mean error was 4.3% (± 0.9%, S.E.M.) and 6.1% (± 0.9%) for the hard and soft continuous surfaces respectively. The error was not larger on the alternating surface: 4.2% (± 0.7%, hard sections) and 5.7% (± 0.8%, soft sections). Runners maintained normal spring-like dynamics despite surface property differences by using a greater leg stiffness on the soft versus the hard surface (16.1 ± 3.5 kN/m vs. 12.1 ± 2.5 kN/m, $p < 0.05$) as observed previously (Ferris et al., 1998),

SUMMARY

A spring-mass model predicts the COM trajectory with errors less than 6.1% regardless of surface properties. Thus, it is reasonable to model leg force generation with a linear spring. This observation suggests that runners somehow coordinate the force generation by many muscles so that the overall leg behaves like a spring on a range of surfaces. The spring-mass model should provide quantitative information about the determinants of running dynamics, and thus advance our understanding of the control of locomotion.

REFERENCES

Farley, C.T. et al. (1993). *J. exp. Biol.* **185**, 71-86.
Farley, C.T. & O. Gonzalez. (1996). *J. Biomech.* **29**, 181-186.
Ferris, D.P. et al. (1998). *Proc. Royal Soc. B.* **265**, 989-994.
McMahon, T.A., Cheng, G.C. (1990). *J. Biomech.* **23**, 65-78.

ACKNOWLEDGEMENTS

Supported by NIH (AR44008) and NSF (ECS-9873474) to C.T.F.

PLANTAR PRESSURES, SHOCK AND REARFOOT MOTION DURING RUNNING ARE THESE MEANINGFUL QUANTITIES FOR THE PREDICTION OF RUNNING INJURIES ?

Ewald M. Hennig
Biomechanics Laboratory, Universitaet Essen
Essen, Germany, ewald.hennig@uni-essen.de

INTRODUCTION

Injury surveys on runners have concluded that the occurrence of overuse injuries is the most common reason for runners to quit running and to continue with other kinds of physical exercise (Koplan et al., 1995). Among many other authors Messier et al. (1988), Duffey et al. (2000), Hreljac et al. (2000), and Bennett et al. (2001) showed that excessive rearfoot motion and increased shock can be identified as risk factors for injuries in runners. Therefore, pronation control and cushioning are still considered to be the main concepts for injury prevention in running shoe design. However, conclusive epidemiological and clinical proofs for these concepts are still missing. Plantar in-shoe pressure measurements provide comprehensive information about the interaction of the individual foot anatomy with the shoe. No studies, however, have identified specific pressure patterns with running injury risk to date.

METHODS

During the last 12 years our laboratory has performed 7 running shoe tests for a consumer product test agency in Germany. On the basis of more than 12000 measurements (140 runners) the biomechanical properties of 116 different shoe constructions were evaluated with regard to plantar in-shoe pressures, shock, and pronation properties. All products in the shoe tests were also worn by each of the participating runners for a distance of 10 km on varying terrain. Perception scale (15 point) shoe property ratings were given by the participants after completion of the 10 km run. All shoes were also tested mechanically, using an impacter devices to quantify midsole material properties. Comparing the technical and biomechanical data with the subjective evaluations from the runners in a questionnaire, several conclusions could be drawn.

RESULTS

Data from 17 pairs of shoes (test from the year 2000) showed that neither the subjective rating of shock ($r^2 = 0.01$) nor the peak tibial accelerations from the biomechanical tests ($r^2 = 0.08$) showed relationships to the impacter peak g results. The subjective perception of rearfoot motion control revealed only low correlations with the biomechanically determined maximum pronation ($r^2 = 0.20$) or pronation velocity ($r^2 = 0.01$). From the biomechanical tests it was found that maximum pronation ($r^2 = 0.04$) and peak pronation velocity ($r^2 = 0.01$) did not show any relationship to shock, as measured by the peak acceleration. This finding defies assumptions that good shock absorbing shoes do not provide sufficient support against overpronation. The highest correlations between any of the perception against the biomechanical variables were found for plantar pressure data (figure 1). Footwear with reduced forefoot pressures were rated by the runners as better overall performing shoes.

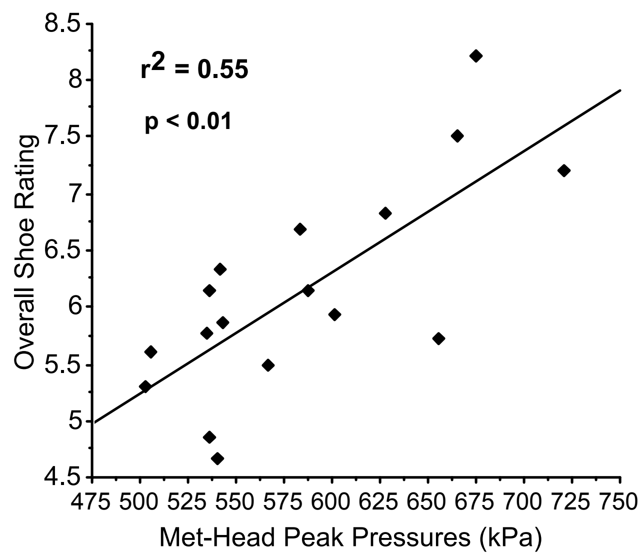

Figure 1: Shoe Performance Rating vs. Forefoot Pressures

Our shoe tests during the last 12 years showed that overall performance rating is closely related to the perception of comfort. Therefore, peak plantar pressures seem to be a key variable for the perception of comfort. It is unlikely, however, that this variable is a strong indicator for the occurrence of injuries. The influence of running shoe design on the loading behavior of the foot is best described with a relative load analysis. Such an analysis will identify percentile load bearing of anatomical structures across the plantar surface. Relative load analyses would be well suited to draw conclusions from load patterns of specific shoe designs with running shoe based injury surveys.

REFERENCES

Bennett JE, Reinking MF, Pluemer B et al. (2001) *J Orthop Sports Phys Ther* **31**. 504-510.
Duffey MJ, Martin DF, Cannon DW et al. (2000) : *Med Sci Sports Exerc* **32**. 1825-1832.
Hreljac A, Marshall RN, Hume PA (2000): *Med Sci Sports Exerc* **32**. 1635-1641.
Koplan JP, Rothenberg RB, Jones EL (1995*). Med Sci Sports Exerc* **27**:1180-1184.
Messier SP, Pittala KA (1988). *Med Sci Sports Exerc* **20**. 501-505.

INDIVIDUAL VS. GROUP ANALYSES IN DISTANCE RUNNING BIOMECHANICS

Keith R. Williams
Human Performance Laboratory, University of California, Davis, Davis, CA, USA (krwilliams@ucdavis.edu)

INTRODUCTION

The goal of much research in distance running biomechanics is to identify mechanical mechanisms inolved in injury occurrence or in metabolic energy expenditure (economy). In addition to the general goal of furthering knowledge, there is the ultimate aim of understanding more about how to improve an individual's ability to perform or to run injury free.

Clinicians have often used a case-study approach to identify relationships with injury, but these methods have been little used in scientific studies due to an inability to statistically verify implied relationships. Many biomechanical studies have involved groups of runners, sometimes using subsets based on injury, sometimes comparing groups differing in economy or the magnitude of impact forces. While such studies have identified some likely causal relationships, statistical results are often relatively weak and usually provide few specific guidelines applicable to individual runners. This paper addresses some of these issues as they relate to furthering our understanding of the relevant mechanisms in distance running.

METHODS

Examples of published and new data are used to examine the relevance of relationships among variables to individuals, focusing on interactions between selected biomechanical data and measures of economy or incidence of injury.

RESULTS AND DISCUSSION

An example of group analyses related to injury can be found in work published by Viitasalo and Kvist (1983) and Messier and Pittala (1988), who found shin splints to be related to excessive pronation or pronation speed. Table 1 shows several biomechanical measures for a subset of elite female distance runners who all had a history of shin splints. Maximum pronation angles were not excessive, and while two showed high pronation speed values, most pronation measures were within normal ranges. The general premise from the group studies did not hold well for these individuals.

Another example can be found for group studies evaluating biomechanical measures and running economy. Heise and Martin (2001) and Williams and Cavanagh (1987) both found relatively weak but significant correlations between ground reaction force (GRF) measures and economy. The vertical force patterns from two trained runners with similar economy measures shown in Figure 1 illustrate that large differences can exist in GRF's with little effect on metabolic costs.

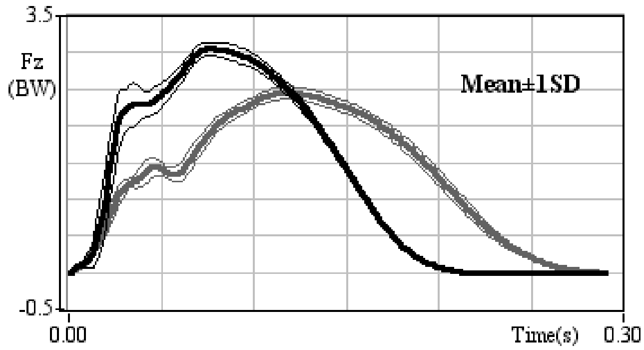

Figure 1: Vertical ground reaction forces from 20 trials for each of two subjects who had similar running economy.

SUMMARY

These and other examples highlight the difficulty in applying results from group studies to individuals. An alternative that can be more successful is to evaluate specific relationships within the individual. This method may also provide a further and perhaps more successful means of identifying mechanistic relationships between biomechanical measures and injury or metabolic energy expenditure.

REFERENCES

Heise,GD & Martin,PE (2001) *Eur J Appl Physiol* 84:438-442
Messier, SP & Pittala, KA.(1988) *Med Sci Sports Exerc* 20: 501-505.
Viitasalo, JT and Kvist, M (1983) *Am J Sp Med* 11:125-130
Williams, KR and Cavanagh, PR (1987) *J Appl Physiol* 63:1236-45.
.

Table 1: Selected biomechanical measures from running at 5.36 m•s^{-1} for five elite female distance runners. Mean statistics are from a database of elite female distance runners.

	Stride Length	Peak Fz	Strike Index	Thigh @FS	MaxKnee Flex Supt	Knee @FS	Max Dorsi Flexion	Ankle @FS	RearAng @FS	Max Pron Ang	Amt of Pronation	Max Pron Spd
Subject	%LL	BW	%	°	°	°	°	°	°	°	°	°/s
S1	4.15	2.83	56.8	34.5	57.3	23.2	115.0	80.0	20.6	-4.5	25.1	-1171
S2	3.74	3.04	31.5	29.2	38.5	16.4	98.7	71.9	13.0	-7.5	20.5	-822
S3	4.13	3.41	72.5	29.4	45.3	16.4	107.2	74.1	15.8	-8.5	24.3	-995
S4	3.66	2.75	34.5	26.9	44.6	18.9	103.7	82.6	21.3	-6.3	27.6	-1239
S5	3.36	3.09	71.2	21.3	34.3	5.8	…	66.7	9.3	-5.3	14.6	-437
Mean	3.93	3.17	39.6	29.8	46.5	19.9	108.9	81.7	14.4	-8.7	23.1	-896
SD	0.24	0.26	20.6	3.7	6.5	6.6	6.6	9.2	6.2	4.2	5.5	282.2
N	49	53	50	38	50	38	40	38	48	48	46	27

DYNAMIC VARIABLES AND RUNNING INJURIES

Gert-Peter Brüggemann, Adamantios Arampatzis, Wolfgang Potthast Institute for Biomechanics, German Sport University of Cologne, Cologne, Germany, brueggemann@dshs-koeln.de

INTRODUCTION

Excessive impact forces, overpronation, excessive mileage and previous injuries have been proposed as major factors for acute and chronic running injuries (e.g. van Mechelen 1992, Robbins et al. 1990). The running shoe was identified to influence impact forces, foot eversion and hence the eversion moments at the ankle joint. Consequently running shoes have been designed to control the impact forces, the eversion moment at the ankle joint, and the torsional moment at the tibia. Recent prospective studies did not support the general and strong association between impact force, eversion moment, tibia shear stress, and running injuries.
The purpose of this paper is to approach to an understanding of a possible association between dynamic variables in heel-toe running, running injuries and performance enhancement.

DYNAMIC VARIABLES

Impact forces in heel-toe running occur when the foot hits the ground and reach their maximum earlier than 50ms after the first ground contact. The magnitude of the vertical impact force peak varies substantially for different running velocities. Unexpected results are that the hardness of the shoe midsole has only a minimal systematic influence on the external impact force peaks (Bates 1989). The resultant internal forces and moments in the structures of the lower extremities are not systematically determined by the hardness of the midsole of running shoes (Cole et al. 1995). Calculations indicate higher joint contact forces in the push-off phase than during the impact. Based on these calculations it was speculated that non excessive impact forces and the related internal joint contact forces during running might not be a major factor for the development of injuries in running (Scott & Winter 1990). Results of a prospective study do not show differences of short term running injuries between subjects with high or low external impact force peaks (Bahlsen 1989). Foot inversion does not act as predictor for an increase in running injuries. From the findings on impact peak forces and the associated foot eversion one can speculate that the eversion moment has no strong relation to running injuries.

INJURIES AND FUNCTIONAL ADAPTATION

Runners did not show a higher incidence of osteoarthistis than non-runners (e.g. Eichner 1989). Some studies showed that in certain cases shock-absorbing insoles reduce the frequency of injuries (e.g. Milgrom et al. 1992). A decrease of impact forces or internal joint loading due to the insoles was not quantified in these studies. Interestingly shock-absorbing insoles did not reduce the incidence of stress fracture (Gardner et al 1988). The unsystematic results lead to the conclusion that shock attenuation might not be the ultimate reason for running induced injuries.
Biological responses to impact loading have been shown to improve bone quality (Grimston & Zernicke 1993). While the thickness of cartilage was not found to adapt to mechanical stimulation through running, the joint size was shown to be modulated during growth (Eckstein et al. 2001).
Based on these findings one cannot conclude that the dynamic variables impact force and loading rate are the most important factors in the development of chronic or acute running–related injuries.

DYNAMIC VARIABLES AND PERFORMANCE

The surface stiffness affects significantly the running economy (Kerdok et al. 2002). Running with comfortable and cushioning shoes might be combined with less energy consumption (Nigg 2001). From that one can conclude that muscle force production must be more efficient under the more comfortable footwear conditions. A comfortable shoe condition can be assumed to be associated with a cushioned midsole or a lateral crashpad. Recent in vivo measurements of Achilles tendon force indicate a faster and more pronounced decrease of the Achilles tendon stress during impact phase in running with harder and non comfortable shoes than in comfortable and cushioning shoes. From the pronounced plantar flexion of the ankle joint at foot strike with the non cushioning footwear one can conclude that the triceps surae muscle shortens and works at the ascending limb of the force length relationship. When running in comfortable shoe condition the contractile element can work at a length closer to the plateau of the force length relation.
The deformation of the midsole or the crashpad of a running shoe decreases the plantarflexion moment at foot strike, the rate of length change of the muscle tendon unit of the triceps surae and allows the contractile element to work more close to the optimal length. From that one can conclude that a decrease of impact peak force and the loading rate through a cushioning midsole or a lateral heelpad of a running shoe will increase the force production potential of the plantarflexors of the ankle joint and therefor increase the economy of musclar work and performance.

REFERENCES

Bates, B.T. (1989). *J. Biom.*, **22**, 963-965.
Bahlsen, A. (1989). PhThesis, University Calgary.
Cole, G.K. et al. (1995). *J. Appl. Biom.*, **11**, 25-46.
Eckstein, F. et al. (2001). *Osteoarthritis & Cartilage*, 1-7.
Eichner, E.R. (1989). *Phys Sportmed.*, **17**, 147-154.
Gardner, L.I. et al (1988). *Am J Public Health*, **78**, 1563-1567.
Grimston, S.K., Zernicke, R. (1993). *J Appl Biom*, **9**, 2-14
Kerdok, A.E. et al. (2002). *J Appl Physiol*, **92**, 469-478.
Robbins, S.E. et al. (1990). *Sports Med*, **9**, 76-85.
Scott, S.,Winter, D.(1990).*Med Sci Sports Exerc*, **22**, 357-369.
Milgrom, C. et al. (1992). *Clin Orthop Rel Res*, **281**, 189-192
Nigg, B.M. (2001). *Clin.J.Sport Med.,* **11**, 2-9.
van Mechelen, W. (1992). *Sports Med.*, **14**, 320-335.

THE INFLUENCE OF VEHICLE ROLL RATE ON NECK LOADING DURING CONTROLLED VEHICLE-TO-GROUND IMPACTS

Catherine Ford Corrigan[1], Peter A. Cripton[1], Jeffrey Croteau[2]
Exponent Failure Analysis Associates, [1]Philadelphia, PA; [2]Natick, MA

INTRODUCTION

Cervical spine injury potential during vehicle rollovers is a function of numerous variables, several of which are associated with the dynamics of the rolling vehicle. Significant roof-to-ground impacts that occur adjacent to an occupant's seated position have been associated with the potential for severe cervical spine injury in both crash test series and field studies (Orlowski, 1985, Bahling, 1990, Huelke, 1983). Consultants in the applied biomechanics field are often asked to determine the cervical spine injury mechanisms associated with a specific rollover accident. However, the extent to which specific dynamic parameters associated with the rolling vehicle contribute to cervical spine injury potential has not been well-documented. This is in large part due to limitations in previous rollover test procedures, which did not allow for controllable and repeatable roof-to-ground impacts. In this study, a novel and highly accurate rollover test apparatus was used to produce pre-defined vehicle to ground impacts. We report on the first use of this apparatus to investigate the effect of vehicle roll rate on neck loading.

METHODS

The Controlled Rollover Impact System (CRIS) (Cooper, 2000) utilizes a modified semi-trailer to release a suspended vehicle from a pre-determined drop height and roll angle. The CRIS apparatus incorporates mechanisms that allow the vehicle's initial roll, pitch, yaw, lateral translational and vertical kinematics to be predetermined by the investigators. Two tests were performed using the same make and model vehicle to examine the effect of vehicular roll rate on neck axial loading. To mitigate potential differences in roof deformation between the tests, each vehicle was tested with a reinforced roof. Both tests utilized a nominal 6.7 m/sec lateral translation velocity (passenger-side leading), a 46 cm drop height, and impacted the ground at a roll angle of 190 degrees. In the first test (Trans-Drop), the vehicle was released with zero roll velocity. In the second test (Spin-Drop), a constant 360 degree per second roll rate was introduced, with all other variables associated with the roof-to-ground impact held constant.

Hybrid III 50th percentile anthropomorphic test devices (ATDs) instrumented with upper neck load cells were restrained in the driver's seated position for each test. The ATDs were held in position by additional harnesses while the desired translational and rotational velocities were achieved. Once vehicle velocities were stabilized prior to vehicle release, the harnesses were pneumatically released so that the ATDs would be restrained only by the vehicle's three-point belt system during the roof-to-ground impact. Both onboard and ground-based high speed cameras were utilized to capture details of the roof-to-ground impacts. All data were collected in accordance with Society of Automotive Engineers J211.

RESULTS

In both tests, the ATD's head was in contact with the vehicle's roof just prior to vehicle release. In the Trans-Drop test, release of the vehicle resulted in a small displacement of the ATD's head away from the roof, after which the ATD and the vehicle fell at essentially the same velocity. Peak axial neck load occurred 24 msec after impact in the test and 22 msec after impact in the Spin-Drop test. Addition of the 360 degree per second roll rate increased the peak axial neck load 21.6% relative to the Trans-Drop test (9120 N versus 7500 N, Fig. 1).

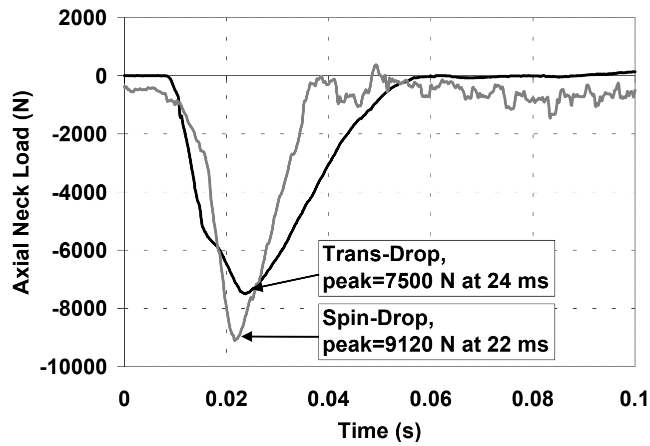

Figure 1: Axial neck load versus time

DISCUSSION

Biomechanical studies have identified velocity-based injury criteria when the neck is called upon to stop the moving torso (McElhaney, 1979). In the case of vehicular rollovers, a vehicle's roll rate can add substantially to the roof's and to the occupant's velocity relative to the ground just prior to impact, thus increasing the injury potential that results from the moving torso transmitting force to the cervical spine. The data presented here directly demonstrate the importance of considering a vehicle's roll rate, in addition to its translation rate and drop height, when evaluating injury potential of specific rollover accidents.

Future testing with the CRIS apparatus will allow detailed study of occupant, vehicle, restraint and injury prevention parameters in a controlled and repeatable fashion. This will result in an improved overall understanding of neck injury mechanisms that occur during rollover accidents.

REFERENCES

Orlowski, K.F. *et al* (1985). SAE 851734.
Bahling, G.S. *et al* (1990). *Proceedings of the 34th Stapp Car Crash Conference*, 101-112.
Huelke, D.F., Compton, C.P. (1983). Accident Analysis and Prevention, **XIV**, No. 5.
Cooper E.R. *et al* (2000). SAE 01B-261.
McElhaney J.H. *et al* (1979). SAE 790137.

BIOMECHANICAL ANALYSIS OF ACUTE LUMBAR INTERVERTEBRAL DISC LOADING

Dan Girvan and Elaine R. Serina

Piziali and Associates, San Carlos, California, USA

INTRODUCTION

Lumbar intervertebral disc (IVD) injuries are often claimed as a result of vehicular, industrial, or other types of incidents. These injuries can result in significant financial costs, physical disability, and loss of productivity. Biomechanical testing can be used to determine the magnitude and type of loading experienced by the lumbar spine in a particular incident or during a specific activity. In particular, acceleration measurements can be useful to assess lumbar loading on subjects exposed to sudden vertical motions. A biomechanical analysis can then be performed to assess whether the claimed lumbar IVD injuries resulted from a particular incident.

METHODS

Because axial compression tends to be a significant factor in causing lumbar IVD injuries, it is most useful to measure z-axis (vertical) accelerations. For seated vehicle or equipment occupants, an accelerometer (Kistler Type 8304B10 10 g) was placed between the operator's buttocks and the seat to measure vertically applied accelerations. The accelerometer was mounted in an ISO 7096-1982 seat pad. In tests with a standing occupant (e.g., elevator emergency stops), the accelerometer was mounted to the floor next to the test subject. The data was collected with an IOtech DaqBook 216 16-bit data acquisition system (1000 Hz sampling frequency).

RESULTS AND DISCUSSION

The tested activities included operating a fork lift in which a wheel dropped through a wooden floor, operating a railroad tie remover/inserter machine, driving over railroad tracks and speed bumps, and emergency elevator stops. Figure 1 shows the vertical acceleration time-history produced at the seat-buttocks interface while operating a railroad tie remover/inserter machine.

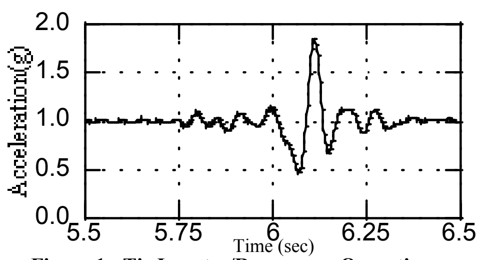

Figure 1: Tie Inserter/Remover -- Operation

These measurements can be compared to the accelerations produced during typical activities such as sitting down into a seat. The results show that sitting down in the operator's seat produced higher peak vertical loading than the machine operation (Figure 2). The forces applied to the spine in the incident under study can be determined by multiplying the measured accelerations by the effective mass (i.e., the upper body mass). The peak applied force can be compared to static spinal forces produced during daily activities. The lumbar compressive forces during activities such as lifting and postural changes can be predicted by computer models of the low back (Chaffin and Andersson, 1991).

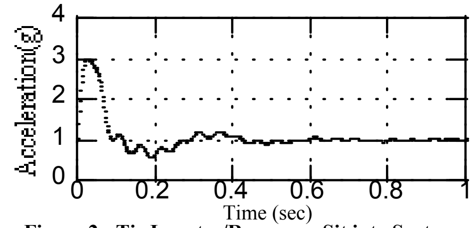

Figure 2: Tie Inserter/Remover--Sit into Seat

This analysis technique can be a useful tool in determining whether a lumbar IVD was injured in a particular incident. If the measured loads in a particular incident are comparable to or less than the loading experienced during activities of daily living, there is no biomechanical rationale for how the given incident could have caused the lumbar IVD injury. Further analysis may be necessary if the incident loads are greater than activities of daily living.

This methodology analyzes the magnitude of loads applied to the lumbar spine. Further evaluation of the nature of the loading and IVD disc injury mechanics should be considered. Some studies indicate that disc bulges and herniations result primarily from degeneration or fatigue loading (Adams and Hutton, 1985; Gordon, *et al.*, 1991). Investigators that have produced disc injuries from acute loading have found that these injuries are accompanied by other bony or ligamentous injuries (Adams and Hutton, 1981). Therefore, a comprehensive biomechanical evaluation should consider IVD injury mechanisms as well as an analysis of the loading.

SUMMARY

Vertical acceleration measurements can help in assessing whether a particular event caused lumbar IVD injuries. The measured accelerations can be compared to accelerations produced in typical activities. Additionally, the forces applied to the spine can be estimated and compared to forces produced by lifting and postural changes.

REFERENCES

Adams, M.A., Hutton, W.C. (1981). *Spine*, 7:3, 184-191.
Adams, M.A., Hutton, W.C. (1985). *Spine*, 10:6, 524-531.
Chaffin, D.B., Andersson, G.B. (1991). *Occupational Biomechanics*, John Wiley & Sons.
Gordon, S.J., *et al.*, (1991). *Spine*, 16:4, 450-456.

BIOMEDICAL ASPECTS OF HELMET DESIGN

James McElhaney[1] and William Newberry[2]

[1]Department of Biomedical Engineering, Duke University, Durham, NC, USA
[2]Exponent® Failure Analysis Associates, Phoenix, AZ, USA, wnewberry@exponent.com

INTRODUCTION

Brain and cervical injuries from contact sports and vehicular accidents are a continuing major problem in our high-speed society. The use of helmets is an attempt to reduce the risk of injury in various activities including motorcycle, bicycle and equestrian riding, football, baseball, ice hockey, rock climbing, certain hazardous industrial operations and, of course, the military. Helmets are quite effective in distributing the force of a head impact over the head thus reducing the risk of skull fractures. Their spherical shape sheds blows changing what would have been a direct blow into a glancing blow. The deformation of the helmet liner manages the energy of the blow and reduces the force or stress applied to the head. But helmets offer little protection to the cervical spine. This paper will discuss the limitations of designing a helmet that offers both head and cervical spine protection in head impact situations.

METHODS

Head and neck injury criteria were developed from the literature. Experiments that developed load-deflection criteria for representative helmet types were performed. Experiments that developed cervical spine deformation and force transmission characteristics were performed. Experiments that compared neck loads in the helmeted and unhelmeted Hybrid III ATDs when swung into a rigid barrier were performed. These various experimental data were analyzed to better understand the biomechanical limitations of helmets to provide significant protection from catastrophic cervical injuries.

RESULTS AND DISCUSSION

Load-deflection tests indicate that the typical football, bicycle, equestrian, baseball and motorcycle helmet with a deformable liner produce a stiffening curve when loaded between an external surface and the head. Since the area under the load-deflection curve is the energy/work expended in producing the deformation, this is an undesirable characteristic that occurs because the area of the crush surface increases during deformation.

Using head deceleration of 250 g as a brain injury threshold, the available helmet crush stiffness would be optimized by having the liner bottom out at a force equivalent to 250 g times the head and helmet weight. For the 50% male head, this would equate to approximately 14,500 N applied to the helmet. A typical motorcycle helmet liner bottoms out at approximately 2 cm deformation. This establishes an energy management level of approximately 150 Nm for the liner, when optimized for head protection. However, because in an axial compression mode the average male's cervical spine fails at approximately 3,800 N, the linear helmet only manages approximately 10 Nm before a compression fracture of the cervical vertebrae occurs.

In addition, catastrophic axial compression of the cervical spine occurs when the neck is aligned with the head and torso and trapped so that the inertia force is transferred through the cervical spine. This so-called torso augmentation means that instead of simply managing the kinetic energy of the head and helmet to protect the neck, the helmet must also manage the dynamic mass of the neck and torso. To further compound the problem, cadaver tests and mathematical models indicate that the head starts to rebound before the peak neck loads occur.

This analysis was verified by experiments using a Hybrid III ATD with a six-axis cervical load cell. The dummy was swung like a pendulum into a wall with and without a helmet. The results indicate that a helmet reduces HIC values by 86% but reduces neck compression by only 22%. Since our tests indicate the Hybrid III neck is much stiffer than a human neck, neck loads in humans under similar circumstances would be reduced by a lesser amount.

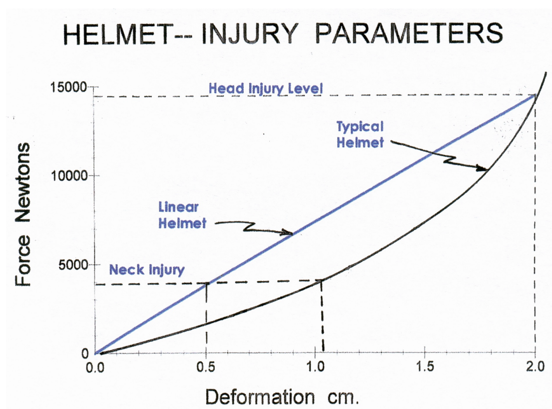

SUMMARY

Helmets cannot provide significant protection to the cervical spine in axial compression because: 1) the tolerance levels of the brain and skull are so much higher than the cervical spine; 2) the torso augmentation factor requires the helmet to manage four to five times more energy for cervical spine protection; and, 3) the phasing of cervical spine loading lags the peak helmet loads so that the helmet is unloading before cervical failure occurs.

REFERENCES

Torg, J.S., et al. (1979). *JAMA* 1477-1479.
McElhaney, J.L., Myers, B.S. (2001). *Accidental Injury Biomechanics and Prevention*, Springer Press 324-373.
Nightingale, R.W., et al (1977). *Spine* 2380-2387.

THEORETICAL MODEL STUDIES OF FLUID-SOLID INTERACTIONS IN THE CERVICAL SPINE DURING LOW-SPEED POSTERIOR SHOULDER IMPACTS

Peter F. Niederer[1], Kai-Uwe Schmitt[1], Markus H. Muser[2], Felix H. Walz[2]

[1] Institute of Biomedical Engineering, ETH Zurich, Switzerland
[2] Working Group for Accident Mechanics, Zurich, Switzerland

INTRODUCTION

Minor soft tissue injuries of the cervical spine which are caused by posterior shoulder impacts at a low loading level represent an important public health issue because they are sometimes associated with long-term impairment ("Whiplash-Associated Disorders"). Such injuries are typically conveyed during low-speed rear-end automobile impacts. A number of hypotheses has been formulated in order to explain the occurrence of potentially harmful neck injuries at apparently subtraumatic loading levels. Among them, interactions between fluid compartments and solid structures have been postulated, in that relative motions of fluids *vs.* solids cause viscous shear stresses and pressure peaks which may have an adverse influence, *e.g.*, on cellular membranes. This hypothesis is supported by a number of experimental findings [1, 2].

METHODS

Mathematical modeling approaches lend themselves for a quantification of fluid/solid interactions under loading conditions which have to be expected under typical impact situations of interest here. In the present study, two modelling strategies have been applied. First, an idealized fluid/solid system is considered which is exposed to an acceleration pulse. The geometry (Figure 1) is chosen such as to represent a fluid-filled tube whereby an analytic solution can be found. Second, a neck model on the basis of a Finite Element formulation has been developed which includes vertebrae, discs, muscles, tendons as well as a representative fluid space (part of the *plexus venosus*, Figure 2). Initial and boundary conditions are applied which correspond to typical low-speed rear-end impacts (change of velocity Δv = 15 km/h, maximal acceleration level $a_0 = 5$ g).

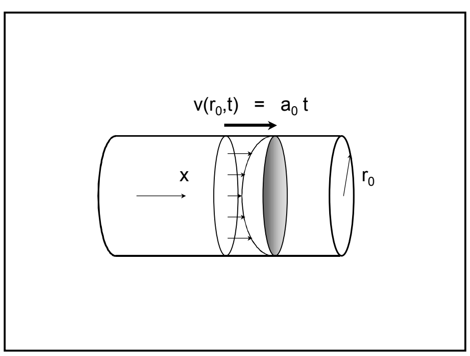

Figure 1. Fluid-filled tube [radius r_0, axial flow velocity $v(r,t)$] which is subjected to an acceleration pulse, a_0.

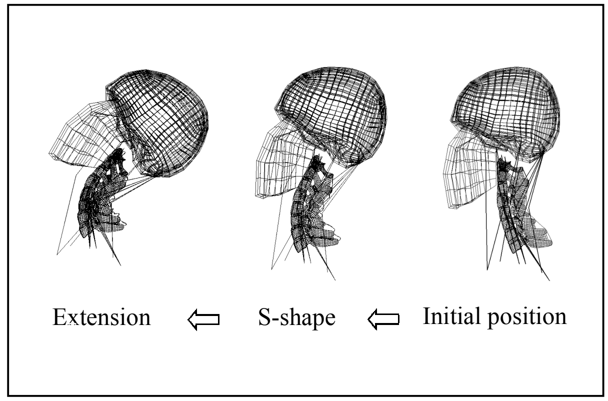

Figure 2. FE model of the human neck: Calculated motion sequence resulting from a Δv = 15 km/h posterior impact. The model of a venous blood vessel is included which runs along the cervical spine (The "S-shape" configuration characterizes a momentary shape of the cervical spine during the impact response and corresponds to the phase which is presently asumed to be critical).

RESULTS

The analytical model shows, that the level of shear stresses caused by fluids and acting on accelerated surfaces in fluid-filled bodies depends essentially on the size and orientation of the fluid space under consideration. Accelerations thereby exhibit a stronger influence than the duration during which they act [3]. On the basis of the presently available information with respect to cellular tolerances it cannot be excluded that critical levels are reached even in a low speed impact scenario. Calculated pressure peaks, in turn, were compared [4] with measurements performed in animal (pig) as well *post mortem* human subjects and they were found to remain within physiological limits.

REFERENCES

1. Oertengren T., *et al.*, J. Neurotrauma, 13 (1996) pp. 171ff
2. Morrison B., *et al.*, J. Neurotrauma, 15 (1998) pp. 911 - 928
3. Niederer P., *et al.*, IMECE 2001
4. Schmitt K.-U., *et al.*, Med & Biol Eng & Comp, 37 (1999) suppl 2, pp. 274ff

BIOMECHANICS IN THE DESIGN AND DEVELOPMENT OF AN ABDOMEN FOR CRASH TEST DUMMIES

Stephen W. Rouhana

Ford Motor Company, Dearborn, Michigan, USA

INTRODUCTION

Crash test dummies are important tools in the development and assessment of automotive safety systems. However, to obtain reasonable results, the mechanical response of these devices to impact should be similar to that of the human body, a characteristic known as biofidelity (Rouhana 2001). The objective of this work was to develop a dummy abdomen with injury assessment capability and good biofidelity. This was a multi-faceted research program encompassing biomechanics, instrumentation and mechanical design (Rouhana et al 2001).

METHODS

Previous biomechanical studies demonstrated the need for rate-sensitivity to achieve abdominal biofidelity and some past efforts with fluid-filled elements gave promising results. Therefore, a fluid-filled bladder concept was chosen for the new crash dummy abdomen. After a significant development effort, a silicone gel-filled, silicone shell abdominal insert design was selected for further test and evaluation (Figure 1).

The biomechanical response targets (force-deflection corridors) used to design the new abdominal inserts were obtained from a human cadaver study performed under contract at the University of Michigan Transportation Research Institute (UMTRI; see Hardy et al 2001). This study utilized a variety of loading conditions that might be encountered in an automotive collision. The new abdominal inserts were tested on the bench and *in situ* in Hybrid III dummies. Most of the in-dummy tests were performed at UMTRI, under identical test conditions as the cadaver study, utilizing a powered pendulum, pneumatic lap-belt loading device and/or airbag impact simulator.

RESULTS AND DISCUSSION

Figure 2 shows the force-deflection response of the silicone gel-filled, silicone shell abdominal insert compared with the force-deflection corridor developed from the UMTRI lap belt loading condition tests.

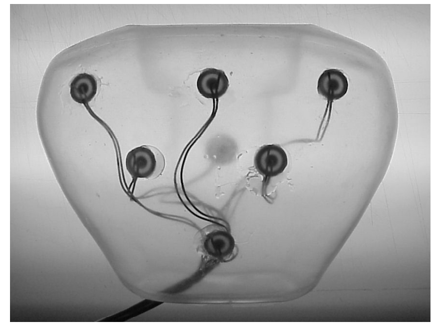

Figure 1: Front view of abdominal insert with electrodes bonded inside of the bladder for deflection measurement.

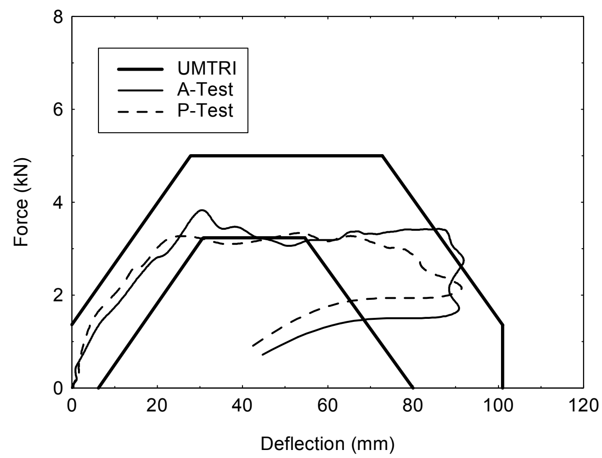

Figure 2: Force-deflection response of abdominal insert in a belt test compared with the human cadaver belt corridor.

The response of the abdominal insert was an aggregate response of the dummy's entire abdominal area and did not address differences in upper versus lower abdominal response, or solid versus hollow organs. While the abdomen developed demonstrated good biofidelity, some work remains to be done before it can be used in crash testing.

SUMMARY

While the amount of rate-sensitivity achieved was not large, when tested as a system with abdomen *in situ* and the dummy chest jacket on, the rate sensitivity was adequate and appropriate for the automotive environment. Moreover, the biofidelity of the abdominal insert in rigid-bar, seat belt and simulated airbag loading conditions was good.

REFERENCES

Hardy, W. N., Schneider, L. W., Rouhana, S. W. (2001) Abdominal impact response to rigid-bar, seatbelt, and airbag loading. *Stapp Car Crash Journal,* **45**, 1-32.
Rouhana, S.W. (2001) Biomechanics of abdominal trauma. In *Accidental Injury: Biomechanics & Prevention*, A.M. Nahum and J.W. Melvin, Eds. 391-428. Springer-Verlag, New York.
Rouhana, S.W., Elhagediab, A.M. et al (2001) Development of a Reusable, Rate-Sensitive Abdomen for the Hybrid III Family of Dummies. *Stapp Car Crash Journal*, **45**, 33-60.

CUMULATIVE LOADING AS AN INJURY MECHANISM: TISSUE CONSIDERATIONS

Jack P. Callaghan
Department of Human Biology and Nutritional Sciences, University of Guelph, Guelph, Ontario, Canada jcallagh@uoguelph.ca

INTRODUCTION

Research examining cumulative loading of the spine has demonstrated the potential to identify individuals more likely to report low back pain (LBP) (Kumar, 1990; Norman et al., 1998). These studies have examined cumulative exposure in the workplace and compared the reporting of low back pain in case subjects to the magnitude of exposure in a control population. This approach, while beneficial for establishing a relationship between LBP and cumulative loading, has done little to develop a standard or threshold tolerance value for cumulative loading exposure. To date cumulative loading is calculated as the unweighted integration of low back joint forces without any consideration to tissue modifying factors such as magnitude (percent of maximum strength) or rate (rest work interaction).

Historically the investigation into tissue tolerance has primarily focused on single cycle destructive compressive testing of spinal motion segments in-vitro. While it is acknowledged that compressive tolerance values can be modified by factors such as loading rate, gender, and age a single tolerance has been adopted for acute compressive loading (i.e. NIOSH). Repetitive loading has recently gained increased attention by both ergonomists and researchers. While there has been a relative scarcity of in-vitro tissue testing, it has been examined by researchers as early as the 1950s (Hardy et al., 1958). Both Liu et al. (1983) and Adams and Hutton (1983) demonstrated that in-vitro repetitive compressive loading can generate injuries at a submaximal level. However, neither of these studies reported the relationship between magnitude of loading and the number of cycles to failure.

The purpose of this paper is to examine current tissue research to determine if there is support for the cumulative injury scenario and provide a tissue-based rationale for developing a single threshold tolerance value based on tissue injury mechanisms in the low back.

METHODS & RESULTS

An examination of data from recent research was performed, in some cases additional calculations were performed to determine the cumulative spine loading. The work of Hansson et al. (1987) and Brinckmann et al. (1988) demonstrated a non-linear relationship between the repetitive in-vitro compressive testing and cycles to failure (Figure 1). When cumulative loading to failure is calculated for the data of Brinkmann et al. (1988) a linear trend is evident in the samples that failed within 5000 loading cycles (Figure 1). This lack of a single cumulative compression magnitude linked to injury was also present in the work of Callaghan and McGill (2001) examining disc herniation in a repetitive loading scenario (Figure 2).

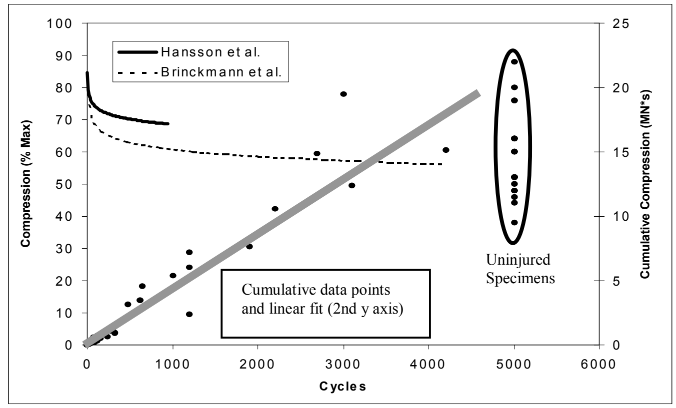

Figure 1: Left Y Axis: Non-linear trend between magnitude of compressive loading and cylces to failure. **Right Y Axis:** Cumulative compression and cycles to failure (adapted from Brinckmann et al., 1988).

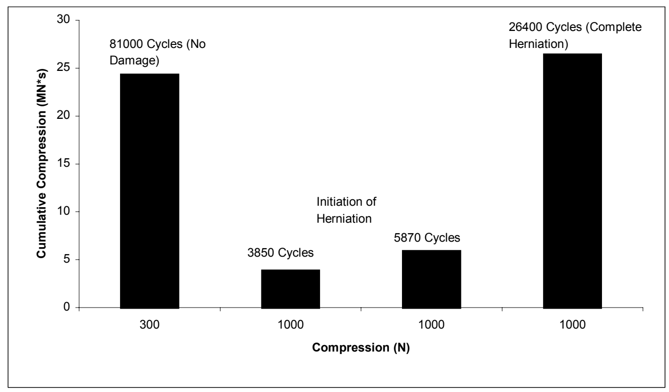

Figure 2: Cumulative loading for two spine specimens.

DISCUSSION & CONCLUSION

An unweighted single cumulative threshold tolerance value is not supported by current in-vitro research. The interplay between magnitude and cycles to failure (Hansson at al., 1987; Brinckmann et al., 1988) when taken together with the lack of a single cumulative value corresponding with injury (Callaghan & McGill, 2001) , indicates that the magnitude of cumulative exposure will need to be incorporated in work towards setting a standard for cumulative exposure.

REFERENCES

Adams, M.A. et al. (1983). *J Bone Joint Surg(B)*, 65, 199-203.
Brinckmann, P. et al. (1988). *Clin Biomech*, 3 Suppl 1, s1-s23.
Callaghan, J.P. & McGill, S. (2001). *Clin.Biomech*,16, 28-37.
Hansson, T.H. et al. (1987). *J Orthop Res*, 5, 479-487.
Hardy, W.G. et al. (1958). *Surg Forum*, 9, 690-695.
Kumar, S. (1990). *Spine*, 15, 1311-1316.
Liu, Y.K. et al. (1983). *Spine*, 8, 857-865.
Norman, R.W. et al. (1998). *Clin Biomech*, 13, 561-573.

USING CUMULATIVE SPINAL LOADING TO ASSESS JOBS, ENGINEERING, AND ADMINISTRATIVE CONTROLS: A SPINAL PERSPECTIVE

Mardy Frazer
Ergonomics Initiative, Faculty of Applied Health Sciences, University of Waterloo, Waterloo, Ontario, Canada

INTRODUCTION

Peak and cumulative forces on spinal structures have been identified as significant and statistically independent risk factors for reporting low back pain (LBP) (Norman et al., 1998). However, current field tools do not account for cumulative spinal loading explicitly so this risk factor is not easily quantified. Thus, when making change to reduce risk, the impact of any specific engineering or administrative control remains unknown. For example, job rotation is often cited as an administrative control for reducing cumulative loading risk, but, evidence of this is difficult to find. This presentation uses a software based, biomechanical modeling approach to calculate, combine and interpret both peak and cumulative spinal loading parameters for two manufacturing jobs to illustrate the risk of injury associated with peak and cumulative loading. The effect of job rotation, and a specific engineering intervention are also evaluated.

METHODS

A 2-D link segment model is used to estimate the L4/L5 moment and reaction forces. The job being analyzed is broken down into specific actions. The number of repetitions, and duration of, each action are entered. For each action the mannequin is positioned to match the job's posture. The direction and magnitude of the forces acting on each hand are entered. The model then estimates the peak and cumulative spine loads. Cumulative spinal loading is estimated by modeling the spinal load time history as a sequence of square waves. These values are compared against an epidemiological database for the reporting of low back pain and presented as a Low Back Pain Reporting Index (LBPRI) score ranging from 0.0 to 1.0 (the lower the score the better). A Combined LBPRI score is also produced from peak (hand load, reaction shear) and cumulative (moment) variables. Two automotive manufacturing jobs were assessed using the software. The effect of a specific engineering change, which stood workers more upright, was assessed for one of the jobs. Finally, a series of job rotation scenarios were simulated and evaluated.

RESULTS AND DISCUSSION

The peak and cumulative spinal loading parameters and their respective LBPRI are presented in Table 1. If only peak loading is considered, the risk of reporting LBP is minimal. For job B-Pre the cumulative moment LBPRI of 0.88 reflects a different scenario. The Combined LBPRI of 0.81 indicates a high probability of LBP being reported due to the demands of this job. The engineering intervention reduced the Combined LBPRI to 0.54 (Job B-Post). Job rotation did not result in an even redistribution of risk (Figure 1). A worker that spends 99% of their time on job A and only 1% on job B-Pre has a Combined LBPRI of 0.61, a 33% increase compared to the 0.46 score if they only worked at Job A.

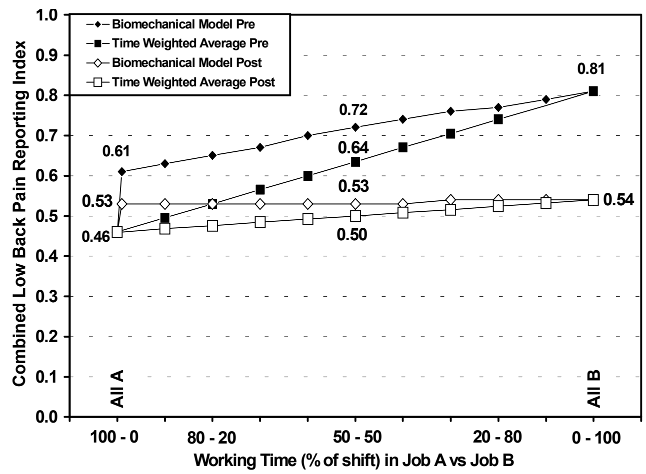

Figure 1 Combined LBPRI scores, as a result of job rotation, calculated pre and post engineering intervention, using a linear time weighted average model and a biomechnical model.

SUMMARY

It is not sufficient to only consider the impact of a single peak. The cumulative effect of many small peaks that are held for long durations and/or performed many times in a shift must also be considered. Measuring cumulative loading allows the effects of interventions to be quantified. Biomechanical diversity of tasks is needed for success with job rotation.

REFERENCES

Norman, R.W. et al (1998). Clin Biomech, **13**, 561-573.

Table 1: The peak and cumulative spinal loading parameters, and their associated LBPRI scores.

Job	Peak								Cumulative		Combined LBPRI
	Compression (N)	LBPRI	Moment (N.m)	LBPRI	Hand Load (N)	LBPRI	Reaction Shear (N)	LBPRI	Moment (MN.m.s)	LBPRI	
A	1356	0.28	56	0.27	29	0.34	118	0.21	1.00	0.71	0.46
B-Pre	2243	0.36	124	0.38	50	0.35	362	0.41	1.48	0.88	0.81
B-Post	1739	0.31	85	0.32	50	0.35	229	0.29	1.00	0.71	0.54

TOWARDS THE DEVELOPMENT OF A CUMULATIVE TRAUMA METRIC FOR OCCUPATIONALLY-RELATED MUSCULOSKELETAL DISORDERS

W. S. Marras

Biodynamics Laboratory, Institute for Ergonomics, The Ohio State University, Columbus, Ohio
Professor and Director, marras.1@osu.edu

INTRODUCTION

A continuing problem for society has been the control of occupationally-related musculoskeletal disorders. It is well established that most occupationally-related low back disorders (LBDs) are associated with manual materials handling (MMH) tasks. However, our ability to characterize overall risk associated with the various dimensions of LBD risk is rather poorly understood. For example, a recent study compared the ability of two commonly used risk metrics for LBD against a database of industrial injury data and found the ability of these tools to characterize risk to be moderate at best [1]. A evaluation of the structure of these metrics indicated that these tools were particularly weak at characterizing risk associated with cumulative trauma. This discussion will consider the contributions to work-related LBD in an attempt to better understand the components of cumulative trauma disorders (CTDs) that must be considered to characterize risk.

LOAD-TOLERANCE AND CTDS

The physical requirements of a lifting task, psychosocial pressures of work, as well as individual factors have all been implicated in the causality of LBDs [2]. Hence all of these risk dimensions should have some influence on cumulative trauma of the low back. If we accept the premise that all risk of LBD is related to a load-tolerance imbalance within the tissues of the trunk then we can begin to formulate how these various dimensions of risk might influence cumulative trauma. The concept of load–tolerance suggests that cumulative trauma may influence this relationship in several ways. Tolerance levels can be exceeded by: 1) increases in the applied load on a tissue; 2) decreases in the tolerance over time; or 3) a combination of both mechanisms occurring simultaneously.

LOAD DETERMINATION

The literature suggests that there may be several mechanisms responsible for increased tissue loading as a result of cumulative trauma. Recent literature indicates that a common link between the various risk dimensions (physical loading, psychosocial factors, and individual factors) involves increases in trunk muscle coactivation. We have known for some time that changes in the physical requirements of work can influence spine loading. However, we must understand how the temporal aspects of exposure to repeated trauma might affect this loading. For example, repeated exertions have demonstrated that the nature of spine loading changes from compressive loading to shear loading [3]. In addition, factors such as task experience, personality, psychosocial stress, mental concentration, and age can all influence how the muscles are recruited and subsequently affect spine tissue loading. We must begin to understand how the quantifiable components of these various dimensions can interact and increase loading of the spinal structures in 3-D space.

TOLERANCE SPECIFICATION

In a similar manner, these same risk factors can affect tolerance of the spinal tissue. It has been well established that individual factors such as age, gender, and conditioning can influence the tolerance of spinal tissues [4]. We also know that tolerances are diminished with greater frequency of exposure [5]. Recent work by the McGill group has also shown how the combination of spine position and frequency is an important component of spine tolerance [6]. Here again, it is well established that the better we can quantify these parameters the better we can understand and quantify the risk dimension.

ADAPTATION

One characteristic that makes the quantification of risk particularly challenging is our poor understanding of adaptation. We must begin to understand how components of these risk dimensions influence our ability to strengthen or weaken tissue due to exposure and rest cycles. Human adaptation may influence either the loading or tolerance. .

CONCLUSION

In summary, we must begin to precisely quantify the influence of physical work requirements, psychosocial influences, and individual factors upon both the loading of the spinal tissue and the tolerance of these tissues if we are to develop meaningful metrics of risk. These metrics will be truly useful if they are able to determine how much exposure to work is too much exposure given individual characteristics and the multidimensional work environment. The real challenge in this endeavor is to account for the dynamic nature of the exposure and the individual's ability to adapt to stress.

REFERENCES

1. Marras, W.S., et al., (1999) *Ergonomics*, **42**(1): 229-45.
2. (NRC), N.R.C., (2001) *Muscusloskeletal disorders and the workplace: low back and upper extremity*. National Academy Press.
3. Marras, W.S., Granata, K.P. (1997) *Spine*, 1997. **22**(21) 2564-70.
4. Jager, M., A. et. al. (1991) *Int J Indust Ergo,* **8**: 261-77.
5. Brinkmann, P., et al.(1988) *Clin Biomech* 1988. **3,** S1-S23.
6. Callaghan, J., McGill, S. (2001) *Clin Biomeh*, **16**(1), 28-37.

LOCOMOTION RESEARCH WITHIN AN ORTHOPAEDICS FRAMEWORK: SUCCESSES AND CHALLENGES

Janet Ronsky, Barbara Loitz-Ramage, Carol Scovil, Anne Gildenhuys, Jessica Maurer, Craig Good, and Ron Zernicke
Mechanical & Manufacturing Engineering, Human Performance Laboratory, McCaig Centre for Joint Injury and Arthritis Research, University of Calgary, Calgary, AL, Canada, jlronsky@ucalgary.ca

INTRODUCTION

A person's locomotion forms a distinct signature that can be recognized qualitatively by a trained observer, but a quantitative description that captures the continuous nature of that locomotion and enables inter-subject comparisons and evaluation of interventions remains a significant challenge . Human locomotion studies have investigated normal gait and elucidated cause-effect relations leading to abnormal gait. Increasingly, gait and locomotor function assessments are being incorporated into orthopaedic diagnoses, treatment planning and evaluations. While we acquire vast quantities of data, questions remain whether the appropriate advantages and insights are being gained for the purpose of influencing orthopaedic decisions and functional outcomes.

ADVANCES

During the past few decades, key advances have enabled new research questions to be tackled, and new linkages to be forged between locomotion analyses and clinically oriented orthopaedic questions. Technical improvements in hardware associated with acquisition of kinematic, kinetic, strength, and muscle activation patterns have enabled simultaneous collection of signals related to external loading, 3D movement, and muscle activation, with recent improvements enabling more accurate analyses in real time. Computers and software advances facilitate rapid data processing and analysis, with user-friendly interfaces that broaden the range of potential users. Increased data storage capacities and computational speed have enabled analysis of larger sample sizes in reasonable cost and time. More advanced statistical approaches have enabled more sophisticated data analyses and identification of key factors relating gait characteristics to an orthopaedic condition (e.g., Deluzio et al., 1997). Computational advances have also led to the development of complex numerical simulations of 2D (e.g., Pandy and Berme, 1988; Piazza and Delp, 1996)and 3D gait simulations (e.g., Scovil et al., 1999). Locomotion studies with animal injury models have also been used successfully by our group (e.g., Frank et al., 2002) and others to investigate relations among joint injury, joint mechanics alterations, and development of degenerative joint disease.

ACCOMPLISHMENTS

Pioneering work with cerebral palsy treatment planning and evaluation (e.g., Gage et al., 1984) assisted in establishing the role of gait analysis in orthopaedics. Successes in providing objective treatment planning and evaluation of outcome in that patient population prompted the widespread development of clinical gait laboratories. Integrated approaches to assessment of joint health and functional status using multiple imaging modalities and dynamic methods are providing promising new insights. Andriacchi and coworkers (e.g., Hurwitz et al., 2002) have reported numerous insights by examining key relations between static alignment, radiological measures of joint degeneration, pain scales, and measures of dynamic function to identify linkages with predictors of dynamic joint function (e.g., knee adduction moment). In a population with tibial rotational malunion, we recently applied similar approaches to identify dynamic variables (ankle eversion moments, hip vs. knee moment) that provide the best indicator of interlimb tibial rotation (Ronsky et al., 2000). Despite these accomplishments, however, clinicians, biomechanists, and orthopaedic specialists continue to have difficulty achieving consensus on interpretation and utility of gait analysis data.

CHALLENGES AND DIRECTIONS

Key challenges related to current movement analysis approaches stem from the fundamental simplifying assumptions associated with representing the complex biological system with a rigid body dynamics model. All such biomechanical models rely on the choice of appropriate geometries and properties for elements of the musculoskeletal system in healthy and clinical populations. Determining these values is currently a barrier to the effective use of locomotion measurements for orthopaedics. Other barriers include person-specific geometry, funding for clinical studies, validation of numerical simulations of locomotion, and appropriate tracking and evaluation of outcome measures. Current and future research that will enable locomotion studies to play a more effective and central role in orthopaedic treatment planning and evaluation must be focused on: 1) techniques for person-specific multi-modal imaging, integration and fusion of anatomical data (obtained with medical imaging) under functional loading, 2) improved technical and computational techniques for representing bony segmental motion based on non-invasive external markers, and 3) standardized, clinically relevant outcome measures.

REFERENCES

Deluzio, K.J. et al. (1997). *Human Mov. Sci.*, **16**, 201-217.
Frank,C. et al., (2002) *Trans. 48th. ORS meeting*, 665.
Gage, J. et al., (1984) *J. Ped. Orthop.* **4(6)**, 715-725.
Hurwitz, D.E. et al. (2002) *J. Orthop. Res.* **20**, 101-107.
Pandy, MG., Berme, N. (1988). *J.Biomech.,* **21**, 1053-1060.
Piazza, S.J., Delp, S.L. (1996). *J.Biomech.,* **29**, 723-733.
Ronsky, J.L. et al. (2000) *Proc. 34th CORS meeting,* 57.
Scovil, C. et al. (1999). *Proc. XVIIth ISB Congress*, 575.

ACKNOWLEDGEMENTS

Financial: NSERC, CRCP, GEOIDE NCE, CHR.

NEURAL CONTROL OF LOCOMOTION: PRESENT KNOWLEDGE & FUTURE DIRECTIONS

Jaynie F. Yang

Department of Physical Therapy and University Centre for Neuroscience
University of Alberta, Edmonton, AB, Canada, T6G 2G4, jaynie.yang@ualberta.ca

INTRODUCTION

Locomotor movements performed by all animals are graceful, rhythmic, efficient and adaptable. Evolution has perfected these movements that are essential for survival. Much progress has been made to understand how the nervous system produces these movements. Much also remains to be done. In this abstract, I will focus on the main principles that have emerged from this body of work. Emphasis will be placed on the generation of rhythmic movements. Equilibrium and goal-directed aspects of locomotion will not be considered here.

PATTERN GENERATORS

The rhythmic movements of locomotion are produced by a group of interneurons, called the pattern generator. The pattern generator requires only tonic excitation to operate. Patterned input is unnecessary.

The design and operation of pattern generators for locomotion have been explicitly shown in invertebrates and lower vertebrates. Key elements in the pattern generator, their intrinsic and network properties important for the production of the behaviour are known (Marder & Calabrese 1996). In mammals up to lower primates, the existence of these generators have been confirmed (Grillner 1981). Elements in the generator, however, remain to be identified. Evidence from the last few years have provided strong support for the existence of these generators in the human. One of the challenges for the future will be the identification of key elements in the pattern generator for mammals, and their working principles.

ROLE OF SENSORY INPUT

The output of the pattern generator is strongly molded by sensory and descending input in the intact animal. Indeed, the output patterns of the generator in isolation are never identical to that in the intact animal. The ability of the pattern generator to adapt on a moment-to-moment basis to changes in the environment is essential for the animal to navigate through changing environments.

Considerable progress has been made in understanding the role of peripheral sensors in locomotion, for both simple and complex animals (Rossignol 1996). Sensory input contributes to the timing, amplitude and dynamics of motoneuron activity. Sensory input can initiate or terminate locomotion. Phase transitions in locomotion (such as transition from the stance to the swing phase in walking) are controlled by sensory input. Interestingly, in animals as diverse as insects to humans, similar sensory inputs are used for controlling phase transitions (Prochazka 1996).

ADAPTABILITY OF THE PATTERN GENERATOR

Pattern generators are not dedicated for one type of movement. In both invertebrates and lower vertebrates, elements in pattern generators can be reconfigured to produce different motor behaviours. These reconfigurations can be brought about by descending input and their neuromodulators, or by specific types of sensory input (Marder 2000). Indirect evidence supports a similar type of flexibility in mammalian pattern generators for different forms of walking in the cat, and for different directions of stepping in the human infant.

Pattern generators also adapt to sustained changes in the nervous system, such as occurs with maturation, injury or disease. After either central or peripheral lesions in the nervous system, the remaining system adapts to allow locomotion to continue. For example, after peripheral lesion to a muscle nerve, the synergistic muscle and the strength of its afferents change to allow functional compensation. These changes are dependent on use of the neural pathways (Pearson et al. 1999). Similarly, after spinal cord transaction, locomotor training can partially restore this function in a variety of mammals (Rossignol 2000).

FUTURE DIRECTIONS

What does the mammalian pattern generator look like? How does it operate? What aspects can we manipulate, particularly after injury? Which neurotransmitters alter its function? How can it be altered with use? These are all questions for the future. Although much remains to be done, our current knowledge has already led to the development of new treatment strategies for individuals with injury to the nervous system (Barbeau et al. 1998). Exciting developments are likely in the near future.

REFERENCES

Barbeau et al. (1998) Neuroscientist 4:14-24
Grillner (1981) Handbook of Physiology, Sec 1, pp.1179-1236
Marder (2000) Curr Opin Neurobiol 10:691-698
Marder & Calabrese (1996) Physiol Rev 76:687-717
Pearson et al. (1999) J Neurophysiol 82:370-381
Prochazka (1996) Handbook of Physiology, Sec 12, Rowell & Sheperd (eds), Am Physiol Soc, pp.89-127
Rossignol (1996) Handbook of Physiology, Sec 12, Am Physiol Soc, pp.173-216
Rossignol (2000) Curr Opin Neurobiol 10:708-716

LOCOMOTOR RESEARCH: PRESENT STATE AND FUTURE DIRECTIONS FOR REHABILITATION

Sandra J. Olney
School of Rehabilitation Therapy and Human Mobility Research Group
Queen's University, Kingston, ON, Canada, K7L 3N6, olneys@post.queensu.ca

INTRODUCTION

Research in locomotion is relevant to the field of rehabilitation to the degree that it can assist with the rehabilitation process. There are four primary ways in which the rehabilitation process can use information about locomotion in normal and pathological conditions: to provide a basic understanding of locomotion; to assist in movement diagnosis; to inform treatment selection, and to evaluate effectiveness of treatments. In each of these categories we can consider the information as being applied either to a group of people with similar conditions, or to individual patients. In each circumstance we can also consider whether locomotion analysis techniques or simpler clinical methods, including observation, are being used. The purpose of this presentation is to evaluate the present state and future direction of research in locomotion in rehabilitation.

BASIC UNDERSTANDING

From Muybridge, through Eberhart and Inman, Perry, Gage, Winter, Andriacchi, and so many more, each has contributed uniquely to this body of knowledge, with the need for knowledge inseparably linked to the introduction of new methods and technology. Basic understanding also includes evaluating the change naturally occurring over time, such as the recovery of persons with stroke (Richards, 1996). From a rehabilitation perspective, information related to kinetics, which can be influenced by therapeutic methods, has provided more useful information than spatio-temporal or kinematic methods. A number of investigators have made landmark contributions by establishing methodologies for understanding locomotion in cerebral palsy, stroke and other specific pathologies. Methodologies are frequently condition-specific.

Future directions for providing basic understanding include relating biomechanical measures to other performance measures such as metabolic analyses.

ASSIST MOVEMENT DIAGNOSIS

Two approaches are used: direct application of gait analysis, usually including kinematic, kinetic and frequently EMG data, with interpretation of findings by a skilled team, and indirect application, using visual observational analysis sometimes assisted by simple aids.

Important future directions for locomotor research to assist movement diagnosis include development of less complex methods of analysis.

INFORM TREATMENT SELECTION

Research in locomotion has made many contributions that can inform selection of treatment. One area that has made a very large contribution is the use of power analyses in identification of compensations and adaptations in pathological conditions (Winter et al., 1990).

Some important future directions of research to inform treatment selection are the development of clinically applicable analytic methods; routine use of power analysis for treatment of cerebral palsy and stroke and computer modeling to predict the results of training interventions.

EVALUATE EFFECTIVENESS OF TREATMENT

To effectively determine difference in treatments, it is important to have methods that are as precise as possible, and recent technical and procedural innovations have facilitated this. Included here are improved methods of determining joint centers and methods of minimizing the effects of skin motion artifact (Andriacchi, 1998). This capacity has been well used by researchers in rehabilitation, and well worth the expense involved.

Important future directions to aid evaluation of effectiveness of treatment include further advances in accuracy of motion analysis techniques, use of combinations of performance measures with locomotor analyses and general use of investigations of locomotion on sloped, rough, and other natural surfaces and on stairs.

CONCLUSION

Analysis of locomotion has provided powerful methods to analyze locomotion, assist in diagnosis, inform treatment and evaluate effectiveness of treatment, but is limited in application in all of these ways. Future research that targets these applications will assist in solving locomotor problems in rehabilitation.

REFERENCES

Richards, C., Olney, S.J. (1996). *Gait and Posture* **4,** 149-162.
Winter, D.A., et al. (1990) *in Multiple Muscle Systems*: Winters and Woo (eds), Springer-Verlag
Andriacchi et al (1998). *J Biomechanical Engineering,* **120**, 743-749.

THE USE OF ROBOTS IN BIOMECHANICS – FUTURE DIRECTIONS

Savio L-Y. Woo, Ph.D., D.Sc., Richard E. Debski, Ph.D., Zong-Ming Li, Ph.D.
Musculoskeletal Research Center, Department of Orthopaedic Surgery, University of Pittsburgh
P.O. Box 71199, Pittsburgh PA, 15213, 412-687-5913 Email: decenzod@msx.upmc.edu Web: http://www.pitt.edu/~msrc

INTRODUCTION

Knee and shoulder joint injury frequently occurs through different forms of activity. However, in order for physicians to properly treat the injuries to the structures in the joint, knowledge of joint mechanics and specific function of the ligaments are needed in order to understand injury mechanisms, improve surgical procedures and design better post-surgical rehabilitation protocols.

THE ROBOTIC/UFS TESTING SYSTEM

A robotic/universal force-moment sensor (UFS) testing system was developed in order to examine joint kinematics in multiple degree-of-freedom (DOF) and the *in situ* forces in normal ligaments as well as the distribution of these forces in a non-contact manner. A major advantage of the robotic/UFS testing system is the ability to determine and repeat the paths of motion. When operated in the force control mode, the testing system applies a known load to the intact joint while the motion and force data are recorded. After transection of a ligament, the system is used in position control mode and the recorded motion for the intact joint is repeated while new force and moment data is recorded by the UFS. Since the robot reproduces the identical initial position as well as path of joint motion before and after a ligament is transected, the *in situ* force in the ligament is indeed the difference in the two sets of force and moment data measured by the UFS. Additionally, changes in kinematics can be measured when a known force is applied to the intact knee while the kinematics are recorded. After transection of a ligament, the same force is applied while the kinematics are again recorded. Testing in this mode is similar to the clinical examination in diagnosing ligament injury or deficiency. Also, the procedure can be extended to examine those for the replacement grafts by using the same specimen, so as to limit the inherent specimen-to-specimen variation.

Using this system, the distribution of *in situ* forces in the anterior cruciate ligament (ACL) as well as the effects of axial compression, quadriceps and hamstring co-contraction and rotatory loads on *in situ* forces in the ACL can be determined. In addition, variables of ACL reconstruction such as location of graft fixation, type of graft, and type of reconstruction are also examined. Similar studies have been performed in the posterior cruciate ligament and shoulder.

3D FINITE ELEMENT MODEL

Currently, a three-dimensional finite element model has been constructed based on serial CT/MRI scans of a knee specimen. The same specimen was tested on the robotic/UFS testing system and the *in situ* forces in the ACL in response to an anterior tibial load were determined. Based on the same anterior tibial load, the model was used to calculate these forces and the values matched well with those from the experiment. Thus, this model was validated and is now being used for predicting knee joint behavior under other external loading conditions. This combined experimental and computational approach has also been used for the shoulder, forearm, and spine.

IN VIVO APPLICATION

Future developments will focus on *in vivo* applications. Input data will be collected during gait analysis or throwing activities using the point cluster technique in order to yield accurate kinematic data. The robotic/UFS testing system can be programmed to reproduce these joint kinematics on young human cadaveric specimens in order to generate a database for *in situ* forces in the ligaments, or ligament replacements grafts. With appropriate computational models, the stresses and strains in these tissues *in vivo* can also be predicted for more complex loading conditions such as sports activity or rehabilitation. Potential application of this combined approach includes pre-operative surgical planning, improvement of surgical procedures as well as development of appropriate post-operative rehabilitation protocols. (**Fig 1**)

FUTURE DIRECTIONS

In the future, it is hoped that we can use this technique to study injury mechanisms, as well as examine the validity of arthrometers and other instruments. However, greater emphasis will also need to be placed in research on rehabilitation and neuromuscular training. The ultimate goal of this strategy is to improve patient outcomes following ligament reconstructions.

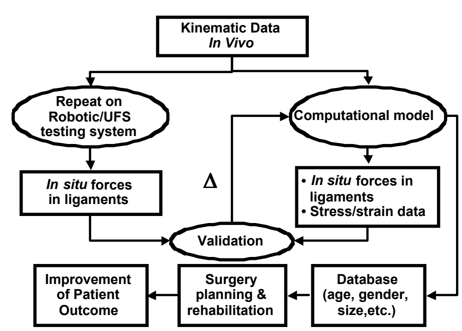

Figure 1: Flow chart describing future directions

DYNAMIC, IN-VIVO FUNCTION OF HEALTHY, ACL-DEFICIENT AND ACL-RECONSTRUCTED KNEES: NEW INSIGHTS USING HIGH FRAME–RATE STEREO–RADIOGRAPHY

Scott Tashman and William Anderst
Bone & Joint Center, Henry Ford Hospital, Detroit MI USA, tashman@bjc.hfh.edu

INTRODUCTION

Accurate in-vivo assessment of skeletal kinematics is essential for understanding normal and pathological joint function. We have developed techniques combining kinematics from high frame-rate stereo-radiography with bone geometry from static CT for precise assessment of in-vivo joint behavior.

We are applying these techniques to the study of ACL insufficiency and reconstruction. Preliminary results from an ongoing study of ACL-deficient human subjects indicate that significant dynamic abnormalities may persist even after ligament reconstruction. Parallel studies with an ACL-deficient canine model suggest that these abnormalities may be related to the increased risk of osteoarthritis associated with ACL loss and reconstruction.

METHODS

Kinematic data is collected using a unique biplane radiographic system. A minimum of three radiopaque markers are implanted into each bone to be tracked. Stereo pairs of radiographs are acquired during movement at up to 1000 frames/s, using synchronized high-speed video cameras coupled to 30cm image intensifiers. 3D coordinates of the markers are reconstructed using a modified DLT method, with

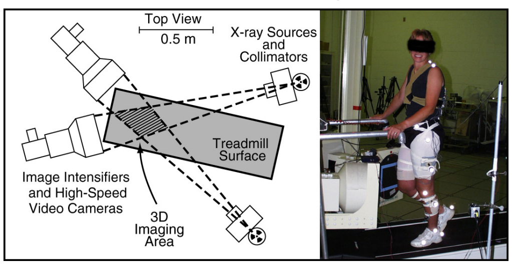

Biplane X-ray configuration for human running trials.

3D tracking accuracy of ±0.1mm.

To interpret this data in an anatomically relevant context, high-resolution knee CT scans are acquired after marker implantation. Bone surface geometry is determined, and related to the coordinates of the implanted markers. Thus, the anatomical motion of the joint surfaces can be completely reconstructed from the dynamic stereo-radiographic data.

For the human study, three 1.6mm tantalum spheres were implanted into the distal femur and proximal tibia of the both the ACL-deficient and uninjured limbs of subjects undergoing ACL reconstruction. Kinematic data was acquired at 250 frames/s during the impact phases of downhill running (2.5 m/s) and forward one–legged hopping. 3D knee kinematics were determined for both limbs and compared. For the canine study, markers were implanted in the right hindlimbs of 23 female foxhounds. Kinematic data was acquired during treadmill gait before and serially for 2 years after ACL transection. Joint condition was assessed visually at the conclusion of the study, and related to knee kinematics.

RESULTS AND DISCUSSION

For the human studies, anterior tibial translation curves were similar for intact and reconstructed limbs. No significant differences were found during running or hopping. Though internal/external tibial rotation plots were also grossly similar in appearance between intact and reconstructed limbs, the reconstructed curves were shifted towards external rotation. The effect was greater during hopping than running (see figure below), but all differences were significant (paired t, $p<0.05$) except for run min. This shift towards external rotation suggests that common reconstruction techniques may fail to restore normal rotational motion, leading to altered interactions of the articulating joint surfaces.

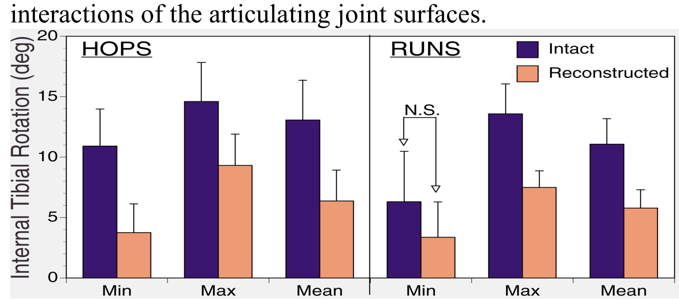

Though the long term effects of these abnormal motion patterns are not known, they could have important implications for long-term joint health. Our canine studies have shown that there are distinct patterns of abnormal joint motion after ACL loss that are predictive of rapid cartilage degeneration. With the combined dynamic X-ray/CT method, we are able to estimate the path of joint contact (see figure below); the average velocity of the contact point on the medial femoral condyle 2 months after ACL loss is highly correlated ($r^2=0.81$) with femoral cartilage damage at 2 years.

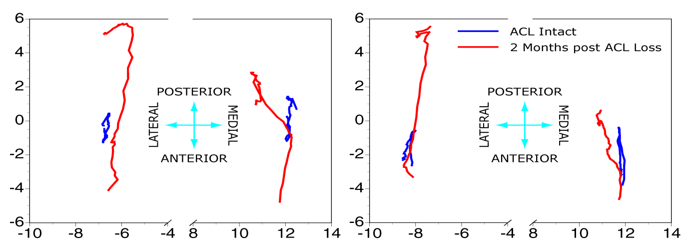

Estimated femoral contact point paths for 2 ACL-deficient dogs. Note differences in medial path length. Two years later, dog on left had full-thickness cartilage loss; dog on right had healthy femoral cartilage.

Our preliminary results suggest that these techniques have great potential for identifying mechanical factors responsible for increased risk of joint disease after ACL injury. This may assist in the development of improved treatments and better long–term outcome.

ACKNOWLEDGEMENTS

Funded in part by NIH grants AR46387 & AR43860.

BIOMECHANICS OF KNEE REPLACEMENT – FROM IN VITRO TO IN VIVO

A.B. Zavatsky[1,3], A.J. Price[2], H.S. Gill[2], P.T. Oppold[1], T. Ward[1], D.W. Murray[2], and J.J. O'Connor[1]
[1]Department of Engineering Science, University of Oxford, Oxford, UK [2]Nuffield Department of Orthopaedic Surgery, University of Oxford, Oxford, UK [3]Email: amy.zavatsky@eng.ox.ac.uk, Web: www.eng.ox.ac.uk/~kneabz/

INTRODUCTION

Knee replacement is now a highly successful operation, with the clinical survivorship of some devices reported to be greater than 96% at 7–10 years (Biomet, 2002). However, complications such as infection, wear, loosening, and patellar instability and pain do occur, particularly in younger patients.

Over the years, we have completed a number of in vitro experiments and theoretical modelling studies of both the intact and replaced knee joint (e.g. Gill and O'Connor, 1996; Feikes et al., 2000; Lu et al., 1998; Miller et al., 1998; O'Connor et al., 1990; Wilson et al., 1998; Wilson et al., 2000; Zavatsky et al., 1999). These studies have shown a relationship between the geometry of the knee ligaments and articular surfaces and passive knee kinematics. They have also highlighted the importance of retaining the cruciate ligaments in medial uni-compartmental knee arthroplasty.

In addition, we have found that some total knee replacements which are very successful clinically have abnormal kinematics when compared to intact knees in vitro (Miller et al., 1998; Zavatsky et al., 1999). This result is a puzzling one, given that the abnormal in vitro kinematics might be expected to translate into serious clinical problems after implantation in vivo. In vitro studies are, of course, limited in that only simple activities using a small number of muscles can be simulated, and resultant joint forces tend to be low compared to those in vivo. Nevertheless, they provide a controlled environment in which specific hypotheses about knee mechanics can be tested. A full picture of knee replacement biomechanics requires an understanding of experimental results both in vitro and in vivo and an explanation of how such data relates to clinical outcomes.

In our present work, we are addressing the problem of patellofemoral complications in total knee replacement by performing studies both in vitro and in vivo. We will be using theoretical models of the knee joint to help us understand the relationship between the two sets of results. At the same time, we will be looking more carefully at relevant clinical outcomes, such as patient satisfaction, mobility, and pain.

METHODS

We have measured simultaneously the tibiofemoral kinematics and patellofemoral kinematics and forces in a supine leg-extension rig in fifteen post-mortem knee specimens both before and after knee arthroplasty (Oppold, 2000). The motions of the patella, tibia, and femur were measured using a five-camera Vicon 370 (Vicon Motion Systems, Oxford, UK). The simulated quadriceps force was measured with a uniaxial tension transducer, and a custom-built six degree-of-freedom force transducer, based closely on the design of Singerman et al. (1994) was used to measure the three forces and three moments acting upon the posterior surface of the patella.

We are using sagittal plane fluoroscopy and image analysis to study knee replacement motion in vivo. So far, a number of patients have been tested in supine leg-extension, and we are currently developing a protocol for stair climbing. A force plate is being incorporated into the step, so that an inverse dynamics type model (Gill and O'Connor, 1996; Lu et al., 1998) can be used to calculate the forces and moments at the knee joint. A software tool is being developed which will fit CAD models to the fluoroscopy images for a more accurate determination of the joint position in vivo. A motion analysis system will be used in conjunction with the fluoroscopy to provide information about any out-of-plane motions.

RESULTS AND DISCUSSION

The in vitro results show that the total knee replacement caused an increase in tibiofemoral adduction and decreases in tibial rotation and patellar tendon angle relative to the intact knee. A sharp change in patellar flexion occurred near 60° tibiofemoral flexion, along with a sharp increase of nearly 100 N in the quadriceps force. Fluoroscopy results on five patients with total knee replacements also show an abnormal patellar tendon angle. The theoretical modelling of the knee joint associated with this experimental work is in progress.

REFERENCES

Biomet Inc. (2002)- www.biomet.com/orthoupdates/
Feikes, J.D. et al. (2000) *Proc 12th Conf ESB*: 195.
Gill, H.S. and O'Connor, J.J. (1996) *Clin Biomech* **11**: 81-89.
Lu T.W. et al. (1998) *J Biomechanics* **31(1)**: 63-69.
Miller, R.K. et al. (1998) *J Bone Jt Surg [Br]* **80(B)**:900-906.
O'Connor, J.J. et al. (1990) *Knee Ligaments*. Raven Press.
Oppold, P.T. (2000) M.Sc. thesis, University of Oxford.
Singerman R. et al. (1994) *J Biomechanics* 27: 233-238.
Wilson, D.R. et al. (1998) *J Biomechanics* **31(12)**:1127-1136.
Wilson, D.R. et al. (2000) *J Biomechanics* **33(4)**: 465-473.
Zavatsky, A.B. et al. (1999) *Proc Intl Conf on Knee Replacement 1974-2024* (IMechE, London): 230-233.

ACKNOWLEDGEMENTS

Much of this work was funded in part by Biomet, Inc.

BIOMECHANICAL SIMULATION OF FRACTURE HEALING

Patrick Prendergast and Damien Lacroix

Bioengineering Group, Department of Mechanical Engineering, Trinity College, Dublin 2, Ireland. pprender@tcd.ie

INTRODUCTION

To better understand the influence of mechanical loading on the differentiation of tissues in the fracture callus, finite element modelling has been used to determine the spatial variation of biophysical stimuli and correlate it with tissue phenotype; e.g. Carter et al (1989) and Claes et al (1994) However, no study has yet addressed whether or not (i) the healing process can be simulated using biophysical stimuli as regulators of tissue differentiation and (ii) the healing process can be simulated in realistic 3D fractures.

The hypothesis to be investigated in this paper is that fracture healing can be simulated over time in three-dimensional model of a fractured tibia using the biphasic mechano-regulation rule presented in Prendergast et al (1997). If this would be true then it opens the possibility of using such biomechanical analyses to assess the possibilities of using finite element models to pre-operatively predict the best fixation treatments for healing of a patient's fracture.

METHODS

The concept of biphasic mechano-regulation is that both solid phase and fluid phases may contribute to stimulation of mesenchymal stem cells (MSCs)– high values of these stimuli cause the cells to differentiate into fibroblasts forming fibrous connective tissue, intermediate values stimulates chondrocytes and cartilage, and low values stimulate osteoblast differentiation and therefore bone formation. Depending on the combination of these two stimuli, differentiation of the MSCs is then determined.

A finite element model was used to represent a bone fracture. The model was constructed based on a CT scan of a composite tibia. An external fixator was used to fixate the fracture, as shown in Fig. 1. The properties of the callus was specified as "granulation tissue" at the beginning and an iterative procedure was used to change the properties of the callus according to the combination of biophysical stimuli in each element.

RESULTS AND DISCUSSION

Richardson et al (1994) proposed that sagittal plane bending could be used as a measure of the success of fracture healing. For that reason, the sagittal plane bending stiffness (in Nm/deg) was calculated during the simulation. The simulation was carried out with under two different loading magnitudes: 300 N and 500 N, see Fig. 2. In addition, the simulations predict the change in tissues appearing and disappearing in the external callus and the fracture gap during healing.

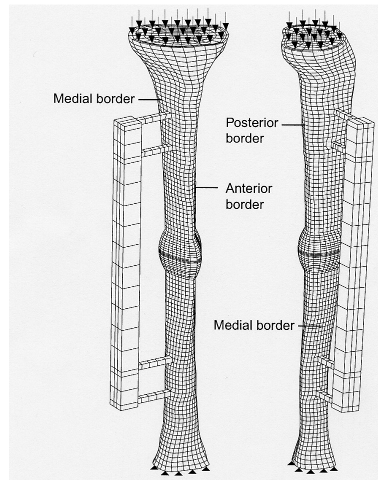

Fig. 1: 3D FEM of the fractured tibia with external fixation.

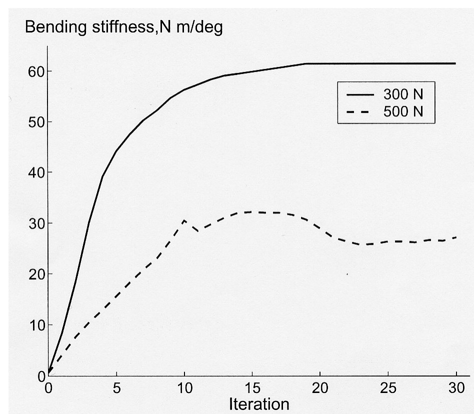

Fig 2: Predicted change in bending stiffness under loading of 300 N and 500 N.

SUMMARY

In conclusion, fracture healing can be simulated using tissue strain and interstitial fluid flow as mechano-regulatory variables. 3D models of real fractures can be generated, and these can predict the influence of loading magnitude. This makes the use such computer simulations a clinical possibility.

REFERENCES

Carter, D.R., et al (1998). *Clin. Orthop.,* **355S**, S41-S55
Claes, L.E, Heigele, C.A., (1999). *J. Biomech,.* **32**, 255-266
Prendergast, P.J., et al (1997) *J. Biomech.* **30**, 539-548
Richardson, J.B., et al (1994). *J.B.J.S.* **76B**, 389-394

MONITORING OF THE REHABILITATION OF PATIENTS AFTER FRACTURE

Franz Burny[1], Wivine Burny[1], Monique Donkerwolcke[1], Francoise Moulart[1], Robert Puers[2], Michael Catrysse[2], Koenrad Van Schuylenbergh[2], Markus Behrens[3], Randy Kauten[3], Jacques Mata[3]

[1] Cliniques Universitaires de Bruxelles, Hôpital Erasme, Brussels, Belgium, fburny@ulb.ac.be
[2]ESAT-MICAS, K.U.Leuven, Leuven, Belgium
[3] Styker Trauma, Plan Les Ouates, Geneva, Switzerland

THE MONITORING CONCEPT

Transducers to assess locomotion structures are poorly represented in the classification of diagnostic instruments. Mechanical measurements of the locomotion system, however, represent a diagnostic tool. A pioneer work has been done by our group in clinical application of the monitoring of implant deformation as a diagnostic tool (Burny et al., 1993, 2000). We present the results of some twenty-five years of monitoring using "smart implants". In this review abstract we present the two main applications of monitoring in our department. We aim to accelerate the rehabilitation (early weight bearing) while avoiding
the risk of overloading.

METHOD

The monitoring of patient rehabilitation allows avoiding dangerous overloads. For this it is mandatory to know the ultimate mechanical characteristics of the fixation (a plate, an external fixation) and limit values which must never be surpassed during exercise to avoid a failure of the system. The implant deformations are measured with a Wheatstone bridge and the signal is transferred to a personal computer for processing and display via a hard-wired connection (a telemetry system is being implemented).

External fixation monitoring

Figure 1: the concept, external fixation

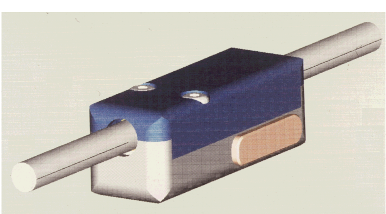

The deformation measurements, throughout the healing process help to quantify the mechanical strength of the callus, an information complementary to the X-ray images. The measurement of the bending and torsion moments at the articulations of a frame fixation is straightforward, once the necessary coefficients are introduced into the system. The dynamic monitoring of the patient rehabilitation is a unique tool to identify hazardous overloads and to anticipate failure during rehabilitation and daily living activities.
The monitoring may also take place after the achievement of a limb lengthening procedure, to control the effectiveness of a distraction osteogenesis.

Conclusion 1:
Early controlled weight bearing, when possible, significantly reduces the healing time (table 1).

Table 1: tibia fracture, retrospective study, and delay of healing

Healing	Monitoring -	Monitoring +
N	75	74
Mean time	180 days	142 days
Variance	4081	1470

$P < 0.001$

Internal implant monitoring

Femoral implants have been instrumented with a "sensing cell" (resistive strain gauges), and carefully calibrated in vitro, before implantation. The fatigue limit is defined for each implant as the half of the signal at the elastic limit. The clinical data already available are presented in table 2.

Table 2: failure of internal fixation, retrospective study
R : regular osteosynthesis
MO : monitoring, measured overloading
MNO : monitoring, no overloading

	R	MO	MNO
N total	618	17	144
N failure	53 (7,9 %)	7 (29,2 %)	3 (2,0 %)

$P < 0.001$

Conclusion 2:
The monitoring of internal implants reduces the rate of failure, when the patient respects the instruction (MNO).

CLINICAL RELEVANCE

Extensive clinical experience has been built up using orthopaedic implants instrumented with strain gauges. This shows the relevance of the monitoring of the deformation of implants to assess nursing and rehabilitation exercises, to identify dangerous overloads and to anticipate implant failure. We consider now combining the results of the mechanical evaluation and of the imaging as a decision making aid.

Burny F., Puers R. (1993). *Monitoring of Orthopedic Implants. A Biomaterials-Microelectronics Challenge.* European Materials Research Society Monographs, Vol. 7. Elsevier Science Pub., Amsterdam.
Burny F., M. Donkerwolcke M., Moulart F., et al. (2000). *Med. Eng. Physics,* **22**: 469-479.

INSTRUMENTATION OF A HEAD FOR THE DETECTION OF LOOSENING BY VIBRATION ANALYSIS

Michael Catrysse[1], Michel De Cooman[1], Robert Puers[1], Siegfried V.N. Jaecques[2], Georges Van der Perre[2], Monique Donkerwolcke[3] and Franz Burny[3]

[1]ESAT-MICAS, K.U.Leuven, Leuven, Belgium, michael.catrysse@esat.kuleuven.ac.be
[2]BMGO, K.U.Leuven, Leuven, Belgium
[3]Service d'Orthopédie-Traumatologie, Hôpital Erasme, ULB, Bruxelles, Belgium

INTRODUCTION

The functional life of orthopedic implants is generally limited to 10-15 years due to aseptic loosening and mechanical failure. Conventional imaging based techniques do not have satisfactory diagnostic sensitivity to detect loosening (Georgiu & Cunningham 2001, Li et al 1995). Therefore, vibration analysis is proposed as a diagnostic method for the monitoring of total hip replacement (THR) loosening.

METHODS

A well-fixed implant and the surrounding bone behave as a linear dynamic system when subjected to a mechanical stimulus. When the implant gets loose, non-linear behavior develops. Loosening is diagnosed by detecting distortion of a sinusoidal excitation signal applied externally to the condyle.
The distorted response is captured by an accelerometer, placed in the THR head. In this way, distortion, introduced by soft tissue between the prosthesis and an externally applied accelerometer are avoided. A telemetry circuit is also implanted, to transmit the measured data to a base unit.
The packaging of this implanted circuit should be biocompatible, hermetic and sufficiently strong and the dimensions minimized (Barbosa et al 1993).

RESULTS AND DISCUSSION

The circuit is placed on hybrid boards inside a Ti can (Figure 1). For telemetric readout, coils are wound around the can, connected to the circuit by feedthroughs in the can. The can is mounted in a cavity of a dedicated ZrO_2 THR head, allowing telemetry and protecting the circuit from mechanical stress. The cavity is filled with Epotek 301.
He leakage tests were performed, according to the MIL-STD-883. 80% of the assembled packages passed the test. The static compression resistance of the heads is higher than the FDA standard (Stryker Howmedica Osteonics 2000). The instrumented head has not been implanted in patients and hence the detection protocol has not been tested yet in a clinical situation. However, on model femora with well-controlled simulated loose stems, it was possible to discriminate between secure, early and late loose stems with an elaborate analysis protocol (Jaecques et al 2001). In a clinical situation, resonance frequency shifts could also be used as an indication of early loosening.

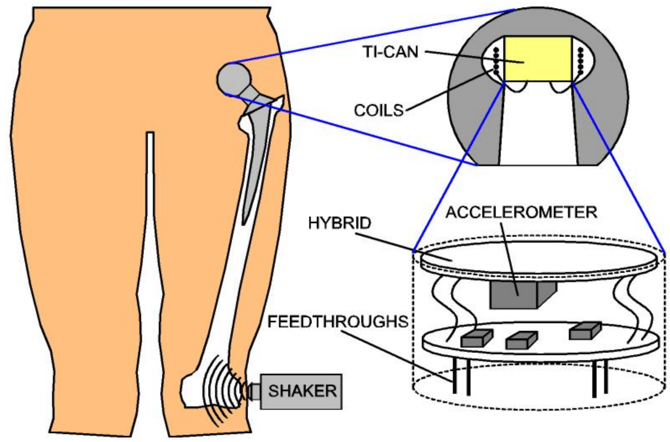

Figure 1: Schematic overview of the instrumented THR

SUMMARY

The presented instrumentation of the THR head fulfils the requirements for implantable systems. The detection method proved to be successful on model femora. Future work will include per-operative testing of the instrumented THR head.

REFERENCES

Georgiu, A.P., Cunningham, J.L. (2001). *Clin. Biomech.*, **16**, 315-323.
Li, P.L.S. et al (1995). *J. Bone Joint. Surg.*, **77**, 640-644.
Barbosa, M.A. et al (1993). In: Burny, F., Puers, R. (eds.). *Monitoring of Orthopedic Implants – A Biomaterials-Microelectronics Challenge*, 222-240.
Stryker Howmedica Osteonics (2000). *Internal Report* No. 441.
Jaecques, S. et al (2001). *Proc. Belgian Day Biomed. Eng.*, in press.

ACKNOWLEDGEMENTS

This research project has been supported by the European Community (BMH4-CT97-2173), K.U.Leuven (COF/97/03 and COF/97/05) and Stryker Howmedica Osteonics.

MONITORING OF FRACTURE HEALING AND IMPLANT INTEGRATION BY VIBRATION AND ULTRASOUND MEASUREMENTS

Georges Van der Perre [1], Arne Borgwardt Christensen [2] and Franz Burny [3]

[1]Division Biomechanics, K.U.Leuven, Belgium Georges.Vanderperre@mech.kuleuven.ac.be
[2] Frederiksberg Hospital, Copenhagen, Denmark
[3] Cliniques Universitaires de Bruxelles, Hôpital Erasme, Brussels, Belgium

BONE CONSOLIDATION

In vivo evaluation of bone consolidation is clinically relevant for the monitoring of fracture healing and assessment of bone consolidation after distraction osteogenesis. In both cases, the evaluation of the effect of BMP's has become of recent interest.

Clinical measurements were made after tibia elongation, and showed interesting correlation between US-velocities measured at different sites within the elongation zone and consolidation time (Lowet 1993). A practical limitation is that tibia measurements can only be taken at the medial face, limiting the relevance of the measurement to that side, while the healing progress could differ over the cross section. On top of that, due to the surgical procedure, a small gap can develop at that site, affecting the precision of determination of the US pathway and hence the velocity. Combining US with Vibration Analysis (VA) could solve those problems, since vibration analysis measures the stiffness of the bone as a whole (hence the whole cross-section).

However, although convincing clinical data on the feasibility of vibration analysis for monitoring of fracture healing were published (Nakatsuchi et al. 1996), skepticism in leading fracture research circles against VA is even stronger than that against US, the leading idea being that the future for bone assessment is in advanced imaging techniques combined with advanced FEM. Apart from the cost of such an approach, the first proof that it can produce a quantitative prediction of bone stiffness or strength remains to be given. In the meantime, ultrasound acoustic imaging (i.e. based upon mechanical properties) has already produced promising clinical results (Moed et al. 1998)

MONITORING OF PROSTHESIS STABILITY

RoentgenStereophotogrammetric Analysis (RSA) is applied to monitor prosthesis migration in clinical studies. Ryd (1992) provided data proving that long-term success or failure of prosthesis can be predicted from migration in an early stage. Hence, it makes sense to use RSA in animal studies and clinical evaluations of prosthesis designs. Routine clinical application of RSA (or rather simplified versions of it) could be justified by the argument that if loosening is predicted in an early stage, it is better to remove the prosthesis before bone damage is caused. Furthermore, it is argued that such a generalized application would contribute significantly to our knowledge on long-term prosthesis behavior.

An alternative to RSA is the so-called "smart" prosthesis, integrating sensor(s) to monitor loosening directly. Such an approach is developed in the STIMULUS project, based upon vibration measurements (Denayer et al, 2000). Two different principle approaches are evaluated. One is based upon the distortion of a sine wave as a result of a non-linear contact between prosthesis and bone. The other is based upon changes in resonant frequencies and damping values, and is similar to the approach used in the monitoring of dental implant fixation (Meredith et al., 1996)

From all these studies, it has become clear that there is a lack of understanding of basic phenomena and mechanisms. What is loosening, or better, which different types of loosening can be distinguished and how can they be identified and detected mechanically? What is the interaction between residual mobility (as measured by vibration analysis), migration (as measured by RSA) and loosening?

REFERENCES

Denayer I, Jaecques S.V.N. et al (2000). Measurement of implant stability and osseointegration: non linearities and resonance frequencies in "Proceedings of the 12th Conference of the European Society of Biomechanics", P. J. Prendergast, T. C. Lee, A. J. Carr, eds., Dublin, 151.

Lowet G. (1993). Vibration and ultrasound wave propagation analysis in long bones, *PHD Thesis*, Katholieke Universiteit Leuven.

Meredith N., Alleyne D. et al (1996). Quantitative determination of the stability of the implant-tissue interface using resonance frequency analysis, *Clin. Oral Impl. Res,* ***7,*** *261-267.*

Moed B.R., Subramanian S. et al (1998). Ultrasound for the early diagnosis of tibial fracture healing after static interlocked nailing without reaming: Clinical results. *Journal of Orthop. Trauma*, **12**, 3, 206-213.

Nakatsuchi Y., Tsuchikane A. et al (1996). Assessment of fracture healing in the tibia using the impulse response method, *Journal of Orthop. Trauma*, **10**,1, 50-62

Ryd L (1992). Roentgen stereophotogrammetric analysis of prosthetic fixation in the hip and knee joint. *Clin Orthop Mar*: **276**, 56-65.

.

MONITORING OF BONE LENGTHENING. AN EXPERIMENTAL STUDY IN SHEEP.

Francisco Forriol
Orthopedic Research Laboratory, Department of Orthopedic Surgery, Clinica Universitaria de Navarra
Facultad de Medicina, Universidad de Navarra, Pamplona, Spain, fforriol@unav.es

AIM OF THE STUDY

The aim is to investigate the mechanical behavior of the lengthening process, and to discern whether any characteristic pattern is followed.

MATERIAL AND METHOD

Four two-to three-month- old sheep, weighting 20-25 Kg, were operated on, by performing a 3cm progressive lengthening of the left tibia. The surgical procedure was performed under general anesthesia. A unilateral external fixator was fitted to the tibia (Monotube-Triax®, Stryker Trauma, Geneva).

Strain gauges were incorporated into the external fixator by replacing a section of the lengthening bar with a sensor consisting of a metal piece instrumented with four strain gauges to form a complete Wheatstone bridge. The 5mm diameter pins were attached to the bone at the proximal and distal metaphysis of the tibia, using an image intensifier. A longitudinal incision 2 cm in length was performed on the lateral side at the middle third of the posterior leg.
Distraction was performed at the same time on six days each week in four sheep that were kept in isolated cages. The lengthening was carried out at a rate of 1 mm/day in one step and the lengthening procedure commenced one week after the operation.

The fixator was connected by means of a cable to a computer (Macintosh IIfx) with an analogical-digital converter for the acquisition and processing of data (Lab View2, National Instruments). This was equipped with an amplifier (San-ei) to pick up the microvolts transmitted through the bar of the fixator every 20 minutes for 24 hours a day, equivalent to 80 readings a day. For each reading, the program performed an average of 500 data points taken in 1 second, then transformed the information into the corresponding value in kilograms. This measurement was carried out without interruption over the lengthening procedure, and always at the same time of the day (10 AM).

The measurement system was checked every day before the lengthening was carried out. When a technical problem was detected, the experiment was stopped. Lengthening procedures performed for less than 3 weeks were not included in the results.

RESULTS

The forces began to increase around day 10, and were clearly higher once the third week after surgery had been reached, that is, after the bone had already been lengthened for a week. The forces continued to rise until day 21, to a value of over 8 Kg (40-50% of the animal's weight).

The force increases each day, rising dramatically after lengthening and then slowly falling until it reaches a value slightly greater than the final force on the previous days. The forces follow a common pattern in every case. The maximum daily force starts to drop one hour after distraction, and continues to decrease gradually throughout the day until it reaches a value slightly greater than the initial force on the previous day; the mean daily force thus increases little by little.

DISCUSSION

The progressive increase obtained is just the result of distracting the muscles and other soft tissues.
In our study, the obtained pattern shows that no differences exist between day and night, because the sheep does not lean on the limb during the lengthening period. This pattern is produced by distraction of the soft tissues, which gradually adapt to their new situation owing to their elasticity, thus reducing the amount of tension.

KEY WORDS
Bone lengthening, external fixator, monitoring

LOADS ON AN INTERNAL SPINAL FIXATOR DURING SITTING

A. Rohlmann, F. Graichen and Georg Bergmann

Biomechanics Laboratory, University Hospital Benjamin Franklin, Free University of Berlin, Germany, rohlmann@biomechanik.de

INTRODUCTION

It is assumed that spinal load in the lumbar region depends on the degree of lordosis and the inclination of the pelvis. Sitting may involve different degrees of lordosis and pelvic inclination. Thus spinal load may depend on the type of seat and the sitting posture. The aims of this study were to measure implant loads in ten patients for sitting on different types of seats and to compare implant loads for sitting erect and relaxed.

MATERIAL AND METHODS

Telemeterized bisegmental internal spinal fixators were used for in vivo measurements of spinal loads (Rohlmann et al., 1994). The inductively powered fixators were implanted in ten patients and allowed the measurement of three force components and three moments. The patients were videotaped during the measurements, and the load-depended signals of the two telemetries were stored on the same videotape. Forces and moments were calculated from the telemetric signals and shown online on a computer monitor.

During a measuring session, patients successively sat on a stool, a chair, an office chair, a bench, a physiotherapy ball, and a knee-stool. While sitting on a stool or chair, the patients were asked to sit relaxed and afterwards to straighten and extend their back. This exercise was repeated during several measuring sessions. Previous studies (Rohlmann et al., 1999, 2000) have shown that the bending moment in the sagittal plane is the most important load component. Thus, only the bending moments in the fixators are compared here.

RESULTS

The type of seats had only a minor effect on bending moments in the fixators. Implant loads differed considerably in some patients when they changed the type of seat. However, a significant difference was only found between sitting on a bench and on a knee-stool with slightly higher values for the latter.

Sitting erect and actively straightening the spine as taught in some back schools increased the bending moment in the fixators by an average of about 11% compared to sitting relaxed (Fig.1). There were marked interindividual differences in load changes.

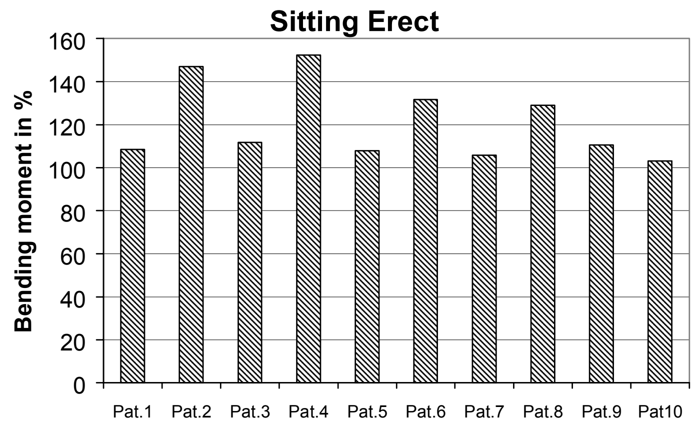

Figure 1: Comparison of normalised fixator bending moments for sitting relaxed (100%) and erect.

DISCUSSION

Loads on internal spinal fixation devices caused by sitting were measured in ten patients. There was marked interindividual variation, partially due to differences in the indication for surgery (compression fracture, degenerative instability) and the surgical procedure performed (compression or distraction of the bridged region) (Rohlmann et al., 1999, 2000). Load differences were negligible for sitting on different types of seats. Intradiscal pressure likewise varied only slightly for sitting on different types of seats (Wilke et al., 1999).

Sitting erect and actively straightening the spine led to higher implant loads than sitting relaxed. Intradiscal pressure was about 10% higher for sitting erect than relaxed (Wilke et al., 1999). Sitting erect requires additional muscle forces which cause higher spinal load and implant loads. The fact that the loads for sitting are lower than for walking and much lower than for lifting a weight (Wilke et al., 1999) argues against the assumption that the higher load for sitting erect is the reason for low back pain, which sometimes occurs during sitting.

ACKNOWLEDGEMENTS

Funding for this study was obtained from the Deutsche Forschungsgemeinschaft (Ro 581/7-2).

REFERENCES

Rohlmann, A. (1994) *J Biomech* **27**, 961-967.
Rohlmann, A. et al. (1999) *Eur Spine J* **8**, 354-359.
Rohlmann, A. et al. (2000) *Spine* **25**, 2981-2986.
Wilke, H.-J. et al (1999) *Spine* **24**, 755-762.

THREE DIMENSIONAL COMPUTER MODELLING OF THE HUMAN ANATOMY

Panayiotis Diamantopoulos[1] , John D. Richardson[2] and Simon Holden[3]

[1] Research Manager, Biomedical Modelling Unit, University of Sussex, Brighton BN1 9QT, UK
P.Diamantopoulos@sussex.ac.uk, www.sussex.ac.uk/Units/biomodel
[2] Lecturer, School of Engineering, University of Sussex, Brighton BN1 9QT, UK
[3] Team Leader - RF Biological Effects, DSTL Chemical and Biological Sciences, Porton Down, Salisbury SP4 OJQ, Wilts, UK

INTRODUCTION

The United Kingdom Ministry of Defence is undertaking a programme of research to address issues raised by long term exposure to low level or novel electromagnetic fields. A key element of this is the development of a computer model of the whole human anatomy to serve as an input to electromagnetic simulation software. Such computer model of the human anatomy would similarly be valuable for the biomechanical analysis of anatomical structures.

METHODS

Magnetic Resonance Imaging (MRI) and Computed Tomography (CT) images of various parts of the human anatomy, including the head, thorax, arms, legs and feet, were utilised as the input data to an image processing software system. The general method used for processing available data included the processing of the images; the identification of anatomical tissues; the extraction of geometrical information; and the interface of the data to an appropriate file format. Parametric and polygonal modelling techniques were investigated.

RESULTS AND DISCUSSION

Most of the anatomical structures and tissues of the human anatomy were successfully processed and modelled. A specific methodology was investigated and satisfactory results were achieved (Fig. 1). Potential difficulties, when dealing with such large-scale modelling, were identified. Those were the image processing time and manual segmentation of medical data; the identification of tissue boundaries and tissue classification; the accuracy requirements of the resulting model; the file format for interfacing the model to a design or analysis code; and the required computer resources.

SUMMARY

The aim of this work has been the processing of medical images regarding the extraction of anatomical geometrical information and the development of a 3D human model.

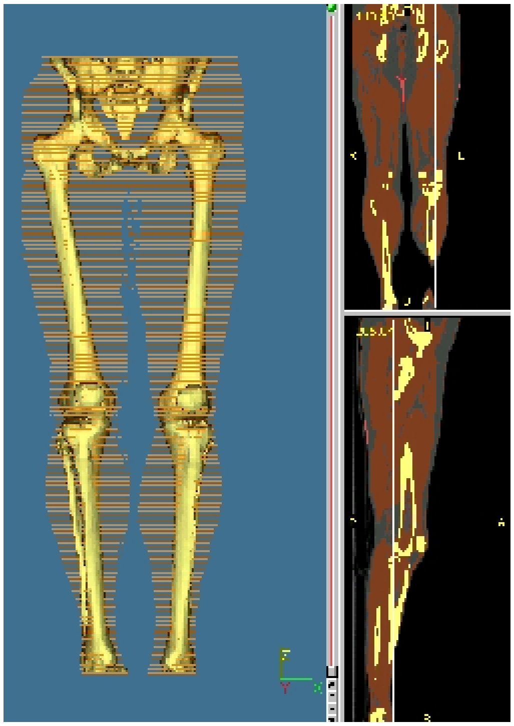

Figure 1: Example of image processing and 3D modelling of the lower body: hard tissues are shown on the left, while identified tissues are depicted on the right.

REFERENCES

Dimbylow, P.J., (1997). FDTD calculations of the whole-body averaged SAR in an anatomically realistic voxel model of the human body. *Phys. Med. Biol.* **42**, 479-490.

Diamantopoulos, P., Richardson, J.D., (2001). Integrating Medical Imaging, FEA, CAD and RP. In: *Computer Methods in Biomechanics and Biomedical Engineering - 3*, Middleton, J., et al. editors, Gordon & Breach Publishers, pp.501-508.

ACKNOWLEDGEMENTS

Surgeon Commander P. Buxton RN of the Royal Hospital Haslar, UK
The work has been supported by the United Kingdom Ministry of Defence

INTEGRITY OF COMPRESSION MOULDED UHMWPE COMPONENTS FOR JOINT REPLACEMENT

J.J Wu[1], C.P Buckley[1], J.J and O'Connor[1,2],
University of Oxford, Department of Engineering Science, Oxford OX1 3PJ, England[1].
Oxford Orthopaedic Engineering Centre, Oxford OX3 7LD, England[2]
Correspondence to: j.oconnor@btconnect.com

INTRODUCTION

Ultra-high molecular weight polyethylene (UHMWPE), formed into a solid by compression moulding, has been in use for approximately three decades in total hip and knee joint replacement prostheses. Generally these perform well, but there is a small and significant failure rate from wear and fatigue. Evidence from retrievals has implicated "fusion defects", remaining in the UHMWPE from the moulding process, as possible initiators of failure. In an attempt to improve understanding of this problem and to develop a viable strategy to overcome it, a systematic study has been carried out of the integrity of a medical grade UHMWPE (Hifax 1900H) following compression-moulding.

EXPERIMENTAL METHODS

As-received powder was moulded at 20Mpa in instrumented, cylindrical, matched-die moulds, with maximum temperatures from 145°C to 200°C, and dwell times at the maximum temperature between 10 minutes and 90 minutes. Constant extension-rate tensile tests at 37°C were performed of specimens manufactured from material at the surface of the moulding and in the centre. Low voltage scanning electron microscopy (SEM) was used to study the specimens before and after elongation to break.

EXPERIMENTAL RESULTS

We identified two distinct forms of fusion defect. Type 1 defects were residual voids observed at the lowest moulding temperatures (up to 165°C) and shortest times. It proved impossible to manufacture tensile specimens from material from the centre of mouldings formed at 145°C.

No voids were found at higher moulding temperatures: mouldings were apparently defect-free, when observed in the SEM as-moulded. Moreover, in tensile tests at 37°C these samples showed highly ductile behaviour, with mean values of elongation to break exceeding 400% for each mould temperature. When the free surfaces were examined in the SEM, from samples after elongation to break, linear surface features were observed on the same length scale as the original particle size (ca 150 μm) where no such features had been observed prior to loading.

These markings were identified as Type 2 fusion defects, where there was incomplete inter-particle molecular diffusion during moulding, leaving compliant particle boundaries rendered visible on machining marks by their relative shearing displacement during the large elongations. The severity of these defects reduced with increase in mould temperature, as evidenced by a peak in elongation to break occurring near 175°C, beyond the point where voids ceased to be visible. The reduction at the highest temperatures was attributed to oxidation revealed by infra-red spectroscopy.

THEORETICAL METHODS

A strategy was devised for quantifying the severity of Type 2 fusion defects, for components of given shape, subject to a given process history. A numerical method was developed to compute the progress of interparticle diffusion, employing a finite element model of heat transfer during moulding, together with results from the theory of polymer self-diffusion by reptation. *Reptation Time* is the diffusion time required for the current conformation of a long-chain molecule to bear no correlation to its initial conformation. It depends on Molecular Weight to the power of 3.4. For a given length of time spent above the melting temperature during temperature rise and dwell and above the recrystallisation temperature during temperature fall, molecules above a certain molecular weight – the Maximum Reptated Molecular Weight (MRMW in g/mol) – will not have fully reptated. The distribution of MRMW was calculated for a variety of surface thermal histories (Rise, Dwell, Fall).

THEORETICAL RESULTS

As an example, we describe the calculated temperature and MRMW distributions in a cylindrical moulding 30mm diameter, 15mm thick, formed from powder of initial viscosity-average molecular weight 4.9 to 5.9 x 10^6 g/mol and melting temperature 141°C. The assumed surface temperature rose from 20°C to 175°C in 25 minutes, followed by a dwell at 175°C for 15 min and a fall to 20°C in a further 28 min, a total processing time of 68 min. The material at the surface started to melt after 12 min, reaching a final MRMW of 2.23 x 10^6. The material at the centre did not start to melt until 21 min, reaching a final MRMW of 1.96 x 10^6. Both values of final MRMW lie far below the initial minimum viscosity molecular weight. Final MRMW increased with dwell time and temperature. Increasing the dwell time to 90 min gave a final MRMW of 3.37 x 10^6 for the surface.

DISCUSSION

Compression moulding requires the polymer powder to be melted and fully compacted under pressure. Full integrity of the solid is then achieved only after the molecules in neighbouring particles have diffused across their interfaces, knitting the particles together and leaving no memory of the interfaces. The shearing movements detected in Type 2 defects after one loading, if repeatedly reversed under oscillatory loading, could lead to the initiation of fatigue cracks and subsequent failure. Our calculations explained the experimental observation of Type 2 defects, by showing that the moulding conditions, although spanning the range thought to be used commercially, were insufficient to allow reptation of the majority of the molecular population. The computational tool has potential in the design of components and process conditions, to achieve specified levels of integrity and MRMW in the UHMWPE components of knee and hip prostheses.

MOLECULAR BIOLOGY OF BIOMATERIAL INCORPORATION WITH BONE

Hannu Aro, Heli Salminen, Taija Helminen and Eero Vuorio

Department of Surgery and Medical Biochemistry/Molecular Biology, University of Turku, Turku, Finland, hannu.aro@utu.fi

INTRODUCTION

Bioactive glasses (BG) are a group of surface-active silica-based synthetic biomaterials which are highly osteoconductive and their surface provides the bonding interface with the bone tissue. The surface reactions of BGs occur very rapidly within minutes and it involves a sequence of reactions - including ionic translocations, allowing an exchange of ions with the physiologic milieu. The process leads to the formation of two reaction layers: an internal silica-rich layer and an exterior biologically active hydroxyapatite layer. The hydroxyapatite phase is equivalent chemically and structurally to the mineral phase in bone and this equivalence is responsible for interfacial bonding. Determination of mRNA levels for specific bone matrix components and their degradation enzymes provides a novel way to accurately determine the bioactivity of the BG materials and to characterize remodeling of the bonded new bone. Using such an approach, this study compared the capacity of bioactive glass and titanium microspheres to serve as a substratum for new bone formation and subsequent remodeling.

METHODS

To create the bone defect 75 female Harlan Sprague Dawley rats (age 15-16 weeks, weight 195-274 g) underwent the following surgical procedure. The proximal metaphyseal areas of both tibias were exposed on the medial side. One hole (Ø 3-mm) and 5 mm distally an other hole (Ø 1-mm) were drilled into the anteromedial cortex of the tibia below the medial collateral ligament. Bone marrow was removed by rinsing with 0.9% saline through both holes. The cortical holes and the marrow cavity were filled with bioactive glass microspheres (Ø 250-300 μm) or titanium microspheres (Ø 250-300 μm) through the Ø 3-mm hole using a pipet. Sodium hyaluronate (Healon® at 10 mg/ml) was used as the carrier for both microspheres. At a random order, one tibia of each animal received bioglass glass microspheres and the contralateral tibia titanium microspheres. The selected bioactive glass composition is an intra-institutional product for research purposes only. The study protocol was approved by institutional animal care committee. Paired comparison of bone healing was performed at 1, 2, 4, 8, and 18 weeks. Ten animals at each time point were used for molecular biologic analyses and five animals for comparative histologic analysis. The bone segment was cut above the Ø 3-mm hole and below the Ø 1-mm hole and immediately frozen in liquid nitrogen. For extraction of total RNA using the guanidinium isothiocyanate method, bone tissue was powderized under liquid nitrogen. This yielded sufficient amounts of material to allow analysis of individual animals and subsequent statistical analysis. The expression of various genes for matrix components (type I, II and X collagens, osteonectin, osteocalcin) and proteolytic enzymes (cathepsin-K, MMP-9, MMP-13) were determined by Northern analysis of the respective mRNAs. The histologic hard-tissue specimens were analyzed for new bone formation using operator-assisted histomorphometry. The bone-biomaterial interface was delineated in DEXA mode with a scanning electron microscope. Means for bioactive glass and titanium microspheres were compared with paired Student´s t-test at each time period.

RESULTS AND DISCUSSION

Histomorphometric analysis showed a significantly increaced formation of new bone in bones filled with bioactive microspheres as compared with those filled with titanium microspheres. Significant differences in total bone-mass per cent of bone marrow became evident already at two weeks and was significant at eight weeks ($p<0.01$). The difference in the amount of neew bone was evident still at eighteen weeks ($p<0.01$).

Significant differences in the mRNA levels for specific bone matrix components became evident at 8 weeks: type I collagen ($p<0.001$) and osteonectin ($p<0.01$) mRNAs were higher in defects filled with BG microspheres than in those filled with titanium microspheres. No expression of cartilage specific collagens (type II and X collagens) were seen in any of the samples. The mRNA levels for cathepsin K demonstrated a significant increase of in BG samples both at 4 weeks ($p<0.05$) and at 8 weeks ($p<0.01$). The MMP-13 mRNA levels tended to be elevated in BG samples throughout the healing period, reaching a statistically significant level at 8 weeks ($p<0.01$). By 18 weeks, the differences between the mRNA levels of the GB and titanium samples became insignificant and approached the control mRNAs levels of intact bone specimens.

SUMMARY

The current study confirms that the cellular activities of biomaterial-bone interfaces can be quantitatively studied at the molecular level. The surface activities of the BG material were shown to significantly enhance the expression of genes coded for bone formation and resorption. The model described here is useful for systematic comparative studies of different bioactive materials as it provides sufficient material for measurement of specific mRNA levels for bone matrix components and proteolytic enzymes in individual samples.

ARE THERE THRESHOLD VALUES FOR SAFE PLANTAR PRESSURES ON NEUROPATHIC FEET?

Peter R. Cavanagh and Jan S. Ulbrecht
The Center for Locomotion Studies, Penn State University
University Park, PA 16802, USA
prc@psu.edu, jsu1@psu.edu

INTRODUCTION

Plantar pressure measurement is becoming a more common part of the evaluation and screening for people with diabetes. Ideally, such screening would identify feet that are "at risk" for tissue injury because of high plantar pressures that are not perceived due to diabetic sensory neuropathy. Unfortunately, such a threshold has not yet been identified. This paper discusses issues involved in the definition of thresholds.

BAREFOOT MEASUREMENT

A number of authors have suggested threshold values to distinguish normal from abnormal feet based on the measurement of barefoot plantar pressures. Boulton et al. (1987) suggested that a value of 1080 kPa on an optical pedobarograph was such a threshold. Veves et al. (1991) used a value of 1207 kPa to make a similar distinction, and found in a prospective study (Veves et al., 1992) that patients who proceeded to ulcerate all had plantar pressures greater than 1108 kPA during walking. The only study that has attempted to define a specific threshold for ulceration is that of Armstrong et al. (1998) who used an EMED SF platform to collect plantar pressures during walking in controls and in patients with a history of ulceration. Peak pressures were significantly higher in patients with a history of ulceration compared to controls (831 ± 247 kPa vs. 627 ± 244 kPa). The optimal cut-off point, which balanced sensitivity and specificity in the data, was 700 kPa. However, this value was only 70% sensitive and 65% specific, leaving the authors to conclude that there was no clear value that could be used in screening to predict ulceration. Rather, the higher the pressure, the greater the risk.

As we have discussed elsewhere (Cavanagh et al., 2001) there are a number of reasons why threshold defined in this manner may differ between investigators. These include different element sizes of different platforms, different thresholds in different parts of the foot, different thresholds depending upon tissue status, variations in shear pressures, and the fact that the duration of loading is usually not accounted for. Duckworth et al. (1985) and Shaw and Boulton (1996) have included loading duration in their analyses.

It is reasonable to ask whether barefoot pressure measurement will ever be able to reliably predict an ulceration threshold. Ideally, neuropathic patients should never let their feet touch the ground without shoes. Indeed, in most clinics they are strongly urged to avoid barefoot walking. If this ideal were to be achieved, barefoot pressure would only be a predictor of the actual pressure experienced by the foot (the in-shoe pressure) in activities of daily living if all shoes reduced pressure by the same amount. This is clearly not the case – since there are patients in good shoes and those in bad shoes. It is, therefore, likely that we need to look toward the measurement of in-shoe pressure to gain a better estimate of threshold.

IN-SHOE PRESSURE MEASUREMENT

It is now quite feasible to obtain accurate and reproducible measurements of pressure distribution inside the shoes of ambulating patients. In collaboration with our colleagues in Sweden (Cavanagh et al. 2002) we have used the PEDAR device to measure in-shoe pressure in a group of 53 patients with a history of ulceration, but who had remained ulcer free while wearing therapeutic footwear. Although barefoot pressure measured with the EMED SF revealed greater peak pressures at ulcer sites under the first metatarsal head (MTH1) compared to the hallux (692 ± 330 kPa, n=18 vs. 486 ± 242 kPa, n=17) this trend disappeared for the in-shoe measurements (unadjusted peak pressures of 204 ± 63 kPa vs. 214 ± 71 kPa at MTH1 and hallux respectively). In-shoe peak pressures at all of the different prior ulcer sites were remarkably close to 200 kPa, suggesting that the reduction of in-shoe pressure below this value is necessary to maintain healing. If such a threshold were to be prospectively validated, it would be extremely useful in footwear design as long as plantar pressure monitoring were available prior to the shoes being dispensed.

OTHER FACTORS

In-shoe plantar pressure measurement alone will never predict all of the variance in ulceration threshold. For example, patients with extremely low plantar pressures can injure their feet by non-compliant behavior, and those with extremely high pressures can prevent injury by inactivity. It is, therefore, likely that in addition to in-shoe plantar pressure and the factors mentioned above, both compliance and activity level would need to be taken into account.

REFERENCES

Armstrong DG, Peters EJG, Athanasiou KA et al. (1998) J Foot Ankle Surg 37:303-307
Boulton AJM, Betts RP, Franks CI et al. (1987) Diabetes Res 5:73-77
Cavanagh PR, Ulbrecht JS, Caputo GM (2001) In: The Diabetic Foot; Mosby, Inc. 6th ed:125-196
Cavanagh PR, Ulbrecht JS, Apelqvist J et al. (2002) ADA Abstract (submitted)
Duckworth T, Boulton AJM, Betts RP et al. (1985) JBJS 67-B: 79-85
Shaw JE, Boulton AJM (1996) Diabet Med 13(Suppl 7):S22
Veves A, Fernando DJS, Walewski P et al. (1991) Foot 2:89-92
Veves A, Murray H, Young MJ, et al. (1992) Diabetologia 35:660-663

ACKNOWLEDGEMENTS

This work was supported in part by NIH (RO1 HD37433) and by a grant from DIApedia LLC.

PLANTAR PRESSURE MEASUREMENTS AS AN OUTCOME MEASURE FOR INTERVENTIONS USED TO TREAT FOREFOOT AND MIDFOOT PAIN

Thomas G. McPoil
Gait Research Laboratory, Department of Physical Therapy, Northern Arizona University,
Flagstaff, Arizona, USA, tom.mcpoil@nau.edu

INTRODUCTION

Forefoot and midfoot pain as a result of orthopaedic problems are both painful and debilitating. Although numerous interventions have been suggested for the management of forefoot and midfoot pain, the success of these treatment techniques is often based on patient self-reported pain reduction. Plantar pressure measurements offer the clinical researcher the ability to assess the effectiveness of the various interventions available for the conservative treatment of forefoot and midfoot pain. Just as importantly, pressure measurements serve as an effective outcome measurement tool to validate if a reported reduction in pain corresponds to a decrease or modification of the plantar pressures acting on the painful plantar region of the foot. The purpose of this presentation is to review the etiology of forefoot and midfoot pain as well as the use of plantar pressure assessment as both a research and outcome measurement tool.

FOREFOOT PAIN

Forefoot pain, or metatarsalgia, is defined as pain in or about the head of the metatarsal, the metatarsophalangeal joint, and surrounding soft tissue structures. Next to heel pain, metatarsalgia is one of the most frequent causes of pain in the foot. The causes of metatarsalgia fall into four major groups: 1) localized disease processes (i.e.; Morton's neuroma, interdigital neuroma, Freiberg's disease, stress fracture), 2) systemic diseases with specific symptoms in the forefoot region (i.e.; rheumatoid arthritis), 3) toe deformities (i.e.; claw toe, hammer toe, mallet toe), and 4) alteration in normal forefoot biomechanics. Groups 3 and 4 are often referred to as primary metatarsalgia, while groups 1 and 2 are considered secondary types of metatarsalgia. Specific factors that can influence and alter normal forefoot mechanics include: 1) overload of anterior support (i.e.; high heeled shoes, equinus foot, cavus foot) and 2) irregularity in the distribution of metatarsal head loading (i.e.; first ray overload syndrome, overload of a central ray, first ray insufficiency syndrome, Morton's toe).

FOREFOOT PAIN INTERVENTIONS

Both primary and secondary forms of metatarsalgia can respond well to conservative treatment interventions if initiated early in the course of the patient's symptoms. Common conservative interventions include: cushioned insoles, metatarsal pads, foot orthoses, cushioned hosiery, and external and internal metatarsal bars. Previous studies using both traditional research methods as well as single-subject design models have demonstrated that: a) metatarsal pads and insole materials decrease plantar pressures effectively and in a similar manner but that arch taping to control first ray insufficiency actually causes an increase in plantar pressure (Childs, 1996), b) padded hosiery can significantly reduce forefoot plantar pressures but that pressure reductions were not uniform across the entire forefoot (Flot, 1995), c) total contact foot orthoses are effective in decreasing plantar pressures irrespective of whether rearfoot posting is utilized (Cornwall, 1992), and d) the use of foot orthoses constructed from lower density materials provide a greater reduction in forefoot loads during walking than higher density materials (McPoil, 1991). Clinical outcome studies using plantar pressure measurements have also shown that a) internal metatarsal bars can be effective in the management of forefoot pain associated with toe deformities and b) total-contact cushioned foot orthoses can decrease forefoot pressures in athletes with a cavus foot structure.

MIDFOOT PAIN

Midfoot pain can occur as a result of overuse repetitive stress in activities such as ballet and volleyball. A more common cause of midfoot pain is trauma to the region as a result of motor vehicle accidents, occupational/industrial injuries, and athletic competition.

MIDFOOT PAIN INTERVENTIONS

In most cases, the conservative treatment for midfoot pain as a result of overuse or acute injury is foot orthotics that provide both cushioning and stabilization to the joints and soft tissues in the midfoot region. Although plantar pressure assessment provides little information on the effectiveness of this type of treatment intervention, plantar pressure measurements serve as an important functional outcome tool to determine progress of the patient in their reacquisition of a normal gait pattern. In addition to temporal measures, plantar pressure data can also provide valuable information on the pattern and sequencing of plantar surface loading.

REFERENCES

Childs, R.A. et al (1996). *Lower Extremity*, **3**, 25-29.
Cornwall, M.W., McPoil, T.G. (1992). *J. Am. Podiatr. Med. Assoc.*, **82**, 371-374.
Flot, S. et al (1995). *Lower Extremity*, **2**, 201-205.
McPoil, T.G., Cornwall, M.W. (1991). *J. Am. Podiatr. Med. Assoc.*, **81**, 638-642.

RELATIONSHIP OF PERCEPTION VS. THE MEASUREMENT OF PLANTAR PRESSURES – A NEUROSENSORY APPROACH

Thomas L. Milani & Stefan Kimmeskamp
University of Essen, Department of Human Locomotion
45131 Essen, Germany; thomas.milani@uni-essen.de

INTRODUCTION

Human balance is controlled by afferent information based on visual, vestibular and somatosensory input systems (van Deursen et al., 1999). Studies have focused on the specific role of vestibular, visual or muscular sensory information, but few research studies have been performed to date to investigate the role of cutaneous sensibility from the foot soles (Kavounoudias et al., 1998). The contribution of the plantar sensory systems to balance control has been discussed indirectly by researchers that studied sensory deficiencies based on neuropathic (e.g. diabetes) or artificial (e.g. icing/cooling) perturbations. Research with Diabetes patients revealed that diabetic neuropathy lead to a loss of protective sensation (Simoneau et al., 1996). The loss of protective sensation in combination with the continually repeated stress onto the plantar surface in daily walking have been observed as main factors for ulceration. Using anesthesia procedures the importance of cutaneous afferent input from the plantar surface in controlling rapid compensatory stepping reactions could be shown (Perry et al., 2000).

Since the foot mechanoreceptors are the boundary systems between the body and the ground it can be assumed that they play an important role in controlling the human balance. While mechanoreceptors of human skin are specific for different stimuli the identification and contribution of the specific foot sensors for balance control is of interest. Whereas Merkel corpuscles and Ruffini are sensitive for the intensity of pressure, vibratory stimuli are mediated by Meissner (low frequencies of 10 – 50 Hz) and Pacinian (high frequencies of 100 – 300 Hz) corpuscles.

METHOD

A direct approach for studying the relationship between foot sensation and posture control can be performed by using sensor stimulation procedures. For different groups of subjects, sensitivity and posture control measurements were performed. Health youth adults (mean age: 26y), senior adults (64y) and patients with Parkinson disease (67y) participated in these studies. Subjective sensibility thresholds under five foot structures (heel, midfoot, I. & V. metatarsus head and Hallux) of different mechanoreceptors (intensity, vibration) were determined by using a vibration exciter (30 Hz, 125 Hz) and Semmes Weinstein-microfilaments. The sensitivity of intensity mechanoreceptors were analyzed by using a 4-2-1-algorithm. Control of human posture was measured by pressure sensitive insoles (Novel GmbH, Munich). The postural stability was tested under various sensory conditions with increasing level of demand (one leg standing/eyes open – closed/head upright – tilted back/lean forward). A sensitivity parameter for each subject was determined by averaging vibration resp. intensity thresholds of five foot locations. Sensitivity variables and balance control variables were evaluated by regression analyses.

RESULTS & DISCUSSION

Sensitivity threshold measurements revealed significant differences (p<.01) between the various foot areas for both stimulus modalities (intensity & vibration). Comparisons between the different groups revealed significant differences in sensory threshold data (Fig.1).

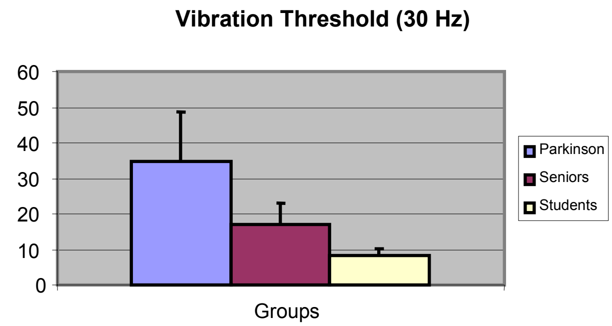

Fig.1: Vibration (30 Hz) threshold diff. between groups

Regression analyses of the threshold data and Center of Pressure (CoP) data revealed that subjects with more sensitive feet show less motion amplitudes of the Center of Pressure (Fig.2).

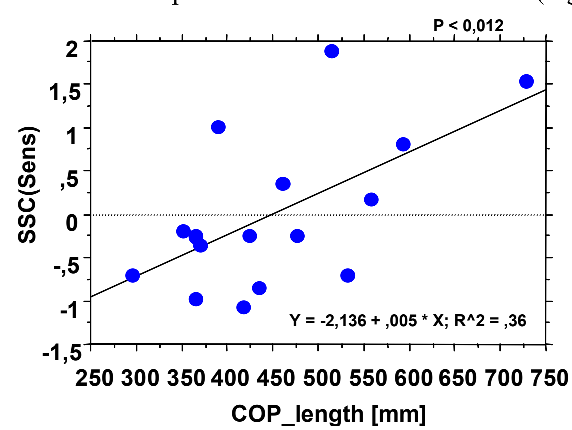

Fig.2: Sensitivity (SSC) vs. Length of CoP in students

REFERENCES

Van Deursen, R.W. et al (1999). *Orthop. & Sports Phys. Ther.*, **29**(12): p. 718-726.

Kavounoudias, A. et.al., (1998). *Neuroreport* **9**(14): p. 3247-52.

Simoneau, G.G., et al., (1996). *Arch Phys. Med. Rehab.,* **77**(5): p. 453-60.

Perry, S.D. et al., (2000). *Brain Res*, **877**(2): p. 401-406.

PRESSURE PATTERNS UNDER THE FEET OF CHILDREN, ADULTS AND OVERWEIGHT PERSONS - THE INFLUENCE OF GENDER -

Ewald M. Hennig
Biomechanics Laboratory, Universitaet Essen
Essen, Germany, ewald.hennig@uni-essen.de

INTRODUCTION

Results from various plantar pressure studies on adults and children, performed at our laboratory and in cooperation with international partners are presented here. Specifically, the influence of gender on foot pressures will be discussed.

ADULTS

An early study determined the pressures during bipedal standing and walking (approx. 1 m/s) under the symptom-free feet of 49 women and 62 men (Hennig et al., 1993). During standing and walking the highest pressures under the forefoot were found under the third metatarsal head. It was concluded that during weight bearing no transverse arch across the metatarsal heads is apparent. Therefore, a tripod theory of foot loading as it had been mentioned in many anatomy text books can not be confirmed by plantar pressure measurements. Similar to findings of Cavanagh et al. (1987) under none of the investigated anatomical regions a relationship between peak pressures and body weight were found across subjects. When grouping the subjects according to gender, however, a relationship ($r = +0.65$, $p < 0.01$) was found for the comparison of body weight against the peak pressures under the longitudinal arch of the women's feet during walking. Because this phenomenon was only present for the women, it was speculated that weaker ligamentous structures in women's feet result in a higher collapse of the longitudinal arch with increased body weight. This hypothesis has recently been supported by a study comparing foot function of women and men during running (Hennig, 2001). Midfoot loading as well as the amount of rearfoot pronation were increased for the women.

CHILDREN

Plantar pressures during barefoot walking and running were determined for 15 infants (7 male, 8 female) between the ages of 14 and 32 months (Hennig & Rosenbaum, 1991). Compared to the plantar pressures in adults, considerably reduced peak pressures in the infant group were observed. These could be attributed to the softer foot structure as well as a lower body-weight to foot-contact area ratio. An almost three times higher relative load under the midfoot of the infant foot shows that the longitudinal foot arch is still a weak structure in this age group. Across the age range of the children it was observed that with increasing age the relative load under the midfoot decreases while it becomes more pronounced under the third and fifth metatarsals. In a later study peak pressures and relative loads under the feet of 125 children (64 boys, 61 girls) between 6 and 10 years of age were determined (Hennig et al, 1994). These results were compared to the data from adults. The school children showed considerably lower peak pressures under all anatomical structures. These lower pressures could mainly be attributed to the larger foot dimensions per kg body mass for the children. Reduced loading of the first metatarsal head in the younger children was attributed to a valgus knee condition with hyperpronation of the foot and a reduced stability of the first ray. No reduction in pressures under the longitudinal arch with an increase of age suggests that foot arch development is almost complete before the age of six. Contrary to the findings in adults, body weight was identified to be of major influence on the magnitude of the pressures under the feet of school children. Between boys and girls no differences in the peak pressure or relative load patterns were present.

OVERWEIGHT PERSONS

Hills et al. (2001) investigated the plantar pressure differences between obese and non-obese adults during standing and walking. Thirty-five men (67–179 kg) and 35 women (46–150 kg) were divided into an obese (body mass index (BMI) 38.8 kg/m2) and a non-obese (BMI 24.3 kg/m2) group. The obese subjects showed an increase in the forefoot width to foot length ratio, suggesting a broadening of the forefoot under increased weight loading conditions. In spite of the increased load bearing contact area of the foot with the ground, the obese men and women had substantially higher pressures under the heel, midfoot, and forefoot during standing and walking. In the static as well as the dynamic loading situations, the highest pressure increases for the non-obese group were found under the longitudinal arch of the foot. The influence of body weight on increased midfoot pressures was much stronger for the women as compared to the men. This gender related influence of body weight on the flattening of the arch may be the consequence of a reduced strength of the ligaments in women's feet.

REFERENCES

Cavanagh PR, Rodgers MM, Iiboshi A (1987) Foot & Ankle **7**. 262-276
Hennig EM, Rosenbaum D (1991) Foot & Ankle **11**.306-311
Hennig EM, Milani TL (1993) Z Orthop **131**. 279-284
Hennig EM, Staats A, Rosenbaum D (1994). Foot & Ankle **15**.35-40
Hennig E (2001) Proc. 5th Symp. on Footwear Biomechanics. Zuerich: 44-45
Hills AP, Hennig EM, McDonald M et al. (2001) Journal of Obesity **25**.1674-1679

PRESSURE DISTRIBUTION MEASUREMENT AND THE RHEUMATOID ARTHRITIC FOOT

James Woodburn
Rheumatology & Rehabilitation Research Unit, School of Medicine,
University of Leeds, Leeds, UK

INTRODUCTION

Rheumatoid arthritis (RA) is a chronic inflammatory arthritis associated with widespread synovial joint involvement and systemic features. It is both persistent and destructive and manifests itself early in the feet causing pain, deformity, functional impairment and disability. Synovitis, tenosynovitis, bursitis are responsible for pes planovalgus deformity, hallux valgus, claw and hammer toe deformity of the forefoot, subluxation of the metatarsophalangeal joints with plantar callosities, bursitis and ulceration, and more rarely neurological and vascular deficit.

The Rheumatology Research Unit at the University Leeds conducts a clinical research foot and ankle program for patients with RA foot disease. The gait laboratory utilises both platform (Emed- Novel GmbH) and in-shoe (Pedar- Novel GmbH) plantar pressure measurement (PPM) systems and the suite of NovelWin analytical software. The aim of this presentation is to provide a brief overview of RA and its common manifestations in the feet and to demonstrate justification for PPM. Application in routine clinical practice will be described, illustrated with case histories. An overview of past, current and future research projects will be provided.

CLINICAL APPLICATIONS OF PPM IN RA

PPM is used routinely in the RA foot clinic to evaluate overall foot geometry- midfoot collapse, forefoot splaying, absent toe contact, prominence of metatarsal heads, etc- (fig 1 & 2), foot loading patterns- medial heel loading, medial midfoot loading, antalgic gait, etc- (fig 2), the magnitude and distribution of forefoot pressures- Hughes loading patterns, peak and time integrals of pressure and force, etc. We derive a core set of quantifiable PPM measurements and combine this information with standard outcomes for foot pain, deformity and disease activity to both inform and evaluate diagnosis and therapy.

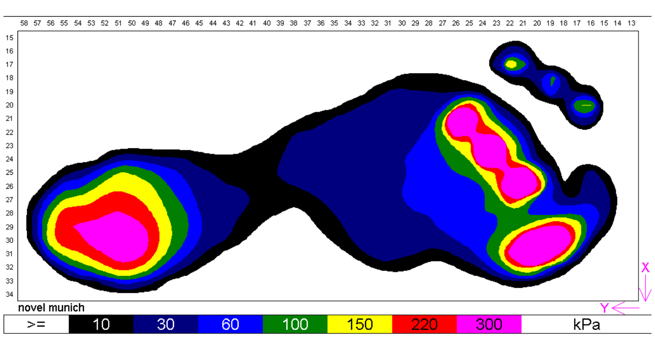

Fig 1. Abnormal plantar pressure distribution in RA showing elevated forefoot pressures, reduced toe contact and partial collapse of the medial longitudinal arch.

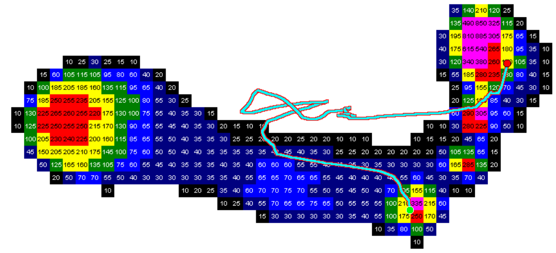

Fig 2. Antalgic gait pattern in RA- absent toe contact, elevated forefoot peak pressures and abnormal loading pattern (CoP).

PPM RESEARCH IN RA

Foot structure and function in RA

Various PPM and footprint parameters have been used in RA to study the structural and functional changes associated with RA disease. Results of these studies will be described. Our group is interested in the interaction between local inflammatory and biomechanical factors causing persistent localised disease activity. We are studying the ability of PPM in very early RA to predict future distribution and severity of localised forefoot synovitis and bone pathology, pressure lesions, pain, deformity and functional impairment.

Tissue Viability

PPM has been used to study the effects of tissue debridement for forefoot lesions in RA and findings will be presented[2].

Orthotic management

Redistributing plantar pressures is a stated goal in orthotic management. Literature will be reviewed and results from our own cross-sectional and longitudinal studies presented[3].

Future research

An MRI-based method for determining foot structure in RA has been developed. Preliminary findings will be presented investigating the relationship between PPM/footprint derived structure and function and *in vivo* foot architecture derived from MRI analysis.

SUMMARY

PPM is a useful clinical and research tool to study foot structure and function in RA foot disease.

REFERENCES

[1] Woodburn J, Helliwell PS (1996). *Ann Rheum Dis*, 55: 806-810.
[2] Woodburn J, Stableford Z, Helliwell PS (2000). *Rheumatology*, 39: 652-654.
[3] Woodburn J, Helliwell PS (2001). *Arthritis and Rheumatism*, 44; 9: S371.

NEURONAL CO-ORDINATION OF ARM AND LEG MOVEMENTS DURING HUMAN LOCOMOTION

Karim Fouad[1,2], Catharina Maria Bastiaanse[1,3] and Volker Dietz[1]

[1]ParaCare, Paraplegic Centre University Hospital Zurich, Switzerland,
[2]University of Alberta, Faculty of Rehabilitation Medicine, T6G 2G4 Edmonton, Canada, Karim.fouad@ualberta.ca
[3]Catholic University Nijmegen, Dept. of Medical Physics and Biophysics, Nijmegen, The Netherlands

INTRODUCTION

The evolution of upright stance and gait in association with the differentiation of hand movements represents the basic requirement for human development. An unresolved question of this development is whether or not there are still residual functions of quadrupedal locomotion during human bipedal gait reflected in a neuronal linkage between leg and arm movements. Therefore, the aim of this study was to examine the interlimb co-ordination between leg and arm movements in walking humans.

METHODS

To study the neuronal co-ordination of lower and upper limb muscles the effect of small leg displacements during gait on leg and arm muscle electromyographic (EMG) activity was evaluated. During walking on a split-belt treadmill (velocity 3.5 km/h), short accelerations or decelerations were randomly applied to the right belt during the mid or end stance phase. Alternatively, trains of electrical stimuli were delivered to the right distal tibial nerve. The EMG activity of tibialis anterior (TA), gastrocnemius medialis (GM), deltoideus (Del), triceps (Tric) and biceps brachii (Bic) of both sides was analysed. For comparison, impulses were also applied during standing and sitting.

RESULTS AND DISCUSSION

The displacements were followed by specific patterns of right leg and bilateral arm muscle EMG responses. Most arm muscle responses appeared with a short latency (65 to 80 ms) and were larger in Del and Tric than in Bic. They were strongest when deceleration impulses were released during mid stance, associated with a right compensatory TA response. A similar response pattern in arm muscles was obtained following tibial nerve stimulation. The arm muscle responses were small or absent and when stimuli were applied during standing or sitting. The arm muscle responses correlated more closely with the compensatory TA than with the compensatory GM responses. The amplitude of the responses in most arm muscles correlated closely with the background EMG activity of the respective arm muscle.

The observations suggest the existence of a task-dependent, flexible neuronal coupling between lower and upper limb muscles. The results showed a stronger connection between flexor activity in the legs and activity in arm muscles than between leg extensors and arm muscles. The results are compatible with the assumption that the proximal arm muscle responses are associated with the swinging of the arms during gait, as a residual function of quadrupedal locomotion.

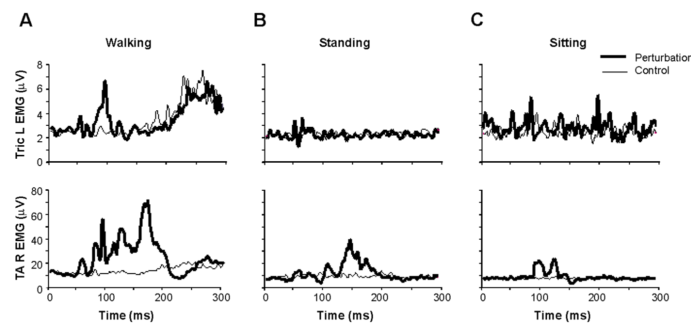

Figure 1: Comparing walking, standing and sitting. Rectified and averaged right TA and left Tric EMG response to a deceleration impulse during walking (A) a backward translation of the right belt during standing (B) and during sitting (C). Thin lines represent EMG recordings without perturbation.

CONCLUSION

In conclusion we would suggest a functional gating of neuronal pathways between lower and upper limb muscles during human locomotion. It remains a future task to define these neuronal connections more precisely.

ACKNOWLEDGEMENTS

This study was supported by the Swiss National Science Foundation (No. 31-53526.98 and No. 3152-062025)

ARE RHYTHMIC ARM MOVEMENTS CONTROLLED BY A CENTRAL OSCILLATOR?

E. Paul Zehr
Neurophysiology Laboratory, University of Alberta, Edmonton, Alberta, Canada, pzehr@ualberta.ca

INTRODUCTION

The neural control and sensory regulation of arm movement in humans has received comparatively scarce attention when compared to studies on the lower limb during locomotor movements such as treadmill walking or leg cycling (for reviews see Duysens and Tax, 1994; Brooke *et al.*, 1997). Such studies have shown extensive modulation of reflexes evoked by stimulation of muscular (e.g. H-reflexes) and cutaneous afferents during leg movement and have contributed greatly to our understanding of the sensory control of rhythmic movement. Mechanisms controlling the patterns of reflex modulation observed during leg movements (e.g. phase-dependent modulation, task-dependency, reflex reversal, and nerve specificity) have been ascribed to the activity of spinal central rhythm generating networks (Duysens and Van de Crommert, 1998). The working hypothesis in my laboratory has been that neural mechanisms controlling rhythmic movement are conserved between the human lumbar and cervical spinal cord. Therefore the neural control mechanisms and thus patterns of reflex modulation observed during rhythmic arm movement should be similar to that previously documented for leg movement during locomotor tasks. We have developed a model for studying rhythmic human arm movements and have been testing our hypothesis by evaluating the control of cutaneous and H-reflexes during these arm movements. Additionally we have also studied cutaneous reflex modulation during the rhythmic arm swing occurring during treadmill walking.

METHODS

All subjects participated in the experiments with informed, written consent. Subjects performed rhythmic arm cycling on a custom made hydraulic ergometer in which the two arms could be constrained to move together (180° out of phase) or could rotate independently. In different experiments, cutaneous reflexes were evoked with trains (5 x 1.0 ms pulses @ 300 Hz) of electrical stimulation delivered at non-noxious intensities (~ 2 x threshold for radiating parasthesia) to the superficial radial (SR), the median, and the ulnar nerves innervating distinct cutaneous fields in the hand. H-reflexes in forearm flexor carpi radialis (FCR) were evoked with single 1.0 ms pulses of constant current stimulation applied just proximal to the medial epicondyle of the humerus. Electromyographic recordings were made bilaterally from muscles acting at the shoulder, elbow, and wrist. Reflexes were evoked during rhythmic movement as well as during static contraction at matched positions. For the experiments during walking, subjects walked on a motorized treadmill while the SR nerve was stimulated pseudorandomly throughout the step cycle. Analysis was conducted on specific sections of the step cycle after phase-averaging contingent upon the occurrence of stimulation in the step cycle.

RESULTS AND DISCUSSION

During arm cycling, cutaneous reflexes were modulated with the movement cycle (i.e. there was phase-dependency; Zehr and Chua, 2000, Zehr and Kido, 2001). Also prominent phase-modulated cutaneous reflexes were typically observed in arm muscles during treadmill walking (Zehr and Haridas, 2001). Nerve and task-specificity of cutaneous reflexes was also seen as cutaneous reflexes were of larger amplitude or inhibitory during arm cycling movement when compared to static contraction (i.e. reflex reversal; Zehr and Kido, 2001). Additionally, forearm H-reflexes were attenuated during arm cycling as compared to static contraction. Thus, task-dependent modulation of H-reflexes was observed in the arm as previously demonstrated in the leg (Frigon et al. 2002).

SUMMARY

It is concluded that reflexes are modulated similarly during rhythmic upper and lower limbs suggesting similar motor control mechanisms. However, there are some differences between this pattern and that previously observed in the lower limb. It is suggested that these small differences arise from the difference in biomechanical constraints seen when comparing articulation at the wrist vs. ankle joints in humans. The data support the assertion that mechanisms regulating reflex pathways during rhythmic movement are similar in the human upper and lower limbs.

REFERENCES

Brooke,J.D., et al. (1997) *Prog Neurobiol* **51,** 393-421.
Duysens,J., Tax,T. (1994) *Interlimb coordination: neural, dynamical, and cognitive constraints.* Academic Press, Inc.
Duysens,J., Van de Crommert,H.W. (1998). *Gait Post.* **7,** 131-141.
Frigon, A., Collins, D.F., Zehr, E.P. (2002). *Proc. World Cong. Biom. (this volume).*
Zehr,E.P., Chua,R. (2000). *Exp Brain Res* **135,** 241-250.
Zehr,E.P., Haridas,C. (2001). *Soc Neurosci Abs* **27,** 305.9.
Zehr,E.P., Kido,A. (2001). *J. Physiol.* **537,** 1033-1045.

ACKNOWLEDGEMENTS

Supported by the Natural Sciences and Engineering Research Council of Canada and the Alberta Heritage Foundation for Medical Research.

INTER-LIMB COORDINATION IN HUMAN LOCOMOTION WITH ADDED MASS.

J. Duysens[1,2], S.F. Donker[1], S. M. P. Verschueren[3] and S. P. Swinnen[3]
[1]Sint Maartensclinic Research, Nijmegen, The Netherlands
[2]Dept. of Biophysics, K.U.Nijmegen, The Netherlands j.duysens@mbfys.nl
[3]Motor Control Laboratory, Department of Kinesiology, FLOK, Katholieke Universiteit Leuven, Belgium

INTRODUCTION

During gait there is a continuous interaction between sensory input and motor circuits generating the locomotor patterns (Duysens et al., 2000). From animal models it is known that proprioceptive information from a limb affects not only the kinematics of the limb involved but also the inter-limb coordination. During walking in crabs, for example, the activation of load receptors in one leg induced changes not only in the perturbed leg but also in the non-perturbed legs (Libersat et al. 1987). In human walking and running the addition of mass (load) to one leg leads to substantial changes in the structure of the step cycle (increased duration of swing; decrease in duration of double support period) although very little effect on cadence has been observed (Bonnard and Pailhous 1991; Cavanagh and Kram 1989). Little is known, however, concerning changes in the relation between upper limbs and between upper and lower limb activity as a result of selective loading to a single segment.

METHODS

In the present experiments, adaptations in arm amplitude and arm muscle activity to mass perturbations were studied in 7 participants during walking on a treadmill. Four different perturbation conditions (no perturbation, mass added to both wrists, to the right wrist, and to the right ankle) were employed randomly. During each experimental condition 10 different belt speeds (from 0.5 to 5.0 km/h) were tested, while the arm movements and the electromyographic (EMG) activity of the posterior and anterior deltoids were measured.

RESULTS AND DISCUSSION

No differences were found for stride frequency. However, loading the arm resulted in a significant decrease in movement for that particular arm. In addition, loading one arm increased the movements on the contralateral left arm. Loading the leg resulted in a significant increase of the movements of both arms as compared to the control condition. The highest increase in EMG activity was found for deltoids of the arm to which the weight was added. Remarkably, loading one arm yielded a significant increase in the (non-loaded) left arm. Additionally, in the condition in which a load was added to one leg a significant increase in EMG was found also in the deltoids of both (non-loaded) arms.

SUMMARY

The results indicate that during gait the added mass not only yielded an increase in arm muscle activity and in a decrease of movement amplitude of the perturbed arm, but also in alterations in the non-perturbed arm. The effects were not limited to the arms. Notably, adding mass to the ankle induced adaptive changes in both arms.

In conclusion, during gait the loading of one of the limbs induces adaptations in inter-limb coordination in the 3 remaining limbs despite rhythm constancy (stable cadence). This is in line with experiments on sitting subjects. Serrien and Swinnen (1998) showed that inter-limb synchronization remained possible after loading the limbs although the synchronization between homologous limbs was more robust than between non-homologous limbs. The results from the Swinnen laboratory along with the present ones point towards the existence of neural circuits which allow for stable interlimb coordination despite extensive changes in limb loading.

REFERENCES

Bonnard M, Pailhous J (1991). Intentional compensation for selective loading affecting human gait phases. *J Mot Behav,* **23**, 4-12.

Cavanagh PR, Kram R (1989). Stride length in distance running: velocity, body dimensions, and added mass effects. *Med Sci Sports Exerc,* **21**, 467-479.

Duysens J, Clarac F, Cruse H (2000). Load-regulating mechanisms in gait and posture: compararive aspects. *Physiol Rev,* **80**,83-133.

Libersat F, Clarac F, Zill S (1987). Force-sensitive mechanoreceptors of the dactyl of the crab: single-unit responses during walking and evaluation of function. *J Neurophysiol,* **57**, 1618-1637.

Serrien DJ, Swinnen SP (1998). Load compensation during homologous and non-homologous coordination. *Exp Brain Res*, **121**, 223-229.

ACKNOWLEDGEMENTS

Supported by the Dutch N.W.O. and Belgian Onderzoeksfonds K.U.L.

MUSCLE WORK AND FORCE: ENERGETICS OF HUMAN WALKING

Arthur D. Kuo[1], Jiro Dokeh[1], and J. Maxwell Donelan[2]
[1]Dept. of Mechanical Engineering, University of Michigan, Ann Arbor, Michigan USA (artkuo@umich.edu)
[2]Centre for Neuroscience, Dept. of Physiology, University of Alberta, Edmonton, Alberta, Canada

INTRODUCTION

What determines the metabolic cost of walking? Movement is produced by muscles, and muscles consume energy to produce work and force. Although the muscle work is known to consume energy, work is insufficient to explain the net metabolic cost of walking. It also does not explain the relationship that step length and walking speed that humans typically prefer (Elftman, 1966). This may be due to the consumption of energy to produce muscle force without performing work. We use a simple mathematical model of bipedal walking, along with experimental measurements of metabolic cost, to examine how work and force might be used in human walking.

METHODS

We developed a simple model of actively powered bipedal locomotion, based on the passive dynamics of the legs (Fig. 1; Kuo, 2001). The model is actively powered by an impulsive toe-off push, applied along the trailing leg axis, just prior to heel strike of the leading leg. A torsional spring acts between the legs. This model walks stably on level ground, with the toe-off push providing propulsion, and the torsional spring adjusting step length and step frequency.

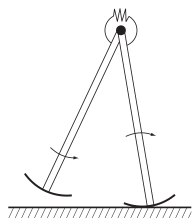

Figure 1. Bipedal walking model.

The model dissipates mechanical energy in the collision between the swinging foot and ground. During each step the center of mass (located near the hip) moves in an arc. Energy loss occurs between steps, as the center of mass is redirected from the downward arc of one step to the upward arc of the next. The redirection is due to negative work performed by the trailing leg. In order to walk at steady speed, an equal amount of positive work must be performed each step. The rate of positive and negative work due to collisions should increase with the fourth power of step length if step frequency is kept fixed, with a proportionate metabolic cost.

Collisions alone do not explain the metabolic cost of walking, because collisions could be minimized by taking very short but frequent steps. Instead, humans increase both step length and step frequency with walking speed, indicating that there is an energetic cost to high step frequencies, perhaps for the muscle activity required to move the legs quickly. We therefore examined the possibility that such movement, which is produced at no energetic cost by the model's torsional spring, comes at a substantial cost in humans. But the work needed to move the legs, if assumed to exact a proportionate metabolic cost, does not properly predict the preferred step length vs. speed (Kuo, 2001). Instead, an energetic cost for moving the legs—proportional to force and inversely proportional to duration of force—appears to predict optimal step length. This assumes that muscle force is the dominant cost, with work performed by elastic tendons. A prediction arising from this model is that metabolic cost should increase with the fourth power of step frequency, if step length is kept constant.

We tested these predictions by measuring human metabolic energy consumption with three types of walking. First, we asked subjects (N=7) to walk at increasing speed by changing step length alone. Metabolic cost should increase with the fourth power of step length. Second, we asked the same subjects to walk at increasing speed by changing step frequency alone. Metabolic cost should increase with the fourth power of step frequency. Finally, we asked subjects to walk at increasing speed without restrictions. The combined metabolic costs at the preferred step length should increase approximately with speed raised to the 2.4 power.

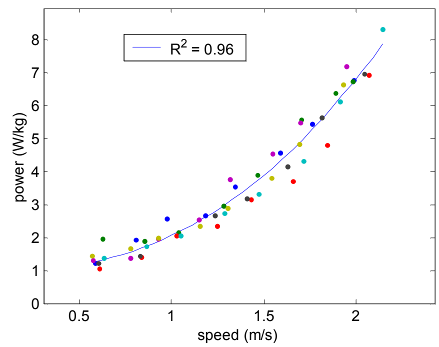

Fig. 2. Net metabolic power vs. speed at freely selected step lengths, with model prediction (speed raised to 2.4 power).

RESULTS AND DISCUSSION

We found that when subjects increased speed by changing only step length, metabolic power increased with the fourth power of step length (R^2 = 0.95). When they increased speed by changing only step frequency, metabolic power also increased with the fourth power of step frequency (R^2 = 0.91). Finally, when they increased speed using their freely selected step lengths, metabolic power increased with speed raised to the 2.42 power (Fig.2; R^2 = 0.96).

CONCLUSION

These results are consistent with our predictions that mechanical work is performed to redirect the center of mass between steps (collisions), and mechanical force is produced by muscles to move the legs, with both contributions exacting a proportional metabolic cost.

REFERENCES

Elftman, H. (1966) Biomechanics of muscle, *J. Bone Joint Surg.* **48-A**: 363-377.

Kuo, A. D. (2001) A simple model of bipedal walking predicts the preferred speed-step length relationship, *J. Biomech. Eng.*, **123**: 264-26.

ACKNOWLEDGEMENTS

This research was supported in part by NIH grant DC0231201A1 to ADK, and NSERC fellowship to JMD.

MUSCLE FUNCTION DURING FORWARD AND BACKWARD WALKING

S.A. Kautz[1, 3], R.R. Neptune[1, 2] F.E. Zajac[1, 3, 4], L. Worthen[1] and C.A. Dairaghi[1]

[1] Rehabilitation R & D Center, VA Palo Alto HCS, Palo Alto, CA
[2] Department of Mechanical Engineering, University of Texas, Austin, TX
[3] Departments of Functional Restoration and [4] Mechanical Engineering, Stanford University, Stanford, CA
Email: kautz@rrdmail.stanford.edu

INTRODUCTION

Numerous studies have described the differences in kinematic, kinetic and EMG variables between forward and backward human walking. Many aspects of the backward pattern appear to be a time-reversal of the forward pattern, with many similarities observed between initial and late stance in forward walking and late and initial stance, in backward walking, respectively. However, since initial and late stance are associated with net resistive and propulsive ground reaction forces, respectively, and the directions of joint rotations will be opposite during the two gait modes, it is unclear whether the observed similarities represent similar muscle actions. Winter et al. (1989) suggested that "temporal cycling of muscle contraction would be reversed: Concentric muscle activity in forward walking would become eccentric activity in backward walking, and vice versa." While their EMG results generally supported those findings, other studies have found the differences in muscle activity patterns between forward and backward walking more complex (e.g., Grasso et al., 1998). In the present study, we explicitly test the hypothesis that individual muscle activity will switch from from concentric to eccentric, and vice versa, in backward walking.

METHODS

Bilateral ground reaction forces, 3D kinematics, and unilateral EMG from eight muscles (tibialis anterior, soleus, medial gastrocnemius, vastus medialis, rectus femoris, biceps femoris, semimembranosus, and gluteus maximus) were collected from 12 subjects walking forward and backward at their self-selected speed. To assess muscle length, a forward dynamical simulation that emulated observed planar walking kinematics and kinetics of young adult subjects was produced. The musculoskeletal model and simulation were developed using SIMM/Dynamics Pipeline (MusculoGraphics, Inc.) and SD/FAST (PTC). The contact between the foot and the ground was modeled with discrete visco-elastic elements located on the bottom of the foot. The individual muscle excitation patterns were modeled as block patterns and an optimization framework systematically varied the muscle controls to replicate the experimental data.

RESULTS AND DISCUSSION

During backward walking, tibialis anterior, soleus, medial gastrocnemius, and gluteus maximus showed peak activity during muscle lengthening and the hamstrings, vastus and rectus femoris showed peak activity during shortening (Fig 1). During forward walking, only hamstrings showed peak activity during the same region, with all others being reversed.

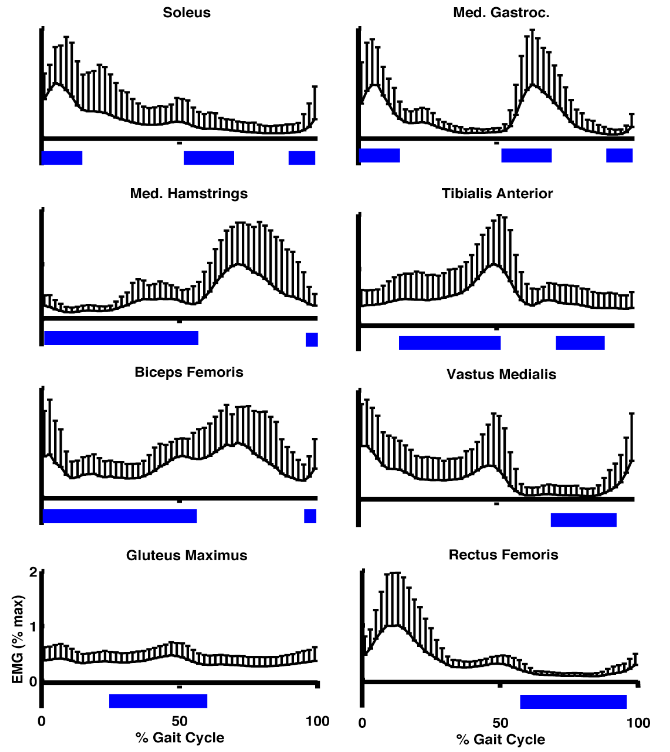

Figure 1: EMG activity during backward walking (mean + SD), normalized as percent of max for forward walking. Gait cycle begins with ground contact and ends with final swing. Bars represent regions of muscle-tendon unit lengthening.

SUMMARY

The hypothesis of Winter et al. (1989) was mostly supported. A change from predominantly concentric to eccentric activity, and vice versa, was found in nearly all muscles when walking backward. Different mechanisms of propulsion and support were observed during forward and backward walking. Analysis of simulation results will be presented to contrast the mechanical effects of concentric and eccentric action by individual muscles in the two walking tasks.

REFERENCES

Grasso, R. et al. (1998). *J Neurophysiol* **80**:1868-1885.
Neptune, R.R. et al. (2001). *J Biomech* **33**:155-164.
Winter, D.A. et al. (1989). *J Mot Behav* **21**:291-305.

ACKNOWLEDGEMENTS

This work was supported by NIH grant NS17662 and the Rehab R&D Service of the Dept. of Veterans Affairs (VA).

QUADRUPLE JUMPS IN FIGURE SKATING

Deborah King, Ph.D.

Biomechanics Lab, Montana State University, Bozeman, Montana
Email: dking@montana.edu

INTRODUCTION

The "quad", a quadruple revolution figure skating jump, has become a commanding presence in figure skating. However, the completion percentage of quadruple jumps remains low, only 13 of 24 attempted quadruple jumps were successfully landed at the 2000 State Farm Figure Skating Championships analyzed for this study.

Successfully completing any figure skating jump requires, at a minimum, the skater to coordinate time-in-the-air with average rotational velocity. Albert and Miller (1996) found an increase in angular velocity from single to double Axels with only minor variations in time-in-the-air. The increase in angular velocity was predominantly due to decreases in moments of inertia of the skaters as opposed to increase in angular momentum (Albert and Miller, 1996). However, King (1997) found an increase in jump height and time-in-the-air from single to double to triple Axels with more highly rated jumps having higher jump heights than more lowly rated jumps. Moreover, due to physiological limitations in generating vertical velocity (maximizing jump height), minimizing moment of inertia, and generating angular momentum, completing triple jumps may require different strategies than completing quadruple jumps. Thus, the purpose of this study was to determine critical technique elements for successful completion of quadruple jumps.

METHODS

Data were collected during the 2000 State Farm Figure Skating Championships. Written informed consent along with age, height, and weight were obtained from participating skaters. The approach through landing of quadruple and triple jumps were recorded using four high speed (120-pictures/second) pan and tilt cameras (Peak Performance Technologies, Inc.). A calibration was performed at the beginning of each day of testing using survey poles. Data were manually digitized and 3D coordinates were calculated using the Peak Motus pan and tilt procedure. The 3D coordinates were filtered using a quintic spline algorithm and then analyzed using software written in LabView (National Instruments, Inc.). Four men attempted a total of 24 quadruple jumps resulting in a total of 6 landed and 6 fallen quads being analyzed along with 7 corresponding triples. All jumps were toe-loops and Salchows. Results from 4 landed quad toe-loops, 4 fallen quad toe-loops, and 4 triple toe-loops are presented.

RESULTS AND DISCUSSION

Jump heights were similar between triple and quadruple jumps, though time-in-the-air (*FlightTime*) was longer for quadruple jumps (Table 1). This seeming incongruity is explained by a lower, or slightly seated, landing position for the quads. Similar to the findings of Albert and Miller (1996), the minimum moments of inertia (I_{min}) during flight were smaller for quad jumps as compared to triple jumps, and angular momentum values at take-off (H_{to}) were similar between jump types, especially after removing one outlying triple, which changes the H_{to} triple average to 29.9 kgm^2 (Table 1). Moreover, the average moment of inertia during flight (I_{avg}) was smallest for the landed quad jumps as compared to the fallen quads or triples (Table) allowing for faster angular velocities during flight. Smaller toe-pick distances (*PickDist*) at the instant of tap for the landed quads (Table), were likely influential for the skaters controlling their moments of inertia and angular velocities during take-off. Lastly, in landed quadruple jumps, skaters initiated on average 64 degrees more rotation on the ice (*PreRot*) as compared to triple jumps. The average number of revolutions for the landed quadruple jumps was 3.1 as compared to 2.5 for the triple jumps (Table), so that the quads were actually only 0.6 more revolutions than the triples.

SUMMARY

Additional revolutions during quadruple jumps were from a combination of increased time-in-the-air and smaller moments of inertia during flight. However, due to a more pre-rotation, the quad jumps in this study had only 0.6 more revolutions than the triples.

REFERENCES

Albert, W.J., Miller, D.I. (1996). *J. Applied Biomech*, **12**, 72-87.

King, D.L. (1997). *Professional Skater*, **Jan/Feb**, 10-12.

Table 1: Basic Characteristics for Triple and Quadruple Toe-Loops. Values are mean ± SD.

Jump Type	Height (m)	FlightTime (s)	I_{to} (kgm^2)	I_{avg} (kgm^2)	I_{min} (kgm^2)	PickDist (m)	H_{to} (kgm^2/s)	PreRot (deg)
Triples	0.46 ±0.02	0.634 ±0.024	2.02 ±0.12	1.47 ±0.12	1.12 ±0.06	0.99 ±0.13	32.5 ±6.6	135 ±31
Quads (land)	0.47 ±0.02	0.648 ±0.018	1.63 ±0.11	1.14 ±0.19	0.84 ±0.18	0.77 ±0.35	28.5 ±5.8	199 ±25
Quads (fall)	0.46 ±0.06	0.652 ±0.022	1.66 ±1.02	1.24 ±0.26	0.79 ±0.12	0.99 ±0.11	29.9 ±3.8	217 ±42

SEARCHING FOR OPTIMAL KNEE EXTENSION TIMING IN DIVES FROM THE REVERSE GROUP

Eric Sprigings[1] and Doris I. Miller[2]

[1]College of Kinesiology, University of Saskatchewan, Saskatoon, Saskatchewan, Canada
[2]Professor Emerita, University of Western Ontario, London, Ontario, Canada

INTRODUCTION

Reverse rotating dives require divers to face forward yet generate backward somersault angular momentum during the takeoff phase. These requirements place major importance on the positioning of the lower legs and timing of the knee extension. The optimal changes that should take place in these two variables when progressing from a reverse 1½ to a 2½ pike have yet to be determined. The purpose of this study was to develop a mathematical model to simulate the diver's springboard or platform contact during the takeoff phase of dives from the reverse group.

METHODS

The diver was modeled in 2-D space as a 5-segment linked system: feet, lower legs, thighs, head & torso, arms. The springboard was modelled as a mass-spring element with no damping (Sprigings et al., 1990). Effective mass and spring stiffness of the board model were set at 9.5 kg and 3500 N/m ('soft' board), respectively. Torque generators that adhered to activation rates and force-velocity properties of human muscle were inserted at ankle, knee, hip and shoulder joints allowing the model to control energy to the system. The force-length property of muscle was expected to play a 2nd order role in the outcome of the performance (Caldwell, 1995) and, as such, was not included in the simulation model. Activation rate and force-velocity properties associated with human muscle were implemented using calculated instantaneous isometric torque predicted from a linearized Hill model structure as input to the force-velocity approach described by Alexander (1990). Parameter values for segment lengths, masses and moments of inertia for a representative diver with body mass of 54.0 kg and standing height of 1.62 m, were obtained from de Leva (1996). Equations of motion for the diver-springboard system were written using a Newtonian formulation in combination with the known equations of constraint for a system linked with pin joints. A 5th order Runge-Kutta-Fehlberg algorithm with variable step size was programmed in FORTRAN and used to numerically solve the 2nd order differential equations for the corresponding angular position and velocity values of the 5 segments. Thirteen control variables, consisting of the times of onset and the length of activation time of each of the muscle torque generators, plus the body tilt angle, were used in the optimization process. The total angular displacement, as measured from the start of dive flight until the piked model's CG passed the level of the takeoff surface, along with any accrued penalties from inappropriate behaviour by the model, served as the objective function to be minimized.

RESULTS AND DISCUSSION

The simulation model suggested a controlled knee extension, which commenced late in the springboard's depression phase, was best. This is contrary to the fact that most divers begin knee extension early in depression. Delaying knee extension until the board has nearly reached its maximum deflection due to the diver's downward momentum has the advantage of allowing muscular efforts to be exerted against a stiffer surface. The two-phase knee extension velocity strategy observed in a number of world class divers (Miller, 2000) may be related to the optimization results. From an energy perspective, delayed knee extension produces a greater deflection in the board, thus increasing the storage of strain energy to be returned to the diver during the recoil phase. The optimization process suggests that as the number of required somersaults increases both the angle of the lower leg with respect to the springboard and the angle of knee extension at the completion of the takeoff should decrease (Figs. 1 and 2).

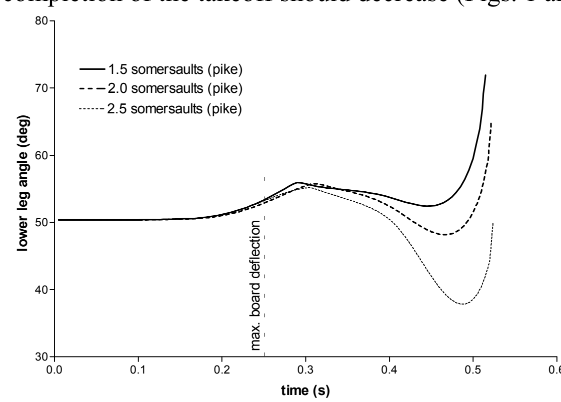

Fig. 1: Lower leg angle relative to the board during takeoff.

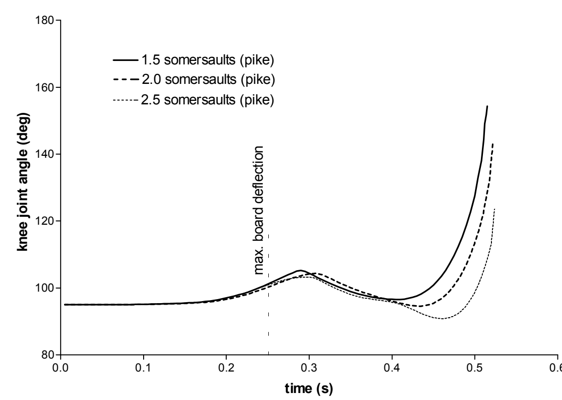

Fig. 2: Knee joint angle during takeoff.

REFERENCES

Alexander, McN. (1990). *Phil. Trans. Royal Soc.*, **329**, 3-10.
Caldwell, G.E. (1995). *J. Applied Biomech.*. **11**, 1-24.
de Leva, P. (1996). *J. Biomech.* **29**, 1223-1230.
Miller, D.I. (2000). In *Biomechanics in Sport*, 335-336.
Sprigings, E.J. et al (1990). *Int. J. Sport Biomech.*, **6**, 325-335.

ACKNOWLEDGEMENT

Funded by the United States Diving Foundation.

EFFECT OF THE DIRECTION OF THE SOMERSAULT ROTATION ON THE AMOUNT OF TWIST ROTATION IN HIGH JUMPING

Jesús Dapena

Department of Kinesiology, Indiana University, Bloomington, IN 47405, USA (dapena@indiana.edu)

INTRODUCTION

At the end of the takeoff, a high jumper is upright, and facing approximately along the bar. For an effective bar clearance, at the peak of the jump the athlete needs to be horizontal and facing upward. This requires the athlete to make a twisting somersault rotation in the air. The twist rotates the body about its longitudinal axis, and the somersault rotates the body about an axis perpendicular to the longitudinal axis. The twist rotation is generated by the component of angular momentum aligned with the longitudinal axis (H_{TW}) and through rotational action-and-reaction ("catting") (Dapena, 1997). A defective twist rotation can produce a tilted position at the peak of the jump with one hip lower than the other. This will reduce the effectiveness of the bar clearance. To solve the problem, it is first necessary to understand its causes. A tilted position at the peak of the jump can be due to deficiencies in H_{TW} or in the catting (Dapena, 1995). The purpose of this project was to investigate the possibility that the tilt might also be affected by the direction of the somersault rotation.

THEORETICAL CONSIDERATIONS

Figure 1 shows an overhead view of a hypothetical high jumper at takeoff and after 90° of pure somersault rotation (no twist) in three different directions. A typical somersault about an axis parallel to the bar would produce the position shown in image b, which would require in addition 90° of twist for a face-up orientation. A somersault about an axis aligned with the final direction of the run-up would produce the position shown in image a, which would require only 45° of twist for a face-up orientation. A somersault about a horizontal axis perpendicular to the final direction of the run-up would produce the position shown in image c, which would require 135° of twist for a face-up orientation. The implication is that the somersault rotation of image c would require 90° more of twist in the air than the somersault rotation of image a to reach a face-up position at the peak of the jump.

PROCEDURES

Two trials with markedly different orientations of the angular momentum vector relative to the bar (overhead view) were selected for analysis. Body landmark locations were obtained using 3D film analysis. Center of mass location and angular momentum were calculated with a method based on Dapena (1978). The orientation of the longitudinal principal axis was computed for each airborne frame. The cumulative twist rotation of the hips about the longitudinal axis between takeoff and the peak of the jump was calculated, as well as the twist orientations of the hips at takeoff and at the peak of the jump.

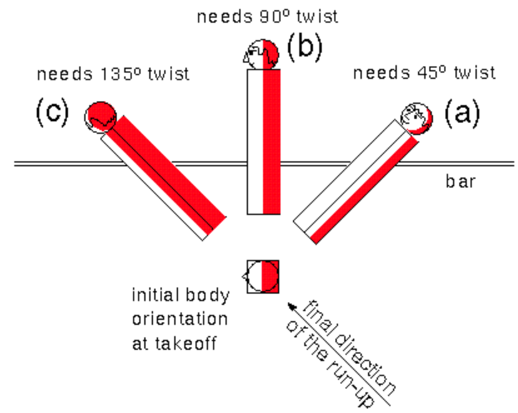

Figure 1: Body positions after pure somersault rotations.

RESULTS AND DISCUSSION

The horizontal component of the angular momentum vector of subjects #1 and #2 pointed, respectively, 21° counterclockwise and 41° clockwise relative to the bar. At takeoff, the subjects' hips faced, respectively, 31° and 27° counterclockwise relative to the bar. In the air, subject #1 twisted through a cumulative angle of 76°, and his hips were level at the peak of the jump. Subject #2 twisted through a cumulative angle of 8°, and ended up with the hips 6° short of level at the peak of the jump. Thus, an additional 6° of twist rotation would have leveled his hips at the peak. If subject #2 had taken off facing the same direction as subject #1 (31° rather than 27°), he would have needed (8+6-4 =) 10° of twist rotation in the air to reach a level position at the peak of the jump, while subject #1 needed 76° of twist rotation for the same outcome.

The results indicate that high jumpers with angular momentum vectors oriented more counterclockwise relative to the bar in the view from overhead may need to twist through substantially larger angles to reach a level position of the hips at the peak of the jump. This could make it impossible for some jumpers to reach such a position.

REFERENCES

Dapena, J. (1978). *J. Biomechanics*, **11**:251-256.
Dapena, J. (1995). *Conference Proceedings ASB*, 35-36.
Dapena, J. (1997). *J. Applied Biomechanics*, **13**:239-253.

ACKNOWLEDGEMENTS

This project was funded by grants from the U.S. Olympic Committee and U.S.A. Track & Field.

THE CONTROL OF TWISTING SOMERSAULTS USING ASYMMETRICAL ARM MOVEMENTS

Maurice R. Yeadon

School of Sport and Exercise Sciences, Loughborough University, Loughborough, United Kingdom (M.R.Yeadon@lboro.ac.uk)

INTRODUCTION

Twist may be initiated during the aerial phase of a somersault by using asymmetrical arm movements to tilt the body away from the vertical plane of the somersault (Yeadon, 1993). A reversal of the asymmetrical arm movement can also remove the tilt and stop the twist. Since there will be some variation in the movement initiating the twist, it will be necessary to make in-flight adjustments in order to complete the required amount of twist. Adjustments in arm asymmetry have been shown to be capable of controlling twist in unstable non-twisting somersaults (Yeadon and Mikulcik, 1996). This study investigates whether the same type of control can control the twist in the final phase of a twisting somersault.

METHODS

An 11-segment computer simulation model of aerial movement (Yeadon et al., 1990) was used to produce a backward somersault with one twist. The arms each moved from an initial symmetrical position through 90^{o} until one was by the side of the body and the other was overhead (Figure 1). The arm movements were later reversed so that the tilt was removed and the twist ceased after one revolution had been completed. The arm movement initiating the twist was perturbed by reducing the amplitude of the movement by 5^{o}. This resulted in less tilt and a slower twist. The timing of the arm reversal in this perturbed movement was the same as that in the original simulation and lead to insufficient twist.

A control system was introduced into the model whereby arm asymmetry was adjusted with arm abduction acceleration being a function of twist angular velocity and acceleration (Yeadon and Mikulcik, 1996). With zero feedback time delay in the control system, the perturbation was accomodated with the required amount of twist being completed. With a time delay of 0.2 somersaults problems were encountered arising from the high rate of twist with the arms in the asymmetrical position. To overcome this difficulty the arms were abducted through 50^{0} from the asymmetrical position before the control system was activated.

The procedure was repeated for a perturbation in which the simulation overtwisted.

RESULTS

The original simulation produced 1.00 twists with a final tilt angle of 0.2^{o} after one somersault (Figure 1a). The perturbation resulted in a final twist angle of 0.86 revolutions and a final tilt angle of 7.0^{o} (Figure 1b). With zero time delay the control system was able to compensate automatically for the perturbation, producing final amounts of 1.01 revolutions of twist and 0.4^{o} of tilt (Figure 1c). With a time delay of 0.2 somersaults and a spreading of the arms in mid-flight, the control system was at its limit in coping with the disturbance producing final amounts of 1.00 revolutions of twist and 2.3^{o} of tilt (Figure 1d). Similar results were obtained when a perturbation was used to produce too much twist.

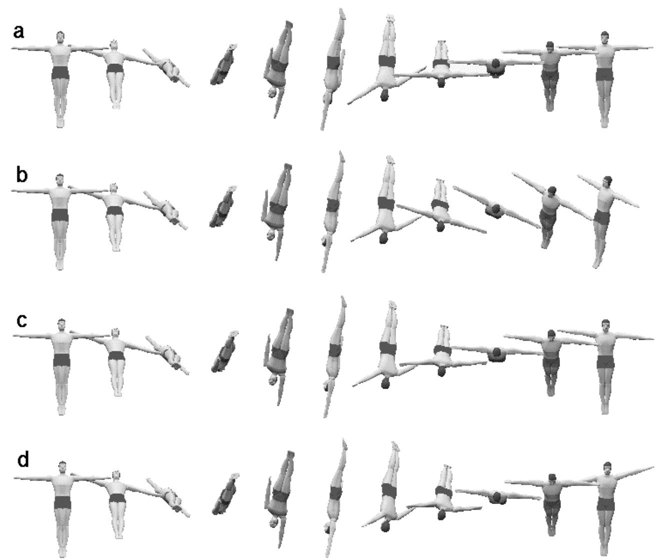

Figure 1: Simulation of a full twisting somersault (a) with change resulting from perturbation (b) and subsequent correction using control system with feedback delays of zero (c) and 0.2 somersaults (d).

DISCUSSION

There are few reports of difficulty in controlling the twist when gymnasts or trampolinists first attempt double somersaults in the straight position. This suggests that the method of control has been learnt prior to the attempt at the unstable movement. It may be speculated that gymnasts learn this method of twist control in single somersaults with twist.

SUMMARY

A feedback control system for making in-flight adjustments to the twist in twisting somersaults has been shown to be capable of effecting control for time delays of up to 0.2 somersaults.

REFERENCES

Yeadon, M.R. (1993). *J. Biomechanics*, **11**, 209-218.
Yeadon, M.R. et al. (1990). *J. Biomechanics* **23**, 85-89.
Yeadon, M.R. and Mikulcik, E.C. (1996). *J. Biomechanics* **29**, 1341-1348.

ASSESSMENT OF TECHNIQUES USED IN CALCULATING CELL-MATERIAL INTERACTIONS

Y.F. Missirlis* and A.D. Spiliotis
Biomedical Engineering Laboratory, Department of Mechanical Engineering,
University of Patras, Rion Achaia, 26500, Greece

A review of the techniques used in measuring the forces of de-adhesion of cells that have been adhering on substrate surfaces will be presented. Two categories of techniques will be described. The first category involves techniques that utilize fluid flow against an adhered cell population and subsequently count the percentage of cells that detach (global tests). The second category of techniques involve manipulation of single cells in various configurations which lend themselves to more specific force application and provide the basis for theoretical analysis of the receptor-ligand mechanics.

Starting from the simple static assays, where centrifugation is used to detach the cells, the parallel-plate flow chamber technique is dealt with in some detail due to its popularity in studying cell-substratum attachment. Steady-state or dynamic shear stresses are responsible for the detachment of cells in this case. The techniques of micropipette aspiration or the microplate versions are discussed next, with the new feature of handling single cells (one cell at a time) instead of populations of cells. Other techniques include the use of magnetic beads as a means of exerting the required force on the cell, the optical tweezers (utilizing optical forces) and the shear forces applied on single cells by manipulating microcantilevers (such as those used in atomic force microscopes).

The relative range of applied forces, and the merits and pitfalls of each technique are discussed in an attempt to make useful comparisons possible.

BIOMATERIALS AS EXTRACELLULAR (ECM) MATRICES

Dr. Tim McGloughlin
Biomedical Engineering Research Centre, Dept. of Mechanical & Aeronautical Engineering University of Limerick, Ireland.

INTRODUCTION

The loss or failure of organs/tissues remains one of the most severe human health problems. Standard treatment is organ transplantation but there is an inadequate supply of organs available for transplantation to meet the needs of the 36,000 patients on organ waiting lists, and in the last 5 years 10,000 people have died while on such lists (Fentiman 1994). There is an increasing need for an adequate alternative to transplantation. It is believed that tissue engineering has great potential to overcome the shortcomings of conventional treatment.

Tissue engineering is an emerging multi-disciplinary field, which embraces a diverse range of disciplines including cell biology, polymer chemistry and engineering. It is intended to be used in the development of bio-artificial organs/tissues and also to assist in the tissue remodelling process with the purpose of repairing or enhancing tissue/organ function (Nerem et al 1995).

Conventional cell culturing involves growing cells in an artificial environment, which enables them to proliferate into larger colonies. These cell cultures are intended for diagnostic use and do not become organised into tissues and organs. In the body cells are continuously bombarded with environmental cues including mechanical, chemical and electrical signals, which tell the cells how to behave. The cells are also exposed to structural cues due to the interaction with the extracellular matrix (ECM) (Ratcliffe 2000). It is believed that the physical communication between cells and their ECM directly and indirectly impacts cell shape and function. As a result it is believed that these signals are necessary for normal cellular activity. It is now usual to employ a 3-D ECM scaffold in the engineering of new tissues/organ.

Scaffold guided tissue regeneration involves seeding highly porous biodegradable extracellular matrix (ECM) scaffolds with donor cells and/or growth factors followed by culturing and implantation of the scaffolds to induce and direct growth of new tissue. These scaffolds are required to provide structural support and a suitable substrate for cell adhesion and proliferation to the new developing tissue. The scaffold may also be required to release bioactive substances at a controlled rate or to directly influence the behaviour of incorporated or ingrowing cells (Sundararajan 1999).

There a number of issues which must be considered prior to selection of a biomaterial as a tissue engineering scaffold including mechanical properties, surface morphology, porosity, degradation and chemistry of the material. Each of these parameters plays a significant role in cell attachment, proliferation, differentiation and secretion of proper ratios of ECM molecules. The ability of the material to perform the appropriate and specific function for which it is intended (biofunctionality) and also the compatibility of the material within the body (biocompatibility) must also be assessed (Marques 2002).

ECM scaffolds may be synthetic or natural in origin. Polylactide (PLA) and polyglycolic acid (PGA) are examples of biodegradable synthetic polymers, which have been used in applications such as sutures, and orthopaedic fixation. Natural polymers include collagen, alginate, and heparin etc which have been used in cardiovascular applications and in the development of skin substitutes.. Recently biological scaffolds such as acellularised aortic conduits have been used (Chen 2001).

To date only tissue engineered skin has been commercialised. Tissue engineered skin products include epithelial replacements such as Epicel (Genzyme), dermal replacements such as Dermagraft (Advanced Tissue Sciences) and full thickness replacements (Organogenesis Inc.). These have meet with varied success and there are still many issues relating to control of fluid loss, vascularisation etc. which need addressing (Seal 2001).

In orthopaedic applications donor bone cells have been seeded on hydroxyapatite (HA), which is a ceramic scaffold to create small-scale bone. It has been found that the microstructure of coralline HA is very similar to the mineralised component of natural bone ECM. Although this has shown some success there remains a need for improved scaffolding for orthopaedic applications, which address a number of issues relating to strength, toughness, osteoinductivity, osteoconductivity, controlled degradation and inflammatory response (Seal 2001).

Vascular tissue engineering has utilised natural polymer materials such as collagen, which is a tough fibrous protein matrix, and synthetic polymers such as polyglycolic acid (PGA). Attempts have focused on seeding tubular scaffolds with smooth muscle cells and endothelial cells (Hoerstrup 2001). However there remain numerous issues relating to thrombosis in these artificial vessels.

REFERENCES

Fentiman, L.C Organs donations: The failure of altruism. Issues Sci. Technol. Fall 1994,43,1994.

Nerem, R.M., Sambanis A. Tissue engineering: From biology to biological substitute. Tissue Engineering 1995; 1:3-13.

Ratcliffe, R. Tissue engineering of vascular grafts. Matrix biology 19; 2000:353-357.

Sundararajan, V.M., Matthew, H. Porous chitosan scaffolds for tissue engineering. Biomaterials 1999; 20:1133-1142.

Marques, A.P., Reis, R.L, Hunt, J.A. The biocompatibility of novel starch-based polymers and composites: in vitro studies. Biomaterials 2002; 23:1471-1478.

Chen, G, Ushida, T, Tateishi, T. Development of biodegradable porous scaffolds for tissue engineering. Materials Science and Engineering C17; 2001:63-69.

Seal, B.L., Otero, T.C, Panitch, A. Polymeric biomaterials for tissue and organ regeneration. Materials Science and Engineering R 34 (2001) 147-230.

Hoerstrup, S.P., Zund, G., Sodian, R., Schnell, A.M., Grunenfelder, J., Turina M.I. Tissue engineering of small calibre vascular grafts. European Journal of Cardio-thoracic Surgery 2001; 20:164-169.

POTENTIAL FOR COMBINED AND SEQUENTIAL DELIVERY OF GROWTH FACTORS TO CONTROL RESPONSES AT THE CELL-BIOMATERIAL INTERFACE

David A. Puleo and Adrian T. Raiche
Center for Biomedical Engineering, University of Kentucky, Lexington, KY 40506
puleo@uky.edu

INTRODUCTION

Delivery of biomolecules having the ability to control bone cell differentiation and functions directly to the tissue-biomaterial interface has great potential for influencing the fate of implants. Although the optimal mode and profiles for delivering these molecules remain unknown, the natural cascade of growth factor release during fracture healing can be used as a guide. Zero-order release of single biomolecules does not occur. Instead, temporally varying profiles of multiple biomolecules are observed. We hypothesize that combined and sequential delivery of different growth factors with non-zero-order release profiles will more effectively alter cellular activity than zero-order delivery of a single molecule. As a first step in testing this hypothesis, the *in vitro* effects of simultaneously and sequentially delivering two bone growth factors, BMP-2 and IGF-I, were determined.

MATERIALS AND METHODS

A crosslinked gelatin coating system was used to control release of growth factors. BMP-2 and IGF-I were selected because of their roles in bone formation and repair. A mathematical model was used to determine loading and glutaraldehyde crosslinking needed to produce peak release at 2 and 11 days from the top and bottom layers, respectively, of two-layer coatings. Peaks consisted of BMP, IGF, or both if co-immobilized. Unloaded layers were used as controls.

Solutions of 5 wt% gelatin were dissolved in PBS, pH 7.4, at 37°C and BMP-2 and/or IGF-I were added. After adding glutaraldehyde, layers were cast in 24-well tissue culture plates. Free aldehdye groups were blocked by incubation in 200 mM glycine at 4°C for 1 hour. The plates were dried overnight under laminar airflow. Second layers were added on top of blocked dried layers. Finally, plates were sterilized under ultraviolet light for 5 hours.

Three models were used to assess cellular responses: SaOS-2 cells for IGF-I mitogenticity, C3H10T1/2 cells for BMP-2 activity, and bone marrow stromal cells (BMCs) for both growth factors' osteogenic effects. Cells were seeded directly on dried gelatin coatings at a density of 18,000 cells/cm^2 and cultured for up to 4 wk, with weekly feeding. Cell growth was determined using a Hoechst DNA assay, and osteoblastic differentiation was assessed by measuring alkaline phosphatase (AP) activity and matrix mineralization.

RESULTS AND DISCUSSION

Using the two cell lines, non-zero-order profiles were found to stimulate cell responses more effectively than zero-order release. Furthermore, use of both BMP-2 and IGF-I was more effective than either molecule alone. Although differences in responses were observed for the different cell types tested, simultaneous release of both growth factors generally was not as effective as sequential release. For example, using the pluripotent C3H10T1/2 cell line, release of BMP-2 followed by IGF-I induced a significantly greater response ($p<0.01$) than all of the other coatings tested (Figure 1). Similarly, in BMC cultures, multilayered coatings delivering BMP-2 after 2 days and IGF-I after 11 days resulted in significantly greater AP activity compared to controls at 14 days, which subsequently enhanced mineralization at 28 days. Animal studies are being conducted to verify the observed *in vitro* findings.

CONCLUSION

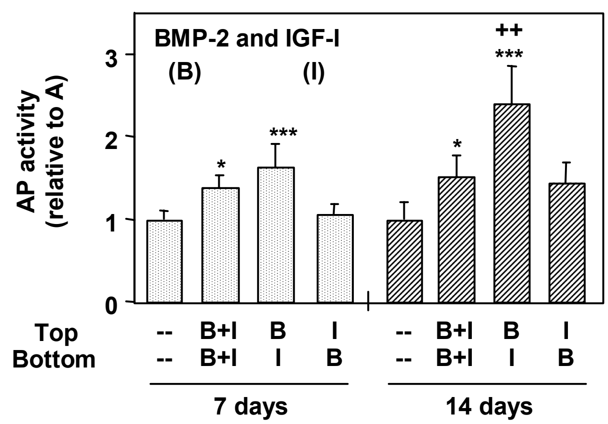

Figure 1. Induction of alkaline phosphatase activity in C3H10T1/2 cultures in response to simultaneous and sequential release of BMP-2 and IGF-I.

More biologically relevant release of growth factors increased osteoblastic cell activity and matrix mineralization *in vitro*. Similar strategies may enhance bone formation *in vivo*, thereby improving implant fixation.

ACKNOWLEDGEMENT

This work was supported by The Whitaker Foundation.

EFFECTS OF SURFACE TOPOGRAPHY ON CELL BEHAVIOUR AND TISSUE ORGANIZATION.

D.M. Brunette,. M. Takekawa and B.Chehroudi. brunette@interchange.ubc.ca
Faculty of Dentistry, University of British Columbia, Vancouver, B.C. Canada

INTRODUCTION

Surface properties, including topography and chemistry, are of prime importance in establishing the response of tissues to biomaterials. Microfabrication techniques have enabled the production of precisely-controlled surfaces to investigate the response of cells to topography. The intent of such studies is to develop principles of cell response to topography that could be used to design surfaces for tissue interaction on implanted devices. Originally produced in silicon (Brunette et al. 1983) the microfabricated surfaces can be replicated in epoxy, and coated with the biocompatible materials such as titanium(Ti). The Ti surfaces can be used as substrata for cell or implanted *in vivo*. Microfabricated surfaces have been used to explore the effects of topography on cell shape, locomotion, and function for epithelial cells, fibroblasts and cells involved in the production of mineralized tissue. The work on cell behaviour and fabrication methods has been reviewed recently (Brunette 2001, Jaeger and Brunette 2001)

Epithelium: Attachment to titanium surfaces on implanted devices and culture substrata is similar and features hemidesmosomes. Epithelial cells have a tendency to be oriented by grooved surfaces but the behaviour of individual cells *in vitro* is modified by the number of cells with which an epithelial cell is in contact. Epithelial downgrowth on implanted percutaneous devices can be inhibited by grooves on the implant surface directed at right angles to the direction of downgrowth.In general it appears that epithelium attached to implants *in vivo* displays several aspects of behaviour similar to those that are apparent *in vitro* , but the behaviour is modified by the connections with other epithelial cells and leads to the epithelium behaving more as a tissue than as individual autonomous units.

Fibroblasts. Fibroblasts exhibit contact guidance *in vitro* and *in vivo*, but the shape of migrating cells differs markedly. Cell culture substratum topography can also alter fibronectin and matrix metalloproteinase expression, orientation of fibronectin and other extracellular-matrix proteins, and cytoskeletal organization.

Mineralized tissue. Micromachined grooved surfaces increase the frequency of bone-nodule production *in vitro* and *in vivo*. Moreover, orientation of the nodules occurs both in culture and on implants.

Harris and Stopak (1982) have demonstrated that fibroblast-generated tractional forces and positive mechanical feedback can evoke the formation of complex connective tissue structures such as ligaments. Our hypothesis is that as structural geometry of extracellular matrix is largely controlled by directed cellular traction, control of cell orientation and attachment on an implant by surface topography should enable control of soft connective tissue organization and the promotion of tissue integration. In this study we adapted the system of Harris and Stopak (1982) to assess the ability of Ti surfaces of varying topographies to promote attachment and orientation of connective tissue.

METHODS

Machined, grit-blasted and blasted and etched (SLA), and micromachined grooved surfaces were replicated in epoxy and coated with ≈50nm Ti as described by Wieland et al. (*in press*). The surfaces were embedded in a type 1 collagen gel containing human gingival fibroblasts and culture medium in a well constructed of filter paper on a polystyrene dish. Cell orientation was determined by nuclear staining with propidium iodide and confocal microscopy.

RESULTS

The collagen gel becomes embedded in the filter paper and, as cell tractional forces develop, the collagen gel contracts away from the Ti surface. The length of time the surface resists the cell-generated forces thus reflects the strength of the collagen gel-fibroblast system (sometimes called tissue equivalent) attachment. There was a statistically signficant ($p<0.05$) difference in the time of attachment betwenn the surfaces in the order SLA> grooved> blasted >etched>machined. Moreover cell orientation differed between the surfaces with the machined surface showing the greatest tendency for orienting fibroblasts parallel to the surface.

CONCLSION

The topography of Ti surfaces can markedly alter the attachment and organization of fibroblast collagen gel tissue equivalents. This in vitro model provides a convenient system to evaluate the ability of surfaces to supportt connective tissue attachment and organization and resist cell tractional forces. There is thus abundant evidence that microfabricated surfaces can control diverse aspects of behaviour of several cell types. Only a few of the many possible topographies that can be produced by microfabrication techniques have been investigated, and there is considerable potential for optimizing cell responses to implanted devices by topographic control of cell behaviour.

REFERENCES

Brunette, D.M *et al.* (1983). *J. Dent. Res*. **62**,1045–1048,.
Brunette, D.M., in *Titanium in Medicine*. ed. by Brunette, D.M., et al. (2001). pp 485-512,Springer Verlag.
Chehroudi, B. *et al.* (1989).*J. Biomedical Materials Res*., **23**:1067–1085,.
Harris, A.K. and Stopak, D. (1982) *Dev. Biol*.,**90**: 383-398
Jaeger N.A.F. , Brunette, D.M. , (2001) in*: Titanium in Medicine*. ed. by Brunette, D.M. *et al*. pp343-374. Springer Verlag
Wieland, M. *et al.* (in press) *J. Biomedical Materials Res*.,

ACKNOWLEDGEMENTS

Supported by the Canadian Institutes of Health Research

DESIGNING SYNTHETIC POLYMERS WITH CELL-ADHESIVE PROPERTIES: N-ISOPROPYLACRYLAMIDE POLYMERS CONTAINING RGD-PEPTIDES FOR OSTEOGENESIS

Hasan Uludag, Erin Smith and Jennifer Yang
Department of Chemical and Materials Engineering, and Department of Biomedical Engineering,
University of Alberta, Edmonton, AB, Canada T6G 2G6.

INTRODUCTION

Synthetic polymers are promising materials to support tissue regeneration. Being synthetic, one can easily manipulate material properties to optimize the properties critical for tissue regeneration. However, a critical drawback of synthetic biomaterials is their inability to interact with mammalian cells; cells simply do not possess cell-surface receptors for material recognition. This limitation can be circumvented by incorporating synthetic peptides, which are recognized by cell receptors, into the biomaterials. Towards this goal, Arginine-Glycine-Aspartic acid (RGD) peptides were grafted onto polymers for cell attachment via integrins [1].

We are designing RGD-containing *N*-isopropylacryl-amide (NiPAM) polymers for bone regeneration. The polymers are thermoreversible: i.e., solubility in aqueous medium varies as a function of temperature. This allows one to inject the biomaterial solution to a specific site, where the biomaterial becomes insoluble at the physiological temperature. These materials, in combinations with Bone Morphogenetic Proteins (BMPs), will direct *in situ* differentiation of osteoprogenitor cells into bone-depositing osteoblasts. The response of osteoprogenitors is expected to be influenced by the nature of the biomaterial, and, in this presentation, we will present data exploring correlation among the physicochemical properties of NiPAM-based biomaterials and *in vitro* osteogenesis in response to BMP treatment.

MATERIALS AND METHODS

NiPAM polymers were prepared by thermal polymerization and characterized by ^{1}H-NMR [2]. RGD-containing peptides were synthesized at Alberta Peptide Institute (Edmonton, AB) or obtained from Bachem. The polymers contained amine-reactive N-acryolxysuccinimide (NASI). Peptide conjugation was characterized by using ^{1}H-NMR and a RP-HPLC method. The bioactivity of the polymers was assessed using cell adhesion studies with C2C12 cells. The cells are myoblastic in origin and exhibit osteblastic phenotype when treated with BMP-2. The cells were seeded onto multiwell plates, which had been previously coated with the desired polymers. The polymers contained NiPAM, hydrophobic alkylmethacrylates and, in some cases, NASI groups. The cellular response to the designed materials were based on (1) extent of cell attachment (direct cell counts and MTT assay); (2) cell proliferation (MTT assay), and; (3) cell differentiation (alkaline phosphatase, ALP, induction) in response to BMP-2 treatment.

RESULTS AND DISCUSSION

The NiPAM/NASI polymers were conjugated to GRGDYS by incubating the reagents in aqueous buffers. The NMR and RP-HPLC techniques indicated that as much as 8.4 peptides/polymer was obtained. The NiPAM/NASI polymer supported little C2C12 attachment in medium with or without serum. A significant increase in cell attachment was observed as a result of GRGDYS grafting (69.6% vs 3.1% after 24 hours). An dose-response study showed that cell adhesion was directly proportional to RGD concentration. An RGE-peptide did not support cell attachment, indicating that attachment was specific to the RGD sequence. Cell proliferation on NiPAM/NASI polymers was relatively slow. Although GRGDS-grafted surfaces enhanced cell proliferation, cells did not proliferate as much as the cells seeded on tissue culture surfaces (**Fig. 1**). Incorporating hydrophobic alkyl (hexyl and lauryl) methacrylates increased cell attachment and enabled better retention of activity on polymer surfaces up to 1 week in culture. Finally, C2C12 cells grown on tissue wells and treated with BMP-2 exhibited an alkaline phosphatase induction that was proportional to the dose of BMP-2. This osteogenic ability of cells were retained on surfaces grafted with GRGDS, albeit to a lower extent than the tissue culture surfaces.

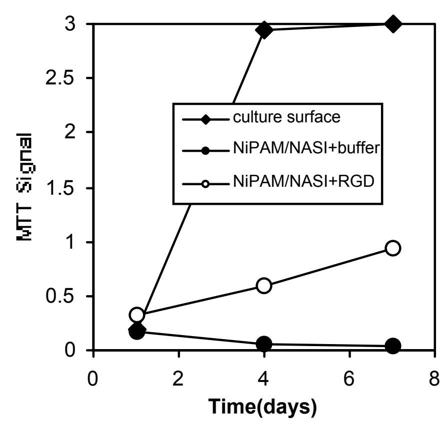

Figure 1. Cell proliferation on tissue culture surface and surfaces coated with NiPAM/NASI polymers. The polymers were treated with either buffer or GRGDS.

CONCLUSIONS

RGD-containing polymers were effective in increasing C2C12 cell adhesion as compared to parent polymers. The cells were able to proliferate on RGD-surfaces and respond to morphogenetic signals (BMP-2). However, cell responses (proliferation and ALP induction) were not as strong as the cells grown on tissue culture polystyrene. Further engineering will be needed to enhance cell-compatibility of the polymers.

REFERENCES

[1] Mann, B.K. et al., Biomat. **1999**,20:2281-2286.
[2] Uludag, H. et al., J. Appl. Poly. Sci. **2000**, 75:583-592.

CORRELATES BETWEEN CONTINUUM AND MICROSTRUCTURAL DESCRIPTIONS OF CENTRAL NERVOUS SYSTEM WHITE MATTER

David F. Meaney
Department of Bioengineering, University of Pennsylvania, Philadelphia, Pennsylvania, USA

INTRODUCTION

With measurements of finite strain material properties for the CNS white matter[1], relationships between the continuum behavior and the underlying structure of the tissue can be developed. In the past, isotropic material descriptions have been used to describe the behavior of the white matter in different testing directions[1]. In this report, we develop a structurally based model for the white matter and compare this description to the isotropic hyperelastic formulation used to model the material behavior of the white matter. For simplicity, we do not account for the time dependent behavior in this analysis. The long-term objective of this analysis is to estimate how properties of individual axons within the white matter can be approximated from continuum material descriptions.

MODEL DEVELOPMENT

In simple extension, the following stress (T) –stretch (λ) is obtained for a first order Ogden material:

$$T = \frac{2\mu}{\alpha}\left(\lambda^{\alpha-1} - \lambda^{-\alpha/2-1}\right) \quad [2]$$

where α and μ are parameters assigned to the material. This material description has been used to model the response of white matter tissue in shear [1]. For the structural model, we use a form of the stress-stretch relationship developed from a single myelinated nerve fiber [2]

$$\sigma_{fiber} = C(\lambda_{fiber} - 1)^2 \quad [3]$$

We assume all axons are aligned in the direction of stretch, and examine simple extension along the axis of the axonal fibers. In the unstretched state, each axon has a unique microstructural appearance, where most axons are undulated (U>1.0) and do not bear tensile force. As the white matter elongates in the direction of the axons, these axons will eventually straighten (U=1.0) and begin to produce a tensile force according to the above relationship [3]. Summing the contribution of the individual axons at a stretch (λ_o), the resulting tensile force is

$$T(\lambda_o) = \sum f_i(U_i) \cdot \Delta U_i \cdot \sigma_{fiber}\left(\frac{\lambda_o}{U_i}\right) \quad [4]$$

where $f(U_i)$ denotes the fraction of axons at an undulation U_i. Measured microstructure of the axonal geometry was used to predict the response of the structural model to the applied tensile loading.

RESULTS AND DISCUSSION

Using the nonlinear constitutive relationship for single, myelinated PNS axons, general stress-stretch response produced by a structurally based model of the material behavior (Figure 1A) could be reproduced by the first order Ogden material. Unlike other simpler descriptions for the individual axonal elements, the tangential stiffness characteristics between the two modeling approaches also agreed (Figure 1B)

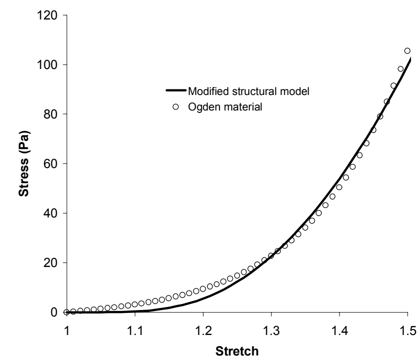

(A)

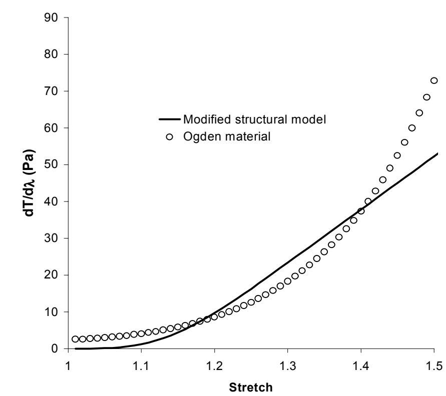

(B)

Figure 1

SUMMARY

Continuum formulations used for brain tissue behavior show a general agreement with stress-stretch relationships derived based on individual fiber behavior. The correspondence between the material behavior developed using these two approaches will lend insight into how continuum descriptions can incorporate structural failure of axons, as well and predicting the deformation of axons at specified macroscopic deformation levels.

REFERENCES

1. Prange, M., and S. Margulies, Regional, directional, and age-dependent properties of the brain undergoing large deformation, *J Biomech Eng*, in press
2. Saatmaan, K.E., Thibault, L.E., 1993, Response of the single myelinated nerve fiber to dynamic stretch," IRCOBI, pp. 216-223.

ACKNOWLEDGEMENTS

Funds for this work were provided by CDC R49/CCR 31271

REDUCTION OF BLAST INDUCED HEAD ACCELERATION AND CONCUSSIVE HEAD INJURY POTENTIAL

Jean-Philippe Dionne, Jeffery Nerenberg, Aris Makris

Med-Eng Systems, Ottawa, Ontario, Canada
Corresponding author: jpdionne@med-eng.com

INTRODUCTION

When an explosive device detonates, a blast wave is generated, compressing the gases behind it and propagating away in all directions. The impact of the blast wave with a person can induce violent accelerative motion of the head. A previous systematic investigation to assess the relevance of this type of injury in the context of demining concluded that blast-induced head acceleration injuries can be fatal for an unprotected deminer facing typical mines (Makris et al, 2000). The present study extends these results to an explosive ordnance disposal scenario, where a bomb technician faces explosive charges of the order of 5 to 17.5 kg at standoff distances of few meters.

METHODS

Anthropomorphic test devices (50th percentile Hybrid II) were fully dressed in protective equipment (EOD-8 and EOD-7B from Med-Eng Systems) or only dressed in light fleece clothing and subjected to blasts from high explosives. The mannequins were supported in the standing position by means of an anchored steel pipe slipped underneath each armpit, allowing a natural response to the blast. Charge sizes ranging from of 5.1 to 17.5 kg of C4 plastic explosive were placed on a stand located 1 m off the ground at distances varying from 2 to 5 meters from the mannequin. Standard blasting caps were used to initiate the detonation. The mannequins were instrumented with a tri-axial cluster of accelerometers in their head and the signals were filtered using a four-pole Butterworth filter set to attenuate signals above 1650 Hz. For each test, the Head Injury Criterion (HIC) was calculated (Versace, 1971) and probabilities of injuries were estimated, based on the Prasad/Mertz probability curves (Prasad, 1985).

RESULTS AND DISCUSSION

The injury analysis based on the HIC indicates that protective equipment drastically reduces the injury outcome. For an explosive charge of 10kg at a 3m standoff, Fig. 1 indicates the probability of injuries, based on the AIS scale for both the protected (EOD-8 helmet) and unprotected cases. Instead of a significant probability of fatal injury, there is a 80% probability of at most a minor injury.

Given the explosive type, charge and distance from the mannequin, the theoretical incident impulse of the blast can be calculated. A linear correlation between the HIC values and the impulse was found, based on tests involving the EOD-7B helmet (see Fig. 2). This linear behavior, which was also assumed for the EOD-8 helmet and unprotected tests, provides a predictive tool to estimate the likeliness and severity of blast-induced head acceleration injury.

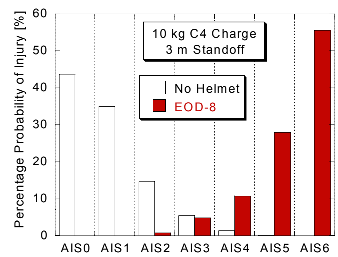

Figure 1: Probability of head acceleration injury for mannequin facing a 17.5kg charge at 3m standoff distance, protected (EOD-8 helmet) and not protected

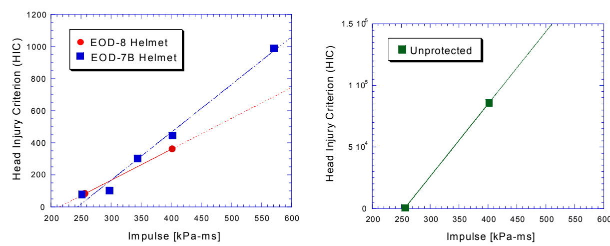

Figure 2: HIC vs Impulse curves for the protected cases (left) and unprotected (right)

SUMMARY

Injury analysis based on the head injury criterion indicates the significant reduction in injury outcome in an explosive ordnance disposal scenario when wearing adequate protection. Moreover, a correlation between the HIC values and the blast impulse was found, yielding a convenient predictive tool for blast-induced head acceleration injury for a general case of explosive charge and standoff distance.

REFERENCES

A. Makris et al., (2000), Reduction of blast-induced head acceleration in the field of anti-personnel mine clearance, 2000 IRCOBI conference, Montpellier, France

Prasad, P., Mertz, H.J., (1985) SAE Paper Number 85-1246, Society of Automobile Engineers, Warrendale, PA

Versace, J., (1971) Proceedings of the Fifteenth Stapp Car Crash Conference, pp. 771-796

ICE IN TISSUES

Locksley E. McGann

Department of Laboratory Medicine and Pathology, University of Alberta, Edmonton, Alberta, Canada

INTRODUCTION

Engineered tissues are being developed for a wide variety of applications in medical, agricultural, and food industries, but our ability to preserve these constructs for distribution is lagging significantly. Cryopreservation is often the only method for preserving physiological structure, viability and function in living tissues for long periods of time, therefore considerable research effort is now required to develop general methods for cryopreservation of tissue systems. Preservation of cell viability, cell-matrix interactions, and properties of the matrix are all required for post-thaw function of living tissues. Research in cryobiology has focused largely on the preservation of cellular viability, but it is now clear that cell-cell and cell-matrix interactions play a major role in low temperature responses of tissue systems.

METHODS

This paper is a synthesis of previous studies on ice in cells and tissue systems, designed to summarize the information and to point to future directions for cryopreservation of tissue systems.

RESULTS AND DISCUSSION

Cell adhesions affect intracellular freezing
Cell-cell and cell-matrix interactions change the responses of the cells at low temperatures (McGann 1993). Notable among these changes are the increased likelihood of intracellular freezing (Acker 1999), and the increased probability of intracellular freezing when an adjacent cell freezes (Acker 1998). Cell damage associated with intracellular freezing occurs during the formation of intracellular ice, but it is not clear whether intracellular ice is the cause or result of membrane damage (Acker 2001a).

Freezing damages cell adhesions
Monolayer systems have also been used to demonstrate that loss of cell adhesion is an independent type of cell damage that requires different modes of cryoprotection (Ebertz 2002).

Ice propagation between cells
For cells in a monolayer with close cell-cell contacts, intracellular ice formation does not necessarily result in the immediate disruption of the plasma membrane (Acker 2000). An equation for capillary freezing-point depression developed to describe the effect of temperature on the equilibrium radius of an ice crystal supports the theory that gap junctions facilitate ice nucleation between cells (Acker 2001b). This introduces the potential for developing strategies to cryopreserve tissues using rapid cooling.

Direct and indirect damage by interstitial ice
Chondrocyte recovery in articular cartilage after cryopreservation is dependent on the location of chondrocytes within the cartilage (Shachar 1999). The observation that physical proximity to a surface leads to higher recovery of cells supports the hypothesis that planar ice growth into the cartilage, with exclusion of solutes by ice, leads to constitutional supercooling deep in the tissue (Muldrew 2000).

SUMMARY

From these studies, it appears that the use of high concentration of cryoprotectants to reduce the amount of ice in the matrix, with rapid cooling to limit movement of water and solutes, is a feasible approach for the cryopreservation of natural and engineered tissues, when coupled with methods to induce innocuous intracellular ice that provides cellular cryoprotection.

REFERENCES

Acker, J.P., McGann, L.E. (1998). *Cryo-Letters*, **19**, 367-374.
Acker, J.P. et.al. (1999). *Cryobiology*, **38**, 363-371.
Acker, J.P., McGann, L.E. (2000). *Cryobiology*, **40**, 54-63.
Acker, J.P., McGann, L.E. (2001a). *Cryo-Letters*, **22**, 241-254.
Acker, J.P., Elliott, J.A.W., McGann, L.E. (2001b). *Biophysical Journal*, **81**, 1389-1397.
Ebertz, S. (2002). PhD Thesis. University of Alberta, Edmonton, Alberta, Canada.
McGann, L.E. et.al. (1993). *Transfusion*, **33**, 611.
Muldrew, K. et al. (2000). *Cryobiology*, **40**, 102-109.
Schachar, N.S. et.al.(1999) *J. Orthopaedic Research*, **17**, 909-919.

THERMO-MECHANICAL STRESS AS A LIMITING FACTOR OF LARGE SCALE CRYOPRESERVATION

Yoed Rabin

Department of Mechanical Engineering, Carnegie Mellon University, Pittsburgh, PA 15213, USA
Email: rabin@cmu.edu, Fax: 412 268 3348

INTRODUCTION

Cryopreservation technologies represent a potential long term and minimally damaging method to preserve both native and engineered tissues. This presentation addresses one of the limiting factors that hinder the widespread use of recent developments in cryopreservation technology to multicellular tissues, namely thermo mechanical stresses.

For example, conventional cryopreservation of allogeneic veins involving freezing is currently being used clinically. However, *in vivo* studies using these grafts in both animal models and patients have demonstrated poor long-term patency rates. Our industrial collaborators, Organ Recovery Systems, Inc., have demonstrated recently that an alternative approach to cryopreservation, involving vitrification that avoids the hazards of ice formation, leads to a markedly improved vascular product in terms of both structure and function. Vitrification (*vitreous* means glassy in Latin) is essentially the solidification of a supercooled liquid by adjusting the chemical composition and cooling rate such that the crystal phase is avoided. This new preservation technology is now being scaled up for clinical applications, and ultimately for use with engineered blood vessels.

Techniques have already been developed to preserve native blood vessels. However, while vitreous cryopreservation has been demonstrated to provide superior preservation compared with conventional freezing methods, cryopreservation of large tissue samples has been hampered by mechanical damage including fractures. Such fractures are attributed to stresses that can arise due to the non-uniform cooling of larger tissues. In fact, the higher cooling rates that facilitate vitrification will typically lead to higher mechanical stresses. The competing needs for vitrification and minimization of mechanical damage demand greater understanding of both vitrification and stress development. Although mechanical stress has long been recognized as an important mechanism of tissue destruction, it has received very little attention in the context of cryobiology.

The current presentation addresses three aspects of thermo mechanical stress in cryopreservation: mathematical modeling, physical properties measurements, and the mechanical response of the frozen tissue to an applied load.

MATERIAL PROPERTIES

The mechanical behavior of slowly freezing tissue specimens (conventional cryopreservation), and glass forming specimens, is inherently different. For the purpose of analyzing thermal stress during conventional preservation, our group has measured thermal expansion, the elastic modulus, and the strength of various frozen tissues (Table 1).

The mechanical behavior of vitrified biomaterial can be modeled as that of a fluid with viscosity value that increases exponentially with the decrease in temperature. This behavior continues until the viscosity reaches such a high value that the material can be considered solid in a typical time scale relevant to cryopreservation. Our group is now focusing on quantifying mechanical properties of glass forming biomaterials.

Table 1: Typical properties of polycrystalline ice water and soft frozen biological tissues in conventional cryopreservation

	Polycrystalline Ice Water @ 101.3 kPa	Frozen Biological Tissues
Thermal Expansion Coefficient: $\beta_1+\beta_2 T$ [1/°C]	$\beta_1=56.3\times10^{-6}$ $\beta_2=2.53\times10^{-7}$ $-180<T<0$°C (Powell, 1958)	$\beta_1=65\times10^{-6}$ $\beta_2=2.89\times10^{-7}$ $-180<T<-20$°C (Rabin et al., 1998)
Elastic Modulus, E [GPa]	8.9 - 9.9 @-5°C (Fletcher, 1970)	14 - 132 @ -196°C (Rabin et al., 1996)

REFERENCES

Dennis, B.H., Dulikravich, G.S., Rabin, Y. (2000). Optimization of organ freezing protocols with specified allowable thermal stress levels, *Advances in Heat and Mass Transfer in Biotechnology*, E.P. Scott, J.C. Bischof (Eds.), HTD-Vol. 368/BED-Vol. 47, ASME, New York, pp. 33-48.

Rabin, Y., Steif, P.S. (1996). Analysis of thermal stresses around a cryosurgical probe. *Cryobiology*, **33**, 276-290.

Rabin, Y. et al. (1996). An experimental study of the mechanical response of frozen biological tissues at cryogenic temperatures, *Cryobiology*, **33**, 472-482.

Rabin, Y. et al. (1997). Gross damage accumulation in frozen rabbit liver due to mechanical stress at cryogenic temperatures, *Cryobiology*, **34**, 394-405.

Rabin, Y., Taylor, M.J., Wolmark, N. (1998). Thermal expansion measurements of frozen biological tissues at cryogenic temperatures," *J. Biomech. Eng.*, **120**, 259-266.

Rabin, Y., Steif, P.S. (1998). Thermal stresses in a freezing sphere and its application to cryobiology, *J. of Appl. Mech.*, **65**, 328-333.

Rabin, Y., Steif, P.S. (2000). Thermal stress modeling in cryosurgery, *Int. J. Solids Struct.* **37**, 2363-2375.

MODELING AND SIMULATION OF MICRO-SCALE PHASE CHANGE AND TRANSPORT PHENOMENA IN CRYOPRESERVATION OF CELLS AND TISSUE

H. S. Udaykumar
Department of Mechanical Engineering, University of Iowa, Iowa City, IA 52242, USA

INTRODUCTION

Successful cryopreservation of cells and tissue critically depends on the thermophysics of ice-cell interaction. The rate at which extracellular ice forms and the resulting solutal environment in which the cell is placed in the cooling process determines cell death due to “solution effects” or “intracellular ice formation (IIF)”. The morphology of the extracellular ice crystals can determine the ability of the cell to navigate the freeze-thaw cycle. The interaction of the ice fronts with the cell membrane can also impact on the nucleation of lethal intracellular ice. Hitherto, modeling of ice cell interactions have relied largely on the theory developed by Mazur (1963), which provides a method to calculate the volume of the cell and the intracellular water content as a function of time (and temperature). Karlsson et al. (1994) have developed techniques to predict cell survival by combining Mazur’s approach with intracellular ice formation models. The present work goes beyond the analytical models of cell response to direct numerical simulation of ice formation and cell response, in order to include non-equilibrium effects on crystal growth and provide better visualization and understanding of the physics of ice-cell interactions.

METHODS

Diffusion-controlled growth of ice crystals from an aqueous salt solution is computed using a numerical method detailed in Udaykumar et al. (1999). The governing equations are solved using a finite-volume scheme that handles arbitrary moving boundaries, including phase change interfaces and membranes. Isothermal conditions are imposed in the computational domain, with cooling rates specified corresponding to typical cryo-protocols. The segregation and transport of salt from the advancing ice front is calculated. The cell is modeled as a fluid region bounded by a semi-permeable membrane. Water loss from the cell is computed using mass flux balance at the cell membrane. Properties of the solution and the cell are obtained from the literature.

RESULTS AND DISCUSSION

Figure 1 shows a sample calculation of the response of a modeled cell to the approach of an extracellular ice front. Initially the intra- and extra-cellular solutions are isotonic. Due to subsequent instability of the ice front the cell is finally attacked by a front with deep finger-like structures. The segregated solute is trapped in the deep grooves between the ice fingers and between the ice and the cell. As the extracellular medium becomes progressively salt-rich, the cell loses water by exosmosis. The ability of the water to escape from the cell is determined by the permeability of the membrane. A detailed study of cell water loss as a function of the controlling parameters (cooling rate, membrane permeability, CPA content etc) will be presented.

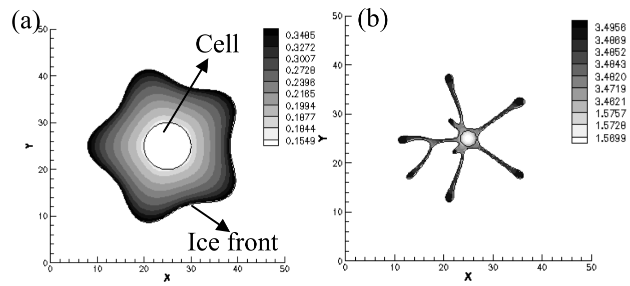

Figure 1: The shrinking of a cell in response to an approaching unstable ice front (a) Early time, (b) Later time. The dark region corresponds to a salt-rich medium.

SUMMARY

A method for the direct numerical simulation of the interactions between a freezing (ice) front in an aqueous medium with a modeled cell has been developed. The method allows the computation of the ice-cell interaction where two-dimensional phase change and heat/mass transport is computed. The method has also been extended to study the interactions in a ternary medium and to predict cell death based on the IIF mechanism.

REFERENCES

Karlsson, J.O.M., Cravalho, E.G., Toner, M. (1994). Model of diffusion-limited ice growth inside biological cells during freezing, *J. Appl. Phys*., **75**, 4442-4455.
Mazur, P. (1963). Kinetics of water loss from cells at subzero temperatures and the likelihood of intracellular freezing, *J. Gen. Physiol*., **47**, 347-369.
Udaykumar, H. S., Mittal, R., Shyy, W. (1999). Computation of solid-liquid phase fronts in the sharp interface limit on fixed grids, *J. Comput. Phys*, **153**, 535-574.

ACKNOWLEDGEMENTS

This work is supported by the National Science Foundation (CAREER program) and the Whitaker Foundation (through a Biomedical Engineering Research Grant). Mr. Leng Mao, graduate research assistant worked on this project.

RATIONAL CONTROL OF ICE DURING VITRIFICATION OF EXTENDED SYSTEMS

Gregory M. Fahy and Brian Wowk
21st Century Medicine, Inc., Rancho Cucamonga, California, USA (www.21cm.com)

INTRODUCTION

The only way to meet the clinical demand for replacement vascularized tissues and organs is to create engineered bioartificial organs. Cryopreserving these organs is a challenge similar to the challenge of preserving natural organs. Current evidence suggests that adequate preservation of large systems will require the elimination of essentially all ice despite cooling to and warming from the glass transition temperature (about –110 to –135^{o}C). This is problematic for several reasons. First, water is an essential constituent of living systems, and removing more than 50% of the water from an organ is normally damaging. Second, even though most ice formation may be prevented by using colligative agents, a few stray heterogeneous nucleators may produce ice crystals that, though occupying only a very small volume fraction of the system, are able to produce unacceptable injury to the system as a whole. To overcome these problems, we have designed solutions that, despite being very high in concentration, are low in toxicity and that, in addition, contain specific molecules that recognize and inactivate most heterogeneous nucleators.

METHODS

The toxicity of multiple candidate vitrification solutions was determined by exposing rabbit renal cortical slices to these solutions, washing the slices free of cryoprotectant, and assaying their K^+/Na^+ ratios after 90 min of incubation at an optimal temperature for ion transport. Solution stability was determined by heating vitrification solutions at a variety of warming rates in a differential scanning calorimeter (DSC) and determining the warming rate required to almost completely suppress ice formation on warming. The influence of solution composition on viability (K^+/Na^+ ratio) was studied by plotting viability against different global compositional variables. An overall figure of merit was constructed as the position of the results for a given composition on a plot of viability vs. stability. For the control of heterogeneous nucleation, a hanging vial technique was developed in which visual observations of the number and size of ice crystals under standardized conditions could be made and photographed. In addition, nucleation spectra were constructed by evaluating the behavior of populations of droplets tested for crystallization using the DSC. Furthermore, computer simulations of potential interactions between successful "ice blockers" and ice-like templates were carried out using Hyperchem.

RESULTS AND DISCUSSION

A polyvinyl alcohol-polyvinyl acetate copolymer (PVA) was found to have broad spectrum antinucleation capacity, whereas polyglycerol was found to specifically inhibit bacterial ice nucleation. The antinucleation effects were complementary, allowing synergistic protection from ice formation when the agents were combined. Molecular dynamics simulations showed an affinity of certain PVA oligomers for ice that may explain the effects of PVA as a disrupter of nascent ice crystals forming on heterogeneous nucleator surfaces.

A linear relationship was found between a compositional variable called qv* and the K^+/Na^+ ratio of slices exposed to vitrification solutions. qv* is the number of cryoprotectant polar groups per water molecule in the solution at the concentration needed to vitrify, and a high value was associated with both a high solution concentration and a high viability, quite contrary to normal expectation. It appears that the inclusion of poor glass formers is advantageous to glass formation, because such agents fail to compete successfully with biological molecules for water, thus allowing living systems to remain hydrated under water-poor conditions. The addition of ice-inhibiting polymers permitted the attainment of solutions that have very low toxicity despite extremely high stability (for example, VM3, which yields ~ 95% viability after 30 min of contact at 0^{o}C, and yet which has a critical warming rate of 10^{o}C/minute). These solutions are believed to be sufficiently stable and sufficiently non-toxic to enable vitrification of bioartificial organs, without electromagnetic warming requirements. Experiments showed that Cordis-Dow Artificial Kidneys could be vitrified and rewarmed at rates consistent with the stability of these solutions, whereas frozen-thawed CDAKs cracked.

SUMMARY

The combination of molecular ice control and biologically gentle water-replacing chemicals has permitted the realization of extraordinarily valuable vitrification solutions that may be equal to the task of permitting both natural and bioartificial organs to be successfully vitrified and recovered for clinical use.

REFERENCES

Kheirabadi, B.S., Fahy, G.M. (2000). *Transplantation*, **70**, 51-57.
Wowk, B. et al (2000). *Cryobiology*, **40**, 228-236.
Wowk, B., Fahy, G.M. (2002). *Cryobiology* (in press).

THE BEHAVIOR OF INDIVIDUAL SARCOMERES AFTER STRETCH IN ACTIVATED SKELETAL MUSCLE MYOFIBRILS

Dilson E. Rassier[1], Walter Herzog[1] and Gerald H.Pollack[2]
[1] Human Performance Laboratory, University of Calgary, Calgary, AB, Canada
[2] Department of Bioengineering, University of Washington, Seattle, WA, USA

INTRODUCTION

Force enhancement after stretch is observed in skeletal muscle and has been associated with instability of sarcomeres (Edman et al, 1982; Morgan, 1994). It has been suggested that during stretch some sarcomeres shorten, being responsible for most of the active force, while other sarcomeres are overstretched, being supported by passive structures. The average force of these sarcomeres would be increased compared to the isometric force at the same length. However, evidence suggests that sarcomeres may be stable, and sarcomere non-uniformity may not account for the force enhancement solely (ter Keurs et al, 1978). Although there has been much controversy, this issue has never been resolved. By studying single myofibrils, and tracking individual sarcomeres, we should be able to resolve this issue.

METHODS

Myofibrils isolated from rabbit psoas muscle were attached to a glass needle at one end and to a nanolever at the other end. The displacement of the nanolever could be monitored, providing force measurements. The image of the myofibrils was projected onto a linear 1024-element photodiode array, which was scanned to produce tracings of light intensity vs. position along the myofibril. Due to the contrast between the A-bands and I-bands, the photodiode array output gave a striation pattern, and the sarcomere length (SL) could be calculated as the span between A-band centroids (Blyakhman et al, 2001). Starting from an average SL of ~2.5 µm, stretches (4% to 10% of average SL, at a velocity of 95 nm·sec^{-1}·SL^{-1} to 350 nm·sec^{-1}) were applied to the myofibrils in relaxing (pCa^{2+} 8.0) and activating (pCa^{2+} 4.0) solutions.

RESULTS AND DISCUSSION

When the myofibrils were activated, and then stretched, force was higher than before stretch (Fig. 1). Since the stretch was performed on the descending limb of the force-length relation, the final length was at a region of less filament overlap. The observed force is therefore higher than expected if the myofibril had been stretched passively to the final length and then activated. It is also higher than the pre-stretch tension (less overlap, but more tension). The passive force after stretch accounted for ~2.5% of total force, similar to what others have reported in this SL range (Bartoo et al, 1993), and was therefore negligible.

Fig. 2 shows that force enhancement was not accompanied by instability of sarcomeres. All sarcomeres in this myofibril stretched (not necessarily by the same amount), and remained at constant length until the myofibril was shortened. There were cases in which some sarcomeres shortened modestly during stretch; however, that was observed in occasional sarcomeres in fewer than 5% of myofibrils.

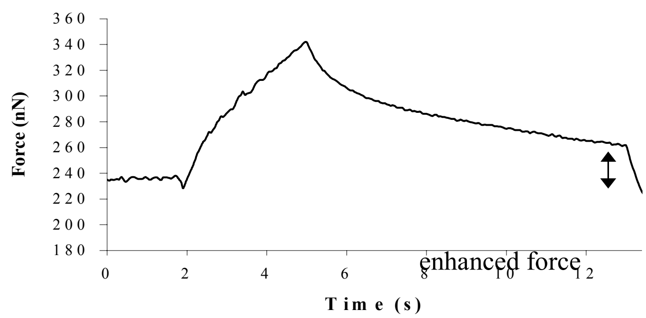

Figure 1: Force enhancement during and after stretch in an activated myofibril. The initial average SL was 2.5 µm. The myofibril was stretched to a final average SL of 2.7 µm.

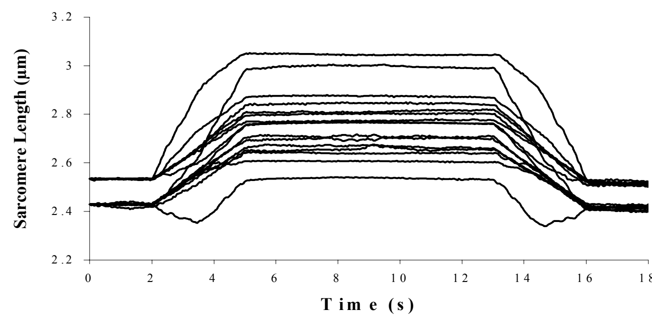

Figure 2: The behavior of all sarcomeres (n = 16) during and after stretch in an activated myofibril.

In conclusion, sarcomeres appear to be stable. Stretch-induced force enhancement in skeletal muscle cannot be explained solely by instability that results in sarcomere non-uniformity.

REFERENCES

Bartoo, M.L. et al. (1993). *J. Musc. Res. Cell Motil.* **273**, C266-C276.
Blyakhman, F. et al. (2001). *Biophys. J.* **81**, 1093-1100.
Edman, K.A.P. et al. (1982). *J. Gen. Physiol.* **80**, 769-784.
Morgan, D.L. (1994). *Exp. Physiol.* **79**, 831-838.
ter Keurs, H.E.D.J. et al. (1978). *J Gen. Physiol.* **72,** 565-592.

THE FORCE-SARCOMERE LENGTH-[CA^{2+}]$_I$ RELATIONSHIP IN RAT HEART

Henk EDJ ter Keurs, Tsuyoshi Shinozaki[+] , Jun Sun, Ying M Zhang, Amir Landesberg[*].
Departments of Medicine Physiology and Biophysics, Cardiovascular Research group, Faculty of Medicine, University of Calgary, Canada. [+]Tohoku Graduate School of Medicine Sendai Japan; [*]Dept of Biomedical Engineering, Technion-Israel Institute of Technology, Haifa Israel.[+]

INTRODUCTION

Sarcomere dependent (SL) Ca^{2+} sensitivity of the myofilaments underlies Starling's law of the Heart and fundamental changes in this interrelationship may be involved in heart disease. The steady state Force-SL relationship in skeletal muscle is determined by filament overlap, but little information is available on the steady state properties of Cardiac muscle. In this study we have analyzed F-SL-[Ca^{2+}]$_i$ relationships of intact and skinned Cardiac Trabeculae from the Rat.

METHODS

We used both intact and skinned trabeculae from LBN Rats. The trabeculae were suspended between a silicon strain gauge and a motor arm. SL was measured using laser diffraction techniques, [Ca^{2+}]$_i$ by fluorescence of Fura-2 injected by iontophoresis.

Tetani were elicited by 2 s stimulus trains at varied SL (1.85- 2.05μm) and at varied [Ca^{2+}]$_o$ (0.3-6 mM). The effects of SL and [Ca^{2+}]$_o$ and tetanic force (F_t) on auto fluorescence were measured. [Ca^{2+}]$_i$ was calculated from fluorescence of Fura-2 after subtraction of auto fluorescence corrected for effects of SL, [Ca^{2+}]$_o$ and F_t . the dependence of Fura-2 fluorescence on [Ca^{2+}] was calibrated in skinned fiber solutions.

Trabeculae were skinned using 1% triton X-100 and activated by solutions with 6 different [Ca^{2+}] with physiological free [Mg^{2+}] (0.7 mM) and following correction for skinning induced myofilament lattice expansion by addition of Dextran. A biochemical scheme, which couples Ca^{2+} binding to troponin-C (Tn-C) with cross bridge (XB) cycling, was established in order to quantify the dependence of Ca^{2+} affinity and XB kinetics on the SL, free [Ca^{2+}] and the generated force. The hypotheses that were tested included: i) SL-dependent Ca^{2+} affinity; ii) interfilament spacing dependent Ca^{2+} sensitivity; iii) force-dependent Ca^{2+} affinity and; iv) Ca^{2+}-dependent XB kinetics.

RESULTS

F_t, SL and [Ca^{2+}]$_i$ reached a steady state in 2s during tetani. Sub maximal activation at [Ca^{2+}]$_o$ 0.3-3 mM revealed F_t-SL relationships identical to those in skinned fibers. F_t at saturating [Ca^{2+}]$_i$ (6 mM) increased from 60 % of F_{max} at SL 1.65 μm to 100% at SL=2.1 μm, following a curve predicted on the basis of the cross-bridge theory, given the sarcomere geometry in rat trabeculae. The F_t-[Ca^{2+}]$_i$ relationship revealed a SL-dependent decrease in EC_{50} (0.95, 0.70 and 0.56 μM at SL 1.65, 1.75 and 1.85 μm, respectively) and increase in F_{max} (62, 85 and 98 mN/mm^2) and increase in Hill coefficient (3.9. 4.7 and 5.5, respectively).

The shape of the F-SL relationship in skinned trabeculae was identical to that previously published. F_{max} , at SL 2.1 μm, was lower in the control muscle than in Dextran treated muscle (78.7±8.1 mN/mm^2 vs. 107.6±6.2 mN/mm^2 (mean±s.e.m), $p<0.001$). EC_{50} decreased with increase of SL in both groups. EC_{50} decreased from 1.55±0.09 μM at SL 1.90 μm to 1.06±0.10 μM at SL 2.15 μm without Dextran and decreased from 1.41±0.06 μM to 1.04±0.09 μM over the same SL range in Dextran treated muscle. EC_{50} at corresponding SL were 0.18 ± 0.03 μM higher in Dextran free solution than that in the presence of Dextran ($p<0.05$). The EC_{50} from both groups were substantially higher than those of intact fibers (EC_{50} 0.56 μM at SL ~1.85 μm and 0.38 μM at SL ~2.20 μm).

Using the biochemical scheme, it appeared that SL-dependent and Ca^{2+}-dependent mechanisms were unable to explain the measured stress-length-[Ca^{2+}] relationships. However, for all trabeculae, an identical, unique relationship between Ca^{2+} affinity and developed stress demonstrated that an increase in the generated stress is associated with a proportional increase in apparent Ca^{2+} affinity.

CONCLUSION

Filament overlap determines SL-dependence of cardiac force development at saturating [Ca^{2+}]. Correction of [Mg^{2+}] and colloid osmotic pressure in the skinning solutions increases F_{max}, but neither eliminates SL-dependent Ca^{2+} sensitivity, nor does it increase Ca^{2+} sensitivity to the level of intact cardiac muscle suggesting the presence of a Ca^{2+} sensitizer in the cytosol of the cardiac myocyte. The dependence of Ca^{2+} affinity on the number of force generating XBs is the dominant mechanism that regulates XB recruitment and SL-dependent generated stress in cardiac muscle at physiological cytosolic [Ca^{2+}].

CONTRACTION OF SINGLE MYOFIBRILLAR SARCOMERES OCCURS IN 2.7-NM STEPS AND INTEGER MULTIPLES THEREOF

Olga Yakovenko[1], Felix Blyakhman[1] and Gerald H.Pollack[2]

[1] Department of Physics, Ural State University, Ekaterinburg, Russia
[2] Department of Bioengineering, University of Washington, Seattle, WA, USA

INTRODUCTION

In deducing the underlying nature of contraction, considerable emphasis has been placed on determining the elemental contractile step. Early on, muscle contraction was noted to occurr in steps (Pollack et al., 1977). Since then, we have continually refined methodologies, and are now able to follow the time course of shortening and lengthening in individual sarcomeres of single myofibrils, with nanometer resolution.

METHODS

Myofibrils isolated from rabbit cardiac muscle and honeybee flight muscle were attached between the tips of glass needles, one of which could be moved by a piezoelectric motor. The image of the myofibril was projected onto a linear 1024-element photodiode array, which was scanned to produce tracings of light intensity vs. position along the myofibril. Sarcomere length could be calculated as the span between A-band centroids (Blyakhman et al, 2001). Myofibrils were placed in activating solution, and put through ramp-stretch-release cycles, and the length of each sarcomere was tracked.

RESULTS AND DISCUSSION

Although the myofibril was programmed to change length by a ramp waveform, the sarcomere-length change was consistently stepwise. Examples are shown in Fig. 1. We computed step size by taking the sarcomere-length decrement between successive pauses, determined by least squares fit.

Results are shown in Fig. 2. Note that the primary step size is 2.7 nm. All other step sizes are integer multiples of that value. Thus, each sarcomere can step by any of a series of values, but the values are always integer multiples of 2.7 nm. The same was found for stretch—always integer multiples of 2.7 nm. And, the same paradigm was found in honeybee flight muscle. Hence, the 2.7-nm stepping paradigm appears general.

Why 2.7 nm? The value 2.7 nm is the molecular repeat along the thin filament. (Although the repeat along the individual actin strand is 5.4 nm, the two strands that make up the filament are displaced by half of 5.4 nm, giving a linear repeat of 2.7 nm.) Hence each step is related to the actin-monomer repeat. But, each step can be two, or three, or *n* times the repeat. A simple model to explain these results will be presented (see: Pollack, 2001).

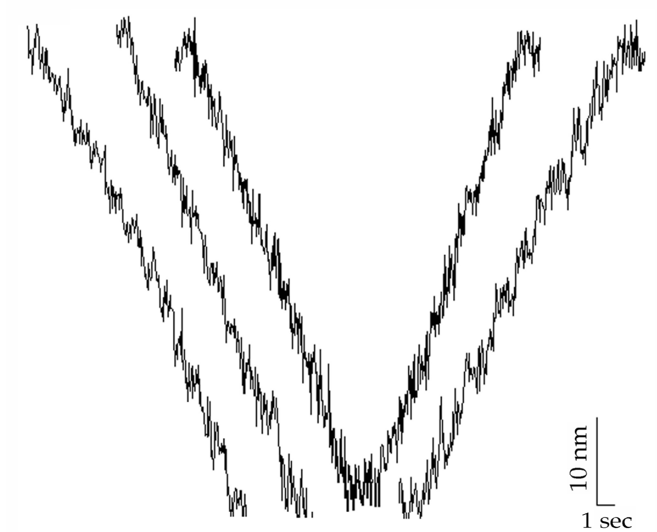

Figure 1: Representative traces of sarcomere-length change during motor-imposed trapezoid in rabbit cardiac muscle. First, second and fourth traces show segments of record; third trace shows entire record.

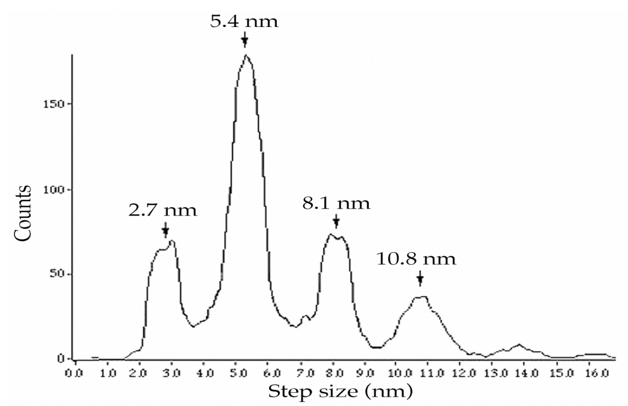

Figure 2: Histogram of shortening steps obtained from activated rabbit cardiac muscle. Histogram includes 493 steps from 75 sarcomeres in 25 myofibrils.

REFERENCES

Blyakhman, F., Tourovskaya, A., and Pollack, G.H. Biophys J. 81: 1093-1100, 2001.
Pollack, GH, Cells, Gels and the Engines of Life, Ebner and Sons, Seattle, 2001. www.cellsandgels.com.
Pollack, GH, Iwazumi, T., ter Keurs, HEDJ, and Shibata, EF, *Nature* 268: 757-759, 1977.

CLASS VI MYOSIN MOVES PROCESSIVELY ALONG ACTIN FILAMENTS BACKWARDS WITH LARGE STEPS.

Mitsuhiro Iwaki*, Yasunori Komori*, So Nishikawa*, Kazuaki Homma, Atsuko H. Iwane, Junya Saito, Reiko Ikebe, Mitsuo Ikebe and Toshio Yanagida*

* *Single molecule process project, ICORP, JST, 2-4-14, Senba-Higashi, Mino Osaka Japan562-0035. Department of Biophysical Engineering*, *Osaka University Machikaneyama, Toyonaka, Osaka 560-8531, Japan. Department of Physiology, University of Massachusetts Medical School, 55 Lake Avenue North, Worcester, Massachusetts 01655-0127, USA. Department of Physiology and Biosignaling, Osaka University Graduate School of Medicine, 2-2, Yamadaoka, Suita, Osaka, 565-0871, Japan.*

Among a superfamily of at least 18 known classes of myosin, class VI myosin is recently found to move actin filaments backwards in the surface gliding assay (Wells et al., Nature 401, 505-'99). Here we observed movement of single molecules of myosin VI with GFP fused along actin filaments by total internal reflection fluorescence microscopy. Single myosin VI molecules moved processively towards the pointed (-) end of actin filament (backwards). Furthermore, using optically-trapping nanometry, it was found that myosin VI produces several successive steps along an actin filament with ~38 nm steps. These mechanical properties of myosin VI are quite similar to those of myosin V, except for the directionality. The extended long (23 nm) neck domain (lever arm) of myosin V has been thought to be essential for its large processive step, based on the lever arm model. However, since myosin VI has only one IQ motif thus its neck domain is extremely short, it is unlikely that the myosin VI takes this scenario. Recently we have shown that the directionality of myosin VI is irrespective to the neck domain (Homma*, et al*. Nature 412, 831- '01). These results indicate that the motor domain and/or actin-mysoin interface, not the neck domain, determine the processive 36 nm steps and directionality of myosin VI.

PASSIVE ELASTIC RECOIL OF TITIN ADDS TO THE SHORTENING SPEED OF SKELETAL MUSCLE FIBERS

Ave Minajeva, Ciprian Neagoe, Michael Kulke, and Wolfgang A. Linke
Institute of Physiology and Pathophysiology, University of Heidelberg, Im Neuenheimer Feld 326, D-69120 Heidelberg, Germany,
wolfgang.linke@urz.uni-heidelberg.de, webpage: http://www.physiologie.uni-hd.de/linke/

INTRODUCTION

The shortening velocity of skeletal-muscle fibers is determined principally by actin and myosin. However, these contractile proteins are in parallel with elastic elements, whose main structural basis is thought to be the titin filaments. If titin is stretched, it may contribute to sarcomere shortening simply because it can recoil passively. Thus, titin truly is a 'contractile' protein. Here, the titin-based contribution to shortening velocity (V_p) was quantified in single rabbit psoas myofibrils. Results were used to estimate the importance of titin elastic recoil for the shortening speed of actively contracting rabbit psoas fibers.

METHODS

Single rabbit psoas myofibrils were suspended between a rigid needle and a micromotor, and the image was projected onto a linear CCD array (Fig. 1). Nonactivated specimens were rapidly released from different initial sarcomere lengths (SLs) by steps of 150, 250, or 450 nm/sarcomere. During buckling of the myofibril, the regular intensity-profile pattern disappeared, but was spontaneously restored as the slack was taken up. V_p was calculated from release amplitude and time to slack reuptake.

Method to Measure the Speed of Passive Elastic Recoil

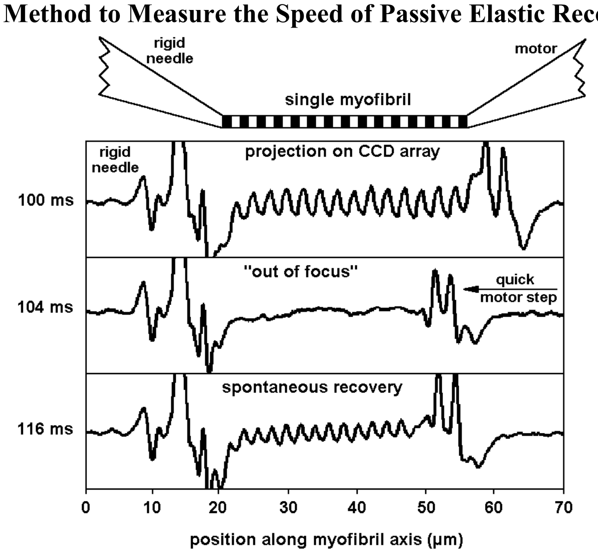

Figure 1: Example of measurement of V_p of relaxed myofibril.

RESULTS AND DISCUSSION

V_p progressively increased (upper limit of detection, ~60 µm× s^{-1}×sarcomere^{-1}) between 2.2 and 3.0 µm initial SL (Fig. 2), albeit much steeper than passive tension (*cf.*, Linke, 2000). Already at very low passive-tension levels (<1-2 mN/mm^2), V_p could greatly exceed the active unloaded shortening velocity measured in fully Ca^{2+}-activated skinned rabbit psoas fibers (11.8 (15°C) or 14.5 (23°C) µm×s^{-1}×sarcomere^{-1}), if release steps were sufficiently small. Degradation of titin by low doses of trypsin (0.05 µg/ml; 23°C, 5 min) drastically decreased V_p.

Summary of V_p Measurements on Single Myofibrils

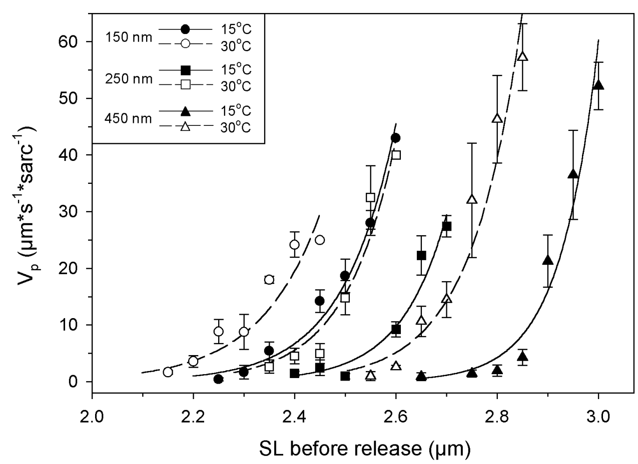

Figure 2: Passive shortening speed (mean±SEM, n=9-11), calculated for release steps of 150, 250, 450 nm/sarcomere, and temperatures of 15°C or 30°C (Minajeva et al., 2002).

In intact myofibrils, average V_p was the faster, the smaller the release step applied. Also, V_p was much higher at 30°C than at 15°C (Q_{10}: 2.0-3.04-6.15, for releases of 150-250-450 nm/sarcomere, respectively). Viscous forces opposing the shortening are likely to be involved in determining these effects (Kulke et al., 2001). The results support the idea that the contractile system imposes a braking force onto the passive recoil of elastic structures. However, elastic recoil may aid active shortening during phases of high elastic energy utilisation (Minajeva et al., 2002), *i.e.*, immediately after the onset of contraction under low or zero load or during prolonged shortening from greater physiological SLs.

SUMMARY

Measurements of the passive elastic recoil of single psoas myofibrils revealed that stretched titin filaments are sufficiently powerful molecular springs to make a significant contribution to the shortening speed of Ca^{2+}-activated muscle fibers. Under physiological conditions this contribution may be important in that it acts as an additional driving force on the contractile system at small releases and during shortening from longer SLs.

REFERENCES

Kulke, M. et al. (2001). *Circ. Res.*, **89**, 874-881.
Linke, W.A. (2000). *Histol. Histopathol.,* **15**, 799-811.
Minajeva, A. et al. (2002). *J. Physiol.*, in press.

ANGULAR MOMENTUM OF THE NON-THROWING ARM IN THE JAVELIN THROW

Michele LeBlanc
Pepperdine University, Malibu, CA 90263
michele.leblanc@pepperdine.edu

INTRODUCTION

Javelin throwers are instructed to “block” with their non-throwing side and to “reach for their wallet” during the final phase of the throw to enhance their throw’s distance. The purpose of this study is to determine the effectiveness of the motion of the non-throwing arm (NTA) during a javelin throw by examining its angular momentum.

METHODS

At the end of the run-up, a right-handed thrower makes a cross-over step, lands on the right foot (RTD), plants the left foot (LTD), and releases the javelin. The athlete is in single-support (SS) between RTD and LTD, and generally, in double-support (DS) between LTD and release. Two throws for each of eight elite-level male javelin throwers were used for this study. Data was collected at 100 Hz using standard 3D film analysis procedures.

Digitized data from the film images were used to calculate the coordinates of 21 body landmarks and three javelin landmarks. The 3D coordinates were expressed in a fixed orthogonal reference frame with the X-axis perpendicular to the run-up (pointing to the right), Y-axis along the run-up, and Z-axis pointing upward. The coordinate data were smoothed using quintic spline. Center of mass locations and angular momentum values of the body segments and of the javelin were calculated following a method based on Dapena (1978). The location of the javelin c.m. was computed using information from Hubbard and Bergman (1989).

The SS and DS phases were each divided into two equal time periods. The 3D angular momentum values of the system (body-plus-javelin) and the NTA, all relative to the whole-body c.m., were calculated for five instants: (1) RTD, (2) the midpoint of SS, (3) LTD, (4) midpoint of DS, and (5) release.

RESULTS AND DISCUSSION

Average angular momentum values for the 16 throws are shown in Table 1. To facilitate this discussion, the terms “clockwise” (CW) and “counterclockwise” (CCW) will replace the signs of the X, Y and Z angular momentum components; the directions will correspond to views from the right, from behind and from overhead for the H_X, H_Y and H_Z angular momentum components, respectively.

During SS and DS, the system obtains more and more CW H_X. The NTA minimally contributes to the system H_X. The c.m. of the NTA is located just slightly in front of the body c.m. and moves from shoulder level to approximately the height of the body c.m., creating a small amount of CW H_X.

The amount of system CCW H_Y increases throughout SS, in large part due to the motions of the extended NTA as it sweeps horizontally across the thrower’s body, away from the throwing arm. During DS, the system CCW H_Y remains relatively fixed. The NTA transfers its CCW H_Y to the trunk throughout DS. The trunk transfers the CCW H_Y to the throwing arm-plus-javelin segment (TAJ) later in DS.

During SS, the system has a small amount of CCW H_Z and the NTA generates CCW Hz by the sweeping motion of the extended arm across the body. During the early portion of DS, the NTA’s CCW H_Z is transferred through the trunk to the TAJ.

CONCLUSIONS

During SS the motions of a javelin thrower’s NTA create angular momentum that is transferred to the TAJ via the trunk during DS. The NTA has little angular momentum at release. The effectiveness of a javelin thrower’s NTA action can be assessed by noting the amount of angular momentum generated and transferred, as well as noting the timing of the transfer of angular momentum to the trunk and TAJ.

Table 1: Angular momentum of the system and NTA ($kg \cdot m^2/s$). (Means ± s.d.)

Times	1	2	3	4	5
	(RTD)		(LTD)		(Release)
H_X					
System	13 ± 4	-15 ± 5	-35 ± 7	-49 ± 5	-67 ± 9
NTA	0 ± 2	-3 ± 2	-4 ± 2	-3 ± 2	-1 ± 1
H_Y					
System	8 ± 4	-6 ± 5	-23 ± 6	-16 ± 7	-21 ± 6
NTA	-3 ± 2	-6 ± 3	-11 ± 3	-6 ± 2	0 ± 1
H_Z					
System	3 ± 4	0 ± 3	3 ± 3	17 ± 5	23 ± 9
NTA	2 ± 1	3 ± 1	5 ± 2	1 ± 2	1 ± 1

REFERENCES

Dapena, J. (1978) *J. Biomechanics*, **11**, 251-256
Hubbard, M., Bergman, C.D. (1989) *Int. J. Sport Biomechanics*, **5**, 40 – 59

ACKNOWLEDGMENTS

This work was supported by a grant from USA Track & Field.

OPTIMAL DISCUS RELEASE CONDITIONS INCLUDING PITCHING-MOMENT-INDUCED ROLL

Mont Hubbard

Sports Biomechanics Laboratory, University of California, Davis, California, USA
mhubbard@ucdavis.edu

INTRODUCTION

Besides its roughly parabolic flight path, the next most apparent feature of discus flight to the keen observer is the slow rolling of the discus attitude from right to left (when viewed from behind). Although this motion has apparently not yet been measured quantitatively, it appears that tens of degrees of roll occur in a typical flight and that the women's discus is perhaps more susceptible to it than the men's. This rolling motion changes the direction of the lift vector and consequently the trajectory from an otherwise vertical plane, and the smaller vertical component of lift reduces range. Most previous discus simulation studies have assumed that attitude is unchanged during flight, however, relying on the assumption that large angular momentum due to spin about its axis of symmetry will resist completely the effects of aerodynamic torques and maintain the initial release discus attitude constant. Even Frohlich (1981), who clearly described the precessional effects of torques due to any offset between centers of pressure and mass, neglected these in simulations.

Only the calculations of Soong (1976) have considered the possibility of general rotational motion. He derived equations for flight including not only large axial spin, but also wobble about the other two axes, and used experimental lift and drag force data of Stilley (1972) for a frisbee-like disc. Because he was unable to find information in the literature on discus pressure distributions, Soong calculated these using the classical velocity potential for an approximate rotating ellipsoid. These were used to calculate aerodynamic moments in the trajectory integrations. Unfortunately, no numerical results were given for the dependence of the moments on translational and rotational velocities that would allow for comparison with experimental data.

METHODS

In this work, equations of motion were derived for discus flight including the assumption that attitude changes (mainly in roll) due to precession of spin angular momentum by nonzero pitching moments. The initial angular velocity vector is assumed parallel to the axis of symmetry, i.e. there is no initial wobble. Although other authors have measured discus lift and drag (Cooper, et al., 1959; Ganslen, 1964), for consistency we use the experimental aerodynamic force results of Kentzer and Hromas (1958), who also measured pitching moment as a function of angle of attack, α. Other realistic features observed in their data are stall and consequent abrupt decrease in lift near $\alpha = 28$ deg. Recent studies of the aerodynamics of Frisbee and other similar circular planform objects (Potts and Crowther, 2000; Hubbard and Hummel, 2000) support the assumption that even large spin produces negligible rolling moment. Thus, in the calculations, the precession of spin angular momentum is due only to pitching moment, and discus attitude changes occur in roll only. Optimization in the initial condition parameter space allows calculation of release conditions producing maximum range including initial pitch and roll attitude, and angle of attack.

RESULTS AND DISCUSSION

It is optimal to release with the discus rolled significantly to the right ($\phi_o = 15$ deg) so that the lift vector remains near vertical throughout much of the flight. Maximum range (when v_o=25 m/s and h_o=1.8 m) is more than 73 m. Roll angle excursions during the optimal trajectory exceed 35 deg ($-20 < \phi(t) < 15$ deg). Optimal release conditions found here neglect the possible dependence of release velocity and spin, since no such dependence has yet been documented. It is also likely that release velocity is dependent on release angle as in the shot put (Hubbard, et al., 2001) and even angle of attack. This motivates further study of these dependencies.

SUMMARY

Discus roll changes substantially during flight as a result of the precessional effects of nonzero pitching moments and must be accounted for in simulations. Optimal release conditions include non-zero initial roll and allow the mean lift to stay nearly vertical, especially near the end of flight.

REFERENCES

Cooper, L. et al. (1959). *Flight of the discus.* Division of Engineering Science, Purdue University.
Frohlich, C. (1981). *Am. J. Phys*. **49**, 1125-1132.
Ganslen, R.V. (1964) *Athletic Journal*, **44**, 50.
Hubbard, M., Hummel, S.A. (2000). *5th Conf. on Math.and Sport*, G.Cohen (Ed.), Univ. of Technology Sydney, 124-134.
Hubbard, M. (2001) *J. Biomechanics* **34**, 449-456.
Kentzer, C. P., Hromas, L. A. (1958). *Discobolus* **4**, 1, Available in 2001 from Barry Willis, 14 Bluebridge Avenue, Brookmans Park, Hatfield, Herts. UK.
Potts, J.R., Crowther, W.J. (2000). The flow over a rotating wing, *Proc RAeS Aero. Res. Conf.*, London, UK.
Soong, T.-C. (1976). *J. Applied Mechanics*, **98**, 531-536.
Stilley, G.D. (1972). AD-740117, Naval Ammunition Depot, Crane, IN.

TWIST ANGULAR MOMENTUM DURING THE POLE VAULT TAKE OFF

Peter M. McGinnis

Department of Exercise Science and Sport Studies, SUNY College at Cortland, Cortland, New York, USA (pmcginnis@cortland.edu)

INTRODUCTION

Pole vaulting is an exciting and complex athletic event. During a successful vault, rotations occur about several axes. Following takeoff, rotation around the transverse or somersault axis occurs as the vaulter swings on the pole and continues to rotate into an inverted position. This somersaulting rotation reverses direction later in the vault as the vaulter pushes off the pole. Just prior to this, rotation about the vertical or twist axis occurs as the vaulter extends and prepares to push off the pole. On initial examination, it appears that this is the only time during the vault when a vaulter has angular momentum about the vertical or twist axis. However, upon closer examination, it seems that a pole vaulter might have some angular momentum about the twist axis during the takeoff phase of the vault as well, due to the forward swinging action of the lead leg at the instant of takeoff. This angular momentum would be in the opposite direction of the twist angular momentum the vaulter possesses when he turns and pushes off the pole.

Most analyses of the pole vault have only been 2-dimensional, a few have been 3-dimensional, and even fewer have reported the angular momentum of a vaulter in 3-dimensions. Morlier and Cid (1996) did measure the angular momentum of a pole vaulter in 3-dimensions. Their results indicated that the vaulter had a slight amount of twist angular momentum at the instant of takeoff. Their study was limited to only one vault at 4.80 m, however.

The purpose of this study was to measure the twist angular momentum generated during the takeoff phase of successful competitive vaults by elite pole vaulters .

METHODS

Two gen-locked video cameras operated at 60 hz recorded the last step and take off phases of vaults during the men's pole vault competitions at the USA Track and Field Championships in 1999 and 2001. A Peak Motus video digitizing system was used to manually digitize 20 anatomical landmarks in each frame of the selected videorecords. The digitized coordinate data were filtered and then transformed into global 3-dimensional coordinates using the DLT method. The following global coordinate system was used: the X-axis was directed forward and horizontally along the direction of the runway, the Y-axis was directed to the left horizontally across the runway, and the Z-axis was directed upward. A total of 9 vaults (one by each by 9 different vaulters) were analyzed. These vaults represented the highest successful vaults by each vaulter in the two competitions. The heights of the analyzed vaults ranged from 5.50 m to 6.02 m. The average height of the analyzed vaults was 5.71 m.

The vaulter model included the following 11 segments: head, neck, and trunk; 2 forearms and hands; 2 upper arms; 2 thighs; 2 legs; and 2 feet. Anthropometric data from Zatsiorsky and Seluyanov (1983) and Plagenhoef et al. (1983) were used to describe the inertial characteristics of the vaulter. The angular momentum of the pole vaulter about his center of mass was computed using the technique described by Dapena (1978). A composite history of the angular momentum was computed by averaging the angular momentum of the 9 vaulters using the instant of takeoff as the synchronizing event.

RESULTS

The angular momentum about the Z-axis was negative at foot strike and generally changed toward positive throughout the stance phase of the takeoff foot for all 9 vaulters. All 9 vaulters had positive angular momentum about the Z-axis at the instant of takeoff as did the vaulter in Morlier and Cid's (1996) study. This angular momentum reached a maximum at takeoff or within one frame of takeoff in 7 of the 9 vaults. The composite angular momentum about the Z-axis was minimum and negative at the instant of foot strike (H_z = -3.9 kg.m^{2}s^{-1}) and maximum and positive at the instant of takeoff (H_z = 7.3 kg.m^{2}s^{-1}). The most significant contribution to the positive angular momentum about the Z-axis at takeoff came from the swing leg.

DISCUSSION AND CONCLUSIONS

The positive angular momentum about the Z-axis possessed by pole vaulters at takeoff is not large, but it must be reversed later in the vault to execute the turn. The total change in angular momentum about the Z-axis during the vault may thus be significant. This change in momentum may be difficult for some vaulters to produce. Qualitative examination of videos of the elite vaulters in this study indicates that this is not a problem for them. However, some less skilled vaulters may have difficulty producing this change in momentum. As a result, their turning action may be incomplete or late, thus adversely affecting their performance.

REFERENCES

Dapena, J. (1978). *J. Biomechanics*, **11**, 251-256.
Morlier, M., Cid, M. (1996). *J. Biomechanics*, **29**, 1085-1090.
Plagenhoef, S. et al. (1983). *RQES*, **54**,169-178.
Zatsiorsky, V, Seluanov, V. (1983). In Matsui & Kobayashi (eds.), *Biomechanics VIII-B*, Human Kinetics, 1152-1159.

ACKNOWLEDGEMENT

This study was financially supported by USA Track and Field.

KINEMATICS AND KINETICS IN POLE VAULTING: ENERGY STORAGE AND RETURN

Gert-Peter Brüggemann, Adamantios Arampatzis, Falk Schade
Institute for Biomechanics, German Sport University of Cologne, Cologne, Germany, brueggemann@dshs-koeln.de

INTRODUCTION

Pole vaulting at national and international levels was subjected to numerous biomechanical studies in the past (e.g. Gross & Kunkel 1990, Angulo-Kinzler et al. 1994). Most biomechanical analyses were restricted to the description of selected parameters of the performance. Only a few model oriented studies were carried out to explain the effect of energy storage by pole bending and of energy re-utilization by the athletes in a later stage of the movement (McGinnis & Bergmann 1986, Ekevad & Lundberg 1997). Due to the fact that calculations of the energy of the pole based on pure kinematic sources are extremely sensitive to noise and errors, most of the energy and power research is based on a relatively restricted data base. No kinetic data are available from elite pole vaulters in training or competitive situations. Only a very small amount of kinetic data (ground reaction forces at the pole box) has been reported from sub-elite athletes in training situations (Woznik 1992).

The objective of the study is the explanation of the effect of energy storage in the pole by bending, and of energy re-utilization by the athletes in a later stage of the movement, on the final performance in pole vaulting.

METHODS

For the analysis, the pole vault was divided into the following phases: (1) The energy production phase. This phase starts with the approach and ends with contact of the jump foot against the ground at take-off. (2) The energy exchange phase. This phase is from the first contact of the takeoff foot with the ground at take-off to the athlete's release of the pole at the end of the jump. During the first part of the energy exchange phase, elastic energy is transferred into the pole while decreasing the athlete's energy. The difference between the decrease in the athlete's energy and the maximum pole energy indicates if the pole elasticity was effectively used (Criterion 1). During the second part of the energy exchange phase the stored energy is re-utilized through transfer from the pole to the athlete. The athlete's energy increases. The difference between the returned energy and the energy gain of the athlete indicates to what extent the athlete used muscular work to increase his/her energy (Criterion 2). The two criteria were applied to identify energy storage and return strategies of elite athletes in two separate competitions.

In the study, 6 top national jumpers (5 male, 1 female) performed 4 to 11 trials each, at 90% of their respective personal records. All trials were recorded using four synchronized and genlocked video cameras operating at 50 fps. The ground reaction forces exerted on the bottom of the pole were measured with an instrumented planting box (three 3D Kistler force transducers). Pole deformation and force data allowed the calculation of energy transmitted into the pole and re-utilized by the athlete.

RESULTS AND DISCUSSION

From the energy data, one can derive an energy loss of 7–10% during pole bending and extending (Fig. 1). Different athletes use different energy storage and return strategies while reaching similar energy amounts at the end of the pole phase. Differences in the final energy at release can be determined through different motor behavior in the two phases.

The results show that the chosen criteria are sensitive to differentiate between top athletes and to identify individual deficits (Figs. 1, 2). The criteria are repeatable and reliable.

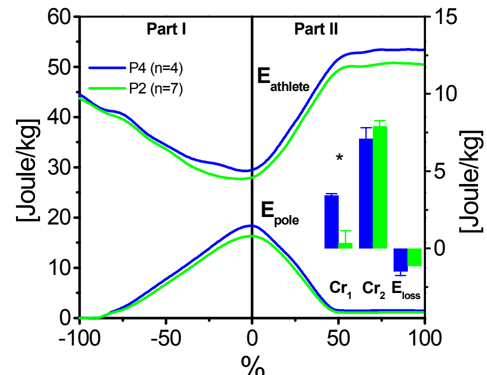

Figure 1: Mechanical energy of the athlete and of the pole during pole bending and extending of two athletes (means of 4 and 7 trials, respectively). Criteria 1 (Cr_1) and 2 (Cr_2) are completely different in the two athletes.

Figure 2: The two criteria (Cr_1 and Cr_2) and the energy loss analyzed

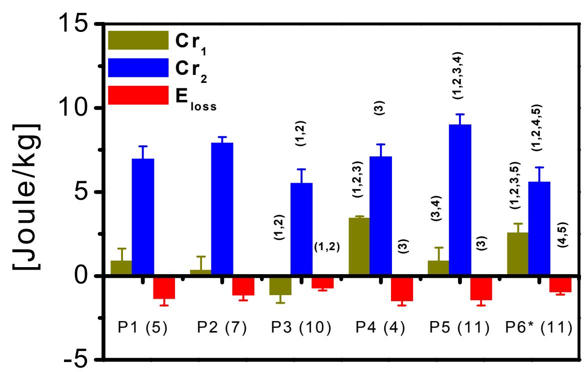

in the trials of six athletes demonstrate subject-dependent energy storage and re-utilization strategies. The numbers in the graph indicate significant ($p<.05$) differences between the individual athletes: (1,2) different from athletes 1 and 2; (1,2,3) different from athletes 1,2,3.

REFERENCES

Angulo-Kinzler, R.M. et al. (1994). *J.Appl.Biom.*,**10**, 147-165.
Ekevad, M., Lundberg, B. (1997). *J. Biom.*, **30**, 259-264.
Gross, H.J., Kunkel, V. (1990). *Int. Am.Athl.Federation.*
McGinnis, P.M., Bergman, L.A. (1986). *Int. J.Sport Biom.*, **2**, 186-201.
Woznik, T. (1992). Sportwiss. Tpraxis., *SFT*, Erlensee.

ORTHODONTIC BRACKET DEBONDING: IN VIVO AND IN VITRO DEBONDING STRENGTH AND THE RELATED TOOTH DAMAGE

Tamar Brosh, Ofer Sarne, Alexander D Vardimon
Department of Orthodontics, School of Dental Medicine, Tel Aviv University, Tel Aviv Israel

INTRODUCTION

Debonding strength of orthodontic brackets and their related tooth damage are of concern to bracket developers, engineers, dental material researchers and orthodontics. The in vitro studies, as well as numerical models, cannot simulate the oral environment and its affect on the debonding characteristics. This presentation introduces results obtained from in vivo and in vitro bracket debonding and their related tooth damage.

METHODS

Orthodontic debonding pliers were modified and a strain gauge was bonded to one of its handles. After calibration, in vivo bracket debonding force measurement could be performed.

In vivo study: Metal brackets were debonded after full orthodontic treatment (about 24 mo) from 50 patients using pliers. Brackets from 30 of these patients were scanned using SEM and EDAX and scaled for Adhesive Remnants Index (ARI) (0-3) and Calcium Remnant Index (CRI) (0-3). Only premolars were used for comparison.

In vitro study: Metal brackets were bonded to the buccal side of 20 premolars after acid-etching procedure and then divided into 2 groups which differed in water storage duration: Group A - 48 h, Group B - 12 mo. Before bracket debonding using the pliers connected to a loading machine, all specimens underwent thermo-cycling procedure. All brackets were scanned and scaled as in the in vivo study.

Student t-test was applied to evaluate differences between debonding strengths, ARI and CRI. Correlations between debonding strength and ARI or CRI were performed for both studies.

RESULTS AND DISCUSSION

Table 1 presents the mean values of the determined parameters of all tests. No significant differences ($p>0.05$) were found between debonding strength or ARI. However, calcium remnants on brackets debonded in the in vivo study were significantly higher than those observed in the in vitro study after 48 h ($p=0.05$) and also higher than the 12 mo water storage of specimens. One of the brackets debonded with a large enamel chip is presented in Figure 1. Significant negative correlations were found between debonding strength and ARI or CRI (Table 2).

Debonding strength was not affected by the clinical environment (orthodontic forces, saliva ect.) compared to in vitro measurements. This fact alone allows further determining strength values by using laboratory models. However, more tooth damage was observed when brackets were debonded after the long orthodontic treatment.

Higher debonding strength values do not indicate higher tooth damage (Table 2). Debonding site can occur at various locations: (i) cohesive at the adhesive-bracket interface, where the adhesive remains on tooth enamel; (ii) adhesive through the adhesive layer; and (iii) cohesive at the adhesive-enamel interface. Almost none of these categories appear alone and a combination of more than one appears. If debonding occurs according to (i) no tooth damage occurs. Most importantly, debonding strength between the bracket and the adhesive is higher than required to debond the bracket according to (ii) or (iii). This conclusion is an outcome of the negative correlations found between debonding strength and ARI or CRI. However, high values of debonding strengths indicate large amounts of adhesive remnants on tooth enamel. In these cases, scaling using orthodontic tools should be performed and damage may occur.

SUMMARY

Teeth are prone to damage when low debonding strength is required, since debonding occurs at the enamel-adhesive interface. This interface is weaker than the bonding interface between the adhesive material and the metal bracket. Moreover, in vitro studies can indicate debonding strength, however, their indication for tooth damage is limited.

Table 1: Debonding strength, adhesive (ARI) and calcium (CRI) remnant index (mean ± SD)

	In vivo study	In vitro study	
Test after	24 mo	48 h	12 mo
Debonding strength (MPa)	17.2 ± 6.6	15.2 ± 4.6	15.9 ± 2.7
ARI	1.9 ± 1.3	2.2 ± 1.2	1.9 ± 1.4
CRI	1.0 ± 1.0	0.2 ± 0.4	0.6 ± 0.9

Table 2: Correlations between parameters

	Debonding strength		
	In vivo	In vitro	
	24 mo	48 h	12 mo
ARI	-0.34	-0.75	-0.75
CRI	-0.24	-0.36	-0.49

Figure 1: Bracket base covered with adhesive and a large scale of enamel chip (arrow)

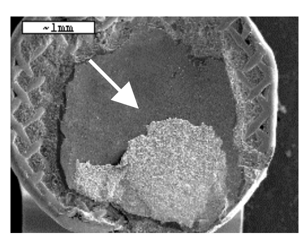

EXPERIMENTAL AND NUMERICAL STUDY ON THE MECHANICAL BEHAVIOUR OF THE PERIODONTAL LIGAMENT UNDER ORTHODONTIC LOADING

Christoph Bourauel

Department of Orthodontics, University of Bonn, 53111 Bonn, Germany
Head Orthodontic Biomechanics Laboratory, bourauel@uni-bonn.de

INTRODUCTION

Inital tooth deflections under orthodontic loads are the mechanical key stimulus to trigger bone remodeling processes in the dento-alveolar complex. In particular the elasticity properties of the periodontal ligament (PDL) have a great impact on stresses and strains induced in the PDL and the surrounding bony structures and thus control the orthodontic tooth movement. It was the objective of the presented study to determine linear and nonlinear elasticity parameters desribing the mechanical behaviour of the PDL regarding the initial tooth mobility. Though the parameters are well known for teeth and bony structures, a wide range of values for Young's modulus of the PDL can be found in literature. In a combined experimental and numerical approach, the behaviour of different human and animal models was determined.

MATERIALS AND METHODS

Ten non-fixed preparations of human front and canine teeth, five canines from mini pigs (genus Yucatan, Troll), each with surrounding bone and ligament, and twelve mandibular segments of Wistar rats were investigated. The specimens were measured in a 3-D laser-optical set-up (**MO**bility **M**easurement **S**ystem, *Hinterkausen* et al., 1998) to determine force/ deflection characteristics. The crowns of the teeth were loaded with forces of up to 0.1 N (rat specimens), 1.0 N (human) and 3.5 N (pig). A very slow force rate was chosen to simulate the orthodontic load case and to ensure that hydrodynamic flow processes have decayed. The maximum load was applied in up to 100 steps within one hour of measurement time.
Subsequently, the specimens were cut into sections, microphotographs were taken and 3-D finite element (FE) models were generated semi-automatically with a specialized software (*Vollmer et al.*, 2000). Using measured force/deflection diagrams and the FE models of the experimentally investigated preparations, material parameters of the PDL have been determined in an iterative procedure. Constant values of the material parameters were assumed for all other structures (tooth: 20 GPa, cortical bone: 15 GPa, spongious bone: 1 GPa). Calculations were performed with the FE package COSMOS/M (Versions 2.5 – 2.6) using its 3D solid element.

RESULTS AND DISCUSSION

Initial tooth deflections under orthodontic loads is dominated by the material parameters of the periodontal ligament.

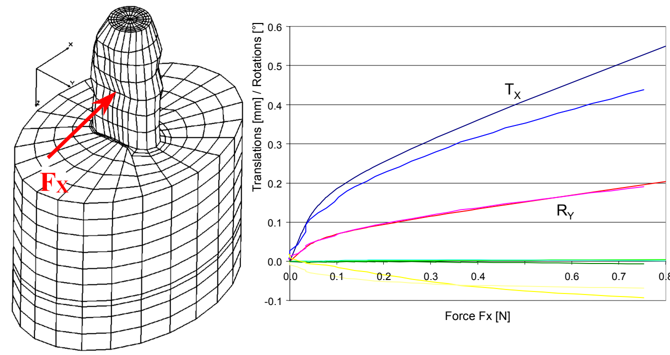

Figure 1: FE model of a human canine (left) and numerical load/deflection curve fitted to the experimental one (right).

However, the experimental load/deflection curves could not be reproduced satisfactory with the assumption of a linear behaviour (Young's modulus E = 0.1 MPa, Poisson's ratio ν = 0.3). A bilinear approach representing the nonlinear behaviour of the PDL could be fitted to the force/deflection curves of all preparations. Two Young's moduli seperated by an ultimate strain ε_{12} were determined. The first, E_1, represents an initial regime with high mobility, and the second Young's modulus, E_2, is approximately four times higher and the tooth reacts stiffer on force application. The means and standard deviations of the parameters are listed in the table below for all preparations. Only minor variations were determined between human and pig material parameters of the PDL, while the values for the rat seem to differ significantly especially with respect to the start value (ε_{12}) and the modulus (E_2) of the second elastic regime.

REFERENCES

Hinterkausen, M., Bourauel, C., Siebers, G. et al. (1998). *Med. Eng. Phys.*, **20**, 40-49.
Vollmer, D., Haase, A., Bourauel, C. (2000). *Biomed. Tech.*, **45**, 62-69.

Table 1: Elasticity parameters of the PDL determined in this study.

	Human	Pig	Rat
E_1 [MPa]	0.05 ± 0.02	0.05 ± 0.01	0.04 ± 0.03
E_2 [MPa]	0.28 ± 0.12	0.22 ± 0.05	0.12 ± 0.06
ε_{12} [%]	7.5 ± 2.4	7.5 ± 1.5	12.5 ± 6.0

ON THE RELATIONSHIP BETWEEN BONE-REMODELING RATE AND ORTHODONTIC STRAINS WITHIN THE PERIODONTAL LIGAMENT

Christopher G. Provatidis

Mechanical Engineering Department, National Technical University of Athens, Athens, Greece
Associate Professor, prowaton@central.ntua.gr
9, Heroes of Polytechnion Avenue, GR-15773, Athens, Greece

INTRODUCTION

Analytical closed formulas for the calculation of strains within the periodontal ligament (PDL) in case of intrusion were previously reported by Provatidis (1999). In this particular (and very simple) case it was shown that if the bone remodeling rate along the interface between the PDL and the alveolar bone is assumed to be proportional to *both* the normal and the tangential strain components, the PDL reserves its shape and it continuously follows the tooth during its long-term orthodontic movement". This result is in the opposite direction to bone remodeling assumptions for long bones; a differentiation firstly made by Middleton et al (1996). This paper extends the theory to bodily tooth movement.

METHODS

Following Provatidis (2001), translation (u) of a tooth with a paraboloidal root is related to only a normal (ε_{nn}) and two shear strains ($\gamma_{nt}, \gamma_{n\vartheta}$), which are approximated as follows:

$$\varepsilon_{nn} = -{}^{u_n}\!/_{\delta}, \ \gamma_{nt} = -{}^{u_t}\!/_{\delta}, \ \gamma_{n\vartheta} = -{}^{u_\phi}\!/_{\delta} \qquad (1)$$

where δ is the PDL thickness and u_n, u_t, u_ϕ are tooth displacement components with respect to local coordinate (tooth-fixed) system.

It is here hypothesized that the PDL reserves both its shape and thickness and it continuously follows the tooth during its long-term orthodontic movement. This assumption establishes a relationship between bone remodeling rate ($\dot{\vec{u}}_{bone}$) and tooth displacement (u) given as (λ =constant):

$$\dot{\vec{u}}_{bone} = \lambda \vec{u} \qquad (2)$$

A combination between (1) and (2) leads to ($c = -\lambda\delta$):

$$\left[\dot{u}_n, \dot{u}_t, \dot{u}_\phi\right]^T_{bone} = c\left[\varepsilon_{nn}, \gamma_{nt}, \gamma_{n\theta}\right]^T \qquad (3)$$

The theory is here validated by a numerical example on an upper central incisor using FEM analysis. A structured mesh of 1156 nodes and 768 elements was generated by cutting root in 24 equidistant slices. The PDL/bone interface was moved in accordance to (3) using c=1000, mainly for visual purposes.

RESULTS AND DISCUSSION

It is clearly shown in **Figure 1** that the interface between PDL and alveolar bone reserves the shape of the tooth.

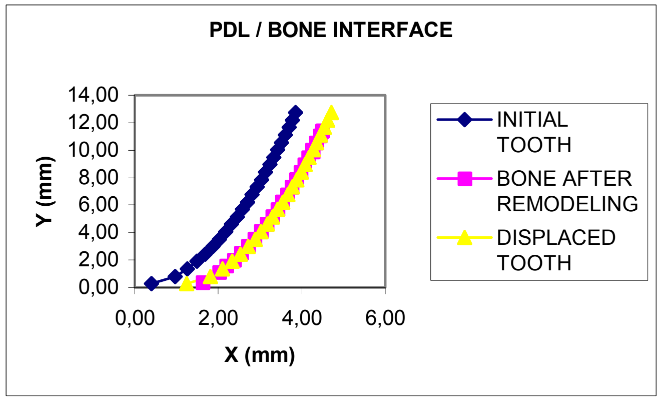

Figure 1: Initial tooth-root surface (blue) and new position of the alveolar bone (pink). The tooth is then shifted to depict that tooth shape is reserved (yellow).

The limitation of the proposed approach is that it is reduced to linear elastic considerations. It is remarkable that according to the above considerations, if the bone displacement is larger than its corresponding on the adjacent tooth surface in such a way that these displacements are related through a common *constant* ratio, then the PDL is *uniformly* enlarged according to the same ratio.

SUMMARY

Closed-formed analytical formulas for single-rooted teeth offer the background for the development of a simple bone remodeling theory in orthodontics. Tooth roots characterized by more complex geometries can be further analyzed using finite element analysis. Comparison with clinical and histological findings will further validate the proposed theory.

REFERENCES

Provatidis, C.G. (1999). *Proceedings 6th FEM Workshop in Biomedicine*, Ulm, Germany (ISBN-3-9806183-2-3), 144-158.
Provatidis, G.G. (2001). *Int. J. Eng Sci*, **39**, 1361-1381.
Middleton et al. (1996), *Am J Orthod Dentof Orthop*, **109**, 155-62.

DELAYED VERSUS EARLY VERSUS IMMEDIATE LOADING OF ORAL IMPLANTS

Els De Smet[1], Siegfried Jacques[2], Joke Duyck[1], Jos Vander Sloten[2], Ignace Naert[1]

Katholieke Universiteit Leuven, Belgium
[1]School of Dentistry, Oral Pathology and Maxillofacial Surgery, Department of Prosthetic Dentistry,
E-mail: els.desmet@uz.kuleuven.ac.be
[2]Division of Biomechanics & Engineering Design (BMGO)

INTRODUCTION

The classic osseointegration method is based on a two-stage surgical protocol and delayed loading (3-6 months). Over the years this has proven to be a highly succesful and predictable treatment. However attempts have gradually been made to simplify the protocol and to reduce the treatment time. Techniques have e.g. been suggested for one-stage approaches as well as early (weeks) and immediate loading (days) of the oral implants. Loading is an important factor concerning implant success/failure. In a clinical study these three treatment concepts are prospectively followed during the first year of loading, concerning type of loading and the related effect on (re)modelling of the peri-implant bone. At the same time the effect of mechanical loading on early loaded implants is investigated in an animal study. Both studies are part of a larger project to analyse adaptive bone (re)modelling around implants, using a combination of clinical and animal experiments and individualized finite element models.

METHODS

In the clinical study a miniature bite forc is used to measure bite forces. Strain gauged supra-osseous parts on the implants measure the accompanying type (axial/moment) and amplitude of loading of the implants. Digital intra-oral peri-apical and tomographic radiographs are used to follow the peri-implant bone (re)modelling.
In the animal study percutaneous titanium implants are placed in both tibiae of skeletally mature guinea pigs. Using an electromechanical shaker implants are mechanically stimulated with a sinusoidally varying bending moment, frequency 30 Hz, for 1800 cycles. Already 4 experimental groups with a force amplitude of 10 Nmm, 20 Nmm, 40 Nmm and 80 Nmm respectively are performed. Stimulation was applied unilaterally, during 4 weeks, starting one week post-operatively. The contra-lateral leg was used as control. Bone(re)modelling of both test and control implants are followed by in vivo (1 week post-op, before loading and two weeks after loading) and post mortem micro-focus computer tomography.

RESULTS AND DISCUSSION

Both clinical and animal study are not completed yet, but interim results show that bite forces increase during the first year of function in all three patient groups. Marginal bone loss takes place meanly during the first three months of loading. In the early and immediate loading patient groups mean marginal bone loss (1.07 mm) is larger than in the delayed loading group (0.47 mm).
In the animal study micro-CT images are qualitatively scored on the amount of new bone formation. Using a non-parametric test, mechanical stimulation has a positive effect on bone (re)modelling around early loaded implants in guinea pigs for the 10, 20 and 40 Nmm group. Using a 80 Nmm force amplitude, test implants showed non-integration, probably due to overload.

SUMMARY

Although bite forces increase over time, the rate of mean marginal bone loss decreases during the first year of function. Early and immediate loaded implants show more bone (re)modelling than delayed loaded implants.
In an animal study stimulation of bone(re)modelling can be shown. Quantification of the positive effect will be done by means of histomorphometric analysis of the post mortem bone with implant specimens.

REFERENCES

Brånemark, P.-I. et al (1985). *Quintessence Publishing Co, Chicago.*
Adel, R. et al (1990). *Int J Oral Maxillofac Impl,* 5: 347-359.
Jemt, T. et al (1996). *Int J Oral Maxillofac Impl,* **11**: 291-298.
Schnitman, P.A. (1990). *J Oral Implantol*, **16**: 96-105.
Brånemark, P.-I. et al (1999). *Clin Implant Dent & Rel Res,* **1**: 2-16.
Duyck, J. et al (2000). *J Oral Rehab,* **27**: 744-53.
Jansen, J.A. & de Groot K. (1988). *Biomaterials,* **9**: 268-272.

ACKNOWLEDGEMENTS

Supported by K.U.Leuven grant VIS/99/012 “IMFIX”.

NUMERICAL SIMULATION OF THE POLYMERIZATION OF TOOTH/RESIN INTERFACE FOR CLASS V RESTORATIONS

Estevam Barbosa de Las Casas[1], Tulimar Pereira Machado Cornacchia[2], Fabiano de Carvalho Filho[1], Priscila Azeredo[2] and Carlos Alberto Cimini Jr.[1]

[1]School of Engineering and Dentistry, Federal University of Minas Gerais, Brazil
[2]School of Dentistry, Federal University of Minas Gerais, Brazil

INTRODUCTION

Composite resins are nowadays the most used materials in dental restorations, due to their aesthetic advantages and mechanical characteristics. These materials are usually light-cured and their polymerization induces a significant volumetric shrinkage, varying between 1 and 3%. The process of polymerization and its related constrained shrinkage produces a state of residual stresses which can lead to failure in the involved materials, post-operative pain or fracture of the margins of restoration, leading to leakage of fluids and caries.

In order to reduce the effects of the shrinkage, incremental techniques were developed as an option to the unique incremental procedure. Different manners of filling the restoration cavity have shown to result in different stress distributions of the residual stresses, as observed by the clinical results in terms of success. The choice of the best filling technique is the dentist-surgeon function, and there are not very clear guidelines as to how to proceed.

METHODS

In this paper, step-by-step analysis of the transient stresses induced for different filling techniques is performed. In the model the accumulated stresses are considered, as well as the leakage in the event of reaching local stresses higher than the shear bond between tooth and resin. Mastication load is then introduced, to improve understanding of the behavior of the restoration with residual stresses under functional loads. The three techniques are shown in Figure 1 - uniform, WI and bulk.

A similar analysis procedure was described by Winkler and co-workers in 1996. Our results show that the final stress distribution is dependant on the filling technique, as expected in a nonlinear phenomenon.

RESULTS AND DISCUSSION

The results indicate that the bulk technique results in larger interfacial stresses, while the WI provided the best results.

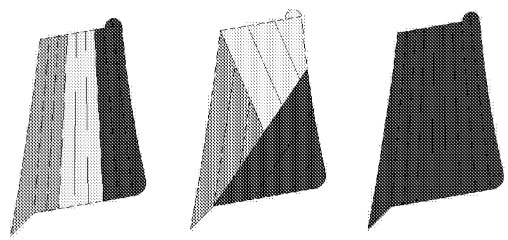

Figure 1: Filling techniques - uniform, WI and bulk

A larger number of failures is expected when using the bulk filling, which agrees with clinical practice. High values of principal tensile stresses are obtained in all cases. The first principal stresses that arise during the polymerization and the final residual stresses are shown in Table 1.

Table 1: Stresses during filling and at the end of the process.

[MPa]	$S_{1\,residual}^{\max imum}$	$S_{1\,transient}^{\max imum}$	$S_{1\,transient}^{\max imum} / S1_{residual}^{\max imum}$
BULK	181,863	265,365	1,459
HI	173,656	255,784	1,473
WI	193,736	256,737	1,325
Uniform	138,420	138,420	1

REFERENCE

Winkler, M. M. , Katona, T. R. and Paydar, N. H. (1996) J. Dent. Res. **75**(5):1477-1483

ACKNOWLEDGEMENTS

The authors would like to acknowledge the support of FAPEMIG through grant TEC 352/99 and ANSYS for the use of the program.

A NONLINEAR ELASTIC TRANSVERSELY ISOTROPIC CONSTITUTIVE LAW FOR THE PDL: ANALYTICAL AND COMPUTATIONAL ASPECTS

Georges Limbert and John Middleton
Biomechanics Research Unit, University of Wales, College of Medicine, Cardiff, UK, LimbertG@cardiff.ac.uk

INTRODUCTION

A thorough knowledge of the periodontal ligament (PDL) is vital in understanding the mechanics of tooth mobility, soft tissue response and proposed treatment plans (Middleton et al., 1996]. In order to overcome the limitations exhibited by the existing constitutive models of the PDL (Pietrzak et al., 2002), we propose a new model of the PDL that captures simultaneously its essential mechanical features: non-linear behaviour, large deformations, anisotropy, distinct behaviour in tension and compression, and fibrous characteristics.

METHODS

Due to the composite nature of the PDL (collagen fibres embedded in a gel-like solid matrix) the framework of a continuum theory of fibre-reinforced composite (Limbert and Taylor, 2002) was used. Let **F** be the deformation gradient and J its determinant. **C**, the right Cauchy-Green deformation tensor admits three principal invariants I_1, I_2 and I_3. To model the preferred mechanical direction from which anisotropy arises a local unit vector $\mathbf{n_0}$ defining the fibre direction is introduced. This leads to the definition of a fourth invariant I_4: $I_4 = (\mathbf{n_0} \otimes \mathbf{n_0}) : \mathbf{C}$. The following notations are introduced:

$$\overline{\mathbf{F}} = J^{-\frac{1}{3}}\mathbf{F},\ \det(\mathbf{F}) = 1 \quad \Rightarrow \quad \overline{\mathbf{C}} = J^{-\frac{2}{3}}\mathbf{C} \tag{1}$$

$\overline{I}_1, \overline{I}_2$ and $\overline{I}_3$ are the principal invariants of $\overline{\mathbf{C}}$. The existence of a strain energy density $\psi(\overline{I}_1, \overline{I}_2, \overline{I}_3, \overline{I}_4)$ is postulated. It is further hypothesised that the strain energy function can be represented by the uncoupled sum of the isotropic deviatoric, anisotropic deviatoric and isotropic volumetric strain energy functions:

$$\psi = \psi(\overline{I}_1, \overline{I}_2, I_3, \overline{I}_4) = \psi^m_{dev} + \psi^f_{dev} + \psi^m_{vol} \tag{2}$$

For the matrix contribution a simple Mooney-Rivlin type strain energy function is chosen:

$$\psi^{matrix}_{dev} = c_1(\overline{I}_1 - 3) + c_2(\overline{I}_2 - 3) \tag{3}$$

To capture the distinct behaviour of the PDL in tension and compression (Pietrzak et al., 2002), the following convex function I_3 is used:

$$\psi^m_{vol} = \kappa f(I_3) = \begin{cases} \dfrac{\kappa}{4\alpha^2}(I_3^{\alpha} - 1 - \alpha \ln I_3) & \text{if } I_3 \le 1 \\ -\dfrac{\kappa}{4\beta^2}(-I_3^{-\beta} + 1 - \beta \ln I_3) & \text{if } I_3 \ge 1 \end{cases} \tag{4}$$

To represent the mechanical contribution of the collagen fibres the following convex function is proposed:

$$\psi^f_{dev} = g(\overline{I}_4) = \begin{cases} 0 & \text{if } \overline{I}_4 \le 1 \\ \dfrac{c_3}{2c_4}[e^{c_4(\overline{I}_4 - 1)^2} - 1] & \text{if } \overline{I}_4 \ge 1 \end{cases} \tag{5}$$

c_1, c_2, c_3, c_4, κ, α and β are material parameters that were determined by identification with experimental/analytical curves (Pietrzak et al., 2002). Stress and elasticity tensors are respectively obtained by first and second differentiation of ψ with respect to **C**.

The constitutive law was implemented into the finite element (FE) code ABAQUS/Standard (HKS Inc., Pawtucket, RI, USA) via a customized subroutine. An idealized FE model of the PDL was then built and several FE analyses were carried out in order to simulate various mechanical physiological conditions the PDL is subjected to.

RESULTS AND DISCUSSION

The constitutive law exhibited the typical non-linear stiffening in the fibre direction as well as being capable of capturing the distinct highly non-linear stress-strain characteristics in tension and compression. Essential constitutive requirements were also verified. Excellent agreement was found between the analytical and numerical solutions therefore providing a solid basis for further FE analyses. The FE analyses of the PDL model demonstrated the relevance of the continuum mechanics formulation adopted in this work. The anisotropy of the PDL has also provided a much more accurate insight into the complexity of its mechanical behaviour. The proposed model adds significant improvement to the current analytical and numerical models of the PDL through being able to capture the directional and non-linear properties of the ligament for the finite strain regime. Further experimental data will permit the constitutive law to be extended to encompass both time-dependent and transport effects. Accurate geometrical definition of the PDL-tooth-bone complex will also be required for the simulation of more realistic *in-vivo* physiological conditions.

REFERENCES

Middleton, J. et al. (1996). *Am. J. Orthod. & Dentofac. Orthop.,* **109**, 2, 155-162.
Pietrzak, G. et al. (2002), *Comp. Meth. Biom. Biomed. Eng*., **5**.
Limbert, G, Taylor, M. (2002). *Int. J. Sol. Struct*., to appear.

SIMULATION OF OVERLOAD-INDUCED MARGINAL BONE RESORPTION USING ANATOMICAL FINITE ELEMENT MODELS

Hans Van Oosterwyck[1], Tom De Wilde[1], Jos Vander Sloten[1], Joke Duyck[2], Ignace Naert[2]
[1]Division of Biomechanics and Engineering Design, KU Leuven, Leuven, Belgium, hans.vanoosterwyck@mech.kuleuven.ac.be
[2]Department of Prosthetic Dentistry, KU Leuven, Leuven, Belgium

INTRODUCTION

Pathological overload has been suggested as an important etiological factor for marginal bone loss around oral implants. (Duyck et al 2001). Recently overload-induced marginal bone resorption was simulated for a simple non-anatomical finite element model of a cylindrical implant (Van Oosterwyck et al 2001). In order to compare simulated resorption with in vivo observed resorption into more detail anatomical finite element models are needed. In the present study the simulation algorithm was applied to anatomical models. The hypothesis was tested whether pathological overload alone is sufficient to explain marginal bone loss.

METHODS

An iterative feedback algorithm was developed to simulate bone adaptation around an oral implant (Van Oosterwyck et al 2001). It was assumed that the rate of change of apparent bone density can be expressed as a function of the difference between the actual strain and a reference strain (fig. 1). The corresponding change in (isotropic) E-modulus was then calculated (Carter & Hayes 1977).

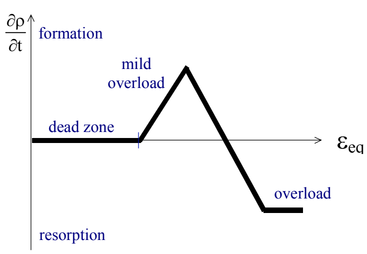

Figure 1: Bone adaptive response, expressed as the rate of change of apparent bone density as a function of strain.

The algorithm was applied to anatomical finite element models. A first model was taken from a previous study that investigated the influence of adverse dynamic loading on the bone response around a screw-shaped implant, placed in a rabbit tibia (Duyck et al. 2001). The interface between bone and implant was assigned a finite tensile strength. A second model was created from spiral tomographic images of an implant, placed in a patient's mandible. For the latter model the implant was simplified to a cylinder and a fixed bond was assumed between implant and bone. For both models a bending moment was applied to the implant.

RESULTS

The implementation of a finite strength resulted in debonding at the proximal (tensile) side for the model of the rabbit tibia. As a result, an asymmetric resorption pattern was predicted (fig 2, left). In reality resorption craters were present at both the proximal (tensile) and distal (compressive) side. The discrepancy between simulated and observed resorption pattern could indicate that overload was not the only factor, responsible for marginal bone loss. Possibly, relative motion could also play a role in bone resorption, as was already previously hypothesised (Duyck et al. 2001). Relative motion was not yet included in the algorithm as a stimulus.
A symmetric resorption pattern was predicted for the model of the patient's mandible: resorption craters were predicted at the mesial and distal implant side. The simulated resorption could however not be validated due to the lack of radiographic data of sufficient quality.

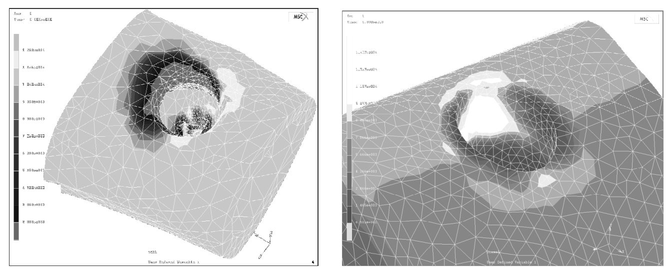

Figure 2: Simulated distribution of E-modulus in rabbit tibia (left) and human mandible (right) around an oral implant. Dark zones in the marginal bone region represent a decrease in bone density, light zones represent an increase.

CONCLUSION

Marginal bone resorption was predicted for both a clinical and animal experimental case. Based on the animal experimental case it is hypothesised that other factors, apart from pathological overload, might be responsible for marginal bone loss.

ACKNOWLEDGEMENTS

This study was financially supported by the Research Council of the K.U. Leuven (OT 98/30). Hans Van Oosterwyck is a postdoctoral fellow of the Fund for Scientific Research Flanders.

REFERENCES

Duyck, J. et al (2001). *Clin Oral Impl Res*, **12**, 207-218.
Van Oosterwyck, H. et al (2001). *Fifth Int. Symp. on Computer Meth. in Biomech. and Biomed. Eng.*, Rome, Italy.
Carter, D.R., Hayes, W.C. (1977). *J Bone Joint Surg*, 59-A, 954-962.

BIOMECHANICAL MODELING OF OVERLOAD AT THE BONE-ORAL IMPLANT INTERFACE

John B. Brunski[1], Do Gyoon Kim[2], Ajit Prabhu[1] and Chia-Ju Yang[2]
Department of Biomedical Eng. [1]; Department of Mechanical, Aeronautical and Nuclear Eng.[2]
Rensselaer Polytechnic Institute, Troy, NY 12180-3590

INTRODUCTION

Several studies have suggested that it is possible to "overload" the bone-oral implant interface (e.g., Isidor, 1999). While clinical overload seems to involve bone loss at the crestal region, mechanisms underlying that bone loss remain unclear. Possible mechanisms have been explored in experiments and computer-simulations, and here we outline a recent series of computer simulations of possible biomechanical mechanisms. A major distinction between our simulations and related previous models of bone adaptation at interfaces (e.g., van Rietbergen *et al.* 1993) is that our model accounts for changes in the bone microstructure during the remodeling process itself, i.e., we account for the fact that remodeling occurs via A-R-F = Activation of osteoclasts, Resorption by osteoclasts, and Formation of bone by osteoblasts. Also, we assume that microdamage (MDx) occurs in bone when maximum or minimum principal strain reaches ~0.5% (5,000 $\mu\varepsilon$), and that MDx triggers A-R-F.

METHODS: REALITY VS. SIMULATION

An unrealistic aspect of some previous models of bone adaptation is that once a certain stress/strain signal is presumed to trigger remodeling, A-R-F (and its presumed adaptive effect on bone properties) is assumed to happen essentially instantaneously, with no recognition of the step-by-step A-R-F cycle that unfolds over weeks to months (Roberts, 1988). Therefore, such models do not allow for the possibility that bone near a site of A-R-F might respond to signals during the weeks to months required for a remodeling cycle. To address this shortcoming, our model explicitly simulates the A-R-F process; it allows for the possibility that holes from the initial A-R- step may alter local stress-strain states, and in turn, subsequent remodeling events. Using this idea, we have formulated several finite element models of bone-implant interfaces in 2- and 3-dimensions. We have simulated remodeling events under the rule that A-R-F is triggered at regions where the maximum or minimum principal strains exceed a magnitude of ~0.5% (5,000 $\mu\varepsilon$).

RESULTS AND DISCUSSION

Examples simulations (Figs 1-2, plus others to be reviewed) illustrate that one outcome consistent with overload is a situation of *positive feedback*, which develops as follows: 1) implant loading produces high strain levels and MDx at some osteons in the interfacial microstructure; 2) A-R- is triggered at MDx sites, thereby producing a hole in the bone; 3) the hole from step 2) may then concentrate strain nearby, possibly inducing new high strains, new MDx, and new sites of A-R- (which outpaces the –F stage); and 4) increasing A-R- causes another cycle of high strains, more MDx, more A-R-, etc., causing diminished bone support and, eventually, frank failure of the majority of the interfacial bone.

REFERENCES

Isidor, F. (1999) Occlusal loading in implant dentistry. in *Proc. 3rd European Workshop on Periodontology* (N.P. Lang, T. Karring and J. Lindhe, Eds.) Quintessence, Chicago IL, 358-375.
Roberts, W.E. (1988) *J. Dent. Educ*. 52:804-809.
Van Rietbergen, B. *et al.* (1993) *J. Biomech.* 26:369-382.

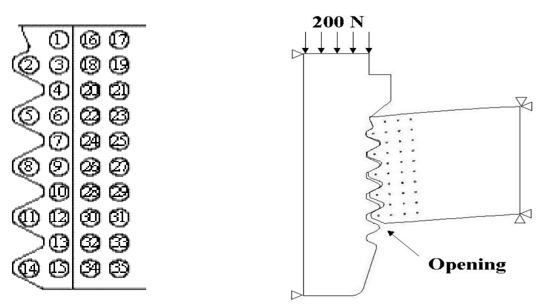

Fig. 1 (left) Schematic microstructure with 35 osteons in an interface; (right) loading/boundary conditions in a simulation with a non-bonded interface that allows gap-

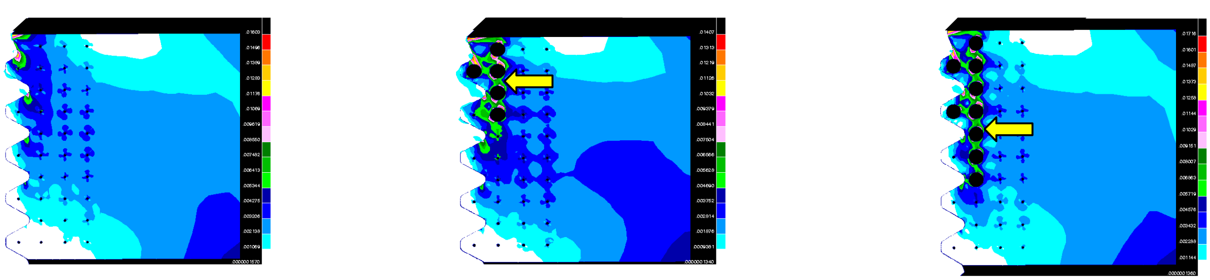

Fig. 2 An example interface showing increasing development (left to right) of the A-R- phase of remodeling (arrows) due to increasing

NEW INSIGHTS INTO ORTHODONTIC LOAD TRANSFER AND ALVEOLAR BONE REMODELING

Michel Dalstra[1], Paolo M. Cattaneo[1], Felix Beckmann[2] and Birte Melsen[1]

[1]Dept. of Orthodontics, Royal Dental College, University of Aarhus, Aarhus, Denmark
[2]Hamburger Synchrotron Laboratorium (HASYLAB at DESY), Hamburg, Germany
mdalstra@odont.au.dk

INTRODUCTION

Moving teeth through the use of orthodontic appliances, like braces etc., is perhaps one of the most direct applications of biomechanical principles in clinical practice. By carefully choosing a force system (forces & moments) for a particular tooth, the orthodontist can provoke this tooth to move (translate & rotate) in the desired direction. The tooth can actually move inside the jaw, because the alveolar bone around the tooth starts to remodel due to the perturbations in the normal loading pattern caused by the presence of the orthodontic load.

In the orthodontic field, the classical view on alveolar bone remodeling still largely persists that, if a tooth is pushed against one side of the alveolus, on this side the bone is in a state of compression, while on the opposite side the bone is in tension. As the tooth moves in the general direction it is loaded in, bone in compression must thus be getting resorbed, while bone is tension gives rise to new bone formation. This, however, is in total contrast with bone remodeling laws, which are employed in the field of orthopaedics. By using new techniques to, on the one hand, create highly geometrically accurate finite element (FE) models of tooth/bone configurations and on the other to determine the alveolar bone architecture, it is the aim of this study to shed new light on orthodontic load transfer mechanisms and give new insights into alveolar bone remodeling.

METHODS

Segments of human mandibles containing three or four teeth were obtained at autopsy and embedded in blocks of methyl-metacrylate. These blocks were scanned with a table-top micro-CT scanner at a spatial resolution of 30 µm. These scans were used for the creation of FE models. First they were read into Mimics software (Materialise, Leuven, Belgium). With this visualization/CAD software, masks were created of the different anatomical structures, which could be transformed into 3D geometrical entities. These shapes were then read into the COSMOS/M FE package (SRAC, Los Angeles, CA), where a mesh was then automatically generated. The material properties of the periodontal ligament (PDL) were assumed to be non-linear (Bourauel et al., 1999), while the Young's moduli of the individual bone elements were directly linked to the local bone densities given by the gray values in the CT-scans (Cattaneo et al., 2001). External loading simulated various orthodontic loading regimes.

The same blocks were scanned with a micro-tomograph attached to the DORIS synchrotron-ring at HASYLAB/DESY at a spatial resolution of 7 µm. The individual scans were read into VGL software (Volume Graphics, Heidelberg, Germany) for three-dimensional (3D) reconstruction and further analysis.

RESULTS AND DISCUSSION

The orthodontic load transfer is more complex than the classical view of having opposite zones of tension and compression. Firstly this is caused by the very shape of the jaw. Due to its irregular form, the teeth are not supported uniformly by the alveolar bone. Especially near the alveolar edge, the cortical bone can be very thin and when this shell is loaded perpendicular to its thickness, secondary load transfer mechanisms become activated causing the bone to behave almost like a Roman arch. This means that normal tensile stresses are transformed into circumferential compressive stresses and vice versa, and that the nature of loading becomes the opposite of what one might expect intuitively. Secondly, the inner surface of the alveolar bone is not smooth and homogeneous. The 3D reconstructions of the micro-CT scans show a very porous surface with rough and sharp edges. This means that the stresses here are much higher than previously assumed.

SUMMARY

By using state-of-the-art techniques the orthodontic load transfer from teeth to alveolar bone has been re-examined and compared to the traditional views. The classical zones of tension and compression in the alveolar bone, still believed by many in the orthodontic field to be the origin for alveolar bone remodeling during orthodontic loading, can no longer be identified as such. This means that new hypotheses on alveolar bone remodeling must be raised, more in line with those in use in the orthopaedic view (Melsen et al. 2001).

REFERENCES

Bourauel, C. et al. (1999) *J Orofac Orthop/Fortschr Kieferorthop*, **60**: 136-51.

Cattaneo, P.M. et al. (2001) *Proc Inst Mech Eng [H]*, **215**: 203-13.

Melsen, B. et al. (2001) *J Paradont & Impl Orale*, **20**: 313-29.

THE DEVELOPMENT OF ABFRACTION LESIONS IN TEETH

J S Rees, M Hammadeh and D C Jagger

University of Bristol Dental School, Lower Maudlin Street, Bristol BS1 2LY, UK
Corresponding Author: j.s.rees@bristol.ac.uk

INTRODUCTION

Cervical tooth surface loss is particularly common resulting in poor aesthetics and sensitivity and this problem is likely to increase as the population ages and retains their teeth for longer. This type of tooth surface loss has traditionally been attributed to gingival recession and toothbrush abrasion. More recently, Grippo (1996) has suggested that occlusal loading causes strains in the cervical region of the crowns of teeth. These high surface strains initiate microcracks and eventually propagate, resulting in bulk enamel loss. Grippo has coined the term "abfraction" to describe this process.

Clinically, abfraction lesions are sharp, angular wedge-shaped defects that occur more commonly on the buccal surface of teeth compared to the lingual surface. They are also found more commonly in bruxists and are more commonly found on incisor and premolar teeth (Rees, 2000).

METHODS

The Bristol group has carried out a number of finite element studies to broaden understanding of this clinical problem. Various aspects have been investigated, including:

- Varying the position and magnitude of the occlusal load
- Comparison of cervical stresses in incisor, canine and premolar teeth
- Effect of undermining of the amelo-dentinal junction by erosive liquids on the buccal aspect of teeth
- The exacerbating effect of an occlusal restoration.

RESULTS AND DISCUSSION

Initial studies found that a typical bruxing load of 500N produced cervical shear stresses of 30 MPa, a figure that is close to the known failure stresses for enamel. Obliquely applied loads also produced much higher cervical stresses.

A comparison of the cervical stresses in different tooth types found that the highest stresses were evident in the premolar, followed by the incisor, with the lowest stresses in the canine. This correlates well with clinical studies that show a higher prevalence of abfraction lesions in premolar and incisor teeth and is likely to be related to variations in tooth morphology and the area of the supporting periodontal ligament.

The effect of the presence of a coronal amalgam restoration was modelled and it was found that the cervical stresses increased by a factor of 2 or 3. This effect is probably due to the weakening effect of the amalgam restoration, resulting in increased cuspal flexure under occlusal loading. This ultimately produces greater cervical stresses.

SUMMARY

In conclusion, high occlusal loads, obliquely applied occlusal loads, and the presence of coronal amalgam restorations seem likely to contribute to the development of abfraction lesions. Incisor and premolar teeth also seem more susceptible to the development of abfraction lesions compared to canine teeth, due to the natural variation in their morphology.

REFERENCES

Grippo, J.O. (1996) Bioengineering seeds of contemplation. A private practitioner's perspective. *Dent. Mater.*, **12**, 198-202.

Rees, J.S. (2000) A review of the biomechanics of abfraction. *Eur. J. Prosthodont. Rest. Dent.*, **8**, 139-144.

REGISTRATION METHODS FOR COMPUTER-ASSISTED SURGERY

RE Ellis PhD, Departments of Computing and Information Science, Mechanical Engineering, and Surgery, Queen's University, Kingston, Canada K7L 3N6

Computer-assisted surgery allows a surgeon to navigate inside a patient's body through tiny incisions. Figure 1: Navigation from a CT image and a 3D model to excise a deep bone tumor in the tibia.

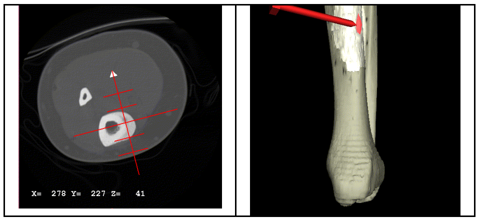

Figure 1: Navigation from a CT image and a 3D model to excise a deep bone tumor in the tibia.

Registration is the process of finding a transformation equation from patient data to a medical image. Typically, the patient data are gathered in the operating room by touching bone surfaces with a calibrated probe that is tracked by a three-dimensional localizer (such as the Optotrak optoelectronic system of Northern Digital, Waterloo, Canada). The transformation is found by optimizing an objective function, such as the least-square error, between the patient data and the medical image. The image is commonly a computed tomography (CT) or magnetic resonance image (MRI) of the patient, taken days or weeks before the surgical procedure.

Early registration methods matched pairs of points, so the locations of pre-implanted markers [0] or distinct anatomical landmarks needed to be selected from the medical image. Examples of markers and landmarks are shown in CT images in Figure 2.

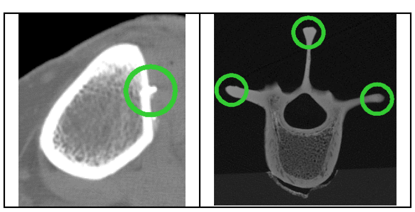

Figure 2: A tantalum bead used as a marker in a patient's tibia, and distinctive landmarks on a plastic model of a lumbar vertebra. These are matched to points on a patient's anatomy for image-guided surgery.

Current registration methods use numerous surface points from the bone, which are matched to a triangulated mesh derived from the medical image. The iterated closest point (ICP) algorithm [0] iteratively solves the matching problem, determining the mesh point closest to the data, and the optimization, which is a least-squares process. Our preferred method for registering a patient to his/her preoperative image is mathematically robust [0], and automatically discards statistical outliers (which are poorly collected data).

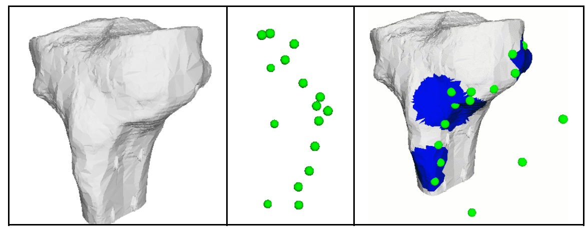

Figure 3: A mesh of a tibia, surface data, and the data registered by our robust method. The spurious data were automatically discarded; the blue "spotlight" areas guide the surgeon in finding an initial registration.

Our most recent method is a deformable transformation to an *atlas*, which is an average model developed from images of volunteers. This method does not require a scan of the patient, which saves time, cost, and is logistically simpler for both the patient and the medical team.

REFERENCES

R.E. Ellis, S. Toksvig-Larsen, M. Marcacci, D. Caramella, and M. Fadda. Use of a biocompatible fiducial marker in evaluating the accuracy of CT image registration. *Investigative Radiology*, 1(10):658–667, 1996.

P.J. Besl and N.D. McKay. A method for registration of 3-D shapes, IEEE Transactions on Pattern Analysis and Machine Intelligence, 14(2):239-256, 1992.

B. Ma, R.E. Ellis, and D.J. Fleet. Spotlights: A robust method for surface-based registration in orthopedic surgery. In *Medical Image Computing and Computer-Assisted Intervention -MCCAI'99*, pages 936–944. Springer Lecture Notes in Computer Science #1496, 1999.

IMAGING TECHNOLOGY FOR COMPUTER AIDED SURGERY

Gabor Székely

Computer Vision Laboratory, Swiss Federal Institute of Technology Zürich, Switzerland

INTRODUCTION

Computer aided surgical procedures crit-ically depend on available information about the anatomy, physiology and path-ology of the patient, which can be gener-ated by pre- and inter-operative imaging procedures. The talk will provide a short introduction of available radiological methods and their applicability for opti-mally supporting surgical interventions.

IMAGING METHODS

The basic principles of interaction between electromagnetic radiation and human tis-sue will be summarized. The resulting properties and limitations will be dis-cussed for the most important imaging modalities like X-Ray, Computer Tomog-raphy, Magnetic Resonance Imaging or Ultrasound.

IMAGE PROCESSING

A short overview will be given about the most important methods of image analysis allowing the preparation of raw image data for optimal usage during interventions. The most important concepts of segmen-tation and registration will be explained.

VISUALIZATION

The results of the whole image acquisition and processing scheme discussed above must be presented in an intuitive and non-obstructive manner in order to enable the surgeon to fully utilize the information ex-tracted from the radiological data. Recent achievements in computer graphics, especially in virtual and augmented reality technology will be presented, together with selected examples about their utilization in minimizing the invasiveness of medical interventions

SIMULATION-BASED DESIGN OF KNEE REPLACEMENT SURGERY

Scott L. Delp and Stephen J. Piazza*

Biomechanical Engineering Division, Mechanical Engineering Department, Stanford University, Stanford, CA, USA
*Departments of Kinesiology, Mechanical Engineering, and Orthopaedics and Rehabilitation, and the Center for Locomotion Studies, The Pennsylvania State University, University Park, PA, USA
E-mail: delp@stanford.edu Web: http://www.stanford.edu/group/nmbl

INTRODUCTION

The primary goal of most three-dimensional planning systems for total knee replacement is to align the centers of the hip, knee, and ankle. We have developed a system that extends the capability of the surgical planning process by allowing one to study the effects of implant design and placement on knee kinematics and stability. We illustrate the utility of our technique by analyzing effects of implant design parameters and posterior tilting of the tibial component on the kinematics of posterior-cruciate substituting knees.

METHODS

Planar implant kinematics were determined from sagittal-plane profiles of the component geometry (Piazza et al, 1998). Three assumptions were employed to simulate motion of the implant during knee flexion: first, the most inferior point on the femoral condylar profile contacted the tibial well at its most inferior point when the knee was extended and remained there until the knee was flexed enough for the cam to contact the spine; second, contact – either condylar or between cam and spine – was maintained once initiated as the knee flexed; and third, tangents to sagittal implant profiles at points of contact were collinear. These assumptions can be stated as kinematic constraint equations. Vector addition (Fig. 1) gives

$$\mathbf{p} + \mathbf{f}(v) = \mathbf{t}(u), \tag{1}$$

and collinearity of tangents yields

$$\frac{d\mathbf{t}}{du} \times \frac{d\mathbf{f}}{dv} = \mathbf{0}, \tag{2}$$

where u and v are the tibial and femoral spline parameters used to fit the implant geometry. These vector equations were converted to a system of three scalar equations and solved for the position of the femoral component relative to the tibial component as knee flexion angle was increased from full extension to maximum flexion in 1° increments. Equations similar to Eqs. (1) and (2) described contact between the cam and spine and were solved to determine both the knee flexion angle at which the cam initially contacted the spine and the tibiofemoral kinematics once this contact had occurred.

We used the simulation to study the effects of five design parameters (tibial spine height, spine anterior-posterior position, femoral component posterior radius, and femoral cam anterior-posterior and distal-proximal position) on tibiofemoral kinematics and prosthesis stability. Prosthesis stability was characterized by a "dislocation safety factor," defined as the vertical distance from the bottom of the femoral cam to the top of the tibial spine. We also studied the effect of posterior tilt of the tibial component on the flexion angle at which the cam and spine engaged.

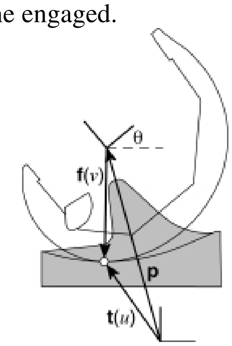

Figure 1. Sagittal plane implant geometry.

RESULTS AND DISCUSSION

Computer simulations revealed that posterior substituting knees are most likely to dislocate at maximum knee flexion. Prosthesis stability can be improved by increasing the tibial spine height and moving the femoral cam posteriorly. Our results suggest there is a tradeoff between maximum knee flexion and prosthesis stability. We found that relatively small gains in maximum knee flexion, made through design changes, may cause substantial decreases in prosthesis stability (Delp et al., 1995). (1)

The simulations revealed that even small degrees of posterior tilt of the tibial component reduced rollback by limiting the interaction between the cam and spine; tilting the component posteriorly by 5° caused the cam (2) to contact the spine at a flexion angle that was 18° higher than in the untilted case. The results suggest that posteriorly tilting the tibial component in posterior-cruciate substituting knee replacement may not produce the same beneficial effects that have been reported for tilting in posterior cruciate-retaining knee replacement.

Incorporating kinematic models into the surgical planning process reveals the relationships between implant design, surgical technique, and knee kinematics.

REFERENCES

Delp, S.L. et al., (1995), *J. Biomech*. **28**, pp. 1155-1166.
Piazza, S.J., et al. (1998), *J. Orthop. Res*. **16**, pp. 264-270.

ACKNOWLEDGMENTS

Dr. David Stulberg and Dr. Steven Stern.

SURGICAL NAVIGATION

Lutz P. Nolte

Center for Computer Assisted Surgery, M.E. Müller Institute for Biomechanics, University of Bern, CH
E-mail: Lutz.Nolte@memot.unibe.ch

INTRODUCTION

The recent advent of new computer assisted surgery technology has bridged the gap between preoperative diagnosis and planning and intraoperative manipulations. This is achieved by a so-called navigator that establishes a link between preoperative images and the intraoperative anatomy (registration), and maintains that link during motion of the patient (referencing). Surgical navigation technology allows to perform accurate and safe surgical actions through image-interactive control of tools actions.

TECHNICAL ASPECTS

Initially the focus of research and development was on navigation technology, which is purely based on preoperatively acquired 3D tomographic image data sets. These techniques require intraoperatively a surgeon-generated transformation between the surgical object and the associated image based virtual object, the so-called registration procedure. A wide variety of associated matching algorithms have been developed adapted to different clinical applications. Free-hand navigation systems using active or passive optolectronic tracking technology are then used to image-interactively perform various surgical actions.

The need for an often additional CT scan, the applied X-ray radiation dose and the rather difficult and time-consuming registration procedure has led to a novel approach to computer assisted orthopaedic surgery, in which intraoperative images, such as fluoroscopy complement or replace preoperatively acquired 3D tomographic image data. For this purpose the imaging devices or device components had to be integrated into the rigid body navigation concept. In addition internal and external device calibrations had to be realized in order to overcome physical image distortions. The resulting so-called registered 2D images can effectively be used for navigation by superimposing onto them the action of tracked surgical tools.

Also the concept of 'surrogate variables' was introduced into surgical navigation. By identifying important morphological landmarks from registered patient images or by direct digitization on the available bony anatomy or even indirect through pivoting procedures, variables, such as clinical axes, orientations (anteversion, inclination,…), etc. can accurately be determined at the OR table and then related to the subsequent surgical action. This has led to a variety of successful image-free surgical navigation systems.

Another challenge is the use of surgical navigation for novel minimal access surgery in orthopaedics. This requires accurate and reliable percutaneous registration procedures. Various research groups currently investigate the effectiveness of co-registering preoperative CT scans with intraopeatively acquired registered fluoroscopic and ultrasound images.

CLINICAL APPLICATIONS

Various clinical applications for both strategies will be presented in different anatomical areas, such as spine, hip, shoulder, and knee. Surgical interventions ranging from joint reconstruction and replacement to trauma treatment will be covered. A variety of systems have emerged from the laboratory and are being clinically used.

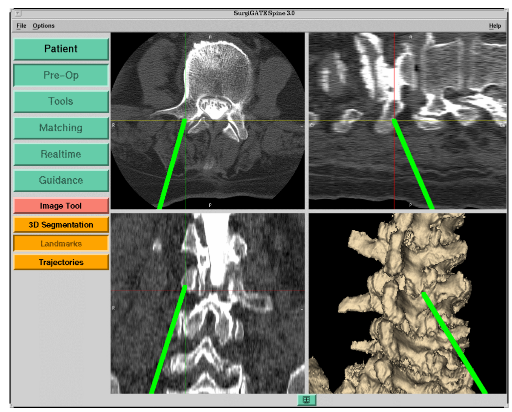

Figure 1: Example of an early CT based surgical navigation system - Transpedicular screw holes are prepared interactively using tracked surgical instruments.

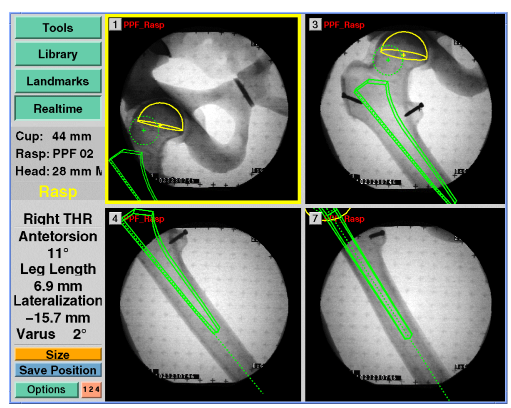

Figure 1: Example of a novel CT free navigation system – The spatial position of both joint components is optimized (antetorsion, varus, …) in registered fluoroscopic images.

FUTURE PERSPECTIVES

Future surgical navigation systems will bring (a) automated cross-registration and complementary use of 1D, 2D, and 3D imaging modalities, (b) see-through vision for the surgeon during the whole treatment process, and (c) a new breed of computer based implants and instruments.

COUPLING INFORMATION TO ACTION IN THE 21'ST CENTURY

Russell H. Taylor, Ph.D.
Center for Computer-Integrated Surgical Systems and Technology, Johns Hopkins University, Baltimore, Maryland, USA
Center Director, rht@cs.jhu.edu

INTRODUCTION

The impact of Computer-Integrated Surgery (CIS) on medicine in the next 20 years will be as great as that of Computer-Integrated Manufacturing on industrial production over the past 20 years. A novel partnership between human surgeons and machines, made possible by advances in computing and engineering technology, will overcome many of the limitations of traditional surgery. By extending human surgeons' ability to plan and carry out surgical interventions more accurately and less invasively, CIS systems will address a vital national need to greatly reduce costs, improve clinical outcomes, and improve the efficiency of health care delivery.

The evolution of these systems will be synergistic with the development of patient-specific surgical simulation for planning as well as for training and surgical augmentation systems transcending human sensory-motor limitations in the performance of surgical tasks.

THE INFORMATION FLOW OF CIS SYSTEMS

Figure 1 shows the information flow associated with CIS systems [1, 2]. Information from medical images and other sources is combined with generic information in anatomical atlases to produce patient-specific models that are used do developed optimized surgical plans. The plans, models, and images are combined in the operating room with intraoperative images and other sensing to update the models and register them to the patient. Once this is done, the plans can be updated and a variety of appropriate means, including robots, navigational aids, and interactive displays can be used to assist the surgeon in carrying out the surgical plan. The same system components can also be used intraoperatively to verify that the plan has been executed and also to assist in postoperative assessment and follow-up.

SURGICAL CAD/CAM SYSTEMS

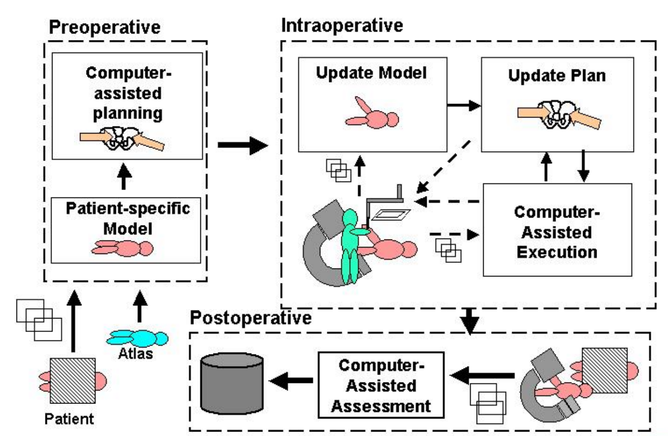

Figure 1: CIS Systems Information Flow

We refer to the process described in the previous section as *Surgical CAD/CAM*, stressing the analogy with Computer-Integrated Manufacturing. Indeed, the analogy can be taken further by noting that the greater consistency and information gathering made possible by computer-integrated planning, execution, validation, and follow-up can enable us to improve surgical processes and evaluate new therapies more efficiently. We refer to this process as *Surgical Total Quality Management (Surgical TQM).*

This talk will provide numerous examples of Surgical CAD/CAM, but will emphasize the development of "one stop shopping" systems that integrate modeling, planning, and therapy delivery in an interventional scanner, as shown in Figure 2 (Left).

SURGICAL ASSISTANTS

A second way of looking at CIS systems emphasizes their role as *Surgical Assistants* that work cooperatively with surgeons in carrying out highly interactive surgical procedures. This talk will also discuss examples of such systems, emphasizing our work on cooperatively controlled systems for microsurgical augmentation such as shown in Figure 2 (right).

ACKNOWLEDGMENTS

The support of the National Science Foundation under grants EEC9731478 and IIS9801684 is gratefully acknowledged.

REFERENCES

1. Joskowicz, L. and R. Taylor, *Computers in Imaging and Guided Surgery.* Computing in Science and Engineering, 2001(September/October): p. 65-72.
2. Taylor, R.H. and L. Joskowicz, *Computer-Integrated Surgery and Medical Robotics*, in *Biomedical Engineers' Handbook*, M. Kutz, Editor. 2002, McGraw-Hill. p. (in press).
3. Solomon S, et al., *CT Guided Robotic Needle Biopsy: A Precise Sampling Method Minimizing Radiation Exposure.* Radiology, 2001. **(Accepted-to appear)**.
4. Taylor, R., et al., *Steady-hand robotic system for microsurgical augmentation.* International Journal of Robotics Research, 1999. **18**(12): p. 1201-1210.

Figure 2: (Left) In-scanner percutaneous therapy [3]; (Right) Cooperative Steady-Hand robot for microsurgical assistance.[4]

MECHANICAL ENERGY OUTPUT BY RED MUSCLE FIBRES

Nancy Curtin[1]*, Roger Woledge[2] and Fang Lou[3]

[1]Biomedical Sciences, Imperial College, London SW7 2AZ UK
[2]University College London, Institute of Human Performance, Stanmore HA7 4LP UK
[3] Dept. Biosciences, University of Hertfordshire, Hatfield AL10 9AB UK
*Email: n.curtin@ic.ac.uk

Dogfish myotomal muscle consists of three fibre types, white, red and superficial fibres. Each fibre type has a distinct histological, biochemical and energetic profile, which at least for white and red fibres seems well matched to its function during swimming.

Two questions are addressed: (1) Are red fibres as strong as white fibres during isometric contraction? (2) Can we predict the force and power output during sinusoidal movement (work-loops), which mimic swim-like contractions of red fibres? Successful predictions have been made for the white fibres of dogfish based on observations of the behaviour of crossbridges and series elasticity of the fibres, and a reasonable assumption about the time-course of activation (Curtin et al, 1998).

Experiments were done on bundles of red and white fibres isolated from dogfish, *Scyliorhinus canicula* (L.). Intact fibre bundles were stimulated electrically and their length controlled by a motor, while force, length change and stimuli were recorded.

Maximum isometric tetanic force produced by red muscle fibres was 142.4 ±10.3 $kN.m^{-2}$ (N=35); this is significantly less than that produced by white fibres 289.2 ±8.4 $kN.m^{-2}$ (N=25). (All values mean ± S.E.M.) Part, but not all, of the difference is due to the higher mitochondrial content of the red fibres (Lou et al, in press).

The stiffness of the elasticity in series with the contractile component (crossbridges) was measured in step-and-ramp shortenings of fully active fibres. Force was measured during shortening and lengthening at different velocities (Lou et al, in press). The force-shortening velocity relationship was hyperbolic, as expected, with force intercept of P_0*/P_0 = 1.228 ±0.053, velocity intercept, V_{max} = 1.814 ±0.071 L_0/s, and other constants, a/P_0* = 0.225 ±0.024, and b = 0.404 ±0.041 L_0/s (N=7 for all values). The maximum power was 0.107 ±0.005 P_0V_{max} and was produced during shortening at 0.297 ±0.012 V_{max}.

These results show that although the red fibres have a lower P_0 (49%) and V_{max} (48%), compared to white fibres, the shapes of the force-velocity curves are very similar (Curtin & Woledge, 1988). Thus the white and red fibres have equal capacities to produce power within the limits set by the isometric force and maximum velocity of shortening of each fibre type.

In separate experiments, force and power output were measured during patterns of movement and stimulation that mimic what occurs during swimming. (Sinusoidal movement at 0.75 Hz with stimulation during 0.33 of each mechanical cycle, starting at different times in the cycle.). These results will be compared with predictions based on the elastic and force-velocity properties of red muscle, and an assumed time-course of activation.

REFERENCES

Curtin, N.A. et al (1998). *J. exp. Biol.* **201**, 103-114.
Lou, F. et al (in press). *J. exp. Biol.*
Curtin, N.A., Woledge, R.C. (1988). *J. exp. Biol*. **140**, 187-197.

ACKNOWLEDGEMENTS

This work was supported by the Biotechnology and Biological Sciences Research Council, UK.

NEW ENERGETICS APPROACHES TO ELUCIDATING MECHANISMS OF CONTRACTION AND RELAXATION

Lawrence C. Rome*, Iain S. Young, Claire L. Harwood, Boris Tikunov and Andrei A. Klimov

Department of Biology, University of Pennsylvania, Philadelphia PA 19104 &
The Marine Biological Laboratory, Woods Hole MA 02543
*Email: lrome@sas.upenn.edu

Vertebrate muscle must perform mechanical work to power locomotion, pump blood or produce sound energy. The frequency at which the work must be generated varies dramatically from less than 1Hz for some slow-twitch skeletal and cardiac muscles to more than 200 Hz for super-fast sound producing muscles. We have found that no single muscle fiber type can perform all activities (Rome & Lindstedt, 1998; Young & Rome, 2001) rather that specific molecular modifications are necessary to enable different muscles to operate at different frequencies

It is clear from our previous studies (Rome et al, 1996; 1999) that the kinetics of the crossbridges and the kinetics of sarcoplasmic reticulum (SR)-Ca^{2+} pumping are two major determinants of twitch speed: to relax quickly you must have a fast crossbridge detachment rate constant and a fast Ca^{2+} uptake rate. Because crossbridge force generation and Ca^{2+} pumping involve rapid utilization of ATP, measurement of ATP utilization during contraction can serve as an important window on understanding these mechanisms. For ATP utilization measurements to be useful, however, it is necessary to be able to partition the contribution made by crossbridges and the SR-Ca^{2+} pumps. For nearly a decade, specific and potent SR-Ca^{2+} pump blockers (e.g., TBQ, CPA) have been used extensively to knock out the SR-Ca^{2+} pump ATPase (Stienen et al. 1995). This has permitted the direct measure of crossbridge ATPase, which in turn, has permitted the determination of crossbridge detachment rate constants (i.e., ATPase /number of attached crossbridges; Rome et al. 1999).

Until now, there has not been an analogous crossbridge blocker that could be used to knock out crossbridge ATPase so that ATP utilization of SR-Ca^{2+} pumps could be measured directly. SR-Ca^{2+} pump ATPase is generally measured indirectly as the difference of total ATPase and crossbridge ATPase (Stienen et al., 1995), or directly over a limited range of Ca^{2+} concentrations [Ca^{2+}]s in toadfish swimbladder muscle (Rome & Klimov, 2000) because of its low affinity force-[Ca^{2+}]. Recently Young *et al.* (2002) have shown that the crossbridge blocker BTS (N-benzyl-P-toluene sulfonamide; Cheung *et al.* 2002) can be used at low concentrations in skinned toadfish fibers to eliminate at least 96% of the force and crossbridge ATPase, without affecting the SR-Ca^{2+} pump ATPase. Thus, by measuring the SR-Ca^{2+} pump ATPase one can determine the total Ca^{2+} pumping rate as well as the pump turnover rate (ATPase / number of pumps) in an intact SR.

Using BTS in intact fibers has opened up additional opportunities to study Ca^{2+} release and reuptake. Although Ca^{2+} transient measurements are very useful in determining free [Ca^{2+}], they do not measure the amount of Ca^{2+} released. Using a combination of high-energy phosphate measurements as well as recovery metabolism measurements, we are able to determine how much Ca^{2+} is released per stimulus. In addition, we can determine the fate of the released Ca^{2+}, that is, whether it is pumped back into the SR immediately or left bound temporarily in the myoplasm at the time of mechanical relaxation. This information, coupled with measurements of the muscle stimulation pattern in calling toadfish, permits unprecedented insights into muscle Ca^{2+} usage and budgeting during normal motor behaviour.

REFERENCES

Cheung et al. (2002). *Nature Cell Biol*. **4**: 83-88.
Rome, L.C., Klimov, A.A. (2000). *J. Physiol. (Lond.),* **526**, 279-298
Rome, L.C., Lindstedt, S.L. (1998). *News Physiol. Sci.,* **13**, 261-268
Rome, L.C. et al (1999). *Proc. Natl. Acad. Sci.,* **96**, 5826-5831
Rome, L.C. et al (1996). *Proc. Natl. Acad. Sci.,* **93**, 8095-8100
Stienen, G. J. M. et al. (1995*). J. Physiol. (Lond),* **482**, 109-122
Young, I.S., Rome, L.C. (2001). *Proc. Roy. Soc. B,* **268**, 1975-1980
Young, I.S. et al (2002). *Biophys. J.,* **82**, 366a

ACKNOWLEDGMENTS

This work is supported by NIH grants AR38404 and AR46125 (LCR), MBL Summer Fellowships (ISY) and by the Wellcome Trust UK (CLH).

THE RELATIONSHIP BETWEEN FILAMENT MOVEMENT AND ATP SPLITTING IN SKELETAL MUSCLE: CROSS-BRIDGE STEP SIZE AT DIFFERENT SHORTENING VELOCITIES

C. J. Barclay

School of Physiotherapy and Exercise Science, Griffith University, Gold Coast Campus
PMB 50 Gold Coast Mail Centre, Queensland 9726, Australia, Email: C.Barclay@mailbox.gu.edu.au

INTRODUCTION

Worthington & Elliott (1996) described a method for quantifying the contractile filament sliding generated per ATP hydrolysed in skeletal muscle by calculating the ratio of the velocity of filament sliding to the rate of ATP splitting along a single actin filament. Using this analysis, the amount of filament movement per ATP used was necessarily 0 in an isometric contraction (*i.e.* no filament movement) and increased as the load against which the muscle shortened decreased, reaching ~2 nm for unloaded shortening. Those authors used these data to support a model of muscle contraction in which only a single cross-bridge was attached to a thin filament at any instant (*i.e.* cross-bridges work sequentially); in this case, the filament movement per ATP used corresponds to the amount of movement generated in each cross-bridge cycle. They further claimed that the small amount of filament movement generated for each ATP split was inconsistent with the more generally accepted cross-bridge models of the type proposed by Huxley and colleagues in which the amplitude of the fundamental power stroke is typically assumed to be 10-15 nm (Huxley & Simmons, 1971).

The purpose of this study was to demonstrate that the relationship between net filament sliding per ATP used and load can be explained quantitatively in terms of a cross-bridge model in which multiple cross-bridges are attached along each thin filament simultaneously.

METHODS

The amount of movement each cross-bridge imparts to the thin filament in one ATP-splitting cycle (cross-bridge step size, D_{ATP}) was calculated from the net filament movement per ATP used (z) and the number of cross-bridges attached simultaneously along one thin filament (N):

$$D_{ATP} = z \cdot N$$

z was calculated from published measurements of the rate of enthalpy output from shortening frog sartorius muscle (Hill. 1964) and the fast-twitch EDL and slow-twitch soleus muscles from the mouse (Barclay, 1996) and making corrections for non-cross-bridge energy use and the extracellular fraction of fibre volume. N in an isometric contraction and its variation with shortening velocity were estimated by assuming that (i) 50 % of all cross-bridges were attached in an isometric contraction (Linari et al. 1998), (ii) muscle fibre stiffness decreased linearly with load (Julian & Sollins, 1975) and (iii) 50 % of sarcomere compliance was due to cross-bridges and the remainder was due to other compliant structures in series with the cross-bridges.

RESULTS AND DISCUSSION

D_{ATP} was estimated for each muscle shortening against a range of loads. In an isometric contraction (load = $1P_0$) D_{ATP} is 0, by definition. D_{ATP} increased as load decreased (that is, as shortening velocity increased) reaching values over 20 nm when load was < $0.1P_0$ (Fig. 1). Over much of the load range, D_{ATP} was between 10 and 15 nm in all three muscles and the dependence of D_{ATP} on relative load was similar for all three muscles, despite distinct differences in their energetic profiles.

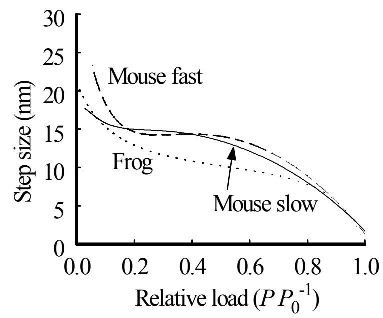

Figure 1: Variation in estimated cross-bridge step size with relative load.

At loads >$0.2P_0$, the magnitude of D_{ATP} is consistent with the magnitude of the cross-bridge power stroke estimated from a variety of experiments. Assuming these estimates are accurate, then over this range each power stroke must be associated with hydrolysis of one ATP. The high values of D_{ATP} at low loads is consistent with the idea that under these conditions cross-bridge cycles can occur without ATP use (*e.g.* Barclay, 1999).

SUMMARY

The relationship between net filament displacement and load described by Worthington & Elliott (1996) is consistent with a model in which many cross-bridges attach simultaneously along each thin filament and in which cross-bridges produce 10-15 nm of movement for each ATP split across much of load range.

REFERENCES

Barclay, C.J. (1996). *J. Physiol.* **497**, 781-794.
Barclay, C.J. (1999) *J. Mus. Res. Cell Motil.*, **20**, 163-176.
Hill, A.V. (1964). *Proc. R. Soc. B.* **159**, 297-318.
Huxley, A.F., Simmons, R.M. (1971) *Nature*, **233**, 533-538.
Julian, F.J., Sollins, M.R. (1975). *J. Gen.Physiol.* **66**, 287-302.
Linari, M. et al. (1998). *Biophys. J.*, **74**, 2459-2473.
Worthington, C.R., Elliott, G.F. (1996). *Int. J. Biol. Macromol.*, **18**, 123-131.

QUANTIFYING ISOMETRIC FORCE-DEPENDENT ENERGY RELEASE IN WHITE MUSCLE BY COMPARING CONTRACTION ENERGETICS IN INTACT AND SKINNED FIBRES

Tim West[1]*, Nancy Curtin[1], Mike Ferenczi[1], He-Zhen He[2], Yin-Biao Sun[3], Malcolm Irving[3] & Roger Woledge[4]

[1]Imperial College, London SW7 2AZ; [2]National Institute for Medical Research, London NW7 1AA;
[3]King's College London SE1 1UL,[4]UCL Institute of Human Performance, Stanmore HA7 4LP, UK , *Email: t.west@ic.ac.uk.

INTRODUCTION

Energy release in contracting muscle is complex because force-dependent and force-independent components are enmeshed into the time-course of total energy output. We have compared isometric contraction energetics in intact and skinned fibres to (i) establish the time-course of force-dependent energy production and (ii) quantify the actomyosin ATPase contribution to total energy output.

METHODS

White fibres were isolated from the dogfish (*Scyliorhinus canicula* L.). Energy release during a 3.5s tetanus was monitored as heat production in intact fibre bundles (4 – 12 fibres) at optimal length (Lo). Force-dependent energy release was determined from heat production at Lo and at longer fibre lengths (i.e., decreased filament overlap). Plots were made of relative energy release at selected time-points in the tetanus *vs.* relative force production and the slopes from these plots were used to model the force-dependent component of total energy release.

Energy production was also monitored in single Triton-permeabilised fibres using two independent fluorescent assays. These fibres contain the contractile filament array but no functional membrane ATPases. Initial rates of energy release were calculated from the binding of Pi to MDCC-labelled protein following initiation of contraction by the photolytic release of ATP from NPE-caged ATP (He *et al.* 1997). The final, stable rate of energy release was determined from NADH oxidation coupled to ADP production in a linked enzyme assay (Sun et al. 2001). Comparisons with intact fibres were made by assuming 34 kJ/mol Pi or ADP released (Woledge *et al.* 1985) and fibre density = 1.06 g/ml.

RESULTS & DISCUSSION

Initially energy is released by intact fibres at a high rate (210 μJ/mg·s, slope in Fig 1); this declines to a slower stable rate (45 – 50 μJ/mg·s, data not shown) by about 1.5s. The initial rate of energy release by skinned fibres was 150 μJ/mg·s (Pi-binding protein assay, Fig 1A). It is likely that activation processes involving Ca^{++} account for the difference in the initial rates.

Fig. 1A also shows that energy release in the Pi-binding study agrees with the force-dependent energy release in intact fibres, indicating that the ATP hydrolysis in skinned fibres matches the actomyosin ATPase activity in the intact system. Fig.1B shows that the rate of force-dependent energy release by intact fibres declines during an isometric tetanus. The ATPase activity late in the contraction time-course (31 μJ/mg·s; NADH-assay, n = 4) is 1/5th of that determined in the first 0.1s (Pi-binding assay). The two independent skinned-fibre assays concur with the intact fibre result.

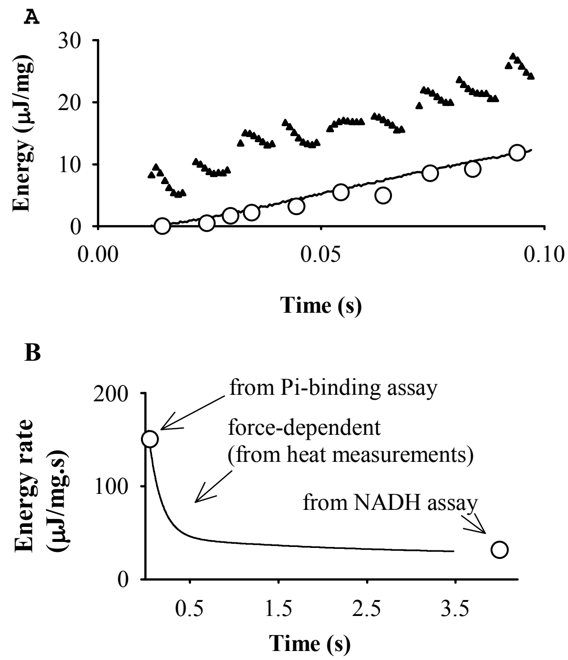

Figure 1: A. Mean energy release in intact (black triangles, n=8) and skinned (black line, n=15) fibres. Force-dependent energy release (open circles) from a separate group of intact fibres (n=9). **B.** Rates of force-dependent and skinned-fibre energy release during contraction.

CONCLUSIONS

- The initial energy turnover is greater in intact than in skinned fibres; probably due to activation processes.
- The actomyosin ATPase rate slows down during isometric contraction.

REFERENCES

He, Z.-H. et al (1999). *J. Physiol. (Lond),* 517, 839-854.
Woledge, R.C. et al (1985). *Energetic Aspects of Muscle Contraction*. Academic Press.
Sun, Y.B. et al (2001). *J. Physiol. (Lond),* **531**, 781-791.

APPLICATIONS OF MAGNETIC RESONANCE TECHNIQUES TO SKELETAL MUSCLE ENERGETICS AND BIOMECHANICS

Robert W. Wiseman

Molecular Imaging Research Center, Departments of Physiology and Radiology,
Michigan State University, East Lansing, MI 48824
Email: rwiseman@msu.edu

Magnetic resonance studies of skeletal muscle can provide unique information useful for biomechanical studies that may be otherwise unattainable. Magnetic resonance imaging (MRI) methods can provide quantitative morphometry on parameters such as cross-sectional area and tissue composition (e.g. muscle, fat, connective). In addition, more specialized "functional" MRI techniques provide information on the relative involvement (recruitment) of individual muscle groups in a particular mechanical task (Meyer & Prior, 2000). Magnetic resonance spectroscopy (MRS) provides invaluable information on the metabolic aspects of muscle function. For example, phosphorus MRS can be used to measure muscle content of ATP, PCr, Pi and free ADP as well as intracellular pH (Wiseman & Kushmerick, 1995; Wiseman et al, 1996). Thus the control and regulation of ATP free energy homeostasis and direct measurement of some of the key reactions in cellular energy metabolism are possible *in vivo* (Jeneson et al, 1997). When coupled with concurrent measurements of force production estimates of contractile costs can be derived.

In muscle, ATP production during the first few seconds of contraction is known to be almost entirely via the creatine kinase reaction (Harkema et al, 1997). Thus, the ATP cost of contraction can be estimated from the initial PCr change. In this study to investigate the ATP cost associated with contraction, we examined the initial rate of PCr depletion during stimulation using gated NMR, which enables sub-second time resolution of metabolic events (Foley & Meyer, 1993). C57B mice were anaesthetized with 50 mg/kg sodium pentobarbital and prepared for in situ stimulation via the sciatic nerve. ^{31}P-NMR spectra were acquired at 162 MHz by gating the acquisitions (8000 Hz sweep width, 1K data) to times 200 ms and 20, 40, 60, 80, 100, 120, and 140 s after a 2 s burst of isometric twitch contractions at 5 Hz (10-11 twitches total). After a final 20 s delay, the sequence was repeated for a total of 8 scans per time point. In addition, time-averaged spectra (8 scans, TR=2 s) were acquired during 2.1 min of continuous stimulation at 5 Hz. Relative changes in PCr were computed by the method of natural linewidths (Heineman et al, 1990).

The resting PCr/ATP ratio was 2.97 ± 0.13, mean ± SE (n=7). Assuming an ATP content of 7.5 μmol/g muscle, these changes correspond to initial PCr hydrolysis rates of 1.08 ± 0.17 umol/g/s. Peak twitch force after 2 s of 5 Hz stimulation was 95.6±1.6 % of initial in control muscles. Thus, in this study, as in previous studies of rat muscles (Foley & Meyer, 1993), the result is about 0.2 μmol/g/ twitch.

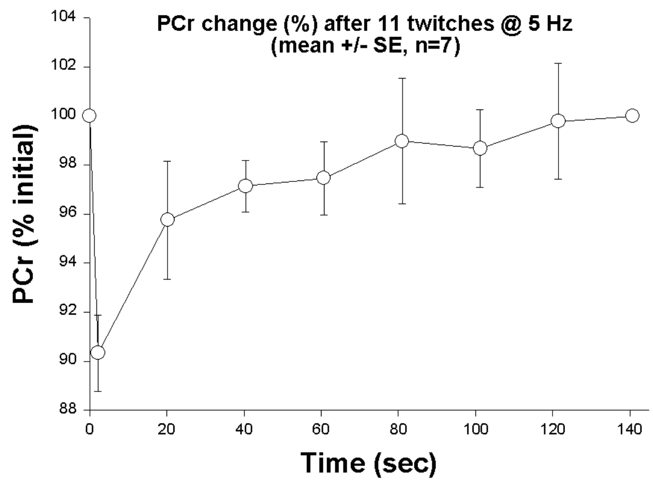

REFERENCES

Meyer, R.A., Prior, B.M. (2000). *Ex. Sport Sci. Rev.* **28**, 89-92.
Wiseman, R.W., Kushmerick. M.J. (1995). *J Biol. Chem.* **270**, 12428-38.
Wiseman, R.W. et al (1996). *Am. J. Physiol.* **271**, C878-86.
Jeneson, J.A.L. et al (1997). *Mol. Cell. Biochem.* **174,** 17-22.
Harkema, S.J. et al (1997). *Am. J. Physiol.*, **272**, C485-490.
Foley, J.M., Meyer, R.A. (1993). *NMR in Biomed.*, **5**, 32-38.
Heineman, F.W. et al (1990). *Magn. Reson. Med.*, **13**, 490-497.

ACKNOWLEDGEMENTS

Supported by NSBRI MA00210

BIOMECHANICAL ASPECTS OF TUMOR MICROCIRCULATION: WITH SPECIAL EMPHASIS ON LEUKOCYTE-ENDOTHELIUM INTERACTIONS

Norio Ohshima[1], Chika Miyoshi, Toshishige Suzuki, Kennichi Yanagi
Department of Biomedical Engineering, Institute of Basic Medical Sciences, University of Tsukuba,
Tsukuba Science City, Ibaraki, Japan. [1]ohshima@md.tsukuba.ac.jp

INTRODUCTION

Blood flow in the microvasculature plays an important role in governing the growth of the tumor tissue. Thus, more detailed knowledge of hemodynamics in the microcirculation is needed to obtain sound guidelines for diagnosis and treatment of malignant tumors. Direct observation of these dynamic processes *in vivo* has been extremely difficult mainly due to methodological limitations of the microscope optics. On the other hand, recent development in technologies of intravital microscope system, in particular, the use of a confocal laser-scanning microscope (CLSM) system combined with the use of a variety of fluorescent tracers has made it possible to visualize the microcirculatory blood flow *in vivo* even in a solid tumor tissue with a considerable depth.

As an experimental animal model to observe tumor microcirculation intravitally, the aurhors have established a solid tumor model called "peritoneal disseminated tumor model rat." This model has a distinct advantage to allow observation of the three-dimensionally grown-up tumor microcirculation under physiological conditions.

Using CLSM and the peritoneal disseminated tumor model, we have performed a series of experiments to analyze quantitative features of the vascular architecture of the tumor microvasculature, hemodynamics of the blood flow and behavior of leukocytes in the tumor microcirculation.

MATERIALS AND METHODS

Tumor model:
Tumor cells of a tumor cell line; RCN-9 (Riken Cell Bank, Tsukuba, Japan), established from Fischer 344 rat colon carcinoma, were intraperitoneally inoculated according to the method developed by the authors. Briefly, $1x10^7$ cells were inoculated into the peritoneal cavity of 7 week-old male Fischer 344 rats (Charles River, Kanagawa, Japan).

Intravital microscopic observation:
The mesenteric microvasculature was observed under an intravital microscope system (BHWI; Olympus Optical Co., Tokyo, Japan) equipped with a real time confocal laser-scanning optics (InSIGHT plus; Meridian Instrument Inc., Okemos, MI) and an image processing unit. Microvascular architecture and microhemodynamics of the formed elements were fluorescently visualized selectively by injecting a bolus of an appropriate fluorescent dye through the right jugular vein. Hemodynamic parameters were determined off-line by play-back analysis of the videotape.

RESULTS AND DISCUSSION

Angiogenic growth of the microvasculature:
After inoculation of the tumor cells into the peritoneal cavity of rats, tumor growth with an angiogenesis was microscopically observable within a few days. The inoculated tumor cells were then gradually became to be supplied by the mesenteric microvasculature with the progression of angiogenesis.

The branching pattern of the vascular network was analyzed based on the Horton's law of bifurcation. Arterioles and venules were given an order of branching separately according to the Strahler's nomenclature, and the number of vessel segment (N) having the same order number was counted. A vascular density index (VDI) and a bifurcation ratio (BR) were calculated from a semilogarithmic plolt of the vessel density against the vessel order. Values of VDI in both arterioles and venules showed a significant increase with time after the tumor cell inoculation. The rate of increase in the venular VDI was larger than that of the arteriolar VDI. Moreover, the arteriolar BR remained almost constant, whereas the venular BR showed an increase with time.

Microhemodynamic parameters in the tumor microvessels:
As a consequence of morphological abnormality, tumor microvessels also showed an altered hemodynamics. Fluorescent labeling of the erythrocytes (labeled by fluorescein isothiocyanate (FITC)), leukocyte (labeled by rhodamine 6G) and blood plasma (labeled by FITC-dextran) enabled quantitative measurements of microhemodynamic parameters such as flow velocity, blood cell flux and vessel diameter in both the normal and tumor microvascuatures.
In the vessels of the tumor-bearing mesentery, the centerline velocity of erythrocytes was significantry lower than that of the tumor-free rats. The wall shear rate of the tumor microvasculature also significantly decreased as compared with the normal control.

Leukocyte-endothelial cell interactions in the angiogenic vessels:
Selective labeling of leukocytes with rhodamine 6G enabled visualization of leukocytes even in the complexed microvasculature of the tumor tissue. Measurements of the flux of the rolling leukocytes and density of the adhered leukocytes revealed that these values were significantly lower in the tumor microcirculation than in the normal controls. Decrease in the baseline levels of these leukocyte-endothelial cell interactions was prominent in the venules located inside the tumor nodule.

Effect of NO inhibition on microhemodynamics:
To elucidate the mechanisms of these hemodynamic changes in the tumor microcirculation, effects of inhibition of nitric oxide (NO) production were examined. Although reduction of the baseline levels of leukocyte-endothelial cell interactions that was observed in the tumor veneules were markedly suppressed by inhibition of NO synthase (NOS), these increases in leukocyte interactions were scarcely found in the tumor-free rats. These results suggest that exposure to a high level of NO creates the tumor-specific micro-environment, thereby modulating leukocyte behavior in the angiogenic tumor vessels.

REFERENCES

Yanagi, K., Ohshima, N. (1996). *Microvasc. Res*., **51**, 15-28.
Suzuki, T. et al (1998). *Ann. Biomed. Eng*., **26**, 803-811.
Miyoshi, C., Ohshima, N. (1999). *in vivo*, **15**: 233-238.

ACKNOWLEDGEMENTS

Partly supported by a Grant for "Research for the Future Program" (JSPS-RFTF 96I00202) from the Japan Society for the Promotion of Science (JSPS), and a Grant-in-Aid from Japanese Ministry of Education, Science and Culture.

SIMULTANEOUS MEASUREMENT OF RED CELL VELOCITY AND PRESSURE IN MICROVESSELS REVEALED ADVANCEMENT IN PHASE OF FLOW PULSE RELATIVE TO THE PRESSURE PULSE BY π/4

Junji Seki[1], Yasuhiko Satomura[1,2] and Yasuhiro Ooi[3]
[1]Department of Biomedical Engineering, National Cardiovascular Center Research Institute, Suita, Osaka, Japan, ekij@ri.ncvc.go.jp
[2]Division of Physiology and Biosignaling, Osaka University Graduate School of Medicine, Suita, Osaka, Japan
[3]Division of Pathogenesis and Control of Oral Disease, Osaka University Graduate School of Dentistry, Suita, Osaka, Japan

INTRODUCTION

Red cell velocity in microvessels especially in arterioles has been found to pulsate rather largely originating from heart beats, and it propagates along the vessel as a pulse wave with phase delay (Seki, 1994). It is predicted theoretically that the flow pulse in microvessels advances the pressure pulse in phase by π/4 (45°) unless the microvessel is completely rigid, assuming that the Reynolds number and the frequency parameter of blood flow in microvessels are much smaller than one. However, the experimental results obtained so far showed the coincidence between the two within 10-15° (Intaglietta, et al., 1971). In this study, the red cell velocity in the rat pial arterioles was measured by the laser-Doppler method which has a higher temporal resolution than the dual-slit method used by Intaglietta et al. (1971) to reconcile the discrepancy between the experimental results and the theoretical prediction.

METHODS

Five male Wistar rats weighing 220-250 g were used for cerebral preparations. After animals were anesthetized and the respiration was controlled by a respirator, a cranial window of 3x5 mm^2 was created in the parietal region. Systemic arterial pressure was monitored in the femoral artery. Pressure in the pial arterioles was measured with a servonull pressure measuring system (IPM, San Diego, USA). Red cell velocity was measured with the fiber-optic laser-Doppler anemometer microscope (FLDAM) (Seki, 1990) in the upstream vicinity of the micro-pipette used for the pressure measurement. Temporal resolution of the velocity measurement was 5-10 msec. Time lag of the velocity relative to the pressure was calculated from cross-correlation.

RESULTS AND DISCUSSION

Measurements were made in 7 pial arterioles with diameter ranging from 41 to 53 μm. The Reynolds number based on the temporal mean velocity ranged from 0.04 to 0.15, and the frequency parameter ranged from 0.05 to 0.08, both of which were actually much smaller than one.

An example of the experimental results obtained in a pial arteriole with 44 μm in diameter is shown in Fig. 1. The microvascular velocity and pressure, and the femoral arterial pressure in this example all show distinctive pulsation with the same period. As estimated from the cross-correlation between the velocity and pressure (Fig. 1 (b)), the velocity wave preceded the pressure wave by 28.4 ms, which corresponds to 47.5° in this arteriole.

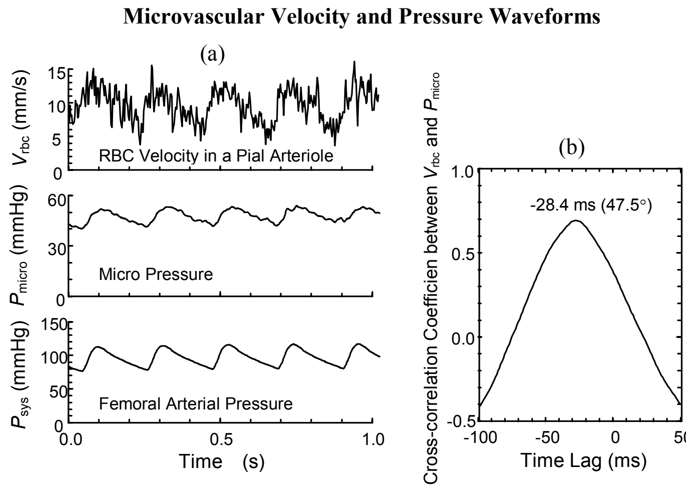

Figure 1: (a) Example of simultaneous measurement of red cell velocity and intravascular pressure in a rat pial arteriole of 44 μm in diameter and the femoral arterial pressure. (b) Cross-correlation coefficient between the microvascular velocity and pressure, indicating precedence of the velocity pulse relative to the pressure pulse.

In all the measured arterioles, the velocity in the arteriole preceded the intravascular pressure by 18.7-43.6 ms. The precedence of the velocity to the pressure was statistically significant. The corresponding phase difference, which is calculated from the time difference and the pulsation period, ranged from 28° to 56°. The average phase difference was 42.2° with the standard deviation of 7.6°, which is in accordance with the theoretical prediction, 45°.

The difference in the experimental results between ours and Intaglietta et al. (1971) is considered to come from the difference in the temporal resolution of velocity measurements between the laser-Doppler method and the dual-slit method, since the method to measure microvascular pressure used in this study was the same as in theirs.

REFERENCES

Intaglietta, M., Richardson, D. R., and Tompkins, W. R., *Amer. J. Physiol.*, **221**, 922-928, 1971.
Seki, J., *Microvasc. Res.*, **40**, 302-316, 1990.
Seki, J., *Amer. J. Physiol.*, **266**, H811-H821, 1994.

IMPLICATIONS OF A THICK ENDOTHELIAL CELL GLYCOCALYX FOR MICROVASCULAR FUNCTION IN MICE.

Hans Vink, Bernard van den berg, Alina Constantinescu, and Jos Spaan
Department of Medical Physics, Cardiovascular Research Institute Amsterdam
Academic Medical Center / University of Amsterdam, PO Box 22700, 1100 DE, Amsterdam, The Netherlands

INTRODUCTION

Vascular endothelial cells are shielded from direct exposure to flowing blood by a highly hydrated mesh of membrane associated proteoglycans, glycosaminoglycans, glycoproteins, and glycolipids. This anionic endothelial cell glycocalyx contributes to the selective permeability barrier of the vascular wall, regulates leukocyte- and thrombocyte- adherence, and specifically interacts with plasma proteins essential for vascular function.Numerous factors are described that may modulate the integrity of the endothelial cell glycocalyx. Elevation of vascular wall shear stress is reported to stimulate glycocalyx synthesis, while degradation of endothelial glycocalyx constituents is observed upon ischemia-reperfusion, during hypoxia, and by exposure to atherogenic plasma levels of oxidized low-density lipoprotein (oxLDL). Acurate assessment of glycocalyx thickness is therefore essential to relate dimensional glycocalyx changes to modulation of endothelial function. In the present study, we determined capillary glycocalyx dimension and tube hematocrit in Apo E3-Leiden mice supplied with an atherogenic diet for 3 months

METHODS

Mice (ApoE3-Leiden after 3 months of high fat diet, and wild type C57Bl/6 controls) were anesthetized with a single intraperitoneal injection of ketamine hydrochloride (125 mg/kg BW) and xylazine (7.5 mg/kg BW). The anesthesia was maintained with intraperitoneal injections of ketamine hydrochloride (15 mg/kg BW) administered at 1h interval. Atropine was supplemented subcutaneously. The trachea was cannulated to ensure a patent airway and the jugularis vein was cannulated for injection of lipoproteins. Body temperature was monitored with an intraesophageal thermometer and maintained at 37°C using a heating lamp. The right cremaster muscle was prepared for visualization of the microcirculation by longitudinal incision without cutting the connection with the epididymis. The muscle was continuously superfused at 34°C (5 ml/min) with a bicarbonate-buffered physiological salt solution (composition: 131.9 mM NaCl, 4.6 mM KCl, 2.0 mM $CaCl_2$, 1.2 mM $MgSO_4$, and 20 mM $NaHCO_3$) which was gas-equilibrated with 5% CO_2 and 95% N_2 to obtain a pH of 7.35 to 7.45. Succinylcholine (10^{-5} M, Sigma) was added to the superfusion solution to reduce spontaneous skeletal muscle contractions. In vivo glycocalyx dimension and capillary hematocrit were measured as previously described.

RESULTS AND DISCUSSION

In 9 out of 14 capillaries of Apo E3-Leiden mice (n=4), numerous lipid particles with diameters between 0.7 - 1.2 μm were present in the subendothelial space. In these capillaries, the dimension of the endothelial cell glycocalyx averaged 0.3 ± 0.1 μm, as compared to 0.5 ± 0.1 μm in non-fat Apo E3-Leiden capillaries, and 0.6 ± 0.1 μm in capillaries of wild type mice (C57Bl/6). Respective capillary tube hematocrits averaged 0.27 ± 0.03, 0.17 ± 0.04 and 0.15 ± 0.02 during control conditions, and increased to 0.34 ± 0.02, 0.34 ± 0.04 and 0.32 ± 0.02 after topical administration of bradykinine (10^{-5} M).

SUMMARY

It is concluded that reduced dimension of the endothelial cell glycocalyx in atherogenic Apo E3-Leiden mice is associated with increases in capillary tube hematocrit and subendothelial lipid accumulation.

REFERENCES

Desjardins, C. & Duling, B.R. Heparinase treatment suggests a role for the endothelial cell glycocalyx in regulation of capillary hematocrit. *Am. J. Physiol.* 258, H647-H654 (1990).

Vink, H. & Duling, B.R. Identification of distinct luminal domains for macromolecules, erythrocytes, and leukocytes within mammalian capillaries. *Circ. Res.* 79, 581-589 (1996).

Vink, H., Constantinescu, A.A. & Spaan, J.A. Oxidized lipoproteins degrade the endothelial surface layer : implications for platelet-endothelial cell adhesion. *Circ.* 101, 1500-1502 (2000).

EXCLUSION OF NEUTRAL AND POLYANIONIC PLASMA TRACERS BY THE CAPILLARY GLYCOCALYX IN EQUILIBRIUM AND DEFORMED CONFIGURATIONS PREDICTS MECHANO-ELECTROCHEMICAL PROPERTIES *IN VIVO*

Edward R. Damiano[1], Thomas M. Stace[1,2], and Hans Vink[3]

[1]Department of Mechanical and Industrial Engineering, University of Illinois at Urbana-Champaign, damiano@uiuc.edu
[2]Cavendish Laboratory, Cambridge University
[3]Department of Medical Physics, University of Amsterdam

INTRODUCTION

The interface between blood and the vascular endothelium represents one of the most complex, dynamic, and fundamentally important interfaces in mammalian physiology. Strategically located at this interface is a glycocalyx surface layer that is regulated by and expressed on capillary endothelial cells. In order to investigate the properties of this structure, we have combined analytical modeling with intravital brightfield and fluorescence microscopy. In our analysis, we have assumed that the glycocalyx consists of a mixture of electrostatically charged macromolecules hydrated in an electrolytic fluid. Disturbances arising from mechanical deformation are introduced as perturbations away from a nearly electroneutral equilibrium environment. In the case of mechanical compression of the layer, such as might occur on the passing of stiff leukocytes through capillaries, fluid flux into the compressed layer, driven by electrochemical potential gradients of the ions and glycocalyx macromolecules, results in rehydration of the layer and a restoration of its equilibrium dimensions. An analysis of the equilibrium configuration of the layer predicts that polyanionic fluorescent plasma tracers would be partially excluded by the glycocalyx by vitue of their charge. It further predicts, quantitatively, the degree to which this exclusion would occur as a function of tracer valence, glycocalyx fixed-charge density, and the ionic strength of blood plasma. This exclusion would result in a reduction in fluorescence intensity within the glycocalyx relative to luminal intensity levels, and could therefore be detected using epifluorescence illumination *in vivo*.

METHODS

To investigate the fixed-charge density and permeability of the glycocalyx, distributions of 20 and 40 kDa neutral and polyanionic plasma tracers were obtained over the cross section of capillaries in the mouse cremaster muscle using wide-field intravital fluorescence microscopy. Three-dimensional fluorescence recordings were made by moving the microscope objective lens through 150 steps along the *z* axis in 20 nm increments (where *xy* planes correspond to sagittal planes through the vessel). Out-of-focus light was removed from the three-dimensional recordings of the capillaries using iterative constraint deconvolution software. Using different optical filters, fluorescence intensity distributions were obtained for both neutral and polyanionic tracers of the same molecular weight that were simultaneously present within the same capillary segment.

RESULTS AND DISCUSSION

Results reveal a charge-mediated exclusion by the glycocalyx of polyanionic tracers within an approximately 0.5-micron-thick region adjacent to the vessel wall. This exclusion was measured by the attenuation in fluorescence intensity of near-wall polyanionic tracers, which was found to be 46% relative to the centerline polyanionic tracer intensity and 30% relative to the near-wall neutral tracer intensity. When combined with our electrochemical model of the glycocalyx (Stace and Damiano, 2001), these measurements provide an estimate of the glycocalyx fixed-charge density of between 0.7 and 1.3 mEq/l. Based on this estimate of the fixed-charge density, and a recovery time of the layer of approximately 1 s after the passage of a single leukocyte (Vink et al., 1999), our mechano-electrochemical model of the glycocalyx (Damiano and Stace, 2002) estimates the glycocalyx permeability to be approximately 10^{-11} cm^4/dyn-s. This result is consistent with an independent estimate of permeability made by Feng and Weinbaum (2000) using a fiber matrix model based on the Brinkman equation. Results under iso-osmolar conditions of low, normal, and high plasma ionic strength will also be presented.

REFERENCES

Damiano, E.R., Stace, T.M. (2002). *Biophys. J.*, (to appear).
Feng, J., Weinbaum, S. (2000). *J. Fluid Mech.*, **422**, 281-317.
Stace, T.M., Damiano, E.R. (2001). *Biophys. J.*, **80**, 1670-1690.
Vink, H. et al. (1999). *FASEB. J.*, **13**, 3.14, p. A11 (Abstr).

ACKNOWLEDGEMENTS

Partial support for this work was provided by the Whitaker Foundation (RG-98-0524) and NSF (BES-0093985).

RECONSTITUTION OF GPIbα-MEDIATED PLATELET BEHAVIOR IN MICROCIRCULATION

Makoto Suematsu, Tomihiro Katayama, Takako Nishiya, Satoshi Kashiwagi,
Mitsuru Murata, Makoto Handa, Yasuo Ikeda

Department of Biochemistry and Integrative Medical Biology, and Department of Internal Medicine, School of Medicine, Keio University, Tokyo 160-8582, Japan
msuem@sc.itc.keio.ac.jp

INTRODUCTION

Analyses of behavior of circulating platelets in microvessels in vivo have been difficult technically through multiple reasons. High magnification and cell-specific labeling are necessary to visualize individual platelets, while such optical conditions causes difficulties in time resolution for visualization of the rapid-moving cells in circulation.

METHODS

To overcome these difficulties, we have established a novel method to stain platelets with the fluorophore and to visualize their individual traffics with a resolution sufficient enough to determine site-specific velocity and density in a single vessel of organ microcirculatory system. High-speed intensified video microscopy in rats allowed us to visualize fast-moving platelets at videorates of 300-1000 frames/sec, and normospeed replay of the video images at 30 frames/sec demonstrated that behavior of individual platelets in microvessels differ greatly between the cells flowing at centerline region and those flowing in the periendothelial space.

RESULTS AND DISCUSSION

Our results demonstrate that, under high shear rates greater than 600 sec^{-1} (e.g. arterioles), platelets tend to form microaggregates and to flow along the periendothelial space, exhibiting transient skipping and rolling on the endothelium. They utilize GPIbα on their surface for these shear-dependent interactions with the surface of the endothelium through its affinity to vWF. In venules, GPIbα-mediated platelet adhesion appeared to occur transiently on the surface leukocytes. These specific events were reproducible in vivo by mimicking platelets with liposomal particles coated with human recombinant GPIbα were injected into circulation. Furthermore, liposomes coated with M239V GPIbα, the gain-of-function mutant protein losing shear-sensing ability showed transient adhesion not only to arterioles but also to venules, and most of them were captured finally on leukocytes immediately after the injection. These results suggest a critical role of GPIbα as a major determinant of shear-specific microvascular distribution of platelets and their behavior.

REFERENCES

Katayama, T., et al. (2000) Circ Res 86, 1031-1037, 2000.

FORCE ENHANCEMENT DURING AND FOLLOWING ECCENTRIC MUSCLE CONTRACTION

Walter Herzog
Faculties of Kinesiology and Engineering, University of Calgary, Calgary, Alberta, Canada

INTRODUCTION

Cross-bridge models of muscle typically predict well the loss of force during concentric contractions, and the increase in force during eccentric contractions (Huxley, 1957). However, they do not contain, except in isolated cases, a description of the steady-state force depression/force enhancement that follows shortening/stretch contractions (Abbott and Aubert, 1952;Edman et. al., 1982), and no cross-bridge model contains a biological explanation of how such force depression/enhancement may be caused. For lack of understanding these well-accepted phenomena, structural mechanisms, not related to the mechanism of contraction, have typically been assumed to cause force depression/enhancement. The most widely accepted mechanism is the sarcomere length non-uniformity theory (Morgan, 1990). Although this theory was originally proposed on scarce evidence, it has provided a framework for hypothesis testing that has persisted in time. Here, we provide evidence that the sarcomere length non-uniformity theory alone cannot account for the observed phenomena.

HYPOTHESES:

One of the pillars of the sarcomere length non-uniformity theory is the hypothesis that force enhancement following muscle stretch cannot exceed the isometric force at the optimum muscle length (the length at which peak active isometric force is produced).

METHODS

Over the past five years, we measured force enhancement following muscle stretch in single fibres of frog tibialis anterior (TA) and flexor digitorum brevis (FDB), in cat soleus and semitendinosus, and in human knee extensors and adductor pollicis. Stretch contractions were always performed following achievement of the full active state, and forces following stretching were measured long enough for transient force changes to disappear. Force enhancement was defined as the steady-state isometric force following stretch minus the purely isometric force obtained at the same length and at the same time of contraction as that for the stretch tests.

RESULTS AND DISCUSSION

We found that the steady-state force enhancement can clearly exceed (10%) the purely isometric force at optimum length in frog single fibers (TA and FDB), in cat soleus, and in human adductor pollicis (Figures 1 and 2). Furthermore, we found a persistent passive component that contributed to the total force enhancement in all muscle preparations tested (Figure 1).

The results of this study indicate that force enhancement cannot be solely attributed to the development of non-uniformities in sarcomere length, because sarcomeres cannot exert more force than they do at optimum length. Initially, we thought that perhaps force enhancement above the peak isometric force could be associated with the newly discovered passive force enhancement. However, preliminary analysis indicates that this is likely not the case.

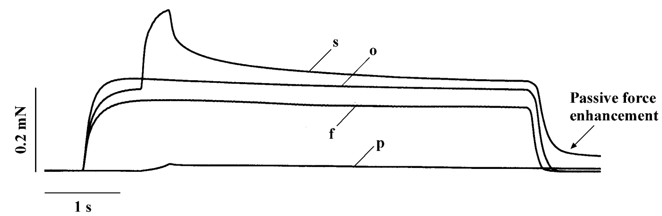

Figure 1: Force enhancement (s) above optimal (o) and ifnal length (f) isometric force. Frog FDB; p = passive stretch

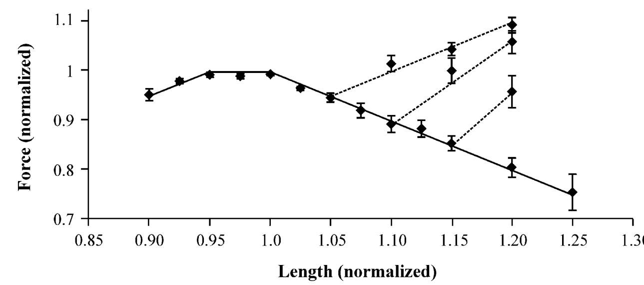

Figure 2: Force-length relation of frog FDB fibres (n=22) and the force enhancement following stretch exceeding the isometric force at optimum length.

CONCLUSION:

We conclude that although the sarcomere length non-uniformity theory cannot be dismissed as a mechanism to contribute to force enhancement, it appears unlikely that it can explain the full extent of force enhancement observed experimentally. We speculate that sarcomere length non-uniformity may play a minor (if any) role in force enhancement, and that force enhancement may be associated with the elementary, molecular mechanism of muscle contraction.

REFERENCES

Abbott,B.C.,Aubert,X.M. (1952). *J Physiol* 117, 77-86.
Edman,K.A.P. et al. (1982). *J Gen Physiol* 80, 769-784.
Morgan,D.L. (1990). Biophys J 57, 209-221.
Huxley, A.F. (1957) Prog.Biophys.Biophys.Chem. 7:255-318

NEURAL CONTROL OF ECCENTRIC CONTRACTIONS

E. Paul Zehr

Neurophysiology Laboratory, University of Alberta, Edmonton, Alberta, Canada, pzehr@ualberta.ca

INTRODUCTION

Eccentric, or lengthening, muscle contractions have been suggested to require distinctive neural control strategies (Enoka, 1996). Supraspinal, spinal, and neuromuscular properties have been suggested as possible loci for mechanisms underlying the neural control of eccentric contractions although data has been lacking particularly for CNS mechanisms. Recently, however, numerous studies have identified altered features of both cortical (Fang *et al.*, 2001) and corticospinal tract excitability (Sekiguchi *et al.*, 2001) during eccentric contractions. Also, there are data to support altered H-reflex excitability during active (Nardone and Schieppati, 1988) and passive (Pinniger *et al.*, 2001) eccentric contractions of the human triceps surae. To address further the issue of spinal reflex mechanisms and muscle activation levels we have been studying cutaneous reflex modulation and EMG amplitudes during eccentric and concentric contractions of the human ankle flexor and extensor muscles.

METHODS

Subjects participated in the experiments with informed written consent. In separate experiments subjects performed both isolated and rhythmic isometric or isotonic plantar- (PF) and dorsiflexions (DF). To evaluate differences in the patterns of muscle activation (EMG) during eccentric and concentric contractions, subjects performed isotonic PF at different velocities (slow to near maximum) with loads of 40% of isometric plantarflexion MVC. Evaluations were made of peak and average EMG activity as well as temporal occurrence of the peak EMG during eccentric and concentric contractions. In the experiments focused upon reflex mechanisms, subjects performed eccentric and concentric contractions of the triceps surae and tibialis anterior (TA) muscles against a constant load (~20% MVC), while EMG was collected continuously. Additionally, both isotonic and isometric contractions were studied. Cutaneous reflexes were evoked by applying trains (5 x 1.0 ms pulses @ 300 Hz) of isolated constant current electrical stimulation to the sural nerve. The stimulation was typically applied pseudorandomly throughout the movement cycle. Reflexes were then phase-averaged dependent upon the time of occurrence of the stimuli within the movement cycle. Additionally, in some experiments stimulation was applied at the midpoint of the movement cycle and positions were matched when comparing eccentric and concentric contractions. Cutaneous reflexes were evaluated at early (~50-70 ms), middle (~75-110 ms), and late (>120 ms) latencies post-stimulation. Additionally, the net effect of stimulation over a 150 ms post-stimulus window was calculated.

RESULTS AND DISCUSSION

Our results on EMG amplitudes extend to higher submaximal loads the observation that greater muscle activation is required to produce a concentric than an eccentric contraction. Interestingly, while the EMG amplitude scaled with contraction velocity during concentric contractions, there was no scaling during eccentric contractions (Gillies *et al.*, 2000). Cutaneous reflex amplitude was differentially modulated during eccentric and concentric contractions in triceps surae. Typically, reflexes were inhibitory during concentric but excitatory during eccentric contractions (Haridas *et al.*, 2000). Interestingly, cutaneous reflex reversal was not typically observed in the ankle flexor muscle TA (Haridas *et al.*, 2001). Taken together, our recent experiments suggest that EMG and cutaneous reflex amplitudes are differentially modulated during eccentric and concentric contractions, at least in extensor muscles of the leg. These observations fit with the observations on reflex control documented in other laboratories.

SUMMARY

The preponderance of evidence, particularly that obtained recently from many different laboratories, supports the assertion that eccentric contractions are treated as distinctly different actions by the nervous system. The biomechanical implications for this distinction as applied to functional motor tasks is currently the study of investigation.

REFERENCES

Enoka,R.M. (1996). *J Appl.Physiol.* **81,** 2339-2346.
Fang,Y. et al. (2001). *J Neurophysiol* **86,** 1764-1772.
Gillies,E. et al. (2000). *Can J Appl Physiol* **25,** 374.
Haridas,C. et al. (2001). *Can J Appl Physiol* **26,** 484.
Haridas,C., et al. (2000). *Soc Neurosci Abs* **26,** 1232.
Nardone,A. & Schieppati,M. (1988). *J.Physiol.* **395,** 363-381.
Pinniger,G.J. et al. (2001). *J Physiol* **534,** 913-923.
Sekiguchi,H. et al. (2001). *Neurosci.Lett.* **312,** 83-86.

ACKNOWLEDGEMENTS

Supported by the Natural Sciences and Engineering Research Council of Canada and the Alberta Heritage Foundation for Medical Research.

EFFECTS OF CONTRACTION HISTORY ON FASCICLE BEHAVIOR IN SHORTENING CONTRACTIONS

Taija Finni, Janne Avela and Paavo V. Komi
Neuromuscular Research Center, Department of Biology of Physical Activity, University of Jyväskylä, Finland

INTRODUCTION

The force produced by a skeletal muscle is dependent on length, velocity and activity level, but also on previous contraction history. For example, enhanced force production following stretching phase is well established in the literature (Noble 1992). The stretch-shortening cycle of muscle function that occurs frequently in natural locomotion potentially benefits from the force enhancement mechanism, although the issue is controversial. In the present study, muscle-tendon interaction in the triceps surae muscle was examined during controlled ankle flexion-extension movements. On the basis of previous findings on the knee extensor muscles (Finni et al. 2001) it was hypothesized that the previous eccentric phase elongates muscle fascicles to a length longer than in corresponding isometric condition, thereby affecting force production in the consequent shortening phase (Meijer et al. 1997).

METHODS

Plantarflexion torque and fascicle lengths from gastrocnemius medialis muscle were measured from nine volunteers during isometric-concentric (IC) and eccentric-concentric (EC) contractions performed on a motor driven ankle ergometer. Subjects gave informed consent to participate in the study, which was approved by the University Ethics Committee. During the procedure, the subjects were seated in a chair with their right leg relaxed and fixed to the ergometer. The axis of rotation of the ankle was aligned with the axis of rotation of the ankle ergometer as well as possible. Plantarflexor muscles were activated by applying electrical stimulation via self-adhesive stimulation electrodes (5×5cm) that were placed over proximal and distal part of the muscle bellies. The intensity of the current was 10% MVC (ankle 90°), and was the same in IC and EC. Furthermore, IC contractions were repeated with an intensity that produced the same force as was recorded in the EC condition just prior to the shortening phase. Mean (SD) torques and fascicle lengths in different phases of the performance were calculated and the differences were tested with two-way ANOVA with Tuckey HSD Post Hoc Test.

RESULTS AND DISCUSSION

As expected, torque was significantly higher just before the concentric phase in EC as compared to IC (36 vs. 12 Nm, respectively, $p<0.05$), when muscles were stimulated with the same intensity (Fig. 1). The fascicle lengths, however, did not differ (4.3 vs. 5.1 cm, ns.). When the torque level was the same in EC and IC, the fascicle length in the isometric phase of IC was 4.4 ± 0.9 cm (Fig. 2). The major difference in fascicle behavior in EC and IC was that during EC the fascicle continued to lengthen in the early plantarflexion phase although the length remained unchanged in IC. After the

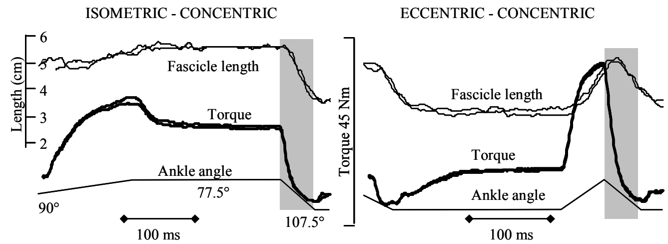

Figure 1: Example of recordings from one individual. Two repetitions from both IC (left) and EC (right) conditions are shown. The shaded area indicates the concentric plantarflexion movement. Stimulation intensity was 10% MVC and the same in both conditions.

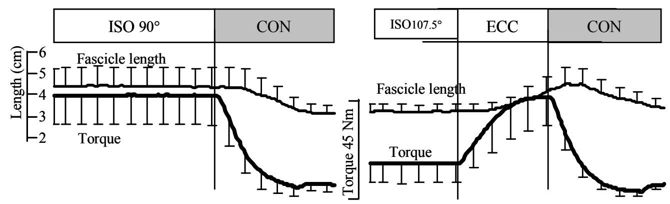

Figure 2: Group mean (SD) torque and fascicle length curves in IC (left) and EC (right) conditions. In IC, the stimulation intensity was set to produce the same force as in the end of eccentric phase of EC.

elastic tissues had shortened taking up the slack in the muscle-tendon unit, also the fascicles started to shorten. Shortening of the fascicles during the first 15° of plantarflexion movement was more pronounced in IC than in EC ($p<0.05$). Consequent effects on force production, however, were not seen. The lack of observation of stretch-induced force-enhancement phenomenon is attributed to the low stimulation intensity used in the present experiment. In the measurements to follow we intend to use greater force levels to confirm our earlier findings that were done with the knee extensor muscles.

SUMMARY

Benefits of stretch-shortening cycle (SSC) muscle function may come through different interactive mechanisms. With controlled ankle flexion-extension movements this study showed that the fascicles of the gastrocnemius medialis muscle behave differently during plantarflexion movement when it is initiated from pre-stretched or pre-isometric contraction. In pre-stretch condition, the fascicles continued to stretch during early plantarflexion movement. Longer initial length may affect force production during shortening phase of SSC.

REFERENCES

Finni, T. et al. (2001). *Acta Physiol Scand* **173**, 369-377
Meijer et al. (1997). *J Appl Biomech* **13**, 164-181.
Noble, M.I.M. (1992). *Exp Physiol* **77**, 539-552.

NEUROMUSCULAR FATIGUE DURING AND AFTER ECCENTRIC AND CONCENTRIC EXERCISES

Paavo V. Komi and Vesa Linnamo
Neuromuscular Research Center, Department of Biology of Physical Activity, University of Jyväskylä, Finland

INTRODUCTION

Considerable controversy exists regarding fatigue effects of repeated concentric and eccentric exercises. In discussing these controversies one should keep in mind that the maximal force produced during eccentric actions may sometimes be even twice that developed during concentric action and that the mximal EMG activities may not necessarily be different between these forms of actions. This high mechanical load concept in individual muscle fibres and connective tissues put Asmussen (1956) among the very first ones to quantify the performance and muscle soreness differences between fatiguing concentric and eccentric exercises. He was able to demonstrate for both arm (triceps brachii) and leg (quadriceps femoris) muscles that muscular soreness was always present 1 or 2 days after the eccentric exercise, but hardly ever after the concentric exercise. This finding has formed a basis – although often without reference to Asmussen´s work – for the concept of delayed muscle soreness (DOMS), typically occurring in relation to unaccustomed exercises, including specifically eccentric exercises.

METHODS

The experiments of Asmussen (1956) on the "mechanical stress" concept for muscle soreness stimulated us to design studies, in which EMG activities and muscle forces were followed in forearm flexors and knee and leg extensors with repeated maximal eccentric and concentric actions with special dynamometers with controlled stretching and shortening velocities of the specific muscle groups (Komi & Rusko, 1974; Komi & Viitasalo, 1977; Linnamo et al, 2000). Depending on the study, the number of repeated maximal muscle actions were either 40 or 100. The two types of fatiguing exercises were separated by a minimum of two weeks. The individual contractions (either concentric or eccentric) were always produced by maximal preactivation.

RESULTS AND DISCUSSION

In the two earlier studies the fatiguability was clearly greater in eccentric than in concentric modes, and the eccentric induced reduction in performance was associated with DOMS. This is presented in fig. 1, which shows that both the force-time characteristics and EMG/force ratio during isometric actions presented a delayed recovery from eccentric fatigue but not concentric fatigue. This same association with DOMS and delayed recovery was confirmed in the later study by Linnamo et al (2000).

In all these studies the eccentric actions started with maximal preactivation similar to the model of Edman (1978) in isolated muscle fibres/sarcomeres. Linnamo et al (in preparation) showed that if eccentric action is started with 50% or 0% preactivation, the maximal and average eccentric force remained lower compared with when maximal preactivation was used. Therefore, if the fatigue protocol in the eccentric mode is started with zero preactivation (e.g. Hortobagyi et al, 1996; Tesch et al, 1990) it is natural to expect that the overall eccentric loading is less than the full preactivated mode in our experiments. In the latter case the "mechanical load concept" of Asmussen (1956) is followed and the overall duration of eccentric action is much higher and the resulting fatigue response is usually greater than after concentric exercise. Equal metabolic loading between eccentric and concentric exercises in these conditions are in line with this observation as indicated by almost similar oxygen consumption (Komi & Rusko, 1974), blood lactate values, and muscle glycogen depletion (Komi & Viitasalo, 1977). Additional prerequisite in these fatigue studies is that the maximal EMG activation is similar in both exercise modes.

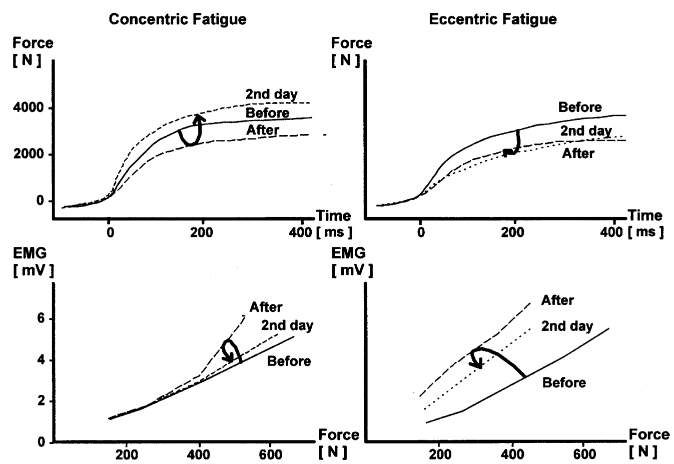

Figure 1: Influence of 40 repeated maximum concentric and eccentric actions on the isometric force-time curve of the bilateral leg extension (upper graphs) and on EMG-force relationship in unilateral knee extension (lower graph). Note the delayed recovery of muscle performance following the eccentric fatigue (from Komi & Viitasalo, 1977).

REFERENCES

Linnamo et al (2000) *J Electrom Kinesiol* **10(5)**, 293-300
Hortobagyi et al (1996) *Int J Sports Med* **17(6)**, 409-414
Tesch et al (1990) *Acta Physiol Scand* **138**, 263-271
Komi & Viitasalo (1977) *Acta Physiol Scand* **100**, 246-254
Edman (1978) *J Physiol* **281**, 139-155
Komi & Rusko (1974) *Scand J Rehab Med* **3**, 1121-126
Asmussen (1956) *Danish National Association for Infantile Paralysis, Hellerup, Denmark*, **20**, 3-11

SCALING OF DAMPING: IMPLICATIONS FOR STABILITY

Robert J. Full[1] , Anne M. Peattie[1], Mariano S. Garcia[1], Art D. Kuo[2], Paul C. Wang[1], Thomas M. Libby[1]and Daniel Dudek[1]

[1]Department of Integrative Biology, University of California at Berkeley, USA
[2]Department of Mechanical Engineering, University of Michigan, USA

INTRODUCTION

Rapid running insects are remarkable at negotiating rough terrain. Experiments have shown that animals maintain their preferred speed and gait, even when challenged with obstacles that exceed three times the height of their center of mass. Theoretical models of animals demonstrate passive, dynamic self-stabilization without sensing of the environment (Schmitt et al.). These horizontal plane models consist of a mass and a laterally projecting spring representing three legs acting as one. Biologically inspired robots or physical models using simple, damped-springy legs have become extremely effective at traversing irregular terrain (Altendorfer et al.; Cham et al.).

To determine one parameter often implicated in contributing to stability, we measured leg damping in the cockroach (*Blaberus discoidalis*). We hypothesized that damping provides stability by rejecting perturbations to legs in the swing phase, thus allowing simpler control of foot position. We wondered whether this hypothesized advantage was specific to insects or was a more general phenomenon based on size. Therefore, we determined the scaling of damping.

METHODS

We used three methods to measure damping in cockroach legs. First, we perturbed the free tibia and recorded its motion with a high-speed video camera until it returned to an equilibrium position. Second, we fixed the femur and attached the tibia to a lever. We oscillated the leg at a range of frequencies in the plane of the joint while measuring force. Damping in the plane of the joint was measured with and without passive muscles. Third, we fixed the body and attached the end of the tibia to a lever. We oscillated the whole leg out of the plane of the joint while measuring force.

RESULTS AND DISCUSSION

Insect joints and legs were highly overdamped, whether or not the perturbation occurred from the side in the plane of the joint or vertically out of the plane of the joint. The femur tibia joint was highly overdamped, both with and without passive muscles (damping ratio near 10). The exoskeleton was responsible for approximately 70% of the damping. Damping was independent of perturbation frequency.

When we modeled the limb as a cylinder oscillating at its natural frequency operating with a viscously damped joint, we found that stiffness and damping scaled proportionally with length. Damping ratio scaled inversely with the length and mass. Therefore, as limb length decreases damping ratio increases. At large scales, damping is negligible and limbs swing like a pendulum. As size decreases, pendulum behavior gives way to self-stabilization without overshoot. Although data are insufficient to formalize a scaling relationship, measurements on humans lend support to the principle.

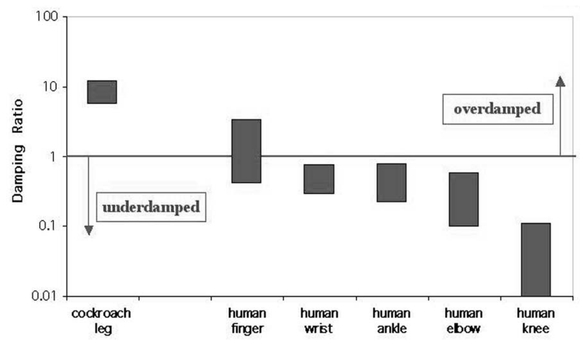

Figure 1. Damping ratio for segments that differ in size. Data from Garcia M.S., et al., 2000; Coveney V.A., et al., 2001; Lebiedowska M.K. & Fisk J.R., 1999; Milner T.E. & Cloutier C., 1998; Lacquaniti F., et al., 1982; Hunter I.W. & Kearney R.E., 1982; Hajian A.Z. & Howe R.D., 1997; Agarwal G.C. & Gottlieb C.L., 1977.

SUMMARY

Cockroach legs in the swing phase are overdamped. Damping ratio increases with decreasing limb mass and length. Large passive, damping in small appendages has implications for control. Perturbations to small limbs can be dissipated with less neural feedback. Muscle activation could be regarded more as a simple position or velocity command rather than a force command. A self-stabilizing limb favors the use of simple feedforward control strategies for locomotion.

REFERENCES

Altendorfer, A. et al. *J Autonomous Robots,* In press.
Schmitt, J. et al. *Bio. Cyber.* In press
Cham, J.G. et al. *Int J of Robotics Research.* In press.

ACKNOWLEDGEMENTS

Supported by DARPA/ONR N00014-98-1-0747 and ONR N00014-98-1-0669.

SELF-STABILITY MECHANISMS FOR SENSOR-CHEAP LEGGED LOCOMOTION

Daniel Koditschek[1], Richard Altendorfer[1], Raffaele Ghigliazza[2], and Philip Holmes[2]
[1]Deparment of Electrical Engineering and Computer Science, University of Michigan, Ann Arbor, MI 48109-2110
[2]Department of Mechanical and Aerospace Engineering, Princeton University, Princeton, NJ 08544

INTRODUCTION

It is now well established that running animals' mass centers exhibit the characteristics of a Spring Loaded Inverted Pendulum (SLIP) in the sagittal plane (Blickhan and Full, 1993). What control policy accomplishes this collapse of dimension by which animals solve the "degrees of freedom problem" (Bernstein, 1967)? How valuable might this policy be to gait control in legged robots?

A general framework for "anchoring" virtual spring loaded inverted pendulum (SLIP) mechanics in the far more elaborate morphologies of real animals' bodies (Full and Koditschek, 1999) has been motivated by successful implementation in laboratory robots (Buehler et al., 1990; Nakanishi et al., 2000; Rizzi and Koditschek, 1996). However these implementations appear to demand sensing, actuation, and computation that may be unrealistic relative to the resources that animals and practical robots might be expected to have on hand.

Can we account for stable running animal gaits without recourse to such "expensive" control techniques? If so, can we introduce such "cheap" controllers to robotics and hope to obtain similarly high performance legged locomotion?

METHODS

A new hexapedal robot, endowed with passive compliant legs and sprawled posture in essential conformance with the functional properties of exemplary cockroach runners (Full et al., 1998), exhibits mobility over general terrain exceeding that of any previous (scientifically documented) power autonomous legged machine (Saranli et al., 2001). When this machine's mechanical and control parameters are properly tuned, its mass center also exhibits pronounced SLIP characteristics (Altendorfer et al., 2001). Notably, this stable dynamical regime is achieved by a feedforward controller that drives the machine's few (only six) actuators without the benefit of any proprioceptive data (beyond the motor shaft angle measurements used to enforce the desired open loop hip position profile).

RESULTS AND DISCUSSION

At present, we do not understand enough about this robot's mathematical models to select desired gaits by first principles analysis. Stable steady state SLIP behavior is adjusted at present by systematic but almost purely empirical parameter tuning methods.

Mathematical analysis (Schmitt and Holmes, 2000) of the (simplified) horizontal plane mechanics of a running cockroach (Kubow and Full, 1999) has revealed that self-stabilization can occur in two and three degree of freedom lossless mechanisms. These models are mechanically very similar to a horizontal plane version of SLIP, motivating a search for self-stabilized gaits in the sagittal plane. Analogous study of the sagittal plane SLIP model now reveals that it too indeed includes parameter regimes that yield self-stabilizing gaits. Algebraic approximations of this parameter regime suggest the possibility of computation- and sensor-cheap feedforward control by means of parameter set points appropriate to a desired control target.

SUMMARY

The wider range of maneuvers and larger stability margins active controls can afford may well justify a greater investment in sensory technology and internal models and computation on the part of robot designers. Similarly, there is growing evidence in the animal motor literature that biological solutions to these same problems span a design space that includes both active and passive stabilizing strategies (Klavins et al., 2001). A better understanding of the tradeoffs – of just how "cheap" a machine might suffice to accomplish just what level of locomotion performance – seems essential to better robot design as well as deeper insight into animal evolution. The talk will review our growing interest and slowly increasing understanding respecting the role of self-stability mechanisms in sensor-cheap "passive" locomotion behavior.

REFERENCES

Altendorfer, R., et al. (2001). *J. Au..t Rob.* **11**, 207-213.
Bernstein, N. (1967). Coordination and Regulation of Movements. Pergamon Press.
Blickhan, R. & Full, R. J. (1993). *J. Comp. Physiol., A* **173**, 509-517.
Buehler, M., et al. (1990). *IEEE Cont. Sys. Mag.* **10**, 16-22.
Full, R. J., et al. (1998). *American Zoologist* **38**, 81A.
Full, R. J. & Koditschek, D. E. (1999).*J. Exp. Bio.* **202**, 3325 –3332.
Klavins, E., et al. (2002). In *Neurotechnology for Biomimetic Robots*, eds J. Ayers J. Davis and A. Rudolph). Boston, MA: MIT.
Kubow, T. M. & Full, R. J. (1999). *Phil. Trans. R. Soc. Lond. B* **354**, 849-862.
Nakanishi, J., & Fukuda et al. (2000).. *IEEE Trans. Rob. Aut.* **16**, 109-123.
Rizzi, A. A. & Koditschek, D. E. (1996). *IEEE Trans. Rob Aut.* **12**, 697-713.
Saranli, U., et al. (2001). *Int. J. Rob. Res* **20**, 616-631.
Schmitt, J. & Holmes, P. (2000). *Biol Cybern* **83**, 517-27.

ACKNOWLEDGEMENTS

This work is supported in part by DARPA/ONR under grant N00014-98-1-0747.

RUNNING STABILITY: LIMB ROTATIONAL CONTROL IN QUADRUPEDAL ANIMALS

Hugh M. Herr, Andre Seyfarth and Gregory T. Huang

Artificial Intelligence Laboratory, MIT, Cambridge, MA, USA

INTRODUCTION

Our goal is to understand the biological strategies used by humans and animals in locomotion. In running, the spring-like axial behavior of the limbs during stance is a well-known and remarkably general feature (e.g., Blickhan and Full, 1993). Here we consider how the *rotational* behaviors of limbs affect running stability. It is commonly observed that running animals retract their limbs just prior to ground contact (Muybridge, 1957) and exert proximal hip and shoulder torques throughout stance (Lee et al., 1999; Herr and McMahon, 2000). Measurements on trotting dogs show that just prior to touch-down the limbs retract towards the ground, and after touch-down, the stance-limb hip tends to exert a thrusting torque while the stance-limb shoulder predominantly brakes. More recently, a dynamic model of running quadrupeds constrained to give smooth, periodic solutions exhibited swing-phase limb retraction and stance thrusting and braking at the proximal limb joints over a wide range of body size (Herr et al., 2002). The mechanism by which these behaviors may influence stability is not fully understood. In this talk we discuss the idea that late swing-phase retraction, together with hip thrusting and shoulder braking during stance, improve quantitatively the stability of running quadrupeds (Figure 1). As a secondary issue, we consider the mechanical work expended at the hip and shoulder and test whether this work may be used by animals to stabilize gait with a manageable energetic cost.

METHODS

To address these questions, we study three dynamic models, each obeying the laws of Newtonian mechanics, in a hierarchy of complexity: (1) A structurally realistic quadruped model with distributed mass and ten degrees of freedom (DOF) (Herr and McMahon, 2000), where the mechanical assumptions are that stance limbs act as springs and forward motion is controlled by active hip and shoulder torques; (2) a simplified quadrupedal model with a rigid trunk, springy massless legs, and eight DOF; and (3) a further simplified spring-mass model with a single DOF. The models operate in two dimensions; motions are restricted to the sagittal plane. In the first and second models, we perform a linearized stability analysis for small perturbations of the state variables about periodic solutions and examine the eigenvalues of the system, and for the simplified third model, we compute a system return map to characterize model stability.

RESULTS AND DISCUSSION

For each model, simulations are run with and without the rotational control features. We find that limb retraction during the flight phase is a highly stabilizing strategy, independent of model complexity. Results show that leg retraction compensates for errors in leg position and allows the system to adapt the angle of attack corresponding to internal (e.g leg stiffness variations) and external disturbances (e.g. ground level variations). As for limb control during stance, the eigenvalue associated with body pitch is sensitive to the exact combination of fore and hind limb torques. If the legs are constrained to act (axially) in a passive spring-like manner, then there is a quantifiable advantage to commanding a torque to the animal's front end that generally acts to decelerate the mass of the body during early ground contact. Results suggest that this coordinated limb rotational control is crucial for pitch stability and may be used by animals to stabilize gait for a manageable energetic cost. These findings should be applicable to legged robots designed to traverse irregular terrain (Saranli et al., 2001). A control scheme for a robot that includes swing-phase limb retraction and thrusting and braking during each stance period may prove to be self-stabilizing.

Limb Rotational Control in a Trotting Horse

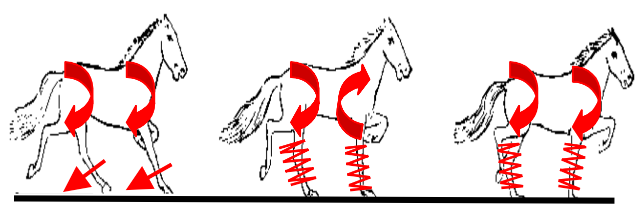

Figure 1: Stabilizing behaviors: limb retraction just prior to ground contact (left), thrusting torque at the hip and braking torque at the shoulder during early stance (center), and thrusting torques at both joints during late stance (right). The limbs behave as passive springs in the axial direction.

REFERENCES
Blickhan, R., Full, R.J. (1993). *J. Comp. Physiol. A* **173**, 509-517.
Herr, H.M., et al. (2002). *J. Exp. Biol*., in press.
Herr, H.M., McMahon, T.A. (2000). *Int. J. Robot. Res.* **19**, 566-581.
Lee, D.V., et al. (1999). *J. Exp. Biol*. **202**, 3565-3573.
Muybridge, E. (1957). *Animals in Motion* (ed. L.S. Brown). Dover.
Saranli, U., et al. (2001). *Int. J. Robot. Res.* **20**, 616-631.

DOES LEG RETRACTION SIMPLIFY CONTROL IN RUNNING?

Andre Seyfarth[1,2], Hartmut Geyer[1,2], Reinhard Blickhan[2], Hugh Herr[1]

[1]MIT LegLab, 200 Technology Square, Cambridge MA 02139, USA (seyfarth@ai.mit.edu)
[2]Movement Science Group, University of Jena, Seidelstr. 20, 07749 Jena, Germany

INTRODUCTION

In fast locomotion (running, hopping, jumping) the leg operation during the stance phase can be described by a simple linear spring (Cavagna et al., 1964; Blickhan, 1989). For periodic running with a spring-like leg, the orientation of the angle of attack α_0 must be carefully adjusted to the chosen leg stiffness k (Seyfarth et al., 2002). For example in human running at 5 m/s the angle of attack must be kept within a range of ±1° (assuming fixed leg stiffness).

But how is the leg adjusted during the swing phase to guarantee such an angle of attack precision? Here we propose leg retraction (velocity ω_R, Fig. 1) as a simple mechanism to reduce the control effort in leg angle adjustment.

Using this approach we address following questions:
(1) Is leg retraction capable to adjust the angle of attack?
(2) Does leg retraction enhance the stability of running?
(3) Does leg retraction support low running speeds?

METHODS

The trajectory of the center of mass in running is described by the gravitational acceleration (during flight and contact phases) and by the force produced by the stance leg (during contact) which is here represented as a linear spring.

Leg retraction (angular velocity ω_R) starts at the apex of the flight phase (Fig. 1) assuming a given initial retraction angle α_R. This allows a simple stride to stride analysis in terms of a *return map* of the apex height of two successive flight phases $y_{i+1}(y_i)$. Here self-stabilized running requires a stable fixed point with (1) $y_{i+1} = y_i$ and (2) $dy_{i+1}(y_i) / dy_i = (-1, 1)$.

The robustness of running is examined by measuring the number of successful steps after disturbance (e.g. change in ground level, leg stiffness etc.).

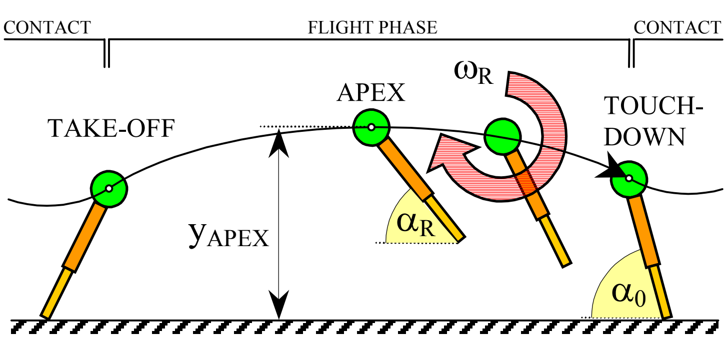

Fig. 1: Leg retraction (velocity ω_R) starts at apex with an initial retraction angle α_R. The angle of attack α_0 at touch-down is not a constant but influenced by the apex height y_{APEX}.

RESULTS

In Fig. 2A the return map $y_{i+1}(y_i)$ for a moderate retraction speed $\omega_R = 50°/s$ in human running is presented. The control effort of the retraction angle is clearly reduced (α_R-range for stable running > 12°) in comparison to the critical angle of attack adjustment without retraction.

The robustness of running with different retraction speeds ω_R is shown in Fig. 2B. Already a moderate retraction speed is sufficient to guarantee stable running for large stiffness variations. At high retraction speeds (> 100 °/s) lower leg stiffness is of advantage.

Moreover, the minimum speed for stable running is largely reduced by leg retraction (e.g. ca. 3.5 m/s without retraction, less than 2 m/s with ω_R = 50 °/s).

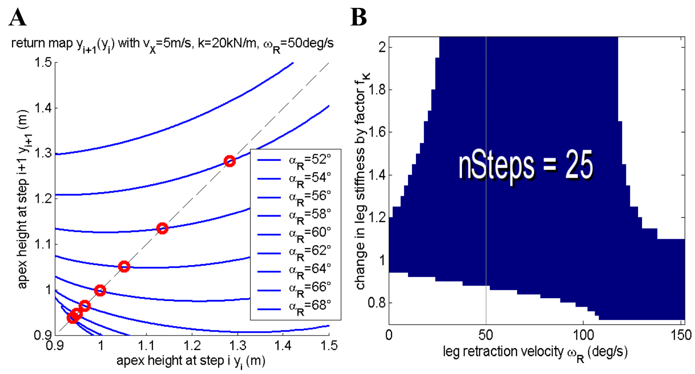

Figure 2: A Return map $y_{i+1}(y_i)$ with stable fixed points (o) for human running with ω_R = 50°/s. **B** Area with 25 successful steps after a sudden change in leg stiffness by factor f_K.

DISCUSSION

Leg retraction proves to be a powerful strategy to adjust the appropriate angle of attack resulting in an increased robustness of running with respect to external and internal disturbances. It is a universal mechanism observed in nature and requires a further understanding.

Acknowledgements. This research is supported by the German Science Foundation (DFG SE1042-1, A. Seyfarth) and by the German Academic Exchange Service (DAAD, H. Geyer).

REFERENCES

Blickhan, R. (1989) *J. Biomech.* 32(12), 1349-1353.
Cavagna, G.A., et al., (1964) *J. Appl. Phys.* 19(2), 249-256.
Seyfarth, A., et al., (2002) *J. Biomech.*, in press.

STABLE STRATEGIES FOR MUSCLE SKELETAL SYSTEMS

Heiko Wagner, Tobias Siebert and Reinhard Blickhan

Institute of Sports Science, Dept. Motion Science, Friedrich-Schiller-University Jena, D-07749 Jena
heiko.wagner@uni-jena.de

INTRODUCTION

Voluntary movements of humans and animals are based on muscular contractions. In this view muscles are reduced to simple force generators and the skeletal system transfers the forces to the environment. Within the last few years several studies have shown that the muscle-skeletal system (MSS) is tuned in a way that it works not only as a simple force generator but as a controller system (Dickinson et al. 2001, Wagner and Blickhan 1999, 2001ab, submitted) stabilizing small perturbations without the need of a neuronal feedback. Here we give an overview of different studies in which we have been able to show the stabilizing ability of the muscle skeletal system.

METHODS

In order to quantify the stability of a system (e.g. muscle tendon complex, human leg, arm and trunk) we use the well established Ljapunovian method and calculate the eigenvalues of the systems equation of motion. These eigenvalues must be negative for a self-stabilized movement. If one eigenvalue is positive the system is unstable. In general we describe the force production of the muscles with a Hill-type muscle model including the force-velocity relation (FVR), the force-length relation (FLR) and a series elastic component (SEC). The geometric model is adapted to the different situations.

RESULTS AND DISCUSSION

<u>Muscle (Fig. 1A):</u> An isotonic contraction (e.g. of rat M. triceps brachii) can be interpreted as a simple perturbation with respect to a given external moment. We found that the system is stable and moves towards a new equilibrium point. The model calculations show that a FVR and operation at the ascending limb of the FLR is required.

<u>Leg and arm (Fig. 1B,C):</u> Here again, we found solutions where the MSS is able to self-stabilize the prescribed trajectories. However, it was necessary that the system is adapted to the special tasks. For vertical knee-bends (simplification of walking and running) we have shown that i) bi-articular muscles, ii) co-activation of antagonistic muscles (quadrizeps and hamstrings), and iii) the moving center of rotation of the knee-joint contribute to stability. For cyclic vertical arm movements (juggling) it is important that the biceps muscle works on the ascending limb of the FLR.

<u>Trunk (Fig. 1D):</u> For lateral bending of the trunk the geometric arrangement of the muscles represents an important factor for stability. The muscles should not be in parallel to the spine but should be arranged obliquely with a slope between 25° - 40°. Nearly all muscles responsible for lateral bending of the spine have such a slope (multifidus, obliguus ext./int.).

SUMMARY

Surprisingly, all the properties necessary to generate self-stabilized movements are realized in the muscle-skeletal system, e.g. the negative slope of the FVR, the ascending limb of the FLR, the moving center of rotation of the knee joint, co-activation of antagonistic muscles, bi-articular muscles, the geometric arrangement of the muscles within the skeletal system (trunk). In conclusion, the muscle skeletal system should not be reduced to a simple force generator but it must be seen as a complex self-stabilized controller system unburdening the neuronal reflexive system.

REFERENCES

Dickinson M. H. et al., (2000) *Science* **288**, 100-6.
Wagner H., Blickhan R. submitted to *Biol.Cybern*.
Wagner H., Blickhan R., (2001a) *J. Morphol* **248**, 3, p.297.
Wagner H., Blickhan R., (2001b) *Proceedings of the XVIIIth Congress of the ISB* O426
Wagner H., Blickhan R. (1999) *J Theor Biol.* **199**, 163-179.

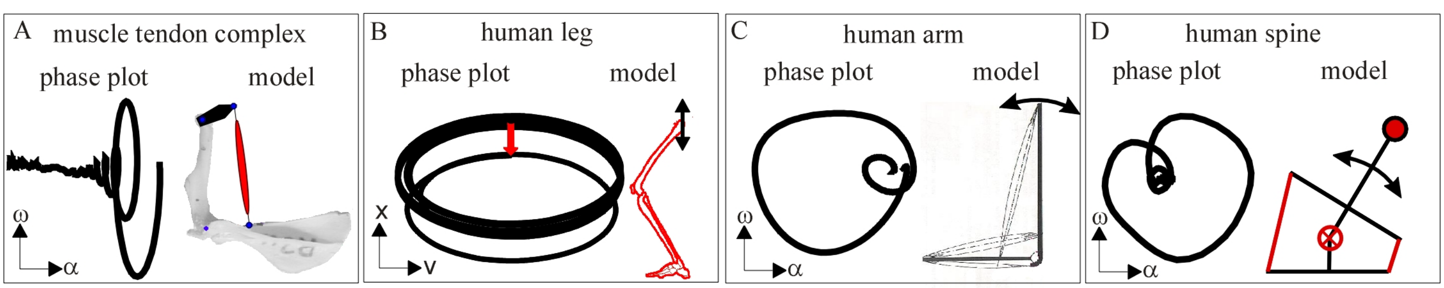

Figure 1: Schematically representation of four different models describing, A the muscle tendon complex of a rat, B the human leg, C the human arm and D the human spine. Examples of typical phase plots of the movement following a perturbation are shown (A,C,D measurements, B simulation).

PASSIVE DYNAMIC STABILITY IN HUMAN WALKING

Arthur D. Kuo
Dept. of Mechanical Engineering, University of Michigan, Ann Arbor, Michigan USA (artkuo@umich.edu)

INTRODUCTION

As shown by McGeer (1990), the passive dynamics of the legs are sufficient to walk down a gentle slope with no external control, and no external energy input save from gravity. Here we consider different models based on passive dynamics, including actively powered models that still make use of passive dynamic principles. We consider the stability of these models, and the implications on human central nervous system control.

MODELS

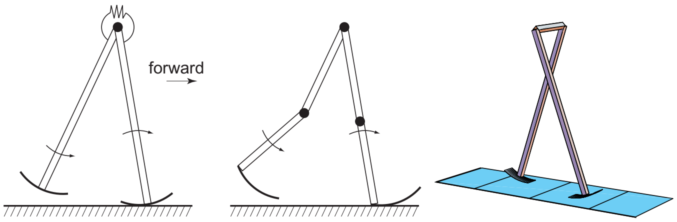

Fig. 1. Passive dynamic walking models. Left to right: planar stiff-legged model (McGeer, 1990; Kuo, 2001), planar kneed model, 3-d stiff-legged model (Bauby & Kuo, 2000).

Models of passive dynamic walking (Fig. 1) use the natural pendular motion of the legs to generate a single stance phase that advances one step. At the end of that phase, the swing foot comes into contact with the ground. Modeled as a perfectly inelastic collision, the impact shifts weight onto the new foot and alters the velocities of the legs so that the conditions at the beginning of the previous step are repeated. This cyclical motion, known as a limit cycle in dynamical systems, is found by appropriate selection of inertial properties and initial conditions. The inertial properties of a human work well in generating a limit cycle.

Passive dynamic stepping is not necessarily stable. Perturbations to the system may cause it to veer away from the limit cycle, resulting in an unstable gait. But computational and physical models of passive walking show that, in the sagittal plane, the gait is stable in response to small perturbations. The stability is retained even with the addition of knees to the legs. However, frontal plane motion appears to be unstable in a 3-d model that can move side-to-side, even though the sagittal plane motion is still stable. In the absence of active control, bipeds would be expected to fall laterally. Of many possible stabilizing mechanisms, lateral adjustment of foot placement appears to be especially simple.

Experiments suggest that humans use lateral foot placement as part of their stabilization strategy (Bauby & Kuo, 2000). Human subjects exhibit higher variability of foot placement in the lateral direction than fore-aft, indicative of highly sensitive lateral dynamics. This difference is magnified when subjects walk with their eyes closed, perhaps because the feedback stabilization is operating on less than optimal information.

IMPLICATIONS

Passive dynamics have several implications for central nervous system control. We propose a reinterpretation of the role of central pattern generators, and examine how passive dynamics change at different size scales.

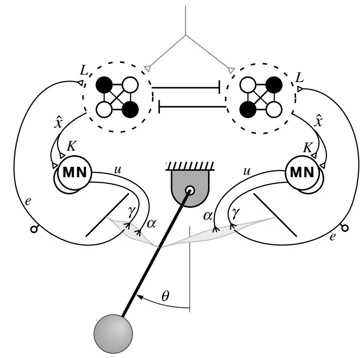

Fig. 2. Central pattern generator with sensory feedback.

Central pattern generators (CPGs) are often interpreted as providing rhythmic commands to the periphery. But the legs themselves may already have an inherent rhythm. Mismatch between two rhythms will tend to adversely affect performance. Presumably sensory feedback (Fig. 2) allows the CPG to adjust its rhythm accordingly. But that feedback also implies that the CPG should not be interpreted as a feedforward controller. Instead, the need for an external rhythm generator is called into question, because feedback alone is sufficient to modulate and power walking. It is possible that the CPG's role is to help filter sensory information in the presence of noise (Kuo, 2002).

At small size scales, mass becomes less dominant as viscous and elastic effects become more dominant. Geometric scaling predicts that small animals will have limbs that are more highly damped than their larger counterparts. This implies that smaller animals such as insects cannot rely on a pendular action to move the legs, and must instead move the legs quite deliberately. This drawback is offset by the possible advantage of greater self-stability in legs of small animals.

CONCLUSIONS

Passive walking highlights the importance of dynamics in walking. The natural pendular motion of the legs appears to have little use of a CPG as a command generator, but might instead use a CPG to filter sensory signals. These effects change in relative priority for animals of different size scales.

REFERENCES

Bauby, C. E. & Kuo, A. D. (2000) *J. Biomech.* **33**: 1433-1440.
McGeer T (1990) *Int. J. Robot. Res.* **9**: 68-82.
Kuo, A. D. (2001) *J. Biomech. Eng.*, **123**: 264-26.
Kuo, A. D. (2002) *Motor Control*, in press.

ACKNOWLEDGEMENTS

This research was supported in part by NIH grant DC0231201A1 to A.D. Kuo.

NONLINEAR TIME SERIES MEASURES FOR QUANTIFYING LOCAL DYNAMIC STABILITY DURING WALKING

Jonathan B. Dingwell

Department of Kinesiology and Health Education, The University of Texas, Austin, TX
Email: jdingwell@mail.utexas.edu Web: http://www.utexas.edu/education/kinesiology/motorbe/dingwell.html

INTRODUCTION

The basic control task in walking is to maintain stability across multiple consecutive strides. Gait analyses typically examine only a single "average" stride, inherently disregarding the continuous nature of gait. Understanding locomotor control requires understanding how the nervous system (CNS) controls locomotion *from one stride to the next*. Here, we describe a relatively new set of techniques that have been successfully used to quantify locomotor stability defined as the system's capacity to respond to infinitesimal (i.e. "local") perturbations (Dingwell & Cusumano, 2000). We believe these techniques can help illuminate important aspects of locomotor behavior and control that cannot be assessed by other means.

METHODS

First, an appropriate state space for each time series is constructed using delay-embedding (Fig. 1A&B; Kantz & Schreiber, 1997). The effects of local perturbations to the dynamics are tested by quantifying the Euclidean distance between initially "nearest neighbor" trajectories as the system evolves over time (Fig. 1C). The exponential *rate* of divergence, averaged over many neighboring trajectories, defines the maximum *finite-time Lyapunov exponent* (λ*) for the time series (Fig. 1D; Rosenstein et al., 1993; Kantz & Schreiber, 1997):

$$\ln\left[d_j(i)\right] \approx \lambda^*(i\Delta t) + \ln\left[D_j\right] \qquad (1)$$

Local dynamic stability (λ*) was quantified in young healthy subjects during continuous over-ground and treadmill walking (Dingwell et al., 2001) and in a group of diabetes patients with peripheral neuropathy (NP) who have a far greater risk of falling than healthy controls (CO) (Dingwell et al., 2000).

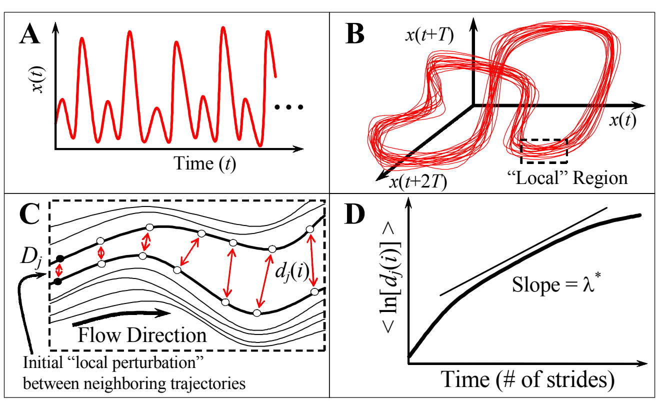

Figure 1: ***A:*** Original time series, $x(t)$. ***B:*** Embedded time series. ***C:*** Local divergence in embedded time series. ***D:*** λ* defined as the average exponential rate of local divergence.

RESULTS AND DISCUSSION

Local perturbations, on average, led to continued divergence of neighboring trajectories across ≥ 10 strides (Fig. 2A) in all subjects. Although NP patients exhibited increased variability relative to CO subjects (Dingwell & Cavanagh, 2001), they were more locally stable (Fig. 2B). In fact, slower speeds appear to be a compensatory strategy used by NP patients to maintain upper body stability during level walking (Dingwell et al., 2000). Correlation analyses of mean standard deviations and λ* in these patients revealed no discernable relationship between variability and local stability measures (Fig. 2C), similar to findings in younger subjects (Dingwell et al., 2001).

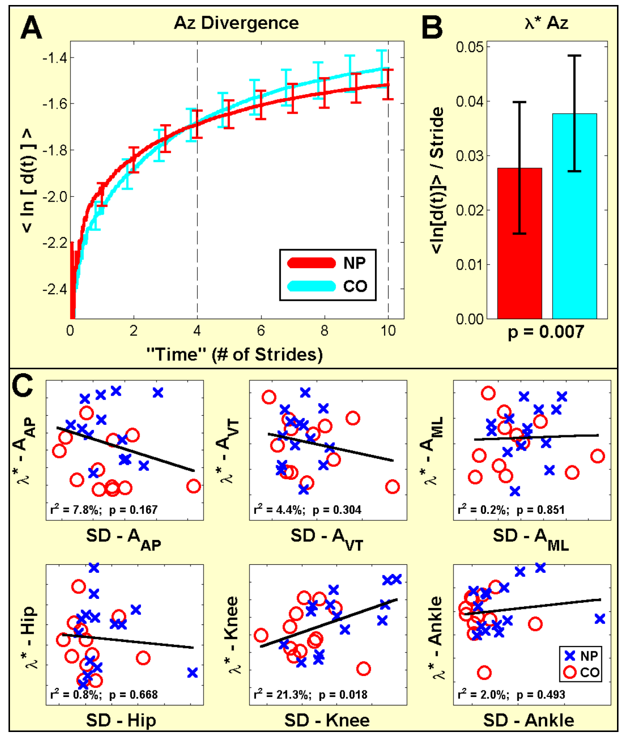

Figure 2: Mean exponential divergence curves (*A*) and λ* exponents (*B*) for medio-lateral upper body accelerations in NP and CO subjects. *C*: Correlations between variability and stability measures for all subjects and variables recorded.

SUMMARY

The results of these studies demonstrate that: (1) Locomotor control of stability acts over multiple (≥ 10) strides; (2) Traditional measures of variability do *not* quantify the capacity of a system to respond to perturbations; and (3) in NP patients, λ* may provide a better indicator of CNS compensatory strategies than more traditional gait analysis approaches. These and related techniques may provide important new insights into the control of locomotion and other similar movements.

REFERENCES

Dingwell JB & Cavanagh PR (2001) ***Gait & Posture***, 14 (1): 1-10.
Dingwell JB & Cusumano JP (2000) ***Chaos***, 10 (4): 848-63.
Dingwell JB et al. (2000) ***J. Biomech.***, 33 (10): 1269-77.
Dingwell JB et al. (2001) ***J. Biomech. Eng.***, 123 (1): 27-32.
Kantz H & Schreiber S (1997) ***Nonlinear Time Series Analysis***, Cambridge, UK: Cambride University Press.
Rosenstein MT et al. (1993) ***Physica D***, 65: 117-34.

LOCAL FEEDBACK MECHANISMS FOR STABLE BOUNCING

Hartmut Geyer[1,2], Andre Seyfarth[1,2], Reinhard Blickhan[1], and Hugh Herr[2]

[1]Dept. Motion Science, Institute of Sport Science, Friedrich-Schiller University, D-07749 Jena, Germany
[2]MIT Leg Laboratory, Massachusetts Institute of Technology, Cambridge, MA 02139, USA (hartmut@ai.mit.edu)

INTRODUCTION

Most studies addressing local feedback mechanisms are focused on posture and walking (Orlovsky et al. 1999), but only little is known about their role in fast locomotion.
Fast periodic movements like hopping and running are characterized by an almost sinusoidal shape of the ground reaction force with its maximum approximately at half contact time. This global feature of leg operation can be described by a simple spring-mass template (Blickhan, 1989) and has been successfully applied to predictions of experimental results. But it remains unclear, how this behavior is generated by the biomechanical system on the muscle-skeleton level.
We investigate to what extent local muscle reflex loops can suitably adapt the dynamic properties of muscle actuators to result in spring-like behavior on the global leg level.

METHODS

A three-segment model using Hill-type muscles is equipped with sensory feedback pathways to analyze the contribution of simple, single loop muscle reflexes to the generation of spring-like leg operation during fast periodic movements.
Each proprioceptive reflex pathway transmits only one of three possible signals from the muscle receptors: muscle fiber length or velocity from the muscle spindles, and muscle force from the Golgi tendon organ (representing Ia, II and Ib afferences, respectively). The signals are applied either as positive or negative feedbacks. Multiple reflex signals affecting one muscle are summed.
The excitation-contraction coupling, delaying the muscle activation behind its neural stimulation, links proprioceptive signals to muscle force production. For each muscle a stimulation bias is considered.
The control parameters - feedback time delay and signal gain for each reflex pathway and stimulation bias for each muscle - are mapped to find an optimal adjustment for a stable periodic hopping pattern.

CURRENT RESULTS AND DISCUSSION

So far the model contains two Hill-type muscles: knee and ankle extensor. Without reflexes, the muscle stimulation must be centrally adapted to result in periodic hopping.
With a constant stimulation bias, i.e. lacking a central signal adaptation, the model leg can be tuned to operate spring-like, if both muscles are governed by separate positive force feedbacks (Fig. 1). The movement pattern is robust with respect to changes in ground level.
This result coincides with former model investigations using a two-segment system including one Hill-type extensor muscle (Geyer et al. 2001) and suggests that positive muscle force feedback could be a powerful and fast mechanism to facilitate spring-like leg behavior in periodic movements.
However, in comparison to the system without feedbacks, the inner leg stability is not clearly improved using the separate force feedbacks. The system still tends to destabilize as predicted for a mechanical three-segment system (Seyfarth et al. 2001), if the muscle or feedback parameters are altered.
With a special focus on muscle reflexes, the goal of further investigations is to find the minimal neuromuscular architecture, which provides both spring-like leg behavior and inner leg stability in fast bouncing tasks.

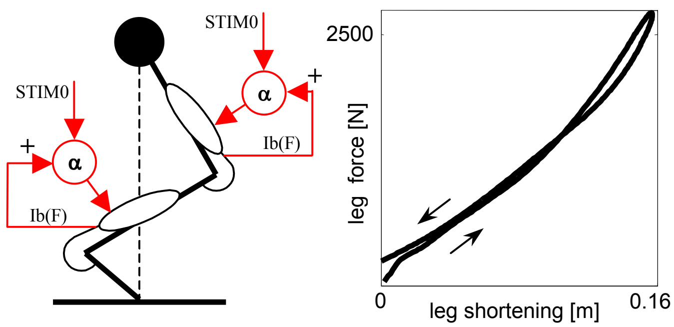

Figure 1: Spring-like leg behavior in hopping using separate positive force feedbacks ($Ib(F)^+$). The three-segment model is equipped with knee and ankle extensor muscles. The feedback motor commands are not influenced by central adaptations during stance (STIM0 = const).

Acknowledgements. This research is supported by the German Academic Exchange Service (DAAD, H. Geyer) and by the German Science Foundation (DFG SE1042-1, A. Seyfarth).

REFERENCES

Blickhan, R. 1989. *J. Biomech*. **32**(12), 1349-1353.
Geyer, H., Seyfarth, A., Blickhan, R. (2001). *Proc. 18th Congress of ISB.*
Orlovsky, G.N., Deliagina, T.G., Grillner, S. (1999) *Neuronal Control of Locomotion*. Oxford University Press.
Seyfarth, A., Guenther, M., Blickhan, R. (2001). *Biol. Cybern.*, **84**, 365-382.

BIOMIMETIC APPROACHES TO STABLE SYSTEMS FOR FUNCTIONAL ELECTRICAL STIMULATION

Gerald E. Loeb, Rahman Davoodi, Ian E. Brown, Milana Mileusnic and Emo Todorov
Medical Device Development Facility
A.E. Mann Institute for Biomedical Engineering at the University of Southern California
Los Angeles, CA 90089 USA; http://ami.usc.edu; gloeb@usc.edu

INTRODUCTION

Humans learn to use their limbs for a wide range of tasks requiring dexterity, accuracy, efficiency and stability. Presumably their strategies take advantage of features of the muscle fibers, the musculoskeletal architecture, somatosensory feedback and spinal cord reflexes. Those structures form a hierarchy of control with the brain at the top. Neural prosthetic systems to reanimate paralyzed limbs by functional electrical stimulation (FES) have to anticipate the relevant features of the components that remain (muscles and their skeletal linkages) and replace those that are no longer available (sensors, feedback circuitry and motor planning). We hypothesize that subjects will find it easier to learn to control such prosthetic systems if they incorporate the same principles of operation as the biological components that have been replaced.

METHODS

Our general strategy is to build computer models of the subsystems that must be incorporated or replaced in an FES system and to conduct virtual experiments in model systems in order to understand how the properties of those subsystems contribute to the performance that we desire for our prosthetic systems. To this end, we are developing three modeling tools:

- Virtual Muscle™ (Cheng et al., 2000) is a program written in Matlab® that accepts morphometric data for musculotendinous structures and generates Simulink® blocks that reproduce accurately the force production and energy consumption of muscles responding to dynamic conditions of either neural or FES activation under the full range of physiological kinematics.
- Musculoskeletal Modeling in Simulink (MMS™; Davoodi and Loeb, 2001) is a program written in C++ that converts models of musculoskeletal anatomy and dynamics created in SIMM® (Musculographics, Inc.) and SD-FAST® (Symbolic Dynamics, Inc.) into Simulink blocks that can be linked to Virtual Muscle blocks and simulated sensors and control systems.
- A motion capture and animation environment that permits sensors of residual limb movements (e.g. shoulder and scapular motion) to be converted into command signals that operate a virtual prosthetic arm whose control systems can be adaptively trained to reproduce the desired limb trajectories.

SUBSYSTEMS CONTRIBUTING TO STABILITY

Mechanical Properties of the Musculoskeletal Subsystem: Force production and energy consumption by muscles depend strongly on sarcomere velocity and the firing rates of motor units. Both of these reflect details of cross-bridge kinetics that appear to have evolved to improve the stability and efficiency of motor behavior. We use the term “preflexes” to identify force changes resulting directly from kinematic perturbations because they occur instantaneously, without the delays associated with synaptic transmission in reflex pathways, propagation of action potentials in nerve and muscle fibers, and excitation-contraction coupling (Brown and Loeb, 2000).

Adaptive Sensitivity Control of the Proprioceptive Subsystem: Biological sensorimotor systems employ much higher aggregate data rates for sensing than for controlling muscle activation. Muscle spindles provide the most important kinesthetic information for stabilizing posture. They further optimize the information available by actively shifting the dynamic range of these sensors through fusimotor control.

Adaptive Gain Control of the Segmental Interneuronal Subsystem: Most of the descending control from the brain to the motoneurons is routed through spinal cord interneurons, where it converges with somatosensory feedback and is distributed widely to increase or inhibit the activation of many different muscles. This pattern of connectivity also accounts for the often profound gating and even reversals of net reflex effects produced by external perturbations when delivered during different motor tasks or phases of tasks. Functionally, this subsystem appears to act as a programmable regulator (He et al., 1991).

REFERENCES

Cheng, E., Brown, I.E. and Loeb, G.E. (2000) Virtual Muscle: A computational approach to understanding the effects of muscle properties on motor control. *J. Neurosci. Methods,* 101:117-130.

Davoodi, R. and Loeb G. E. (2001) Conversion of SIMM for Faster Development of Musculoskeletal Models. 6th Annual Conference of the International Functional Electrical Stimulation Society, June 16-21, 2001, Cleveland, Ohio.

He, Jiping, Levine, W.S. and Loeb, G.E. (1991) Feedback gains for correcting small perturbations to standing posture. *IEEE Trans on Automatic Control,* 36:322-332.

Brown, I.E. and Loeb, G.E (2000). A reductionist approach to creating and using neuromusculoskeletal models. Chapter in: *Neuro-Control of Posture and Movement*, (Eds.) J. Winters and P. Crago, pp 148-163.

STABILITY OF BIPEDAL STANCE; THE CONTRIBUTION OF CO-CONTRACTION AND SPINDLE FEEDBACK

W. P. (Wouter) Haenen and A.J. (Knoek) van Soest

Faculty of Human Movement Sciences and IFKB, Free University, Amsterdam, The Netherlands

INTRODUCTION

The human motor control system is hierarchically organized, and it is generally thought that control is delegated to the lowest possible hierarchical level. Thus, it is worthwhile to analyze the potential contribution of well-defined low level mechanisms when thinking about the control structure for any task. In this study, we investigate the contribution of two low level mechanisms often referred to, co-contraction and spindle feedback, to the control of bipedal stance in humans. Given the destabilizing effect of gravity in this "inverted pendulum" task, assuring local stability around an equilibrium is an obvious first objective for the control system. Therefore, the aim of this study is to assess the maximal contribution of co-contraction and spindle feedback to local stability.

METHODS

The 2-D forward dynamical model of the human musculoskeletal system used in this study consists of 4 rigid segments (foot, lower legs, upper legs, upper body), actuated by 9 Hill-type "muscles" (tibialis anterior, soleus, gastrocnemius, vasti, rectus femoris, hamstrings, biceps femoris caput breve, glutaeus maximum, iliopsoas). Motion between foot and ground is neglected. Input of the open loop model is the stimulation of the muscles; output is the resulting behavior (kinematics and kinetics). First, a reference state was defined in which the joints are slightly flexed, and in which muscle stimulation is chosen such that equilibrium is maintained at a low level of co-contraction. Local stability of the open-loop controlled reference system around this equilibrium position was investigated by linearizing the state space model of the system at the equilibrium, and calculating the eigenvalues of the resulting system matrix. The effect of co-contraction was assessed by comparing the results for the reference state with those for a maximally co-contracted system. Spindle feedback was applied to the reference system; spindle feedback was modeled as local proportional time-delayed feedback of contractile element length and contractile element velocity. The time delay of 0.035 s. was modeled as a 5^{th} order Padé filter. The 2 (length and velocity) x 9 (muscles) feedback gains were determined using a parallel genetic algorithm for optimization. As the sign of the maximum of the real parts of the eigenvalues is indicative of stability, the optimization criterion was chosen as max(real(eig(Afb))), where Afb is the system matrix of the linearized feedback-controlled system.

RESULTS

In the reference state, max(real(eig(A))) equalled +4.71, indicating an unstable system; imposing maximal co-contraction reduced this value to +2.62, again indicating an unstable system. For the feedback-controlled system with a time delay of 0.035 s, the optimal choice of feedback gains resulted in a max(real(eig(Afb))) of +0.06, indicating a marginally unstable system. The optimal feedback gains were also calculated for the system without time delays, resulting in a max(real(eig(Afb))) of –0.97, indicating a stable system. As the (nonrealistic) nondelayed spindle feedback system is the only one considered that yields a stable system, we investigated for this system how well the behavior of the linear system matches with that of the nonlinear system. In the Figure, the response in terms of the horizontal position of the body center of mass is plotted for this system after application of a velocity perturbation of 0.01 rad/s to the trunk. Qualitatively, the responses are very similar.

DISCUSSION

In literature, co-contraction is often mentioned as an important first line of defense against destabilizing external forces (e.g. Hogan 1984). Here it is found that in the context of bipedal stance, co-contraction does contribute to joint stiffness, but to a limited extent. Moving up one level in the hierarchy of the motor control system, local muscle spindle feedback was considered. Given the strong emphasis on position feedback in several theories of motor control (e.g. Feldman 1986) it is surprising that locally stable bipedal stance cannot be obtained even when the spindle feedback gains are chosen optimally with respect to local stability.

As expected on theoretical grounds, the time delay limits the contribution of spindle feedback to stability; given the fact that transmission delays are inherent to neural conduction, it is unfortunate that in the comparable study by He et al. (1991) time delays were not included.

In future work we will investigate the potential contribution of non-local spindle feedback (afference of muscle A influencing stimulation of muscle B) and the potential contribution of force feedback, as mediated through Golgi tendon organs.

REFERENCES

Feldman AG (1986) J. Motor Beh. 18, 17-54.
He J et al. (1991) Trans. Aut. Control 36, 322-332.
Hogan N (1984) Trans. Aut. Control 29, 681 – 690.

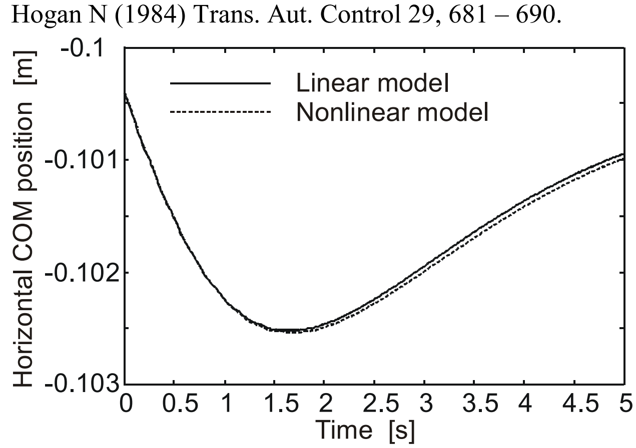

CLINICAL AND BASIC SCIENCE STUDIES OF THE DELTOID TO TRICEPS TENDON TRANSFER

Jan Fridén and Richard L. Lieber
Department of Hand Surgery, Department of Orthopaedics and Bioengineering
Göteborg University, SWEDEN and University of California, San Diego, USA
e-mail: jan.friden@orthop.gu.se

INTRODUCTION

The posterior deltoid muscle is surgically transferred to the triceps insertion to replace lost elbow extension in patients with C5 and C6 level tetraplegia (Freehafer et al. 1991; Hentz et al.1983). Considering the large range of motion of both the elbow and shoulder joints, a risk exists for overstretching the repair sites, exceeding the range over which the muscle can operate and thereby jeopardizing the torque-producing capability of the new motor due to active insufficiency. For more than 15 years we have placed stainless steel markers into the tendons proximally and distally to the attachments during tendon transfer surgery. The distance between markers can be radiologically measured at various time intervals after surgery to provide quantitative measurement of repair site slippage. We have used this approach to evaluate two post-operative protocols—use of an arm restraint on the wheelchair that restricts shoulder adduction and nonuse of the arm restraint. In addition, we have developed methods to measure the detailed muscle fiber architecture of both the posterior deltoid and triceps muscles (Lieber et al. 1992). Thus, the purpose of this study was to quantify the magnitude of tendon slippage after postoperative deltoid-to-triceps tendon transfer and to mathematically model the transfer based on detailed architectural study of cadaveric specimens. .

METHODS

Twelve patients (mean 26, range 20 - 35 years, 10 males and 2 females) had thirteen tendon transfers of the posterior deltoid-to-triceps brachii muscle secondary to traumatic spinal cord injury. The average interval from the time of injury to the procedure was 3.4±0.9 years. Surgery was performed under brachial plexus anesthesia combined with an axillary nerve block. The posterior deltoid border was mobilized and the interval between middle and posterior deltoid identified. The distal tibialis anterior was cut at its insertion, the tendon was then cut proximally at the myotendinous junction and removed through an anterior incision on the distal portion of lower leg. A subcutaneous tunnel was created from the level of deltoid insertion to the distal triceps tendon via a dorsal incision to the level of olecranon. The distal deltoid tendon and the tendon graft were placed with an overlap of 5 cm and sutured to each other using 5-0 Ethibond running sutures along the sides of the graft and host tendons. Stainless steel sutures (6-0) were placed in four positions: the deltoid tendon (marker #1), proximal tendon graft (marker #2), distal tendon graft (marker #3) and triceps tendon (marker #4) at a spacing of ~3 cm. Subsequently, 10 posterior deltoid and triceps muscles were harvested from cadaveric specimens for detailed quantification are muscle fiber length and cross-sectional area using methods previously developed for upper extremity muscles (Lieber et al. 1992).

RESULTS AND DISCUSSION

Total distance between markers, taken as a measure of muscle-tendon unit (MTU) length, measured 6 months postoperatively was 23±3.7 mm for patients without arm rests while the corresponding value measured for patients with the arm rest was significantly lower (8.4±3.0 mm, $p<0.05$). Average muscle fiber length of the posterior deltoid was 113±15 mm while that of the triceps was only 60±10 (mean±SEM, n=8). Two cadaveric specimens were excluded due to poor quality of fixation.

The two main results of this study are (1) use of a shoulder adduction protection armrest significantly reduces slippage of the deltoid-triceps tendon repair and (2) the very long deltoid fiber length (113 mm) renders it highly suitable for this type of transfer in which high excursion is required, due to the large shoulder and elbow mobility of these patients.

The present data suggest that elongation of the deltoid-triceps transfer occurs secondary to overstretch of the muscle-tendon unit during recovery. Significant tendon elongation was found within the first 4-6 weeks after surgery but even more intriguing was the fact that the elongation continued over the next months. This could have been due to the fact that the plaster was removed after four weeks and caused an increased mobility (although restricted by orthosis) in many directions and thereby caused at the repair site. The fact that the posterior deltoid has very long (i.e., >100 mm) muscle fibers suggests that it would be difficult to suture the muscle in a position where it would not generate significant tension over the entire range of elbow extension. Of course, a definitive test of this comment requires the measurement of actual posterior deltoid passive tension as well as its normal and transferred sarcomere length operating range.
original muscle.

REFERENCES

Freehafer et al. *J. Hand Surg. (Am.)* **16A**:804, 1991
Hentz et al. *J. Hand Surg. (Am.)* **8A**:119, 1983
Lieber et al. *J. Hand Surg. (Am.)* **17A**:787, 1992

ACKNOWLEDGMENT

This work has been generously supported by the, Swedish Medical Research Council, the NIH and the Department of Veterans Affairs Rehabilitation Engineering Research & Development Service.

RELATIONSHIP BETWEEN JOINT MOMENT ARMS AND MUSCLE FUNCTION

Kai-Nan An, Ph.D.
Biomechanics Laboratory, Department of Orthopedics, Mayo Clinic/Mayo Foundation
200 First Street SW, Rochester, MN 55905, e-mail: an.kainan@mayo.edu

INTRODUCTION

Biomechanically, muscle is considered to be an actuator, which provides force and power for the movement and balance of the musculo-skeletal structures. The anatomic arrangement of the muscle in relation to skeletal structure determines the mechanical behavior and efficiency of the function. In general, a muscle can cross several joints, and there can be numerous muscles spanning one given joint. The recruitment of the muscle and also the magnitude of the muscle force exerted for a given task are therefore dependent on both muscle physiology as well as the mechanical arrangement of the musculo-skeletal system. Biomechanically, the function of muscle has been regarded as a segmental mover and also a joint stabilizer. The function of mover and stabilizer can be described respectively based on the moment arms and line of action considered in the equilibrium equations.

MUSCLE AS SEGMENT MOVER

To achieve equilibrium of rotation, the resultant moment generated by the external loading has to be balanced with the moment generated by the muscle contraction. The moment generated by the muscle is equal to the muscle force multiplied by the moment arm of the muscle force to the joint axis of rotation. The larger the moment arm, the greater the mechanical advantage of that muscle and thus less force is required to resist a fixed amount of external loading.

Muscle crosses a joint in a three dimensional fashion. In other words, in general, muscle contraction will generate moments about all three axes of rotation of a given joint. However, when the constraints of other peri-articular soft tissues are not available, the muscle will have primary responsibility for maintaining balance of the joint rotation. For example, the flexors and extensors of the elbow joint are the primary elements responsible for resisting any flexion and extension joint moment due to external loading. The contractions of elbow flexors and extensors will also generate valgus and varus moments about the elbow joint. However, within normal anatomic conditions, when the varus and valgus rotation of the elbow joint are restricted by the collateral ligaments and the joint articulating surfaces, the contribution of muscle moments are not manifested.

For joints with additional degrees of freedom, where the caspulo-ligamentous constraints are not important, the contribution of muscle moment in multiple planes is greater. For example, the wrist joint has two degrees of freedom, namely flexion-extension and radial-ulnar deviations. Contraction of FCR causes both flexion and radial deviation, and contraction of ECU causes both extension and ulnar deviation.

For muscles crossing multiple joints, muscle activity depends on the moments of all the joints spanned by the muscle. The concept of multiple-joints muscle is extremely important in the clinical setting. For example, the tendons of extrinsic flexors and extensors of the hand span both the wrist joint and as well as the metacarpal-phalangeal and inter-phalangeal joints. Contraction of the muscle coordinates the movement of all these joints. The concept of dynamic tenodesis effect has been adopted for controlling hand prosthetics and consideration in mobilization after tendon repair. Co-contraction of quadriceps and hamstrings, due to the principle of two joint muscle, at the knee joint results in reduced anterior joint shear force, hence reduced tension in anterior cruciate ligament considered in rehabilitation after reconstructive surgery.

MUSCLE AS JOINT STABILIZER

To achieve equilibrium of translation, the resultant joint forces due to external loading must be balanced by the summation of forces generated by individual muscles across the joint. In a three dimensional situation, such force equilibrium equations have to be satisfied along each of the three directions or axes. In other words, a given muscle force at a given joint can be decomposed into three components which are commonly used to represent the lines of action of the muscle. If the muscle force component is in the direction to contribute to the balance of the resultant joint force, then the muscle is a joint stabilizer. On the other hand, if the muscle force component is not in favor of balancing the resultant joint force, but rather in the same direction as the resultant joint force, then this muscle may even facilitate joint subluxation and dislocation.

COMPUTER SIMULATION OF THE EXTENSOR CARPI ULNARIS TRANSFER TO EXTENSOR CARPI RADIALIS BREVIS

Scott L. Delp and Ariel M. Herrmann
Biomechanical Engineering Division, Mechanical Engineering Department
Stanford University, Stanford, California, USA, delp@stanford.edu

INTRODUCTION

Tendon transfers are often performed to improve the functional capacity of the hand and wrist after spinal cord injury. The restoration of voluntary active grasp is one of the major goals of these procedures. To provide a stable platform for digital flexion, strong active wrist extension is necessary. Wrist extension strength can be augmented by transfer of the extensor carpi unlaris (ECU) to the extensor carpi radialis brevis (ECRB). Keith et al. (1989) reported the effects of this transfer on the moment generated by the ECU at the neutral wrist position in one spinal cord injury patient. We developed a computer simulation of this procedure to study its affects on the moment-generating capacity of the ECU throughout a range of wrist positions. This computer model provides a basis for an inquiry into the elements of a successful tendon transfer design.

METHODS

A graphics-based computer model was developed from anatomical measurements of the muscle-tendon paths before and after transfer (Figure 1; Herrmann and Delp, 1999). This model, based on a model of normal wrist mechanics (Gonzalez et al., 1997), calculates the lengths and moment arms of the muscles over a range of wrist flexion-extension, and represents the muscles' force-generating characteristics from measurements of their physiologic cross-sectional areas, fiber lengths, and pennation angles (Lieber et al., 1990).

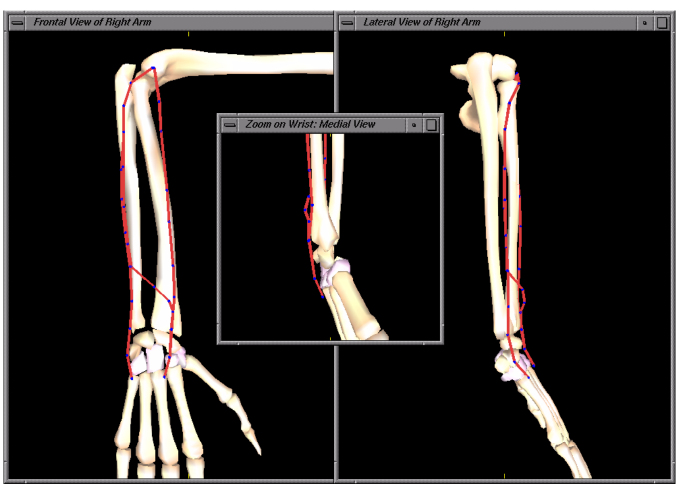

Figure 1. Musculoskeletal model depicting the path of the ECRB and of the ECU before and after transfer to the ECRB. The left window shows a frontal view in the neutral wrist position. The inset shows a medial view (wrist in 25° flexion). The right window shows a lateral view (wrist in 25° extension).

RESULTS AND DISCUSSION

Analysis of the computer model revealed that the maximum isometric extension moment of the ECU at the neutral wrist position increased from 0.50 N-m to 1.72 N-m after transfer to the ECRB. The deviation moment shifted from 2.72 N-m ulnar deviation to 1.42 N-m radial deviation. The extension moment generated by the ECU varied more with wrist flexion angle after transfer due to its greater range of operating length.

The simulations highlighted the need for proper intraoperative tensioning of the ECU to maximize the isometric force-generating potential of the transferred muscle over the functional range of motion (Figure 2).

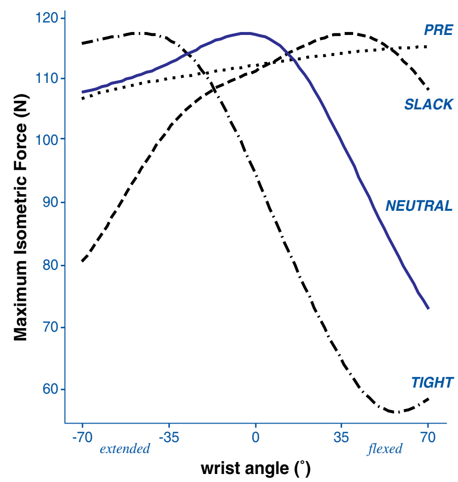

Figure 2. Force vs wrist flexion angle curve of ECU postoperatively after adjustment of tendon slack length to yield maximum force at the neutral wrist position (solid line) and after a 1-cm increase (dashed line) and decrease (dot-dashed line) from this value. Preoperative force profile of ECU (dotted line) provided for comparison.

REFERENCES

Gonzalez et al., J Biomech, **30**, 707-712, 1997.
Herrman and Delp, J. Hand Surg, **24A**, 1083-1090, 1999.
Kieth et al., J Hand Surg, **14A**, 524-530, 1989.
Lieber et al., J. Hang Surg, **15A**, 244-250, 1990.

ACKNOWLEDGEMENTS

This work has been supported by grants from the Whitaker Foundation and the Powell Foundation. We thank Dr. Wendy Murray and Dr. Charles Carroll for assistance with this study.

HUMAN UPPER EXTREMITY ARCHITECTURE: IMPLICATIONS FOR FUNCTION AND SURGICAL RECONSTRUCTION

Richard L. Lieber and Jan Fridén
Department of Orthopaedics and Bioengineering, Department of Hand Surgery
University of California, San Diego, USA and Göteborg University, SWEDEN
e-mail: rlieber@ucsd.edu

INTRODUCTION

Recently, the architectural differences between whole muscles have been investigated and quantified in a number of animal species (see reading list below) These studies suggest that skeletal muscle architecture is the most profound determinant of whole muscle function and that muscles are composed of different fiber types which reflect the developmental process and level of muscle use. This would obviously have significant implications for surgical procedures in which muscles are transferred from one position to another. The purposes of our studies in human upper extremity muscles has been to define the architecture of upper extremity muscles for use in surgical tendon transfer and to provide objective criteria for decision-making in tendon transfer cases.

METHODS

To perform architectural analysis, cadaver extremity specimens are typically amputated well above the elbow and skinned and mounted to a board with the elbow fixed at 90° of flexion, the wrist in the neutral position and the forearm supinated. The fingers are not immobilized and assumed a flexed position during fixation. Each specimen is immersed in 10% phosphate-buffered Formalin for 24 to 48 hours to fix the muscle tissue and then rinsed in phosphate buffer for another 24 hours to remove residual Formalin. Muscles are then placed in mild sulfuric acid to partially digest both the connective tissues surrounding the muscles and especially the endomysium around the muscle fibers. Muscle fiber bundles (consisting of 5-50 muscle fibers) are isolated from the proximal, middle and distal muscle regions and fiber length measured. It is important to normalize architectural properties to a reference sarcomere length which may be measured by optical microscopy or laser diffraction.

RESULTS AND DISCUSSION

Upper extremity skeletal muscles demonstrated a remarkable degree of architectural specialization in terms of fiber length and physiological cross-sectional area (PCSA). This specialization appears to be well-suited to each muscle in order that it might perform its task (Fig. 1). The longest and largest muscles, by far, are the digital flexors to the middle finger (mass=16.3±1.7 g, length=200±8 mm) and the brachioradialis (mass=16.6±2.8 g, length=175±8 mm) Individual digital and thumb extensors were very similar in architectural features and are characterized as relatively long muscles (100-150 mm) composed of moderately long fibers (40-60 mm) oriented at a small pennation angle (2-6°) relative to the axis of force generation and possessing a moderate PCSA (50-100 mm2). The individual muscles of the deep and superficial digital flexors are also similar to one another with a moderate fiber length (~60 mm) and intermediate PCSA (150-250 mm2).

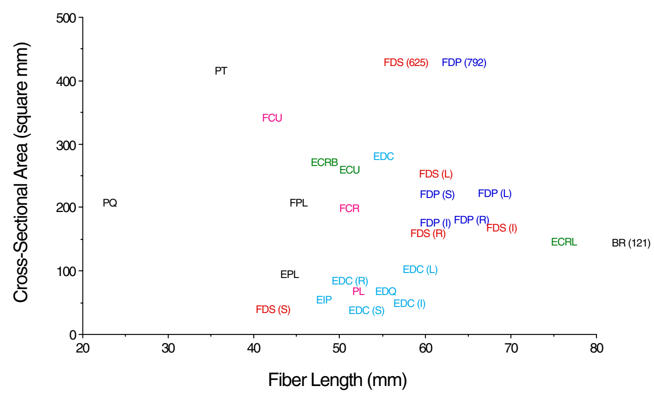

Figure 1: Scatter graph of some of the major upper extremity muscles in terms of fiber length (FL) and physiological cross-sectional area (PCSA). FL is a good predictor of muscle excursion while PCSA is a good predictor of peak force.

In addition to improving our understanding of muscle anatomy and function, elucidation of human muscle architecture may ultimately provide information useful for selection of muscles used in tendon transfers. To substitute a lost muscle function, it would seem reasonable to select a donor muscle with similar architectural properties as the original muscle.

READING LIST

Brand, P. W. et al. *J. Hand Surg.* **3**: 209-219, 1981.
Burkholder, T. J. et al. *J. Morphol.* **220**: 1-14, 1994.
Jacobson, M. D. et al. *J. Hand Surg.* **17**: 804-809, 1992.
Fridén, J. et al. *Clin. Orthop. Rel. Res.* **383**:152-161, 2001
Fridén, J. and R.L. Lieber. *J. Hand Surg. (Am.)* **26A**:147-155.
Lieber, R. L. . *J. Hand Ther.* **6**: 105-113, 1993.
Lieber, R. L., and F. T. Blevins. *J. Morphol.* **199**: 93-101, 1989.
Lieber, R. L., and C. C. Brown. *J. Biomech.* **25**: 557-560, 1992.
Lieber, R. L. et al. *J. Hand Surg.* **15A**: 244-250, 1990.
Lieber, R. L. et al. *J. Hand Surg.* **17A**: 787-798, 1992.
Powell, P. L. et al. *J. Appl. Physiol.* **57**: 1715-1721, 1984.
Sacks, R. D., and R. R. Roy. *J. Morphol.* **173**: 185-195, 1982.

ACKNOWLEDGMENT

This work has been generously supported by the NIH and the Department of Veterans Affairs Rehabilitation Engineering Research & Development Service.

INTRAMUSCULAR PRESSURE IS AN INDICATOR OF MUSCLE FORCE

Kenton R. Kaufman[1], Jennifer Davis[2], Tom Wavering[3], Duane Morrow[1], Richard L. Lieber[2]
[1]Mayo Clinic/Mayo Foundation 200 First Street SW, Rochester, MN 55905 USA
[2]University of California, San Diego
[3]Luna Innovations
e-mail: kaufman.kenton@mayo.edu

INTRODUCTION

Knowledge of forces produced by individual muscles during normal locomotion is important for understanding muscle mechanics, muscle physiology, musculoskeletal mechanics, neurophysiology, and motor control. Direct measurement of muscle force *in-vivo* has been performed using a buckle transducer surgically implanted around the Achilles' tendon (Komi 1990). A fiber optic method has also been developed for direct *in-vivo* tendon force measurements (Komi, 1996). This approach has been used to measure Achilles' tendon forces in a human during walking (Laitinen, 1997). However, most recently the accuracy of this fiber optic measurement system has been questioned (Erdemir, 2001).

Intramuscular pressure (IMP) is a measurable mechanical parameter related to muscle force that is less invasive to obtain. Hill (Hill 1948) showed that mechanical pressures develop inside a muscle when it contracts. This observation led to measurement of intramuscular pressure as a direct measure of muscle force. Numerous studies have shown a linear relationship between intramuscular pressure and joint torque. However, these studies have not confirmed the underlying physiologic mechanisms. Further, routine measurements of intramuscular pressure have been limited by the relatively large catheter diameter static pressure artifacts associated with using saline filled catheter lines. This abstract reports recent advances which have eliminated these limitations.

METHODS

A new fiber optic pressure microsensor has been developed that measures 360µm in diameter and is based on an extrinsic Fabry-Perot interferometric technique. The relationship between intramuscular pressure and muscle stress has been quantified during active isometric and passive conditions. The experimental model was the tibialis anterior of the New Zealand white rabbit. Muscle length, muscle tension, and intramuscular pressure were recorded at relative muscle lengths from L_0 –50% to L_0 +50%.

RESULTS AND DISCUSSION

Microsensor performance characteristics of the were evaluated. The microsensor has an accuracy, repeatability, and linearity better than 2% full scale output (FSO) and a hysteresis of 4.5% FSO. The small size allows simple, minimally traumatic and highly precise measurement of intramuscular pressure.

The length-tension curve for isometric contractions (Figure 1) was mimicked by the length-pressure curve (Figure 2) for both active and passive contractions. The correlation between muscle stress and intramuscular pressure was quantified for both active contractions and passive conditions. Pressure-stress coefficients of determination for active contractions ranged from 0.215 to 0.956 (mean = 0.70 ± 0.27) and from 0.045 to 0.948 (mean = 0.83 ± 0.05) for passive conditions. Correlations were higher for the descending limb of a length-tension curve compared to the ascending limb. These data demonstrate that intramuscular pressure reflects the total tension (active + passive) of muscle.

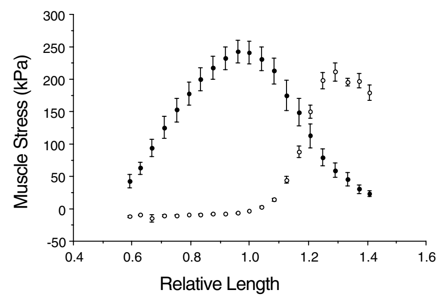

Figure 1

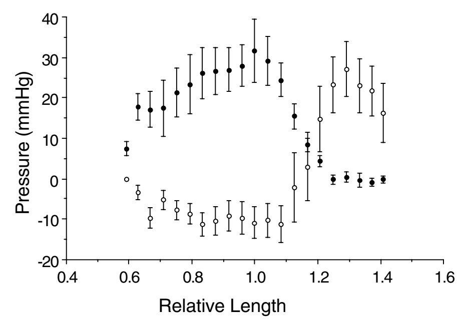

Figure 2

Measurement of intramuscular pressure provides a viable technique for *in-vivo* muscle force measurement. A linear relationship between IMP and muscle force exists during isometric muscle contraction. Therefore, IMP provides data which are more physiologically relevant than EMG. This technique may be used to gain insight into the function and mechanical behavior of human skeletal muscle during locomotion.

REFERENCES

Erdemir, A., et al. (2001). *Proceedings ISB*: 165.
Hill, A. V. (1948). *J. Physiol.* **107**: 518-526.
Komi, P. V. (1990). *J. Biomech.* **21**(1): 23-34.
Komi, P. V., et al. (1996). *Eur J Appl Physiol* **72**(3): 278-280.
Laitinen, T., et al. (1997). *Proceedings ISB*.

ACKNOWLEDGMENT

Funding provided by NIH Grants AR40050 and HD31476 and the Department of Veterans Affairs

THERAPEUTIC ELECTRICAL STIMULATION WITH BIONS TO REHABILITATE SHOULDER AND KNEE DYSFUNCTION

FJR Richmond[1], A-C Dupont[1], SD Bagg[2], S Chun[4], JL Creasy[2], C Romano[3], D Romano[3], RL Waters[4], CL Wederich[4] and GE Loeb[1]
[1]A.E. Mann Institute for Biomedical Engineering, University of Southern California, Los Angeles, CA 91201, USA
[2]Queen's University, Kingston, Ontario, Canada; [3]Istituto Ortopedico Gaetano Pini, Milan, Italy
[4]Rancho Los Amigos National Rehabilitation Center, Downey, CA, USA

INTRODUCTION

The recent development of microminiature, single channel stimulators (BIONs) has provided a flexible tool by which weakened muscles can be stimulated intramuscularly. The leadless devices are controlled and powered from an external magnetic field. Implantations can therefore be conducted as outpatient procedures by injecting devices near nerve bundles or motor points through a large gauge needle. We are currently using BIONs in three pilot clinical applications in which safety and efficacy of the devices can be assessed with relative ease.

Table 1: Current sites of clinical trials

Subacute shoulder subluxation	Kingston, Canada
Chronic Shoulder subluxation	Los Angeles, CA
Knee Osteoarthritis	Milan, Italy

METHODS

Subacute shoulder subluxation: Hemiplegic subjects are randomized 3-12 weeks after stroke into a control or experimental group. In experimental subjects, two BIONs are implanted into the middle deltoid and supraspinatus muscles, respectively. These are used to stimulate muscles daily for 6 weeks. Treatment is followed by a 'non-stimulation' period of 6 weeks. Control subjects receive only conventional physiotherapy for 6 weeks. If control patients meet inclusion criteria after this 6-week period, they are offered BION therapy. Outcome measures included shoulder subluxation, arm strength, arm range of motion, pain (Visual Analogue Score) and muscle thickness measured by ultrasound.

Chronic shoulder subluxation: A longitudinal repeated measures design will be used for subjects with stable shoulder subluxation resulting from a stroke more than 6 months before they enroll in the study. The first patient is currently under baseline testing and will be implanted February 2002.

Quadriceps Stimulation for Knee Osteoarthritis: Using a repeated measures design, subjects are first observed for 12 weeks to determine baseline state. They are evaluated with the Western Ontario-McMaster (WOMAC) knee function scale, Knee Society Function tests and Visual Analogue Scale for pain. Muscle cross-sectional areas are assessed using MRI. A BION is implanted next to the femoral nerve.

In all studies, stimulation starts with 3 10-minute sessions per day, increasing gradually to 30 minutes per session. We use low frequency (2-5pps) trains of stimuli (2-5s on/1-3s off) at an intensity sufficient to recruit most or all of the motor units in the target muscles (typically 2-8 times motor threshold).

RESULTS AND DISCUSSION

Fifteen subjects implanted with BIONs have been satisfied with the simple implantation procedure and absence of complications. A single subject did not complete the trial because of worsening mental confusion following his stroke. One BION was removed from a second subject after completing the experimental phase of the osteoarthritis trial because she experienced unpleasant but not painful sensations when soft tissues folded around the device, in the groin. Stimulation thresholds remain constant over time, indicating a stable foreign body reactionand little or no migration of the BIONs. Autopsy tissue from one stroke patient who died of unrelated causes after two years of successful BION treatment showed a little foreign-body response. The main problem to date has been the sensitivity of devices to the position of the RF coil. This problem should be corrected by a new data transmission system developed recently.

Sub-acute subluxation: A significant decrease was found between subluxation levels before and after 6 weeks of BION therapy ($p < 0.05$). If no BION therapy was administered, no significant changes occurred. Muscle thickness stayed the same or improved slightly with BION therapy, but tended to decrease without the electrically induced exercise.

Knee osteoarthritis: Significant improvement of Knee Society Scores, WOMAC scores and pain levels were found after 12 weeks of BION therapy for the 3 patients who have completed the trial ($p<0.05$). One subject has cancelled knee replacement surgery because of the improvement.

Typically, BION patients were compliant with their therapy and found it pleasant to receive. Patients self-administered the therapy at home, avoiding the cost of a medical professional administering the therapy and making it a practical treatment for patients who may need chronic electrical stimulation to maintain the health and function of muscles and joints that cannot be exercised voluntarily due to upper motoneuron damage.

ACKNOWLEDGEMENTS

Funded by the Canadian Institutes for Health Research and the A.E. Mann Institute for Biomedical Engineering. BION technology was developed in collaboration with the A.E. Mann Foundation for Scientific Research (J.H. Schulman, co-P.I.) and Illinois Institute of Technology (P.R. Troyk, co-P.I.) and has been licensed to Advanced Bionics Corp., CA.

A LEG-PROPELLED WHEELCHAIR: BIOMECHANICS, ENERGETICS AND MODELING

RB Stein[1], KB James[1], A Kido[1], SL Chong[1], LA Tubman[2] , GJ Bell[3]
[1]Centre for Neuroscience, University of Alberta, Edmonton, AB Canada
[2] Faculty of Kinesiology, University of Calgary, Calgary AB Canada
3 Faculty of Physical Education, University of Alberta, Edmonton AB Canada

INTRODUCTION

Conventional wheelchairs have been widely accepted by persons with motor disabilities and sufficient arm strength for propulsion. However, problems remain: 1) Many, if not most long-term wheelchair users, develop overuse injuries of their arms, as a result of the strenuous and somewhat unnatural movements that are needed to propel a wheelchair with the arms. 2) The disuse of the legs for persons who spend much of their time in a wheelchair leads to atrophy of leg muscles and osteoporosis of the long bones of the legs and an increased rate of bone breakage. 3) The lack of whole body exercise leads to a decrease in cardio-respiratory fitness and an increased incidence of heart disease. 4) Sitting in a chair all day can lead to pressure sores and other skin problems that are difficult and costly to treat. The purpose of these studies was to test a new, leg-propelled wheelchair to see if it could provide increased mobility and fitness for wheelchair users who retained some voluntary leg movements or who required functional electrical stimulation (FES) to move their legs.

METHODS

A commercially available wheelchair (Pro-SA, Invacare Inc., Cleveland OH) was modified for these tests [1]. Essentially, a single mobile footrest, which allows flexion/extension of the legs around the knee center, replaced the two stationary footrests. Both legs were attached to the new footrest by straps at the toe and heel. Rotation of the lower legs was coupled to the wheelchair. A steering lever was added that attached to one of the front, castor wheels. Rotation of the lever turned the direction of this wheel and hence the chair.

Subjects wheeled with the arms or the legs and walked (where possible) for 4 min. periods in random order with approximately 10 min. rest periods in between. The subjects included persons with complete spinal cord injury (SCI; n=9), other motor disorders (retaining some voluntary control of the legs, n=13) and control subjects (n=13). The physiological cost index (PCI) and oxygen consumption were measured. PCI is computed as the change in heart rate during exercise divided by the speed of movement.

RESULTS AND DISCUSSION

Arm-wheeling took significantly more effort (mean PCI = 0.52 beats/m.) than walking (0.33) in control subjects [2]. Leg-wheeling was most efficient (0.23), requiring less than half the effort of arm-wheeling and 30% less effort than walking. For SCI subjects leg-wheeling with FES required less than half the effort (0.18) of arm-wheeling (0.40). This group could not walk. The voluntary group walked, but with substantial effort (1.81) compared to arm- (0.76) or leg-wheeling (0.64). The effort required during leg-wheeling for the voluntary group depended on the presence or absence of spasticity. Results for oxygen consumption were similar to those for PCI

For individual subjects we measured the passive properties of the legs and foot at rest (effective stiffness and viscosity), the length-tension (torque-angle) properties of the active muscle groups, as well as their force-velocity curve and their activation and fatigue rates. The measured values were inserted into a model of the leg-propelled wheelchair. The model could predict the performance of individual subjects accurately and was used to optimize the thresholds for switching between stimulating knee extension and flexion and vice-versa for subjects using FES.

Finally, we tested the capabilities of the wheelchair using 9 able-bodied female subjects, who performed a graded exercise protocol up to maximal levels using leg-wheeling and arm-wheeling on custom-designed rollers that simulated the effort of wheeling over ground. Leg-wheeling elicited significantly higher peak cardio-respiratory values than arm-wheeling. Yet, leg-wheeling was more efficient, since the cardio-respiratory responses were significantly less than arm-wheeling at all levels of sub-maximal work. Thus, subjects could propel a wheelchair longer and faster with the legs than the arms.

CONCLUSION

Better efficiency and increased mobility can be obtained for many disabled individuals, while exercising the leg muscles voluntarily or with FES. Biomechanical measurements can be incorporated into a simple model that can be used to optimise the performance of individual subjects. The greater efficiency allows subjects to wheel further and faster with the legs than the arms, as well as getting a better cardio-respiratory workout. We are now testing the usefulness of this device in the community.

REFERENCES

[1] James, KB. (2002) Leg-propelled wheelchair U.S. Patent, pending.
[2] Stein, RB, Chong SL, James KB, Bell, GJ. (2001) Arch Phys Med Rehab 82:1198-1203.

ACKNOWLEDGEMENTS

Funded by the Canadian Institutes for Health Research and the Alberta Heritage Foundation for Medical Research.

ARM STIFFNESS AND STABILITY IMPROVED BY FNS IN C5-C6 SCI

Robert F. Kirsch[1] and Eric J. Perreault[2]
[1]Case Western Reserve University, Cleveland, Ohio, USA rfk3@po.cwru.edu
[2]Northwestern University, Chicago, IL, USA e-perreault@northwestern.edu

INTRODUCTION

Estimates of the dynamic endpoint stiffness of the human arm were obtained in this study to quantify the mechanical properties of the arm and to investigate arm stability. Endpoint stiffness, defined as the relationship between externally applied displacements of the hand and the resulting forces, characterizes the mechanical interface humans use to interact with their environment. Endpoint stiffness is thus closely related to postural stability. Numerous studies have quantified endpoint stiffness properties in able-bodied individuals (e.g., Mussa-Ivaldi et al. 1985). Recently developed techniques (Perreault et al. 1999) have allowed us to examine postural arm stability in individuals with spinal cord injuries.

METHODS

Two subjects (three arms) with complete cervical level spinal cord injuries (C5 or C6 level) function were examined. None had voluntary elbow extension and all had voluntary elbow flexion. A single electrode delivered biphasic, 20mA current pulses from an implanted stimulator to the triceps muscle, which was fatigue resistant due to months of electrical exercise. The endpoint stiffness of the arm was estimated using 2 cm peak-to-peak stochastic displacement perturbations applied by a two-joint robotic manipulator. All measurements were made at a single location: the arm was held in a horizontal plane passing through the glenohumeral joint, with the hand positioned between the sternum and acromion at a distance approximately 0.45m anterior to the acromion. Endpoint stiffness measurements made with the subject at rest and during combined voluntary and stimulated muscle activation that resulted in zero net endpoint force. Two-dimensional stiffness dynamics were estimated using a previously described nonparametric system identification algorithm (Perreault et al. 1999). A second order system model was then fit individually to each of the four resulting transfer functions to extract elastic stiffness, viscosity, and inertia for each. The directional qualities of the 2D endpoint stiffness were represented graphically by transforming the inertial, viscous and elastic matrices into ellipses, as was first demonstrated by Mussa-Ivaldi et al. (1985). 2D compliance impulse responses were generated by simulating the endpoint trajectories resulting from a 1N force impulse applied at 16 orientations in the measurement plane. The path length of the resulting endpoint displacement trajectories was used as a quantitative measure of endpoint stability.

RESULTS AND DISCUSSION

Figure 1 summarizes the effects of triceps stimulation on the stiffness, viscosity, and stability of the arm of a subject with a C5 level injury. Results on the left are for when the arm was at rest, and those on the right are for when the triceps was being stimulated and subjects voluntarily contracted elbow flexor muscles to compensate for the FNS-induced elbow extension moment. The endpoint elasticity and viscosity are shown by the ellipses at the top of the figure. Arm position is indicated by the stick figures. The 2D compliance impulse responses are shown at the bottom. The number in the *FNS+Voluntary* trajectory ring is the ratio of the average trajectory path length with no stimulation to that during stimulation. The average path length decreased by a factor of 3.0 for this arm, and across all arms by an average of 2.3.

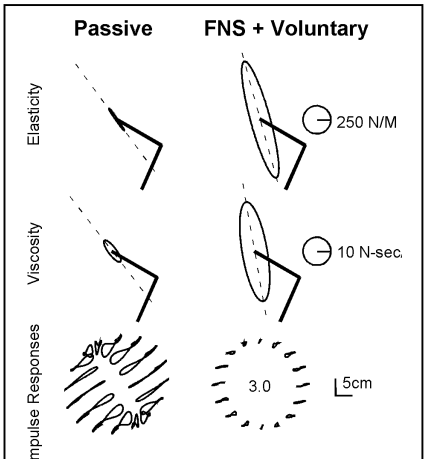

Figure 1: Effects of triceps FNS on endpoint stiffness, viscosity, and stability.

SUMMARY

We found that the endpoint dynamics of the SCI-impaired arm can be adequately described by a linear model with inertial, viscous, and elastic parameters, and that triceps FNS improved arm stability for all tested conditions. Our results indicate that the additional information regarding arm function provided by the stiffness estimates should provide valuable information for the development of task-specific FNS control mechanisms that provide high stiffness when desirable and low stiffness when that is more appropriate.

REFERENCES

Mussa-Ivaldi, FA, Hogan, N, and Bizzi, E (1985). *J Neurosci.* 5: 2732-2743.

Perreault, EJ, Kirsch, RF, and Acosta, AM. (1999). *Biol Cybern*, 80:327-337.

ACKNOWLEDGEMENTS

This work was supported by the Department of Veterans Affairs, Rehabilitation Research and Development Service. Additional support was provided by NIH (HD32653) and by the Whitaker Foundation.

FUNCTIONAL INTRASPINAL MICROSTIMULATION FOR RESTORING LIMB MOVEMENTS AFTER SPINAL CORD INJURY

VK Mushahwar[1], DM Gillard[2], MJA Gauthier[2] and A Prochazka[2]
Departments of [1]Biomedical Engineering and [2]Physiology, University of Alberta, Edmonton, AB, Canada

INTRODUCTION

Recovery of function after spinal cord injury (SCI) remains a daunting medical challenge. The difficulty in achieving regeneration of functional neural connections in the central nervous system prompted the development of systems that use electrical stimulation of muscles or nerves to improve respiration, micturition and motor function. However, the electrical restoration of whole limb movements remains elusive. Intraspinal microstimulation (ISMS) may provide an alternative. The spinal cord is distant from moving muscles, so electrodes implanted therein are less likely to be dislodged or damaged. Moreover, the lumbar enlargement of the cord is relatively short (~5cm in adult humans), allowing activation of the main limb muscles and spinal locomotor neural networks by electrodes implanted in a small, protected region. Since 1992 we have been testing the feasibility of using this novel approach for generating functional movements of the legs. We found that ultra-fine electrodes placed in the ventral horn can activate limb muscles through ensembles of interneurons and motoneurons. Smooth and graded muscle contractions with little fatigue are obtained. ISMS through some electrodes generates single-joint movements while stimulation through others produces coordinated whole-limb synergies. Generated extensor synergies are powerful enough to bear the cats' weight. The implanted microwires remain securely in place for long periods of time and the implantation procedure causes minimal neural damage. These results suggested that ISMS may be a feasible approach for restoring motor function after SCI. It could also be used in conjunction with other rehabilitation approaches (e.g., treadmill locomotor training, regeneration and pharmacology) to maximize the functional benefits after injury. However, the feasibility of using ISMS for restoring functional walking remained untested. The following experiments were conducted to address this issue.

METHODS

Under pentobarbital anesthesia, the lumbosacral region of the spinal cord in 3 adult cats was exposed. Twelve insulated microwire electrodes (30 µm dia., 30-100 µm bared tips) were implanted in each side of the cord. The electrode tips targeted motoneuronal and premotoneuronal regions within the ventral horn. These locations were chosen based on results obtained in awake chronically-implanted animals in which ISMS through wires in the ventral horn produced functional flexor and weight-bearing extensor movements with no apparent discomfort. However, ISMS through dorsally located wires generated paw shakes and flexion-withdrawals but no weight-bearing extensor movements. Behavioral responses indicated that the cats perceived the stimuli in these cases.

The electrodes were anchored to the spinous process of vertebra L3 or L4 with dental acrylic and terminated in an external connector. The back wound was sutured shut in layers.

The cats were then placed in a sling leaving all limbs pendant. Trains of electrical stimuli (biphasic, charge-balanced, 2-300µA, 200µs, 25 or 50 pulses/s) were delivered through each electrode separately and the elicited limb movements were documented. Two to four electrodes in each side of the spinal cord that generated limb flexion or extension were selected. An open-loop controller was used to modulate the timing and amplitude of pulse trains through each electrode, to produce bilateral alternating stepping.

RESULTS AND DISCUSSION

In most cases, limb movements elicited by stimulating through individual electrodes could be predicted based on the anatomical distribution of motoneuron pools. However, stimulating through 1/3 of the electrodes generated full limb flexor or extensor synergies which were primarily attributed to the activation of spinal interneuronal networks. Phasic, amplitude modulated, ISMS through as few as 2 electrodes in each side of the spinal cord (one eliciting limb flexion and the other limb extension) generated near normal bilateral stepping. Typical stride lengths were 25cm (cf. ~30cm in normal cats) and ample foot clearance was achieved during swing. Mean ground reaction force during stance was 36.4 N and was sufficient for lifting the animals' hindquarters. However, stimulation through only 2 electrodes in each side of the cord to produce bipedal stepping required that the stimuli be delivered at high repetition rates (50 pulses/s) to elicit fused muscle contractions. This resulted in the early onset of muscle fatigue (typically after 15 steps). Muscle fatigue was circumvented by stimulating through 4 electrodes in each side of the spinal cord (2 generating flexor movements and 2 extensor movements) and interleaving the stimuli (25 pulses/s) between the electrodes that elicited similar mechanical actions. At the expense of doubling the number of electrodes, this stimulation strategy resulted in no observable muscle fatigue throughout the duration of the experiments (15 hrs).

The results show that by stimulating through relatively few intraspinal microwires and using simple control strategies, load-bearing walking could be achieved. The efficacy of ISMS in restoring functional stepping after chronic SCI is currently under investigation.

ACKNOWLEDGMENTS

This work was supported by Alberta Heritage Foundation for Medical Research and Canadian Institutes of Health Research.

CONTROL OF ELECTRICAL THERAPY SYSTEMS FOR REACHING AND GRASPING AFTER STROKE

Mirjana Popović[1,2] and Dejan Popović[1]

[1]Department of Health Science and Technology, Aalborg University, Denmark, dbp@smi.auc.dk
[2]Institute for Medical Research, Belgrade, Yugoslavia, mira@imi.bg.ac.yu

INTRODUCTION

Many control schemes, such as optimal control, prediction control, sample-data control, model-based control, and adaptive control have been suggested often focusing on possible use on humans with disability [1]. Our hypothesis was that a neural prosthesis for upper extremities would contribute the most to the recovery of functions if it implements life-like control, that is, if it is integrated in the biological movement scheme. The reasons behind this hypothesis are that life-like control will maximise reorganisation, i.e. provide the augmentation to an inherent capacity to self-organise sensory-motor systems throughout life.

REACH / GRASP / RELEASE COORDINATION MODEL

The biological control of reaching and grasping relies on high connectivity between individual joint movement that is, muscle activation during functional movements. This connectivity is being developed through a skill acquisition procedure, mostly in childhood. This connectivity allows that a single decision at the brain level is appropriately distributed to end organs. This co-ordination is achieved by the hierarchical and parallel organisation of the CNS, yet it can be assessed in different phase spaces (e.g., force space, EMG space, angular velocity space).

The co-ordination model that we introduce comprises three automatic, and one biological control level [2]. The highest control levels (decision and planning) allow the user to select an action and the modality of operation. The top automatic level co-ordinates spatial and timing synergies between joints; it applies a discrete rule-base control. This rule-base controller implements the state model of movement that is heuristically cloned using data acquired in able-bodied humans; thereby mimicking life-like movement. The lower co-ordination implements synergies at the joint level, that is, machine determined mappings between the arm segment angular velocities. The lowest, actuator level deals with patterning functional electrical stimulation (FES) of muscle groups being responsible for the flexion or the extension of a single joint, or potentially biarticular muscles. The actuator level uses continuous feedback control, and is fully model-based [3].

The implementation of this model has two phases. Phase 1 is general: it applies machine learning with the inputs and outputs generated from able-bodied kinematics when performing slowed down reaching and grasping of daily utilities. Phase 2 is individual and relates to customising of the stimulation map to a specific user. The customising relates to biomechanical parameters and muscle properties (recruitment, force vs. length, and force vs. velocity nonlinearities) [3].

An example of the stimulation map designed for grasping of a can, bottle, or cup; drinking form it, and returning it to the original post is shown in Fig. 1. The user should voluntarily select the task (keypad), and the flexible goniometer measuring the shoulder movement would then govern the whole sequence of stimulation required for the accomplishment of the task. The number of tasks is infinite, yet many of them can be accomplished with the same strategy; thus, it was possible to use a practical size keypad for selection of the activity. The shoulder sensor generates information that drives the elbow, forearm and hand; a threshold with hysteresis was applied to eliminate switching noise (Fig. 1).

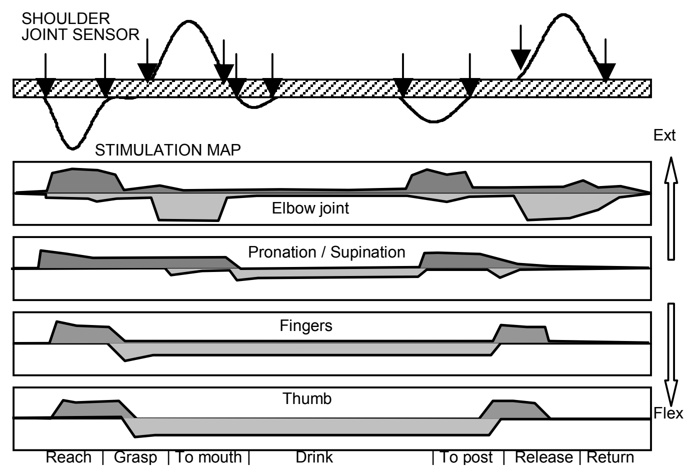

Fig. 1: Stimulation pattern for drinking from a cup. The activations were normalized. Arrows show the timing. Spatial synergy was used for the elbow. Ext - extension (dark), Flex - flexion (light fields).

CONLUSION

The co-ordination model of reaching and grasping that we developed for upper extremity neural prostheses relies on analysed behaviour of functional movements in able-bodied subjects. The model allows the design of life-like control for FES that is preferential specially for neurorehabilitation because it provides synchronised activation of both afferent and efferent sensory pathways with the voluntary activity of preserved sensory-motor mechanisms [4].

REFERENCES

1. Winters J, Crago PE. (Eds.) *Biomechanics and Neural Control of Posture and Movement*, Springer Verlag, 2002.

2. Popovic MB, Popovic DB. Cloning biological synergies: Improved control of elbow neuroprostheses, *IEEE EMBS Magazine*, 20(1):74-81, 2001.

3. Popovic M, Jovanovic N, Schwirtlich L. Identification of parameters for assistive systems, *J Aut Control*, 4:31-45, 1994.

4. Popovic DB, Popovic MB, Sinkjær T. Neurorehabilitation of upper extremities in humans with sensory-motor impairment. *Neuromod*, 5(1):1-13, 2002.

MAXIMAL CYCLING POWER CAN BE SLIGHTLY INCREASED BY CONSTRAINING LEG KINEMATICS

A.J. "Knoek" van Soest (1) and Andy Ruina (2)
(1) Faculty of Human Movement Sciences and IFKB, Free University, Amsterdam, The Netherlands
(2) Dept. of Theoretical and Applied Mechanics and Mechanical Engineering, Cornell University, Ithaca, NY, USA

INTRODUCTION

In steady state bicycle riding the average crank power equals average muscle power (neglecting the dissipation in the joints and other soft tissue). Muscle power depends on muscle length and muscle stimulation as a function of time. Modeling the bike-crank-leg system as a 2D 5-bar linkage, there are two degrees of freedom, e.g. the crank angle and the ankle angle. When a suitable pattern of muscle stimulation (as a function of crank angle) is prescribed, and given a load model for the crank, periodic kinematics and power output are obtained. To what extent is the muscular potential for power production compromised by the requirement of producing a kinematic pattern that does not, say, hyperflex any joints? In other words, by how much could power output be enhanced if the leg kinematics were fully prescribed as a function of crank kinematics? Constraining the leg to a kinematic pattern it is already following does not alter the energetics of its present muscle use, but does allow new choices in muscle use. Thus, prescription of the current kinematics and subsequent re-optimization of muscle stimulation has to lead to an equal or (most likely) greater power output. To quantitatively measure the effect of constraint addition we performed power optimizations for a model without and again with an extra kinematic constraint.

METHODS

Numerical simulations were performed using a model of the musculoskeletal system. The skeleton was represented by a rigid foot, lower leg, upper leg, trunk, with the ball of the foot being attached to the crank through a hinge joint. The skeletal model is actuated by 8 Hill-type "muscles" per leg. The input of the model is the stimulation of the muscles; the output of the model is the resulting kinematics, kinetics and power output. The neural inputs are optimized with respect to the mechanical power output (while demanding periodicity) using a genetic algorithm for optimization. Optimization results for a standard, unconstrained model of 120 RPM isokinetic sprint cycling (van Soest and Casius, 2000) are compared to those for a model in which the leg kinematics (taken from the optimal solution for the standard model) is prescribed as a function of crank kinematics. A similar comparison is made for an arbitrary suboptimal stimulation pattern that yields 50% of optimal power in the absence of a kinematic constraint.

RESULTS AND DISCUSSION

For the optimal solution, total muscle power per leg for the normal (N) model increases from 537.9 W to 550.2 W (a 2% increase) when kinematics is constrained (C), the improvement largely being produced by Tib. Ant.. In contrast, the improvement caused by imposing kinematics is substantial when starting from a somewhat random stimulation pattern that results in 50% of maximal power (see Table). These results are reflected in a small effect of constraint addition on the tangential pedal force for the optimal solution, and a substantial effect for the 50% power solution (see Figure).

	OPTIMAL		50% POWER	
	N	C	N	C
Tib Ant	12.2	20.0	-2.9	5.6
Soleus	53.6	54.0	-3.3	4.2
Gastroc	18.6	19.1	-3.7	11.2
Vasti	140.1	141.3	54.6	123.5
Rectus Fem	49.0	49.2	-28.8	46.4
Glut max	110.5	110.9	130.8	138.2
Hamstrings	56.8	56.9	66.7	79.3
Iliopsoas	97.0	98.6	55.4	70.0
TOTAL	**537.9**	**550.2**	**268.8**	**478.5**

It has been argued (Raasch et al., 1997) that in cycling, the activity of some muscles (mostly mono-articulars) is geared towards power production, whereas the activity of others (mostly biarticulars) is geared towards ensuring smooth transitions near top and bottom dead center. The negligible improvement in power output that results from constraining the kinematics for the optimal solution suggests that the optimal stimulation pattern results in kinematics in which all muscles perform near-optimally in terms of power production. In other words, even though biarticulars are not the most important power sources (see Table), their coordination is still geared towards production of power.

It remains to be investigated if the optimal kinematics for the normal, unconstrained system is also optimal for the constrained system and, if not, what the optimal constrained kinematics and the corresponding power output are.

REFERENCES

Raasch CC et al. (1997) J. Biomech. 30, 595-602
Soest AJ van and Casius RC (2000) MSSE 32, 1927-1934

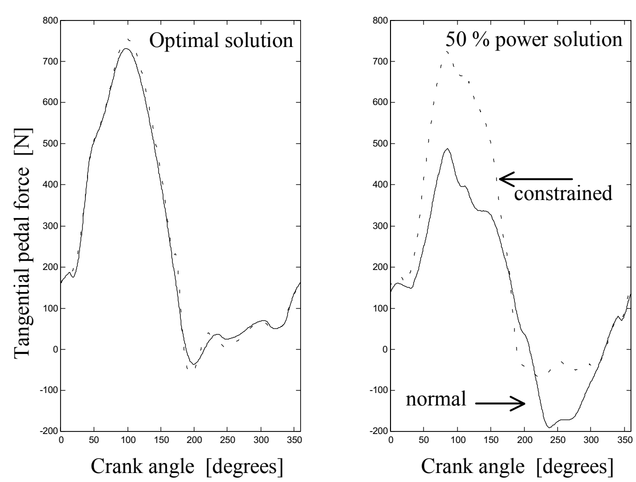

THE MUSCULAR COMPONENT OF PEDALING FORCE IS NOT WELL DEFINED

Jim Papadopoulos[1] and Andy Ruina[2]
[1] Paper Converting Machine Co., Green Bay, Wisconsin
[2] Theoretical and Applied Mechanics, Cornell University

Ruina@cornell.edu, http://www.tam.cornell.edu/~ruina/hplab

INTRODUCTION

Multi-axis load-sensing pedals make it possible to determine the foot forces applied to the pedals as riders aim for certain goals in controlled circumstances such as maximum power at a given rpm and heart rate, the Wingate test, etc. As an example of what is now generally recognized now as a misuse of such data, some early investigators proposed that any radial force component (perpendicular to the pedal path) was harmful to performance. Given that pedal force data is collected and is subject to such misinterpretation, one would like a rational way to evaluate pedal force profiles. What identifies desirable or undesirable pedal forces?

Towards the end of better understanding pedal forces there have been a few attempts to decompose them into parts due to gravity, inertial reactions, and muscle forces. Ross and Miller (1980) proposed a scheme to determine the purely mechanical (gravity and inertia) component of a measured foot force. Kautz and Hull (1993) also proposed a force-decomposition method, which has been used by many researchers. Both of these methods are based on a 2D five-bar linkage model of the pedaling system (bike, crank, foot, calf, thigh). Another decomposition was proposed by Papadopoulos (1987) based on a four-bar linkage approximation (foot and calf combined).

We show that the two five-bar methods are effectively identical, being based (at least implicitly) on an artificial external torque on the foot. From a fundamental standpoint, other equally well defined measures could be defined by instead applying other artificial torques instead, for example to the calf or thigh. In all of these cases the decomposition fails to pass the reasonableness criterion that the net work of claimed muscle-based forces being equal over a revolution of periodic motion to the actual work of the foot on a pedal. On the other hand, the four-bar model is explicitly approximate.

METHODS

In all cases we assume the pedaling system is well modeled as an actuated planar linkage of rigid bodies. Thus all analysis is of the robotics type, being based on momentum and energy balance of a system of interacting rigid bodies.

RESULTS

If an actuated mechanism has one degree of freedom, all joint forces, including for example the force on the pedal, can be rigorously decomposed into a sum three sets: one from gravity, one from inertial terms, and one from actuation (muscle forces). In this case, the work of the foot on the pedal over a cycle is equal to the work of the muscular (actuated) component over a cycle. The four bar linkage model fits this criterion. However a five bar linkage, having two degrees of freedom, does not allow such a unique decomposition. The ficticious torque approach to making a five bar linkage determinate unfortunately leads to an explicit violation of energy balance; the work of the foot on the pedal is mismatched to the calculated work of the muscular component by the amount of work performed by the ficticious torque.

Another view of the ficticious-torque approach is as a ficticious kinematic constraint. But equally legitimate constraints, on other parts than the foot give rise to different force decompositions (which also violate the energy reasonableness criterion) and give different muscular component of foot forces.

The lack of definition of muscular force comes from the extra kinematic freedom of the five-bar system. Without muscle forces the kinematics would be wild and nothing like actual pedaling. Thus the muscles are needed for postural reasons.
The force without muscles is not defined, because the motion could not occur. And with muscles there is no way to fundamentally separate postural from propulsive muscular contractions.

SUMMARY

Because a useful pedal force decomposition ought to be usable for calculating net muscular power, we conclude that all the five-bar methods must be viewed as either wrong or essentially approximate. And the four-bar method, while theoretically better grounded, is explicitly approximate.

We doubt the existence of a well defined muscular component of pedal force and thus question any but approximate reasoning based on the concept.

REFERENCES

Kautz, S. A.,.Hull, M. L (1993), *J. Biomechanics*, **26**, 155-165
Miller, N. R., Ross, D (1980), *J. Mech. Des.*, **102**, 711-717
Papadopoulos, J. M. (1987), in *Biomechanics in Sports – A 1987 Update* (Edited by Rekow, E. D., Thacker, J. G., and Erdman, A. G.) BED-Vol. 6, 83-92, American Society of Mechanical Engineers, New York

MECHANICAL ENERGY FLOW DURING MAXIMAL CYCLING

James C. Martin and Bruce M. Wagner

Neuromuscular Function Laboratory, The University of Utah, Salt Lake City, Utah

INTRODUCTION

Internal work has been defined as the work done to accelerate the limb segments (Winter, 1979) and has been assumed to do no external work during gait. Internal work is also thought to be lost during cycling (Wells et al., 1986). However, Ingen Shenau et al. (1990) reported that net joint muscular power during cycling was equal to the sum of power delivered to the crank and the rate of change of mechanical energy in the limb segments (E dot). The sign of the E dot term varied within each crank cycle, indicating that energy was transferred to and from the limb segments and thus may perform external mechanical work. The purpose of this investigation was to determine the quantity of energy lost and transferred as external work to the cranks via the limb segments.

METHODS

Five male cyclists (76±5 kg) performed maximal cycling trials during which pedaling rates ranged from 58 to 190 rpm. The right pedal was equipped with two 3-component piezoelectric force transducers (Kistler 9251) and the pedal and crank were equipped with position sensors (Vishay Spectrol 601-1045). Peal forces, and pedal and crank position were recorded at a frequency of 200Hz. Two dimensional leg kinematics were determined from the geometric relationships of a five-bar linkage (Hull and Jorge, 1985). Velocity and acceleration terms were determined by finite differentiation. Net joint moments at the ankle, knee, and hip were determined using inverse dynamic techniques (Elftman, 1939). Joint power was calculated as the product of joint moment and joint angular velocity. Pedal forces were decomposed into muscular, gravitational, and inertial components (Kautz and Hull, 1993). Non-muscular crank power was calculated from the gravitational and inertial pedal forces and moments, and crank and foot angular velocity. Kinetic and potential energy in each limb segment were determined from the mass, position and velocity of the center of mass, moment of inertia, and angular velocity of each segment. E dot was determined by finite differentiation. Finally, gravitational and inertial pedal forces and moments were used to determine the net joint moments required to produce those observed non-muscular pedal forces and moments.

RESULTS AND DISCUSSION

Summed joint power was equal to the sum of total crank power and E dot throughout the crank cycle. The non-muscular component of crank power was equal in magnitude but opposite in direction to E dot. Joint power associated with non-muscular pedal forces was equal to the sum of non-muscular power delivered to the pedal and E dot.

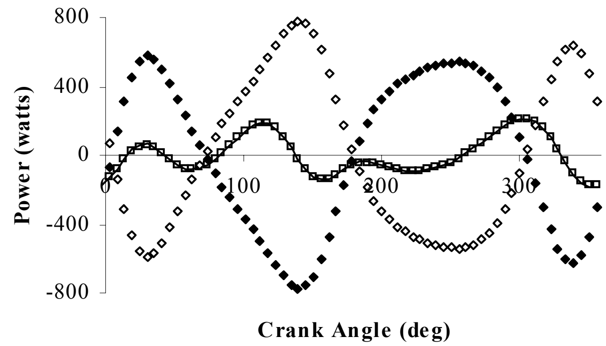

Example data for 1 revolution at a pedaling rate of 190 rpm. The rate of change of mechanical energy stored in the limbs (E dot; ♦) was equal and opposite to the crank power generated by non-muscular pedal forces (◇). The sum of all joint powers which contributed to non-muscular pedal forces (□) was equal to the sum of the crank power and E dot (—).

In this investigation, we used force decomposition to explore the relationships among E dot, net joint power, and non-muscular crank power. We conclude that the energy delivered to the limb segments is conserved rather than lost. That energy is stored for some portion of the crank cycle and subsequently exits the limb segments to perform external work. The ability of the limbs to transfer kinetic and potential energy into external work at the cranks supports the conclusions of Ingen Schenau et al. (1990) who wrote that "…the majority of the power associated with the decrease of segmental energy benefits the power transferred to the pedal…"

These data might be interpreted to suggest that the cost of moving the limbs during cycling should be zero. However, it has been reported that the metabolic cost of producing zero power output increases with increasing pedaling rate (Sidossis et al., 1992). Although some investigators have attributed that increase to mechanical energy losses, the present data do not support that explanation. Rather, they suggest some other phenomena, most likely viscous loss in muscle tissue, are responsible for the that increase in metabolic cost.

REFERENCES

Elftman H (1939) *Am J Physiol* 125, 357-366
Hull ML, Jorge M (1985) *J Biomech* 18, 631-644
Ingen Schenau GJ, van et. al., (1990) *Eur J Appl Physiol Occup Physiol* 61, 11-19
Kautz SA, Hull ML (1993) *J Biomech* 26:155-165
Sidossis LS et al. (1992) *Int. J Sports Med* 13, 407-411
Wells R, Morrissey M, Hughson R (1986) *Eur J Appl Physiol Occup Physiol* 55, 295-301
Winter DA (1979) *J Appl Physiol* 46, 79-83

THE METABOLIC EQUIVALENT OF INTERNAL WORK IN CYCLING

Alberto E. Minetti
Centre for Biophysical and Clinical Research into Human Movement
Manchester Metropolitan University, UK, a.e.minetti@mmu.ac.uk

INTRODUCTION

While the concept of mechanical internal work (W_{INT}) comes from the straightforward need to account for reciprocal acceleration of body segments (not affecting the trajectory of the overall centre of mass, BCOM), its use in walking/running has been debated in relation to the potential interference with external work. This paper is about W_{INT} estimation and its metabolic relevance in cycling, where the movement of lower limbs is supposed not to remarkably affect the overall BCOM.

MATERIALS AND METHODS

In a previous paper (Minetti et al. 2001) we measured W_{INT} by 3D motion analysis of a stationary cyclist pedalling at different rates. We concurrently developed a rationale for the theoretical estimation of the internal work in cycling, which ended up in the following model equation:

$$\dot{W}_{INT} = k\, freq^3$$

where $\dot{W}_{INT}$ is in watt per kilogram, $freq$ in Hz and k reflects the inertial characteristics of the moving segments (lower limbs). The experimental $\dot{W}_{INT}$ data was fitted by the model which proved to be sound (resulting in k = 0.153).

In order to get information about the metabolic equivalent of $\dot{W}_{INT}$ we recently undertook the re-elaboration of data from Francescato et al. (1995). The authors measured the oxygen consumption ($\dot{V}_{O2}$, W) of subjects pedalling on a cyclo-ergometer at different combinations of external power ($\dot{W}_{EXT}$, range 20-125 W) and pedalling frequency (range 40-100 RPM). A second set of experiments was done by applying the same protocol to the same subjects after having loaded the lower limb segments with additional mass (+40%).

The model equation for $\dot{W}_{INT}$ was incorporated in a new one,

$$\dot{V}_{O2} = \frac{(\dot{W}_{EXT} + 75k\, freq^3)}{eff}$$

representing the main determinants of oxygen consumption, where the brackets contain the total mechanical work (assuming the complete separation between the external and internal parts). The value 75 means the mass of a typical subject (since our previous equation was expressed in W/kg, while the data from Francescato et al are in W).

This equation was used as a non-linear multiple regression (Systat, USA) to fit the experimental data from Francescato et al. (1995) and estimate the two unknowns: k (see $\dot{W}_{INT}$ model equation) and eff, namely the efficiency of the conversion of metabolic into mechanical work.

RESULTS AND DISCUSSION

For the unloaded (UL) set of experiments from Francescato et al (1995) the results of the regression were k_{UL} = 0.150 (very close to our previous estimation) and eff = 0.270 (R^2 = 0.980, n= 20). When the same procedure is applied to the loaded experiment (L), the results are k_L = 0.241 and eff = 0.284 (R^2 = 0.942, n= 20).

The results show that: a) the variability of $\dot{V}_{O2}$ can be almost entirely explained by the different contribution of $\dot{W}_{EXT}$ and $\dot{W}_{INT}$, both in UL and L conditions, b) k_L is close to what expected on the basis of limb loading (k_L = 1.4, k_{UL} = 0.21, the difference being probably due to the mass positioning on the limbs), c) R^2 values are high enough to suggest a small effect of assuming, in the regression equation, a constant eff for all the pedalling frequencies and external work. The obtained results allow one to compute the metabolic equivalent of the mechanical internal work of cycling as:

$$\underset{\text{(W/kg)}}{\dot{V}_{O2.INT}} = 0.556\underset{\text{(Hz)}}{freq^3} \quad \text{or} \quad \underset{\text{(mlO}_2\text{/(kg min))}}{\dot{V}_{O2.INT}} = 1.66\underset{\text{(Hz)}}{freq^3}$$

The re-processing of data from Francescato et al (1995), obtained by using a model equation for $\dot{W}_{INT}$ (Minetti et al 2001) indicates that the internal work in cycling can represent a remarkable portion of the metabolic energy expenditure, particularly at high pedalling rates (e.g. about 13.3 mlO_2/(kg min) at 120 RPM).

REFERENCES

Francescato M. P., Girardis M., di Prampero P.E. Oxygen cost of internal work during cycling. Eur J Appl Physiol 72(1-2): 51-57, 1995.
Minetti A. E., J. Pinkerton and P. Zamparo. From bipedalism to bicyclism: evolution in bioenergetics and biomechanics of historic bicycles. Proc. R. Soc. B 268: 1351-1360, 2001.

BIOMECHANICAL DETERMINANTS OF PEDALING ENERGETICS: INTERNAL AND EXTERNAL WORK ARE NOT INDEPENDENT

S.A. Kautz[1, 3] and R. R. Neptune[1, 2]
[1] Rehabilitation R & D Center, VA Palo Alto HCS, Palo Alto, CA
[2] Department of Mechanical Engineering, University of Texas, Austin, TX
[3] Department of Functional Restoration, Stanford University, Stanford, CA
Email: kautz@rrdmail.stanford.edu

INTRODUCTION

The total mechanical work done by muscles during a given locomotor task is often assumed to include two independent quantities: "external work" (work done to overcome external resistance, which can be accurately measured) and "internal work" (putative work done to accelerate and decelerate the leg segments, which cannot be directly measured). However, recent pedaling simulation studies have illustrated how muscle forces generate and redistribute energy within the musculoskeletal system to overcome the external workload (e.g. Neptune et al., 2000). Muscle force can cause significant energy transfer from the legs to the environment at given instants during the pedaling cycle such that the external power (rate of doing external work) exceeds the mechanical muscle power. We hypothesize that muscles accelerate and decelerate the legs as an integral part of performing external work, and that there is no ***additional independent*** mechanical cost associated with moving the legs (i.e., internal work).

METHODS

To investigate this hypothesis, a forward dynamics simulation that emulated observed pedaling kinematics and kinetics of young adult subjects was used (Neptune et al., 2000). The musculoskeletal model and simulation were developed using SIMM/Dynamics Pipeline (MusculoGraphics Inc.) and consisted of a fixed pelvis and right and left legs. Each leg consisted of a thigh, shank, foot and fourteen individual Hill-type musculotendon actuators. The hip, knee and ankle joints were modeled as frictionless revolutes.

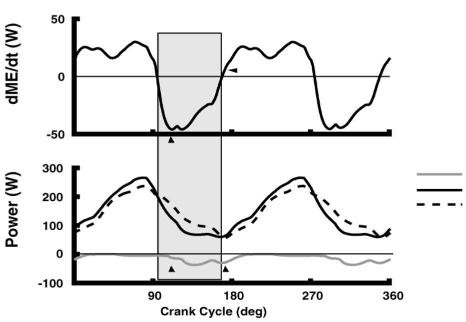

Figure 1: From approximately 350-95°, muscles generated more power than was delivered to the crank, resulting in an increase in leg power (dME/dt is positive). From 95-170°, even though muscles perform significant positive work and little negative work, the energy of the legs decreased as the muscles transferred more energy from the legs to the crank than was generated by the muscles themselves.

RESULTS AND DISCUSSION

The putative "basis" for calculating internal work is that decreases (increases) in the total mechanical energy during pedaling (Fig. 1) are due to mechanical energy absorption (production) of muscles. However, total mechanical energy decreases are coincident with both external work done at the crank and negative muscle power (Fig. 1). Furthermore, the negative muscle power is not closely matched to the decreasing total energy, with the peak decrease at 110° coinciding with relatively little negative muscle power and substantial negative muscle power occurring with increasing energy at 180°. The most powerful deceleration of the legs is caused by concentric activity in the ankle plantar flexors (e.g., Fig 2.). By acting to decelerate the leg, they transfer energy from the leg to the crank that allows them to deliver much more energy to the crank than they produce.

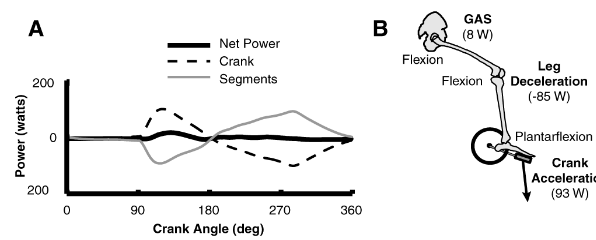

Figure 2: A) Between 90-180°, the gastrocnemius (GAS) transfers significantly more power from the legs to the crank than it produces. **B)** GAS acts to accelerate the foot powerfully into plantar flexion, which creates a pedal reaction force that accelerates the crank and intersegmental forces that decelerate the leg, and therefore reduce its energy.

While muscle forces increase and decrease the leg energy, the energy lost in the deceleration of the legs can and does generate a pedal force tangential to the crank, and thus does positive external work against the environment. As a result, the muscle work done to *increase* the total energy of the legs (considered to be one component of internal work) can be subsequently recovered as external work during the *decrease* in total leg energy (considered to be the other component of the internal work). Therefore, the internal work hypothesis is invalid as a direct measure of the mechanical energy cost associated with moving the legs in pedaling.

REFERENCES

Neptune, R.R. et al. (2000). *J Biomech* **33**:155-64.

ACKNOWLEDGEMENTS

Supported by NIH grant HD37996 and the Rehabilitation R&D Service of the Department of Veterans Affairs (VA).

THE "EVOLUTION" OF BICYCLE DESIGN AND ITS EFFECTS ON THE EFFICIENCY AND ECONOMY OF CYCLING

P. Zamparo [1,2] A.E.Minetti [1]

[1] Centre for Biophysical and Clinical Research into Human Movement, Manchester Metropolitan University, UK
[2] Dipartimento di Scienze e Tecnologie Biomediche, Università degli Studi di Udine, I, p.zamparo@mmu.ac.uk

INTRODUCTION

During the whole nineteenth century the combination of the need for individual mobility at an affordable price and the current technological advances produced a rapidly flourishing "evolution" of the bicycle towards higher speeds and better riding economy. In the 1820-1890 time span the speed gain was the result of concurrent technological advancements of wheeled human-powered vehicles and of the "smart" adaptation of the same actuator (the muscle) to different operational conditions (Minetti et al. 2001). The evolution of bicycle design was investigated by measuring the total mechanical work and the energy cost of riding the most relevant historical bicycles.

METHODS

Experiments were performed by 5 subjects (56 ± 11 years, 1.7 ± 0.4 m height and 68 ± 3 kg mass) riding historical bicycles at sub maximal speeds, on a flat concrete road. The investigated bicycles were the Hobby Horse (HH, 1820s), the Bone Shaker (BS, 1860s), the High Wheeler (HW, 1870s), the Rover (RO, 1880s), the Safety (SA, 1890s) and a modern bike (MB, 1970s) as a mean of comparison. For each bicycle: 1) the work to overcome rolling resistance (W_R) was calculated by means of coasting down experiments; 2) the work to overcome air resistance (W_A) was obtained from air density, frontal area and assuming a drag coefficient of 1.1; 3) the mechanical internal work (W_{INT}) was computed from 3D motion analysis (Minetti, 1998); and 4) the economy of progression (C, J m^{-1}) was calculated from the ratio of net metabolic power expenditure (VO_{2NET}) to the speed (v). The net mechanical efficiency (η) of riding each bicycle was computed from the ratio of total mechanical work (W_{TOT} (J m^{-1}) = $W_R + W_A + W_{INT}$) to the net energy cost (C).

RESULTS AND DISCUSSION

At an average net metabolic power of 350 W (e. g. about 1 lO_2 min^{-1}) the improvement in bicycle design allowed one to double the speed of progression: from 2.8 to 5.6 m s^{-1} in HH and MB, respectively. The increase in speed was obtained by decreasing the work spent against rolling resistance (W_R: from 24 - 26 J m^{-1} in HH and BS to 6.6 - 6.7 J m^{-1} in SA and MB) and the internal work (W_{INT} from 9.8 to 2.5 J m^{-1} in HH and MB, respectively) whereas the work spent against air resistance (W_A) increased according with the increase in speed (from 2.3 in HH to 9.4 J m^{-1} in MB). The decrease of W_{TOT} from HH to MB (from 36.3 to 18.5 J m^{-1}) was matched by a proportional decrease of C (from 136 to 70 J m^{-1}) so that the efficiency of cycling remained fairly constant from the nineteenth century to the modern times (0.27 ± 0.01). The relationship between η and progression speed was found to be a downward parabola in each bicycle; its maximum value was attained at increasing speeds (from 2.2 to 5.0 m s^{-1} in HH and MB, respectively) but at a similar pedalling frequency (of about 1 Hz), a rate which was suggested to be the optimum one for Type I fibers in cycling (Sargeant and Jones, 1995). This finding indicates that bicycle design was not only effective in decreasing the frictional forces residing outside the body, but also allowed the muscles to contract in their optimal operational conditions.

Among the other aspects in bicycle design not considered in this study, two further improvements played an important role in the evolution of cycling: 1) the introduction of the multiple gear system by which muscle contraction speed was made independent from the progression speed; and 2) the adoption of streamlined fairing by which the work spent against air resistance was dramatically reduced (Gross et al., 1984).

REFERENCES

Gross A.C., Kyle C.R., Malewicki D.J. (1983) Scientific American 249: 142-152.
Minetti A.E. (1998) J Biomech. 31: 463-468.
Minetti A.E., Pinkerton J., Zamparo P. (2001) Proc R Soc B 268: 1351-1360.
Sargeant A.J. and Jones D.A. (1995) In: Neural and neuromuscular aspects of muscle fatigue. Plenum press, NY, 323-338.

PEDAL MOTION DIRECTION AND THE CONTROL OF FOOT FORCE DURING PEDALING

Kreg G. Gruben

Departments of Kinesiology, Biomedical Engineering, and Mechanical Engineering
University of Wisconsin-Madison, Madison, Wisconsin, USA
gruben@education.wisc.edu

INTRODUCTION

Upright human posture is critically dependent on the control of leg muscles to generate force against the ground with appropriate direction and magnitude. The direction of this force must be controlled independent of limb motion. The purpose of this study was to examine the preferred directional control of force for a variety of limb motions at a given limb posture.

Total foot force results from inertia and forces of gravity and muscle while only the muscle component of foot force is directly controlled by the nervous system. Thus, study of nervous system control requires isolating the muscular component of foot force. We accomplish this by constraining limb motion so that the contributions of gravity and inertia are constant. Any changes in total foot force are then due exclusively to muscle action.

Previously we have shown that humans increase foot force with a directionally invariant strategy while pushing against both stationary and moving pedals (Gruben 1999, Gruben & Lopez-Ortiz 2000a, 2000b). The path of the tip of the foot force vector is well-described by a straight line. The orientation of the force path varies around the crank cycle in a pattern that appears to track the changes in pedal velocity direction (Gruben 1999). This changing orientation may be due to changes in limb posture or an attempt by the nervous system to align foot force with the pedal motion to increase mechanical efficiency of power transfer to the crank. However, these effects covary during the task of circular pedaling. Here we determine the effect of pedal motion direction on the orientation of the force path lines.

METHODS

Five healthy adult humans performed pushing efforts against a pedal while it moved in a reciprocating manner along a linear path. A motor controlled pedal motion to be independent of foot force (travel=±0.165m at 40 cycles per second). While lying on their right side on a horizontal platform, participants generated force against a moving pedal with their left foot to match five force target levels. Five directions (40,50,...,80°) of linear pedal motion that passed through a common reference pedal position were tested in sequence. Lines at the extreme angles passed anterior to the knee or posterior to the hip. The pedal measured the sagittal-plane components of the foot force. For each participant and each pedal motion direction, we constructed a force path as the set of foot forces measured at the instant the pedal passed through the reference pedal position. The orientation of each force path was determined by principal components analysis.

RESULTS

The force paths were well characterized by straight lines. Force path orientation was not affected by the direction of the pedal motion (Fig. 1). The line-of-action of the force paths passed anterior to the hip joint and posterior to the knee joint. The mean force path orientation passes within 0.01m of the whole body center-of-mass (CM) of the typical participant.

SUMMARY

Force path linearity and consistency in direction suggest that the motor control system has a preferred pattern of force output that is independent of limb motion and is directed approximately at the CM. Consistently directing foot force toward the CM is critical for upright posture. Observation of this control in a task that did not require foot force to provide any postural support indicates that this control strategy may be a critical component of a variety of lower limb actions.

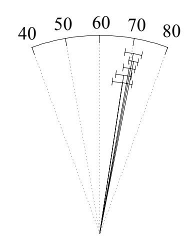

Fig. 1 Force Path Orientation Force path orientation (mean±sd) was independent of pedal motion direction (p=0.18). Each line is the mean of the five participants for one pedal motion direction.

REFERENCES

Gruben, K.G. (1999) *Progress in Motor Control-II*, State College, PA, USA, 84-85.
Gruben, K.G., López-Ortiz, C. (2000a). *J Motor Behavior*, **32**(2):151-162.
Gruben K.G., López-Ortiz, C. (2000b). *American Soc. of Biomechanics Annual Mtg.*, Chicago, IL, USA, 25-26.

CYCLING BY MEANS OF FES: SIMULATION AND PRACTICAL APPLICATION

Margit Gföhler[1], Thomas Angeli[1] and Peter Lugner[2]
[1]Department of Machine Elements, Vienna University of Technology, Vienna, Austria, email: margit.gfoehler@tuwien.ac.at
[2]Department of Mechanics, Vienna University of Technology, Vienna, Austria

INTRODUCTION

Functional Electrical Stimulation (FES) has been explored as a means of restoring lost function in the spinal cord injured (SCI). Specific training with FES combines the physiological benefits of the muscle training with the psychological incentive of independent locomotion. In this study, cycling on a tricycle for SCI-subjects using multi-channel FES was investigated in a forward dynamic simulation. The efficiency of the movement is increased by an optimized pedal path, which is realized by a four bar linkage (Angeli et al., 1999). Besides this pedal path, the overall performance is essentially influenced by a number of configuration and stimulation parameters that may be different for each subject.

METHODS

For the dynamic simulation, the rider-cycle system was modeled as a planar rigid body system with frictionless pin joints (Fig. 1). The muscle forces are applied as joint moments. The musculotendon actuators were modeled by a Hill-type mechanical model that was enlarged to provide the proper FES-stimulation behavior.

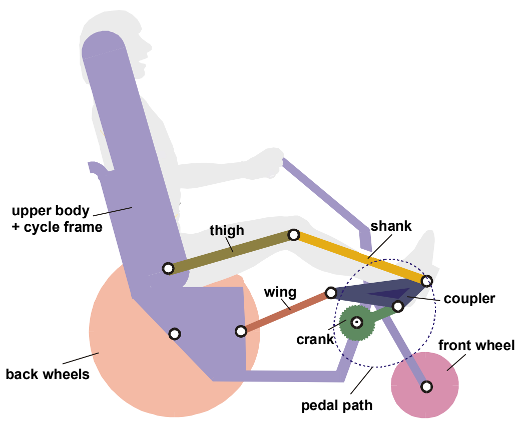

Figure 1: Scheme of the rider-cycle system with three bar linkage for realization of the optimized pedal path.

Activation patterns for the stimulated muscles / muscle groups gluteus maximus, quadriceps, hamstrings alone and hamstrings and iliopsoas together activated by pereonaeus reflex were optimized for maximum power output with respect to the angular velocity of the crank. Forward dynamic simulations of steady state cycling and a startup with 50% of maximum muscle activation were used to analyze drive torques and mean power per cycle and the resulting riding performance of the rider-cycle system. A number of individual parameters are considered in the simulation.

RESULTS AND DISCUSSION

The simulation provides information on the optimal stimulation patterns (Fig. 2), drive torques and power applied to the pedal by the stimulated muscles.

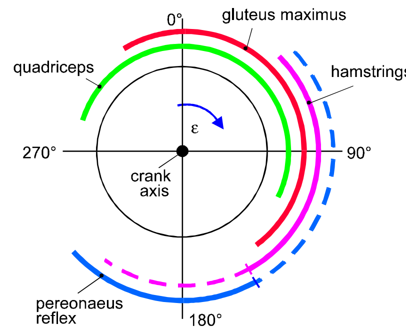

Figure 2: Optimized stimulation patterns for averaged user-specific parameters at crank angular velocity 150 °/s.

The results of the simulation and practical tests on a mobile tricycle have shown that SCI-subjects are able to move a tricycle independently with muscle force generated by FES. Still, there are parameters like electrode placement, spasm activity and fatigue which are difficult to predict.

SUMMARY

In this study, FES-cycling on a tricycle was investigated in a forward dynamic simulation. The stimulation patterns were optimized with respect to drive power efficiency for surface stimulation of gluteus maximus, quadriceps, hamstrings, and peronaeus reflex assuming averaged individual parameters. The results can be used not only for estimating the riding performance of an individual SCI-subject, but also for the layout of a controller for FES-cycling.

REFERENCES

Angeli T. et al. (1999). *Med. & Biol. Eng. & Comp.*, **37**, Supp. 2, 326-327.

ACKNOWLEDGEMENTS

This work was sponsered by the Austrian Science Foundation.

MUSCLE FIBER TYPE EFFECTS ON ENERGETICALLY OPTIMAL PEDALING CADENCE

Brian R. Umberger[1], Karin G.M. Gerritsen[2], & Philip E. Martin[1]

[1]Exercise & Sport Research Institute, Arizona State University, Tempe, AZ, USA (brian.umberger@asu.edu)
[2]Human Performance Laboratory, University of Calgary, Calgary, AB, CANADA

INTRODUCTION

Metabolic energy expenditure exhibits a curvilinear dependence on pedaling rate during steady-state, submaximal cycling. The most economical cadence typically occurs around 50-60 rpm, and has recently been shown to be significantly higher (by 6-7 rpm) in explosively-trained athletes than in endurance athletes (Hintzy et al., 1999). Muscle fiber type differences between subjects were suggested to cause the observed differences in energy optimal pedaling rates, but were not directly assessed. Such experimental investigations are complicated by factors such as individual variations in training history, or difficulties in measuring muscle fiber type distribution. These problems can be circumvented using computer modeling and simulation techniques. Specifically, muscle fiber type distribution can be precisely controlled for each muscle, and studied in isolation from other potentially confounding effects. The purpose of this study was to assess whether differences in muscle fiber type, *per se*, affect most economical cadences as proposed in the literature.

METHODS

Forward dynamic simulations were generated of steady-state pedaling (200 W) at cadences from 40-120 rpm by solving a combined tracking/energy-minimization problem using numerical optimization. The cyclist and bicycle were modeled as 9 rigid segments (trunk, 2 thighs, 2 shanks, 2 feet, crank, frame) actuated by 12 Hill-type muscles per leg. Frictional and inertial loads were applied at the crank to simulate the dynamics of overground riding. Dynamic properties of the muscles (force-velocity relations and active state dynamics) were scaled with fiber type to produce a slow twitch model and a fast twitch model. Static properties (e.g., force-length relations) were identical between models. Metabolic energy expenditure, which also depended on muscle fiber type, was estimated using a model of human muscle energy expenditure (Umberger et al., 2001). Muscle excitation patterns were optimized to minimize the differences between simulated and experimental crank torque and pedal angle data, while simultaneously minimizing energy expenditure. Separate optimizations were conducted for both models at all cadences.

RESULTS AND DISCUSSION

Both the fast twitch and slow twitch models were able to pedal at the target power and cadences (within ±1%), while reproducing the major features of experimental pedaling data. Optimized muscle excitation patterns also showed broad agreement with experimental EMG data. The dependence of total body energy rate (including heat liberated by the head, arms, and trunk) on pedaling cadence for the two models is shown in Figure 1, along with group mean data taken from several experimental studies (e.g., Marsh & Martin, 1993). The energy rates predicted by the two models tended to bound the published experimental values, consistent with muscle fiber type distributions higher than, and less than, average.

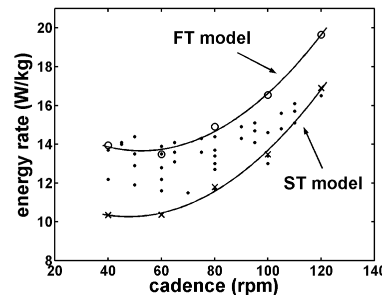

Figure 1: Whole body energy rate at different cadences for models with fast twitch (o) and slow twitch (x) muscles, along with experimental data (.) from various studies.

Predicted most economical cadence was higher for the fast twitch model (53 rpm) than for the slow twitch model (48 rpm); a deviation similar to that reported by Hintzy et al. (1999). Differences in the two economy curves can largely be explained by the dependence of muscle mechanical efficiency on pedaling rate in the two models. Mechanical efficiency was higher for the slow twitch model and peaked at a lower cadence than in the fast twitch model. Other factors that influenced the shapes of the global economy curves with increasing cadence were the growing contribution that muscle energy liberation made to total energy, and increasing work done against joint viscosity.

SUMMARY

Differences in energetically optimal pedaling rates have been proposed to be due to variations in muscle fiber type. However, fiber type distribution has usually not been adequately characterized. The results of this computer simulation study suggest that between-subject differences in muscle fiber type do indeed contribute to differences in energetically optimal cadences as suggested in the literature.

REFERENCES

Hintzy, F et al. (1999). *Eur. J. Appl. Physiol.*, **79**, 426-432.
Marsh, A, Martin, P. (1993). *Med. Sci. Sp. Ex.*, **25**, 1269-1274.
Umberger, B et al. (2001). *Proceedings of ASB 2001*, 319-320.

ACKNOWLEDGEMENT

This work was supported by NSF IGERT grant DGE9987619.

MUSCLE FIBRE PROPERTIES AND OPTIMAL CADENCE IN CYCLING

Anthony J. Sargeant

Centre for Biophysical and Clinical Research into Human Movement,
Manchester Metropolitan University, ST7 2HL, United Kingdom. a.j.sargeant@mmu.ac.uk

INTRODUCTION

The identification of optimal cadences for human movement has been the subject of many investigations dating back to, and beyond, Benedict and Cathcart (1913). In this paper the optimal cadence for cycling is considered in relation to three aspects of muscle function; generation of maximum muscle power; muscle fatigue during sustained exercise; and the energy cost of generating muscle power.

Optimal cadence and Maximum Muscle Power:
The optimum velocity of muscle contraction for maximum power output is a frequently used reference point in isolated muscle studies, but its significance in human locomotory exercise has been less widely recognized (despite e.g. A.V.Hill 1922). However, using an isokinetic cycle ergometer system it was possible to identify an optimal pedaling rate of ~120 revs/min for maximum power output during cycling in a large group of male and female subjects (Sargeant, Hoinville and Young, 1981). Subsequently it has been shown that the optimal cadence can be influenced by the effect of, for example, changes in muscle temperature and exercise induced fatigue, a phenomenon which has been termed "acute plasticity" (for review see e.g. Sargeant 1999).

Optimal cadence and the delay of muscle fatigue in sustained exercise:
Human performance is usually dependent upon the ability of skeletal muscle to both generate power, and sustain that power – that is, resist fatigue. At the level of the whole muscle it will be obvious that in sustained exercise a critical factor will be the proportion of the maximum 'available' power that is required for the task. Recently it has been reported that in a group of normal healthy males the proportion of the maximum available muscle power required at maximum oxygen uptake when pedaling at 40, 60, 80, 100 and 120 rev/min was respectively 55, 45, 38, 35 and 29% (Zoladz, Rademaker, and Sargeant, 2000): This is simply a consequence of the parabolic nature of the maximum power/velocity relationship but it implies a much greater 'reserve' of muscle power at the faster pedaling rates. At first sight this would suggest an advantage to also choosing the optimal pedaling rate for maximum power during submaximal sustained exercise. This however ignores the impact of possible changes in the relative contribution of different muscle fibre types with their different levels of fatigue resistance and mechanical efficiency. Clearly any potential benefit of choosing fast pedaling rates and maintaining a high 'reserve' of muscle power generating capability will be negated if there were a disproportionate increase in energy cost or a reduced resistance to fatigue.

In very short sprints requiring power to be sustained for ~10 s there is typically a reduction of a ~25% in delivered power due to fatigue of a small population of the most powerful but also most fatigue sensitive type II muscle fibres. That fatigue is associated with depletion of high-energy phosphates as shown by analysis of single human fibres isolated from needle biopsy following sprint exercise (Karatzaferi, De Haan, van Mechelen, and Sargeant 2001)

Optimal cadence for generating mechanical power at minimal energy cost:
If exercise is to be sustained for more than a few contractions the efficiency with which chemical energy is transformed into mechanical energy may be of critical importance. Unfortunately little is known about the mechanical efficiency/velocity characteristics of human muscle fiber types. It could be expected that maximal efficiency would occur at a velocity close to, but slightly less than that for maximum power. This suggests an optimal pedaling rate for maximum mechanical efficiency of ~60 rev/min for type I human muscle fibres and ~130 rev/min for the mean of type II. In agreement with this suggestion we have recently been able to show that in high intensity aerobic exercise where type I fibres make the dominant contribution to power output increasing leg muscle temperature results in a decrease in efficiency at 60 rev/min but an increase in efficiency at 120 rev/min Such opposite changes would be consistent with a rightward temperature shift in the efficiency/velocity relationship (Ferguson, Ball, and Sargeant 2002).

REFERENCES

Benedict, F.G., Cathcart, E.P. (1913) *Muscular Work.* Publications of the Carnegie Institute, No. 187.
Ferguson, R.A., Ball, D., Sargeant, A.J. (2002) *J.Exp.Biol.* **205**, (in press)
Hill, A.V. (1922) *J. Physiol.* **56**, 19-30.
Karatzaferi, C., de Haan, A., van Mechelen, W., Sargeant, A.J. (2001) *Exp Physiol.* **86.3**, 411-415
Sargeant, A.J. (1999) In: *Physiological Determinants of Exercise Tolerance in Humans.* Eds. Whipp, B.J. and Sargeant A.J. Physiological Society/Portland Press. London. pp.13-28.
Sargeant, A.J., Hoinville, E., Young, A. (1981) *J.Appl. Physiol.* **51**, 1175-1182.
Zoladz, J., Rademaker, A. and Sargeant, A.J. (2000). *Exp Physiol.* **85.** 117-124.

EXAMINATION OF KNEE CONTROL VIA TWO INDUCED ACCELERATION MODELS

Thomas M. Kepple, Karen Lohmann Siegel, and Steven J. Stanhope

National Institutes of Health, Physical Disabilities Branch, Bethesda, MD, USA, tkepple@cc.nih.gov

INTRODUCTION

Although induced acceleration methods can be powerful tools for analyzing the control of the knee joint during walking (Siegel et al., 2001), the results obtained from these models depend on the selection of an appropriate foot-floor constraint. Kepple et al. (1995) previously compared a constraint system that fixed the foot to the floor during foot-flat with one that allowed the foot to rotate about the center of pressure. The fixed-foot model produced a discontinuity in the induced acceleration data when the constraint was released at heel-off. It is not known if this discontinuity is physically realistic. The alternative method of allowing the foot to rotate about the center of pressure produces no discontinuity but does result in increased knee accelerations which may indicate an under estimation of the contribution of the knee extensors to the ground reaction force (Kepple et al., 1995). Neptune et al. (2001) used a visco-elastic foot-floor model in an attempt to more accurately represent the actual foot-floor interface during a simulated walk. The purpose of this paper was to apply a similar visco-elastic model in an induced acceleration analysis and compare it to the previous fixed-foot model.

METHODS

Using a six-camera Vicon system (Oxford Metrics Inc.), data were collected from a single female adult subject walking at a self-selected pace. The subject supplied informed consent under an IRB approved protocol. For each frame of video data, Visual3d software (C-Motion Inc) generated a Solver dataset, which was loaded into ADAMS software (Mechanical Dynamics Inc.). The data set contained a three-dimensional biomechanical model derived from that of Kepple et al. (1997). This model included seven anatomical segments: two feet, two legs, two thighs and a single head-arms-trunk segment. The knees were modeled as revolute joints, the hips were modeled as spherical joints and the ankles were modeled as a universal joints with one medial/lateral axis and one anterior/posterior axis.

Two foot-floor constraints were used and compared. The first constraint (fixed-foot constraint) fixed the foot to the floor during foot flat and allowed the foot to rotate about the center of pressure after heel off. The second constraint was an eight element visco-elastic model based on Gerritsen et al. (1995). The Gerritsen model was modified slightly so that the coefficient used on the vertical displacement in the damping term was reduced to a first order. This change was required in order to allow the visco-elastic deformations to build up in a short enough time period so that there was little change in the position of the segments.

RESULTS AND DISCUSSION

The data indicate that there is generally good agreement between the two models. The mean differences between the models were 27.3 rad/s^2. The sources of knee acceleration for both models are presented in Figure 1. The fixed-foot model produced the expected discontinuity at heel-off while the visco-elestic model tended to make this transition more smoothly.

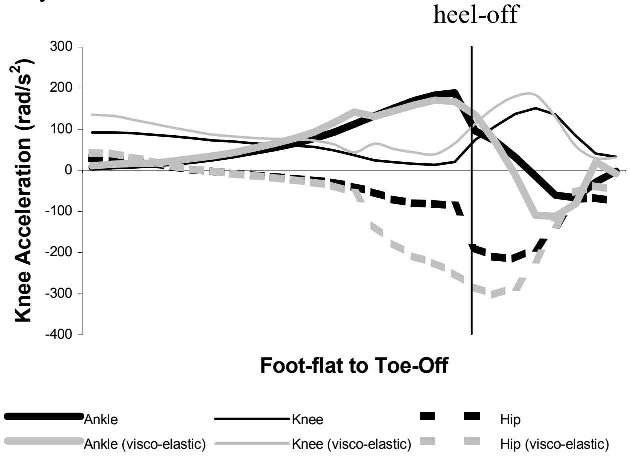

Figure 1. Acceleration induced at the knee by the lower extremity joint moments. Data from the fixed-foot model are in black and data from visco-elastic model are in gray.

SUMMARY

Although the visco-elastic model produced a smoother roll-off, the general shapes of the induced acceleration histories were very similar, increasing the confidence that the fixed-foot model correctly estimates the role of the knee extensors during foot-flat. These results are also important because the fixed-foot model produces similar results to the more difficult to implement and computationally expensive visco-elastic model.

REFERENCES

Gerritsen et al. (1995), *J Biomech*, **28**, 661-668.
Kepple et al. (1995), *Gait & Posture,* **5**, 172-173.
Kepple et al. (1997), *Gait & Posture*, **6**, 1-8.
Neptune et al. (2001), *J Biomech*, **34**, 1387-1398.
Siegel et al. (2001), *Gait & Posture*, **10**, 255-256.

GENERATING DYNAMIC SIMULATIONS OF MOVEMENT USING COMPUTED MUSCLE CONTROL

Frank C. Anderson[1], Darryl G. Thelen[2], and Scott L. Delp[3]

[1,2,3] Department of Mechanical Engineering, Stanford University, Stanford, California, USA, [1] fca@stanford.edu
[2] Honda Fundamental Research Laboratories, Mountain View, California, USA

INTRODUCTION

Dynamic simulation is a powerful approach for investigating how the elements of the neuromusculoskeletal system interact to produce movement; however, computing neural excitation patterns that produce coordinated movements is difficult. Using dynamic optimization to solve this problem can be computationally costly (Neptune and Hull, 1998) and difficult to implement (Kaplan and Heegaard, 2001). Yamaguchi et al. (1995) devised a pseudo-inverse method for computing muscle forces, but this method does not incorporate the dynamic properties of musculotendon actuators and requires the use of a specific optimization performance criterion. In this paper, we introduce a new approach to computing muscle excitation patterns which we term computed muscle control (CMC). We illustrate the algorithm by computing a set of muscle excitations for pedaling.

METHODS

The CMC algorithm is applied at each time step during a forward dynamic simulation (Figure 1). In a manner similar to computed torque control (Lewis et al., 1993), feedback is used with linear gains (k_v, k_p) to drive the kinematic trajectory of a dynamic model ($\vec{q}, \dot{\vec{q}}$) toward a set of desired experimental kinematics ($\ddot{\vec{q}}_{exp}, \dot{\vec{q}}_{exp}, \vec{q}_{exp}$). Static optimization is used to resolve actuator redundancy by computing a set of desired muscle activations ($\vec{a}^*$) that would generate a set of desired accelerations ($\ddot{\vec{q}}_d$) when steady-state conditions within the muscles are present. Then, an excitation controller is used to transform the desired activations into the excitations ($\vec{u}$) that drive the forward dynamics model.

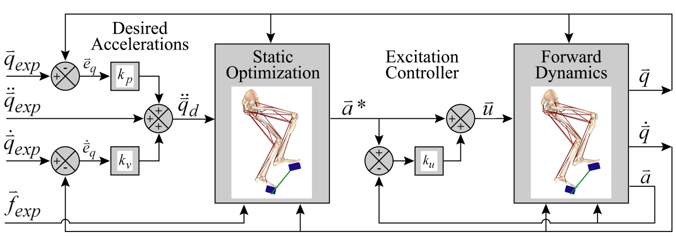

Figure 1: Computed Muscle Control Algorithm.

The pedaling model had 3 degrees of freedom and was driven by 30 musculotendon actuators (Neptune and Hull, 1998). Activation dynamics was modeled as a first order process with activation and deactivation times of 15 ms and 50 ms, respectively. Average crank angles and pedal forces from Neptune et al. (1997) were used as experimental input. In the static optimization problem, the sum of squared muscle activations was used as the performance criterion (Anderson and Pandy, 2001), with additional equality constraints included to track the experimental pedal forces ($\vec{f}_{\text{exp}}$).

RESULTS

A set of muscle excitations that produced a coordinated pedaling simulation was found using 15 minutes of computer time on a 1.7 GHz Pentium 4. Simulated kinematics were within one degree of experimental values, simulated pedal forces were within two standard deviations of measured forces (Figure 2(a)), and computed excitations were similar in timing to electromyographic (EMG) patterns (Figure 2(b)).

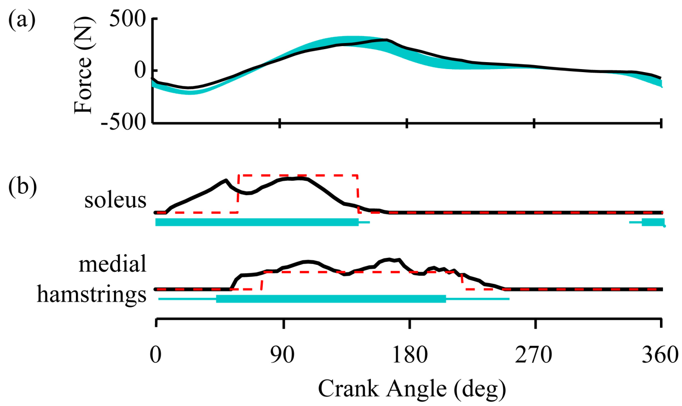

Figure 2: **(a)** Computed (black line) and experimental (shaded area) radial pedal forces. **(b)** Computed muscle excitations for two muscles (solid black lines). A simulated annealing solution (dashed lines) and on-off times from EMG signals (shaded bars) are also shown (Neptune and Hull, 1998).

DISCUSSION

The speed and ease of implementation of the CMC algorithm greatly improves the feasibility of using detailed musculoskeletal models to simulate and analyze movement. The CMC algorithm predicts continuously varying excitations and is approximately two orders of magnitude faster than a simulated annealing approach (Neptune and Hull, 1998). The improvement in speed derives from the fact that only a single forward integration of the state equations is needed, in contrast to the thousands typically required by dynamic optimization.

REFERENCES

Anderson FC, Pandy MG (2001). *J. Biomech.*, **34**, 153-161.
Kaplan ML, Heegaard JH (2001). *J. Biomech.*, **34**, 1077-1083.
Lewis FL et al. (1993). *Control of Robot Manipulators*. Macmillan Publishing Company.
Neptune RR et al. (1997). *J. Biomech.*, **10**, 1051-1058.
Neptune RR, Hull ML (1998). *J. Biomech. Eng.*, **120**, 334-41.
Yamaguchi GT et al. (1995). *J. Biomech.*, **28**, 999-1005.

ACKNOWLEDGEMENTS

NIH R01 HD38962, NIH R15 AG13759-01, NSF BES-9702275, Rick Neptune, and Jill Higginson.

FORWARD DYNAMIC MODELING OF ACUTE INJURY: EFFECTIVE METHODS FOR OPTIMIZATION, VALIDATION, AND EXPERIMENTATION

A. J. (Ton) van den Bogert, Anne Su, Scott G. McLean, Xuemei Huang

Department of Biomedical Engineering, Cleveland Clinic Foundation, Cleveland OH, USA
bogert@bme.ri.ccf.org, http://www.lerner.ccf.org/bme/

INTRODUCTION

When human subjects are used to study mechanisms of acute musculoskeletal injury, we are limited to performing experiments that are within the limits of safety. Computational modeling is the only technique that allows the injury mechanism itself to be studied, and has already found widespread acceptance for simulation of passive movements during vehicle collisions. Only recently have computational models been used to study an acute injury during active movement (ankle sprain, Wright *et al*., 2000).

The current state of the art has a few limitations that we are trying to overcome. Optimization of a model to fit human movement data typically takes weeks of computer time (Neptune et al. 2000) and it is generally not known if a global optimum has been found. Validation experiments must be added to guard against overfitting, which could produce a good fit of the target movement but poor predictions of other movements such as injuries. Finally, experimentation with acute injury mechanisms requires a statistical approach so that conclusions are not based on a single case that was simulated.

COMPUTATIONAL METHODS

A software library was written for forward dynamic musculoskeletal modeling, including Hill muscle models, contact force calculations, and equations of motion generated by SD/FAST (PTC, Needham MA). The easy to use API allows short project-specific driver programs (~500 lines of C code) to be developed quickly. During initialization, the library reads a model description from a text file. The library was optimized for speed, mainly in the muscle modeling computations. Instead of a 3-D muscle path based on geometry, fast regression equations compute only muscle length and its derivatives, the moment arms, as a function of joint angles. The effect of muscles on joint reaction loads is not needed for movement simulation but can still be computed during postprocessing. Occasional extreme stiffness of the differential equations for muscle contraction was overcome by lower bounds on the isometric contractile element force (10 N) and on active state (1%).

RESULTS AND DISCUSSION

Results are shown from a model that was developed to simulate anterior cruciate ligament (ACL) injury during sidestepping. Movement was simulated for 200 ms after heelstrike, and muscle stimulation patterns were optimized using a simulated annealing algorithm to fit a subject's mean movement and ground reaction forces (Neptune et al., 2000). Optimization required 165,000 simulations, 36 hours on a 800 MHz Pentium III. Repeated optimizations confirmed that the optimum was global.

The ability of the optimized model to predict the effect of perturbed initial conditions was quantified by performing simulations starting with the initial conditions of each movement trial. In forward dynamic simulations of unstable systems the prediction error tends to grow exponentially over time. A predicted variable was considered "useful" until the time when the prediction error exceeded the between-trial standard deviation (Fig. 1b). For most variables, predictions were useful for about 100 ms.

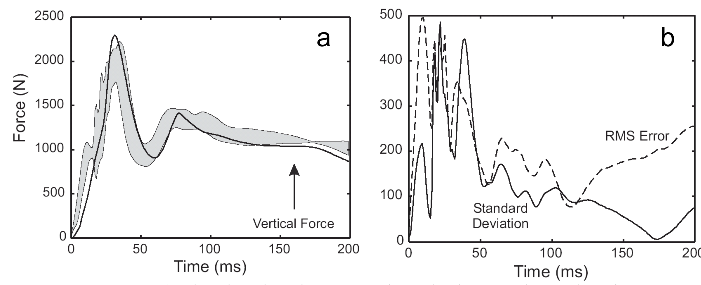

Figure 1: (a) Simulated and measured vertical ground reaction force. (b) RMS prediction error and variability. Note that prediction errors rise to 250 N in 200 ms, while the fit error is much smaller.

Once validated, 50,000 more simulations with randomly perturbed initial conditions were performed to study the potential effect of joint angles and angular velocities at heelstrike on ACL injury (Fig. 2). Such Monte Carlo simulations are an effective method to generate a statistically meaningful sample of simulations that can then be further analyzed to quantify probability of injury and study input-output relationships.

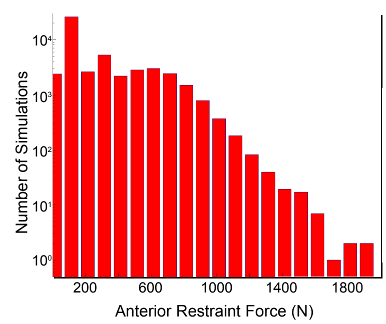

Figure 2: Histogram of peak ACL loads obtained by Monte Carlo simulation (N=50,000). Note the logarithmic vertical scale.

We conclude that acute musculoskeletal injury can be effectively studied using validated computational methods. Computation speed is essential, and so is the use of statistical methods for validation and experimentation.

REFERENCES

Wright IC et al. (2000) *J Biomech* **33**:513-519.
Neptune RR et al. (2000) *Comp Meth Biomech Biomed Engng* **3**:321-334.

Acknowledgement: Supported by NIH (AR47039).

A KINEMATICALLY CONSTRAINED METHOD FOR DETERMINING SUBJECT SPECIFIC JOINT PARAMETERS

Michael Schwartz[1,2,3] (schwa021@tc.umn.edu) and Adam Rozumalski[1,2]

[1] Department of Orthopaedic Surgery, University of Minnesota, Minneapolis, Minnesota, USA
[2] Graduate Program in Biomedical Engineering, University of Minnesota, Minneapolis, Minnesota, USA
[3] Gillette Children's Specialty Healthcare, St. Paul, Minnesota, USA

INTRODUCTION

Joint centers and axes of rotation, referred to here as "joint parameters", are fundamental elements of quantitative gait analysis. Joint parameters derived in the traditional manner are influenced by significant random and systematic errors [Leardini 1999]. In this study we present a new method for determining joint parameters, based on the application of kinematic constraints. The functional method is the most well known alternative method for locating hip centers. Imaging studies and simulations have shown the functional method to be accurate [Leardini 1999, Piazza 2001]. However, recent data indicate that the functional method's variability may be unacceptably large for clinical gait analysis [McDermott 2001]. The functional method is also limited by its restriction to spherical joints, thereby excluding hinge-like joints such as the knee. The results of this study show that the kinematically constrained (KC) method is repeatable and objective for the estimation of both hip and knee parameters.

METHODS

Assume the point $\mathbf{q}$ is a joint center, and is therefore shared by adjacent segments. A motion that maps the segments from time t_k to time t_l satisfies the kinematic constraint,

$$\left(\mathbf{T_p} - \mathbf{T_d}\right)\mathbf{q} = \mathbf{T_p}\mathbf{O_p} - \mathbf{T_d}\mathbf{O_d} + (\widetilde{\mathbf{O}}_\mathbf{d} - \widetilde{\mathbf{O}}_\mathbf{p})\,. \quad (1)$$

$\mathbf{T_{p,d}}$ describe the re-orientation of the adjacent segments during the interval, while $\mathbf{O_{p,d}}$ and $\widetilde{\mathbf{O}}_\mathbf{p,d}$ are the segment origins at the interval's end-points. The axis of rotation $\mathbf{L}_{kl}$, passing through $\mathbf{q}$ at t_k is found using the singular value decomposition theorem. By choosing a second interval with the same starting time, (t_k, t_m), a second axis of rotation can be found ($\mathbf{L}_{km}$). The joint center $\mathbf{q}_k$ at time t_k is the mutual intersection of all such axes; determined by first finding the intersections of each pair of axes, and then finding the mode of these pair-wise intersections [Fig. 1]. The average axis of rotation is defined as the mode of the instantaneous axes.

Table 1: Trial-to-Trial Variation: Repeatability

	H_X	H_Y	H_Z	K_X	K_Y	K_Z	Θ_X	Θ_Y	Θ_Z
			[mm]					[deg]	
Mean	-60.2	73.1	-94.1	14.3	18.9	-12.6	84.4	6.2	92.0
SD	3.6	2.3	3.7	3.1	14.8	0.6	1.1	0.9	1.0
Range	12.4	7.1	12.1	9.3	43.2	1.4	3.5	2.6	2.8

Table 2: CS-to-CS Variation: Objectivity

	H_X	H_Y	H_Z	K_X	K_Y	K_Z	Θ_X	Θ_Y	Θ_Z
			[mm]					[deg]	
SD	0.6	0.7	1.5	2.6	9.6	1.4	0.4	0.6	0.8
Range	1.5	2.0	4.3	8.3	41.8	4.3	0.9	1.5	2.1

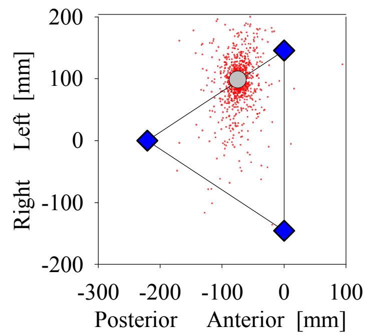

Figure 1. A transverse plane view of the Pelvis (diamonds are the L/R ASIS and PSIS). The KC based hip center (circle) is located at the mode of the of pair-wise axis intersections (dots).

Repeatability and objectivity were evaluated using a single healthy adult. The subject donned a standard clinical marker set with additional markers on the thigh and shank that permitted four independent segmental coordinate systems (CS) to be defined. During each session, 10 hip-centering trials (bi-lateral circumduction) and 10 knee-centering trials (flexion-extension) were conducted. Hip centers were calculated using one pelvic CS and four thigh CS. Knee centers and average knee axes were calculated using four thigh CS and four shank CS.

RESULTS

Hip centers are expressed in the Pelvic CS: Orig. = mid-ASIS, (X,Y,Z) = (ant, lat, sup). Knee parameters are expressed in the Thigh CS: Orig. = mid-condylar, Y = bi-condylar axis (lat), (X,Z) ≅ (ant, sup). Trial-to-trial variations in joint parameters were calculated to assess repeatability [Table 1]. Within trial variations, due to choice of coordinate system (CS-CS), were calculated to measure objectivity [Table 2]. For the CS-CS data, SD and range were calculated for each trial over all CS-CS combinations, and then averaged over the 10 trials.

DISCUSSION

The joint parameters derived with the kinematically consistent method are repeatable and objective. The medial lateral position of the knee center (K_Y) is not well localized by the KC method (1.5 cm SD, 4cm total range). The objectivity data indicate that CS-CS outliers contribute to the high K_Y uncertainty (Range/SD > 4.0). In contrast, the knee axis is well defined. Thus, a hybrid of KC and traditional methods could be used to better locate K_Y. The objectivity and repeatability results suggest that inter-observer consistency should be similar to the inter-trial results. This has been seen in an earlier study [Schwartz 2001]. Further trials are currently being analyzed to re-confirm this hypothesis. The experimental design does not allow for a direct evaluation of accuracy (*e.g.* RSA, MRI). Indirect measures, including comparisons with regression based hip centers, the mid-condylar point and the bi-condylar axis, are favorable.

REFERENCES

Leardini A., *et al.*, *J Biomech*, **32**, 99-103, 1999.
McDermott B., *et al.*, *Gait Posture*, **14**, 181, 2001.
Piazza S., *et al.*, *J Biomech*, **34**, 967-73, 2001.
Schwartz M. and Rozumalski A., 2002 *GCMAS Ann Mtg*.

EFFECTS OF FEMORAL COMPONENT ROTATIONAL PLACEMENT ERROR IN A DYNAMIC MUSCULOSKELETAL SIMULATION OF TOTAL KNEE REPLACEMENT MOTION

Stephen J. Piazza[1,2,3,4] and Ahmet Erdemir[1,4]

Departments of [1]Kinesiology and [2]Mechanical Engineering, The Pennsylvania State University, University Park, PA, USA
[3]Department of Orthopaedics and Rehabilitation, The Pennsylvania State University, Hershey, PA, USA
[4]Center for Locomotion Studies, The Pennsylvania State University, University Park, PA, USA
e-mail: *steve-piazza@psu.edu* www: *http://www.celos.psu.edu*

INTRODUCTION

Total knee replacement (TKR) has proved to be effective in the elimination of pain associated with degenerative osteoarthritis. Some TKR recipients, however, experience patellofemoral problems, including anterior knee pain, patellar dislocation, and mechanical inefficiency of the extensor mechanism that may limit functional performance postoperatively. Placement of the femoral component in internal-external rotation is both technically challenging and likely to directly influence patellofemoral mechanics. The purpose of this study was to investigate the effects of this surgical error on the actions of muscles using a computer simulation of a seated knee extension task in TKR.

METHODS

The three-dimensional musculoskeletal model upon which the simulation was based included 5 segments (pelvis, femur, patella, tibia, and foot), locked hip and ankle joints, and 6 DOF each at the patellofemoral and tibiofemoral joints. The forces produced by 10 muscles crossing the knee were predicted using a muscle model that incorporated force-velocity as well as active and passive force-length relationships (Delp et al, 1990; Schutte et al., 1993). Medial collateral, lateral collateral, and patellar ligaments were modeled as nonlinear elastic tensile springs (Wismans et al, 1980). Knee extension was driven in open-loop fashion by an excitation signal supplied to rectus femoris (RF) and vastus lateralis (VL), intermedius (VI) and medialis (VM) that was derived from measured EMG (Wilk et al, 1996).

Equations of motion were developed and integrated forward in time using the SIMM/Dynamics Pipeline (MusculoGraphics, Inc.) and SD/FAST (Parametric Tech. Corp.) software packages. A rigid-body contact model was used that permitted multiple frictionless contacts at the patellofemoral and tibiofemoral interfaces. Contacts occurring with an approach velocity normal to the implant surfaces that was above a certain threshold were treated as impacts that were handled by stopping the integration, reassigning velocities using an experimentally determined coefficient of restitution, and restarting the integration. Implant surfaces (IB-II; Zimmer) were located with respect to the bones with the assistance of an orthopaedic surgeon. Misplacement of the femoral component was performed by internally and externally rotating it by 5° about the axis defined by the center of the femoral head and the midpoint of the transepicondylar axis. The initial position was determined in each case by performing preliminary simulations in which no muscles were active.

RESULTS AND DISCUSSION

Muscle forces and patellofemoral contact forces were smaller when the femoral component was rotated either internally or externally when compared to forces in the unrotated case (Table 1). VM forces were reduced more by internal rotation than they were by external rotation (–10% vs –7%), but the opposite was true for VI (–6% vs –15%) and VL (–9% vs –18%). Internal rotation medially shifted the patella by 4 mm and medially rotated it by 4°. Changes opposite and approximately equal in the patellar motions occurred when the femoral component was rotated externally.

	5° IR	**unrotated**	**5° ER**
peak RF force (N)	21.5	23.4	21.0
peak VM force (N)	98.7	110.1	102.2
peak VI force (N)	104.5	111.3	94.9
peak VL force (N)	147.4	161.2	132.4
peak PF force (N)	352.6	397.2	334.1

Table 1: Simulated peak forces in quadriceps muscles and at the patellofemoral (PF) interface with femoral component internally rotated (IR), unrotated, and externally rotated (ER).

These results demonstrate the manner in which component malalignment may affect implant kinematics, but also show how the interaction between the implant and the musculoskeletal system is altered. Similar effects on patellar kinematics were simulated by Heegard et al. (2001) for internal rotation but not for external rotation. This difference may be due to the use of a more sophisticated contact model or the assumption of constant quadriceps forces.

REFERENCES

Delp, SL et al (1998). *IEEE Trans Biomed Eng*, 37, 757-767
Heegaard JH et al (2001) *Clin Biomech*, 16, 415-423
Schutte, LM et al. (1993) *IEEE Trans Rehab Eng*, 1, 109-125
Wilk, KE et al (1996) *Am J Sports Med*, 24, 518-527
Wismans et al (1980) *J Biomechanics*, 13, 677-685

ACKNOWLEDGMENTS

The authors wish to thank Steven H. Stern, MD.

ON LOW-COST STRATEGIES FOR REDUCING FALL-RELATED INJURIES IN THE ELDERLY

James A. Ashton-Miller, Ph.D.

Department of Mechanical Engineering, Department of Biomedical Engineering, Institute of Gerontology, University of Michigan, Ann Arbor, Michigan, USA [jaam@ umich.edu]

INTRODUCTION

Fall-related injuries are projected to reach an annual cost of $85 billion in the United States by the year 2020 (Englander 1996). Direct medical costs are highest in those over 65 years. Fall-related injuries become more serious with advancing age: for example, twice as many individuals 85 years and older die from falls as do those 65 years and younger. Tinetti found that one-third of community-dwelling elderly fall each year. Some 15 % of these result in serious injury, with women at increased risk. Two-thirds of elderly fallers sustain minor injuries. Even when no injuries result, increased fear of falling can limit activities. Slips and trips cause approximately 50% of these falls, the most common fall direction is forwards, and the upper extremity is the most frequent injury site. However, as Hayes and others have shown, a fall onto the hip will often result in fracture if the impact load exceeds the capacity of the bone to withstand it; these injuries have the greatest morbidity and mortality. So Rule 1 (to avoid a hip fracture) might be: "Avoid hip impact with the ground".

THE APPROACH

A central tenet of our work is that fall-related injuries are not inevitable: a significant proportion may be prevented using a variety of low-cost strategies. That hypothesis remains to be tested. But given that "an ounce of prevention is worth a pound of cure", what might that "ounce" of prevention be? How about starting with a set of rules to fall safely by – whether forwards, sideways or backwards. These rules should be based on impact dynamics, and how age affects neuromuscular control and physical and cognitive capacities, learning and memory.

Our low-cost interventions aim to involve a few minutes intervention to yield a lasting change in behavior. The individual must see value in the intervention, learn the skill, and then retain it over months or, preferably, years. A recent doctoral student in my laboratory showed that healthy young males can learn in 10 minutes how to arrest a standardized forward fall with 27% smaller impact forces than normal and 40% less than with straight arms (DeGoede & Ashton-Miller, 2002). These results suggest Rule 2 (for avoiding wrist injury): "Avoid using a straight arm to arrest a fall". Specifically, for a given fall velocity, it is the combination of elbow flexion angle and wrist-ground relative velocity that determines the impact force. A more recent study showed that some young males retained the ability to arrest a forward fall with reduced impact for several months without practice (McCabe et al. 2001). My own recent experience, tripping at a fast walking speed, showed me that it is possible to fall onto a cement sidewalk without sustaining so much as a scratch. But exactly how this was accomplished is not understood yet in physical terms. However, we conclude that there is usually plenty of time for the elderly to deploy their arms to protect themselves in a fall (DeGoede et al. 2001).

Traditionally, all falls are viewed as "bad". But the above studies raise the possibility that healthy individuals may actually need to fall every so often in order to retain the ability to arrest falls safely. A 1-year prospective study in 1100 community-dwelling elderly showed that the mean proportion of falls resulting in serious injury was 7, 4, and 1% for those reporting 1, 2 or >=3 falls per year, respectively (Tinetti et al., 1995), a trend that supports the above contention.

Our studies of forward fall arrests using the lower extremity showed highly significant age and gender differences, and considerable leg strengths being required for rapid stepping responses (Thelen et al, 1997 & 2000, Wojcik et al. 2000 & 2001). Rapid rates of torque development are needed to accelerate the limb, and considerable joint power is required to complete a large step in time, underlining the need for the elderly to retain as much physical capacity as possible.

We have shown that healthy elderly, and even healthy young adults, can unintentionally fall over a stripe of light (when asked to avoid stepping on it, should it suddenly come to their attention, Chen et al, 1994). Healthy elderly could not avoid it reliably if their attention was divided between stepping over it and responding to a secondary (visual-oral reaction time) task (Chen et al. 1996). Neuropsychological measures of executive function were predictive of difficulty with this task (Persad et al. 1995). Thus, Rule 3 (for avoiding fall-related injuries) might be: "Do not allow yourself to be distracted when approaching any hazard/obstacle (that can cause you injury)".

REFERENCES

Chen HC, et al. 1994, *J Gerontol Med Sci* **49**, M258-263.
Chen HC, et al. 1996, *J Gerontol Med Sci* **51**, M116-22.
DeGoede K & Ashton-Miller JA. 2002, *J. Biomech*. In press.
Englander F et al. 1996, J Foren Sci **41**, 733-64
McCabe G, et al. *Am. Soc Biomech*, 2001.
Persad C. et al. 1995, *J Gerontol Psychol Sci* **50**, 272-7.
Tinetti ME, et al. 1995, *JAGS,* **43**, 1214-21.
Thelen DG et al., 1997, *J Gerontol Med* Sci **52**, M88-93.
Thelen DG et al., 2000, *J EMG & Kines* **10**, 93-101
Wojcik L et al, 2000, *J Gerontol Med* Sci **54**, 44-50
Wojcik L et al., 2001, *J. Biomech* **34**, 67-73.

ACKNOWLEDGEMENTS

Many of these studies were supported by PHS Grants PO1 AG10542 and P60 AG08808.

TAI CHI EXERCISE AND THE PREVENTION OF FALLS IN ELDERLY TRANSITIONING TO FRAILTY

Robert J. Gregor[1,2], Steve L. Wolf[3]

[1]School of Applied Physiology, Georgia Institute of Technology, Atlanta, GA
[2]Center for Human Movement Studies, Georgia Institute of Technology, Atlanta, GA
[3]Department of Rehabilitation Medicine, Emory University School of Medicine, Atlanta, GA

INTRODUCTION

Ninety percent of hip fractures reported in the United States occur in people over the age of 65. Cost estimates for hip fractures alone are extremely high with most fractures due to falling. In light of these statistics, development of innovative and/or alternative approaches to reduce the severity or incidence of falls appears warranted. Recent emphasis in the exercise and rehabilitation communities has focused on interventions designed to delay or reduce the risk of falling in older adults. In a recent review of exercise programs and their impact on falls risk (Gregg, et al., 2000) physical activities, specifically activities focused on balance and lower extremity strength, were highlighted. For example, the FICSIT trials (Wolf, et al., 1996) were reviewed. The FICSIT trials explored novel interventions including balance, flexibility, endurance, resistance training and physical therapy exercise. Among the balance training therapies was a 16-week Tai Chi intervention that resulted in a 47.5% delay in the onset of first or multiple falls, compared to a 16-week Wellness education or computerized balance training groups. Results from recent studies also suggest an intense Tai Chi training program may improve strength, balance, and flexibility and reduce blood pressure and resting heart rate.

While there is a need for practitioners of geriatric medicine to develop new therapeutic approaches designed to preserve functional ability and to prevent falls in older adults, much of the current information reported is on generally healthy, robust older adults. This investigation was undertaken to study the effects of an intense Tai Chi intervention on older adults transitioning to frailty (Speechley, M. and M.E. Tinetti, 1991).

METHODS

Data reported here represent measurements taken on a group of 50 older adults, volunteers, transitioning to frailty. The group is a self-selected subset of a larger group of 286 older adults recruited at 20 different congregate living facilities to participate in a clinical trial to compare fall rates in an intense Tai Chi exercise intervention group against an education wellness program group as controls (Wolf, et al., in review).

Knee extensor strength assessments were made on a Kin Com isokinetic device and gait and balance measures made using two force platforms (Kistler) and a high-speed motion capture system (Peak Performance Technologies). Gait analysis included trials focused on initiating gait in three discrete directions, gait kinematics and kinetics at a self-selected walking speed and a series of trials (50) involving unexpected turns in three discrete directions as a vehicle to induce unexpected perturbations.

All measures were made during a baseline session before intervention, every four months during the 48-week intervention (Tai Chi twice a week or a Wellness Education class once a week) and then every four months during a one-year follow-up. A total of seven testing sessions over a two-year period were conducted for each of the 50 subjects.

RESULTS AND DISCUSSION

For most of the baseline characteristics the subset of 50 volunteers were similar to the rest of the larger group. There were significant differences however, in two aspects, i.e. the subset of volunteers walked for exercise more regularly and took fewer sedatives than did the larger group. Because of these differences, the subgroup, while remaining in the broadly defined population of “transitioning to frailty” (Speechley, M. and M.E. Tinetti, 1991) was slightly more robust than the larger group. Gait features in the subgroup were also more variable supporting the hypothesis that older adults transitioning to frailty will have greater variability in their gait. The implications these results have on our interpretation of kinematic and kinetic aspects of gait and balance in this subset of 50 subjects will be discussed.

SUMMARY

These data represent results from an extensive analysis on an underrepresented population of older adults, i.e. those transitioning to frailty. Additionally, an intense exercise Tai Chi intervention had very positive effects on rates of falls and selected gait related variables compared to the data from the Wellness Education group. Finally, a more refined set of parameters must be utilized to better define certain subsets in the elderly, i.e. transitioning to frailty.

REFERENCES

Gregg, et al., (2000), JAGS, 48: 883-93.
Speechley, M, and M.E. Tinetti, (1991). JAGS, 39: 46-52.
Wolf, et al., (1996). JAGS, 44:489-497.
Wolf et al., (in review). JAMA.

EFFECT OF HIP PROTECTORS AGAINST HIP FRACTURES

Jes Bruun Lauritzen

Department of Orthopedic Surgery, Traumatology & Hip Clinic, Hvidovre Hospital,
University of Copenhagen, Denmark
Associate Professor DMSc, jblauritzen@dadlnet.dk

INTRODUCTION

Increased research and understanding of the biomechanics of hip fracture has made hip protection a recommended strategy by The European Commission in the ”Report on Osteoporosis in the EC – action for Prevention 1998”, and a Cochrane review (1999) concludes, that hip protectors seem to reduce the occurrence of hip fractures in selected populations with high risk.

NURSING HOMES RESIDENTS

The positive effect of external hip protectors against hip fractures has been studied in five randomized trials in nursing homes (table 1) and one combined nursing home/ home-dweller study (Cameron).

HOME-DWELLERS

Data are sparse among home-dwellers. Our controlled case cohort study among elderly orthopedic in-patients indicate a comparable effect among those with risk factors for hip fracture (Hindsø & Lauritzen, 2001). Follow-up 1 to 1½ year; n 1590. Primary acceptance was 57%. Users reported 143 falls with impact on the hip protector, and no hip fractures occurred. Two hip fractures occurred while the patients used their hip protectors, but no impact on the hip was reported.

PRIMARY ACCEPTANCE AND ADHERENCE

Compliance has been questioned with the first prototypes, but improved in later studies. Primary acceptance may reach 75 to 100 %. Long-term adherence at two years was 40% in the home-dweller study by Hindsø & Lauritzen (2001).

COST-SAVING

Preliminary, the hip protectors seem cost-saving among elderly women or men.

SUMMARY

Hip protectors are an important supplement in the prevention of hip fractures among nursing home residents, and may also prove to be beneficial among elderly frail home-dwellers.

REFERENCES

Lauritzen, J.B. et al (1993) *Lancet* **341,** 11-13
Ekman, A. et al (1997) *Lancet* **350,** 563-564 Heikinheimo, R. et al (1997). *Proceeding of the 13th Treenieal Congress of the International Ergonomics Association.* Tampere, Finland 576-578. Kannus, P. et al (2000) *New Engl J M* **343,** 1506-1513 Harada, A. et al (2001) *Osteoporos Int* **12**, 215-212 Kumar, B.A., Parker, M.J. (2000) *Injury* **31,** 693-695

Table 1: Intervention studies with hip protectors against hip fractures

Study	Follow-up(mths)	No of hfx / subjects: Intervention	Control	RR	95%CL	Hip fractures avoided: No
Lauritzen 1993	11	8 / 247	31 / 418	0.44	0.20-0.95	10
Ekman 1997	11	4 / 302	17 / 442	0.34	0.12-1.0	7
Heikinheimo 1997	12	1 / 36	5 / 36	0.20		4
Kannus et al 2000	18	13 / 653	67 / 1148	0.4	0.2-0.8	15
Harada 2001	19	1 / 65	8 / 68	0.13		5
Cameron 2001	18	8 / 86	7 / 88	1.46	0.53-4.51	- Haz.Risk

RR; relative risk. CL; confidence limits. Hfx; hip fractures

TO FALL OR NOT TO FALL: THE THRESHOLD OF BALANCE RECOVERY FROM A FALL

Cécile Smeesters, Ph.D.
Mechanical Engineering, University of Sherbrooke, Sherbrooke, Quebec, Canada [cecile.smeesters@gme.usherb.ca]
Research Centre on Aging, Sherbrooke Geriatric University Institute, Sherbrooke, Quebec, Canada

INTRODUCTION

It is only recently that researchers have focused their attention on the biomechanics of responses of both young (YA) and old (OA) adults to postural disturbances that are large enough that balance recovery was not always possible, and on the **mechanisms** responsible for balance recovery during these large postural disturbances. This limited subset of studies on the threshold of balance recovery from a fall is described here.

DISCUSSION

Hsiao and Robinovitch (1998) showed that YA (22-33yrs), who attempted to prevent a fall after the gymnasium mattress they stood upon was abruptly translated, were more likely to fall after *anterior* translations of the feet (63%) when compared to *posterior* (22%) or *lateral* (28%) translations. Most of those who recovered took more than one step.

Wojcik et al. (1999) showed that the maximum *forward* lean angles, YA (19-29yrs) and OA (67-81yrs) could be suddenly released from and still recover balance by taking a single rapid step, were 31.6º and 20.1º, respectively. **Step velocity** and lean angle WERE strongly correlated, but volitional **strengths** in plantarflexion and hip flexion as well as **reaction time** WERE NOT (Wojcik *et al.*, 2001).

Using a concealed obstacle, Pavol et al. (1999; 2001) induced *forward* trips during gait in OA (72±5yrs) who were allowed to use multiple steps. Falls occurred in 16% of trips and WERE associated with faster walking speed and more anterior head-arms-torso centre of mass at the time of the trip, **delayed support limb loading**, excessive lumbar flexion, and/or buckling of the recovery limb. In a similar study with YA males (27±6yrs) and females (29±15yrs), they DID NOT find relationships between voluntary eccentric **strength** of the trunk or hip extensors, voluntary or automatic **reaction time**, **activation amplitudes** and trunk kinematics (Grabiner *et al.*, 1996). Furthermore, in a study similar to that by Wojcik et al. (1999) using the same OA, these authors showed that **postural steadiness** and **stability limits** WERE NOT related to the maximum *forward* lean angle of 15.5º (Owings *et al.*, 2000). Finally, they induced slips during gait in YA (27±4yrs) (Brady *et al.*, 2000). Falls *backwards* occurred in 54% of slips and WERE associated with longer slip durations and displacements, faster velocities of the slipping foot, and smaller angles between the shank and the floor at heel-strike.

Pai (1999) determined a 62% failure rate for balance recovery in YA (22-40yrs) who stood on a platform that suddenly and unexpectedly slipped during the termination of a sit-to-stand task, producing a *forward* translation of the feet. Fourteen (14) of the 15 subjects initiated a backward step and all but one used multiple steps. The authors showed that a **delay in the step initiation** MIGHT HAVE contributed to substantial descent of the centre of mass, leading to falls by limb collapse.

Cham and Redfern (2001) induced slips in YA (19-30yrs) during gait and showed that the corrective strategies involved in balance recovery included increased knee flexion and hip extension. Falls *backwards* occurred in 25% of slips.

We studied recovery of YA (18-36yrs) from *forward* trips of sustained duration and showed that the threshold trip duration for which balance recovery with a single rapid step is not possible IS associated with volitional hip flexor **strength** and volitional **foot lift-off time** (Smeesters *et al.*, 2001).

CONCLUSIONS

Therefore, the knowledge on the threshold of balance recovery from a fall is still very limited and discrepancies exist between studies on the **mechanisms** responsible. To expand the body of knowledge in this area, we recently complete studies on the effect of age and gender on maximum hip flexion **power** at low and high velocities (Smeesters *et al.*, Submitted) as well as on the abilities of YA and OA to adjust *medio-lateral* step location during a *forward* fall (Thelen *et al.*, Submitted). Results from both of these studies will be presented at this congress.

REFERENCES

Brady, R.A. *et al.* (2000). *J Biomech*, **33**, 803-808.
Cham, R., Redfern, M.S. (2001). *J Biomech*, **34**, 1439-1445.
Grabiner, M.D. *et al.* (1996). *J Biomech*, **29**, 735-744.
Hsiao, E.T., Robinovitch, S.N. (1998). *J Biomech*, **31**, 1-9.
Owings, T.M. *et al.* (2000). *J Am Geriatr Soc*, **48**, 42-50.
Pai, Y.C. (1999). *J Biomech*, **32**, 1377-1382.
Pavol, M.J. *et al.* (1999). *J Gerontol*, **54A**, M103-108.
Pavol, M.J. *et al.* (2001). *J Gerontol*, **56**, M428-437.
Smeesters, C. *et al.* (Submitted). IVth World Congr Biomech.
Smeesters, C. *et al.* (2001). *J Biomech*, **34**, 589-595.
Thelen, D.G. *et al.* (Submitted). IVth World Congr Biomech.
Wojcik, L.A. *et al.* (1999). *J Gerontol*, **54A**, M44-50.
Wojcik, L.A. *et al.* (2001). *J Biomech*, **34**, 67-73.

ACKNOWLEDGEMENTS

The studies by this author were supported by grants from NIH (AG08808, AG10542, AG13587, AG13759, AR40321) and NSF (BES9702275), as well as by a scholarship from NSERC.

PHYSICAL PERFORMANCE FACTORS AND FALLS BY OLDER ADULTS: WHAT IS THE WEAKEST LINK?

Tammy M. Owings[1], Michael J. Pavol[2], Mark Grabiner[3],
[2]Department of Physical Therapy[3] and [3]School of Kinesiology, University of Illinois at Chicago, Chicago, Illinois and
[3]Department of Biomedical Engineering, Cleveland Clinic Foundation, Cleveland, Ohio, grabiner@uic.edu

INTRODUCTION

Despite explicit objectives & targets for HP2000, the hospitalization rate for hip fractures was not improved during the 1990's. The Healthy People 2010 program has 28 focus areas, one of which relates to injury prevention, in general and death from falls and hip fractures, in particular. Hip fractures account for about 60% of total hospitalizations for fractures. Since 90% of hip fractures result from falls, the failure to achieve improvement in this public health issue underscores the need for continued research efforts to uncover treatable causes of falls.

Highly visible and widely disseminated position statements regarding exercise and physical activity as means to improve resistance to falls explicitly endorse postural stability and muscle strength as risk factors for falls. For example, "Physical activity...appears to be protective against falling...probably by increasing muscle strength and balance" (US Department of Health and Human Services, 1996). Further, the American College of Sports Medicine maintains that "… benefits from exercise include...improved postural stability, thereby reducing the risk of falling...and fractures".

Age-related changes to postural control and muscle strength likely contributes to the increased incidence of falls by some populations of older adults, perhaps most notably in frail older adults. It reasonable to expect that age-related changes in postural control influence the likelihood of requiring a stepping response following a postural perturbation. However, it may not be reasonable to expect changes to postural control, in and of themselves, to directly influence the success of the stepping response, which represents a time critical coordination of multiple joint systems.

In contrast, it does seem reasonable that changes in muscle strength and/or power would influence the success of the stepping response. However, a threshold below which strength and/or power must decrease to significantly increase the probability of falls has not been defined. Indeed, in a study of healthy older adults subjected to unexpected trip induced under laboratory conditions, both the strongest and the weakest were unable to avoid falling (Pavol et al., in press).

We previously reported that the contribution of lower extremity coordination to performance of a time critical task was independent of lower extremity strength and accounted for a similar amount of variance (Tomioka et al, 2001). This suggests that even in the presence of adequate strength, the ability to avoid a fall following a large perturbation can be significantly diminished by inadequate lower extremity coordination.

METHODS

A group of 79 older adults were subjected to unexpected accelerations of a motorized treadmill to 0.89 m/s in about 150 ms (Owings et al, 2002). A previously described algorithm based on data from an instrumented safety harness was used to determine if the recovery effort from each trial was successful. Five recovery attempts were collected, with each trial lasting five seconds. The initial attempt was considered an "untrained" response.

RESULTS AND DISCUSSION

Repeated exposure to the treadmill perturbation resulted in a rapid adjustment of recovery biomechanics that resulted in a substantial improvement in the recovery rate. Of the 23 subjects who fell during the perturbation of the first trial, 18 successfully recovered during the second attempt. The modified recovery responses closely approximated the successful initial recoveries. Specifically, the successful, modified recoveries were marked by a faster reaction time, increased recovery step length, smaller trunk flexion angle at toe-off and at recovery foot ground contact, and smaller trunk flexion velocity at toe-off and at recovery foot ground contact, as compared to the failed initial attempt. The rapidity of the response suggests that it occurred independently of changes in muscle strength and or power, and postural control. Collectively, these findings suggest the potential for developing and using the protocol as a clinical tool.

REFERENCES

Mazeo et al: Exercise and physical activity for older adults. Med Sci Sports Exerc, 30:992-1008, 1998.

Owings Mechanisms of failed recovery following postural perturbations on a motorized treadmill mimic those associated with an actual forward trip, Clin Biomechanics, 16:813-819, 2001.

Pavol et al: Influence of lower extremity strength of healthy older adults on the outcome of an induced trip. J Am Geriat Soc, in press.

Tomioka et al: Lower extremity strength and coordination are independent contributors to maximum vertical jump height. J Appl Biomechanics, 17:181-187, 2001.

US Department of Health and Human Services, Physical Activity and Health: A Report of the Surgeon General. Atlanta, GA: US Department of Health and Human Services, Centers for Disease Control and Prevention, National Center for Chronic Disease Prevention and Health Promotion, p.132, 1996.

ACKNOWLEDGEMENTS

The authors gratefully acknowledge funding from NIH AG10557 (MDG).

SCALING OF HUMAN POSTURAL CONTROL RESPONSES DUE TO BIOMECHANICAL CONSTRAINTS

[1]Arthur D. Kuo, [1]Sukyung Park, and [2]Fay B. Horak
[1]Dept. of Mechanical Engineering, University of Michigan, Ann Arbor, Michigan USA (artkuo@umich.edu)
[2]Neurological Sciences Institute, Oregon Health Sciences Institute, Portland, Oregon, USA

INTRODUCTION

Postural responses are typically described as a pattern of muscle activations or a trajectory of joint motions, each triggered by a disturbance. Although these descriptions are highly useful, one drawback is that they do not describe the biomechanical constraints that limit possible responses. These constraints, such as the maximum allowable ankle torque, imply that postural responses cannot simply scale with perturbation magnitude. Instead, they must change behavior in such a way as to accommodate constraints while still maintaining stability. We devised a continuous feedback control model to test whether postural responses, to backwards perturbations of the support surface, can be described in terms of feedback control gains, and whether these responses are scaled appropriately to accommodate biomechanical constraints.

METHODS

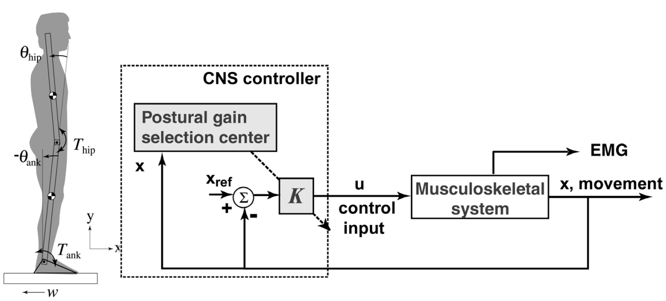

Fig. 1. Feedback control model.

We used a simplified model of human body dynamics in the sagittal plane, incorporating ankle and hip joints. These dynamics were stabilized by a continuous feedback loop, using a set of linear state feedback gains that are selected according to perturbation magnitude. The length of the foot relative to body weight places a constraint on the maximum allowable ankle torque that can be exerted against the support surface, making feedback gains that are used for small perturbations inappropriate for larger perturbations.

We applied fast backward perturbations to 13 healthy young human subjects to provide data for comparison with model. There were five perturbation magnitudes ranged 3 – 15 cm, applied in random order, with each magnitude applied five times in a block. Subjects were asked to maintain balance without stepping or lifting the heels. We measured kinematics and ground reaction forces, and used inverse dynamics to estimate joint torques. For each magnitude, we identified a set of model feedback gains that best matched the kinematics and joint torques, and resulted in a stable closed-loop system. We then examined whether these gains are scaled to accommodate biomechanical constraints on ankle torque.

RESULTS

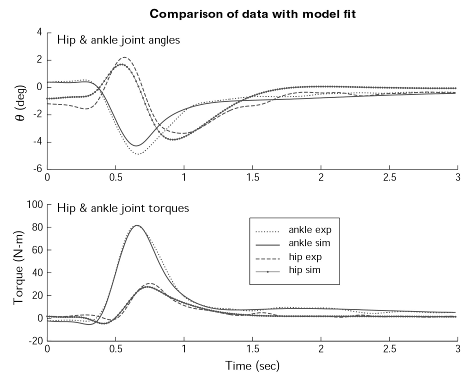

Fig. 2. Experimental kinematics and joint torques compared with feedback model fit.

We found that the simple model was able to reproduce experimental responses reasonably well (Fig. 2), with an average fit $R^2 = 0.91 \pm 0.04$ (s.d.).

We next tested whether these gains are scaled by the central nervous system to accommodate the constraint on allowable ankle torque. We found that all feedback gains changed as a function of perturbation magnitude. In particular, ankle torque response to ankle motion (ankle gain T_{ank}/θ_{ank}) decreased as perturbations increased. In the absence of constraints, a single set of gains will stabilize the body for any perturbation magnitude. But with constraints, the allowable ankle torque would be exceeded for larger perturbations. The reduction of ankle gain ($p < 0.01$) indicates that the constraint is accommodated as expected.

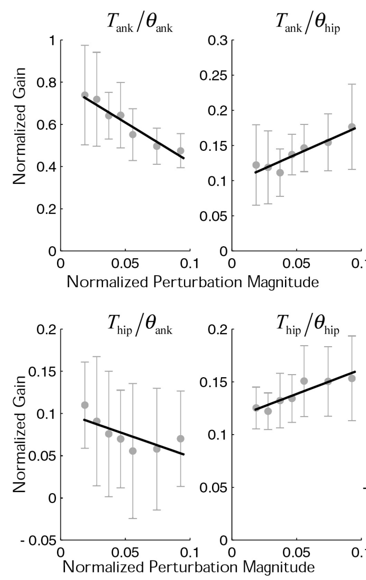

Fig. 3. Feedback control gains vs. perturbation magnitude.

CONCLUSIONS

The results show that the trajectories of joint angles and joint torques are gradually scaled with perturbation magnitude. Feedback gains were found to be multivariate in character, meaning that the torque produced at any joint is generally a function of motions not only at the same joint, but other joints as well. The gains also scaled nearly linearly with perturbation magnitude, in accordance with biomechanical limitations on ground reaction torque. The postural adjustments can be described as a feedback scheme with scalable gains.

ACKNOWLEDGEMENTS

This research was supported in part by NIH grants R29DC0231201 and R01AG06457.

IMPORTANCE OF PLANTAR-SURFACE MECHANORECEPTION IN POSTURAL CONTROL.

Stephen D. Perry[1], Brian E. Maki[2], William E. McIlroy[2,3] and Aftab E. Patla[4]

[1]Department of Kinesiology & Physical Education, Wilfrid Laurier University, Waterloo, ON Canada (sperry@wlu.ca), [2]Centre for Studies In Aging, Sunnybrook & Women's HSC, Toronto, ON Canada, [3]Department of Rehabilitation Science, University of Toronto, Toronto, ON Canada, [4]Department of Kinesiology, University of Waterloo, Waterloo, ON Canada

INTRODUCTION

Sensation from the bottom of the feet has primarily been overlooked as an important contributor to the control of balance. The age-related loss of this sensation has been well documented. In addition to the age-related loss of plantar-surface cutaneous sensation excessive cushioning, found in present day athletic footwear, may further impair this sensation. Our studies and others have demonstrated the contribution of plantar-surface mechanoreception to postural control.

Methods used to understand the role of plantar-surface cutaneous sensation have involved both patients with loss of sensation (e.g. diabetic neuropathy (Inglis et al, 1994), surgical reconstruction of the plantar skin flap(Hamalainen et al, 1992), experimentally induced changes in sensitivity (e.g. hypothermia (Magnusson & al, 1990), standing on foam rubber (Wu and Chiang, 1997), anesthetic (Do et al, 1990)) and facilitation (with ball bearings (Watanabe and Okubo, 1981)). Many studies of postural control have focussed on the measurement of sway during quiet, unperturbed stance. Each study has demonstrated some evidence of a role for mechanoreception in balance control. Recently, vibration applied to the heel and metatarsal region of the sole of the foot induced leaning in the direction opposite to the vibratory stimulus (Kavounoudias et al, 1998), providing a strong indication of the involvement of cutaneous sensation from the bottom of the foot in control of unperturbed stance. To date, very little is known about the contribution of plantar cutaneous mechanoreceptors to dynamic postural control in response to unpredictable perturbations during gait. The potential importance of cutaneous afference in controlling foot-contact is supported by observations that cutaneous sensitivity is up-regulated at the end of the swing phase, just prior to foot contact, during gait (Duysens et al, 1995). Additionally, Zehr and Stein (1999) have suggested that cutaneous reflexes may play important roles during specific phases of the gait cycle. Foot contact and loading information, in combination with information about the distribution of foot pressure relative to the anatomical boundaries of the foot, may also contribute to an internal representation of the location and motion of the centre-of-mass with respect to the base-of-support (Dietz, 1992; Massion, 1992).

Our recent collection of studies has employed either reduction or facilitation of the sensation from the bottom of the feet. These have demonstrated its importance in compensatory stepping (Maki et al, 1999; Perry et al, 2000), terminating gait (Perry et al, 2001) and travelling effectively over uneven terrain (Perry and Patla, 2001). During compensatory stepping in response to a postural disturbance (young adults), reduced sensation led to an increase in number of steps required to recover balance and a delay in the initiation of the stepping reaction (Perry et al, 2000). Conversely, facilitation (in older adults with moderately insensitive feet) decreased the number of steps required to recover balance and, during continuous perturbations, reduced the extent to which the center of foot pressure approached the edges of the base of support (Maki et al, 1999). During gait termination, reduced sensation led to increased loading and poorer precision/control of foot placement during the last two steps of termination (Perry et al, 2001). Initial results from reduced sensation during uneven terrain have demonstrated an impaired control of side-to-side movement of the body when attempting to walk along a simulated uneven terrain (Perry and Patla, 2001).

INTERVENTIONS

Based upon the initial studies demonstrating the importance of this sensation in balance control (Maki et al, 1999; Perry et al, 2000), we have developed a balance-enhancing insole (Maki et al, 2001). The purpose of this insole is to mechanically facilitate stability-related sensation from the soles of the feet. The targeted population are older adults having age-related loss of this sensation. This population would benefit from this sensory facilitation in order to improve their balance control. The development of this intervention is in its early stages and requires clinical trials to test its efficacy.

ACKNOWLEDGEMENTS

Supported by grants from MRC (operating-BEM, Studentship-SDP), CIHR (PDF-SDP), NIH (operating-BEM), NSERC (operating-AEP).

REFERENCES

Dietz. (1992). *Physiol Rev, 72*(1), 33-69.
Do et al. (1990). *Exp Brain Res, 79*, 319-324.
Duysens et al. (1995). *Exp Brain Res, 105*, 423-431.
Hamalainen et al. (1992). *Hum Mov Sci, 11*, 549-561.
Inglis et al. (1994). *Exp Brain Res, 101*, 159-164.
Kavounoudias et al. (1998). *NeuroReport, 9*, 3247-3252.
Magnusson et al. (1990). In: Disorders of Posture and Gait.
Maki et al. (2001). United States Patent US 6,237,256 B1
Maki et al. (1999). *J Gerontol, 54*(6), M281-287.
Massion. (1992). *Prog Neurobiol, 38*(1), 35-56.
Perry et al. (2000). *Brain Res, 877*(2), 401-406.
Perry and Patla. (2001). Society for Neuroscience Congress
Perry et al. (2001). *Brain Research, 913*(1), 27-34.
Watanabe and Okubo (1981). *Ann NY Acad Sci, 374*, 855-864.
Wu and Chiang. (1997). *Exp Brain Res, 114*, 163-169.
Zehr and Stein. (1999). *Prog Neurobiol, 58*, 185-205.

UTILIZING BIOMECHANICS TO PREVENT SLIPS AND FALLS

Mark S. Redfern[1,2] and Rakié Cham[1]
[1]Department of Bioengineering and [2]Department of Otolaryngology
University of Pittsburgh, Pittsburgh, PA, USA

INTRODUCTION

Falls are the leading cause of injury requiring medical attention and are associated with the most severe occupational injuries (Courtney and Webster, 1999). Slipping is the dominant cause of falls. Courtney et al. (2001) reported that slips account for 32 % of falls in young adults and 67 % of falls sustained by the elderly. The causes of slips and falls are complex, involving interactions of environmental and human factors. (Redfern, et al., 2001) The environmental factors include properties of the floor surface (e.g. roughness compliance and topography) and shoe (e.g. material properties and tread), as well as lighting, housekeeping, and changes in elevation. Human factors include the biomechanics of gait, mental set (i.e. attention and alertness), as well as the health of musculoskeletal and sensory systems. When there is a mismatch, the result can be a slip or trip, often resulting in an injurious fall. An ergonomics approach to the prevention of falls is to attempt to design the environment to match the requirements of the person. This involves understanding the physical requirements of the tasks performed (such as standing, walking or carrying) and ensuring that the environment meets the requirements for those tasks. Biomechanical analyses of gait and slipping can be used to understand the physical interactions of the environment and person that leads to falls. The purpose of this presentation is to discuss the role of biomechanics in developing intervention strategies to prevent slips and falls.

ENVIRONMENTAL FACTORS

The dominant methods to prevent slipping have focused on evaluation of the frictional properties of the shoe-floor-contaminant interface using various testing equipment. Many of these devices attempt to measure the coefficient of friction (COF); however, there is no consensus on the best methodology for such testing. Current methods have begun to focus on making the measurements as *biofidelic* as possible, i.e. measure COF under conditions as close to actual gait conditions as possible. In order to accomplish this goal, the biomechanics of gait, specifically of the foot-floor interactions, must be measured through gait analysis.

Studies in our laboratory have defined foot dynamics during various walking conditions. (i.e. Cham and Redfern, 2001). Variables such as heel velocities and accelerations, as well as shear and normal forces, at contact have been established. These studies provide detailed information useful in the design and use of slip resistance measurement devices.

HUMAN FACTORS

Biomechanical studies of the postural reaction to slips and falls are also important to understand the human response. These types of studies are useful in understanding how different populations respond during a slip event.

We have conducted studies to investigate the postural reaction of subjects to slips on different surfaces and how different factors, such as anticipation of slippery conditions, impact those reactions. (Cham and Redfern, 2001). In these studies, subjects were equipped with a safety harness and instructed to walk naturally across a vinyl tile walkway instrumented with two Bertec force plates (FP). Ground reaction forces and whole body motion (Optotrak-3020 motion measurement system) were recorded. After initial dry trials, a soap solution was applied to the floor without the subject's knowledge. The moments generated during the slip are of particular interest in understanding the postural reaction. Flexion moments at the knee and extension moments at the hip have a characteristic response in young, healthy subjects (Cham & Redfern, 2001a) and this response is affected by the expectations of the floor condition by the subject (Cham and Redfern, 2001b). Figure 1 shows an example of the knee moment response during slip. Successful recovery is dependent on the timing and magnitude of this response.

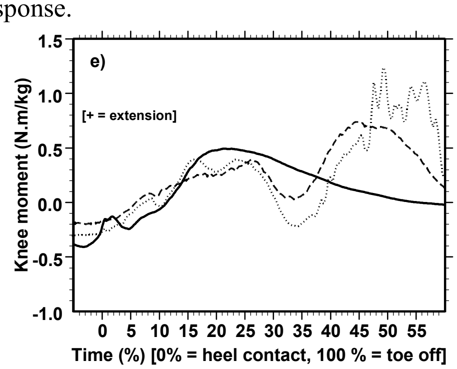

Figure 1: Knee moments during no slip (solid), slip w/ recovery (dashed), and slip w/ fall (dotted). Arrow indicates moment generated in response to slip attempting to recover

REFERENCES

Redfern, MS, et al (2001). *Ergonomics,* **44** (13), 1038-1166.
Cham, R & Redfern, MS (2001). *J Biomech*, **34**, 1439-1445.
Cham, R & Redfern, MS (2002). *Gait & Posture, In Press*.
Courtney, TK & Webster, BS (1999) *J Occup and Environ Med*, **41**, 60-69.
Courtney, et al, (2001) *Ergonomics*, **44**(13).

ADAPTATION TO SLIPPING AND FALL PREVENTION

(Clive) Yi-Chung Pai and Michael J. Pavol
Department of Physical Therapy, University of Illinois at Chicago,
Chicago, IL 60612-7251, e-mail: cpai@uic.edu

INTRODUCTION

A health threat facing the older adult population is their increasing susceptibility to falling. It is highly likely that the likelihood of suffering a fall depends upon the robustness of one's protective mechanisms and upon the adaptation that can take place to enhance one's protection against falls. We examined this adaptive behavior by investigating whether the central nervous system, when faced with a potential postural perturbation, employs feedforward adjustments to reduce the near-term and overall likelihood of balance loss.

METHODS

Slips were induced, using bilateral low-friction platforms, during a sit-to-stand task in 60 safety-harnessed young adults. Subjects underwent a block of slipping trials, a block of non-slipping trials, then a "random" block of trials. After the first novel and unexpected slip, subjects were aware that a slip "may or may not occur." The state (i.e. horizontal position and velocity) of the body center of mass (COM) at seat-off and the direction of balance loss (forward, no loss, backward) were determined for each trial. Feedforward adjustments were identified as between-trial changes in COM state at seat-off. Effects of these feedforward adjustments on the likelihood of balance loss were quantified using logistic regression.

RESULTS AND DISCUSSION

The likelihood of balance loss in each direction (forward, backward) under each condition (slipping, non-slipping) was significantly related to the COM state at seat-off. After experiencing the first, unexpected slip, subjects adjusted their task execution to increase their COM velocity and shift their COM anteriorly at seat-off (Fig 1), reducing the probability of a backward balance loss. Such adaptive changes in the COM state prior to the slip onset suggest feedforward control.

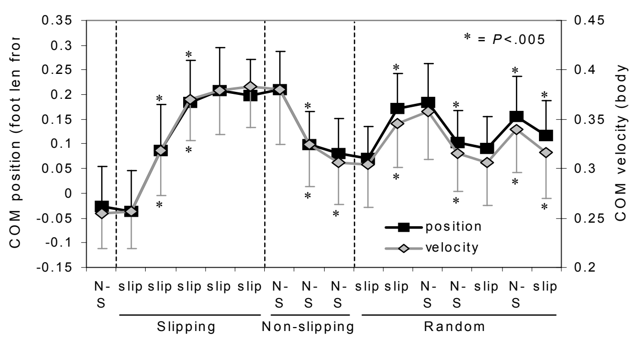

***Fig. 1**:* Adaptation of the center of mass (COM) position-velocity state at seat-off. Means and standard deviations of COM state are shown for the slipping and non-slipping (N-S) trials within the three blocks of trials performed. Significant changes versus the preceding trial are indicated.

In the subsequent non-slipping and random blocks, subjects readjusted their COM state at seat-off after each unexpected change in the experimental conditions (Fig 1). Adjustments to non-slipping and to slipping conditions respectively acted to reduce the probability of a forward or backward balance loss. Over the longer term, subjects also adapted their COM state at seat-off to decrease their overall likelihood of balance loss in either direction under either condition (Fig. 2).

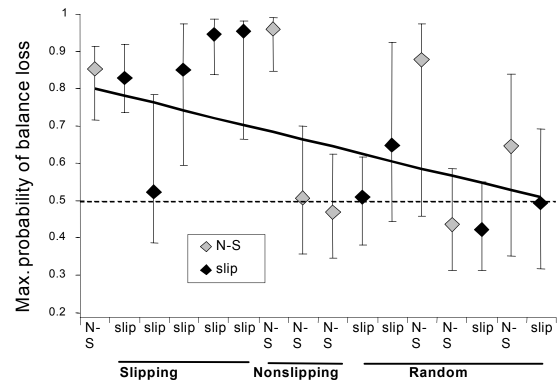

Fig. 2. Adaptation decreased the probability of balance loss in either a forward or backward direction under either slipping (slip) or nonslipping (NS) conditions. Medians and interquartile ranges of the maximum probability of balance loss, predicted from the COM state at seat-off using logistic relationships, are shown for the three blocks of trials performed.

These findings revealed that the CNS can adapt to the uncertainties in an environment by acquiring "desirable" movement options. Consistent with theoretical predictions [1], such movement options entailed the adjustment of the COM state so that a person had neither the tendency to fall forward during non-slipping conditions nor the tendency to fall backward during a slip. Our findings suggest that, through training similar to the present protocol, it may be possible to induce adaptations in task performance that would increase stability and reduce the likelihood of falling upon a slip.

SUMMARY

Healthy young adults rapidly learned how to improve stability through repeated exposure to a slipping perturbation. This learning was characterized by feedforward adjustments that altered the COM state. Individuals further learned to adapt their task performance to remain stable under both perturbed and unperturbed conditions.

REFERENCES

[1] Pai, Y.-C., Iqbal, K. (1999) *J Biomech*, 32, 779-786.

ACKNOWLEDGEMENTS

The work was funded by NIH R01-AG16727 and by the Whitaker Foundation RG 95-0293.

AGE DIFFERENCES IN ABILITY TO ABSORB IMPACT ENERGY IN THE UPPER EXTREMITIES DURING FALLS

Stephen N. Robinovitch, Paula J. Stotz, Sarah C. Normandin
Injury Prevention and Mobility Laboratory, School of Kinesiology
Simon Fraser University, Burnaby, B.C., Canada

INTRODUCTION

While over 90 percent of hip fractures are caused by falls, the vast majority of falls do not result in hip fracture. The strongest determinant of whether fracture occurs is fall severity, as defined by the configuration and velocity of the body at impact (Schwartz et al., 1998; Nevitt and Cummings, 1993). Our previous studies suggest that young subjects tend to reduce fall severity by absorbing energy through contraction of the lower extremity muscles during descent (as one does while sitting or squatting), and by "braking the fall" by impacting the ground with the outstretched hands (Hsiao and Robinovitch, 1998). Exercise programs that seek to enhance these responses have a strong likelihood for reducing hip fractures in the elderly. The efficacy of the upper extremity (UE) response depends on how quickly the hands can be moved into a protective position, and on the faller's ability to absorb energy in the UE muscles during impact. In the present study, we examined whether declines occur with age in the capacity to absorb energy in the UE muscles during a simulated forward fall.

METHODS

A total of 12 young (Y) women (of mean age 77 ± 6 yrs) and 12 elderly (E) women (of mean age 21 ± 3 yrs) participated in the study. During the experiment, the subject stood leaning at an angle θ from the vertical (initially set to 15°) with her arms fully extended and each hand contacting a force plate (Fig 1). She was instructed to then slowly lower her body weight (similar to the descent phase of a push-up). If she was able to complete the task at a given angle, the experiment was repeated with θ increased by 15°, up to a maximum of 90°. Three trials were acquired for each angle. During each trial, a 7-camera, 60 Hz motion measurement system (Qualisys Inc.) acquired the positions of 27 skin surface markers. Simultaneous reaction forces on each hand were acquired from two force plates (MU2535, Bertec Corp.) at 960 Hz.

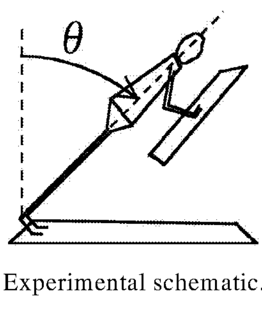

Fig. 1. Experimental schematic.

For each trial, we estimated UE energy absorption (for the dominant side) as the integral of the in-line component of hand contact force and the change in length of a vector connecting the hand centre-of-pressure and the acromium. We normalized force by body mass (which averaged 68 ± 11 kg for E and 57 ± 11 kg for Y), deflection by body height (which averaged 1.59 ± 0.75 m for E and 1.65 ± 0.75 m for Y), and energy by the product (body mass * body height) (which averaged 108 ± 21 kg*m for E and 94 ± 21 kg*m for Y).

RESULTS AND DISCUSSION

Peak magnitudes of energy absorption in the dominant UE, over the entire range of tested angles, were greater for Y than for E (mean = 0.389 ± 0.054 (SD) versus 0.252 ± 0.092 J/(kg*m); mean difference = 0.138 J/(kg*m); $p < 0.001$). This reflected young subjects' ability to generate greater contact forces (3.31 ± 0.41 versus 2.24 ± 0.74 N/kg; $p = 0.001$), since no difference existed between Y and E in peak arm deflection (0.128 ± 0.02 versus 0.123 ± 0.036 m/m; $p = 0.69$; Fig. 2).

To put these data in context, consider that during recent experiments in our laboratory with young women (n = 7) undergoing forward falls onto a gym mat (with the knees impacting before the wrists), whole-body kinetic energy at the instant of wrist impact averaged 0.590 ± 0.338 J/(kg*m). Therefore, if individuals can absorb similar energy in the non-dominant and dominant UE, these combined results suggest that young but not elderly adult females can absorb sufficient energy in their UE muscles to halt downward movement of the body during a fall, and thereby prevent impact to the head or pelvis. Strengthening of upper extremity muscles should enhance the effectiveness of the UE response in elderly individuals.

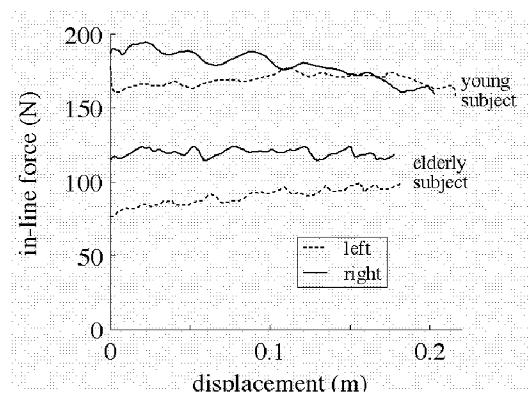

Fig 2. Force-deflection trace for typical young and elderly subjects.

ACKNOWLEDGEMENTS

This research was supported by grants from the CDC (R49CCR019355), NIH (R01AR46890), CIHR, and MSFHR.

REFERENCES

Hsiao, E.T., Robinovitch, S.N. (1998). *J. Biomech.*, **31**, 1-9.
Nevitt, M.C., Cummings, S.R. (1993). *J. Am. Geriart. Soc.*, **41**, 1226-1234.
Schwartz, A.V. et al (1998). *Osteoporos Int.*, **8**, 240-6.

3D MOTION RECONSTRUCTION FROM UNCALIBRATED 2D VIDEO SEQUENCES - APPLICATION TO FREESTYLE ACL INJURY SITUATIONS

Tron Krosshaug[1], Stig Heir[1,2] and Roald Bahr[1]
[1]Oslo Sports Trauma Research Center, PO Box 4014 Ullevaal Stadion, 0806 Oslo, Norway
[2]Martina Hansens Hospital, Box 23, N-1306 Baerum, Norway

INTRODUCTION

Various injury mechanisms have been proposed for alpine skiing, both for ACL and other ligament injuries (Natri et al. 1999), but the emphasis so far has mainly been on recreational skiing. Much less is known about the mechanisms for serious knee injuries among elite skiers. During recent years, off-piste skiing seems to be growing in popularity. Skiing resorts leave trails ungroomed – giving rise to natural mogul courses that make jumping and "trick-skiing" possible, thereby challenging the more advanced recreational skiers. In our opinion, several biomechanical characteristics of these new trends of skiing compare well with those of freestyle skiing. *We therefore consider freestyle skiing (moguls and aerials) as a suitable model for extreme skiing.*

So far, interviews and visual inspection of videos have been the most common way of extracting information about injury mechanisms. Although other approaches, like mathematical modelling and simulation (e.g. Gerritsen et al. 1995) have been undertaken, a significant problem is that reliable kinematic information from actual injury situations is lacking. Since elite level sports is regularly taped for TV, systematic collection of tapes from injury situations may potentially provide a source of valuable information.

The purpose of this project is to arrive at better 3D descriptions of knee injury mechanisms in elite freestyle skiing through analysis of 2D video sequences, and to describe the events leading up to injury situations.

METHODS

Questionnaires were handed out to all WC teams prior to the season to provide information on former serious knee injuries. A representative at each WC-meeting records the injuries and collects videos retrospectively and prospectively. So far we have received 8 videos (mostly from prior seasons), but we expect to collect at least 15 videos by the end of the season.

An interactive model-based image-matching method will be used for the estimation of 3D motion from 2D video sequences. The commercially available 3D modelling program Poser® provides the environment for image matching. The matching procedure consists of the following steps:

- Measuring (if possible) or estimating the anthropometry of the subject and building a customized computer-model (e.g. by changing segment dimensions of an existing model).
- If possible, obtain measures of landmarks in the surroundings (e.g. floor, walls, lines, objects etc.) and build a virtual environment similar to the original.
- "Calibrating" the Poser-cameras at each time step (e.g. adjust the pose and focal length parameters until the virtual surroundings matches the video footage)
- Matching the model to the background person.

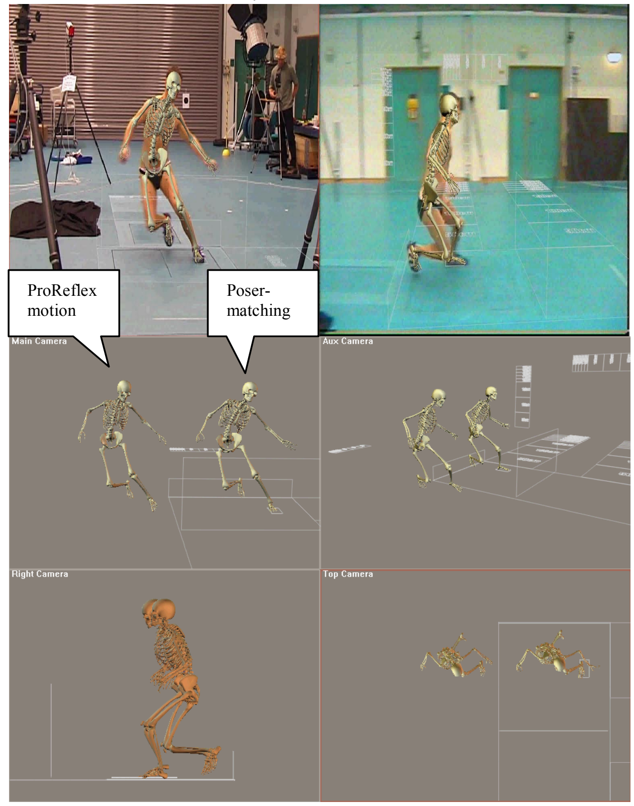

Figure 1: A Poser model matching the video sequences, and the comparison with the recorded ProReflex motion.

PRELIMINARY RESULTS

At present, we are comparing results from the method with a 7-camera infra-red 240Hz marker based system (ProReflex, Qualisys, Inc.). Preliminary results indicate that we get a reasonably good match when two camera views are available. However, when only one camera view is available, it is more difficult to make a reliable matching.

REFERENCES

Gerritsen, K. G. M., van den Bogert, A. J., Nachbauer, W. (1997) *Skiing Trauma and Safety: Eleventh International Symposium, ASTM STP 1289*, R. J. Johnson, C. D. Mote, Jr. and Ekeland A. (Eds.), 133-140

Natri, A, Beynnon, B. D., Ettlinger, C. F., Johnson, R. J. And Shealy, J. E. (1999). *Sports Med.* **28**(1), 35-48

ACKNOWLEDGEMENTS

The Oslo Sports Trauma Research Center has been established through generous grants from the Royal Norwegian Ministry of Culture, the Norwegian Olympic Committee & Confederation of Sport, Norsk Tipping AS, and Pfizer AS. This project is supported by a grant from the IOC/Pfizer Olympic Research Program.

DYNAMIC ANALYSIS OF JOINT LOADING DURING SKIING

A. J. (Ton) van den Bogert
Department of Biomedical Engineering, Cleveland Clinic Foundation, Cleveland OH, USA
bogert@bme.ri.ccf.org, http://www.lerner.ccf.org/bme/

INTRODUCTION

Large loads can be applied to the joints during skiing. Inverse dynamic analysis (van den Bogert, 1994) can be applied to estimate these joint loads from external forces and kinematics. This can be an effective method to study chronic problems such as overuse injuries. Human subject tests can be done to determine how such injuries can be prevented or treated. For acute injuries, such as fractures or ligament tears, this type of analysis is generally not useful, unless the experimenter is "lucky" enough that an injury happens while the analysis is being performed. Forward dynamic analysis (van den Bogert, 1994) is based on the same laws of dynamics, but it has the potential to generate theoretical movements that are possible, but not observed. Forward analysis requires good constitutive equations that describe how the forces in muscles and skis are generated. For muscles, it is important that the theoretical model response realistically to changes in muscle length and activation. For skis and boots, it is important that force-deformation properties are represented.

In this paper, we will present (1) an inverse dynamic analysis of hip joint loading during cross country and alpine skiing, and (2) a forward dynamic analysis of knee joint loading during the landing from a jump during downhill skiing.

HIP JOINT: INVERSE DYNAMICS

Total hip replacement (THR) is a common and effective treatment for osteoarthritis. With advances in technology, implants last longer and THR is now considered for yonger and more active patients. This raises the question which activities can be potentially damaging, and specifically: can skiing lead to loosening of the implant?

Intersegmental forces and moments at the hip joint were determined in nine subjects using accelerometry (van den Bogert et al., 1996), during walking, running, cross-country skiing (two techniques) and alpine skiing (four conditions). Magnitude of the resultant hip joint contact force was estimated by assuming an effective muscle moment arm of 0.06 m (van den Bogert et al., 1999). The results for walking (Fig. 1) agree with recent data from instrumented prostheses.

Distinct differences between the activities were found (Fig. 1), especially between the different conditions of alpine skiing. Under controlled skiing conditions, the contact force was not much larger than for walking. However, the intersegmental force vector indicated that the A-P loading was much larger during downhill skiing. This exerts a torsional load on the stem of the femoral component. Further research is needed to determine whether loosening of the implant should be expected in the long term.

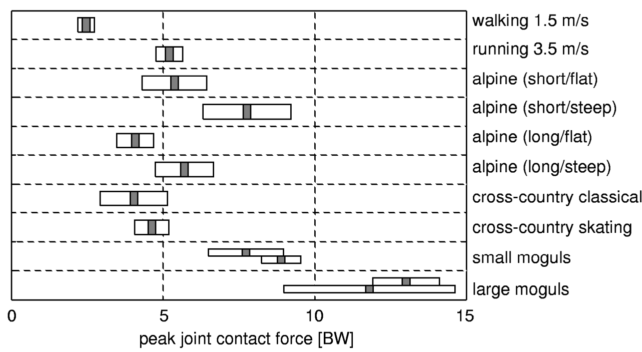

Figure 1: Mean and standard deviation of peak hip joint contact force for the nine subjects. From van den Bogert et al., 1999.

KNEE JOINT: FORWARD DYNAMICS

A two-dimensional musculoskeletal model was used to simulate a landing from a jump during downhill skiing (Gerritsen et al., 1996). The model's inputs were the initial positions and velocities of the body segments just before landing, and the muscle activation levels during the landing. The activation levels were optimized until an optimal match with an observed movement was obtained.

This baseline movement was then perturbed to initiate a backwards fall. When the quadriceps was activated to simulate an attempt at recovery, large quadriceps and external forces occurred that both pushed the tibia anteriorly (Fig. 2). In this particular example, peak anterior force was 2566 N, of which 75% came from the external force. This mechanism is unique to skiing. Similar force magnitudes occur in other sports, but never with the tibia leaning backwards relative to the ground reaction force.

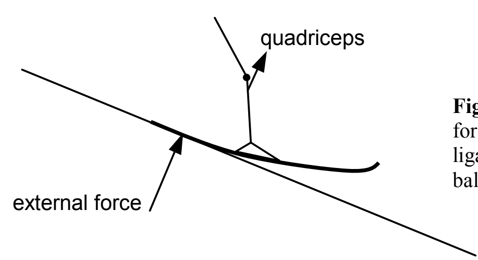

Figure 2: Mechanism for anterior cruciate ligament injury during a balance recovery.

REFERENCES

Bergmann et al. (2001) *J Biomech* **34**:859-871.
van den Bogert (1994) *Exerc Sport Sci Rev* **22**:23-51
Gerritsen *et al.* (1996) *J Biomech* **29**:845-854.
van den Bogert *et al.* (1996) *J Biomech* **29**:949-954.
van den Bogert *et al.* (1999) *Med Sci Sports Exerc* **31**:131-142.

ACKNOWLEDGEMENT: Supported by the Swiss Society for Orthopedics (SGO) and by the Austrian Ski Federation.

SKI BINDING SETTINGS AND DIFFERENCES BETWEEN SEX

Dr. Marc-Hervé Binet * - (Avoriaz- France)
Dr. Jean Dominique Laporte – (Les Angles - France)
A Bally – (Lausanne – Suisse)

INTRODUCTION

Skiers in France have basically been poorly informed on the standards of adjustement binding and the necessity of their application.

For the last ten years the results of the Médecins de Montagne epidemiological network (this group of 70 physicians established in ski resorts analyse more than 20.000 winter sports injuries each season since 1992) have put forward that the number of knee injuries has increased especially in the female population. The specific risk for a cruciate ligament injury is 3 times greater for adult females than males. This injury occurs with more than 60 % of non release of the ski bindings.

Ski binding adjustment surveys have shown that many skiers were able to ski with lower release levels than those indicated by the international standards, without complaining of inadvertent release. This established fact was confirmed afterwards during many seasons by testing voluntary lower binding setting levels.

These findings have motivated a work group of the AFNOR to suggest an improvement of the ISO standard 11088 for binding adjustments; a documentation leaflet was published (under the number FD S 52-748) proposing a simplification of the ISO table. The adjustments of the ski binding international standards for women and low weights have been lowered . A specific table for women and another for men have been established on the basis of weight, size of the shoe and a correction factor correlated to the type of skier. 7 different types of skiers are described in the AFNOR leaflet..

	Position initiale de l'indicateur de réglage / Adjustment indicator value					
Pointure française/French size	<33	34/35	36/38	39/41	42/44	>45
Mondopoint	<20,5	21/22	22,5/24	24,5/26	26,5/28	>28,5
Poids skieur/Skier weight en Kg						
10/17		3/4				
18/21	1 1/4	1	3/4			
22/25	1 1/2	1 1/4	1 1/4	1		
26/30	2	1 3/4	1 1/2	1 1/4	1 1/4	
31/35	2 1/2	2 1/4	2	1 3/4	1 1/2	1 1/2
36/41	3	2 3/4	2 1/2	2 1/4	2	1 3/4
42/48		3 1/2	3 1/4	2 3/4	2 1/2	2 1/4
49/57		4 1/4	4	3 3/4	3 1/2	3
58/66		5 1/2	5	4 1/2	4	3 1/2
67/78		6 1/2	6	5 1/2	5	4 1/2
79/94		7 1/2	7	5 1/2	6	5 1/2
>94			8 1/2	8	7	6 1/2
			10	9 1/2	8 1/2	8
			11 1/2	11	10	9 1/2

Profil du skieur Skier type	Corrections à apporter aux tableaux Correction to apply to upper chart
• Débutant adulte (plus de 25 ans) • Skieur de plus de 50 ans • Adult beginner (age : 25 and over) • Skier aged over 50 years old	Monter d'une ligne Move up one line
• Débutant jeune et enfant (moins de 25 ans) • Niveau débrouillé, avec faible condition physique • Bon skieur, style souple et coulé, privilégiant la sécurité • Young beginner and child (less than 25) • Average level, in poor physical condition • Good skier, with a smooth style, for whom safety is important	Pas de correction No correction
• Bon skieur jeune, style souple et coulé • Niveau débrouillé, bonne condition physique • Good young skier, with a smooth style • Average level, in good physical condition	Descendre d'une ligne Move down one line
• Bon skieur, ski d'attaque sur tous terrains • Good skier, aggressive skiing on all terrains	Descendre de deux lignes Move down two lines
• Très fort skieur, sur terrains engagés • Excellent skier, on difficult terrains	Descendre de trois lignes Move down three lines

Because the actual international standards were badly applied or simply unknown, a large information campaign supported by the national French health insurance was launched aiming skiers and ski equipment renters. For the first year of the mass public campaign a television spot of 30 seconds and 1 000 000 documentation leaflets where distributed by tour-operators, skiing equipement renters and tourist offices. A specific information campaign aimed the ski equipment renters. This campaign has started in autumn 2000 but will continue up to 2003 winter season informing public and renters on the new standards.

RESULTS and DISCUSSION

The evaluation of the impact of the first campaign on the public and on the professionals concerned 2203 interviews on the slopes using a randomised survey method concerning 1597 alpine skiers. 204 interviews aiming ski renters were performed by telephone. It shows that the required binding settings for both female and beginners can be lowered by 15 % whithout more accidents occuring because an inadvertent release. One an other hand a first effect of the campaign after only one winter season was the first diminution after ten years of augmentation of ACL injuries, but no correlation with the binding settings has been prooven. The evaluation of modifications of the settings in the control group shows an important shift of the setting values to lower values for 2001 compared to 1998 and 1999 in the control group that rent skis but there is no significant change in the setting values amongst equipment owners.

CONCLUSION

This suggest that a new definition of ski binding international standards for females with a more attractive presentation could improve the injury situation in alpine skiing.

EXPERIMENTS WITH AN *IN VITRO* LOAD SIMULATOR FOR CORRELATING KNEE KINEMATICS, LIGAMENT STRAIN AND ALPINE SKI BINDING LOADS

Veit Senner[1], Rick Greenwald[2], Mirko Barone[3]

BASIS GmbH Applied Biomechanics, c/o TUEV Product Service, Ridlerstr. 65, D-80686 Munich, Germany
[1] General Manager BASIS GmbH, vsenner@t-online.de
[2] General Manager, SIMBEX LLC, New Hampshire, USA
[3] Surgeon, AGATHARIED Hospital, Hausham, Germany

INTRODUCTION

In Alpine skiing, two primary rotary mechanisms have been identified for anterior cruciate ligament (ACL) injuries to the knee: one with the knee in hyperflexion with rotation (phantom foot), the other in hyperextension with rotation. To date, Alpine ski bindings are not developed to protect the soft tissues in the knee. The long term goal of this research is to determine whether there is a correlation between knee positions and binding forces during likely injury events such that a unique release paradigm for Alpine ski bindings can be prescribed to protect the knee. The objective of this study is (1) to develop and validate a physical model that can be used to investigate situations, which are believed to be crucial for ACL injuries in skiing, (2) systematically apply external and muscular loads to cadaver knees in order to find out the relationship between the resulting knee ligament strain and the binding forces present in that situation.

MATERIAL AND METHODS

An *in vitro* load simulator (Fig. 1) was developed to simultaneously apply 6 degree of freedom loading to a cadaver knee joint and measure knee kinematics, anterior cruciate ligament strain and Alpine ski binding forces and moments.

Figure 1: Device to apply external loads and quadriceps forces to cadaver knee joints with simultaneous measurement of ski binding forces and moments.

Quadriceps muscle loading is used to set the knee flexion angle and was applied via a tissue clamp attached directly to the quadriceps tendon and controlled by a closed-loop linear actuator. Varus/valgus moments are applied via weights attached to the femur. Superior/inferior motion of the femur with respect to the fixed tibia is permitted, allowing unconstrained motion of the knee joint during application of external rotations to the ski. Anterior cruciate ligament strain is measured directly with a DVRT inserted i.e. into the anteromedial bundle of the ligament. Knee kinematics is measured with an Instrumented Spatial Linkage (ISL) mounted directly to the knee. The cadaver knee is potted and rigidly coupled to a ski boot via a custom-made prosthesis that prevents rotation of the leg within the boot. The boot is mounted onto a multi-axis instrumented ski binding, which is in turn mounted on a test ski attached to the loading frame. The loading frame has a stepper motor which can drive internal/external rotation of the ski about the axis of the tibia.

FIRST RESULTS

Repeatability testing of the device was performed on young male cadavers at flexion angles of 110 and 130 degrees. Internal and external rotation of the ski to +/- 30 degrees was performed with incremental quadriceps muscle loading of 700 N to 2400 N. Three trials of at each loading condition were performed. ACL strain, knee kinematics, and binding loads were synchronously recorded. Repeatability was within 5% for repeated trials. The tests performed were below failure levels. Low levels of ACL strain (~2-3%) were recorded, yet measured binding loads were extremely low, and well below release limits. Increasing the level of quadriceps force at these flexion angles and applied rotation angles had little effect on ACL ligament strain, but these results cannot be extrapolated to higher angles of internal/external tibio-femoral rotation or to other knee flexion angles.

STEPS CURRENTLY PERFORMED

Currently numerous tests with additional cadavers are conducted and sensitivity analyses for the different parameters in test are performed. The results from this systematic variation of loading conditions, which also takes into account the different fibre bundles of the ACL will be presented and discussed.

RELEASE SETTING FOR AN ELECTRONIC ALPINE SKI BINDING

Werner Nachbauer[1] , Kurt Schindelwig[1], and Herwig Schretter[2]
[1]Department of Sport Science, University of Innsbruck, Innsbruck, Austria
[2]HTM Sport- und Freizeitgeräte AG, A-2320 Schwechat, Austria

INTRODUCTION

For several years ski binding companies have made attempts to develop electronically controlled ski bindings. This kind of binding generally consists of a transducer to convert physical variables into electrical signals, a micro controller to process the transducer signal, and an electromechanical release device. The incidence of anterior cruciate ligament (ACL) ruptures has increased in the last decade in ski racing as well as in recreational skiing. One major ACL injury mechanism identified is called the phantom foot injury. The purpose of this investigation was to identify the characteristic loading of the binding for the phantom foot injury mechanism and to develop a release criterion for an electronic ski binding.

METHODS

14 subjects imitated the phantom foot injury mechanism in laboratory and field tests. To make sure that no ACL rupture occurred during the tests, the falls were stopped by a trained supervisor and an extra release mechanism allowed the subject to release the boot from the ski by squeezing a lever switch on the ski pole. During the falls the three components of the force acting on the toe and the heel pieces of the binding were measured by using two force plates (Kistler) at a sampling rate of 200 Hz. With the same force plates the forces of 30 subjects were measured during 137 regular runs on different terrain (flat, steep, moguls, ...), on a wide range of snow conditions (coarse, deep snow, icy, ...), and at different speed.

The data analysis consisted of the identification of the characteristic forces on the binding during the phantom foot injury imitation and the comparison of these forces with the forces apparent during regular skiing in order to determine a release criterion for the phantom foot release mechanism.

RESULTS

The falls investigated showed a high tractive and lateral force on the toe piece of the binding. Fig. 1 shows two video frames of the imitation of the injury situation with the normal and lateral forces on the toe piece of the binding. The arrow marks the forces when the binding was released by the subject.

In the following the 137 regular runs were systematically examined with respect to the observed tractive and lateral force on the toe piece of the binding. When only considered the magnitude of these forces then the release criterion was

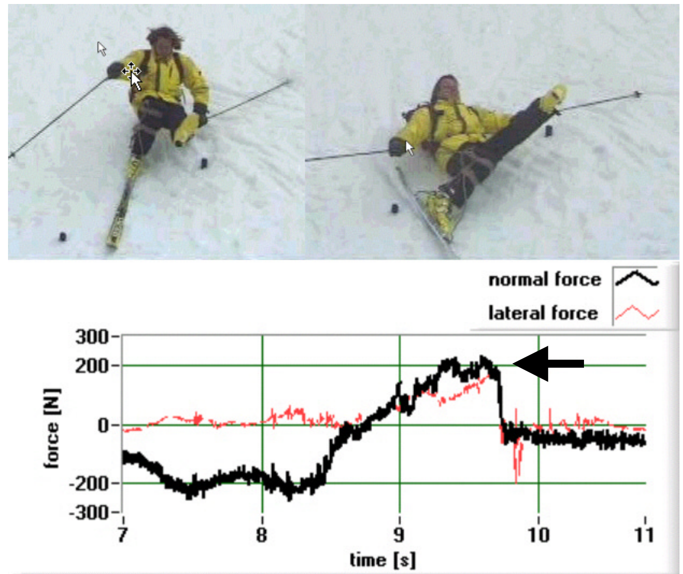

Figure 1: Normal and lateral forces during the imitation of a phantom foot injury situation.

violated during regular skiing which would cause inadvertent releases. By introducing the time interval of the tractive force the following release criterion for the toe piece of the binding was determined: (a) tractive force greater than 400 N, (b) lateral force greater than 150 N, and (c) the running interval of the tractive force over 0.5 s greater than 50 Ns.

DISCUSSION

A release criterion for the phantom foot injury mechanism was developed. A major problem in determining the release criterion is that the imitation of the injury situation has to be done in a way that no injury can happen. So the forces measured during the imitation give an assumption of what happens during the real injury situation. The high variability in the measured forces during the imitation might be due to differences in the imitation of the falls. Consequently, the release criterion was chosen so that during the 137 regular runs the criterion was not fulfilled. The tentative criterion was implemented into the micro processor of a prototype of an electronic binding. During the winter season 2001/02 first tests with the prototype were conducted. Besides these tests efforts are made to adapt the criterion to different skiing levels or physiques of the skiers.

MODELING OF SLOPE AND TRAJECTORY IN ALPINE SKIING

Joachim Mester, Ralf Roth, Florian Seifriz

German Sport University Cologne, Cologne, Germany

INTRODUCTION

Due to modern computer development, various presentation techniques have been made available in the last years. This refers to digital videos taken from real sport environments as well as to modeling, simulation and animation of movements. Although the scientific background for these techniques has been improved remarkably, there is a delay of penetration into media and even into training in top performance sports.

METHODS

During the last winter FIS-Championships and the Ski-World-Championships 2001 and 2002 for the alpine racing events and for ski-jumping the following groups of techniques were used: At the level of models, deterministic biomechanical models and non-conventional approaches by means of genetic algorithms (GA) for determination and simulation of performance, e.g. "optimal trajectory," were calculated. The necessary data for the individual skiers result from anthropometrical measurements. The slopes were roughly surveyed with satellite scanning data and additionally with high resolution GPS (LEICA) (see figure 1). These data were processed in 3D-Studio MAX and then used for visualization and animation of the runs (see figure 3). Finally digital videos were manipulated in terms of blending and superimposing two runners into one video (see figure 2).

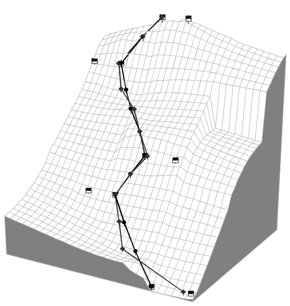

Figure 1: Model of Slope

RESULTS

Deterministic modeling of the trajectory with individual parameters from the athletes and the various conditions of the slopes is faced with the large number, complexity and interdependence of "independent" variables. Genetic algorithms help to optimize the trajectory. Evolution studies of the algorithms, fitting for run time and/or for distance, show that saturation effects occur rather early, e.g. after approx. 50 steps (see table 1). A comparison between calculated and real trajectories and run times of world-class athletes demonstrates realistic settings.

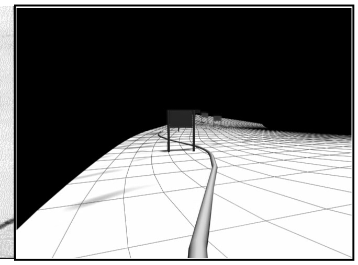

Figure 2: Digital video superimposing

Figure 3: Model-based irtual trajectory

	GA fit for distance		GA fit for time	
Evolution	Distance	Time	Distance	Time
1 st Step	259.78 m	10.68 s	266.89 m	10.40 s
50 th Step	225.75 m	9.08 s	237.99 m	8.96 s
100 th Step	224.38 m	9.04 s	238.36 m	8.88 s

Table 1: Evolution of GA

DISCUSSION

These scientific findings and developments raised remarkable interest not only in the various groups of athletes but also in mass media and supplying television companies. This adds new perspectives to research in sport science as these techniques can contribute to an improvement of media presentation as well as to an optimization of athletic training and performance. Especially non-conventional approaches such as GA seem to promise new insights into the complex structure of sport performance.

REFERENCES

Sakata, T., Ito, T. (1998). Simulation of ski turn. In: Haake, S. J. (ed.), *The Engineering of Sport Design and Development.* Blackwell Science, Oxford, 361-368.

Seifriz, F. (2000). *Simulation im alpinen Skisport.* Dissertation.de, Berlin.

DYNAMIC SKIING: INFLUENCES OF SNOW AND SKI PROPERTIES

Franz Bruck[1], Lukas Magerl[1], Heinz-Bodo Schmiedmayer[1], Peter Lugner[1], and Herwig Schretter[2]
[1]Institute of Mechanics, Vienna University of Technology, Austria
[2]Tyrolia HTM, Schwechat, Austria

INTRODUCTION

To be able to investigate by means of simulation how the turn radius performed by a skier is affected by ski properties and/or by the type of snow, a model for the contact between ski and snow is needed.

METHODS

Based on snow measurements similarly to Casolo et al. a contact model was developed that describes the forces that are exerted from the snow to the ski due to the penetration depth and the shearing behaviour. For the validation of this snow force model a ski sledge was used consisting of a pair of skis and a rigid frame, which is fixed to the ski bindings and allows to choose a certain value for the edge angle of the skis. This sledge was put on a slope and autonomously performed a circular-like turn. At the same time the snow conditions were measured on the slope. Sledge runs were carried out for two kinds of skis, a giant slalom ski and a slalom ski. For both ski types the snow model was used to calculate the path of the ski sledge (modelled as a multibody system), and a comparison shows that measured and simulated trajectories coincide very well, see also Bruck et al..

RESULTS AND DISCUSSION

Using the verified contact model the influence of snow hardness on the average curve radii of the sledge was analysed. Two certain kinds of snow are investigated more closely, one can be characterized as “hard snow”, the other one as “soft snow” according to the measured range of snow properties. For both the slalom and the giant slalom ski it is studied how ski properties like bending and torsional stiffness or damping characteristics can change the radius of turn being made by the ski sledge. By the means of simulation it is possible e. g. to look into the difference it makes to use a ski with high bending stiffness and low torsional stiffness, or to have a ski with low bending, but high torsional stiffness. In addition it is investigated whether it could be advantageous to have a stiffness distribution along the ski differing from a normally used distribution. Besides the direct comparison of average turn radii a further criterion for the assessment of a certain variation of the system is the energy dissipated during a run.

SUMMARY

Using the methods of multibody system dynamics this investigation shows the influence of ski and snow properties on the average turn radius of a ski sledge.

REFERENCES

Casolo, F., Lorenzi, V., Vallatta, A., and Zappa, B. (1997). *Simulation Techniques Applied to Skiing Mechanics.* Science and Skiing, First International Congress on Skiing and Science (St. Christoph am Arlberg, Austria), pp. 116-130.

Bruck, F., Lugner, P., and Schretter, H. (submitted for publishing). *A Dynamic Model for the Performance of Carving Skis.* International Society for Ski Trauma and Safety, 14th International Symposium, Queenstown, New Zealand, 2001.

EVALUATION OF THE RELEVANT PARAMETERS TO PREDICT THE BEHAVIOUR OF ALPINE SKIS

Federico Casolo* and Vittorio Lorenzi**
*Politecnico di Milano (casolo@mech.plimi.it) **Università degli Studi di Bergamo (vlorenzi@unibg.it)

Ski trajectory in carved turns is related to ski edging and to snow and ski mechanical and geometrical parameters. Thus, any analytical approach requires to identify the crucial factors and to set a protocol for their experimental evaluation. A first approximation formula by Howe[1] may be used to roughly estimate the mean curvature of an edged ski on a rigid flat surface, knowing only the ski length and the max value of the side-cut. However, we adopt a more refined approach and take into account ski and snow mechanic characteristics and the whole ski shape-camber, side-cut and length-. We estimate ski deformation and trajectory by means of the following differential equat. where only torsional flexibility (ski torsion<1°) and "generalized skidding" (absent in ideal turns) are neglected.

$$EJ(x)\cdot y^{IV}(x)+EJ'(x)\cdot y'''(x)+2\cdot EJ''(x)\cdot y''(x)+q(x)=0 \quad ◙$$

$$y(x)=y_0(x)+y_N(x)$$

$$y_0(x)=camber(x)+\tan(\vartheta)\cdot\left(carving(x)-\frac{(sc_A-sc_D)\cdot(l-x)}{l}\right)$$

$$sc_A=\frac{width_A-width_{min}}{2} \qquad sc_D=\frac{width_D-width_{min}}{2}$$

where EJ is the local ski bending stiffness and the other parameters [2] *are shown in the following figures*: .

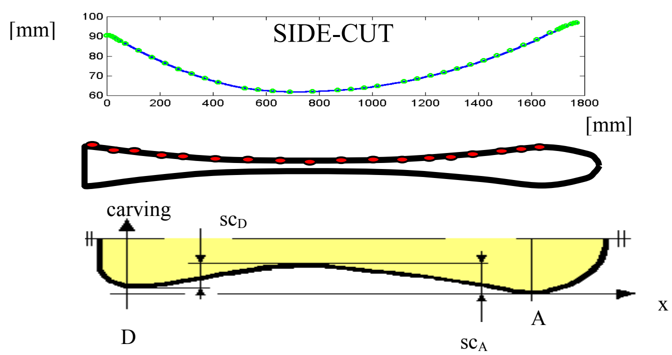

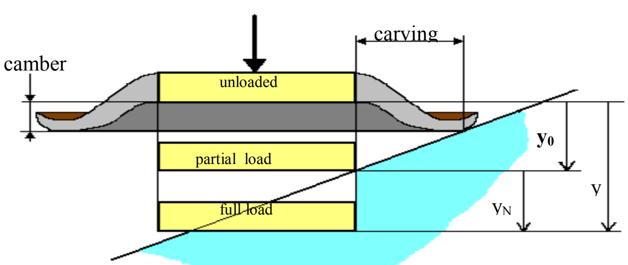

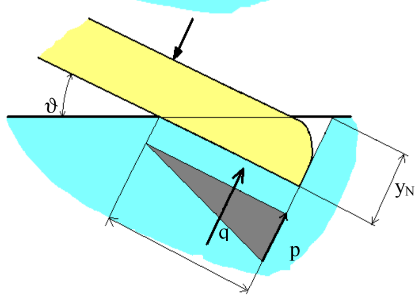

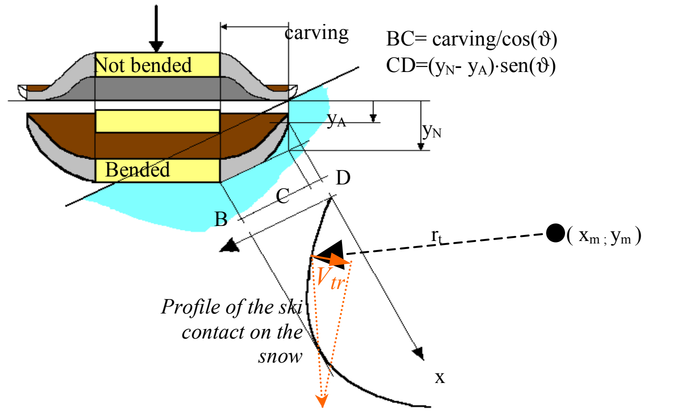

The "local skidding", where only portions of the skis skid, is on the contrary, unavoidable and always occurs because the ski contact on the snow is never perfectly circular. This is one of the causes of the power loss during a turn and its effect can be evaluated by:

$$\int_0^l q\cdot V_{tr}\cdot k\cdot dl$$

where V_{tr} is the velocity component of a ski point in the direction of the local center of curvature of the ski-snow contact line.

The bending stiffness used in eq.◙ for a ski with bindings, boot and anti-vibrating platform, varies very much along the ski length and should be evaluated for each ski set-up: for this aim we use a simple testing apparatus to flex and measure the deflection of the ski segments, compensating the influence of the weight of the not-bent ski portions. The critical point is the evaluation of the snow static and viscous characteristics and of its pressure distribution on the transversal ski section(p) For them, up to now, we use approximate literature data. The computer simulation of alpine ski tracks [2] shows that the ski stiffness plays an important role on the skier´s trajectory. The same model can be used for other aims, such as, to design the ideal side-cut which, for given ski stiffness and a specific ski edge, produces a circular contact line and thus avoids local skidding (e.g. for carving races). In order to validate our simulation system we designed a device for measuring pressure distribution and contact line path of an edged ski (below fig.).

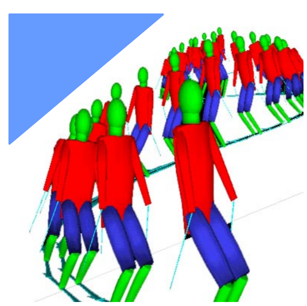

Computer simulation output

REFERENCES

1-John Howe Skiing Mechanics, Poudre (1983)
2-Casolo, Lorenzi Science and Skiing II, ed. E. Muller, Kovac (2001)

SNOW FRICTION AND DRAG IN ALPINE DOWNHILL RACING

Peter Kaps, Werner Nachbauer, Martin Mössner
University of Innsbruck, Innsbruck, Austria

INTRODUCTION

For training purposes we want to visualize an Alpine downhill slope from the view of an elite skier. As slope we have chosen the Streif, a famous and difficult Alpine downhill run in Kitzbühel, Austria. The surface of the slope between the starting area and the end of the Steilhang was geodetically surveyed. The length is approximately 700 m, the difference in height 300 m. The first 30 runners of the FIS World Cup downhill event 2002 were recorded by video cameras. With direct linear transformation we obtained the trajectory of the fastest skier as a function of the time. We call the trajectory with the time history a path. It depends not only on the trajectory but also on the velocity of the skier. It is well known that the speed depends on the drag and the snow friction. These parameters depend strongly on the situation and the skill of the skier. Minimal values occur during straight running when the skier takes an egg position. The snow friction is considerably increased during turns when the skier edges, especially, if the turn is not optimally carved. The drag is increased during difficult parts of the track when the skier takes an upright position. Additionally, the optimal path depends on the strength of the skier. The skier has to exert forces onto the snow to keep his trajectory. These forces are limited due to the constitution of the skier and the consistency of snow.

METHODS

For the fastest skier, a video analysis was performed. A typical frame is given in Fig. 1. Here, the trajectory is represented, additionally. In each frame, the positions of the toe pieces of the bindings as well as the visible control points were manually digitized. With help of the direct linear transformation the position of the skier was obtained in real 3D object coordinates. Finally, the path was obtained by smoothing. For dynamic analyses, the skier is modeled as a mass point. The equation of motion is established in descriptor form (1). The constraint g is given by the trajectory of the skier.

$$\begin{bmatrix} I & 0 & 0 & 0 \\ 0 & I & 0 & 0 \\ 0 & 0 & 0 & 0 \\ 0 & 0 & 0 & 0 \end{bmatrix} \begin{bmatrix} x \\ v \\ a \\ \lambda \end{bmatrix}' = \begin{bmatrix} v \\ a \\ Ma - f - r \\ Gv - g^1 \end{bmatrix} \qquad (1)$$

$$g(x,t) = 0\,, \quad G = \frac{\partial g}{\partial x}, \quad g^1 = \begin{pmatrix} 0 \\ 0 \end{pmatrix}$$

The applied forces f are assumed in the form

$$f = \begin{pmatrix} 0 \\ 0 \\ -mg \end{pmatrix} - \mu N t - \frac{1}{2} c_d A \rho v^2 t\,, \text{ with } t = \frac{v}{\|v\|}$$

For the reaction forces r and the normal force N it holds $r = -G^T \lambda\,,\ \ N = \|r\|$.

We assume that the drag $c_d A$ and the snow friction μ are piecewise constant. The values are determined by a least squares argument: the error between measured and computed positions is minimal.

RESULTS

We have computed snow friction and drag for the turn in Fig. 1. The turn starts at t=0 end ends at t=1.92. The results are given in Table 1. The mean error is less than 4 mm.

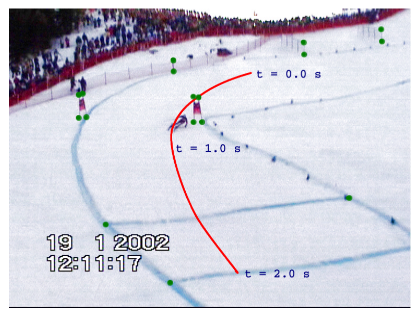

Figure 1: Video frame with trajectory of the ski racer

	t<0.58	t>0.58
μ	0.40	0.10
$c_d A$	0.90	0.55

Table 1: Snow friction and drag for the turn in Fig. 1

DISCUSSION

Despite of the short time passed since data collection we can present some preliminary results on a small portion of the investigated slope. We plan to visualize the downhill race from the view of a skier. We hope that the results can be used by the Austrian ski team for training purposes.

ACKNOWLEDGEMENT

The research was supported by a Top Sport Austria project of the Austrian Ski Federation.

BIOMECHANICAL RESEARCH METHODOLOGY IN SKIJUMPING: OVERVIEW AND PERSPECTIVES

Hermann Schwameder and Erich Müller
Institute of Sport Science, University of Salzburg, Salzburg, Austria

INTRODUCTION

Biomechanical research in skijumping has a long tradition. This may be caused by the restrictions and constraints in skijumping which makes it relatively easy to biomechanically describe and analyse the movements. Biomechanical studies primarily proceed within five areas: (1) field studies of hill jumps, (2) lab studies of simulation jumps, (3) wind tunnel experiments, (4) computer simulations of the flight phase and (5) material testing. This paper presents an overview of the biomechanical methods used in these areas. Furthermore, the strength and restrictions of the methods are discussed. Finally, some ideas concerning perspectives in skijumping research methodology will be presented.

METHODOLOGY IN SKIJUMPING

Kinematic methods

Both, in hill and simulation jumps kinematic methods (film and video techniques) are the most frequently used ones. In hill jumps primarily the take-off and the flight phase were analysed. Depending on the point of interest 2D and 3D approaches were used. While the kinematic methods are standardized routines and easy to handle in a lab, the analysis of the flight phase in the field is – due to the large space of movement - a challanging task. The problem has been used by operating with cameras in a series or by panning the cameras. The main pruposes of filming hill jumps are to serve an accurate description and to find the most important kinematic parameters related to performance. The analysis of simulation jumps is primarily concentrated on basic research and to compare the coordination pattern between hill and simulation jumps. An important advantage of kinematic methods is that the skijumper are not influenced by any filming device. So these methods can even be used during competitions. The most severe restictions of kinematics are the sampling rate and the accuracy to determine the marker and/or joint positions.

Dynamic methods

Two methods are used to measure an analyse hill jumps dynamically. Force plates mounted to the take-off table allow to measure take-off forces with a high sampling frequency. As the skijumper is not influenced by the measuring device this method can even be used during competitions. The disadvantages of the method are the high costs and the high sensitivity to failure and errors at low temperatures. The second type of dynamic methods used in hill jumps are bindings equipped with load cells and insoles instrumented with measuring sensors. Load cell bindings could yield to the most accurate and most distinct data. The device itself, however, influences the mechanics and the weight balance of the ski-binding system substantially. Sensor instrumented insoles, however, are easy to handle and the jumper is hardly irritated by it. Certain restrictions are usually given by the storage device with respect ot weight and size. Furthermore, only forces between foot and boot perpendicular to the sole can be measured.

The force plate is the dominant dynamic measurement system used in simulation jumps. By that the forces and their application points can be measured at a high sampling rate in 3D. For comparative aspects in few studies also mobile dynamic systems (see above) were used in simulation jumps. To estimate aerodynamic forces during take-off in recent studies simulation jumps were measured in wind tunnels.

Electromyography (EMG)

EMG has been successfully used both, in hill and simulation jumps. In combination with kinematic and kinetic data the EMG gives important information of the muscle activity and the muscle coordination during skijumping.

Wind tunnel experiments

The purpose of wind tunnel experiments are to measure and optimize the aerodynamic forces during the flight phase. Studies were presented using both, athletes and models.

Computer simulation of the flight phase

Computer simulations are used to optimize the aerodynamic forces, to serve basics for hill constructions and to estimate the influence of body positions and material to the flight path.

Material properties, construction and design

The development and optimization of material (jumping suit, boots, bindings and skis) is an important issue in skijumping. Both, companies and research institutions work in this area. There are, however, hardly any results available in the literature.

FUTURE ASPECTS AND PERSPECTIVES

Two aspects seem to be important for skijumping research in the future. The first one is referred to the dynamic methods used in hill jumps. An important progress could be made by measuring the horizontal ground reaction forces during take-off, as these components influence the forward body rotation and therefore the quality of the jumps substantially. Another improvement would be the reduction of size and weight of mobile storage devices (e.g. insole systems, EMG).

The second aspect is related to the correlation of material properties with flight length. This information is an important basis for meaningful regulations in skijumping. Regulations regarding to (1) the importance of the jumpers' athletics vs. material, (2) the attraction of competitions both, for athletes and spectators and (3) the safety for the athletes.

THE TRANSITION FROM TAKE-OFF TO EARLY FLIGHT PHASE IN SKI-JUMPING

Gert-Peter Brüggemann[1], Gianpiero DeMonte[1], Paavo V. Komi[2], Juha Isoletho[2], Wolfgang Potthast[1], M. Virmavirta[2]
[1]Institute for Biomechanics, German Sport University of Cologne, Cologne, Germany, brueggemann@dshs-koeln.de
[2]Neuromuscular Research Center, University of Jyväskylä, Finland

INTRODUCTION

The early flight phase in ski-jumping is characterized as the transition from take-off into a stable flight. This phase covers the first 15 to 25 meters or 0.7 to 1.0 seconds, respectively, depending on the size of the jumping hill.

The recently published data on the early flight kinematics (Arndt et al. 1995, Schwameder/Müller 1995, Schwameder/ Müller 2001) reported that less than 15% of the variance of total performance (distance jumped) can be explained by the CM parameters (position, velocity) of the take-off. The explained variance at 15m after the take-off through the CM ballistic variables was shown to be less than 20%. When adding five parameters describing the body configuration and indicating aerodynamic variables the explained variance of total performance increased up to about 85% (Arndt et al. 1995. These results demonstrate that the early flight or the transition take-off to stable flight should be the most sensitive phase to determine the total performance in ski jumping. The use of drag and lift forces and gravity acting on the jumper-ski-system in this transition from take-off to early flight are not well or completely understood.

The purpose of this paper was to summarize the results of the biomechanical studies performed at the 1994 and the 1998 Olympic Games in Lillehammer and Nagano, respectively, and to increase the knowledge of the identification of performance limiting factors in the transmission from take-off to flight.

METHODS

The jumps of all participants of the 90m and the 120m hills were recorded by three synchronized cameras. A highspeed video camera filmed the sagittal plane of the take-off at 250 fps (1998 in Nagona) and 200 fps (1994 in Lillehammer). Two cameras operating at 50 fps were genlocked and recorded the take-off and the early flight of the jumpers. The cameras were panned and tilted in order to allow a small object field. The panning and the tilting were controlled via well calibrated landmarks in the background. A specific DLT routine (Drenk 1994) was used to transform the digitized data into the metric space coordinate system. Twenty trials of each competition were chosen for further analysis. Joint centers, reference points on the ski and calibration points were digitized manually using the Peak Motus System. The cutoff frequencies of a second-order Butterworth filter was set at 4 Hz for raw date smoothing. Data of segments' relative mass and moment of inertia were taken from Hanavan's model (Hanavan 1964).

RESULTS AND DISCUSSION

The take-off movement is determined by the strength and power abilities of the jumper and the quality of the take-off. The crucial point for the jumper during the take-off is to adjust to the external forces (aerodynamic forces, friction between ski and track, ground reaction forces) and to control the posture during the take-off to achieve the best initial conditions for the early flight. Different groups of athletes can be identified using different and individual strategies to solve the problem. The correlations between vertical or resultant release velocity and the total distance jumped show different results and are not very consistent. Among other reasons the different results are due to the various conditions in which the data were collected. The direction of the release velocity vector under the various condition seems to play the dominant role. The direction of the take-off and the release velocity vector has a higher effect on the rotational component than on the linear component. The rotational component determines the angular momentum of the body's forward rotation during the take-off substantially. From that one can conclude that the angular momentum of the body rotation during the take-off play the major important role concerning the preparation of the early flight. A high angular momentum at take-off is more important than a high release velocity in order to reach an early compact flight position. From the results we can conclude that there exists an optimum of the angular momentum for the early flight which means that there is an optimal relationship between ballistic and aerodynamic take-off parameters. The optimum angular (somersault) momentum will ensure the early compact flight position and thus the necessary lift and the drag forces for an optimum flight.

SUMMARY

The take-off and the transition to early flight are the dominant prerequisites for total performance in ski-jumping. An optimum angular momentum at take-off brings the athlete in an advantageous position in the early flight for an optimum use of lift and drag forces. It is substantial for the jumping performance to optimize angular momentum during the take-off in accordance with the torque due to the air steam after take-off, which has to stop the forward rotation at the right moment.

REFERENCES

Arndt, A. et al. (1995). *J. Appl. Biom.*, **11**, 224-237.
Drenk, V. (1994). Angew. TrWiss. **1**, 130-142.
Hanavan, E.P.(1964). AMRL-TR-64-102, Ohio.
Schwameder, H, Müller E. (1995*). Spectr. Sp.Wiss.*, **71**, 5-36.
Schwameder, H, Müller E. (2001*). Eur. J. Sport Science, **1**,1*

ACKNOWLEDGEMENT

These studies were made through the support of the Medical Commission of the IOC and Pfizer.

AN EXPERT SYSTEM FOR TALENT IDENTIFICATION AND SUCCESSFUL PERFORMANCE IN SKI JUMPING

Bojan Jost, Janez Pustovrh, Maja Ulaga
Faculty of Sport, University of Ljubljana, Slovenia, bojan.jost@sp.uni-lj.si

INTRODUCTION

The object of the current research has been to establish the model structure of competitive and potential performance of top Slovenian ski jumpers. The knowledge base of a reduced potential performance model of ski jumpers (RPPM) was formed so as to include variables of the morphological and motor sub-spaces. The frame of reference for the variables of the reduced potential performance model was set on the basis of the theories dealing with the issues of the morphological-motor behavior of man. The problem and goal of the research has been to establish the structure of the dimensional configuration of the variables of the competitive and reduced potential model of performance of ski jumpers (RPPM) and to establish the connection between the dimensions of the RPPM (=model variables) and competitive performance in ski jumping. The basic hypothesis of the research was that the individuals in the used sample of ski jumpers significantly differed in their attained competitive performance in the 2001 season and that the differences in performance were associated with the measured variables.

METHODS

To solve the problem of the task and to verify the basic hypothesis of the research, the shell of the expert system "Sport Expert - SPEX" was used. The basic structure of the expert system SPEX is described in Jost, Pustovrh, and Ulaga (1998). The sample included 45 best Slovene ski jumpers, 15 years of age and above. The sample of independent variables represented elementary (n=17) and derived (n=14) motor variables, 4 elementary and 3 derived morphological variables and 2 elementary special morphological-motor index variables. By means of the method of expert decision-making (Chankonk, & Haimes, 1983) we established the heuristic rules of conclusion-drawing and decision-making. By means of the computer program we calculated the results on the derived variables of the potential performance model (i.e. the aggregated criteria of the decision tree). The criterion variable of performance was determined on the basis of the mark of competitive performance of ski jumpers in the Slovenian National Championship in the 2001 season.

RESULTS AND DISCUSSION

In the space of the variables (table 1) by which the aggregated mark of the sub-criterion (POTENTIAL PERFORMANCE) was calculated, the mark of the basic motor status (MOTORICS) dominated from the aspect of correlation with the criterion of performance of ski jumpers, with the value of the coefficient of correlation ($r=0.46$; $p<0.01$). The mentioned variable - which was obtained by means of the mechanism of conclusion drawing according to the SPEX method as a linear combination of the elementary motor variables - explained approximately 21% of the variance of performance of the ski jumpers. The variables which formed the linear multiple function in the morphological space of the psychosomatic status of ski jumpers (MORPHO) have also shown a statistically significant contribution to the performance of ski jumpers ($r=0.40$; $r^2=0.16$; $p<0.01$). In the analysis of performance of ski jumpers we should not neglect the importance of morphological indexes, calculated on the basis of the anticipated functional relations to the physical environment in which ski jumps are realized. In this research, the morphological index of the take-off of ski jumpers showed the largest correlation ($r=0.53$; $p<0.01$). The mentioned index points to a relative relationship between the body weight and leg length. It is assumed that the ski jumpers with a higher relative leg length in comparison to body height have a poorer predisposition for successful take-off and transition into flight.

REFERENCES

Jost, B., Pustovrh, J., & Ulaga, M. (1998). The Follow-up of the Development of a Competitive and Potentially Successful Performance of a Top Sportsman with the aid of the »Sport-Expert« System. *Kinesiology*, 30(2), 17-22.
Chankong, V., & Haimes, Y.Y. (1983). *Multiobjective Decision - Making. Theory and Methodology*. North-Holland.

Table 1: Correlations of the criterion variable with the derived and elementary variables (**p<=0.01, *p<=0.05).

	r	r^2
POTENTIAL PERFORMANCE	0.56**	0.31
MOTORICS	0.46**	0.21
jump over Swedish bench	0.26	0.07
abdominal crunches (45 degrees)	0.02	0.00
long jump from a standstill	0.43**	0.19
vertical jump = the abalac test	0.48**	0.23
high jump explosiveness	0.28	0.08
push off power	0.06	0.00
triple jump from a standstill	0.41**	0.17
balance in sagital plane	0.35*	0.12
balance in frontal plane	0.43**	0.18
tapping with the right foot	0.13	0.02
tapping with the left food	0.13	0.02
forward bend	0.43**	0.19
forward bend – relative	0.42**	0.18
angle (shank–base) of the ankle	0.01	0.00
hurdle – jumping	0.17	0.03
»figure-of-eight« with bending	0,22	0,05
polygon backwards	0,21	0,05
MORPHO	0.40**	0.16
body weight	0.21	0.04
body height	0.19	0.04
aerodynamic index	0.09	0.01
morphological index of the take-off	0.53**	0.28
SPECIAL MORPHOLOGICAL – MOTORIC INDEX	0.48**	0.23
basic morphological index	0.20	0.04
special morphological – motoric index	0.52**	0.27

COMPUTER SIMULATED SKI JUMPING: THE TIGHTROPE WALK TO HIGH PERFORMANCE

Wolfram Müller and Bernhard Schmölzer

Institute of Medical Physics and Biophysics, Karl-Franzens University Graz, Austria
Communicating author, wolfram.mueller@uni-graz.at

INTRODUCTION

Straumann (1927) developed a first analytical model of ski jumping. Jump length optimisation (using a simplified approach) has been discussed by Remizov (1984). We have developed a modelling concept that contains the dependency of the aerodynamic lift and drag areas functions L(t) and D(t) to the flight position (Müller et al. 1995; Müller et al. 1996).

METHODS

For the simulation of the effects of parameter and initial value variations on the jump length a reference jump that had been described in detail before (Schmölzer and Müller, 2002) has been used as a starting point. Characteristics of the reference jump: Approach velocity $v_0 = 26$m/s; take-off velocity perpenticular to the ramp v_{p0} = 2.5m/s; mass of athlete with his equipment m = 65kg. All simulations use the new profile of the jumping hill in Innsbruck (K = 120; Müller and Schmölzer, 2002).

RESULTS AND DISCUSSION

The Figures 1 to 3 point out that the jump length is substantially influenced by several factors: v_0, v_{p0} (due to the athlete's jumping force), L(t) and D(t), by the wind u blowing, and by the mass m. Ski jumpers are very light (Müller, 2002). L and D depend on the individual flight style and the equipment.

SUMMARY

The simulation of the flight phase in ski jumping enables a detailed investigation of the effects of all initial value and parameter variations that influence the flight and gives us a deeper insight into the extremely difficult multidimensional optimisation problem a ski jumper has to solve in real time.

REFERENCES

Straumann, R. (1927). In: *Jahrbuch des Schweizerischen Skiverbandes*, 34-64.
Remizov, L. P. (1984) *J. Biomech*; **17**, 167-171.
Müller, W. et al. (1995). *Nature*, **375**. 455.
Müller, W. et al. (1996) *J. Biomech*, **8**. 1061-68.
Schmölzer, B., Müller, W. (2002) *J. Biomech*, (accepted).
Müller, W., Schmölzer B. (2002). *Proceedings of WCB 2002*
Müller, W. (2002) Proceedings ACSM 2002 (in press)

ACKNOWLEDGEMENTS

Supported by: IOC, FIS, FWF (P14388,P15130),Land Stmk.

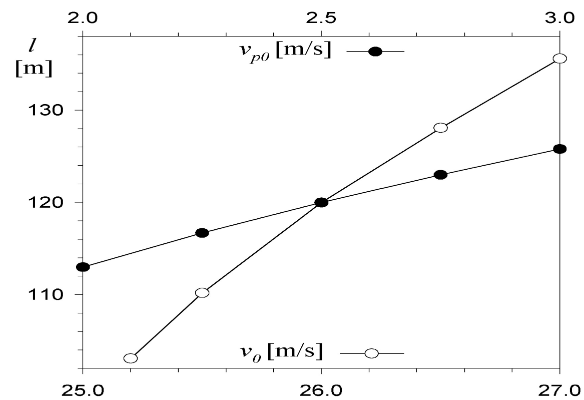

Figure 1: Jump length l, in-run velocity v_0, velocity perpendicular to the ramp v_{p0}. Slopes at l=120m: 16.2m/ms^{-1};12m/ms^{-1}

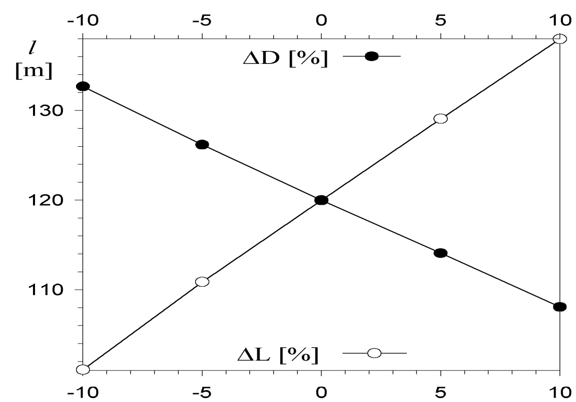

Figure 2: Effects of shifts of L(t) and D(t) functions on the jump length. Slopes: L: 1.8 m/ %; D: -1.2 m/%.

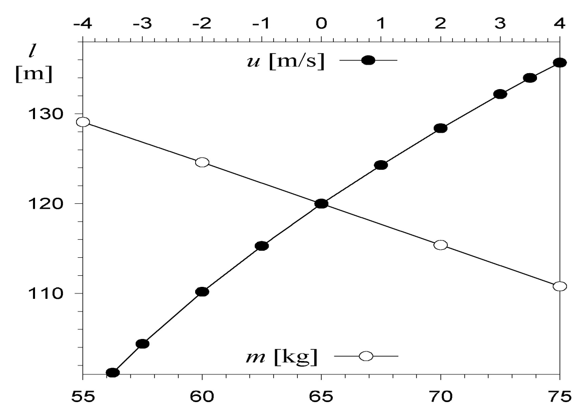

Figure 3: Mass m, wind u ; u positive for wind blowing constantly up the hill (ζ = 130°, with respect to x-axes) and neg for wind from behind (320°). Slopes: -0.9m/kg ; 4.3m/ms^{-1}

CHANGES IN MECHANICAL PROPERTIES OF HUMAN TIBIALIS ANTERIOR MUSCLE FOLLOWING REPEATED ECCENTRIC CONTRACTIONS

Yasuo Kawakami, Toshiyuki Kurihara, Kentaro Chino, Toshiaki, Oda, Kazunori Nosaka*, and Tetsuo Fukunaga
Department of Life Sciences (Sports Science), The University of Tokyo, Komaba, Tokyo, Japan
*Graduate School of Integrated Science, Yokohama City University, Kanagawa, Japan
E-mail: kawakami@idaten.c.u-tokyo.ac.jp

INTRODUCTION

It has been recognized that skeletal muscles are prone to microstructural injury after eccentric contractions. Evidence from humans and other animals points to disruption at the level of sarcomeres as an early step in the damage process (Fridén and Lieber, 1992; Jones et al., 1997) that alters mechanical characteristics of muscle fibers (Morgan, 1990). In the present study, we investigated changes in mechanical properties of human muscle following repeated eccentric contractions by directly looking at muscle fiber behavior *in vivo*.

METHODS

The subjects were six healthy women and men (18 - 21 yr). Each subject performed maximal voluntary eccentric, unilateral dorsiflexion exercises (100 times) by using an isokinetic dynamometer (Con-Trex, Switzerland) at 60 deg/s. The range of motion of the ankle joint was between -15 and 45 deg of plantar flexion. Before and immediately after the exercise, and after 1, 2, 3, and 4 days (n=3 for day 4), the maximal isometric dorsiflexion torque was measured with ankle positioned at -5, 0, 5, 10, 15, 20, 25, and 30 deg. During the measurement, longitudinal ultrasound images were taken from the tibialis anterior muscle (TA) and fascicle length was determined.

RESULTS

Muscle soreness emerged immediately after the exercise, then peaked after 1 day, and gradually subsided thereafter. The decrease in the range of ankle joint motion followed a similar pattern. The maximal isometric torque decreased after the exercise, then began to increase from day 1 through day 3 but did not fully recover to the initial level. The relationship between ankle angles and passive dorsifllexion torque did not change over the testing period (Fig. 1). The relationship between TA fascicle length and dorsiflexion torque showed a clear shift downward (to lower torque) and to longer fascicle length after the exercise, which gradually came back to the initial position (Fig. 2).

DISCUSSION

The decrease in the maximal torque associated with muscle soreness clearly indicates occurrence of muscle damage by the eccentric exercise (Nosaka et al., 1996). The shift in fascicle length – torque relationship is in concert with the model by Morgan (1990), i.e., "popping sarcomeres" due to excessive lengthening that results in transformation of some sarcomeres into passive elastic tissue. The shift in the length-torque curve downward to longer fascicle length could have been due to an increase in series compliance (damaged sarcomeres) within the fascicle, and a decrease in elongation of external series elastic component (tendons). This change, however, was not evident from observations at the joint level.

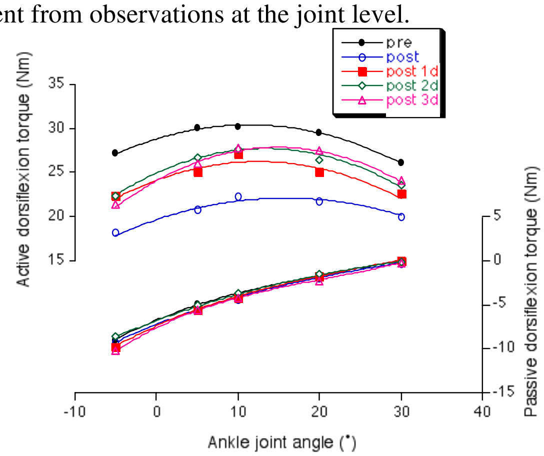

Figure 1: The isometric torque–ankle angle relationship before, immediately after, and 1, 2, 3, 4 days following eccetntric exercise (average of six subjects)

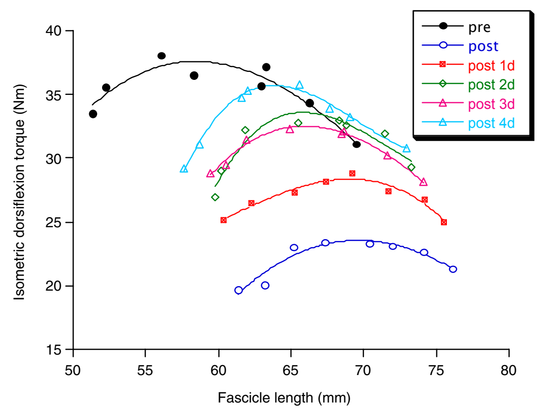

Figure 2: The isometric torque–fascicle length relationship (an example from one subject)

REFERENCES

Fridén, J., Lieber, R. L. (1992). *Med. Sci. Sports Exerc.,* **24**, 521-530.
Jones, C. et al. (1997). *Eur. J. Appl. Physiol.,* **76**, 21-31.
Morgan, D. L. (1990). *Biophys. J.,* **57**, 209-221.
Nosaka, K., Clarkson, P. M. (1996). *Med. Sci. Sports Exerc.,* **28**, 953-961.

MECHANICAL COUPLING OF HUMAN MUSCLES AT VERY LOW FORCES

S.C. Gandevia[1] and R. D.Herbert[2]
[1]Prince of Wales Medical Research Institute, University of New South Wales, and [2]School of Physiotherapy, University of Sydney, Sydney, Australia (s.gandevia@unsw.edu.au)

INTRODUCTION
The neural output to muscle and sensory feedback from it will be influenced by the mechanical coupling of muscle fibres and tendons. This has been studied extensively at high forces, but much less at the very low forces used in many everyday motor tasks. The present studies were designed to examine the coupling behaviour of muscle fibres and tendons at very low levels of tension.

METHODS
In the main studies we used ultrasonography to measure changes in the length of muscle fascicles in the relaxed muscles operating at the human ankle (tibialis anterior and medial gastrocnemius). Anthropometric data were used to derive changes in total length of the muscle-tendon unit across a range of ankle (and knee) angles (for detail see Herbert et al. 2002). In additional studies the transmission of forces within muscle was examined indirectly using the contraction of single motor units during weak voluntary contractions of the multitendoned flexor digitorum profundus (< 2% maximum). Spike-triggered averages of the forces under each finger were measured. Lateral force transmission should mean that forces from a motor unit associated with voluntary movement of one finger spread to adjacent fingers.

RESULTS AND DISCUSSION
Overall there was a quasi-linear relation between the changes in fascicle length and the total change in muscle-tendon length. However, in relaxed muscles, the muscle fascicles underwent much smaller changes in length than the muscle-tendon unit. The slope of the relationship between fascicle length and total length was 0.55 ± 0.13 for tibialis anterior and 0.27 ± 0.09 for medial gastrocnemius. These slopes remained well below unity for a range of muscle conditioning manoeuvres. These values could not be fully explained by muscle pennation, or by slackness at the shortest lengths we examined. This suggests that the tendency for passive movement to be taken up by the tendon was greater for gastrocnemius than tibialis anterior ($P<0.01$).

Simple calculations show why changes in tendon length must occur at low forces. Changes in muscle length that accompany passive rotation across the full physiological range often greatly exceed the rest length of muscle fascicles. If tendons were inextensible at low forces, muscle fibres would experience impossibly large strains. We deduced that tendons may undergo changes in length that are greater than changes in muscle fascicle length, even though tendons experience smaller strains. This is because the rest length of tendons is often much greater than that of their muscle fascicles.

In the second study, the forces triggered by the discharge of single motor units in flexor digitorum profundus were not uniformly distributed to the fingers. For example, units associated with the index finger distributed more than 90% of their force to the index finger. The ring finger behaved similarly. However, units in the little finger appeared to distribute a greater fraction of their force to the ring finger.

The results suggest that for muscles that do not become slack across parts of their working range, some degree of 'in-series' compliance takes up a significant amount of total length changes. Furthermore, the study of multitendoned muscles may help to place an upper limit on the degree to which intramuscular force transmission at low forces affects performance.

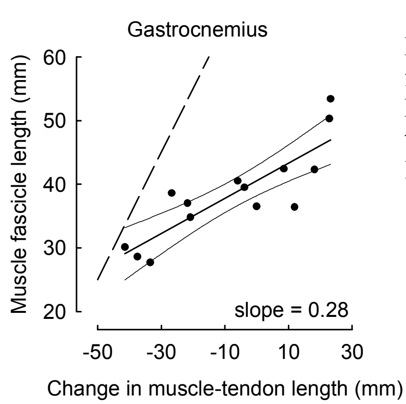

Figure 1. Data from one subject. Fitted slope is less than one (dashed line).

REFERENCES
Herbert, R.D., Mosley, A.M., Butler, J.E. and Gandevia, S.C. (2002). *Journal of Physiology,* **539**, 637-645.

ACKNOWLEDGEMENTS
We are grateful to NHMRC for support, and to S. Kilbreath and R. Gorman for the data relating to finger muscles.

JUMPING INTENSITY DETERMINES THE BEHAVIOR OF THE FASCICLE AND TENDON PARTS OF THE VASTUS LATERALIS MUSCLE

Paavo V. Komi, Masaki Ishikawa and Taija Finni
Neuromuscular Research Center, Department of Biology of Physical Activity, University of Jyväskylä, Finland

INTRODUCTION

Power output of the human skeletal muscle is under influence of muscle-tendon elasticity. In normal stretch-shortening cycle (SSC) activities the interaction between contractile (fascicle) and tendon structures are somewhat controversial. The basic definition of the eccentric part of SSC refers to lengthening of the muscle while it is activated. This concept refers naturally to the entire muscle tendon unit (MTU), but its validity has been questioned to apply to the contractile tissue (Griffits, 1991; Belli & Bosco, 1992). The present study was designed to examine the behavior of both the contractile (fascicle) and tendon parts of the vastus lateralis (VL) muscle during varying intensity SSC jumps performed in a special sledge apparatus.

METHODS

Eight young male subjects performed one-legged drop jumps (DJ) from the predetermined constant dropping height in a sledge apparatus (Kyröläinen & Komi; 1995). Four different rebound heights were designed as low (80% maximum squat jumping height; SJH), middle (90% of SJH), high (110% of SJH) and maximum intensities. The knee angular movement from contact to lowest position was kept the same in all jumping conditions. The subjects were given visual feedback to control the predetermined lowest position with the knee and ankle angles and the target jumping height. Measurement of EMG activities of the vastus lateralis muscle (VL) was made simultaneously with ultrasound recording of the fascicle length changes. In addition, one subject performed all jumps with an optic fiber inserted into his patellar tendon for in vivo force recordings. During trials kinematic, force plate, ultrasonographic, EMG and patella tendon force data were time synchronized.

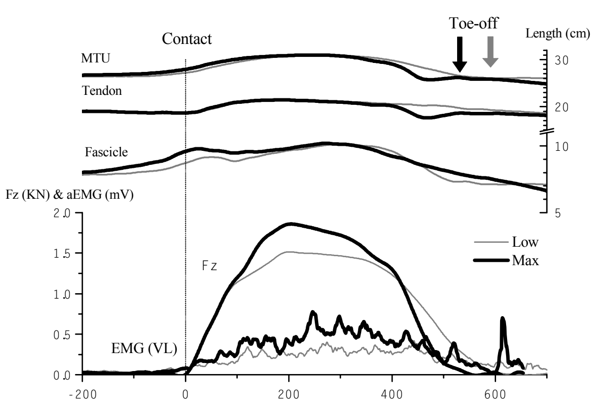

Figure 1: Length changes of MTU, tendon and fascicle drawn together with ground reaction force and EMG recordings during low and maximal jumps.

RESULTS AND DISCUSSION

The results indicated that in all conditions the fascicle, tendon and MTU were stretched during the braking (eccentric phase) and shortened during the subsequent concentric phase. Fig. 1 presents these results for the low and maximum intensity rebound conditions. When the VL force was plotted against the MTU velocity (fig. 2) the obtained curves represent the expected F-V relationship for SSC activities (Komi; 1990; Finni et al, 2001). A more detailed examination of the fascicle and tendon length changes revealed that their behavior was different when jumping (rebound) intensity was varied. The fascicles followed different response curves compared to either tendon or MTU. As expected the fascicles demonstrated higher stiffness in the braking phase and the tendon shortening increased in the push off phase with increased jumping intensities.

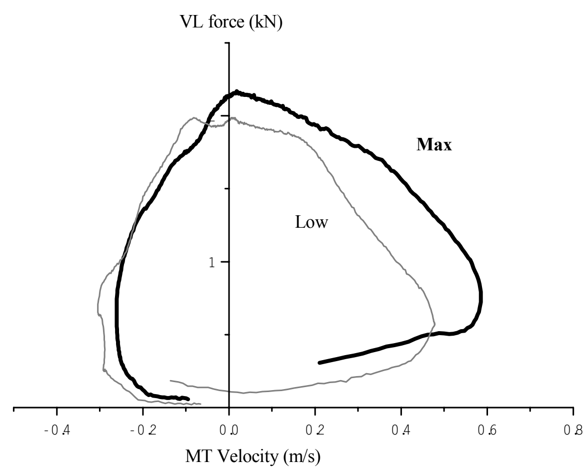

Figure 2: Instantaneous force-velocity curves of the vastus lateralis muscle in the two intensity jumps.

The observed results must be interpreted to apply to the VL muscle only and to the used SSC exercises. Within this limitation the results confirm the hypothesis that in SSC exercise the performance potentiation results partly from increased muscle stiffness operating efficiently to make the tendon recoil during the push off phase.

REFERENCES

Finni et al (2001) *Acta Physiol Scand* **173**, 369-377
Kyröläinen & Komi (1995) *Eur J Appl Physiol* **70**, 36-44
Belli & Bosco (1992) *Acta Physiol Scand* **144**, 401-408
Griffits (1991) *J Physiol* **436**, 219-236
Komi (1990) *J Biomechanics* **23(1)**, 23-34

MUSCLE CELLULAR AND ARCHITECTURAL CHANGES DUE TO CHRONIC SPASTICITY

Richard L. Lieber and Jan Fridén
Department of Orthopaedics and Bioengineering, Department of Hand Surgery
University of California, San Diego, USA and Göteborg University, SWEDEN
e-mail: rlieber@ucsd.edu

INTRODUCTION

Spasticity that occurs after brain injury can cause severe joint deformity and dramatically affect quality of life. While muscle spasticity is neural in origin there is good evidence that spastic muscles are themselves abnormal. However, there are a paucity of objective data available regarding the properties of normal and spastic human muscle and muscle cells. Thus, the purpose of these studies were to measure sarcomere length-joint angle and isolated material properties of normal and spastic hum muscle.

METHODS

Twelve subjects with radial nerve palsy were used to represent flexor carpi ulnaris (FCU) sarcomere length of "normally innervated" muscle, even though the patients themselves required surgical treatment. While the extensor muscles were denervated, the FCUs had normal central and peripheral innervation. Patients with spasticity ranged in age from 13 to 34 and were receiving tendon transfers secondary to cerebral palsy (n=5) or head injury (n=1). Muscle biopsies were also obtained from normal (n=25) or spastic muscles (n=15) secondary to other surgical procedures. Sarcomere length was measured by intraoperative laser diffraction (Lieber et al. 1994) and cellular passive mechanical properties by in vitro biomechanics (Magid and Law, 1983)

RESULTS

Spastic FCU muscles had extremely long sarcomere lengths with the wrist fully flexed (3.48 ± 0.44 μm) compared to the FCU muscles of patients with radial nerve injury (2.41±0.31 μm; Fig. 1

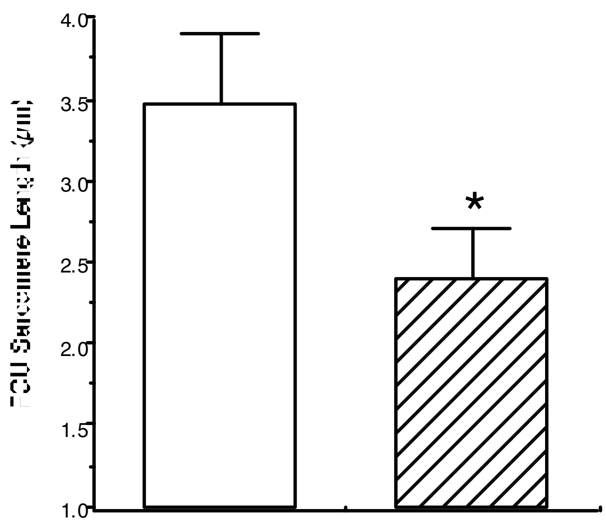

Figure 1: Sarcomere length of normal FCU (hatched bar) compared to spastic FCU. Spastic FCU sarcomere length was significantly longer than normal (asterisk).

In three of the patients with spastic wrist flexion contractures, the slope of the FCU sarcomere length-joint angle relationship was measured and found to be, essentially, normal (0.017±0.005 μm/°, n=3) suggesting that serial sarcomere number (and therefore muscle fiber length) was unchanged in spite of the dramatic absolute sarcomere length change.

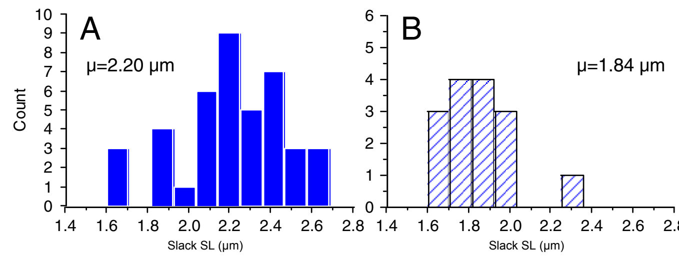

Figure 2: Histogram of resting sarcomere length of normal muscle cells (A) compared to spastic muscle cells (B). Spastic resting sarcomere length was significantly shorter than normal.

DISCUSSION

The most dramatic effect observed between cell types, was the consistent and relatively large resting sarcomere length difference between groups. While normal fibers had a resting sarcomere length of 2.20±0.04 μm, spastic fibers were about 20% shorter with an average resting sarcomere length of only 1.84±0.05 μm (Fig. 2, p<0.001). Tangent modulus of the sarcomere length-stress relationship in spastic fibers (55.00±6.61 kPa) was almost double that measured in normal fibers (28.25±3.31 kPa, p<0.001). Overall, these results indicate that spasticity results in a major alteration of normal muscle-joint anatomical relationships. Such an alteration appears unprecedented in either the muscle plasticity or neuromuscular disease literature. In addition, the fact that spastic muscle cells have a shorter resting sarcomere length and increased modulus suggests dramatic remodeling of muscle structural components. While there is evidence in the literature for significant remodeling of muscle after spasticity (Rose et al. 1994; Sinkjaer et al 1993) he details of this remodeling remains to be elucidated.

LITERATURE REFERENCES

Lieber, R. L. et al. J. Neurophysiol. **71**, 874-881;1994.
Magid, A. & Law, D. J. Science **230**, 1280-1282;1985.
Rose, J. et al. J. Orthop. Res. **12**, 758-768;1994.
Sinkjaer, T. et al. J. Muscle & Nerve **16**, 69-76;1993.

ACKNOWLEDGMENTS

This work was supported by the NIH and the Department of Veterans Affairs Rehabilitation Engineering Research & Development Service.

EFFECTS OF RESISTANCE AND STRETCHING TRAINING PROGRAMS ON THE VISCOELASTIC PROPERTIES OF TENDON STRUCTURES IN VIVO

Tetsuo Fukunaga, Keitaro Kubo, and Yasuo Kawakami
Department of Life Science (Sports Sciences), University of Tokyo,
Komaba 3-8-1, Meguro-ku, Tokyo 153-8902, Japan

INTRODUCTION

Resistance training and stretching have been commonly used for increasing the performances during various human movements. However, we have little knowledge on the influences of these exercise programs on human tendon structures. Recent our observations showed that the execution of either muscle contractions or stretching changed transiently the tendon properties (Kubo et al. 2001a,b). Therefore, it is likely that the tendon properties will be changeable through regular resistance and/or stretching exercises. The present study examined whether resistance and stretching training programs altered the viscoelastic properties of human tendon structures in vivo.

METHODS

Eight subjects completed 8 weeks (4 days /week) of resistance training which consisted of unilateral plantar flexion at 70% of one repetition maximum with 10 repetitions per set (5sets/day). They performed the resistance training on one side (TR) and the resistance training and static stretching training (10 min/day, 7 days/week) on the other side (TRST). Other 8 subjects performed the static stretching training (10 min/day, 7 days/week) on one side (ST) and served as control on the other side. Before and after training, the elongation of the tendon structures in the medial gastrocnemius muscle was directly measured using ultrasonography, while the subjects performed ramp isometric plantar flexion up to the voluntary maximum, followed by a ramp relaxation. The relationship between estimated muscle force (Fm) and tendon elongation (L) was fitted to a linear regression, and then the slope of which was defined as stiffness of the tendon structures. The hysteresis was calculated as the ratio of the area within the Fm−L loop to the area beneath the load portion of the curve.

RESULTS AND DISCUSSION

The stiffness increased 25 ± 13 % for TR and 23 ± 20 % for TRST, respectively. There was no significant difference in the relative increase of stiffness between TR and TRST. The hysteresis, on the other hand, decreased 17 ± 20 % for TRST, but unchanged for TR. For ST, the stretching training produced no significant change in stiffness, but decreased hysteresis 37 ± 26 % . In addition, we investigated the effects of resistance and stretching training on the electromechanical delay, rate of torque development, plantar flexion torque with and without prior stretch. These results suggested that the resistance training increased the stiffness of tendon structures as well as muscle strength and size, and the stretching training affected the viscosity of tendon structures but not the elasticity.

REFERENCES

Kubo, K. et al (2001a) J Appl Physiol, **90**, 520-527.
Kubo, K. et al (2001b) J Appl Physiol, **91**, 277-282.

ANKLE AND SUBTALAR KINEMATICS OF THE ANKLE JOINT WITH INTACT, INJURED, AND RECONSTRUCTED LATERAL LIGAMENTS

D. Rosenbaum[1], H.P. Becker[2], R. Schmidt[2], A. Wilke[3], E. Cordier[3], S. Neller[3], L. Claes[3], C. Bertsch[1], E. Eils[1]
[1] Movement Analysis Lab, Orthopaedic Department, University Clinics Münster, Münster, Germany, diro@uni-muenster.de
[2] Chirurgische Abteilung, Bundeswehrkrankenhaus Ulm, [3] Unfallchirurgische Forschung & Biomechanik, Universitätsklinikum Ulm

INTRODUCTION

Foot motion occurring in the ankle joint complex takes place in two separate joints, the ankle (or talocrural) and the subtalar (or talocalcaneal) joint. In vivo range of motion measurements of the relative involvement of the two joints is impossible with non-invasive methods. Therefore, it appeared valuable to measure the complex ankle joint motion under well-controlled laboratory conditions and determine the relative involvement of the two joints in the three main movement directions. The present study investigated the 3-D kinematics of the ankle and subtalar joint under intact joint conditions, after sectioning of the lateral ligaments and after reconstruction procedures with anatomical repair and tenodeses.

METHODS

The effect of ligament injuries and subsequent surgical treatment was investigated in fresh lower leg specimens. The specimens were mounted in a foot movement simulator that imposed computer-controlled moments in one direction of rotation allowing unconstrained motion in the other dimensions. Range of motion measurements were performed in the ankle and subtalar joint with two goniometer linkage systems measuring the relative motion between tibia-talus and talus-calcaneus. The measurements were repeated with the same specimens after ligament sectioning and reconstruction procedures in order to allow for intra-individual comparisons. After testing the intact joint the measurements were repeated following simulated ligament injuries by cutting the anterior talofibular and calcaneofibular ligament (condition **LC**).

In the first part of the project, three types of tenodeses were performed according to Evans (**EV**), Watson-Jones (**WJ**) and Chrisman-Snook (**CS**).

In the second part, the ligaments were fixed with different anatomical reconstruction procedures: direct repair (**DR**), peroneus tendon transplant (**TT**), carbon fiber graft (**CF**).

RESULTS

Ligament lesions led to an increased inversion and internal rotation predominantly in the ankle joint (Fig. 1). The reconstruction procedures with tenodeses reduced the range of motion in the ankle joint complex but achieved this stabilizing effect by reducing the range of motion in the subtalar joint to an non-physiologic level without correcting the ankle joint instability (Fig. 2). The most pronounced influence was seen after Evans tenodesis whereas the least interfering reconstruction was achieved with the Watson-Jones procedure In general, the anatomical repairs led to a better restoration of joint kinematics than the tenodeses. In the ankle and subtalar joint the direct repair achieved the best result.

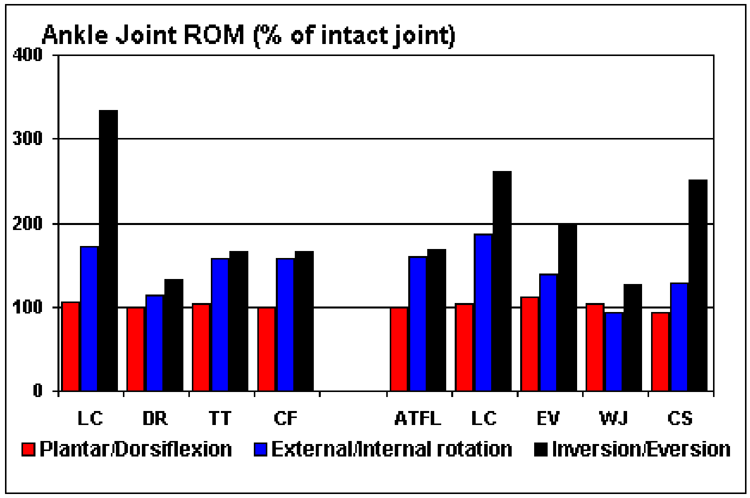

Fig. 1: Changes in ankle joint range of motion normalized to the intact joint (for abbreviations see text).

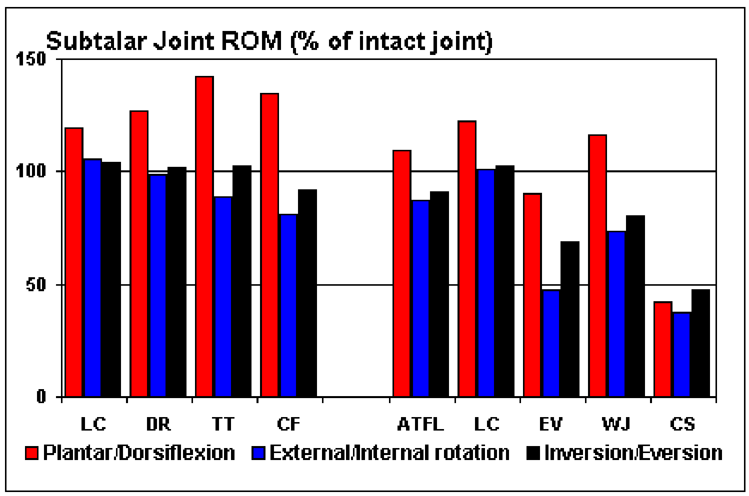

Fig. 2: Changes in subtalar joint range of motion normalized to the intact joint (for abbreviations see text).

DISCUSSION AND CONCLUSION

The presented results reveal that tenodeses restored ankle joint complex stability at the expense of overcorrecting at the subtalar joint. Anatomical procedures resulted in more physiologic joint kinematics. In general, these findings underline the necessity for anatomical treatment of chronic ankle instability that appears superior to the investigated tenodeses.

ACKNOWLEDGEMENT:

This project was supported by the German Research Society (DFG grant # CL77/3-2).

THE EFFECT OF DAMAGE TO THE LIGAMENTOUS SUPPORT OF THE ARCH ON THE FUNCTION OF THE POSTERIOR TIBIALIS TENDON.

Carl Imhauser, M.S.[1], Nicholas A. Abidi, M.D.[2], David Z. Frankel[3], Sorin Siegler, Ph.D[4].

[1]Drexel University, Department of Mechanical Engineering and Mechanics, carl.imhauser@drexel.edu
[2]Attending Physician, Dominican Hospital, Orthopedic Surgeons of Santa Cruz
[3]Medical Student, Jefferson Medical College

INTRODUCTION

The posterior tibialis tendon (PTT) has been described in the clinical literature as a stabilizer of the medial longitudinal arch and of the hindfoot, particularly during the heel-off phase of gait (Baumhauer,1997). Specifically, this muscle counteracts forces and moments, which evert and plantarflex the hindfoot and flatten the arch. Consequently, PTT dysfunction often leads to progressive flatfoot deformity (Gould,1980). This deformity is often associated with excessive stretching of several ligaments, namely the Spring Ligament, Deltoid Ligament, Long Plantar Ligament and Plantar Aponeurosis (Kitaoka,1998). It was hypothesized that disruption of the ligaments reduces the PTT's ability to control the stability of the arch resulting in a progressive collapse of the arch. However, little work has been done to investigate how disruption of these ligaments affects the ability of the PTT to maintain the geometry of the arch. The purpose of this study was to test this hypothesis.

METHODS

An experiment was conducted on five fresh frozen cadaveric lower limbs. The experimental system provided a model of the loading conditions on the foot during heel-off. It consisted of a loading frame interfaced to a tensile testing machine. The tensile machine provided the axial load, and the muscle forces were applied through a system of weights, cables and pulleys. Each specimen was configured in the heel-off position and the load on the PTT was removed to simulate total tendon disruption. Each specimen was tested in the intact condition and after each of the ligaments was sectioned. The order of ligament sectioning was changed between specimens. Geometric data was recorded after each unloading stage. Arch architecture describing the geometric relationship between the bones of the medial longitudinal arch was analyzed from a sagittal projection of the bones (Figures 1,2).

RESULTS AND DISCUSSION

In the intact state, the most significant effects of the PTT on arch architecture were in dorsiflexing the talus and increasing the height of the navicular and medial cuneiform. After the Spring Ligament was sectioned, the PTT still controlled the height of the arch, but its effectiveness in controlling the talus and the height of the navicular was compromised (Figure 1). The PTT still acted to control the inclination of the talus after the plantar ligaments were sectioned but its effectiveness in controlling arch height was compromised as it could not restore the medial cuneiform to its original intact height (Figure 2).

The Effect of the PTT after Sectioning the Spring Ligament

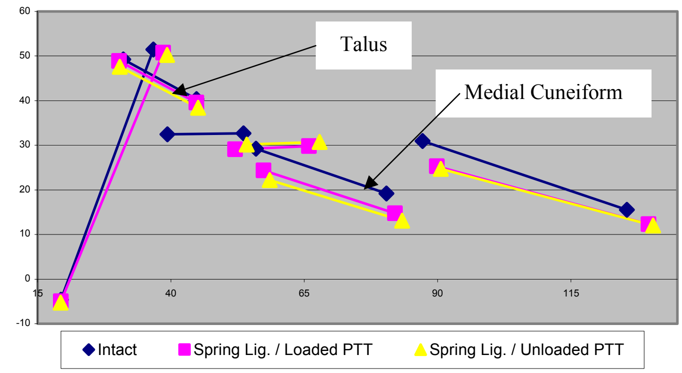

Figure 1

The Effect of the PTT after Sectioning the Plantar Ligaments

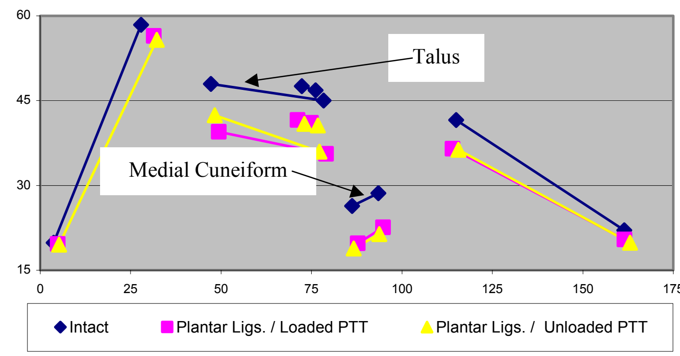

Figure 2

SUMMARY

Similar to previous studies, it was found that the PTT controls arch architecture primarily by dorsiflexing the talus and increasing the height of the navicular and cuneiform bones (Kitaoka,1998). Sectioning the plantar ligaments compromised the PTT's ability to control the height of the medial cuneiform. Sectioning the spring ligament compromised the PTT's ability to control the height of the navicular and dorsiflex the talus. These results suggest that surgical treatment of advanced stages of PTT dysfunction must address both the dysfunction of the PTT as well as the collapsed arch.

REFERENCES

Baumhauer, JF. (1997). Foot and Ankle Clinics, 2(2)
Gould, N, et al (1980) Foot Ankle, 1(1)
Kitaoka, HB, et al (1998). Foot Ankle Int, 19(7)
Kitaoka, HB, et al (1997). Foot Ankle Int, 18(1)

FINITE ELEMENT MODELING OF TOTAL ANKLE REPLACEMENTS FOR CONSTRAINT AND STRESS ANALYSIS

Terence E. McIff [1], Greg A. Horton [1], Charles L. Saltzman [2], Thomas D. Brown [2]
[1] Orthopedic Research Laboratory, University of Kansas Medical Center, Kansas City, Kansas, USA, tmciff@kumc.edu
[2] Orthopaedic Biomechanics Laboratory, University of Iowa, Iowa City, Iowa, USA

INTRODUCTION

Interest in ankle joint replacement has increased due to the encouraging survival rates reported of lately in the literature and at professional conferences. Less-than-satisfactory results with a variety of implant designs had previously left the orthopedic community apprehensive about including ankle replacement among the recommended treatments for painful ankle. In comparing early implants with those of the more recent successful implants, several design and technique distinctions can be made. Many of these characteristics, particularly low constraint, are now credited with contributing to the increased success being seen. Nevertheless, since most total ankle implants were originally developed without the aid of concerted engineering design efforts, little is known about their biomechanics. Likewise, due to the many early failures experienced, lower number of ankles replaced, and few retrievals available, objective long-term clinical assessment of the ankle arthroplasty lags far behind that of hip and knee replacement. Now with more ankles being replaced annually, a closer engineering examination of current ankle replacement designs and techniques is warranted in the hopes of averting any potential long term failure, improving design, and encouraging acceptance of this potentially beneficial treatment option. This paper reports on the use of FE methods to examine the relationship between intrinsic constraints, polyethylene stress, and wear in two types of total ankle replacements. A two-component low-constraint device (Agility) and a mobile bearing device (STAR) were examined.

METHODS

Finite element models of the total ankle implants were constructed using Patran 2000 based on manufacturer supplied geometry in the form of IGES files. Analysis was performed using Abaqus 6.1. All software ran on a high performance NT based workstation. Tibial and talar metallic components were modeled as rigid bodies. Polyethylene components were modeled using a finite element mesh comprised of reduced-integration, 8–node Hex elements, or modified 10-node Tet elements, and used an elastic-plastic constitutive model. In the case of the two-component device, (Fig. 1) the superior surface of the polyethylene device is constrained by the metallic tibial backing so contact was modeled between the polyethylene and talar component only. Models of the mobile bearing device (Fig. 2) required two contact interfaces, one at the polyethylene superior surface and one at the inferior surface. The polyethylene bearing in the mobile bearing device is, once loaded, constrained solely by friction and the topography of the contact surfaces. In both models a finite-sliding contact formulation was used at the contact interfaces. The intrinsic constraints provided by each implant were evaluated by observing relative displacement as a function of applied load. To examine relative contact mechanics and wear potential, quasi-static ankle loading and displacement conditions, representative of those found in normal gait, were applied to the models. Contact and internal stress distributions were recorded for each implant.

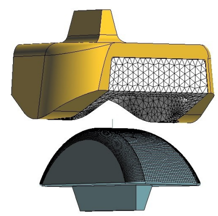

Fig 1. Two-Component Device

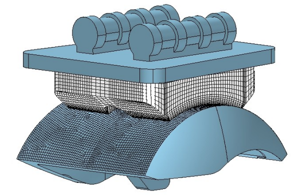

Fig 2. Mobile Bearing Device

RESULTS AND DISCUSSION

The contact stress distribution of the two-component device is highly sensitive to relative position and orientation of the components. In this device, high polyethylene contact and internal stresses result when congruency is lost. Several loading configurations, most notably those including internal/external rotational torque in the physiologic range, resulted in loss of congruent contact between polyethylene bearing surface and the talar component. This phenomenon resulted in point and line contact yielding very high contact and internal stresses (> 96 MPa at 5X body weight) in the polyethylene that are predictive of local wear and plastic deformation. Once loss of contact is initiated through torsional rotation, inversion/eversion stability is increasingly lost. Polyethylene yield stresses were reached with as little as 1X body weight axial load and 1.3 Nm torque. Based on the stresses predicted, permanent polyethylene deformation and high local wear can be expected to occur during many physiologic loading activities. In the mobile bearing device, wear is predicted to occur primarily on the inferior surface of the polyethylene bearing where both larger motion and larger contact stresses were found. Despite the maintenance of congruency, contact stresses were not evenly distributed across contact areas and were a function of loading configuration. During flexion of this mobile bearing device, max contact stresses (over 30 MPa were predicted at 5X body weight) were elevated (up to 2X) by friction forces during flexion and by applied shear forces or version moments.

MECHANICAL STABILITY OF ANKLE BRACES UNDER PASSIVE AND DYNAMIC LOADING CONDITIONS

Eric Eils[1], Dieter Rosenbaum[1], Christina Demming[1], Guido Kollmeier[1], Lothar Thorwesten[2], Klaus Völker[2]
[1]Movement Analysis Lab, Orthopaedic Department, [2]Sports Medicine
University Clinics Münster, Münster, Germany, eils@uni-muenster.de

INTRODUCTION

Mechanical stability of ankle braces may either be evaluated under passive or dynamic conditions (Podzielny/Hennig 1997; Siegler et al. (1997). Passive condition refers to a situation where the ankle joint complex is moved passively in different directions in an unloaded situation. Dynamic condition refers to a situation where subjects are subjected to a fast inversion event on a tilting platform simulating an ankle sprain. These two tests provide objective information about the stabilizing effects of various ankle braces either under laboratory or more realistic conditions. However, at this point it remains unclear, if the obtained findings describing the stability of braces under laboratory conditions can be transferred to a more realistic situation when the foot-ankle complex is loaded with bodyweight. Therefore, the aim of the present investigation was to compare the stability of ten different ankle braces under passive and dynamic loading conditions.

METHODS

24 subjects with chronic ankle instability participated in the project (23±3 yrs, 70±12 kg, 177±8 cm). A mechanical fixture was developed to test passively induced stability of ankle braces in three planes with a standardized torque. Rotation axes for plantar/dorsiflexion, inversion/eversion and internal/external rotation were set perpendicular to each other in alignment with the intermalleolar axis, the long axis of the foot on the level of the estimated location of the subtalar joint and the longitudinal axis of the tibia, respectively. To determine individual torques, the leg was fixed without brace and rotated in each direction to the limits of comfort. The maximum torque for each direction was then used for all conditions and the rotational displacement were measured with potentiometers fixed to the axes. For dynamic stability tests a trap door with a tilting angle of 30° in the frontal plane was used to simulate lateral ankle sprains. A customized goniometer was used to measure the hindfoot inversion angle inside the shoe. Ten commercially available ankle braces were used in all subjects. Models were subdivided into three categories (rigid, semi-rigid and soft). One shoe model was used in these investigations and the order of testing conditions was randomized. For comparison , the restriction of motion in relation to the no-brace condition was calculated for each direction. A repeated measures ANOVA with the alpha-level set to 5% and the Scheffe post-hoc test were used for statistical analysis.

RESULTS

Under passive and dynamic loading conditions, all braces restricted the range of motion significantly compared to the no-brace condition (Tab. 1). The most distinct reduction was obtained for inversion. Differences between most semi-rigid and soft braces were significant. A high correlation between passively induced and dynamic inversion was found (r=0.78; p=0.0031). The stabilizing effect was less pronounced during dynamic inversion as compared to passive inversion (Tab. 1).

DISCUSSION

All tested braces significantly restrict range of motion compared to the no-brace condition in passive and dynamic situations. The present results provide an objective basis about mechanical stabilizing characteristics of braces. Correlation between passive and dynamic results for inversion showed that dynamic characteristics are reflected by passive testing but the amount of restriction for dynamic inversion is less than for passively induced movements. Therefore, it should be considered that recommending braces only on the basis of passive support characteristics may be not sufficient for dynamic movements.

REFERENCES

Podzielny, S. and Hennig, E.M. (1997) Clin Biomech, 12, 253-258.
Siegler et al. (1997) J Orthop Sports Phys Ther, 26, 299-309.

Table 1: Passive and dynamic range of motion in % relative to condition without brace. The lower the value, the more effective the restriction.

%±SD	%		01	02	03	04	05	06	07	08	09	10
		No-brace	rigid	semi-rigid					soft			
Passive	Inversion	100	38±10	40±8	37±13	44±10	38±12	54±12	54±12	57±13	56±12	47±11
	Eversion	100	42±10	58±9	53±18	56±12	52±12	70±10	66±12	61±13	71±10	62±11
	Plantar flexion	100	27±13	49±9	47±14	64±8	51±11	60±8	80±8	71±10	77±9	64±10
	Dorsiflexion	100	66±10	52±15	50±20	48±17	51±20	58±15	60±15	52±17	72±15	44±18
	Internal rotation	100	55±22	63±18	61±18	69±19	66±14	75±13	64±20	57±17	69±19	73±17
	External rotation	100	81±13	83±14	79±15	81±12	77±14	86±14	85±11	87±12	87±11	85±12
Dy-namic	Inversion	100	77±10	51±8	51±8	54±10	56±8	69±10	85±13	79±13	85±13	74±10

A FINITE ELEMENT MODEL OF THE FOOT AND ANKLE: VALIDATION OF QUIET STANCE

William R. Ledoux, Ph.D.[1,2], Daniel L. A. Camacho, M.D., Ph.D.[1], Randal P. Ching, Ph.D.[1,2], Bruce J. Sangeorzan, M.D.[1,2]

[1] RR&D Center for Excellence in Limb Loss Prevention and Prosthetic Engineering, VA Puget Sound, Seattle, WA, USA
[2] Department of Orthopaedics and Sports Medicine, University of Washington, Seattle, WA, USA, wrledoux@u.washington.edu

INTRODUCTION

Finite element (FE) models of the foot and ankle are becoming increasingly sophisticated. Our laboratory has developed an anatomically accurate FE model that incorporates physiological material properties. In this abstract we describe the current development and validation of our FE foot and ankle model for simulations of quiet stance.

METHODS

The addition of cartilage bodies and the increased degrees of freedom in the model (allowing more bones to move relative to each other) represents an improvement of our laboratory's FE foot and ankle model (Ledoux et al 2000a; Camacho et al 2001). The bones were modeled as rigid bodies; geometries were obtained from CT scans of a 67-year-old male. The ligaments were modeled as springs and dashpots that were anatomically located (Sarrafian 1993); properties were extrapolated from ankle ligament data (Siegler et al 1988). The plantar soft tissue was modeled with hyperelastic elements; the geometry was obtained from the CT scans and the properties from the literature (Lemmon et al 1997). The anatomical description of the cartilage bodies was obtained from the space between bones. The material properties were not physiologic, but were estimated as 100x stiffer than the plantar soft tissue. The foot bones proximal to the metatarsals were free to move independently. The bones of the first ray were grouped together, as were the bones of the 2nd through 5th rays. The mesh was generated with Truegrid v2.1 and the simulation was run with LS-DYNA v960 (Figure 1).

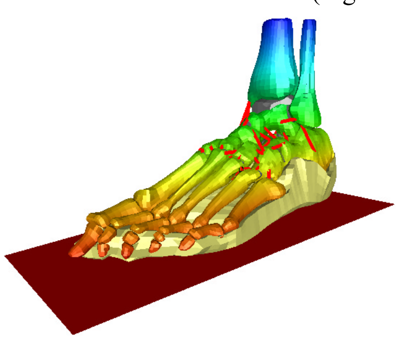

Figure 1: The FE foot and ankle model.

The validation data were collected via a custom designed pneumatic foot-loading frame (Niki et al 2001). The apparatus supported the foot in midstance; a compressive load was applied to the tibia while the tensile forces were applied to the extrinsic muscles. Motion of the bones of the foot (calcaneus, talus, navicular, cuboid, first metatarsal and fifth metatarsal) were quantified with a FastTrak™ Motion Analysis System. Data were collected for a compressive load (400 N) on the tibia and a tensile load (200 N) on the Achilles tendon (Ledoux et al 2000b). For 10 cadaveric feet, the mean and standard deviation (SD) of the motion of the 6 bones in the 3 cardinal planes, representing 18 performance metrics, were quantified and compared to the predicted motion of the model.

RESULTS AND DISCUSSION

The predicted motion of the FE model paralleled the motion measured of the cadaveric study in the sagittal plane (Figure 2). The two bones that were out of range, the 1st and 5th metatarsals, actual dorsiflexed too much because the model lacks any passive structures on the dorsum of the foot to restrict motion. Overall, the motion of the model was within 1 SD for 14 of the 18 motions, and within 2 SD for 17 of 18.

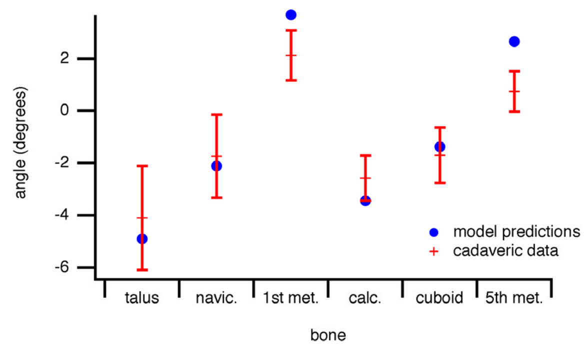

Figure 2: Sagittal plane motion (dorsiflexion = positive, plantar flexion = negative) of the foot bones for the model and cadaveric specimens (mean +/- 1 SD).

SUMMARY

The ability of the FE foot and ankle model to accurately predict bone movement under postural load has been demonstrated in comparison to experimental measures.

REFERENCES

Camacho D.L.A. et al (2002) *J Reh Res & Dev*, **in press**.
Ledoux W.R. et al (2000a) *Proceedings of The World Congress on Med. Physics and Biomedical Eng.*, TH-G325
Ledoux W.R. et al (2000b) *Proceedings of the ASB*, 242-43
Lemmon D. et al (1997) *J. of Biomechanics*, **30**, 615-620.
Niki H. et al (2001) *Foot & Ankle Int*, **22**, 292-300.
Sarrafian SK (1993) In *Anatomy of the foot and ankle: Descriptive, topographic, functional*. J. B. Lippincott
Siegler S. et al CD (1988) *Foot & Ankle*, **8**, 234-242.

ACKNOWLEDGEMENTS

Department of Veterans Affairs, grant A0806C

THE LOCOMOTOR BIOMECHANICS OF LARGE TERRESTRIAL VERTEBRATES

John R. Hutchinson

Biomechanical Engineering, 209 Durand, Stanford CA 94305-4038
jrhutch@stanford.edu

INTRODUCTION

As body mass (m_b) increases during ontogeny or evolution, it is increasingly precarious to maintain locomotor performance (e.g., maximum forward velocity) at the same level, especially when m_b >>100 kg (Garland, 1983). Increasing the relative cross-sectional areas of bones, muscles, and tendons, or the relative lengths of muscle moment arms, is an anatomical specialization that forestalls reduction of locomotor performance at larger sizes. Similarly, adopting a more upright (graviportal, or columnar) limb orientation or using a higher duty factor are behavioral specializations (Alexander, 1985; Biewener, 1990) that can maintain performance. Although the earliest dinosaurs were relatively small ($m_b<10^2$ kg), multiple lineages of dinosaurs such as sauropods, duckbill dinosaurs, and tyrannosaurs evolved gigantism ($m_b>10^3$ kg; approaching 10^5 kg in the case of sauropods; Sereno, 1997). Likewise, elephants secondarily evolved gigantism. I ask, as gigantism evolved in these lineages, did locomotor performance decrease as a consequence of increasing m_b, or did anatomical or behavioral specializations keep performance relatively constant despite increasing m_b?

METHODS

A quasi-static model of *Tyrannosaurus* and other tetrapods was used to estimate the joint moments at mid-stance of rapid bipedal running (Hutchinson & Garcia, in press). These moments, combined with data on muscle anatomy, permitted calculation of how much muscle mass (as a proportion of m_b) would be required to maintain static equilibrium in a given limb orientation. The ratio of the muscle mass dedicated to limb extensors to muscle mass required to balance the limb joints during rapid running is crucial. For extant animals, we used dissections to gather necessary anatomical data, and entered joint angles based on published kinematics. For extinct tetrapods such as *Tyrannosaurus* and smaller dinosaurs, we entered our best estimates of anatomical data and used sensitivity analysis to see how much possible variation in joint angles, muscle fiber lengths and moment arms, and other uncertain parameters changed estimates of the required muscle masses. We also studied healthy elephants in captivity (Hutchinson et al., in press) to see how fast they could move and what gait(s) they used. Trainers in America and Thailand guided 48 elephants (4 African; 44 Asian; m_b~500-5000 kg; age ~2-50 yrs) past stationary cameras (25-200 Hz) to collect kinematic data from ~5-20 trials per elephant.

RESULTS AND DISCUSSION

Giant tetrapods face a particular problem in terms of body composition. As m_b increases, the proportion of m_b that must be dedicated to extensor muscles (and skeletal elements) supporting the body increases. Because total muscle mass is usually ~50% m_b (Hallgrímsson & Maiorana, 2000); less than 40% m_b as extensors; and skeletal mass is <20% m_b (Christiansen, 2001), eventually no more mass can be allocated to extensor muscles or limb bones. In *Tyrannosaurus*, we (Hutchinson & Garcia, in press) showed that roughly 80-90% m_b was required as extensors in order to run quickly with bent limbs. This is impossible, so large dinosaurs like *Tyrannosaurus* presumably straightened their limbs and reduced their relative locomotor performance. Elephants demonstrate that rapid locomotion (>6 m/s, duty factor <0.40, and Froude number >3.0; Hutchinson et al., in press) is possible with columnar limbs but no true aerial phase, which would incur greater impact forces. Elephants maintain walking kinematics as they increase speed, keeping one foot on the ground, but available data suggest that the underlying kinetics switch from walking to running. As size increases, terrestrial vertebrates often first evolve anatomical, then behavioral specializations for maintaining locomotor performance. However, at giant sizes relative and eventually absolute locomotor performance inevitably decline because no specializations can maintain locomotor performance at high levels. Therefore, giant animals are generally restricted to less extreme limb morphologies, gaits, and speeds.

REFERENCES

Alexander, R.McN. (1985). The maximum forces exerted by animals. *J. Exp. Biol.*, **115**, 231-238.

Biewener, A.A. (1990). Biomechanics of mammalian terrestrial locomotion. *Science*, **250**, 1097-1103.

Christiansen, P. (2002). Mass allometry of the appendicular skeleton in terrestrial mammals. *J. Morphol.*, **251**, 195-209.

Garland, T., Jr. The relation between maximal running speed and body mass in terrestrial mammals. *J. Zool.*, **199**, 157-170.

Hallgrímsson, B., Maiorana, V. (2000). Variability and size in mammals and birds. *Biol. J. Linn. Soc.*, **70**, 571-595.

Hutchinson, J.R., Garcia, M. (2002). Could *Tyrannosaurus* run? *Nature*. **415,** 1018-1021.

Hutchinson, J.R., Famini, D., Kram, R., Lair, R. (in press). Do elephants run? *Amer. Zool.*, 2002 abstract volume.

Sereno, P.C. (1997). The origin and evolution of dinosaurs. *Annu. Rev. Earth Planet. Sci.*, **25**, 435-489.

ACKNOWLEDGEMENTS

I thank my collaborators Mariano Garcia, Dan Famini, Rodger Kram, and Richard Lair, and my Ph.D and postdoctoral advisors Kevin Padian (Berkeley) and Scott Delp (Stanford). Part of this material is based on work supported by the National Science Foundation under a grant awarded in 2001.

MECHANICAL POWER PRODUCTION FOR ACCELERATION: THE CHALLENGES OF BEING A BIPED

Thomas J. Roberts

Zoology Department, Oregon State University, Corvallis, OR
robertst@bcc.orst.edu

INTRODUCTION

Running animals face challenges associated with the transition from steady-speed running, where net mechanical power output is low, to acceleration, where muscle function must be altered to maximize power output. Two features of this transition may present particularly difficult challenges for bipedal runners. First, balance must be maintained during acceleration while the direction of the ground reaction force changes significantly. Accelerating quadrupeds can transfer more weight to the hindlimbs to maintain the alignment of the ground reaction force and the center of mass (Lee et al., 1999), and human runners lean forward to position their center of mass anterior of the point of force development (Harland and Steele, 1997). Birds must use an alternative mechanism for maintaining balance, because their body posture cannot be altered to position the center of mass more anterior to the hip. Another challenge facing accelerating bipeds is the potentially limited availability of muscles specialized for work vs. power production. Quadrupeds use the large, long-fibered muscles of the hindlimbs to power jumping and accelerations, while distal muscles with long tendons appear to be specialized for spring-like function (Alexander, 1974). Birds have a large concentration of muscle mass in the distal ankle extensors, and must either use these spring-like muscles to perform net work during acceleration, or power acceleration with only a fraction of their available muscle motor.

This paper presents results from high-speed video and force plate measurements of accelerating turkeys. These measurements were used to determine how accelerating bipeds produce the power for acceleration while still maintaining balance.

METHODS

High speed video and force plate measurements were made for 5 wild turkeys accelerating over a 10 meter trackway. Joint positions were determined by analysis in NIH Image. Joint power outputs for single footfalls were calculated from the joint velocity and joint moment measured from coordinated joint position and ground reaction force measurements. Measurements were taken for single footfalls across a range of accelerations, from steady-speed running to the maximal elicited acceleration.

RESULTS AND DISCUSSION

Peak accelerative horizontal ground reaction forces during maximal accelerations were as much as 50% of peak vertical force. With increasing rate of acceleration, turkeys increased their angle of limb protraction and decreased the angle of limb retraction. The change in limb angles positioned the center of mass more anterior to the point of force application during accelerations, thereby maintaining alignment of the ground reaction force and the center of mass. Total stance limb excursion did not change significantly with acceleration.

Net power output at the ankle increased as a function of acceleration. Approximately half of the total power output required to accelerate the body was produced at the ankle. The high net power output at the ankle is consistent with the idea that the relatively short-fibered, spring-like ankle extensors contribute significant net power during acceleration. Analysis of possible transfer of power from knee extensors to the ankle via biarticular muscles indicates that the relatively limited range of knee extension during stance makes significant power transfer to the ankle unlikely.

SUMMARY

Running turkeys alter limb kinematics to produce the high propulsive forces required for acceleration. This appears to be a sufficient alternative to quadrupeds' redistribution of force between the hindlimbs and forelimbs during acceleration. Turkeys use the muscles of the ankle as force-producing springs during steady-speed running and as power producing motors during acceleration. This adaptability in muscle function may be particularly critical for maximizing accelerative power in avian runners because ankle extensors make up nearly one third of the turkeys' hindlimb muscle mass. Birds meet the challenges of bipedal acceleration with flexibility in limb kinematics and adaptability of function in individual muscles.

REFERENCES

Alexander, R. McN. (1974). *J. Zool. Lond.* **173**, 549-573.
Harland, M. J.,Steele, J. R. (1997). *Sports Med.* **23**, 1 11-20.
Lee, D. V. et al. (1999). *J Exp Biol* **202**, 3565-73.

ACKNOWLEDGEMENTS

Supported by NIH AR46499.

CHANGES IN FLIGHT MORPHOLOGY INFLUENCE THE SHAPE OF THE AVIAN POWER CURVE

Matthew W. Bundle[1] and Kenneth P. Dial
[1] mbundle@selway.umt.edu
Flight Laboratory, University of Montana, Missoula, MT, USA

INTRODUCTION

Investigations into the metabolic cost of flight have yielded power curves of two types, those with a strong dependence upon flight speed (U-shaped) and those that are independent of speed(flat) (Ellington '91). A number of aerodynamic models exist to predict the cost of flight, and all predict power curves that are U-shaped. However, the most accepted of these models (Rayner '93, Pennycuick '89) do not account for changes in airfoil geometry that occur as birds fly across a range of speeds. The influence of airfoil size on the power curve of a flying object can be significant, and birds change their size and shape to an astonishing degree as they fly across their speed range.

Here, we test the hypothesis that birds who dramatically change the surface area of their wings and tail will have a flat power curve. Alternatively, birds with a restricted morphology will have a narrow range of speeds over which they fly economically and will conform to predictions based on aerodynamic theories.

METHODS

Four Budgerigars(38.7g), three Cockatiels(80.5g) and two Black Billed Magpies(190.5g) were trained to fly across a range of speeds in a variable speed wind tunnel while wearing light weight masks designed to capture their expired air. Oxygen consumption and carbon dioxide production were measured using the open flow technique. Simultaneous wing-beat kinematics were obtained from lateral and dorsal high-speed video cameras(500fps).

RESULTS AND DISCUSSION

The budgie and cockatiel power curves show a pronounced U-shape(fig 1). The magpie metabolic power curve by contrast is nearly independent of flight speed. Preliminary kinematic data suggest that magpies reduce the surface area of their wings and tail by 35% as they fly from the slowest to fastest speeds in their range, compared to only 12% for cockatiels.

If a commercial aircraft was able to affect these graduated shape changes, a broad region of flight speeds with no increase in fuel consumption would be produced(thick line fig 2). We suggest that the morphing ability of some bird species may allow them to fly across a range of speeds with little increase in cost, and that this phenomena may explain the existing dichotomy between empirical and aerodynamic studies. We further suggest that avian morphology may play an under appreciated role in influencing the cost of flight.

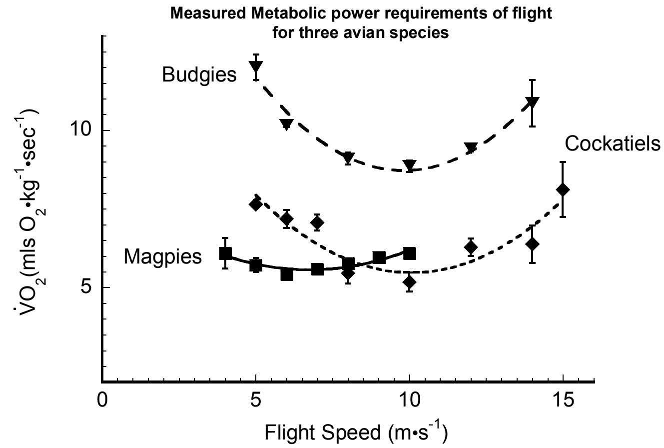

Figure 1: This is the first time where power curves that are qualitatively different have been obtained using the same methodology. These results suggest that a biological rather than experimental event is influencing the shape of the avian power curve.

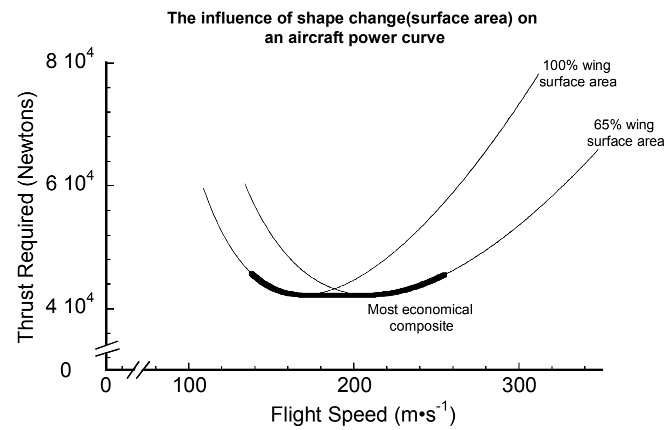

Figure 2: Power curves for a commercial aircraft and for the same aircraft if wing area is reduced by 35%. The thick line shows the power curve that would be produced if an airplane were able to perform graduated shape changes similar to those of a magpie.

REFERENCES

Ellington C.P. (1991) *J. Exp. Biol.*, **160**:71-91.
Pennycuick C.J. (1989). Bird Flight Performance, Oxford University press.
Rayner J.M.V. (1993). *Contemp. Math*, 141:351-400.

CERVICAL SPINE FACET CAPSULAR LIGAMENT STRAIN IN MIDSAGITTAL AND THREE DIMENSIONAL WHIPLASH-LIKE LOADING

Barry S. Myers[1], MD, PhD, Beth A. Winkelstein[2], PhD, Ed K. Chung[1], BS, Roger W. Nightingale[1], PhD, Gunter Siegmund[3], PhD

[1]Department of Biomedical Engineering, Duke University, Durham, NC, USA, barry.myers@duke.edu
[2]Department of Bioengineering, University of Pennsylvania, Philadelphia, PA, USA
[3]MacInnis Engineering Associates & University of British Columbia, Vancouver, BC, Canada

INTRODUCTION

Cervical spine facet capsular ligaments are thought to be an anatomic site of whiplash injury. Biomechanical studies have shown that whiplash loading is complex and includes phases of combined compression-bending and shear. Epidemiology studies have shown that out-of plane loading as a result of pre-impact head rotation also contributes to risk. In-vitro studies, however, have shown that capsular ligaments have little effect on the mechanical properties of motion segments. As a result, low-grade injury to this ligament would have no effect on segmental kinematics despite potentially serving as a source for whiplash symptoms. Accordingly, our goals were to examine the potential for injury by comparing the full-field capsular ligament strain under, one, two and three dimensional in-vitro loads, similar to those that occur in whiplash, to the strains required to produce injury in the ligament.

METHODS

Twenty-five cervical spine C3-C4 and C5-C6 motion segments were mounted in a test frame in the neutral anatomic position. Specimens were mechanically stabilized and then tested in pure flexion-extension bending; and combined posterior shear, extension and compression. Each test was performed with and without an axial torque. Posterior shear loads varied from 0 to 135 N, compression loads varied from 0 to 325 N, flexion/extension moments from 0 to 2.5 Nm, and axial pre-torques were either 0 or 1 Nm. Two photo absorptive target arrays mounted to the facet capsular ligament and the anterior surface of the vertebral body were stereo-imaged to calculate facet capsular ligament Lagrangian large strain field and motion segment kinematics respectively. Strain to failure was measured by isolating the right facet joint of each motion segment and loading it to failure in axial tension or shear at constant velocity (0.0083 mm/s, 10 mm/s, or 100 mm/s). Failure strain was defined by the maximum principal strain measured at a decrease in load with increasing deformation. Failure was defined as sub-catastrophic if the load subsequently increased. Mechanical quantities were then compared using ANOVAs and paired t-tests ($\alpha = 0.05$)

RESULTS

Strain fields were complex and the site of maximum strain varied with donor, motion segment, and loading condition. Maximum strain did not, however, vary between motion segments ($p>0.09$). The addition of an axial pre-torque significantly increased facet capsular ligament strain ($p<0.01$). Strain to catastrophic failure in tension was insensitive to loading rate. Strain to both catastrophic failure (94±84%) and sub-catastrophic failure (35±21%) in shear were significantly larger than strains measured during whiplash-like loading (17.8±5.8%) ($p<0.006$). Two specimens from different donors, however, showed larger strains during whiplash-like loading than at sub-catastrophic failure (Figure 1).

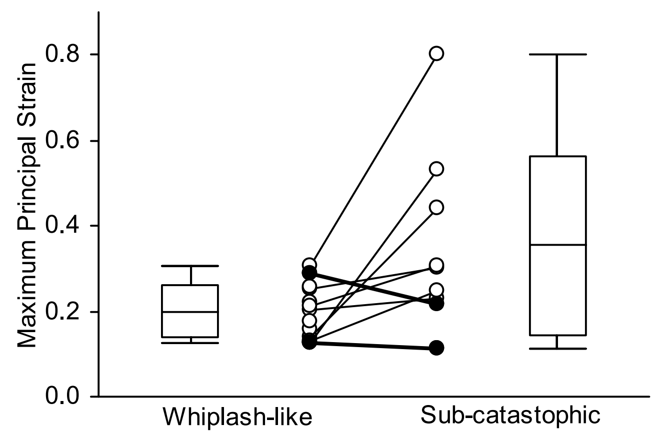

Figure 1. Individual strain data, and mean, range, and variance for nine specimens. While the mean data show no risk for injury, comparison of individual data points illustrates potential sub-catastrophic injury risk in two (heavy line) cases.

DISCUSSION

Although strategies to prevent whiplash are being advocated, the risk for injury, the mechanism of injury, and the site of injury remains unknown. This series of experiments showed that some subjects experienced strains during whiplash-like loading that can cause sub-catastrophic capsular ligament failure. The results also suggested that axial rotation of the head increased injury risk. With the additional strain imposed by muscles that insert directly onto the capsular ligaments, these data provide a biomechanical explanation for injuries to the facet capsular ligaments of some subjects during whiplash collisions.

ACKNOWLEDGEMENTS

This research was supported by the CDC, ISB, NSERC, and the Science Council of British Columbia.

EFFECT OF BUMPER DESIGN ON WHIPLASH INJURY RISK AS MEASURED BY BIORID

David S. Zuby[1] and Adrian K. Lund[2]

Insurance Institute for Highway Safety, Arlington, Virginia, United States
[1]Vice President, Vehicle Research Center, dzuby@iihs.org
[2]Chief Operating Officer

INTRODUCTION

Soft tissue neck injuries, commonly called whiplash, are a frequent and costly consequence of vehicle crashes. The U.S. Department of Transportation estimates 805,000 whiplash cases occur annually, and U.S. insurers pay more than $7 billion yearly to treat these injuries. Efforts to address whiplash include improving vehicle seat and head restraint designs. Special whiplash dummies like BioRID exist, but currently there are no standard test protocols for evaluating the injury protection performance of new designs. A standard test protocol should anticipate the acceleration likely to be encountered in real crashes. This study examines how different bumper designs attached to the same car model affect the car's acceleration in a rear crash and, in turn, whether the differences in vehicle acceleration affect the injury measures recorded on a BioRID in the car's front seat.

METHODS

Four 32 km/h front-to-rear crash tests were conducted with Volkswagen New Beetles, two of which were equipped with standard U.S. bumpers and two with standard European bumpers. The design difference is that hydraulic dampers attach the U.S. bumpers to the car, while crushable steel box elements attach the European bumpers. Each pair of crashes involved cars with the same bumpers. Sensors fixed to the floor of each struck car recorded crash acceleration.

A BioRID was seated in a front seat of each rear-struck car. Sensors on the dummy's head and first thoracic vertebrae (T1) recorded accelerations used to calculate the neck injury criterion (NIC). A multi-axis force sensor recorded forces applied to the head by the neck.

RESULTS AND DISCUSSION

Figure 1 shows the vehicle accelerations. The differences between U.S. and European bumpers resulted because the front of the striking European cars slid up over the rear of the struck car, thus delaying the struck car's acceleration until stiff parts of both striking and struck cars were engaged. In contrast, the U.S. striking car fronts pushed solidly against the rear of the struck cars without over-riding them.

Table 1 summarizes injury measures recorded from BioRID sensors. On average, the European bumpers produced higher loads on BioRID's neck, but test-to-test variability was nearly as great as differences between tests with different bumpers.

SUMMARY

Differences in vehicle acceleration timing like those resulting in tests with different bumpers described here do not have a strong influence on neck injury risk as measured by BioRID.

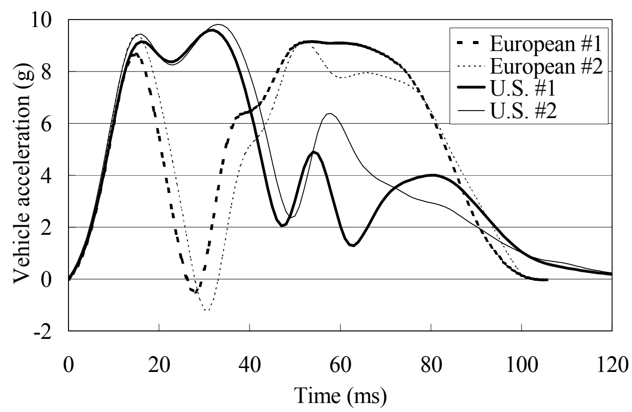

Figure 1: Struck car accelerations, 32 km/h impact by same model.

REFERENCES

Bostrom, Ola et al. (1996). A new neck injury criterion candidate based on findings in the cervical spinal ganglia after experimental neck extension trauma. *Proceedings of the 1996 International IRCOBI Conference*. Bron, France: IRCOBI.

Davidsson, J. (2000). Developmment of a mechanical model for rear impacts (doctoral thesis).

Insurance Research Council. (1994). Auto injuries: claiming behavior and its impact on insurance costs. *Federal Register* vol. 66, no. 3, pp. 968-99, January 4, 2001. Oak Brook, IL.

Table 1: Summary of neck injury measures, 32 km/h rear crash tests

	NIC	Maximum Anterior-Posterior Neck Force (N)	Maximum Neck Tension (N)
European #1	28	384	910
European #2	20	285	821
U.S. #1	22	225	861
U.S. #2	18	300	679

MINOR NECK INJURY MECHANISM IN LOW SPEED REAR IMPACT BASED ON HUMAN CERVICAL VERTEBRA MOTIONS

Koshiro Ono [1], Koji Kaneoka [2]
[1] Japan Automobile Research Institute, Karima, Tsukuba, Japan kono@jari.or.jp
[2] Dept. of Orthopaedic Surgery, University of Tsukuba, Tennoudai, Tsukuba, Japan

INTRODUCTION

In order to understand minor neck injury mechanisms, it is said that an in-depth analysis of the relationship among the neck muscular response, motions of cervical vertebrae, intervertebral disc and facet joint injuries is necessary. In this regard, it was decided to conduct experiments using volunteers for the sled tests in low speeds and to compare and analyze the motions of cervical vertebrae upon impact with those under normal physiological conditions. Furthermore, for the parameter study of the head/neck/torso and spine responses, the impact speed, seat stiffness, neck muscle tension, and the alignment of the cervical spine were selected. The main objectives of the study are as follows: 1) to better understand minor cervical spine injury mechanism, 2) to quantify the motion of each vertebra during rear-end impact, and 3) to verify the head/neck/torso kinematics and the spine response under the different conditions.

METHODS

An X-ray cineradiographic system was used to analyze motions of cervical vertebrae of volunteers subjected to rear impacts. The mini-sled was developed that it could simulate the impact accelerations when the rear end of vehicle was collided. Accelerations were measured on the sled, the head, chest (above the first thoracic spine: T1) and front chest of each volunteer. With the application of the head four-channel acceleration measurement (Ono & Kanno, 1996), the shear & axial forces and the bending moment on the occipital condyle were analyzed. The electromyographic responses were measured with EMG electrodes at the sternoclaidomastoid (SCM) on each side of neck, trapezius (TZM) and the paravertebral (PVM) muscles on the left side. In order to analyze the volunteers' motions during rear impacts, motions of head/neck/torso were photographed with high speed camera (MEMORECAM: NAC Inc.) at the speed of 500 frames per second, and then fed into a system called ImageExpress (NAC Inc.) .

RESULTS AND DISCUSSIONS

The five series of experiments on twenty-five volunteers conducted under this study are shown in Table 1. Some volunteers were involved twice in different series of experiment. The aim of the experiments was to determine the effect of the difference in seat performance (standard or rigid) on motions of cervical vertebrae at the impact speeds of 4, 6 and 8 km/h, respectively. It may be said that the foregoing study discusses the mechanism of spine straightening. The influences of the spine motions on the neck injuries are expressed in patterns per phase of timing after impact as shown in Figure 1, together with the human impact responses. In the initial phase of impact, lumbar and thoracic vertebrae flex and extend, resulting in their straightening and torso ramp-up motion. Due to the motions of spine and torso, the neck is pushed up during the initial phase and middle phase of impact, and the lower cervical vertebrae extend sharply, resulting in the extension of upper cervical vertebrae and S-shape deformation of neck. Since the rotation axis of the lower vertebrae travels upward because of the above, the facet joint injury mechanism and synovial fold impingement are apt to occur.

SUMMARY

A series of experiments simulating low speed rear-end impacts have been conducted on volunteers. Motions of the cervical vertebrae have been analyzed by means of X-ray cineradiography. Results of the analysis have been compared with those in physical state, and the influences of spine motions on the risk of neck injuries have been discussed. The findings have been obtained on the risk of minor neck injuries based on clinical knowledge, according to the characteristics of human motions during rear-end impacts.

REFERENCES

Ono K. and Kanno M., (1996). *Accident Analysis and Prevention, Vol.28, No,4,* pp. 493-499
Kaneoka K. et al (1999), *Spine Vol.24, Number.8*, pp.763-770

Figure 1. Human response

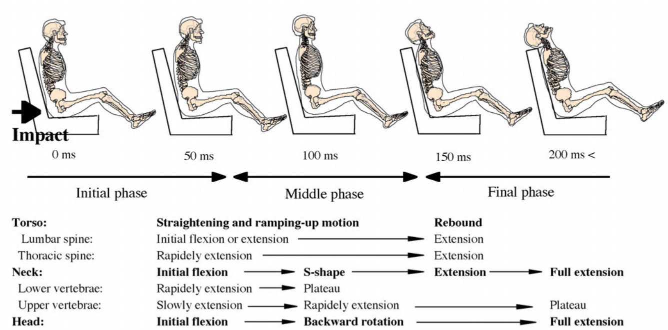

Table 1 Matrix on JARI Volunteer Tests from 1996 to 1999

	Series A	Series B	Series C	Series D	Series E
No. of Subjects	10	3	8	1	7
Impact Speed (km/h)	4	2/4/6	4/6/8	6	4/6/8
Type of Seat	Std.	Rigid	Std./Rigid	Rigid	Std./Rigid
Muscle Tone	w/o	w/o	w/o or with	w/o	w/o
Neck Alignment	Neutral	Neutarl	Neutral	Fl./Ne./Ex.	Neutral
Sitting Position	Std.	Std.	Std.	Std.	Std.
Headrest	w/o	w/o	w/o or with	w/o	w/o

EFFECTS OF MUSCLE ACTIVATION AND SEATING POSTURE IN REAR END IMPACT USING A HUMAN MODEL WITH A DETAILED NECK

Jack van Hoof, Riske Meijer, and Marike van der Horst
TNO Automotive, Crash Safety Centre, Delft, The Netherlands

INTRODUCTION

Neck injuries resulting from rear-end impact rank among the top vehicle safety problems and have serious implications for our society. The mechanisms causing these neck injuries are still not clearly understood. The main reason for this is that it is hard to characterize whiplash both clinically and experimentally. Numerical models of the human body can partly solve this problem, since they provide a relatively cheap and efficient means of gaining insight into the parameters that determine the response of the human body during impact.

METHODS

In this study, a human body model including a detailed model of the neck was used to study the mechanics of the neck during rear-end impact. This model has been validated previously for frontal, lateral, and rear-end impact with responses of volunteers and post mortem human subjects (PMHSs) (Van der Horst *et al.* 2001; Kroonenberg e*t al*. 1998). Data in literature indicates that neck muscle activity (Siegmund & Brault 2000) and initial seating posture (Aibe *et al.* 1982, Szabo 2000) are two of the main factors affecting the response of the neck under rear impact conditions. The objective of this study was to use the human model with detailed neck to evaluate the effects of neck muscle activation and seating posture on the head-neck kinematics. The effects predicted by the model were verified with two sets of volunteer rearward sled tests. The model is shown in Figure 1

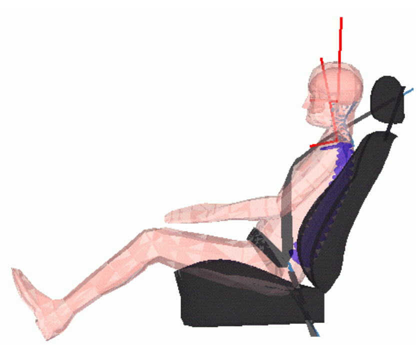

Figure 1: Human model with detailed neck seated in car seat

RESULTS AND DISCUSSION

In general, the response of the numerical model corresponded well with that of the volunteers. The ramping up observed for the volunteers was slightly higher than predicted by the model. The muscle activation level was found to influence the head kinematics significantly. A higher muscle activation level resulted in a smaller maximum head angle, whereas a longer reflex delay resulted in a larger maximum head angle. The position of the head relative to the head restraint was also found to significantly affect the head and neck kinematics. A forward bent seating posture combined with a low head restraint resulted in a larger head and neck rotation, and a higher neck extension than a straight seating posture with high head restraint. The results of this study indicated that the model can be used in seat design studies to mitigate whiplash injuries.

SUMMARY

In this study, a human body model including a detailed model of the neck was used to study the effects of neck muscle activation and seating posture on the mechanics of the neck during rear-end impact. The effects predicted by the model were verified with two sets of volunteer rearward sled tests. In general, the response of the numerical model corresponded well with that of the volunteers. The results of this study indicated that the model can be used in seat design studies to mitigate whiplash injuries.

REFERENCES

Aibe, T., *et al.* (1982). *Proc. 26th Stapp Car Crash Conference*, 231-238

Horst, M.J. van der, *et al.* (2001). *2001 ESV Conference*.

Kroonenberg, A.J. et al. (1998). *Proc. 42nd Stapp Car Crash Conference*.

Siegmund, G.P., and Brault, J.R. (2000). *Frontiers in whiplash trauma, clinical and biomechanical*, IOS Press.

Szabo, T.J. (2000). *Frontiers in whiplash trauma, clinical and biomechanical*, IOS Press.

FINITE ELEMENT HUMAN MODEL FOR LOW SPEED REAR IMPACT SIMUATION

Hyung-Yun Choi[1], In-Hyeok Lee[2], Eberhard Haug[3] and Jin-Hee Lee[4]

[1]Mechanical System Design Engineering Dept., Hong-Ik University, Seoul, Korea, hychoi@hongik.ac.kr
[2]Hankook ESI, Seoul, Korea, [3]ESI Software, Paris, France, [4]IPS-i, Seoul, Korea

INTRODUCTION

Low speed rear-end impact of motor vehicle tend to produce a whiplash injury of the occupants. Whiplash injury is known to be one of the minor injuries occurring to the crash victims. However, the enormous societal cost and incompleteness of the basic information of injury mechanisms make this whiplash injury as one of the most urgent issues to be investigated in the occupant safety field. Various hypotheses for the cause of injury have been proposed based on the experimental and analytical studies. Thus, the supporting findings for the hypotheses would make further progresses of the study like development of whiplash injury criteria and implementation of proper countermeasures. For this purpose, a finite human model has been developed in this study to analyze the kinematics and deformations of body parts during the rear impact.

FINITE ELEMENT MODELING

The model was built on 50% male geometry and consists of deformable neck and torso to which the rigid head and limbs were articulated. Since the main body parts for rear impact event are the neck and torso, they are thus anatomically depicted in detail. The hard and soft tissues in the neck and torso such as vertebrae, muscles, ligaments, organs, discs and fatty tissues were modeled by using the various kinds of finite elements and material properties to represent adequate mechanical behaviors of each component. The other body parts were also included but rather in simplified forms. Rigidly modeled head and limbs are articulated to the neck and torso. Fig. 1 shows the FE human model developed in this study.

VALIDATION

Range of motion for each motion segment of spine (cervical, thoracic, and lumbar) was calculated by applying the moment of flexion/extension and axial rotation, respectively. And it coincided well with the physiological representative values from the open literature. The kinematic motions of head-neck unit due to the frontal, rear and lateral impacts were also validated with the published results of volunteer tests.

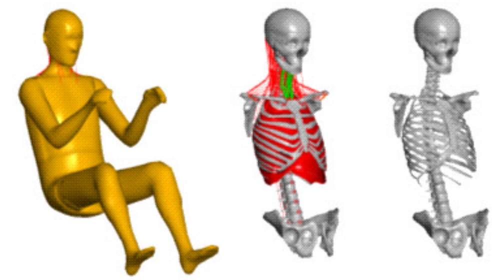

Figure 1: FE Human model for rear impact simulation

LOW SPEED REAR IMPACT SIMULATION

As shown in Fig. 2, a simulation of 4g rear impact with rigid seat was performed to evaluate the overall behavior of the model. The correlation of head CG and T1 accelerations between volunteer tests and simulation showed fairly good agreement. The kinematic changes of spine curvature were qualitatively reviewed as well.

REFERENCES

Robbins, D.H., *"Anthropometry of Motor Vehicle Occupants"* Vols. 2-3, University of Michigan, UMTRI-83-53-2, 1983

White III A. A., M. M. Panjabi, Clinical Biomechanics of the Spine, J.B. LIPPINCOTT COMPANY, 2nd Edition, 1990

ACKNOWLEDGEMENTS

This study was supported, in part, by Korean ministry of science and technology. (Project No.: M1-0139-00-0005)

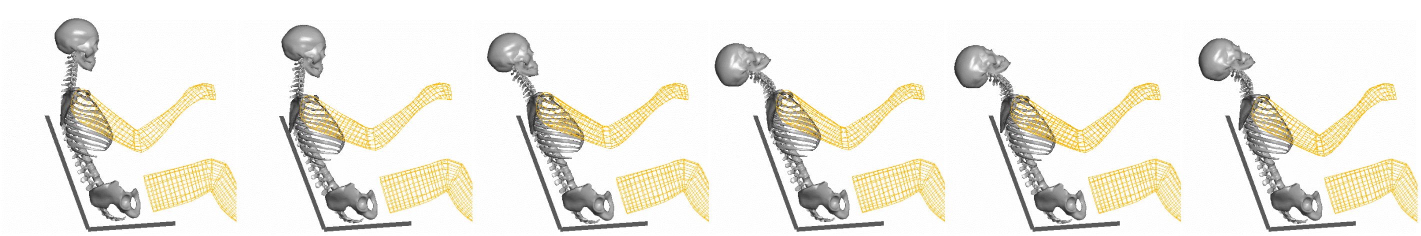

0 ms. 60 ms. 120 ms. 180 ms. 240 ms. 300 ms.

Figure 2: 4g rear impact simulation

THE EFFECT OF HEAD RESTRAINT PROPERTIES ON TISSUE DEFORMATIONS IN THE CERVICAL SPINE IN REAR-END MOTOR VEHICLE IMPACTS

AF Tencer, SK Mirza, P Huber
Dept of Orthopedics and Sports Medicine, University of Washington, Seattle, WA, USA

INTRODUCTION In several volunteer and cadaveric studies of rear-end impacts, alternative explanations of the effects of impact forces on cervical spinal tissues, related to the mechanism of whiplash, have been proposed. However these different tissue deformations have not been directly compared in the same study. Only a few studies have addressed the effect of properties of the head restraint although the motion of the head and therefore the deformation of the cervical spine are related to the interaction of the head with the head restraint.

METHODS Each of 11 cervico-thoracic spine specimens, with an artificial instrumented skull, was mounted on a sled, which was impacted through its bumper by a pendulum. This caused forces similar to those in a vehicle-to-vehicle rear impact, by comparison to a previous study using volunteers. Each specimen was subjected to 5 sequential tests. At a 2g peak impact acceleration, using a standard head restraint, the effects of head to restraint distances of 4cm and 8 cm were compared. At a 4g acceleration, the effects of a standard and a modified head restraint with initial head to restraint contact and energy absorption were determined. Chest and head accelerations, and shear force at the base of the specimen were measured. Tissue strains monitored included transient local pressure around the C5-6, C6-7 and C7-T1 nerve roots using micro pressure transducers, peak articular facet joint pressures using pressure sensitive film, and facet and vertebral intersegmental planar displacements and rotations from high speed video recordings. Two tailed t tests were used to determine significant differences in measured parameters.

RESULTS Tissue deformations with increasing acceleration Similar to other studies, the lower end of the cervical spine was pushed forward under the initially stationary head due to the rear impact. After the head interacted with the head restraint, it was pushed forward of the spine causing flexion and shear loading. The chest accelerations of this experiment matched those measured in volunteers in a previous study well but the head accelerations were higher, demonstrating the effect of completely passive head motion with no muscle control. Pressure pulses occurred around the lower cervical nerve roots, ranging in peak magnitude from 2.7kPa to 10kPa, and occurring generally after chest but before peak head acceleration. Facet pinching varied with spinal level, with C4-5 and C5-6 having the highest probability (64% and 71% respectively) of pinching. Vertebral intersegmental extension rotations (4 to 9.5 deg) and posterior translations (3.7 to 8.9 mm) peaked near maximum head excursion into the head restraint, at the time of peak head acceleration. Intersegmental shear translations were most sensitive to increasing impact acceleration. **The effect of head restraint properties** Decreasing the head-to-head restraint distance from 8cm to 4cm, with a standard head restraint changed spinal kinematics, for example decreasing C4 -C5 extension from a mean of 7.15deg to 5.53deg and C7-T1 posterior shear from a mean of 2.62mm to 1.95mm. Using a modified head restraint significantly decreased head acceleration, from a mean of 5.73g to 3.58g and shear force, from 168N to 120N, at head to restraint contact. Peak C7-T1 foramenal pressure decreased, from 10kPa to 6.6kPa, as did C6-7 extension, from 9.45deg to 6.85 deg, and posterior intersegmental shear displacement at all levels, by about 20%.

CONCLUSIONS (1) Vertebral rotation, intersegmental shearing, facet pinching, and nerve root compression all occurred with rear impact forces. (2) As the peak impact acceleration doubled, intersegmental shear translations showed the greatest increases. (3) Shear deformations peaked near the time of contact of the head with the head restraint. (4) Decreasing head to head restraint gap reduces spinal shear force and changes spinal kinematics, reducing cervical spine extension and posterior shear. (5) Allowing initial head to restraint contact decreased cervical spine extension and posterior shear, while allowing energy absorption at head contact decreased head acceleration, shear force, and local pressures around the cervical nerve roots.

Parameter	4cm	8 cm	p
Superior head acceleration in Z (g)	0.69	0.38	0.044
Shear force in X direction (N)	98.5	120.8	0.048
Post. head acceleration in X (g)	-2.28	-1.23	0.0001
C4-5 extension rotation (deg)	5.53	7.15	0.022
C4 on C5 anterior translation (mm)	1.90	0.60	0.039
C5 on C6 anterior translation (mm)	0.85	0.40	0.038
C7onT1 posterior translation (mm)	-1.95	-2.62	0.020
C5-6 distraction in Z (mm)	0.55	1.10	0.038

Parameter	Std	Mod	p
Ant. chest acceleration in X (g)	4.25	3.51	0.0002
Ant. head acceleration in X (g)	5.73	3.58	0.0001
Anterior shear force in X (N)	167.9	120.3	0.009
Post. head acceleration in X(g)	-3.72	-3.17	0.013
Superior head acceleration, Z (g)	-3.81	-3.11	0.039
C7-T1 nerve root pressure (kPa)	10.05	6.61	0.037
C6-7 extension rotation (deg)	9.45	6.85	0.049
C3 on C4 posterior trans, X (mm)	-8.94	-7.14	0.017
C4 on C5 posterior trans, X (mm)	-7.88	-6.42	0.0003
C5 on C6 posterior trans, X (mm)	-6.46	-5.32	0.002
C6 on C7 posterior trans, X (mm)	-5.52	-4.89	0.022
C7 on T1 posterior trans, X (mm)	-3.72	-3.04	0.025

Table 1. Means of peak values (Upper) Effect of changing the pre-impact head to head restraint distance from 4 cm to 8 cm (lower) effect of a standard (Std) with 4 cm head to restraint gap, or modified (Mod) head restraint (0 cm head to restraint gap, energy absorbing) (p = t test result, X = forward, anterior direction, Z = upward, superior direction)

+INFLUENCE OF LIGAMENTOUS INJURIES ON THE UPPER CERVICAL SPINAL KINEMATICS

Karin Brolin, karin@flyg.kth.se

Department of Aeronautics, Royal Institute of Technology, Stockholm, Sweden

INTRODUCTION

Cervical spinal injuries may be very severe, since they have the potential to damage the spinal cord. The upper cervical spine is a frequent location for spinal injuries, Brolin and von Holst 2002. It is important to prevent these injuries and to increase the knowledge of injury mechanisms and how injuries influence the spinal behavior. Stability of the upper cervical spine is highly dependent on ligamentous structures. The interaction of these ligamentous structures with the skeletal system allows extensive motion in the occipitoatlantal and atlantoaxial joints.

The goal of this project was to evaluate how ligamentous injuries influence the motion of the upper cervical spinal joints.

METHODS

An anatomically detailed Finite Element (FE) model of the intact ligamentous upper cervical spine was developed and validated against experiments by Panjabi et al (1991). The developed model included the cortical and trabecular bone of the occiput, atlas, axis, and C3 and all soft tissues structures, such as the disc and ligaments. The occipitoatlantal, atlantoaxial, and facet joints were modeled with sliding contacts and the intervertebral disc was modeled as an anisotropic structure with an incompressible nucleus pulposus.

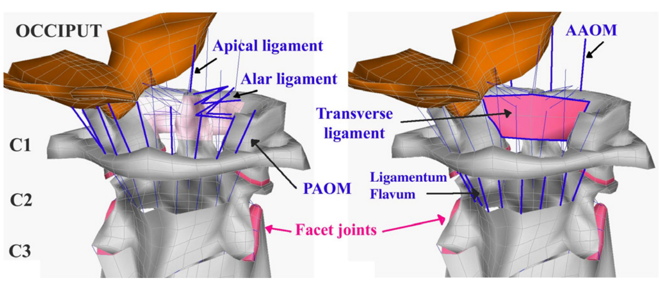

Figure 1: Posterior views of the intact FE model of the upper cervical spine.

The FE model was modified to incorporate rupture of the ligaments. Transection of all the upper cervical ligaments were implemented in separate models. The FE models were subjected to flexion, extension, lateral bending, and axial rotation by applying moments of 1.5 Nm at the occiput. The resulting rotations and translation of the occipitoatlantal and atlantoaxial joints were compared for the intact and injured models.

RESULTS AND DISCUSSION

The FE model of the upper cervical spine correlated well with the experimental data, see Table 1. Rupture of the transverse ligament significantly altered spinal kinematics for all load cases. Axial rotations were significantly influence by rupture of the alar ligaments, the capsular ligaments, the tectorial membrane, and the posterior atlantoaxial ligament. Extension increased with injuries on the anterior and central ligaments, while flexion was more dependent on the posterior structures. This correlates with *in-vitro* experimental studies, where transection of spinal ligaments have been studied by among others Panjabi et al 1991.

Load case	Joint		Panjabi et al	**FE model**
Axial rotation	C0-C1	degrees	1.0 - 10.5	**6.1**
	C1-C2	degrees	24.2 - 46.4	**23.3**
Flexion	C0-C1	degrees	10.8 - 17.2	**18.2**
	C1-C2	degrees	9.8 - 16.2	**11.3**
Extension	C0-C1	degrees	10.8 - 17.2	**10.5**
	C1-C2	degrees	6.0 - 16.0	**14.0**
Lateral bending	C0-C1	degrees	2.6 - 8.6	**3.0**
	C1-C2	degrees	3.8 - 19.6	**6.0**

Table 1: Results from the validation of the intact FE model.

It is concluded that FE models of the upper cervical spine can contribute to the understanding of spinal injuries.

SUMMARY

The objectives of this study were to analyze the effect of spinal injuries on the motion of the upper cervical spinal joints using FE-models. It was concluded that ligamentous injuries can be studied successfully with the FE method and the transverse ligament was confirmed to play a significant role in the stability of the upper cervical spine. Rupture of several ligamentous structures simultaneously are a potential threat to spinal stability.

REFERENCES

Brolin K, von Holst H (2002), Cervical Injuries in Sweden, a National Survey of Patient Data from 1987 to 1999, submitted to *Injury Control and Safety Promotion.*

Panjabi et al (1991), Flexion, Extension, and Lateral Bending of the Upper Cervical Spine in Response to Alar Ligament Transection, *J. Spinal Disorders* **4**: 157-167

Panjabi et al (1991), Effects of Alar Ligament Transection on Upper Cervical Spine Rotation, *J. Orthopaedic Research* **9**: 584-593

COMPARISON OF RELATIVE MOTION BETWEEN THE BRAIN AND SKULL OF THE HUMAN CADAVER FOR ROTATION IN THE CORONAL AND SAGITTAL PLANES

Albert I. King[1], Warren N. Hardy, Matthew J. Mason, and Scott Tashman[2]
Bioengineering Center, Wayne State University, Detroit, Michigan, USA
[1]Distinguished Professor and Director, king@rrb.eng.wayne.edu
[2]Henry Ford Hospital Bone and Joint Specialty Center

INTRODUCTION

Understanding of head injury mechanisms can lead to appropriate preventative measures. This study examines relative brain motion with respect to the skull using high-speed, biplane x-ray and neutral density targets (NDTs), and builds upon the work reported by Hardy et al. (2001).

METHODS

Inverted, perfused, human cadaver heads were subjected to impacts generating either sagittal or coronal rotation. Specimens were stopped against a rigid surface from steady-state motion. NDTs were implanted in multiple columns of 5 or 6 targets, with 10 mm between targets in each column. The columns are designated as either anterior or posterior ("a" or "p"), and right or left ("R" or "L"), as shown in Figure 1.

RESULTS AND DISCUSSION

Figure 2 shows the brain displacements in the right-posterior NDT column for sagittal plane rotation (SAE 180 Hz: -3519 r/s^2, -21 r/s). The primary direction of motion for each target is the Major Displacement Axis (MDA). Perpendicular bisectors from each MDA intersect at the Average Instant Center (AIC) of rotation. The orientation the MDAs also rotates from inferior to superior. Similar phenomena are evident in Figure 3, which shows NDT motion in three columns for coronal rotation (SAE 180 Hz: -7695 r/s^2, -26 r/s).

SUMMARY

The local brain motions follow loop or figure eight patterns, with peak displacements on the order of ± 5 mm. These displacements seem to be related to an Average Instant Center. Motion for sagittal and coronal plane rotation is remarkably similar, as is the angular speed of each test. The brain motions exhibit interesting anterior-posterior and right-left symmetry.

REFERENCES

Hardy, W., Foster, C., Mason, M., Yang, K., King, A., Tashman, S. (2001). *Stapp Car Crash Journal*, **45**, 337-368.

ACKNOWLEDGEMENTS

This work was supported in part by the Centers for Disease Control and Prevention, National Center for Injury Prevention and Control Grant No. R49/CCR503534-12.

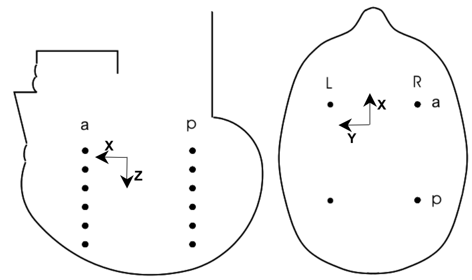

Figure 1: NDT implant scheme, showing lateral and superior perspectives. Not all locations are used in all tests.

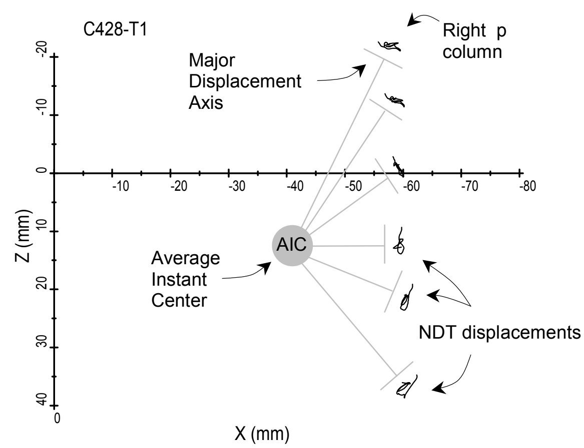

Figure 2: Sagittal plane rotation test for cadaver 428 showing motion in the right posterior NDT column.

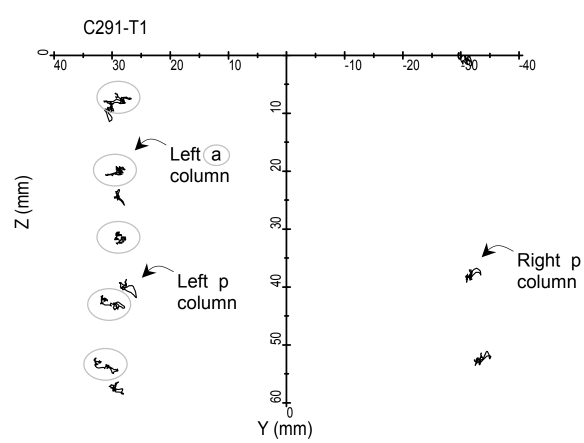

Figure 3: Coronal plane rotation test for cadaver 291 showing motion in the right and left posterior and left anterior NDT columns. Some NDT data are missing.

BIOMECHANICAL CHARACTERISTICS OF FACIAL FRACTURE IN CHILDREN

Kristy B. Arbogast and Flaura K. Winston

TraumaLink, The Children's Hospital of Philadelphia, Philadelphia, PA
arbogast@email.chop.edu

INTRODUCTION

Facial injuries in children rank high in importance to parents due to the potential for these injuries to result in disfigurement and occur often in motor vehicle crashes. These injuries have been shown to be related to the use of restraints, however the detailed injury mechanism has not been delineated. (Murphy, 2001) An understanding of the injury mechanism must incorporate the changing biomechanical structure of the child's face, i.e. the development of the jaw, the growth and pneumatization of the sinuses, and the emergence of the teeth. (McCarthy, 1990). The objective of this paper is to identify common mechanisms of facial trauma to children in motor vehicle crashes. It was hypothesized that pediatric facial development effects the mechanical compliance of the face and influences the fracture patterns seen after impact.

METHODS

A case-series analysis of 15 children sustaining facial fractures was performed. Cases were identified through the Partners for Child Passenger Safety (PCPS) study between 3/98-3/01, an on-going child-focused motor vehicle crash surveillance system that includes children 15 years or younger in crashes involving 1990 and newer vehicles reported to State Farm Insurance Companies in 15 states and Washington, D.C. Injury and vehicle damage descriptions (included in the claims data) were reviewed to select potential cases for a full-scale on-site crash investigation. Medical, crash, and child characteristics of documented pediatric facial bone fractures were analyzed. The site of facial fracture was further classified as upper (supraorbital bone), middle (nasal, zygomatic, maxillary, and infraorbital bones), or lower face (mandible). Fracture patterns were examined above and below 6 years of age due to this age as a transition point in facial development.

RESULTS AND DISCUSSION

Fourteen crashes involving fifteen children with facial fractures were studied by on-site crash investigation. All children were restrained by an adult seat belt. 11/15 either placed the shoulder belt behind their back or sat in a position only equipped with a lap belt. Nasal fractures were the most common (8/15 children), followed by zygomatic/maxillary fractures (4/15 children), orbital fractures (5/15 children), and mandible fractures (3/15 children). These injuries resulted from excessive torso and head excursion with facial impact. The lap only belt configuration provided little restraint for the upper torso and resulted in greater forward motion and acceleration over the lap belt and greater relative energy upon impact. Children are at particular risk for this jackknife motion as a greater proportion of their body mass lies above the level of the lap belt. The distribution of fracture location (upper, middle, and lower) with respect to age is shown in Figure 1. In the younger children, less than 6 years of age, all areas of the face are represented in the fracture distribution. In the older school age children, 12/13 fractures occurred to the mid-face. These changes in fracture patterns are associated with changes in facial structure.

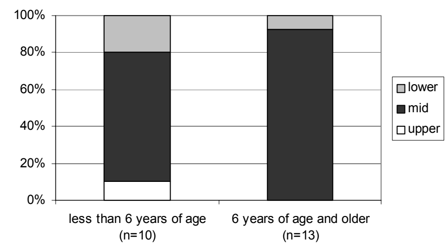

Figure 1: Region of facial injury by age group.

In order to develop potential countermeasures for these injuries, a surrogate child face is necessary. The combination of the field crash data and pediatric facial development would suggest that a structure representing the mid-face may be appropriate for an anthropometric surrogate representing the pre-teen. A young school age dummy presents more of a challenge due to the transitional nature of this age in facial development.

SUMMARY

This paper demonstrated that the patterns of facial fracture vary by child age due to the changing structure of the pediatric face. These differences must be incorporated into an appropriate engineering tool to evaluate pediatric facial injury risk and potential countermeasures. This may require different facial construction for dummies of different ages.

REFERENCES

Murphy, R, et al. (2001). *Plast Reconstr Surg*. **107**, 34-37.
McCarthy, J. (1990) *Plastic Surgery*. Saunders.

ACKNOWLEDGEMENTS

This study was funded by State Farm Insurance Companies.

INFLUENCE OF IMPACT DIRECTION AND DURATION TO THE HUMAN HEAD IN EVALUATION OF HEAD INJURY CRITERIA: A NUMERICAL STUDY

Svein Kleiven[1] and Hans von Holst[1,2]
[1]Department of Aeronautics Royal Institute of Technology
[2]Department of Clinical Neuroscience Karolinska Institute
Stockholm, Sweden.

INTRODUCTION

For people younger than 45 years, the frequency of death or severe injury from road accidents is about six times higher than that from cancer (ETSC, 1999). In Sweden, head injuries causes about 78% of the deaths in motor vehicle accidents. When evaluating the consequences of an impact to the head, different injury criteria are used. However, present injury criteria do not take into consideration rotational or directional dependency. Recently a new global head injury criteria, called the Head Impact Power (HIP) was presented (Newman *et al*., 2000). In that study, it was proposed that coefficients for the different directions could be chosen to normalize the HIP with respect to some selected failure levels for a specific direction. The aim of the present investigation was to study the influence of inertial forces to all the degrees of freedom of the human head evaluated with a detailed FE model.

METHODS

A detailed and parameterized Finite Element (FE) model of the adult human head has been developed. It includes the scalp, skull, brain, meninges, cerebrospinal fluid (CSF), and eleven pairs of parasagittal bridging veins. Separate representations of gray and white matter, and inclusion of the ventricles were also implemented. This model has been described in Kleiven and von Holst (2001). The description of the status of the head model is also available on the home page: http://www.flyg.kth.se/ (Division of Neuronic Engineering). A total of nine acceleration pulses (pure translation and angular, respectively) were applied to all the non-symmetrical directions of the head. In the study of the angular acceleration components, a squared sinusoidal pulse *(sin^2)* with an amplitude of 20 krad/s^2 and a duration of 5 ms, resulting in a peak angular velocity of 50 rad/s, and a HIP_{max} of 17.3 kW. To obtain a comparison with the angular impulses, a squared sinus with an amplitude of 1580 m/s^2 and a duration of 5 ms was used for the translational impulses resulting in a HIC of 295 and a HIP_{max} of 17.3 kW. In addition, the durations of the sagittal translational and rotational impulses were varied between 2.5 and 20msec while keeping the HIC and HIP_{max} constant. The models were used to investigate the differences in terms of engineering strain in the bridging veins, ε, and the effective stresses, σ_e, and shear strains, ε_{shear}, in the brain, due to variation in impact direction and duration.

RESULTS, DISCUSSION AND SUMMARY

The largest strains occurred in the brainstem for the axial impulses. Axial accelerations are usually caused by accidents due to fall, and clinical observations shows that this may lead to DAI in the brainstem (Dirnhofer *et al.*,1979).

Table 1: Summary of the results from the comparison of translational and angular impulses in different directions.

	Cortex		*Corpus Call.*		*Brain Stem*		*Bridg*
V. Direction	ε_{shear}	σ_e	ε_{shear}	σ_e	ε_{shear}	σ_e	ε
A.P.	0.20	19.1	0.10	7.9	0.16	30.5	0.02
P.A.	0.33	26.2	0.10	8.2	0.12	21.7	0.05
S.I.	0.19	15.3	0.12	8.4	0.30	48.1	0.00
I.S.	0.19	15.4	0.12	8.4	0.28	45.7	0.03
Lat.	0.29	19.6	0.12	6.3	0.07	15.8	0.06
A.P. Rot.	0.25	19.6	0.14	10.8	0.18	28.6	0.09
P.A. Rot.	0.23	17.6	0.15	10.6	0.19	27.8	0.16
Axial Rot.	0.27	20.4	0.17	12.8	0.08	12.3	0.07
Lat. Rot.	0.19	15.3	0.21	15.2	0.22	32.7	0.09

The findings of larger stresses and strains in the corpus callosum for the lateral angular acceleration support conclusions drawn by Gennarelli (1983). The maximal effective stresses and shear strains in the brain occurred at a later time than the maximal strain in the bridging veins, which also is in agreement with Gennarelli (1983). The present results also verifies a study by Fruin *et al.* (1984) who reported that six out of eight cases with known trauma sites were due to occipital impacts. The shorter durations resulted in a slightly lower values of the stresses/strains in the brain compared to the longer durations for the translational impulses. The opposite occured for the rotational impulses. However, the differences due to variation in impulse duration were small, corroborating the validity of impulse criteria such as HIC and HIP. No significant differences in the strain of the bridging veins were found for the various impulse durations.

REFERENCES

Dirnhofer, R. *et al.* (1979). Zur Mechanischen Belastbarkeit des Tentorium Cerebelli, Z. Rechtsmed. **82**, 305-311.

European Transport Safety Council (1999). Reducing the Severity of Road Injuries through Post Impact Care. ISBN: 90-76024-07-3.

Fruin, A. *et al.* (1984). Interhemispheric subdural hematoma. J. Neurosurg. **60**, 1300-1302.

Gennarelli, T.A. (1983). Head injuries in man and experimental animals: Clinical aspects. Acta Neurochir Suppl **32**, 1-13.

Kleiven, S. and von Holst, H. (2001). Consequences of Head Size following Trauma to the Human Head. Accepted for publication in J. Biomech.

Newman, J.A. *et al.* (2000). A Proposed New Biomechanical Head Injury Assessment Function - The Maximum Power Index, in: *44th Stapp Car Crash Conf.,* SAE Paper No. 2000-01-SC.

BEHIND ARMOR BLUNT TRAUMA

Cameron R. 'Dale' Bass

Research Assistant Professor, bass@virginia.edu
Center for Applied Biomechanics, University of Virginia, Charlottesville, Virginia

INTRODUCTION
Traditionally, helmets and body armor have been used to stop or blunt penetration of ballistic projectiles, bullets or shrapnel, into the human body. However, the introduction of modern high impact strength deformable materials into helmets and body armor for such ballistic impact protection has increased the potential for significant backface deformation under ballistic impact. Further, for most helmet and body armor systems there is limited space available for such backface deformation. So, systems that suffer no penetration may have a substantial risk of producing severe head or thorax injury from blunt backface trauma, even in systems that to not suffer ballistic defeat. Further, the desire to use even lighter weight head or thorax protection with greater ballistic penetration resistance may lead to increased risk of backface impact injuries. There is, however, no widely accepted, widely available, and sufficiently validated objective technique for evaluating the risk of impact head trauma from helmet backface deformation.

This overview discusses the history and current progress in elucidation of mechanisms of injuries from Behind Armor Blunt Trauma (BABT). This includes a detailed examination of proposed injury mechanisms from high rate cranial trauma and high rate thoracic trauma. The applicability of existing automobile injury criteria, blast injury criteria, and high rate ultrasonic injury criteria is critically examined, and theoretical and experimental progress in understanding high rate head and thoracic injury is discussed.

METHODS
To develop objective test methodologies to assess BABT, an approach for all body regions was developed that includes the common elements:

- **Biofidelic surrogate** – a dummy that is robust, gives a repeatable physical response, and responds in a human manner. Generally, a surrogate should be as simple as possible while still representing the relevant human response.
- **Engineering measurement** – a physical parameter such as force or acceleration that may be used to quantify the physical response of the dummy. Dummies may be instrumented to produce accepted or proposed injury criteria.
- **Injury risk evaluation** – a correlation between an engineering measurement and some injury model.
- **Validation by injury model** – a correlation between the injury risk evaluation and a physical model of injury. An injury risk model has limited value without successful validation using 1) physical reconstruction of an actual injury event, 2) an animal injury model, or 3) a cadaveric human injury model.

RESULTS AND DISCUSSION
This study uses backface deformation of a helmet into a human skull to elucidate the special circumstances in assessing injury risk in high rate blunt trauma. This includes results from helmet dummy and cadaver experiments and mine blast (thorax) biomechanics (Figure 1). The efforts include the verification of physical surrogate models and indication of current model deficiencies.

Figure 1: Simulated Antipersonnel Mine Blast with Hybrid III Surrogates

SUMMARY
To adequately assess the risk of injury from BABT, the development of high rate biomechanical injury models is required. In addition, the establishment of a relationship between a robust surrogate for injury and a validated injury model is crucial in the success of this approach. A roadmap is proposed toward development of comprehensive high rate injury criteria suitable for use with BABT. This roadmap emphasizes the most critical deficiencies in the current research.

ACKNOWLEDGEMENTS
The author gratefully acknowledges the U.S. Army Soldier Center, Natick and U.S. Army CECOM for partial support of the work that led to this overview.

COMPARATIVE NECK LOAD MEASUREMENTS IN AN INSTRUMENTED MANIKIN EXPOSED TO PARACHUTE DROPS FROM A UH-60 BLACK HAWK HELICOPTER

B. Joseph McEntire, Frederick T. Brozoski, and Nabih Alem

U.S. Army Aeromedical Research Laboratory, Aircrew Protection Division, Fort Rucker, Alabama
Joe.mcentire@se.amedd.army.mil

BACKGROUND

Paratroopers are exposed to unique injury risks. Some of these risks are associated with the dynamics of parachute opening shock and the parachutist's landing fall. A particularly vulnerable body region is the neck, because the head is likely to flail as the inertial loads overcome voluntary muscular control, loading the neck bony and tissue structure. The addition of head or helmet mounted devices could increase the transmitted neck loads during airborne operations, increasing neck injury risk.

Even soft tissue injuries such as neck strains and sprains could affect soldier performance. Typical acute neck strain symptoms include: stiffness, headache, neck pain, dizziness, nausea, double vision, impaired concentration, impaired memory, irritability, weakness, and others. A soldier experiencing these symptoms would not be expected to complete a mission as efficiently or effectively as they would if they did not experience the symptom. Of course, more serious injuries could have greater operational impact as well as disability and occupational implications.

METHOD

An investigative study was conducted to measure the inertia neck loads during parachute opening shocks. An instrumented Hybrid III test dummy was used in all dynamic tests to sense and record the response loading. This manikin was modified with an articulated spine and internal data acquisition system. Data was recorded at a sample rate of 4000 Hz. After each test, data was downloaded onto a laptop PC and archived. The manikin provides the capability to record 32 data channels, of which 30 were instrumented for recording. Video recordings of the manikin's exit and parachute openings were reviewed and the neck load data were screened to identify occurrences of the parachute riser snagging on the head and helmet. Exits where a head/helmet snag occurred were excluded from the data set as the loads transmitted through the riser contaminated the pure inertia loads under evaluation.

An Army UH-60A Black Hawk helicopter was used to obtain the desired release altitude (700 feet above ground level) and airspeed (110 knots indicated airspeed) for these tests. A standard Army circular, static line deployed, parachute system was used during all aircraft exits. Two different head borne device conditions were utilized to apply discrete mass and mass position conditions to the test dummy. These were the standard airborne helmet (3.56 pounds), and a modified helmet with an additional electronic device (4.30 pounds). Each condition was exposed to 17 repetitions for a total of 34 tests.

ANALYSIS

Two data analysis methods were used. First, a comparison of means was conducted to determine if the addition of the head-mounted weights produced a statistically significant difference ($P \leq 0.05$) in the transmitted neck loads. Within each group, a one-way analysis of variance (ANOVA) was used to compare the means and standard deviations. Then, the peak neck loads and forces were compared to the published injury assessment reference values.

RESULTS AND DISCUSSION

The UH-60 Black Hawk proved to be an efficient means to conduct multiple aircraft exits in a short time period. Repeated manikin aircraft exits were conducted in less than 15-minute cycles. However, attempts to control the manikin's response upon entering the wind-stream proved less successful. Nine helicopter-exit data sets subsequently were eliminated from the analysis for signal contamination resulting from riser snag. The mean moments and forces measured at the C1 load cell are provided in Table 1. None of the peak values exceeded the injury assessment reference values recommended by NHTSA. The associated Nij values, combined loading injury criteria, remain to be calculated.

Table 1: Transmitted neck loads during parachute opening shock (mean, SD) (Units are inch-pounds and pounds)

Dependent Variables	Standard (n=14)		Modified (n=13)		P value
Lateral Bend, +Mx	127.8	75.8	142.6	85.2	.64
Lateral Bend, -Mx	-146.6	60.7	-148.6	80.2	.94
Flexion, +My	104.6	51.2	184.4	123.1	.04
Extension, -My	-73.4	50.1	-59.7	36.1	.42
Forward shear, +Fx	83.4	31.7	73.1	38.2	.45
Rearward shear, -Fx	-88.8	23.2	-93.7	35.7	.67
Lateral shear, +Fy	39.0	14.7	39.5	30.1	.95
Lateral Shear, - Fy	-54.7	19.4	-58.2	28.1	.71
Tension, +Fz	179.3	88.7	177.8	81.1	.96
Compression, -Fz	-39.9	34.0	-52.2	29.2	.33

REFERENCES

Wehrly, David. Low Altitude, High Speed Personnel Parachuting: Medical and Physiological Issues, USAARL Report 87-3, February 1987.

Amoroso, et.al. 1997. Injury among female and male Army parachutist, Aviation, Space, and Environmental Medicine, Vol. 68, No. 11

Paschal, et al., Evaluation of the Head Injury Hazard During Military Parachuting, USAARL Report 90-6, March 1990.

INFLUENCE OF HELMET MASS PROPERTIES ON HEAD/NECK FORCES DURING HIGH-SPEED EJECTION

G Paskoff
In-Flight Escape Systems Branch, Naval Air Warfare Center - Aircraft Division, Patuxent River, MD

INTRODUCTION

High-speed ejection from the cockpit is a highly chaotic event that is affected by a multitude of factors including airspeed, elevation, pitch, sink, and roll rates, temperature, seat stabilization, parachute type, aircrew weight, and many others. Mission enhancement devices worn on the helmet are used for air-to-air and air-to-ground targeting, night vision, forward looking infra-red views, and flight control information. However, as the number of features increases, the total weight of the system increases. Earlier systems that provided a number of features, in addition to the basic functions of a helmet, weighed close to 6 pounds. More modern systems are approaching 4.8 pounds or less. While the total weight is important, the major factor in the injury potential is the location of the CG of the head and helmet system combined. Typically the CG is placed forward of the occipital condyles and results in high pitch moments about the occipital condyles and C7/T1 which are consistent with cervical injuries reported during ejections. As a result of the expanded aircrew population, the potential exists for smaller anthropometric individuals, male and female, to be at a greater risk of injury during high-speed escape and crash scenarios. The objective of the study was to determine safe requirements for helmet mass properties (weight, center of gravity, and moments of inertia) based on predictions of inertial loads during ejection.

METHODS

A parametric simulation study consisting of hundreds of simulations was performed using the Articulated Total Body (ATB) model to determine the effect that varying helmet weight, center of gravity, and moments of inertia had on head and neck forces during ejection (Ref. 1). This model was able to evaluate the 3-D dynamic response of a system of rigid bodies when subjected to a dynamic environment consisting of applied forces and interactive contact forces (Ref. 2). In addition, tests were conducted on the Navy's ejection tower facility using advanced tactical helmets and compared with results from tests using baseline helmets (Ref. 3).

RESULTS

Simulation results indicated that the head/helmet center of gravity was the most dominant variable in affecting head/neck loading during ejection. The total head supported mass and head/helmet moments of inertia were found to have lesser effects. Test results supported the simulation data and demonstrated that the forward center of gravity of the advanced display helmet resulted in significantly greater tensile loading and flexion moment on the head/neck versus the baseline helmet, during the catapult stroke of ejection.

CONCLUSIONS AND FUTURE WORK

Minimizing head/neck loads during ejection is critical to protecting the life of the aviator. The location of the center of gravity was found to have a major impact on the resultant head/neck forces and moments, particularly in ejection systems that exhibited inherent instabilities. However, many other factors affect the overall dynamics of the ejection that directly impact the loads that are transferred to the aviator. Research in ejection seat technology has proven that improving seat stability during ejection can reduce head/neck loads to tolerable limits even with added head mass and at higher ejection airspeeds. Programs that improve the stability of the ejection seat system will ultimately reduce the likelihood of severe neck injury, even as advances in materials and optics technology result in lighter weight and improved performance helmet systems.

REFERENCES

1. Marquette, T.M., Paskoff, G.R. and McConnell, R. "Tactical Helmet Mass Properties Study." NAWCADPAX Draft Report, NAWCAD, Pax River, MD: September, 1996.
2. Obergefell, L.A., Gardner, T. R., Kaleps, I., and Fleck, J.T., "Articulated Total Body Model Enhancements, Vol. 2, Users Guide", Armstrong Aerospace Medical Research Laboratory, AAMRL-TR-88-043, January, 1988.
3. Paskoff, G.R. and Dillon, T.J. "Joint Helmet Mounted Cueing System Ejection Tower Evaluation for F/A-18 Configuration." NAWCADPAX-99-52-RTR, NAWCAD, Pax River, MD: June, 1999.

TABLE 1: Max/Min Parameter Values for Ejection Tower Evaluation of Advanced Display Tactical Helmet vs. Baseline Helmet

Test No.	Manikin Size	Helmet Config.	CAT_GZ (G)	HFX (N)	HFZ + (N)	HFZ - (N)	HMY + (N-m)	HMY - (N-m)	NFX (N)	NFZ + (N)	NFZ - (N)	NMY + (N-m)	NMY - (N-m)
44	5th %ile Male HIII	Baseline	12.24	146	791	-528	9.60	-27.44	686	856	-798	339.3	-72.19
46	5th %ile Male HIII	Advanced Display	11.33	130	905	-484	8.71	-32.53	738	969	-758	361.3	-74.11
47	95th %ile Male HIII	Baseline	12.64	154	752	-582	10.43	-24.64	780	662	-1044	307.8	-82.25
48	95th %ile Male HIII	Advanced Display	12.68	130	975	-629	12.63	-29.49	967	739	-1011	338.8	-83.83

THE STUDY OF DYNAMIC BIOMECHANICAL EVENTS USING DIGITAL FLASH RADIOGRAPHY

Jeffrey A. Adams[1], Peter C. Laurence[2], and T. Ellory Sanderson[3]

[1]Senior Engineering Technician, jadams@atc.army.mil
[3]Senior Test Engineer, tsanders@atc.army.mil
U.S. Army Aberdeen Test Center, Aberdeen Proving Ground, Maryland

[2]Senior Imaging Specialist, Peter.Laurence@enfish.com
Titan Systems Corporation, Pulsed Sciences Division, San Leandro, California

INTRODUCTION

The Aberdeen Test Center has a long history of using flash radiography as a premier diagnostic tool aiding in the design and development of armor and anti-armor weapon systems. Current trends in this testing arena are moving towards the evaluation of personal protection systems used by the warfighter. This type of testing requires an objective re-evaluation of the diagnostic tools and techniques used to obtain the required data. Several legitimate digital techniques will be discussed in this paper as they have been applied in real test scenarios involving high-speed dynamic impact and blast effects on biomechanical specimens.

BACKGROUND

Over the better part of the past three decades, the typical flash x-ray workload at ATC consisted of dynamic test and evaluation of "hard" military materiel including targets, projectiles, guns, and shaped charges. Within the past few years we have realized a shift in this tradition with a significant portion of the projected workload focused on "soft" specimens within the arena of biomechanical studies. With this type of testing, the areas of interest are typically smaller, more detail is often required, and so the ability to digitally extract and enhance information not visible on film is proving invaluable. The first viable digital flash radiography system was fielded by ATC for tank ammunition testing circa 1996, and used Kodak™ storage phosphor screens as the imaging medium. The use of this system on ballistic impact studies at the University of Virginia's Automobile Safety Laboratory will be discussed in detail. Another hybrid system successfully fielded by ATC was comprised of a standard flash x-ray system, a custom-built multi-anode x-ray tube, and a high-speed digital video camera. This combination of technologies was melded into an effective data collection system used to study biomechanical response to blast effects for The Institute of Surgical Research from Fort Sam Houston Texas. The unique circumstances and site-specific test set-up shall be discussed as well.

RESULTS AND DISCUSSION

The use of diagnostic digital imaging has become commonplace in medical institutions throughout the world. Various methods are now available to the medical professional including MRI, CAT Scan, CR, and standard x-ray. One common and very beneficial trait they share is the ability to access the information in the digital domain, and fortunately this characteristic transfers with the techniques used in digital flash radiography. Although many of the principles used for high-speed studies are anchored in medical imaging, the standard hardware and software packages available to the medical community are virtually useless in the world of high-speed imagery. The duration of some of the slower high-speed events is on the order of a few milliseconds (10^{-3}sec) during which time as many as eight x-ray exposures may be taken. A typical "fast" single exposure in a clinical x-ray setting might be on the order of a few tenths of a second (10^{-1} sec). The challenge of capturing and recording images of high-speed dynamic events while attempting to maintain medical image quality becomes significant. In addition, the need to protect the x-ray equipment and imaging sensors from collateral damage is sometimes a serious challenge in and of itself. These challenges have resulted in the development of many innovative techniques, but more work is needed to further refine the quality of the acquired images. As the medical community becomes more intimately involved with ballistic testing, the need to improve the spatial resolution of digital flash radiographs becomes more apparent. Further investigation into the optimization of x-ray sources and digital imaging techniques has become a priority for ATC. Investigative studies are currently underway and will be discussed in detail.

SUMMARY

In less than a decade, ATC has made considerable progress in its migration from film-based flash radiography into the realm of digital x-ray imaging. With the exception of the high-speed digital video camera, the imaging technologies used in these efforts are hand-me-downs from the medical community. We are realizing an increased interest in biomechanical studies from the military medical community as they relate to soldier systems such as body armor, helmets, and footwear. The inevitable collaboration of the medical and test communities can only foster increased sharing of related technologies. The studies discussed in the paper are a solid representation of this collaborative effort as it plays out in the military test community. These efforts are bound to have far reaching effects on the biomechanical research community in the foreseeable future.

NUMERICAL MODELING OF HUMAN OCCUPANTS AND AUTOMOTIVE SAFETY

King H. Yang and Albert I. King
Bioengineering Center, Wayne State University, Detroit, MI, USA

INTRODUCTION

Locomotion is an essential element of human existence. Because moving on foot is rather inefficient, the idea of utilizing power-propelled vehicles arose fairly early in human history. with the invention of automobiles humans were able to fulfill the desire to move both farther and faster. However, the speed and weight of the vehicles became an inherent safety hazard to their occupants and other road users. Special design considerations are needed to improve the safety of human beings who live in today's automobile-saturated environment.

In 1955, Ford Motor Company promoted a slogan of "Lifeguard Design" advocating automotive safety. Unfortunately, safety did not translate into sales, as consumers were more into style than safety. In the late 1960s, Ribicoff's landmark congressional hearing, the Nader testimony, and the subsequent creation of the National Highway Traffic Safety Administration established a set of minimum standards that auto manufacturers need to meet before they can sell any particular vehicle.

Establishment of safety standards and performance criteria requires the understanding of human responses and tolerances to impact loading. Research methods include but are not limited to: accident and clinical investigations, animal, cadaver, and volunteer testing, and theoretical, physical, and mathematical modeling. Results from these studies were used to design anthropomorphic crash dummies, which in turn were also used to develop and evaluate new concepts for active and passive injury prevention systems. Unfortunately, each of the aforementioned methods has its limitations and, as a result, the dummies currently in use were designed for limited purposes such as for frontal and lateral impact, scenarios that are unlikely to occur in real world crashes. Additionally, significant differences exist between the dummy and the human, for instance, the stiffness of body segments and the inability of the dummy to fully simulate bony fractures. Dummies are made of steel and rubber while the human is mainly composed of bone and muscle.

With the rapid advances in computing power, sophisticated vehicular and dummy models are routinely employed in the design and evaluation of new prototypes. Dummies are mechanical devices that could be simulated accurately. However, the lack of biofidelity associated with mechanical dummies is also reflected in dummy models. Even though the application of dummies and their numerical counterparts have greatly improved crash safety for subjects that are similar in sizes to these dummies in full frontal and lateral impacts, protection provided for other collision directions or for occupants of non-standard sizes is not fully effective. Numerical human surrogates simulating both genders and of different sizes can be used to study impacts from all directions and can offer the general population more protection than what is available now.

The development of such a surrogate requires comprehensive knowledge of human anatomy, the constitutive laws governing a large variety of human tissue, and injury thresholds. Additionally, response data at different loading rates, similar to real world crashes, are needed for model validation. This paper summarizes regional models of the human body, from head to foot, developed at Wayne State University (WSU) over the last decade (1-8). In general, strengths of these models are that they employ an accurate and detailed geometry of the body region, thus rendering it suitable for investigation of injury mechanisms. Some of these models are being used to improve vehicular seat and restraint system design.

COMPUTER MODELS

The WSU brain model simulates all the essential substructures of the head and brain and has been validated against available intracranial pressure, ventricular pressure, and relative displacement between the skull and the brain (1, 8). It is being used to evaluate the efficacy of current helmet designs. The neck model, which includes all seven cervical vertebrae, intervertebral discs, and 15 pairs of passive muscles, has been validated against data obtained in vertical head drop and rearend impact test results (7). It has been applied to study the neck responses when interacting with an airbag. The chest model includes descriptions of the rib cage, heart, lung, and major blood vessels. It has been validated against pendulum impact data from frontal and lateral impacts as well as against lateral sled test data when whole body cadavers slid into a rigid or padded wall (4, 6). The model has been used to determine the mechanism of aortic rupture as well as injury to the upper arm interacting with a side airbag. The abdominal model includes detail descriptions of vital solid organs and major blood vessels while other hollow organs were lumped into three "body bags" to transfer loads (5). This model could be used to simulate the interaction between the seat belt and the abdomen. The lower extremity model includes all main anatomical structures from the pelvis to foot (2, 3). It has been validated against 21 different sets of experimental data and has been applied to study dynamic interactions between the knee and a knee bolster.

DISCUSSION

Around the world, human occupant models, either at the component or whole body level, are also being developed. However, models developed elsewhere emphasize its direct integration into vehicular models. As a result, detailed anatomical representation was sacrificed in favor of the inclusion of the vehicular model. On the other hand, the weakness of WSU models is their high computational cost. Nevertheless, biofidelity issues still exist in models developed at either WSU or elsewhere for impact directions and severities not tested in the model validation process. This concern arises primary because the experimental data available for model validation vary greatly due to large variations in biological tissue response. Additionally, existing constitutive laws implemented in simulation software packages are not well suited for modeling human tissues.

Through various in-house and international collaborative projects, these deficiencies are being corrected by studying the epidemiology of automotive related injuries and the material properties of human tissue. More importantly, new experiments are being designed and conducted guided by model predicted results to advance our understanding in injury biomechanics. Once detailed bony kinematics and tissue deformation become available to validate these models rigorously, it is expected that human models will become an efficient tool to assess injury risk of passengers in transportation systems, pedestrians, and other road users.

REFERENCES

1) Al-Bsharat, A.; Hardy, W.N.; Yang, K.H.; Khalil, T.; Tashman, S. and King, A.I. (1999) "Brain/Skull Relative Displacement magnitude due to Blunt Head Impact: New Experimental Data and Model" proceedings of the 43rd Stapp Car Crash Conference, San Diego, California, pp. 321-332.
2) Beillas, P.; Lavaste, F.; Nicolopoulos, D.; Kayventash, K.; Yang, K.H. and Robin, S. (1999) "Foot and ankle finite element modeling using actual articular surfaces" proceedings of the 43rd Stapp Car Crash Conference, San Diego, California, pp. 171-184.
3) Beillas, P.; Begeman, P.C.; Yang, K.H.; King, A.I.; Arnoux, P.J.; Kang, H.S.; Kayvantash, K.; Brunet, C.; Cavallero, C.; Prasad, P. (2001) "Lower Limb: Advanced FE Model and New Experimental Data" *Stapp Car Crash Journal* 45:469-493.
4) Iwamoto, M.; Mike, K.; Mohammad, M.; Nayef, A.; Yang, K.H.; Begeman, P.C. and King, A.I. (2000) "Development of a Finite Element Model of the Human Shoulder"; *Stapp Car Crash Journal,* 44:281-297.
5) Lee, J.B. and Yang, K.H. (2001) "Development of a Finite Element Human Abdomen Model"; *Stapp Car Crash Journal* 45:79-100.
6) Shah, C.; Yang, K.H.; Hardy, W.N.; Wang, H.K. and King, A.I. (2001) "Development of a Computer Model to Predict Aortic Rupture due to Impact Loading"; *Stapp Car Crash Journal* 45:161-182.
7) Yang, K.H.; Zhu, F.; Luan, F.; Zhao, L. and Begeman, P.C. (1998) "Development of a Finite Element Model of the Human Neck"; Proceedings of the 42nd Stapp Car Crash Conference, Tempe, Arizona, pp. 195-205.
8) Zhang, L.; Yang, K.H.; Dwarampudi, R.; Omori, K.; Li, T.; Chang, K.; Hardy, W.N.; Khalil, T.B. and King, A.I. (2001) "Recent Advances in brain Injury Research: A New Human Head Model Development and Validation" *Stapp Car Crash Journal* 45:369-393.

LOWER EXTREMITY FORCES DURING AN AUTOMOBILE COLLISION: THE INFLUENCE OF MUSCLE PROPERTIES

E. C. Hardin, A. Su and A. J. van den Bogert, hardine@bme.ri.ccf.org
Department of Biomedical Engineering, Cleveland Clinic Foundation, Cleveland, Ohio, USA

INTRODUCTION

Cadavers, dummies and computational models have been used to study automobile collision injuries to the legs (Digges *et al*., 1995; Rudd *et al*., 1998). In lieu of active muscles, joint friction and joint torque are generally employed. Considering that muscle tensing could affect injuries (Digges *et al*., 1995; Parenteau *et al*., 1996; Rudd *et al*., 1998; Tencer *et al*., 2002), models without muscle properties might be incomplete. The purpose of this study was to compare peak lower extremity forces in models with joint friction, joint torque and muscle properties during an automobile collision.

METHODS

A 2-D musculoskeletal model was developed which had seven body segments and six functional right-side muscle groups (glutei, hamstrings, rectus femoris, vasti, gastrocnemius, and soleus) each represented by a three-element Hill model. Vehicular contact surfaces were line segments while body segments contacting these surfaces were given contact elements from the literature (Wright *et al*., 1998; Digges *et al*., 1995). The model was implemented in C code using the SD/FAST library for forward dynamics. For the frontal crash simulations, vehicle motion data were obtained from the National Highway Transportation and Safety Administration (crash #2075) and were applied to the contact surfaces. Five models were tested: maximal muscle activation (MX, panic braking), minimal muscle activation (MN), no muscles (NM), joint friction (JT) and joint torque (JT). MN activation values were found by optimizing a weighted cost function using a 4-second dynamic simulation of static driving, resulting in a realistic equilibrium posture and pedal force at minimal muscle activation. Muscles were eliminated from NM, JF and JT. Moments calculated for JF and JT were nonlinear functions of angle and angular velocity, respectively, with saturation levels specified for each joint (Digges *et al*., 1995). The forces of interest during the crash were those from the ankle joint (A), knee joint (K), rearfoot ground reaction force (RF), Achilles tendon (AT), and calcaneus (C = RF + AT).

RESULTS

Peak joint forces (A and K) were greatest in the panic braking model (MX), yet this model also had the lowest peak RF force (Table 1, Fig. 1). Peak AT and C force were 4.5 times and 3 times greater, respectively, during panic braking compared to minimal activation (MX and MN, Table 1). Results for MN and NM were similar, as well as were those for JF and JT.

Table 1: Peak forces (N) in the five models.

Model	*A*	*K*	*RF*	*AT*	*C*
MX	4125	3147	629	6445	6941
MN	2001	1073	1202	1430	2569
NM	1451	917	1178	-	-
JF	2783	1813	1547	-	-
JT	2809	1815	1596	-	-

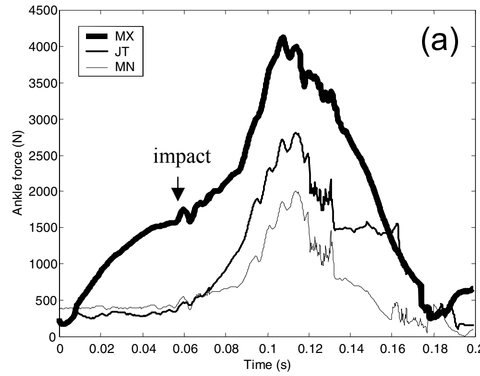

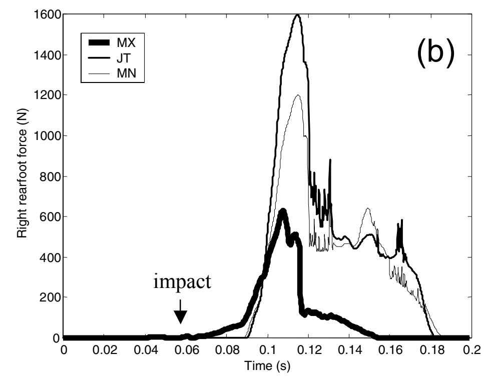

Figure 1: Right ankle force (a) and rearfoot force (b) for MX, JT and MN during the crash.

DISCUSSION

Muscle activation affected peak joint force, as others have suggested (Parenteau *et al*., 1996; Rudd *et al*., 1998; Tencer *et al*., 2002), and would likely exacerbate injuries. A relatively simple method to model muscles is to use joint friction (JF) or joint torque (JT) functions, both of which seem to predict similar joint forces to a model with moderately activated muscles (Fig. 1a). Unfortunately, RF force is overestimated with JT or JF (Fig. 1b). We think this is caused by the saturation of joint torque in these models, effectively resulting in zero muscle stiffness during the dorsiflexion at impact. We conclude that computational models for prediction of lower extremity injury in vehicle collisions require a realistic representation of muscle properties and muscle activation.

REFERENCES

Digges, K.H. *et al*. (1995) *Int Conf Pelvic and Lower Ext Inj* Washington, D.C.
Parenteau, C.S. *et al*. (1996) *Accid Anal Prev* **28**:607-617.
Rudd, R.W. *et al*. (1998) *Mechanics of Protection,* SAE, **1355**:75-81,125-132.
Tencer, A.F. *et al*. (2002) *Accid Anal Prev* **34**:1-11.
Wright, I.C. *et al*. (1998) *Clin Biomech* **13**:521-531.

ACKNOWLEDGMENT Funded in part by the Aircast Foundation.

OPTIMAL PROTECTION OF HUMANS FROM IMPACT

Walter D. Pilkey

Center for Applied Biomechanics, University of Virginia,
122 Engineer's Way, P.O. Box 400746, Charlottesville, VA 22904-4746
wdp@virginia.edu

INTRODUCTION

The severity of certain injuries often can be reduced if vehicles, seats, sports helmets, etc., are equipped with effective impact isolators. A shock isolator is an engineering device placed between the body to be protected and a base subjected to a transient load. The isolator generates a control force that reduces the intensity of the force transmitted to the body. An important step in the optimal design of shock isolators is a limiting performance analysis.

A limiting performance analysis can be employed to determine the absolute optimal performance of the system with shock isolators. As part of the design process, it is advantageous to know the physical response possibilities (limiting response), irrespective of the actual design configuration. In setting up the limiting performance study, a mathematical model is established in which the isolator is replaced by a generic, time-dependant control function. The limiting performance analysis involves the computation of the time history of the control function corresponding to the minimum of an objective function, while satisfying prescribed response constraints, e.g., a rattlespace.

This talk discusses problems of the limiting performance analysis of systems intended to reduce impact-induced injuries.

METHODS

Analytical limiting performance analyses are possible for limited degree of freedom systems. For complex systems, computational optimal methods are necessary. In particular, linear programming or quadratic programming methods often can be employed.

Critical to a limiting performance study for injury mitigation is a biomechanical injury model. This paper is not concerned with the development of new injury models. Established injury models are used to illustrate the limiting performance analysis.

RESULTS AND DISCUSSION

Limiting performance problems for the success of seats in preventing spinal injuries, the use of seatbelts in reducing thoracic injuries, and the effectiveness of sports helmets in mitigating head injuries are considered. In addition, leg injuries from automobile toepan intrusion are used to illustrate the potential improvement in impact isolation if a pre-impact sensor is available so that the optimal isolator can be "cocked" prior to impact.

It is often contended that injury prevention systems, such as seatbelts, should be constant force systems. This issue is addressed for single and multi degree of freedom systems subject to various pulses.

For the limiting performance of seat systems, the dynamic response index (DRI) is used to predict thoracolumbar-spine fracture injuries. The so-called Lobdell injury models are used to study the dynamics of the human thorax in a crash of a vehicle. The Stalnaker head injury models are utilized in the helmet limiting performance analysis studies.

SUMMARY

It is shown that limiting performance analyses can be used to study the potential injury prevention characteristics of safety devices. It is also shown that preview control can improve considerably the injury reduction potential of an impact isolation system. Finally, the investigation into constant force isolators demonstrates that optimal isolators occur for single degree-of-freedom systems subject to impulse loading. For more realistic models, constant force isolators are not optimal.

REFERENCES

Balandin, D., Bolotnik, N., and Pilkey, W.D. (2001). *Optimal Protection from Impact, Shock, and Vibration*, Taylor and Francis, Philadelphia.

A NUMERICAL MODEL PREDICTING UPPER EXTREMITY FRACTURES DUE TO AIRBAG DEPLOYMENT

Jack van Hoof[1], Lex van Rooij [1, 2], and Jeff Crandall [2]

[1] TNO Automotive, Crash Safety Centre, Delft, The Netherlands
[2] University of Virginia, Center for Applied Biomechanics, Charlottesville, Virginia

INTRODUCTION

Forearm fractures are commonly observed in cases where the arm of the driver was close to the airbag door at the time of deployment. Even though these injuries are not life threatening, they can result in long-term disabilities for the victims. Numerical modelling can be used as an efficient and flexible tool to further enhance airbag designs, so that the severity of forearm fractures can be reduced in future. The current paper presents a numerical model that provides an efficient and accurate prediction of forearm fractures due to airbag deployment.

METHODS

The current paper presents a hybrid multibody-finite element model, which provides an optimal combination of efficiency and detailed injury predictions. The main part of the model was taken directly from the MADYMO multibody model of a mid-size male, but the arm was replaced with a detailed finite element arm model adopted from the MADYMO full finite element human body model. The multibody part of the hybrid model provided a biofidelic kinematic response, whereas the finite element arm enabled accurate predictions of the injurious deformations. The model is shown in Figure 1, where it is interacting with a side airbag.

Prior to application, the hybrid model was validated for the same range of multi-directional impact conditions as used for the full multibody and finite element models. The detailed arm model was validated with quasi-static and dynamic 3-point bending tests on cadaver upper extremities. Once the model was validated it was used in applications with airbag models to predict arm fractures resulting from airbag deployment. Published data on failure strains of the bones of the arm were used in injury criteria for arm fractures resulting from airbag deployment.

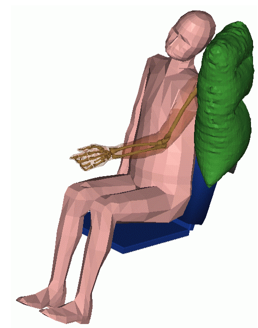

Figure 1: Multibody human model with FE upper extremity interacting with side airbag

RESULTS AND DISCUSSION

The results obtained in this study showed that the model presented in this paper provided an efficient and accurate prediction of arm fractures due to airbag deployment.

SUMMARY

A hybrid multibody-finite element human model has been developed and validated. The model was used in applications with airbags and provided accurate predictions of arm fractures due to airbag deployment.

REFERENCES

Happee R., *et al*. (1998). *Proceedings STAPP Conference*.
Happee R., *et al*. (2000). *Proceedings IRCOBI Conference*.

DESIGN OF A BIOFIDELIC, INSTRUMENTED 2.5 KG INFANT DUMMY

N. Rangarajan, J.McDonald, T. Shams, R. Delbridge[1] and T. Fukuda, Y-M. Liu, K. Kawasaki, H. Morishima, Y. Tokushige[2]

[1] GESAC, Inc. nrangarajan@gesacinc.com
[2]Aprica Kassai, Inc.

INTRODUCTION

This paper describes the design, development and testing of a biofidelic infant dummy weighing 2.5 kg. The dummy can be used to evaluate the efficacy of child seats when used to protect infants.

METHODS

Anthropometric data were obtained from literature and children in a pediatric hospital [Table 1]. Dynaman© 3-D lumped mass occupant simulation model was used to obtain joint loads and other design parameters. Joint ranges of motion were obtained from literature also. Impact response data were also obtained from literature and scaled as needed.

Table 1 : Sample anthropometric data

Parameter	Units	Design Goal
Mass	Grams	2600
Height	mm	450
Arm length (arm to tip of hand)	mm	180
Leg length (crotch to heel)	mm	150
Head Circumference	mm	349
Neck Circumference	mm	172
Neck Length	mm	54
Upper Arm Circumference	mm	80
Leg at Hip Circumference	mm	130
Head Weight	grams	800
Upper Arm Weight	Grams	29
Lower Arm Weight	Grams	22
Upper Leg Weight	Grams	82
Lower Leg (w/Foot) Weight	Grams	48

RESULTS AND DISCUSSION

Preliminary static tests indicate that the dummy is biofidelic in its response [Fig. 2]. A number of sled tests have been conducted in a variety of child seats. Sleds tests indicate that the dummy and instrumentation are robust and that the dummy yields repeatable results. Repeat static tests indicate that the dummy provides repeatable response. Tests on two dummies indicate that the dummy is reproducible as both dummies provide very similar responses under similar loading conditions [Figs. 3 & 4].

Figure 1: Infant dummy

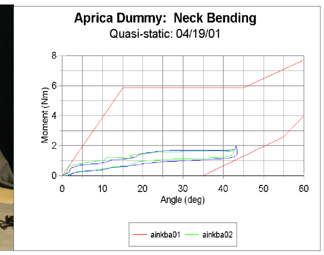

Figure 2: Neck bending response with corridor

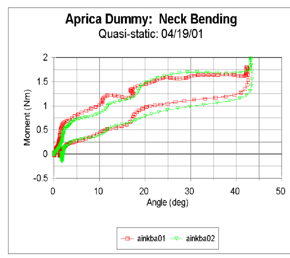

Figure 3: Neck bending Response for 2 dummies

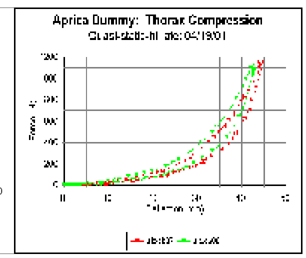

Figure 4: Thorax compression in repeat tests

SUMMARY

A twelve segment, instrumented, biofidelic infant dummy has been developed. It weights 2.5 kg and is instrumented with five tri-axial accelerometers. Data from tri-axial accelerometers at the base and top of the neck can be used to calculate the Neck Injury Criterion (NIC). Head Injury Criterion (HIC) can be calculated using data from the tri-axial accelerometers in the head. The dummy can be used to evaluate the safety potential of various types of child seats to transport infants.

HEAD IMPACTS: ANALYTICAL, NUMERICAL AND EXPERIMENTAL MODELS.

Philippe G. Young

Department of Engineering, University of Exeter, Exeter, EX4 4QF, UK
Senior Lecturer in Biomechanics. philippe.g.young@ex.ac.uk

INTRODUCTION

An overview of some of the work carried out at The University of Exeter on the response of the human head to blunt impact will be presented. Simple analytical expressions were derived to predict global impact characteristics (e.g. duration of impact, peak force transmitted, peak acceleration, HIC) for a fluid-filled spherical shell impacting with a projectile. In addition approximate analytical formulae to predict the onset of a dynamic response in the brain (onset of high intra-cranial pressure and shear transients) were also proposed. The analytical models were based on a number of simplifying assumptions and, in order to test their applicability when complicating effects were considered, realistic patient specific finite element and rapid prototyped models were generated based on 3D medical imaging data. The numerical and physical replica models were tested under a range of impact conditions and results obtained compared with the predictions from the analytical models.

METHODS

A high-resolution T1-weighted whole head MRI scan of a normal young male volunteer was obtained *in vivo* (see Figure 1.a). A three-dimensional finite element (FE) model was generated automatically from the 3D data sets using an in-house developed technique adapted from the marching cubes approach (see Figure 1.b). A rapid prototyped (RP) model based on the same dataset was also generated in parallel (see Figure 1.c).

1(a)

1(b)

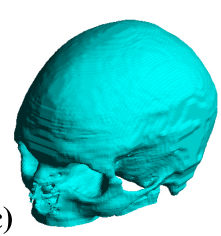

1(c)

Figure 1: (a) Rendered image of MRI data acquisition.
(b) Photograph of rapid prototyped skull generated
(c) Rendered image of finite element mesh generated.

RESULTS AND DISCUSSION

The RP model was filled with water to simulate the brain and subjected to low velocity impacts with a range of steel balls of different masses. These impacts were also simulated using the FE model and in Figure 2 the impact durations obtained using both these approaches as well as impact durations predicted by the analytical model are plotted for impact masses ranging from 45 g to 250 g. Excellent agreement is seen between the FE and RP results which in turn are in good agreement with the predictions from the simple analytical model.

SUMMARY

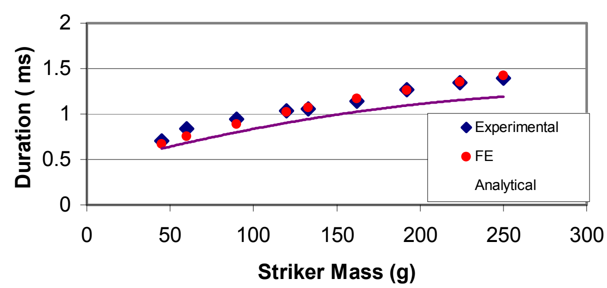

Figure 2: Comparison of FE, experimental and analytical impact durations.

A simple analytical model for key impact characteristics was validated using finite element and rapid prototyped models. As the mass of the projectile decreases the impact duration also decreases and, below a threshold value, it can be shown that there is an increasing likelihood of potentially deleterious pressure and shear strain transients occurring.

ACKNOWLEDGEMENTS

The author wishes to acknowledge the following all of whom have contributed to the work presented: Sergio Rodriguez Diaz, Ricardo Villanueva, Terry Beresford West, Emma Johnson, John Dry and Luca Zunarelli,

EFFECT OF VENTILATION ON INSTILLED LIQUID TRANSPORT IN THE PULMONARY AIRWAYS OF RATS

Joseph C. Anderson[1], Christopher A. Dawson[2,3], Robert C. Molthen[2,3], Steven T. Haworth[2,3], Matthew R. Glucksberg[4], and James B. Grotberg[1]

[1]Department of Biomedical Engineering, University of Michigan, Ann Arbor, MI 48109, [2]Marquette University and Medical College of Wisconsin, Milwaukee 53201, [3]Zablocki Veterans Affairs Medical Center, Milwaukee, Wisconsin 53295, and [4]Department of Biomedical Engineering, Northwestern University, Evanston, Illinois 60208
Email: grotberg@umich.edu

INTRODUCTION

Liquid can be instilled into the pulmonary airways during medical procedures such as surfactant replacement therapy, partial liquid ventilation and pulmonary drug delivery. For all cases, understanding the dynamics of liquid distribution in the lung will increase the efficacy of treatment. Recently, Cassidy et al (2001) developed an imaging technique for the study of real-time liquid transport dynamics in the pulmonary airways of rats. This study uses those imaging methods to investigate the effect of respiratory rate on the distribution of an instilled liquid, surfactant, in a rat lung.

METHODS

Lungs from 10 anesthetized Sprague-Dawley rats (~300 g) were removed, cannulated., vertically suspended via the cannula, and placed on 4 cmH_2O positive end-expiratory pressure. A bolus (0.05 ml) of exogenous surfactant (Survanta, Ross Laboratories, Columbus, OH) mixed with radiopaque tracer was instilled as a plug into the trachea of each lung. The lungs were ventilated with a 4 ml tidal volume for 20 breaths at one of two respiratory rates: 20 or 60 breaths/min. During the first five breaths, the movement of radiopaque surfactant in the lungs was imaged at 30 images/s using a microfocal X-ray source and an image-intensifier. After 20 breaths, the lungs were placed on 4 cmH_2O positive pressure and rotated at 2°/s while imaging with the microfocal X-ray device. A 3-D image of the lung was reconstructed using the images acquired during rotation and compared to the 2-D images collected at breath 20.

Transport dynamics of surfactant during the first few breaths were quantified statistically using the center of mass, standard deviation, skewness, and kurtosis of the spatial distribution of surfactant. Additionally, the lung was divided into four regions to examine the homogeneity index, and fraction reached.

RESULTS AND DISCUSSION

Respiratory rate influenced the distribution of instilled surfactant within the airways of the rat lung. Surfactant distribution was more homogeneous throughout the first 5 breaths in lungs respiring at 60 breaths/s than at 20 breaths/s. Figure 1 shows the distribution of surfactant (black regions) in a rat lung after breathing 20 breaths at 60 breaths/min. Notice that surfactant was located throughout the lung whereas in lungs respiring at 20 breaths/min (not shown), the surfactant resided in the center of the lung.

Figure 1: X-ray image of surfactant + radiopaque tracer (black regions) in a rat lung that was ventilated at 60 breaths/min.

After 20 breaths, surfactant reached a greater portion of the lower lobes than upper lobes of lungs respiring at either frequency. Using the 3-D lung reconstruction, the spatial distribution of surfactant was located and quantified for analysis and comparison with the 2-D images.

REFERENCES

Cassidy, K.J. et al (2001). *J. Appl. Physiol.*, **90**, 1955-1967.

ACKNOWLEDEGMENTS

Supported by NIH grant HL41126, and Ross Laboratories.

LIMITATION OF EXPRIATORY FLOW IN LIQUID VENTILATION

Joseph L. Bull[1,2], Craig A. Reikert[3], E. Komori[3], S. Tredici[3], J.B. Grotberg[1], and R.B. Hirschl[3]
[1]Biomedical Engineering Department, University of Michigan, Ann Arbor, MI,
[2]E-mail: joebull@umich.edu
[3]Department of Surgery, University of Michigan, Ann Arbor, MI

INTRODUCTION

Total liquid ventilation involves filling the lungs with a perfluorocarbon (PFC) liquid, and ventilating with a liquid tidal volume. Liquid ventilation has shown promise for treating acute respiratory distress syndrome (Hirschl 1996). Flow limitation can occur during expiration of the PFC, causing difficulty in achieving the desired minute ventilation, and can result in "breath stacking" in which the end-inspiratory lung volume increases with time. Flow limitation occurs when airway pressures become low enough that airways collapse. Flow limitation (also known as "choked" flow) and airway flutter have been studied extensively in the context of gas ventilation (Elad 1987, Elliot & Dawson 1977, Knudson 1983, Larose & Grotberg 1998, Luo & Pedley 1998), but few studies have investigated flow limitation in liquid ventilation. In this work, we investigate flow limitation in liquid ventilation.

METHODS

New Zealand White rabbits (n=56, mean weight = 3.1 kg ± 0.3 kg) were anesthetized, heparinized, and euthanized. A tracheostomy was performed and one of four different PFCs (PFOB, PP4, FC77, or PFDEC) was instilled into the lungs to an end-inspiratory lung volume (EILV) of either 40 ml/kg or 20 ml/kg. The enodotracheal tube was connected to a computer-controlled piston pump which provided a constant flow expiration. The PFC volume remaining in the lungs at choke, V_{ch}, was measured three times for each of three different expiratory flow rates (2.5, 5.0, 7.5 ml/s). The PFC properties are listed in Table 1. Additionally, we have developed a theoretical model of choke in liquid-filled lungs. The model is based on a modified Bernoulli equation, and accounts for the effects of gravity.

RESULTS AND DISCUSSION

Figure 1 contains a plot of V_{ch} vs. flow rate for each PFC with (a) EILV = 40 ml/kg, (b) EILV = 20 ml/kg. V_{ch} does not follow an obvious relationship based on fluid properties. For example, the densities and viscosities of PFOB and PP4 are similar, yet a PFOB-filled lung has a much lower V_{ch} for a given flow rate. We are currently measuring the resistance and compliance of PFC-filled lungs. Our preliminary measurements suggest these may depend on PFC type, possibly involving PFC interactions with surfactant or with the aqueous lining of the lungs. Our model indicates these parameters affect V_{ch}.

SUMMARY

Flow limitation in PFC-filled lungs does not correlate directly with PFC fluid properties. Using our theoretical model, we are currently investigating the reasons for this behavior.

REFERENCES

Elad, D., et al (1987) *J. Biomech. Eng.* **109**:1-9.
Elliot, E.A., Dawson, S.V. (1977) *J. Appl. Physiol.* **43**:516-22.
Hirschl, R.B. (1996) *Critical Care Medicine* **24**:1001-1008.
Knudson, R.J., et al (1983) *Resp. Phsyiol.* **52**(1): 113-123.
Larose, P.G., Grotberg, J.B. (1998) *J. Fluid Mech.* **331**:37-58.
Luo, X.Y., Pedley, T.J. (1998) *J. Fluid Mech.* **363**:253-280

ACKNOWLEDGEMENTS

J.L. Bull is a Parker B. Francis Fellow in Pulmonary Research. This research is funded by NIH grant HL64373.

Table 1 PFC properties.

	PFDEC	PP4	FC77	PFOB
Formula	$C_{10}F_{18}$	C_9F_{18}	$C_8F_{18}O$	$C_8F_{17}Br$
MW	462	450	415	441
Vapor Pressure, Torr	14	7.2	85	11
Density, g/cm^3	1.93	1.89	1.78	1.92
Kinematic viscosity, cS	2.90	1.20	0.8	1.10
Surface tens., dyne/cm	19	17.7	15	18

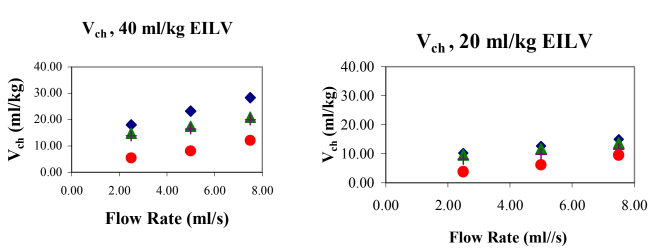

Figure 1 V_{ch} vs. flow rate. PFDEC ♦, PP4 ▲, FC77 +, PFOB ●.
(a) EILV = 40 ml/kg, (b) EILV = 40 ml/kg.

ANATOMICALLY BASED MODELS OF BLOOD FLOW IN THE HUMAN PULMONARY MICROCIRCULATION

Kelly Burrowes, Merryn Tawhai, and Peter Hunter

Bioengineering Institute, The University of Auckland, Auckland, New Zealand
k.burrowes@auckland.ac.nz

INTRODUCTION

An anatomically based mathematical model of the human pulmonary micro-vasculature and blood flow within this network is being constructed as part of the Lung Physiome (http://www.bioeng.auckland.ac.nz/physiome/physiome.php). The real capillary network is continuous throughout several alveolar units and at least throughout a single acinus; the model capillary network generated covers a small number of alveolated airways. Blood flow equations are solved through this network, and results are compared with in vivo measurements of red blood cell and neutrophil transit times from Presson et al. (1995).

METHODS

The alveolar structure is modeled using a Voronoi mesh that fills a given volume, with faces removed to form alveolar ducts, alveoli, and sacs. The capillary network is generated to be continuous over these alveolar surfaces. A 2D Voronoi network is generated over the surface of a ¾ sphere. This mesh is then texture-mapped onto the alveoli geometry. The Voronoi capillary junctions usually comprise, but are not restricted to, 3 segments. The Voronoi meshing method ensures mesh continuity between the septa of adjacent alveolar faces.

The method described by Huang et al. (2001) and Dhadwal et al. (1997) is implemented for the solution of blood flow in the capillary mesh. The resistance is calculated in each capillary segment and mass conservation balances are carried out at each junction. Pressure boundary conditions are applied at the inlet and outlet nodes of the network.

An iterative solution procedure is used: a linear solution of the pressure-flow equations is followed by rheological analysis to update hematocrit values. The rheological analysis takes into account the flow rate solution and feed hematocrit (volume fraction of red blood cells entering the network) to estimate an updated hematocrit field. This process also considers the uneven distribution of red blood cell fluxes.

The resulting pressures throughout the capillary network in turn induce cross sectional dimensional changes in the thin distensible vessels. These effects are taken into account iteratively. The influence of junctional resistances and the difference in flow through corner vessels is also accounted for in the solution procedure.

Calculation of red blood cell and neutrophil transit times through their preferred pathways are used to compare model solutions with in vivo measurements.

RESULTS AND DISCUSSION

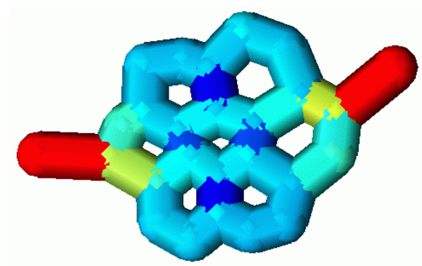

Figure 1: Normalised flow fields in a test capillary mesh. Red corresponds to 100% of inlet flow; dark blue is zero flow.

The Voronoi meshing procedure has been used to create alveolated airway meshes, and capillary networks. The resulting meshes compare well with recorded anatomical data (Weibel 1963, Sobin et al. 1980, Staub and Schultz 1968).

An advantage of using the texture-mapping procedure to generate the capillary mesh is that the method can be extended to mapping imaged capillary beds to the alveolar surface. That is, the texture-mapping method will ultimately be used to create capillary bed models from images of normal or diseased pulmonary capillaries.

Solution of blood flow and pressure equations has been implemented in the developed capillary network. The accuracy of the model is analyzed by comparison with *in vivo* measurements of red blood cell transit times.

This capillary system will be used to develop a lumped parameter model of pulmonary capillary bed pressure drop, to enable coupling of blood flow solutions in models of the pulmonary arterial and venous trees. The lumped parameter model will provide a pressure transfer function between the arterioles and draining venules. Blood flow in the large vessels is described by solution of Navier Stokes equations with pressure boundary conditions at the main pulmonary artery and vein.

REFERENCES

Dhadwal, A., et al. (1997). *J Appl Physiol*., **83(5)**, 1711-1720.
Huang, Y., et al. (2001). *J Appl Physiol*., **90**, 545-564.
Presson, R.G. Jr., et al (1995). *J Appl Physiol.*, **79**, 382-388.
Sobin, S.S., et al. (1980). *Microvasc. Research*, **19**, 217-233.
Staub, N.C., Schultz, E.L. (1968). *Resp. Physiol.,* **5**, 371-378.
Weibel, E.R.. (1963) *Morphometry of the Human Lung*, Springer-Verlag, Germany.

A MULTI-SEGMENTAL MODEL OF THE COUPLING OF INSPIRATORY FLOW WITH THE COMPLIANT NOSE STRUCTURE ASSESSED IN VIVO.

Redouane Fodil[1], Lydia Brugel [1, 2], Daniel Isabey[1], Alain Harf[1, 2], Bruno Louis[1]

[1] INSERM UMR 492, Faculté de Médecine et Faculté des Sciences et Technologies, Créteil, France
[2] Service de Physiologie - Explorations Fonctionnelles, CHU Henri Mondor, Créteil, France
redouane.fodil@creteil.inserm.fr

INTRODUCTION

Nasal flow limitation has often been reported in the patho-physiological literature in many circumstances including hyperventilation and, in case of nasal valve pathologies, during quiet inspiratory breathing (Bridger *et al*., 1970; Proctor, 1977). We have developed a discrete multi-segmental model describing the coupling between inspiratory flow and the nasal wall distensibility. This model has been initially developed to describe the flow-structure coupling in pharyngeal airways with at least two-compliant compartments in series (Fodil *et al*., 1997), but it has never been applied at the nose level. In the present study, the local wall compliance has been estimated in normal subjects, from longitudinal nasal area profiles obtained, by acoustic reflection, at various predetermined negative values of nasal pressure.

MATERIAL AND METHOD

The two-microphone acoustic reflection method was used to assess the inner geometry of the nose in terms of cross-sectional area versus the distance along the longitudinal airway axis (Louis *et al*., 2001). This method, associated to the generation of a negative nasal pressure (negative pressures values generated at the nose were -2, -4, -6, -8 and –10 hPa below atmospheric pressure), permitted to assess the relationship between the local nose area and the values of the negative pressure in the nose. Then, the local nasal compliance could be deduced from the slope of the relationship between the local area variation and the various values of constant negative pressure inside the nasal cavity.

MODEL

The developed nasal model only considers the coupling in a part of the nose where the area can be inferred by the acoustic method. Indeed, due to artifacts associated to paranasal sinuses, only the nasal portion of 6 cm-long from the nostril, i.e., the so-called anterior part of the nose, could be explored (Hilberg *et al*., 1996). The discrete segmental model of the anterior part of the nose included 19 compliant elements in series, which correspond to the spatial resolution of the acoustic method. Each element represents an individualized nasal segment coupled to the inspiratory flow. Area at 0 hPa and compliance of each segment were obtained from acoustic data. For a given value of negative pressure drop between the two ends of the nose, flow and local cross-sectional areas in each nasal segment were numerically computed from flow conservation principle and the generalized form of Bernoulli's equation.

RESULTS

Nasal compliance was found to increase as longitudinal distance from nose entry increases. This softening phenomenon was found to linked to the amount of vaso-erectil tissues in the nose. Indeed, the variation in compliance with the distance disappeared when a vasoconstrictor was dispensed to the subject. The pressure-flow relationship predicted with the model exhibited a systematic flow limitation pattern. The model also shows that this flow limitation was associated with a major collapse localized in the anterior part of the inferior turbinate. The model results reveal that flow limitation occurs through the coupling between area-variation pressure changes, which is essentially associated to kinetic energy variation, and the local nasal compliance.

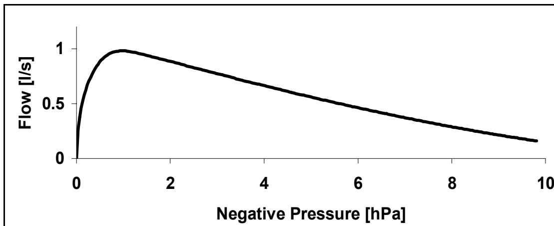

Pressure flow relationships obtained with proposed model in a subject

CONCLUSION

Although the proposed model oversimplifies the anatomical reality, it appears consistent with the reported flow limitation and area constriction phenomena. Noteworthy, maximum flow predicted by the model for pressure value between 1 and 2 hPa, was in agreement with the reported physiological observations. Thus, the proposed multi-segmental model appears to provide a rationale for flow limitation phenomena though the nose while classical models, based upon rigid wall properties, failed to describe such pathological features.

REFERENCES

Bridger G.P., et al. (1970) *Ann Otol Rhinol Laryngol* **79**, 481-488.
Fodil R., et al. (1997) *Med Biol Eng Comput* **35**, 638-648.
Hilberg O., et al. (1996) *J Appl Physiol* **80**, 1589-1594.
Louis B., et al, (2001) *J Appl Physiol* **90**, 630-637.
Proctor D.F., (1977) *Am Rev Respir Dis* **115**, 97-129.

STEADY FLOW AND PARTICLE DEPOSITION IN NON-PLANAR AIRWAY BIFURCATION MODEL

Hideki Fujioka[1] and Robert C. Schroter[2]

[1]Biomedical Engineering Department, University of Michigan, Michigan, USA, fuji@umich.edu
[2]Department of Bioengineering, Imperial College of Science, Technology and Medicine, London, UK

INTRODUCTION

Diseases such as asthma are often treated with drugs inhaled as an aerosol; controlling particle deposition pattern within the lung airways is, therefore, vitally important. Studies of particle movement in the airflow and local deposition patterns within the lung will be also aid understanding of the early stages of lung diseases. The geometry of a bronchial bifurcation can be characterized by a bifurcating tube with smoothly curving surface and varying cross-sectional area. Because the velocity distribution within the boundary layer can affect the particle deposition, the surface variation will be very important - an idealized, planar geometry will be inadequate to improve understanding of the particle deposition characteristics. In this study, we aim to construct a realistic model of a bifurcation, with smoothly curved surface, particularly at the flow divider, and to investigate the particle trajectory and deposition on the wall using this model.

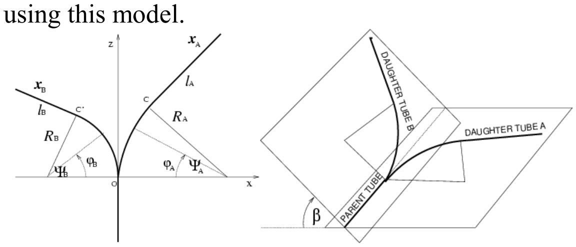

Figure 1: Bifurcating tube axes. In present study, geometric parameters are $R_A=R_B=10$, $\Psi_A=\Psi_B=35^\circ$, $\gamma=3$. The radius ratio between the parent and daughter tube is 0.775.

METHODS

To describe the curved surface of the model, $\mathbf{x}_A$ and $\mathbf{x}_B$ are defined as two tube axes, which provide density space ϕ_A and ϕ_B around each axes defined by following equations.

$$\phi_A = \frac{G(\mathbf{x}_A)}{r_A} \qquad \phi_B = \frac{G(\mathbf{x}_B)}{r_B} \qquad (1)$$

$G_A(\mathbf{x}_A)$ and $G_B(\mathbf{x}_B)$ are functions associated with the radius of the tube. The model surface, $\mathbf{x}_S$ is defined to be satisfied when the summation of γ^{th} powers of these density spaces is equal to unity.

$$\Phi(\mathbf{x}_S) = \phi_A{}^{\gamma}(\mathbf{x}_A) + \phi_B{}^{\gamma}(\mathbf{x}_B) = 1 \qquad (2)$$

γ is a parameter to control the sharpness of flow divider. This method can be easily adapted to construct non-planar models by defining two planes, one for each daughter tube axis, as illustrated in Fig. 1.

We calculated steady flow in three bifurcation models, planar ($\beta=0^\circ$), and non-planar $\beta=45^\circ$ and 90°. NS-equations were solved with the SIMPLER algorithm, supposing the fluid is incompressible Newtonian fluid. Particle trajectories and deposition on the wall were also calculated using resultant velocity fields.

RESULTS AND DISCUSSION

In the planar bifurcating tube the secondary flow at the daughter tube forms a pair of symmetrical vortex. This symmetry was broken when the bifurcation is non-planar, as shown in Fig. 2. The particle deposition pattern was slightly changed by β as shown in Fig. 3, while the deposition efficiencies in each model were almost equivalent in the range of the Stokes number between 0.01 and 1.0.

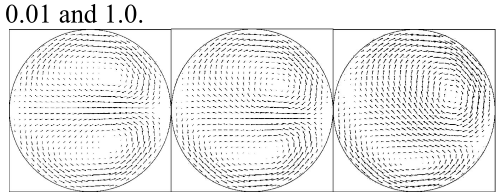

Figure 2: Secondary flows at the daughter tubes at Re=1000. From the left, $\beta=0^\circ$, $\beta=45^\circ$ and $\beta=90^\circ$.

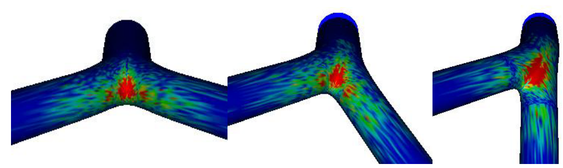

Figure 3: Particle deposition pattern at Stokes number=0.5 and Re=1000. From the left, $\beta=0^\circ$, $\beta=45^\circ$ and $\beta=90^\circ$.

SUMMARY

It is necessary to define a reproducible geometry of any model employed because the geometry is an important factor determining local flow features, especially within the bifurcation. In this study we present a formula based method to describe a bifurcation model with non-planar geometry. The steady inspiratory flow field in the non-planar bifurcating tube showed asymmetrical secondary flow pattern in the daughter tube. This caused a change of particle deposition pattern but did not affect to the deposition efficiency. The deposition efficiency increased with Stokes number just as in the planar bifurcating tube.

REFERENCES

Pedley, T.J. (1977). *Ann Rev Fluid Mech*, **114**, 228-250.

EFFECT OF TISSUE VISCOELASTICITY AND LUNG SURFACTANT ON EUSTACHIAN TUBE MECHANICS

Samir N. Ghadiali[1,2] (ghadiali@pitt.edu), J. Douglas Swarts[2], William J Federspiel[1]

[1]Department of Chemical Engineering, University of Pittsburgh, Pittsburgh, PA, USA
[2]Department of Pediatric Otolaryngology, Children's Hospital of Pittsburgh (CHP), Pittsburgh, PA, USA

INTRODUCTION

The development of Otitis media (OM), a common childhood disease, has been associated with Eustachian tube (ET) dysfunction. The collapsible ET is similar to respiratory airways in that the lumen contains a fluid layer, the muscosa, and is surrounded by various soft tissue elements. An impaired ability to open the ET results in negative middle ear (ME) pressures, ME fluid accumulation, and subsequent infection and inflammation. Impaired ET opening may be due to abnormal mechanical properties such as ET elasticity, E_{tube}, and hysteresis, η. E_{tube} may depend on the elasticity of the surrounding tissue and on the mucosa-air surface tension, while η may depend on viscoelastic tissue properties and on surface tension hysteresis due to the presence of surfactant. In this study, the relative importance of tissue and surface tension mechanics is determined by experimentally altering specific structural elements and subsequently measuring E_{tube} and η.

METHODS AND MATERIALS

A modified force-response protocol (Ghadiali et al, 2000) was performed to assess ET mechanics in sedated and anesthetized cynomolgus monkeys (*Macaca fascicularis,* 2-4 kg). During this protocol the ME was inflated at a constant flow rate until the ET opened at the opening pressure, P_{open}. The syringe pump was then programmed to produce a sinusoidal flow rate and pressure transients were measured until stable pressure-flow oscillations were observed. Data for analysis consisted of the pressure and flow rate during the final oscillation cycle, which are plotted as a pressure-flow (P-Q) hysteresis loop in Figure 1. These experimental P-Q loops were analyzed with a simple model of flow in a collapsible tube (Ghadiali et al, 2001). In this model, the pressure drop in the ET, Δp, is related to the flow rate, Q, by a Poiseuille relationship,

$$\Delta p = p(t) - p_d = KQ(t)\big/A(t)^2\ , K = 8\pi\mu L \qquad (1)$$

where p_d=0 is the reference downstream pressure, μ is the viscosity of air, A(t) is the collapsed area, and L is the length of the collapsed segment. The solid mechanics is described by,

$$p(t) - p_{ext} = E_{tube}A(t) + \eta\, dA\big/dt \qquad (2)$$

where p_{ext} is the external tissue pressure. Once A(t) is calculated from eqn. (1) and dA/dt is estimated with finite-differences, eqn. (2) can be correlated with experimental measurements (solid line in Figure 1). As a result, the ET's compliance, C=1/E_{tube}, and hysteresis, η, can be determined.

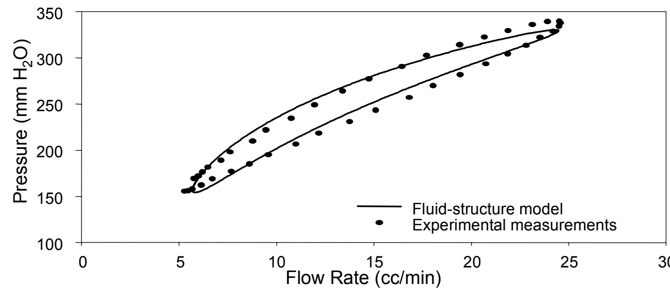

Figure 1: Experimental/theoretical P-Q hysteresis loop

ET mechanical properties (P_{open}, C, η) were measured in two groups of monkeys. The first group (n=12) was used to investigate tissue mechanics by performing measurements before and after paralysis of the left tensor veli palatini (TVP) muscle. The right ear of the second group (n=6) was used to investigate the influence of the mucosa-air surface tension by performing measurements under normal conditions, after washing out the mucosa with saline, and after the installment of a pulmonary surfactant (Infasurf). All protocols were approved by the CHP Animal Research and Care Committee.

RESULTS AND CONCLUSIONS

Results of these experiments are summarized in Table 1 where statistical differences were documented using analysis of variance. Muscle paralysis resulted in a decrease in P_{open}, an increase in C, and a decrease in η. The removal of the normal mucosal layer did not significantly alter P_{open}, but did result in a decrease in C and η. Treatment of the mucosa with Infasurf reduced P_{open} and was effective in increasing C and η to baseline values. The large change in C during TVP paralysis indicates that ET elasticity is primarily determined by tissue mechanics. ET hysteresis, however, appears to be equally affected by tissue and surface tension mechanics. Knowledge of how specific structural components affect ET mechanics may lead to improved treatment strategies.

REFERENCES

Ghadiali et al (2002) *Auris Nasus Larynx*, **29**(1), 1-5
Ghadiali et al (2001) *Ann. Biomed. Eng*. in review

ACKNOWLEDGEMENTS

NIDCD P01 DC01260, CHP Research Fellowship, Ony Inc.

Table 1: Mechanical parameter values under various conditions (mean ± SD). $^*p<0.05$, $^\wedge p<0.01$ with respect to normal.

	Normal TVP	Paralyzed TVP	Normal Mucosa	Saline Wash	Surfactant
P_{open} (mm H_2O)	396 ± 72	$^\wedge$272 ± 77	471 ± 72	476 ± 91	$^\wedge$356 ± 82
$Cx10^{-7}$(cm^2/mm H_2O)	18.4 ± 7.8	$^\wedge$42.9 ± 27	20.6 ± 3.8	*13.7 ± 5.0	18.2 ± 7.5
$\eta x10^8$ (Poise/cm^2)	1.32 ± 0.80	*0.78 ± 0.45	1.94 ± 0.76	*0.724 ± 0.58	1.78 ± 0.39

THE INFLUENCE OF CELL TOPOGRAPHY ON EPITHELIAL CELL STRESSES DURING AIRWAY REOPENING

Anne-Marie Jacob and D. P. Gaver

Department of Biomedical Engineering, Tulane University, New Orleans, LA, ajacob@tulane.edu

INTRODUCTION

The lung consists of a series of liquid-lined airways that act as conduits for air traveling from the outside environment to the remainder of the respiratory system. Under both normal and pathological conditions, these compliant tubes may collapse, impeding gas exchange. This results in a liquid occlusion whose surface tension, under extreme conditions, becomes quite large, requiring the excessive pressures of mechanical ventilation to peel apart the airway walls as they reopen. This exerts mechanical stresses on the pulmonary epithelial cells that could potentially lead to damage or modification of their biological function. This study is designed to quantify these stresses on the cellular level in order to better understand the dynamic behavior of the pulmonary system during airway reopening.

METHODS

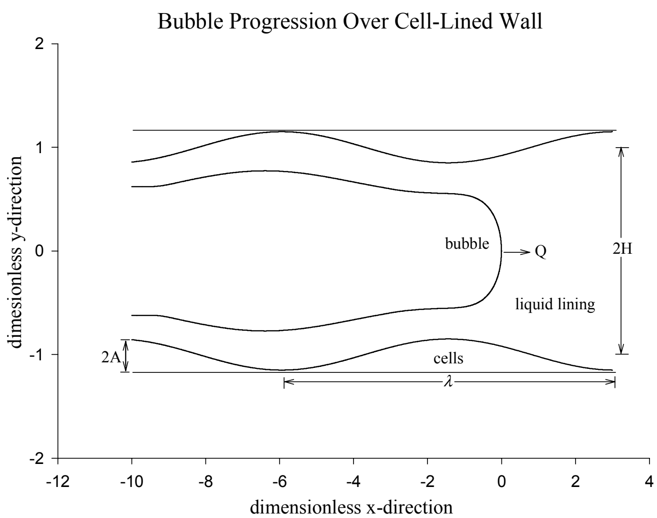

Figure 1: Schematic diagram of a semi-infinite bubble progressing through a cell-lined airway

We present a 2-D computational model for the flow-driven progression of a semi-infinite bubble through a liquid-occluded airway. The system is modeled as a horizontal channel whose walls, separated by a mean distance 2H, are sinusoidal with an appropriate amplitude, A, and wavelength, λ, to mimic the real geometry of a cell-lined airway (Figure 1). The liquid film is assigned a constant viscosity, μ, and density, ρ, and the air-liquid interface is characterized by a constant surface-tension, γ. We employed the boundary element method (BEM) in conjunction with lubrication approximations to solve the Stokes flow equations for the steady-state stresses acting on the cells. Relevant dimensionless parameters examined include:

- ʅ $= \frac{A}{H}$, which relates the height of the cells to the average distance separating the airway walls. The relevant values vary from 0.01 in the respiratory bronchioles to 0.75 in more collapsed airways.
- $Ca = \frac{Q\gamma}{2H\mu}$, the capillary number (Q is the 2-D flow rate), which represents the ratio of viscous forces to surface-tension forces. We examined the system's behavior at Ca = 0.5, where both viscosity and surface-tension are important.

RESULTS AND DISCUSSION

A characteristic curve of the shear stress acting on the cells lining the model's airway walls is given in Figure 2 for the bubble orientation depicted in Figure 1. The magnitude of this

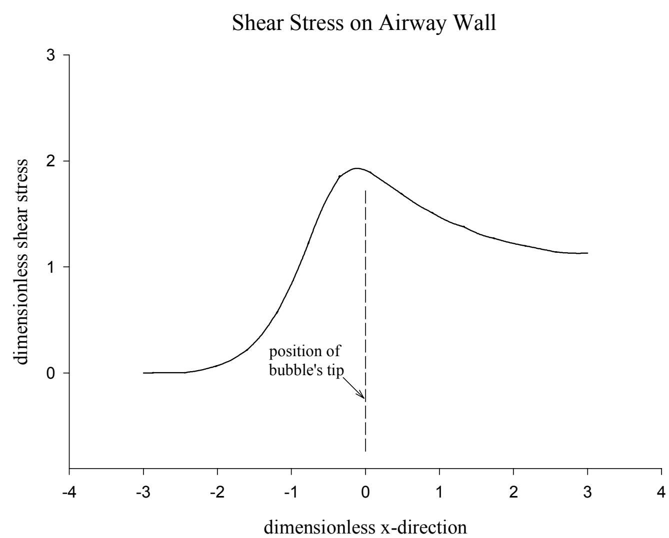

Figure 2: Dimensionless shear stress along cell-lined airway wall corresponding to Figure 1

stress is maximum at the tip of the bubble (x=0) and approaches a Poiseuille shear stress downstream. Our results indicate that corrugations of the airway wall may amplify stresses and result in alterations in cell function.

ACKNOWLEDGEMENTS

Funded by NSF grant BES-9978605, and the NASA Physical Sciences Research Division. Computational resources provided by the U.S. DOE through the Livingston Digital Millennium Center for Computational Science at Tulane and Xavier Universities, award #DE-FG-02-01ER633196

USE OF COMPUTATIONAL FLUID DYNAMICS TO STUDY INHALED GAS AND PARTICLE TRASPORT IN THE NASAL PASSAGES

Julia S. Kimbell[1], Rebecca A. Segal, and Bahman Asgharian

CIIT Centers for Health Research, Research Triangle Park, NC, USA, www.ciit.org
[1]kimbell@ciit.org

INTRODUCTION

The nasal passages represent the main portal of entry for inhaled gases and particles and contain considerable capacity for uptake, filtering, metabolism, and clearance of inhaled material. For certain air pollutants such as highly water-soluble or reactive gases, respiratory tract airflow patterns can play a major role in determining sites of uptake by the airway lining. These uptake patterns influence the distribution and severity of toxic response and account in part for interspecies differences in susceptibility to associated respiratory tract disease. To better characterize respiratory airflow, uptake, and deposition patterns among species, three-dimensional, anatomically accurate computational fluid dynamics (CFD) models of the F344 rat, rhesus monkey, and human nasal passages were constructed (Kimbell et al., 1997a; Kepler et al., 1998; Subramaniam et al., 1998). The models can be used to test hypotheses about dominant transport mechanisms. Uptake and deposition predictions can be used to assess human health risks. Examples of gas and particle transport simulations are presented here.

METHODS

Three-dimensional computational meshes were reconstructed from serial sections of fixed rat and monkey nasal specimens and from human MRI scans. Steady-state inspiratory airflow simulations were conducted using the commercial software FIDAP (Fluent, Inc., Lebanon, NH) to solve the Navier-Stokes equations for laminar flow. Flow rates corresponding to resting breathing minute volumes were simulated using a uniform velocity profile at the nostrils. Simulation results agreed with observations and measurements of dye streaklines and airflow in hollow nasal molds (Kimbell et al., 1993; Kimbell et al., 1997a; Kepler et al., 1998; Subramaniam et al., 1998).

As an example of gas transport, nasal uptake of inhaled formaldehyde was simulated using FIDAP in the rat, monkey, and human with a condition specifying that flux at nasal walls is proportional to concentration near nasal walls. Formaldehyde gas is quite water-soluble, so constants of proportionality for this condition were determined for mucus- and nonmucus-coated nasal regions from experimental data (Kimbell et al., 2001).

As an example of particle transport, nasal deposition simulations were conducted in the rat, monkey, and human for spherical particles between 0.5 and 10 μm in mass median aerodynamic diameter. A CIIT computer program in which impaction was the dominant transport mechanism (Asgharian and Anjilvel, 1994) was used to predict particle trajectories and deposition sites. Particles were assumed to have no effect on inspiratory airflow patterns.

RESULTS AND DISCUSSION

Formaldehyde simulations predicted that nasal flux patterns were species-specific. Regions where flux was predicted to be high correlated with areas of nasal tissue damage in formaldehyde-exposed rats and monkeys (Kimbell et al., 1997b; Kepler et al., 1998). These results support the hypothesis that species-specific patterns of nasal tissue damage observed in formaldehyde-exposed laboratory animals are determined by species-specific patterns of formaldehyde uptake. Particle simulations at resting breathing rates predicted as expected that near complete filtration of particles by the nose occurred at a smaller particle size in the rat than in the human. In the rat, predicted nasal deposition efficiencies generally agreed with experimental data, but human simulations overpredicted nasal deposition efficiencies at small Stokes numbers. Potential effects of airflow velocity profiles imposed at the nostrils are being explored.

REFERENCES

Asgharian, B., Anjivel, S. (1994). *Aerosol Sci Technol,* **20**, 177-193.

Kepler, G.M. et al (1998). *Toxicol Appl Pharmacol,* **150**, 1-11.

Kimbell, J.S. et al (1993). *Toxicol Appl Pharmacol,* **121**, 253-263.

Kimbell, J.S. et al (1997a). *Toxicol Appl Pharmacol,* **145**, 388-398.

Kimbell, J.S. et al (1997b). *Mut Res,* **380,** 143-154.

Kimbell, J.S. et al (2001). *Toxicol Sci,* **64,** 100-110.

Subramaniam, R.P. et al (1998). *Inhal Toxicol,* **10**, 91-120.

ACKNOWLEDGMENTS

The authors would like to thank Dr. Kevin Morgan, Betsy Gross, Regina Richardson, Donald Joyner, and Darin Kalisak for their contributions to this research.

PREDICTING THE MIXING OF ULTRA-FINE PARTICLES IN A MODEL LUNG ACINUS

Angus Leeming[1] and Robert C. Schroter[2]

Department of Bioengineering, Imperial College of Science, Technology and Medicine, London, SW7 2BX, U.K.
[1] a.leeming@ic.ac.uk, [2] r.schroter@ic.ac.uk

INTRODUCTION

Heyder *et al.* [1973] showed that during normal quiet breathing 10% of all particles reaching the acinar regions of the lung deposit, independent of particle size. These rates of deposition cannot be explained by classical transport mechanisms. Flow in the acinus is Stokesian and both the Brownian diffusivity and gravitational settling of such particles are negligibely small.

New insight was provided by Butler and Tsuda [1997] when they demonstrated convective stretch-and-fold mixing patterns in a rat lung filled with silicone. The mixing associated with these patterns can be very rapid, even for particles with only a small Brownian diffusivity. Nevertheless, the mechanism driving this mixing is still not clear.

One plausible source, geometric hysteresis of the alvolar wall motion over the course of a breath, was illustrated by Tsuda *et al.* [1999] using a model alveolar duct. It consisted of a T-shaped junction of three short, straight, square ducts. The model was filled with silicone oil and alveolar wall motion was simulated by pistons in the two horizontal ducts. The pistons were driven to generate a low Reynolds number, cyclic flow. Their motion had a small amount of asynchrony, adjusted to match the degree of geometric hysteresis found in rabbit lungs. Tsuda *et al.* demonstrated that this system would stretch-and-fold a line of tracer dye, leading to progressively more complex patterns as the cycle number increased.

THE PRESENT STUDY

A realistic structural model of the acinar region is a necessary precursor to truly realistic simulations of the flow processes occuring within the lung. Our group has created just such a model over several years [Denny and Schroter, 1995, 2000]. It provides us with an opportunity to calculate particle dispersions in a alveolar duct model with realistic geometry and dynamic behaviour.

The present study, however, reproduces numerically Tsuda *et al.*'s experimental results, thereby providing a strenuous test of our flow-solver and particle tracking codes. Figure 1 is an illustrative snapshot of the particle field after 40 cycles.
Both the original experiment and this simulation followed the evolution with time of a line of non-diffusive tracer. Real particles in alveolar air have a small but finite diffusivity that will smear out and mix these purely convective patterns. By applying the methods of Wonhas and Vassilicos [2001], the original Tsuda *et al.* analysis can be extended to provide a predictive tool capable of describing the mixing of such diffusive particles as a function of time.

The mixing properties of the field are determined by the fractal dimension D' of a cut through the interface, a variable that can be calculated from snapshots such as Figure 1. Thereafter, the variance of the particle field scales like

$$E(0) - E(\kappa) \propto \sqrt{\kappa}^{\,1-D'}$$

where κ is the diffusivity of the particles. Moreover, if, as here, the line of tracer grows linearly with time, then the variance varies like

$$\frac{\partial}{\partial t}[E(0) - E(t)] \propto \sqrt{\kappa}^{\,1-3D'}$$

Both relations are valid for particles whose diffusive length scales lie within the range where the interface has a well-defined fractal dimension.

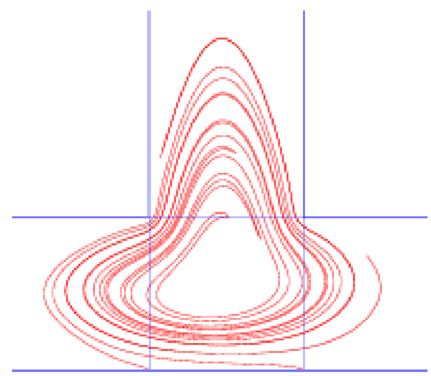

Figure 1: Particle dispersion after 40 cycles. The original tracer position is shown across the mouths of the three ducts.

REFERENCES

Butler, J.P., Tsuda, A. (1997). *J Appl Physiol*, **83**, 800-809.
Denny, E., Schroter, R.C. (1995). *J Biomech Eng*, **117**, 254-261.
Denny, E., Schroter, R.C (2000). *J Biomech Eng*, **122**, 1-9.
Heyder, J., et al. (1973). *J Aerosol Sci*, **4**, 191-208.
Tsuda, A. et al. (1999). *J Appl Physiol*, **86**, 977-984.
Wonhas, A., Vassilicos, J.C. (2001). *J Geophys Res*, (submitted).

PULMONARY EPITHELIAL CELL-MATRIX SIGNALLING VIA ALPHA-6/BETA-4 INTEGRIN

Susan Margulies[1], Michele Hawk[1] and Valerie Weaver[2]

Departments of Bioengineering[1] and Pathology[2], University of Pennsylvania, Philadelphia PA, USA, margulies@seas.upenn.edu

INTRODUCTION

Previously we have demonstrated that primary pulmonary alveolar epithelial cells (AEC's) that were seeded on fibronectin and maintained in culture for five days demonstrated a significant resistance to stretch-induced death compared to those maintained for only one day in culture (Tschumperlin et al, 2000). Furthermore, when seeded on lamanin-rich extracellular matrix (ECM) obtained from 5-day cells rather than fibronectin, the AEC's had a stretch tolerance similar to 5-day cells (Oswari et al, 2001). We hypothesized that AEC's have alpha-6/beta-4 integrins at the cell membrane, offering them the opportunity to utilize the unique mechanotransduction pathway between laminin and the intermediate filaments (Green and Jones, 1996). Transferring the load to the intermediate filaments, with larger ultimate strains than actin (Janmey et al, 1990), may be associated with the AEC's ability to tolerate large deformations.

METHODS

Lungs were excised from anesthetized male Sprague-Dawley rats (200-350g), and AEC's were dissociated and isolated, as described previously (Tschumperlin et al, 2000). Cells were seeded at $1.0x10^6$ cells/cm^2 on silastic membranes coated with fibronectin (40µg/ml, Boerhinger Mannheim). Wells were cultured in minimum essential medium (MEM), supplemented with 24ug/ml gentamicin and 10% fetal bovine serum (all from Life Technologies). Cells were studied at days 1, 2, and 5 days after isolation, with four cell isolations per time point.

Surface proteins were labeled in the following manner: monolayers were washed 6 times with DPBS (with calcium and magnesium ions) and incubated on ice with Sulfo *N*-Hydroxysuccinimide-Biotin (Pierce, Rockford, IL) for 1h. The cells were washed 3 times with ice cold 50mM DPBS glycine solution and solubilized in RIPA lysis buffer (1% IGEPAL CA-630, 0.25% deoxycholate, 0.1% SDS, 150mM NaCl, 50mM Tris-HCL, pH 7.4) containing 4.8mM EDTA and a cocktail of protease inhibitors. Equivalent amounts of rat protein extracts were preadsorbed by an overnight incubation at 4° C with rabbit IgG coupled to agarose beads (Sigma, Saint Louis, Mo) followed by a 1h incubation with protein A coupled to agarose beads (Invitrogen, Grand Island, NY) at room temperature. Beta-4 integrins were immunoprecipitated from the precleared supernatant by incubation for 2h at room temperature with rabbit anti-integrin beta-4 subunit polyclonal serum, (Chemicon International, Temecula, CA) and protein A coupled to agarose beads. Immunocomplexes bound to protein A agarose beads were washed repeatedly with RIPA lysis buffer eluted in SDS-PAGE sample buffer and separated on 7.5% SDS polyacrylamide gels under nonreducing conditions. Resolved protein was transferred to polyvinylidene difluoride (PDVF) membranes and incubated with streptavidin HRP (Dako, Carpinteria, CA). Labeled bands were detected using enhanced chemiluminescence (ECL™)(Amersham Pharmacia Biotech UK Limited,Little Chalfont Buckinghamshire, England) and ECL™ Hyperfilm™ and quantified using densitometry.

RESULTS

Data indicate that lung AEC's express detectable levels of beta-4 integrins at 1, 2 and 5 days in culture, as confirmed by a band migrating at the same molecular weight in human mammary epithelial cells (positive control; (Weaver et al 1997)) and its absence in murine fibroblasts (negative control). Band density on each film was normalized to cells at day 1. Across all four gels surface beta-4 levels averaged 168% of day 1 levels by 2 days in culture, and 128% of day 1 levels after 5 days. Data across timepoints were statistically indistinguishable ($p > 0.25$, unpaired Student's t analysis).

DISCUSSION

Our immunoprecipitate data demonstrating expression of the beta-4 integrin subunit on the surface of lung AEC's support our hypothesis that the IF's, when ligated to a laminin-rich ECM via the alpha-6/beta-4integrin, could play a major role in distributing the applied load throughout the cytoskeleton structure. In a similar manner, mechanical integrity and cell viability in keratinocytes in vivo is conveyed primarily through the laminin receptor, alpha-6/beta-4integrin, and is mediated via intermediate filament-beta 4 integrin interactions (Dowling et al 1996; Jones and Green 1991; Spinardi et al 1995). Ongoing studies are targeting new therapeutic interventions to prevent or ameliorate deformation-induced AEC injury via modulators of the alpha-6/beta-4integrin mechanotransduction pathway.

REFERENCES

Dowling, J. et al (1996). *J Cell Biol,* **134**, 559-72.
Green, K.J. and Jones, J.C.R. (1996). *FASEB J,* **10**, 871-881.
Janmey, P.A. et al (1990). *Nature (Lond),* **345**, 89-92.
Jones, J.C., Green K.J (1991). *Curr Opin Cell Biol,* **3**, 127-32.
Oswari, J. et al (2001). *AJP-Lung,* **281**, L1068-1077.
Spinardi L. et al. (1995). *J Cell Biol,* **129**, 473-87.
Tschumperlin, D.J. et al (2000). *AJRCCM,* **152**, 357-362.
Weaver, V.M. et al (1997). *J Cell Biol,* 137, 231-245.

ACKNOWLEGEMENTS

Funding was provided by NIH HL57204 and the University of Pennsylvania.

FINITE ELEMENT GEOMETRIC MODELS OF THE HUMAN LUNG AND DIAPHRAGM

Premakumar Mithraratne, Geoff Carden, Merryn Tawhai, and Peter Hunter

Bioengineering Institute, The University of Auckland, Auckland, New Zealand
p.mithraratne@auckland.ac.nz

INTRODUCTION

Accurate representation of the geometry of organs is an important factor when modeling their physiological behavior. Here we present anatomically accurate finite element meshes of the human lung and diaphragm derived from the visible human (VH) data (Ackerman, 1998). Development of these high order (cubic Hermite) geometric models forms part of a project aiming to study the integrated performance of lung soft-tissue mechanics, airflow, and pulmonary circulation. The geometric fitting method has been applied successfully to fit finite element surface meshes of various organs of the body (Bradley et al., 1997), and is used to fit a surface mesh to the diaphragm model. The lungs are fitted as a volume mesh - this is the first time that the geometry fitting method has been extended to fit a finite element volume mesh.

METHODS

CMISS, a computational and visualization software package developed by the Bioengineering Institute at the University of Auckland, was used to extract geometric coordinates of data points from visible human (VH) slices. The anatomical images at 5 mm intervals were read into a CMISS graphical window and the circumference of both the lungs were digitized. A total number of 46 images from 300 to 525 mm (0 mm is the uppermost image at the head, and 1871 mm is lowest image at the foot) were used to digitize 3103 data points. For the diaphragm, a similar procedure was adopted and 28098 data points were collected from 95 images. All images were linearly transformed in the xy-plane with respect to the three 'markers' present on each image prior to the digitization, to ensure correct alignment of the sections.

An initial linear volume mesh was fitted to the data iteratively until the root mean square (RMS) error converged to an acceptable value. The first step in this fitting process is to calculate the shortest distance from each data point to the surface of an initial (in this case linear) mesh. An error function is then set up as the summation of the squares of all these distances. The nodal parameters (nodal value and derivatives) that minimize the error function are evaluated by differentiating the error function with respect to each nodal parameter, and equating the resulting expression to zero. This process yields the necessary number of linear equations to determine the nodal parameters. The set of linear algebraic equations thus obtained is solved using a Newton-Raphson method.

The scale factors are held constant during the minimization of the error function. Because the scale factors depend on the nodal position and derivatives, if they were allowed to vary during the minimization process then one would end up with a computationally expensive non-linear problem. The approach that we have adopted is to hold the scale factors constant during a fit, then update the scale factors post-fit with respect to the new nodal parameters. Because the scale factor update alters the fitted element shape, the fitting and scale factor updates must be repeated iteratively until the overall RMS error reaches a pre-specified limit. For further details of the mathematical formulation of the problem and the various element parameters, the reader is referred to the paper by Bradley et al., (1997).

RESULTS AND DISCUSSION

Figure 1 depicts the fitted bi-cubic Hermite finite element mesh of the diaphragm. The final form of the mesh was obtained after four iterations. The mesh consists of 302 nodes and 124 elements.

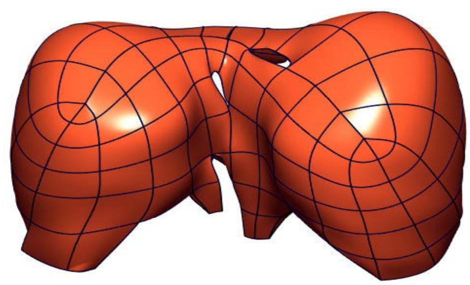

Figure 1: Fitted finite element surface meshes (bi-cubic Hermite) of the diaphragm.

It is to be noted that the data derived from the VH images represent partially collapsed lungs and diaphragm as the VH images were obtained from a cadaver. However, these models can be considered as generic geometric models and be can readily be transformed into patient-specific models using imaging data. This technique is currently being applied to customize the VH geometry to fit the Auckland skeleton, with the help of 'land mark points' from the VH images and skeleton model.

REFERENCES

Ackerman, M.J. (1998). *Proc. IEEE*, **86**, 504-511.
Bradley, C.P., Pullan, A.J., Hunter, P.J. (1997). *Ann. Biomed. Eng.*, **25**, 96-111.

ACKNOWLEDGEMENTS

This work was funded by The Royal Society of NZ Marsden Grant 01-UOA-070 MIS, and the Health Research Council of New Zealand. The authors would like to thank Carey Stevens, Jackie Lee, and Steve Thrupp for their contribution to this work.

COMPUTATIONAL ANALYSIS OF INSPIRATORY HEAT AND WATER VAPOR FLUXES IN THE HUMAN NOSE

Sara Naftali[1], Moshe Rosenfeld[1], Michael Wolf[2] and David Elad[1]

[1]Department of Biomedical Engineering, Faculty of Engineering, Tel-Aviv University, Tel-Aviv, 69978, Israel, sara@eng.tau.ac.il
[2]Department of Otorhinolaryngology, Sheba Medical Center, Tel-Hashomer, 52621, Israel

INTRODUCTION

Nasal inspiration is important for maintaining the internal environment of the lung, since it equilibrates ambient air with alveolar conditions (body temperature and fully saturated water vapor) on reaching the nasopharynx. The nose has a complex three-dimensional geometry and its inner surface is lined with a layer of wet and warm ciliated mucosa. Numerous studies were aimed at evaluation of the functional role of the nose in health and disease in terms of its temperature and relative humidity (RH) characteristics. However, the complex structure and relative inaccessibility of the nasal cavity have prevented detailed *in vivo* studies of nasal transport characteristics. Accordingly, we developed a complex *nose-like* model in order to study the dynamic capacity of the human nose to warm and humidify environmental air during inspiration.

METHOD

The physical domain of the problem is a *nose-like* model that incorporates the anatomical aspects of the nasal cavity that most affect gas transport patterns, and allows for the removal or addition of functional nasal features as required by the analysis (Naftali *et al*., 1998). The governing equations are the continuity and Navier-Stokes equations for laminar flow of an incompressible air with constant viscosity and thermal conductivity and the energy conservation (thermal) and convection-diffusion equations. These equations were simultaneously solved for different boundary conditions by implementing the finite volume numerical software of FLUENT. The mesh of the *nose-like* model was composed of 290,115 tetrahedral cells and 607,088 triangular wall faces. The inner walls were assumed to be at alveolar conditions (e.g., 37^{o}C and 100% RH). The flow for quiet breathing was chosen to fit a tidal volume of 0.41 L and 15 breathes per min. The inlet conditions for normal ambient air at the nasal nares was assumed to be 20% RH and 25°C.

RESULTS

Normal breathing was chosen to be the reference case, and then, we investigated the influence of physiological, environmental and pathological variations. Simulation of the reference case showed that during a day long of quiet breathing a total of 216 kcal of heat and 330 ml of water are transferred from the nasal walls into the inspired air. The fluxes that would bring the inspired air to alveolar conditions (37 ^{0}C and 100% RH) were computed from psychrometric data to be 248 kcal of heat and 364 ml of water vapor. Thus, the *nose-like* model is capable of conditioning the inspired air into about 90% of alveolar condition, which is similar to the normal *in vivo* data that the inspired air is normally conditioned to 80-90% of alveolar condition before reaching the nasopharynx. Numerical simulations at different extreme environments (e.g., hot-dry, cold-wet) showed that the inspired air was conditioned in the nasal cavity to about 90% of alveolar conditions regardless of the environmental conditions. The results of daily fluxes from noses after surgical interventions of turbinectomy are summaries in Table 1. The heat and water vapor fluxes from the nasal walls after turbinectomy of the middle or inferior turbinates are about 12-16% smaller than in the normal nose. After turbinectomy of both inferior and middle turbinates, the fluxes are reduced by about 23%.

DISCUSSION

The healthy nose can easily condition the inspired air within about 10% of alveolar conditions regardless of environmental surroundings. The turbinates increase the rate of local heat and moisture transport by improving mixing and by maintaining narrow passages. In problematic noses that require surgical intervention such as turbinectomy, it has been demonstrated that removing of either the inferior or middle turbinate reduces nasal efficacy to condition the inspired air by 12-16%. These results are very useful for evaluation of nasal efficacy at different environmental conditions and for both of planning and assessment of pharmaceutical or surgical intervention.

REFERENCES

Naftali, S. et al. (1998). *Ann Biomed Eng*, **26**: 831–839.

ACNOWLEDGEMENT

Funded by the US-Israel binational science foundation (BSF).

Table 1. Heat and water vapor fluxes in the normal nose ("reference") and after surgical interventions. Percentage compared to the "reference" case.

Case	Reference	Turbinectomy of Middle Turbinate		Turbinectomy of Inferior Turbinate		Turbinectomy of Middle & Inferior Turbinates	
	[kCal]	[kCal]	[%]	[kCal]	[%]	[kCal]	[%]
Heat Flux [kCal]	216	190	88	181	84	165	77
Water Flux [ml H2O]	330	291	88	277	84	254	77

AN ASYMPTOTIC MODEL OF UNSTEADY AIRWAY REOPENING

S. Naire[1], M.K. Horsburgh[2] and O.E. Jensen[1]

[1]Centre for Mathematical Medicine, University of Nottingham,
Nottingham NG7 2RD, U.K. Email: Oliver.Jensen@nottingham.ac.uk
[2]DAMTP, University of Cambridge, Silver Street, Cambridge CB3 9EW, U.K.

INTRODUCTION

Airway reopening is a fundamental process in pulmonary mechanics. It involves the propagation of a bubble of air into a liquid-filled collapsed airway at a pressure (P_b) sufficiently large to overcome the adhesive effects of viscosity and surface tension, yet sufficiently low to minimize damage to delicate airway walls. Understanding the mechanics of reopening is important in developing ventilation strategies and in reducing the risk of ventilator-induced lung injury.

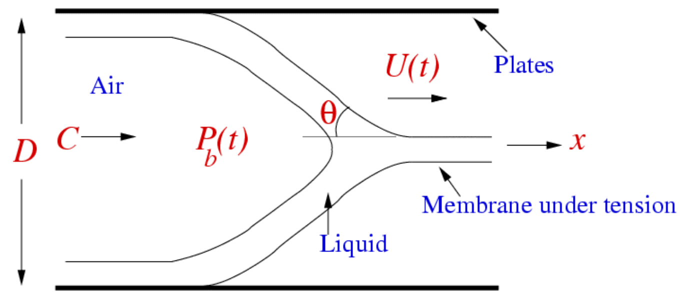

Figure 1: A physical model of airway reopening. The bubble propagates to the right, its volume increasing at rate C, peeling apart wet membranes held under longitudinal tension.

Pioneering work in understanding airway reopening was carried out by Gaver and co-workers (1990, 1995) using bench-top models such as that in Fig. 1. During the initiation of reopening in their experiments, when the bubble is driven into the channel by a constant flow-rate piston, P_b can transiently overshoot its final steady value. This transient pressure peak is physiologically and clinically significant since it might lead to dangerously large stresses being imposed on the airway walls. Our aim is to use a theoretical model to understand and characterise this behavior.

ASYMPTOTIC MODEL

A computational model for the steady reopening problem was developed by Gaver *et al*. (1996), who showed that reopening can be regarded as a peeling process. More recently, Jensen *et al*. (2002) described this problem using an asymptotic model based on the assumption that the membrane tension is large, so that the wall slopes are uniformly small. The model incorporated accurate expressions for the film thickness and the pressure drop near the bubble tip. We extend this asymptotic model to describe reopening as an unsteady initial-value problem for the configuration illustrated in Fig. 1, where the membranes lie between a pair of smooth parallel plates separated by a distance D. The model for unsteady reopening reduces to a fourth-order nonlinear PDE for the evolution of the width of the channel $H(x,t)$ ahead of the bubble tip, subject to four boundary conditions. Starting from a small initial peeling angle, we seek the evolution of the bubble pressure $P_b(t)$, the bubble speed $U(t)$ and the membrane shape $H(x,t)$.

RESULTS

The results show the following two types of behavior. First, there is the transient peak behavior, similar to that seen by Perun & Gaver (1995). At early times θ and P_b rise slowly and the channel inflates without the bubble tip advancing significantly. At a critical time they both increase rapidly and the bubble begins to accelerate. This causes the channel walls some distance ahead of the bubble tip to bend sharply and correspondingly the fluid pressure there falls rapidly. This low pressure provides a strong adhesive force pulling the walls together and P_b must rise to overcome this resistance. P_b overshoots its steady value; U does the same shortly afterwards. Eventually, P_b settles back down to its steady value. The second type of behavior is when P_b does not exhibit a peak, but simply rises and settles immediately on its steady value. The type of behavior and magnitude of the pressure peak were recorded for a wide range of values of C and D. A monotonic response in P_b occurred when C and D were both low or both high.

DISCUSSION

Our asymptotic model captures transient bubble pressure peaks during the initiation of airway reopening and agrees qualitatively with experiments. The results suggest that it is feasible to avoid transient overshoot by suitably tuning the model parameters, although whether this is physiologically realistic is not yet clear. This model provides a first step towards understanding this phenomenon in a variety of reopening configurations.

REFERENCES

Gaver III, D.P. *et al*. (1990). *J. Appl. Physiol.*, **69**, 74-85
Perun, M.L. & Gaver III, D.P. (1995). *J. Biomech. Eng.*, **117**, 245-253
Gaver III, D.P. *et al*. (1996). *J. Fluid Mech.*, **319**, 25-65
Jensen, O.E. *et al*. (2002). *Phys. Fluids,* **14,** 443-457

ACKNOWLEDGEMENTS

This work was supported by The Wellcome Trust.

ALVEOLAR TRANSPORT DURING TOTAL LIQUID VENTILATION

Ryan C. Patterson, Hsien-Hung Wei, Vinod A. Suresh, and James B. Grotberg

Department of Biomedical Engineering,
University of Michigan, Ann Arbor, MI 48109-2125, USA.
E-Mail: grotberg@umich.edu

INTRODUCTION

During normal, air-breathing respiration diffusive effects dominate alveolar gas transport, because the Peclet number, Pe, for transport of O_2 and CO_2 is much smaller than unity. However, during ventilation with perfluorocarbon liquids Pe >>1, because of small molecular diffusivities, D, in liquid. Understanding the fluid dynamics and mass transport within an alveolus during total liquid ventilation with perfluorocarbon can lead to an understanding of the mechanisms that affect gas exchange as well as delivery of larger molecules such as medications or genetic material.

METHODS

The alveolus is assumed to be an oscillating sphere of radius $R(t) = R_0(1 + \delta \sin\ )$ where δ is a measure of the tidal volume to functional residual capacity ratio. We use a dimensionless time, $=\omega t$, where t is dimensional time and ω is the breathing frequency. The flow field inside the alveolus is in the radial direction only with a point source at $r = 0$.

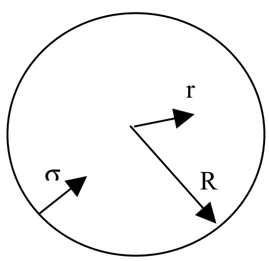

The concentration field is governed by the convection-diffusion equation, which we solve asymptotically in the limit of Pe >>1. The corresponding mass transfer is discussed in detail with respect to the parameters δ and Pe.

The fluid velocity field is given by Equation 1, and the concentration boundary conditions are C = 0 on the alveolar wall and C = 1 in the alveolar interior.

$$u_r = \frac{R^2 \dot{R}}{r^2} \qquad (1)$$

The transport equation governing this model can be transformed into a Lagrangian reference frame with the local coordinate σ, as shown.

$$\frac{\partial C}{\partial \tau} = \frac{1}{Pe}\frac{\partial}{\partial \sigma}\left[\left(3\sigma + R^3\right)^{4/3}\frac{\partial C}{\partial \sigma}\right] \qquad (2)$$

Assuming $Pe = \omega R_0^2/D >>1$, Equation 2 can be solved using the method of matched asymptotic expansions to obtain an inner and outer solution.

RESULTS AND DISCUSSION

An example of the solution for oxygen concentration at full expiration and full inspiration are shown below. Transport is enhanced at end inspiration because the concentration boundary layer is thin, yielding steep gradients for outward diffusion. Therefore, one way to enhance gas transport during total liquid ventilation may be to include an inspiratory pause in the ventilator duty cycle.

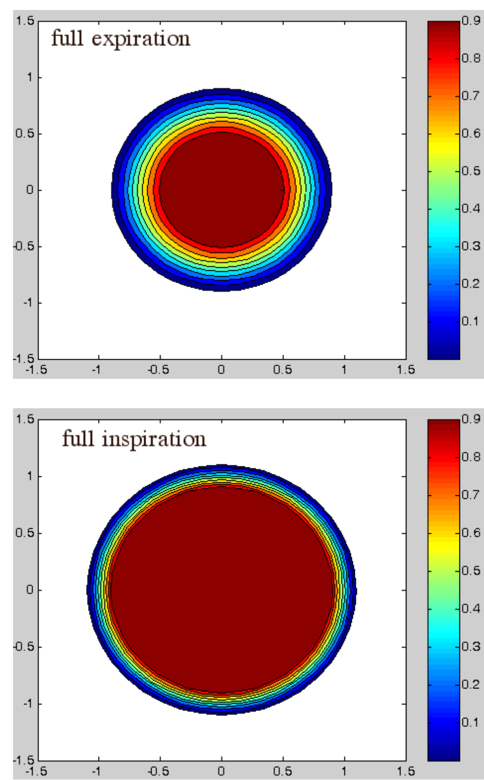

ACKNOWLEDGEMENTS

This research is supported by the Whitaker Foundation and NIH grants HL41126 and HL64373.

A REALISTIC MECHANICAL MODEL OF THE HUMAN CHEST WALL

Anat Ratnovsky, Uri Zaretsky and David Elad
Department of Biomedical Engineering, Faculty of Engineering, Tel-Aviv University, Tel-Aviv 69978, Israel
anatrat@post.tau.ac.il

INTRODUCTION

The respiratory muscles constitute the respiratory pump which determines the efficacy of ventilation. Any functional disorder in their performance may cause insufficient ventilation. The human chest wall is a complex structure and the contribution of its different components to efficient respiration has been the subject of many simplified models. However, the existing models did not evaluate the performance of individual groups of respiratory muscles and did not calculate the forces generated by them. Furthermore, most of the models used mechanical analogs which could not differentiate between the rib cage and the accessory muscles, and thus, precluded any evaluation of their contribution to respiration in lung disease. In this study we developed a two-dimensional (2D) realistic model of the human chest wall in order to explore the relative contribution of major groups of respiratory muscles in healthy subjects.

THE CHEST MODEL

A 2D mechanical model is proposed for simulations of the mechanical performance of the complex chest wall in the sagittal plan. The model is composed of the major stationary and mobile elements of the chest wall. The stationary elements include the bones of the vertebral column, skull, iliac crest and pelvis. The rib cage forms the mobile part of the model and is composed of ten ribs. Each rib is connected by hinge joints to the vertebral column and sternum at its posterior and anterior ends, respectively (Fig. 1). The respiratory muscles act as actuators of the mobile rib cage.

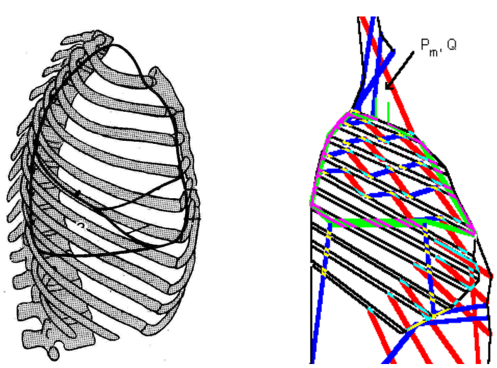

Figure 1: Rib cage anatomy (left) and the 2D model (right). The black lines represent bones, the green line represents the lung, the red lines represent muscles whose forces were derived from Hill model, and the blue lines represent the muscles whose forces will be derived from this model.

The following major groups of the respiratory muscles are incorporated in the model: diaphragm (costal and crural), external and internal intercostals, scalene, sternomastoid, rectus abdominis, external and internal oblique, and the transverse abdominis muscles. The lungs opening is inserted in the skull and its caudal end is attached to the diaphragm. Parameters of the model geometry such as the ribs angle at different lung volumes, ribs length and muscles length and position were derived from the literature as well as from radiological fluoroscopy and observation of cadavers in the school of medicine.

RESULTS AND DISCUSSION

The model can be utilized to simulate quasi-static breathing of different respiratory efforts. The governing equations of the model include the force balance equations for the rib cage and the central tendon of the diaphragm, and the work done by the muscles ($\int Fdx$) compared with the work of the respiratory system ($\int PdV$). The number of unknowns is larger than the number of governing equations, thus, we incorporated in the set of input parameters all the variables that can be measured in vivo from the lungs and respiratory muscles (Ratnovsky *et al.*, 1999; 2001). These inputs include the following variables, which were simultaneously measured from healthy subjects while performing different breathing maneuvers: mouth pressure, airflow rate (lung volume) and the forces generated by the sternomastoid, external intercostal, rectus abdominis and external oblique muscles. Muscle forces were computed by a Hill-type muscle model from measurements of EMG signals and geometry parameters of the respiratory muscles (Ratnovsky *et al.*, 2001). As a result, the present model for the chest wall can be used to derive the forces generated by the scalene, internal intercostal, internal oblique, diaphragm (costal and crural) and the transverse abdominis muscles at different breathing maneuvers. This new realistic model of the human chest wall may be utilized along with in vivo measurements of breathing variables and EMG signals from easily accessed respiratory muscles in practical procedures for analysis of the relative contribution of major groups of respiratory muscles to lung performance during different maneuver. Then, it may be employed for either clinical diagnosis of the respiratory muscles, as well as monitoring of disease progression or follow up after surgical intervention.

REFERENCES

Ratnovsky, A. *et al*. (1999). *Physiol Measur,* **20,** 37-51.
Ratnovsky, A. *et al*. (2001). *Proc XVIIIth Cong Int Soc Biomech*, Zurich, P. 375.

EFFECTS OF BOUNDARY CONDITIONS ON PARTICLE DEPOSITION PREDICTIONS IN HUMAN NASAL PASSAGES

Rebecca A. Segal and Julia S. Kimbell
CIIT Centers for Health Research, Research Triangle Park, NC, USA, www.ciit.org, kimbell@ciit.org

INTRODUCTION

Research in the computation of airflow patterns and particle deposition in human nasal passages is being used to provide information about specific nasal deposition sites and nasal filtering capabilities for lung protection. The goals of these research efforts are both toxicologic and therapeutic in nature. Information on nasal deposition and filtering can lead to knowledge regarding potential toxic effects of exposure to inhaled materials. The same information can also lead to the development of better nasal drug delivery methods.

In previous research, a three-dimensional nasal airway model was reconstructed from digitized MRI data for a healthy human. Steady-state nasal airflow patterns were simulated using the commercial finite element code FIDAP (Fluent, Inc., Lebanon, NH) to solve the computational fluid dynamics flow equations. Simulations were conducted at 7.5 L/min assuming a uniform flow profile at the nostrils and were confirmed by comparison with hot film anemometry data (Subramaniam et al., 1998; Hahn et al., 1993). The flow results were then used as input for an in-house particle deposition computer program (Asgharian and Anjivel, 1994). Predictions of deposition efficiency generally agreed with experimental measurements made by Heyder and Rudolf (1977); however, the simulations overestimated deposition for smaller particles (< 2 μm in mass median aerodynamic diameter (MMAD)). One hypothesis for this discrepancy is that the uniform flow profile imposed at the nostrils artificially enhanced deposition due to impaction.

METHODS

To test this hypothesis, additional airflow simulations were conducted at 7.5 L/min in which a fixed pressure was imposed at the outlet of the model to achieve a realistic pressure drop across the nasal passages. Due to the complexity of the problem, only solutions for the first-order Navier-Stokes problem have converged to date. Nasal particle deposition efficiencies were calculated using simulated airflow velocities from the first-order solutions.

RESULTS AND DISCUSSION

Simulated airflow at the nostrils when flow was pressure- driven showed a nonuniform profile in contrast to the uniform flow field previously imposed (Fig. 1). Deposition efficiencies computed using pressure-driven flow were closer to experimental values than deposition efficiencies calculated using flow computed under uniform profile conditions for particles between 0.5 and 2 μm (MMAD) (Table 1). These results suggest that particle deposition in the nasal passages is probably sensitive to initial particle velocity for particles less than 2 μm in MMAD. The accuracy of airflow simulations at the nostrils may have a significant impact on the accuracy of nasal deposition efficiency predictions.

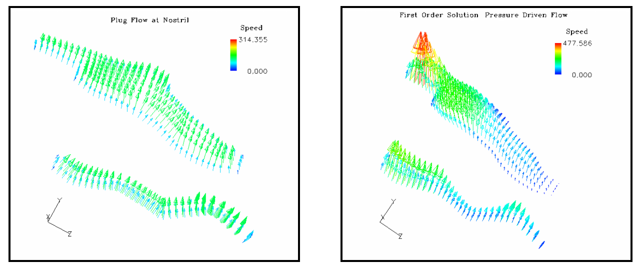

Figure 1: Velocity vectors at the nostril surface. (Left) Plug flow at the nostril surface. (Right) Velocity vectors at the nostril for the first-order solution to flow with pressure boundary conditions. Note the nonuniformity of the velocity field in the pressure-driven flow indicated by the color change.

Table 1: Deposition efficiency values for flow simulations. Note that the pressure-driven results are computed from a first-order solution

MMAD(μm)	Plug Flow	Pressure-Driven	Experiment
0.5	0.254419	0.130702	0.020
1.0	0.256924	0.124073	0.023
2.0	0.284501	0.123687	0.093

CONCLUSION

More realistic boundary conditions describing flow in the human nasal passages leads to more accurate modeling of particle deposition and hence to better models of nasal toxicity and drug delivery.

REFERENCES

Asgharian, B. and Anjival, S. (1994). *Aerosol Sci Tech,* **20**, 177-193.
Hahn, I., et al (1993). *J Appl Physiol,* **75**, 2273-2287.
Heyder, J. and Rudolf, G. (1977). *Inhaled Particles IV, Part 1* (W.H. Walton, ed.) Oxford: Pergamon, pp:107-125.
Subramaniam, R.P., et al. (1998). *Inhal Toxicol*, **10**, 91-12.

GRAVITY EFFECTS ON LIQUID PLUG TRANSPORT AND DISTRIBUTIONS IN AIRWAY MODELS

Vinod Suresh and James B. Grotberg

Department of Biomedical Engineering,
University of Michigan, Ann Arbor, MI 48109-2125, USA.
E-Mail: grotberg@umich.edu

INTRODUCTION

Surfactant replacement therapy (SRT), which is commonly used to treat pulmonary surfactant deficiency in infants, and liquid ventilation both involve the instillation of a liquid bolus into the trachea. When the bolus forms an air-blown plug, optimal delivery of the surfactant or perfluorocarbon to various regions of the lung can depend on uniform dispersion through bifurcating airways. In this work we determine the effect of gravitational and surface tension forces on plug shape, which in turn affects the mass split ratio of the plug at successive bifurcations.

METHODS

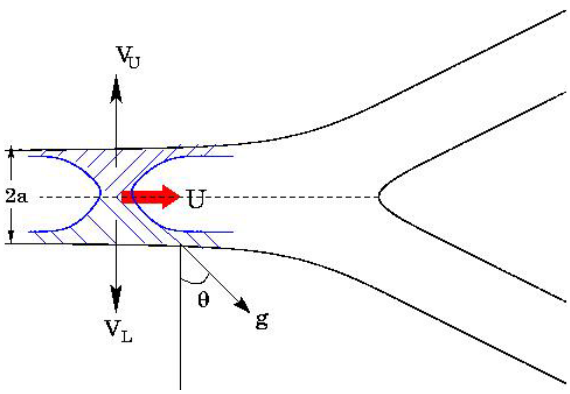

Figure 1: Schematic of a liquid plug in a bifurcating airway.

A simplified theoretical model is used, involving the pressure and gravity driven quasi-steady motion of a liquid plug of density ρ through a liquid-lined, rigid cylindrical tube. A schematic of the plug in a bifurcating airway is shown in Figure 1. The relative orientation of the parent airway to gravity is given by the angle θ. Close to the body of the plug, a static balance between pressure and surface tension forces determines the shapes of the front and rear interfaces. As seen in Figure 1, the interface shapes are not symmetric about the centerline of the airway due to gravitational effects. These effects are quantified by defining a volume ratio, $\lambda = V_U / V_L$, as the ratio of the plug volume above the centerline to that below the centerline.

RESULTS

Figure 2 plots the volume ratio, λ, as a function of the Bond number ($Bo=\rho g a^2/\sigma$), which is a measure of the ratio of gravitational force to surface tension, σ, force. These results correspond to an angle $\theta = 0°$. Volume ratios are determined for various orientations of the airway with respect to gravity. The range of Bond numbers considered are typical for SRT in infants (Cassidy *et. al.*). The ratio shows a strong dependence on the Bond number and differs significantly from unity, indicating a highly non-uniform fluid distribution in the plug. The volume ratio in turn affects the quantity of surfactant delivered to each airway at a bifurcation.

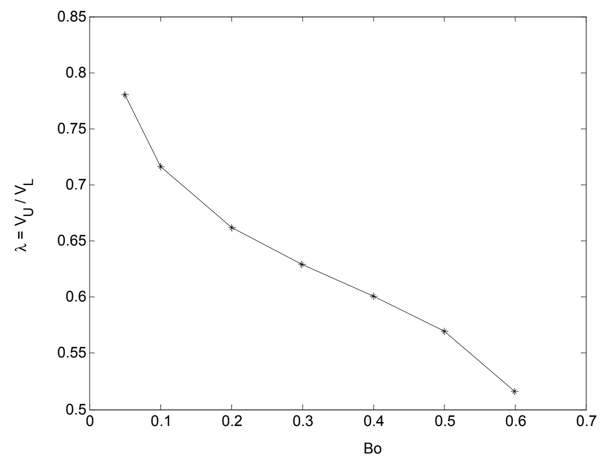

Figure 2: Ratio of plug volumes above and below the centerline of the airway for various *Bo*, $\theta = 0°$.

REFERENCES

Cassidy, K. J. et al. (2001). *J. Appl. Physiol.,* **90**, 1955-1967.

ACKNOWLEDGEMENTS

Supported by NIH grants HL41126, HL64373, NSF grant BES-9820967 and NASA grant NAG3-2196 .

THREE-DIMENSIONAL AIRWAY CLOSURE: SURFACE-TENSION-DRIVEN NON-AXISYMMETRIC INSTABILITIES OF LIQUID-LINED ELASTIC TUBES

Joseph P. White[1] and Matthias Heil[2]
Department of Mathematics, University of Manchester, UK
[1]jwhite@maths.man.ac.uk; http://www.ma.man.ac.uk/~jwhite
[2]M.Heil@maths.man.ac.uk; http://www.ma.man.ac.uk/~mheil

INTRODUCTION

The airways of the lung are thin-walled elastic vessels which are lined with a thin liquid film. This liquid film can undergo a surface-tension-driven fluid-elastic instability which may lead to airway closure via the formation of an occluding liquid bridge. Halpern & Grotberg (1992) studied this problem in an axisymmetric geometry and determined the volume of liquid required to occlude the airways. For physiologically realistic parameter values, the pressure drop across the air-liquid interface can be large enough to cause non-axisymmetric buckling of the airway. Heil (1999) showed that in non-axisymmetrically buckled airways, occluding liquid bridges can be formed with a fraction of the fluid volume required to occlude a corresponding axisymmetric airway. However, the existence of such non-axisymmetric occluding liquid bridges of small volume does not guarantee that they can be realised in the course of the system's evolution from the initially uniform axisymmetric state. We aim to determine if liquid-lined elastic airways that do not contain enough fluid to form an axisymmetric occluding liquid bridge can undergo a non-axisymmetric instability that leads to airway closure.

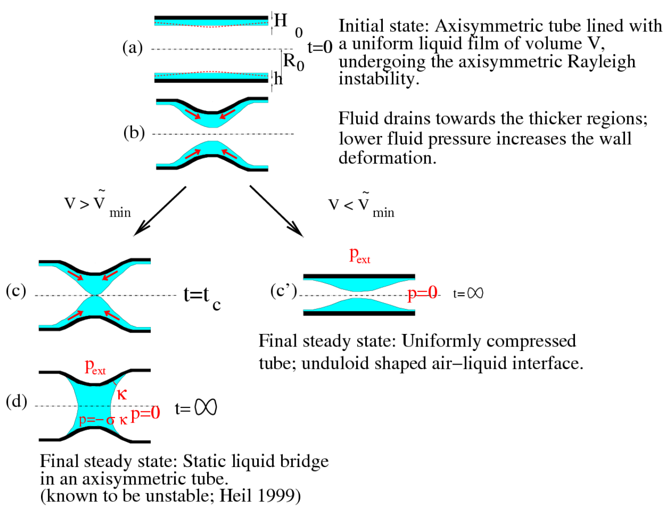

Figure 1: Sketch of axisymmetric airway closure. Axisymmetric occlusion depends upon the liquid volume.

THE COMPUTATIONAL MODEL

Figure 2 illustrates the model problem. A thin-walled elastic tube is initially lined with a viscous liquid of uniform thickness. Following Heil & White (2002) we model the liquid using an exactly volume-conserving lubrication theory. The airway wall is modelled using geometrically nonlinear Kirchhoff-Love shell theory. The governing equations are solved by a fully coupled finite element method.

RESULTS

The uniform liquid layer is unstable to the Rayleigh instability which leads to the formation of axisymmetric lobes as shown in Fig. 1. The curvature of the air-liquid interface is larger where the lobes are thickest and this increases the compression of the airway wall. If the compression exceeds a critical value then the airway buckles non-axisymmetrically. This increases the liquid surface curvature and thus the tube's compression even further. We show that this feedback mechanism can lead to occlusion of the airway and demonstrate that airway closure is possible at relatively small liquid volumes.

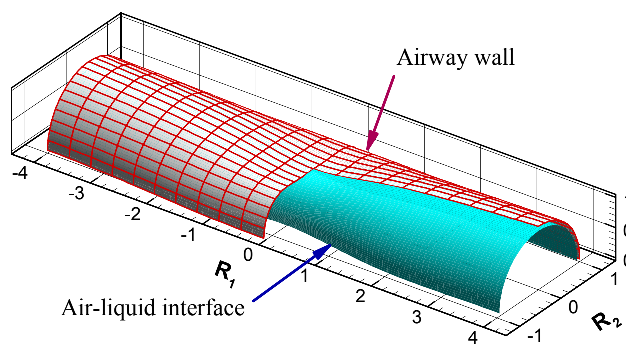

Figure 2: Airway wall and air-liquid surface. A section of the tube wall is not shown.

REFERENCES

Halpern D. & Grotberg J.B. (1992) *Journal of Fluid Mechanics* **244**, 615-632.

Heil, M. (1999) *Journal of Fluid Mechanics* **380**, 309-337.

Heil, M. & White J.P. (2002) *Journal of Fluid Mechanics* (in press).

MODULATION OF CYTOCHROME P450 (CYP) 1A1 and 1B1 and CTGF EXPRESSION BY SHEAR STRESS

S. G. Eskin, N. A. Turner, L. V. McIntire,
Department of Bioengineering, Rice University, Houston, TX , USA

INTRODUCTION

Traditionally, we have chosen genes in endothelial cells to study based on our presupposition of their significance in vascular disease processes. Using DNA microarrays provided changes in unanticipated genes, which might be crucial to cell function and help us to unravel the signalling pathways involved in understanding the effects of shear stress on gene regulation in endothelial cells. For example, the most strongly up-regulated genes, cytochrome P450 CYP 1A1 and 1B1, have only been reported differentially expressed in HUVEC using DNA microarrays. [1]The cytochrome P450 gene families have classically been associated with cellular detoxification mechanisms. Cytochrome P450 1A1 (CYP 1A1) has been postulated to participate in endogenous signaling of oxidative processes. [2] Loss of CYP 1A1 in cultured endothelial cells has been correlated with dedifferentiation. [3] A comparison of senescent fibroblast, epithelial, and HUVEC cell lines reveal that CYP1B1 was up-regulated in HUVEC alone among senescent cell lines.

Connective tissue growth factor (CTGF) was initially purified from HUVEC-conditioned medium, and is elevated in fibrotic lesions, thus may play a role in the development of fibrotic diseases. It is highly expressed in vascular cells of atherosclerotic lesions, but not in normal arteries. CTGF has been found to be down-regulated in shear stressed HUVEC by microarrays. [1]

METHODOLOGY

Third passage HUVEC, seeded on glutaraldehyde cross-linked gelatin coated glass slides, were subjected to 25 dynes/cm^2 for 24 h in a parallel plate flow chamber in complete medium (M199, 20% fetal calf serum, and antibiotics). Matched control cells were maintained in static conditions. For the β-naphthoflavone treatment, P3 HUVEC were seeded as for shear stress experiments, then maintained in stationary culture in complete medium containing 6 μg/ml β-naphthoflavone and 1 μl/ml DMSO, or complete medium with 1 μl/ml DMSO alone for 72 hours.

RESULTS

Gene expression levels of CYP 1A1, CYP 1B1, CTGF, and ET-1 in P3 HUVEC exposed to shear stress (25 dynes/cm^2, 24 hrs.). Values are normalized to GAPDH values, then ratios of values for shear stressed to matched static cultured cells are calculated, then the 3 ratios are averaged. Note that the fold changes for CTGF and ET-1 are less than 1, thus these genes are down-regulated. Values are mean +/- S.E.M. n = 3.

Gene	Primary HUVEC	P3 HUVEC
CYP 1A1	12.6 ± 3.9	10.8 ± 2.1;
CYP 1B1	15.3 ± 6.0	23.1 ± 3.7;
CTGF	0.14 ± 0.04	0.8 ± 0.08;
ET-1	0.17 ± 0.0	0.7 ± 0.05;

Below are gene expression fold differences in P3 HUVEC incubated with 6 μg/ml •-naphthoflavone in DMSO relative to DMSO alone for 72 hours (β-NF); and in P3 HUVEC incubated under static conditions in conditioned medium from 24 hr. shear stressed cells. Results were compared to untreated cultures and expression levels were normalized to GAPDH. Values are mean ± se, n= 3.

Gene	β-NF	Shear Stress Conditioned Medium with cells
CYP 1A1	18.3 ± 4.2;	5.8 ± 1.4;
CYP 1B1	4.1 ± 0.3;	5.8 ± 0.9;
CTGF	0.8 ± 0.05;	1.3± 0.1;

DISCUSSION and CONCLUSIONS

The genes that shear stress strongly up-regulated and down-regulated in P3 were consistent with the results obtained in primary HUVEC, although CTGF and ET-1 were less dramatically down-regulated in the passaged cells.

Because the CYP genes were increased so much, and the increases were unexpected, we exposed static cells to •-naphthoflavone. CYP 1A1 was increased 18-fold in response to •-naphthoflavone, compared to an 11-fold increase induced by shear stress. CYP 1B1 was more strongly upregulated by shear stress (15-fold) than by •-naphthoflavone (4-fold), consistent with •-naphthoflavone's selectivity for CYP 1A1.

To assess the presence of CYP 1A1 inducers in the circulating medium, we asked whether conditioned medium from shear stressed cells could induce CYP genes in static HUVEC. CYP 1A1 and 1B1 both showed a 5 fold increase in static cells exposed to conditioned medium from shear stressed cells, whereas CTGF was unchanged.

REFERENCES

[1] S. M. McCormick, S. G. Eskin, L. V. McIntire, C. L. Teng, C.-M. Lu, C. G. Russell, and K. K. Chittur, "DNA microarray reveals changes in gene expression of shear stressed human umbilical vein endothelial cells," *Proc Natl Acad Sci*, vol. 98, pp. 8955-8960, 2001.

[2] A. Dey, J. E. Jones, and D. W. Nebert, "Tissue- and cell type-specific expression of cytochrome P450 1A1 and cytochrome P450 1A2 mRNA in the mouse localized in situ hydridization," *Biochem Pharmacol*, vol. 58, pp. 525-537, 1999.

[3] T. Thum, A. Haverich, and J. Borlak, "Cellular dedifferentiation of endothelium is linked to activation and silencing of certain nuclear transcription factors: implications for endothelial dysfunction and vascular biology," *FASEB J.*, vol. 14, pp. 740-751, 2000.

SHEAR STRESS–INDUCED STRAIN FOCUSING IN THE ENDOTHELIAL CYTOSKELETON

Brian P. Helmke (helmke@virginia.edu)[1], Amy B. Rosen[2], and Peter F. Davies[2]

[1]Department of Biomedical Engineering, Cardiovascular Research Center, University of Virginia, Charlottesville, Virginia, USA
[2]Institute for Medicine and Engineering, University of Pennsylvania, Philadelphia, Pennsylvania, USA

INTRODUCTION

The endothelium at the blood-tissue interface plays a critical role in the regulation of both physiological and pathological responses to changes in blood flow. A large number of cellular adaptations in gene and protein expression (Chien et al., 1998; Gimbrone et al., 1997), cell shape and orientation (Levesque and Nerem, 1985), and intracellular structure (Dewey et al., 1981) correlate spatially to both the predicted blood flow force profile along the arterial tree and locations of atherosclerotic lesion development (Ross, 1995). Endothelial cells (ECs) sense the local hemodynamic force profile to generate biochemical signals at multiple intracellular locations (Davies, 1995; Helmke and Davies, in press), but mechanisms that modulate spatial integration of force transmission and signal transduction within the cell remain unclear.

METHODS

ECs expressing green fluorescent protein (GFP) fused to either vimentin or actin were grown to confluence and assembled into a parallel plate flow chamber maintained at 37 ºC (FCS2, Bioptechs). High-resolution fluorescence optical sections were acquired every 90 s for 15 min (DeltaVision, Applied Precision). A step increase in unidirectional laminar flow was imposed so that wall shear stress was 12 dyn/cm^2, and image acquisition continued at the same rate for an additional 30 min. Out of focus light intensity was repositioned using a 3-D constrained iterative deconvolution algorithm (softWoRx, Applied Precision). Deconvolved fluorescence optical sections were exported to Matlab for analysis.

The magnitude of GFP-vimentin and GFP-actin displacement during the interval from t_i to t_j in spatial subregions of the cell was measured in 3-D using a displacement index (Helmke et al., 2001) defined as

$$DI(t_i, t_j) = 1 - \frac{\mathrm{Cov}[I(x,y,z,t_i), I(x,y,z,t_j)]}{\sqrt{\mathrm{Var}[I(x,y,z,t_i)] \cdot \mathrm{Var}[I(x,y,z,t_j)]}}$$

where the covariance and variance are computed between pairs of 3-D images I.

In order to compute the spatial distribution of cytoskeletal deformation (Helmke, in press), GFP-vimentin optical sections were skeletonized, and vertices connecting adjacent filament segments were tracked in time. The Lagrangian strain tensor E_{ij} was computed from relative displacements among triads of adjacent vertices, and principal values and axes were mapped as a function of time and intracellular location.

RESULTS AND DISCUSSION

Small magnitude random direction displacements of cytoskeletal elements were measured at steady state. Onset of shear stress induced significant displacement of GFP-vimentin–labeled filaments within 3 min that was often most pronounced in apical and downstream regions of the cytoplasm. Bending and shortening of GFP-actin filaments was observed near cell edges after onset of shear stress. In addition, increased displacement of GFP-actin was observed that was consistent with lamellipod extension near the edge of the cell in the upstream direction. Thus, shear stress acting at the apical cell surface induces displacement of cytoskeletal filaments that may modulate rapid shape changes.

Spatial maps of cytoskeletal strain magnitude as a function of time revealed localized peak concentrations at discrete sites throughout the cytoplasm, including near the coverslip. Strain focusing was only detectable in these high-resolution maps and not in spatial averages over larger cytoplasmic regions. Onset of shear stress caused an increase in angular dispersion of strain direction, often eliminating a whole-cell preferred orientation that existed before flow onset. In local regions near cell edges, however, preferred strain direction was rotated from parallel to perpendicular to the cell edge, implying that shear stress directly alters mechanical interactions among adjacent cells.

SUMMARY

Onset of shear stress induces rapid displacement and deformation of both vimentin and actin cytoskeletal components. Increased edge motility and shape changes indicate altered actin dynamics. Cytoskeletal network strain focusing at discrete intracellular locations associated with molecular signaling complexes may play a crucial role in initiation of cellular mechanotransduction.

REFERENCES

Chien, S. et al. (1998). *Hypertension*, **31**, 162-169.
Davies, P.F. (1995). *Physiol. Rev.*, **75**, 519-560.
Dewey, C.F. et al. (1981). *J. Biomech. Eng.*, **103**, 177-188.
Gimbrone, M.A. et al. (1997). *Ann. NY Acad. Sci.*, **811**, 1-10.
Helmke, B.P. et al. (2001). *Biophys. J.*, **80**, 184-194.
Helmke, B.P. (in press). *Conf. Rec. 35th Asilomar Conf. Signals Sys. Comp.*
Helmke, B.P., Davies, P.F. (in press). *Ann. Biomed. Eng.*
Levesque, M.J., Nerem, R.M. (1985). *J. Biomech. Eng.*, **107**, 341-347.
Ross, R. (1995). *Annu. Rev. Physiol.*, **57**, 791-804.

ACKNOWLEDGEMENTS

GFP-vimentin was a gift from R. D. Goldman (Northwestern Univ. Med. School). Supported by NIH grants HL10058 (BPH) and HL36049 (PFD) and Univ. of Virginia Dept. of Biomed. Eng. and Cardiovascular Research Center (BPH).

CONTROL MECHANISMS OF THE FLUID SHEAR RESPONSE IN CIRCULATING LEUKOCYTES

Shunichi Fukuda, Peter Marschel, Geert W. Schmid-Schönbein

Department of Bioengineering, University of California San Diego, La Jolla, CA 92093-0412
gwss@bioeng.ucsd.edu

INTRODUCTION

The majority of leukocytes in the circulation are in a spherical state. This is a requirement for free passage of these cells through capillaries. After activation, for example in the presence of pseudopods, the cells become trapped in the microcirculation

While numerous biochemical mediators serve to either down- or upregulate leukocytes, we have identified fluid shear stress to play a central role in this process [1]. Our investigation is designed to identify the mechanisms and consequences of the fluid shear response in leukocytes.

METHODS OF APPROACH

We exposed freshly isolated leukocytes (1g sedimentation) to steady fluid shear at low Reynolds number under controlled flow conditions. Isolation of leukocytes by centrifugation was avoided, since exposure of the cells to accelerations of 300 g or above, even for only a few minutes, serves to suppress or reverse the fluid shear response [1]. We observed under high-resolution light microscopy the cell shape and active pseudopod formation while applying a controlled fluid flow from an adjacent micropipette. The order of magnitude of the fluid shear stress over the surface of the cell (about 1 dyn/cm^2) was determined by numerical solution of the Stokes approximation for a Newtonian fluid (buffer) around the cell [2]. As an alternative approach, suspensions of leukocytes were exposed to controlled fluid shear stress (5 dyn/cm^2) in a cone-and-plate shear device in whole blood without any isolation. The cells were kept in heparin as anticoagulant. The distribution of the membrane adhesion molecule CD18 was investigated by labelling with a fluorescently conjugated monoclonal antibody and observation under confocal microscopy or with flow cytometry.

RESULTS AND DISCUSSION

Application of fluid shear over the surface of activated and migrating leukocytes (mostly neutrophils and monocytes) leads to retraction of pseudopods. The expression of CD18 integrin on the membrane is reduced at locations with elevated fluid shear, by a process that in part may involve proteolytic enzymes. After stimulation of the cells with inflammatory mediators (platelet activating factor or the tripeptide f-met-leu-phe) the number of leukocytes that respond by retraction of pseudopod is reduced in a concentration dependent fashion. This reduction in the response to fluid shear is accompanied by spreading of the cells and can be simulated by depletion of cGMP in the cell cytoplasm [3]. In contrast, elevation of the cGMP level with cGMP analogous or with nitric oxide donors leads to restoration of the fluid shear response. The ability of cGMP to enhance the fluid shear response is not associated with CD18 expression, because cGMP has no effect on CD 18 expression under shear. The fluid shear response is also sensitive with respect to the particular membrane integrin. Adhesion of leukocytes via β_2 integrins serves to preserve the shear response, while in contrast adhesion via β_1 integrins inhibits the fluid shear response [4]. This evidence suggests that inflammatory mediators have the ability to suppress the fluid shear response while cGMP may serve to maintain the response even in inflammation. The migration of lymphocytes across endothelium is enhanced by fluid shear even in the absence of chemotactic gradients [5].

SUMMARY

Important biomechanical properties of leukocytes in the circulation are controlled by fluid shear. There exists an interaction between fluid shear and traditional inflammatory mediators or cytokines that serve to activate the cells. These observations are of importance in regards to immune functions of leukocytes, microvascular entrapment of leukocytes and organ function in many diseases, atherosclerotic lesion formation, and tissue repair mechanisms.

REFERENCES

[1] Fukuda, S., Schmid-Schönbein, G.W.: Centrifugation annihilates the fluid shear response of circulating leukocytes. J. Leuk. Biol., in press, 2002.

[2] Moazzam, F., DeLano, F. A. , Zweifach, B. W., Schmid-Schönbein, G. W. : The leukocyte response to fluid stress. Proc. Nat. Acad. Sci. USA, 94: 5338-5343, 1997.

[3] Fukuda, S., Yasu, T., Predescu, D. N., Schmid-Schönbein, G.W.: Mechanisms for regulation of fluid shear stress response in circulating leukocytes. Circ. Res. (UltraRapid Communication), 86: E13- E18, 2000.

[4] Marschel, P., Schmid-Schönbein, G.W.: Control of fluid shear response in circulating leukocytes by integrins. J. Biomech. Eng., in review, 2002.

[5] Cinamon, G., Shinder, V., Alon, R.: Shear forces promote lymphocyte migration across vascular endothelium bearing apical chemokines. Nature Immunology, 2: 515-522, 2001.

ACKNOWLEDGEMENT

NIH Grant PO1 HL 43026 supported this research.

DIFFERENTIAL MODULATION OF FOCAL ADHESION DYNAMICS BY SHEAR STRESS AND SERUM DURING ENDOTHELIAL CELL MIGRATION

Song Li[1] and Shu Chien[2]

[1]Department of Bioengineering, UC Berkeley, Berkeley, CA 94720-1762, songli@socrates.berkeley.edu
[2]Department of Bioengineering and The Whitaker Institute of Biomedical Engineering, UC San Diego, La Jolla CA 92093-0427

INTRODUCTION

The migration of vascular endothelial cells (ECs) plays an important role in angiogenesis and wound healing. The focal adhesions (FAs) and cytoskeleton respond to diverse extracellular signals and regulate cell migration. At FAs, focal adhesion kinase (FAK), via its phosphorylation at tyrosine 397 [p-FAK(Y397)], mediates the FA dynamics and signaling in response to growth factors and integrin-ligand binding. ECs are constantly subjected to fluid shear stress due to blood flow, but the effect of shear stress on the molecular dynamics of FAs during EC migration remains to be determined.

METHODS

Bovine aortic ECs (BAECs) were seeded on fibronectin (1 $\mu g/cm^2$)-coated slides in DMEM containing 0.5% serum for 3 hr at ~10% confluence; they were subjected to fluid shear stress, stimulated with 10% serum in DMEM, or kept as static control. To apply fluid shear stress, the slide with BAECs was mounted in a rectangular flow channel created by sandwiching a silicone gasket (0.015-cm thick) between the slide and an acrylic plate. Laminar shear stress was generated by the flow resulting from hydrostatic pressure difference between two reservoirs. The shear stress applied was 12 dyn/cm^2, a level found in arteries and capillaries.

Cell migration was monitored by time-lapse phase contrast microscopy, and the dynamic motion of individual cells was analyzed by using Dynamic Image Analysis System software. DNA plasmids encoding green fluorescence protin (GFP)-FAK were transfected into ECs by using GenePorter reagent. The dynamics of GFP proteins were monitored by time-lapse confocal microscopy. To detect FAK activation at FAs, BAECs were fixed and stained with a monoclonal anti-p-FAK(Y397) antibody.

RESULTS AND DISCUSSION

Under static condition, ECs showed random migration without any preferential direction. Serum did not significantly affect EC migration. The application of shear stress for 1 hr caused >90% of cells to migrate in the flow direction with a 30% increase ($p<0.05$) of speed. We use "mechanotaxis" to describe the directional migration of cells induced by mechanical forces, analogous to chemotaxis and haptotaxis.

Time-lapse confocal microscopy showed that serum induced lamellipodia and new FAs in many directions, and caused a sustained increase in total FA area. In contrast, shear stress induced lamellipodia and new FAs preferentially in the flow direction (Fig. 1). Then the pre-existing FAs merged, moved, disappeared and/or segregated from the cells. The total number of FAs decreased by 60% ($p<0.05$), suggesting that shear stress induces FA disassembly. Under continuous shearing, ECs migrated persistently in the flow direction with new FAs forming at the leading edge, and these FAs either turned over quickly or remained stationary until the cell body glides over.

Dynamics of FAK stimulated by serum and shear stress

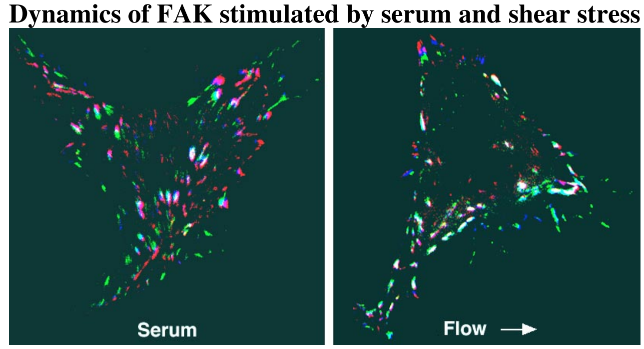

Figure 1: Dynamics of FAK in ECs stimulated by serum or shear stress. Time-lapse confocal microscopy images taken at three time periods at 15-min intervals are pseudocolored sequentially as red, blue and green. The formation of new focal adhesions (green) is random with serum stimulation, but polarized to the right under flow.

Shear stress induced p-FAK(Y397) phosphorylation under the lamellipodia in the flow direction. Serum induced p-FAK(Y397) in many directions, and the total p-FAK(Y397) level was higher ($p<0.05$) than that induced by shear stress. These results suggest that the polarized change of p-FAK(Y397) at the cell periphery, rather than the total level of p-FAK(Y397), is necessary for effective directional migration.

SUMMARY

We showed that fluid shear stress enhanced EC migration in flow direction (mechanotaxis). We demonstrated the differential regulation of FA dynamics by shear stress (polarized) and serum (random). Our findings indicate that the spatial dynamics of signaling at FAs is critical in directional migration, and that mechanotaxis is an important mechanism controlling EC migration in addition to chemotaxis and haptotaxis.

REFERENCES

Sheetz, M.P. et al (1999) *Biochem Soc Symp* **65,** 233-43.
Hsu, P. et al (2001) *Biochem Biophy Res Comm* **285,** 751-759.
Cary, L.A. et al (1999) *Histol Histopathol* **14,** 1001-9.

HYDRODYNAMIC SHEAR AND TETHERING ON E-SELECTIN SIGNALS ADHESION OF HUMAN NEUTROPHILS

Scott Simon[1], Daniel McDonough[1], Fiona McIntosh[2], Harry Goldsmith[2]:
[1]Department of Biomedical Engineering, UC Davis, Davis, CA, [2]Montreal General Hospital, Montreal, Quebec, Canada.

INTRODUCTION Neutrophil recruitment to sites of inflammation from the blood stream is a multistep process involving tethering via selectins and firm adhesion through activation of integrins. At least two critical steps are identified; the first an efficiency of neutrophil capture by tethering via selectins, and next, an efficiency of subsequent transition to firm adhesion through activation and binding of β_2-integrins. Recently we have reported that tethering and rolling of neutrophils in shear flow over a substrate of E-selectin signals activation of β_2-integrins and firm adhesion (Simon et al., 2000). Here we study heterotypic and homotypic aggregation in suspension between neutrophils and murine pre B-cells expressing E-selectin (300.19-E) or L-selectin (300.19-L) using cone-plate viscometry to apply a defined shear environment and fluorescence flow cytometry to quantitate aggregation over the time course of shear and activation. The objective of these studies was to examine the molecular mechanisms and shear dependence underlying the transition from tethering to firm adhesion during collisional interactions between neutrophils and 300.19 target cells. Adhesion efficiency was determined by applying two-body collision theory to predict the time course of heterotypic aggregation Two-body collision doublet lifetime and capture efficiency was also directly observed in shear using in-line a transparent cone plate rheometer and videomicroscopy.

METHODS Human neutrophils (PMN) were isolated from fresh blood and stored in Ca^{++} free buffer prior to the experiment. 300.19 cells, an immortalized murine pre-B-cell line transfected to express either E-selectin or L-selectin expressed similar receptor levels. We used cone plate viscometry to apply a defined shear rate to cell suspensions of neutrophils and either 300.19-E or 300.19-L. Selectin mediated tethering and neutrophil firm adhesion to 300.19-selectin targets were quantified using videomicroscopy and flow cytometry respectively.

Neutrophil-300.19 activation and firm adhesion in a sheared cell suspension was quantitated using two-color flow cytometric analysis of fixed samples over the time course of activation and shear. Cell suspensions were stimulated with low doses (~2.5nM) of formyl peptide, and sheared at G=600 s^{-1}. Using a model of aggregation based on two body collision theory the efficiency of aggregation was extracted from the kinetic data. Collision frequency is computed based on the experimental parameters of cell radius, concentration and the applied shear rate. The efficiency is then defined as the aggregation rate normalized by the total number of collisions per unit time.

High speed video of (250-500 fps) PMN-300.19 collisional interactions were obtained using a transparent counter-rotating cone and plate rheoscope mounted on an inverted microscope(Goldsmith et al., 2001). Heterotypic doublets were observed in the sheared suspension and collisional duration was measured. Doublets rotating past the orientation of predicted break-up for inert spheres ($\Phi = 90^0$) were considered to be tethered.

RESULTS AND DISCUSSION Flow cytometric analysis of two color aggregation at shear rate G=600 s^{-1} stimulated with 2.5nM FMLP elicited formation of both heterotypic and homotypic aggregates. 300.19-E proved to be more efficient targets than 300.19-L under identical experimental conditions as shown by the fraction of neutrophils recruited (20% for 300.19-E *vs.* 5% for 300.19-L) The efficiency of firm adhesion for capture of 300.19E was 4.5% , as compared to 1% for 300.19-L.

Varying the 300.19 cell concentration in suspension revealed a striking difference in the adhesion efficiency for E-selectin versus L-selectin. While the efficiency of PMN-300.19L aggregation remained constant at a value of ~1% over a range of 300.19 concentrations from 0.3:1 up to 5:1 300.19:PMN, the efficiency of PMN-300.19E aggregation decreased three-fold from 4.6% to 1.6%. It was hypothesized that this drop in adhesion efficiency is due to the longer collisional lifetime of PMN-300.19E doublets. This limits the number of available singlets in the cell suspension as compared to the theoretical model, which is based on elastic collisions between inert spheres. The resulting aggregation kinetics were fit with an apparent efficiency of adhesion that decreased four-fold over a ratio of. 300.19:PMN was increased from 0.3:1 up to 5:1 300.19:PMN.

Rheometric observations of collisional interactions confirmed a high efficiency of doublet formation for 300.19E ε_{hetero} = 28%. The mean lifetime of homotypic doublets was equivalent to that predicted for inert spheres ($\tau_{exp} = \tau_{theor}$), whereas for heterotypic doublets $\tau_{exp} = 5\times\tau_{theor}$. Shear stress was increased from 1.1 dyn/cm^2 up to 6.4 dyn/cm^2 at a shear rate of 100 s^{-1} by addition of Ficoll to the suspending media. The lifetime of colliding doublets increased four-fold, along with the efficiency of stable adhesion. These data confirmed by direct observation that shear stress promotes stable adhesion initiated through E-selectin.

The longer lifetime of adhesion via E-selectin also correlated with a greater stability of PMN-300.19E aggregates. To test whether this resistance to disaggregation was due to an increased engagement of activated β_2-integrins, we assessed active β_2-integrin expression on neutrophils in heterotypic suspensions. Using mAb 327C, which reports on the active conformation of β_2-integrin, we found expression to be up to three-fold greater on PMN-300.19E than on aggregates with 300.19L or on homotypic aggregates.

SUMMARY Neutrophil capture of E-selectin expressing target cells (300.19E) exhibited a greater efficiency of adhesion that correlated with a longer adhesive lifetime as compared to L-selectin expressing targets (300.19L). A distinct dependence of integrin activation on the magnitude of shear rate suggests a coupling between fluid mechanical effects of shear and signaling of adhesion.

REFERENCES

Goldsmith, H.L., et al. (2001). Biophys. J., 81:2020-2034.
Simon, S.I., et al. (2000). J. Immunol., 164:4348-4358.

FLOW REGULATION OF GAP JUNCTIONAL COMMUNICATION AND THE FUNCTIONAL COMPARTMENTALIZATION OF VASCULAR ENDOTHELIUM

Natacha DePaola[1], Lucio Florez[1], Eno Essien[1], Denise Polacek[2], and Sanghee Kim[1]
[1]Biomedical Engineering Department, Rensselaer Polytechnic Institute, Troy, New York, USA
[2]Institute for Medicine and Engineering, University of Pennsylvania, Philadelphia, PA, USA

INTRODUCTION

The localization of atherosclerotic lesions coincides with regions of disturbed blood flows where endothelial cells of altered phenotype are adjacent to normal endothelium. *Functional Compartmentalization* of the endothelium refers to the occurrence of neighboring regions with distinctively different cell function.

The endothelium is recognized as a mechanical signal-transduction interface between flowing blood and the vessel wall (Davies et al 1997). However, the cellular and molecular mechanisms by which hemodynamics might alter endothelial cell function leading to lesion development remain unclear. The decentralized model of endothelial mechanotransduction (Davies 1995) predicts that endothelial mechanosensors associated with the conversion of shear stress forces to signals are not restricted to the lumenal surface but located at multiple sites throughout the cell, including cell junctions (Osawa et al 1997).

Gap junctions, the only communicating intercellular junctions, allow the direct transport of ions and second messenger molecules between adjacent cells. Connexin proteins forming endothelial gap junctions have been demonstrated to be regulated by shear stress *in vivo* (Polacek et al 1997, Gabriels and Paul 1998) and *in vitro* (Cowan et al 1998, DePaola et al 1999). We hypothesize that fluid shear stress associated with disturbed flows, induce regional changes in endothelial gap junctional communication (GJIC) which in turn, affect cell phenotype, contributing to Functional Compartmentalization of the endothelial monolayer *in vivo* and *in vitro*.

METHODS

Human aortic endothelial cells were exposed to controlled fluid forces in experimental flow chambers that recreate each type of shear stress gradients found at atherogenesis-prone sites. The various components of the stress gradients were studied at several magnitudes either in isolation or in combination. Regulation of the gap junctional proteins Cx43 and Cx40 in the various flow-defined regions was assessed by *in situ* immunolocalization. Regional GJIC was evaluated by single cell microinjections. Immunocytochemistry and image analysis were used to assess the occurrence of endothelial Functional Compartmentalization by regional evaluation of cell shape, proliferation and migration. A GFP-Cx43 construct was used to evaluate Cx43 protein redistribution in real time. GJIC inhibition studies were conducted to determine which of the evaluated cell functions are dependent on functional GJIC.

RESULTS AND DISCUSSION

Simultaneous immunostaining (double-labeling) of the gap junctional proteins Cx43 and Cx40 demonstrated different levels of baseline expression and flow regulation after 6 hours exposure to flow. Both Cx43 and Cx40 were disrupted at cell borders and partially relocated to the cytoplasm in areas of high shear stress gradients. The observed disruption of Cx40 protein at cell borders was more pronounced than that of Cx43. When at cell borders, Cx40 remained co-localized with Cx43. The disassembly of gap junctions by CX43 protein redistribution under flow was evaluated in real time with a GFP-Cx43 construct in transfected cells. The regional differences in connexin protein expression and organization were reflected in inhibition of intercellular communication (dye transfer). A significant decreased in the rate of cell motion was observed in regions of simultaneous high shear and high shear gradients when compared with the average motion rates observed in regions of simultaneous low shear and high shear gradients, where cell motion was not only significantly increased with exposure to flow but persisted for up to 36 hours after flow removal. Protein synthesis inhibition by monolayer pretreatment with cycloheximide resulted in inhibition of cell motion in response to flow. Areas of significant increase in cell motility coincided with areas exhibiting aberrantly localized connexin protein expression.

SUMMARY

The data suggest a prominent role for shear gradients in regulating endothelial cell communication and provide evidence that there are cell signaling processes initiated by flow which continue to alter cell function after cessation of the stimulus. Altered communication rate correlated with areas of altered cell function.

REFERENCES

Davies, P.F. et al (1997). *Annual Review of Physiology* 59:527-549. Davies, P.F. (1995). *Physiol. Rev.* 75:519-560.

Osawa, M. et al (1997). *Eur. J. Cell Biol,* 72:229-237.

Polacek, D. et al (1997). *J. Vasc. Res.,* 34:19-30.

Gabriels, J.E., Paul, D.L. (1998). *Circ. Res.,* 83:636-643.

Cowan, D.B. et al (1998). *Circ. Res.,* 82:786-793.

DePaola, N. et al (1999). *Proc. Natl. Acad. Sci.,* 96(6):3154

ACKNOWLEDGEMENTS

This work is supported by NIH HL64728 (NDP).

FLUID-STRUCTURE INTERACTION AND COLLAGEN REMODELING IN THE AORTIC HEART VALVE

Frank Baaijens, Ralf Boerboom, Carlijn Bouten, Niels Driessen, Debbie Gawlitta, Jurgen de Hart, Gerrit Peters and Jacques Huyghe

Department of Biomedical Engineering, Eindhoven University of Technology, PO Box 513, 5600 MB Eindhoven, The Netherlands
e-mail: f.p.t.baaijens@tue.nl

INTRODUCTION

.
In vitro mechanical conditioning has been demonstrated to be of critical importance in the tissue engineering of heart valves[1]. Therefore, after static culturing, cell seeded constructs are placed in a bioreactor and subjected to pulsatile flow conditions. The objective is to stimulate cell proliferation and differentiation as well as extra cellular matrix production. In particular for aortic heart valves, the leaflets have to carry substantial hemodynamic loads, both during the systolic and the diastolic phase. Since collagen fibers are known to provide a substantial part of the structural integrity of the heart valves, the production of sufficient amounts of appropriately aligned collagen fibers appears mandatory. The production and alignment of collagen fibers is known to be strain sensitive, which suggests that the strain distribution, i.e. deformation modes, inside the leaflets must be controlled carefully during *in vitro* conditioning. Furthermore, at implantation the heart valves may not necessarily have to be morphologically identical to the native heart valves, they, however, should be sufficiently functional.

METHODS

Numerical analysis, using the finite element method, of the motion of the leaflets induced by the blood flow[3,4,5], provides crucial information about the stresses and strains within the developing tissue as well as the shear stresses imposed on the leaflet surfaces. The numerical method is based on the so-called fictitious domain method[3]. Fluid-structure interaction between the leaflets and the fluid is achieved via the introduction of Lagrange multipliers on non-conforming meshes, while the dispensability of the aortic wall is accounted for via the Arbitrary Lagrange Euler (ALE) formulation.

Particular emphasis is given on the modeling of the collagen fiber reinforcement of the leaflets. For this purpose a structural approach is adopted that distinctively accounts for the contribution of the matrix and collagen fibers. The impact of fiber reinforcement and aortic wall flexibility on the hemodynamics of the valve is examined. Fiber reinforcement not only substantially reduces the stresses in the matrix, it also stabilizes the motion of the leaflets.

RESULTS AND DISCUSSION

Understanding the impact of mechanical loads as imposed on the tissue inside a bioreactor on the collagen fiber organization is one of the key challenges in the regeneration of the leaflet tissue. Motivated by the work of Peskin and McQueen[6], it is assumed that remodeling of the collagen fiber network is strain modulated. A rate equation for the volume fraction of a particular fiber is formulated composed of a synthesis and degradation expression. An initially random, isotropic, fiber distribution is assumed that is allowed to remodel according to this rate equation. By imposing physiological loads on the leaflet, the collagen fibers remodel and show a structure that closely resembles the fiber structure of the natural leaflet. This is a first step towards understanding how the mechanical loading in a bioreactor should be modulated to obtain optimal mechanical tissue properties

REFERENCES

S.P. Hoerstrup, R. Sodian, S. Daebritz, J. Wang, E.A. Bacha, D.P. Martin, A.M. Moran, J. Guleresian, J.S. Sperling, S. Kaushal, J.P. Vacanti, F.J. Schoen and J.E. Mayer. *Functional living trileaflet heart valves grown in vitro.* Circulation, 102:III-44-III-49, 2000, suppl III

A.A.J.H. Sauren. *The mechanical behaviour of the aortic heart valve*, PhD thesis, Eindhoven University of Technology, 1981

F.P.T. Baaijens, *A fictitious domain/mortar element method for fluid-structure interaction*, Int. J. Num. Meth. Fluids, 35 , 743-761, (2001)

G. Cacciola, G.W.M. Peters, F.P.T. Baaijens, *A synthetic fiber-reinforced stentless heart valve.,* J. Biomech., 33 653-658, (2000)

J. de Hart, G.W.M. Peters, P.J.G. Schreurs, F.P.T. Baaijens, A two-dimensional fluid-structure interaction model of the aortic valve, J. Biomech., 33 , 1079-1088, (2000)

Peskin CS, McQueen*, Mechanical equilibrium determines the fractal fiber architecture of aortic heart valve leaflets,* Am J Physiol. 1994 Jan;266(1 Pt 2):H319-28

DEVELOPING A COMPOSITE, TISSUE-ENGINEERED AORTIC VALVE

Ivan Vesely, Ph.D., Yaling Shi, M.S., Anand Ramamurthi, Ph.D.

Department of Biomedical Engineering, The Cleveland Clinic Foundation, Cleveland, Ohio, USA
vesely@bme.ri.ccf.org

INTRODUCTION

A tissue-engineered valve will need to incorporate the complex microstructure of the aortic valve if it is expected to offer durability comparable to that of conventional bioprosthetic valves. Native aortic valve cusps contain three layers of morphologically distinct tissue: fibrosa, spongiosa, and ventricularis. The fibrosa contains large, bifurcating collagen fiber bundles; the ventricularis consists of multiple sheets of elastin; and the spongiosa consists of collagen, elastin, and glycosaminoglycans (GAGs). Collagen fiber bundles are surrounded by tubular sheaths of elastin, which are linked together by elastin struts. Given the complexity of native aortic valve cusps, our approach to tissue engineering the aortic valve has been to fabricate cusps from the basic building blocks: (i) branching collagen fiber bundles; (ii) elastin sheets and tubes; and (iii) a highly hydrated GAG matrix.

METHODS

We have developed the following building blocks:
Collagen fiber bundles were fabricated using the principle of directed collagen gel shrinkage. Fibroblasts were mixed with acid-solubilized rat tail collagen and cast into silicon rubber wells with microporous holders to entrap the gel. Since the gel is constrained in the longitudinal direction, it contracts only laterally forming well-aligned collagen fiber bundles.
The viscoelastic matrix that integrates these components together has been fabricated from divinyl sulfone-crosslinked high molecular weight hyaluronan (hylan) [1], texturized by UV irradiation to enhance cell attachment.
Elastin sheets were grown atop the hylan gels and around the collagen fiber constructs by way of long-term cultures of neonatal rat aortic smooth muscle cells.

RESULTS AND DISCUSSION

Collagen gel contraction increased with higher cell seeding density, the optimal value being 1 million cells/ml. The optimal collagen concentration was 2 mg/ml, producing a failure strength as high as 2 MPa. Branched bundles were formed using appropriately shaped wells (Fig 1).
UV-irradiated gels had highly extended cells throughout their thickness. The confocal studies indicate that cells atop and within the gels actively proliferate. The hylan matrices had stiffness values as high as 40 kPa, and strain to failure in excess of 150%.

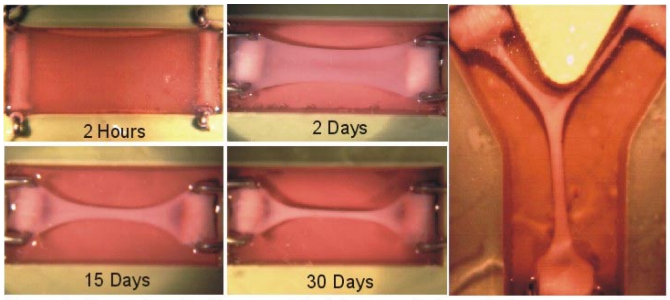

Figure 1: Examples of collagen gel shrinkage and a branched constructs (right)

Transmission electron microscopy showed the presence of a uniform elastic membrane at the surface of UV-exposed gels. We also found that an elastin sheath developed around the collagen core after 6 weeks of culture (Fig 2).

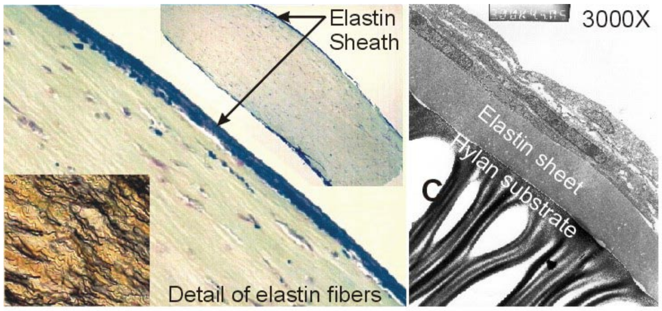

Figure 2: Examples of elastin sheath surrounding a collagen fiber bundle (left), and a flat sheet of elastin bound to the texturized hylan gel (right)

CONCLUSIONS

We have therefore fabricated the basic building blocks of the structure of the native aortic valve using tissue engineering principles. These are: (i) strong collagen fiber bundles that branch, (ii) sheets of elastin adherent to an underlying matrix, (iii) tubes of elastin that surround collagen fiber bundles, and (iv) a highly biocompatible, elastic matrix that can integrate all of these components. We are enhancing the mechanical properties of these components further through dynamic tissue culture. Entire leaflets can thus be fabricated from these constructs by growing each of individually, and assembling them together to make the composite tissue-engineering aortic valve cusp.

REFERENCES

[1] Ramamurthi A., Vesely I., Smooth muscle cell adhesion on crosslinked hyaluronan gels. J. Biomed.Mater.Res., (in press).

FABRICATION AND CHARACTERIZATION OF FIBRIN-BASED TISSUE-EQUIVALENT VALVES

Michael Neidert[1], Theodore Oegema[2], and Robert Tranquillo[1]

University of Minnesota, Minneapolis, Minnesota, U.S.A.
[1]Department of Biomedical Engineering (corresponding author: tranquillo@cems.umn.edu)
[2]Department of Orthopaedic Surgery

INTRODUCTION

Heart valve replacement surgeries account for over 70,000 surgeries in the U.S. alone each year. The majority of those replacement valves are either mechanical (mhv) or bioprosthetic (bhv) each of which present different complications post-surgery either bleeding (mhv), calcification (bhv), or thromboembolism (bhv and mhv). Furthermore, both mechanical and bioprosthetic valves are incomplete solutions for children who require replacement valves. Therefore, there is a great demand for living tissue-engineered valves that would be able to grow and respond to the *in vivo* environment.

To date, we have fabricated tissue-engineered heart valves using the tissue-equivalent approach of entrapping human fibroblasts within a forming collagenous network (producing a valve-equivalent, or VE). A solution of cells and collagen monomers is injected into an appropriate mold (patent pending) and gelled. Entrapped cells then begin to compact the network by exerting traction. Appropriate constraint of the compaction produces constructs with the collagen fibrils aligned in a prescribed direction (Barocas et.al.) mimicking the commissure-to-commissure alignment of native valve leaflets and circumferential alignment of the adjoining root.

While the current generation of tissue-engineered valves are geometrically correct and possess the correct collagen fiber alignment, they are significantly weaker due to the lack of extracellular matrix components and general organization of native heart valve leaflets (Vesely et.al.). Thus, we have pursued methods to induce cell-mediated remodeling of the original biopolymer scaffold such that the entrapped cells will replace it with a highly organized, mechanically competent, tissue-like matrix. To effect this change, we use biochemical cues (using fibrin as a scaffold protein combined with growth factors) and mechanical cues (i.e. leaflet bending) to produce tissue engineered valves, and we present the resultant biaxial mechanical, bending, and compositional data.

METHODS

A mold predominantly composed of 5% agarose gel (formed around mounting surfaces) to prevent fibrin adhesion is constructed using an appropriate negative mold. A solution of 3.3 mg/ml bovine fibrin (Sigma) and human foreskin fibroblasts at 1×10^6 cells/ml is injected into the mold, gelled, and incubated for up to 4 weeks in M199 (Gibco) supplemented with 1 ng/ml TGF-β (R&D Systems), 2 ug/ml insulin (Sigma), 0.01 U/ml plasmin (Calbiochem), 10% FBS (HyClone) and 50 ug/ml ascorbic acid (Sigma). After incubation, the VE is carefully removed and characterized using uniaxial (MTS Systems), planar biaxial (Instron), and bending mechanical tests. Furthermore, VE leaflet sections are histologically characterized using a Masson's trichrome stain and elastin antibody staining.

RESULTS AND DISCUSSION

Preliminary testing of adherent fibrin hemispheres incubated with TGF-β, insulin, and plasmin show definite bands of cell-synthesized collagen and elastin aligned similarly to the compacted fibrin matrix (Figure 1). Furthermore mechanical testing of fibrin samples incubated with growth factors show improved mechanical properties relative to collagen samples and approaching those of cardiovascular tissues.

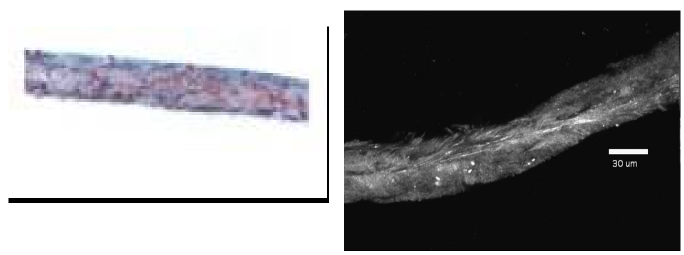

Figure 1: Left: Trichrome stain of fibrin construct showing cell-deposition of collagen (blue-green) along the top of the construct. Right: Confocal micrograph of a fibrin construct staining showing immunofluorescent staining for elastin.

SUMMARY

We have developed and characterized a fibrin-based tissue-engineered heart valve that is mechanically stronger than a collagen-based valve and more closely resembles the matrix composition and microstructure of the native valve.

REFERENCES

Barocas, V.H. et.al. (1997). *J.Biomech.Eng.* **119**, 137-145.
Vesely, I. (1998) *J. Biomech.* **31.** 115-123.

THE ROLE OF DYNAMNIC STRESSES DURING INCUBATION IN INCREASING TEHV TISSUE STRENGTH

Michael S. Sacks[1], Kristine Gulesarian[2], David Martin[3], John E. Mayer, Jr.[2]
[1]Department of Bioengineering, 749 Benedum Hall, University of Pittsburgh, Pittsburgh PA 15261
[2]Childrens Hospital, Harvard Medical School, Boston, MA; [3]TEPHA, Cambridge, MA

INTRODUCTION: The need for improved heart valve prostheses is especially critical in pediatric applications, where growth and remodeling are essential. Tissue engineered heart valves (TEHV) have functioned in the pulmonary circulation of growing lambs, and thus can potentially overcome limitations of current prosthetic heart valves. Despite these promising results, significant questions remain. In particular, the role of mechanical incubation conditions is largely unexplored. The following study was conducted provide fundamental information for optimizing TEHV biomaterials.

METHODS: Tri-leaflet valve constructs were fabricated from poly-4-hydroxybutyrate coated polyglycolic acid seeded with ovine endothelial and carotid artery medial cells and first cultured under static conditions for 4 days under static conditions. Next, the valves were either cultured for an additional 14 days under static conditions or under dynamic flow conditions, for a total in both cases of 18 days. A total of six groups were evaluated: 4 days static with and without cells, 18 days static with and without cells, and 18 dynamic with and without cells.

After incubation, valves were removed and shipped in chilled culture media to the Tissue Mechanics Lab for flexural mechanical testing. We utilized the flexure testing device as previously described (Gloeckner, Billiar et al. 1999). A 2 mm x 10 mm circumferentially-oriented specimen was prepared from each leaflet and placed in 100% normal saline, and 15 ~200 μm diameter graphite markers were attached to one edge. Each specimen was bent in both directions, notated as the "against-curvature (AC)" and "with-curvature (WC)", with respect to the TE leaflet's shape. Video images of the specimen were acquired during the test from which the loads and marker displacements were determined. We then utilized the moment-curvature relation for beams undergoing large displacements to determine the effective bending stiffness,

$$E_{eff}: \quad M = E_{eff} I \, \Delta\kappa \qquad (1)$$

where $\Delta\kappa$ is the change in specimen curvature, I is the 2nd moment of inertia, M is the bending moment, and E_{eff} the effective tissue stiffness. From the marker positions $\Delta\kappa$ was computed using a spline fit. E_{eff} is determined over the entire bending path by plotting M/I vs. $\Delta\kappa$ so that the slope of the curve at each point is equivalent to E_{eff}. Due to the potential for transmural structural heterogeneity, it is understood that the value of E_{eff} represents the specimen's bending stiffness only for the AC and WC bending directions, respectively. Flexural data from a fresh ovine pulmonary valve are also presented.

RESULTS: The 4 day unseeded control specimens were ~25% stiffer than the seeded controls with no directional differences (Fig. 1). By 18 days under static conditions this trend was reversed, with the seeded specimens almost double in stiffness compared to the corresponding controls (Fig. 1). Interestingly, under dynamic conditions there was not only a greater drop in stiffness, but also a substantial directional dependence, with the AC stiffness only ~1/2 that of the WC stiffness. Further, the dynamically condition tissues were more similar to the very compliant native pulmonary valve tissue (Fig. 1). When the seeded/unseeded specimen modulus ratios were examined, the dynamically conditioned tissue was ~3 times stiffer than the unseeded control, compared to only ~2 fold change for the statically incubated tissue (Fig. 2).

DISCUSSION: This study reported the effects of static and dynamic incubation conditions for a tissue engineered heart valve biomaterials. Under static culture conditions, we demonstrated that the presence of the deposited extracellular matrix and cellular material can increase the effective stiffness of the TE leaflet by ~two fold. Further, dynamic culture conditions can increase the TE leaflet stiffness by a factor of three compared to unseeded controls. Clearly, mechanical conditions during in-vitro incubation have a dramatic effect on tissue engineered construct's mechanical properties.

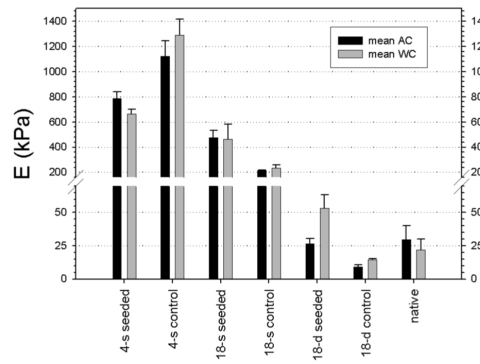

Figure 1: Effective stiffness results for all 6 TEHV groups.

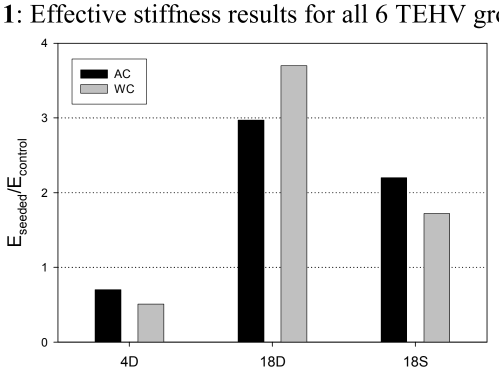

Figure 2 – Ratio of the effective stiffness between the seeded and unseeded controls, indicating that dynamic conditions can increase the effective stiffness by a factor of three.

Acknowledgements: This research was supported by NIH grants HL-68-816-01 (MSS) and HL-97-005 (JEM).

REFERENCE: Gloeckner, D. C., K. L. Billiar, et al. (1999). ASAIO J **45**(1): 59-63.

BIOMECHANICS & HYDRODYNAMICS OF DECELLULARISED PORCINE AORTIC HEART VALVES

Sotiris Korossis[1], Cath Booth[2], Helen Wilcox[2], Kevin Watterson[3], John Kearney[4], Eileen Ingham[2], John Fisher[1]
[1] School of Mechanical Engineering, University of Leeds, Leeds, UK menskoro@leeds.ac.uk,
[2] Division of Microbiology, University of Leeds, Leeds, UK, [3] Leeds General Infirmary, Leeds, UK,
[4] Yorkshire Regional Tissue Bank, Pinderfields Hospital, Wakefield, UK

INTRODUCTION

There is no adequate heart valve substitute for long term implantation for the majority of patients (Korossis 2000). For elderly patients bioprosthetic tissue valves with a life expectancy of 10-15 years provide a satisfactory solution. The heart valve substitute of choice for patients with a greater life expectancy is the mechanical heart valve. However, these valves require long-term anticoagulation therapy. For young adults and children there is a need to deliver a heart valve that will develop with the patient. Homograft valves have been used in this patient group, but they do not retain viability following transplantation. Tissue engineered heart valves coupled with recellularisation have the potential to grow with the patient. An approach is to use natural tissue matrices, either of xenograft or allograft nature. The major challenge in this approach is to develop effective decellularisation techniques to remove foreign cellular elements while retaining the biomechanical integrity of the valvular matrix. This study investigated the effect of sodium-dedocyl-sulfate (SDS), as a decellularisation treatment, on the biomechanical integrity and hydrodynamics of porcine aortic heart valves.

METHODS

Left coronary leaflets were dissected from fresh porcine aortic valves within 4 hours of slaughter. The leaflets were divided into 6 groups and treated according to the protocols listed in Table 1. Haematoxylin and eosin histological staining was performed to all the groups to assess the degree of decellularisation. Circumferential and radial specimens were cut from each of the 6 leaflet groups and tested under uniaxial tensile loading to failure. Whole porcine aortic roots were also treated with 0.1% (w/v) SDS in hypotonic buffer and their functionality was assessed by pressurising them to physiological pressures (120 mmHg) and by subjecting them to simulated pulsatile flow.

Table 1: Leaflet treatments used in the biomechanical study.

Fresh (control)
Isotonic buffer (control)
Hypotonic buffer (control)
Isotonic buffer + 0.03%(w/v) SDS (control)
Hypotonic buffer + 0.03%(w/v) SDS
Hypotonic buffer + 0.1%(w/v) SDS

RESULTS AND DISCUSSION

Isotonic buffer or isotonic buffer with SDS did not alter the biomechanical properties. However, they were not effective decellularisation treatments. Treatment with 0.03% and 0.1% (w/v) SDS in hypotonic buffer produced complete accellularity while retaining the network of elastin, collagen and glycosaminoglycans (Booth 2002). These protocols produced modest changes in the biomechanics of the leaflets by reducing their elastin and collagen phase slopes, as well as by increasing their transition and failure strains. However, the treatments did not affect the strength of the leaflets (Korossis 2002). Whole porcine aortic roots treated with 0.1% (w/v) SDS in hypotonic buffer and pressurized to 120mmHg presented complete leaflet competence, whereas, when they were subjected to pulsatile flow showed reduced transvalvular pressure gradients (Figure 1) and similar regurgitation volumes compared to fresh, untreated roots. Regarding leaflet kinematics, the treated roots exhibited similar levels of leaflet free edge bending strains compared to the fresh control, as well as physiological opening and closing actions (Figure 2).

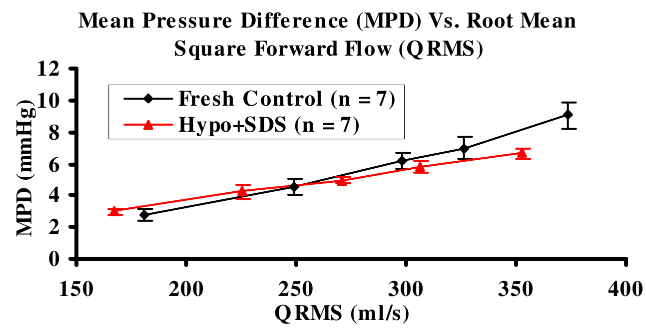

Figure 1: Pressure difference vs. root mean square forward flow for fresh and SDS-treated aortic roots (mean ± 95% C.I.).

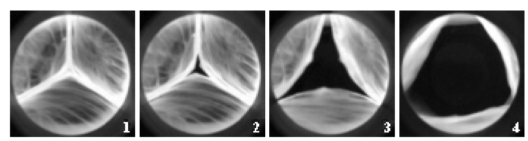

Figure 2: Leaflet kinematics of SDS-treated aortic valve.

SUMMARY

The decellularisation protocol used in this study, incorporating SDS in hypotonic buffer, produced complete accellularity of porcine aortic leaflets, causing modest changes in their extensibility. The absence of dead cells as foci for calcification, the retention of the elastin, collagen and glycosaminoglycans, as well as the promising leaflet kinematics and the retention of the leaflet matrix compliance and strength, form a promising platform for further studies. Further work will investigate whether the treated leaflets have adequate durability and will consider *in vitro* recellularisation and penetration of the cells in the leaflet matrix.

REFERENCES

Korossis, S.A. et al (2000). *Bio-Med Mat Eng*, **10**, 83-124.
Booth, C. et al (2002). *J Heart Valve Dis* (In press)
Korossis, S.A. et al (2002). *J Heart Valve Dis* (In press)

MODULATION OF ANABOLIC AND CATABOLIC MECHANICAL SIGNALS IN BONE: FROM MECHANICS TO GENETICS

Stefan Judex
Department of Biomedical Engineering
State University of New York, Stony Brook, NY

A link between mechanical forces and skeletal morphology was first recognized by Galileo Galilei in the early 1600's. Almost four centuries later, the interdependence of form and function to explain the intricate architecture of the skeleton and the changes in bone mass with altered mechanical demands are yet to be elucidated. This incomplete understanding of mechanotransduction from the organ- down to the molecular-cellular level has crippled our efforts to design effective mechanical interventions that promote bone formation without significant side-effects.

Although there is little argument that bone can readily respond to mechanical stimuli, it is more than likely that the inconclusive results of whether exercise is efficacious in increasing bone mass or in preventing its decline reflect our limited understanding of which specific component of the mechanical signal is perceived as osteogenic by the resident bone cells populations. Using *in vivo* strain gaging together with finite element modeling, the ability of candidate mechanical parameters to predict the specific sites of bone formation was tested in an animal exercise-model. We found that a very brief daily running regime was capable of activating periosteal surfaces in the tarsometatatarsal middiaphysis of adult roosters. Spatial correlations indicated that new bone was deposited primarily at sites experiencing the least rather than greatest strain magnitudes; regions in which circumferential strain gradients were large. While it is counterintuitive from an engineering perspective that bone formation is activated at sites subjected to low strains, physiologically, it is important to point out that strain gradients are proportional to fluid flow in bone, a byproduct of strain which has been implicated to play an important role in mechanotransduction in bone. Further experiments in growing roosters subjected to both running as well as jump exercises substantiated the importance of mechanical parameters that may be associated with interstitial fluid flow.

The prevailing tenet is that mechanical stimuli have to be large in magnitude to elicit an adaptive response. Recent studies indicated, however, that extremely low magnitude (inducing <10 microstrain in the matrix) mechanical signals readily stimulate bone formation and ameliorate mechanical properties. These potentially clinically relevant stimuli, when applied as low-level whole body vibration to the rat skeleton for 10 min/day, were anabolic to trabecular bone of the proximal tibia while mechanical disuse reduced bone formation rates. This suppression of bone formation was only slightly curbed when disuse was interrupted by 10 min/d of weight-bearing. In contrast, disuse interrupted by 10 min/d of low-level mechanical vibration normalized bone formation rates to values seen in age-matched controls. At the molecular level, the expression of a gene that is a critical factor for osteoclastogenesis (RANKL) was quantified. Mechanical stimulation for 10 min/d decreased RANKL mRNA levels. Disuse increased RANKL transcripts while disuse interrupted by 10 min of daily mechanical stimulation decreased RANKL levels. Bone formation rates were inversely related to RANKL expression levels across groups (r^2=0.79). This work indicated that the low-level stimulus may provide an effective biomechanical intervention for the bone loss which plagues long-term space flight, bedrest, or immobilization and that gene expression is modulated by its mechanical environment.

Murine models of bone adaptation are critical for an integrative biomechanical/molecular/genetic approach to elucidate the adaptive skeletal processes as the mouse genome has been extensively deciphered, specific mouse strains with different bone phenotypes are available (e.g., high and low bone mineral density), and gene function can be tested through selective knockouts or inducible gene expression. While the influence of genetic variations on attaining and retaining bone mass is well established in both mice and humans, it is entirely possible that genetic make-up is also a strong determinant of bone's sensitivity to mechanical stimuli. Three genetically distinct strains of mice were subjected to either 10 min/d of whole body vibration or mechanical disuse. The extremely low-level mechanical stimuli superimposed upon normal daily activities were highly anabolic in the proximal tibia of both low bone mineral density (BMD) and mid BMD mice, while no significant effect of this specific stimulus was detected in the high BMD mice. Disuse diminished bone formation rates and bone volume in mid BMD mice, but failed to significantly influence bone's formative response in the other two strains. This genetic basis of bone's mechano-sensitivity at the tissue level was essentially mirrored at the molecular level. For instance, inducible nitric oxide synthase was significantly down-regulated by a similar percentage in mechanically stimulated mice of those strains that had responded to mechanical stimulation at the tissue level. Extrapolating these results to the human skeleton may provide insight into the inconsistent efficacy of treatment regimens as well as into the individual variation in the pathogenesis of osteoporosis.

In summary, the sensitivity of bone to mechanical stimuli is apparent but the design of interventions that will maximize tissue strength in young adults and prevent its loss in the elderly will require approaches combining biomechanics and genetics at the level of the tissue and the cell. The discovery of genes involved in regulating the skeletal response to mechanical stimuli may uncover novel drug targets that are not addressed by current pharmacological interventions and may also enable rapid advances in tissue engineering.

These studies were kindly supported by NSERC, NSBRI, NASA, and AHFMR.

MOLECULAR MECHANICS OF CARDIAC TITIN'S PEVK AND N2B SPRING ELEMENTS

Kaori Watanabe[1], Siegfried Labeit[2], Henk Granzier[1].

[1]VCAPP, Washington State University, Pullmann, WA, 99164-6520, USA, [2]Anesthesiology and Intensive Operative Medicine, University Hospital Mannheim, D-68135 Mannheim, Germany.

Email: Granzier@wsunix.wsu.edu

INTRODUCTION

Titin is a giant elastic protein that is responsible for the majority of passive force generated by the myocardium. Titin's force is derived from its extensible I-band region, which, in the cardiac isoform, comprises three main extensible elements: tandem Ig segments, the PEVK domain, and the N2B unique sequence (N2B-Us). Using atomic force microscopy (AFM), we characterized the single molecule force-extension curves of the PEVK and N2B-Us spring elements, which together are responsible for physiological levels of passive force in moderately to highly stretched myocardium.

RESULTS AND DISCUSSION

Molecules were stretched using a molecular force probe (Asylum Research, Santa Barbara, CA), an AFM specialized for stretching molecules. Force *versus* displacement curves were collected in repeated stretch and release cycles. Stretch-release force-extension curves of both the PEVK domain and N2B-Us displayed little hysteresis: the stretch and release data nearly overlapped. The force-extension curves closely followed worm-like chain behavior. Histograms of persistence length (measure of chain's bending rigidity) indicated that the single molecule persistence lengths are ~1.4 and ~0.65 nm for the PEVK domain and N2B-Us, respectively. Using these mechanical characteristics and those determined earlier for the tandem Ig segment (assuming folded Ig domains), we modeled the cardiac titin extensible region in the sarcomere and calculated the extension of the various spring elements and the forces generated by titin, both as a function of sarcomere length. In the physiological sarcomere length range, predicted values and those obtained experimentally were indistinguishable.

SUMMARY

AFM studies revealed that the PEVK domain and N2B-Us both behave as entropic springs, but with different persistence lengths. Persistence length histograms allow the single molecule persistence lengths to be determined; and using the obtained PEVK domain and N2B-Us values, a model of the extensible region of cardiac titin can be constructed that simulates very closely the complex extension of titin in the sarcomere and the unique passive force-sarcomere length relation of cardiac myocytes.

REFERENCES

Freiburg, et al. (2000). *Circulation Research,* 86(11):1114-21.

Bang et al., 2001. *Circulation Research*, 89, 1065-1072

Granzier, and Labeit, S. (2002). *J. Phys*;541:335-42.

Watanabe, Nair, Labeit, Kellermayer, Greaser, Labeit, and Granzier (2002A). *J. Biological Chemistry*, 227, 11649-11558.

Watanabe, Muhle-Goll, Kellermayer, Labeit and Granzier (2002B). *J. Structural Biology*, 137-248-258.

TITIN DEFICIENCY – LESSONS FROM KNOCKOUT MODELS

Michael Gotthardt[1], Henk Granzier[1], Siegfried Labeit[2]

[1]VCAPP, Washington State University, Pullmann, WA, 99164-6520, USA, [2]Anesthesiology and Intensive Operative Medicine, University Hospital Mannheim, D-68135 Mannheim, Germany.

Email: labeit@embl-heidelberg.de

INTRODUCTION

The giant elastic protein titin is found in vertebrate muscle, where it spans the half-sarcomere and integrates into the Z-disc and M-line through the N-and C-terminus, respectively.

Titin has been proposed to function as a molecular ruler and as a scaffold for several sarcomeric proteins, including alpha-actinin, myosin, C-protein, T-cap, myomesin, and MURF-1 (Granzier and Labeit, 2002).

Its subdomains perform distinct functions (Gregorio et al., 1999). The N-terminus appears to regulate the assembly of the Z-disc. Titin's I-band region is responsible for the elastic response of the sarcomere. A-band titin has been proposed to serve as a molecular scaffold to coordinate the proper assembly of the thick filament. Titin's c-terminus integrates into the M-line lattice and contains a serine/threonine kinase domain, which shares homology with the catalytic serine/threonine kinase domain of smooth muscle myosin light chain kinase (MLCK). This domain is conserved in evolution and present in titin- like proteins in C. elegans and Drosophila (Champagne et al., 2000) but no physiological catalytic function has yet been shown.

RESULTS AND DISCUSSION

To investigate the importance of this domain for muscle development, sarcomere stability and function, we have used gene targeting and the cre/lox recombination system to create knockout mice, which can be induced to express titin molecules deficient in the kinase domain. Tissue specific expression of the Cre recombinase has enabled the generation of heart- and striated muscle specific knockout animals.

In heart the kinase domain knockout interferes with embryonic development, while the striated muscle knockout animals survive to term but develop progressive myopathy and die at 5 weeks of age. Morphological and expression profiling analysis suggests that the kinase domain is essential to preserve sarcomere structure, but dispensable to elicit the hypertrophic gene response.

SUMMARY

Our results define a critical role for the titin kinase region in maintaining the structural integrity of the sarcomere. We have generated an animal model in which the role of titin and its binding partners in human disease can be explored, as well as titin's proposed role in stretch-dependent signaling.

REFERENCES

Granzier, H. and Labeit, S. (2002). *J. Phys.*, in press.
Gregorio, et al. (1999). *Curr. Opin. Cell Biol.* 11, 18-25
Champagne, et al. (2000) *J. Mol. Biol.* 4, 759-77

NEW APPROACHES TO INTEGRATING MUSCLE FUNCTION AND DESIGN FROM MOLECULAR BIOPHYSICS TO WHOLE-ANIMAL

Lawrence C. Rome*

Department of Biology, University of Pennsylvania, Philadelphia PA 19104 &
The Marine Biological Laboratory, Woods Hole MA 02543
*Email: lrome@sas.upenn.edu

Muscle must perform mechanical work over a wide range of speeds to pump blood, power locomotion, or produce sound energy. My laboratory has been trying to understand how muscular systems are modified for their function. Two central concepts dictate that our experimental approaches must be integrative. First, one cannot understand how a muscle is designed without knowing exactly what it does during normal behavior and second, many of the modifications of muscle for different motor activities take place at the molecular level. Hence our long-standing goal has been to understand, from the level of molecular biophysics to whole-animal biomechanics, how muscular systems are designed to power different movements. This goal has only become feasible recently, because of a technological revolution in two areas: biophysics and musculoskeletal modelling.

The development of new biophysical technologies (e.g., Ca^{2+}-sensitive dyes, caged compounds, single fiber energetics and mechanics) has enabled us, for the first time, to measure the kinetics of pertinent molecular processes of muscle contraction and relaxation. For instance, by using these technologies on the muscles of toadfish, whose twitch speed varies over 50-fold, we (Rome et al 1996, 1999) have been able to demonstrate that 3 modifications are necessary to increase the rate of relaxation: First, the Ca^{2+} transient duration must be sped up, and this is achieved by having many SR-Ca^{2+} pumps and a high concentration of the Ca^{2+}-binding protein, parvalbumin. Second, Ca^{2+} must come off troponin, soon after the fall of myoplasmic Ca^{2+}, and this is achieved by a low affinity troponin which is endowed with a fast Ca^{2+} off-rate. Finally, there must be a modification of the myosin to provide a fast cross-bridge detachment rate constant, ***g***. We found that the super-fast swimbladder muscle which is used to produce a mating call at 200 Hz has the fastest Ca^{2+} transient, the lowest affinity force- [Ca^{2+}] relationship, and by far the fastest ***g***.
However, there is a cost for speed: the superfast ***g*** is accompanied with only a normal attachment rate constant, ***f***. Thus in the steady state, only a small fraction of the cross-bridges are attached at any one time and hence the force generated by the swimbladder muscle is only about 1/10 that generated by locomotory muscles. This trade-off of force for speed (Rome et al. 1999) results in mutually exclusive designs (Young & Rome, 2001): The superfast sound producing muscles generate too little force for powering locomotion, while the locomotory muscles relax too slowly for powering sound production. These biophysical approaches are very powerful and will soon lead to a mechanistic model of muscle contraction that is based on principles of chemical kinetics.

An ultimate goal of this integrative approach is to understand enough about the molecular and macroscopic components of muscular systems, so that we can develop the first comprehensive model that enables us to predict and understand how alterations in one molecular parameter (e.g., ***g***) might affect whole animal motor performance. For this goal, we are using frogs because their muscle length changes and overall body mechanics during jumps are relatively easily quantified. Previously, by examining the length changes and stimulation pattern of the semimembranosous (a hip extensor), we were able to show that this muscle is designed to generate maximum power during jumping (Lutz & Rome, 1994).

Still, a significant obstacle to integrating from muscle function to locomotion is that the musculoskeletal system of any animal is complex. Frog hindlimbs have in excess of 15 muscles that contribute to overall performance, and these muscles may perform different types of contractions. Thus it is difficult to appreciate and predict whole animal movements from the mechanics of a single (or even several) muscles. Musculoskeletal modeling can be an enormous help by keeping track of the forces generated by multiple muscles, so that the net action of all the muscles can be determined.

My laboratory has recently constructed a realistic skeletal model of jumping frogs containing the bones, joints, masses and moments of inertia of body segments (Kargo et al. 2002). The power of this overall approach is that we can alter components of the muscular system and test how this alteration affects the frog's ability to jump. For instance, by varying the joint degrees of freedom in the model and applying realistic torques around the joints, forward dynamic simulations enabled us to test hypotheses about how the skeletal system of frogs is modified for jumping (i.e., frog has extra joints and extra joint degrees of freedom than humans). As modeling progresses, we will add the muscles (their mass, fiber orientation, placement of the origin and insertion and physiological properties). We will then be able to turn the muscles on in their measured sequence (i.e., EMGs) and the virtual forces and torques will make the frog move. The addition of a molecular model of muscle will then provide us with an unprecedented ability to test how changes in single amino acids of myofibrillar proteins might alter jumping performance. The interactive nature of this model will also make it an excellent platform for teaching biomechanics.

References

Kargo, W.J. et al (2002) *J.Exp.Biol.* In Press.
Lutz G.J., Rome L.C.(1994) *Science* 263, 370-372.
Rome, L.C. et al. (1999) *Proc.Natl.Acad.Sci.* 96, 5826-5831.
Rome, L.C. et al. (1996) *Proc.Natl.Acad.Sci.* 93, 8095-8100.
Rome, L.C. (2002) *Clin. Ortho.Rel. Res.* In Press.
Young I.S., Rome, L.C. (2001) *Proc.Roy.Soc.B.* 268, 1975-1980.

MOLECULAR MECHANISMS FOR DEVELOPMENT OF TENDINITIS

James H-C. Wang, Ph.D., Guoguang Yang, M.S., David Stone, M.D., Savio L-Y. Woo, Ph.D., Zhaozhu Li, M.D.

Musculoskeletal Research Center, Department of Orthopaedic Surgery
University of Pittsburgh, P.O. Box 71199, Pittsburgh, PA 15213
412-648-9102, 412-648-2001 (FAX), Wanghc@pitt.edu

Tendinitis affects millions of people both in the workplace and athletic settings in the United States. The etiology of tendinitis is largely unknown, but it is believed to result from excessive repetitive mechanical loading of tendons, which results in tendon inflammation and degeneration. However, because of the lack of a reliable experimental model, the cellular and molecular mechanisms responsible for the development of tendinitis remain unclear.

We hypothesize that tendon fibroblasts are responsible for the development of tendinitis by producing high levels of PGE_2 and LTB_4, which are regulated by increased expression levels of PLA_2, COX and 5-LO. To test this hypothesis, we have developed a novel model system to study inflammatory responses of human tendon fibroblasts, thereby elucidating developmental mechanisms for tendinitis at the molecular level. The model system consists of a stretching apparatus (**Fig. 1A**) silicone dishes to grow and stretching tendon fibroblasts. A unique feature of this system is that the silicone dishes contain microgrooved surfaces instead of commonly used smooth culture surfaces (**Fig. 1B**). We have shown that the alignment, shape and mechanical loading conditions of the human patellar tendon fibroblasts (HPTFs) in this model system are similar to those *in vivo* (**Fig. 2**).

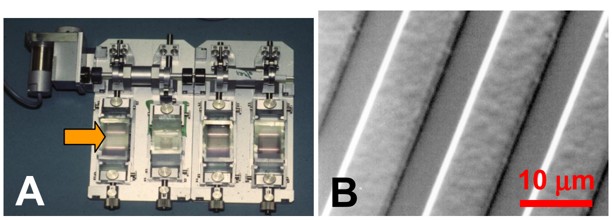

Fig. 1 A model system to study molecular mechanisms for tendinitis.

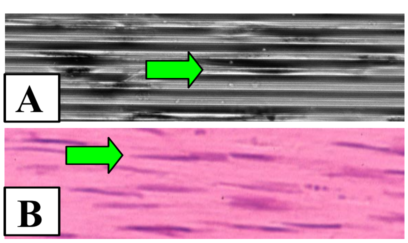

Fig. 2 Tendon fibroblasts in microgrooves are elongated and aligned under cyclic uniaxial stretching, which is similar to the cells *in vivo* (H&E staining). Note that arrows point the fibroblasts in the microgrooves (**A**) and tendon (**B**).

Using the novel model system, we have studied the production of PGE_2 by HPTFs in response to cyclic mechanical stretching. It was found that cyclic stretching of the tendon fibroblasts induces high levels of PGE_2 in a stretching-magnitude dependent manner. We have also found that cyclic stretching of HPTFs increases expression levels of COX and PLA_2, which mediate synthesis of PGE_2. Cyclic stretching was also found to induce high levels of LTB_4 production and expression of 5-LO, the enzyme that mediates cellular production of LTB_4. In addition, inhibiting COX with indomethacin to block PGE_2 production further increases LTB_4 production by stretched tendon fibroblasts, suggesting that cellular production of PGE_2 is related to that of LTB_4.

In future, the effect of cyclic mechanical stretching on the expression of other inflammatory genes (e.g., IL-1, IL-6 and TNFα) will be investigated using our model system. Further, with an multidisciplinary approach based on mechanobiology, molecular biology, and biomechanics, the effect of stretching-induced PGE_2 and LTB_4 on the biological, biochemical and biomechanical properties of the tendon will be evaluated on an animal model.

REFERENCES

1. Almekinders LC., Banes AJ., Ballenger CA. 1993. Effects of repetitive motion on human fibroblasts. Medicine & Science in Sports & Exercise. 25:603-7.
2. Archambault JM., Wiley JP., Bray RC. 1995. Exercise loading of tendons and the development of overuse injuries. A review of current literature. [Review]. Sports Medicine. 20(2):77-89.
3. Banes AJ. Horesovsky G. Larson C. et al., Tsuzaki M. et al., 1999. Mechanical load stimulates expression of novel genes *in vivo* and *in vitro* in avian flexor tendon cells. Osteoarthritis & Cartilage. 7(1):141-53.
4. Wang JH-C., Stone D., Jia F., Woo SL-Y. 2001. Cyclic stretching of human tendon fibroblasts induces high levels of prostaglandin E2, *ORS Conference 2001* (Abstract).

ACKNOWLEDGEMENT

The studies are supported in part by the Whitaker Biomedical Engineering Grant, Arthritis Investigator Award and NIH AR 47372-01 (JHCW).

COMPUTATIONAL SIMULATION OF TREATMENTS USED FOR PATELLOFEMORAL PAIN AND INSTABIITY

John J. Elias[1] and Andrew J. Cosgarea[2]

[1]Biomechanics Laboratory, Medical Education and Research Institute of Colorado, Colorado Springs, CO, elias@meric.info
[2]Department of Orthopaedic Surgery, Johns Hopkins University, Baltimore, MD

INTRODUCTION

Lateral patellar instability and anterior knee pain are often attributed to a large Q-angle. The lateral component of the resultant force applied to the patella by the quadriceps muscle group and the patella tendon increases as the Q-angle increases. Surgical and non-surgical treatment methods are used to reduce the lateral force acting on the patella. Computational simulation can be used to evaluate how these treatment methods influence the patellofemoral contact pressure distribution. For this study, two treatment methods were evaluated: surgical medialization of tibial tubercle to reduce the Q-angle and vastus medialis strengthening to decrease the lateral force acting on the patella.

METHODS

A surface model of a knee was created using CT data from the Visible Human Male (National Library of Medicine). Origin, insertion and wrapping points were identified for the vastus medialis, vastus intermedius, vastus lateralis, rectus femoris, and patella tendon. The tibia was flexed about the femur to model a dual limb knee squat. The patella was flexed, and aligned with the femur by aligning the posterior patella with a parallel surface within the trochlea. The quadriceps force was divided among the four muscles (Ahmed, 1983). At each flexion angle, the quadriceps muscles created a knee moment representing a dual limb knee squat (Cohen, 2001). The patella tendon force was determined based on the quadriceps force and the flexion angle (Huberti, 1984). For these input forces, the patellofemoral pressure distribution was quantified using the discrete element analysis technique (Elias, 2002). Surgical variation of the Q-angle was modeled by shifting the patella tendon attachment point on the tibia in the medial/lateral direction. Vastus medialis strengthening was modeled by increasing the percentage of the quadriceps force applied by the vastus medialis by 50%.

RESULTS AND DISCUSSION

The lateral component of the force acting on the patella, the total force applied to the lateral cartilage and the area of cartilage subjected to more than 4 MPa of pressure all increased with the flexion angle. The peak lateral contact pressure was larger than the peak medial contact pressure, with relatively little variation in the peak lateral contact pressure from 70º to 90º of flexion (Fig. 1). At 90º of flexion, the lateral force acting on the patella, the total force applied to the lateral cartilage, and the area of cartilage subjected to more than 4 MPa of pressure decreased by 10%, 5%, and 13%, respectively, as the Q-angle decreased from 25º to 10º. The maximum lateral pressure did not decrease with the Q-angle (Fig. 2). Medializing the tibial tubercle increased the moment acting to rotate the distal pole of the patella medially, offsetting the expected peak pressure decrease due to a lateral force decrease.

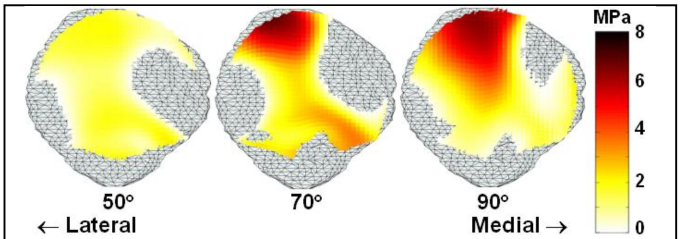

Fig. 1: Variation in the patellofemoral contact pressure distribution during flexion.

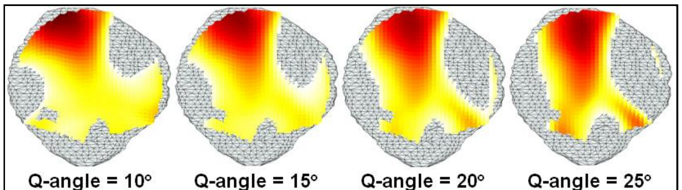

Fig. 2: Influence of the Q-angle on the patellofemoral contact pressure distribution at 80° of flexion.

Increasing the vastus medialis force decreased the lateral component of force acting on the patella and the total force acting on the lateral cartilage, but increased the peak pressure by approximately 4% for the four Q-angles. The peak pressure increased despite the decrease in the lateral force due to the increased medial rotation moment caused by the increased vastus medialis force.

SUMMARY

Although both vastus medialis strengthening and surgical medialization of the tibial tubercle reduced the force tending to sublux the patella laterally and the total force acting on the lateral cartilage, the peak pressures did not decrease due to the moments acting on the patella. This study shows that computational modeling may help surgeons get a better understanding of how prescribed treatments influence the patellofemoral contact pressure distribution.

REFERENCES

Ahmed, A.M., et al (1983). *J Biomech Eng*, **105**, 226-236.
Cohen, Z.A., et al (2001). *Am J Sports Med*, **29**, 480-487.
Huberti, H.H., et al (1984). *J Orthop Res*, **2**, 49-54.
Elias, J.J., et al (2002). *Transactions of ORS '02*, 896.

ACKNOWLEDGEMENTS

Funding was provided by a research grant from the Whitaker Foundation.

SINGLE MOLECULE MECHANICS AND THE MYOSIN FAMILY OF MOLECULAR MOTORS

James A. Spudich, William Shih, Coleen Murphy, Amit Mehta, Ron Rock, Sarah Rice, Tom Purcell and Matthias Rief.

Stanford University School of Medicine, Stanford, CA 94305.

Employing a combination of biophysical, biochemical and biological approaches, we have examined the role of myosin, actin, and associated regulatory proteins in these processes. Our focus has been on how the myosin family of molecular motors work and the roles that they play *in vivo*. This has involved the development of *in vitro* motility assays, whereby individual filaments of actin move along purified myosin molecules in an ATP-dependent manner, as well as single molecule analyses using laser trapping.

It has been hypothesized that the molecular motor myosin acts by binding to actin and swinging its light-chain binding region through a large angle to provide a ~10-nm step in motion coupled to changes in the nucleotide state at the active site. Direct dynamic measurements to date, however, have largely failed to reveal changes of that magnitude. We used a cysteine engineering approach to create a high-resolution FRET-based sensor that reports a very large ~70-degree nucleotide dependent angle change of the light-chain binding region. The combination of steady-state and time-resolved (with Zygmunt Gryczynski and Joseph Lakowicz, Univ Maryland) fluorescence resonance energy transfer measurements unexpectedly revealed two distinct prestroke states. The measurements also show that bound Mg.ADP.Pi, and not bound Mg.ATP, induces the myosin to adopt the prestroke states.

It is thought that Switch II of myosin, kinesin and G-proteins plays a critical role in relating the nucleotide state to the protein conformation. We examined S456L myosin-II from *Dictyostelium*, a mutant of the Switch II region, whose mechanical activity is uncoupled from the chemical energy of ATP hydrolysis so that actin filament gliding velocities are only one-tenth that of wild type. The mutant myosin exhibits an extended strongly-bound state time and a shorter step size, which together account for the decrease in *in vitro* velocity.

Myosin-V and myosin-VI are quite different from myosin-II and also different from one another. We showed that these motors move processively along their actin tracks. With Mark Mooseker (Yale), Richard Cheney (Univ North Carolina), and Lee Sweeney (Univ Pennsylvania) we employed a feedback-enhanced optical trap to examine the stepping kinetics of these movements. By analyzing the distribution of time periods separating discrete ~36 nm mechanical steps for myosin-V, we characterized the number and duration of rate-limiting biochemical transitions preceding each such step. Based on this, we propose a model for myosin-V processivity involving a tightly coupled motor whose cycle time is limited by ADP release.

HEMODYNAMICS AND ATHEROSCLEROSIS: ARTERIES TO CELLS, AND BACK AGAIN

Don P. Giddens

Wallace H. Coulter Department of Biomedical Engineering
Georgia Institute of Technology and Emory University, Atlanta, GA 30332-0536, USA

Hemodynamics has attracted biomechanics investigators for decades. Early studies made simplifying assumptions, since neither experimental methods nor mathematical/computing tools were sufficiently advanced to allow accurate modeling of actual blood vessels. The simplest approximation, Hagen-Poiseuille flow, was followed by oscillatory (Womersley) flow in a long tube. Gradually, more sophisticated modeling was performed, both computationally and in the laboratory, and flow through stenoses and idealized branches and bifurcations – first with steady and then pulsatile flow – led to a deeper understanding of phenomena that might be relevant to blood flow in real arteries. Gradually, the assumptions of vessel rigidity, Newtonian fluids and idealized geometries have been relaxed as fluid dynamicists tackled increasingly more complex, and relevant, issues. These studies have resulted in a much clearer view of the relative importance of simplifying assumptions and, importantly, when these assumptions can and cannot be made.

Currently, it is possible to perform experiments in laboratory models in which fluid velocity and wall shear are measured using optical techniques in fairly realistic geometric models that mimic the shape and motion of individual vessels. A completely realistic representation of blood is still elusive, not so much due to an inability to employ fluids that model viscoelastic behavior as determined in rheological measurements, but because non-Newtonian blood viscosity results largely from the formation of RBC rouleaux – and the characteristic time for cells to form rouleaux under a given shear condition is different than that for breaking these down.

As hemodynamic modeling advanced, knowledge gained was "correlated" with biological observations. In the case of localization of early atherosclerotic plaques, a number of laboratories produced evidence that not only were plaques localized in curves, branches and bifurcations of arteries, but more specifically these were localized at sites where the fluid dynamic wall shear stress was low – often below 5 dynes/cm^2. Usually, these locations also corresponded to oscillations in wall shear during the pulsatile cycle. This observation was particularly evident in the human carotid bifurcation where early plaques invariably develop along the outer wall of the carotid sinus rather than at the flow divider itself, although there is also clear evidence of this association in other arteries. Thus, two decades of research by biofluid dynamicists posed – and settled – the issue of "low shear" versus "high shear" as participating in atherogenesis. It is worth adding that this knowledge is still not pervasive in the "rank and file" of physicians, some of whom still attribute atherosclerotic plaque localization to turbulence and high shear stress.

Recognizing that correlations are often not the same as mechanisms, studies of the effects of fluid dynamics on cellular behavior began to abound, spurred both by the realization that mechanical factors could affect cell function and by new knowledge and tools in cellular and molecular biology. Endothelial cells, in particular, were of great interest; and a body of knowledge gradually developed that showed fluid dynamic effects on cell shape, migration, signaling and molecular and genetic expression. Literally thousands of papers have been published and presented dealing with various – and increasingly detailed – observations of mechanical effects on endothelial cells. How much of this information is relevant to human pathophysiology in general, and to atherogenesis in particular, is still being sorted out. Nonetheless, it is abundantly clear that there is a strong interplay between the local hemodynamic environment in the vicinity of a cell and the structure and function of that cell.

Thus, hemodynamics has provided insight into the pathophysiology of the artery, and it is being used commonly as a tool to probe the molecular biology of cells. Perhaps now is the time for hemodynamics to return to the arteries – and specifically to the arteries of individual human subjects.

Fortunately, our investigative tools are now permitting this. With MRI, for example, we can obtain geometry and flow conditions in individual human vessels, albeit with difficulties in accuracy and resolution. Our computational tools allow description of pulsatile, 3D flows in hours rather than weeks, and our ability to transfer image data to a rapid prototyping device for constructing realistic arterial models is becoming extremely useful. Simultaneously, molecular biology tools that use very small tissue samples to measure infinitesimal amounts of cellular material are giving us "biological" spatial resolution comparable to our computational resolution. Ultimately, noninvasive imaging technology may be able to supplant harvesting tissue samples.

Thus, there is now the potential for a convergence of computing technology, experimental methodology, imaging and molecular biology that may enable us to return to the artery in order to unravel the mystery of atherosclerosis. Perhaps a decade from now we will be able to define specific mechanisms through which vessels remodel, arteries develop plaques and bypass grafts fail.

CELL STRUCTURE AND FUNCTION: PLENTY OF ROOM FOR BIOMECHANICS

Jean-Jacques Meister

Cellular Biophysics and Biomechanics Laboratory,
Swiss Federal Institute of Technology, Lausanne, Switzerland
e-mail: Jean-Jacques.Meister@epfl.ch

INTRODUCTION

Most of the functions performed by cells ultimately involve internal forces, deformations and movements as well as mechanical interactions between the cell and its environment. Moreover, cells are constantly exposed to external forces which may modify their structure, shape and functions.

The rapid growth of molecular and cellular biomechanics is mainly driven by novel experimental techniques, which allow manipulation of single molecules and subcellular components, to measure piconewton forces or nanometer displacements and to dynamically image cell elements. Added to theoretical models, these experimental results allow determination of the mechanical properties of cells and cell components, to understand the building and remodelling of cell structures, to describe the role played by mechanics in cell functions like motility, adhesion or division and to analyze cellular mechanisms of external force sensing and transmission.

This information is of utmost importance to understand the relationship between mechanical forces and cellular functions, to advance techniques in molecular and cellular engineering as well as to design engineered tissues and organs.

BIOMECHANICS AT THE WHOLE CELL LEVEL

The information gained by stressing and deforming a whole cell is twofold. First, mechanical properties and constitutive laws of the cell may be obtained by applying a theoretical model of its principal components (nucleus, cytoskeleton) to the experimental results. Second, the mechanisms involved in the sensing of external forces, in force transmission into the cell as well as its consequences in terms of structural and functional changes of the cell may be studied. Recent results showed for instance that the nucleus is deformed under a deformation of the cell substrate, that the cytoskeleton is remodelled under external stretch or stress and that the constitutive law of the cell is strongly influenced by the ability of the cytoskeleton to deform, flow and reorganize.

MECHANICS OF CELL COMPONENTS

The cell is a complicated structure built with elements of very diverse materials. The knowledge of the mechanical properties of its different components is necessary to predict cell behavior and to analyze the interactions between components. This challenging task has already started. At the level of a single molecule for instance, force-deformation curves of a DNA molecule, obtained by using an optical trap or an atomic force microscope, has revealed conformational transitions from 50 to 150 pN and unzipping around 20 pN. At the level of the nucleus, its elastic modulus (about 5 kN/m^2) has been measured by the compression of a single nucleus between two microplates. Other nice works were performed on isolated cytoskeleton filaments, e.g. measurement of the force-velocity relation of growing microtubules. The cytoskeleton is a three-dimensional deformable dynamic scaffold made of different filaments. There is still a challenge to measure the mechanical properties of the different organizations of this scaffold as well as to build a theoretical model (tensegrity, glassy material) describing the mechanisms of force transmission from the cell membrane to the nucleus and cytoskeleton remodelling.

INTRACELLULAR FORCES AND MOVEMENTS

Different functions of the cell involve internal forces, deformations and movements, which have to be analyzed: the transport of different cargos along microtubules, the deformation of contractile cells like hair and muscle cells, the motion of chromosomes during cell division (mitosis), etc. As an example, the recent real time imaging of molecules transported within chemosensory neurons of C-elegans address interesting questions in biomechanics: mechanisms of transport, relationship between frequency of transport events and chemotaxis, forces and energy involved in this transport, link between characteristics of transport and locomotor response, etc.

CELL MOTILITY

Cell locomotion usually requires active protrusion, adhesion and retraction. The protrusion and the retraction are created by a profound structural and geometrical modification of the cytoskeleton, mainly created by actin polymerization and actin-myosin II contraction, respectively. The knowledge of the mechanical properties of the cytoskeleton during cell locomotion is fundamental to understand the resulting production of coordinated protrusive and contractile forces. Focal adhesions serve as points of traction over which the cell moves. Biomechanics may help to determine the cell-substratum force and to understand the mechanisms that regulate the formation of points of adhesion at the cell front and their release at the rear.

STRUCTURE-FUNCTION RELATIONSHIPS

The ultimate goal of molecular and cellular biomechanics is to identify the relationships between cell shape, structure, mechanical properties and functions. This knowledge is essential to better understand cell physiology during cell growth, cell division, cell motility and signal transduction, as well as cellular pathologies like inflammation, changes of phenotype and cell death.

FUNCTIONAL ADAPTATION AND REMODELING OF BIOLOGICAL SOFT TISSUES

Kozaburo Hayashi
Biomechanics Laboratory, Division of Mechanical Science, Graduate School of Engineering Science
Osaka University, Toyonaka, Osaka 560-8531, Japan, hayashi@me.es.osaka-u.ac.jp

INTRODUCTION

There are many evidences indicating that living organs, bio-logical tissues, and cells are skillfully and optimally designed, and remodel functionally adapting themselves to stress and force. The ability of remodeling and functional adaptation is characteristic of living systems. This lecture deals with a part of our studies on the biomechanical and morphological responses of such biological soft tissues as tendon/ligament and vascular wall to stress and force. The knowledge of these phenomena should contribute much not only to better understanding of basic biology and physiology as well as the improvement of practical medicine but also to the development of new areas in mechanical design and engineering.

EFFECTS OF STRESS ON THE BIOMECHANICAL PROPERTIES OF TENDONS AND LIGAMENTS

Effects of stress deprivation, resumption of stress after stress deprivation, and stress enhancement on the mechanical proper-ties and dimensions of the patellar tendon (PT) were experi-mentally studied in the rabbit.

A newly developed stress shielding technique was directly applied to the PT for completely releasing stress (complete stress shielding) or partially reducing stress (partial stress shielding, 70% reduction from normal). Both stress shielding very rapidly and markedly decreased the material strength of the PT. The structural strength (load at break) was also much decreased by complete stress shielding; however, it was kept at control level in the case of partial stress shielding. Essentially similar phenomena were observed in the canine anterior cruciate ligament, and also in the rabbit frozen PT for a graft model.

To know the roles of substructural components, the mechanical properties of collagen fascicles (300 μm in diameter) and collagen fiber (1 μm) obtained from the stress-shielded rabbit PT were studied. Stress shielding significantly decreased the tangent modulus and tensile strength of collagen fascicles; however, these changes were smaller than those observed in bulk tendons. There were no changes in the mechanical prop-erties of collagen fibers. These results indicate that ground substances and mechanical interaction between collagen fibers have important roles in the remodeling of tendons and ligaments.

Stress resumption induced after complete stress shielding gradually recovered tendon strength, although the strength did not return to control level. Overstressing to 133 % of normal stress (33 % overstressing), that was induced by removing the medial and lateral one-eighth width of the PT, did not change the material strength, but increased the structural strength to that of the whole intact tendon due to the increase in the cross-sectional area. In the case of 100 % overstressing, which was induced by removing the medial and lateral one-fourth, strength increased in some tendons but decreased in others.

These results indicate that tendons and ligaments have the ability of adapting themselves to stress changes, although the adaptation does not occur if stress exceeds an allowable range.

RESPONSE OF CULTURED COLLAGEN FASCICLES TO STRESS

To obtain information on the mechanisms of the remodeling of tendons and ligaments, stress effects on the mechanical prop-erties of collagen fascicles were studied using in vitro tissue culture methods. Collagen fascicles obtained from the rabbit PT were cultured under static (24 hours per day) or cyclic (4 Hz, 1 hour per day) stress for 1 and 2 weeks. In each case, a parabolic relation was observed between applied stress and tensile strength. The tensile strength and tangent modulus of the fascicles cultured under zero stress were 50 % of each control level. They were maximal at the applied stresses that are equivalent to 50 and 100 % of the in vivo peak stress in the intact PT in the static and cyclic cases, respectively. Smaller and larger applied stresses than these stresses deteriorate the mechanical properties. The maximum strength and modulus were at control levels in both cases. Thus, cultured collagen fascicles also have an ability of mechanical and structural adaptation to stress.

VASCULAR WALL REMODELING DEVELOPED BY BLOOD PRESSURE AND BLOOD FLOW CHANGES

Biomechanical responses of the common carotid artery to hypertension (HT), low and high blood flow (BF), and the combinations of HT with these BF changes were studied in the rat. Wall thickness was larger in HT animals than in normo-tensive ones; due to the wall hypertrophy, wall circumferential stress was kept at control level. Except for the case of the combination of HT with low BF, the inner diameter of wall was decreased by low BF, and increased by high BF, which kept wall shear stress at control level. Therefore, the arterial wall very well adapts itself to HT regardless of BF. Diameter response to a vasoconstrictor was larger in HT animals than in normotensive and control ones, which suggests that smooth muscle tone is enhanced by HT and it takes an important role in the wall remodeling. Wall properties including wall elasticity and diameter response were also adapted to HT regardless of BF changes, and rather normal properties were retained at high pressure range in HT animals. Essentially similar adaptation phenomenon to HT was also observed in the rabbit femoral vein.

THE NOVEL AERODYNAMICS OF INSECT FLIGHT: APPLICATIONS TO MICRO AIR VEHICLES

Charles Ellington

Department of Zoology, University of Cambridge, Cambridge, England
c.ellington@zoo.cam.ac.uk

The design of small flying machines can take inspiration from the insects and small vertebrate fliers (birds and bats). The flapping wings of these animals produce much greater forces than conventional wings, but the aerodynamic mechanisms responsible for these large forces have only been investigated for insects.

Some butterflies rely on pressure drag for vertical take-off and slow forward flight, and the lift contribution is small. It is ironic that a drag-based mechanism of flight is found for such large insects. It has been postulated that tiny insects, flying at very low Reynolds numbers (*Re*), must 'swim' through the air because viscosity should reduce their lift-to-drag ratios below unity. However, they rely instead on the lift of their wings, augmented by the fling mechanism, for weight support. Hoverflies, dragonflies and small vertebrates (except hummingbirds) hover with their flapping motion inclined to the horizontal by some 30 degrees. They use dynamic stall on the downstroke to support their weight, and the required lift-to-drag ratio is necessarily low: less than 2.

Most insects (and hummingbirds) hover with an approximately horizontal stroke plane, using lift on both the downstroke and upstroke to support their weight. Their flapping wings must typically produce 2-3 times more lift than can be achieved in steady motion. A leading-edge vortex (LEV) created by dynamic stall is responsible for most of the enhanced lift production. A strong spanwise flow is also generated by the pressure gradients on the flapping wings of medium and large insects, stabilising the LEV and causing it to spiral out to the wingtip. At the laminar *Re* appropriate to these insects, we have discovered that the spiral LEV can be maintained indefinitely on rotary wings. The vortex is therefore a steady 3-D rotary wing phenomenon, and not an unsteady flapping mechanism as previously thought. Force coefficients for steady propeller rotation are remarkably insensitive to *Re* and wing characteristics: camber, twist and leading-edge construction. The flow separation causes a loss of leading-edge suction, and the resultant aerodynamic force is approximately normal to the wing surface. The lift-to-drag ratio is therefore low, typically less than 2, at the angles of attack normally used.

For all of the high-force aerodynamic mechanisms employed by insects at laminar *Re*, an enhanced lift is only obtained at the expense of a large drag force and poor lift-to-drag ratios. These ratios are appallingly low for conventional aerodynamic designs, and would necessarily entail high power consumption and low aerodynamic efficiency for fixed and rotary wing flight systems. However, insects can incline their wing motion to take advantage of the high drag force, using the resultant aerodynamic force instead of just lift to support their weight. The mechanical power expended against wing drag is therefore incorporated in the induced power, greatly improving aerodynamic efficiency. For small flying machines to exploit the high-force aerodynamic mechanisms of insects to improve their lifting capacity with good efficiency, flapping flight with full control over the wing motion will be essential.

SKIING WITH CARVED SKIS: CHALLENGES ON PERFORMANCE AND SAFETY

Erich Müller, Hermann Schwameder, Christian Schiefermüller
Institute of Sport Science, University of Salzburg, Salzburg, Austria

INTRODUCTION

In recent years many dramatic changes have taken place in Alpine skiing. In ski racing as well as in recreational skiing skis have become much shorter, their side cut has increased to a great extent and binding plates (risers) have been fixed between the ski and the binding. In addition the stiffness of the ski has changed, too. This evolution has, of course, also changed the movement patterns of performing ski turns but might also have changed the risk of sustaining injuries. This paper will present the results of various projects dealing with these aspects.

CHALLENGES ON PERFORMANCE

Carving turn vs traditional turn

An excellent carving ski racer and former world cup ski racer performed 8 test runs on a well prepared piste with both carving (side cut radius: 14 m) and traditional giant slalom skis (side cut radius: 32 m). Kinematic analysis of the runs was done using 3 video cameras and the Peak 3D system. Ground reaction forces were measured by implementing bilateral mobile pedar insoles (Novel) into the boots of the subject. EMG data of 7 leg muscles were collected with the mobile biovision system.

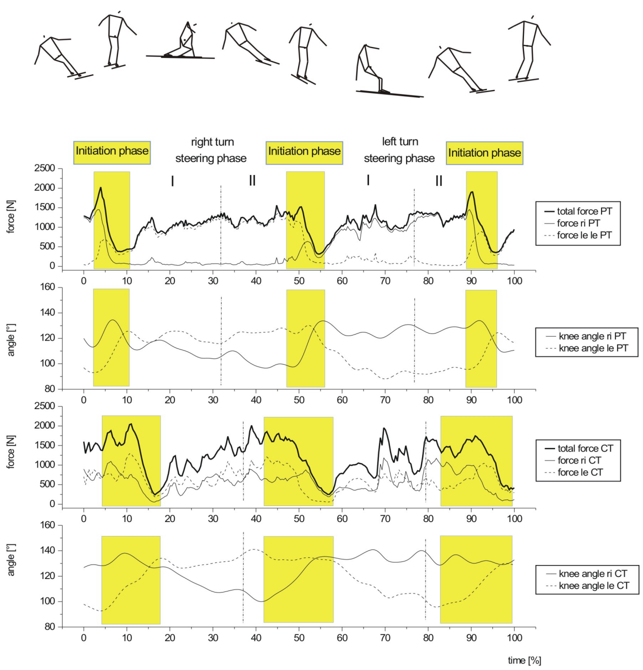

Fig. 1: Comparison between traditional parallel turns and carving turns

Turns with carving skis (CT) in comparison to traditional skis (PT) have higher inward leaning angles (50 – 55°), higher ski edging angles (65 – 70°), higher inside ski load during the steering phase with higher activities of the M. peroneus and M. tibialis anterior. Turns with carving skis demand obviously a better sagittal balance ability as well as an improved edge steering ability in order to be able to stay centrally positioned over the ski.

The influence of riser height on performance

Ski racers are convinced to be able to race faster using so called risers. So in a further project we had to prove this hypothesis and to try to find the mechanism which might increase the racer's performance. In a field test three different riser heights (0 cm, 1 cm, 2 cm) were used. The course was standardized by gates. 12 runs, using the different ski systems alternatively were performed by a world cup racer. The following parameters were measured: running time, ground reaction forces normal to the ski, anterior/posterior moments or lateral moments respectively. There was a significant decrease of the running time in dependence on the riser height. No significant differences for forces and moments could be found between the different riser heights analysing the whole turn. But if the turn is divided into a steering phase and a very short edge changing phase, the values of the steering phase remain nearly constant, whereas the values of the edge changing phase decrease significantly using higher risers. Therefore risers help to reduce running time as the edge changing can be managed in a shorter time period.

CHALLENGES ON SAFETY

Carving turns and risks of sustaining injuries.

The aim of skiing with carving skis is to perform turns with a small turning radius without any skidding. The turning radius depends on the side cut radius of the ski, the edging angle and the stiffness of the ski and the piste. The smaller the turning radius and the higher the speed the bigger becomes the skier's load. Skiing turns with small radii on high speed might exceed the skier's physiological capacity soon. The use of carving skis with binding plates also increases the probability of catching an edge. The higher the risers between the ski and the binding the smaller edging angle is needed to initiate the catching of an edge and due to the smaller side cut radius of the ski the distance of the lateral deviation from the intended skiing direction becomes too big within a short period of time and therefore makes a successful correction movement impossible. The binding plates are also considered to increase the acting moments in the knee due to the lenthening of the lever arms of the lower leg. As a consequence of these findings the F.I.S limited the maximum standing position for ski racing.

References: Müller, E., Lindinger, S., Raschner, C., Schwameder, H., Kornexl, E., (2001), Science and Skiing II, Kovac, Hamburg

THE ENGINEERING OF VASCULAR SUBSTITUTES

Robert M. Nerem

Georgia Tech/Emory Center for the Engineering of Living Tissues
Petit Institute for Bioengineering and Bioscience
Atlanta, GA 30332-0363, U.S.A.

The engineering of a blood vessel substitute has for a quarter of a century been a "holy grail" within the cardiovascular research community. There is no more important example of the role of biomechanics in all of tissue engineering than that of a blood vessel substitute. Although for some tissues there has been frequently too little attention paid to what today is termed "functional tissue engineering" and in particular to the role of mechanics, the engineering of functional tissue substitutes has in a sense always been the goal of those engaged in tissue engineering.

To address the challenges posed by this "holy grail," a number of concepts are being pursued. These range from acellular approaches to cell-seeded scaffolds and include the use of collagen-based, polymeric, and cell-secreted materials. As important as the various approaches and contributions have been, each of the currently available concepts falls short in achieving at least one of the important, functional characteristics. So what are these desirable characteristics?

To start with, a primary failure mode of small diameter blood vessel substitutes made from synthetic materials is thrombotic closure. Thus, a critical, issue is to provide for non-thrombogenicity. This suggests having an endothelium, or at least an "endothelial-like" cell layer. Such an interfacial, cellular monolayer should be adherent, confluent, and biologically non-activated. In all of these, there is a role of biomechanics. In this a key issue is the identification of a source for the endothelial cells to be used. Are these to be autologous, perhaps recruited from surrounding vessels or obtained either from adipose tissue or from circulating endothelial cells? Or is one's strategy to be the employment of allogeneic endothelial cells in which case the engineering of immune acceptance will be critical? Long term stem cell technology offers considerable potential. Whatever the case, the functional characteristics including how the cells respond to mechanical forces will be important. Although vascular endothelial cells have been studied extensively in this regard, little is yet known about the effects of mechanical stimuli on circulating endothelial cells and stem cells.

If one seeks to engineer a blood vessel substitute which mimics the complete functionality of a native artery, vasoactivity is a desired functional characteristic. The vascular smooth muscle cell (SMC), the natural neighbor of the endothelial cell is responsible for generating the contractile force necessary to change vessel dimensions. For such vasoactivity to be exhibited, the vascular smooth muscle cell must exist in the appropriate contractile phenotype. In addition, these cells must be oriented in a circumferential direction within the blood vessel wall. Finally, as noted earlier, vascular SMCs are the natural neighbors to the endothelial cells. As such, another important role for SMCs may be to provide through their presence a more natural environment for the endothelial cells. In doing so, if patency is enhanced, then this may be even more important, than providing for vasoactivity.

There are at least two important mechanical properties for a blood vessel substitute. The first and most basic of these is ultimate strength, frequently denoted simply as burst pressure. For native arteries this is in excess of 2000 mm Hg, and several of the tissue engineering approaches have resulted in burst pressures on this order. A second, potentially very important characteristic has been more difficult to achieve. This is to engineer into a construct a viscoelasticity that matches that of native vessels. The various tissue engineering approaches pursued to date have resulted in constructs with a very limited amount of elastin; thus, a critical problem has been the incorporation of elastin into the wall of the construct.

When a tissue-engineered blood vessel substitute is implanted, there is an integration into the host system which takes place, and associated with this there will be a remodeling. Thus, six months after implantation the characteristics of the blood vessel substitute should not be expected to be the same as those exhibited at the time of surgery. There also is a remodeling, however, which can be induced prior to implantation as part of the process used to grow the tissue. Thus, the in vitro environment can be used to advantage in engineering the remodeling of the tissue substitute. In this it will be critical to understand how biomechanical stimulation can be used and how the biology and the biomechanics integrate with one another in the remodeling which takes place.

Taking all the relevant issues together, we are still a decade away from having an FDA approved, tissue-engineered blood vessel substitute. Of course, not all of the issues are ones related to biomechanics; however, the biomechanical ones are of real significance and thus are deserving of the attention of the entire cardiovascular tissue engineering research community.

MECHANICAL ADAPTATION OF BONE MASS AND ARCHITECTURE: TOWARDS A UNIFIED THEORY

Rik Huiskes & Ronald Ruimerman
Dept. Biomedical Engineering, Eindhoven University of Technology, The Netherlands, r.huiskes@tue.nl

After the cartilaginous bone tissue has mineralized in the embryo, the tissue is modeled to bone by invading bone-forming osteoblasts and bone-resorbing osteoclasts. This *modeling* process continues during growth, producing trabecular patterns that seem mechanically optimized in density and directionality, relative to the external forces. In maturity, the trabeculae are continuously *remodeled* through resorption and apposition of bone tissue at free surfaces, repairing micro-cracks, while maintaining structural optimality relative to external loads. Later in life trabecular number and thickness gradually decrease, when musculo-skeletal activities reduce. So still, the relationship between structure and mechanical loading seems to be maintained. The lasting association between quality and its mechanical demands is a great evolutionary asset, but it also has negative side effects in the increase of fracture risk in the elderly through osteoporosis, and bone resorption around orthopaedic implants through abnormal load transfer (stress shielding.)

We developed and validated an empiric theory to predict periprosthetic bone-density changes due to 'stress shielding', assuming them to be coupled to post-operative changes in the local strain-energy density (SED) [1-6]. We used a similar theory to explain density distributions in the proximal femur as adapted to natural load transfer [7]. Although realistic, the results were mathematically invalid due to trabeculation of the FEA mesh, where it was formulated as a continuum. The solution was a separation of actor and sensor functions: osteocytes within the bone trabeculae were assumed as SED sensors, signaling Basic Multicellular Units (BMU's) of osteoclasts and osteoblasts at trabecular surfaces to add or remove net bone mass [8,9]. This alternative theory explained alignment of trabecular structure to the external loads (modeling) and re-alignment for alternative loads (adaptation).

We have now refined and unified the theory to include the separate activities of osteoclasts and osteoblasts in both *modeling* and *remodeling* of trabecular structure [10,11]. We use dynamic loading variables (SED-rate) which activate osteocytes in the bone matrix to transfer osteoblastic bone-formation stimuli to trabecular surfaces, through the canalicular network. The stimulus received at the surface depends on osteocyte density, mechano-sensitivity and signal decay by distance. Bone is formed at the surface where and while the stimulus exceeds a threshold value. Concurrently, osteoclasts are assumed to resorb bone which is (micro)damaged, the sites of which are determined at random per iteration. Coupling between osteoclastic and osteoblastic activities in remodeling is governed *implicitly* by the mechanics through SED concentrations around resorption cavities, due to a notching effect [10,11].

Applied in an FEA computer simulation of a bone cube, starting from a conceptual morphology representing the post-mineralized fetal stage, the theory produces a mature trabecular structure, aligned to the external loads, as shown in the figure. The bone volume fraction of the cube initially rises sharply, overshoots, and then stabilizes, as also found with density measurements in growing pigs [12]. Other structural and dynamic predictions were realistic as well.

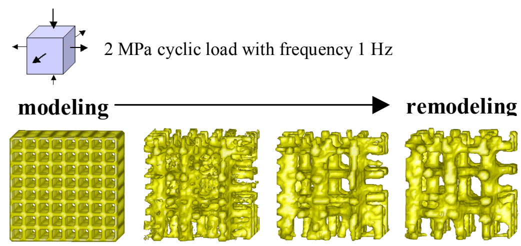

Based on these results we propose that the mechanical regulation of *modeling* and *remodeling, growth* and *adaptation* of trabecular structure can be explained with a unified theory, assuming coupling between osteoclasts and osteoblasts to occur only *implicitly* through the mechanics of load transfer. This implies that modeling and remodeling are just different expressions of the same metabolic cascade. Obviously, many complex biochemical cell-signaling events will play a role in the execution of these metabolic processes; the theory is only a regulatory framework. Our present work is directed at validating the theory by attempts to explain morphological expressions of normal and abnormal metabolic processes that are known to occur in reality.

1. Huiskes et al., 1987, *J Biomech*, 20:1135-1151; **2**. Weinans et al., 1993, *J Orthop Res*, 11:500-513; **3**. van Rietbergen et al., 1993, *J Biomech*, 26:369-382; **4**. Kerner et al., 1999, *J Biomech* 32: 695-703; **5**. van Lenthe et al., 1997, *J Bone Joint Surg* 79-B:117-122; **6**. van Rietbergen & Huiskes, 2002, *J Arthroplasty* 16, Suppl. 1:55-63; **7**. Weinans et al., 1992, *J Biomech* 25: 1425-1441; **8**. Mullender & Huiskes, 1995, *J Orthop Res* 13:503-512; **9**. Huiskes, 2000, *J Anat* 197:145-156; **10**. Huiskes et al., 2000, *Nature* 405:704 – 706; **11**. Ruimerman et al., 2001, *Comp Meth in Biomech & Biomed Engr* 4:433-448; **12**. Tanck et al., 2001, *Bone* 28:650-654..

HAS COMPUTER SIMULATION OF LOCOMOTION DELIVERED ALL ITS PROMISE IN THE PAST 20 YEARS ?

Christopher L Vaughan

Hyman Goldberg Professor of Biomedical Engineering, University of Cape Town, South Africa
Director: MRC/UCT Medical Imaging Research Unit, kvaughan@cormack.uct.ac.za

MODELLING vs SIMULATION

Computer modelling and simulation of locomotion have been utilised by biomechanics researchers for over three decades (Vaughan, 1984). Although often used synonymously, the terms do have different meanings:

> *Computer modelling* refers to the setting up of mathematical equations to describe the system of interest, the gathering of appropriate input data, and the incorporation of these equations and data into a computer program.
>
> *Computer simulation* is restricted to mean the use of a validated computer model to carry out "experiments", under carefully controlled conditions, on the real-world system that has been modelled.

It is clear that computer simulation cannot take place without first developing a computer model. Some of the advantages of computer simulation in locomotion research include: safety; time; optimal performance can be predicted; expense; and the ubiquitous availability of microcomputers. However, there also some important limitations: validation is difficult (Panjabi, 1979); advanced mathematics are often required; and the results can often be difficult to translate into practicality.

Almost two decades ago, I stated: "Of one thing we can be certain: the power of computers, particularly the readily available and portable microcomputer, will expand beyond all recognition. We can certainly look forward with confidence to the exciting challenges and benefits that computer simulation of human motion will bring" (Vaughan, 1984). The purpose of this paper is to review the progress that has been made in both the technology of computer simulation and its application to our understanding of locomotion.

THE PROGRESS IN TECHNOLOGY

Whilst the earliest studies on computer simulation of locomotion were performed on mainframe computers, and hand-held calculators have been used in some simple cases (Vaughan, 1983), the vast majority of models have been implemented on personal computers. The changing face of the microcomputer is illustrated in the table above which compares the vital statistics of the original IBM PC in 1981 with its direct descendent, an entry-level machine 20 years later. In all categories, except boot-up time, the improvements have been dramatic, by two or more orders of magnitude.

There have also been outstanding software tools that have become available: SIMM by MusculoGraphics, ADAMS by Mechanical Dynamics, SD/FAST and DADS (Pandy, 2001).

Vital Statistic	1981	2001
CPU speed	4.77 MHz	933 MHz
RAM	64 KB	128MB
Storage	160 KB floppy drive	20 GB hard drive, CD-R, 1.44MB floppy drive
Display	11.5" monochrome text monitor	17" graphic monitor with 16.7 million colours
Operating System	DOS 1.0	Windows 2000
OS Requirements	16KB	32 MB
Boot-up Time	16 seconds	51 seconds
Price	$3,000	$1,500

THE PROGRESS IN SIMULATING LOCOMOTION

Locomotion researchers have been the first to embrace cutting edge technologies: (1) *artificial neural networks* have provided insight into the linkage between control and effect, and neuromuscular stimulation (Vaughan, 2002); (2) *dynamic optimisation* has predicted novel and emergent behaviour, including muscle excitation patterns based on minimising metabolic cost (Pandy, 2001); (3) *3D visualisation* has allowed a unique view into the complex integration of EMG, kinematic and dynamic variables; and (4) *finite element analysis* has demonstrated the temporal effects of mechanical loading on bones and other tissues.

There is no doubt that the insights we have gained from computer simulation over the past 20 years have provided startling insights that would not otherwise have been possible. These relate to: basic theories of bipedal gait; the relationship between mechanical energy and muscle coordination strategies; the biomechanical consequences of soft tissue surgery; and the effect of design parameter changes on joint replacement implants. In conclusion, the answer to the question posed by this paper is a resounding "yes". It will certainly be interesting to see what the next 20 years bring.

REFERENCES

Pandy MG (2001) "Computer modeling and simulation of human movement", *Annual Reviews in Biomedical Engineering*, 3: 245-273.

Panjabi M (1979) "Validation of computer models", *Journal of Biomechanics*, 12:238.

Vaughan CL (1983) "Simulation of a sprinter", *International Journal of Biomedical Computing*, 14: 75-83.

Vaughan CL (1984) "Computer simulation of human motion in sports biomechanics", *Exercise and Sports Science Reviews*, 12: 373-416.

Vaughan CL (2002) Theories of bipedal gait: an odyssey, *Journal of Biomechanics*, 35 (in press).

FEATURE OF ARTERIAL BLOOD FLOW ASSOCIATED WITH THE BIOLOGICAL FUNCTIONS

Kazuo Tanishita
Department of System Design Engineering, Keio University, Yokohama, Japan, tanishita@sd.keio.ac.jp

MACROSCOPIC APPROACH

The feature of arterial blood flow is characterized by the geometry and mechanical properties of vessel and its peculiar pulsatility, and is associated with the physiological and clinical implications. This motivated to study the fluid mechanics of arterial blood flow. Previously many fluid mechanical studies have been preceded by the idealistic geometries such as constant curvature, bifurcation, branching, taper and planer flow. This approach contributed to establish the fundamentals of the physiological fluid mechanics. For instance, the aortic blood flow is characterized by the strong curvature and intermittent flow waveform developing the peculiar secondary flow (1).

On the other hand, prospective studies became necessary, because they are directly correlated in a subject-specific manner. Recently we focused on the blood flow in the cerebral aneurysms based on the CT-images of patients to anticipate the possibility of rupture and intravascular surgery. We built anatomically realistic models of cerebral aneurysm by the photoforming method and measured the velocity profiles in the aneurysms by LDV and PIV methods. Figure 1 is one of the velocity profiles in the basilar tip aneurysm with small aspect ratio (depth/neck width) (2). This prospective study for the individual patient offers the pertinent information of aneurysm fluid mechanics that is required for the diagnosis and treatment of cerebral aneurysms.

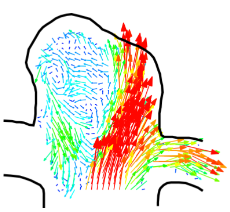

Figure 1. Velocity vectors in the basilar tip aneurysm obtained by PIV

MICROSCOPIC APPROACH

The microscopic viewpoint is essential to understand the function of arterial blood flow, because many previous studies revealed the important bio-chemical process occurred in the endothelial cells and other vessel components associated with the shear stress stimulus by the blood flow. Firstly we focused on the macromolecule transfer process in the endothelial cells with the shear stress stimulus, because transport of macromolecule such as LDL causes to precede the atherosclerotic development. We measured the albumin uptake into the endothelial cells by confocal laser scanning microscopy and obtained the interesting feature of albumin uptake. At 10 dyne/cm^2, the shear stress increased the albumin uptake by 30 %. The albumin uptake decreased in proportion as shear stress increased, and minimum uptake was quarter of the control value (3). This albumin uptake process is regulated during the mechano-transduction process and associates with the energy-consuming process in the mitochondria. This brings to measure the activating process of mitochondria by measuring the membrane potentials of mitochondria (4). Low shear stress (10 dyne/cm^2) increased mitochondrial membrane potential by 30%. On the contrary, high shear stress (60 dyne/cm^2) decreased it by 20%. This observation was consistent with the ATP-dependent albumin uptake into endothelial cells; in other words, the ATP synthetic activity is related to the albumin uptake into the endothelial cells.

The specific mechanisms of mechano-biological interactions alternating shapes and functions have not been fully identified in the individual cells cells, because of the lack of a detailed description of microscopic flow near the cell surfaces. We therefore developed the velocimetry using the expanded cell models and demonstrated the microscopic flow depending on the three-dimensional cell shape, then determined the wall shear tress distribution on cultured endothelial cells experimentally (5).

Responses of endothelial cells to shear stress due to blood flow are basically heterogeneous. Namely the shear stress distribution on a cell has close correlation not only with the surface geometry of the cell but also with that of surrounding cells, and varied from cell to cell (6).

CONCLUDING SUMMARY

Both macroscopic and microscopic viewpoints indicate that the arterial blood flow is closely involved in the biological function of blood vessels and its integrative viewpoint is essentially important.

REFERENCE

(1) Naruse, K. and Tanishita, K., Trans. ASME, J. Biomech. Eng., 118(1996)180-186.
(2) Tateshima, S. et al., J Neurosurg. 95 (2001) 1020-7
(3) Kudo, S. et al., Trans. JSME, B64 (1998) 367-374
(4) Kudo, S. et al., BBRC, 270 (2000) 616-621
(5) Fukushima, S. et al. Trans. ASME, J Biomech Eng. (to appear)
(6) Fukushima, S. et al. JSME Int J., 44 (2001) 972-981

BIOMECHANICS IN OCEANOGRAPHY

T J Pedley

Department of Applied Mathematics and Theoretical Physics, University of Cambridge, Silver Street, Cambridge CB3 9EW, UK
Email: T.J.Pedley@damtp.cam.ac.uk

INTRODUCTION

The oceans contain more than 50%, by mass, of life on earth. Understanding the locomotion of, nutrient uptake by, and interactions between aquatic organisms is important for fisheries predictions and global warming, for example. This talk will summarise a variety of problems in fluid mechanics and mass transfer in which the author has been involved and which in a small way contribute to the required understanding.

LOCOMOTION

Lighthill (1960, 1975) and Wu (1961) pioneered the analysis of undulatory fish swimming at large Reynolds number. Wu's was a two-dimensional, small-amplitude theory which took account of the vortex sheet shed at the trailing edge. The lateral fluid motions generated by the body undulations were necessarily in the plane of the flow; if the body were removed they would look like a series of vortices, though how they would be shed into the wake remains unclear. Lighthill's "elongated-body theory" was intrinsically three-dimensional and easy to extend to large amplitude, but ignored the effect of the vortex wake on the pressure distribution on the fish body. In this case the lateral fluid motions resembled more a series of potential dipoles in planes perpendicular to the fish centreline. Recent full computations using a panel method (Zhu et al, 2002) and recent experimental measurements (Müller et al, 1997) indicate that the Wu picture, although apparently much more idealised, is closer to the truth, at least for some fish species. The mechanism of vortex shedding is still an open question. Other recent work shows how to relate the pressure distribution around the swimming fish to the variable bending moments generated by the swimming muscles; fish body inertia is a crucial ingredient (Pedley & Hill, 1999).

Micro-organism swimming is a low-Reynolds-number problem. For most flagellates the simple resistive-force theory of Gray & Hancock (1955) is accurate enough, and can also be coupled to a description of the internal generation of bending moments, though there have been numerous more refined calculations. Similarly for ciliates, the envelope model (e.g. Blake, 1971) is accurate enough though more detailed theories can be performed.

NUTRIENT UPTAKE

The effect of a micro-organism's swimming on its nutrient uptake has usually been assessed as if the cell were being translated through the fluid at constant speed by an external force (Karp-Boss et al, 1996). The dimensionless mass transfer (Sherwood number, *Sh*) is estimated as a function of dimensionless speed (Peclet number, *Pe*). However, one might expect that the active movements of a cell's swimming apparatus would stir the concentration boundary layer around the cell and enhance the mass transfer. We have investigated this question using the simplest possible (non-realistic) model of a swimming cell: a spherical squirmer (Lighthill, 1952; Blake, 1971). Indeed, at values of *Pe* that are not small, the nutrient uptake is considerably enhanced (Magar et al, 2002).

ENCOUNTER RATE

Both phytoplankton and the zooplankton that prey on them perform random walks, both by swimming and because the ocean is turbulent (weakly so except very near the surface). An over-simple formula for the encounter rate proposed by Rothschild & Osborn (1988) has been widely used. We revisited the problem, proposed a somewhat more well-founded formula and tested it successfully against a computational simulation of swimmers in a turbulent flow. We have also used it to predict capture rate – not the same as encounter rate because predators have a variable probability of capturing their prey once they have spotted them (Lewis & Pedley, 2000, 2001). Depending on the turbulence level there are two optimal hunting strategies, "cruise" and "ambush", both of which are found in Nature.

REFERENCES

Blake, J.R. (1971). *J. Fluid Mech.*, **46**, 199-208.
Gray, J., Hancock, G.E. (1955). *J. Exp. Biol.*, **32**, 802-814.
Karp-Boss, L., Boss, E., Jumars, P.A. (2000). *Ann. Rev. Oceanogr. Mar. Biol.*, **34**, 71-107.
Lewis, D.M., Pedley, T.J. (2000; 2001). *J. Theor. Biol.*, **205**, 377-408; **210**, 347-365.
Lighthill, M.J. (1952). *Comm. Pure Appl. Math.*, **5**, 109-118.
Lighthill, M.J. (1960). *J. Fluid Mech.*, **9**, 305-317.
Lighthill, J. (1975). *Mathematical Biofluiddynamics*. SIAM.
Magar, V., Goto, T., Pedley, T.J. (2002). *Quart. J. Mech. Appl. Math.* (submitted).
Müller, U., van den Heuvel, B., Stamhuis, E., Videler, J.J. (1997). *J. Exp. Biol.*, **200**, 2893-2906.
Pedley, T.J., Hill, S.J. (1999). *J. Exp. Biol.*, **202**, 3431-3438.
Rothschild, B.J., Osborn, T.R. (1988). *J. Plankton Res.*, **10**, 465-474.
Wu, T.Y. (1961). *J. Fluid Mech.*, **10**, 321-344.
Zhu, Q., Wolfgang, M.J., Yue, D.K.P., Triantafyllou, M.S. (2002). *J. Fluid Mech.* (in press).

THE CONVERGENCE OF CARDIOVASCULAR GENOMICS AND ENDOTHELIAL BIOMECHANICS

Peter F. Davies[1]: pfd@pobox.upenn.edu
Brian P. Helmke[2], Natacha DePaola[3], Congzhu Shi[1], Amy B. Rosen[1], Denise C. Polacek[1]
[1]Institute for Medicine & Engineering, University of Pennsylvania [2]Department of Biomedical Engineering, University of Virginia, and [3]Rensselaer Polytechnic Institute, NY

The focal origin of atherosclerosis and its localization to predictable locations in the arterial tree is strongly correlated with regions of complex hemodynamics that include flow separation/reattachment and flow instabilities. The spatial and temporal distribution of forces acting at the haemodynamic interface, the endothelium, can be measured over regions of many cells, or for smaller groupings extending down to the single cell. Mechanotransduction in the endothelium therefore needs to be considered over several scale lengths. This presentation outlines spatial cell and molecular studies of haemodynamic force interactions with endothelial cells.

At a regional level, gene expression, protein organization, and functional differences are illustrated for the cell communication molecule *connexin43* in relation to shear stress gradients and flow separation *in vitro*. This is an example of one gene studied in many cells. Through the use of customized cardiovascular microarrays, the transcription of many genes as a function of regional haemodynamics can be measured by differential transcription profiling ("spatial genomics"). Recent developments in nucleic acid amplification techniques permits refinement to the study of smaller groups of cells. We surmise that the dynamic and large spatio-temporal gradients of shear stress may contribute to regional variability of gene expression *in vivo*.

The hemodynamic force-generating system itself operates over a range of length scales determined both by the geometry of the vasculature (bulk flow characteristics; μm-cm) and the topography of the individual cells (force distribution; sub-μm scale). The flow combines with cell micro-topography to distribute forces across the cell surface (sub-μm) to cytoskeletal elements and connecting proteins (nm-μm) involved in the mechanotransduction signaling and adaptive gene expression. Furthermore, individual cells are part of an interconnected monolayer capable of cell-cell communication extending over mm-cm. Information obtained at finer scales must therefore be integrated and understood in the context of larger scale events.

Structural and biochemical studies of endothelial mechanotransduction using living cells have provided some mechanistic insights relevant to the genomics studies. Atomic force microscopy defined the surface topography of endothelial cells permitting the calculation of shear stress distribution at subcellular distances over the cell surface. The use of fluorescent prrotein gene constructs (eg GFP) transfected into cells revealed positional displacement of the cytoskeleton in response to shear stress. And interference optical techniques allowed visualization of adhesion site dynamics in real time demonstrating basal responses to apical flow forces. These studies have led to the *decentralization model* of endothelial mechanotransduction:- hemodynamic forces are transmitted throughout the cell via the cytoskeleton to multiple sites where conversion of mechanical forces to electrophysiological, biochemical, and genetic responses occur. The decentralized model for subcellular haemodynamic responses is outlined and discussed.

Supported by NIH grants HL36049MERIT, HL62250, HL64388 and a Sponsored Research Agreement with AstraZeneca Pharmaceuticals.

REFERENCES

Davies, P.F. 1995. Flow-mediated endothelial mechanotransduction. *Physiol. Rev.* 75:519-560.

Davies, P.F., Polacek, D.C., Handen, J.S., Helmke, B.P., DePaola, N. 1999. A spatial approach to gene expression profiling: mechanotransduction and the focal origin of atherosclerosis. *Trends in Biotechnology* 17:347-351.

DePaola, N., Davies, P.F., Pritchard, W.P., Polacek, D. 1999. Spatial regulation of gap junction connexin 43 in endothelial cells exposed to disturbed flows *in vitro*. *Proc. Natl. Acad. Sci. USA* 96:3154-3160.

Helmke, B.P., Thakker, D., Goldman, R.D., Davies, P.F. 2001. Quantitative spatial analysis of flow-induced intermediate filament displacement in living endothelial cells. *Biophysical J.* 80:184-194.

STRUCTURE FUNCTION PROPERTIES OF BONE: THE INFLUENCE OF MECHANICAL AND BIOLOGIC STIMULI

Steven A. Goldstein, Ph.D.

Orthopaedic Research Laboratories, University of Michigan, Ann Arbor, Michigan

Investigators have been diligently studying the mechanical behavior of bone for more than 100 years and, specifically, searching to identify the mechanisms that guide its abilities to adapt to physical forces. While the potent influences of mechanical stresses on bone tissue behavior has been characterized and even quantified to a limited extent by a number of laboratories, the specific mechanisms associated with the translation of mechanical forces into regulatory signals mediating cell activity remain incompletely known. As a result, advances in the development of therapies for conditions that might be influenced by physical forces such as fracture healing, implant fixation and perhaps osteoporosis have been limited.

The purpose of this presentation will be to present a series of studies designed to characterize the hierarchical properties of bone and the influence that mechanical and potentially biologic stimuli have on these properties. From a mechanical perspective, the most striking feature of bone is its multi-scale organization. The precise morphology and architectural features at each level of hierarchy have been assumed to play a substantial role in bone's ability to minimize damage, repair rapidly, adapt to changes in physical and biochemical signals, and participate in mineral homeostasis. We have utilized a hierarchical paradigm to study the properties of bone in an effort to gain insight into its dynamic behavior. Our desire to characterize the structure function properties of bone is motivated by two specific interests: (1) to support approaches for the treatment of fragility disorders ranging from osteoporosis to osteogenesis imperfecta and, (2) to evaluate hypothesized mechanisms through which bone receives and adapts to mechanical stimuli. The rationale for this latter motivation comes from the fact that bone extracellular matrix serves as the medium through which all mechanical signals are transmitted to the included cells.

The initiation of bone formation involves the commitment, clonal expansion, and differentiation of progenitor cells, followed by the expression and organization of extracellular matrix proteins in a manner which results in the deposition and eventual mineralization of the tissue. In an effort to quantitatively study the influence of local mechanical or biological stimuli on bone formation, remodeling and adaptation, we have utilized several in vivo models in which both the mechanical and biologic environments were experimentally controlled. The models have included a novel hydraulically activated bone chamber, fracture repair studies that utilize specialized external fixators that allow application of controlled perturbations, as well as, in vitro organ culture systems that enable isolated mechanical or biologic effects to be measured. In all of these studies, we have attempted to quantify and control the local stress or biochemical environment while measuring outcomes across several hierarchical scales of the tissue. These studies have been extended to test whether mechanical factors also play a role during growth and development of the skeleton.

Results of these studies demonstrated that mechanical forces play an important epigenetic role in regulating shape and morphology of bone structure. Newly formed bone is particularly sensitive to applied mechanical forces which appear to trigger integrin mediated signaling cascades incorporating the formation of focal adhesions, and enacting both src tyrosine kinase and MAP kinase activity. We have also found that we can stimulate analogous bone formation cascades through the local delivery of regulatory biofactors using gene-based technologies. Taken together, these studies have provided some insight into the strategies that may be employed by bone related cells to regulate matrix properties and organization.

ACKNOWLEDGEMENTS

This paper will summarize work from a large group of investigators and their trainees. In particular, I acknowledge Dr. Maria Moalli and Dr. Barbara McCreadie from the University of Michigan. The work was funded by NIH (AR20557, AR34399, AR31793, AR46024), Selective Genetics, Inc., and The Whitaker Foundation.

THE SMALL PROTEOGLYCAN IN TENDON

Kathryn G. Vogel

Dept. of Biology, The University of New Mexico
Albuquerque, NM 87131 kgvogel@unm.edu

INTRODUCTION

It has been nearly 20 years since we undertook the isolation of proteoglycans from bovine deep flexor tendon during my sabbatical year in Sweden. We found that the predominant tendon proteoglycan was a small dermatan-sulfate PG and, of greatest interest, that the core protein of this tendon proteoglycan had a remarkable ability to inhibit the *in vitro* fibrillogenesis of both type I and type II collagen (Vogel et al 1984). This small tendon proteoglycan was later given the name decorin (because it appeared to “decorate” collagen fibrils) and it is now only one of a family of proteoglycans in which the core proteins are characterized by the presence of repeating sequence motifs with high leucine content. Biglycan, fibromodulin and lumican are other members of this family of small leucine-rich proteoglycans, and most of these have a similar ability to affect collagen fibrillogenesis. During this talk I will discuss some of the observations which indicate that decorin plays an important role in regulating the orderly assembly of the extracellular matrix, and therefore the biomechanical properties, of many tissues - including tendon and ligament.

DECORIN BINDS TO COLLAGEN

That decorin binds to collagen was easily demonstrated. It has been much more difficult to figure out just what part of the decorin core protein binds to collagen, and to what part of the collagen it is bound. The decorin core protein is modeled as having a three-dimensional shape like an arch. It is believed that this arch or U-shaped molecule wraps itself crosswise around the long, skinny, collagen triple helix. The correct three-dimensional shape of decorin is necessary for efficient binding to collagen, and regions of decorin core protein important in binding have been identified by recombinant techniques. There are probably multiple points of interaction in more than one of the leucine-rich repeats. The site on the type I collagen molecule to which decorin binds is near the C terminus, within the CB6 fragment of the $\alpha1$(I) chain (Keene et al, 2000). Because this location is very close to one of the major intermolecular cross-linking sites of collagen heterotrimers it is hypothesized that decorin might be in a position to regulate collagen fibril stability.

DECORIN AFFECTS COLLAGEN FIBRILLOGENESIS

Purified soluble collagen placed in permissive conditions of salt concentration and temperature will self assemble into fibrils that show the same fine structure as the collagen in tissue. This shows that proteoglycans are not necessary for fibrils to form. However, when decorin is added to soluble collagen the fibrils form more slowly and are thinner in diameter. The core protein has this effect on collagen fibrillogenesis even after the GAG is removed, but the free GAG does not affect fibril formation *in vitro*. The GAG chains of decorin can be visualized by electron microscopy as filaments sticking out from the surface of the collagen fibril. This image suggests that GAG chains coat the surface of the fibril and could inhibit the lateral association of fibrils. On the other hand, these GAG chains might interact with each other and thereby enhance fiber stability. Collagen fibers formed in the presence of decorin showed an increased ultimate tensile strength compared to fibers formed without added decorin, perhaps as a result of decorin facilitating fibrillar slippage during deformation (Pins et al., 1997). So which is it? Do the GAGs of decorin stick fibrils together, or do they keep them apart? For best function should tissues have more decorin, or less?

THE ROLE OF DECORIN IN TISSUE

That decorin plays a role in fibrous tissue organization was demonstrated by the fragile skin of the transgenic mouse lacking decorin expression (Danielson et al, 1997). In addition, the collagen fibrils of tendon in this knock-out mouse showed large, irregular profiles in cross section and non-uniform axial mass distribution. This observation could result from lateral aggregation of fibrils and is consistent with the *in vitro* result showing that added decorin promotes thinner fibrils, perhaps by inhibiting lateral aggregation. Because thicker collagen fibrils are correlated with greater tensile strength, it is argued that removing decorin could promote the maturation of healing tendon or ligament. In contrast, increased decorin content might disrupt collagen fibers (not a good thing for tendon). On the other hand, added decorin might bind and thus sequester growth factors that would otherwise enhance the formation of weak scar tissue or fibrous adhesions (a good thing for tendon healing).

REFERENCES

Danielson K.G. et al (1997) *J. Cell Biology*, **136**, 729-743.
Keene D.R. et al (2000) *J. Biol. Chem*. **275**, 21801-21804.
Pins G.D et al (1997) *Biophysical J*. **73**, 2164-2172.
Vogel et al (1984) *Biochem J*. **223**, 587-597.

MOLECULAR BASIS OF CELLULAR RESPONSES TO MECHANICAL FORCES

Shu Chien

Departments of Bioengineering and Medicine and
The Whitaker Institute of Biomedical Engineering, University of California, San Diego.
La Jolla, California 92093-0427, U.S.A.

There is increasing evidence that cells can sense and respond to mechanical stimuli such as pressure and flow, as well as chemical stimuli such as hormones and growth factors. The endothelial cells (ECs) in blood vessels play significant roles in regulating vascular functions in health and disease. The fluid shear stress resulting from blood flow can modulate EC functions by activating sequentially the mechano-sensors, intracellular signaling pathways, and specific transcription factors to modulate gene expression and protein, and hence cellular functions. The vascular endothelial growth factor receptor (VEGFR) on the luminal side of ECs and integrins on the abluminal side have been shown to be mechano-sensors. Other potential EC membrane mechano-sensors are G-proteins, ion channels, and intercellular junction proteins. The activation of these mechano-sensors by mechanical stimuli such as shear stress leads to the triggering of phosphorylation cascades of signaling molecules. For example, the Ras-JNK signaling pathway mediates the shear stress-activation of the expression of monocyte chemotactic protein-1 (MCP-1) gene and protein in response to shear stress. A sustained application of laminar shear stress results in only a transient activation of this signaling pathway and a transient MCP-1 expression followed by its down-regulation. Sustained laminar shear stress also activates the genes that inhibit vessel wall growth. When ECs are subjected to complex flow patterns simulating these seen in the branch points, the down-regulation of MCP-1 in response to sustained flow does not occur, and the sustained activation of genes such as MCP-1 in the areas with complex flow contributes to atherogenesis. Furthermore, EC mitosis and apoptosis are accelerated in the areas with complex flow. Such accelerated cell turnover leads to an enhanced macromolecular permeability. The temporal and spatial variations in shear stress and flow pattern play important roles in endothelial functions such as monocyte chemoattraction, macromolecular permeability, and cell migration, and hence can play important roles in tissue engineering. The results of interdisciplinary studies at the interface of biomedical sciences and engineering mechanics help to enhance our understanding of the fundamental process of mechano-chemical transduction and the pathophysiological mechanisms underlying cardiovascular diseases.

INJURIES IN SPORT: REDUCTION THROUGH A BIOMECHANICAL INTERVENTION

Bruce Elliott

The School of Human Movement and Exercise Science, The University of Western Australia, Australia
Bruce.Elliott@uwa.edu.au

INTRODUCTION

Research which identifies causal mechanisms associated with injury requires input from many specialists. Winston et al. (1996) proposed that the biomechanist should be an integral part of what they termed 'epidemiological research', if injury control mechanisms were to be understood. This would seem to be essential as most injuries have a mechanically related etiology. van Mechelen et al. (1992) reviewed risk factors involved in sport and suggested a four step prevention process, namely:

1. The collection of epidemiological data (nature, extent and severity of injury) to identify the problem
2. Identify the etiology of the problem
3. Educate the relevant population as to the techniques needed for prevention
4. Evaluate the effectiveness of preventative measures.

This paper will discuss the role of biomechanics in the above approach, as it is applied to reducing the incidence of back injuries in the cricket fast bowler.

EPIDEMIOLOGY

Epidemiological data have clearly shown that the lumbar spine of the cricket fast bowler is the area at greatest risk of injury. The incidence of lumbar stress fractures and disc abnormalities was particularly high in this population of sportspeople.

ETIOLOGY

A prospective and several longitudinal studies using videography and magnetic resonance imaging (MRI) have shown that shoulder alignment counter-rotation during the delivery stride was associated with the development of lumbar stress fractures and disc degeneration (Foster et al., 1989; Elliott et al., 1992; Burnett et al., 1996).

EDUCATION

An annual half day clinic and 6 small group coaching sessions spread over the season were held to assist the bowlers reduce the level of shoulder counter-rotation over a 3-year period. All players had the level of shoulder counter rotation assessed from video and disc status determined from a MRI scan of the lumbar spine on an annual basis.

EVALUATION

Data showed that small group coaching significantly reduced the level of shoulder alignment counter-rotation in young fast bowlers from 35.4° to 21.3° over the 3-year period. The incidence and progression of lumbar disc degeneration were also reduced in parallel with this decreased shoulder counter rotation. Figure 1 shows the differences in MRI data from this study with that of Burnett et al. (1996), where young players were tracked for 3-years with no coaching intervention.

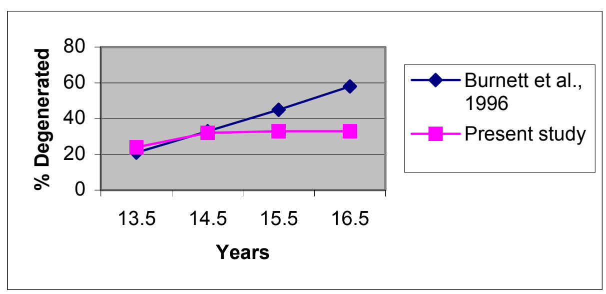

Figure 1: Comparison of MRI data from the lumbar discs

REFERENCES

Burnett, A. et al. (1996). *Clin Biom*, **11**, 305-310.
Elliott, B. et al. (1992). *Sport Med Train Rehab*, **3**, 113-130.
Foster,D. et al. (1989). *Brit J Sports Med*. **23**, 150-154.
Van Mechelen,W. et al. (1992). *Sports Med*. **14**, 82-99.
Winston, F. (1996). *J Trauma Inj Inf Crit Care*, **40**,820-824.

APPLICATION OF MODELS TO UNDERSTAND THE INTEGRATION OF CORONARY VASCULAR CONTROL MECHANISMS.

Jos AE Spaan

Department of Medical Physics, CardioVascular Research Institute Amsterdam
Academic Medical Center, University of Amsterdam
Meibergdreef 15, 1105 AZ, Amsterdam, the Netherlands.

INTRODUCTION

Coronary blood flow must meet the demands of the heart for supply of nutrients for a large range of cardiac work. In a healthy myocardium such is not a problem and resistance vessels can dilate to increase coronary flow by a factor 4 over the value at rest. This flow reserve, however, can be compromised by disease in the larger coronary arteries as arteriosclerosis or in the microcirculation.
The control of coronary flow is the result of interactions of several mechanisms some related to control of vascular smooth muscle tone in resistance vessels and others to mechanical factors related to heart contraction. These mechanisms do vary in nature and strength over the different types of vessels in the arterial tree and different locations in the myocardium. In order to arrive at a clear picture of the interaction between these different mechanisms and at different locations within the vascular tree, models are required.

MECHANICAL FORCES

The compressing force of cardiac contraction reduces intramural blood volume periodically causing the coronary arterial and venous flow to be phasic with about a 180^{o} phase shift. On average, intramural blood volume is lower at a higher HR resulting in an increased coronary resistance component. These compressive forces have a stronger effect on the inside of the heart muscle (sub-endocardium) than on the outside (sub-epicardium). Compressive forces are related to a change of the stiffness properties of the myocardium when the heart goes from diastole into systole and to tissue pressure related to Left Ventricular pressure which transmission through the tissue depends on wall stiffness as well.
The distending force of arterial pressure becomes especially clear when dynamic pressure- flow relations are studied in a non-beating myocardial preparation. That coronary resistance depends on arterial pressure is generally accepted but is mostly implemented in models by taking a constant resistance with a value dependent on the mean pressure of the phasic pressure signal. Interpretation of pressure-flow Bode plots demonstrate clearly a dependence of arterial pressure but interpretation with a model of resistance constant during the pressure variation underestimates intramural compliance 10-20 fold. Including the variation of resistance during the pressure wave results in much better estimates of intramural compliance. This obviously complicates modeling the resistance distribution in the coronary vasculature but is a necessity when one wants to relate measured signals to physical properties of the circulation.

VASCULAR RESPONSES

Normally smooth muscle tone is continuously adjusted as to match flow to myocardial oxygen consumption and adjusting for flow compromising mechanisms like cardiac contraction and disease in the larger coronary arteries. There are many processes involved in this tone regulation and their effect on local tone are dependend on the vessel segment location within the tree. Since overall coronary resistance is adjusted in arteries between 20 and 400 μm the interactions of these mechanisms in vessel segments and between segments along the tree have to be known.
Models are used here to translate findings from isolated resistance artery studies to studies on the intact heart. A typical example is the interaction of metabolic factors active on the smallest arterioles and flow dependent dilation of upstream vessels having myogenic tone. Hence, flow is a signal integrating downstream and upstream regulatory processes.

DISCUSSION

In the development of comprehensive understanding of coronary blood flow regulation and how this regulation is compromised by disease, a distributed model of the intramural vasculature is needed. This vascular tree should consist out of segments having control properties with input-output relations allowing for inter-segmental communication of control signals and mechanical interaction with the contracting muscle.

REFERENCES

1)Cornelissen AJ, Dankelman J, VanBavel E, Stassen HG, Spaan JA. Am J Physiol Heart Circ Physiol. 2000 278(5):H1490-9. 2) Spaan JA, Cornelissen AJ, Chan C, Dankelman J, Yin FC. Am J Physiol Heart Circ Physiol. 2000 Feb;278(2):H383-403.

ACKNOWLEDGEMENTS

This presentation is the result of longstanding cooperation with Prof. Jenny Dankelman*, Dr. Ed van Bavel and Dr. Annemiek Cornelissen. *Dept. of Biomedical Engineering and Mechanics, University of Technology Delft.

BIOMECHANICS OF VERY SOFT TISSUES

Lynne Bilston

Prince of Wales Medical Research Institute
Barker St, Randwick, 2031. Sydney, Australia
l.bilston@unsw.edu.au

INTRODUCTION

Understanding and characterising soft biological tissues is an important part of biomechanics. The "very" soft biological tissues, such as the central nervous system and abdominal organs, have been less thoroughly characterised, and modelling efforts have been frustrated by the complexity of their mechanical responses. Here, I describe our efforts to both measure the viscoelastic properties of some of these tissues, and discuss modelling progress and remaining challenges.

METHODS

Fresh tissue samples (brain, spinal cord, kidney and liver) were obtained soon after death, in order to minimise the effects of biological decay on measured tissue properties. All tissues were bathed during transport, preparation and testing with an appropriate fluid to avoid dehydration. Shear tests were conducted in a Bohlin shear rheometer. Tensile tests were conducted in a benchtop testile testing machine. Elongational/compression tests were conducted in a custom-designed lubricated squeeze rheometer. There has been considerable debate about the use of preconditioning, however it has two great advantages - it produces a repeatable, predictable initial stress state in the tissue at the beginning of testing, and reduces the variability in the test data obtained. It was used in all these data discussed here. Coarse sandpaper on the platens in shear tests was used to prevent slip. Tensile specimens were bonded between tabs using cyanoacrylate adhesive. Testing protocols include shear oscillation, stress-relaxation, creep tests, and constant strain rate tests. Together, this battery of tests allows sufficient data to be collected to determine the linear and nonlinear viscoelastic properties of the tissues.

RESULTS AND DISCUSSION

For all the tissues, the linear viscoelastic limit was found be to of the order of 0.1% strain. Clearly, this is such a small strain that these tissues must be considered to be nonlinearly viscoelastic for all practical loading levels. Moreover, they all demonstrate significant strain-rate sensitivity, as shown in Figure 1. Other key characteristics include the observation that their relaxation moduli and the long-term modulus are dependent on both strain and also, in some cases (eg spinal cord), loading rate, as shown in Figure 2. Indeed, even the shape of the relaxation moduli curves depends on strain, rendering the tissues strain-time inseparable. Various approaches to constitutive modelling for these tissues have been investigated, with varying degrees of success. What is clear, however, is that the simple linear and quasilinear models that have been commonly used for ligaments and tendons are inadequate for these tissues, because they are nonlinear, and not strain-time separable. Nonlinear differential constitutive models have been used with some success, but their applicability is limited because of the complexity required to accurately reproduce the very complex mechanical response of these tissues. So far, no models of these tissues have incorporated the hydraulic stiffening due to perfusion in living tissues.

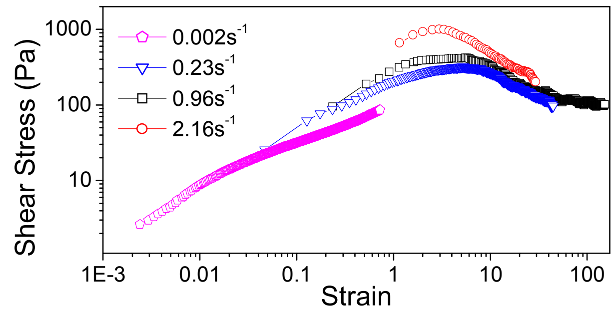

Figure 1: Shear response of bovine brain tissue.

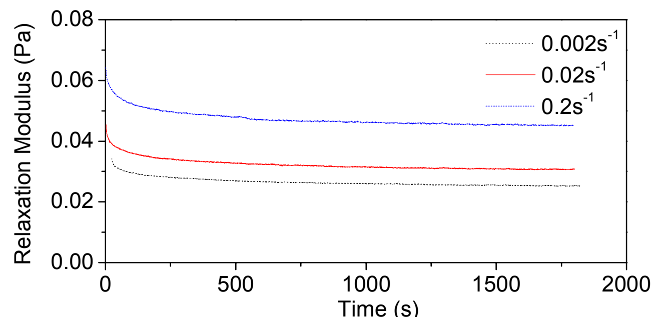

Figure 2: Relaxation moduli at 5% strain for rat spinal cord tissue, showing long-term moduli dependent on strain rate.

SUMMARY

Very soft biological tissues pose experimental and theoretical challenges. They are very nonlinear, often strain-time inseparable, and it is difficult to capture all of their complex mechanical behaviour in a constitutive model that is not prohibitively complex. Future challenges include obtaining consistent constitutive models for multiple types of loading (shear, elongation, etc) across a broad range of loading rates, determining the structural mechanisms for their complex behaviour, and measuring and modelling the effects of perfusion on tissue properties.

ACKNOWLEDGEMENTS

This work was supported by the Australian Research Council and the University of Sydney

EFFECT OF VISCOUS FLUID STRESSES ON CELLS AND BIO-ARTIFICIAL CAPSULES

Dominique Barthès-Biesel

Biomécanique et Génie Biomédical, UMR CNRS 6600, Université de Compiègne, Compiègne, France
dbb@utc.fr

INTRODUCTION

A capsule consists of an internal medium (pure or complex liquid), enclosed by a deformable membrane. In Biomedical Engineering, bio-artificial capsules are used in drug delivery systems, artificial organs or cell therapy. A liquid filled capsule is also an appropriate model for a simple cell such as a red blood cell. When such particles are suspended in a flowing liquid, they are deformed by viscous fluid stresses and may sometimes burst. The modeling of this process has two main applications. One is the prediction of cell response to physiological flows and the diagnosis of pathological states. The other is bio-artificial capsule design, with appropriate control of the deformation and breakup. The motion and deformation of a capsule in flow depends on the stress-free initial geometry, the membrane mechanical properties and the rheology of the internal medium. It is the aim of this presentation to study the effect of such intrinsic physical properties on the deformation and burst of cells and bio-artificial capsules suspended in different flow fields.

MEMBRANE MECHANICS

A major issue is the determination of the mechanical properties of the membrane, as these control the resistance of the capsule to applied stresses. Those properties have to be inferred from experiments such as squeezing between two plates for large capsules or micropipette aspiration for cells. In many cases the membrane is very thin and treated as a two-dimensional solid with hyperelastic or visco-elastic properties. Popular membrane constitutive laws include the Mooney-Rivlin (MR) law that assumes that the membrane is an infinitely thin sheet of a 3D incompressible material. For biological membranes, which are almost area incompressible Skalak et al.(1973) law (SK) is usually preferred as it accounts for shear deformation and area dilatation of the material. Recent experiments have shown that gelatin membranes reinforced with a polymer network, are also well described by SK law where the area dilatation and shear modulus are of the same order. However, MR and SK laws lead to quite different membrane behaviors for large deformations (Barthes-Biesel et al. 2002).

MOTION OF A CAPSULE IN FLOW

The general problem consists in analyzing the motion of a capsule freely suspended in another liquid subjected to a known flow field in the limit of small Reynolds numbers. Two free surface flow problems (motion of the internal liquid and of the suspending fluid) and a solid mechanics problem (deformations of the membrane) must be solved simultaneously. An efficient method consists in recasting the Stokes equations in integral form and in using the boundary integral technique. The effect of the membrane rheology on the capsule response can then be assessed by comparing two capsules subjected to the same flow but with different membrane constitutive laws.

Unbounded linear shear flow

Results have been obtained for capsules suspended in elongational flow and in simple shear flow. A capsule with a SK membrane can sustain higher shear stresses than a capsule with a MR membrane. The latter always bursts when the shear stress exceeds a critical value. The model also provides values of the elastic tensions in the membrane and can thus help to predict burst for a given failure criterion of the material.

Pore flow

A capsule is forced to flow through a long cylindrical tube (filtration process or microciculation). The deformed profile of the particle, the steady pressure drop and center of mass velocity can be computed as functions of geometry, flow rate and membrane rheology. The model predictions are in very good agreement with recent experimental observations of the flow of an artificial capsule in a tube. They can also be used to analyze filtration data on red blood cells in a cell transit analyzer, or to provide a model for erythropoiesis (Diaz et Barthès-Biesel 2002).

REFERENCES

Barthès-Biesel D. et al.(2002) *J. Fluid Mech.*
Diaz A. et Barthès-Biesel D. (2002) *Comp. Meth. Eng. Sc.*
Skalak, R et al. (1973) *Biophys. J.* **13**, 245-264.

INFRASTRUCTURE FOR THE IUPS PHYSIOME PROJECT

Peter Hunter

Chair, IUPS Physiome Commission.
Bioengineering Institute, The University of Auckland, Auckland, New Zealand
p.hunter@auckland.ac.nz

INTRODUCTION

In 1998 the International Union of Physiological Sciences (IUPS) established the "Physiome Commission" whose aim is to: *"Promote anatomically and biophysically based computational modeling for analysing integrative physiological function in terms of underlying structure and molecular mechanisms. Closely coupled to this is the need to establish web-accessible physiological databases dealing with genomic data through bioengineering data to clinical data."* This talk will present an overview of the current status of the IUPS Physiome Project and, in particular, current plans for developing an infrastructure and industry consortium to support the project on a larger scale than has previously been possible.

METHODS

Ontologies and markup languages

An ontology is the vernacular and rules needed to describe a body of knowledge and a 'markup language' provides the structure for capturing this and other information relevant to describing a mathematical model in a machine readable form. The ontologies (and associated markup languages) being developed for the Physiome Project are:

(a) The mathematical modelling framework for describing the boundary value problem associated with some aspect of physiological function (PhysioML).
(b) The parameterized anatomical description of organs and organ systems (AnatML).
(c) The description of tissue composition, structure and function (TissueML).
(d) The description of cell composition, structure and function (CellML).

Model databases

A large variety of models of physiological function have been published by the worldwide community of bioengineers and physiologists. These models are often difficult for anyone other than the originator to use and are usually difficult to use in combination with other models. The development of the markup languages for encapsulating these models at the cell, tissue, organ and whole organism level will help in overcoming these obstacles but clearly there is also a need for databases of such models which can be downloaded freely from the web. Three-dimensional finite element models of all major anatomical structures in the body are currently being developed (see www.bioeng.auckland.ac.nz) and this should be complete in 2-3 years. About 100 models of cell electrophysiology, signal transduction pathways and metabolic pathways have now been created in CellML format and are available from www.cellml.org. A primary focus for the Physiome Project over the next two years will be completing the TissueML markup language and establishing a database of tissue models.

Web interfaces and simulation tools

The databases of publications, experimental data and models for the Physiome Project will be substantial. The accessibility and usefulness of these databases will depend crucially on the software tools for accessing them via the web and displaying information. A software development effort is now underway to develop open-source tools for this purpose. Equally important will be access to simulation packages for running the models. A number of such packages are available freely for academic use (see www.bioeng.auckland.ac.nz for a list) and the emphasis now is on developing application programming interfaces (APIs) for the markup languages to allow the authors of these simulation packages to add the code needed to read the markup language files. A related issue is access to high performance computing and in particular 'grid computing' (or 'e-Science' as it is called in the UK). Web interfaces have been developed to access the PhysioML files defining a model, to run the model on a high performance computer, and to display the results via visualization software.

Model validation

The primary criterion for including a model in the database of markup language files is that it has been published in a refereed journal. It is likely, however, that further curation of this database will be necessary to provide expert judgement on the benefits and limitations of all models in a given area of physiology. A proposal for how this is done and by whom will be presented.

REFERENCES

Bassingthwaighte, J.B. (2000) Strategies for the Physiome Project. Ann. Biomed. Eng. 28:1043-1058.
Bock, G. & Goode, J. (2002) (Eds) *In Silico Simulation of biological processes*. Novartis Foundation Symposium, **247**. London:. John Wiley (in press).
Kohl P., Noble D., Winslow R.L. & Hunter P.J. (2000) Computational modelling of biological systems: tools and visions. *Phil Trans R Soc Lond A,* **358**, 579-610.
Kohl P., Noble D., and Hunter P.J. (2001) (Eds). The Integrated Heart: Modelling Cardiac Structure and Function. *Phil.Trans R Soc Lond A*, **359**, 1047-1337.
Hedley, W.J.H., Nelson, M.R., Bullivant, D.P., Nielsen, P.F. (2001) "A short introduction to CellML" *Phil Trans Roy Soc Lond A*, **359**, 1073-1089.

EXPLORING STRUCTURE/FUNCTION RELATIONSHIPS IN ARTICULAR CARTILAGE USING NOVEL EXPERIMENTAL APPROACHES

Neil Broom

Biomechanics Laboratory, School of Engineering, University of Auckland, New Zealand, nd.broom@auckland.ac.nz

ABSTRACT

The durability of most high performance engineering components derives from the fact that they are precisely shaped from materials with clearly defined physical properties and in which structural inhomogeneities and anisotropies are largely eliminated (directional composites are an obvious exception). In such components maximum service stresses can be predicted to a high degree of accuracy. They are designed to function almost exclusively over a quite narrow deformation range (typically strains of less than 0.001). Importantly, this involves mostly one type of deformation mechanism - purely elastic stretching of interatomic or intermolecular bonds in mostly regular crystalline arrays. Stress singularities at interfaces are generally minimized by ensuring material property compatibility, thus allowing the engineer to predict accurately and thus control the stresses to which a crucial component is exposed. Also, conventional materials are generally put into service in a condition of minimal internal residual stress, again so as to enhance the engineer's control of the component's total stress environment.

Almost everything about articular cartilage transgresses these engineering rules. Between its major zones the tissue is highly inhomogeneous and anisotropic at the macro, micro and ultramicroscopic structural levels. Even within each major zone there are major structural inhomogeneities and strong directional effects in terms of both intrinsic extensibility and ease of rupture. Major structural/mechanical discontinuities exist between the surface layer and the underlying general matrix and, most severely, between cartilage and its much more rigid substrate – the subchondral bone. Compared to a conventional precision-engineered component the anatomical environment in which cartilage is required to function over a life time is somewhat imprecise.

Cartilage is also subjected to a wide range of loading rates during normal function. Quite different mechanisms of deformation operate when cartilage is loaded either dynamically or statically. At high rates the tissue behaves approximately as a large-strain elastic material. At lower rates high levels of deformation are attainable via a mechanism involving the time-dependent outflow of fluid through a matrix of ultra-low permeability and this can be approximated as a process of consolidation. Large-scale deformation and rearrangement of the matrix components occurs under such conditions. Cartilage in its unloaded state is also pre-stressed. Residual stresses are built into its structure by virtue of the swelling of the proteoglycan component against the constraining 3-dimensional network of collagen fibrils. Its total response to an external load is therefore a combination of both the stiffness generated by this intrinsic swelling potential and the resistance to fluid outflow. Articular cartilage is thus a highly complex load-bearing material, and it possesses remarkable durability.

This talk will describe a number of novel experimental approaches we have developed in our biomechanics laboratory both to reveal and quantify the complex structural/mechanical properties of normal articular cartilage and to track what appear to be significant changes in these properties resulting from ageing and degeneration. Specifically the deformation and rupture properties of the articular surface, the relationship between fibrillar network configuration, directional rupture behaviour and swelling propensity of the general matrix, and the toughness or resistance to fracture of the osteochondral region will be discussed.

SELECTED REFERENCES

Broom, N.D., (1986). The collagenous architecture of articular cartilage - a synthesis of ultrastructure and mechanical function. *Journal of Rheumatology*, **13**, 142-152.

Oloyede, A., Broom, N.D., (1994). The complex nature of stress inside loaded articular cartilage. *Clinical Biomechanics*, **9**, 149-156.

Oloyede, A., Broom, N.D., (1994). The generalised consolidation of articular cartilage: an investigation of its near-physiological response to load. *Connective Tissue Research*, **31**, 75-86.

Flachsman, R., Broom, N.D., Hardy, A.E., Moltschaniwskyj, G., (2000). Why is the adolescent joint particularly susceptible to osteochondral shear fracture? *Clinical Orthopaedics and Related Research*, **381**, 212-221.

Flachsmann, R., Broom, N.D., Hardy, A.E., (2001). Deformation and rupture of the articular surface under dynamic and static compression. *Journal of Orthopaedic Research*, **19**, 1131-1139.

Broom, N.D., Chen, M-H., Hardy, A.E., (2001). A degeneration-based hypothesis for interpreting fibrillar changes in the osteoarthritic cartilage matrix. *Journal of Anatomy*, **199**, 683-698.

TENDON EXCURSION AND GLIDING MECHANISM

K. N. An, C. F. Zhao, M. E. Zobitz, P. C. Amadio

Biomechanics Laboratory, Division of Orthopedic Research
Mayo Clinic/Mayo Foundation, Rochester, MN 55905

As integral components of the musculoskeletal system, the primary function of tendons is to transmit muscle force to the skeletal system. Tendon excursion and the gliding mechanism of the tendon, which have direct clinical significance, will be addressed.

TENDON EXCURSION

A pulley type system keeps the tendon path close to the bone when the tendon crosses a joint. In normal anatomy, there is an intimate relationship between tendon excursion and joint rotation that maintains the mechanical advantage of the tendon while preserving the passive and active muscle tension during joint motion. Disturbance of the normal pulley-tendon unit could potentially lead to abnormal joint motion and muscle function. Tendon excursion influences the functional length of the muscle-tendon unit. Due to the length-tension interaction of the muscle contraction, the potential tension generated by the muscle will therefore be influenced by the joint position and tendon excursion. For the postoperative treatment of flexor tendon injury, it has been demonstrated that synergistic wrist motion could eliminate tendon slackness in the palm and improve tendon excursion during passive finger joint motion.

GLIDING RESISTANCE

A tendon sliding through the pulley is analogous to a belt wrapped around a fixed mechanical pulley. Assume that the total arc of contact between the belt and pulley is •, and the tensions on the belt on each side of the pulley are F_2 and F_1. If the impending motion of the cable is from F_1 to F_2, then F_2 is greater than F_1, $F_2 = F_1 e^{¨}$, where • is a frictional coefficient. The frictional force $f = F_2 - F_1$.

Based on this theoretical consideration, an experimental system was developed that allows direct measurement of friction at the tendon-pulley interface. To allow tendon excursion, the force applied to the tendon needs to overcome the finger resistance, which includes internal sources such as friction, and external sources such as resistance due to joint stiffness or edema. These sources, combined, make up the work of flexion (WOF). A device has been further constructed which can precisely evaluate these components and be a reliable tool for the evaluation of finger function after flexor tendon repair in experimental model.

LUBRICANT

Hyaluronate or proteoglycan, in the synovial membrane and the matrix of the tendon, may act as a boundary lubricant, facilitating the gliding by reducing the resistance. The gliding resistance increased significantly after the tendon had been treated with a hyaluronidase solution.

The gliding ability of the flexor digitorum profundus tendon and of the palmaris longus tendon through the A2 pulley was compared. The average gliding resistance between the palmaris longus tendon and the A2 pulley was found to be greater than that of the flexor digitorum profundus tendon. Intrasynovial tendons possess a boundary lubricant on their surfaces. The extrasynovial tendon does not have a synovial membrane, instead it has a paratenon of loose connective tissue.

Further investigation was performed to improve the gliding surface using hyaluronic acid (HA). The gliding resistance of extrasynovial tendons treated with chemically modified HA remained significantly lower than that of tendons treated either with saline or unmodified HA.

TENDON REPAIR AND REHABILITATION

Different suture repair techniques result in various amounts of gliding resistance and thus, the amount of excursion during post-operative rehabilitation can be affected. An in vivo study has been performed comparing a synergistic wrist motion therapy to an immobilized tendon. The results showed the adhesion grade and the adhesion breaking strength in the synergistic wrist motion group was significantly less than those of the wrist fixed group.

REFERENCES

Cooney, W.P. et al (1989). *J. Hand Ther,* pp. 102-106.
Lin, G-T. et al (1989). *J. Hand Surg.,* 14A(6):949-956.
Momose, T. et al (2002), *J. Biomed Mater. Res.* 59:219-224.
Uchiyama, S.et al (1997). *J. Bone Joint Surg.,* 79A:213-218.
Zhao, C. et al (2001*) J. Orthop. Res.* 19:580-586.

MECHANICAL STIMULI AND ENDOTHELIAL CELL MECHANICS

Masaaki Sato

Biomechanics Laboratory, Graduate School of Mechanical Engineering, Tohoku University, Sendai, Miyagi, Japan
sato@biomech.mech.tohoku.ac.jp

INTRODUCTION

It is well known that endothelial cells respond to mechanical stimuli and show changes in cytoskeletal structure, mechanical properties of cell body, cell shape, cell functions, and so on (Davies, 1995). One of those responses are prescribed by mechanical properties of the cell such as stiffness, elasticity, and viscosity. Measurements of the response of cell to mechanical stimuli can provide information on the structure of cytoskeleton, focal adhesion and cell membrane. However, less frequently examined are the mechanical properties of the cells, the cytoskeletal components and the organelles. We have been interested in and have studied the mechanical responses of cultured endothelial cells to flow-imposed shear stress (Sato et al., 1987, 1990, 2000; Kataoka et al., 1998).

In this presentation I would like to show you that the changes in dynamic behavior of actin filaments in living endothelial cells and mechanical stiffness measured by AFM by exposing to shear stress.

CYTOSKELETAL RESPONSES IN LIVING CELLS DURING EXPOSING TO SHEAR STRESS

A plasmid encoding GFP fused to the amino terminus of actin (the vector was cordially provided by Dr. G. Marriott, Max-Planck-Institute for Biochemistry, Germany) was transfected into cultured bovine aortic endothelial cells (BAECs) using a liposomal method. All experiments were performed with confluent monolayers of cell. Cells expressing GFP-actin were observed in flow condition. Fluid shear stress of 2 Pa was applied using the parallel plate flow chamber. Distribution and dynamic behavior of actin filaments in a cell were observed under a confocal laser scanning microscope and the images were recorded on a computer through a high resolution digital CCD camera.

It was already confirmed by separate experiments that localization of GFP-actin coincided with the F-actin filaments stained by rhodamine-phalloidin in ordinary method. The cytoskeletal reorganization during endothelial exposure to flow preceded changes in cell shape. In one example, actin bundles located upstream side in a cell were disrupted and started to align to the flow direction within 30 min. Fine network structure of actin filaments at the downstream side was partly destroyed within 60 min and became the thick bundles along the peripheral edges within 90 min. These bundles started to align to flow direction at around 240 min. Since the focal adhesion proteins, integrins, should play important roles in reorganization of actin filaments, we need to simultaneously observe the dynamic movements (Urbich et al., 2000). At present, we also need more examples to conclude general moving process of actin filaments in shear stress condition.

CHANGES IN STIFFNESS OF SHEAR EXPOSED CELLS MEASURED BY AFM

Morphology and mechanical properties of BAECs were measured, using a novel atomic force microscope (AFM) system, developed in our laboratory, in conjunction with an inverted confocal laser scanning microscope (Sato et al., 2000). We used this system to examine endothelial cell both in static cultures and exposed to a shear stress of 2 Pa. Initially, the three-dimensional topography of a cell was measured by the AFM and a location was selected for the subsequent measurement of the mechanical response of the cell.

The surface of statically cultured cell was smooth. The cell height was significantly decreased by exposure to shear stress. A relationship between external force, F, and the indentation depth, δ, was obtained for several different locations on a cell. This force-indentation response was modeled using a quadratic equation, $F=a\delta^2+b\delta$, indicating that two parameters, a and b, will be constants which are representative of the mechanical response. Endothelial cells cultured at static conditions demonstrated a polygonal shape and less stiff mechanical characteristics around the nucleus compared to those at peripheral regions. The stiffness of the endothelial cells exposed to shear stress increased with the duration time of exposure. At 6-hour exposures, the stiffness was higher at upstream side of the cell than the downstream side. However, after 24-hour exposure, the stiffness was similar on both sides of the cell. These changes in the stiffness of endothelial cells when those are exposed to shear stress were suggested to correspond with the distribution of stress fibers in the cell.

REFERENCES

Davies, P.F. (1995). *Physiol. Rev.*, **75**, 519-560.
Kataoka, N., et al. (1998). *Med. & Biol. Eng. & Comput.*, **36**, 122-128
Sato, M., et al. (1987). *Arteriosclerosis* **7**, 276-286
Sato, M., et al. (1990). *J. Biomech. Eng.,* **112**, 263-268.
Sato, M., et al. (2000). *J. Biomech.,* **33**, 127-135.
Urbich, C., et al. (2000). *Circ. Res.*, **87**, 683-689.

ACKNOWLEDGEMENTS

I thank Professor T. Nishino, Dept. Biomolec. Eng., and Dr. T. Ohashi, Messrs. K. Tsuyuki and M. Yamamoto, Biomech. Lab., Tohoku University, for their technical assistances to do the experiments. This work was supported in part by a research grant from the Ministry of Education, Culture, Sports, Science and Technology, Japan (#12480257).

CRITICAL ISSUES IN THE BEHAVIOR OF HUMAN SKELETAL MUSCLE DURING SSC ACTIVITIES

Paavo V. Komi

Neuromuscular Research Center, Department of Biology of Physical Activity, University of Jyväskylä, Finland

It is believed that stretch-shortening cycle (SSC) in human skeletal muscle is the only normal way of muscle function (e.g. Komi, 2000). Isolated forms of isometric, concentric or eccentric actions do not occur often in real life. Running, walking and hopping are typical examples in human locomotion of how external forces (e.g. gravity) lengthens the muscle. In this lengthening phase the muscle is acting eccentrially, then a concentric (shortening) action follows. The true definition of eccentric action indicates that the muscle(s) must be active during stretch. The combination of eccentric and concentric actions forms the muscle function called stretch-shortening cycle of SSC. This type of sequence in muscle function also involves the important features of preactivation and variable activation. SSC function has a well-recognized purpose: enhancement of performance during the final phase (concentric action) when compared to the isolated concentric mode.

The in-vivo force measurement systems, buckle transducer technique (Komi, 1990), and optic fiber technique (Komi et al, 1996; Finni et al, 2001) have revealed that a nonfatiguing SSC exercise demonstrates considerable performance enhancement with increased force at a given shortening velocity. Characteristic to this phenomenon is very low EMG activity in the concentric phase of the cycle, but a very pronounced contribution of the short-latency stretch-reflex component. The stretch reflex contributes significantly to force generation during the transition (stretch-shortening) phase in SSC action such as hoppping and running (e.g. Komi & Gollhofer, 1997).

The common assumption has been that in SSC activities both the muscle fiber compartment and the tendon would change their lengths in phase. This assumption has been challenged, because muscle fibers have been estimated to stay at a constant length (Belli & Bosco, 1992) or they can even shorten (Griffiths, 1991) while the whole muscle-tendon complex may be lengthening. It can therefore be questioned whether the definition of SSC applies equally to two parts of the muscle-tendon complex.

Several studies undertaken to examine the fascicle and tendon length changes combining ultrasound (fascicle length) and optic fiber (tendon force) for the vastus lateralis (VL) and gastrocnemius (GA) muscles simultaneously using different types of jumps and effort intensities. The purpose was to examine further the hypothesis that in the eccentric phase of slow SSC actions the VL fascicle demonstrates much greater increase in length as compared to a faster SSC. Fig. 1. gives representative examples of the behavior of VL and GA fascicles during counter-movement and drop jumps. The following important findings were observed: (1) the fascicle lengthening / shortening does not occur in phase in the two muscles; (2) the fascicle behavior, in addition to the expected effort dependence, is also very much muscle and joint dependent; and (3) these changes in the fascicle (and tendon) are also dependent on the type of muscle action and movement. Consequently, in multijoint action it is possible that the fascicles of some muscles may demonstrate differences from the "general" rule of lengthening (eccentric mode) and shortening (concentric mode). For example, if the VL fascicle is being lengthened in the braking phase of CMJ, GA may demonstrate either no change in length or even shortening of the fascicle.

Isolation of the fascicle and tendon of the muscle-tendon complex can reveal specific roles the tendon and aponeurosis play in performance potentiation in SSC. But their potential and individual contribution may be clearly dependent on the type of SSC movement and muscle in question. Thus it is difficult to generalize muscle mechanical behavior in SSC from single experimental conditions only.

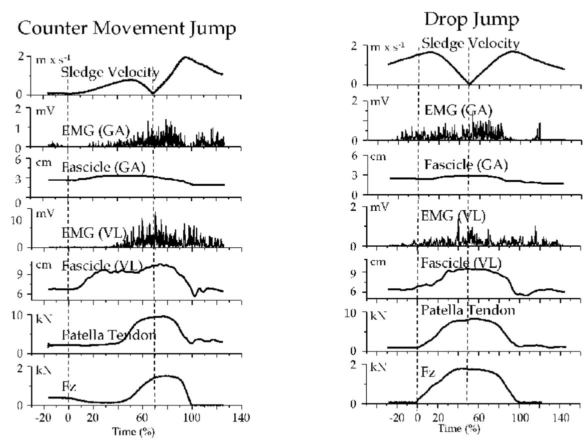

Figure 1: Examples of the fascicle length changes in the VL and GA muscles in counter movement jumps (left) and drop jump (right) on the sledge. The figures show also respective EMG activities as well as the patella tendon force (optic fiber technique) and the sledge force plate force. The second dashed line refers to the end of the braking phase in the countermovement and drop jump conditions (Ishikawa et al, in progress).

REFERENCES

Belli A & Bosco C (1992) *Acta Physiol Scand* **144**, 401-408
Finni et al (2001) *Acta Physiol Scand* **173**, 369-377
Griffits RI (1991) *J Physiol* **436**, 219-236
Komi PV (1990) J Biomech **23** (Suppl. 1), 23-34
Komi et al (1996) *Eur J Appl Physiol* **72**, 278-280
Komi PV & Gollhofer A (1997) *J Appl Biom* **13**, 451-460
Komi PV (2000) *J Biomech* **33**, 1197-1206

WHAT CAN WE LEARN FROM LOOKING AT BIOLOGICAL PROCESSES, ONE MOLECULE AT A TIME

Steven Chu
Stanford University

Virtually all knowledge of chemical and biochemical processes has been deduced from studies of a large number of molecules. The ability to look at individual molecules has given us new insights into biological processes. As an example, our polymer studies using DNA have fundamentally altered our thinking of polymer dynamics by showing that identical molecules placed under identical conditions take several distinct paths to a new equilibrium state.

We have been applying sensitive fluorescence microscopy to study the behavior of individual biomolecules. Using energy transfer between two dye molecules, a change in relative fluorescence from the two dyes can be used to measure the distance between two locations of a bio-macromolecule. This technique has proven to be particularly powerful in linking molecular structural information with biological activity measured with molecular biology methods.

Examples of how this work is allowing us to test mechanistic models of how biological systems function will be given. This talk may include our work on the observation an RNA enzyme folding into a biologically active structure, and the discovery of “molecular memory” in the fluctuations of another RNA enzyme, and real-time observation of the unwinding of DNA by a Helicase enzyme. A preview of our work with more complex interacting systems such as the manufacture of proteins by the ribosome, and vesicle fusion that occurs in at the synapse between neurons will also be given.

MECHANISMS OF MECHANOTRANSDUCTION IN CELL PROCESSES AND MICROVILLI

Sheldon Weinbaum

Departments of Biomedical and Mechanical Engineering
New York Center for Biomedical Engineering
Weinbaum@ccny.cuny.edu
City College of New York, CUNY
New York, NY 10031 USA

INTRODUCTION

In contrast to the actin cytoskeleton in the main body of the cell, where the actin network forms a gel-like structure that is isotropic, many cells have slender microvilli or cell processes in which the actin net work is highly organized into cross-linked axial arrays or bundles in which the long axes of the actin filaments are parallel to one another. Four prominent examples of such structures are the stereocilia in the inner ear, the microvilli in the brush border epithelia of the proximal tubule and small intestine and the cell processes of osteocytes. In this presentation we shall examine the relationship between structure and function in each cellular extension with a view toward developing new insight into the fluid flow induced mechanosensory mechanisms that may be operative in brush border microvilli and osteocyte cell processes. In particular, we shall compare the detailed structures of the filament bundles, the stress and strain amplification that results from fluid dynamic loading, the magnitude of the forces and strains required to activate membrane ion channels and elicit intracellular electrical and chemical responses and the coupling of the cell membrane to intracellular and extracellular matrix structures.

METHODS

Much more is known about the structure and function of the the actin filament bundles in stereocilia and the molecular structure of the the microvilli in the small intestine than the brush border microvilli in the kidney or the cell processes of osteocytes. This anatomical information has been used in Guo et al. (2000) and Yu et al. (2001) to construct new models to quantitatively explore whether the cellular extensions on kidney and bone cells can serve as mechanotransducers when subject to hydrodynamic forces *in vivo*.

RESULTS AND DISCUSSION

The model for kidney microvilli develops a new theoretical approach for predicting the forces and torques in a dense network of brush border microvilli. The elastic modulus of individual actin filaments and their observed cytoskeletal organization are then used in a an elastic beam model to predict the deformation of microvilli and the strain amplification that is experienced in the terminal web of the cytoskeletal structures at the base of the micoovilli. The model provides a quantitatively feasible new hypothesis for the afferent sensory mechanism in glomular-tubular balance and perfusion-absorbtion balance in proximal tubule. The model predicts that the forces on the microvilli are only of the order of 0.01 pN, that they are relatively stiff structures which deform less than 5 nm at their tips, but that there is a 40 fold stress amplification at the base of the microvilli which should be sufficient elicit intracellular responses.

The model for the osteocyte cell processes attempts to resolve a long standing paradox, as to why whole tissue strains in bone are at least an order of magnitude smaller than the cellular level strains required in tissue culture to elicit intracellular biochemical responses. The model is based on a new hypothesis and experimental observation that the cell processes are tethered at regular intervals to the canalicular wall by transverse filaments in the pericellular matrix. The model is the first, to our knowledge, to relate flow induced strains on extracellular matrix to the deformation of the actin cytoskeleton and predicts that the effective elastic modulus of the cell process is 200 times stiffer than the measured modulus in the cell body. Thus, the processes should not be sensitive to fluid shear stress as now assumed by many investigators. However, the fluid drag on the transverse tethering elements can create hoop strains in the actin filament bundle of the process which are up to 100 times whole tissue strains. These strains should be sufficient to open membrane ion channels and activate intracellular signaling.

These results are summarized in a recent review paper Weinbaum *et al*. (2001).

REFERENCES

Guo, P. et al (2000). *Am. J. Physiol. Renal* **279,** F698-F712.
Weinbaum et al (2001). *Biorheol.* **23**, 119-142.
You, L. et al (2001). *J. Biomech.* **34,** 1375-1386.

CARTILAGE MECHANICS, DIAGNOSTICS AND REPAIR

Michael D. Buschmann

Department of Chemical Engineering and Biomedical Engineering Institute
Ecole Polytechnique, PO 6079, Station Centre-ville
Montreal, Quebec, Canada, H3C 3A7
mike@grbb.polymtl.ca

INTRODUCTION

Articular cartilage of the knee and hip is often considered to be the main tissue affected by Osteoarthritis and other debilitating joint diseases. Thus its normal structure, composition and biomechanical function are of great interest in addition to understanding disease-induced alterations. Once articular cartilage is degenerated or completely removed via erosion to bone, therapies to resurface the joint by cartilage implantation or stimulation of cartilage growth at the eroded site are desired. In this presentation, the biomechanical roles of cartilage components will be reviewed and recent data presented. Strategies to resurface degenerated or denuded articular cartilage will also be discussed as well as biomechanical evaluation of cartilage function in a non-destructive manner in intact joints.

CARTILAGE MECHANICS

Most of the observed mechanical behavior of articular cartilage can be explained within the framework of biphasic theory or poroelasticity. One necessary constitutive characteristic is to consider collagenous and non-collagenous (mainly proteolgycan) components of the solid phases independently since this allows for 1) the description of the well known tension-compression nonlinearity (~10× stiffer in tension) and 2) the very high ratio of dynamic to equilibrium stiffness (~10:1) in compression. The high density of proteoglycan is also essential to 1) furnish about half of the equilibrium stiffness via electrostatic repulsion and 2) to create nanometer sized pores that endow cartilage with its extremely low permeability to fluid flow. Another important characteristic to consider is depth-dependent composition and structure where proteoglycan density increases with depth and collagen fibril orientation changes systematically. Some recent experimental and theoretical results arising from depth-dependent composition and structure include zone-dependent strains, pressurization, and a shifting of strain from zone to zone that do not occur in the absence of depth-dependence. Finally, nonlinear stiffening of collagen fibrils when they are stretched has been recently measured. This stiffening of collagen in tension can exert a great influence on cartilage compressive stiffness since the level of isotropic fluid pressurization under compression depends to a large extent on the stiffness of the solid matrix in the direction of fluid flow.

CARTILAGE REPAIR

Focal erosion of articular cartilage down to the underlying bone in an area larger than $1cm^2$ is considered clinically treatable. Current treatments mainly involve penetration of subchondral bone to induce bleeding and subsequent tissue repair, or osteochondral grafting, or cell-based methods. Recently much effort has been focused on growing cartilage tissue in vitro that could then be implanted. Cell sources include autologous chondrocytes, and stem cells derived from autologous tissue. One goal in this approach is often that the in vitro grown tissue achieves the mechanical properties of normal articular cartilage before implantation. Once this outcome is optimized, tissue implantation, integration with the surrounding cartilage, and its ability to remodel to meet local functional requirements become the main obstacles. Although not yet entirely successful, these approaches are showing promise. Particular attention must be made towards cell selection for phenotype control and the use of an appropriate scaffolding to guide tissue growth.

CARTILAGE DIAGNOSTICS

Unfortunately the most accurate methods to determine cartilage composition, structure and function require tissue removal and destructive analysis. Non-destructive methods can be based on imaging, biochemical markers, or involve direct estimation of mechanical function. In the latter category measurements can be purely mechanical or include electromechanical phenomena. Many of the problems encountered to date in these technologies are similar and involve accurate control and/or measurement of force, displacement, orientation and electrical parameters and a subsequent analysis that provides a useful description of tissue function. A recently developed electromechanical device solves some of these problems and provides a simple diagnostic parameter through a robust user-friendly system. This device allows measurement of non-visible degradation of articular cartilage and can map out focal cartilage degeneration that is both visible and non-visible through the arthroscope.

HOW DO BIOLOGICAL MOTORS WORK?

E. Katayama[1], T. Q. P. Uyeda[2], A. Hikikoshi Iwane[3], and Mitsuo Ikebe[4], T. Yanagida[5] ,

[1] Institute of Medical Science, The University of Tokyo, [2] Gene Discov. Res. Ctr., Nat. Inst. Adv. Ind. Sci. Tech. [3] Graduate School of Medicine, Osaka University. [4] University of Massachusetts Medical School. [5] Single molecule process project, ICORP, JST

Myosin V moves processively with large (~36nm) steps and it is believed that myosin V strides along the actin helical repeat using its two heads each with an unusually long neck domain. However, we have recently shown that a deletion myosin V mutant, in which five out of the six IQ motifs were removed (Tanaka et al. Nature 415, 2002), and myosin VI, which naturally has only one IQ motif, both move processively with ~36 nm steps (Nishikawa, et al.BBRC,2002: Rock, et al. PNAS 98, 2001). Thus, the long neck domain is critical to neither the processivity nor the large step. We discovered by electron microscopy that an S1 form of a mutant *Dictyostelium* myosin II, in which the 680^{th} Gly is replaced by Val so that it forms a long-life actomyosin complex in the presence of ATP like myosins V and VI, periodically binds along one side of an actin filament at ~36 nm intervals in the presence of ATP. Myosin VI was also found to cooperatively bind to an actin filament at ~36 nm intervals in the presence of ATP. These results suggest that the binding of an activated myosin head evokes “hot spots” on the actin filament~~s~~ that attract free myosin heads. Based on these findings, we propose that myosin V and VI step on these “hot spots” at every helical pitch along actin filaments, thus producing processive movement with 36 nm steps.

CELLS, GELS AND THE ENGINES OF LIFE: A FRESH APPROACH TO BIOLOGICAL MOTION

Gerald H. Pollack. Dept. of Bioengineering, University of Washington, 357962, Seattle WA 98195

The cell is broadly envisioned to be an aqueous solution in which solutes are freely diffusible. Many mechanisms build on this assumption. Yet, it is well known that the cell is a gel, and not an aqueous solution. Gels and aqueous solutions are quite different: Gels are polymer matrices to which water clings—that's why the cracked egg feels gooey, and why gelatin dessert does not shrivel up despite upwards of 95% water content.

The concept of a gel-like cytoplasm is replete with power. Partitioning of ions between the inside and outside of the cell is directly explainable from the cytoplasm's gel-like character; such partitioning requires zero maintenance energy, unlike ion-pumping mechanisms. The cell's electrical potential is also explainable: substantial potentials are measured in gels, as well as in cells stripped of their membrane. Hence, gel properties can go far in explaining the most fundamental of the cell's static properties.

Polymer gels also undergo phase-transition—transformation from one physical state to another. In so doing, they change volume, ion content, solvency, permeability, etc.—changes similar to those experienced by organelles within the functioning cell. The polymer-gel phase transition therefore has the potential to be a central paradigm for mediating many aspects of basic cell function.

These ideas are explored in depth in a recent book (Pollack, "Cells, Gels and the Engines of Life," 2001 www.cellsandgels.com), and will be outlined at the meeting. In short, it appears that many features of cell function are explained in a straightforward way by the phase-transition mechanism.

A question particularly relevant to those at the biomechanics meeting is whether the phase-transition might be the underlying basis of biological motion. When phase-transitions take place in polymer gels, all constituents move: the polymer (i.e., protein) moves, water moves, and ions move. Thus, a "byproduct" of the transition is vectorial movement of all components. It is shown in the above-mentioned book that such movements constitute a promising candidate for all kinds of biological motions ranging from muscle contraction to cell motility, fluid streaming and transport along microtubules. Further, physical properties of tendons and cartilage, which involve water movements, are also readily explained by this kind of mechanism.

Thus, the gel mechanism provides simple explanations for the genesis of biological motion, which are consistent with available data. These mechanisms are substantially different from those in textbooks, all of which are based essentially on aqueous solution behavior, not on gel behavior.

CARTILAGE NANOMECHANICS, MECHANOTRANSDUCTION, AND TISSUE ENGINEERING

Alan Grodzinsky, Christine Ortiz, Joonil Seog, Delphine Dean, Laurel Ng, Moonsoo Jin, John Kisiday, and Eliot Frank

Departments of Mechanical Engineering, Electrical Engineering and Computer Science,
Materials Science and Engineering, and Biological Engineering Division
Massachusetts Institute of Tecnology, Cambridge MA, USA alg@mit.edu

INTRODUCTION and OVERVIEW

Cells in articular cartilage synthesize an extracellular matrix (ECM) of proteoglycan aggregates and collagens in order to create a dense woven tissue that can withstand joint loading *in vivo*. At the same time, mechanical forces acting on the cells during motion of both healthy and osteoarthritic cartilage can differentially modulate the nanostructure of these ECM molecules which are continually synthesized and secreted by the cells. This feedback system is extremely important for maintenance of healthy cartilage, and for the success of cartilage tissue engineered constructs being developed for the repair of cartilage defects.

METHODS and RESULTS

We have therefore used high resolution force spectroscopy to quantify the electrostatic and steric interactions between glycosaminoglycan (GAG) molecules, a critically important component of cartilage ECM. GAGs have now been end-grafted to the substrate and probe tip of a Molecular Force Probe (MFP), and the measured GAG repulsive forces (fig. 1) have been compared to a hierarchy of theoretical models for the electrostatic repulsive interactions between GAGs using the Poisson Boltzmann equation. In addition, novel AFM imaging of aggrecan proteoglycan (PG), hyaluronan (HA), and PG-HA aggregates are now revealing the structures of these native ECM components that may be more relevant to the physiological wet state without using preparative staining, coating or freezing for traditional electron microscopy. Using a self-assembling peptide hydrogel scaffold, chondrocytes have been subjected to a range of dynamic compressive loads to simulate mechanical forces during joint loading. Appropriate loading regimes have been identified which can stimulate sustained, enhanced synthesis and accumulation of GAG-rich proteoglycans capable of providing cartilage-like stiffness to the neo-cartilage tissue growing within the peptide scaffold (Fig. 2).

DISCUSSION

Cartilage is subjected to wide range of mechanical forces associated with joint loading *in vivo*. These mechanical forces can dramatically alter chondrocyte synthesis, assembly, and degradation of extracellular matrix. Recent studies suggest that there are multiple regulatory pathways by which chondrocytes in cartilage can sense and respond to mechanical stimuli. Chondrocyte mechanotransduction is critically important in the cell-mediated feedback between joint loading, the molecular structure of newly synthesized ECM collagens

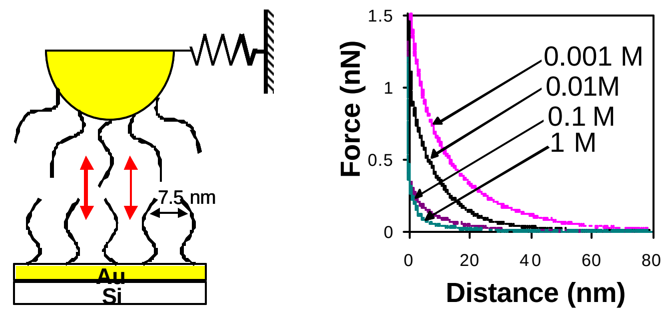

Fig. 1. Repulsive forces between charged GAG chains quantified using MFP.

and proteoglycans, and the resulting functional biomechanical properties of cartilage. Current approaches to creating tissue engineered cell-scaffold implants for cartilage repair are incorporating mechanical loading of the developing constructs to optimize their biological and mechanical properties.

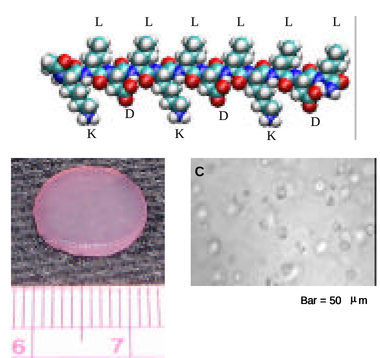

Fig. 2 A. KLD-12 peptide structure
B. disk specimen for biomechanical tests and loading-induced biosynthesis
C. Encapsulated chondrocytes

REFERENCES

Kisiday, J et al. (2002) *PNAS*, (in press)
Seog et al., (2002) *Macromolecules*, (in press).
Jin et al., (2001), Archiv Biochem Biophys., **395**:41-48

ACKNOWLEDGEMENTS

Supported by NIH Gants AR33236 and AR45779, the DuPont MIT Alliance, and the Cambridge-MIT Institute.

FLUID SHEAR STRESS AFFECTS VASCULAR SMOOTH MUSCLE CELL FUNCTION

John M. Tarbell[1,2], Shigeru Tada[3], Jeff Garanich[1], Kristy Ainslie[2], and Mete Civelek[2]
Departments of Bioengineering[1](jmt@psu.edu) and Chemical Engineering[2], The Pennsylvania State University;
Department of Mechanical Engineering and Science[3], Tokyo Institute of Technology

INTRODUCTION

Vascular smooth muscle cells (SMC) are not normally exposed to the direct shearing forces of blood flow because they lie beneath the arterial intima and its endothelial lining layer. When the intima is damaged, as in angioplasty or vascular grafting, SMC are exposed directly to blood flow shear stress. In the intact vessel, SMC are also exposed to fluid shear stress associated with transmural interstitial flow driven by the transmural pressure differential. Interstitial shear stresses have been estimated to be comparable in magnitude to blood flow shear stresses on endothelial cells (order 10 dyne/cm^2) and the most superficial layer of SMC may experience significantly higher levels due to entrance effects associated with flow distribution through the fenestral pores of the internal elastic lamina (Tada and Tarbell, 2002).

We have hypothesized that fluid flow shear stress on SMC affects two important functions of the cells: (1) cell migration, which is fundamental to intimal hyperplasia and re-stenosis; and (2) cell contraction, which is essential for blood flow control in response to pressure changes (myogenic response). We have developed in vitro systems to assess migration and contraction in response to well defined shear stress fields as described below.

METHODS

Primary rat aortic SMC were expanded in cell culture flasks containing DMEM + 10% FBS. Then, depending on the experiment, SMC were treated in one of two ways in order to maintain them in a specific cell phenotype. For the "proliferative phenotype", SMC were maintained in DMEM + 10% FBS throughout the duration of the experiment. For the "contractile phenotype" SMC were "starved" (maintained in DMEM, no FBS) in culture flasks for two days and then on quartz slides for two more days prior to experiments that were also run serum-free.

To study cell contraction in response to shear stress, serum-starved cells were plated at sub-confluent density on quartz slides and exposed to a defined level of steady shear stress in a parallel plate flow chamber for 30 minutes while being photographed under a microscope with a video camera. Reduction in cell area was interpreted as cell contraction and quantified in terms of percent area reduction. Intra-cellular calcium (Ca^{2+}) was imaged under flow in the parallel plate chamber using the calcium sensitive dye fura-2.

To study cell migration, polycarbonate filters with 8µm pores were coated with Matrigel, an extracellular matrix formulation containing type IV collagen, laminan and other components, and a monolayer of SMC in the proliferative phenotype was plated on top of the Matrigel. PDGF-BB was placed in the well beneath the filter to serve as a chemoattractant. Migration was quantified by counting the number of cells that migrated to the bottom of the filter. Defined shear stress was applied to the SMC monolayer using a rotating disk apparatus (Sill et al., 1995).

RESULTS AND DISCUSSION

Cells in the contractile phenotype that were exposed to 25 dyne/cm^2 shear stress decreased their area significantly within 3 minutes and by more than 30% after 30 minutes. The threshold for contraction was about 7 dyne/cm^2. To our surprise, this contraction response was not accompanied by a response of intracellular Ca^{2+}. Additional experiments in calcium free media and with intracellular Ca2+ chelators also displayed a significant contraction response to shear stress confirming that shear-induced contraction is not mediated by intracellular Ca^{2+}. Additional pharmacological experiments suggested that the shear-induced contraction is mediated primarily through a Rho-kinase intracellular signaling pathway. In contrast, cells in the proliferative phenotype did not contract in response to shear stress but did display a marked intracellular Ca^{2+} response to shear.

Migration of SMC through Matrigel was significantly inhibited by shear stress in a time- and dose-dependent manner. Four hours of exposure to 20 dyne/cm^2 inhibited migration by 90%. Inhibition of migration over this time frame was still significant at 10 dyne/cm^2 shear stress but not at 1 dyne/cm^2. The inhibition of migration is believed to be at least partially due to the restricted action of matrix metallo-proteinase-2 (MMP-2). Latent levels of MMP-2 released by SMC were not affected by shear stress whereas active MMP-2 was significantly inhibited by increased shear stress.

Taken together these experiments demonstrate the potential for fluid shear stress on SMC to influence the myogenic response and intimal hyperplasia.

REFERENCES

Tada, S., Tarbell, J.M. (2002). *Am. J. Physiol.*, **282**, H576-H584.
Sill, H.W., et al (1995). *Am. J. Physiol.*, **268**, H535-H543.

ACKNOWLEDGEMENTS

Supported by NIH NHLBI Grant HL-35549.

ORTHOTICS ALTER LOWER EXTREMITY JOINT COUPLING: A DYNAMICAL SYSTEMS APPROACH

R. Ferber[1], I. McClay Davis [1,2,] D.S. Williams III[3]

[1]University of Delaware, Newark, DE, USA 19716 email: reedferb@udel.edu
[2]Joyner Sportsmedicine Institute, Mechanicsburg, PA, USA 17111
[3]Department of Physical Therapy, East Carolina University, Greenville, NC, USA 27858

INTRODUCTION

Foot orthoses are often prescribed for lower extremity injuries. The method by which orthotics relieve symptoms is not well understood as most studies have focused solely on rearfoot motion. However, the rearfoot and knee are linked by their common articulation with the tibia resulting in a necessity for coordination between their motions. Disruption of this coordination is thought to be one of the causes of running-related injuries (Nigg et al, 1993, McClay et al., 1997). Restoration of rearfoot-knee coordination may be a way in which orthotics provide relief of symptoms. One method of investigating joint coordination is through a dynamical systems theory (DST) approach (Hamill, 1999). These authors believe that variability in joint coupling is important and suggest that injured subjects exhibit less variability in their movement patterns. Therefore, the purpose of this study was to compare joint coupling during the stance phase of running in a group of runners treated with two types of orthotic devices. It was hypothesized that coordination would improve with orthotic intervention.

METHODS

Eleven injured runners, presenting to a single physical therapist, volunteered for the study. Each was initially fitted with a standard (STD) custom-molded graphite foot orthoses, but symptoms were not resolved. The subjects were then fitted with inverted (INV) orthoses posted between 15° and 25° which resulted in relief of symptoms. Kinematic and kinetic data were collected from 5 trials and for 3 conditions: no orthotics (NO), STD, and INV. Data from 11 healthy runners served as the controls (CON). They were randomly chosen from a normative database of runners previously collected under a similar experimental protocol. Coordination of rearfoot eversion/inversion and tibial internal/external rotation (RF-Tib) were examined using a DST analysis. Continuous relative phase (CRP) plots were calculated for each condition. For each trial, the CRP plot was divided into 4 phases according to discrete ground reaction force (GRF) events. Phase 1: heel strike to F1, phase 2: F1 to GRF max, phase 3: GRF max to ~75% of stance, phase 4: ~75% of stance to toe off. Mean CRP and variation of CRP was analyzed for each phase. Repeated measures ANOVAs were used to determine differences, if any, in mean CRP and CRP variability between the orthotics conditions (NO, STD, INV). Orthogonal contrasts were used to detect differences compared to the CON group.

RESULTS AND DISCUSSION

The injured runners during the NO condition displayed out of phase coupling compared to CON who exhibited relatively tight coupling throughout the stance phase (Fig 1). However, during the NO condition, the injured group also presented with greater CRP variability which is in contrast to the findings of Hamill et al. (1999) who reported lower variability in their injured population. They suggested that a lack of flexibility in coordinated movement patterns may lead to overuse injuries. In general, both orthotic conditions (STD, INV) resulted in greater in-phase motion of the RF-Tib and lower variability of coupling compared to the NO condition. This brought the coupling parameters closer to that of the CON group (Fig 1). It is interesting to note that the greatest differences occurred during phase 2 which represents an important transition where the rearfoot and knee reverse their motions. It was surprising to find that the STD condition demonstrated greater in phase joint coupling than the INV during phase 2 yet the latter provided the greatest relief of symptoms. In terms of variability, both orthotic conditions reduced the variability of coupling in phase 2, bringing it closer to the CON group. Again, the STD device resulted in a greater reduction of variability than the INV (Fig 1). It is possible that there is an optimal coordination pattern and an optimal variability of coordination that minimizes the risk of overuse injuries in runners.

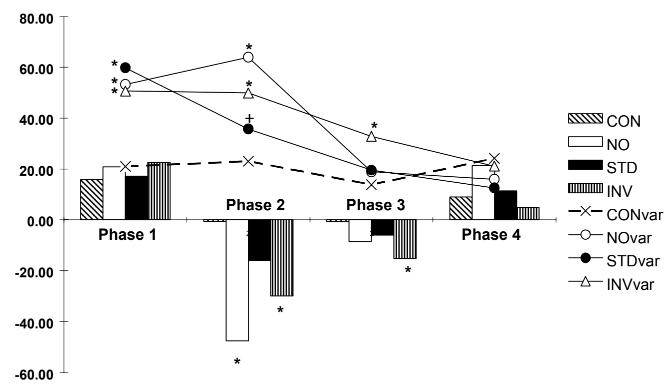

Figure 1: RF-Tib CRP means (bars) and variability (lines) for the CON and orthotic groups across the 4 phases of stance. (* significantly different than CON, + significantly different than NO: $p<0.05$)

SUMMARY

These data suggest that 1) rearfoot and knee motion are tightly coupled during the stance phase of running, and 2) a custom fitted orthotic device can alter the lower extremity joint coupling, as well as variability of that coupling, in a group of injured subjects. More studies using DST are needed to understand the nature of joint coordination in injured runners.

REFERENCES

Hamill J. (1999). Clin Biomech, **14**, 297-308
McClay, I.S. (1997). J App Biomech, **13**, 109-124
Nigg, B.E. (1993). J Biomech, **26**, 909-916

THE EFFECT OF AXONAL INJURY ON THE MATERIAL PROPERTIES OF BRAIN TISSUE

Kurosh K. Darvish, James R. Stone[1], and Jeff R. Crandall

Impact Biomechanics Laboratory (auto-safety.mech.virginia.edu), [1]Department of Neurosurgery
University of Virginia

INTRODUCTION

It has been shown previously that the instantaneous linear shear modulus of brain tissue, in simple shear tests *in vitro*, reduces with strain (Darvish and Crandall, 2002). This softening effect, after about 15% Lagrangian shear strain, which is believed to be the threshold of traumatic axonal injury (Thibailt et al, 1990), is permanent. In this study, the strain softening phenomenon was investigated using an animal injury model. This phenomenon can explain why secondary head injuries are more harmful and also provides a means to predict axonal injury based on changes in the material properties.

MATERIALS AND METHOD

The impact acceleration weight drop model was used to produce traumatic axonal injury in rat brain stem. Two points were selected on dissected brain stems for determination of material properties. Point 1, the most rostral point was at the basilar pons. Point 2, the most caudal point, was the caudal medullary pyramids, at the region of the pyramidal decussation. The most axonal damage has been observed at Point 2 (Stone et al, 2000).

The material properties were determined using indentation test. A cylindrical indentor (1.56 mm dia.) was pushed 1.0 to 1.5 mm onto the selected points of the samples using a linear servo system. The ramp time was 50 ms and the hold time was 1 second. The force at the tip of the indentor was measured using an inertially compensated load cell. The viscoelastic shear relaxation function was determined by applying the correspondence principle to the solution of the linear indentation problem in half-space (Sneddon, 1951):

$$L(t) = \frac{4a}{1-\nu}\int_0^t \mu(t-\tau)h(\tau)d\tau \qquad \textbf{(1)}$$

It was assumed that the Poisson's ratio ν remains constant (ν = 0.49). $L(t)$ is the time history of the applied force, a is the radius of the indentor, $\mu(t)$ is the shear relaxation function, and $h(t)$ is the time history of the indentor displacement. The relaxation function was assumed in the form of Prony series with three terms (Darvish et al, 1999). The material properties were determined by solving equation (1) numerically, using the actual indentor displacement, and minimizing the difference between the model and the experimental force histories.

RESULTS AND DISCUSSION

The results of the instantaneous and long term shear moduli, $\mu_0=\mu$ (t=0) and $\mu_\infty=\mu$ (t→∞), for three samples are shown in Table 1. Figure 1 shows representative experimental and model results. These preliminary results showed that in relation to axonal injury, there was significant reduction in the shear moduli at both Points 1 and 2. However, reductions in the shear moduli at Point 2, which sees more axonal damage, were 13% to 15% more. The reduction in the instantaneous shear modulus *in vitro*, for 20% Lagrangian shear strain, was reported to be about 70% (Darvish and Crandall, 2002). Therefore, it can be concluded that in the impact acceleration weight drop model the level of shear strain in brain stem went beyond 20%. The significant difference between the material properties at Points 1 and 2 can be attributed to the difference in the microstructural arrangement of the axons.

Table 1. The instantaneous and the long term shear moduli

Sample	Injury	μ_0 (kPa)		μ_∞ (kPa)	
		Point 1	Point 2	Point 1	Point 2
1	Injured	4.13	4.57	1.85	2.23
2	Non-injured	14.41	36.17	7.29	19.21
3	Non-injured	14.99	32.71	8.67	24.82
Average Reduction (%)		72	87	77	90

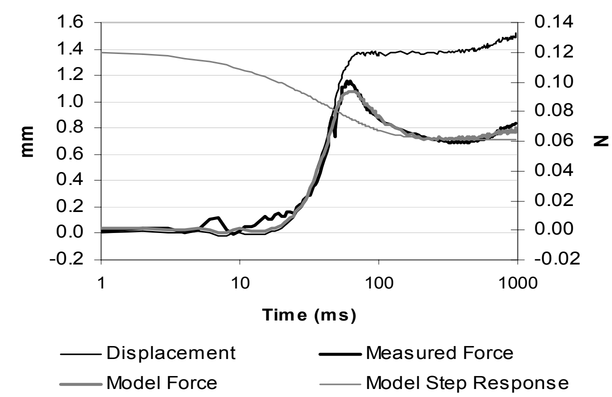

Figure 1. Experimental and Model Results of Sample 2 at Point 1

REFERENCES

Darvish, K.K., Crandall, J.R. (2002). *Medical Eng. & Phys.*, in press.
Thibault, L.E. et al (1990). *Proceedings* of *IRCOBI 1990*.
Stone, J.R. et al (2000). Brain Res. **21**:871(2), 288-302.
Sneddon, I.N. (1951). *Fourier Transforms*, McGraw Hill.
Darvish, K.K., et al (1999). *J. Mat. and Manufact.*, **108**(5), 209-215.

A 3D FINITE ELEMENT MODEL OF AN IMPLANTED SCAPULA USING CADAVERIC DATA FOR EVALUATION

Nathalie Maurel[1], Amadou Diop[1], Mercedes Irujo[1] and Jean Grimberg[2]

[1] Ecole Nationale Supérieure d'Arts et Métiers, 151 Bd de l'Hôpital, 75013 Paris, nathalie.maurel@paris.ensam.fr
[2] Centre Hospitalier de Meulan, 1 rue du Fort, 78250 Meulan

INTRODUCTION

Biomechanical investigations are yet necessary to better understand the origin of the glenoïd loosening which is the main reason for revision surgery. Some experimental tests have been done. Nevertheless, either they represent only postoperative situations when they are done on cadaveric specimen which is not sufficient to completely study loosening phenomenon or they use bone substitute to study fatigue phenomenon. Moreover, using such tests, it is difficult to appreciate the behaviour inside the bone. Some finite element models of scapula can be found in the literature, but few models were validated using experimental data. So, the aim of this study is to develop a finite element model of a scapula whose behaviour will be validated using global and local results issued from experimental data.

MATERIAL AND METHOD

During a previous in vitro experimental study (Maurel et al.,2002), tests were done on intact and implanted scapulae. Each scapula was placed in a specific box with a cross which allowed to define a referential system bound to the scapula. Nine loads of 500N were applied on the implanted scapulae (eight regularly applied around the prosthesis and one applied in the centre). Two kinds of measurements were done: Strains around peripheral cortex of the glenoïd using 6 strains gages placed on precise points and displacements of 4 points (posterior, anterior, superior, inferior) of the implant using 2 CCD cameras (figure 1).
Before experiments, each scapula was scanned in order to obtain the geometry of the tested scapulae. Before scanner, little balls were placed on the scapula to materialise the future position of the gages.
The finite element model was then developed using the ANSYS finite element software. Eight node elements were used for spongious bone and prosthesis. Shell elements were used for cortical. The Young modulus are 300MPa for spongious bone, 16000MPa for cortical bone and 1000MPa for implant (figure 2).

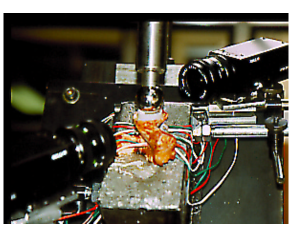

Figure 1: In vitro experimental test

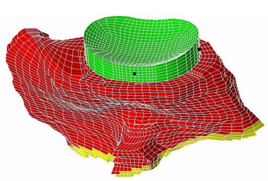

Figure 2: Finite element model

Same loads as in the experimental study were applied on the implant.
Principal strains calculations were done where gages were positioned during in vitro tests and the four implant displacements were calculated.

RESULTS:

The preliminary results were qualitatively coherent with experimental results (figure 3 and 4).

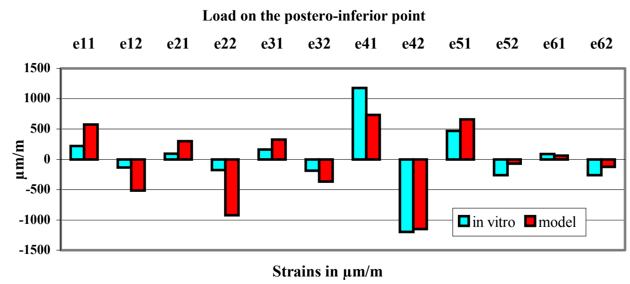

Figure 3: Comparison of principal strains for the 6 gages

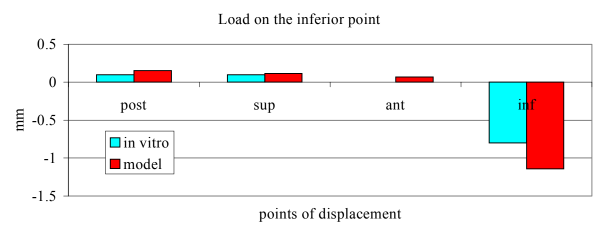

Figure 4: Comparison of the displacement of the four points of the implant

CONCLUSION :

We have developed a 3D finite element model of an implanted scapula. Both displacements and strains were used to evaluate the model. Improvements are still necessary and are in progress. When validated, such a model should be useful for better understanding implanted scapula behaviour and for giving information inside the bone. And later, it should allow us to introduce remodelling process in order to analyse implanted scapula behaviour at different delays.

REFERENCES :

N. Maurel et al, J. of Biomechanics (2002, in revision)

ACKNOWLEDGEMENTS :

Depuy France for its financial support.

EFFECT OF STRAIN RATE ON CERVICAL SPINE TENSILE MECHANICS

David Nuckley, Suzanne Hertsted, and Randal Ching
Applied Biomechanics Laboratory, University of Washington, Seattle, Washington, USA
Contact: dnuckley@u.washington.edu

INTRODUCTION

Injury criteria used in computational and anthropomorphic test dummy simulations is typically based on experimentally collected biomechanical data. Unfortunately, many of these studies are performed at quasi-static loading rates despite the fact that loading rate and strain rate have been implicated in the underestimation of mechanical properties for dynamic events. Increasing strain rate has been shown to increase the stiffness, modulus, and failure loads of ligamentous tissues [Noyes, 1974; Peterson, 1986; Woo, 1997].

Therefore, this study examined the effects of strain rate on cervical functional spinal units to elucidate the functional range and failure mechanics of these tissues. These efforts provide data for the generation of rate sensitive models which will more accurately represent spinal injury mechanics and support improved injury prevention.

METHODS

Ten fresh cadaveric baboon cervical spines were obtained through the Washington Regional Primate Research Center. The specimens were all male, age 10±0.6-human equivalent years based upon radiographic assessment of their skeletal maturity. Each specimen was dissected free of all musculature, then sectioned into functional spinal units: Occiput-C2, C3-4, C5-6, and C7-T1. These were then wired and embedded in polymethylmethacrylate for tensile loading. Each functional spinal unit was randomized to a loading rate group (N=8) to minimize the effect of inter-specimen variability and distinguish rate effects alone. The loading rates investigated were 0.5-mm/sec, 5-mm/sec, 50-mm/sec, 500-mm/sec, and 5,000-mm/sec.

Tensile inputs were provided by a servohydraulic testing frame (Model 810 Bionix, MTS Corp., Eden Prairie, MN) which supplied a constant velocity to failure. An inferiorly mounted six-axis load cell measured the force/moment response and the displacement was recorded using a LVDT and high-speed video camera (Eastman Kodak Company, Motion Analysis Systems Division, San Diego, CA). These data were recorded up to 40,000-Hz and filtered with a CFC 1000 (Butterworth low pass 1650-Hz cutoff) digital filter.

RESULTS AND DISCUSSION

The tensile failure load significantly increased (ANOVA, $p < 0.0001$) with increasing loading rate (Figure 1). Within two orders of magnitude there is no difference in failure loads; however statistical contrasts revealed significant differences in failure loads two orders of magnitude or more away. Further, differences between the various cervical spinal levels were observed. The stiffness and modulus of elasticity also increased with enhanced loading rates; however, not to the same magnitude as the tolerance values. Modulus of elasticity demonstrated a two-fold increase between 0.5-mm/sec and 5,000-mm/sec. The tensile failure strains (1.07 ±0.31-mm/mm strain) were not significantly correlated with loading rate, suggesting strain-based failure criteria instead of stress.

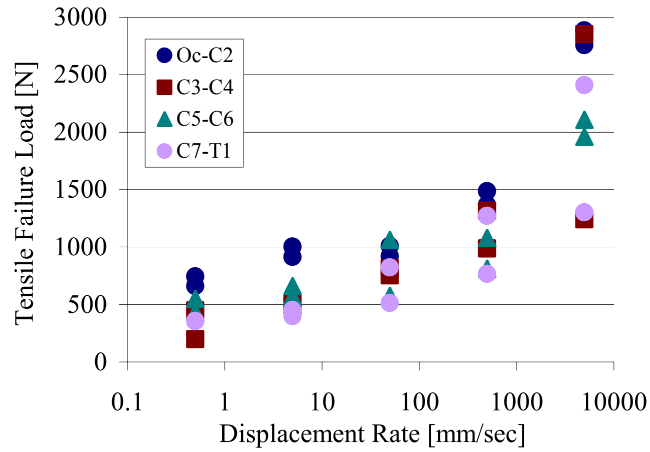

Figure 1: *Tensile Failure Load by Displacement Rate. This plot depicts spinal-level and loading rate differences in the tensile tolerance of the 10-year old spine.*

SUMMARY

Both the functional and tolerance biomechanics of the cervical spine were found to be significantly related to the displacement rate of loading. The failure load tolerance of the neck was most affected by increased rates, while the failure strains appeared insensitive to loading rate. This suggests that cervical functional spinal units fail as a result of excessive strains rather than extreme loads. These data have implications for the functional response of the spine (both structural and material properties) by loading rate and spinal level. Thus, the relationships generated herein suggest that strain rate or loading rate consideration is imperative in modeling efforts aimed at mitigating dynamic neck injuries.

REFERENCES

Noyes, FR, et al. (1974) *J Bone Joint Surg Am*, **56**, 236-53.
Peterson, RH et al. (1986) *J Biomech Eng*, **108**, 365-7.
Woo, SLY, et al. (1997) *Basic Orthopaedic Biomechanics*. Lippincott – Raven.

ACKNOWLEDGEMENT

National Highway Traffic Safety Administration

ULTRASONIC ASSESSMENT OF WHITE MATTER PROPERTIES AS A FUNCTION OF AXONAL DIRECTION

Elizabeth M. Rang[1] and Michele J. Grimm[2]

Bioengineering Center, Wayne State University, Detroit, Michigan, United States of America
[1]Graduate Research Assistant, rang@rrb.eng.wayne.edu
[2]Assistant Professor, grimm@rrb.eng.wayne.edu

INTRODUCTION

The material properties of neuronal white matter are believed to vary depending on the orientation of the axon. Ultrasonic techniques provide a non-destructive method for the characterization of the material properties of tissues, which make them ideal for investigating brain. Acoustic microscopy can be used to measure the velocity of an ultrasonic wave, which can then be related to the tissue material properties. The objective of this study was to evaluate the variation in wave velocity and material properties as a function of axonal orientation for white matter. In order to do this, tissue was obtained from two regions of the brain. The corpus collosum consists of nerve fibers with primarily transverse orientation. Conversely, the brain stem is composed of axons that are oriented longitudinally.

METHODS

The specimen used for testing was fresh lamb brain, obtained locally. The sample was retrieved from the slaughter house and immediately returned to the lab. The skull was opened with a roto-zip saw, and the brain was removed intact from the cranium. Within 1 hour of death, the brain was removed, and the corpus collosum and brain stem were separated from surrounding tissue by blunt dissection. The brain stem was sliced to obtain transverse sections. The tissue was weighed and the volume was measured in order to determine the density (ρ) of the sample. The specimen was sandwiched between plexiglas and aluminum plates, secured, and placed in a bath filled with artificial CSF (Sugawara, 1996) (Fig. 1).

Figure 1: Experimental setup

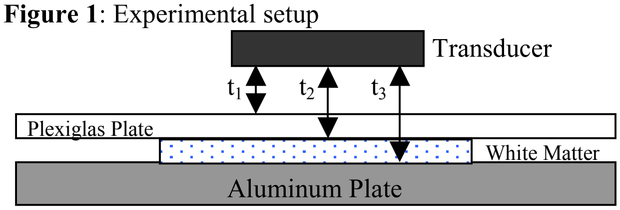

Each sample was scanned using a Sonix acoustic microscope at a frequency of 90 MHz. Three gates were set up to measure the time of flight (t_1, t_2, and t_3) of the wave to the plexiglas, to the plexiglas/white matter interface, and then to the white matter/aluminum interface. The wave velocity (c_p) was calculated from the thickness of the specimen and the time difference between the second and third reflected waves. A combination of bulk and shear moduli (K + 4G/3) was then calculated using the measured wave speed and tissue density, from the equation: $c_P = [(K + 4G/3)/\rho]^{1/2}$.

RESULTS AND DISCUSSION

The values obtained for wave velocity and combined modulus (K + 4G/3) are given in Table 1 for the two axon orientations. There is a significant difference in both the modulus and velocity values between the two tissue structures. When the ultrasonic wave traveled down the length of the axon in the brain stem sections, the combined modulus was significantly higher than the values obtained for waves traveling perpendicular to the axon orientation in the corpus collosum. As the bulk modulus of a tissue is by definition independent of orientation, the variation in combined modulus can be used to estimate the differences in the shear moduli of the tissue depending on the orientation of the axons. It should be noted that the shear modulus estimated for a transversely isotropic material using an applied pressure wave will be characteristic of shearing along the direction of wave propagation – not perpendicular to the wave front as would normally be expected. Thus, the data indicate a higher shear modulus for white matter for displacements along the axis of the axon (longitudinal samples) compared to shear displacements perpendicular to the axon axis (transverse samples).

	Corpus Collosum				**Brain Stem**					
Sample	**1**	**2**	**3**	**4**	**1**	**2**	**3**	**4**	**5**	**6**
c_p [m/s]	452	535	649	529	1299	1442	1377	1349	1411	1442
K + 4G/3 [MPa]	277	237	417	379	1967	2422	2121	2035	2302	2404

Table 1: Results for corpus collosum (transverse axons) and brain stem (longitudinal axons).

SUMMARY

The resistance to shear is greater along the axis of the axon compared to perpendicular to the fiber. This confirms what would be expected based on the fibrous structure of the white matter. Acoustic microscopy allows for the characterization of material differences in small tissue specimens without the problems associated with traditional mechanical testing.

REFERENCES

Osamu Sugawara, et. al. (1996). *Spine* **21**, 18, 2089-2094,.

ACKNOWLEDGEMENTS

This work was supported by a grant from the Centers for Disease Control, National Center for Injury Prevention and Control (CCR-503534-11).